COMPREHENSIVE BIOMATERIALS

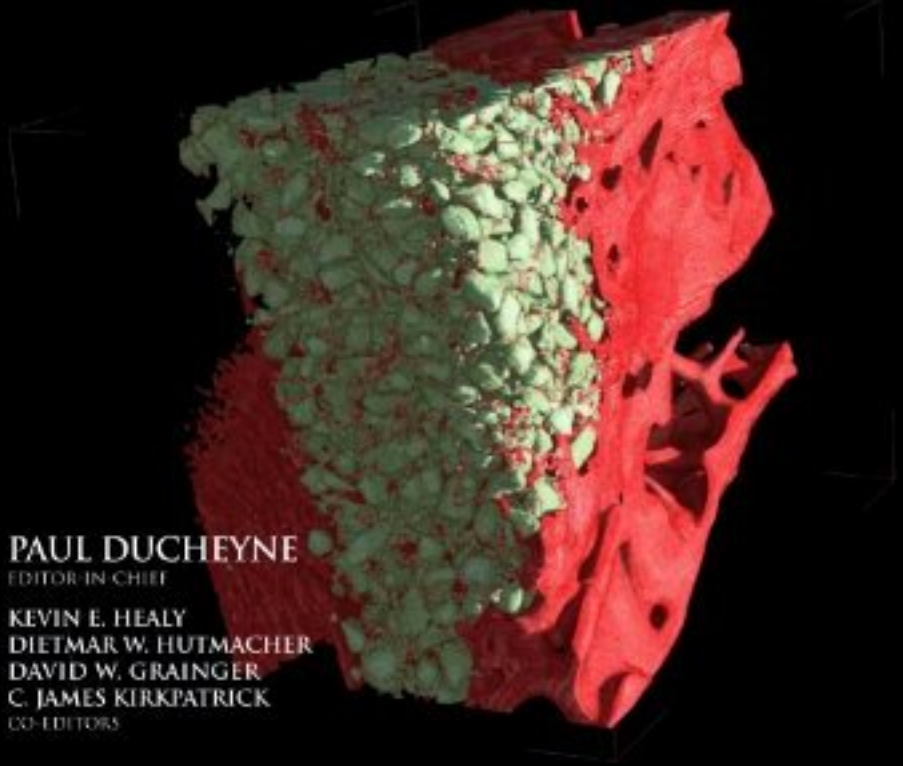

PAUL DUCHEYNE
EDITOR-IN-CHIEF

KEVIN E. HEALY
DIETMAR W. HUTMACHER
DAVID W. GRAINGER
C. JAMES KIRKPATRICK
CO-EDITORS

EDITOR-IN-CHIEF

PAUL DUCHEYNE
University of Pennsylvania, Philadelphia, PA, USA

CO-EDITORS

KEVIN E. HEALY
University of California, Berkeley, Berkeley, CA, USA

DAVID W. GRAINGER
University of Utah, Salt Lake City, UT, USA

DIETMAR W. HUTMACHER
Queensland University of Technology, Brisbane, QLD, Australia

C. JAMES KIRKPATRICK
Johannes Gutenberg University Medical Center, Mainz, Germany

Elsevier
Radarweg 29, PO Box 211, 1000 AE Amsterdam, Netherlands
The Boulevard, Langford Lane, Kidlington, Oxford OX5 1GB, UK
225 Wyman Street, Waltham, MA 02451, USA

Copyright © 2011 Elsevier Ltd. All rights reserved.

No part of this publication may be reproduced, stored in a retrieval system or transmitted in any form or by any means electronic, mechanical, photocopying, recording or otherwise without the prior written permission of the publisher.

Permissions may be sought from Elsevier's Science & Technology Rights department in Oxford, UK:
phone (+44) (0) 1865 843830; fax (+44) (0) 1865 853333; email: permissions@elsevier.com
Alternatively you can submit your request online by visiting the Elsevier website at http://elsevier.com/locate/permissions and selecting *Obtaining permission to use Elsevier material*.

Notice
No responsibility is assumed by the publisher for any injury and/or damage to persons or property as a matter of products liability, negligence or otherwise, or from any use or operation of any methods, products, instructions or ideas contained in the material herein. Because of rapid advances in the medical sciences, in particular, independent verification of diagnoses and drug dosages should be made.

British Library Cataloguing in Publication Data
A catalogue record for this book is available from the British Library

Library of Congress Control Number: 2011933642

ISBN: 978-0-08-055302-3

For information on all Elsevier publications
visit our website at elsevierdirect.com

Cover Image: Rack, A.; Zabler, S.; Müller, B. R.; Riesemeier, H.; Weidemann, G.; Lange, A.; Goebbels, J.; Hentschel, M.; Görner, W. High resolution synchrotron-based radiography and tomography using hard X-rays at the BAMline (BESSY II). *Nuclear Instruments and Methods in Physics Research A.* **2008**, *586*(2) 327–344. DOI 10.1016/j.nima.2007.11.020

Printed and bound in Italy
11 12 13 14 10 9 8 7 6 5 4 3 2 1

Working together to grow libraries in developing countries
www.elsevier.com | www.bookaid.org | www.sabre.org
ELSEVIER BOOK AID International Sabre Foundation

Editorial: Graham Nisbet, Louisa Hutchins, Anne Collett, Claire Byrne
Production: Justin Taylor

EDITOR-IN-CHIEF BIOGRAPHY

Paul Ducheyne

Paul Ducheyne is currently Professor of Bioengineering and Professor of Orthopaedic Surgery Research at the University of Pennsylvania, Philadelphia, PA, USA, and Director of its Center for Bioactive Materials and Tissue Engineering. He is also Special Guest Professor at K.U. Leuven, Belgium.

Ducheyne graduated from K.U. Leuven in Materials Science and Engineering (M.Sc.: 1972; Ph.D.: 1976). With fellowships from the National Institutes of Health (International Postdoctoral Fellowship) and the Belgian American Educational Foundation (Honorary Fellowship), he performed postdoctoral research at the University of Florida.

Over a diverse research career, he has organized a number of significant symposia and meetings, including the Fourth European Conference on Biomaterials (1983), the Engineering Foundation Conference on Bioceramics (1986) and the 6th International Symposium on Ceramics in Medicine (1993). The 1986 meeting led directly to the New York Academy of Sciences publications *Bioceramics, material characteristics versus in vivo behavior* (1988). He has lectured around the world and currently serves, or has served on, the editorial board of more than ten scientific journals in the biomaterials, bioceramics, bioengineering, tissue engineering, orthopaedics and dental fields. He has been a member of the editorial board, and then an Associate Editor, of *Biomaterials* (Elsevier), the leading biomaterials journal, since its inception in the late 1970s. He has authored more than 300 papers and chapters in a variety of international journals and books, and he has edited ten books. He has also been granted more than 40 US patents with international counterparts. His papers have been cited about 7,000 times; his ten most visible papers have been cited more than 2000 times.

Ducheyne started his career in Europe. While at K.U. Leuven (1977–1983), he was one of the co-founders of the Post-Graduate Curriculum in Bioengineering. This program is now a full M.Sc. program in the School of Engineering and Applied Sciences. In those initial years, he was also chairman-founder of the chapter on Biomedical Engineering of the Belgian Engineering Society (Flemish section) and director of Meditek, the Flemish Government body created to promote Academia to Industry Technology Transfer in the area of Biomedical Engineering.

He founded Gentis, Inc., which focuses on breakthrough concepts for spinal disorders. Previously, he founded Orthovita (NASDAQ: VITA) in 1992 and served as Chairman of its Board of Directors until 1999. Orthovita focuses on bioceramic implant materials for orthopaedics.

Ducheyne has been Secretary of the European Society for Biomaterials, is Past President of the Society for Biomaterials (USA) and Past President of the International Society for Ceramics in Medicine. He has been recognized as a fellow of the American Association for the Advancement of Science (AAAS), fellow of the American Institute of Medical and Biological Engineering (AIMBE), and fellow of the International Association of Biomaterials Societies. He was the first Nanyang Visiting Professor at the Nanyang Institute of Technology, Singapore and he has received the C. William Hall Award from the Society for Biomaterials.

Many of Ducheyne's PhD students and postdoctoral fellows have become leaders of the next generation. Among his students are Professors at the University of California at Berkeley, the University of Michigan, Columbia University, Georgia Institute of Technology, Kyushu University and K.U. Leuven. Among the six U.S. Associate Editors of the *Journal for Biomedical Materials Research* (Wiley and Society for Biomaterials), three were his PhD students.

CO-EDITOR BIOGRAPHIES

Kevin E. Healy

Kevin E. Healy, Ph.D., is the Jan Fandrianto Distinguished Professor in Engineering at the University of California at Berkeley in the Departments of Bioengineering and Materials Science and Engineering. He received a BSc. in Chemical Engineering from the University of Rochester in 1983. He obtained graduate degrees in Bioengineering from the University of Pennsylvania (M.Sc.: 1985; Ph.D.: 1990).

His research interests include the design and synthesis of biomimetic materials that actively direct the fate of embryonic and adult stem cells, and facilitate regeneration of damaged tissues and organs. Major discoveries from his laboratory have centered on the control of cell fate and tissue formation in contract with materials that are tunable in both their biological content and mechanical properties. These materials find applications in medicine, dentistry, and biotechnology.

Healy has authored or coauthored more than 200 published articles, abstracts, or book chapters. He is a named inventor on numerous issued United States and international patents relating to biomaterials, and has founded several companies to develop materials for applications in biotechnology and regenerative medicine.

He is currently an Associate Editor of the Journal of Biomedical Materials Research. He has served on numerous panels and grant review study sections for N.I.H. He has given more than 200 invited lectures in the fields of Biomedical Engineering and Biomaterials. He has chaired the Gordon Research Conference on Biomaterials and Tissue Engineering.

He was elected a Fellow of the American Institute of Medical and Biological Engineering (AIMBE) and was recently honored with the Clemson award for outstanding contributions to basic biomaterials science.

Dietmar W. Hutmacher

Dietmar W. Hutmacher is currently Professor and Chair in Regenerative Medicine at the Institute of Health and Biomedical Innovation, Queensland University of Technology, Brisbane, Australia. He holds Adjunct Professorships at the Georgia Institute of Technology and the Humboldt University, Berlin, Germany. Before this, he was at the National University of Singapore, where he also obtained his Ph.D. (2001). His undergraduate degree is in Biomedical Engineering (1988) and he was awarded an MBA from the Henley Management College, United Kingdom.

With a strong research focus in the field of biomaterials, tissue engineering, and regenerative medicine, Hutmacher developed an accomplished international profile that exemplifies the main challenge in the field of biomedical sciences, namely crossing traditional boundaries to nurture and initiate research and educational programs across different disciplines, and especially the boundaries between engineering, biology, and medicine.

Outcomes from Hutmacher's research have resulted in high-profile scientific and academic contributions as well as patents and commercialization. He was ranked 45 in the list of the world's top 100 materials scientists compiled by Thomson Reuters in 2010. Dr. Hutmacher has published more than 180 journal articles and 30 book chapters and edited three books. His citation record includes more than 5700 citations, with an h-index of 40. Hutmacher serves on the editorial board of *Biomaterials*, *Tissue Engineering*, *Journal of Biomaterials Sci. – Polymer Edition*, *Artificial Organs* (Associate Editor) and *Polymers International* (Associate Editor). Over the last ten years, Hutmacher has presented more than 30 invited international lectures and has served on more than 20 organizing committees of international conferences. Most recently, he was Chair of *Tissue Engineering and Regenerative Medicine International Society – Asia Pacific (TERMIS-AP) 2010*, and Chair of the *Australasian Society of Biomaterials and Tissue Engineering (ASBTE) 2010* meeting.

David Grainger

David W. Grainger is the *George S. and Dolores Doré Eccles Presidential Endowed Chair in Pharmaceutics and Pharmaceutical Chemistry*, Chair of the Department of Pharmaceutics and Pharmaceutical Chemistry, and Professor of Bioengineering at the University of Utah.

Grainger received his Ph.D. in Pharmaceutical Chemistry from the University of Utah in 1987. With an Alexander von Humboldt Fellowship, he undertook postdoctoral research under Prof. Helmut Ringsdorf, University of Mainz, Germany.

Grainger's research focuses on improving implanted medical device performance, drug delivery of new therapeutic proteins, nucleic acids and live vaccines, nanomaterials interactions with human tissues, low-infection biomaterials, and innovating diagnostic devices based on DNA and protein biomarker capture. He also has expertise in perfluorinated biomaterials and applications of surface analytical methods to biomedical interfaces, including surface contamination, micropatterns, and nanomaterials.

Grainger has published over 130 research papers at the interface of materials innovation in medicine and biotechnology, and novel surface chemistry. He has organized many international scientific symposia and chaired the Gordon Research Conference in Biomaterials and Tissue Engineering. He frequently lectures worldwide, including delivering many named, keynote, and plenary presentations.

Grainger serves on the editorial boards of four major journals in the biomedical materials field. He is currently Chair of the *Emerging Bioanalytical and Imaging Technologies* scientific review group (SRG) at the NIH, and has served on many other national and international review panels, including the NIH's *Surgery and Bioengineering* SRG. He remains active on academic scientific advisory boards for many academic programs in the United States, Asia, and Europe, including major research centers at the Universities of Wisconsin-Madison and of

Washington, the AO Foundation and EMPA, Switzerland, several other competence centers in Europe, and Waseda University's ASMeW Research Center, Japan. Grainger also sits on the scientific advisory boards for four biomedical companies and actively consults internationally with industries in applications of materials in biotechnologies and medicine.

His scientific and technical accomplishments are widely recognized, both at his institution and worldwide. Among several citations, Grainger is fellow of *the American Association for the Advancement of Science* (AAAS), the *American Institute of Medical and Biological Engineering* (AIMBE), and the *International Union of the Societies of Biomaterials Science and Engineering*. He has also been honored with the *2007 Clemson Award for Basic Research*, Society for Biomaterials, and the 2005 American Pharmaceutical Research and Manufacturer's Association's award for '*Excellence in Pharmaceutics*'.

Charles James Kirkpatrick

C. James Kirkpatrick is Professor of Pathology and Chairman of the Institute of Pathology at the Johannes Gutenberg University of Mainz, Germany, having taken up this position in 1993. He is also honorary professor at the Peking Union Medical College, Beijing and the Sichuan University, Chengdu, both in China.

Kirkpatrick is a graduate of the Queen's University of Belfast and holds a triple doctorate in science and medicine (PhD: 1977; MD: 1982; DSc: 1992). Previous appointments were in pathology at the University of Ulm, where he did postdoctoral research in experimental pathology, Manchester University (Lecturer in Histopathology) and the RWTH Aachen (Professor of Pathology & Electron Microscopy).

On moving to Aachen in 1987, he established a cell culture laboratory which began using modern methods of cell and molecular biology to study how human cells react to biomaterials. Since then, his principal research interests continue to be in the field of biomaterials in tissue engineering and regenerative medicine, with special focus on the development of human cell culture techniques, including novel 3D coculture methodology for biomaterials and the application of modern molecular pathology techniques to the study of biofunctionality of biomaterials.

Kirkpatrick is author/coauthor of more than 380 publications in peer-reviewed journals and has made more than 1000 presentations to scientific meetings worldwide. He is a former president of both the German Society for Biomaterials (2001–2005) and the European Society for Biomaterials (2002–2007) and has served on its council since 1995. He is also a member of the Council of the European Chapter of the Tissue Engineering & Regenerative Medicine International Society (TERMIS-EU).

Kirkpatrick is a long-standing member of the editorial board of the premier journal *Biomaterials* and is currently associate editor (since 2002). He has also served as associate editor of the leading *Journal of Pathology* (2001–2006). In total, he serves or has served as an editorial board member of 18 international journals in pathology, biomaterials, and tissue engineering.

Kirkpatrick was the Scientific Programme Committee Chair for the 8th World Biomaterials Congress in Amsterdam in 2008.

Kirkpatrick is a member of the Scientific Advisory Board of a number of research institutes, centres of excellence and companies in biomaterials and regenerative medicine in Europe, as well as the Medical Technology Committee, Federal Ministry of Education & Research in Germany (BMBF) (since 2005) and the German Federal Institute for Drugs & Medical Devices (BfArM)(since 2007).

Kirkpatrick has been recognized for his contributions. He is a Fellow of the Royal College of Pathologists, London and a Fellow of Biomaterials Science & Engineering (FBSE) of the IUS-BSE (International Union of Societies for Biomaterials Science & Engineering). He received the Research Prize of the State of Rhineland-Palatinate for Research on Replacement and Alternative Methods for Animal Research. He was the recipient of the George Winter Award from the European Society for Biomaterials (2008), and in 2010, he received, as first medical graduate, the Chapman Medal from the Institute of Materials, Minerals & Mining in London for "distinguished research in the field of biomedical materials".

PREFACE

Biomaterials is a dynamic, changing field that influences modern medicine and therapeutics in diverse ways. In view of the major expansion of the field of Biomaterials over the last decade, it was considered most timely to publish the present work, *Comprehensive Biomaterials*, with the intent to bringing together the myriad facets of biomaterials in one, major series of six edited volumes that would cover the field of biomaterials in a major, extensive fashion.

Experts from around the world in hundreds of related biomaterials areas have contributed to this publication that addresses the current status of most biomaterials in the field. The contributions discuss their strengths and weaknesses, their appropriate analytical methods and testing, and their device applications and performance. The chapters treat the subjects not only from a retrospective lens but one that is truly prospective, with many articles examining forthcoming materials as disruptive future technologies.

From the outset, it was our goal to review materials in the context of medical devices and tissue properties, biocompatibility and surface analysis, tissue engineering and controlled release. It was also the intent both, to focus on material properties from the perspectives of therapeutic and diagnostic use, and to address questions relevant to state-of-the-art research endeavors. Thus, in this publication, conventional, clinically used biomaterials as well as current emerging prototypes, studies and new ideas, along with visionary predictions of future biomaterials compositions and capabilities have been extensively covered by many colleagues in the field. The editorial team is cognizant of the major efforts our contributors have made in this regard, and appreciates the many, very insightful chapters received.

It was the objective of the editorial team to compose the publication with chapters that would provide strategic insights for those working in diverse biomaterials applications, research and development, regulatory management, and industry. Furthermore, we solicited papers written for a broad, cross-disciplinary audience, such that the work would include up-to-date information in a scholarly, readable and critical style. We are truly grateful to all authors, each of them leading experts in their own right, who dedicated their time to pursuing this goal.

In the first chapter "Biomaterials", the genesis of the structure of this publication is described. Materials are reviewed from the basic building blocks across the formulations and chemistry of *Metals*, *Ceramics and Polymers* to *Biologically Inspired and Biomolecular Materials*, *and Materials of Biological Origin*. Properties are analyzed on the basis of advanced *Methods of Analysis*. Unique aspects of *Biocompatibility*, *Surface Engineering*, *and Delivery of Drugs*, *Genes and Other Molecules* are covered. Materials uses in tissue engineered constructs and devices and implants are treated in *Tissue and Organ Engineering* and *Biomaterials and Clinical Use*. This chapter does not contain any references, as all the 200 chapters in these volumes are unique references in their own right.

From concept to print, this publication was developed and implemented over a five year time span. Even though at times, the editors may have entertained the thought to add some more chapters, it would not have been fair to all our colleagues who submitted their contributions in a timely manner to extend the development time any further.

The publishing field is undergoing major changes at this time. By way of example, scientific society memberships oftentimes provide electronic subscription to their journals, and members more often than not subscribe to this electronic format of journals exclusively. In addition, libraries have shifted to ordering books, compendia, monographs and major reference works in electronic format, and frequently not in printed form. It cannot be denied, though, that the learning process is also one that takes place by leafing through printed publications. Thus, with the goal of achieving the highest possible impact on knowledge dissemination that could result from

this Major Reference Work in the field of biomaterials, a printed format was also deemed necessary. The editorial team and Elsevier have worked closely together to make this publication available in two formats:

- online via the Science Direct platform guaranteeing worldwide distribution via an established medium;
- a printed version with printing-on-demand runs determined by orders received.

This dual publication actually also lends itself very well to publishing updates and additions such as video clips. Elsevier and the editorial team have already discussed some of the concepts in this regard and will be moving on this in the near future.

Comprehensive Biomaterials started with a very innocuous email from a publishing consultant requesting input for a project under discussion at Elsevier. After some soul-searching and corporate restructurings at Elsevier (what's really new in the corporate world?), the project got on track, and it has been my and the editorial team's delight to work with outstanding publishing professionals. David Sleeman was our first publisher. Interestingly, he also moonlighted as a football reporter which reminded me that there was always life after science (yes America, the whole world calls this football). He was succeeded by Graham Nisbet who gave up the trappings of a Politics major for science publishing. Louisa Hutchins and Anne Collett managed most of the editorial flow, ably assisted by Joanne Williams and Marise Willis. With the time difference between the UK and the US, matters had mostly been handled before the day broke on this side of the pond. Once we moved to production, Justin Taylor took charge. There was not a single email that went unanswered. Closer to home, actually in my professional home, the Department of Bioengineering at the University of Pennsylvania, Tabitha Hymans first, and then Jennifer Leung managed my paper flow.

As editors, we want to express a special word of thanks to our colleague, Professor Teruo Okano, Tokyo, Japan, who suggested quite a few interesting topics and excellent contributors when we launched the project. We also relied on a number of referees, among whom we want to single out Ravi Radhakrishnan, Jeremy Gilbert and Christine Knabe.

Lastly, and very importantly, as Editor-in-Chief, it is my pleasure mentioning that it was my privilege to work with a team of colleagues as co-editors. Their enthusiasm was infectious and their insight masterful!

Paul Ducheyne
University of Pennsylvania
Philadelphia, PA, USA

FOREWORD

Almost from the beginning of recorded time, humans have attempted – and often failed – to deploy a wide variety of substances and materials to treat their diseases and traumas. But only within the past few decades, as technologies have matured and materials selection and use diversified, have scientists and therapists discovered the ability to create artificial compounds suitable for *in vivo* usage. The concept of *biomaterials* was introduced no more than fifty years ago, around the mid-1960s. During a conference in 1986 in Chester (UK), colleagues and I struggled mightily to elaborate a consensual definition of biomaterials under D. F. Williams' leadership. This now accepted definition states: "*a biomaterial is a non-viable substance used in a medical device, intended to interact with biological systems.*"

With this definition in mind, one might wonder whether there is a science dedicated to *biomaterials*? Two notions present in this definition are important: utility, and interaction with living systems. *Per se*, they are enough to claim that biomaterial science does not exist. Of course, that is not to say the field itself does not exist. Demonstrably, biomaterials research now straddles such fundamental disciplines as chemistry, physical chemistry, physics, materials science – with its numerous sub-divisions, biology – with its yet-more-numerous sub-divisions. Biomaterial studies include applications in surgery, dentistry, and, more recently, pharmacology with the development of medicated devices. The field extends to scaffolds to support tissue cultures, and degradable and bioresorbable systems to avoid storage after completion of the function. Diversifying the field yet further from these fundamental aspects of "biomaterials" is the necessary, and now extensively developed, set of bioengineering precepts that pushes the field forward.

Today "biomaterials" is a maturing research area. As scientists, our enterprise stretches well beyond the very purest of research characterizing the early "gold rush" days. Furthermore, we are well beyond the initial generations of prosthetic and therapeutic devices made of industrially derived materials. With materials developed for other purposes, rather remarkable therapeutic successes were achieved. This period is now over. Today the challenges are in designing novel therapeutic systems, or finding the means to minimize the few percent of failures observed in systems which have reached the clinic. Having a common vision of such an enormous domain that groups various sciences, methodologies and technologies is a necessity, but it is difficult to achieve by people active in the domain. Individually, there is no chance, for sure. The future depends on interdisciplinary approaches involving top specialists from the diverse specialties that are capable of sharing tasks and thus are capable of understanding each others disciplines and approaches. One can hardly find a textbook, however, to train them and at the same time, to provide initiation to novices. All that has been available to date have been books composed of a collection of some articles and reviews that capture a segment of this expansive, and sometimes confusing, literature.

Comprehensive Biomaterials seeks to provide just such a common vision for the presently vast, and mushrooming domain of biomaterials, embracing numerous perspectives in an expansive, inherently interdisciplinary major reference work to support effective current research in a sometimes bewilderingly complex environment. Significantly, it is written by a panorama of the world's experts in hundreds of related biomaterials areas. The result is a continuum of rich information appropriate for many audiences. The work addresses the current status of nearly all biomaterials in the field, their strengths and weaknesses, their future prospects, appropriate analytical methods and testing, device applications and performance, emerging candidate materials as competitors and disruptive technologies, and strategic insights for those entering and operational in diverse biomaterials applications, research and development, regulatory management, and commercial aspects.

The question may be asked: in such an information-rich environment, what is the interest of this huge collection of 200 contributions? It offers the authority – and the vision – of well-known specialists in the field.

What is the originality of the content? While I have not read all of the contributions, those that I have appear remarkable with contents that are far beyond what reviews usually provide, thanks to clear efforts in updating the knowledge and a didactic writing style. Reading these articles, I felt ignorant but learnt something from each. I see *Comprehensive Biomaterials* as an excellent tool for training those new to the different disciplines and for expanding our numerous specialists' knowledge. Professor Ducheyne and colleagues are to be commended for this extraordinary enterprise.

Michel Vert
University of Montpellier
France

PERMISSION ACKNOWLEDGMENTS

The following material is reproduced with kind permission of Nature Publishing Group

Figure 2 of Fluorinated Biomaterials
Figure 2 of Dynamic Hydrogels
Figure 4 of Dynamic Hydrogels
Figure 5 of Dynamic Hydrogels
Figure 6 of Bio-inspired Silica Nanomaterials for Biomedical Applications
Figure 7 of Engineering Viruses For Gene Therapy
Figure 8 of Engineering Viruses For Gene Therapy
Figure 9 of Engineering Viruses For Gene Therapy
Figure 11 of Engineering Viruses For Gene Therapy
Figure 3 of Phages as Tools for Functional Nanomaterials Development
Figure 6 of Extracellular Matrix: Inspired Biomaterials
Figure 1 of Materials as Artificial Stem Cell Microenvironments
Figure 2 of Materials as Artificial Stem Cell Microenvironments
Figure 3 of Materials as Artificial Stem Cell Microenvironments
Figure 5 of Materials as Artificial Stem Cell Microenvironments
Figure 6 of Materials as Artificial Stem Cell Microenvironments
Figure 7a of Materials as Artificial Stem Cell Microenvironments
Figure 1 of Molecular Imaging
Figure 3 of Biological Microelectromechanical Systems (BioMEMS) Devices
Figure 7 of Biological Microelectromechanical Systems (BioMEMS) Devices
Figure 10 of Intracellular Probes
Figure 4 of Hydrogels in Biosensing Applications
Figure 13 of Hydrogels in Biosensing Applications
Figure 15 of Conjugated Polymers for Biosensor Devices
Figure 1 of Vaccine and Immunotherapy Delivery
Figure 12 of Sol–Gel Processed Oxide Controlled Release Materials
Figure 5 of Porous Metal–Organic Frameworks as New Drug Carriers
Figure 6 of Porous Metal–Organic Frameworks as New Drug Carriers
Figure 7 of Porous Metal–Organic Frameworks as New Drug Carriers
Figure 10 of Porous Metal–Organic Frameworks as New Drug Carriers
Figure 13 of Porous Metal–Organic Frameworks as New Drug Carriers
Table 2 of Porous Metal–Organic Frameworks as New Drug Carriers
Figure 7 of Bone Tissue Engineering: Growth Factors and Cytokines
Table 1 of Biomaterials for Central Nervous System Regeneration
Figure 7 of Finger
Figure 3 of From Tissue to Organ Engineering
Figure 4 of Kidney Tissue Engineering
Figure 1 of Liver Tissue Engineering
Figure 2 of Liver Tissue Engineering
Figure 5 of Trends in Materials for Spine Surgery

Figure 25 bottom of Degradable Polymers
Figure 5 of Peptoids: Synthesis, Characterization, and Nanostructures
Figure 15a of Patterned Biointerfaces
Figure 15b of Patterned Biointerfaces
Figure 16a of Patterned Biointerfaces
Figure 17a of Patterned Biointerfaces
Figure 17b of Patterned Biointerfaces
Figure 5 of Quantifying Integrin–Ligand Engagement and Cell Phenotype in 3D Scaffolds
Figure 6 of Quantifying Integrin–Ligand Engagement and Cell Phenotype in 3D Scaffolds

http://www.nature.com/nature

The following material is reproduced with kind permission of American Association for the Advancement of Science

Figure 1 of Bio-inspired Silica Nanomaterials for Biomedical Applications
Figure 7a of Magnetic Resonance of Bone Microstructure and Chemistry
Figure 7b of Magnetic Resonance of Bone Microstructure and Chemistry
Figure 16 of Biological Microelectromechanical Systems (BioMEMS) Devices
Figure 10 of Hydrogels in Biosensing Applications
Figure 11a of Patterned Biointerfaces
Figure 11b of Patterned Biointerfaces
Figure 19 of Surface Engineering Using Peptide Amphiphiles
Figure 13 of Shape-Memory Polymers

www.aaas.org

The following material is reproduced with kind permission of Taylor & Francis

Figure 5 of Shape Memory Alloys for Use in Medicine
Figure 8 of Shape Memory Alloys for Use in Medicine
Figure 9 of Shape Memory Alloys for Use in Medicine
Figure 2 of Materials as Artificial Stem Cell Microenvironments
Figure 6 of Surface Engineering Using Peptide Amphiphiles
Figure 4 of Development of Contact Lenses from a Biomaterial Point of View – Materials, Manufacture, and Clinical Application

www.taylorandfrancisgroup.com

1.101. Biomaterials

P Ducheyne, University of Pennsylvania, Philadelphia, PA, USA

© 2011 Elsevier Ltd. All rights reserved.

No one really knows when Adam and Eve left Earth's Paradise. But would it really be important? Millennia forward, no one really agrees when Biomaterials came into existence. But does it really matter? The fragmented historical record indicates that even centuries ago, this is before Lister established the principles of aseptic surgical technique, materials were occasionally used to help in the treatment of injured or lost tissues.

In the era of rebuilding that followed the Second World War, innovators in the treatment of painful arthritic joints were using corrosion-resistant metals to restore motion and function to the joint. Half a century ago, a key consideration for the use of materials in surgery was the minimal reactivity of the material when implanted in the body. It was the principle that when foreign materials and devices would be implanted, there should be no adverse response, either in the local tissues or systemically, and this could best be achieved with materials that would not or would only minimally react when inserted in biological milieus.

Almost all metals used in the body, with the exception of the noble metals, derive their benign tissue response from the formation of a tenacious oxide film that forms spontaneously on their surface and thereby shields the underlying metal from further oxidation; this is corrosion. Thermodynamically, metals such as stainless steels, cobalt chromium alloys, and titanium and its alloys are not in their lowest state of energy, but the initially formed oxide film forms a protective layer that renders the kinetics of further oxidation extremely slow. This holds true as long as the oxide film is present and not compromised. Obviously, achieving this under any circumstance is still a major issue, as can be evidenced by reviewing the performance of some orthopedic joint replacement device designs today.

The advances in technical ceramics prompted their pursuit for medical use. The thinking went that to achieve minimal reactivity in tissues, ceramics were inherently better suited than metals, which can still be reactive in conditions in the body. In contrast, ceramics are materials that are composed of ionic compounds, and as such are thermodynamically very stable. This formed the first impetus for their use. Technical ceramics also possessed excellent wear and friction properties that made them uniquely attractive as a material of choice for artificial joints. It was expected, in an at the time unbeknownst way, that less wear particulates would be produced and as such that there would be less of a possibly adverse tissue response. This work was very prescient, since as it stands today, the prognosis for successful functioning of a total hip replacement is set at some 15 years, and the key limiting factor for longer successful performance is the osteolytic tissue response to the accumulated wear debris produced in the artificial joint.

A new school of thought emerged in the 1970s. It was held that, since any material implanted into the body will elicit a response, materials should be designed for directing a favorable tissue response and to guide the healing. Thus, bioactive ceramics were first formulated. Even though these materials are also composed of ionic compounds, they are reactive, and their reactivity, as well as the control of their reactivity is at the basis of their unique *in vivo* properties. When bioactive ceramics such as hydroxyapatite and bioactive glass were first described, their *in vivo* tissue response was barely understood. Initially, studies relied on materials science methodologies to describe surface reactions, more often than not focusing on inorganic material reactions. It was not for long, though, until fundamental advances in cellular and molecular biology pushed along the quest for a better and more thorough understanding. These studies revealed that molecules known to play important roles in cell function and cell signaling adsorb onto - and into - the surface reaction layers that form *in vivo* on bioactive ceramics. These events, in tandem with dissolution from the inorganic material, then prompt the cellular activity and enhance tissue formation.

A conceptually opposite path, but one the field followed in parallel, was the engineering of materials surfaces. New materials were created with molecules in order to specifically drive cell function. Studies focused on the biomimetic modification of materials to alter a material's compatibility with a biological system. The insight emerged that controlling cell behavior in contact with biomaterials critically depended on the material providing the correct chemical and physical signals to the cells. Cell adhesion and proliferation were controlled by designing the material to incorporate biomimetic chemistry that regulated cell function. Molecules such as peptides and growth factors were covalently coupled to an inorganic material's surface so that the cells surrounding the material recognized it through a normal biomolecular pathway.

Today, the field of Biomaterials is replete with studies and discussions of treatments that make use of biological processes to interact with materials, and, in so doing, aid in tissue formation and regain of bodily functions. Actually, the concept of 'smart materials', this is, materials that elicit and stimulate tissue formation, has become a mainstay in the field, as can be witnessed from the myriad of studies involving all classes of materials, including metals, ceramics, polymers, and composites. Materials have a surface composition intended to interact with biological pathways and cellular functions. Biological functionality is also built into material structures or is grafted onto material surfaces. New materials are designed to mimic biological structures or functions, giving rise to the class of biomimetic materials. And lest we forget we cannot possibly improve on Mother Nature, we also use materials of biological origin such as collagens, fibrin, and hyaluronic acid polymers.

Not only does surface chemistry have an effect on biological response, surface structures can be engineered to guide and direct a desirable biological outcome. Patterned material surfaces have been developed with the goal, first, to pursuing a fundamental understanding of how surface geometries and physical properties on a micro- and nanoscale affect cellular

biology. A second, not less important goal, is to define interfacial properties that optimally achieve repair with implanted materials. To mention an example, data has been published demonstrating that the shapes of nuclei of primary cells on microfabricated substrata are controlled by confining attachment and spreading isolated cells on adhesive islands. Gene expression, protein synthesis, and cell differentiation on such substrates are then altered by changing the nuclear shape of cells present within the substrate features. Thus, biomaterials studies have led to the discovery that nuclear shape, and not cell shape, is a predominant component affecting cell fate decisions in contact with materials.

From here, it is only a small step to conceive of therapies purely based on material concepts to upregulate a cellular response, and this without relying on any drugs or growth factors. In this context, the word 'theramer' has been used in studies of polymers with this built-in capability. Furthermore, bioactive ceramics, which have the inherent ability to adsorb and potentiate cellular ligands and growth factors as a critical step toward tissue formation and repair, also represent a class of materials uniquely illustrating this very principle of biomaterials. Theramers are integrated into tissue structures; and, bioactive ceramics react, are being transformed and are resorbed along with the remodeling tissues.

Even though there is major interest in material responses by themselves, there is also widespread focus on materials that are combined with therapeutic molecules and with various cells. These interests have evolved alongside with the development of Controlled Release (of drugs and other therapeutic molecules) and Regenerative Medicine and Tissue Engineering.

Controlled release was first pursued with the goal of achieving drug blood plasma concentrations that would vary much less than with intermittent bolus administration, even to the extent of staying constant. It was the hope that with continuous delivery, a concentration could be maintained that would not be less than the minimum therapeutic dose and also would not exceed the toxic threshold concentration. Today, Controlled Release as a field is much vaster in scope and pursues its goals in part by designing materials concepts for optimal delivery. Areas of interest include superior biological tolerance ('biocompatibility') of the materials in which molecules are embedded; local drug delivery with implanted materials for greater treatment efficacy by achieving much greater local drug concentrations than possible with systemic administration; targeted delivery of therapeutics with controlled release particles that hone in on cell membrane receptors uniquely expressed by cancer cells; release subsequent to site-specific enzymatic degradation of the delivery material; local delivery to eliminate risks of systemic toxicity associated with oral and parenteral therapies; delivery of water-insoluble drugs to increase bioavailability; protection of molecules with a short half life, such as growth factors; convenience (anticonceptive); avoidance of compliance issues in treating mental disorders; and tunable delivery to achieve space- and time-dependent delivery. A whole plethora of materials are used in this regard: polymers, ceramics, even metals. In fact, surface modifications of metals are designed in order to incorporate molecules that, upon release, produce a bactericidal effect.

The explosion of the biological sciences and the quest for using this wealth of new knowledge for better treatments also did not leave biomaterials untouched. As was indicated earlier, it advanced the understanding of the modes of action of bioactive ceramics and materials with engineered biomimetic surfaces. But, there is also the converse of this path. In the pursuit of treatments to regenerating tissues and organs, cell biology has been unraveling answers to questions such as how to deliver cells, in what state, from which source, and subject to what prior treatment. These studies include many aspects of stem cell biology and cell signaling. This field, oftentimes captured by the words 'Regenerative Medicine', has come to suggest the importance of cell carrier materials vis-à-vis excellent cellular preparation, proper cell signaling, and successful delivery of cell constructs into *in vivo* tissue beds. This represents the next frontier in biomaterials: rather than deciphering reactions to materials, the mechanistic understanding of cellular stimulation is now used to advance delivery of cells and pursue optimal cell and tissue engineering treatments.

At its core, tissue engineering integrates aspects of advanced cell biology, of delivery and release of various molecules that signal cellular function, and of materials that act both as optimal scaffolds for cellular functional expression and as vehicles for release of any biological molecule relevant in this process. This essence of tissue engineering reveals a critical aspect of modern biomaterials, namely the complex interplay among various components ('cells, signals, and scaffolds'), where solutions to the difficult problems the field addresses derive from information in a multiplicity of related fields. In tissue engineering studies, one can easily discern the core principle of materials science, which is the materials science triad. This principle reflects the interdependency among processing, composition and structure, and properties. Focusing on tissue engineering and, within it, the unique biomaterials aspect, the methodology of scaffold material synthesis critically determines composition and surface structures, which in their turn affect molecule release and cellular stimulation (to name but a few of the scaffold properties). All aspects are coupled, and modification of one of the parameters in this materials universe typically will affect many other parameters and outcomes.

Over the many years that the field of Biomaterials has evolved, there has been the overarching focus on contributing to better medical care. There has been an evolution from extraneous repair by replacing tissues to intrinsic repair by stimulating tissue formation and regeneration. A merger of these evolutions is underway, as devices continuously co-opt biological functionality. The example of drug-coated stents is the one that jumps most readily to mind. The field is also moving inexorably into nanoscience, and in this instance, it is again the result of a logical evolution. Even though nanotechnology at large is at the forefront of many engineering disciplines, it evolved in a gradual and natural way. In fact, nanotechnology, at large, involves using the typical engineering skills of analysis, quantification, synthesis, and design, but then at ever smaller levels of organization. The evolution came about with ever better tools and methods being developed. In Biomaterials, these tools enable probing at the smallest levels of organization of materials and tissues and make it possible to design and synthesize materials with ever smaller dimensions. In the context of biomaterials, it may be apparent that modifying surfaces with molecules and physical features having

nanodimensions in order to stimulate biological response is one but an outstanding illustration of this principle. Other, not less revealing examples are materials which by themselves have nanodimensions, such as quantum dots, nanoparticles for controlled and targeted delivery, and nanofibers that are incorporated in tissue engineering scaffolds.

Advances in methods, tools, and techniques have contributed critically to the progress in biomaterials. Obviously, there are the methods derived from Cellular and Molecular Biology alluded to earlier. There are also the advances in microscopic and spectroscopic techniques that enable probing materials and tissues, and very importantly, the interface between materials and tissues. New imaging techniques have evolved that enable the study of materials and devices *in vivo* with unprecedented richness of information. And there are the computational methods, both in mechanics and in chemistry that use sheer computational power to address fundamental questions of the effects of physical and chemical properties on any detail of material tissue interaction.

Understanding and guiding the biological response is at the core of the field of Biomaterials. In the mid-eighties, the field actually tried to capture this essence by defining biocompatibility this way. At the Consensus Conference "Definition in Biomaterials" of the European Society for Biomaterials in Chester, England, March 1986, one came to define biocompatibility as "the ability of a material to perform with an appropriate host response in a specific application". As a corollary today, can it then not be stated that biocompatibility is existential to modern Biomaterials Science?

The definition of biocompatibility also emphasized the application. This observation carries with it important consequences. First and foremost is the need to study materials in functional forms reflecting actual treatments *in vivo*. In so doing, medical aspects such as issues associated with trauma, pathology, patient variability, and patient compliance enter into the analysis. It is interesting to revisit the early evolution of Biomaterials in the post-Second World War era. At the time, the standard-of-care for treating painful, arthritic hip joints was arthrodesis, this is, a 'stiffening' of the joint. Today, one still uses this approach of removing motion, but then in the treatment of painful spines. Spinal fusion entails the removal of the intervertebral disk and the coalescence of bone tissue from the neighboring vertebrae. In so doing, motion and function of the 'spinal motion segment' are severely reduced. Notwithstanding the fact that arthrodesis is long past in the treatment of arthritic hip joints, but conversely is actively practiced in spinal surgery, it is interesting to note that the past advances in the joint replacement field are regularly invoked to rationalize developments in spinal care. At first sight, this is surprising, given that anatomical structures, tissue properties, and surgical details are all vastly different in the spine and the joints of the lower extremities. However, even though the same materials are used to advance spinal care as were used in joint replacement surgery, including various metals, polymers and ceramics, the materials properties are now studied in view of these significantly different uses.

Analysis of clinical performance is part of the field of Biomaterials. Today, it is well established that for new materials, new devices, or new material-based treatment concepts to be introduced clinically, a five-pronged evaluation scheme needs to be addressed: (i) *in vitro* evaluation of biocompatibility in simple, a-functional conditions; (ii) *in vitro* evaluation of acceptable performance in conditions mimicking functional *in vivo* conditions; (iii) *in vivo* evaluation of biocompatibility in simple, a-functional conditions; (iv) *in vivo* evaluation of satisfactory performance in functionally relevant conditions (typically appropriate animal models are then used); and (v) evaluation of materials and devices in well-conceived clinical trials. During these studies, one addresses questions not just related to material properties *per se*, but properties in view of surgery(or other procedure)-related characteristics, tissue properties, trauma or illness-related conditions, and patient factors. Today, with the advent of personalized medicine, we may be, perhaps, at the verge of having to include considerations of genomic variations.

Biomaterials is a field that bears testimony to the adage that paradigm-shifting fields are situated at the cross-section of various existing disciplines. In Biomaterials, advanced materials science with its chemical, mechanical, and physical components, crosses into biology and makes this knowledge all its own, and this with the intent on furthering medical care and contributing to medicine.

How does one structure such a vast, dynamic, and complex field? Materials technologies spanning the continuum from academic and industrial research to clinical applications in devices, drug delivery, tissue engineering, and regenerative medicine occupy an enormous intellectual and technological bandwidth. The field embraces fundamental linkages within device and regenerative medicine innovation. Contemporary biomaterials science encompasses molecular, computational, recombinant and biotechnological, nanotechnological, hybrid composite, microbial and cell- and tissue-based approaches.

The question begs repeating. How does one structure such a vast, dynamic, and complex field? In this 200-chapter publication, the modern aspects of biomaterials are described from basic science to clinical applications. Materials are reviewed from the basic building blocks across the formulations and chemistry of **Metals, Ceramics and Polymers** to **Biologically Inspired and Biomolecular Materials, and Materials of Biological Origin**. Properties are analyzed on the basis of advanced **Methods of Analysis**. The unique aspects of **Biocompatibility, Surface Engineering, and Delivery of Drugs, Genes and Other Molecules** are covered. Materials uses in tissue-engineered constructs and devices and implants are treated in **Tissue and Organ Engineering** and **Biomaterials and Clinical Use**.

By the very nature of the field of Biomaterials, these subjects are extensively interrelated, and as such, it may appear as though there is some overlap. However, this is only appearance, as typically, there are different vantage points from which one can review the information. Thus, overlap must not be confused with complementarity. As a case in point, there are chapters on "Fretting Corrosion of Orthopedic Implants" and "Electrochemical Behaviour of Metals in Biological Milieus". In the former, the emphasis is on the actual fretting corrosion/mechanically assisted corrosion that has been documented in orthopedic implants. In the latter, there is limited focus on actual implant construct behavior, but extensive focus on the fundamental mechanisms of corrosion. In the former, there is ample discussion of implant testing and metallic ion release

analysis. In the latter, the basic mechanisms of oxidation and reduction, and the shifts in electrical potential that occur during oxide abrasion are described.

Health care and the commitment to excellent care are typical characteristics of advanced countries. In *Comprehensive Biomaterials*, some major advances in medicine and health care that came about by studying and using materials in medicine are covered. The publication provides many examples from the main medical disciplines to which Biomaterials has contributed: cardiovascular care, orthopedics and dentistry, to name but a few. This publication, however, is not a comprehensive description of all matters 'Biomaterials'. It cannot be, by virtue of the field's enormous reach and ever-changing dynamics. Rather it is a current, broad-based review of the salient directions of the field.

Biomaterials Science is very much a part of the broader discipline of Biomedical Engineering. Whereas Engineering, and Materials Science by extension, used to derive their foundation from mathematics, physics, and chemistry, Biomedical Engineering and Biomaterials have also embraced biology as a basic science on which they build. Thereby, the scope of the parent disciplines is expanded in a way no other activity in engineering currently does or currently achieves with the thoroughness of the biomedical engineering or biomaterials community. The major advances in the biological sciences are followed in lockstep. With the twenty-first century turning into the age of biology, Biomedical Engineering and Biomaterials contribute to society by building on the advances in this critical science. Biomedical Engineering, and within it Biomaterials, is advancing as a discipline worldwide. Full-fledged Biomedical Engineering educational programs at the undergraduate level have been started worldwide and departments in biomedical engineering are continuously being created.

The foray of biomedical engineers and biomaterial scientists into areas, such as heart pacing, joint replacement, and imaging brain function, and so many more challenges seemed daunting beyond comprehension half a century ago. Many of these challenges have been conquered, all while progress continues. Other areas of great complexity are now related to the universe of genes and stem cells and are also being tackled by the biomedical engineering and the biomaterials community. This publication shows the strides made and the challenges that remain.

1.102. Metals for Use in Medicine

P J Andersen, Andersen Metallurgical LLC, Madison, WI, USA

© 2011 Elsevier Ltd. All rights reserved.

1.102.1.	**Introduction**	6
1.102.2.	**General Requirements for Long-Term Implantation**	6
1.102.3.	**Key Metallurgy Concepts**	6
1.102.4.	**Chemical Composition and Structure**	7
1.102.4.1.	Stainless Steels	7
1.102.4.2.	Cobalt Base Alloys	8
1.102.4.3.	Titanium Base Alloys	9
1.102.4.4.	Other Implantable Metals	10
1.102.5.	**Mechanical Properties**	10
1.102.5.1.	Static Properties	10
1.102.5.2.	Fatigue	11
1.102.6.	**Processing Effects**	14
1.102.6.1.	Metal Processing Overview	14
1.102.6.2.	Process Effect Examples	15
1.102.6.2.1.	Work hardening and annealing	15
1.102.6.2.2.	Wrought versus cast alloys	17
1.102.6.2.3.	Precipitation hardening	17
1.102.6.2.4.	Surface condition effects	17
1.102.7.	**Future Developments**	18
1.102.8.	**Summary**	18
References		18

Glossary

Alloy A material composed of at least two chemical elements. At least one of these elements must be metallic and the alloy must have metallic characteristics.

ASTM International ASTM develops standards for a wide range of activities including materials and testing procedures used in the medical device field.

Crystal structure The arrangement of atoms in simple, repeated, three-dimensional arrays. Almost all metals are crystalline (as opposed to amorphous).

Dislocation(s) Dislocations are extended defects in the structure of a crystal (e.g., edge dislocations are represented by an extra partial row of atoms in the crystal). Dislocation behavior is critical to deformation of metals.

Fatigue Progressive localized damage due to repeated applications of load. This can lead to crack formation, crack growth, and component failure.

Fracture mechanics The study of the behavior of structures in terms of the stress conditions and defects (e.g., cracks or flaws) in the structure.

ISO The International Organization for Standardization develops standards in a variety of fields including materials and tests for the medical device industry.

Recrystallization Formation of new, ductile grains from previously worked metal grains by heating the metal to an elevated temperature. This increases ductility and decreases strength of the metal.

Abbreviations

BCC Body centered cubic
FCC Face centered cubic
FDA Food and drug administration
HCP Hexagonal close packed
MRI Magnetic resonance imaging
PSB Persistent slip bands
α Alpha, in titanium alpha phase refers to the hexagonal closed packed crystal structure
β Beta, in titanium beta phase refers to the body centered cubic crystal structure

1.102.1. Introduction

Implantable materials make critical contributions to modern medicine. Many of the treatments we now take for granted (joint replacement, pacemakers, heart valves, stents) would not have been possible without the advanced metals, polymers, and ceramics that are available to the medical device community.

The human body presents a very challenging environment for materials engineers because of the need for implants that are highly corrosion resistant and, in many applications, able to withstand millions of high stress load cycles. This chapter focuses on implantable metals, with the emphasis on their composition, mechanical properties, and the relationships between processing methods (i.e., the techniques used to produce the implant) and mechanical properties. As the field is so broad, this discussion primarily covers metals used in load bearing applications for structural components.

1.102.2. General Requirements for Long-Term Implantation

Any implantable metal must be well tolerated by the host tissue. Therefore, metals of interest must be nontoxic and biocompatible (various aspects of the biological response to implants are discussed in **Chapter 4.401, The Concept of Biocompatibility**; **Chapter 4.402, Biocompatibility and the Relationship to Standards: Meaning and Scope of Biomaterials Testing**; **Chapter 4.403, The Innate Response to Biomaterials**; **Chapter 4.404, Adaptive Immune Responses to Biomaterials**; **Chapter 4.405, Leukocyte–Biomaterial Interaction *In Vitro***; **Chapter 4.406, Protein Interactions with Biomaterials**; **Chapter 4.407, Bacterial Adhesion and Biomaterial Surfaces**; **Chapter 4.408, Integrin-Activated Reactions to Metallic Implant Surfaces**; **Chapter 4.409, Surfaces and Cell Behavior**; and **Chapter 3.319, Characterization of Nanoparticles in Biological Environments**). In this regard, composition and corrosion resistance are the key factors for metallic materials. With the exception of noble metals such as platinum and gold, implantable metals form very thin, passive oxide films that reduce their corrosion rates to extremely low levels.

Implantable materials must exhibit mechanical properties that are appropriate for specific applications. High fatigue strength is needed for devices such as femoral hip stems and pacemaker leads; metallic suture wires must be relatively soft and ductile.

Only a limited number of metals can be safely implanted for long periods of time; the metals made in the greatest commercial quantities (steels, aluminum alloys, copper alloys) are not suitable for use as implants.

In many cases a material is chosen for an implant application because of a unique property or combination of properties. For example, platinum or palladium alloys are used in a variety of applications where radiopacity is important (i.e., marker bands). Wear behavior is a critical aspect of devices that articulate, and the choice of material for these applications is often made on the basis of wear characteristics; cobalt base alloys, oxidized zirconium, and aluminum oxide ceramics are often used in these applications because of their wear behavior. **Table 1** provides a broad overview of implantable metals along with their important attributes and typical applications.

1.102.3. Key Metallurgy Concepts

The atoms in metals are arranged in simple, repetitive, long-range, three-dimensional crystal structures. For the metals of interest in this chapter, the relevant crystal structures are body centered cubic (BCC), face centered cubic (FCC), and hexagonal close packed (HCP). The nature of atomic bonding in metals is quite different from that found in other materials. Metallic bonding involves the sharing of valence electrons between closely packed atomic cores. The mobility of shared electrons is crucial to the electrical and thermal conductivity of metals. As the bonds are not localized, individual metal atoms or planes of atoms can move, or slip, relatively easily with respect to one another.

Permanent, or plastic, deformation of metal crystals occurs most frequently by dislocation motion. Dislocations are defects in the crystal; edge dislocations (an extra half plane of atoms) are a common type (**Figure 1**). If the applied loads are high enough, atomic bonds break in a sequential fashion and the dislocation moves through the crystal. Dislocations move most favorably on close packed planes within the crystal. Metals with the FCC structure have more close packed planes than BCC and HCP structures and therefore are generally more ductile. While dislocation theory is a complex subject beyond the scope of this chapter, it is important to note that the approaches used to alter the strength and ductility of metals

Table 1 Overview of some major groups of implantable metals and their applications

Alloy family	*Reason for medical use*	*Some typical uses*
Stainless steels	Fatigue strength, corrosion resistance	Fracture fixation, stents, hip stems, spinal implants, cables
Cobalt base alloys	Fatigue strength, corrosion resistance, wear resistance	Joint replacement, stents, pacemaker conductor wires, spinal disc replacements, dental bridgework
Titanium alloys	Fatigue strength, corrosion resistance, ability to bond to bone (osseointegration)	Joint replacement, dental implants, fracture fixation, spinal fusion implants, spinal disc replacements
Nitinol	Shape memory	Stents
Tantalum	Corrosion resistance, radiopacity	Porous structures for bone ingrowth, X-ray markers
Zirconium	Wear resistance of oxidized zirconium	Joint replacement
Platinum alloys	Radiopacity, electrical properties, corrosion resistance	Pacemaker electrodes, guide wire marker bands, aneurysm coils
Gold alloys	corrosion resistance, radiopacity	Crowns, inlays, guide wire marker bands

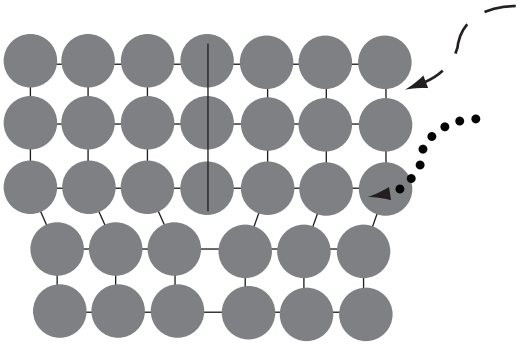

Figure 1 Dislocation motion is the most common mechanism for plastic deformation in metals. In this schematic, an edge dislocation (extra row of atoms) is shown by the solid line. It is easier to break bonds between atoms one at a time along the plane indicated by the dotted line than it is to break all the bonds at one time along the plane indicated by the dashed line. Illustration with permission from Haggard, W. O.; *et al*. In *Surgery of the Hip*; Berry, D. J., Leiberman, J. R. Eds.; Elsevier, (in press).

rely on mechanisms that alter the ability of dislocations to move through the crystal structure. Deformation by twinning is another deformation mode in some metals. The deformation behavior of Nitinol (the major shape memory alloy) is quite different from that of conventional metals; Nitinol deformation involves phase transformations and reversible twinning processes (Nitinol is discussed in **Chapter 1.104, Shape Memory Alloys for Use in Medicine**).

Most metal objects contain large numbers of individual grains. The orientation of the crystal within each grain is generally different from the orientation in adjacent grains. This mismatch between grains is accommodated by grain boundaries, which are thin disordered regions. Grain size is an important factor in the mechanical strength of metals. In general, finer grains lead to higher strength. A well-known equation describing this behavior is the Hall–Petch relationship, $\sigma_y = \sigma_o + kD^{-1/2,}$ where σ_Y is the yield stress of the metal, σ_o is a frictional stress required to move dislocations, k is the Hall–Petch slope, and D is the grain size.[1]

Pure metals are typically quite soft and ductile; extremely pure metals are also very expensive to produce as it is difficult to avoid contamination by small amounts of impurities. Therefore, the vast majority of metals are alloys with more than one ingredient. The major constituent may be thought of as the solvent and the minor constituents as solute atoms. Metallic alloying elements generally take the place of the solvent atoms at random locations in the crystal structure; they are referred to as substitutional alloying elements. (Nitinol is an exception to random alloying element locations. NiTi has an ordered structure with the Ni and Ti atoms alternating in the lattice.) As the substitutional alloying elements are not the same atomic size as solvent atoms, the crystal lattice is distorted by the addition of these elements. This makes dislocation motion more difficult and increases the strength of the metal. Small atoms such as nitrogen, oxygen, and carbon tend to be located in the regions (or interstices) between the solvent atoms; these are known as interstitial alloying elements. Interstitial alloying elements 'pin' dislocations very effectively, so small additions of these elements can have a large impact on mechanical properties. Chemical composition is also an important determinant of the crystal structure of the material. The crystal structure of a metal determines how many and which slip systems are available; this in turn affects deformation behavior and response to mechanical loading.

Another technique to improve the strength of metals is to increase the number, or density, of dislocations within the crystal. There are a number of mechanisms which produce additional dislocations within a metal crystal as the crystal is deformed. As dislocation density increases, the dislocations begin to interact, and further dislocation motion becomes more difficult. This behavior forms the basis for strengthening metals by work hardening (also known as cold working or strain hardening).

1.102.4. Chemical Composition and Structure

The metals most frequently used for implants include iron-based stainless steels, cobalt-based alloys, titanium-based alloys, and nickel–titanium (Nitinol) shape memory alloys. Shape memory materials are the subject of **Chapter 1.104, Shape Memory Alloys for Use in Medicine**. There is limited use of zirconium, tantalum, and a variety of noble metals (platinum, gold, etc.).

1.102.4.1. Stainless Steels

Implantable stainless steels are iron-based alloys. Although other types of stainless steels exhibit BCC or duplex (BCC+FCC) crystal structures, the implantable alloys exhibit a FCC crystal structure referred to as austenite. Austenite is nonmagnetic; given the widespread use of MRI techniques, this is a critical requirement for implantable materials today. Stainless steels with lower amounts of alloying ingredients (e.g., 302 and 304) can transform to the magnetic martensite phase during cold working operations. If part of a catheter or guide wire made from these materials breaks off in a patient, it could lead to serious consequences. A portion of the FDA warning about unretrieved device fragments is related to this (http://www.fda.gov/MedicalDevices/Safety/AlertsandNotices/PublicHealthNotifications/ucm062015.htm).

Typical stainless steel alloying ingredients include chromium (Cr), nickel (Ni), molybdenum (Mo), manganese (Mn), and nitrogen (N). Chromium is added primarily to enable the alloys to form a protective chromium oxide layer (passive film). Passive films in stainless steels and cobalt–chromium alloys are often thought of as being simply Cr_2O_3 layers, but they are more complex as they may contain small amounts of other oxide species and may interact with the human environment postimplantation. Additional information on the nature and behavior of passive layers may be found in Gilbert.[2] Ni and/or Mn additions are necessary to stabilize the nonmagnetic FCC crystal structure. Nitrogen additions also help stabilize austenite and improve strength and corrosion resistance while Mo improves corrosion resistance (particularly pitting corrosion). Although carbon is a key alloying ingredient in conventional steels, carbon is kept at low levels in these alloys to reduce the possibility of chromium carbide formation (a phenomenon known as sensitization) during slow cooling

Table 2 Chemical composition of common implantable stainless steels

Alloy designation	*Cr (wt%)*	*Ni (wt%)*	*Mn (wt%)*	*Mo (wt%)*	*N (wt%)*	*Minor elements*
316L (ASTM F 138[5], ISO 5832 Part 1[6])	17.00–19.00	13.00–15.00	2.00 max	2.25–3.00	0.10 max	0.03 C max 0.75 Si max 0.50 Cu max
Rex 734™[7] (ISO 5832 Part 9[8])	19.5–22.00	9.0–11.00	2.00–4.25	2.0–3.00	0.25–0.50	0.25–0.80 Nb 0.08 C max 0.75 Si max 0.50 Cu max
22-13-5™[9]	20.50–23.50	11.50–13.50	4.00–6.00	2.00–3.00	0.20–0.40	0.10–0.30 Nb 0.10–0.30 V 0.03 C max 0.75 Si max 0.50 Cu max
BioDur® 108[10]	19.00–23.00	0.05 max	21.00–24.00	0.50–1.50	0.85–1.10	0.08 C max 0.75 Si max 0.25 Cu max

Table 3 Chemical composition of common implantable cobalt base alloys

Alloy designation	*Cr (wt%)*	*Ni (wt%)*	*Mo (wt%)*	*W (wt%)*	*Fe (wt%)*	*N and/or C (wt%)*	*Minor elements*
Cast Co–Cr–Mo (ASTM F 75, ISO 5832 Part 4)	27.0–30.0	0.050 max	5.0–7.0		0.75 max	0.35 C max 0.25 N max	1.0 Mn and Si max
Wrought Co–Cr–Mo (ASTM F 1537, ISO 5832 Part 12)	26.0–30.0	1.0 max	5.0–7.0		0.75 max	Either 0.25 N max and 0.14 C max, or 0.15–0.35 C and 0.25 N max	1.0 Mn and SI max
L-605 (ASTM F 90, ISO 5832 Part 5)	19.0–21.0	9.0–11.0		14.0–16.0	3.00 max	0.05–0.15 C	1.0–2.0 Mn 0.4 Si max
MP35N (ASTM F 562, ISO 5832 Part 6	19.0–21.0	33.0–37.0	9.0–10.5		1.00 max	0.025 C max	1.0 Ti max 0.15 Mn and Si max
Elgiloy™/phynox™ (ASTM F 1058, ISO 5832 Part 7)	19.0–21.0 or 18.5–21.5	14.0–16.0 or 15.0–18.0	6.0–8.0 or 6.5–7.5		Specifications for this alloy call out 39.0–42.0 Co Balance Fe	0.15 C max	Mn 1.5–2.5 or 1.0–2.0 1.2 Si max Be 0.10 or 0.001 max

from elevated temperatures. Formation of these carbides reduces the Cr content along grain boundaries making sensitized stainless steels more likely to experience intergranular corrosion.

The use of stainless steels for implants began in the mid 1920s[3] with the use of Fe–18% Cr–8% Ni screws. The 18-8 alloy was quickly replaced with an improved version that contains additions of Mo for better corrosion resistance. This type of alloy was used for a variety of fracture fixation devices as well as an early total hip replacement developed by Wiles.[4] Over time, 316L stainless steel emerged as the most commonly implanted stainless steel. Common applications for 316L include fracture fixation products and stents.

Stainless steels with improved mechanical properties and superior corrosion resistance to 316L appeared in the 1980s. These alloys contain higher levels of Cr, Mn, and N than 316L. An example of this alloy is Rex 734™ which is used for hip stems. The most recent implantable stainless steels contain very low Ni content; these alloys were created in response to concerns about patient sensitivity to nickel. These low nickel alloys contain high levels of Mn and N to stabilize the desired austenitic phase. Table 2 lists the chemical composition of some implantable stainless steels along with their ASTM and/or ISO standards.

1.102.4.2. Cobalt Base Alloys

Cobalt base alloys share many similarities with stainless steels. Under most conditions, they exhibit an FCC crystal structure and often contain the same alloying elements (Cr, Ni, Mo, N) used in stainless steels. As with stainless steels, the corrosion resistance of these alloys is due to the formation of a thin chromium oxide passive film. Low levels of nitrogen (0.25% max) increase strength. Nickel additions stabilize the FCC crystal structure.[11,12] Deformation of cobalt base alloys can cause some of the FCC structure to transform to the less ductile HCP phase; this is somewhat less prevalent if nickel is added to these alloys. The cobalt base alloys that are generally used in product forms that require extensive amounts of deformation (e.g., wire, tubing,

and thin strip) commonly contain nickel. The cobalt alloys used to produce orthopedic implants such as hip stems and knee replacements contain much lower nickel content than the other implantable cobalt base alloys. Table 3 lists the chemical composition of commonly implanted cobalt base alloys.

Unlike implantable stainless steels, some of these alloys contain significant levels of carbon (up to 0.35%) which results in the formation of carbide particles throughout the material. Carbides are intermetallic compounds with fixed ratios of metal and carbon atoms. In the cobalt base alloy used in orthopedics, the presence of carbon results in formation of primarily $M_{23}C_6$-type carbides. In this carbide, the metal atoms (M) are primarily Cr.[13] The size and the distribution of the carbides depend on the manufacturing process used to produce the alloy. Carbides in cast versions of this alloy are much coarser than those found in wrought material of the same composition.

The initial use of cobalt base alloys was in dental appliances; a paper by Venable published in 1937 demonstrated favorable response to a Co–Cr–Mo alloy when implanted in a canine model.[14] This alloy, which came to be known as Vitallium® among other trade names, found its initial implant use in hip 'molds' (a cup placed over the head of the femur to eliminate bone-to-bone contact).[15] As joint replacement procedures evolved, the use of this type of alloy became common in hip and knee replacements. Other cobalt base alloys are used to produce pacemaker leads, stents, heart valve cages, and a variety of other implants.

1.102.4.3. Titanium Base Alloys

Titanium alloys are often divided into categories based on the crystal structure of the alloy. The three categories that are used in medical devices are alpha (α), which has HCP crystal structure (e.g., CP titanium), alpha plus beta (α+β) which contains both HCP and BCC structures (e.g., Ti–6Al–4V and Ti–6Al–7Nb), and beta (β) alloys such as Ti–12Mo–6Zr–2Fe. The crystal structure of these alloys depends on the chemical composition of the alloy and processing conditions such as the cooling rate from elevated temperatures. Some alloying elements (e.g., Al, O) act to stabilize the α phase; such elements are referred to as α stabilizers. Other elements (e.g., Mo, V, and Nb) stabilize the β phase, so they are referred to as β stabilizers. These beta alloys are sometimes referred to as metastable as they rely on rapid cooling from elevated temperatures to retain the β crystal structure. If α+β alloys are cooled in this manner, they will transform to a martensitic structure with undesirable mechanical properties. Table 4 lists the chemical compositions of some of the most widely used titanium alloys.

The internal microstructure of α+β and β titanium alloys can be altered over a very wide range by control of deformation parameters (amount of deformation, deformation temperature), cooling rates, and the use of heat treatment. This allows airframe and jet engine manufacturers to tailor alloys for specific mechanical demands such as high fracture toughness or resistance to high-stress-low-cycle fatigue. The ASTM and ISO standards for alloys such as Ti–6Al–4V require fine dispersions of equiaxed α and β phases because this condition offers excellent high-cycle fatigue performance.

A key aspect of microstructure control in Ti alloys involves the temperature at which the β phase transforms to a mixture of α+β (the β transis temperature). In α+β alloys, cooling from above the β transis leads to lamellar structures; faster cooling rates result in finer lamellae. The fine grain equiaxed α+β microstructure generally used in implants results from deformation below the β transis followed by recrystallization and annealing cycles(or a single 'mill anneal' cycle), also below the β transis. A complete review of the relationships between processing, structure, and properties can be found in Lütjering and Williams.[21] The microstructural changes associated with processing above the β transis mean that operations such as welding or other high-temperature processes (sintering to apply a porous coating) will lead to formation of lamellar microstructures. This may cause some reduction in high-cycle fatigue strength.

The corrosion resistance of these alloys is due to the formation of titanium dioxide (TiO_2) passive layers. Titanium is extremely reactive, so the passive film forms extremely rapidly. The high reactivity of titanium means that any melting or elevated temperature fabrication processes must be done

Table 4 Chemical composition of common implantable titanium Alloys

Alloy designation	*Crystal structure*	*Al (wt%)*	*V (wt%)*	*Nb (wt%)*	*Mo (wt%)*	*Zr (wt%)*	*Fe (wt%)*	*O (wt%)*
Commercially pure Ti (ASTM F 67[16], ISO 5832 Part 2[17])	Alpha						0.20 max Grade 1 0.50 max Grade 4	0.18 max Grade 1 0.40 max Grade 4
Ti–6Al–4V ELI (ASTM F 136)[a]	Alpha plus beta	5.50–6.50	3.5–4.5				0.25 max	0.13 max
Ti–6Al–4V (ASTM F 1472, ISO 5832 Part 3)	Alpha plus beta	5.50–6.75	3.5–4.5				0.30 max	0.20 max
Ti–6Al–7Nb (ASTM F 1295, ISO 5832 Part 11)	Alpha plus beta	5.50–6.50		6.50–7.50			0.25 max	0.20 max
Ti–15Mo (ASTM F 2066[18])	Metastable beta				14.0–16.0		0.10 max	0.20 max
Ti–12Mo–6Zr–2Fe (ASTM F 1813[19])	Metastable beta				10.0–13.0	5.0–7.0	1.50–2.50	0.008–0.28
Ti–15Mo–5Zr–3Al (ISO 5832 Part 14[20])	Metastable beta	2.50–3.50			14.0–16.0	4.5–5.5	0.35 max	0.20 max

[a]The composition of ELI Ti–6Al–4V falls within the ranges specified by ISO 5832 Part 3.

under strictly controlled conditions to avoid contamination and resultant reduction of mechanical properties.

As a viable production process for titanium and its alloys did not become available until after World War II, development and use of titanium implants lagged behind the use of stainless steels and cobalt alloys. Reports by Leventhal and Down cover some of the earliest uses of titanium and its alloys for implant applications.[22,23]

An active area of research in medical materials involves new titanium alloys. Most of this work involves β alloys. The interesting attributes of β alloys include low elastic modulus, ability to utilize large oxygen additions without brittle failure, lower notch sensitivity in fatigue, and the ability to work harden and cold form shapes.

Metallic joint replacements alter the stresses experienced by the surrounding bone; this can lead to loss of bone density. The difference between the stiffness of bone and the stiffness of an implant is an important factor in this bone loss.[24,25] The elastic modulus of femoral cortical bone is on the order of 17–20 GPa,[26,27] significantly lower than the values for stainless steels (~190 GPa), cobalt base alloys (~230 GPa), and α+β titanium alloys (~110 GPa). The Ti–35Nb–4SN β alloy has been processed to result in elastic modulus levels of 40–60 GPa[28]; it remains to be seen if low modulus Ti alloys will yield clinical benefits for human patients.

Current titanium alloys contain low levels of oxygen (0.13–0.28% max depending on the alloy) because of loss of ductility with further increases in oxygen content. Higher oxygen contents (up to 0.68%) have been studied in a Ti–35Nb–7Zr–5Ta alloy. Yield strength of this alloy at 0.68% oxygen is over 1050 MPa with a high level of ductility (over 20%).[29]

The fatigue strength of α+β alloys declines significantly if the material has surface discontinuities or notches; this behavior is known as notch sensitivity. In general, β titanium alloys are less sensitive to notches. For example, Murray *et al.* reported a 585 MPa 10^7 million cycle endurance limit for smooth Ti–6Al–4V samples in a rotating beam fatigue test. The endurance limit decreased to 280 MPa for specimens with a notch (stress concentration factor of 1.6). For the β alloy Ti–12Mo–6Zr–2Fe, the smooth and notched values were 585 and 410 MPa, respectively.[30]

As the BCC structure of the β alloys offers more slip systems than the HCP α phase, these alloys are easier to deform at low or room temperature. Thus, the β alloys offer more possibilities for strengthening by work hardening. Jablokov *et al.* have published tensile property data on cold worked, and cold worked and aged Ti–15Mo. In this study, a 40% reduction in area increased the ultimate tensile strength from 758 MPa (solution treated) to 1104 MPa. Further increases in strength were achieved by aging the alloy.[31]

The ability to deform β alloys at low temperatures has led to efforts to form parts at room temperature (as opposed to the more common hot forging process).[28] More information on the range of β titanium alloys that have been studied can be found in Niinomi.[32]

1.102.4.4. Other Implantable Metals

Some of the earliest attempts to use metals in surgery, dating back to around 150 AD, involved gold suture wire.[33] Gold was also reportedly used in the 1500s and 1600s.[34] Today, applications of noble metals such as gold, platinum, and palladium are limited; the high cost of noble metals tends to limit their applications to very small devices or components of devices. In addition to cost, many of these materials exhibit relatively low mechanical properties further limiting their range of applications.

In the past decade, porous tantalum (Ta) and an oxidized zirconium (Zr) alloy have been used in orthopedic applications. The porous Ta structure is used in applications where bony ingrowth is desired; it may be used as a free standing material or bonded to implants.[35,36] Ta is also used in some devices to provide radiopaque markers and it has been used to produce other types of implants. The oxidized Zr alloy is used in articulating applications (total knee replacements, femoral heads for hip stems) due to the wear resistance of its zirconium oxide (Zr_2O_3) surface layer.[37]

1.102.5. Mechanical Properties

Any implant must have mechanical properties that enable it to perform its function for the desired lifetime of the implant. The properties of interest are specific to each application and depend on design of the implant and the properties of the material used to produce the implant. The factors that control mechanical properties are the material composition and the processes used to fabricate the implant. Processing choices (e.g., using a cast part vs. a forged part) can have a dramatic effect on the final properties of the implant.

Mechanical properties can be divided into properties determined by a single load application such as a tensile test and fatigue properties determined by repeated application of loads. These categories are often referred to as static and dynamic properties. As many medical devices routinely see millions of loading cycles over their lifetimes, fatigue properties are especially important.

1.102.5.1. Static Properties

Static properties are generally measured using laboratory specimens that are loaded using specialized testing machines. The most common loading condition applies tensile loads, but testing in compression, shear, or torsion is also possible. Typical data reported from this testing are yield and ultimate stress, elongation, and modulus of elasticity. Yield stress is sometimes reported as proof stress or yield strength, and ultimate tensile stress may be referred to as tensile strength or ultimate tensile strength.

The materials standards published by groups such as ISO and ASTM include minimum standards for tensile properties of implantable metals. Table 5 shows the ASTM requirements for minimum tensile properties of selected metal alloys. The data in the table demonstrate the impact of some processing variables. For 316L and Rex 734™ stainless steels, it is clear that as a result of work hardening, the cold worked (or medium hard) condition exhibits higher strength and lower ductility as expected. Cobalt alloys such as MP35N exhibit similar behavior. The properties of wrought, warm worked Co–Cr–Mo are much higher than those of investment cast material because

Table 5 Tensile properties of some common implantable metal alloys

Alloy designation	*Yield strength (min.) (MPa)*	*Ultimate strength (min.) (MPa)*	*Elongation (min.) (%)*	*Reference*
316L stainless (annealed)	190	490	40	ASTM F 138
316L stainless (cold worked)	690	860	12	ASTM F 138
Nitrogen strengthened stainless steel (REX 734™); annealed	430	740	35	ASTM F 1586
Nitrogen strengthened stainless steel (REX 734™); medium hard	700	1000	20	ASTM F 1586
'Nickel free' stainless steel (BioDur 108®); annealed	517	827	35	ASTM F 2229
'Nickel free' stainless steel (BioDur 108®); cold worked	827	1034	20	ASTM F 2229
Investment cast Co–Cr–Mo	450	655	8	ASTM F 75
Co–Cr–Mo (wrought, warm worked)	827	1192	12	ASTM F1537
Commercially pure Ti	170 (grade 1) 483 (grade 4)	240 (grade 1) 550 (grade 4)	24 (grade 1) 15 (grade 4)	ASTM F 67
Ti–6Al–4V (ELI)	795	860	10	ASTM F 136
Ti–12Mo–6Zr–2Fe (solution annealed)	897	931	12	ASTM F 1813

of structure refinements (much smaller grain size, smaller carbides in the versions of this alloy, which contain carbon), and the development of a worked structure within the grains.

Under some conditions, the strength of work hardened cobalt alloys can be further increased by aging treatments. As per ASTM F562, the yield strength of cold worked MP35N is 1000 MPa (minimum) in the hard condition (ASTM specifications do not specify the amount of cold work or reduction of area). In the cold worked and aged condition, the minimum yield strength is 1596 MPa.

The static mechanical properties of titanium alloys depend on chemical composition and processing history. Oxygen content has a large impact on the strength of these alloys, which can be seen in the strength levels of the various grades of commercially pure titanium (**Table 5**). The amount of oxygen that can be added to current titanium alloys is limited because excessive amounts of oxygen result in low ductility. As was mentioned earlier, recent work with a Ti–35Nb–7Zr–5Ta alloy suggests that higher amounts of oxygen can be tolerated in Ti alloys that contain large amounts of other alloying ingredients. Although at least some of the titanium alloys respond to work hardening or heat treatment (aging), the effect of these treatments is not specified in either the ASTM or ISO specifications for these alloys.

1.102.5.2. Fatigue

The study of fatigue began in the mid-nineteenth century after failures of locomotive axles caused fatal accidents. The disastrous Comet airliner crashes in the 1950s are another example of historically significant fatigue failures. In the device industry, the most devastating fatigue failures involved the Björk Shiley 60° Convexo-Concave (BSCC) heart valve. There have been hundreds of deaths associated with the fracture of the outlet struts which were welded to the main body of the device: failure of the struts resulted in the carbon disc no longer functioning as a valve. Welding quality issues and higher than anticipated stresses have both been implicated in this tragic case.[38]

Modern medical implants are not free from fatigue failures. Implants used for fracture fixation or spinal fusion may fail if the location that is being stabilized does not heal. Fracture of segments of stents is also observed.[39] Forces at the hip joint can be as high as eight times body weight during running and three times body weight while walking.[40] These forces can lead to fatigue fractures of femoral hip stems. Hip stem fracture becomes more likely if the proximal region of the implant is not supported by bone. This lack of support increases the moment arm acting on the device leading to high stresses. Overall statistics on the rate of hip stem or other orthopedic implant fractures are not readily available, but the MAUDE (Manufacturer and User Facility Device Experience) database on the FDA website can be searched to find reports of fractures in specific devices (http://www.accessdata.fda.gov/scripts/cdrh/cfdocs/cfMAUDE/search.CFM).

A basic definition for fatigue is "... a degradation of mechanical properties, leading to failure of a material or component under *cyclic* loading."[1] The stresses needed to create damage by fatigue are typically lower than the overall yield strength of the material. The fatigue process involves three stages: crack initiation, crack growth, and final failure due to overload. As many implants experience millions of load cycles over their lifetime, it is not surprising that mechanical failures of metallic implants are almost always because of fatigue. The possibility of fatigue failure depends primarily on the design of the component, the fatigue strength of the material used to produce the component, and the nature of the surface of the device (e.g., surface roughness, residual stresses, stress concentration sites such as sudden transitions in section size and sharp radii, and surface flaws such as cracks and inclusions).

Wöhler, a German engineer working in the Prussian railway system, is generally credited with pioneering the systematic study of the relationships between applied stress and the number of loading cycles a component could withstand. In this method, a number of samples are tested at different loads and the applied stress (S) is plotted against the log of the number of loading cycles (N) to yield an S/N (or Wöhler) curve. Shütz has prepared an extensive review of the development of our understanding of metal fatigue.[41]

A feature of the metals discussed in this chapter is that they exhibit a fatigue or endurance limit. If the maximum stress level is below the endurance limit, the material can be cycled indefinitely without failure. Fatigue tests are generally run to 10^7 million loading cycles to establish an endurance limit (cardiovascular stents are often tested to 4×10^8 million cycles as a heart rate of 60 beats per minute translates to over 30 million cycles per year).

Table 6 Some published values for 10^7 million cycle fatigue strength of common implantable metals

Material	*Material condition*	*10^7 cycle endurance limit (MPA)*	*References*
Co–Cr–Mo (ASTM F 75[42], ISO 5832-4[43])	Investment cast	200 (min)–450	44–46
Co–Cr–Mo (ASTM F 1537[47], ISO 5832-12[48])	Forged or warm worked	656–930	34, 44, 49
Ti–6Al–4V (ASTM F 136[50], ISO 5832-3[51])	Wrought	500–800	34, 46, 49, 52
Ti–6Al–7Nb (ASTM F 1295, ISO 5832-11[53])	Wrought	540–750	52

It is important to realize that there is variation in S/N fatigue test outcomes; a large number of specimens are needed to obtain good statistics. Sources of variability include variation in the processes used to produce the test material and the test sample, and the random nature of flaws such as inclusions. Fatigue crack initiation generally begins at, or very close to, a surface of the sample as stresses are generally highest at the surfaces. This makes surface finish and the presence (or absence) of residual surface stresses factors which can affect the test results. The type of fatigue test used may also result in different results. As a result, different investigations may result in different estimates of the endurance limits of implantable metals; **Table 6** contains a few examples of published values for some common alloys. Implant designers should keep this variability in mind when deciding what material properties to use for implant strength calculations.

Starting in the 1960s, fracture mechanics methods began to be applied to studies of component life under fatigue loading conditions. This approach assumes that flaws are inherent in the material and seeks to predict the response of the flaw to the loading conditions. This approach is generally referred to as damage tolerant design; the US Air Force requires key airframe and engine components to be designed to damage-tolerance guidelines (the US Air Force Handbook for damage tolerant design is on-line at http://www.afgrow.net/applications/DTDHandbook/sections/page1_0.aspx).

Application of the fracture mechanics approach to airframes and jet turbine components was driven by unanticipated component failure. The fracture mechanics approach assumes all components have flaws and then characterizes the behavior of the flaws when loads are applied to the component. This analysis relies on understanding the crack growth behavior of the material and it demands accurate modeling of the high stress regions of the component. The original Paris relationship between crack growth rate and loading conditions is $da/dN = C(\Delta K)^m$, where da/dn is the crack growth rate, ΔK is the stress intensity factor at the crack tip, and C and m are empirical constants.[54,55] Since Paris published this work, it has been widely used even though there are several issues with it. Shütz summarizes the issues as follows: "... it contains neither the influence of mean stress on crack propagation, nor the static fracture on reaching the fracture toughness K_{1c}, nor the 'fracture mechanics fatigue limit' AK_0, that is the stress-intensity range below which no fatigue–crack propagation occurs."[41] If fatigue crack growth rates (da/dN) are known as a function of the stress intensity factor (ΔK), it is possible to calculate a threshold cyclic stress intensity factor (ΔK_{TH}) for cracks of various sizes. For medical devices this information may be used to calculate the size of a flaw that will not propagate under the highest stress conditions experienced by the part (this is referred to as the critical flaw size). As long as the component can be inspected to insure that any flaws are smaller than this critical size, flaws at or below the critical flaw size will not grow (or will require billions of load cycles to grow); thus the component should not fail.

The fracture mechanics approach has been used to model a heart valve and a stent but the method is not in general use for medical devices.[56,57] A complete description of this method is beyond the scope of this chapter; see Shütz for a review and list of references on this approach.

The vast majority of medical device fatigue evaluations continue to rely on the S/N approach. The fracture mechanics approach focuses on crack growth calculations and, in the case of aircraft components, utilizes periodic inspections to monitor crack length. Most medical device designs seek to avoid crack initiation as once a crack starts in a medical device, it is likely to propagate until the device fails; crack size inspection for implanted devices is not possible and the cost of implant failure is high. Another issue with the fracture mechanics method involves assessing the maximum stress conditions. For highly stressed components like femoral hip stems, patient variability (weight, activity level, bone size, and bone quality) makes it difficult to determine a true worst case stress situation. Conservative estimates for all of these factors might result in impractical designs (i.e., large components that would not be useful for many patients).

As the classic S/N approach is commonly reported in the medical device literature, it will be the focus of further discussion. S/N curves are usually generated with laboratory specimens as (opposed to testing complete devices). This testing is generally done in air as opposed to simulated body fluids such as Ringer's solution. Testing in air may result in higher observed fatigue strengths for stainless steels,[58] but there does not appear to be a difference when testing Ti alloys in air and in Ringers.[52,59] If the component of interest is large enough, it may be possible to machine test specimens from actual implants.[60] This can help capture the influences of the production processes on fatigue. It is more common to machine test specimens from more convenient product forms such as round or flat bars of the material of interest; care must be taken with this approach to ensure that the raw material used is as representative as possible of the material condition found in the device of interest.

Testing methods to measure fatigue strength include rotating bending (with either a constant bending moment or a cantilever loading situation), flat plate cantilever bending, and axial testing. An example of a rotating test with a constant bending moment is the R.R. Moore method; this creates a sinusoidal loading condition with equal maximum tensile and compressive loads. In this case, the mean stress is zero and the ratio of the minimum to maximum stress (the R value) is -1.0. As this type of test generally uses an hour glass shaped

specimen, the volume of the specimen exposed to the maximum load is very small. Another issue with rotating bending tests is that many implants do not experience reverse bending while in service. In spite of these issues, its relative ease and the simple, robust testing equipment involved make rotating bending a common screening method. Flat plate cantilever bending and axial loading tests make it possible to apply a mean stress. In these types of tests, a stress ratio of 0.1 is often used and the specimen is never loaded in compression. These tests have the advantage of testing a greater volume of material than a standard rotating sample with an hour glass cross-section; if there are flaws within the material, tests that involve additional material in high stress regions are more likely to result in failures initiated by the flaws. The differences between these testing methods, therefore, may lead to different fatigue strength outcomes depending on the test protocols that are used.

Another type of fatigue of interest for medical devices is fretting fatigue. Fretting involves low amplitude cyclic rubbing between two surfaces that are in contact. Surface damage can occur under these conditions making crack initiation easier. Modular joint replacements, fracture fixation devices, and spinal fusion products all have multiple parts that are assembled in the operating room. When these components undergo loading in the body, relative motion and fretting can occur at the junctions between the parts. Fretting corrosion may be observed under these conditions; this is discussed in **Chapter 6.607, Fretting Corrosion of Orthopedic Implants**. In general, the fatigue strength of metals under fretting conditions is expected to be lower than the strength levels obtained from smooth laboratory samples. A paper by Neu provides an excellent review of this topic for Ti–6Al–4V.[61] A decline in the fatigue strength of Ti–6Al–4V from ~550 to 175 MPa because of fretting has been observed.[62]

These results were generated using a flat cantilever bending test; for the fretting tests, two cylinders were clamped across the test specimen yielding a cylinder on flat contact situation. ASTM F 1875 describes two methods for evaluating fretting corrosion; one of these methods can also be used to determine fatigue strength of the junction between a femoral hip stem and a modular head.

While laboratory specimens provide useful information, testing of finished components provides more assurance that the product will meet its performance requirements. Final component testing takes into account design features, surface conditions, and processing effects that are difficult to mimic in a laboratory test specimen. Final component tests can also apply more complex loading conditions than those found in simple rotating beam or cantilever bending tests. For example, testing of completed stents ensures that postlaser cutting processes such as electropolishing have adequately removed any recast layer associated with laser cutting operations while testing hip stems in their final form ensures that any effects of the actual manufacturing processes are accounted for.

Typical fatigue tests of finished components seek to approximate the loading conditions experienced in clinical service. In the case of femoral hip stems, 'the validity of these methods has been empirically established through the reasonably good correlation of test results with historical clinical data.'[63] If there are implants with excellent clinical histories (in terms of mechanical failure rates), the performance of these implants in standard tests can be used to establish performance requirements for subsequent implants. Standards organizations such as ISO and ASTM have written test method standards for a variety of finished implants. Examples include ISO 7206 parts 4[64] and 6[65] and ASTM F 1612[66] for hip stems, and ASTM F 2477[67] for stents.

Finished component testing is generally performed to establish that the implant in question meets specified performance requirements. Determination of an endurance limit for specific devices is uncommon. In the case of orthopedic implants, a potential problem for this type of test is the reliance on historical clinical data. Thus, major changes in the patient population such as greater numbers of obese patients and increasing use of joint replacements in younger, more active patients may result in higher stresses than those observed in the historic joint replacement population.

In both laboratory testing and in the clinical setting, fatigue crack initiation is generally the critical stage. If a crack initiates on a medical implant, it is likely that the implant will experience enough additional loading cycles to lead to failure. Fatigue cracks generally initiate at or near the surface of implants. If there are flaws on the surface of a device in a highly stressed region, they may act as crack initiation sites. Examples of this include porosity, laps or cracks in the material, and inclusions (foreign materials, typically oxide particles, which were entrapped in the material in the early stages of production). **Figure 2** shows SEM micrographs of fatigue initiation in 177 μm MP35N wire; in one case, the fracture initiated near a small Al_2O_3 inclusion and in the other example, the failure initiated at a surface tool mark.

Design and manufacturing issues can also provide potential crack initiation sites; sudden changes in section size or sharp

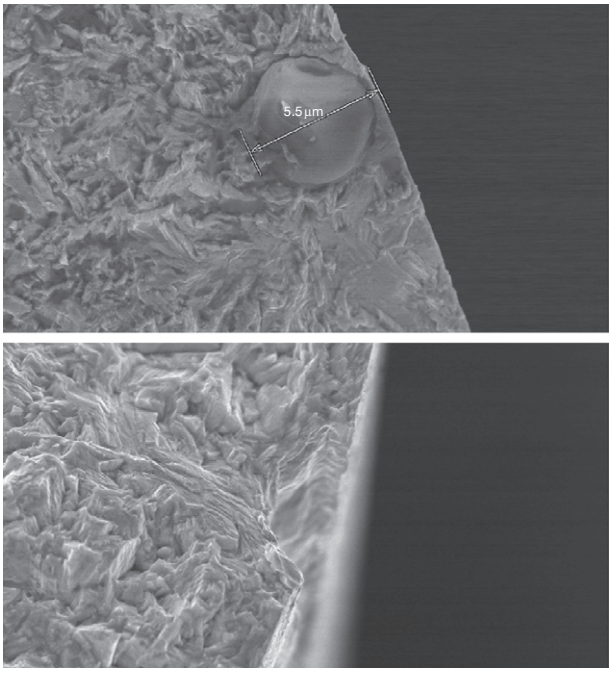

Figure 2 SEM micrographs showing fatigue initiation sites in 177-μm MP35N wire. The top image shows an alumina inclusion very near the initiation site while the bottom image shows initiation from a tool mark on the surface of the wire. Images provided by Mr. Jeremy Schaffer, Fort Wayne Metals, used with permission.

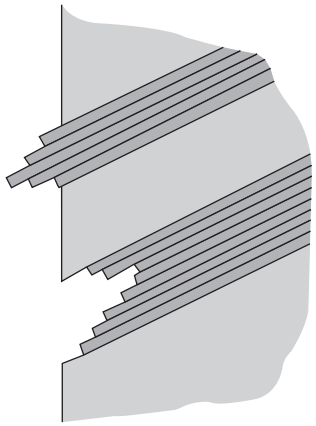

Figure 3 Intrusions and extrusions formed by slip on the surface of a metal. These surface features may act as stress concentrators and crack initiation sites.

radii are examples of design issues that result in stress concentrations and potential failure. Some machining operations (e.g., aggressive grinding) can result in microstructural change due to overheating or formation of small cracks on the surface; a reduction in the endurance limit for Ti–6Al–4V from 596 MPa (polished) to 310 MPa (abusively ground) has been reported.[68] In the absence of any of these discontinuities, localized slip processes can lead to formation of persistent slip bands (PSBs) followed by formation of intrusions and extrusions on the surface which may act as stress concentration sites (Figure 3); PSBs and intrusions/extrusions may also interact with other discontinuities to initiate cracks. Thoughtful implant design, stringent control over manufacturing processes, and careful inspection methods all help to minimize the risk of implant fatigue failure.

Figure 4 shows SEM micrographs of a failed 316L bone screw. This screw exhibited multiple initiation sites followed by a crack growth phase (as evidenced by the fatigue striations) and final overload once the cross-sectional dimensions of the screw were reduced to the point that it could no longer support the load.

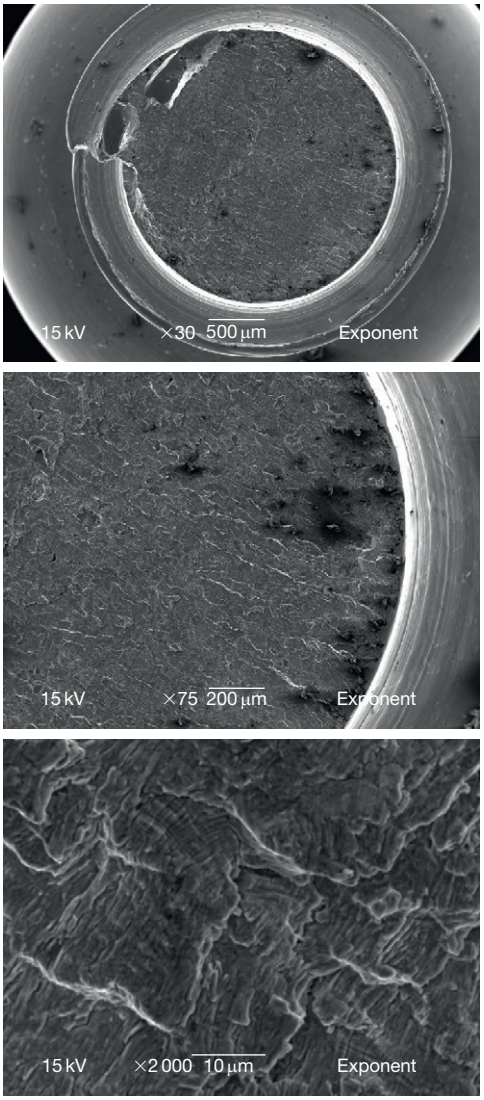

Figure 4 SEM micrographs of a 316L bone screw that failed because of fatigue. The top view shows the overall screw surface; multiple initiation sites are evident in the middle image; the crack then grew by fatigue as indicated by the striations in the lower image. Images supplied courtesy of Brad James PhD Exponent, used with permission.

1.102.6. Processing Effects

For a given chemical composition, the choice of process routes has an enormous effect on mechanical properties. Processing choices influence factors such as grain size, hardness, extent of cold work within grains, and the presence of texture (i.e., preferred orientation of the crystal structure, leading to mechanical properties that are anisotropic). Processes also influence properties by altering the nature of the surface of the device in question. Internal structure alterations influence dislocation motion. Surface modifications, such as shot peening and application of porous surface layers, affect the ease of initiating cracks. Processing can also introduce flaws into an implant. Examples include inclusions that are introduced in melting operations, porosity in castings, cracks in forgings or extruded tubing, surface damage due to laser marking, etc. Figure 5 shows examples of processing related flaws.

1.102.6.1. Metal Processing Overview

Nearly all metals, including those used to fabricate implants, require a melting operation as part of their production. In some applications, components are made to near net dimensions by pouring molten metal into a shaped cavity, or mold, which mimics the shape of the desired object. A version of the casting process known as investment casting is in wide use for production of orthopedic implants such as femoral knees. Other metal products begin with the casting of large (~500–5000 kg for specialized implantable alloys) ingots. The main constituent and the desired alloying ingredients are melted together to achieve the desired overall chemical composition. As-cast ingots have very large grains; some alloys may also exhibit segregation of the alloying elements at this stage. Control of the melting process is crucial to minimize

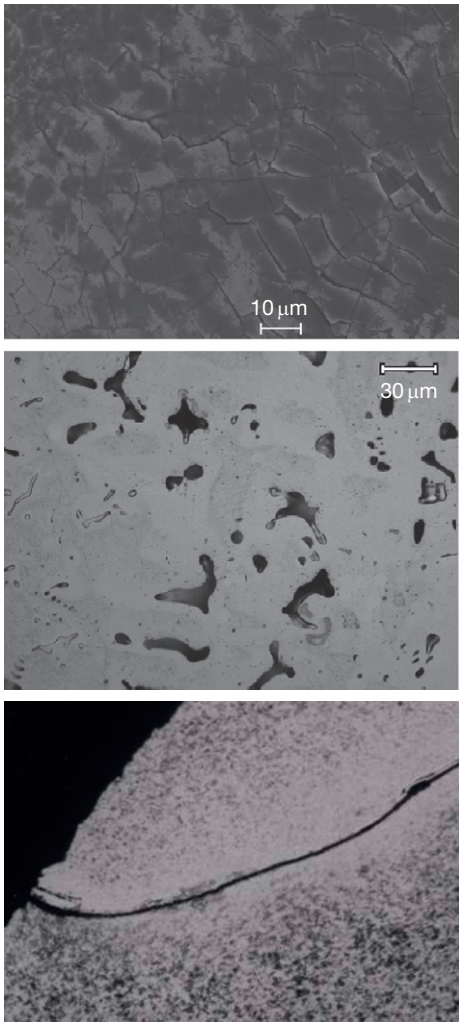

Figure 5 Processing of metals may result in flaws which can impact the mechanical properties of the device. The top image shows the development of surface cracks in a laser etched part number on a titanium implant. The middle image shows porosity observed in an investment cast stainless steel hip implant (with permission from Griza). The lower image shows a surface crack found in a Ti–6Al–4V forging during routine inspection.

entrapment of oxide particles or other undesirable inclusions and reduce alloy segregation. The alloys of interest for medical devices are generally melted under protective atmospheres (i.e., vacuum or inert atmospheres) to eliminate formation of oxide particles and they are routinely melted several times to improve chemical homogeneity. Excessive inclusion content may harm corrosion resistance and mechanical properties; ASTM and ISO specifications for implantable stainless steels and some cobalt base alloys include 'microcleanliness' requirements that limit the number of large, nonmetallic inclusions that may be present in these alloys. The impact of inclusions on mechanical properties depends on the location of the inclusion and, to some extent, the size of the implant. A 5–10 μm inclusion in a 15-mm-diameter hip stem may not impact mechanical properties, but a similar inclusion in a device with very small dimensions (e.g., wires in pacing leads, stents) may have large effects on fatigue strength. The benefits due to reducing inclusion size in small devices have been demonstrated in MP35N wire. Here, the Ti content in the alloy was reduced from 1.0% to 0.01%, which reduced the size and number of titanium nitride (TiN) inclusions in the material. Rotary beam fatigue testing was done on work hardened 177 μm MP35N wire. At a stress of 758 MPa, the average fatigue life of the conventional high Ti content wire was 1 154 000 cycles; for the low Ti content wire, the average fatigue life was 33 470 000 cycles.[69]

A recent report of Ti–6Al–4V bar stock containing unalloyed or incompletely alloyed regions underscores the need to achieve a high level of chemical homogeneity prior to subsequent working operations.[70] In this case, supplies of this material reached a number of medical device producers before the problem was discovered.

After casting, large ingots must be reduced to useable sizes. Dislocation motion is necessary for the deformation process and additional dislocations are generated during deformation; if the initial breakdown of the ingot were to take place at room temperature, the metal would fracture before a significant amount of reduction took place. Thus, the bulk of the size reduction steps (i.e., press forging, rotary forging, and rolling) are done at elevated temperatures. The forces required to deform metals are much lower at high temperatures and the metals are more ductile. During deformation processes above a critical temperature range, dislocations are annihilated as new grains form. These new grains contain low dislocation densities, so they can be readily deformed. This cycle of deformation and formation of new stress-free, deformable grains is common to the materials of interest in this chapter. The deformation steps may occur in sequence (i.e., deformation operations followed by separate annealing cycles) or in a continuous operation. The temperature at which new, stress-free grains will develop from heavily worked, high dislocation density grains is known as the recrystallization temperature. This is not a fixed temperature and it is different for different metal alloys. Besides the alloy composition, factors influencing recrystallization behavior include the extent of deformation, the time at temperature, and the presence of second phase particles. Metals that have been processed through this series of deformation and recrystallization steps are referred to as wrought materials. For some product forms, the final deformation steps may occur at relatively low temperatures or even at room temperature to produce work hardened material. Overall, these processes reduce the grain size of the material and improve chemical homogeneity.

1.102.6.2. Process Effect Examples

1.102.6.2.1. Work hardening and annealing

The key factor in work hardening are the interactions between dislocations and the generation of additional dislocations during plastic deformation. As the number of dislocations in a metal increases, the dislocations begin to interact and tangle. As more and more dislocations are produced during deformation, these interactions become increasingly complex, and resistance to further deformation increases. If this deformation continues beyond a critical level, voids will begin to form in the metal followed by cracking and failure. The details of these

processes are quite complex; material science textbooks can be consulted for more information.[1,71] Since dislocations are defects, they have stresses and strains associated with them. As the number of dislocations increases, the total energy in the crystal increases. This increased energy provides the driving force to recrystallize the metal by heating (or annealing) it. Thus, in broad terms, grain size, hardness, and resultant mechanical properties of metals can be altered by controlling the amounts of deformation and the thermal cycles used, if any, to recrystallize the material.

Implantable austenitic stainless steels are strengthened by alloying effects and work hardening. While 316L is still the most common implantable stainless steel, more recently developed alloys such as Rex 734™ and BioDur 108® contain higher amounts of key alloying elements, which improve both mechanical behavior and corrosion resistance. In the annealed condition, these alloys are all relatively soft and ductile. Deformation of these alloys at temperatures below the recrystallization temperature causes increased levels of hardness, tensile and fatigue strength, and decreased ductility. The amount of deformation is routinely described in terms of percent reduction in area: $(A_I - A_f/A_I)100$ where A_I is the initial cross-sectional area and A_f is the final cross-sectional area. Table 5 shows the impact of cold working on mechanical properties of some representative stainless steel and cobalt base alloys.

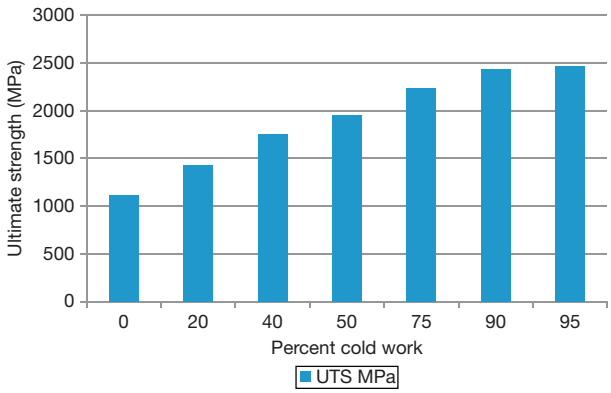

Figure 6 Response of MP35N wire to cold work. Note the wide range of strength depending on the amount of cold work. The initial wire diameter was 5.1 mm. Data provided by Fort Wayne Metals; used with permission. MP 35N® is a registered trademark of SPS Technologies.

The data in Table 5 show the normal trade off between strength and ductility in cold worked metals. As strength is increased by cold work the ductility decreases. It should be noted that it is very difficult to achieve uniform amounts of cold work through the entire cross section of large components. In the case of large cross sections, it is likely that the material at or near the surface will be more heavily worked than the material at the core. Annealed stainless steels are used where a high level of ductility may be required (e.g., balloon expandable stents, suture wire); various levels of work hardening can be specified for devices that require higher strength.

Figure 7 shows the microstructure of 316L in both the annealed and cold worked conditions. Indications of deformation (slip) within the grains of the cold worked specimen are evident. These images were obtained by polishing the samples to provide smooth, flat surfaces. The samples are then chemically etched using various acids or other solutions which preferentially attack grain boundaries or second phases within the sample. After the samples are prepared, they are examined at high magnification using light or scanning electron microscopy. The resultant images reveal features such as grain size, distribution of different phases (e.g., α and β in titanium alloys), cleanliness of the material (i.e., inclusion content), flaws (porosity, cracking), and the extent of deformation within grains.

Cobalt alloys such as L-605 and MP35N respond in a similar manner as stainless steels to work hardening. Figure 6 shows the relationship between ultimate tensile stress and the percent reduction of area for MP35N wire. Heavily cold worked MP35N is routinely used for pacemaker leads.

Closed die forging is a common technique to produce orthopedic implants. This process uses a sequence of shaped dies mounted in a press. The shape of the final die is close to the shape of the desired part and the press supplies the force needed to deform the metal into the shape of the cavity. This is generally done at elevated temperatures to reduce the forces required and maximize the ductility of the metal being deformed. The use of elevated temperatures suggests that forgings should exhibit annealed structures and properties but this is often not the case. Published data on forged Rex 734™ hip stems[60] show tensile properties well above annealed levels

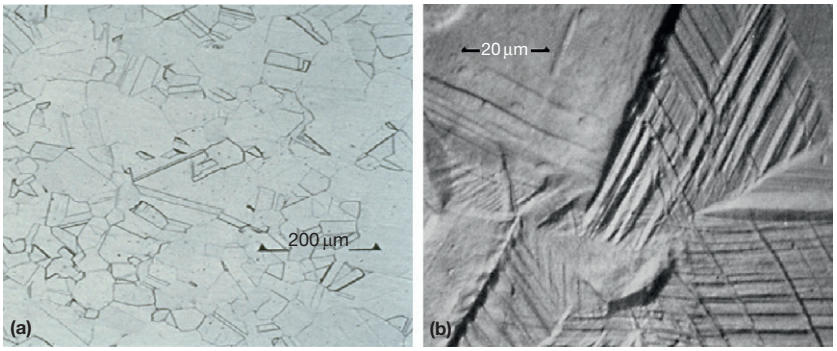

Figure 7 Microstructures of annealed (a) and cold worked (b) 316L stainless steel. Note evidence of slip within the grains of the cold worked material. (b) Reproduced from Brunski, J. B. In *Biomaterials Science*; Ratner, B. D., Hoffman, A. S., Schoen, F. J., Lemons, J. E., Eds.; Elsevier: Amsterdam, 2004; p 142, with permission from Elsevier.

indicating that these forgings are work hardened. Cobalt alloy forgings also have higher properties than these alloys in the annealed condition; minimum ultimate tensile strength for forged Co–28Cr–6Mo alloy is 897 MPa in the annealed condition and 1172 MPa in the warm worked condition per ASTM F 1537. ASTM F 799 (Cobalt–28 Chromium–6 Molybdenum Alloy Forgings for Surgical Implants) does not describe forging parameters, but the mechanical property, grain size, and hardness requirements ensure that the forging process results in a work hardened metal. Details of the structure changes that occur in Co–C–Mo alloys during hot deformation can be found in Immarigeon *et al.*[72] and Yamanaka *et al.*[73]

Production of bar stock, tubing, and wire used in implant applications utilizes a series of deformation and annealing operations. The annealing processes can be tailored to produce either fine or coarse grain structures. Fine grain materials result from annealing at lower temperatures and/or shorter times while grain growth will occur with increases in temperature or time. In general, finer grain materials are preferred for typical medical products. For example, balloon expandable cardiovascular stents are often made by laser cutting thin walled tubing. Desirable attributes of the tubing include uniform, equiaxed small grain size, and high ductility. These attributes can be obtained by a series of low temperature tube drawing steps followed by controlled annealing cycles (i.e., short cycles at temperatures that do not cause rapid grain growth). Details of the response of L-605 stent tubing to different amounts of cold work and different annealing temperatures can be found in Poncin *et al.*[74]

It is important to remember that heating a work hardened material above the recrystallization temperature will result in the formation of new, soft, ductile grains. This causes strength levels to decrease while ductility increases. Common high temperature processes such as welding or sintering a porous coating on a work hardened device will cause dramatic reductions in both static and fatigue strength.

1.102.6.2.2. Wrought versus cast alloys

Cast cobalt alloys are common in orthopedic and dental applications. Investment cast stainless steel hips, although once fairly common, are rarely used today because of their relatively low strength (a recent report discusses fatigue failure of a cast 316L hip stem).[75] Figure 8 compares the microstructure of an investment cast Co–Cr–Mo alloy with the microstructure of a wrought alloy of similar composition. The cast material contains very large carbides and the grain size is much larger than that of the wrought material. The wrought material has a much smaller grain size, a very fine carbide distribution, and a higher dislocation density because of the deformation involved in forming the part. These structural differences lead to the large differences in tensile and fatigue strength shown in Tables 5 and 6.

1.102.6.2.3. Precipitation hardening

A process known as precipitation hardening, or aging, can be used in some cobalt and titanium base alloys. The aging process involves heating the metal to a temperature at which a second phase can precipitate out of the matrix. If the precipitates are small enough they will interact with dislocations and increase strength. The specific response of an alloy to this type of treatment depends on the alloy system and the details of both the heat treatment and prior conditions such as the deformation history of the material. Implantable austenitic stainless steels do not respond to heat treatment (although stainless steels used to make surgical instruments are hardened by heat treatment). Cobalt base alloys can be heat treated to alter properties. Formation of small HCP precipitates within the FCC matrix is an important feature in these alloys.[76,77] ASTM specifications F 562 and F 1058 include mechanical property information for MP35N and Elgiloy™ in the cold worked and aged condition. The ultimate tensile strength of thin (0.110–0.469 mm) Elgiloy™ strip increases from 1725 to 2170 MPa. Beta titanium alloys can be strengthened by aging treatments that result in formation of a fine dispersion of α within the β matrix. Ti–15Mo has shown an increase in ultimate tensile stress from 770 MPa in the solution annealed condition to 1280 MPa in the solution annealed plus aged condition; for Ti–15Mo–5Zr–3Al, the ultimate tensile stress increases from ~950 to ~1500 MPa because of aging.[78,79]

1.102.6.2.4. Surface condition effects

Altering the surface of an implant can have either negative or positive effects. Negative effects are often due to the presence of features that act to concentrate stresses in a critical region of a

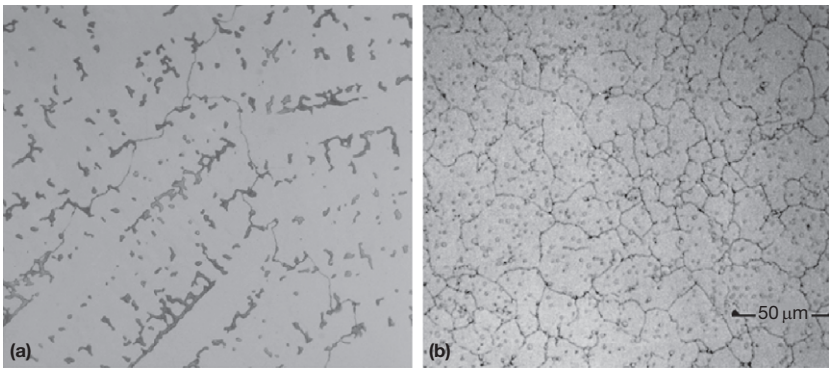

Figure 8 Microstructures of as-cast (a) and forged Co–Cr–Mo (b); ASTM F 75 and ASTM F 1537, respectively. The cast material contains large carbides (the dark phase) which form in the interdentdritic regions and along the grain boundaries. The grains are very large in the cast material. The forged microstructure contains very fine carbides and much smaller grains. (b) Reproduced from Brunski, J. B. In *Biomaterials Science*; Ratner, B. D., Hoffman, A. S., Schoen, F. J., Lemons, J. E., Eds.; Elsevier: Amsterdam, 2004; p 142, with permission from Elsevier.

device. This includes design features as well as surface conditions that result from the processes used to make the implant. Undesirable design features include sudden transitions in the dimensions of the component and sharp radii at corners. Processing issues include undetected flaws in the material such as surface cracks or porosity. Laser cutting and marking operations can also create surface damage. The fatigue strength of wrought cobalt and titanium alloys can be reduced by 60–70% by using lasers to apply part numbers if the laser marked surface is loaded in tension.[44,80] Several authors have reported hip implant failures associated with laser marking.[81,82] Marking lasers can create a fine network of surface cracks as seen in **Figure 5**; if these small cracks are located in high stress regions, they may grow and lead to fatigue failure. ASTM F 86 'Standard Practice for Surface Preparation and Marking of Metallic Surgical Implants' advises that part markings be located in low stress areas.[83]

When laser cutting is used to machine stents from thin wall tubing, a thin recast layer is formed on the cut edges. This layer may be brittle and somewhat rough, so it is removed by electropolishing or mechanical operations such as light grit blasting or tumbling.

Surface damage can also occur in the operating room. Simulated contouring of Ti spinal rods has been shown to form cracks.[84] Care must also be taken in the operating room to avoid striking implant surfaces with sharp surgical instruments as this could create notches on the implant surface.

Porous layers are routinely applied to orthopedic implants to allow for fixation by bony ingrowth; this topic is covered in detail in **Chapter 6.605, Porous Coatings in Orthopedics**. It should be noted that most coating application methods have substantial impact on mechanical properties of devices. High temperature sintering results in structural changes in the implant that reduce strength. The bond sites between the porous layer and the implant can act as stress raisers. Designers of these devices must incorporate these effects when analyzing the strength of porous coated implants.

Residual surface stresses can have either positive or negative effects depending on the nature of the stress and the loading conditions that the part experiences in service. Most orthopedic implants experience tensile loading in their high stress regions, so creating residual compressive stresses in these regions can improve fatigue resistance. This can be achieved by operations such as shot peening, laser shock peening, and low plasticity burnishing.[85]

1.102.7. Future Developments

The metals currently used for medical implants are highly successful and the costs associated with developing and commercializing new alloys are quite high. This combination tends to limit development of new metal alloys for implants. Most of the alloys used by the device community were developed for other purposes and then applied to implants. However, trends toward less invasive surgery (which can require smaller, easier to insert devices) and the application of implants in younger, more active patients increase the likelihood that future devices will have to withstand higher stresses and survive for longer times. This may lead to efforts to develop higher strength materials.

Trends in implantable stainless steels over the past several decades have been toward more corrosion resistant alloys that can be processed to higher strengths than 316L. These alloys rely on additions of nitrogen and, in recent days, contain minimal amounts of Ni because of concerns about nickel sensitivity. It is possible that additional stainless steels will be developed along these lines.

As mentioned previously, there is a significant amount of research aimed at developing new β titanium alloys. These alloys appear to offer opportunities for higher strength or lower elastic modulus than current Ti alloys.

Another area with potential for improving mechanical properties involves creating materials with extremely small grain sizes. The techniques to achieve this involve extensive amounts of deformation under carefully controlled conditions. Yamanaka has reported grain sizes below 1 μm for a heavily deformed Co–Cr–Mo alloy.[73] Titanium grain sizes less than 500 nm have been reported by Valiev and a β titanium alloy with grain size in the 50 nm range has been reported by Hao;[86,87] if these methods can be commercialized, they could result in higher strength alloys.

1.102.8. Summary

Successful long-term metallic implants must be able to withstand both mechanical and environmental stresses. There are a limited number of metal alloys with the appropriate combination of corrosion resistance and mechanical properties necessary to survive in the body. The major alloy systems in use in load bearing applications are austenitic stainless steels, cobalt–chromium alloys, and titanium alloys.

The corrosion resistance of the major implantable alloys depends on formation of thin oxide films. Corrosion behavior is primarily controlled by the composition of the alloy; secondary factors such as inclusion content can influence corrosion.

Mechanical properties of devices depend on the product design, the properties of the material used to make the product, and the details of the processes used to fabricate the device. A wide range of properties can result from a given chemical composition because of these processing effects.

Fatigue is the most common cause of mechanical failure of medical devices. Variation in fatigue strength is inherent in materials. Rigorous control of raw materials and production processes can reduce but not totally eliminate this variability.

References

1. Meyers, M. A.; Chawla, K. K. *Mechanical Behavior of Materials*. Cambridge University Press: Cambridge, UK, 2007.
2. Gilbert, J. L. In *The Adult Hip*; Callaghan, J. J., Rubash, H. E., Rosenberg, A. G., Eds.; Lippencott-Raven: New York, 2005; Vol. 1, p 138.
3. Park, J. B. *Biomaterials Science and Engineering*. Plenum: New York, 1984.
4. Scales, J. T. *Proc. Institut. Mech. Eng.* **1966–1967**, *181*(Pt 3J), 66.
5. ASTM Standard F 138, *Standard Specification for Wrought 18 Chromium–14 Nickel–2.5 Molybdenum Stainless Steel Bar and Wire for Surgical Implants*. ASTM International: West Conshohocken, PA, 1997 (2008).
6. ISO Standard 5832-1, *Implants for Surgery – Metallic Materials, Part 1: Wrought Stainless Steel*. International Organization for Standardization: Geneva, Switzerland, 1997 (2007).
7. ASTM Standard F 1586, *Standard Specification for Wrought Nitrogen Strengthened 21 Chromium–10 Nickel–3 Manganese–2.5 Molybdenum Stainless*

Steel Alloy Bar for Surgical Implants. ASTM International: West Conshohocken, PA, 1995 (2008).
8. ISO Standard 5832-9, *Implants for Surgery – Metallic Materials, Part 9: Wrought High Nitrogen Stainless Steel*. International Organization for Standardization: Geneva, Switzerland, 1992 (2007).
9. ASTM Standard F 1314, *Standard Specification for Wrought Nitrogen Strengthened 22 Chromium–13 Nickel–5 Manganese–2.5 Molybdenum Stainless Steel Alloy Bar and Wire for Surgical Implants*. ASTM International: West Conshohocken, PA, 1995 (2007).
10. ASTM Standard F 2229, *Standard Specification for Wrought Nitrogen Strengthened 23 Manganese–21 Chromium–1 Molybdenum Low-Nickel Stainless Steel Alloy Bar and Wire for Surgical Implants*. ASTM International: West Conshohocken, PA, 2002 (2007).
11. Klarstrom, D. L. *J. Mat. Engr. Perf.* **1993**, *2*(4), 524–530.
12. Sullivan, C. P.; *et al*. *Met. Engr. Q.* **1969**, 16–28.
13. Gomez, M.; *et al*. *BioMed. Mat. Res.* **1997**, *34*, 157–163.
14. Venable, C. S.; *et al*. *Ann. Surg.* **1937**, *105*, 917–938.
15. Smith-Peterson, M. N. *JBJS* **1939**, *21*, 269–288.
16. ASTM Standard F 67, *Standard Specification for Unalloyed Titanium for Surgical Implant Applications*. ASTM International: West Conshohocken, PA, 2000 (2006).
17. ISO Standard 5832-2, *Implants for Surgery – Metallic Materials, Part 2: Unalloyed Titanium*. International Organization for Standardization: Geneva, Switzerland, 1993 (1999).
18. ASTM Standard F 2066, *Standard Specification for Wrought Titanium–15 Molybdenum Alloy for Surgical Implant Applications*. ASTM International: West Conshohocken, PA, 2000 (2007).
19. ASTM Standard F 1813, *Standard Specification for Wrought Titanium–12 Molybdenum–6 Zirconium–2 Iron Alloy for Surgical Implant*. ASTM International: West Conshohocken, PA, 2006; 1997e1.
20. ISO Standard 5832-14, *Implants for Surgery – Metallic Materials, Part 14: Wrought Titanium 15–Molybdenum 5–Zirconium 3–Aluminium Alloy*. International Organization for Standardization: Geneva, Switzerland, 2007.
21. Lütjering, G.; Williams, J. C. *Titanium*. Springer: New York, 2007.
22. Down, G. M. *Eng. Med.* **1973**, *2*(3), 51–57.
23. Leventhal, G. S. *Am. J. Surg.* **1957**, *94*, 735–740.
24. Glassman, A. H.; *et al*. *Clin. Ortho. Rel. Res.* **2006**, *453*, 64–74.
25. Huiskes, R.; *et al*. *Clin. Ortho. Rel. Res.* **1992**, *274*, 124–134.
26. Cuppone, M.; *et al*. *Calcif. Tissue Int.* **2004**, *74*, 302–309.
27. Rho, J. Y.; *et al*. *J. Biomech.* **1993**, *26*(2), 111–119.
28. Matsumoto, H.; *et al*. In *Proceedings of the Materials & Processes for Medical Device Conference, November 14–16*; Venugopalan, R., Wu, M., Eds.; ASM International: Boston, MA, 2005; p 9.
29. Jablokov, V. R.; *et al*. In *Titanium, Niobium, Zirconium, and Tantalum for Medical and Surgical Applications, STP 1471*; Zardiackas, L. D., Kraay, M. J., Freese, H. L., Eds.; ASTM International: West Conshohocken, PA, 2006; p 40.
30. Murray, N. G. D.; *et al*. In *Titanium, Niobium, Zirconium, and Tantalum for Medical and Surgical Applications STP 1471*; Zardiackas, L. D., Kraay, M. J., Freese, H. L., Eds.; ASTM International: West Conshohocken, PA, 2006; p 3.
31. Jablokov, V. R.; *et al*. In *Titanium, Niobium, Zirconium, and Tantalum for Medical and Surgical Applications, STP 1471*; Zardiackas, L. D., Kraay, M. J., Freese, H. L., Eds.; ASTM International: West Conshohocken, PA, 2006; p 83.
32. Niinomi, M. *J. Mech. Behav. Biomed. Mater.* **2008**, *1*, 30–42.
33. Ratner, B. D. In *Biomaterials Science*; Ratner, B. D., Hoffman, A. S., Schoen, F. J., Lemons, J. E., Eds.; Elsevier, 2004; 2nd ed., p 10.
34. Shetty, R.; Ottersberg, W. In *Encyclopedic Handbook of Biomaterials and Bioengineering- Part B Applications*; Wise, D. L., Ed.; CRC: London, 1995; pp 509–540.
35. Medlin, D. J.; *et al*. In *Titanium, Niobium, Zirconium, and Tantalum for Medical and Surgical Applications STP 1471*; Zardiackas, L. D., Kraay, M. J., Freese, H. L., Eds.; ASTM International: West Conshohocken, PA, 2006; p 30.
36. Zardiackas, L. D.; *et al*. *Biomed. Mater. Res. Appl. Biomater.* **2001**, *58*, 180–187.
37. Hunter, G.; *et al*. In *Titanium, Niobium, Zirconium, and Tantalum for Medical and Surgical Applications STP 1471*; Zardiackas, L. D., Kraay, M. J., Freese, H. L., Eds.; ASTM International: West Conshohocken, PA, 2006; p 16.
38. Eiselstein, L. E.; James, B. In *Proceedings of the Materials & Processes for Medical Device Conference*; Venugopalan, R., Wu, M., Eds.; ASM International: USA, 2006; p 3.
39. Nakazawa, G. *J. Am. Coll. Cardiol.* **2009**, *54*, 1924–1931.
40. Simon, S. In *Biomechanics of the Musculoskeletal System*; Buckwater, J. S., Einhorn, T. A., Simon, S. R., Eds.; American Academy of Orthopaedic Surgeons: Rosemont, IL, 2000; p 790.
41. Shütz, W. *Eng. Fracture Mech.* **1996**, *54*, 263–300.
42. ASTM Standard F 75, *Standard Specification for Cobalt–28 Chromium–6 Molybdenum Alloy Castings and Casting Alloy for Surgical Implants*. ASTM International: West Conshohocken, PA, 1998 (2007).
43. ISO Standard 5832-4, *Implants for Surgery – Metallic Materials, Part 4: Cobalt–Chromium–Molybdenum Casting Alloy*. International Organization for Standardization: Geneva, Switzerland, 1978 (1996).
44. Berlin, R. M.; *et al*. In *Cobalt-base Alloys for Biomedical Applications STP 1481*; Disegi, J. A., Kennedy, R. L., Pilliar, R., Eds.; ASTM International: West Conshohocken, PA, 1999; p 62.
45. Georgette, F. S.; Davidson, J. A. *JBMR*. **1986**, *20*, 1229–1248.
46. Semlitsch, M.; Panic, B. *Eng. Med.* **1983**, *12*, 185–198.
47. ASTM Standard F 1537, *Standard Specification for Wrought Cobalt–28 Chromium–6 Molybdenum Alloys for Surgical Implants*. ASTM International: West Conshohocken, PA, 2000 (2007).
48. ISO Standard 5832-12, *Implants for Surgery – Metallic Materials, Part 12: Wrought Cobalt–Chromium–Molybdenum Alloy*. International Organization for Standardization: Geneva, Switzerland, 1996 (2007).
49. Brunski, J. B. In *Biomaterials Science*; Ratner, B. D., Hoffman, A. S., Schoen, F. J., Lemons, J. E., Eds.; Elsevier: Amsterdam, 2004; p 142.
50. ASTM Standard F 136, *Standard Specification for Wrought Titanium–6 Aluminum–4 Vanadium ELI (Extra Low Interstitial) Alloy for Surgical Implant Applications*. ASTM International: West Conshohocken, PA, 2008; 1998e1.
51. ISO Standard 5832-3, *Implants for Surgery – Metallic Materials, Part 3: Wrought Titanium 6–Aluminium 4–Vanadium Alloy*. International Organization for Standardization: Geneva, Switzerland, 1990 (1996).
52. Niinomi, M.; *et al*. In *Titanium, Niobium, Zirconium, and Tantalum for Medical and Surgical Applications STP 1471*; Zardiackas, L. D., Kraay, M. J., Freese, H. L., Eds.; ASTM International: West Conshohocken, PA, 2006; p 135.
53. ISO Standard 5832-11, *Implants for Surgery – Metallic Materials, Part 11: Wrought Titanium 6–Aluminium 7–Niobium Alloy*. International Organization for Standardization: Geneva, Switzerland, 1994.
54. Paris, P. C.; *et al*. *Trend Eng.* **1961**, *13*, 9.
55. Paris, P. C. Dissertation, Lehigh University, 1962.
56. Marrey, R. V.; *et al*. *Biomaterials* **2006**, *27*, 1988–2000.
57. Ritchie, R. O.; Lubock, P. *J. Biomech. Eng.* **1986**, *108*(2), 153–160.
58. Zardiackas, L. D.; *et al*. In *Stainless Steels for Medical and Surgical Applications, STP 1438*; Winters, D. L., Nutt, M. J., Eds.; ASTM International: West Conshohocken, PA, 2003; p 194.
59. Roach, M. D.; *et al*. In *Titanium, Niobium, Zirconium, and Tantalum for Medical and Surgical Applications, STP 1471*; Zardiackas, L. D., Kraay, M. J., Freese, H. L., Eds.; ASTM International: West Conshohocken, PA, 2006; p 183.
60. Windler, M.; Steger, R. In *Stainless Steels for Medical and Surgical Applications, STP 1438*; Winters, G. L., Nutt, M. J., Eds.; ASTM International: West Conshohocken, PA, 2003; p 39.
61. Neu, R. W. *Materials* **2008**, *378–379*, 147–162.
62. Shepard, M. J.; *et al*. Effects of surface treatment on fretting fatigue performance of Ti–6Al–4V. In *Proceedings of the 8th National Turbine Engine High Cycle Fatigue (HCF) Conference, Monterey CA*, 2003.
63. Humphrey, S. M.; Gilbertson, L. N. In *Composite Materials for Implant Applications in the Human Body; Characterization and Testing, STP 1178*; Jamison, R. D., Gilbertson, L. N., Eds.; ASTM International: West Conshohocken, PA, 1993; pp 27–40.
64. ISO Standard 7206-4, *Implants for Surgery – Partial and Total Hip Joint Prostheses, Part 4: Determination of Endurance Properties of Stemmed Femoral Components*. International Organization for Standardization: Geneva, Switzerland, 1989 (2007).
65. ISO Standard 7206-6, *Implants for Surgery – Partial and Total Hip Joint Prostheses, Part 6: Determination of Endurance Properties of Head and Neck Region of Stemmed Femoral Components*. International Organization for Standardization: Geneva, Switzerland, 1992.
66. ASTM Standard F 1612, *Standard Practice for Cyclic Fatigue Testing of Metallic Stemmed Hip Arthroplasty Femoral Components with Torsion*. ASTM International: West Conshohocken, PA, 1995 (2005).
67. ASTM Standard F 2477, *Standard Test Methods for in vitro Pulsatile Durability Testing of Vascular Stents*. ASTM International: West Conshohocken, PA, 2006 (2007).
68. Reitz, E. Surface finishes: Methods and metrics for production, Medical Device and Diagnostic Industry. Available at http://www.devicelink.com/mddi/archive/07/09/023.html, 2007.

69. Bradley, D.; *et al*. In *Proceedings of the Materials & Processes for Medical Device Conference, Anaheim, CA*; Shrivastava, S., Ed.; ASM International: Philadelphia, PA, 2004; p 301.
70. Haflich, F. *Am. Met. Market August* **2009**, *3*, 2009.
71. Smallman, R. E.; Bishop, R. J. *Modern Physical Metallurgy and Materials Engineering*; Butterworth Heinemann: Oxford, UK, **1999**.
72. Immarigeon, J.-P.; *et al*. *Met. Trans.* **1984**, *15A*, 339–345.
73. Yamanaka, K.; *et al*. *Trans A* **2009**, *40*, 1980–1994.
74. Poncin, P.; *et al*. In *Proceedings of the Materials & Processes for Medical Device Conference*; Helmus, M., Medlin, D., Eds.; ASM International: Minneapolis, MN, 2005; p 279.
75. Griza, S.; *et al*. *Eng. Fail. Anal*. **2008**, *15*, 981–988.
76. Drapier, J. M.; *et al*. *Cobalt* **1970**, *49*, 171–186.
77. Vander Sande, J. B.; *et al*. *Metall. Trans. A* **1976**, *7A*, 389–397.
78. Marquardt, B.; Shetty, R. In *Titanium, Niobium, Zirconium, and Tantalum for Medical and Surgical Applications STP 1471*; Zardiackas, L. D., Kraay, M. J., Freese, H. L., Eds.; ASTM International: West Conshohocken, PA, 2006; p 71.
79. Nishimura, T. In *Materials Properties Handbook: Titanium Alloys*; Boyer, R., Collings, E. W., Welsch, G., Eds.; ASM International, 1994; p 949.
80. Anon, Do you know the fatigue strength of your components? In Robert Mathys Stiftung Newsletter, N02/07. Available at http://www.rms-foundation.ch/uploads/media/newsletter_e-nr0207.pdf, 2007.
81. Grivas, T. B.; *et al*. *J. Med. Case Rep*. **2007**, *1*, 174–180.
82. Woolson, S. T.; *et al*. *Report ten cases JBJS* **1997**, *79*, 1842–1848.
83. ASTM Standard F 86, *Standard Practice for Surface Preparation and Marking of Metallic Surgical Implants*. ASTM International: West Conshohocken, PA, 2000 (2004).
84. Dick, J. C.; *et al*. *Spine* **2001**, *26*, 1668–1672.
85. Hornback, D. J.; *et al*. In *Fatigue and Fracture of Medical Metallic Materials and Devices*; Mitchell, A., Jerina, B., Eds.; ASTM International: West Conshohocken, PA, 2007; p 45.
86. Hao, Y. L.; *et al*. Nanostructured β-type titanium alloy for biomedical applications. In *Proceedings of the Materials & Processes for Medical Device Conference*; Venugopalan, R., Wu, M., Eds.; ASM International: Philadelphia, PA, 2006; p 21.
87. Valiev, R. Z.; *et al*. In *Proceedings of the Materials & Processes for Medical Device Conference Anaheim CA*; Shrivastava, S., Ed.; ASM International: USA, 2004; p 362.

1.103. Electrochemical Behavior of Metals in the Biological Milieu

J L Gilbert, Syracuse University, Syracuse, NY, USA

© 2011 Elsevier Ltd. All rights reserved.

1.103.1.	**Introduction**	22
1.103.2.	**Metals Currently Used in Medical Devices**	23
1.103.2.1.	Titanium Alloys	23
1.103.2.2.	Co–Cr–Mo Alloys	23
1.103.2.3.	Stainless Steel	23
1.103.3.	**Metallic Biocompatibility**	24
1.103.3.1.	Immune Response and Haptens	24
1.103.3.2.	Wound Healing and Biocompatibility	24
1.103.3.3.	The Reduction Half-Cell in Biomaterials Corrosion	24
1.103.4.	**The Biological Milieu**	24
1.103.4.1.	The *In Vitro* Approximation to the Biological Milieu	25
1.103.5.	**Basic Electrochemistry Concepts**	25
1.103.5.1.	Active Corrosion Theory: Oxidation and Reduction	25
1.103.5.2.	Passivating Metal Surface Behavior	29
1.103.5.3.	Polarization Testing	30
1.103.5.3.1.	Linear polarization and R_p	31
1.103.5.3.2.	Cyclic and anodic polarization testing	31
1.103.6.	**Passive Oxide Films and Semiconducting Electrochemistry**	32
1.103.6.1.	Introduction to Passive Oxide Films	32
1.103.6.2.	High Electric Field Oxide Growth	33
1.103.6.3.	Redox Electrochemistry at Oxide–Solution and Oxide–Metal Interfaces	34
1.103.6.4.	Oxide Semiconductor Theory for Thin Oxide Films Between Metals and Solutions	36
1.103.7.	**Electrical Double Layer**	37
1.103.8.	**Electrochemical Impedance Spectroscopy (EIS) of Metallic Biomaterials**	37
1.103.8.1.	The Methods of EIS	37
1.103.8.2.	Time-Based Methods	39
1.103.8.3.	Impedance Behavior of Ti, CoCr, and 316L SS: Effects of Solution, Voltage, and Time	40
1.103.9.	**Mechanically Assisted Corrosion**	42
1.103.9.1.	Modeling the Electrochemical Response to Scratching	42
1.103.9.2.	The Consequences of Mechanically Assisted Corrosion *In Vivo*	43
1.103.10.	**Effects of Prior Electrochemical History**	44
1.103.11.	**Oxide Film Structure and Formation**	44
1.103.12.	**Effects of Solution Redox System**	45
1.103.13.	**Biological Consequences: Oxidation and Reduction**	45
1.103.14.	**Summary**	46
1.103.15.	**Appendix: Derivation of Mott–Schottky Equation**	46
References		47

Abbreviations

Ag/AgCl	Silver–silver chloride reference electrode
Co–Cr–Mo	Cobalt–chromium–molybdenum alloys
$CoO–Cr_2O_3$	Cobalt oxide, chromium oxide
cp-Ti	Commercially pure titanium
EMF	Electromotive force
FCC	Face-centered cubic
NHE	Normal hydrogen electrode
NiTi	Nickel titanium alloy (typically in the range of 50:50 wt%)
OCP	Open circuit potential
PBS	Phosphate-buffered saline
SBF	Simulated biological fluid
SCE	Saturated calomel electrode
Ti–6Al–4V	Titanium, 6 wt% aluminum, 4 wt% vanadium
Ti–6Al–7Nb	Titanium 6 wt% aluminum, 7 wt% niobium
TiO_{2-x}	Titanium dioxide with anion deficit
TMFZ	Titanium, molybdenum, zirconium, iron alloy
zcp	Zero current potential

Symbols

A^*	Complex admittance
A'	Real admittance
A''	Imaginary admittance
b	Constant related to charge of moving ion and jump distance in high-field oxide growth
C	Oxide capacitance
C_i	Concentration of ith species
D_i	Diffusivity of ith species
$\mathrm{d}V/\mathrm{d}x$	Gradient of potential (electric field)
e^-	Charge of an electron 1.6e −19C
E_{corr}	Corrosion potential
E_f^M	Fermi energy level in the metal
E_f^{ox}	Fermi energy level in oxide
E_{fb}	Flat-band potential
E^{eq}	Equilibrium potential
E^o	Standard potential
E_{pp}	Passivating potential
F	Faraday's constant (96 500 coul mol^{-1})
i	Current density
i	Imaginary number ($\sqrt{-1}$)
i_{corr}	Corrosion current density
i_{diss}	Dissolution current density
i_{diss}^o	Exchange current density for dissolution reaction
i_{film}	Current density associated with oxide film formation
i_o	Exchange current density
J_i	Flux of ith specie
k	Boltzmann's constant
L	Laplace operator
M_w	Molecular weight of oxide film
n	Valence
N_D	Number of charge carrier per volume in oxide
[Ox]	Oxidized species activity
Q	CPE impedance
R	Ideal gas constant 8.314 J $mol^{-1}K^{-1}$
[Red]	Reduced species activity
R_s	Solution resistance
R_p	Polarization resistance
Tanδ	Tangent of the phase angle, δ
w	Activation energy for atom jumping in an oxide film
Z^*	Complex impedance
Z'	Real impedance
Z''	Imaginary impedance
Z_{CPE}	Impedance of the constant phase element
α	CPE exponent
β	Tafel slope
β_M^a	Anodic Tafel slope for metal half-cell reaction
β_o^c	Cathodic Tafel slope for oxygen half-cell reaction
ΔG_{ox}	Gibbs free energy of oxidation
ΔG_{red}	Gibbs free energy of reduction
ε	Dielectric constant
ε_o	Permittivity of free space
η	Overpotential
Φ_M	Work function of a metal, M
κ^{-1}	Debye thickness
μ	Chemical potential
θ	Area fraction covered by oxide
ρ	Density of oxide film, or charge density
ω	Frequency
v	Volume of oxide

1.103.1. Introduction

Metallic biomaterials have been, and will continue to be, used in implants spanning all areas of use in the human body. Whether one considers orthopedic, spinal, dental, cardiovascular, neural, urological, or other implant applications, metals are central to the success of these devices. Metallic biomaterials will remain central to these applications because of their unique properties compared to those of other classes of materials. Electrical behavior and mechanical properties are the main reasons for this uniqueness. Whether we are interested in delivering electrical energy (e.g., pacemaker leads), or providing structural support (e.g., hip replacements), metals will continue to be used for the foreseeable future. However, a major concern with metals is their susceptibility to corrosion and the associated problems corrosion processes cause in the biological system.

This chapter provides a current state-of-knowledge assessment of the nature of metallic biomaterial surfaces in the biological milieu. This includes descriptions of the electrochemical nature of surfaces, the basic concepts of electrochemistry, the effects of the presence of metal–oxide thin films, the electrical semiconducting nature of the surface, adsorption of proteins, interactions of cells and surfaces, and the complex interplay between surface mechanical processes (e.g., fretting and wear) and electrochemical processes.

The *central paradigm* of metallic biocompatibility has been: "The more corrosion resistant, the more biocompatible." That is, the primary concerns of metal corrosion in the biological milieu have been the release of ions and particles and the effect of these ions and particles on the biological system. While this view still has merit and is discussed in this chapter, it is not a complete and inclusive view of the electrochemical interaction of metals in the body. Other factors, including the interaction of surface mechanics and corrosion, and the role of reduction reactions, are important to understand. In this chapter, we expand on this central paradigm and include the effects of mechanical processes (fretting and wear), and the role of reduction reactions on metallic corrosion and biocompatibility. As shown subsequently, biological behavior at metallic implant surfaces is dramatically affected by reduction reactions that occur at metallic biomaterial surfaces which have not been previously appreciated.

Therefore, the goals of this chapter are to discuss the metallic biomaterials in use today. Observations of corrosion from retrieval studies and the consequences of corrosion are discussed. The basic materials science of metallic biomaterial surfaces is described including the presence of metal–oxide

thin films and includes their structure, voltage-dependent growth, and their electrical double layer as well as protein adsorption. Next, the concepts of the biological milieu are presented to discuss the complex and variable environment to which devices are exposed. This includes discussion of variations in the environment because of wounding, location, protein adsorption, and the presence of inflammatory species including reactive oxygen species (ROS). This chapter then moves on to describe some basic electrochemistry including passive oxide film electrochemical character and electrochemical impedance spectroscopy (EIS), and then presents current concepts of mechanically assisted corrosion. Finally, this chapter discusses the biological consequences of electrochemical processes and the electrochemical consequences of biological processes. This chapter is not intended to comprehensively review the literature compiled over 40 years on the corrosion of metallic biomaterials, but rather to describe the nature of the electrochemical interface in the biological milieu based on the experience and understanding of the author.

1.103.2. Metals Currently Used in Medical Devices

There are several metals and alloys used in the human body. The three major alloy systems in use today are based on titanium (Ti), cobalt–chromium–molybdenum (Co–Cr–Mo), and stainless steel (316L SS). Other metals that are seeing increased use include zirconium (Zr), tantalum (Ta), platinum (Pt), gold (Au), and others.[1] Recently, some newer alloys are being investigated for use as degradable metals including those based on magnesium (Mg) where corrosion is purposeful and planned for. Most of these metals have complex surfaces in terms of structure and chemistry. In particular, metal–oxide thin films (also known as passive films) are present on the surface of most of these alloys, and it is these oxide thin films that are the key to understanding corrosion. These so-called passive films are not in the strict sense 'passive.' They are dynamic structures that can change in chemistry, thickness, defect density, and resistance to corrosion and are susceptible to change in response to the biological environment and the overall voltage drop across them. Furthermore, metal–oxide thin films experience mechanical perturbations including fretting, wear, and fatigue which require understanding of the mechanical behavior of these films and corrosion consequences of disruption.

By far, the first three listed alloy systems make up the largest fraction of alloys used in medical devices. Therefore, most of this chapter focuses on the behavior of these materials. However, other metal alloys are gaining in interest and others are used in smaller amounts but in circumstances where electrochemical behavior is an important element in their use.

1.103.2.1. Titanium Alloys

Titanium, universally viewed as the 'most biocompatible metal,' has several alloys that are in use today in medical devices including cp-Ti (commercially pure titanium), Ti–6Al–4V, TMZF (Ti–Mo–Zr–Fe), Ti–6Al–7Nb, NiTi (shape memory alloy), and others. Each of these alloys has specific chemical and structural features that make them similar and some that separate them from each other. For example, most alloys of Ti owe their corrosion resistance to the presence of the passive oxide film TiO_{2-x} (an anion-deficit, n-type semiconducting oxide) that spontaneously forms on their surface. The substrate alloy has two typical crystal structures: alpha, which is a hexagonal close packed (HCP) crystal, and beta, which is a body-centered cubic structure. Elements such as Mo, Nb, and V are beta stabilizers while Al is an alpha stabilizer. The oxides that form on these surfaces are impacted by the substrate in terms of their structure.

Ti surfaces have been studied more than any other metal surface and we know much about the oxides that form[2–5] For the most part, Ti-oxides are TiO_2 at the surface and change to more reduced forms toward the metal. Native oxides of Ti are of 2–10 nm thickness and are mostly thought to be nanocrystalline or amorphous. As the anion deficit character results in excess electrons in donor energy levels of the energy band gap, they are good electron conductors but do not transport positive charge easily.

1.103.2.2. Co–Cr–Mo Alloys

The alloys based on Co–Cr–Mo are more complex metallurgically (composition, grain size and structure, carbide chemistry and structure). The alloys of Co–Cr–Mo can be cast (large grained with large carbides at grain boundaries), forged, wrought, or powder consolidation products, where the microstructure is small grained with discrete blocky carbides.[2] The crystal structures possible with Co–Cr–Mo alloys include face-centered cubic (FCC), HCP, and other nonequilibrium and carbide phases.[6] Much less is known about the oxides on Co–Cr–Mo in terms of their chemistry, structure, and electrochemical properties or how these change with time and exposure. The basic oxide is thought to be comprised primarily of $Cr_{2-x}O_3$ (a cation-deficit, p-type semiconducting oxide); however, there is evidence that during immersion, the oxide takes on n-type semiconducting behavior. There is some evidence that the chemistry of these oxides can change over time with immersion and with the electrochemical potential established at its surface. There is also some evidence that the oxide film on these alloys may be mixed oxides such as $CoO–Cr_2O_3$ (a spinel oxide) or a heterogeneous amorphous oxide with varying chemistry with depth into the surface as well as variability over the surface.[2] For example, long-term immersion tends to result in increased Cr in the oxide. There is also uncertainty related to the nature of the surface oxide on the carbide surfaces present in these alloys.

1.103.2.3. Stainless Steel

Alloys of stainless steel include 316L stainless, as well as low Ni high nitrogen stainless steel.[2] Stainless steels are primarily austenitic (FCC) structures and derive their corrosion resistance as a result of the formation of Cr_2O_3 oxides that can be mixed with Fe_2O_3 oxides and others. These oxides are complex and susceptible to chemical variations due to immersion, time, and voltage.

1.103.3. Metallic Biocompatibility

While this chapter is not meant to be focused specifically on metallic biocompatibility, it is worthwhile to mention some elements of biocompatibility here and to acknowledge the relationship between corrosion behavior and biocompatibility.

The biocompatibility of any material is defined as the ability of the biomaterial to perform its intended function with an appropriate host response. For metals, the following is the main paradigm for metallic biocompatibility: *The more corrosion resistant, the more biocompatible*. That is, for well over 50 years, metal alloys successfully used in the body have been those materials that have a high resistance to the release of metal ions and metal oxidation products (oxides, chlorides, etc.). Indeed, virtually all of the studies in orthopedics (where the literature of metallic biocompatibility is most extensive) have focused on the toxicological effects of metal ions and the local and systemic effects of metal and metal oxide particulates released into the peri-implant space.[7]

It is known, for example, that metallic ion and particle release associated with modular taper connections in orthopedic devices results in osteolysis.[8] Modular tapers are metal–metal connections in orthopedic implants such as hip and knee replacements where a conical male tapered component is fitted tightly into a female counterpart to assemble the device *in situ*. These modular implants provide great flexibility in materials and design selection to result in the optimal device for a specific patient. However, as is discussed in greater detail below, these tapers can induce particularly severe corrosion reactions when they are mechanically loaded. The corrosion products and local environment resulting from these reactions can then affect the tissue adjacent to the implant and impact the success or failure of the device.

Metallic biocompatibility, as with other biomaterials, is dependent on the specific medical device application. In blood-contacting devices, the requirements of the surface (and its corrosion behavior) can be very different than what is required in, say, a dental implant. In the former, blood clotting and neointimal hyperplasia (high rates of tissue growth at the intimal lining of the vessel) may be most important, whereas the dental implant may require good bone-cell attachment and mineralization capabilities.

1.103.3.1. Immune Response and Haptens

In the paradigm of 'the more corrosion resistant, the more biocompatible,' the concern relates specifically to how metallic ions (e.g., Co^{2+}, Cr^{3+}, Cr^{6+}, Ni^{2+}, Fe^{2+}, Mo^{2+}, Ti^{4+}, Al^{3+}, etc.) interact with the biological system. We know, for example, that Cr ions can complex with many biological molecules forming haptens,[9] which can induce an immune response in some patients with highly wear-prone CoCr joint replacements. There have also been recent reports of elevated metal-ion levels in blood, serum, and urine in patients with highly wear-prone and corroding hip resurfacing implants or total joint replacements and that there is an established correlation between the extent of wear and corrosion, and the measured ion levels.[10]

1.103.3.2. Wound Healing and Biocompatibility

For most implant alloys, the biocompatibility reactions are associated with the wound healing processes taking place after implantation. Surgical intervention to place a medical device results in damage to the surrounding soft and hard tissues of the body (depending on the site). Therefore, wound healing, comprised of the processes of blood clotting (hemostasis), acute inflammatory response, and chronic inflammatory responses, critically impacts on the ultimate metal–tissue interface that gets established. For most metallic devices, some form of fibrous capsule is ultimately developed to encase the metallic biomaterial. This is the typical end state of the wound healing response when an implant material is present. However, when significant ions and/or particles are released, then more aggressive chronic inflammatory reactions can and do take place. Under these conditions, the local solution constituents may be dramatically altered from the normal extracellular solution and may, as a result, alter the electrochemical reactions associated with the metal surface. That is, corrosion *in vivo* can be altered by the inflammatory state of the local solution. These changes include the presence of oxidizing proteins, enzymes, and molecules such as superoxide anions (i.e., ROS). These latter molecules can include byproducts such as hydrogen peroxide, hypochlorous acid, and peroxynitrite, all of which can act as oxidizing agents for the implant metals.

Another element of the biocompatibility of metals relates to the size. Small particles (on the scale of the cell or smaller) will induce a biological response far different from that induced by large size metals. The type and severity of the response will depend on the size, shape, and chemistry of the particles.

1.103.3.3. The Reduction Half-Cell in Biomaterials Corrosion

Recently, work by the author, Ehrensberger and Gilbert,[11] and that by others, Kalbacova *et al.*,[12] have shown that cellular biocompatibility *in vitro* is affected by the reduction processes that are present on metallic biomaterial surfaces. Indeed, these recent observations (to be described in greater detail below) have opened up a whole host of questions related to metallic biocompatibility which have yet to be recognized or addressed in the biomaterials community. When cells are cultured on metallic surfaces (either Ti or CoCr, for example), and the voltage of these surfaces is held slightly cathodic of the open circuit potential (OCP), the cells die within several hours of the onset of this condition. This observation is important because metallic medical devices which are subject to wear or surface oxide abrasion can experience large sustained cathodic voltage shifts that can result in reduction reactions taking place on a majority of the implant surface. Thus, reduction reactions appear to play a significant role in the viability and behavior of cells adjacent to these surfaces.

1.103.4. The Biological Milieu

Primarily, the biological milieu is one of a 0.9% NaCl solution. That is, we are bags of salt water. Many early corrosion studies,

therefore, utilized 0.9% NaCl (isotonic saline) as the corrosion environment. Of course the biological milieu is highly complex and highly variable. The complexity comes from the range of ions, the presence of biomolecules (proteins, enzymes, ROS), location in the body (vascular, brain, orthopedic, dental, etc.), severity of the wound used to introduce the device, the potential for bacterial infection, and a whole range of other factors.

1.103.4.1. The *In Vitro* Approximation to the Biological Milieu

Most corrosion studies of metallic biomaterials have utilized pH 7.4, aerated or deaerated saline solutions. Mostly inorganic salts in the absence of organic species are used in these studies. The range of inorganic salt solutions utilized to study biomaterial corrosion include 0.9% NaCl, Ringer's solution, Hanks balanced salt solution, phosphate-buffered saline (PBS), and other simulated biological fluids (SBFs) – see Table 1 for compositions of these solutions.

In some experiments, additions of single proteins or serum to ionic electrolytes have been used, and pH adjustments using HCl to as low as pH 2 have been explored as specific modifications of the biological environment. There has been much less focus on the role of other organic and inorganic species on the corrosion behavior of metallic biomaterials; however, these could be important to explore the effects of wound healing environments and infection. For example, additions of hydrogen peroxide as the electrolyte in corrosion tests may help to explore highly inflammatory conditions and may bring to light differences in surface oxides and corrosion rates.

Serum and other protein additions have been investigated in terms of their effects on corrosion reaction and in terms of wear–corrosion behavior. The literature in this regard is somewhat conflicting. In some cases serum additions appear to increase corrosion rates while in others, particularly where wear and fretting are present, proteins seem to inhibit the corrosion.[13] There is consistent evidence that OCPs of titanium tend to become more negative in the presence of serum proteins compared to measurements made in PBS.[14]

Very little work has been done to systematically explore the effects of inflammatory species on the corrosion behavior of medical alloys. Messer *et al.*[15] recently looked at the effects of IL-1b on the corrosion of Ti and found increased susceptibility of a Ti alloy to this cytokine. Others have investigated the effects of hydrogen peroxide (a ROS generated during inflammation) and its role in cell-alloy surface interactions. Some work has appeared looking at corrosion in the presence of hydrogen peroxide where increased corrosion rates were observed for all tested alloy surfaces.[16]

Clearly, simulation of the biological milieu is complex and challenging. It depends on the site to be approximated and the nature of the peri-implant tissue activity. Significantly more work is needed to understand the role of local factors and the range of local chemical and biological conditions present on the corrosion processes of these alloys.

Table 1 Summary of physiological solutions typically used in corrosion testing of biomaterials

Solution	*0.9% NaCl*	*HBSS*	*RS*	*PBS*
DI H_2O (ml)	1000	400	1000	800
NaCl (g)	9.000	4.000	6.300	8.000
KCl (g)	–	0.200	0.347	0.200
$MgCl_2$-$6H_2O$ (g)	–	0.111	0.230	–
$MgSO_4$ (g)	–	–	0.086	–
Na_2HPO_4 (g)	–	0.021	0.071	1.440
$NaH_2PO_4.H_2O$ (g)	–	–	0.069	–
Glucose (g)	–	0.500	–	–
KH_2PO_4 (g)	–	0.027	–	0.240
$CaCl_2$ (g)	–	0.096	–	–
$NaHCO_3$ (g)	–	0.176	–	–

1.103.5. Basic Electrochemistry Concepts

The basis for understanding the corrosion of metallic biomaterials comes from several disciplines including electrochemistry, materials science of surfaces, physics of semiconducting thin film oxides (passive oxides), biological phenomena at surfaces, and electrical phenomena at interfaces. These disciplines, each having arisen somewhat independently, combine to provide insight into the electrochemistry in the biological milieu. Each part of this interdisciplinary subject provides important theoretical underpinnings and therefore each needs to be presented to give a good picture of what transpires at the metallic biomaterial interface. This section will provide some of the basic principles and equations required to understand corrosion. This will include the development of electrified interfaces, the driving force for corrosion including both oxidation and reduction. We will discuss the mixed-potential theory of corrosion and explore the Butler–Volmer equation for corrosion of active metal surfaces. Then, the structure, chemistry, and physics associated with semiconducting passive oxide thin films on metal surfaces and adjacent to an aqueous electrolyte solution will be described. The electrified nature of this interfacial region, with its high electric fields, electronic and ionic transport mechanisms across the metal–oxide–solution interface, and growth and reductive dissolution mechanisms will be described including the role of voltage on the properties of the interfaces. Next, the techniques to measure the electrochemical character of metal surfaces will be discussed including polarization testing methods (potentiodynamic polarization, linear polarization, and cyclic polarization). Then, EIS methods will be presented to show how the metal–oxide–solution interface can be analyzed on the basis of its frequency response to small scale voltage excursions.

1.103.5.1. Active Corrosion Theory: Oxidation and Reduction

During corrosion, two basic sets of reactions must be present. These are oxidation and reduction. Each is one half of the overall process of corrosion, and thus, is referred to as a half-cell reaction. It is important to understand that one cannot have corrosion (oxidation) without the corresponding reduction half-cell reactions accounted for as well. Each has influence over the other as the overall process requires both to

take place. Indeed, a central tenet of corrosion, in the absence of any externally applied potentials, is that the sum of all currents generated by oxidation reactions must balance with the sum of all currents generated by reduction reactions on a metal surface. This governing rule, called the 'Mixed-Potential Theory,'[17] is central to our understanding of corrosion in general and in corrosion of metallic biomaterials, in particular. It holds for all cases, even when oxide films are present and has consequences for how the voltage of a metal surface varies with changes in the rates of either oxidation or reduction reactions. Before we explore the mixed-potential theory, let us discuss the basic concepts of oxidation and reduction.

The basic concepts of corrosion have to do with the susceptibility of metals to increase their valence state from atomic element to ion. This process is called oxidation and the metal atoms increase their valence state to become metal ions (or cations). Two typical types of oxidation reaction for elemental metal to its cationic form are shown in eqn [I] below.

$$\mathrm{M} \rightarrow \mathrm{M}^{+} + ne^{-} \qquad \text{(ionic dissolution)}$$

$$n\mathrm{M} + m\mathrm{H_2O} \rightarrow \mathrm{M}_n\mathrm{O}_m + 2m\mathrm{H}^{+} + ne^{-} \quad \text{(oxide formation)} \qquad [\mathrm{I}]$$

These are only meant to be representative of oxidation reactions and not exhaustive of all the types of oxidation processes possible. In the first, metal atoms transit the interface from the metal to the solution to become ions in solution while the electrons liberated remain behind in the metal (see **Figure 1**). In the second, metal atoms transit the interface and react with water to become metal oxides (or hydrated metal oxides), and liberate both hydrogen ions into the solution and electrons into the metal.

In all oxidation reactions, the characteristic increase in the valence state of the metal to become a cation is associated with electrons remaining behind in the metal. Thus, oxidation reactions result in a buildup of positive charge in the solution and negative charge left behind in the metal. The oxide formation reaction may result in oxides in solution or the development of an oxide film on the surface.

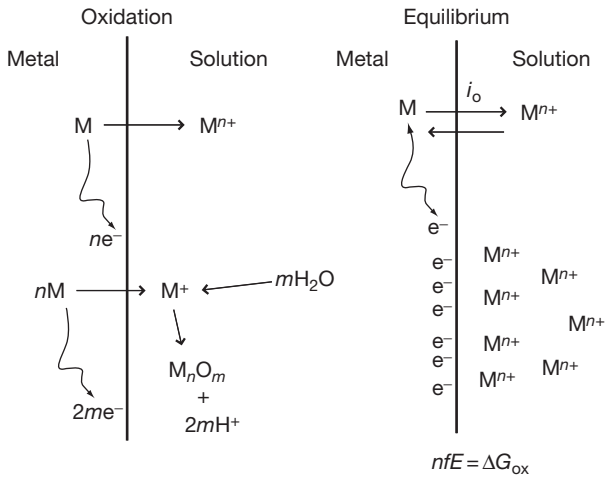

Figure 1 Simplified representation of a half-cell reaction across a metal–solution interface. Metal atoms get oxidized to ions in solution and leave electrons behind in the metal. Also metals can react with water to form oxides (either in solution or as films). A build-up of charge occurs across the interface whose electrical energy balances the oxidation energy driving the reaction at equilibrium.

There are two main thermodynamic forces at play that will balance each other when the oxidation reaction reaches equilibrium (i.e., equal forward and reverse reactions) and there are no other reactions at play. These two forces are the Gibbs free energy driving the oxidation reaction (ΔG_{ox}), or the negative of the Gibbs free energy change for the opposite reaction (reduction), that is, $\Delta G_{red} = -\Delta G_{ox}$. The second force arises from the separation of charge that is established across the interface – much like the charging of a capacitor – which gives rise to an electrical energy (nFE, where n is the valence of the ion, E is the potential across the interface, and F is Faraday's constant, 96 500 coul mol^{-1} of electrons). At equilibrium, these two terms are equal and the so-called Nernst equation results:

$$nFE = -\Delta G_{red} \quad \text{or} \quad E^{eq} = E^{o} + \frac{RT}{nF} \ln\left[\frac{[\mathrm{Ox}]}{[\mathrm{Red}]}\right] \qquad [1]$$

where R is the ideal gas constant, T is temperature, and [Ox] and [Red] are the activities of the oxidized and reduced forms of the half-cell reaction, respectively. E^{eq} is the equilibrium potential for the half-cell reaction and E^{o} is the potential of the half-cell when the activities of the oxidized and reduced forms are equal to 1 or equal to each other (i.e., where the natural log term equals 1).

The Nernst equation shows that there is a voltage that gets established across a metal–solution interface as a result of the accumulation of charge separation across the interface that depends on the free energy driving the oxidation. The greater the chemical driving force for oxidation, the more negative this potential (i.e., greater build-up of charge) is. This scale, called the electromotive force (EMF), or electrochemical series, provides a relative scale of the thermodynamics driving oxidation. On the most positive side of this scale are metals such as gold and platinum while on the most negative side are metals such as Na, Mg, Ti, Cr, Fe, Co. It is important to note that many of the metals used in medical alloys today have high negative EMFs including titanium (−1.6 V vs. the normal hydrogen electrode (NHE, which is arbitrarily defined as 0.0 V)). That is, metals used as biomaterials typically have high driving forces for corrosion and given the opportunity they will oxidize very rapidly. As we will discuss, the presence on the surface of a very thin layer of oxide – called the passive oxide film – prevents this rapid oxidation from taking place. The passive film is a kinetic barrier preventing the high driving forces of oxidation from oxidizing the metal. This is important to understand when we discuss mechanical disruption of oxides and their repassivation.

When a half-cell reaction (such as metal ion release in **Figure 1**) is at its equilibrium Nernst potential, there is still a current per unit area (referred to as an exchange current density (i_o)) which reflects the reaction rate constant for the oxidation and reduction reactions of metal changing to cation and cation changing back to metal across the interface. The exchange currents are equal and opposite at equilibrium, but they are NOT zero. In fact, the exchange current density is important to

consider when the voltage of the interface deviates away from the Nernst potential as it will when a second half-cell reaction is introduced.

For a single half-cell reaction (e.g., metal oxidation), one can derive, using the activated complex theory (see Bard and Faulkner[18] for a good description), a relationship between the current density, i, the exchange current density, i_o, and the potential deviation away from the Nernst potential for that half-cell reaction, η (the over potential). This equation, when diffusion and mass transport rates are assumed to be high relative to the rate of the interfacial reactions (i.e., the reactions are 'activation limited') is called the Butler–Volmer equation:

$$i = i_o\left(10^{\eta/\beta_a} - 10^{-\eta/\beta_c}\right) \qquad [2]$$

where η is $(E-E_M^{eq})$ the overpotential, or deviation away from the Nernst potential for the half-cell reaction, and β_a and β_c are the anodic and cathodic Tafel slopes for the half-cell reaction. These slopes can be visualized on a so-called Evans diagram which plots the potential versus Log base 10 of the current density (see Figure 2). In this figure, each term in the Butler–Volmer equation is plotted as voltage versus Log_{10} (current density), with the equilibrium Nernst potential at −500 mV and the exchange current density at 0.1 μA cm^{-2}.

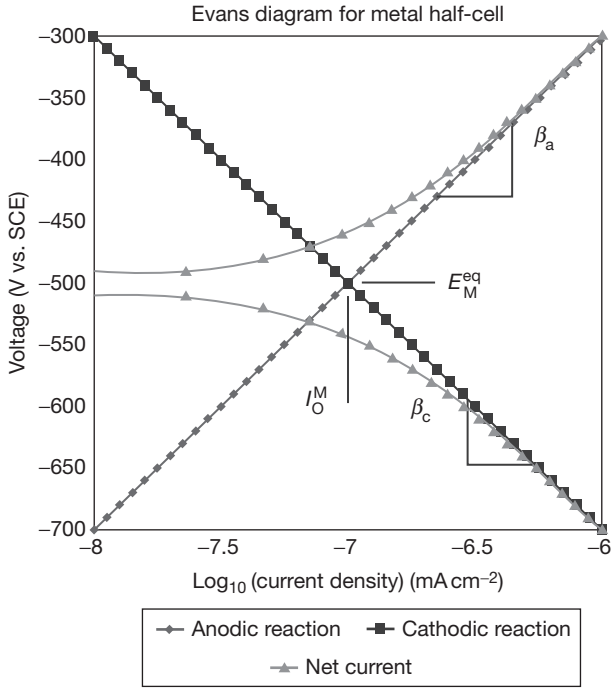

Figure 2 Evan's diagram for the metal half-cell reaction. This is a plot of V versus Log(i) and represent the Butler–Volmer equation. The two straight lines represent the current densities that arise when the voltage of the electrode is moved away from the equilibrium (Nernst) voltage (the overpotential). Increases in either anodic (oxidation) or cathodic (reduction) current densities arise. The net current at any voltage is just the sum of the anodic and cathodic currents. The intersection represents the exchange current density which is a measure of the inherent rate of the reaction. The slopes of the lines are the Tafel constants for oxidation and reduction.

The Tafel slopes are assumed to be 200 mV per decade of current. The net current density, i, when one deviates away from the equilibrium potential, E_M^{eq}, is the sum of the anodic and cathodic current densities at the potential of interest. One can see that as the potential approaches the equilibrium (where η goes to 0), the net current density approaches zero and the $Log_{10}(i)$ goes to negative infinity.

The Evans diagram's graphical representation of one half-cell reaction is helpful in identifying the important features of the Butler–Volmer equation. However, in virtually all corrosion conditions, there are usually at least one oxidation half-cell and one reduction half-cell present on the surface. When multiple half-cell reactions are taking place, then one must write a Butler–Volmer equation for each half-cell and the mixed-potential theory states that the total interfacial anodic and cathodic currents must balance for the sum of all anodic and cathodic processes. The Evans diagram for two half-cell reactions and the associated interfacial reaction schematics are shown in Figure 3 where a second reaction has been added to the half-cell reaction in Figure 2. Also shown is a schematic of the metal surface where both reactions are present, as is an oxide film.

If we assume in this example that the anodic reaction is metal oxidation and the reduction reaction is an oxygen reaction

$$\frac{1}{2}O_2 + H_2O + 2e^- \rightarrow 2OH^- \qquad [II]$$

for example, then the Evans diagram for both reactions results in Figure 3. In this case, the two half-cell reactions must be in balance if there is no external flow of current (i.e., equal oxidation and reduction currents), the electrons 'liberated' during the metal oxidation reaction (eqn [I]) must be consumed at an equal rate in the reduction reaction (eqn [II]). This condition requires that the two currents be equal (or the two current densities should be equal if the entire surface can participate in both reactions). Note that if the areas upon which the anodic reactions and the cathodic reactions occur are different, then it is the total anodic (oxidation) current that must balance the total cathodic (reduction) current. Therefore, the point of intersection of the metal oxidation curve with the oxygen reduction curve is where the two currents are equal and this is the corrosion current (or corrosion current density) of the two combined reactions. Note that as long as there is oxygen (or some other species) available to consume the electrons liberated in the oxidation reaction, the oxidation will continue; however, if the reduction reaction cannot continue, then the net oxidation will cease. This shows the importance of having reducible species available to depolarize the metal surface (sweep up the electrons) to force a continuation of the corrosion process. The voltage of the point of intersection is referred to as the OCP (or corrosion potential, E_{corr}) of the surface and the current density is the corrosion current density, i_{corr}.

It is important to emphasize that the OCP of a surface that can engage in redox reactions is dictated by the condition where the net anodic and cathodic currents passing an electrochemical interface are equal as can be seen in the Evans diagram of Figure 3. That is, when Faradaic (redox) reactions are present, the surface voltage is determined by the balance of all

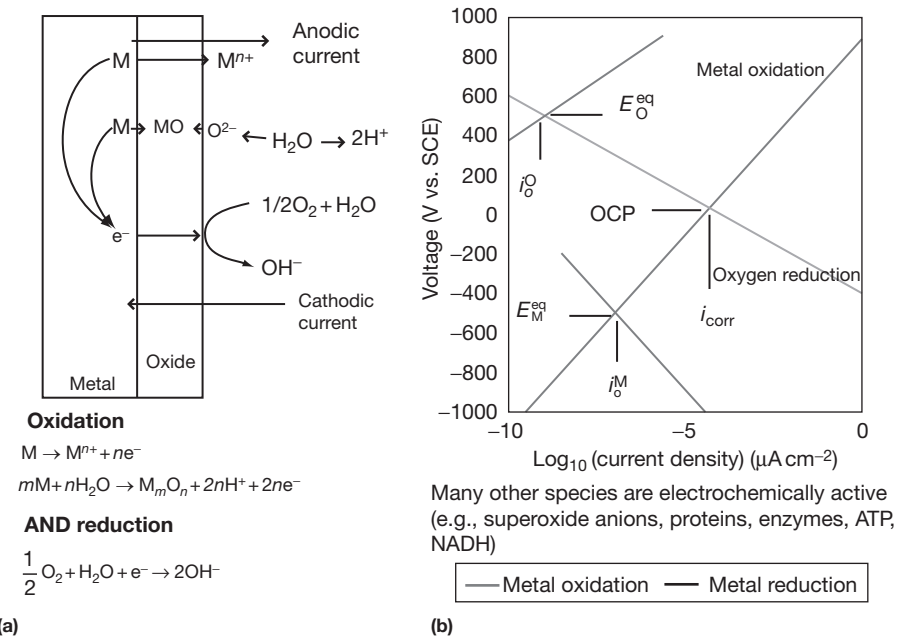

Figure 3 Schematic of a metallic biomaterial electrode (with oxide present) that presents oxidation and reduction reactions to show the overall process required for corrosion. Both oxidation and reduction are required. (a) Schematic of the half-cell reactions, the movement of ions, and electrons and the corresponding currents. (b) Evan's diagram for two ideal (Butler–Volmer based) reactions, both an oxidation half-cell and a reduction half-cell, showing that they intersect at the open circuit potential (OCP) and result in a corrosion current i_{corr}. The reduction half-cell consumes the electrons liberated in the oxidation reactions and continues to drive the corrosion of the metal.

of the anodic and cathodic currents and there is a resistance that one can measure called the charge transfer resistance, R_{ct}, which is sometimes referred to as the polarization resistance, R_P, described below (but is strictly not the same). This is a fundamental aspect of the mixed-potential theory[17] and the activated complex theory.[18] This condition on OCP is true regardless of whether the surface is an active metal, a metal with a passive film, or a semiconducting metal–oxide–solution interface. The OCP of an electrode surface is determined by the voltage required to balance the flow of anodic and cathodic currents across the interface. We will revisit this concept when we discuss mechanically assisted corrosion where mechanical disruption of the surface oxide can dramatically increase the oxidation reactions and result in a large negative excursion in the voltage as a consequence. If no electrochemical currents (no Faradaic processes) are present, the electrode is said to be a 'polarizable' electrode and the voltage of the surface is dictated by the charge at the surface, not the current. When both charge transfer across the interface (Faradaic process) and charge accumulation (non-Faradaic process) can occur, then the interface takes on characteristics of both a charging interface (e.g., a capacitor) and a charge transfer interface (e.g., a resistor). However, the OCP in this case is still defined by the sum of currents. This combined interfacial electrical character will be discussed in the section on impedance.

The Evans diagram can now help understand how and why OCP and corrosion rates can vary with changes in the electrochemical system. For example, if the exchange current density for the oxygen reaction is increased (moves to the right in Figure 3), then the reduction currents that arise when the voltage moves away from the equilibrium voltage for the oxygen half-cell also increase. This will cause the metal oxidation curve to intersect the reduction curve at a higher voltage (more positive OCP), and will result in a higher corrosion rate. Similarly, the equilibrium potential for the reduction reaction can shift due to changes in the concentration of oxygen in solution. For instance, if the oxygen level decreases, the equilibrium potential for oxygen will decrease (on the basis of the Nernst equation) and the reduction currents will be reduced as well. This will cause the OCP to become more negative and the corrosion rate to decrease. Similar thought experiments can be done with the metal parameters (exchange current density and equilibrium potential); however, some different outcomes will occur. For example, if the exchange current density of the metal increases, then the Evans diagram plot for the metal will shift to the right and the point of intersection between the metal oxidation curve and the oxygen reduction curve will shift to higher currents and lower voltages. Thus, the OCP will shift more positive or more negative depending on the changes that are taking place for either the oxidation half-cell or the reduction half-cell.

Some other important observations from the Evans diagram include the fact that voltages more negative than OCP do NOT stop corrosion processes from occurring. They may be decreased, but the corrosion will continue, albeit at a lower rate, until the voltage drops below the equilibrium potential for the metal, which can be very negative. Also, the curves plotted in Figure 3 represent only cases where the metal surfaces are active and no film or oxide layer is present to introduce other kinetic barriers to the process. This is, of course, not

representative of most metallic biomaterials used today where oxide thin films cover the surfaces and interfere with the activation-limited processes giving rise to the Butler–Volmer behavior.

The role of the reduction reaction in corrosion needs to be emphasized. The example used above only considered oxygen reduction as the cathodic half-cell; however, there are many other reducing species (also known as oxidizing agents) potentially available in the body to help increase the rate of corrosion. ROS, in particular, needs to be mentioned. Inflammatory cells can release ROS molecules that can react to form a variety of strong oxidizing agents (species available for reduction). These include hydrogen peroxide (a very strong oxidizing agent), hypochlorous acid, and peroxynitrite.[19] Local concentrations of these species near metallic biomaterial surface may become very large and may be influenced by other factors (e.g., infection, autoimmune disease, presence and severity of the chronic inflammatory reaction). Very little is known about the range and specific concentrations of these oxidizing agents or their effect on corrosion. We do know that hydrogen peroxide increases the rate of corrosion of most metallic biomaterials (see below).

Active metal corrosion behavior is not seen in many medical alloy systems. Those that may exhibit close to active corrosion condition include the noble metals (Au, Pt), or alloys such as those of Mg. However, the noble metal equilibrium potentials are so positive that there are few reduction reactions available to induce corrosion. That is, there is very low free energy available to drive oxidation of these alloys. Most metallic biomaterials are passive oxide film coated and therefore, the concepts outlined above, while useful, need to be modified to account for this important difference.

1.103.5.2. Passivating Metal Surface Behavior

When the surface of a metal becomes covered with a highly adherent compact thin oxide film, it is said to become passivated. These passive films result in several changes to the Evans diagrams shown above (see Figure 4). In this schematic (Figure 4(a)), the active region is at the bottom of the plot and in this potential range no oxide film will grow if the oxide is removed from the metal surface. (We should note that passive films may reductively dissolve if the surfaces are maintained at or below these potentials for sufficient periods of time.) If the potential is raised from its equilibrium level, active corrosion will occur up to the passivating potential (E_{pp}) where the first onset of oxidation reactions results in oxide film formation. As oxides cover the metal surface, they result in a physical barrier that kinetically limits continued ion release and the currents drop significantly. Superimposing a reduction reaction results in Figure 4(b) which is what is typically measured in polarization tests. Note that the active region of the metal may be hidden by the overlaid reduction reaction but it is still present and can lead to adverse (and poorly understood) mechanisms of attack.

An example of this behavior is seen with Co–Cr–Mo alloy (see Figure 5). Once the oxide film forms on the surface, the surface is said to be passivated; however, this does not mean that there are no ongoing reactions taking place. The oxide film will continue to grow with increasing potential, the chemistry of the oxide may change, ions may continue to be released into solution, the valence states of the ions may change, and the defect structure may be altered too. Polarization tests provide only incomplete information about the nature of the oxide surface, and the methods often adopted in performing polarization tests will not reveal the active region or the active-to-passive transition. This is because the potential range where these reactions occur is often more negative than the range of OCP which is typically used to determine the starting potential for anodic polarization testing (e.g., typically scans will start 200 mV cathodic of OCP and scan forward); however, the active-to-passive transition for CoCr surfaces is from −800 to −500 mV, and its OCP is typically in the −200 to +100 mV range (vs. Ag/AgCl).

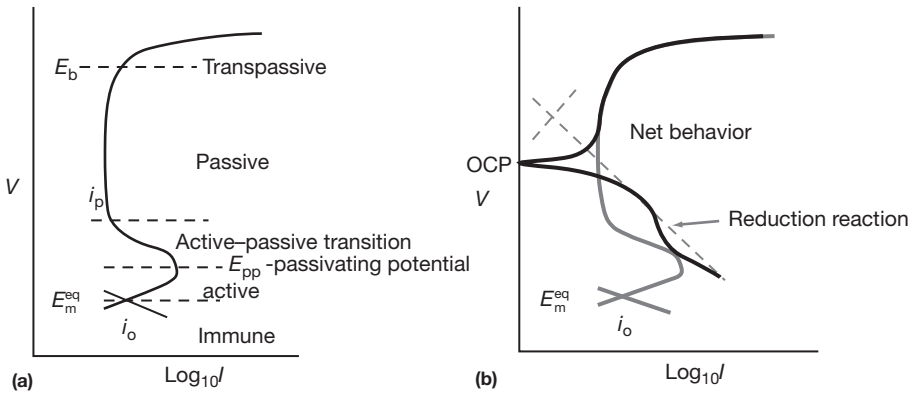

Figure 4 (a) Modified Evans diagram for a metal that undergoes both active corrosion and passivation to form an oxide on its surface. Note that the metal initially (at negative voltages, but above E^{eq}) engages in active corrosion, but when the voltage reaches the passivating potential, oxide film begins to form on the surface which kinetically limits the corrosion and decreases the current density. The active–passive region is where the oxide partially covers the surface and the passive region is where the oxide completely covers the surface. At the transpassive potential (sometimes referred to as the breakdown potential when pitting is involved), the oxide film loses its protective ability and the surface corrodes much more rapidly. Note that no reduction half-cell is present. (b) The same active–passive behavior with a reduction reaction overlaid to show the total behavior typical for such electrodes. Note that sometimes the active–passive region is hidden or masked by the dominating reduction reaction.

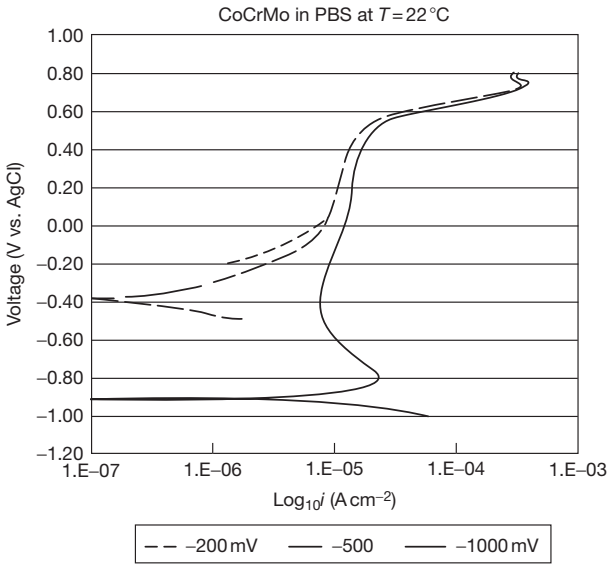

Figure 5 Anodic polarization test results for Co–Cr–Mo (ASTM F-1537) in PBS at room temperature. Note that three tests are shown, starting at three different potentials: −200, −500, and −1000 mV and scanned to +800 mV at 1 mV s^{-1}. The behavior changes slightly with starting potential, where the crossing potential (zero current potentials) shifts more negative with starting potential, and the active–passive transition from −800 to −500 mV arises when starting at −1000 mV.

The surface is fully passive between −500 and +200 mV. As the potential of the surface continues to increase beyond 200 mV, the oxide film can begin to enter into the transpassive region (see Figure 4 or 5).[20] Here, one or more of several events can occur depending on the metal and the condition of the oxide. Either the surface can begin to undergo pitting attack (typically seen in stainless steel) in which case the transpassive potential is known as the breakdown potential, or the oxide film can begin to react to the voltage by changing the valence state of the cations in the oxide (e.g., Cr(III) to Cr (VI)) and lose its passivity. In this case, the surface is said to go transpassive. It is clear that the polarization behavior of oxide film covered surfaces is significantly different from that of active surfaces; however, the Evans diagram can help understand how passive oxide surfaces behave in the presence of other redox species. Interestingly, it is very unlikely that the potential of metallic biomaterials will rise up to the levels needed to induce transpassive or breakdown behavior *in vivo*. Indeed, these surfaces are more likely to have a voltage established that is more negative than their resting OCP because of ongoing mechanical abrasion processes likely being present, especially in orthopedic and spinal devices (as well as others where metal–metal contact and relative motion can occur – see Section 1.103.9). In these cases, the OCP may shift into more active corrosion potentials especially for Cr-based oxides.

1.103.5.3. Polarization Testing

At this point, it is useful to introduce the concepts of potentiodynamic polarization testing including linear polarization and the concept of the polarization resistance. In potentiodynamic polarization testing, the working electrode (the sample) is connected to a potentiostat, which is an electrical device that can control the voltage of the working electrode and measure the current required to maintain that voltage with respect to a reference electrode. Typical polarization testing requires the use of a three electrode system where the first electrode is the working electrode, the second is a reference electrode, and the third is the counter electrode. The reference and counter electrodes are present to provide a stable datum or reference voltage from which to base the voltages of the working electrode, and the counter is present to provide an electrode surface through which the currents coming from the working electrode can be transported back into the electrolyte to complete the circuit. In some experiments, the reference electrode serves both purposes; however, if the currents get large enough, then the voltage of the reference will deviate due to the currents passing over its surface and it will no longer be stable. Thus, the potentiostat provides an electronic circuit that can isolate the reference electrode from any of the currents in the system, and complete the current path through the counter electrode while maintaining a high fidelity reference voltage.

Typically, reference electrodes are made from saturated calomel electrodes (SCE, a mercury–mercury chloride electrode), or a saturated silver–silver chloride (Ag/AgCl) electrode. Both have the characteristic of being nearly ideal nonpolarizable electrodes (their voltage remains relatively fixed even when small currents are passing through their interfaces). On the other hand, counter electrodes typically need to have relatively large surface areas compared to the working electrode and to be able to pass charge (either by capacitive charging or by Faradiac reactions) into the solution without degrading to complete the electrochemical circuit. Typical counter electrodes include platinum and carbon. Both materials are polarizable electrodes (their voltage changes rapidly with small currents) and the potentiostatic circuit will drive these electrodes to whatever potential is required to deliver the current necessary to maintain the working electrode at its set potential (i.e., to complete the circuit).

The solution in which these electrodes sit, besides influencing the chemical state or the surface and the reactions at the working electrode, provides the medium through which ionic charges can complete the electrical circuit for the test. There is a small amount of resistance associated with all ionic solutions (known as the solution resistance (R_s)) which depends on their ionic strength. Most solutions used in biomaterials corrosion testing have relatively low resistances (in the range of 20–70 Ω cm^{-2}). This solution resistance may affect the actual potential across the working electrode depending on the magnitude of the currents in the solution ($V = IR$). So, for example, if 10 μA of current is flowing through a solution with a 50 Ω resistance, then 5e-4 volts (or half of a millivolt) will be present across the solution and the remaining voltage drop will take place across the working electrode. Thus, for most experiments, the solution resistance plays a very minor role (if at all) in the polarization tests of metallic biomaterials. However, if high resistivity solutions (DI water) are used, then large voltage drops in the solution will be present and will affect the voltage at the interface.

In a typical potentiodynamic polarization test, the working electrode is placed in the SBF and its OCP is monitored for up

to 1 h to allow any short-time transient effects to settle out. It should be noted that OCP will continue to vary for days or even weeks after immersion as the interface continues to change upon immersion. After 1 h, the working electrode is brought to a fixed potential, which is suggested by typical corrosion test standards to be a few hundred millivolts cathodic to the OCP, but in reality can be any voltage desired as the starting potential. Then, after a conditioning time, the potential is typically scanned anodically (positively) at some fixed rate (0.167 up to 1 mV s^{-1} is typical). Differences in the starting potential, the scan rate, and the peak positive potential are on the basis of the type of test to be performed. For a linear polarization test, the voltage is typically moved only about 10 mV cathodic to OCP and scanned very slowly through OCP to about 10 mV above. Cyclic polarization and anodic polarization tests typically start at the potential 200–700 mV cathodic to OCP and scan either to a fixed positive potential (e.g., 1000 mV) or until the current density reaches a critical level (e.g., 2 mA cm^{-2}); then the voltage scan is either reversed (for cyclic polarization) or the test is terminated (anodic polarization).

1.103.5.3.1. Linear polarization and R_p

Linear polarization testing is used to try to determine the polarization resistance of the working electrode interface. In linear polarization, the assumption is made that the Butler–Volmer equation holds for the interface. Then, this equation is simplified to a linear equation by taking the Taylor series expansion of the current density and assuming that only the first (linear) term of the expansion is required. Then, a linear relationship between the current density and the voltage is obtained that is called the polarization resistance.

Starting with the Butler–Volmer equation for the case in Figure 3 (where two half-cell reactions are in equilibrium), we can rewrite this equation with the starting potential at the OCP and the overpotential defined as the deviation of the voltage away from OCP. In this case, two things change in the equation. The Tafel slopes for the equation are the anodic slope for the metal oxidation and the cathodic slope for the oxygen reduction, and the exchange current density is replaced by the corrosion current density, i_{corr}.

$$i = i_{corr}\left(10^{(E-OCP)/\beta_a^M} - 10^{-(E-OCP)/\beta_c^O}\right) \quad [3]$$

Now, converting to the natural exponent and taking the Taylor series expansion of this function yields

$$i = i_{corr}\left(1 + 2.3026\frac{(E-OCP)}{\beta_a^M} - \left(1 - 2.3026\frac{(E-OCP)}{\beta_c^O}\right)\right) \quad [4]$$

Taking the derivative of i with respect to E

$$\frac{di}{dE} = \frac{1}{R_p} = 2.3026 i_{corr}\left[\frac{1}{\beta_a^M} + \frac{1}{\beta_c^O}\right] \quad [5]$$

or

$$R_p = \frac{1}{2.3026 i_{corr}}\left[\frac{\beta_a^M \beta_c^O}{\beta_a^M + \beta_c^O}\right] \quad [6]$$

Thus, linear polarization, by measuring the Tafel slopes away from OCP and the slope of the I versus E curve through the OCP, allows one to relate the corrosion current density (i_{corr}) to the polarization resistance (R_p). This method, of course, presumes an active metal interface (not a passive film covered surface) and thus it is questionable whether one can use this method to directly link R_p with i_{corr}. However, even for passive film covered surfaces, there is likely to be an inverse relationship between the corrosion rate and the polarization resistance of the interface. The rate at which one scans to obtain the I versus E plot is important and with passive oxide film surfaces, this is particularly true.

1.103.5.3.2. Cyclic and anodic polarization testing

Cyclic polarization testing and anodic polarization testing are methods where the sample is swept through a range of potentials and the current is measured. These plots are developed to provide information about the passive and transpassive behavior of the surface. In cyclic polarization, reverse scanning is done after a sample has reached a vertex potential (usually around 800–1000 mV vs. SCE) to measure current response on reversal of scanning. If there had been any deleterious pitting attack of the surface, the reverse potential scan will remain at high current levels and will not retrace the forward scan currents. This indicates that unstable pitting attack is taking place and the current is said to develop a hysteresis (see Figure 6 for typical polarization plots). The extent of this hysteresis behavior indicates the susceptibility of the surface to sustained pitting attack. Indeed the voltage difference between the breakdown potential and the repassivating potential is a measure of the susceptibility to pitting. Most metallic biomaterials in use today do not suffer from pitting corrosion in cyclic polarization tests. The exceptions to this are 316L stainless steel and NiTi shape memory alloys. Even these surfaces can sometimes be prepared to resist pitting in

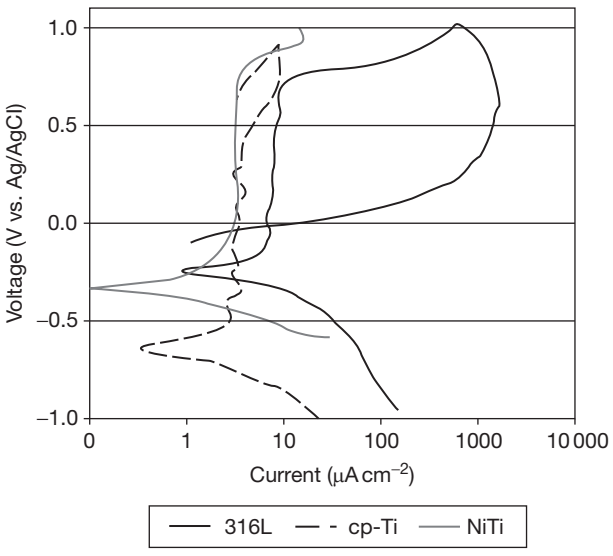

Figure 6 Polarization plots for 316L stainless steel, NiTi shape memory alloy, and commercially pure Ti. Note the hysteresis in the 316L SS plot showing the onset of pitting corrosion attack above about 700 mV.

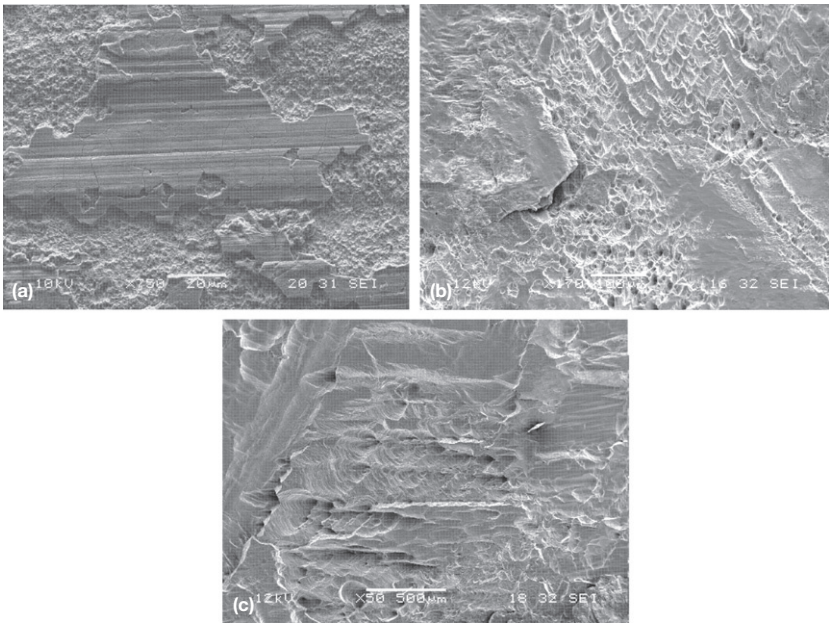

Figure 7 Scanning electron micrographs of retrieved Ti-6Al-4V alloy hip replacements in the modular taper interface showing severe corrosion attack of the Ti-alloy surface. (a), (b), and (c) represent different retrieved devices and both the male and female taper surfaces. The opposing taper alloy was also Ti-6Al-4V indicating that these corrosion processes are not galvanic in nature but result from the combination of fretting and crevice corrosion. Severe pitting is also observed.

these tests (by, e.g., increasing the nitrogen content in the steel, or pulsed anodization of the NiTi to drive the Ni ions out of the film and leave only TiO_2 on the surface). However, it is important to note that ALL metallic biomaterials have been shown to pit inside the human body under certain circumstances. Recent work by Rodrigues *et al.*[21] has shown that even Ti–6Al–4V can be induced to pit in modular taper interfaces of Ti–Ti modular body total hip stems *in vivo* (see Figure 7). Co–Cr–Mo alloys have been documented to undergo pitting, intergranular corrosion, selective dissolution and, corrosion fatigue failure *in vivo*.[22] This will be discussed in more detail below.

Typical polarization results for 316L SS, cp-Ti, Co–Cr–Mo, and NiTi are shown in Figures 5 and 6. These tests were performed in PBS at room temperature at a scan rate of $1\,mV\,s^{-1}$. These curves and their details will depend on the specifics of the solution, prior electrochemical history (voltage, solution, time path), and the starting voltage of the experiment. For example, the OCP for Ti is shifted to more negative potentials when proteins are added to the electrolyte; however, when hydrogen peroxide is added, the OCP shifts to more positive potentials. As the surfaces of these medical alloys have a semiconducting thin film on them that has a significant capacitance, the rate of scanning will affect the measured currents. The starting potential will affect the current response as well. If one starts a polarization test at more negative voltages (e.g., −1000 mV, held for 10 min), the voltage at which the current passes from cathodic to anodic state will shift to more negative potentials (see Figure 5). This point of zero current (zcp, zero current potential) can shift to as low as −800 mV for CoCrMo in PBS but no lower. Thus, the zcp appears to depend on starting potential up to a certain range and starting from a more negative value than that potential does not further alter the zcp. The shape of the curve may also change as well because of alterations in the surface oxide by way of voltages that may drive reductive dissolution or other changes in the oxide film (e.g., modifications in defect density).

1.103.6. Passive Oxide Films and Semiconducting Electrochemistry

1.103.6.1. Introduction to Passive Oxide Films

Oxide films are extremely thin (in the range of 2–10 nm) and are compact and tightly adhered to the metal substrates. We call these oxide thin films 'passive' films as they act to 'passivate' the surface and reduce the rate of corrosion. As we will see, these films are not 'passive' but are rather dynamic in terms of thickness, chemistry, and properties, and responsive to their environment. The thickness, resistivity, and chemistry are all affected by solution chemistry, voltage, and prior electrochemical history. The presence of the oxide thin films alters the polarization behavior of active metals as shown above, but also develops several other important differences that impact on the interaction with the biological system.

Oxides that result from the reaction of metallic titanium or chromium with water (i.e., TiO_{2-x}, $Cr_{2-x}O_3$) release extremely large amounts of energy during their oxidation. For example, the equilibrium voltage for titanium E_{Ti}^{eq} is about −1.6 V (vs. NHE), and gives off four electrons per cation. The energy released in the oxidation of a mole of Ti ($47.9\,g\,mol^{-1}$) is $\Delta G_{ox} = nFE\ (4 \times 96500 \times -1.6) = -620\,kJ\,mol^{-1}$. This is a very high amount of energy associated with this reaction.

It implies that if the reaction were allowed to proceed without any barrier effect of the oxide, the rate of the reaction would be extremely high. It has been reported that the oxide free Ti surface can generate current densities between 0.3 and 150 A cm^{-2}.[23–25]

The barrier concept is critical in understanding the behavior of these surfaces and their response to effects such as mechanical abrasion. To date, there is no simple theory that can describe the electrochemistry of metallic biomaterials with passive thin films. This is due to the complexity and multiplicity of physical and chemical processes that transpire at these interfaces. To begin to understand oxide thin films and their barrier effects on corrosion in the biological milieu, we must introduce several different concepts. These include high-electric field oxide thin film growth, semiconductor electrochemical behavior, ionic and electronic transport mechanisms in oxides, defects, internal stress distribution, adhesion theory, impedance behavior, electrical double layer, surface chemistry (adsorption/desorption), etc. Even areas of quantum mechanics (e.g., tunneling, molecular orbital theory, Fermi energies, energy band theory of semiconductors, band bending, etc.) play a role.

The following sections will provide background in many of the subjects listed above to serve as the foundation upon which a more complete understanding of metal–oxide thin films and their effects on electrochemistry in the biological milieu can be obtained. First, a simplified view of this surface is required. Figure 8 shows a schematic representation of the atomistic view of an oxide film. These films arise from the high-energy

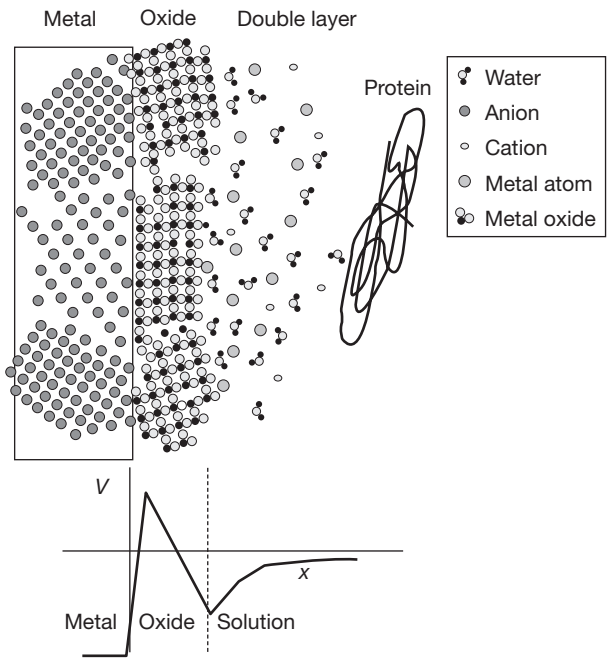

Figure 8 Atomistic view of the metallic biomaterial metal–oxide–solution interface. Crystalline metal grains intersect the surface and convert to oxide that is only a few atom layers thick. The surfaces of these oxides interact with water, ions, proteins, and other species. There is a voltage variation across this interface that promotes the oxidation of the metal.

reactions that take place between fresh metal atoms and virtually any oxygen that is available including that from water. In air, oxygen molecules will react in as little as a few milliseconds to convert the surface metal atoms to a metal oxide. Cabrera and Mott[26] were the first to propose a mechanism by which this occurs that depends on the development of a very high electric field which drives electromigration of the cations and anions through the film to react to grow the oxide.

1.103.6.2. High Electric Field Oxide Growth

The basic premise of Cabrera and Mott's theory is that high electric fields are developed across the oxide. Electrons from the metal tunnel through the surface and are captured by (and capture) oxygen at the surface. Oxygen serves as an electron trap providing a low-energy site for the electron. The deficit of electrons at the metal–oxide interface (i.e., the oxidation of the metal to metal ions) and accumulation of electrons in the oxygen ions at the solution–oxide surface result in very high electric fields across the interface (about 10 MV cm^{-1}). This field drives metal cations through the forming oxide by means of cation vacancy motion or cation motion as interstitial atoms in the oxide. The process of field driven motion is known as electromigration and is characterized by the Nernst–Plank equation[27] This equation comes from definition of activity, C_i, in terms of electrochemical potential, the flux equation (j_i) for ionic species, and the continuity equation in the absence of generation or elimination of species.

$$C_i = e^{(\mu_i - \mu_i^o - n_i FV)/RT}$$

Nernst–Plank equation:

$$j_i = -D\nabla C_i = -\frac{D}{RT}C_i\nabla\mu_i - \frac{n_i FD_i}{RT}C_i\nabla V$$

Nernst–Plank–Fick equation:

$$\frac{\partial C_i}{\partial t} = -\nabla\cdot j = \nabla\cdot D_i\nabla C_i + \frac{n_i FD_i}{RT}\nabla\cdot C_i\nabla V \qquad [7]$$

And the current density is

$$i = \sum n_i F j_i = -F\sum n_i D_i\nabla C_i - F^2\nabla V\sum\frac{D_i}{RT}C_i n_i^2 \qquad [8]$$

where C_i is the activity (concentration) of the ith species, D_i is the diffusivity (Note, $D = uRT$, where u is known as the mobility – the Nernst–Einstein equation), n_i is the charge per ion, F is Faraday's constant, μ_i is the chemical potential of the ith species, and V is the voltage. This equation provides insight into the forces driving ions through either oxides or solutions and may be helpful in understanding the high-field growth behavior of oxides.

Similarly, anion vacancies (and therefore anions) can also migrate from the solution–oxide interface inward, because of the electric field developed, by anion vacancy motion. When cations and anions combine, the result is growth in the oxide. The overall model and the variation of the voltage with position from metal through the oxide to the solution are schematically represented in Figure 9. In Figure 9, metal atoms at the

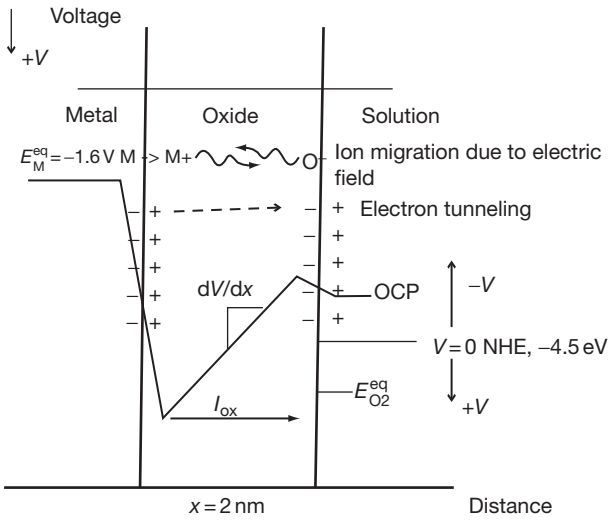

Figure 9 Schematic of the voltage variation across the metal–oxide–solution interface driving oxide thin film growth. High electric fields are developed because of the energy of oxidation and the tunneling of electrons from the metal to the oxide–solution interface. This leads to the high-field growth models of Cabrera and Mott.

metal–oxide surface tend to get oxidized because of the large free energy change associated with oxidation (−1.6 V for Ti); this creates cations at the metal–oxide interface and a separation of charge with some electrons remaining in the metal and some tunneling to the solution interface to be captured by oxygen. The resulting electric field through the oxide, dV/dx (see Figure 9), with positive charge at the oxide–metal interface, and negative charge at the oxide–solution interface then causes cations to migrate from the metal into the oxide and anions to migrate from the solution into the oxide because of the Nernst–Plank equation. Thus, the metal potential, dictated by its free energy of oxidation, changes across the metal–oxide interface, which is acting like a capacitor and becomes very positive just inside the oxide. Cations and anions will feel a high field in the oxide which itself is now acting like a leaky capacitor with charge distributed across the oxide from metal to solution, and ions will migrate toward one another and react to grow new oxide. The voltage at the oxide–solution interface (i.e., the measured OCP) is determined by the condition where the sum of all anodic and cathodic currents is balanced and therefore depends on the transport of both positive and negative charges (as cations and anions, and electrons and holes). There is an additional charged layer and capacitance, referred to as the electrical double later that forms on the basis of the net charge at the oxide–solution interface (see below). There is also a net flow of charge (i.e., an oxidation current) associated with ion transport through the oxide.

The rates of ion transport depend on the extent of ionic defects and the intrinsic mobility of the ions in the oxides. Indeed, Wagner[28] was an early contributor to the concept of electromigration, and anion and cation mobilities to provide a theory for oxide film growth. As the film thickens, the field decreases and lowers the driving force for continued oxidation until a limiting oxide thickness where the transport rates drop to very low levels. This thickness turns out to be only a few nanometers. It has been reported, for instance, that Ti-oxide films will grow at a rate of about 2 nm V^{-1} (the so-called anodization rate). This implies that the limiting field strength is about 5×10^6 V cm^{-1} below which the oxide's growth becomes limited. Similar anodization rates are seen for the other major alloys as well (CoCr and SS).

In Cabrera and Mott's theory, they proposed the following equation:

$$i_{film} = \frac{nF\rho A}{M_w}\frac{dx}{dt} = Ae^{-\left(w - b\frac{dV}{dx}\right)/kT} \quad [9]$$

where x is the oxide thickness, w is the activation energy for diffusion, dV/dx is the electric field, k is Boltzmann's constant, and T is the absolute temperature. A is related to the frequency of attempted ion jumps, the number of ions available to jump, while b relates to the charge of the ion and the jump distance (qa). Integration of this equation results in the so-called inverse-logarithmic growth law ($1/x$ = B-Alnt).[29]

Other models were proposed by Eley and Wilkinson,[30] and Gunterschulze and Betz.[31] These models, also referred to as high-field growth models, appear to have similar concepts related to their development and are reasonable estimates of the high field behavior seen. Eley and Wilkinson proposed a different term in the exponent of Cabrera and Mott ($w + ux$) where the activation energy for ionic jumping is proposed to increase as the thickness, x, of the oxide increases. This results in the logarithmic growth law ($x = A\ln(1 + Bt)$. Gunterschulze and Betz proposed an empirically derived equation, $I = ae^{-bx}$ similar to Cabrera and Mott equation.

1.103.6.3. Redox Electrochemistry at Oxide–Solution and Oxide–Metal Interfaces

This high-field view of oxide film growth is generally accepted as the process by which metal–oxide thin films form and grow on alloy surfaces. However, when one thinks about semiconductor electrochemistry theory in the absence of these growth processes or the underlying reactive metal, there are some different concepts that arise to explain how semiconductors allow electron transport so that solution-based redox reactions can occur.

Semiconducting electrochemistry theory is on the basis of electron energy band theory and typically presumes that the semiconductor is a bulk material whose only contribution to electrochemical processes is to provide a source or sink of electrons and holes (positive charge carriers in the valence band). Thus, knowledge of electron and hole movement in the semiconductor in response to voltage changes is central when considering semiconducting electrochemistry. This section lays out basic semiconducting electrochemistry theory and ignores changes in the oxide film because of growth effects. Overall synthesis of both field-assisted growth and semiconducting electrochemistry needs to occur for a more general theory to emerge.

Redox electrochemistry at bulk semiconductor surfaces can occur when a solution-bound redox half-cell is present. To understand these processes, the band theory of electrons is needed (see Figure 10). Here, the oxide is positioned between a metal phase and a solution phase. The band theory of

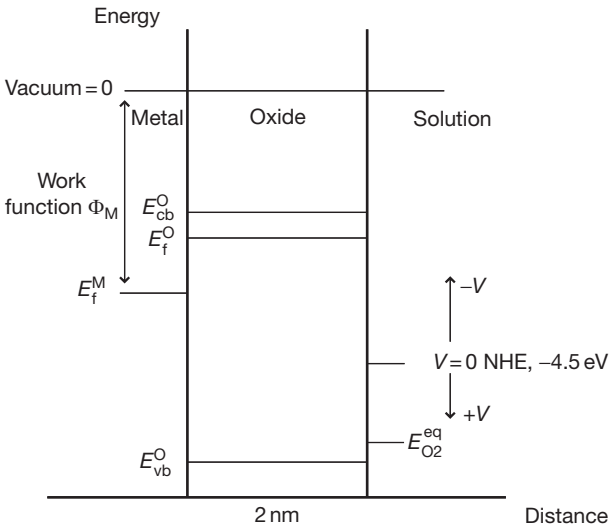

Figure 10 Electron energy diagram for the metal, oxide, and solution when they are not in contact or at equilibrium. Shown is the vacuum energy (= 0), the Fermi energy levels, E_f for each phase, and the conduction and valence bands for the oxide semiconductor. Also shown is the sense of electrochemical voltage in the solution and the energy equivalent for the normal hydrogen electrode (NHE).

electrons in a phase is used here. Electrons occupy discrete electron energy levels from the lowest up to the highest occupied energy level – known as the Fermi energy level. The energy of electrons in a material like a metal fill up to the Fermi energy of the metal, E_f^M. Thus, to remove an electron from this metal, additional energy is needed to raise the electron to the vacuum energy. This is known as the work function (Φ_M,) (see Figure 10). Each phase has a different Fermi energy level (as shown, Figure 10). In the case of the oxide, E_f^{ox} sits between the filled valence band and the unoccupied conduction band of the oxide. Its location within the band gap depends on the defect density giving rise to acceptor (for p-type), or donor levels (n-type) in the oxide. Electron energy is denoted by the vertical axis, where the top is the energy of vacuum (i.e., the energy needed to pull an electron out of the surface – the work function, Φ_M). In the oxide, the Fermi level sits between the filled valence band and the conduction band in the band-gap region and depends on the presence of donor or acceptor sites in the oxide as well as dopants and surface energy states.[32]

In the solution, the Fermi energy level is replaced by the concept of an equilibrium potential for the solution-based redox reaction of interest. Half-cell potentials and electron energies have been related to one another and it has been shown that the normal hydrogen electrode potential sits at about −4.5 eV on the electron energy axis (see Figure 10). Thus, one can relate electron energies in the oxide to the redox potentials of solution-based redox systems. Above and below the solution redox potential sit energy states for the oxidized and reduced forms of the redox system, respectively. As the redox voltage shifts negatively (upwards in Figure 10) more oxidized states convert to reduced states (i.e., more reduced form is present).

In general, the Fermi energy levels (or equilibrium potentials, i.e., $E_f^M \neq E_F^O$) for the different phases are not equal when the phases are not in contact, as shown in Figure 10. When the bulk (not thin film) oxide phase is brought into contact with the metal phase (see Figure 11(a)), or the solution phase (see Figure 11(b)), electron equilibrium (no net electron flow) requires that the Fermi levels become equal. This occurs by movement of electrons across the phase boundary until the E_f's are equal across the interface. In the metal case as shown in Figure 11(a), which is typical for implant alloy–oxide interfaces, as the Fermi level of the oxide is higher than that of the metal, electrons move from oxide to metal and the metal surface has a net negative charge while the oxide at the metal surface is depleted in electrons. This condition is known as a Schottky barrier.[33] The conduction and valence bands of the oxide have two conditions to which that they must hold. First, the energies of these bands must remain fixed at the oxide surfaces, and second, inside the oxide the relationship between the Fermi energy level and the band energies must remain constant. These two conditions result in what is known as band bending (see Figure 11). For the metal–oxide case (with no solution phase nearby), the oxide develops a space-charge region which is the depth into the oxide where the band bending is taking place. The thickness of this space-charge region, known as the Garrett-Brittain space-charge layer, is determined by the Poisson–Boltzmann equation just like in the case of the solution double layer.[34] It is important to note that the metal–oxide semiconductor discussion has not included any sort of redox processes of the metal to form oxide, and as the oxide is considered to be 'thick' the energy levels flatten out into the bulk. Neither of these is the case with the thin oxide films we are discussing.

For the case of a bulk oxide coming into contact with the solution phase, similar arguments hold (see Figure 11(b)). Here we have drawn the redox potential of the solution-based species to be more positive (lower electron energy) than the oxide Fermi Level. This is typical for TiO_2 in an oxygen-containing saline (E_{O2}^{eq} ~0.4 V NHE, E_{fb} Ti ~−0.4 V). Again, electron equilibrium (redox equilibrium) between the phases requires that the Fermi levels become equal and the oxide bands again bend to develop a depletion of electrons at the surface. Of course, if the redox potential is more negative than the oxide Fermi level, then the oxide bands will bend upward moving away from the surface, and an accumulation of electrons will occur at the surface. If the two levels are equal, then the oxide bands do not bend and this potential is known as the flat-band potential (E_{fb}).

The thickness of the space-charge layer in the oxide can be calculated; the approach is similar to the solution electrical double layer (see Appendix) and is known to depend on the number of charge carriers present per volume, N_D,

$$\kappa^{-1} = \left[\frac{\varepsilon\varepsilon_o kT}{N_D e^2}\right]^{1/2} \quad [10]$$

The typical value for the density of donor states is between 10^{17} and 10^{22} cm^{-3}. Using typical values for TiO_2 semiconductors, the space-charge layer is between 0.5 and 15 nm. From direct capacitance measurements, TiO_2 film thickness on cp-Ti

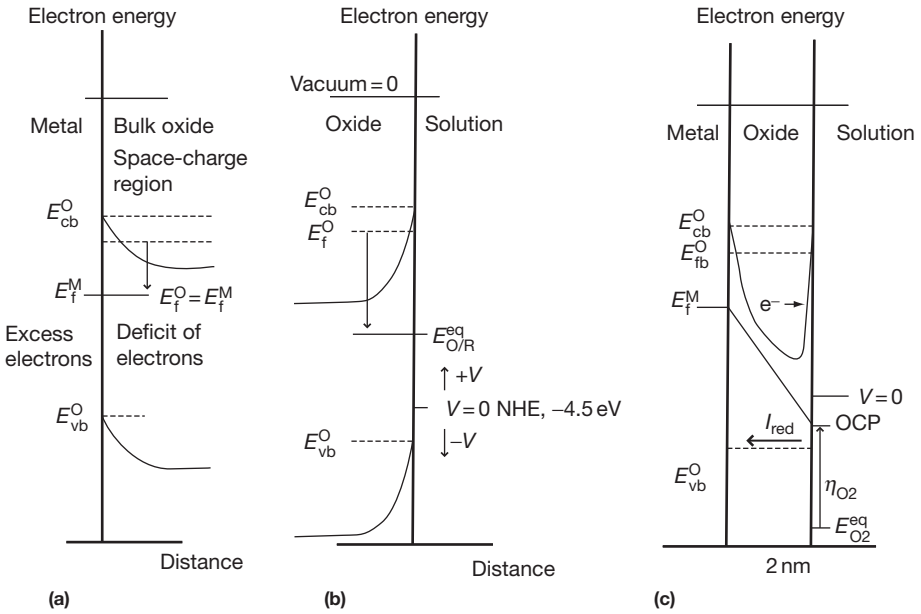

Figure 11 (a) Electron energy diagram for a metal–oxide junction demonstrating the electron energy band bending that gives rise to a Schottky barrier and a depleted space-charge region in the oxide. Electron equilibrium (no current) requires that the Fermi energy levels of the metal and oxide must be equal which requires that the valence and conduction bands bend at the oxide surface. (b) Electron energy diagram for bulk oxide–solution interface. The Fermi energy for the solution-based redox reaction is replaced by the Nernst potential. Again, equilibrium between the oxide and the solution-based species requires band bending and an electron-depleted zone in the oxide. The thickness of this space-charge region can be calculated (eqn [12]). (c) When the metal–oxide–solution construct is developed, where the oxide thickness is only a few nanometers, the combined electron energy diagram is shown. In this figure, the Fermi levels of the metal and solution are different thereby giving rise to a gradient in electron energy through the oxide. This will give rise to a current providing electrons to the redox reaction and causing reduction.

is about 4 nm at 0 mV versus Ag/AgCl. Thus, the space charge thickness is on the order of the thin film oxide thickness.

The space-charge region we have discussed so far gives rise to a capacitance of the oxide known as the space-charge capacitance, or oxide capacitance. The relationship between the oxide capacitance, the charge carrier density, the voltage of the interface, and the flat-band potential is known as the Mott–Schottky equation and is derived from the Poisson–Boltzmann equation (see Appendix Gelderman *et al.*[35]).

$$\frac{1}{C^2} = \left[\frac{2}{\varepsilon\varepsilon_o N_D e}\right]\left(V - V_{fb} - \frac{kT}{e}\right) \qquad [11]$$

where C is the oxide capacitance, ε is the dielectric constant, ε_o is the permittivity of free space, e is the electron charge, k Boltzmann's constant, T temperature, N_D is the number of donor levels (or charge carriers) per volume, V is the voltage of the interface, and V_{fb} is the flat-band potential. This equation is very useful in electrochemical impedance analysis of oxide film covered metallic biomaterials and has been used by a number of investigators to describe the character of the oxide film. The capacitance of the oxide is measured (see EIS discussion below) over a range of voltages and plotted as C^{-2} versus V to find N_D and V_{fb}. It is important to note that the above discussion assumed equilibrium. If a voltage is enforced on the oxide–solution interface and equilibrium is not attained, then the Fermi energy will slope through the oxide and charge will flow until equilibrium is reestablished.

1.103.6.4. Oxide Semiconductor Theory for Thin Oxide Films Between Metals and Solutions

The picture of semiconducting electrochemistry becomes more complicated when both a metal phase and a solution phase sandwich a very thin oxide phase (see **Figure 11(c)**). Here, we are not considering any oxidation effects of the metal, but simply assuming that the Fermi energy levels of the metal and solution are at different levels. When the oxide comes into contact with metal and solution under these circumstances, the Fermi energy level of the oxide must equal the metal Fermi level on the one hand, and the oxide–solution energy levels must be equal, but will likely be at a different level. The Fermi energy in the thin oxide will, therefore, be sloped such that electrons will move from metal through oxide to solution to reduce the solution-based redox system. This will be the case until the solution redox potential shifts to higher energies to bring all of the Fermi energy levels into equilibrium. As can be seen, the valence and conduction bands will be bent on both sides of the interface and indeed the two space-charge regions may overlap significantly depending on the thickness of these layers. With the conditions shown, one can see depletion of electrons on both sides of this oxide and under these conditions the oxide will not easily transport electrons across to participate in the reaction. This is what is seen under anodic conditions ($V > V_{fb}$) for, for example, titanium oxide thin films. The anodic currents are typically very low and the oxide acts much like an insulator.

It is clear from this discussion that the theory of semiconducting electrochemistry is not completely reconciled with the theory of oxide thin film growth discussed earlier. In the absence of oxide film growth and metal oxidation effects, the voltage (energy) distributions through the oxides are not the same as required for film growth. The differences arise because of the thin film character where electron tunneling can take place, and in the oxidation energy associated with taking metal atoms and converting them to cations. The high-field growth models require high electric fields which are positive at the metal–oxide interface and negative at the oxide–solution interface whereas the semiconductor theory only requires the conditions of equilibrium of Fermi energy levels and band bending. The former causes oxide growth, the latter allows only electronic charge to be transported to engage in a redox reaction in the solution. These views of the surface electrochemical processes need to be reconciled to have a more holistic understanding of thin-film oxide corrosion behavior for metallic biomaterials.

1.103.7. Electrical Double Layer

The net-charge distribution in the oxide established because of these processes also results in a distribution of charge in the solution adjacent to the oxide and is known as the electrical double layer which will have a capacitive character and the distribution of charge and voltage through this double layer is determined by the Poisson–Boltzman equation[34]

$$\nabla^2 V = \frac{1}{\varepsilon\varepsilon_o}\sum n_i F e^{-}\mathrm{e}^{-[nFV/RT]} \qquad [12]$$

where n_i is the valence of the ith species; the solution of this equation under conditions of a 'small' voltage results in the Debye–Huckel equation and the Debye thickness for the double layer.

$$V = V_o \mathrm{e}^{[-\kappa x]} \qquad [13]$$

$$\kappa^{-1} = \left[\frac{\varepsilon\varepsilon_o kT}{Ne^2}\right]^{1/2} \qquad [14]$$

where N is the number density of charged species (number per volume). It is important to note that the establishment of the electrical double layer on metallic biomaterial surfaces is determined by the voltage required to balance the anodic and cathodic currents and is not, as the theory lays out, on the basis of the static charge. Thus, zeta potentials of bulk oxides in no way represent the zeta potential of oxide thin films with underlying metals present. The electrical double layer could have a local solution layer with excess positive charge or negative charge. As V_{fb} is the potential with no net charge, if OCP is greater than V_{fb}, the solution at the surface will have a net negative charge (to balance the net oxide positive charge), and a double-layer capacitance will be present. In general, the metal–oxide–solution interface will have three different capacitances: the metal–oxide capacitance (Schottky barrier), the oxide capacitance, and the double-layer capacitance. The overall interface capacitance will, therefore, be a series combination of these three capacitances. In this case, as capacitances sum as the reciprocal, the total interfacial capacitance will be dominated by the smallest of these three capacitances. In most cases (i.e., at most potentials), the oxide capacitance will be the smallest of the three. However, the double-layer capacitance will become the smallest of these at negative voltages below about −700 mV (vs. Ag/AgCl).

1.103.8. Electrochemical Impedance Spectroscopy (EIS) of Metallic Biomaterials

The study of metallic biomaterials in the biological milieu has increasingly used the techniques associated with EIS to explore the behavior of these interfaces. Therefore, this section will briefly summarize the theory and methods of EIS and present some of the relevant findings related to biomaterials.

1.103.8.1. The Methods of EIS

EIS is a technique used to determine the impedance characteristics of an electrochemical interface. It has been used increasingly in biomaterials studies to understand the interactions between the surface and the biological environment. As discussed above, electrodes, either with or without an oxide thin film, can either accumulate charge at the interfaces, and/or can transport charge across the interface. Thus, all electrochemical interfaces can be thought of as being comprised of resistive and capacitive elements connected in series and/or parallel. EIS directly measures the frequency-based impedance of the interface and then typically attempts to relate the response to some resistive–capacitive circuit model to infer behavior. The technique typically applies a small (10 mV) sinusoidal voltage overtop of a static voltage using a range of frequencies typically from 10^5 to 10^{-3} Hz. The current response is then monitored and the current amplitude and phase (δ) are used to obtain the impedance of the interface. The impedance of any electric circuit is defined by its transfer function:

$$Z^*(\omega) = Z'(\omega) + \mathrm{i}Z''(\omega) = \frac{L(V(t))}{L(I(t))} \qquad [15]$$

$$\tan\delta = \frac{Z''}{Z'} \qquad [16]$$

where $Z^*(\omega)$ is the complex impedance and L represents the Laplace operator. One can see that the impedance of a circuit is comprised of a real (or resistive) term, and an imaginary (capacitive and/or inductive) term. The phase angle, δ, is a measure of the shift in time (the phase lag) between the input and the output and can be determined by the ratio of imaginary to real impedance.

The electrode interface can have one of several electrical analog models associated with it, depending on the complexity of the surface. These can range from a simple capacitive response, indicating an ideally polarizable electrode where no Faradaic currents are passed across the interface (see **Figure 12(a)**), to a parallel combination of a resistive and capacitive elements representing the charging and charge transfer processes possible at typical electrode surfaces (see **Figure 12(b)**, Randle's circuit), to more complex circuits that may be used to represent more complex interfaces with

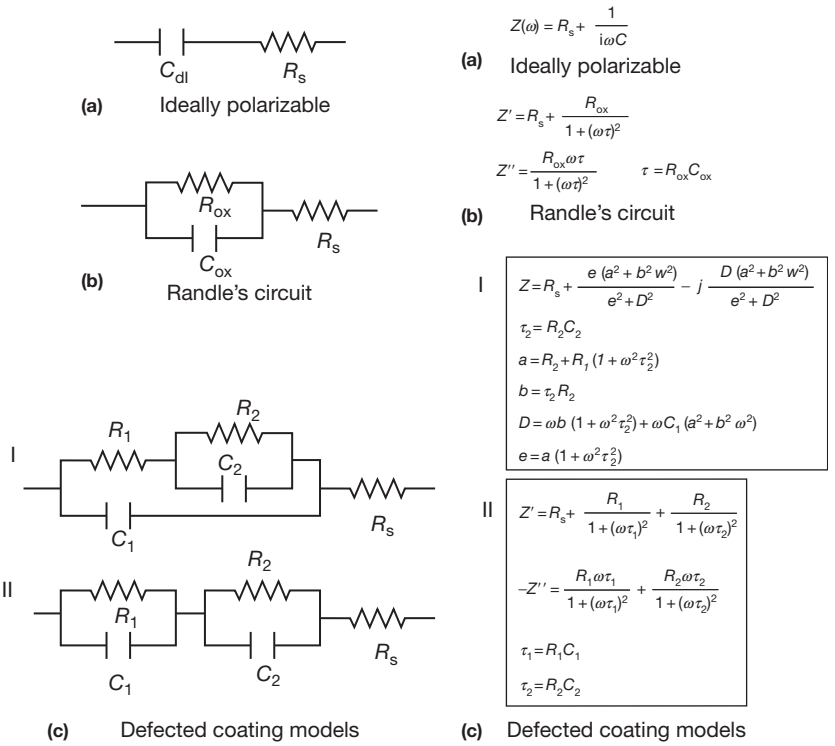

Figure 12 Circuit models used to analyze metallic biomaterial surface electrochemical impedance properties. (a) Ideally polarizable electrodes where no currents transit the interface. (b) Randle's circuit – typically used to describe oxide thin film surfaces. (c) Defected coating models used to analyze thicker coatings on metal surfaces. The impedance equations used to decrease each of these models are to the right of the figure.

defective coatings (see Figure 12(c)). The impedance of these electrical equivalent circuits can be found by defining $Z_R = R$ and $Z_c = 1/i\omega C$ (where $i = \sqrt{-1}$) and remembering that series impedances add, while parallel impedances sum as the reciprocal. Figure 13 shows the Bode and Nyquist representations for the two defect coating models assuming ideal circuit elements.

Real metallic biomaterial interfaces are often not adequately represented by ideal circuit elements. Real electrode interfaces have a distribution of behaviors and heterogeneity over the area of the electrode. This results in a distribution of capacitive and resistive character. To account for this heterogeneity, the concept of a constant phase element (CPE) has been introduced. Here, the capacitive elements of the electrode model are replaced with an impedance of the form[27]

$$Z_{CPE} = \frac{1}{((i\omega)^{\alpha}Q)} \qquad [17]$$

where α is the constant phase exponent which can vary from 1 to 0 and Q is the capacitive-like value of the CPE. When α is 1, the CPE acts like an ideal capacitor, while at values less than 1, the CPE takes on more and more of a resistive character.

The CPE substitutes for the capacitors in the ideal circuits discussed above and can be mathematically dealt with by knowing that

$$i^{\alpha} = \left[e^{\left(i\frac{\pi}{2}\right)}\right]^{\alpha} = e^{\left(i\alpha\frac{\pi}{2}\right)} = \cos\left(\alpha\frac{\pi}{2}\right) + i\sin\left(\alpha\frac{\pi}{2}\right) \qquad [18]$$

For a Randle's circuit with a CPE the impedance equations are

$$Z' = R_s + \frac{R_p\left(1+R_pQ\omega^{\alpha}\cos\left(\alpha\frac{\pi}{2}\right)\right)}{\left(1+R_pQ\omega^{\alpha}\cos\left(\alpha\frac{\pi}{2}\right)\right)^2 + \left(R_pQ\omega^{\alpha}\sin\left(\alpha\frac{\pi}{2}\right)\right)^2} \qquad [19]$$

$$Z'' = \frac{R_pQ\omega^{\alpha}\sin\left(\alpha\frac{\pi}{2}\right)}{\left(1+R_pQ\omega^{\alpha}\cos\left(\alpha\frac{\pi}{2}\right)\right)^2 + \left(R_pQ\omega^{\alpha}\sin\left(\alpha\frac{\pi}{2}\right)\right)^2} \qquad [20]$$

where Q is the magnitude of the CPE, thought to be related to the oxide capacitance (or space-charge capacitance), and α is the CPE exponent which is a measure of the deviation from ideality. R_p and R_s, for oxide thin film surfaces, are typically thought to be related to the oxide resistance (or polarization resistance) and solution resistance, respectively. These equations are used to fit the impedance response data generated in an EIS experiment and a nonlinear least squares regression method is typically used to fit these functions to the data.

The modified Randle's circuit (Figure 14(a)–14(c)) is the most commonly used circuit in modeling the metallic biomaterial interface impedance where the CPE replaces the capacitor in the model. A typical plot of the impedance and phase angle versus log of the frequency (known as Bode plots), and the plot of $-Z''$ versus Z' (the Nyquist plot) are shown in Figure 14(c) for typical values of the parameters. The Bode plot for impedance becomes more spread over frequency as α decreases from 1, while the Nyquist plot becomes a more-depressed semicircle as α decreases.

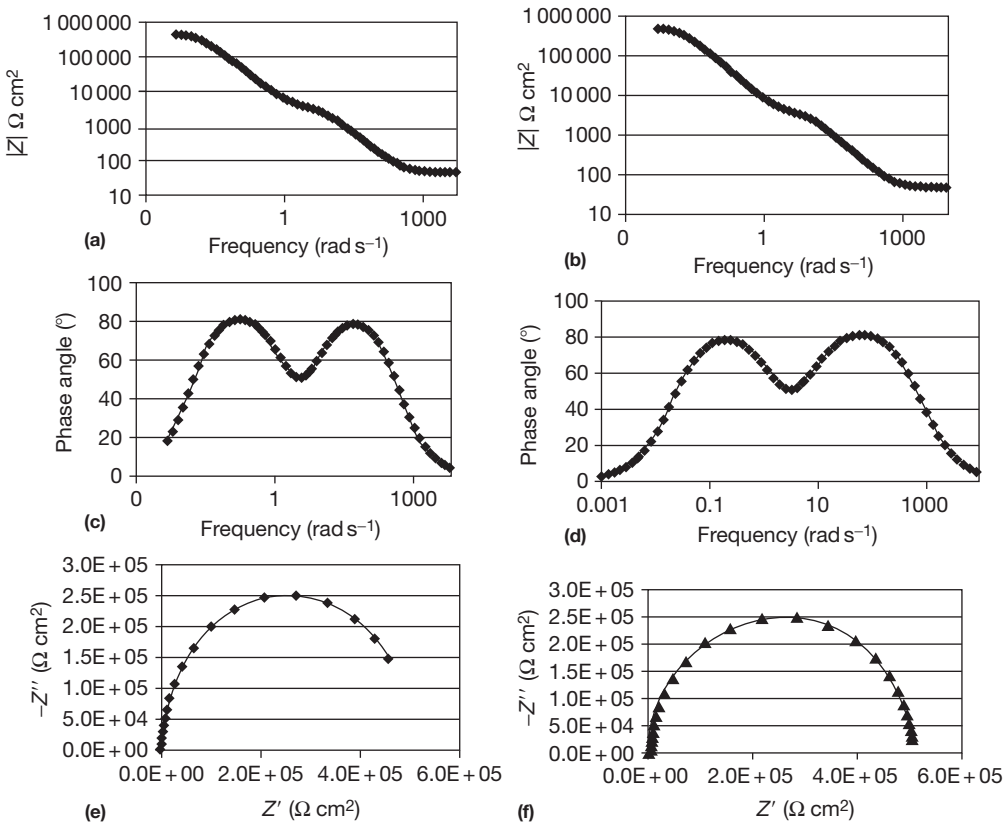

Figure 13 Bode plots (a,b,d,e) and Nyquist diagrams (c and f) for the defected coating models in **Figure 12**. (a) Model I, (b) Model II (both with $R_s = 50$, R1 = 5000, R2 = 5e5, C1 = 3e-5, C2 = 1e-4). The Bode plots are impedance and phase plotted as a function of log of the frequency, while the Nyquist plots show the imaginary versus the real impedance. These two models, with the appropriate values for the elements can model the same impedance behavior (compare with **Figure 15**).

1.103.8.2. Time-Based Methods

Impedance analysis can also be performed by obtaining the time-dependent response of the electrode interface and performing a time–frequency transform on the time-domain response. Here, potential step current-transient methods have been developed[36,37] for these studies. A benefit of using time-transient methods is that it allows one to explore a range of static voltage conditions by sequentially stepping through a range while capturing the current transient at each step. This so-called step-polarization impedance spectroscopy (SPIS) method can help provide information related to the voltage-dependent impedance behavior of these surfaces. Here, the reciprocal of the impedance, known as admittance ($A^*(\omega) = 1/Z^*(\omega)$), is found from the current transient that results from a small (25–50 mV) step from some initial potential.

$$A^*(\omega) = \frac{1}{\Delta V}\left(\int_0^\infty \frac{di(t)}{dt} e^{i\omega t} dt + i(t=0)\right) \qquad [21]$$

where $i(t)$ is the time-dependent current density response to the voltage step, ΔV.

The current is captured over several intervals of time (from 10^{-5} to 10^{2} s) and is analyzed with a numerical transform to obtain the admittance, while the late currents can be used to obtain the polarization plots for the surface. The earliest current response is a measure of the solution resistance (e.g., $I(t=0^+) = I(0) + \Delta V/R_s$), while the latest time currents relate to the sum of solution resistance and polarization resistance, R_p (e.g., $I(t\to\infty) = I(0) + \Delta V/(R_s + R_p)$).

Other time-based methods have also recently been published (see Haeri *et al.*[38] for example). Gettens and Gilbert[39,40] used the time-based solution of the Randle's circuit to a step in potential, and modified the exponential terms to be stretched exponentials of the form of the KWW function.[41] The stretched exponential raises the exponential terms of the time-domain solution to the differential equation, to a power, n (where n is between 0 and 1), that stretches the time response. The exponent, n, has similar characteristics to those of α in the CPE elements described above, and allows for a better fit of the data with the function.

The stretched exponential model proposed by Gettens and Gilbert[42] is

$$I(t) = I(0) + \frac{\Delta V}{R_s} e^{-(t/\tau)^n} + \frac{\Delta V}{R_p + R_s}\left(1 - e^{-(t/\tau)^n}\right) \qquad [22]$$

where this function is the solution to the differential equation of Randle's model (when $n = 1$), τ is the time constant and is related to the capacitance and the resistances of the model,

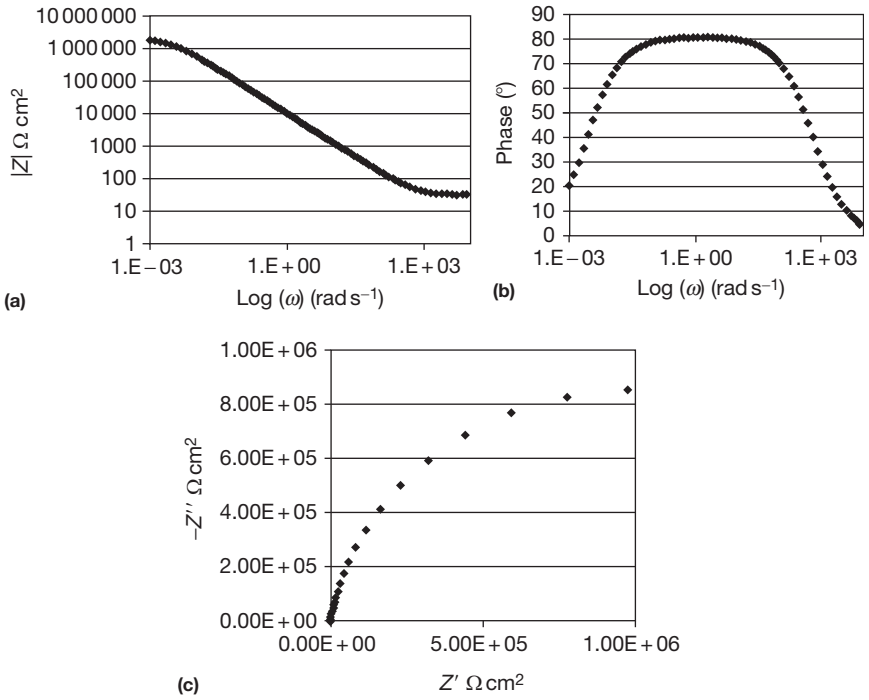

Figure 14 Bode (a and b) and Nyquist (c) plot for a Randle's circuit with a constant phase element. The values of the elements used ($Q = 1e\text{-}4$, $R_p = 2e6$, $R_s = 30$, $\alpha = 0.8$) are similar to that seen for typical oxide thin film covered metallic biomaterials.

and n is the stretch exponent. This method has been used to explore the impedance and polarization response of 316L SS immersed in PBS and PBS with fibrinogen[40] over a range of potentials from −1000 to 800 mV versus (Ag/AgCl). It was shown that the presence of fibrinogen did not significantly affect the overall impedance response except at very negative potentials, while the stretch exponential, n, was affected by the presence of fibrinogen at several potentials.

Other methods include a hybrid time–frequency method proposed by Ehrensberger and Gilbert[43] where the time-based transients are used to find the resistances and the time constant for the decay response, and the frequency-transformed behavior is used to determine the CPE exponent, α.

One benefit of these time-based methods is the ability to capture a range of voltages (by potential steps). From these voltage-dependent measurements, equations such as the Mott–Schottky equation (eqn [13]) can be used to determine the flat-band potential and the density of charge carriers in the oxide.

1.103.8.3. Impedance Behavior of Ti, CoCr, and 316L SS: Effects of Solution, Voltage, and Time

Typical examples of the EIS response for Ti–6Al–4V and Co–Cr–Mo can be seen in Figure 15(a)–15(c) which shows the Bode and Nyquist plots for Ti–6Al–4V and Co–Cr–Mo alloys in PBS after 24 h immersion at OCP and 37 °C. Impedance behavior of Ti-alloy, CoCr, and 316L SS interfaces all exhibit some degree of CPE behavior that varies with voltage, and each has a range of frequencies where it is acting very much like an ideal capacitor (where the phase angle is close to 90°).

It is also important to recognize that the impedance of an interface will be affected by factors including time of immersion, voltage experienced, and solution conditions (e.g., pH, temperature, proteins, inflammatory species, superoxide anions, etc.). It has been shown, for example, that the polarization resistance (oxide resistance) varies with time of immersion and can either increase or decrease with time depending on the voltage of the interface. For example, Ehrensberger and Gilbert[14] have shown that cp-Ti impedance in PBS at 24 h immersion is highly voltage dependent (see Figure 16). At potentials above about 0 mV versus Ag/AgCl, Rp remains high, well above 1 MΩcm^2. However, as the potential of the interface is held at more cathodic potentials, R_p of the surface decreases exponentially and drops to about 10 kΩcm^2 for potentials of −700 mV or more negative. These results show that the oxide film impedance characteristics are highly voltage and time dependent. CoCrMo and 316L SS both have voltage-dependent impedances.

The semiconducting character of the oxides of Ti and CoCr alloys can be obtained from their impedance behavior as a function of voltage (see Figure 17(a) for Co–Cr–Mo, and Figure 17(b) for cp-Ti). The oxide resistances of CoCrMo and cp-Ti are measured versus voltage and show significant variations over the range. Ehrensberger and Gilbert,[43] and others, have shown that the flat-band potential for Ti alloys is between −300 and −500 mV versus Ag/AgCl; for CoCr it is around −450 mV and for 316L SS it is around −100 mV.[39,40] The charge carrier density typically determined from Mott–Schottky analyses ranges from 10^{17} to 10^{22} cm^{-3}. A typical Mott–Schottky analysis of cp-Ti from Ehrensberger and Gilbert[43] can be seen in Figure 18.

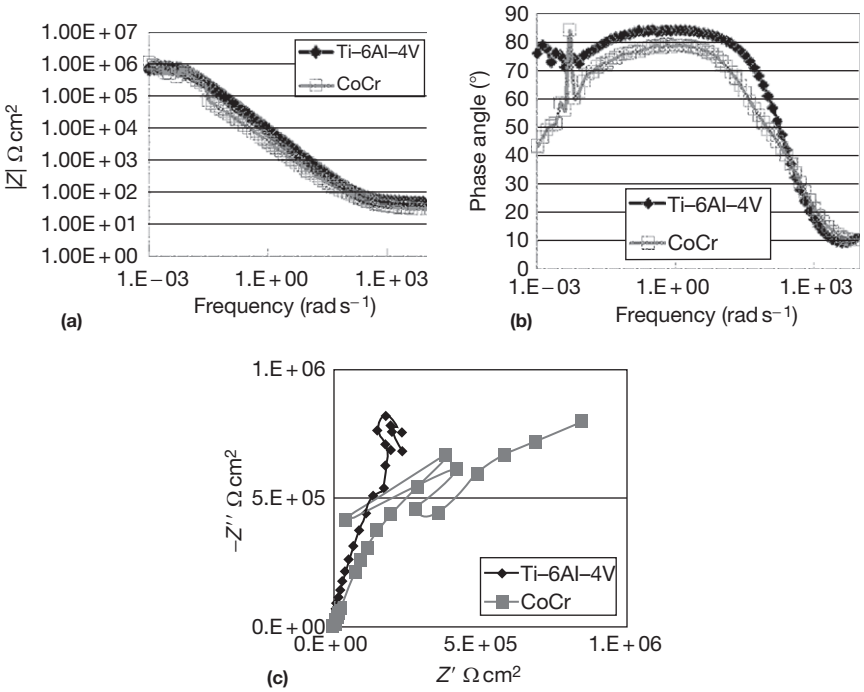

Figure 15 Impedance results (Bode: a,b; Nyquist: c) for Co–Cr–Mo and Ti–6Al–4V. Each of them has similar behavior that is mostly capacitive and the low frequency resistance (the oxide resistance) approaches 1 MWcm^2. Note the similarity between these actual data and the modified Randle's circuit in **Figure 14**.

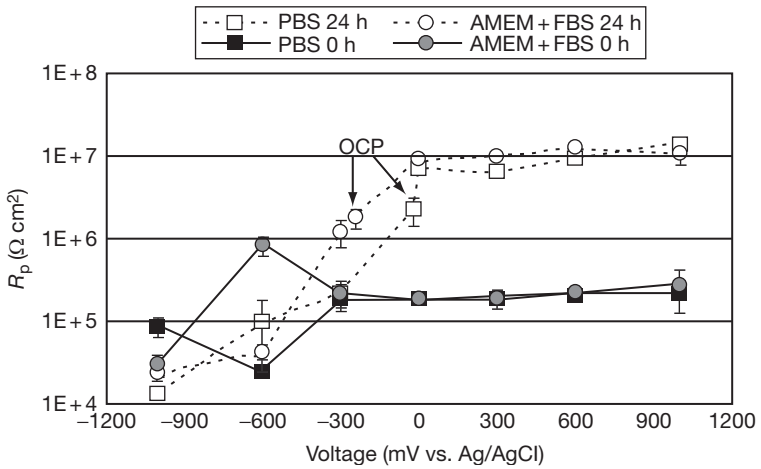

Figure 16 Plots of the polarization resistance of cp-Ti at 0 and 24 h held at fixed voltages. Both PBS and AMEM + FBS solutions were studied. Note the differences between 0 and 24 h. There is a significant increase in R_p for 24 h for both solutions above −300 mV. Also note that the R_p at 24 h shows an approximate log-linear decrease with decreasing voltage and drops almost three orders of magnitude over 1 V change. Reproduced from Ehrensberger, M. T.; Gilbert, J. L. *J. Biomed. Mater. Res. B* **2009**, with permission from J. Wiley and Sons.

It is important to note that the flat-band potential (as discussed above) represents the voltage where the oxide electron energy bands are not bent upward or downward. The voltage of the interface, however, is dictated by the balance of the redox reactions (net Faradaic currents sum to zero) and the potential can range from above the flat band (typical when the interface is not mechanically abraded) to below the flat-band potential (when abrasion processes are ongoing). When the potential drops below the flat band, the oxides become very capable of transporting negative charge via electrons and the oxide significantly decreases its resistance. However, it is likely that ionic transport through the oxides is also altered under reducing conditions.[44] In fact, studies of oxides have shown that they may undergo reductive dissolution with negative voltage, reducing the thickness of the oxide.[45]

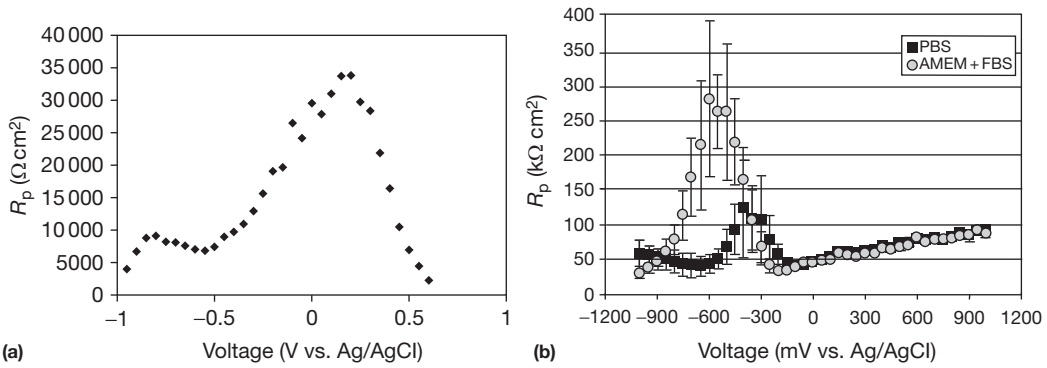

Figure 17 Polarization resistances measured for (a) CoCrMo in PBS and (b) cp-Ti in AMEM and FBS + AMEM using the step-polaization impedance spectroscopy method. Note the different scales for each. Each was tested starting at −1 V and scanning anodically. The impedance values are lower than is typical because of the scanning nature of the experiment but are consistently observed. The variation with voltage shows how the oxide films on each alloy is changing its electrical character with voltage. The peak in R_p for CoCr shows the oxide transitioning from a well coated surface oxide to a more defected oxide that ultimately breaks down above +200 mV. The Ti variations show changes in oxide behavior around the flat-band potential. (b) Reproduced from Ehrensberger, M. T.; Gilbert, J. L. JBMR-A **2010**, with permission from J. Wiley and Sons.

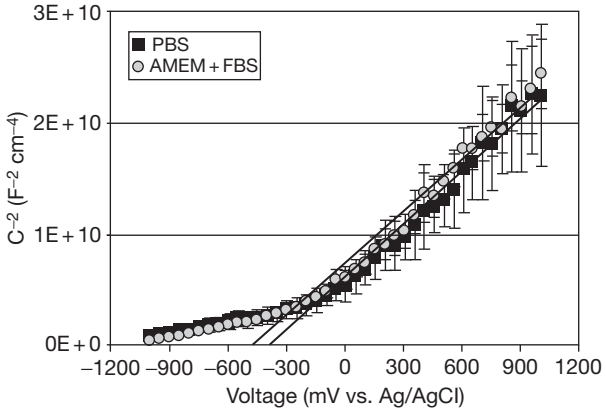

Figure 18 Mott–Schottky plot of cp-Ti in PBS and AMEM with 10% fetal bovine serum. Note that the extrapolation of C^{-2} versus V to the voltage axis yields a flat-band potential of about −400 mV. The slope of this line yields a charge carrier density of about 2.5e + 21 cm^{-3}, which is very high – approaching a metallic surface. Reproduced from Ehrensberger, M. T.; Gilbert, J. L. *J. Biomed. Mat. Res. A*, **2010**, with permission from J. Wiley and Sons.

1.103.9. Mechanically Assisted Corrosion

In the biological milieu, there are significant mechanical factors typically at play when metallic biomaterials are placed. These mechanical factors, besides the direct consequence of their presence (e.g., generation of wear particles), can significantly and dramatically impact electrochemical processes. In loaded medical device applications, the high cyclic-stress nature of the biological environment can give rise to a number of surface mechanical events that may result in mechanical disruption of the oxide film. These events include fretting (small scale cyclic motion between two materials – one of which is oxide covered alloy), wear, and substrate deformation (elastic and plastic). Fretting is a significant problem in devices where there are hard surfaces in contact with the metal device that can both create abrasive fretting of the oxide and develop a restricted crevice geometry. The hard opposing surface may be another metal, or a ceramic. Examples of fretting–crevice corrosion susceptible devices include all modular tapers in total joint prostheses[46–48] crevices created by the bone cement–metal implant interface,[49] screw-countersink geometries,[50,51] and other contact sites in fracture fixation devices and spinal instrumentation, and overlapping vascular stents. Wear processes are also sites where oxide mechanical disruption can occur. These include cases where metal–metal wear surfaces are present (e.g., hip resurfacing, metal-on-metal total hip replacements).

1.103.9.1. Modeling the Electrochemical Response to Scratching

When oxide films are disrupted, the exposure of the underlying metal to the biological milieu results in some very significant electrochemical events. Immediately after oxide disruption (see **Figure 19**) there are three main reactions that appear or increase dramatically. First, the active dissolution reaction (metal to metal ions in solution) increases at the site of disruption. Second, the oxide film reaction proceeds to reform the oxide and recover the site of the breach. Third, both of the above oxidation reactions release free electrons that remain behind in the metal. This results in an overall decrease in the OCP of the implant and an increase in the rate of the reduction reactions present on the surface that eventually consume these excess electrons and bring the surface back into overall dynamic equilibrium (i.e., where the sum of all anodic and cathodic currents balance). It is important to note that during and immediately after oxide disruption, the interface is not in overall equilibrium. Anodic reactions (repassivation and ionic dissolution) will occur at rates that have been measured to be up to 10^8 times those present at intact oxide films.

There have been several models proposed for the behavior of the oxide film during and after mechanical disruption. A relatively simple and direct model was first proposed by Ambrose.[52] Here, the surface starts in a complete oxide-devoid

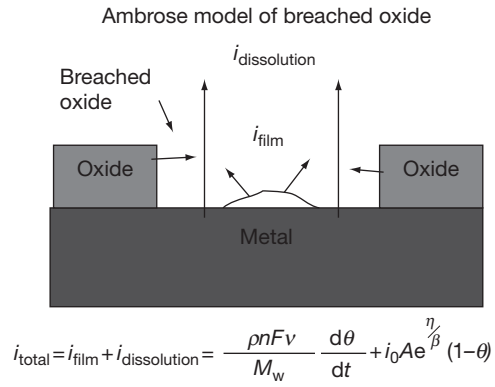

Figure 19 Ambrose's representation of a breached oxide and the repassivation currents that arise. Both film currents and dissolution currents are present and the fraction of surface disrupted, θ, varies with time as the surface repassivates. Reprinted, with permission, from STP 1301 – Modularity of Orthopedic Implants, © ASTM International, West Conshohocken, PA.

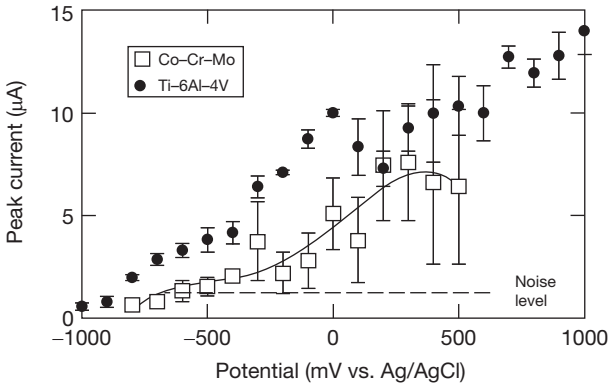

Figure 20 Scratch test results at fixed load and scratch length and varying potential for Co–Cr–Mo and Ti–6Al–4V in PBS at room temperature. Note that the peak scratch currents increase with voltage (Co–Cr–Mo from −500 mV and Ti–6Al–4V from −900 mV). Above +500 mV, CoCrMo loses its passive oxide and the peak currents drop (not shown). Ti peak currents continue to increase across voltage range tested. Note the similarity in the R_p (**Figure 18**) and these peak currents. The peak depends on the area scratched, the thickness of the oxide reforming, and the valence of the cation. Reprinted, with permission, from STP 1301 – Modularity of Orthopedic Implants, ©ASTM International, West Conshohocken, PA.

state. The fraction of volume repassivated (θ) varies with time. It is assumed that the ionic dissolution reaction follows a Tafel-like behavior through the breached surface.

$$i_{diss} = i_o^{diss}(1-\theta)e^{\frac{V-V^{eq}}{\beta}} \quad [23]$$

and the oxide film currents, i_{film}, depend on Faraday's law and the time rate of regrowth of the oxide film

$$i_{film} = \frac{nF\rho v}{M_w}\frac{d\theta}{dt} \quad [24]$$

where ρ is the film density, υ is the total volume of oxide to grow, M_w is the molecular weight of the film, and n is the charge per cation. Thus, the total current associated with the oxidation processes of repassivation is just the sum of the film and dissolution currents densities:

$$i = i_{film} + i_{diss} = \frac{nF\rho v}{M_w}\frac{d\theta}{dt} + i_o^{diss}(1-\theta)e^{\frac{V-V^{eq}}{\beta}} \quad [25]$$

where i_O^{diss} is the dissolution exchange current density across bare metal, V is the voltage away from the equilibrium potential for the bare metal dissolution reaction (for $V_{Ti}^{eq} = -1.6\,V$), and β is the Tafel constant for this reaction. This first-order differential equation results in an exponential time decay of the total current (i.e., $i = i^{max}e^{-t/\tau}$)[53] when the surface is held at a fixed potential. While there are many assumptions associated with this model, it gives a good interpretation of the process and it has been used to explore the voltage, solution, and oxide surface dependent responses to high speed scratching of the surface oxide.[53–55] It does not account for the voltage excursions nor does it deal with the reduction reactions that must increase as a result of the sudden increase in electronic charge in the metal. To study the current transient response under fixed voltage, we developed an electrochemical scratch test system that imparts a small (50 μm) scratch in about 0.5 ms under the conditions of controlled contact load and geometry, solution chemistry, and applied voltage. The results of this work have shown, for instance, that there is a contact stress of about 1 GPa required to disrupt the oxides, that the repassivation process is highly dependent on the voltage and can detect the voltage below which oxides do not repassivate. These results also show the upper potential (for 316L SS and CoCr) where the oxides begin to lose their passivating ability (note Ti surfaces do not exhibit a similar effect – the oxides on Ti surfaces repassivate up beyond 1000 mV). Goldberg and Gilbert[54] found that the addition of proteins increase the repassivation time constants from about 1–2 ms to about 4–5 ms. The effect of voltage on the peak scratch current for Ti and CoCr surface in PBS are shown in **Figure 20**. Here, one can see that Ti does not show scratch currents below −1 V, while for Co–Cr–Mo the cutoff is −600 mV.

1.103.9.2. The Consequences of Mechanically Assisted Corrosion *In Vivo*

There are numerous reports of severe corrosion in metallic biomaterials when mechanically assisted corrosion processes are present. These began many decades ago in the study of retrieved fracture fixation devices.[56] Starting in the early 1990s evidence of modular taper corrosion began to appear in retrieved components. This form of corrosion has since been found to occur for all major alloy types, regardless of the alloy combination and can occur in stainless steel modular intramedullary rods.[57] The consequences of this type of corrosion include induction of osteolysis. It is important to note that osteolysis can be induced even in the absence of any other source of particles. Examples of modular taper corrosion are shown in the micrographs of **Figure 7**. Numerous types of corrosion processes have been observed including pitting attack of 316L SS, CoCr and Ti, selective dissolution from CoCr, and intergranular corrosion of CoCr ultimately leading to fracture.[58] In a recent study, we were able to show that such

severe, low pH conditions could be developed with Ti–6Al–4V and that hydrogen uptake and embrittlement are possible *in vivo*.[21]

There have been studies of the mechanism of mechanically assisted corrosion[59–61] of modular tapers where laboratory experiments were performed with electrochemically instrumented total hip replacements. Here, modular hip implants were placed into a cyclic loading condition and the head–neck junction was isolated in terms of its electrochemistry. The current generated at the taper, and the overall shift of the implant voltage can be directly measured in these tests. Typical results from such an investigation shows currents that are biphasic in relationship to the applied load (i.e., currents increase on the increasing and decreasing loading phases of the loading cycle). The voltage of the overall device shows a progression to more negative potentials as the loading increased. This overall shift in potential can be explained by the increased rate of oxidation that occurs due to repassivation and ionic dissolution through the breached zone. This increases the number of liberated electrons present, lowering the potential and increasing the reduction currents until they can consume the free electrons. As long as the mechanically assisted corrosion increases the oxidation rate, the potential of the implant will become more cathodic (negative) to increase the reduction rate and maintain quasi-equilibrium. The overall change in implant voltage will depend on the extent of oxidation currents and the area available for reduction reactions to consume the generated free electrons. If the overall reduction area available is small, or the overall area fraction abraded is large, then the voltage shifts will be much larger and can approach −1000 mV or more depending on the material.

Thus, an important result that must be clearly understood is that when metallic implants are loaded and their oxides are abraded, the voltage of the implant *in vivo* can vary through a wide range of potentials. This result is very important in terms of how the biological milieu reacts to these voltage excursions. Large negative potentials may have adverse effects on the local adsorbed proteins and any adjacent living cells (see below).

1.103.10. Effects of Prior Electrochemical History

Oxide thin films on metallic biomaterials, as can be seen from the above, are complex and affected by a complex set of behaviors and reactions. This complexity is compounded by several other factors related to the biological milieu. The main medical alloys, namely Ti-alloys (Ti–6Al–4V, cp-Ti, NiTi, TiAlNb, TMZF), Co–Cr–Mo, stainless steels, Zr alloys, Ta alloys, etc., all form oxides via the high-field growth behavior. In several of these cases, the oxide is dominated by a single chemistry (e.g., cp-Ti has TiO-based oxides) and in others the chemistry of the oxide is variable and comprised of more than one cation (e.g., Co–Cr–Mo oxides, Fe–Cr–Mo oxides, etc.). A few words related to the chemistry of these medical alloy oxides is in order. Ti-oxides are thought to be comprised primarily of TiO_2 type oxides with some reduced oxides possibly present toward the metal–oxide interface (e.g., Ti_2O_3, TiO, etc., Pan *et al.*[62]). Indeed, titanium is known to have a number of reduced forms of oxides that are possible[44] and these may arise within the thin film depending on the voltage conditions. For Co–Cr–Mo oxides, the chemistry of these oxides can vary from predominantly Cr_2O_3 to mixed oxides of Cr_2O_3, CoO, etc. Through-thickness and lateral variations of the chemistry of these oxides are possible. Indeed there is some evidence that prolonged exposure of Cr-containing alloy oxides will tend to become more enriched in Cr-oxides than in the other elements due to the strong passivating tendency of Cr on the surface.[63] NiTi surfaces are also known to show changes in oxide chemistry with prior electrochemical treatment and immersion with the Ni constituent becoming depleted with time and leaving behind primarily TiO_2.

Another important parameter that affects the oxide chemistry and properties is what can be referred to as the 'prior electrochemical history,' by which is meant the voltage–solution–time history of the surface. Electrochemical history will also affect oxide thickness, chemistry, and properties. For example, anodization of Ti using high voltage will lead to the growth of oxides. However, many other electrochemical histories should be acknowledged. For example, mechanical abrasion of oxides is known to induce significant shifts toward cathodic potentials, and sustained cathodic bias can dramatically reduce the impedance of the oxide surface and will alter its electrochemical interaction with the biological system as a consequence. Our recent work has shown that oxide growth in solution will depend on the enforced voltage applied across the metal–oxide–solution interface. In fact, oxide growth during repassivation processes will depend on the voltage across the interface. Electrochemical scratch test methods have shown that there are potentials above which oxide films repassivate and below which they do not (see **Figure 20**). For Ti surfaces, this voltage is about −1000 mV while for Co–Cr–Mo it is about −600 mV (vs. Ag/AgCl).

Another aspect of electrochemical history has to do with the hydration processes associated with oxide thin films.[4,64] Here, we know that when oxides go from nonhydrated to hydrated, the surface morphology of the oxides is altered and this likely indicates additional changes in structure, chemistry, and properties of the oxide films. This hydration process is voltage dependent.

1.103.11. Oxide Film Structure and Formation

Oxides grow in processes that depend on the substrate crystal structure, the relative mismatch between oxide and metal (i.e., the so-called Pilling Bedworth ratio of volume of oxide per cation to volume of metal per atom). Typically the PD ratio is greater than 1 and thus the oxide film tends to be put into compressive residual stress as it grows from the metal. These stresses and the lattice mismatch can result in different types of oxide growth which can be categorized as layer-by-layer growth (Frank–Van der Merwe), Island growth (Volmer–Weber), and layer-by-layer followed by island growth (Stransky–Krastinow). Ti-oxide on titanium appears to be governed by the third mechanism and results in a compressive residual stress in the oxide. These stresses and the general mechanics of the oxide–metal interface are important in terms of dictating the resistance of the surface to mechanical abrasion. For example, Ti-oxides are relatively poorly adhered to their metallic substrates while CoCrMo oxides are highly

adherent. This difference, along with differences in metal modulus, work hardening, and metallurgical state, is a main reason why Ti surfaces do not work well as wear surfaces, while CoCr surfaces are excellent. Thus, the mechanics of these thin films are important in terms of the overall electrochemical behavior in the biological milieu.

1.103.12. Effects of Solution Redox System

The biological milieu may have significant effects on the overall electrochemistry of the interface and the susceptibility of the metal to corrosion. In particular, the biological system can bring to bear large quantities of superoxide anions and other ROS when it is stimulated by any number of factors (e.g., particles, ions, infection, recent implantation, etc.). The role and effect of ROS-based species on the corrosion of implant surfaces has not been well studied even though there have been efforts to modify Ti oxides with hydrogen peroxide, and there have been studies of the catalytic effect of oxides on reduction of super oxide anions.[65] Montague *et al.*[66] looked at the effect of H_2O_2 on fretting corrosion and found increased corrosion rates in the presence of H_2O_2. Recent work by the author has shown that hydrogen peroxide, in conjunction with cathodic conditioning voltages can induce selective dissolution of the beta phase of Ti–6Al–4V[16] with the proper combination of hydrogen peroxide concentration and prior voltage history. Recent retrieval studies have shown severe pitting of Ti–6Al–4V alloys which appears to have the features of selective dissolution of the beta phase present (see **Figure 21**). Thus, conditions which give rise to large inflammatory responses may add to the factors that lead to severe corrosion attack of these alloys. To demonstrate this effect, we tested Ti–6Al–4V in PBS solutions containing various levels of hydrogen peroxide. The resulting polarization plots (**Figure 21**) clearly show that there are increases in corrosion sensitivity with moderate increases in hydrogen peroxide levels (0.003 M) and as the molarity of the solution increases, the corrosion rates increase, as do the reduction currents (depending on the voltage applied). Thus, it is likely that ROS-based chemistry will significantly affect the corrosion characteristics of the alloys *in vivo*.

1.103.13. Biological Consequences: Oxidation and Reduction

It is clear that the main known consequences of corrosion of implant materials are the effects of the metal ions (cations) and particles that result from the oxidation half-cell. Clearly these ions and particles have serious biological consequences which we are only now beginning to understand. For example, metal ions and particles can themselves induce osteolysis in adjacent bone. Metal ions can have both immunogenic effects and inflammatory effects. Recent work by Caicedo *et al.*[67] have indicated that there may well be a new pathway of effect of metal ions beyond the simple and simplistic metal sensitivity ideas described to date. Also, in recent reports related to hip resurfacing arthoplasty, Clayton *et al.*[68] indicate that severe pseudotumor formation can occur adjacent to the metal-on-metal articulating implants used in these applications.

Clearly, cations and particles are deleterious to the biological milieu and more work is needed to fully understand the consequences of their presence both in the peri-implant space, and more systemically. However, there are other potential consequences to the electrochemistry of metallic biomaterials that have been ignored or not appreciated until recently. This includes the reduction half-cell reactions and their consequences on the adjacent biology. Gilbert *et al.*[69] published a paper: "The reduction half-cell in biomaterials corrosion" which looked at the consequences of having increased reduction reactions at an implant surface. In that work, it was shown that oxygen levels can be significantly altered as the voltage of the implant became more negative and they were virtually

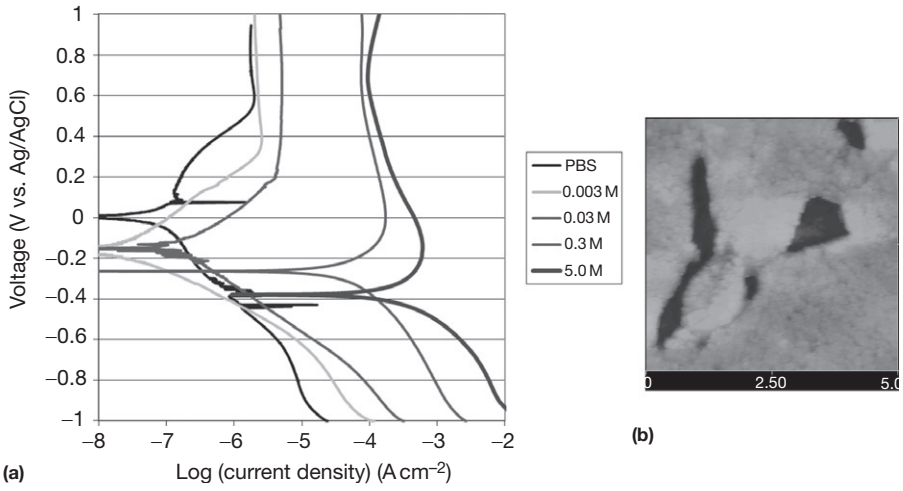

Figure 21 (a) Polarization plot for Ti–6Al–4V in PBS with varying levels of H_2O_2 present representing different levels of inflammatory species. Note that even 0.003 M solution increased oxidation and reduction currents and at high concentrations (over 0.3 M), the surface became very active. (b) 5 um AFM image of Ti–6Al–4V after exposure to 0.3 M H_2O_2 showing selective dissolution of the beta phase and thickening of the oxide film.

depleted at −1000 mV. This severe potential was also shown to have adverse (albeit not well characterized) effects on bone-like cells cultured directly on Ti surfaces held at −1000 mV for 2 h. Recent work, by Ehrensberger and Gilbert,[11] has revisited this study to show that Ti is NOT 'the most biocompatible' material, as is mentioned in virtually all scientific articles on this material, when the voltage of the surface is controlled and held below −300 mV (vs. Ag/AgCl). That is, if bone-like cells are cultured on cp-Ti surfaces held at fixed potentials, the cells will die when the potential is held below −300 mV for prolonged periods (see **Figure 22**). Here, MC3T3 cell viability was assessed using an MTT assay and showed that cells cultured below −300 mV for 24 h died, whereas cells on cp-Ti above −300 mV were not affected. Cell death can be induced in as little as 2–4 h when the potential is held below −600 mV.[70] This work shows that reduction reactions ongoing at an implant surface can induce bone-like cells to die if they are adjacent to the polarized surface. This is in contrast to the well know DC electrical bone stimulation devices which apply a cathodic bias via electrodes in proximity to a fracture non-union and are shown to induce bone formation.[71,72] Clearly, there are differences in the two situations. In DC stimulators, the electrodes are near to, but not in contact with the cells, and the entire living system was available to respond to the electrodes, whereas the *in vitro* tests were more constrained. *In vitro* is clearly not representative of the biological milieu. Nonetheless, these *in vitro* studies clearly point to the strong effects that reduction currents and reduction potentials have on the biological system (see **Figure 22**, from Ehrensberger and Gilbert[11]).

Thus, the paradigm of metallic biocompatibility needs to be reconsidered to include the strong effects reduction reactions have on the biological system. These effects have not seen significant investigation as most biocompatibility studies have focused only on the products of oxidation and not the consequences of reduction currents ongoing at implant surfaces. There are numerous ways that the biological system can be affected by reduction currents. Protein adsorption and blood clotting,[39,40,73] for example, are known to be sensitive

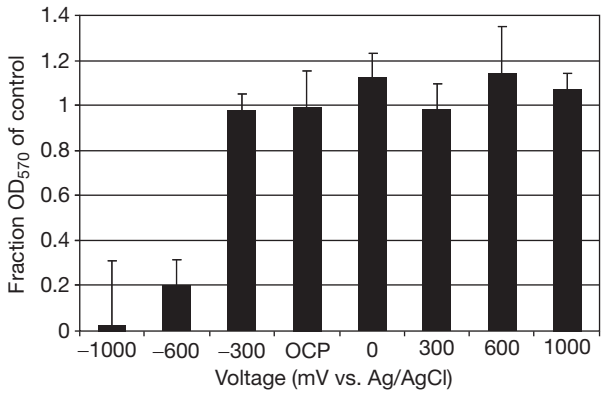

Figure 22 MTT viability assay for MC3T3-E1 cells cultured on cpTi for 24 h at different voltages. Viability was compared with a tissue culture plastic control. Note that the cells were viable for 24 h for voltages between −300 and +1000 mV. An approximate 80% decrease in viability was shown between −300 and −600 mV. Reproduced from Ehrensberger, M. T.; Gilbert, J. L. *JBMR-A* **2009**, with permission from J. Wiley and Sons.

to the potential of the interface. Electrochemical atomic force microscopy studies have recently shown[39,40] that voltage affects the rate and morphology of fibrinogen adsorption. Stankovich and Bard,[74] showed that proteins are susceptible to reduction reactions; in particular, the disulfide bonds that often make up the backbone of the protein can be reduced to sulfur–hydrogen bonds. The possibility of alteration of adhesion proteins, amino acids, membrane potentials, and behavior, as well as the possibility of direct charge transfer into the living cell may all act to disrupt and alter cellular life processes. As degradable metals (e.g., Mg) whose OCP can range as low as −1.5 V are being considered for implantation, the increased reduction reactions that will accompany the use of these alloys need to be carefully and completely understood. At present, there is very little known about the effects of reduction on the biological milieu because of the lack of appreciation of its consequences and a lack of understanding of how implant voltages and oxidation reactions may give rise to large increases in reduction reactions.

1.103.14. Summary

This chapter has attempted to provide a broad background and underpinning to the theory and behavior of metallic biomaterials and their electrochemical behavior in the biological milieu. The surfaces of these materials are highly complex, governed by numerous high energy and dynamic processes that can elicit significant effects within the biological system. To understand metallic biomaterial surfaces, one needs to appreciate the oxide thin film, its semiconducting properties, its high electric field growth characteristics, the consequences of its mechanical breach, and the processes and events that can occur when these surfaces are exposed to the biological milieu. In real medical devices where high cyclic loads are applied throughout the life of the device, the metal surface can be exposed to severe environments that can lead to severe corrosion and even hydrogen embrittlement. Understanding how these processes arise and what factors govern their appearance may help in designing surfaces that are better able to withstand the harsh and unforgiving conditions developed by the body. Recent work has been presented that shows that the consequences of the oxidation reactions (i.e., ions and particles) can have significant deleterious effects on the biological system and that the Faradaic currents themselves and the associated reduction reactions that are present may have profound effects. This leads to a new paradigm of metallic biocompatibility where it is not ONLY "the more corrosion resistant the more biocompatible" that defines the success of these devices. Oxidation AND reduction are both important and mechanical factors, in conjunction with biologically based reduction processes, may result in severe attack and degradation of metallic medical devices.

1.103.15. Appendix: Derivation of Mott–Schottky Equation

The Mott–Schottky equation comes from an analysis of the space-charge layer in a semi-infinite oxide adjacent to a surface

charge – much like the analysis of the electrical double layer in a solution adjacent to a charged surface.

Starting with the 1D Poisson's equation for the voltage distribution in a charged material

$$\frac{d^2V}{dx^2} = -\frac{\rho}{\varepsilon\varepsilon_o}$$

where ρ is the charge density, ε is the dielectric constant, and ε_o is the permittivity. For a semiconductor, the charge density for an n-type semiconductor can be approximated as

$$\rho = eN_D\left(1 - e^{-\frac{eV}{kT}}\right)$$

Thus, Poisson's equation becomes

$$\frac{d^2V}{dx^2} = \frac{eN_D}{\varepsilon\varepsilon_o}\left(1 - e^{-\frac{eV}{kT}}\right)$$

Using the identity

$$2\frac{dV}{dx}\frac{d^2V}{dx^2} = \frac{d}{dx}\left(\frac{dV}{dx}\right)^2$$

Integrating (with $V = dV/dx = 0$ in the bulk) yields

$$\left(\frac{dV}{dx}\right)^2 = \frac{2eN_D}{\varepsilon\varepsilon_o}\left(V - \frac{kT}{e}\left(1 - e^{-\frac{eV}{kT}}\right)\right)$$

Using Gauss' law for a charged surface

$$\frac{dV}{dx} = \frac{Q}{A\varepsilon\varepsilon_o}$$

The space-charge layer forms when V deviates from the flat-band potential (V-Vfb), and the capacitance is defined as

$$C = \frac{dQ}{dV}$$

which yields the Mott–Schottky equation:

$$C^{-2} = \frac{2}{A^2\varepsilon\varepsilon_o eN_D}\left(V - V_{fb} - \frac{kT}{e}\right)$$

Acknowledgments

The author would like to thank all of the students and colleagues without whom this chapter would not have been possible: Eugene P. Lautenschlager, Joshua J. Jacobs, MD, Robert Urban, Danieli Rodrigues, Robert Gettens, Mark Ehrensberger, Jane Bearinger, Spiro Megremis, Christine Buckley, Jay Goldberg, Morteza Haeri, Shiril Sivan, Jua Kim, Ivan Lockward, Daniel Pressl, Zhijun Bai, and Nithya Chandrasekaran.

References

1. Gilbert, J. L. In *The Adult Hip*, 2nd ed.; Callaghan, J. J., Rubash, H. E., Rosenberg, A. G., Eds.; Lippencott-Raven Press: New York, 2006; Vol. 1; Chapter 8.
2. Bai, Z.; Gilbert, J. L. In *Corrosion: Materials, Environments, and Industries*, *ASM International Handbook*; ASM: Metals Park, OH, 2006; Vol. 13C, pp 837–852.
3. Healy, K. E.; Ducheyne, P. *J. Colloid Interface Sci.* **1992**, *150*, 404–417.
4. Healy, K. E.; Ducheyne, P. *Biomaterials* **1992**, *13*, 553–561.
5. Healy, K. E.; Ducheyne, P. *J. Biomed. Mater. Res.* **1992**, *26*, 319–338.
6. Kilner, T.; Pilliar, R. M.; Weatherly, G. C.; Allibert, C. *J. Biomed. Mater. Res.* **1982**, *16*(1), 63–79.
7. Jacobs, J. J.; Gilbert, J. L.; Urban, R. M. *J. Bone Joint Surg.* **1998**, *80A*(2), 268–282.
8. Jones, D.; Marsh, J. L.; Nepola, J. V.; *et al. J. Bone Joint Surg.* **2001**, *83A*(4), 537–548.
9. Black, J. *Biological Performance of Materials: Fundamentals of Biocompatibility*, 4th ed.; CRC Press: New York, 2006; p 231.
10. De Smet, K.; De Haan, R.; Calistri, A.; *et al. J. Bone Joint Surg.* **2008**, *90A*(Suppl. 4), 202–208.
11. Ehrensberger, M. T.; Gilbert, J. L. *J. Biomed. Mater. Res. A* **2009**.
12. Kalbacova, M.; Roessler, S.; Hempel, U.; *et al. Biomaterials* **2007**, *28*, 3263–3272.
13. Merritt, K.; Brown, S. A. *J. Biomed. Mater. Res.* **1988**, *22*(2), 111–120.
14. Ehrensberger, M. T.; Gilbert, J. L. *J. Biomed. Mat. Res. B* **2009**, *93B*, 106–112.
15. Messer, R. L.; Tackas, G.; Mickalonis, J.; Brown, Y.; Lewis, J. B.; Wataha, J. C. *J. Biomed. Mater. Res. B* **2009**, *88*(2), 454–481.
16. Gilbert, J. L.; Bai, Z.; Chandrasekaran, N. Method for preparing biomedical surfaces. Patent Application No. 2007/0187253, 2007.
17. Jones, D. A. *Principles and Prevention of Corrosion*; MacMillan: New York, 1992; pp 85–91.
18. Bard, A. J.; Faulkner, L. R. *Electrochemical Methods: Fundamentals and Applications*; John Wiley: New York, 1980.
19. Ratner, B.; Hoffman, A.; Schoen, F.; Lemons, J. *Biomaterials Science*, 2nd ed.; Academic Press: New York, 1996; pp 249–252.
20. Gilbert, J. L.; Bai, Z.; Bearinger, J.; Megremis, S. *Proceedings of the ASM Conference on Medical Device Materials*; Shrivastava, S., Ed.; ASM International: Metals Park, OH, 2004, 139–143.
21. Rodrigues, D. C.; Urban, R. M.; Jacobs, J. J.; Gilbert, J. L. *J. Biomed. Mater. Res. B* **2009**, *88B*(1), 206–219.
22. Gilbert, J. L.; Buckley, C. A.; Jacobs, J. J. *J. Biomed. Mater. Res.* **1993**, *27*(12), 1533–1544.
23. Burstein, G. T.; Guo, G. *J. Electrochem. Soc.* **1991**, *138*(9), 2627–2630.
24. Kolman, D. G.; Scully, J. R. *J. Electrochem. Soc.* **1995**, *142*(7), 2179–2188.
25. Gilbert, J. L.; Jacobs, J. J. In *Modularity of Orthopedic Implants*, ASTM STP 1301; Parr, J. E., Mayor, M. B., Marlow, D. E., Eds.; American Society for Testing and Materials: Philadelphia, PA, 1997; pp 45–59.
26. Cabrera, N.; Mott, N. F. *Rep. Prog. Phys.* **1948**, *12*, 163.
27. MacDonald, J. R. *Impedance Spectroscopy: Emphasizing Solid Materials and Systems*; Wiley InterScience: New York, 1987; pp 43–45.
28. Smeltzer, W. W. In *Oxidation of Metals and Alloys*; ASM: Metals Park, OH, 1971; pp 115–136.
29. Felner, F. P.; Mott, N. F. In *Oxidation of Metals and Alloys*; ASM: Metals Park, OH, 1971; pp 37–60.
30. Eley, D. D.; Wilkinson, P. R. *Proc. R. Soc. London Ser. A* **1960**, *254*, 327.
31. Gunterschulze, A.; Betz, H. *Z. Phys.* **1932**, *74*, 681.
32. Gerischer, H. *Electrochem. Acta* **1990**, *35*(11/12), 1677–1699.
33. Rhoderick, E. H.; Williams, R. H. *Metal-Semiconductor Contacts*. Clarendon Press/Oxford University Press: Cambridge, UK, 1988; pp 20–48.
34. Bokris, J. O. M.; Reddy, A. K. N. *Modern Electrochemistry*; Plenum: New York, 1976; Vols. 1 and 2.
35. Gelderman, K.; Lee, L.; Donne, S. W. *J. Chem. Ed.* **2007**, *84*(4), 685–690.
36. Gilbert, J. L. *J. Biomed. Mater. Res.* **1998**, *40*, 233–243.
37. Mopsik, F. *IEEE Trans. Dielect. El. In.* **2002**, *9*(5), 829–837.
38. Haeri, M.; Gilbert, J. L. *Corrosion Sci.* **2011**, *53*(2), 582–588.
39. Gettens, R. T.; Gilbert, J. L. *J. Biomed. Mater. Res. A* **2009**, *90*(1), 121–132.
40. Gettens, R. T.; Gilbert, J. L. *J. Biomed. Mater. Res. A* **2008**, *85*(1), 176–187.
41. Williams, G.; Watts, D. C. *Trans. Faraday Soc.* **1970**, *66*(565), 80–85.
42. Gettens, R. T.; Gilbert, J. L. *J. Biomed. Mat. Res. (A)* **2009**, *90A*(1), 121–132.
43. Ehrensberger, M. T.; Gilbert, J. L. *J. Biomed. Mat. Res. A* **2009**, DOI 10.1002/jbm.a.32550.
44. Diebold, U. *Surf. Sci. Rep.* **2003**, *48*(5–8), 53–230.
45. Bearinger, J. P.; Orme, C. A.; Gilbert, J. L. *Biomaterials* **2003**, *24*(11), 1837–1852.
46. Collier, J. P.; Mayor, M. B.; Jensen, R. E.; *et al. Clin. Orthop. Relat. Res.* **1992**, *285*, 129–139.
47. Goldberg, J. R.; Gilbert, J. L.; Jacobs, J. J. *Clin. Orthop. Relat. Res.* **2002**, *401*, 149–161.
48. Mathiesen, E. B.; Lindgren, J. U.; Blomgren, G. G.; Reinholt, F. P. *Br. J. Bone Joint Surg.* **1991**, *74*(4), 569–575.
49. Willert, H. G.; Brobakc, L. G.; Buchhorn, G. H.; *et al. Clin. Orthop. Relat. Res.* **1996**, *333*, 51–57.

50. Piehler, H. R.; Portnoff, M. A.; Sloter, L. E.; Vegdahl, E. J.; Gilbert, J. L.; Weber, M. J. *Corrosion-Fatigue Performance of Hip Nails: The Influence of Materials and Design*, ASTM STP 859; Fraker, A. C., Griffin, C. D., Eds.; 1985; pp 93–104.
51. Brown, S. A.; Hughes, P. J.; Merritt, K. *J. Orthop. Res.* **1988**, *6*(4), 572–579.
52. Ambrose, J. In *A Treatise on Materials Science and Technology, Aqueous Processes and Passive Films*; Scully, J. C., Ed.; Academic Press: New York, 1980; Vol. 23, pp 175–204.
53. Gilbert, J. L.; Buckley, C. A.; Lautenschlager, E. P. In *Medical Applications of Titanium and its Alloys: The Materials and Biological Issues*, ASTM STP 1272; American Society for Testing and Materials: Philadelphia, PA, 1996; pp 199–215.
54. Goldberg, J. R.; Lautenschlager, E. P.; Gilbert, J. L. *J. Biomed. Mater. Res.* **1997**, *37*(2), 421–433.
55. Goldberg, J. R.; Gilbert, J. L. *Biomaterials* **2004**, *25*(5), 851–864.
56. Bechtol, C. O.; Ferguson, A. B.; Laing, P. G. *Metals and Engineering in Bone and Joint Surgery*; Williams and Wilkins: Baltimore, 1959.
57. Jones, D.; Marsh, J. L.; Nepola, J. V.; *et al*. *J. Bone Joint Surg.* **2001**, *83A*(4), 537–548.
58. Gilbert, J. L.; Jacobs, J. J.; Buckley, C. A.; Bertin, K. C.; Zernich, M. *J. Bone Joint Surg.* **1994**, *76A*(1), 110–115.
59. Gilbert, J. L.; Mehta, M.; Pinder, B. *J. Biomed. Mater. Res. B* **2009**, *88B*(1), 162–173.
60. Goldberg, J. R.; Gilbert, J. L. *Appl. Biomater.* **2003**, *64B*(2), 78–93.
61. Brown, S. A.; Flemming, C. A.; Kawalec, J. S.; *et al*. *J. Appl. Biomater.* **1995**, *6*(1), 19–26.
62. Pan, J.; Leygraf, C.; Thierry, D.; Ektessabi, A. M. *J. Biomed. Mater. Res.* **1997**, *35*, 209–218.
63. Kocijan, A.; Milosev, I.; Pihlar, D. *J. Mater. Sci. Mater. Med.* **2004**, *15*, 643–650.
64. Bearinger, J. P.; Orme, C. A.; Gilbert, J. L. *Surf. Sci.* **2001**, *491*, 370–387.
65. Suzuki, R.; Frangos, J. A. *Clin Orthop. Relat. Res.* **2000**, *372*, 280–289.
66. Montague, A.; Merritt, K.; Brown, S. A.; Payer, J. *J. Biomed. Mater. Res.* **1996**, *32*(4), 519–526.
67. Caicedo, M. S.; Desai, R.; MacAlister, K.; Reddy, A.; Jacobs, J. J.; Hallab, N. *J. Orthop. Res.* **2009**, *27*(7), 847–854.
68. Clayton, R. A.; Beggs, I.; Salter, D. M.; Grant, M. H.; Patton, J. T.; Porter, D. E. *J. Bone Joint Surg. Am.* **2008**, *90*(9), 1988–1993.
69. Gilbert, J. L.; Zarka, L.; Chang, E.; Thomas, C. *J. Biomed. Mater. Res.* **1998**, *42*, 321–330.
70. Sivan, S.; Gilbert, J. L. Voltage-time dependence morphological response of MC3T3 pre-osteoblast cells on Ti-6Al-4V due to electrochemical stimulation. Transactions Society for Biomaterials Annual meeting, San Antonio, TX, 2009.
71. Baranowski, T. J. J.; Black, J.; Brighton, C. T. In *Electrochemical Society Extended Abstracts*, Electrochemical Society: Pennington, NJ, 1983; p 993; Extended Abstracts, Spring Meeting, Electrochemical Society, San Francisco, CA, 1983.
72. Black, J.; Baranowski, T. J., Jr.; Brighton, C. T. *Bioelectrochem. Bioenerg.* **1984**, *12*, 323–327.
73. Sawyer, P. N. *Ann. N. Y. Acad. Sci.* **1983**, *416*, 561–583.
74. Stankovich, M. T.; Bard, A. J. *J. Electroanal. Chem.* **1978**, *86*, 189.

1.104. Shape Memory Alloys for Use in Medicine

B O'Brien and M Bruzzi, National University of Ireland, Galway, Ireland

© 2011 Elsevier Ltd. All rights reserved.

1.104.1.	**Introduction**	50
1.104.2.	**Fundamentals of Shape Memory Systems**	50
1.104.3.	**Practical SMAs**	51
1.104.4.	**Manufacturing, Processing, and Performance of Nitinol**	52
1.104.4.1.	Melting Methods and Compositional Effects	52
1.104.4.2.	Production of Semifinished Wrought Products	52
1.104.4.3.	Heat Treatment to Control Performance	53
1.104.4.4.	Characterization Methods and Some Basic Material Properties	54
1.104.4.4.1.	Transformation temperatures	54
1.104.4.4.2.	Tensile behavior	56
1.104.5.	**Minimally Invasive Device Applications for Nitinol**	56
1.104.5.1.	Cardiovascular Stents	56
1.104.5.1.1.	Deployment considerations	56
1.104.5.1.2.	Manufacturing methods	58
1.104.5.1.3.	Cardiovascular stents: clinical examples	59
1.104.5.2.	Other Cardiovascular Devices	62
1.104.5.3.	Nonvascular Stents	62
1.104.6.	**Orthodontic Applications for Nitinol**	64
1.104.7.	**Orthopedic Applications for Nitinol**	64
1.104.8.	**Clinical Imaging of Nitinol Medical Devices**	65
1.104.9.	**Long-Term Durability and Biocompatibility of Nitinol**	66
1.104.9.1.	Fatigue Behavior of Nitinol	66
1.104.9.2.	Corrosion Behavior of Nitinol	68
1.104.9.3.	Biocompatibility Aspects of Nitinol	69
1.104.10.	**Summary and Future Directions**	70
References		70

Glossary

Hysteresis The lag in response exhibited by a body in reacting to changes in the forces.

Minimally invasive procedure Any procedure (surgical or otherwise) that is less invasive than open surgery used for the same purpose.

Orthodontics The dental specialty and practice of preventing and correcting irregularities of the teeth.

Pseudoelasticity An elastic (reversible) response to an applied stress, caused by a phase transformation between the austenitic and martensitic phases of a crystal.

Shape memory alloy An alloy that 'remembers' its original, cold-forged shape, returning to the predeformed shape by heating.

Stent A wire metal mesh tube used to prop open an artery during angioplasty.

Abbreviations

Af	Austenite finish
As	Austenite start
BFR	Bend and free recovery
COF	Chronic outward force
CT	Computed tomography
DSC	Differential scanning calorimetry
HAZ	Heat-affected zone
ISM	Induction skull melting
Mf	Martensite finish
MRI	Magnetic resonance imaging
Ms	Martensite start
NiTi	Nickel–titanium
PBS	Phosphate-buffered saline
RRF	Radial resistive force
SFA	Superficial femoral artery
SHS	Self-propagating high-temperature synthesis
SMA	Shape memory alloy
SVG	Saphenous vein graft
TTT	Time–temperature–transformation
VAR	Vacuum arc remelting
VIM	Vacuum induction melting

1.104.1. Introduction

This chapter will provide an introduction to shape memory alloy (SMA) systems with an emphasis on nickel–titanium alloys. Unique performance characteristics and manufacturing technologies will be reviewed, followed by a description of significant applications in cardiovascular, orthopedic, and orthodontic fields. Long term *in vivo* durability of the material will be addressed, including fatigue and corrosion performance, as well as biocompatibility aspects.

1.104.2. Fundamentals of Shape Memory Systems

The unique properties of SMAs revolve around what is known as the martensite transformation, whereby a solid state change from one phase to another is induced through a change in temperature or stress. Irrespective of the alloy system, the higher temperature phase is identified as austenite, while the lower temperature state is martensite. The transformation is diffusionless, with no long-range diffusion of atoms, but is instead due to a small, but long-range, shift in the crystallographic structure. In most commercial SMAs, the crystal structure of the austenite is a cubic B2 or caesium chloride (CsCl) while the martensite is a more complex twinned monoclinic structure. The transformation is thermoelastic, with the martensite structure growing continuously as the temperature is reduced and converting back to austenite as the temperature is reversed. It is first important to note that the transformation itself does not provide shape change, but it does provide the twinned martensitic structure that is central to shape memory and superelastic behavior. At a microstructural level, this twinned martensite structure has a platelike appearance. From a crystallographic perspective, the opposing sides of the twin boundaries of the structure are mirror images of each other. Figure 1 schematically illustrates the austenite-to-martensite transformation, with changes in temperature. In addition, this diagram demonstrates how the transformation is exploited to bring about macroscopic shape changes. When the structure is deformed in the martensite condition, the twin boundaries readily shift such that the twins are predominantly oriented in one preferential direction; this process is known as de-twinning. In the case of the NiTi system, twinned martensite can be deformed to a strain of ~8%, and importantly, this is achieved with no dislocation movement or the development of slip bands. If the strain goes beyond this, the de-twinned martensite will start to elastically deform and ultimately plastically deform. Upon heating of the deformed martensite, the structure reverts to austenite as it becomes more thermodynamically stable; in doing so, the deformation induced in the martensite fully recovers with the material returning to its undeformed state – thereby giving the shape memory effect. Once the shape has recovered, thermal cycling will not cause further shape change, and the material would need to be deformed in the martensitic state again in order to reactivate the effect.

The transition between the two phases does not occur sharply, but is typically spread over several degrees with proportional volume fractions of the phases coexisting within this range. The other feature of note is that the 'forward' and 'reverse' transformations do not occur at the same temperature, that is, the austenite-to-martensite change occurs at a lower temperature than the reverse martensite-to-austenite transition. This hysteresis effect and the incremental nature of the transformation are both schematically shown in Figure 2. The critical temperature points here are the austenite start (As), austenite finish (Af), martensite start (Ms), and martensite finish (Mf). These characteristic temperatures are central to most discussions on SMAs and are critical in accurate specification of the materials.

The shape memory effect now described could be considered as being primarily a thermal memory in that application of heat activates the deformed martensite to change shape. However, a mechanical memory effect is also achievable, with martensite being stress induced by deformation of the material in the austenite condition. At a crystallographic level, the transformation is the same as thermally inducing martensite, and therefore recoverable strains of up to ~8% can also be achieved in this manner. In effect, the stress is transforming the austenite into martensite and immediately de-twinning the martensite, to provide the high levels of deformation. Once the stress is released, the material reverts to the more

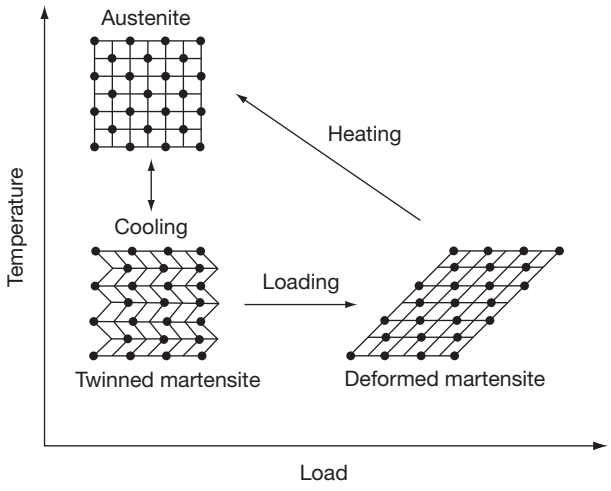

Figure 1 Schematic of the shape memory effect, showing the influence of temperature and stress on the crystal structure and shape.

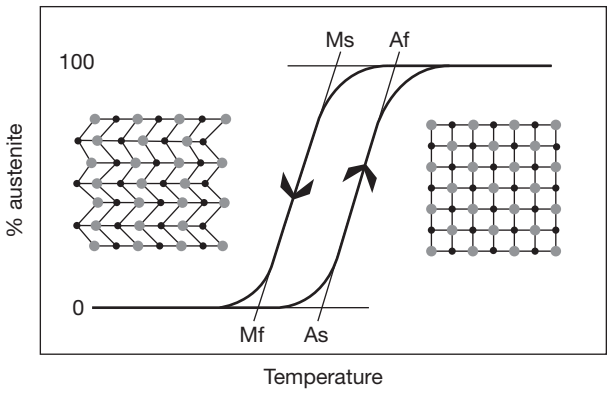

Figure 2 Transformation temperatures and the hysteresis effect.

thermodynamically stable austenite condition and the induced deformation fully recovers. While the mechanism of attaining this level of recoverable strain is not hookean or elastic, the effect is most widely known as superelasticity or is occasionally known as pseudoelasticity. Similar to that already described for thermally induced martensite, if the level of recoverable strain is exceeded, the stress-induced de-twinned martensite will start to deform elastically and ultimately deform plastically.

Just as there is a hysteresis effect with thermally induced transformations, there is similarly a hysteresis when the transformation is stress induced. This superelastic hysteresis is illustrated in **Figure 3** which shows the superelastic strain being induced up to Point A. If the stress is released, the hysteresis can be seen, whereby the superelastic strain recovers at a lower stress level than at which it is induced. These stress levels are respectively identified as the loading and unloading plateau stresses. If the material is stressed above the load plateau, the de-twinned martensite elastically and plastically deforms and ultimately fails, as indicated by Point B in **Figure 3**.

There is, however, an optimum temperature range over which superelastic behavior is observed. The stresses required to induce martensite and de-twinning are lowest at the Af point; at increasing temperatures above Af, the austenite becomes more thermodynamically stable such that higher stresses are required to transform the material to martensite. This has the effect of raising the level of the load and unload plateaus and it can therefore be seen that shifting the Af point, relative to the operating temperature, is one method of influencing mechanical capability of the material. At higher temperatures, a point is reached where the austenite is so stable that martensite cannot be stress induced and the austenite starts to deform by conventional slip mechanisms with no superelasticity present.

In summary, it can be seen that the structure and behavior of shape memory materials is highly dependent upon the inherent transformation temperatures of the material, as these in effect control the materials' response to applied stress and temperature. For example, a material which operates typically in the shape memory mode can be made to behave superelastically by either reducing Af or increasing the ambient temperature. This introduction to the principles of shape memory and superelasticity is brief, but is sufficient background for the biomaterials scientist or engineer needing to get an appreciation of medical applications for the materials. There is an extensive quantity of literature available describing the crystallographic and mechanistic aspects of the underlying transformations; the reader is referred to the reviews of either Wayman and Duerig[1] or Hodgson *et al.*[2] for further introductory material on these aspects.

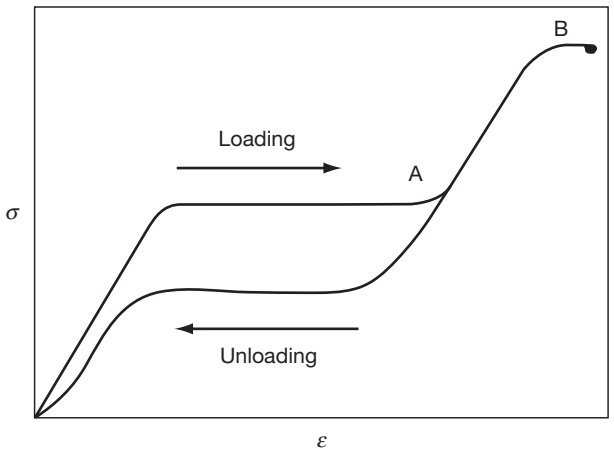

Figure 3 Superelastic behavior for a material above its Af temperature.

Finally, a brief mention needs to be given to the two-way shape memory effect. As indicated earlier, shape memory is primarily a one-way process, that is, after heating and recovery of deformed martensite, no further shape change will be obtained unless the cooling and deformation step is repeated. Under certain conditions, some shape memory materials can be processed to give a two-way memory effect, such that the material changes shape solely due to control of temperature. Extensive thermomechanical treatments are needed to induce this behavior, usually involving thermal cycling, from below Mf to above Af, with the material constrained in one of the configurations required.[3] Applications for this effect have, however, been limited due to the relatively low recoverable strain achievable (typically <3%) as well as the loss of the effect with increased thermal cycling.[4] The majority of commercial medical device applications for shape memory materials rely on the conventional one-way effect and on superelasticity.

1.104.3. Practical SMAs

There are several alloy systems that exhibit shape memory effects, though very few have achieved successful engineering application; fewer still have been used in medical device applications. There are a number of copper-based shape memory systems, with Cu–Zn–Al and Cu–Al–Ni being the most commercially successful. Copper-based alloys have traditionally been viewed as relatively inexpensive due to low raw material costs and easy processing. These materials have found applications mainly in engineering actuators;[5] however, a Cu–Al–Mn alloy has been utilized for development of a cardiovascular guidewire, exhibiting ductility and superelastic properties similar to conventional guidewire materials.[6] There are also a number of iron-based shape memory materials, including Fe–Mn–Si and Fe–Mn–Si–Cr–Ni, though these materials tend to have low recoverable strain and require complex thermomechanical treatments.[7]

However, by far the most significant SMA to date is that based on equiatomic and near-equiatomic nickel and titanium compositions. These NiTi materials have accounted for the majority of commercial applications, particularly in the medical device industry, and this trend is likely to continue. NiTi has been successfully used in engineering actuator applications since the 1970s, but it was not until the early 1990s that its potential in the medical device field started to become realized. The material was originally developed at the US Naval Ordnance Laboratory, leading to it being now widely known as NiTiNOL. The early historical development of nitinol is reviewed by Kauffman and Mayo,[8] presenting a unique insight into the somewhat fortunate discovery and initial development of the material.

From a metallurgical perspective, NiTi is classified as an intermetallic material with the respective atoms bonded to each other in a long-range ordered structure; this is unlike many common alloys where the solute atoms randomly substitute for atoms of the solvent crystal structure or sit in the interstices of the crystal structure. The properties and performance of the material are highly sensitive to the ratio of nickel and titanium and therefore the composition needs to be very tightly specified; the most widely used NiTi material has 50.8 at.% nickel and 49.2 at.% titanium. In addition to thermomechanical treatments, small adjustments in this composition can be used to shift the characteristic transformation temperatures of the material.

1.104.4. Manufacturing, Processing, and Performance of Nitinol

1.104.4.1. Melting Methods and Compositional Effects

Normally, details of melt practices and compositional control are of little interest to the scientist or engineer developing specific medical device applications. However, given the high sensitivity of NiTi to these particular aspects, a brief review is useful. NiTi is most usually produced by either vacuum induction melting (VIM) or vacuum arc remelting (VAR). The VIM process involves placing the charge materials in a graphite crucible and applying heat via external induction coils. The stirring effect of the induction field leads to highly homogenous melting and mixing; however, the main disadvantage of this method is that the material tends to pick up small amounts of carbon from the graphite crucible. This usually results in the formation of TiC inclusions. The VAR process involves compacting the charge materials into a consumable electrode and striking an arc between this electrode and the base of the crucible. The crucible is copper lined, with water cooling, eliminating the risk of carbon contamination. As molten metal is formed, the relative electrode position is adjusted, thereby moving the molten zone along its length; this has the effect of pulling all impurities into the final molten zone (which can be discarded), leading to a very high-purity material. The main disadvantage of the VAR process is that only part of the ingot is molten at any one time, thereby resulting in less alloy homogenization than is possible with VIM. This creates the risk of transformation temperature variations throughout the material; multiple repeat VAR steps can be used to address this aspect. A VIM/VAR combination process can also be used to produce NiTi, with the initial homogenous induction melted material being remelted to reduce impurities. However it should be noted that contamination from oxygen is also highly detrimental to NiTi materials and each additional melting or remelting step increases the risk of such contamination. The potential benefits of an induction skull melting (ISM) process have been reported by Kramer.[9] ISM has features of both VIM and VAR in that the charge is induction melted within a copper water-cooled crucible. As the charge melts, a thin solidified skin or 'skull' forms at the crucible walls, around the material, protecting the molten material from contamination. Exceptionally high power is needed to achieve induction effects through the copper crucible, but a clean and homogenous material is achieved. The study by Kramer did show that the ISM material had a lower carbon content and a lower number of overall inclusions, compared to VIM material, but the inclusions tended to be larger in size. This was attributed to nonoptimized forging of the ISM material, which would be further addressed. In any event, it is important to note that ISM is not yet used to manufacture commercial material and the VIM and VAR processes are being widely and successfully used. However, in instances where composition and inclusion content becomes critical to fatigue, corrosion, or transformation temperatures, then an insight into these melting options can be useful.

While the effect of contaminants and inclusions on aspects such as fatigue may be widely appreciated, the secondary effects are more subtle, though just as significant. To appreciate this it must first be realized that shifting nickel content (to a Ni-rich composition) by only 1.0% can decrease transformation temperatures by as much as 100 °C, also illustrating how composition may need to be controlled to levels of 0.01% to achieve sufficient control on transformation behavior.[10] This is schematically illustrated in Figure 4.

Most impurity elements, including oxygen and carbon, tend to preferentially react with the titanium, creating titanium-based inclusion compounds. This leaves the adjacent matrix material richer in nickel and therefore it can produce a significant drop in transformation temperatures. In addition to oxides or carbides, which are the most common, the formation of hydrides or nitrides leads to similar effects, as does the presence of trace levels of iron, cobalt, or chromium. In virtually all of these instances, the precipitated compound also results in an increase in strength, but with an associated drop in ductility.[11]

1.104.4.2. Production of Semifinished Wrought Products

After melting, the cast ingot is processed, using primarily conventional metalworking technologies, to obtain wrought

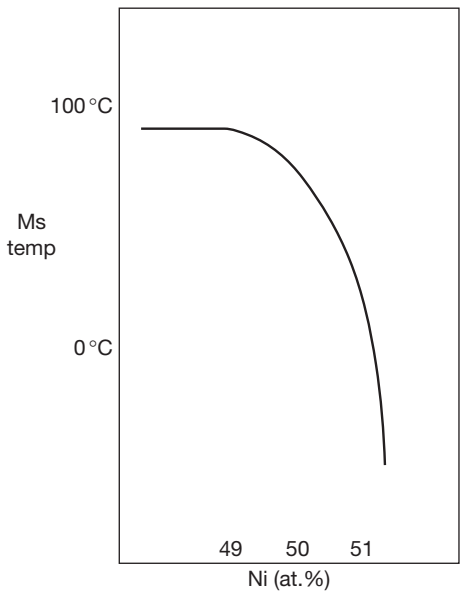

Figure 4 Illustration of dramatic effect that nickel content has on transformation temperature.

products such as wire, strip, or tubing.[12] The ingot is typically hot rolled or forged in the temperature range 800–950 °C, breaking down and refining the cast structure and thereby improving the mechanical properties. Once reduced to a suitable size, the bar or rod is further processed by cold working methods such as drawing and rolling. However, nitinol has a high work-hardening rate, and several passes with interstage anneals (600–800 °C) are needed to get the material down to the required dimensions. The final tube, wire, or strip products are usually available with a variety of polished or oxided surface finishes and there are now several suppliers worldwide. However, it should be noted that there are fewer facilities producing the original ingot material, and often, material from different suppliers can originate from a single melt source and therefore have similar melt chemistries and inclusion contents. The subsequent hot and cold working may have altered inclusion size and distribution as well as altered mechanical properties through control of residual cold work. The level of cold work is usually in the 30–45% range.

1.104.4.3. Heat Treatment to Control Performance

Cold worked nitinol does not exhibit full shape memory or superelastic behavior and needs to be heat treated to activate these effects. While the heat treatment itself is not particularly complex, there are a number of metallurgical phenomena taking place, all of which combine to control the thermal and mechanical properties of the final structure. At the most basic level, the heat treatment is used to set the final desired shape of the product, that is, the shape to which it would thermally recover after being deformed in a martensitic state, or mechanically (superelastically) recover after being released from a constrained condition. This shape setting is achieved through the annealing effects that take place during the treatment; the release of cold work through dislocation recovery allows the material to retain this heat-treated shape. In addition, the reduction in dislocation density allows for easier crystallographic movement, in particular allowing the austenite–martensite transitions to take place. Longer times or higher temperatures tend to provide better shape retention, but of course a balance needs to be achieved in order to avoid full annealing or recrystallization effects, as some residual cold work is needed in order to maintain optimum material strength levels. In addition to annealing and recovery processes, the heat treatment is also used to tune in the transformation temperatures of the material. While chemical composition and residual cold work will have already defined a window for transformation behavior, this heat treatment serves to further tune transformations to the desired level, through nucleation and growth of nickel-rich precipitates. Pelton *et al.*[13] have presented an excellent overview of these heat treatments for nitinol wire, particularly with respect to obtaining properties and transformation temperatures generally suitable for medical devices. The temperature for such treatments can range from 300 to 600 °C, though most are typically at 500 °C. Durations can be as short as 2 or 3 min or as long as 2 or 3 h, though they are typically in the 5–30 min range, depending on the temperature and the desired properties. The interaction of time and temperature and its effect on transformation temperature is explained through the manner in which the nickel-based precipitates form during the treatment, particularly for the widely used nickel-rich 50.8 at.% Ni composition. At lower temperatures, diffusion processes are slow, and while precipitates do nucleate they are slow to grow to significant sizes. Relatively long durations are therefore required to obtain measureable effects on transformation behavior. At high temperatures, the more rapid diffusion processes somewhat inhibit precipitate nucleation, with the outcome being similar to low temperatures, that is, relatively long durations are needed. Therefore, at intermediate temperatures the diffusion and nucleation process provide a better balance, leading to more rapid precipitation effects. Such heat treatment effects can be best presented in a nitinol time–temperature–transformation (TTT) diagram as shown in **Figure 5**.

In the example shown here, peak precipitation is at ~400 °C, with Af being shifted by 20 °C for durations of up to 70 min. Often however, in production environments, the slightly slower precipitation region of ~500 °C is selected in order to give less sensitivity to time deviations, that is, to give a more robust manufacturing process. This higher region is also preferred over the lower temperatures so as to ensure adequate recovery and shape setting as described earlier. The shifts in Af relate directly to the manner in which the nickel-rich precipitates deplete nickel from the adjacent material, creating a titanium-rich matrix. These nickel-based precipitates do also contain titanium, but the composition is typically such that more nickel is consumed than titanium. There are a number of different precipitates that may form, but the most predominant composition is Ni_4Ti_3; Khalil-Allafi *et al.*[14] have performed a thorough study of the formation and evolution of this Ni_4Ti_3 precipitate during aging of nitinol. In addition, analysis of precipitate volume fractions was used to calculate the extent of matrix nickel depletion and this was correlated with observed shifts in transformation temperature. With higher temperature treatments (i.e., 500–600 °C) the precipitate chemistry shifts, initially the Ni_3Ti_4 dissolves and this is followed by precipitation of Ni_3Ti_2 and Ni_3Ti. Pelton *et al.*[13] have used this precipitation sequence to explain the 'cusp' observed

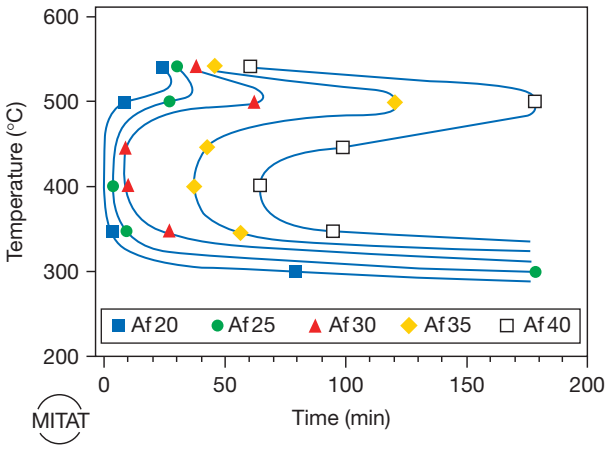

Figure 5 Time–temperature–transformation diagram for 50.8 at.% Ni–49.2 at.% Ti wire. This particular material had an Af of 11 °C before the aging treatments. Reproduced from Pelton, A. R.; DiCello, J.; Miyazaki, S. *Minim. Invasive Ther. Allied Technol.* **2000**, *9*(1), 107–118.

above 500 °C in the TTT diagrams, such as seen in Figure 5. As the Ni_3Ti_2 and Ni_3Ti become the more favored composition, they draw even more nickel from the matrix, thereby leading to an overall faster shift upwards in the transformation temperatures. Related to this, there is an intermediate set of conditions where the Ni_3Ti_4 has dissolved, but the more Ni-rich precipitates have not yet formed. This is reported by Drexel *et al.*,[15] showing lower Af values from treatments at 550 °C for 2–20 min, while obtaining similar shaped TTT diagrams. Beyond 20 min, the Af rapidly shift upwards again. The specific treatments and transformation temperature response described here will not hold for every material or device, due to influences of composition and residual cold work; however, the general trends will be observed and need to be appreciated when developing a heat treatment process and performance requirements for any device.

At this stage, a brief mention needs to be given to the R-phase, which is an intermediate rhombohedral crystal structure sometimes detected upon cooling from austenite down to martensite. The transition from austenite to R-phase is a martensitelike transformation, involving small crystallographic displacements, with Otsuka[16] describing this phase as effectively being in competition with martensite. Its presence is promoted by heat treating of cold-worked materials in the 400–500 °C range or by aging of slightly nickel-rich compositions in the same range. As with the martensite transformation, the austenite to R-phase transformation also provides for shape memory and superelastic effects. However some differences are observed, most notable being that the recoverable strain for the R-phase transformation is typically <1%, providing much less scope for actuation of engineering or medical devices. As a result, this transformation has not been widely investigated or understood. Another key difference is the low hysteresis involved, that is, the reverse transformation occurs at nearly the same temperature, unlike martensite–austenite transitions which have extensive hysteresis effects. As a consequence of its more subtle presence, the R-phase is often not clearly observed in mechanical tests of materials or devices. However, a study by Šittner *et al.*[17] suggests that it cannot be completely ignored, as a minimum in elastic modulus was observed at the Rf temperature. This could have implications for device performance should this Rf temperature coincide with the operating temperature.

Finally, some practical considerations relating to heat treatment. As can now be appreciated, the performance of any nitinol medical device is highly dependent on the temperature and duration of heat treatment. Therefore, equipment and methods need to be used that will allow sufficiently tight control over these parameters. As a general rule, techniques that allow for rapid heat up and cooling are preferred, thereby minimizing ramp-up and cool-down durations, which could lead to uncontrolled or undesired effects. Equipment such as fluidized baths and salt baths are therefore most often used, with water quenching usually employed at the end of the cycle. The other key aspect of the heat treatment is the fixturing that is used to keep the structure in the desired final shape. The design and operation of this will be specific to each type of device, but again the effect that the fixturing may have on heat-up and cool-down rates needs to be understood in order to achieve proper process control.

1.104.4.4. Characterization Methods and Some Basic Material Properties

1.104.4.4.1. Transformation temperatures

Given the extreme sensitivity of nitinol to the nickel and titanium contents, as well as to the thermomechanical history, accurate measurement and specification of performance can be challenging. While precise chemical analysis is essential at the ingot development stage, the chemistry becomes a secondary factor as the material is processed through to semifinished product and ultimately to the final device configuration. Specification of the transformation temperatures then becomes important and in many instances, for the semifinished product, these are more critical than composition. In most

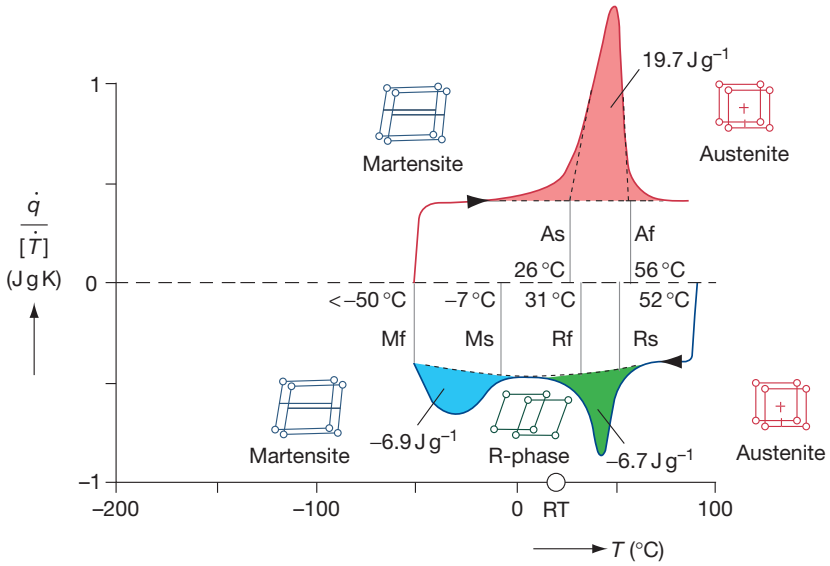

Figure 6 Schematic differential scanning calorimetry curve showing all crystal structures and transition points. Reproduced from Shaw, J. A.; Churchill, C. B.; Iadicola, M. A. *Exp. Tech.* **2008**, *32*, 55–62.

situations a high degree of interaction is needed between the material supplier and the device developer so that target transformation temperatures and mechanical properties can be accurately achieved, at the end of all the processing and shape setting steps that may be involved. The performance of wire or tubing will shift considerably during device manufacture and while a supplier will only guarantee properties of the 'as-received' material, knowledge of the subsequent processing will allow better tuning of earlier thermomechanical treatments so that the desired performance can be achieved. Agreement on the specification and on measurement method for transformation temperatures is therefore essential. Normally the Af point is the most important to specify for medical devices, that is, for shape memory actuation, the Af may need to be below body temperature and the difference between the two temperatures may define the level of the actuation force obtained. In many instances, the start and finish temperatures for both austenite and martensite phases may be specified.

Differential scanning calorimetry (DSC) is widely used for measurement of all the transformation temperatures, usually scanning down in temperature first to capture Ms and Mf and then scanning up to record As and Af. **Figure 6** schematically presents a typical nitinol DSC curve, also showing the presence of R-phase.

While DSC methods are widely used for measurement of thermal events in many materials, there are several test factors that can influence the data obtained. Marquez *et al.*[18] and Shaw *et al.*[19] have presented detailed reviews of the critical factors involved in nitinol sample preparation and in test parameters. For example, care must be taken not to induce additional cold work into the sample during preparation and oxides should be removed as they may impact heat transfer during the test, thereby affecting the measured transformation values. High heating rates can give sharp peaks, but may induce hidden thermal lag effects, leading to inaccurate values. In any event, scope for discrepancies have been reduced in recent years with the introduction of an ASTM,[20] specific to nitinol. This method, and the technique in general, does however have limitations in that it is really only suitable for material in an annealed condition and does not well capture effects of residual or applied stress, which on a macroscopic scale can increase transformation temperatures.

An alternative approach for measuring transformations is to use what are known as 'active' methods. These are active in the sense that they measure recovery motion on a sample as it transforms from martensite back to austenite. It is, therefore, more appropriate in many situations where the ultimate performance of a device involves shape memory or superelastic actuation at a given temperature; it is a more direct measure and captures the complete processing history of the sample or device. It is, therefore, suitable for use on as-received semifinished material or on processed devices. Rice and Sczerzenie[21] initially developed such a technique for wire samples while Chen *et al.*[22] developed a similar approach for tubes and cylindrical stent structures. The methods simply involve cooling of the sample to the martensite phase and deforming to a controlled strain, followed by heating back up to above the Af temperature. As the sample heats up and the material transforms, it recovers to its original shape. A transducer is used to measure this recovery motion, giving a plot of displacement versus temperature. The precise profile of the curve will of course depend on the sample configuration and the nature of the deformation or strain imparted to it, but typically the austenite transformation points, both start and finish, are readily identified. **Figure 7** illustrates this schematically. The test can also be used to detect R-phase transition points, if these are present in the material.

As the actual measured Af is dependent on the applied strain, it is always advisable to use a method that captures strain and motions representative of how the device will be clinically used. For example in the case of stents, it can be useful to deform the stent to a configuration similar to that which it may experience when loaded in a delivery system. As with the use of DSC, an ASTM[23] has been developed to provide guidance and consistency for performing these tests. Of note, the methods are generally known as bend and free recovery (BFR) tests, to distinguish from methods that involve recovery into a constrained configuration. (In these tests, the force generated by a recovering but constrained sample is measured, to discern the transformation points.) Drexel *et al.*[24] have performed a critical evaluation of the ASTM BFR method, highlighting and assessing the key test variables; overall, this study confirmed the value of the test and the standard methodology. Finally, it should be noted that transformation temperatures measured by DSC are not likely to correspond exactly with those obtained by BFR methods, though correlations may be established. Either method can be used for specification purposes, once the merits of the respective approaches are appreciated.

In relation to specific transformation temperature values, there are no standard recommendations for medical device applications; the interaction of device design, actuation forces requirements and the transformation temperature itself make each situation different. However, when considering peripheral vascular stents, currently the main medical application for nitinol, it is usual to have an Af value at least 5–10 °C below body temperature. This ensures that the device is fully

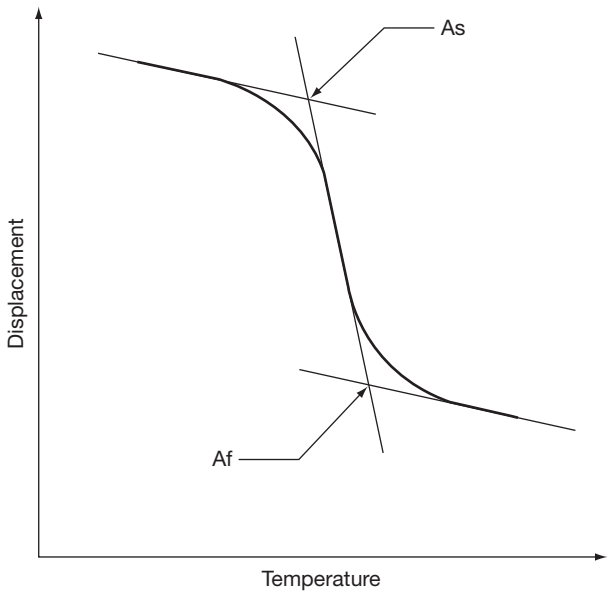

Figure 7 Displacement versus temperature curve from an active Af test, indicating the austenite start and finish temperatures.

deployed and exerting an optimum force against the vessel wall at body temperature. Depending on the profile of the austenite transformation peak, the As point may be a further 10–20 °C below the Af. In this situation, the Ms and Mf temperatures may be down in the −50 to −80 °C region. The mode of actuation obtained with these characteristic temperatures would be classified as shape memory, with the device needing to reach body temperature to achieve the precise performance required. However, it would not be unusual for devices to have much lower austenite transformation temperatures than these (i.e., Af well below room temperature), such that the deployment behavior is primarily superelastic.

1.104.4.4.2. Tensile behavior

Aside from characterization of transformation temperatures, it should now be evident that measurement and control of tensile behavior is equally important and is tightly related to the transformations. The shape memory and superelastic responses have already been described, and given the virtually infinite number of combinations on cold work, heat treatment, and composition, the literature abounds with endless data for tensile mechanical properties. In some respects these data are of little use to the biomedical scientist or engineer conceptualizing or developing a new device, unless there is some very specific aspect of this new application directly comparable to the literature. Some generalizations and useful specific examples can of course be highlighted. First however, some specific aspects of tensile testing of nitinol need mention. The shape and magnitude of the curve will of course depend on the relationship between the test temperature and the transformation temperatures, that is, whether the material is exhibiting shape memory or superelasticity. When tested in the martensitic condition, nitinol will have a relatively low elastic modulus and will superelastically deform at low load (by de-twinning of the martensite). If unloaded, the superelastic deformation will be retained but can be thermally recovered upon heating (i.e., shape memory). If loading had been continued beyond the end of the superelastic deformation point, the martensite would now start to elastically deform and ultimately fail due to tensile overload. When testing close to the Af temperature, with a predominantly austenite structure, martensite will be stress induced at the loading plateau, giving recoverable strains of up to about 8%. Upon unloading, this deformation will recover at the lower (unloading) plateau, giving the characteristic superelastic performance. Again, if loading had been continued, the martensite would then behave elastically, before plastically deforming and failing. Testing of nitinol above the Af temperature will continue to provide a superelastic effect, but the level of the load and unload plateau will increase with temperature. This increase in plateau levels with increasing temperature is due to the increasing stability of the austenite and the associated difficulty in transforming it to martensite. This is known as the 'stress rate' effect; it is widely documented, and the investigations of McKelvey and Ritchie[25] and Gall *et al.*[26] provide a detailed insight for some practical nitinol materials. With further increases in temperature, the deformation obtained is due to an increasing amount of austenite plastic deformation and reducing superelastic effect, such that some permanent set takes place when the load is released. Eventually a temperature is reached where martensite cannot be stress induced and deformation of the austenite is purely elastic or plastic. This full range of tensile behavior is shown in the set of curves presented in Figure 8.

Given the unusual tensile behavior on nitinol, compared to conventional metals, there are a number of specific issues to be aware of when performing such tests. Perhaps most obvious, but still meriting mention is that the test temperature needs to be appropriate for the intended use of the data and that the temperature needs be measured accurately. Next, monitoring of strain needs to be carefully considered to ensure that the superelastic region and any additional elastic and plastic regions are fully recorded. One of the other main potential complications arises from the thermal nature of the transitions; as austenite is stress induced to martensite, heat is given off which has the potential to influence load measurements, that is, based on the influence of temperature on load plateaus. Similarly, on reverse loading through the transition, heat is absorbed. The standard approach to addressing this problem has been to use relatively slow strain rates, allowing time for this heat to transfer to the ambient environment, whatever that temperature may be. As with other aspects of nitinol, an ASTM[27] has recently been introduced to provide guidance and consistency in all these aspects. However, Johe[28] has performed a detailed strain rate study and proposes that some of the strain rates specified in this standard are unnecessarily conservative. It is, therefore, an area in which there are likely to be ongoing revisions.

1.104.5. Minimally Invasive Device Applications for Nitinol

1.104.5.1. Cardiovascular Stents

1.104.5.1.1. Deployment considerations

The extensive use of nitinol in cardiovascular stent applications can be directly attributed to its characteristic shape memory and superelastic behavior. The possibility of achieving small compressed device configurations, inserting these with minimal trauma, and then having them recover to their larger deployed functional configuration has intrigued physicians and device designers for many years now. In addition, the unique superelastic 'durability' has made nitinol even more attractive in applications where device flexibility, conformance, and crush resistance are critical. However, to fully appreciate how nitinol is ideally suited to stent applications, the strains and loads involved during all stages of stent deployment need to be considered. Duerig *et al.*[29] have presented an excellent overview of this from the perspective of superelastic stent design, as well as introduced the concept of 'biased stiffness.' Details of stent delivery systems are beyond the scope of this chapter, but in summary, the stent is first compressed down to a small diametrical profile and retained within the delivery tube or sheath. Upon tracking of the catheter to the treatment site, the stent is deployed in the artery by either pushing out the stent or retracting the sheath. The stent is usually oversized, so that the unconstrained diameter of the stent would be larger than that of the vessel, thereby developing a force between the stent and the vessel wall which keeps the stent in position. All of these steps can be considered further with reference to Figure 9, which illustrates a plot of stent hoop force versus stent diameter. It can initially be seen that the shape of this plot mirrors the

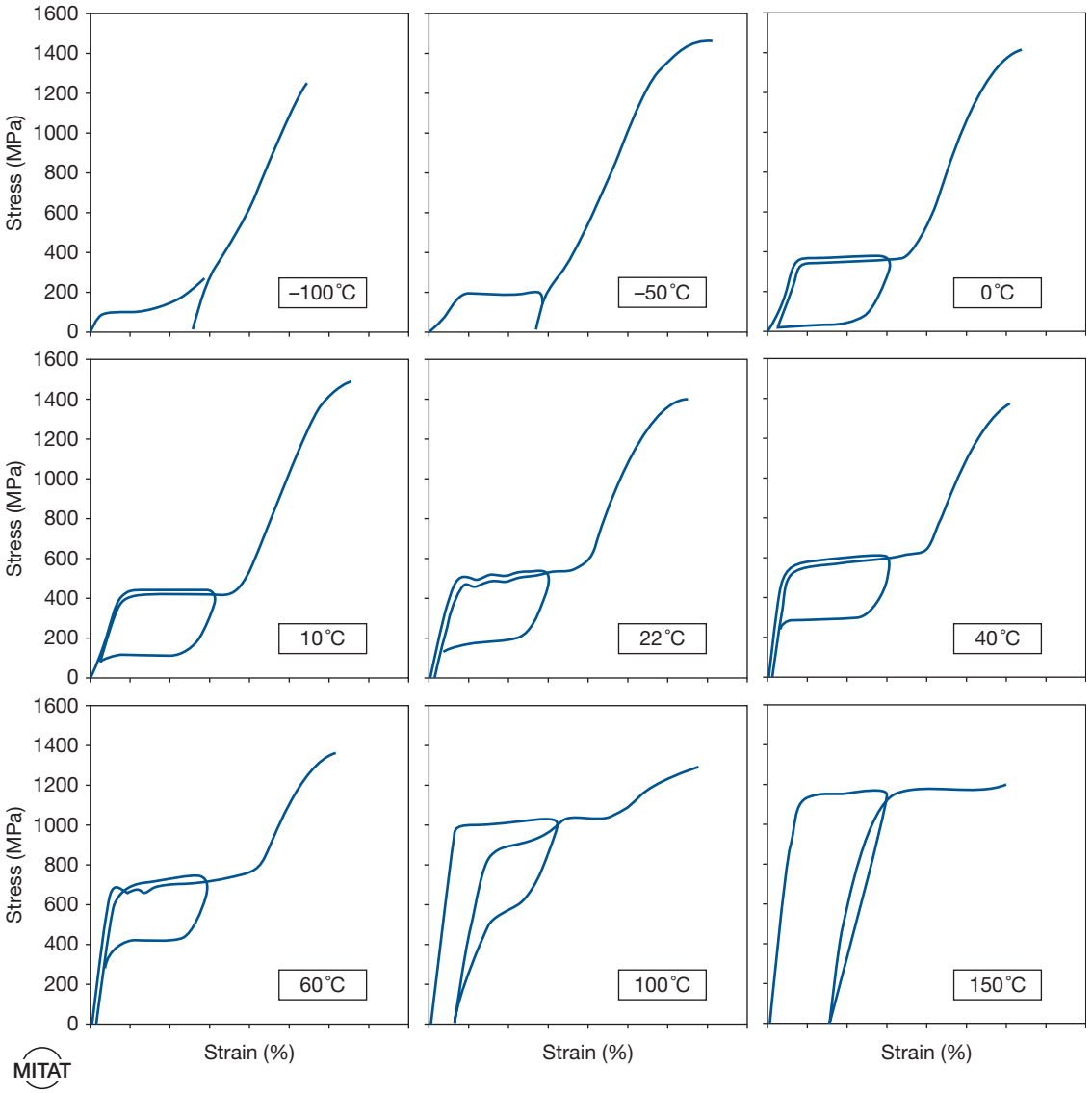

Figure 8 Influence test temperature on tensile properties, for a material with As of −22 °C and Af of 11 °C. Reproduced from Pelton, A. R.; DiCello, J.; Miyazaki, S. *Minim. Invasive Ther. Allied Technol.* **2000**, *9*(1), 107–118.

typical uniaxial stress–strain curve of superelastic nitinol. Upon loading, the stresses and strains arise from the hoop forces that develop within the stent structure as the stent is deformed during crimping into the catheter sheath. Upon unloading, the stresses and strains relax as the stent is released from the constraining catheter sheath and expands within the lumen.

As the stent is initially compressed to fit into the catheter, it deforms elastically and when the stress reaches the level of the load plateau, the superelastic deformation commences. This accounts for the bulk of the deformation strain taken by the stent during crimping. There may be some further elastic deformation of the stress-induced martensite also taking place, but this obviously needs to be controlled to avoid the risk of plastic deformation which could affect subsequent stent size and shape. As the stent is released from the catheter, the stresses drop, following the path of the unloading curve. As the expanding stent reaches the vessel diameter, the expansion process stops (Point C in Figure 9), and the opening force exerted by the stent against the vessel wall is now defined by the level of the unloading plateau. This is known as the chronic outward force (COF) and it can now be appreciated that this COF will remain constant against the vessel wall for a substantial range of oversizing, that is, depending on stent design, the difference between the vessel diameter and the unconstrained (larger) stent diameter may be range of a number of millimeters, but the force exerted will remain constant. This is an exceptionally attractive feature of stent design, that can only be achieved with nitinol; it provides some tolerance on stent sizing when selecting a device diameter to suit a particular vessel size. Furthermore, as diameters are likely to vary more in diseased vessels than in healthy ones, it gives some assurance that consistent forces will still be obtained irrespective of the vessel profile along the stented segment. This is not to underestimate the importance of vessel sizing, which is still a

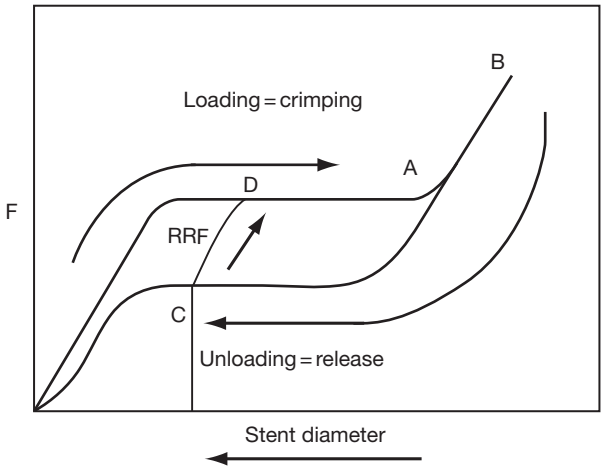

Figure 9 Superelastic stress–strain behavior for a stent (8 mm) being loaded into a catheter and then deployed with a vessel, of smaller diameter. Adapted from Duerig, T. W.; Tolomeo, D. E.; Wholey, M. *Minim. Invasive Ther. Allied Technol.* **2000**, *9*(3/4), 235–246.

critical aspect that can affect tissue response and stent fatigue life; but it does provide more consistency to designers and physicians.

Returning to Figure 9, further unique features of nitinol can be seen when the effect of external compression forces on the vessel are considered. The stent will rapidly develop a resistance to such compression forces, as stresses in the nitinol will follow the path from Points C to D, returning to the load plateau level. Therefore, depending on the magnitude of the load plateau, it can be seen that substantial resistance stresses will be generated before superelastic deformation would recommence. This is known as the radial resistive force (RRF) and essentially provides crush resistance to superelastic nitinol devices (and to shape memory-activated devices, provided they are operating above Af). This crush resistance feature is important for most stents, but is particularly significant for carotid stents. The carotid arteries have less protective tissue (bone, muscle, or organs) around them than most other stented vessels. This risk of stent deformation from external forces or injuries is therefore high and the effect could be critical, if blood supply to the brain becomes restricted. As a general rule for all stents, it is therefore desirable to have high RRF values and relatively low COF levels, highlighting the importance of measurement and control of the load and unload plateaus in the material. This ability of nitinol stents to provide different behavior depending on the loading conditions as described is known as 'biased stiffness.'

To close on deployment aspects, a brief comparison with balloon-expandable stents needs to be mentioned. When a balloon-expandable stent is deployed in a vessel, there is a small elastic recoil, as the balloon is deflated and withdrawn. This causes the stent diameter to reduce slightly and in an extreme case could result in the stent dislodging. Designers can minimize this effect through optimization of the stent pattern and design, while physicians sometimes try compensating for it through slight overinflation of the device. In any event, it cannot be fully eliminated. On the other hand, nitinol stents show no recoil when deployed in a vessel; the combination of superelastic strain and vessel to stent sizing ratio will ensure that the device exerts an outward force, keeping it fully open. This is a significant clinical procedural advantage that nitinol offers over balloon-expandable stent materials.

1.104.5.1.2. Manufacturing methods

Given the extensive use of nitinol in cardiovascular stents and bearing in mind the high sensitivity of the material to heat treatment, a brief review of stent-manufacturing processes is useful. The majority of nitinol stents are now laser cut from tubes, typically using Nd-YAG lasers. The effect of heat absorbed by the material during this process needs to be carefully considered. Schuessler[30] has presented an overview of laser processing of nitinol and has included an assessment of thermal effects in the laser cut heat-affected zone (HAZ). This HAZ can extend several micrometers deep, and metallurgical evaluations confirm the structure to be substantially altered; evaluations of Af reported by Schuessler[30] indicate that transformation temperatures can be pushed upwards by several degrees. This highlights the importance of fully removing the HAZ layer during subsequent electropolishing. Removal of laser-cutting dross and surface oxidation by electropolishing is just as essential for nitinol devices as it is for other materials. In addition to implications for fatigue and corrosion resistance, which will be described later, smooth and clean electropolished surfaces minimize thrombogenic and inflammatory responses. Electopolishing of nitinol is typically performed in mixtures of alcohols and acids, though most processes tend to be proprietary and there is a scarcity of detailed published information. Hassel[31] does briefly describe the use of nitric or sulfuric acid with methanol, or perchloric acid with ethanol, as techniques that have been successfully used. The nitric and methanol mixture is usually run at −30 °C, which in many instances will mean that the material is in the martensitic state during polishing. This leads to another interesting feature, specific to nitinol, though not widely investigated or reported; Pohl *et al.*[32] have shown that the surface finish and texture of electropolished nitinol are influenced by the crystal structure present during the process. Specifically it was shown that surfaces polished in the martensitic state develop a relief pattern, as the structure warms up and converts to austenite. While both processes were deemed to give satisfactory surfaces, it was also noted that polishing in the martensitic state seemed to give better results than processing in the austenite condition, when more material needs to be removed. Finally, electropolished devices are most often passivated, to improve corrosion resistance and enhance biocompatibility. There are many ways to implement this surface treatment, but the process objective is to remove free surface nickel and to preferentially oxidize the titanium, thereby creating a predominantly titanium oxide surface. Treatments in oxidizing chemicals such as nitric acid are widely employed, as reported by Trepanier *et al.*[33] and O'Brien *et al.*[34]

While nitinol heat treatment has already been described, the positioning of this step in the overall process flow needs to be considered. Normally, heat treatment is carried out after laser cutting and before surface finishing. This ensures that any chemical pickling or cleaning step, employed as a pretreatment for electropolishing, will remove all dross and oxides including

those oxides that may develop during heat treatment. However, the number of heat treatment steps required will depend on the tube diameter selected, relative to the desired final stent diameter. One option is to laser cut from a tube size of the same diameter as the finished stent size. This configuration requires only one heat treatment step, primarily to tune in the transformation temperatures and to impart some stress relief and shape setting. The other alternative is to laser cut from a smaller tube diameter and to gradually expand out the stent to the required diameter. This expansion may take several steps, with the stent being put on increasing-sized mandrels for each step and being given a shape setting and stress relief heat treatment each time, typically at ~500 °C. Once the desired size is achieved, the device is given the final heat treatment, to tune in transformation behavior. This has the obvious disadvantage of adding more steps to the overall manufacturing process, as well as requiring development of an initial laser cutting tool path that is different to the ultimate stent geometry required. This approach does, however, generate less scrap metal during laser cutting, and the smaller diameter tubes are also usually less expensive. Originally this sequence developed as only small diameter tubes were available, but now, even though larger tubes are readily available, some manufacturers continue with this gradual expansion route, for the reasons outlined. Aside from cost aspects, there may, however, be some device performance issues also to be considered when deciding upon the processing route. Favier *et al.*[35] compared the two routes, by simulating the different aging effects that occur in stent sections that are exposed to several such deformation and heat treat cycles and in sections that are not strained during the process. The study showed that strained and heat-treated material aged more rapidly than material that was just heat treated, thereby increasing Af at a more rapid rate in these regions. This effect can of course be accounted for during the development of an overall heat treatment schedule for a device. It does, however, point to the potential for inhomogenous material properties across the device, as well as less scope for intentional shifting of transformation temperature, if it is already being pushed upward by the expansion steps.

1.104.5.1.3. Cardiovascular stents: clinical examples

While there is a vast number of nitinol stents developed and approved, there are surprisingly few available for cardiovascular use. The majority are approved for nonvascular indications, such as biliary stenting, and do not meet the regulatory requirements for cardiovascular devices. This situation developed over time, due to off-label use of these nonvascular stents in vascular applications, resulting in devices with the lowest level of design and development input being used in the most challenging anatomical applications. The end result was a high number of device failures, leading ultimately to tighter control of such off-label use.[36] The situation has therefore improved in recent years with an increasing number of stents being specifically designed and developed for a whole range of peripheral vessel anatomies. Even still, there are many design challenges to be addressed in these applications.

Some of the initial nitinol stent designs and features have been reviewed by O'Brien[37] and Stoeckel *et al.*[38] While many new additional designs are being developed, the basic principal features remain the same. These cardiovascular devices

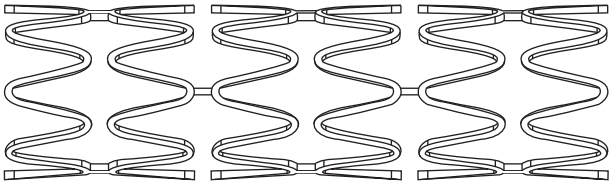

Figure 10 Typical stent pattern showing individual segments and connectors.

are mainly tube-based designs, that is, laser cut, as already described. (Wirebased designs are more widely used in nonvascular applications and will be reviewed in a later section of this chapter.) These tube-based designs typically consist of cylindrical segments or rings composed of several struts spanning around the device circumference. The mechanical performance of this ring will primarily control the radial stiffness of the device. These rings are connected to each other via 'connector' or 'bridge' struts; the design and number of these will influence the axial stiffness or flexibility of the stent. Figure 10 schematically illustrates these stent design features.

While the Radius™ stent was the first nitinol stent developed specifically for coronary arteries, it enjoyed only moderate clinical and commercial success. Angiographic studies suggested that the device continued to slightly expand for a number of months after implantation, leading to a greater neointima formation.[39] While this neointima had minimal effect on lumen diameter, the trend was undesirable and usage of the device diminished. A variation of this device was developed specifically for stenting of saphenous vein grafts (SVGs). These vessels have a high incidence of reocclusion after the bypass surgery; in addition, stenting of these is known to be problematic due to risk of dissection and embolization of plaque particulate. Fabric-covered stents were therefore developed with the aim of trapping any particulate against the vessel wall. The Symbiot™ nitinol stent was such a device, with a poly tetra-fluoro ethylene (PFTE) covering on the inner and outer surfaces. Ultimately, however, clinical studies on this covered device failed to show an advantage over conventional stents, with regard to reducing embolization; covered balloon-expandable devices fared similarly in this indication.[40] Perhaps these initial setbacks in coronary applications had an impact, as there have been no significant approvals for nitinol coronary stents in several years. However, as nitinol technologies and expertise have continued to develop, the inherent flexibility of the material is now being exploited in a much wider spread of demanding applications in the peripheral vasculature. This ongoing evolution of the technology and a growing appreciation for its benefits have also given a recently renewed interest in coronary applications. A number of novel devices for stenting of coronary bifurcations are in development[41] as well as a unique low-profile, small-vessel stent which is electrolytically detached from a guide wire, rather than deployed from a sheath.[42]

Without doubt, however, the area of biggest application development for nitinol over the last 10 years has been the field of peripheral artery stenting. Balloon-expandable stents were being used in many peripheral indications for several years, but the only competing self-expanding product was

the Wallstent, a braided device made from Elgiloy, the cobalt–chromium alloy. This stent derived its self-expanding capability from the high elasticity of the material (high elastic modulus and high strength), rather than from superelasticity. An early review of vascular stent usage in carotid, subclavian, renal, iliac, femoral, and popliteal arteries shows the majority of devices to be either Palmaz balloon-expandable or Wallstent devices, with nitinol stents barely getting a mention.[43] Nitinol, however, provided designers with much more scope for control and tuning of deployment, flexibility and radial force characteristics, and it was only a matter of time before competitive nitinol devices appeared. One of the first and most widely used nitinol peripheral vascular devices was the SMART® (Shape Memory Alloy Recoverable Technology) stent. This laser cut device has a typical zigzag strut pattern, with the segments connected to each other by bridging struts. The end struts are slightly flared to aid securement against the vessel. Phatouros *et al.*[44] describe the device and one of the first clinical uses of it, which was in a carotid stenting application. The high conformability of the device to the vessel curvature was noted as being a significant advantage over other devices, which tended to straighten and stiffen the stented artery. The longer-term outcome with using the SMART® stent in carotid arteries has also been demonstrated in a number of studies; for example, Drescher *et al.*[45] showed exceptionally low restenosis rates at 6-month follow-up. By way of illustration, **Figure 11** shows angiographic images of a stenosed internal carotid artery before stenting, immediately after stenting and at 6-month follow-up.

The SMART stent has since also been included in several clinical trials covering a wide range of peripheral applications. Sabeti *et al.*[46] reported on a femoropopliteal artery trial comparing a number of nitinol devices, including the SMART stent, against the Wallstent and concluded that the nitinol devices performed better with higher vessel patency at long-term follow-up. The case for nitinol stents was also strengthened by a similar study, using the absolute design, which showed superior outcomes compared to balloon angioplasty when used in the superficial femoral artery (SFA).[47]

There have now been a number of other nitinol stents developed and approved for various peripheral indications. Some of these may have only been initially approved for nonvascular biliary applications, but as off-label use of these stents has now been restricted, manufacturers have been going back, gathering data, and obtaining the approvals for vascular indications. Readers are advised to refer to manufacturers' current literature or to check regulatory agency websites, to verify approved indications for any particular device. However, these peripheral vascular applications did suffer a temporary setback in recent years when it became apparent that a high incidence of strut fractures was being observed. As mentioned, this was in part due to use of stents designed and verified for other anatomies, but was also due to a fundamental lack of understanding of the loading condition present in many of these peripheral vessels, that is, even devices like the SMART® stent, developed and tested initially for peripheral (iliac) applications, showed a significant incidence of strut fracture, especially in the SFA. This was first reported by Duda *et al.*[48] at 6-month follow-up in a trial comparing drug-coated and bare SMART® stents in the SFA. Stent fractures were observed in 6 out of 33 patients, with a fracture defined as one or more broken struts per stent. The fracture rate was evenly split between the two test groups, but it was observed that fractures typically occurred in overlapping stents. In addition, the possible role of vessel 'compression and movement' was acknowledged, this perhaps being the earliest recognition of the challenges with this particular vessel. A follow-up trial restricted the use of overlapping stents and significantly lower fracture rates were observed.[49] However, the failures are not attributable purely to stent overlap, but more to the exceptional nonpulsatile forces exerted on the vessel during regular ambulatory motion. Allie *et al.*[50] present an overview of the anatomy in the vicinity of the SFA, summarizing the compression, torsion, tension, and bending loads to which the vessel is subjected. In addition, the same study reviewed repeat angiography on over 100 patients with nitinol stents implanted in the SFA (not just the SMART® stent); fractures were detected in 72 out of 110 patients. The study concluded that flexible

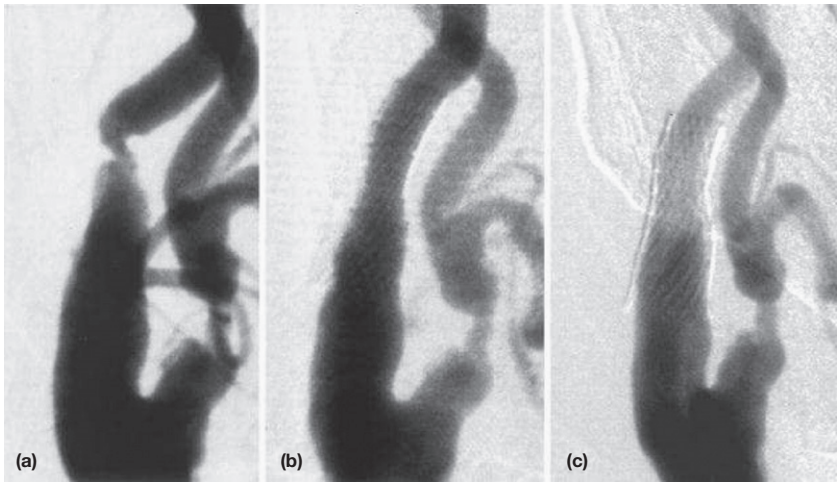

Figure 11 X-ray angiographic images of internal carotid artery (a) before stenting, (b) immediately after SMART® stent placement, and (c) at 6-month follow-up showing high vessel patency. Reproduced from Drescher, R.; Mathias, K. D.; Jaeger, H. J.; *et al. Eur. Radiol.* **2002**, *12*, 2451–2456.

stent designs resulted in less fractures. The significance of the fractures was put even more into perspective by Scheinert *et al.*[51] when it was established that strut fractures increased the risk of restenosis: a particularly challenging finding, given the typically high restenosis rates and the ineffectiveness of drug-coated devices in this indication.

It must, however, be emphasized that nitinol is not particularly susceptible to fracture. The failures observed in the SFA, and even in other coronary and peripheral vessels, are recognized to be due to the vessel-specific multiaxial loading, to which the implanted stents are subjected. Such a variety of loading conditions was not previously recognized and was largely ignored during device development and particularly during fatigue testing. Significant challenges do exist in relation to understanding and quantifying the appropriate loads and deformations of the relevant vessels, as well as translating that information to realistic *in-vitro* fatigue tests. Fatigue and long-term durability aspects of nitinol will be dealt with in more detail in a later section of this chapter. However, in summary, device developers and regulatory agencies now have a high awareness of these issues, and as new devices come to the market, they are being subjected to an increased level of scrutiny.

There are a number of other important vascular anatomies in which nitinol stents are being implanted, most notable being the placement of stent grafts in the abdominal and thoracic aorta, for aneurysm treatment. These devices typically consist of a nitinol frame to which the graft fabric is attached. Once implanted, this device seals off the weakened aneurysm section of the vessel, reducing the risk of rupture and ultimately allowing the aneurysm to repair. By way of illustration Figure 12 shows a CT image of an infrarenal aortic aneurysm, showing the severely dilated vessel, as well as an angiogram and CT image after placement of the stent graft. Treatment of aneurysms in the thoracic aorta is usually done with a conventional straight stent-graft,[52] while treatments in the abdominal region often use modular devices,[53] consisting of an upper body component and individual lower parts that can extended through the bifurcation region, into the individual iliacs if necessary. However, such stent-graft devices have had their own share of problems during development and clinical trials; some have even been taken off the market.

From a nitinol perspective, early concerns revolved around observations of corroded and fractured struts, noted on X-rays or on explanted devices.[54] Ultimately these observations were attributed to poor surface finishing and lack of adequate passivation on early devices – material quality and heat treatments may also have played a role. It is clear, however, that while subsequent devices may have had other issues, the corrosion aspect was addressed and has not since been observed. Jacobs *et al.*[55] present a detailed review of these corrosion aspects and other difficulties encountered with development of early versions of the devices; the most significant problem has been wear and fatigue damage of the graft material, which can ultimately lead to leakage back into the region between the fabric and the vessel wall. Device migration can also be an issue. Strut fractures are still observed, though these are usually associated with regions of high tortuosity in the vessel – pointing again to the need for better understanding of vessel deformations and optimization of designs. While several of these nitinol devices have been developed and explored in clinical trials, very few have achieved regulatory approval. However, as computed tomography and magnetic resonance imaging provide more accurate information on vessel anatomy and deformations, device designs are continuing to evolve and nitinol will be extensively used in this application.

The field of intracranial stenting also merits mention here, though it might be more accurately classified as relating to the neurovascular system rather than cardiovascular. Similar to coronary and peripheral vessels, the intracranial arteries are prone to atherosclerotic disease, and this may be a contributory factor in the occurrence of stroke. Balloon-expandable stents have been used to treat these lesions; some have been coronary devices, used off-label, while others have been designed specifically for intracranial applications. The Wingspan stent system is a nitinol device developed for this indication. Bose *et al.*[56] describe this stent and the outcome of the key clinical trial in which it was used. The results proved promising and the advantages of nitinol over balloon-expandable systems are cited as key factors in the outcome; these included flexibility, conformance to variable diameters and tortuous lesions, and the avoidance of high deployment pressures. Nitinol stents are also being used in conjunction

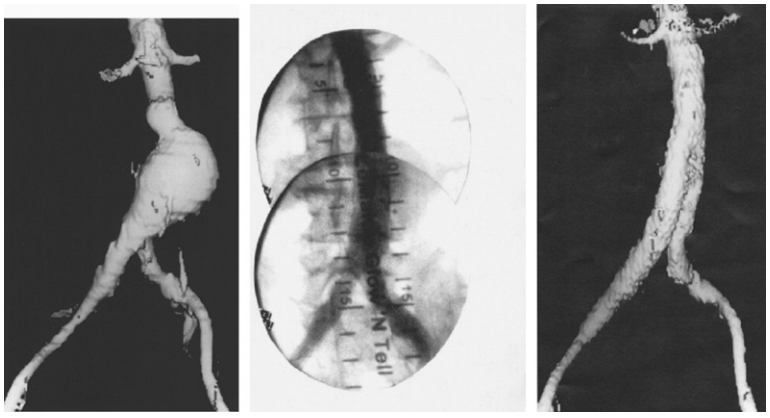

Figure 12 Stent-graft treatment of aortic aneurysm showing CT image of initial condition (on left) and angiogram and CT image after treatment. Reproduced from Allen, R. C.; White, R. A.; Zarins, C. K.; Fogarty, T. J. *J. Endovasc. Surg.* **1997**, *4*, 195–202.

with detachable coil treatment of wide-necked intracranial aneurysms. The treatment involves deployment of a fine coil of wire within the aneurysm to intentionally embolize and seal the defect. In the case of wide-necked aneurysms, the use of a stent can help with positioning and retention of the coils. The Neuroform stent has been developed for this treatment. Akpek *et al.*[57] present details of this stent and initial experiences with using the device in conjunction with embolization coils. Again, the flexibility and conformability of the nitinol device are indicated to be significant advantages over balloon-expandable stents in this application. However, given the high risks associated with neurovascular interventions, it should be noted that like the Wingspan device, this stent has a very restricted scope of use.

1.104.5.2. Other Cardiovascular Devices

In addition to stents, there is a wide range of existing and developing cardiovascular applications for nitinol, with many of these developed even before stenting became a standard procedure. The use of nitinol in vena cava filters goes back to the 1980s with the introduction of the Simon Nitinol Filter™.[58] Vena cava filters are implanted for prevention of pulmonary embolism – being placed in the vena cava to trap and break down blood thrombi, before they reach the lungs. Typically they are used in patients for whom anticoagulation therapy is not feasible. Several different materials have been successfully used for vena cava filters, but nitinol devices offer lower delivery catheter profiles, due to the manner in which the nitinol filter structure can be readily folded down into a small shape and recover upon deployment, either through shape memory or superelasticity. Figure 13 illustrates a number of different filter configurations, showing the conical or umbrella-shaped structures that trap the blood clots.

Interestingly, the Simon Nitinol Filter™ was initially deployed using a chilled saline infusion, thereby converting the material to martensite and reducing the device stiffness during tracking to the delivery site. Developments in both catheter and filter mean this is no longer necessary, but this filter is still in use today, although there are now several other competing nitinol filters available. Some of these are designed to be retrievable, where the flexibility of nitinol can again be an advantage.

More recently, the use of nitinol in filters has been in relation to development of embolic protection devices. These have been developed mainly for use during carotid stenting where the impact of embolized plaque debris could be fatal. They typically consist of a metal frame structure, to which a fine porous polymer membrane is attached. This device is deployed distal to the lesion, and during the stenting procedure, any loose plaque particles are trapped within the filter, which allows blood to pass through. At the end of the procedure, the filter is then collapsed and retrieved through the catheter, with the trapped debris retained. The self-expanding and flexibility aspects of nitinol are key features in such designs and it is probably reasonable to conclude that nitinol actually enabled development of these devices. The only other option available prior to this was to use occlusion balloons to seal off the artery during the procedure – not an ideal solution due to risks associated with temporarily stopping cerebral blood flow. Several such filter devices are now available, all utilizing nitinol frames[59]; clinical studies have demonstrated their safety and efficacy, and they are also being used in other stenting applications where there is a risk of plaque rupture.

The diversity of nitinol applications in the cardiovascular anatomy is highlighted by the final two uses described herein. A relatively early application has been its use in the mesh frame of a septal occluder device, used for closing of atrial septal defects. Fischer *et al.*[60] describe the features and experiences with the Amplatzer® system, one of the first occlusion devices to use nitinol – and still widely used today. The device consists of two disk-shaped structures, woven from fine nitinol wire, with polyester fabric attached, to aid in thrombus formation and sealing of the defect. The connected disks are deployed sequentially from a catheter, positioning one at each side of the chamber wall. The use of nitinol provides for easier deployment and smaller delivery systems, which is a critical aspect, as the treatment is most often required in smaller, pediatric patients. There are now several such occluder devices on the market. Finally, to briefly mention heart valve replacement, a highly challenging application where nitinol is starting to be used. Heart valve disease has traditionally been treated using replacement mechanical valves, which have provided good durability but have been susceptible to thrombosis. The use of more compatible biological materials has therefore evolved in recent years, with either human or animal tissue being utilized. When using animal tissue, usually either bovine or porcine, the tissue itself is supported on a metal frame for implantation – this is in effect a stent structure, but with the valve attached. Grube *et al.*[61] describe initial experiences with the CoreValve device, one of these first bioprosthetic-nitinol valves. While balloon-expandable stent frames have been used in this application, the advantages of nitinol and self-expansion are cited as being better securement, lower risk of leaks or migration, and a reduced risk of damaging the valve leaflet material itself during deployment.

1.104.5.3. Nonvascular Stents

There is a wide range of nonvascular vessels and tracts within the body where nitinol devices are being used, mainly utilizing superelastic behavior. These include biliary, ureteral, esophageal, and pulmonary applications, with stenting usually being a palliative treatment to open up a vessel that is being obstructed by a tumor or by other degenerative diseases. Many of these stents were developed before laser cutting became the stent-manufacturing norm, and therefore they are made from wire, using knitting, braiding, and winding technologies. Miyazawa *et al.*[62] describe use of the Ultraflex™ stent in treatment of malignant bronchial occlusions. In this application, the 'biased stiffness' feature of nitinol is again worth mentioning; as a tumor presses against the structure, a high-compression resistance will develop while a much lower radial force will be exerted away from the obstruction, preventing damage to the mucosa lining. In addition, the superelasticity of nitinol is a key feature of this device. During coughing events, these airway vessels can completely collapse before recovering to full diameter – the highly superelastic device

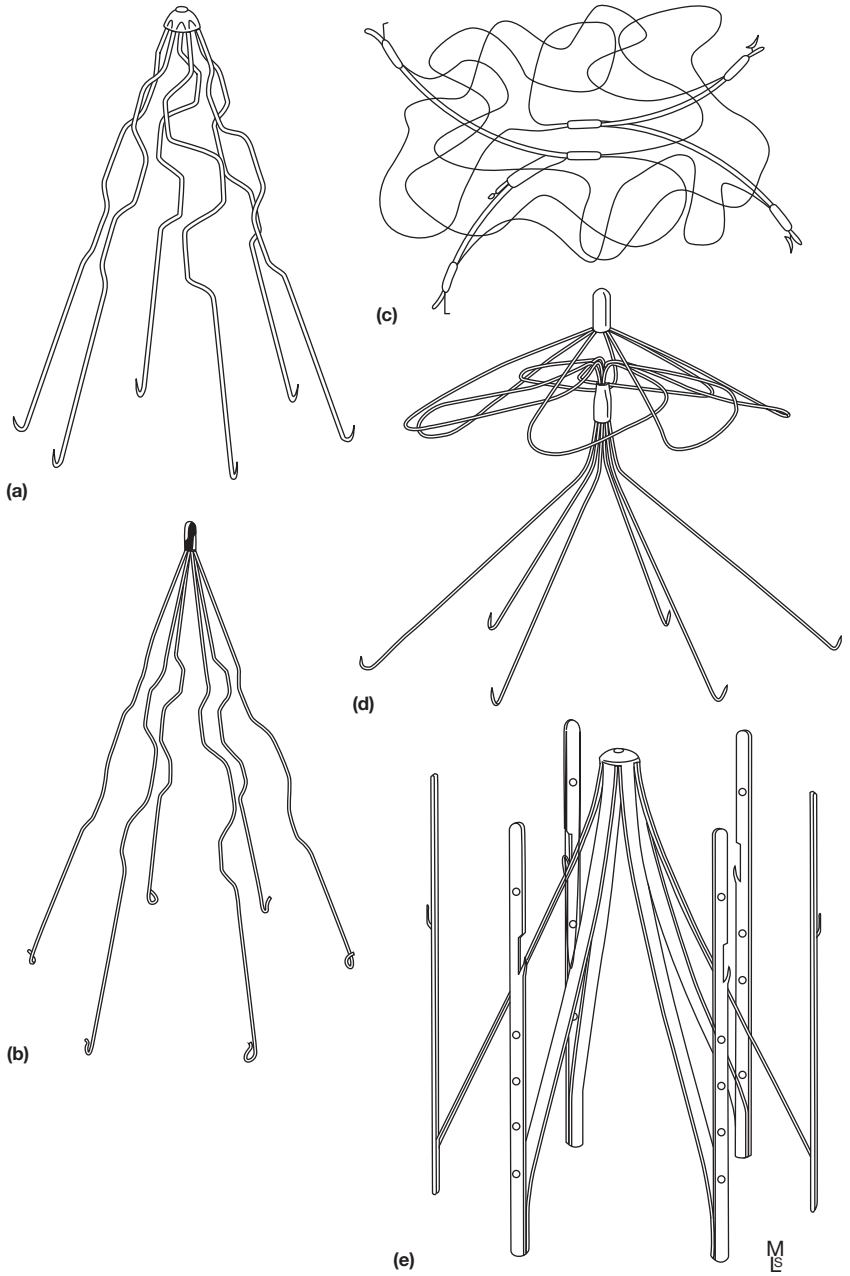

Figure 13 Example of a number of different vena cava filters: (a) stainless steel greenfield, (b) titanium greenfield, (c) bird's nest (stainless steel), (d) Simon nitinol filter, and (e) Vena Tech (Phynox). Reproduced from Streiff, M. B. *Blood* **2000**, *95*, 3669–3677.

handles this well, opening back fully, with no permanent deformation. The Ultraflex design is also used for esophageal stents, where similar challenges exist. The peristaltic motion of swallowing creates high repetitive deformations that few other materials could readily handle. Cwikiel *et al.*[63] describe initial experiences with the stent. Covered versions of the device were subsequently developed to minimize tumor in-growth through the knitted wire structure. Aside from the Ultraflex devices, there are many other nonvascular stents on the market, with an increasing amount being made from nitinol. Lee[64] describes the features and selection aspects of several of these, specifically those designed for esophageal treatments. Kozarek[65] reviews a number of balloon expanding and self-expanding designs used for treatment of biliary obstructions. While long-term durability and fatigue aspects are not seen as critical for nonvascular devices, there have been instances of wire breaks and device fragmentation. Rasmussen *et al.*[66] report on biliary stenting patient follow-ups, ranging from 1 to 21 months, and observed fractures in 8% of patients. In addition, it was suggested that fracture could be a contributory factor in recurrent obstruction. Reddy *et al.*[67] and Chhetri *et al.*[68] report on observations of fractures in esophageal stents. While it is noted that such fractures are a rare occurrence, these findings do suggest that there is scope for continued improvement of device designs and material processing aspects.

1.104.6. Orthodontic Applications for Nitinol

Though perhaps not as popularized as cardiovascular applications, nitinol has been widely used in orthodontic applications for several decades now. Kusy[69] presents a thorough review of the historical evolution of orthodontic materials, indicating the significant role that nitinol now has in this market. Nitinol is an ideal material for archwires. By tuning of the unload plateau level, nitinol archwires can be applied to give a continuous force against the teeth. As the teeth gradually realign to the desired position, this level of force is kept constant over a substantial strain range. This provides an improved level of comfort to the patient as well as minimizing the number of readjustments needed over time. In addition, the shape memory effect can be used where fitting and adjustments are made in the soft martensitic condition, and when the device warms up to body temperature high retaining forces are developed, as the material converts to the austenitic phase.

There are a wide range of nitinol archwire products on the market, utilizing shape memory and superelastic effects, with ranges of unload forces (and therefore transformation temperatures) tuned to suit many different patient needs. Wires with Af at approximately body temperature are classified as martensitic, typically imparting low forces and therefore often used in early-stage treatments. Devices with lower Af (i.e., at room temperature) are classified as austenitic, providing higher forces at body temperature and often used in later stages of a treatment. While mechanical aspects may be reasonably predictable, long-term corrosion and surface degradation are the main challenges facing these devices. The ideal archwire surface needs to be smooth with minimal friction against the brackets to which it is attached. Friction at this interface can inhibit the gradual sliding adjustment that is necessary to accommodate the realignment of the teeth and maintain a constant level of force. Any deterioration of the surface condition may therefore have an impact on the overall efficiency of the device. Therefore, aside from potential implications for biocompatibility performance, corrosion is also undesirable due to the manner in which it can impact the surface and mechanical behavior of the device. Huang[70] has studied the surface characteristics and corrosion response of a number of commercial archwires in artificial saliva with a range of acidities. Significant differences between the wires were observed, with some showing relatively poor pitting and crevice corrosion resistance – especially in lower pH environments. However, this study did not show any link between as-received surface roughness and corrosion performance, with the roughest of the wires performing well in the corrosion tests. Es-Souni *et al.*[71] studied two different commercial archwires, showing that the wire with a rougher surface and with more inclusions present did have a worse corrosion resistance. While these findings may seem at odds with each other, direct comparisons are difficult given the variety of materials and test methods used. Overall, however, such studies do suggest that the level of control and consistency on surface condition is not as high on some of these components as it is for cardiovascular devices. Eliades *et al.*[72] examined retrieved archwires that had been *in vivo* for up to 6 months, noting extensive degradation of the surfaces. Roughness was increased due to the presence of mineralized deposits, microcracks, and due to both pitting and crevice corrosion. However, the study did not correlate these observations with clinical performance of the devices. The effect of fluoride ions on archwire corrosion performance has also been studied, given the widespread use of fluoride-containing mouthwashes. A detailed study by Schiff *et al.*[73] compared several archwire and bracket material combinations in a number of different commercial mouthwash solutions. Interestingly, the study did show that some mouthwashes were more corrosive than others, with the nitinol archwires exhibiting high nickel ion release when used with stainless steel or cobalt–chromium brackets. The investigators suggest that orthodontists should consider prescribing specific mouthwashes depending on the archwire and brackets materials being used. Nitinol archwire fractures have also been observed *in vivo*, though a detailed investigation by Zinelis *et al.*[74] did not determine the precise failure mechanism, other than noting that all failures were typically brittle in nature. To conclude, nitinol is being widely and successfully used in orthodontic applications, though longer-term mechanical performance and biocompatibility of these devices merits continued exploration.

1.104.7. Orthopedic Applications for Nitinol

Nitinol is of interest for orthopedic applications due to its high strength combined with superelastic strain recovery, as well as its lower elastic modulus, compared to other traditional implanted metals. This lower modulus provides for the possibility of less 'stress shielding' effects between load-bearing implants and the adjacent bone. While monolithic nitinol devices are of interest for such applications, greater potential lies in the use of porous nitinol structures, which can additionally provide enhanced osseointegration. Bansiddhi *et al.*[75] have presented a comprehensive review of developments in this field. Work in this area is focused on methods for producing the porous structures, on surface modifications to reduce nickel release, and on studies to assess and optimize the biological response. There are several powder metallurgy-based methods for producing porous nitinol, but the most widely used method is self-propagating high-temperature synthesis (SHS). This process involves the ignition of a compressed powder mixture to produce an exothermic self-sustaining reaction, which propagates through the material to create the final porous structure. Nickel and titanium powder ratio, powder size and shape, as well as preheating temperature and ignition technique can all influence the nature of the porosity obtained. Chu *et al.*[76] and Bassani *et al.*[77] describe both production and characterization of porous nitinol structures created by SHS. The objective is to maximize the amount of interconnected porosity while retaining good compressive strength; most target applications are compressive load-bearing structures. Chu *et al.*[76] report on creating a material with 57% porosity, giving a compressive strength of 208 MPa (higher than compact human bone) and with an elastic modulus of only 2.26 GPa, which matches well with 1–2 GPa for bone.

One concern with these structures is the potential for increased nickel ion release, due to the large surface area obtained with the open porosity. While nickel release from cardiovascular nitinol devices has often been debated, it has

never been established to be a significant aspect of device biocompatibility. On the other hand, with surface areas of these porous structures being orders of magnitude greater than typical cardiovascular devices, the risks are more substantial. Incomplete synthesis may also leave some residual elemental nickel or nonstoichiometric compounds in the structure. Approaches for minimizing nickel release typically focus on enhanced oxidation of titanium in order to create a protective titanium oxide layer – these include thermal oxidation and oxygen ion implantation techniques. Vapor-deposited coatings of titanium nitride and titanium oxide have also been explored, as well as hydroxyapatite coatings. Bansiddhi *et al.*[75] include a review of these approaches, particularly those for which nickel release data are obtained. While all show promise, aspects such as long-term durability and impact on shape memory or superelastic properties also need to be considered.

Several *in vivo* animal studies have been performed to assess bone in-growth with these porous structures. Ayers *et al.*[78] report on a study in which samples with varying amounts of porosity were implanted in rabbit craniums, to assess potential applications in the field of craniofacial reconstruction surgery. Analysis 6 weeks after implantation demonstrated immature bone in-growth to all structures, with no evidence of macrophage reactions. In a similar study, aimed at assessing suitability for load-bearing bone grafts, Kujala *et al.*[79] implanted samples in rat femur, but for a much longer duration of 30 weeks. The best bone–implant contact was obtained in the samples with the highest level of porosity. Likibi *et al.*[80] compared bone fusion for a commercially available porous nitinol (Actipore™) against a conventional titanium intervertebral lumbar fusion device, in a sheep model. While both components performed well, the porous nitinol demonstrated better osseointegration. The Actipore™ material is currently the only commercially available porous nitinol and is being explored in clinical trials for spinal fusion procedures. Munroe *et al.*[81] investigated the corrosion response of this Actipore™ material with a number of different surface passivation treatments. A combined process of etching followed by boiling in water and nitric acid passivation gave the best corrosion resistance. **Figure 14** illustrates some typical porous nitinol structures including those present in the Actipore™ material.

In addition to these applications for porous material, some unique orthopedic applications are also being considered for conventional nitinol. Kujala *et al.*[82] report on the possibility of using a nitinol intramedullary nail to help correct bone deformities. A study of this concept in rat femurs involved implanting of the device in a straightened martensitic condition; upon heating up to the austenite phase, the device changes to a slightly curved shape, thereby applying a gradual bending force to the bone. The ability to remodel the bone in this manner was demonstrated. Nitinol is already being widely used in commercial orthopedic staples, with a number of different types now approved by regulatory bodies. After positioning across a fractured bone, these staples can be activated through shape memory or superelasticity, to apply a compressive force that pulls the fracture faces together. Russell[83] presents a thorough review of the design approaches and clinical aspects for some of the main commercially available staples. There are many other orthopedic fixation applications currently being explored, where the unique force control of nitinol is being exploited. These include devices such as a long-bone fracture fixation component described by Fu *et al.*[84] and superelastic rings for cranioplasty procedures presented by Morawiec *et al.*[85]

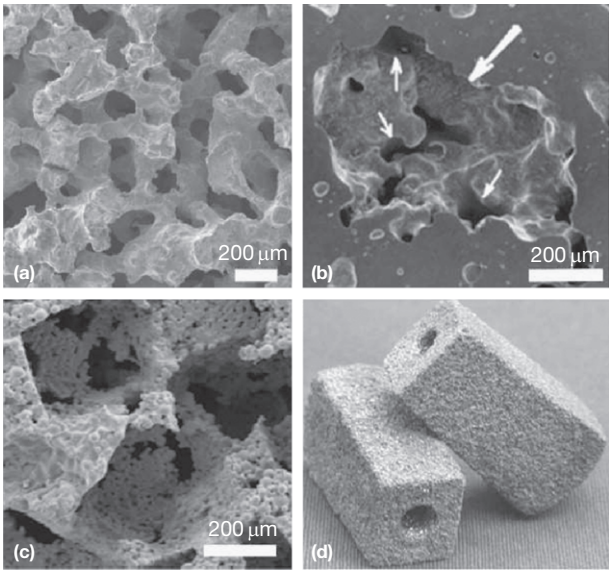

Figure 14 Images of porous nitinol produced by (a) self-propagating high-temperature synthesis, (b) hot-isostatic pressing with argon, (c) metal injection molding with NaCl spacers, and (d) commercially available self-propagating high-temperature synthesis Actipore™. Reproduced from Bansiddhi, A.; Sargeant, T. D.; Stupp, S. I.; Dunard, D. C. *Acta Biomater.* **2008**, *4*, 773–782.

1.104.8. Clinical Imaging of Nitinol Medical Devices

Accurate imaging of medical devices is an important aspect during and after interventional procedures. This is particularly critical for small minimally invasive devices, such as stents and filters, as physicians rely heavily on imaging techniques to visualize deployment of the devices. Similarly, for any monitoring or follow-up procedures, the device needs to be accurately imaged. X-ray has long been the standard method and is adapted for real-time imaging through fluoroscopic techniques. The method relies on attenuation of X-rays by the device structure, and in this regard, nitinol has only moderate X-ray attenuation compared to stainless steel or cobalt–chromium. The density of a material can be used as an approximation for X-ray attenuation; 6.5 g cm^{-3} for nitinol compares unfavorably with 8.0 g cm^{-3} for 316L stainless steel or 9.1 g cm^{-3} for L605 cobalt–chromium. Therefore under fluoroscopic angiography, nitinol devices can be difficult to observe, particularly those with relatively thin strut designs. There have been several different approaches to enhancing the radiopacity of these small devices, but the most widely used method is the attachment of small 'markers' of highly radiopaque materials in the form of bands, clips, or rivets to the stent structure at specific locations. Often these are put at each end of the stent so that the precise length of the device can be clearly visualized even if the main stent structure is not so visible. Stoeckel *et al.*[38] describe some of the usual materials and configurations used

for a number of commercial nitinol devices. Tantalum has the advantage that it does not generate significant galvanic interaction with nitinol. In addition, it is possible to weld the tantalum markers to the nitinol, if required. Siekmeyer *et al.*[86] present a useful study comparing the features of welded and riveted marker bands, using tantalum and gold.

Platinum or platinum–iridium alloys are also used where higher radiopacity is needed, though they do have the potential to generate more galvanic effects. Wiskirchen *et al.*[87] present a comparative *in-vitro* imaging study on a number of nitinol and stainless steel stents, highlighting the influences of stent design, mass, and strut thickness on visibility as well as illustrating the benefits of tantalum markers. Coating of nitinol with radiopaque materials has also been explored; however, this can lead to additional considerations for biocompatibility and also raises the possibility of galvanic corrosion at coating defects, where unfavorable cathode-to-anode ratios could develop. Process complexity and cost must also be considered when exploring such options. Cheng *et al.*[88] report on a tantalum coating applied to nitinol, using physical vapor deposition techniques; significant improvements in device visibility were demonstrated. Another perhaps more promising approach, though limited to wire-based devices, is the use of composite tube structures, with nitinol on the outside and a radiopaque core on the inside. This approach preserves the nitinol outer surface, thereby not altering biocompatibility aspects. In addition, the risk of galvanic effects is significantly reduced as exposure of the more cathodic radiopaque materials is minimized. Schaffer and Gordon[89] have described development and characterization of such a composite tube, using platinum as the radiopaque core. These NiTi-DFT®-Pt materials demonstrate excellent visibility, though care must be taken in selecting the appropriate size of core so that expected shape memory or superelastic properties are not impaired.

X-ray fluoroscopy will continue to be the imaging technique of choice during minimally invasive interventions. However, for noninterventional imaging, such as for prescreening or follow-up procedures, techniques such as CT and MRI are being increasingly used. The compatibility of nitinol devices with these imaging modalities is therefore of increasing interest. During clinical CT imaging, metallic structures can create image artifact which is typically proportional to the radiopacity of the material. In the case of some devices, this can obscure clinical interpretation of the data, such as assessing stent lumen patency for evaluation of restenosis. In this instance, the modest radiopacity of nitinol is actually an advantage as it leads to low levels of artifact. Maintz *et al.*[90] have presented a comprehensive *in-vitro* study assessing the CT imaging compatibility of several different coronary stent designs. Only two nitinol devices were evaluated, but these were among only a small number of devices that showed good compatibility. It should be noted, however, that the presence of radiopaque marker bands can somewhat negate this advantage, as these can lead to image artifact at specific points.[91]

A different set of challenges arise with MR imaging of devices. Here the magnetic characteristic of the material and the electrical conduction paths throughout the device become critical features. Material magnetic susceptibility is an important characteristic for all implants, as it can impact on device safety through magnetic-induced movements or heating effects. In addition, inherent device magnetism can produce image atifact due to localized disruption of the magnetic fields within the MRI scanner. Fortunately, nitinol has relatively low magnetic susceptibility due to the absence of ferromagnetic elements such as iron. Magnetic susceptibility-induced artifacts are therefore relatively low. However in the specific case of stents, or other devices with mesh-based patterns, additional MR-specific issues arise. These structures can attenuate the radio-frequency signals, which are integral to the MR imaging process, such that signal from the inside of these devices can be diminished. In effect this can impair MR visualization within the device, such as required for assessment of restenosis within stents or characterization of thrombus within filters. Melzer *et al.*[92] have presented an overview of both the magnetic and shielding effects for a range of nitinol devices, illustrating clearly the levels of artifact that can be created. Lenhart *et al.*[93] have carried out an evaluation on a range of commercial stents, including several made of nitinol. The nitinol devices typically resulted in the lowest image artifact, with the best lumen visibility. The extent of the shielding artifact is highly design-dependent and the problem is not unique to nitinol, but nitinol has the greatest potential to be part of the solution to this issue, as a low magnetic susceptibility material is still essential. Immel and Melzer[94] describe some of the novel approaches to altering the shielding behavior of devices; integrating these with nitinol shows promise in terms of achieving full lumen visualization.

1.104.9. Long-Term Durability and Biocompatibility of Nitinol

1.104.9.1. Fatigue Behavior of Nitinol

The fatigue response of nitinol has long been of interest, given the potential for unique effects from different phases and from stress-induced transformations. The subject has become even more important in recent years, given the increased occurrence of peripheral cardiovascular stent fractures, as already discussed. In addition to the near-endless combinations of material properties, microstructure, loading conditions, temperatures, and surface finishes being tested, there are also several different test methodologies to deal with. These include options on testing of actual devices or testing of material coupons and whether to use the traditional fatigue life approach (i.e., strain–life curves) or to use fracture mechanics approaches to evaluate critical stress intensities and crack growth rates. The fracture mechanics methodology has primarily been explored by Robertson and Ritchie[95], establishing fatigue crack growth thresholds and crack growth rates for nitinol in a variety of loading conditions. While this approach generates fundamentally sound data, it is difficult to utilize this information for the majority of nitinol devices, especially for stents. Using the data to predict device lifetime depends on having accurate information on the shape, dimensions, and location of flaws such as microcracks or inclusions in the material. This can be practically very difficult for such small components, where stent strut dimensions are typically $<100\,\mu m$. The critical crack size in such instances is therefore relatively small, and given that small cracks tend to grow at much faster rates, Paris Law crack growth rates are not highly relevant. Gong *et al.*[96] and James and Sire[97] have recently

clarified that traditional fatigue life approaches are therefore best for vascular devices, and in this regard, these methods are therefore also applicable to most current discussions on fatigue behavior of nitinol.

As with any material, there are a number of useful studies in the literature reporting on the traditional factors that influence fatigue performance, such as inclusion content,[98] hydrogen contamination,[99] and surface roughness.[100,101] However, the similarities with conventional metallic materials do not go much further, with some unique behavior being observed in nitinol. Foremost among these is the influence of mean strain and strain amplitude on the number of cycles to failure. First it should be noted that when the fatigue data relates to nitinol stent applications, the mean strain comes from the oversizing of the stent within the vessel, while the strain amplitude is controlled by the range of vessel diameter change, between the systolic and diastolic pressures. It can therefore be appreciated that the mean strain is generally compressive and the extent of this would vary depending on the degree of oversizing. The zero-mean strain condition has little relevance to nitinol stents, though is sometimes tested to put other data into perspective. Perry and Kugler[102] were among the first to investigate mean and amplitude relationships, using samples representative of the cell geometry of a specific stent, thereby representing the mean and amplitude strains that the cell structure experiences. Among the findings was the unusual observation that fewer samples failed when tested at a mean strain of 3.4% compared to those tested at a mean strain of 2.0%, when applying an alternating strain of 0.6%. This is unlike conventional metallic materials where higher mean strains generally result in more failures, for a given alternating strain, that is, as described by the traditional Goodman relationship. However, there is some doubt about the applicability of the data for stent applications as it appears that in this instance, the mean strain has been applied in a tensile mode, that is, opening out the cell structure rather than compressing it, as would occur when a stent is *in vivo*. Subsequent studies by Pelton *et al.*[103,104] have made these aspects clearer, in addition to presenting finite element analysis (FEA) analysis to support the strain conditions selected. These studies evaluated uniaxial fatigue behavior of samples representing individual cells (diamonds) of a stent structure, as well as pulsatile fatigue evaluation of complete stents. A range of mean strains and alternating strains were applied and all were tested at 37 °C. The subcomponent cells and the stents had Af in the range 26–32 °C. Extensive data were obtained and presented in a number of graphs for strain amplitude versus number of cycles to failure; however, the best insight is obtained when these data are presented as a constant life diagram as shown in **Figure 15**. This diagram shows data for the individual subcomponent cells (or diamonds) at the various conditions of mean strain (zero and compressive) and alternating strain. The data shows that these nitinol samples have a constant fatigue life at a strain amplitude of ±0.4%, for mean strains up to about 1.5%. At higher mean strains, the fatigue life is shown to actually increase, contrary to expectations based on traditional metals.

The mean and alternating strain values applied to the stents covered the same range as tested for the subcomponents, though it was noted that this included values that would exceed those expected under typical *in vivo* conditions. The stent data

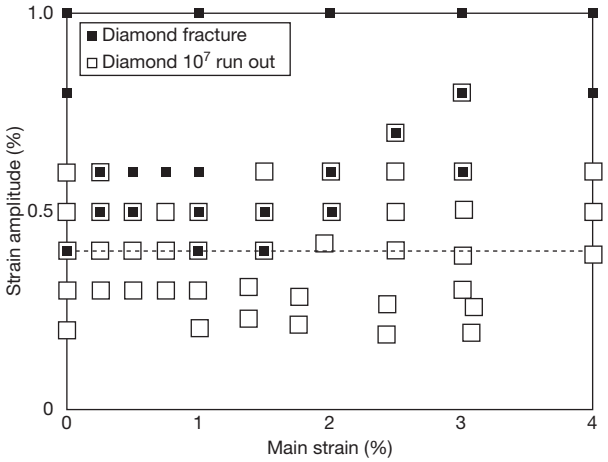

Figure 15 Constant-life diagram for stent cell subcomponents. Samples that survived beyond 10^7 cycles are shown as open squares, while samples that failed at $<10^7$ cycles are shown as solid shaded squares. A 10^7 fatigue strain limit at 0.4% alternating strain is shown. Reproduced from Pelton, A. R.; Schroeder, V.; Mitchell, M. R.; Gong, X. Y.; Barney, M.; Robertson, S. W. *JMBBM* **2008**, *1*, 153–164.

supported the subcomponent findings in that no failures were again observed below the strain amplitude of ±0.4%. This study did not include microstructural or crystallographic evaluations, but the investigators suggest that the observation of improved performance, above ~1.5% mean strain, is attributable to the formation of stress-induced martensite and the ability of this phase to better accommodate the cyclic deformations. A fatigue study by Morgan *et al.*[105] on nitinol wire with an Af of 12 °C did find some trends consistent with these mean strain observations. The results showed that higher mean strains (within the range 2–6%) gave longer fatigue life, when tested at low strains amplitudes (±1.0% and below). A constant life limit for strain amplitude was not described.

The impact of phase transformations was also highlighted in a study by Wick *et al.*[106] in which materials with different Af values were tested. The data showed that nitinol with higher Af performed better, consistent with the argument that martensitic structures have better fatigue resistance. In addition, it is proposed that nontransforming martensite (i.e., martensite that exists at the test temperature without needing to be stress induced) is superior to transforming martensite.

In summary, the fatigue behavior of nitinol is highly complex, with performance influenced by a wide range of material and test variables. While some data, which point to alternating strain limits at various mean strains are emerging, more data are needed to verify these findings. This subject is particularly important in the field of cardiovascular stents, where the influence of multiaxial loading now also needs to be fully considered. Traditionally stents were tested in purely pulsatile mode, normally with the stent held in a straight configuration. This will need to shift to include additional multiaxial loading and for testing of devices in curved and tortuous configurations. In addition, device manufacturers will need to demonstrate a broader understanding of the conditions that actually induce fatigue failures rather than just aiming to pass a specific minimum number of cycles.[96,107]

1.104.9.2. Corrosion Behavior of Nitinol

At the outset it must be stated that nitinol is in general a highly corrosion-resistant material with an *in vivo* performance that is typically comparable to stainless steel or titanium materials. However, its corrosion resistance is highly sensitive to material impurities and to the nature and integrity of the oxide that is created by surface processing. This fact was highlighted in the early stages of nitinol stent development, with reports of pitting corrosion on explanted aortic aneurysm stent grafts.[54,108] These findings were ultimately attributed to poor surface finishing and passivation of these early devices, and no further cases of *in vivo* corrosion failures have been reported in the literature.

The influence of ingot melt practice on inclusion content has already been described, and this is an important aspect when considering corrosion resistance. These carbide and oxide inclusions are regularly the sites of corrosion attack; Shabalovskaya *et al.*[109] have presented an analysis of the different types of inclusions present, clearly illustrating the manner in which they may act as initiation sites. Localized composition variations in the surrounding matrix (i.e., depletion of matrix constituents) can be sufficient to create galvanic effects between the particles and the matrix. These inclusions will be present even on well-polished and passivated surfaces. Though an ASTM[110] for nitinol does provide limits on the size and volume fraction of inclusions, there is some doubt as to whether the limits are sufficiently stringent.

While use of materials with minimum inclusion content is the first step towards optimizing corrosion performance, the next objective is to develop a passive surface through enhancement of the native titanium oxide layer. Given the manner in which titanium readily and rapidly oxidizes, there will always be some titanium oxide present on the surface. The precise composition, uniformity, distribution, and thickness of this surface oxide will, however, depend on the material processing route and especially on final surface treatments. As a general rule, the best corrosion performance is obtained from surface oxides with minimal free nickel or oxidized nickel contents, that is, maximizing the titanium oxide. Furthermore, thicker oxide layers are not necessarily good as these tend to be brittle and readily crack; optimum corrosion resistance is typically obtained from oxide layers that are <10 nm thick. Shabalovskaya *et al.*[111,112] and Pérez *et al.*[113] have presented extensive studies of oxide composition and the related corrosion performance from a wide range of surface treatments, including thermally oxided, chemically etched, sand blasted, mechanically polished, and electropolished. It is immediately clear upon reviewing these data that a significant spread in performance is obtained; for example, values for breakdown potential, as measured by cyclic potentiodynamic polarization testing, can range from as low as 100 mV to over 1000 mV. Interpreting trends and establishing correlations is complicated, not just by the differences in the specific surface treatments, but also by the differences in test coupons (geometry and manufacture), material compositions, inclusion contents and test environment. Pound[114] carried out a study of mechanically polished and electropolished wire and demonstrated that use of either 0.9% NaCl solution or phosphate-buffered saline (PBS) will give significantly different results, with the NaCl generally being the more severe environment. This study also included a review of data obtained in other media such as Hank's solution, further highlighting the variations in performance. However, from the perspective of implantable nitinol devices, some of the published data can be disregarded – particularly surfaces that would not be considered suitable for implantation. For example, cardiovascular applications usually demand smooth surfaces, to meet expectations in relation to fatigue, thrombogenicity, and delivery system interactions. Electropolishing is therefore the usual process of choice, irrespective of corrosion implications – though of course the corrosion performance of electropolished surfaces can be modified through appropriate passivation treatments. On the other hand, some nonvascular applications may have lower surface finish expectations and mechanically polished or chemically etched surfaces may suffice. In summary, device developers are strongly advised to focus on their specific application and environment and to carry out their own assessment to ensure that all material, design, thermomechanical, and surface treatment effects are appropriately captured. The published literature does then provide a useful guide in understanding the effects of the many variables and in identifying performance targets from surfaces or devices with some relevance to the application. In addition to the forementioned studies, Shabalovskaya *et al.*[115] have presented a comprehensive review of nitinol surface treatments encompassing typical as-received, heat-treated, and polished surfaces, through to surfaces modified with ion beams, laser treatments, or surface coatings.

As indicated, however, electropolished surfaces are often the most relevant to implantable devices, and these therefore merit some further detail. First, it must be stated that the corrosion performance of a well-electropolished surface can be hampered by the presence of inclusions. Shabalovskaya *et al.*[111] highlight this well, with a comparison to chemically etched surfaces. These etched surfaces may be rougher, but for the samples concerned, had better corrosion resistance than the electropolished surfaces. This was attributed to the etched surfaces having lower inclusion content due to the manner in which etching removes some of the soluble inclusions as well as regions of matrix inhomogeneity around them. Electropolishing, on the other hand, removes only the conductive metal around the inclusions, leaving more of them revealed at the surface. This can help explain why a surface that appears to be well polished, and perhaps passivated, results in an occasional low breakdown potential when polarization tested.

Perhaps one of the most comprehensive studies of electropolished nitinol surfaces is that of Eiselstein *et al.*[116] which compared mechanically polished and electropolished samples (with similar inclusion levels) in a series of long-term immersion and cyclic polarization tests. In summary, all mechanically polished samples showed breakdowns at potentials <800 mV ($n = 130$), while only 13% of the electropolished samples ($n = 290$) showed breakdown. Interestingly, the study did also show that extended immersion of nitinol in such physiological solutions actually increases the measured breakdown potentials. This indicates that the solution has a passivating effect, most likely leaching out free nickel and allowing additional titanium oxide to form. Similar observations have been reported by Warner,[117] who recorded a shift in breakdown potential from an average of 446 mV up to 680 mV after 672 h immersion in PBS, for surfaces with a thermally grown

oxide. Finally, in relation to electropolished surfaces, additional passivation treatments are always recommended, to maximize the amount of titanium oxide at the surface. As already reviewed in the section relating to stent manufacture, relatively simple treatments in oxidizing chemicals such as nitric acid work well, leaching out residual surface nickel and oxidizing additionally exposed titanium.

While there are other corrosion tests that can be used to assess nitinol for implant applications, measurement of the breakdown potential, in cyclic polarization tests, is by far the most widely used. There is, however, often debate as to what is an acceptable level, not just for nitinol, but for any metallic implant. In summary, there is no clinically or regulatory based minimum established, however, a minimum value of 600 mV has been proposed.[118,119] Data sets from nitinol testing have been used in establishing this proposed minimum.

Considering that it is a relatively 'new' implant material, the corrosion performance of nitinol is being rapidly understood and accepted in most situations. There are, however, some aspects for which there is very little information. Specifically, these relate to the performance of the material in situations where either fretting corrosion or galvanic effects (or both) may be possible. A fretting situation could arise, for example, in cardiovascular stenting where overlapping stents are used; the pulsatile-induced motion of the stents may be enough to cause oxide breakdown and wear damage at the overlap. Similarly, galvanic effects could arise should a nitinol stent be in direct contact with another stent, of a different material. In a fundamental study of mechanical damage and repassivation effects, Schroeder[120] has evaluated the performance of fresh mechanically abraded surfaces at different time-points in PBS. The results showed that a passive film started to reform relatively fast and developed progressively for ~6 days, at which point it leveled off. While this is a very positive finding, breakdown potentials were not measured, neither did the study assess how repeated abrasion/fretting may impact performance. A more practical study performed by Trépanier *et al.*,[121] evaluated the breakdown potential on nitinol stents that had been overlapped with each other during axial fatigue testing. The results showed that the breakdown potential decreased from ~900 to 650 mV due to the induced fretting damage. Again, however, the long-term *in vivo* corrosion response during fretting or abrasion cannot be accurately predicted from this data. However, on a positive note, this work did also demonstrate that nitinol repassivates well in situations of cervice-induced pitting.

In relation to the potential for galvanic interactions between nitinol and other materials, Venugopalan and Trépanier[122] have measured corrosion currents from coupling of nitinol to stainless steel, titanium, tantalum, platinum, platinum–iridium, and gold–palladium alloy. Equal cathode and anode areas were used. Perhaps not surprisingly, the current densities measured were exceptionally low ($<35\ \mathrm{nA\,cm^{-2}}$) when nitinol was connected to stainless steel, tantalum, or titanium. When coupled with the more noble metals, currents were over an order of magnitude higher, with NiTi–Pt giving the highest value of $836\ \mathrm{nA\,cm^{-2}}$. Still, these currents are exceptionally low and were insufficient to initiate corrosion of the nitinol. A study by Carroll and Kelly[123] showed similarly low levels of current for nitinol–gold couples. In addition, these findings were supported by inspection of nitinol–gold couples that had been immersed in saline for up to 12 months; no evidence of corrosion was observed. Thus while galvanic effects under stable oxide conditions seem most unlikely, there is probably a need for more information on the possibility of galvanic coupling in situations where oxides are being damaged through fretting or wear contact.

1.104.9.3. Biocompatibility Aspects of Nitinol

The generally biocompatible nature of nitinol has now been well demonstrated; many years of preclinical and clinical experience have been gained in a range of different biological environments. These applications have been supported by many fundamental cellular interaction studies. Ryhanen *et al.*[124] performed extensive cell proliferation studies in osteoblast and fibroblast cell cultures, using samples of nitinol that had only been mechanically polished. No inhibition of cell proliferation or cell growth was observed due to contact with the metal. This study also monitored nickel release and while levels of nickel ions were initially higher than that observed for stainless steel samples, the release rate dropped after 4 days to the same level as the steel. This behavior correlates well with observations of increased passivity and corrosion resistance, during immersion in physiological solutions, as described earlier. In further agreement with such observations, Shabalovskaya[125] has ranked nitinol has having lower pathological potential than stainless steel. While it is well recognized that nitinol does release nickel ions, even when no visible corrosion is occurring, the extent of this is put into perspective by a study from Okazaki and Gotoh.[126] This investigation measured ion release from a number of stainless steels, cobalt–chromium alloys, and nitinol in a variety of simulated physiological solutions. The nitinol showed lower release of nickel ions than the stainless steels or the cobalt–chromium alloys in cell culture medium, PBS, 0.9% NaCl and Ringers solution. Higher release from the nitinol was only observed, with 0.9% NaCl, when the pH was pushed below 4.0 by adding HCl. Similarly, a study by Messer *et al.*[127] showed nitinol to have the lowest nickel ion release into endothelial cell culture, compared to stainless steel and cobalt–chromium.

However, while there has been several other cell assay studies that establish the biocompatibility of nitinol,[128–131] it must be recognized that there have also been some reports of allergic response to nitinol implants. Kim *et al.*[132] report on the allergic reaction of a patient after having a nitinol ductal occluder device (a similar device to the septal occluder, described earlier) implanted. The skin lesions that developed in this instance were readily treated with medication, and a skin patch test did confirm that the patient had a hypersensitivity to nickel. Interestingly, when medication was stopped after 3 months, the symptoms did not reoccur. This is perhaps further support of the data that show nickel release rapidly diminishing over time. In a review of sensitivity reactions to metallic endovascular devices, Honari *et al.*[133] documents two further cases where allergic response was directly attributable to implantation of such closure devices. While acknowledging that such reactions are rare and sometimes relatively minor or transient, the authors provide recommendations on metal sensitivity tests for patients prior to receiving any metallic implant. In this regard it is worth noting that nickel sensitivity

reactions are not limited to nitinol, and Honari *et al.*[133] also document studies relating to stainless steel and cobalt–chromium stents. The issue of nickel sensitivity and possible correlations to in-stent restenosis has long been debated, though never clearly resolved. Koster *et al.*[134] presented some of the first data on this subject, suggesting a possible link on the basis that patients with positive patch test results had a higher frequency of in-stent restenosis. However subsequent studies by Norgas *et al.*[135] and Iijima *et al.*[136] failed to show a correlation between positive patch test results and restenosis. All of these studies were primarily concerned with coronary stenting, and no nitinol stents were included in the test groups. However, given that nitinol typically releases less nickel than stainless steel or cobalt–chromium, it seems unlikely that nitinol devices could have restenosis issues directly attributable to their nickel content or to nickel release. To conclude, while each device may have its own unique features, including important surface oxide characteristics, in general the biocompatibility of nitinol is at least comparable to that of many typical implantable materials.

1.104.10. Summary and Future Directions

Shape memory effects can be observed in several alloys but from a medical device perspective, nitinol is the only significant shape memory material. The use of nitinol in a diverse array of medical devices has been described. The majority of the applications to date have been in the cardiovascular field, and this trend is likely to continue given the growing demand for peripheral interventional technologies. However, it is likely that ongoing developments in the production of porous structures will also enable an increasing number of applications in orthopedics.

There are many aspects of current nitinol technologies that require further investigation and development. These range from continuous improvements needed in design and manufacturing methodologies through to collection and understanding of more extensive fatigue data. Thermomechanical treatments merit further development – particular those aimed at producing refined grain structures. Schaffer[137] describes how nanocrystalline structures can provide an increase in the amount of superelastic recoverable strain as well as improvements in fatigue resistance.

Given the sensitivity of the material to precise nickel concentration there will probably be very little shift from the mainstream equiatomic or slightly nickel-rich compositions. There are, however, some novel developments under way that could eventually see broader application. These include a number of different ternary alloy compositions, with the third element being added to modify specific characteristics. For example, Haider *et al.*[138] report on exploration of NiTiTa alloys to improve radiopacity and NiTiCu compositions to increase corrosion resistance. Lin *et al.*[139] describe NiTiPt alloys also aimed at enhancing radiopacity; these alloys have shown narrower hysteresis between load and unload plateau which may also provide additional design options for devices. To conclude, nitinol has proven to be a unique material, enabling many highly worthy medical device developments, and this trend is likely to continue.

References

1. Wayman, C. M.; Duerig, T. W. In *Engineering Aspects of Shape Memory Alloys*; Duerig, T. W., Melton, K. N., Stoeckel, D., Wayman, C. M., Eds.; Butterworth-Heinemann: London, 1990; pp 3–20.
2. Hodgson, D. E.; Wu, M. H.; Biermann, R. J. In *Metals Handbook, Properties and Selection: Nonferrous Alloys and Special Purpose Materials*, 10th ed.; ASM International: Materials Park, OH, 1990; Vol. 2, pp 897–902.
3. Liu, Y.; Liu, Y.; Van Humbeeck, J. *Acta Mater.* **1999**, *47*, 199–209.
4. Scherngell, H.; Kneissl, A. C. *Scr. Mater.* **1998**, *39*, 205–212.
5. Huang, W. *Mater. Des.* **2002**, *23*, 11–19.
6. Sutou, Y.; Omori, T.; Furukawa, A.; *et al. J. Biomed. Mater. Res. B Appl. Biomater.* **2004**, *69B*, 64–69.
7. Wen, Y. H.; Yan, M.; Li, N. *Scr. Mater.* **2004**, *50*, 441–444.
8. Kauffman, G. B.; Mayo, I. *Chem. Educ.* **1996**, *2*, 1–21.
9. Kramer, G. M. *J. Mater. Eng. Perform.* **2009**, *18*(5–6), 479–483.
10. Melton, K. N. In *Engineering Aspects of Shape Memory Alloys*; Duerig, T. W., Melton, K. N., Stoeckel, D., Wayman, C. M., Eds.; Butterworth-Heinemann: London, 1990; pp 21–35.
11. Pelton, A. R.; Russell, S. M.; DiCello, J. *J. Met.* **2003**, 33–37.
12. Wu, M. H. *Mater. Sci. Forum* **2002**, *394–395*, 285–292.
13. Pelton, A. R.; DiCello, J.; Miyazaki, S. *Minim. Invasive Ther. Allied Technol.* **2000**, *9*(1), 107–118.
14. Khalil-Allafi, J. K.; Dlouhy, A.; Eggeler, G. *Acta Mater.* **2002**, *50*, 4255–4274.
15. Drexel, M. J.; Selvaduray, G. S.; Pelton, A. R. In *Proceedings of the International Conference on Shape Memory and Superelastic Technologies*, May 7–11, 2006; Berg, B., Mitchell, M. R., Proft, J., Eds.; ASM International: Materials Park, OH, 2008 pp 447–454.
16. Otsuka, K. In *Engineering Aspects of Shape Memory Alloys*; Duerig, T. W., Melton, K. N., Stoeckel, D., Wayman, C. M., Eds.; Butterworth-Heinemann: London, 1990; pp 36–45.
17. Šittner, P.; Landa, M.; Lukáš, P.; Novák, V. *Mech. Mater.* **2006**, *38*, 475–492.
18. Marquez, J.; Slater, T.; Sczerzenie, F. In *Proceedings of the Second International Conference on Shape Memory and Superelastic Technologies*, Mar 2–6, 1997; Pelton, A., Hodgson, D., Russell, S., Duerig, T., Eds.; International Organisation on SMST: Pacific Grove, CA, 1997 pp 13–18.
19. Shaw, J. A.; Churchill, C. B.; Iadicola, M. A. *Exp. Tech.* **2008**, *32*, 55–62.
20. ASTM F2004-05. Standard test method for transformation temperature of nickel–titanium alloys by thermal analysis. ASTM International: West Conshohocken, PA, 2005.
21. Rice, C.; Sczerzenie, F. In *Proceedings of the Second International Conference on Shape Memory and Superelastic Technologies,* Mar 2–6, 1997; Pelton, A., Hodgson, D., Russell, S., Duerig, T., Eds.; International Organisation on SMST: Pacific Grove, CA, 1997; pp 19–22.
22. Chen, J.; Duerig, T.; Pelton, A.; Stoeckel, D. *J. Phys. IV* **1995**, *5*(2), 1247–1252.
23. ASTM F2082-06. Standard test method for determination of transformation temperature of nickel–titanium shape memory alloys by bend and free recovery. ASTM International: West Conshohocken, PA, 2006.
24. Drexel, M.; Proft, J.; Russell, S. *J. Mater. Eng. Perform.* **2009**, *18*, 620–625.
25. McKelvey, A. L.; Ritchie, R. O. *Philos. Mag. A* **2000**, *80*, 1759–1768.
26. Gall, K.; Tyber, J.; Brice, V.; Frick, C. P.; Maier, H. J.; Morgan, N. *J. Biomed. Mater. Res.* **2005**, *75A*, 810–823.
27. ASTM F2516-07e2. Standard test method for tension testing of nickel–titanium superelastic materials. ASTM International: West Conshohocken, PA, 2007.
28. Johe, R. *J. Mater. Eng. Perform.* **2009**, *18*, 836–842.
29. Duerig, T. W.; Tolomeo, D. E.; Wholey, M. *Minim Invasive Ther. Allied Technol.* **2000**, *9*(3/4), 235–246.
30. Schuessler, A. In *Proceedings of the International Conference on Shape Memory and Superelastic Technologies, Apr 30–May 4, 2000*; Russell, S. M., Pelton, A., Eds.; International Organisation on SMST: Pacific Grove, CA, 2000; pp 25–32.
31. Hassel, A. W. *Minim Invasive Ther. Allied Technol.* **2004**, *13*(4), 240–247.
32. Pohl, M.; Heßing, C.; Frenzel, J. *Mater. Sci. Eng. A* **2004**, *378*, 191–199.
33. Trepanier, C.; Tabrizian, M.; Yahia, L'.H.; Bilodeau, L.; Piron, D. L. *J. Biomed. Mater. Res. Appl. Biomater.* **1999**, *43*, 433–430.
34. O'Brien, B.; Carroll, W. M.; Kelly, M. J. *Biomaterials* **2001**, *23*, 1739–1748.
35. Favier, D.; Liu, Y.; Orgéas, L.; Sandal, A.; Debove, L.; Comte-Gaz, P. *Mater. Sci. Eng. A* **2006**, *429*, 130–136.
36. Bridges, J.; Maisel, W. *Am. J. Ther.* **2008**, *15*(1), 12–18.
37. O'Brien, B. In *Proceedings of the First European Conference on Shape Memory and Superelastic Technologies*; Van Moorleghem, W., Besselink, P., Aslanidis, D., Eds.; ASM International, Materials Park, OH, 1999; pp 171–180.
38. Stoeckel, D.; Pelton, A.; Duerig, T. *Eur. Radiol.* **2004**, *14*, 292–301.

39. Kobayashi, Y.; Honda, Y.; Christie, L. G.; *et al*. *J. Am. Coll. Cardiol*. **2001**, *37*, 1329–1334.
40. Blackman, D. J.; Choudhury, R. P.; Banning, A. P.; Channon, K. M. *J. Invasive Cardiol*. **2005**, *17*, 609–612.
41. Jilaihawi, H.; Farah, B.; Laborde, J. C. *EuroInterv* **2009**, *4*, 669–675.
42. Abizaid, A. C.; de Ribmar Costa, J., Jr.; Whitbourn, R. J.; Chang, J. C. *EuroIntervention* **2007**, *3*, 154–157.
43. Duda, S. H.; Wiesinger, B.; Koenig, C.; Wiskirchen, J.; Dietrich, T.; Tepe, G. *Minim. Invasive Ther. Allied Technol*. **2002**, *11*(4), 193–201.
44. Phatouros, C. C.; Higashida, R. T.; Malek, A. M.; *et al*. *Am. J. Neuroradiol*. **2000**, *21*, 732–738.
45. Drescher, R.; Mathias, K. D.; Jaeger, H. J.; *et al*. *Eur. Radiol*. **2002**, *12*, 2451–2456.
46. Sabeti, S.; Schillinger, M.; Amighi, J.; *et al*. *Radiology* **2004**, *232*, 516–521.
47. Schillinger, M.; Sabeti, S.; Loewe, C.; *et al*. *N. Engl. J. Med*. **2006**, *354*, 1879–1888.
48. Duda, S. H.; Pusich, B.; Richter, G.; *et al*. *Circulation* **2002**, *106*, 1505–1509.
49. Duda, S. H.; Bosiers, M.; Lammer, J.; *et al*. *JVIR* **2005**, *16*, 331–338.
50. Allie, D. E.; Hebert, C. J.; Walker, C. M. *Endovasc. Today* **2004**, *2004*(7/8), 22–34.
51. Scheinert, D.; Scheinert, S.; Sax, J.; *et al*. *J. Am. Coll. Cardiol*. **2005**, *45*, 312–315.
52. Dake, M. D. *Eur. J. Radiol*. **2001**, *39*, 42–49.
53. Steingruber, I. E.; Neuhauser, B.; Seiler, R.; *et al*. *Eur. J. Radiol*. **2006**, *59*, 384–392.
54. Riepe, G.; Heintz, C.; Kaiser, E.; *et al*. *Eur. J. Vasc. Endovasc. Surg*. **2002**, *24*, 117–122.
55. Jacobs, T.; Teodorescu, V.; Morrissey, N.; *et al*. *Semin. Vasc. Surg*. **2003**, *16*, 103–112.
56. Bose, A.; Hartmann, M.; Henkes, H.; *et al*. *Stroke* **2007**, *28*, 1531–1537.
57. Akpek, S.; Arat, A.; Morsi, H.; Klucznick, R. P.; Strother, C. M.; Mawad, M. E. *Am. J. Neuroradiol*. **2005**, *26*, 1223–1231.
58. Simon, M.; Athanasoulis, C. A.; Kim, D.; *et al*. *Radiology* **1989**, *172*, 99–103.
59. Cremonesi, A.; Mannetti, R.; Setacci, F.; Setacci, C.; Castriota, F. *Stroke* **2003**, *34*, 1936–1941.
60. Fischer, G.; Masura, J.; Heiner Kramer, H.; Gavora, P. *Prog. Pediatr. Cardiol*. **1998**, *9*, 119–124.
61. Grube, E.; Laborde, J. C.; Gerckens, U.; *et al*. *Circulation* **2006**, *114*, 1616–1624.
62. Miyazawa, T.; Yamakido, M.; Ikeda, S.; *et al*. *Chest* **2000**, *118*, 959–965.
63. Cwikiel, W.; Stridbeck, H.; Tranberg, K. G.; *et al*. *Radiology* **1993**, *187*, 661–665.
64. Lee, S. H. *Br. J. Radiol*. **2001**, *74*, 891–900.
65. Kozarek, R. A. *World J. Gastroenterol*. **2000**, *6*, 643–646.
66. Rasmussen, I. C.; Dahlstrand, U.; Sandblom, G.; Eriksson, L. G.; Nyman, R. *Acta Radiol*. **2009**, *50*, 730–737.
67. Reddy, A. V.; Alwair, H.; Trewby, P. N. *Gastrointest. Endosc*. **2003**, *57*, 138–139.
68. Chhetri, S. K.; Selinger, C. P.; Greer, S. *Endoscopy* **2008**, *40*, E199.
69. Kusy, R. P. *Angle Orthod*. **2002**, *72*, 501–512.
70. Huang, H. H. *J. Biomed. Mater. Res*. **2005**, *74A*, 629–639.
71. Es-Souni, M.; Es-Souni, M.; Fischer-Brandies, H. *Biomaterials* **2002**, *23*, 2887–2894.
72. Eliades, T.; Eliades, G.; Athanasiou, A. E.; Bradley, T. G. *Eur. J. Orthod*. **2000**, *22*, 317–326.
73. Schiff, N.; Mickaël Boinet, L.; Morgon, M. Lissac; Dalard, F.; Grosgogeat, B. *Eur. J. Orthod*. **2006**, *28*, 298–304.
74. Zinelis, S.; Eliades, T.; Pandis, N.; Eliades, G.; Bourauel, C. *Am. J. Orthod. Dentofacial Orthop*. **2007**, *132*, 84–89.
75. Bansiddhi, A.; Sargeant, T. D.; Stupp, S. I.; Dunard, D. C. *Acta Biomater*. **2008**, *4*, 773–782.
76. Chu, C. L.; Chung, C. Y.; Lin, P. H.; Wang, S. D. *Mater. Sci. Eng*. **2004**, *A366*, 114–119.
77. Bassani, P.; Giuliani, P.; Tuissi, A.; Zanotti, C. *J. Mater. Eng. Perform*. **2009**, *18*, 594–599.
78. Ayers, R. A.; Simske, S. J.; Bateman, T. A.; Petkus, A.; Sachdeva, R. L. C.; Gyunter, V. E. *J. Biomed. Mater. Res*. **1999**, *45*, 42–47.
79. Kujala, S.; Ryhänen, J.; Danilov, A.; Tuukkanen, J. *Biomaterials* **2003**, *24*, 4691–4697.
80. Likibi, F.; Assad, M.; Jarzem, P.; *et al*. *Eur. J. Orthop. Surg. Traumatol*. **2004**, *14*, 209–213.
81. Munroe, N.; Pulletikurthi, C.; Haider, W. *J. Mater. Eng. Perform*. **2009**, *18*, 765–767.
82. Kujala, S.; Ryhänen, J.; Jämsä, T.; *et al*. *Biomaterials* **2002**, *23*, 2535–2543.
83. Russell, S. M. *J. Mater. Eng. Perform*. **2009**, *18*, 831–835.
84. Fu, Q. G.; Liu, X. W.; Xu, S. G.; Li, M.; Zhang, C. C. *JMPEG* **2009**, *18*, 797–804.
85. Morawiec, H. Z.; Lekston, Z. H.; Kobus, K. F.; Wegrzyn, M. C.; Drugacz, J. T. *J. Mater. Eng. Perform*. **2009**, *18*, 818–823.
86. Siekmeyer, G.; Steegmüller, R.; Schrader, B.; Hegel, A.; Strobel, M.; Schuessler, A. In *Proceedings from the Materials & Processes for Medical Devices Conference*, Nov 14–16, 2005; Venugopalan, R., Wu, M., Eds.; ASM International, Materials Park, OH, 2006 pp 57–62.
87. Wiskirchen, J.; Kraemer, K.; König, C.; *et al*. *J. Vasc. Interv. Radiol*. **2004**, *15*, 843–852.
88. Cheng, Y.; Cai, W.; Li, H. T.; Zheng, Y. F. *J. Mater. Sci*. **2006**, *41*, 4961–4964.
89. Schaffer, J. E.; Gordon, R. In *Proceedings of the International Conference on Shape Memory and Superelastic Technologies*, May 5–8, 2003; Pelton, A. R., Duerig, T., Eds.; ASM International, Materials Park, OH, 2004 pp 109–118.
90. Maintz, D.; Seifarth, H.; Raupach, R.; *et al*. *Eur. Radiol*. **2006**, *16*, 818–826.
91. Létourneau-Guillon, L.; Soulez, G.; Beaudoin, G.; *et al*. *J. Vasc. Interv. Radiol*. **2004**, *15*, 615–624.
92. Melzer, A.; Michitsch, S.; Konak, S.; Schaefers, G.; Bertsch, T. *Minim. Invasive Ther. Allied Technol*. **2004**, *13*(4), 261–271.
93. Lenhart, M.; Volk, M.; Manke, C.; *et al*. *Radiology* **2000**, *217*, 173–178.
94. Immel, E.; Melzer, A. *Minim. Invasive Ther*. **2006**, *15*(2), 85–92.
95. Robertson, S. W.; Ritchie, R. O. *Biomaterials* **2007**, *28*, 700–709.
96. Gong, X. Y.; Chwirut, D. J.; Mitchell, M. R.; Choules, B. D. *J. ASTM Int*. **2009**, *6*(7), 1–10.
97. James, B. A.; Sire, R. A. *Biomaterials* **2010**, *31*, 181–186.
98. Patel, M. M.; Plumley, D. L.; Bouthot, R. J.; Proft, J. L. In *Proceedings of the International Conference on Shape Memory and Superelastic Technologies*, May 7–11, 2006; Berg, B., Mitchell, M. R., Proft, J., Eds.; ASM International, Materials Park, OH, 2008 pp 43–52.
99. Sheriff, J.; Pelton, A. R.; Pruitt, L. A. In *Proceedings from the Materials & Processes for Medical Devices Conference*, Aug 25–27, 2004; Helmus, M., Medlin, D., Eds.; ASM International, Materials Park, OH, 2005 pp 38–43.
100. Lin, Z. C.; Denison, A. In *Proceedings from the Materials & Processes for Medical Devices Conference*, Sept 8–10, 2003, ASM International, Materials Park, OH, 2004 pp 205–208.
101. Patel, M. M.; Gordon, R. F. In *Proceedings of the International Conference on Shape Memory and Superelastic Technologies*, May 7–11, 2006; Berg, B., Mitchell, M. R., Proft, J., Eds.; ASM International, Materials Park, OH, 2008 pp 397–403.
102. Perry, K. E.; Kugler, C. *Exp. Tech*. **2002**, *26*, 37–38.
103. Pelton, A. R.; Gong, X. Y.; Duerig, T. In *Proceedings of the International Conference on Shape Memory and Superelastic Technologies*, May 5–8, 2003; Pelton, A. R., Duerig, T., Eds.; ASM International, Materials Park, OH, 2004 pp 293–302.
104. Pelton, A. R.; Schroeder, V.; Mitchell, M. R.; Gong, X. Y.; Barney, M.; Robertson, S. W. *JMBBM* **2008**, *1*, 153–164.
105. Morgan, N. B.; Painter, J.; Moffat, A. In *Proceedings of the International Conference on Shape Memory and Superelastic Technologies*, May 5–8, 2003; Pelton, A. R., Duerig, T., Eds.; ASM International, Materials Park, OH, 2004 pp 303–310.
106. Wick, A.; Gong, X. Y.; Fino, J.; Sheriff, J.; Pelton, A. R. In *Proceedings from the Materials & Processes for Medical Devices Conference*, Aug 25–27, 2004; Helmus, M., Medlin, D., Eds.; ASM International, Materials Park, OH, 2005 pp 15–20.
107. Cavanaugh, K. J.; Holt, V. M.; Goode, J. L.; Anderson, E. *J. ASTM Int*. **2006**, *3*(6), 110–116.
108. Heintz, C.; Riepe, G.; Birken, L.; *et al*. *J. Endovasc. Ther*. **2001**, *8*, 248–253.
109. Shabalovskaya, S.; Anderegg, J.; Van Humbeeck, J. *Mater. Sci. Eng. A* **2008**, *481/482*, 431–436.
110. ASTM F2063-05. Standard specification for wrought nickel–titanium shape memory alloys for medical devices and surgical implants. ASTM International: West Conshohocken, PA, 2005.
111. Shabalovskaya, S.; Rondelli, G.; Anderegg, J.; Xiong, J. P.; Wu, M. *J. Biomed. Mater. Res. B Appl. Biomater*. **2004**, *69B*, 223–231.
112. Shabalovskaya, S. A.; Rondelli, G. C.; Undisz, A. L.; Anderegg, J. W.; Burleigh, T. D.; Rettenmayr, M. E. *Biomaterials* **2009**, *30*, 3662–3671.
113. Pérez, L. M.; Gracia-Villa, L.; Puértolas, J. A.; Arruebo, M.; Irusta, S.; Santamaria, J. *J. Biomed. Mater. Res. B Appl. Biomater*. **2009**, *91B*, 337–347.
114. Pound, B. G. *J. Biomed. Mater. Res*. **2006**, *77A*, 185–191.

115. Shabalovskaya, S.; Anderegg, J.; Van Humbeeck, J. *Acta Biomater.* **2008**, *4*, 447–467.
116. Eiselstein, L. M.; Steffey, D.; Nissan, A.; *et al. JMPEG* **2009**, *18*, 768–780.
117. Warner, C. P. *J. Mater. Eng. Perform.* **2009**, *18*, 754–759.
118. Corbett, R. A. In *Proceedings of the Materials and Processes for Medical Devices Conference*, Sept 8–10, 2003; Shrivastava, S., Ed.; ASM International, Materials Park, OH, 2004 pp 133–138.
119. Rosenbloom, S. N.; Corbett, R. An assessment of ASTM F2129 electrochemical testing of small medical implants – lessons learned. In *NACE Corrosion 2007*, Mar 11–15, 2007; Paper No. 07674.
120. Schroeder, V. *J. Biomed. Mater. Res.* **2009**, *90A*, 1–17.
121. Trépanier, C.; Gong, X. Y.; Ditter, T.; Pelton, A.; Neely, Y.; Grishaber, R. In *Proceedings of the International Conference on Shape Memory and Superelastic Technologies*, May 7–11, 2006; Berg, B., Mitchell, M. R., Proft, J., Eds.; ASM International, Materials Park, OH, 2008 pp 265–276.
122. Venugopalan, R.; Trépanier, C. In *Proceedings of the International Conference on Shape Memory and Superelastic Technologies*, Apr 30–May 4, 2000; Russell, S. M., Pelton, A., Eds.; International Organisation on SMST: Pacific Grove, CA, 2000 pp 261–270.
123. Carroll, W. M.; Kelly, M. J. *J. Biomed. Mater. Res.* **2003**, *67A*, 1123–1130.
124. Ryhanen, J.; Niemi, E.; Serlo, W.; *et al. J. Biomed. Mater. Res.* **1997**, *35*, 451–457.
125. Shabalovskaya, S. A. *Int. Mater. Rev.* **2001**, *46*(4), 1–18.
126. Okazaki, Y.; Gotoh, E. *Corrosion Sci.* **2008**, *50*, 3429–3438.
127. Messer, R. L.; Wataha, J. C.; Lewis, J. B.; Lockwood, P. E.; Caughman, G. B.; Tseng, W. Y. *J. Long Term Eff. Med. Implants* **2005**, *15*(1), 39–47.
128. Bogdanski, D.; Köller, M.; Müller, D.; *et al. Biomaterials* **2002**, *23*, 4549–4555.
129. Es-Souni, M.; Fischer-Brandies, H.; Es-Souni, M. *J. Biomed. Mater. Res.* **2007**, *80A*, 159–166.
130. Rocher, P.; El Medawar, L.; Hornez, J. C.; Traisnel, M.; Breme, J.; Hildebrand, H. F. *Scr. Mater.* **2004**, *50*, 255–260.
131. Wever, D. J.; Veldhuizen, A. G.; Sanders, M. M.; Schakenraad, J. M.; van Horn, J. R. *Biomaterials* **1997**, *18*, 1115–1120.
132. Kim, K. H.; Park, J. C.; Yoon, N. S.; *et al. Int. J. Cardiol.* **2008**, *127*, e98–e99.
133. Honari, G.; Ellis, S. G.; Wilkoff, B. L.; Aronica, M. A.; Svensson, L. G.; Taylor, J. S. *Contact Dermatitis* **2008**, *59*, 7–22.
134. Koster, R.; Vieluf, D.; Kiehn, M.; *et al. Lancet* **2000**, *356*, 1895–1897.
135. Norgas, T.; Hobikoglu, G.; Serdar, Z. A.; *et al. Tohoku J. Exp. Med.* **2005**, *206*, 243–246.
136. Iijima, R.; Ikari, Y.; Amiya, E.; *et al. Int. J. Cardiol.* **2005**, *104*, 319–325.
137. Schaffer, J. E. *J. Mater. Eng. Perform.* **2009**, *18*, 582–587.
138. Haider, W.; Munroe, N.; Pulletikurthi, C.; Singh Gill, P. K.; Amruthaluri, S. *J. Mater Eng. Perform.* **2009**, *18*(5/6), 760–764.
139. Lin, B.; Gall, K.; Maier, H. J.; Waldron, R. *Acta Biomater.* **2009**, *5*, 257–267.

Relevant Websites

http://smst.asminternational.org/portal/site/smst/ – International Organization on Shape Memory and Superelastic Technologies (SMST).
www.nitinol.com – Material supplier with library of published data.
http://www.smit.de/R08/index.htm – Society for Medical Innovation and Technology (SMIT).

1.105. Alumina

C Piconi, Catholic University, Roma, Italy; Tor Vergata University, Roma, Italy

© 2011 Elsevier Ltd. All rights reserved.

1.105.1.	**Introduction**	74
1.105.2.	**Properties of Alumina**	77
1.105.2.1.	Physical Properties	77
1.105.2.2.	Mechanical Properties	77
1.105.2.3.	Stability in Wet Environment	78
1.105.2.4.	Wear Behavior of Alumina	79
1.105.2.4.1.	Simulator tests on alumina-on-PE bearings	80
1.105.2.4.2.	Simulator tests on alumina-on-alumina bearings	80
1.105.2.4.3.	Microseparation tests on alumina-on-alumina bearings	80
1.105.2.5.	Biocompatibility	81
1.105.2.5.1.	*In vitro* tests	81
1.105.2.5.2.	*In vivo* tests	81
1.105.2.5.3.	Carcinogenecity	82
1.105.2.6.	Reaction to Ceramic Wear Debris	82
1.105.3.	**Clinical Application of Alumina Ceramics**	83
1.105.3.1.	Technology of Alumina for THR Bearings	84
1.105.3.2.	Design of Ceramic THR Bearings	84
1.105.3.3.	Clinical Results	86
1.105.3.4.	Complications	87
1.105.3.4.1.	Failures in THR bearings	87
1.105.3.4.2.	Noises in THR bearings	88
1.105.3.5.	Tips and Tricks in Alumina Bearings	89
1.105.3.6.	Revision Strategies	90
1.105.3.7.	Alumina in Knee Replacements	90
1.105.3.8.	Alumina in Other Medical Devices	91
References		92

Glossary

Arthroplasty The surgical intervention aimed to restore the function of a body joint, for example, hip arthroplasty, knee arthroplasty, etc.

Sintering A thermal treatment process aimed to reduce the free surfaces of the body, achieving its densification. During sintering mass transport takes place depending on the differences in surface energy into the porosity, by diffusion due to the gradient in concentration of the chemical species into the body mass. The process takes place between one-half and two-thirds of the melting temperature, and is then suitable for shaping refractory materials.

Total hip replacement A medical device aimed at the substitution of the hip joint. It is formed by a stem to be inserted into the femur, which is surgically adapted to its shape, by a socket (or cup) to be fixed into the acetabulum after reaming, these two components form a spherical bearing (or joint).

Total knee replacement A medical device aimed at the substitution of the knee joint. It is formed by a femoral component that is fixed to the distal end of the femur replacing both condyles, by a tibial component (tibial tray) fixed to the proximal part of the tibia which is hosting the tibial plateau (fixed or mobile) onto which the femoral component is sliding. A fourth component of the implant is the patellar one, to be implanted in the inner part of the patella and articulating against the troclea between the femoral condyles.

Abbreviations

AMC	Alumina–matrix composite
ATZ	Alumina-toughened zirconia
CoC	Ceramic-on-ceramic THR bearing. Also synonym of alumina-on-alumina THR bearing
CoP	Ceramic-on-polyethylene THR bearing
FDA	United States Food and Drug Administration
IDE	Investigational device exemption
LPSN	Liquid-phase-sintered silicon nitride
LTD	Low-temperature degradation
Mg-PSZ	Magnesia-stabilized partially stabilized zirconia

MHRA	Medicine and Healthcare products Regulatory Agency	**THR**	Total hip replacement
MoP	Metal-on-polyethylene THR bearing	**TKA**	Total knee arthroplasty
PE	Polyethylene (all medical-grade types)	**TKR**	Total knee replacement
RBSN	Reaction-bonded silicon nitride	**UHMWPE**	Ultra high molecular weight polyethylene
ROM	Range of motion	**XLPE**	Cross-linked PE
TD	Theoretical density	**Y-TZP**	Yttria-stabilized tetragonal zirconia polycrystal
THA	Total hip arthroplasty	**ZTA**	Zirconia-toughened alumina

1.105.1. Introduction

Dense, hard and stable also in chemically aggressive environment at elevated temperature, alumina ceramic seemed the ideal material to the pioneers of the biomaterials science, when chemical stability and biologic inertia of the implants were the main requirements to be satisfied.

In orthopedic applications, alumina is a well-established material, with 40 years of clinical record so far, as components of the joints of total hip replacements (THR); newer applications can be foreseen in the near future, thanks to the introduction of high-performance alumina matrix composites. The success of alumina in THR bearings is relevant, especially in some European countries (Austria, France, Germany, Italy, Switzerland) where more than 50% of the hip implants make use of ceramic ball heads, and in Asian countries such as Korea where 72% of THRs have an alumina ball. Also, in countries where the introduction of ceramic bearing components took place later (USA, China, India, Eastern European countries) the use of ceramic heads and CoC bearings shows a growing trend (Table 1).

The use of alumina is so common in orthopedics that in scientific papers the use of the term 'ceramic' without any other specification to indicate alumina is accepted. The use of the term may be tricky because of the many ceramics that are, or have been, or are proposed to be used in the fabrication of bearing for joint replacements besides alumina (e.g., Y-TZP, Mg-PSZ, Si3N4, ZTA, ATZ, etc.). In this chapter we will follow the current use, that is 'ceramic' will mean 'alumina,' if not specified otherwise (Figure 1).

The first mention of the use of alumina as a biomaterial can be traced back to the German patent application made by Rock,[1] but alumina remained unexploited in clinical applications until the 1960s, when Lyman W. Smith[2] developed Cerosium, a silica aluminate containing up to 65% porosity filled with epoxy resin, to be used as a bone substitute. In the same year, Eyring and Campbell[3] developed alumina temporary osteotomy spacers, which were implanted in a small number of patients, while Sandhaus[4] developed and started the clinical use of a screw-shaped alumina dental implant, the concept of which originated several designs in the following years.[5]

During the 1960s, the hip arthroplasty procedure was gaining importance among the orthopedic community, addressing hip-related problems in millions of patients facing pain, disability, and limitation of activity. However, this procedure, which has proved to be one of the greatest successes in the field of surgery in recent times, did not produce the expected outcomes in the early stages. Catastrophic bearing wear was the most critical complication of the early devices, and many scientists concentrated their efforts on the research of better bearing couples.

In the early 1970s, alumina was the most advanced ceramic material, thanks to the availability of the high alumina powder, Degussit Al23, which helped to overcome many limitations of the earlier ceramic precursors. It was in this context that Dr. Pierre Boutin, an orthopedic surgeon working in Pau, a town in southern France, had the opportunity to discuss the feasibility of an alumina-on-alumina THR bearing with one of his patients, a top manager of CGE France, whose factory was

Table 1 Use of ceramic components in THR bearings in selected countries

	USA	*Germany, Austria, Switzerland*	*UK*	*France*	*Italy*	*Korea*
Ceramic-on-Ceramic bearings %	5	14	10	25	20	70
Ceramic heads %	10	56	24	50	53	72

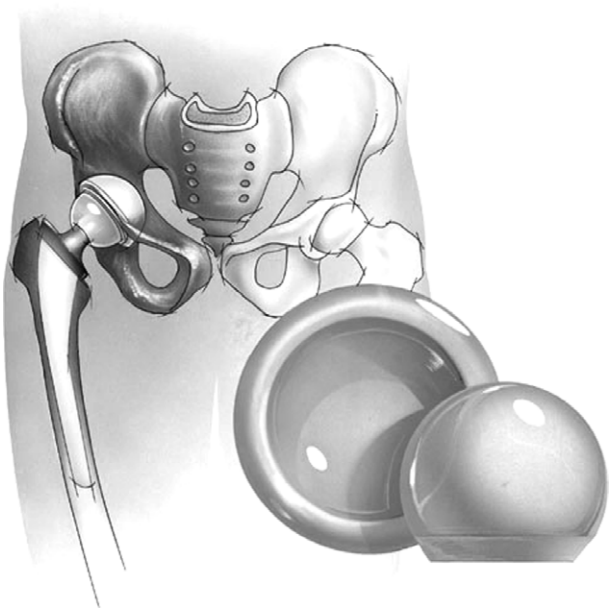

Figure 1 Schematic of a total hip replacement, with evidence of the ceramic ball head and insert forming the bearing (Courtesy CeramTec AG, Plochingen, Germany).

situated nearby. Their combined efforts led to the production of the first alumina-on-alumina bearing for total hip arthroplasty (THA).[6] Both the stem and the cup were fixed to the bone by cement (Figure 2).

In the same years, several pioneers like Langer in Keramed, Heimke in Friedrichsfeld, Dörre in Feldmüle, and Maier in Rosenthal were working in a big research program launched in Germany to develop alumina clinical implants. Both the stem and the cup of the hip replacements were designed to achieve cementless fixation in the host bone, that is, by a screw-like profile of the cup (Figure 3).

Some of the early devices, for example, hip replacements completely made out of polycrystalline alumina,[7] never went beyond the developmental stage but the device named 'femoral cap endoprostheses' completely made out alumina was used in eight cases of massive bone resections following chondrosarcoma or carcinoma metastases, and resurfacing alumina cups were used for hemiarthroplasty of the hip[8] (Figure 4).

As these developments were in progress in Europe, Japanese researchers were also developing alumina devices, some of them by using single crystal alumina.[9] The most impressive devices obtained by this original approach were single crystal alumina stems used for hip replacements implanted after resection of bone tumors, while polycrystalline alumina knee condyles, coupled to a alumina tibial plateau hosting an ultra high molecular weight polyethylene (UHMWPE) tibial component were used in alumina knee replacements and talar component has been used in ankle prostheses since the early 1980s.[10] Single crystal alumina was also used to manufacture blade and screw-shaped dental implants.[5]

The clinical use of these early large and heavy monolithic devices allowed surgeons and engineers to assess the clinical advantages of alumina-on-alumina bearings in terms of wear reduction and absence of particle-induced osteolysis. Unsatisfactory outcomes were due to the component design or to failures in the cementation. Nevertheless, in younger patients with good bone quality – in whom good primary stability in the cortical bone was achieved – several positive clinical results had been reported.[11–13]

Along the 40 years of clinical use of alumina, many improvements had been introduced in the material technology, which aimed to increase reliability of the products by increasing the ceramic density – result obtained by reducing and by making more homogeneous the grain size – and by increasing the purity of the material. In the beginning, the

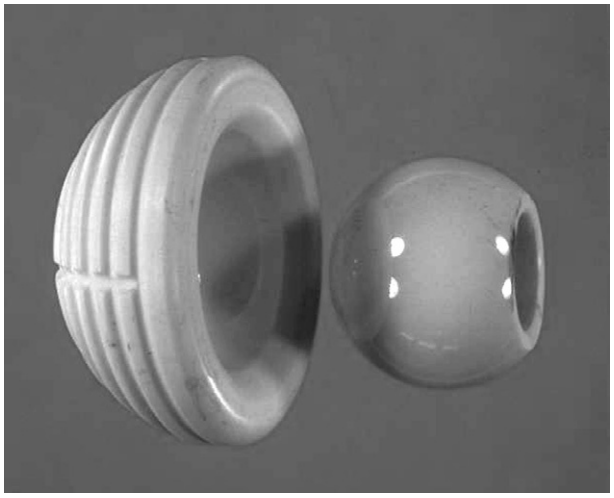

Figure 2 The Dr. Boutin's alumina-on-alumina bearing. The cup is designed for cementation into the acetabulum (Courtesy Dr. C. Rieker, Zimmer Gmbh, Winterthur, CH).



Figure 3 The Prof. Mittelmeier's alumina-on-alumina bearing. Note the design of the cup, intended to achieve the device integration by the acetabular bone.



Figure 4 The Prof. Saltzer's 'recapping device,' to be implanted onto the surgically shaped femural shaft.

developments were focused on the selection of appropriate raw materials. The proper selection of the raw materials represents a critical step in any technology, and in the case of medical grade alumina a significant milestone in the development process was reached around 1980 when, thanks to the introduction of high purity powders for ceramic production and to the improvements in process control, the so-called 'second generation alumina' was obtained.

A significant step in the development of medical-grade alumina was marked by the introduction of hot isostatic pressing (HIP) in the production, a thermal treatment performed at extremely high pressures (about 1000 MPa) with temperature slightly below the sintering temperature, and this allows the obtaining of high density, limiting the development of the grain size. A further improvement that contributed to significantly increase the reliability of alumina components was the use of the laser for engraving the component's identification marks. Marks to identify, for example, manufacturer, size, and production lot were historically done by engraving the component before firing. Concerns arose about the effects of these marks that could act as stress risers on the service life of the component when combined with the notch sensitivity and brittleness inherent in alumina. The application of the new laser marking technique has allowed manufacturers to reduce the effect of markings on the mechanical behavior of the ceramic components, as it allows for a more rounded, less deep, and smoother profile on the markings, demonstrating an important addition to the reliability of alumina ceramic components in clinical use.

But the single most important development in improving the reliability of ceramic components was the introduction of proof test, a nondestructive test to be performed as a part of the final control on finished components, aimed to discard all those components where a flaw larger than a predetermined critical size may hamper the expected lifetime and performances. It is known that both the strength and lifetime of ceramic components is determined by the number of flaws within the material.

The development of the test on the basis of the fracture mechanics theory has been extensively discussed by Kleer *et al.*[14] and by Schaefer *et al.*[15]

Briefly, it has been shown that the two main stresses in the head are a tensile stress in the upper part of the inner bore (the dome) due to the forces transmitted by the cup, and a tensile orthoradial (hoop) stress in the taper due to the force exerted by the spigot on the ceramic. To obtain such a stress distribution close to the load bearing capability of the component under test, it has to be overloaded in a manner that ensures that the parts are not damaged in any way during the test, yet eliminating the possibility of an internal flaw not being detected.

Forces must be applied to the ceramic surfaces without damaging the component (head or cup) or the finish of the articulating surface, for example, by hydrostatic pressure, as explained by Schaefer *et al.*[12]

The introduction of laser marking, HIP, and proof testing of components in the manufacturing process around 1995 lead to 'third generation alumina,' which is still today on the market.

The key developments described above are only a few in the list of constant improvements made to alumina–ceramic components over the years, and are a part of the overall Quality Assurance System that encompasses the whole design, development, manufacturing, and post marketing monitoring of this kind of products. The Quality Control System, which monitors the compliance with the specifications of chemical composition, grain size, density, geometrical parameters, surface finish, sphericity, and such other aspects, throughout the manufacturing process, is only a part of it.

The definition of a set of reference standards for medical grade alumina played a pivotal role in this process. The first standard on alumina for clinical implants was issued in Germany in 1979 as DIN 58835. The standard ISO 6474, largely based on DIN 58835, was issued in 1980, and was followed by the similar standard ASTM F603. The current version of ISO 6474 was released in 1994, and is today under revision due to the improvements introduced in the manufacturing process. ISO 6474 is circulating as a DIS (Draft International Standard), while a ISO 6474 – Part 2 is under preparation to provide a reference for composite alumina–zirconia materials now available for biomedical applications, and known as ZTA (zirconia-toughened alumina) if alumina is the main constituent, or as ATZ (alumina-toughened zirconia) when the main constituent is zirconia.[16,17]

The main disadvantage of alumina is its brittle fracture mechanics that limits the flexibility of ceramic components during design. The persistent demand placed upon the implant manufacturers for new ceramic devices with increased reliability and longevity and sometimes a challenging design has pushed the industry to develop composite ceramic materials of higher strength, obtained by the introduction of zirconia as a reinforcing and toughening phase into the alumina matrix. Zirconia, notwithstanding its much lower hardness (1200 GPa), is characterized by toughness and bending strength that is twice that of the alumina due to the phase transformation toughening peculiar to this material.[18]

Considerable work was conducted during the second half of the 1980s in France and in the 1990s in Italy on ZTA as a biomaterial.[19–22] In ZTA, the constrained phase transition of zirconia grains from tetragonal to monoclinic (the native crystallographic form of zirconia) has to overcome stiffness of the alumina matrix which is much higher than that of zirconia. The compressive field, forming an energy barrier to cracks, is then enhanced by increasing the toughness of the material in a manner comprehensively described by De Aza *et al.*[23] An optimum compromise has to be sought between alumina and zirconia grain size, the zirconia–alumina ratio, and the additives.[21,22] Moreover, the increase in toughness and bending strength due to the presence of zirconia comes at the price of the decrease in hardness, related to the zirconia concentration in ZTA.

ZTAs have been proposed for dental and orthopedic applications.[23–26] Begand *et al.*[27] developed a zirconia–alumina composite mostly constituted by zirconia, a material belonging to the class of ceramics and identified by the general name ATZ. This material, which is now in use for the manufacture of THR ball heads, is a result of the dispersion of alpha–alumina (20 wt%), in a matrix of yttria-stabilized tetragonal zirconia polycrystal (Y-TZP), mostly tetragonal (66 wt%) and cubic (12 wt%), the balance being monoclinic zirconia and Yttria with an homogeneous structure and average grain size less than 0.5 μm.

So far, the alumina–zirconia composite with the longest clinical record is known by the trade name BIOLOX®delta.[28]

On February 2010, more than 1 million BIOLOX®delta components had been released in the market worldwide. BIOLOX®delta has a peculiar microstructure, constituted by a matrix of fine grained alumina (average grain size about 4.5 μm) containing a second phase of Y-TZP grains (average grain size about 0.3 μm) and a third phase of platelet-shaped crystals of strontium aluminate having a maximum length of 5 μm.[29] In this composite, the toughening and reinforcing actions are performed by two independent synergic mechanisms, that is, phase transformation of the fine and evenly dispersed Y-TZP grains (about 17 vol%) and crack bridging due to the presence of platelet-shaped grains that constitute about 3 vol% of the material, the balance being alumina and other oxides of which the CrO_2 forms a solid solution with alumina that gives the characteristic pink color to BIOLOX®delta. It is used to compensate for the decrease in hardness, thus allowing the use of this composite in the manufacture of CoC bearings (Table 2).

1.105.2. Properties of Alumina

1.105.2.1. Physical Properties

The clinical application of alumina is based on its biocompatibility, density, strength, and wear resistance. Alumina (aluminum oxide, Al_2O_3) may occur in many metastable phases. All these phases irreversibly transform into alpha–alumina if heated above 1200°C, a close-packed hexagonal arrangement of oxygen ions which is a very high thermodynamically stable phase, and is the material selected for biomedical application. α-Alumina (known also as corundum, or emery if containing impurities) forms several gemstones, for example, ruby, the red color of which is caused by the presence of Chromium and sapphire, the blue color of which is due to Titanium. Alpha–alumina is aluminum metal in its highest oxidative state where no more oxidative reactions are possible and the chemical and physical stability of the material being the maximum achievable. The strong ionic and covalent chemical bonds between Al_3^+ and O_2^- gives the material a high melting point, hardness, and resistance to the attack of strong inorganic acids, such as orthophosphoric or hydrofluoric acid.

In the lattice of alpha–alumina, each aluminum cations Al_3^+ is surrounded by oxygen anions O_2^- forming two regular triangles on both sides, twisted by 180° and lying on parallel planes. The surface layer of O_2^- anions allow the chemisorption on the surface of OH^+ groups, and the bonding of water molecules or proteins. In other words, the surface has an high wettability, higher than that of several metallic alloys.

This behavior, coupled with the high hardness of alumina (2000–2200 GPa), makes this ceramic an ideal material for the components of the arthroprostheses joints. The high hardness makes the alumina components extremely resistant to scratching from foreign bodies thus saving the extremely smooth surface finish achievable by diamond polishing (typical values: $R_a = 0.02$ μm, $R_t = 0.5$ μm). Both these characteristics (wettability and hardness) are prerequisites for the extreme low wear of the prosthetic bearings making use of alumina components.

Further physical characteristics of alumina which are relevant for *in vivo* behavior are density and porosity, both important for the mechanical performances of the ceramic products. Especially, the open porosity fraction that allows the penetration of liquids and gases below the surface and inside the ceramic has a strong influence on the long-term strength of alumina and is a characteristic to be carefully controlled in view of the use of alumina devices in the physiologic environment.

Medical grade alumina may contain a maximum concentration of 0.5 wt% sintering additives. These are mainly Magnesium and Chromium oxides. Magnesium oxide (MgO) is used as sintering additive to control the deleterious discontinuous grain growth and to achieve optimum results in terms of density and grain size, while Chromium Oxide (Cr_2O_3) is introduced in the matrix to compensate the decrease in hardness due to the introduction of MgO (Table 3; Figures 5 and 6).

1.105.2.2. Mechanical Properties

Alumina shares several characteristics with other polycrystalline ceramic materials, such as moderate tensile and bending resistance and the brittle fracture behavior, which is the main disadvantage of the mechanical properties of alumina.

Alumina is a ionic-covalent solid that does not yield under load as metals and alloys do. The strong chemical bonds in alumina are the roots of several of its characteristics such as the

Table 2 Synopsis of the evolution of alumina ceramics as a biomaterial

Material generation	*Chemical composition*	*Marking*	*Densification route*	*Reference standards*	*Grain size (μm)*	*Bending strength (MPa)*	*Notes*
First (from 1970)	Pure alumina + (MgO, Cr_2O_3)	Engraving	Pressureless sintering	None	<7	>300	
Second (from 1985)	Pure alumina	Engraving	Pressureless sintering	DIN 58835 (from 1979) ISO 6474 (from 1980)	<4	>350	
Third (from 1995)	Pure alumina	Laser	Pressureless pre-sintering + HIP	ISO 6474:1994	<2	>500	
Current (from 2000)	Alumina matrix composite	Laser	Pressureless pre-sintering + HIP	ISO 6474-1 ISO 6474-2 Circulating as drafts	Submicron and nanometric	>1000	Phase transformation toughened material

low electric and thermal conductivity, the high melting point that makes it practically impossible to shape alumina by casting, and the high hardness that characterizes this material and makes its machining complex and costly.

The brittleness of alumina is the main concern of engineers while designing alumina components. In metals, crack energy is dissipated by yielding at the crack tip, while alumina components may fail without any previous plastic deformation at the location of high tensile stresses, such as surface defects, notches, internal flaws, or on the occurrence of thermal shocks. Moreover, as polycrystalline ceramics contain a number of flaws characterized by a large scatter in size and by a random location within the solid body, the relationships between stress distribution, failure probability, and strength in ceramics need to be discussed on statistical basis.[32]

As a biomaterial, alumina ceramic has undergone great improvements in its mechanical properties during the 40 years of clinical use as described in **Section 1.105.1**. The remarkable increase in bending strength (from less than 400 MPa to more than 630 MPa in pure alumina components) is due to the improvements in the selection of raw materials used as precursors and in the sintering process that resulted in marked reduction in grain size and in the increase in density, which is close to the theoretical one.[29]

However, it was the introduction of the alumina composite in clinics that made it possible to overcome the limits of alumina in terms of mechanical properties, for example, the toughness and bending strength of BIOLOX®delta are more than twice that of the former BIOLOX®forte (**Table 4**).

Table 3 Physical properties of alumina

Property	*Units*	*Value*
Crystallography	–	Hexagonal
Lattice parameter a	nm	0.476
Lattice parameter c	nm	1.299
Melting point	K	2310
Density (theoretical)	g cm^{-3}	3.986
Thermal expansion coeff.	–	6.5
Thermal conductivity (298 K, >99.9%TD)	W m^{-1} K	30
Specific heat (298 K)	J Kg^{-1} K	$8–10\times10^{-4}$

Based on data from Dörre and Hübner[30] Li and Hastings,[31] and Munz and Fett.[32]

1.105.2.3. Stability in Wet Environment

Among the characterstics that form the rationale behind the use of alumina in clinical application, the key point is the long-term stability of this material within the human body. The strength degradation of alumina in a wet environment is strongly dependent on density and on open porosity as discussed by several authors.[33,34,35] The liquids that may permeate the material through the open porosity may interact with the microstructural defects (flaws) that are intrinsic to

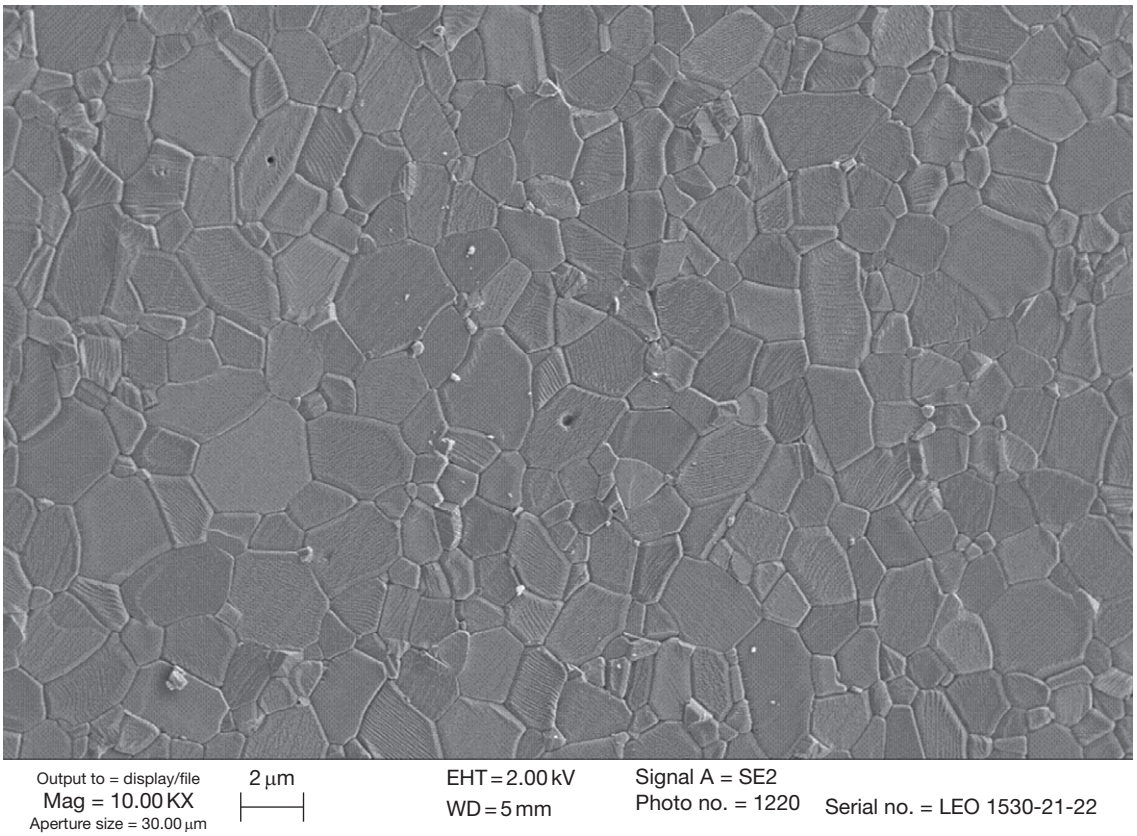

Figure 5 Microstructure of a contemporary medical-grade HIP-treated alumina (Courtesy Dr. L. Pilloni, ENEA, Rome, Italy).

ceramics because of their production technology. In a brittle material – such as alumina – subcritical cracks or flaws may grow at a speed much lower than the one leading to instantaneous failure. This behavior – known as subcritical crack growth (SCG) – depends on several variables (e.g., chemical species concentration, environment, temperature) and leads to the strength degradation of the component until it fails, thereby limiting its service life (see **Chapter 1.106, Zirconia as a Biomaterial**).

Especially during the early years of use of alumina ceramics in clinical applications, SCG was a relevant problem, although not of the same level for all the materials manufactured at that time. The introduction of high purity powders, and limiting to 0.1 vol% the content in calcia, alkali, and silica by the standard ISO 6474 in 1980, allowed for the control of the problem of strength degradation in alumina.

To achieve the grained, homogeneous, high-density, pore-free structure that characterizes medical grade alumina, the ceramic precursors used must be free from impurities such as CaO, NaO, and SiO_2 that play an important role on stability. CaO interactions with the aqueous environment, calcium migration, and segregation were found responsible for strength degradation by Sinkaroy *et al.*[36] and by Osterholm and Day,[37] while SiO_2 increased indirectly the risk of fatigue fracture, as during sintering it limits densification and promotes grain growth. Moreover, silica and alkalis (e.g., NaO) may segregate at grain boundaries and their dissolution in physiologic liquids may lead to accelerated fatigue fracture.[30] For the same reason, the content in MgO and the thermal cycle have to be tuned to avoid increase in solubility of the MgO in alumina, which leads to the formation of AlMgO spinel.

The issue of hydrothermal stability was also carefully investigated for the new alumina composites because of the presence of Y-TZP in their matrix and of the low temperature degradation behavior of this ceramic in the presence of the wet environment. It is noted that in BIOLOX®delta, due to the low content of Y-TZP (17 vol%) and to the stiffness of the alumina matrix, this behavior is very much limited and also the accelerated aging treatments in the most severe conditions (grinding, polishing, aging at 134°C in water up to 100 h) have been almost ineffective on the mechanical behavior of the material.[29]

In the case of ATZ, the situation is quite different because of the higher content in zirconia. Notwithstanding the presence of alumina in the composite that operates a limiting action on the extent of the phase transformation,[38] the increase in monoclinic phase is significant (monoclinic phase increase from 0.6 wt% to 58 wt%) with detrimental effects on the mechanical properties. The mean bending strength of the material shows a marked decrease in time, that is, 11% after 30 h and 18% after 30 or 100 h aging, respectively.[27]

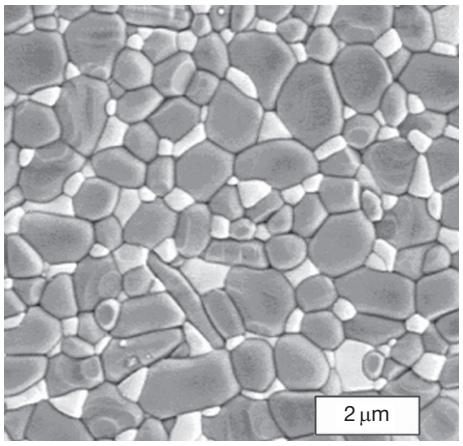

Figure 6 Micrograph of BIOLOX®delta, showing the platelets and the zirconia grains (white) forming the reinforcing and toughening phase in the alumina matrix (Courtesy Ceramtec Gmbh, Germany).

1.105.2.4. Wear Behavior of Alumina

In the processes leading to osteolysis and aseptic loosening of the implants, a relevant role is played by the cascade of cellular events following the release of large amounts of small particles in the joint, for example, due to the wear of the bearing. Aseptic loosening is the main cause of arthroprostheses failures, a problem of particular economic and social relevance, as revision arthroplasty is a costly and challenging surgery, with outcomes poorer than the primary surgery.

The relevance of the problem fostered wear studies aimed to predict the clinical performances of bearings in well-controlled laboratory conditions and to make a screening of the behavior of the different bearings. This resulted in a challenging task in terms of the difficulty in modeling the complexity of human articular joints. For this reason simulator testing of arthroprostheses' bearings needs to control a relevant number of parameters. A review on wear of orthopedic bearings[39] enlist 37 different parameters influencing laboratory tests, such as

Table 4 Mechanical properties of medical grade alumina and alumina composites

Property	*Units*	*Alumina (1970s)*	*BIOLOX® (since 1974)*	*BIOLOX®forte (since 1995)*	*BIOLOX®delta*	*ATZ*	*ISO 6474:80*	*ISO 6474:94*
Al_2O_3 content	Vol %	99.1–99.6	99.7	>99.8	80	20	≥99.5	≥99.5
Density	g cm^{-3}	3.90–3.95	3.95	3.97	4.37	n.s.	≥3.90	≥3.94
Av. grain size	µm	≤4.5	4	1.75	0.54	<0.5	≤7	≤4.5
Flexural strength	MPa	>300	400	630	1390	1090	>380	>400
Young modulus	GPa	380	410	407	n.s.	n.s.	380	–
Hardness	HV	1800	1900	2000	1760	n.s.	–	–

Data from Kuntz *et al.*[29] and Begand.[27]

the status of the surfaces, the type of contact between the surfaces, the materials, the geometrical characteristics of the joint, the loads and their variation in time, and the motion patterns. Deionized water, used in the early tests in joint simulator, does not represent the synovial fluids. The composition of the serum that forms the joint environment during the tests and of the additives mixed in it are further variables making the comparison between different laboratories sometimes difficult. The degradation of the serum for the heating due to the surface friction may strongly bias the results of wear tests: that is, the precipitation of calcium phosphates in the heated serum may alter the roughness of the ceramic head surface and increase the wear of polyethylene, while the formation of proteins layers may protect the cup in a way that does not occur *in vivo*.

The differences that can be remarked upon, between the results of laboratory tests performed in well-controlled conditions and clinical wear of bearings may be explained in terms of patient-related factors that influence clinical wear, for example, age, activity, pathology, etc. Moreover, in the laboratory setting there are no third bodies that may scratch the surface of heads and increase the wear of the bearing. This led to the development of 'nonstandard' simulator test for a better reproduction of the clinical situation, where studies on the effects on wear of third bodies, or of the microseparation of the bearing surfaces during the swing phase of the gait cycle due to the laxity of the joint can be performed.

1.105.2.4.1. Simulator tests on alumina-on-PE bearings

There is general agreement that when coupled with ceramic heads the wear of UHMWPE (PE) cups is reduced in comparison with metallic heads. The comprehensive review of laboratory and clinical data made by Clarke and Gustafson[40] shows that ceramic-on-polyethylene (CoP) bearings have in average half the wear of metal-on-polyethylene (MoP) bearings. The results obtained in laboratory tests of CoP bearings "document dramatic reductions in wear volume offering the prospect of increase polyethylene longevity and decreased potential for osteolytic response."[41]

About 70% of hip implants make use of PE for the acetabular component. As PE wear strongly depends on the roughness of the counterpart (the ball head), substantial effort has been devoted to improve the surface finish in the development of surface treatments of metallic heads (i.e., ion implantation, nitriding, etc.). Nevertheless, only the use of alumina heads so far allows 50% reduction of PE wear, thanks to the smooth finish and to the resistance to scratching of the alumina surface, and to the lubrication of the bearing due to alumina wettability.[42]

Third bodies, such as wear or cement debris and bone chips, can be present in the joint and remain embedded in the surface of the polyethylene cup, transported through the bearing interface, damaging the surfaces of metallic ball heads, for example, the presence of zirconia of barium sulphate particles, introduced in the bone cement to make it opaque to X-rays, may enhance the abrasive action of the debris. Alumina ball heads, because of their resistance to scratching, have proven to be extremely effective in preventing the negative effect of third bodies on PE wear.

The study of Minakawa *et al.*[43] clearly highlights these aspects. The Author measured the roughness of metallic and ceramic ball heads retrieved during revision surgeries. The roughness of alumina heads in damaged zones (0.023 μm) was about 1/20 of the roughness of damaged metallic heads ($R_{pm} = 0.4–0.556$ μm).

Similar observations were made by Wang *et al.*[44] who reported that when coupled with cross-linked PE (XLPE) cups and in presence of bone cement particles the wear rate of CoCr/XLPE bearings was 118 mm^3/million cycles while that of Alumina/XLPE was 35 mm^3/million cycles, indicating a lower potential for wearing of PE acetabular cups in the long term because of the superior resistance to surface damage of ceramics.

1.105.2.4.2. Simulator tests on alumina-on-alumina bearings

The biphasic behavior that characterize the wear of ceramic-on-ceramic bearings was already described by Boutin,[6] who reported a relatively high linear wear in the first million cycle while in the test the wear was 'undetectable.' The presence of an initial wearing-in phase (the run-in phase) was observed in the first 0.5–1 million cycle by several other investigators, and was analyzed in detail by Clarke *et al.*[45] who also reviewed the results of previous authors.

Nevelos *et al.*[46] studied the wear of BIOLOX®forte ceramic-on-ceramic bearings (CeramTec AG, Plochingen, Germany) using different joint clearances. In the first million cycles the run-in wear behavior was observed (0.14 mm^3/million cycles) followed by extremely low steady state wear (0.05 mm^3/million cycles). In former tests performed by the author in the same experimental conditions, the wear of metal/PE was 35 mm^3/million cycles. No difference depending on the clearances of the bearings tested (20 and 30 μm) was detectable. The reduction in wear using CoC bearings was also shown by the already cited study of Wang *et al.*[44] who measured alumina-on-alumina wear rate of 0.1 mm^3/million cycles, while the wear rate of alumina/XLPE and of MoM bearings tested in the same experimental conditions were 5.62 and 7.40 mm^3/million cycle, respectively.

Hip simulator tests also show favorable wear performances of the bearings based on the alumina matrix composites, although not all the materials show similar performances. The results of the study by Kaddick and Pfaff[47] demonstrated the very low wear of ceramic-on-ceramic BIOLOX®delta bearings, with a 150× reduction in wear debris volume of several orders of magnitude with respect to the alumina-PE bearings. In hip simulator tests, the volume of PE wear particles released when coupled with the alumina matrix composite BIOLOX®delta resulted in 60% of the one released when coupled with pure alumina (BIOLOX®forte).

1.105.2.4.3. Microseparation tests on alumina-on-alumina bearings

The wear tracks in alumina-on-alumina bearings frequently appear as stripes of variable width. Nevelos *et al.*[46] correlated this feature (stripe wear) with the separation of the bearing surfaces during the swing phase of the gait. If the soft tissue allows enough laxity to the joint, the ball will hit the rim of the acetabular cup before its relocation after the heel strikes the ball. The repeated impacts may damage the surface finish and

cause grain pullout eventually resulting in the stripe wear on the ceramic-on-ceramic joint. This behavior explains the differences that can be observed between the wear measured in some retrieved explants (up to 1 mm^3/year) and the wear measured in hip simulators.

The model of microseparation was implemented in a hip wear simulator in Leeds allowing researchers to observe for the first time in a laboratory test wear patterns and rates similar to the ones observed clinically by Nevelos *et al.*[46] Further studies performed with surface separation up to 500 µm show that steady state wear of alumina-on-alumina bearing is increased from 0.05 mm^3/million cycles in standard simulation mode, to 1.3 mm^3/million cycles in severe separation mode.[48]

The mechanical behavior of alumina matrix composite resulted in a very low wear in tests performed in microseparation mode. Stewart *et al.*[49] – who tested in microseparation BIOLOX®delta bearings – measured wear rates of 0.32 mm^3/million cycles in the run-in phase and 0.12 mm^3/million cycles in the steady state wear phase. BIOLOX®forte bearings tested in the same microseparation conditions were showing higher wear rate of one order of magnitude. Also, the wear stripes on the components were different between the two ceramic tested: the wear stripes on BIOLOX®delta were more shallow than the ones observed on BIOLOX®forte heads; this behavior appears to be related to the improved mechanical properties of the nanocomposite BIOLOX®delta.

Other zirconia-toughened alumina (NZTA) ceramics tested under the same conditions (microseparation mode) show wear rates almost twice that of BIOLOX®delta. No significant differences in hardness and fracture toughness between the NZTA tested and BIOLOX®delta were observed, but the flexural strength was two-third only. In comparison to NZTA, BIOLOX®delta has a much finer and homogeneous alumina matrix grain size and evenly distributed zirconia grains, these latter forming large agglomerates in NZTA.[50]

1.105.2.5. Biocompatibility

The *in vivo* biocompatibility of alumina is an already well established behavior since the beginning of the seventies.[51,52] The high oxidative status of alumina gives high chemical inertia to alumina ceramics, that are frequently taken as negative reference in biocompatibility testing of orthopedic biomaterials (see **Chapter 4.401, The Concept of Biocompatibility**; **Chapter 4.402, Biocompatibility and the Relationship to Standards: Meaning and Scope of Biomaterials Testing**; **Chapter 4.403, The Innate Response to Biomaterials**; **Chapter 4.404, Adaptive Immune Responses to Biomaterials**; and **Chapter 4.405, Leukocyte–Biomaterial Interaction *In Vitro***).

1.105.2.5.1. In vitro *tests*

Extraction procedures performed by media suitable for cell culture have shown the absence of release from alumina, and a very low cellular reactivity. The *in vitro* tests were performed using different cell lines (e.g., macrophages, lymphocytes, fibroblasts and osteoblasts), different cell conditions during the tests, and materials different both in physical forms (powders or dense ceramics) and with different chemical–physical characteristics (e.g., reactive surface, chemical composition, impurity content, etc.).[53]

The concentration of powders resulted relevant for cellular response. Dose dependent cytotoxicity was observed on human lymphocytes stimulated with phytohemoagglutinine in the presence of partially stabilized zirconia and alumina powders,[54] as well as on fibroblasts cocultured with ceramic extracts.[55] Similar dependence of cellular response on ceramic powders concentration was observed for macrophages apoptosis[56] and more recently by Kranz *et al.*[57] who observed cytotoxic reactions to corundum particles challenged to murine macrophages depending on particle size, the more cytotoxic being the nanometric ones because of their very high reactive surface for a given volume (see **Section 1.105.2.6**) (**Table 5**).

1.105.2.5.2. In vivo *tests*

The *in vivo* tests were performed on ceramics in different physical forms and in several sites of implantation, to analyze adverse reactions in soft tissue and/or bone, and systemic toxicity.

When implanted in soft tissues, dense alumina ceramics are surrounded by a layer of connective tissue that transforms in a fibrous membrane. Implants of alumina in bone performed in non-loaded sites show that bone comes into contact

Table 5 Summary of *in vitro* tests on alumina(A) and zirconia(Z)

References	*Physical form*	*Cell type*	*Test type*
Harms and Mausle[58]	Powders	Macrophages, limphocytes	Direct contact
Pizzoferrato *et al.*[59]	Ceramics	HeLa, 3T3	Direct contact
Bukat *et al.*[60]	Ceramics	3T3	Direct contact
Greco *et al.*[54]	Powders	Human limphocytes	Inhibition of cell mitogenesis after PHA induction
Ito[61]	Wear debris	L929	Cell proliferation
Li *et al.*[62]	Powders and ceramics	Human Oral Fibroblasts	Direct contact, MTT test
Dion *et al.*[63]	Powders	HUVEC, 3T3	Indirect contact, MTT tests
Harmand *et al.*[64]	Powders	Fibroblasts	MTT test
Takami[55]	Extracts	Fibroblasts	Citoxicity
Catelas[56]	Powders	Macrophages	Apoptosis
Mebouta *et al.*[65]	Powders	Human monocytes	Cell differentiation
Torricelli *et al.*[66]	Powders	Osteoblasts	Direct contact, MTT test, ALP
Lohmann *et al.*[67]	Powders	Osteoblasts	Cell proliferation

Based on data from Piconi *et al.*[53]

with the ceramic without fibrous interposition. A thin proteoglycan layer is present at the bone–biomaterial interface, as expected from a 'nearly inert' material. Bone apposition at implant interface is enhanced by the stresses due to loading.[70]

The tissue reaction to the injection of alumina particles in several animal sites is characterized by the absence of acute toxicity: granulocytes and lymphocytes have been observed in numbers lower than after the injection of metals. Also at the higher reactive surface alumina elicit the weakest tissue response in comparison to metals and polyethylene: it was remarked that alumina particles did not induce the fibrosis observed after injection of polymeric or metallic particles.[70]

This behavior of ceramic powders was observed also by Warashina *et al.*[71] who implanted in rat calvaria powders of alumina, zirconia, polyethylene and Ti-alloy (Ti6Al4V).

Absence of acute or systemic toxicity was also observed after the implant of alumina or zirconia in bone. Hulbert *et al.*[51] observed the absence of systemic toxicity after the implantation of ceramic disks and tubes of different porosity in the paraspinal muscles of rabbits, and the dependence on pore size of the tissue ingrowth in ceramics.

Absence of acute sistemic adverse tissue reactions to ceramics were also reported after subcutis, intramuscular or intraperitoneal and intra-articular injection of alumina and zirconia powders in rats and/or mice, as well as by implants made into the paraspinal muscles of rabbits, rats or in rabbit's bone (see Piconi and Maccauro[53] for a comprehensive review) (Table 6).

1.105.2.5.3. Carcinogenecity

The issue of cancer development after joint replacement, especially related to metallic implants, was raised long time ago. So far, the only (and alone) case concerning a possible carcinogenic effect of ceramic in about 40 years of clinical use was that described by Ryu *et al.*[72] who associated the presence of a ceramic hip implant to soft tissue sarcoma.

Griss *et al.*[52] who analyzed the long term *in vivo* reactions to ceramics did not describe tumours and reported the absence of tumor induction by alumina powders. No carcinogenic reaction was observed after the subcutaneous injection of alumina powder in Sprague-Dawley rats[69] (Table 7).

Table 6 Summary of *in vivo* tests of alumina

References	*Physical form*	*Animal model*	*Implant site*
Hulbert *et al.*[51]	Porous and nonporous disks and tubes	Rabbit	Paraspinal muscle
Griss *et al.*[52]	Slurry	Swiss mice	Subcutis, knee
Harms and Mausle[58]	Powders	Mice	Intraperitoneal, intramuscular
Wagner[68]	Pins	Rat	Femur
Christel *et al.*[69]	Pins	Rat	Paraspinal muscle
Christel[70]	Pins	Rabbit	Femur
Warashina *et al.*[71]	Powders	Rat	Calvaria

Based on data from Piconi *et al.*[53]

1.105.2.6. Reaction to Ceramic Wear Debris

In spite of the excellent outcomes of the great majority of arthroplasties, the wear of the bearing surfaces is still among the major problem that limit their long term survival. Schmalzried and Callaghan[73] calculated that a well-functioning metal-on-polyethylene hip bearing may produce about 500,000 wear particles per step. The cascade of cellular events following the release of such large amounts of small particles in the joint leads to bone loss (osteolysis) and to implant loosening, which is the main cause of arthroprostheses failures, a problem of particular economic and social relevance, as revision arthroplasty still is a challenging surgery with outcomes poorer than primary surgery.

The reactions to wear debris had been described exhaustively by several comprehensive reviews.[73–76] The evidence collected show that size, shape, and nature of the debris, influence the rate of bone loss. In the case of polyethylene debris, the hypothesis that osteolysis takes place only if the density of debris in the tissue is above a threshold value was advanced and this resulted in the interest for bearings with a reduced wear rate.

Besides local effects, systemic effects of wear debris are relevant. Due to the pressure gradients generated by the motion of the articular joint during daily activity of the patient the wear debris dispersed in the fluid surrounding the joint can be transported by the fluids into body regions that form the 'effective joint space.'[73] A similar behavior had been reported formerly by Willert and Semlitsch[77] who observed that particles accumulate in periarticular tissues, leading eventually to granulomas associated with necrosis and fibrosis, can also migrate through vessels giving rise to systemic reactions.

Wear debris from hard-on-hard bearings (metal-on-metal and ceramic-on-ceramic) are characterized by a very fine size, most of their total volume being constituted by micron- or sub micron-size grains. Hard-on-hard bearings are intended for use in younger patients as they are the ones with longer life expectations, and the study of the chronic effects of these small particles has become very relevant.[74,78] Concerns had been raised especially about wear debris coming from metal-on-metal bearings,[79–81] while it is acknowledged that local and systemic reactions to alumina wear debris are reduced, in comparison to the ones observed in the presence of metal and polyethylene (UHMWPE) debris.

Table 7 Summary of carcinogenicity tests of alumina and zirconia

References	*Physical form*	*Experimental model*	*Description*
Griss *et al.*[52]	Disks, powders	Sprague-Dawley rats	Long-term test in subcutis
Ryu *et al.*[72]	Ceramic	Clinical observation	Hip
Takami[55]	Ceramic	*In vitro*	Mutagenicity, Ames test
Maccauro *et al.*[26]	Ceramic	*In vitro*	Mutagenesis, carcinogenesys

Based on data from Piconi *et al.*[53]

Alumina wear debris have been found less active than UHMWPE debris in promoting the differentiation of osteoclasts, especially in the low concentration typical of the low wear of alumina bearings.[82] These findings correspond well to the ones reported by Fisher *et al.*[83] who demonstrated the negligible biological activity of ceramic-on-ceramic wear debris in comparison with standard polyethylene (60×) and to cross-linked polyethylene (13×).

The results reported by these Authors are in agreement with the ones reported formerly by Germain *et al.*[84] who observed that at equivalent volume concentration, the CoCr debris was more cytotoxic than the alumina ones, while Mattews *et al.*[85] reported that a concentration of alumina wear debris ten times higher than the one of polyethylene debris of the same size is necessary to stimulate osteolytic cytokines production by human peripheral blood mononuclear cells.

On the other hand, Krantz *et al.*[77] observed that cytotoxic reaction depends on particle size in murine macrophages challenged with corundum particles; the nanometric ones being the more cytotoxic. It is noted that depending on the grain size, ceramic powders may develop a significant surface area per mass unit, a feature that enhances the reactivity of powders in comparison to sintered ceramics. Especially the nanometric powders may develop specific surface area of some hundreds of square meters per gram.

A critical role in the transport of debris from the site of production into the peripheral organs is played by the blood vessels.[86] The presence of many vessels in the periprosthetic membrane containing debris may be considered an inflammatory aspect of the tissue response, typical of reaction to metals[88] related to the cytotoxicity of the particles and to the release of humoral factors after phagocytosis by macrophages. This behavior was observed also by Maccauro *et al.*[87] using an *in vivo* model designed for the gradual release of ceramic debris in the articular joint. This author reported the formation of fibrous tissue as 'poor' in vessels in the absence of contaminations from metals or polymers. Few giant cells were observable, a finding in agreement with Lerouge *et al.*[88] who reported that foreign body cells are typically associated to polyethylene, PMMA, and large metal particles, but rarely to ceramics. This finding was reported also by Christel[70] who in autoptic observations made on stable THR after 12 years of clinical use noted that ceramic debris were concentrated around capillaries in the ligament capsule in presence of a low local inflammatory reaction, while in failed THRs lymphocytes and plasma cells infiltrates were observed only when metallic debris were simultaneously found.

Baldini *et al.*[89] never observed massive osteolysis in a series of 30 failed alumina-on-alumina arthroplasties. Bone resorption leading to failure was due to infections either to secondary implant instability or malpositioning. In this series, a few ceramic wear debris were detectable, without any tissue reactions. Also in the few cases of severe wear foreign body multinucleated cells were absent, this being the main difference with failed metal-PE THAs.

In observing the tissues retrieved during 134 revision surgeries of ceramic-on-ceramic THRs implanted between 1974 and 1993. Fritsch *et al.*[90] noted that giant cells – considered strictly related to osteolysis – were detected only in a few cases, associated to bone cement particles in cemented THRs. Histology of this series of negative cases put in evidence no tissue necrosis and only slight fibrosis was detected indicating the high biocompatibility of alumina wear debris (0.5–2 μm), present within active macrophages.

The absence of vessels in the periprosthetic tissue surrounding alumina particles in alumina–alumina joints led De Santis *et al.*[91] to hypothesize that ceramic debris did not migrate from the production site. These findings, coupled with the chemical stability of ceramic oxides higher than the one of metals may be considered as indicative of the absence of systemic toxicity of ceramic debris in the long term (see **Chapter 6.606, Biological Effects of Wear Debris from Joint Arthroplasties**).

1.105.3. Clinical Application of Alumina Ceramics

The early alumina-on-alumina bearings had clinical outcomes that can be defined as 'mixed' at best. The review of the results of the French clinical series made by Nizard *et al.*[92] show that in 172 patients with more than 10-year follow-up, the revision of 15 acetabular cups for aseptic loosening was necessary and that there had been five component fractures. These results match the ones of the review of the German experience[93]: in the first series (109 patients, minimum 10-year follow-up) the aseptic loosening of the femoral component accounted for 24 revisions along with five fractured components.

Several lessons could be learned from these early clinical experiences. The failures observed were essentially related to the poor clinical performance of the acetabular component (French series) or of the femoral component (German and USA series) and were not related to the use of alumina on alumina bearings: the series reported by Miller *et al.*[94] consisted of 102 patients who experienced 26% aseptic loosening for the femoral stem but no fracture of any of the ceramic components within the first 3 years after implantation. It is also noted that the high incidence of fractures (3–13%; see Piconi *et al.*[95]) of the generation of alumina heads belongs to materials made in absence of any voluntary or consensus standard, and that the fractures reported in some series took place in components made by companies that are no more operational.[96] Besides this, the wear rate of these early alumina ceramic couple was very low compared to metal-UHMWPE couples (2.6 μm/year for the cup; 5.4 μm/year for the head), and complications related to aseptic loosening was drastically decreased by the application of ceramic in younger patients.

The solutions to these problems become the reference targets of the orthopedic ceramic manufacturers in the 1980s. Improved design of the fixations of both the acetabular and the femoral components reduced the incidence of loosening, as well as the adoption of patient selection criteria by the surgical community (younger, more active). Moreover, some ceramic manufacturers who were determined to continue in the field of orthopedics devoted their efforts first to standardize and then to improve alumina ceramics.

The experience in the United States with the early ceramic-on-ceramic (CoC) monolithic cup and cementless stems (Autophor) was poor and eventually led to the removal of the system from the market. Nevertheless, THRs using ceramic femoral heads coupled to polyethylene (CoP bearings) have

been used in the United States from 1989, when FDA gave its clearance limited to these devices. The experience cumulated by surgeons in non-US countries was demonstrating the benefits of modern CoC bearings for young and active patients with a dynamic lifestyle. Leading surgeons in Europe and in Japan, aware of the benefit this technology, offered it to their patients and continued to use CoC joints in THR since the 1980s, contributing in this way to the well-being of their patients and to the development of alumina as a biomaterial.

1.105.3.1. Technology of Alumina for THR Bearings

The use of alumina in the fabrication of ball heads and inlays for THR bearings is the main application of this ceramic as a biomaterial, and is today among the European leading technologies in biomedical engineering. The main manufacturer worldwide (CeramTec AG, Plochingen, Germany) alone is quoted to have sold more than 6 million alumina components of the different alumina BIOLOX® types so far (July 2010). Alumina components for THR bearings are manufactured by several companies worldwide each one making use of its proprietary process, characterized by specific choices in terms of starting materials, consolidation route, machining tolerances, quality control, and acceptance criteria. It is worthwhile then to outline the generic flow sheet which is used for the production of medical grade alumina components (Table 8).

The technology of alumina – and of most advanced ceramics – is based on the consolidation of powders, a process that can be summarized in three steps: pre-processing of the powder, shaping, and firing of the ceramic body.

Depending on the consolidation route and on the desired behavior of the final product the powder undergo several treatments that may include the blending of sintering aids (i.e., MgO forming a liquid phase that enhances mass transport at high temperature, thus allowing for the control of grain growth), of processing additives specific to the shaping process (i.e., waxes, as plasticizers of the mass and lubricant of the dyes), and of additives that will give peculiar properties to the ceramic.

The most common route for shaping ball heads and inlays is dye-pressing the 'ready-to-press' powders in cylindrical dyes. To optimize the feeding of the dye, the powder should have a good flowability. To this aim, the powders and the additives are blended in a slurry, which is then granulated by spray-drying to obtain particles uniform in size, that should be weak enough to be crushed, leaving no voids in the product. The dye-pressing product is the so-called 'green body,' with density being 50–60% of the theoretical density (TD). As the green body volume exceeds the one of the final component, the shrinkage that occurs during sintering due to the migration of porosity out of the ceramic must accurately be taken into account in designing the dyes.

Notwithstanding its low density, the green body has enough mechanical resistance to be handled and machined in the form of ball heads or of inlays. The machined parts are then submitted to a thermal treatment (sintering) that will bring them to high density. Sintering is usually performed in an oxidizing atmosphere in gas-heated kilns but continuous (tunnel) furnaces are also in use for high volume production. In these furnaces the green bodies are loaded on trays that are transported by a belt conveyor across a kiln tunnel formed by a series of chambers (zones) heated at different temperatures: time-temperature sequence depends on the speed of the conveyor and on the length of the chambers.

However, process parameters for sintering (temperature and time) alone do not guarantee that density, median grain size and grain size distribution can be optimized at the same time. For this reason, optimized grain size and distribution is obtained at a reduced sintering temperature, while the final density is achieved by a further thermal treatment performed under high pressures at a relatively high temperature (slightly below the sintering temperature), the so-called HIP. It is noted that HIP-treated BIOLOX®forte alumina made by CeramTec AG has a density of 3.97 $g\,cm^{-3}$ and average grain size less than 1.8 μm, while the former pressureless sintered BIOLOX®II had density of 3.95 $g\,cm^{-3}$ and average grain size of 4 μm (see Table 4).

After cooling, the spherical surface is diamond polished to the desired grade, the inner cone is ground to the expected tolerances in terms of roundness and linearity.

An alternative route consists in sintering balls of the desired diameter and then to hard machine the conical bore in the balls. This option allows a great flexibility in production to ceramic manufacturers, as ball diameters are standard, while the tapers – whose specification depend on the type of implant – can be machined on demand.

After machining and finishing, identification marks are engraved by laser. This marking method, as explained above, was a remarkable improvement in the reliability of alumina ceramic components, as engraved markings were acting as notches in the surface of the component. This step is followed by proof testing to detect the presence of internal flaws. It is noted that this testing procedure is not applied to 100% of the product by all the manufacturers of THR alumina components.

Table 8 Manufacturers of alumina ball heads

Name	*Country*
CeramTec AG	Germany
Ceraver SA	France
C5 MedicalWerks	USA
Dynamic Ceramic Ltd	UK
JMM	Japan
Keramed	Germany
Mathis	CH
Morgan Advanced Ceramics	UK

1.105.3.2. Design of Ceramic THR Bearings

The optimization in design and the evolution in technology have made available today's modular implants where the optimal material and size combination can be selected, depending on the options of the surgeon. Thanks to the taper connection, a stem may host metallic or ceramic heads that can be coupled with ceramic, metal, or polyethylene inserts hosted in modular acetabular sockets. Due to the number of available size this give rise to a family of bearings, providing the selection of the wear couple that better suits the

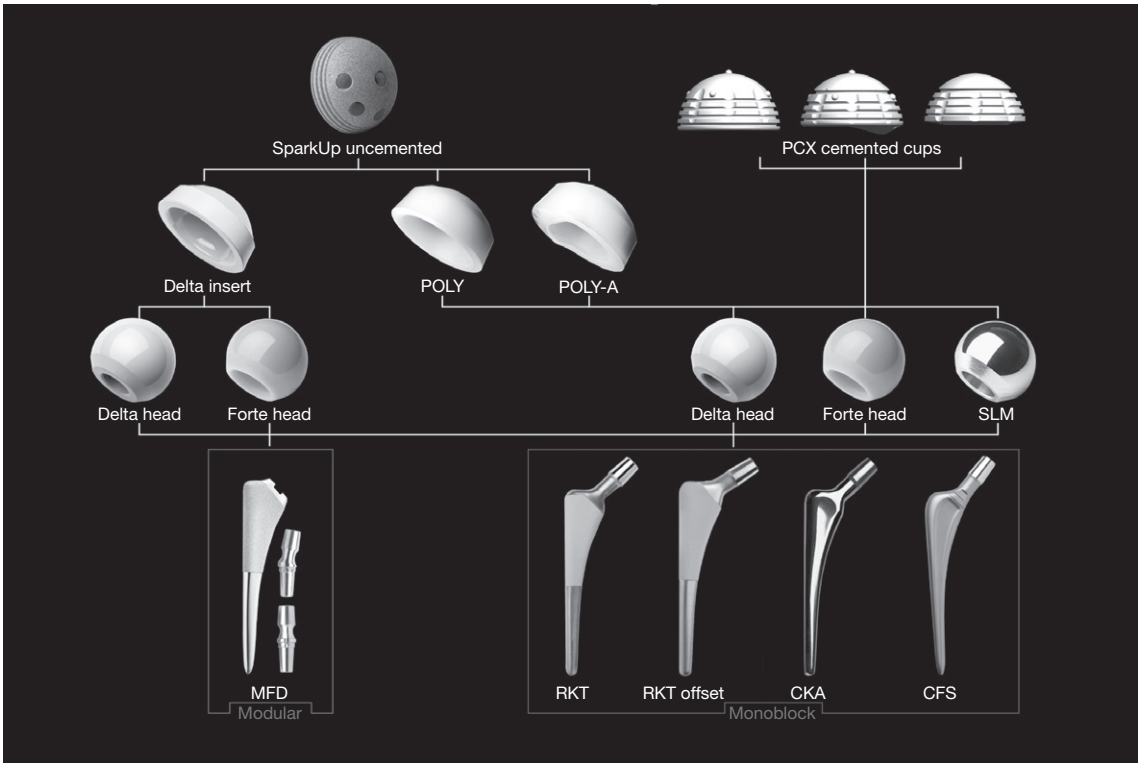

Figure 7 A modern modular Total Hip Replacement system, showing the different bearing solutions (Courtesy SAMO Biomedica SpA, Bologna, Italy).

needs and the anatomy of the patients. It is noted, however, that couplings shall not be made at random, but carefully following the instructions given by the implant manufacturer (Figure 7).

The introduction of ceramic ball heads raised the problem of metal–ceramic fixation, that found its solution by the introduction in THR technology of the Morse taper connection, made by German researchers in the early 1970s. The taper connection is stable in the long time, since ball-to-stem movement are eliminated. It is easy and quick to perform, easing the handling of the implant in the surgical theatre. Moreover, it makes no use of adhesives or solders that may pose problems of stability in the long term.[96]

Alumina ball heads are manufactured in five diameters from 28, 32, 36, 40, 44 mm. For any diameter, the internal depth of the conical bore can be selected in four steps, identified by the resulting neck length of the implant, that is, +5 (XL, Extra Long neck), +3.5 mm (L, Long neck), 0 mm (M, Medium neck), and –3.5 mm (S, Short neck).

The loads due to patient activity are transferred to the ceramic head generating two main tensile stresses in the ceramic head, for example, in the head dome, and homoradial (hoop) stresses close to the taper surface.[97,98] The stress distribution and intensity within the ceramic head depend on the friction between the taper surfaces and on the design of head, – for example, it is known that the frequency of fracture of 28 mm heads is higher than the one of 32 mm heads or bigger, and that the fracture frequency of medium neck (M-neck) heads is lower than the one of L- and S-neck heads. Although much of the attention is devoted to the ceramic, the metallic trunnion also plays a major role because stresses depend on taper characteristics such as stiffness, extent of the contact, cone angle, surface roughness, roundness, and straightness. It is noted that as the perfect matching of the metal trunnion and of the ceramic taper is only an ideal representation of the reality, the unavoidable tolerances in machining the metallic and ceramic surfaces through which the loads are transferred are relevant for the stress distribution in the system.[96]

To compensate the deviations due to machining tolerances, implant manufacturers take advantage of the ductility of metals, that is, providing grooves in the trunnion surface ('structured' taper). Provided that the angle of the bore into the head is slightly wider than the trunnion one, when the head is positioned onto the trunnion and loaded the tip of the grooves will be deformed progressively. In this way the contact area is increased and stress concentrations are avoided. Richter *et al.*[99] reported that the burst loads of alumina heads coupled to titanium alloy tapers is higher than the one observed for CoCr alloys due to the higher ductility of titanium alloys, and that the fracture load is higher in tapers with higher roughness. Also the head-trunnion friction torque is increased by the plastic deformation of the metal, improving the rotational stability of the coupling. A real diffusion joint is obtained in this way, as it is evident observing the marks of transferred metal in the taper of retrieved ceramic heads.[100]

Most of the considerations made above can be extended to the acetabular component of ceramic-on-ceramic bearing. Contemporary ceramic sockets for THA are metal backed devices, made out of a metallic shell hosting the ceramic insert. The socket may be pre-assembled (the so-called monoblock cups) or may have a modular design: a ceramic insert (or inlay)

is fixed into the metal back by a taper connection. Each implant system is characterized by its own design details, for example, presence of a rim to protect the ceramic from impingement, intermediate shells or rings between the ceramic and the metal back, etc. Morse taper must be self-locking, but it must also be possible to remove the components intraoperatively, or at the time of revision surgery, if necessary. For this reason 1:3 taper (about 18°) was selected for sockets, allowing the ceramic insert removal by, for example, a stroke on the rim of the metal back[96] (**Figure 8**).

The safety of modular sockets hosting ceramic liners depends on the roundness, straightness, roughness of the metal-ceramic interface, in a way similar to the one already described for ball heads. Moreover, the design of the mechanical interlock between the liner and the metal back has to assure the stability of the inlay, for example, when seated into the metal back the inlay has to resist to pull out, to torsion moments, to lever out moment due to the forces exerted on it when implanted.

Besides the taper connection, the manufacturers of ceramic-on-ceramic bearings have to take care of the clearance of the joint, for example, the difference between the head diameter and the inner diameter of the socket. This parameter is of paramount relevance for the performance of the bearing, as it allows the wedging of fluids in the bearing interface, assuring, in this way, the joint lubrication. To assure the optimal lubrication properties, the ball head should have a diameter slightly smaller than the cup's head; if equal, or bigger, the ball will stick into the cup, or will wear in a catastrophic way at the best, while a too large clearance may have a catastrophic influence on the stress distribution, due to the load concentration in the top of the insert dome.[99] Today, thanks to the improvements in the manufacturing process, deviation from roundness are in the order of a micron, allowing for the control of the clearance of ceramic-on-ceramic bearings, where the optimal value is between 20 and 80 μm.

The contemporary trend in THR design is to increase the bearing diameter, and ball heads 36 or 40 mm in diameter are now common in hip arthroplasty. This option has proven to be effective in the reduction of implant dislocations that are among the major complications in THR.[101,102] The increase of the head diameter is an effective way to increase the 'jumping distance' of the joint, for example, the displacement necessary to permanently dislocate the head from the socket. A further advantage of the increase of the head-to-neck diameter ratio is an increased range of motion (ROM), with reduction of the risk of impingement and consequent damage of the cup rim and of the stem neck. This is especially relevant for young and active patients, or for patients demanding high joint mobility due to their resting position (squatting).

It is noted, however, that the benefits of ROM are not directly proportional to the increase in ball head diameter, that is, the gain in ROM passing from 32 to 42 mm is lower that the gain when the diameter is increased from 22 to 32 mm. Moreover, the anatomy of the patient may be a limiting factor. The best benefit/diameter ratio looks to take place for a bearing diameter no more than 40–44 mm, a value that also allows to limit the overall diameter of the implant, a feature relevant both to save the patient's bone stock and for the implant intended for smaller anatomies (e.g., female or Asian patients).

The independence of the wear of THR ceramic bearings on the diameter[103] makes them interesting candidates for large diameter bearings, but the mechanical behavior of pure alumina did not allow the manufacture of components having the small wall thickness requested. This has been made possible by the introduction of alumina matrix composites in clinics and so far a relevant part of ceramic bearings for THR is manufactured 36 mm in diameter or more.

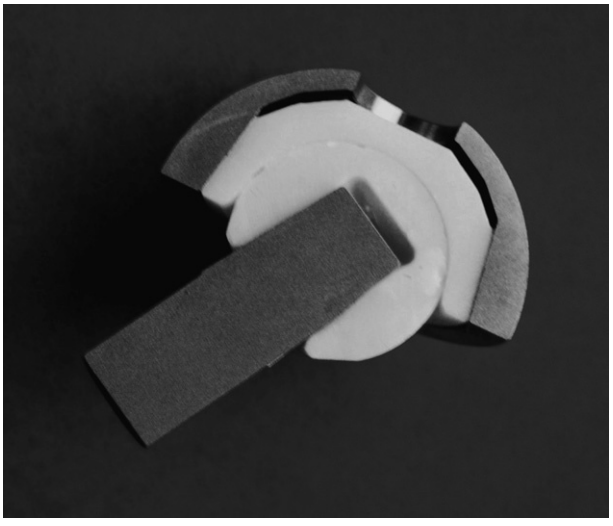

Figure 8 Cross-section of a ceramic-on-ceramic bearing, showing the ceramic-to-metal taper connections.

1.105.3.3. Clinical Results

The review of the long-term French experience in alumina THR bearings reported by Sedel[12] is very impressive, especially taking into account the state of the art in the early 1980s, the time of implant production. The results at 20-year follow-up reported were excellent: taking revision surgery for whatever reason as endpoint, the survival rate of cups was 85.6% (cementless cups) and 61.2% for cemented cups, while survival rate of cementless stems was 84.9% in comparison to 87.3% for the cemented ones. The wear of the ceramic components was undetectable. A further retrospective analysis of improved implants, implanted from 1990 to 1992 in young patients (mean age 46) was showing 93% survival rate at 9 years (taking revision surgery for any cause as endpoint), while taking aseptic loosening as endpoint the survival rate was 98.4%.

Long-term results obtained by a THR implant belonging to the first generations (Autophor 900-S) have also been reported by Petsatodis *et al.*[11] who reviewed at 22.25 years (mean survival time) a cohort of patients who underwent the implant of this cementless THA. The cumulative rate of survival (84.4% at 20.8 years) is remarkable, and the few cases of focal osteolysis leading to revision demonstrate the effectiveness of alumina bearings especially in young and active patients. The results are of special interest because they were obtained from an Autophor implant. The design of this device underwent several changes in time, with a significant evolution in clinical results. Mittelmeier *et al.*[104] in the retrospective analysis of

4000 Autophor THR at a maximum of 19 years reported the decrease in incidence of aseptic loosening from 35% using Autophor Type 1 (1974–7) to 15% with Type 2 (1976–84) and then to 2% with Type 3, implanted after 1984.

Alumina heads give positive clinical outcomes, and when coupled to PE they decrease the wear rate of the polymeric counterface. The reduction of wear debris-induced osteolysis can, for example, be observed also in the results reported by Suckel *et al.*[105] who evaluated retrospectively a series of 320 CoP THRs implanted in 303 patients, at a mean follow-up of 15 years, observing a 98% survival rate of both the femoral and of the acetabular components of the implants, as well as in the work of Ihle *et al.*[106] who analyzed a cohort of 93 consecutive uncemented THRs performed with the same PE cup running against alumina or CoCr-alloy ball heads, both at 32 mm diameter. At an average 19.3-year follow-up, the revision rate in the CoP group was 13.8%, while it was 46.2% in the MoP group. The wear rate of the PE cup when coupled with metallic heads, measured by computerized analysis of XR images, was 0.190 mm/year and 0.107 mm/year when coupled with ceramic heads, about 40% less linear wear.

However, it is in ceramic-on-ceramic bearings that the wear behavior of alumina are exploited at their best. This is shown, for example, by the work by Benazzo *et al.*[107] who retrospectively analyzed their 10-year experience with contemporary alumina implants. In their clinical series of 511 ceramic-on-ceramic THRs there were no cases of aseptic loosening, no radiological sign of cup or stem mobilization, the three implant revision performed were due to infection (two cases) or periprosthetic fracture (one case). Similar findings were reported by Lewis *et al.*[108] who investigated in a prospective randomized study the clinical outcomes of CoC bearings versus CoP bearings. Fifty-six THRs were followed with annual controls, the X-radiographs taken on the interview underwent computerized analysis. The results at 10-year follow-up show that the average ceramic/PE wear is fivefold the one of ceramic-on-ceramic bearings, while the two revision performed (one in each patient group) were not related to the type of bearing implanted.

An interesting insight on CoC bearings is given by the analysis of a series of 2984 CoC and 3432 MoP implants by Toni *et al.*[109] At 7-year follow-up the survival for THR with CoC bearings was 96.07% versus 92.61% for the MoP ones. The global incidence of aseptic loosening in THR with CoC bearings was less than one-half (45.5%) of the one observed in THR with MoP bearings, leading the Author to remark that the decreased risk of revision due to the use of alumina-on-alumina bearings instead of metal/polyethylene bearings justifies the selection of ceramic bearings on an economical basis.

A modern alumina-on-alumina THR bearing was approved for use in the USA on February 2003 by the Food and Drug Administration. The review by D'Antonio *et al.*[110] of the results in the 5 years range (5–8 years) found signs of femoral osteolysis only in 0.6% of the patients treated with CoC implants in comparison to 22.1% of the patients used as control and treated with MoP bearings. The corresponding revision rates were 1.8% versus 7.4% for CoC and MoP groups, respectively. These data were confirmed by the report, of Murphy *et al.*,[111] about the outcomes of 194 THRs implanted in 173 patients enrolled in the prospective Investigational Device Exemption study performed under the supervision of FDA which shows that the survivorship of CoC implants in hips that did not experience prior surgery was 99.3% at a maximum 9-year follow-up.

The complication rates of a CoC cementless implant that was the object of the FDA pre-market clinical trial were recently retrospectively analyzed by Mesko *et al.*[112] A total of 930 THRs implanted in 848 patients by nine surgeons was analyzed at 5- to 10-year follow-up, confirming the positive advantage of alumina-on-alumina bearings on the metal/PE control bearings. The Kaplan–Meier survivorship at 10 years taking revision of any component of the implants for any reason was 96.8% in the ceramic-on-ceramic group, while it was 92.1% in the metal/PE group (see **Chapter 6.604, Ceramic Prostheses: Clinical Results Worldwide**).

1.105.3.4. Complications

1.105.3.4.1. Failures in THR bearings

There is a little but finite risk of fracture in the use of ceramic component in THR bearings. This risk is low in comparison to the risk of fracture of stems, either to the catastrophic wear of PE inserts, and has to be weighted against the reduction of the risk of wear debris induced osteolysis. The Swedish Arthroplasty Register data show that loosening and osteolysis accounts for more than 80% of the THR revisions 6 years postoperatively onward.[113]

The fracture of the ceramic head is today a rather rare event, associated with severe traumas like road accidents or accidents in sports such as skiing, soccer playing, horse riding. If on the one side this testifies the sense of well-being and the good general health condition of THRs bearers today, it is noted that a few fractures are still too much.

Before 1980 the frequency of ceramic heads fractures was absolutely too high especially for the products of some manufacturers that have stopped to market ceramic components for THR bearings since a long time ago. The introduction in 1980 of the ISO 6474 standard for medical grade alumina established a set of quality requirements that limited the number of failures[95] but a wide scatter is still present in the data reported in the literature during the following years, indicative of the uncertainties present in this kind of evaluations. This behavior appears linked to the size of the study: numerous series do not show fractures, while the small ones show higher fracture rates, and it may be then hypothesized that some follow-up studies may present a bias depending on technical factors linked to the surgery.[96]

It is noted that the reliability of ceramic heads, belonging to the first generations, is higher than the one of other THR components – that is, of stems, of PE inlays – in the same age and that perception of the risk of fracture of ceramic components overestimate the real incidence of this event. It can be speculated if the spontaneous association of the concepts of 'brittleness' and 'ceramic' is coming from the everyday experience with dishes and cups. The study performed by Heck *et al.*[114] that involved about one-half of the members of the American Association for Hip and Knee Surgeons shows that taking as reference the observed rate of head fractures (0.22%),

the probability of fracture of the metallic stem or of catastrophic failure of the PE insert are respectively about 22 and 32% much higher. It is noted that 3 out of the 11 ceramic fractures were related to femoral heads implanted on suboptimal quality tapers.[115] Then the adjusted rate of head fractures (non-HIP-treated alumina) results are 0.15%. The low incidence of fractures of ceramic components is put in evidence also in the analysis by Castro *et al.*[116] of 1717 adverse events related to THRs reported to the FDA. The results shows that only 1% of adverse events was related to ceramic failures, while 18% were related to the failure of the femoral component (stem fracture, head dissociation, neck fracture, head wear) and 38% were failures of the acetabular cup. It is noted that these last figures may be biased by the low number of ceramic heads in use in the USA at that time.

Both the abovementioned studies are related to ceramic heads made before 1995, belonging to the so-called 'second generation alumina.' The data related to the HIP-treated 'third generation alumina' demonste the effectiveness of the improvements introduced in the manufacturing process. BIOLOX®forte heads[115] show a well-defined trend in the reduction of the number of fractures from 2000 to 2005, which is today about 0.02% (2/10,000). Most of the fractures are related to 28 mm diameter heads with neck length other than medium size (see **Section 1.105.3.2**). The increase in femoral head diameter, besides the advantage on stability and range of motion of the joints, brings an increase in reliability of the heads, the failure rate of 28 mm alumina heads being about fourfold the 32 mm one. The decreasing trend reported may then be due to several synergistic factors, for example, due to the improvements in the overall manufacturing process and quality control, to the extension in the use of 32 mm heads, and to the surgeon's improved knowledge on the use of ceramic bearings. The use of ceramic components requires the knowledge of several procedures to be carefully followed during their handling in the surgical theatre to avoid disastrous failures.[117]

The results of the investigational device exemption (IDE) study of a 28 mm CoC bearing made out of the alumina matrix nanocomposite BIOLOX®delta have been recently reported by Hamilton *et al.*[118] The prospective, randomized, multicenter trial was focused on a single model of cementless acetabular component (Pinnacle®, DePuy, Warsaw, IN) coupled to five different cementless stems. The study enrolled 263 patients (264 hips) who were treated in eight centres. A CoP (XLPE) bearing was implanted in the control group. There were four revisions in the CoC group and two in the control group. Four events related to the ceramic liners and the surgeon's difficulty in obtaining a correct seating into the metallic shell had been reported. In three cases, the problems were settled intraoperatively, while the correction of fourth one – a liner eccentric in the shell at the time of surgery, fractured 12 months postoperatively – demanded the revision surgery. The implant survival rate is similar in the two groups (97.6% CoC, 97.7% CoP).

A further cohort of patients who too were a part of the IDE study was reviewed at a mean follow-up of 6 years.[119] The bearing in the implants under study was formed by a BIOLOX®delta head articulating in a BIOLOX®forte insert. The socket was of the sandwich type. The control group received a Y-TZP head articulating on XLPE insert. Six years postoperatively the two groups did not show significant difference. The major event was the atraumatical fracture of a BIOLOX®delta head (28 mm, S-neck). It is, however, noted that the introduction in clinics of the new ceramic nanocomposite BIOLOX®delta has a positive effect on the head reliability: the rate of fracture of BIOLOX®delta ball heads is 0.003% or 3/100,000 based on the reports received by the manufacturer on 650,000 ball heads of this material released to market on February 2010.[120]

In the acetabular side, the fracture of ceramic inlays is a rather uncommon event. The reported frequency of rim chipping during surgery due, for example, to errors in the alignment of the inserts into the metal shells during surgeries was about 0.018% in the period 2000–5. Garino *et al.*[115] remark that in comparison to BIOLOX®forte heads the failure rate of BIOLOX®forte inserts decreased from 2000 to 2006, and it can be speculated as to how much the 'learning curve' of surgeons using CoC bearings may have contributed to this trend.

Nevertheless, it is noted that the safety of the insert depends on the design of the whole acetabular component: the introduction of a new design originated an unexpected high number (up to 2.6%) of intraoperative rim chipping in a series of devices in the USA, as did the use of compliant fiber metal cup that led to 1.3% fracture rate.[121] High incidence of insert fractures (3–6%) was also reported for some design of the so-called sandwich cups.[119] In these devices a PE cup is placed between the metal back and the insert – sometimes the PE is molded directly on the outer part of the insert – to reduce the dynamic stresses at the bone-shell interface.

It was hypothesized that in some design the high flexibility of the metal back and its deformation by the loads of the gait – especially in case of rim loading of the inlay due to malpositioning of the socket – may lead to the dislocation of the insert within the metal back,[122] to load concentration in the rim zone, and to fracture. The deformation of the metallic shell can be enhanced by the underreaming of the acetabular bed. Laboratory tests have shown[123] that the retentive forces do not change significantly, but questions arise on the insert stability in the long term due to the shell deformations observed on the testing apparatus. It is noted that this was observed in components positioned in a laboratory setting, then in conditions quite different from the surgical theatre ones.

1.105.3.4.2. Noises in THR bearings

In the last 5 years the orthopedic community, especially in the USA, has focused its interest on the noises that can come from hip replacements. The incidence of this almost always transient behavior is rather low overall (0.5%), but in some studies much higher values has been reported. In the beginning noises (e.g., squeaking) were associated with hard-on-hard bearings only, but several reports (see, e.g., Glaser *et al.*[124]) have shown that noises of several nature can be audible from whatever type of THR bearing.

Several hypotheses had been advanced about the nature of the phenomenon that looks multifactorial. A landmark was put by the study of Walter *et al.*[122] by acoustic analysis. They tested four different types of femoral and four acetabular components observing absence of emission of audible

frequencies from well-assembled modular components, either from any of the unassembled ceramic heads or liners. The implant tested had different thickness, as the use of thinner components in modular implants is a solution adopted both to save the patient bone stock and to improve the stress distribution in bone. An 'audible resonance' was on the other hand generated by the shells made out of titanium alloy, the frequency of the sound was inversely related to the shell thickness (and stiffness). Also the titanium stems tested generated audible frequencies. It is noted that some implants generate *in vivo* squeaking noises at the extreme of their range of motion, where edge loading on the insert can occur. It is also noted that in a number of retrieved noisy implants there are evidences of impingement – more evident in some cup design with protected insert rim – and of edge loading due to malpositioning. Most of the ceramic components retrieved had transfers of metal on the articulating surfaces. These findings led the author to see the concurrent origins of the noises in liner malpositioning on surgery, in edge loading, or in joint laxity.

The results of this study have a good correspondence with the ones presented by Restrepo *et al.*[125] who observed a seven times higher incidence of noisy hips in patients implanted with a low stiffness THR, in comparison with patients who underwent the implant of a much stiffer stem and cup. These findings led this author to hypothesize that the frictional forces generated at the ball–insert interface by an interruption of the lubricating fluid film, due to metal contamination of the ceramic surface, decreasing its wettability, or the alteration of the surface finish due to edge loading, microseparation, and stripe wear, are transmitted to the elastic metallic components that start vibrating in the audible range of frequencies. The low stiffness of the implant due to its construction by titanium–molybdenum–zirconium–iron (TMZF) alloy instead of the traditional Ti–Al–V alloy, the use of a smaller taper for head fixation, the design of stem and of implant neck justify this hypothesis.

Till date, the multifactorial nature of noise generation is debated and its incidence also seems to be sharply decreasing. It is noted that in the EU Countries where the use of ceramics has become a well-established practice, this phenomenon was registered only episodically and does not, however, compromise the integrity of the implants.

1.105.3.5. Tips and Tricks in Alumina Bearings

The ability of a ceramic bearing to satisfy the patient demand for a long time depends on several factors such as the manufacturing, implant design, and surgery. The proof testing adopted in production today, allows for the elimination of defective parts before their release to the market. The effectiveness of this control procedure is demonstrated by the progressive reduction of fractures reported in the last years. Moreover, it was remarked by Garino *et al.*[115] that almost one-half of the fractures takes place within 12 months from surgery, then it is likely that the origin of the failure lies in the abnormal stress distribution in the head, for example, disturbance of the head–trunnion interface that will lead to stresses higher than fracture strength of the material should a sudden overload take place after the implantation.

This may happen for several reasons, linked to the modularity of the implants and to their handling in the surgical theatre, as underlined by the MHRA in the UK.[126] It is of uppermost relevance to avoid the contamination of the taper: it has been shown[120] that particles of bone cement, serum, bone chips, fat tissue, or water in the taper interface can decrease the burst load of ceramic heads down to 40% of the original value, while the residual burst load of the head on a taper that has been scratched during the THR handling is only 20% of the original one.

The reliability of the ceramic components can also be compromised by a number of other actions,[117] for example, the use of metallic mallets in positioning of ball heads on metallic taper or by thermal shock due to fast cooling after autoclave sterilization.

A third critical aspect to achieve the expected implant performances depends on the surgical technique: both extreme accuracy and careful attention to the smallest details are demanded.

In handling the acetabular metallic shell, attention should be paid to not to damage both the inside rims of the taper. Should the use of additional screws be necessary, it is mandatory to check that there is no screw head protrusion inside the acetabular cup. The removal of the soft tissues close to the cup rim is recommended to avoid the contamination of the taper interfaces, as well as repeated washing and drying to remove any fat and clots. The liner shall be gently placed into the shell. Special care has to be taken about orientation, as edge loading of the socket and impingement upon the components depend on this parameter: perfect THR component adaptation and orientation, and soft tissue tension are required.

In ceramic–ceramic, the positioning of the cup is critical, as it influences the stress distribution of the bearing interface. Both the inclination and the anteversion of the cup shall be taken into account.

Inclination is related to the position of the cup in the sagittal (lateral) plane: when the cup is too vertical, the concentration of stresses in the rim may originate edge wear, while dislocation may happen both for too horizontal or for too vertical cups. Anteversion of the cup is also very important, as a malpositioning can cause dislocation, early wear, and also impingement of the neck zone of the stem with the socket rim. It is important to remember that not only the too vertical cup but also a too anteverted or retroverted cup is a cause of stress concentration and potentially early wear.[96] Moreover, would the cup be too anteverted the stress will be concentrated on a small portion of the bone.

The most common mistakes in cup positioning are placing the cup too vertical and too retroverted: this appears relevant for the risk of dislocation. That is, a malpositioned cup raises the rate of short-term and long-term complications, but a too vertical cup increases the stresses on the rim of the ceramic insert, with potential problems of wear. On the other hand when the cup is too horizontal, the anterior wall and the superior wall are far out from the bone, and this of course decreases the stability of the component.

To avoid impingement and to obtain the maximum range of motion, there is a range of socket anteversion for each couple of socket abduction and femoral anteversion angles. The papers by Pitto *et al.*[127] and by Garino[128] constitute an

exhaustive review of the issue of cup orientation, and what the optimum positioning is, is still a topic of debate. The recommendations expressed by different authors reported by Pitto *et al.*[127] indicate cup abduction angles in the range from 30° to 50° and anteversion angles between 10° and 30°, both depending on the patient's anatomy.

A further parameter to be carefully controlled is the correct seating of the insert in the metal back because any tilting of the insert in the metal shell will cause the insert failure. Passing the finger of the socket rim to check that the rim of the shell and the rim of the insert are flush, then correcting any malpositioning, is a simple and effective way to enhance intraoperatively the reliability of the implant.

Care is to be taken in avoiding the pairing of components from different manufacturers, or in selecting wear couples unauthorised by the manufacturer of the device. That is, besides the nominal diameter, manufacturing tolerances are unavoidable and are different for each implant and for the same manufacturer also. Randomised coupling may lead to catastrophic wear and to the failure of the implant: it is noted that the now abandoned ASTM F 1636-95 standard was listing 29 different taper angles in the range from 4° to 6° for use in THRs, a difference quite impossible to note by the naked eye, but that changes dramatically the stress distribution should mistakes be made in coupling.[129]

1.105.3.6. Revision Strategies

The revision of ceramic components[130] is characterized by several specific features as the cause of revision are usually not related to osteolysis due to the little debris production in ceramic-on-ceramic joints, but more often to mechanical aseptic loosening of the socket, bearing dislocation, impingement, or to the fracture of the ceramic components. In case of socket loosening, if the revision is performed in a short time, few ceramic debris may be expected, and it may be possible to retain socket and head. For longer loosening time, if socket is damaged or tilted it has to be replaced, while the head substitution may be avoided if the ceramic is undamaged.

In case of fracture of the ceramic insert, the best choice is to replace it by a new one, and to replace the ceramic ball head too: it is likely that the insert debris constrained in this case between two hard surfaces may have damaged the articular surface of the head.

In the case of a fractured ball head, besides the need of fragments removal, the replacement of the insert by a new one, whatever its nature (polyethylene or ceramic), is recommended. The insert replacement also must be performed if the preexisting insert appears in good conditions at visual examination. Allain *et al.*[131] recommend cup substitution even if it appears undamaged in case of a fracture of ceramic head, and the implant of a CoCr-alloy head, joined to the extensive removal of the synovia to eliminate the maximum of debris. This option is valuable only if it is not possible to implant a new ceramic ball head, for the residual risk of early failure of revision surgery due to severe wear of the metallic heads by the ceramic debris that remained trapped in the polyethylene cup surface, as in the several cases that have been already reported.[132–134]

The substitution of the fractured ball head by a new ceramic one if the taper looks undamaged was performed in selected cases from more than 20 years. Sedel[135] reported not to have had fractures in a 15-year follow-up of ceramic heads implanted on tapes that resulted undamaged at the time of revision surgery. Nevertheless, the manufacturers of ceramic bearings and MHRA[126] recommend not to install a new ceramic head on the used taper because of the damage made to the taper surface by the fragments of the broken ceramic components. The ridges at the scratch rims will act as stress risers at the taper interface compromising the reliability of the new ceramic head. To install a new ceramic head, if the implant does not have modular neck/taper component, the stem substitution is demanded. This decision to remove a usually stable stem is not an easy one: stems holding ceramic bearings are usually stable because of the absence of debris-induced osteolysis.

The solution has come with the introduction in the market of ceramic heads of special design, to be implanted on the used taper with an intermediate titanium sleeve, provided that the level of taper damage allows this technique. In this way, the taper becomes much larger in diameter, which corresponds to a decrease in thickness of the ball head wall, then the use of the new alumina composites for the construction of these devices (e.g., BIOLOX®option, CeramTec AG) was necessary. The sleeves are designed to obtain different neck length, in such a way that during surgery it would be possible to select the correct lateralization of the implant. Moreover, with such sleeves it is possible to have additional neck length (from +5 to +7 mm) adding extra-length size to ceramic heads. The early clinical results reported show the positive outcomes of this technique, that may also be suitable for primary implants[136,137] (**Figure 9**).

1.105.3.7. Alumina in Knee Replacements

The implant of a total knee replacement (TKR) is today a standard surgical procedure to overcome the mobility limits



Figure 9 BIOLOX®option ball heads, with internal titanium alloy sleeve (Courtesy CeramTec AG, Plochingen, Germany).

in patients suffering from osteoarthritis of the knee that have already been treated for a long time to reduce pain and control inflammation of the joint. TKR has proven to be overall a successful surgical procedure, with positive outcomes in terms of function and correction of deformities, if any. So far, about 900 000 TKR implants are performed each year worldwide, and in some counties the yearly number of TKR implants is higher than that of THRs.

The first use of alumina in the knee is due to Langer, who performed the implants of unicondylar ceramic tibial components in 73 cases from 1972 to 1980 in the Orthopedic Clinic of the University of Jena.[138] The use of these devices, made by the company Hermsdorf in the former German Democratic Republic, was stopped in the 1980s, due to the availability of modern TKR in that country. It is then acknowledged that the path for the development of a ceramic TKR was started in Japan in the late 1970s by Prof. Hironobu Oonishi, a pioneer in the development of ceramic devices, who implanted a first series of devices manufactured by the company Kyocera. These TKRs (the so-called KOM-1) were made of an alumina tibial plateau hosting a polyethylene platform on which was articulating an alumina femoral component, and were implanted cementless in 134 patients.

Several versions of this implant were set up in time:[139] the kinematics was improved, a titanium-alloy tibial tray was introduced and design was modified for cemented fixation of both the tibial and of the femoral components. These improved versions have been implanted in 534 joints until 2006. The latest evolution of the KOM (KU type, JMM Co) with the femoral components made in Y-TZP has been implanted since 2001 in Japan.

The use of a ceramic knee replacement has several potential advantages; first, an improved lubrication of the articulating surface due to the high wettability of ceramic surface by the synovia liquid and then a lower wear rate of the PE liner of the tibial component. A reduction in PE wear can also be expected for the better scratching resistance of the ceramic surfaces, in comparison to metallic alloys, that will save the polished surface of the articulating condyles. Moreover, it is known that the degree of finish achievable in ceramic surfaces is far beyond the ones achievable in metals. The absence of scratching or of increased roughness on the condyles of a KOM-type femoral component implanted in 1979 in a young patient and retrieved after 23 years of clinical use was reported by Oonishi *et al.*[140] who on the other hand, observed worn areas of different severity in CoCr femoral components retrieved after 3 years of clinical use.

The issue of wear is becoming more and more relevant as more younger patients are today candidates for TKR. These patients not intended to change their active lifestyle and have high expectations from surgery, that is, to recover their original conditions and be able to practice sports like downhill skiing or golf.

A further reason for the selection of ceramics is linked to the growing incidence of allergic reactions to metal ions, and of the wide metallic surface that patients may develop for the presence of different metallic implants in several anatomical districts of the body.

Notwithstanding the improvements introduced in the technology, the intrinsic brittleness of alumina was the bigger limit for the development of a knee replacement out of this material. Thanks to the higher strength and impact resistance of alumina matrix composite[141] it was possible to start the manufacture of alumina TKR devices with reduced thickness, reducing the patient's bone resections.[142] The early clinical results of a first device of this kind (Multigen Plus, Lima Corp.) have been reported recently.[143] Forty patients had been treated in two centers on the basis of a common selection and surgical protocol. The implant is made by a femoral ceramic component (BIOLOX®delta, CeramTec AG), a PE tibial component, and a Ti-alloy tibial tray. The femoral component and the tibial tray are both cemented to the bone. Twelve months postoperatively, there were no device-related complications in the patient cohort under study, and significant improvement of the physical functions was reported both in the 3- and 12-month evaluations (**Figure 10**).

1.105.3.8. Alumina in Other Medical Devices

On the wake of the promising results obtained by the alumina dental implants by Sandhaus, several researchers started the development of alumina dental implant devices. In the United States, Hulbert, Klawitter, Driskell developed different devices but the largest success was obtained by the so-called Tübingen implant, made by the company Friedrichsfeld (Mannheim) under the trademark Frialit®.[5] The comprehensive research program launched in Germany that led to the development of BIOLOX® alumina heads and sockets for THRs, also led to the development of several prototypes of alumina devices for other applications, such as middle ear implant for the replacement of the ossicular chain, keratoprostheses. Anchor- and screw-shaped dental implants have also been developed by the company Feldmüle (now CeramTec AG, Plochingen) (**Figure 11**) (see **Chapter 6.619, Materials in Dental Implantology**).

The mechanical behavior of alumina was the main limit for all those devices. Especially for dental implants the high stiffness of alumina did not allow the expected load transfer to the host bone. Besides this, to support masticatory loads, the implants were rather bulky, the transverse sections sometimes exceeded the thickness of normal maxillae.

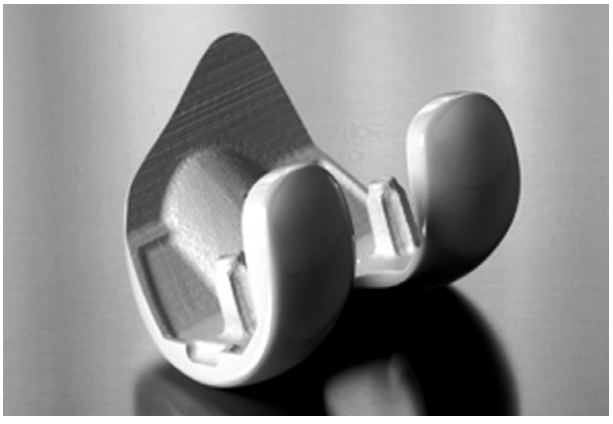

Figure 10 Ceramic (BIOLOX®delta) femoral component for total knee replacement (Courtesy CeramTec AG, Plochingen, Germany).



Figure 11 Alumina endodontic pins, anchor- and screw-shaped dental implants manufactured during the 1970s and 1980s (Courtesy CeramTec AG, Plochingen, Germany).

The Japanese approach to the alumina dental implants was based on the technology of synthetic sapphire (alumina single crystals). Blade-, tap-, and screw-type dental implants made out of synthetic sapphire were manufactured by Kyocera and were in clinical use in Japan since 1972, and in the United States since 1980. These implants had relevant aesthetic advantages on the metallic contemporary device, their gingival emergence being clear and transparent. Recently, Takahashi *et al.*[144] reported the follow-up of a series of 65 tap-type porous sapphire dental implants, three of them still in place after 21–23 years.

However, alumina dental implants have been outpaced by the modern titanium implants: new momentum to this technology in dentistry was given by the introduction of Y-TZP in dental implant production.[5]

So far, the only application of alumina medical devices within the human body besides the orthopedic ones is in orbital implants. These devices must have high biocompatibility, high porosity (to reduce overall weight), and hardness to provide movement of the artificial eye.[145]

Another aluminum oxide application had been attempted as a porous coating of the struts of drug eluting vascular stents, aimed to host and release the drug inhibiting the restenosis of the blood vessel. The coating was obtained by oxidation of pure aluminum metal that was applied on the stent's struts.[146]

New applications can come only by contemporary alumina matrix composites and extending the flexibility in design will allow engineers and surgeons to set up new ceramic components. An example of the design flexibility allowed by the new alumina–matrix composite ceramics is the Self-Adjusting Cup System,[147] a three-component bearing designed to achieve implant stability against dislocation in the most difficult situation. The bipolar system is composed of two ceramic-on-ceramic bearings (22.22 and 32 mm in diameter), the insert external diameter being limited to 41 mm only. Also application in the cervical spine[148] and in dental implants[149] are under study and will soon be tested in clinics.

References

1. Rock, M. German Patent DRP n°583 589, 1933.
2. Smith, L. W. *Clin. Orthop.* **1992**, *282*, 4–9.
3. Eyring, E. J.; Campbell, W. *Ceramic Prostheses, News in Engineering*. Ohio State University Publishing: Ohio, 1969; pp 4–7.
4. Sandhaus S. Bone Implants and Drills and Taps for Bone Surgery, British Patent n°1,083,769, 1965.
5. Piconi, C.; Rimondini, L.; Cerroni, L. *La Zirconia in Odontoiatria*. Elsevier Masson: France, 2008.
6. Boutin, P. *Rev. Chir. Orthop.* **1972**, *58*, 230–246.
7. Stock, D.; Geissler, M. In *Osseo-Integrated Implants*. Heimke, G., Ed.; CRC Press: Boca Raton, 1990; Vol. 1, pp 127–152.
8. Salzer, M.; Locke, H.; Plenk, H.; Punzet, G.; Stärk, N.; Zweimüller, K. In *Artificial Hip and Knee Joint Technology*; Schaldach, M., Hohmann, D., Eds.; Springer: Berlin, 1976; pp 459–474.
9. Kawahara, H.; Yamagami, A.; Hirabajashi, M. In *Proceedings of 1st Symposium of the Japanese Society of Implant Dentistry*, 1975; pp 187–196.
10. Oonishi, H. In *Osseo-Integrated Implants*; Heimke, G., Ed.; CRC Press: Boca Raton, 1990; Vol. 1, pp 171–186.
11. Petsatodis, G. E.; Papadopoulos, P. P.; Papavasiliou, K. A.; Hatzokos, I. G.; Agathangelidis, F. G.; Christodoulou, A. G. *J. Bone Joint Surg. Am.* **2010**, *92*, 639–644.
12. Sedel, L. In *Bioceramics in Joint Arthroplasty*; Lazennec, J. Y., Dietrich, M., Eds.; Steinkopff: Darmstadt, 2004; pp 17–20.
13. Willmann, G. *Biomed. Tech.* **1998**, *43*, 342–349.
14. Kleer, G.; Sóltesz, U.; Siegele, D. In *Advances in Biomaterials 6, Biological and Biomechanical Performances of Biomaterials*; Christel, P., Meunier, A., Lee, A. J. C., Eds.; Elsevier: Amsterdam, 1986; pp 489–494.
15. Schaefer, R.; Sóltesz, U.; Siegele, D. In *Bioceramics*; Heimke, H., Ed.; Deusche Keramische Geselshaft: Köln, 1990; Vol. 2, pp 172–179.
16. International Standards Organization, 2009. ISO-DIS 6474-1.2 Implants for surgery – ceramic materials – part 1: ceramic materials based on high purity alumina.
17. International Standards Organization, 2009 ISO-DIS 6474-2 Implants for surgery – ceramic materials – part 2: composite material based on high purity alumina matrix with zirconia reinforcement.
18. Piconi, C.; Maccauro, G. *Biomaterials* **1999**, *20*, 1–25.
19. Affatato, S.; Testoni, M.; Cacciari, G. L.; Toni, A. *Biomaterials* **1999**, *20*, 1925–1929.
20. Mandrino, A.; Eloy, R.; Moyen, B.; Lerat, J.-L.; Treheux, D. *J. Mater. Sci. Mater. Med.* **1992**, *3*, 457–463.
21. Rieu, J.; Goeuriot, P. *Clin. Mater.* **1993**, *12*, 211–217.
22. Salomoni, A.; Tucci, A.; Esposito, L.; Stamenkovich, I. *J. Mater. Sci. Mater. Med.* **1994**, *5*, 651–653.
23. De Aza, A. H.; Chevalier, J.; Fantozzi, G.; Schehl, M.; Torrecillas, R. *Biomaterials* **2002**, *23*, 937–945.
24. Ban, S.; Sato, H.; Suehiro, Y.; Nakanishi, H.; Nawa, M. *J. Biomed. Mater. Res. B Appl. Biomater.* **2008**, *87B*, 492–498.
25. Begand, S.; Oberbach, T.; Glien, W. *Key Eng. Mater.* **2007**, *330–332*, 1207–1210.
26. Maccauro, G.; Bianchino, G.; Sangiorgi, S.; *et al. Int. J. Immunopathol. Pharmacol.* **2009**, *22*, 773–779.
27. Begand, S.; Oberbach, T.; Glien, W. *Key Eng. Mater.* **2005**, *284–286*, 983–986.
28. Burger, W.; Richter, H. G. *Key Eng. Mater.* **2001**, *192–195*, 545–548.
29. Kuntz, M.; Masson, B.; Pandorf, T. In *Strength of Materials*; Mendes, G., Lago, B., Eds.; Nova Science: New York, 2009; pp 133–158.
30. Dörre, H.; Hübner, H. *Alumina: Processing Properties and Application*. Springer: Berlin, 1984; pp 9–79.
31. Li, J.; Hastings, G. In *Handbook of Biomaterial Properties*; Black, J., Hastings, G., Eds.; Chapman and Hall: London, 1998; pp 340–354.
32. Munz, D.; Fett, T. *Ceramics: Material Properties, Failure Behavior, Materials Selection*. Springer: Berlin, 1999; pp 9–18.
33. Frakes, J. T.; Brown, S. D.; Kenner, G. H. *J. Am. Ceram. Soc.* **1974**, *53*, 183–187.
34. Krainess, F. E.; Knapp, W. J. *J. Biomed. Mater. Res.* **1978**, *12*, 241–246.
35. Ferber, M. K.; Brown, S. D. *J. Am. Ceram. Soc.* **1980**, *63*, 424–429.
36. Sinkaroy, S.; Levenson, L. L.; Day, D. E. *Am. Ceram. Soc. Bull.* **1979**, *58*, 464–466.
37. Osterholm, H. H.; Day, D. E. *J. Biomed. Mater. Res.* **1981**, *15*, 279–288.
38. Schneider, J.; Begand, S.; Kriegel, R.; Kaps, C.; Glien, W.; Oberbach, T. *J. Am. Ceram. Soc.* **2008**, *91*, 3613–3618.
39. Sauer, W. L.; Anthony, M. E. In *Alternative Bearing Surfaces in Total Joint Replacements ASTM STP1346*; Jacobs, J. J., Craig, T. L., Eds.; American Society for Testing and Materials: Pennsylvania, 1998; pp 1–29.
40. Clarke, I. C.; Gustafson, A. *Clin. Orthop.* **2000**, *379*, 34–40.

41. Greenwald, S. A. In *Proceedings of 68th AAOS Meeting*, San Francisco, CA, 2001; pp 30–31.
42. Streicher, R. M. In *Modern Trends in THA Bearings*; Cobb, J., Ed.; Springer: Berlin, 2010; pp 9–13.
43. Minakawa, H.; Stone, M. H.; Wroblewski, B. M.; Lancaster, J. G.; Ingham, E.; Fisher, J. *J. Bone Joint Surg. Br.* **1998**, *80B*, 894–899.
44. Wang, A.; Dumbleton, J. H.; Manley, M. T.; Serekian, P. In *Bioceramics in Joint Arthroplasty*; Zippel, H., Dietrich, M., Eds.; Steinkoppf: Darmstadt, 2003; pp 49–62.
45. Clarke, I. C.; Williams, P. A.; Shishido, T.; Good, V.; Oonishi, H.; Gustafson, A. In *Bioceramics in Joint Arthroplasty*; Garino, J. P., Willmann, G., Eds.; Thieme: New York, 2002; pp 20–26.
46. Nevelos, J. E.; Ingham, E.; Doyle, C.; *et al*. *J. Arthroplasty* **2000**, *15*, 793–795.
47. Kaddick, C.; Pfaff, H. G. In *Bioceramics in Joint Arthroplasty*; Garino, J. P., Willmann, G., Eds.; Thieme: New York, 2002; pp 16–20.
48. Stewart, T. P.; Tipper, J. L.; Streicher, R. M.; Ingham, E.; Fisher, J. *J. Mater. Sci. Mater. Med.* **2001**, *12*, 1053–1056.
49. Stewart, T. P.; Tipper, J. L.; Insley, G.; Streicher, R. M.; Ingham, E.; Fisher, J. *J. Biomed. Mater. Res. Appl. Biomater.* **2003**, *66B*, 567–573.
50. Insley, G. M.; Turner, I.; Fisher, J.; Streicher, R. M. In *Bioceramics in Joint Arthroplasty*; Garino, J., Willmann, G., Eds.; Thieme: New York, 2002; pp 26–31.
51. Hulbert, S. F.; Morrison, J. S.; Klavitter, J. J. *J. Biomed. Mater. Res.* **1972**, *6*, 347–374.
52. Griss, P.; von Andrian-Werbung, H.; Kempien, S.; Heimke, G. *J. Biomed. Mat. Res. Symp.* **1973**, *4*, 453–462.
53. Piconi, C.; Maccauro, G.; Muratori, F.; Brach del Prever, E. *J. Appl. Biomater. Biomech.* **2003**, *1*, 19–32.
54. Greco, F.; Piantelli, S.; Maccauro, G.; Arena, M.; Piconi, C. *Minerva Ortop. Traumatol.* **1993**, *44*, 913–918.
55. Takami, Y.; Yamane, S.; Makinouchi, K.; *et al*. *J. Biomed. Mater. Res.* **1998**, *40*, 24–30.
56. Catelas, I.; Petit, A.; Zukor, D. J.; Marchand, R.; Yahia, L. H.; Huk, O. L. *Biomaterials* **1999**, *20*, 625–630.
57. Kranz, I.; Gonzalez, J. B.; Dorfel, I.; *et al*. *J. Biomed. Mater. Res.* **2009**, *89A*, 390–401.
58. Harms, J.; Mausle, E. *J. Biomed. Mater. Res.* **1979**, *13*, 67–87.
59. Pizzoferrato, A.; Vespucci, A.; Ciapetti, G.; Stea, S. *Biomaterials* **1985**, *6*, 346–351.
60. Bukat, A.; Fassina, P.; Greco, F.; Piantelli, S.; Piconi, C.; Zaghini, N. In *Bioceramics 3. Proceedings of the 3rd Symposium on Ceramics in Medicine*; Hulbert, J. E., Hulbert, S. F., Eds.; The Rose Hulmann Institute of Technology, 1990; pp 355–365.
61. Ito, A.; Tateishi, T.; Niwa, S.; Tange, S. *Clin. Mater.* **1993**, *12*, 203–209.
62. Li, J.; Liu, Y.; Hermansson, L.; Soremark, R. *Clin. Mater.* **1993**, *12*, 197–201.
63. Dion, I.; Bordenave, L.; Lefebvre, F.; *et al*. *J. Mater. Sci. Mater. Med.* **1994**, *5*, 18–24.
64. Harmand, M. -F.; Naji; A.; Lorini, G.; Priem, Th.; Piconi, C. In *Abstracts of the 12th Conference of the European Society for Biomaterials*, Oporto, Portugal, 1995; The European Society for Biomaterials, Sept 2006; p 141.
65. Mebouta, Nkamgueu E.; Adnet, J. J.; Bernard, J. *J. Biomed. Mater. Res.* **2000**, *52*, 587–594.
66. Torricelli, P.; Verné, E.; Brovarone, C. V.; *et al*. *Biomaterials* **2001**, *22*, 2535–2543.
67. Lohmann, C. H.; Dean, D. D.; Koster, G. *Biomaterials* **2002**, *23*, 1855–1863.
68. Wagner, W.; Rixecker, H.; Wahlmann, U. W. In *Biological and Biomechanical Performance of Biomaterials*; Christel, P., Meunier, A., Lee, A. J. C., Eds.; Elsevier: Amsterdam, 1986; pp 129–134.
69. Christel, P.; Meunier, A.; Dorlot, J.-M.; *et al*. *Ann. N. Y. Acad. Sci.* **1988**, *523*, 234–256.
70. Christel, P. *Clin. Orthop.* **1992**, *282*, 10–18.
71. Warashina, H.; Sakano, S.; Kitamura, S.; *et al*. *Biomaterials* **2003**, *24*, 3655–3661.
72. Ryu, R. K.; Bovill, E. G.; Skinner, H. B.; *et al*. *Clin. Orthop.* **1987**, *216*, 207–212.
73. Schmalzried, T. P.; Callaghan, J. J. *J. Bone Joint Surg. Am.* **1999**, *81A*, 115–136.
74. Archimbeck, M. J.; Jacobs, J. J.; Black, J. *Clin. Orthop.* **2000**, *379*, 12–21.
75. Ingham, E.; Fisher, J. *Proc. Instn. Mech. Engrs. Part H* **2000**, *214H*, 21–37.
76. Dumbleton, J. H.; Manley, M. T.; Edidin, A. A. *J. Arthroplasty* **2002**, *17*, 649–661.
77. Willert, H. G.; Semlitsch, M. *J. Biomed. Mater. Res.* **1977**, *11*, 157–164.
78. Jacobs, J. J.; Hallab, N. J.; Urban, R.; Skypor, A. In *World Tribology Forum in Arthroplasty*; Rieker, C., Oberholzer, S., Wyss, U., Eds.; Hans Huber: Switzerland, 2001; pp 77–82.
79. Lindgren, L. *J. Bone Joint Surg. Br.* **2008**, *90B*, 7–10.
80. Crawford, D.; Ranawat, C. S.; Rothman, R. H. *J. Arthroplasty* **2010**, *25*, 1–2.
81. Medicines and Healthcare products Regulatory Agency (MHRA). *All Metal-on-Metal (MoM) Hip Replacements*; MHRA: London, 2010; MDA/2010/033.
82. Granchi, D.; Amato, I.; Battistelli, L.; *et al*. *Biomaterials* **2005**, *26*, 2371–2379.
83. Fisher, J.; Jin, Z.; Tipper, J.; *et al*. *Clin. Orthop.* **2006**, *453*, 25–34.
84. Germain, M. A.; Hatton, A.; Williams, S.; *et al*. *Biomaterials* **2003**, *24*, 469–479.
85. Mattews, J. B.; Green, T. R.; Stone, M. H.; Wroblewski, B. M.; Fisher, J.; Ingham, E. *J. Mater. Sci. Mater. Med.* **2001**, *12*, 249–258.
86. Willert, H. G.; Broback, L. G.; Buchan, G. M.; *et al*. *Clin. Orthop.* **1996**, *333*, 51–75.
87. Maccauro, G.; Piconi, C.; Muratori, F.; De Santis, V.; Burger, W. In *Bioceramics in Joint Arthroplasty*; Zippel, H., Dietrich, M., Eds.; Steinkoppf: Darmstadt, 2003; pp 81–88.
88. Lerouge, S.; L'H, Yahia; Huk, O.; *et al*. In *Bioceramics 8*; Wilson, J., Hench, L. L., Greenspan, D., Eds.; Elsevier: Amsterdam, 1995; pp 145–150.
89. Baldini, N.; Ciapetti, G.; Giunti, A.; Savarino, L. Wear and tissue reaction in retrive ceramic-on-ceramic THA. In *Abstract F68, 10th EFORT Congress*, Vienna, Austria, June 3, 2009.
90. Fritsch, E.; Remberger, K.; Mittelmeier, H. In *Die Keramikpaarung BIOLOX in der Hüftendoprotetik*; Puhl, W., Ed.; Henke: Kansas, 1996; pp 12–17.
91. De Santis, E.; Maccauro, G.; Proietti, L.; *et al*. *Key Eng. Mater.* **2001**, *192–195*, 995–998.
92. Nizard, R. S.; Sedel, L.; Christel, P.; Meunier, A.; Soudry, M.; Witvoet, J. *Clin. Orthop.* **1992**, *282*, 53–63.
93. Mittelmeier, H. *Acta Orthop. Belg.* **1985**, *51*, 367–376.
94. Miller, E. H.; Heidt, R. S.; Welch, M. C.; Harding, W. G.; Heidt, R. S., Jr.; Lawhon, S. M. *Instr. Course Lect.* **1986**, *35*, 188–202.
95. Piconi, C.; Labanti, M.; Magnani, G.; Caporale, M.; Maccauro, G.; Magliocchetti, G. *Biomaterials* **1999**, *20*, 1637–1646.
96. Piconi, C. *Ceramic Biomaterials in Total Hip Arthroplasty*. DePuy International, 2004; Technical Monograph n. 9070-50-000.
97. Andrisano, A. O.; Dragoni, E.; Strozzi, A. *Proc. Instn. Mech. Engrs. Part H* **1990**, *204H*, 157–167.
98. Middleton, J.; Pande, G. N.; Richter, H. G.; Willmann, G. *J. Mater. Sci. Mater. Med.* **1994**, *5*, 503–506.
99. Richter, H. G.; Willmann, G.; Weick, K. In *Alternative Bearing Surfaces in Total Joint Replacements – ASTM STP 1346*; Jacobs, J. J., Craig, T. L., Eds.; American Society for Testing and Materials: Pennsylvania, 1998; pp 173–185.
100. Masson, B. *Int. Orthop.* **2009**, *33*, 359–363.
101. Zagra, L.; Giacometti-Ceroni, R.; Corbella, M. In *Bioceramics in Joint Arthroplasty*; Lazennec, J. Y., Dietrich, M., Eds.; Steinkopff: Darmstadt, 2004; pp 163–168.
102. Amlie, E.; Hoevik, O.; Reikeras, O. *J. Orthop. Traumatol.* **2010**, *11*, 111–115.
103. Pandorf, T. In *Bioceramics and Alternative Bearings in Joint Arthroplasty*; Chang, J. D., Billau, K., Eds.; Steinkopff: Darmstadt, 2007; pp 91–98.
104. Mittelmeier, H.; Fritsch, E.; Heisel, J.; Siebel, T.; Deimel, D. In *Die Keramikpaarung BIOLOX in der Hüftendoprotetik*; Puhl, W., Ed.; Henke: Kansas, 1996; pp 4–10.
105. Suckel, A.; Geiger, F.; Kinzl, L.; Wuelker, N.; Gabrecht, N. *J. Arthroplasty* **2009**, *24*, 846–853.
106. Ihle, M.; Mai, S.; Siebert, W. In *Modern Trends in THA Bearings*; Cobb, J., Ed.; Springer: Berlin, 2010; pp 169–178.
107. Benazzo, F.; Rossi, S. M. P.; Piovani, L.; Combi, A.; Russo, C. In *Modern Trends in THA Bearings*; Cobb, J., Ed.; Springer: Berlin, 2010; pp 191–194.
108. Lewis, P. M.; Al-Belooshi, A.; Olsen, M.; Schemlitsch, E. H.; Waddell, J. P. *J. Arthroplasty* **2010**, *25*, 392–397.
109. Toni, A.; Stea, S.; Bordini, B.; Sudanese, A. In *Bioceramics in Joint Arthroplasty*; Garino, P., Willmann, G., Eds.; Thieme: New York, 2002; pp 75–80.
110. D'Antonio, J. A.; Capello, D.; Manley, M.; Naughton, M.; Sutton, K. *Clin. Orthop.* **2005**, *436*, 164–171.
111. Murphy, S. B.; Ecker, T. M.; Tannast, M. *Clin. Orthop.* **2006**, *453*, 97–102.
112. Mesko, J. W.; D'Antonio, J. A.; Capello, W. N.; Bierbaum, B. E.; Naughton, M. In *Modern Trends in THA Bearings*; Cobb, J., Ed.; Springer: Berlin, pp 209–217.
113. Garellick, G.; Kaerrholm, J.; Rogmark, C.; Herberts, P. *Annual Report 2008*. Swedish Arthroplasty Register, 2009.
114. Heck, D. A.; Partridge, C. M.; Reuben, J. D.; Lanzer, W. L.; Lewis, C. G.; Keating, E. M. *J. Arthroplasty* **1995**, *10*, 575–580.
115. Garino, J.; Rahaman, M. N.; Sonny, Bal B. *Semin. Arthro.* **2006**, *17*, 113–119.
116. Castro, F. P.; Chimento, G.; Munn, B. G.; Levy, R. S.; Timon, S.; Barrack, R. L. *J. Arthroplasty* **1997**, *12*, 765–771.
117. Piconi, C.; Maccauro, G.; Logroscino, G. *Key Eng. Mater.* **2005**, *284–286*, 975–978.

118. Hamilton, W. G.; McAuley, J. P.; Dennis, D. A.; Murphy, J. A.; Blumenfeld, T. J.; Politi, J. *Clin. Orthop.* **2010**, *468*, 358–366.
119. Lombardi, A. V.; Berend, K. R.; Seng, B. E.; Clarke, I. C.; Adams, J. B. *Clin. Orthop.* **2010**, *468*, 367–374.
120. Pandorf, T. In *Modern Trends in THA Bearings*; Cobb, J., Ed.; Springer: Berlin, 2010; pp 97–102.
121. Tateiwa, T.; Clarke, I. C.; Willams, P. A.; *et al. Am. J. Orthop.* **2008**, *37*, E26–E31.
122. Walter, W. L.; Walters, T. S.; Gillies, M.; *et al. J. Bone Joint Surg. Am.* **2008**, *90A*, 102–111.
123. Postak, P. D.; Rosca, M.; Greenwald, A. S. *J. Bone Joint Surg. Am.* **2009**, *91A*(S6), 129–133.
124. Glaser, D.; Komistek, R. D.; Cates, H. E.; Mahfouz, M. R. *J. Bone Joint Surg. Am.* **2008**, *90*, 112–120.
125. Restrepo, C.; Post, Z. D.; Kai, B.; Hozack, W. J. *J. Bone Joint Surg. Am.* **2010**, *92*, 550–557.
126. Medicines and Healthcare products Regulatory Agency (MHRA), *Best Practice in Use of Ceramic Femoral Heads in Hip Replacement Implants*. MDA SN2002(05) MHRA: London, 2002;.
127. Pitto, R. P.; Schmidt, R.; Meller, S.; Petzold, R.; Willmann, G. In *Bioceramics in Joint Arthroplasty* ; Toni, A., Willmann, G., Eds.; Thieme: New York, 2001; pp 34–38.
128. Garino, J. P. In *Bioceramics in Joint Arthroplasty*; Toni, A., Willlmann, G., Eds.; Thieme: New York, 2001; pp 6–10.
129. American Society for Testing and Materials, *ASTM F 1636-95 Standard Specification for bores and cones for modular femoral heads*. ASTM: West Coshohocken, PA, 1995.
130. Sedel, L. In *Reliability and Long Term Results of Ceramics in Orthopedics*; Sedel, L., Willmann, G., Eds.; Thieme: New York, 1999; pp 75–76.
131. Allain, J.; Roudot-Thoraval, F.; Delecrin, J.; Ancrat, P.; Migaud, H.; Goutallier, D. *J. Bone Joint Surg. Am.* **2003**, *85*, 825–830.
132. Gozzini, P. A.; Schmid, C.; Dalla, Pria P. *Hip Int.* **2002**, *12*, 37–42.
133. Hasegawa, M.; Sudo, A.; Uchida, A. *Acta Orthop.* **2006**, *77*, 833–835.
134. Matziolis, G.; Perka, C.; Disch, A. *Arch. Orthop. Trauma Surg.* **2003**, *123*, 48–50.
135. Sedel, L. In *Surgical Techniques in Orthopedics and Traumatology*, Edition Scientifiques et Medicales; Elsevier SAS: Paris, 2001; 55-430-E-10.
136. Chang, J.-D.; Kamdar, R.; Yoo, J.-H.; Hur, M.; Lee, S.-S. *J. Arthroplasty* **2010**, *24*, 1231–1235.
137. Lazennec, J.-Y.; Boyer, P.; Rousseau, M. A.; *et al*. In *Modern Trends in THA Bearings*; Cobb, J., Ed.; Springer: Berlin, 2010; pp 103–106.
138. Langer, G. In *Bioceramics in Joint Arthroplasty*; Garino, J. P., Willmann, G., Eds.; Thieme: New York, 2002; pp 128–130.
139. Lee, M. C.; Ahn, J. W. In *Bioceramics and Alternative Bearings in Joint Arthroplasty*; Chang, J. D., Billau, K., Eds.; Steinkoppf: Darmstadt, 2007; pp 123–132.
140. Oonishi, H.; Oonishi, H.; Kim, S. C.; *et al. Semin. Arthro.* **2006**, *17*, 134–140.
141. Heimke, G.; Leyen, S.; Willmann, G. *Biomaterials* **2002**, *23*, 1539–1551.
142. Dalla, Pria P.; Giorgini, L.; Kuntz, M.; Pandorf, T. In *Bioceramics and Alternative Bearings in Joint Arthroplasty*; Benazzo, F., Falez, F., Dietrich, M., Eds.; Steinkoppf: Darmstadt, 2006; pp 115–123.
143. Bergschmidt, P.; Lohmann, C.; Bader, R.; *et al*. In *Modern Trends in THA Bearings*; Cobb, J., Ed.; Springer: Berlin, 2010; pp 239–244.
144. Takahashi, T.; Sato, T.; Hisanaga, R.; *et al. Bull. Tokyo Dent. Coll.* **2008**, *49*, 23–27.
145. Noiri, A.; Hoshi, F.; Murakami, H.; Sato, K.; Kawai, S.; Kawai, K. *Fol. Ophthalmol. Jpn.* **2002**, *53*, 476–480.
146. Wieneke, H.; Sawitowski, T.; Wendt, S.; *et al. Herz* **2002**, *27*, 518–526.
147. Lazennec, J.-Y.; Qingshan, C.; Nan, A. K.; Masson, B. In *Bioceramics in Joint Arthroplasty*; Lazennec, J. Y., Dietrich, M., Eds.; Steinkoppf: Darmstadt, 2004; pp 51–55.
148. Graessel, M. In *Bioceramics and Alternative Bearings in Joint Arthroplasty*; Chang, J. D., Billau, K., Eds.; Springer: Berlin, 2007; pp 261–268.
149. Kohal, R. J.; Wolkewitz, M.; Mueller, C. *Clin. Oral Implant Res.* **2010**, *21*, 1345–1352.

1.106. Zirconia as a Biomaterial

J Chevalier and L Gremillard, Université de Lyon, Villeurbanne, France

© 2011 Elsevier Ltd. All rights reserved.

1.106.1.	**Introduction**	95
1.106.1.1.	The Discovery of Phase Transformation in the 1970s: A Revolution in the Ceramic Field	95
1.106.1.2.	The Logical Development as a Structural Bioceramic	96
1.106.1.3.	Phase Transformation and Aging: The Two Sides of Zirconia	96
1.106.2.	**Crystallography and Phase Transformation of Zirconia**	97
1.106.2.1.	Crystallography and Phases Stability	97
1.106.2.2.	Stress-Induced Phase Transformation and Toughening	99
1.106.2.3.	Surface Transformation in the Presence of Water and LTD	99
1.106.3.	**Different Types of Zirconia and Zirconia-Based Composites**	100
1.106.3.1.	Alloy Additives for Zirconia	100
1.106.3.2.	Partially Stabilized Zirconia Ceramics	102
1.106.3.3.	Tetragonal Zirconia Polycrystals	102
1.106.3.4.	Zirconia-Dispersed Ceramics	103
1.106.4.	**The Use of Zirconia as a Biomaterial: Current State of the Art**	103
1.106.4.1.	The Use of Zirconia in Orthopedics: From Yttria-Doped Zirconia to Zirconia-Toughened Alumina	103
1.106.4.2.	The Use of Zirconia in the Dental Field: From Dental Restoration to Implants	104
1.106.5.	**Future Directions**	105
1.106.5.1.	Tough, Strong, and Stable Zirconia Ceramics and Composites: The Necessary Challenge	105
1.106.6.	**Conclusion**	107
1.106.7.	**Further Reading**	107
References		107

Abbreviations

3Y-TZP	Tetragonal zirconia polycrystal stabilized with 3 mol% yttrium oxide (Y_2O_3)
c-phase/structure	Cubic phase/structure of zirconia
CAD/CAM	Computer-assisted design and machining
Ca-PSZ	Calcium-doped partially stabilized zirconia
Ce-TZP	Tetragonal zirconia polycrystal stabilized with cerium oxide (CeO_2)
LTD	Low-temperature degradation
m-phase/structure	Monoclinic phase/structure of zirconia
MAJ	Mehl–Avrami–Johnson
Mg-PSZ	Magnesium-doped partially stabilized zirconia
PSZ	Partially stabilized zirconia
t–m	Tetragonal to monoclinic phase transformation
t-phase/structure	Tetragonal phase/structure of zirconia
TZ3Y-E	A kind of 3Y-TZP powder containing silica and alumina dopants (easy sintering grade from Tosoh Ltd)
TZP	Tetragonal zirconia polycrystal
UHMWPE	Ultra-high-molecular-weight polyethylene
XRD	X-ray diffraction
ZTA	Zirconia-toughened alumina

1.106.1. Introduction

1.106.1.1. The Discovery of Phase Transformation in the 1970s: A Revolution in the Ceramic Field

Zirconia has been one of the most important ceramic materials for well over a century. The discovery of transformation toughening in 1975[1] heralded visions of new high-performance applications of zirconia, ranging from bearing and wear applications to, most recently, biomedical applications. Garvie and his colleagues discovered transformation toughening in calcia-stabilized zirconia, as described in their famous 'ceramic steel' paper. It was followed by intense efforts to understand and describe the mechanisms of phase transformation, its effect on mechanical properties, and its application in a large variety of zirconia ceramics with different alloying elements. In this respect, without being exhaustive, the pioneering works of Garvie, Swain, and Hannink in Australia and Lange, Green, and Evans in the United States form the groundwork of today's knowledge (see, e.g., Green *et al.*,[2] Lange,[3] and McMeeking and Evans[4]). The idea behind phase transformation toughening was first to maintain the tetragonal phase of zirconia in a metastable state after sintering, thanks to the addition of a stabilizing oxide (e.g., CaO, MgO, and Y_2O_3). The tetragonal phase could then transform to the stable monoclinic one under stress. Associated to a large volume expansion inducing compressive stresses, the stress-induced phase transformation

created the conditions for an increase of strength and toughness never reached before with ceramics. Toughness and strength of more than 6 MPa √m and 1 GPa, respectively, could be obtained with yttria-doped zirconia, to compare with 4 MPa √m and 600 MPa for the best alumina ceramics, opening a new avenue for structural applications.

1.106.1.2. The Logical Development as a Structural Bioceramic

Following the fundamental work of the late 1970s, attempts to apply zirconia as a biomaterial were conducted as early as 1984[5] in the form of magnesia partially stabilized zirconia (PSZ). However, mainly based on higher strength at room temperature, 3 mol% Y_2O_3-stabilized zirconia (3Y-TZP, TZP standing for tetragonal zirconia polycrystal) became the material of clinical choice in the 1990s, for the large-scale processing of hip joint femoral heads.[6] Its use made possible the production of small hip implants (such as 22.22 mm femoral heads, leading to a reduction of volumetric wear of UHMWPE sockets) and knee joints that did not have adequate mechanical resistance when made with alumina. There is experimental evidence that the ultimate compressive load of zirconia ball heads is 2–2.5 times higher than that of alumina ball heads of the same diameter and neck length.[6] More than 600 000 zirconia hip joint heads were implanted between 1990 and 2001, but its use in orthopedic surgery has since been reduced by more than 90% after a failure episode in 2001–2002 described below, highlighting the lack of long-term stability of 3Y-TZP *in vivo*.[7] Given the lack of mechanical properties of alumina alone and the critical lack of stability of 3Y-TZP alone *in vivo*, companies developing orthopedic implants turned to composite materials with the aim of reinforcing alumina with zirconia phase transformation toughening.[8] At the same time, zirconia in dental application has been booming during the last 10 years, based on three main properties: better esthetics and corrosion resistance than metals and better crack resistance than other ceramics. The use of zirconia allows the fabrication of long bridges, abutments, and even implants with a sufficient mechanical resistance.[9] The failure episode of zirconia femoral heads had a clear negative impact in orthopedics, but almost none in the dental field. It is undoubtedly because of the lower criticality of a dental device failure for the patient and also a lack of information exchange between the two communities.

1.106.1.3. Phase Transformation and Aging: The Two Sides of Zirconia

The main features of phase transformation and aging are given in Figure 1. The best mechanical properties of zirconia are achieved only if some grains are able to transform under

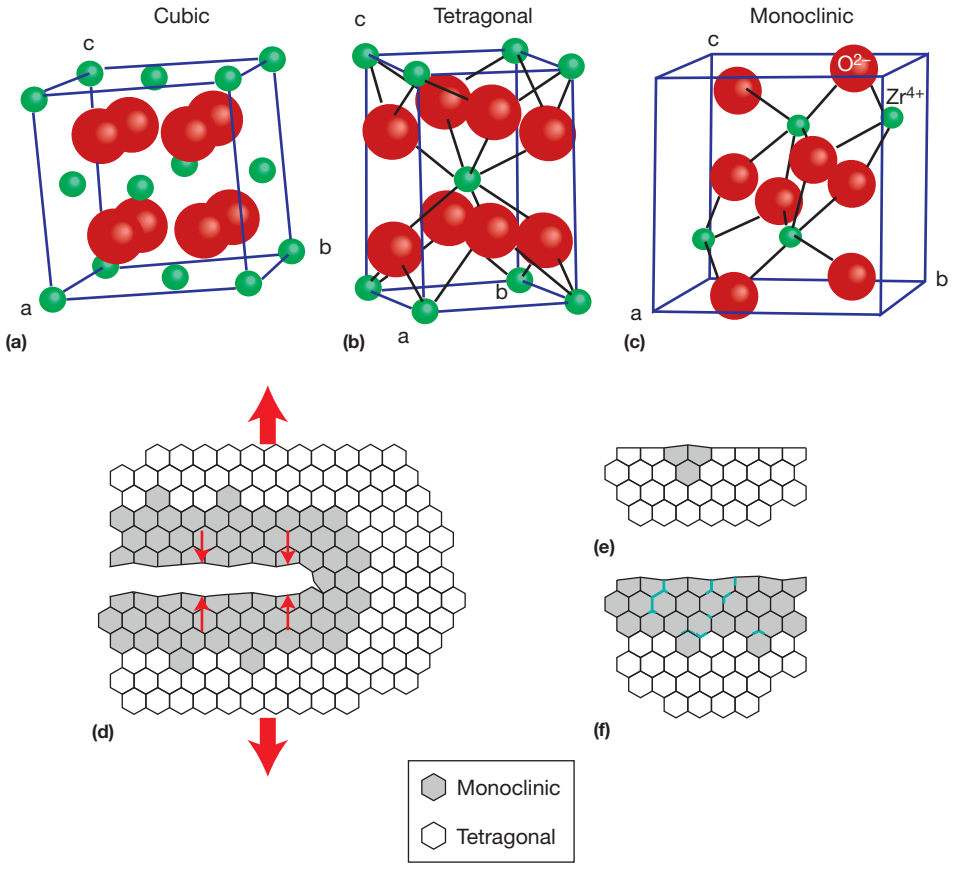

Figure 1 (a–c) The three major polymorphs of zirconia and the two alternative means by which metastable tetragonal phase can transform to monoclinic phase. (d) Phase transformation toughening and (e, f) aging.

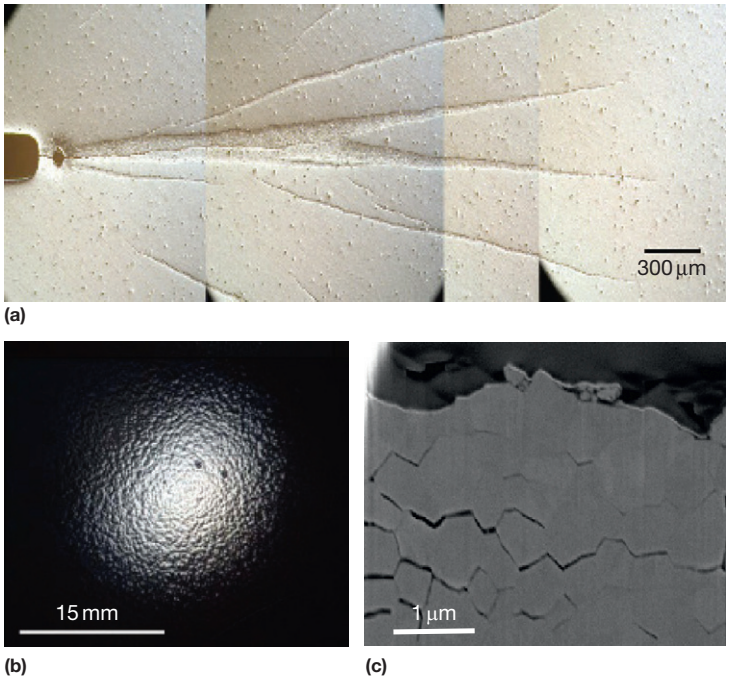

Figure 2 (a) Scanning electron microscopy picture of phase transformation around a propagating crack in a ceria-doped zirconia. Reproduced from El Attaoui, H.; Saâdaoui, M.; Chevalier, J.; Fantozzi, G. *J. Eur. Ceram. Soc.* **2007**, *27*(2–3), with permission from Elsevier. (b) Optical microscopy image (Nomarski contrast) of a 3Y-TZP femoral head after 20 h aging at 134 °C in autoclave. Courtesy D. Douillard, INSA-Lyon. (c) Focused ion beam slice of a 3Y-TZP dental implant after severe aging, showing microcracking beneath the surface. Courtesy B. Van De Moortele, ENS-Lyon.

stress from the tetragonal metastable state toward the stable monoclinic one. This is the concept of phase transformation toughening. Without the help of phase transformation, cubic zirconia, for example, exhibits toughness on the order of 2 MPa √m. In other words, zirconia can be used as a structural bioceramic only if it is not completely stable. However, this necessary metastability of the tetragonal phase at room temperature can result in the transformation of the surfaces in contact with water (or body fluids). This phenomenon, which was first described by Kobayashi *et al.*[10] at 250 °C, is known as 'aging' or 'low-temperature degradation' (LTD) and is partly responsible for the failure episode of 2001–2002 in orthopedics, when hundreds of 3Y-TZP femoral heads processed under specific conditions failed after 1–2 years *in vivo*.[11] Stress-induced transformation and aging are in fact two alternative means by which the metastable tetragonal phase can transform to monoclinic. The positive side is the phase transformation under stress, which enables zirconia to resist high loads, while the negative is the possible transformation at the surface, leading to microcracking and roughening, as will be discussed later. Figure 2 illustrates these two sides of the phase transformation, with a positive, large transformation zone around a propagating crack in (ceria-doped) zirconia, and detrimental roughening of a Y-TZP femoral head and microcracking beneath the surface after aging. The stake is therefore to process zirconia ceramics able to transform under applied stresses but with the lowest sensitivity to water. *A posteriori*, knowing now the effect of yttria on tetragonal phase stability in the presence of water, it becomes quite clear that the choice of Y-TZP for orthopedics might not have been the best one.

1.106.2. Crystallography and Phase Transformation of Zirconia

Many of the properties of zirconia ceramics are related to their crystallography, and in particular to the phase transition from a tetragonal phase to the monoclinic one. (Other properties, such as ionic conductivity that makes zirconia ceramics so useful for solid electrolyte fuel cells and oxygen sensors, are a result of the presence of numerous oxygen vacancies, introduced by the presence in the material of trivalent cations stabilizing the cubic phase at low temperature.)

In this section, we describe the crystallography of zirconia phases, and show its influence on the two major properties that control the lifetime of zirconia-implanted devices: resistance to crack propagation (influenced by the transformation toughening) and hydrothermal aging (also called LTD).

1.106.2.1. Crystallography and Phases Stability

There are at least five known solid phases of zirconia ceramics. Under normal processing conditions (pressureless or low-pressure environment and conventional thermal cycles), only three phases (cubic, tetragonal, and monoclinic) are generally observed, depending on temperature and addition of a stabilizing oxide. We will focus here only on these three phases as they are the only ones of interest for biomedical applications. They are schematically described in Figure 1.

In pure zirconia (i.e., without any stabilizing oxide), from low to high temperature, the stable phases are the monoclinic (m) phase (up to 1170 °C), the tetragonal phase (t)

(from 1170 to 2370 °C), and the cubic (c) phase (above 2370 °C and up to the melting point at 2680 °C).

The c-structure is a calcium fluorite-type structure (face-centered cubic, 225, $Fm3m$), where the zirconium ions occupy the summits of the cube and the center of the faces, while oxygen ions are located in the tetrahedral sites. However, the O ions are slightly displaced from the (0.25,0.25,0.25) position toward a higher z (typically 0.25,0.25,0.28), which may be due to the tendency of the Zr atoms to form sevenfold coordination.

Compared to the c-structure, the t-structure presents an elongated c-axis and can thus be described as a distorted calcium fluorite structure (zirconium ions being organized in a face-centered tetragonal lattice). This description facilitates comparison to the 'parent' cubic phase. However, considering half the face-centered lattice, one obtains a body-centered tetragonal organization of the Zr ions, described in the $P4_2/nmc$ (137) space group (**Figure 1**). Both descriptions are commonly used in the literature, and, for example, the (111) plane in the face-centered description corresponds to the (101) plane in the body-centered one.

It is not yet sure whether the m-structure is a homogeneous single phase or if it forms a series of incommensurate, solid solutions. However, it can be described in the $P2_1/c$ space group. In this structure, the Zr atoms are in sevenfold coordination with the O sublattice (eightfold in the CaF_2 structure).

Sintering zirconia generally involves temperatures above the tetragonal-to-monoclinic (t–m) transformation temperature. Thus, zirconia is tetragonal at the sintering temperature and the t–m transformation occurs during cooling. This transformation results in a very large volume increase (around 5%) that inevitably provokes a cracking of dense, pure zirconia bodies. It is possible to avoid transformation-induced cracking by either sintering below 1170 °C (the material remains monoclinic during the whole sintering cycle, which leads to non-transformable, low strength and tough ceramic) or retaining the tetragonal or the cubic phases at room temperature by alloying with alliovalent cations (which avoids the t–m transformation during cooling). The latter approach is the basis of the use of zirconia as a technical ceramic, and was first described by Ruff and Ebert[12] almost a century ago. The tetragonal phase is in fact metastable, and may be able to transform to monoclinic, if either mechanical or chemical energy is provided, to t-grains. This is the basis of phase transformation toughening, but also of aging.

The t–m transformation is martensitic in nature. It is most often described by the phenomenological theory of martensitic crystallography.[13,14] Shortly, crystallographic correspondences exist between the parent (tetragonal) and the product (monoclinic) phase. They can be described by habit planes and directions (shape strain). The three possible lattice correspondences in zirconia are ABC, BCA, and CAB, which correspond to a change of the (a_t, b_t, c_t) lattice axis of the t-phase into the (a_m, b_m, c_m), (b_m, c_m, a_m), and (c_m, a_m, b_m) axes of the m-phase, respectively. Each of these lattice correspondences may occur along two different habit planes. This leads to six different configurations, and in total 24 variants (as in the tetragonal symmetry, a, b, $-a$, and $-b$ are crystallographically equivalent). Note that variants are auto-accommodating: even if for each variant a shear strain of around 0.16 results from the transformation, for two auto-accommodating variants the resulting shear strain is near zero, and only the dilatational strain (~0.05) has to be taken into account. This means that the transformation-induced cracking is mostly because of the dilatational component of the transformation strain.

The first thermodynamic model of t–m transformation in zirconia was proposed by Lange,[3] considering a rather idealized case (a spherical tetragonal particle). The change of total free energy (ΔG_{t-m})as a result of the transformation is given by eqn [1]:

$$\Delta G_{t-m} = \Delta G_c + \Delta U_{SE} + \Delta U_S \quad [1]$$

where ΔG_c (<0 at low temperature) is the chemical free energy (dependent on temperature and composition), ΔU_{SE} (>0) is the strain energy associated with the transformed particles (dependent on the surrounding matrix, the size and shape of the particle, and the presence of stresses), and ΔU_S (>0) the change in energy associated with the surface of the particle (creation of new interfaces and microcracking).

The balance between ΔU_S and ΔG_c explains why it is possible to retain tetragonal pure zirconia powders at room temperature (ΔU_{SE} is zero), up to grain sizes around 24 nm.[15,16] In bulk-sintered ceramics, such low grain sizes are almost impossible to retain. Associated with possible internal residual stresses, this makes it impossible to stabilize the tetragonal phase without the help of stabilizing oxides that increase ΔG_c (or decrease $|\Delta G_c|$), or without the existence of additional compressive stresses (due, e.g., to a stiff matrix) that decrease ΔU_{SE}.

Bulk monolithic zirconia ceramics of practical use for engineers can only be obtained by stabilizing the t-phase by a number of stabilizing oxides (or dopants). In view of this model, one can expect the dopants to stabilize t-zirconia by decreasing $|\Delta G_c|$.

When considering zirconia alloyed with another oxide, the transformation temperature for pure zirconia does not hold true anymore. In fact, in most of the zirconia-stabilizer systems, we have to take into account two kinds of phase diagrams to be able to predict the exact phase composition of the systems.[11] The first one is the classical phase equilibrium diagram that indicates the composition and amounts of the different phases at equilibrium. The most recent version of this diagram is shown in **Figure 3**. It indicates, for example, that a 3 mol% Y_2O_3-stabilized zirconia held at high temperature (i.e., 1500 °C) should be constituted of 88% of tetragonal phase containing 2.4 mol% Y_2O_3 and 12% cubic phase with 7.5 mol% Y_2O_3. The same zirconia with an overall 3 mol% Y_2O_3 content should be constituted at room temperature of a monoclinic phase containing almost no Y_2O_3 and a cubic phase containing 18 mol% Y_2O_3. But reaching this equilibrium should take hours at high temperatures and many thousand years at room temperature. Thus, metastable phase diagrams are also needed and are being considered today. These diagrams indicate the t–m transformation temperatures for each composition of the tetragonal grains (see **Figure 3**). These t–m transformation temperatures in the metastable phase diagram are called T_0^{t-m}. Above T_0^{t-m}, the tetragonal phase is stable (referring to the thermodynamic approach of Lange, $\Delta G_c > 0$). Below T_0^{t-m}, the stable phase is monoclinic ($\Delta G_c < 0$), although a metastable tetragonal phase can be retained ($\Delta G_c < 0$, but $\Delta U_{SE} + \Delta U_S > |\Delta G_c|$; thus, $\Delta G_{t-m} > 0$).

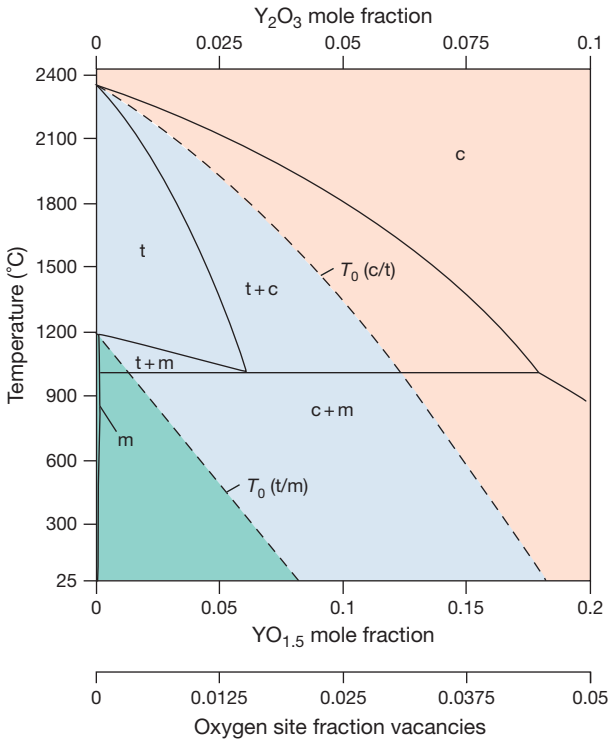

Figure 3 Most recent zirconia–yttria phase diagram (continuous lines) and metastable phase diagram (dotted lines). Reproduced from Chevalier, J.; Gremillard, L.; Virkar, A. V.; Clarke, D. R. *J. Am. Ceram. Soc.* **2009**, *92*, 1901–1920, with permission from Wiley.

For example, the following features are seen in **Figure 3**:

- Starting with a homogeneous powder containing 3 mol% Y_2O_3, sintering at 1400 °C for only 5 h will not allow reaching the equilibrium phase diagram at this temperature. The sintered body will still present at 1400 °C a homogeneous distribution of yttria. Thus, the t–m transformation temperature to be taken into account is the one related to the tetragonal phase containing 3 mol% Y_2O_3 (around 400 °C). In this case, the tetragonal phase is stable above 400 °C (T_0^{t-m} temperature for 3 mol% Y_2O_3), but only metastable below 400 °C.
- Sintering at higher temperature (e.g., 1500 °C for 5 h) will result in the high-temperature equilibrium being reached (a mixture of tetragonal phase containing 2.4 mol% Y_2O_3 and cubic phase containing 7.5 mol% Y_2O_3). Thus, upon cooling, the t-phase becomes metastable below 600 °C (the cubic phase becoming metastable below around 750 °C; see T_0^{c-t}). (For more detailed information on the use of stable and metastable diagrams, please refer to Chevalier *et al.*[11] (Figure A3).)

Such T_0^{t-m} temperatures give a clear indication of the stability of the t-phase as a function of the thermal history followed during processing: sintering at high temperatures for long durations results in a higher T_0^{t-m} temperature traducing a lower (meta)stability of the t-phase at room temperature. As the tetragonal phase is only metastable at room temperature, an additional driving force (e.g., tensile stresses) may trigger the t–m transformation.

1.106.2.2. Stress-Induced Phase Transformation and Toughening

Stress-induced phase transformation and phase transformation toughening have been described in detail by Green *et al.*[2] We give here only the necessary basics. As described earlier, the presence of tensile stresses in the vicinity of a crack relieves some or all of the mechanical constraints on the metastable tetragonal phase and allows it to transform to the monoclinic phase, leading to the formation of a transformation zone (see **Figure 1**). Obviously this cannot occur if the t-phase is stable, but takes place only in its metastability range, below the T_0^{t-m} temperature. The transformation induces compressive stresses that act to hinder crack propagation, as schematized in **Figure 1**. In the phase transformation toughening model developed by McMeeking and Evans,[4] the stress-induced phase transformation leads to a shielding K_{Ish} of the applied stress intensity factor K_I, meaning that the real stress intensity factor at the crack tip K_{Itip} is lower than that applied by the external forces, according to eqn [2]:

$$K_{Itip} = K_I - K_{Ish} \quad [2]$$

Both this theoretical model and experimental results[17] show that increasing the applied stress intensity factor leads to a larger transformation zone and thus larger shielding effect, which is in fact proportional to the applied K_I (eqn [3]):

$$K_{Ish} = C_{sh}K_I \quad [3]$$

where the proportionality constant C_{sh} depends on the Young modulus (E), Poisson ratio (ν), volume fraction of the transformable particles (V_f), volume expansion associated to the transformation (e^T), and a critical local stress leading to transformation (σ_m^c), via the following equation:

$$C_{sh} = \frac{0.214EV_f e^T(1+V)}{(1-V)\sigma_m^c}\left(\frac{\sqrt{3}}{12\pi}\right) \quad [4]$$

A given zirconia will be all the more tough if the critical local stress leading to phase transformation (σ_m^c) is low. In turn, σ_m^c depends on the magnitude of the undercooling below the T_0^{t-m} temperature: large undercooling below T_0^{t-m} will result in a high propensity toward t–m phase transformation, and thus in low σ_m^c and large transformation toughening.

The effect of phase transformation toughening is seen while comparing crack propagation velocities in different zirconia ceramics in V–K_I diagrams. For example, the difference between the good crack propagation resistance of 3Y-TZP (TZPs stabilized with 3 mol% Y_2O_3) and the modest one of cubic zirconia comes from phase transformation toughening.[18] It was also seen that increasing the grain size in 3Y-TZP results in increased phase transformation toughening efficiency,[17] and thus better resistance to crack propagation and better toughness. This could originate from the higher sintering temperature and soaking time used for the coarser-grained zirconia ceramics, that should have resulted in a higher phase partitioning (Y-rich cubic phase plus Y-poor tetragonal phase), resulting in turn in a higher T_0^{t-m} temperature (thus a higher undercooling and a lower σ_m^c).

1.106.2.3. Surface Transformation in the Presence of Water and LTD

The presence of water can trigger the t–m phase transformation at the surface of zirconia. This is especially true and well

documented in the case of Y-TZP. In contrast with the t–m transformation 'in the bulk' in the vicinity of a propagating crack, t–m transformation 'at the surface' in the presence of water leads to degradation of the materials properties. The main features of this 'aging' process are given in Figure 1.

The mechanism by which the presence of moisture leads to a transformation of Y-TZP remains to be firmly established. One of the hypotheses currently most favored is that the filling of oxygen vacancies by 'water-derived species' (hydroxyl, oxygen, or hydrogen ions) probably leads to both decrease of ΔG_c (by modifying the local oxygen configuration around Zr ions) and an accumulation of internal tensile stresses (decrease of ΔU_{SE}) in the grains in contact with water (with the maximum tensile stresses in those grains roughly estimated at 300–500 MPa[19]). However, some authors claim that exposure to moisture increases lattice parameters of the tetragonal phase[20] while others claim that lattice parameters decrease under the same conditions. More detailed experimental work and computational atomic scale simulations are necessary to resolve this crucial issue. In any case, it is clear today that diffusion of water-derived species leads to a progressive change of the stability of the tetragonal grains: metastable t-grains at the surface can become unstable and transform to the m-phase after a certain exposure time. The volume increase accompanying the transformation results in a surface uplift and large stresses that can provoke the creation of cracks along the grain boundaries.[7,11] In turn, tensile stresses appear in the neighboring grains and cracks facilitate the penetration of moisture further into the material: the process is repeated as moisture ingress goes on and tensile stresses are accumulated. As it is likely that the moisture can flow through grain boundary cracks much faster than by diffusion, it is likely that the observed activation energy for LTD is determined by diffusion of the moisture species into the lattice of the individual grains.

Aging kinetics may be characterized by quantifying the amount of monoclinic phase on zirconia surface versus time, using techniques such as X-ray diffraction (XRD) or Raman spectroscopy. All the results obtained to date show that the kinetics can be fitted with the standard Mehl–Avrami–Johnson (MAJ) equations for a nucleation and growth process (eqn [5]):

$$f_m = 1 - \exp\left(-(bt)^n\right) \quad [5]$$

where f_m is the fraction of tetragonal phase that has transformed to monoclinic phase, t is the time of exposure to moisture, and the exponent, n, and the value of the constant, b, depend on the microstructural features of the material and on the temperature. Values of n range between 0.5 and 4.[21]

For 3Y-TZP, aging is faster around 250 °C. At lower temperatures (say below 150 °C), the phenomenon is thermally activated and the value of the constant, b, follows an Arrhenius law:

$$b = b_0 \exp\left(-\frac{Q}{RT}\right) \quad [6]$$

where b_0 is a constant, Q is an apparent activation energy, R is the gas constant, and T is the absolute temperature. The reported activation energies are around 100 kJ mol^{-1} (~1 eV), similar to the activation energy for oxygen vacancy diffusion extrapolated from higher temperatures.[22]

At temperatures higher than 250 °C, aging becomes slower. Combining experimental data at different temperatures on a time–temperature plot shows that transformation kinetics form 'C-shaped' curves. This behavior can be interpreted in terms of balance between the driving force for t–m transformation (which is larger at lower temperature, where the undercooling of the t-phase below the T_0^{t-m} temperature is high) and the growth rate (lower at low temperature due to lower diffusion kinetics).

The nucleation and growth of small monoclinic spots on tetragonal zirconia surfaces exposed to water, fully consistent with the MAJ kinetics, can be observed by techniques such as optical interferometry[22] or atomic force microscopy.[23] Observations by scanning electron microscopy further show that transformation first extends at the surface and then into the bulk. Careful atomic force microscopy observations also indicate that nucleation occurs preferably at the grain junctions and corners (where the residual tensile stresses are higher), and that the transformation then extends across individual grains.[23] The transformation then proceeds by a neighbor-to-neighbor propagation, as shown in the movie in Annex 1.

Although hydrothermal aging has been known since the early 1980s, its influence on the durability of orthopedic implants was neglected until the early 2000s, when a series of fractures of zirconia ball heads occurred early after implantation (around 2 years). These failures were later determined to have been caused by an accelerated aging of balls that were not sufficiently densified during sintering.[11] It appears now that femoral heads processed under 'normal' conditions might also suffer aging.[24,25] The mechanism and its effect on dental devices are less documented but there is evidence that some specific processing or surface modification might promote aging in dental grade zirconia. This will be the subject of Section 1.106.4.2.

Aging is intrinsic to 3Y-TZP. However, it depends largely on the microstructure and hence on the process. It can be minimized under the following conditions:

- The grain size remains small.
- The density is high, and more importantly there is no percolative porosity.
- There are no tensile residual stresses in the parts of the material exposed to water.
- There is no cubic phase (the t-grains that surround cubic grains are depleted in yttrium, and can transform more easily).

1.106.3. Different Types of Zirconia and Zirconia-Based Composites

Figures 4 and 5 schematically present the typical microstructure of different zirconia ceramics and their denomination, together with their standard temperature, composition, and processing conditions. The different types of zirconia ceramics differ in the dopant and its concentration, and the temperature of processing.

1.106.3.1. Alloy Additives for Zirconia

The oxides stabilizing zirconia tetragonal or cubic phase can be classified in several categories, depending on the valence of the cation and on the solubility of the stabilizer in the zirconia

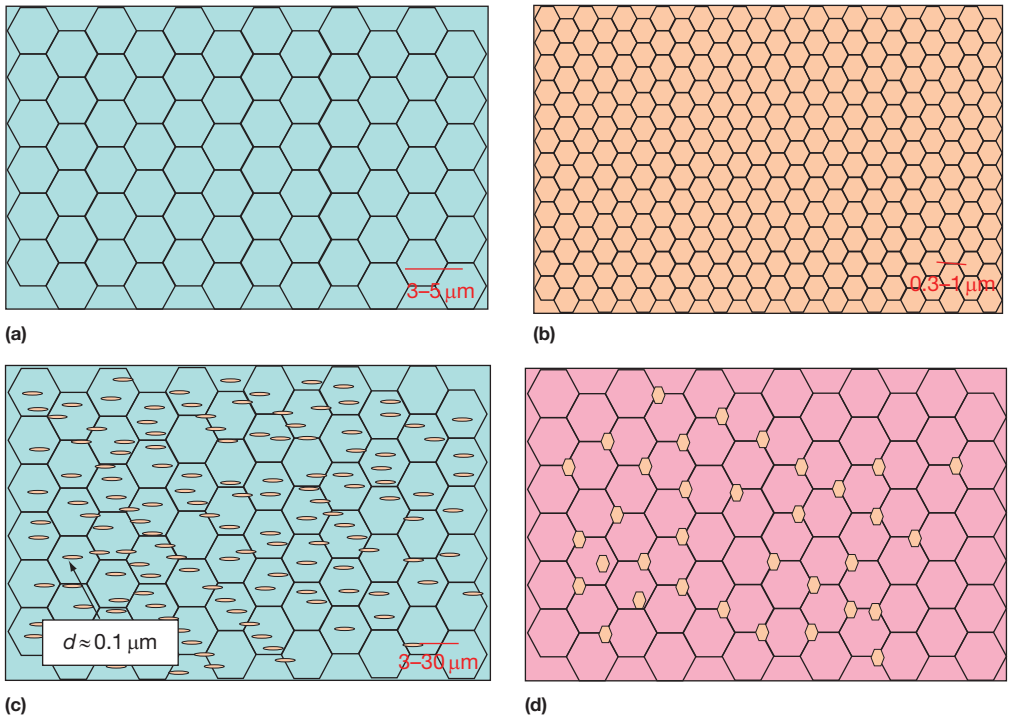

Figure 4 Schematic representation of the microstructures of the main types of zirconia ceramics and composites. Only TZP, PSZ, and ZTA exhibit phase transformation toughening. (a) Cubic, fully stabilized zirconia (FSZ; i.e., with 8 mol% Y_2O_3); (b) tetragonal zirconia polycrystal (TZP; i.e., with 3 mol% Y_2O_3 or 12 mol% CeO_2); (c) partially stabilized zirconia (PSZ), with tetragonal precipitates in a cubic matrix (i.e., with 8 mol% MgO); (d) zirconia-toughened alumina (ZTA), with tetragonal zirconia grains in an alumina matrix.

lattice. Calcium and magnesium are the only divalent cations used; they are of low solubility in zirconia at sintering temperatures, and they generally form PSZ ceramics, which consist of tetragonal grains in a cubic matrix (see **Figures 4** and **5**), at high temperature. This structure can be retained at low temperature or tetragonal precipitates can transform toward the monoclinic symmetry upon cooling, depending on the temperature and time of sintering. Some 'aging' treatments (say 'long thermal treatments' after sintering) can be conducted to favor the presence of the monoclinic phase at ambient temperature. In this case, the PSZ is no more prone to phase transformation toughening (tetragonal precipitates are already transformed after cooling). Trivalent cations of interest are mostly yttrium, but scandium, gadolinium, gallium, and iron can be found in special applications. They possess an intermediate solubility, and give rise to either tetragonal zirconia polycrystals (TZP) or PSZ ceramics, depending on the thermal history (see **Figures 4** and **5**). Tetravalent dopants such as cerium possess the highest solubility in zirconia and produce TZP ceramics. For example, zirconia can dissolve up to 15% of titanium oxide in the tetragonal phase and up to 18% in the cubic phase, and tetragonal zirconia doped with 18 mol% ceria can be found. Both Ce and Ti stabilize efficiently the tetragonal phase (although not as efficiently as Y).

Moreover, costabilization of t-zirconia with yttrium and Ti or Ce has also been considered. In these materials, the grain size is increased by the presence of Ce or Ti; however, because of the higher stability of the Ce- or Ti-doped Y-TZP, large tetragonal grains may remain stable (up to 10 μm grains, as compared to the maximum tetragonal grain size of 1.5 μm in a 3Y-TZP). Aging resistance of Y-TZP is improved by the addition of either Ti or Ce,[26] but the mechanical properties decrease, as can be expected from the higher stability.

Most stabilizers of zirconia tetragonal phase act through a decrease of 'oxygen overcrowding' around zirconium cations, either through the introduction of oxygen vacancies[27] or through the expansion of the cations lattice. In a very good series of two papers, Li *et al.*[28,29] used X-ray absorption spectroscopy to examine the effect of trivalent and tetravalent dopant ions on the local environment of zirconium ions. Local atomic structures around the Zr^{4+} and around dopant cations in zirconia solid solutions were determined. These included undersized (Fe^{3+}, Ga^{3+}) and oversized (Y^{3+}, Gd^{3+}) trivalent ions as well as undersized (Ge^{4+}) and oversized (Ce^{4+}) tetravalent ions. They concluded that in the presence of trivalent dopants, oxygen vacancies are generated for charge compensation. These vacancies are associated with the Zr cations in the case of oversized dopants, and with two dopant cations in the case of undersized dopants. With both configurations, the number of zirconium cations coordinated by seven oxygens (instead of eight) increases, which stabilizes the tetragonal or even the cubic phases. The closer association of oxygen vacancies with Zr is responsible for the more effective stabilization effects of oversized trivalent dopants (around twice as effective as with undersized trivalent cations). In tetravalent cations-doped zirconia, oxygen vacancies are scarce and cannot account for the stabilization of the tetragonal phase. Instead, it was shown that adding oversized cations dilates the cation network and thus decreases the oxygen overcrowding around Zr ions.

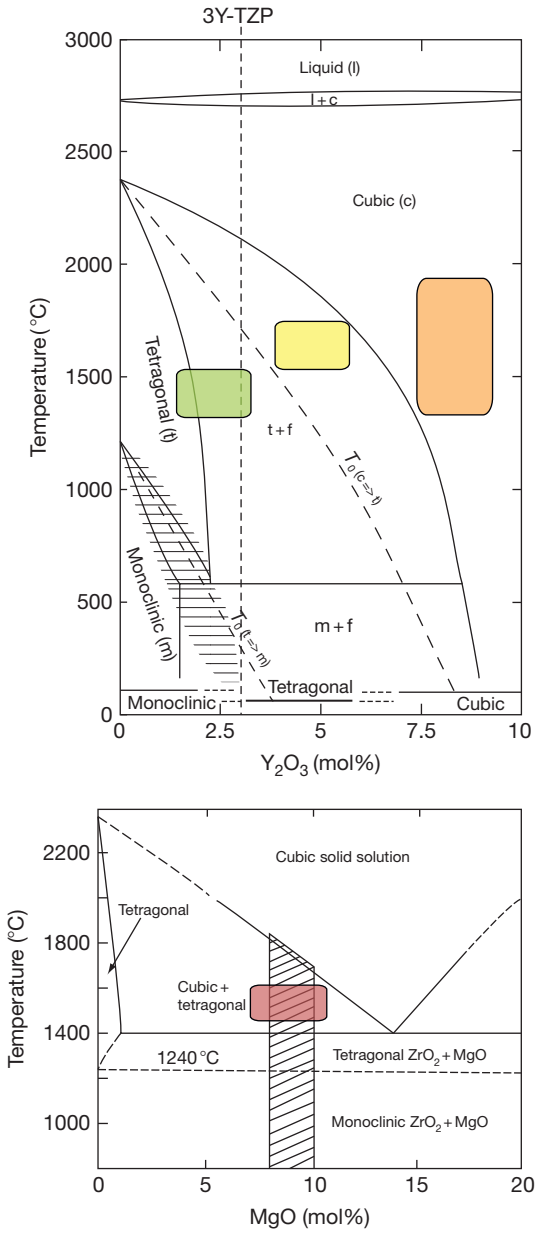

Figure 5 Temperature and compositions ranges for the process of (a) Y-TZP (green area), Y-PSZ (yellow area), and Y-FSZ (orange) ceramics and (b) Mg-PSZ (pink) ceramics.

Thus, doping with trivalent oversized cations, such as Y^{3+}, is most efficient in relieving the oxygen overcrowding (via both oxygen vacancies generation and dilatation of the cation network). The same stabilizing efficiency is obtained with 1.5 mol% of Y_2O_3 or 10 mol% of CeO_2; this exemplifies the crucial role of oxygen vacancies in stabilizing t-zirconia (the presence of Ce^{4+} brings no vacancies) and explains the prevalent use of yttria-stabilized zirconia ceramics in practical applications. On the other hand, it is clear that Y_2O_3 is not the only dopant able to stabilize the t-phase at room temperature.

Other stabilizing mechanisms exist, such as the creation of ordered phases (as is the case when doping with undersized tetravalent ions such as Ge^{4+} or Ti^{4+}), but this mechanism is of less interest when considering zirconia as a biomaterial (to our knowledge, Ge-stabilized zirconia only exist in the laboratories, and do not provide sufficient mechanical properties).

As mentioned above, one of the major difficulties in processing and using zirconia ceramics is maintaining the delicate balance between the t-phase stability necessary to resist aging and the t-phase transformability necessary for phase transformation toughening. However, it is possible to get out of this compromise by creating zirconia ceramics that possess a constant stability with time, even in the presence of water: within certain limits, a high transformability is preferable if the material is insensitive to aging. One way to achieve it is to use zirconia stabilized with tetravalent ions (e.g., Ce^{4+}) or with mixed tri- and pentavalent ions (e.g., $Y^{3+} + Nb^{5+}$). This way, the t-phase can be stabilized at room temperature but is readily transformable under applied stress, while the absence of oxygen vacancies will prevent the occurrence of aging.

1.106.3.2. Partially Stabilized Zirconia Ceramics

Divalent cations such as Mg^{2+} and Ca^{2+} were historically the first to be used for 'technical' zirconia ceramics. Indeed, phase transformation toughening was discovered in Ca-doped zirconia, and Mg-doped zirconia was the first one to be used in orthopedics. Most Mg- and Ca-doped zirconia are PSZ. PSZ is composed of nanometric precipitates of tetragonal or monoclinic phase embedded in a cubic matrix (see **Figures 4** and **5**). Such zirconia ceramics are generally obtained with the addition of lime or magnesia. They are often submitted to a second thermal treatment (so-called 'aging,' with no relation with the aging process described as an LTD in the presence of water) after sintering in order to control the number, crystallography (tetragonal and/or monoclinic), and size of the precipitates. Note that yttria-stabilized zirconia can also be obtained in the PSZ form, if it contains enough yttria (between 4 and 7 mol% Y_2O_3), is thermally treated at a temperature high enough to be fully cubic, and then cooled in a way that allows the formation of small tetragonal precipitates.

Although it possesses a lower strength than 3Y-TZP, Mg-PSZ is a valid alternative for the realization of heads of hip prostheses, because of its higher toughness[30] and higher crack propagation threshold (respectively 8 and 6 MPa $\sqrt{m}$, vs. 5 and 3.5 for 3Y-TZP). It was considered for orthopedic applications as early as 1984, but set aside for Y-TZP on strength arguments. There is a renewed interest in this material, as, compared to Y-TZP, Mg-PSZ is immune to aging.[31] Mg-PSZ prostheses explanted after 5 years *in vivo* do not show any sign of aging.[32] On the other hand, it has been shown that at around 200 °C, exposure to water can lead to a depletion of Mg from the surface and thus a transformation of the surface tetragonal precipitates to the monoclinic phase,[33,34] which seems not to be relevant so far, for usual industrial applications. Its deep yellow to orange color impairs its possible application in the dental field (especially when crowns and bridges are considered).

1.106.3.3. Tetragonal Zirconia Polycrystals

Tetragonal zirconia polycrystals (TZPs) are often considered monoliths of the tetragonal phase, although the phase diagram

and the sintering conditions for Y-TZP dictate that they most often contain a secondary cubic phase (see Figure 3 or 5). Most of the TZPs investigated so far are those stabilized with yttria or ceria, sintered at temperatures at which the tetragonal phase is the major or the only phase. Y-TZP is of special interest, as this is the one chosen for the processing of hip prosthesis heads and, more recently, of dental devices. This choice initially results from the higher strength of Y-TZP as compared to Mg- and Ca-PSZ. It was later made easier by the availability of high-quality powders. Actually, after the original work on PSZ, most of the practical knowledge on phase transformation toughening and on aging has been acquired on Y-TZP.

3Y-TZP possesses the best combination of toughness and strength among oxide ceramics, as a direct benefit of fine grain size (sintering fully dense, submicron 3Y-TZP is much easier to achieve than for other oxide ceramics) and transformation toughening. Being easy to polish, 3Y-TZP became in the 1990s the natural candidate for the fabrication of ceramic hip joints. Unfortunately, all these advantages are today balanced with its lack of stability in the presence of water. Ce-TZP (typically 10 and 12 mol% Ce-TZP) does not possess such hardness and strength as 3Y-TZP mainly because its grain size is larger. However, being stabilized by a tetravalent cation, the t-phase can transform under stress (transformation toughening) but remains essentially stable in the presence of water (no aging *in vivo* for realistic durations).

1.106.3.4. Zirconia-Dispersed Ceramics

Taking advantage of phase transformation toughening is also possible in composites containing particles of transformable zirconia tetragonal phase in a nontransformable matrix. This is possible if the size of the zirconia particles ranges between two critical values: the highest is the size for spontaneous transformation to the m-phase during cooling, and the lowest is the size for which no transformation to the m-phase is possible (even under stress). Both critical sizes depend on the stiffness of the matrix, the amount of zirconia particles, and the composition of the zirconia particles. Generally zirconia particle size of a few tenths of microns is adequate.

PSZ materials can be considered one of these composites, where the nontransformable matrix is made of cubic zirconia. But the most used is undoubtedly zirconia-toughened alumina (ZTA) (in which tetragonal zirconia particles are embedded in an alumina matrix, as schematically shown in Figure 4).

In such composites, zirconia particles have to be stabilized in the tetragonal phase. This can be done classically by using a stabilizing oxide (yttria of course, but ceria is more widespread).[35,36] Another approach is to let the high stiffness alumina matrix stabilize pure zirconia particles (simply by increasing ΔU_{SE}): the composites can then be completely insensitive to aging, as the zirconia phase is devoid of oxygen vacancies.[37] Of course, the stability of the tetragonal phase is more difficult to handle: on the one hand, small zirconia particle size and no agglomeration of the zirconia particles are mandatory to retain the tetragonal phase; on the other hand, too small t-zirconia particles will not transform even under stress, leading to a composite with poor mechanical properties.

1.106.4. The Use of Zirconia as a Biomaterial: Current State of the Art

1.106.4.1. The Use of Zirconia in Orthopedics: From Yttria-Doped Zirconia to Zirconia-Toughened Alumina

The story of zirconia in orthopedics started with Mg-PSZ in 1984, mainly in the United States and Australia, without reaching large-scale clinical application. The rapid shift toward 3Y-TZP in the late 1980s was due to a much better strength, lower grain size resulting in supposedly better wear properties, and technical advantages in terms of sintering. 3Y-TZP possesses strengths at least twice that of Mg-PSZ and grain sizes as low as 0.3 μm even under standard sintering conditions (as compared to 30–40 μm for the cubic grains of Mg-PSZ), and can be processed at temperatures as low as 1400 °C, versus 1800 °C for Mg-PSZ. Besides, ultra-pure 3Y-TZP powders were available in large quantities, while Mg-PSZ powders often contained silica impurities. One must remember that at that time, aging of Y-TZP had already been discovered, as described by Kobayashi at 250 °C, but not considered as relevant for orthopedic applications.

From the early 1990s to 2002, more than 600 000 zirconia hip joint heads were implanted worldwide. Main producers were Saint-Gobain Desmarquest in France, Kyocera in Japan, Metoxit in Switzerland, and Morgan Technical ceramics in the United Kingdom. If in the first decade, 3Y-TZP was considered the 'new ceramic solution' by many orthopedic surgeons, several critical issues finally put a stop to its use in the early 2000s. First, in May 1997, the US Food and Drug Administration (FDA) reported on the critical effect of the standard steam sterilization procedure (134 °C, 2 bar pressure) on the surface roughness of zirconia implants for the first time. This occurred because 'exposure to steam and elevated temperatures may lead to a phase transformation in the crystal structure of the zirconia material.' FDA and other sanitary agencies over the word then strongly advised against resterilization of zirconia femoral heads in hospitals. Second, in August 2001, the Therapeutic Goods Administration in Australia issued a 'hazard alert' on 'spontaneous disintegration of zirconia femoral heads' in some batches manufactured in a new tunnel furnace in 1998 by Saint-Gobain Desmarquest. More than 800 failures were reported, most of them occurring 12–36 months after implantation. In some specific batches (i.e., TH 2957 or TH 93038), the failure rate was higher than 30%. All sanitary agencies recommended immediate recall of all unimplanted zirconia femoral head prostheses manufactured by Saint-Gobain Desmarquest and advised orthopedic surgeons to inform all patients implanted with a Saint-Gobain Desmarquest Prozyr® head prosthesis that they should seek urgent medical attention. The fabrication of Prozyr® heads (90% of the market of zirconia heads), even with the reliable batch furnace (BH) process, was stopped in early 2002. The different panels of experts constituted by Saint-Gobain, orthopedic companies, and sanitary agencies later clearly demonstrated that the 'spontaneous disintegrations' were in fact failures due to an accelerated aging in these particular batches, related to a lack of densification in the center of the heads. More information on these process-related failures can be found in Chevalier *et al.*[11,24] These dramatic events shed light on the strong

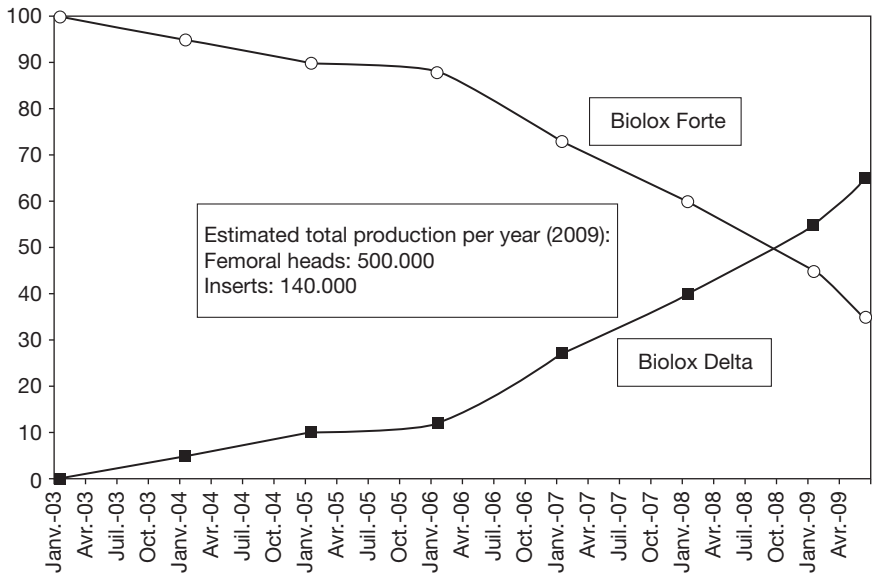

Figure 6 Evolution of the production (in %) of Biolox Forte® (Alumina) and Biolox Delta® (zirconia-toughened alumina) during the past 7 years.

influence of process parameters on the stability of zirconia *in vivo* and the question of the 'natural' aging of 'good' heads remained open.[7] Recent reports unfortunately suggest that significant aging occurs even *in vivo* at the surface of implants processed under 'normal' conditions, leading to increased wear and aseptic loosening.

Concurrent to the 'fall' of zirconia, the need for high mechanical performance ceramic for femoral heads and other orthopedic components led to the development of ZTA composites. Starting from the early 2000s, being more or less confidential until 2005, this material took a more and more important part of the ceramic heads market. The market share of ZTA femoral heads is now roughly equivalent to that of alumina heads and is still growing. Biolox Delta® produced by Ceramtec AG (which is a ZTA material containing strontium platelets and chromium oxide as reinforcing agents), represents two-thirds of their ceramic production for orthopedic devices (see Figure 6). ZTA heads compensate for their higher price by increased mechanical performances as compared to alumina heads (thus allowing more critical designs) and better stability as compared to zirconia. The microstructure of Biolox Delta® together with two examples of products not realizable with alumina are shown in Figure 7. Note the pink color due to the addition of some chromium oxide in the composition. Although it should be emphasized that the stability of such yttria-stabilized ZTA composites versus hydrothermal aging may not be complete,[38,39] to our knowledge no *in vivo* study has yet demonstrated any critical effect.



Figure 7 Two examples of ceramic orthopedic products processed with Biolox Delta® to meet highly demanding applications (top: thin-walled insert; bottom: knee joint). Courtesy: Meinhard Kuntz, Ceramtec AG.

1.106.4.2. The Use of Zirconia in the Dental Field: From Dental Restoration to Implants

In addition to mechanical specifications, dental applications require esthetic properties. For example, strength of more than 500 MPa is generally required for posterior crowns and must be accompanied by translucency and appropriate color. The white to ivory color of most oxide ceramics gives them a clear advantage versus metals, which is the reason why metal-free dental prosthetic restorations have been strongly developed in the past 10 years. It is assumed (even if difficult to quantify) that 15 000–20 000 zirconia restorations are made every day. Indeed, metal-free restorations preserve soft tissue color closer to the natural one than porcelain fused to metal restorations. Moreover, ceramics do not suffer corrosion and/or galvanic coupling as do metals. The clinical demand for all-ceramic

restoration is increasing and ceramics are becoming important restorative materials in dentistry. Y-TZP ceramics possess the best combination of mechanical and esthetical properties among polycrystalline oxide ceramics. 3Y-TZP ceramics with a translucency reaching 12–15% are available,[40] and their color is easily adjustable by doping, for example, with iron or rare earth, meeting the demand for long-lasting, natural-like restoration. In addition, it cannot be underemphasized that 3Y-TZP can be easily shaped by CAD/CAM process.[41,42] Basically, a wax model of the patient's teeth is made and 3D measurements of the model are entered in a computer. These data are then used to control the precise machining necessary to obtain pieces with the right shape. The machining can be done either on presintered[43–45] or on fully dense zirconia blocks.[46] By presintered 'blanks,' we mean zirconia blocks thermally treated so as to form necks between the zirconia grains in the first sintering stage, thus being much stronger than green bodies but much easier to machine than fully dense pieces. Presintering is generally performed around 1100 °C, leading to a density of roughly 55%. The shrinkage that occurs during sintering imposes to machine presintered pieces with dimensions approximately 20% larger than the final dimensions; thus the final dimensions (after sintering) are not fully controlled. Machining of fully dense blocks is technically more difficult, wears the machining hardware at a much higher rate, and may introduce microcracks in the material.[47] However, it offers higher precision and simpler thermal treatments as only one-step sintering is sufficient. For technical (and economical) reasons, CAD/CAM on presintered blanks is now most often preferred. Most current zirconia restorations are veneered with a glass-ceramic to achieve perfect matching with natural teeth. An example is shown in **Figure 8**. However, the translucency and colors reached today by some zirconia offer the possibility to develop unveneered restorations in the future, in which zirconia ensures both mechanical functions and esthetical properties.

The long-term clinical success of 3Y-TZP for dental restorations has recently led several companies to develop zirconia dental implants as an alternative to the 'gold standard' titanium or titanium alloys. If the esthetic interest of zirconia for restorations or even abutments is indisputable, it appears less clear for implants, inserted in the jaw, except in some clinical cases (e.g., front teeth and 'gingival smile'). Expected advantages are a perfect resistance to galvanic corrosion (which is discussed without consensus for titanium) and the possibility to avoid the presence of any metal in the mouth. The osteointegration of zirconia is as good as titanium, thanks to the oxide nature of the surface,[48] but certainly not intrinsically better. The search for a still better integration has led researchers and companies to develop methods to increase surface roughness and/or to create microporosity. Among them, we may cite sandblasting,[49] chemical etching,[48] spraying of a bioactive phase, or coating by a porous zirconia layer. The development of zirconia for dental implants is young, and there is a dearth of clinical studies assessing its long-term reliability versus titanium.



Figure 8 Hybrid (crown and inlay retained), full-ceramic three-unit bridge showing the zirconia core and the veneering, esthetic layer. Reproduced from Höland, W.; Schweiger, M.; Watzke, R.; Peschke, A.; Kappert, H. *Expert Rev. Med. Devices* **2008**, *5*, 729–745, with permission of Expert Reviews Ltd.

If aging has been very well documented in orthopedic applications, as clearly controlling the lifetime of implants, the lack of studies for dental applications is striking. Even though a few general papers devoted to dental zirconia underline the need to 'keep in mind that some forms of zirconia are susceptible to aging and that processing conditions can play a critical role on the LTD of zirconia,'[50] the problem of aging in dental zirconia is still underemphasized so far. In part, this is due to the availability of new aging resistant 3Y-TZP, such as TZ3Y-E from Tosoh. It is also certainly due to a lack of exchanges from one community to another. The aging consequences are much less dramatic in dental applications, especially when restorations are concerned, but large-scale failure events such as those of Prozyr® heads in 2001 would be a critical issue for the material and ceramics in general. A recent paper by Lughi and Sergo[51] critically reviews the relevant aspects of aging in dentistry and provides some engineering guidelines for the use of zirconia as dental materials.

We have to keep in mind that every step of the process is influencing the microstructure, hence the stability of zirconia versus aging. The trends followed by companies to obtain highly translucent zirconia (sintered at high temperatures, with large grains and sometimes partially cubic) or porous surfaces to enhance bone in-growth or chemical and mechanical treatments at the surface (in the company, the dental laboratory or by the clinician himself) will inevitably affect its stability.

The bad story of 3Y-TZP in the orthopedic field has had at least one positive output: the aging mechanisms are now well understood and several tools are now available to assess the resistance of a given zirconia to aging. We recommend, for example, the use of XRD combined with accelerated aging tests in autoclave to systematically assess the stability of process/product combination. In parallel, the search for aging-free and robust zirconia must be pursued.

1.106.5. Future Directions

1.106.5.1. Tough, Strong, and Stable Zirconia Ceramics and Composites: The Necessary Challenge

The differences observed both *in vitro* and *in vivo* from one zirconia to another have shown that some 3Y-TZP zirconia products behave well. It is difficult to talk about 'aging-free' zirconia as the transformation occurring upon aging consists of a 'natural' return to the monoclinic equilibrium state.

However, the transformation kinetics can be much affected by microstructural issues and they can be sufficiently low to avoid any problem during the lifetime of the product. Recent revision of the ISO standard for 3Y-TZP (ISO 13356, revised in 2008) now includes the critical issue of aging and accelerated tests to assess the long-term reliability of a given zirconia. Such accelerated tests are mandatory before launching a given 3Y-TZP to the market. They are simple: 1 h of autoclave treatment at 134 °C has roughly the same effect as 2–4 years *in vivo*[22]; 5 h steam sterilization avoids heavy and long experiments to assess the aging sensitivity of a given zirconia prior to commercialization. XRD analysis was traditionally used to follow quantitatively the transformation. More sensitive methods were proposed in recent years. In particular, optical interferometer and atomic force microscopy, generally used for roughness measurements, are powerful tools to quantify the first stages of aging. Raman spectroscopy is also a powerful tool to monitor transformations at the surface or even in-depth and transformation-induced stresses.[52] Associated with standard scanning electron microscopy and XRD analysis, they should be conducted also for the scientific analysis of explanted materials. 3Y-TZP as a dental material should benefit from these new developments and from the knowledge acquired by scientists on this material over the last 10 years as a result of the unfortunate problems encountered in orthopedics. On the other hand, it seems clear that the strong negative events in orthopedics have definitively put an end to 3Y-TZP in this field and other options must be found. It has to be said that the issue of aging stands to the use of yttria as a dopant. Yttrium, as a trivalent ion, creates oxygen vacancies that help hydroxyl group diffusion in the lattice. Ceria-doped zirconia ceramics exhibit superior toughness (up to 20 MPa $\sqrt{m}$) and reduced aging sensitivity (due to the tetravalent character of cerium ion). There is thus still a door open for zirconia ceramics improved with a good combination of toughness and stability. The major drawbacks of Ce-TZP ceramics as compared to Y-TZP are the lower strength (typically 600 MPa as compared to 1000 MPa for Y-TZP) and the lack of translucency. Both aspects are certainly related to the difficulty of producing Ce-TZP with a grain size as small as that of 3Y-TZP. Grain size of (almost) fully dense Ce-TZP generally lies above 1.5–2 µm, when 3Y-TZP can exhibit grain size lower than 0.5 µm with full density. Efforts should be made to process Ce-TZP with sufficiently high density and small grain size to develop tough, strong, and stable zirconia ceramics. Unfortunately tetravalent Ce^{4+} is reduced to Ce^{3+} under reducing atmosphere, leading again to stability problems. Therefore, innovative sintering techniques such as spark plasma sintering or even hot isostatic pressing are hardly applicable to reduce grain size and improve densification. Composites, based on Ce-TZP with another oxide, may be a promising alternative at least to refine their microstructure and improve their strength (unfortunately, they will remain opaque). This is the case of Ce-TZP–alumina composites.[35,36] One approach to avoid oxygen vacancies introduced by yttria doping is to select co-dopants and to combine trivalent and pentavalent ions to minimize the total concentration of vacancies required for charge compensation. Works have focused on Y^{3+}/Nb^{5+}[53] or Y^{3+}/Ta^{5+}[54] co-doping. The resistance to LTD of equimolar $YO_{1.5}$–$TaO_{2.5}$-stabilized tetragonal ZrO_2 ceramics in air has been demonstrated to be highly superior to that of the standard 3Y-TZP. However, further effort is required on the new co-doped zirconia ceramics before going for practical use in medical devices. Indeed, not only aging, but also toughness, strength, wear resistance (orthopedics), and esthetic properties (dental) are required for such applications.

Composites, based on the combination of zirconia with another oxide, may be clearly the way to benefit from zirconia transformation toughening without the major drawback associated with its transformation under steam or body fluid condition. In the recent literature concerning alumina–zirconia composites for biomedical applications, different compositions have been tested, from the zirconia-rich to the alumina-rich side. Major ceramic companies are developing such materials and the composites developed may be ATZ (alumina-toughened zirconia) or ZTA (zirconia-toughened alumina). ATZ composites are a combination of 3Y-TZP and alumina. They are therefore sensitive to aging even if the kinetics are significantly slower than that of 3Y-TZP as a monolith.[55] The impact of the transformation is also less negative, as roughness is not strongly affected even after long duration of aging. ZTA are either a combination of undoped or yttria-doped zirconia with alumina. Being the minor phase, the content of Y_2O_3 in zirconia can be lowered. It depends on the zirconia content: the larger the zirconia content, the larger is the amount of Y_2O_3 needed. Undoped zirconia can be stabilized in a zirconia matrix provided the grain size and the zirconia content are sufficiently low. Stabilization is possible thanks to the stiff alumina matrix, but high zirconia contents cannot be reached (tensile stresses due to thermal mismatch balancing the benefit of the stiff matrix). The optimum zirconia content for high toughness stands around 10 vol.%.[56] With such compositions, toughness higher than 3Y-TZP and full stability are achieved. Very few studies have been devoted to aging in ZTA systems, but they show that, even if limited, some degree of degradation can be observed, depending on microstructural features. As an example, aging may be significant in a 3Y-TZP–alumina composite, above 16 vol.% zirconia.[57] This critical content is related to the percolation threshold above which a continuous path of zirconia grains allows transformation to proceed. The presence of zirconia aggregates, especially if the zirconia is stabilized with yttria, should also be avoided.[58] Biolox Delta®, which is an advanced version of ZTA composites produced by Ceramtec and the new standard in orthopedics, is not fully 'aging free.'[38] Accelerated aging tests and extrapolations toward *in vivo* situations predict a slow transformation of Biolox Delta® products, and we might foresee an increase of monoclinic content from 10 to 15 vol.% in heads before implantation to 15–25 vol.% after 10 years. There is a dearth of retrieval analysis performed on Biolox Delta® heads to assess this issue and give a clear indication of *in vivo* kinetics. This is fortunately because of the very low failure rate associated with Biolox Delta®. Of importance also is the mechanism by which the transformation proceeds as compared to that in 3Y-TZP monoliths and the consequences of the transformation: the composite does not show large surface uplifts, as it is the case for 3Y-TZP and no loss in strength is observed even after long aging treatments, equivalent to 40 years *in vivo*.[38]

In conclusion, aging and its consequences must be investigated for each specific zirconia-containing material, without prior speculative assumptions, as kinetics and impacts may

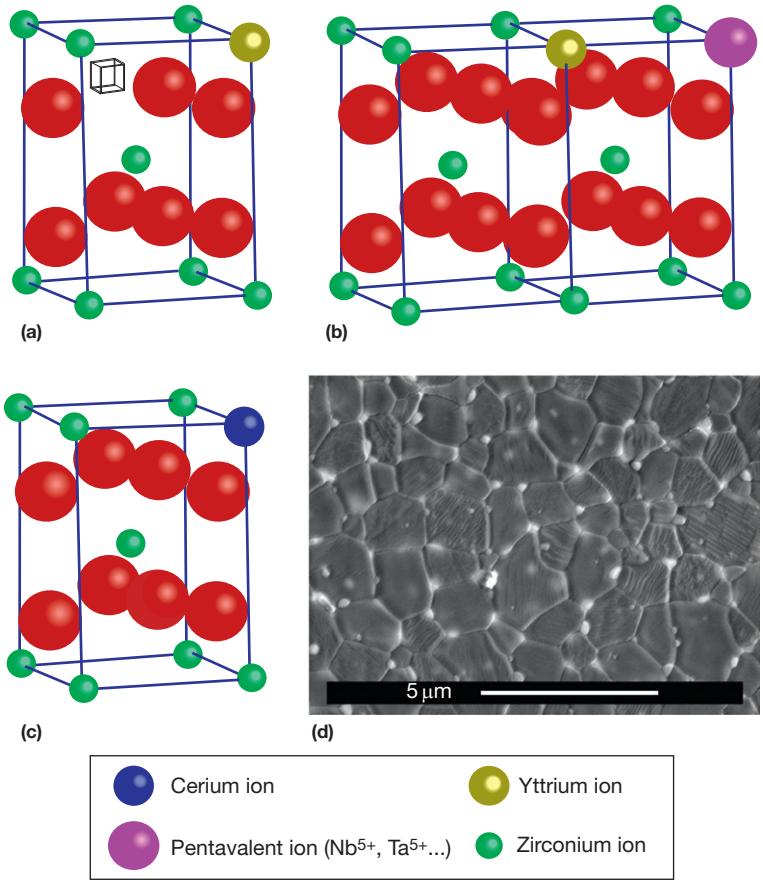

Figure 9 The search for tough and stable zirconia-based ceramics: from (a) yttria-stabilized zirconia (with oxygen vacancies) toward (b) zirconia stabilized by a combination of tri- and pentavalent ions or (c) ceria-doped zirconia ceramics or composites or (d) zirconia-toughened alumina.

vary from one composition to another. It appears also that there is no commercial zirconia-based material today fully free of aging. Such tough, strong, and stable zirconia ceramics and composites are options for the next decade. They are schematically presented in Figure 9.

1.106.6. Conclusion

Among biomaterials, biomedical grade zirconia has led to a major controversy among scientists, industrialists, and clinicians. On the one hand, biomedical grade zirconia exhibits the best mechanical properties of oxide ceramics; this is the consequence of phase transformation toughening, which increases its crack propagation resistance. On the other hand, because of this ability to transform, zirconia is prone to aging in the presence of water: this has been unfortunately verified *in vivo* with some critical consequences. These two sides of zirconia have been described here.

3Y-TZP as a monolithic ceramic has disappeared from the orthopedic field because of aging-related failure events in some particular products. In the absence of any clinical report of aging in dental applications, 3Y-TZP still has a strong potential as a biomaterial, because of its excellent mechanical and esthetic properties. Because scientists and companies are now aware of aging and because of the improvement in the monitoring of the degradation, one should expect that no critical issue appears in this field in the future, provided sufficient attention is given to it.

1.106.7. Further Reading

This short chapter highlights the two major aspects of zirconia ceramics: phase transformation toughening beneficial for mechanical properties and aging (or LTD) that can be considered as its Achilles heel. More in-depth understanding of transformation toughening is possible from the book 'Transformation Toughening of Ceramics,' from Green *et al.*[2] and from the recent review paper from Kelly and Rose.[14] The authors of the current chapter have recently published a review on aging and its negative impact on orthopedic implants[24] and on the two sides of the t–m phase transformation in a feature paper.[11,38] Clinical data and retrieval analysis may also be obtained from Clarke *et al.*[25] Review papers on the use of zirconia in dental applications can be found in Denry and Kelly[50] and Höland *et al.*[41]

References

1. Garvie, R. C.; Hannink, R. H.; Pascoe, R. T. *Nature* **1975**, *258*, 703–704.
2. Green, D. J.; Hannink, R. H. J.; Swain, M. V. *Transformation Toughening of Ceramics*; CRC: Boca Raton, FL, 1989.

3. Lange, F. F. *J. Mater. Sci.* **1982**, *17*, 225–234.
4. McMeeking, R. M.; Evans, A. G. *J. Am. Ceram. Soc.* **1982**, *65*, 242–246.
5. Garvie, R. C.; Urbani, C.; Kennedy, D. R.; McNeuer, J. C. *J. Mater. Sci.* **1984**, *19*, 3224–3228.
6. Piconi, C.; Maccauro, G. *Biomaterials* **1999**, *20*, 1–25.
7. Chevalier, J. *Biomaterials* **2006**, *27*, 535–543.
8. Rahaman, M. N.; Yao, A.; Bal, B. S.; Garino, J. P.; Ries, M. D. *J. Am. Ceram. Soc.* **2007**, *90*, 1965–1988.
9. Manicone, P. F.; Rossi Iommetti, P.; Raffaelli, L. *J. Dent.* **2007**, *35*, 819–826.
10. Kobayashi, K.; Kuwajima, H.; Masaki, T. *Solid State Ionics* **1980**, *3*(4), 489–493.
11. Chevalier, J.; Gremillard, L.; Virkar, A. V.; Clarke, D. R. *J. Am. Ceram. Soc.* **2009**, *92*, 1901–1920.
12. Ruff, O.; Ebert, F. *Z. Anorg. Allg. Chem.* **1929**, *180*, 19–41.
13. Deville, S.; Guenin, G.; Chevalier, J. *Acta Mater.* **2004**, *52*, 5697–5707.
14. Kelly, P. M.; Rose, L. R. F. *Prog. Mater. Sci.* **2002**, *47*, 463–557.
15. Garvie, R. C. *J. Phys. Chem.* **1978**, *82*, 218–224.
16. Pitcher, M. W.; Ushakov, S. V.; Navrotsky, A.; *et al. J. Am. Ceram. Soc.* **2005**, *88*, 160–167.
17. Chevalier, J.; Olagnon, C.; Fantozzi, G. *J. Am. Ceram. Soc.* **1999**, *82*, 3129–3138.
18. Chevalier, J.; De Aza, A. H.; Gremillard, L.; Zenati, R.; Fantozzi, G. *Mater. Eng.* **2001**, *12*, 159–178.
19. Schubert, H.; Frey, F. *J. Eur. Ceram. Soc.* **2005**, *25*, 1597–1602.
20. Guo, X.; Schober, T. *J. Am. Ceram. Soc.* **2004**, *87*, 746–748.
21. Gremillard, L.; Chevalier, J.; Epicier, T.; Deville, S.; Fantozzi, G. *J. Eur. Ceram. Soc.* **2004**, *24*, 3483–3489.
22. Chevalier, J.; Cales, B.; Drouin, J. M. *J. Am. Ceram. Soc.* **1999**, *82*, 2150–2154.
23. Deville, S.; Chevalier, J. *J. Am. Ceram. Soc.* **2003**, *86*, 2225–2227.
24. Chevalier, J.; Gremillard, L.; Deville, S. *Annu. Rev. Mater. Res.* **2007**, *37*, 1–32.
25. Clarke, I. C.; Manaka, M.; Green, D. D.; *et al. J. Bone Joint Surg. A* **2003**, *85*, 73–84.
26. Gremillard, L. Ph.D. Thesis, Institut National des Sciences Appliquées de Lyon, 2002.
27. Fabris, S.; Paxton, A. T.; Finnis, M. W. *Acta Mater.* **2002**, *50*, 5171–5178.
28. Li, P.; Chen, I. W.; Penner-Hahn, J. E. *J. Am. Ceram. Soc.* **1994**, *77*, 118–128.
29. Li, P.; Chen, I. W.; Penner-Hahn, J. E. *J. Am. Ceram. Soc.* **1994**, *77*, 1281–1288.
30. Nagl, M. M.; Lhanes, L.; Fernandez, R.; Anglada, M. In *Fracture Mechanics of Ceramics*; Bradt, R. C., *et al.* Eds.; Plenum: New York, 1996; Vol. 12, pp 61–76.
31. Roy, M. E.; Whiteside, L. A.; Katerberg, B. J.; Steiger, J. A. *J. Biomed. Mater. Res.* **2007**, *83A*, 1096–1102.
32. Roy, M. E.; Whiteside, L. A.; Katerberg, B. J.; Steiger, J. A.; Nayfeh, T. *Clin. Orthop. Relat. Res.* **2007**, *465*, 220–226.
33. Sato, T.; Endo, T.; Shimada, M.; Mitsudome, T.; Otabe, N. *J. Mater. Sci.* **1991**, *26*, 1346–1350.
34. Swain, M. V. *J. Mater. Sci. Lett.* **1985**, *4*, 848–850.
35. Benzaid, R.; Chevalier, J.; Saâdaoui, M.; *et al. Biomaterials* **2008**, *29*, 3636–3641.
36. Tanaka, K.; Tamura, J.; Kawanabe, K.; *et al. J. Biomed. Mater. Res.* **2002**, *63*, 262–270.
37. Deville, S.; Chevalier, J.; Fantozzi, G.; *et al. J. Eur. Ceram. Soc.* **2003**, *23*, 2975–2982.
38. Chevalier, J.; Grandjean, S.; Kuntz, M.; Pezzotti, G. *Biomaterials* **2009**, *30*, 5279–5282.
39. Pezzotti, G.; Yamada, K.; Sakakura, S.; Pitto, R. P. *J. Am. Ceram. Soc.* **2008**, *91*, 1199–1206.
40. Baldissara, P.; Llukacej, A.; Ciocca, L.; *et al. J. Prosthet. Dent.* **2010**, *104*, 6–12.
41. Höland, W.; Schweiger, M.; Watzke, R.; Peschke, A.; Kappert, H. *Expert Rev. Med. Devices* **2008**, *5*, 729–745.
42. Ritzberger, C.; Appel, E.; Höland, W.; Peschke, A.; Rheinberger, V. M. *Materials* **2010**, *3*, 3700–3713.
43. Filser, F.; Kocher, P.; Weibel, F.; Luthy, H.; Scharer, P.; Gauckler, L. J. *Int. J. Comput. Dent.* **2001**, *4*, 89–106.
44. Papanagiotou, H. P.; Morgano, S. M.; Giordano, R. A.; Pober, R. *J. Prosthet. Dent.* **2006**, *96*, 154–164.
45. Suttor, D.; Bunke, K.; Hoescheler, S.; Hauptmann, H.; Hertlein, G. *Int. J. Comput. Dent.* **2001**, *4*, 195–206.
46. Besimo, C. E.; Spielmann, H. P.; Rohner, H. P. *Int. J. Comput. Dent.* **2001**, *4*(243), 262.
47. Luthardt, R. G.; Holzhuter, M. S.; Rudolph, H.; Herold, V.; Walter, G. A. *Dent. Mater.* **2004**, *20*, 655–662.
48. Depprich, R.; Zipprich, H.; Ommerborn, M.; *et al. Head Face Med.* **2008**, *4*, 30.
49. Yamashita, D.; Machigashira, M.; Miyamoto, M.; *et al. Dent. Mater. J.* **2009**, *28*, 461–470.
50. Denry, I.; Kelly, R. *Dent. Mater.* **2008**, *24*, 299–307.
51. Lughi, V.; Sergo, V. *Dent. Mater.* **2010**, *26*, 807–820.
52. Pezzotti, G.; Porporati, A. *J. Biomed. Opt.* **2004**, *9*, 372–384.
53. Kim, D. J.; Jung, H. J.; Jang, J. W.; Lee, H. L. *J. Am. Ceram. Soc.* **1998**, *8*, 2309–2314.
54. Shen, Y.; Clarke, D. R. *J. Am. Ceram. Soc.* **2010**, *93*, 2024–2027.
55. Schneider, J.; Begand, S.; Kriegel, R.; Kaps, C.; Glien, W.; Oberbach, T. *J. Am. Ceram. Soc.* **2008**, *91*, 3613–3618.
56. De Aza, A. H.; Chevalier, J.; Fantozzi, G.; Schehl, M.; Torrecillas, R. *J. Am. Ceram. Soc.* **2003**, *86*, 115–120.
57. Pecharroman, C.; Bartolome, J. F.; Requena, J.; *et al. Adv. Mater.* **2003**, *15*, 507–511.
58. Gutknecht, D.; Chevalier, J.; Garnier, V.; Fantozzi, G. *J. Eur. Ceram. Soc.* **2007**, *27*, 1547–1552.

1.107. Carbon and Diamond

R D Boehm, C Jin, and R J Narayan, University of North Carolina and North Carolina State University, Raleigh, NC, USA

© 2011 Elsevier Ltd. All rights reserved.

1.107.1.	**Introduction**	110
1.107.2.	**Pyrolytic Carbon**	111
1.107.2.1.	Introduction	111
1.107.2.2.	Production of Pyrolytic Carbon	112
1.107.2.2.1.	Fluidized-bed production of pyrolytic carbon	112
1.107.2.2.2.	Tumbling and stationary bed production of pyrolytic carbon	112
1.107.2.3.	Mechanical Properties of Pyrolytic Carbon	113
1.107.2.4.	Biological Properties and Biomedical Applications of Pyrolytic Carbon	113
1.107.2.4.1.	Cardiovascular applications of pyrolytic carbon	113
1.107.2.4.2.	Orthopedic applications of pyrolytic carbon	114
1.107.2.4.3.	Shortcomings of pyrolytic carbon	114
1.107.3.	**Diamond-Like Carbon**	115
1.107.3.1.	Introduction to DLC	115
1.107.3.2.	Production and Characterization of DLC	115
1.107.3.2.1.	Raman spectroscopic characterization of DLC	116
1.107.3.2.2.	Nuclear magnetic resonance and electron energy loss spectroscopy of DLC	116
1.107.3.3.	Properties of DLC	116
1.107.3.3.1.	Electronic properties of DLC	116
1.107.3.3.2.	Mechanical properties of DLC	117
1.107.3.4.	Applications and Biological Properties of DLC	117
1.107.3.4.1.	Orthopedic applications of DLC	117
1.107.3.4.2.	Cardiovascular applications of DLC	118
1.107.3.4.3.	Additional applications of DLC	119
1.107.4.	**Microcrystalline, Nanocrystalline, and Ultrananocrystalline Diamond**	119
1.107.4.1.	Introduction to MCD, NCD, and UNCD	119
1.107.4.2.	Production of MCD, NCD, and UNCD	120
1.107.4.2.1.	CVD and film growth	120
1.107.4.2.2.	Hot-filament CVD of diamond films	121
1.107.4.2.3.	Microwave PECVD of diamond films	122
1.107.4.2.4.	Additional diamond film production methods	122
1.107.4.3.	Mechanical and Biological Properties of MCD, NCD, and UNCD	122
1.107.4.4.	Biomedical Applications of MCD, NCD, and UNCD	123
1.107.4.4.1.	Biosensor applications	123
1.107.4.4.2.	Orthopedic applications	123
1.107.4.4.3.	Further biomedical applications	124
1.107.5.	**Summary of Carbon and Diamond**	124
References		124

Glossary

Carbon The number six element in the periodic table. It consists of six valence electrons, which are arranged in the $1s^2 2s^2 2p^2$ electronic configuration. Carbon can be found in a variety of forms, including in nearly completely amorphous materials and in entirely crystalline materials.

Chemical vapor deposition (CVD) The process in which a high-purity material is deposited onto a substrate as a result of a chemical reaction or as a result of decomposition of a volatile precursor.

Diamond-like carbon (DLC) A variety of amorphous carbon films, which contain sp^3-hybridized atoms. In addition, these materials may contain varying degrees of hydrogenation as well as alloying materials.

Fluidized-bed reactor A furnace chamber in the form of a vertical cylinder, which contains ceramic particles suspended in a fluid-like form by an inert gas. Substrates are suspended on the fluidized bed of particles; coating of the substrate occurs by means of chemical vapor deposition after introduction of a volatile precursor gas.

Microcrystalline diamond (MCD) A crystalline form of carbon containing a high fraction of sp^3-hybridized atoms; grain sizes on the order of 0.5–2.0 μm are observed. It should be noted that sp^2-hybridized atoms as well as

amorphous carbon are commonly observed at the grain boundaries.

Nanocrystalline diamond (NCD) A crystalline form of carbon-containing sp^3-hybridized atoms; grain sizes below 100 nm are observed. This material has a lower degree of sp^3 bonding compared to microcrystalline diamond due to sp^2-hybridized atoms and amorphous carbon at the grain boundaries.

Pyrolysis The thermal decomposition of a substance into more basic compounds. Pyrolysis is the form of decomposition used for chemical vapor deposition of pyrolytic carbon from fullerenes or from hydrocarbon gases.

Pyrolytic carbon A turbostratic form of carbon, which consists of randomly layered graphene sheets that are formed with sp^2-hybridized atoms. Pyrolytic carbon is similar in form to graphite; however, defects in the graphene layers result in kinked sheets or curved sheets.

Thin film Surface coating with a thickness of between a fraction of a micrometer and a few micrometers. Thin films are deposited on substrate materials in order to modify the surface properties of the substrate materials.

Ultrananocrystalline diamond (UNCD) A crystalline form of carbon-containing sp^3-hybridized atoms; grain sizes below 10 nm are observed. Among MCD, NCD, and UNCD, UNCD has the lowest fraction of sp^3-hybridized atoms due to sp^2-hybridized atoms and amorphous carbon at the grain boundaries.

Abbreviations

a-S:H	Hydrogenated amorphous silicon
CVD	Chemical vapor deposition
DLC	Diamond-like carbon
EELS	Electron energy loss spectroscopy
ELAM-1	Endothelial cell adhesion molecule-1
FTIR	Fourier transform infrared
ICAM-1	Intercellular cell adhesion molecule-1
LIBAD	Low incidence beam angle X-ray diffraction
LTI	Low-temperature isotropic
MCD	Microcrystalline diamond
MEMS	Microelectromechanical systems
MPECVD	Microwave plasma-enhanced chemical vapor deposition
MWNT	Multi-walled nanotube
NCD	Nanocrystalline diamond
NMR	Nuclear magnetic resonance
PDMS	Polydimethylsiloxane
PECAM-1	Platelet endothelial cell adhesion molecule-1
PECVD	Plasma-enhanced chemical vapor deposition
PF_4	Platelet factor 4
PLD	Pulsed laser deposition
PMMA	Polymethylmethacrylate
PTFE	Polytetrafluoroethylene
RDF	Radial distribution function
RF PA CVD	Radio frequency plasma-activated chemical vapor deposition
SWNT	Single-walled nanotube
ta-C	Tetrahedral amorphous carbon
ta-C:H	Hydrogenated tetrahedral amorphous carbon
TXB_2	Thromboxane B_2
UHMWPE	Ultrahigh molecular weight polyethylene
ULTI	Ultra-low-temperature isotropic
UNCD	Ultrananocrystalline diamond
UV	Ultraviolet
XPS	X-ray photoelectron spectroscopy

1.107.1. Introduction

Carbon is the sixth most common element found on earth; it is found in greater than 90% of all known chemical substances.[1,2] What makes carbon interesting from a biomaterials standpoint is the range of forms in which it is found. Carbon has two naturally occurring crystalline allotropic forms, graphite and diamond. It can be found in a variety of forms, including entirely amorphous materials and completely crystalline materials.[3] In recent years, fullerene (C_{60}) and carbon nanotube materials have been synthesized; these materials have attracted a significant amount of attention from the research community.

The existence of carbon structures with a variety of physical and chemical properties is attributed to the electronic behavior of the carbon atom. Carbon is the number six element in the periodic table. It contains six electrons, which are arranged in the electronic configuration of $1s^2 2s^2 2p^2$. In the ground state of a carbon atom, two 2p electrons occupy $2p_x^1$ ($m = 1$) and $2p_y^1$ ($m = -1$) states. When a carbon atom forms covalent bonds with other atoms (e.g., hydrogen atoms or other carbon atoms), not only the two 2p electrons but also the 2s electrons may participate in bond formation. The energy gap between the 2s levels and the 2p levels in carbon atoms is only 8 eV. The 2s electron of the carbon atom can be easily excited to the 2p level, forming four unpaired electrons. The four unpaired electrons form chemical bonds with other atoms by means of hybrid orbitals. A hybrid orbital is a linear combination of atomic orbitals. A carbon atom may exhibit one of the three types of hybrid orbitals: sp-hybridized orbitals, sp^2-hybridized orbitals, and sp^3-hybridized orbitals. In sp orbital hybridization, mixing of the s orbital and the p_x orbital takes place; two equivalent sp hybrid orbitals with an angle of 180° result. Two of the four unpaired electrons occupy the two hybrid sp orbitals; the other two electrons occupy the 2p orbitals. The sp hybrid orbitals can form two σ bonds. The other two 2p electrons can give two relatively weak π bonds. In the sp^2 hybridization, three electrons in the s, p_x, and p_y orbitals form three hybrid orbitals.

Three of the four unpaired electrons are in the hybrid orbitals and the other one is in the 2p orbital. The angle between the orbitals is 120°. Three sp^2 hybrid orbitals create three σ bonds; one 2p electron gives a π bond. All of the four unpaired electrons of the carbon atom participate in sp^3 hybridization by forming four sp^3 hybrid orbitals in the arrangement:

$$\left.\begin{aligned}\varphi_1 &= s + p_x + p_y + p_z\\ \varphi_2 &= s + p_x - p_y - p_z\\ \varphi_3 &= s - p_x + p_y - p_z\\ \varphi_4 &= s - p_x - p_y + p_z\end{aligned}\right\} \quad [I]$$

The angle between the sp^3 orbitals is 109.5°. The four sp^3 orbitals give four strong σ bonds when the carbon atom creates covalent bonds with other atoms. The three types of orbital hybridizations for a carbon atom are schematically illustrated in Figure 1.

The hybrid orbitals of a carbon atom commonly form σ bonds when carbon atoms undergo chemical bonding with other atoms. The electrons in the 2p orbitals contribute to π bonds. In acetylene (C_2H_2), the two hybrid sp orbitals of the carbon atom form two σ bonds with one hydrogen atom and another carbon atom. The two singly occupied 2p electrons form two π bonds between the two carbon atoms (H–C≡C–H).

One of the carbon polymorphs is graphite. The crystalline structure of graphite is hexagonal (6/m 2/m 2/m), with a lattice parameter of $a = 2.461$ Å and $c = 6.708$ Å. In each hexagonal plane, three unpaired electrons of a carbon atom form three σ bonds with the three nearest neighbor carbon atoms by means of sp^2 hybrid orbitals. These σ bonds are stronger than those in diamond. The electrons in the p_z orbitals form distributed π bonds within the hexagonal sheet. The π bonds are weaker and the electrons forming these bonds are delocalized; due to this electronic arrangement, graphite is an electrically conducting material. The hexagonal sheets are connected with one another through weak Van der Waals forces. The weak Van der Waals forces facilitate slipping of graphene sheets past one another. On account of this arrangement, graphite is a soft material. In addition, the layered structure of graphite allows it to exhibit lubricating behavior.

Diamond is another polymorph of carbon. The lattice structure is named diamond structure, with a lattice constant of 3.567 Å. Diamond is the hardest known material. The high hardness of diamond comes from its crystalline structure and from the strength of the chemical bonds that hold the carbon atoms together. The carbon atoms within diamond exhibit sp^3 hybridization. The four unpaired electrons of each carbon atom form four σ bonds with the four nearest carbon atoms.

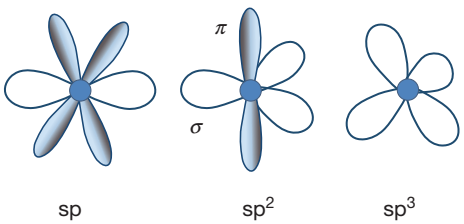

Figure 1 Schematic showing sp, sp^2, and sp^3 hybridization from s orbitals and p orbitals.

The covalent sp^3 bonds of diamond make it extremely hard; the material behaves as a single isotropic covalent molecule.[4] The rigid network of covalent bonds in carbon makes it an excellent material for applications such as cutting or grinding. In addition, the high wear resistance of diamond makes it an attractive material for hip prostheses, knee prostheses, and other joint prostheses.

Fullerenes are another form of crystalline carbon which will be covered extensively in Chapter 5.523, Carbon Nanotubes: Applications for *In Situ* Implant Sensors. Buckyballs are a type of fullerene that comprise a family of spheroid or geodesic carbon molecules containing five-membered pentagonal rings and six-membered hexagonal rings. They require 12 pentagonal rings in order for the structure to close into a spheroid. Buckyballs possess a variable number of hexagonal rings.[5] This class of carbon materials has been evaluated for use in a variety of technological applications (e.g., plastic solar cells, donor–acceptor systems, and quantum computing), biological applications (e.g., DNA photocleavage, HIV protease inhibition, neuroprotection, and apoptosis), and medicinal applications (e.g., improvements to magnetic resonance imaging contrast agents and encapsulation of radiopharmaceutical drugs for nuclear medicine).[6] The carbon nanotube is another class of carbon material that is receiving significant interest in the scientific community (see Chapter 3.330, Carbon Nanotube-Based Sensors: Overview). In nanotubes, rolled graphene sheets form cylinders with high length to radius ratios, excellent strength, and unusual electrical properties. Single-walled nanotubes (SWNT) and multi-walled nanotubes (MWNT), which consist of concentric cylinders, have been demonstrated. Carbon nanotubes have numerous technological and biological applications, including uses in nanoelectronics; field emitters; composite materials; and physical, chemical, and biological sensors, among others. Carbon can exist in other allotropes, including amorphous carbon, carbyne, and lonsdaleite.

This chapter focuses on the use of carbon materials in biomedical applications. Specifically, the use of pyrolytic carbon, diamond-like carbon (DLC), microcrystalline diamond (MCD), nanocrystalline diamond (NCD), and ultrananocrystalline diamond (UNCD) in medical applications is described. Pyrolytic carbon is a form of turbostratic carbon formed from pyrolysis of hydrocarbons or fullerene gases. DLC is an amorphous carbon material, which contains sp^3-hybridized carbon atoms; in addition, it may contain a variable amount of hydrogen. MCD, NCD, and UNCD are composed of sp^3-hybridized carbon crystals with microscale or nanoscale grain sizes. The structure, mechanical properties, biological properties, production processes, and biomedical applications of these carbon materials are addressed in detail. While the focus is placed on the use of these carbon materials in thin films and coatings, attention is also given to the general properties of carbon and its applications as a biomaterial.

1.107.2. Pyrolytic Carbon

1.107.2.1. Introduction

Pyrolytic carbon is an allotropic form of carbon that consists of turbostratic graphene sheets. This material is produced via pyrolysis of hydrocarbon precursors. Pyrolytic carbon is a

man-made material that was originally considered for use in biomedical devices over 40 years ago by the company General Atomics.[4] It is primarily utilized as a coating material, which can be applied to substrate materials such as graphite, carbon fibers, and carbon–carbon composites.[5] Types of pyrolytic carbon materials that are commonly used in biomedical engineering applications include low-temperature isotropic (LTI) carbon and ultra-low-temperature isotropic (ULTI) carbon.

Pyrolytic carbon exhibits a turbostratic structure. In this structure, sp^2-hybridized crystals form graphene sheets that are layered in a random manner. In some respects, the structure of pyrolytic carbon resembles that of graphite. Both allotropes are composed of graphene sheets; the graphene sheets in graphite demonstrate consistency in the hexagonal crystal structure throughout each layer. On the other hand, pyrolytic carbon exhibits defects in the lattice structure within the layers. These defects result in curved or kinked sheets. The term 'turbostratic' refers to the kinked or curved crystalline structure of the material layers, which causes larger gap distances between the layers than would be present if the sheets were perfectly parallel. The layer spacing between graphene layers in graphite is 3.35 Å; in comparison, the layer spacing is 3.48 Å in pyrolytic carbon.[4] In a similar manner to graphite, the layered sheets of graphene in pyrolytic carbon are held together by Van der Waals forces. It should be noted that graphite exhibits consistently smooth layers of graphene, which allow the layers to slip past one another and endow graphite with lubricating behavior. On the other hand, the kinks and defects within the graphene layers of pyrolytic carbon prevent the graphene layers from easily slipping past one another. As a result, the strength, hardness, and wear resistance properties of pyrolytic carbon are greater than those of graphite. In addition, pyrolytic carbon exhibits crystallite sizes of 25–40 Å.[4] Small crystallites form during the deposition process; the resulting polycrystalline features exhibit a random orientation. The isotropic behavior of pyrolytic carbon is attributed to the random orientation and the small crystallite sizes of these growth features.

1.107.2.2. Production of Pyrolytic Carbon

The term 'pyrolysis' refers to thermal decomposition of a substance; pyrolytic carbon coatings are produced using this mechanism. This material is formed via thermal breakdown and dehydrogenation of gaseous hydrocarbon or fullerene precursors in an oxygen-free environment. Examples of hydrocarbon precursors that are commonly used in the production of pyrolytic carbon are propane, propylene, acetylene, and methane. In the presence of oxygen, hydrocarbon gases decompose into water and carbon dioxide. By thermally decomposing hydrocarbons in the absence of oxygen, the carbon atoms go through a decomposition cascade in which the carbon atoms from the gaseous precursor can form arrays that exhibit crystallite growth features.[4]

1.107.2.2.1. Fluidized-bed production of pyrolytic carbon

Pyrolytic carbon is commonly deposited on a substrate using what is known as a fluidized-bed reactor. A fluidized-bed reactor consists of a furnace chamber in the shape of a vertical tube that is heated to 1000–2400 °C.[4,7] The fluidized bed is created using ceramic particles within the furnace chamber. A carrier gas (e.g., argon, nitrogen, or helium) is pumped through the chamber, suspending the particles. As the gas flows between the particles, they move throughout the chamber in a fluid-like manner. The hydrocarbon precursor is added to the gas flow, enabling pyrolysis to occur within the furnace. The fluid-like bed of particles provides a mechanism for suspending the substrate material that is to be coated.

The microstructure of pyrolytic carbon is dependent on the fluidized-bed reactor deposition parameters. In particular, the characteristics of the pyrolytic carbon produced from fluidized-bed reactors are affected by the pyrolysis conditions. The variables of interest for controlling the structure of pyrolytic carbon have been discussed by Bokros[3]; they include the nature and concentration of the hydrocarbon precursor, the pyrolysis temperature, the time in which the gaseous precursor is exposed to temperatures that result in pyrolysis, and the ratio of the deposition substrate surface area to the volume of gas in the pyrolysis chamber.

Laminar, isotropic, or granular pyrolytic carbon may form depending on the processing conditions. Generally, laminar structures form at low temperatures and high pressures, granular structures form at high temperatures and low pressures, and isotropic structures fall in the middle range; it should be noted that variations in hydrocarbon gas concentration and the area of the fluidized bed can influence processing parameters.[8] Laminar structures are created due to aligned deposition of planar molecules, which form in the gas phase during pyrolysis.[8] Granular structures with distinct grains form during ordered growth, which are associated with a temperature gradient between the substrate and the decomposing gas, low supersaturation of the gas phase, and high mobility of molecule deposition on the substrate surface.[8] Isotropic pyrolytic carbon forms as a result of random deposition of gas-phase carbon droplets onto the substrate surface; this material is of greatest interest for biomedical applications.[8]

Owing to the high processing temperature, it is difficult to fabricate components entirely made of pyrolytic carbon, and it is not possible to produce thick pieces of pyrolytic carbon that can be machined into desired geometries.[7] As pyrolytic carbon is commonly used in coating form, an acceptable substrate material must be selected that is compatible with chemical vapor deposition (CVD) pyrolysis conditions. A material that is often used as a substrate for pyrolytic carbon coatings is polycrystalline graphite; this material is capable of withstanding the temperatures and pressures associated with the fluidized-bed reactor process. Polycrystalline graphite is a substrate material that can be levitated within the fluidized bed by the ceramic materials; uniform deposition of the pyrolytic carbon coating is possible, as hydrocarbon precursors pyrolyze around the substrate material. This material also exhibits a coefficient of thermal expansion closely matching that of pyrolytic carbon, which results in minimal extrinsic (thermal) stress and good coating adhesion.[7]

1.107.2.2.2. Tumbling and stationary bed production of pyrolytic carbon

Fluidized beds are commonly used to produce pyrolytic carbon.[3,7–13] Production using tumbling beds and stationary beds has also been investigated. Tumbling bed reactors use a rotating

coating chamber that allows the substrate material to move slowly along the chamber wall during rotation. The substrate material tumbles back to a neutral position, allowing coating of the material during collisions with the carbon gas-phase droplets.[14–20] This coating process allows for deposition of isotropic pyrolytic carbon. The bed tumbles at low speeds (0.2–100 rpm).[14–19] Stationary beds have also been used for pyrolytic carbon deposition; in this case, the substrate material is held in an immobile position. While stationary beds may be used for deposition of isotropic pyrolytic carbon,[17] there is greater difficulty in promoting collisions between gas-phase droplets of the carbon species and the substrate material during pyrolysis. As a result, stationary beds often produce pyrolytic carbon with columnar, granular, or filamentous structures that contain soot by-products; these materials exhibit poor mechanical properties in comparison with isotropic pyrolytic carbon.[8,18]

1.107.2.3. Mechanical Properties of Pyrolytic Carbon

Pyrolytic carbon used in biomedical applications must exhibit appropriate mechanical properties, including strength, modulus of elasticity, toughness, hardness, wear resistance, and fatigue resistance. Alterations in pyrolytic carbon-processing parameters may be used to modulate density, porosity, degree of anisotropy, as well as mechanical properties.

A material used in biomedical applications must exhibit sufficient strength to function in the environment in which it is utilized. The flexural strength of pyrolytic carbon, the stress prior to fracture during bending, is high enough to support structural components for various implant applications. It should be noted that the mechanical properties of materials required for an implant will vary depending on the implant application. Table 1 contains a comparison of glassy carbon, vapor-deposited carbon, silicon-doped LTI carbon, as well as LTI pyrolytic carbon, which is the most common type of pyrolytic carbon used in biomedical applications. Silicon is utilized as a doping agent in order to modulate the mechanical properties of pyrolytic carbon.

Table 1 Comparison of properties of low-temperature isotropic (LTI), glassy, and vapor-deposited turbostratic carbons

Property	*Glassy carbon*	*Vapor-deposited carbon*	*LTI carbon*	*LTI carbon with silicon*[a]
Density ($g\,cm^{-3}$)	1.4–1.6[b]	1.5–2.2[c]	1.7–2.2[c]	2.04–2.13
Crystallite size (L_c) (Å)	10–40	8–15	30–40	30–40
Flexural strength, ($\times$ 1000 psi)	10–30[b]	50 to >100[c]	40–80[c]	80–90
Young's modulus ($\times 10^6$ psi)	3.5–4.5[b]	2.0–3.0[b]	2.5–4.0[c]	4.0–4.5
Strain to fracture (%)	0.8–1.3	2.0 to >5.0[c]	1.6–2.1	2.0
Fatigue limit/ fracture strength	1.0	1.0	1.0	1.0
Strain energy to fracture ($\times$ 100 psi)	1–2	>10	4–8	8
Hardness, DPH	150–200[b]	150–250[c]	150–250[c]	230–370[c]

Source: Reprinted from Bokros, J. C. *Carbon* **1977**, *15*, 355–371. Copyright (1977), with permission from Elsevier.
[a]Specification range 5.0–12.0 wt% Si.
[b]Not adjustable; varies randomly.
[c]Adjustable through process control.

1.107.2.4. Biological Properties and Biomedical Applications of Pyrolytic Carbon

1.107.2.4.1. Cardiovascular applications of pyrolytic carbon

Pyrolytic carbon has been considered for use in biomedical devices because of favorable evidence regarding its interaction with tissues, cells, and proteins. In particular, pyrolytic carbon has been considered for use in cardiovascular medical devices due to its excellent hemocompatibility. Early studies demonstrated that pyrolytic carbon possesses excellent blood compatibility; these properties were attributed to adsorption of proteins onto the surface of the material.[4] Studies involving adsorption of blood proteins suggested that pyrolytic carbon adsorbed proteins onto its surface; as a result, the material did not induce coagulation or thrombogenesis.[21] In a more recent study, the interaction between endothelial cell adhesion proteins and polyethylene terephthalate coated with pyrolytic carbon was investigated.[22] This study evaluated human umbilical vein endothelial cell expression of several molecules, including platelet endothelial cell adhesion molecule-1 (PECAM-1), endothelial leukocyte adhesion molecule-1 (ELAM-1), and intercellular adhesion molecule-1 (ICAM-1). PECAM-1 helps regulate adhesion of endothelial cells to other endothelial cells as well as to leukocytes. ELAM-1 is involved in adhesion of neutrophils, monocytes, and lymphocytes to endothelial cells. ICAM-1 plays a role in the adhesion of leukocytes to endothelial cells. Cenni *et al.* investigated the expression of these molecules by human umbilical vein endothelial cells, because they reflect inflammation associated with cell–material interaction. Cytofluorometry was used to measure the presence of PECAM-1, ELAM-1, and ICAM-1 molecules in cultures of human umbilical vein endothelial cells on pyrolytic carbon-coated polyethylene terephthalate. Their results showed no significant changes in expression of PECAM-1, ELAM-1, or ICAM-1, indicating that pyrolytic carbon-coated polyethylene terephthalate did not result in unfavorable expression of proteins that could disrupt connections between endothelial cells or stimulate an inflammatory response. These results are important in evaluating the use of pyrolytic carbon in applications that involve endothelialization.

Cenni *et al.*[23] examined adhesion of platelets and stimulation of coagulation factors by pyrolytic carbon-coated polyethylene terephthalate. Platelet adhesion was determined using plasma-rich protein. Platelet aggregation was examined using thromboxane B_2 (TXB_2) and platelet factor 4 (PF_4) immunoassays; TXB_2 and PF_4 are involved in the blood coagulation cascade. The results of this study indicate that pyrolytic

carbon-coated polyethylene terephthalate exhibited a reduction in platelet adsorption, as well as lower levels of TXB_2 and PF_4. However, platelet adsorption and expression of aggregation factors were significantly higher in pyrolytic carbon-coated polyethylene terephthalate than in control materials. Although pyrolytic carbon improved the hemocompatibility of polyethylene terephthalate, aggregation of proteins on the pyrolytic carbon surface was noted.

Over the last 40 years, pyrolytic carbon has been used as a coating on prosthetic heart valves and other cardiovascular medical devices due to its chemical inertness and biocompatibility. A study by Fernandez *et al.*[24] indicated positive results in 90% of the 110 patients who received a pyrolytic carbon tilting disk Bjork–Shiley aortic prosthesis. The study indicated beneficial results when compared to previous heart valve designs, which were associated with thrombogenesis, occluded blood flow, or implant deterioration. A reduction in thrombogenesis was also attributed to the use of pyrolytic carbon. It should be noted that some of the successes of pyrolytic carbon-coated prosthetic heart valves are attributed to reduced valvular regurgitation, which is associated with a reduction in clearance in pyrolytic carbon-coated disk occluder/orifice ring designs when compared with polyoxymethylene disk occluder/orifice ring designs.

The wear properties of heart valve prostheses containing pyrolytic carbon have also been considered. An implant retrieval study by Schoen *et al.*[25] compared the wear properties of eight pyrolytic carbon disk occluder and cage prostheses with those of a Teflon disk and cage prosthesis. Seven of the eight replacements had been implanted for a range of 30–85 months and one had been implanted for 44 days. The Teflon prosthesis was obtained postmortem from a patient who had the prosthesis for 34 days. Examination using dissecting microscopy, scanning electron microscopy, and analytical surface profilometry showed that there was insignificant wear on the occluders and struts of the pyrolytic carbon prosthetic valves. On the other hand, the Teflon valve demonstrated wear on the struts. Their study provided further evidence regarding the efficacy of pyrolytic carbon in prosthetic valve applications.

Antoniucci *et al.*[26] evaluated tubular stainless steel stents that were coated with turbostratic carbon. These stents, which went by the trade name Carbostent™ (Sorin Biomedica, Sallugia, Italy), were implanted in 112 patients; angiographic follow-up examinations at 6 months were performed in 108 patients.[26] The carbon-coated stents demonstrated low rates of 10% and 11% for target lesion revascularization and restenosis, respectively. The results of the study indicate that carbon-coated stents may be useful for minimizing thrombus formation and restenosis. A later study by Bartorelli *et al.*[27] examined the efficacy of stenting procedures involving the Carbostent™ and aspirin therapy for treatment of coronary artery disease. This study, termed the Aspirin alone Treatment After Carbostent Stenting (ANTARES) study, sought to determine the effectiveness of the carbon coating on the Carbostent™ device for prevention of thrombus formation. A total of 165 Carbostents™ in 110 patients were examined in this study. Postoperative analysis indicated that stenting with the Carbostent™ and antithrombotic therapy with aspirin were associated with an absence of thrombosis at the 30-day follow-up.[27]

1.107.2.4.2. Orthopedic applications of pyrolytic carbon

Pyrolytic carbon has been investigated for use in orthopedic medical devices. Isotropic pyrolytic carbon is alloyed with silicon in order to improve wear resistance and to better match the mechanical properties of bone. Pyrolytic carbon has been utilized in interphalangeal joint prostheses, which are used to reduce joint pain and improve movement in arthritic joints. Mixed results have been noted for pyrolytic carbon-containing proximal interphalangeal joint prostheses with regard to pain relief and range of motion following joint arthroplasty. In a 13-month postoperative follow-up study involving 18 joints in eight patients by Tuttle *et al.*,[28] only 50% reported a reduction in pain. There was no net increase in the average range of motion following surgery. There were also reports of squeaking in several of the joints; in addition, two of the joints experienced loosening. In another report, 50 proximal interphalangeal joints in 35 patients were studied at least 2 years after implantation.[29] In this study, 79% overall patient satisfaction was reported. In addition, statistically significant improvement in both pinch strength and grip strength was noted. There were also reports of improved range of motion; however, this trend did not reach levels of statistical significance. Secondary procedures were necessary for 28% of the joints; in addition, revision arthroplasty was necessary for 8% of the joints. **Figure 2** displays images of the proximal interphalangeal joint prostheses used in the study.[29] Although secondary procedures were required in some cases, the overall results indicated that there was potential for the use of pyrolytic carbon in proximal interphalangeal joint replacement prostheses. In addition, pyrolytic carbon has been investigated for use in metacarpophalangeal joints,[30] in scaphoid trapezium implants,[31] in the femoral head articulating surfaces of hip joint prostheses,[32] and in femoral implants to enhance bone ingrowth.[33–35]

1.107.2.4.3. Shortcomings of pyrolytic carbon

Although pyrolytic carbon has demonstrated utility in a variety of biomedical applications, concerns regarding the mechanical



Figure 2 (a and b) Views of the pyrolytic carbon prostheses. Note the bicondylar semiconstrained articulation similar to a total knee arthroplasty design. The distal component is on the left of the figure and the proximal component is on the right of the figure. Reprinted from Bravo, C. J.; Rizzo, M.; Hormel, K. B.; Beckenbaugh, R. D. *J. Hand Surg.* **2007**, *32*A(1), 1–11. Copyright (2007), with permission from Elsevier.

and biological properties of this material have been described in the literature. A lack of bone fixation to pyrolytic carbon-coated proximal interphalangeal joint prostheses may lead to loosening of the implants, failure of the implants, and need for revision surgeries.[36] In addition, blood flow and impact stress may lead to cavitation and pitting of pyrolytic carbon heart valves. Pitting of pyrolytic carbon heart valves can lead to fracture of the material and failure of the implant.[37] Infection is also a concern for pyrolytic carbon heart valves; for example, endocarditis can lead to serious health complications or death.[38,39] Bacterial biofilms (e.g., *Staphylococcus aureus*, *Staphylococcus epidermidis*, and *Pseudomonas aeruginosa*) have been shown to form on the surfaces of pyrolytic carbon heart valves.[40] Adhesion of platelets on the surfaces of pyrolytic carbon heart valves has also been raised as a concern. Despite reports that pyrolytic carbon is favorably hemocompatible, platelet activation on the surfaces of pyrolytic carbon heart valves has been noted; activation of platelets plays an important role in thrombus formation.[41,42]

1.107.3. Diamond-Like Carbon

1.107.3.1. Introduction to DLC

'DLC' is a term that is used to refer to a range of amorphous carbon films that contain sp^3-hybridized carbon atoms; these materials may contain varying degrees of hydrogenation as well as alloying components. DLC is a man-made product that can exhibit properties similar to those of diamond. Diamond-like hydrocarbon was first identified in the early 1950s by Schmellenmeir; significant efforts involving processing and characterization of DLC began in the 1990s.[1] Significant progress involving industrial production of diamond has also taken place in the past 20 years.[1] The use of DLC in biomedical devices (e.g., as a coating on implant components such as cardiac stents and joint replacements) is an emerging area of investigation.[1] The high hardness, wear resistance, and favorable biological properties of DLC have made it an interesting option for use in biomedical applications. DLC draws its unusual properties from the sp^3-hybridized carbon atoms within the material. DLC films exhibit large variations in several parameters, including the sp^3-hybridized carbon atom/sp^2-hybridized carbon atom ratio, the degrees of hydrogenation, and the presence of doping elements; these parameters have significant effects on biomedically relevant properties (e.g., mechanical properties).[43] Tetrahedral amorphous carbon (ta-C) and hydrogenated ta-C (ta-C:H) are forms of DLC that contain high percentages of sp^3-hybridized carbon atoms. ta-C:H is similar to ta-C; hydrogen atoms bonded to some of the carbon atoms in hydrogenated ta-C.

1.107.3.2. Production and Characterization of DLC

Several thin film deposition techniques have been utilized for depositing DLC films.[44,45] DLC is a thermodynamically metastable material; formation of sp^3-hybridized carbon atoms requires nonequilibrium processing technologies due to the high activation energy barrier for converting sp^2-hybridized carbon atoms to sp^3-hybridized carbon atoms. Films obtained using electron beam evaporation, an equilibrium process, contained 100% sp^2-hybridized carbon.[45] Commonly used methods for DLC growth include cathodic arc deposition, ion beam deposition, sputtering deposition, plasma-enhanced CVD (PECVD), and pulsed laser deposition (PLD). A common feature of DLC-processing methods is that DLC films are obtained from carbon or hydrocarbon ions that possess energies of ~100 eV.[44] Ion bombardment is considered to be a critical physical process for producing sp^3-hybridized carbon atoms in DLC films. Robertson proposed that the formation mechanism of sp^3 bonds is low-energy subsurface implantation or 'subplantation.' Subplantation of carbon ions during film growth is associated with an increase in mass density and formation of sp^3-hybridized carbon atoms.[44] At high ion energies, thermal effects are produced that lead to a reduction in the fraction of sp^3-hybridized carbon atoms.

Another key factor is the ordering of sp^3 sites in DLC; this ordering determines the electronic properties of the material.[44,45] Data on ordering of sp^3 sites in DLC films can be obtained using X-ray, neutron, and electron diffraction techniques. The structure and chemistry of DLC films can be characterized using diffraction techniques, electron energy loss spectroscopy (EELS), nuclear magnetic resonance (NMR), X-ray photoelectron spectroscopy (XPS), Fourier transform infrared spectroscopy (FTIR), visible Raman spectroscopy, or ultraviolet (UV) Raman spectroscopy.[44,45] Diffraction techniques, including X-ray, electron, and neutron diffraction, are commonly used to analyze the structure of amorphous materials; neutron diffraction provides a higher resolution than the other two techniques. Using diffraction, bond length and the number of nearest neighbors can be obtained from a radial distribution function (RDF). RDF or reduced density function describes the variation of atomic density as a function of distance. The RDF may be obtained from the Fourier transformation of reduced elastic scattering intensity, $\varphi(s)$, using the following equation[46,47]:

$$G(r) = 4\pi r[\rho(r) - \rho_0] = 8\pi \int_0^\infty \varphi(s) \sin(2\pi rs) \mathrm{d}s \qquad [1]$$

$\varphi(s)$ related to diffraction intensity $I(s)$ by means of the following relationship:

$$\varphi(s) = s\left[I(s) - Nf^2\right] / \left(Nf^2\right) \qquad [2]$$

In this equation, Nf^2 is the scaled atomic scattering intensity. The reciprocal quantity is given by $s = 2 \sin\theta/\lambda$. In this equation, θ is the angle between the incident and the scattering beam and λ is the wavelength.

The RDF consists of a series of local maxima.[44] The first peak is attributed to first neighbor or directly bonded atoms; the distance obtained from the first peak corresponds to the bond length (r_1). The coordination number of the first neighbor (N_1) can be obtained by calculating the area under the first peak. The bond angle (ϕ,) can be obtained from the distance of the first neighbor (r_1) and the second neighbor (r_2,) using the following relationship: $r_2 = 2r_1 \sin(\phi/2)$. The coordination number of the second neighbor (N_2) can be obtained using the following relationship: $N_2 = N_1(N_1 - 1)$. ta-C films showed values similar to those of diamond in terms of first nearest neighbor distances, second nearest neighbor distances, and coordinate numbers,

which indicated that ta-C contains a high fraction of sp^3-hybridized carbon atoms. Glassy carbon exhibited values closest to those of graphite.

1.107.3.2.1. Raman spectroscopic characterization of DLC

Raman spectroscopy is a nondestructive light scattering technique that is commonly used for examining the bonding between carbon atoms in DLC films and other carbon-containing solids. Many Raman spectroscopy studies have involved the use of the 514.5 nm line of an argon-ion laser. The Raman peak at 1332 cm^{-1} in diamond is attributed to the zone center optical phonon mode of T_{2g} symmetry.[44] Single crystalline graphite exhibits two Raman active modes with E_{2g} symmetry; however, the energy difference between these two modes is so small that the frequency separation is often not measurable. The two E_{2g} modes of graphite are observed as a single peak around 1580 cm^{-1}.[45] This Raman peak is frequently referred to as the G- or graphite band. Graphite is also associated with a small peak around 1350 cm^{-1}, which is known as the D- or disordered band; this band is attributed to the A_{1g} mode of graphite. It is attributed to small crystallites or boundaries.[45]

As pointed out by Ferrari and Robertson,[48] the G-mode is associated with in-plane bond stretching motion of sp^2-hybridized carbon atoms in pairs and the D-mode is associated with breathing motion of sp^2-hybridized carbon atoms in rings. The atomic behavior associated with each mode is shown in Figure 3. G-mode motion can occur in any pair of sp^2-hybridized carbon atoms. D-mode motion is prohibited in perfect graphite; it is observed in rings. G- and D-bands have been observed in the visible Raman spectra of many disordered carbon films. It is interesting to note that none of the features in the visible Raman spectra of disordered carbon materials is directly related to sp^3-hybridized carbon atoms.[45] Information about the presence of sp^2-hybridized carbon atoms in carbon-containing materials can be indirectly determined by analyzing the G- and D-Raman bands. Ferrari and Robertson[48] have classified the Raman spectra of disordered carbon materials into three categories, which describe variations in the peak positions of the G- and D-bands and the I(D)/I(G) ratios as a function of the degree of disorder. In the first category, the G-band position increases from 1580 to 1600 cm^{-1} as the carbon grain size progressively decreases from perfect graphite to nanocrystalline graphite. Because the degree of disorder increases as the grain size decreases, the D-peak intensity increases from zero and the I(D)/I(G) ratio increases. In the second category, the vibration density of states decreases as a result of the loss of aromaticity as well as increased disorder.

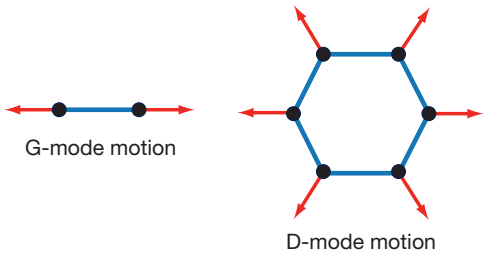

Figure 3 Schematic indicating carbon atom motion in G- and D-Raman modes.

The G-peak position shifts to lower energies; in addition, the I(D)/I(G) ratio is reduced. Materials in the third category contain a large fraction of sp^3-hybridized carbon atoms; in these materials, the I(D)/I(G) ratio is near zero. Instead of rings, the sp^2-hybridized carbon atoms are found in chains.[44] Spectra of materials containing a large fraction of sp^3-hybridized carbon atoms exhibit symmetric G-peaks.[44]

UV Raman spectra are obtained through the use of a frequency-doubled argon-ion laser ($\lambda = 244$ nm), which has a relatively high photon energy (5.1 eV) that can effectively excite the σ states from both sp^2-hybridized carbon atoms and sp^3-hybridized carbon atoms. Direct observation of sp^3 bonding in DLC films has been reported using UV Raman spectroscopy. A Raman peak at 1050–1200 cm^{-1} has been observed in the UV Raman spectra of materials with a high sp^3 content[44,45]; this peak, which is known as the T peak, has been attributed to sp^3 bonding.

1.107.3.2.2. Nuclear magnetic resonance and electron energy loss spectroscopy of DLC

NMR and EELS are commonly used for evaluating the structure of DLC and other carbon-containing materials. NMR is used to observe alterations in magnetic resonance frequencies that are associated with chemical bonding. The NMR signal is only obtained from C^{13} atoms, which make up approximately 1.1% of all of the carbon atoms. NMR spectroscopy requires large sample sizes to reach a satisfactory signal. This requirement limits the use of NMR spectroscopy with DLC thin films. EELS is commonly used for determining the sp^3/sp^2 ratio.[44] Both low energy loss spectra and near K edge ionization spectra may be used to obtain information on chemical bonding states. It should be noted that EELS requires very thin samples and is a destructive technique.

1.107.3.3. Properties of DLC

The mechanical, electronic, and optical properties of DLC are closely related to the sp^3/sp^2 ratio, which in turn is dependent on the substrate material, growth method, and growth parameters (e.g., growth temperature and ion energy). Theoretical and experimental information on the electronic structure of DLC is extensively discussed elsewhere.[44,45,49]

1.107.3.3.1. Electronic properties of DLC

Theoretical simulations of DLC materials have been performed using cluster model and direct calculation of carbon networks.[44] In the cluster model, σ and π states are separately considered.[49] In this model, the sp^2 sites are located in planes within a sp^3 bonded matrix. The optical gap and electronic properties are determined by the arrangement of the sp^2 sites; the sp^3 matrix is responsible for the mechanical properties of the material. A simple relationship has been derived for the band gap of the aromatic cluster,[44]

$$E_g \approx \frac{2\gamma}{M^{1/2}} \approx \frac{2\gamma}{L_a} \qquad [3]$$

In this equation, γ is the nearest neighbor $V(pp\pi)$ interaction, M is the number of sixfold rings in the cluster, and L_a is the cluster diameter or the in-plane correlation length. A wide

energy gap is formed by sp^3-hybridized carbon atoms; on the other hand, the gap associated with sp^2-hybridized carbon atoms varies with the configuration of the cluster. Both experimental and simulation results showed that the band gap of DLC decreased with an increasing fraction of sp^2-hybridized carbon atoms.[44] The optical gap (E_g) can be extracted from the optical absorption spectra. The relationship between absorption coefficient (α), photon energy (E), and optical gap is as follows:

$$\alpha E = B\left(E - E_g\right)^2 \quad [4]$$

In this equation, B is a constant.[44,45] The undoped DLC film is a p-type material in which the Fermi level is 0.22 eV above the effective valence band edge semiconductor.[44,45,50,51] A narrow $\pi-\pi^*$ gap is located between the wider $\sigma-\sigma^*$ gap. The π states in these materials are localized due to the orientation dependence of π interaction.[44] The mobility gap is determined by the σ states. Two types of defects exist in DLC films. Weak form disorders create localized band tails. Defects such as dangling bonds usually form deep levels. The electrical properties of DLC film can be modified by the introduction of dopants. For example, nitrogen has been introduced into DLC as an electron donor; however, the doping efficiency of nitrogen is poor.[44]

1.107.3.3.2. Mechanical properties of DLC

In general, DLC exhibits high hardness values. The mechanical properties of DLC are determined by the fraction of sp^3-hybridized carbon atoms. An empirical relationship for hardness (H) can be written as

$$\frac{H}{Y} = 0.07 + 0.06 \ln\left(\frac{E}{Y}\right) \quad [5]$$

In this equation, Y and E are yield stress and Young's modulus, respectively.[44] For DLC, the relationship between H and E is $H = 0.16E$; consequently, hardness is proportional to Young's modulus. Using the constraint-counting model, the Young's modulus of DLC has the following relationship with the average coordination number $\langle r \rangle$,[44]

$$E = -k(\langle r \rangle - 2.4)^{1.5} \quad [6]$$

This relationship between elastic modulus and coordination number has been experimentally confirmed.[51] The average coordination number increases with the sp^3/sp^2 ratio; consequently, DLC films with larger sp^3 fractions have higher hardness values. A hardness value of ~60 GPa can be obtained when the fraction of sp^3-hybridized carbon atoms exceeds 80%.

Internal compressive stresses as high as 10 GPa commonly exist in DLC films. Owing to the internal compressive stresses, DLC films demonstrate poor adhesion on many substrates. Three-dimensional molecular dynamic simulation has indicated that compressive stresses arise from competition between generation and recovery of defects[52]; these compressive stresses are dependent on the kinetic energies of the incident ions. Intrinsic compressive stresses limit the use of DLC films in several technical applications, including use as protective hard coatings. Adhesive failure takes place when the mechanical energy density of the film exceeds the energy required to create two new surfaces.[45] Depending on the nature of the interface between the DLC film and the substrate, there is a critical film thickness; delamination takes place if the thickness of the coating is larger than the critical thickness. Several studies have evaluated mechanisms for increasing DLC film thickness. One mechanism for obtaining DLC films with high thicknesses involves increasing the interfacial strength between the DLC film and the substrate. Argon ion cleaning has been used to produce fresh substrate surfaces and improved interfacial strength.[53] Buffer layers have also been utilized for increasing the adhesion of DLC films. For example, buffer layers containing silicon, tungsten, and chromium form carbides during deposition that increase interfacial bonding.[44,45,53,54] One approach for increasing the film thickness involves reducing internal compressive stresses. Stress relaxation may be accomplished by means of thermal annealing.[55–57] Complete stress relaxation was achieved after the materials were annealed at a temperature of 600–700 °C. EELS and Raman spectroscopy studies showed that this annealing process was associated with minimal structural modification.[45] Stress relaxation can be also achieved by incorporating dopants within DLC films; for example, codeposition of DLC and metals such as tungsten or titanium has been shown to be an effective method to reduce the internal stresses.[45]

1.107.3.4. Applications and Biological Properties of DLC

DLC is utilized in a variety of technological applications. For example, incorporation of DLC within field-effect transistors has been proposed.[58] Other electronic applications include the use of DLC in antifuses, field emission displays, and ULSI devices.[44] DLC has also been investigated for use in stretchable electronic devices (e.g., biomedical sensor arrays), which may be used to conform to surfaces with arbitrary geometries.[59] Electronic components may be applied to stiff subcircuit components (e.g., those fabricated out of DLC), which are placed on elastomeric stretchable substrates; conformational changes to the device can be performed while limiting strain to the electronic components that are located on the stiff DLC subcircuit components.[59]

Many applications of DLC involve the use of this material as a protective coating. For example, DLC films have been commercially utilized as protective coatings in the microelectronics industry.[45,60] DLC can be used as protective coatings on magnetic storage disks. As DLC films exhibit high hardness, wear resistance, and chemical inertness, they are very attractive for use as coating material for biomedical devices.[61]

1.107.3.4.1. Orthopedic applications of DLC

DLC has high wear resistance and a low friction coefficient. For amorphous hydrogenated DLC, the friction coefficient varies between 0.05 under vacuum and 0.1–0.15 under normal atmospheric humidity.[44] For ta-C, the friction coefficient is 0.1–0.15 under vacuum and slightly decreases under normal atmospheric humidity. The use of DLC films in artificial joint prostheses has been evaluated by several investigators.[62–65] One issue facing conventional articulating joint prostheses is the formation of wear debris. Ultrahigh molecular weight polyethylene (UHMWPE) particulates in knee and hip joint prostheses may be formed at a rate of 10^{10} particulates per year.[61] As DLC provides high wear resistance and low

coefficient of friction, this material is being considered for use on the articulating surfaces of joint prostheses.[61] Several studies have been performed to evaluate the efficacy of DLC as a coating material for use in total joint prostheses. Saikko *et al.*[63] investigated the wear properties of UHMWPE using an anatomical hip wear simulator. Femoral heads fabricated out of Co–Cr–Mo alloy, alumina, and DLC-coated Co–Cr–Mo alloy were examined against UHMWPE acetabular cups in bovine serum without additives; the results of this study indicate that the wear properties of these femoral heads are similar.

Sheeja *et al.*[64] evaluated the wear properties of DLC-coated Co–Cr–Mo alloy disks on UHMWPE pins and uncoated Co–Cr–Mo alloy disks on UHMWPE pins in simulated body fluid. Similar wear rates were observed for sliding pairs containing DLC-coated Co–Cr–Mo alloy and uncoated Co–Cr–Mo alloy; it should be noted that the corrosion resistance and the hardness of DLC-coated Co–Cr–Mo alloy were higher than those of uncoated Co–Cr–Mo alloy. The corrosion rate of DLC-coated Co–Cr–Mo alloy was reduced by approximately a factor of 10 000 in comparison with uncoated Co–Cr–Mo alloy. Furthermore, the sliding life was significantly reduced for DLC coatings applied to Co–Cr–Mo substrates with surface roughness values greater than 35 μm.[64] Another study by Sheeja *et al.*[66] examined the effect of coating Co–Cr–Mo alloy disks as well as UHMWPE pins. The wear on both surfaces was greatly reduced with DLC-coated Co–Cr–Mo alloy disks and UHMWPE pins compared with uncoated Co–Cr–Mo alloy disks and UHMWPE pins. If only the UHMWPE pin is coated, the wear rate for the pin is reduced; however, the Co–Cr–Mo disks undergo increased wear. The results of these two studies indicate that coating only one surface of a UHMWPE/Co–Cr–Mo sliding pair with DLC does not significantly improve wear performance. On the other hand, pin-on-disk testing showed improved wear properties for sliding pairs that contain DLC-coated UHMWPE and DLC-coated Co–Cr–Mo alloy.[66]

On the other hand, work by Oñate *et al.*[67] suggests that DLC is appropriate for reducing wear. DLC-coated Co–Cr alloy was examined; the wear performance of this material against UHMWPE in a knee wear simulator was investigated. Materials in this study were tested in a knee wear simulator for up to 5 million cycles; distilled water was used as a lubricant. DLC-coated Co–Cr alloy, titanium nitride-coated Co–Cr alloy, and uncoated Co–Cr alloy were compared. Nitrogen ion implantation was also utilized for modification of Co–Cr alloy and UHMWPE. The result of the study indicated that the DLC-coated material was able to reduce the wear of UHMWPE compared to uncoated material or titanium nitride-coated material. Ion implantation of Co–Cr alloy and UHMWPE was also shown to be an effective mechanism for reducing wear.[67] Tiainen *et al.*[68] also indicated favorable wear and corrosion properties for DLC-coated implant materials. DLC-coated metal femoral heads on UHMWPE acetabular cups were shown to reduce wear by a factor of 10–600 compared with that of uncoated metal femoral heads on UHMWPE acetabular cups. DLC-on-DLC-coated metal surfaces demonstrated a 10^5–10^6 lower wear rate in comparison with metal-on-metal surfaces. DLC-coated metallic implants can reduce the corrosion rate by a factor of 100 000 in comparison with uncoated metallic components. Despite the variability of the data in previous studies, DLC offers significant promise as a coating material for orthopedic applications.

1.107.3.4.2. Cardiovascular applications of DLC

Biomaterials used in cardiovascular implants (e.g., stents or guidewires) must demonstrate appropriate hemocompatibility, particularly an absence of platelet activation and thrombosis (as discussed in **Chapter 4.401, The Concept of Biocompatibility** and **Chapter 4.406, Protein Interactions with Biomaterials**). DLC has been investigated for use as a coating material in cardiovascular applications due to its favorable blood interaction properties. In addition, DLC may serve as a protective coating on metallic implants due to the fact that it can limit corrosion of metallic implant materials.

Interactions between an implant material and blood may lead to platelet activation.[69] In the case of metallic implant materials, release of metallic ions from the implant surface can lead to platelet activation and thrombus formation.[69,70] For example, Ferguson *et al.*[71] examined the release of ions from commonly used medical implant alloys, including alloys of chromium, cobalt, iron, molybdenum, nickel, titanium, and zirconium. Metallic cylinders of these materials were implanted into the skeletal muscle of albino rabbits; after 4–6 months, the materials were removed. Increased metal ion levels in peri-implant tissues were noted for metal alloys, including metal alloys that are considered to be corrosion-resistant. Particularly high metal ion concentrations were observed in tissues that surrounded titanium implants. These results suggest that the biological environment plays a significant role in implant degradation. In addition, cobalt, chromium, and nickel ions may serve to stimulate the release of E-selectin, GMP-140, and ICAM-1; these molecules are involved in adhesion of cells such as leukocytes and platelets to endothelial cells.[70] For example, interactions between an implant material may result in adhesion of platelets to the surface of the material; this process may be followed by platelet activation and release of granule materials (e.g., ADP).[72] Such interactions are unfavorable and could result in formation of a thrombus (blood clot).

DLC coatings have been deposited on the surfaces of stents and guidewires for the purpose of limiting platelet activation and minimizing thrombus formation. Gutensohn *et al.*[69] examined the hemocompatibility of uncoated 316L steel intracoronary stents and DLC-coated 316L steel intracoronary stents; release of metal ions (e.g., chromium, nickel, molybdenum, and manganese) was evaluated. Atomic adsorption spectrophotometry revealed that release of chromium and nickel ions was significant in uncoated stents; minimal release of these ions was observed in DLC-coated stents. Furthermore, flow cytometry showed that the concentrations of activation-dependent antigens, CD62p and CD63, were higher for uncoated stents than for DLC-coated stents. These results indicate that DLC coatings may be used to provide an increase in biocompatibility and a decrease in thrombogenicity.

Schaefer *et al.*[73] evaluated nickel–titanium shape memory alloy (nitinol) stents that were coated with DLC in a small clinical trial (see **Chapter 1.104, Shape Memory Alloys for Use in Medicine** for further details on shape memory alloys); in this study, DLC-coated stents were used for treatment of two

patients with superficial femoral artery occlusions. Implantation of the DLC-coated nitinol stents was successful; 6-month and 12-month postoperative follow-up studies for the two patients indicated no restenosis and 100% primary patency.[73] The authors of this study acknowledged that additional work is necessary to further confirm the efficacy of DLC-coated nitinol stents for treatment of peripheral artery occlusive disease.[73]

Blood-contacting biomaterials may also undergo interactions with macrophages and other inflammatory cells. Ball *et al.*[74] investigated the interaction between vascular stents and the J774 macrophage cell line. In this study, the metabolic activity of the macrophages in response to uncoated 316L stainless steel stents, ta-C-coated stainless steel stents, and polyurethane-coated stainless steel was investigated. Cells were shown to become activated at higher levels on uncoated stainless steel stents than on polyurethane-coated steel or ta-C-coated stents. The metabolic activity of macrophages on the ta-C-coated surfaces was comparable to that on the commercially available polyurethane-coated surfaces. These results indicate that ta-C-coated stainless steel elicits a lower inflammatory response from macrophages than did uncoated stainless steel.

Medical guidewires may also benefit from DLC coatings. These devices are utilized for placement of stents, catheters, or other medical devices into the body. Guidewires must exhibit several properties, including biocompatibility, chemical inertness, flexibility, low surface roughness, and low coefficient of friction values.[75,76] Medical grade stainless steel is commonly used for medical guidewire devices; this material is utilized in both uncoated and polymer-coated forms.[75] Various polymers (e.g., polytetrafluoroethylene, PTFE) have been investigated for use as guidewire coatings; however, poor adhesion between the polymer coating and the steel substrate has been noted.[77,78] As previously mentioned, the release of metal ions from a medical device can result in platelet activation and inflammation. The use of DLC as a coating material for stainless steel guidewires can reduce metal ion release, provide a chemically inert surface, and impart low coefficient of friction values. McLaughlin *et al.*[75] investigated deposition of DLC coatings onto stainless steel guidewires by means of PECVD. DLC-coated medical grade 306V stainless steel was shown to exhibit better adhesion and lubricity than did PTFE-coated material; no decrease in guidewire stiffness was noted.[75] Hasebe *et al.*[79] described deposition of DLC and fluorinated DLC (F-DLC) coatings on SUS316L stainless steel wires. A radio frequency PECVD process was utilized to deposit 40–50-μm-thick DLC and F-DLC coatings. *In vitro* studies indicated that DLC steel wires and F-DLC steel wires exhibited lubricity improvements of ~30% when compared with uncoated steel wires. Incorporation of fluorine or silicon within DLC films can serve to improve blood-contacting properties as well as film adhesion to steel wires.[76]

Although DLC has shown beneficial properties for use in cardiovascular medical devices, cracks in DLC films and delamination of DLC films remain significant concerns. Cracking and spallation of DLC coatings may occur as a result of tensile strains and shear strains on DLC-coated devices.[80,81] To address these issues, studies have investigated pretreatment of the substrate material, incorporation of a silicon interlayer between the substrate and DLC coating, and doping of the DLC coating with silicon.[80,81] Doping of DLC with silicon and incorporation of a hydrogenated amorphous silicon (a-Si:H) interlayer were associated with improved adhesion of DLC coatings to stainless steel substrates as well as crack prevention.[81] Attachment of platelets was decreased and attachment of microvascular endothelial cells was increased in silicon-doped hydrogenated DLC in comparison with undoped hydrogenated DLC. It should be noted that immersion of silicon-doped hydrogenated DLC-coated materials in biofluids resulted in a reduction in film adhesion of up to 75%.[81] Spallation of DLC coatings on 304 stainless steel substrates was decreased by incorporating a silicon interlayer with a thickness of at least 32 nm.[80] In addition, a pretreatment protocol involving argon plasma cleaning of steel substrates was shown to reduce spallation of DLC coatings.[80] Efforts are underway to improve adhesion of DLC films so that these materials can successfully endure stresses that are associated with implantation and use in the body.

1.107.3.4.3. Additional applications of DLC

DLC coatings may find use in other medical devices, including soft contact lenses.[60] *In vitro* studies have shown DLC to be chemically inert; *in vitro* studies involving macrophages, monocytes, fibroblasts, and osteoblasts have shown that DLC is associated with an absence of cytotoxicity and inflammatory stimulation.[82] DLC-coated materials may also be used for treatment of complex bone fractures.[82] In addition, DLC-coated materials may be used to increase longevity and improve effectiveness of medical probes, catheters, and coronary implants.[82] DLC has also been alloyed with antimicrobial metals such as silver; not only does incorporation of silver reduce compressive stresses, but also silver provides antibacterial activity.[83–85] Although significant work has already been completed, continued investigation is necessary to develop and commercialize DLC-based medical devices.

1.107.4. Microcrystalline, Nanocrystalline, and Ultrananocrystalline Diamond

1.107.4.1. Introduction to MCD, NCD, and UNCD

MCD, NCD, and UNCD are carbon-based coating materials that have been considered for use in a variety of medical applications. Diamond exhibits many characteristics that make it appropriate for use in medical applications, including high hardness, chemical inertness, biological inertness, and high wear resistance. MCD thin films exhibit grain sizes that are on the order of micrometers; typical grain sizes are between 0.5 and 2.0 μm.[86,87] NCD thin films commonly contain grain sizes below 100 nm; 50–100 nm grain sizes are commonly observed.[88] Thin films containing diamond grains with sizes below 10 nm, commonly between 3 and 5 nm, are known as UNCD films.[88]

MCD, NCD, and UNCD thin films consist of sp^3-hybridized diamond crystallites; the grain sizes of these materials are in the micrometer to nanometer range. The grain boundaries between crystallites contain sp^2-hybridized carbon impurities and hydrogenated carbon species. Materials with smaller grain sizes contain a higher number of grain boundaries as well as a higher percentage of sp^2-hybridized carbon atoms and amorphous carbon impurities.

1.107.4.2. Production of MCD, NCD, and UNCD

As previously mentioned, graphite and diamond are crystalline allotropes of carbon. At normal atmospheric temperatures and pressures, graphite is the stable crystalline form of carbon and diamond is a metastable form of carbon. At high temperatures and pressures (e.g., thousands of degrees Celsius and gigapascals of pressure), diamond is the stable crystalline form. High temperatures and pressures must be utilized in order to create diamond under thermodynamic equilibrium conditions. Single crystal and polycrystalline diamond aggregates have been produced by means of static compression of materials such as C_{60}, graphite, glassy carbon, and amorphous carbon under high pressures (8–20 GPa) and high temperatures (1000–3000 °C).[89]

Carbon materials may be dissolved within catalyst materials, which reduce the pressure and temperature necessary for diamond processing. Catalyst materials include transition metals belonging to Group VIII of the Periodic Table, alloys of carbide-forming elements, magnesium, oxygen-containing materials, and hydrides.[89] Processing of carbon in conjunction with catalyst materials requires temperatures and pressures on the order of 1200–1500 °C and 5–6 GPa, respectively.[89]

MCD and NCD thin films are commonly produced by vapor deposition processes, which involve decomposition of hydrocarbon or fullerene precursor gases. Growth of diamond thin films on substrates can be achieved through the use of a carbon source gas in conjunction with a carrier gas (e.g., argon, hydrogen, or nitrogen); the gas is heated to radicalize the hydrocarbon or fullerene precursor materials and form reactive species. The radicalized carbon species interact with the surface of the substrate and form the diamond thin film.

1.107.4.2.1. CVD and film growth

There are a few methods that have been utilized for processing of NCD and MCD thin films. CVD is an approach that is commonly used for processing diamond thin films; it involves the use of a carbon-containing gas that is mixed with a carrier gas (e.g., hydrogen or argon). The size of the grains in diamond thin films can be modified by altering the processing parameters. Based on the chemical composition of the gas mixture, the renucleation process can either be suppressed or maintained. During the CVD process, the crystals grow larger and the film becomes thicker; the nanocrystalline grains increase in size and form microcrystalline grains. If the film thickness is kept sufficiently thin, then the grain sizes will fall within the size range of NCD.

As mentioned by Williams *et al.*,[88] renucleation can be suppressed during diamond thin film growth through the use of a dilute methane and hydrogen gas mixture. The high concentration of the hydrogen in the mixture results in preferential etching of graphite; hydrogen also acts to terminate carbon dangling bonds, abstract hydrogen from carbon–hydrogen bonds, and etch sp^2-hybridized carbon from the thin film surface.[87] Graphite formed during processing is more favorably degraded, resulting in growth of the diamond layer.[90]

Renucleation of the crystals can be suppressed through the use of a hydrogen-rich gas mixture; renucleation can also be encouraged for processing of diamond thin films with grain sizes that correspond to the UNCD size range. Through the use of a mixture with a lower concentration of hydrogen, the formation of graphitic bonding can take place, typically along grain boundaries. By allowing these sp^2-bonded regions to be created, without the degrading action of the hydrogen gas, additional nucleation sites can form in the film. The renucleation process is therefore able to commence, allowing for smaller crystallite sizes, and subsequently smaller grain boundaries. Figure 4 displays the concept of renucleation with differences in grain sizes between nanocrystalline and UNCD. The constant renucleation process allows for grain boundaries characteristic of NCD without limiting the thickness of the film. According to Gruen,[91] it is generally agreed upon that without renucleation, grain size of thin film diamond increases as the film thickness increases. However, by ensuring high renucleation rates (on the order of $10^{10}\,cm^{-2}\,s^{-1}$) during the growth of the film, NCD films can be deposited in excess of 1 μm in thickness. Gruen[91] noted, however, that to ensure that heterogeneous nucleation of the crystallites and thus NCD thin films, the deposited films generally needed to be produced with thicknesses greater than 3 μm. Films with thicknesses beyond this value that maintain their nanocrystallinity ensure that the renucleation is proceeding appropriately. When films are produced in this manner, the grain sizes can be kept low on the nanoscale and UNCD can be produced. Figure 5 displays SEM images of nanocrystalline and UNCD produced via CVD.

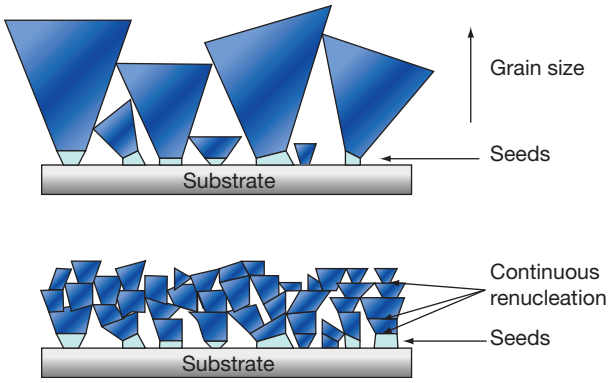

Figure 4 Schematic of the difference between nanocrystalline diamond (NCD) and ultrananocrystalline diamond (UNCD) nucleation. Reprinted from Williams, O. A.; *et al*. *Diam*. *Relat*. *Mater*. **2008**, *17*, 1081. Copyright (2008), with permission from Elsevier.

In the same way as NCD, applying MCD films to desired substrates can be accomplished by combining a hydrocarbon gas with an inert gas during the CVD process. Controlling the renucleation process by adjusting the chemical composition of the gas mixture used to form the CVD plasma, the substrate temperature, and the system pressure can allow control of the grain size. As discussed with regard to NCD and UNCD, frequent renucleation allows for smaller grain sizes, maintaining diamond films with features within the nanometer size range. However, if the renucleation phase is not reinitiated as frequently, the grain sizes increase and allow the diamond grain growth to cross into the microcrystalline size range. As the diamond is deposited and grows thicker, the crystallites compete with one another during their growth process.[92,93] If the renucleation is suppressed, the crystallites will continue to grow and impede the growth of one another. Crystals with

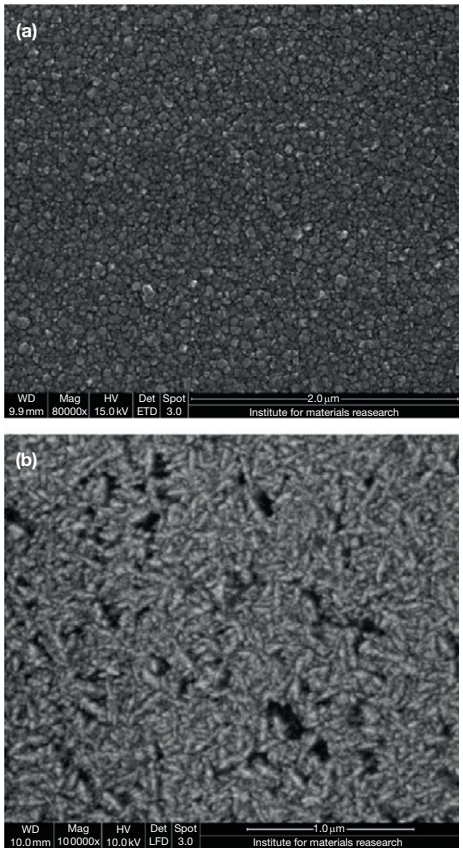

Figure 5 Scanning electron micrographs of (a) nanocrystalline diamond and (b) ultrananocrystalline diamond. Reprinted from Williams, O. A.; *et al*. *Diam. Relat. Mater.* **2008**, *17*, 1083. Copyright (2008), with permission from Elsevier.

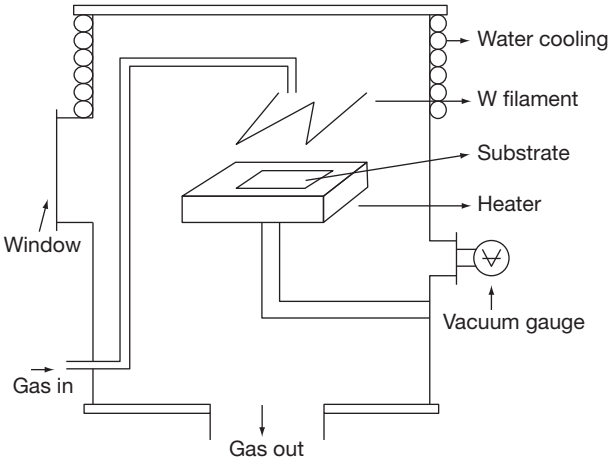

Figure 6 Schematic diagram of a hot-filament-assisted chemical vapor deposition (CVD) system. Reprinted from Narayan, R. J.; *et al*. *J. Adhes. Sci. Technol*. **2004**, *18*(**12**), 1346. Copyright (2004), with permission from Koninklijke Brill NV.

rapid growth rates in directions normal to the substrate surface will overtake the crystals growing in other orientations, they will grow larger, and the number of crystals will decrease as the film is grown thicker.[93] Eventually, instead of having many nanometer-size crystallites, a smaller number of larger crystallites are formed within the micrometer size range.

As discussed with NCD, initiation of the renucleation phase can be suppressed during diamond thin film growth by employing a high percentage of hydrogen within the carrier gas mixture.[88] Higher concentrations of the hydrogen result in etching of sp^2-hybridized graphitic material; diamond growth is continued. With hydrogen present in the mixture, sp^2-hybridized carbon species are limited, reducing the prevalence of nucleation sites deposited on the growing diamond crystallites, allowing the crystals to grow larger and grain sizes to form in micrometer dimensions.[90] As the film grows thicker, so do the sizes of the crystal grains.

1.107.4.2.2. Hot-filament CVD of diamond films

Several types of CVD processes are utilized for deposition of MCD, NCD, and UNCD thin films. Hot-filament CVD is a process that involves the use of a heated filament or wire for decomposition of a hydrocarbon precursor gas.[94–96] Figure 6 shows a schematic of a hot-filament CVD system. Initial work involving hot-filament CVD of diamond microcrystals on silicon, silica, diamond, and molybdenum substrates was performed by Matsumoto *et al.*[96] Using a gas mixture containing methane and hydrogen (0.05–0.005, CH_4–H_2 ratio), a flow rate range of 4–200 $cm^3\,min^{-1}$ at standard temperature and pressure, a chamber pressure of 0.5–750 torr, and substrate temperatures of 600–1000 °C, Matsumoto *et al.*[96] were able to deposit diamond microcrystals with various morphologies. Diamond crystal morphology may be varied by altering the hydrocarbon precursor gas, reaction chamber pressure, substrate temperature, and other processing parameters.

Kang *et al.*[97] demonstrated deposition of both microcrystalline and NCD thin films on silicon wafer substrates, which had been seeded with diamond particles from 0.5 µm diamond slurry. In one study, the chamber pressure was varied from 40 to 400 torr; the hydrogen gas flow rate (100 sccm), methane gas flow rate (4 sccm), and a temperature of 1100 °C were maintained at constant values.[97] MCD was successfully deposited in a pressure range between 40 and 200 torr; NCD was obtained above 200 torr.[97] In addition, NCD and MCD films were successfully deposited by varying the substrate deposition temperature between 1020 and 1220 °C under a constant pressure of 200 torr. NCD was observed at 1140 °C and MCD was observed at 1200 °C; the transition from NCD to MCD occurred over the temperature range between these two temperatures.[97] MCD features were observed up to a temperature of 1220 °C.

Amaral *et al.*[98] described processing of NCD films and MCD films on Si_3N_4 substrates by means of hot-filament CVD. Gas mixtures containing argon, methane, and hydrogen; gas flow ratios of $Ar/H_2 = 1.2$ and $CH_4/H_2 = 0.04$; and gas flow rates of either 50 or 100 $ml\,min^{-1}$ were utilized in this study. The filament and substrate temperatures were maintained at 2200 and 650 °C, respectively. The filament was located 5 mm from the substrate. A constant gas pressure of 5 kPa was used in this study. NCD films were successfully grown into continuous films using a deposition time of 4 h. Micro-Raman spectroscopy and low-incidence beam angle X-ray diffraction (LIBAD)

confirmed the composition of the NCD films. Abreu *et al.*[94] described the use of a hot-filament CVD process to produce nanocrystalline films on Si_3N_4 substrates. In this study, an argon–methane–hydrogen gas mixture with volume ratios of $Ar/H_2 = 0.1$ and $CH_4/H_2 = 0.04$ as well as a gas flow rate of 50 ml min^{-1} were used.[94] A tungsten filament temperature of 2300 °C, a substrate temperature of 750 °C, and a chamber pressure of 50 mbar were used in this study. A 18-μm-thick NCD film was obtained using a deposition time of 22 h.[94]

1.107.4.2.3. Microwave PECVD of diamond films

Microwave PECVD (MPECVD) is another type of CVD process that can be used to prepare MCD, NCD, and UNCD thin films.[99–106] In this process, the precursor gas mixture is ionized to form a plasma; microwave energy is used to modulate film deposition. A bias voltage is applied to the substrate material, which serves to attract the ionized species to the substrate surface. MPECVD can be used at lower substrate temperatures than other deposition processes. Furthermore, it can be used to coat surfaces with deep depressions, complex geometries, or three-dimensional topologies.

Liu *et al.* described processing of UNCD using MPECVD. In this study, the H_2 concentration was varied from 0 to 20%. The CH_4 level was maintained at 1% and the Ar concentration was varied to maintain a 250 sccm flow rate. An input power of 800 W, a chamber pressure of 13.3 kPa, and a substrate temperature of ~900 °C were used in this study.[103] Achatz *et al.* utilized MPECVD for deposition of UNCD thin films using an argon-rich $Ar/N_2/CH_4$ gas phase. Flow of CH_4 gas was maintained at 1.4 sccm; the argon and N_2 flow rates were varied in order to maintain an overall flow rate of 100 sccm. The quartz substrate was maintained at 800 °C.[99,107] Xiao *et al.*[108] described deposition of UNCD thin films on silicon substrates using MPECVD at substrate temperatures between 400 and 800 °C; a gas mixture containing 1% methane and 99% argon was used in this study.

1.107.4.2.4. Additional diamond film production methods

Radio frequency plasma-activated CVD (RF PA CVD) is another method that has been utilized for depositing NCD thin films onto substrate surfaces. Mitura *et al.*[109,110] reported processing of NCD coatings using this approach; in this study, they utilized a radio frequency (13.56 MHz) plasma to decompose a methane source. Mitura *et al.*[110] described deposition of NCD coatings containing 97% diamond onto 316L stainless steel substrates. Deposition of MCD has also been reported using direct ion beam deposition.[111] For example, Feng *et al.* generated argon, hydrocarbon, and hydrogen ions with a Kaufman ion source; MCD films (particle size ~1 μm) in an amorphous carbon matrix were grown on (100) silicon substrates. PLD is another method that has been used for processing of NCD thin films. PLD is a type of physical vapor deposition process, which involves ablation of material using laser energy in a vacuum chamber. After vaporization of the material, an energetic plasma plume is produced; this plume subsequently forms a film on the substrate. Hara *et al.*[112] described processing of 4–5-μm-thick NCD films on diamond substrates using PLD. In this study, an ArF excimer laser (energy = 200 mJ) was used to ablate a rotating graphite target.

1.107.4.3. Mechanical and Biological Properties of MCD, NCD, and UNCD

MCD, NCD, and UNCD thin films must exhibit appropriate mechanical and biological properties for use in the human body. Bulk diamond exhibits several desirable properties, including high hardness (Vickers hardness = 10 400 kg mm^{-2}), wear resistance, corrosion resistance, stable electrical resistance, and excellent thermal conductivity.[113–115] In addition, diamond also exhibits low coefficient of friction values ($u(s) < 0.1$).[113–115] Owing to these desirable properties, diamond has been considered for use in several biomedical applications.

In addition, diamond shows more favorable biological properties than many other materials that are commonly utilized in biomedical applications. For instance, many polymeric and metallic materials elicit a response from immune cells when introduced into the body (as discussed in **Chapter 4.403, The Innate Response to Biomaterials**; **Chapter 4.404, Adaptive Immune Responses to Biomaterials**; and **Chapter 4.405, Leukocyte–Biomaterial Interaction *In Vitro***); on the other hand, diamond has been shown to induce limited responses from neutrophils, polymorphonuclear leukocytes, and monocytes.[116–120]

Several studies have evaluated the hemocompatibility, cytotoxicity, and *in vitro* behavior of cells in contact with diamond materials. Tang *et al.*[119] compared the biocompatibility of CVD-prepared MCD with that of titanium and 316 stainless steel; titanium and 316 stainless steel are commonly utilized in implantable medical devices. Their investigation examined adsorption and denaturation of fibrinogen. They also evaluated adhesion and activation of cells by means of *in vitro* and *in vivo* studies; less cell adhesion and activation was observed on diamond than on the other materials. The diamond was shown to adsorb and denature small amounts of fibrinogen. Garguilo *et al.*[121] used contact angle goniometry to examine fibrinogen adhesion to the surface of MPECVD-prepared polycrystalline diamond. In their study, titanium-coated silicon substrates experienced notable fibrinogen adhesion; on the other hand, fibrinogen adsorption on diamond was negligible.

Neuronal cell growth on diamond has also been investigated. For example, Specht *et al.*[122] coated single crystal diamond surfaces with laminin; these surfaces were seeded with mouse cortical neuron cells; proliferation of neurites on the laminin-coated diamond surface was observed. Ariano *et al.*[123] demonstrated that rat hippocampal neurons and chick ciliary ganglion neurons are able to survive, proliferate, and function on diamond surfaces, which were coated with adhesion molecules such as poly-D-lysine, poly-DL-orthonine, or laminin.

Nordsletten *et al.*[118] investigated the monocyte interaction with diamond particles. In this study, interleukin-1β production and release by monocytes after exposure to particles of hydroxyapatite, silicon carbide, and diamond was examined. Phagocytosis of each type of particle was observed; diamond was noted to not stimulate the production and release of interleukin-1β, which is associated with bone resorption and orthopedic implant loosening.[118]

Amaral *et al.*[124] investigated the growth of L929 fibroblast cells and human gingival fibroblast cells on NCD thin films. Adhesion, proliferation, and viability of cells on NCD thin

films were evaluated; these films were deposited on silicon nitride (Si_3N_4) substrates using hot-filament CVD. In this study, materials were evaluated using the MTT assay, scanning electron microscopy, and confocal laser scanning microscopy. Scanning electron microscopy and confocal laser scanning microscopy revealed that cell morphology and adhesion of cells on NCD-coated substrates and standard tissue culture plates were comparable. MTT assays indicated that proliferation rates of L929 fibroblasts and gingival fibroblasts on NCD thin films and polystyrene culture plates were similar.

In another study, Amaral *et al.*[125] investigated the biocompatibility of NCD films using MG63 osteoblast-like cells and human bone marrow cells. Cells were grown in culture on NCD, which was deposited on silicon nitride (Si_3N_4) using hot-filament CVD. Microscopic examination of cell morphology, MTT analysis of proliferation and viability, and analysis of alkaline phosphatase activity showed better cell function on NCD-coated materials than on control materials. The authors suggest that the surface of the NCD-coated film, which has a surface roughness similar to that of bone, may facilitate osteoblast proliferation and function. Kalbacova *et al.*[126] evaluated the effect of NCD surface termination on osteoblast cell survival and growth. Osteoblast cells grown on hydrophilic oxygen-terminated NCD films exhibited improved viability and proliferation in comparison with as-deposited hydrogen-terminated NCD films.

Smisdom *et al.*[127] evaluated the growth of transfected Chinese hamster ovary cell cultures using hydrogen-terminated MCD thin films, oxygen-terminated MCD thin films, hydrogen-terminated NCD thin films, oxygen-terminated NCD thin films, and glass control materials. This work sought to determine whether transfected Chinese hamster ovary cells could be successfully cultured on diamond film surfaces without treatment with laminin, collagen, poly-D-lysine, or poly-L-lysine; laminin, collagen, poly-D-lysine, and poly-L-lysine are commonly used as surface treatments to promote cell attachment and growth.[127] Direct diamond-tissue contact would facilitate the use of diamond in implantable biosensor applications.[127] Hydrogen-terminated MCD and NCD films were deposited on silicon substrates using MPECVD; films were terminated with oxygen using potassium nitrate and sulfuric acid treatment. MTT, flow cytometry, and [^{3}H]-thymidine assays at 5 days of culture indicated no statistically significant differences in transfected Chinese hamster ovary cell proliferation, viability, or protein content on MCD surfaces or NCD surfaces than on glass control materials.[127] Some differences in cell proliferation and viability were observed at 7 days of culture. Additional investigation regarding the use of diamond in biological applications is necessary.

1.107.4.4. Biomedical Applications of MCD, NCD, and UNCD

1.107.4.4.1. Biosensor applications

Diamond electrodes have been considered for use in biosensor applications due to the semiconducting behavior, chemical inertness, and biological inertness of diamond. For example, diamond thin films have been investigated for use in biosensors for electrochemistry and biological molecule detection applications. Chatterjee *et al.*[128] evaluated the use of high-purity MCD films, low-phase purity MCD films, and NCD thin film electrodes for electrochemical analysis of riboflavin redox reactions. Their work examined the effectiveness of boron-doped microcrystalline hot-filament CVD-grown films and boron-free nanocrystalline films, which were grown using MPECVD techniques. Chatterjee *et al.* noted that adsorption of molecules and fouling of electrode surfaces pose a problem during the electrochemical analysis of biological molecules. The nonfouling properties of diamond suggest that it may be appropriate for use as an electrode material. Chatterjee *et al.* reported that high-phase purity MCD had very limited riboflavin adsorption, low-phase purity MCD had a moderate degree of riboflavin adsorption, and NCD had a high degree of riboflavin adsorption.[128] Adsorption of biological molecules on the electrode surface may be associated with difficulty in acquiring accurate information on an electrochemical reaction. The presence of nondiamond phases at grain boundaries in low-phase purity MCD films and NCD films may contribute to riboflavin adsorption. These efforts indicate that diamond films may be useful for electrochemical analysis of biological molecules; this material may find use in *in vitro* and *in vivo* biosensing applications.

NCD thin film electrodes have also been investigated; in many biosensor applications, attachment of biological molecules to the NCD surface is desirable. For example, Hartl *et al.*[129] described the use of green fluorescent protein and catalase in combination with NCD for use in amperometric measurements of solutions that contain hydrogen peroxide. Hydrogen peroxide is a by-product of many oxidase enzyme reactions in the body (e.g., breakdown of glucose); sensing of this molecule may be useful for detection of biological activities. Green fluorescent protein emits green light after absorbing blue light, enabling detection of protein attachment to an NCD surface with conventional fluorescence microscopy techniques. Hartl *et al.* confirmed protein molecule immobilization on an NCD electrode surface using green fluorescent protein. This study also demonstrated immobilization of catalase, which catalyzes the breakdown of hydrogen peroxide into water and oxygen, on the surfaces of NCD electrodes; hydrogen peroxide was amperometrically measured in concentrations between 0.3 and 150 mM using the electrodes.[129] In a similar study, Rubio-Retama *et al.*[130] immobilized horseradish peroxidase onto an NCD electrode for measurement of solutions containing hydrogen peroxide. The immobilized horseradish peroxidase allows for electron transfer and amperometric measurement of H_2O_2 in solution. In addition, Jian *et al.*[131] successfully demonstrated immobilization of glucose oxidase on UNCD electrode surfaces; these materials have potential use in *in vivo* glucose sensing applications. Popov *et al.*[106] modified NCD/amorphous carbon composite films with chemical linkers (e.g., 1-amino-3-cyclopentene hydrochloride) using UV irradiation. Ribonucleic acid molecules were subsequently attached; these structures may have potential use in bioanalytical assays.

1.107.4.4.2. Orthopedic applications

The high hardness, wear resistance, corrosion resistance, and low coefficient of friction values for diamond make it a promising material for use in orthopedic implant coating applications. In particular, diamond is being considered for use in articulating joint surfaces that encounter stresses because

of movement of the implant during its functional lifetime. Diamond is the hardest known material and exhibits excellent wear resistance. Diamond also exhibits low friction values. For applications in which one implant surface experiences contact with another implant surface (e.g., the articulating surface of a ball-and-socket joint), high wear resistance and low coefficient of friction values may serve to minimize production of wear particles and degradation of the implant surface. Deposition of diamond thin films onto the articulating surfaces of a joint prosthesis could reduce the friction and wear, thereby increasing the life span of the prosthesis and reducing the need for revision surgeries.[132] NCD and UNCD are desirable for this application because of their small grain sizes and low surface roughnesses.[133] Fries *et al.*[132] discussed the use of NCD as a coating on temporomandibular joint prostheses. They have suggested the need for the implant coatings to have low roughness, high hardness, corrosion resistance, and strong adhesion to the joint surface. Fries *et al.*[132] successfully demonstrated deposition of NCD on a Ti–6Al–4V substrate, which exhibited a geometry similar to that of a temporomandibular joint prosthesis component, by means of microwave plasma CVD.

1.107.4.4.3. Further biomedical applications

In addition to the biosensor and implant coating applications mentioned previously, diamond is being considered for use in a variety of other biomedical applications. On account of its favorable characteristics, including high chemical inertness, optical transparency, high thermal conductivity, and hydrophobicity in hydrogen-terminated form, NCD has been investigated for use in microfluidic lab-on-a-chip devices and microelectromechanical systems (MEMS).[134,135] Diamond can be made to resist nonspecific binding by DNA; hydrophobic surfaces may be created through hydrogen termination and fluorine termination. Khanna *et al.*[135] investigated the use of NCD for developing a chromatin immunoprecipitation lab-on-a-chip device. Chromatin immunoprecipitation is important for understanding cancer biology and diagnosing cancer. Nonspecific binding of DNA on NCD as well as a variety of materials typically used in microfluidic device fabrication (e.g., silicon, silicon dioxide, polydimethylsiloxane (PDMS), polymethylmethacrylate (PMMA), SU-8, and glass) was investigated. The results of the study indicated that nonspecific DNA binding was lowest on NCD, indicating that it is the most appropriate material for use in a high-sensitivity microfluidic device.

UNCD may be used as a surface coating in MEMS as well as MEMS that is used for biological applications (bioMEMS).[134] Bajaj *et al.*[134] compared cell growth on UNCD with that on platinum/titanium and (100) p-type silicon wafers. Platinum/titanium and (100) p-type silicon wafers are typically used in MEMS. Their work indicated that HeLa, PC12, and MC3T3 cells most favorably interacted with UNCD with respect to cell attachment, cell spreading, nuclear coverage, and cell rounding.[134] The high surface roughness of UNCD and the hydrogen termination of the UNCD surface may have contributed to the high biocompatibility of UNCD. Although additional testing is needed to better understand the cell–UNCD surface interactions, UNCD shows promise for use in bioMEMS applications (see **Chapter 3.315, Biological Microelectromechanical Systems (BioMEMS) Devices** for examples of bioMEMS devices).

There are many possibilities available for the use of diamond in biomedical applications due to its excellent biocompatibility and mechanical properties. For example, diamond has favorable blood interactions, leading to potential use in blood-contacting applications. Diamond thin films show promise in applications such as heart valves, vascular grafts, and stents.[69] For example, Jowzik *et al.*[136] developed an NCD-coated titanium alloy artificial heart valve using plasma-assisted CVD. The diamond coating remained on the entire surface after mechanical fatigue testing.

1.107.5. Summary of Carbon and Diamond

Carbon has been used as a biomaterial for many decades due to its unusual chemical, biological, and mechanical properties. Pyrolytic carbon, DLC, MCD, NCD, and UNCD have been considered for use in medical device applications. Pyrolytic carbon was the first carbon material to find extensive use in biomedical device applications, including cardiovascular and orthopedic devices. Initial studies involving pyrolytic carbon suggested that it was a hemocompatible material; as a result, pyrolytic carbon has found extensive use in prosthetic heart valves. More recent studies involving protein adhesion have brought the hemocompatibility of pyrolytic carbon into question. Long-term anticoagulant therapy is required for patients with pyrolytic carbon-coated heart valve prostheses in order to prevent thrombogenesis. Diamond and DLC have also garnered attention for use in orthopedic, cardiovascular, and sensor devices due to their unusual chemical, biological, and mechanical properties. Polycrystalline diamond coatings with micrometer-scale grains were initially investigated. In recent years, the biological properties of NCD and UNCD have been investigated. In the future, DLC, NCD, and UNCD will find use in medical device applications. In addition, pyrolytic carbon will continue to see a significant role in medical device applications. Scalable methods for the growth of DLC, NCD, and UNCD must be developed for these materials to be successfully translated to commercial use.

References

1. Donnet, C.; Erdemir, A. In *Tribology of Diamond-Like Carbon Films: Fundamentals and Applications*, Springer: New York, 2007; pp 1–9.
2. Erdemir, A.; Donnet, C. *J. Phys. D Appl. Phys.* **2006**, *39*, R311–R327.
3. Bokros, J. C. In *Chemistry and Physics of Carbon*; Walker, P. L., Ed.; Marcel Dekker: New York, 1969; Vol. 5, pp 1–118.
4. More, R.; Haubold, A. D.; Bokros, J. C. In *Biomaterials Science: An Introduction to Materials in Medicine*, 2nd ed.; Ratner, B., Hoffman, A. S., Schoen, F. J., Lemons, J. E., Eds.; Elsevier Academic Press: San Diego, CA, 2004; pp 170–181.
5. Pierson, H. O. In *Handbook of Carbon, Graphite, Diamond, and Fullerenes: Properties, Processing, and Applications*; Pierson, H. O., Ed.; Noyes Publications: Park Ridge, NJ, 1993; pp 356–373.
6. Tagmatarchis, N.; Prato, M. *Fullerene Based Materials, Structure and Bonding*; Mingos, D. M. P., Prassides, K., Eds.; Springer-Verlag: Berlin, Heidelberg, 2004; Vol. 109, pp 1–39.
7. Bokros, J. C. *Carbon* **1977**, *15*, 355–371.
8. Bokros, J. C. *Carbon* **1965**, *3*, 17–29.
9. Kaae, J. L. *Carbon* **1971**, *9*, 291–299.

10. Kaae, J. L. *Carbon* **1975**, *13*, 55–62.
11. Kaae, J. L. *Carbon* **1985**, *23*, 665–673.
12. Lopez-Honorato, E.; Meadows, P. J.; Xiao, P. *Carbon* **2009**, *47*, 396–410.
13. Meadows, P. J.; Lopez-Honorato, E.; Xiao, P. *Carbon* **2009**, *47*, 251–262.
14. Choon, H. O.; Lee, J. Y.; Oh, S. M. *Carbon* **1985**, *23*, 487–492.
15. Je, J. H.; Lee, J. Y. *Carbon* **1984**, *22*, 563–570.
16. Je, J. H.; Lee, J. Y. *J. Mater. Sci.* **1985a**, *20*, 839–844.
17. Je, J. H.; Lee, J. Y. *J. Mater. Sci.* **1985b**, *20*, 643–647.
18. Lee, J. Y.; Je, J. H.; Ryu, W. S.; Kim, H. S. *Carbon* **1983**, *21*, 523–533.
19. Oh, S. M.; Lee, J. Y. *Carbon* **1986**, *24*, 411–415.
20. Pesakova, V.; Klezl, Z.; Balik, K.; Adam, M. *J. Mater. Sci. Mater. Med.* **2000**, *11*, 793–798.
21. Nyilas, E.; Chiu, T. H. *Artif. Organs* **1978**, *2*(Suppl.), 56–62.
22. Cenni, E.; *et al*. *Biomaterials* **1995a**, *16*, 1223–1227.
23. Cenni, E.; *et al*. *Biomaterials* **1995b**, *16*, 973–976.
24. Fernandez, J.; Morse, D.; Maranhao, V.; Gooch, A. S. *Chest* **1974**, *65*, 640–645.
25. Schoen, F. J.; Titus, J. L.; Lawrie, G. M. *J. Biomed. Mater. Res.* **1982**, *16*, 559–570.
26. Antoniucci, D.; *et al*. *Am. J. Cardiol*. **2000**, *85*, 821–825.
27. Bartorelli, A. L.; *et al*. *Catheter Cardiovasc. Interv.* **2002**, *55*, 150–156.
28. Tuttle, H. G.; Stern, P. J. *J. Hand Surg.* **2006**, *31*, 930–939.
29. Bravo, C. J.; Rizzo, M.; Hormel, K. B.; Beckenbaugh, R. D. *J. Hand Surg.* **2007**, *32*, 1–11.
30. Cook, S. D.; Beckenbaugh, R. D.; Redondo, J.; Popich, L. S.; Klawitter, J. J.; Linscheid, R. L. *J. Bone Joint Surg. Am.* **1999**, *81A*, 635–648.
31. Pegoli, L.; Zorli, I. P.; Pivato, G.; Berto, G.; Pajardi, G. *J. Hand Surg. Br. Eur.* **2006**, *31*, 569–573.
32. Cook, S. D.; Thomas, K. A.; Kester, M. A. *J. Bone Joint Surg. Br.* **1989**, *71B*, 189–197.
33. Anderson, R. C.; Cook, S. D.; Weinstein, A. M.; Haddad, R. J. *Clin. Orthop. Relat. Res.* **1984**, *182*, 242–257.
34. Thomas, K. A.; Cook, S. D. *J. Biomed. Mater. Res.* **1985**, *19*, 875–901.
35. Thomas, K. A.; *et al*. *J. Biomed. Mater. Res.* **1985**, *19*, 145–159.
36. Herren, D. B.; Schindele, S.; Goldhahn, J.; Simmen, B. R. *J. Hand Surg. Br. Eur.* **2006**, *31B*, 643–651.
37. Kafesjian, R.; Howanec, M.; Ward, G. D.; Diep, L.; Wagstaff, L. S.; Rhee, R. *J. Heart Valve Dis.* **1994**, *3*(Suppl. 1), S2–S7.
38. Arvay, A.; Lengyel, M. *Eur. J. Cardiothorac. Surg.* **1988**, *2*, 340–346.
39. Vongpatanasin, W.; Hillis, L. D.; Lange, R. A. *N. Engl. J. Med.* **1996**, *335*, 407–416.
40. Litzler, P.; *et al*. *J. Thorac. Cardiovasc. Surg.* **2007**, *134*, 1025–1032.
41. Goodman, S. L.; Tweden, K. S.; Albrecht, R. M. *J. Biomed. Mater. Res.* **1996**, *32*, 249–258.
42. Goodman, S. L. *J. Biomed. Mater. Res.* **1999**, *45*, 240–250.
43. Park, J. B. In *Bioceramics: Properties, Characterizations, and Applications*, Springer: New York, NY, 2008; pp 198–218.
44. Robertson, J. *Mater. Sci. Eng. R* **2002**, *37*, 129–281.
45. Wei, Q.; Narayan, J. *Int. Mater. Rev.* **2000**, *45*, 133–164.
46. Cockayne, D. J. H.; McKenzie, D. R. *Acta Cryst.* **1988**, *A44*, 870–878.
47. Green, D. C.; McKenzie, D. R.; Lukins, P. B. *Mater. Sci. Forum* **1990**, *52*, 103–124.
48. Ferrari, A. C.; Robertson, J. *Phys. Rev. B* **2000**, *61*, 14095–14107.
49. Robertson, J. *Adv. Phys.* **1986**, *35*, 317–374.
50. Maeng, S. L.; *et al*. *Diam. Relat. Mater.* **2000**, *9*, 805–810.
51. Schultrich, B.; Scheibe, H. J.; Drescher, D.; Ziegele, H. *Surf. Coat. Technol.* **1998**, *98*, 1097–1101.
52. Zhang, S.; Johnson, H. T.; Wagner, G. J.; Liu, W. K.; Hsia, K. J. *Acta Mater.* **2003**, *51*, 5211–5222.
53. Anttila, A.; Lappalainen, R.; Tiainen, V. M.; Hakovirta, M. *Adv. Mater.* **1997**, *9*, 1161–1164.
54. Dimigen, H.; Klages, C. P. *Surf. Coat. Technol.* **1991**, *49*, 543–547.
55. Ferrari, A. C.; Kleinsorge, B.; Morrison, N. A.; Hart, A.; Stolojan, V.; Robertson, J. *J. Appl. Phys.* **1999**, *85*, 7191–7197.
56. Friedmann, T. A.; *et al*. *Appl. Phys. Lett.* **1997**, *71*, 3820–3822.
57. Sullivan, J. P.; Friedmann, T. A.; Baca, A. G. *J. Electron. Mater.* **1997**, *26*, 1021–1029.
58. Clough, F. J.; Milne, W. I.; Kleinsorge, B.; Robertson, J.; Amaratunga, G. A. J.; Roy, B. N. *Electron. Lett.* **1996**, *32*, 498–499.
59. Lacour, S. P.; Wagner, S.; Narayan, R. J.; Li, T.; Suo, Z. G. *J. Appl. Phys.* **2006**, *100*, 014913–014918.
60. Kobayashi, A.; *et al*. *Surf. Coat. Technol.* **1995**, *72*, 152–156.
61. Dearnaley, G.; Arps, J. H. *Surf. Coat. Technol.* **2005**, *200*, 2518–2524.
62. Lappalainen, R.; Anttila, A.; Heinonen, H. *Clin. Orthop. Relat. Res.* **1998**, *352*, 118–127.
63. Saikko, V.; Ahlroos, T.; Calonius, O.; Keranen, J. *Biomaterials* **2001**, *22*, 1507–1514.
64. Sheeja, D.; Tay, B. K.; Lau, S. P.; Nung, L. N. *Surf. Coat. Technol.* **2001**, *146–147*, 410–416.
65. Xu, T.; Pruitt, L. *J. Mater. Sci. Mater. Med.* **1999**, *10*, 83–90.
66. Sheeja, D.; Tay, B. K.; Nung, L. N. *Surf. Coat. Technol.* **2005**, *190*, 231–237.
67. Oñate, J. I.; *et al*. *Surf. Coat. Technol.* **2001**, *142–144*, 1056–1062.
68. Tiainen, V. M. *Diam. Relat. Mater.* **2001**, *10*, 153–160.
69. Gutensohn, K.; *et al*. *Thromb. Res.* **2000**, *99*, 577–585.
70. Klein, C. L.; *et al*. *J. Mater. Sci. Mater. Med.* **1994**, *5*, 798–807.
71. Ferguson, A. B.; Laing, P. G.; Hodge, E. S. *J. Bone Joint Surg. Am.* **1960**, *42*, 77–90.
72. Haycox, C. L.; Ratner, B. D. *J. Biomed. Mater. Res.* **1993**, *27*, 1181–1193.
73. Schaefer, O.; Lohrmann, C.; Winterer, J.; Kotter, E.; Langer, M. *Clin. Radiol.* **2004**, *59*, 1128–1131.
74. Ball, M.; O'Brien, A.; Dolan, F.; Abbas, G.; McLaughlin, J. A. *J. Biomed. Mater. Res. A* **2004**, *70A*, 380–390.
75. McLaughlin, J. A.; Meenan, B.; Maguire, P.; Jamieson, N. *Diam. Relat. Mater.* **1996**, *5*, 486–491.
76. Roy, K. R.; Lee, K. R. *J. Biomed. Mater. Res. B* **2007**, *83B*, 72–84.
77. Judkins, M. P.; Hinck, V. C.; Dotter, C. T. *Am. J. Roentgenol. Ra* **1968**, *104*, 223–224.
78. Takayasu, K.; Muramatsu, Y.; Moriyama, N.; Ohtsu, T.; Catapia, F. C. *Radiology* **1988**, *166*, 545–546.
79. Hasebe, T.; *et al*. *Diam. Relat. Mater.* **2006**, *15*, 129–132.
80. Choi, H. W.; Lee, K. R.; Wang, R. Z.; Oh, K. H. *Diam. Relat. Mater.* **2006**, *15*, 38–43.
81. Maguire, P. D.; *et al*. *Diam. Relat. Mater.* **2005**, *14*, 1277–1288.
82. Grill, A. *Diam. Relat. Mater.* **2003**, *12*, 166–170.
83. Marciano, F. R.; Bonetti, L. F.; Santos, L. V.; Da-Silva, N. S.; Corat, E. J.; Trava-Airoldi, V. J. *Diam. Relat. Mater.* **2009**, *18*, 1010–1014.
84. Morrison, M. L.; *et al*. *Diam. Relat. Mater.* **2006**, *15*, 138–146.
85. Narayan, R. J.; Scholvin, D. *J. Vac. Sci. Technol. B* **2005**, *23*, 1041–1046.
86. Narayan, R. J. *J. Adhes. Sci. Technol.* **2004**, *18*, 1339–1365.
87. Zhou, D.; Gruen, D. M.; Qin, L. C.; McCauley, T. G.; Krauss, A. R. *J. Appl. Phys.* **1998**, *84*, 1981–1989.
88. Williams, O. A.; *et al*. *Diam. Relat. Mater.* **2008**, *17*, 1080–1088.
89. Kanda, H.; Sekine, T. In *Properties, Growth, and Applications of Diamond*; Nazaré, M., Neves, A., Eds.; INSPEC, the Institution of Electrical Engineers: London, UK, 2001; pp 247–255.
90. Frenklach, M. *J. Appl. Phys.* **1989**, *65*, 5142–5149.
91. Gruen, D. *Annu. Rev. Mater. Sci.* **1999**, *29*, 211–259.
92. Wild, C.; *et al*. *Diam. Relat. Mater.* **1993**, *2*, 158–168.
93. Wild, C.; Herres, N.; Koidl, P. *J. Appl. Phys.* **1990**, *68*, 973–978.
94. Abreu, C. S.; Amaral, M.; Oliveira, F. J.; Gomes, J. R.; Silva, R. F. *Diam. Relat. Mater.* **2009**, *18*, 271–275.
95. Amaral, M.; Salgueiredo, E.; Oliveira, F. J.; Fernandes, A. J. S.; Costa, F. M.; Silva, R. F. *Surf. Coat. Technol.* **2006**, *200*, 6409–6413.
96. Matsumoto, S.; Sato, Y.; Tsutsumi, M.; Setaka, N. *J. Mater. Sci.* **1982**, *17*, 3106–3112.
97. Kang, M.; Lee, W.; Baik, Y. *Thin Solid Films* **2001**, *398*, 175–179.
98. Amaral, M.; Oliveira, F. J.; Belmonte, M.; Fernandes, A. J. S.; Costa, F. M.; Silva, R. F. *Surf. Eng.* **2003**, *19*, 410–416.
99. Achatz, P.; *et al*. *Phys. Status Solidi A* **2007**, *204*, 2874–2880.
100. Benedic, F.; Duten, X.; Syll, O.; Lombardi, G.; Hassouni, K.; Gicquel, A. *Chem. Vapor Depos.* **2008**, *14*, 173–180.
101. Ikeda, T.; Teii, K. *Diam. Relat. Mater.* **2006**, *15*, 635–638.
102. Liu, C. M.; Kungen, T.; Sung, T. L.; Ting, K.; Teii, S. *IEEE Trans. Plasma Sci.* **2009**, *37*, 1172–1177.
103. Liu, Y. K.; Tzeng, Y.; Liu, C.; Tso, P.; Lin, I. N. *Diam. Relat. Mater.* **2004**, *13*, 1859–1864.
104. Narayan, R. J.; *et al*. *Diam. Relat. Mater.* **2006**, *15*, 1935–1940.
105. Popov, C.; Bliznakov, S.; Kulisch, W. *Diam. Relat. Mater.* **2007**, *16*, 740–743.
106. Popov, C.; *et al*. *Diam. Relat. Mater.* **2008**, *17*, 882–887.
107. Achatz, P.; *et al*. *Appl. Phys. Lett.* **2006**, *88*, 101908–101910.
108. Xiao, X.; Birrell, J.; Gerbi, J. E.; Auciello, O.; Carlisle, J. A. *J. Appl. Phys.* **2004**, *96*, 2232–2239.
109. Mitura, S. *Proc. SPIE* **1997**, *3179*, 79–86.
110. Mitura, S.; Mitura, A.; Niedzielski, P.; Couvrat, P. *Chaos Solitons Fractals* **1999**, *10*, 2165–2176.

111. Feng, J. Y.; Shang, N. G.; Sun, X. S.; Bello, I.; Lee, C. S.; Lee, S. T. *Diam. Relat. Mater.* **2000**, *9*, 872–876.
112. Hara, T.; *et al*. *Diam. Relat. Mater.* **2004**, *13*, 679–683.
113. Amaral, M.; Mohasseb, F.; Oliveira, F. J.; Benedic, F.; Silva, R. F.; Gicquel, A. *Thin Solid Films* **2005**, *482*, 232–236.
114. Beck, C. M.; Brearley, C. J. *GEC Rev.* **1999**, *14*, 115–123.
115. Panizza, M.; Cerisola, G. *Electrochim. Acta* **2005**, *51*, 191–199.
116. Aspenberg, P.; *et al*. *Biomaterials* **1996**, *17*, 807–812.
117. Hedenborg, M.; Klockars, M. *Lung* **1989**, *167*, 23–32.
118. Nordsletten, L.; Hogasen, A. K. M.; Konttinen, Y. T.; Santavirta, S.; Aspenberg, P.; Aasen, A. O. *Biomaterials* **1996**, *17*, 1521–1527.
119. Tang, T. L.; Tsai, C.; Gerberich, W. W.; Kruckeberg, L.; Kania, D. R. *Biomaterials* **1995**, *16*, 483–488.
120. Tse, R. L.; Phelps, P. *J. Lab. Clin. Med.* **1970**, *76*, 403–415.
121. Garguilo, J. M.; Davis, B. A.; Buddie, M.; Kock, F. A. M.; Nemanich, R. J. *Diam. Relat. Mater.* **2004**, *13*, 595–599.
122. Specht, C. G.; Williams, O. A.; Jackman, R. B.; Schoepfer, R. *Biomaterials* **2004**, *25*, 4073–4078.
123. Ariano, P.; *et al*. *Diam. Relat. Mater.* **2005**, *14*, 669–674.
124. Amaral, M.; Gomes, P. S.; Lopes, M. A.; Santos, J. D.; Silva, R. F.; Fernandes, M. H. *Acta Biomater.* **2009**, *5*, 755–763.
125. Amaral, M.; *et al*. *J. Biomed. Mater. Res. A* **2008**, *87A*, 91–99.
126. Kalbacova, M.; *et al*. *Phys. Status Solidi B* **2007**, *244*, 4356–4359.
127. Smisdom, N.; *et al*. *Phys. Status Solidi A* **2009**, *206*, 2042–2047.
128. Chatterjee, A.; Foord, J. *Diam. Relat. Mater.* **2009**, *18*, 899–903.
129. Hartl, A.; *et al*. *Nat. Mater.* **2004**, *3*, 736–742.
130. Rubio-Retama, J.; *et al*. *Langmuir* **2006**, *22*, 5837–5842.
131. Jian, W.; Firestone, M. A.; Auciello, O.; Carlisle, J. A. *Langmuir* **2004**, *20*, 11450–11456.
132. Fries, M. D.; Vohra, Y. K. *Diam. Relat. Mater.* **2004**, *13*, 1740–1743.
133. Zhang, L.; Sirivisoot, S.; Balasundaram, G.; Webster, T. J. In *Advanced Biomaterials: Fundamentals, Processing, and Applications*; Basu, B., *et al*. Eds.; Wiley: Hoboken, NJ, 2009; pp 205–241.
134. Bajaj, P.; *et al*. *Biomed. Microdevices* **2007**, *9*, 787–794.
135. Khanna, P.; *et al*. *Diam. Relat. Mater.* **2006**, *15*, 2073–2077.
136. Jozwik, K.; Karczemska, A. *Diam. Relat. Mater.* **2007**, *16*, 1004–1009.

1.108. Wear-Resistant Ceramic Films and Coatings

I Gotman and E Y Gutmanas, Department of Materials Engineering, Israel Institute of Technology, Haifa, Israel
G Hunter, Smith & Nephew, Inc., Memphis, TN, USA

© 2011 Elsevier Ltd. All rights reserved.

1.108.1.	**Introduction**	127
1.108.2.	**State of the Art – Processing, Microstructure, Biocompatibility, and Mechanical Properties of Ceramic Coatings**	128
1.108.2.1.	Surface Modification Processes	128
1.108.2.1.1.	Ion implantation	129
1.108.2.1.2.	Physical vapor deposition	129
1.108.2.1.3.	Diffusion surface modification	130
1.108.2.2.	Specific Wear-Resistant Surface Modification Processes	130
1.108.2.2.1.	Oxidized zirconium	130
1.108.2.2.2.	Titanium nitride (TiN) coatings	132
1.108.2.2.3.	Diamond-like carbon coatings	137
1.108.2.2.4.	Multicomponent hard coatings	138
1.108.2.3.	Simulation and Testing of Wear-Resistant Surface Modifications	138
1.108.2.3.1.	Durability comparisons	138
1.108.2.3.2.	Wear simulation tests	140
1.108.2.4.	*In Vivo* Performance of Wear-Resistant Ceramic Coatings	150
1.108.2.4.1.	Animal studies	150
1.108.2.4.2.	Clinical performance	151
1.108.3.	**Future Trends**	152
References		152

Abbreviations

AEPVD	Arc evaporative PVD
AIP	Arc ion plating
ASF	Artificial synovial fluid
CoCr	Co–28 wt% Cr–6 wt% Mo alloy
CVD	Chemical vapor deposition
DLC	Diamond-like carbon
EB, E-beam	Electron beam
FCVA	Filtered cathodic vacuum arc
ICP	Inductively coupled plasma
IIAMS	Ion implantation assisted magnetron sputtering
LFIT	Low friction ion treatment
Mc	Million cycles
MoM	Metal-on-metal
MuBiNaFs	Multicomponent, bioactive nanostructured films
OXINIUM, OxZr	Oxidized zirconium
PE	Polyethylene
PACVD	Plasma-assisted CVD
PAPVD	Plasma-assisted PVD
PIIID	Plasma immersion ion implantation and deposition
PIRAC	Powder immersion reaction-assisted coating
PN	Plasma-nitrided
PVD	Physical vapor deposition
r.f.-PECVD	Radio frequency plasma-enhanced chemical vapor deposition
SEM	Scanning electron microscope
SHS	Self-propagating high-temperature synthesis
Ti–6Al–4V	Ti–6 wt% Al–4 wt% V alloy
TiN, Ti_2N	Titanium nitride
THA	Total hip arthroplasty
THR	Total hip replacement
TJR	Total joint replacement
TKA	Total knee arthroplasty
TKR	Total knee replacement
UHMWPE	Ultra-high-molecular-weight polyethylene

1.108.1. Introduction

Total joint arthroplasty is a successful and accepted procedure for the treatment of advanced osteoarthritis. Improvements in the implants are desired despite this success to keep pace with the increasing demands and expectations of patients. One limitation for the longevity of joint replacements is related to articular wear, the debris from which can lead to osteolysis and subsequent aseptic loosening. A detailed discussion of wear-related osteolysis can be found in the **Chapter 6.606, Biological Effects of Wear Debris from Joint Arthroplasties**. Efforts to reduce wear have focused primarily on improving

implant design and the quality of the ultra-high-molecular-weight polyethylene (UHMWPE) often used as one of the bearing surfaces. It is also important to consider the influence of the hard bearing counterface surface that articulates against the polyethylene (PE) in order to reduce the generation of wear debris even further and thereby reduce the potential for osteolysis and loosening.

The hard bearing surface can produce wear of the PE surface during articulation through both abrasive and adhesive mechanisms. Wear mechanisms of polyethylene that apply to prosthetic joints are reviewed in the **Chapter 6.603, Ultra-high Molecular Weight Polyethylene Total Joint Implants**. Positive asperities on the hard counterface can abrade the PE surface, which is softer, producing abrasive wear debris. Friction between the articulating surfaces shears off particles, producing adhesive wear debris. Improved lubrication reduces friction and tends to reduce adhesive wear. Hard 'third-body' particles in the joint space that intrude between the articulating surfaces can embed in the PE producing abrasive wear of the hard counterface, with the resulting increased hard surface roughness in turn tending to increase friction and abrasive wear of the PE.

Examination of explanted arthroplasty components has shown that roughening of the hard counterface occurs clinically, and that many observed scratches have a shape and orientation that can increase PE wear.[1–11] Not only does volumetric wear of PE increase with increasing counterface roughness, but it also has been found that increasingly sharp peaks associated with counterface scratches increase the tendency for the production of submicron debris that may be related to osteolysis. These findings suggest that a hard counterface that resists roughening and provides lower friction with PE should reduce abrasive and adhesive wear and thereby prolong the lifetime of the joint replacement.

A metallic cobalt–chromium (CoCr) alloy (Co–28% Cr–6% Mo) is the standard material for hard bearing joint replacement components. The oxide ceramics alumina and zirconia are the most popular alternatives to CoCr. Their harder surfaces resist roughening and tend to produce less friction by having better 'wetting' characteristics with lubricating fluids in the joint. These ceramics have demonstrated improved wear performance over metal surfaces in laboratory and clinical investigations.[12–20] The adaptation of monolithic ceramics has been slow because their brittle nature has limited implant designs and created concerns for component fracture.

The desired alternative would combine the fracture toughness of metals with the wear performance of ceramics. One approach for achieving this is to combine a thin ceramic surface on a metallic substrate. While simple in concept, providing a clinically and commercially successful combination has proven challenging.[21] Besides having the desired tribological wear properties already discussed, the materials must be biocompatible and have suitable mechanical properties and structural stability. As a practical matter, these components must be fabricated with reliable consistency and at a reasonable cost.

A critical feature for alternative technology is the durability of the ceramic film on the metallic substrate. The ceramic must adhere to the metal so that it does not chip or spall from the surface under the stress and strain experienced during surgical implantation and clinical use. The film itself must be cohesive within itself to resist fracture and shear during articulation with PE and third-body particles. Not only would adhesive or cohesive failure of the ceramic film negate its potential wear advantages, but also it would liberate hard third-body particles into the joint that could increase abrasive wear of the unprotected metal. Because no material is damage-proof, it is desirable that the film be able to tolerate localized accidental damage to the surface without progressive adhesive or cohesive failure.

In some applications, it is desirable to avoid the use of a PE bearing altogether. This is the motivation for the hard–hard bearing combinations of metal-on-metal (MoM) and ceramic-on-ceramic (CoC) that use monolithic metal and ceramic. One important example is hip resurfacing (HR) arthroplasty where MoM is currently the only option. Both MoM and CoC bearings generate orders of magnitude less wear debris than the standard CoCr–UHMWPE articulation.[22–24] Concerns with CoC bearings include a small risk of brittle fracture and the squeaking phenomenon, whereas MoM bearings have been associated with elevated metal ion levels. Because the metals and ceramics used are less compliant than PE, the resulting mechanical loading is much more demanding in hard–hard applications. This challenge is illustrated by the fact that hard–hard applications have been introduced for hips and not for knees. The ball-in-socket nature of a hip implant produces lower and more consistent stress concentrations on the surfaces. Thus, a ceramic thin film application that could be used in a hard–hard application, while desirable, would be even more challenging than for bearing against PE.

1.108.2. State of the Art – Processing, Microstructure, Biocompatibility, and Mechanical Properties of Ceramic Coatings

1.108.2.1. Surface Modification Processes

There are countless variations of processes and materials that have been proposed, investigated, or implemented to create ceramic films on the surface of a metal.[21] One type of method is to deposit or overlay a ceramic coating onto the metal surface (**Figure 1**). This can be thought of as an 'exogenous' film. The mechanical properties of the ceramic are typically much different from those of the metal, causing a potential for adhesive failure between the two materials under load or during

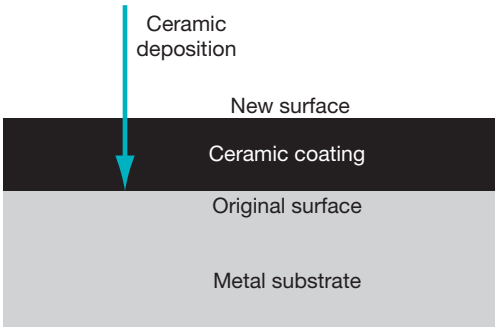

Figure 1 Depositing a ceramic layer onto the original metal surface produces an 'exogenous' ceramic surface film. Examples of this are physical vapor deposition and chemical vapor deposition.

articulation. Sometimes, multiple coatings are deposited to enhance adhesion or to make the transition in properties more gradual. Another method of creating the ceramic film is to diffuse or inject a nonmetallic element such as nitrogen into the surface and cause a phase transformation of the surface from metal to ceramic (Figure 2). This can be thought of as an 'autogenous' film. The rate of diffusion typically restricts this process so that either the film is very thin or the processing time is very long. One advantage of this approach is that a diffusional gradient with an associated gradient in properties often underlies the film to aid in adhesion. These exogenous and autogenous approaches can be used together as well. For example, a ceramic can be deposited onto the surface and then diffused partly or fully into the metal, or a diffusion zone can be created on the surface of the metal before a coating is applied.

1.108.2.1.1. Ion implantation

The basic concept of ion implantation is to use a highly energetic beam of ions to bombard a surface and become incorporated on and into it.[25] This modifies the surface structure and chemistry, but does not modify component dimensions or bulk material properties because it is conducted at low temperature (Figure 3). With sufficiently high beam energy, atoms in the surface can be sputtered away and the crystal structure can be disrupted. At lower energies, a nonmetallic element can be implanted into a metal surface to increase its hardness and wear resistance, and to reduce friction.

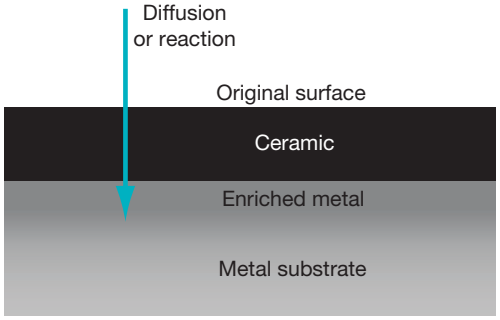

Figure 2 Diffusing a nonmetallic element into the original metal surface beyond its saturation limit transforms it into an 'autogenous' ceramic surface film. Examples of this are thermally driven oxidation and electrochemically driven anodization.

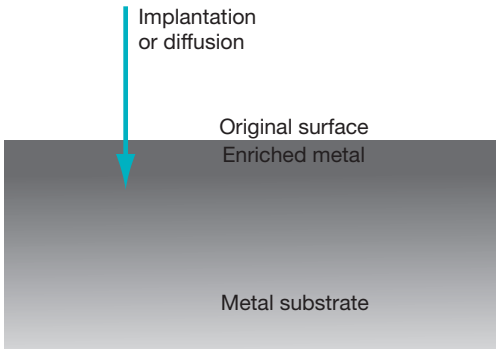

Figure 3 Diffusing a nonmetallic element into the original metal surface below its saturation limit modifies the surface composition and properties without causing a phase transformation. An example of this is nitrogen-ion implantation.

The ion implantation process is conducted in a vacuum chamber and consists of three basic steps. First, ionized plasma is formed by stripping electrons from source atoms. Each ion is typically a single atom or molecule. Next, the ions are accelerated and focused into a beam using a potential gradient column and a series of electrostatic and magnetic lens elements. Lastly, the ion beam is directed onto and scanned over the target surface. This implants the ions onto the surface and into the crystalline structure of the target surface. The concentration of the ion species at the surface increases with implantation time. It is a line-of-sight process, so specialized fixturing is needed for uniform treatment of complex geometries. The energy and composition of the ions and the composition of the target affect the depth of ion penetration. Typically, this depth is less than a micron.

The primary commercialization of ion implantation in the orthopedic industry involves implanting nitrogen ions into CoCr alloy (LFIT – low friction ion treatment, Stryker, Mahwah, NJ), although it also has been applied to Ti alloys.[26,27] In this application, insufficient nitrogen is implanted to create a continuous ceramic nitride film. It is discussed in this chapter to illustrate the potential of altering the metal surface properties. The ions penetrate to a depth of 200 nm into the CoCr metal, creating crystalline lattice strains that harden the metal. One measurement indicated that the microhardness of the surface was doubled by the treatment.[27] The ions also increase the surface energy of the metal, causing the surface to become more hydrophilic, so the synovial fluids can more effectively lubricate the interface. In one case, laboratory testing indicated a reduction in the coefficient of friction against UHMWPE to be approximately 25%.[27] These types of effects are typical of the general features intended by creating a ceramic film.

1.108.2.1.2. Physical vapor deposition

Deposition methods of surface modification are based on adding a new material to the surface as a coating and do not involve the substrate material constituents. The coating substance is transported from a source material and deposited on the substrate surface. Physical vapor deposition (PVD) is a generic term for a large family of vacuum deposition techniques where a solid source (target) is converted into vapor by physical means.[28,29] Typical source materials are pure metals or alloys such as titanium, zirconium, chromium, and titanium–aluminum. To produce a hard coating, a reactive gas (nitrogen, oxygen, or hydrocarbon) is introduced during the evaporation process. The gas reacts with the ionized metal vapor to form a compound that is then deposited on the substrate as a thin film. The coating process consists of three main steps: (1) evaporation – removal of material from the target; (2) transportation of the plasma constituents to the substrate; and (3) condensation of the coating on the substrate.

The available PVD methods differ in the means of producing metal vapor, the main technologies being sputtering, electron beam (E-beam) evaporation, and arc evaporation (AE). Depending on the technology used, plasma material of different quality is generated. The positively charged constituents of

plasma tend to travel to the negatively charged substrate in straight lines making PVD a 'line-of-sight' process. This means that only areas exposed to the plasma will be coated.

Sputtering is one of the most versatile PVD processes available for various metallic and ceramic (carbide and nitride) thin films preparation.[30] In PVD by sputtering, the source material is converted into vapor by bombarding with high-energy particles or ions. A glow discharge is produced in an argon atmosphere at low pressure, with the target being the cathode. The argon ions are accelerated in the direction of the target by the electrical field and knock atoms out of the target. The addition of concentrated magnetic fields near the target increases the deposition rate (magnetron sputtering) by increasing the density of the plasma and power density on the target surface. Sputtered films are typically denser and have a better adhesion on the substrate than evaporated films; however, they have higher compressive stresses and a higher level of impurities as the inert sputtering atoms can be built into the growing film.

In PVD by evaporation, the conversion into vapor phase is achieved by applying heat to the source material.[31] In electron-beam evaporation (EB-PVD), metal vapor plasma is produced by melting the source material in a crucible using a focused high kinetic energy beam of electrons. Coatings produced by EB-PVD are smooth, dense, and defect free. The coating thickness, however, is limited to the volume of the crucible, and film adhesion is weak because of the low level ionization of metal vapor achieved by the e-beam.

In cathodic arc PVD, an electric arc is used to vaporize materials from a solid target. The cathodic spot is small (0.1–10 μm) and the resulting high current densities lead to the local melting of the cathode surface and subsequent evaporation and ionization of the source material. The arc spot continuously moves on the cathode surface because of the different resistance to current flow of a liquid versus a solid. Magnets are used to confine the arc to the cathode surface and influence its motion. Here, a solid cathode source allows placement of cathodes in any orientation to ensure proper plasma density leading to coating uniformity at the substrate. A major drawback of this technique is the emission of micrometer-sized liquid droplets of the target material from the arc spot. These macroparticles can be trapped in the growing film and extend through the coating, thereby strongly deteriorating its physical and mechanical properties.

PVD processes are typically carried out at low substrate temperatures (180–500 °C), which allows for coating deposition without detrimentally affecting bulk properties. On the other hand, only physical (rather than chemical) bond is created between the coating and the substrate often leading to weak coating adhesion.

1.108.2.1.3. Diffusion surface modification

Diffusion surface treatments aim to produce corrosion-resistant, wear-resistant, and hardened surface layers by superficially diffusing new elements (nitrogen, carbon) into the substrate at elevated temperatures. In contrast to deposition techniques (e.g., PVD), substrate material constituents are actively involved in the modified layer formation. Nitriding – diffusing nitrogen atoms into the metal surface – is one of the most widely used surface hardening techniques. The diffused nitrogen reacts with the metal and forms metal nitrides to impart hardness on the surface up to a certain depth determined by the metal properties. There are several commercial nitriding methods, the difference lying in nitrogen supply. In salt bath nitriding, the source of nitrogen is molten salt; in gas nitriding, nascent nitrogen is produced by dissociation of ammonia, and in plasma nitriding (ion nitriding), molecular nitrogen is split into ions in an electromagnetic field.[32,33] Plasma nitriding is the preferred nitriding route for stainless steels and titanium alloys. The process is conducted in a heated vacuum chamber in a glow discharge at a very low pressure and under high voltage. High-voltage electrical energy is used to form plasma through which nitrogen ions are accelerated to impinge on the workpiece.[34] This ion bombardment heats the workpiece and cleans the surface providing active nitrogen which then penetrates inside by diffusion. The nitriding current, temperature, and process time determine the depth of the nitride case. Plasma nitriding, by nature, is faster than traditional gas nitriding because of activation of the main reactive species. The benefits of plasma nitriding include lower processing temperatures and correspondingly lower mechanical distortion, as well close control of microstructure allowing nitriding with or without compound layer (TiN–Ti_2N in the case of titanium substrate) formation. Because of the growth of the layer from the bulk material, there is no danger of the layer spalling off as in the case of PVD treatments. Furthermore, a hardened diffusion zone supports the compound layer.

PIRAC (powder immersion reaction-assisted coating) nitriding has been proposed as an alternative nitriding method.[35] In PIRAC nitriding, a workpiece is annealed in a chromium steel container that prevents oxygen penetration while allowing for inward diffusion of atmospheric nitrogen. As a result, oxygen-free monatomic nitrogen environment is created on-site, without the use of vacuum pumps and nitrogen gas supply.

1.108.2.2. Specific Wear-Resistant Surface Modification Processes

1.108.2.2.1. Oxidized zirconium

Oxidized zirconium was developed for orthopedic applications to provide improvements over CoCr alloy for resistance to roughening and frictional behavior, and for biocompatibility without the mechanical limitations of brittle monolithic ceramics.[36–39] The manufacturing process begins with zircon-containing beach sand as the raw material that is refined to zirconium metal which then is fabricated into a prosthetic joint replacement (Figure 4). The wrought zirconium alloy (Zr–2.5% Nb) is oxidized by thermal diffusion in heated air to create a cohesive and adherent zirconium oxide ceramic surface of about 5 μm thickness (Figure 5). The oxide is not an externally applied coating, but rather a transformation of the original metal surface into zirconia ceramic. The oxide is thick enough to provide the desired tribological properties against UHMWPE or cartilage, but is thin enough that the component retains its metallic toughness and resilience. This technology has been in global commercial use for over 10 years under the trade name OXINIUM (Smith & Nephew Orthopaedics, Memphis, TN), and is used for in both knee and hip applications.

Although similar in manufacture and properties to titanium, zirconium exhibits several unusual processing attributes,



Figure 4 Zircon-containing sand (left) is the raw material that is refined to zirconium metal which is then fabricated to make an oxidized zirconium implant (right). Reproduced with permission from Hunter, G.; Dickinson, J.; Herb, B.; Graham, R *Titanium, Niobium, Zirconium, and Tantalum for Medical and Surgical Applications*, ASTM STP 1471; Zardiackas, L. D., Kraay, M. J., Freese, H. L., eds.; American Society for Testing and Materials: West Conshohocken, PA, 2006; pp 16–29.

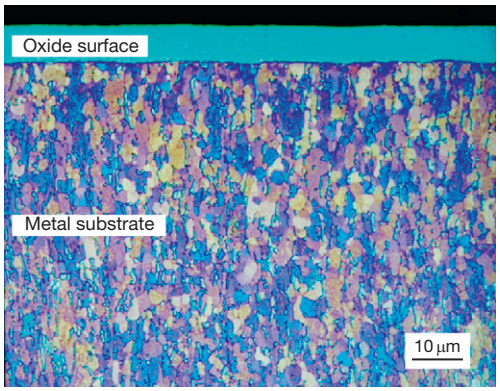

Figure 5 Oxygen naturally diffuses into the zirconium alloy when the alloy is heated in air, causing the original metal surface to transform to zirconium oxide (zirconia) ceramic (the outer surface is at top in this cross-sectional optical micrograph that is heat-tinted to show the metal microstructure). Reproduced with permission from Hunter, G.; Dickinson, J.; Herb, B.; Graham, R. *Titanium, Niobium, Zirconium, and Tantalum for Medical and Surgical Applications*, ASTM STP 1471; Zardiackas, L. D., Kraay, M. J., Freese, H. L., eds.; American Society for Testing and Materials: West Conshohocken, PA, 2006; pp 16–29.

including its oxidation behavior.[40,41] Small amounts of niobium and oxygen are alloyed with the zirconium metal to create a two-phase microstructure of hexagonal close-packed α-Zr and body-centered cubic β-Zr with sufficient strength and other mechanical properties for use as an orthopedic prosthesis.[42] Like titanium, the metallic elements of zirconium and niobium are very biocompatible with minimum biological availability and electrocatalytic activity because of their passive oxide layers with extremely low solubility and excellent protective ability.[43–45] The biocompatibility of the alloy both with and without an oxide was found to be at least equivalent to that of titanium alloy (Ti–6% Al–4% V) and CoCr.[36,38]

The ceramic surface is formed by heating the zirconium alloy in air to a temperature above 500 °C to allow oxygen to diffuse into the surface. Once the surface becomes saturated

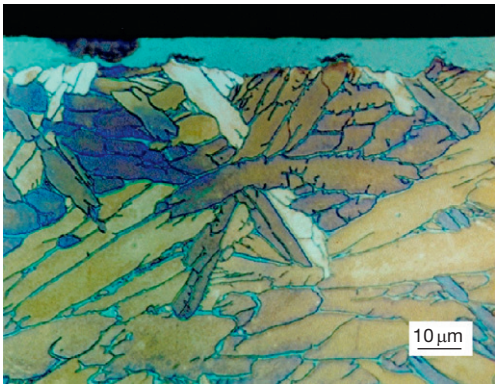

Figure 6 This centrifugal casting of the zirconium alloy produced a nonuniform oxide with internal cracks (the outer surface is at the top in this cross-sectional micrograph that is heat-tinted to show the coarse cast microstructure). Reproduced with permission from Hunter, G.; Dickinson, J.; Herb, B.; Graham, R. *Titanium, Niobium, Zirconium, and Tantalum for Medical and Surgical Applications*, ASTM STP 1471; Zardiackas, L. D., Kraay, M. J., Freese, H. L., eds.; American Society for Testing and Materials: West Conshohocken, PA, 2006; pp 16–29.

with oxygen, the metallic surface transforms into a dense ceramic that is predominantly monoclinic zirconia.[40,41] This crystal structure is fully stable, unlike the metastable tetragonal crystal structure of yttria-stabilized zirconia components.[46] Individual grains in the microstructure of stabilized zirconia have a tendency to transform to the monoclinic structure under certain conditions such as those during autoclave sterilization procedures. The transformation can result in reduced strength and increased surface roughness. This cannot happen to the monoclinic oxide on oxidized zirconium.

The desired oxide cohesiveness is created by the proper combination of many factors at the original metal surface.[37] Castings have a coarse microstructure that allows nonuniform oxide growth, which can lead to crack formation within the oxide (Figure 6). During oxidation, very smooth or contaminated surfaces can produce esthetic and functional flaws in the oxide. An appropriate selection of time and temperature during oxidation can produce an oxide of uniform thickness without internal flaws. Continuing oxidation at a given temperature eventually leads to a transition in oxidation behavior during which the oxide starts cracking and growing rapidly and nonuniformly. Therefore, clean and moderately rough articular surfaces on fine-grained wrought material are oxidized at a tightly controlled time and temperature in order to produce a high integrity oxide of consistent thickness.

Oxidized zirconium components are made from wrought alloy because the local rate of oxide growth and the resulting oxide microstructure are affected by the metallic microstructure.[37] The refined metallic microstructure produces a fine-grained (essentially nanostructural) oxide (Figure 7). The fine-grained structure provides some effective ductility so that the oxide can deform modestly without cracking. The diffusion process allows for a uniform oxide layer to form, even on complex shaped components. This oxide is comprised primarily of a staggered columnar microstructure oriented perpendicular to the outer surface.[40,41] It is left in a compressive stress state without pores or voids internally or at the

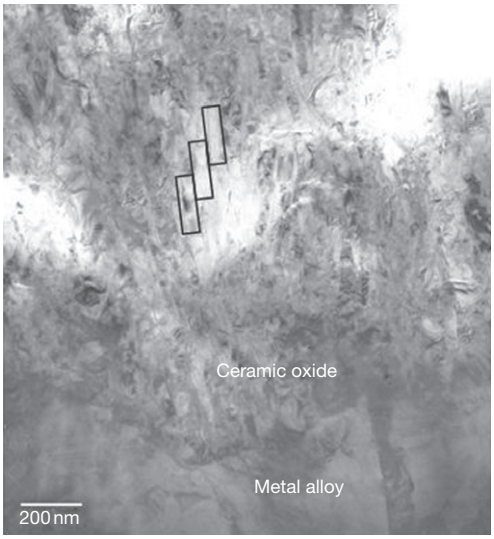

Figure 7 The oxide on zirconium exhibits excellent integrity which is due in part to grains that are columnar, staggered, nanostructural in size, and generally perpendicular to the surface. Three examples of the oxide grains are outlined in this transmission electron micrograph from the ceramic–metal interface. Reproduced from Benezra, V.; Mangin, S.; Treska, M.; Spector, M.; Hunter, G.; Hobbs, L. W. In *Biomedical Materials*, MRS Symposium Proceedings; Neenan, T., Marcolongo, M., Valentini, R. F.; Materials Research Society: Warrendale, PA, 1999; Vol. 550, pp 337–342.



Figure 8 The component does not break and the oxide remains adherent after an oxidized zirconium knee femoral component condyle is bent 45° under continuous loading to 20 kN. Reproduced from Hunter, G.; Jones, W. M.; Spector, M. In *Total Knee Arthroplasty*; Bellemans, J., Ries, M. D., Victor, J., eds.; Springer Verlag: Heidelberg, Germany, 2005; pp 370–377, with permission from Springer.

interface. An oxygen diffusion gradient beneath the oxide provides a gradual transition to the underlying metal mechanical properties. All of these microstructural features enhance cohesion and adhesion of the oxide even under shear and mechanical strain.

Because of the strength, toughness, and stability of oxidized zirconium, it can be used to produce components that duplicate the design of ones made from CoCr. In contrast to the limitations exhibited by monolithic ceramics such as alumina and zirconia, oxidized zirconium heads do not exhibit brittle fracture during crush tests.[46] Biomechanical testing and finite element analysis demonstrate that knee femoral components made from oxidized zirconium and CoCr have equivalent device fatigue strength, with both exceeding a strength of 450 MPa for 10 million cycles (Mc).[47] Continuous loading of a single oxidized zirconium knee condyle up to 20 kN can cause it to bend to an angle of 45°, but the condyle does not break and the oxide remains attached and functional (Figure 8). Having oxidized zirconium components with the same designs as CoCr components allows a surgeon the flexibility of offering the advantages of a ceramic bearing with metallic component strength using a similar design that obviates the need for unique surgical procedures and associated training.

Like other oxide ceramics, oxidized zirconium can reduce friction (and thereby adhesive wear of UHMWPE) relative to that of metal surfaces by roughening less and better maintaining a lubricating film.[12] Laboratory studies have shown that the oxide exhibits better wetting behavior in lubricating fluids (Figure 9) and can produce up to 50% less friction against UHMWPE than does CoCr.[48–53] In the joint, lubrication is provided by synovial fluid wetting the counterfaces. The lubricating quality of synovial fluid can vary greatly between individuals, placing the prostheses at greater risk for wear in certain patients.[53] Oxidized zirconium also was found to be less sensitive than CoCr to these variations, and maintained a lower coefficient of friction when articulated with UHMWPE even in poor lubricants. Other laboratory studies have shown that oxidized zirconium may provide similar benefits for reducing friction during direct articulation against cartilage.[54]

1.108.2.2.2. Titanium nitride (TiN) coatings

Hard ceramic coating with the longest (over 15 years) clinical history of use in joint arthroplasty is titanium nitride, TiN. Already in 1988, a patent was granted for a method of applying a thin layer of TiN onto orthopedic implants.[55] Joint replacements (hip, knee, ankle) with TiN or Ti(Nb)N-ceramized articulating surfaces are commercially available from Corin Medical, Endotec and Van Straten (Figure 10).

1.108.2.2.2.1. PVD TiN coatings

TiN-based layers are applied by means of a PVD process on CoCr or Ti alloy, each company using its own proprietary procedure. For example, Endotec uses a proprietary, reproducible PVD process to deposit a 6–10 µm thick UltraCoat® TiN coating on articulating surfaces of its hip, shoulder, and knee systems. TiN-coated surfaces are designed to articulate against UHMWPE or against similarly coated metallic components. The rationale behind using titanium nitride as a wear-resistant coating is its high hardness (HV 2400–2800), high scratch resistance, low friction coefficient, and enhanced wettability characteristics with synovial fluids. TiN is FDA approved: it is considered to be physiologically inert, it is not listed as a carcinogen, and neither acute nor chronic exposure induces toxic effects. TiN coatings are golden colored, and they can be deposited on CoCr or titanium alloy joint replacement components. One disadvantage of CoCr alloys is that Co, Cr, and a small amount of Ni that they always contain are known to cause allergic reactions. Coating CoCr articulating surfaces with TiN has been reported to reduce the release of these metal ions into the body fluids while preserving the alloy wear resistance characteristics.[56,57] Alternatively, CoCr alloy can be

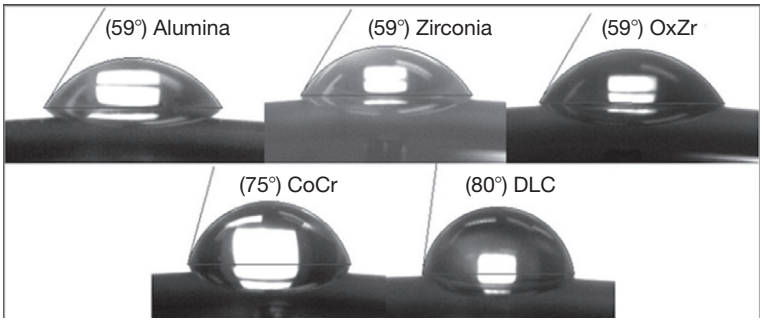

Figure 9 Oxide ceramics are wetted better than is CoCr by a serum–water solution, as indicated by lower sessile drop contact angles, thereby improving lubrication. Reproduced from Salehi, A.; Tsai, S.; Pawar, V.; *et al*. In *Bioceramics*; Nakamura, T., Yamashita, K., Neo, M., eds.; Trans Tech Publicaton: Uetikon-Zuerich, Switzerland, 2006; Vol. 18; *Key Eng. Mater*. **309–311**, 1199–1202, with permission from Trans Tech Publication.

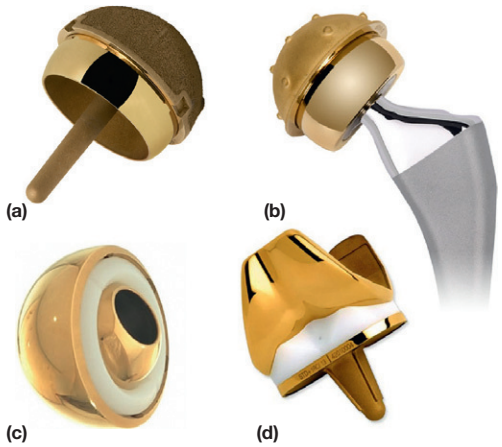

Figure 10 (a) TiNbN-coated CoCoMo alloy ACCIS hip resurfacing device (Van Straten Medical); (b) TiNbN-coated CoCoMo alloy total hip replacement (Van Straten Medical); (c) TiN-coated Ti alloy articulating unit of total hip replacement (Endotec); and (d) TiN-coated Ti alloy total knee replacement (Endotec).

substituted altogether with a Ti alloy. Titanium alloys (e.g., Ti–6Al–4V) are currently used in implant surgery because of their low density, relatively low elastic modulus, and excellent biocompatibility and corrosion resistance. However, their tribological behavior has frequently been reported to be poor, because of a high coefficient of friction and poor performance under abrasive and adhesive wear.[58] The coating of articulating joint replacement components made of Ti alloys with a thin TiN layer is expected to provide them with the required high wear resistance. TiN-coated Ti alloy parts are offered as substitutes to the traditional CoCr components in both knee and hip systems for nickel-sensitive patients or where large-diameter femoral heads are indicated (heavy, active patients).

A crucial factor for the length of life and the performance of the coated component is the coating's adhesion to the substrate.[59] Failure of a hard coating–soft substrate system under many tribological situations is seldom caused by conventional wear but by fracture of the coating (cohesive failure) or debonding of the coating from the substrate (adhesive failure).[60] Practical adhesion of a coating to the substrate is a function of fundamental adhesion (i.e., chemical bonds across the interface) and numerous other factors such as stresses in the coating, thickness and mechanical properties of the coating, and mechanical properties of the substrate. As the low-temperature PVD process does not generally involve diffusion phenomena and chemical reactions, the adhesion between the substrate and the hard layer is weak. To facilitate the formation of strong chemical bonds at the coating–substrate interface, modern PVD processes entail thorough and expensive cleaning operations that remove contaminations from the substrate surface thereby increasing surface reactivity.

To date, there are very few open literature reports concerning the examination of TiN-coated bearing surfaces of joint replacements that have been recovered following surgical revision. *In vivo* data on wear performance of TiN coatings is also very limited. Despite incidental clinical and simulator test evidence of the durability of TiN-coated femoral components,[61–63] the majority of available retrieval observations and joint simulation results show that coating breakthrough and detachment (adhesive failure) of PVD TiN films can occur in the body thereby reducing the wear properties of the implant (**Figure 11**).[57,64–68]

Premature coating detachment in areas where the coated surface is exposed to mechanical wear is the dominant and most worrisome failure mode as the flaking of the hard coating can lead to an aggravated wear situation. The underlying (softer) substrate becomes exposed and partial delamination of the coating leads also to surface roughening which increases the wear rate of the counterpart material. In addition, hard coating flakes can work as abrasive particles on the surfaces in tribological contact.

High residual stresses associated with ceramic PVD coatings on metal substrates[69] could be one of the reasons of TiN layer failure. Tensile stress in the coating causes through-thickness microcracking while compressive stress tends to promote microcrack propagation along the interface. It has been shown by a scratch test that 1.2–1.7 μm thick TiN coatings applied on Ti alloy substrates by arc ion plating (AIP) are prone to localized adhesive failure.[70] In addition, the wear behavior of TiN layer, both in abrasion and adhesion, is strongly deteriorated by the presence of coating defects such as pinholes and embedded microparticles (**Figure 12**).[50,71] These defects are typically formed because of deposition of droplets during the coating process and their subsequent removal or leveling-off by postcoating polishing.

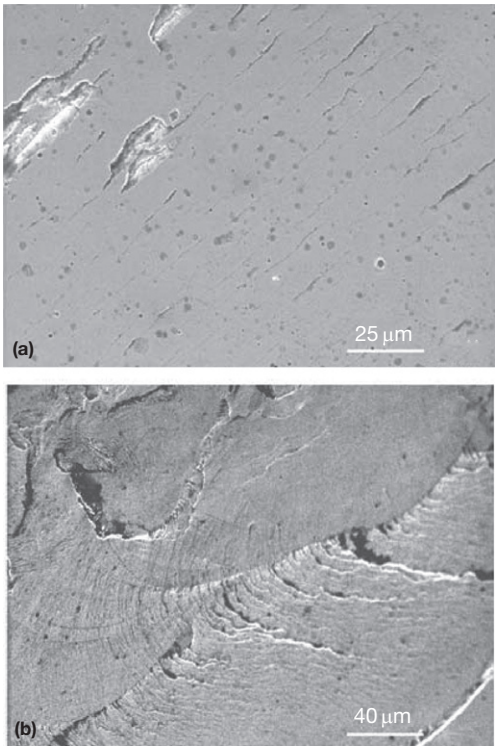

Figure 11 SEM micrographs of AEPVD TiN-coated femoral head after 2 million cycles articulation against TiN-coated insert in a hip simulator. Coating detachment is clearly visible. Reproduced from Fisher, J.; Hu, X. Q.; Stewart, T. D.; *et al*. *J*. *Mater*. *Sci*. *Mater*. *Med*. **2004**, *15*, 225–235, with permission from Springer.

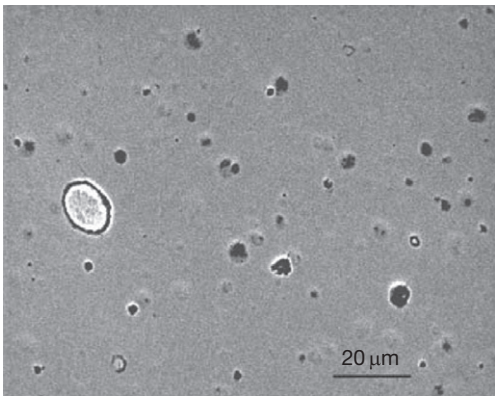

Figure 12 SEM micrograph of AEPVD TiN-coated Co–Cr alloy demonstrating coating defects – pinholes (dark) and embedded microparticles (white). Reproduced from Fisher, J.; Hu, X. Q.; Stewart, T. D.; *et al*. *J*. *Mater*. *Sci*. *Mater*. *Med*. **2004**, *15*, 225–235, with permission from Springer.

Under the synergistic action of corrosion and wear, both pinholes and prior mechanical damage (caused, e.g., by third-body abrasion *in vivo*) make TiN-coated implant surfaces more vulnerable to subsequent corrosion. In these defects, galvanic corrosion between the relatively passive coating and the relatively active small exposed substrate surface can lead to blistering and localized loss of the TiN coating (Figure 13(a)).[70,71]

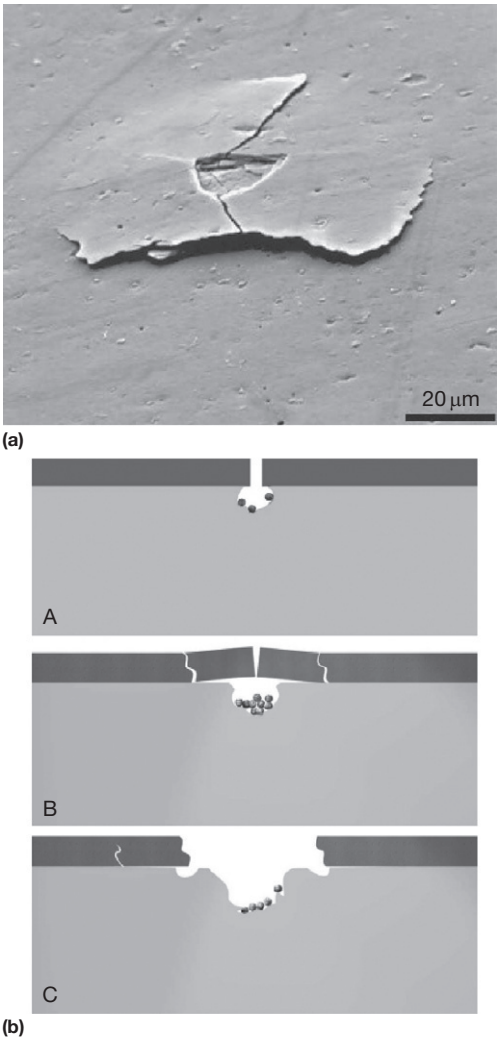

Figure 13 (a) Corrosion damage on TiN-coated (by arc ion plating) titanium alloy with prior damage, after cyclic polarization in 0.89% NaCl at 37 °C: blister with associated cracks due to the release of compressive residual stress in TiN coating. Reproduced from Komotori, J.; Lee, B. J.; Dong, H.; Dearnley, P. A. *Wear* **2001**, *251*, 1239–1249, with permission from Elsevier. (b) Schematic of the effect of pinholes on coating delamination under corrosive conditions: A – small corrosion pit generated below the coating; B – debonding of the coating caused by corrosion at the interface; C – formation of a circular blister and release of corrosion products. Reproduced from Lappalainen, R.; Santavirta, S. S. *Clin*. *Orthop*. *Relat*. *Res*. **2005**, *430*, 72–79, with permission from Lippincott Williams & Wilkins.

Figure 13(b) schematically displays how coating defects gradually lead to delamination of the coating.

Accelerated corrosion of the underlying substrate at microdefects present in PVD TiN coating was observed for both Ti alloy and CoCr substrates.[70,72] The process of the localized TiN layer loss is assumed to be further promoted by the relaxation of residual stress in the coating.

The less than optimal wear performance of PVD TiN-coated articulating implants is also attributed to the low hardness of the substrate immediately beneath the hard nitride thin film and the sharp transition of hardness and elastic modulus

across the PVD coating–substrate interface.[73] The sudden change of properties is due to the fact that little or no diffusion across the film–substrate interface and, subsequently, no subsurface strengthening take place at the low temperature of the PVD coating process. When load is applied to the hard TiN PVD film on a relatively soft, metallic substrate, plastic deformation is always initiated in the substrate material at the coating–substrate interface. The yielding substrate is unable to support the coating while the hard TiN film is unable to accommodate the deformation, so the coating fractures just like the shell of a boiled egg and triggers catastrophic third-body wear.[74] This typically occurs under point contact loading caused by debris particles between the articulating surfaces, or contact with hard components like the rim of the metal shell of the cup, or in the area of point-and-line contact in total knee arthroplasty (TKA). The 'eggshell-effect' is more pronounced for the softer substrates, for example, Ti alloy. The failure of EB-PVD TiN films (Tecvac Ltd, Cambridge) on Ti6Al4V substrates after cyclic loading tests[58] demonstrates the need to provide substrates with enhanced load-supporting characteristics.

1.108.2.2.2.2. Diffusional TiN coatings

It has been suggested that surface treatments that modify the surfaces to an increased depth are capable of providing better wear resistance than plain TiN PVD-coating deposition.[75,76] Nitrogen-ion implantation, for example, is able to convert Ti alloy surface into a hardened compound nitride layer; however, the depth of modification at typical energies of 50–100 keV is only 0.1–0.2 μm providing little improvement in load support from the substrate.[77–79] The required support to the hard TiN coating may be achieved by nitrogen-diffusion-hardening methods providing a more gradual hardness change across the subsurface layer (**Figure 14**). Depending on the nitriding temperature and time, a several micrometer thick compound layer is obtained on the surface followed by a several tens of micrometers thick diffusion zone – solid solution of nitrogen in titanium, α-Ti(N).[80–85] The compound layer consisting of two distinct titanium nitrides (TiN and Ti_2N) and the α-Ti(N) zone are clearly seen in **Figure 15**. Unlike the case of PVD, the compound (nitride) layer that grows from the bulk material is supported by the hardened diffusion zone so that there is no danger of the layer spalling off. At relatively low temperatures (≤700 °C), no continuous titanium nitride layer is formed on the surface and the increase in hardness is attributed only to the diffusion of nitrogen into the alloy.[86] For successful diffusion treatment, nitrogen has to be in the atomic or ionic state. This is achieved by ammonia dissociation (in gas nitriding) or plasma excitation (in plasma nitriding). Compared to gas nitriding, plasma nitriding is more environmentally friendly (does not use ammonia that may be harmful to the workers) and results in less surface roughening. Still, plasma nitriding has several important drawbacks including limited temperature control, inhomogeneous plasma distribution, and expensive equipment.

A method that can become an attractive alternative to conventional nitriding techniques is PIRAC. In PIRAC nitriding, highly reactive monatomic nitrogen is supplied by decomposition of an unstable nitride (e.g., Cr_2N) and/or by selective diffusion of the atmospheric nitrogen.[35,87,88] Ti alloy parts to be coated are placed in a stainless steel container, sealed and

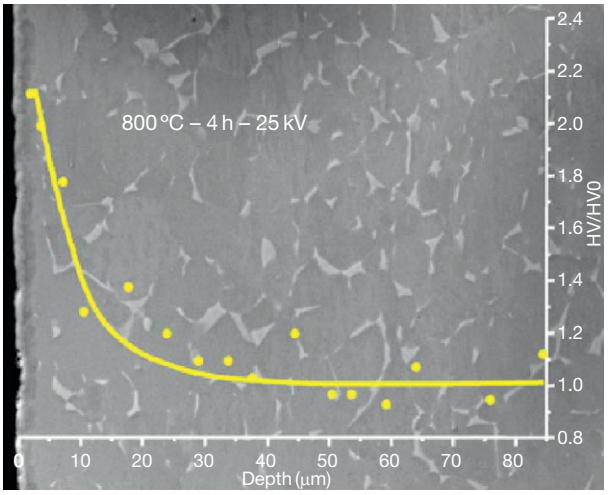

Figure 14 SEM micrograph and microhardness profile obtained on Ti6Al4V alloy nitrided by plasma immersion ion implantation at 800 °C, for 4 h. Reproduced from Fouquet, V.; Pichon, L.; Drouet, M.; Straboni, A. *Appl. Surf. Sci.* **2004**, *221*, 248–258, with permission from Elsevier.

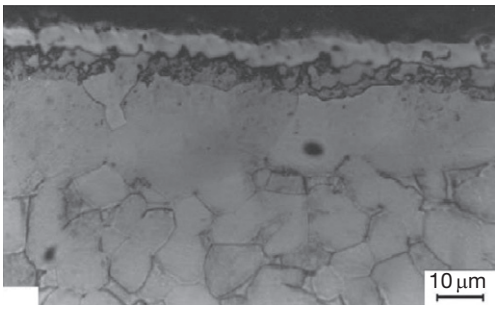

Figure 15 Optical micrograph of the cross-section of Ti6Al4V alloy plasma nitrided for 12 h at 900 °C. Reproduced from Taktak, S.; Akbulut, H. *Vacuum* **2004**, *75*, 247–259, with permission from Elsevier.

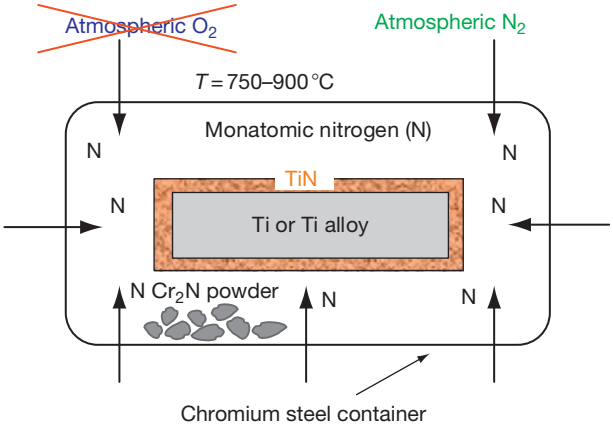

Figure 16 A schematic of PIRAC nitriding process.

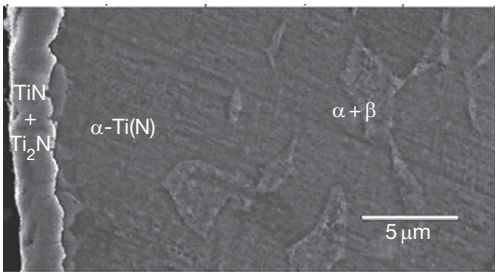

Figure 17 SEM micrograph of Ti6Al4V alloy PIRAC nitrided at 900 °C, for 4 h. Reproduced from Shenhar, A.; Gotman, I.; Gutmanas, E. Y.; Ducheyne, P. *Mater. Sci. Eng. A* **1999**, *268*, 40–46, with permission from Elsevier.

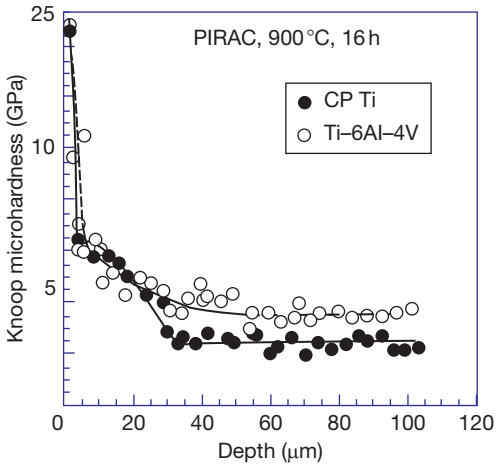

Figure 18 Microhardness profile obtained on CP Ti and Ti6Al4V alloy PIRAC nitrided at 900 °C, for 16 h. Reproduced from Shenhar, A.; Gotman, I.; Gutmanas, E. Y.; Ducheyne, P. *Mater. Sci. Eng. A* **1999**, *268*, 40–46, with permission from Elsevier.

annealed at 700–900 °C (Figure 16). In addition, the container is filled with a chromium nitride (Cr_2N) powder. The steel of the container has a high content of chromium that reacts with the atmospheric oxygen to form a stable Cr oxide, Cr_2O_3. This reaction prevents oxygen from penetrating through the container walls, so that a very low partial O_2 pressure ($\leq 10^{-5}$ Pa) is maintained inside the container without application of any vacuum pumps.[35] At the same time, N atoms can easily diffuse through the container walls because of the rather low affinity of Cr (which is the only nitride-forming element in the foil) for nitrogen. The diffusion of N from the atmosphere leads to a gradual build-up of monatomic nitrogen pressure inside the container. This is accompanied by the decomposition of the Cr_2N powder as long as nitrogen pressure has not reached the equilibrium pressure of Cr_2N dissociation at the corresponding temperature (e.g., ~3 Pa at 900 °C.[89] Reactive diffusion of nitrogen atoms into titanium alloy results in the formation of a Ti–N coating. As PIRAC is not a line-of-sight process it allows uniform coating of complex shape parts. Similarly to plasma-nitrided (PN) surfaces, PIRAC nitrided Ti surface consists of a several micrometers thick outer compound layer (TiN–Ti_2N) and a several tens of microns thick inner solid solution layer (α-Ti(N)) (Figure 17). Beneath the ceramic, a nitrogen-enriched Ti gradually transforms into the metal alloy, preventing an abrupt mismatch in properties. This hardened N-rich titanium layer (Figure 18) provides an optimal support for the ceramic coating and prevents its collapse and delamination. The low level of residual stresses in PIRAC coatings on Ti6Al4V substrate compared to the PVD TiN layers[88] is an additional factor in the excellent adhesion of PIRAC coatings. In contrast to PVD, PIRAC coatings are not externally applied layers but are grown from the substrate itself and are characterized by an excellent conformity and strong adhesion. Strong adhesion of PIRAC TiN coatings was demonstrated by the absence of delamination in a three-point bending test (Figure 19).[88]

1.108.2.2.2.3. Duplex TiN coatings

To improve the ability of PVD TiN-coated Ti alloys to bear highly localized loads, 'duplex' treatments which combine PVD (or chemical vapor deposition (CVD)) coating with a diffusion treatment (nitriding) of the underlying surface have been proposed.[90–92] The nitrided layer confers graded properties with increasing hardness from the substrate to the

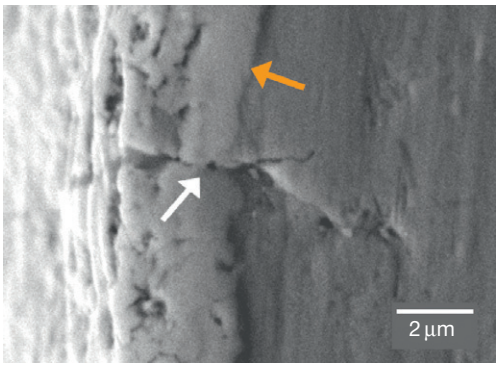

Figure 19 SEM cross-section of Ti6Al4V alloy PIRAC nitrided at 900 °C, for 2 h after bending test illustrating excellent TiN coating adhesion. Note the absence of cracks at the coating–substrate interface. Reproduced from Shenhar, A.; Gotman, I.; Radin, S.; Ducheyne, P.; Gutmanas, E. Y. *Surf. Coat. Technol.* **2000**, *126*, 210–218, with permission from Elsevier.

outermost surface thus providing the required support to the hard PVD coating. It has been reported that plasma nitriding pretreatment of Ti6Al4V and Ti5Al2.5Fe2 substrates provided an optimal support of TiN layer produced by plasma-assisted CVD (PACVD) and a good adhesion.[93] Along the same lines, it has been shown by indentation tests that the adhesion of TiN coatings deposited by plasma-enhanced CVD (pulsed d.c. PCVD) on PN Ti6Al4V alloy was substantially stronger than TiN adhesion to the untreated substrate.[94] As a result, a marked improvement in the wear resistance of PN-PCVD duplex treated alloy in pin-on-disk test against a steel ball was achieved.

Cassar *et al.*[95] compared the reciprocating-sliding wear performance of ~3 μm thick PAPVD TiN coatings deposited on bare and duplex triode PN Ti6Al4V alloy. Duplex-coated disks exhibited a strongly improved wear resistance compared to the PVD-coated ones. Moreover, prenitriding process was beneficial even when the coating had been partially worn. While the

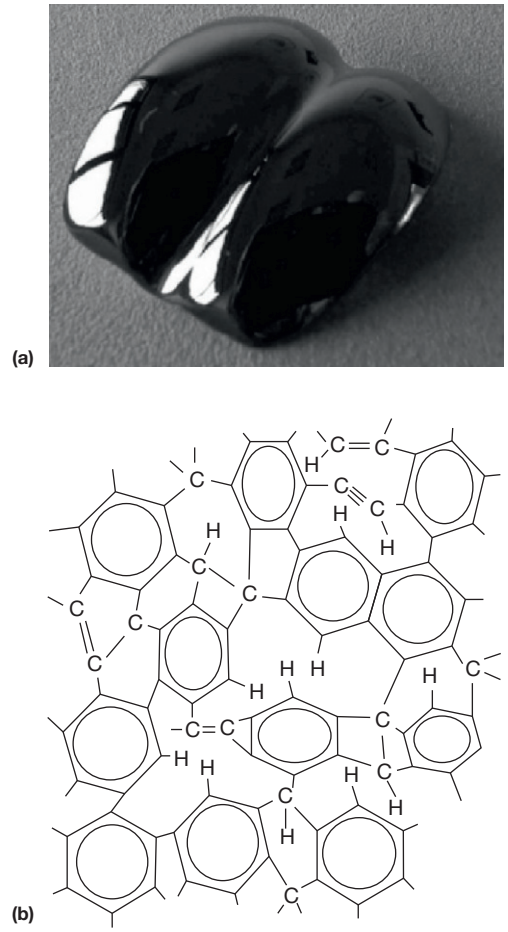

Figure 20 (a) DLC-coated talar component of ankle joint. Reproduced from Hauert, R. *Diam. Relat. Mater.* **2003**, *12*, 583–589, with permission from Elsevier. (b) Structure of DLC (http://www.diameterltd.co.uk/DLC.htm).

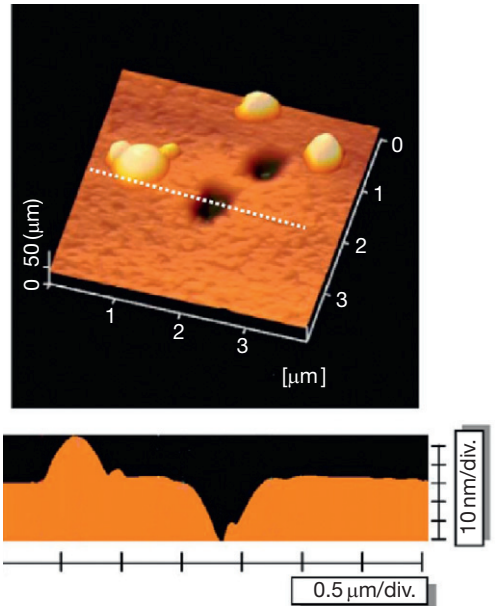

Figure 21 Scanning probe microscope (SPM) image of pinhole defects (dark) and tubercles (while) in DLC film prepared by plasma-based ion implantation technique. The lower picture is the cross-sectional view along the dotted line in the upper one. Reproduced from Yatsuzuka, M.; Tateiwa, J.; Uchida, H. *Vacuum* **2006**, *80*, 1351–1355, with permission from Elsevier.

coatings directly deposited on Ti alloy were quickly removed across the entire contact area, the wear of the duplex coatings was constrained to within the central region and the coating adjacent to this region was still capable of supporting the applied load.

1.108.2.2.3. Diamond-like carbon coatings

Diamond-like carbon (DLC) (Figure 20) has emerged as a potential coating material for joint replacements because of its high hardness (1500–3500 HV), low frictional coefficient, high wear and corrosion resistance, biocompatibility, and excellent smoothness. A comprehensive overview of biomedical applications on DLC coatings can be found in Hauert,[96] Grill,[97] Hauert,[98] Dearnaley and Arps,[99] Roy and Lee[100]. DLC film comprises a mixture of sp^2 (graphitic-like) and sp^3 (diamond-like) carbon bonds (Figure 20(b)) and is deposited by using high energy carbon species.[101,102] DLC films are produced by a number of techniques such as ion beam deposition, radio frequency plasma-enhanced CVD (r.f.-PECVD), filtered cathodic vacuum arc (FCVA), ion plating, plasma immersion ion implantation and deposition (PIIID), magnetron sputtering, ion beam sputtering, pulsed laser deposition, and mass selected ion beam deposition. For detailed description of DLC deposition methods, see Chapter 1.107, Carbon and Diamond. The hydrogen content in DLC films varies up to 40%. Because of its amorphous structure, DLC films can be easily doped and alloyed with different elements. This leads to a wide range of properties depending on its sp^3, sp^2, and hydrogen content together with element incorporation.

The tribological behavior of DLC is different from that of other hard materials. Under tribological conditions, usually the softer of the two materials will be worn. In the case of DLC, the wear products have a graphitic nature and are transferred to the partner surface forming a so-called transfer layer on the partner surface.[102] The DLC then slides on this transfer layer that protects the softer partner surface from wear and the harder DLC-coated surface wears off at an extremely low rate. Additionally, the graphitic wear products of DLC act also as a solid lubricant. The build up and especially the adhesion of this transfer layer depend critically on the environmental conditions.[100,102]

Despite the excellent tribological behavior of DLC in dry air, catastrophic failure of DLC coatings is often observed when sliding in aqueous environments.[103,104] The instability of DLC coatings in aqueous environment is believed to be caused by the degradation of the interfacial strength because of water molecules penetration via through-film defects. A representative example of DLC film defects is given in Figure 21.[105] Here, the large hole was possibly formed from the ejection of a microparticle. The smaller pinhole was formed as a result of the film growth mechanism.

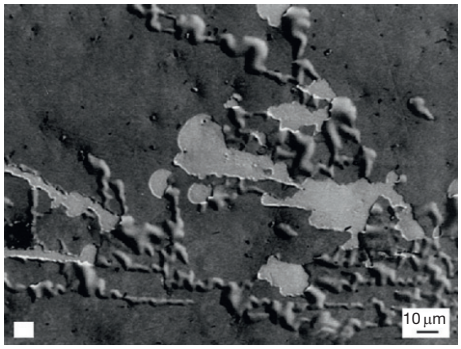

Figure 22 SEM micrograph showing delamination of 100 nm thick DLC coating on Ti6Al4V alloy disk after 1 million cycles sliding against UHMWPE pin in distilled water. Reproduced from Xu, T.; Pruitt, L. *J. Mater. Sci. Mater. Med.* **1999**, *10*, 83–90, with permission from Springer.

Improvement of the deposition technique (e.g., multistep coating) can be effective in reducing the through-film defects and enhancing the film stability. In addition, DLC coatings can exhibit a wide range of atomic bond structure and properties depending on the deposition condition. Another aspect to be addressed is the adhesion of DLC coating with biomaterials. Because of high residual compressive stress, the coating can spontaneously delaminate if the adhesion is insufficient (Figure 22).[106] The spallation, delamination, and corrosion of the DLC coatings during their long-term use in medical implants are to be carefully considered for the future biomedical applications.

1.108.2.2.4. Multicomponent hard coatings

An exciting and novel area of research deals with the synthesis of multicomponent, bioactive nanostructured films (MuBiNaFs) by sputtering of composite self-propagating high-temperature synthesis (SHS) targets.[107–111] SHS provides a highly dense, uniform structure that exhibits the required mechanical, thermal, and electrical properties needed for such composite PVD target materials. A radically new approach in the development of new nanostructured materials is to add nanocomponents. It has been shown that the introduction of nanosized powders into electrode material can modify the material structure favorably affecting the quality of produced coatings.[112]

MuBiNaFs were deposited by magnetron sputtering of composite targets $TiC_{0.5} + X$ and $(Ti,Ta)C + X$ {where $X = CaO$, TiO_2, $Ca_{10}(PO_4)_6(OH)_2$, ZrO_2, Si_3N_4, and $Ca_3(PO_4)_2$} in an Ar atmosphere or reactively in a gaseous mixture of $Ar + N_2$. The application of ion implantation assisted magnetron sputtering (IIAMS) of SHS composite targets offers a flexible approach to surface improvement of metal implants. This technique facilitates the production of dense, well-adhered films with controlled elemental composition. TiC/CaO nanocomposite films were also deposited by means of a hybrid PVD/plasma activated CVD(PACVD) technique, which combines dc magnetron sputtering of a SHS composite target $TiC_{0.5} + CaO$ with a subsequent high density inductively coupled plasma (ICP) in order to excite and ionize the sputtered species to a higher degree.[113–115]

By varying the target compositions and PVD process parameters, the structure and properties of films can be elegantly engineered and the size of crystallites can be reduced to nanometer scale.[116] This extremely small crystallite size results in a significant fraction of atoms locating at the grain boundaries. The effect of the film–biomedium interaction depends on surface characteristics, such as composition, charge, and structure. These characteristics can be adjusted over a wide range depending on different ion–plasma deposition conditions.

The MuBiNaFs films exhibit excellent tribological properties that, in combination with high level of biocompatibility and bioactivity, make them promising candidates for load-bearing implants.[117–122]

1.108.2.3. Simulation and Testing of Wear-Resistant Surface Modifications

1.108.2.3.1. Durability comparisons

Durability of surface modifications is a key performance attribute. The typically hard and chemically inert nature of ceramic surfaces makes them ideal for resisting the roughening influences of third-body abrasives and of corrosive wear that affect metal surfaces. As one example, nanohardness testing indicates that the zirconia surface on oxidized zirconium is over twice as hard as CoCr on the articular surface.[123] Other ceramics, such as titanium nitride and alumina, can be even harder.[21] Harder surfaces are more scratch resistant, but this alone does not mean that they are more abrasion resistant. The hard surface also must resist shear during articulation and cracking during loading.

A bone cement abrasion test was developed to assess the resistance of various materials to an aggressive third-body abrasive challenge.[124] Bone cement particles represent some of the most abrasive third bodies that might be present in a joint because of the crystalline nature of the polymer and the inclusion of radiopaque powder such as zirconia or barium sulfate.[5] The abrasive effect of third-body debris is approximated by rubbing the tip of bone cement pins against flat plates of the hard counterface material, simulating the counterface abrasion caused by a particle of bone cement embedded in the PE component (Figure 23). The pins are made with a spherical tip so that the initial Hertzian contact stress is 82 MPa which, as the tip is worn flat, drops through the range of stress during testing that would be found in prosthetic joints. One million cycles (Mc) of this test is assumed to be equivalent to 1 year for a typical joint arthroplasty patient, but that assumption is unimportant when comparing different surfaces using a test of fixed length.

Plates of conventional CoCr and oxidized zirconium were subjected to 10 Mc of this bone cement abrasion test.[125] The ceramic surfaces on the oxidized zirconium plates were not penetrated and exhibited over 4900 times less volumetric wear and over 160 times less roughening than the CoCr plates (Figure 24). This indicated that the oxide ceramic surface provides superior resistance to roughening compared to CoCr as well as being durable in the presence of bone cement debris.

Vapor deposited nitride coatings on both CoCr and titanium alloy plates representing a variety technologies used or proposed for use on orthopedic bearing surfaces were subjected to this bone cement abrasion test.[124,126] The coatings

also tended to improve abrasive resistance relative to non-coated plates, but all of the tested coatings were compromised within 1 Mc (Figure 25). It was common to find debris from the abraded coatings embedded in the bone cement pins. It is reasonable to suppose that the wear volume for these specimens would have increased significantly if the tests had continued to 10 Mc because the hard protective coating would no longer have been present on the plates to resist abrasion from the pins and embedded coating debris. On the basis of these test results, the nitride coatings appeared to have less resistance to the shear of articulation despite their greater hardness relative to oxidized zirconium. The nitride coatings did not chip or delaminate away from the plates, indicating that they had good adhesion, but the coatings appeared to rub off over time, indicating that they had poor cohesion.

This difference in performance might be due the differences in their microstructures.[21,126] The nitride coatings subjected to this test have a heterogeneous structure with numerous nodules and pores (Figure 26). The heterogeneous structure may be inherent in the vapor deposition process because of embedment of solid particles, or chemical segregation from the elevated temperatures and long processing durations. By contrast, the transformed ceramic on oxidized zirconium has a uniform, nanostructural, high integrity grain structure with a perpendicular orientation relative to the articular motion.[40,41] It is reasonable to suppose that an applied nitride

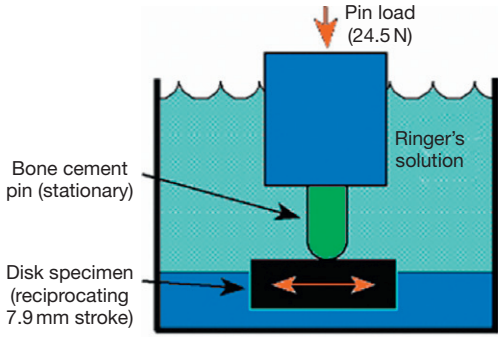

Figure 23 The abrasion test simulates third-body bone cement debris rubbing against the counterface during articulation of the joint. Reproduced from Hunter, G.; Pawar, V.; Salehi, A.; Long, M. In *Medical Device Materials*; Shrivatsava, S., ed.; ASM International: Materials Park, OH, 2004; Vol. 1, pp 91–97, with permission from ASM International.

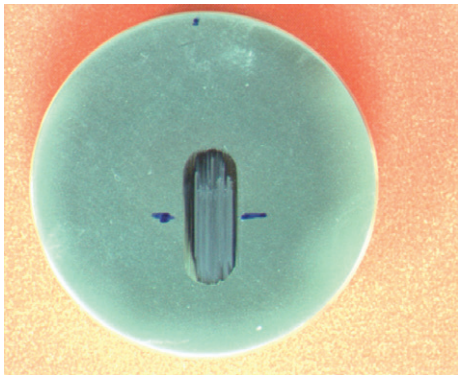

Figure 25 Vapor-deposited nitride coatings, such as on this TiNbN-coated CoCr plate, were breached within 1 million cycles of the bone cement abrasion test. Reproduced from Hunter, G.; Pawar, V.; Salehi, A.; Long, M. In *Medical Device Materials*; Shrivatsava, S., ed.; ASM International: Materials Park, OH, 2004; Vol. 1, pp 91–97, with permission from ASM International.

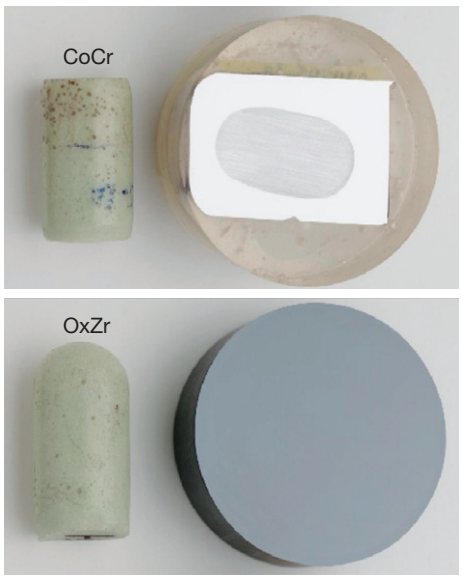

Figure 24 An oxidized zirconium plate (lower right) exhibits 4900 times less volumetric wear when compared with a CoCr plate (upper right) after 10 million cycles of articulation against spherical-tipped bone cement pins (remains on left of the plates). Reproduced from Hunter, G.; Jones, W. M.; Spector, M. In *Total Knee Arthroplasty*; Bellemans, J., Ries, M. D., Victor, J., eds.; Springer Verlag: Heidelberg, Germany, 2005; pp 370–377, with permission from Springer.

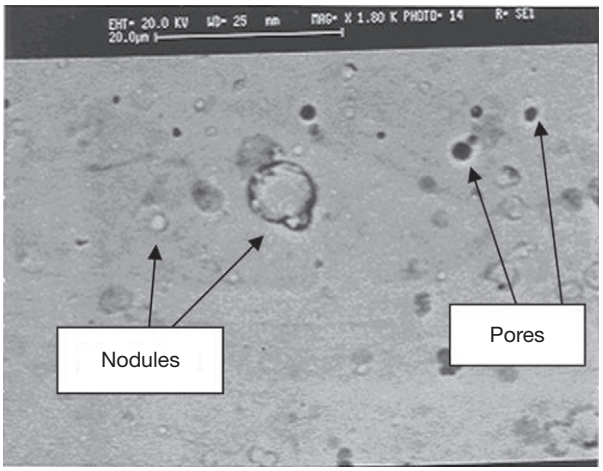

Figure 26 A heterogeneous structure with numerous nodules and pores, such as seen in this scanning electron microscope image of the TiNbN-coated CoCr plate in Figure 25, is typical of vapor-deposited coatings. Reproduced from Hunter, G.; Pawar, V.; Salehi, A.; Long, M. In *Medical Device Materials*; Shrivatsava, S., ed.; ASM International: Materials Park, OH, 2004; Vol. 1, pp 91–97, with permission from ASM International.

coating with a homogeneous, fine-grained, high integrity microstructure might exhibit improved durability in this test.

The behaviors of diamond and DLC coatings have been more difficult to interpret because their characteristics differ on the basis of processing technology and composition.[21,127] Some of these coatings are difficult to polish after application to a curved surface, and when these coatings were subjected to a bone cement abrasion test without being polished first, they caused rapid wear of the bone cement pins.[124,126] Most diamond and diamond-like coatings were not penetrated after 10 Mc of testing unless they had inclusions such as graphite nodules, indicating that heterogeneous coatings tend to have poor cohesion. It was not uncommon to find that a cohesive coating which was not breached during testing had flaked off of small regions either in the wear track or around the edges of the plates. This suggests that adhesion can be more of a challenge than cohesion for diamond and diamond-like coatings.

A popular method of assessing the adhesion of coatings to a substrate involves using a hardness test indenter to push an indentation crater into the surface.[21,128] The material displaced from the crater heaves up around it and under the coating, providing an aggressive challenge to adhesion of the coating to the substrate. Oxidized zirconium and most nitride coatings used in orthopedics perform very well in this test. Although cracks are often observed around the crater because of the extensive plastic deformation of the substrate, evidence of chipping or delamination typically is not observed (Figure 27). The extreme hardness of diamond and diamond-like coatings makes it challenging to create an indentation crater using a hardness test indenter, so they are difficult to assess in this test.

A modification of the bone cement abrasion test was used for a more vigorous adhesion test of whether the ceramic surface on oxidized zirconium plates would chip or spall if damaged.[128] Before testing, a groove was milled through the oxide and aligned perpendicular to the pin motion so that the bone cement pin crossed the groove with each stroke. The milled groove had not widened after 10 Mc, indicating that the oxide around it remained adherent and could tolerate localized damage or loss without catastrophic failure (Figure 28).

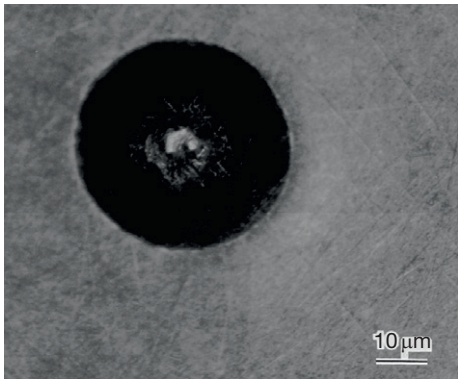

Figure 27 The absence of chipping and spalling around the indentation test crater on oxidized zirconium indicates excellent adhesion of the oxide despite extensive deformation of the substrate. Reproduced from Hunter, G. *Trans. Soc. Biomater.* **2001**, *24*, 540, with permission from Society for Biomaterials.

A galvanic relationship is created by placing different materials in contact, such as occurs between the ceramic film and a metal substrate or a mating component in a taper junction. This relationship can cause accelerated corrosion if the galvanic potentials are significantly different, particularly if relative mechanical articulation (fretting corrosion) or restricted spaces (crevice corrosion) are involved. Ceramic coatings can provide good protection against these types of corrosion, but the presence of pinhole defects in the coatings also can lead to localized blistering and pitting.[21,127,200] Laboratory testing is recommended in conditions that are at least as demanding as those encountered in the intended application.

Oxidized zirconium samples were subjected to a series of corrosion tests to characterize their behavior in static and dynamic conditions, both in neutral and acidic environments.[129–131] The zirconium alloy behaved as the anode when coupled with the other orthopedic alloys, helping to protect them. This behavior is attributed to a high thermodynamic activity but slow electrochemical reaction kinetics in the passive state. In static tests, the concentrations of zirconium and niobium ions in the solution were below detection limits, indicating that the anodic current on the zirconium alloy was consumed mainly by the formation of a passive film. This helps protect breaches in the oxide from galvanic attack. An extreme test combines the cyclic loads of a taper junction fretting test with the potential of crevice corrosion from an acidic solution under elevated temperature.[132] In this test, oxidized zirconium heads produced fewer features of chemical attack on stainless steel trunnions than did the clinically acceptable combination of stainless steel heads and trunnions (Figure 29). This indicates that oxidized zirconium should perform at least as well as other orthopedic material combinations under clinical conditions.

1.108.2.3.2. Wear simulation tests

Determining if hard coatings are effective in reducing the wear of joint replacements requires the use of reliable wear testing techniques. Joint simulators are the standard tools for

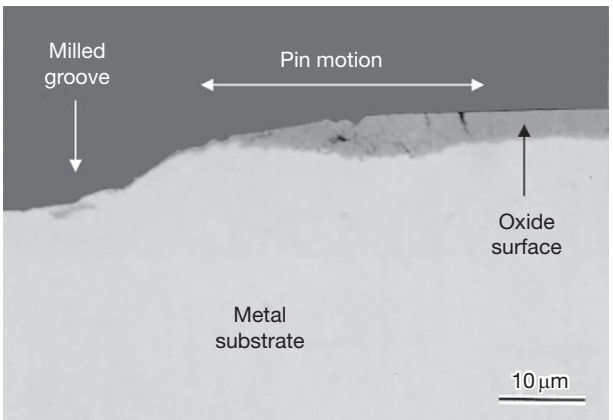

Figure 28 The oxide tolerated localized damage without catastrophic failure by protecting the bone cement abrasion test surface within the wear track on an oxidized zirconium plate right up to the edge of a milled groove, as seen in this cross-sectional optical micrograph. Reproduced from Hunter, G. *Trans. Soc. Biomater.* **2001**, *24*, 540, with permission from Society for Biomaterials.

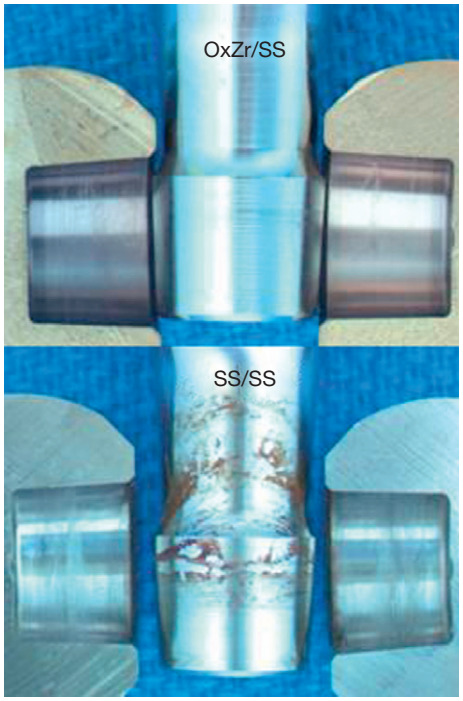

Figure 29 Minor fretting scars and minimal chemical activity are evident after an extreme fretting corrosion test with oxidized zirconium heads on stainless steel trunnions (above). Extensive chemical activity is evident under the same conditions with stainless steel heads on stainless steel trunnions (below). Reproduced from Pawar, V.; Jones, B.; Sprague, J.; Salehi, A.; Hunter, G. In *Medical Device Materials*; Helmus, M., Medlin, D., eds.; ASM International: Materials Park, OH, 2005; Vol. 2, pp 403–408, with permission from ASM International.

evaluation of wear resistance. Joint simulators are designed to reproduce the physiological kinematics and physical forces acting on the joint during movement; however, they are still limited in their ability to simulate the lubrication conditions, the loads, and the motions that occur over a broad range of daily activities. Moreover, tribology and wear mechanisms are different for different joints, so results obtained on a hip simulator are not always relevant for a knee (or other joint) replacement. Thus, in order to properly assess the potential of a hard coating to reduce *in vivo* wear rates, simulator tests should be conducted under a variety of conditions.

1.108.2.3.2.1. Oxidized zirconium

Knee simulator tests have been used to help understand how OxZr counterfaces compare to the standard CoCr counterfaces for wear of the PE components. The pioneering study was conducted using a simulator that mimics the rolling and plowing motions of knee prosthesis kinematics.[133] Early OxZr prototypes made from castings were used in this study, and the oxide was thinner and had less integrity than that developed later. In addition, the PE liners were gamma irradiated in air. Despite these material limitations, the OxZr components produced significantly fewer wear features and none of the macroscopic PE delamination observed in the tests with CoCr components. It also was noted that the CoCr surfaces became roughened during testing while the OxZr surfaces were not affected.

After full development of the manufacturing processes, a study was conducted using a four-axis, displacement-controlled, physiologic knee simulator.[134] Components were tested for 6 Mc of 90% walking-gait and 10% stair-climbing activity, and PE wear was measured periodically during the test by weight loss and by wear particle characterization. In comparison to CoCr, OxZr produced an aggregate wear rate of PE that was 85% less. This comparison had a 90% confidence level because the test parameters generated lower wear rates and more measurement variability than desired. It was noted that all of the OxZr components generated lower PE wear rates and produced less burnishing of the inserts. In contrast to the OxZr surfaces, the CoCr surfaces were found to have become roughened during testing even though the lubricant was filtered before testing. Analysis of the wear debris also indicated that OxZr produced fewer small PE particles and less total volume of particles, but the sample size was too limited for statistical significance.

A separate study was conducted on a different component design in the same type of simulator, but the test parameters were modified to produce greater wear rates and less measurement variability using just a walking-gait motion.[135] In comparison to CoCr, OxZr produced a mean wear rate that was 42% less when measured either gravimetrically or volumetrically. This reduction is substantial, although less than the 85% comparison of the previous study. The later study may be more representative of the 'normal' performance advantage of OxZr knees because it achieved a 95% confidence limit and the relative performance is similar to that found with hip simulators.[136] This study continued, however, to show that the knee wear rates were sensitive to test conditions. The wear rate using OxZr was 62% less than that using CoCr under conditions of greater rotation and an additional varus moment. This indicated that the performance advantage for OxZr might increase for conditions associated with 'more demanding' patient kinematics.

Besides kinematics, another 'more demanding' condition occurs commonly as the femoral component surface becomes roughened. CoCr femoral components were tumbled in an abrasive alumina powder before simulator testing.[137] The resulting roughness values were within the clinically relevant range. The components were tested for 5 Mc using the same displacement-controlled simulator protocol as used with the first test series. OxZr components tumbled using the same procedure became roughened less, and produced an aggregate wear rate of PE that was 89% less ($p < 0.05$). Because the components were preroughened, particle analysis was conducted on the wear debris without the complicating presence of numerous abrasive particles in the test lubricant. In comparison to CoCr, OxZr produced 44% fewer PE particles ($p < 0.05$). A separate test with preroughened components was conducted for 5 Mc using a force-controlled simulator.[138] Compared to CoCr, OxZr produced an average wear rate that was 82% less ($p < 0.001$) in this test.

Lee *et al.*[139] compared the effects of OxZr and CoCr total knee replacement (TKR) femoral components of a similar design (Genesis II, Smith & Nephew) on the wear of UHMWPE inserts (on CoCr baseplates) using a force-controlled knee simulator during an enhanced force walk cycle simulation. The enhanced walking cycle is more aggressive than the standard

walking cycle and provides a 25% increase in anterior–posterior shear force and 25% increase in external–internal rotation. Simulation tests were run in 30% fetal calf serum for 4 Mc, and PE wear was assessed gravimetrically.

OxZr components showed increased resistance to scratching compared to CoCr. This difference was evident already after 1 Mc. The wear of UHMWPE tibial inserts articulating against OxZr femoral components was measurably lower than for CoCr femoral components (Figure 30), probably as a consequence of reduced scratching. The results suggest that the increased scratch resistance of OxZr has the potential to increase the longevity of TKRs.

DesJardins *et al.*[140] conducted knee joint simulator study using conventional UHMWPE to quantify the effect of surface roughening of OxZr and CoCr on TKR wear performance. OxZr and CoCr femoral components of a similar design (Genesis II, Smith & Nephew) were tumbled in an abrasive alumina powder before simulator testing. The tests were run against cruciate-retaining UHMWPE tibial inserts on Ti6Al4V baseplates in 50% bovine calf serum. PE wear was assessed gravimetrically.

After 5 Mc of wear testing, the roughened OxZr femoral components were found to reduce the rate at which UHMWPE wear debris was generated by 82.0% when compared to the roughened CoCr femoral components (Figure 31). The average weight loss rates for the roughened OxZr and the roughened CoCr groups were 16.6 ± 7.6 and $92.0 \pm 24.4\ \text{mg Mc}^{-1}$, respectively ($p < 0.00001$).

Collectively, these knee simulator tests indicate that OxZr components can reduce wear of the PE counterface by 40–90% depending on test conditions. Similar wear reductions have been found for monolithic ceramic femoral components in knee simulator tests.[141,142] These results indicate that OxZr may contribute to reducing wear-related clinical complications such as debris-induced osteolysis. It is interesting to note that the performance advantage for OxZr relative to CoCr seems to increase as the testing conditions become more demanding. This trend indicates that OxZr may be of particular help to 'high demand' patients who are most in need of assistance for prolonging the survival of their prostheses.

Hip simulator comparisons of OxZr to traditional metal CoCr alloy also have been important in anticipating its *in vivo* properties for PE wear. The earliest study was conducted with 32-mm heads in 100% bovine serum using a displacement-controlled, physiologic hip simulator.[136] Both nonirradiated UHMWPE and highly crosslinked PE were tested, as well as both smooth and roughened heads. Components were tested for at least 5 Mc at 1 Hz using ISO and Bergmann loading profiles alternating every 100 000 cycles. PE wear was measured periodically during the test by weight loss and by wear particle characterization. In comparison with CoCr, OxZr produced wear rates of nonirradiated UHMWPE that were 45% less with smooth heads and 61% less with roughened heads ($p < 0.01$), with fewer particles in both cases (Figure 32). With crosslinked PE, wear rates were not detectable except for the roughened CoCr heads, but OxZr heads produced 27 and 63% fewer particles when comparing smooth and roughened heads, respectively (Figure 32). Even

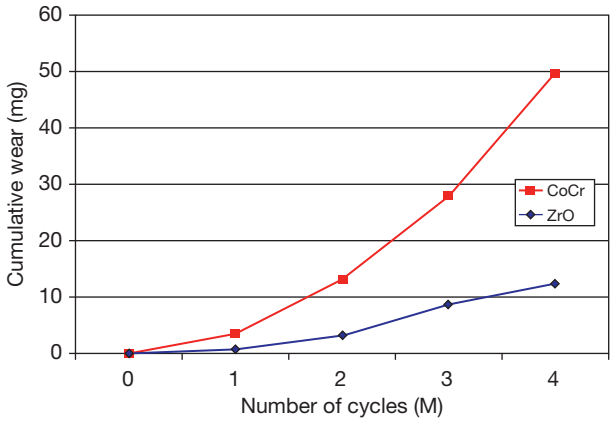

Figure 30 Cumulative wear of UHMWPE tibial inserts articulating against CoCr and OxZr ('ZrO') femoral components as a function of number of cycles in a knee wear simulator. Reproduced from Lee, J. K. L.; Maruthainar, K.; Wardle, N.; Haddad, F.; Blunn, G. W. *The Knee* **2009**, *16*, 269–274, with permission from Elsevier.

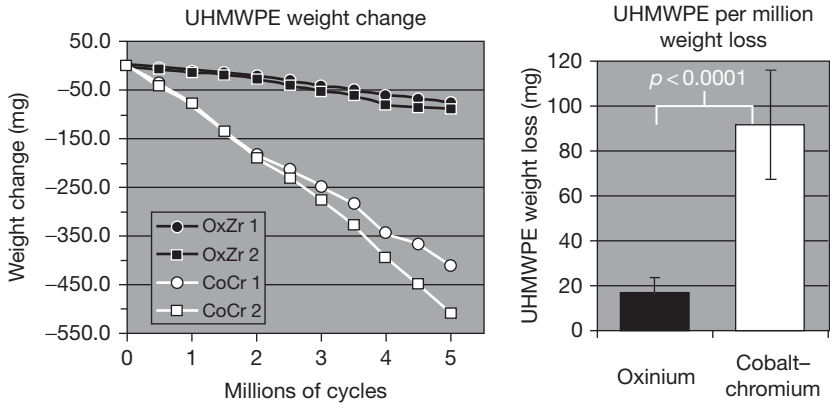

Figure 31 Weight changes of UHMWPE tibial components cycled against roughened OxZr and CoCr femoral components. The average per-million weight loss measures between 0 and 5 million cycles were statistically different ($p < 0.0001$), with the roughened OxZr femurs offering an 82.0% reduction in wear rate when compared to the roughened CoCr femurs. Reproduced from DesJardins, J. D.; Burnikel, B.; LaBerge, M. *Wear* **2008**, *264*, 245–256, with permission from Elsevier.

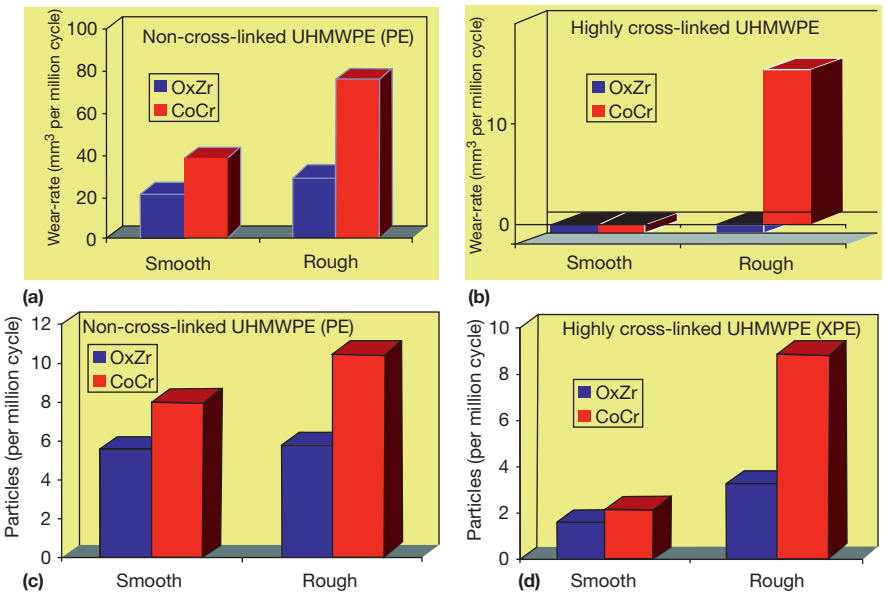

Figure 32 Wear rates of polyethylene acetabular liners (a,b) and number of particles generated per million cycles (c,d) through 5 million cycles hip simulator test against CoCr and OxZr femoral heads: a, c – nonirradiated UHMWPE; b, d – cross-linked UHMWPE. Reproduced from Good, V.; Ries, M.; Barrack, R. L.; Widding, K.; Hunter, G.; Heuer, D. *J. Bone Joint Surg.* **2003**, *85A*(S4), 105–110.

after extending the test to 20 Mc, a linear regression of oxide thickness measurements on roughened OxZr heads indicated that less than 0.0023 μm Mc^{-1} of oxide thickness was removed, a change so small that it was within the resolution of the spectrometer system.[143] Therefore, the thickness of the ceramic oxide should be durable over the life of the implant.

A study by Clarke *et al.*[144] evaluated both smooth and roughened 36-mm heads made of OxZr and CoCr coupled to highly crosslinked PE acetabular liners. A total of 6 Mc of testing were done for each combination in the physiologic environment of 50% alpha-serum (400 ml). The authors concluded that smooth CoCr and both types of OxZr heads produced negligible amounts of weight loss (less than the fluid absorption by the liners). However, roughened CoCr heads produced a 'dramatic' wear rate for the highly crosslinked liners.

Bourne *et al.*[145] assessed the roughening damage to heads that can occur as a result of postoperative dislocation. They noted that the damage on any material can be of significant extent, but that the damage tends to occur on the inferior half of the head where the effect on wear would be less critical. Using profilometry and scanning electron microscopy, they found that the resulting metal transfer on CoCr heads produced mostly peaks surface while the OxZr heads produced more valleys below the articulating surface. Testing a laboratory model of a dislocation event on the crown of the heads (the worst case location) using a hip simulator showed that the wear of nonirradiated UHMWPE produced by damaged OxZr heads was not statistically distinct from that produced by smooth CoCr heads and was reduced over tenfold by using highly crosslinked liners.

A study by Lee *et al.*[146] assessed OxZr bearings for their resistance to aggressive abrasion and wear performance as compared to zirconia toughened alumina (Biolox(r) Delta)

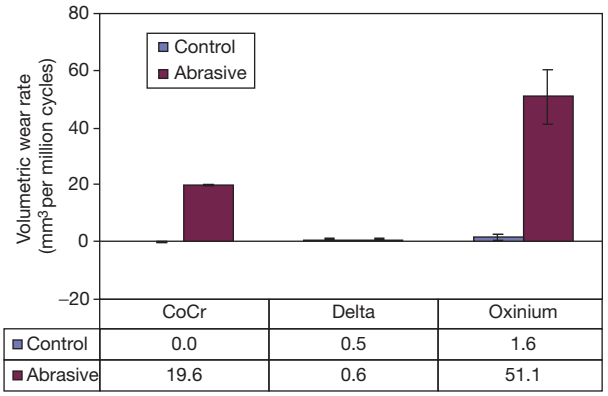

Figure 33 Wear rates (over 2 million cycles hip simulation) of crosslinked UHMWPE sockets articulating against pristine (control) and abraded CoCr, alumina (Delta), and OxZr (Oxinium) femoral heads. Reproduced from Lee, R.; Essner, A.; Wang, A.; Jaffe, W. L. *Wear* **2009**, *267*, 1915–1921, with permission from Elsevier.

and ion treated CoCr in a hip wear simulator for 2 Mc. Wear rates of the crosslinked PE liners were low and near zero when worn against nonabraded femoral components (all less than 1.6 mm^3 Mc^{-1}) (Figure 33). There was no statistical difference in wear rates using these three different femoral head materials ($p = 0.18–0.37$). A force-controlled diamond indenter was then utilized to produce damage on the femoral heads similar to that found in OxZr clinical retrievals with repeated head dislocation. Abrasion of the femoral component with the diamond indenter markedly increased PE wear rates for OxZr and CoCr bearings (51.1 and 19.6 mm^3 Mc^{-1}, respectively), and had no effect on PE wear for the bulk ceramic bearings (0.6 mm^3 Mc^{-1}). The soft metallic substrate of OxZr

yielded to the pressure of the indenter and caused the surface film to be compromised. The damage of OxZr components exceeded that of the CoCr control components because the substrate metal was softer. The study indicated that increased liner wear can be expected if the surface film is compromised within the bearing area on an OxZr head.

1.108.2.3.2.2. Titanium nitride coating

A limited number of hip or knee simulator comparisons of TiN-coated materials to traditional CoCr alloy or other coating options can be found in open literature, and their results are rather contradictory. First hip simulator studies of titanium nitride coatings running against UHMWPE were conducted by Pappas *et al.* back in 1990s.[147,148] The coatings were applied on wrought Ti6Al4V alloy by a proprietary PVD process, and the tests were conducted in distilled water. The average wear of UHMWPE obtained in these two studies is shown in **Figure 34**. The results of the earlier, 10 Mc study[147] showed that under the same testing conditions, the wear of UHMWPE articulating against TiN-coated 32 mm femoral heads was three times lower than for the CoCr alloy heads of the same diameter. In the second study,[148] 47 mm diameter femoral HR cups with a polished 8 μm thick TiN coating were run against UHMWPE inserts for 48 Mc. The wear of the TiN coating was <2 μm, and no delamination was observed. Minor wear, scratching, and burnishing of the TiN surface were visible to the naked eye after 35 Mc. As no reference CoCr femoral cups were used in this 48 Mc test, the wear of UHMWPE was compared to the results for the CoCr heads from the previous, 10 Mc study, and was found to be significantly lower. Because of the different geometry of the femoral components (47 mm diameter TiN-coated Ti6Al4V cups vs. 32 mm diameter CoCr heads), however, the validity of such a comparison is questionable.

Another hip simulator study[149] compared, among others, the wear performance of TiN coatings on 28 mm diameter CoCr femoral heads articulating against UHMWPE acetabular cups. Approximately 10 μm thick TiN layers were deposited by arc evaporative PVD (AEPVD). Simulation studies were run for up to 5 Mc in 25% (v/v) bovine serum. Wear loss of PE was determined volumetrically.

The wear volume change of the UHMWPE acetabular cups as a function of time and the mean steady state UHMWPE wear rates (2–5 Mc) are shown in **Figure 35(a)** and **35(b)**. It can be seen that TiN-coated heads produced PE wear two times higher than the control uncoated heads. Although the authors observed no coating failure, a strong increase and a large scatter of the total height of the surface roughness profile, R_t (from 0.490 ± 0.240 μm before testing to 2.063 ± 5.077 μm after testing), strongly suggest that localized loss of the TiN coating has occurred. At the same time, no roughening of the uncoated CoCr heads was observed after 5 Mc which might explain the lower UHMWPE wear associated with these heads compared to the TiN-coated heads.

The same authors observed cohesive failure of a similar ~10 μm thick AEPVD-deposited TiN coating on a 28 mm CoCr femoral head (**Figure 36**), after 2 Mc wear simulation against an uncoated CoCr insert.[150] The wear of the TiN-coated heads was lower than that of the uncoated heads, but it caused relatively high wear of the corresponding CoCr inserts. It was hypothesized that droplets remaining on the as-deposited TiN coating surface might have been an initial originator of cohesive failure.

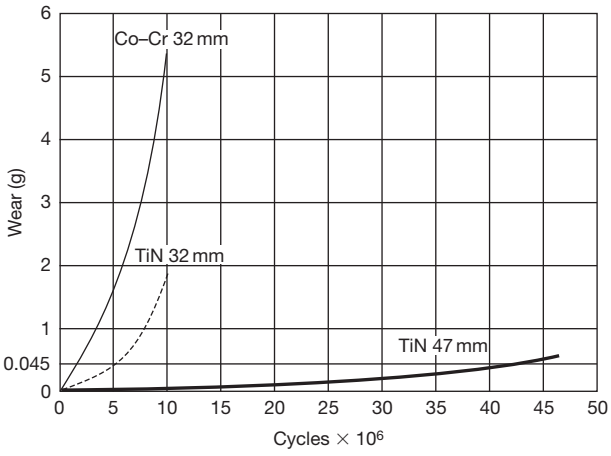

Figure 34 Wear of UHMWPE sockets articulating against 32 and 47 mm diameter CoCr- and TiN-coated Ti6Al4V femoral heads as a function of number of cycles in a hip wear simulator. Reproduced from Pappas, M. J.; Makris, G.; Buechel, F. F. *Clin. Orthop.* **1995**, *317*, 64–70, with permission from Lippincott Williams & Wilkins.

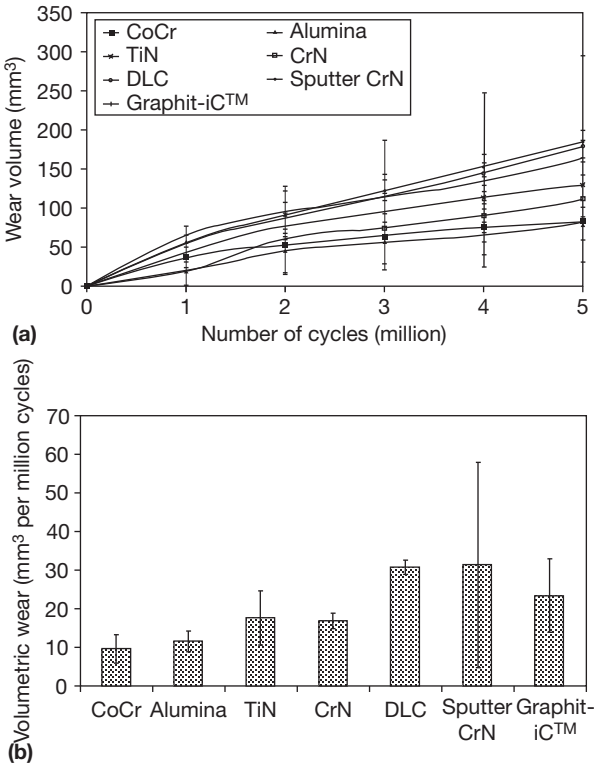

Figure 35 Wear of UHMWPE sockets articulating against alumina, CoCr, and coated CoCr femoral heads as a function of number of cycles in a hip wear simulator (a) and the mean steady state UHMWPE wear rates (2–5 million cycles) (b). Reproduced from Galvin, A.; Brockett, C.; Williams, S.; *et al. Proc. IMechE H J. Eng. Med.* **2008**, *222*, 1073–1080.

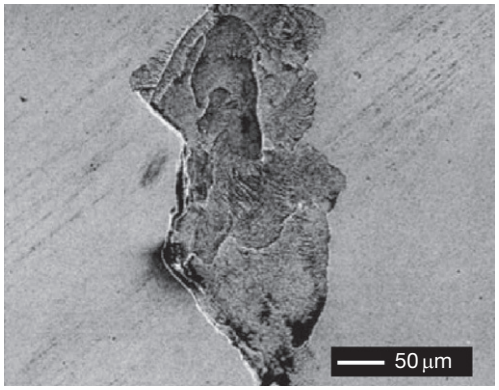

Figure 36 Cohesive failure of TiN coating on CoCrMo femoral head after 2 million cycles articulation in a hip wear simulator against CoCrMo insert. Reproduced with permission from Fisher, J.; Hu, X. Q.; Tipper, J. L.; *et al. Proc. IMechE H J. Eng. Med.* **2002**, *216*, 219–230.

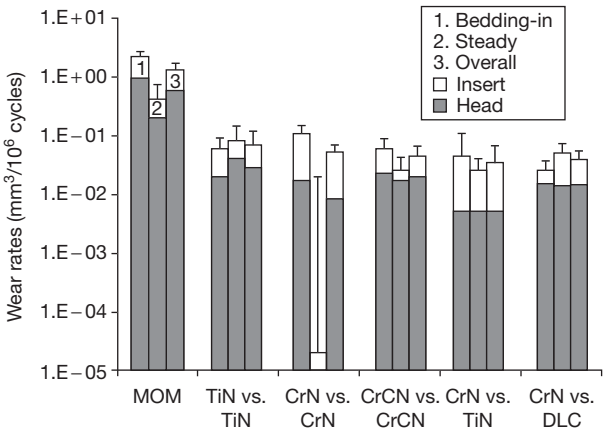

Figure 37 Wear rates of surface engineered and uncoated MoM (CoCr) prostheses over three different stages of hip wear simulator test. Reproduced from Fisher, J.; Hu, X. Q.; Stewart, T. D.; *et al. J. Mater. Sci. Mater. Med.* **2004**, *15*, 225–235, with permission from Springer.

In a different study,[57] the same authors tested AEPVD TiN-coated 28 mm diameter CoCr femoral heads articulating against similar coated CoCr inserts in 25% (v/v) bovine serum. Wear loss was determined gravimetrically and converted into volume loss. The wear rates (+95% confidence limits) for the first Mc (bedding-in), the second 1 Mc (steady state) and over 2 Mc (overall) are shown in Figure 37. It can be seen that both the coated heads and the coated inserts demonstrated much lower wear compared to the traditional MoM prostheses. By the end of the 2 Mc period, the overall wear of the coated couples was ~20-fold lower than for the uncoated ones. Also, the concentrations of Co, Cr, and Mo ions from the TiN-coated combination were at least 20-fold lower. At the same time, some localized damage to the TiN coating (Figure 11) was seen on the coated heads even after the relatively short period of 2 Mc corresponding to no more than 2 years *in vivo*. It may be hypothesized that larger areas of coating delamination and correspondingly higher wear would be observed if the test was continued for a longer time period.

Oñate *et al.*[151] tested the wear behavior of TiN coating in a simplified knee wear testing machine where the contact between femoral condyles and tibial plates is approximated by a ball-on-plate geometrical contact. A 3–4 μm thick TiN layer was produced by a proprietary ion plating PVD process. TiN-coated and -uncoated CoCr femoral heads of 32-mm diameter were subjected to a combined rolling-sliding motion against UHMWPE plates. The tests were run in distilled water as the lubricant for up to 5 Mc. Wear evaluation of UHMWPE plates was carried out by weight loss measurements. High wear loss occurred in the case of PVD TiN-coated CoCr wearing against UHMWPE (Figure 38). After 5 Mc, TiN coating induced a UHMWPE wear five times higher than the control (uncoated) material. When the worn surfaces of the TiN-coated balls were observed, small areas of approximately 70 μm without a coating were detected. These areas corresponded to hard phases of the CoCr microstructure in which the coating had not nucleated or adhered properly. According to the authors, detachment of the coating particles from these areas

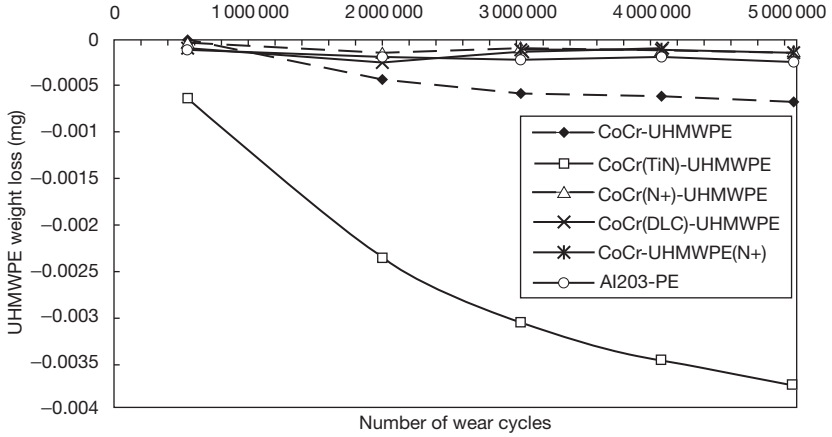

Figure 38 Weight loss of UHMWPE plates articulating against alumina, CoCr, and surface engineered femoral heads as a function of number of cycles in a knee wear simulator. Reproduced from Oñate, J. I.; Comin, M.; Braceras, I.; *et al. Surf. Coat. Technol.* **2001**, *142–144*, 1056–1062, with permission from Elsevier.

was responsible for the presence of scratches and the high weight loss of the UHMWPE plates.

Very recently, Weisenburger *et al.*[152] reported the results of extended simulator testing of total hip replacements (THRs) and TKRs metallic components with PVD TiN-based coatings. MoM THRs comprising TiN-coated heads and liners (44 mm diameter) were tested on a hip simulator, and TiNbN-coated 65 mm femoral components were tested on a force-control knee simulator against conventional UHMWPE tibial inserts. As claimed by the authors, the tested TiN-based coatings are commercially available for clinical use in some parts of the world including Europe. The tests were conducted in bovine serum ($20\,g\,l^{-1}$ protein) at 37 °C, and wear was measured gravimetrically. Uncoated MoM THR components and TKR femorals were used as controls.

Over 5 Mc, the TiN-coated THRs wore at a rate of ~8.5 mg Mc^{-1} while uncoated THR components wore at a lower rate of ~3.2 mg Mc^{-1}. Over 8 Mc, UHMWPE tibial inserts paired with TiN-coated femoral components wore at ~11.2 mg Mc^{-1} while the control insert wore at ~9.0 mg Mc^{-1}. Remarkably, all TiN-coated components clearly showed loss of coating in the articulating region which increased in size as the tests progressed. The higher wear observed with TiN-coated specimens must have been caused by third-body wear (evidenced by scratches) from the coating removal debris. The authors suggested that the coating process had to be altered to create a more durable coating able to withstand many years of articulation within the body.

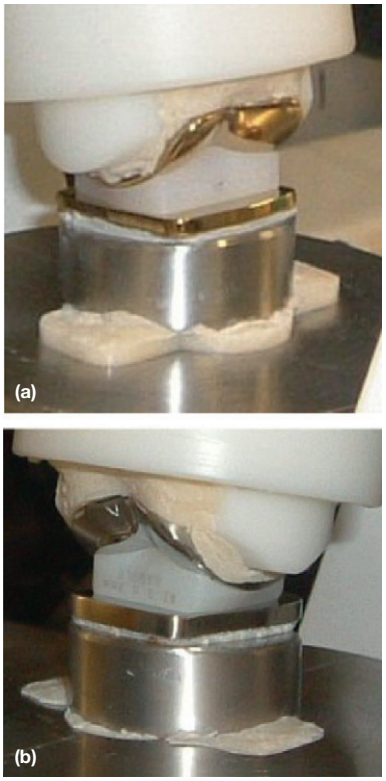

Figure 39 Wear simulation test set-up of a total ankle replacement (TAR): (a) TiN-coated Ti alloy (Buechel Pappas, BP); (b) CoCr alloy (Mobility, DePuy International). Reproduced from Bell, C. J.; Fisher, J. *J. Biomed. Mater. Res. Appl. Biomater.* **2007**, *81B*, 162–167, with permission from Wiley.

Bell and Fisher[153] performed wear simulation comparison of a total ankle replacement (TAR) whose talar and tibial components were CoCr alloy (Mobility, DePuy International) with the Buechel Pappas (BP) TAR whose metallic components were made of PVD TiN-coated titanium alloy (**Figure 39**). It is important to mention that TiN-coated BP prosthesis is one of the few TAR designs with a good clinical history. The simulator tests were run in 25% (v/v) bovine serum for 6 Mc. No statistically significant difference was observed between UHMWPE wear bearing against TiN-coated titanium alloys and that against uncoated CoCr alloy.

The results of different wear simulation tests with PVD TiN-coated joint prostheses are summarized in **Table 1**.

As mentioned in **Section 1.108.2.2**, surface treatments that modify the surfaces to an increased depth are capable of providing better wear resistance than plain TiN PVD-coating deposition. Unfortunately, practically no wear joint simulation studies of nitrogen-diffusion-hardened bearing surfaces have been reported in literature. The only exception is the work of Gutmanas and Gotman[160] where 32 mm diameter PIRAC nitrided Ti6Al4V femoral heads (with a 2–2.5 μm thick titanium nitride layer) were tested against UHMWPE cups in a hip simulator. After 2 Mc in distilled water, PIRAC TiN–UHMWPE couples produced approximately five times less PE wear than the control 316L steel–UHMWPE couples. Importantly, no signs of coating delamination were observed after 4 Mc suggesting better adhesion than for PVD TiN layers.

1.108.2.3.2.3. DLC coating

1.108.2.3.2.3.1. DLC-coated metal against UHMWPE

Saikko *et al.*[154] coated 28 mm diameter CoCr femoral heads with a 3 μm thick DLC layer by a proprietary, hybrid PVD–CVD process. The heads were tested in a hip simulator against metal-backed UHMWPE cups in Calf serum diluted 1:1 with distilled water (protein content close to that of synovial fluid). Wear of UHMWPE was estimated gravimetrically. Uncoated CoCr and alumina heads were used as controls. DLC produced the highest average gravimetric PE wear rate over 3 Mc; however, the differences between the three head materials were not large (~58, 56, and 48 mg/10^6 cycles for DLC-coated CoCr, uncoated CoCr, and Al_2O_3, respectively). After the tests, all heads proved to be practically unchanged in visual and microscopical examination. The authors concluded that, as a counterface for PE, their experimental DLC coating was fairly similar to alumina and CoCr.

Dowling *et al.*[155] carried out wear tests of DLC-coated 22 mm diameter stainless steel femoral heads against UHMWPE cups in a multistation hip simulator in distilled water. DLC films of 150–200 nm thickness were deposited using the saddle field source. UHMWPE wear was evaluated by the change in dimensions of the plastic cups. DLC-coated heads exhibited significantly lower wear than their uncoated counterparts (~5 vs. 70 mm^3 after 6 Mc). The wear observed with DLC coatings was comparable to that obtained with femoral heads made from zirconia.

Dorner-Reisel *et al.*[156] tested DLC-coated CoCr femoral segments for total knee joint replacements against UHMWPE inlays in knee wear simulator in bovine serum solution for

Table 1 A summary of literature reports on wear simulation tests of PVD TiN-coated and DLC-coated joint prostheses

Material couple	*Conditions*	*Result*	*References*	*Remarks*
TiN-coated Ti6Al4V THR head against UHMWPE insert	Hip simulator, distilled water, 10×10^6 cycles	Less wear than with uncoated CoCr alloy	147	
TiN-coated Ti6Al4V HR cup against UHMWPE insert	Hip simulator, distilled water, 48×10^6 cycles	Less wear than with uncoated CoCr alloy	148	TiN-coated 44 mm HT cup compared to 32 mm CoCr head from Ref.148
TiN-coated CoCr THR head against UHMWPE insert	Hip simulator, 25% v/v bovine serum, 5×10^6 cycles	More wear than with uncoated CoCr alloy	149	Roughening of TiN-coated head – TiN layer delamination?
TiN-coated CoCr THR head against CoCr insert	Hip simulator, 25% v/v bovine serum, 2×10^6 cycles	More wear than with uncoated CoCr alloy	150	Cohesive failure of TiN layer
TiN-coated CoCr THR head against TiN-coated CoCr insert	Hip simulator, 25% v/v bovine serum, 2×10^6 cycles	Less wear than for uncoated MoM pair	57	Localized damage to TiN coating
TiN-coated Co–Cr femoral head against UHMWPE plate	Knee simulator, distilled water, 5×10^6 cycles	More wear than with uncoated CoCr alloy	151	Some TiN layer detachment
TiN-coated femoral head against TiN-coated acetabular liner	Hip simulator, bovine serum, 5×10^6 cycles	More wear than with uncoated CoCr alloy	152	Loss of TiN coating Substrate material not reported (Ti6Al4V or CoCrMo?)
TiNbN-coated femoral component against UHMWPE insert	Knee simulator, bovine serum, 5×10^6 cycles	More wear than with uncoated CoCr alloy	152	Loss of TiN coating Substrate material not reported (Ti6Al4V or CoCrMo?)
TiN-coated CoCr talar/tibial components against UHMWPE bearing	Ankle simulator, 25% v/v bovine serum, 6×10^6 cycles	Same wear as for uncoated CoCr alloy	153	
DLC-coated CoCr femoral head against UHMWPE cup	Hip simulator, diluted calf serum, 3×10^6 cycles	Similar wear as with uncoated CoCr alloy and alumina	154	
DLC-coated 316L femoral head against UHMWPE cup	Hip simulator, distilled water, 6×10^6 cycles	Less wear than with uncoated 316L steel	155	
DLC-coated CoCr femoral segment against UHMWPE inlay	Knee simulator, bovine serum solution, 5×10^6 cycles	Less wear than with uncoated CoCr alloy for thin DLC More wear than with CoCr alloy for thicker DLC	156	
DLC-coated CoCr femoral head against UHMWPE cup	Hip simulator, 25% v/v bovine serum, 5×10^6 cycles	More wear than with uncoated CoCr alloy	149	Possible delamination of DLC layer
DLC-coated CoCr femoral head against UHMWPE plate	Knee simulator, distilled water, 5×10^6 cycles	Less wear than with uncoated CoCr	151	
DLC-coated Ti6Al4V cup against alumina ball	Hip simulator, ASF and calf serum, 6×10^6 cycles	DLC coating failed after 100×10^3 cycles	157	
DLC-coated CoCr ball-on-socket pairs	Hip simulator, bovine serum based fluid, 20×10^6 cycles	Less wear than with uncoated CoCr alloy	158	
DLC-coated 316L ball-on-socket pairs	Hip simulator, diluted bovine serum, 15×10^6 cycles	Very low wear	159	No control uncoated pairs were tested
DLC-coated CoCr THR head against CoCr insert	Hip simulator, 25% v/v bovine serum, 2×10^6 cycles	Less wear than with uncoated CoCr alloy	150	

5 Mc. DLC-coatings were deposited by plasma decomposition of the gaseous hydrocarbon methane in three different thicknesses – 0.8, 2.7, and 4.5 μm. Wear loss was estimated by weighing the UHMWPE inlays. The test results are shown in **Figure 40**. In comparison to the uncoated CoCr femoral segments, DLCs with a thickness of 0.8 and 2.7 μm on the CoCr femoral components reduced the UHMWPE wear. Surprisingly, the 4.5 μm thick DLC coating caused a drastically increased wear. This result was explained by changes in the heat transfer. The authors assumed that the heat transfer might be reduced with DLC coating thickness and because of lower fraction of defects, such as pinholes, in thicker DLC coatings.

Galvin *et al.*[149] reported a hip simulator study of 28 mm diameter CoCr femoral heads coated with a ~10 μm thick amorphous DLC (aDLC) film by PACVD. Simulation studies were run against UHMWPE acetabular cups in 25% (v/v) bovine serum for 5 Mc. As can be seen in **Figure 35**, DLC-coated heads produced PE wear three times higher than the control uncoated heads. It is worth mentioning that an increase and, especially, large scatter of the total height of the surface roughness profile, R_t, obtained following the simulation test suggest that local delamination of the DLC layer had occurred.

DLC-coated 32-mm diameter CoCr femoral heads were tested in a simplified knee wear testing machine against

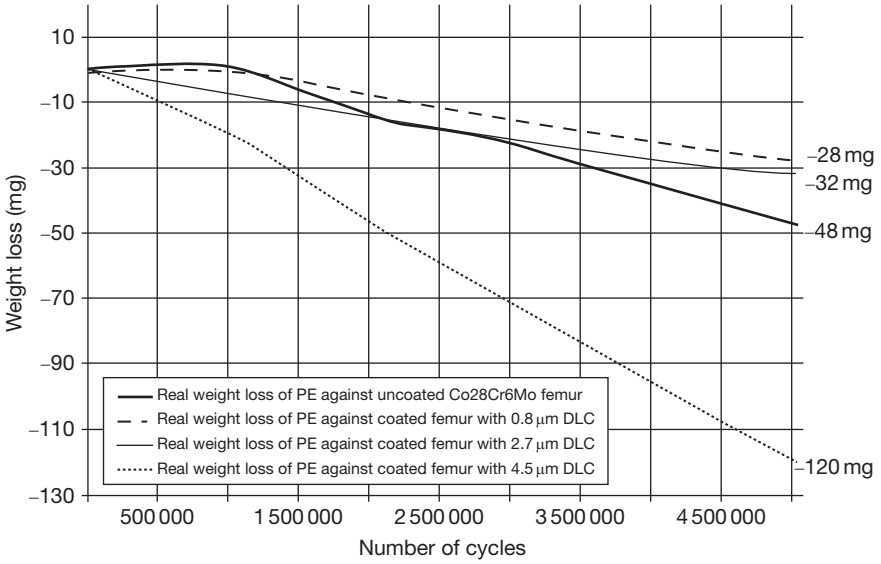

Figure 40 Weight loss of UHMWPE inlays articulating against uncoated and DLC-coated Co28Cr6Mo femoral segments as a function of number of cycles in a knee wear simulator. Reproduced from Dorner-Reisel, A.; Schürer, C.; Müller, E. *Diam. Relat. Mater.* **2004**, *13*, 823–827, with permission from Elsevier.

UHMWPE plates.[151] DLC coating of 3–4 µm thickness was PVD deposited from acetylene in a radio frequency (RF) plasma discharge on a metallic interlayer. The tribological tests were run in distilled water for 5 Mc. As shown in Figure 38, the weight loss of UHMWPE articulating against DLC-coated CoCr head was significantly lower than in the case of uncoated CoCr (0.130 vs. 0.690 mg). PE material on the DLC coating was almost negligible.

1.108.2.3.2.3.2. DLC coating in hard-on-hard bearings

Österle *et al.*[157] ran hip simulator tests of DLC-coated Ti6Al4V cups against 44 mm diameter alumina composite ceramic balls (BIOLOX® delta, CeramTec AG) in artificial synovial fluid (ASF) and new born calf serum. DLC (a-C:H) coating of 2 µm thickness was deposited on a 0.5 µm Ti interlayer by high-frequency PACVD. Three of four joints failed during hip simulator testing already during the first 100×10^3 cycles, because of peeling off the coating from large areas of the cups. The authors concluded that the premature failure of DLC-coated cups during hip simulator testing was due to insufficient polishing of the parts prior to coating. One such failure is shown in Figure 41 revealing local delamination of the coating at the substrate–coating interface.

It was claimed that, in the case of the nonwear-resistant titanium alloy substrates, the sole application of a thin hard coating is not sufficient. A possible solution might be surface modification of a several microns thick supporting layer, for example, by plasma nitriding prior to coating with DLC.

In Thorwarth *et al.*,[158] 4 µm thick DLC (a-C:H) layers (hardness of 23 GPa) were grown in an acetylene plasma on ball-on-socket implant pairs made from CoCr (radius of curvature 14.5 mm). Metallic interlayers were used to provide stable layer adhesion. For comparison, a rough 16 µm DLC layer exhibiting 'cauliflower' structure ('rough DLC') was also investigated. Hip simulator tests were run in 30 g l^{-1} protein-containing bovine serum based wear testing fluid at 37 °C.

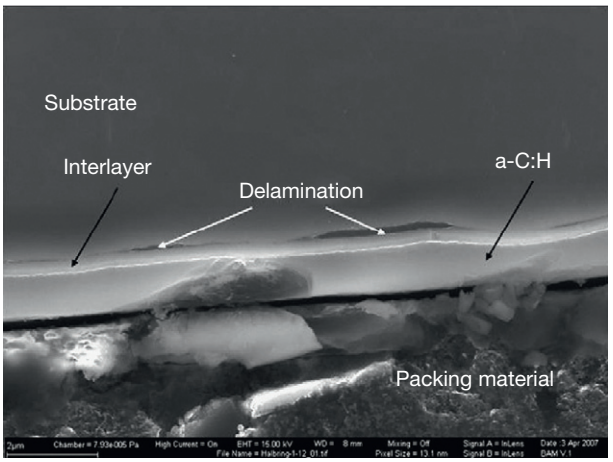

Figure 41 Local delamination of DLC coating on Ti6Al4V cup after 100 000 cycles articulation against alumina ball in a hip simulator. Reproduced from Österle, W.; Djahanbakhsh, M.; Hartelt, M.; Wäsche, R. *Wear* **2008**, *265*, 1727–1733, with permission from Elsevier.

Total wear volumes for uncoated MoM and DLC-on-DLC (DoD) friction pairs up to the full test runtime of 20 Mc are shown in Figure 42. The smooth DoD friction pairs exhibited significantly reduced wear ($p < 0.001$) compared to the uncoated variants. In comparison, the 16 µm 'cauliflower' DLC layer, having a much higher surface roughness from the beginning, showed a wear volume much higher than the smooth DLC coatings ($p < 0.05$) but still half of the MoM pairs ($p < 0.001$).

The low wear resistance of uncoated implants led to a large increase of metal wear after about 7 Mc. After roughening, MoM pairs required additional, tribologically active molecules (e.g., proteins) to establish a sufficient surface separation. Without these compounds, stick–slip was observed, leading

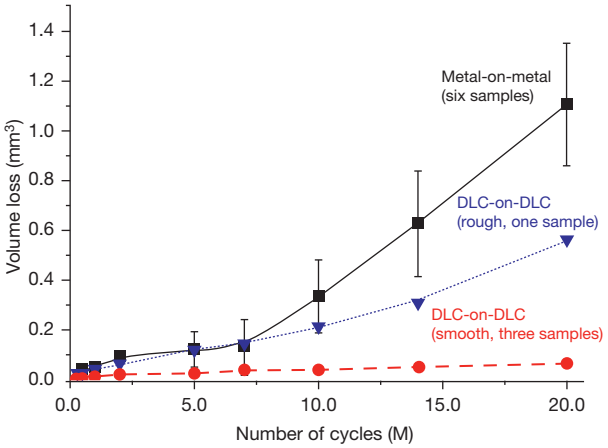

Figure 42 Volume wear loss of ball-on-socket implant pairs made from uncoated and DLC-coated Co28Cr6Mo alloy as a function of number of cycles in a hip wear simulator. Reproduced from Thorwarth, G.; Falub, C. V.; Müller, U.; *et al*. *Acta Biomater*. **2010**, *6*, 2335–2341, with permission from Elsevier.

to significantly higher wear generation. In contrast, DLC-coated implants were much more tolerant toward the absence of such molecules. A few scratches that did not penetrate into the substrate and sparse local defects were observed on smooth DLC surfaces after 20 Mc. These defects appeared at about 1 Mc and did not lead to layer delamination for DLC coatings with good interfaces not susceptible to stress corrosion cracking (SCC).

Lappalainen *et al.*[159] deposited 40–100 µm thick amorphous diamond (AD, 80–85% diamond bonding) coatings on custom made stainless steel acetabular cups and 28- or 35-mm femoral heads by the filtered pulsed plasma arc discharge method. Proper intermediate layers and high plasma ion energies were used in the beginning to achieve extreme adhesion. Wear testing was done in commercial hip joint simulator in diluted bovine serum (protein content of 35 mg ml^{-1}) for 15 Mc. No uncoated controls were tested. Linear wear rates were evaluated by the change in the depth of 60–200 nm deep marker scratches on the surfaces of the balls. An extremely low volumetric wear (estimated on the basis of the linear wear) of 10^{-4} mm^3 Mc^{-1} was obtained. Comparing this *in vitro* wear rate with the clinical data for conventional metal-on-UHMWPE and MoM hip prostheses, the authors conclude that high-quality AD coatings can reduce the amount of wear debris from articulating surfaces so as to be close to negligible.

Fisher *et al.*[150] performed hip simulator studies of 28 mm diameter CoCr head-on-socket couples where the femoral heads were modified using 2 µm thick PACVD DLC coating. After 2 Mc articulation in 25% (v/v) bovine serum, the wear of such half-coated couples was at least one order of magnitude lower compared with that of the traditional MoM reference bearings. Correspondingly, the concentration of three major elements Co, Cr, and Mo in the serum lubricant of the DLC-half-coated couple was reduced by an order of magnitude.

The results of literature reported wear simulation tests with DLC-coated joint prostheses are summarized in **Table 1**. It can be seen that the results on the wear of DLC–UHMWPE articulating couples are contradictory. The common trend in these studies is that when the experiments are done in water, the wear of PE is somewhat reduced. However, when protein-containing fluid (e.g., serum) is used, no significant improvement compared to uncoated control samples can be seen. It has been hypothesized that with protein-containing lubricants and real loads (used in hip simulators) the formation of the transfer layer responsible for wear protection of the softer surface sliding against DLC is inhibited.[127] In these authors' opinion, the approach in improving the wear of UHMWPE articulating components via DLC coating of the partner surface is a dead-end. The superior way of realizing the potential of DLC in joint replacements is, therefore, to use DLC coatings on both articulating surfaces. Indeed, in joint simulation tests, DoD couples exhibited a significantly reduced wear. It is important to mention, however, that DLC coatings might be successful in simulator experiments but still fail *in vivo*. This is due to the existence of pinholes providing corrosion paths through the coating to the substrate. Such corrosion paths can lead to galvanic effects, delamination, and eventual failure of the coating.[127] Furthermore, it takes a long time for the lubricating fluid to diffuse through microscopic pinholes. As simulator experiments are strongly accelerated compared to the *in vivo* situation, their duration might be too short for the corrosion processes to have effect. To reduce the probability of existence of through-film defects, the application of thicker DLC coatings has been advocated.[127]

1.108.2.3.2.4. Chromium nitride based coatings

Chromium nitride (CrN) and carbonitride (CrCN) PVD-deposited coatings were studied in simulation tests as bearing surfaces for hip replacements. These coatings are claimed to generally have better cohesive strength and toughness compared to TiN, with only slightly reduced hardness.[57]

CrN-coated (AEPVD, ~10 µm) 28 mm diameter CoCr femoral heads were tested against UHMWPE acetabular cups in 25% (v/v) bovine serum for 5 Mc.[149] Similar to TiN- and DLC-coated heads, the CrN-coated heads showed no reduction in PE wear compared to uncoated CoCr (**Figure 35**). An increase of the total height of the surface roughness profile, R_t, might suggest some local loss of the CrN surface layer.

A different picture emerged for CrN-coated MoM articulations. In Fisher *et al.*,[57] 28 mm diameter CrN- and CrCN-coated (AEPVD, ~10 µm) CoCr femoral heads were tested against similarly coated CoCr inserts in 25% (v/v) bovine serum. After 5 Mc, the coated THR combinations showed a 36-fold reduction in wear rate compared to the MoM control. Although no significant damage was found to the coating, several isolated cohesive coating failures on femoral heads already occurred after 2 Mc.

Another paper reports wear simulation study of AEPVD CrN-coated (>10 µm) 39 and 55 mm diameter HR CoCr devices in 25% (v/v) bovine serum.[161] After 10 Mc, the CrN-coated bearings had 80% lower wear than the MoM controls. The Cr and Co ion levels in the lubricant of the CrN bearings were 73 and 98% lower than in the MoM controls. No damage to the CrN coating was mentioned. It has been concluded that thick AEPVD CrN coatings have great potential for the reduction of wear and ion release of MoM hip replacement implants.

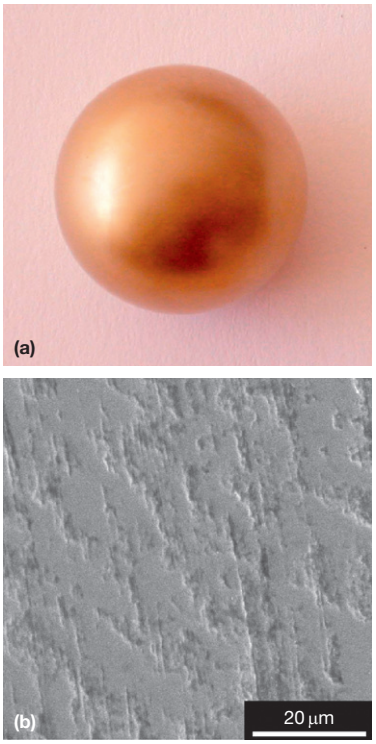

Figure 43 Postmortem retrieved TiN PIRAC-coated femoral head of canine THR: optical (a) and SEM (b) micrographs.

1.108.2.4. *In Vivo* Performance of Wear-Resistant Ceramic Coatings

1.108.2.4.1. Animal studies

There is a dearth of animal studies evaluating the efficacy of hard ceramic coatings in reducing the wear of joint prostheses. This could be due to the lack of accepted animal models for human total joint replacement (TJR) performance.[162–164] The existing reports on *in vivo* performance of hard coatings for orthopedic applications are limited to the assessment of their biocompatibility.[165–168]

In a pilot animal study,[169] 12 dogs received THRs with TiN PIRAC-coated Ti6Al4V femoral heads articulating against UHMWPE acetabular cups. Two animals were lost to analysis because of postoperative complications. The other ten dogs retained normal walking, running, and jumping capabilities until sacrificed 2–3.5 years after the total hip arthroplasty (THA) surgery. No radiographic or clinical signs of aseptic loosening were observed during the follow-up period. The excised TiN-coated heads preserved the initial golden color and were only lightly abraded as observed under scanning electron microscope (SEM) (**Figure 43**). Importantly, no delamination of the TiN layer occurred *in vivo*. Histological findings included a fairly small amount of metal/PE debris and active osteoblastic (bone-building) activity around the implants.

In another research, *in vivo* performance of TiN PIRAC-coated MoM THR was studied in a rat model.[170] The animals were sacrificed 18 weeks after THA surgery, following daily treadmill exercise that amounted to approximately 7 million

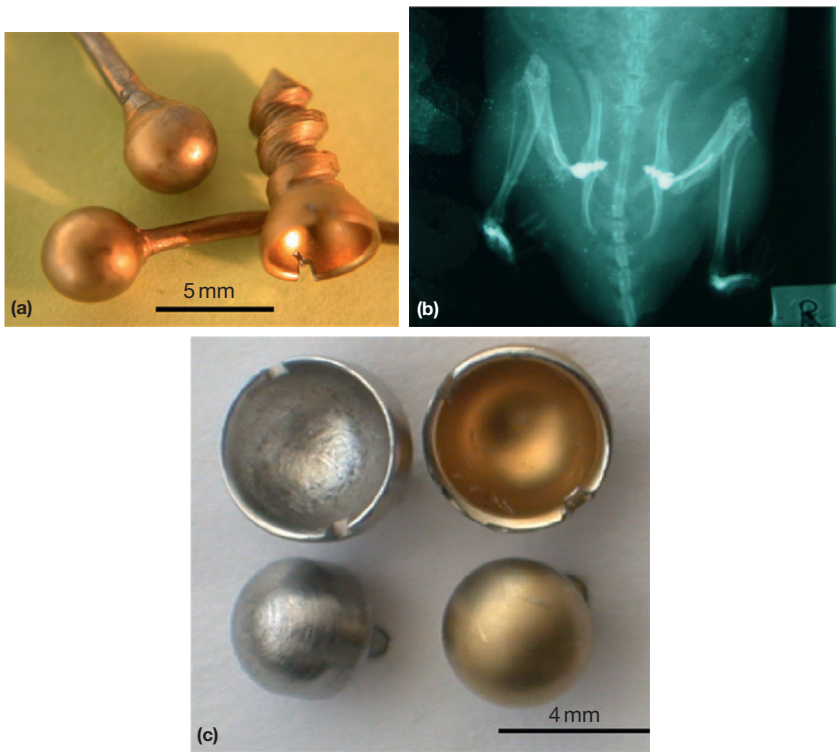

Figure 44 (a) PIRAC TiN-coated Ti6Al4V rat THR prostheses; (b) an X-ray of a rat after bilateral THA; (c) postmortem retrieved rat stainless steel (left) and TiN-coated Ti6Al4V (right) THR prostheses. Surface scratches in (c) are an artifact of the retrieval procedure.

stress cycles on hip joint. The excised TiN-coated articulating components remained smooth and did not show any sign of coating delamination. This is in contrast to the control steel-on-steel (316L) joint prostheses where pronounced surface roughening was observed (**Figure 44**). The encouraging results of the two animal studies with PIRAC TiN coatings[169,170] suggest that hard diffusion coatings are a promising alternative to PVD ceramic coatings.

1.108.2.4.2. Clinical performance

The primary purpose of bearing surface modifications is to decrease wear, both to reduce the debris produced that can elicit a potentially negative biologic response, such as particles and metal ions, and to reduce changes in the bearing geometry that can impact gait kinematics. This should provide increased longevity and survivorship of the prosthetic devices. Laboratory testing can indicate how the surface modifications may behave, but ultimate verification must rely on clinical performance. There are few publications dealing with clinical performance of surface modifications considering the number of technologies and devices that have been used clinically. The following is a review of some of these publications.

The clinical behavior of orthopedic components with articular surfaces modified by ion implantation provides insight into how components with a ceramic surface film may provide benefits. One short-term study (minimum 3-year follow-up) reported that nitrogen ion treated CoCr heads produced approximately 28% less linear penetration into UHMWPE liners than nontreated CoCr heads did.[26] The advantage of this radiographic approach is that it can provide a measure of bearing wear without surgical intervention. Another study examined the surfaces of clinically retrieved hip components.[171] The nitrogen ion implanted CoCr heads had harder surfaces and, while they exhibited scratches, the scratches tended to have less depth. It also was noted that the surface hardness and depth of nitrogen enrichment tended to decrease with length of implantation, with some heads showing no evidence of the ion treatment remaining. It would be interesting to see if the wear advantage of the ion implanted heads seen in the radiographic study was maintained or if it diminished with longer term follow-up. In either case, the greater potential durability and resistance to roughening of a ceramic film might provide even better clinical performance.

Assessing the performance of ceramic coatings is complicated by the variety of coating compositions, substrate compositions, coating processes, coater expertise, and component types.[21,127] Very few clinical studies are published comparing coated and conventional bearing components directly, particularly considering the large number of coated components that have been used globally for decades. Some publications involve only retrieved components from a small number of patients, potentially skewing the understanding of that coating toward anecdotal experience rather than typical performance.

Only one published study was found with a direct comparison of bearing prostheses with nitride coatings to those of noncoated CoCr.[66] Titanium nitride coatings were found to have been breached on the modular heads of several revised hip components, but the comparison was complicated by issues involving the bone cement and cementing technique. Some studies of titanium nitride coated components report good clinical outcomes, but they do not describe the condition of the articulating surfaces in any detail.[61,63,172] It is difficult from this to assess whether the nitride coating will be durable long-term or provide significant reductions in UHMWPE wear in a THR or TKR. Two retrieval analyses reported scratching or breaching of the titanium nitride coating on modular heads at short to medium durations.[64,65] These studies described features that questioned the adhesive and cohesive durability of the coatings even in low demand use.

Very few publications are available on the clinical performance of diamond and DLC coatings as well. Those reports that have been published indicate poor clinical performance.[21,98,173,174] Poor adhesion between the coating and substrate is noted in each case. In at least one case, this appeared to involve corrosion between the coating and metal substrate. In others, stress states existing within the coating or produced between the articulating surfaces were implicated. Recommendations have been made about how to address these deficiencies in coating performance, but a successful clinical implementation has not been reported.

In contrast, the clinical performance of the autogenic ceramic surface film on oxidized zirconium is the subject of various types of published investigations. Comparisons of functional scores and survivorship in THRs and TKRs indicate that oxidized zirconium components are at least comparable to CoCr components in short- and medium-term follow-up.[175–184] One of these studies uniquely reported faster recovery for patients with oxidized zirconium components, but the advantage did not persist.[175] Another study found no difference in volume, size, and shape of UHMWPE wear debris between oxidized zirconium and CoCr hips, but it is not clear if the small amount of retrieved debris was representative of all the debris.[180] Many of the investigators noted that longer term observations will be needed to determine if there are significant differences in outcomes.

Several investigations observed aspects of the clinical behavior of oxidized zirconium components for comparison with reported laboratory test behavior. Radiographic evaluation of THRs indicated trends of less linear penetration into the liner with oxidized zirconium heads than with CoCr heads, in some cases with statistical significance.[183–185] Analysis of components retrieved after clinical use indicated fewer wear features on components articulating with oxidized zirconium than with CoCr, and less roughening of oxidized zirconium surfaces than of CoCr surfaces.[186,187] Synovial fluid temperature in TKR patients was lower with oxidized zirconium components than with CoCr components, indicating less friction with oxidized zirconium.[188] These clinical results were consistent with expectations from laboratory studies and provide some optimism for future performance.

One behavior of concern that has been noted is significant damage and removal of the ceramic surface on oxidized zirconium heads that have been revised subsequent to dislocation and attempts at closed reduction.[145,189–195] This damage was caused by contact of the head with the edge of the acetabular shell, and prompted recommendations for caution and careful monitoring of such patients because of the possibility of greatly increased liner wear. Some of these studies noted that CoCr and ceramic heads also were damaged significantly by this type of event, although not in the same way. An initial

study indicated that the increased liner wear caused by this damage would not be catastrophic, and that the damage of the oxide would not be progressive.[145] Another study that placed the retrieved heads in a hip wear test simulator indicated that the liner wear could be severe, but the orientation of the head was not controlled.[194] When the same type of test was conducted with the heads in their clinical orientation, the increase in liner wear was small because the damage was on the inferior side of the head and outside of the main area of liner contact.[195] It is worth noting that these heads were revised for instability, and long-term liner wear was not a concern. Nevertheless, the articular surface of any material may be damaged by contact with the acetabular shell, so patients who have dislocations with closed reduction should be monitored with care.

Two other performance advantages were noted for oxidized zirconium over CoCr in clinical use. Hypersensitivity to metal ions has been identified as a possible cause of arthroplasty failure in certain patients.[196] Ceramic or nitride-coated components have been used in such cases as a means of limiting ion exposure to the patient. One clinical study of metal-sensitive patients demonstrated that oxidized zirconium components can be used for such patients with cost or performance advantages over the traditional alternatives.[197] The other advantage involves magnetic resonant imaging of patients. It has been demonstrated that oxidized zirconium components can produce less image distortion than CoCr.[175,198,199]

1.108.3. Future Trends

Optimizing the bearing surfaces of joint replacements is an urgent socioeconomic need because of the increasing life expectancy and increased performance demands from the growing number of younger patients to whom the surgery is indicated. Ceramic surface films have a great potential to improve the tribological performance and longevity of artificial joints as they provide the metallic components with a hard, wear-resistant surface while preserving their toughness and fracture resistance. Titanium nitride (TiN) and DLC are the most extensively studied hard coatings for orthopedic applications. Despite their high hardness, excellent biocompatibility, and promising laboratory test results, the worrisome premature failure of such coatings has been observed in clinical and some wear simulation studies. Insufficient adhesion and inadequate load-bearing capacity of the underlying softer metallic substrate are believed to be the major obstacles on the way to successful implementation of hard coatings into clinical practice. Next generation technologies aiming to alleviate the shortcomings of single-layer hard coatings include the introduction of interlayers to reduce residual stresses and improve adhesion, development of multilayer coatings to reduce residual stresses, and application of duplex surface treatments involving primary substrate surface hardening (e.g., plasma or PIRAC nitriding) followed by hard coating (TiN or DLC) deposition. Another direction is changing the coating structure and composition, for example, development of multicomponent coatings, Cr-based (CrN, CrAlN, and CrCN) coatings, and nanocrystalline and nanocomposite coatings. Further improvements in coating processes and process control to ensure the elimination of pinholes and structural inhomogeneities should contribute to the better performance of hard-coated artificial joint components operating in the corrosive clinical environment under tribological contact.

Clinical evidence is growing so that the autogenic ceramic surface on oxidized zirconium is an appropriate technology for orthopedic components that articulate with PE bearings, except maybe in the case of recurrent dislocations with closed reduction. The next step is to determine from longer term studies if oxidized zirconium can reduce PE wear to a significant extent, and if that will result in improved clinical outcomes. Another possibility might be to see if an autogenic ceramic surface like that of oxidized zirconium can be developed for self-articulation in a hard-on-hard bearing application for hips, eliminating PE debris without introducing greater risk for metal ion debris or catastrophic component fracture. This would appear to require a thicker oxide or a harder or stiffer substrate than the zirconium alloy currently in use for oxidized zirconium fabrication.

References

1. Dowson, D.; Taheri, S.; Wallbridge, N. C. *Wear* **1987**, *119*, 277–293.
2. Fisher, J.; Firkins, P.; Reeves, E. A.; Hailey, J. L.; Isaac, G. H. *Proc. Inst. Mech. Eng. H* **1995**, *209*, 263–264.
3. Levesque, M.; Livingston, B. J.; Jones, W. M.; Spector, M. *Trans. Orthop. Res. Soc.* **1998**, *23*, 247.
4. Que, L.; Topoleski, L. D. *J. Biomed. Mater. Res.* **2000**, *50*, 322–330.
5. Davidson, J. A.; Poggie, R. A.; Mishra, A. K. *Biomed. Mater. Eng.* **1994**, *4*(3), 213–229.
6. Jasty, M.; Bragdon, C. R.; Lee, K.; Hanson, A.; Harris, W. H. *J. Bone Joint Surg.* **1994**, *76B*, 73–77.
7. Hailey, J. L.; Ingham, E.; Stone, M.; Wroblewski, B. M.; Fisher, J. *Proc. Inst. Mech. Eng. H* **1996**, *210*, 3–10.
8. Dwyer, K. A.; Topoleski, L. D. T.; Bauk, D. J.; Nakielny, R.; Engh, G. A. *Trans. Orthop. Res. Soc.* **1993**, *18*, 82.
9. Barrack, R. L.; Castro, F. P., Jr.; Szuszczewicz, E. S.; Schmalzried, T. P. *Orthopedics* **2002**, *25*(12), 1–6.
10. Sychterz, C. J.; Engh, A.; Swope, S. W.; McNulty, D. E.; Engh, C. A. *Clin. Orthop.* **1999**, *38*, 223–234.
11. Hall, R. M.; Siney, P.; Unsworth, A.; Wroblewski, B. M. *Med. Eng. Phys.* **1997**, *9*(8), 711–719.
12. Davidson, J. A. *Clin. Orthop.* **1993**, *294*, 361–378.
13. Schmalzried, T. P.; Scott, D. L.; Zahiri, C. A.; *et al*. *Trans. Orthop. Res. Soc.* **1998**, *23*, 275.
14. Sychterz, C. J.; Moon, K. H.; Hashimoto, A. Y.; Terefenko, K. M.; Engh, C. A.; Bauer, T. W. *J. Bone Joint Surg.* **1996**, *78A*, 1193–1200.
15. Oonishi, H.; Takayaka, Y.; Clarke, I. C.; Jung, H. *J. Long Term Eff. Med. Implants* **1992**, *2*, 37–47.
16. Oonishi, H.; Kadoya, Y. *J. Orthop. Sci.* **2000**, *5*, 223–228.
17. Wroblewski, B. M.; Siney, P. D.; Fleming, P. A. *J. Bone Joint Surg.* **1999**, *81B*(1), 54–55.
18. Skinner, H. B. *Clin. Orthop.* **1999**, *369*, 83–91.
19. Willmann, G. *Clin. Orthop.* **2000**, *379*, 22–28.
20. Bal, B. S.; Garino, J.; Ries, M.; Oonishi, H. *J. Knee Surg.* **2007**, *20*(4), 261–270.
21. Dearnley, P. A. *Proc. Inst. Mech. Eng. H* **1999**, *213*, 107–135.
22. Willmann, G. *Adv. Eng. Mater.* **2000**, *2*(3), 114–122.
23. Savarino, L.; Greco, M.; Cenni, E.; *et al*. *J. Bone Joint Surg. Br.* **2006**, *88B*, 472–476.
24. Greenwald, S.; Garino, J. *J. Bone Joint Surg.* **2001**, *83A*(Suppl. 2, Part 2), 68–72.
25. Fenske, G. R. In *Friction, Lubrication, and Wear Technology*, ASM Handbook; ASM International: Materials Park, OH, 1992; Vol. 18, pp 850–860.
26. Maruyama, M.; Capello, W. N.; D'Antonio, J. A.; Jaffe, W. L.; Bierbaum, B. E. *Clin. Orthop.* **2000**, *370*, 183–191.

27. Sioshansi, P.; Tobin, E. J. Surgical Implants and Method. U.S. Patent 5,123,924, 1992.
28. Mahan, J. E. *Physical Vapor Deposition of Thin Films*; Wiley: New York, 2000.
29. Sree Harsha, K. S. *Principles of Physical Vapor Deposition of Thin Films*; Elsevier: Oxford, 2006.
30. Brown, I. *Ann. Rev. Mater. Sci.* **1998**, *28*, 243–269.
31. Kelly, P. J.; Arnell, R. D. *Vacuum* **2000**, *56*, 159–172.
32. O'Brien, J. M.; Goodman, D. In *Heat Treating*, *ASM Handbook*; ASM International: Materials Park, OH, 1996; Vol. 4, pp 420–424.
33. Michel, H.; Czerwiec, T.; Gantois, M.; Ablitzer, D.; Ricard, A. *Surf. Coat. Technol.* **1995**, *72*, 103–111.
34. Czerwiec, T.; Renevier, N.; Michel, H. *Surf. Coat. Technol.* **2000**, *131*, 267–277.
35. Shenhar, A.; Gotman, I.; Gutmanas, E. Y.; Ducheyne, P. *Mater. Sci. Eng. A* **1999**, *268*, 40–46.
36. Davidson, J. A.; Asgian, C. M.; Mishra, A. K.; Kovacs, P. In *Bioceramics*; 1992; Vol. 5, pp 389–401.
37. Hunter, G.; Dickinson, J.; Herb, B.; Graham, R. In *Titanium, Niobium, Zirconium, and Tantalum for Medical and Surgical Applications*, ASTM STP 1471; Zardiackas, L. D., Kraay, M. J., Freese, H. L., Eds.; American Society for Testing and Materials: West Conshohocken, PA, 2006; pp 16–29.
38. Hunter, G.; Jones, W. M.; Spector, M. In *Total Knee Arthroplasty*; Bellemans, J., Ries, M. D., Victor, J., Eds.; Springer: Heidelberg, Germany, 2005; pp 370–377.
39. Sheth, N. P.; Lementowski, P.; Hunter, G.; Garino, J. P. *J. Surg. Orthop. Adv.* **2008**, *17*(1), 17–26.
40. Hobbs, L. W.; Rosen, V. B.; Mangin, S. P.; Treska, M.; Hunter, G. *J. Appl. Ceram. Technol.* **2005**, *2*(3), 221–246.
41. Benezra, V.; Mangin, S.; Treska, M.; Spector, M.; Hunter, G.; Hobbs, L. W. In *Biomedical Materials*, MRS Symposium Proceedings; Neenan, T., Marcolongo, M., Valentini, R. F., Eds.; Materials Research Society: Warrendale, PA, 1999; Vol. 550, pp 337–342.
42. Schemel, J. H. *ASTM Manual on Zirconium and Hafnium*, ASTM STP 639; ASTM International: West Conshohocken, PA, 1977.
43. Kovacs, P.; Davidson, J. A. In *Medical Applications of Titanium and Its Alloys*, ASTM STP 1272; Brown, S. A., Lemons, J. E., Eds.; American Society for Testing and Materials: West Conshohocken, PA, 1996; pp 163–178.
44. Haygarth, J. C.; Graham, R. A. In *Review of Extraction, Processing, Properties & Applications of Reactive Metals*; Mishra, B., Ed.; The Minerals, Metals & Materials Society: Warrendale, PA, 2001; pp 1–72.
45. Blumenthal, W. B. *J. Sci. Ind. Res.* **1976**, *35*(7), 485–490.
46. Sprague, J.; Aldinger, P.; Tsai, S.; Hunter, G.; Thomas, R.; Salehi, A. In *ISTA 2003*; Brown, S., Clarke, I. C., Gustafson, A., Eds.; International Society for Technology in Arthroplasty: Birmingham, AL, 2004; Vol. 2, pp 31–36.
47. Tsai, S.; Sprague, J.; Hunter, G.; Thomas, R.; Salehi, A. *Trans. Soc. Biomater.* **2001**, *24*, 163.
48. Poggie, R. A.; Wert, J. J.; Mishra, A. K.; Davidson, J. A. In *Wear and Friction of Elastomers*, ASTM STP 1145; Denton, R., Keshavan, M. K., Eds.; American Society for Testing and Materials: Philadelphia, PA, 1992; pp 65–81.
49. Walker, P. S.; Blunn, G. W.; Lilley, P. A. *J. Biomed. Mater. Res.* **1996**, *33*(3), 159–175.
50. Galetz, M. C.; Seiferth, S. H.; Theile, B.; Glatzel, U. *J. Biomed. Mater. Res. B Appl. Biomater.* **2010**, *93*(2), 468–475.
51. Salehi, A.; Tsai, S.; Pawar, V.; *et al*. In *Bioceramics*; Nakamura, T., Yamashita, K., Neo, M., Eds.; Trans Tech Publication: Uetikon-Zuerich, Switzerland, 2006; Vol. 18, pp 1199–1202; *Key Eng Mater. 309–311*.
52. Salehi, A.; Aldinger, P.; Sprague, J.; *et al*. In *Medical Device Materials*; Shrivatstava, S., Ed.; ASM International: Materials Park, OH, 2004; pp 98–102.
53. Mazzucco, D.; Spector, M. *Clin. Orthop.* **2004**, *429*, 17–32.
54. Patel, A. M.; Spector, M. *Biomaterials* **1997**, *18*(5), 441–447.
55. Suire, R.; Malet, C.; Speri, R. J.; Bermard, C. U.S. Pat. 4,790,851, 1988.
56. Türkan, U.; Öztürk, O.; Eroğlu, A. E. *Surf. Coat. Technol.* **2006**, *200*, 5020–5027.
57. Fisher, J.; Hu, X. Q.; Stewart, T. D.; *et al*. *J. Mater. Sci. Mater. Med.* **2004**, *15*, 225–235.
58. Liu, C.; Bi, Q.; Matthews, A. *Surf. Coat. Technol.* **2003**, *163–164*, 597–604.
59. Gerth, J.; Wiklund, U. *Wear* **2008**, *264*, 885–892.
60. Sun, Y.; Bloyce, A.; Bell, T. *Thin Solid Films* **1995**, *271*, 122–131.
61. Buechel, F. F., Sr.; Buechel, F. F.; Helbig, T. E.; D'Alessio, J.; Pappas, M. J. *J. Arthroplasty* **2004**, *19*, 1017–1027.
62. Buechel, F. F., Sr.; Buechel, F. F., Jr.; Pappas, M. J. *Foot Ankle Int.* **2003**, *24*(6), 462–472.
63. Saxler, G.; Temmen, D.; Bontemps, G. *Knee* **2004**, *11*, 349–355.
64. Raimondi, M. T.; Pietrabissa, R. *Biomaterials* **2000**, *21*, 907–913.
65. Harman, M. K.; Banks, S. A.; Hodge, W. A. *J. Arthroplasty* **1997**, *12*, 938–945.
66. Massoud, S. N.; Hunter, J. B.; Holdsworth, B. J.; Wallace, W. A.; Juliusson, R. *J. Bone Joint Surg. Br.* **1997**, *79*, 603–608.
67. Ward, L. P.; Subramanian, C.; Strafford, K. N.; Wilks, T. P. *Proc. Inst. Mech. Eng. H* **1998**, *212*, 303–315.
68. Williams, S.; Tipper, J. L.; Ingham, E.; Stone, M. H.; Fisher, J. *Proc. Inst. Mech. Eng. H* **2003**, *217*, 155–163.
69. Wiklund, U.; Gunnars, J.; Hogmark, S. *Wear* **1999**, *232*, 262–269.
70. Komotori, J.; Lee, B. J.; Dong, H.; Dearnley, P. A. *Wear* **2001**, *251*, 1239–1249.
71. Lappalainen, R.; Santavirta, S. S. *Clin. Orthop. Relat. Res.* **2005**, *430*, 72–79.
72. Bolton, J.; Hu, X. *J. Mater. Sci. Mater. Med.* **2002**, *13*, 567–574.
73. Nolan, D.; Huang, S. W.; Leskovsek, V.; Braun, S. *Surf. Coat. Technol.* **2006**, *200*, 5698–5705.
74. Willmann, G. *Adv. Eng. Mater.* **2001**, *3*(3), 135–141.
75. Venugopalan, R.; George, M. A.; Weimer, J. J.; Lucas, L. C. *Biomaterials* **1999**, *20*, 1709–1716.
76. Dearnley, P. A. *Surf. Coat. Technol.* **2005**, *198*, 483–490.
77. Wilson, A. D.; Leyland, A.; Matthews, A. *Surf. Coat. Technol.* **1999**, *114*, 70–80.
78. Wei, R.; Booker, T.; Rincon, C.; Arps, J. *Surf. Coat. Technol.* **2004**, *186*, 305–313.
79. Rahaman, M. N.; Yao, A. *J. Am. Ceram. Soc.* **2007**, *90*(7), 1965–1988.
80. Zhecheva, A.; Sha, W.; Malinov, S.; Long, A. *Surf. Coat. Technol.* **2005**, *200*, 2192–2207.
81. Fouquet, V.; Pichon, L.; Drouet, M.; Straboni, A. *Appl. Surf. Sci.* **2004**, *221*, 248–258.
82. Lanning, B. R.; Wei, R. *Surf. Coat. Technol.* **2004**, *186*, 314–319.
83. Fouquet, V.; Pichon, L.; Straboni, A.; Drouet, M. *Surf. Coat. Technol.* **2004**, *186*, 34–39.
84. Raaif, M.; El-Hossary, F. M.; Negm, N. Z.; Khalil, S. M.; Schaaf, P. *J. Phys. Condens. Matter* **2007**, *19*, 1–12.
85. Taktak, S.; Akbulut, H. *Vacuum* **2004**, *75*, 247–259.
86. Avelar-Batista, J. C.; Spain, E.; Housden, J.; Matthews, A.; Fuentes, G. G. *Surf. Coat. Technol.* **2005**, *200*, 1954–1961.
87. Shenhar, A.; Gotman, I.; Radin, S.; Ducheyne, P. *Ceram. Int.* **2000**, *26*, 709–713.
88. Shenhar, A.; Gotman, I.; Radin, S.; Ducheyne, P.; Gutmanas, E. Y. *Surf. Coat. Technol.* **2000**, *126*, 210–218.
89. Chase, M. W. *J. NIST-JANAF Thermochemical Tables*, 4th ed.; American Chemical Society: Woodbury, NY, 1998.
90. Meletis, E. I.; Erdemir, A.; Fenske, G. R. *Surf. Coat. Technol.* **1995**, *73*, 39–45.
91. Casadei, F.; Pileggi, R.; Valle, R.; Matthews, A. *Surf. Coat. Technol.* **2006**, *201*, 1200–1206.
92. Dong, H. In *Heat Treating Including Advances in Surface Engineering,* An International Symposium in Honor of Professor Tom Bell and Professor Jerome B. Cohen Memorial Symposium on Residual Stresses in the Heat Treatment Industry Proceedings of the 20th Conference; Funatani, K., Totten, G. E., Eds.; 2001; Vol. 1, pp 170–176.
93. Rie, K.-T.; Stucky, T.; Silva, R. A.; *et al*. *Surf. Coat. Technol.* **1995**, *74–75*, 973–980.
94. Ma, S.; Xu, K.; Jie, W. *Surf. Coat. Technol.* **2004**, *185*, 205–209.
95. Cassara, G.; Avelar-Batista Wilson, J. C.; Banfield, S.; Housden, J.; Matthews, A.; Leyland, A. *Wear* **2010**, *269*, 60–70.
96. Hauert, R. *Tribol. Int.* **2004**, *37*, 991–1003.
97. Grill, A. *Diam. Relat. Mater.* **2003**, *12*, 166–170.
98. Hauert, R. *Diam. Relat. Mater.* **2003**, *12*, 583–589.
99. Dearnaley, G.; Arps, J. H. *Surf. Coat. Technol.* **2005**, *200*, 2518–2524.
100. Roy, R. K.; Lee, K. R. *J. Biomed. Mater. Res. Appl. Biomater.* **2007**, *83B*, 72–84.
101. Robertson, J. *Mater. Sci. Eng.* **2002**, *R37*, 129–281.
102. Erdemir, A.; Donnet, C. *J. Phys. D Appl. Phys.* **2006**, *39*, R311–R327.
103. Park, S. J.; Lee, K.-R.; Ahn, S.-H.; Kim, J.-G. *Diam. Relat. Mater.* **2008**, *17*, 247–251.
104. Manhabosco, T. M.; Müller, I. L. *Tribol. Lett.* **2009**, *33*, 193–197.
105. Yatsuzuka, M.; Tateiwa, J.; Uchida, H. *Vacuum* **2006**, *80*, 1351–1355.
106. Xu, T.; Pruitt, L. *J. Mater. Sci. Mater. Med.* **1999**, *10*, 83–90.
107. Shtansky, D. V.; Lyasotsky, I. V.; D'yakonova, N. B.; *et al*. *Surf. Coat. Technol.* **2004**, *182*, 204–214.
108. Levashov, E. A.; Larikhin, D. V.; Shtansky, D. V.; *et al*. *J. Mater. Synth. Process.* **2002**, *10*, 319–330.
109. Shtansky, D. V.; Levashov, E. A.; Sheveiko, A. N.; Moore, J. J. *Metall. Mater. Trans.* **1999**, *30A*, 2439–2447.
110. Shtansky, D. V.; Levashov, E. A.; Sheveiko, A. N.; Moore, J. J. *J. Mater. Synth. Process.* **1999**, *7*, 187–193.
111. Shtansky, D. V.; Levashov, E. A.; Sheveiko, A. N.; Moore, J. J. *J. Mater. Synth. Process.* **1998**, *6*, 61–72.

112. Levashov, E. A.; Kudryashov, A. E.; Vakaev, P. V.; *et al*. *Surf. Coat. Technol*. **2004**, *180–181*, 347–351.
113. Kulisch, W.; Colpo, P.; Gibson, P. N.; *et al*. *Surf. Coat. Technol*. **2004**, *188–189*, 735–740.
114. Kulisch, W.; Colpo, P.; Rossi, F.; Shtansky, D. V.; Levashov, E. A. *Surf. Coat. Technol*. **2004**, *188–189*, 714–720.
115. Kulisch, W.; Colpo, P.; Gibson, P. N.; *et al*. *J. Appl. Phys. A* **2006**, *82*, 503–507.
116. Shtansky, D. V.; Kaneko, K.; Ikuhara, Y.; Levashov, E. A. *Surf. Coat. Technol*. **2001**, *148*, 206–215.
117. Shtansky, D. V.; Gloushankova, N. A.; Sheveiko, A. N.; *et al*. *Biomaterials* **2005**, *26*, 2909–2924.
118. Shtansky, D. V.; Bashkova, I. A.; Levashov, E. A.; *et al*. *Dokl. Biochem. Biophys*. **2005**, *404*, 336–338.
119. Shtansky, D. V.; Gloushankova, N. A.; Bashkova, I. A.; *et al*. *Surf. Coat. Technol*. **2006**, *201*, 4111–4118.
120. Shtansky, D. V.; Gloushankova, N. A.; Bashkova, I. A.; *et al*. *Biomaterials* **2006**, *27*, 3519–3531.
121. Shtansky, D. V.; Bashkova, I. A.; Kiryukhantsev-Korneev, Ph.V.; *et al*. *Dokl. Biochem. Biophys*. **2008**, *418*, 8–10.
122. Shtansky, D. V.; Gloushankova, N. A.; Bashkova, I. A.; *et al*. *Surf. Coat. Technol*. **2008**, *202*, 3615–3624.
123. Long, M.; Riester, L.; Hunter, G. *Trans. Soc. Biomater*. **1998**, *21*, 528.
124. Mishra, A. K.; Davidson, J. A. *Mater. Technol*. **1993**, *8*(1/2), 16–21.
125. Hunter, G.; Long, M. In *Sixth World Biomaterials Congress Transactions*; Society for Biomaterials: Minneapolis, MN, 2000; Vol. 835.
126. Hunter, G.; Pawar, V.; Salehi, A.; Long, M. In *Medical Device Materials*; Shrivatsava, S., Ed.; ASM International: Materials Park, OH, 2004; Vol. 1, pp 91–97.
127. Alakoski, E.; Tiainen, V.; Soininen, A.; Konttinen, Y. T. *Open Orthop. J*. **2008**, *2*, 43–50.
128. Hunter, G. *Trans. Soc. Biomater*. **2001**, *24*, 540.
129. Marek, M.; Pawar, V.; Tsai, S.; *et al*. In *Medical Device Materials*; Venugopalan, R., Wu, M., Eds.; ASM International: Materials Park, OH, 2006; Vol. 3, pp 195–201.
130. Pawar, V.; Jones, B.; Sprague, J.; Salehi, A.; Hunter, G. In: *Medical Device Materials*; Helmus, M., Medlin, D., Eds.; ASM International: Materials Park, OH, 2005; Vol. 2, pp 403–408.
131. Tsai, S.; Heuer, D.; Pawar, V.; Salehi, A. *Trans. Soc. Biomater*. **2005**, *28*, 85.
132. Bhambri, S. K.; Gilberston, L. N. In *Modularity of Orthopedic Implants*, ASTM STP 1301; Marlowe, D. E., Parr, J. E., Mayor, M. B., Eds.; American Society for Testing and Materials: West Conshohocken PA, 1997; pp 146–156.
133. White, S. E.; Whiteside, L. A.; McCarthy, D. S.; Anthony, M.; Poggie, R. A. *Clin. Orthop*. **1994**, *309*, 176–184.
134. Spector, M.; Ries, M. D.; Bourne, R. B.; Sauer, W. S.; Long, M.; Hunter, G. *J. Bone Joint Surg*. **2001**, *83A*(S2), 80–86.
135. Hermida, J. C.; Patil, S.; D'Lima, D. D.; Colwell, C. W., Jr.; Ezzet, K. A. *Am. Acad. Orthop. Surg. Ann. Mtg. Proc*. **2004**, *5*, 449.
136. Good, V.; Ries, M.; Barrack, R. L.; Widding, K.; Hunter, G.; Heuer, D. *J. Bone Joint Surg*. **2003**, *85A*(S4), 105–110.
137. Ries, M. D.; Salehi, A.; Widding, K.; Hunter, G. *J. Bone Joint Surg*. **2002**, *84A*(S2), 129–135.
138. DesJardins, J. D.; LaBerge, M. *Trans. Soc. Biomater*. **2003**, *26*, 364.
139. Lee, J. K. L.; Maruthainar, K.; Wardle, N.; Haddad, F.; Blunn, G. W. *Knee* **2009**, *16*, 269–274.
140. DesJardins, J. D.; Burnikel, B.; LaBerge, M. *Wear* **2008**, *264*, 245–256.
141. Alberts, L. R.; Neff, J. R.; Webb, J. D. *Trans. Orthop. Res. Soc*. **2001**, *26*, 1101.
142. Oonishi, H.; Hanatate, Y.; Tsuji, E.; Yunoki, H. In *Bioceramics*; Oonishi, H., Aoki, H., Sawai, K., Eds.; Ishiyaku EuroAmerica: Tokyo, 1989; Vol. 1, pp 219–224.
143. Vittetoe, D. A.; Rubash, H. E. *Semin. Arthroplasty* **2002**, *13*(4), 344–349.
144. Clarke, I. C.; Green, D. D.; Williams, P. A.; *et al*. In *Transactions of the Seventh World Biomaterials Congress*; Australian Society for Biomaterials: Victoria, Australia, 2004; p 1138.
145. Bourne, R. B.; Barrack, R.; Rorabeck, C. H.; *et al*. *Clin. Orthop. Relat. Res*. **2005**, *441*, 159–167.
146. Lee, R.; Essner, A.; Wang, A.; Jaffe, W. L. *Wear* **2009**, *267*, 1915–1921.
147. Pappas, M. J.; Makris, G.; Buechel, F. F. *Trans. Biomater*. **1990**, *13*, 36.
148. Pappas, M. J.; Makris, G.; Buechel, F. F. *Clin. Orthop*. **1995**, *317*, 64–70.
149. Galvin, A.; Brockett, C.; Williams, S.; *et al*. *Proc. IMechE H J. Eng. Med*. **2008**, *222*, 1073–1080.
150. Fisher, J.; Hu, X. Q.; Tipper, J. L.; *et al*. *Proc. IMechE J. Eng. Med*. **2002**, *216*, 219–230.
151. Oñate, J. I.; Comin, M.; Braceras, I.; *et al*. *Surf. Coat. Technol*. **2001**, *142–144*, 1056–1062.
152. Haider, H.; Weisenburger, J.; Garvin, K. In *Presented at 2010 Annual Meeting of American Academy of Orthopaedic Surgeons*, New Orleans, Louisiana, Mar 9–13, 2010.
153. Bell, C. J.; Fisher, J. *J. Biomed. Mater. Res. Appl. Biomater*. **2007**, *81B*, 162–167.
154. Saikko, V.; Ahlroos, T.; Calonius, O.; Keränen, J. *Biomaterials* **2001**, *22*, 1507–1514.
155. Dowling, D. P.; Kola, P. V.; Donnelly, K.; *et al*. *Diam. Relat. Mater*. **1997**, *6*, 390–393.
156. Dorner-Reisel, A.; Schürer, C.; Müller, E. *Diam. Relat. Mater*. **2004**, *13*, 823–827.
157. Österle, W.; Djahanbakhsh, M.; Hartelt, M.; Wäsche, R. *Wear* **2008**, *265*, 1727–1733.
158. Thorwarth, G.; Falub, C. V.; Müller, U.; *et al*. *Acta Biomater*. **2010**, *6*, 2335–2341.
159. Lappalainen, R.; Selenius, M.; Anttila, A.; Konttinen, Y. T.; Santavirta, S. S. *J. Biomed. Mater. Res. Appl. Biomater*. **2003**, *66B*, 410–413.
160. Gutmanas, E. Y.; Gotman, I. *J. Mater. Sci. Mater. Med*. **2004**, *15*, 327–330.
161. Leslie, I. J.; Williams, S.; Brown, C.; *et al*. *J. Biomed. Mater. Res. Appl. Biomater*. **2009**, *90B*, 558–565.
162. Powers, D. L.; Claassen, B.; Black, J. *J. Invest. Surg*. **1995**, *8*(5), 349–362.
163. Kuo, T. Y.; Skedros, J. G.; Bloebaum, D. *J. Biomed. Mater. Res*. **1998**, *40*, 475–489.
164. Skurla, C. P.; James, S. P. *J. Biomed. Mater. Res. Appl. Biomater*. **2005**, *73B*, 260–270.
165. Allen, M.; Myer, B.; Rushton, N. *J. Biomed. Mater. Res. Appl. Biomater*. **2001**, *58*, 319–328.
166. Hayashi, K.; Matsuguchi, N.; Uenoyama, K.; Kanemaru, T.; Sugioka, Y. *J. Biomed. Mater. Res*. **1989**, *23*, 1247–1259.
167. Scarano, A.; Piattelli, M.; Vrespa, G.; Petrone, G.; Iezzi, G.; Piattelli, A. *Clin. Implant Dent. Relat. Res*. **2003**, *5*, 103–111.
168. Sovak, G.; Weiss, A.; Gotman, I. *J. Bone Joint Surg. [Br]* **2000**, *82B*, 290–296.
169. Gotman, I.; Fuchs, D.; Onalla, J.; *et al*. In *Book of Abstracts of the 19th European Conference on Biomaterials, European Society for Biomaterials*, Sorrento, Italy, Sept 11–15, 2005, T183.
170. Gotman, I.; Fuchs, D.; Gutmanas, E. Y. In *Book of Abstracts of the 19th European Conference on Biomaterials, European Society for Biomaterials*, Sorrento, Italy, Sept 11–15, 2005, P 404.
171. McGrory, B. J.; Ruterbories, J.; Pawar, V.; Thomas, R.; Salehi, A. *Am. Acad. Orthop. Surg. Ann. Mtg. Proc*. **2005**, *6*, 379.
172. Buechel, F. F., Sr.; Buechel, F. F., Jr.; Pappas, M. J. *Clin. Orthop*. **2004**, *424*, 19–26.
173. Taeger, G.; Podleska, L. E.; Schmidt, B.; Ziegler, M.; Nast-Kolb, D. *Materwiss. Werksttech*. **2003**, *34*(12), 1094–1100.
174. Joyce, T. J. *Wear* **2007**, *263*, 1050–1054.
175. Laskin, R. S. *Tech. Knee Surg*. **2007**, *6*(4), 220–226.
176. Nava, W. A. *Informe Médico*. **2005**, *7*(11), 517–520.
177. Masonis, J. L.; Kuremsky, M.; Odum, S. M.; Springer, B. D. *Am. Acad. Orthop. Surg. Ann. Mtg. Proc*. **2008**, *9*, 481.
178. Karachalios, Th.; Giotikas, D.; Roidis, N.; Poultsides, L.; Bargiotas, K.; Malizos, K. N. *J. Bone Joint Surg*. **2008**, *90B*(5), 584–591.
179. Innocenti, M.; Civinini, R.; Carulli, C.; Matassi, F.; Villano, M. *Clin. Orthop*. **2010**, *468*, 1258–1263.
180. Kim, Y. H.; Kim, J. S.; Huh, W.; Lee, K. H. *Clin. Orthop*. **2010**, *468*(5), 1296–1304.
181. Sah, A. P.; Ready, J. E. *J. Arthroplasty* **2007**, *22*(8), 1174–1180.
182. Lewis, P. M.; Moore, C. A.; Olsen, M.; Schemitsch, E. H.; Waddell, J. P. *Orthopedics* **2008**, *31*(12S), 109–112.
183. Garvin, K. L.; Hartman, C. W.; Mangla, J.; Murdoch, N.; Martell, J. M. *Clin. Orthop*. **2009**, *467*(1), 141–145.
184. Haddad, F. S.; Tahmassebi, J.; Fernandez, J. A. S.; Wardle, N. S.; Hossein, F. S.; Patel, S. *Am. Acad. Orthop. Surg. Ann. Mtg. Proc*. **2010**, *11*, P067.
185. Li, M. G.; Zhou, Z. K.; Wood, D. J.; Rohrl, S. M.; Ioppolo, J. L.; Nivbrant, B. *Trans. Orthop. Res. Soc*. **2006**, *31*, 643.
186. Heyse, T. J.; Davis, J.; Haas, S. B.; Chen, D. X.; Wright, T. M.; Laskin, R. S. *J. Arthroplasty* **2010**, on-line: doi:10.1016/j.arth.2009.11.024.
187. Sebastian, A. M.; Roy, M. E.; Whiteside, L. A.; Azzam, M. G. *Trans. Orthop. Res. Soc*. **2008**, *33*, 1778.

188. Pritchett, J. W. *Clin. Orthop.* **2006**, *442*, 195–198.
189. Kop, A. M.; Whitewood, C.; Johnston, D. J. *J. Arthroplasty* **2007**, *22*, 775–779.
190. Evangelista, G. T.; Fulkerson, E.; Kummer, F.; Di Cesare, P. E. *J. Bone Joint Surg.* **2007**, *89*, 535–537.
191. Wright, T.; Danoff, J.; Bostrom, M.; Pellicci, P. *Trans. Orthop. Res. Soc.* **2008**, *33*, 1899.
192. Mai, K.; Verioti, C.; D'Lima, D. D.; Colwell, C. W., Jr.; Ezzet, K. A. *Am. Acad. Orthop. Surg. Mtg. Proc.* **2009**, *10*, 471.
193. Sakona, A. S.; MacDonald, D. W.; Sharma, P.; Medel, F.; Kurtz, S. M. *Trans. Orthop. Res. Soc.* **2010**, *35*, 2358A.
194. Jaffe, W. L.; Strauss, E. J.; Cardinale, M.; Herrera, L.; Kummer, F. J. *J. Arthroplasty* **2009**, *24*(6), 898–902.
195. Bragdon, C. R.; Wannomae, K. K.; Lozynsky, A.; Micheli, B.; Malchau, H. *Trans. Orthop. Res. Soc.* **2009**, *34*, 2337.
196. Nasser, S. In *Total Knee Arthroplasty*; Bellemans, J., Ries, M. D., Victor, J., Eds.; Springer Verlag: Heidelberg, Germany, 2005; pp 343–353.
197. Nasser, S.; Mott, M. P.; Wooley, P. H. *Am. Acad. Orthop. Surg. Ann. Mtg. Proc.* **2007**, *8*, 437.
198. Lee, K. Y.; Slavinsky, J. P.; Ries, M. D.; Blimenkrantz, G.; Majumdar, S. *J. Magn. Reson. Imaging* **2005**, *21*, 172–178.
199. Raphael, B.; Haims, A. H.; Wu, J. S.; Katz, L. D.; White, L. M.; Lynch, K. *Am. J. Roentgenol.* **2006**, *186*(6), 1771–1777.
200. Goldberg, J. R.; Gilbert, J. L. *J. Biomed. Mater. Res. B Appl. Biomater.* **2002**, *64*(2), 78–93.

1.109. Bioactive Ceramics

A El-Ghannam, University of North Carolina at Charlotte, Charlotte, NC, USA
P Ducheyne, University of Pennsylvania, Philadelphia, PA, USA

© 2011 Elsevier Ltd. All rights reserved.

1.109.1.	**Bioactivity**	158
1.109.2.	**Bone Formation at the Interface with Bioactive Materials**	159
1.109.3.	**Testing Bioactivity *In Vitro***	159
1.109.4.	**Methods of Analysis of the Dissolution–Precipitation Reaction**	160
1.109.5.	**Bioactive Glasses**	162
1.109.5.1.	Composition of Bioactive Glasses	162
1.109.5.2.	Structure of Bioactive Glass	163
1.109.5.3.	Description of *In Vitro* Bioactivity	163
1.109.5.3.1.	Ion exchange and dissolution–precipitation reaction	163
1.109.5.3.2.	Protein adsorption	164
1.109.5.3.3.	Bone cell interaction with bioactive glass *in vitro*	164
1.109.5.4.	Effect of Preparation Methods of Glass on Its Bioactivity	165
1.109.5.4.1.	Melting method	165
1.109.5.4.2.	Sol–gel method	165
1.109.6.	**Bioactive Glass Ceramics**	166
1.109.7.	**Calcium Phosphate Ceramics**	167
1.109.7.1.	Composition of Hydroxyapatite	167
1.109.7.2.	Structure of Hydroxyapatite	168
1.109.7.3.	Calcium Deficient Hydroxyapatite	168
1.109.7.4.	Preparation of Hydroxyapatite	169
1.109.7.5.	Composition and Structure of β-TCP	169
1.109.7.6.	Synthesis of β-TCP	170
1.109.7.7.	Effect of Composition, Dissolution, Protein Adsorption, and HA Crystal Size on Bioactivity	170
1.109.7.8.	Apatite Formation and Bone Bioactivity of β-TCP	171
1.109.8.	**Silica-Calcium Phosphate Nanocomposite**	172
1.109.8.1.	Composition	172
1.109.8.2.	Crystalline Structure	173
1.109.8.3.	Structure and Bioactivity Relationship	174
1.109.8.3.1.	Effect of structure and composition on protein adsorption	175
1.109.8.3.2.	Effect of structure and composition on bone cell function and tissue formation	175
1.109.9.	**Silica-Xerogel**	176
1.109.10.	**Conclusion**	177
References		178

Glossary

Amorphous material The atomic structure of amorphous materials lacks the long-range atomic order, that is, noncrystalline. Bioactive glass is characterized by an amorphous silicate structure that facilitates a dissolution–precipitation reaction on the material surface in contact with physiological solution.

Bioactive ceramic A chemically active biocompatible ceramic. The chemical reactivity is in favor of cell function and tissue formation. Bone tissues bond directly to the surface of the bioactive ceramic.

Bioactivity A material property that refers to the ability to bond directly to the bone and enhance bone formation.

Crystalline material Crystallized materials are characterized by a long-range atomic order. The crystallization of bioactive glass reduces the rate of bioactivity reactions in physiological solution.

Solid solution Incorporation of foreign atoms within the crystalline structure of the host material. The formation of solid solution affects the chemical stability and the bioactivity property of bioactive ceramics. Silicate–phosphate ionic substitution in hydroxyapatite ceramic enhances the bioactivity property of the material.

Abbreviations

A-W	Apatite-wollastonite
CDHA	Calcium-deficient hydroxyapatite
EDXA	Energy dispersed X-ray analysis
FTIR	Fourier transform infrared spectroscopy
HA	Hydroxyapatite
ICP-OES	Inductively coupled plasma-atomic emission spectrometry
KGC	Ceravital glass ceramic
OHA	Oxyhydroxyapatite
SBF	Simulated body fluid
SCPC	Silica–calcium phosphate nanocomposite
s-HA	Stoichiometric hydroxyapatite
TMOS	Tetramethoxysilane
TTCP	Tetracalcium phosphate
TEOS	Tetraethoxysilane
TCP	Tricalcium phosphate
TRAP	Tartrate-resistant acid phosphatase
XRD	X-ray diffraction analysis

Bioactive ceramics is a family of materials including various calcium phosphates, bioactive glasses, and bioactive glass ceramics. Common property for these materials is the ability to bond to bone and enhance bone tissue formation within this class of materials. The rate of bone bonding, the stimulatory effect on cell function, and the resorbability vary significantly due to structural and compositional variations. The objective of this chapter is to describe the various bioactive ceramics and the methods used to make them and to analyze the effect of compositional and structural variations on their bioactive behavior. In Table 1 we have compiled a summary of most bioactive ceramics together with their typical composition.

1.109.1. Bioactivity

The bioactivity property refers to the ability of the materials to bond directly to bone and enhance bone formation. The bone-bonding ability of bioactive ceramics is extensively described elsewhere (**Chapter 1.114, Bioactivity: Mechanisms**). In essence, if a calcium phosphate layer is not present on the surface at the time of implantation, various reactions will lead to such a surface. These reactions very much involve proteins and cells within the biological environment. The material also releases ions including calcium. Proteins, including attachment proteins adsorb onto its reacting surface and enable cell adhesion, which in its turn triggers an intracellular reaction cascade that promotes bone tissue formation.

Table 1 Chemical composition of selected bioactive ceramics

	Chemical formula/composition
Stoichiometric hydroxyapatite	$Ca_5(PO_4)_3OH$ or $Ca_{10}(PO_4)_6(OH)_2$
Calcium deficient hydroxyapatite	$Ca_{10-x}(HPO_4)_x\,(PO_4)_{6-x}\,(OH)_{2-x}$, with $0 < x \leq 1$
Carbonate hydroxyapatite	$Ca_5(PO_4)_{2.5}(CO_3)_{0.5}(OH)$ or $Ca_5(PO_4, CO_3)_3(OH)$
Fluorapatite	$Ca_5(PO_4)_3F$
Tricalcium phosphate	$Ca_3(PO_4)_2$
Tetracalcium phosphate	$Ca_4P_2O_9$
Octacalcium phosphate	$Ca_8H_2(PO_4)_6 \cdot 5H_2O$
Rhenanite	$NaCaPO_4$
Oxyapatite	$Ca_{10}(PO_4)_6O$
Oxyhydroxyapatite	$Ca_{10}(PO_4)_6(OH)_{2-2x}(O)_x(\blacksquare)_x$, where ▪ represents a vacancy
Apatite-wollastonite (A-W) glass ceramic	In mol%: 34.2 SiO_2, 16.3 P_2O_5, 44.9 CaO, 0.5 CaF_2, and 4.6 MgO
Ceravital glass ceramic (KGC)	In mol%: 46.2 SiO_2, 20.2 CaO, 25.5 $Ca(PO_3)_2$, 4.8 Na_2O, 2.9 MgO, and 0.4 K_2O
Silica-calcium phosphate nanocomposite (SCPC)	In mol%: 3–33 SiO_2,11–31 P_2O_5, 23–62 CaO, and 3–33 Na_2O

Bioactive ceramics are characterized by a dynamic surface. The ionic dissolution of the material surface is closely linked to precipitation of a calcium phosphate (Ca-P) layer. In fact, the deposition of a Ca-P layer on the surface of bioactive ceramics in physiological solution is well documented for bioactive ceramics with enhanced dissolution properties. In general, the dissolution property of these main classes of bioactive ceramics decreases in the order:

Bioactive glass > Hydroxyapatite > Bioactive glass ceramic

Each of the above materials has compositional and processing parameters that affect the dissolution rate. These parameters will be discussed in detail in the following sections. As mentioned, the dissolution of the surface of bioactive ceramics is associated with precipitation of a Ca-P layer onto the surface of bioactive materials. By virtue of this new surface layer bone integrates directly with the material surface. During the deposition of the Ca-P layer onto the material surface other ions present in the biological milieu, including Mg^{2+}, K^+, CO_3^{2-}, and Cl^- are also incorporated. The characteristics of the deposited Ca-P mimic those of the mineral phase of bone in many aspects. The crystals of the calcium phosphate layer are small in size, defective, and formed at the body temperature. Bone cells attach directly to the adsorbed protein on the surface layer.

Bone deposition is enhanced by the high pool of calcium ions provided by the bioactive ceramic. Measurements of the ionic concentrations of tissue culture medium incubated with bone marrow stem cells attached onto silica-calcium phosphate nanocomposite (SCPC) showed that the cells did not affect the dissolution behavior of the material.[1] However, the attached bone marrow stem cells interfered with the back precipitation reaction and inhibited the formation of a Ca-P layer on the material surface.[1] Scanning electron microscope-energy dispersive X-ray analyses showed that, in the absence of cells, a Ca-P layer formed on the surface of the material because of the dissolution–precipitation reaction.[1] Therefore, the role of the Ca-P surface layer in bone tissue is unique in that it enhances specific cell adhesion and that it provides a high pool of

Ca ions. The effect of bioactive ceramics on osteoblast phenotypic expression and mineralized bone tissue formation are well documented.

1.109.2. Bone Formation at the Interface with Bioactive Materials

Owing to the similarity between the mineral phase of bone and the surface chemistry of bioactive materials a fibrous capsule is not formed around the implant. Instead, bone cells attach and deposit extensive bone matrix directly on the material surface. The integrated nature of surface and tissues leads to a strong interfacial bond. Figure 1 is a histomicrograph showing the intimate bonding between bioactive glass and bone. By way of example, the bond strength at the interface between bioactive glass and bone reaches values of 15–25 MPa, much higher than 0.5 and 2 MPa for inert glass and smooth titanium.[2] Most biocompatible ceramics, metals, and polymers are not bioactive, that is, they do not have the ability to bond to bone. Tissue response is typically fibrous encapsulation. Figure 2 shows a fibrous capsule at the interface with polymethylmethacrylate bone cement inserted into bone.[3]

As bioactive ceramic stimulates the activity of bone cells in direct contact with the material, it also stimulates cells away from the material surface. The dissolution of the surface of bioactive ceramic increases the ionic concentration of, for example, Ca and/or Si in the interfacial tissue fluids. These ions have a well known strong effect on bone cell function.[4–7] Therefore, bone cells in the neighborhood of the bioactive ceramic and those in direct contact with the material surface are stimulated to deposit new bone. It has been shown repeatedly that bone defects grafted with granules of bioactive ceramic are filled with bone.[6,8,9] The new bone formation starts at the surface of the granules of bioactive ceramic and continues to grow until it fills the interspace between the granules.[8] Bone growth inside porous bioactive ceramic implanted in bone defects is also common. Bone formation begins at the wall of the pores and continues to grow until it fills the pores. Certain bioactive ceramics such as SCPCs are resorbable with a controlled rate of degradation inside the implantation bed. As the graft material resorbs, it leaves a space for bone cells to deposit new bone.[6] Therefore, using resorbable bioactive ceramics as a bone graft will allow complete tissue regeneration (Figure 3).[6] The mechanism of new bone formation in defects grafted with bioactive ceramic is rather complex. Therefore, extensive studies have addressed this issue by analyzing separately each event that takes place during the interaction between bioactive ceramics and the biological system. The data from these studies provided extensive foundation to the mechanism of bone bonding and tissue formation at the interface with bioactive ceramics.

1.109.3. Testing Bioactivity *In Vitro*

The mechanism of the formation of the hydroxyapatite (HA) layer on the surface of bioactive ceramics was widely studied *in vitro* by immersing the material in physiological solution and analyzing both the material surface as well as the composition of the solution. The most common physiological solution used for bioactivity analysis *in vitro* is the simulated body fluid (SBF). SBF is a tris buffer with pH and ionic concentration similar to the plasma of the blood.[10] Table 2 shows the ionic composition of the SBF and the plasma of the blood. Interestingly, immersion of bioactive ceramic in SBF produces a HA layer on the material surface similar in many aspects to that of biological apatite. The ability of a biomaterial to

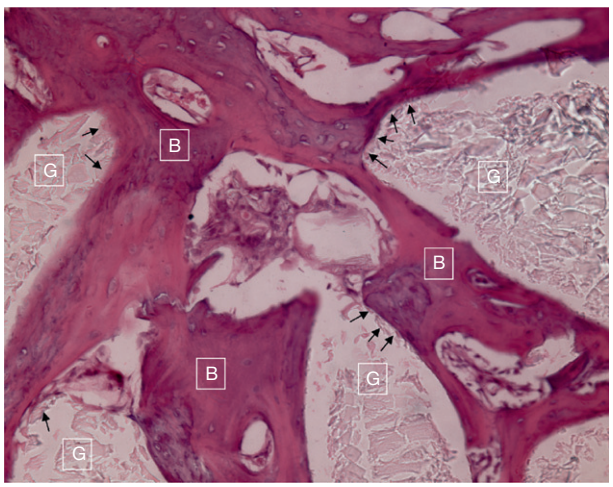

Figure 1 Histomicrograph of rabbit femoral bone defect grafted with bioactive glass granules for 3 weeks. The interspaces between the bioactive glass particles (G) are filled with new mature bone tissue (B) containing haversian systems and blood vessels. Some areas showed high cellular activity and immature woven bone. The arrows point to areas showing direct bonding between the bioactive glass and the new bone. The granules of bioactive glass shattered into small pieces during cutting and processing of the slide due to the brittleness of the material. (H&E stain).

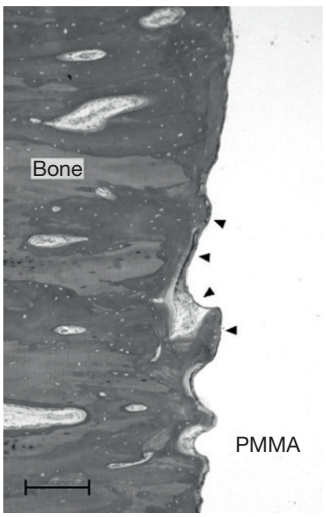

Figure 2 The interface between PMMA bone cement and bone after 2 weeks of implantation in the cortical bone of the tibial diaphysis in goats. A thin fibrous layer (arrow heads) was always present at the interface between bone and PMMA implant. Bar = 200 mm. Reproduced from Ooms, E.; Wolke, J.; Van de Heuvel, M.; Jeschke, B.; Jansen J. *Biomaterials* **2003**, *24*(6), 989–1000, with permission from Elsevier.

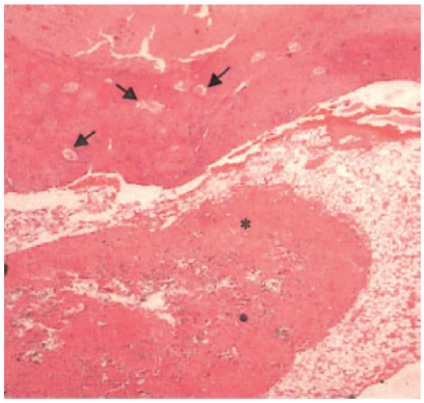

Figure 3 Histology analysis of critical size bone defect created in the rabbit femur and grafted with granules of silica–calcium phosphate nanocomposite (SCPC75) for 3 weeks. The grafted defect was extensively filled with new bone. Bone formed in the internal side of the defect has been completely remodeled and few vascular cavities (arrows) remained. New bone (*) is also present within the marrow cavity that was initially filled with graft material. The architecture of the remodeled cortical bone and marrow resembles that of normal healthy bone. Reproduced from El-Ghannam A. *J. Biomed. Mater. Res. A* **2004**, *69*(3), 490–501, with permission from Wiley.

Table 2 The ionic concentration of simulated body fluid and human blood plasma

Ion	*Simulated body fluid (SBF) (mM)*	*Human blood plasma (mM)*
Na^+	142	142
K^+	5	5
Mg^{2+}	1.5	1.5
Ca^{2+}	2.5	2.5
Cl^-	148.8	103
HOC_3^-	4.2	27
HPO_4^{2-}	1	1
SO_4^{2-}	0.5	0.5

develop a HA surface layer in SBF is indicative of its chemical reactivity and hence, correlates well with the ability of the material to bond to bone *in vivo*. Moreover, the rate of formation of the HA surface layer in SBF correlates well with the rate of bone bonding *in vivo*.[11] Therefore, the rate of development of a HA layer on the material surface when immersed in SBF can be taken as a measure of the degree of bioactivity of bone implant materials. Whereas the actual formation of a surface layer in SBF lends credence to the effect on bone cell function *in vivo*, this *in vitro* test is still not a full simulation of the *in vivo* conditions, and therefore cannot universally address *in vivo* effects of materials and *in vivo* sequences of surface reactions and intracellular events. More details on the validity of the SBF for evaluating bone-bonding ability are described in **Chapter 1.113, Bioactive Layer Formation on Metals and Polymers**.

The deposition of HA layer on the surface of bioactive ceramic in physiological solution *in vitro* involves two components: dissolution of the material surface and precipitation of a Ca-P layer. The dissolution of Ca and P ions into the physiologic solution raises the local ionic concentration of biological fluid at the interface with the implant material to a level that exceeds saturation. The result is the precipitation of amorphous calcium phosphate layer that matures by time to the more thermodynamically stable HA. To the extent that the surface is not a carbonate apatite, the initial rapid dissolution of the material surface is important to initiate the formation of reactive surface layer. If the rate of ion release is slow, the time required for the interfacial ionic concentration to reach the super saturation level may be indefinitely extended. As a result, slow dissolution may delay the formation of the surface layer or in some cases make its deposition impossible due to diffusion of ions away from the surface. Thus, having an implant material with a surface composition made of stable calcium phosphate is not enough to trigger conditions that stimulate the first step to bone formation. The implant material has to have a controlled chemical reactivity that facilitates initial high rate of dissolution. The controlled high rate of dissolution expedites the precipitation of a Ca-P layer that matures into HA (see **Chapter 1.111, Bioactive Ceramics: Physical Chemistry**).

The formation of the amorphous calcium phosphate or HA layer in SBF can be taken as a measure of the chemical reactivity of the material surface and not necessarily as part of the mechanism of bone formation *in vivo*. The last statement is justified by two important facts: First, the presence of serum protein inhibits the formation of the calcium phosphate layer[12,13] and second, attached cells interfere with the deposition of a calcium phosphate layer.[1] Moreover, the dissolution–precipitation reactions are dependent on the properties of both the bioactive material and the simulated physiological solution. Material-related parameters include chemistry, crystalline structure, surface charge, porosity, and surface area. Solution related parameters include protein content, ionic concentration, pH, buffer capacity, and temperature.

1.109.4. Methods of Analysis of the Dissolution–Precipitation Reaction

The surface modifications during the dissolution–precipitation reactions at the interface between bioactive materials and SBF can be analyzed using various methods. The ionic concentration of the physiological solution is typically measured by inductively coupled plasma-atomic emission spectrometry (ICP-OES). The modifications in the surface chemistry and morphology can be analyzed by Fourier transform infrared spectroscopy (FTIR) and scanning electron microscopy with energy dispersed X-ray analysis (SEM-EDXA). **Figure 4(a)** demonstrates the rate of Si release from various bioactive SCPCs immersed in a SBF.[14] **Figure 4(b)** shows a decrease in Ca concentration in the solution due to the precipitation of Ca onto the material surface.[14] FTIR analyses showed that in conjunction with the high rate of Ca uptake by SCPC50 the surface of the material was covered with a HA layer as shown in **Figure 5**.[14]

The dissolution–precipitation reactions can also be followed by recording the changes in the surface charge of the material using ζ-potential measurements. Lu *et al.*[15] measured the ζ-potential of bioactive glass in a SBF. The changes in the

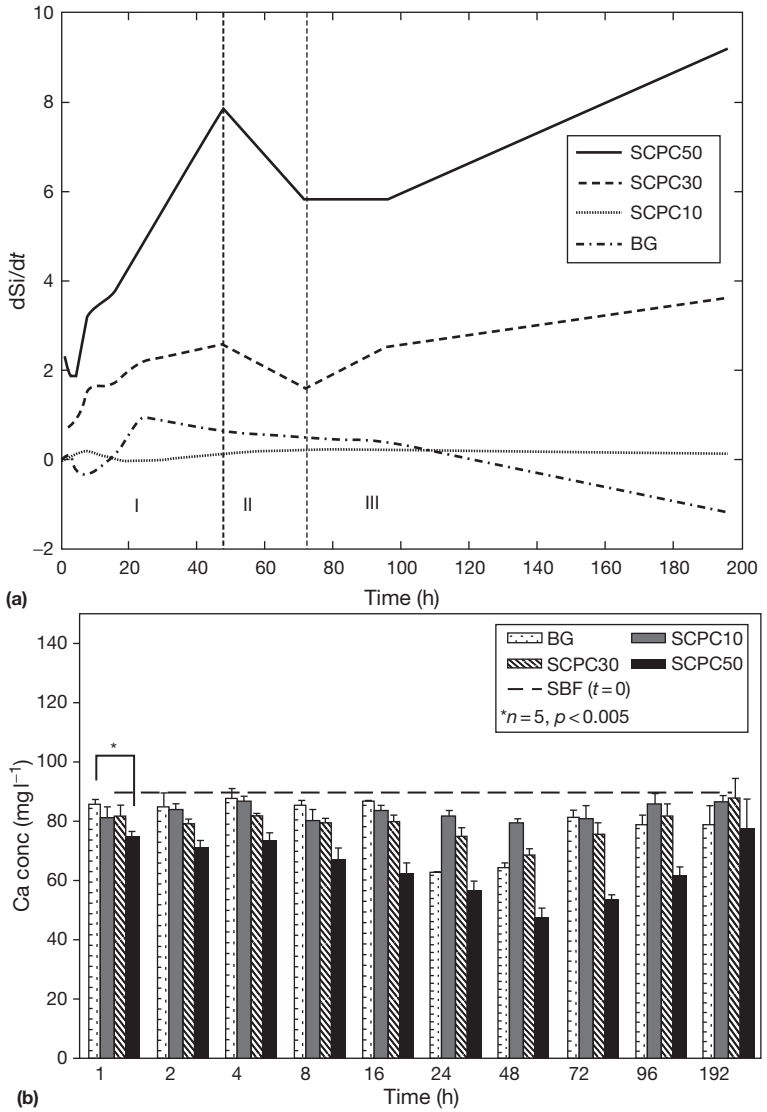

Figure 4 (a) ICP analyses of the Si concentration in SBF incubated with bioactive silica–calcium phosphate nanocomposite (SCPC). The weight ratio of silica/calcium phosphate components are 1/9, 3/7, and 5/5 for SCPC10, SCPC30, and SCPC50, respectively. The rate of Si release has been taken as a measure of the dissolution kinetics of the bioceramics. The dissolution kinetics of SCPC30 and SCPC50 has been divided into three stages. Stage I (0–48 h) was characterized by a high rate of Si release from SCPC30 and SCPC50 due to initial material dissolution. Stage II (48–72 h) involved a marked reduction in the dissolution rate because of the precipitation of the calcium phosphate layer on the material surface. Stage III (72–192 h) was characterized by a controlled bulk degradation of SCPC30 and SCPC50, which resulted in a linear increase in the rate of Si release. SCPC10 showed minimal dissolution in SBF at all time points. Bioactive glass (BG) exhibited a high initial dissolution rate up to 24 h of immersion. However, the dissolution rate was almost zero during 24–48 h, and continued to decrease thereafter up to 192 h. Thus, BG unlike SCPC, showed no evidence of bulk-degradation behavior. (b) ICP analysis of Ca^{2+} concentrations in SBF incubated with various SCPC formulations (see Figure 5a for details) and BG particles (90–425 mm). SCPC50 exhibited significantly higher Ca-uptake compared to BG or other SCPC samples up to 96 h of immersion. During the first 48 h of immersion, the average rate of Ca-uptake from SBF was in the order: BG (1.32 mg/L/h) < SCPC10 (2.04 mg/L/h) < SCPC30 (2.67 mg/L/h) < SCPC50 (4.94 mg/L/h), which indicated a faster initial kinetics of Ca-uptake in SBF solutions incubated with SCPC samples compared to those incubated with BG. Between 48 and 96 h, the kinetics of Ca-uptake decreased markedly for all samples, and after 192 h of immersion, there was no significant difference in the Ca^{2+} concentrations of SBF incubated with the different bioceramic samples. ($^*n = 5$, $p < 0.005$). Reproduced from Gupta, G.; Kirakodu, S.; El-Ghannam, A. *J. Biomed. Mater. Res. A* **2007**, *80*(2), 486–496, with permission from Wiley.

surface charge of bioactive glass were found to correlate well with the modifications in the surface chemistry as analyzed by SEM-EDX, and FTIR during the dissolution–precipitation steps as measured by the ionic concentration of the solution. Initially, the surface of bioactive glass was negatively charged, and then during 3 days of immersion two reversals of the sign of the surface were detected. Figure 6 demonstrates the variations in the ζ-potential of bioactive glass as a function of immersion duration in SBF.[15] The dynamic shift in the sign of the ζ-potential from an initially negative surface to a positively charged surface directly corresponded with the formation of an amorphous Ca-P surface layer. As the amorphous Ca-P

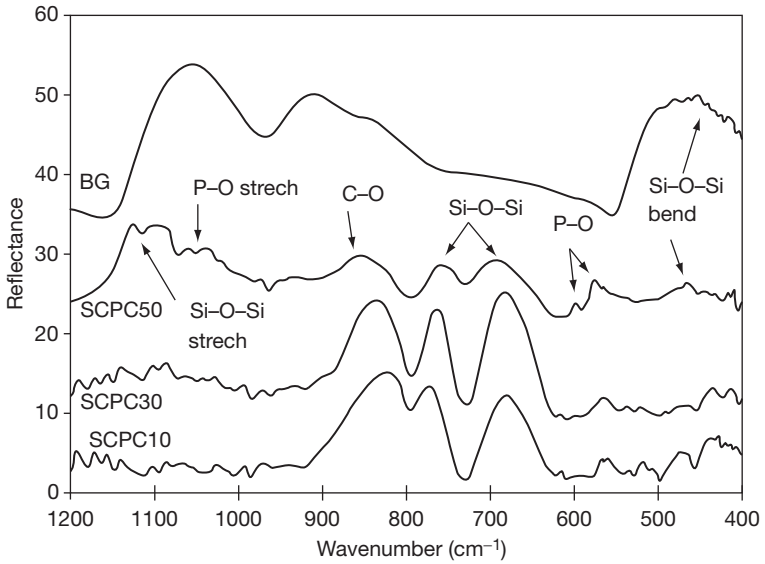

Figure 5 FTIR analysis of various formulations of SCPC after a 2-hr immersion in SBF. Distinct orthophosphate (570 and 590 cm^{-1}) and carbonate (850 cm^{-1}) peaks corresponding to a biological HA were detected on the surface of SCPC50. However, these peaks were not detected for SCPC10, SCPC30, or BG after the same time period. This indicated a much faster kinetics of bioactivity reactions on the surface of Si-rich SCPC50 compared to the other bioactive ceramic samples. Reproduced from Gupta, G.; Kirakodu, S.; El-Ghannam, A. *J. Biomed. Mater. Res. A* **2007**, *80*(2), 486–496, with permission from Wiley.

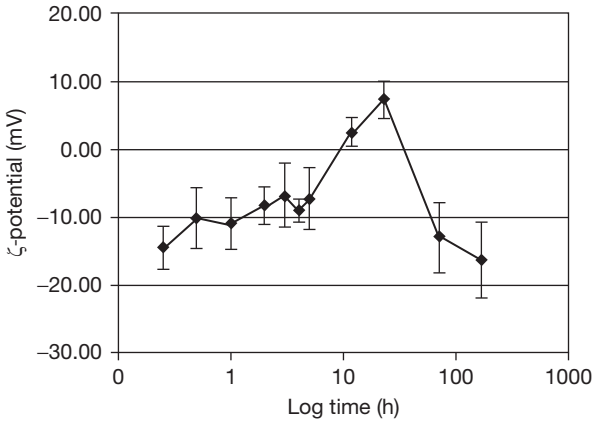

Figure 6 Zeta potential of 45S5 bioactive glass particles as a function of immersion time in simulated body fluid. The immersion ratio equals 1 mg/mL. Each data point in the graph is calculated based on the average electrophoretic mobility values obtained from nine sets of electrophoretic mobility histograms (n = 9). The error bars represent standard deviations of the means. Reproduced from Lu, H.; Pollack, S.; Ducheyne, P. *J. Biomed. Mater. Res. A* **2000**, *51*(1), 80–87.

matured into a crystalline HA layer, the surface charge changed from a positive to a negative surface.[15] Methods to enhance the chemical reactivity of bioactive ceramics include modifications of the chemistry, crystal lattice parameters and porosity. Porosity of bioactive materials provides high surface area in contact with tissue fluids and therefore enhances dissolution and back precipitation of a HA surface layer.

Mercury porosimetry is widely used to measure percent porosity, pore size distribution and pore area. BET gas adsorption method is used to measure porosity and specific surface area for nanoporous materials.

1.109.5. Bioactive Glasses

1.109.5.1. Composition of Bioactive Glasses

Bioactive glass first synthesized by Hench and associates[16] is the generic name of a class of amorphous material covering a wide range of bioactivity arising from variations of the chemical composition. The most common components of bioactive glass are SiO_2, CaO, Na_2O, and P_2O_5. Figure 7 shows the location of the composition of 45S5 bioactive glass on a ternary SiO_2–CaO–Na_2O phase diagram with a constant 6 wt% P_2O_5. The SiO_2 content determines the chemical stability and bioactivity of the glass. Melt-derived glass which has SiO_2 content larger than 60 wt% is chemically stable and hence is not bioactive. (45S5) bioactive glass with 45 wt% SiO_2 is characterized by a high rate of bioactivity. Figure 8 is a ternary SiO_2–CaO–Na_2O phase diagram showing the bioactivity boundaries of various glass compositions.[17]

Push out test data of glass coupons in rat tibia led to the formulation of a ternary diagram, first published in a review paper.[17] Glass compositions that fall in region A are characterized by a high rate of bioactivity in that a high interfacial bond strength is established within 30 days. Glass compositions in region B contain high silica content and therefore, they are chemically stable and behave as inert materials. Glass compositions in region C are degradable inside the body and can be resorbed in 10–30 days. Compositions in region D have high ratios of $(Na_2O + CaO)/SiO_2$ and therefore they either devitrify or produce nonpractical glasses with very short workability range.

Many additives including MgO, K_2O, B_2O_3, Al_2O_3, Zr_2O_3, CaF_2, and Ta_2O_5 can be added to bioactive glass to improve its mechanical and thermal properties or to enhance the workability range. However, a boundary condition that limits the modification of the composition of bioactive glass is the bioactivity property. For example, addition of more than

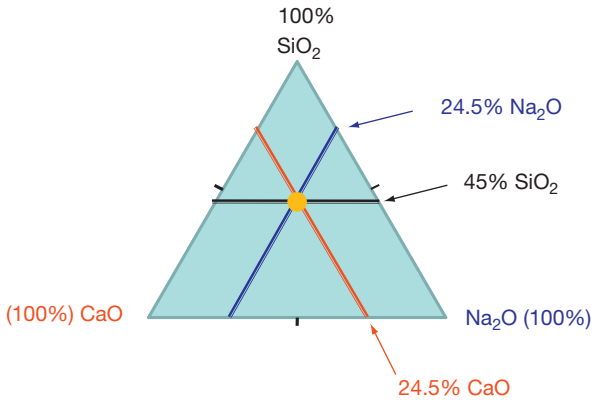

Figure 7 A ternary phase diagram for silicate glass in the system SiO_2–Na_2O–CaO. The composition of a bioactive glass containing 24.5% Na_2O, 24.5% CaO, and 45% SiO_2 in weight percent (at a fixed 6% P_2O_5, not shown) is identified in the diagram.

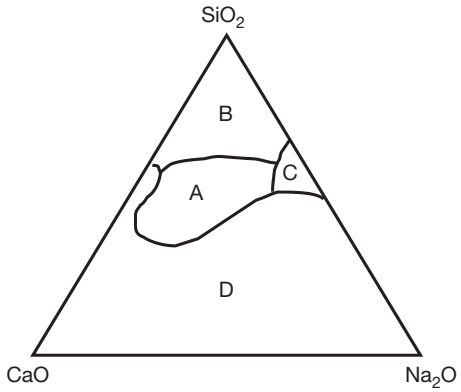

Figure 8 Phase diagrams for Na_2O–CaO–SiO_2 showing four composition regions A, B, C, D, and the corresponding bone-bioactivity property. Reproduced from Hench, L. *J. Am. Ceram. Soc.* **1991**, *74*(7), 1487–1510, with permission from Wiley.

1.0–1.5 wt% Al_2O_3 or 1.5–3.0 wt% multivalent ions such as Ta^{5+} enhances the workability range and the thermomechanical properties of the material. However, Al^{3+} and Ta^{5+} ions have an adverse effect on bone cell viability and function, thereby inhibiting the bone-bonding ability.[18] The substitution of MgO for CaO enhances the chemical stability of bioactive glass and hence lowers the rate of dissolution and overall bioactivity reactions. The decreased solubility of Mg-containing bioactive glass is attributed to the low electronegativity of Mg compared to Ca. Therefore, the percent of ionic character in Mg–O bond is lower than that in the Ca–O bond, which makes the former glass more stable in physiologic solution.

1.109.5.2. Structure of Bioactive Glass

Bioactive glass is like any glass, an amorphous material with short range atomic order. This structure is opposite to the long range atomic order found in crystalline materials. The SiO_2 in bioactive glass serves as a network former giving the glass structure its chemical stability. The CaO and Na_2O serve as network modifiers, which facilitate glass melting during processing and bioactivity in contact with the biological system. A schematic representation of the bonds between SiO_2 and Na_2O and CaO in bioactive glass is shown in Figure 9.

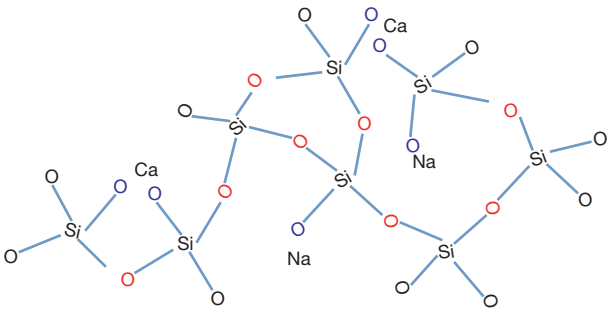

Figure 9 A schematic showing the silicate structure of bioactive glass. The bridging oxygen in the Si–O–Si bond stabilizes the material. Nonbridging oxygen in the -Si–O–Na and -Si–O–Ca- enhances the dissolution in physiological solutions.

The oxygen atom (red color) that connects two silicon atoms in the silicate structure (Figure 9) is called bridging oxygen, while that which connects silicon atom to Ca or Na atom is called nonbridging oxygen. The ratio of bridging oxygen to nonbridging oxygen in the bioactive glass controls the rate of bioactivity reaction *in vitro* and the resorbability of the material. The ratio of the percent of the ionic character to that of covalent character in these bonds increases in the order Na–O > Ca–O > Si–O. Therefore, the bridging oxygen that is connected to two silicon atoms (Si–O–Si) is responsible for the stability of bioactive glass. Bioactive glasses with high percentage of SiO_2 are chemically stable due to the domination of the strong Si–O–Si bond in the material. As the concentration of the SiO_2 in bioactive glass decreases and the Na_2O or CaO increases, the chemical stability decreases and the rate of reactivity increases. However, at a critical low SiO_2 concentration, the high concentration of cations breaks down the silicate structure and the material will lose its ability to make glass (region D in the Figure 8). In such case, as the temperature of the melt cools down, it experiences uncontrolled crystallization (i.e., devitrification).

1.109.5.3. Description of *In Vitro* Bioactivity

Many studies have immersed bioactive glass in SBF (Table 2) and analyzed dissolution kinetics and modifications in the surface properties of the material. Immersion of bioactive glass in SBF revealed one aspect of the mechanism of bioactivity that includes ion exchange and dissolution–precipitation reaction.

1.109.5.3.1. Ion exchange and dissolution–precipitation reaction

Immersion of bioactive glass in the SBF results in an initial partial dissolution of the material surface associated with a precipitation of a calcium phosphate that resembles the mineral phase of bone.[19] As the ionic character in Na–O bond is high (85%), Na ions can easily exchange with H^+ of the H_2O molecule upon contact with tissue fluids. On the other hand, the ionic character in the Si–O bond is about 55% with the

remaining 45% being covalent in nature. The high covalent character of the Si–O bond limits the dissolution of silica. The strength of the Si–O bond renders the release of Si ions from bioactive glass much lower than the release of the Na. The enhanced release of Na ions from the bioactive glass surface has a dual effect: First; it renders the material surface rich on $Si–O^-\ldots{}^+H$ groups and second, it increases the pH of the interfacial fluids. Both the surface Si–OH and the alkaline pH work synergistically to enhance the precipitation of a Ca-P layer on the material surface. The disruption of the silicate network as a result of Na and Ca ions release increases the concentration of hydrated silica (silanol ≡ Si–OH). The Si–OH groups form a highly porous silica gel surface layer that traps Ca ions. Figure 10 is a schematic showing the formation of the silica gel layer and the nucleation and the deposition of a calcium phosphate layer on the materials surface. The calcium phosphate layer starts as amorphous with high Ca/P ratio. However, as the dissolution–precipitation continues the amorphous calcium phosphate layer crystallizes into defective, carbonate-containing HA.[19]

1.109.5.3.2. Protein adsorption

The dissolution–precipitation reactions at the interface between bioactive glass and tissue fluids take place in the presence of serum protein. The range for total protein concentration in serum is 60–85 $g\,l^{-1}$. Calcium binding proteins such as fibronectin (FN) and vitronectin are present in minor concentrations in serum and serve as cell attachment proteins.

Immersion of bioactive glass in tissue culture medium that contains 10% serum slows down the formation of the HA surface layer.[20] The inhibition of the formation of the HA layer is attributed to the chelation of calcium by calcium binding proteins such as albumin.[21] Subjecting bioactive glass to two immersion treatments: first in SBF without proteins, and then in tissue culture medium, significantly enhanced serum protein adsorption.[22] Interestingly, the calcium phosphate layer formed on the surface of bioactive glass shows high affinity to serum FN an attachment protein known to enhance bone cell adhesion and function. As described by Knabe *et al.* (**Chapter 1.114, Bioactivity: Mechanisms**) the concentration of FN on the calcium phosphate layer of bioactive glass facilitates bone cell adhesion and deposition of bone tissue directly onto the material surface.

1.109.5.3.3. Bone cell interaction with bioactive glass in vitro

Some *in vitro* studies have shown an unfavorable cell response to bioactive glass; obviously such data are against the favorable tissue response *in vivo*. Such findings were related to the accumulation of the dissolved ions released from bioactive glass into the tissue culture medium, specifically the hydroxyl ions, which raise the pH of the medium to a level that lyses the cells.[20] Accumulation of dissolved ions does not occur *in vivo* due to the fluid turn over and blood circulation. Therefore, the effect of the accumulation of dissolved ions can be eliminated by reacting the glass in SBF before cell seeding as well as using a high ratio of medium to glass surface area. Seeding bone cells on the surface of bioactive glass that has been covered by a calcium phosphate layer and adsorbed serum protein stimulated bone cell adhesion, proliferation, differentiation, and bone tissue formation *in vitro*.[20–22] A porous template made of bioactive glass with a modified surface was able to reproduce the mechanism of bone formation when seeded with bone cells within 7 days.[20]

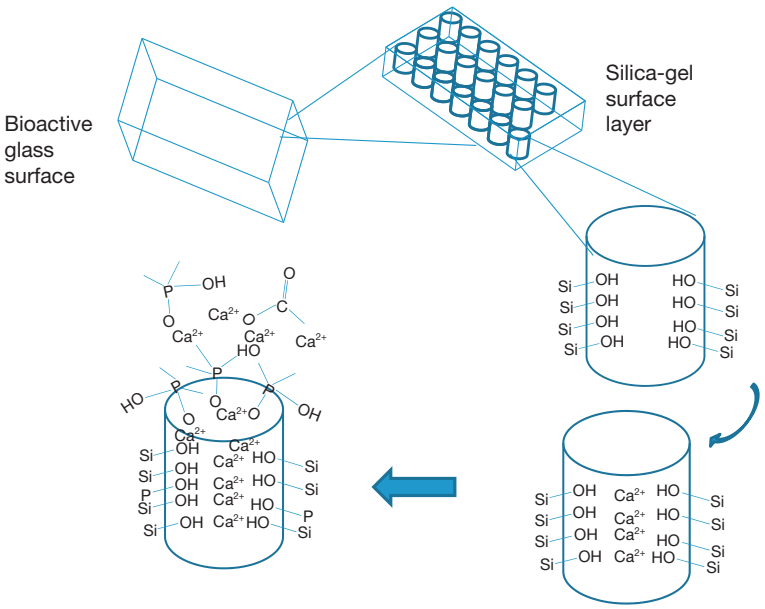

Figure 10 A schematic showing the surface modifications of bioactive glass due to interaction with simulated body fluid. The initial cations release leaves behind a highly porous glass surface rich in silanol groups (silica gel). The pores of the silica gel nucleate calcium-phosphate precipitation onto the material surface. The structure of the deposited calcium phosphate starts as amorphous and then matures into carbonate containing hydroxyapatite.

1.109.5.4. Effect of Preparation Methods of Glass on Its Bioactivity

1.109.5.4.1. Melting method

Bioactive glass is usually prepared by melting. The source of SiO_2 is sand with 99.99% purity. Na_2O and CaO are derived from the corresponding carbonate compounds. Heating up Na_2CO_3 and $CaCO_3$ during glass melting produces fresh and active Na_2O and CaO respectively according to equations [I] and [II] below.

$$CaCO_3 \rightarrow CaO + CO_2 \quad [I]$$

$$Na_2CO_3 \rightarrow Na_2O + CO_2 \quad [II]$$

The byproduct is CO_2 that diffuses as bubbles through the glass melt into the air. Diffusion of the CO_2 bubbles help mixing the melt together to produce homogenous glass. P_2O_5 can be added to the glass batch before melting as an oxide or can be derived from any calcium phosphate compound. The raw materials and corresponding oxide weight and mole percentages used for the preparation of 45S5 bioactive glass are shown in Table 3.

Bioactive glass batch is melted at 1350–1400 °C in a Pt–Rh crucible. After homogenization, the melt is poured in a mold. The rapid cooling of the glass creates strains within the material that deteriorates the mechanical stability. To relieve any strains, the glass is subjected to an annealing treatment at 450–550 °C depending on the glass composition and glass softening temperature. The annealing temperature is usually determined based on the differential thermal analysis of the glass. Figure 11 is a schematic showing the melting and annealing of bioactive glass.

Table 3 Chemical composition and selected raw materials used for bioactive glass preparation

Oxides (wt%)	*Oxides (mol%)*	*Raw material*
45 SiO_2	46.1	Sand (SiO_2)
24.5 Na_2O	24.4	Na_2CO_3
24.5 CaO	26.9	$CaCO_3$
6 P_2O_5	2.6	P_2O_5

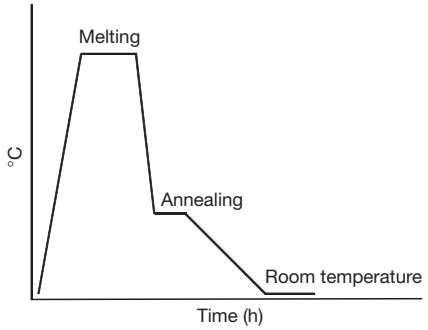

Figure 11 A schematic showing the processing steps involved in the synthesis of bioactive glass by melting. Solid glass objects are required to be annealed after melting to release strains created during cooling the melt. For the preparation of bioactive glass granules, the melt may be quenched in DI water; no annealing treatment is required in that case.

Bioactive glass prepared by melting is dense and does not contain any remnants of organic components or water. Therefore, melt-derived bioactive glass has limited surface area in contact with tissue fluids when used in bulk as an implant. However, using bioactive glass as granules increases the surface area in contact with tissue fluids and cells and therefore facilitates surface reactivity and bone formation.

1.109.5.4.2. Sol–gel method

Preparation of bioactive glass by a sol–gel method is based on a solution reaction between chemical reagents that contain Si, Na, and Ca components at room temperature. The most widely used precursor for silica is tetraethoxysilane (TEOS, $Si(O–C_2H_5)_4$) which is usually reacted with soluble salts of sodium (NaCl) and calcium (Ca_2NO_3). These precursors undergo various forms of hydrolysis and polycondensation reactions. The silicon alkoxide $Si–(OR)_4$ where R is C_2H_5 for TEOS (and CH_3, when the precursor is tetramethoxysilane (TMOS)), is insoluble in water. Therefore, adding water to TEOS will form a sol, that is, a solution with TEOS suspension. The addition of an acid or a base as a catalyst allows the silane to mix with the water and catalyzes the formation of a network of polymers and cross-linkages that leads to the creation of a gel. Using an acid leads to longer chains and fewer cross-linkages, resulting in a gel with smaller pores, while an alkaline catalyst promotes cross-linkages and leads to larger pore-sizes. Hydrolysis of TEOS in water involves attachment of hydroxyl ions to the silicon atom. The degree of hydrolysis of the TEOS may vary from partial to full. Depending on the amount of water and the presence of catalyst, hydrolysis may proceed to completion as represented by the following equation:

$$Si(O-C_2H_5)_4 + 4H_2O \rightarrow Si(OH)_4 + 4C_2H_5OH \quad [III]$$

The hydrolyzed $Si–(OH)_4$ can undergo a condensation (polymerization) reaction to produce a gel.

$$(OH)_3Si-OH + HO-Si(OH)_3 \rightarrow (OH)_3Si-(O-Si-O)_n-Si(OH)_3 \quad [IV]$$

Soluble sodium and calcium ions are added slowly during the hydrolysis step to create Si–O–Na and Si–O–Ca–O–Si bonds. When the particles in the sol form long *polymers* (chains) that span the entire sol, a gel is formed. The gelation reaction proceeds slowly; the sol–gel is usually left for sometime for an ageing process to allow for complete cross-linking of the silicate. The gel is typically heated to 110 °C in order to remove water and alcohol and is then subjected to annealing thermal treatment to create the glass. This treatment is typically performed at temperatures between 350 and 700 °C.[23] The properties of the final bioactive glass product are controlled by processing parameters such as: molecular weight of the reactants, solution pH, solvent concentration, gelation temperature, and duration and drying conditions.

Foaming of sol–gel derived bioactive glasses provides the potential to make a scaffold with hierarchal interconnected porous structure to promote cell adhesion, tissue ingrowth, and nutrient delivery.[24,25] Porosity and structure of foamed sol–gel can be engineered by controlling processing parameters such as temperature at which the foaming process is carried out, surfactant type and concentration, gelling agent type and

concentration, added water concentration and glass composition.[26,27] Example of the foaming technique was described by Jones and Hench,[26] were aliquots of 50 ml 58S sol (60 mol% SiO_2, 36 mol% CaO, 4 mol% P_2O_5) were foamed by vigorous agitation with the addition of 1.5-ml surfactant (Teepol, a detergent containing a low-concentration mixture of anionic and nonionic surfactants), de-ionized water (improves foamability of surfactant), and 5 vol% hydrofluoric acid (HF, a catalyst for polycondensation).[25] It has been shown that small changes in added water concentration can be used at constant temperature and constant concentrations of surfactant and gelling agent to produce different pore networks at reproducible gelling times. The amount of water added to aid the surfactant produced a simplest control over pore size of the foams.[25] Although the foaming process changes the sol–gel process slightly, compared to the production of monoliths and powders, the 58S foam is still highly bioactive as indicated by the deposition of a carbonate-HA layer after 2 h immersion in SBF at 37 °C and 175-rpm agitation.[25]

A major advantage of the sol–gel method over the melting method is the purity of the final product and the ability to expand the compositional range of bioactivity for glasses in the system SiO_2–CaO–Na_2O. The gel-derived glasses contain entrapped nanopores that significantly increase the surface area of the material in contact with tissue fluids. Moreover, the low processing temperature of the gel-derived glass maximizes the number of the silanol (Si–OH) groups on the material surface. The silanol group is critical for the bioactivity reaction of the material. In addition, gel-derived bioactive glass may contain high energy silicate ring structures, which further activate the material's reactivity.

Primary human osteoblasts seeded on porous 58S scaffolds formed mineralized nodules within 10 days of culture.[28] Osteoblasts attached and proliferated on the foams as demonstrated by SEM. Mineralization was also observed when cells were incubated with medium supplemented with certain dilutions of the dissolution products of 58S foam. However, undiluted dissolution products from the foams were toxic to the cells and caused significant apoptosis (programmed cell death).[28] Earlier *in vitro* studies by El-Ghannam *et al.*[20] have demonstrated a similar adverse effect on bone cell function of the accumulation of the degradation products of porous bioactive glass prepared by melting. To alleviate the undesirable modifications in the medium pH and composition due to ion release from the bioactive substrate, it was necessary to preimmerse the bioactive glass in SBF before cell culture and to use high ratio of medium volume to scaffold surface area during cell culture.[7,20]

1.109.6. Bioactive Glass Ceramics

Bioactive glass ceramic is made by subjecting bioactive glass to thermal treatment in order to transform its structure from amorphous to crystalline. The crystallization of bioactive glass improves the mechanical strength significantly. Table 4 is a list of various bioactive glass ceramics and the corresponding mechanical properties.[29] Bioactive glass ceramics bond to bone and have been successfully used as load bearing implants.[10] The crystallization of bioactive glass limits the dissolution rate of the material and, therefore, slows down the surface reactivity.[30] Figure 12 demonstrates the significant decrease in the solubility of bioactive glass as the percentage of crystallization increased.[30] In addition, the negative ζ-potential of bioactive glass ceramic containing as little as 5% crystallization was significantly higher than that of amorphous bioactive glass ($p < 0.02$) (Figure 13(a)).[30] The high surface negativity of bioactive ceramic reduced the amount of protein adsorbed onto the material surface significantly. Figure 13(b) demonstrates the change in the ζ-potential and corresponding amount of protein adsorbed onto the surface of bioactive glass ceramic.[30] Moreover, significant changes in the protein conformation was observed; the ratio of (amide I)/(amide II) functional groups of all proteins adsorbed onto amorphous bioactive glass was greater than that of proteins adsorbed onto

Table 4 Mechanical properties of A/W and bioverit bioactive glass ceramics

Properties	*A/W glass ceramic*	*Bioverit I*	*Bioverit II*	*Bioverit III*
Pending strength (MPa)	215	140–180	90–140	60–90
Compressive strength (MPa)	1080	500	450	–
Young's modulus (GPa)	118	70–88	70	45
Vickers hardness (HV)	680	5000	8000	–
Fracture toughness ($MPa\,m^{1/2}$)	2	1.2–2.1	1.2–1.8	0.6

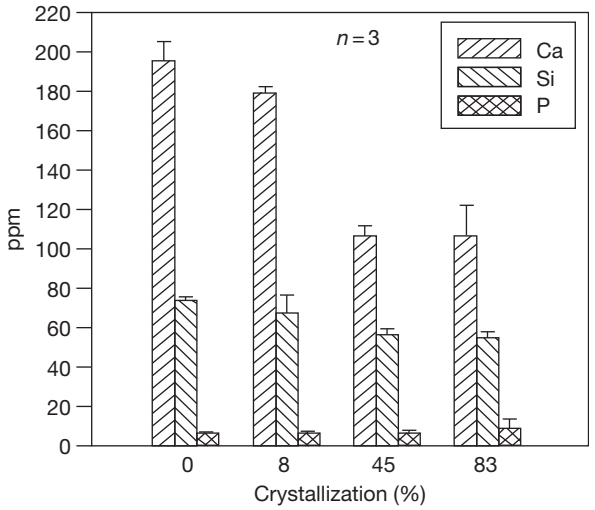

Figure 12 ICP concentration analyses of Ca, Si, and P ions in SBF after immersion of bioactive glass containing different crystallization percentages for 24 h. The amount of Ca and Si ions released from bioactive glass containing 8% crystallization was slightly lower than that released from control untreated bioactive glass. However, the amount of Ca and Si ions released from bioactive glass containing 45% or 83% crystallization was significantly lower than that released from control untreated bioactive glass ($p < 0.001$). P concentration in SBF increased as the crystallization percentage in the immersed bioactive glass increased; however, this increase was not statistically significant. Values shown are means ± standard deviation (SD) of three determinations. Reproduced from El-Ghannam, A.; Hamazawy, E.; Yehia, A. *J. Biomed. Mater. Res.* **2001**, *55*(3), 387–395, with permission from Wiley.

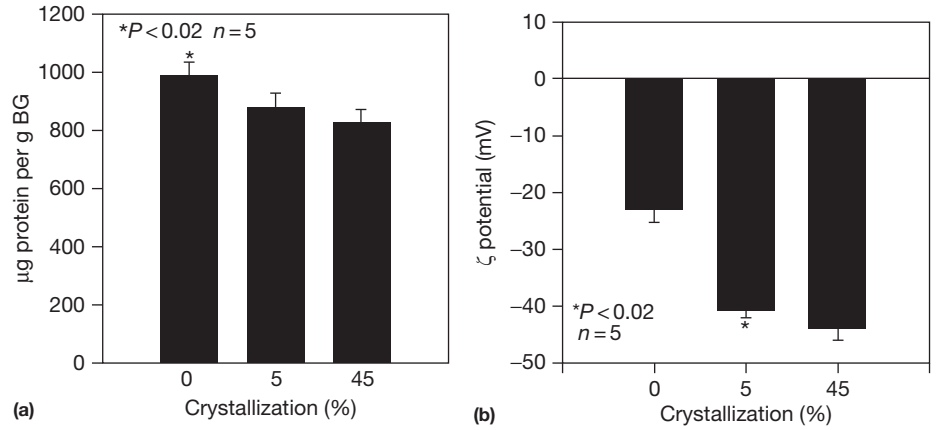

Figure 13 (a) Comparison of the amount of serum protein adsorbed onto thermally treated and control untreated bioactive glass. Control untreated bioactive glass adsorbed a statistically significant higher amount of serum protein than bioactive glass samples containing 5% crystallization ($p < 0.02$). Moreover, there was no significant difference between the amount of serum protein adsorbed onto bioactive glass containing 5% or 45% crystallization. Values shown are means ± SD of five determinations. (b) Zeta potential measurements of bioactive glass immersed in SBF. Bioactive glass containing 5% crystallization had a statistically significant higher negative zeta potential value than control untreated bioactive glass ($p < 0.02$). Moreover, statistical analysis showed that the difference in surface charge between bioactive glass samples containing 5% and that containing 45% crystallization was not significant. Values shown are means ± SD of five determinations. Reproduced from El-Ghannam, A.; Hamazawy, E.; Yehia, A. *J. Biomed. Mater. Res.* **2001**, *55*(3), 387–395, with permission from Wiley.

Table 5 FTIR band intensity and area under the peak ratios of amide I/amide II for various proteins adsorbed on amorphous and crystalline bioactive glass

Protein solutions	*Amorphous*		*Crystalline*	
	Area ratio	*Intensity ratio*	*Area ratio*	*Intensity ratio*
BSA	1.70 ± 0.25	1.75 ± 0.15	0.36 ± 0.14	0.54 ± 0.19
FBS	0.40 ± 0.12	0.52 ± 0.13	0.05 ± 0.02	0.08 ± 0.05
FN	4.21 ± 1.03	4.29 ± 0.92	1.30 ± 0.83	1.43 ± 0.80

Reproduced from Buchanan, L.; El-Ghannam, A. *J. Biomed. Mater. Res. A* **2010**, *93*(2), 537–546, with permission from Wiley.

crystallized bioactive glass (Table 5).[31] The Gaussian curve fitting analysis suggests that the significant expression of amide I, rich in charged and flexible unordered secondary structure of adsorbed FN, stimulated bone cell adhesion and spreading on the surface of amorphous bioactive glass. Bioactive glass ceramic enforces protein conformation that exposes amide II, rich in neutral and stable β-sheet structure and α-helix; this limited cell adhesion and spreading.[31]

1.109.7. Calcium Phosphate Ceramics

Calcium phosphates are crystalline materials with chemical composition similar to the mineral phase of bone, therefore, they are capable of inducing a direct bond with bone. Table 6 shows the main composition of the inorganic components of enamel, dentin, and bone as compared to stoichiometric HA.[32] The rate of bone bonding is enhanced by the controlled dissolution rate of the material. The solubility and bioactivity depends on the Ca/P ratio, inclusion of dopants, and crystallinity of the material. A variety of calcium phosphate ceramics have been employed as implant material. Among them, HA ($Ca_{10}(PO_4)_6(OH)_2$) and tricalcium phosphate (TCP, $Ca_3(PO_4)_2$) are the most widely used.

Table 6 Concentration of the inorganic components of enamel, dentin, bone, and stoichiometric HA

Composition (wt%)	*Enamel*	*Dentin*	*Bone*	*HA*
Calcium	36.5	35.1	34.8	39.6
Phosphorus	17.7	16.9	15.2	18.5
Ca/P (molar ratio)	1.63	1.61	1.71	1.67
Sodium	0.50	0.60	0.9	–
Magnesium	0.44	1.23	0.72	–
Potassium	0.08	0.05	0.03	–
Carbonate (as CO_3^{2-})	3.5	5.6	7.4	–
Fluoride	0.01	0.06	0.03	–
Chloride	0.30	0.01	0.13	–
Crystallographic properties: lattice parameters (±0.003 Å)				
a-axis (Å)	9.441	9.421	9.41	9.430
c-axis (Å)	6.880	6.887	6.89	6.891

Reproduced from Kannan, S.; Goetz Neunhoeffer, F.; Neubauer, J.; Ferreira, J. *J. Am. Ceram. Soc.* **2008**, *91*(1), 1–12, with permission from Wiley.

1.109.7.1. Composition of Hydroxyapatite

Stoichiometric HA has a rigid hexagonal dipyramidal crystalline structure[33] with a molecular formula $Ca_5(PO_4)_3OH$. The crystal unit cell of HA has ten Ca ions ($10Ca^{2+}$) and therefore, its chemical formula is usually written as $Ca_{10}(PO_4)_6(OH)_2$. Stoichiometry of HA refers to exact atomic ratio of Ca/P (10/6 or 1.67) in the unit cell. Deviation from the exact Ca/P ratio destabilizes the crystal and enhances the dissolution of the material. Thus, calcium deficient HA with a Ca/P ratio of 1.60 is slightly more bioactive than stoichiometric HA with a Ca/P ratio of 1.67.

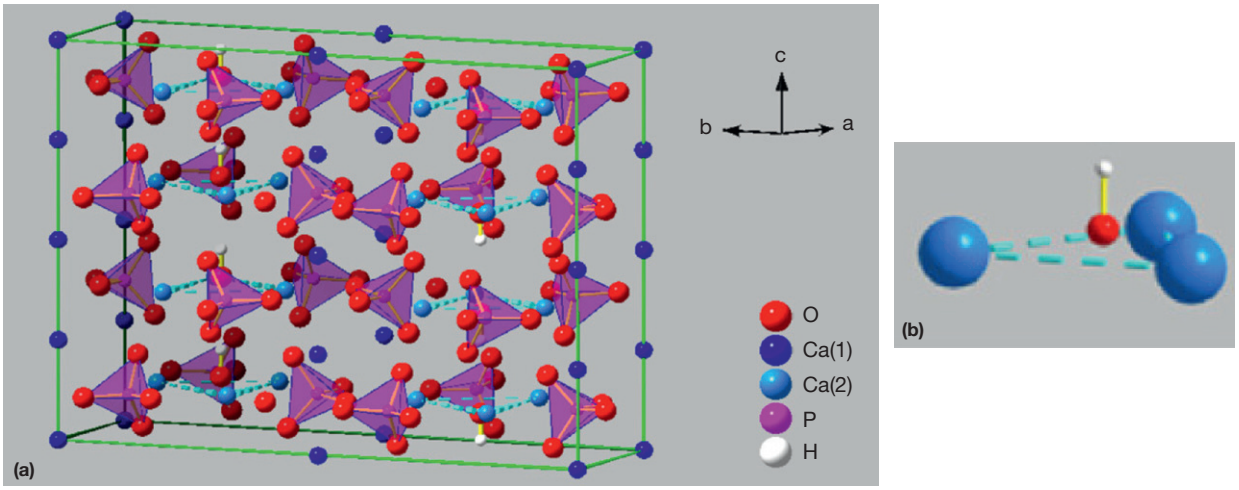

Figure 14 (a) Defect-free 1×1×2 supercell of the monoclinic modification of hydroxyapatite as obtained from full geometry optimization. The phosphate ions are illustrated as transparent tetrahedra. Two types of calcium ions are discriminated, that is, Ca(1) sites which are located between the phosphate ions and Ca(2) sites which form staggered triangles (dashed lines) resulting in channels parallel to the c-axis. Figure 14(b) illustrates that each Ca(2)-triangle embeds a hydroxide ion. Reproduced from Zahn, D.; Hochrein, O. *J. Solid State Chem.* **2008**, *181*(8), 1712–1716, with permission from Elsevier.

1.109.7.2. Structure of Hydroxyapatite

Phosphorous occurs in apatite in tetrahedral coordination, with the central P atom in the 6 h special position. The strong atomic bonds in the phosphate polyhedra are responsible for the rigidity of the apatite structure. Apatite has two types of calcium ions: Ca(1) sites which are located between the phosphate ions and Ca(2) sites which form staggered triangles resulting in channels parallel to the *c*-axis (**Figure 14(a)** and **14(b)**).[33]

Each of the three Ca(2) atoms at the corners of the triangles is bonded to the central anion, for example, OH^-, F^-, or Cl^- in HA, fluorapatite, or chloroapatite, respectively (**Figure 15**).[34] The diameter of these anions correlates well with the chemical stability of the material. The diameter of F^- ion is small enough to fit in the Ca(2) triangle without introducing appreciable alteration of the apatite structure. Therefore, fluoroapatite is a highly stable material with limited bioactivity properties. This also explains the stability of biological fluoroapatite that naturally exists in tooth enamel and which contributes to the protection against tooth decay. The OH^- anion is too large to fit within the rigid plane of the Ca(2) triangle. Therefore, the OH^- anion is displaced above or below the plane causing strains that results in shifts in the position of the Ca(2) ions without affecting the stoichiometry of HA. The accommodation of the OH^- is enhanced by the presence of vacancies and impurity atoms in the material. The atomic rearrangement required to accommodate the hydroxyl group makes stoichiometric HA slightly less stable than fluorapatite.[34]

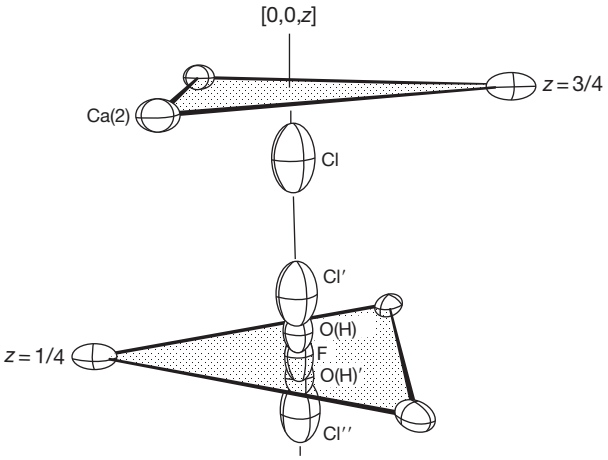

Figure 15 Depiction of possible anion positions in the hexagonal ternary apatite structure. Stippled planes represent mirror planes at $z = 1/4$, 3/4, each containing a triangle of Ca2 atoms (connected by 'bonds'). Atom Cl represents a Cl atom disordered below the mirror plane at $z = 3/4$, and other column anions represent five possible anion neighbors associated with the mirror plane at $z = 1/4$ (Cl′ = Cl disordered above plane; O(H) = OH oxygen disordered above that plane; F = fluorine atoms at 0,0, 1/4; O(H)′ and Cl″ represent OH and Cl disordered below the mirror plane at $z = 1/4$). Reproduced from Hughes, J.; Rakovan, J. *Rev. Mineral. Geochem.* **2002**, *48*(1), 1, with permission from Mineralogical Society of America.

1.109.7.3. Calcium Deficient Hydroxyapatite

Synthetic calcium deficient HA (CDHA) has a Ca/P ratio in the average range 1.5–1.6. The general chemical formulas are usually written as:

$$Ca_{10-x}(HPO_4)_x(PO_4)_{6-x}(OH)_{2-x}(H_2O)_x \quad \text{with } 0 < x \leq 1$$

or

$$Ca_{10-x}(HPO_4)_x(PO_4)_{6-x}(OH)_{2-x}$$

When one Ca ion is missing, it leaves behind two negative charges that need to be balanced in order to keep the neutrality of the crystal.[33] The crystal neutrality is restored by either protonation of one (PO_4^{3-}) group and one OH^- group or by protonation of (PO_4^{3-}) and removal of an OH^- ion, respectively.

The structure and chemistry of apatite allow for cationic (e.g., Na^+, Mg^{2+}, Zn^{2+}, Sr^{2+}) and anionic (e.g., SO_4^{2-}, CO_3^{2-}, SiO_4^{4-}) substitutions. The metal cations substitute for Ca^{2+} and the anions replace PO_4^{3-} and to a limited extent the OH^-. Substitutions in the apatite structure for Ca^{2+}, PO_4^{3-}, or OH^- groups modifies the crystal lattice parameters and changes the solubility and bioactivity properties of the material.

Solid state nuclear magnetic resonance (NMR) spectroscopy showed that natural bone contains only about 20% of the OH ions present in pure HA.[35] The carbonate ions in biological apatite accounts for 3–8 wt% of the material.[36] Carbonate (CO_3^{2-}) can substitute for either the (OH^-) or the (PO_4^{3-}) groups, designated as type A or type B substitution respectively.[37] Polarized infrared (IR) studies suggested that for A type substitution to occur, the planar CO_3^{2-} ions in the anion channels are oriented approximately parallel to the *c*-axis to minimize the steric strain related to the incorporation of this large ion. On the other hand, the substitution of the smaller CO_3^{2-} group for the larger tetrahedral PO_4^{3-} group cause a contraction in the *a*-axis and expansion in the *c*-axis compared to the CO_3^{2-} free apatite.[37] The changes in the crystal lattice parameters introduced by the incorporation of the carbonate group renders the material more soluble and bioactive than carbonate-free apatite.

1.109.7.4. Preparation of Hydroxyapatite

As is described in length in the chapter by Rey *et al.*, solid state reaction between $Ca(OH)_2$ or $CaCO_3$ and $CaHPO_4 \cdot 2H_2O$ or β-$Ca_3(PO_4)_2$ above 950 °C forms HA.[38,39] Formation of HA by wet precipitation method is achieved by the dropwise addition of phosphoric acid (H_3PO_4) to an aqueous suspension of calcium hydroxide ($Ca(OH)_2$) under constant stirring.[40–42] The pH of the solution is maintained by the addition of NH_4OH to ensure the formation of HA according to eqn [III].

$$10Ca(OH)_2 + 6H_3PO_4 \rightarrow Ca_{10}(PO_4)_6(OH)_2 + 18H_2O \quad [V]$$

An alternate method is to mix solutions of calcium nitrate tetrahydrate and di-ammonium hydrogen orthophosphate at pH ~11 according to eqn [IV].

$$10Ca(NO_3)_2 \cdot 4H_2O + 6(NH_4) \cdot 2HPO_4 + 8NH_4OH \rightarrow Ca10(PO_4)_6(OH)_2 + 20NH_4NO_3 + 6H_2O \quad [VI]$$

The precipitate is dried and calcined at 400 °C for 1 h to obtain HA.[43,44] The nature and crystallinity of HA depends significantly on the processing parameters such as temperature, pH, and reaction durations.[45–47] **Figure 16** shows the typical X-ray diffraction analysis (XRD) spectra for HA prepared by wet precipitation method and calcined at 1200 °C.[48]

HA can also be prepared by the hydrolysis of $CaHPO_4$, β-$Ca_3(PO_4)_2$, α-$Ca_3(PO_4)_2$, $Ca_2PO_4(OH)_2H_2O$, $Ca_8H_2(PO_4)_6 \cdot 5H_2O$, or $Ca_3(PO_4)_2 \cdot CaO$ at low temperature (usually <100 °C) resulting in micron sized needle-like crystals. The HA produced by hydrolysis is highly nonstochiometric with the Ca/P ratio in the range of (1.5–1.71).[49] The morphology of HA crystals affects the bioactivity properties and can be controlled by treatment temperature.[50–52] Single phase HA crystallites (10–60 nm) in diameter have been prepared by mixing $Ca(NO_3)_2 \cdot 4H_2O$, and $(NH_4)_2HPO_4$ at 200 °C under saturated water vapor pressure.[53] Micron size HA granules (50–1000 μm) have been prepared by hydrothermal treatment of α-TCP at 105–200 °C.[54,55] HA powder prepared by this method is characterized by a high degree of crystallinity with a Ca/P ratio close to stoichiometric value.

1.109.7.5. Composition and Structure of β-TCP

The TCP family comprises of three polymorphic structures: β-TCP, α-TCP, and α′-TCP; all of which have higher resorption rate than most other calcium phosphate ceramics. Of the TCPs, β-TCP and to a lesser extent α-TCP have widely been used as bone grafts. The stoichiometric formula of β-TCP is $Ca_3(PO_4)_2$ with a Ca/P ratio of 1.5 and a O/P ratio of 4.0. The crystal structure of β-TCP has been well characterized by X-ray and neutron powder diffraction methods.[56–58] β-TCP has a rhombohedral crystal structure with unit cell parameters ($a = b = 10.4352$ Å, $c = 37.4029$ Å, $\alpha = \beta = 90°$, and $\gamma = 120°$).[58] The crystal structure is in the form of two independent columns, column 'A' containing two Ca and one P atoms and a second slightly distorted column 'B' containing six Ca and four P atoms. A schematic of the two columns is shown in **Figure 17**.[58] Ca atoms are located in five crystallographic sites labeled Ca(1)–Ca(5) within the two columns, however, with variable coordination numbers and different energy states.[58,59]

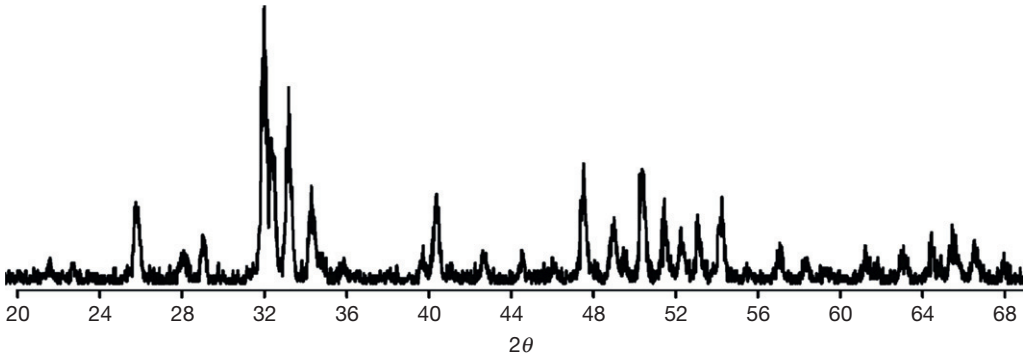

Figure 16 X-ray diffraction patterns of hydroxyapatite prepared by wet method and sintered at 1200 °C showing exclusively sharp, clear reflections corresponding to hydroxyapatite, which confirm the phase purity and high degree of crystallinity. Reproduced from Afshar, A.; Ghorbani, M.; Ehsani, N.; Saeri, M.; Sorrell, C. *Mater. Des.* **2003**, *24*(3), 197–202, with permission from Elsevier.

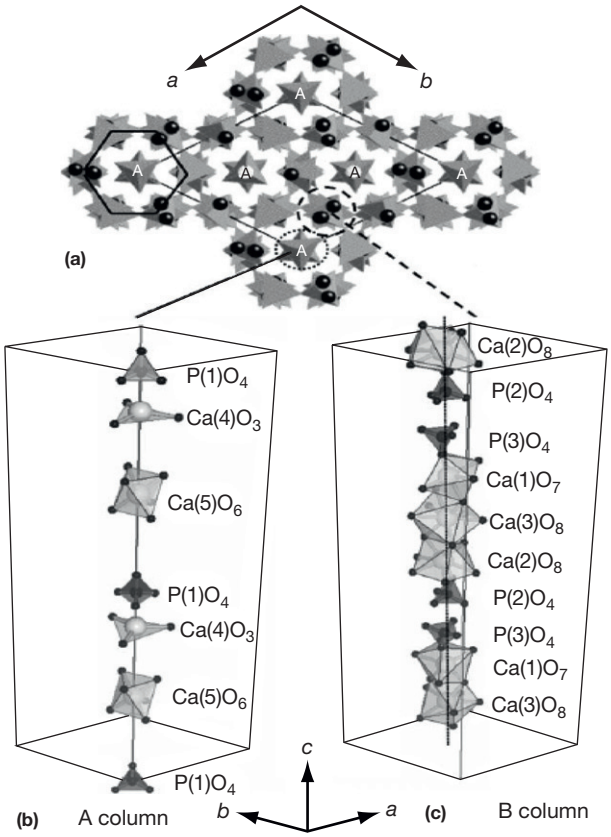

Figure 17 (a) Projection of the crystal structure of β-$Ca_3(PO_4)_2$ on the (001) plane, showing the A and B columns. 'A' denotes the A column, while no indication is given for the B column. The rhombus in (a) denotes the hexagonal unit cell of β-$Ca_3(PO_4)_2$. (b) and (c) are the configurations of CaO_n and PO_4 groups in the A and B columns, respectively, along the c-axis of the hexagonal cell (n ¼ 3; 6, 7, and 8). (b) and (c) were made using a computer program VICS. Reproduced from Yashima, M.; Sakai, A.; Kamiyama, T.; Hoshikawa, A. *J. Solid State Chem*. **2003**, *175*(2), 272–277, with permission from Elsevier.

1.109.7.6. Synthesis of β-TCP

β-TCP can be prepared via a wet precipitation method by mixing stoichiometric ratios of $Ca(NO_3)_2$ with $(NH_4)_2HPO_4$ at pH 10 at 60 °C for 2 h, followed by aging at boiling point for 2 h.[60] It can also be produced by a solid state reaction between $CaCO_3$ and $Ca_2P_2O_7$ or $CaHPO_4$ at 1350 °C for 3.5 h or 1000 °C for 24 h respectively.[58,61] **Figure 18(a)** shows the XRD spectra of β-TCP calcined at 1150 °C for 4 h.[62] In addition, amorphous TCP nanoparticles (α-TCP, chemical formula: $Ca_3(PO_4)_2$) can be prepared by flame spray pyrolysis.[63,64] **Figure 18(b)** shows the FTIR spectra of as-prepared and sintered TCP nanoparticles produced by flame spray synthesis. Broad absorption bands for as-prepared powder transformed into distinct peaks characteristic for crystallized β-TCP after calcination at 900 °C.[64]

Dopants can be introduced in the β-TCP crystal structure prepared using either method. Mg or Zn substituted β-TCP is produced by including $Mg(NO_3)_2 \cdot 6H_2O$ or $Zn(NO_3)_2 \cdot 6H_2O$ in the wet precipitation synthesis route respectively.[56,65] Sr substitution in β-TCP has been achieved by sintering β-TCP and α-$Sr_3(PO_4)_2$ at 1000 °C for 15 h.[66] Similarly, Li-, Na-, and K-substituted β-TCP is produced by a solid state reaction between Li_2CO_3, Na_2CO_3, and K_2CO_3 respectively at 1000 °C for 24 h.[57] Discs of β-TCP containing both Sr and Mg substitution have been produced by mixing MgO and SrO with pure β-TCP followed by powder compaction and sintering at 1250 °C for 2 h.[67]

1.109.7.7. Effect of Composition, Dissolution, Protein Adsorption, and HA Crystal Size on Bioactivity

Calcium phosphate ceramics can be transformed into biological apatite by virtue of its reactivity and the associated dissolution, precipitation, and ion exchange in physiological media. Materials undergoing high dissolution in simulated physiological solution also induce back precipitation of a biologically equivalent apatite on their surface.[4] The formation of a bioactive surface layer of apatite on HA *in vitro* depends on the physicochemical characteristics of the material which can be controlled by processing parameters such as temperature and pressure.

Interesting data follow from an experiment in which amorphous HA was calcined at 600 or 900 °C to produce small, defective, or mature undefective crystalline material respectively.[68] The samples were immersed in SBF and the calcium uptake (decrease in Ca concentration in the solution) was taken as an indicator of the deposition of the apatite layer on the material surface. The uptake of Ca by HA decreased with the increase in the pretreatment temperature of HA. This indicates that an increase in the crystallinity of HA aggravates the deposition of surface apatite layer due to the enhanced stability of the material. Moreover, the HA pretreated at low temperature has small and defective crystals and hence, high surface energy. The high surface energy would facilitate rapid formation of surface apatite layer. On the other hand, well crystallized HA prepared at high temperature would require to undergo an initial dissolution to reach the critical super saturation essential for the deposition of the surface apatite layer.[68]

Substitution of Ca by Mg, Zn, Si, and Y has been reported to enhance solubility and bioactivity properties of HA ceramic.[69–74] The dissolution rate of stoichiometric HA (s-HA), β-TCP, α-TCP, oxyhydroxyapatite (OHA), tetracalcium phosphate (TTCP) and of a commercial CDHA was evaluated in tris buffer.[75] In terms of the dissolution of calcium the rate of dissolution decreased in the order:

$$\text{TTCP} > \alpha\text{-TCP} > \text{OHA} > \beta\text{-TCP} > \text{CDHA} > \text{s-HA}$$

However, in terms of the dissolution of phosphate the order was[75]:

$$\alpha\text{-TCP} > \text{CDHA} \approx \beta\text{-TCP} > \text{OHA} \approx \text{s-HA} > \text{TTCP}$$

On the other hand, the Ca/P ratio in the different ceramics varied as follows:

$$\text{TTCP} > \text{OHA} > \text{s-HA} > \text{CDHA} > \alpha\text{-TCP} > \beta\text{-TCP}$$

The differences in the rate of dissolution of Ca and P among these materials have been attributed to the precipitation of another calcium phosphate phase, particularly on CDHA, OHA, and TTCP.

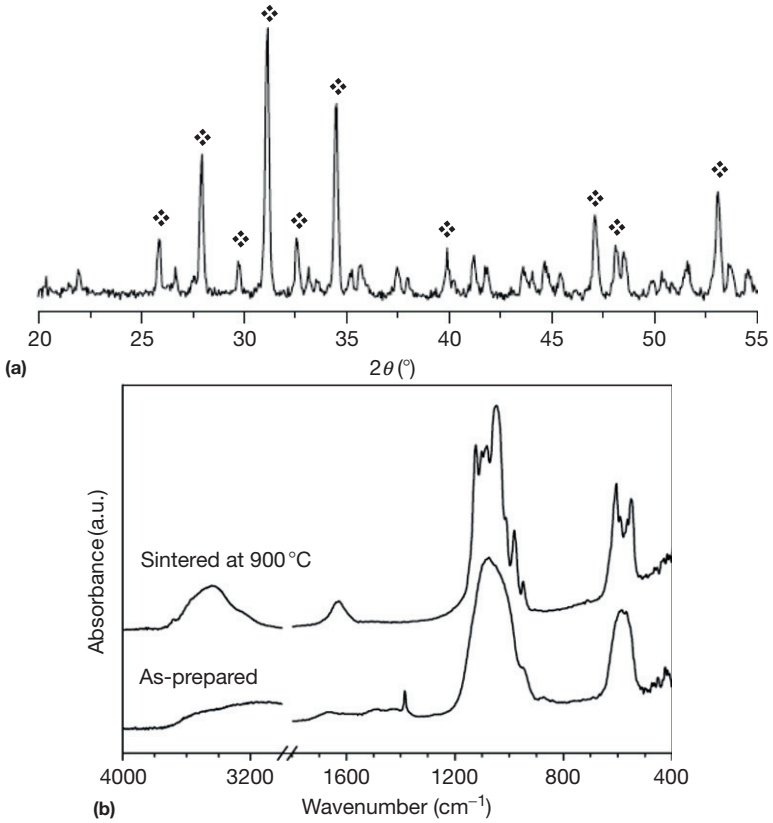

Figure 18 (a) XRD spectra of β-TCP samples after calcinations at 1150 °C for 4 h. The ten most intense diffraction peaks are shown on the patterns. The three maximum diffraction peaks corresponding to the planes (0 2 10), (2 2 0), and (2 1 4) of β-TCP were observed at 31.0°, 34.4°, and 27.8°. (b) FTIR spectra of as-prepared and sintered tricalcium phosphate nanoparticles produced by flame spray synthesis. Broad absorption bands for as-prepared amorphous TCP powder transform into distinct peaks characteristic for β-TCP after crystallization by calcination at 900 °C. Adapted from Dos Santos, E.; Farina, M.; Soares, G.; Anselme, K. *J. Mater. Sci. Mater. Med.* **2008**, *19*(6), 2307–2316, with permission from Springer; Loher, S.; Reboul, V.; Brunner, T.; *et al. Nanotechnology* **2006**, *17*, 2054, with permission from IOP Publishing Ltd.

Ceramic dissolution is a causative factor for the bone-bonding ability of HA.[4,76] The degradation of HA depends on its composition, crystal size, porosity, and preparation methods.[37] De Bruijn *et al.*[77] have reported the bioactivity of HA of varying crystallinity after implantation in rat femora for up to 4 weeks. It was found that amorphous HA coating demonstrates a gradual surface degradation while the high crystallinity HA coating showed negligible degradation. Degradation was also related to the bone apposition, as high bone apposition was present on the amorphous HA coating compared to highly crystalline HA coating.[77]

Protein adsorption onto the surface of bioactive ceramic and the initial cell response and tissue integration with the implant are closely related. The high affinity between functional protein groups like R–COO^- and $R-NH_3^+$ and the Ca^{2+} and PO_4^{3-} sites on the calcium phosphate ceramics enhances protein adsorption.[78,79] It has been proposed that the affinity of the (COO^-) protein functional group to the Ca^{2+} site of the ceramic is larger than that of the (NH^{3+}) of proteins to the PO_4^{3-} sites.[80] However, the hydrophobic segments on the protein molecule can also interact with the surface of inert ceramics and contribute to protein adsorption. Greater adsorption of serum proteins has been observed on HA than on bioactive glass or metals such as titanium (cp-Ti) or stainless steel.[22,81] Figure 19 shows a comparison of the amount of serum proteins adsorbed on HA as compared to untreated or SBF treated bioactive glass.[22] However, there is a difference in the adsorption profile of HA and bioactive glass as described in greater detail in **Chapter 1.114, Bioactivity: Mechanisms**.

1.109.7.8. Apatite Formation and Bone Bioactivity of β-TCP

The bone-bonding ability of β-TCP is well documented,[11,82–84] however, there has been a considerable debate on the apatite-forming ability of β-TCP upon immersion in SBF.[11,84–86] The formation of an apatite layer on β-TCP after immersion in SBF has been demonstrated (Figure 20).[85] Small apatite crystals appeared after immersion for 7 days and continued to grow into larger apatite clusters until day 14.[85] Other studies however, have reported that both β-TCP and natural calcite do not form apatite on their surfaces *in vitro* or *in vivo*.[11] These authors suggested that the bone-bonding ability of β-TCP is related to its high rate of resorbability.[11] The discrepancies in the results related to the *in vitro* deposition of the HA surface layer can easily be understood in view of the differences in the experimental design, conditions under which the material was prepared, and the sensitivity of the SBF. In any event, the formation of the

surface HA should be looked at as an indicator of bioactivity but not necessarily the only indicator. One main attribute for the HA layer that deposits on the surface of a bioactive material is to provide calcium ions necessary for bone cell function and tissue formation. Therefore, the high rate of dissolution of β-TCP will provide calcium ions.

Several studies have shown that the degradation of TCP is solution-mediated and cell-mediated.[82,87,88] However, in view of the high solubility product (2.30×10^{-30}) of β-TCP, solution-mediated resorption is expected to be dominating. The variations in the coordination number and bond energy of the Ca–O bonds in β-TCP enhances atomic debonding of β-TCP in physiological solution, the collapse of the crystal structure, and the initiation of bulk degradation. Although the Ca^{2+} and PO_4^{3-} ions are released rapidly from β-TCP into the physiological solution, the dynamic degradation of the material surface would not enhance the nucleation and crystallization of an apatite layer. It is also possible that the initial calcium phosphate that precipitates on β-TCP is thermodynamically unstable and would not allow persistent apatite crystallization.[86]

Macrophages are triggered and participate in the bulk degradation of the material contributing to the cell-mediated resorption. Many studies have reported that tartrate-resistant acid phosphatase (TRAP) positive multinucleated cells and macrophages adhered to β-TCP after implantation.[82,88] The presence of TRAP-positive cells indicates the role of osteoclasts in the resorption process as TRAP is associated with osteoclastic activity. Moreover, osteoblastic differentiation markers such as type I procollagen and osteopontin have also been detected along with osteoclasts suggesting that bone formation and β-TCP resorption are concurrent processes.

A common method to stabilize the structure of β-TCP is by doping it with metal ions such as Mg, Zn, Sr, Si, etc.[56,59,66] These metal ions substitute some of the Ca bound to the PO_4^{3-} polyhedra and improve thermal stability during processing, mechanical properties, dissolution, and bioactivity characteristics of the material. Yoshida *et al.*[57] have proposed a mechanism for the substitution of up to 9.1 mol% Ca in β-TCP by monovalent or trivalent metal ions, while the divalent metals can substitute up to 13.6 mol% Ca. **Figure 21** shows the decrease in the dissolution rate of β-TCP upon substitution of Ca with 0.1–1.0 mol% Zn indicating the significant improvement in material's stability.[65] It has been suggested that the adsorption of Zn and Mg ions from physiologic solution onto the β-TCP surface enhances Ca substitution and inhibits ceramic dissolution.[89]

The ability of calcium phosphate ceramics to adsorb proteins is an important factor that mediates initial cell response to the material. Many studies have shown that biphasic HA-TCP composite adsorbs significantly higher serum protein than pure HA as shown in **Figure 22**.[90,91] Moreover, it has been shown that β-TCP adsorbs more FN than dense HA; however, the difference was not statistically significant,[62] most probably due to the interference of other parameters including ceramic dissolution and its effect on the medium pH.

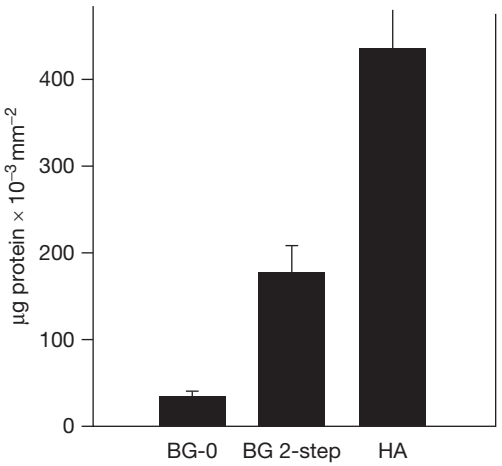

Figure 19 Quantitative analysis of serum protein adsorption onto the surface of bioactive ceramics immersed in tissue culture medium containing 10% serum. HA ceramic adsorbed significantly more serum protein than SBF-treated bioactive glass covered with hydroxyapatite layer (BG 2-step) or control untreated bioactive glass (BG-0) without a hydroxyapatite surface layer. Bioactive glass covered with hydroxyapatite layer adsorbed a significantly higher amount of serum protein than unmodified bioactive glass.

1.109.8. Silica-Calcium Phosphate Nanocomposite

1.109.8.1. Composition

SCPC is a family name for a series of compositions in a multiphase bioactive ceramic system.[1,6,14,92] **Table 7** shows the

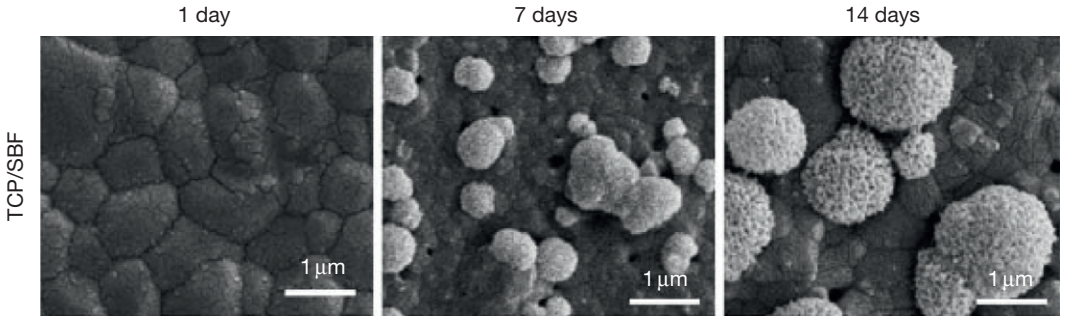

Figure 20 SEM images of apatite growth on the surface of β-TCP when soaked in SBF. Most of the apatite crystals remained submicron-sized, whereas others grew into larger apatite clusters. Reproduced from Juhasz, J.; Best, S.; Auffret, A.; Bonfield, W. *J. Mater. Sci. Mater. Med.* **2008**, *19*(4), 1823–1829, with permission from Springer.

composition of selected formulations of SCPC. Interestingly, SCPC formulations with high content of silica are more bioactive than calcium phosphate-rich SCPC compounds, HA ceramic or bioactive glass.[1,6,14] The excellent bioactivity and resorbability of the Si rich SCPC are due to the physicochemical properties of its mineral constituents as well as the controlled release of Si from the substrate. Figure 4(a) demonstrates the controlled release of Si from SCPC50 as compared to that released from bioactive glass and other SCPC formulations. Although silica is an essential component of SCPC, the bioactivity property of the material is not dependent on the ionic diffusion from the bulk to the surface as is the case with bioactive glass. Critical size bone defects implanted with SCPC showed extensive bone regeneration and graft material resorption 3 weeks postoperatively.[6] On the other hand, defects grafted with bioactive glass particles for the same time period showed bone formation but with only initial resorption of the graft material.

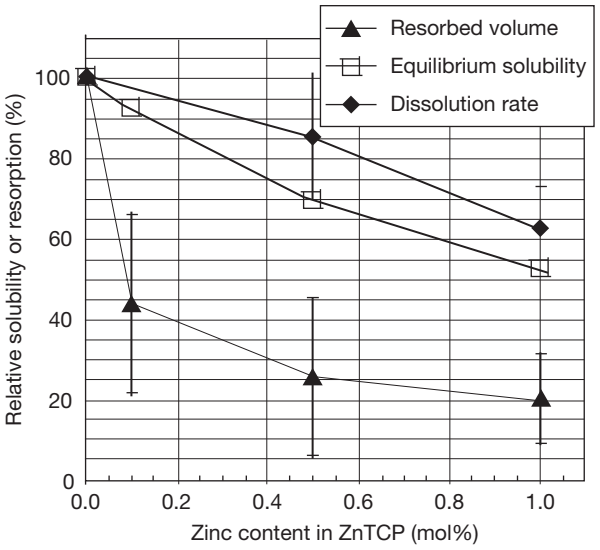

Figure 21 Dissolution rates for TCP discs doped with Zn in the concentration range from 0 to 10 mol%. The samples were immersed in 35 mL of 0.08 M acetic acid and sodium acetate buffer solution at pH 5.5 and 25 ± 3°C in polystyrene bottles for 300 min with a stirring rate of 440 ± 10 rpm. The pH value of the immersing solution was selected to be similar to that associated with osteoclastic resorption. Reproduced from Ito, A.; Senda, K.; Sogo, Y.; Oyane, A.; Yamazaki, A.; LeGeros, R. *Biomed. Mater.* **2006**, *1*, 134, with permission from IOP Publishing Ltd.

1.109.8.2. Crystalline Structure

The crystalline structure of SCPC is complex, as it contains solid solutions instead of pure phases. Depending on the initial chemical composition and processing parameters, the SCPC may contain a combination of two or more of the following phases ('ss' stands for solid solution): α-quartz (SiO_2) ss, β-quartz (SiO_2) ss, α-crystobalite (SiO_2) ss, cyclosilicate $Na_3CaPSiO_7$ (clinophosinaite) ss, β-$NaCaPO_4$ (rhenanite) ss, Na_2CaSiO_4 ss, γ-$Ca_2P_2O_7$ ss, β-$Ca_2P_2O_7$ ss, and α- or β-$Ca_3(PO_4)_2$ ss. Among these phases, β-$NaCaPO_4$ ss and α-cristobalite ss are the most thermodynamically stable phases. Formation of solid solutions in SCPC ceramic phases underlies the excellent bioactivity and resorbability properties of SCPC. Solid solutions form during thermal processing of SCPC, when ion diffusion at the grain boundaries between the calcium phosphate and silica takes place. The silicate-phosphate ionic diffusion is an example of the crystal modification during processing. This ionic diffusion results in substitution of solid solution due to the similarity between the ionic radii of silicon ion (0.04 nm) and that of phosphorous ion (0.035 nm). The effect of silicate-phosphate ion substitution is threefold: first, it lowers the crystallization temperature of the silicate and calcium phosphate phases. Crystalline phases that form at low temperature are known to be more bioactive than crystals that form at high temperature. Second, incorporation of foreign atoms (Si or P) in the host phase (calcium phosphate or silica, respectively) introduces strains within the crystal that enhances the fatigue and mechanical strength of the material. But most importantly, the incorporation of the impurity atoms in the

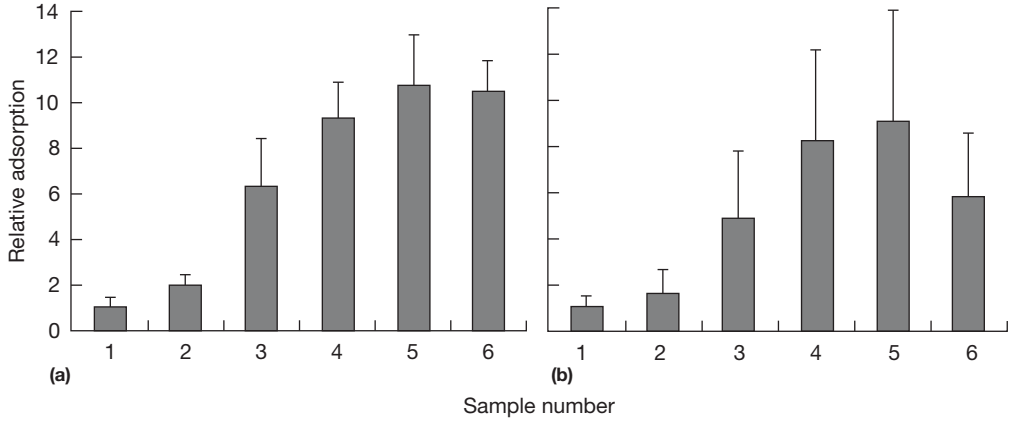

Figure 22 Histogram showing the adsorption of (a) fibronectin and (b) BMP-2 on various biphasic ceramics. The amount of protein adsorbed on each sample has been normalized to the amount adsorbed on dense pure HA (Sample (1)). The biphasic ceramics are (1) 100% HA; (2) 95% HA/5% β-TCP; (3) 25%β-TCP/70% α-TCP/5% $Ca_2P_2O_7$; (4) 30%β-TCP, 70%α-TCP; (5) 90%β-TCP/ 10% HA, and (6) 85%β-TCP/15%HA. All ratios are in wt%. Reproduced from Kubarev, O.; Komlev, V.; Maitz, M.; Barinov, S. *Dokl. Chem.* **2007**, *413*(1), 72–74, with permission from Springer.

Table 7 Chemical composition in mol% of selected formulations of silica-calcium phosphate nanocomposite

Sample	*SiO_2*	*P_2O_5*	*CaO*	*Na_2O*
SCPC10	3.31	31.13	62.25	3.31
SCPC30	10.74	26.18	52.34	10.74
SCPC50	19.49	20.34	40.68	19.49
SCPC75	32.9	11.4	22.8	32.9

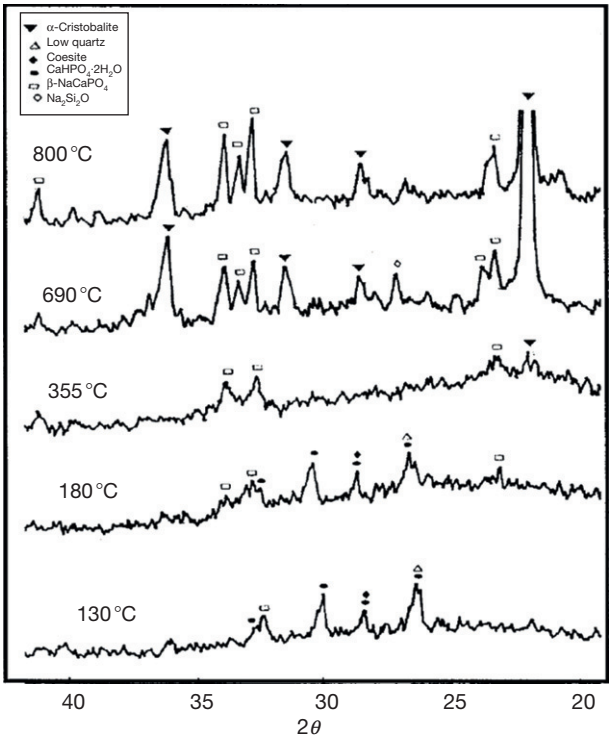

Figure 23 XRD analysis of SCPC75 treated at 130° or 180 °C showed ill crystallization and comprised of brushite ($CaHPO_4$), L-quartz (SiO_2) ss, and rhenanite (β-$NaCaPO_4$) ss. After treatment at 355 °C, $CaHPO_4$ transformed into β-$NaCaPO_4$ ss and low quartz ss transformed into α-cristobalite ss. The intensity of the signal characteristic of β-$NaCaPO_4$ ss and α-cristobalite ss increased, after treatment at 690° and 800 °C, indicating maturation of the crystalline structure of these two phases. Reproduced from El-Ghannam A. *J. Biomed. Mater. Res. A* **2004**, *69*(3), 490–501, with permission from Wiley.

quartz or cristobalite solid solutions enhances the dissolution of the material. In the absence of impurities, quartz is highly stable (beach sand is high purity quartz). The dissolution and bioactivity of (quartz ss) can be controlled by the amount of impurities incorporated in its crystal structure during thermal treatment.

The phases that form when the SCPC reactants are mixed together and treated at temperatures in the range 180–350 °C are highly defective and immature. The ill crystallization at low temperature is reflected on the XRD diagrams, which show broad and low intensity diffraction patterns (Figure 23).[6] This is particularly true for SCPC compounds rich in calcium phosphate where the blend of phases that form at low

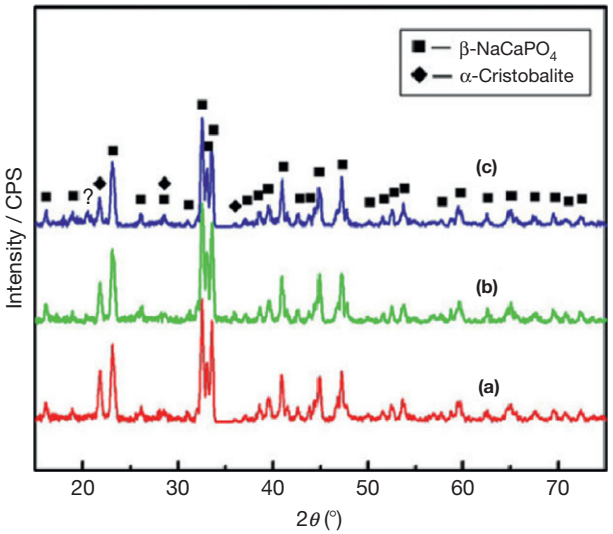

Figure 24 XRD patterns of SCPC50 pressed at 200 MPa and sintered at (a) 900 °C, (b) 1000 °C, and (c) 1100 °C for 3 h. The crystalline phases of the SCPC were mainly composed of β-$NaCaPO_4$ ss and α-cristobalite ss. Reproduced from Liu, X.; El-Ghannam, A. *J. Mater. Sci. Mater. Med.* **2010**, *21*, 2087–2094, with permission from Springer.

temperature includes $CaHPO_4$ and β-$Ca_2P_2O_7$ ss, which are thermodynamically unstable and hence highly biodegradable. When the SCPC material is heated at higher temperature, these preliminary calcium phosphate phases transform into the more stable β-rhenanite.[5] The silica phase that forms at low temperature is α-quartz ss which transforms into α-cristobalite at higher temperature. The most thermodynamically stable phases in the SCPC system are α-cristobalite (SiO_2) ss and β-rhenanite ($NaCaPO_4$) ss. This can easily be noticed as the two phases (α-cristoblaite and β-rhenanite) are consistently formed in all SCPC chemical formulations after thermal treatment at 900–1200 °C (Figure 24).[93] Detailed studies on the effect of temperature and pressure on the crystallization behavior of SCPC have been described elsewhere.[93]

1.109.8.3. Structure and Bioactivity Relationship

The SCPC is composed of nanocrystals of resorbable minerals, which induce unique bioactivity and mechanical properties. Transmission electron microscopy (TEM) analyses showed that the grain size of the SCPC75 is 50 nm (Figure 25).[92] The high density of grain boundaries in SCPC would provide preferential sites for protein adsorption and cell adhesion. X-ray microanalysis of the elemental distribution along the grain boundary showed maximum counts for Ca, Na, and P, whereas the grain bulk was rich in Si (Figure 26). These results indicate that calcium phosphate-containing phases preferred to distribute along the boundaries of the silica grains. The migration of Ca, P, and Na atoms to the grain boundaries may be enhanced by the low melting points of the β-$NaCaPO_4$ and $Na_3CaPSiO_7$ phases.[92] Therefore, unlike bioactive glass, both the surface and the bulk of the SCPC acquired bioactive structure and composition that facilitated bioactivity on the nanoscale level.

1.109.8.3.1. Effect of structure and composition on protein adsorption

SCPC formulations containing $CaHPO_4$ ss adsorbed significantly higher amount of serum proteins than those containing γ-$Ca_2P_2O_7$ ss and α-$Ca_3(PO_4)_2$ ss (Figure 27).[6] The enhanced protein adsorption on $CaHPO_4$ could be attributed to the high ratio of Ca-to-P sites on the material surface.[94] On the other hand, the inhibition of protein adsorption onto the surface of SCPC containing pyrophosphates and TCP is due to the low ratio of Ca-to-P and high surface negativity of $(P_2O_7)^{4-}$ and $[(PO_4)_2]^{6-}$ respectively. The increase in surface negativity of the material makes adsorption of negatively charged glycoprotein molecules a thermodynamically unfavorable reaction ($\Delta G > 0$).[95] On the other hand, as $Ca_2P_2O_7$ ss is transformed into β-$NaCaPO_4$ ss serum protein adsorption is enhanced.[6] The affinity of β-$NaCaPO_4$ ss toward serum proteins would be higher than that of $Ca_2P_2O_7$ ss due to the presence of labile Na atom in the former compound. Protein adsorption was also significantly affected by the crystallization and phase transformation of the silica phase(s). In all SCPC composites, the crystallization of amorphous silica inhibited protein adsorption. However, the degree of inhibition varied depending on the concentration and nature of the crystalline silica phase. Composites that contained α-cristobalite ss adsorbed a significantly higher amount of serum proteins than those contained α-quartz ss. The enhancement of protein adsorption correlates well with the fact that α-cristobalite ss has a comparatively open atomic structure, whereas the atoms in quartz are more closely linked.[96] Moreover, α-cristobalite ss is characterized by a tetragonal structure, with a low degree of symmetry than the hexagonal structure of α-quartz ss. Therefore, in biological solutions, α-cristobalite ss becomes more polar than α-quartz ss and can easily bind to the active sites of the protein molecules. In addition, the formation of crystal defects and solid solutions is expected to increase after treatment at high temperature ($\geq$800 °C), which further activates the material by providing charged surface sites favorable for protein binding. It is also possible that the surface characteristics of SCPC dictate a favorable protein conformation that enhances cell–material interaction and tissue integration.

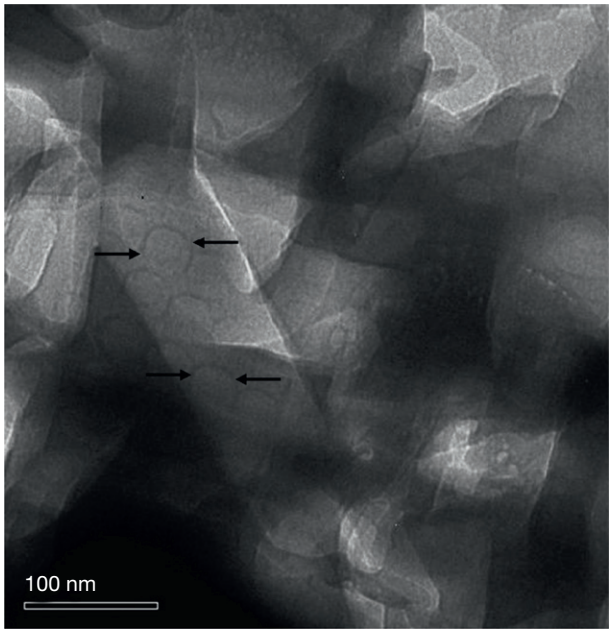

Figure 25 TEM micrograph showing SCPC nanocrystals within the size range of 50 nm. The arrows point to the edge of 50-nm crystals. The scale bar is 100 nm. Reproduced from El-Ghannam, A.; Ning, C.; Mehta, J. *J. Biomed. Mater. Res. A* **2004**, *71*(3), 377–390, with permission from Wiley.

1.109.8.3.2. Effect of structure and composition on bone cell function and tissue formation

The effect of silica-rich SCPC compounds on bone cell function and tissue formation is related to the two crystalline phases that make up the material; β-$NaCaPO_4$ ss and

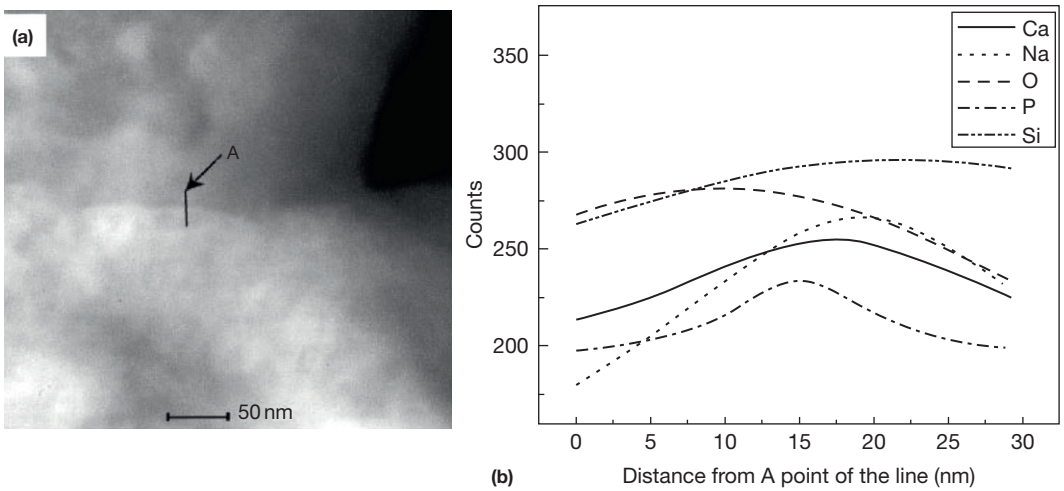

Figure 26 (a) A grain boundary in the SCPC nanocomposite. (b) Lorentzian fitting curves of elemental distributions along the grain boundary in (a). X-ray microanalysis showed that the grain boundary had maximum counts for Ca, Na, and P, whereas the grain bulk was rich in Si. These results indicate that calcium-phosphate–containing phases preferred to distribute along the boundaries between silica grains. Reproduced from El-Ghannam, A.; Ning, C.; Mehta, J. *J. Biomed. Mater. Res. A* **2004**, *71*(3), 377–390, with permission from Wiley.

α-cristobalite (SiO_2) ss. β-$NaCaPO_4$ ss phase has enhanced bioactivity compared to other calcium phosphate phases including TCP due to the presence of the labile sodium (Na), which can easily be exchanged with a proton in the aqueous physiological solution, rendering the surface biologically active thereby promoting osteogenesis and matrix calcification.[6]

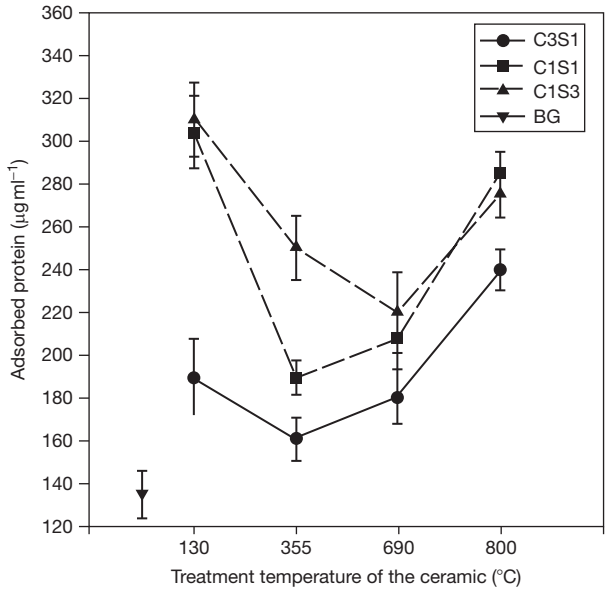

Figure 27 Total protein analysis showed that SCPC adsorbed a significantly higher amount of serum protein than bioactive glass ($p < 0.00001$). Silica-rich C1S3 (SCPC75) adsorbed significantly higher amounts of serum protein than calcium phosphate-rich C3S1 (SCPC25) ($p < 0.003$). The XRD structures of the SCPC ceramics after each thermal treatment are found in [6]. These results indicate that the porosity and modified crystalline structure of silica-rich SCPC enhanced protein adsorption. Reproduced from El-Ghannam A. *J. Biomed. Mater. Res. A* **2004**, *69*(3), 490–501, with permission from Wiley.

As is described in Chapter 1.114, Bioactivity: Mechanisms. It has been shown that β-$NaCaPO_4$ has stimulatory effect on the differentiation of human bone-derived cells, inducing mRNA and protein expression of osteopontin, osteocalcin, osteonectin, and bone sialoprotein, suggesting later osteoblast differentiation.[97,98] In terms of bioresorption, β-$NaCaPO_4$ ss contains Na ions that weaken the bond between Ca^{2+} and the PO_4^{3-} in the crystal surface and, hence, facilitate solution-mediated resorption. Previous studies reported that β-$NaCaPO_4$ has improved bioactivity compared to HA due to its higher rate of solubility in the body.[99,100] Because of its enhanced solubility, β-$NaCaPO_4$ ss can act as a weak interphase for α-cristobalite ss and provide an easy path for structure debonding of SCPC, which facilitates silica dissolution as demonstrated in Figure 4(a). In conjunction with the enhanced silica release, rapid bone regeneration was observed.

SCPC is characterized by high porosity with a unique hierarchical porous structure (50 nm–650 mm) as shown in Figure 28(a) and 28(b).[92] Previous *in vivo* and *in vitro* studies have shown that protein adsorption and cell adhesion increase manyfold when in contact with porous nanobiomaterials compared to in contact with conventional biomaterials.[101,102] The enhanced biological effects were attributed to the high surface area in contact with tissue fluids and cells.

1.109.9. Silica-Xerogel

Earlier in this chapter we described bioactive glass prepared by the sol–gel processing routes. Essential processing steps were drying typically at about 100 °C and sintering in the temperature range 350–700 °C. Sol–gel processing as a processing methodology has existed for a long time.[103] This method has also been pursued to controlled release materials, as described in Chapter 4.428, Sol–Gel Processed Oxide Controlled Release Materials. A critical aspect of the overall processing is to omit any heat treatment steps that would damage the biological

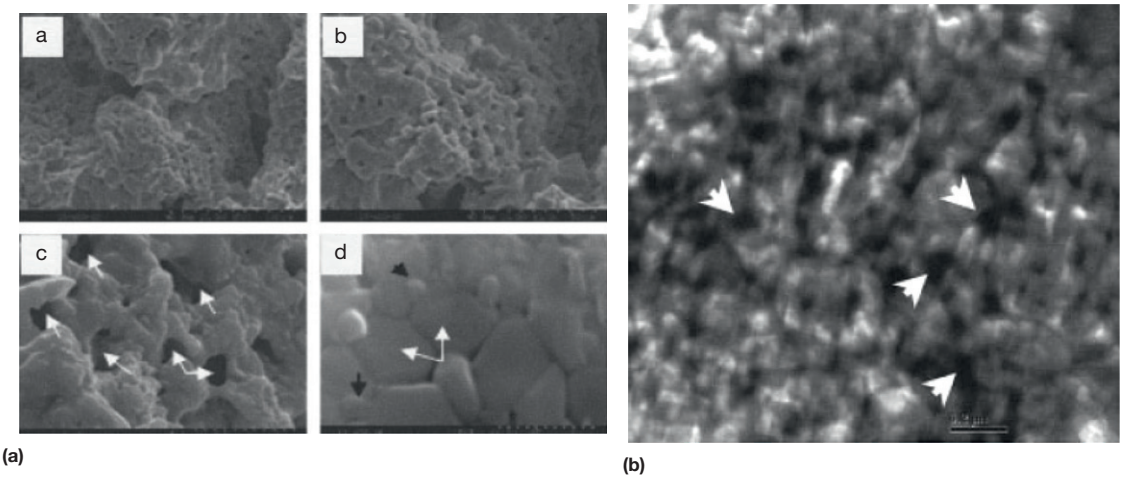

Figure 28 (a) SEM micrographs of the SCPC at different magnifications. (a) Two pores 100 μm in diameter on the surface of the material. (b) The walls of the large pores are very porous. (c) Higher magnification of the wall of the pores demonstrating homogeneously distributed interconnected pores 3 μm in diameter (arrows). (d) Single hexagonal calcium phosphate crystals (0.7 μm) (white arrows) and round-shaped silica crystals (0.2 μm) (black arrows) are in intimate interaction. (b) TEM micrograph of the porous structure of SCPC showing nanopores in the size range 50–100 nm (arrows). Reproduced from El-Ghannam, A.; Ning, C.; Mehta, J. *J. Biomed. Mater. Res. A* **2004**, *71*(3), 377–390, with permission from Wiley.

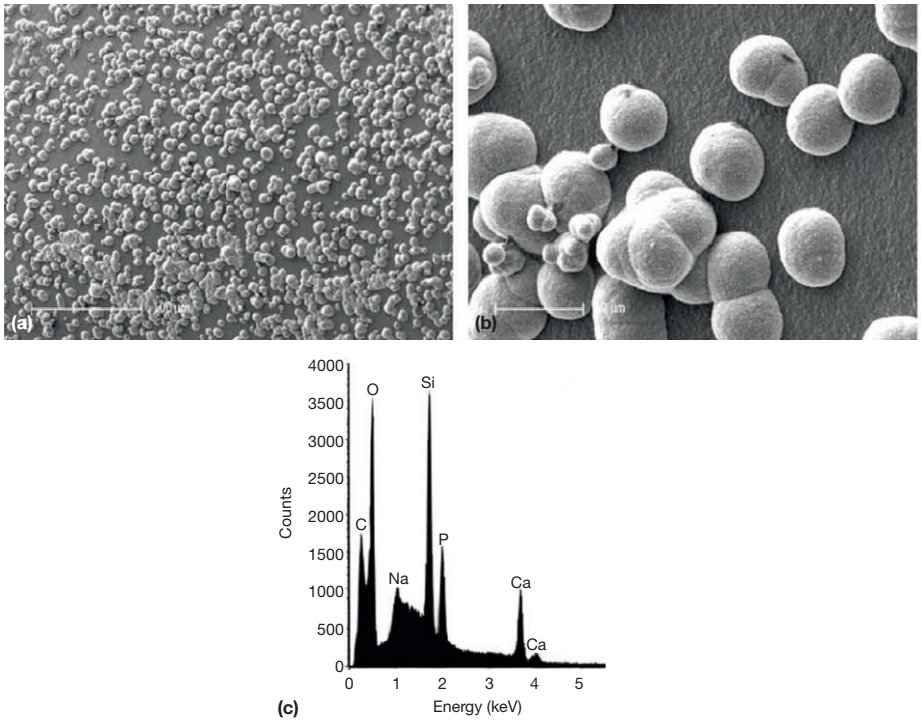

Figure 29 (a) SEM image of the silica xerogel surface after immersion in SBF for 7 days showing the formation of apatite crystals; (b) higher magnification of the apatite crystals. (c) EDX spectra of the surface showed a Ca/P ratio of 1.61 confirming the presence of apatite. Reproduced from Heinemann, S.; Heinemann, C.; Bernhardt, R.; *et al*. *Acta Biomater*. **2009**, *5*(6), 1979–1990, with permission from Elsevier.

function of the molecules being incorporated. By and large, processing conditions also have to be modified from those for synthesizing sintered bioactive glass, in order to achieve release kinetics appropriate for the intended uses. Sol–gel processed materials that are not heat treated are also called xerogels.

Silica xerogels has a highly porous matrix. The nanostructure of silica xerogels can be controlled in various ways, including modifying the molecular ratio of water to alkoxides, such as TEOS and TMOS and by type of catalyst, or by thermal treatment of the xerogels.[104–111]

It is interesting to address whether these materials can have bioactive properties. Various silica xerogels have been studied. They included a 100% silica and silica xerogels with various amounts of Ca and P oxides. Immersion of sol–gel derived silica xerogels in SBF resulted in the precipitation of a HA layer on the material surface.[112–114] Silica xerogel cylinders were immersed in 1× modified SBF.[114,115] The solution was exchanged every 24 h to ensure constant ion concentration and a pH of 7.4. After 7 days of immersion, SEM analyses (**Figure 29(a)** and **29(b)**) showed apatite formation on the material surface.[114] EDX spectroscopy revealed the Ca/P ratio on the surface to be 1.61 (**Figure 29(c)**), which was close to that of HA (Ca/P = 1.67).[114] The formation of the HA layer was attributed to the presence of a large number of silanol groups (Si–OH) on the material surface. The reaction of surface silanols with phosphate is thought to lead to complexation of both phosphate and calcium ions through heterogeneous nucleation.[116] Addition of minor concentrations of Ca and P oxides to silica xerogels accelerated the deposition of the HA layer onto the material surface. FTIR analyses showed a more intense band characteristic for Si–OH group in the Ca-P containing xerogels.[112] In conjunction of the higher expression of the Si–OH group on the material surface, all Ca-P containing xerogels showed a deposition of a HA layer within 24 h. The enhanced precipitation and growth of HA at the surface of Ca-P containing xerogels was preceded by calcium and phosphate release from the xerogels that contained it, and which resulted in supersaturation of the solution.

Other studies have correlated the amount of apatite precipitation on Ca-containing xerogels to the ionic product (IP) of HA.[113] The IP of the HA can be defined as:

$$\mathrm{IP} = \gamma\left(\mathrm{Ca}^{2+}\right)^{10}\gamma\left(\mathrm{PO}_4^{3-}\right)^{6}\gamma\left(\mathrm{OH}^{-}\right)^{2} \times \left[\mathrm{Ca}^{2+}\right]^{10}\left[\mathrm{PO}_4^{3-}\right]^{6}\left[\mathrm{OH}^{-}\right]^{2}$$

where γ is the activity coefficient. $\gamma(\mathrm{Ca}^{2+})$, $\gamma(\mathrm{PO}_4^{3-})$, and $\gamma(\mathrm{OH}^{-})$ at physiological ionic strength are 0.36, 0.06, and 0.72 respectively. The solubility product (K_{sp}) of the HA in an aqueous solution is $10^{-117.2}$ at 37 °C. After soaking silica xerogels containing various Ca contents, all immersing solutions were supersaturated with variable degrees depending on the Ca concentration released from the material during immersion. As the Ca content in the silica xerogel increased, the initial Ca ion concentration of the solution rose, which promoted the early deposition of apatite.

1.109.10. Conclusion

Bioactive ceramics have chemical reactivity in favor of cell function and tissue formation. Ions released from bioactive

ceramics such as Ca and Si have a stimulatory effect on bone cell function and tissue formation. Therefore, the level of bioactivity of ceramic implants depends on the enhanced and controlled solubility of the material. Amorphous bioactive materials have open structure, which facilitates ion release and bioactivity reactions at the interface with tissue fluids and cells. The bioactivity and resorbability of the amorphous bioactive glass is controlled by the atomic bond strength of the material. For crystalline bioactive ceramics the bioactivity and resorbability depend on the atomic arrangement in addition to the atomic bond strength. Parameters such as crystal size, shape, and impurity can be engineered to enhance the bioactivity and resorbability of calcium phosphate ceramics. The SCPCs are designed with modified crystalline phases in the form of solid solutions. The modified crystalline structure and porosity of the material induced excellent bioactivity and resorbability properties.

Immersion of bioactive ceramics in SBF results in the formation of a surface Ca-P layer relatively similar to the mineral phase of bone. The prior formation of this layer stimulated bone cell differentiation and tissue formation. The advantage of the Ca-P layer is twofold: it provides bone cells with a ready meal of calcium ions and it enhances selective adsorption of serum FN, an attachment protein known to enhance bone cell adhesion and function. The mechanism of bioactivity *in vivo* is complicated by the presence of high protein concentration and the presence of multiple kinds of cells. Both proteins and cells interfere with the precipitation of the Ca-P layer on the bioactive ceramic surface. Employment of sol–gel techniques to process bioactive ceramics has enhanced the bioactivity and resorbability properties of the material. Bioactive ceramics prepared by the sol–gel method are highly porous and can be used as a scaffold for drug delivery. Most bioactive ceramics are brittle materials and cannot be used as load bearing orthopedic implants. Bioactive glass ceramic and silica-calcium phosphate nano composite have high mechanical properties suitable for load bearing.

References

1. El-Ghannam, A.; Ning, C. *J. Biomed. Mater. Res. A* **2006**, *76*(2), 386–397.
2. Hench, L.; Andersson, O. In *An Introduction to Bioceramics*; Hench, L. L., Wilson, J., Eds.; World Scientific: Singapore, 1993; p 41.
3. Ooms, E.; Wolke, J.; Van de Heuvel, M.; Jeschke, B.; Jansen, J. *Biomaterials* **2003**, *24*(6), 989–1000.
4. Ducheyne, P.; Qiu, Q. *Biomaterials* **1999**, *20*(23–24), 2287–2303.
5. Pietak, A.; Reid, J.; Stott, M.; Sayer, M. *Biomaterials* **2007**, *28*(28), 4023–4032.
6. El-Ghannam, A. *J. Biomed. Mater. Res. A* **2004**, *69*(3), 490–501.
7. El-Ghannam, A. *Expert Rev. Med. Devices* **2005**, *2*(1), 87–101.
8. Mastrogiacomo, M.; Scaglione, S.; Martinetti, R.; *et al*. *Biomaterials* **2006**, *27*(17), 3230–3237.
9. Le Nihouannen, D.; Daculsi, G.; Saffarzadeh, A.; *et al*. *Bone* **2005**, *36*(6), 1086–1093.
10. Kokubo, T. *Biomaterials* **1991**, *12*(2), 155–163.
11. Kokubo, T.; Takadama, H. *Biomaterials* **2006**, *27*(15), 2907–2915.
12. Radin, S.; Ducheyne, P.; Falaize, S.; Hammond, A. *J. Biomed. Mater. Res. A* **2000**, *49*(2), 264–272.
13. Radin, S.; Ducheyne, P. *J. Biomed. Mater. Res. A* **1996**, *30*(3), 273–279.
14. Gupta, G.; Kirakodu, S.; El-Ghannam, A. *J. Biomed. Mater. Res. A* **2007**, *80*(2), 486–496.
15. Lu, H.; Pollack, S.; Ducheyne, P. *J. Biomed. Mater. Res. A* **2000**, *51*(1), 80–87.
16. Hench, L.; Splinter, R.; Allen, W.; Greenlee, T. *J. Biomed. Mater. Res.* **1971**, *5*(6), 117–141.
17. Hench, L. *J. Am. Ceram. Soc.* **1991**, *74*(7), 1487–1510.
18. Gross, U.; Strunz, V. *J. Biomed. Mater. Res.* **1985**, *19*(3), 251–271.
19. Filgueiras, M.; La Torre, G.; Hench, L. *J. Biomed. Mater. Res.* **1993**, *27*(12), 1485–1493.
20. El-Ghannam, A.; Ducheyne, P.; Shapiro, I. *J. Biomed. Mater. Res.* **1995**, *29*(3), 359–370.
21. El-Ghannam, A.; Ducheyne, P.; Shapiro, I. *J. Biomed. Mater. Res. A* **1997**, *36*(2), 167–180.
22. El-Ghannam, A.; Ducheyne, P.; Shapiro, I. *J. Orthop. Res.* **1999**, *17*(3), 340–345.
23. FitzGerald, V.; Martin, R.; Jones, J.; *et al*. *J. Biomed. Mater. Res. A* **2009**, *91*(1), 76–83.
24. Freyman, T.; Yannas, I.; Gibson, L. *Prog. Mater. Sci*. **2001**, *46*(3–4), 273–282.
25. Jones, J.; Hench, L. *J. Biomed. Mater. Res. B Appl. Biomater.* **2004**, *68*(1), 36–44.
26. Jones, J.; Hench, L. *J. Mater. Sci*. **2003**, *38*(18), 3783–3790.
27. Jones, J.; Ehrenfried, L.; Hench, L. *Biomaterials* **2006**, *27*(7), 964–973.
28. Gough, J.; Jones, J.; Hench, L. *Biomaterials* **2004**, *25*(11), 2039–2046.
29. Höland, W.; Vogel, W. In *An Introduction to Bioceramics*, pp 125–137.
30. El-Ghannam, A.; Hamazawy, E.; Yehia, A. *J. Biomed. Mater. Res.* **2001**, *55*(3), 387–395.
31. Buchanan, L.; El-Ghannam, A. *J. Biomed. Mater. Res. A* **2010**, *93*(2), 537–546.
32. Kannan, S.; Goetz Neunhoeffer, F.; Neubauer, J.; Ferreira, J. *J. Am. Ceram. Soc.* **2008**, *91*(1), 1–12.
33. Zahn, D.; Hochrein, O. *J. Solid State Chem.* **2008**, *181*(8), 1712–1716.
34. Hughes, J.; Rakovan, J. *Rev. Mineral. Geochem.* **2002**, *48*(1), 1.
35. Cho, G.; Wu, Y.; Ackerman, J. *Science* **2003**, *300*(5622), 1123.
36. Dorozhkin, S.; Epple, M. *Angew. Chem.* **2002**, *114*(17), 3260–3277.
37. LeGeros, R.; LeGeros, J. In *An Introduction to Bioceramics*, World Scientific: Singapore, 1993; pp 139–180.
38. Asaoka, N.; Best, S.; Knowles, J.; Bonfield, W. *Bioceramics* **1995**, *8*, 331–337.
39. Toriyama, M.; Ravaglioli, A.; Krajewski, A.; Celotti, G.; Piancastelli, A. *J. Eur. Ceram. Soc.* **1996**, *16*(4), 429–436.
40. Santos, M.; Oliveira, M.; Souza, L.; Mansur, H.; Vasconcelos, W. *Mater. Res.* **2004**, *7*, 625–630.
41. Rapacz-Kmita, A.; Paluszkiewicz, C.; Slosarczyk, A.; Paszkiewicz, Z. *J. Mol. Struct.* **2005**, *744*, 653–656.
42. Andronescu, E.; Tefan, E.; Dinu, E.; Ghitulica, C. *Key Eng. Mater.* **2001**, *206*, 1595–1598.
43. Rodriguez-Lorenzo, L.; Vallet-Regi, M. *Chem. Mater.* **2000**, *12*(8), 2460–2465.
44. Rodriguez-Lorenzo, L.; Vallet-Regí, M.; Ferreira, J. *Biomaterials* **2001**, *22*(6), 583–588.
45. Raynaud, S.; Champion, E.; Bernache-Assollant, D.; Thomas, P. *Biomaterials* **2002**, *23*(4), 1065–1072.
46. Arends, J.; Christoffersen, J.; Christoffersen, M.; *et al*. *J. Cryst. Growth* **1987**, *84*(3), 515–532.
47. Ahn, E.; Gleason, N.; Nakahira, A.; Ying, J. *Nano Lett.* **2001**, *1*(3), 149–153.
48. Afshar, A.; Ghorbani, M.; Ehsani, N.; Saeri, M.; Sorrell, C. *Mater. Des.* **2003**, *24*(3), 197–202.
49. Fulmer, M.; Brown, P. *J. Mater. Res.* **1993**, *8*(7), 1687–1696.
50. Lazi, S.; Zec, S.; Miljevi, N.; Milonji, S. *Thermochim. Acta* **2001**, *374*(1), 13–22.
51. Prakash, K.; Ooi, C.; Kumar, R.; Khor, K.; Cheang, P. In *Proceedings of Emerging Technologies – Nanoelectronics: IEEE*, 2006 pp 345–349.
52. Guo, L.; Huang, M.; Zhang, X. *J. Mater. Sci. Mater. Med.* **2003**, *14*(9), 817–822.
53. Earl, J.; Wood, D.; Milne, S. *J. Phys. Conf. Ser.* **2006**, *26*, 268–271.
54. Ioku, K.; Kawachi, G.; Sasaki, S.; Fujimori, H.; Goto, S. *J. Mater. Sci.* **2006**, *41*(5), 1341–1344.
55. Suchanek, W.; Yoshimura, M. *J. Mater. Res.* **1998**, *13*(1), 94–117.
56. Kannan, S.; Ventura, J.; Ferreira, J. *Ceram. Int.* **2007**, *33*(4), 637–641.
57. Yoshida, K.; Hyuga, H.; Kondo, N.; *et al*. *J. Am. Ceram. Soc.* **2006**, *89*(2), 688–690.
58. Yashima, M.; Sakai, A.; Kamiyama, T.; Hoshikawa, A. *J. Solid State Chem.* **2003**, *175*(2), 272–277.
59. Wei, X.; Akinc, M. *J. Am. Ceram. Soc.* **2007**, *90*(9), 2709–2715.
60. Cuneyt Tas, A.; Korkusuz, F.; Timucin, M.; Akkas, N. *J. Mater. Sci. Mater. Med.* **1997**, *8*(2), 91–96.
61. Viswanath, B.; Raghavan, R.; Gurao, N.; Ramamurty, U.; Ravishankar, N. *Acta Biomater.* **2008**, *4*(5), 1448–1454.
62. Dos Santos, E.; Farina, M.; Soares, G.; Anselme, K. *J. Mater. Sci. Mater. Med.* **2008**, *19*(6), 2307–2316.
63. Loher, S.; Stark, W.; Maciejewski, M.; *et al*. *Chem. Mater.* **2005**, *17*(1), 36–42.
64. Loher, S.; Reboul, V.; Brunner, T.; *et al*. *Nanotechnology* **2006**, *17*, 2054.

65. Ito, A.; Senda, K.; Sogo, Y.; Oyane, A.; Yamazaki, A.; LeGeros, R. *Biomed. Mater.* **2006**, *1*, 134.
66. Bigi, A.; Foresti, E.; Gandolfi, M.; Gazzano, M.; Roveri, N. *J. Inorg. Biochem.* **1997**, *66*(4), 259–265.
67. Banerjee, S.; Tarafder, S.; Davies, N.; Bandyopadhyay, A.; Bose, S. *Acta Biomater.* **2010**, *6*, 4167–4174.
68. Shi, D.; Jiang, G.; Bauer, J. *J. Biomed. Mater. Res. B Appl. Biomater.* **2002**, *63*(1), 71–78.
69. Gineste, L.; Gineste, M.; Ranz, X.; *et al. J. Biomed. Mater. Res. B Appl. Biomater.* **1999**, *48*(3), 224–234.
70. Kaplan, F.; Hayes, W.; Keaveny, T.; Boskey, A.; Einhorn, T.; Iannotti, J. In *Orthopaedic Basic Science*; Simon, S. R., Ed.; American Academy of Orthopaedic Surgeons: Rosemont, IL, 1994; pp 127–185.
71. Porter, A.; Patel, N.; Skepper, J.; Best, S.; Bonfield, W. *Biomaterials* **2003**, *24*(25), 4609–4620.
72. Webster, T.; Ergun, C.; Doremus, R.; Bizios, R. *J. Biomed. Mater. Res.* **2002**, *59*(2), 312–317.
73. Tian, J.; Zhang, S.; Shao, Y.; Shan, H. In *Proceedings of the Bioceramics: Materials and Applications II Symposium*, 1995 pp 107–114.
74. Serre, C.; Papillard, M.; Chavassieux, P.; Voegel, J.; Boivin, G. *J. Biomed. Mater. Res. A* **1998**, *42*(4), 626–633.
75. Ducheyne, P.; Radin, S.; King, L. *J. Biomed. Mater. Res.* **1993**, *27*(1), 25–34.
76. Duheyne, P.; Beight, J.; Cuckler, J.; Evans, B.; Radin, S. *Biomaterials* **1990**, *11*(8), 531–540.
77. De Bruijn, J.; Bovell, Y.; Van Blitterswijk, C. *Biomaterials* **1994**, *15*(7), 543–550.
78. Wassell, D.; Hall, R.; Embery, G. *Biomaterials* **1995**, *16*(9), 697–702.
79. Yongli, C.; Xiufang, Z.; Yandao, G.; Nanming, Z.; Tingying, Z.; Xinqi, S. *J. Colloid Interface Sci.* **1999**, *214*(1), 38–45.
80. Luo, Q.; Andrade, J. *J. Colloid Interface Sci.* **1998**, *200*(1), 104–113.
81. Kilpadi, K.; Chang, P.; Bellis, S. *J. Biomed. Mater. Res.* **2001**, *57*(2), 258–267.
82. Jensen, S.; Broggini, N.; Hj, H. E.; Schenk, R. K.; Buser, D. *Clin. Oral Implants Res.* **2006**, *17*, 237–243.
83. Okuda, T.; Ioku, K.; Yonezawa, I.; *et al. Biomaterials* **2007**, *28*(16), 2612–2621.
84. Xin, R.; Leng, Y.; Chen, J.; Zhang, Q. *Biomaterials* **2005**, *26*(33), 6477–6486.
85. Juhasz, J.; Best, S.; Auffret, A.; Bonfield, W. *J. Mater. Sci. Mater. Med.* **2008**, *19*(4), 1823–1829.
86. Ribeiro, C.; Rigo, E.; Sepulveda, P.; Bressiani, J.; Bressiani, A. *Mater. Sci. Eng. C* **2004**, *24*(5), 631–636.
87. Chazono, M.; Tanaka, T.; Kitasato, S.; Kikuchi, T.; Marumo, K. *J. Orthop. Sci.* **2008**, *13*(6), 550–555.
88. Kondo, N.; Ogose, A.; Tokunaga, K.; *et al. Biomaterials* **2005**, *26*(28), 5600–5608.
89. Tang, R.; Wu, W.; Haas, M.; Nancollas, G. *Langmuir* **2001**, *17*(11), 3480–3485.
90. Kubarev, O.; Komlev, V.; Maitz, M.; Barinov, S. *Dokl. Chem.* **2007**, *413*(1), 72–74.
91. Zhu, X.; Zhang, H.; Fan, H.; Li, W.; Zhang, X. *Acta Biomater.* **2010**, *6*(4), 1536–1541.
92. El-Ghannam, A.; Ning, C.; Mehta, J. *J. Biomed. Mater. Res. A* **2004**, *71*(3), 377–390.
93. Liu, X.; Ei-Ghannam, A. *J. Mater. Sci. Mater. Med.* **2010**, *21*, 2087–2094.
94. Ohta, K.; Monma, H.; Takahashi, S. *J. Biomed. Mater. Res.* **2001**, *55*(3), 409–414.
95. Latour, R., Jr.; Rini, C. *J. Biomed. Mater. Res.* **2002**, *60*(4), 564–577.
96. Berry, L.; Mason, B.; Dietrich, R. In *Mineralogy: Concepts, Descriptions, Determinations*; Dietrich, R. V., Ed.; W. H. Freeman: New York, 1983.
97. Berger, G.; Gildenhaar, R.; Ploska, U. *Bioceramics* **1995**, *453*.
98. Knabe, C.; Berger, G.; Gildenhaar, R.; Howlett, C.; Markovic, B.; Zreiqat, H. *Biomaterials* **2004**, *25*(2), 335–344.
99. Kangasniemi, I.; Vedel, E.; de Blick-Hogerworst, J.; Yli-Urpo, A.; De Groot, K. *J. Biomed. Mater. Res.* **1993**, *27*(10), 1225–1233.
100. Kangasniemi, I.; Groot, K.; Wolke, J.; *et al. J. Mater. Sci. Mater. Med.* **1991**, *2*(3), 133–137.
101. Webster, T.; Ergun, C.; Doremus, R.; Siegel, R.; Bizios, R. *J. Biomed. Mater. Res. A* **2000**, *51*(3), 475–483.
102. Webster, T.; Ejiofor, J. *Biomaterials* **2004**, *25*(19), 4731–4739.
103. Brinker, C. J.; Scherer, G. W. In *Sol–Gel Science*; Brinker, C. J., Scherer, G. W., Eds.; Academic Press: New York, 1989.
104. Curran, M.; Stiegman, A. *J. Non Cryst. Solids* **1999**, *249*(1), 62–68.
105. Ro, J.; Chung, I. *J. Non Cryst. Solids* **1991**, *130*(1), 8–17.
106. Kortesuo, P.; Ahola, M.; Kangas, M.; Yli-Urpo, A.; Kiesvaara, J.; Marvola, M. *Int. J. Pharm.* **2001**, *221*(1–2), 107–114.
107. Czarnobaj, K.; Czarnobaj, J. *J. Biomed. Mater. Res. B Appl. Biomater.* **2008**, *87*(1), 114–120.
108. Ahola, M.; Kortesuo, P.; Kangasniemi, I.; Kiesvaara, J.; Yli-Urpo, A. *Int. J. Pharm.* **2000**, *195*(1–2), 219–227.
109. Nicoll, S.; Radin, S.; Santos, E.; Tuan, R.; Ducheyne, P. *Biomaterials* **1997**, *18*(12), 853–859.
110. Santos, E.; Radin, S.; Shenker, B.; Shapiro, I.; Ducheyne, P. *J. Biomed. Mater. Res. A* **1998**, *41*(1), 87–94.
111. Falaize, S.; Radin, S.; Ducheyne, P. *J. Am. Ceram. Soc.* **1999**, *82*(4), 969–976.
112. Radin, S.; Falaize, S.; Lee, M.; Ducheyne, P. *Biomaterials* **2002**, *23*(15), 3113–3122.
113. Wu, X.; Wei, J.; Lu, X.; *et al. Biomed. Mater.* **2010**, *5*, 035006.
114. Heinemann, S.; Heinemann, C.; Bernhardt, R.; *et al. Acta Biomater.* **2009**, *5*(6), 1979–1990.
115. Oyane, A.; Kim, H.; Furuya, T.; Kokubo, T.; Miyazaki, T.; Nakamura, T. *J. Biomed. Mater. Res. A* **2003**, *65*(2), 188–195.
116. Radin, S.; El-Bassyouni, G.; Vresilovic, E.; Schepers, E.; Ducheyne, P. *Biomaterials* **2005**, *26*(9), 1043–1052.

1.110. Bioactive Glass-Ceramics

R G Hill, Queen Mary, University of London, London, UK

© 2011 Published by Elsevier Ltd.

1.110.1.	AW Glass-Ceramic	181
1.110.2.	Apatite–Mica Glass-Ceramics	183
1.110.3.	Apatite–Mullite Glass-Ceramics	184
References		185

Abbreviations

AM	Apatite–mullite
AU	Arbitary units
AW	Apatite–wollastonite
CAD/CAM	Computer-aided design/computer-aided manufacturing
FAP	Fluorapatite
GDR	German Democratic Republic
HA	Hydroxyapatite
HCA	Hydroxycarbonated apatite
OA	Oxyapatite
SBF	Simulated body fluid
SEM	Scanning electron microscopy
SLS	Selectively laser sintered
VHN	Vickers hardness number
XRD	X-ray diffraction

Symbols

T_{Growth}	Crystal growth temperature
$T_{Nucleation}$	Nucleation temperature

Hydroxyapatite (HA) has been extensively studied as a bioceramic. HA is closely related to the mineral phase of bone and HA-based ceramics exhibit good biocompatibility and osseointegrate with bone. However, HA ceramics exhibit poor flexural strength typically below 100 MPa and low fracture toughness values typically <1.0 MPa $\sqrt{m}$ compared with cortical bone at ~ 6 MPa $\sqrt{m}$. Consequently, HA-based materials are generally used only as bone substitutes in low loaded situations. Another disadvantage of HAs is that they are produced by a sintering route and are prone to decomposition during sintering and it is difficult to form the complex shapes required for prostheses without resorting to subsequent machining using diamond tipped tooling.

Apatite glass-ceramics are an attractive alternative to sintered HAs. A glass-ceramic may be defined as a polycrystalline solid produced by the controlled crystallization of a glass. Two steps are involved in conversion of a glass to a glass-ceramic.

1. Nucleation
2. Crystal growth

The classic glass-ceramic processing route involves casting the glass to the desired shape followed by a two-step heat treatment. The first step involves crystal nucleation and the second crystal growth. The classic glass-ceramic processing route is shown in Figure 1. Figure 2 shows the rates of crystal nucleation and crystal growth as a function of temperature, and the nucleation temperature $T_{Nucleation}$ and the crystal growth temperature T_{Growth} are marked on the plot.

One of the advantages of this classic glass-ceramic processing route is the ease of forming complex shapes; another is the ability to control the volume fraction of crystal phase(s), size of crystals, microstructure, and residual glass phase composition.

There have been numerous studies of apatite-based glass-ceramics by the ceramics community; however, on very few of these apatite glass-ceramics is there any published information with regard to their biological behavior, either *in vitro* or *in vivo*. A notable exception is the apatite–wollastonite (AW) glass-ceramic.

1.110.1. AW Glass-Ceramic

In 1982, Kokubo *et al.*[1] found that the heat treatment and sintering of glass powder compacts in the system $CaO–MgO–SiO_2–P_2O_5–CaF_2$ resulted in a dense, homogeneous glass-ceramic composed of apatite and β-wollastonite crystals. This type of apatite–wollastonite has become known as AW glass-ceramics and has been very extensively studied (Figure 3). The commercially available material was based on a $SiO_2–P_2O_5–CaO–MgO–CaF_2$ glass of the composition expressed in weight percent as 34.0% SiO_2, 16.2% P_2O_5, 44.7% CaO, 4.6% MgO, and 0.5% CaF_2. This composition is given in mole percent in Table 1.

Favorable properties of this glass-ceramic include good mechanical strength and fracture toughness[2,3] and it possesses the ability to chemically bond with bone.[1,4,5] The mechanical properties of this glass-ceramic are summarized in Table 2.

As a result, the AW glass-ceramic has been used clinically in bone fillers and as a structural material in prosthetic applications.[1,6,7] However, it is important to note that this

glass-ceramic is processed not by the classic glass-ceramic route shown in Figure 1 by first forming the component in the glassy state, but by a sintering route. The glass is formed, ground to a fine powder, and then sintered. The small particle size and large surface area result in surface nucleation of a large number of small wollastonite crystals, which are restricted in size by the particle size.

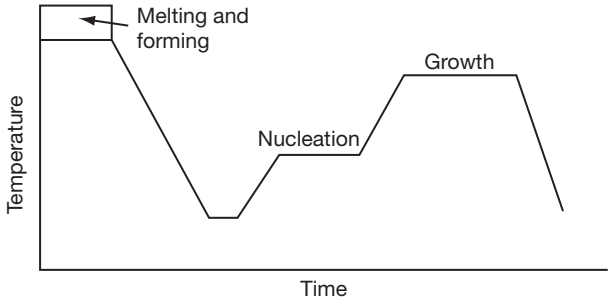

Figure 1 Controlled two-step crystallization process.

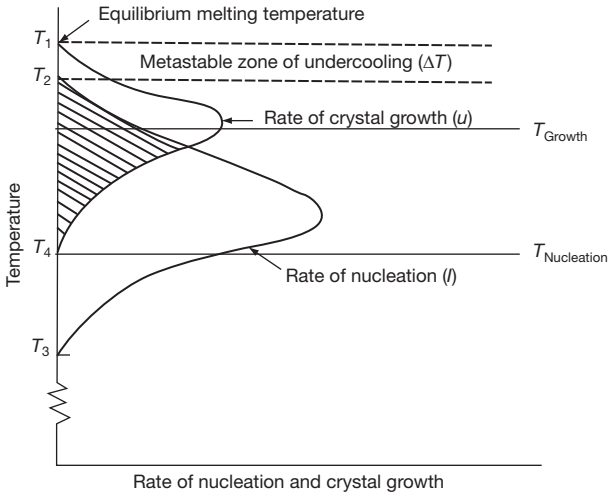

Figure 2 Nucleation and crystal growth rates.

Analysis of a cast bulk crystallized sample of AW glass-ceramic revealed that the surface nucleation and rapid growth of large β-wollastonite crystals caused internal cracks. A similar analysis of heat-treated powder compacts revealed that sintering and full densification occurs at a temperature much lower than the first crystallization temperature (~800 °C).[3] Cast AW components exhibited poor mechanical properties due to cracks at crystal boundaries. However, sintered AW components are difficult and expensive to machine, as a result of the hardness of the material. This made the fabrication of complex shapes required for prostheses expensive and as a result, the AW material is no longer produced commercially.

The apatite phase present in the AW glass-ceramic is thought to be a mixed fluorapatite (FAP)/oxyapatite (OA)/HA. However, as it is impossible to distinguish between these three forms of apatite easily by conventional X-ray diffraction (XRD), the exact nature of the apatite phase is unclear. Examination of the AW glass composition expressed in mole percent is enlightening. The Ca:P:F ratio is 7.03:1:0.05; thus, the composition is calcium rich with respect to the apatite stoichiometry (Ca:P = 1.67) and highly fluorine deficient with regard to the FAP $Ca_5(PO_4)_3F$ stoichiometry (P:F = 3:1). Only about one-sixth of the phosphorus present in the AW composition can be converted to FAP. Given that fluorine is frequently included in low dielectric loss glass compositions to drive out hydroxyl groups, the idea of FAP and HA or mixed hydroxy/FAP crystals being formed in the heat-treated AW glass-ceramic can be discounted. It is more likely, that the apatite present is FAP and OA or a solid solution of these two phases. It must be noted however that OA converts to HA in the presence of water and this may occur at the surface by reaction with atmospheric water prior to X-ray powder diffraction being carried out.

The most useful feature of the AW glass-ceramic is that it combines high bioactivity with good mechanical properties and consequently it has been used clinically for vertebral bodies and to replace bone in the iliac crest.

The final glass-ceramic following heat treatment contains in weight percent Wollastonite 28% ($CaO{\cdot}SiO_2$), Oxy/FAP 34 %

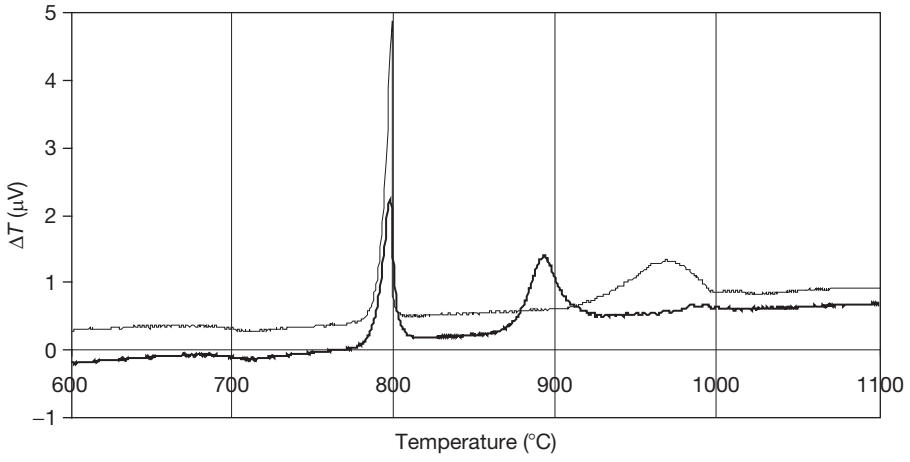

Figure 3 Differential thermal analysis traces of the apatite–wollastonite glass. The bold line indicates a particle size of <45 μm and the lighter line a particle size of 45–100 μm. The first peak corresponds to the crystallization of apatite and the second to apatite and wollastonite.

($Ca_{10}(PO_4)_6(O,F_2)$), and 28% glass of composition MgO 17%, CaO 24%, and SiO_2 59 % by weight.

Kokubo also developed a rapid method of ranking the bioactivity of bioactive ceramics. Kokubo and coworkers developed a simulated body fluid (SBF) solution of similar composition to that of human blood plasma. It was found that, when samples of the AW glass-ceramic were immersed in the SBF, a hydroxyl carbonated apatite layer formed on the surface and the rate at which this occurred could be correlated with the likely activity of the sample *in vivo*. Figure 4 shows a typical glancing angle XRD patterns before and after immersion in SBF of a bioactive glass showing the formation of hydroxycarbonated apatite (HCA) after soaking in SBF. The ability of the AW glass-ceramic to form HCA in SBF solution is thought to result largely from the dissolution of the residual glass phase, which is highly disrupted and has a network connectivity close to 2.0 and therefore would be expected to dissolve releasing calcium ions in a fashion similar to that of bioactive glass. A large number of studies have subsequently utilized Kokubo's SBF as a means of assessment of bioactivity and an ISO standard now exists for this test.

Other workers have developed machinable and castable apatite glass-ceramics, but these systems are based on alumina-containing compositions and release of small amounts of aluminum in soluble form is known to result in defective mineralization of osteoid. Care must be taken to ensure that no aluminum is present in soluble form in the final glass-ceramic. The machinable glass-ceramics are based on apatite and mica.

Table 1 Glass compositions studied in mole percent

Component/name	*MgO*	*CaO*	*SiO_2*	*P_2O_5*	*CaF_2*
AWK1	7.11	49.88	35.46	7.15	0.4

1.110.2. Apatite–Mica Glass-Ceramics

Apatite–mica glass-ceramics were developed as an alternative to the AW system by Vogel and coworkers. Mica glass-ceramics based on tetrasilicic micas and trisilicic mica phases are the basis of commercial machinable glass-ceramics for industrial

Table 2 Comparison of the physical properties of apatite glass-ceramics with cortical bone and hydroxyapatite

Glass-ceramic	*Crystal phases*	*Density*	*Thermal expansion coefficient ($\times 10^{-6}\,K^{-1}$)*	*Flexural strength (MPa)*	*Young's modulus (GPa)*	*Fracture toughness (MPa $\sqrt{m}$)*
Cortical bone	Substituted hydroxyapatite	2–3	–	100–200	7–20	5–7
HA	Hydroxapatite		–	60–120	70 GPa	0.8–1.05
AW	Apatite and wollastonite	3.07	8–10	215	118	2.0
Bioverit I	Apatite and mica	2.8	8–12	140–180	70–88	1.2–2.1
Bioverit II	Apatite and mica	2.5	8–12	90–140	70	1.2–1.8
Bioverit III	Apatite and $AlPO_4$	2.7–2.9	14–18	60–90	45	0.6
AM	Fluorapatite and mullite	2.7–3.3	8–10	90–330	70–90	1.0–3.3

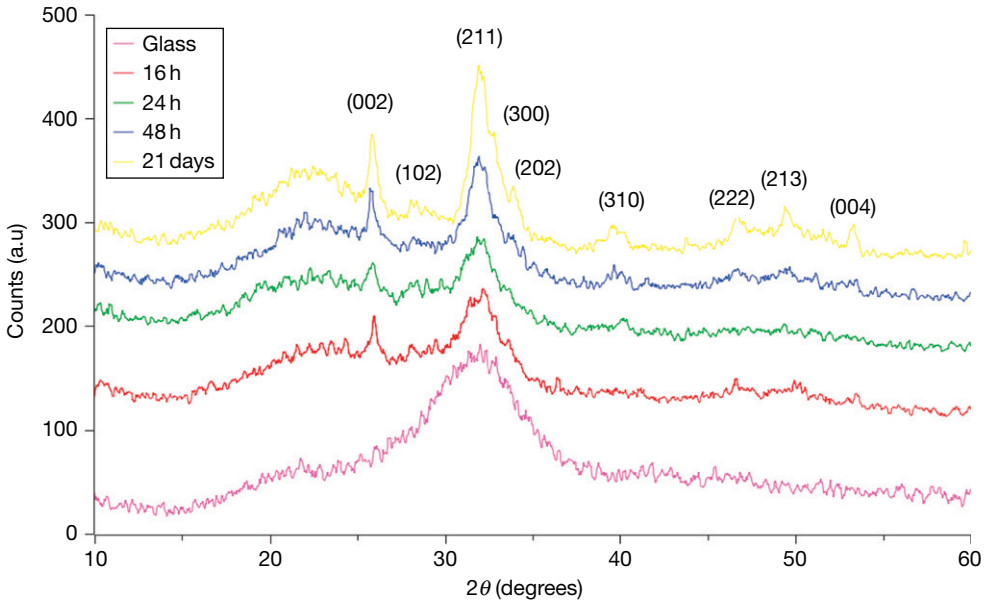

Figure 4 Formation of hydroxycarbonated apatite in simulated body fluid with time of immersion.

and dental applications. The incorporation of a mica phase is designed to impart machinability to the apatite–mica glass-ceramic. The mica phase is readily cleaved during fracture and redirects the propagating crack preventing catastrophic fracture during machining. However, in machinable glass-ceramics a high volume fraction >50% and an interconnected house-of-cards microstructure are required for good machinability. These materials have a low hardness typically <250 Vickers hardness number (VHN) which generally correlates with machinability. Incorporating a hard apatite phase will disrupt the interconnected mica crystal structure and will increase the hardness and result in much reduced machinability. Vogel and Hoeland produced two apatite–mica glass-ceramics Bioverit I and Bioverit II and one apatite–aluminum phosphate glass-ceramic. Bioverit III is based on a silica-free phosphate glass and exhibits mechanical properties inferior to dense HAs; consequently, it has not been studied in any great detail with regard to its *in vivo* behavior.

Bioverit I contains apatite crystals with a diameter of 1–2 μm and large mica crystals of 10–20 μm. The mica crystals can be trisilicic fluorphlogopite type $Mg_3(AlSi_3O10F_2)K/Na$ or tetrasilicic mica $Mg_3(Si_4O10F_2)K/Na$. Bioverit II consists of apatite crystals and curved fluorphlogopite mica crystals. One of the advantages of Bioverit I and II is that they can be shaped by the surgeon prior to implantation.

All three glass-ceramics exhibit high levels of osseointegration in animal implant experiments. All three glass-ceramics exhibit limited solubility. While data is available for Na^+, K^+, Ca^{2+}, Mg^{2+}, and PO_4^{3-} release from these materials, no data is available for Al^{3+} release. This poses a concern over the long-term release of aluminum from these materials.

Despite this concern, Bioverit I and Bioverit II were widely used in the former German Democratic Republic (GDR) and Bioverit I is marketed and sold today for custom made computer-aided design/computer-aided manufacturing (CAD/CAM) implants.

1.110.3. Apatite–Mullite Glass-Ceramics

Hill and coworkers[8–10] developed castable FAP-mullite glass-ceramics from the SiO_2–Al_2O_3–P_2O_5–CaO–CaF_2 system that bulk-nucleated, via prior amorphous phase separation. The needle-like apatite crystals in these materials give these glass-ceramics high fracture toughness and high strength.[8,11] The high aspect ratio of the FAP crystals which are thought to grow by a screw dislocation mechanism in the *c*-axis is thought to result in high fracture surface energies. Figure 5 shows a fracture surface showing the elongated nature of the hexagonal FAP crystals. The mechanical properties are superior to the AW system. These glass-ceramics can be readily cast to shape using a lost-wax casting process and can be used to form complex shapes

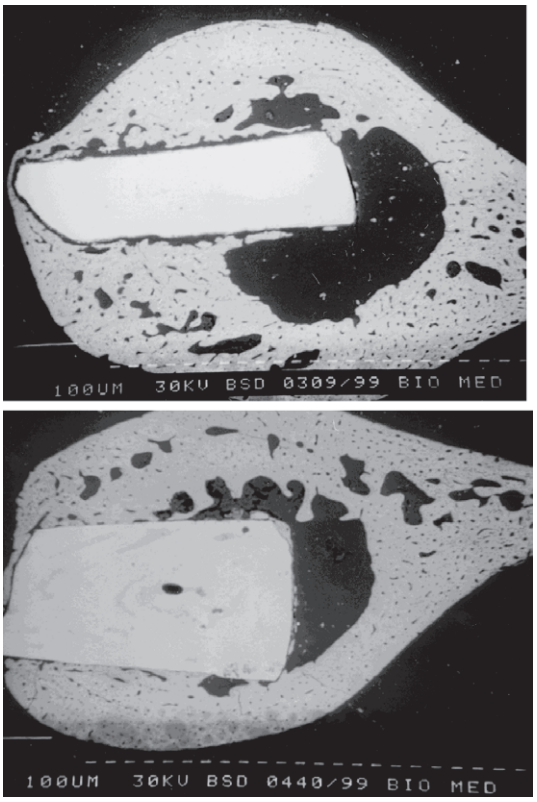

Figure 6 Backscattered scanning electron micrographs of implanted glass (top) and the implanted glass following crystallization to fluorapatite and mullite (bottom).

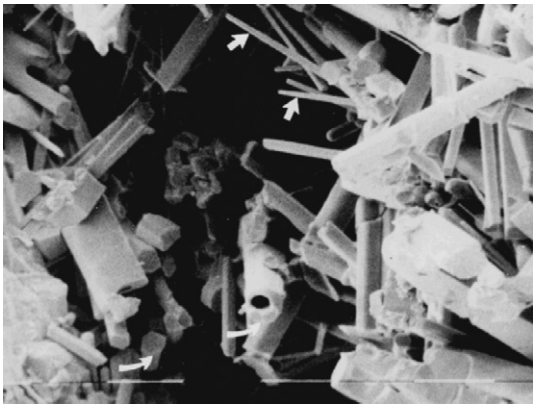

Figure 5 Scanning electron micrograph of elongated fluorapatite (FAP) crystals in a FAP glass-ceramic.

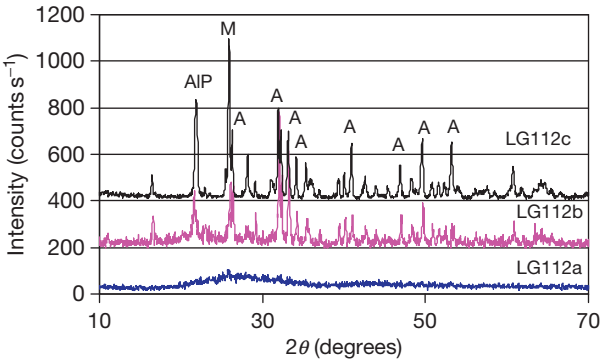

Figure 7 X-ray diffraction patterns of glass (LG112a), low temperature heat treatment (LG112b), and high temperature heat treatment (LG112c). A, FAP; M, mullite; and AlP, aluminum phosphate.

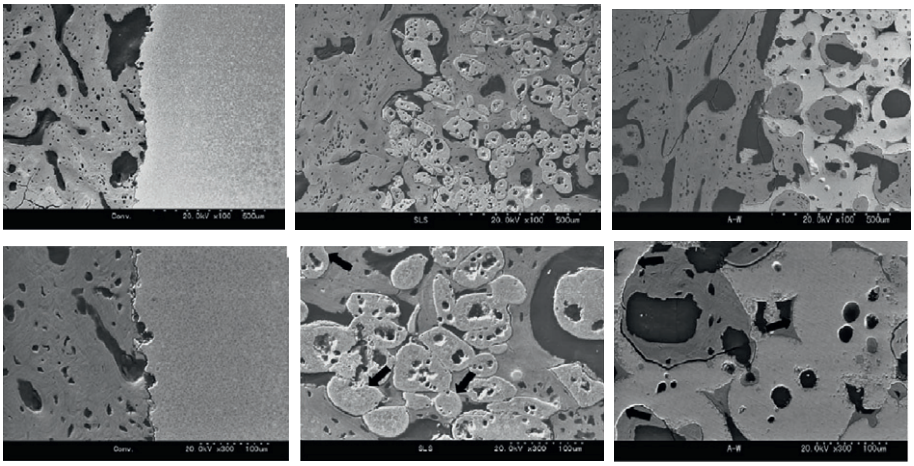

Figure 8 Scanning electron micrographs after 4 weeks of implantation of cast apatite–mullite glass-ceramic (Cast A–M), selectively laser sintered apatite–mullite glass-ceramic (SLS A–M), and apatite–wollastonite glass-ceramic (A–W). Micrographs courtesy of Ruth Goodridge.

with near-nett shapes, overcoming the drawbacks of the AW system. The second phase to form in these glass-ceramics is mullite ($2SiO_2{\cdot}3Al_2O_3$) which is chemically very stable and serves to lock away the aluminum in a chemically stable inert form. The glass-ceramics are chemically stable following appropriate heat treatment; the residual glass phase has a high network connectivity and low aluminum content, and is chemically stable. They do not release any aluminum ions into solution.

The glass-ceramics do not form HCA in Kokubo's SBF test but do osseointegrate *in vivo* without any apparent formation of a fibrous capsule layer. In contrast, some of the glasses are degradable and do form HCA in SBF but do not osseointegrate *in vivo*. An example of an apatite–mullite (AM) glass-ceramic implanted into the femur of a rat and the equivalent amorphous glass of exactly the same chemical composition are shown in Figure 6.

The AM glass-ceramic osseointegrates,[12] while the amorphous glass does not osseointegrate and has been fibrous encapsulated. Glass-ceramics, which crystallized to FAP, but which had not crystallized to mullite in addition to FAP, osseointegrated poorly. Figure 7 shows the XRD patterns for three samples that were implanted; LG112a is the amorphous glass. This sample did not osseointegrate at all. LG112b has been heat treated to give FAP and LG112c has been heat treated to give mullite and a small amount of aluminum phosphate (see also **Chapter 1.109, Bioactive Ceramics**; **Chapter 1.111, Bioactive Ceramics: Physical Chemistry**; **Chapter 1.112, Calcium Phosphate Coatings**; **Chapter 1.113, Bioactive Layer Formation on Metals and Polymers**; **Chapter 1.114, Bioactivity: Mechanisms**; **Chapter 1.115, Calcium Phosphates for Cell Transfection**; **Chapter 4.430, Silica-Based Mesoporous Nanospheres**; **Chapter 1.116, Bioactive Ceramics: Cements**; and **Chapter 1.117, Phosphate-Based Glasses**. LG112b osseointegrated poorly while LG112c exhibited better osseointegration and evidence of osteoconduction from the marrow cavity. It is clear that the presence of FAP can give rise to osseointegration provided there is no release of aluminum.

Goodridge *et al.*[13] investigated both AM glass-ceramics and AW glass-ceramics in the same *in vivo* implant study in the tibae of rabbits. In addition, they also studied the porous selectively laser sintered (SLS) samples for use as tissue-engineered scaffolds. The AM glass-ceramics also did not form HCA after immersion in SBF, nor was there any pH change following immersion and no significant ion release into the SBF solution. Any Al release was below the background levels found in the SBF solution of ~0.2 ppm.

Figure 8 shows the scanning electron micrographs. The cast and heat treated AM glass-ceramic osseointegrates, as does the porous selectively sintered AM glass-ceramic.

The *in vivo* response of apatite glass-ceramics and their ability to stimulate bone formation and to osseointegrate can be summarized as follows:

The *in vivo* response depends on the presence of the apatite phase and the residual glass phase. Increasing the apatite volume fraction in the glass appears to increase the osseointegration. The residual glass phase may add to the osseointegration by promoting apatite formation or may hinder osseointegration if the glass phase degrades and releases ions such as Al^{3+} that are known to inhibit biological mineralization. In the case of aluminum-containing glass-ceramic compositions, it is important that all the aluminum is either locked away in either a chemically inert glass phase or a chemically inert crystalline phase as even trace amounts of the order of 1 ppm of aluminum are known to inhibit the mineralization of the newly forming osteoid.[14]

The SBF test developed by Kokubo is widely used as a predictor of bioactivity and the ability of a bioceramic to osseointegrate. While this test is of value for bioactive glasses and AW glass-ceramics, its value with regard to aluminum-containing glasses and glass-ceramics must be questioned.

References

1. Kokubo, T.; Nagashima, Y.; Tashiro, M. *J. Jpn. Ceram. Soc.* **1982**, *90*, 151.
2. Kokubo, T.; Ito, T. S.; Sakka, S.; Yamamuro, T. *J. Mater. Sci.* **1986**, *21*, 536.
3. Kokubo, T.; Ito, S.; Shigematsu, M.; Sakka, S.; Yamamuro, T. *J. Mater. Sci.* **1985**, *20*, 2001.
4. Ono, K.; Yamuro, T.; Nakamura, T.; Kokubo, T. *Biomaterials* **1990**, *11*, 265–271.

5. Kokubo, T.; Kushitani, H.; Ohtsuki, C.; Sakka, S.; Yamamuro, T. *J. Mater. Sci. Mater. Med.* **1992**, *3*, 79–83.
6. Nakamura, T.; Yamamuro, T.; Higashi, S.; Kokubo, T.; Ito, A. *J. Biomed. Mater. Res.* **1985**, *19*, 685–698.
7. Ono, K.; Yamamuro, T.; Nakamura, T.; Kakutani, Y.; Kitsugi, T.; Kokubo, T. *J. Biomed. Mater. Res.* **1988**, *22*, 869–885.
8. Hill, R.; Clifford, A.; Rafferty, A.; Wood, D.; Samuneva, B.; Dimitrova-Lukacs, M. *J. Am. Ceram. Soc.* **2000**, *83*, 2833–2838.
9. Hill, R.; Wood, D. *J. Mater. Sci. Mater. Med.* **1995**, *6*, 311–318.
10. Hill, R.; Goat, C.; Wood, D. *J. Am. Ceram. Soc.* **1992**, *75*, 778.
11. Dimitrova-Lukacs, M.; Gillemot, L. In *Third Euroceramics*; Duran, P., Fernandez, J. F., Eds.; Editrice Iberica SL: Spain; 1993; Vol. 3, pp 778–785.
12. Freeman, C. O.; Brook, I. M.; Johnson, A.; Hatton, P. V.; Hill, R. G.; Stanton, K. *J. Mater. Sci. Mater. Med.* **2003**, *14*, 985–990.
13. Goodridge, R. D.; Wood, D. J.; Ohtsuki, O.; Delgano, K. W. *Acta Biomater.* **2007**, *3*, 221–231.
14. Blades, M. C.; Hill, R.; Moore, D. P.; Revell, P. *J. Mater. Sci. Mater. Med.* **1998**, *9*, 701–706.

1.111. Bioactive Ceramics: Physical Chemistry

C Rey, C Combes, C Drouet, and D Grossin, University of Toulouse, Toulouse, France

© 2011 Elsevier Ltd. All rights reserved.

1.111.1.	**Introduction**	188
1.111.2.	**Calcium Orthophosphates Used as Biomaterials: Composition, Occurrence, and Brief Synthesis Description**	189
1.111.2.1.	Calcium Phosphates Obtained by Wet Synthesis Methods	189
1.111.2.1.1.	Monocalcium phosphates	189
1.111.2.1.2.	Dicalcium phosphates	189
1.111.2.1.3.	Tricalcium phosphate, whitlockite, and amorphous tricalcium phosphate	190
1.111.2.1.4.	Octacalcium phosphate	191
1.111.2.2.	Calcium Phosphate Obtained by Dry Synthesis Methods	191
1.111.2.2.1.	Crystalline tricalcium phosphates: α- and β-TCP	191
1.111.2.2.2.	Tetracalcium phosphate	191
1.111.2.3.	Apatites	192
1.111.2.3.1.	Well-crystallized apatites	192
1.111.2.3.2.	Nanocrystalline apatites	192
1.111.2.3.3.	Synthesis and formation of apatites	193
1.111.2.4.	Other Phosphate Compounds	194
1.111.3.	**Characterization Methods of Calcium Phosphates**	194
1.111.3.1.	Chemical Analysis	195
1.111.3.1.1.	Major ions	195
1.111.3.1.2.	Minor and trace elements	196
1.111.3.1.3.	Meaning of the Ca/P ratio	196
1.111.3.2.	Diffraction Methods	196
1.111.3.3.	Electron Microscopy Techniques	198
1.111.3.4.	Vibrational Spectroscopies	199
1.111.3.5.	Solid-State Nuclear Magnetic Resonance	200
1.111.4.	**Properties of Calcium Phosphates**	202
1.111.4.1.	Thermal Properties of Calcium Phosphates	202
1.111.4.1.1.	Reversible decomposition of stoichiometric apatites	202
1.111.4.1.2.	Irreversible decomposition of nonstoichiometric apatites	203
1.111.4.2.	Solubility	204
1.111.4.3.	Hydrolysis and Aqueous Conversion	205
1.111.4.4.	Surface Charge and Surface Energy	206
1.111.4.4.1.	Surface charge	206
1.111.4.4.2.	Interfacial energy	207
1.111.4.5.	Chemical Alterations of the Surface	207
1.111.4.5.1.	Ion exchange	207
1.111.4.5.2.	Adsorption	208
1.111.4.6.	Nucleation Properties	209
1.111.5.	**Biological Response and Physical–Chemical Characteristics**	209
1.111.5.1.	Active and Passive Biomaterials with Regard to Ca-P Nucleation	210
1.111.5.2.	Simulated Body Fluid Testing	211
1.111.5.3.	Biodegradation	212
1.111.6.	**Examples of Applications and Processing**	213
1.111.6.1.	Porous Ceramics	213
1.111.6.2.	Coatings, Example of HA-Plasma Spraying	214
1.111.6.3.	Cements	215
1.111.6.4.	Examples of Composite Materials with Collagen	216
1.111.7.	**Other Bioactive Ceramic Materials**	216
1.111.7.1.	Oxide- and Hydroxide-Based Bioactive Ceramics	216
1.111.7.2.	$CaCO_3$-Based Bioactive Ceramics	217
1.111.7.3.	$CaSO_4$-Based Bioactive Ceramics	218
1.111.8.	**Conclusion and Future Perspectives**	219
References		219

Glossary

Isomorph Compounds with identical crystalline structure.
Metaphosphate Salt of the hypothetic metaphosphoric acid HPO_3, often corresponding to chain or cyclic polyphosphates ($P_nO_{3n+1}^{(n+2)-}$ and $P_nO_{3n}^{n-}$ ions).
Nonstoichiometry Always relative to a given stoichiometric composition (see stoichiometry). Compound exhibiting ions or elements ratios different from that of the given composition.
Orthophosphate Salts of the orthophosphoric acid: H_3PO_4.
Polymorph Compounds with identical composition but different crystalline structures.
Pyrophosphate (also called diphosphate) Salts of the pyrophosphoric acid $H_4P_2O_7$.
Rietveld analysis Series of computing techniques permitting to extract from X-ray diffraction patterns of powders of crystalline substances information relative to the size, strains, preferential orientations of crystals, phases ratios, and, in favorable cases, the atoms locations and site occupancy relative to a model structure (these last points were in fact at the origin of Rietveld refinements techniques).
Stoichiometry Proportion of ions or elements in a given compound.

Abbreviations

AAS	Atomic absoption spectroscopy
ACP	Amorphous calcium phosphate
ATCP	Amorphous tricalcium phosphate
BMP	Bone morphogenetic protein
ClA	Chlorapatite
Ca-P	Calcium phosphate
CHN	Carbon, hydrogen, nitrogen analyser
CS	Calcium sulfate
CSD	Calcium sulfate dihydrate (or gypsum)
CSH	Calcium sulfate hemihydrate
DC	Direct current
DCPA	Dicalcium phosphate amorphous
DCPD	Dicalcium phosphate dihydrate
DSC	Differential scanning calorimetry
DTA	Differential thermal analysis
EDS	Energy dispersive spectroscopy
EDTA	Ethylene diamine tetracetic acid
FA	Fluorapatite
FGF	Fibroblast growth factor
FTIR	Fourier transform infrared spectroscopy
HA	Hydroxyapatite
ICDD	International centre for diffraction data
ICP	Inductively coupled plasma
ISO	International organization for standardization (this is not really an accronym but it is an abbreviation)
JCPDS	Joint committee for powder diffraction standards
lzc	Line of zero charge
MES	Metastable solubility equilibrium
MCPA	Monocalcium phosphate anhydrous
MCPM	Monocalcium phosphate monohydrate
NMR	Nuclear magnetic resonance
nsHA	Nonstocihiometric hydroxyapatite
OCP	Octacalcium phosphate
OCPt	Octacalcium phosphate triclinic phase
PLLA	poly-L lactic acid
PMMA	Polymethylmethacrylate
pzc	Point of zero charge
SAED	Selected area electron diffraction
SBF	Simulated body fluid
SEM	Scanning electron microscopy
TCP	Tricalcium phosphate
TEM	Transmission electron microscopy
TRIS	Trishydroxymethyl aminomethane
TTCP	Tetracalcium phosphate
VEGF	Vascular endothelial growth factor
WDS	Wavelength dispersive spectroscopy
XRD	X-ray diffraction

1.111.1. Introduction

Bioactive ceramics based on calcium orthophosphates (Ca-P) have considerably developed in the last decades; their applications have progressively spread, worldwide, and they have become the most implanted bioactive ceramics. The initial use of Ca-P as bioceramics was based on their analogy of composition with bone mineral and the need for versatile and risk-free bone substitute materials immediately available without the constraint of bone graft. One of the major properties of most Ca-P materials is their osteoconductivity, their ability to favor bone healing and to bind firmly to bone tissue. In addition, some Ca-P materials have been shown to be able to initiate bone formation *de novo* in nonosseous sites. Today, Ca-P compounds are mainly used as bone substitute materials in the form of porous ceramics, coatings on metallic prostheses, composite materials with organic macromolecules, injectable calcium phosphate cements and scaffolds for tissue engineering. They are also used in nonosseous applications such as ocular implants, allowing eyes movements. Many other applications have been proposed: drug carriers, tubing for nerve reconstruction, transfection support for cell therapy, adsorption substrates in some types of cancer treatments triggering the immune system. This chapter presents the different Ca-P compounds and their main physical–chemical properties of importance for biomedical applications. This chapter is primarily intended to describe the physical chemistry of these materials. In its last part, this chapter briefly presents other, non-Ca-P, bioactive materials, which are not treated in other parts of this chapter (see also **Chapter 1.109, Bioactive Ceramics**).

1.111.2. Calcium Orthophosphates Used as Biomaterials: Composition, Occurrence, and Brief Synthesis Description

Calcium orthophosphates result from the neutralization of the different acidities of phosphoric acid (H_3PO_4). Different calcium salts are formed corresponding to the progressive replacement of acidic protons by calcium ions. The chemical composition of these calcium phosphates with indications of composition and structures are reported in Table 1. The presentation is divided into two parts: calcium phosphates obtained by low-temperature wet synthesis methods and those obtained by high-temperature dry synthesis methods. Apatites, among the most important calcium phosphate compounds, which can be obtained by these two routes will be treated separately. All of these calcium phosphates do not give bioactive ceramics, but they are involved as intermediary phases or compounds in different types of biomaterials and/or they may appear as impurities.

1.111.2.1. Calcium Phosphates Obtained by Wet Synthesis Methods

1.111.2.1.1. Monocalcium phosphates

The first acidic proton of H_3PO_4 corresponds to a strong acid. The associated calcium salts, monocalcium phosphates, exist as hydrated and anhydrous crystalline phases. The soluble monohydrated monocalcium phosphate (MCPM) can be prepared by partial neutralization of the phosphoric acid with calcium hydroxide, followed by evaporation of water at low temperature, in acidic conditions.[13] The hydrated monocalcium phosphate crystallizes as platelets elongated along the c axis of the triclinic structure. Generally, monohydrated monocalcium phosphate can be obtained by gentle evaporation of acidic calcium- and phosphate-containing solutions.

The anhydrous phase can be obtained with the same method but at a higher phosphoric acid concentration. Some commercial products appear, in fact, as a mixture of the two monocalcium phosphates. Monocalcium phosphate anhydrous (MCPA) also forms by slow thermal dehydration of the hydrated phase above 100 °C. This reaction is reversible and, in moist air MCPA, can be converted back into MCPM. Monocalcium phosphates can incorporate many different mineral ions in their lattice (NH_4^+, K^+, Cl^-, Br^-).[14]

The monocalcium phosphate crystals do not form in living organisms, but these salts are used in biomedical mineral cement compositions.

1.111.2.1.2. Dicalcium phosphates

The second acidity of phosphoric acid corresponds to a weak acid. The neutralization of two acidities of phosphoric acid

Table 1 Main calcium phosphate compounds

Name and chemical formulae	*Most used abbreviations and mineralogical name*	*Structural characteristics (unit-cell dimensions in angstrom)*	*Density ($g\,cm^{-3}$)*	*References*
Monocalcium phosphate monohydrate: $Ca(H_2PO_4)_2$, H_2O	MCPM	Triclinic $P\bar{1}$ $a = 5.6261$; $b = 11.889$; $c = 6.4731$ $\alpha = 98.633$; $\beta = 118.262$; $\gamma = 83.344$	2.23	1
Monocalcium phosphate anhydrous: $Ca(H_2PO_4)_2$	MCPA	Triclinic $P\bar{1}$ $a = 7.5577$; $b = 8.2531$; $c = 5.5504$ $\alpha = 109.87$; $\beta = 93.68$; $\gamma = 109.15$	2.57	2
Dicalcium phosphate dihydrate: $CaHPO_4$, $2H_2O$	DCPD brushite	Monoclinic Ia $a = 5.812$; $b = 15.180$; $c = 6.239$ $\beta = 116.25$	2.3	3,4
Dicalcium phosphate anhydrous: $CaHPO_4$	DCPA monetite	Triclinic $P\bar{1}$ $a = 6.916$; $b = 6.619$; $c = 6.946$ $\alpha = 96.18$; $\beta = 103.82$; $\gamma = 88.34$	2.93	5
Amorphous tricalcium phosphate: $Ca_3(PO_4)_2$, nH_2O	ATCP (ACP)	$Ca_9(PO_4)_6$ clusters, S_6 symmetry	–	6
Octacalcium phosphate (triclinic structure): $Ca_8(PO_4)_4(HPO_4)_2$, $5H_2O$	OCP (OCPt)	Triclinic $P1$ $a = 19.692$; $b = 9.523$; $c = 6.835$ $\alpha = 90.15$; $\beta = 92{,}54$; $\gamma = 108.65$	2.67	7
β-tricalcium phosphate $Ca_3(PO_4)_2$	β-TCP	Trigonal $R3c$[a] $a = 10.439$; $b = 37.375$	3.07	8,9[b]
α-tricalcium phosphate $Ca_3(PO_4)_2$	α-TCP	Monoclinic $P2_1/a$ $a = 12.887$; $b = 27.280$; $c = 15.219$ $\beta = 126.20$	2.86	10
Tetracalcium phosphate $Ca_4(PO_4)_2O$	TTCP (TeTCP)	Monoclinic $P2_1$ $a = 7.023$; $b = 11.986$; $c = 9.473$ $\beta = 90{,}90$	3.05	11
Phospho-calcium hydroxyapatite: $Ca_{10}(PO_4)_6(OH)_2$	Hydroxyapatite	Hexagonal $P6_3/m$[c] $a = 9.418$; $c = 6.881$	3.16	12

[a]Hexagonal settings.

[b]Neutron diffraction on powder, Rietveld refinement.

[c]The structure of pure stoichiometric HA at room temperature is monoclinic; however, in biomaterials, it is essentially the hexagonal form which is encountered.

with calcium hydroxide leads to dicalcium phosphates. Two crystalline forms exist: dicalcium phosphate dihydrated (DCPD), also called brushite by mineralogists, and dicalcium phosphate anhydrous (DCPA), also called monetite. These sparingly soluble calcium phosphates have some biological importance. Brushite may form as an intermediary phase in ectopic mineralization occurring in slightly acidic media, for example, in dental calculi or urinary calculi.[15] DCPD and DCPA are largely used as biomaterials in mineral cements and coatings and also in composite materials, but these compounds have other applications also, in tooth paste, for instance. These compounds crystallize easily and they can be obtained industrially with a very high purity. They are often used for the preparation of other calcium phosphates.

DCPD crystals can be prepared simply by neutralization of phosphoric acid with calcium hydroxide at pH between 3 and 4 at room temperature. Generally, DCPD can be obtained by double decomposition between calcium and phosphate-containing solutions in slightly acidic media. It can also be formed by conversion of calcium phosphate salts, in acidic media, or by reaction of calcium salts such as calcium carbonate in acidic orthophosphate solutions.

DCPA is most conveniently obtained by dehydration of DCPD at 180 °C. However, it may also be directly precipitated in aqueous acidic solutions (pH 3–4) at mild temperature (60 °C).

The dicalcium phosphates can accommodate different biologically relevant ionic substitutes. Calcium, for example, can be replaced by Sr^{2+} ions and HPO_4^{2-} ions by SO_4^{2-} ions. These phases appear generally stoichiometric and no report has mentioned the existence of cationic or anionic vacancies in these compounds, to our knowledge.

Dicalcium phosphate also exists as an amorphous solid, with interesting properties. This phase can be obtained in nonaqueous media and by mechanosynthesis.[16,17]

1.111.2.1.3. Tricalcium phosphate, whitlockite, and amorphous tricalcium phosphate

The third acidity of orthophosphoric acid is very weak and, although the PO_4^{3-} exists only in a very small amount at pH lower than 11, tricalcium phosphate salts (TCP) can precipitate due to their very low solubility. The term TCP is used here in its strict chemical meaning to designate phases with a chemical composition represented by $Ca_3(PO_4)_2$ with a Ca/P ratio close to 1.5. Several different phases with a composition close to TCP exist (**Table 1**): crystalline TCP (α- and β-TCP) form only at high temperature and it is generally considered that crystalline, pure, TCP salt cannot be obtained by direct precipitation from aqueous media.[18] Although a publication reports the formation of crystalline β-TCP in aqueous media,[19] this result has to be considered with caution, as very often, minor impurities such as magnesium in calcium salts can lead to the formation of whitlockite, a calcium-magnesium phosphate, occurring in nature, isostructural to β-TCP. Although very often the term whitlockite is used to designate the β-TCP, this confusion should be avoided, as significant differences exist between these two phases in terms of composition and properties despite a structural analogy.[20]

Whitlockite forms very easily in biological media and it contains an appreciable amount of Mg^{2+} ions and HPO_4^{2-} ions. The composition can be represented by the following chemical formula:

$$Ca_{18}Mg_2H_2(PO_4)_{14}$$

but other compositions exist. The crystal structure of whitlockite can be accessed on a number of mineralogical Web sites.

In mammals, whitlockite generally appears in ectopic calcifications, for example, in joints and in calculi.

Several preparation methods of whitlockite generally involving coprecipitation of a calcium and magnesium solution with a phosphate solution have been described.[21] The structure of whitlockite has been determined, but its solubility is not clearly known. The conversion of whitlockite into apatite in aqueous solution has never been described and this compound might be possibly considered as one of the most insoluble calcium phosphate-based compounds.[20]

Aqueous precipitation of TCP generally leads to an amorphous phase often designated as amorphous calcium phosphate (ACP) or more accurately as amorphous tricalcium phosphate (ATCP). It is obtained most conveniently by double decomposition between calcium and phosphate solutions in alkaline media.[22] ACP is considered as one of the most important calcium phosphates in living organisms. It has been found in calcifications occurring in primitive organisms[23] and it has also been described as an intermediary phase in the formation of bone mineral in vertebrates.[24] Although it has, since then, been shown that in most cases no amorphous phase could be detected in bone,[25] the existence of this phase as a precursor of bone mineral formation is still debated.[26,27] ATCP is being used as a major or minor phase in calcium phosphate self-setting injectable cements for bone substitution and it also occurs in calcium phosphate coatings obtained by plasma-spray. Owing to its reactivity, it has also been proposed as a remineralizing agent in toothpaste and in several composite materials for dental restoration.[28]

ATCP exhibits a short-range organization of mineral ions, very similar to that occurring in apatite and other calcium phosphates, often referred as Posner's clusters.[29] It has been shown that these clusters correspond to the most stable association of calcium and phosphate ions.[6]

ATCP accepts different mineral ion substitutes and often impurities, which are not always considered and taken into account. Many different ions can replace calcium or phosphate ions in ATCP. For example, cations of biological importance such as Mg^{2+}, Sr^{2+}, Zn^{2+}, or anions like CO_3^{2-} can be incorporated.

It is often difficult to prepare very pure ATCP and several ionic impurities like HPO_4^{2-} and CO_3^{2-} may lead to Ca/P under or above 1.5 respectively. The best method to test the composition of TCP is probably calcination and transformation into crystalline phases as explained in the section relative to high-temperature TCPs.

In addition to ATCP, crystalline TCPs with an apatitic structure exist and have been named 'apatitic TCP.' Some industrial TCP products correspond, in fact, to apatitic TCP. Such compounds are described in the apatite section.

Other ACP phases may exist with lower Ca/P ratio than TCP (and thus containing HPO_4^{2-} and PO_4^{3-}). Several reviews on ACP have been recently provided.[30,31]

1.111.2.1.4. Octacalcium phosphate

In addition to amorphous phases, several crystalline calcium phosphate phases associate HPO_4^{2-} and PO_4^{3-} ions such as whitlockite, octacalcium phosphate, and apatite. Octacalcium phosphate has been the subject of a book edited by Chow and Eanes.[32] The term 'OCP,' refers to a chemical composition, but it is also considered to designate most generally the triclinic crystalline phase associated with this composition (noted here as OCPt). Very often this confusion makes some publication or patents rather imprecise. Like for TCP, OCP represents *stricto sensus*, a chemical composition, and this term has been used to name any compound with a close chemical composition; thus, 'apatitic OCP' or 'amorphous OCP' have been described.[33,34]

The original triclinic phase, OCPt, has initially been obtained by hydrolysis of DCPD in slightly acidic media at 40 °C,[35] but other preparation methods have been developed, especially the double decomposition between a calcium and a phosphate solution in slightly acidic medium at mild temperatures.[36] The structure of OCPt is characterized by the association of alternated apatite layers and hydrated layers containing Ca^{2+} and HPO_4^{2-} ions.[7] OCP has been proposed as a precursor of apatite in several biological mineralization processes, for example, in bone tissue and tooth enamel but also in dental calculi, although some of these identifications appear rather incomplete and uncertain and have not always been reproduced. The use of OCP in biomaterials has been proposed, in injectable bone mineral cements, or for the preparation of thin coatings, due to its high reactivity. OCP coatings have been found to exhibit an osteoinductive behavior.[37] However due to difficulties of preparation and conservation OCP does not seem to have yet found any large-scale industrial use.

The hydration degree of OCP depends on the preparation and storage conditions, and two types of OCP differing by the amount of attached water molecules have been described by Fowler *et al.*[38]

Little is known about the incorporation of mineral ions within the OCPt structure. Most data concern OCP hydrolysate's conversion into apatite.[39] Most OCP preparations lead to a partly hydrolyzed phase that contains an excess of HPO_4^{2-} and OH^- observable by Fourier transform infrared spectroscopy (FTIR) and solid-state nuclear magnetic resonance (NMR). OCP has the ability to incorporate dicarboxylic acids in the hydrated layer.[40] However, these interactions between OCP and organic molecules have not found applications in the biomaterial field.

A last but important type of calcium phosphate compound can be precipitated in aqueous media: apatite, which will be described in a specific section.

All these phases obtained from aqueous preparations exhibit a thermal decomposition at moderate temperature and cannot be transformed into bioceramics by conventional high-temperature treatments (see the thermal properties section). This is not the case of calcium phosphates obtained at high temperature, which can easily be processed and sintered by traditional methods used by ceramists.

1.111.2.2. Calcium Phosphate Obtained by Dry Synthesis Methods

The monohydrogen phosphate and dihydrogen phosphate groups are unstable and condense respectively into metaphosphate and pyrophosphate ions. Thus, all calcium orthophosphates obtained by dry synthesis methods contain the PO_4^{3-} ion. Two main compositions: TCP, tetracalcium phosphate (TTCP), in addition to apatites, are obtained. None of these compositions is naturally present in biological systems.

1.111.2.2.1. Crystalline tricalcium phosphates: α- and β-TCP

Two main crystalline phases belong to this category: α- and $\overline{\alpha}$-TCP, in addition to a very high temperature and unstable $\overline{\alpha}$-TCP phase. A review on TCP has recently been published.[41]

The TCP form easily by heating precipitated TCP (amorphous TCP or apatitic TCP) at high temperatures, or by dry preparation, heating mixtures of any calcium phosphate/carbonate with a 1.5 Ca/P ratio such as, for example,

$$CaCO_3 + Ca_2P_2O_7 \rightarrow Ca_3(PO_4)_2 + CO_2$$

but many other combinations with Ca/P = 1.5 are possible such as

$$Ca_{10}(PO_4)_6(OH)_2 + Ca_2P_2O_7 \rightarrow 4Ca_3(PO_4)_2 + H_2O$$

β-TCP is obtained at temperatures between 850 °C and the transition temperature to the α-TCP, 1125 °C. The metastable α-TCP is most conveniently obtained by quenching TCP heated above the transition temperature. However, heating ATCP between 650 and 700 °C results, also, in the formation of α-TCP. The $\overline{\alpha}$-TCP exists only at high temperature (above 1430 °C) and, unlike α-TCP, it does not seem to have been quenched at room temperature.

Several ion substitutions can occur in each of these phases and may modify the transition temperature. Mg^{2+} and other bivalents ions substituting for calcium, such as Zn^{2+}, Mn^{2+}, and Fe^{2+} ions, for example, stabilize the β-TCP structure, whereas silicate ions substituting for phosphate stabilize the α-TCP structure. Alkali metals -containing β-TCP with a higher solubility than regular β-TCP have also been evidenced and studied.[42,43]

The main impurities associated with TCP can be apatite or calcium pyrophosphate corresponding to a Ca/P ratio respectively higher or lower than that of regular TCP. Apatite can be easily detected by X-ray diffraction (XRD); however, this is not the case of pyrophosphate which is best evidenced by FTIR spectroscopy.

TCP phases are, with apatites, among the most widely used Ca-P biomaterials, mainly as bioresorbable ceramics.[41]

1.111.2.2.2. Tetracalcium phosphate

This phase is easily obtained by heating at high temperature a mixture of calcium and phosphate salts with a Ca/P ratio close to 2, for example,

$$2CaCO_3 + Ca_2P_2O_7 \rightarrow Ca_4(PO_4)_2O + 2CO_2$$

The reaction has, however, to be carried out under dry atmosphere in order to avoid, in the presence of water vapor, the decomposition of TTCP into hydroxyapatite (HA) according to the reversible reaction:

$$3Ca_4(PO_4)_2O + H_2O \leftrightarrow Ca_{10}(PO_4)_6(OH)_2 + 2CaO$$

The TTCP formed at high temperature is generally quenched to prevent any evolution. It is used as an alkaline, Ca-rich

component in multicomponent mineral cements. Owing to the alkaline pH generated by dissolution of TTCP in water, this phase transforms very easily into apatite. Ion substitutions in this phase do not seem to have been much studied.

1.111.2.3. Apatites

The apatites are the most frequently encountered crystalline biological calcium phosphates, and they are also among the most used Ca-P compounds as biomaterials. Apatite is also one of the most extensively studied phases.[20] Apatites are found in all mineralized tissues of mammals and more generally in mineralized tissues produced by vertebrates (bones, tooth enamel fish scales, antlers, defenses, roster of whales) except for egg shell. The presentation is divided into two parts: well-crystallized apatites and nanocrystalline apatites for which surface structure and composition have to be considered.

1.111.2.3.1. Well-crystallized apatites

The chemical composition of apatites is given by the generic formula:

$$Me_{10}(XO_4)_6Y_2$$

where Me represents a bivalent metallic ion such as Ca^{2+}, Sr^{2+}, Ba^{2+}, Cd^{2+}, Pb^{2+}; XO_4 a trivalent anion such as PO_4^{3-}, AsO_4^{3-}, VO_4^{3-}; and Y a monovalent anion such as OH^-, F^-, Cl^-, Br^-. The composition of apatites may include many foreign ions and several solid solutions are possible. The bivalent cations may be replaced partly by trivalent cations (e.g., La^{3+}, Eu^{3+}) or monovalent ones (e.g., Na^+) or by cationic vacancies. The trivalent anions can be partly replaced by bivalent or tetravalent ones such as CO_3^{2-} (type B carbonate apatite), HPO_4^{2-}, or SiO_4^{4-}. The monovalent anions can be replaced partly by bivalent anions such as CO_3^{2-} (type A carbonate apatite), O^{2-}, or anionic vacancies. No large amounts of vacancies have been reported in trivalent anionic sites, probably because of the instability of the lattice resulting from the creation of bulky defects. The maximum amount of cationic and/or monovalent anionic vacancies can be rather large and it may reach 2 per unit formula. This means that apatite with all monovalent anionic sites empty can exist. It seems, however, that such sites in apatites obtained in aqueous media are not empty and can be occupied by water molecules as suggested by Rietveld analyses of calcium-deficient apatites[44] or solid-state NMR studies.

Apatites containing vacancies or ionic substituents can be easily prepared in aqueous media. In order to preserve the electroneutrality of the solid, several charge compensation mechanisms are observed. Only a few examples related to calcium phosphate apatites and biological applications will be given.

For example, the replacement in part of bivalent cations by trivalent ones can be compensated for by the increase of the charge of monovalent anions or by that of trivalent anions:

$$Ca_8La_2\ (PO_4)_6O_2$$

$$Ca_8La_2\ (PO_4)_4(SiO_4)_2(OH)_2$$

The replacement of trivalent PO_4^{3-} anions by bivalent ones results in the formation of both a cationic vacancy (represented by squares in the chemical formulas) and an anionic vacancy in monovalent site, for HPO_4^{2-}- and CO_3^{2-}-containing apatites:

$$Ca_{10-x}\square_x\quad (PO_4)_{6-x}(HPO_4)_x\quad (OH)_{2-x}\square_x$$

$$Ca_{10-x}\square_x\quad (PO_4)_{6-x}(CO_3)_x\quad (OH)_{2-x}\square_x\quad \text{with}\ \ 0\le x\le 2$$

Bone mineral composition has been approximated with some success using such chemical formulas.[45]

However, other phenomena can disturb this rather simple compensation mechanism. For example, additional Ca^{2+} and OH^- ions can be incorporated in the lattice at alkaline pH in carbonate apatites:

$$Ca_{10-x+u}\square_{x-u}\quad (PO_4)_{6-x}(CO_3)_x\quad (OH)_{2-x+2u}\square_{x-2u}$$
$$\text{with}\ \ 0\le x\le 2\quad \text{and}\quad 0\le u\le x/2$$

An internal hydrolysis of PO_4^{3-} groups (giving rise to hydrogen phosphate ions and additional OH^- ions) may also occur with residual water molecules associated with the solid:

$$Ca_{10-x}\square_x\quad (PO_4)_{6-x-y}(HPO_4)_{x+y}(OH)_{2-x+y}\square_{x-y}$$

The precise composition of the apatite unit-cell can be obtained traditionally by determining the density of the solid and the unit-cell dimensions. Although Rietveld refinements can be performed to determine the site occupancy, the simulation becomes rapidly rather complex when several possibilities of charge compensation have to be considered. A homogeneous distribution of foreign atoms is generally assumed, although heterogeneous distribution and atoms clustering can occur in the structure. This is especially the case for nanocrystalline apatites.

Apatite corresponds also to a structure, or more precisely, to a series of structures. Most apatites crystallize in a hexagonal structure and belong to the $P6_3/m$ group.[46] In this structure, the calcium ions can occupy two sites labeled as I and II. Calcium I sites are on the trigonal axis of the structure at (1/4, 3/4, 1/2 and 3/4, 1/4, 1/2 positions). The Ca II ions form equilateral triangles at $z = 1/4$ and $z = 3/4$, on the 6_3 axis of the structure. These ions constitute part of the walls of 'channels' where the monovalent sites are located. They correspond to the narrowest part of the channels with a diameter of 0.27 nm for Ca-P apatites. At $z = 1/2$, the channels appear slightly larger (0.29 nm) and they are limited by a distorted hexagon of oxygens belonging to PO_4^{3-} ions. Owing to the existence of these channels, apatites have sometimes been compared to zeolithes; the channels appear, however, smaller than those generally found in zeolithes and they are monodimensional and obstructed by ions, which limit considerably the exchanges at low temperature and the trapping of molecules. Nevertheless, it has been shown that small molecules such as O_2 and possibly, CO_2 or small organic molecules like glycine, formate ion, and even acetate ions can be trapped in these channels. In addition to the hexagonal structure, several Ca-P apatites, always stoichiometric, such as HA, chlorapatite, and type A carbonate apatite crystallize in the monoclinic structure, $P2_1/b$ group, due to an ordering of the monovalent anions (or bivalent anions and vacancies) in the channels of the structure.[20]

1.111.2.3.2. Nanocrystalline apatites

Except for enamel and a few other mineralized tissues, most biological apatites are nanocrystalline. Several data support the

concept that apatite nanocrystals exhibit a surface hydrated layer very different from the apatite structure forming the core of the crystals. The first model of an apatite surface was provided by Brown who suggested that the surface was close to the hydrated layer found in OCPt structure.[47] Specific surface reactions have been studied in the early fifties by Neuman and Mulryan,[48] and these conceptions have been developed and refined since then to explain spectroscopic data and chemical behavior.[49]

Spectroscopic data suggest that biomimetic apatite nanocrystals are constituted by an apatite core (generally, a nonstoichiometric apatite phase) and a hydrated surface layer mainly constituted by bivalent ions such as Ca^{2+}, HPO_4^{2-}, or CO_3^{2-} (**Figure 1**).

The proportion of hydrated layer has been found to be particularly important in freshly precipitated apatites. Upon aging in solution, the more stable apatitic domains develop, progressively, incorporating ions from the hydrated layer, if they can be inserted in the apatite lattice.

The ions in the hydrated layer appear to be relatively mobile and they can be very easily exchanged by other mineral ions or charged organic groups in adsorption reactions (see **Sections 1.111.4.5.1** and **1.111.4.5.2** on surface properties). In addition, the possibilities of ionic substitutions appear much more numerous in the hydrated layer than in the apatite lattice; thus, ions like magnesium, for example, can easily replace calcium ions in the hydrated layer but they are only incorporated in minute quantities in the apatite lattice; they are preferably located on the hydrated surface of the crystals and then always remain, for a major part, exchangeable.

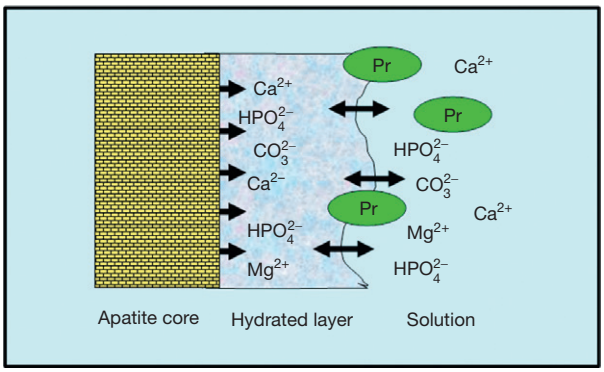

Figure 1 Model of the surface of biological and synthetic biomimetic apatite. The core of the nanocrystals is made of a nonstoichiometric apatite domain constituting a rigid and stable crystalline lattice. The surface is formed by a fragile structured hydrated layer which is destroyed by drying. This layer contains mainly bivalent mineral ions. On aging (maturation) in aqueous media, the very stable apatite domain grow (arrows) incorporating the mineral ions of the hydrated layer which can be inserted in the apatite lattice. The ions of the hydrated layer can be rapidly and reversibly exchanged by ions of the solutions (double arrows) and such reactions alter strongly the structure of the hydrated layer. Charged groups of macromolecules and proteins (labeled Pr) can also participate to such ion exchanges leading to adsorption of molecules on the crystals. The adsorption (or ion exchange) affinity and the amount of molecules (or ions) which can be adsorbed (or exchanged) vary with the extent of the hydrated surface domains. Adapted from Rey, C.; Combes, C.; Drouet, C.; Lebugle, A.; Sfihi, H.; Barroug, A. *Mat Wiss U Werkostofftech* **2007**, *38*, 996–1002.

The surface hydrated layer has been found to be structured in aqueous media, using wet spectroscopic characterization methods with ambivalent features: FTIR spectroscopy suggests the existence of OCPt-like environments, whereas NMR indicates the presence of mineral ions in an environment close to that in DCPD structure.[50] Upon drying, these surface structures are strongly altered and the surface environments appear amorphous-like. These observations point out the necessity to use various techniques to accurately characterize nanocrystalline apatites. It also appears that conclusions regarding the presence of foreign phases cannot be drawn from spectroscopic data alone.

1.111.2.3.3. Synthesis and formation of apatites

Apatites can be prepared by wet and dry methods.

1.111.2.3.3.1. Wet preparations

Wet preparation methods of apatites include direct neutralization reaction between $Ca(OH)_2$ and H_3PO_4 solutions, double decomposition between soluble calcium and phosphate salts, hydrolysis reactions of nonapatitic calcium phosphate phases, or else the conversion of other calcium or phosphate salts; in addition, several sol–gel and nonaqueous methods have been proposed. The neutralization method does not leave any counter-ion residue and any by-product to discard. It thus appears as a good method for industrial preparations; however, it generally gives precipitated apatites with carbonate ions impurities. Double decomposition seems to be the preferred method at the laboratory level and it is often used, also, for industrial production. Continuous precipitation processes using double decomposition have been studied, giving apatites with different chosen compositions (from TCP to stoichiometric HA).[51] Calcium nitrate and ammonium phosphate are the preferred starting salts. Although tiny proportions of nitrate or ammonium ions can be trapped in the precipitate during synthesis, they are easily eliminated by heating. Hydrolysis reactions are also relatively clean methods: they are generally based on the hydrolysis of DCPD or DCPA.[52] However, they require a large amount of water and part of the phosphate is lost in the waste water. Conversion methods are mostly based on calcium carbonate treatment in phosphate-containing solution.[53]

The important parameters for wet methods are the pH, temperature, maturation time in solution, and the way of addition of the reactants, in case of double decomposition. It has been shown that the rate of growth of apatite crystals is rather low, and in many cases, apatite formation proceeds through the hydrolysis of precursor phases, essentially ACP and OCP, having a higher rate of formation but a lower stability.

Apatites are generally obtained at slightly acidic or alkaline pH. The solubility isotherms indicate that HA is the most stable Ca-P compound in aqueous solution at pH greater than 4 at 37 °C. The nonstoichiometry of apatites is directly related to the pH value, and, at neutral or slightly acidic pH, the solids generally contain a large amount of HPO_4^{2-} ions and are nonstoichiometric.

The synthesis temperature also affects the chemical composition, degree of nonstoichiometry, and crystallinity of apatites. The crystallinity is, in general, greatly improved when the apatites are synthesized at rather high temperature, although

the rate of formation and the supersaturation ratio are also important. At, or under, room temperature, the first precipitate formed is, most of the time, an amorphous phase, which is then transformed into more stable apatites at a rate strongly related to temperature and pH. At constant pH, the elevation of temperature leads to apatites closer to stoichiometry.

The importance of the maturation time or aging time in solution is related to the process of formation of apatites involving intermediate nonapatitic phases and/or nonstoichiometric apatite precursors. Aging is associated with an evolution of the apatite toward more stable less soluble ones. Different processes seem, however, to be involved depending on the type of apatites. Three types of aging mechanisms can be distinguished: (i) the development of the apatite domains at the expense of the less stable surface hydrated domains, especially active in nanocrystals, (ii) the chemical evolution leading to more stable apatites closer to stoichiometry, and (iii) the Ostwald ripening process, based on the decrease of interfacial energy of crystals, which favors the growth of large crystals at the expense of smaller ones. The fastest process, especially active in biological systems, seems to be the first one.

The order of addition of the reactants and relative proportions also seem to be important parameters in apatite preparation: when a calcium excess is present in the solution, the apatites obtained are generally closer to stoichiometric ones, whereas such a stoichiometric composition seems more difficult to obtain in the presence of an excess of phosphate ions.

Some impurities are often present in apatites synthesized by wet methods: magnesium, carbonate, and HPO_4^{2-} ions are among the most important ones.

Magnesium is always the major cation impurity, found in variable concentrations, in most commercial calcium salts. Very disappointingly, some providers of such salts do not think it useful to signal the presence of this impurity. We encourage the different actors in the biomaterial field to determine and control the magnesium impurities in their products. This element has some chemical and biological effects, which may modify the properties of biomaterials. It has an inhibitory effect on apatite nucleation and crystal growth and it alters the apatite crystal morphology. It can be located on the surface of the crystals and be readily available, modifying the biological behavior of implants and scaffolds for tissue engineering.

Carbonate impurities are related to reactions with atmospheric CO_2 during preparation and washing of precipitated apatites. Surface carbonation may also occur by simple contact with carbonate-containing solutions. Like magnesium, carbonate is an inhibitor of apatite crystals nucleation and growth. Carbonate can be eliminated by heating at temperature close to 900 °C with a possible partial decomposition of the apatite phase.

Hydrogen phosphate ions result from the precipitation reaction or the internal hydrolysis reaction of PO_4^{3-} ions by water molecules. They are eliminated on heating (see Section 1.111.4.1 on thermal stability of apatites), but as in the case of carbonate, decomposition of the apatite may occur.

1.111.2.3.3.2. Dry preparation

Several dry preparation methods of apatites have been published, essentially for stoichiometric apatites. Basically, they consist in calcination between 900 and 1100 °C of solid reactants in the stoichiometric ratio (Ca/P = 1.67). HA, for example, can be obtained by heating a mixture of calcium carbonate and TCP at 1000 °C under water vapor:

$$CaCO_3 + 3Ca_3(PO_4)_2 + H_2O \rightarrow Ca_{10}(PO_4)_6(OH)_2 + CO_2$$

Fluorapatite (FA) or Chlorapatite (ClA) can be prepared with similar reactions:

$$CaF_2 \text{ (or } CaCl_2) + 3Ca_3(PO_4)_2 \rightarrow Ca_{10}(PO_4)_6(F \text{ or } Cl)_2$$

But many other reactants can also be chosen such as pyrophosphate in preparation of hydroxy- or fluorapatite:

$$4CaCO_3 + 3Ca_2P_2O_7 + H_2O \rightarrow Ca_{10}(PO_4)_6(OH)_2 + 4CO_2$$

or a more complex reaction[54]:

$$14CaF_2 + 18Ca_2P_2O_7 \rightarrow 5Ca_{10}(PO_4)_6F_2 + 6POF_3$$

releasing POF_3 as a gas.

Other interesting processes, concerning apatites, are ion substitutions at high temperature (900–1000 °C). It is thus possible to convert a HA into carbonated (type A), chlorinated or fluoridated apatites, for example,

$$NH_4Cl + Ca_{10}(PO_4)_6(OH)_2 \rightarrow Ca_{10}(PO_4)_6Cl_2 + NH_3 + H_2O$$

NH_4Cl is here sublimated in the oven and if the reaction is made in dry atmosphere, a stoichiometric ClA is obtained. These rather fast reactions do not change the crystal or ceramic characteristics; however, in bulk ceramics, only the surface might be modified due to slow diffusion of the ions.

1.111.2.4. Other Phosphate Compounds

Several other phosphates are of potential interest for biological applications either because they may appear as impurities in Ca-P compounds or because of their properties.

Calcium pyrophosphates contain the $P_2O_7^{4-}$ anion. Dicalcium pyrophosphates $Ca_2P_2O_7$ may appear as an impurity in TCP. Calcium pyrophosphates may also form in ectopic calcifications. Several polymorphs of these pyrophosphates exist. Pyrophosphates have been tested as biomaterials; they are bioresorbable and seem well tolerated.[55]

Polyphosphates can exist as linear chains of phosphate groups: $[P_2O_7(PO_3)_n]^{(n+4)-}$ or cyclic anions $(PO_3)_n^{n-}$. Cyclic polyphosphates give soluble complexes with calcium and they are mainly used in washing powders. Linear polyphosphates may give amorphous glasses or crystalline substances and some of them have been proposed as biomaterials.[56]

Several other calcium-containing orthophosphates are of potential interest:

Rhenanite (or Buchwaldite), $NaCaPO_4$ or Chlor-spodiosite, Ca_2PO_4Cl which could possibly be used in cements; Merillite: $Ca_{18}Na_2Mg_2(PO_4)_{14}$, Brianite $Na_2CaMg(PO_4)_2$.

1.111.3. Characterization Methods of Calcium Phosphates

Characterization of calcium phosphates can be the easiest or the most difficult task depending on the type of compound and the extent of information required. The characterization of DCPD or DCPA phases, for example, is rather straightforward and can be obtained by different techniques. Systems such as

nanocrystalline apatites prepared in close-to-physiological conditions have been shown to exhibit a rather complex composition and structure, involving an apatitic core (generally nonstoichiometric) and a hydrated surface layer-containing anions and cations in positions which do not correspond to the regular apatite structure (see Section 1.111.2.3.2). In this case, no single characterization technique can provide sufficient data, as it only enables to determine one characteristic of the system. Therefore, the conjoint use of several techniques along with chemical analyses is of foremost importance in the quest for precise characterization of complex Ca-P materials. Chemical composition is the first step, followed by XRD, electron microscopy, and spectroscopic techniques such as FTIR, Raman and solid-state NMR spectrometries.

1.111.3.1. Chemical Analysis

The thorough physicochemical characterization of calcium phosphate-based ceramics (as for any other advanced materials) requires, as one of the main steps, to determine precisely the nature and relative amounts of the chemical elements composing the system. Such data then allow deriving the overall chemical formula of the compound studied. This consideration appears especially essential for apatitic materials, which can accommodate a large number of ionic vacancies and which can also tolerate many ionic substitutions.

It is possible to distinguish three types of ions in calcium phosphates of biological origin and in many synthetic apatites:

- major ions like Ca^{2+}, orthophosphates, including PO_4^{3-} and HPO_4^{2-}, CO_3^{2-}, and OH^-,
- minor ions like Na^+, Mg^{2+},
- trace elements such as Sr^{2+}, Zn^{2+}, F^-

The techniques which are possible to use depend on the abundance of the elements.

1.111.3.1.1. Major ions

1.111.3.1.1.1. Calcium

The amount of calcium contained in a given specimen can be drawn by way of many techniques such as atomic absorption spectroscopy (AAS), inductively coupled plasma (ICP) emission spectroscopy, ionometry using a specific electrode, ion chromatography, old but competitive chemical methods like complexometry (e.g., with a complexing agent such as ethylene diamine tetracetic acid (EDTA)), or even X-ray fluorescence or electron microscopy-based techniques (microprobe analyses, energy-dispersive X-ray analyses). Although the latter offer the possibility to observe the spatial distribution of the elements (s) across the sample, they require a precise preliminary calibration step and do not appear generally accurate enough to distinguish phases with close composition or to determine a departure from stoichiometry. The other techniques cited above are thus more frequently used for the routine determination of the amount of calcium contained in a specimen. Determinations based on AAS or ICP seem to provide relatively accurate data, and these techniques are more specific than complexometry where the complexation of other cations may simultaneously occur during the titration, thereby leading to nonspecific cationic content measurements. Direct determinations of calcium ions in solution can also be made by ion chromatography or by ionometry. These methods are not as accurate as AAS or ICP-related methods, but they can be useful for a follow-up of calcium concentration in solutions in contact with Ca-P.

1.111.3.1.1.2. Phosphorus

Phosphorus contained in calcium phosphates is generally present either under the form of orthophosphate ions (PO_4^{3-}, HPO_4^{2-}, $H_2PO_4^-$) or as pyrophosphate ions $P_2O_7^{4-}$. It is then such oxygenated phosphorus species that are generally followed. The total phosphorus content can be determined by some of the methods, which can also be used for calcium such as ICP, or electron microprobe analysis. However, these methods do not allow discrimination between orthophosphate and other phosphorus-containing molecules or ions. Ion chromatography can be used in such a situation.

Orthophosphate ions can usually be satisfactorily and specifically titrated by spectrophotometry of the phosphovanado-molybdenum complex either directly (yellow coloration) or after reduction (blue coloration).[57] All orthophosphate ions present in the system, under any form, are analyzed. Other phosphate groups such as pyrophosphate ions or metaphosphates are not analyzed. When such ions are present, however, a slow hydrolysis may occur in the aqueous medium needed for the analysis, and it is advised to carry out the determination using these spectrophotometric methods just after dissolution. Such hydrolysis reactions could also occur with esters of phosphoric acid.

The HPO_4^{2-} content appears as an important characteristic in several calcium phosphates, especially in dicalcium phosphates, ACP, or octacalcium phosphates. In apatites, the amount of HPO_4^{2-} ions is related to nonstoichiometry, and in nanocrystalline apatites, it may also appear as a characteristic of the surface composition. HPO_4^{2-} in calcium orthophosphates can be determined after thermal conversion into pyrophosphate ions as shown by Gee and Dietz.[58,59] Samples are heated at 500 °C for 3 h (or preferably at 600 °C for 1 h). The amount of pyrophosphate ions is then determined either after separation on an ion exchange resin or simply by difference between the amount of orthophosphate before and after pyrophosphate formation. A limitation to this determination of the HPO_4^{2-} content, however, exists in the simultaneous presence of carbonate ions as side reactions between HPO_4^{2-} and carbonate ions may interfere. Another difficulty is the possible internal hydrolysis of PO_4^{3-} with water molecules attached to the solid during heating. An alternative to the rather time-consuming analytical method proposed by Gee and Dietz exists for nanocrystalline apatite where most of the HPO_4^{2-} ions belong to a surface hydrated layer. The HPO_4^{2-} content can be evaluated from the mathematical decomposition of the ν_4PO_4 band of the FTIR spectrum.[60] Indeed, a rather good correlation could be obtained between the amount of HPO_4^{2-} drawn from chemical analyses and by this FTIR-based method. However, the curve-fitting parameters need probably to be refined for obtaining more precise determinations.

1.111.3.1.1.3. Carbonate

Several methods can be used to determine the carbonate content of calcium phosphate samples. One of the best methods is probably coulometry. The carbonate content of Ca-P samples can be determined using a CO_2 coulometer measuring the CO_2

released upon sample dissolution in acidic media or heating of the sample. The CO_2 released is transferred into a photometric cell in a nonaqueous medium and titrated through an acid–base reaction.[61] A second method is the CO_2 analysis through gaz chromatography or a carbon-hydrogen-nitrogen (CHN) classical analysis system, releasing the CO_2 by heating, although the heating parameters have to be adjusted to be sure to decompose all carbonate ions.[62] Thermogravimetric determination of the CO_2 evolved can be carried on; however, generally, CO_2 and water loss cannot be easily separated, and in this case also, gas chromatography can be used. Another method for total carbonate content is FTIR spectroscopy. The spectral lines intensity of carbonate is determined relatively to that of phosphate bands. The accuracy seems lower than that of chemical methods; however, FTIR spectroscopy allows the determination of the type of carbonate (type A and/or B, see Section 1.111.2.3.1) involved.

1.111.3.1.4. Hydroxide ions

For HAs, the evaluation of the amount of OH^- ions is also important, although this determination is rarely made. The chemical method proposed by Trombe and Montel[63] consists in a substitution of OH^- ions by F^- ions at 1000 °C; when HA or oxy-HAs are heated in the presence of an excess of CaF_2 in a dry atmosphere, FA is formed and H_2O is released:

$$CaF_2 + Ca_{10}(PO_4)_6(OH)_2 \rightarrow Ca_{10}(PO_4)_6F_2 + CaO + H_2O$$

The mass of the released water corresponds to the amount of OH^- ions initially present in the solid. An excess of CaF_2 is used (up to 20%) to be sure that the reaction is completed. The application of this method supposes, however, that there are no other possibilities of reactions. The decomposition of HA at high temperature under vacuum appears also as a possible method, although it does not seem to have been utilized much:

$$Ca_{10}(PO_4)_6(OH)_2 \rightarrow Ca_{10}(PO_4)_6O + H_2O$$

Among other methods, the relative intensity of FTIR OH^- lines at 3570 or 633 cm^{-1} can also be used and applications have been developed for the determination of OH^- in oxy-HA coatings,[64] which can be extended to bone and nanocrystalline apatites. An alternative method is to use the Raman OH^- stretching band at 3570 cm^{-1}. These necessitate, however, calibration curves obtained with well-characterized reference samples (or mixtures of samples) in a preliminary step.

1.111.3.1.2. Minor and trace elements

The determination of minor and trace elements is usually performed by spectroscopic methods such as AAP or ICP-related methods using emission spectroscopy or mass spectroscopy. In some cases, neutron activation analyses have also been used to determine trace elements in biological samples. Fluoride is often found in apatites of biological origin and in the case of a bone disease, fluorosis. This ion is generally determined quite accurately by ionometry using a specific electrode.

1.111.3.1.3. Meaning of the Ca/P ratio

The Ca/P ratio of calcium phosphates is generally considered as one of their major characteristics. The Ca/P ratio of most calcium phosphate phases is generally restrained to a narrow domain of variations. In the case of apatites, however, the Ca/P ratio may vary in a wide domain and it is frequently used to characterize the apatite composition. Two cases shall be considered:

The first one concerns nonstoichiometric apatites with Ca/P ratios lower than that of the stoichiometric composition (Ca/P = 10/6 = 1.667), which occur when the apatite contains HPO_4^{2-} ions in place of PO_4^{3-} ions, as discussed in the section on apatite composition. Considering that phosphate sites do not accommodate large amounts of vacancies, the Ca/P ratio represents then the amount of cationic vacancies.

The second one concerns nonstoichiometric apatites with carbonate ions replacing phosphate groups (type B carbonate apatites). In this case, the Ca/P ratio does not represent the amount of cationic vacancies and it has no simple meaning. However, considering that there are only a few vacancies in the trivalent anionic sites of the apatite structure (all six sites are occupied either by phosphate or by carbonate groups), it is the Ca/(P+C) ratio (where C represents the amount of carbonate ions replacing phosphate groups) which represents the departure from stoichiometry and the cationic vacancies.

In more complex compositions when other cations than calcium, for example Sr^{2+}, are present in the apatite, the atomic ratio related to vacancies to consider is (Ca+Sr)/(P+C).

For nanocrystalline biomimetic apatites, the situation is even more complex due to the surface composition, which cannot be neglected, and which is different from the core of the crystals. An important proportion of bivalent ions is on the surface, but this amount is difficult to estimate, and there is no adequate model describing these compounds. In this case, the (cations)/(P+C) ratio does not have a meaning and it has no correlation with the amount of vacancies in the apatite domains.

Special techniques for the determination of Ca/P ratio using XRD have also been developed and standardized in the case of HA ceramics and coatings (see Section 1.111.3.2).

1.111.3.2. Diffraction Methods

XRD is an essential method for the characterization of calcium phosphate materials. XRD experiments have been performed on monocrystals, polycrystalline bulk ceramics, coatings, or powder samples.[65] The first point is not be discussed here, although it has been involved in the determination of most Ca-P structures (see Table 1 for references). The peak position of XRD diffraction patterns allows the identification of all crystalline calcium phosphate compounds as recorded in the databases of diffraction patterns such as International centre for diffraction data (ICDD), Joint committee for powder diffraction standards (JCPDS) or other. In everyday uses, some specific intense peaks are used to recognize the main Ca-P phases (Table 2).

The identification of phases has been standardized for several biological applications (ISO Standard 13779-3), mainly related to high-temperature processing of apatites as coatings or ceramics. The proposed method is based on the use of reference samples and single peaks integrated intensity ratios and needs the establishment of a standardization curve using known mixtures of phases in presence. However, other

methods have now been developed using the integrated intensity of all the peaks of phases in presence and involving Rietveld analysis. These methods a knowledge of the crystallographic structure, including atomic positions of each crystallized phase.

The determination of the amorphous Ca-P phase content existing in plasma-sprayed coatings, for example, however remains an open question. The standards define only a crystallinity ratio not necessarily related to the amount of amorphous phase as it has been shown in the case of bone mineral 30 years ago. The methods using standardization curves ACP/HA appear rather inaccurate and the best method at present is probably the determination of the heat of crystallization of the amorphous phase by differential scanning calorimetry (DSC) or differential thermal analysis (DTA).[66,67]

Among the difficulties related to phase identification is the distinction of poorly crystalline apatites and OCPt, due to XRD patterns analogies and peak broadening. However, the most intense peak of OCPt, (100), corresponding to a 1.868 nm *d* spacing, has been shown to be characteristic of this phase, although its position may vary with partial dehydration. The observation of this peak might need special settings of the diffractometer to reach low angle. Another difficulty arises from the preferential orientation of the crystals due to several causes, such as the preparation of the samples for XRD, a preexisting crystal orientation like in biological tissues (bone, dental enamel), or the processing of the Ca-P-based biomaterial. Such preferential orientations can considerably change the intensity of the different peaks and can make phase identification and quantification difficult.

In addition to phase recognition, XRD can be used to determine the unit-cell dimensions of the different crystallized Ca-P compounds. These crystallographic parameters can also be used to estimate the effect of ion substitutions on the structure. Such effects have been particularly well documented for the apatite structure. It is well established that the substitution of cation by a bigger one induces an increase of both dimensions of the hexagonal unit-cell. The replacement of a trivalent anion by a bigger one has the same influence. However, when a monovalent anion is replaced by a larger one, it induces an increase of the hexagonal *a* unit-cell dimension and a decrease of the *c* dimension. Generally, substitutions in apatite follow the Vegard's law, and the increase or decrease of the unit-cell dimensions is linearly proportional to the amount of ions introduced. Thus, increments can be determined for different ions of biological interest as shown by McConnel[68] (**Table 3**).

Important information brought by XRD concerns the crystal size and strains, which induce a peak broadening. Basic application in the biological field for the crystal size determination uses Scherrer's method neglecting the contribution of microstrains.[69] More elaborated treatments can be performed considering the effect of microstrains and crystal sizes, which are now included in Rietveld analysis of the XRD diagrams available from different Web sites. Such analysis allows the determination of crystal size in different crystallographic directions, microstrains, unit-cell dimensions, phase composition but also structural information such as the atomic position of substitutes or vacancies in favorable cases. For example, the orientation of carbonate species in carbonate apatites (type A and type B) has been solved using Rietveld analysis of XRD data and the location of vacancies in nonstoichiometric apatites has been determined.[44] The location of Sr in Sr-containing apatites has been determined using Rietveld analysis.[70] Although these very powerful methods have brought valuable information on calcium phosphates, they may sometimes lead to unrealistic solutions, and a critical examination of the data is advised. One of the difficulties, especially annoying in the case of apatites, is that these treatments do not consider the possibilities of a distribution of solid solutions with variable compositions, which is known to exist in bone and synthetic preparations (in fact in all Rietveld analyses, the phases are considered as homogeneous).

Table 2 Useful X-ray diffraction lines for the identification of main Ca-P phases and impurities in ceramics, thermal coatings, and powders

Phase	*JCPDS folder*	hkl	dhkl *(Å)*	*2θ(λ_{Cu} = 1.5406 Å)*
α-Tricalcium phosphate	09-0348	4 4 1	2.905	30.753
β-Tricalcium phosphate	09-0169	0 2 10	2.88	31.027
Tetracalcium phosphate	25-1137	0 4 0	2.995	29.807
Calcium oxide	82-1690	2 0 0	2.405	37.361
Hydroxyapatite	09-0432	2 1 0	3.08	28.967
Hydroxyapatite	72-1243	2 1 1	2.81	31.820
DCPA-Monetite	09-0080	− 1 1 2	2.958	30.189
DCPD-Brushite	09-0077	0 2 0	7.57	11.681
DCPD-Brushite	09-0077	1 2 1	4.24	20.935
OCP	26-1056	0 1 0	18.7	4.722

Table 3 Increments of crystallographic parameters (in Å) of the apatite unit-cell related to cationic and monovalent anionic substitutions for biologically relevant ions

a parameter	F	Δ(OH → F)	OH	Δ(Cl → OH)	Cl	Δ(Cl → F)
Ca	9.370	0.025	9.420	0.105	9.630	0.130
Δ(Sr → Ca)	0.034		0.034		0.024	
Sr	9.710	0.025	9.760	0.055	9.870	0.080
c parameter	F	Δ(OH → F)	OH	Δ(Cl → OH)	Cl	Δ(Cl → F)
Ca	6.880	0.000	6.880	− 0.050	6.780	− 0.050
Δ(Sr → Ca)	0.040		0.040		0.024	
Sr	7.280	0.000	7.280	− 0.045	7.190	− 0.045

The increments are determined for one atom substituted (Δ) (according to McConnel[68]).

Such samples would exhibit peaks broadening falsely interpreted as strains and size effects.

A special, very accurate technique, for the determination of the Ca/P ratio by XRD has been developed and standardized for Ca/P ratios between 1.50 and 2 (ISO standard 13779). Nonstoichiometric apatites are not stable and they decompose on heating at 900–1100°C depending on their Ca/P ratio. If the Ca/P ratio is lower than 1.67, the heated sample is constituted by β-TCP and stoichiometric HA. If the Ca/P ratio is higher than 1.67, a mixture of stoichiometric apatite and calcium oxide is observed. For a Ca/P ratio equal to 1.67, no decomposition is observed.[71] The foreign phases (β-TCP and calcium oxide) can be detected with high precision by XRD and quantified. The accuracy of the method lies on the observation that when the chemical Ca/P atomic ratio varies by about 10% between 1.50 (pure TCP) and 1.67 (pure HA), the phase composition varies by 100%.

A similar technique can be used for the determination of the purity of TCP. Heating at 900 °C shall give only β-TCP phase. Samples with a Ca/P lower than 1.5 give an additional Ca-pyrophosphate phase and samples with a Ca/P ratio higher than 1.5 contain stoichiometric apatite as explained above. However, in this case, the detection of pyrophosphate by FTIR appears much more sensitive than by XRD.

1.111.3.3. Electron Microscopy Techniques

Electron microscopy techniques are widely used by materials scientists with several objectives:

- determination of the crystal morphology, their size and organization, including pores distribution in ceramics
- identification of phases at the microscopic level using electron diffraction
- composition determination using Energy Dispersive Spectrometry (EDS) or Wavelength Dispersive Spectrometry (WDS)
- analyses of crystal defects through lattice imaging at high resolution

Most Ca-P exhibit specific crystal morphologies, which can be used for their identification. Mathew and Takagi[72] (2001) proposed a classification of the most used Ca-P into three major structural types: (1) the apatite-type structure also including apatite-related structures such as OCP and TTCP, (2) the glaserite-type structure in which all the TCP polymorphs can be included, and (3) the Ca-PO_4 sheet-containing compounds including dicalcium and monocalcium phosphate phases. However, this classification cannot be used to determine the crystal morphology of these compounds, as other parameters can control nucleation and crystal growth of these Ca-P phases leading, for example, in the cases of apatite or DCPD, either to needle-like or platelet-like morphologies. Some of the typical and most common morphologies are shown in Figure 2.

Some crystals can show a variable morphology depending on their formation conditions; however, some morphologies can be considered as recurrent: this is the case, for example, of OCPt crystals appearing as platelet crystals forming imbricated leaflet with irregular edges comparable to 'sand-roses.' However, OCPt can hydrolyze into apatite, without change of crystal habit, and these morphologies may also be associated with apatites. DCPD also forms platelet crystals with, generally, larger dimensions than OCP crystals. Precipitated ATCP appears most generally as spherical units (diameter between 20 and 300 nm). Well-crystallized apatites generally exhibit a needle-like morphology with crystals elongated along the c axis of the hexagonal structure. Platelets hexagonal crystals with a short dimension along c have also been reported in special preparation conditions.[73] Upon heating, the morphology of apatite crystals changes considerably: the length is reduced and the width-thickness is increased, resulting in a lower crystal surface energy. The hexagonal shape, however, remains recognizable. Some preparations such as hydrothermal synthesis, slow hydrolysis of more soluble Ca-P salts (DCPD, TCPs), and reactions in fused salts may give apatite crystals a very high aspect ratio (length/width ratio) that can be considered as fibers.[74] In most preparations, the needle-like crystals have the tendency to form dendritic spherical units. Tooth enamel crystals show the typical morphology of apatite with very elongated crystals. Bone crystals, however, appear essentially as platelet crystals with a rather irregular shape, elongated along the c axis of the hexagonal structure, but with different perpendicular dimensions along *a* and *b*. This very unlikely morphology for hexagonal crystals (supposed to possess equivalent *a* and *b* directions) has been considered as an indication of the formation of OCP precursor phases.[20] This morphology is also observed in nanocrystalline synthetic apatites precipitated at physiologic pH and it is not confined to the growth of apatite crystals in bone matrix.

- Identification of phases at the microscopic level using electron diffraction, selected area electron diffraction (SAED), can be performed on Ca-P samples. All these observations can be disturbed by beam damage especially when fragile hydrated phases or nanocrystalline compounds are present.[75]
- Composition determinations using EDS or WDS are often performed. These techniques are used for the determination of main constituents of biomaterials and biological Ca-P compounds: essentially Ca, Mg, P, F, seldom C. Their accuracy is, however, linked to the stability of the Ca-P compound and the sample characteristics (surface roughness, conditions of analyses), and even with the use of adequate standards, the determination of the apatite nonstoichiometry, using these methods, remains difficult.
- High-resolution transmission electron microscopy (TEM) is also a common technique often difficult to perform on very small unstable crystals sensitive to beam damage. The lattice fringes allow an identification of the crystallographic planes, the determination of the d-spacings, the orientations of crystals, and the observation of crystal defects. Amorphous domains have also been observed, at high resolution, at the surface of apatite nanocrystals corresponding probably to the dehydration of the structured layer existing in wet media (see spectroscopic characterizations).

One of the problems of these techniques is the beam damage, which is frequently observed especially with hydrated Ca-P and may lead to the decomposition of hydrated phases or even to the volatilization of phosphorus.[76,77] As calcium phosphates are nonconductive, it is necessary to limit the charge effect. In scanning electron microscopy (SEM), several techniques can be used: (1) coating with an electrically conductive layer, (2) working at low accelerating voltage at short working

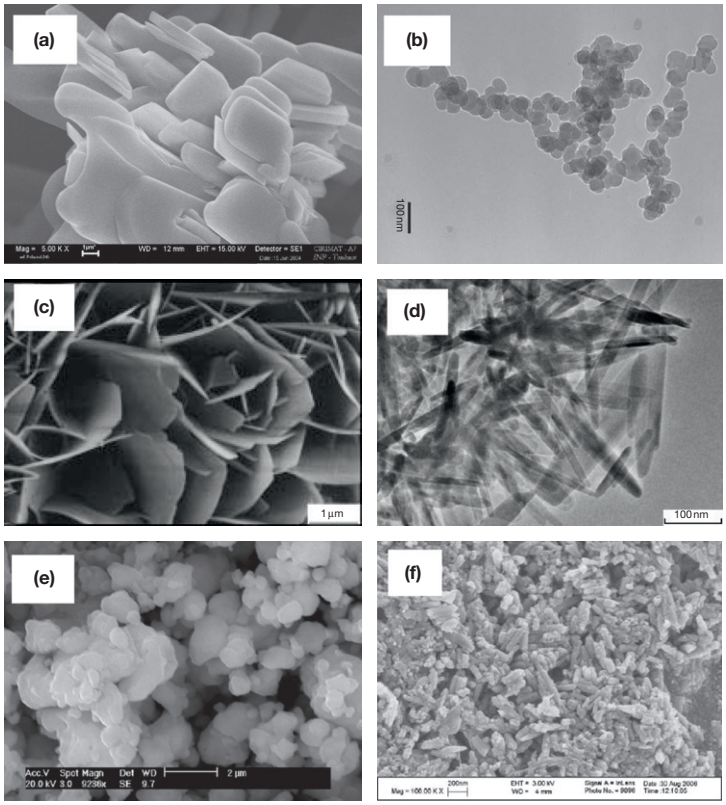

Figure 2 Example of typical morphologies of Ca-P compounds. (a) Scanning electron microscopy (SEM) image of DCPD crystals; (b) transmission electron microscopy (TEM) image of ACP (reproduced from Kim, S.; Ryu, H.-S.; Shin, H.; Jung, H. S.; Hong, K. S. *Mater. Chem. Phys.* **2005**, *91*, 500–506, with permission); (c) SEM image of OCP crystals (reproduced from Combes, C.; Rey, C.; Frèche, M. *J. Mater. Sci. Mater. Med.* **1999**, *10*, 153–160, with permission); (d) TEM image of apatite crystals (reproduced from Suvorova, E. I; Buffat, P. A. *Crystallogr. Rep. Kristallografiya* **2001**, *46*(5), 722–729, with permission); (e) SEM image of β-TCP crystals (reproduced from Choi, D.; Kumta, P. N. *Mater. Sci. Eng. C* **2007**, *27*(3), 377–381, with permission); (f) SEM image of TTCP crystals (reproduced from Pan, H. B.; Darwell, B.W. *Arch. Oral. Biol.* **2007**, *52*, 618–624, with permission).

distance, and (3) working under alterated vacuum. The solution (1) is preferred for morphology examination. The high vacuum may also alter the hydrated Ca-P phases; however, environmental microscopes can be used.

1.111.3.4. Vibrational Spectroscopies

FTIR and Raman spectroscopies allow the identification of most calcium phosphate phases. Generally, these methods focus on the use of internal vibrational levels of molecules and ions which may vary according to the short-range environments of these molecules or ions. Phosphate, carbonate, hydroxide ions, and water molecules are the main species detected by FTIR and Raman spectroscopies.

The PO_4^{3-} group has four main vibrational domains: ν_1 (at about 950 cm^{-1}), ν_2 (400–470 cm^{-1}), ν_3 (1000–1150 cm^{-1}), ν_4 (500–620 cm^{-1}). The main characteristic bands of the FTIR and Raman spectra of different calcium phosphates are shown in Tables 4 and 5.

The phases that cannot be easily distinguished by XRD can be discriminated using FTIR or Raman spectroscopies. This is the case, for example, of OCP and apatite or HA, oxy-HA, and amorphous phases present in plasma-sprayed coatings.[84] In addition to phase identification, these vibrational spectroscopies can be used for phase quantification using standard mixtures and standardization curves based on line intensity ratios. However, the principal advantage of vibrational spectroscopies over XRD is the identification of fine structural details, especially concerning apatites, such as the location of carbonate species on the different sites of the apatite structure, the presence of HPO_4^{2-} species, the quantification of the amount of OH^- ions, or the fine characterization of nanocrystalline apatites.

Carbonate ions, like phosphate, have four main vibrational domains: ν_1 (at about 1050 cm^{-1}), ν_2 (820–900 cm^{-1}), ν_3 (1400–1550 cm^{-1}), and ν_4 (650–750 cm^{-1}). Carbonate ions are always present in biological apatites and they may occupy different types of sites historically labeled as A and B: site A corresponds to monovalent anionic sites of the apatite structure and site B corresponds to trivalent anionic sites (Table 6). However, in addition to these main carbonate locations, several slight deviations have also been distinguished corresponding to different combinations with vacancies or water molecules or simply the combination of the two carbonate substitutions.[87] It has been shown that carbonate may also be incorporated in the surface hydrated layer of nanocrystalline apatite.

One of the most powerful uses of vibrational spectroscopies concerns apatite nanocrystals and poorly crystalline apatites for which XRD lacks accuracy. These methods are able to distinguish surface species and allow their quantification in simple cases. Surface HPO_4^{2-} have been shown to exhibit a specific

Table 4 FTIR spectral characteristics of phosphate ions in different calcium phosphate salts (wavenumbers in cm^{-1})

	DCPD	*DCPA*	*OCP*	*ATCP*	*β-TCP*	*α-TCP*	*HA*	*TTCP*
ν_3PO_4		1400 w						
		1350 w						
	1215 m		1295 w					
		1175 m, sh	1193 w					
	1132 s	1128 s	1137 vw					
			1121 s		1119 s			
			1103 s					1105 w
					1094 w, sh		1092 s	1093 w
	1070 s		1077 s		1080 w, sh			1073 w
	1060 s	1064 s	1055 s			1055 s		1062 s
				1040 s	1041 vs	1039 s	1040 vs	1046 s
			1037 s			1025 s		1033 m
			1023 s			1013 s		
	1000 w, sh		1000 vvw		1010 w, sh	997 s		1010 s
						984 s		
ν_1PO_4	984 s	992 m			972 s			989 s
			962 w				962 w	962 w
				949 w, sh		954 m		956 w
					945 m			946 w
								941 w
P-OH st. of HPO_4^{2-}			917 w					
	872 m	892 m	861 w					
ν_4PO_4			627 vw			613 m		620 w
			601 m		602 m	597 m	601 m	594 w
					589 w	585 m		
	577 m	576 s	575 w			563 m	575 m, sh	571 s
		563 s	560 m	560 m	550 m	551 m	561 m	
	526 s	525 m	524 w		541 m			501 w
ν_2PO_4		480				471 w	472 vw	471 m
			466 vw			463 w		
						454 w		
	418 sh	428 vw	449 vw		432 vw	430 w		450 w
	400 m	405 m				415 w		429 w
		398 sh						399 m
References	78	79	79		79	80	79	81

Intensity of the bands: vw: very weak; w: weak; m: medium; s: strong; sh: shoulder.

band, at 534 cm^{-1} in the ν_4 domain of the ion. When carbonate species are included in the hydrated layer of nanocrystalline apatite, they frequently appear in an 'amorphous-like' environment. In addition, FTIR and Raman spectroscopies can be used on wet samples revealing specific structural environments, which are lost upon drying, as shown in **Figure 3**.

Concerning OH^- ion, there is only one vibrational domain corresponding to the stretching of the O–H bond (3400–3650 cm^{-1}). However, a libration line, corresponding to a rotational energy level of the ion in the lattice, is also observed (630–750 cm^{-1}). OH^- bands are essentially detected in apatites and related compounds like partly hydrolyzed OCP. The OH^- stretching and libration movements are very sensitive to hydrogen bonding, and it has been shown in fluoride- and chloride-containing apatites that the OH bands can be considerably shifted away from their position in HA. The OH^- vibration and libration modes are also very sensitive to the nature of the surrounding cations.

Water molecules exhibit three vibrational modes: the symmetric stretching mode (ν_s) and the antisymmetric stretching mode (ν_{as}) have very close energy and they are difficult to distinguish. They generally give a broad absorption band on FTIR spectra (3000–3700 cm^{-1}). The bending movement around 1640 cm^{-1} gives a narrower band. Like OH^-, the water molecules are very sensitive to hydrogen bonding. In some calcium phosphates such as DCPD, the lines due to water molecules appear very specific and allow a clear identification. In other calcium phosphates (OCP, apatite, ACP), however, the water bands appear rather unspecific. Recently, a study of water molecules in nanocrystalline apatites has been published.[88] (see also **Chapter 3.322, Infrared and Raman Microscopy and Imaging of Biomaterials**.)

1.111.3.5. Solid-State Nuclear Magnetic Resonance

Solid-state NMR allows the identification of the short-range environment of different nuclei possessing a magnetic moment, such as ^1H, ^{13}C, ^{31}P, ^{19}F, which can be found in calcium phosphates.[89]

Table 5 Raman spectral characteristics of phosphate ions in different calcium phosphate salts (Raman shifts in cm^{-1})

	DCPD	*DCPA*	*OCP*	*ATCP*	*β-TCP*	*α-TCP*	*HA*	*TTCP*
ν_3 PO_4	1132 vw	1131 m						
	1119 vw			1118 w				1119 vw
			1112 w					1101 w
	1079 w	1094 m	1079 vw		1090 w	1077 w	1077 w	1091 sh
	1061 m						1064 w	1076 vw
			1052 w			1058 w	1057 w	
			1048 w	1050 w			1048 w	1045 vw
							1041 w	
			1036 vw				1034 w	
			1027 vw			1027 w	1029 w	1026 w
			1011 m		1015 w	1012 w		1008 w
			1005 w, sh			998 w		
ν_1 PO_4						976 s		983 vw
	986 s	988 s	966 s		970 s	964 s	964 vs	961 vs
			959 vs		948 s	954 sh		956 vs
				951 s				946 s
								940 s
P-OH st. of HPO_4^{2-}		900 m	916 w					
	878 m		874 w					
ν_4 PO_4			619 vw			620 w	614 w	615 vw
			609 mw		612 w	610 w	607 w	608 vw
	588 w	588 m	591 m	594 m		593 w	591 w	597 w
		563 m	577 m			577 w	580 w	576 vw
						563 w		566 sh
					549 w			556 vw
	525 w		523 w, b					495 sh
ν_2 PO_4					480 w			481 sh
			451 m	451 m		451 w	448 w	463 sh
					439 w		433 w	449 w
		420 w	427 m	419 m		421 w		414 sh
	411 w		409 m		408 w			407 w
	381 w	394 w	353 w					389 w
References	82	83	38	Leroy, personnal communication	82	80	82	81

Intensity of the bands: sh, shoulder; vw, very weak; w, weak; m, medium; s, strong.

Table 6 FTIR and Raman spectral characteristics of carbonate ions in different calcium phosphates (wavenumbers in cm^{-1})

	Type A carbonate		*Type B carbonate (in HA)*		*Type B (in FA)*	*Carbonate in ACP*
	FTIR	Raman	FTIR	Raman	FTIR	FTIR
ν_3CO_3	1542 s					1480 s
	1465 s		1462 s		1452 s	
			1412 s		1425 s	1417 s
ν_1CO_3		1107 m		1070 m		
ν_2CO_3	883 m		872 m		862 m	866 m
ν_4CO_3	757 vw[85]		718 vw[85]		716 vw[85]	
	670 vw[85]		692 vw[85]		695 vw[85]	
References	86	82	86	83	86	86

Intensity of the bands: sh, shoulder; vw, very weak; w, weak; m, medium; s, strong.

This very powerful technique also gives information on magnetic interactions between neighbor magnetic species. The main lines detected in calcium phosphates and the corresponding assignments are reported in **Table 7**.

Like FTIR, NMR spectrometry is particularly suitable for the study of nanocrystalline and poorly crystalline apatites. Recent data involving spin diffusion have confirmed the concept of the hydrated layer rich in HPO_4^{2-} ions.[91] In bone, several types of water species have been distinguished.[92]

The study of carbonate species by NMR spectrometry has confirmed the existence of the two main types of carbonate sites in apatite named A and B (**Table 7**). In addition, a third

type of carbonate species has been detected in nanocrystalline apatites, confirming the FTIR results. Two-dimensional NMR analysis of carbonated apatites has also established the location of carbonate species in a hydrated domain.[93]

^{19}F solid-state NMR studies of fluoride-containing carbonated apatites have clearly indicated the existence of two crystallographic sites corresponding to fluoride ions in monovalent sites and close to type B carbonate ions.[93]

Solid-state NMR spectroscopy also proved to be particularly useful in the study of the evolution of amorphous phases and the formation of apatite nuclei undetectable by other techniques.

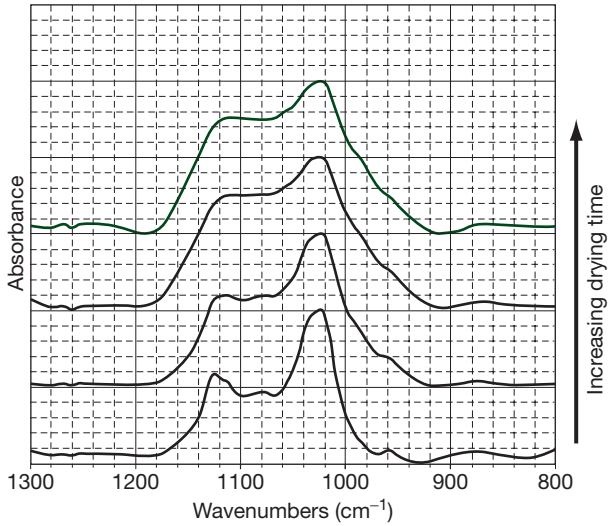

Figure 3 Example of FTIR PO_4^{3-} lines in the ν_3 domain of wet nanocrystalline apatite samples progressively dried in the spectrometer. The fresh wet samples (bottom) show very narrow well-resolved lines which can be associated to phosphate groups belonging to the hydrated layer. On drying (in minutes), the lines become broadened and poorly resolved indicating the destruction of the surface structure and resulting in amorphous-like environments of the phosphate ions.

1.111.4. Properties of Calcium Phosphates

1.111.4.1. Thermal Properties of Calcium Phosphates

The thermal properties of Ca-P are important parameters to consider when processing phosphate materials, or simply when preparing biological samples for different types of analyses. They are schematized in Figure 4.

The monocalcium phosphate monohydrate loses water at 108 °C and the MCPA obtained decomposes into calcium dihydrogen pyrophosphate, and then, due to continuous water loss, into calcium metaphosphate above 186 °C.

The DCPD loses water at 180 °C and transforms into DCPA. At higher temperature, another water loss is observed corresponding to the formation of calcium pyrophosphate.

The ATCP loses water up to its crystallization into α-TCP first and then β-TCP above 800 °C. The formation of the metastable α-TCP before the stable β-TCP might appear surprising. In fact, this phenomenon is rather common and it is observed also, for example, with amorphous zirconium dioxide or in the crystallization of polymeric substances. It is known as 'Ostwald's step rule' or law of successive reactions, stating that in any crystallization process, the state that is generally observed is not the most stable state but the least stable state that is closest in terms of free-energy change to the original state.[94]

The decomposition of OCP is more complex and involves the formation of DCPA and HA, and at higher temperature calcium pyrophosphate, which then partly reacts on HA to give β-TCP.

Considering apatites, two different types of decomposition reactions can be distinguished: reversible decomposition affecting stoichiometric apatites at very high temperature and irreversible decomposition related to nonstoichiometric apatites or apatites-containing thermally unstable ions such as carbonate and HPO_4^{2-}, for example.

1.111.4.1.1. Reversible decomposition of stoichiometric apatites

The stoichiometric HA is thermally very stable and it can be sintered at 1200–1250 °C without strong alteration. However,

Table 7 Solid-state NMR isotropic chemical shifts of ^{31}P and ^{1}H in calcium phosphates (in ppm relative to H_3PO_4 and TMS (tetramethylsilane), respectively

Nuclei	*MCPM*	*MCPA*	*DCPD*	*DCPA*	*OCP*	*ATCP*	*β-TCP*	*α-TCP*	*TTCP*	*HA*
^{31}P	− 4.6									
				− 1.5						
	− 0.1	− 0.5		0.0	-0.3			− 0.23		
		0.5					0.6	0.04; 0.35		
								0.66; 0.95		
								1.15; 1.40		
			1.7		2.0		1.7	1.7; 1.92		
					3.2	3.0		2.53; 2.99		2.8
					3.5			3.44; 3.97	3.8	
							5.1	4.22; 4.68	4.7	
^{1}H				16.2						
				13.6	13.0					
			10.4		9.6					
			6.5							
			5.0		5.5					5.6
					0.2					0.18
References	89	89	89	89	89	89	89	90	89	89

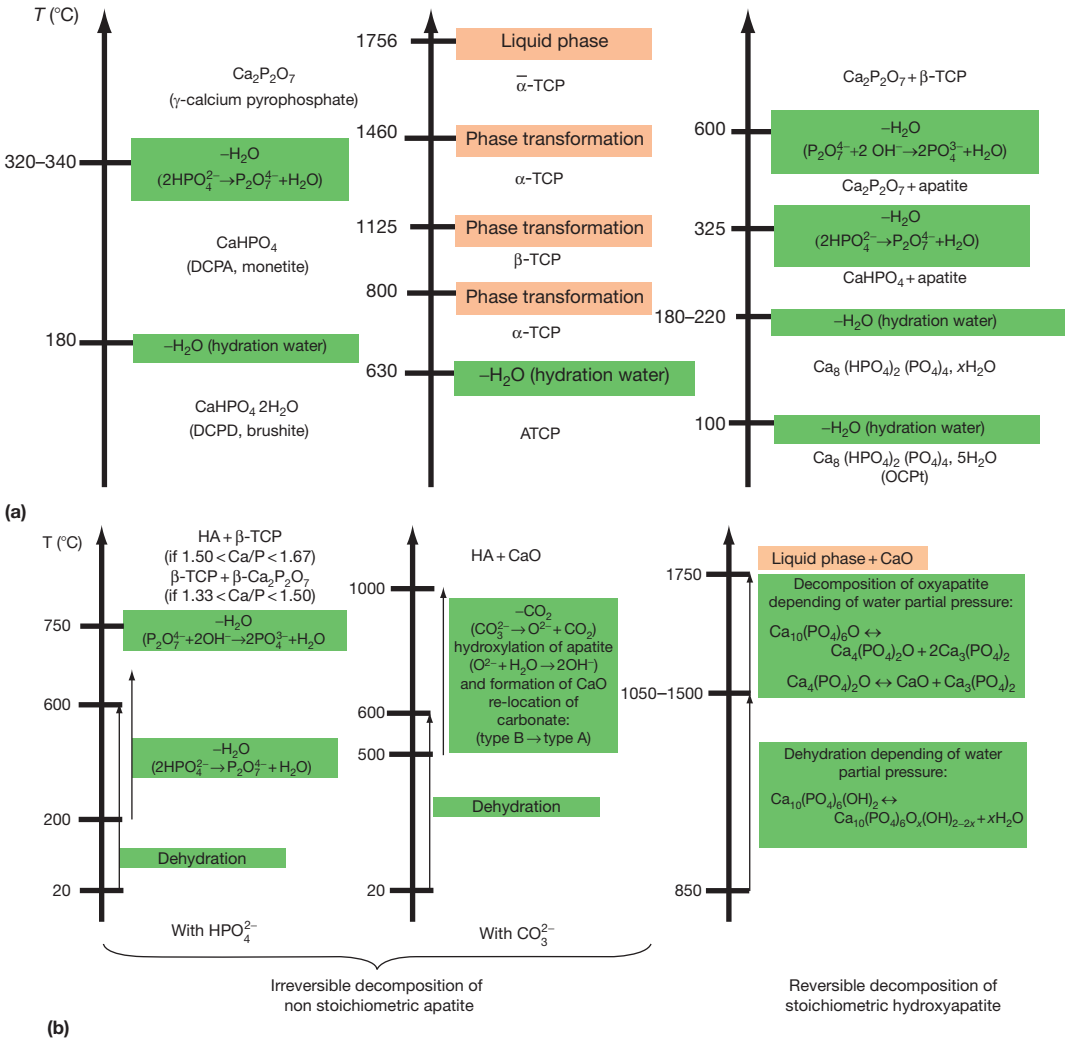

Figure 4 (a) Thermal decomposition of DCPD, DCPA, ATCP, and OCPt. (b) Thermal decomposition of apatites. Depending on their composition (HPO_4^{2-} or CO_3^{2-} or both) vacancies-containing apatite decompose differently, these reactions are always irreversible. At high temperature (above 850 °C) stoichiometric hydroxyapatite decomposes reversibly into different Ca-P compounds depending on the temperature and water partial pressure.

HA is considered to begin to lose water at 850 °C at a very low H_2O partial pressure leading to the formation of oxyapatite.[63] This loss is strongly dependent on the water partial pressure. Then, oxyapatite decomposes into TCP and TTCP at about 1050 °C and, at higher temperature (1720 °C), TTCP decomposes into CaO and a liquid phase.

All these reactions are theoretically reversible and, on cooling under an adequate water partial pressure, the HA structure is reformed, provided there is no fast quenching which prevents the completion of the reverse reaction. A problem which has been raised is the volatilization of P at very high temperatures, for example, in plasma spraying processes.

1.111.4.1.2. Irreversible decomposition of nonstoichiometric apatites

Nonstoichiometric apatites exhibit a complex decomposition behavior depending on their initial composition, as shown in Figure 4(b). All these reactions are related to the instability of calcium-deficient apatites and they are irreversible. The decomposition involves the formation of pyrophosphate in the case of HPO_4^{2-}-rich apatites and the formation of oxide ions in the case of carbonate-containing apatites

$$2HPO_4^{2-} \rightarrow P_2O_7^{4-} + H_2O$$

$$CO_3^{2-} \rightarrow O^{2-} + CO_2$$

Curiously, the pyrophosphate ions are not easily detected in the apatite structure but they can be evidenced by chemical methods. It is only at high temperature that calcium pyrophosphate crystallizes as a separate phase when the Ca/P ratio of the apatite is under 1.5. The formation of oxide ions can lead to the formation of OH^- in the apatite structure, or, in highly carbonated type B apatites with a Ca/P ratio above 1.67, to the separation of a CaO phase.

When HPO_4^{2-} and CO_3^{2-} are both present, cross-reactions can be observed such as

$$2HPO_4^{2-} + CO_3^{2-} \rightarrow 2PO_4^{3-} + CO_2 + H_2O$$

or

$$P_2O_7^{4-} + CO_3^{2-} \rightarrow 2PO_4^{3-} + CO_2$$

In the case of nanocrystalline apatite, the first reactions can occur at very low temperature 100–200 °C.

The end products at 900–1000 °C of the irreversible decomposition of nonstoichiometric Ca-P apatites are only related to the initial Ca/P ratio:

- for Ca/P < 1.5, β-TCP and β-calcium pyrophosphate are obtained
- for 1.5 < Ca/P < 1.67, a mixture of β-TCP and stoichiometric HA is obtained
- for 1.67 < Ca/P, a mixture of stoichiometric HA and CaO is obtained.

These decomposition reactions can be used to determine the Ca/P ratio of an unknown Ca-P phase and some of them have been standardized (see **Section 1.111.3.2**).

The irreversible decomposition of calcium-deficient apatites can be used to prepare biphasic ceramics made of TCP and HA.

1.111.4.2. Solubility

Per definition, the solubility of a solid in an aqueous solution is characterized by an equilibrium between the solid surface and the species in solution, which exhibit a constant ion activity product corresponding to the solubility product (K_{sp}). The K_{sp} is characteristic of a solid compound and is related to its composition; it is not directly representative of the amount of solid dissolved, which may change as the species in solution vary, due, for example, to protonation or deprotonation of orthophosphate groups, the formation of ion pairs in solution, or the change of the activity coefficients of the different ions due to alterations of the ionic strength. The speciation of different entities present in the solution is an important factor. Such alterations are considered in computer programs available on the web. In several cases, however, authors have not really evidenced an equilibrium and they report solubility data, which might correspond to a dissolution rate rather than to real solubility equilibrium. In the case of phases that cannot form in the conditions of the dissolution experiments, for example in physiological conditions (37 °C, pH = 7.4) such as α- and β-TCP, DCPA, and TTCP, an apparent dissolution equilibrium is reached; however, the risk exists to precipitate non detectable amounts of more stable Ca-P phases. The determination of K_{sp} of unstable calcium phosphates, which can be easily hydrolyzed into more stable phases in aqueous media, is particularly delicate (e.g., OCP, ACP) and, in fact, several different solubility products have been reported in these cases.[20,30] Another confusion arises from apparent solubilities often determined in conditions where an equilibrium is not really reached, for example, because of uncontrolled release of CO_2 in dissolution studies of carbonated phases. Other problems of reliability include uncontrolled impurities levels, the consideration of different ion pair formations or ion activities corrections, which are responsible for discrepancies of K_{sp} of sparingly soluble solid phases. Recently, Nancollas has raised a new concern regarding the dissolution process of crystals.

Table 8 Solubility products of different calcium phosphates

Ca-P compound	*Common abbreviation*	*$-log\ K_{sp}$ at 25 °C*	*References*
$CaHPO_4$, $2H_2O$	DCPD (monoclinic)	6.59	96
$CaHPO_4$	DCPA (triclinic)	6.90	97
$Ca_8(PO_4)_4(HPO_4)_2$, $5H_2O$	OCP (triclinic)	96.6	98
α-$Ca_3(PO_4)_2$	α-TCP (monoclinic)	25.5	99
β-$Ca_3(PO_4)_2$	β-TCP (trigonal)	28.9	100
ATCP	Noncrystalline	25.5	
$Ca_{10}(PO_4)_6(OH)_2$	HA (stoichiometric)	116.8[a]	101
$Ca_{10}(PO_4)_6F_2$	FA (stoichiometric)	121[a]	102
$Ca_4(PO_4)_2O$	TTCP (monoclinic)	38	103

[a]Expressed for a chemical formula in '$Ca_{10}(PO_4)_6Y_2$.'

A stepwise dissolution behavior has been shown in the case of well-crystallized OCPt assigned to the need of additional energy for the formation of dissolution kinks on a flat crystal surface and resulting in difficulties to determine a solubility equilibrium.[95] In the case of solid solutions and nanocrystalline apatites, other difficulties have been raised, as discussed later in this paragraph. Nevertheless, the solubility products of most stoichiometric well-crystallized calcium phosphates have been determined (**Table 8**), although divergences and discussion are still existing. A recent direct method, especially based on the total dissolution of increasing amounts of crystals until the detection of residual crystals in suspension[104], has given solubility products much lower values than those generally admitted, but this rather unconventional procedure could be biased due to the stabilization of crystals in undersaturated solutions as shown by Tang and Nancollas.[95]

The solubility isotherms of stoichiometric Ca-P compounds have been studied in detail by several authors.[105,106] At physiological pH, the solubility, expressed as the amount of Ca^{2+} and orthophosphate ions in solution at the equilibrium, is found to decrease in the order TTCP > α-TCP > DCPD > DCPA ~ OCP > β-TCP > HA, while FA is itself less soluble than HA. Moreover, among the nonfluorinated Ca-P compounds, stoichiometric HA is the least soluble phase in a wide range of pH values down to pH close to 4. Below this value, DCPA becomes the least soluble phase, although it does not form generally in these conditions, and DCPD appears as the stable phase in solution.

These data permit some general observations. For the same composition, phases with lower density show a higher solubility, for example, considering the dicalcium phosphates or the crystalline TCP, in relation with the hydration or simply the structure. This observation can be related to the degree of cohesion of the structure, assuming that the main factor involved in the cohesion of Ca-P crystals is the electrostatic attraction between anions and cations and if we neglect the events occurring in solution (protonation, ions pairs), which, for the same or similar compositions, should not be crucial. Such a reasoning can be extended to apatites; thus, Ca-P apatites with the smaller unit-cells and, therefore, the higher the cohesion forces the lesser the solubles, and FA is less soluble than HA. Similarly, Ca-P apatites are less soluble than strontium-phosphate apatites, with larger unit-cell

dimensions. This behavior can probably be generalized to apatites-containing vacancies: apatites with a high vacancies content should be more soluble than those with a low vacancies content. Considering carbonate and HPO_4^{2-}-containing apatites with similar Ca vacancies content, type B carbonated apatites, with a smaller unit-cell, should be less soluble and they have been found, in fact, to form preferentially during maturation.[107] The cohesion forces can also be increased by raising the electric charge of the constitutive ions, thus, silicate- and lanthanide-containing apatites are less soluble than regular Ca-P apatites. These considerations neglect, however, the existence of partial covalent bondings between ions in the apatite crystals and the ions interactions with the solution and, although they are indicative, no definitive conclusion should be made based only on electrostatic cohesion forces.

It is also worth mentioning that the presence of foreign ions in the composition of a given Ca-P compound or even in the surrounding solution may noticeably modify the dissolution behavior. For example, in the case of HA, the incorporation of fluoride ions was found to decrease the solubility, while carbonate or else magnesium ions induced an increase in the apparent solubility.[108,109] In the presence of fluoride ions in solution, a decrease in solubility is also observed probably related to a surface alteration of the HA. Such phenomenon involving a very low amount of surface ions impurities may considerably affect the solubility behavior of apatites and they are used in the biomedical field, such as in fluorinated tooth paste, for example, or in apatite coatings of prosthetic devices.

Besides the above considerations, dealing with stoichiometric Ca-P compounds, the solubility behavior of nonstoichiometric, biomimetic, nanocrystalline apatites is also interesting to address due to their resemblance with bone mineral and their high potential in the bioceramic field. However, the physicochemical characteristics of apatite nanocrystals highly depend on their conditions of formation. Several factors can influence the solubility, such as the composition/nonstoichiometry of the nanocrystals and, probably, the surface structure and composition. A detailed analysis of the solubility behavior of such biomimetic apatites indicates that, unlike stoichiometric HA, they do not reach a constant solubility product. In fact, the apparent equilibrium which is attained depends on the amount of solid dissolved (Figure 5); the ionic product at the apparent equilibrium state shifts progressively toward that of stoichiometric HA as the amount dissolved increases. This observation has led to the concept of 'Metastable Equilibrium Solubility' (MES). This behavior has been evidenced and studied in various works (e.g., Baig *et al.*,[111] Chhettry *et al.*,[112] and Hsu *et al.*[113]) and has been related to the level of microstrains in the crystals.[110] However, other explanations are possible such as a variable surface composition and structure or the existence of mixed crystals population with different size, composition, and solubility.

Noncongruent dissolution (i.e., dissolution leading to a mineral ion composition of the solution different from the solid) has often been reported in the case of calcium phosphates. This phenomenon can have several causes, for example, a surface hydrolysis or the preferential dissolution of undetected impurities possibly on the surface of the crystals. In the case of high solid/solution ratios with solids of high specific surface area, noncongruent dissolution can also be related to surface reactions such as adsorption of constitutive ions, as discussed in Section 1.111.4.4.1, or surface hydrolysis or precipitation; but these experimental conditions, favoring the detection of surface reactions, and depending on solid/solution ratios, do not necessarily correspond to an anomaly of dissolution. It shall be emphasized that a dissolution of a homogeneous phase leads to a congruent dissolution as it is most commonly found. Subsequent surface equilibrations of the residual mineral surfaces can alter the composition of the solution and this alteration is dependent on the solid/solution ratio. In the case of phase with an heterogeneous distribution of atoms, however, a 'noncongruent' dissolution may be observed.

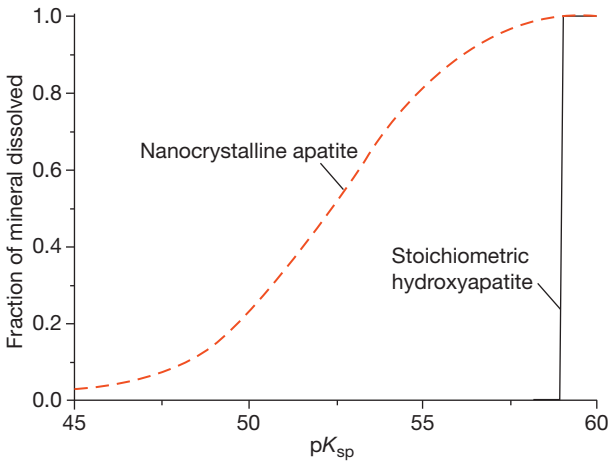

Figure 5 Illustration of the Metastable Equilibrium Solubility (MES) of biomimetic apatites.[110] For a stoichiometric hydroxyapatite, the ion activity product in solution is independent of the amount dissolved. For biomimetic nanocrystalline apatites (from biological or synthetic origin), the ion activity product in solution decreases as the amount of dissolved apatite increases leading to a MES. The shape and position of the MES curves depend on the maturation time.

1.111.4.3. Hydrolysis and Aqueous Conversion

The most soluble Ca-P compounds (ACP, DCPD, DCPA, OCP, TTCP, nonstoichiometric HA) can be transformed into more stable phases in aqueous media. The important parameters are pH, calcium and phosphate concentrations, and temperature. Most generally from slightly acidic pH to alkaline pH, the end term of these conversion reactions is apatite, in agreement with the dissolution isotherms. However, these reactions can lead to apatites with very different compositions depending on the mineral ions in the solution. Thus, in the presence of carbonate and/or fluoride, carbonated and/or fluorinated apatites can be obtained.

Several reaction mechanisms have been proposed for the hydrolysis reactions. Dissolution–reprecipitation seems to be the dominant process for hydrolysis involving phases transformations. Although at physiologic pH, the most stable, least soluble, phase is apatite, even stoichiometric apatite, this phase is rarely obtained in solution, in these conditions, and generally, metastable nonstoichiometric apatites are formed

especially at human body temperature. These conversion reactions may involve intermediary phases according to the Ostwald step rule (see Section 1.111.4.1); thus, the transformation of ACP into apatite at neutral pH is considered to occur through an OCP precursor at pH close to neutrality. In the case of OCP hydrolysis into apatite, a topotactic transformation which could give rise to interlayered crystals of OCP and apatite has been suggested.[114] The HA crystals formed can appear in this case as pseudomorphs of OCP crystals. In the case of apatite nanocrystals with a surface hydrated layer, the evolution in aqueous media appears more complex and is often called 'maturation.' In this case, the hydrolysis is associated with an alteration of crystals characteristics. At physiological pH, maturation has been found to be related to the hydrated layer. The apatite domains develop at the expense of the ions in the hydrated layer and when the hydrated layer has practically vanished, the process stops.[107] Even when maturation has stopped, slower evolution processes remain active like Ostwald ripening. However, if they play a role at geological time scale, their implication in biological minerals is questionable.

Aqueous conversions of Ca-P are mainly used in self-setting Ca-P cements. One may distinguish rapidly hydrolyzable Ca-P such as ACP, α-TCP, which can lead to apatites in less than 1 h at 37 °C and can be used in neutral monocomponents mineral Ca-P cements, and slowly hydrolyzable Ca-P such as DCPD, DCPA, and OCPt, which need generally longer reaction times, higher temperature, or an alkaline pH to react rapidly. These are used in 'acid–base' cements in combination with TTCP, which hydrolyzes relatively rapidly and generates an alkaline pH. This distinction between rapidly and slowly hydrolyzable Ca-P is, however, rather artificial and depends essentially on the characteristics of the crystals, especially the crystal dimensions.

1.111.4.4. Surface Charge and Surface Energy

Interfacial phenomena play a major role regarding the biological properties of Ca-P, especially in adsorption and cell adhesion, and surface charge and surface energy have often been considered as the most important physical characteristics of the surface.

1.111.4.4.1. Surface charge

The surface charge of solids, at the origin of 'zeta potential,' arises from different phenomena: the preferential adsorption/desorption of the constituting ions of this solid in solution, the protonation of surface species like PO_4^{3-} ions, for example, or the surface adsorption of foreign ions or molecules from the solution. For ionic solids such as calcium phosphates, the surface charge is closely related to the concentration, in the surrounding fluid, of specific ions that can interact with the surface of the solid. Such ions are often referred to as 'potential-determining.' A difficulty is the time-dependent variation of the zeta potential, which may result in discrepancies.[115]

The point of zero charge (pzc) defines the conditions of the solution (in particular, the pH value) for which the surface density of positive charges (contribution of cations) equals that of negative charges (anions). It is often regarded as a characteristic parameter for a given surface in a given aqueous solution.

When considering calcium phosphates, most studies have been dedicated to the determination of the surface charge of stoichiometric HA. It should be added here that as HA involves at least three types of potential-determining ions (calcium, phosphate, and hydroxide or proton), a variety of concentration conditions exist for conducing to a condition of zero surface charge,[116] which therefore leads to define a *line* of zero charge (lzc) in the calcium–phosphate–hydroxyl ternary diagram. Chander and Fuerstenau[116] have, for example, calculated the position of this lzc for HA and compared it to experimental data reported by several authors. Some discrepancies were observed between calculated and experimental points, which is probably due to dissimilar affinities of calcium, phosphate, and OH^- ions for the surface (assumed identical in the calculations). The calculated pzc value is found to be around pH 8.5; however, experimental values are often slightly lower. The isoelectric point of stoichiometric HA, for example, is close to pH 7.[117] Generally speaking, it may be stated that the pzc for HA is found in the range 6.4–8.5.[118] The conditions of preparation, washing, and storage of the apatite material as well as the presence of impurities and structural defects seem indeed to play a nontrivial role in the electrochemical properties[118,119] of the surface, which constitute the basis of most zeta potential measurements. In all cases, a negatively charged surface is observed, for HA, beyond the pH corresponding to the isoelectric point and a positively charged surface below it. It is interesting to point out that, under constant pH and ionic strength, a change in the calcium or phosphate concentrations can affect the surface charge of HA significantly. Indeed, an increase of calcium concentration will, in every case, lead to a surface charge shifted toward more positive values (traducing the adsorption of calcium ions on the surface of the solid), while an increase of phosphate concentration would render the surface more negative. These effects were indeed experimentally observed by Somasundaran and Wang.[119]

Ionic substitutions and apatite composition also play a role in the modification of apatite surface charge. For example, the following order was found for the pH values of the pzc of four apatite samples: FA < HA < strontium-HA < barium-HA.[120] Interestingly, this order also corresponds to the order of increasing solubility of the four apatites. For example, the pzc of FA is found in the range 4.5–6.9.[118] Other types of ionic substitutions were also investigated; for example, the surface charge of silicated-HA was found[121] to be noticeably more negative than regular HA in similar conditions, which was assigned to the presence of tetravalent silicate ions exposed on the surface of the solid rather than phosphate ions. Nonstoichiometry may affect the surface charge of apatites, and Ca-deficient apatites, more soluble than stoichiometric ones, have been found to exhibit zeta potential greater than stoichiometric HA.[122]

It is also worth noting that the adsorption of organic molecules on the surface of solids can significantly modify the surface charge of the particles, especially when the molecules exhibit charged functional end-groups (or at least strongly electropositive or electronegative elements). An example of this effect was reported by Mangood *et al.*[123] referring to the adsorption of acetaminophen on HA, leading to a surface noticeably more negatively charged. In contrast, the adsorption

of amino acids[124] or an amine-terminated phospholipid moiety[125] on calcium-deficient apatites were found to lead to surface charges shifted toward more positive values. It must, however, be stated that, in the case of nonstoichiometric nanocrystalline apatites prepared in biomimetic conditions (low temperature, physiological pH, etc.), the existence of a nonapatitic surface layer on the apatite nanocrystals (see previous section on the 'preparation of Ca-P compounds') leads to a more complex system that cannot anymore be adequately defined by using the regular HA surface model, which thus makes it difficult to appreciate the amounts of phosphate or calcium ions actually exposed on the surface (as they are bound to vary depending on the conditions of formation and storage).

Apart from these data regarding apatitic compounds, only the surface charge data related to other calcium phosphate compounds are scarce. Among such works, however, zeta potential measurements have been interestingly performed on octacalcium phosphate (OCP) in solutions equilibrated with respect to that phase.[126] The results of this study pointed out the positively charged surface of OCP under a wide range of pH values (from 5 to 11). In addition, measurements carried out in a solution with increasing Ca/P ratios led to increasingly positive zeta potential values (at a given pH) suggesting the specific adsorption of calcium ions. In contrast, a decreasing zeta potential was observed when decreasing the Ca/P ratio of the solution, possibly related to a more extensive adsorption of phosphate ions in these conditions.

1.111.4.4.2. Interfacial energy

Interfacial energy is also an important parameter to consider when dealing with interactions between a solid surface and the surrounding solution. Yet, only few data are available in the literature on this matter in the case of calcium phosphates. Generally, two main components of the interfacial tension are distinguished, determined by the type of interactions with the surface polar (dielectric bondings) and apolar (van der Waals bonding) components, sometimes completed by a hydrophilic parameter related to hydrogen bonding. Such interfacial energies (with respect to water) have been reported for HA, FA, OCPt, and DCPD, with respective values: 9.0, 18.5, 4.3, and 0.4 $mJ\,m^{-2}$.[127,128] Interestingly, among those four compounds, the lowest interfacial tensions were found for the hydrated phases (OCP and DCPD). A value for the interfacial tension in water was also reported for β-TCP: 3.8 $mJ\,m^{-2}$,[129] also pointing out a lower value than for the apatites HA or FA. The surface tension of a carbonated apatite sample (well crystallized, 3 wt.% CO_3) was also determined,[130] with a value (9.0 $mJ\,m^{-2}$) found similar to that of HA. In all cases, the surface tension of these calcium phosphate compounds was found to correlate well with their solubility in water, the lowest surface tensions being observed for the most soluble phases.

1.111.4.5. Chemical Alterations of the Surface

Two main chemical alterations of the surface of Ca-P have been described in addition to preferential adsorption of constitutive ions discussed in Section 1.111.4.4.1: ion exchange and the adsorption of molecules.

1.111.4.5.1. Ion exchange

The term 'ion exchange' can be used to describe ion substitutions inside an apatite lattice. This is not, however, what is intended here, and ion exchange corresponds to a reaction specifically affecting the accessible ions on the surface of given crystals.

The surface ion exchanges are of utmost relevance in the case of nanocrystalline calcium phosphate apatites, which were found to exhibit a structured, metastable, nonapatitic surface layer that was shown to be highly reactive (see Section 1.111.2.3.2). These phenomena were first studied by Neuman and Mulryan[48] who suggested the possibility of carbonate-HPO_4^{2-} exchanges in biological nanocrystalline apatites. Several studies have explored surface ion exchange capabilities of biomimetic apatites, as illustrated recently in the case of Ca/Mg and Ca/Sr exchanges[88,131], where Mg^{2+} and Sr^{2+} are biologically active ions. Other ion sorptions were also investigated for HA. For instance, exchanges of part of the Ca^{2+} ions with metal ions Cu^{2+}, Cd^{2+}, Pb^{2+}, or else Zn^{2+} were studied.[132,133] The exchange isotherms may generally be well described by using the Langmuir model, and two main constants K and N representing respectively the affinitiy constant and the maximum exchangeable amount have been derived for exchanges performed either on carbonated or noncarbonated apatites. The ion exchange capabilities of nanocrystalline apatites have been related to the development of the surface hydrated layer. Thus, higher amount of ions are exchanged in freshly precipitated nonmatured apatites, where the surface hydrated layer may contain up to 20% of the exchangeable ions; in matured apatites where the apatite domains have developed at the expense of the hydrated layer, the ion exchange capabilities can be considerably reduced especially for carbonate–hydrogen-phosphate or anion exchanges. Curiously, cation exchanges appear to always involve higher amounts than anion exchanges. All these exchange reactions are very fast (the equilibrium is reached in a few minutes) and they do not alter the main characteristics of the apatite domains (crystal size and nonstoichiometry).[134] The ion substitution capabilities in the hydrated layer are considerably larger than those of a Ca-P apatite lattice. Thus, a considerable amount of surface Ca^{2+} can be replaced by Mg^{2+}, whereas Mg^{2+} ions can only substitute for a very small amount of Ca^{2+} ions in the apatite lattice. The reversibility of ion exchange reactions is always very high when the reverse reaction immediately follows the direct exchange reaction. However, when a maturation period occurs after the exchange, two kinds of behavior have been distinguished. When the mineral ion introduced in the hydrated layer can substitute calcium ions in the apatite domains, the reverse exchange reaction can only exchange back decreasing amounts of foreign ions still present in the decreasing hydrated layer. This is the case of Sr–Ca exchanges. When the mineral ion introduced cannot substitute in appreciable proportion the calcium ion in the apatite domain, they stay in the decreasing hydrated layer and remain almost totally exchangeable. This is the case of Mg–Ca exchanges.[135]

Another interesting feature related to ion exchanges is the role of foreign ions either on the promotion or the inhibition of apatite crystal growth. Several ions such as pyrophosphate, carbonate, or magnesium, among others, were thus shown to act as growth inhibitors for apatite crystals.[136]

It is often difficult to determine if the ion exchange reaction corresponds really to a surface ion exchange or to a dissolution–reprecipitation process involving a reequilibration of the surface. This distinction is especially difficult in the case of apatites where continuous solid solutions exist and where surface exchange can modify the surface composition to reach an equilibrium with the solution by modifying only the first surface atomic layers.

1.111.4.5.2. Adsorption

Adsorption phenomena on calcium phosphates are also of major interest, as molecules interacting with these compounds can play a key role in the recruitment and expression of cells, and they are strongly involved in the biointegration of implants. This is especially true for apatites due to their biomimetic nature and their numerous potentialities in the biomedical field.

The adsorption of proteins or other active molecules on apatites is also considered to play a determining role in mineralized tissues as it may control apatite crystal growth and dissolution *in vivo*, and it also appears as a clever way to associate drugs (e.g., antibiotics, antiosteoporotic agents, etc.) and other active agents (growth factors, etc.) to control their range of action. Such adsorption phenomena have thus been the object of a great number of studies. Proteins like osteocalcin, osteopontin, or else, albumin, and other biomolecules (phospholipid, growth factors such as fibroblast growth factor (FGF), vascular endothelial growth factor (VEGF), bone morphogenetic protein (BMP)) have, for example, been shown to adsorb on apatite and interact strongly with its surface (e.g., Boskey *et al.*,[137] Hauschka and Wians,[138] and Romberg *et al.*[139]). Also, as was mentioned above for substituting ions, several macromolecules were found to act either as promotors or inhibitors of crystal precipitation.[136] It has been shown, however, that such classifications can be misleading. Of course, an adsorbed molecule on a given calcium phosphate surface appears to delay in most cases the growth of the corresponding crystalline face; however, adsorption also stabilizes crystal nuclei with a subcritical size, and paradoxically low concentrations of adsorbing molecules in solution were shown to increase the nucleation rate and accelerate precipitation, whereas high concentrations inhibit precipitation.[140] All these adsorption reactions exhibit some common characteristics: they are generally well described by a Langmuir adsorption isotherm and they appear irreversible by dilution, which is often considered as an anomaly with regard to the Langmuir model (Figure 6).

Several factors have been shown to be involved in the adsorption properties of molecules on calcium phosphates either related to the solid surface or to the molecules themselves: surface energy, surface charge, functional chemical groups of the molecules, conformation, competition with other potential adsorbents, etc.

Historically, interfacial energy has been one of the first parameters to be considered in adsorption and, according to Gibbs, adsorption may be considered as determined by a decrease of the interface energy. This global physical view, of interest when weak interactions are involved with the adsorbate, neglects the possibility of strong chemical interactions at the atomic level which very often occur with the surface of Ca-P and determine the major adsorption processes of importance in biology.

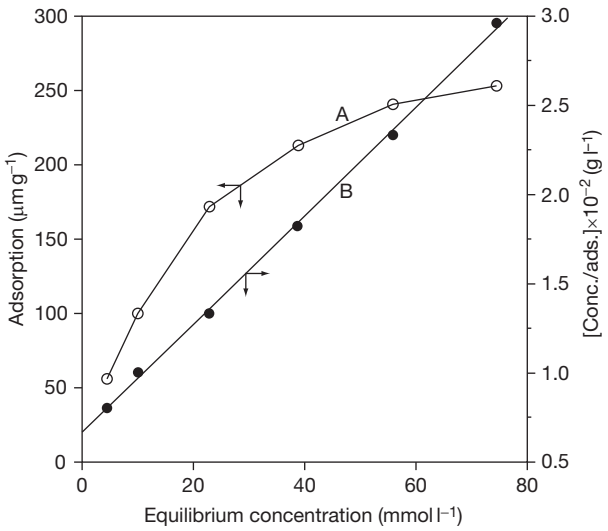

Figure 6 Example of an adsorption isotherm of citrate molecular ions, on apatite from aqueous solutions (22 °C). The isotherms (curve A) correspond to a Langmuir adsorption equation: $Q = KNC/(1 + KC)$ where Q is the amount adsorbed (ordinate), and C is the equilibrium concentration (abscise). Two parameters characterize the adsorption reaction: K, the affinity constant, and N, the maximum amount adsorbed at saturation. Generally, the Langmuir equation is linearized to extract more conveniently the adsorption parameters (curve B): $C/Q = C/N + 1/KN$. Reproduced from Misra, D. N. *Colloids Surf.* **1998**, *141*, 173–179, with permission from Elsevier.

Indeed, due to the ionic nature of Ca-P compounds, two main types of interactions have been distinguished corresponding to electrostatic attraction between negatively charged end-groups and calcium ions on the one side, and/or positively charged end-groups and phosphate ions on the other side. The zeta potential of apatites has thus been and is still considered to play a major role in the adsorption process and most adsorption behaviors have been related to this surface parameter. Once again, however, the correlation between this global physical parameter describing the total surface charge of apatite particles and chemical interactions with specific ions or charged groups at an atomic level is not straightforward. It appears that the global charge of a particle does not give any information on the local distribution of cations and anions on a mineral surface, and as a matter of fact, the zeta potential does not appear to be a decisive parameter: for example, the adsorption of positive molecules on a globally positive apatite surface and, inversely, negative molecules on a globally negative apatite surface have been described.[141,142] Adsorption is also observed on neutral Ca-P surfaces near their pzc. Similarly, the isoelectric point of proteins, by itself, does not give specific information on the ionization state of the different functions of a molecule and should be considered with caution when predicting the adsorption behavior related to a chemical interaction.

Interestingly, the nature of the functional chemical groups exposed by the adsorbent is one of the key parameters to take into account when considering the interaction with a calcium phosphate surface. Phosphate esters and similar groups especially interact strongly with apatite surface, and phosphorylated compounds are considered to play an important role in biomineralization. Among the other functional groups

considered to interact strongly with apatite surfaces are silicate and sulfate. In general, carboxylate groups interact weakly, except when they are associated in polyacids.[143,144] Positively charged groups can also adsorb on apatites but generally less strongly than negatively charged ones.

In numerous examples, the adsorption of negative molecular ions has been related to the release of phosphate ions, demonstrating a chemical ion exchange reaction with the apatite surface. This process has been described in different instances, as for example in the adsorption of polyacids[145], citrate ions[146], zoledronate[147], or serum proteins on apatites. This chemical process seems rather general and supports a chemical description of the adsorption reaction rather than a physical one based on global electrostatic interactions or pure interfacial energy considerations. Adsorption could thus be represented, for example, as a chemical equilibrium as follows (in the case of a one-to-one exchange with surface phosphate groups):

$$A_{sol} + P_{ap} \Leftrightarrow A_{ap} + P_{sol}$$

with A being the adsorbate in a given ionic state either in solution (sol) or on the apatite surface (ap), and P being the phosphate group in a given ionic state either in solution or on the apatite surface. Other ion exchange possibilities have been discussed by Misra[146] in the case of citrate adsorption. These descriptions seem consistent with the use of apatites in chromatography where negatively charged molecules are desorbed using phosphate solutions and positively charged ones using calcium solutions. It has been shown that this ion exchange process could be described by a Langmuir-type isotherm, often observed, and could also explain the apparent irreversibility of the adsorption on dilution of the solution.[148]

Here again, like for ion exchanges, surface reaction and dissolution–reprecipitation can be considered as possible competitive processes. However in this case, unlike for ion exchange on apatites, no solid solutions are generally possible between the calcium phosphate and the phosphate salt of the molecules. Thus, in the case of insoluble calcium salts formation and precipitation with the adsorbate molecules, the apatite phase is progressively destroyed as the new phase forms, leading to the release of phosphate into the solution until a new equilibrium is reached. This event does not generally give a Langmuir-type isotherm with a typical saturation domain. On the contrary, the increase of the amount of adsorbate results in more precipitation of its calcium salt and more destruction of the apatite. In some cases, however, this process could result in a Langmuir-like adsorption behavior, with an apparent saturation domain if there is coating of the apatite surface by the new phase, preventing further reaction. Observation of the solid phase by XRD or electron microscopy generally allows the formation of new phases to be detected (For more details on proteins adsorption, see also **Chapter 3.311, Molecular Simulation Methods to Investigate Protein Adsorption Behavior at the Atomic Level**.)

1.111.4.6. Nucleation Properties

Nucleation and crystal growth are processes involved in normal and pathological biological mineralization; these processes are also of primary importance when calcium phosphate-based bioceramics are in contact with a calcium and phosphate supersaturated solution such as human blood plasma (ceramics implanted *in vivo*) or the considered equivalent synthetic solutions such as simulated body fluid (SBF) or other similar solutions used to test ceramics *in vitro*.

Crystallization at surfaces, that is, heterogeneous crystallization, may be induced at supersaturations lower than those required for spontaneous precipitation (homogeneous crystallization). This phenomenon is generally considered to be related to the lower overall free energy in the formation of nuclei of critical size at the surface of a substrate[149] and it has been related to the interfacial energies. Crystallization on foreign substrates is generally preceded by an induction period which is markedly related to the supersaturation, the temperature, and the presence of additives or impurities. This period has been considered by many authors to be the time needed for the formation of nuclei of critical size, that is, stable nuclei able to grow.

The growth of one crystalline phase on the surface of another may be important especially in physiological mineralization processes. The epitaxial relationships and kinetics of growth of HA on calcium phosphate crystalline phases or on other compounds such as the ones involved in bioactive ceramics (especially $CaCO_3$) have been investigated by Koutsoukos and Nancollas.[150] Epitaxy or oriented crystal growth is a special case of heterogeneous crystallization in which the crystal formation on the substrate is determined by the atoms mapping that offers a good crystal lattice match facilitating the nucleation of a foreign phase. The authors showed that HA can be grown on different calcium salts as substrates (DCPD, calcium fluoride, and calcite) from calcium and phosphate solutions with a low supersaturation; moreover, they showed that the crystallization kinetics are similar to that of HA on HA seed crystals whatever the substrate. However, epitaxial growth of HA on these substrates was not confirmed due to the difficulty to well characterize the grown microcrystalline apatite on the HA. β-TCP on the contrary appears as a poor nucleation substrate for HA[151], although it can be used in heteronucleation of OCPt.

The heterogeneous nucleation of apatite crystals on organic substances has been related to functional groups. Thus, phosphate groups have been found to favor the nucleation of apatite on collagen matrix.[152] More recently, Toworfe *et al.*[153] have shown that apatites form preferentially on surfaces rich in –OH terminal groups, whereas surfaces with $-NH_2$ groups exhibited a low induction capability. Such findings have been associated with the polarization of the surfaces and especially, the acceleration of crystal growth on a negative surface evidenced by Yamashita *et al.*[154] and discussed by Calvert and Mann.[155]

In vitro and *in vivo* crystallization processes can differ substantially. Indeed, two main differences can be noted between *in vitro* and *in vivo* crystallization: (i) the rate of precipitation which is usually faster *in vitro* compared to *in vivo* and (ii) the presence of many proteins and ions *in vivo* that can promote or inhibit mineralization and can alter crystal morphology.

1.111.5. Biological Response and Physical–Chemical Characteristics

Physical–chemical characteristics of materials are directly related to some of their biological properties and determine in part biointegration, biological activity, and biodegradation

of materials. The biointegration of an implant is a crucial property, especially in the case of bone substitutes, and a poor biointegration is responsible for most implant failures. The biointegration of implants is determined on the one hand by mechanical factors: the interlocking of implant surface and biological tissue and on the other hand by chemical factors: the chemical bonding to the tissue constituent. The mechanical integration is mostly determined by the roughness and porosity of biomaterial surfaces initially created on the medical device and it may also be the result of biodegradation irregularities. The chemical bonding to the tissue seems a determining factor and it appears mainly related, in actual bone substitutes, to the ability of the surface to bind directly to the mineral fraction of bone tissue.

Even if bioactivity has different meanings depending on the authors, it is generally recognized that bioactive materials have the property to bind directly to bone tissue without any fibrous interface. Bioactivity is also used to name materials favoring an accelerated tissue repair. These definitions are related to different biological phenomena, namely implant–tissue interactions and implant–cell interactions that can possibly be or not be combined in the same material. It seems important to insist on these two properties. Cell culture dishes, for example, which have been specially treated to favor cell adhesion, allow osteoblast cells to proliferate and produce bone tissue. However, their bone-bonding ability is limited and the materials they are made of will never be a good bone substitute. In fact, once osteoblast cells have reconstructed bone, the interface is essentially implant/tissue and it is mainly the strength of this interfacial interaction which insures bone bonding. Most calcium phosphate compounds involved in bioceramics are not in equilibrium with biological fluids; several reactions will thus occur on the Ca-P ceramic surface. As biological fluids are supersaturated with respect to apatite, the Ca-P ceramics may also serve as templates for the formation of carbonated apatite crystals.

1.111.5.1. Active and Passive Biomaterials with Regard to Ca-P Nucleation

It has been shown that all bioactive materials that bind chemically to bone tissue and promote the formation of a stable interface ('bone-bonding materials') also have the ability to initiate nucleation of Ca-P from biological fluids at their surface. This layer of Ca-P shows characteristics analogous to bone mineral and appears to be composed of nanocrystalline carbonated apatite with a high reactivity. The association of the layer with specific bone proteins enables osteoblast cells (responsible for bone tissue formation) adhesion and activity.[156] Their activity is, however, related to nutritive fluid supply. For some authors, this process is similar to that involved in bone remodeling and the neoformed layer would present a composition analogous to the cement line at the edge of an osteon.[157] However, one can note that the formation of this layer is desirable at the biomaterial surface only for applications as bone substitutes and not for articular or cardiovascular applications for which any calcium phosphate nucleation and deposit must be avoided.

The ability to form this layer is generally considered as a measurement of the biological activity of bioceramics. Two main classes of biomaterials can be distinguished depending on the processes inducing the formation of apatite nanocrystals (see **Table 9** and **Figure 7**): in one case, the implant is only a substrate favoring the heterogeneous nucleation ('passive' biomaterials) and in the other case, it releases mineral ions that locally increase the supersaturation of biological fluids and thus contribute to the fast formation of the apatitic layer ('active' biomaterials) adding mineral ions from the material to the ions of the body fluids (**Figure 7**).

Assuming that the formation of an apatite layer determines the biological activity, 'active' biomaterials could be considered more efficient than 'passive' ones and in fact such a conclusion has been drawn by Hench comparing bioactive glass and HA.[158] However, bone is a living tissue with a remodeling process and one may wonder what may happen at the interface of the 'active' biomaterials and bone after successive remodeling processes. Is the release of mineral ions from the biomaterials still active or is it no more existing after the first contact resulting in surface depletion of active mineral ions? 'Active' biomaterials are probably superior for bioabsorbable implants, whereas 'passive' ones, which will essentially keep their intrinsic nucleation properties even after multiple remodeling events, could be preferred for permanent implants.

Table 9 Classification of biomaterials based on their ability to promote the formation of an apatitic layer analogous to bone mineral on their surface

	Biomaterial	*Active ions*	*Induction process*
'Active' biomaterials	Bioglasses	Ca^{2+}	Diffusion outside the bioglass
	Coral	Ca^{2+}, CO_3^{2-}	Dissolution
	Plaster of Paris	Ca^{2+}	Dissolution
	Ca-P cements	Ca^{2+}, PO_4^{3-}, OH^-	Dissolution
	Alkaline hydrogels	OH^-	Hydrolysis
	Biomaterial	Nucleation ability	Induction process
'Passive' biomaterials	Sintered apatites	Excellent	Epitaxy
	Titanium	Average	Hydrolysis, PO_4^{3-} and Ca^{2+} uptake
	Neutral hydrogels	Good	PO_4^{3-} uptake
	Collagen	Good	Phosphorylated entities
	Polyactiv®	Good	Ca^{2+} uptake

Source: From Cazalbou, C.; Combes, C.; Rey, C. *J. Aust. Ceram. Soc.* **2004**, *40*, 58–67.

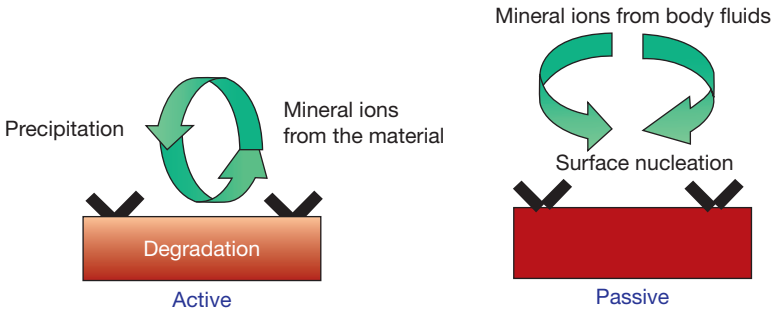

Figure 7 Illustration of 'active' and passive bioactive materials with regard to the nucleation of Ca-P apatites. In active biomaterials, the mineral ions needed for the precipitation of apatite crystals at the surface of the biomaterial can come in part from the material, either by dissolution or by diffusion leading to a surface depletion. In passive biomaterials, the formation of the apatite crystals involves only ions from the supersaturated body fluids, and nucleation ability is exclusively an inherent surface property.

Table 10 Ionic composition of blood plasma and SBF solutions

	Concentration 10^{-3} mol l^{-1}							
	Na^+	K^+	Ca^{2+}	Mg^{2+}	HCO_3^-	Cl^-	HPO_4^{2-}	SO_4^{2-}
SBF	142.0	5.0	2.5	1.5	4.2	148.8	1.0	0.5
Blood plasma	142.0	5.0	2.5	1.5	27.0	103.0	1.0	0.5

Source: Kim, H. M.; Miyazaki, T.; Kokubo, T.; Nakamura, T. *Key Eng. Mater.* **2001**, *192–195*, 47–50; Kim, H. M.; Kim, Y. S.; Woo, K. M.; Park, S. J.; Rey, C.; Kim, Y.; Kim, J. K.; Ko, J. S. *J. Biomed. Mater. Res.* **2001**, *56*, 250–256; Kokubo, T.; Hata, K.; Nakamura, T.; Yamamuro, T. In: *Bioceramics*; Bonfield, W., Hastings, G. W., and Tanner, K. E., Eds.; Butterworth-Heinemann Ltd: London, 1991; Vol. 4, pp 113–120.

1.111.5.2. Simulated Body Fluid Testing

Considering the importance of nucleation and formation of an apatite layer on bioactive materials, an international standard (ISO standard 23317, 2007) has recently been published to evaluate the apatite-forming ability on the surface of biomaterials in a model solution: simulated body fluids (SBF). The SBF solution, proposed by Kokubo *et al.* in the 1990s, contains mineral ions at concentrations nearly equal to those of human blood plasma (see **Table 10**).[159] Indeed it has been shown that this apatite layer can be reproduced on the surfaces of material in SBF solutions and that nanocrystalline apatite thus formed is quite analogous to bone mineral. This inexpensive and fast test has been largely used to estimate the potential biological activity of a material and it is presented as useful for evaluating in a quantitative manner bone-bonding ability of a biomaterial preliminary to animal experiments, although it shall be acknowledged that there are no quantitative studies correlating SBF tests and the *in vivo* biological activity and performance.

The test is quite simple and consists in the immersion of the material to be tested in a SBF solution at 37 °C up to 4 weeks. The formation of the biomimetic carbonated apatite on the surface of the biomaterial can be detected by thin film XRD spectrometry and/or SEM and the rate of formation can be followed by chemical analyses of the solution. This test is commonly considered as a measurement of the bioactivity of a biomaterial; as bioactivity increases, apatite is supposed to form on the material surface in a shorter time in proportion to this increase.

The protocol for the use of this solution to test bioceramics or more generally, biomaterials, is detailed in the ISO standard, although several errors exist in the available version at this date: the amount of trishydroxymethyl aminomethane (TRIS), used to buffer the solution, for example, is incorrect and the way of obtaining the SBF solution appears rather awkward, leading to the elimination of carbonate ions and risks of precipitation. A safer and more correct procedure would consist in preparing two buffered solutions, a cations solutions (half of the sodium chloride, potassium chloride, magnesium chloride, calcium chloride, buffered with half the amount of HCl recommended and TRIS) and an anion solution (half of the sodium chloride, dipotassium hydrogen phosphate, sodium sulfate, buffering the other half of HCl and TRIS, the sodium bicarbonate is added, last, in the buffered anion solution without alteration of the pH) and mixing them just before use.

SBF solutions differ in several points from the composition of blood plasma: the carbonate content is not adequate and proteins are absent. These constituents of blood plasma are important and they have been shown to alter strongly the nucleation and crystal growth process of apatites. The composition of SBF solution has been revised with a view to getting closer to mineral ion concentrations in human blood plasma by decreasing Cl^- concentration and increasing HCO_3^- concentration compared to concentration in conventional SBF solution.[160]

However, reaching the carbonate composition of real blood plasma would need to work under CO_2 partial pressure to avoid a decrease of carbonate content related to its dissociation at physiological pH in solution:

$$HCO_3^{2-} + H^+ \leftrightarrow H_2CO_3 \leftrightarrow H_2O + CO_2$$

Whatever the type of SBF solution (conventional or revised) considered, there is still a major difference between this model solution and human blood plasma: many proteins are present in plasma and the ionic concentrations in SBF solution have been established considering the ionic content of plasma, which includes compounds formed between mineral ions and organic molecules (soluble complexes, ion pairs) of serum altering the amount of free ions in solution and the activities of the mineral ions. It has been demonstrated that ultrafiltrated fractions of blood plasma (excluding mineral ions linked to proteins) had in fact, an ionic product close to that of OCP[161], whereas the actual SBF solutions exhibit a much larger one.

Another criticism made to SBF testing is that the mineral ions concentrations is not constant in the batch as it would be *in vivo* and circulating SBF testings have been proposed. However, the test is supposed to measure the apatite nucleation ability of an implant surface and not really a crystal growth kinetic. In this sense, the batch procedure seems adequate. SBF testing is the only chemical model presented as a measure of the biological activity of an implant surface based on the assumption that the apatite nucleation ability of a surface is related to its bioactivity. As it is an inexpensive and rather rapid testing method, it will probably continue to be extensively used, although it cannot replace animal implantation. The SBF test has been recently criticized by Bohner and Lemaitre who have proposed some improvements.[162]

The chemical reproduction of the reactions occurring on an implant surface placed in the body seems difficult to achieve: the body response to an implantation is a complex phenomenon which varies as time elapses. From a chemical–physical point of view, the composition and pH of the body fluids at the vicinity of an implant surface after the surgical operation is not really known. It is believed that the surgical trauma induces acidic pH, which could be responsible for accelerated degradation of Ca-P materials, but the intensity and duration of these events are difficult to predict, making a modeling of the behavior of an implant surface difficult.

1.111.5.3. Biodegradation

Biodeterioration and biodegradation of implants determine their durability. The first term is generally used when the alteration of the implant is not necessarily wanted and the second when it is one of its advantages. Several processes contribute to biodeterioration and biodegradation: mechanical wear, spontaneous reactions of the implant materials with body fluids, and cell-mediated alterations. Mechanical wear is of course occurring at the interface between mobile parts of a medical device but it is also observed at the tissue–implant interface, and appears mainly related to micromovements (fretting) and results in abrasion wear residues and possible inflammatory reaction. This phenomenon is limited when there is a strong interfacial bonding between the implant and the tissue.

In addition to mechanical wear and surface abrasion, two main processes can be distinguished: one is purely physicochemical (ionic crystal dissolution) and the other one is linked to cellular (and enzymatic) activity at the implantation site (activated resorption).[163] In fact, both aspects are bound to the intrinsic properties of the ceramic, including its grain shape and size, porosity, solubility, structure and microstructure, and also the degradation residues of various constituents in combined materials such as composites or heterogeneous materials.

The overall biodegradation rate *in vivo* has often been directly linked to the solubility behavior of the compound(s) constituting the bioceramic.[164] The different Ca-P compounds exhibit solubility products that greatly differ from one another (see **Section 1.111.4.2**). Compared with blood plasma, with an ionic activity product generally considered to be very close to OCP[161], the calcium phosphate phases, that should spontaneously dissolve are TTCP, DCPD, DCPA, ACP, and α-TCP, in addition to the two very soluble monocalcium phosphates. The other calcium phosphates should not spontaneously dissolve and on the contrary could exhibit a crystal growth. However, the most stable phase remains apatite, and an evolution of OCP and β-TCP toward apatite by surface or topotactic transformation cannot be excluded.

Spontaneous dissolution does not mean, however, that the implant, made of the most soluble Ca-P, necessarily disappears. The supersaturations that are reached locally are so high in body fluids that spontaneous precipitation occurs most of the time and the formation of apatites is observed. On experimental grounds it has been found that the implants containing the most soluble Ca-P (excluding the very soluble calcium monophosphates) are effectively transformed rather rapidly after implantation into poorly crystalline apatites.

The cell activity has also to be considered in biodegradation. Multinucleated giant cells involved in the defense response of the organism and osteoclast-like cells are frequently found in the vicinity of Ca-P bioceramics. These cells have the property to generate very acidic pH, and all Ca-P, including apatites, become rather soluble below pH 4, which explains their progressive dissolution, for example, within osteoclastic resorption pits. In this case, the rate of dissolution becomes the main parameter determining the biological degradation. It is related not only to the solubility product of the Ca-P and more precisely to the undersaturation achieved locally, but also to the crystals characteristics (size, strains) and the implant characteristics (surface exposed, porosity). The undersaturation appears as a crucial factor. The rate of dissolution of stoichiometric HA, for example, is very low and this Ca-P is often considered as a nonresorbable or at least a very slowly resorbable compound. This is only valid, however, for stoichiometric highly crystalline HA and it is not an inherent property of the structure itself. In the case of calcium-deficient HA, the biodegradation can be very high, like in some biomimetic cements, for example. On the contrary, β-TCP is considered to give rapidly resorbing ceramics.

Generally, bioceramics made of Ca-P are made of a multitude of crystals bound to one another, and they are sometimes multiphasic compounds. Several additional physical–chemical phenomena affecting biodegradation can then be involved. The most obvious is probably the decohesion of the material related to the preferential dissolution of the most rapidly soluble constituent, leading to the release of crystals or particulates of the least soluble, more stable, phase. These phenomena

have been found, for example, in the case of HA plasma-sprayed coatings, and they can also manifest in biphasic HA/β-TCP ceramics or in composite materials. Depending on their size these particles can induce different body responses. When the released particles are small enough, they can be phagocitized and they are eventually eliminated. However, when the elimination is not possible or when too numerous particles are released, they may initiate an inflammatory response sometimes devastating. This can occur, for example, with poorly sintered materials or when a Ca-P ceramic is associated with a rapidly absorbed matrix. When the fragments are big enough and cannot be further fragmented, they might remain in place, enkisted in the tissue. Biphasic compounds, especially, have considerably developed in the last years and their resorption can be regulated by the phase ratio. This is the case, for example, of biphasic HA/β-TCP ceramics where the degradation rate can be tailored by modifying the proportion of the more soluble phase, namely β-TCP, which seems to be degraded preferentially upon cellular activity.

The degradation behavior of nonstoichiometric nanocrystalline apatites is also interesting to consider, although apatite nanocrystals may exhibit varying physicochemical characteristics depending on their conditions of formation, which then account for differences in resorption rates *in vivo*. Various parameters can indeed influence the dissolution and biodegradation processes: in particular, the nonstoichiometry of the nanocrystals is a major factor to consider, as the dissolution of such ionic compounds depends on the amount of vacancies. A second effect could be related to the important interfacial energy and the evolution of the dissolution rate with the crystal size. As already mentioned, the presence of foreign ions in the composition of a given Ca-P compound may greatly modify its dissolution behavior. For instance, the solubility and *in vivo* degradation rates of zinc-enriched TCP were found to be significantly lowered as compared to pure TCP.[165] Also, the dissolution of calcium pyrophosphates was found to increase in the presence of ions such as Mg^{2+} or albumin,[166] although the *in vivo* degradation is mostly due to enzymatic activity of those compounds.

Other physical–chemical parameters have been shown to determine the degradation rate of implants *in vivo* such as the porosity and the crystallinity. Considering the porosity, macroporosity (pore diameter in the range 150–500 μm) seems to play a major role especially in the case of ceramics made of insoluble Ca-P in body fluids. The macropores allow cell invasion and increase the number of dissolution sites. The effect of microporosity is more difficult to apprehend: a first effect seems primarily related to a lesser content in material; a second effect is related to the increase of the surface area and of the related dissolution rate. Thus, for the same composition, highly microporous mineral cements are faster absorbed than less porous ones. Crystallinity has been shown to play also a role probably related to the increase of the surface area and dissolution rate but also to crystalline defects and possibly amorphous phase content, as these different characteristics are often considered in the global 'crystallinity' parameters.

A last parameter of importance in biodegradation is cell adhesion. In order to be active, the osteoclast-like cells involved in the biodegradation of Ca-P materials have to adhere to the materials and find favorable conditions. Alkaline pHs especially have been found to strongly inhibit osteoclast activities.[160,167] Thus, Ca-P generating alkaline pH on hydrolysis, like TTCP, for example, found in some mineral cements, may inhibit osteoclasts activity, as long as they are present.

1.111.6. Examples of Applications and Processing

1.111.6.1. Porous Ceramics

Porous Ca-P ceramics are among the most used synthetic bone substitute materials. They are generally obtained by natural sintering at a high temperature of HA, β-TCP, or a mixture of them and stabilized α-TCP. Several types of porosity are found in such ceramics. The definition of porosity in bioceramics appears historically different from the uses determined for other substances like zeolithes. In bioceramics, macroporosity is generally between 200 and 400 μm and allows cell rehabilitation. In addition, microporosity (1–10 μm) is frequently present depending on the sintering conditions: longer sintering time and higher temperatures generally decrease the microporosity. The macroporosity of most industrial ceramics is obtained by replication from a porous polymer, the use of calibrated porosity agents or with foaming agents. Other types of porous Ca-P ceramics have been obtained from natural compounds like the sintering of cow bone, for example, or the conversion of corals (calcium carbonate) skeleton.[168] Several shapes exist for different surgical uses: granules, cylinders, parallelepipeds, edges. Other techniques have been proposed to obtain a more regular porosity, however, they do not seem to have been commercialized yet. The total porosity; of porous Ca-P ceramics is generally comprised between 30 and 80%. As usually observed, the compressive strength decreases when the porosity increases for similar compounds.

HA ceramics are considered as nonbioresorbable and, although osteoclasts adhere on such surfaces effectively, they have difficulties to spread and create resorption pits.[169] HA ceramics may contain two impurities: CaO and TCP, which can be determined by XRD according to ISO standards. CaO rehydrates as $Ca(OH)_2$ in aqueous media with a 40% increase in volume. This phenomenon may result in the fragilization and cracking of the ceramic. TCP is a bioresorbable Ca-P, which might dissolve *in vivo* and facilitate the bioresorption as in biphasic ceramics, as discussed earlier. HA ceramics have been associated with very low levels of SiO_2 that have been shown to improve their biological activity.[170] However, the reasons for these effects remain obscure. The improvements obtained with silicate-substituted apatite at higher ratios have been assigned to the effect of released silicate (for more details on Si-containing apatites, see **Chapter 1.119, Silicon-Containing Apatites**).[171] It seems interesting to mention that the doping of HA with foreign elements cannot be considered as straightforward as for glasses or alloys. For example, if a mixture of HA with SiO_2 is heated, it will result in a mixture of HA and β-TCP due to the fact that it is SiO_4^{4-} anions which will be incorporated and that these anions will substitute for PO_4^{3-} anions in the apatite structure. For example:

$$2.5Ca_{10}(PO_4)_6(OH)_2 + SiO_2 \rightarrow 5Ca_3(PO_4)_2 + Ca_{10}(PO_4)_5(SiO_4)OH + H_2O$$

If one wants to get Zn doped HA by heating HA and ZnO, one has to consider that Zn^{2+} will substitute for Ca^{2+} in the apatite structure and the result will be HA doped with Zn and CaO:

$$Ca_{10}(PO_4)_6(OH)_2 + xZnO \rightarrow Ca_{9-x}Zn_x(PO_4)_6(OH)_2 + xCaO$$

Heating with different oxides may lead to different results and impurities, depending on substitution abilities in the apatite structure.

β-TCP ceramics have been especially developed by Jarcho *et al.*[172] They are bioresorbable. However, unlike it is sometimes written, they cannot spontaneously dissolve in body fluids at physiologic pH. β-TCP can hydrolyze and be converted into apatite in aqueous solution, but this reaction already rather slow at 100 °C (at least 48–72 h are needed) is inappreciably slow at 37 °C. It is only cell activity after implantation, producing acidic pH, which can dissolve β-TCP. As its biodegradation is determined by osteoclast cells activity, like in regular bone, it appears as a ceramic, which adapts to the remodeling rate of bone at the loci of the implantation. Unlike some other Ca-P, like DCPD, for example, β-TCP is unable to favor apatite nucleation by epitaxy. Although the reported data are not consistent, due to its rate of dissolution in acidic media linked to its solubility product, it is considered as a fast resorbing implant; this resorption rate could, however, depend on its composition and especially the Mg content, a major impurity in calcium salt. The main impurities in β-TCP are calcium pyrophosphate and apatite. They can be determined with high accuracy by FTIR spectroscopy and XRD respectively. β-TCP has been associated with active ions such as Zn^{2+}. In some cases, behavior akin to osteoinduction has been suggested for β-TCP;[173] however, the reason of this behavior is not really known.

Biphasic HA-β-TCP ceramics have been proposed by Daculsi and LeGeros.[174] They are bioresorbable and it has been shown that the bioresorption rate was related to the β-TCP content.[175] Generally, this content varies between 20 and 60% in industrial products. All these ceramics are osteoconductive and some of them, generally sintered at low temperature, have been shown to be osteoinductive. (see also **Chapter 5.521, Calcium Phosphates and Bone Induction** treating of calcium phosphates and osteoinduction.) Unlike in pure β-TCP, the presence of HA facilitates the nucleation of apatite in body fluids, and these ceramics, like pure HA ceramics, can bind firmly to bone tissue. The biodegradation has been reported to involve a faster dissolution of the β-TCP phase, followed by HA crystals elimination. Curiously, these biphasic Ca-P are unlikely to contain any other crystalline phase: excess of CaO in the HA fraction would lead to additional HA by reaction on β-TCP at sintering temperature and excess of pyrophosphate in β-TCP would lead to additional β-TCP by reaction with HA.

The high-temperature ceramics can be associated with drugs and growth factors; however, because of their very low specific surface area there is no strong surface interaction and the release is mainly controlled by diffusion through the pores and physical parameters. This release process can be interesting for some substances like antibiotics, for example, but it might appear as a drawback for very active substances like growth factors, compared to other Ca-P materials where adsorption occurs and where the release remains localized and under the control of the organism.

1.111.6.2. Coatings, Example of HA-Plasma Spraying

One of the most efficient solutions to favor biological integration and bioactivity of prostheses and orthopedic implants consists in coatings with Ca-P ceramics. Many different techniques have been proposed and used to deposit such coatings, but plasma spraying of HA appears as one of the most applied and most developed at an industrial scale.[84]

This is a technique in which a DC electric is struck between two electrodes, while a stream of mixed gasses (generally H_2 and Ar) passes through this arc. The arc turns these gas into an ionized mixture (plasma) of high temperature and with a high speed of up to 400 m s^{-1}. The temperature of the plasma rapidly decreases as a function of distance from 20.000 K close to the arc to 2000–3000 K at 6 cm outside the electrodes. A ceramic powder suspended in a carried gas can be incorporated into the plasma and impinged in a partially molten state toward a surface. Many surfaces of metals or ceramics can be coated with a relatively thick layer (50–300 μm) of composition close to that of the powder. Ideally, only a thin outer layer of powder particles gets into the molten state which is necessary to ensure dense and adhesive coatings. The bonding of the coating is mainly due to mechanical interlocking.

HA appears certainly as the major plasma-sprayed Ca-P. One of the main difficulties in HA plasma spraying is the thermal decomposition of HA at high temperature and the mixture of phases, which constitute the coating (**Table 11**).[176] These phases are heterogeneously distributed in the particle reaching the surface and in the coating. At contact with the metal and on the surface, a rapid quenching of the molten fraction leads mainly to an amorphous phase, a slower quenching inside the particle may allow the crystallization of high-temperature phases in their order of stability: CaO (with a very high melting point: above 2500 °C), TTCP and α-TCP, and then β-TCP and oxy-HA. However, when a second pass is made, the surface is reheated and a recrystallization may proceed again. In addition to this decomposition, volatilization of phosphorus has also been evidenced, especially in H_2-rich flames, resulting in a change in stoichiometry; thus, even when using pure HA in the plasma spraying, the resulting coatings may contain an excess of calcium appearing as CaO or TTCP. Depending on processing parameters, many different coatings can be obtained and ISO standards have been published regarding some important physical–chemical characteristics of the coating: the Ca/P ratio, the content in

Table 11 Phases found in plasma-sprayed coating of HA

Phases	*Formation*
Calcium oxide	Decomposition of HA and TTCP Volatilization of P
Calcium hydroxide and calcium carbonate	Reaction of CaO with humidity and CO_2 (on contact with air or body fluids)
Amorphous calcium phosphate	Melting of HA and quenching
α-Tricalcium phosphate	Thermal decomposition of HA
β-Tricalcium phosphate	Phase transition on cooling from α-TCP
Tetracalcium phosphate	Thermal decomposition of HA
Oxyhydroxyapatite	Dehydration of HA
Hydroxyapatite	–

crystalline impurities, and a crystallinity index (ISO 13779-2 and 3), but curiously not really the amorphous phase content. Although several post-treatments have been proposed as remedial and have been shown to restore the apatite structure, they all have some drawbacks and weaken at some point the coating cohesion and adhesion to the metal surface.

The decomposition of HA and the formation of different Ca-P phases, especially the amorphous phase, can have a positive effect, especially on biological activity, as most of these phases will spontaneously release mineral ions and will thus 'activate' the coating (see **Section 1.111.4.1**).[84] However, these phases weaken the coating which may degrade and lead to a deterioration of the implant–bone interface. In addition, the metal-coating interface appears as the weak point of the process and delamination of the coating may occur.[177] In fact, the adhesion of the coating on the metallic substrate is mainly due to mechanical interlocking on the porous implant surface, although chemical bonding cannot be totally excluded. High levels of amorphous phase in the coating lead to improved interfacial adhesion on the metal and biological activity but poor durability. Raising the crystalline HA content, on the contrary, lowers the biological reactivity and weakens the metal-coating interface but the coating can last longer. The solution to this dilemma could be a coating made of several layers with different characteristics as proposed by different authors.[178] (see also **Chapter 1.112, Calcium Phosphate Coatings** and **Chapter 1.113, Bioactive Layer Formation on Metals and Polymers**)

1.111.6.3. Cements

The fast-setting calcium phosphate cements have emerged as an attractive concept essentially as bone filling and reinforcement biomaterials. Ca-P bone cements have developed considerably in the last few years due to their excellent biocompatibility and bioactivity.[105] The applications for the filling of bone defects are very promising, whether in the form of a molded paste placed in the surgery site or in the form of an injectable paste hardening *in situ*.

Several types of reactions can be involved in the Ca-P self-setting materials, which lead to the formation of two main classes of Ca-P cements depending on the end product: apatite cements consisting of more or less crystallized apatite and brushite cements.[105,179] Some examples of apatite and brushite cements are given in another chapter of this volume. It shall be noticed that brushite is not stable in body fluids and that it shall inevitably be transformed more or less rapidly, depending on the size of the implant, into nanocrystalline apatite.

The hardening of mineral cements is generally attributed to the growth of interlaced crystals. This has been shown in the case of some apatite cements where long needle-like crystals can be seen by SEM and in the case of brushitic cement, interlaced large plate-like crystals isomorphous to gypsum crystals responsible for the hardening of plaster can be observed. This mechanism, however, does not seem to be involved in biomimetic cements resulting in nanocrystalline apatite analogous to bone mineral. The high specific surface area and strong interactions between nanocrystals could be, in this case, the main factor of hardening.

Two major types of reaction are involved in phosphocalcium cements formation. The first consists in a reaction between one or more 'basic' calcium compound (i.e., rich in calcium) such as TTCP or even $Ca(OH)_2$ and one or more 'acidic' calcium phosphates (i.e., rich in phosphate) such as MCPM, H_3PO_4, DCPD. In aqueous medium, the reaction between these phases leads to less soluble new phases, whose crystallization brings about the setting. The second type of reaction takes advantage of the metastability of a Ca-P phase in aqueous medium and its rapid conversion into apatite. Two phases, α-TCP and ACP, can be used. Various cement formulations have been proposed, sometimes mixing different Ca-P phases and hardening reactions, and several cements are commercialized: SRS®, Bonesource®, Cementek®, Biobon®, α-BSM® (see **Chapter 1.116, Bioactive Ceramics: Cements**).

Several properties characterize a biological cement, like construction cements, although most of them have not been standardized which do not allow comparison between formulations. The workability is the time during which the paste can be mixed and kept before use; this property is related to the characteristics of the reactions involved in the setting. The ACP conversion, for example, is extremely slow at room temperature, which is related to a long working time. For some brushitic cements, like for plaster of Paris, mixing the paste for too long may break the growing crystals involved in the setting process and may result in lower mechanical properties. Additives, which delay the reactions between constituents at room temperature, can be used to increase the workability. The setting time has been standardized (Gillmore needle test) and corresponds to the time needed to get a compact block. Generally, the chemical reactions are not achieved at the setting time. Several factors determine this property related essentially to the rate of reactions. The addition of soluble phosphate salts in the liquid phase, for example, has been shown to shorten the setting time of 'acid–base' cements, probably through the reaction with TTCP or other calcium-rich phase. The addition of apatite nuclei can also be used like in ACP-based cements, for example.[180] Fluoride ions, through their effect on apatite solubility, may also accelerate the apatite formation and shorten the setting time. The hardening time is related to the evolution of the cement after setting: in construction cements, it corresponds to the time needed to get the nominal mechanical properties, for biological cements, this parameter is not always determined and the mechanical properties may possibly degrade after completion of the chemical reactions. Injectability is an important parameter for biological cements and several techniques have been proposed to determine this parameter in conditions as close as possible to those of the surgical use. One of the difficulties in the injection of an aqueous suspension of a solid phase is the filter-press effect responsible for a variation of the solid/liquid ratio during the injection and eventually the impossibility to continue the injection by applying a reasonable pressure on the syringe. The injectability is related to the viscosity of the suspension and especially the solid/liquid ratio, and the stability of the suspension obtained. Several additives have been used to improve the injectability. The wash-out phenomenon corresponds to the disaggregation or dispersion of the paste during or after its placement; this property is not an intrinsic characteristic of the cement and is also related to the viscosity of the medium in which the cement paste is introduced. It has been shown that the viscosity of the paste has to be higher than that of the medium it is injected in to avoid

dispersion. *In vivo*, wash-out can also be due to the action of blood on the nonset paste. Additives such as gelling agents can be used to avoid wash-out, provided they do not interfere with the setting reaction. The mechanical properties of hardened Ca-P cements depend on their microstructure and especially their porosity related to the solid/liquid ratio. They vary in a large domain in commercial cements (reported compression resistance from 5 to 80 MPa) and they are not suitable for implantation in locations where mechanical loads are high. In addition to these physical chemical properties, biological properties of the Ca-P cements have to be determined and, here also, the absence of standardized methods does not generally allow comparison between different formulations. Among these properties, the most important is bone reconstruction ability associating bone formation with cement resorption. Like in the case of bioceramics, the cohesion of the hardened cement is a determining factor for avoiding the release of too numerous particles and the development of uncontrolled inflammatory reactions. Generally, cement are considered to behave like bone tissue and their degradation has been defined as 'centripetal' resulting in irregular degradation and bone formation from the surface of the implant to the interior with possible cement residues remaining encysted in the newly formed bone. The degradation of apatite cements is related to the microstructural and physical–chemical characteristics of the hardened material. The degradation is faster when the porosity is higher, the crystal size is smaller, and the amount of vacancies in the structure is higher. The amount of vacancies is not simply related to Ca/P ratio as explained earlier (**Section 1.111.3.1**), but to the substitution ratio of trivalent PO_4^{3-} ions by bivalent ones (essentially CO_3^{2-} and HPO_4^{2-} ions). Biphasic cements have been proposed, in analogy with biphasic ceramics, to vary the bioabsorption properties.[181]

The main advantages of Ca-P ionic cements are their easiness of use, their biodegradation combined with the progressive replacement by bone neoformed tissue. Besides, they can easily be associated with therapeutic and/or biologically active components (antibiotics, growth factors, platelets, etc.). Radio-opacifier can also be added to the paste provided they are bioabsorbable; Sr salts have also been proposed. One of the main drawbacks of actual cements are the small size of pores which does not favor cell rehabilitation; the poor mechanical properties and the variability in characteristics and procedures for paste preparation compared to polymeric cements.

1.111.6.4. Examples of Composite Materials with Collagen

Associations of Ca-P compounds and polymers represent an interesting way to confer calcium phosphates' advantageous cohesiveness and mechanical properties in relation with the imitation of bone tissue. In this context, apatite/collagen hybrid systems have been particularly studied by many research groups. The possibility for molecules such as collagen to interact with the ions from the highly reactive surface layer on apatite nanocrystals through ionic functions of proteins (mostly anionic groups) has already been mentioned in this chapter (**Section 1.111.4.5.2**).

Many studies have been aimed at producing biomimetic artificial bone-like tissue involving apatite and collagen taken in varying forms: fiber, gel, or gelatin.[182–186] Several protocols have been used to prepare apatite/collagen hybrids. Testing two methods of preparation of such composites (dispersion of HA in collagen gel or direct nucleation of apatite on collagen fibers), Tampieri *et al.*[186] have shown that the bioinspired method based on the direct nucleation of apatite leads to composites analogous to calcified tissue and exhibits strong interactions between apatite and collagen. Some researchers mentioned the preliminary phosphorylation of collagen in order to generate nucleation sites for mineralization, followed by a subsequent step of apatite nucleation and growth on the collagen by immersion in SBF.[187] Other techniques were also tested, such as electrospinning.[188] They showed that this technique was useful for obtaining composite fibers up to about 30 wt.% loading with HA, while beyond this amount, a preferred bead-like morphology was observed.

In vivo evaluation in weight-bearing sites (in the dog) were performed for testing apatite/collagen composites prepared by a coprecipitation method. The results led to interesting conclusions, especially when associated with BMP-2 growth factor.[189] The controlled release of BMP-2 from the implant was indeed found to facilitate the early formation of callus and hence of newly formed bone, enabling early weight bearing. Nishikawa *et al.*[190] have examined the biodegradation of HA/collagen composites implanted in dogs by a tissue labeling method, and these authors showed that this novel composite allowed bone augmentation.

The interactions between the collagen fibrils and the Ca-P (most generally apatite) are not really known. Quite recently, Dos Santos *et al.*[191] have expressed the possibility to study the apatite–collagen interface by using a FRET technique with luminescent europium-doped apatite. This is a promising idea for deriving a new tool for investigating the interface between collagen and apatite.

These associations have not, however, given materials with the mechanical properties of bone and they have not resulted in decisive advantages compared to bioceramics bone substitutes. (For composite-ceramics associations see also **Chapter 5.520, Bioactive Ceramics and Bioactive Ceramic-Composite-Based Scaffolds**.)

1.111.7. Other Bioactive Ceramic Materials

A number of other bioactive ceramics have been designed more or less specifically for biomedical applications and are used in different implantable systems because of their physical–chemical properties and their good biocompatibility. We limit our presentation to examples of three main types of bioactive ceramics: oxide- and hydroxide-, calcium sulfate- or calcium carbonate-based ceramics.

1.111.7.1. Oxide- and Hydroxide-Based Bioactive Ceramics

As it has been suggested that the hydrated silica layer formed at the surface of implanted bioactive glasses and glass-ceramics plays a very important role in the formation of the bone-like apatite layer, the idea of using pure silica hydrogels as bioactive compounds has emerged. It has been shown that gels of silica, and also other gels of titania or zirconia, after being subjected to heat treatment, can induce the formation of apatite when

these are immersed in a metastable solution analogous to biological fluids.[192] Such bioactive materials are generally obtained by sol–gel processes and they have been shown to favor the heterogeneous nucleation of the apatite. However, when the silica gel is heated to a temperature greater than 900 °C, the formation of the apatite is delayed. The rate of rehydroxilation and the amount of hydroxyl group on the surface of the silica gel appear to control the formation of apatite.[193]

We chose to develop in this subsection the case of titania-based biomaterials, which has been studied in depth especially by Professor Kokubo's group.

It has been shown that sufficiently hydrated titanium dioxide with Ti–OH groups on the surface can join with the bone while it is placed in an osseous site. This property offers the possibility to confer a bioactivity to titanium by a treatment leading to the formation of a gel or a highly hydrated layer at the surface of the implant.[193]

Titania-based materials are easily formed on titanium metal and its alloys by chemical and thermal treatments. Titania gels can be prepared by sol–gel method including a thermal treatment in the range 500–800 °C. Titanium metal with an oxide–hydroxide layer on its surface formed after treatment in NaOH solution and subsequent water or acid treatment can show a high apatite-forming ability in biological environment and bond to bone.[192] The first formation of sodium hydrogen titanate phase on the metal surface has been evidenced by XRD and Raman spectroscopy. It is then transformed into sodium titanate and rutile TiO_2 after heat treatment. The dehydration of sodium titanate and titanium oxide after the final heat treatment is considered to favor apatite formation *in vivo*.

Takadama *et al.* proposed a mechanism describing the apatite formation on titania-based materials.[194] When immersed in SBF solution, the release of sodium ions from the surface occurred via ion exchange with H_3O^+ ions from the solution leading to a local alkalinization of the solution associated with the formation of a large number of negatively charged Ti–OH groups on the surface which can react with positively charged calcium ions from the solution to form calcium titanate. As its concentration increases on the surface, calcium is supposed to react then with hydrogen phosphate from the solution and a calcium phosphate nucleates and grows to give an apatite analogous to bone mineral. Similar mechanisms have been proposed in other studies on the nucleation and growth of Ca-P on titanium surfaces involving either calcium or phosphate binding.[127,195–197]

When implanted *in vivo*, titania-based implant surface showed osteoconductivity, and more recently, osteoinductivity has been evidenced.[198]

Recently, associations of titania with polymer to prepare flexible polyethylene terephtalate fiber-titania) or self-setting composites (polymethylmethacrylate-titania) have been reported.[192] (See also **Chapter 1.113, Bioactive Layer Formation on Metals and Polymers**.)

1.111.7.2. $CaCO_3$-Based Bioactive Ceramics

Different types of natural substitutes for bone tissue are available on the market, generally of animal origin. These are subjected to physical, chemical, or biochemical processes before utilization as biomaterials. Calcium carbonates ($CaCO_3$), particularly those produced by marine organisms such as coral and mother of pearl, have been shown to be biocompatible and bioactive biomaterials, and they have been used for more than 20 years as bone substitutes in the form of powders, porous ceramics, or gels.[199–205]

Three crystalline phases of anhydrous calcium carbonates are encountered in nature: calcite, aragonite, and vaterite. Natural calcium carbonates from certain corals and nacre present the aragonite structure.

The idea that coral can replace defective parts of bone comes from the similarity in the structure of some coral skeletons with cancellous bone allowing colonization by cells and blood vessels penetration.[206] The exoskeleton of coral polyps constitutes blocks of calcium carbonates with regular and interconnected porosity, according to a structure specific for each species. After selecting, cleaning, and shaping, these materials can be implanted in bone locations to serve as a framework for the new bone tissue.

The calculation of the ionic product of blood plasma indicates that it is supersaturated with respect to the three calcium carbonate varieties, although for vaterite, the oversaturation is much smaller than for calcite or aragonite. Then, these compounds cannot dissolve spontaneously. However, in the presence of phosphate ions, the apatite remains the most stable phase and all the three calcium carbonate varieties should transform, at least superficially, into apatite. The main degradation process of calcium carbonate has been assigned to a carbonic anhydrase enzyme, which induces a local dissolution and leave place for newly synthesized bone tissue.[203] Many *in vivo* studies reported that calcium carbonate-based macroporous bioceramics, prepared by physical–chemical treatment of coral, promote bone ingrowth and resorption.[203,205] Another example is coralline HA, a carbonated HA, which is prepared by the hydrothermal conversion of calcium carbonate from coral in the presence of ammonium phosphate.[206,207] It has been suggested that controlling the thickness of HA on a $CaCO_3$ matrix could control the rate of resorption of the implant and its replacement by newly formed bone.

Despite a good mechanical strength, this is not sufficient to allow their use in bones subjected to high mechanical stresses (load-bearing bones). Moreover, their structure is fixed with the considered species and their chemical composition is not well controlled, particularly, with respect to trace elements, and residual organic matrix and implant rejection have been observed possibly due to the presence of organic matter residue.

The mother of pearl, also composed of calcium carbonate and an organic matrix, has been proposed as a substitute for bone. Mother of pearl powder implanted in a bone defect has shown behavior similar to that of a coral.[200]

Although several attempts have been made to produce synthetic calcium carbonate bioceramics, sintering proves to be difficult, and calcium carbonate-based cements, prepared by mixing calcium carbonate phases with an aqueous medium, offer an interesting alternate way to prepare low-temperature carbonate-containing bioceramics. Recently, Combes *et al.* demonstrated the feasibility of calcium carbonate-based biomedical cements consisting of 100% $CaCO_3$ or of a mixture of $CaCO_3$ and calcium phosphate.[181,208] Calcium carbonate compounds have a higher solubility compared to that of apatite and the use of very large proportions of calcium carbonate

(≥20% (w/w) in the dry powder ingredients) opens new possibilities which have not yet been exploited. Cements, unlike materials obtained by high-temperature sintering or natural materials, can be intimately associated with biologically active molecules (specific proteins, antibiotics, etc.) to improve bone reconstruction.[209,210]

1.111.7.3. $CaSO_4$-Based Bioactive Ceramics

Calcium sulfate hemihydrate ($CaSO_4 \cdot 1/2H_2O$), known as plaster of Paris, has been used as a building material for at least 5000 years and used by Egyptians to decorate burial tombs of pharaohs.[211] Dreesman was the first to report a study on the implantation of plaster of Paris as a bone filler material in eight patients.[212] Since this first clinical success, several groups of research have studied different bioactive ceramics for bone filling and repair involving calcium sulfate hemihydrate (CSH) as cement, preset granules, or resorbable composites (CSH-HA or CSH-polymer).[213,214]

The plaster of Paris is prepared from gypsum (calcium sulfate dihydrate (CSD): $CaSO_4 \cdot 2H_2O$) which is mined from the earth or synthesized. When heated at about 160 °C, gypsum is converted in its hemihydrate form (CSH) which is used in plaster of Paris. The chemical reaction responsible for the setting and hardening of calcium sulfate cement is based on the rehydration of CSH:

$$CaSO_4 \cdot 1/2H_2O + 3/2H_2O \rightarrow CaSO_4 \cdot 2H_2O$$

This reaction involving a dissolution–reprecipitation process is slightly exothermic and the resulting bioceramic/cement consists of a network of entangled rod-like CSD (or gypsum) crystals.

CSH exists in two forms, α and β. The α-form is used as dental materials and requires less water and thus leads to denser CSD cement, whereas the β-form uses large amounts of water and leads to less dense material than with the α-form.

Only the dense α-form should be used as bone filler and in non-load-bearing bone sites to guarantee the performance of the cement. In addition, CSH intended for biomedical application must be well characterized and carefully produced.

In vivo, the presence of proteins influences the calcium sulfate-based cement setting, that is, the dissolution and crystallization processes involved, and it has been shown that cement set in these conditions dissolved more quickly. As it is really difficult to avoid bleeding during surgery, the use of preset calcium sulfate cement can lead to slower cement degradation once implanted. Another way to prevent the effect of blood proteins on the setting reaction is to use setting accelerants such as NaCl or K_2SO_4.

The concentration of sulfate ions in blood plasma is not sufficient to reach the solubility product of CSD, thus, calcium sulfate materials should spontaneously dissolve in the body and they are in fact rapidly absorbed.

An interesting review of the clinical use of calcium sulfate as cements or preset granules is presented by Ricci and Weiner.[211] The most recent studies showed that calcium sulfate is fully resorbed *in vivo* within 4–7 weeks in most applications and that its bioactivity is related to the release of calcium ions, local decrease of pH, and local carbonated apatite precipitation. Ricci *et al*. proposed a schematic representation summarizing the processes involved in calcium sulfate-based bone substitute bioactivity (see **Figure 8**).

The main criticism of calcium sulfate as bone substitute is its limitation to small defect filling and rapid resorption exceeding the rate of bone growth into the defect. With a view to extending and controlling the calcium sulfate-based biomaterial resorption properties, composites of calcium sulfate and poly-L-lactic acid (PLLA) consisting either of a nanocomposite of both constituents or of granules of CS coated with a thin layer of PLLA have been studied by Madmidwar *et al*.[213] The authors showed that the full resorption of a nanocomposite consisting of 4% PLLA and 96% of calcium sulfate occurred after 4 months *in vivo*.

Association of this composite or of calcium sulfate cement with biologically active components (growth factors, platelets, antibiotic, etc.) has also been investigated as local controlled release system.[214–216]

In addition to the bioactivity, additional properties of CS have also been pointed out by several authors: CS acts as a barrier membrane in the defect area and allows bone

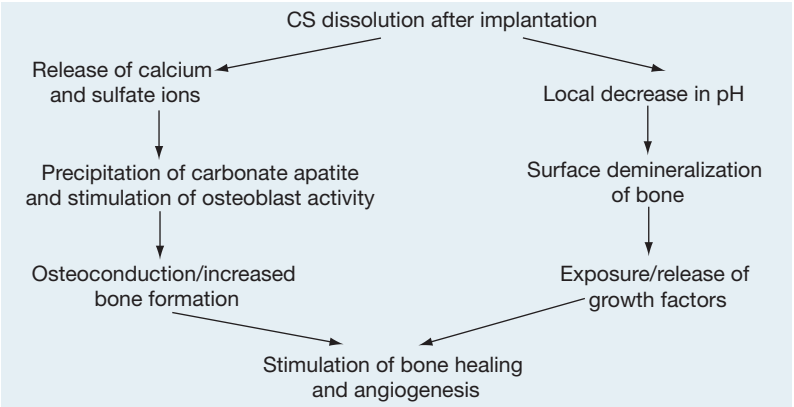

Figure 8 Schematic representation of the proposed pathways of biological activity involving calcium sulfate and stimulating bone formation: calcium and sulfate ions release (left) and pH decrease (right). Reproduced from Ricci, J. L.; Weiner, M. J. In *Bioceramics and Their Clinical Applications*; Kokubo, T., Ed.; CRC/Woodhead: Boca Raton, FL, 2008; pp 302–325, with permission from Woodhead, Cambridge, UK.

generation during healing as an hemostatic agent, probably due to the release of calcium ions known as a coagulant, and as an angiogenic agent.[211]

1.111.8. Conclusion and Future Perspectives

The evolution in the last decade has shown the emergence of substituted Ca-P, and more generally, chemically modified Ca-P, with improved biological properties such as apatite with silicate ions, TCP with Zn ions, and other products. It is probable that such trials to improve the biological activity will be pursued with possibly other types of ions with a biological action or combination of ions. Simultaneously, the mechanisms relaying the improved biological activity related to chemically modified Ca-P are not yet perfectly known in many cases, and the distinction between several effects of doping related to bulk properties of crystals, microstructural characteristics of the ceramics, and surface alterations probably needs to be clarified.

A second route of development concerns nanocrystalline apatites, which exhibit a very high and peculiar reactivity and constitute the main component of bone substance. Advances in this field will probably result in a better understanding of bone biology also which in many cases has focused on cell activity and organic macromolecules specificities, forgetting that the mineral with its high surface area and strong potential interactivity is probably an important actor in several bone regulation mechanisms. Ca-P-based bioceramics with osteoconductive and osteoinductive properties have attracted back the attention of researchers on the role of Ca-P minerals in living organisms, and advances are expected in this field. In addition to their involvement in nanomaterials, Ca-P nanocrystals can also be used in different applications for imaging or cell therapy. The development of the use of nanocrystals raises the problem of their accurate characterization, evolution, and surface properties, and regulations and standards will probably flourish.

A third development domain, already active, concerns the associations of bioceramics with active molecules for different purposes, for example, antiseptic activity or improvement of cell response using growth factors or associations of growth factors with sequenced controlled release.

The Ca-P bioceramics and composite materials are an interesting substrate for scaffolding in tissue engineering, and there is no doubt that these intense research activities will develop our knowledge of cell–material interactions and will probably allow the distinction of crucial parameters involved in cell colonization and differentiation determined by materials with, here also, interesting returns in the domain of bone biology.

References

1. Dickens, B.; Bowen, J. S. *Acta Crystallogr. B* **1971**, *27*, 2247–2255.
2. Dickens, B.; Prince, E.; Schroeder, L. W.; Brown, W. E. *Acta Crystallogr. B* **1973**, *29*, 2057–2070.
3. Jones, D. W.; Smith, J. A. S. *J. Chem. Soc.* **1962**, 1414–1420.
4. Curry, N. A.; Jones, D. W. J. *Chem. Soc. A* **1971**, *23*, 3725–3729.
5. Dickens, B.; Bowen, J. S.; Brown, W. E. *Acta Crystallogr. B* **1972**, *28*, 797–806.
6. Treboux, G.; Layrolle, P.; Kanzaki, N.; Onuma, K.; Ito, A. *J. Phys. Chem. A* **2000**, *104*, 5111–5114.
7. Mathew, M.; Brown, W. E.; Shroeder, L. W.; Dickens, B. *J. Crystallogr. Spectrosc. Res.* **1988**, *18*, 235–250.
8. Dickens, B.; Schroeder, L. W.; Brown, W. E. *J. Solid State Chem.* **1974**, *10*, 232–248.
9. Yashima, M.; Sakai, A.; Kamiyama, T.; Hoshikawa, A. *J. Solid State Chem.* **2003**, *175*, 272–277.
10. Mathew, M.; Shroeder, L. W.; Dickens, B.; Brown, W. E. *Acta Crystallogr. B* **1977**, *33*, 1325–1333.
11. Dickens, B.; Brown, W. E.; Kruger, G. J.; Stewart, J. M. *Acta Crystallogr. B* **1973**, *29*, 2046–2056.
12. Kay, M. I.; Young, R. A.; Posner, A. S. *Nature* **1964**, *204*, 1050–1052.
13. van Wazer, J. R. *Phosphorus and Its Compounds*. Interscience: New York, 1958.
14. Brown, W. E.; Smith, J. P.; Lehr, J. R.; Frazier, A. W. *J. Phys. Chem.* **1958**, *62*, 625–627.
15. Johnsson, M. S. A.; Nancollas, G. H. *Crit. Rev. Oral Biol. Med.* **1992**, *3*, 61–82.
16. Layrolle, P.; Lebugle, A. *Chem. Mater.* **1994**, *6*, 1996–2004.
17. Tofighi, A.; Palazzolo, R. *Key Eng. Mater.* **2005**, *284–286*, 101–104.
18. Heughebaert, J.-C.; Zawacki, S.; Nancollas, G. *J. Cryst. Growth* **1983**, *63*, 83–90.
19. Tonkovic, M.; Sikiric, M.; Babic-Ivancic, V. *Colloids Surf.* **2000**, *170*, 107–112.
20. Elliott, J. C. *Structure and Chemistry of the Apatites and Other Calcium Orthophosphates*. Elsevier, 1994.
21. Hamad, M.; Heughebaert, J.-C. *J. Cryst. Growth* **1986**, *79*, 192–197.
22. Heughebaert, J.-C.; Montel, G. *Calcif. Tissue Int.* **1982**, *34*, 103–108.
23. Lowenstam, H. A. *Science* **1981**, *21*, 1126–1131.
24. Termine, J. D.; Posner, A. S. *Calcif. Tissue Res.* **1967**, *1*, 8–23.
25. Glimcher, M. J.; Bonar, L. C.; Grynpas, M. D.; Landis, W. J.; Roufosse, A. H. *J. Cryst. Growth* **1981**, *53*, 100–119.
26. Rey, C.; Combes, C.; Drouet, C.; Glimcher, M. J. *Osteoporos. Int.* **2009**, *20*, 1013–1021.
27. Weiner, S.; Sagi, I.; Addadi, L. *Science* **2005**, *309*, 1027–1028.
28. Skrtic, D.; Antonucci, J. M. *J. Biomater. Appl.* **2007**, *21*, 375–393.
29. Betts, F.; Posner, A. S. *Mater. Res. Bull.* **1974**, *9*, 353–360.
30. Combes, C.; Rey, C. *Acta Biomater.* **2010**, *6*, 3362–3378.
31. Eanes, E. D. In *Octacalcium Phosphate*; Chow, L. C., Eanes, E. D., Eds.; Karger: Basel, 2001; pp 130–147.
32. Chow, L. C.; Eanes, E. D. *Octacalcium Phosphate: Monographs in Oral Science*. Karger: Basel, 2001.
33. Lebugle, A.; Zahidi, E.; Bonel, G. *Reactivity Solids* **1986**, *2*, 151–161.
34. Rodrigues, A.; Lebugle, A. *J. Solid State Chem.* **1999**, *148*, 308–315.
35. Brown, W. E.; Lehr, J. R.; Smith, J. P.; Frazier, A. W. *J. Am. Chem. Soc.* **1957**, *79*, 5318–5319.
36. LeGeros, R. Z. *Calcif. Tissue Int.* **1985**, *37*, 194–197.
37. Habibovic, P.; van der Valk, C. M.; van Blitterswijk, C. A.; de Groot, K.; Meijer, G. *J. Mater. Sci. Mater. Med.* **2004**, *15*, 373–380.
38. Fowler, B. O.; Markovic, M.; Brown, W. E. *Chem. Mater.* **1993**, *5*, 1417–1423.
39. Tomazic, B. B.; Mayer, I.; Brown, W. E. *J. Cryst. Growth* **1991**, *108*, 670–682.
40. Markovic, M. In *Octacalcium Phosphate*; Chow, L. C., Eanes, E. D., Eds.; Karger: Basel, 2001; pp 77–93.
41. Rey, C.; Combes, C.; Drouet, C.; Somrani, S. In *Bioceramics and Their Clinical Applications*; Kokubo, T., Ed.; CRC/Woodhead: Boca Raton, FL, 2008; pp 326–366.
42. Obadia, L.; Deniard, P.; Alonso, B.; *et al*. *Chem. Mater.* **2006**, *18*, 1425–1433.
43. Yoshida, K.; Hyuga, H.; Kondo, N.; *et al*. *J. Am. Ceram. Soc.* **2006**, *89*, 688–690.
44. Wilson, R. M.; Elliott, J. C.; Dowker, S. E. P.; Rodriguez-Lorenzo, L. M. *Biomaterials* **2005**, *26*, 1317–1327.
45. Legros, R.; Balmain, N.; Bonel, G. *J. Chem. Res.* **1986**, (S), 8–9.
46. White, T. J.; Zhili, D. *Acta Crystallogr. B* **2003**, *59*, 1–16.
47. Brown, W. E.; Mathew, M.; Chow, L. C. In *Adsorption and Surface Chemistry of Hydroxyapatite*; Misra, D. N., Ed.; Plenum: New York, 1984; pp 13–28.
48. Neuman, W. F.; Mulryan, B. J. *J. Biol. Chem.* **1951**, 843–848.
49. Rey, C.; Combes, C.; Drouet, C.; Sfihi, H.; Barroug, A. *Mater. Sci. Eng., C* **2006**, *27*, 198–205.
50. Eichert, D.; Sfihi, H.; Combes, C.; Rey, C. *Key Eng. Mater.* **2004**, *254–256*, 927–930.
51. Chaair, H.; Heughebaert, J.-C.; Heughebaert, M.; Vaillant, M. *J. Mater. Chem.* **1995**, *4*, 765–770.
52. Obadia, L.; Rouillon, T.; Bujoli, B.; Daculsi, G.; Bouler, J.-M. *J. Biomed. Mater. Res. B* **2006**, *80*, 32–42.
53. Verwilghen, C.; Chkir, M.; Rio, S.; Nzihou, A.; Sharrock, P.; Depelsenaire, G. *Mater. Sci. Eng. C* **2009**, *29*, 771–773.

54. Montel, G. *Colloq. Sek. Anorg. Chem. Intern. Union Reine u. Angew. Chem. Munster* **1955**, 178–183.
55. Lee, J. H.; Lee, D. H.; Ryu, H. S.; Chang, B. S.; Hong, K. S.; Lee, C. K. *Key Eng. Mater.* **2003**, *240–242*, 399–402.
56. Omelon, S. J.; Grynpas, M. D. *Chem. Rev.* **2008**, *109*, 4694–4715.
57. Charlot, G. *La chimie analytique quantitative*. Masson, 1966.
58. Gee, A.; Dietz, V. R. *Ann. Chem.* **1953**, *25*, 1320–1324.
59. Gee, A.; Dietz, V. R. *J. Am. Chem. Soc.* **1955**, *77*, 2961–2965.
60. Combes, C.; Rey, C.; Mounic, S. *Key Eng. Mater.* **2001**, *192–195*, 143–146.
61. Huffman, E. W. D. *Microchem. J.* **1977**, *22*, 567–573.
62. Godinot, C.; Bonel, G.; Torres, L.; Mathieu, J. *Microchem. J.* **1984**, *29*, 92–105.
63. Trombe, J.-C.; Montel, G. *J. Inorg. Nucl. Chem.* **1978**, *40*, 15–21.
64. Ranz, X. Ph.D. Thesis, Institut National Polytechnique, Toulouse, France, 1996.
65. Ducheyne, P.; van Raemdonck, W.; Heughebaert, J. C.; Heughebaert, M. *Biomaterials* **1986**, *7*(2), 97–103.
66. Feng, C. F.; Khor, K. A.; Gu, Y. W.; Cheang, P. *Mater. Lett.* **2001**, *51*, 88–93.
67. Somrani, S.; Banu, M.; Jemal, M.; Rey, C. *J. Solid State Chem.* **2005**, *178*, 1337–1348.
68. McConnel, D. *Apatite, Its Crystal Chemistry, Mineralogy, Utilization and Geologic and Biologic Occurrences*. Springer: Berlin, 1973.
69. Scherrer, P. *Nachr. Ges Wiss Gottengen* **1918**, 96–100.
70. Bigi, A.; Boanini, E.; Capuccini, C.; Gazzano, M. *Inorg. Chim. Acta* **2007**, *360*, 1009–1016.
71. Balmain, N.; Legros, R.; Bonel, G. *Calcif. Tissue Int.* **1982**, *34*, S93–S98.
72. Mathew, M.; Takagi, S. In *Octacalcium Phosphate*; Chow, L. C., Eanes, E. D., Eds.; Karger: Basel, 2001; pp 1–16.
73. Nagata, F.; Toriyama, M.; Teraoka, K.; Yokogawa, Y. *Chem. Lett.* **2001**, *30*, 780–781.
74. Ioku, K.; Yamauchi, S.; Fujimori, H.; Goto, S.; Yoshimura, M. *Solid State Ionics* **2002**, *15*, 147–150.
75. Suvorova, E. I.; Buffat, P. A. *Crystallogr. Rep. Kristallografiya* **2001**, *46*(5), 722–729.
76. Bres, E. F.; Hutchison, J. L.; Senger, B.; Voegel, J. C.; Frank, R. M. *Ultramicroscopy* **1991**, *35*, 305–322.
77. Rangavittal, N.; Landa-Canovas, A. R.; Gonzalez-Calbet, J. M.; Vallet-Regı, M. *J. Biomed. Mater. Res.* **2000**, *51*, 660–668.
78. Petrov, I.; Soptrajanov, B.; Fuson, N.; Lawson, J. R. *Spectrochimica Acta A* **1967**, *23*, 2637–2646.
79. Fowler, B. O.; Moreno, E. C.; Brown, W. E. *Arch. Oral Biol.* **1966**, *11*, 477–492.
80. Jillavenkatesa, A.; Condrate, R. A. *Spectrosc. Lett.* **1998**, *31*, 1619–1634.
81. Posset, U.; Löcklin, E.; Thull, R.; Kiefer, W. *J. Biomed. Mater. Res.* **1998**, *40*, 640–645.
82. Penel, G.; Leroy, G.; van Landuyt, P.; *et al. Bone* **1999**, *25*(suppl 2), 81S–84S.
83. Penel, G.; Leroy, G.; Rey, C.; Brès, E. *Calcif. Tissue Int.* **1998**, *63*, 475–481.
84. Heimann, R. B. In *Trend in Biomaterials Research*; Pannone, P. J., Ed.; Nova Publishers: New York, 2007; pp 1–80.
85. El Feki, H.; Rey, C.; Vignoles, M. *Calcif. Tissue Int.* **1991**, *49*, 269–274.
86. Vignoles, M.; Bonel, G.; Holcomb, D. W.; Young, R. A. *Calcif. Tissue Int.* **1988**, *43*, 33–40.
87. Barroug, A.; Rey, C.; Trombe, J.-C. *Adv. Mater. Res.* **1994**, *1–2*, 147–153.
88. Bertinetti, L.; Drouet, C.; Combes, C.; *et al. Langmuir* **2009**, *25*, 5647–5654.
89. Yesinowski, J. P. In *Calcium Phosphates in Biological and Industrial Systems*; Amjad, Z., Ed.; Kluwer Academic: Dordrecht, 1998; pp 103–143.
90. Bohner, M.; Lemaître, J.; Legrand, A. P.; d'Espinose de la Caillerie, J.-B.; Belgrand, P. *J. Mater. Sci. Mater. Med.* **1996**, *7*, 457–463.
91. Jäger, C.; Welzel, T.; Meyer-Zaika, W.; Epple, M. *Magn. Reson. Chem.* **2006**, *44*, 573–580.
92. Wilson, E.; Awanusi, A.; Morris, M. D.; Kohn, D. H.; Tecklenburg, M. M. *Biophys. J.* **2006**, *90*, 3722–3731.
93. Sfihi, H.; Rey, C. In *Magnetic Resonance in Colloid and Interface Science*; Fraissard, J., Lapina, B., Eds.; Nato ASI Series; Kluwer Academic: Dordrecht, 2002; Vol. II, pp 409–418.
94. Myerson, A. S. In *Molecular Modelling Applications in Crystallization*; Myerson, A. S., Ed.; Cambridge University Press: Cambridge, 2005.
95. Tang, R.; Nancollas, G. *J. Cryst. Growth* **2000**, *212*, 261–269.
96. Gregory, T. M.; Moreno, E. C.; Brown, W. E. *J. Res. Natl. Bur. Stand.* **1970**, *74A*, 461–475.
97. McDowell, H.; Brown, W. E.; Sutter, J. R. *Inorg. Chem.* **1971**, *10*, 1638–1643.
98. Tung, M. S.; Eidelman, N.; Sieck, B.; Brown, W. E. *J. Res. Natl. Bur. Stand.* **1988**, *93*, 613–624.
99. Fowler, B. O.; Kuroda, S. *Calcif. Tissue Int.* **1986**, *38*, 197–208.
100. Gregory, T. M.; Moreno, E. C.; Patel, J. M.; Brown, W. E. *J. Res. Natl. Bur. Stand.* **1974**, *78A*, 667–674.
101. McDowell, H.; Gregory, T. M.; Brown, W. E. *J. Res. Natl. Bur. Stand.* **1977**, *81A*, 273–281.
102. Moreno, E. C.; Kresak, M.; Zahradnik, R. T. *Caries Res.* **1977**, *11*(suppl. 1), 142–171.
103. Matsuya, S.; Takagi, S.; Chow, L. C. *J. Mater. Sci.* **1996**, *31*, 3263–3269.
104. Pan, H. B.; Darwell, B. W. *Arch. Oral Biol.* **2007**, *52*, 618–624.
105. Chow, L. C. In *Octacalcium Phosphate*; Chow, L. C., Eanes, E. D., Eds.; Karger: Basel, 2001; pp 148–163.
106. Wang, L.; Nancollas, G. *Chem. Rev.* **2008**, *108*, 4628–4669.
107. Rey, C.; Hina, A.; Tofighi, A.; Glimcher, M. J. *Cells Mater.* **1995**, *5*(4), 345–356.
108. Moreno, E. C.; Kresak, M.; Zahradnik, R. T. *Nature* **1974**, *247*, 64–65.
109. LeGeros, R. Z.; Kijkowska, R.; Bautista, C.; LeGeros, J. P. *Connective Tissue Res.* **1995**, *33*, 203–209.
110. Baig, A. A.; Fox, J. L.; Young, R. A.; *et al. Calcif. Tissue Int.* **1999**, *64*, 437–449.
111. Baig, A. A.; Fox, J. L.; Hsu, J.; *et al. J. Colloid Interface Sci.* **1996**, *179*, 608–617.
112. Chhettry, A.; Wang, Z.; Hsu, J.; *et al. J. Colloid Interface Sci.* **1999**, *218*, 57–67.
113. Hsu, J.; Fox, J. L.; Higuchi, W. I.; *et al. J. Colloid Interface Sci.* **1994**, *167*, 414–423.
114. Brown, W. E.; Schroeder, L.; Ferris, J. *J. Phys. Chem.* **1979**, *83*, 1385–1388.
115. Ducheyne, P.; Kim, C. S.; Pollack, S. R. *J. Bomed. Mater. Res.* **1992**, *26*, 147–168.
116. Chander, S.; Fuerstenau, D. W. In *Adsorption and Surface Chemistry of Hydroxyapatite*; Misra, D. N., Ed.; Plenum: New York, 1984; pp 29–50.
117. Somasundaran, P.; Markovic, B. In *Calcium Phosphates in Biological and Industrial Systems*; Amjad, Z., Ed.; Kluwer Academic: Dordrecht, 1998; pp 85–101.
118. Tung, M. S.; Skrtic, D. In *Octacalcium Phosphate: Monographs in Oral Science*; Chow, L. C., Eanes, E. D., Eds.; Karger: Basel, 2001; Vol. 18, pp 112–129.
119. Somasundaran, P.; Wang, Y. H. C. In *Adsorption and Surface Chemistry of Hydroxyapatite*; Misra, D. N., Ed.; Plenum: New York, 1984; pp 29–50.
120. Saleeb, F. Z.; De Bruyn, P. L. *Electroanal. Interfac. Electrochem.* **1972**, *37*, 99–118.
121. Botelho, C. M.; Lopes, M. A.; Gibson, I. R.; Best, S. M.; Santos, J. D. *J. Mater. Sci. Mater. Med.* **2002**, *13*, 1123–1127.
122. Ducheyne, P.; Pollack, S. R.; Kim, C. S. *Electromagn. Med. Biol.* **1991**, 49–52.
123. Mangood, A.; Malkaj, P.; Dalas, E. *J. Cryst. Growth* **2006**, *290*, 565–570.
124. Palazzo, B.; Walsh, D.; Iafisco, M.; *et al. Acta Biomater.* **2009**, *5*, 1241–1252.
125. Bouladjine, A.; Al-Kattan, A.; Dufour, P.; Drouet, C. *Langmuir* **2009**, *25*, 12256–12265.
126. Burke, E. M.; Nancollas, G. H. *Colloids Surf. A* **1999**, *150*, 151–160.
127. Nancollas, G. H.; Wu, W.; Tang, R. In *Mineralization in Natural and Synthetic Biomaterials*; Li, P., Calvert, P., Kokubo, T., Levy, R., Scheid, C., Eds.; Material Research Society; Materials Research Society: Warrendale, PA, 2000; Vol. 599, pp 99–108.
128. Wu, W.; Nancollas, G. H. *Adv. Colloid Interface Sci.* **1999**, *79*, 229–279.
129. Tang, R.; Wu, W.; Haas, M.; Nancollas, G. H. *Langmuir* **2001**, *17*, 3480–3485.
130. Tang, R.; Henneman, Z. J.; Nancollas, G. H. *J. Cryst. Growth* **2003**, *249*, 614–624.
131. Drouet, C.; Carayon, M. T.; Combes, C.; Rey, C. *Mater. Sci. Eng. C* **2008**, *28*, 1544–1550.
132. Chen, X.; Wright, J. V.; Conca, J. L.; Peurrung, L. M. *Water Air Soil Pollut.* **1997**, *98*, 57–78.
133. Fernane, F.; Mecherri, M. O.; Sharrock, P.; Hadioui, M.; Lounici, H.; Fedoroff, M. *Mater. Charact.* **2008**, *59*, 554–559.
134. Rey, C.; Combes, C.; Drouet, C.; Lebugle, A.; Sfihi, H.; Barroug, A. *Mat Wiss U Werkostofftech* **2007**, *38*, 996–1002.
135. Cazalbou, S.; Hina, A.; Rey, C. In *New Aspects of Trace Element Research*, Selected Papers from the Vth ISTERH Conference; Abdulla, M., Bost, M., Gamon, S., Arnaud, P., Chazot, G., Eds.; Smith-Gordon/Nishimura: London/Tokoyo, 1999; pp 58–62.
136. Sallis, J. D. In *Calcium Phosphates in Biological and Industrial Systems*; Amjad, Z., Ed.; Kluwer Academic: Dordrecht, 1998; pp 173–191.
137. Boskey, A. L.; Ullrich, W.; Spevak, L.; Gilder, H. *Calcif. Tissue Int.* **1996**, *58*, 45–51.
138. Hauschka, P. V.; Wians, F. H. *Anat. Rec.* **1989**, *224*, 180–188.
139. Romberg, R. W.; Werness, P. G.; Riggs, B. L.; Mann, K. G. *Biochemistry* **1986**, *25*, 1176–1180.
140. Combes, C.; Rey, C. *Biomaterials* **2002**, *23*, 2817–2823.
141. Barroug, A.; Fastrez, J.; Lemaitre, J.; Rouxhet, P. *J. Colloid Interface Sci.* **1997**, *189*, 37–42.

142. Barroug, A.; Lernoux, E.; Lemaitre, J.; Rouxhet, P. G. *J. Colloid Interface Sci.* **1998**, *208*, 147–152.
143. Barroug, A.; Legrouri, A.; Rey, C. *Key Eng. Mater.* **2008**, *361–363*, 79–82.
144. Benaziz, L.; Barroug, A.; Legrouri, A.; Rey, C.; Lebugle, A. *J. Colloid Interface Sci.* **2001**, *238*, 48–53.
145. Pearce, E. I. *Calcif. Tissue Int.* **1981**, *10*, 123–131.
146. Misra, D. N. *Colloids Surf.* **1998**, *141*, 173–179.
147. Josse, S.; Faucheux, C.; Soueidan, A.; *et al*. *Biomaterials* **2005**, *26*, 2073–2080.
148. Errassifi, F.; Menbaoui, A.; Autefage, H.; *et al*. In Proceedings of the 8th Pacific Rim Conference on Ceramic and Glass Technology, 2010; pp 159–174.
149. Mullin, J. W. *Crystallisation*, 2nd edn.; Butterworths: London, 1972.
150. Koutsoukos, P. G.; Nancollas, G. H. *J. Cryst. Growth* **1981**, *53*, 10–19.
151. Nancollas, G. H.; Wefel, J. S. *J. Dent. Res.* **1976**, *55*, 617–624.
152. Glimcher, M. J. *Biomaterials* **1990**, *11*, 7–10.
153. Toworfe, G. K.; Composto, R. J.; Shapiro, I. M.; Ducheyne, P. *Biomaterials* **2006**, *27*, 631–642.
154. Yamashita, K.; Oikawa, N.; Umegaki, T. *Chem. Mater.* **1996**, *8*, 2697–2700.
155. Calvert, P.; Mann, S. *Nature* **1997**, *386*, 127–129.
156. Dewez, J. L.; Doren, A.; Schneider, Y. J.; Rouxhet, P. G. *Biomaterials* **1999**, *20*, 547–559.
157. McKee, M. D.; Nanci, A. *Microsc. Res. Tech.* **1996**, *33*, 141–164.
158. Hench, L. L.; Hench, J. W.; Greeenspan, D. C. *J. Aust. Ceram. Soc.* **2004**, *40*, 1–42.
159. Kokubo, T.; Hata, K.; Nakamura, T.; Yamamuro, T. In *Bioceramics*; Bonfield, W., Hastings, G. W., Tanner, K. E., Eds.; Butterworth-Heinemann: London, 1991; Vol. 4, pp 113–120.
160. Kim, H. M.; Miyazaki, T.; Kokubo, T.; Nakamura, T. *Key Eng. Mater.* **2001**, *192–195*, 47–50.
161. Eidelman, N.; Chow, L. C.; Brown, W. E. *Calcif. Tissue Int.* **1987**, *40*, 71–78.
162. Bohner, M.; Lemaître, J. *Biomaterials* **2009**, *30*, 2175–2179.
163. De Groot, K. In *Adsorption and Surface Chemistry of Hydroxyapatite*; Misra, D. N., Ed.; Plenum: New York, 1984; pp 97–104.
164. LeGeros, R. Z. *Clin. Mater.* **1993**, *14*, 65–88.
165. Ito, A.; Kawamura, H.; Miyakawa, S.; *et al*. *J. Biomed. Mater. Res.* **2002**, *60*, 224–231.
166. Bennett, R. M.; Lehr, J. R.; McCarty, D. J. *J. Clin. Invest.* **1975**, *56*, 1571–1579.
167. Kim, H. M.; Kim, Y. S.; Woo, K. M.; *et al*. *J. Biomed. Mater. Res.* **2001**, *56*, 250–256.
168. Pena, J.; LeGeros, R. Z.; Rohanizadeh, R.; LeGeros, J. P. *Key Engineering Mater.* **2001**, *192–195*, 267–270.
169. Redey, S. A.; Razzouk, S.; Rey, C.; *et al*. *J. Bone Miner. Res.* **1999**, *45*, 140–147.
170. Hing, K. A.; Revell, P. A.; Smith, N.; Buckland, T. *Biomaterials* **2006**, *27*, 5014–5026.
171. Porter, A. E.; Patel, N.; Skepper, J. N.; Best, S. M.; Bonfield, W. *Biomaterials* **2004**, *25*, 3303–3314.
172. Jarcho, M.; Salsbury, R. L.; Thomas, M. B.; Doremus, R. H. *J. Mater. Sci.* **1979**, *14*, 142–150.
173. Yuan, H.; de Bruijn, J. D.; Li, Y.; Yang, Z.; de Groot, K.; Zhang, X. *J. Mater. Sci. Mater. Med.* **2001**, *12*, 7–13.
174. Daculsi, G.; LeGeros, R. Z. In *Bioceramics and Their Applications*; Kokubo, T., Ed.; Woodhead: Cambridge, England, 2008; pp 395–423.
175. Yamada, S.; Heyman, D.; Bouler, J.-M.; Daculsi, G. *Biomaterials* **1997**, *18*, 1037–1041.
176. Radin, S.; Ducheyne, P. *Mater. Med.* **1992**, *3*, 33–42.
177. Rokkum, M.; Reigstadt, A.; Johansson, C. B. *Acta Orthop. Scand.* **2003**, *74*, 365–368.
178. Goyenvalle, E.; Aguado, E.; Nguyen, J. M.; *et al*. *Biomaterials* **2006**, *27*, 1119–1128.
179. Mirtchi, A. A.; Lemaître, J.; Terao, N. *Biomaterials* **1989**, *10*, 475–480.
180. Knaack, D.; Goad, M. E. P.; Ailova, M.; *et al*. *J. Biomed. Mater. Res.* **1998**, *43*, 399–409.
181. Combes, C.; Miao, B.; Bareille, R.; Rey, C. *Biomaterials* **2006**, *27*, 1945–1954.
182. Itoh, S.; Kikuchi, M.; Takakuda, K.; *et al*. *J. Biomed. Mater. Res.* **2000**, *54*, 445–453.
183. Kikuchi, M.; Ikoma, T.; Itoh, S.; *et al*. *Compos. Sci. Technol.* **2004**, *64*, 819–825.
184. Kim, H. W.; Knowles, J. C.; Kim, H. E. *J. Biomed. Mater. Res. B* **2005**, *74*, 686–698.
185. Kim, S.; Ryu, H.-S.; Shin, H.; Jung, H. S.; Hong, K. S. *Mater. Chem. Phys.* **2005**, *91*, 500–506.
186. Tampieri, A.; Celotti, G.; Landi, E.; Sandri, M.; Roveri, N.; Falini, G. *J. Biomed. Mater. Res.* **2003**, *67*, 618–625.
187. Li, X. K.; Chang, J. *J. Biomed. Mater. Res. A* **2008**, *85*, 293–300.
188. Song, J. H.; Kim, H. E.; Kim, H. W. *J. Mater. Sci. Mater. Med.* **2008**, *19*, 2925–2932.
189. Itoh, S.; Kikuchi, M.; Takakuda, K.; *et al*. *J. Biomed. Mater. Res.* **2002**, *63*, 507–515.
190. Nishikawa, T.; Masuno, K.; Tominaga, K.; *et al*. *Implant Dent.* **2005**, *14*, 252–260.
191. Dos Santos, I.; Mazeres, S.; Freche, M.; Lacout, J. L.; Sautereau, A. M. *Mater. Lett.* **2008**, *62*, 4377–4379.
192. Kokubo, T.; Takadama, T.; Matsushita, T. In *Bioceramics and Their Applications*; Kokubo, T., Ed.; Woodhead: Cambridge, England, 2008; pp 485–500.
193. Li, P.; Ohtsuki, C.; Kokubo, T.; Nakanishi, K.; Soga, N.; de Groot, K. *J. Biomed. Mater. Res.* **1994**, *28*, 7–15.
194. Takadama, H.; Kim, H. M.; Kokubo, T.; Nakamura, T. *J. Biomed. Mater. Res.* **2001**, *55*, 185–193.
195. Combes, C.; Rey, C.; Frèche, M. *Colloids Surf. B* **1998**, *11*, 15–27.
196. Hanawa, T.; Ota, M. *Appl. Surf. Sci.* **1992**, *55*, 269–276.
197. Healy, K. E.; Ducheyne, P. *Biomaterials* **1992**, *13*, 553–561.
198. Fujibayashi, S.; Neo, M.; Kim, H. M.; Kokubo, T.; Nakamura, T. *Biomaterials* **2004**, *25*, 443–450.
199. Arnaud, E.; de Pollak, C.; Meunier, A.; Sedel, L.; Damien, C.; Petite, H. *Biomaterials* **1999**, *20*, 1909–1918.
200. Atlan, G.; Delattre, O.; Berland, S.; *et al*. *Biomaterials* **1999**, *20*, 1017–1022.
201. Begley, C. T.; Doherty, M. J.; Mollan, R. A.; Wilson, D. J. *Biomaterials* **1995**, *16*, 1181–1185.
202. Braye, F.; Irigaray, J. L.; Jallot, E.; *et al*. *Biomaterials* **1996**, *17*, 1345–1350.
203. Guillemin, G.; Patat, J. L.; Meunier, A. *Bull. Inst. Océanogr. Monaco* **1995**, *14*(3), 67–77.
204. Roudier, M.; Bouchon, C.; Rouvillain, J. L.; *et al*. *J. Biomed. Mater. Res.* **1995**, *29*, 909–915.
205. Piatelli, A.; Podda, G.; Scarano, A. *Biomaterials* **1997**, *18*, 623–627.
206. Chiroff, R. T.; White, E. W.; Weber, J. N.; Roy, D. M. *J. Biomed. Mater. Res.* **1975**, *9*, 29–45.
207. Damien, E.; Revell, P. A. *J. Appl. Biomater. Biomech.* **2004**, *2*, 65–73.
208. Combes, C.; Bareille, R.; Rey, C. *J. Biomed. Mater. Res. A* **2006**, *79*, 318–328.
209. Blom, E. J.; Klein-Nulend, J.; Wolke, J. G. C.; Van Waas, M. A. J.; Driessens, F. C. M.; Burger, E. H. *J. Biomed. Mater. Res.* **2002**, *59*, 265–272.
210. Lucas, A.; Gaude, J.; Carel, C.; Michel, J. F.; Cathelineau, G. *Int. J. Inorg. Mater.* **2001**, *3*, 87–94.
211. Ricci, J. L.; Weiner, M. J. In *Bioceramics and Their Clinical Applications*; Kokubo, T., Ed.; CRC/Woodhead: Boca Raton, FL, 2008; pp 302–325.
212. Dreesman, H. *Beitr. Klin. Chir.* **1892**, *9*, 804.
213. Mamidwar, S. S.; Arena, C.; Kelly, S.; Alexander, H.; Ricci, J. *J. Biomed. Mater. Res. B* **2006**, *2*, 1–18.
214. Rosenblum, S. F.; Frenkel, S.; Ricci, J. L.; Alexander, H. *J. Appl. Biomater.* **1993**, *4*, 67–72.
215. Beardmore, A. A.; Brooks, D. E.; Wenke, J. C.; Thomas, D. B. *J. Bone Joint Surg. Am.* **2005**, *87*, 107–112.
216. Intini, G.; Andreana, S.; Intini, F. E.; Buhite, R. J.; Bobek, L. A. *J. Transl. Med.* **2007**, *5*, 1–13.

Relevant Websites

http://www.webmineral.com, or www.mindat.org – Description of mineral structures with tri-dimentional view.
http://www.crystallography.net – Crystallography open database.
http://rruff.info, http://rruff.geo.arizona.edu/AMS/ – Site collecting the diffraction data and Raman and FTIR spectra of minerals.
http://www.lwr.kth.se/English/OurSoftware/vminteq – Site of 'visual MINTEQ' the open access software for the speciation of mineral ions in solution.
http://www.ccp14.ac.uk – Collaborative computational project number 14. Series of open access software for single crystal and powder diffraction. Includes Rietveldt refinements.

1.112. Calcium Phosphate Coatings

P Layrolle, University of Nantes, Nantes, France

© 2011 Elsevier Ltd. All rights reserved.

1.112.1.	Introduction	223
1.112.2.	Calcium Phosphates	224
1.112.3.	Titanium Implants	225
1.112.4.	Plasma Spraying of CaP Coatings	225
1.112.5.	Electrochemical Deposition of CaP Coatings	226
1.112.6.	Biomimetic CaP Coatings	227
1.112.7.	Conclusion and Perspectives	228
References		229

Glossary

Biomimetic A process or substance that mimics biological natural systems. For instance, synthetic hydroxyapatite resembles in composition and structure the mineral of bone.

Electrodeposition A process of depositing films on metal surfaces, such as titanium implants, assisted by current or voltage gradients.

Osteoconduction The direct apposition of bone tissue onto the surface of an implant as the opposite of fibrous tissue encapsulation.

Plasma spraying A high-temperature spraying method for depositing coatings, such as calcium phosphate coatings, on orthopedic implants.

Simulated body fluid A supersaturated protein-free, electrolyte solution with ionic concentrations similar to those found in human blood plasma.

1.112.1. Introduction

As populations age in industrial countries, the market for orthopedic prostheses and dental implants is growing steadily at a rate of 15% per year. For instance, total hip arthroplasties or knee joint replacements have turned into a standard surgical procedure with a relatively high success rate.[1] In response to millions of edentulous patients, artificial dental roots are implanted in the maxillary and mandible bone to restore dentition.[2] Despite a very high success rate of >95% over 5 years, the lifetime of orthopedic and dental implant is limited to 10–15 years and the number of revisions is steadily increasing.

Metals are commonly used for manufacturing orthopedic and dental implants. These medical devices are mostly made out of titanium and alloys due to their high mechanical strength and corrosion resistance in the body. All grades of titanium and alloys exhibit a layer of titanium oxide with a thickness of few nanometers. This titanium oxide layer is rapidly formed upon reaction with oxygen in air and acts as a protective barrier. This oxide layer is very adherent and stable in physiological conditions. Although biocompatible, titanium implants lack bioactivity and osteoconductive properties for a rapid bone apposition. At early implantation time, titanium implants are generally encapsulated by fibrous tissue and are not in direct contact with bone tissue.

Calcium phosphate (CaP) coatings, especially those made with hydroxyapatite (HA, $Ca_{10}(PO_4)_6(OH)_2$), are applied on titanium implants to improve their bone-integrative properties.[3–5] As CaPs are similar in composition as the bone mineral, these materials are bioactive and able to achieve an early and functional bone apposition on the implants.[6–9] Following implantation, the release of calcium and phosphate ions into the peri-implant region increases the saturation of body fluids, leading to the precipitation of a biological carbonated apatite onto the surface of the implant (Figure 1). This layer of biological apatite might incorporate endogenous proteins and serve as a matrix for osteogenic cells' attachment and growth. These cells produce the bone extracellular matrix (ECM), resulting in a direct apposition of bone tissue on the CaP coating on titanium implants. The bone-healing process around the implant is therefore enhanced by this biological apatite layer.[10–12] The combination of the high mechanical strength of titanium with the osteoconductive properties of CaPs has proven efficacy to stimulate an early integration and long-term stability of noncemented orthopedic prosthesis.

There are a number of techniques to apply CaP coatings on titanium implants. The most successful method is plasma spraying of HA on orthopedic devices. However, plasma spraying presents some drawbacks such as high processing temperature, relatively thick and heterogeneous coatings, and poor efficiency on tiny or complex-shaped implants.[5,13] To overcome drawbacks of the commercially provided plasma-sprayed HA coating, several other deposition methods have been proposed. One of them is the biomimetic coating, where CaP is deposited on substrates by immersion in a simulated body fluid (SBF). Electrolytic deposition (ELD) is another promising alternative method to plasma-spraying HA. This chapter reviews the methods to apply CaP coatings on orthopedic and dental implants. It also discusses the advantages and drawbacks of each technique in regards to physicochemical

properties, mechanical strength, *in vitro* behavior in SBF or in cell culture, and *in vivo* bone integration. Future trends in the research of CaP coatings in view of addressing difficult clinical situations are finally proposed.

1.112.2. Calcium Phosphates

CaPs are similar in composition to the mineral part of bones and teeth. CaPs are salts of the phosphoric acid H_3PO_4 and thus can form compounds that contain $H_2PO_4^-$, HPO_4^{2-}, and/or PO_4^{3-} ions (Table 1). Most of the CaP compounds can be precipitated from aqueous solutions, while some are only formed at elevated temperatures. The CaP containing $H_2PO_4^-$ ions, such as monocalcium phosphate monohydrate (MCPM), only form under acidic conditions. The MCPM is usually not found in bones, as body fluids are neutral supersaturated calcium and phosphate solutions. In physiological conditions, CaP containing both HPO_4^{2-} and/or PO_4^{3-} ions such as OCP, CDA, or carbonated apatite are the most thermodynamically stable and insoluble phases. Bone tissue consists of a mineralized collagenous ECM produced by osteoblastic cells. In the bone mineralization process, collagen fibers serve as substrates for the nucleation and growth of carbonated apatite crystals that precipitate from body fluids.[14] The mineral part of bones and teeth is related to a type AB carbonated CaP apatite, which can be tentatively represented by the following formula[15]:

$$Ca_{8.3}\square_{1.7}(PO_4)_{4.3}(CO_3)(HPO_4)_{0.7}(OH,CO_3)_{0.3}\square_{1.7}$$

$\square$ = vacancy

Both the crystallinity and composition of bone mineral may vary considerably with age and skeletal sites. Bone mineral crystals contain nonapatitic carbonate and phosphate groups that are very labile and rapidly exchange with ions contained in body fluids.[15] Furthermore, minor or trace elements, such as magnesium and zinc, are also present in bone mineral. Bone crystallites are essentially plate-shaped, with average dimensions of 35–40 nm.[16] These crystals are believed to reinforce the collagen fibers forming a composite with high mechanical properties, as bone tissue is able to support body load as well as considerable forces during motion.

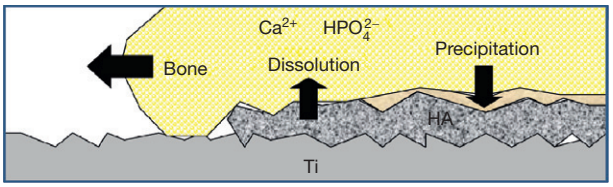

Figure 1 Principle of bioactivity and osteoconduction of CaP coatings on titanium implants. Following implantation, the partial dissolution of HA coating leads to the release of Ca^{2+} and HPO_4^{2-}, precipitation of biological apatite, colonization of osteogenic cells producing the bone extracellular matrix resulting in a direct bone tissue apposition on titanium.

Table 1 Names, abbreviations, composition, Ca/P ratios, solubility, pH, and temperature (°C) stability for synthetic and biological calcium orthophosphates

Name	*Abbreviation*	*Formula*	*Ca/P ratio*	*Solubility −log(K_s)*[a]	*pH and T (°C) stability*
Monocalcium phosphate monohydrate	MCPM	$Ca(H_2PO_4)_2 \cdot H_2O$	0.50	1.14	0.1–2.0 25 °C
Monocalcium phosphate anhydrous	MCPA	$Ca(H_2PO_4)_2$	0.50	1.14	0.1–2.0 > 80 °C
Dicalcium phosphate dihydrate (brushite)	DCPD	$CaHPO_4 \cdot 2H_2O$	1.00	6.59	2.0–5.5 25 °C
Dicalcium phosphate anhydrous (monetite)	DCPA	$CaHPO_4$	1.00	6.90	2.0–5.5 > 80 °C
Octacalcium phosphate	OCP	$Ca_8(HPO_4)_2(PO_4)_4 \cdot 5H_2O$	1.33	96.6	5.5–7.0 25–37 °C
Calcium-deficient apatite	CDA	$Ca_{10-x}[]_x(HPO_4)_x(PO_4)_{6-x}(OH)_{2-x}[]_x$ $(0 < x < 2)$[b]	1.33–1.67	~85.1	6.5–9.5 25–37 °C
Amorphous calcium phosphate	ACP	$Ca_x(HPO_4)_y(PO_4)_z \cdot nH_2O$ ($n = 3$–4.5; 15–20 wt% H_2O)	1.20–2.20	25.7–32.7	5–12 4–37 °C
β-Tricalcium phosphate	β-TCP	$\beta\text{-}Ca_3(PO_4)_2$	1.50	28.9	> 800 °C[c]
α-Tricalcium phosphate	α-TCP	$\alpha\text{-}Ca_3(PO_4)_2$	1.50	25.5	> 1125 °C[c]
Biphasic calcium phosphate	BCP	$\beta\text{-}Ca_3(PO_4)_2 + Ca_{10}(PO_4)_6(OH)_2$	Variable 1.55–1.65	NA	> 800 °C[c]
Hydroxyapatite	HA	$Ca_{10}(PO_4)_6(OH)_2$	1.67	116.8	9.5–12 > 80 °C
Fluoroapatite	FA	$Ca_{10}(PO_4)_6F_2$	1.67	120.0	7–12 > 80 °C
Tetracalcium phosphate	TTCP	$Ca_4(PO_4)_2O$	2.00	38–44	> 1400 °C[c]

NA, not applicable.

[a]The solubility at 25 °C in water is given at the logarithm of the ionic product of the given formula with concentrations in moles per liter.

[b][] represents a vacancy in the crystal lattice of hydroxyapatite.

[c]These compounds cannot be precipitated from aqueous solutions and form only at elevated temperatures.

Synthetic CaP, particularly HA, β-tricalcium phosphate (β-TCP), and mixtures, named biphasic calcium phosphate (BCP), have been successfully used for filling bone defects in various clinical indications. For more than three decades, these biomaterials in dense or porous forms have been clinically applied in orthopedic, spinal, and maxillofacial surgeries as bone substitutes.[17] These ceramics are manufactured starting from well-characterized CaP powders, mixed with pore makers, and sintered at elevated temperatures (e.g., 1000–1300 °C). Following implantation, these CaP ceramics interact with body fluids, partly dissolving and precipitating a biological apatite on their surface that serves as a substrate for osteogenic cells producing the bone ECM. This process, known as bioactivity, guides bone healing into the CaP ceramic by osteoconduction. However, CaP ceramics are intrinsically brittle and relatively weak, making them unsuitable for replacing skeleton parts that experience high loads. Consequently, CaPs have been applied as coatings on mechanically strong metal implants. This approach results in the combination of the high strength of titanium with the biological properties of CaP. Bioactive and osteoconductive CaP coatings applied on titanium devices are able to achieve an early and functional integration of the implant with the surrounding bone.

1.112.3. Titanium Implants

Prior to applying CaP coatings, surfaces of titanium implants are generally grit-blasted with alumina ceramic (Al_2O_3) particles. This treatment consists of blasting with air pressure ceramic particles of 100–200 μm on titanium implants. It aims at increasing the surface roughness to Ra value around 2–5 μm. High surface roughness ensures a good mechanical interlocking of CaP coatings on metals, improving bonding strength and shear resistance. Furthermore, modifying surface roughness has been shown to enhance the osteoblastic differentiation of mesenchymal stem cells and the bone-to-implant contact.[18] Dental implants are often grit-blasted and then etched with strong acids, producing cavities and micropitting on surfaces.[19] Nevertheless, alumina grit-blasting residues are not easily removed from the surface, and alumina particles may interfere with the osseointegration of implants. In order to overcome this drawback, we have recently proposed to use BCP ceramic particles for grit-blasting titanium implants. Grit-blasting titanium implants with BCP ceramic particles gave a high average surface roughness and particle-free surfaces after etching, as CaPs are soluble in acids. Studies conducted both *in vitro* and *in vivo* have shown that BCP grit-blasted surfaces promoted an early osteoblast differentiation and bone apposition as compared to smooth or alumina grit-blasted titanium implants.[20,21]

Alkaline and heat treatments of titanium implants have also been shown to promote CaP deposition *in vitro* from SBF as well as bone apposition. Kokubo and colleagues have treated titanium implants in KOH or NaOH 5 M solutions at 60 °C for 24 h producing an alkali titanate gel, which was stabilized by heating at 500 °C.[22–24] This group developed an SBF, which is a protein-free, electrolyte solution with similar concentrations of ions as in human blood plasma in order to mimic interactions with body fluids (Table 2). SBF is a supersaturated or metastable CaP solution at pH 7.4 and 37 °C. By immersion in SBF, alkali- and heat-treated titanium implants induced the precipitation of carbonated apatite on their surface. Similarly, bone bonding was observed on such treated titanium implants *in vivo*.[25]

1.112.4. Plasma Spraying of CaP Coatings

Plasma-sprayed coatings, mainly HA, have been used in orthopedic surgery to enhance the fixation to the skeleton of noncemented hip and knee prostheses. Many studies have shown that these coatings can successfully favor an early bone apposition on titanium implants.[26] The biological fixation of titanium implants to bone tissue is faster with a CaP coating than without. It is also well recognized that CaP coatings have led to better clinical success rates in the long term than did uncoated titanium implants. These long-term success rates are due to a superior initial rate of osseointegration.[27–29]

Atmospheric plasma spraying (APS) is the most widely applied method to deposit HA coating onto titanium alloy prostheses. As shown in Figure 2, the method consists of injecting the ceramic HA particles into a high-temperature (>10 000 °C) and high-velocity (>800 m s^{-1}) plasma torch. The HA particles partly melt and are projected on the surface of the titanium implants where they condense and fuse together, forming a coating. The plasma-spraying method is highly effective for coating orthopedic prostheses, as CaP layers having a thickness of 50–100 μm can be produced within minutes. However, the high temperature of the plasma torch provokes dehydration and decomposition of HA. The dehydration produces oxyapatite (OA, $Ca_{10}(PO_4)_6O$) and/or oxyhydroxyapatite (OHA, $Ca_{10}(PO_4)_6(OH)_{2-x}O_x[]_x$).[30] The thermal decomposition of HA results also in different phases such as calcium oxide (CaO), α-TCP, tetracalcium phosphate (TTCP, $Ca_4P_2O_9$), and amorphous calcium phosphate (ACP). A sprayed HA particle impacting the titanium surface is composed of a solid core and a solidified shell. Fast cooling at impact results in conservation of high-temperature CaP phases in the solid core, while the solidified shell is mostly composed of an amorphous phase. The fractions of HA, OA-OHA, TTCP, α-TCP, and ACP phases in sprayed coatings is the most important factor that determines the dissolution and biological behavior of coatings. These heterogeneities of CaP phases in plasma-sprayed HA coatings are responsible for differences in dissolution rates *in vivo*. The ACP

Table 2 Ionic composition of human blood plasma and simulated body fluids

Ionic concentration (mM)	Na^+	K^+	Mg^{2+}	Ca^{2+}	Cl^-	HCO^{3-}	HPO_4^{2-}	SO_4^{2-}	pH
Blood plasma	142	5	1.5	2.5	103.8	27	1	0.5	7.2–7.4
SBF	142	5	1.5	2.5	147.8	4.2	1	0.5	7.4

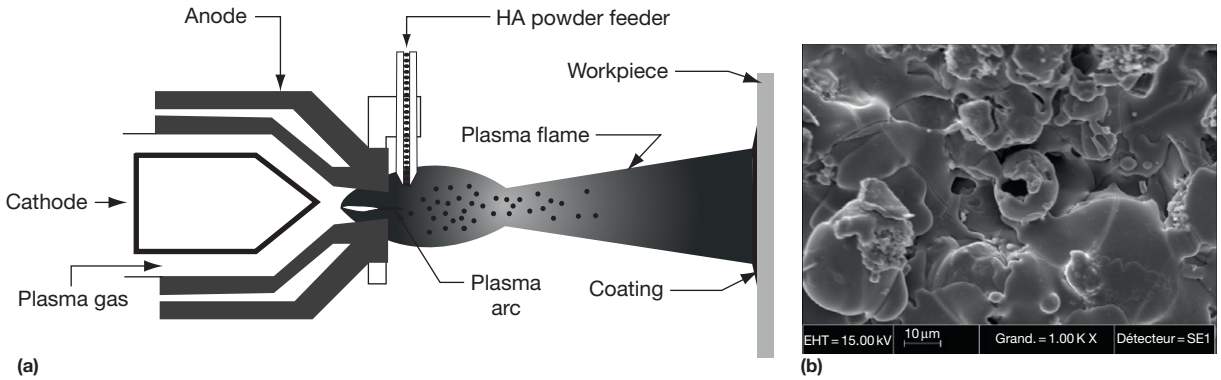

Figure 2 (a) Plasma spraying of HA coating and (b) scanning electron microscopy of a typical HA coating on titanium implants.

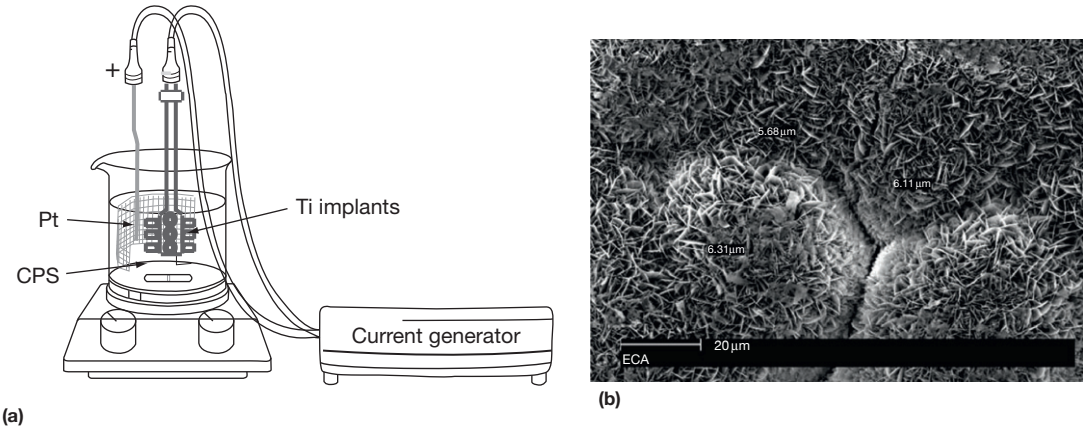

Figure 3 (a) Electrodeposition setup and (b) scanning electron microscopy of a typical ELD coating on titanium.

phase being highly soluble, some crystalline HA particles may be released in the articular synovia, inducing inflammation or delamination of coatings from the titanium implant. Furthermore, the plasma-spraying technique is not very effective for coating tiny dental implants. Coating delamination has been reported in dental situations where the efficacy of plasma spraying is not optimal due to the small size of the dental implants. Loosening of the coating has also been reported, especially when the dental implants have been inserted into dense bone. For all of the aforementioned reasons, the clinical use of plasma-sprayed HA coating on dental implants is marginal. Other drawbacks of the plasma-spraying technique are the impossibility of applying on implants promising CaP phases such as OCP, CDA, or carbonated apatite that precipitate in the body. The high temperatures of plasma spraying prevent the incorporation of biological agents such as antibiotics to prevent postsurgical infections or growth factors to stimulate bone healing. The technique is also not applicable to heat-sensitive implants such as polymers. Finally, plasma spraying is a line-of-sight process that produces uneven coating on porous or beaded metal implants. Therefore, researchers have explored alternative techniques for deposition of CaP coatings onto metal implants. The most promising methods are those that produce CaP coatings at ambient temperatures from aqueous supersaturated solutions.

1.112.5. Electrochemical Deposition of CaP Coatings

Electrodeposition (ELD) is a promising alternative method to plasma-spraying HA. In the ELD process, electrochemical reactions near the electrode induce local pH increase and thus CaP precipitation on the titanium implant. As shown in Figure 3, the ELD process is conducted in supersaturated or metastable CaP solutions and is based on the electrolytic decomposition of water. A platinum electrode (anode) and the titanium implant (cathode) are connected to a current generator. The application of current of several milliamperes results in the following electrochemical reactions. At the titanium cathode, the reduction of water takes place with production of hydrogen gas and rise of pH:

$$2H_2O + 2e^- \rightarrow H_2{}^{\uparrow} + 2OH^-$$

At the platinum anode, the oxidation of water with oxygen gas is observed:

$$2H_2O \rightarrow O_2{}^{\uparrow} + 4H^+ + 4e^-$$

The ELD takes advantage of the pH-dependent solubility of CaP compounds. Resulting from hydroxyl ions' production, the local pH rise leads to an increase in the relative supersaturation of the electrolyte and the precipitation of CaP

on the titanium surface. Most of the ELD have been conducted in acidic CaP solutions and formed brushite coating (dicalcium phosphate dihydrate, DCPD). Such brushite coatings normally need hydrothermal treatments to convert them into apatite. Recently, some studies have reported the direct deposition of apatite coating through ELD in SBF.[31,32] It has been found that the deposited CaP coating was composed of CA, or OCP that converted into CA with increasing time and temperature. Owing to physiological conditions (aqueous solutions, pH, and temperature), the incorporation of bioactive molecules such as proteins into CaP coatings is possible. For instance, bovine serum albumin–DCPD, collagen–OCP, and chitosan–apatite composite coatings were produced by using ELD. Nevertheless, the relatively low solubility of CaP at neutral pH is a limiting factor for ELD. Indeed, supersaturated solutions contain low concentrations of Ca^{2+} and HPO_4^{2-} ions, typically 2.5 and 1 mM, at neutral pH (Table 2). The precipitation of CaP coatings on titanium implants requires a sufficient volume of electrolyte to surface ratio. Based on a rough calculation, approximately 20 ml of electrolyte are needed to coat 1 cm^2 of implant. Applying CaP coatings through ELD on a large number of implants is therefore a challenging issue for industrial applications. Additionally, the hydrogen gas production hampers the deposition of CaP because of the formation of bubbles on the titanium surface. It results in nonuniform and relatively thin CaP coatings (around 10 μm). In order to overcome this problem, Legeros's group has developed a pulsed galvanostatic method to deposit CaP coatings on Ti6Al4V and Co–Cr alloys.[33] This method makes possible a perfect control of the thickness of the deposit on all kinds of complicated surfaces. The time required for coating is very short, and the process presents high reproducibility and efficacy. Other interesting methods to apply CaP coatings on metal implants using current are the electrophoretic deposition (EPD) process and the electrostatic spray deposition (ESD). The first EPD method consists of suspending CaP powders in nonaqueous solutions (e.g., isopropanol, ethanol) and applying an electric field ~10 V cm^{-1} between an electrode and the implant to be coated.[34] As CaPs are predominantly positively charged particles, they are displaced onto the negative metal substrate forming a layer. However, the stabilization of CaP suspensions is not an easy task. The second ESD method is based on the generation of an aerosol composed of organic solvents containing inorganic precursors under the influence of high voltages.[35] Spray droplets are generated by pumping a solution through a nozzle and attracted by a grounded and heated substrate. Leeuwenburgh and colleagues have used the ESD method to produce CaP coatings on titanium. Calcium nitrate or chloride and phosphoric acid were dissolved in ethanol and/or butyl carbitol and processed by ESD while substrate was heated at 300–450 °C. Interestingly, different spray droplets of carbonated apatite were produced on titanium. Both the EPD and ESD methods are efficient processes, as typical deposition time is in the range of minutes. However, the initial adherence of the CaP coatings is poor, and EPD is followed by postheating at 800–1200 °C for 1 h, while ESD requires *in situ* heating at 300–450 °C. The incorporation of bioactive molecules is therefore not possible using ESD and EPD methods. DCPD coatings on orthopedic prostheses and dental implants processed by ELD have reached clinical applications and are commercially available (BIONIT®, DOT GmbH). Nanocrystalline HA coatings have been applied by ELD on orthopedic acetabulum prostheses (BoneMaster®, BIOMET Corp.) and showed higher bone mineral density than that of plasma-sprayed HA-coated devices.

1.112.6. Biomimetic CaP Coatings

In order to avoid the drawbacks of plasma-sprayed HA coatings, scientists have developed a new coating method inspired by the natural process of biomineralization. In this biomimetic method, the precipitation of CaP apatite crystals was obtained onto the titanium surface from SBF. This method involves the heterogeneous nucleation and growth of bone-like crystals on the surface of the implant at physiological temperatures and pH conditions. In order to overcome the problem of low saturation of SBF, calcium and phosphate concentrations were increased by bubbling a weak acid gas, namely, carbon dioxide (Figure 4). Upon exchange of CO_2 with air, the pH of the solution rises and thus saturation of the solution increases, causing the precipitation of CaP coatings onto the implants.[36] The heterogeneous nucleation and crystal growth of the CaP coatings on the titanium surface is initiated by the chemical bonding of nano-sized clusters, forming an interfacial unstructured matrix, stabilized by the presence of magnesium and carbonate ions.[37] The method resulted in uniform and well-attached coating of carbonated apatite on titanium implants, as shown in Figure 4. In addition, this physiological method broadens the variety of CaP phases that can be deposited, such as OCP or bone-like carbonate apatite.[38] It has been shown that such biomimetic coatings are more soluble in physiological fluids and resorbable by osteoclastic cells than high-temperature coatings such as plasma-sprayed HA.[39,40] The osseointegration of titanium implants coated with biomimetic CaP has been investigated in preclinical comparative models. These studies have demonstrated a higher bone-to-implant contact for biomimetic CaP coatings than for uncoated titanium implants.[41] As shown in Figure 5, noncoated metal implants were encapsulated by fibrous tissue, while direct bone apposition was observed on biomimetic CaP-coated implants. Despite these positive results, the osseointegration of titanium implants coated biomimetically has not yet been compared with other surface treatments in preclinical models.

Owing to the physiological conditions of formation, biomimetic CaP coatings may incorporate bone-stimulating agents such as growth factors in order to enhance the bone-healing process in the peri-implant region.[42] Members of the transforming growth factor-β (TGF-β) superfamily, and in particular, bone morphogenetic proteins (BMPs), TGF-β1, platelet-derived growth factor (PDGF), and insulin-like growth factors (IGF-1 and -2), are some of the most promising candidates for this purpose. Experimental data, in which BMPs have been incorporated into dental implants, have been obtained from a variety of methodologies.[43] The limiting factor is that the active product has to be released progressively and not in a single burst. Another possibility may be the adjunction of a plasmid containing the gene coding for a BMP. This possibility is limited due to the poor efficacy of inserting plasmids into the cells and the expression of the protein. In addition, overproduction of BMPs by cells might not be desirable after the bone-healing process. The surface of

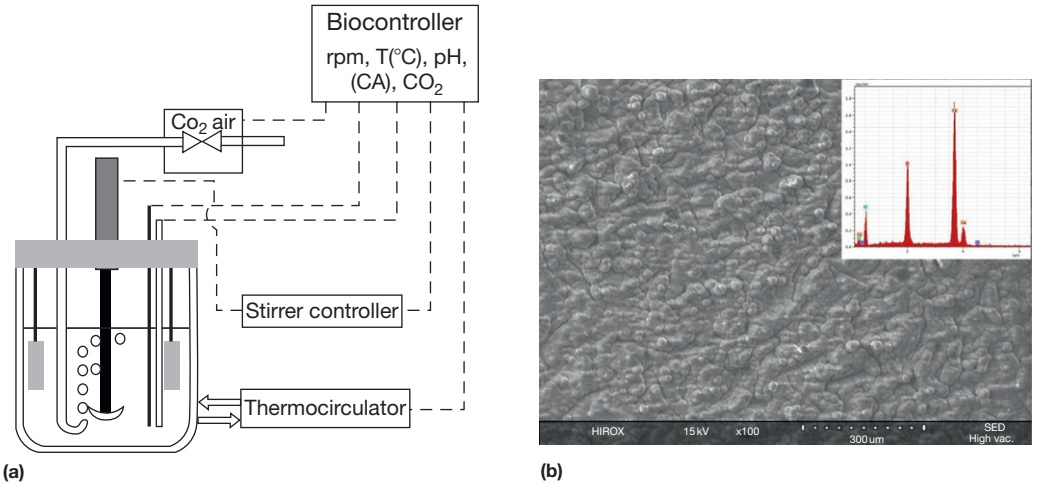

Figure 4 (a) Bioreactor for biomimetic coating of the metal implants and (b) scanning electron microscopy of a typical carbonated apatite coating on titanium. Insert: EDX spectrum of the biomimetic CaP coating.

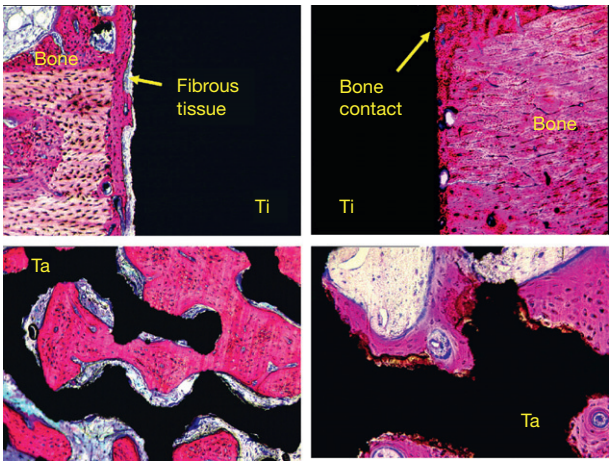

Figure 5 Comparison of bone-integrative properties of noncoated (left) and biomimetic calcium phosphate-coated metal implants (right) after implantation in the femur of goats for 6 weeks.

implants could also be loaded with molecules controlling the bone-remodeling process. Incorporation of bone antiresorptive drugs, such as biphosphonates, might be very relevant in clinical cases lacking bone support, for example, resorbed alveolar ridges. It has been shown recently that a biphosphonate incorporated onto titanium implants increased bone density locally in the peri-implant region.[44] The effect of the antiresorptive drug seems to be limited to the vicinity of the implant. Experimental *in vivo* studies have demonstrated the absence of negative effects but only a slight increase in dental implant osseointegration. Other experimental studies using plasma-sprayed HA-coated dental implants immersed in pamidronate or zoledronate demonstrated a significant increase in bone contact area. The main problem lies in the grafting and sustained release of antiresorptive drugs on the titanium implant surface. On account of the high chemical affinity of biphosphonates for CaP surfaces, incorporation of the antiresorptive drug onto dental implants could be achieved by using the biomimetic coating method at room temperatures. However, the ideal dose of antiresorptive drug will have to be determined, because the increase in peri-implant bone density is biphosphonate concentration-dependent. In order to prevent postsurgical infections around orthopedic or dental implants, antibiotics may be incorporated into biomimetic CaP coatings. The antibiotic can be gradually coprecipitated with the CaP crystals, forming a layer on the metal implants. This creates the possibility to incorporate an antibiotic uniformly within the biomimetic coating and release it at a controlled rate, thus preventing or stopping local infection postoperatively. Different antibiotics were incorporated into the carbonated apatite coatings and their release was studied *in vitro*. The antibiotics were effective to stop locally the growth of bacteria. These studies evidenced the benefits of using a biomimetic method for coating medical implants. The incorporation of various bioactive molecules into CaP coatings at physiological conditions allowed their sustained, local release and bioactivity in the peri-implant region concomitantly with an improved osseointegration.

1.112.7. Conclusion and Perspectives

Metal implants are only biocompatible and have no osteogenic properties in order to promote bone healing. Their osteointegration or biological anchoring to the skeleton is improved by CaP coatings. The aim is to provide metal implants with surface biological properties for the adsorption of proteins, the adhesion of cells, and the bone apposition. Direct bone-to-implant contact is desired for a biomechanical anchoring of implants rather than fibrous tissue encapsulation. These bioactive coatings on titanium implants are resorbable and stimulate bone apposition onto the implant surface. The biomimetic approach has four main advantages: (i) it is a low-temperature process applicable to any heat-sensitive substrate including polymers; (ii) it forms bone-like apatite crystals having high bioactivity and good resorption characteristics; (iii) it is evenly deposited on, or even into, porous or complex implant geometries; and (iv) it can incorporate bone-growth-stimulating factors.

References

1. *European Spine Implants Market 2008-2010*, 5th edn., Avicenne Market Reports, 2009.
2. *European Markets for Dental Implants and Final Abutments*, Millenium Research Group's Reports, 2005.
3. Geesink, R. G. T.; De Groot, K.; Klein, C. P. A. T. *Clin. Orthop.* **1987**, *225*, 147–170.
4. Leon, B.; Jansen, J. A. *Thin Calcium Phosphate Coatings for Medical Implants*. Springer: New York, 2009.
5. Serekian, P. *Hydroxyapatite Coatings in Orthopaedic Surgery*. Raven Press: New York, 1993.
6. Chow, L. C.; Eanes, E. D. *Octacalcium Phosphate*. Karger: Basel, 2001.
7. de Groot, K. *Bioceramics of Calcium Phosphate*. CRC Press: Boca Raton, FL, 1983.
8. Driessens, F. C. M. *Monographs in Oral Science*; Karger: Basel, 1982; Vol. 10.
9. Legeros, R. Z. In *Monographs in Oral Science*; Karger: Basel, 1991; Vol. 15.
10. Ducheyne, P.; Radin, S.; King, L. *J. Biomed. Mater. Res.* **1993**, *27*, 25–34.
11. Ducheyne, P.; Qiu, Q.-Q. *Biomaterials* **1999**, *20*, 2287–2303.
12. Radin, S.; Ducheyne, P. *J. Biomed. Mater. Res.* **1993**, *27*, 35–45.
13. Wolke, J. G. C.; Blieck-Hogervorst, J. M. A.; Dhert, W. J. A.; Klein, C. P. A. T.; De Groot, K. *J. Therm. Spray Technol.* **1992**, *1*, 75.
14. Burger, C.; Zhou, H. W.; Wang, H.; *et al*. *Biophys. J.* **2008**, *95*, 1985–1992.
15. Rey, C.; Combes, C.; Drouet, C.; Glimcher, M. J. *Osteoporos Int.* **2009**, *20*, 1013–1021.
16. Boskey, A. L. *Calcif. Tissue Int.* **2003**, *72*, 533–536.
17. Daculsi, G.; Legeros, R. Z.; Nery, E.; Lynch, K.; Kerebel, B. *J. Biomed. Mater. Res.* **1983**, *23*, 883–894.
18. Lavenus, S.; Ricquier, J. C.; Louarn, G.; Layrolle, P. *Nanomedicine (Lond.)* **2010**, *5*, 937–947.
19. Le Guehennec, L.; Soueidan, A.; Layrolle, P.; Amouriq, Y. *Dent. Mater.* **2007**, *23*, 844–854.
20. Citeau, A.; Guicheux, J.; Vinatier, C.; *et al*. *Biomaterials* **2005**, *26*, 157–165.
21. Le Guehennec, L.; Goyenvalle, E.; Lopez-Heredia, M. A.; Weiss, P.; Amouriq, Y.; Layrolle, P. *Clin. Oral Implants Res.* **2008**, *19*, 1103–1110.
22. Kokubo, T.; Kushitani, H.; Abe, Y.; Yamamuro, T. *Bioceramics* **1989**, *2*, 235–242.
23. Li, P.; Kangasniemi, I.; de Groot, K.; Kokubo, T. *J. Am. Ceram. Soc.* **1994**, *77*, 1307–1312.
24. Li, P.; Ducheyne, P. *J. Biomed. Mater. Res.* **1998**, *41*, 341–348.
25. Kokubo, T.; Kim, H. M.; Kawashita, M.; Nakamura, T. *J. Mater. Sci. Mater. Med.* **2004**, *15*, 99–107.
26. Goyenvalle, E.; Aguado, E.; Nguyen, J. M.; *et al*. *Biomaterials* **2006**, *27*, 1119–1128.
27. De Groot, K.; Geesink, R. G. T.; Klein, C. P. A. T.; Serekian, P. *J. Biomed. Mater. Res.* **1997**, *21*, 1375–1381.
28. Ducheyne, P.; Hench, L. L.; Kagan, A.; Martens, M.; Mulier, J. C.; Burssens, A. *J. Biomed. Mater. Res.* **1980**, *14*, 225–237.
29. Geesink, R. G.; de Groot, K.; Klein, C. P. *J. Bone Joint Surg. Br.* **1988**, *70*, 17–22.
30. Radin, S.; Ducheyne, P. *Mater. Med.* **1992**, *3*, 33–42.
31. Lopez-Heredia, M. A.; Weiss, P.; Layrolle, P. *J. Mater. Sci. Mater. Med.* **2007**, *18*, 381–390.
32. Wang, J.; Layrolle, P.; Stigter, M.; de Groot, K. *Biomaterials* **2004**, *25*, 583–592.
33. Lin, S.; LeGeros, R. Z.; LeGeros, J. P. *J. Biomed. Mater. Res. A* **2003**, *66*, 819–828.
34. Gottlander, M.; Johansson, C. B.; Wennerberg, A.; Albrektsson, T.; Radin, S.; Ducheyne, P. *Biomaterials* **1997**, *18*, 551–557.
35. Leeuwenburgh, S. C.; Wolke, J. G.; Schoonman, J.; Jansen, J. A. *Biomaterials* **2004**, *25*, 641–649.
36. Habibovic, P.; Barrere, F.; van Blitterswijk, C. A.; de Groot, K.; Layrolle, P. *J. Am. Ceram. Soc.* **2002**, *85*, 517–522.
37. Barrere, F.; Snel, M. M.; van Blitterswijk, C. A.; de Groot, K.; Layrolle, P. *Biomaterials* **2004**, *25*, 2901–2910.
38. Barrere, F.; van Blitterswijk, C.; de Groot, K.; Layrolle, P. *Biomaterials* **2002**, *23*, 2211–2220.
39. Barrère, F.; van der Valk, C. M.; Dalmeijer, R. A.; van Blitterswijk, C. A.; de Groot, K.; Layrolle, P. *J. Biomed. Mater. Res. A* **2003**, *64*, 378–387.
40. Leeuwenburgh, S.; Layrolle, P.; Barrère, F.; *et al*. *J. Biomed. Mater. Res.* **2001**, *56*, 208–215.
41. Barrere, F.; van der Valk, C. M.; Meijer, G.; Dalmeijer, R. A.; de Groot, K.; Layrolle, P. *J. Biomed. Mater. Res. B Appl. Biomater.* **2003**, *67*, 655–665.
42. Liu, Y.; Layrolle, P.; de Bruijn, J.; van Blitterswijk, C.; de Groot, K. *J. Biomed. Mater. Res.* **2001**, *57*, 327–335.
43. Liu, Y.; Hunziker, E. B.; Layrolle, P.; De Bruijn, J. D.; De Groot, K. *Tissue Eng.* **2004**, *10*, 101–108.
44. Peter, B.; Pioletti, D. P.; Laïb, S.; *et al*. *Bone* **2005**, *36*, 52–60.
45. Stigter, M.; Bezemer, J.; de Groot, K.; Layrolle, P. *J. Control. Release* **2004**, *99*, 127–137.
46. Stigter, M.; de Groot, K.; Layrolle, P. *Biomaterials* **2002**, *23*, 4143–4153.

1.113. Bioactive Layer Formation on Metals and Polymers

T Kokubo and S Yamaguchi, Chubu University, Kasugai, Aichi, Japan

© 2011 Elsevier Ltd. All rights reserved.

1.113.1.	**Introduction**	231
1.113.2.	**Bioactive Layers**	231
1.113.2.1.	Bioactive Layers on Metals	231
1.113.2.1.1.	Bioactive layers on titanium metal and its alloys	231
1.113.2.1.2.	Bioactive layers on Zr metal	240
1.113.2.1.3.	Bioactive layers on Nb metal	240
1.113.2.1.4.	Bioactive layers on Ta metal	241
1.113.2.2.	Bioactive Layers on Organic Polymers	241
1.113.3.	**Future Perspectives**	242
1.113.4.	**Additional Reading**	242
References		242

Abbreviations

AES	Auger electron spectroscopy
EDX	Energy dispersive X-ray analysis
EVOH	Ethylene-vinyl alcohol
HMWPE	High-molecular-weight polyethylene
PE	Polyethylene
PET	Poly(ethylene terephthalate)
PTFE	Poly(tetrafluoroethylene)
SBF	Simulated body fluid
SEM	Scanning electron microscopy
TEM	Transmission electron microscopy
Ti	Titanium
$TiCl_4$	Titanium tetrachloride
XPS	X-ray photoelectron spectroscopy

1.113.1. Introduction

Various kinds of bone-bonding, bioactive ceramics have been developed and are being used clinically as important bone substitutes.[1] Although they can be glass, glass–ceramic, or polycrystalline ceramics, all of them contain calcium, and the majority contain calcium phosphate. They are intrinsically brittle and have poor fracture toughness. Some orthopedic and dental applications need tough and ductile bioactive materials. Metals coated with calcium phosphates have been developed using various methods, such as plasma spraying, sputtering, sol–gel deposition, biomimetic deposition,[2] and alternate soaking processes.[3] Some are already being used clinically under load-bearing conditions. However, the coated hydroxyapatite has a distinct boundary against the metallic substrate; hence, it does not remain stable in the body for long periods (see **Chapter 1.102, Metals for Use in Medicine**; **Chapter 1.109, Bioactive Ceramics**; **Chapter 1.110, Bioactive Glass-Ceramics**; **Chapter 1.111, Bioactive Ceramics: Physical Chemistry**; and **Chapter 1.112, Calcium Phosphate Coatings**).

It has been shown that some gels, such as silica[4] and titania[5] gels, can form bone-like apatite on their surfaces in simulated body fluid (SBF) having ion concentrations nearly equal to those of human blood plasma,[6] as shown in **Figure 1**. This indicates that functional groups, such as Si–OH and Ti–OH, abundant on the gels, induce nucleation of the apatite within the body. Therefore, if their surfaces could be modified with functional groups that enable effective apatite nucleation, it is expected that even tough metallic materials and soft organic polymeric materials could form the bone-like apatite on their surfaces in the body and bond to living bone through this apatite layer.

In the next section, various methods for producing bioactive layers, which form apatite on metallic and polymeric substrates in the body, are reviewed.

1.113.2. Bioactive Layers

1.113.2.1. Bioactive Layers on Metals

1.113.2.1.1. Bioactive layers on titanium metal and its alloys

1.113.2.1.1.1. Sodium titanate layer

Titanium (Ti) metal is generally covered with a thin layer of titanium oxide. It is expected that if Na^+ ions are incorporated into the titanium oxide layer, the resultant sodium titanate layer could form Ti–OH groups on its surface in the body by exchanging its Na^+ ions with the H_3O^+ ions in the body fluid and thus induce apatite formation (see **Chapter 1.114, Bioactivity: Mechanisms** and **Chapter 6.605, Porous Coatings in Orthopedics**).

Kokubo *et al.*[7] were the first to show that a sodium titanate layer is formed on the surface of Ti metal when the metal is soaked in NaOH solution and then heat treated, and that the treated Ti metal forms a bone-like apatite on its surface in SBF. The effects of varying concentration, temperature, periods of soaking in the NaOH solution, and the temperature of the heat treatment on the apatite-forming ability of the Ti metal in SBF were

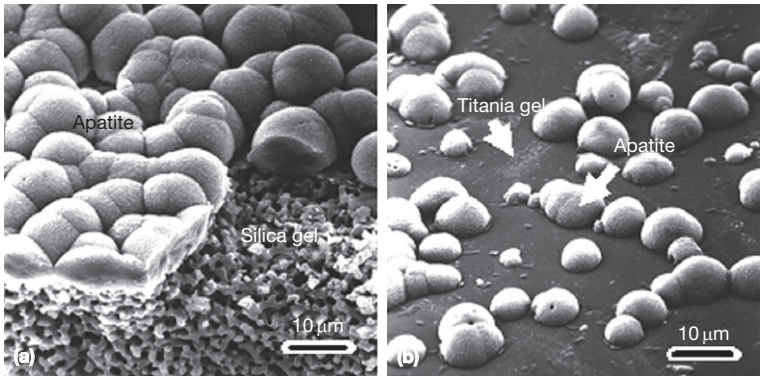

Figure 1 Scanning electron microscopy photographs of surfaces of (a) silica gel and (b) titania gel after soaked in simulated body fluid for 14 days. Reproduced from Li, P.; Ohtsuki, C.; Kokubo, T.; Nakanishi, K.; Soga N.; de Groot, K. J. *Biomed. Mater. Res.* **1994**, *28*, 7–15, with permission from John Wiley and Sons.

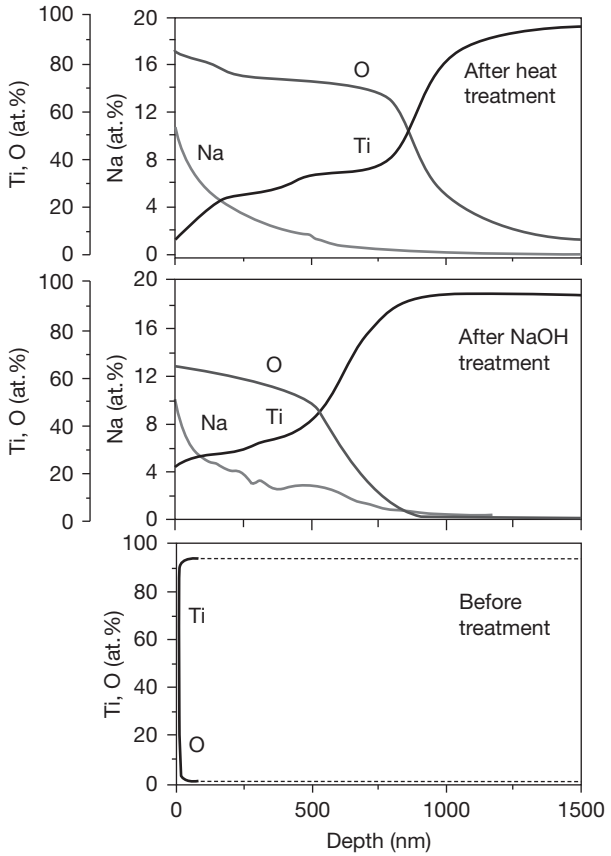

Figure 2 Auger electron spectroscopy depth profiles of surfaces of Ti metals untreated and those subjected to NaOH and heat treatments. Reproduced from Kim, H. M.; Miyaji, F.; Kokubo, T.; Nishiguchi, S.; Nakamura, T. *J. Biomed. Mater. Res.* **1999**, *45*, 100–107, with permission from John Wiley and Sons.

investigated.[8,9] These studies showed that soaking in a 5 M NaOH solution at 60 °C for 24 h and heat treatment at 600 °C for 1 h were standard treatments, and that these treatments are also effective in inducing the apatite-forming ability of Ti-based alloys, such as Ti–6Al–4V, Ti–6Al–2Nb–Ta, and Ti–15Mo–5Zr–3Al.[10]

Auger electron spectroscopy (AES) showed that the sodium and oxygen ions penetrated the surface of the Ti metal to a depth of 1 μm after NaOH treatment, and that only oxygen ions penetrated a little deeper during the subsequent heat treatment, as shown in Figure 2.[11] The concentration of both ions continued to decrease gradually with increasing depth from the surface. A distinct boundary was not formed between the surface layer and the metallic substrate. Similar graded surface structures were observed for Ti–6Al–4V[12] and Ti–15Mo–5Zr–3Al alloys[13] subjected to the NaOH and heat treatments. During the NaOH treatment, alloy elements, such as Al, V, Mo, and Zr, were selectively released from the surfaces of these alloys.

Using thin-film X-ray diffraction,[10] it was initially assumed that the phase formed on the Ti metal by the NaOH treatment was sodium titanate hydrogel, and those formed by the subsequent heat treatment were amorphous sodium titanate and rutile. Using detailed analyses of thin-film X-ray diffraction and Raman spectroscopy, Kawai *et al.*[14] later found that the sodium titanate hydrogel and amorphous sodium titanate were actually nano-sized crystalline sodium hydrogen titanate ($Na_xH_{2-x}Ti_yO_{2y+1}$; $0 < x < 2$ and $y = 2$, 3, or 4) and nano-sized crystalline sodium titanate layers ($Na_2Ti_yO_{2y+1}$; $y = 5$, 6, etc.), respectively.

The NaOH treatment formed a fine network structure on the surface of the Ti metal, and subsequent heat treatment did not essentially change this, as shown in Figure 3. The fine network structure was shown to consist of featherlike phases that were elongated perpendicular to the substrate, about 1 μm in length, and the structure was further densified by the subsequent heat treatment, as shown in Figure 4.[15] The structural changes due to the NaOH and heat treatments are shown schematically in Figure 5.

The adhesive strength[16] and scratch resistance[14] of the surface layer formed on the Ti metal by the NaOH treatment increased with the subsequent heat treatment.

When the NaOH- and heat-treated Ti metal was soaked in SBF, apatite started to precipitate in the deep region of the interspaces of the featherlike phases. The apatite filled the interspaces and integrated with the featherlike phases to form a dense composite of apatite and titanate, which grew over the surface layer, fully covering the surface, as shown in Figure 6.[15]

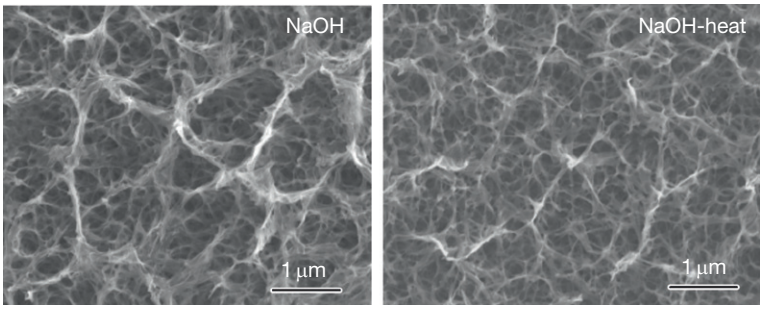

Figure 3 Scanning electron microscopy photographs of surfaces of Ti metals subjected to NaOH and heat treatments.

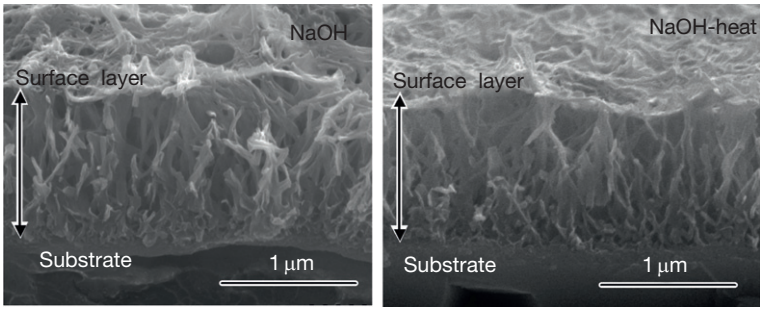

Figure 4 Scanning electron microscopy photographs of cross-sections of surfaces of Ti metals subjected to NaOH and heat treatments. Reproduced from Yamaguchi, S.; Takadama, H.; Matsushita, T.; Nakamura, T.; Kokubo, T. *J. Ceram. Soc. Jpn.* **2009**, *117*, 1126–1130, with permission from The Ceramic Society of Japan.

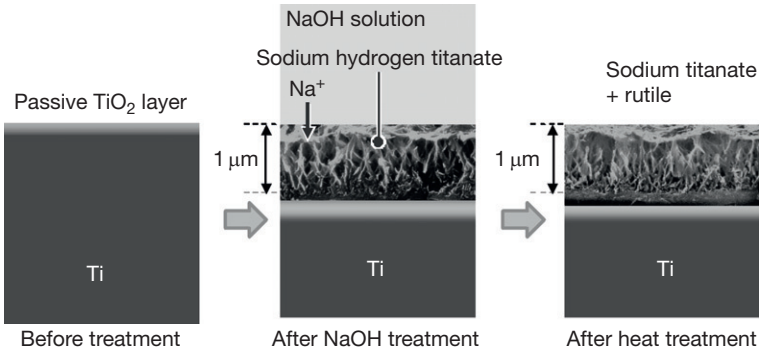

Figure 5 Structural change of surface of Ti metal due to NaOH and heat treatments.

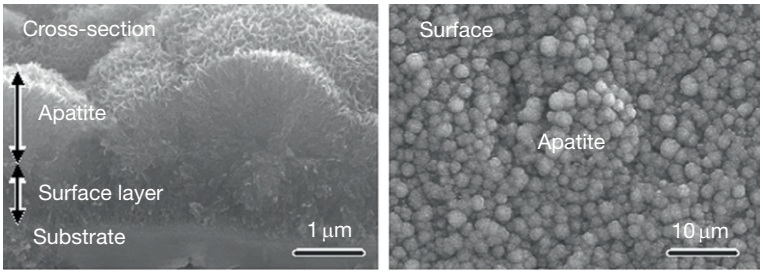

Figure 6 Scanning electron microscopy photographs of cross-section and surface of NaOH- and heat-treated Ti metal after soaking in simulated body fluid for 1 day. Reproduced from Yamaguchi, S.; Takadama, H.; Matsushita, T.; Nakamura, T.; Kokubo, T. *J. Ceram. Soc. Jpn.* **2009**, *117*, 1126–1130, with permission from The Ceramic Society of Japan.

There was no distinct boundary between the apatite–titanate composite and the metallic substrate. Transmission electron microscopy (TEM) confirmed the fact that the apatite so formed took a needle-like shape and had a composition similar to bone mineral, with a Ca/P atomic ratio of 1.65 and small amounts of Na and Mg, as shown in Figure 7.[17]

With respect to the mechanism of apatite formation on the thus-treated Ti metal, Uchida *et al.* first showed that a specific

structure is required for the formation of apatite on sodium titanate in SBF.[18] Later, X-ray photoelectron spectroscopy (XPS),[19] TEM observation,[17] and zeta potential measurement[20] showed that apatite is formed on the treated Ti metal in SBF by a process that is shown in **Figure 8**. Sodium ions are released from the surface of the sodium titanate via exchange with H_3O^+ ions in the SBF to form Ti–OH groups on the surface of the titanate. The Ti–OH groups thus-formed are negatively charged because the pH of the surrounding SBF is increased by the released sodium ions[21]; these then combine with the positively charged calcium ions to form a calcium titanate. As the calcium ions accumulate on the surface of the titanate, the surface is positively charged, and hence, it combines with the negatively charged phosphate ions to form amorphous calcium phosphate. This calcium phosphate is metastable and eventually transforms into a crystalline bone-like apatite. Using XPS[22] and TEM[23] studies, Takadama *et al.* confirmed that a similar process of apatite formation occurs on a Ti–6Al–4V alloy subjected to the NaOH and heat treatments. Using TEM observations, Conforto *et al.*[24] examined the process of apatite formation on Ti metal subjected to NaOH treatment, but not to the heat treatment, in SBF, and they confirmed the formation of calcium titanate prior to the formation of apatite.

Strnad *et al.* showed that preliminary acid treatment enables effective and uniform apatite formation in Ti metal subjected to NaOH treatment but not to the heat treatment, in SBF.[25,26] Müller *et al.*[27] also found that the preliminary acid treatment effectively enabled apatite formation on a Ti–13Nb–13Zr alloy treated with an NaOH solution, in SBF.

Jonášová *et al.* raised concerns over an inflammatory response of the surrounding tissues that could be induced by the sodium ions released from the sodium titanate. They showed that even NaOH-treated Ti metals, which released a fair amount of sodium ions, do not decrease their apatite-forming ability in SBF.[28] This result is applicable to Ti metals subjected to the NaOH treatment, but not to the heat treatment. Kawai *et al.*[14] showed that the subsequent heat treatment greatly increases the apatite-forming ability of NaOH-treated Ti metal in SBF, and that the NaOH- and heat-treated Ti metal displays a high apatite-forming ability even when the sodium ions in the surface layer are decreased, but not completely released. It should be noted here that the sodium ions in the surface layer of the treated Ti metal are liable to be released when the treated Ti metal is stored in a humid environment as it is exchanged with the H_3O^+ ions in the atmosphere. This decreases the apatite-forming ability of the treated Ti metal. However, according to Kawai *et al.*,[14] if the sodium ions on the top surface of the sodium titanate are removed by water treatment after the NaOH treatment, the apatite-forming ability of the treated Ti metal does not decrease, even after the treated Ti metal has been stored in a humid environment for a long period.

Krupa *et al.*[29] showed that the NaOH-treated Ti metal displays high corrosion resistance after heat treatment.

By using these chemical and heat treatments, the bioactive layer can easily be formed uniformly, even on the irregular inner surfaces of porous materials.[30] Both heat treatment for fabrication of the porous body and subsequent treatments for inducing bioactivity can incorporate fairly large amounts of oxygen ions into the Ti metal. However, the incorporated oxygen does not have any adverse effect on the apatite-forming ability of the Ti metal in SBF.[31]

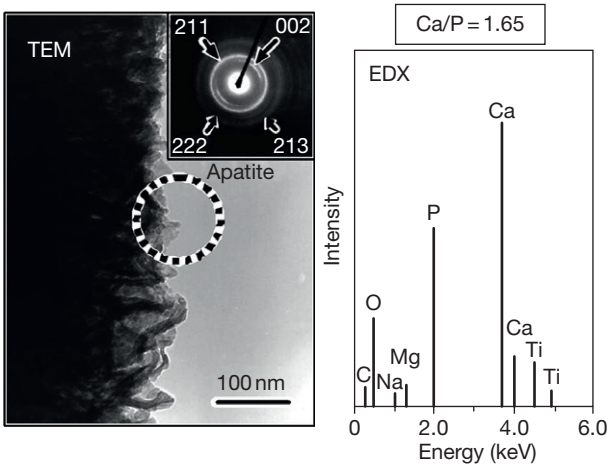

Figure 7 Transmission electron microscopic photograph and energy dispersive X-ray analysis (EDX) spectrum of the surface of the NaOH- and heat-treated Ti metal after soaking in simulated body fluid for 5 days (dotted circle: area of electron diffraction and EDX analysis). Reproduced from Takadama, H.; Kim, H. M.; Kokubo, T.; Nakamura, T. *J. Biomed. Mater. Res.* **2001**, *57*, 441–448, with permission from John Wiley and Sons.

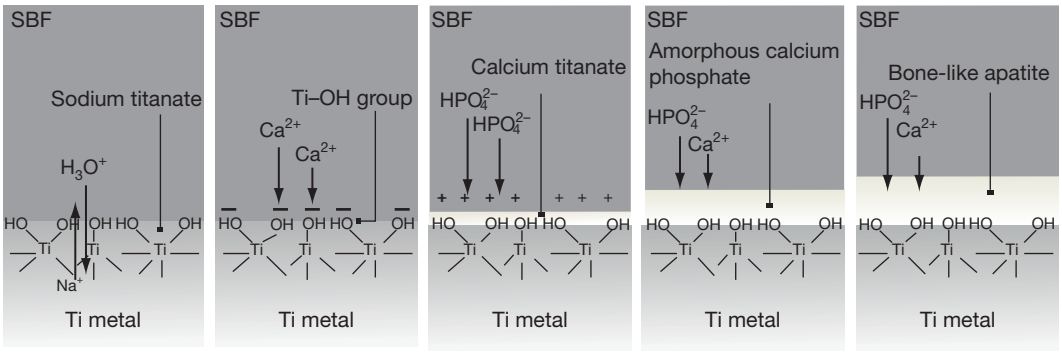

Figure 8 Process of apatite formation on NaOH- and heat-treated Ti metal in simulated body fluid. Reproduced from Kim, H. M.; Himeno, T.; Kawashita, M.; Lee, J.-H.; Kokubo, T.; Nakamura, T. *J. Biomed. Mater. Res.* **2003**, *67A*, 1305–1309, with permission from John Wiley and Sons.

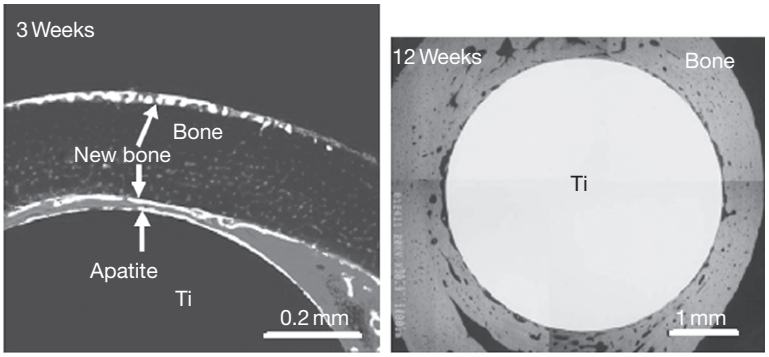

Figure 9 Confocal laser scanning microscopic photograph (left-hand side) and SEM photograph (right-hand side) of the cross-section of the NaOH- and heat-treated Ti metal rod implanted into rabbit femur for 3 and 12 weeks, respectively. Reproduced from Nishiguchi, S.; Fujibayashi, S.; Kim, H. M.; Kokubo, T.; Nakamura, T. *J. Biomed. Mater. Res.* **2003**, *67A*, 26–35, with permission from John Wiley and Sons.

Cell culture experiments have shown enhancements in both differentiation of osteoblasts and bone nodule formation on the apatite layer formed by the NaOH- and heat-treatments in Ti metal, in SBF.[32,33]

These *in vitro* data indicate that the NaOH- and heat-treated Ti metal forms a bone-like apatite layer on its surface, even in the living body, and that it tightly bonds to the living bone through this apatite layer. Actually, when the NaOH- and heat-treated Ti metal was implanted into the tibia of a rabbit, it formed a bone-like apatite on its surface and tightly bonded to the living bone.[34] Under tensile stress, the failure load of the treated Ti metal bonded to the living bone was much higher than that of the untreated Ti metal, higher than that of only NaOH-treated Ti metal, and almost equal to that of the Ti metal formed with apatite on its surface, in SBF.[34–36] The failure load increased with an increase in the period after implantation. Ti-based alloys, such as Ti–6Al–4V, Ti–6Al–2Nb–Ta, and Ti–15Mo–5Zr–3Al, which were subjected to NaOH and heat treatments and implanted into the tibia of a rabbit, also displayed high failure loads under tensile stress.[37] When implanted into a canine femur,[38] the Ti metal and its alloys, subjected to the same treatments, showed high bonding strengths, even under shear stress. An NaOH- and heat-treated Ti metal rod implanted into the medullary canal of a rabbit femur was observed to form a bone-like apatite on its surface within 3 weeks, and to be completely surrounded by newly grown bone within 12 weeks, as shown in **Figure 9**.[39] The push-out failure load of the treated Ti metal was much higher than that of the untreated Ti metal, and it increased with an increase in the period after implantation, as shown in **Figure 10**.[39] At 12 weeks after implantation, the treated Ti metal rod could not be pulled out without being accompanied by bone fragments, as shown in **Figure 11**.

Porous Ti metals subjected to NaOH and heat treatments were fully penetrated, and they bonded with new bone derived from the surrounding bone.[40]

Based on these animal experiments, NaOH and heat treatments were applied to a porous Ti metal layer on the outer cup and on part of the stem of a Ti–6Al–2Nb–Ta alloy of a total artificial hip joint. After successful clinical trials, the resultant bioactive artificial joint has been in clinical use in Japan since 2007, as shown in **Figure 12**.[41]

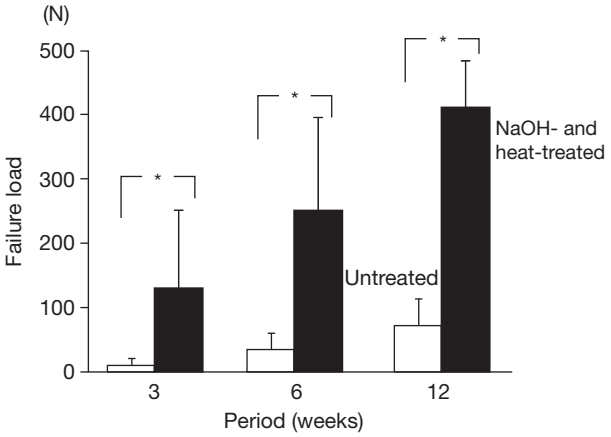

Figure 10 Pull-out failure loads of the Ti metal rod implanted into medullary canal of femur of rabbit for periods of 3, 6, and 12 weeks, for Ti metals untreated and subjected to NaOH and heat treatments prior to implantation. Reproduced from Nishiguchi, S.; Fujibayashi, S.; Kim, H. M.; Kokubo, T.; Nakamura, T. *J. Biomed. Mater. Res.* **2003**, *67A*, 26–35, with permission from John Wiley and Sons.

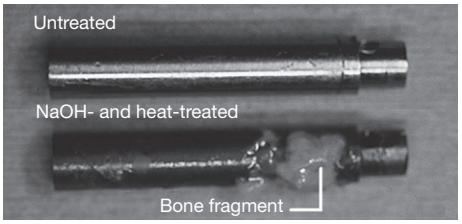

Figure 11 Surfaces of the untreated and the NaOH- and heat-treated Ti metal rods after the pull-out tests at 12 weeks after implantation. Reproduced from Kokubo, T.; Kim, H. M.; Kawashita, M.; Nakamura, T. *J. Mater. Sci. Mater. Med.* **2004**, *15*, 99–107, with permission from Springer.

1.113.2.1.1.2. Calcium titanate layer

The NaOH and heat treatments described above are simple treatments for inducing bioactivity in Ti metal and its alloys. However, some problems remain unresolved. The sodium ions in the sodium titanate are easily released from the surface, not

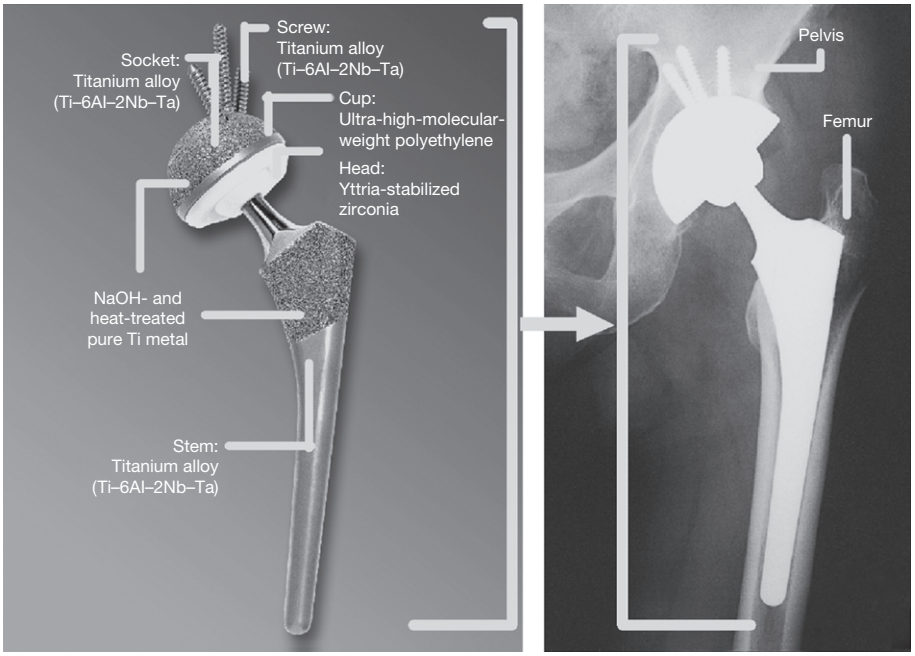

Figure 12 Clinical application of NaOH- and heat-treated Ti metal in hip joint. Reproduced from Kokubo, T. *Mater. Sci. Eng. C* **2005**, *25*, 97–104, with permission from Elsevier.

only in the body after implantation, but also in a humid environment, before implantation, as described in Section 1.113.2.1.1.1. This decreases the apatite-forming ability of the treated Ti metal after implantation and is a problem when the implant is stored in a humid environment for a long time period before implantation. Although partial removal of the sodium ions on the top surface solves this problem, for the clinical artificial joint, it is desirable to develop a more stable, highly bioactive layer.

On the other hand, the release of sodium ions from sodium titanate in the body is liable to be suppressed by the contamination of its surface layer with some other ions, such as calcium, thus decreasing the apatite-forming ability of the treated Ti metal. The aim is, therefore, to develop a highly bioactive layer that is not disturbed by contamination.

The NaOH and heat treatments are effective in inducing the bioactivity of the conventional Ti-based alloys, such as Ti–6Al–4V, Ti–6Al–2Nb–Ta, and Ti–15Mo–5Zr–3Al, but not of the new kind of Ti–Zr–Nb–Ta alloys. Effective treatments for these alloys need to be developed. The formation of a calcium titanate layer on the metal is expected to meet these requirements because the calcium ions can better promote apatite formation in the body by increasing the ionic activity product of the apatite, compared with the sodium ions. The calcium ions might be more stable than the sodium ions and may stay in the surface layer, even in a humid environment.

Hanawa *et al.*[42] were the first to attempt an implantation of calcium ions into the surface of the Ti metal, and they were later followed by Armitage *et al.*[43] and Nayab *et al.*[44] They showed that the calcium ions are incorporated into the surface of Ti metal up to a depth of about 100 nm at a dose of 1×10^{17} ions cm^{-2} under 40 keV, and that the calcium-implanted Ti metal gives greater bone-surface contact by activating bone cell function. However, this method of ion implantation requires expensive and large apparatus.

Sul[45] showed that about 11 at.% Ca ions are incorporated into the TiO_2 layer with a thickness of about 1300 nm on the surface of the Ti metal by micro-arc oxidation in a calcium-containing mixed electrolyte system. The resultant dental implant had a higher removal torque compared with the untreated implant. However, this higher torque cannot be simply attributed to the formation of the calcium-containing TiO_2 layer on the Ti metal because the micro-arc oxidation forms a porous structure with a number of craters on the surface of the Ti metal. Fröjd *et al.*[46] later reported that the calcium-incorporated titanium oxide layer formed on Ti metal by micro-arc oxidation gives larger bone contact than the calcium-free oxide layer. However, Song *et al.*[47] did not observe apatite formation in SBF on the calcium-containing titanium oxide formed by the micro-arc oxidation, but on the surface layer formed with amorphous $Ca(OH)_2$ by the subsequent hydrothermal treatment with water at 250 °C for 2 h.

Nakagawa *et al.*[48] also attempted the incorporation of calcium ions into Ti metal by hydrothermal treatment. They showed that a small quantity of calcium ions could be incorporated into the surface of the Ti metal by hydrothermal treatment with a $CaCl_2$ solution at 200 °C for 24 h, and that the so-treated Ti metal forms an apatite layer on its surface in SBF. Park *et al.*[49] incorporated larger amounts of calcium ions onto the surface of a Ti–6Al–4V alloy by forming $CaTiO_3$ through hydrothermal treatment with NaOH and CaO solution at 180 °C for 24 h. The alloy thus-treated also formed apatite on its surface in Hank's solution and showed an increase in bone-to-implant contact. Ueda *et al.*[50] have observed apatite formation in SBF on Ti metal that was first

treated with a H_2O_2/HNO_3 solution at 80 °C for 50 min and then hydrothermally treated with $Ca(OH)_2$ solution at 180 °C for 12 h. Chen *et al.*[51] showed that calcium ions can be incorporated onto the surface of porous Ti metals by hydrothermal treatment with 0.2 M $Ca(OH)_2$ solution at 250 °C for 8 h.

However, both the micro-arc oxidation and hydrothermal treatments described above need expensive apparatus especially designed for applying electric fields or high pressure.

Rakngarm *et al.*[52] tried to incorporate calcium ions into the surface of the Ti metal and Ti–6Al–4V alloy by simple chemical treatments. The Ti metal and its alloy were soaked in a 5 M NaOH solution at 60 °C and then in a $Ca(OH)_2$ solution at 60 °C. The Ti metal thus-treated and its alloy formed apatites on their surfaces in SBF. However, the solubility of $Ca(OH)_2$ in water is low, and the method used to incorporate calcium ions into the surface of the Ti metal was not revealed. The scratch resistance of the surface layer was expected to be low because the chemically treated Ti metal was not subsequently subjected to heat treatment.

Kizuki *et al.*[53] soaked the Ti metal in a 5 M NaOH solution at 60 °C for 24 h and then in a 100 mM $CaCl_2$ solution at 40 °C for 24 h. Sodium hydrogen titanate, formed on the Ti metal by the NaOH treatment, was isomorphously transformed into calcium hydrogen titanate by the subsequent $CaCl_2$ treatment. Although the Ti metal thus-treated formed apatite on its surface in SBF, the scratch resistance of the surface layer was very low. It was remarkably increased by subsequent heat treatment at 600 °C for 1 h. Unfortunately, the apatite-forming ability in SBF of the Ti metal was lost due to the heat treatment because the calcium hydrogen titanate was converted to calcium titanate and rutile, as shown in Figure 13. Its apatite-forming ability was recovered by subsequent water treatment at 80 °C for 24 h, as shown in Figure 14. A small amount of the calcium ions in the calcium titanate was exchanged with H_3O^+ ions during the water treatment, as shown in the depth profile of the Auger electron spectra in Figure 15. As a result, the calcium ions in the calcium titanate are easily released into the SBF, forming an apatite layer on the surface of the titanate by the same process as that of sodium titanate shown in Figure 8. The final water treatment can be replaced with autoclave treatment for sterilization before implantation. The Ti metal thus-treated maintains its high apatite-forming ability, even after it is stored in a humid environment for a long period of time.

These NaOH, $CaCl_2$, heat, and water treatments were effective in inducing bioactivity not only in Ti metal, but also in the new Ti–Zr–Nb–Ta alloys, such as Ti–15Zr–4Nb–4Ta, Ti–37Nb–2Ta–3Zr–0.3O, and Ti–29Nb–13Ta–4.6Zr.[54,55]

Animal experiments using rabbit tibia confirmed that the treated Ti metal bonded tightly to living bone, without the intervention of fibrous tissue.[138]

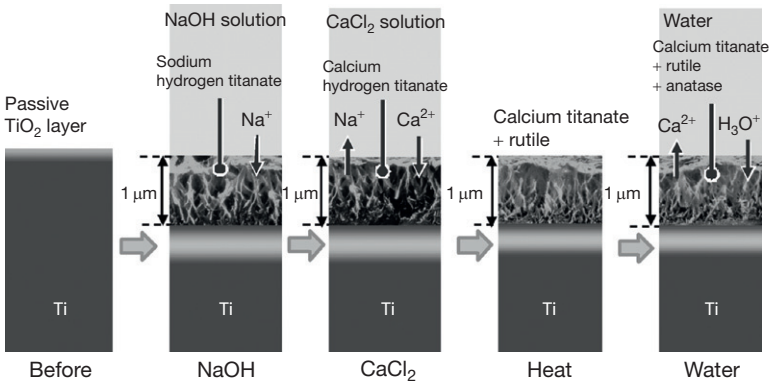

Figure 13 Structural change of surface of Ti metal due to NaOH, $CaCl_2$, heat, and water treatments. Reproduced from Yamaguchi, S.; Takadama, H.; Matsushita, T.; Nakamura, T.; Kokubo, T. *J. Mater. Sci. Mater. Med.* **2010**, *21*, 439–444, with permission from Springer.

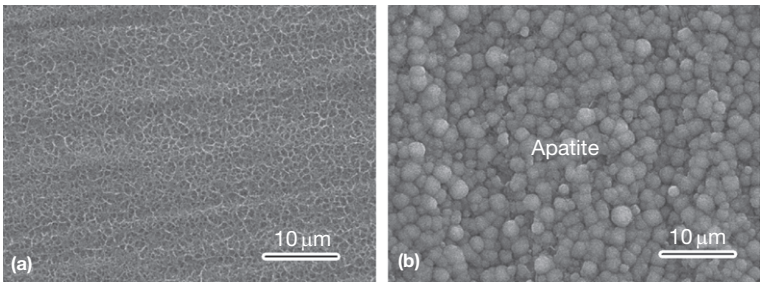

Figure 14 Scanning electron microscopy photographs of surfaces of Ti metal soaked in simulated body fluid for 1 day (a) after NaOH, $CaCl_2$, heat treatments and (b) subsequent water treatment. Reproduced from Kizuki, T.; Takadama, H.; Matsushita, M.; Nakamura, T.; Kokubo, T. *Acta Biomater.* **2010**, *6*, 2836–2842, with permission from Elsevier.

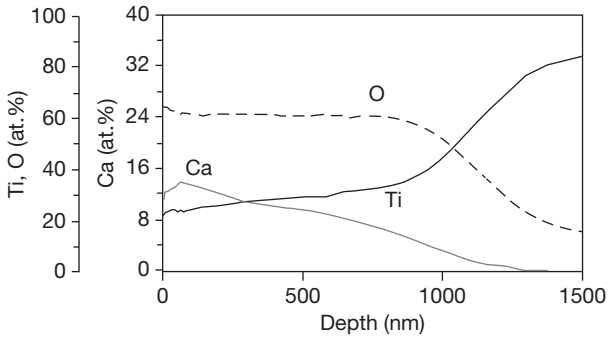

Figure 15 Auger electron spectroscopy depth profile of surface of Ti metal subjected to NaOH, $CaCl_2$, heat, and water treatments. Reproduced from Kizuki, T.; Takadama, H.; Matsushita, M.; Nakamura, T.; Kokubo, T. *Acta Biomater*. **2010**, *6*, 2836–2842, with permission from Elsevier.

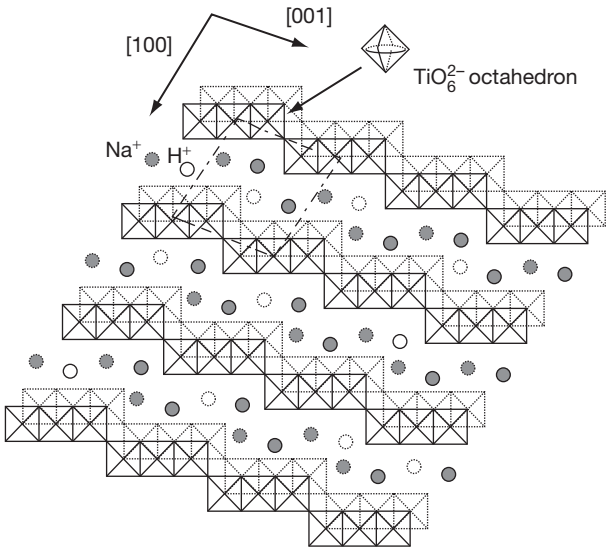

Figure 16 Structure of sodium hydrogen titanate. Reproduced from Kokubo, T.; Yamaguchi, S. *Materials* **2010**, *3*, 48–63, with permission from Molecular Diversity Preservation International.

1.113.2.1.1.3. Titanium oxide layer

Both sodium titanate and calcium titanate layers release ions, as previously described, which increase the pH of the surrounding body fluid. This could be an unfavorable condition for the cells in the surrounding tissues, especially in the narrow spaces of porous materials. Therefore, it is desirable that a bioactive layer containing no soluble ions is formed on porous materials. Titanium oxides have extremely low solubility in aqueous environments, and some of them exhibit an apatite-forming ability in SBF, as shown for a titania gel in **Figure 1** (see **Chapter 6.610, Trends in Materials for Spine Surgery**).

However, it is not yet clear what kind of titania phase shows the highest apatite-forming ability in the body. Uchida *et al.*[56] showed that a titania gel of an anatase phase has a higher apatite-forming ability in SBF compared with either an amorphous or rutile phase. Rohanizadeh *et al.*[57] reported that an anatase–gelatin slurry displays a higher apatite-forming ability in a supersaturated calcium phosphate solution compared with a rutile–gelatin slurry. On the other hand, Moritz *et al.*[58] reported that a TiO_2 gel layer permits a higher apatite-forming ability in SBF when transformed into a rutile phase from an anatase phase by laser beam irradiation.

Zhao *et al.*[59,60] showed that a plasma-sprayed TiO_2 coating layer with a rutile phase gave a high apatite-forming ability in SBF when treated with acid solutions, such as H_2SO_4 and HNO_3. Wang *et al.*[61] reported that Ti metal, treated with an H_2O_2/HCl solution and heat treated to around 400–500 °C to form anatase, precipitated apatite on its surface in SBF. Wang *et al.*[62] reported that Ti metal, treated with an HF/HNO_3 solution and heat treated to around 400–500 °C to form rutile, precipitated apatite, but only in a narrow gap. Wu *et al.*[63] showed that Ti metal, treated with H_2O_2/$TaCl_2$ solutions at 80 °C after HF–HNO_3 mixed acid treatment to form anatase and rutile, precipitated apatite on its surface in SBF, even without subsequent heat treatment. Lu *et al.*[64] showed that Ti metal, treated with a nitric acid solution (65% HNO_3:H_2O=1:1 in volume ratio) at 60 °C for 600 min but not subjected to heat treatment, also precipitated apatite on its surface in SBF, although the oxide phase was not detected on its surface. Lu *et al.*[65] reported that Ti metal, treated with H_2SO_4/HCl solutions and heat treated at 500 °C to form rutile, precipitated apatite on its surface in SBF. Sugino *et al.*[66] reported that a Ti–15Zr–4Ta–4Nb alloy, which was heat treated at 500 °C to form rutile without acid treatment, precipitated apatite in SBF, but only in the internal surface of the microgrooves. Sul *et al.*[67] reported that a Ti metal dental implant, formed with a thick layer of anatase and/or rutile on its surface by anodic oxidation in a 0.1 M CH_3COOH solution, showed a high removal torque when implanted into the tibia of a rabbit. Yang *et al.*[68] and Cui *et al.*[69] have shown that Ti metal, formed with anatase and rutile on its surface by anodic oxidation with a spark discharge in H_2SO_4 and Na_2SO_4 solutions, precipitated apatite on its surface in SBF.

It is difficult to derive the principle that governs the apatite-forming ability of titanium oxide from these data. However, it seems that acid and/or heat treatments are effective, except in some cases, in inducing the apatite-forming ability of titanium oxide in SBF irrespective of the kind of crystalline phase.

As described above, Ti metal forms sodium hydrogen titanate on its surface when treated with a 5 M NaOH solution at 60 °C for 24 h. The sodium hydrogen titanate has a layered structure, shown in **Figure 16**.[70] It is expected that by using water or acid treatment, the Na^+ ions located in the interlayers of this structure could easily be replaced with H_3O^+ ions to form hydrogen titanate, and that the hydrogen titanate could be transformed into anatase or rutile by subsequent heat treatment. Uchida *et al.*[71] showed that the Na^+ ions in the sodium hydrogen titanate, formed on Ti metal by the NaOH treatment, are completely exchanged with H_3O^+ ions by water treatment at 40 °C for 48 h, and that both anatase and rutile are formed on the surface of the Ti metal by subsequent heat treatment at 600 °C for 1 h. The apatite-forming ability of the sodium hydrogen titanate in SBF was decreased by its transformation into hydrogen titanate and the removal of the Na^+ ions, but was increased by its transformation into anatase and rutile upon subsequent heat treatment. Pattanayak *et al.*[72] found that if the Ti metal was treated with an HCl solution, instead of water, after the NaOH treatment, the apatite-forming ability of the subsequently heat-treated Ti metal roughly increased

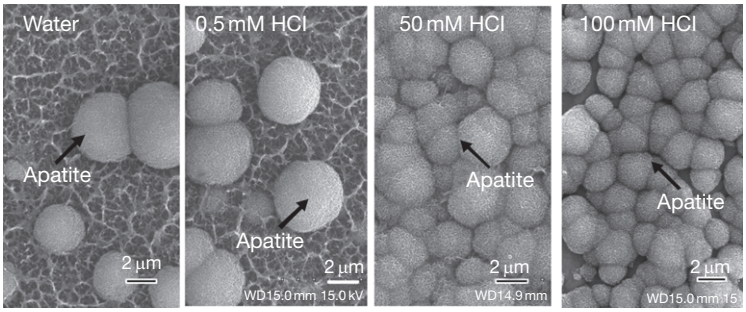

Figure 17 Scanning electron microscopy photographs of surfaces of Ti metals soaked in simulated body fluid for 1 day after NaOH, water or HCl solutions with various concentrations, and heat treatments. Reproduced from Pattanayak, D. K.; Kawai, T.; Matsushita, T.; Takadama, H.; Nakamura, T.; Kokubo, T. *J. Mater. Sci. Mater. Med.* **2009**, *20*, 2401–2411, with permission from Springer.

with an increase in the concentration of the HCl solution in the range of 0.5–100 mM, as shown in Figure 17. The ratio of rutile to anatase, formed after the heat treatment, changed with HCl concentration. However, the apatite-forming ability of the treated Ti metal did not depend upon the rutile/anatase ratio. When HNO_3 or H_2SO_4 solutions replaced the HCl solution, the apatite-forming ability of the subsequently heat-treated Ti metal again increased with an increase in the concentration of these solutions. Further, their apatite-forming abilities did not depend upon the kind of acid solution used.[73] As the concentration of the HCl, HNO_3, and H_2SO_4 solutions increased from 0.5 to 100 mM, their pH decreased from 3.46, 3.50, and 3.10 to 1.16, 1.15, and 1.05, respectively. Titanium oxide has been reported to have a positive surface charge in an aqueous solution with a low pH, as shown in Figure 18.[21] Therefore, it is expected that the Ti metals treated with HCl, HNO_3, or H_2SO_4 solutions (with low pH) after the NaOH treatment could be positively charged on their surface in SBF, after they are subsequently heat treated to form the titanium oxide because Cl^-, NO_3^-, or SO_4^{2-} ions might be adsorbed on their surfaces, only to be dissociated in SBF.

If their surfaces are positively charged in SBF, apatite could be formed on the surfaces by the following process. They would first combine with the negatively charged phosphate ions. As the phosphate ions accumulated, their surfaces would become negatively charged and they could combine with the positively charged calcium ions, thus forming calcium phosphate. The calcium phosphate thus-formed would eventually transform into a crystallite bone-like apatite. This process of apatite formation has been confirmed by XPS spectra of the surface of a Ti metal subjected to NaOH, 50 mM HCl, and heat treatments, as a function of soaking time, in SBF, as shown in Figure 19.[74] This process of apatite formation on positively charged titanium oxide is in contrast with that formed on negatively charged sodium titanate given in Figure 8.

The Ti metals, formed with the titanium oxide by the NaOH, acid, and heat treatments, have practical, useful, high scratch-resistant surface layers, and their high apatite-forming abilities are maintained, even after exposure to a humid environment for long periods.

Fujibayashi *et al.*[75] showed that after implantation into rabbit tibia, Ti metal, formed with anatase on its surface by the NaOH, water, and heat treatments, has a higher bone-bonding ability than Ti metal formed with sodium titanate by NaOH and

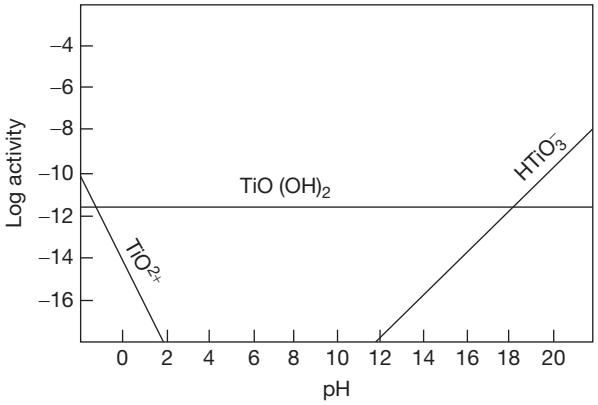

Figure 18 The pH dependence of activity of TiO_2 phase in aqueous solution. Reproduced from Kokubo, T.; Takagi, H.; Tashiro M. *J. Non-Cryst. Solid* **1982**, *52*, 427–433, with permission from Elsevier.

heat treatments at an early stage. Liang *et al.*[76] showed that Ti metal, formed with anatase on its surface by anodic oxidation in a H_2SO_4 solution, also gives a high bone-bonding ability, which is comparable to that of the Ti metal formed with anatase by NaOH, water, and heat treatments.

When the Ti metal cage, which was subjected to the NaOH, water, and heat treatments, was used to segmentally replace a defect in the long bone of a rabbit femur, it was observed to tightly bond to the surrounding bone.[77] Porous Ti metal, subjected to the NaOH, water, and heat treatments, showed greater penetration of newly grown bone compared with untreated porous Ti metal, and it bonded to the newly grown bone in a rabbit femur.[78] Otsuki *et al.*[79] investigated the dependence of bone growth into pores on the microstructure of the porous Ti metal that has been subjected to NaOH, water, and heat treatments. Interestingly, within 12 months[80] of implantation into the muscle of a dog, the same porous Ti metal formed bony tissue. This kind of osteoinduction was observed only to a small extent in the porous Ti metal subjected to the NaOH and heat treatments, whereas, it is more active in porous Ti metal subjected to NaOH, 0.5 mM HCl, and heat treatments, as shown in Figure 20.[81] When it was applied as an implant in the spinal interbody fusion of a canine, the porous Ti metal subjected to the NaOH, HCl, and heat treatments was tightly fixed to the surrounding bone, as shown in Figure 21.[82]

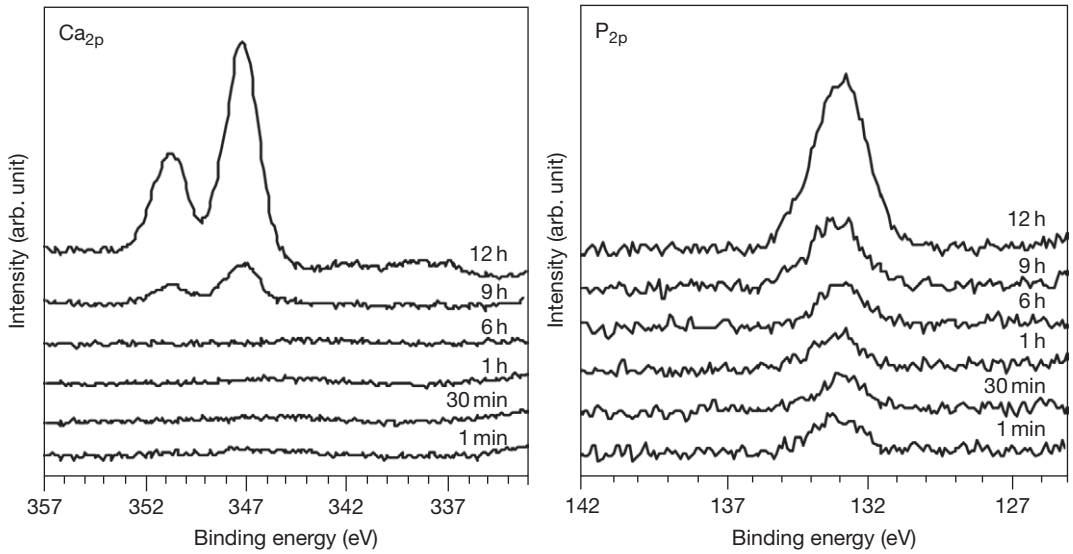

Figure 19 X-ray photoelectron spectra of surface of Ti metal subjected to NaOH, 50 mM HCl and heat treatments, as a function of soaking time in simulated body fluid. Reproduced from Kokubo, T.; Pattanayak, D. K.; Matsushita, T.; Takadama, H.; Nakamura, T. Effect of HCl treatment on apatite-forming ability of NaOH-treated Ti metal; In *Proceedings of 22nd European Conference on Biomaterials*, 2009; T6–T231, with permission from European Conference on Biomaterials.

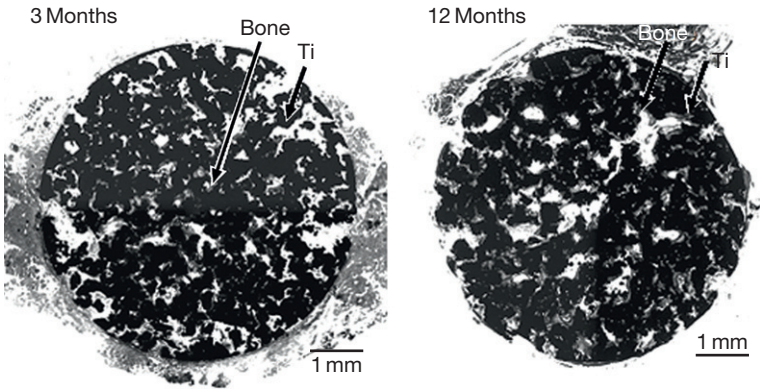

Figure 20 Bone formation in porous Ti metal subjected to NaOH, HCl, and heat treatments, 3 and 12 months after implantation into muscle of beagle dog. Reproduced from Takemoto, M.; Fujibayashi, S.; Neo, M.; *et al*. *Biomaterials* **2006**, *27*, 2682–2691, with permission from Elsevier.

On the basis of these animal experiments, this porous bioactive Ti metal was successfully applied to clinical trials as a spinal interbody fusion device.

1.113.2.1.2. Bioactive layers on Zr metal

Zirconia gel, prepared by a sol–gel method, was also found to form apatite on its surface, in SBF.[83] When it was heat treated up to 600–800 °C, in order to be converted into the tetragonal and monoclinic crystalline phases, it formed apatite more easily.[84] These results indicate that the bioactivity of the zirconium metal can also be induced by some surface treatments. However, zirconium metal only formed apatite on the surface that faced the bottom of the vessel when it was soaked in a 5 M NaOH solution at 95 °C for 24 h.[85] Chen *et al.*[86] reported that zirconium metal forms apatite on its surface, in SBF, when soaked in a 10 M NaOH solution at 60 °C for 24 h and then heat treated at 600 °C for 1 h in vacuum. Hang *et al.*[87] reported that zirconium metal forms apatite on its surface, in SBF, when subjected to micro-arc oxidation in an aqueous electrolyte containing 0.2 M calcium acetate monohydrate and 0.02 M β-glycerophosphate disodium salt pentahydrate at 500 V for 5 min, in order to form a zirconia containing CaO and a phosphate layer on its surface.

1.113.2.1.3. Bioactive layers on Nb metal

Niobium oxide gel, prepared by a sol–gel method, also forms apatite on its surface, in SBF, as long as it is not heat treated above 1000 °C, in order to be transformed into the monoclinic phase.[88] This indicates that some surface treatments can induce bioactivity in the niobium metal also.

However, it does not form apatite on its surface in SBF, even when sodium niobate is formed on its surface by soaking it in 1 M NaOH solution at 60 °C for 24 h.[88] Later, Wang *et al.*[89] reported that niobium metal formed apatite on its surface in

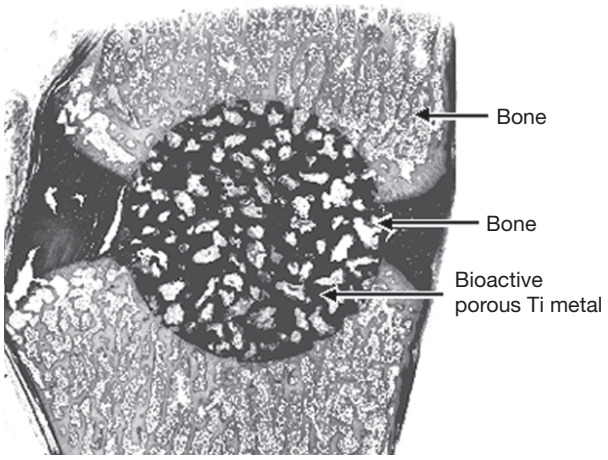

Figure 21 Fusion of spine of dog by a bioactive porous Ti metal. Reproduced from Takemoto, M.; Fujibayashi, S.; Neo, M.; *et al. J. Neurosurg. Spine* **2007**, *7*, 435–443, with permission from American Association of Neurosurgeons.

SBF when it was soaked in a 0.5 M NaOH solution at 80 °C for 24 h and then heat treated at 600 °C for 1 h in vacuum.

1.113.2.1.4. Bioactive layers on Ta metal

Tantalum oxide gel, prepared by a sol–gel method, also forms apatite on its surface in SBF, and its apatite-forming ability increases with an increase in the sodium content of the gel.[90]

Tantalum metal will form apatite on its surface, in SBF, without any chemical treatment, although apatite formation takes a long time. If it is soaked in a 0.2–0.5 mM NaOH solution at 50 °C for 24 h to form a sodium tantalite hydrogel on its surface, the induction period for the apatite formation is largely decreased.[91] When it is subsequently subjected to heat treatment at 300 °C for 1 h, the bonding strength of the surface layer to the substrate is increased without any appreciable decrease in its apatite-forming ability.[92,93] The reason why the NaOH and heat treatments could enhance the apatite-forming ability of the Ta metal was interpreted in terms of apatite nucleation induced by the Ta–OH groups formed on the Ta metal in SBF.[94]

The Ta metal, subjected to the NaOH and heat treatments, was confirmed to bond tightly to the living tibial bone of a rabbit within 16 weeks of implantation.[95]

When the Ta metal was soaked in a 100 mM $CaCl_2$ solution at 80 °C for 24 h after the NaOH treatment, and then heat treated at 500 °C for 1 h, its apatite-forming ability increased appreciably.[96]

1.113.2.2. Bioactive Layers on Organic Polymers

Bakker *et al.*[97] showed that a poly (ethylene oxide)/poly (butylene terephthalate) copolymer forms calcium phosphate on its surface in the body that bonds to living bone through calcium phosphate when implanted into the femur of a goat. However, it was found to swell in an aqueous environment.

Although other organic polymers have not been shown to bond to living bone, it is speculated that any kind of organic polymer can bond with living bone by forming apatite on its surface in the body, if its surface is modified with functional groups that are conducive for apatite nucleation, such as Si–OH, Ti–OH, Zr–OH, Nb–OH, and Ta–OH. By using self-assembled monolayers, Tanahashi *et al.*[98] showed that $COOH^-$ and $H_2PO_4^{2-}$ groups are also effective in enabling apatite nucleation. Subsequently, many attempts to form functional groups on various kinds of organic polymers have been made.

Early attempts were made to form a silicate ion cluster on polymers, such as poly(methyl methacrylate),[99] poly(ethylene terephthalate) (PET), polyether sulfone (PES), polyamide 6 (Nylon 6), polyethylene (PE), poly(tetra fluoro ethylene) (PTFE), and poly(vinyl alcohol) hydrogel, by placing the polymers on $CaO–SiO_2$[100] or $Na_2O–SiO_2$[101] glass particles in SBF. In this method, the $CaO–SiO_2$ or $Na_2O–SiO_2$ glass releases silicate ions that attach to the surface of the polymers. The attached silicate ions induce apatite nucleation on polymers by combining with the calcium ions to form calcium silicate, and then combining with the phosphate ions to form calcium phosphate. This calcium phosphate then transforms into apatite.[102] The polymers thus-treated form apatite on their surface in SBF,[103] or in 1.5 SBF, which has ion concentrations at 1.5 times that of SBF. The adhesive strength of the apatite layer and the polymers was increased by preliminary surface treatment of the polymers with NaOH solution,[104] HCl solution,[105] glow discharge,[106] and ultraviolet irradiation.[107] The PES plates, formed with apatite in 1.5 SBF on its surface by this method, were confirmed to be tightly bonded to the tibial bone of a rabbit.[108,109]However, the silicate ions attached to the polymers by this method are not tightly bonded to the surfaces of the polymers.

In order to obtain polymers modified with Si–OH groups that bond tightly to polymers, tetraethoxysilane, dispersed in silicone, was subjected to partial hydrolysis and polycondensation. However, the red silicone thus-prepared did not form apatite on its surface in SBF, but did so in 1.5 SBF.[110] In addition, the Si–OH groups, formed on ethylene-vinyl alcohol (EVOH) by hydrolysis and polycondensation of tetraethoxysilane, did not form apatite in SBF,[111] but did so only in 1.5 SBF. A calcium silicate layer, formed by the sol–gel method on EVOH pretreated with a silane-coupling agent, formed apatite on its entire surface, in SBF, within 1 day. This is because many of the Si–OH groups are formed on the surface of EVOH by the exchange of the Ca^{2+} ions with the H_3O^+ ions in SBF, and the released calcium ions increase the ionic activity product of the apatite on its surface.[112] However, this calcium silicate is not stable in the body for a long period.

Kawashita *et al.*[113] showed that the carboxyl (–COOH) group-containing polymer gels form apatite on their surface in SBF if they are preliminarily treated with a $Ca(OH)_2$ solution. Based on this result, alginate fibers, containing the carboxyl groups, were shown to form apatite on their surfaces in SBF only when first treated with $Ca(OH)_2$ solution.[114–116]

Kawai *et al.*[117] showed that polyamides containing sulfonic ($–SO_4H$) groups form apatite on their surfaces in 1.5 SBF, but not in SBF. They showed that the apatite-forming ability of the sulfonic groups is lower than that of the carboxyl group.[118] Leonor *et al.*[119] have shown that high molecular weight PE (HMWPE) and EVOH, modified with sulfonic groups upon exposure to sulfonic acid or chlorosulfonic acid, form apatite

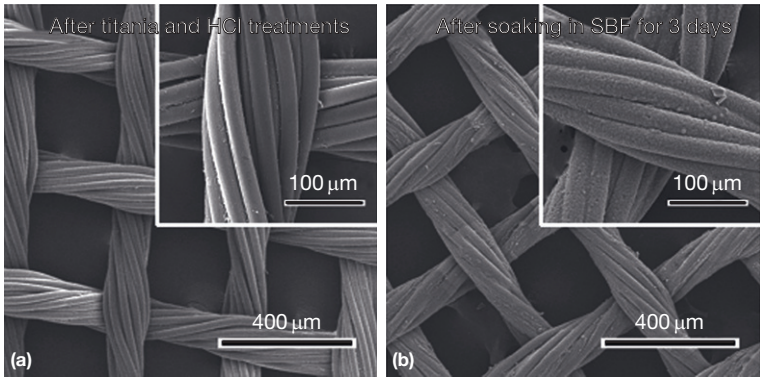

Figure 22 Scanning electron microscopy photographs of poly(ethylene terephthalate) fabric (a) as-treated with titania sol and HCl solution, and subsequently (b) soaked in simulated body fluid for 3 days. Reproduced from Kokubo, T.; Ueda, T.; Kawashita, M.; Ikuhara, Y.; Takaoka, G.G.; Nakamura, T. *J. Mater. Sci. Mater. Med*. **2008**, *19*, 695–702, with permission from Springer.

on their surfaces in SBF when they were preliminarily treated with a $Ca(OH)_2$ solution. However, their apatite-forming abilities in SBF were relatively low.

A titania gel layer, formed by a sol–gel method on EVOH,[120] PET, and Nylon 6[121] treated with a silane-coupling agent, formed apatite on its entire surface in SBF. Here, the titania layer was treated with a 0.1 M HCl solution at 80 °C for 8 days to be transformed into anatase from the amorphous phase. However, the silane-coupling agent can sometimes have a cytotoxic effect. Wu *et al.*[122] showed that a titania layer of the rutile phase is formed on PTFE by dipping the polymer into a solution of titanium tetrachloride ($TiCl_4$) at 60 °C for 3–60 h, and the titania layer thus-formed forms apatite on its surface, in SBF. Balas *et al.*[123] showed that a titania layer, formed by a simple sol–gel method, can strongly adhere to PE, PET, and Nylon 6 without the aid of a silane-coupling agent, and that they fully form apatite on their surfaces in SBF, after the HCl treatment. A two-dimensional fabric of PET fine fibers, which were coated with a titania sol after preliminary treatment with NaOH solution and then subjected to the HCl treatment, was able to be sharply bent without the 'peeling off' of the titania layer, and it fully formed apatite uniformly on the individual fibers in SBF, as shown in **Figure 22**.[124] This indicates that the TiO_2-coated PET fabric forms a bone-like apatite on its surface in the body, and that it bonds to living bone. Actually, when it was implanted into the tibia of a rabbit, it was in direct contact with the living bone, whereas, a fibrous tissue encapsulated the untreated PET. A large load was required for producing a failure at the interface between the TiO_2-coated PET and the bone.[125] This kind of flexible bioactive PET fabric is useful as a unique bone substitute.

1.113.3. Future Perspectives

It is apparent from the cases described above that various kinds of bioactive layers, which form apatite on their surfaces in the living body and bond to living bone, can be formed on different kinds of metals by simple chemical and heat treatments. The so-formed bioactive layers are gradually changed to their metallic substrates without a distinct boundary against the substrates, thus giving high bonding strength to the substrates. In addition, such bioactive layers can be formed on organic polymers by simple chemical and heat treatments. The bioactive layers thus-formed can tightly bond to organic substrates, although their bonding mechanism has not yet been revealed.

The bioactive layers can be formed uniformly, even on the complex inner surfaces of porous materials by the above mentioned chemical and heat treatments. Various kinds of ions, having different novel functions, can be incorporated into the bioactive layers by selecting appropriate solutions for the chemical treatments. In the future, various kinds of bioactive metals and organic polymers with different novel functions could be developed by using these chemical and heat treatments.

Metals and organic polymers, formed with these novel bioactive layers on their surfaces, are expected to be useful in various applications in the orthopedic and dental fields because of their high fracture toughnesses and ductility, properties that are lacking in bioactive ceramics, as well as their high bioactivity.

1.113.4. Additional Reading

Other review papers regarding bioactive layer formation on metals and polymers have been published by the same authors elsewhere.[126–137]

References

1. Kokubo, T. *Bioceramics and Their Clinical Applications*; Woodhead: Cambridge, 2008.
2. Leeuwenburgh, S. C. G.; Wolke, J. G. C.; Jansen, J. A.; de Groot, K. In *Bioceramics and Their Clinical Applications*; Kokubo, T., Ed.; Woodhead: Cambridge, 2008; p 464.
3. Taguchi, T.; Muraoka, Y.; Matsuyama, H.; Kishida, A.; Akashi, M. *Biomaterials* **2001**, *22*, 53–58.
4. Li, P.; Ohtsuki, C.; Kokubo, T.; *et al*. *J. Am. Ceram. Soc.* **1992**, *75*, 2094–2097.
5. Li, P.; Ohtsuki, C.; Kokubo, T.; Nakanishi, K.; Soga, N.; de Groot, K. *J. Biomed. Mater. Res.* **1994**, *28*, 7–15.
6. Kokubo, T.; Kushitani, H.; Sakka, S.; Kitsugi, T.; Yamamuro, T. *J. Biomed. Mater. Res.* **1990**, *24*, 721–734.

7. Kokubo, T.; Miyaji, F.; Kim, H. M.; Nakamura, T. *J. Am. Ceram. Soc.* **1996**, *79*, 1127–1129.
8. Kim, H. M.; Miyaji, F.; Kokubo, T.; Nakamura, T. *J. Ceram. Soc. Jpn.* **1997**, *105*, 111–116.
9. Kim, H. M.; Miyaji, F.; Kokubo, T.; Nakamura, T. *J. Mater. Sci. Mater. Med.* **1997**, *8*, 341–347.
10. Kim, H. M.; Miyaji, F.; Kokubo, T.; Nakamura, T. *J. Biomed. Mater. Res.* **1996**, *32*, 409–417.
11. Kim, H. M.; Miyaji, F.; Kokubo, T.; Nishiguchi, S.; Nakamura, T. *J. Biomed. Mater. Res.* **1999**, *45*, 100–107.
12. Kim, H. M.; Takadama, H.; Miyaji, F.; Kokubo, T.; Nishiguchi, S.; Nakamura, T. *J. Mater. Sci. Mater. Med.* **2000**, *11*, 555–559.
13. Kim, H. M.; Takadama, H.; Kokubo, T.; Nishiguchi, S.; Nakamura, T. *Biomaterials* **2000**, *21*, 353–358.
14. Kawai, T.; Kizuki, T.; Takadama, H.; *et al. J. Ceram. Soc. Jpn.* **2010**, *118*, 19–24.
15. Yamaguchi, S.; Takadama, H.; Matsushita, T.; Nakamura, T.; Kokubo, T. *J. Ceram. Soc. Jpn.* **2009**, *117*, 1126–1130.
16. Kim, H. M.; Miyaji, F.; Kokubo, T.; Nakamura, T. *J. Biomed. Mater. Res. (Appl. Biomater.)* **1997**, *38*, 121–127.
17. Takadama, H.; Kim, H. M.; Kokubo, T.; Nakamura, T. *J. Biomed. Mater. Res.* **2001**, *57*, 441–448.
18. Uchida, M.; Kim, H. M.; Kokubo, T.; Nakamura, T. *J. Am. Ceram. Soc.* **2001**, *84*, 2969–2974.
19. Takadama, H.; Kim, H. M.; Kokubo, T.; Nakamura, T. *J. Biomed. Mater. Res.* **2001**, *55*, 185–193.
20. Kim, H. M.; Himeno, T.; Kawashita, M.; Lee, J. H.; Kokubo, T.; Nakamura, T. *J. Biomed. Mater. Res.* **2003**, *67A*, 1305–1309.
21. Kokubo, T.; Takagi, H.; Tashiro, M. *J. Non-Cryst. Solid* **1982**, *52*, 427–433.
22. Takadama, H.; Kim, H. M.; Kokubo, T.; Nakamura, T. *Sci. Technol. Adv. Mater.* **2001**, *2*, 389–396.
23. Takadama, H.; Mizuno, M.; Kim, H. M.; Kokubo, T.; Nakamura, T. In *Ceramic Engineering and Science Proceedings*; Lin, H. T., Single, M., Eds.; , 20021953–1961 p 753.
24. Conforto, E.; Caillard, D.; Müller, L.; Müller, F. A. *Acta Biomater.* **2008**, *4*, 1934–1943.
25. Jonášová, L.; Müller, A. F.; Hlebrant, A.; Strnad, J.; Greil, P. *Biomaterials* **2004**, *25*, 1187–1194.
26. Strnad, J.; Protivínský, J.; Mazur, D.; *et al. J. Therm. Anal. Calorim.* **2004**, *76*, 17–31.
27. Müller, A. F.; Bottino, M. C.; Müller, L.; *et al. Dent. Mater.* **2008**, *24*, 50–56.
28. Jonášová, L.; Müller, A. F.; Hlebrant, A.; Strnad, J.; Greil, P. *Biomaterials* **2002**, *23*, 3905–3101.
29. Krupa, D.; Baszkiewicz, J.; Mizera, J.; *et al. J. Biomed. Mater. Res.* **2008**, *88A*, 589–598.
30. Kim, H. M.; Kokubo, T.; Fujibayashi, S.; Nishiguchi, S.; Nakamura, T. *J. Biomed. Mater. Res.* **2000**, *52*, 553–557.
31. Pattanayak, D. K.; Doi, K.; Takadama, H.; Nakamura, T.; Kokubo, T. *Mater. Sci. Eng. C* **2009**, *29*, 1974–1978.
32. Isaac, J.; Loty, S.; Hamdan, A.; *et al. J. Biomed. Mater. Res. A* **2009**, *89*, 585–593.
33. Nishio, K.; Neo, M.; Akiyama, H.; *et al. J. Biomed. Mater. Res.* **2000**, *52*, 652–661.
34. Yan, W. Q.; Nakamura, T.; Kobayashi, M.; Kim, H. M.; Miyaji, F.; Kokubo, T. *J. Biomed. Mater. Res.* **1997**, *37*, 267–275.
35. Nishiguchi, S.; Nakamura, T.; Kobayashi, M.; Kim, H. M.; Miyaji, F.; Kokubo, T. *Biomaterials* **1999**, *20*, 491–500.
36. Yan, W. Q.; Nakamura, T.; Kawanabe, K.; Nishiguchi, S.; Oka, M.; Kokubo, T. *Biomaterials* **1997**, *18*, 1185–1190.
37. Nishiguchi, S.; Nakamura, T.; Kobayashi, M.; Kim, H. M.; Miyaji, F.; Kokubo, T. *J. Biomed. Mater. Res. (Appl. Biomater.)* **1999**, *48*, 689–696.
38. Nishiguchi, S.; Kato, H.; Fujita, H.; *et al. Biomaterials* **2001**, *22*, 2525–2533.
39. Nishiguchi, S.; Fujibayashi, S.; Kim, H. M.; Kokubo, T.; Nakamura, T. *J. Biomed. Mater. Res.* **2003**, *67A*, 26–35.
40. Nishiguchi, S.; Kato, H.; Neo, M.; *et al. J. Biomed. Mater. Res.* **2001**, *54*, 198–208.
41. Kawanabe, K.; Ise, K.; Goto, K.; *et al. J. Biomed. Mater. Res. B Appl. Biomater.* **2009**, *90B*, 476–481.
42. Hanawa, T.; Kamimura, Y.; Yamamoto, S.; *et al. J. Biomed. Mater. Res.* **1997**, *36*, 131–136.
43. Armitage, D. A.; Mihoc, R.; Tate, T. J.; *et al. Appl. Surf. Sci.* **2007**, *253*, 4085–4093.
44. Nayab, S. N.; Jones, F. H.; Olsen, I. *J. Biomed. Mater. Res.* **2007**, *83A*, 296–302.
45. Sul, Y. T. *Biomaterials* **2003**, *24*, 3893–3907.
46. Fröjd, V.; Franke-Stenport, V.; Meirelles, L.; Wennerberg, A. *Int. J. Oral Maxillofac. Surg.* **2008**, *37*, 561–566.
47. Song, W. H.; Ryu, H. S.; Hong, S. H. *J. Am. Ceram. Soc.* **2005**, *88*, 2642–2644.
48. Nakagawa, M.; Zhang, L.; Udoh, K.; Matsuya, S.; Ishikawa, K. *J. Mater. Sci. Mater. Med.* **2005**, *16*, 985–991.
49. Park, J. W.; Park, K. B.; Suh, J. Y. *Biomaterials* **2007**, *28*, 3306–3313.
50. Ueda, M.; Ikeda, M.; Ogawa, M. *Mater. Sci. Eng. C* **2009**, *29*, 994–1000.
51. Chen, X. B.; Li, Y. C.; Plessis, J. D.; Hodgson, P. D.; Wen, C. *Acta Biomater.* **2009**, *5*, 1808–1820.
52. Rakngarm, A.; Miyashita, Y.; Mutoh, Y. *J. Mater. Sci. Mater. Med.* **2008**, *19*, 1953–1961.
53. Kizuki, T.; Takadama, H.; Matsushita, M.; Nakamura, T.; Kokubo, T. *Acta Biomater.* **2010**, *6*, 2836–2842.
54. Yamaguchi, S.; Kizuki, T.; Takadama, H.; Matsushita, T.; Nakamura, T.; Kokubo, T. In *Proceedings in the 31st Annual Meeting of the Japanese Society for Biomaterials*; Japanese Society for Biomaterials, Ed.; Hokuto Print: Kyoto, 2009; p 247.
55. Yamaguchi, S.; Takadama, H.; Matsushita, T.; Nakamura, T.; Kokubo, T. *J. Mater. Sci. Mater. Med.* **2010**, *21*, 439–444.
56. Uchida, M.; Kim, H. M.; Kokubo, T.; Fujibayashi, S.; Nakamura, T. *J. Biomed. Mater. Res.* **2003**, *64A*, 164–170.
57. Rohanizadeh, R.; Al-Sadeq, M.; LeGeros, R. Z. *J. Biomed. Mater. Res.* **2004**, *71A*, 343–352.
58. Moritz, N.; Areva, S.; Wolke, J.; Peltola, T. *Biomaterials* **2005**, *26*, 4460–4467.
59. Zhao, X.; Liu, X.; Ding, C. *J. Biomed. Mater. Res.* **2005**, *75A*, 888–894.
60. Zhao, X.; Liu, X.; You, J.; Chen, Z.; Ding, C. *Surf. Coat Technol.* **2008**, *202*, 3221–3226.
61. Wang, X. X.; Hayakawa, S.; Tsuru, K.; Osaka, A. *Biomaterials* **2002**, *23*, 1353–1357.
62. Wang, X. X.; Yan, W.; Hayakawa, S.; Tsuru, K.; Osaka, A. *Biomaterials* **2003**, *24*, 4631–4637.
63. Wu, J. M. *J. Am. Ceram. Soc.* **2004**, *87*, 1635–1642.
64. Lu, X.; Zhao, Z.; Leng, Y. *Mater. Sci. Eng. C* **2007**, *27*, 700–708.
65. Lu, X.; Wang, Y.; Yang, X.; *et al. J. Biomed. Mater. Res.* **2008**, *84A*, 523–534.
66. Sugino, A.; Ohtsuki, C.; Tsuru, K.; *et al. Acta Biomater.* **2009**, *5*, 298–304.
67. Sul, Y. T.; Johansson, C. B.; Jeong, Y.; Wennerberg, A.; Albrektsson, T. *Clin. Oral Implants Res.* **2002**, *13*, 252–259.
68. Yang, B.; Uchida, M.; Kim, H. M.; Zhang, X.; Kokubo, T. *Biomaterials* **2004**, *25*, 1003–1010.
69. Cui, X.; Kim, H. M.; Kawashita, M.; *et al. Dent. Mater.* **2009**, *25*, 80–86.
70. Sun, X.; Li, Y. *Chem. Eur. J.* **2003**, *9*, 2229–2238.
71. Uchida, M.; Kim, H. M.; Kokubo, T.; Fujibayashi, S.; Nakamura, T. *J. Biomed. Mater. Res.* **2002**, *63*, 522–530.
72. Pattanayak, D. K.; Kawai, T.; Matsushita, T.; Takadama, H.; Nakamura, T.; Kokubo, T. *J. Mater. Sci. Mater. Med.* **2009**, *20*, 2401–2411.
73. Pattanayak, D. K.; Matsushita, T.; Takadama, H.; Nakamura, T.; Kokubo, T. In *Proceedings in the 31st Annual Meeting of the Japanese Society for Biomaterials*; Japanese Society for Biomaterials, Ed.; Hokuto Print: Kyoto, 2009; p 130.
74. Kokubo, T.; Pattanayak, D. K.; Matsushita, T.; Takadama, H.; Nakamura, T. Effect of HCl treatment on apatite-forming ability of NaOH-treated Ti metal. In *Proceedings of 22nd European Conference on Biomaterials*, 2009; T6-231.
75. Fujibayashi, S.; Nakamura, T.; Nishiguchi, S.; *et al. J. Biomed. Mater. Res.* **2001**, *56*, 562–570.
76. Liang, B.; Fujibayashi, S.; Neo, M.; *et al. Biomaterials* **2003**, *24*, 4959–4966.
77. Fujibayashi, S.; Kim, H. M.; Neo, M.; Uchida, M.; Kokubo, T.; Nakamura, T. *Biomaterials* **2003**, *24*, 3445–3451.
78. Takemoto, M.; Fujibayashi, S.; Neo, M.; Suzuki, J.; Kokubo, T.; Nakamura, T. *Biomaterials* **2005**, *26*, 6014–6023.
79. Otsuki, B.; Takemoto, M.; Fujibayashi, S.; Neo, M.; Kokubo, T.; Nakamura, T. *J. Biomater.* **2006**, *27*, 5892–5900.
80. Fujibayashi, S.; Neo, M.; Kim, H. M.; Kokubo, T.; Nakamura, T. *Biomaterials* **2004**, *25*, 443–450.
81. Takemoto, M.; Fujibayashi, S.; Neo, M.; *et al. Biomaterials* **2006**, *27*, 2682–2691.
82. Takemoto, M.; Fujibayashi, S.; Neo, M.; *et al. J. Neurosurg. Spine* **2007**, *7*, 435–443.
83. Uchida, M.; Kim, H. M.; Kokubo, T. *J. Am. Ceram. Soc.* **2001**, *84*, 2041–2044.
84. Uchida, M.; Kim, H. M.; Kokubo, T.; Tanaka, K.; Nakamura, T. *J. Ceram. Soc. Jpn.* **2002**, *110*, 710–715.
85. Uchida, M.; Kim, H. M.; Miyaji, F.; Kokubo, T.; Nakamura, T. *Biomaterials* **2002**, *23*, 313–317.

86. Chen, X. B.; Nouri, A.; Li, Y. C.; Lin, J.; Hodgson, P. D.; Wen, C. *Biotechnol. Bioeng.* **2008**, *101*, 378–387.
87. Hang, Y.; Yan, Y.; Lu, C.; Zhang, Y.; Xu, K. *J. Biomed. Mater. Res.* **2009**, *88A*, 117–127.
88. Miyazaki, T.; Kim, H. M.; Kokubo, T.; Ohtsuki, C.; Nakamura, T. *J. Ceram. Soc. Jpn.* **2001**, *109*, 929–933.
89. Wang, X. J.; Li, Y. C.; Lin, J. G.; Yamada, T.; Hodgson, P. D.; Wen, C. E. *Acta Biomater.* **2008**, *4*, 1530–1535.
90. Miyazaki, T.; Kim, H. M.; Kokubo, T. *J. Sol-Gel Sci. Technol.* **2001**, *21*, 83–88.
91. Miyazaki, T.; Kim, H. M.; Miyaji, F.; Kokubo, T.; Kato, H.; Nakamura, T. *J. Biomed. Mater. Res.* **2000**, *50*, 35–42.
92. Miyazaki, T.; Kim, H. M.; Kokubo, T.; Miyaji, F.; Kato, H.; Nakamura, T. *J. Mater. Sci. Mater. Med.* **2001**, *12*, 683–687.
93. Miyazaki, T.; Kim, H. M.; Kokubo, T.; Ohtsuki, C.; Kato, H.; Nakamura, T. *J. Mater. Sci. Mater. Med.* **2002**, *13*, 651–655.
94. Miyazaki, T.; Kim, H. M.; Kokubo, T.; Ohtsuki, C.; Kato, H.; Nakamura, T. *Biomaterials* **2002**, *23*, 827–832.
95. Kato, H.; Nakamura, T.; Nishiguchi, S.; *et al. J. Biomed. Mater. Res. (Appl. Biomater.)* **2000**, *53*, 28–35.
96. Pattanayak, D. K.; Matsushita, T.; Takadama, H.; Nakamura, T.; Kokubo, T. In *Proceedings of the 29th Annual Meeting of the Japanese Society for Biomaterials*; Japanese Society for Biomaterials, Ed.; Ishikawa Tokushu Kyukyu Seihon: Osaka, 2007; p 213.
97. Bakker, D.; de Wijin, J. R.; Vrouenraets, C. M. F.; Hesseling, S. C.; Grote, J. J.; van Blitterswijk, C. A. *Polym. Med. Surg.* **1989**, *VI*, 11–16.
98. Tanahashi, M.; Matsuda, T. *J. Biomed. Mater. Res.* **1997**, *34*, 305–315.
99. Abe, Y.; Kokubo, T.; Yamamuro, T. *J. Mater. Sci. Mater. Med.* **1990**, *1*, 233–238.
100. Tanahashi, M.; Yao, T.; Kokubo, T.; *et al. J. Am. Ceram. Soc.* **1994**, *77*, 2805–2808.
101. Tanahashi, M.; Yao, T.; Kokubo, T.; *et al. J. Ceram. Soc. Jpn.* **1994**, *102*, 822–829.
102. Takadama, H.; Kim, H. M.; Miyaji, F.; Kokubo, T.; Nakamura, T. *J. Ceram. Soc. Jpn.* **2000**, *102*, 822–829.
103. Hata, K.; Kokubo, T.; Nakamura, T.; Yamamuro, T. *J. Am. Ceram. Soc.* **1995**, *78*, 1049–1053.
104. Tanahashi, M.; Yao, T.; Kokubo, T.; *et al. J. Appl. Biomater.* **1994**, *5*, 339–347.
105. Tanahashi, M.; Yao, T.; Kokubo, T.; *et al. J. Mater. Sci. Mater. Med.* **1995**, *6*, 319–326.
106. Tanahashi, M.; Yao, T.; Kokubo, T.; *et al. J. Biomed. Mater. Res.* **1995**, *29*, 349–357.
107. Liu, G. J.; Miyaji, F.; Kokubo, T.; Takadama, H.; Nakamura, T.; Murakami, A. *J. Mater. Sci. Mater. Med.* **1998**, *9*, 285–290.
108. Nagano, M.; Kitsugi, T.; Nakamura, T.; Kokubo, T.; Tanahashi, M. *J. Biomed. Mater. Res.* **1996**, *31*, 487–494.
109. Tanahashi, M.; Yao, T.; Kokubo, T.; Nakamura, T.; Katsura, Y.; Nagano, M. *Biomaterials* **1996**, *17*, 47–51.
110. Oyane, A.; Minoda, M.; Nakanishi, K.; *et al. Biomaterials* **1999**, *20*, 79–84.
111. Oyane, A.; Minoda, M.; Miyamoto, T.; *et al. J. Biomed. Mater. Res.* **1999**, *47*, 367–373.
112. Oyane, A.; Kawashita, M.; Nakanishi, K.; *et al. Biomaterials* **2003**, *24*, 1729–1735.
113. Kawashita, M.; Nakao, M.; Minoda, M.; *et al. Biomaterials* **2003**, *24*, 2477–2484.
114. Kokubo, T.; Hanakawa, M.; Kawashita, M.; *et al. Biomaterials* **2004**, *25*, 4485–4488.
115. Kokubo, T.; Hanakawa, M.; Kawashita, M.; *et al. J. Mater. Sci. Mater. Med.* **2004**, *15*, 1007–1012.
116. Kokubo, T.; Hanakawa, M.; Kawashita, M.; *et al. J. Ceram. Soc. Jpn.* **2004**, *112*, 363–367.
117. Kawai, T.; Ohtsuki, C.; Kamitakahara, M.; *et al. Biomaterials* **2004**, *25*, 4529–4534.
118. Kawai, T.; Ohtsuki, C.; Kamitakahara, M.; *et al. J. Ceram. Soc. Jpn.* **2005**, *113*, 588–592.
119. Leonor, I. B.; Kim, H. M.; Balas, F.; *et al. J. Mater. Sci. Mater. Med.* **2007**, *18*, 1923–1930.
120. Oyane, A.; Kawashita, M.; Kokubo, T.; Minoda, M.; Miyamoto, T.; Nakamura, T. *J. Ceram. Soc. Jpn.* **2002**, *110*, 248–254.
121. Balas, F.; Kawashita, M.; Nakamura, T.; Kokubo, T. *Biomaterials* **2006**, *27*, 1704–1710.
122. Wu, J. M.; Liu, J. F.; Hayakawa, S.; Tsuru, K.; Osaka, A. *J. Mater. Sci. Mater. Med.* **2007**, *18*, 1529–1536.
123. Balas, T.; Kawashita, M.; Nakamura, T. *J. Mater. Sci. Mater. Med.* **2007**, *18*, 1167–1174.
124. Kokubo, T.; Ueda, T.; Kawashita, M.; Ikuhara, Y.; Takaoka, G. G.; Nakamura, T. *J. Mater. Sci. Mater. Med.* **2008**, *19*, 695–702.
125. Saito, T.; Takemoto, M.; Fukuda, A.; *et al. Acta Biomater.* **2010**, in press.
126. Kokubo, T. *Eur. J. Solid State Inorg. Chem.* **1995**, *32*, 819–827.
127. Kokubo, T. *Thermochim. Acta* **1996**, *280/281*, 479–490.
128. Kokubo, T. *Anales de Química Int. Ed.* **1997**, *93*, S49–S55.
129. Kokubo, T. *Acta Mater.* **1998**, *46*, 2519–2527.
130. Kokubo, T.; Kim, H. M.; Kawashita, M. *Biomaterials* **2003**, *24*, 2161–2175.
131. Kokubo, T.; Kim, H. M.; Kawashita, M.; Nakamura, T. *J. Mater. Sci. Mater. Med.* **2004**, *15*, 99–107.
132. Kokubo, T. *Mater. Sci. Eng. C* **2005**, *25*, 97–104.
133. Kokubo, T.; Matsushita, T.; Takadama, T. *J. Eur. Ceram. Soc.* **2007**, *27*, 1553–1558.
134. Kokubo, T.; Takadama, H.; Matsushita, T. In *Bioceramics and Their Clinical Applications*; Kokubo, T., Ed.; Woodhead: Cambridge, 2008; p 485.
135. Kokubo, T.; Matsushita, T.; Takadama, H.; Kizuki, T. *J. Eur. Ceram. Soc.* **2009**, *29*, 1267–1274.
136. Kokubo, T.; Yamaguchi, S. *Materials* **2010**, *3*, 48–63.
137. Kokubo, T.; Pattanayak, D. K.; Yamaguchi, S.; *et al. J. R. Soc. Interface* **2010**, *7*, S503–S513.
138. Fukuda, A.; Takemoto, M.; Saito, T.; *et al. Acta Biomater.* **2010**.

1.114. Bioactivity: Mechanisms

C Knabe, Philipps University Marburg, Marburg, Germany
P Ducheyne, University of Pennsylvania, Philadelphia, PA, USA

© 2011 Elsevier Ltd. All rights reserved.

1.114.1.	**Introduction**	245
1.114.2.	**Mechanisms of Bioactive Behavior**	246
1.114.2.1.	Surface Transformation and Protein Adsorption Events of Bioactive Ceramics and Glasses	246
1.114.2.2.	The Effect of Bioactive Ceramics on the Expression of the Osteoblastic Phenotype *In Vitro*	248
1.114.2.3.	Solution-Mediated Effects of Bioactive Behavior	249
1.114.2.4.	Intracellular Signaling Events Regulating the Stimulatory Effect of Bioactive Ceramics on Cell Function	249
1.114.2.5.	Correlation of *In Vitro* and *In Vivo* Events: The Effect of Bioactive Ceramics on the Osteoblastic Phenotype *In Vivo*	252
1.114.3.	**Mechanisms of Biodegradation of Bioactive Ceramics**	254
1.114.4.	**Summary**	256
References		257

Abbreviations

AAS	Absorption spectrophotometry
AFM	Atomic force microscopy
AP-1	Activator protein-1
Bcl-2	Antiapoptotic factor
Bcl-xL	Antiapoptotic factor
BG 45S5	Bioactive glass 45S5
BSA	Bovine serum albumin
BSP	Bone sialoprotein
c-Ap	Carbonate containing hydroxyapatite
Col I	Type I collagen
ERK	Extracellular signal-regulated kinase
FAK	Focal adhesion kinase
Fn	Fibronectin
FTIR	Fourier Transform Infrared Sprectroscopy
Grb2	Growth factor receptor-bound protein 2
HA	Hydroxyapatite
MAPK	Mitogen-activated protein kinase
PI3K	Phosphatidylinositol 3-kinase
p-jnk	Phosphorylated c-Jun N-terminal kinase
RBS	Rutherford backscattering spectroscopy
SOS	Son of sevenless
T	0.05M tris buffer
β-TCP	β-tricalcium phosphate
TE	T supplemented with physiological electrolytes
TES	TE supplemented with 10% fetal calf serum
TRAP	Tartrate Resistant Acid Phosphatase
Vn	Vitronectin

1.114.1. Introduction

The ability to bond to bone tissue and stimulate bone formation at their surface is a unique property of bioactive ceramics. This has led to their wide clinical use in both orthopedics and dentistry. Bioactive ceramics are used as bone grafting materials and as coatings for titanium and its alloy. These coatings have been shown to accelerate initial stabilization of implants by enhancing bony ingrowth and stimulating osseous apposition to the implant surface, thereby promoting a rapid fixation of the devices to the skeleton.[1–7] Most commonly, long-term stable calcium phosphates that display a low biodegradability such as hydroxapatite are utilized for fabricating bioactive calcium phosphate coatings.[1–7] As **Chapter 4.402, Biocompatibility and the Relationship to Standards: Meaning and Scope of Biomaterials Testing** is specifically dedicated to calcium phosphate coatings, this topic is only briefly discussed in this chapter.

The current gold standard for bone reconstruction in orthopedics and cranio-maxillofacial surgery is the use of autogenous bone grafts.[8–10] Of the more than 1 million fractures that are treated with osteosynthetic materials each year in the United States, ~80% of these require adjuvant grafting.[9] Resorption of the alveolar ridge after tooth extraction frequently mandates site development by augmentation before dental implants can be placed.[11–13] Although autogenous bone grafts are currently the standard of care, bone substitute materials are extensively studied in order to avoid harvesting autogenous bone, as there are several disadvantages associated with using autogenous grafts: the additional surgical site, donor site morbidity exceeding that at the treatment site, often times insufficient volume of harvested bone, and, in dentistry, the need for general anesthesia to harvest extraoral bone.[14–16] Among alternative graft choices, synthetic bone substitutes are superior to freeze-dried human allografts or bovine-deproteinized bone xenografts in several respects. They excel in terms of safety profile, as there is no risk of disease transmission or immunological challenges.[17] Consequently, there has been an increasing demand and an ongoing search for synthetic, biodegradable bone substitute materials that degrade in a timely fashion, that is, rather rapidly, but still stimulate osteogenesis at the same time, thereby resulting in bone repair defect regeneration and replacement by fully functional bone tissue[1,16]

Because of their ability to stimulate bone formation, bioactive calcium phosphate ceramics and bioactive glasses (BGs) are excellent candidate grafting materials for bone augmentation.[3,18–21] Among the bioactive ceramics most commonly investigated for use in bone regeneration are β-tricalcium phosphate (β-TCP),[19–26] hydroxyapatite (HA),[3,21,27,28] and BG.[3,18,29,30] All of these materials are biocompatible[19–21] and osteoconductive.[3,18–30] However, they differ considerably in the rate of resorption. HA resorbs very slowly compared to β-TCP[21–26,28] and BG.[3,18,29,30]

Recent improvements in TCP ceramics include products with a high-phase purity (>99%) and homogenous solubility characteristics, so as to prevent premature separation of microparticles from the structural compound.[31] In the past, these types of microparticles have been shown to elicit inflammatory tissue responses.[31] Furthermore, the use of TCP particles with increased porosity has been proposed in order to increase the biodegradability.[31,32] These particles exhibit a material structure with micro-, meso-, and macropores, which is designed to enhance the degradation process. This structure allows for a reduced bulk density. The microporosity allows circulation of biological fluids, increases the specific surface area, and thus accelerates the degradation process. The interconnectivity of the pores creates a capillary force that actively draws cells and nutrients in the center of the particles. The macroporosity is created to encourage the ingrowth of bone by permitting penetration of cells and vascularization.[31]

Particularly, in nonload-bearing applications, a biomaterial used as a bone substitute should be a temporary material serving as a scaffold for bone remodeling. The material must degrade in a controlled fashion into nontoxic products that the body can metabolize or excrete via normal physiological mechanisms.[21] Moreover, this substance should be resorbable and should undergo complete remodeling and substitution by newly formed functional bone tissue.[10,16,21,23] Thus, ideally bioactive calcium phosphate ceramics for use in bone augmentation should exhibit good bone-bonding behavior by stimulating enhanced bone formation at the interface in combination with a high degradation rate, thereby meeting a balance between rapid bone formation and rapid biodegradation.

In modern dentistry, the use of oral implants has become a common treatment to replace missing or lost teeth.[11] Furthermore, resorption of the alveolar ridge after tooth extraction frequently mandates site development by augmentation before implants can be placed.[11–13] Among the various techniques to reconstruct or enlarge a deficient alveolar ridge, the concept of guided bone regeneration (GBR) and sinus floor augmentation procedures has become well-established surgical approach for localized lateral ridge augmentation.[8] Furthermore, augmentation of the maxillary sinus floor with autogenous bone grafts has become a predictable and well-documented approach for alveolar ridge augmentation of the posterior maxilla.[33] Over the last 15 years, the use of TCP and BG45S5 particles as alloplastic bone graft materials for alveolar ridge augmentation and sinus floor elevation procedures has received increasing attention in implant dentistry.[22–26,29,30,32,34–36] This is due to an overall effort to develop augmentation procedures that involve reduced surgical effort, thereby increasing patient comfort in addition to decreasing treatment cost, while yielding the same clinical success rates as conventional procedures that utilize autogenous bone grafts. As a result, over the last decade, an increasing number of clinical studies have been published that provide valuable data regarding the biodegradability as well as the bone regenerative capacity of these materials in a clinical setting as these data were derived from histological studies of human biopsies[22,24–26,29,30,32,34–36] (see also **Chapter 6.620, Dental Graft Materials** for further details).

Even with β-TCP and BG45S5, biodegradation has been reported to be incomplete 9.5, 12, and 25 months after grafting in the human mandible or sinus floor.[25,26,29,30] Collectively, these studies showed that these materials resorb within 1–2 years (see **Chapter 6.620, Dental Graft Materials** for details). Hence, given the clinical findings with current bone grafting materials,[22,24–26,29,30,32,34–36] there continues to be an interest in bone substitute materials that degrade more rapidly, but still stimulate osteogenesis at the same time.[10,16]

As a result, considerable efforts have been undertaken to produce rapidly resorbable bone grafting materials that exhibit good bone-bonding behavior by stimulating enhanced bone formation at the interface in combination with a high degradation rate.

This has led to the synthesis of a series of bioactive, rapidly resorbable glassy crystalline calcium–alkali–orthophosphate materials.[37–47] These are glassy crystalline calcium-alkali orthophosphates that exhibit stable crystalline $Ca_2KNa(PO_4)_2$ phases.[37,38,47,48] These materials have a higher solubility than TCP and therefore they are designed to exhibit a higher degree of biodegradability than TCP.[37,38,47] On this basis, they are considered as excellent candidate materials for alveolar ridge augmentation.[39–46]

Furthermore, various calcium phosphate materials with addition of silicon have been developed with the intent to enhance their bioactivity and mechanical stability.[49–51]

As outlined above, bioactive calcium phosphate ceramics and glasses are known to stimulate bone tissue formation at their surfaces.[52–54] Over the past 15 years, increasing efforts have focused on understanding the underlying mechanisms. In these studies, attention was directed toward the atomic and molecular phenomena occurring at the material surface and their effects on the reaction and signaling pathways of cells and tissues. This implied studies that elucidated any of the cellular activities leading up to tissue formation, including protein adsorption, cell adhesion, differentiation, and extracellular-matrix formation.[52]

Given the great clinical need, obtaining this understanding is of critical importance, as once these mechanisms are identified and studied, it should be possible to alter biomaterial molecular components and surface characteristics in ways that promote optimal cell adhesion, proliferation, and differentiation leading to more expeditious and enhanced bone formation in combination with a desirable biodegradability, and thus, to create bioactive calcium ceramics and glasses that are optimally tailored toward their clinical application.

1.114.2. Mechanisms of Bioactive Behavior

1.114.2.1. Surface Transformation and Protein Adsorption Events of Bioactive Ceramics and Glasses

The nature of the biomaterial and its surface characteristics play important roles in determining bone adaptation to the

implant material. Surface reactivity is one of the common characteristics of bone bioactive ceramics and glasses. It contributes to their bone-bonding ability and their enhancing effect on bone tissue formation. During implantation, reactions occur at the material–tissue interface that lead to time-dependent changes in the surface characteristics of the implant material and the tissues at the interface.[52] With bioactive ceramics and glasses, solution-mediated surface reactions take place after immersion in biological fluids. These reactions include dissolution, reprecipitation, and ion-exchange phenomena in combination with protein adsorption events occurring at the bioactive ceramic surface (**Figure 1**).[52,55–62] A key element of bone bioactive behavior is the development of a carbonated apatite surface after immersion in biological fluids.[52,57–59] Previous review papers summarized these events that were reported to occur at the bioactive ceramic–tissue interface.[52,63] The following list does not imply a ranking in terms of time sequence or importance: (1) dissolution from the ceramic,[57–59,61–68] (2) precipitation from solution onto the ceramic,[57–59,61–68] (3) ion exchange and structural rearrangement at the ceramic–tissue interface,[57–59,61,62,64–66] (4) interdiffusion from the surface boundary layer into the ceramic,[69] (5) solution-mediated effects on cellular activity,[70–72] (6) deposition of either the mineral phase or the organic phase, without integration into the ceramic surface,[67,73–76] (7) deposition with integration into the ceramic,[67,73] (8) chemotaxis to the ceramic surface,[77] (9) cell attachment and proliferation,[69,76,78] (10) cell differentiation,[76] and (11) extracellular-matrix formation.[75–78]

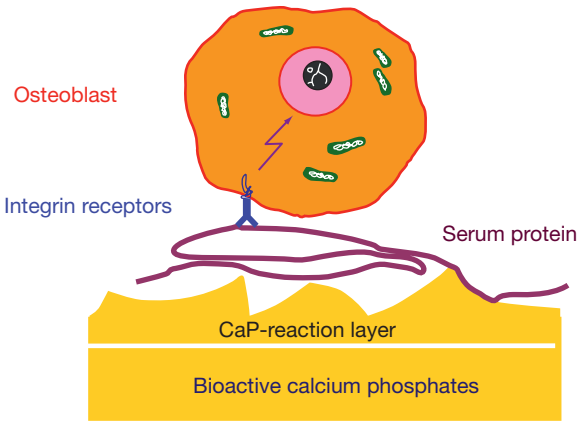

Figure 1 Schematic diagram illustrating the events that take place at the interface between the bioactive ceramics and the surrounding biological milieu and thereby establish bioactive behavior. Contact with biological fluids leads to dissolution and reprecipitation phenomena and results in the formation of a calcium phosphate surface reaction layer and serum protein adsorption. The nature of this surface reaction layer that in its turn influences the structure of the adsorbed protein modulates the structure of the adsorbed serum protein. Thereby, specific adhesive motifs within the molecule are exposed to osteoblasts and osteoprogenitor cells that are migrating to the implant surface, which then has an effect on subsequent cell adhesion via integrin receptors and activation of intracellular signaling pathways. Activation of these intracellular signaling mechanisms modulates cellular differentiation, bone matrix formation, and mineralization resulting in bone bonding and a stimulatory effect on bone tissue formation.

The observation of what occurs at the interface, however, does not represent a mechanistic explanation for the effect that bioactive ceramics and glasses ceramics have on bone tissue formation. We can focus on mechanisms by relying on an increasing body of evidence that suggests that bone-bonding and bone tissue ingrowth enhancement are the result of multiple, parallel, and sequential reactions at the material–tissue interface. These interactions are related to either physicochemical phenomena that occur in the presence or absence of cells or reactions affected by the cellular activity. An important aspect of the overall reaction sequence between these materials and tissues is that in the absence of a biologically equivalent, calcium-deficient, carbonate-containing hydroxyapatite (c-Ap) surface upon implantation, dissolution, precipitation, and ion exchange reactions leads to a biologically equivalent apatitic surface on the implanted material (**Figure 1**). This reaction does not proceed by itself, but is accompanied by parallel reactions, such as adsorption and incorporation of biological molecules and attachment of surrounding cells. Furthermore, cells that have adhered to the ever-reacting material surface interact with the material and produce some of the surface changes. In the inverse direction, that is, from material to environment, there is both a solution-mediated as well as a surface-controlled effect on cellular activity such as cell adhesion and differentiation, organic matrix deposition, and mineralization. The gradual change of the ceramic surface to become a biologically equivalent HA with small crystal dimensions is a rate-determining step in the cascade of events underlying bioactive behavior. All these phenomena, collectively, lead to the gradual incorporation of the bioactive implant material into developing bone tissue.

Moreover, for mechanisms to be uniquely identified, it is important to establish the extent of each of these reactions and the sequence in which they occur.

Formation of a biologically equivalent apatitic surface, a common characteristic of bioactive materials, can be reproduced *in vitro* by immersion experiments using a simulated physiological solution that mimics the typical ion concentrations in body fluids. These *in vitro* physicochemical analyses are useful to explain the observations on *ex vivo* specimens.[59,64,65] Such experiments have shown that the materials with high solubility also readily induce the precipitation of a biologically equivalent apatite on their surface. Using this *in vitro* immersion methodology, considerable evidence has been obtained revealing the mechanisms of surface reactions.[57–59,67] The reactions include dissolution, precipitation, and ion exchange accompanied by adsorption and incorporation of biological molecules.[55,56,71,79,80]

Furthermore, it has been demonstrated that this surface reaction layer does not form as a result of inorganic reactions first, followed by biologically driven events next, but that serum proteins do have a major effect on the properties of the surface reaction layer.

To explore the effect of proteins on the formation of surface reaction layers on BG, the atomic and molecular changes in BG45S5 surface during immersion in protein-free buffer solution and protein-containing culture medium were examined using various complementary techniques including atomic force microscopy (AFM), Rutherford backscattering

spectroscopy (RBS), and Fourier transform infrared sprectroscopy (FTIR).[56] When immersed in serum-free solutions, AFM showed that the surface of BG reacted nonuniformly. After 5 min of immersion, the glass surface showed a rough texture due to the formation of particles on the surface. With increasing immersion time, the particles increased in size and number. Unlike the reaction on the substrates immersed in serum-free solution, a uniform layer of globules, presumably proteins, covered the substrates immersed in serum-containing solutions. As the immersion time increased, the density of globules increased and the layer thickened. RBS of the outermost surface layers revealed that substrates formed Si-rich surface layers in the first hour of immersion in the absence or presence of serum proteins. In addition, the RBS spectra showed that the formation of the calcium phosphate layer was different in serum-containing solutions compared with that in serum-free solutions. FTIR analysis revealed that, in the serum-free solution, crystalline HA was formed by transformation from the initially formed amorphous calcium phosphate. In contrast, immersion in serum-containing solutions only produced an amorphous calcium phosphate.

Given the repeated observation of the absence of crystalline HA when proteins coadsorb, it is unlikely that, *in vivo*, adsorption of biological molecules will take place subsequent to the transformation of an amorphous calcium phosphate-rich layer to carbonated apatite, as was previously suggested.[18] The present data suggest that serum proteins adsorb in tandem with the occurrence of solution-mediated reactions leading to the formation of a silica gel. Amorphous calcium phosphate phases accumulate in this Si-rich matrix.

In solutions more closely approaching the physiological state, the maturation of amorphous calcium phosphate to crystalline HA does not take place readily. The proteinaceous layer that adsorbs onto the glass interferes with the solid to liquid interaction of the amorphous calcium phosphate layer. Whereas amorphous calcium phosphate can form exclusively as the result of physicochemical phenomena in the solid glass phase, it is suggested here that adsorbed serum proteins impede the nucleation and growth reactions by which it would transform to carbonated apatite. The physicochemical reactions in the glass are not blocked however, as Ca and P diffusion leads to a continuously thickening of the Ca–P-rich zone under the adsorbed protein layer. In this context, it is an important aspect that the surface composition and structure of the surface reaction layer in their turn influence serum protein adsorption. There is support for the view that the enhanced cellular and tissue responses to bioactive ceramics are related to enhanced fibronectin (Fn) adsorption at their surfaces.[55,80] Also it is noteworthy that surface chemistry of the biomaterial surface, that is, the surface reaction layer in the case of bioactive ceramics, modulates the structure and activity of adsorbed Fn (**Figure 1**).[81] Hence, the adsorption of the protein layer is also critical in terms of providing attachment sites for bone cells such as osteoblasts and their progenitors (**Figure 1**). The cell adhesion and intracellular signaling events are the subject of **Section 1.114.2.4**.

In addition, the solution-mediated effects require adequate consideration. This involves first, analyzing the release of soluble ions from these bioactive substrata and second, investigating their effect on the cellular response,[52,63,70,82–84] which are discussed in more detail in **Section 1.114.2.3**.

1.114.2.2. The Effect of Bioactive Ceramics on the Expression of the Osteoblastic Phenotype *In Vitro*

Calcium phosphate ceramics[2,4,21,22,24,32] and glass ceramics[29,30,66,85] are known to bond to bone. Differences among these materials are reflected in the rate of bone formation on their surfaces.[4,21,22,24,27,33,34,54] Bioactive calcium phosphate ceramics stimulate bone formation.[4,24,27,32,42,43,54,86] This requires the ability to differentiate osteoprogenitor cells into osteoblasts at their surfaces. Thus, in order to evaluate the stimulatory potential of bioactive ceramics on osteogenesis, it is logical to examine the effect of these materials on osteoblastic differentiation. Consequently, over the last 15 years, various assays have been developed and used, which permit studying the effect of bioceramics on the expression of osteogenic markers *in vitro*.[40,42,52,70,76,87–89]

Osteoblast differentiation is defined by three principal biological periods: cellular proliferation, cellular maturation, and matrix mineralization.[90–92] Differentiating osteoblasts are known to synthesize type I collagen, alkaline phosphatase (ALP), and other noncollagenous extracellular bone matrix proteins such as osteonectin, osteocalcin, osteopontin, and bone sialoprotein.[90–93] These bone–matrix proteins have proven to be particularly useful osteogenic markers to characterize the different stages of osteoblast differentiation.[92] Type I collagen is expressed during the initial period of proliferation and extracellular-matrix synthesis, whereas ALP is expressed during the post proliferative period of extracellular-matrix maturation, and the expression of osteopontin, osteonectin, osteocalcin, and bone sialoprotein occurs later during the third period of extracellular-matrix mineralization.[90–93] Osteopontin peaks twice – during proliferation and then later but prior to BSP and osteocalcin.[91,93] Osteonectin is found in preosteoblasts, osteoblasts, osteocytes, and the newly formed osteoid in matrix.[94] This protein has the ability to bind to collagen and promote HA formation *in vitro*.[94] Bone sialoprotein is characterized by its ability to mediate initial formation of hydoxyapatite crystals[95] and is transiently expressed very early,[91,92,95] and then upregulated again in differentiated osteoblasts actively involved in mineralization.[91,92,95] Consequently, as there is no specific single marker for osteoblasts, the cellular expression of a range of noncollagenous and collagenous proteins as well as ALP has to be assayed, when examining cellular differentiation.

When studying the effect of bioactive ceramics for bone regeneration on cellular behavior it is important to examine cell proliferation and differentiation, first, because these materials should posses the ability to differentiate osteoprogenitor cells into osteoblasts and, second, because proliferation and differentiation of osteoblasts are affected by the chemistry of substrata.[96,97] As a result, numerous authors studied the response of osteoblasts or bone marrow stromal cells to various bioactive ceramics in terms of messenger RNA and translated proteins that form an array of osteogenic parameters as a measure of phenotypic differentiation. It has been demonstrated that various bioactive calcium phosphates significantly affected cellular growth and the temporally dependent expression of an array of bone-related genes and proteins.

Moreover, various investigators were able to show that BGs and glass ceramics,[42,52,63,70–72,76,84,88,89,98] HA,[7,99] various calcium phosphates,[7,99] and calcium-alkali orthophosphate ceramics[40,42,87,88] stimulated osteoblast differentiation *in vitro*.

El-Ghannam *et al.* studied the cellular response to BG45S5 disks that were preconditioned by a two-step procedure that resulted in the transformation of the BG surface to a crystalline, carbonated calcium phosphate apatite onto which serum proteins were adsorbed in a second step.[70,71] The authors demonstrated the greater differentiation for osteoblasts, which were grown on the preconditioned BG45S5 compared to when identical cells were cultured on the native glass[70] or HA surfaces.[71] These findings were corroborated by a study,[89] in which enhanced ALP activity of rat bone marrow stromal cells was demonstrated when these cells were grown on preconditioned BG45S5 disks compared to when identical cells were cultured on tissue culture plastic, that is, polystyrene controls.

In recent years, several studies have been performed that examined the effect of rapidly resorbable calcium-alkali orthophosphate bone substitute materials on the expression of osteogenic markers characteristic of the osteoblastic phenotype and compared this behavior with that of the currently clinically used materials such as β-TCP and BG45S5. These studies showed that several calcium-alkali orthophosphates supported osteoblast differentiation to a greater extent than TCP.[40,87,88] Recently, it was demonstrated that the glassy-crystaline calcium-alkali orthophosphate material GB9, which contains the crystalline phase $Ca_2KNa(PO_4)_2$ and a small amorphous portion containing silica phosphate, had a significantly greater stimulatory effect on osteoblastic proliferation and differentiation compared to β-TCP,[42,87] preconditioned BG45S5,[42] and other calcium-alkali orthophosphate materials of varying composition[42,87] (see **Chapter 6.620, Dental Graft Materials** for more details).

1.114.2.3. Solution-Mediated Effects of Bioactive Behavior

In this context, it is also of considerable interest to explore the effect of soluble ions released from these bioactive ceramics on the cellular response.[71,72] Several investigators used experimental setups and *in vitro* models that allowed for dissociating between solution-mediated and surface-mediated effects on the cellular response. This is in contrast to the *in vivo* setting, in which it is not possible to dissociate between these two effects. Hence, when addressing this issue, utilizing adequate *in vitro* models offers a significant advantage over *in vivo* experiments.[52,71,72,83] Xynos *et al.*[84] demonstrated that BG45S5 stimulated osteoblast proliferation and differentiation when culturing primary human osteoblasts on the BG ceramic substrate. Ducheyne *et al.*[63] and El-Ghannam *et al.*[71] had shown this effect with a rodent cell line and shown it to be associated with cell membrane receptor activation. In order to determine whether this stimulation of osteogenesis by BGs occurs through direct contact between substrate and cells or through ions released during their biodegradation, Xynos *et al.* studied the relationship between this stimulation of osteogenesis and ionic products of BG dissolution.[82,83] They reported that these ionic products increased osteoblast proliferation.[83] They suggested that this effect was mediated by insulin-like growth factor II whose expression was upregulated.[83] Furthermore, they observed enhanced gene expression of various growth factors and extracellular-matrix regulators including cell surface receptors, signal transduction factors, and transcription factors.[82]

Radin *et al.*[89] performed a study in which rat bone marrow stromal cells were cultured in the presence but not in contact with BG45S5 disks. These cells showed enhanced osteoblast differentiation compared to cells, which were grown in the presence of tissue culture plastic controls. However, even greater osteoblast differentiation was noted, when cells were cultured in physical contact with the BG45S5 disks. They also examined the release of BG dissolution products into the cell culture medium and concluded that both surface- and solution-mediated effects play a major role in the osteogenic effect of BG. These data emphasize the synergistic nature of the solution- and the surface-mediated effects of BG45S5 on osteoblast function. Yao *et al.*[72] took these experiments a step further and showed that cells that were cultured on porous BG45S5 substrata released signaling factors into the cell culture medium that caused enhanced cell differentiation of osteoblasts, which were cultured in the presence of these cell-seeded scaffolds but physically separated at the bottom of the cell culture dish. This enhancement of cellular differentiation was greater compared to when cells were solely cultured in the presence of the BG45S5 scaffold.[72]

1.114.2.4. Intracellular Signaling Events Regulating the Stimulatory Effect of Bioactive Ceramics on Cell Function

To decipher the complexity of the reactions at the bioactive ceramic–bone interface, it is logical to first analyze the surface transformation and protein adsorption events and then to study the cellular response of osteoblasts to these bioactive surfaces (**Figures 1** and **2**). Although numerous studies have investigated cellular responses to bioactive ceramics, little is known about the intracellular signaling events that take place in osteoblasts at these bioceramic surfaces. As outlined above, numerous authors were able to show that BGs and glass ceramics, HA, various calcium phosphates, and calcium-alkali orthophosphate ceramics were able to stimulate osteoblast differentiation *in vitro*.[7,32,40,42,43,52,63,70–72,76,84,86–89,98–100] However, the intracellular signaling events that follow osteoblast attachment to these bioactive ceramics, leading to differences in osteoblast activity and function, are not known. Because cell signaling affects cell proliferation and differentiation, it is important to understand the cell signaling pathways, which are affected or activated by osteoblast–implant material interactions.[101]

The cellular interactions between osteoblasts and the biomaterial surface are thought to be mediated primarily by membrane-associated adhesion receptors belonging to the integrin superfamily.[101–104] Integrins are transmembrane heterodimers composed of an α- and a β-subunit and are connected to the cytoskeleton.[105,106] Bone cells express the following integrin receptors: $\alpha_1\beta_1$, $\alpha_2\beta_1$, $\alpha_3\beta_1$, $\alpha_5\beta_1$, $\alpha_v\beta_3$, and $\alpha_v\beta_5$.[106–108,107–109] The interaction of osteoblasts with implant surfaces is mediated largely by the β1 subfamily.[101,103,104] It is furthermore noteworthy that surface

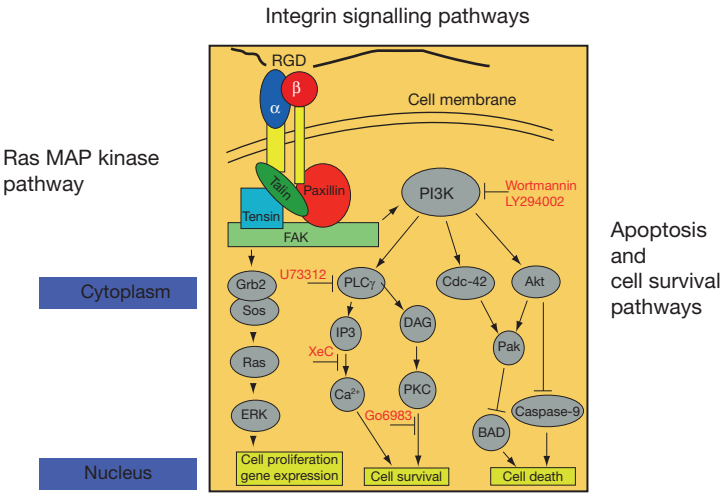

Figure 2 Integrin signaling pathways. Binding of the integrin receptor activates focal adhesion kinase (FAK) along with other focal adhesion proteins. FAK activates the cell differentiation (Extracellular signal-regulated kinase or Ras/MAPkinase) pathway in addition to PI3K (phosphatidylinositol 3-kinase)-cell survival pathway, which results in the depression of apoptosis.

chemistry of the biomaterial surface modulates the structure and activity of adsorbed Fn.[81,110]

Integrins $\alpha_5\beta_1$ and $\alpha_v\beta_3$ bind to and compete for the central cell-binding domain of the Fn molecule.[112] The differences in Fn conformation alter integrin binding and therefore can lead to selective binding of the $\alpha_5\beta_1$ integrin or $\alpha_v\beta_3$ integrin or binding of both $\alpha_5\beta_1$ and $\alpha_v\beta_3$ integrin.[81,111] Furthermore, osteogenic cells require signals from non-RGD-binding integrins, notably $\alpha_2\beta_1$, for robust differentiation. The GFOGER recognition site of type I collagen specifically targets the $\alpha_2\beta_1$ integrin receptor, thereby supporting focal adhesion kinase (FAK) activation, expression of osteoblast-specific genes, and matrix mineralization. Recent findings suggest that selective binding of the $\alpha_5\beta_1$ integrin or $\alpha_2\beta_1$ integrin[113,114] leads to upregulation of osteoblastic differentiation and matrix mineralization as well as enhanced bone formation *in vivo*.[113–118] In addition to their role as adhesion receptors, integrins are also involved in transducing signals from the extracellular matrix to the interior of the cell,[119,120] resulting in the activation of cascades signaling molecules and pathways and thereby regulation of gene expression, thus modulating cellular migration, proliferation, differentiation, and apoptosis (**Figures 1** and **2**).[106,120–122]

Interaction between osteoblasts and bone matrix components via integrins leads to a rearrangement of cytoskeletal components and activation of specific signaling proteins localized at focal adhesions and FAK (**Figure 2**).[101,123] Activation of FAK is considered to play a critical role in the control of adhesion-dependent cell survival and proliferation.[122,123] It has been demonstrated that osteoblast adhesion to titanium alloy and Fn resulted in the activation of FAK and mitogen-activated protein (MAP) kinase signal transduction pathways.[101] FAK associates with several signaling proteins (e.g., the src-family of protein-tyrosine kinases: Src-homology collagen (Shc) and growth factor receptor-bound protein 2 (Grb2)) (**Figure 2**). One downstream signaling protein in the integrin-generated signaling pathway is the adaptor protein Shc. Mitogen-activated protein kinase (MAPK) p44 (extracellular signal-regulated kinase 1 (Erk1)) and p42 MAPK (Erk2) are important mediators of cellular responses to intracellular signaling proteins. FAK interaction with Shc creates a Grb2-binding site thus linking FAK to the Ras/MAPK (mitogen-activated protein kinase) pathway (**Figure 2**).[124] The Shc–Grb2 complex induces Ras activation via Grb2-associated son of sevenless (SOS), a cytoplasmic GTP (guanosine triphosphate) exchange protein.[125] Ras then stimulates the Erk1/Erk2 MAP kinase cascade, which plays an important role in cellular differentiation and growth (**Figure 2**). Activated MAP kinases (Erk1/2) translocate to the nucleus and are then able to phosphorylate and activate transcription factors including c-fos and c-jun, members of the activator protein-1 (AP-1) transcription factor complex, which control gene expression (**Figure 2**).[101,102] The AP-1 complex initiates early transcription events that lead to cell proliferation and/or can affect differentiation. Moreover, AP-1 has an important role in osteoblast differentiation and bone development. AP-1 sites are known to be present in the promoters of many bone-specific genes such as type I collagen, ALP, osteocalcin, and osteopontin.[101,102] In addition, possible interaction with the p38 pathway is important.[126,127] Ivaska and coworkers[128] demonstrated a novel signaling mechanism in human osteosarcoma cells (SaOS-2) mediated by $\alpha_2\beta_1$ integrin involving isoform-specific activation of the p38 signaling protein. More recent data suggest a possible interaction between the Ras/MAPK pathway and the p38 pathway.[126]

Moreover, the effect on apoptosis is of importance. Activation of the PI3K/Akt (phosphatidylinositol-3-kinase/protein kinase B) survival pathway results in the depression of apoptosis.[129] Consequently, activation of this pathway would be expected by bioactive ceramics, which stimulate osteogenesis. Thus, studying the activation of various antiapoptotic factors such as Bcl-2 and Bcl-x_L is also of considerable importance.

The effect of bioactive bone substitute materials on these signaling pathways controlling osteoblast function and differentiation is not fully understood at present. Elucidation of these reactions has been hampered by the inadequacy of the experimental techniques that could be used. Excellent

techniques to study integrin-mediated adhesion and the intracellular pathways that are triggered were only recently established[101,103,127,129–133] In addition, advanced surface analytical methods have been combined with molecular biological techniques only over the last decade. Doing so, however, greatly contributed to achieving a better understanding of the surface transformations of bioactive, resorbable ceramics, and the protein adsorption events associated with the immersion in biological fluids.[52,55,56,59–62] Recent research efforts combined these two powerful analytical methodologies (advanced surface analytical methods and molecular biological assays). The understanding resulting from combining these methods to examine integrin-mediated cell adhesion and intracellular signaling mechanisms with methods to analyze protein adsorption events and surface and solution-mediated reactions has greatly helped to unravel the complex reactions at the bioactive ceramic–bone interface. Hence, a series of studies was performed to elucidate the mechanisms by which various bioactive calcium phosphates including four calcium-alkali orthophosphate materials (**Table 1**), TCP, BG45S5, and a bovine-derived HA (commercial name BioOss), whose excellent osteoconductive properties have been demonstrated by numerous *in vivo* studies, stimulate the intracellular signaling pathways, which regulate osteoblast differentiation and cell survival.[44–46,134] This included investigating: (1) solution-mediated surface transformations, (2) serum protein adsorption events, (3) integrin-mediated cell adhesion mechanisms, and (4) intracellular signaling mechanisms. To this end, in order to first reveal the precipitation mechanisms, the kinetics of formation and the composition, and thickness and morphology of the reaction layer which forms on the ceramic surfaces in a biological milieu, two measurements were performed on these bioactive calcium phosphates: (1) analysis of the surface characteristics of the bioceramics by FTIR, scanning electron microscopy, and energy dispersive X-ray analysis (2) and determination of the ions released from the resorbable ceramics by atomic absorption spectrophotometry (AAS) and UV-visible spectrophotometry. These immersion experiments were intended to quantify, first, the resorption of the bioceramics and, second, the phenomenon of reprecipitation. These dissolution/precipitation experiments for immersion times were run up to 3 weeks.

Three types of solutions were used for these immersion experiments including 0.05 M Tris buffer (T), T supplemented with physiological electrolytes (TE), and TE supplemented with 10% fetal calf serum (TES). All materials were immersed at a surface area-to-solution volume ratio of 0.1 cm^{-1}. Postimmersion solutions were analyzed for changes in calcium and silicon concentrations using AAS. After 21 days of incubation, the structure and composition of the surface reaction layers were determined using FTIR.

Subsequently, serum protein adsorption to these novel substrata after immersion in the serum-containing tissue culture medium for 1 and 24 h was determined utilizing sodium dodecyl sulfate–polyacrylamide gel electrophoresis and Western blot analysis using antibodies against Fn, vitronectin (Vn), collagen type I (Col-I), and bovine serum albumin (BSA). This was followed by conducting blocking studies to investigate the role of different integrin molecules in mediating cell attachment of osteoblasts to the different test materials using adhesion blocking monoclonal antibodies against β_1, $\alpha_2\beta_1$, $\alpha_5\beta_1$, and β_3. In addition, Western blot and quantitative densitometric analyses were used to determine the effect of these bioceramics on the expression and activation of key intracellular signaling molecules of the Erk-differentiation pathway, the alternate p38 pathway, the PI3K (phosphatidylinositol 3-kinase)/Akt survival pathway, as well as antiapototic factors in osteoblasts after 30 min, 1, 3, and 24 h of incubation.[44–46,134] This included studying the expression of FAK and phosphorylated-FAK, Erk and phosphorylated Erk, phosphorylated c-Jun N-terminal kinase, (p-jnk), c-fos (Erk-differentiation pathway), p38 mitogen-activated-kinase (p38MAPK) and phosphorylated p38 (alternate p38 pathway), PI3K, Akt, phospho-Akt (PI3K/Akt survival pathway), as well as Bcl-x_L, Bad (apoptosis markers).[46,134]

When immersed in T, all calcium-alkali orthophosphates tested showed a time-dependent dissolution behavior (**Figure 3(a)–3(d)**). When immersed in TE, β-TCP and GB9 showed a time-dependent uptake of Ca ions, whereas GB14 and GB9/25 displayed only a minor uptake (**Figure 3(a)–3(d)**). FTIR spectra of GB14 (**Figure 5(a)**) and GB9 (**Figure 5(b)**) before and after 21 days of immersion showed that bioactive surface transformations occurred both in TE and TES, whereas GB9/25 (**Figure 5(c)**) showed detectable phase transformation that were not associated with HA formation. A crystalline apatitic phase was also observed on BioOss® (**Figure 5(d)**). Hence, the results of these studies showed that GB9 surfaces displayed calcium (**Figure 3(b)**) and silicon ion (**Figure 4**) release as well as calcium uptake (**Figure 3(b)**) and bioactive surface transformations after immersion both in TE and in TES (**Figure 5(b)**). This was associated with considerable Fn (**Figure 6(a)**) and extensive type I collagen serum protein adsorption (already after 1 h) (**Figure 6(b)**), while vitronectin adsorption was minor.[44–46,134] As a result, cell adhesion was mainly mediated through integrin $\alpha_5\beta_1$ and (to a slightly lesser

Table 1 Description of bioactive calcium-alkali orthophosphate ceramic bone grating materials, TCP and Bioglass 45S5

GB14	*GB9*	*GB9/25*	*352i*	*β-TCP*	*Bioglass 45S5™*
Calcium-alkali orthophosphate: $Ca_2KNa(PO_4)_2$ crystalline phase with a small amorphous portion containing magnesium potassium phosphate	Calcium-alkali orthophosphate: $Ca_2KNa(PO_4)_2$ crystalline phase with a small amorphous portion containing silica phosphate	Diphosphate containing calcium-alkali orthophosphate: $Ca_2KNa(PO_4)_2$ crystalline phase and $Ca_2P_2O_7$	Diphosphate containing calcium-alkali orthophosphate: $Ca_{10}[K/Na](PO_4)_7$, crystalline phase with small addition of SiO_2	Tricalcium-phosphate $Ca_3(PO_4)_2$	BG45S5 composition (wt%): SiO_2· 45.0CaO· $24.5P_2O_5$· $6.0Na_2O$·24.5

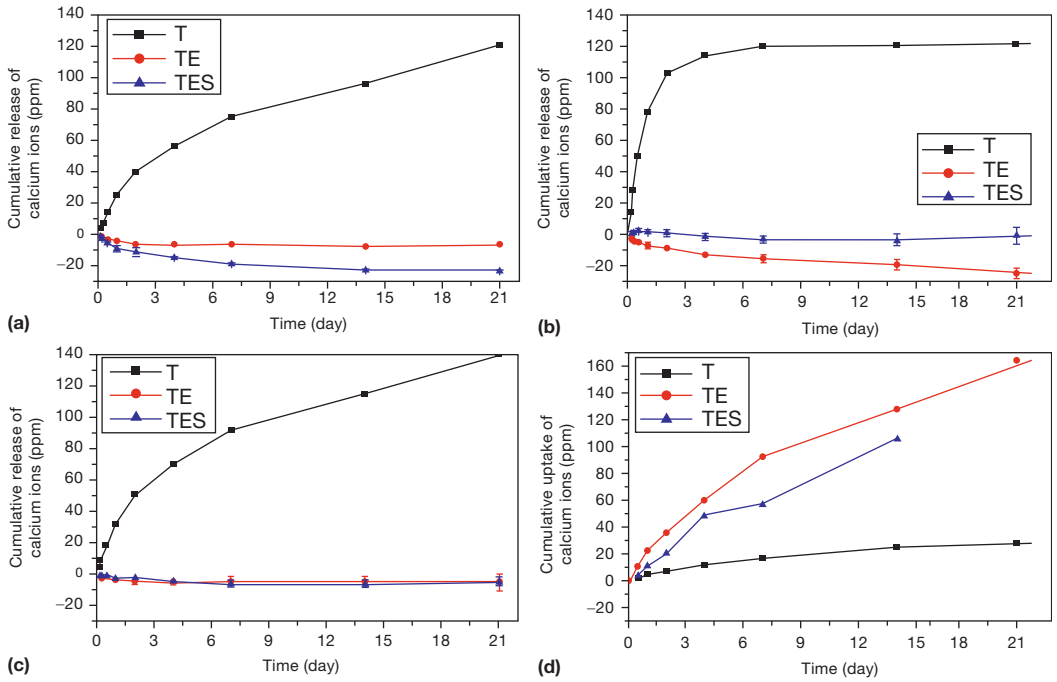

Figure 3 Results of the atomic absorption spectrophotometry (AAS) analysis. Cumulative release of Ca^{2+} ions after 21 days of immersion in 0.05 M Tris buffer (T), T supplemented with physiological electrolytes (TE), and TE supplemented with 10% fetal calf serum (TES): (a) GB14, (b) GB9, (c) GB9/25, and (d) BioOss®. When immersed in T, all calcium-alkali orthophosphates tested showed a time-dependent dissolution behavior. When immersed in TE, β-tricalcium phosphate (β-TCP) and GB9 showed a time-dependent uptake of Ca ions, whereas GB14 and GB9/25 displayed only a minor uptake.

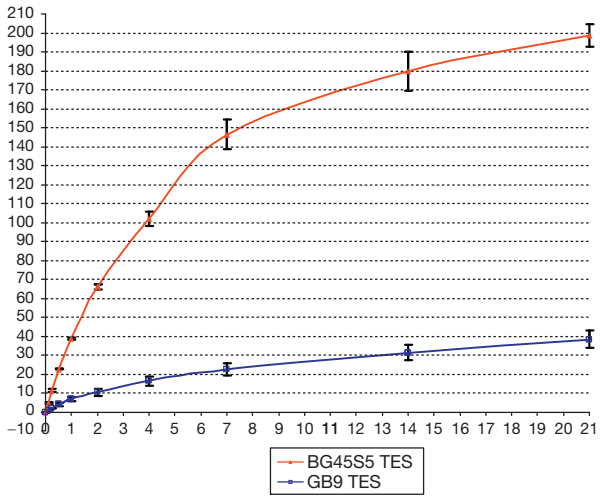

Figure 4 Cumulative release of silicon ions from GB9 and bioactive glass 45S5 (BG45S5) measured by atomic absorption spectrophotometry (AAS) after immersion in TES for 21 days.

degree) through $\alpha_2\beta_1$, while β_3 played a minor role (Figure 7), which in turn then leads to a cumulative or even synergistic effect, that is, enhanced activation of the Ras/MAPkinase pathway (Figure 8(a) and 8(b)) in combination with activation of the p38 pathway (which is thought to be activated after cell adhesion to $\alpha_2\beta_1$) (Figure 8(c)) as well as activation of key signaling factors of the PI3K/Akt-cell survival pathway (Figure 8(d)) and of antiapoptotic factors (Figure 8(e)) and thereby also to the greatest antiapoptotic effect. Consequently, among others, enhanced activation of Erk (Figure 8(a)), c-fos (Figure 8(b)), p38 (Figure 8(c)), Akt (Figure 8(d)), and the antiapoptotic factor Bcl-x_L (Figure 8(e)) was noted.[46,134] Taken together, GB9 displayed the greatest stimulatory effect on the activation of all signaling pathways examined (cell differentiation, cell survival, and p38 pathway) as well as the greatest antiapoptotic effect. This was in agreement with the findings of previous studies outlined above, in which GB9 had a significantly greater stimulatory effect on osteoblastic proliferation and differentiation *in vitro*[42,87,88] as well as the best bone-bonding behavior and the greatest stimulatory effect on bone formation and expression of osteogenic markers *in vivo*,[43,46] while exhibiting the highest biodegradability when compared to β-TCP, BG45S5, and the other calcium-alkali orthophosphate materials.[41,43,46]

1.114.2.5. Correlation of *In Vitro* and *In Vivo* Events: The Effect of Bioactive Ceramics on the Osteoblastic Phenotype *In Vivo*

Correlating *in vitro* data with *in vivo* phenomena adds to our understanding of the bone–bioactive ceramic interface considering the hypothesis that enhanced osteoblastic cell differentiation *in vitro* leads to more and more expeditious and more copious bone formation at the bone–biomaterial interface *in vivo*. In order to test this hypothesis, correlation of the *in vitro* and *in vivo* data is, of course, needed. This includes (1) correlating quantitative expression of the osteogenic markers *in vitro* with the amount of bone formed after bioceramics implantation, and (2) quantifying the expression of these markers in histological sections obtained from *in vivo*

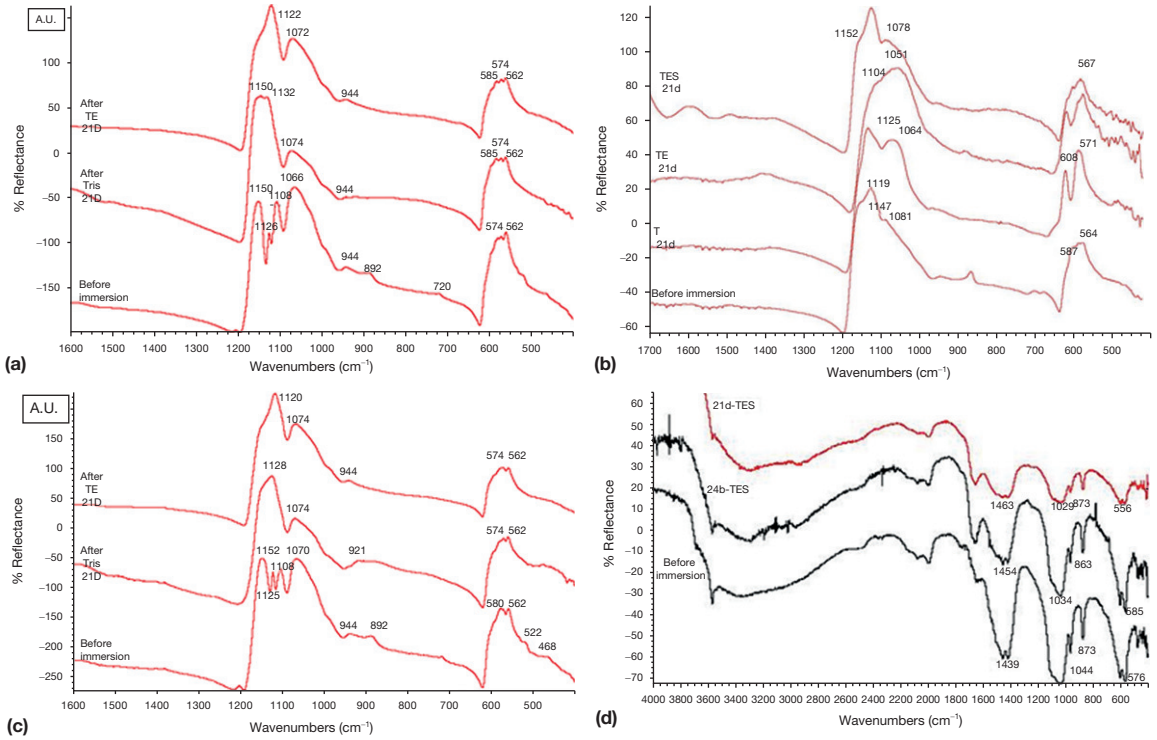

Figure 5 Fourier transform infrared sprectroscopy (FTIR) spectra of the pre- and postimmersion surface analysis after 21 days of immersion in 0.05 M Tris buffer (T), T supplemented with physiological electrolytes (TE), and TE supplemented with 10% fetal calf serum (TES): (a) GB14, (b) GB9, (c) GB9/25, and (d) BioOss®. FTIR spectra of GB14 and GB9 before and after showed that bioactive surface transformations occurred both in TE and in TES, whereas GB9/25 showed detectable phase transformation that were not associated with hydroxyapatite formation. A crystalline apatitic phase was also observed on BioOss®.

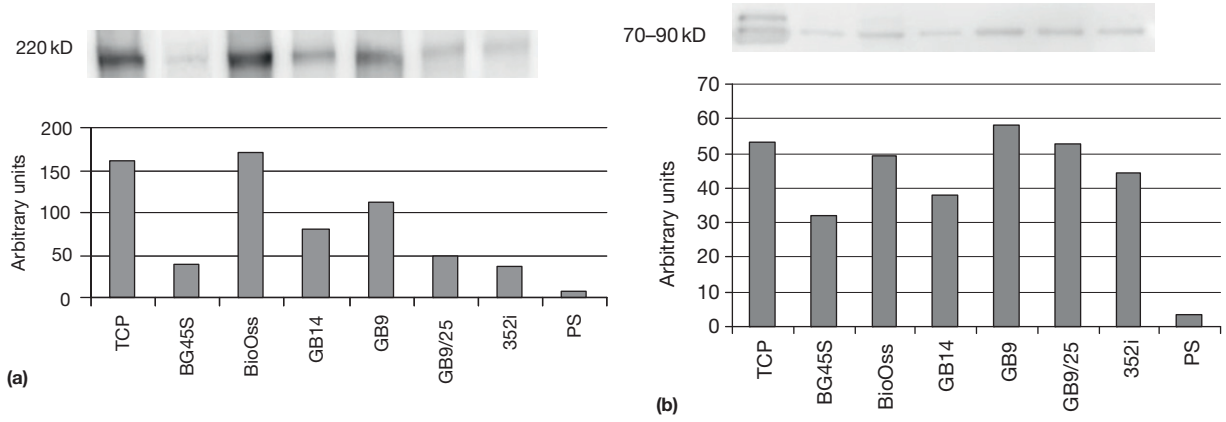

Figure 6 (a) Results of Western blot analysis for serum protein adsorption. Relative amount of Fn adsorbed to various calcium phosphate test materials after 24 h of immersion in serum-containing tissue culture medium (PS: tissue culture polystyrene control surface). (b) Relative amount of type I collagen adsorbed to various calcium phosphate test materials after 1 h of immersion in serum-containing tissue culture medium as determined by Western blot analysis.

experiments in comparison to the expression of the various markers *in vitro*.

To this end, a study was performed, in which the effect of the same selection of bioactive ceramics on the expression of osteogenic markers was studied *in vitro* as well as *in vivo*.[43,46,135] This required the development of an adequate hard tissue histology technique that facilitates immunohistochemical analysis of osteogenic markers on undecalcified sawed resin-embedded sections of bone that contain ceramic implant materials. This rendered it possible to study the effect of ceramic bone substitute materials on osteoblast differentiation and tissue maturation on *ex vivo* specimens by visualizing active osteoblasts in their different stages of differentiation at the bone–biomaterials interface.[136]

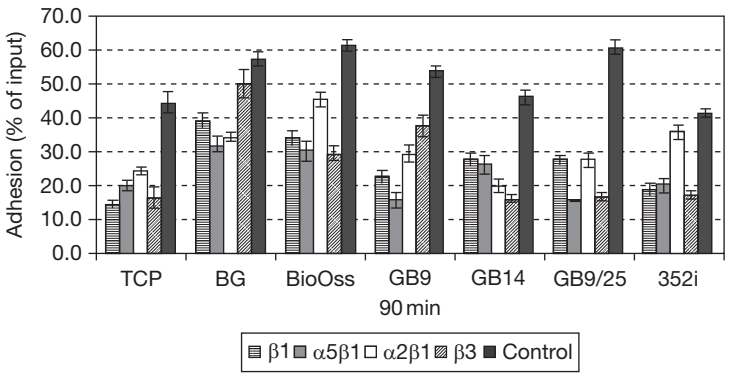

Figure 7 Results of the 90 min adhesion assay for the various calcium phosphate bone grafting materials utilizing functional blocking antibodies against β_1, $\alpha_2\beta_1$, $\alpha_5\beta_1$, and β_3 integrin receptors.

This was in addition to visualizing the expression of various osteogenic markers in the mineralized and unmineralized extracellular-matrix components.[32,43,44,135] Utilizing this novel hard tissue technology rendered it possible to study the effect of identical bioactive ceramics on the expression of osteogenic markers *in vitro* and *in vivo* and to test the above-stated hypothesis.[41–43] In this study, four calcium-alkali orthophosphate ceramic bone substitute materials (**Table 1**) were implanted in the sheep mandible and compared to currently clinically used synthetic bone substitute materials (β-TCP and BG45S5).[41,43,46,135] These materials were selected because previous *in vitro* studies demonstrated that they stimulated greater differentiation of osteoblasts compared to cells grown on TCP ceramic.[42,87,88] (for details, see **Chapter 6.620, Dental Graft Materials**). The various calcium phosphate materials (particle size 300–355 μm) were implanted in the sheep mandible for 1, 4, 12, and 24 weeks to regenerate critical size membrane-protected defects as described by von Arx *et al.*[10] Autogenous bone chips and empty defects, which were filled with collagen sponges, served as controls.[41,43,46,135] This study included examining the above-mentioned calcium-alkali orthophosphate material GB9. As outlined above, *in vitro* GB9 displayed a significantly greater stimulatory effect on osteoblast proliferation and differentiation compared to TCP, BG45S5, and other calcium-alkali orthophosphates.[41,42,46,135] These findings correlated with enhanced bone formation and bone–particle contact (i.e., bone-bonding behavior) *in vivo*, which was accompanied by enhanced expression of type I collagen, osteopontin, osteocalcin, osteonectin, and bone sialoprotein *in vivo*.[41,43,46] This was associated with a significantly greater decrease in particle area fraction over time, that is, a significantly greater biodegradation.[41,43,46] Staining for tartrate-resistant acid phosphatase (TRAP) showed that biodegradation for the various calcium-alkali orthophosphates as well as TCP occurred by dissolution rather than osteoclastic activity.[41,43,46,135] Furthermore, it is noteworthy that with GB9 already after 4 weeks, a significantly greater bone–particle contact was noted compared to all other calcium phosphates. By 12 weeks, defects which were augmented using GB9 displayed greater bone formation compared to defects that were augmented with autogenous bone chips.[41,43,46] These findings are clinically very significant as autogenous bone is considered to be the gold standard. BG45S5 and TCP displayed good bone regenerative capacities and bone-bonding behavior; however, the biodegradability was lower when compared to GB9.[41,43,46] Hence, correlating *in vivo* results with the data from the *in vitro* studies that elucidate the mechanisms by which bioactive ceramics materials induce enhanced osteoblastic differentiation is of great value, because taken together these studies facilitate characterizing the tissue response at the bone–biomaterial interface *in vitro* and *in vivo* at a molecular level and, thus, can contribute significantly to obtaining a fundamental understanding of the processes involved in tissue integration of bioactive implant materials.

1.114.3. Mechanisms of Biodegradation of Bioactive Ceramics

Biodegradation of bioactive ceramics used for bone regeneration can occur either by physicochemical dissolution or by cellular, that is, osteoclastic activity, or by a combination of both. For TCP[24,35] and BG45S5,[30] histological findings from animal studies and human biopsies showed that these materials degrade mainly by physicochemical dissolution and that the role played by osteoclasts was only minor. These results are in agreement with own findings when examining human biopsies[32] and specimens from the sheep study outline above.[41,43,46,135] In these studies, undecalcified histological sections were stained for TRAP activity to identify cells with osteoclastic activity in the vicinity of the various calcium phosphate bone substitute materials. In these sections stained for TRAP activity, no multinucleate TRAP-positive osteoclasts were found in fibrous mesenchym infiltrating the degrading TCP, BG45S5, and calcium-alkali orthophosphate particles or in the mineralized bone tissue in contact with the various calcium phosphate particles, while in the positive controls (experimental fracture-healing sites), numerous multinucleate TRAP positive cells were present. These findings are in agreement with observations by Müller-Mai *et al.*[137] who also noted that degradation of calium-alkali-orthophosphate materials occurred mainly by physicochemical dissolution rather than by osteoclastic activity.[137] With regard to HA-based calcium phosphate materials, however, it has been reported that biodegradation occurs mainly by osteoclastic activity.[77] It has been speculated that these differences in degradation behavior between HA and TCP or BG45S5 are related to the pH, which increases during

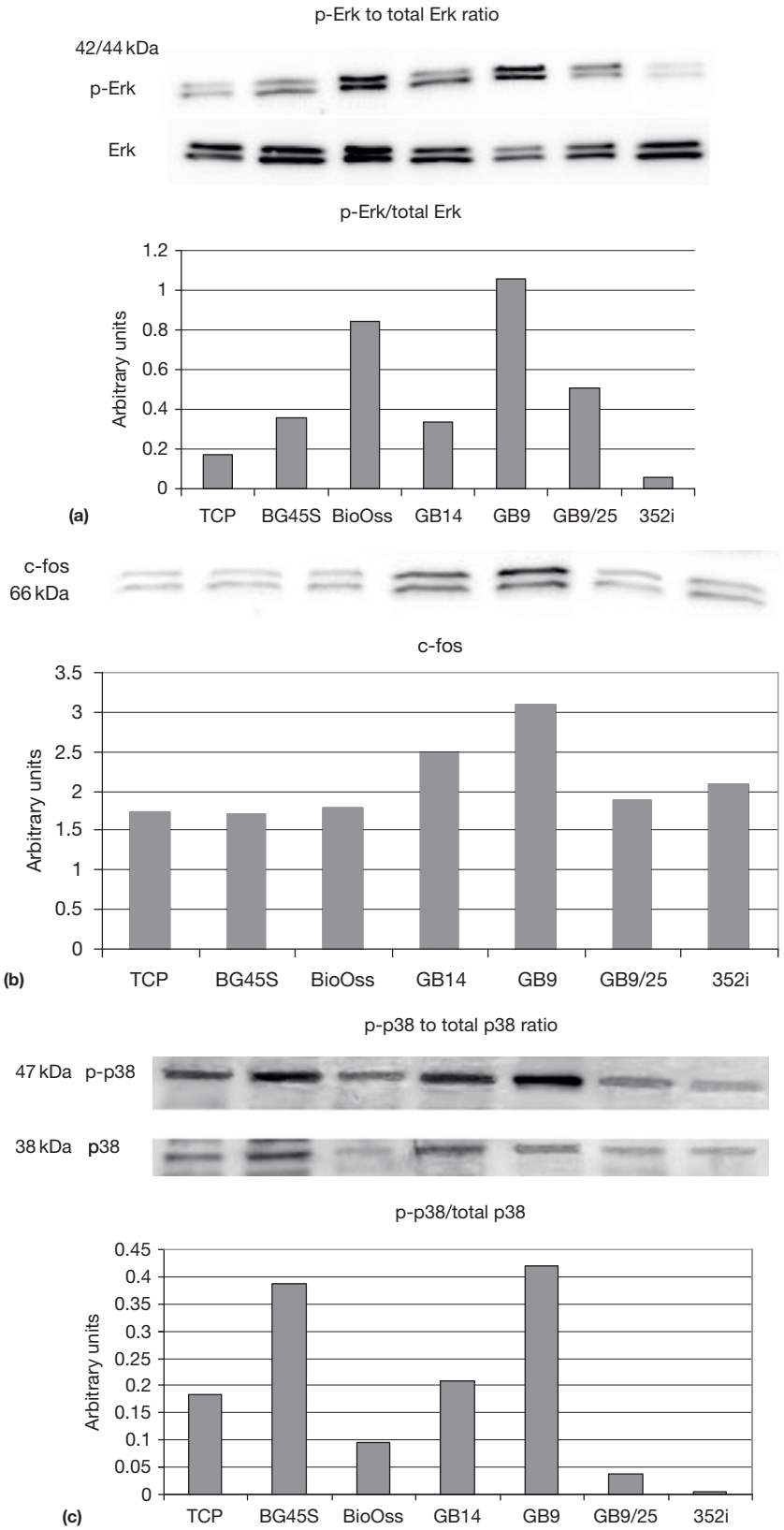

Figure 8 (Continued)

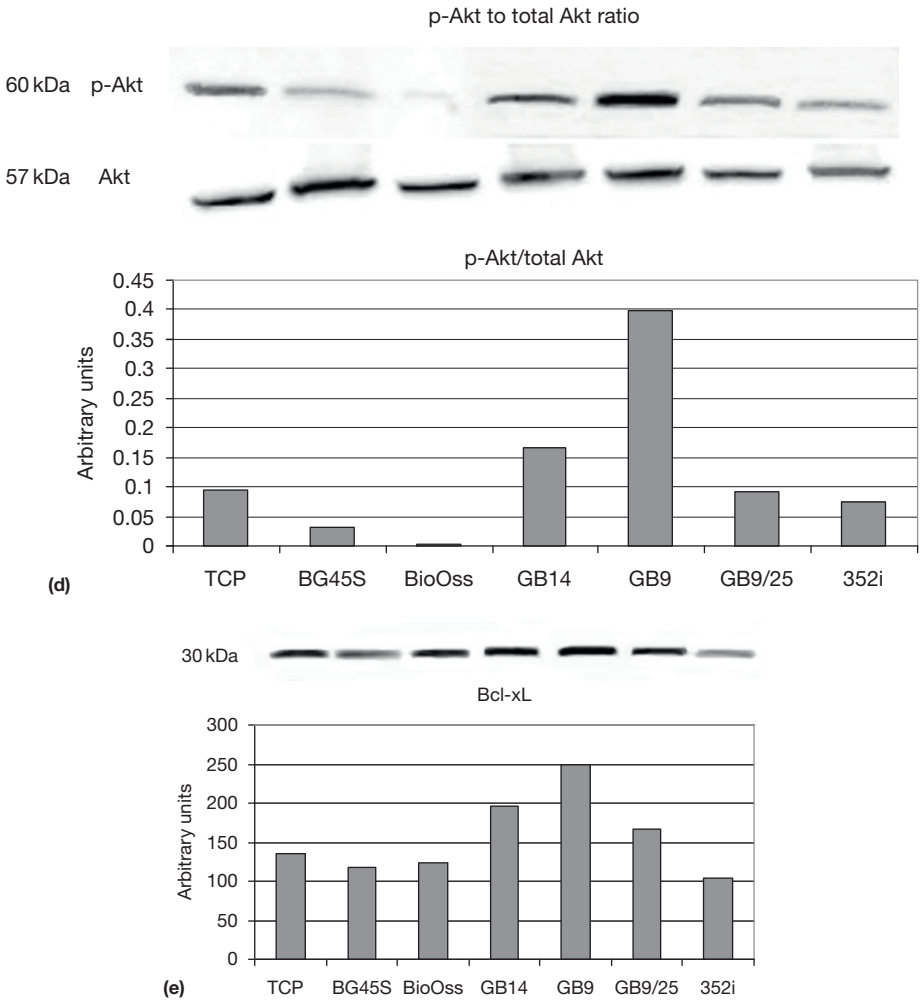

Figure 8 Results of Western blot analysis for activation by tyrosine phosphorylation and/or expression of key signaling factors of the ERK-differentiation pathway (Erk, c-fos), the alternate p38-pathway, the PI3K/Akt cell survival pathway (Akt), as well as of the antiapoptotic factor Bcl-x_L after cultivation of MC3T3-E1 osteoblasts on various bioactive ceramics and glasses. (a) Phospho-Erk to total Erk protein expression ratio after 3 h of cultivation of MC3T3-E1 osteoblasts on various bioceramics. (b) c-fos expression after 24 h of cultivation of osteoblasts on various calcium phosphates ceramics and glasses. (c) Phospho-p38 to total p38 protein expression ratio after 1 h of cultivation of osteoblasts on various calcium phosphates. (d) Phospho-Akt to total Akt protein expression ratio after 24 h of cultivation of MC3T3-E1 bone cells on various bioactive bone substitutes. (e) Protein expression of the antiapoptotic factor Bcl-x_L after 3 h of cultivation of osteoblastic cells on various bioactive calcium phosphates.

the dissolution process.[31] Dissolution of TCP, BG45S5, and calcium-alkali orthophosphates leads to a more alkaline milieu at the material surface, whereas dissolution of HA is associated with a lower pH.[77] This certainly is an interesting issue requiring further investigation.

1.114.4. Summary

Bioactive calcium phosphate ceramics and glasses are known to bond directly to bone and to stimulate bone tissue formation. This has led to their constantly increasing clinical use. Numerous studies have contributed to enhancing our understanding regarding the stimulatory effect of bioactive ceramics on osteoblast function and bone tissue formation. Significant progress has been made in revealing solution-mediated surface reactions that take place close to the surface of bioactive ceramics. Advanced surface analysis methods have been combined with molecular techniques in order to facilitate a better understanding of the surface transformations of bioactive, resorbable ceramics and glasses, and the serum protein adsorption events that are associated with the immersion in biological fluids. A considerable body of knowledge has been generated regarding the effect of various bioactive calcium phosphate ceramics and glasses on osteoblast differentiation *in vitro*. Recent studies provided insight into the effect of various bioactive ceramics on bone cell differentiation and tissue maturation *in vivo*, thereby allowing for correlation of *in vitro* and *in vivo* events. Moreover, techniques have become available to study integrin-mediated cell adhesion and the subsequently activated intracellular signaling pathways that regulate cell function including cellular differentiation and cell survival. As a result, very recent research efforts combined two powerful analytical methodologies (advanced surface

analysis methods and techniques to examine integrin-mediated cell adhesion and signaling mechanisms) to elucidate the mechanisms by which bioactive ceramics and glasses induce enhanced osteoblastic differentiation. Once reaction pathways are clearly identified, the means have become available to alter biomaterial molecular components and surface characteristics in ways that promote optimal cell adhesion, proliferation and differentiation, as well as depression of apoptosis. Thus, new bioactive materials can be created whose surface chemistry and morphology preferentially boosts the osteogenic cascade, thereby leading to more and more expeditious and copious bone formation, which facilitates the creation of bioactive calcium ceramics and glasses that are optimally tailored toward their clinical application.

Acknowledgments

Support over the years from various agencies is gratefully acknowledged. Part of the work was supported by the German Research Foundation DFG (KN 377/2-1, KN377/3-1, KN377/5-1, and KN377/8-1), by the Osteology Foundation, by the European Union (EFRE-grant #10141914 and #10136206), by the NIH (AR-40194, DE-10639, DE-13051, and DE1380), NSF (BCS-9202314 and BCS-9309053), NASA (NAG9-817 and NAG8-1483), and VA (1189-RA).

Furthermore, the authors wish to thank the numerous colleagues who contributed to the work presented in this chapter: Prof. Dr. I. Shapiro, Prof. C. R. Howlett, PD Dr., Dr. M. Stiller, Dr. G. Berger, Dr. S. Radin, Dr. G. Gildenhaar, Dr. A. Houshmand, Dr. A. Bednarek, Dr. Ch. Koch, Dr. H. Renz, Dr. A. El-Ghannam, Ms. A. Kopp, Ms. I. Borchert, Mrs. K. Schulze-Dirksen, Ms. E. Rieger-Rüdiger, and Mrs. I Schwarz.

References

1. de Groot, K.; Wolke, J. G.; Jansen, J. A. *Proc. Inst. Mech. Eng.* **1998**, *212*, 137–147.
2. Denissen, H. W.; Klein, C. P.; Visch, L. L.; van den Hooff, A. *Int. J. Prosthodont.* **1996**, *9*, 142–148.
3. Ducheyne, P. In *Hip Surgery: New Materials and Developments*; Sedel, L., Cabanela, M., Eds.; Martin Dunitz: London, 1998; pp 75–82.
4. Ducheyne, P.; Beight, J.; Cuckler, J.; Evans, B.; Radin, S. *Biomaterials* **1990**, *11*, 531–540.
5. Ducheyne, P.; Hench, L. L.; Kagan, A.; Martens, M.; Mulier, J. C.; Burssens, A. *J. Biomed. Mat. Res.* **1980**, *14*, 225–237.
6. Geesink, R. G. *Clin. Orthop.* **2002**, *395*, 53–65.
7. Knabe, C.; Berger, G.; Gildenhaar, R.; Klar, F.; Zreiqat, H. *Biomaterials* **2004**, *25*, 4911–4919.
8. Buser, D.; Dula, K.; Hess, D.; Hirt, H. P.; Belser, U. C. *Periodontology 2000* **1999**, *19*, 151–163.
9. Praemer, A.; Furner, S.; Rice, D. P. *Musculoskeletal Conditions in the United States*. American Academy of Orthopaedic Surgeons: Park Ridge, 1999.
10. von Arx, T.; Cochran, D. L.; Hermann, J. S.; Schenk, R. K.; Buser, D. *Clin. Oral Implants Res.* **2001**, *12*, 260–269.
11. Belser, U. C.; Mericske-Stern, R.; Bernard, J. P.; Taylor, T. D. *Clin. Oral Implants Res.* **2000**, *11*(Suppl. 1), 126–145.
12. Ganz, S. D.; Valen, M. *J. Oral Implantol.* **2002**, *28*, 178–183.
13. Winkler, S. *J. Oral Implantol.* **2002**, *28*, 226–229.
14. Kalk, W. W.; Raghoebar, G. M.; Jansma, J.; Boering, G. *J. Oral Maxillofac. Surg.* **1996**, *54*, 1424–1429.
15. Kaptein, M. L.; Hoogstraten, J.; de Putter, C.; de Lange, G. L.; Blijdorp, P. A. *Clin. Oral Implants Res.* **1998**, *9*, 321–326.
16. Wheeler, S. L. *J. Oral Maxillofac. Surg.* **1997**, *55*, 1287–1293.
17. Ouhayoun, J. P. Risques de transmission à l'homme de pathologies virale par de substituts oseux d'origine humaine ou animale. In Rapport sur l' état des recherches concernant les risques associés à l'utilisation à des fins thérapeutiques de produits d'origine humaine ou de produits et procédés de substitution, Paris, Edition INSERM, 224–30, 1995.
18. Hench, L. L. *J. Am. Ceram. Soc.* **1998**, *81*, 1705–1728.
19. Hollinger, J. O.; Brekke, J.; Gruskin, E.; Lee, D. *Clin. Orthop.* **1996**, *324*, 55–65.
20. Metsger, D. S.; Driskell, T. D.; Paulsrud, J. R. *J. Am. Dent. Assoc.* **1982**, *105*, 1035–1038.
21. Yaszemski, M. J.; Payne, R. G.; Hayes, W. C.; Langer, R.; Mikos, A. C. *Biomaterials* **1996**, *17*, 175–185.
22. Szabo, G.; Huys, L.; Coulthard, P.; *et al. Int. J. Oral Maxillofac. Implants* **2005**, *20*, 371–381.
23. Wiltfang, J.; Merten, H. A.; Schlegel, K. A.; *et al. J. Biomed. Mater. Res.* **2002**, *63*, 115–121.
24. Zerbo, I. R.; Bronckers, A. L.; de Lange, G.; Burger, E. H. *Biomaterials* **2005**, *26*, 1445–1451.
25. Zerbo, I. R.; Bronckers, A. L.; de Lange, G. L.; van Beek, G. J.; Burger, E. H. *Clin. Oral Implants Res.* **2001**, *12*, 379–384.
26. Zerbo, I. R.; Zijderveld, S. A.; de Boer, A.; *et al. Clin. Oral Implants Res.* **2004**, *15*, 724–732.
27. Ducheyne, P.; de Groot, K. *J. Biomed. Mat. Res.* **1991**, *15*, 441–445.
28. Eggli, P. S.; Muller, W.; Schenk, R. K. *Clin. Orthop. Rel. Res.* **1988**, *232*, 127–138.
29. Tadjoedin, E. S.; de Lange, G. L.; Holzmann, P. J.; Kulper, L.; Burger, E. H. *Clin. Oral Implants Res.* **2000**, *11*, 334–344.
30. Tadjoedin, E. S.; de Lange, G. L.; Lyaruu, D. M.; Kuiper, L.; Burger, E. H. *Clin. Oral Implants Res.* **2002**, *13*, 428–436.
31. Peters, F.; Reif, D. *Materialwiss. Werkstofftech.* **2004**, *35*, 203–207.
32. Knabe, C.; Koch, C.; Rack, A.; Stiller, M. *Biomaterials* **2008**, *29*, 2249–2258.
33. Timmenga, N. M.; Raghoebar, G. M.; van Weissenbruch, R.; Vissink, A. *Clin. Oral Implants Res.* **2003**, *14*, 322–328.
34. Artzi, Z.; Kozlovsky, A.; Nemcovsky, C. E.; Weinreb, M. *J. Clin. Periodontol.* **2005**, *32*, 193–199.
35. Suba, Z.; Takacs, D.; Matusovits, D.; Barabas, J.; Fazekas, A.; Szabo, G. *Clin. Oral Implants Res.* **2006**, *17*, 102–108.
36. Zijderveld, S. A.; Zerbo, I. R.; van den Bergh, J. P.; Schulten, E. A.; ten Bruggenkate, C. M. *Int. J. Oral Maxillofac. Implants* **2005**, *20*, 432–440.
37. Berger, G.; Gildenhaar, R.; Ploska, U. In *Bioceramics*; Wilson, J., Hench, L. L., Greenspan, D. C., Eds.; Butterworth-Heinemann: Oxford, 1995; Vol. 8, pp 453–456.
38. Berger, G.; Gildenhaar, R.; Ploska, U. *Biomaterials* **1995**, *16*, 1241–1248.
39. Knabe, C.; Gildenhaar, R.; Berger, G.; *et al. J. Mater. Sci. Mater. Med.* **1998**, *9*, 337–345.
40. Knabe, C.; Berger, G.; Gildenhaar, R.; *et al. J. Biomed. Mater. Res.* **2004**, *69A*, 145–154.
41. Knabe, C.; Ducheyne, P. In *Handbook of Bioceramics and Their Applications*; Kokubo, T., Ed.; Woodhead: Cambridge, 2008; pp 133–164.
42. Knabe, C.; Houshmand, A.; Berger, G.; *et al. J. Biomed. Mater. Res. A* **2008**, *84*, 856–868.
43. Knabe, C.; Berger, G.; Gildenhaar, R.; *et al.* In *Transactions of the 8th World Biomaterials Congress*, Amsterdam, The Netherlands, May 28–June 1, 2008; p 035.
44. Knabe, C.; Berger, G.; Gildenhaar, R.; *et al.* In *Transactions of the 35th Annual Meeting of the Society for Biomaterials USA*, San Antonio, TX, Apr 22–25, 2009 p 262.
45. Knabe, C.; Kim, J.; Chen, C.; Meausoone, V.; Radin, S.; Ducheyne, P. In *Transactions of the 35th Annual Meeting of the Society for Biomaterials USA*, San Antonio, TX, Apr 22–25, 2009; p 359.
46. Knabe, C.; Berger, G.; Gildenhaar, R.; Ducheyne, P.; Stiller, M. In *Advances in Science and Technology*; Vicenzini, P., Ed.; Trans Tech Publications: Switzerland, 2010; Vol. 76, pp 214–223.
47. Schneider, M.; Gildenhaar, R.; Berger, G. *Cryst. Res. Technol.* **1994**, *29*, 671–675.
48. Berger, G. In *Federal Institute for Materials Research and Testing (BAM) Annual Report*; Federal Institute for Materials Research and Testing: Berlin, Germany, 2003; pp 34–43.
49. Bohner, M. *Biomaterials* **2009**, *30*(32), 6403–6406.
50. Hing, K. A.; Revell, P. A.; Smith, N.; Buckland, T. *Biomaterials* **2006**, *27*, 5014–5026.
51. Komlev, V. S.; Mastrogiacomo, M.; Pereira, R. C.; Peyrin, F.; Rustichelli, F.; Cancedda, R. *Eur. Cell Mater.* **2010 Mar 29**, *19*, 136–146.
52. Ducheyne, P.; Qiu, Q. *Biomaterials* **1999**, *20*, 2287–2303.
53. Hench, L. L. *Bone Implant Interface* **1994**, *9*, 181–190.

54. Ohgushi, H.; Okumura, M.; Tamai, S.; Shors, E. C.; Caplan, A. I. *J. Biomed. Mater. Res.* **1990**, *24*, 1563–1570.
55. El-Ghannam, A.; Ducheyne, P.; Shapiro, I. M. *J. Orthop. Res.* **1999**, *17*, 340–345.
56. Kaufmann, E. A.; Ducheyne, P.; Radin, S.; Bonnell, D. A.; Composto, R. *J. Biomed. Mat. Res.* **2000**, *52*, 825–830.
57. Kokubo, T. In *Bone–Bioactive Biomaterials*; Ducheyne, P. T., Kokubo, T., van Blitterswijk, C. A., Eds.; Reed Healthcare Communications: Leiderdorp, Netherlands, 1993; pp 31–46.
58. Kokubo, T.; Kushitani, H.; Ohtsuki, C.; Sakka, S.; Yamamuro, T. *J. Mater. Sci. Mater. Med. Sci.* **1992**, *3*, 79–83.
59. Radin, S. R.; Ducheyne, P. *J. Biomed. Mat. Res.* **1993**, *27*, 35–45.
60. Radin, S.; Ducheyne, P. *J. Biomed. Mater. Res.* **1996**, *30*, 273–279.
61. Radin, S.; Ducheyne, P.; Berthold, P.; Decker, S. *J. Biomed. Mat. Res.* **1997**, *39*, 234–243.
62. Radin, S.; Ducheyne, P.; Rothman, B.; Conti, A. *J. Biomed. Mat. Res.* **1997**, *37*, 363–375.
63. Ducheyne, P.; El-Ghannam, A.; Shapiro, I. *J. Cell. Biochem.* **1994**, *56*, 162–167.
64. Ducheyne, P.; Bianco, P.; Radin, S.; Schepers, E. In *Bone–Bioactive Biomaterials*; Ducheyne, P., Kokubo, T., van Blitterswijk, C. A., Eds.; Reed Healthcare Communications: Leiderdorp, Netherlands, 1993; pp 1–12.
65. Ducheyne, P.; Radin, S.; King, L. *J. Biomed. Mat. Res.* **1993**, *27*, 25–34.
66. Hench, L.; Splinter, R.; Greenlee, T.; Allen, W. *J. Biomed. Eng.* **1971**, *2*, 117–141.
67. LeGeros, R. Z.; Daculsi, G.; Orly, I.; *et al*. In *Bone-Bonding Biomaterials*; Ducheyne, P., Kokubo, T., van Blitterswijk, C. A., Eds.; Reed Healthcare Communications: Leiderdorp, Netherlands, 1993; pp 201–212.
68. Hench, L. L. *J. Am. Ceram. Soc.* **1991**, *74*(7), 1487–1510.
69. Ducheyne, P.; Kim, C. S.; Pollack, S. R. *J. Biomed. Mat. Res.* **1992**, *26*, 147–168.
70. El-Ghannam, A.; Ducheyne, P.; Shapiro, I. M. *Biomaterials* **1997**, *18*, 295–303.
71. El-Ghannam, A. E.; Ducheyne, P.; Shapiro, I. *J. Biomed. Mater. Res.* **1997**, *36*, 167–180.
72. Yao, J.; Radin, S.; Leboy, P. S.; Ducheyne, P. *J. Biomed. Mater. Res. A* **2005**, *75*, 794–801.
73. Daculsi, G.; LeGeros, R. Z.; Nery, E.; Lynch, K.; Kerebel, B. *J. Biomed. Mat. Res.* **1989**, *23*, 883–894.
74. de Bruijn, J. D.; Bovell, Y. P.; van Blitterswijk, C. A. *Biomaterials* **1994**, *15*, 543–550.
75. de Bruijn, J. D.; Davies, J. E.; Klein, C. P. A. T.; de Groot, K.; van Blitterswijk, C. A. In *Bone-Bonding Biomaterials*; Ducheyne, P., Kokubo, T., van Blitterswijk, C. A., Eds.; Reed Healthcare Communications: Leiderdorp, Netherlands, 1993; pp 57–72.
76. El-Ghannam, A.; Ducheyne, P.; Shapiro, I. M. *J. Biomed. Mat. Res.* **1995**, *29*, 359–370.
77. Schepers, E.; Declercq, M.; Ducheyne, P.; Kempeneers, R. *J. Oral Rehab.* **1991**, *18*, 439–452.
78. Matsuda, T.; Davies, J. E. *Biomaterials* **1987**, *8*, 275–284.
79. Neo, M.; Nakaruma, T.; Yamamuro, T.; Ohtsuki, C.; Kokubo, T. In *Bone-Bonding Biomaterials*; Ducheyne, P., Kokubo, T., van Blitterswijk, C. A., Eds.; Reed Healthcare Communications: Leiderdorp, Netherlands, 1993; pp 111–120.
80. Davies, J. E. Int. *J. Prosthodont.* **1998**, *11*, 391–401.
81. Keselowsky, B. G.; Collard, D. M.; Garcia, A. J. *J. Biomed. Mater. Res. A* **2003**, *66*, 247–259.
82. Xynos, I. D.; Edgar, A. J.; Buttery, L. D.; Hench, L. L.; Polak, J. M. *J. Biomed. Mater. Res.* **2001**, *55*, 151–157.
83. Xynos, I. D.; Edgar, A. J.; Buttery, L. D.; Hench, L. L.; Polak, J. M. *Biochem. Biophys. Res. Commun.* **2000**, *276*, 461–465.
84. Xynos, I. D.; Hukkanen, M. V.; Batten, J. J.; Buttery, L. D.; Hench, L. L.; Polak, J. M. *Calcif. Tissue Int.* **2000**, *67*, 321–329.
85. Schepers, E. J.; Ducheyne, P. *J. Oral Rehabil.* **1997**, *24*, 171–181.
86. Knabe, C.; Stiller, M.; Berger, G.; *et al*. In *For Biomaterials Transactions 2008 Translational Biomaterial Research Symposium*, Atlanta, GA, Sept 11–13, 2008; p 215.
87. Knabe, C.; Berger, G.; Gildenhaar, R.; Howlett, C. R.; Markovic, B.; Zreiqat, H. *Biomaterials* **2004**, *25*, 335–344.
88. Knabe, C.; Stiller, M.; Berger, G.; *et al*. *Clin. Oral Implants Res.* **2005**, *16*, 119–127.
89. Radin, S.; Reilly, G.; Bhargave, G.; Leboy, P. S.; Ducheyne, P. *J. Biomed. Mat. Res.* **2005**, *73A*, 21–29.
90. Aubin, J. E. *Biochem. Cell Biol.* **1998**, *76*, 899–910.
91. Aubin, J. E. In *Bone Engineering*; Davies, J. E., Ed.; em squared: Toronto, Canada, 2000; pp 19–30.
92. Sodek, J.; Cheifitz, S. In *Bone Engineering*; Davies, J. E., Ed.; em squared: Toronto, Canada, 2000; pp 31–43.
93. Fisher, L. W.; Termine, J. D. *Clin. Orthop.* **1985**, *200*, 362–385.
94. Termine, J. D.; Kleinman, H. K.; Whitson, S. W.; Conn, K. M.; McGarvey, M. L.; Martin, G. R. *Cell* **1981**, *26*, 99–105.
95. Oldberg, A.; Franzen, A.; Heinegard, D. *J. Biol. Chem.* **1988**, *263*, 19430–19432.
96. Howlett, C. R.; Chen, N.; Zhang, X.; *et al*. In *Bone Engineering*; Davies, J. E., Ed.; em squared: Toronto, Canada, 2000; pp 240–255.
97. Schwartz, Z.; Boyan, B. D. *J. Cell. Biochem.* **1994**, *56*, 340–347.
98. Salih, V.; Franks, K.; James, M.; Hastings, G. W.; Knowles, J. C. *J. Mater. Sci. Mater. Med. Sci.* **2000**, *11*, 615–620.
99. Knabe, C.; Howlett, C. R.; Klar, F.; Zreiqat, H. *J. Biomed. Mater. Res.* **2004**, *71A*, 98–107.
100. Wang, C.; Duan, Y.; Markovic, B.; *et al*. *Biomaterials* **2004**, *25*, 2507–2514.
101. Krause, A.; Cowles, E. A.; Gronowicz, G. *J. Biomed. Mater. Res.* **2000**, *52*, 738–747.
102. Cowles, E. A.; Brailey, L. L.; Gronowicz, G. A. *J. Biomed. Mater. Res.* **2000**, *52*, 725–737.
103. Gronowicz, G.; McCarthy, M. B. *J. Orthop. Res.* **1996**, *14*, 878–887.
104. Rezania, A.; Healy, K. E. *J. Orthop. Res.* **1999**, *17*, 615–623.
105. Hynes, R. O. *Cell* **1987**, *48*, 549–554.
106. Hynes, R. O. *Cell* **1992**, *69*, 11–25.
107. Gronthos, S.; Stewart, K.; Graves, S. E.; Hay, S.; Simmons, P. J. *J. Bone Miner. Res.* **1997**, *12*, 1189–1197.
108. Hughes, D. E.; Salter, D. M.; Dedhar, S.; Simpson, R. *J. Bone Miner. Res.* **1993**, *8*, 527–533.
109. Saito, T.; Albelda, S. M.; Brighton, C. T. *J. Orthop. Res.* **1994**, *12*, 384–394.
110. Garcia, A. J.; Ducheyne, P.; Boettiger, D. *J. Biomed. Mater. Res.* **1998**, *40*, 48–56.
111. Redick, S. D.; Settles, D. L.; Briscoe, G.; Erickson, H. P. *J. Cell Biol.* **2000**, *149*, 521–527.
112. Danen, E. H.; Aota, S.; van Kraats, A. A.; Yamada, K. M.; Ruiter, D. J.; van Muijen, G. N. *J. Biol. Chem.* **1995**, *270*(37), 21612–21618.
113. Reyes, C. D.; García, A. J. *J. Biomed. Mater. Res.* **2003**, *65A*, 511–523.
114. Reyes, C. D.; García, A. J. *J. Biomed. Mater. Res.* **2004**, *69A*, 591–600.
115. Keselowsky, B. G.; Collard, D. M.; Garcia, A. J. *Proc. Natl. Acad. Sci. USA* **2005**, *102*(17), 5953–9537.
116. Petrie, T. A.; Reyes, C. D.; Burns, K. L.; García, A. J. *J. Cell. Mol. Med.* **2008**, *12*, 1029–1048.
117. Wojtowicz, A. M.; Oest, M. E.; Dupont, K. M.; *et al*. In *Transactions of the Society for Biomaterials 2008 Translational Biomaterial Research Symposium*, Atlanta, GA, Sept 11–13, 2008; p 283.
118. Knight, C. G.; Morton, L. F.; Peachey, A. R.; Tuckwell, D. S.; Farndale, R. W.; Barnes, M. J. *J. Biol. Chem.* **2000**, *275*, 35–40.
119. Juliano, R. L.; Haskill, S. *J. Cell Biol.* **1993**, *120*, 577–585.
120. Rosales, C.; O'Brien, V.; Kronberg, L.; Julinao, R. L. *Biochem. Biophys. Acta* **1995**, *1242*, 77–98.
121. Bates, R. C.; Lincz, L. F.; Burns, G. F. *Cancer Metastasis Rev.* **1995**, *14*, 191–203.
122. Yamada, K. M.; Miyamoto, S. *Curr. Opin. Cell Biol.* **1995**, *7*, 681–689.
123. Richardson, A.; Parsons, J. T. *Bioessays* **1995**, *17*, 229–236.
124. Dedhar, S. *Cancer Metastasis Rev.* **1995**, *14*, 165–172.
125. Harmer, S. L.; DeFranco, A. L. *Mol. Cell. Biol.* **1997**, *17*, 4087–4095.
126. Nohe, A.; Keating, E.; Knaus, P.; Petersen, N. O. *Cell. Signal.* **2004**, *16*, 291–299.
127. Noth, U.; Tuli, R.; Seghatoleslami, R.; Howard, M.; Shah, A.; Hall, D. J. *Exp. Cell Res.* **2003**, *291*(1), 201–211.
128. Ivaska, J.; Reunanen, H.; Westermarck, J.; Koivisto, L.; Kahari, V. M.; Heino, J. *J. Cell Biol.* **1999**, *147*, 401–416.
129. Adams, C. S.; Shapiro, I. M. *Connect. Tissue Res.* **2003**, *44*(Suppl. 1), 230–239.
130. Grigoriou, V.; Shapiro, I. M.; Cavalcanti-Adam, E. A.; Composto, R. J.; Ducheyne, P.; Adams, C. S. *J. Biol. Chem.* **2005**, *280*, 1733–1739.
131. Razzouk, S.; Shapiro, I. M. *J. Bone Miner. Metab.* **2003**, *21*(5), 261–267.
132. Risbud, M. V.; Fertala, J.; Vresilovic, E. J.; Albert, T. J.; Shapiro, I. M. *Spine* **2005**, *30*, 882–889.
133. Szymczyk, K. H.; Shapiro, I. M.; Adams, C. S. *Bone* **2004**, *34*, 148–156.
134. Kim, J.; Berger, G.; Gildenhaar, R.; Shapiro, I.; Ducheyne, P.; Knabe, C. In *Annual Meeting of the Society for Biomaterials*, Seattle, Washington, USA, April 21–24, 2010; p 830.
135. Knabe, C.; Berger, G.; Gildenhaar, R.; *et al*. In *Transactions of the 32nd Annual Meeting of the Society for Biomaterials USA*, Chicago, IL, Apr 18–21, 2007; p 262.
136. Knabe, C.; Kraska, B.; Koch, Ch.; Gross, U.; Zreiqat, H.; Stiller, M. *Biotech. Histochem.* **2006**, *81*, 31–39.
137. Müller-Mai, C.; Berger, G.; Voigt, C.; Bakki, B.; Gross, U. In *Bioceramics*; Sedel, L., Rey, C., Eds.; Butterworth-Heinemann: Oxford, UK, 1997; Vol. 10, pp 53–56.

1.115. Calcium Phosphates for Cell Transfection

P Frayssinet and N Rouquet, Urodelia, Rte de St Thomas, St Lys, France
M Bausero, Polo Tecnologico de Pando, Pando, Uruguay
P O Vidalain, Institut Pasteur, Paris, France

© 2011 Elsevier Ltd. All rights reserved.

1.115.1.	**Introduction**	259
1.115.2.	**Applications of Bioceramic Cell Transfection**	260
1.115.3.	**The Role of Bioceramic Characteristics for their Applications**	261
1.115.3.1.	Bioactivity	261
1.115.3.2.	Degradability	261
1.115.3.3.	Physicochemical Properties	262
1.115.4.	**Traditional Use of Calcium Phosphate for Cell Transfection**	262
1.115.5.	**Hydroxylapatite Ceramics for Cell Transfection**	262
1.115.5.1.	Physicochemistry	262
1.115.5.2.	Transfection of Isolated Cells	263
1.115.5.3.	Transfection of Tissue Culture	263
1.115.5.4.	*In Vivo* Transfection	263
1.115.6.	**Perspectives and Material Evolution**	263
References		264

Abbreviations

APC	Antigen presenting cell
BMP	Bone morphogenic protein
DC	Dendritic cells
HA	Hydroxylapatite
HLA-DR	Major histocompatibilty complex (class II) cell surface receptor whose function is to present peptide antigens, potentially foreign in origin, to the immune system for the purpose of eliciting or suppressing T-(helper)-cell
IL-12	Interleukin 12
Lac-Z	Bacterial enzyme β-galactosidase
MHC	Major histocompatibility complex
MSC	Mesenchymal stem cells
PBS	Phosphate buffered saline
pDNA	Plasmid DNA
TLR4	Toll-like receptor 4
TNF	Tumor necrosis factor

1.115.1. Introduction

Transfection is the process of introducing nucleic acids into cells by nonviral methods, whereas transduction is a term generally used to describe virus-mediated DNA transfer. Naked DNA is not able to significantly transfect cells *ex vivo*, although some limited gene transfer can be detected when injected into muscles.[1] This is the reason why materials and protocols have been developed in order to increase the efficiency of transfection for therapeutic use.

Today, any gene can be artificially synthesized and made readily available for gene therapy. Thus, the challenge is to get a good vector to deliver this gene in the right cell type. Since the first protocol of gene therapy used in humans was approved in September 1990, the number of available vectors has dramatically increased while the ideal vector is still to be found.

Viral vectors have been widely used for clinical trials due to the natural ability of viruses to deliver genetic material into the cell nucleus.[2] They represent the most effective way to deliver DNA, but show limitations regarding cell type targeting, size of carried DNA, production and packaging problems. Furthermore, immunological reactions, cytotoxicity, and hazardous integration events (when using retroviruses as vectors) led to secondary effects and even the death of several patients in clinical trials making viral vectors difficult to use for large-scale clinical research[3] (**Table 1**).

Besides gene delivery methods based on recombinant viruses, there are various alternative methods of introducing foreign DNA into eukaryotic cells. Physical methods have been developed since the permeability of cellular membranes is increased by electric or heat shocks, magnetic force or ultrasounds.[4] Although efficient *in vitro*, these physical methods are difficult to adapt for *in vivo*. Finally, many materials have been used as carriers for DNA transfection, including hydrogel polymers, polycationic lipids, polylysine, polyornithine, dendrimers, histones, and other chromosomal proteins, and precipitated calcium phosphate.[5–7] These different carriers apply the theory and methods of advanced particulate drug delivery to introduce DNA in selective somatic cells.[8] In these systems, DNA is condensed to form nanoparticles which are up taken in the endocytic pathway. Functional molecules can be incorporated in these DNA nanoparticles in order to target a

Table 1 Biological characteristics of viral and nonviral vectors

Viral	*Nonviral*
Cell specificity	No limit on plasmid size
High transfection efficiency	Toxicity predictible
Transportation mechanism of DNA into nucleus	Low immunity
Immune reaction against viral proteins	No integration
Virus infectiosity	Low transfection efficacy
Limitation on gene size	Not always efficient *in vivo*
Random chromosomal insertion: possibility of proto-oncogene activation	Unclear nuclear transport

Table 2 Barriers in gene delivery

Extracellular	*Intracellular*
Plasma nuclease	Endosomal escape
Uptake by reticuloendothelial system	Lysosomal degradation
Opsonization	Cytoplasmic nuclease
Complement activation	Translocation to nucleus

cell type and/or the nucleus. Once in the endosome, the plasmid DNA must be released in the cytosol and escape processing by the cytosolic nucleases.[9] Then, it may enter, through nuclear pores, into the nucleus where gene transcription occurs (Table 2).

Among these transfection agents, liposomes are particularly interesting. Liposomes are spherical vesicles with a diameter ranging from 20 nm to a few thousands nm. These vesicles consist of one or several lipid bilayers that separate an intravesicular space from an external medium. Within these lipid bilayers, like in the biological membrane, motion of phospholipids is observed.[10] Liposomes are easy to prepare. However, liposomes are phagocytosed by macrophages and are rapidly trapped in the liver, spleen, and lung.[11] In addition, liposomes must exhibit membrane-fusion promoting molecules at their surface to enhance the cytoplasmic delivery of pDNA. They can also carry different kinds of surface molecules such as viral glycoproteins, giving them some specificity for an organ or a defined tissue.[12,13]

The synthetic vectors are applicable *in vitro* with isolated cells, but *in vivo* applications are greatly limited by their toxicity or because physicochemical conditions necessary for the transfection are difficult to reach in an open medium. Transfection agents are much less efficient than viral vectors with regard to the transfection yield but they can be used with almost all gene size at the opposite of virus.[14]

1.115.2. Applications of Bioceramic Cell Transfection

Many clinical assays have been carried out in order to correct gene expression deficiencies.[15] However, transfection protocols based on bioceramics could be more useful for two particular applications, DNA vaccination and bone tissue engineering that do not require the integration and long-term expression of the transgene (Table 3).

Table 3 Diseases and conditions of the musculoskeletal system that may be amenable to gene therapy

Inherited	*Acquired*
Osteogenesis imperfecta	Arthritis
Familial osteoarthrosis	Arthrosis
	Delayed unions (pseudarthrosis)
Osteopetrosis	
Certain crystal-deposition arthropathis	Osteosarcomas, chondrosarcomas, bone metastasis
Certain form of osteoporosis	Osteoporosis
Inherited abnomalies of the growth plate	Rheumatic disease
Ehler–Danlos syndrome and other connective-tissue diseases	

DNA vaccination consists in transfection of subcutaneous or muscular cells with a gene coding for a viral or a bacterial protein that will be recognized by the adaptive immune system as a foreign antigen. When transiently expressed by transfected cells, this foreign antigen will trigger an antibody response that provides long term immunity against the corresponding pathogen. Furthermore, the mechanical properties of powdered bioceramics also allow their spray with a gene gun.

Maybe the most important argument for using this material would be to obtain a DNA vaccine that recruits and activates dendritic cells (DC)[16] (Figure 1). In this field, preliminary results suggest that HA particles could both mediate DC transfection and induce their maturation[17] as particulate bioceramics were proven to act as a vaccine adjuvant. DNA vaccination has been highly effective in mice, while less immunogenic in different primates including humans.[18] The efficiency of DNA vaccination depends on appropriate interactions between the foreign antigen, lymphocytes, and antigen presenting cells (APCs). B lymphocytes need helper signals from T lymphocytes to produce antigen-specific antibodies, but the efficient activation of antigen-specific T lymphocytes critically relies on three kinds of biological signals provided by APCs.[19] The APCs must (1) express MHC molecules to present antigen-derived peptidic fragments to T lymphocytes, (2) express suitable costimulatory molecules at their surface like CD80 and CD86, and (3) secrete costimulatory cytokines in their microenvironment such as IL-12. Only DC that have received a maturation signal can express these different signals at optimal levels to mediate T lymphocyte activation.

We have demonstrated that when human immature dendritic cells were grown *in vitro* with hydroxylapatite particles, they maturated within 48 h. The presence of the particles induced the expression of cd 40, 83, 86, and HLA-DR by the cells. It means that the HA bioceramic particles trigger in the APCs a series of events necessary for the priming of T lymphocytes. Interestingly, HA-induced activation of APCs critically relies on TLR4, a membrane receptor well-characterized for its role in the detection of pathogen-associated molecular patterns like bacterial lipopolysaccharides and viral glycoproteins.[20] Associated to the recruitment of APCs in the foreign body reaction, bioceramics can thus be used in combination with

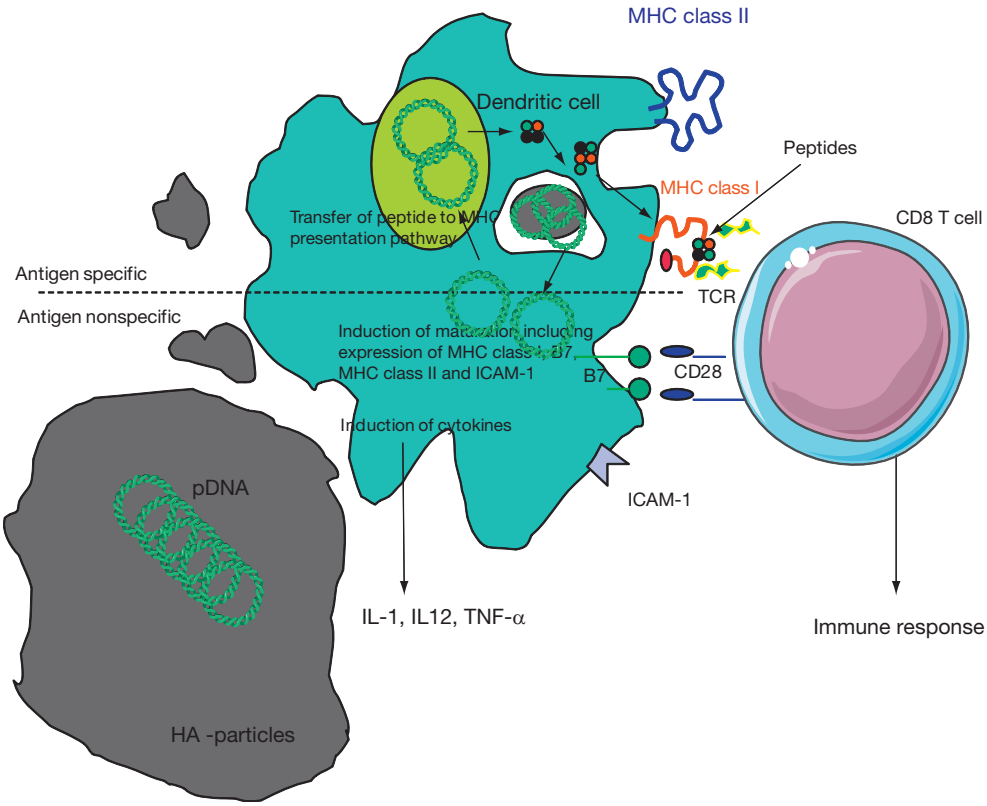

Figure 1 HA particles when in contact with APCs can transfect them with pDNA coding for an antigen which will be expressed and processed at the surface of the MHC class I proteins. The presence of the antigen at the surface of the APC cells will cross prime the CD8 cells. The phagocytosis of HA-fragments triggers the synthesis of costimulation molecules, interleukins, and cytokines like IL-12 necessary for the cross priming.

pDNA to make efficient vaccine in human beings without the need to bring additional signals to trigger the adaptive immune response.

Calcium phosphate bioceramics were used for decades for bone reconstruction and for vectorization of bone cell progenitors.[21,22] In this field, this technology can be used to induce the differentiation of cells grown at the material surface. Differentiation of Mesenchymal Stem Cells (MSCs) in osteoblasts for example using pDNA bearing BMPs genes could be achieved using porous ceramics with high surface area on which the pDNA is immobilized. MSCs are generally dedifferentiated after a culture period even when they are phosphatase alkaline positive, and the presence of morphogenetic proteins at the surface of the material would permit to induce osteoprogenitor cell differentiation and maintain cells in this differentiated state in culture. This type of material would also be useful for direct implantation into connective tissue such as pseudarthrosis fibrous tissue in order to transfect the cells of the surrounding tissue in order to modify their differentiation by transfection.[23]

1.115.3. The Role of Bioceramic Characteristics for their Applications

Bioceramics show biological and physicochemical characteristics, which make possible their use in special applications.

1.115.3.1. Bioactivity

Bioceramics are bioactive materials interacting with bone tissue when implanted inside bone to be totally integrated in several stages and replaced by the neoformed bone.[24] This property makes these materials particularly adapted to the transient transfection of bone cells, in particular osteoblasts and/or osteoclasts which are functionally deficient in some genetic diseases like osteogenesis imperfecta[25] or aging diseases like osteoporosis.[26] There is a number of genetic and acquired bone diseases clearly identified which could benefit from bioceramic transient transfection (**Table 3**).

1.115.3.2. Degradability

Bioceramics are degradable and get replaced by bone following a process of resorption/reconstruction identical to that of natural bone.[24] The ceramic grain boundaries are first resorbed. This degradation of the material allows the release of micro- or even nanoparticles that trigger biological reactions which can be useful for special applications. A good example of this is the transient induction of a foreign body reaction around the microparticles released by the calcium phosphate ceramics (**Figure 2**). The foreign body reaction is constituted by cells of monocytic origin involved in the immune response and in particular antigen presentation to the lymphocytes. Antigen expression

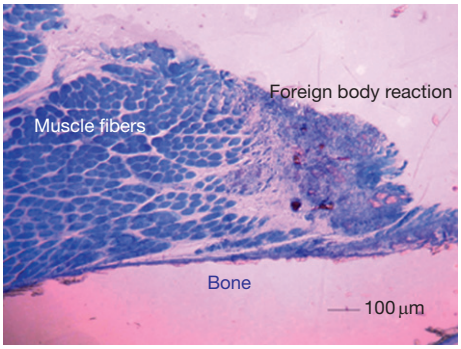

Figure 2 Histological section of the injection site of HA particles in a mice muscle showing the formation of a transient foreign body reaction around the particles.

in antigen presenting cells might enhance immune response.[16] The degradability can thus amplify the foreign body and innate immune reaction.

1.115.3.3. Physicochemical Properties

The biological activity of bioceramics is linked to their physical characteristics, and in particular properties of their surface. We have demonstrated that the toxicity and the inflammatory power of hydroxylapatite (HA) – particles were related to their physical properties, while their chemical composition was the same.[27–29] In the field of vaccination for example, the physical properties of ceramic HA particles, in particular their size and structure of their surface, show a major influence on the synthesis of interleukins and TNF that determine the adjuvant properties of the particles.[30]

Bioceramics can be powdered, porous, or under a bulk material form. Compared to the other transfection tools, the solid state of bioceramics which are implanted in a specific site allows a kind of cell specificity as the transfected cells must come into contact with the material surface. For example, it is of interest for tumor cell transfection since the material can be implanted directly in the tumor.

1.115.4. Traditional Use of Calcium Phosphate for Cell Transfection

Calcium phosphate has been one of the earliest transfection agent under the form of nanoparticles coprecipitated with pDNA. These nanoparticles are obtained by precipitation, through the incubation of pDNA in a supersaturated calcium and phosphate solution. The particles precipitated are nanosized and formed by a coprecipitate of DNA and a poorly characterized calcium phosphate.[31,32] Transfection is achieved when this coprecipitate is contacting a cell monolayer.

This method has a poor transfection yield,[33] with only a few percents of transfected cells being obtained. Above all, this method is only tractable *in vitro* in a closed environment as *in vivo* in an open medium the supersaturation cannot be reached. For this reason, the use of this method for *in vivo* cell transfection must be made in two times. The cells must be first transfected in culture and then injected in the tissue. It is also possible to isolate the nanoparticles from the solution after their formation *in vitro* and inject it in the tissue to be tranfected. However, the migration risk is very high.

Higher transfection yields (60%) can be obtained when the precipitation factors are better controlled.[34] Temperature, DNA concentration, and reaction time were shown to be crucial for better results over standard procedure. Almost 100 000 plasmid molecules could be delivered into individual cells.

Cell cycle is also a key factor for transfection efficiency, and the percentage of cells in S phase when adding the transfection agent correlates with the percentage of transfected cells.[35] The nuclear membrane is dismantled during mitosis, and this probably increases the number of pDNA molecules accessing the nuclear environment.

However, the transfection mechanism is unclear. It seems that the entrapped DNA in the nanoparticles is protected at least partially from the degradation by cellular nucleases, and released by the calcium phosphate degradation in the low pH environment of the endosomes and lysosomes. The way of migration from these cellular compartments into the nucleus is highly speculative.[36]

1.115.5. Hydroxylapatite Ceramics for Cell Transfection

We have developed new hydroxylapatite ceramics for transfection. They have different characteristics from the traditional calcium phosphate nanoparticles obtained by precipitation.

1.115.5.1. Physicochemistry

The calcium phosphate ceramics are different from the nanoparticles obtained by coprecipitation. The ceramics are made of calcium phosphate grains joined by grain boundaries due to the sintering process, with a porosity between the grains that depends on the sintering temperature. This structure makes the material surface area much lower than that of coprecipitates and less reactive. The degradation of the calcium phosphate ceramic is well documented. The degradation of the grain boundaries triggers the release of grains or grain aggregates that are endo- or phagocytosed depending on their size.[37] The internalized particles are then solved inside the low pH cell compartments.[38] Interestingly, we have shown the presence of multinucleated giant cells that contribute actively to the dissolution of the material at the cell–material interface.

DNA is a negatively charged molecule. Calcium phosphate ceramics used in our experiments also show a negatively charged surface. However, we have been able to immobilize pDNA at the surface of calcium ceramics, suggesting that pDNA binding to HA particles is not electrostatic. Numerous theories have been published to describe the interaction between organic molecules and HA. None of them however takes into account the linked water or the modification of surface occurring at the surface when the ceramics are immersed into a saline solution. The epitaxial growth of carbonated apatite at the surface of HA ceramics has been widely described.[39] It is suggested that DNA could be coprecipitated at the surface of the ceramic with the carbonated apatite. The protocol to immobilize pDNA at the ceramic

surface includes the maceration of the powder in a saline solution containing the DNA. Precipitation is then visible at the ceramic surface.[40]

1.115.5.2. Transfection of Isolated Cells

Isolated cells, established or primary cell lines grown in monolayer, were transfected using pDNA loaded ceramic powder. The powder must be introduced into the culture flask and let in contact with the cell layer to transfect for various periods of time. Transfection is generally time dependent. With a constant amount of powder, the percentage of cells expressing the reporter gene is dependent on the time of incubation. The yield of transfection is also dependent on the mass of powder used for the transfection (**Figures 3** and **4**).

1.115.5.3. Transfection of Tissue Culture

Different tissues can be maintained in culture and used to test their behavior in contact with some biomaterials. The interactions between the different cell types is relatively conserved on such biopsies and their differentiated functions maintained, allowing a better understanding of their relationships with the transfection material than when working with isolated cells.

We grew small fragments of bone tissue from rats in contact with HA-beads loaded with pDNA containing a galactosidase reporter gene for two periods of time, 8 and 21 days. The grown bone was made of calvaria, cancellous bone, and growth plate cartilage. The histology of the bone fragments showed that almost no cells were positive at 8 days while all cells expressed the *LacZ* reporter gene at 21 days. It was significantly different from the control made of pDNA in PBS.

The calvaria histology demonstrated that the HA beads were covered by layers of proliferating cells coming from the periosteum of the immature bone formed by a direct ossification process. Some multinucleated cells from monocytic origin were also present at the contact of the HA particles. The cells clearly expressed the *LacZ* gene whatever their distance from the beads (**Figure 5**).

The same results were observed with other types of bone. The cells were stained in blue whether they are proliferating like the mesenchymal cells located inside the pores of the cancellous bone or not as it was shown for the chondrocytes.

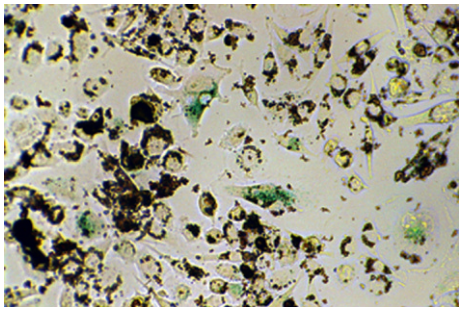

Figure 3 Established murine gliosarcoma cell line grown a few hours in the presence of HA particles showing that many particles were phagocytosed.

1.115.5.4. *In Vivo* Transfection

The same HA particles implanted in a connective tissue such as rabbit bone tissue trigger a foreign body reaction before integration within newly formed bone. Within 3 weeks, the most of the cells of the foreign body reaction at the particle contact expressed the *LacZ* gene (**Figures 6** and **7**). Other cells of monocytic origin were found positive for galactosidase staining. Osteoclasts in Howship's lacunae in the cancellous bone at remote location from the implantation zone were found to express the transgene. Some of these cells were found among the connective tissue present inside the bone pores. Other cells were labeled in this region, including some perivascular and mesenchymal cells, but also some cells of the dental ligament.

The cells labeled at 3 months are different. Fibroblasts of connective tissue and even odontoblasts expressed the galactosidase reporter gene.

1.115.6. Perspectives and Material Evolution

At the opposite of other transfection agents, bioceramics can be shaped. They can even be put in suspension to make solutions of bioceramic powder that can be injected or delivered by spray. Some interesting results were obtained using carboxymethyl cellulose without altering the powder transfection properties. The shaping of the bioceramics will allow their use in the various applications evoked in this chapter.

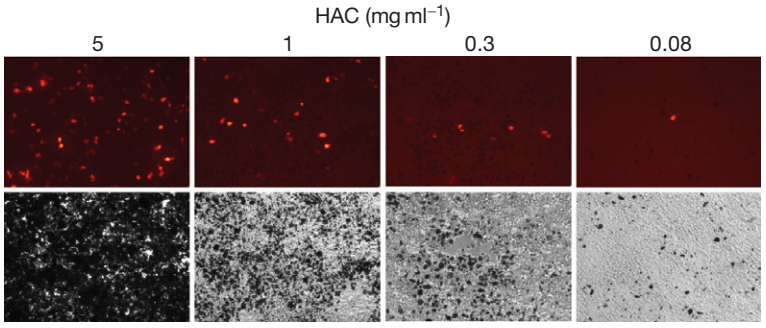

Figure 4 Transfection of a HEK293T cell line with different concentration of HA particles at 24 h. The particles were suspended at different concentrations in 1 ml of culture medium. The percentage of the transfected cells increases with the powder concentration.

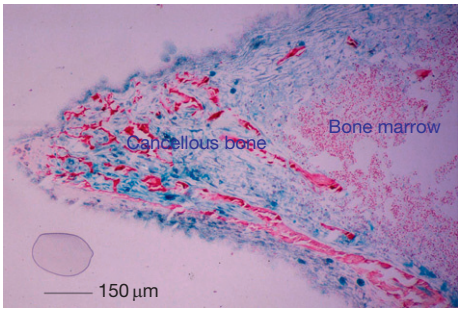

Figure 5 Calvaria tissue grown in the presence of HA particles loaded with a LacZ plasmid. After 3 weeks of culture the histological sections shows that all the cells express the *LacZ* gene.

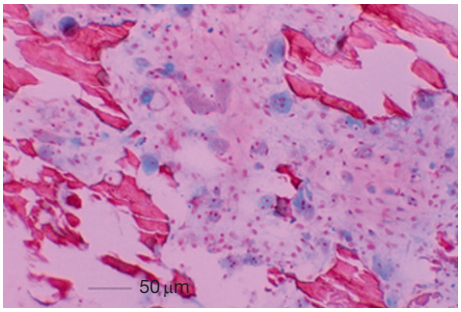

Figure 6 Three weeks after implantation in rabbit jaw, the histological sections shows that the monocytes and the plurinuclear cells of monocytic origin in bone expressed the *LacZ* gene.

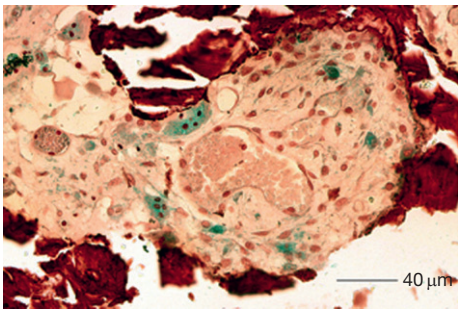

Figure 7 Histological section of a rabbit jaw bone after 3 weeks after implantation of HA particles loaded with pDNA (LacZ). The osteoclasts at the bone surface express the foreign gene.

Highly reactive material able to immobilize more pDNA than the ceramics used in our experiments could be available either by improving the surface area and/or by obtaining a better epitaxial growth at the material surface. This could be reached by associating other phases that are more soluble at physiological pH in the bioceramics.

Ceramic microparticles are not able to circulate in the blood stream for biocompatibility and physical reasons. The size of the particles must be submicronic or even nanometric in order to circulate inside the capillaries of the normal or tumoral tissues. Their density should also be modified in order to keep them in suspension in the blood.

Two other characteristics need to be improved in order to use such particles for *in vivo* transfection. First, particles injected in the blood stream are recognized by the innate immune system and are rapidly cleared by the spleen, the liver, and to a lower extent by the lungs. Thus, it is very important to minimize their recognition by macrophages so that the material is able to reach and enter targeted organs or tissues. Second, in spite of many works that have been published in the last 30 years, it is impossible to achieve transfection of a specific cell type by addressing particles into a specific tissue. This needs to be improved. Associated to a better biocompatibility of the material, humanized antibodies immobilized at the material surface should provide a way to target specific cells. In contrast to their nonhumanized counterparts, these molecules have proved to be able to target specific cells before they get eliminated by the immune system. The chemical molecules bridging these molecules to the material surface should also be eliminated or hidden in the body to minimize that their recognition by the immune system.

References

1. Danko, I.; Williams, P.; Herweijer, H.; *et al*. *Hum. Mol. Genet*. **1997**, *6*(9), 1435–1443.
2. Patil, S. D.; Rhodes, D. G.; Burguess, D. J. *AAPS J*. **2005**, *7*(1), E61–E77.
3. Kahn, A. *Biofutur* **2000**, *202*, 16–21.
4. Plank, C.; Scherer, F.; Schillinger, U.; Anton, M.; Bergemann, C. *Eur. Cells Mater*. **2002**, *3*(Suppl. 2), 79–80.
5. Bonadio, J.; Goldstein, S. A.; Levy, R. J. *Adv. Drug Deliv. Rev*. **1998**, *33*, 53–69.
6. Luo, D.; Saltzman, W. M. *Nat. Biotechnol*. **2000**, *18*, 33–37.
7. Nishikawa, M.; Hashida, M. *Biol. Pharm. Bull*. **2002**, *25*(3), 275–283.
8. Ledley, F. D. *Prod. Hum. Gene Ther*. **1995**, *6*(9), 1129–1144.
9. Zanta, A. M.; Valladier, P. B.; Behr, J.-P. *Proc. Natl. Acad. Sci. USA* **1999**, *96*, 91–96.
10. Laurin, A.; Flore, C.; Thomas, A.; Brasseur, R. *Biotechnol. Agron. Soc. Environ*. **2004**, *8*, 163–176.
11. Dexi, L.; Song, Y. K. *Gene Ther. Mol. Biol*. **1998**, *2*, 59–68.
12. Brigger, I.; Dubernet, C.; Couvreur, P. *Adv. Drug Deliv. Rev*. **2002**, *54*, 631–651.
13. Maruyama, K.; Ishida, O.; Takizawa, T.; Moribe, K. *Adv. Drug Deliv. Rev*. **1999**, *40*(1–2), 89–102.
14. Maitra, A. *Expert Rev. Mol. Diagn*. **2005**, *5*(6), 893–905.
15. Edelstein, M. I.; Abedi, M. R.; Wixon, J.; Edeltein, M. R. *J. Gene Med*. **2004**, *6*, 597–602.
16. Kutzler, M. A.; Weiner, D. B. *J. Clin. Investig*. **2004**, *114*(9), 1241–1243.
17. Frayssinet, P., unpublished results.
18. Surnida, S. M.; McKay, P. F.; Truitt, D. M.; *et al*. *J. Clin. Investig*. **2004**, *114*(9), 1334–1342.
19. Mesher, M. F.; Curtsinger, J. M.; Jenkins, M. In *Vaccine Adjuvants. Immunological and Clinical Principles*; Hackett, C. J., Harn, D. A., Eds.; Humana Press: Totowa, NJ, 2006; pp 49–69.
20. Grandjean-Laquerrière, A.; Tabary, O.; Jacquot, J.; *et al*. *Biomaterials* **2007**, *28*(3), 400–404.
21. Frayssinet, P.; Autefage, A.; Primout, I.; Guilhem, A.; Rouquet, N.; Bonnevialle, P. *J. Mater. Sci. Mater. Med*. **1991**, *2*, 217–221.
22. Frayssinet, P.; Mathon, D.; Rouquet, N. In *Bioceramic*, Giannini, S., Moroni, A., Eds.; Transtech Publications: Zurich, 2001; Vol. 13, pp 471–475.
23. Karsenty, G. *Genes Dev*. **1999**, *13*, 3037–3051.
24. Frayssinet, P.; Trouillet, J. L.; Rouquet, N.; Azimus, E.; Autefage, A. *Biomaterials* **1993**, *14*(6), 423–429.
25. Niyibizi, C.; Smith, P.; Mi, Z.; Robbins, P.; Evans, C. *Clin. Orthop. Relat. Res*. **2000**, *379S*, S126–S133.
26. Evans, C. H.; Robbins, P. D. *J. Bone Joint Surg*. **1995**, *77*(7), 1103–1114.
27. Laquerriere, P.; Grandjean-Laquerriere, A.; Killian, L.; *et al*. *Colloids Surf. B* **2004**, *33*(1), 49–55.

28. Laquerriere, P.; Grandjean-Laquerriere, A.; Guenounou, M.; Lauernt-Maquin, D.; Frayssinet, P.; Nardin, M. *Colloids Surf. B* **2003**, *30*(3), 207–213.
29. Laquerriere, P.; Grandjean-Laquerriere, A.; Jallot, E.; Laurent-Maquin, D.; Frayssinet, P.; Guenounou, M. *Biomaterials* **2003**, *24*(16), 2739–2747.
30. Frayssinet, P.; Laquarrière, P.; Kilian, L.; Grandjean Alexia, A.; Jallot, E.; Bonhomme, P. In *Bioceramics Surfaces – Behavior In Vitro and In Vivo*, 8th Meeting and Seminar on Ceramics, Cells and Tissues; Ravaglioli, A., Krajewky, A., Eds.; IRTEC-CNR: Roma, 2003.
31. Schenborn, E. T.; Goiffon, V. *Methods Mol. Biol.* **2000**, *130*, 135–145.
32. Yang, Y.-W.; Yang, J.-C. *Biomaterials* **1997**, *18*, 213–217.
33. Wurm, F. M.; Jordan, M. Genentech, Inc., U.S. Pat. 5,633,156, 1997, thérapie génique C12N 15/64, 435/172.3.
34. Jordan, M.; Schallhorn, A.; Wurm, F. M. *Nucleic Acid Res.* **1996**, *24*(4), 596–601.
35. Grosjean, F. Ph. D. Thesis, Ecole polytechnique fédérale de Lausanne, 2003.
36. Orrantia, E.; Chang, P. L. *Exp. Cell Res.* **1990**, *190*(2), 170–174.
37. Frayssinet, P.; Hardy, D.; Hanker, J.; Giammara, B. *Cells Mater.* **1995**, *5*(2), 125–138.
38. Frayssinet, P.; Schwartz, C.; Mathon, D.; Rouquet, N. In *Material Research Society Symposium Proceedings*; Materials Research Society: Warrendale, PA, 2000; Vol. 599, pp 3–13.
39. Heughebaert, M.; LeGeros, R. Z.; Gineste, M.; Guilhem, A. *J. Biomed. Mat. Res.* **1988**, *22*, 257–268.
40. Frayssinet, P.; Rouquet, N.; Mathon, D. *J. Biomed. Mater. Res. A* **2006**, *79*(2), 225–228.

1.116. Bioactive Ceramics: Cements

K Ishikawa, Kyushu University, Fukuoka, Japan

© 2011 Elsevier Ltd. All rights reserved.

1.116.1.	**Introduction**	268
1.116.1.1.	Bioactive Cement	268
1.116.1.2.	History of Bioactive Cement	268
1.116.1.3.	Advantages of Bioactive Cement	268
1.116.1.4.	Drawbacks of Bioactive Cement	269
1.116.2.	**Calcium Sulfate**	270
1.116.2.1.	History of Calcium Sulfate	270
1.116.2.2.	Setting Reaction of Calcium Sulfate	270
1.116.2.3.	Tissue Response to Calcium Sulfate	271
1.116.2.4.	Clinical Application of Calcium Sulfate	272
1.116.3.	**Portland Cement and MTA**	272
1.116.3.1.	History of Portland Cement and MTA	272
1.116.3.2.	Composition of Portland Cement and MTA	272
1.116.3.3.	Setting Reaction of Portland Cement and MTA	273
1.116.3.4.	Tissue Response to Portland Cement and MTA	273
1.116.4.	**Apatite Cement**	273
1.116.4.1.	Setting Reaction of TTCP–DCPA Type Apatite Cement	274
1.116.4.2.	Fast-Setting Apatite Cement	275
1.116.4.3.	Antiwashout Apatite Cement	277
1.116.4.4.	Injectability of Apatite Cement	277
1.116.4.5.	Mechanical Strength of Apatite Cement	278
1.116.4.6.	Porous Apatite Cement	280
1.116.4.7.	Premixed Apatite Cement	280
1.116.5.	**Brushite Cement**	281
1.116.5.1.	Setting Reaction of Brushite Cement	281
1.116.5.2.	Effect of Additive on Brushite Cement	281
1.116.5.3.	Tissue Response to Brushite Cement	282
1.116.6.	**Future Direction**	282
References		282

Glossary

Crystal A solid material whose constituent atoms, molecules, or ions are arranged in an orderly repeating pattern extending in all three spatial dimensions.

Cytotoxicity The quality of being toxic to cells.

Osteoblasts Mononuclear cells that are responsible for bone formation.

Periodontal In tissue around tooth.

Porogen An inorganic salt such as sodium chloride, crystals of saccharose, gelatin spheres or paraffin spheres used to create pores in a polymer.

Abbreviations

DDS	Drug delivery system
DFDBA	Demineralized freeze-dried bone allograft
ePTFE	Expanded polytetrafluoroethylene
EBA	Ethoxy benzoic acid
GTR	Guided tissue regeneration
HPMC	Hydroxypropyl methyl cellulose
MMA	Methyl methacrylate
MTA	Mineral trioxide aggregate
PMMA	Polymethyl methacrylate
POP	Plaster of Paris

1.116.1. Introduction

1.116.1.1. Bioactive Cement

The word 'bioactive' is defined in the dictionary as 'having a capacity to interact with a living tissue or system.' It has not been defined yet by any biomaterial related academic societies and, therefore, has been used with different meanings in history. Earlier, the term 'bioactive' was used for materials that are resorbed in the body. After the introduction of Bioglass®,[1] the meaning became synoymous with 'osteoconductive.' In this chapter, bioactive cement is defined as cement that shows osteoconductivity.

'Cement' also has different definitions; however, they are much clearer compared to the definition of 'bioactive.' In general, cement is defined as a fine inorganic powder mixture that sets and hardens independently. In this definition, cement is classified into two categories. One is air-setting cement or nonhydraulic cement and the other is hydraulic cement. In a narrow sense, cement indicates Portland cement, which is a hydraulic cement. A general definition of cement excludes organic materials as there are so many polymeric materials. However, combinations of methyl methacrylate (MMA) and polymethyl methacrylate (PMMA) have been used extensively in medical and dental clinics and thus, the broader definition of cement includes not only inorganic materials, but also organic materials that have hardening ability. Therefore, bioactive cements can be defined as inorganic or organic materials that set and harden independently and whose set mass exhibits osteoconductivity.

1.116.1.2. History of Bioactive Cement

Due to its important self-setting property, cement has been used clinically for a long time. Industrial cements were also used in medical and dental fields. Therefore, the history of bioactive cement runs close to the history of industrial cement. In other words, calcium sulfate or plaster has the oldest history as bioactive cement even though its bioactivity is limited. Portland cement is also used as medical cement for the reconstruction of bone defects. Interestingly, its use as a mineral trioxide aggregate (MTA) for dental treatment is one of the hottest topics in dentistry.

In 1976, Monma and Kanazawa[2] found that α-tricalcium phosphate (α-TCP; α-$Ca_3(PO_4)_2$) set and hardened to form calcium-deficient apatite ($Ca_9(HPO_4)(PO_4)_5(OH)$). LeGeros *et al.* reported calcium phosphate cement as a possible dental restorative material. In 1986, Brown and Chow[3,4] reported that a mixture of tetracalcium phosphate (TTCP: $Ca_4(PO_4)_2O$), and dicalcium phosphate anhydrous (DCPA: $CaHPO_4$) set to form hydroxyapatite (HAp: $Ca_{10}(PO_4)_6(OH)_2$). In 1987, Lemaitre and coworkers[5–7] found that a mixture of β-tricalcium phosphate (β-TCP: β-$Ca_3(PO_4)_2$) and monocalcium phosphate monohydrate (MCPM: $Ca(H_2PO_4)_2{\cdot}H_2O$) or phosphoric acid (H_3PO_4) set to form brushite or dicalcium phosphate dihydrate (DCPD: $CaHPO_4{\cdot}2H_2O$). These findings gave birth to the new history of bioactive cement.

1.116.1.3. Advantages of Bioactive Cement

The advantages of bioactive cements are apparently due to their self-setting property at low temperature or physiological temperature. First, the paste can set and harden, for example, at the bone defect. Therefore, the bone defect can be filled with the cement without leaving a gap between the cement and surrounding bone. In other words, the set cement and surrounding bone have a continuity between them, as shown in Figure 1.

This is extremely important as bone originates from cells, such as osteoblasts, and the migration of osteoblasts should not be prevented by discontinuity between the bone substitute and surrounding bone. Osteoblasts do not migrate if there is a gap between the surrounding bone and bone substitutes. In the case of sintered bioactive block-type ceramics, it is important to shape the ceramic so that it fits snugly into the bone defect to give good clinical results. However, this is very difficult to achieve (Figure 2).

Of course, bioactive cement can fit and follow the contour of the bone defect as the cement paste can be filled into the bone defect to set.

With respect to the continuity, it may be easier to fill the bone defect with granular type ceramics than with the block type. However, micromovement of the granules may prevent

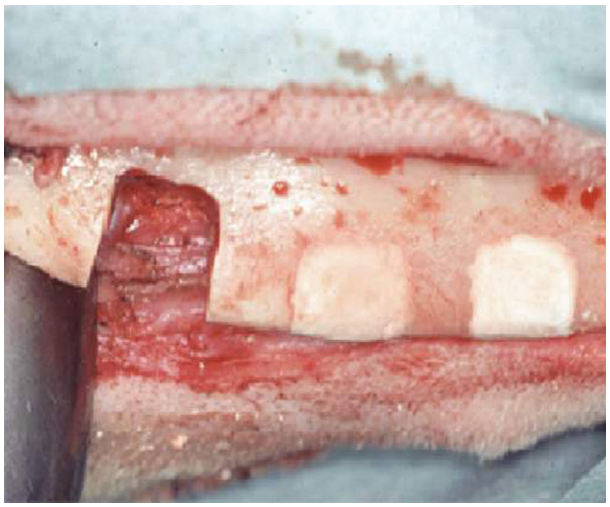

Figure 1 Example of bone defect reconstruction using bioactive cement. Bone defect can be filled with bioactive cement without leaving a gap between the bone and cement due to the cement's self-setting ability.

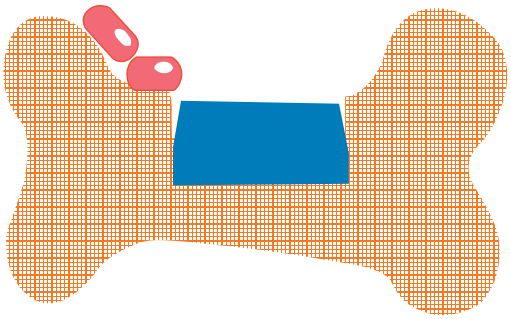

Figure 2 Illustrative view of bone defect reconstruction using the block form of bioactive ceramics. The block should fit into the bone defect to minimize the gap between the bone and the block.

the migration of bone cells. In addition, washout of the granules from the bone defect is a problem. In the case of cement, cement paste sets in the bone defect. Therefore, there is no need to worry about the micromovement or the washout of the set cement (Figure 3). Continuity of the cement and existing bone is presumed to be one of the reasons for the higher osteoconductivity of bioactive cement.

Second, the self-setting property of cement allows of minimum invasive surgery. As shown in Figure 4, the cement can be injected using a syringe.

Minimal invasive surgery has attracted much attention as it provides a better cosmetic result, less blood loss, less infection, a shorter hospital stay, and more effective rehabilitation.[8] However, it should be noted that filling the cement paste using a syringe has some drawbacks, at least with respect to the physical property of cement, including the washout of the paste (except for anti-washout-type cement), and lower mechanical strength of the set mass. Therefore, it is imperative that bioactive cement be used with a good understanding of its advantages and disadvantages and its underlying mechanism.

The third advantage of bioactive cement is that the setting reaction occurs at physiological temperature. As a result, apatite formed by the setting reaction of bioactive cement shows a low crystallinity similar to that of bone apatite. It is known that apatite with lower crystallinity shows higher osteoconductivity even though its mechanism has not been clearly understood till date.[9–11]

A fourth advantage of bioactive cement is that it can be used as a drug delivery system (DDS). Bioactive cement exhibits self-setting properties. Therefore, drug loading can be done by simply mixing the drug into the components of bioactive cement. Release of drug from the bioactive cement is skeleton type even though bioactive cements are known to exhibit adsorption abilities. The mechanical strength of the hardened cement could decrease slightly due to the increase in the porosity of the cement.[12] DDS can be also achieved by the incorporation of resorbable polymer that contains the drug for delivery.[13–15]

Yet another advantage is that bioactive cement can be used as a barrier membrane in guided tissue regeneration (GTR) or guided bone regeneration (GBR). In the case of GBR, bone is regenerated at the bone defect from the existing bone even though the bone defect is larger than critical size, the barrier membrane physically preventing connective tissue ingrowth into the bone defect. In the GBR, 'space making' and complete 'barrier' from the connective tissue are important so that the new bone can be formed at the space without invasion from the connective tissue. These can be achieved by the combination of bone substitute/grafted bone and bioactive cement, as shown in Figure 5. Also, connective tissue integration with the surface of the barrier membrane is important to prevent the separation of connective tissue from the defect. Due to the bioactive nature of bioactive cement, this requirement can also be achieved. Indeed, bone formation inside the bone defect as well as on the bioactive cement layer is facilitated due to the bioactive nature of the cement.

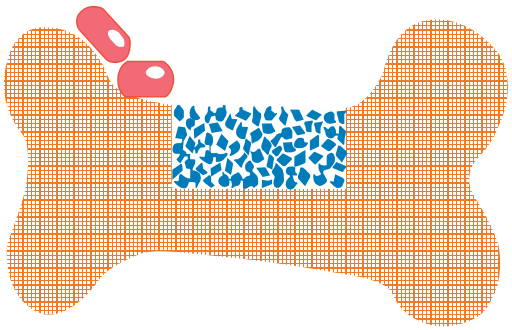

Figure 3 Illustrative view of a bone defect reconstruction using the granular form of bioactive ceramics.

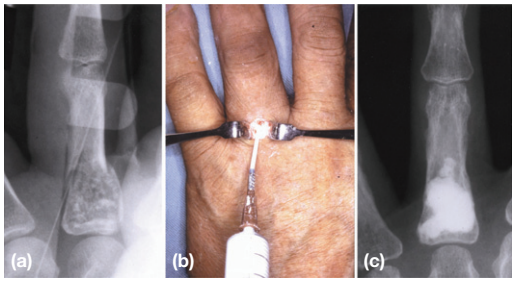

Figure 4 Example of the minimum invasive surgery using bioactive cement.

1.116.1.4. Drawbacks of Bioactive Cement

The main drawback of bioactive cement arises from the fact that the cement is not block but powder before setting. Unfortunately, calcium phosphate powders, including apatite, are known to cause an inflammatory response known as crystalline inflammatory response when they are exposed to soft tissue. Therefore, the setting reaction should be guaranteed for satisfactory clinical results. One of the causes for the disintegration of powder is the external stress before the setting reaction. Bioactive cement shows its inherent mechanical strength upon the setting reaction. As a result, the cement would not free the powder once it set. However, cement paste shows virtually no mechanical strength against external force. It should be pointed out that the cement should be free from external stress before its setting reaction.

Also, exposure of the paste to body fluid causes washout of the cement paste, except for the antiwashout-type or putty-type cement, which can also be used for haemostatic purposes. Washout becomes more problematic when the cement is injected using a syringe. When cement is injected with a syringe, a larger amount of liquid is usually employed than in

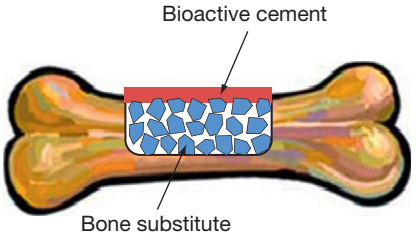

Figure 5 Schematic diagram of guided bone regeneration using bioactive cement instead of barrier membrane.

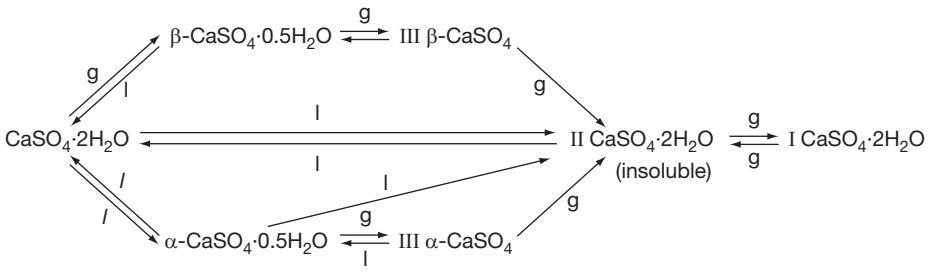

Figure 6 Polymorphism of calcium sulfate.

the packing method. This results in the cement being more sensitive to washout. Also, injected paste from the syringe has a larger area exposed to the body fluid. It should be emphasized that cement shows good tissue response only when it has set.

Another drawback is the lower mechanical strength. At present, the mechanical strength of bioactive cement is much lower compared with that of the sintered bioactive ceramics. Therefore, the cement can be used only in nonload-bearing areas.

1.116.2. Calcium Sulfate

1.116.2.1. History of Calcium Sulfate

Calcium sulfate has the longest history not only for its industrial use but also for its clinical use. The oldest use of calcium sulfate may have been for the hard-setting bandage.[16,17] Later in 1814, Hendrksz used calcium sulfate in the treatment of bone fractures.[16–18] Till date, many clinical *in vivo* and *in vitro* studies have been conducted and their results summarized in review papers.[18–22]

1.116.2.2. Setting Reaction of Calcium Sulfate

Gypsum is the name given to a mineral categorized as calcium sulfate mineral, and its chemical formula is calcium sulfate dihydrate, $CaSO_4 \cdot 2H_2O$. However, a broader definition includes all the calcium sulfates, including calcium sulfate hemihydrate, $CaSO_4 \cdot 0.5H_2O$, which is known as plaster or plaster of Paris (POP). **Figure 6** summarizes the polymorphism of calcium sulfate; 'g' indicates that the transformation reaction occurs in the gaseous phase, while 'l' indicates that the reaction occurs in the liquid phase.[23]

Calcium sulfate dihydrate and II-type calcium sulfate anhydrous, which has no solubility in water, can be taken as ore. When calcium sulfate dihydrate is heated, β- or α-form calcium sulfate hemihydrates are formed, as shown in eqn [I].

$$CaSO_4 \cdot 2H_2O \rightarrow CaSO_4 \cdot 0.5H_2O + 1.5H_2O \qquad [I]$$

The β-form calcium sulfate hemihydrates, whose density is 2.64 g cm^{-3}, are formed when $CaSO_4 \cdot 2H_2O$ is heated dry at round 120–130 °C. In contrast, the α-form, whose density is 2.76 g cm^{-3}, are formed when $CaSO_4 \cdot 2H_2O$ is heated hydrothermally at round 130 °C. At 190 °C, $CaSO_4 \cdot 0.5H_2O$ loses water and becomes calcium sulfate anhydrous, III-type α-$CaSO_4$ and β-$CaSO_4$. Calcium sulfate anhydrous taken as natural ore is stable. However, the calcium sulfate anhydrous formed by heating at 190 °C transforms to its hemihydrates easily by reacting with the humidity in the atmosphere. Further heating to 400 °C results in nonsoluble calcium sulfate anhydrous.

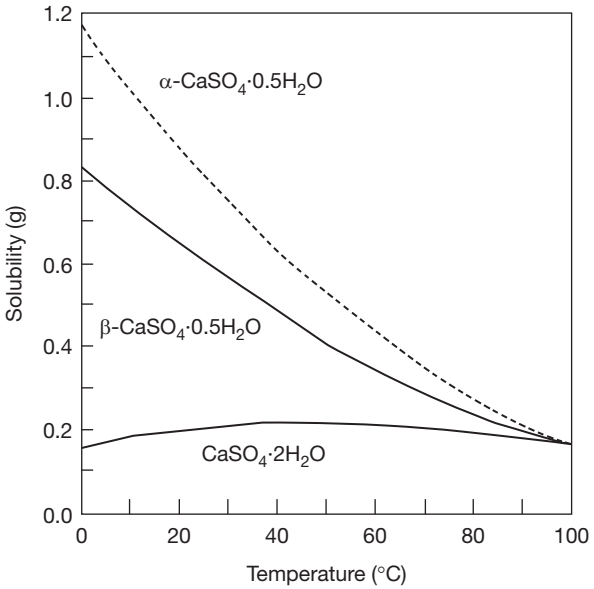

Figure 7 Solubility of α- and β-calcium sulfate hemihydrate and calcium sulfate dihydrate against temperature.

The setting and hardening reaction of calcium sulfate hemihydrate is a phase transformation from calcium sulfate hemihydrates to calcium sulfate dihydrate, and is known as a dissolution–precipitation reaction, as shown in eqns [II] and [III].

$$\alpha CaSO_4 \cdot 0.5H_2O + 1.5H_2O \rightarrow CaSO_4 \cdot 2H_2O + 17.2\,J\,mol^{-1} \qquad [II]$$

$$\beta CaSO_4 \cdot 0.5H_2O + 1.5H_2O \rightarrow CaSO_4 \cdot 2H_2O + 19.3\,J\,mol^{-1} \qquad [III]$$

In this exothermal dissolution–precipitation reaction, the solubility of $CaSO_4 \cdot 0.5H_2O$ and $CaSO_4 \cdot 2H_2O$ plays a very important role (**Figure 7**).

For example, the solubility of α-form calcium sulfate hemihydrate, $CaSO_4 \cdot 0.5H_2O$, and calcium sulfate dihydrate, $CaSO_4 \cdot 2H_2O$, is 0.92 g/100 ml and 0.2 g/100 ml at 20 °C as shown in eqns [IV] and [V], respectively. Therefore, when $CaSO_4 \cdot 0.5H_2O$ is mixed with water, Ca^{2+} and SO_4^{2-} ions, which are equivalent to 0.92 g $CaSO_4 \cdot 0.5H_2O$, are formed in 100 ml solution. If $CaSO_4 \cdot 2H_2O$ does not exist, the solution will be stable, that is, at equilibrium with $CaSO_4 \cdot 0.5H_2O$, and

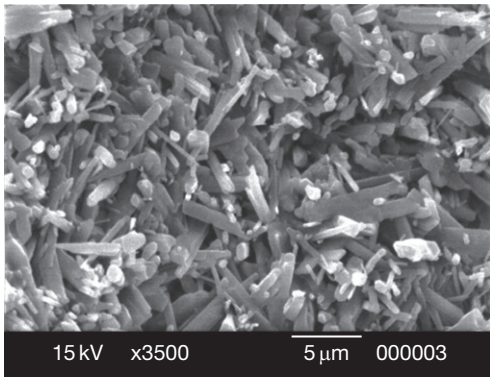

Figure 8 Scanning electron microscopic image of set calcium sulfate hemihydrate.

no further reaction occurs. However, $CaSO_4 \cdot 2H_2O$ exists, and its solubility is 0.2 g/100 ml at 20 °C, as shown in Figure 7.

$$CaSO_4 \cdot 0.5H_2O \rightleftarrows Ca^{2+} + SO_4^{2-} + 0.5H_2O \quad [IV]$$

$$CaSO_4 \cdot 2H_2O \rightleftarrows Ca^{2+} + SO_4^{2-} + 2H_2O \quad [V]$$

This means that the solution that is at equilibrium with $CaSO_4 \cdot 0.5H_2O$ is supersaturated with respect to $CaSO_4 \cdot 2H_2O$. Therefore, Ca^{2+} and SO_4^{2-}, which are equivalent to ~0.72 g $CaSO_4 \cdot 2H_2O$, will precipitate as $CaSO_4 \cdot 2H_2O$ crystals. The precipitation of Ca^{2+} and SO_4^{2-} ions from the liquid results in the undersaturation of the solution to $CaSO_4 \cdot 0.5H_2O$, thus leading to a further dissolution of $CaSO_4 \cdot 0.5H_2O$. In the actual reaction, the concentration of Ca^{2+} and SO_4^{2-} ions does not vary with time and is relatively constant. Anyway, this dissolution–precipitation reaction forms rod-like $CaSO_4 \cdot 2H_2O$ crystals, and the interlocking of these rod-like $CaSO_4 \cdot 2H_2O$ crystals forms the set mass, as shown in Figure 8.

As shown in Figure 7, the difference between the solubility of $CaSO_4 \cdot 0.5H_2O$ and $CaSO_4 \cdot 2H_2O$ becomes smaller with the increase in temperature. As a result of the smaller difference, $CaSO_4 \cdot 0.5H_2O$ does not set at high temperatures of around 100 °C.

Due to the crystal growth of calcium sulfate dihydrate, shown in Figure 8, the plaster exhibits setting expansion, as shown in Figure 9, where setting expansion and absorption expansion are plotted against time after the mixing. Setting expansion is caused by the crystal growth of calcium sulfate dihydrate, as explained earlier. On the other hand, absorption expansion or hygroscopic expansion is observed when the plaster is immersed in aqueous solution during its setting process. The different expansion is explained by the surface tension of water on the crystal surface. When the plaster is allowed to set in the atmosphere, the surrounding water is reduced, and the growing gypsum crystals impinge on the surface of the remaining water, whose surface tension inhibits outward crystal growth. When the water needed for the reaction is used up and the reaction is virtually complete, the growth of gypsum crystals stops, even in its inhibited form.

In contrast, if water is supplied during the setting process, the gypsum crystals can grow further. For absorption expansion, the additional water provided must be presented to the

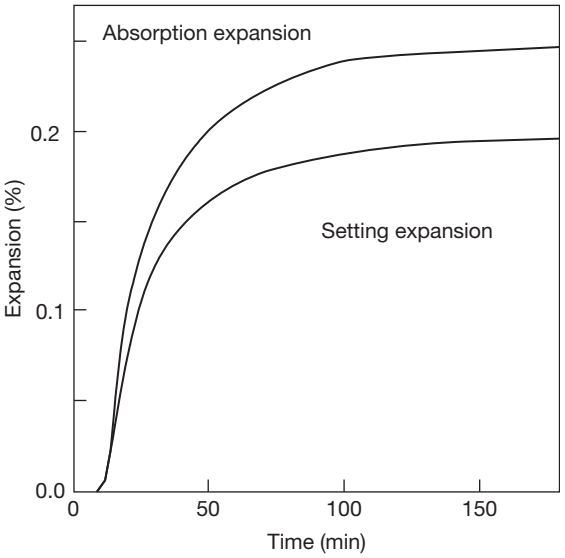

Figure 9 Example of setting and absorption expansion of plaster.

plaster during the setting. This is significantly different than the addition of more water to the premixed plaster.

The setting reaction of the plaster is affected by the additives or by contamination. Some proteins and biological macromolecules are known to retard the setting reaction by preventing full hydration of the hemihydrate, inhibiting seed crystal formation, and forming complexes with the seed crystals.[20,22,24] Contamination of the calcium sulfate with proteins may increase the setting time to 200 min.[25] Also, the set plaster dissolves more quickly in the presence of blood. To minimize the setting retardation and accelerated dissolution, setting accelerators such as NaCl, Na_2SO_4, KCl, and K_2SO_4 are used. However, preset calcium sulfate should be used if the setting cannot be guaranteed.

1.116.2.3. Tissue Response to Calcium Sulfate

Key properties of calcium sulfate are its rapid and complete resorption with minimal inflammatory response.[26–29] Of course, this is due to the high solubility of calcium sulfate dihydrate. Exposure of calcium sulfate paste to blood or body fluids results in significant extension of setting time along with lowered mechanical strength. In addition, washout and heat generation could cause clinical problems and therefore preset calcium sulfate is also used as a calcium sulfate bone substitute.

Replacement of calcium sulfate in bone occurs by the prevention of downgrowth of fibrous connective tissue and resorption of set calcium sulfate, which is followed by formation of bone.

Prevention of downgrowth of fibrous connective tissue or the sealing ability of calcium sulfate may be a common characteristic of cement, but it is an important characteristic, as proved by GTR.[30] The calcium sulfate then disappears from the bone defect. Although the length of resorption varies based on many factors, including the volume, location, accompanying diseases, and setting conditions, it takes ~5–8 weeks.[17,31,32]

Most of the resorption of calcium sulfate is caused by the physicochemical dissolution. However, resorption is accelerated in osteoporosis, indicating that other factors too are involved in the resorption of calcium sulfate.[33,34]

After the resorption of calcium sulfate, new bone is formed from adjacent host bone. The mechanism of bone formation after resorption of calcium sulfate has not been fully elucidated. It may be a complex of many factors. As stated, gradual resorption is thought to contribute to the similar system in GTR. In other words, resorbed calcium sulfate provides space for bone formation. Calcium sulfate also provides a surface to which osteoblasts can attach.[35] The Ca^{2+} that is released upon the dissolution of calcium sulfate can be used as a source of inorganic ions in the formation of new bone.[36,37] Elevated Ca^{2+} concentrations activate osteoblast genesis and function, and they may act as a stimulus in osteoblast differentiation.[20,22] Elevated calcium ion concentrations also exert a mitogenic effect on mesenchymal cells, mediated by the parathyroid/kidney/brain calcium-sensing receptor, PCaR. Similarly, osteoblast proliferation and differentiation, and nodulation of osteoid synthesis are stimulated by elevated calcium ion concentrations.[38]

It has also been found that granular HAp-like calcium phosphate mineral or resorbing calcium sulfate is deposited on the surface.[25,30] The thus-formed HAp-like calcium phosphate mineral may act as an osteoconductive 'trellis.'

1.116.2.4. Clinical Application of Calcium Sulfate

Pure calcium sulfate and its composites with calcium phosphates in the form of preset and cement are available. Many products are available, including Osteoset (Wright Medical Technology, Inc.), BoneGen (Bio-Lok Intl., Inc.), BonePlast (Biomet Inc.), and OsteoCure™ (Tomier Inc.).

Calcium sulfate can be used for the reconstruction of bone defects, to generate bone formation as a GTR membrane, for sinus augmentation, and for ridge preservation. For example, Aichelmann-Reidy evaluated the clinical efficacy of a combination of calcium sulfate as a binder and barrier, and demineralized freeze-dried bone allograft (DFDBA) to polytetrafluoroethylene (ePTFE) and DFDBA for the treatment of human periodontal intrabony defects in each of 19 patients with chronic periodontitis. It was found that calcium sulfate, when used as a binder and barrier in combination with DFDBA, supports significant clinical improvement in intrabony defects, evidenced in the form of reductions in probing depth, gains in clinical attachment level, and defect fill and resolution. The result was slightly better than the ePTTE group, but there was no significant difference.[39]

1.116.3. Portland Cement and MTA

1.116.3.1. History of Portland Cement and MTA

Cement made by heating lime stone and clay was used for large-scale construction of houses at Dadiwan, China around 5800–5400 BC. Many efforts were made to improve the properties of cement that consisted basically of calcined product of lime stone and clay. In 1824, Joseph Aspdin, a British bricklayer, named Portland cement and was granted a patent for the process of making this cement. Portland is derived from Portland stone, a type of building stone that was quarried on the Isle of Portland in Dorset, southern England in the eighteenth century. Due to the self-setting ability of Portland cement, it was used in the past in Egypt to fill bone defects.

MTA, on the other hand, was introduced in 1993 by Mahmoud Torabinejad at Loma Linda University as a dental endodontic cement.[40] The composition of MTA is basically the same as that of Portland cement, except that it has bismuth oxide (Bi_2O_3), which is used as a radiopaque agent. Its clinical application in dentistry has increased rapidly, and several products are available nowadays.

1.116.3.2. Composition of Portland Cement and MTA

There are many types of Portland cement and their compositions are different, depending on the types. However, the European Standard EN197.1 definition goes thus: "Portland cement clinker is a hydraulic material which shall consist of at least two-thirds by mass of calcium silicates ($3CaO{\cdot}SiO_2$ and $2CaO{\cdot}SiO_2$), the remainder consisting of aluminium- and iron-containing clinker phases and other compounds. The ratio of CaO to SiO_2 shall not be < 2.0. The magnesium content (MgO) shall not exceed 5.0% by mass." Tables 1 and 2 show the typical chemical composition of Portland cement and the key components in the Portland cement clinker, respectively. After the raw materials are mixed, they are heated in a cement kiln. The cement kiln rotates slowly with the temperature being

Table 1 Typical chemical composition of Portland cement

Oxide	*CaO*	*SiO_2*	*Al_2O_3*	*Fe_2O_3*	*MgO*	*SO_3*	*($Na_2O + K_2O$)*
Contents (%)	60–67	17–25	3–8	0.5–6	0.1–4	1–3	0.5–1.3

Table 2 Key component in Portland cement clinker

Name	*Composition*	*Code*	*Condition at clinker*	*Reaction rate*	*Heat of hydration ($J\ g^{-1}$)*
Tricalcium silicate	$3CaO{\cdot}SiO_2$	C_3S	Alite	Quick (h)	500
Dicalcium silicate	$2CaO{\cdot}SiO_2$	β-C_2S	Belite	Slow (day)	250
Tricalcium aluminate	$3CaO{\cdot}Al_2O_3$	C_3A	Aluminate	Immediate	850
Tetracalcium aluminoferrite	$4CaO{\cdot}Al_2O_3{\cdot}Fe_2O_3$	C_4AF	Ferrite	Quick (min)	420

increased gradually, to reach 1400–1450 °C in the end. Solid materials produced by the cement kiln stage are called clinker. The cement clinker is crushed, powdered, and added to calcium sulfate to retard the setting reaction, and this mixture is supplied as Portland cement.

The composition of MTA is the same, except for bismuth oxide (Bi_2O_3) which is used as a radiopaque agent. MTA-Angelus® contains 20 wt% bismuth oxide. ProRoot MTA contains 20 wt% bismuth oxide and 5% calcium sulfate.[41] The color of Portland cement is gray. Sometimes, however, gray is not preferred from the esthetic point of view. White MTA is available as ProRoot MTA (white), in which the amount of Fe_2O_3 is reduced.

1.116.3.3. Setting Reaction of Portland Cement and MTA

The setting and hardening reaction of Portland cement is caused by the hydration reaction of the components of the cement, listed in Table 2, with water. MTA shows the same reaction as Portland cement as their compositions are basically the same. For example, the hydration reactions of alite and belite are shown in eqns [VI] and [VII], respectively.

$$2Ca_3SiO_5 + 6H_2O \rightarrow Ca_3Si_2{\cdot}3H_2O + 3Ca(OH)_2 \quad [VI]$$

$$2Ca_2SiO_4 + 4H_2O \rightarrow Ca_3Si_2{\cdot}3H_2O + Ca(OH)_2 \quad [VII]$$

Based on this hydration reaction, amorphous calcium silicate hydrate and calcium hydroxide are formed, as shown in Figure 10, which results in setting and hardening.

1.116.3.4. Tissue Response to Portland Cement and MTA

Portland cement was used in Egypt for the reconstruction of bone defects, and it was discovered that the cement shows osteoconductivity. During the last decade, more attention has been paid to Portland cement, as MTA, in dental fields.[42–44] The composition of Portland cement and MTA is basically the same even though the latter contains bismuth oxide to provide greater radiopacity than dentin.[45] Also, some MTA products contain ~50% gypsum, when compared with the typical Portland cement, to accelerate the setting reaction. The clinical use of MTA in the endodontic field was approved by FDA in 1993.[46]

The advantage of MTA when compared with other dental cements includes its setting expansion. In the case of endodontic treatment, sealing ability, antibacterial effects, and biocompatibility are all equally important. When the cement expands, it increases the sealing ability and is thus beneficial in reducing the bacterial leakage. *In vitro* dye/fluid filtration method leakage studies as well as *in vitro* bacterial leakage studies have demonstrated that MTA allows for less microleakage than traditional dental cements when used as an apical restoration, in fracture repair, and in the treatment of immature apices.

The cytotoxicity evaluation of both freshly mixed and 24-h set MTA extract in human periodontal ligament fibroblasts showed that their cytotoxicity was less when compared to that of amalgam and EBA (ethoxy benzoic acid) cement.[47] It was also found that high pH value of freshly mixed MTA induced cell lysis in L-929 mouse fibroblasts and macrophage cell lines in direct contact with the MTA. However, set MTA demonstrated favorable biocompatibility, with no observed effect on cell morphology, as well as limited impact on cell growth at 72 h.

When the Portland cement and MTA were implanted in bilateral bone cavities prepared at the mandible of pigs, both materials showed the same histological results. At 2 weeks, no noticeable accumulation of inflammatory cells were observed. New bone apposition was observed in direct contact with the materials in both case in the ratio of more than 50% possibility. The remaining case shows new bone apposition on the materials through thin layer of fibrous connective tissue.

Similar histological results are reasonable as the compositions of Portland cement and MTA are almost the same. Although further evaluation of the degree of osteoconductivity is awaited, the usefulness of Portland cement and the need to modify Portland cement-based bioactive cement should be noted.

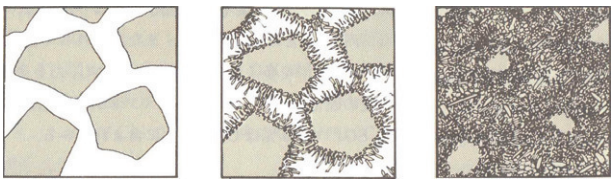

Figure 10 Schematic illustration of the setting and hardening reaction of Portland cement.

1.116.4. Apatite Cement

Although many names have been used so far, apatite cement or HAp cement is used for the calcium phosphate cements, which form apatite following the setting and hardening reaction.

Table 3 summarizes the calcium orthophosphates and their solubility product constants, and Figure 11 summarizes the phase diagram of calcium orthophosphate as a function of pH, using Ca concentration as the solubility index.

In neutral and alkaline regions, apatite is thermodynamically the most stable phase. Therefore, all calcium orthophosphates have the tendency to be precipitated as apatite when suitable conditions are applied. It should be noted that DCPD or brushite, $CaHPO_4{\cdot}2H_2O$ is the most stable phase thermodynamically in acidic regions when pH is 4.3 or lower. Under such conditions, the set cement would be brushite and not apatite.

In 1976, Monma and Kanazawa[2] reported that α-TCP set to form calcium-deficient HAp with Ca/P molar ratio of 1.5 when α-TCP was hydrated in water at 60–100 °C and pH between 8.1 and 11.4 as shown in eqns [VIII] and [IX].

$$3Ca_3(PO_4)_2 + H_2O \rightarrow 3Ca^{2+} + 2PO_4^{3-} + H_2O \quad [VIII]$$

$$3Ca^{2+} + 2PO_4^{3-} + H_2O \rightarrow Ca_9(HPO_4)(PO_4)_5(OH) \quad [IX]$$

Although this was the initial finding of apatite cement, long setting time prevented its clinical use for a long period. To accelerate the initial setting reaction, dicarboxylic acids, such as succinic acid or citric acids[48,49], were employed as liquid phase. In this method, the initial setting is not related to the formation of apatite but based on the formation of a chelate bonding between calcium compound and dicarboxylic acid. Unfortunately, dicarboxylic acid is known to inhibit apatite

Table 3 Calcium orthophosphates and their solubility product constants

Compound	*Abbreviation*	*Chemical formula*	*Ca/P*	*log*Ksp
Monocalcium phosphate monohydrate	MCPM	$Ca(H_2PO_4)_2{\cdot}H_2O$	0.5	Highly soluble
Monocalcium phosphate anhydrous	MCPA	$Ca(H_2PO_4)_2$	0.5	Highly soluble
Dicalcium phosphate dihydrate	DCPD	$CaHPO_4{\cdot}2H_2O$	1.0	6.59
Dicalcium phosphate anhydrous	DCPA	$CaHPO_4$	1.0	6.90
Octacalocium phosphate	OCP	$Ca_8H_2(PO_4)_6{\cdot}5H_2O$	1.33	96.6
α-tricalcium phosphate	α-TCP	$Ca_3(PO_4)_2$	1.5	
β-tricalcium phosphate	β-TCP	$Ca_3(PO_4)_2$	1.5	28.9
Hydroxyapatite	HAP	$Ca_{10}(PO_4)_6(OH)_2$	1.67	116.8
Fluoroapatite	FAP	$Ca_{10}(PO_4)_6F_2$	1.67	121
Tetracalcium phosphate	TTCP	$Ca_4(PO_4)_2O$	2.0	38–44

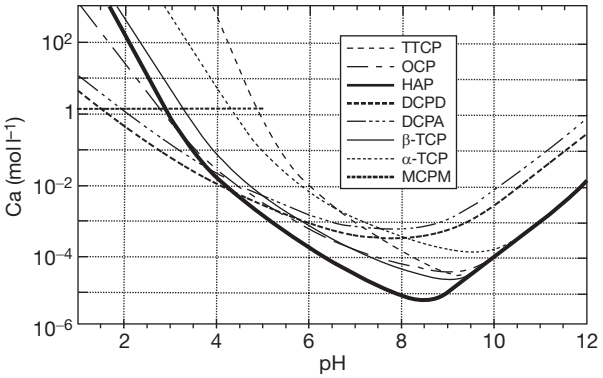

Figure 11 Solubility of Ca in various calcium phosphate compounds versus pH calculated from their solubility products.

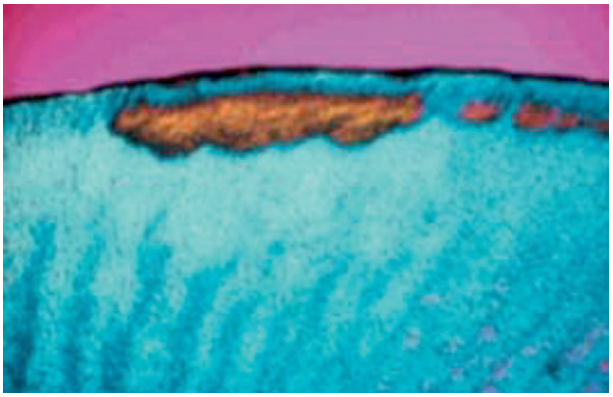

Figure 12 Typical example of subsurface decalcification.

formation. Therefore, compositional transformation from α-TCP to apatite is delayed even when compared to the apatite cement that employs distilled water. However, the amount of calcium phosphates is larger than that of dicarboxylic acid. In other words, dicarboxylic acid is required so that only the surface of the calcium phosphate salt reacts with the acid. Even after the chelate reaction, calcium phosphate under the surface of calcium phosphate particles continues to dissolve to supply Ca^{2+} and PO_4^{3-} ions. As all the dicarboxylic acid has already been used for the chelate reaction with the calcium phosphate salt surface, dissolved Ca^{2+} and PO_4^{3-} ions are supplied to the reaction medium, resulting in supersaturation with respect to Ca-deficient apatite, $Ca_9(HPO_4)(PO_4)_5(OH)$, and thus are precipitated as Ca-deficient apatite crystals. These crystals interlock with each other to harden. The setting reaction of α-TCP cement is exactly the same as that of gypsum when α-TCP cement is free from organic salts.

In 1982, LeGeros *et al.* reported calcium phosphate cement as possible dental restorative material. In 1986, Brown and Chow reported that a mixture of TTCP, and DCPA set within ~30–60 min at physiological temperature and formed apatitic products when mixed with aqueous solution.[3,4]

This apatite cement, which consisted of an equimolar mixture of TTCP and DCPA, was invented independent of the invention by Monma and Kanazawa. Brown and Chow studied the remineralization of decalcified enamel. In the early stage of dental caries, demineralization occurs not on the surface of enamel but below the enamel surface, as shown in Figure 12. At this stage, remineralization is possible if Ca^{2+} and PO_4^{3-} ions can be supplied properly. They chose a TTCP and DCPA mixture to supply Ca^{2+} and PO_4^{3-} ions and found that it set.

Commercially available apatite cements are summarized in Table 4.

1.116.4.1. Setting Reaction of TTCP–DCPA Type Apatite Cement

The setting reaction of apatite cement that consists of an equimolar TTCP and DCPA powder is also the same as that of apatite cement consisting of α-TCP or gypsum, that is, compositional transformation based on a dissolution–precipitation reaction, resulting in the interlocking of the formed apatite crystals. The main difference between the apatite cements consisting of α-TCP and TTCP–DCPA is that the former consist of single calcium phosphate powder whereas the latter consist of two calcium phosphate powders. The Ca/P ratio of TTCP is 2.0 and is higher than that of HAp, which has a Ca/P ratio of 1.67. On the contrary, Ca/P ratio of DCPA is 1.0 and is thus lower than that of HAp.

$$Ca_4(PO_4)_2O + H_2O \rightarrow 4Ca^{2+} + 2PO_4^{3-} + 2OH^- \quad [X]$$

$$CaHPO_4 \rightarrow Ca^{2+} + H^+ + PO_4^{3-} \quad [XI]$$

$$2Ca_4(PO_4)_2O + 2CaHPO_4 \rightarrow 10Ca^{2+} + 6PO_4^{3-} + 2OH^- \rightarrow Ca_{10}(PO_4)_6(OH)_2 \quad [XII]$$

In the case of two-component apatite cements, Ca^{2+} and PO_4^{3-} ions have to be supplied so that the apatite can be

Table 4 Example of the commercially available apatite cement and its composition

Registered name	*Powder*	*Liquid*	*Manufacturer*
Biopex®-R	α-TCP + TTCP + DCPD + HAP + $Mg_3(PO_4)_2$	Succinic acid, chondroitin sulfate and sodium hydrogen sulfite	Mitsubishi Materials
Primafix®	TTCP + DCPA	Sodium dextran sulfate sulfur 5	NGK Spark Plug Co
Cerapaste®	TTCP + DCPA		NGK Spark Plug Co
BoneSource®	TTCP(73%) + DCPA(27%)	Sodium phosphate solution	Stryker
Norian SRS®	α-TCP(85%) + $CaCO_3$(12%) + MCPM(3%)	Disodium phosphate solution	Synthes
Norian CRS®	α-TCP(85%) + $CaCO_3$(12%) + MCPM(3%)	Disodium phosphate solution	Synthes
Norian SRS® Fast Set Putty	Not documented	Not documented	Synthes
Norian SRS® Fast Set Putty	Not documented	Not documented	Synthes
Calcibon®	α-TCP(61%) + DCPA(26%) + $CaCO_3$(10%) + HAP(3%)	Disodium phosphate solution	Biomet
Mimix™	TTCP + α-TCP + $C_6H_5O_7Na_3{\cdot}2H_2O$	Citric acid	Biomet
QuickSet Mimix™	Not documented	Not documented	Biomet
Cementek®	TTCP + α-TCP + $Ca(OH)_2$ + sodium glycerophosphate	Acidic Ca–PO_4	Teknimed
Cementek® LV	TTCP + α-TCP + $Ca(OH)_2$ + sodium glycerophosphate + dimethylssiloxane	Acidic Ca–PO_4	Teknimed
α-BSM®	ACP(50%) + DCPD(50%)	Saline	ETEX
Biobon®[a]	ACP(50%) + DCPD(50%)	Saline	ETEX
Embarc®	ACP(50%) + DCPD(50%)	Saline	ETEX
KyphOs™	α-TCP(77%) + $Mg_3(PO_4)_2$(14%) + $MgHPO_4$(4.8%) + $ScCO_3$(3.6%)	3.5 mol l^{-1} diammonium hydrogen phosphate	Kyphon
Callos™	Not documented	Not documented	Skeletal Kinetics
Rebone	TTCP + DCPA	Water	Shanghai Rebone Biomaterials Co Ltd

[a]Biobon® is the trade name of α-BSM in Europe.

formed. Unfortunately, the dissolution rate of the calcium phosphate is different. When the dissolution rates of TTCP and DCPA are compared, TTCP dissolves quickly, while the dissolution rate of DCPA is slow. Table 5 summarizes the setting reaction of apatite cement consisting of TTCP and DCPA, with their different particle sizes.

As shown in this table, apatite cement that consists of small TTCP and large DCPA does not set. On the other hand, the mechanical strength of apatite cement increases in relation to the diameter ratio of TTCP/DCPA: apatite cement with the highest TTCP/DCPA diameter ratio or apatite cement with large TTCP and small DCPA affords the highest mechanical strength. The results clearly demonstrate that particle size regulation is very important. As stated above, TTCP dissolves faster than DCPA. Therefore, the combination of large TTCP and small DCPA, or TTCP with small specific surface area and DCPA with large specific area is necessary to minimize the dissolution rate of TTCP and DCPA. In the combination of small TTCP and large DCPA, TTCP dissolves quickly as it has a larger specific surface. Dissolution of TTCP supplies more Ca^{2+} ions and increased pH. At high pH, apatite is still the most stable phase themodynamically. Also the degree of supersaturation with respect to apatite is higher when compared to that at relatively lower pH. Too high a supersaturation results in the formation of amorphous calcium phosphate or small apatite crystals, which are too small to be interlocked with each other. The use of larger TTCP and smaller DCPA allows of proper supersaturation, and thus is the key to TTCP–DCPA type apatite cement.

In any case, the supply of Ca^{2+} and PO_4^{3-} by the dissolution of TTCP and DCPA (eqns [X] and [XI]) results in a supersaturated solution with respect to HAp. Therefore, Ca^{2+} and PO_4^{3-} are precipitated as HAp crystals. The precipitation reaction results in the decrease of the Ca^{2+} and PO_4^{3-} concentration, which elicits a further dissolution of the TTCP and DCPA. The dissolution–precipitation continues until all the TTCP and DCPA are consumed for the precipitation of HAp crystals. The precipitated HAp crystals interlock with each other to set and harden. As the mechanism of the setting and hardening reaction of apatite cement is exactly the same as that of gypsum, hardened apatite cement also shows similar morphology, as shown in Figure 13.

Table 5 Effects of particle size on the diametral tensile compressive strength of calcium phosphate cement consisting of tetracalcium phosphate and dicalcium phosphate anhydrous

Average particle diameter (μm)		*Ratio of the average particle diameter of TTCP/DCP*	*Compressive strength (MPa)*
TTCP	*DCPA*		
1.6	11.9	0.13	0 (no setting)
12.4	11.9	1.04	7.1 ± 1.0
1.6	0.9	1.78	21.8 ± 4.4
12.4	0.9	13.78	51.0 ± 4.5

1.116.4.2. Fast-Setting Apatite Cement

Apatite cement consisting of TTCP and DCPA has become clinically available. However, original apatite cement took

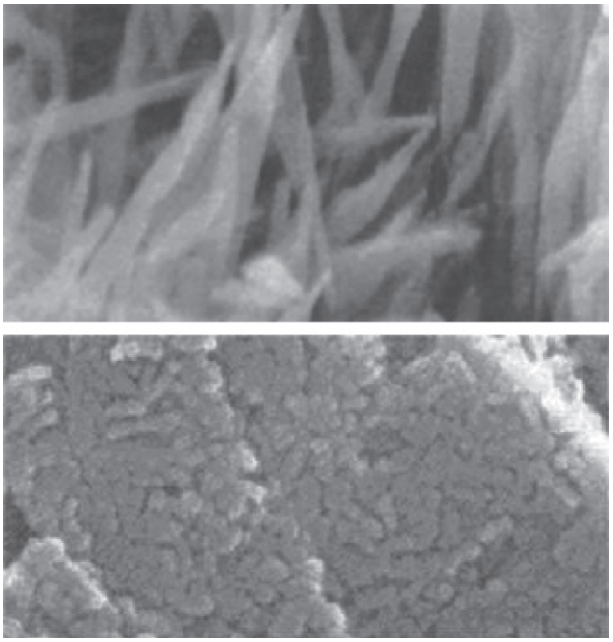

Figure 13 Typical scanning electron microscopic image of apatite cement consisting of tetracalcium phosphate and dicalcium phosphate anhydrous.

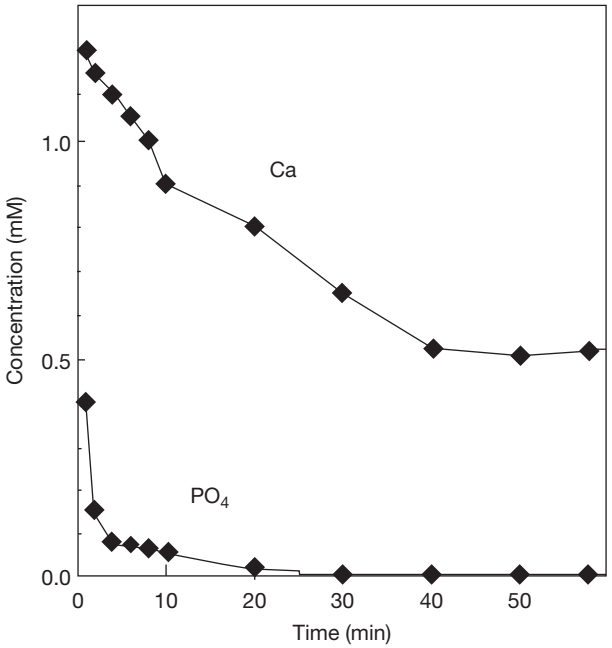

Figure 14 Example of the calcium and phosphate ion concentration in a suspension of apatite cement containing tetracalcium phosphate and dicalcium phosphate anhydrous. Calcium ion kept some concentration whereas phosphate concentration became less than the detection limit with time.

30–60 min to set even though the combination of large TTCP and small DCPA was employed. Setting time of 30–60 min is obviously too long for its clinical use. In addition, apatite cement shows excellent tissue response only when it sets, as stated in the tissue compatibility section. On the contrary, apatite cement causes an inflammatory response known as crystalline inflammatory response when the powders are released into soft tissue. Apatite cement paste can release powder when grazed with covering muscle. As the setting reaction of apatite cement is the same as the setting reaction of gypsum, a similar method can be applied to apatite cement to shorten the setting time. In the case of gypsum, for example, Na_2SO_4 is used as an accelerator. As stated earlier, rod-like crystals of $CaSO_4 \cdot 2H_2O$ are formed because the gypsum suspension is supersaturated with respect to $CaSO_4 \cdot 2H_2O$. Of course, Ca^{2+} and SO_4^{2-} ions have to be supplied for the solution to be supersaturated with respect to $CaSO_4 \cdot 2H_2O$. When Na_2SO_4 is introduced, it increases the ion product of $[Ca^{2+}][SO_4^{2-}]$ by increasing the concentration of SO_4^{2-} ions.

In the case of TTCP–DCPA apatite cement, a combination of large TTCP and small DCPA is employed to minimize the different dissolution rates. However, the dissolution of DCPA is still slower than the dissolution of TTCP, as shown in Figure 14.

In this figure, concentrations of Ca^{2+} and PO_4^{3-} ions in apatite cement suspension were plotted against time. As can be seen, concentration of PO_4^{3-} ions decreased significantly, while Ca^{2+} ion concentration showed a relatively stable value. In the case of cements with more than one component, addition of ions of less concentration is much more efficient. In the case of the TTCP–DCPA cement system, supply of PO_4^{3-} ions based on the dissolution of DCPA is the rate determining step. Note that further reduction of DCPA particle size is not practical as DCPA has already been ground to obtain the smallest particle size.

Table 6 Effects of liquid phase on the setting time of apatite cement that consists of TTCP and DCPA

Liquid	*Concentration (mol l^{-1})*	*Setting time[a] (min)*
Distilled water	–	30–60
$Na_{1.8}H_{1.2}PO_4$	0.2	5
$Na_{1.8}H_{1.2}PO_4$	0.6	5
$Na_{1.8}H_{1.2}PO_4$	1.0	5
$K_{1.8}H_{1.2}PO_4$	0.2	5
$K_{1.8}H_{1.2}PO_4$	0.6	5

[a]Setting time was measured using Vicat needle method at 37° and powder was mixed with liquid at the powder-to-liquid ratio of 4.

Table 6 summarizes the effect of neutral phosphate salt solution on the setting time of TTCP–DCPA apatite cement.[50]

For example, 0.2 mol l^{-1} $Na_{1.8}H_{1.2}PO_4$ aqueous solution was prepared by mixing 0.2 mol l^{-1} Na_2HPO_4 and 0.2 mol l^{-1} NaH_2PO_4 so that its pH became 7.4. Recently, Na_2HPO_4 salt has also been used instead of $Na_{1.8}H_{1.2}PO_4$, for simplicity. Na_2HPO_4 solution is slightly more alkaline than physiological pH, but there is no significant difference on its effect on setting time and the tissue response. As can be seen in Table 6, the setting time of TTCP–DCPA apatite cement shortened significantly from 30–60 to 5 min by employing neutral phosphate salt, regardless of the type and the concentration of neutral phosphate salts. Although the use of neutral phosphate salt solution is the principal method for the regulation of apatite cement, another approach based on the

dissolution– precipitation-based compositional transformation reaction is also possible to shorten the setting time. One such method is the introduction of apatite as seed crystals into the powder phase. Although the effect is limited when compared to the use of neutral phosphate salt solution in liquid phase, addition of the seed apatite into the powder phase allows of freedom for the regulation of liquid phase. Again, the shortening of the setting time, based on seed apatite addition, is the same as gypsum's setting reaction time. In the case of gypsum, the crystals formed by the dissolution–precipitation reaction are $CaSO_4 \cdot 2H_2O$. Therefore, $CaSO_4 \cdot 2H_2O$ is introduced in the powder phase to reduce the setting time. Of course, a shortened setting time is preferable for clinical use.

1.116.4.3. Antiwashout Apatite Cement

Upon the introduction of phosphate salts or dicarboxylic acid, apatite cement becomes less liable to be crumbled. Once apatite cement is hardened, it will not be crumbled. Therefore, apatite cements show excellent tissue response and good osteoconductivity. However, it should be noted that apatite cement takes time to set and the paste would be washed out if it came in contact with body fluid before its initial hardening reaction. Washout of the paste is a problem, especially when the paste is transferred into the bone defect using a syringe or tube as a larger specific surface is exposed to the body fluid.

Two reactions occur in the apatite cement placed in the bone defect, as shown in Figure 15.[51–54]

One is the compositional transformation to apatite based on the dissolution–precipitation reaction. This reaction is the key to the setting of apatite cement and can be accelerated by using neutral phosphate salt solution as the liquid phase. The other reaction is the penetration of the body fluid into the cement paste. This reaction is unavoidable and, unfortunately, induces the washout of the cement paste.

The overall reaction is decided as a result of the two reactions. Therefore, both acceleration of compositional transformation to apatite and inhibition of liquid penetration should be done for the apatite cement to acquire antiwashout property. As stated earlier, compositional transformation to apatite can be accerelated by employing a neutral phosphate salt. Therefore, the other method is the inhibition of body fluid penetration into the cement paste.

One of the effective methods to inhibit the penetration of body fluid into the cement paste is to employ a gelling agent.[51,53,55,56] Components of the cement powder have no bonding with the surrounding powder when the cement is free from the gelling agent. Therefore, body fluid can penetrate into the cement paste because of simple diffusion or osmotic pressure. On the contrary, when a gelling agent is introduced to the liquid phase, cement powder tends to have some bonding strength, even though the bonding strength is very weak. Second, body fluid cannot penetrate easily into the cement paste as the gelling agent that exists between the cement powder prevents such penetration.

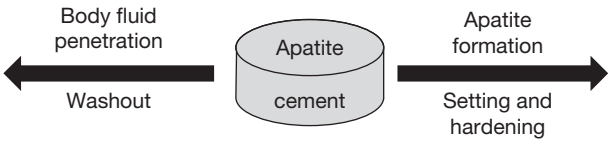

Figure 15 Illustration of the reaction of apatite cement paste when exposed to body fluid. Two different reactions proceeded. Right-hand side, setting and hardening reaction of the cement, which is closely related to cement conversion to apatite. Left-hand side, washout reaction induced by the penetration of body fluid into cement paste.

There are some requirements for the gelling agent to fabricate antiwashout-type apatite cement.

First, the gelling agent should have enough capability to prevent the body fluids from penetrating into the cement. Basically, all gelling agents prevent body fluid penetration into the cement. Therefore, concentration of the gelling agent is the factor.

Second, a gelling agent should enable some bonding between the calcium phosphate particles. For example, sodium alginate forms a weak bonding between the calcium phosphate particles by the formation of calcium alginate.

Third, the gelling agent should not show any toxic response, but instead should show good tissue compatibility. Tissue response depends on the concentration of the added gelling agent. Therefore, the effect of the added gelling agent on tissue response will be minimum when the amount of added gelling agent is small.

Fourth, the gelling agent should not decrease the mechanical strength. However, a slight decrease always occurs, at least with the gelling agents studied till date. Therefore, a slight decrease in mechanical strength should be accepted as acquired antiwashout property has higher priority.

Fifth, addition of gel should not decrease the handling property. With respect to this, the added gel seems to contribute to a better handling property.

Sixth, the gelling agent should not inhibit the conversion of cement to apatite. This is also difficult as basically all gelling agents inhibit the process of dissolution of the calcium phosphate powder as well as the diffusion of Ca^{2+} and PO_4^{3-}. Therefore, acceleration of apatite formation or the hardening process has to be employed at the same time.

Figure 16 summarizes the effect of the gelling agent (sodium alginate) on the antiwashout property of the paste, using the percentage of remaining cement as the index. As shown in this figure, fast-setting apatite cement or apatite cement using neutral sodium phosphate in its liquid phase acquires complete antiwashout property when the liquid phase contains 0.5% sodium alginate.

1.116.4.4. Injectability of Apatite Cement

As the names apatite cement or calcium phosphate cement indicate, the key advantage of the cement is its self-setting reaction. This enables the use of apatite cement with minimum invasive surgery, by using a syringe (Figures 4 and 17). In other words, bone defects can be filled with apatite cement using a syringe needle. In such case, injectability or how easily the cement paste can be injected from the syringe into the bone defect becomes an important factor.

Injectability is governed by many factors, including the syringe needle size. Surely, the use of a syringe with a larger needle diameter allows better injectability. However, the use of

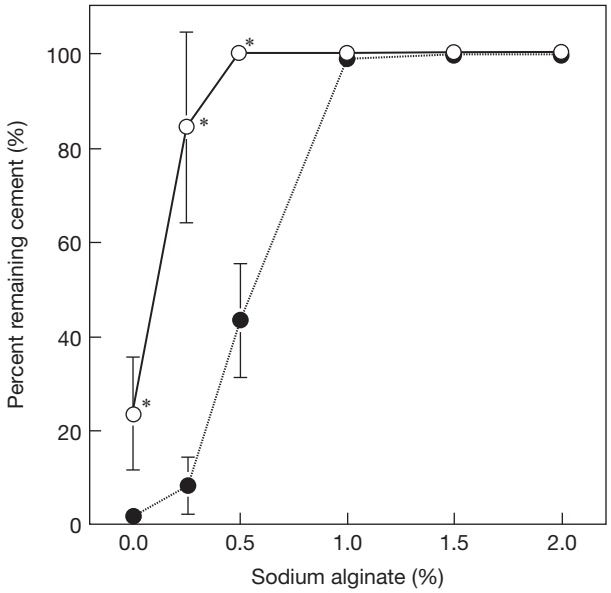

Figure 16 Effect of sodium alginate on the percentage of remaining cement paste after 24 h. The cement paste was immersed in serum at 37 °C immediately after mixing. Open circle employed fast-setting apatite cement as base cement. Closed circle employed conventional apatite cement as base cement.

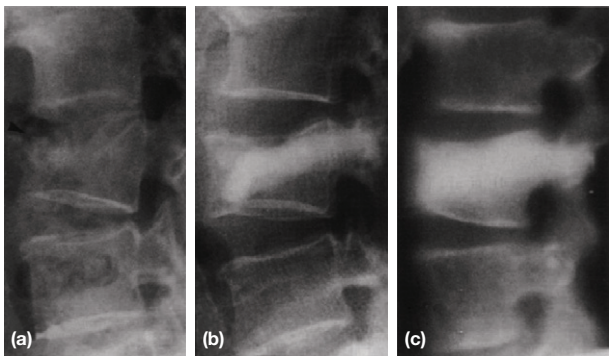

Figure 17 Clinical case of fixation of repositioned compression fracture with apatite cement. Osteoporotic compression fracture of the third lumbar vertebra shown in (a) was reconstructed with apatite cement paste as shown in (b) and (c). Photos courtesy of Kochi Medical University.

a syringe with too large a needle diameter results in less benefit for minimum invasive surgery.

Therefore, fabrication of apatite cement with better injectability is strongly desired. At first, viscosity of the paste should be regulated for the fabrication of injectable apatite cement. Apatite cement paste that is free from gelling agent or viscous additive is very difficult to be injected through a syringe with a small diameter. In such case, pushing the syringe piston results in the selective injection of the paste component from the syringe. In short, the liquid phase is selectively pushed out from the syringe, resulting in the apatite cement powder phase and a smaller liquid phase to remain. This selective injection happens because the syringe needle acts like a filter

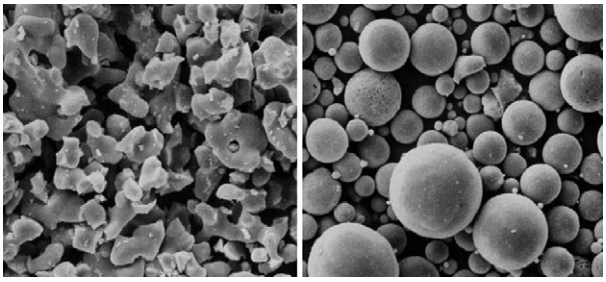

Figure 18 Irregular shape tetracalcium phosphate (left) and spherical tetracalcium phosphate (right) made using the plasma spherical method.

in the absence of a gelling agent. Basically, such a paste, that is, a paste with less liquid, is more difficult to be injected. Therefore, the cement powder phase remains uninjected in the syringe.

When gelling agent is added to the paste, less powder–liquid separation occurs and thus, cement paste is injected when some load is applied on the piston. As expected, the higher the viscosity, the less the powder–liquid separation, which results in higher injectability.

In the case of commercial products, concentration of the gelling agent cannot be regulated by the surgeon. On the other hand, the surgeon can change the liquid-to-powder mixing ratio. A higher liquid-to-powder mixing ratio results in a paste with higher injectability. It should be noted that higher liquid-to-powder mixing ratios result in lower mechanical strength and the paste becomes more sensitive to washout when exposed to body fluid. When apatite cement is injected into bone defect, the paste comes in contact with body fluid. Therefore, the liquid-to-powder mixing ratio should be minimum for better clinical results.

Injectability is also governed by the shape of the powder phase.[57,58] As can be expected, spherically shaped powder is easier to be injected when compared to powder of irregular shape. It is known that the mechanical strength is higher when using powder of irregular shape and the cement sets to form the core-matrix structure. However, the setting reaction of the apatite cement is a dissolution–precipitation reaction and thus, using a spherical powder has no drawback. Figure 18 shows the spherical TTCP, which is a component of TTCP–DCPA type apatite cement. The injectability of apatite cement containing spherical TTCP is known to be much easier when compared to that of apatite cement containing irregular shaped TTCP.

1.116.4.5. Mechanical Strength of Apatite Cement

The mechanical strength of apatite cement is governed by several factors, including powder size, powder-to-liquid mixing ratio, and the type of additives into the liquid and powder phases. Particle size may be the first factor to be regulated for a higher mechanical strength. As stated earlier in Section 1.116.4.2, combination of the particle size so that the supply of necessary ions for the precipitation of apatite is important. In the worst case, the combination of small TTCP and large DCPA would result in the cement not setting even when the Ca/P ratio of the powder was close enough to that of apatite, as shown in Table 6. Therefore, particle size should be regulated so that the particles can supply ions for apatite crystals to grow.

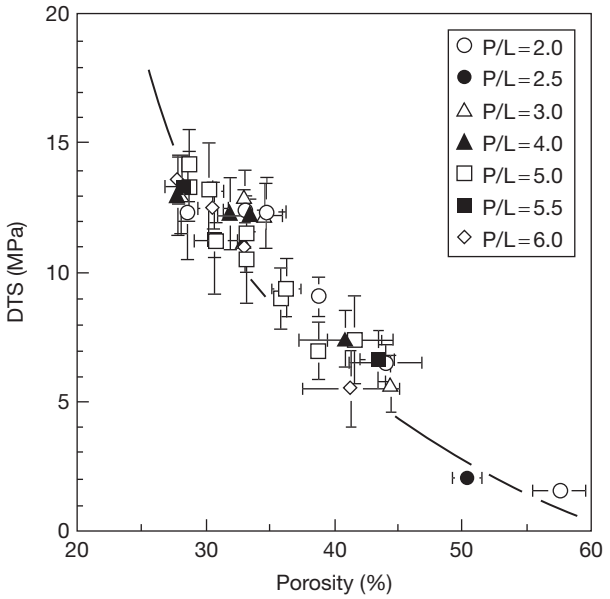

Figure 19 Relationship between wet DTS value and porosity of tetracalcium phosphate–dicalcium phosphate anhydrous type apatite cement specimen kept in an incubator at 37 °C and 100% relative humidity for 24 h.

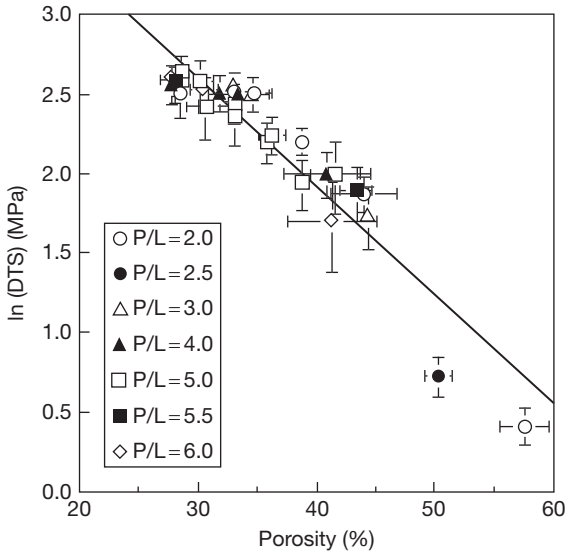

Figure 20 Relationship between logarithm of wet DTS value and porosity of tetracalcium phosphate–dicalcium phosphate anhydrous type apatite cement specimen kept in an incubator at 37 °C and 100% relative humidity for 24 h.

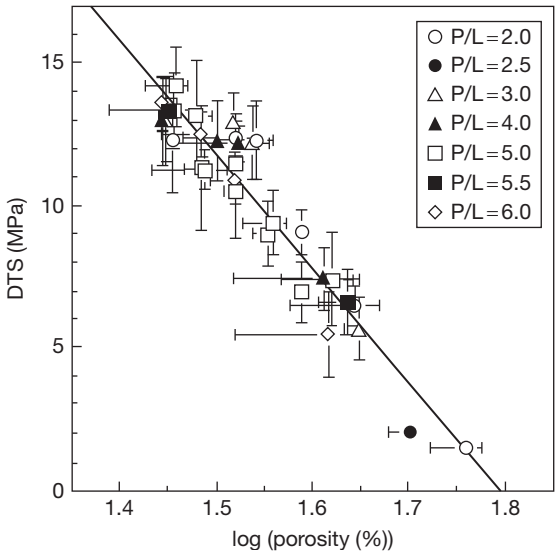

Figure 21 Relationship between wet diametral tensile strength value and the logarithm of the value for the porosity of the apatite cement specimen kept in an incubator at 37 °C and 100% relative humidity for 24 h.

Small particles are used for the component that has a limited dissolution rate. However, it should be noted that small particles result in low bulk density of the powder. In addition, small particles need more liquid to become wet and thus, a large liquid-to-powder mixing ratio becomes necessary to have good handling property. Unfortunately, a larger liquid-to-powder mixing ratio results in less interlocking of the precipitated crystals, which results in a lower mechanical strength.

It has been found that the mechanical strength of TTCP–DCPA type apatite cement is governed by the porosity of the set mass, as shown in **Figure 19**.[59]

An empirical equation for the relationship between the porosity and mechanical strength presented by Duckworth is shown in eqn [1].

$$S = S_0 \exp(-bP) \qquad [1]$$

where S is the observed mechanical strength of the porous material, S_0 is the ideal mechanical strength when there is no porosity, P is the porosity, and b is an empirical constant. By taking the natural logarithm of eqn. [1], eqn. [2] can be obtained:

$$\ln S = \ln S_0 - bP \qquad [2]$$

On the basis of the comparison of the equation obtained from **Figure 20** and eqn. [2], the ideal diametral tensile strength (DTS) value of the TTCP–DCPA type apatite cement is 103 MPa, which is approximately the same as the DTS value of sintered HAp.

Also, critical porosity can be calculated from eqn. [3].

$$S = Q \log (P_{cr}/P) = Q \log P_{cr} - Q \log P \qquad [3]$$

where S is the observed mechanical strength of the porous materials, Q is the strength of the skeleton (called the quality factor), P_{cr} is the critical porosity when S is equal to zero, and P is the porosity. Comparison of eqn [3] with the equation from **Figure 21** shows 62% as the critical porosity.

Addition of inorganic and/or organic materials into the components of apatite cement also affects the mechanical strength of apatite cement. For example, DTS increases when sodium hydrogen phosphate is added into the liquid phase as shown in **Figure 22**.[52]

Although the detailed mechanism of the increased mechanical strength has not been clarified, fast-setting calcium

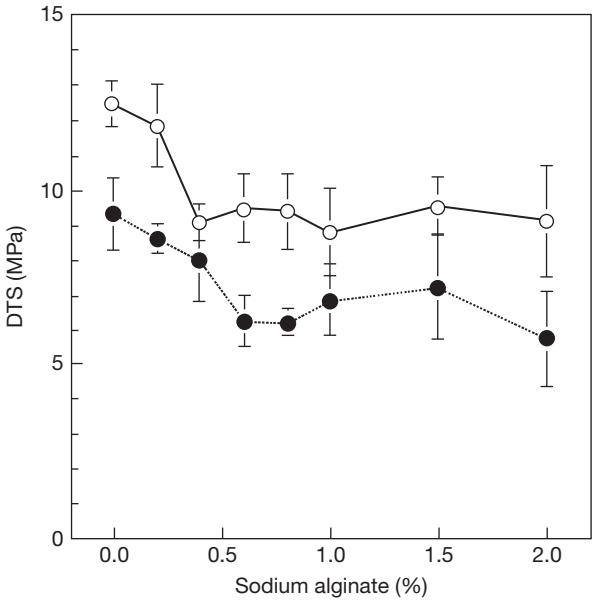

Figure 22 Effect of sodium alginate added to the liquid phase on the wet diametral tensile strength of tetracalcium phosphate–dicalcium phosphate anhydrous type apatite cement after being kept in an incubator at 37°C for 24 h. The powder-to-liquid mixing ratio is 4.0. Open circle: liquid contains 0.2 mol l^{-1} $Na_{1.8}H_{1.2}PO_4$. Close circle: distilled water.

phosphate cement or TTCP–DCPA type apatite cement containing sodium hydrogen phosphate in its liquid phase shows a higher mechanical strength than conventional apatite cement or apatite cement using distilled water as its liquid phase. Incorporation of additional phosphate may contribute to the increased mechanical strength.

On the other hand, organic component introduction usually decreases the mechanical strength. This may be due to the inhibitory effect of apatite crystal growth. For example, antiwashout-type apatite cement containing sodium alginate shows slightly decreased mechanical strength.

It should be emphasized that the addition of a gelling agent is required to obtain antiwashout properties. However, addition of a gelling agent prevents crystal growth and this results in a slight decrease in mechanical strength.

1.116.4.6. Porous Apatite Cement

The importance of macropores in HAp and other biomaterials to enhance bone ingrowth and implant fixation has been pointed out since the early 1970s.[60–63] Especially, macropores (>100 μm) allow ingrowth of bone tissue with Haversian systems and facilitate osteoconduction in the case of calcium phosphates.[64–70]

In the case of apatite cement, *in situ* macroporous fabrication is possible with the use of suitable porogens or macropore-forming materials. Key requirements of porogen are its complete dissolution after implantation and nontoxicity. Also, porogens are expected not to retard the setting reaction significantly. Several porogens have been studied to date, including sucrose, sodium hydrogen carbonate, disodium hydrogen phosphate, mannitol, polyglactin, poly(ε-caprolactone), poly (DL-lactic-*co*-glycolic acid), poly(L-lactic acid), and gelatin.[13–15,66–69,71–82] It should be noted that the mechanical strength of apatite cement decreases significantly with the introduction of macropores. For example, premixed apatite cement consisting of TTCP, DCPA, MCPM, glycerol, and hydroxypropyl methylcellulose (HPMC) shows 6.6 ± 1.8 MPa as flexural strength. However, the value decreases to 3.8 ± 0.3 and 0.7 ± 0.2 when 10% and 40% mannitol is added to the cement.[79] The introduction of bioresorbable fiber, however, contributes to increased mechanical strength. When 25% absorbable fiber (Vicryl) is introduced to the premixed cement, flexural strength increases to 11.7 ± 1.5 MPa. Mannitol-added cement also shows a higher value, 7.3 ± 1.8 MPa (10%) and 7.3 ± 1.8 (40%).[79] It should be noted that bioresorbable fiber acts not only as reinforcement for the cement but also as porogen.

As macropore is effective in tissue response, a balance should be achieved with mechanical strength for its clinical application.

Another aspect of porogen is the possibility that it can be used for drug delivery. So far, porogen has been introduced into the cement only to form macropores. As porogen dissolves at the implanted site, its use in drug delivery may increase the usefulness of porous apatite cement.

Porous apatite can also be made by gas foaming, using gases such as CO_2 and O_2 although problems of the excess gas, such as gas pocket formation and gas embolism need to be solved.[83] For the formation of CO_2, for example, NaH_2PO_4 and $NaHCO_3$ can be reacted.[84–86] For the formation of O_2, decomposition of hydrogen peroxide (H_2O_2) can be used.[87]

Also, surfactant such as sodium dodecyl sulphate[88] and albumen[89] can be used to form the pores in the paste. Because a relatively large amount of surfactant is necessary for the pore formation, tissue compatibility of the surfactant is the key requirement for this method.

1.116.4.7. Premixed Apatite Cement

Setting reactions of apatite cement are initiated when its powder phase is exposed to the liquid phase. Therefore, cement paste should be placed into the bone defect before the setting reaction. Homogeneous mixing and mixing methods that do not to introduce pores are required for a higher mechanical strength. Unfortunately, they are not so easy. Also, the mixing process is a problem for the clinician. In addition, as a ground rule, the powder should be kept out of the operation room to keep the room clean.

Therefore, premixed cement that sets only after the paste has been placed into the bone defect is desired. Premixed cement was initially introduced by Sugawara,[90] and improved later.[79,91,92] Basically, premixed cement consists of (a) calcium phosphate setting components, such as TTCP and DCPA; (b) nonaqueous, but water-miscible, liquid carriers, such as glycerol, poly(ethylene glycol), and poly(propylene glycol); (c) gelling agents, such as HPMC; and (d) hardening accelerators, such as sodium hydrogen phosphate.

Nonaqueous, but water-miscible, liquid is the main component in premixed apatite cement. Due to its nonaqueous property, cement powder is stable even when it is mixed with the liquid. Upon exposure to water, the nonaqueous

solution–water exchange occurs and the cement powder is then exposed to water. Once the cement powder is exposed to water, both TTCP and DCPA dissolve and supply Ca^{2+} and PO_4^{3-}; then, the setting and hardening reaction is initiated. Of course, the exchange of the nonaqueous solution and water cannot occur in the blink of an eye but takes some time. Also, most of the nonaqueous solution adsorbed on the surface of the TTCP and DCPA powder inhibits their dissolution and HAp formation. Therefore, an accelerator is required for premixed apatite cement. Usually, sodium hydrogen phosphate is used as the accelerator due to its neutral pH.[50–52] Also, MCPM is known to accelerate the setting reaction of TTCP–DCPA type apatite cement.[79]

1.116.5. Brushite Cement

1.116.5.1. Setting Reaction of Brushite Cement

Brushite or DCPD is the most thermodynamically stable phase when pH is 4.2 or lower (**Figure 1**). Therefore, a mixture of calcium phosphate powder that supplies Ca^{2+} and PO_4^{3-} ions, and in which the pH of the paste is 4.2 or lower could be brushite cement. One of the key components of brushite cement is β-TCP, and thus, sometimes, brushite cement is also called β-TCP cement. Brushite cement was invented by Lemaitre and coworkers.[5–7] Brushite cement basically consists of β-TCP and MCPM or H_3PO_4 and brushite is formed in the setting reaction, as shown in eqn [XIII].

$$\beta\text{-}Ca_3(PO_4)_2 + Ca(H_2PO_4)_2\cdot H_2O + 7H_2O \rightarrow 4CaHPO_4\cdot 2H_2O \quad [XIII]$$

MCPM is a very acidic calcium phosphate and supplies an acidic environment so that the pH of the cement paste becomes 4.2 or lower. Therefore, not apatite but brushite becomes the most thermodynamically stable phase, and thus brushite is formed. The setting reaction of brushite cement is also a compositional change based on a dissolution–precipitation reaction. Upon mixing with water, MCPM dissolves to supply Ca^{2+}, HPO_4^{3-}, and an acidic condition, as shown in eqn [XIV]. The dissolution occurs immediately after mixing as MCPM is a highly soluble salt. This is one of the main differences between apatite cement whose dissolution reaction takes some time and thus, its setting time is longer when compared to brushite cement. β-TCP does not dissolve immediately even when exposed to water, but β-TCP dissolves immediately in the acidic environment supplied by the dissolution of MCPM, as shown in eqn [XV]. The dissolution of β-TCP consumes protons resulting in the increase of pH, which induces precipitation of brushite, as shown in eqn [XVI],[93] and the precipitated brushite bridges the remaining β-TCP.

$$Ca(H_2PO_4)_2\cdot H_2O \rightarrow Ca^{2+} + 2H^+ + 2HPO_4^{3-} + H_2O \quad [XIV]$$

$$Ca_3(PO_4)_2 + 2H^+ \rightarrow 3Ca^{2+} + 2HPO_4^{3-} \quad [XV]$$

$$Ca(H_2PO_4)_2\cdot H_2O + Ca_3(PO_4)_2 + 7H_2O \rightarrow 4Ca^{2+} + 4HPO_4^{3-} + 8H_2O \rightarrow 4CaHPO_4\cdot 2H_2O \quad [XVI]$$

The use of phosphoric acid instead of MCPM shows asimilar but simpler setting reaction, as shown in eqn [XVII].

$$H_3PO_4 \rightarrow 2H^+ + HPO_4^{3-} \quad [XVII]$$

$$Ca_3(PO_4)_2 + 2H^+ \rightarrow 3Ca^{2+} + 2HPO_4^{3-} \quad [XVIII]$$

$$H_3PO_4 + Ca_3(PO_4)_2 + 6H_2O \rightarrow 3Ca^{2+} + 3HPO_4^{3-} \rightarrow 3CaHPO_4\cdot 2H_2O \quad [XIX]$$

In contrast to apatite cement, which showed a long setting time at the time of initial invention, brushite cement exhibited a rapid setting time even at the time of initial invention. The setting time was 30 s from the initiation of mixing.[6] This may have been due, at least in part, to the higher solubility of calcium phosphate under acidic conditions. Also, the mechanical strength of brushite cement was lower when compared to that of apatite cement. DTS of the brushite cement was low (<1 MPa) and decreased upon prolonged aging in 100% relative humidity at 37–40 °C.[6]

Commercially available brushite cements are summarized in **Table 7**.

1.116.5.2. Effect of Additive on Brushite Cement

Due to its rapid setting time, a retarder was added to the brushite cement. One of the additives is pyrophosphate, which is known to inhibit the nucleation and crystal growth of orthocalcium phosphate.[94] For example, 20 wt% addition of calcium pyrophosphate ($Ca_2P_2O_7$) results in a prolonged setting time: ~5 min. However, the addition of calcium pyrophosphate results in a slight decrease in mechanical strength. Calcium sulfate hemihydrate also prolongs the setting time to ~7 min when 20% of it is added. Interestingly, addition of calcium sulfate hemihydrate with 5 wt% calcium pyrophosphate results in a significant increase in mechanical strength. DTS of calcium sulfate hemihydrate with 5 wt% calcium pyrophosphate shows 3 MPa, which is three times larger when compared to DTS of additive free brushite cement.

Table 7 Example of the commercially available brushite cement and its composition

Registered name	*Powder*	*Liquid*	*Manufacturer*
ChronOS™ Inject	β-TCP(73%) + MCPM(21%) + $MgHPO_4\cdot 3H_2O$(5%) + $MgSO_4$(<1%) + $Na_2H_2P_2O_7$(<1%)	0.5% Sodium hyaluronate Sodium dextran sulfate sulfur 5	Norian
Eurobone®	β-TCP(98%) + $Na_4P_2O_7$(2%)	3 mol l^{-1} H_3PO_4 + 0.1 mol l^{-1} H_2SO_4	Kasios
VitalOs	Component 1: β-TCP(1.34 g) + $Na_2H_2P_2O_7$(0.025 g) 0.05 mol l^{-1} pH7.4 PBS Component 2: MCPM (0.78 g) + $CaSO_4\cdot 2H_2O$ + 0.05 mol l^{-1} H_3PO_4		CalciOs

Citrate and magnesium ions are also known to retard the fast-setting reaction.[95,96] The effect of a retarder was also confirmed by thermal analysis.[97]

When 15 wt% calcium sulfate hemihydrate and 5 wt% calcium pyrophosphate was added to brushite cement, small needle-like crystals were formed instead of rather large tabular brushite crystals. The small needle-like crystals interlocked with the larger β-TCP particles. Although the contribution of calcium sulfate hemihydrate, which is well known as POP, to mechanical strength has not been quantified yet, small brushite crystals are also thought to contribute to higher mechanical strength.

1.116.5.3. Tissue Response to Brushite Cement

The key tissue response of brushite cement is its rapid and complete resorption, which is similar to that of calcium sulfate. Initially, brushite cement attracted less attention than apatite cement because it is not brushite but apatite that is the inorganic component of the bone. Also, the weaker mechanical strength and rapid physicochemical dissolution of brushite are thought to be inferior to those of apatite cement. However, *in vitro* and *in vivo* studies have demonstrated that brushite cement was generally well tolerated by the bone and soft tissue environment.[98,99] When bone defect is reconstructed using brushite cement, the brushite dissolves slightly as the body fluid is undersaturated with respect to brushite or DCPD. Dissolution of brushite, which is the acidic calcium phosphate, reduces the pH, and this results in the activation of macrophage. Then, the phagocytic resorption of the hardened brushite cement is effected by mononuclear macrophage. After the phagocytic resorption, carbonate apatite is formed at the bone defect. In contrast to the phagocytic response to brushite, osteoclastic resorption becomes dominant after brushite is converted to carbonate apatite.[98]

It should be noted that the reaction of brushite cement is different up to the implant location. When brushite cement was used for the reconstruction of metaphyseal defects, part of the brushite cement was converted to carbonate apatite in 2 weeks. In contrast, brushite cement used for the reconstruction of diaphyseal defect begins to convert to another calcium phosphate phase only in 4 weeks. Although the mechanisms of these different reactions have not been understood to date, decreased vascular supply in the case of cements in the diaphysis compared with cements implanted in the metaphysis may be one of the reasons. It is assumed that a more active metabolic state, more blood flow, and a higher cement-specific area may be favorable for the higher conversion rate of brushite to carbonate apatite.

1.116.6. Future Direction

The invention of bioactive cements is one of the breakthroughs for biomaterials aimed at the reconstruction of bone defects. Although newly developed bioactive cement provides a number of benefits to patients, much remains to be studied. Future studies should be conducted with a full understanding of the clinical needs and of the findings from previous studies. Obviously, development and improvement of biomaterials should be the primary focus for the benefit and well-being of the patients. Clinicians have lots of information regarding the bioactive cements to be developed and how the current bioactive cements can be improved. MTA, one of the hottest topics in dentistry, may be a good example. In endodontic treatment, the cement's sealing ability and its antibacterial effects are important, as well as its biocompatibility. MTA, which has the same composition as Portland cement, except for the inclusion of radiopaque agent, was found to be ideal for endodontic cement. Initially, gray-colored Portland cement was used as it was. However, gray is not preferable for aesthetic reasons, so white MTA was developed by reducing the content of Fe_2O_3. This modification can be done easily as endodontic cement does not require high mechanical strength. However, this improvement cannot be made without an understanding of the needs of the clinician.

A number of improvements have also to be made in the properties of apatite cements. One of them may be increasing their mechanical strength for wider clinical applications. Some increase could be made possible by the introduction of the already established calcium sulfate technology. Further increase could also be possible by introducing the already established Portland cement technology. In other words, the core-matrix structure observed in Portland cement may be required as the mechanical strength of simple apatite cement is basically governed by the porosity. Not only higher mechanical strength but also flexibility may be preferable for apatite cement. To overcome the brittleness, a composite with collagen is being attempted. However, the current study level may still be far from inventing the ideal cement. Introduction of the concept of 'itacolumite,' which is known as flexible or bendable stone, may be interesting. In such a scenario, future bioactive cement study should be based not only on the harmonious collaboration of material scientists and clinicians, but also on an understanding of the way of nature.

References

1. Hench, L. L.; Splinter, R. J.; Allen, W. C.; Greenlee, T. K. *J. Biomed. Mater. Res.* **1971**, *2*, 117–141.
2. Monma, H.; Kanazawa, T. *Yogyo-Kyokai-Shi* **1976**, *84*, 209–213.
3. Brown, W. E.; Chow, L. C. In *Cement Research Progress*; Brown, P. W., Ed.; American Ceramic Society: Westerville, 1986 p 351.
4. Brown, W. E.; Chow, L. C. Combination of sparingly soluble calcium phosphate cements in slurries and paste as mineralizers and cements. US Patent 4,612,059, 1986.
5. Lemaitre, J.; Mirtchi, A.; mortier, A. *Sil. Ind. Ceram. Sci. Technol.* **1987**, *52*, 141–146.
6. Mirtchi, A. A.; Lemaître, J.; Munting, E. *Biomaterials* **1989**, *10*(9), 634–638.
7. Mirtchi, A. A.; Lemaitre, J.; Terao, N. *Biomaterials* **1989**, *10*(7), 475–480.
8. Goldstein, W. M.; Branson, J. J.; Berland, K. A.; Gordon, A. C. *J. Bone Joint Surg. Am.* **2003**, *85A*(S4), 33–38.
9. Somiya, M.; Niwa, S.; Sawai, K.; *et al. Chubuseisaishi* **1981**, *24*, 15–19.
10. Somiya, M.; Niwa, S.; Sawai, K.; *et al. Chubuseisaishi* **1981**, *24*, 1267–1271.
11. Somiya, M.; Niwa, S.; Sawai, K.; *et al. Chubuseisaishi* **1982**, *25*, 837–839.
12. Takechi, M.; Miyamoto, Y.; Ishikawa, K.; Nagayama, M.; Kon, M.; Asaoka, K.; Suzuki, K. *J. Biomed. Mater Res.* **1998**, *39*(2), 308–316.
13. Plachokova, A.; Link, D.; van den Dolder, J.; van den Beucken, J.; Jansen, J. A. *J. Tissue Eng. Regen. Med.* **2007**, *1*, 457–464.
14. Ruhe, P. Q.; Hedberg, E. L.; Padron, N. T.; Spauwen, P. H.; Jansen, J. A.; Mikos, A. G. *J. Bone Joint Surg. Am.* **2003**, *85*, 75–81.
15. Ruhe, P. Q.; Boerman, O. C.; Russel, F. G. M.; Spauwen, P. H.; Mikos, A. G.; Jansen, J. A. *J. Control. Release* **2005**, *106*, 162–171.

16. van Rens, T. J. G. *Acta Orthop. Belg.* **1987**, *53*, 34–39.
17. Tay, B. K.; Patel, V. V.; Bradford, D. S. *Orthop. Clin. North Am.* **1999**, *30*(4), 615–623.
18. Pietrzak, W. S.; Ronk, R. *J. Craniofac. Surg.* **2000**, *11*(4), 327–333.
19. Peltier, L. F. *Clin. Orthop. Relat. Res.* **2001**, *382*, 3–5.
20. Thomas, M. V.; Puleo, D. A. *J. Biomed. Mater. Res. Part B Appl. Biomater.* **2009**, *88B*, 597–610.
21. Thomas, M. V.; Puleo, D. A.; Al-Sabbagh, M. *J. Long Term Eff. Med. Implants* **2005**, *15*(6), 599–607.
22. Thomas, M. V.; Puleo, D. A. *J. Biomed. Mater. Res. B Appl. Biomater.* **2009**, *88*(2), 597–610.
23. Sekiya, M. *Gypsum*; Tokyo, Japan Kasai Press, 1964.
24. Ricci, J. L.; Weiner, M. J. In *Bioceramics and Their Clinical Application*; Kokubo, T., Ed.; Woodhead Publishing Ltd: Cambridge, UK, 2008; p 302.
25. Ricci, J. L.; Alexander, H.; Nadkarni, P.; *et al*. In *Bone Engineering*; Davies, J. E., Ed.; Em2 Inc: Toronto, 2000; pp 332–344.
26. Orsini, G.; Ricci, J.; Scarano, A.; *et al*. *J. Biomed. Mater. Res. B Appl. Biomater.* **2004**, *68*(2), 199–208.
27. Peltier, L. F.; Bickel, E. Y.; Lillo, R.; Thein, M. S. *Ann. Surg.* **1957**, *146*, 61–69.
28. Bell, W. H. *Oral Surg. Oral Med. Oral Pathol.* **1964**, *17*, 650–657.
29. Shaffer, C. D.; App, G. R. *J. Periodontol.* **1971**, *42*, 685–690.
30. Coetzee, A. S. *Arch. Otolaryngol.* **1980**, *106*, 405–409.
31. Bell, W. H. *Oral Surg. Oral Med. Oral Pathol.* **1964**, *17*, 650–657.
32. Mukopadhayn, B.; Mehtu, M. J. *Indian J. Surg.* **1957**, *6*, 438–440.
33. Wang, M. L.; Massie, J.; Perry, A.; Gafin, S. R.; Kim, C. W. *Spine J.* **2007**, *7*, 466–474.
34. Wang, M. L.; Massie, J.; Allen, R. T.; Lee, Y. P.; Kim, C. W. *Spine J.* **2007**, *8*, 349–350.
35. Sidqui, M.; Collin, P.; Vitte, C.; *et al*. *Biomaterials* **1995**, *16*, 1327–1332.
36. Bahn, S. L. *Oral Surg. Oral Med. Oral Pathol.* **1966**, *21*, 672–681.
37. Lebourg, L.; Biou, C. *Semin. Hop Paris* **1961**, *37*, 1195–1197.
38. Yamauchi, M.; Yamaguchi, T.; Kaji, H.; Sugimoto, T.; Chihara, K. *Am. J. Physiol. Endocrinol. Metab.* **2005**, *288*(3), E608–E616.
39. Aichelmann-Reidy, M. E.; Heath, C. D.; Reynolds, M. A. *J. Periodontol.* **2004**, *75*(3), 340–347.
40. Torabinejad, M.; Watson, T. F.; Pitt Ford, T. R. *J. Endod.* **1993**, *19*(12), 591–595.
41. Juárez Broon, N.; Bramante, C. M.; Assis, G. F.; *et al*. *J. Appl. Oral Sci.* **2006**, *14*(5), 305–311.
42. Coleman, N. J.; Awosanya, K.; Nicholson, J. W. *J. Biomed. Mater. Res. A* **2009**, *90* (1), 166–174.
43. Roberts, H. W.; Toth, J. M.; Berzins, D. W.; Charlton, D. G. *Dent. Mater.* **2008**, *24*(2), 149–164.
44. Srinivasan, V.; Waterhouse, P.; Whitworth, J. *Int. J. Paediatr. Dent.* **2009**, *19*(1), 34–47.
45. Torabinejad, M.; Hong, C. U.; Pitt Ford, T. R.; Kettering, J. D. *J. Endod.* **1995**, *21*(8), 403–406.
46. Schmitt, D.; Lee, J.; Bogen, G. *Pediatr. Dent.* **2001**, *23*(4), 326–330.
47. Keiser, K.; Johnson, C. C.; Tipton, D. A. *J. Endod.* **2000**, *26*(5), 288–291.
48. Unezaki, Y.; Eto, T.; Inoue, H.; Minamigawa, K.; Sugihara, F. *J. Jpn. Prosthodont. Soc.* **1993**, *37*, 61–66.
49. Unezaki, Y.; Ryumon, H.; Inoue, H.; Okuda, H.; Onishi, H.; Minamigawa, K. *Bioceramics* **1996**, *9*, 251–253.
50. Ishikawa, K.; Takagi, S.; Chow, L. C.; Ishikawa, Y. *J. Mater. Sci. Mater. Med.* **1995**, *6*, 528–533.
51. Ishikawa, K.; Miyamoto, Y.; Kon, M.; Nagayama, M.; Asaoka, K. *Biomaterials* **1995**, *16*(7), 527–532.
52. Miyamoto, Y.; Ishikawa, K.; Fukao, H.; *et al*. *Biomaterials* **1995**, *16*, 855–860.
53. Takechi, M.; Miyamoto, Y.; Ishikawa, K.; *et al*. *J. Mater. Sci. Mater. Med.* **1996**, *7*(6), 317–322.
54. Ishikawa, K.; Miyamoto, Y.; Takechi, M.; *et al*. *J. Biomed. Mater Res.* **1999**, *44*(3), 322–329.
55. Cherng, A.; Takagi, S.; Chow, L. C. *J. Biomed. Mater. Res.* **1997**, *35*, 273–277.
56. Miyamoto, Y.; Ishikawa, K.; Takechi, M.; *et al*. *Biomaterials* **1998**, *19*(8), 707–715.
57. Ishikawa, K.; Matsuya, S.; Nakagawa, M.; Udoh, K.; Suzuki, S. *J. Mater. Sci. Mater. Med.* **2004**, *15*(1), 13–17.
58. Ishikawa, K.; Takeuchi, A.; Suzuki, Y.; Koyano, K. *J. Ceram. Soc. Jpn.* **2008**, *116*, 63–67.
59. Ishikawa, K.; Asaoka, K. *J. Biomed. Mater. Res.* **1995**, *29*(12), 1537–1543.
60. Eggli, P. S.; Muller, W.; Schenk, R. K. *Clin. Orthop.* **1988**, *232*, 127–138.
61. Holmes, R. E. *Plast. Reconstr. Surg.* **1979**, *63*, 626–633.
62. Holmes, R. E.; Bucholz, R. W.; Monney, V. *J. Bone Joint Surg.* **1986**, *68*, 904–911.
63. Hulbert, S. F.; Morrison, S. J.; Klawitter, J. J. *J. Biomed. Mater. Res.* **1972**, *6*, 347–374.
64. Cook, S. D.; Thongpreda, N.; Anderson, R. C.; Thomas, K. A.; Haddad, R. J., Jr.; Griffin, C. D. *Clin. Orthop.* **1987**, *223*, 296–302.
65. Schliephake, H.; Neukam, F. W.; Klosa, D. *Int. J. Oral Maxillofac. Surg.* **1991**, *20*, 53–58.
66. Takagi, S.; Chow, L. C. *J. Mater. Sci. Mater. Med.* **2001**, *12*, 135–139.
67. Xu, H. H. K.; Quinn, J. B.; Takagi, S.; Chow, L. C.; Eichmiller, F. C. *J. Biomed. Mater. Res.* **2001**, *57*, 457–466.
68. Xu, H. H. K.; Eichmiller, F.C.; Barndt, P. R. Effects of fiber length and volume fraction on the reinforcement of calcium phosphate cement. *J. Mater. Sci. Mater. Med.* **2001**, *12*, 57–65
69. Xu, H. H. K.; Quinn, J. B.; Takagi, S.; Chow, L. C. *J. Biomed. Mater. Res.* **2004**, *68A*, 725–734.
70. Zhang, Y.; Xu, H. H. K.; Takagi, S.; Chow, L. C. *J. Mater. Sci. Mater. Med.* **2006**, *17*, 437–445.
71. Habraken, W. J. E. M.; Wolke, J. G. C.; Mikos, A. G.; Jansen, J. A. *J. Biomed. Sci. Polym. Ed.* **2006**, *17*, 1057–1074.
72. Link, D. P.; van den Dolder, J.; Jurgens, W. J. F. M.; Wolke, J. G. C.; Jansen, J. A. *Biomaterials* **2006**, *27*, 4941–4947.
73. Ruhe, P. Q.; Hadberg, E. L.; Padron, N. T.; Spauwen, P. H. M.; Jansen, J. A.; Mikos, A. G. *J. Biomed. Mater. Res. A* **2005**, *74*, 533–544.
74. Tajima, S.; Kishi, Y.; Oda, M.; Maruta, M.; Matsuya, S.; Ishikawa, K. *Dent. Mater. J.* **2006**, *25*(3), 616–620.
75. Xu, H. H. K.; Eichmiller, F. C.; Giuseppetti, A. A. *J. Biomed. Mater. Res.* **2000**, *52*, 107–114.
76. Xu, H. H. K.; Quinn, J. B. *Biomaterials* **2002**, *23*, 193–202.
77. Xu, H. H. K.; Simon, C. G. *J. Biomed. Mater. Res.* **2004**, *69*, 267–278.
78. Xu, H. H.; Weir, M. D.; Burguera, E. F.; Fraser, A. M. *Biomaterials.* **2006**, *27*(24), 4279–4287.
79. Xu, H. H.; Carey, L. E.; Simon, C. G., Jr.; Takagi, S.; Chow, L. C. *Dent. Mater.* **2007**, *23*(4), 433–441.
80. Habraken, W. J. E. M.; Wolke, J. G. C.; Mikos, A. G.; Jansen, J. A. *J. Biomed. Sci-Polym. Ed.* **2006**, *17*, 1057–1074.
81. Bodde, E. W. H.; Habraken, W. J. E. M.; Mikos, A. G.; Spauwen, P. H. M.; Jansen, J. A. *Tissue Eng. A* **2009**, *15*(31), 3184–3191.
82. Shimogoryo, R.; Eguro, T.; Kimura, E.; Maruta, M.; Matsuya, S.; Ishikawa, K. *Dent Mater. J.* **2009**, *28*(5), 627–633.
83. Muth, C. M.; Shank, E. S. *N. Engl. J. Med.* **2000**, *342*, 476–482.
84. del Real, R. P.; Wolke, J. G. C.; Vallet-Regi, M.; Jansen, J. A. *Biomaterials* **2002**, *23*, 3673–3680.
85. del Real, R. P.; Ooms, E.; Wolke, J. G. C.; Vallet-regi, M.; Jansen, J. A. *J. Biomed. Mater. Res. A* **2003**, *65A*, 30–36.
86. Hesaraki, S.; Zamanian, A.; Moztarzadeh, F. *J. Biomed. Mater Res. B Appl. Biomater.* **2008**, *86*(1), 208–216.
87. Almirall, A.; Larrecq, G.; Delgado, J. A.; Martinez, S.; Planell, J. A.; Ginebra, M. P. *Biomaterials* **2004**, *25*, 3671–3680.
88. Sarda, S.; Nilsson, M.; Balcells, M.; Fernandez, E. *J. Biomed. Mater. Res.* **2003**, *65A*, 215–221.
89. del Valle, S.; Mino, N.; Munoz, F.; Conzalez, A.; Planell, J. A.; Ginebra, M. P. *J. Mater. Sci. Mater. Med.* **2007**, *18*, 353–361.
90. Sugawara, A.; Chow, L. C.; Takagi, S.; Chohayeb, H. *J. Endod.* **1990**, *16*(4), 162–165.
91. Carey, L. E.; Xu, H. H.; Simon, C. G., Jr.; Takagi, S.; Chow, L. C. *Biomaterials* **2005**, *26*(24), 5002–5014.
92. Takagi, S.; Chow, L. C.; Hirayama, S.; Sugawara, A. *J. Biomed. Mater. Res. B Appl. Biomater.* **2003**, *67*(2), 689–696.
93. Bohner, M.; Van Landuyt, P.; Merkle, H. P.; Lemaitre, J. *J. Mater. Sci. Mater. Med.* **1997**, *8*, 675–681.
94. Grover, L. M.; Gbureck, U.; Young, A. M.; Wright, A. J.; Barralet, J. E. *J. Mater. Chem.* **1995**, *15*, 4955–4962.
95. Bohner, M.; Lemaitre, J.; Ring, T. A. *J. Am. Ceram. Soc.* **1996**, *79*, 1427–1434.
96. Rousseau, S.; Lemaitre, J.; Bohner, M.; Frei, C. GRIBOI, Shanghai, China, 2002; pp 14–17.
97. Bohner, M.; Gbureck, U. *J. Biomed. Mater. Res. B Appl. Biomater.* **2008**, *84*(2), 375–385.
98. Constantz, B. R.; Barr, B. M.; Ison, I. C.; *et al*. *J. Biomed. Mater. Res.* **1998**, *43*, 451–461.
99. Frayssinet, P.; Gineste, L.; Conte, P.; Fages, J.; Rouquet, N. *Biomaterials.* **1998**, *19*(11–12), 971–977.

1.117. Phosphate-Based Glasses

E A Abou Neel and V Salih, University College London, London, UK
J C Knowles, University College London, London, UK; Dankook University, Chungnam, South Korea

© 2011 Elsevier Ltd. All rights reserved.

1.117.1.	**Phosphate Glasses: Physical Properties and Processing**	285
1.117.1.1.	Introduction	285
1.117.1.2.	Glass Synthesis	286
1.117.1.2.1.	Melt-derived glasses	286
1.117.1.2.2.	Sol–gel derived methods	286
1.117.1.3.	Phosphate Glass Structure and Q Speciation	287
1.117.1.4.	Ternary Glass Systems	288
1.117.1.5.	Phosphate Glass Degradation: General Concepts	288
1.117.1.5.1.	Ternary glass degradation	288
1.117.1.5.2.	Phosphate glass dopants: Control of dissolution rate	288
1.117.1.5.3.	Phosphate glass dopants: Additives for antibacterial use	289
1.117.1.6.	Processing of Phosphate Glass Fibers	289
1.117.2.	**Biological Properties of Phosphate Glasses**	290
1.117.2.1.	*In Vitro* Biological Properties	290
1.117.2.1.1.	Introduction	290
1.117.2.1.2.	*In vitro* properties of ternary glass systems	291
1.117.2.1.3.	*In vitro* properties of quaternary glass systems	291
1.117.2.1.4.	Phosphate glass fibers	292
1.117.2.2.	*In Vivo* Biological Properties	293
1.117.2.2.1.	Introduction	293
1.117.2.2.2.	Phosphate glasses as bone substitutes	293
1.117.2.2.3.	*In vivo* response to phosphate glasses	294
1.117.2.2.4.	Human clinical trials on phosphate glasses	294
1.117.3.	**Therapeutic Actions of Phosphate Glasses**	294
1.117.3.1.	Introduction	294
1.117.3.2.	Therapeutic Phosphate Glasses	295
1.117.3.3.	Other Potential Therapeutic Phosphate Glasses	295
References		296

Abbreviations

ALP	Alkaline phosphatase
BSP	Bone sialoprotein
CFU	Colony forming units
ELISA	Enzyme-linked immunosorbent assay
EXAFS	Extended X-ray absorption fine structure
FN	Fibronectin
HOS	Human osteosarcoma cells
MAS-NMR	Magic angle spinning nuclear magnetic resonance
MRSA	Methicillin-resistant *Staphylococcus aureus*
MTT	(3-(4,5-Dimethylthiazol-2-yl)-2,5-diphenyltetrazolium bromide) assay
OP	Osteopontin
ON	Osteonectin
PBG	Phosphate-based glasses
rtQPCR	Real-time quantitative polymerase chain reaction
SEM	Scanning electron microscopy
XANES	X-ray absorption near edge structure

1.117.1. Phosphate Glasses: Physical Properties and Processing

1.117.1.1. Introduction

Phosphate-based glasses are a unique glass system with properties that are not found in other glass systems. They possess, in general, a low dispersity and a high refractive index, and these properties have driven the development of phosphate glasses for optical use. Early work led to their development as achromatic optical components. As the use of optics diverged, it became apparent that phosphate-based glasses also had excellent UV transmission properties. Additionally, fluoride-containing phosphate glasses, doped with rare earth ions, were found to possess considerable applicability in optical and laser use due to their low absorption at particular frequencies.[1–3] However, for all of this work, one of the factors that

limited the widespread uptake of optical phosphate-based glasses was their poor chemical durability.[4] In particular, they can undergo complete breakdown of their structure and thus are completely degradable. However, this fact coupled with the simplicity with which these glasses can be synthesized (having generally, relatively low melting temperatures) has driven their use in a wide variety of other applications, particularly where this reactivity could be utilized. These areas include agriculture and water treatment.

More specialized optical applications have utilized phosphate-based glasses and these include lasers, and in particular, high-powered lasers. More recently, these glasses have also extended their use to more unusual areas such as glass to metal seals, where their high thermal expansion coefficients may be exploited[5]; as discussed in an excellent review by Brow.[6] Zinc phosphates, with unusually low processing temperatures, and iron phosphates, which have excellent chemical durability and low processing temperatures, lend themselves to utilization in the encapsulation of nuclear waste. Interestingly, various compositions of phosphate glasses have been investigated with the goal of vitrifying nuclear waste. Recently, iron-phosphate glass has come to the forefront of this application as a possible solution. Currently, only borosilicate glass has been approved by the US Department of Energy to vitrify high-level nuclear waste. Related to this, iron-phosphate glass with good chemical durability is able to accept more types of nuclear waste and up to 6 times more nuclear waste per unit volume, compared to borosilicate glasses.[7,8]

It is the combination of degradability and control over the rate of the degradation of these materials that makes them so attractive and is driving their development for biomedical use. In this chapter, we focus on their biomedical applications.

1.117.1.2. Glass Synthesis

1.117.1.2.1. Melt-derived glasses

Phosphate-based glasses produced by the conventional melting route are extremely simple to synthesize. The components used are low cost, even for high purity, and the melting temperature required is relatively low. As with most glasses, when melting, rather than using the pure oxides themselves (e.g., sodium oxide (Na_2O) or calcium (CaO)), they tend to be utilized in a different form, such as the carbonate. The starting point is the network-forming oxide (in this case phosphorous pentoxide) which, due to its extreme reactivity, is not usually added in pure form as it absorbs water very rapidly. It is also extremely volatile and can result in significant losses during melting and an altered composition. It is usual to add the phosphate combined with one of the other oxides, for example, NaH_2PO_4. This may be simply thought of as giving:

$$2NaH_2PO_4 \rightarrow Na_2O + P_2O_5 + 2H_2O$$

Thus it contributes to both the addition of Na_2O and P_2O_5. Any residual P_2O_5 that may be required can be added, as the pure oxide and should be added quickly and into a sealed container, in order to minimize water absorption which can be rapid and very exothermic. Once all the components have been thoroughly mixed and added to a suitable refractory container, (e.g., a platinum crucible) the crucible can be placed into the furnace. It is usual to place the crucible directly inside a hot furnace that has already been set to the appropriate melting temperature. This will result in rapid degassing (see equation above) and melting of the components. In general, the melt needs no more than an hour at the melting temperature to produce a homogeneous melt. The degassing that occurs either from loss of water as above or from other sources, for example,

$$CaCO_3 \rightarrow CaO + CO_2$$

can be significantly beneficial to the melt as the loss of gas helps to mix the glass melt and ensure homogeneity. It should be noted that some care should be taken when choosing precursors, as the production of large amounts of gaseous products can cause the melt to extrude over the crucible lip. The melt can now be poured into a preheated split mould constructed of graphite or steel (with a graphite release spray), the mould is then returned to a furnace to anneal and slowly cool the cast glass to produce the desired object in a stress-free form. Alternatively, the glass can be poured directly onto a cold steel plate to give the glass in a cullet form for further processing or measurement.

1.117.1.2.2. Sol–gel derived methods

The sol–gel method offers some significant advantages compared to the melt-derived route in the preparation of phosphate-based glasses and other sol–gel systems as covered in **Chapter 4.428, Sol–Gel Processed Oxide Controlled Release Materials**. However, the chemistry of sol–gel-derived phosphate-based glasses appears to be much more complex compared to the equivalent silicate-based glasses produced by the sol–gel route. While both the silicate- and phosphate-based glasses are based on tetrahedral units, they exhibit significantly different behavior in solution. The monophosphate unit $(PO_4)^{3-}$ is a good glass former but unlike the $(SiO^4)^{4-}$ unit, is not a good gel former. There are a number of possible precursors that may be considered, for example, phosphoric acid (H_3PO_4), but it is highly reactive with water and precipitates, as opposed to the required gelation. Phosphate esters ($PO(OR)_3$), where R = Methyl, Ethyl, or Butyl, can also be considered, but their rate of hydrolysis being extremely slow they are impractical. Alkyl phosphates $(OP(OR)_x(OH)_{3-x}$ where $x = 1, 2$), or phosphoryl chloride ($POCl_3$) could also be used.[9]

To prepare a mixture of mono- and diethyl phosphates, phosphorous pentoxide should be dissolved in ethanol via the following reaction:

$$P_2O_5 + 3EtOH \rightarrow OP(OEt)(OH)_2 + OP(OEt)_2(OH)$$

Using anhydrous inert conditions and dry glassware, ethanol is added dropwise to P_2O_5. This reaction is exothermic and so needs cooling to prevent the loss of ethanol. Refluxing at 78.5 °C for 24 h gives the required precursors. From this point, the phosphate sol may be prepared by adding the appropriate amounts of sodium ethoxide and/or calcium methoxide dissolved in ethylene glycol. Once dissolved, the mixture is then gelled (and this can take up to 2 weeks) followed by drying and a final calcination stage.

More recently,[10] a much more satisfactory reaction has been developed based on the utilization of *n*-butyl phosphate

in conjunction with titanium isopropoxide, and this was specifically used to synthesize glasses with very high TiO_2 content in the $TiO_2 - P_2O_5$ binary system. This particular system is of great interest as it allows compositions to be synthesized that are not normally achievable via the melt-derived route as TiO_2 is very refractory and difficult to get into solution even at high melting temperatures.

The initial step is to react titanium isopropoxide with 2-methoxyethanol. To this, *n*-butyl phosphate is added, very slowly. Once these have been allowed to react, an H_2O/HCl mixture in a solvent is added as an acid catalyst. This reaction may also be carried out as a base catalyzed reaction with *n*-butyl phosphate dissolved in *n*-butanol followed by addition of the titanium isopropoxide. The base catalyst used is ammonia in water with a solvent. These reaction routes are much more satisfactory, with gelation times of <5 min.

This methodology has also been successfully applied to the more complex ternary systems described initially in this section.[11] Using a mixture of mono- and di-substituted *n*-butyl phosphate $(OP(OH)_2(Bu^n)$ and $OP(OH)OBu^n)_2$, this is added to the sodium methoxide and allowed to react and then the calcium methoxide is added. This sol is then allowed to gel for 2 h. It is then aged at 60 °C for a week and dried at 120 °C for a further 2 weeks. It should be noted that the final calcination temperature is extremely low at 250 °C.

1.117.1.3. Phosphate Glass Structure and Q Speciation

As with all conventional glasses, the structural starting point is the network-forming oxide, which in this case, is a network built up of regular orthophosphate tetrahedra. However, in pure phosphate-based glasses, the tetrahedra have three bridging oxygens and a double-bonded nonbridging oxygen. This limits the speciation to a maximum of 3, compared to silica, which has a maximum of 4. Using the Q^i annotation, this maximum of Q^3 thus limits the degree of cross-linking possible within the glass structure and thus contributes to the relatively low resistance of phosphate glasses to water attack. Unlike silica, while of significant fundamental research interest, pure P_2O_5 has little use as a commercial glass due to its extreme reactivity in the presence of moisture. Much of the development work carried out is focused on reducing this reactivity and limiting or controlling the degradation rate.

Thus at the starting point, pure vitreous P_2O_5 consists almost entirely of Q^3 units. To aid in the understanding of the structural changes, initially, the focus will be on simple binary systems and the effects that the addition of modifying oxides and in particular the role of oxides of alkali metals or R_2O type oxides (i.e., oxides of metals from Group I in the Periodic Table), have on glass structure. The addition of R_2O gives rise to depolymerization of the phosphate network and initially the formation of Q^2 units and the loss of Q^3. The formation (and associated loss) follows simple predictions[6] which have also been proven experimentally.[12,13] The region of the compositional range, wherein the R_2O constitutes 50% or less of the total is deemed an ultraphosphate. At the point where the R_2O content is equal to 50%, this glass is deemed a metaphosphate and consists of a phosphorous-oxygen network that is based entirely on Q^2 units. As the incorporation of more R_2O into the glass melt is continued, further depolymerization occurs and the Q^2 chains are now terminated by Q^1 tetrahedra. With further increase in the R_2O content, the ratio of Q^2 units within a chain and the Q^1 termination units change as more and more Q^1 units are formed. When the amount of R_2O constitutes two-thirds of the total glass, the network consists of phosphate dimers, that is, two linked Q^1 tetrahedra. Further addition now results in complete depolymerization and the breakdown of the dimers into individual Q^0 orthophosphate units.

It should be noted that there is no simple linear relationship between composition and dissolution rate in a simple binary system such as $Na_2O-P_2O_5$. Gao *et al.*[14,15] showed that, in this system, the initial dissolution rate for glass in the metaphosphate region, that is, $0.5Na_2O-0.5P_2O_5$ is extremely high and is of the order of $20\,g\,cm^{-2}day^{-1}$. It should be remembered that the metaphosphate composition should consist almost entirely of Q^2 tetrahedra and hence will have infinitely long chains.[12] Increasing the P_2O_5 content by 10 mol% $(0.4Na_2O-0.6P_2O_5)$ into the ultraphosphate region should show the development of Q^3 tetrahedra at the expense of the Q^2 units and the dissolution rate decreases by over four orders of magnitude to $2\,mg\,cm^{-2}day^{-1}$. However, a continued increase in P_2O_5 content $(0.3Na_2O-0.7P_2O_5)$, at the expense of Na_2O, shows an increase in dissolution rate. The initial decrease in dissolution rate may be explained by the increasing numbers of bridging oxygens and branches that occur in the structure and this increasing complexity decreases the aqueous diffusion velocity and hence the reduction in dissolution. This does not explain why, with further additions of P_2O_5 an increase in dissolution rate is seen, and this has been explained by consideration of the resonance stability and its lack thereof.[16]

The complexity increases when considering the role of adding the oxides of alkaline earth metals (i.e., oxides of metals from Group 2 of the Periodic Table) which is due to the 2+ charge associated with them. Generally, it can be seen that replacing R_2O with RO results in an increase in durability of the glass or a decrease in the dissolution rate.[14,15] A recent detailed study by Walter *et al.*[17] investigated the short, medium, and submicroscopic structural features of the $MgO-P_2O_5$ glass system using a combination of X-ray and neutron scattering, in conjunction with ^{31}P magic angle spinning nuclear magnetic resonance (MAS-NMR) as well as the more conventional techniques of differential thermal analysis, to measure bulk properties such as glass transition temperatures. The glass transition temperature shows a clear linear relationship with composition, within the range studied. There is little change seen in both the $P-O_t$ and $P-O_b$ bond lengths with increasing MgO content, but the coordination number increases for the $P-O_t$ bond and decreases for the $P-O_b$ bond. According to van Wazer,[18] phosphate structural units can react according to:

$$2Q^2 \leftrightarrow Q^3 + Q^1$$

$$2Q^1 \leftrightarrow Q^2 + Q^0$$

Excellent agreement was seen by van Wazer between the metaphosphate composition and up to an $MgO:P_2O_5$ ratio of 1.5. However, above this ratio, when a decrease in Q^2 and a concomitant increase in Q^1 were expected, the presence of Q^0 is also actually seen and this is explained by the disproportionation, which is in accordance with the second reaction above.

The change in coordination number was confirmed by MAS-NMR, which shows a decrease in the proportion of Q^2.

1.117.1.4. Ternary Glass Systems

The binary systems described above give us a simple and controlled insight into the effect of additions on the overall phosphate network. Both the $Na_2O-P_2O_5$ and $CaO-P_2O_5$ systems are limited in the compositional variation that can be applied and also show either excessive dissolution rates or are difficult to process due to high thermal expansion coefficients, respectively. To move to more practical systems, it is necessary to increase the complexity and utilize ternary systems. Obviously, the number of systems now available increases significantly and it is our intention to focus on one ternary system that is of biomedical interest, namely that based on the $Na_2O-CaO-P_2O_5$ system.

The immediate logic in utilizing this system for biomedical use can be seen in the composition, as it contains elements that are present throughout the body at relatively high levels and so should be biocompatible. The majority of the work in literature has concentrated on glasses with P_2O_5 contents in the 40–60 mol% range. With contents <40 mol%, there are difficulties in obtaining a homogeneous melt as there is insufficient network former present and contents higher than 60 mol% do not allow sufficient modifying oxides to be added to give the required dissolution (and hence biological) properties. Substitution of the monovalent metal oxide (Na_2O) with the divalent metal oxide (CaO) gives rise to a significant decrease in the dissolution rate of the glass.[14] Examining the compositions around the metaphosphate region[19,20] showed expected relationships in terms of Q speciation and phosphate content. At the metaphosphate composition (i.e., 50 mol% P_2O_5), the glass consists almost entirely of Q^2 tetrahedra. However, there are some small amounts of Q^1 tetrahedra present and this would be expected as the theory states the chains are infinitely long; but in practice they must be terminated, and hence the presence of the small amounts of Q^1. In the ultraphosphate region, that is, at P_2O_5 contents of 55 mol%, again the structure is dominated by Q^2 speciation. Below the metaphosphate composition (45 mol% P_2O_5), the development of significant amounts of Q^1 tetrahedra is seen. However, within the glasses investigated, it can also be seen that the variation in the amounts of CaO and Na_2O also affects the Q speciation with increasing CaO content giving rise to increasing Q^2.

1.117.1.5. Phosphate Glass Degradation: General Concepts

The chemical durability of phosphate-based glasses is dependent on a number of factors, including the thermal history of the glass, the degradation medium in which the glass is placed and environmental conditions such as temperature. However, the most dominant factor is the composition of the glass. There are two well-known interdependent steps that take place during the degradation of phosphate-based glasses and they are analogous to the processes seen in silicate-based glasses[21] Figure 1).

The first of these reactions is a hydration reaction and involves the exchange of Na^+ with H^+ ions. This also leaves

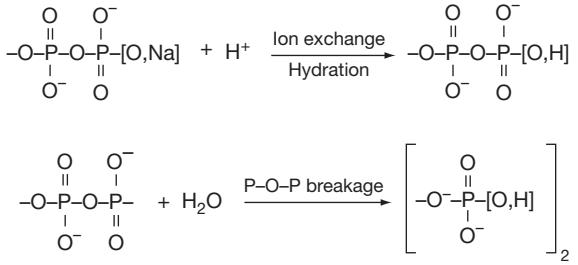

Figure 1 The two interdependent steps in the hydration process in phosphate-based glasses.

an excess of OH^- ions in solution and may account for any initial increases seen in pH.[22] The second stage is concerned with breakage of the phosphorous-oxygen network by hydrogen ions and water molecules. This causes the release of the phosphate chains and molecules into solution. It was proposed by Bunker *et al.*[23] that the dominating reaction was the first one and that the dissolution rate had two kinetic periods. One was proportional to the square root of time and in the second, the mass loss was proportional to time. Bunker also proposed that the dissolution was such that all components in the glass were released at the same time, that is, the solution composition would represent the bulk glass composition at any point in time. However, Gao and coworkers[14,15] indicated that the dominant reaction was the breakdown of the phosphate network and supported the theory of Bunker that dissolution was congruent. However, their work did not measure actual ion release and so this cannot be concluded.

1.117.1.5.1. Ternary glass degradation

Significant work has been carried out to understand the relationship between composition and degradation. In particular, with the advent of new measurement methodologies, not only has it become possible to measure the simple ionic species released but it has also become possible to measure, at least, the more simple mono and polyphosphates released from the glass with time. Recent work investigating glasses with the metaphosphate composition showed clear relationships between glass composition and degradation properties. For glasses in the range $50P_2O_5-(50-x)CaO-xNa_2O$, where x varies from 0 to 50 mol%, with increasing CaO content, the dissolution rate decreased significantly (by over three orders of magnitude). The sodium and calcium ion release also showed a decrease in release rate with increasing CaO content.

The work by Ahmed and coworkers[19,20] gives useful comparative data on the degradation phenomena for compositions on either side of the metaphosphate composition. Glasses below the metaphosphate composition (i.e., <50 mol% P_2O_5 content) showed an initial pH increase and then a slow decrease with time when measured in ultrapure water. Metaphosphate and higher compositions, however, showed a decrease in pH with time.

1.117.1.5.2. Phosphate glass dopants: Control of dissolution rate

A significant amount of work has been carried out to determine the role of dopants on the structure and properties of

phosphate-based glasses and, in particular, to reduce the dissolution rate, as will be discussed later. Three main dopants have been investigated, Al_2O_3, Fe_2O_3, and TiO_2. These are oxides of metals with high valency and this high valency has a significant effect on the glass structure and subsequent physical properties. The utilization of X-ray absorption near edge structure (XANES) analysis gives significant information concerning the structural environment of the titanium ions,[24] and allows elucidation as to whether the titanium is in four, five, or sixfold coordination.

A more detailed study of the role of Fe_2O_3 on the structure of glass was carried out by Qiu *et al.*[25] and they utilized a combination of extended X-ray absorption fine structure (EXAFS) and XANES, with XANES providing coordination and redox state information and EXAFS providing an insight into the local atomic information such as the Fe−O bond length.[26] For glasses in the metaphosphate region with Fe_2O_3 additions up to 5 mol%, the iron is in the Fe(III) oxidation state and has a distorted octahedral coordination geometry.[25] Looking in more detail at the structural information obtained, and in particular the Fe. . .P bond distance, it was inferred that the Fe atoms are incorporated as cross-links into the phosphate network between the phosphate tetrahedra of neighboring metaphosphate-like chains. This translates into a strengthening of the glass network and manifests itself as a significant decrease in the dissolution rate of the glasses.

1.117.1.5.3. Phosphate glass dopants: Additives for antibacterial use

While a number of elements are known to be antibacterial, some are relatively weak in their action. Probably the best known are silver and copper (which has also been discussed in detail in **Chapter 1.118, Calcium Phosphate Ceramics with Inorganic Additives**) and (to a lesser extent) gallium. The exact mechanisms of action for silver and copper have not been elucidated,[27] but it has been suggested that they block an enzyme involved in bacterial respiration. Silver can also bind to DNA. Copper-containing phosphate glasses were originally developed for trace element supplementation in ruminants[28] and also as molluscicides.[29] More recent work has attempted to investigate copper in more complex bacterial biofilm systems that contain single species cultures of *Streptococcus sanguis*.[30] A significant reduction in the number of colony forming units (CFU) can be seen and this improves with increasing copper content up to 24 h. However, if the experiment is extended, this becomes less significant with time and this is a direct reflection of the more complex experiment that was carried out in a constant depth film fermentor designed for conducting biofilm type experiments. This work was extended to investigate the role of silver on single species biofilms.[31] It showed that silver is a much more potent antibacterial ion compared to copper for *S. sanguis*, with only 5 mol% silver causing a 1−1.5 log reduction in CFUs at 6 h. Again, however, when the long-term biofilm experiments were carried out, a significant reduction in CFUs to almost zero was seen at 48 h. After 48 h, however, and for glass containing 10 mol% silver, there was a significant regrowth of bacteria, similar to almost the same level as for the control samples. This regrowth was explained and subsequently imaged (see **Figure 2**) using confocal laser scanning microscopy and quantified[32] as being due to the formation of a dead bacterial layer through which further ion diffusion was hindered, allowing bacteria to continue to grow.

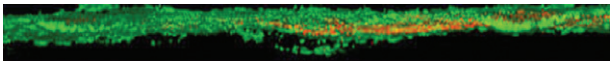

Figure 2 A cross-sectional view of the *S. aureus* biofilm on 20 mol% silver-doped PBGs. Viable (green) and nonviable (red) bacteria.

Further work[32,33] confirmed the effect of silver ions on a host of organisms including methicillin-resistant *Staphylococcus aureus* (MRSA) and the common yeast, *Candida albicans*, as well as the highly resistant *S. aureus*.

Gallium, as an antibacterial agent, functions in a very different way and offers some intriguing possibilities as an antibacterial ion. Infecting bacteria require Fe for growth and proper functioning of key enzymes. Gallium has an ionic radius almost identical to Fe and a similar charge, and thus, bacteria cannot distinguish between Fe^{3+} and Ga^{3+} and so Ga is actively taken up. However, Ga^{3+} cannot be reduced under the same conditions and so the Fe^{3+}-dependent processes are disrupted.[34] Addition of Ga does not change the Q speciation with the expected presence of Q^2 and some Q^1 for glasses with 45 mol% P_2O_5. The utilization of a Ga k-edge XANES coupled with the more unusual ^{71}Ga NMR[35,36] yielded information about the coordination compared to reference spectra for octahedrally coordinated Ga.

1.117.1.6. Processing of Phosphate Glass Fibers

Phosphate-based glasses readily lend themselves to melting and subsequent processing into a variety of forms and this is due to their low melting point, as already mentioned. They also have a relatively large processing window and do not readily crystallize, and thus, further heat treatments may be easily applied. In particular, they have been developed as glass fibers and this has been driven by an interest from the optoelectronics field. Microstructured optical fibers have been developed[37] that have utilized phosphate-based glasses due to their ability to solubilize rare earth components such as ytterbium, which give the fibers their high light absorption and amplification per unit length.[38] The processing of fibers for biomedical use would seem to be an interesting area for development. Fibers with controllable degradation can be utilized to suit the end application, a property not readily achievable with polymeric materials. Initial work utilized data from the glasses and from the structural studies[19] to develop ternary Na_2O−CaO−P_2O_5-based fibers. It is immediately apparent (and obviously so) that the glass structure and, in particular, the Q speciation exert significant control as to whether the glass will form fibers or otherwise.[20] Glasses with compositions below the metaphosphate region could not be converted into fibers. Glasses at the metaphosphate region and above could be readily converted to fibers due to the more polymeric nature of these glasses. Fibers were readily drawn with diameters ranging from ∼40 μm down to 10−12 μm, with both fiber diameter and composition exerting a significant control over the dissolution rate. For example, fibers with a $0.2Na_2O$−$0.3CaO$−$0.5P_2O_5$ composition and ∼37 μm diameter had a dissolution rate of ∼2 mg g^{-1} day^{-1}, but those with ∼17 μm had dissolution

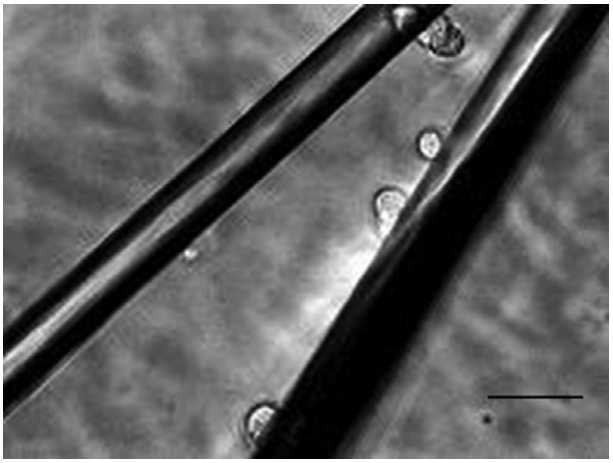

Figure 3 Bovine articular chondrocytes attached after 24 h to glass fibers containing 3% Fe (scale bar = 50 μm).

rate of 7 mg $g^{-1}day^{-1}$. From a biological perspective, these fibers are too soluble as work carried out to investigate the *in vitro* biological properties of the bulk glasses showed that only glasses with very high CaO content did not inhibit cell proliferation. Thus the further development of these fibers centered around the inclusion of dopants that can reduce their dissolution rate.

Phosphate-based fibers of the generic composition $(CaO)_{0.46}-(Na_2O)_n-(Fe_2O_3)_y-(P_2O_5)_{0.50}$ have been evaluated *in vitro* as three-dimensional scaffolds for tissue engineering at the hard–soft tissue interface by assessing fiber solubility and growth and functional gene expression of human cells.[39] Primary human osteoblasts and fibroblasts were seeded onto scaffolds and maintained in culture for up to 21 days. Fluorescent immunolabeling revealed the spread cell morphology and significant proliferation pattern on these fibers, particularly on the 3 mol% Fe_2O_3-containing formulation. Real-time quantitative polymerase chain reaction (rtQ-PCR) analysis of gene expression using TaqMan Probes was preformed and it has been established that committed cell differentiation was maintained by both cell types and was strongly related to the 3 mol% Fe_2O_3 glass composition. These novel, readily manufactured, soluble glass fibers offer a biocompatible and biochemically favorable alternative in the search for suitable degradable materials that can be used in tissue engineering and may offer promising potential for the growth of a variety of different tissue types, including chondrocytes (see Figure 3).

1.117.2. Biological Properties of Phosphate Glasses

1.117.2.1. *In Vitro* Biological Properties

1.117.2.1.1. Introduction

Over the last 50–60 years, biomaterials research has seen a paradigm shift from simply replacing nonfunctioning tissue to one that utilizes application-specific materials. The current ethos is to foster, in three dimensions, normal functionality and structurally compatible tissue. The basic need to replace a functioning joint with a metal prosthesis during the pioneering days of the 1950s has been strikingly enhanced. Nowadays, researchers are actively engaged in developing the biological as well as chemico-physical characteristics of the newer biomaterials in order to enhance the repair, or preferably the regeneration, of diseased or damaged tissues. The phosphate-based glass system represents one such class of innovative materials. Traditionally there has been a very naive belief that materials were typically 'inert' and it has quite correctly been suggested that this is a misleading interpretation, as it became clear that materials could indeed change, both physically and chemically, following implantation.[40] It has become evident that the choice of material is fundamental in enabling the cells to function in an opposite manner to produce the required extracellular matrix; and thus tissue of a desired geometry and normal functional capability. We have previously seen the variety of phosphate glass systems that are currently available in the previous section and here, their *in vitro* evaluations will be highlighted. The discussion will centre on hard tissue applications, although the section on fibers highlights their potential utilization even in soft-tissue applications. The unique solubility profiles of the glasses (from a few hours to several months) make them ideal candidates for a variety of tissue engineering approaches, and their doping with numerous metal oxides can suitably modify their physical properties or even induce specific cellular functions. Specifically, the pool of released ionic products provides an *in vitro* environment which can direct and modulate the biological response of the cells, thereby improving and achieving the desired result. The dissolution of the glass thus provides an environment for direct 'tissue engineering.'

An important consideration to be noted here is that although biodegradability can be a useful property for fixation devices such as orthopaedic pins/screws or tissue scaffolds, *degradable* biomaterials cannot necessarily be considered as truly biocompatible biomaterials unless specific functions of surrounding cells and tissues are considered during the degradation process. To this end, the fact that the phosphate-based glasses can be transformed into biocompatible and active materials by controlling, for example, dimensionality and chemical composition of glass formulations, allows for the incorporation of bioactive substances and ionic species. The subsequent controlled degradation of these glasses would provide time-dependent release of the incorporated bioactive substance and physiological factors and, therefore, a controlled, time-dependent impact on cellular and, ultimately, tissue function. The polymeric network of the phosphate glass species is formed around the tetrahedral phosphate anion; and in the ternary form, $CaO-Na_2O-P_2O_5$, calcium, and sodium oxides are added as modifiers.[20] Clear phosphate glasses can be generated at relatively low melting points provided the phosphorous pentoxide (P_2O_5) content is above 40 mol% in the ternary composition.[41] Solubility measurements have indicated that the degradation trends of these glasses are predictably stable and, by individually modifying each precursor's contribution within the generic glass form, extremely controllable glasses may be synthesized.[42] This flexibility allows the creation of specific solubility profiles that may correspond to the scaffold degradation-tissue formation balance *in vivo*. Solubility rates of these glasses appeared to be primarily dependent on the inhibitory effect of the CaO content as, in several studies, increasing the CaO mol% resulted in reduced glass

solubility.[19,20,22] This phenomenon has been attributed to the saturation of the local environment with the ions released from the least soluble glass constituent, in this case, CaO. However, a more plausible explanation may be the fact that the Ca cations can form cross links between oxygen atoms in different molecular chains within the glass.[41]

Another advantage of the phosphate glass chemical structure is the ability to incorporate a variety of additional elements to produce more complex quaternary compositions, thus further enhancing their physical properties. For example, the introduction of iron oxides to the glass network may lead to more favorable solubility trends and mechanical strength.[43,44]

When the *in vivo* application is targeted, overcoming the mechanical limitations imposed by the brittle nature of the glass is achievable using phosphate-based glasses. With the low melting temperature as an aiding factor, and through reasonably uncomplicated processes, phosphate glasses can be drawn into fibers of considerable tensile strength with flexible physical features so that scaffold systems of suitable shapes and volumes can be constructed.[19,20,45] Hence, the use of soluble phosphate-based glass fibers, doped with various inorganic ions, has been highlighted in several reports as reinforcement for scaffold material for orthopaedic use.[46,47]

1.117.2.1.2. In vitro *properties of ternary glass systems*

The ternary phosphate system containing calcium and sodium is the most common phosphate glass series investigated using *in vitro* analysis.[39,41,48,49] Uo *et al.*, used human pulp cells in a direct contact cytotoxic assay, to assess glass powders, which was quantified with Alamar blue. It was found that increasing the calcium content decreased the cytotoxicity. These studies were accompanied by light microscopy but no attempt was made to investigate the long-term effect of the glass particles on the cells. Salih *et al.*[49] studied calcium/sodium phosphate glass using elution tests using the MG63 and human osteosarcoma (HOS) cells. Along with MTT (3-(4,5-Dimethylthiazol-2-yl)-2,5-diphenyltetrazolium bromide) cytotoxic testing, the effect of the glass upon the expression of bone sialoprotein (BSP), osteonectin (ON), and fibronectin (FN) was also studied using ELISA. The highly soluble glasses with lower calcium concentrations caused some inhibition of growth and bone antigen expression, while extracts from the more durable glasses with higher levels of calcium upregulated proliferation and expression of BSP, ON, and FN. Elsewhere, osteosarcoma cells were cultured on the surface of phosphate glass that contained calcium and sodium.[39] Morphology and cell number were studied using scanning electron microscopy (SEM) and the CyQuant cell proliferation assay kit, respectively. Fluorescence immunocytochemistry was employed to identify BSP, ON, and osteopontin (OP). The most durable compositions supported greater proliferation, and BSP, ON, and OP were also detected. No tests were conducted for longer than 7 days and a quantification of these proteins was not performed. Franks and coworkers[50] studied the effect of exchanging calcium for magnesium in sodium phosphate glass. Elution tests were performed using the MG63 osteosarcoma cells and quantified using the MTT cytotoxic assay. No real difference was observed over a 5-day period. However, no attempt was made to assess any morphological changes or the expression of osteoblastic markers.

All of the previous cell culture studies were short term, despite the fact that the final material applications were to be medium or long term. Some studies looked at the production of particular osteoblast phenotypic markers, but with the exception of OP, all of these are produced early in the osteoblast cell cycle.

Conversely work performed by Gough *et al.*[48] looked at the long-term culture (28 days) of craniofacial fibroblasts seeded on to monolith calcium/sodium phosphate glass surfaces. Along with investigations on cell morphology and proliferation, collagen, ALP, and calcium deposition were also determined. Results from these studies demonstrated how osteoblasts cultured on these glasses progress through all the temporal stages of the osteoblast differentiation cell cycle.

This series of studies highlighted the fact that the degradation and resultant ion species release from these glasses can clearly affect the biocompatibility of these glasses and their efficacy during long-term use. Thus, addition of particular metal oxides to the parent ternary composition has been attempted in order to produce a novel series of quaternary systems that are more stable and potentially useful for biomedical applications.

1.117.2.1.3. In vitro *properties of quaternary glass systems*

By simply substituting K_2O for Na_2O, a monovalent ion for another similar ion of different ionic radius, a quaternary series of glasses were developed.[42] Further partial substitutions of calcium for divalent ions such as Magnesium have also been proposed[50] in quaternary systems and these have emphasized the importance of calcium in the degradation process. Cell proliferation studies showed that such glasses had at least an equal, and sometimes greater effect, on cell proliferation compared to control cells grown in their absence.

Glasses containing Zinc as the dopant have been shown to promote osteoblast cell adhesion.[51] The compositions investigated were P(50)Ca((40−x))Na(10) where $x = 0$, 1, 2, 3, 4, and 5 mol% of zinc. The effect of varying the amounts of zinc was tested on osteoblast adhesion. Furthermore, the dissolution rate and the effect of the pH of glass discs were also investigated and ion release from the glass discs was examined in distilled water at 37 °C up to 7 days, *in vitro*. All the glasses showed a linear decrease in their percentage mass of the glass discs for all compositions for the entire duration of the study, and the dissolution rates were similar for all the compositions. The pH of the glass solutions were slightly reduced; although these experiments were performed in nonbuffered solutions, a normal plasma/blood environment may well act as a suitable buffer under *in vivo* conditions. Cells exhibited attachment to all compositions and cell proliferation increased with an increase in ZnO content.

Previously, glasses with 50% P_2O_5−(20−15%) Na_2O−30% CaO−(0−5 mol%) TiO_2 have been prepared by the conventional melt-quenching process.[52] This study highlighted the importance of the combined addition of titanium ions to calcium ions on the biological activity of human osteoblast-like cells. Indeed the results clearly indicated that addition of TiO_2 in small amounts, up to 5 mol%, enhanced the biocompatibility of these glasses with high levels of cell attachment at 5 mol% of TiO_2 (see **Figure 4**).

The metabolic activity of cells was comparable with control cells up to 21 days in culture and the gene expression study

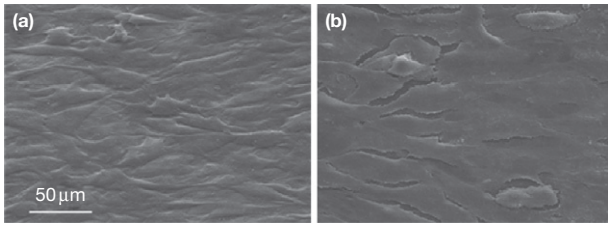

Figure 4 SEM shows MG63 cells after 4 days of culture on the surface of 5 mol% TiO_2-containing phosphate glass disc (a) and Thermanox as a positive control (b). Reproduced from Abou Neel, E. A.; Knowles, J. C. *J. Mater. Sci. Mater. Med.* **2008**, *19*, 377–386, with permission from Springer.

showed that by day 14 in culture, cells had significantly increased gene expression of important bone-associated proteins including alkaline phosphatase, collagen type I and ON. Even though such favorable cell response and gene upregulation were both abundantly evident, these glasses showed no evidence of an apatite layer formation even after incubation for 14 days in simulated body fluid.

Further studies examined the incorporation of strontium to the bulk Ti-based formulations.[53] This study focused on the effect of adding SrO to a Ti-containing quaternary phosphate glass system by incorporating 0, 1, 3, and 5% strontium, respectively. Structural characterization revealed glass transition temperatures in the range of 427–437 °C, and in all the glasses, sodium calcium phosphate was the dominant phase. Degradation and ion release studies conducted over a 15-day period revealed that the Sr-containing glasses showed significantly higher degradation and ion release rates than the Sr-free glass. This release profile was reflected in the cytocompatibility studies performed over a 7-day period using MG63 cells which showed that the addition of 5 mol% SrO yielded glasses with cell viability equivalent to that observed in quaternary TiO_2 glasses. Clearly, the manipulation of these glass compositions is relatively straightforward and the various formulations have profound, biologically relevant effects on human cells *in vitro*.

1.117.2.1.4. Phosphate glass fibers

As the conventional strategies aimed at replacing defective structures suffer many limitations, inductive tissue engineering may present the ideal solution by generating autogenic *de novo* tissue units with biological, histological, and biomechanical properties that match those of the recipient structure. Following injury or disease, clinical problems associated with tendons and ligaments are common and the cell–matrix tissue regeneration approach can potentially succeed in dealing with such problems. It is important to recognize, however, that this approach must be applied so that the structure is generated at the enthesis level as attempting to fuse hard and soft tissues by surgical means is often undermined by inferior integration, and in some cases, failure. Taking the anatomical architecture of the entheses into consideration, and in order to combine two histologically diverse entities so that an interface can be established, and evolved, the constituting cells must be seeded separately on one continuous, incorporating scaffolding system whereby this continuity will later guarantee the establishment of a functional bond between the two tissue elements. Current theories describe two conventional ways of using scaffold implant materials in the repair of bone defects; (1) via direct implantation of the material into the defect area which leads to subsequent repopulation of the scaffold by the surrounding tissues, or (2) via *in vitro* cell culture which involves seeding and incorporation to a porous, three-dimensional structure, followed by the hybrid cell/materials construct being implanted. Thus the *in vitro* conditions were optimized to allow the cells of interest, for example, bone to produce an immature osteoid, leaving the advanced maturation and bone remodeling to continue post implantation *in vivo*.[54,55] The events that occur at the interface of the glass and cells/tissues that lead to integral tissue formation have been previously elegantly described.[56] Essentially, dissolution and reprecipitation of the glass, exchange of ions and the solution-mediated effects on important cell functions, chemotactic events, attachment, proliferation, and differentiation leading to the formation of a functional extracellular matrix, in sequence, are the main processes that must occur to ensure a fully integrated and viable regenerated tissue. One could consider that the phosphate-based glasses, in the form of fibers and seeded with appropriate cell systems, may provide an ideal material which mirrors this concept of a cascade of cellular and material events leading to engineered tissues *in situ*.

Fiber-based matrices are therefore structurally suitable for providing a contiguous base for a coculture/cell transplantation strategy. Apart from the physical configuration, the scaffold structure must be generated from a biocompatible and biodegradable material in a manner that guarantees the survival and function of the seeded cells on one hand and its functional integration into the host tissue on the other. Owing to their biocompatibility and structural properties, phosphate-based glasses have been shown to be potentially excellent scaffold materials for tissue engineering. It is important, at this stage, that this potential is investigated further and developed as a primary, human cell-seeded, fiber-based scaffolding system.

The phosphate family of glasses has, therefore, recently emerged as a potential candidate to create high modulus, resorbable fibers. They possess unique characteristics that are desirable in several biomedical applications. They can be easily manufactured in the laboratory as fibers and they have been shown to exhibit excellent biocompatibility.[39,57] Moreover, they degrade to provide principally phosphate and calcium, which suggests that phosphate glasses in the form of fibers may be potentially osteo-conductive. To highlight this phenomenon, Shah *et al.*[58] utilized iron-based glasses in soft-tissue-engineering applications. They exhibited favorable *in vitro* characteristics, that is, they were nontoxic during degradation but retained their highly controllable degradation profiles.[19] These fibers have a high surface area to volume ratio, which can help increase the area available for the seeded cells to attach. They also have a narrow diameter of ~30 μm which allows for adequate delivery of nutrition and oxygen, and the dissolution products consist of ions that can be incorporated into other normal metabolic and physiological processes. Shah and coworkers[58] also investigated the use of these glass fibers as potential scaffold materials for the *in vitro* engineering of human craniofacial skeletal muscle. The authors concluded that the application of such glass fiber technology to the construction of a muscle organoid is highly suitable due to the structure of skeletal muscle; essentially bundles of fibers surrounded by

fibrous sheaths. This study demonstrated that the cell numbers on the fibers increased with time and that the scaffold mesh configuration as well as cell density aided the attachment of more cells to the fiber construct. Furthermore, the growth conditions were altered to encourage differentiation of the cells which may also have been affected by the glass composition.

Bitar *et al.*[59] investigated the development of a well-characterized, yet contiguous, glass fiber system for regeneration of the hard–soft tissue interface. This latter study evaluated the effect of fiber diameter on the attachment of human osteoblasts and fibroblasts using ternary glass fibers of the composition $0.48CaO-0.02Na_2O-0.50P_2O_5$. Fiber diameter significantly influenced cell attachment and survival, and fibers drawn at 800 revolutions per minute (diameter range of 20–25 μm) were found to be optimal. Using a known composition of iron-phosphate glass fibers (composition $0.46CaO-0.01Na_2O-0.03Fe_2O_3-0.50P_2O_5$), scaffolds were produced. These scaffolds were incorporated within an open laminar flow culture system to provide nutrients, oxygen, and waste removal throughout the culture. The design of the chamber ensured that laminar flow was present; both osteoblast and fibroblast differentiation was neither affected nor enhanced by laminar flow compared to static culture conditions. This system could potentially, therefore, be adapted to construct larger, more complex, three-dimensional iron-phosphate fiber scaffolds for tissue engineering and their performance evaluated *in vitro* with a variety of cells types under varying culture conditions.

A serendipitous finding of the iron oxide-doped phosphate-based glass fiber system was that capillary-like tubules were formed *in vitro* quite simply during their degradation in water.[52] This phenomenon has a unique and potentially important application in several areas including drug delivery, cell transportation, angiogenesis, or even as a conduit for nerve regeneration. These tubes would have great potential for the transportation of nutrients to and waste materials from the sites of tissue regeneration.

More recently, Ahmed *et al.*[60] have compared four more durable phosphate-based formulations for use as reinforcing components of biodegradable polymers like polylactic acid and polycaprolactone. Four invert phosphate-based glasses (PBG) formulations were produced with fixed phosphate and calcium contents at 40 and 25 mol%, respectively. MgO was added at 10–30 mol%, in place of Na_2O. *In vitro* investigations showed that the degradation rates of the glasses decreased by almost two orders of magnitude with an increase in MgO content. In addition, tests on the cytocompatibility of the fibers showed excellent osteoblast responses in terms of metabolic activity and production of alkaline phosphatase for up to 14 days when compared to control cell cultures grown on tissue culture plastic. Glasses containing 20 and 30 mol% MgO displayed optimal protein expression and cell coverage compared to control cells, revealing that the formulations investigated gave a response comparable to tissue cultured on plastic as control.

1.117.2.2. *In Vivo* Biological Properties

1.117.2.2.1. Introduction

Normally, a wide range of *in vitro* studies, including surface, physical, mechanical, and biological testing, are carried out prior to proceeding to *in vivo* experimentation, in order to assess the relevance of a material for clinical applications. Performing *in vitro* studies provides a wealth of information that is necessary to design a material with appropriate function and also to explore the potential toxicity of such a material. These *in vitro* methods, therefore, help to avoid costly and time-consuming *in vivo* procedures on a material that may not progress towards commercialization and eventual clinical use. It is often, however, difficult to extrapolate the *in vitro* behavior of a biomaterial to its *in vivo* performance as the environment that surrounds the material is very different in both the conditions.

Performing *in vivo* experiments, which are regarded as a link between *in vitro* studies and clinical trials, using animal models, is considered as a step towards a better understanding of biomaterial or implant behavior in both the short and long term. The choice of the animal model varies according to the estimated cost and the application of a biomaterial. Generally, small animal models will be employed initially, and then a progression to a higher animal model that has a closer relationship to the actual clinical situation will be performed prior to complex human clinical trials[61] and eventual clinical use. Even though these *in vivo* experiments are important for evaluation of a new material some argue about the use of animals in experimental work and they advocate the use of cell culture studies as a replacement for animal testing instead of supplementing it. They also claim that such animal testing may not be an accurate reflection of what could be expected from the same material in human body due to the expected variations between species.

1.117.2.2.2. Phosphate glasses as bone substitutes

Bone loss resulting from congenital abnormalities, traumatic injury, or disease is a major health care problem worldwide. When this occurs in the craniofacial region, it can also be highly emotive with serious physiological and psychological consequences. The extent of bone loss, commonly requiring reconstruction in the oral and maxillofacial region, varies considerably from small alveolar clefts to large mandibular defects.

As bone substitutes, various types of bone grafts (e.g., autograft, allograft, and xenograft) are regularly used to promote bone healing when insufficient bone is present at the desired surgical site. The limitations associated with them (e.g., limited supply, donor site infection and morbidity, pain, and cost of operation), however, led to the evolution and development of different approaches for the design of new types of synthetic materials as alternatives (see **Chapter 5.521, Calcium Phosphates and Bone Induction** for further reading on alternative types of calcium phosphates for bone induction). There is always a requirement for a biomaterial that can be easily shaped/handled, immunologically safe, and for the degradable materials to be safely eliminated from the body. Phosphate-based glasses provide a wide range of compositions, properties, and forms (e.g., granules, fibers, cloth, tubes, and monoliths of different shapes) for the applications detailed above. Being degradable, a key issue in choosing a biomaterial, this eliminates any concern about any long-term implantation effect. The degradation products, however, dissolve in the surrounding body fluid. When they are doped with oxides with known therapeutic actions, they could enhance new bone formation and reduce the chance of inflammation in the surrounding

tissue, as will be discussed below. Moreover, when they degrade, they provide microroughness and surface irregularities into which the new bone can be deposited and micromechanically bind to them.[62]

1.117.2.2.3. In vivo *response to phosphate glasses*

Although phosphate glasses have been extensively studied *in vitro*, as mentioned in the previous section, there are a limited number of publications that report the *in vivo* performance of this interesting class of materials. From the little information available, it is clear that the ability of these glasses to allow and promote new bone formation is dependent upon glass composition, particularly in the early stages of implantation (see **Figure 5**).[52,63] Some compositions[64] showed early bone formation within a week of implantation while others required several weeks for new bone formation to be detected.[52,63,65] Glasses doped with 1 and 3 mol% TiO_2 showed only soft-tissue formation, presumably due to their relatively higher solubility rate. However, at 5 mol%, bone growth directly on to the glass surface was observed (see **Figure 5**).

With longer implantation times, however, most of the variations between the glass formulations (e.g., solubility variation) could be masked by the physiological environment.[63,66]

Important issues that need to be considered during the selection of appropriate glass composition are when and how the glass is going to resorb and how this will affect the pattern and distribution of bone formation that proceeds to fill the spaces left by the degraded glass. In general, there were no signs of any inflammation or foreign body reaction surrounding the implanted glasses[67] or any soft-tissue intervention observed at the interface between the newly formed bone and the defect margin.[52,63] This newly formed bone also progressed, with time, to show some evidence of calcification and remodeling, as is the case with natural bone.[63,65,66,68] Sometimes, it was also comparable to or had even greater area, length, and density compared to that found on the control side.[63,64]

When these glasses were implanted subcutaneously, they showed a mild nonspecific inflammation, but actually, this mild inflammatory response was attributed to the suture material that was used at that time and not to the glass *per se*.[69,70] Most interestingly, when employed in porous form, they allowed penetration of vascularized tissue throughout the porous implant. These results were considered promising in terms of potential use of these glasses in clinical applications.[69]

1.117.2.2.4. *Human clinical trials on phosphate glasses*

Having materials that can be easily shaped into different forms which also show a potential use in clinical applications led to the development of metacarpophalangeal prostheses of different sizes. These glass prostheses were used in preliminary clinical trials that were carried out on one female patient, aged 44 and suffering from Rheumatoid arthritis. These prostheses were employed as a replacement for the metacarpophalangeal joint of the patient. Rheumatoid arthritis is a chronic, systemic inflammatory condition that may affect many tissues and organs but mainly joints; it can be a painful, disabling condition and can lead to substantial loss of mobility and function. The use of metacarpophalangeal prostheses made from phosphate glasses proved to be successful in pain relief and improved functional capacity with no adverse reactions. It also proved that phosphate glasses could be used without the need for a coating of perichondrium, a layer of dense irregular connective tissue which surrounds the cartilage of a developing bone, which is to be taken from the patient's rib to improve cartilage repair. Using these glass prostheses also eliminated the need for a second revision surgery for implant removal which is the case with conventional Silastic (medical grade silicon) prostheses and hence protected the patient from further complications associated with multiple surgical procedures.[69]

In general and as highlighted above, a lot more effort is still required to cover this area of experimentation. That is, to come up with compositions that could offer effective, safe, lower cost, less demanding, and easy-to-use bone substitutes that could serve a wide sector of population that suffers from bone diseases.

1.117.3. Therapeutic Actions of Phosphate Glasses

1.117.3.1. Introduction

The high temperatures used in the fabrication of these glasses through the conventional melt quench process makes the incorporation of bioactive organic molecules/materials (e.g., proteins, growth factors, genes, and hormones), which are necessary for imparting specific therapeutic action, into the glass structure, impossible. Using the sol–gel route (low-temperature fabrication process),[10,11,71] on the other hand, may make such incorporation possible, but there is still a limitation with the number of organic molecules/materials that can actually be incorporated into the glass network.

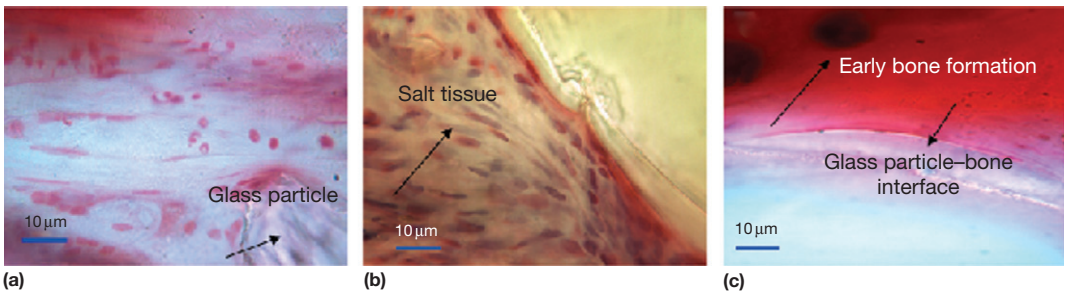

Figure 5 Histology images of glass particles doped with 1, 3, and 5 mol% TiO_2 after implantation in rat calvarium bone defects for 5 weeks (a, b, and c) respectively at ×20 magnification. (Stain: Cole's haematoxylin eosin). Reproduced from Abou Neel, E. A.; Mizoguchi, T.; Ito, M.; Bitar, M.; Salih, V.; Knowles, J. C. *Biomaterials* **2007**, *28*, 2967–2977, with permission from Elsevier.

However, given their dissolution properties, these glasses could be used as a vehicle for controlled delivery of inorganic ions, which may have the same or similar action as organic molecules/materials, as long as they are in contact with the biological environment.

Having this advantage, Standard Telecommunication Laboratories (STL) managed to develop the first phosphate glass releasing inorganic ions with known therapeutic action in the early 1970s.[72] This idea was further adopted, and currently, some of these glasses are under development or are being used for a variety of therapeutic applications, according to the ions being released. This section will deal with the currently commercially available phosphate glasses and then discuss the development of new systems that can potentially treat disease, reduce the risk of infection or help in hastening the healing process.

1.117.3.2. Therapeutic Phosphate Glasses

One of the commercially available therapeutic phosphate glasses is called coseCURE®. It is a soluble glass bolus containing cobalt, selenium, and copper and is used for the treatment of trace element deficiency in animals. This bolus is prepared for oral administration and when it reaches the reticulum, it starts to dissolve continuously over a period of 6 months, leaving no residues behind.[73–75] This bolus provides the animal with the required mineral supplement and guarantees a sustained dose to the animal for the lifetime of the device. These glasses also help in maintaining their offspring by absorbing the toxic molecules that could impair the fertility of the animals.[76–78]

Another example of therapeutic phosphate glasses is that used for treating natural or artificial bodies of water that have been infected with waterborne parasites. These glasses act as a molluscicide and kill the snail which is the intermediate host of the schistosoma parasite. Therefore, they help to reduce the risk of transmission of schistosomiasis, which is the second most socioeconomically devastating parasitic disease affecting humans via human–water contact sites. Thus, these glasses serve a high proportion of the population who are prone to get infected, particularly in developing countries, or those working in endemic areas such as the armed forces.[79–81]

Such an application of these glasses, as well as the metacarpophalangeal joint implant described previously, has also enabled its extension to other clinical areas in humans. Phosphate glasses have been used as a tissue bulking agent to prevent the abnormal flow of urine from the bladder to the kidney, which is essential for the treatment of vesicoureteral reflux.[82] They have also been used to control infection in patients suffering from urinary incontinence, particularly in those who require the use of long-term indwelling catheters. The long-term use of catheters has a significant risk of bacterial colonization and hence bladder infection; a condition that requires the catheter to be regularly changed and hence may impose trauma and additional cost to the patient. For the control of infection, a cartridge with silver containing glass is designed to be inserted, in line, between the catheter and urine collection bag. When in position, the insert is bathed with urine as it flows from the bladder into the collection bag. Then it releases silver ions that kill most of the bacteria that are commonly associated with catheter infection.[82–84] This device has an additional benefit in that it acts as a barrier that prevents bacteria tracking back up the catheter and causing bladder infections.

1.117.3.3. Other Potential Therapeutic Phosphate Glasses

Phosphate glasses could also have enormous potential in other therapeutic applications. They can be effectively used in controlling infections that are resistant to antibiotics (e.g., bone infection) by releasing ions known for their antibacterial actions such as zinc,[85] silver,[33,86] and gallium,[36] since there is no reported bacterial resistance against these ions. They could also be used to prevent bone fracture in osteoporotic patients by releasing ions that are known to strengthen and increase the existing bone mass and density (e.g., strontium),[87–89] or to help in bone healing by enhancing the bone forming ability of bone cells (e.g., zinc).[90]

Incorporation of radioactive ions known to be very effective at killing cancerous cells, for example, $^{90}Sr^{91}$ or $^{191}Pt^{92}$ or $^{90}Y^{93–95}$ into these glasses could also open another avenue for their use in the treatment of localized discrete cancer. Glass microspheres carrying the radioactive isotopes can be easily introduced into a specific organ to treat the cancer.[95] For such an application, they may provide a suitable means of directing these radioactive ions to a specific site and hence reduce the chance of these ions being lost systemically and thus having undesirable side effects on the neighboring healthy tissues. Furthermore, the capacity of these glasses to be X-rayed would be of a considerable asset in monitoring the precise location and degradation of the implant noninvasively.[69]

These therapeutic glasses may also be good candidates for restoring the blood levels of certain ions to their correct levels. They could be designed to correct zinc levels in patients suffering from Crohn's disease, an inflammatory condition of the intestines that can affect any other part of the gastrointestinal tract from the mouth to the anus. They could be also designed to maintain the necessary sodium–potassium balance for carrying out normal body functions in patients on diuretics (drugs that remove water from the body by increasing the amount of urine). In such cases, these glasses could controllably release sodium and potassium ions at the correct ratio and could easily be incorporated with a drip feed in order to avoid any periodic intervention and its subsequent risk of infection.[69]

Glasses releasing ions such as strontium could also be used in dentistry to reduce the prevalence of tooth decay when they are included within cements or in filling materials as these glasses can act as a matrix for the continuous supply of ions that help in remineralization of defective tooth structure.[96] Devices have also been tested to release therapeutic ions directly into the oral cavity to inhibit demineralization and promote remineralization, and this includes strontium mentioned above and also fluoride.

The development of phosphate-based glasses as composite materials for use in endodontic surgery also shows some promise. The rapid release of ions followed by reprecipitation of a calcium phosphate phase at the margin between the tooth and the filling material has been shown to provide an excellent marginal seal around endodontic filling materials by closing

the microgaps that normally exist around endodontic root-filling materials and the surrounding tooth structure. Providing this marginal seal helps to seal the route of ingress of microorganisms at the tooth/restoration interface and hence reduce the incidence of tooth decay.[97,98]

References

1. Ebendorff-Heidepriem, H.; Ehrt, D. *Opt. Mater.* **2002**, *19*, 351–363.
2. Ebendorff-Heidepriem, H.; Riziotis, C.; Taylor, E. R. *Glass Sci. Technol.* **2002**, *75*, 54–59.
3. Philipps, J. F.; Topfer, T.; Ebendorff-Heidepriem, H.; Ehrt, D.; Sauerbrey, R. *Appl. Phys. B Laser. Optic.* **2001**, *72*, 399–405.
4. Morey, G. W. *The Properties of Glass*; Reinhold: New York, 1954.
5. Wei, T. Y.; Hu, Y.; Hwa, L. G. *J. Non-Cryst. Solids* **2001**, *288*, 140–147.
6. Brow, R. K. *J. Non-Cryst. Solids* **2000**, *263&264*, 1–28.
7. Huang, W. H.; Zhou, N.; Day, D. E.; Ray, C. S. *J. Inorg. Mater.* **2005**, *20*, 842–850.
8. Mesko, M. G.; Day, D. E.; Bunker, B. C. *Waste Manag.* **2000**, *20*, 271–278.
9. Carta, D.; Pickup, D. M.; Knowles, J. C.; Smith, M. E.; Newport, R. J. *J. Mater. Chem.* **2005**, *15*, 2134–2140.
10. Pickup, D. M.; Speight, R. J.; Knowles, J. C.; Smith, M. E.; Newport, R. J. *Mater. Res. Bull.* **2008**, *43*, 333–342.
11. Pickup, D. M.; Guerry, P.; Moss, R. M.; Knowles, J. C.; Smith, M. E.; Newport, R. J. *J. Mater. Chem.* **2007**, *17*, 4777–4784.
12. Brow, R. K.; Tallant, D. R.; Hudgens, J. J.; Martin, S. W.; Irwin, A. D. *J. Non-Cryst. Solids* **1994**, *177*, 221–228.
13. Brow, R. K.; Kirkpatrick, R. J.; Turner, G. L. *J. Non-Cryst. Solids* **2000**, *116*, 39–45.
14. Gao, H.; Tan, T.; Wang, D. *J. Contr. Release* **2004**, *96*, 21–28.
15. Gao, H. S.; Tan, T. E.; Wang, D. H. *J. Contr. Release* **2004**, *96*, 29.
16. van Wazer, J. R.; Holst, K. A. *J. Am. Chem. Soc.* **1950**, *72*, 639–644.
17. Walter, G.; Vogel, J.; Hoppe, U.; Hartmann, P. *J. Non-Cryst. Solids* **2003**, *320*, 210–222.
18. van Wazer, J. R. *Phosphorous and Its Compounds*; Interscience: New York, 1958; Vol. I.
19. Ahmed, I.; Lewis, M.; Olsen, I.; Knowles, J. C. *Biomaterials* **2004**, *25*, 491–499.
20. Ahmed, I.; Lewis, M.; Olsen, I.; Knowles, J. C. *Biomaterials* **2004**, *25*, 501–507.
21. Isard, J. O.; Allnatt, A. R.; Melling, P. J. *Phys. Chem. Glasses* **1982**, *23*, 185.
22. Franks, K.; Abrahams, I.; Knowles, J. C. *J. Mater. Sci. Mater. Med.* **2000**, *11*, 609.
23. Bunker, B. C.; Arnold, G. W.; Wilder, J. A. *J. Non-Cryst. Solids* **1984**, *64*, 291.
24. Pickup, D. M.; Abou Neel, E. A.; Moss, R. M.; *et al. J. Mater. Sci. Mater. Med.* **2008**, *19*, 1681–1685.
25. Qiu, D.; Moss, R. M.; Pickup, D. M.; *et al. J. Non-Cryst. Solids* **2008**, *354*, 5542–5546.
26. Greaves, G. N. *J. Non-Cryst. Solids* **1985**, *71*, 203–217.
27. Spacciapoli, P.; Buxton, D.; Rothstein, D.; Friden, P. *J. Periodontal. Res.* **2001**, *36*, 108–113.
28. Allen, W. M.; Drake, C. F.; Sansom, B. F.; Tripp, M. *Ann. Rech. Vet.* **1979**, *10*, 356.
29. O'Sullivan, T. N.; Smith, J. D.; Thomas, J. D.; Drake, C. *Environ. Sci. Technol.* **1989**, *23*, 1102.
30. Mulligan, A. M.; Wilson, M.; Knowles, J. C. *Biomaterials* **2003**, *24*, 1797.
31. Mulligan, A. M.; Wilson, M.; Knowles, J. C. *J. Biomed. Mater. Res.* **2003**, *67A*, 401–412.
32. Valappil, S. P.; Pickup, D. M.; Carroll, D. L.; *et al. Antimicrob. Agents Chemother.* **2007**, *51*, 4453–4461.
33. Ahmed, I.; Ready, D.; Wilson, M.; Knowles, J. C. *J. Biomed. Mater. Res. A* **2006**, *79*, 618–626.
34. Kaneko, Y.; Thoendel, M.; Olakanmi, O.; Britigan, B. E.; Singh, P. K. *J. Clin. Invest.* **2007**, *117*, 877–888.
35. Pickup, D. M.; Valappil, S. P.; Moss, R. M.; *et al. J. Mater. Sci.* **2009**, *44*, 1858–1867.
36. Valappil, S. P.; Ready, D.; Abou Neel, E. A.; *et al. Acta Biomater* **2009**, *5*, 1198–1210.
37. Schülzgen, A.; Li, L.; Temyanko, V. L.; Temyanko, V. L.; Peyghambarian, N. *J. Lightwave Technol.* **2009**, *27*, 1734–1740.
38. Li, L.; Schülzgen, A.; Temyanko, V. L.; *et al. Opt. Lett.* **2005**, *30*, 1141–1143.
39. Bitar, M.; Salih, V.; Mudera, V.; Knowles, J. C.; Lewis, M. P. *Biomaterials* **2004**, *25*, 2283–2292.
40. Anderson, J. M. *J. Mater. Sci. Mater. Med.* **2006**, *17*, 1025–1028.
41. Uo, M.; Mizuno, M.; Kuboki, Y.; Makishima, A.; Watari, F. *Biomaterials* **1998**, *19*, 2277–2284.
42. Knowles, J. C.; Franks, K.; Abrahams, I. *Biomaterials* **2001**, *22*, 3091–3096.
43. Franks, K.; Abrahams, I.; Georgiou, G.; Knowles, J. C. *Biomaterials* **2001**, *22*, 497–501.
44. Wen, H. B.; de Wijn, J. R.; Cui, F. Z.; de Groot, K. *J. Biomed. Mater. Res.* **1998**, *41*, 227–236.
45. Pahler, G.; Bruckner, R. *J. Non-Cryst. Solids* **1982**, *85*, 105–126.
46. Charvet, J. L.; Cordes, J. A.; Alexander, H. *J. Mater. Sci. Mater. Med.* **2000**, *11*, 101–109.
47. Choueka, J.; Charvet, J. L.; Alexander, H.; *et al. J. Biomed. Mater. Res.* **1995**, *29*, 1309–1315.
48. Gough, J. E.; Christian, P.; Scotchford, C. A.; Jones, I. A. *J. Biomed. Mater. Res. A* **2003**, *66*, 233–240.
49. Salih, V.; Georgiou, G.; Knowles, J. C.; Olsen, I. *Biomaterials* **2001**, *22*, 2817–2824.
50. Franks, K.; Salih, V.; Knowles, J. C.; Olsen, I. *J. Mater. Sci. Mater. Med.* **2002**, *13*, 549–556.
51. Salih, V.; Patel, A.; Knowles, J. C. *Biomed. Mater.* **2007**, *2*, 11–20.
52. Abou Neel, E. A.; Mizoguchi, T.; Ito, M.; Bitar, M.; Salih, V.; Knowles, J. C. *Biomaterials* **2007**, *28*, 2967–2977.
53. Lakhkar, N. J.; Abou Neel, E. A.; Salih, V.; Knowles, J. C. *J. Mater. Sci. Mater. Med.* **2009**, *20*, 1339–1346.
54. Jones, J. R.; Tsigkou, O.; Coates, E. E.; Stevens, M. M.; Polak, J. M.; Hench, L. L. *Biomaterials* **2007**, *28*, 1653–1663.
55. Takezawa, T. *Biomaterials* **2003**, *24*, 2267–2275.
56. Ducheyne, P.; Qiu, Q. *Biomaterials* **1999**, *20*, 2287–2303.
57. Parsons, A. J.; Evans, M.; Rudd, C. D.; Scotchford, C. A. *J. Biomed. Mater. Res. A* **2004**, *71*, 283–291.
58. Shah, R.; Sinanan, A. C.; Knowles, J. C.; Hunt, N. P.; Lewis, M. P. *Biomaterials* **2005**, *26*, 1497–1505.
59. Bitar, M.; Salih, V.; Knowles, J. C.; Lewis, M. P. *J. Biomed. Mater. Res. A* **2008**, *87*, 1017–1026.
60. Ahmed, I.; Parsons, A.; Jones, A.; Walker, G.; Scotchford, C.; Rudd, C. *J. Biomater. Appl.* **2010**, *24*, 555–575.
61. Fini, M.; Giardino, R. *J. Appl. Biomater. Biomech.* **2003**, *1*, 155–163.
62. Neo, M.; Kotani, S.; Fujita, Y.; *et al. J. Biomed. Mater. Res.* **1992**, *26*, 255–267.
63. Sanzana, E. S.; Navarro, M.; Macule, F.; Suso, S.; Planell, J. A.; Ginebra, M. P. *Acta Biomater.* **2008**, *4*, 1924–1933.
64. Lee, Y. K.; Song, J.; Moon, H. J.; *et al. Key Eng. Mater.* **2004**, *254–256*, 185–188.
65. Moon, H. J.; Kim, K. N.; Kim, K. M.; *et al. J. Mater. Sci. Mater. Med.* **2006**, *17*, 807–813.
66. Navarro, M.; Sanzana, E. S.; Planell, J. A.; Ginebra, M. P.; Torres, P. A. *Key Eng. Mater.* **2005**, *284–286*, 893–896.
67. Burnie, J.; Gilchrist, T.; Duff, S. R. I.; Drake, C. F.; Harding, N. G. L.; Malcolm, A. J. *Biomaterials* **1981**, *2*, 244–246.
68. Moon, H. J.; Kim, K. N.; Kim, K. M.; *et al. J. Biomed. Mater. Res.* **2005**, *74A*, 497–502.
69. Burnie, J., Ph.D. Thesis, University of Strathclyde, Glasgow, UK, 1982.
70. Burnie, J.; Gilchrist, T. In *Proceedings from 2nd International Symposium on Bioceramics*, Elsevier: Lignano, Italy, 1982.
71. Carta, D.; Knowles, J. C.; Smith, M. E.; Newport, R. J. *J. Non-Cryst. Solids* **2007**, *353*, 1141–1149.
72. Drake, C. F. Continuous and pulsed delivery of bioactive materials using composite system based on inorganic glasses. Consultation on Immunomodulation; Bellagio, Italy, Apr 16–18, 1985.
73. Allen, W. M.; Drake, C. F.; Tripp, M. Use of controlled release system for supplementation during trace element deficiency – The administration of boluses of controlled release glass (CRG) to cattle and sheep. TEMA 5, Jun 29–July 4, 1984, Aberdeen, UK.
74. Allen, W. M.; Sansom, B. F.; Gleed, P. T.; Mallinson, C. B.; Drake, C. F. *Vet. Rec.* **1984**, *115*, 55–57.
75. Telfer, S. B.; Illingworth, D. V.; Anderson, P. J. B.; Zervas, G.; Carlos, G. *Biochem. Soc. Trans.* **1985**, *13*, 529–529.
76. Bedwal, R. S.; Bahuguan, A. *Experientia* **1994**, *50*, 626–640.
77. Kendall, N. R.; Marsters, P.; Scaramuzzi, R. J.; Campbell, B. K. *Reproduction* **2003**, *125*, 657–665.
78. Lyubimov, A. V.; Smith, J. A.; Rousselle, S. D.; *et al. Reprod. Toxicol.* **2004**, *19*, 223–233.
79. Chandiwana, S. K.; Ndamba, J.; Makupa, O.; Taylor, P. *Trans. R. Soc. Trop. Med. Hyg.* **1987**, *81*, 952–955.

80. O'Sullivan, T. N.; Smith, J. D.; Thomas, J. D.; Drake, C. *Environ. Sci. Technol.* **1991**, *25*, 1088–1091.
81. Timothy, N. O. J.; Smith, J. D.; Thomas, J. D. *Environ. Sci. Technol.* **1991**, *25*, 1088–1091.
82. Cartmell, S. H.; Doherty, P. J.; Hunt, J. A.; Healy, D. M.; Gilchrist, T. *J. Mater. Sci. Mater. Med.* **1998**, *9*, 773–777.
83. Gilchrist, T.; Healy, D. M.; Drake, C. *Biomaterials* **1991**, *12*, 76–78.
84. Woodyard, L. L.; Bowersock, T. L.; Turek, J. J.; McCabe, G. P.; DeFord, J. *J. Contr. Release* **1996**, *40*, 23–30.
85. Yamamoto, O. *Int. J. Inorg. Mater.* **2001**, *3*, 643–646.
86. Valappil, S. P.; Knowles, J. C.; Wilson, M. *Appl. Environ. Microbiol.* **2008**, *74*, 5228–5230.
87. Llinas, P.; Masella, M.; Stigbrand, T.; Me'Nez, A.; Stura, E. A.; Le Du, M. H. *Protein Sci.* **2006**, *15*, 1691–1700.
88. Meunier, P. J.; Roux, C.; Seeman, E.; *et al. N. Engl. J. Med.* **2004**, *350*, 459–468.
89. Reginster, J. Y.; Seeman, E.; De Vernejoul, M. C.; *et al. J. Clin. Metab.* **2005**, *90*, 2816–2822.
90. Holloway, W. R.; Collier, F. M.; Herbst, R. E.; Hodge, J. M.; Nicholson, G. C. *Bone* **1996**, *19*, 137–142.
91. Lloyd, R. D.; Angus, W.; Taylor, G. N.; Miller, S. C. *Health Phys.* **1995**, *69*, 272–277.
92. Owens, S. E.; Thatcher, N.; Sharma, H.; *et al. Cancer Chemother. Pharmacol.* **1985**, *14*, 253–257.
93. Cacaina, D.; Ylänen, H.; Simon, S.; Hupa, M. *J. Mater. Sci. Mater. Med.* **2008**, *19*, 1225–1233.
94. Kawashita, M.; Miyaji, F.; Kokubo, T.; *et al. J. Non-Cryst. Solids* **1999**, *255*, 140–148.
95. Sene, F. F.; Martinelli, J. R.; Okuno, E. *J. Non-Cryst. Solids* **2008**, *354*, 4887–4893.
96. Curzon, M. E. J. *J. Dent. Res.* **1985**, *64*, 1286–1388.
97. Alani, A.; Knowles, J. C.; Chrzanowski, W.; Ng, Y. L.; Gulabivala, K. *Dent. Mater.* **2009**, *25*, 400–410.
98. Borbely, P.; Gulabivala, K.; Knowles, J. C. *Int. Endod. J.* **2008**, *41*, 1093–1100.

1.118. Calcium Phosphate Ceramics with Inorganic Additives

L Yang, B Harink, and P Habibovic, University of Twente, Enschede, The Netherlands

© 2011 Elsevier Ltd. All rights reserved.

1.118.1.	**Introduction**	300
1.118.2.	**Bone**	300
1.118.3.	**Current Methods in Bone Regeneration**	301
1.118.3.1.	Natural Bone Grafts	301
1.118.3.2.	Synthetic Bone Graft Substitutes	301
1.118.3.2.1.	Calcium phosphate ceramics	301
1.118.3.3.	Tissue Engineering	301
1.118.4.	**Improvement of Synthetic Bone Graft Substitutes**	303
1.118.5.	**Trace Elements in Bone Metabolism and Processes Related to Bone Formation**	303
1.118.5.1.	Zinc	303
1.118.5.2.	Copper	304
1.118.5.3.	Strontium	304
1.118.5.4.	Fluoride	304
1.118.5.5.	Carbonate	305
1.118.6.	**Inorganic Additives in Calcium Phosphate Ceramics**	305
1.118.6.1.	Methods of Preparation	305
1.118.6.2.	Effect of Inorganic Additives on Ceramic Properties	306
1.118.6.3.	Biological Performance of Ceramics Containing Inorganic Additives	307
1.118.7.	**Future Perspectives**	309
References		309

Glossary

Adipogenic Relating to or derived from the tissue from which fat is developed.
Allograft Graft taken from another individual of the same species as the recipient.
Autograft Graft taken from a source in the individual who receives it; that is, the donor and recipient are the same.
Bioactivity Phenomenon by which a biomaterial elicits or modulates biological activity.
Ceramic Type of material chemically derived from the combination of one or more metallic elements with one or more nonmetallic elements, usually ionically bound, but with a contribution from covalent bonding, characterized in the solid state by extreme brittleness.
Ectopic Located away from normal position.
In vitro Pertaining to a situation that involves the experimental reproduction of biological processes in a more easily defined environment such as a culture vessel.
In vivo Pertaining to a biological process occurring within a living organism or cell.
Orthotopic Occurring at a normal place.
Osteoblast Bone forming cell.
Osteoclast Large, multinuclear cell associated with absorption and removal of bone.
Osteogenic Relating to or derived from the tissue from which bone is developed.
Tissue engineering The application of the principles and methods of engineering and life sciences toward the fundamental understanding of structure/function relationships in normal and pathological mammalian tissues and the development of biological substitutes to restore, maintain, or improve functions.
Trace element Any metal or nonmetal found in minute quantities in the human body which are essential components of the diet, but are harmful if taken in excess.

Abbreviations

ALP	Alkaline phosphatase
BCP	Biphasic calcium phosphate
BMP	Bone morphogenetic protein
CaP	Calcium phosphate
FGF	Fibroblast growth factor
FTIR	Fourier transform infrared spectroscopy
HA	Hydroxyapatite
IGF	Insulin-derived growth factor
MSC	Mesenchymal stromal cell
PDGF	Platelet-derived growth factor
SBF	Simulated body fluid
TCP	Tricalcium phosphate
TGF-β	Transforming growth factor beta
XRD	X-ray diffraction

1.118.1. Introduction

Regenerative medicine, a field that is aimed at restoring rather than replacing the function of damaged and degraded organs and tissues, is becoming increasingly important in our society with aging population. In the areas of orthopedic and craniomaxillofacial surgery, for example, there exists a great demand for bone regeneration strategies. Restoration of bone defects caused by tumor removal, infections, traumas, as well as spinal fusion are frequently performed surgeries in the clinic. Currently, treatments of bone defects include the use of natural bone grafts, synthetic bone graft substitutes, and tissue-engineered constructs (Figure 1).

The goals of these different strategies are to provide an environment that is similar to natural bone and to facilitate bone regeneration in the defect area as optimally as possible. Approaches to bone regeneration are therefore developed on the basis of the properties of bone tissue, which are summarized in the next section.

1.118.2. Bone

Bone is a highly specialized form of connective tissue that is nature's provision for an internal support system in most higher vertebrates. Bone provides for the attachment of the muscles and tendons essential for movement, protects the vital organs of the cranial and thoracic cavities, and encloses the blood-forming elements of the bone marrow. In addition to these mechanical functions, bone plays an important metabolic role as a mobilizable store of calcium and phosphate, which can be drawn upon when needed in the homeostatic regulation of calcium and phosphate in blood and other fluids of the body.[1]

Morphologically, there are two forms of bone: cortical (compact) bone and cancellous (trabecular) bone. Compact bone, which is rigid with little porosity, is found mainly in long bones or shells of other bones. Found predominantly in the epiphyses, ribs, and spine, cancellous bone has a highly porous structure ($>75\%$), with numerous small bone trusses or trabeculae interconnected with each other, and tends to orient along the principal directions in adaptation to the external loading environment.

Bone comprises several cell types. Osteoblasts, osteoclasts, and bone lining cells are present on bone surfaces, whereas osteocytes are present within the mineralized interior. Osteoblasts and bone lining cells originate from local osteoprogenitor cells, whereas osteoclasts arise from the fusion of mononuclear precursors, which originate in the various hemapoietic tissues. Osteoblasts are the fully differentiated cells responsible for the production of the bone matrix and regulation of its mineralization. The osteocyte is a mature osteoblast within the bone matrix and is responsible for the matrix maintenance. Bone lining cells are flat, elongated cells that cover bone surfaces that are undergoing neither bone formation nor resorption. Little is known regarding the function of these cells; however, it has been speculated that bone lining cells can be precursors for osteoblasts. Osteoclasts are large, multinucleated cells, which can resorb bone and its mineral.

By weight, bone contains ~60% mineral, 10% water, and about 30% organic matrix. Type I collagen constitutes ~90% of the organic matrix; the remaining 10% is composed of proteoglycans and numerous noncallogeneous proteins, such as osteocalcin, osteopontin, osteonectin, bone sialoprotein, decorin, and biglycan.[2,3]

The inorganic component of bone mineral consists of nonstoichiometric hydroxyapatite, the exact composition of which varies depending on the location and function in the body,

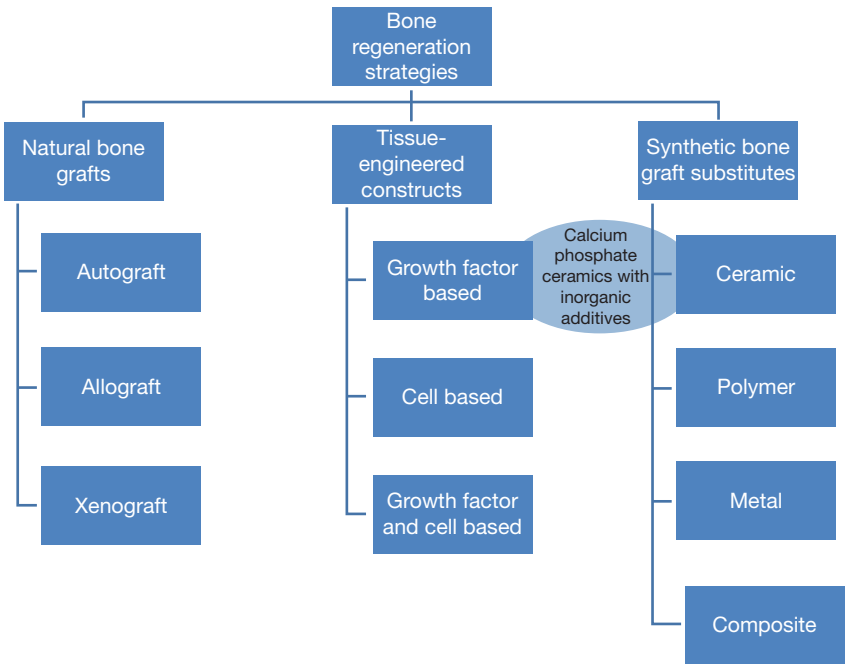

Figure 1 An overview of current strategies in bone repair and regeneration.

species, and age. Carbonate is the most abundant substitute in biological apatite crystal lattice, accounting for 2–8 wt% of total bone mineral in most mammals.[4] Apart from calcium, phosphate, and carbonate, bone mineral contains a great number of other inorganic compounds in varying quantities.

1.118.3. Current Methods in Bone Regeneration

1.118.3.1. Natural Bone Grafts

Patient's own bone meets all the requirements for successful bone regeneration, and it is therefore little surprising that autologous bone is still considered the gold standard in most applications. By its very nature, autologous bone grafts do not cause an immunogenic reaction upon use. Furthermore, they possess a great biological performance in terms of osteogenicity (supply of bone forming cells by the bone marrow),[5] osteoinductivity (initiation of the differentiation of mesenchymal stem cells toward the osteogenic lineage by, e.g., bone morphogenetic proteins (BMPs) present in the graft),[5–8] and osteoconductivity (facilitation of cell and nutrient infiltration through the 3D porous structure).[5,7,9] Several drawbacks are, however, associated with harvesting autologous bone grafts: an additional surgery is required; it is occasionally the cause of donor site morbidity,[5–7,10] chronic postoperative pain,[7,11–13] hypersensitivity,[7] and infections.[8,11,14] In addition to these drawbacks, limited availability of autologous bone is also an important reason why alternative bone regeneration strategies are needed. Other natural bone grafts, allografts and xenografts, are less limited in available quantity, but their performance is often inferior to that of autografts[5,13,15–17] because they need to undergo a number of treatments in order not to cause an immunogenic reaction.[18,19]

1.118.3.2. Synthetic Bone Graft Substitutes

Synthetic bone graft substitutes present an attractive alternative to natural bone grafts, in the first place because of their unlimited and off-the-shelf availability. Second, the fact that they do not cause an immunogenic response and that they can easily be tailored to meet requirements of a specific application explains a great number of substitutes developed in the past few decades. Although all three material types, metals, polymers, and ceramics, and combinations thereof have been used to develop bone graft substitutes, the use of calcium phosphate (CaP)-based biomaterials, mostly ceramics, has garnered the largest interest. The fact that the inorganic component of bone is basically a CaP mineral is the main reason for this interest and emphasizes the fact that the rationale behind a tissue regeneration strategy is often an attempt to create an optimal environment for regeneration.

1.118.3.2.1. Calcium phosphate ceramics

CaP ceramics possess chemical composition similar to that of bone and tooth mineral. In addition to an excellent biocompatibility, their bioactivity is remarkable.

As reviewed by Damien and Parsons,[7] various CaP biomaterials have shown some distinct clinical successes. Hydroxyapatites (HA), for example, both of natural (coral- and bovine bone-derived) and synthetic origin, have widely been tested and successfully used for clinical applications. Owing to its low resorption rate, HA has proven to be a good material for alveolar ridge augmentation, pulp capping, and filling of periodontal defects, where the use of autologous bone, which is resorbable, has been found to be less than optimal. In orthopedics, porous HA blocks have been used for filling defects remaining after tumor excision, as well as in spinal fusion of vertebral bodies. Tricalcium phosphate (TCP) is another widely used ceramic, particularly in applications where degradation of the material is required. Dental applications of TCP ceramics include the filling of defects due to periodontal loss, as well as repairing cleft palates. In orthopedics, TCP has been used in spinal fusion. A ceramic receiving much attention is biphasic calcium phosphate (BCP), consisting of HA and TCP. By altering the ratio of HA to TCP, variable rates of degradation can be achieved, an example of adaptability of synthetic bone graft substitutes to an intended application. Clinically, BCP has been tested for treatment of patient with scoliosis and for filling defects after tumor removal. Currently, CaP ceramics can be made in the form of particles, dense and porous scaffolds,[20,21] and even in more defined shapes using free form fabrication techniques.[22] Their microstructure can be modified by controlling production process, in order to control their bioactivity *in vivo*.[23] **Figure 2** shows an example of CaP ceramic particles (a), macro- (b) and microstructure (c) of porous CaP ceramic, and its bonding to bone (d), which is a sign of bioactivity.

It should be noted that ceramics are intrinsically brittle. This is an important limitation, because restoring the function of bone tissue includes restoration of mechanical properties of bone. However, brittle materials cannot be used in load-bearing applications, where mechanical load needs to be (temporarily) taken over by the implant. In order to overcome this limitation, ceramics are often combined with other materials, such as metals and polymers in the form of coatings[24–28] or composite materials.[29–31]

1.118.3.3. Tissue Engineering

Despite intensive research and continuous improvements of synthetic biomaterials, so far these materials by themselves have not shown a biological performance that is equal to that of autologous bone grafts. Bone conduction over the material surface and the replacement by bone as well as their mechanical properties are usually inferior to autologous bone grafts.[7,15,32–34] Tissue engineering is a relatively recent development, which was, in 1993, defined as an 'interdisciplinary field that applies principles of engineering and life sciences toward the development of biological substitutes that restore, maintain, or improve tissue function' by Langer and Vacanti.[35] In practice, in tissue engineering, attempts are made to create constructs with properties and function similar to that of natural tissue. In other words, rather than using a bioactive CaP ceramic that resembles bone mineral, an additional step is made to add cells and/or growth factors to the ceramic, creating thereby a construct that resembles both mineral and organic component of bone. Bone tissue-engineering construct

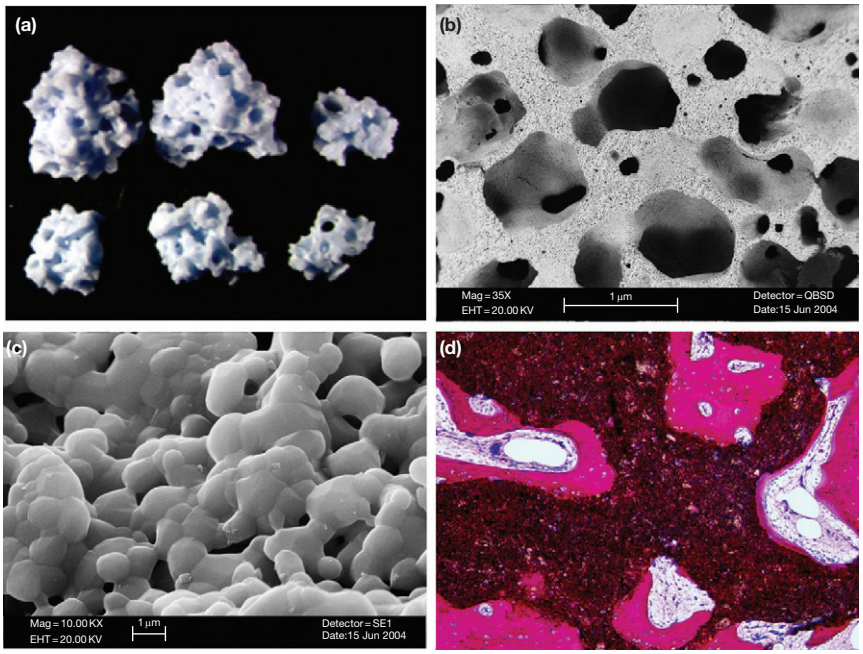

Figure 2 Calcium phosphate ceramic: (a) digital micrograph showing ceramic particles, (b) low magnification scanning electron microscopy micrograph of an open porous macrostructure, (c) high magnification scanning electron microscopy micrograph showing microstructure with ceramic grains among which micropores are found, and (d) light microscopy micrograph of a histological slide showing bone that has formed inside the ceramic pores and is in close contact with ceramic surface.

most often consists of a (synthetic) carrier loaded with bone-inducing substances (chemical stimulation of bone formation-growth factor based tissue engineering), osteogenic cells/tissue (cell-based tissue engineering), or both.[35]

To date, numerous growth factors have been identified and subsequently produced by recombinant gene technology, such as bone morphogenetic proteins (BMPs) and other members of the transforming growth factor β (TGFs-β) family, fibroblast growth factors (FGFs), platelet-derived growth factors (PDGFs), and insulin-derived growth factors (IGFs). Various studies have shown that bone growth factors have several regulating effects on cells from the osteoblastic lineage and *in vivo* studies have demonstrated that some factors can induce bone formation and/or stimulate bone healing. Kirker-Head has reviewed the application of BMPs in a number of animal models at various orthotopic sites, such as in spinal fusion, long bone defects, mandibular and cranial bone defects, fracture healing, as well as periodontal regeneration, alveolar ridge augmentation, and osteointegration of dental implants.[36] In addition, various preclinical and clinical studies have shown positive effects of BMP in nonunions and segmental defects, such as traumatic tibial defects[37,38] and femoral defects.[39]

The combination of autologous cells with carriers is another way to produce tissue-engineered hybrids. Various cell types such as calvarial[40,41] and periostal[42,43] cells, osteoblasts of trabecular bone,[44,45] chondrocytes,[46] and vascular pericytes[47] have been tested as potential sources of bone-forming cells. Nevertheless, the most widely used source of osteogenic cells is bone marrow. Bone marrow has been recognized as a source of osteoprogenitor cells that can differentiate toward bone-forming cells when cultured under adequate conditions.[48–51] In addition, bone marrow has been shown to be the most abundant source of osteoprogenitors, which possess high proliferative ability and great capacity for differentiation.[52,53] Studies in rodents have shown the feasibility of the tissue-engineered hybrids, consisting of a carrier and bone marrow stromal cells, after ectopic[54,55] and orthotopic implantation.[54–58] In larger animals, there are a few studies showing the biological performance of the TE hybrids, in ectopic[59–61] and orthotopic sites.[62–64] In a small number of studies in which cell-based tissue-engineered constructs have been tested in humans, the results obtained showed varying degrees of success.[65]

Although both growth factors-based and cell-based tissue-engineered constructs have shown the capability to enhance bone formation when implanted orthotopically, their biological performance is largely dependent on the construct carrier. For example, when BMPs are implanted without a carrier, they are reported to diffuse too rapidly to be able to induce or to enhance new bone formation. Further, the amount of BMP necessary to achieve a certain dose *in vivo* is also carrier dependent.[66–68] Similarly, a suitable carrier is a prerequisite for the success of a cell-based tissue-engineered construct. For instance, recent studies have shown that bone formation in tissue-engineered constructs is restricted to confined areas of the scaffold. Further, bone bridging between individual tissue-engineered material granules is exceptional. In addition, the findings of the clinically relevant studies suggest that the effect of tissue engineering is moderate and may be irrelevant at long-term implantation intervals.[69] The tissue-engineering technique is also associated with some drawbacks.

The production of recombinant growth factors, collection and transport of the biopsies, and culture of autologous cells are some of the factors that make tissue-engineering time, money, and labor consuming.

1.118.4. Improvement of Synthetic Bone Graft Substitutes

From this overview of the current status of bone regeneration strategies, the following summary can be made: (1) autologous bone is the gold standard with regard to biological performance, but its limited availability creates a need for comprehensive alternatives; (2) synthetic bone graft substitutes have a great advantage of being available in large quantities off-the-shelf and relatively inexpensive, but their biological performance by itself does not position them as an alternative to autograft; and (3) tissue engineering is a strategy with great possibilities, but owing to its complexity, extensive research is needed before tissue engineering will be widely applied in the clinic.

For material scientists, a real challenge lies in the improvement of the biological performance of the existing bone graft substitutes, while retaining their synthetic character. In this chapter, the potential use of inorganic additives to bone graft substitutes will be discussed as 'synthetic growth factors' (Figure 1). These inorganic additives are compounds found in bone mineral as trace elements. As mentioned in the section on bone composition, the inorganic component of bone is nonstoichiometric HA, mainly consisting of calcium (36.6 wt%), phosphorus (17.1 wt%), and carbonate (4.8 wt%). In addition, a number of other components are also found in bone minerals, such as sodium (1 wt%), potassium (0.07 wt%), fluorine (0.1 wt%), chlorine (0.1 wt%), magnesium (0.6 wt%), and strontium (0.05 wt%).[70] In an early work by Becker and coworkers, presence of alumunium, copper, iron, manganese, lead, silicon, tin, vanadium, and zinc has also been determined in human bone.[71] In 1997, El-Amri and El-Kabroun used neutron activation analysis and showed that also barium and bromine are present in human bone.[72] Most of these elements have an effect on properties of bone mineral, such as its mechanical and degradation properties. In addition, a number of them can influence processes of angiogenesis, bone formation, and remodeling, all of which are of importance in the field of bone regeneration. Probably, the best example of use of trace elements in bone regeneration and bone-related diseases is the clinical use of strontium ranelate in patients with osteoporosis. But there is also evidence that other elements can influence processes related to bone formation and remodeling. We have chosen three metallic components (cations), namely, zinc, copper, and strontium, and two nonmetallic components (anions) of bone, namely, fluoride and carbonate, to discuss their potential use in bone regeneration. The occurrence of these five ions in bone is summarized in Table 1. First, their importance will be discussed in bone metabolism and a literature review will be given on their effect on processes related to bone formation and remodeling. Then, a number of methods will be discussed to incorporate these elements in CaP-based ceramics and an overview of studies in which the ceramics with additives were tested with regard to bone formation and resorption will be given. Finally, some future perspectives in the search for and investigations of 'synthetic growth factors' will be given.

Table 1 Occurrence of zinc, copper, strontium, fluoride, and carbonate in bone

Element	*Content*
Zinc	60–85 ppm (in ash of human cortical bone)[71]
	153–266 ppm (in ash of various human bones)[73]
	54–315 ppm (in lyophilized human bone)[72]
Copper	5 ppm (in ash of human cortical bone)[71]
Strontium	62–130 ppm (in ash of human cortical bone)[71]
	11–418 ppm (in lyophilized human bone)[72]
Fluoride	0.1 wt% (in mineral of bovine cortical bone)[70,74]
	0.08–0.69 wt% (in ash of human iliac crest bone)[5]
Carbonate	4.8 wt% (in mineral of bovine cortical bone)[70,74]
	5.1–5.8 wt% (ash of human iliac crest bone)[75]

1.118.5. Trace Elements in Bone Metabolism and Processes Related to Bone Formation

1.118.5.1. Zinc

The amount of zinc in the human body is relatively low, between 1.4 and 2.3 g, on biochemical level; however, its importance has been proven in a number of physiological processes.[73] Zinc is required for the activity of over 300 metalloenzymes, including those involved in nucleic acid and protein synthesis, cellular replication, immune function, and antioxidant systems.[76] It is a constituent of various enzymes and proteins such as alkaline phosphatase (ALP), lactate dehydrogenase (LDH) and carbonic anhydrase, steroid hormone receptors, and transcription factors.[77,78] There exist about 1400 zinc-finger proteins that participate in the genetic expression of a range of proteins.[79] The amount of zinc in bone is relatively high as compared to that in other tissues. As reviewed by Colhoun and coworkers, human bone ash contains between 150 and 250 $\mu g\,g^{-1}$ zinc, depending on the location in body. Zinc deficiency is associated with a number of skeletal anomalies in fetal and postnatal development, such as depressed bone age, which can be treated with zinc supplementation. It was demonstrated that nutritional zinc deficiency results in a decrease of zinc concentrations in bone. Early studies indicated an increase in the uptake of zinc in the areas of bone healing, in particular, in the areas in close proximity to the sites of calcification, as well as during ectopic bone formation, suggesting the influence of zinc in osteogenesis.[73] The role of zinc in the bone has been shown to be twofold: (1) zinc plays a structural role in the bone matrix that consist of HA crystals, which contain zinc complexed with fluoride and (2) zinc is involved in the stimulation of bone formation by osteoblasts and inhibition of bone resorption by osteoclasts.[80]

Yamaguchi and coworkers, for example, showed an increase in Runx-2, osteoprotegerin, and regucalcin mRNA expression by MC3T3-E1 osteoblast-like cells in the presence

of zinc sulfate, at concentrations of 10^{-6}–10^{-4} M.[81] More recently, Kwun and colleagues showed that zinc deficiency reduced osteogenic activity of MC3T3-E1 cells *in vitro* by decreasing bone marker gene transcription through reduced and delayed Runx-2 expression and by reduction of extracellular matrix mineralization through a decrease in alkaline phosphatase (ALP) activity.[82] The effect of zinc on human osteoblast-like cell line SaOS-2 was also investigated, and it was observed that both ALP expression and the formation of mineral nodules were stimulated in presence of zinc at concentrations of 1 and 10 μM but inhibited at concentrations higher than 25 μM.[83] When primary murine bone marrow stromal cells and osteoblast were treated with zinc at concentrations of 10^{-9} M and lower, no effect was observed on proliferation, and inhibitory effect was proven on both osteogenic and adipogenic differentiation.[84]

As recently reviewed by Yamaguchi, zinc has been shown to have an inhibitory effect on bone resorption in tissue culture systems *in vitro* and to suppress osteoclastogenesis of osteoclastic cells derived from bone marrow.[85]

1.118.5.2. Copper

Copper deficiency is generally associated with syndromes of anemia and pancytopenia, as well as with neuro-degeneration in humans and other mammals. In the metabolism of the skeleton, copper performs a key catalytic function in the first step of the maturation of collagen to form stable fibrils.[86,87] This effect can be attributed primarily to the copper-dependent enzyme lysys oxidase, for which copper acts as cofactor. Lysyl oxidase is required for the formation of lysine-derived cross-links in collagen and elastin.[88] Several reports suggested that mild copper deficiency may contribute to bone defects such as osteoporotic-like lesions and bone fragility in humans and animals,[89,90] as well as to a variety of bone developmental defects in preterm infants.[91,92] Oral supplementation with copper, however, resulted in complete healing of fractures and improvement in other bone defects.[91,92]

Copper was shown to affect both the proliferation and differentiation behavior of mesenchymal stem cells (MSCs) *in vitro*. It decreased the proliferation rate of MSCs and induced an increase in their differentiation toward the osteogenic and adipogenic lineage.[93] Copper was also reported to affect the timing of expression of ALP activity, which reached its maximum earlier than in the controls in absence of copper.

Copper also plays a role in the inhibition of bone resorption through its action as a cofactor for superoxidase dismutase, an antioxidant enzyme containing a zinc and a copper atom, which acts as a free radical scavenger, neutralizing the superoxide radicals produced by osteoclasts during bone resorption.[80] While an inhibition in osteoclast function was observed in copper-deficient animals,[94] Wilson suggested that higher concentrations of copper in cell culture medium (10^{-5} M copper sulfate) reduced bone resorption and inhibited hydroxyproline, protein, and DNA synthesis *in vitro*.[95]

In a number of studies, copper was also shown to have an effect on angiogenesis, a process which is of great importance in bone regeneration. Angiogenesis is essential for the survival of osteoblasts, as well as for the regulation of fracture healing and bone remodeling.[96,97] Previous reports showed that copper can enhance growth of endothelial cells *in vivo*,[98–100] and copper found in wound tissues is known to be involved in generation of free radicals during tissue regeneration.[101]

1.118.5.3. Strontium

Strontium is, similar to calcium, a group IIa element and, from a chemical point of view, they behave similarly. Although strontium is not an essential trace element, a substantial amount of research has been performed on its properties and effects due to its chemical analogy to calcium. Strontium is a bone-seeking element, of which 98% in the human body can be found in the skeleton.[102] It is therefore not surprising that among the trace metals present in human bone, strontium was the only one that was correlated with bone compressive strength.[103] Strontium was shown to have dose-dependent effects on bone formation, which was further affected by presence or absence of renal failure. While low doses (0.19–0.34% in drinking water during 9 weeks) were reported to improve the vertebral bone density and stimulate bone formation in rats with normal renal function,[104–106] high doses (> 0.4% in drinking water) were shown to have deleterious effects on bone mineralization.[104,105] However, in animals with chronic renal failure, 0.34% of strontium (as chloride compound) in drinking water induced a bone lesion histologically characterized as osteomalacia.[107] This and further studies on a similar model showed the effect of strontium to be complex and dose dependent.

Similar, dose-dependent effect of strontium was also observed in cell culture experiments. Studies with primary osteoblasts isolated from fetal rat calvaria showed that at low doses (1 μg ml^{-1} strontium in the culture medium) reduced nodule formation occurred in the presence of intact mineralization; at an intermediate concentration (5 μg ml^{-1}), no effect was observed, while at high concentrations (20–100 μg ml^{-1}), intact nodule formation was accompanied by reduced mineralization.[108]

Strontium was also shown to reduce excessive bone resorption in rats with osteopenia, which was associated with a decrease in the number of osteoclasts.[109] Baron and Tsouderos further showed that a distrontium salt, S12911, dissolved into the culture medium inhibited osteoclast differentiation and osteoclast activity in a dose-dependent manner, without affecting the attachment of the osteoclast.[110]

As mentioned before, current clinical use of strontium ranelate for treatment of osteoporosis is an excellent example of application of inorganic trace elements in bone-related conditions. The dual anabolic and antiresorptive role of strontium ranelate has been described *in vitro*.[111] As recently reviewed by O'Donnell and coworkers, there is evidence that supports the efficacy of strontium ranelate in reducing vertebral and, to a lesser extent, nonvertebral fractures in postmenopausal osteoporotic women and in increasing bone matrix density in postmenopausal women with and without osteoporosis.[112,113]

1.118.5.4. Fluoride

Fluoride has been recognized as an important element in mineralized tissues, such as teeth and bone, for over a century.

Initial attention was paid to environmental overexposure to this element as a cause of crippling bone disease. However, research that followed led to some major clinical successes, in particular, in dentistry with eradication of endemic dental fluorosis worldwide and a successful water and topical fluoridation program that has reduced prevalence of dental caries.[114] The role of fluoride in the prevention and control of dental caries in both humans and animals has been shown to be predominant in the maturation stage of enamel formation.[115–119] Fluoride was also found to be the single most effective agent for increasing bone volume in the osteoporotic skeleton[120] and an effective anabolic agent to increase spinal bone density by increasing bone formation and mineralization.[121,122] Similar to strontium, fluoride was shown to have a dose related effect on bone formation: low doses of fluoride (50 mg sodium fluoride daily) increased the trabecular bone density of osteoporotic patients,[123–125] whereas a dose of 75 mg day^{-1} had no beneficial effects on bone mineral density in postmenopausal women.[126] Fluoride intake of 0.8 mg kg^{-1} also stimulated bone formation in rats.[106] Complex and dose-dependent effects of fluoride, together with reports showing an increase in occurrence of osteoporotic hip fractures related to regular fluoride intake, were important reasons for the lack of major achievements of fluoride treatment in orthopedics.

Also *in vitro*, dose-dependent effects of fluoride were observed. Bellows *et al*. demonstrated an increase in proliferation of fetal rat calvarial osteoblasts with increasing dose of sodium fluoride in cell culture medium in concentrations between 10 and 500 μM, with higher concentrations being cytotoxic.[127] A positive effect of 10 μM sodium fluoride on proliferation in culture medium was also observed on embryonic chick calvarial cells, while no effect was found in human osteoblast cultures.[114] Recently, dose-dependent effect of sodium fluoride was found on proliferation and differentiation of caprine osteoblasts: at concentrations below 10^{-5} M of sodium fluoride in cell culture medium, cell proliferation and ALP expression were enhanced, whereas above this dose, apoptosis occurred and a decrease in ALP expression was observed.[128] Burgener and coworkers suggested that fluoride enhances protein tyrosine phosphorylation in osteoblast-like cells UMR-106, by enhancing tyrosine kinase activity, postulating that this signal transduction pathway is involved in the osteogenic effect of fluoride.[129]

The effect of fluoride on the behavior of osteoclasts has been reported in a study where rabbit primary osteoclasts were cultured on thin slices of bovine bone. Sodium fluoride in concentrations of 0.5–1.0 mM in medium decreased the number of resorption lacunae made by individual osteoclasts as well as the resorbed area per osteoclast.[130] It was further shown that the suppression of the resorption was enhanced by increasing the sodium fluoride concentration of the cell culture medium.[131]

1.118.5.5. Carbonate

Carbonate, together with calcium and phosphate, is a major constituent of bone mineral, which makes it, potentially, an interesting compound for the treatment of damaged and degraded bone tissue. Bone mineral of most mammals contains between about 2 and 8 wt% carbonate,[4,70,132] depending on the age of the individual.[133] Type B carbonated apatite (CO_3^{2-} for PO_4^{3-} substitution, coupled with Na^+ for Ca^{2+} substitution) prevails in biological apatites.[132] A small amount CO_3^{2-} is believed to be a substituent for OH^- groups, known as type A substitution.[134] Type A to type B ratio in biological apatites is between 0.7 and 0.9.[135] Introducing carbonate groups in the structure of hydroxyapatite mineral, in general, results in a decrease of crystallinity and increase of solubility *in vitro* and *in vivo*.[136] Direct addition of carbonate to the cell culture medium will mainly affect its pH, which is of relatively little interest. Carbonate will therefore be discussed in more detail in the section on CaP ceramics with inorganic additives.

1.118.6. Inorganic Additives in Calcium Phosphate Ceramics

1.118.6.1. Methods of Preparation

A great advantage of inorganic additives, in comparison with organic compounds such as growth factors, is their thermal stability; that is, inorganic additives do not require physiological conditions to retain their stability and functionality. However, although standard methods of preparation can often be used, processes sometimes need adaptations for various additives to be efficiently incorporated into a CaP ceramic. Method of incorporation determines the way an element is a part of the ceramic and therewith also the release profile and the efficiency of the element upon release.

Powder preparation is often a first step in the process of ceramic production. Depending on the desired ceramic type, the produced powder then undergoes a number of subsequent processes. For sintered, porous, or dense ceramics, for example, calcination, slurry preparation, drying, and sintering are frequently the steps following powder preparation. In the case of nonsintered ceramics or cements, powder is often mixed with a liquid phase to initiate setting of cement. A great number of different coating techniques also exist, which are used to provide surfaces of, for example metallic, implants with a CaP ceramic layer. The most widely used coating method is plasma-spraying,[137,138] but alternative methods such as double decomposition,[139] biomimetic,[140–142] electrolytic deposition,[143,144] sol–gel,[145–147] laser,[148–152] magnetic sputtering,[137] and hydrothermal coating[153–156] have garnered interest in the past few decades. For a number of these methods, powder is a starting point; for others, precipitation of the coating directly from a solution is a part of the process.

Inorganic additives are frequently incorporated into a ceramic (coating) during the process of powder production, either by addition of a salt into the solution from which CaP phase is precipitated or by adding a precursor containing the additive of choice into a sol–gel process. Another way of additive incorporation is in the later stage of ceramic processing, by a solid-state reaction. In this case, a ceramic powder, such as HA or β-TCP, is mixed with a salt of choice, followed by heating at high temperatures, which allows incorporation of the inorganic additive into the ceramic powder.

Metallic ion additives can be doped into the crystal lattice, which is one of the most widely used methods of

incorporation. A maximum exists for the amount of dopant that can be added, above which impurities are formed.

Zinc, for example, is often incorporated into β-TCP ceramics.[157] Incorporation of zinc into β-TCP stabilizes the crystal lattice, preventing conversion to α-tricalcium phosphate,[158] thus increasing the thermal stability of the β-TCP. To manufacture a zinc TCP (ZnTCP) powder, an adapted coprecipitation process as used for the preparation of β-TCP and HA production can be applied. First, to a solution of calcium oxide, zinc nitrate is added with a final molar ratio of 10% in Zn:(Ca+Zn). Up to 12 mol% zinc can be taken up, as at higher concentrations, an impurity appears in the form of $Zn_2Ca(PO_4)_2$. Then, phosphoric acid is added as a source of phosphate, resulting in the precipitation of a zinc-containing powder, which is then used for further ceramic preparation.[157,159] Also sol–gel reactions with, for example, zinc nitrite as a precursor,[160] and solid-state reactions, wherein β-TCP powder was mixed with zinc phosphate powder and heated,[158] were used to produce zinc-containing ceramic.

Incorporation of zinc into HA results in instability of the crystal lattice, because of the lack of adequate atomic sites. Zinc exhibits an inhibitory effect on crystallization of HA, and heat treatment of HA in presence of zinc resulted in conversion into β-TCP, with a reduced lattice constant in comparison to pure β-TCP.[161]

A way to obtain strontium-doped β-TCP is by mixing tristrontium phosphate (α-TSrP/$Sr_3(PO_4)_2$), obtained by solid-state reaction of strontium carbonate and ammonium phosphate at a ratio of 3:2, with β-TCP powders, followed by heat treatment.[158] Strontium has also been added to HA powders, either by a coprecipitation process or sol–gel method. In the coprecipitation process, strontium substitution occurred by the replacement of a part of calcium nitrate with strontium nitrate in the reaction with ammonium phosphate. The overall molar ratio was kept at 10:6 with $(NH_4)_2HPO_4$:(Ca$(NO_3)_2 + Sr(NO_3)_2$), which is the desired Ca/P ratio for HA.[162]

To create a single-phase strontium HA, a sol–gel route was followed. A solution of sodium diphosphate was added to a strontium nitrate solution, with a molar ratio for Sr:P of 2:1. Then, sodium alginate (Na-Alg) was added to the aqueous solution-containing $Sr(NO_3)_2$ and $Na_4P_2O_7$ according to the molar ratio of Sr:P:Na-Alg = 2/1/2.5, followed by drying and calcination of the sol. The phase composition appeared highly dependent on the amount of Na-Alg added. When other ratios were used, phases such as $Sr_2P_2O_7$ and/or $Sr_3(PO_4)_2$ also formed.[163]

In contrast to zinc and strontium doping, a relatively limited amount of work has been done on copper doping of CaP ceramics. In a paper by Belik and coworkers, it was reported that $Ca_{10.5-x}Cu_x(PO_4)_7$ with $x = 0$, 1/6, 1/3, 1/2, 2/3, 5/6, 1, 7/6, 4/3, and 1.5 can be synthesized after the substitution of calcium by copper within the structure of β-TCP through a solid-state reaction.[164]

Fluoridated apatite powders can be readily made by adding a fluoride donor during CaP precipitation process, whereby F^- substitutes the OH^-,[165–167] leading to a reduction in crystal size and an increase in structure stability.[74,75]

Synthetic carbonated apatite type A (CO_3^{2-} for OH^- substitution) has been successfully produced by using a time-consuming process of sintering HA powder under CO_2 supply or by soaking HA powder in an aqueous solution saturated with CO_2.[70,168] Preparation of type B (CO_3^{2-} for PO_4^{3-} substitution, coupled with Na^+ for Ca^{2+} substitution) or type AB is more complex and occurs predominantly via closely controlled aqueous precipitation reactions.[169–173] However, when carbonated apatite powders are sintered to produce highly crystalline, porous ceramics, excessive loss of carbonate may occur[172,174,175] due to thermal instability of carbonated apatites.[176,177]

1.118.6.2. Effect of Inorganic Additives on Ceramic Properties

Effects of incorporation of inorganic additives on the physicochemical and structural properties of CaP ceramics, and consequently their biological behavior, are largely dependent on the way an additive is incorporated into the crystal lattice. HA crystals possess a hexagonal structure with a $P6_3/m$ space group (a space group with a sixfold symmetry axis with a threefold helix and a mirrorplane) and with cell dimensions $a = b = 9.42$ Å and $c = 6.88$ Å, but it can also occur in a similar pseudohexagonal monoclinic form with space group $P2_1/b$ (a space group with a twofold rotation axis and an axial translation of width $b/2$ along (010)). HA consists of a skeleton of PO_4^{3-} tetrahedra, with two oxygen atoms in a horizontal plane, and the other two in the plane parallel to the c-axis. In a crystal unit cell, the PO_4^{3-} tetrahedra are divided into two layers, at ¼ and ¾ of crystal, respectively, in such a way that two columns, perpendicular to the basal plane, exist.[178] Cations at site I, Ca I, are coordinated by nine oxygen atoms belonging to six PO_4^{3-} anions, forming triangles and displaying a columnar arrangement. Cations at site II are heptacoordinated by six oxygen atoms belonging to five PO_4^{3-} anions and one OH^- anion. The smallest distance between a cation and a coordinated oxygen is found at site II, while the smallest Ca–Ca distances are observed between Ca^{2+} ions at site I. Small ions (such as Cd^{2+}, Zn^{2+}, and Mg^{2+}) are incorporated preferentially in the HA structure at Ca I. In contrast, large cations (such as Sr^{2+}, Ba^{2+}, and Pb^{2+}) would first replace Ca^{2+} at Ca II.[162] Small monovalent anions occur in the sixfold symmetry axis, in the center of the Ca(II) triangles. F^- substitution has been shown to include interactions with neighboring OH^- ions via hydrogen bonding.[178] Carbonate ion incorporation into the apatite lattice predominantly occurs through phosphate group substitution (type B), whereas particularly in biological apatites, a small amount of carbonate replaces the OH^- ions (type A substitution).[162] Although the structural location of carbonate ions in the lattice is still incompletely understood, it has been shown that A CO_3^{2-} group is centered on the c-axis, whereas the B CO_3^{2-} group is located at the oblique face of the PO_4 tetrahedron.[178]

Incorporation of zinc into the CaP crystal lattice occurs by substitution of calcium ions. It has been shown that zinc incorporation decreases the lattice parameters a and c because of the Zn^{2+} ionic radius, which is smaller than Ca^{2+} ionic radius; however, there have also been reports suggesting an increase in the size of the a and c axes, at higher zinc contents.[179,180] Zinc generally destabilizes the crystal structure, except for that of β-TCP, which has an atomic site, known as a Mg site, that can incorporate divalent cations with an ionic radius ranging from 0.060 to 0.080 nm, where the ionic radius of zinc belongs to.[181] By heating the zinc-doped β-TCP at

temperatures above 800 °C, the zinc-doped β-TCP started to transform into zinc-doped α-TCP, which had higher solubility than β-TCP.[182] The highest content of zinc in the zinc-doped β-TCP was 6 wt%, which was higher than maximum zinc content of 1.26 wt% in zinc-doped α-TCP at 1450 °C.[183] While the zinc content increases, the solubility of TCP decreases. The negative logarithm of the K_{sp} is expressed as $pK_{sp} = 28.686 + 1.7414C - 0.42239C^2 + 0.063911C^3 - 0.0051037C^4 + 0.0001595C^5$, where C is the zinc content in TCP in mol%.[184] XRD results showed that TCP structure did not undergo great changes after substitution.[157,185,186] Rietveld refinement of the XRD data confirmed that the lattice parameters a and c decreased with an increase of the zinc content in β-TCP from 2 to 9 mol%, leading to contraction in the unit cell volume.[187] This effect on the unit cell volume was consistent with the reports on the effect of magnesium and copper and is probably caused by the lower ionic radius of zinc compared to that of calcium.[188,189] Reports also revealed that the replacement of M(5) site of calcium ions in the β-TCP structure was favored, consistent with reports on copper,[164,187] which can be explained by the fact that the Ca–O bond at M(5) site is the shortest mean distance in the β-TCP structure.[190]

Although substitution of zinc into HA is more difficult than substitution into β-TCP, Chung *et al.* successfully synthesized the ZnHA powders by a sol–gel method through addition of zinc ranging from 200 to 20 000 ppm by atomic ratio versus calcium atoms.[191] The TGA analyses, however, implied that the amount incorporated was relatively small. X-ray diffraction (XRD) results, supported by the Fourier transform infrared spectroscopy (FTIR) analysis showed that the only phase present was that of HA.[186,191,192]

HA was also doped with zinc using a hydrothermal method.[179,192] In this study, it was shown that the crystallinity of HA decreased with an increase in the zinc content from 10 to 20 mol%. Dissolution behavior of HA ceramic was affected in the presence of zinc: while Mayer and Featherstone observed a decrease in dissolution, in another study an increase in solubility was observed, possibly due to differences in production methods.[192–194]

In a study, in which copper-substituted β-TCP was prepared through a solid-state reaction, it was shown that the maximum copper content was 8.5 wt%. XRD data showed that the calcium cations on the M(4) and M(5) sites in the β-TCP structure can be replaced by copper cations and also confirmed the dependence of unit cell parameters on the copper concentration.[164] Replacement of Ca^{2+} with Cu^{2+} reduces the bond lengths between calcium and oxygen atoms in the crystalline lattice mainly because of the lower ionic radius of Cu^{2+} as compared with that of the Ca^{2+}.[188,195] From an energy point of view, the total molecular energy decreases with the replacement of Ca^{2+} with Cu^{2+},[188] meaning that copper ions are theoretically preferred to calcium ions.

In a study wherein single-phase strontium-doped β-TCP was produced by preparing a calcium-deficient apatite through aqueous precipitation and consequent heat treatment at a temperature above 700 °C, substitution of calcium by strontium was shown to have an effect on the lattice constant of the resulting β-TCP.[196] Substitution of calcium by strontium led to a significant expansion in both the *a*- and *c*-axes, which were increased with an increasing strontium content because of the larger ionic radius of strontium of 1.13 Å compared with that of calcium (0.96 Å). β-TCP showed the ability to host up to 80 at.% of strontium without provoking a remarkable rearrangement of the unit cell.[158,196,197] These findings were consistent with studies on strontium-substituted α-TCP.[198]

The substitution of calcium by strontium in the HA was proven possible to an extent of Sr/Ca atomic ratio of 30%. Also here, substitution resulted in larger crystal lattice and increased solubility of the ceramic.[199,200] These findings were consistent with other reports where the XRD and FTIR analyses in strontium-containing HA indicated a substantial expansion of the crystal lattice dimensions as compared to pure HA.[201,202]

Replacement of OH^- with F^- in an apatite lattice can bring about a reduction in the volume of the unit cell and a concomitant increase in structure stability.[70,203] FHA nanopowders with the composition of $Ca_{10}(PO_4)_6OH_{2-x}F_x$ (x in the range of 0–2) were successfully synthesized by mechanical alloying method whereby XRD and FTIR analyses revealed only the presence of apatite.[204] XRD patterns showed that some peaks gradually shifted to the right with the fluoride content increasing in FHA, because of the decrease in *a*-axis of the unit cell, caused by lower ionic radius of F^- compared with that of OH^-.[205–207] Dissolution tests showed that solubility decreased with the increase in fluoride content. The minimum solubility was observed at x values of 0.8–1.1, because the substitution of OH^- by F^- resulted in a stronger hydrogen bond between F^- and nearby OH^-, resulting in a more stable structure with lower solubility.[205,208–210]

An increase of carbonate content in a carbonated apatite by both A and B substitution, resulted in contraction of *a*-axis and expansion of *c*-axis of the unit cell, and therefore, in a decrease in crystal size and an increase in crystal strain, which in turn resulted in a higher solubility.[211,212] **Figure 3** shows microstructure of an HA and a carbonated apatite ceramic, produced using a similar method, from which it is obvious that even a carbonate content of about 5 wt% leads to a great decrease of grain size of the ceramic.

1.118.6.3. Biological Performance of Ceramics Containing Inorganic Additives

In this section, release profiles of the inorganic additives from the ceramics are discussed in physiological conditions as well as their effect in *in vitro* and *in vivo* systems related to bone formation and remodeling.

Studies on the *in vitro* release profiles of zinc for the ZnTCP in simulated body fluid (SBF) showed an initial burst release of zinc, followed by a sustained release over a longer period of time. The amount of zinc released increased with the increasing zinc content of the ceramic ranging from 0.6 to 6 wt%.[185] The rate of zinc release was shown to increase when the calcium content of the release medium was decreased.[185]

In a study by Tas *et al.* it was demonstrated that presence of zinc in β-TCP in concentrations 2900 and 4100 ppm increased viability of murine osteoblast-like cells, whereas further increase in zinc content had an opposite effect. ALP activity of these cells was found to reach its maximum on ceramics containing 4100 ppm zinc.[213] Dose-dependent effects on

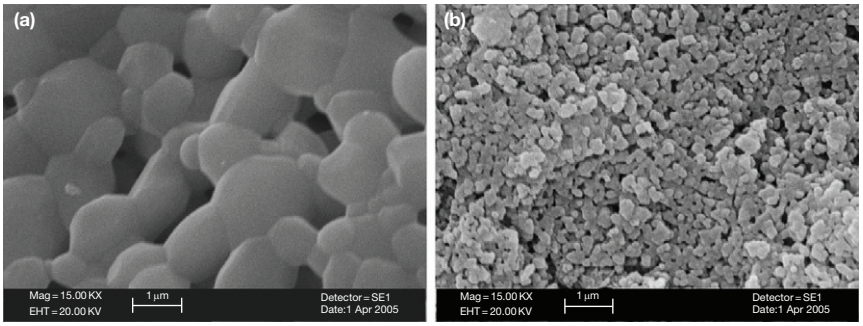

Figure 3 High magnification scanning electron microscopy micrographs showing microstructure of (a) hydroxyapatite and (b) type B carbonated apatite ceramic containing about 4 wt% carbonate, produced using a similar process. Note a significant decrease in crystal size in presence of carbonate.

osteoblastic cell attachment and growth were observed in both zinc-containing HA and β-TCP, with a positive effect up to 1.5 wt% and a negative effect above this level, possibly due to the toxic effects on cells.[186,214] Ito and colleagues also reported a more pronounced MC3T3-E1 osteoblasts proliferation *in vitro* for ZnTCP/HA ceramics with zinc content ranging from 0.6 and 1.2 wt% as compared to the control,[157] which was consistent with other *in vitro* reports.[215,216]

Resorption by mature osteoclasts of ZnTCP with zinc concentrations of 0.316 wt% and especially 0.633 wt%, was lower than resorption of pure TCP, possibly due to an increase in the apoptosis of osteoclasts.[184,217] At a zinc level of 0.633 wt%, the number of apoptotic osteoclasts was 2.8 times higher than on pure TCP after 24 h of culture. These findings were consistent with the laser microscopic measurement experiments on osteoclastic resorption pits, which showed that ZnTCP slightly reduced the resorption area by 15.5%, remarkably reduced the depth of resorption pits by 25.4%, and therewith the volume of resorption pits by 53.9% compared to pure TCP.[218]

In vivo studies in rabbit femora showed that 0.316 wt% of zinc was the optimum concentration at which the largest area of new bone was formed, in both ZnTCP and ZnTCP/HA, whereas zinc content of 0.633 wt% was too high, enlarging the medullary cavity area by stimulated bone resorption.[219] Interestingly, the optimum zinc content *in vivo* was much lower than the zinc amount needed to exert a positive effect of osteoblast proliferation *in vitro*.[157]

Copper-containing CaP ceramics have not been extensively investigated with regard to their bioactivity in bone regeneration; however, simple adsorption of copper ions on a CaP ceramic prepared at room temperature showed a positive effect on angiogenesis *in vitro* and *in vivo*.[220,221] This is an interesting finding because poor vascularization is considered an important reason for failure in timely and complete regeneration of large critically sized bone defects.

In vitro bioactivity studies in SBF showed that Sr-HA, with a strontium content below 10 mol%, showed a more pronounced apatite layer formation on the surface than pure HA, which can be attributed to a higher dissolution rate of strontium-containing ceramic.[200,222] A similar observation was made in strontium-containing TCP.[198] Experiments with osteoprecursor cells (OPC1) showed that both the attachment and proliferation were increased in HA-containing 20 mol% strontium as compared to the control without strontium. Increases in ALP and osteopontin were also seen, suggesting that strontium stimulated osteogenic differentiation of OPC1 cells.[222] Similar findings were also obtained in a study where osteoblast-like cells were cultured on strontium-substituted biphasic CaP ceramic.[223] Pulsed-laser deposition was successfully used to apply a coating of strontium-doped HA, prepared by an aqueous precipitation method, on metallic substrates. Osteogenic differentiation of human osteosarcoma cell line MG-63 was stimulated by strontium (3–7 at.% in the coating), whereas proliferation of osteoclasts was negatively affected.[224]

Injection of strontium-containing CaP cement into rabbit iliac crest cancellous bone revealed that Sr-HA stimulated the formation of osteoblast and osteoid layers, and hence new bone formation.[225]

Fluorinated HA showed a positive effect on proliferation and osteogenic differentiation of cells. In a study by Wang and coworkers, MG-63 cells were cultured on fluorinated HA coatings produced by a sol–gel dipping method. Positive effect of fluoride on cell attachment, as well as ALP and osteocalcin production, was observed in a certain concentration range,[208] at which the ceramic coating had the lowest solubility. A positive effect of fluoride on cell proliferation and osteogenic differentiation was also observed when SaOS-3 rat osteosarcoma cells were cultured on fluorinated HA disks in comparison to fluoride-free controls.[226] In a study by Inoue and coworkers, fluorinated apatite ceramics were tested in a short-term implantation model in rat tibia. A more pronounced bone formation was observed in fluoride-containing ceramic compared to that in an unsintered calcium-deficient apatite ceramic.[227]

Redey and coworkers showed a poor attachment and low collagen production of human primary osteoblasts on carbonated apatite ceramic as compared to that on HA ceramic, possibly caused by the difference in wettability between the two ceramics,[228] which is in agreement with other reports showing a positive correlation between surface energy and attachment of cells.[229–231] After initial cell attachment, however, no significant difference was found in further proliferation of the cells between carbonated and pure HA ceramic. Similar to osteoblast attachment, osteoclast attachment was more pronounced on carbonate-free ceramics compared to the carbonated one, while no difference was observed on the spreading of cells after initial attachment.[232] Doi *et al.* showed that CA was resorbed by osteoclasts in 2-day cultures, while

HA remained unresorbed, suggesting that the presence of carbonate may play a crucial role in osteoclastic resorption,[233] which was in accordance with the results obtained in an *in vivo* experiment in rats.[234] A possible reason could be the released carbonate that stimulates carbonic anhydrase activity and hence promotes acid secretion by osteoclasts.[235] Also Spence and coworkers recently observed an increase in osteoclastic resorption with an increase of carbonate content in an HA ceramic.[236] In an *in vivo* study in rabbits by Landi and coworkers, higher amount of new bone formation was found in sintered carbonated apatite ceramic compared to the pure HA ceramic.[237] An increase in the amount of newly formed bone with increasing carbonate content in an apatite ceramic was also observed in a rat femur model.[238] In a recent study in a critical-size iliac wing model in goats, it was shown that an increase in carbonate content of a ceramic does not necessarily lead to more bone formation if other ceramic properties are not controlled.[177]

Simultaneous incorporation of fluoride and carbonate into apatites led to inhibition of osteoclast proliferation and pit formation *in vitro* as compared to that in pure HA and carbonated apatites, whereas *in vivo*, faster bone remodeling was observed.[239]

1.118.7. Future Perspectives

Incorporation of inorganic additives to improve the biological performance of the existing bone graft substitutes is a complex matter, as we tried to demonstrate in the previous sections, in which we summarized some of the work performed in preparation, characterization, and biological activity assessment of ceramics-containing zinc, copper, strontium, fluoride, and carbonate, respectively. Incorporation of these additives into CaP bone graft substitutes not only adds an additional element into the structure that can exert a certain function but also changes intrinsic properties of the recipient material. The way and the efficiency of incorporation are dependent on the method used. These in turn affect the release profile of the incorporated additive and also the solubility of the recipient itself, and all these affect the behavior of osteoblasts and osteoclasts *in vitro*, as well as the *in vivo* bone formation and remodeling.

Zinc incorporation into β-TCP is responsible for a reduction in cell unit and a decrease in solubility of the ceramic. Zinc has shown positive effects on proliferation and osteogenic differentiation of bone forming cells and decreased osteoclastic resorption *in vitro*, but this effect was dose dependent. Some promising results were observed with regard to bone forming capacity in *in vivo* preclinical models with zinc-doped β-TCP. Copper was shown to have a similar effect on crystal properties as zinc, and although copper-doped ceramics have not been thoroughly tested, there is evidence that copper can stimulate angiogenesis. Strontium replaces calcium in the crystal lattice and increases the size of the unit cell as well as the solubility of the ceramic. Proliferation and osteogenic differentiation of osteoblastic cells were shown to increase in strontium-substituted ceramics, whereas the effect on osteoclast growth was negative. Replacement of OH^- with F^- in an apatite lattice can bring about a reduction in the volume of the unit cell and a concomitant increase in structural stability. Fluorinated apatites can stimulate osteoblast proliferation and osteogenic differentiation, but in a dose-dependent manner. Finally, carbonate is responsible for a decrease in size of an apatitic crystal and an increase in ceramic solubility. Attachment of osteoblastic cells on carbonated ceramics was poorer than on the hydroxyapatite ones, but proliferation was not affected. Osteoclast proliferation and resorption potential were higher on the carbonate-containing CaP ceramics compared to that on the control ceramics without carbonate.

As already mentioned, these are some general remarks about the effects of various additives on properties and efficiency of the existing bone graft substitutes. But due to variations in the preparation and characterization methods and assessment of biological performance of these materials, a comparison among the studies and the results obtained is difficult, and hence general conclusions cannot be drawn. Thus, it behooves the field of biomaterials research to utilize generally accepted, standard methods of study, such that *in vitro* behavior and *in vivo* performance can be correlated. We also suggest that high-throughput study concepts have their place in biomaterials research, such as in the context of quantifying the effect of ionic substitutions with the apatite lattice.

References

1. Fawcett, D. W. In *A Textbook of Histology*, 11 ed.; Bloom, W., Fawcett, D. W., Eds.; W.B. Saunders: Philadelphia, PA, 1986.
2. Derkx, P.; Nigg, A. L.; Bosman, F. T.; *et al*. *Bone* **1998**, *22*, 367–373.
3. Marks, S. C.; Hermey, D. C., Jr. In *Principles of Bone Biology*; Bilezikian, J. P., Raisz, L. G., Rodan, G. A., Eds.; Academic Press: San Diego, USA, 1996.
4. Bigi, A.; Cojazzi, G.; Panzavolta, S.; *et al*. *J. Inorg. Biochem.* **1997**, *68*, 45–51.
5. Lane, J. M.; Tomin, E.; Bostrom, M. P. *Clin. Orthop.* **1999**, *367*(Suppl.), S107–S117.
6. Brown, K. L.; Cruess, R. L. *J. Bone Joint Surg. Am.* **1982**, *64*, 270–279.
7. Damien, C. J.; Parsons, J. R. *J. Appl. Biomater.* **1991**, *2*, 187–208.
8. Urist, M. R. *Science* **1965**, *150*, 893–899.
9. Cornell, C. N.; Lane, J. M. *Clin. Orthop.* **1998**, *355*(Suppl.), S267–S273.
10. Coombes, A. G.; Meikle, M. C. *Clin. Mater.* **1994**, *17*, 35–67.
11. Arrington, E. D.; Smith, W. J.; Chambers, H. G.; Bucknell, A. L.; Davino, N. A. *Clin. Orthop.* **1996**, *329*, 300–309.
12. Cowley, S. P.; Anderson, L. D. *J. Bone Joint Surg. Am.* **1983**, *65*, 1023–1025.
13. Prolo, D. J.; Rodrigo, J. J. *Clin. Orthop.* **1985**, *200*, 322–342.
14. Younger, E. M.; Chapman, M. W. *J. Orthop. Trauma* **1989**, *3*, 192–195.
15. Anderson, M.; Dhert, W.; De Bruijn, J.; *et al*. *Clin. Orthop.* **1999**, *364*, 231–239.
16. Oikarinen, J.; Korhonen, L. K. *Clin. Orthop.* **1979**, *140*, 208–215.
17. Oklund, S. A.; Prolo, D. J.; Gutierrez, R. V.; King, S. E. *Clin. Orthop.* **1986**, *205*, 269–291.
18. Brantigan, J. W.; Cunningham, B. W.; Warden, K.; McAfee, P. C.; Steffee, A. D. *Spine* **1993**, *18*, 1213–1221.
19. Urist, M. R.; Silverman, B. F.; Buring, K.; Dubuc, F. L.; Rosenberg, J. M. *Clin. Orthop.* **1967**, *53*, 243–283.
20. Habibovic, P.; Kruyt, M. C.; Juhl, M. V.; *et al*. *J. Orthop. Res.* **2008**, *26*, 1363–1370.
21. Le Nihouannen, D.; Daculsi, G.; Saffarzadeh, A.; *et al*. *Bone* **2005**, *36*, 1086–1093.
22. Habibovic, P.; Gbureck, U.; Doillon, C. J.; Bassett, D. C.; Van Blitterswijk, C. A.; Barralet, J. E. *Biomaterials* **2008**, *29*, 944–953.
23. Habibovic, P.; Yuan, H.; Van Dervalk, C. M.; Meijer, G.; Van Blitterswijk, C. A.; De Groot, K. *Biomaterials* **2005**, *26*, 3565–3575.
24. Ben-Nissan, B.; Chai, C. S.; Gross, K. A. *Bioceramics* **1997**, *10*, 175–178.
25. Ducheyne, P.; Van Raemdonck, W.; Heughebaert, J. C.; Heughebaert, M. *Biomaterials* **1986**, *7*, 97–103.
26. Havelin, L. I.; Engesaeter, L. B.; Espehaug, B.; Furnes, O.; Lie, S. A.; Vollset, S. E. *Acta Orthop. Scand.* **2000**, *71*, 337–353.
27. Ong, J. L.; Lucas, L. C.; Lacefield, W. R.; Rigney, E. D. *Biomaterials* **1992**, *13*, 249–254.

28. Liu, Y.; Hunziker, E. B.; Layrolle, P.; De Bruijn, J. D.; De Groot, K. *Tissue Eng.* **2004**, *10*, 101–108.
29. Guan, L.; Davies, J. E. *J. Biomed. Mater. Res. A* **2004**, *71*, 480–487.
30. Zardiackas, L. D.; Teasdall, R. D.; Black, R. J.; *et al*. *J. Appl. Biomater.* **1994**, *5*, 277–283.
31. Zhang, R.; Ma, P. X. *J. Biomed. Mater. Res.* **1999**, *44*, 446–455.
32. Blokhuis, T. J.; Wippermann, B. W.; Den Boer, F. C.; *et al*. *J. Biomed. Mater. Res.* **2000**, *51*, 369–375.
33. Boden, S. D.; Martin, G. J., Jr.; Morone, M.; Ugbo, J. L.; Titus, L.; Hutton, W. C. *Spine* **1999**, *24*, 320–327.
34. Zdeblick, T. A.; Cooke, M. E.; Kunz, D. N.; Wilson, D.; McCabe, R. P. *Spine* **1994**, *19*, 2348–2357.
35. Langer, R.; Vacanti, J. P. *Science* **1993**, *260*, 920–926.
36. Kirker-Head, C. A. *Adv. Drug Deliv. Rev.* **2000**, *43*, 65–92.
37. Geesink, R. G.; Hoefnagels, N. H.; Bulstra, S. K. *J. Bone Joint Surg. Br.* **1999**, *81*, 710–718.
38. Johnson, E. E.; Urist, M. R.; Finerman, G. A. *Clin. Orthop.* **1988**, 249–257.
39. Johnson, E. E.; Urist, M. R. *Clin. Orthop.* **2000**, *371*, 61–74.
40. Nefussi, J. R.; Brami, G.; Modrowski, D.; Oboeuf, M.; Forest, N. *J. Histochem. Cytochem.* **1997**, *45*, 493–503.
41. Wada, Y.; Kataoka, H.; Yokose, S.; *et al*. *Bone* **1998**, *22*, 479–485.
42. Miura, Y.; O'Driscoll, S. W. *Cell Transplant.* **1998**, *7*, 453–457.
43. Takushima, A.; Kitano, Y.; Harii, K. *J. Surg. Res.* **1998**, *78*, 68–77.
44. Gundle, R.; Joyner, C. J.; Triffitt, J. T. *J. Mater. Sci. Mater. Med.* **1997**, *8*, 519–523.
45. Robey, P. G.; Termine, J. D. *Calcif. Tissue Int.* **1985**, *37*, 453–460.
46. Bruder, S. P.; Fox, B. S. *Clin. Orthop.* **1999**, *367*(Suppl.), S68–S83.
47. Doherty, M. J.; Ashton, B. A.; Walsh, S.; Beresford, J. N.; Grant, M. E.; Canfield, A. E. *J. Bone Miner. Res.* **1998**, *13*, 828–838.
48. Friedenstein, A. J.; Chailakhyan, R. K.; Gerasimov, U. V. *Cell Tissue Kinet.* **1987**, *20*, 263–272.
49. Maniatopoulos, C.; Sodek, J.; Melcher, A. H. *Cell Tissue Res.* **1988**, *254*, 317–330.
50. Ohgushi, H.; Okumura, M. *Acta Orthop. Scand.* **1990**, *61*, 431–434.
51. Owen, M. *J. Cell Sci. Suppl.* **1988**, *10*, 63–76.
52. Beresford, J. N. *Clin. Orthop.* **1989**, *240*, 270–280.
53. Muschler, G. F.; Boehm, C.; Easley, K. *J. Bone Joint Surg. Am.* **1997**, *79*, 1699–1709.
54. Allay, J.; Dennis, J.; Haynesworth, S.; *et al*. *Hum. Gene Ther.* **1997**, *8*, 1417–1427.
55. Friedenstein, A. J.; Latzinik, N. W.; Grosheva, A. G.; Gorskaya, U. F. *Exp. Hematol.* **1982**, *10*, 217–227.
56. Bruder, S. P.; Kurth, A. A.; Shea, M.; Hayes, W. C.; Jaiswal, N.; Kadiyala, S. *J. Orthop. Res.* **1998**, *16*, 155–162.
57. Cui, Q.; Ming Xiao, Z.; Balian, G.; Wang, G. J. *Spine* **2001**, *26*, 2305–2310.
58. Krebsbach, P. H.; Mankani, M. H.; Satomura, K.; Kuznetsov, S. A.; Robey, P. G. *Transplantation* **1998**, *66*, 1272–1278.
59. Anselme, K.; Noel, B.; Flautre, B.; *et al*. *Bone* **1999**, *25*, 51S–54S.
60. Kruyt, M. C.; De Bruijn, J. D.; Wilson, C. E.; *et al*. *Tissue Eng.* **2003**, *9*, 327–336.
61. Kruyt, M. C.; Dhert, W. J.; Oner, C.; Van Blitterswijk, C. A.; Verbout, A. J.; De Bruijn, J. D. *J. Biomed. Mater. Res.* **2004**, *69B*, 113–120.
62. Bruder, S. P.; Kraus, K. H.; Goldberg, V. M.; Kadiyala, S. *J. Bone Joint Surg. Am.* **1998**, *80*, 985–996.
63. Kruyt, M. C.; Dhert, W. J.; Yuan, H.; *et al*. *J. Orthop. Res.* **2004**, *22*, 544–551.
64. Petite, H.; Viateau, V.; Bensaid, W.; *et al*. *Nat. Biotechnol.* **2000**, *18*, 959–963.
65. Meijer, G. J.; De Bruijn, J. D.; Koole, R.; Van Blitterswijk, C. A. *PLoS Med.* **2007**, *4*, e9.
66. Boden, S. D. *Clin. Orthop.* **1999**, *367*(Suppl.), S84–S94.
67. Hollinger, J. O.; Uludag, H.; Winn, S. R. *Adv. Drug Deliv. Rev.* **1998**, *31*, 303–318.
68. Winn, S. R.; Uludag, H.; Hollinger, J. O. *Clin. Orthop.* **1999**, *367*(Suppl.), S95–S106.
69. Kruyt, M. C. Doctoral Thesis, Department of Orthopedics, University Medical Center Utrecht, 2003.
70. Elliot, J. C. *Structure and Chemistry of the Apatites and Other Calcium Orthophosphates*. Elsevier: Amsterdam, 1994.
71. Becker, R. O.; Spadaro, J. A.; Berg, E. W. *J. Bone Joint Surg. Am.* **1968**, *50*, 326–334.
72. El-Amri, F. A.; El-Kabroun, M. A. R. *J. Radioanal. Nucl. Chem.* **1997**, *217*, 205–207.
73. Calhoun, N. R.; Smith, J. C., Jr.; Becker, K. L. *Clin. Orthop. Relat. Res.* **1974**, *9*, 212–234.
74. Elliot, J. C. *Studies in Inorganic Chemistry: Structure and Chemistry of the Apatites and Other Calcium Orthophosphates*. Elsevier Science: Amsterdam, The Netherlands, 1994.
75. Grynpas, M. D. *J. Bone Miner. Res.* **1990**, *5*(Suppl. 1), S169–S175.
76. Oteiza, P. I.; Mackenzie, G. G. *Mol. Aspects Med.* **2005**, *26*, 245–255.
77. Vallee, B. L.; Auld, D. S. *Biochemistry* **1990**, *29*, 5647–5659.
78. Vallee, B. L.; Falchuk, K. H. *Physiol. Rev.* **1993**, *73*, 79–118.
79. Prasad, A. S.; Bao, B.; Beck, F. W.; Kucuk, O.; Sarkar, F. H. *Free Radic. Biol. Med.* **2004**, *37*, 1182–1190.
80. Lowe, N. M.; Fraser, W. D.; Jackson, M. J. *Proc. Nutr. Soc.* **2002**, *61*, 181–185.
81. Yamaguchi, M.; Goto, M.; Uchiyama, S.; Nakagawa, T. *Mol. Cell. Biochem.* **2008**, *312*, 157–166.
82. Kwun, I. S.; Cho, Y. E.; Lomeda, R. A.; *et al*. *Bone* **2010**, *46*(3), 732–741.
83. Cerovic, A.; Miletic, I.; Sobajic, S.; Blagojevic, D.; Radusinovic, M.; El-Sohemy, A. *Biol. Trace Elem. Res.* **2007**, *116*, 61–71.
84. Wang, T.; Zhang, J. C.; Chen, Y.; Xiao, P. G.; Yang, M. S. *J. Trace Elem. Med. Biol.* **2007**, *21*, 84–91.
85. Yamaguchi, M. *Mol. Cell. Biochem.* **2009**, *338*(1–2), 241–254.
86. O'Dell, B. L. *Philos. Trans. R. Soc. Lond. B Biol. Sci.* **1981**, *294*, 91–104.
87. Tinker, D.; Romero, N.; Rucker, R. In *Trace Element in Man and Animals*; Hurley, L., Keen, C., Lonnerdal, B., Rucker, R., Eds.; Plenum: New York, 1988.
88. Rucker, R. B.; Kosonen, T.; Clegg, M. S.; *et al*. *Am. J. Clin. Nutr.* **1998**, *67*, 996S–1002S.
89. Howell, J. M.; Davison, A. N. *Biochem. J.* **1959**, *72*, 365–368.
90. Strain, J. J. *Med. Hypotheses* **1988**, *27*, 333–338.
91. Paterson, C. R. *J. R. Soc. Med.* **1990**, *83*, 72–74.
92. Allen, T. M.; Manoli, A., II; Lamont, R. L. *Clin. Orthop. Relat. Res.* **1982**, *168*, 206–210.
93. Fromigue, O.; Marie, P. J.; Lomri, A. *J. Cell. Biochem.* **1998**, *68*, 411–426.
94. Rico, H. *Osteoporos. Int.* **1991**, *2*, 20–25.
95. Wilson, T.; Katz, J. M.; Gray, D. H. *Calcif. Tissue Int.* **1981**, *33*, 35–39.
96. Eriksen, E. F.; Eghbali-Fatourechi, G. Z.; Khosla, S. *J. Bone Miner. Res.* **2007**, *22*, 1–6.
97. Ito, H.; Koefoed, M.; Tiyapatanaputi, P.; *et al*. *Nat. Med.* **2005**, *11*, 291–297.
98. Hu, G. F. *J. Cell. Biochem.* **1998**, *69*, 326–335.
99. Parke, A.; Bhattacherjee, P.; Palmer, R. M.; Lazarus, N. R. *Am. J. Pathol.* **1988**, *130*, 173–178.
100. Sen, C. K.; Khanna, S.; Venojarvi, M.; *et al*. *Am. J. Physiol. Heart Circ. Physiol.* **2002**, *282*, H1821–H1827.
101. Halliwell, B.; Gutteridge, J. M. *Meth. Enzymol.* **1990**, *186*, 1–85.
102. Skoryna, S. *Trace Subst. Environ. Health* **1984**, *18*, 3–23.
103. Jensen, J. E.; Stang, H.; Kringsholm, B. *Bone* **1997**, *20*(4), 104–108.
104. Grynpas, M. D.; Marie, P. J. *Bone* **1990**, *11*, 313–319.
105. Marie, P. J.; Garba, M. T.; Hott, M.; Miravet, L. *Miner. Electrolyte Metab.* **1985**, *11*, 5–13.
106. Marie, P. J.; Hott, M. *Metabolism* **1986**, *35*, 547–551.
107. Schrooten, I.; Cabrera, W.; Goodman, W. G.; *et al*. *Kidney Int.* **1998**, *54*, 448–456.
108. Verberckmoes, S. C.; De Broe, M. E.; D'Haese, P. C. *Kidney Int.* **2003**, *64*, 534–543.
109. Marie, P. J.; Hott, M.; Modrowski, D.; de Pollak, C.; Guillemain, J.; Deloffre, P.; Tsouderos, Y. *J. Bone Miner. Res.* **1993**, *8*(5), 607–615.
110. Baron, R.; Tsouderos, Y. *Eur. J. Pharmacol.* **2002**, *450*, 11–17.
111. Canalis, E.; Giustina, A.; Bilezikian, J. P. *N. Engl. J. Med.* **2007**, *357*, 905–916.
112. O'Donnell, S.; Cranney, A.; Wells, G. A.; Adachi, J. D.; Reginster, J. Y. *Cochrane Database Syst. Rev.* **2006**, CD005326.
113. Meunier, P. J.; Roux, C.; Seeman, E.; *et al*. *N. Engl. J. Med.* **2004**, *350*, 459–468.
114. Kleerekoper, M. In *Principles of Bone Biology*; Bilezikian, J. P., Raisz, L. G., Rodan, G. A., Eds.; Academic Press: San Diego, 1996.
115. Richards, A. *J. Dent. Res.* **1990**, *69*, 701–705.
116. Richards, A.; Kragstrup, J.; Josephsen, K.; Fejerskov, O. *J. Dent. Res.* **1986**, *65*, 1406–1409.
117. Kierdorf, U.; Kierdorf, H.; Sedlacek, F.; Fejerskov, O. *J. Anat.* **1996**, *188*(Pt 1), 183–195.
118. Larsen, M. J.; Kirkegaard, E.; Poulsen, S.; Fejerskov, O. *Caries Res.* **1986**, *20*, 349–355.
119. Suckling, G.; Thurley, D. C.; Nelson, D. G. *Arch. Oral Biol.* **1988**, *33*, 361–373.
120. Farley, S. M.; Wergedal, J. E.; Smith, L. C.; Lundy, M. W.; Farley, J. R.; Baylink, D. J. *Metabolism* **1987**, *36*, 211–218.
121. Gabuda, S.; Gaidash, A.; Kozlova, S.; Allan, N. *J. Struct. Chem. Engl. Transl.* **2006**, *47*, 258–266.

122. Mackie, E. J. *Int. J. Biochem. Cell Biol*. **2003**, *35*, 1301–1305.
123. Briancon, D.; Meunier, P. J. *Orthop. Clin. North Am*. **1981**, *12*, 629–648.
124. Mamelle, N.; Meunier, P. J.; Dusan, R.; *et al*. *Lancet* **1988**, *2*, 361–365.
125. Riggs, B. L.; Seeman, E.; Hodgson, S. F.; Taves, D. R.; O'Fallon, W. M. *N. Engl. J. Med*. **1982**, *306*, 446–450.
126. Riggs, B. L.; Hodgson, S. F.; O'Fallon, W. M.; *et al*. *N. Engl. J. Med*. **1990**, *322*, 802–809.
127. Bellows, C. G.; Heersche, J. N.; Aubin, J. E. *J. Bone Miner. Res*. **1990**, *5*(Suppl. 1), S101–S105.
128. Qu, W. J.; Zhong, D. B.; Wu, P. F.; Wang, J. F.; Han, B. *J. Bone Miner. Metab*. **2008**, *26*, 328–334.
129. Burgener, D.; Bonjour, J. P.; Caverzasio, J. *J. Bone Miner. Res*. **1995**, *10*, 164–171.
130. Okuda, A.; Kanehisa, J.; Heersche, J. N. *J. Bone Miner. Res*. **1990**, *5*(Suppl. 1), S115–S120.
131. Taylor, M. L.; Maconnachie, E.; Frank, K.; Boyde, A.; Jones, S. J. *J. Bone Miner. Res*. **1990**, *5*(Suppl. 1), S121–S130.
132. Legeros, R. Z. *Calcium Phosphates in Oral Biology and Medicine*. Basel: Switserland, Karger, 1991.
133. Rey, C.; Renugopalakrishnan, V.; Collins, B.; Glimcher, M. J. *Calcif. Tissue Int*. **1991**, *49*, 251–258.
134. Elliott, J. C.; Holcomb, D. W.; Young, R. A. *Calcif. Tissue Int*. **1985**, *37*, 372–375.
135. Rey, C.; Collins, B.; Goehl, T.; Dickson, M. R.; Glimcher, M. J. *Calcif. Tissue Int*. **1989**, *45*, 157–164.
136. Legeros, R. Z.; Trautz, O. R.; Legeros, J. P.; Klein, E.; Shirra, W. P. *Science* **1967**, *155*, 1409–1411.
137. Massaro, C.; Baker, M. A.; Cosentino, F.; Ramires, P. A.; Klose, S.; Milella, E. *J. Biomed. Mater. Res*. **2001**, *58*, 651–657.
138. Willmann, G. *Adv. Eng. Mater*. **1999**, *1*, 95–105.
139. Bonel, G.; Heughebaert, J. C.; Heughebaert, M.; Lacout, J. L.; Lebugle, A. *Ann. NY Acad. Sci*. **1988**, *523*, 115–130.
140. Barrere, F.; Layrolle, P.; Van Blitterswijk, C. A.; De Groot, K. *Bone* **1999**, *25*, 107S–111S.
141. Barrere, F.; Van, B. C.; De, G. K.; Layrolle, P. *Biomaterials* **2002**, *23*, 2211–2220.
142. Patntirapong, S.; Habibovic, P.; Hauschka, P. V. *Biomaterials* **2009**, *30*, 548–555.
143. Kokubo, T.; Kushitani, H.; Abe, Y.; Yamamuro, T. *Bioceramics* **1989**, *2*, 235–242.
144. Zhitomirsky, I. *Am. Ceram. Soc. Bull*. **2000**, *79*, 57–63.
145. Kim, H. W.; Koh, Y. H.; Li, L. H.; Lee, S.; Kim, H. E. *Biomaterials* **2004**, *25*, 2533–2538.
146. Liu, D. M.; Troczynski, T.; Tseng, W. J. *Biomaterials* **2001**, *22*, 1721–1730.
147. Thian, E. S.; Khor, K. A.; Loh, N. H.; Tor, S. B. *Biomaterials* **2001**, *22*, 1225–1232.
148. Cleries, L.; Fernandez-Pradas, J. M.; Morenza, J. L. *J. Biomed. Mater. Res*. **2000**, *49*, 43–52.
149. Cleries, L.; Fernandez-Pradas, J. M.; Morenza, J. L. *Biomaterials* **2000**, *21*, 1861–1865.
150. Cleries, L.; Fernandez-Pradas, J. M.; Sardin, G.; Morenza, J. L. *Biomaterials* **1999**, *20*, 1401–1405.
151. Cleries, L.; Martinez, E.; Fernandez-Pradas, J. M.; Sardin, G.; Esteve, J.; Morenza, J. L. *Biomaterials* **2000**, *21*, 967–971.
152. Fernandez-Pradas, J. M.; Cleries, L.; Martinez, E.; Sardin, G.; Esteve, J.; Morenza, J. L. *Biomaterials* **2001**, *22*, 2171–2175.
153. Ishizawa, H.; Fujino, M.; Ogino, M. *J. Biomed. Mater. Res*. **1997**, *35*, 199–206.
154. Ishizawa, H.; Ogino, M. *J. Biomed. Mater. Res*. **1995**, *29*, 65–72.
155. Ishizawa, H.; Ogino, M. *J. Biomed. Mater. Res*. **1995**, *29*, 1071–1079.
156. Jolly, W. L., Ed.; In *The Synthesis and Characterization of Inorganic Compounds*; Prentice Hall: Englewood Cliffs, NJ, 1970.
157. Ito, A.; Ojima, K.; Naito, H.; Ichinose, N.; Tateishi, T. *J. Biomed. Mater. Res*. **2000**, *50*, 178–183.
158. Bigi, A.; Foresti, E.; Gandolfi, M.; Gazzano, M.; Roveri, N. *J. Inorg. Biochem*. **1997**, *66*, 259–265.
159. Ito, A.; Kawamura, H.; Otsuka, M.; *et al*. *Mater. Sci. Eng. C* **2002**, *22*, 21–25.
160. Jallot, E.; Nedelec, J. M.; Grimault, A. S.; *et al*. *Colloids Surf. B Biointer*. **2005**, *42*, 205–210.
161. Bigi, A.; Foresti, E.; Gandolfi, M.; Gazzano, M.; Roveri, N. *J. Inorg. Biochem*. **1995**, *58*, 49–58.
162. Li, Z. Y.; Lam, W. M.; Yang, C.; *et al*. *Biomaterials* **2007**, *28*, 1452–1460.
163. Balamurugan, A.; Balossier, E.; Torres, P.; Michel, J.; Ferreira, J. M. F. *Mater. Sci. Eng. C* **2009**, *29*, 1006–1009.
164. Belik, A. A.; Yanov, O. V.; Lazoryak, B. I. *Mater. Reasearch Bull*. **2001**, *36*, 1863–1871.
165. Okazaki, M.; Miake, Y.; Tohda, H.; Yanagisawa, T.; Matsumoto, T.; Takahashi, J. *Biomaterials* **1999**, *20*, 1421–1426.
166. Okazaki, M.; Miake, Y.; Tohda, H.; Yanagisawa, T.; Takahashi, J. *Biomaterials* **1999**, *20*, 1303–1307.
167. Bouslama, N.; Ben Ayed, F.; Bouaziz, J. *J. Mech. Behav. Biomed. Mater*. **2010**, *3*, 2–13.
168. Elliott, J. C. *Clin. Orthop. Relat. Res*. **1973**, *93*, 313–345.
169. Nelson, D. G.; Featherstone, J. D. *Calcif. Tissue Int*. **1982**, *34*(Suppl. 2), S69–S81.
170. Vignoles, M.; Bonel, G.; Young, R. A. *Calcif. Tissue Int*. **1987**, *40*, 64–70.
171. Doi, Y.; Moriwaki, Y.; Aoba, T.; Okazaki, M.; Takahashi, J.; Joshin, K. *J. Dent. Res*. **1982**, *61*, 429–434.
172. Gibson, I. R.; Bonfield, W. *J. Biomed. Mater. Res*. **2002**, *59*, 697–708.
173. Landi, E.; Tampieri, A.; Celotti, G.; Vichi, L.; Sandri, M. *Biomaterials* **2004**, *25*, 1763–1770.
174. Barralet, J. E.; Best, S. M.; Bonfield, W. *J. Mater. Sci. Mater. Med*. **2000**, *11*, 719–724.
175. Ellies, L. G.; Nelson, D. G.; Featherstone, J. D. *J. Biomed. Mater. Res*. **1988**, *22*, 541–553.
176. Barinov, S. M.; Rau, J. V.; Cesaro, S. N.; *et al*. *J. Mater. Sci. Mater. Med*. **2006**, *17*, 597–604.
177. Habibovic, P.; Juhl, M. V.; Clyens, S.; *et al*. *Acta Biomater*. **2010**, *6*(6), 2219–2226.
178. Van Raemdonck, W.; Ducheyne, P.; De Meester, P. In *Metal and Ceramic Biomaterials*; Ducheyne, P., Hastings, G. W., Eds.; CRC: Boca Raton, FL, 1984.
179. Li, M.; Xiao, X.; Liu, R.; Chen, C.; Huang, L. *J. Mater. Sci. Mater. Med*. **2008**, *19*, 797–803.
180. Ren, F.; Xin, R.; Ge, X.; Leng, Y. *Acta Biomater*. **2009**, *5*, 3141–3149.
181. Schroeder, L. W.; Dickens, B.; Brown, W. E. *J. Solid State Chem*. **1977**, *22*, 253–262.
182. Sogo, Y.; Ito, A.; Kamo, M.; *et al*. *Mater. Sci. Eng. C* **2004**, *24*, 709–715.
183. Ito, A.; Otsuka, M.; Kawamura, H.; *et al*. *Curr. Appl. Phys*. **2005**, *5*, 402–406.
184. Ito, A.; Kawamura, H.; Miyakawa, S.; *et al*. *J. Biomed. Mater. Res*. **2002**, *60*, 224–231.
185. Otsuka, M.; Marunaka, S.; Matsuda, Y.; *et al*. *J. Biomed. Mater. Res*. **2000**, *52*, 819–824.
186. Bandyopadhyay, A.; Withey, E. A.; Moore, J.; Bose, S. *Mater. Sci. Eng. C* **2007**, *27*, 14–17.
187. Kannan, S.; Goetz-Neunhoeffer, F.; Neubauer, J.; Ferreira, J. M. F. *J. Am. Ceram. Soc*. **2009**, *92*, 1592–1595.
188. Gutowska, I.; Machoy, Z.; Machalinski, B. *J. Biomed. Mater. Res. A* **2005**, *75*, 788–793.
189. Enderle, R.; Gotz-Neunhoeffer, F.; Gobbels, M.; Muller, F. A.; Greil, P. *Biomaterials* **2005**, *26*, 3379–3384.
190. Dickens, B.; Schroeder, L. W.; Brown, W. E. C. *J. Solid State Chem*. **1974**, *10*, 232–248.
191. Chung, R.-J.; Hsieh, M.-F.; Huang, K.-C.; Perng, L.-H.; Chou, F.-I.; Chin, T.-S. *J. Sol–Gel. Sci. Technol*. **2005**, *33*, 229–239.
192. Webster, T. J.; Massa-Schlueter, E. A.; Smith, J. L.; Slamovich, E. B. *Biomaterials* **2004**, *25*, 2111–2121.
193. Ito, A.; Kawamura, H.; Miyakawa, S.; Layrolle, P.; Aomori, R.; Tsutsumi, S. *Key Eng. Mater*. **2001**, *192–195*, 199.
194. Mayer, I.; Featherstone., J. D. B. *J. Cryst. Growth* **2000**, *219*, 98–101.
195. Shannon, R.; Prewitt, C. *Acta Crystallogr. B* **1969**, *25*, 925–946.
196. Kannan, S.; Pina, S.; Ferreira, J. M. F. *J. Am. Ceram. Soc*. **2006**, *89*, 3277–3280.
197. Bigi, A.; Falini, G.; Foresti, E.; Ripamonti, A.; Gazzano, M.; Roveri, N. *Z. Kristallogr*. **1996**, *211*, 13–16.
198. Saint-Jean, S. J.; Camire, C. L.; Nevsten, P.; Hansen, S.; Ginebra, M. P. *J. Mater. Sci. Mater. Med*. **2005**, *16*, 993–1001.
199. Legeros, R. Z.; Kijkowska, R.; Tung, M.; Legeros, J. P. Effect of strontium on some properties of apatites. In *Enamel Symposium V*; Fearnhead, P. W., Suga, S., Eds.; Elsevier: Amsterdam, 1989; pp 393–401.
200. Christoffersen, J.; Christoffersen, M. R.; Kolthoff, N.; Barenholdt, O. *Bone* **1997**, *20*, 47–54.
201. Verberckmoes, S. C.; Behets, G. J.; Oste, L.; *et al*. *Calcif. Tissue Int*. **2004**, *75*, 405–415.
202. Wang, X.; Ye, J. *J. Mater. Sci. Mater. Med*. **2008**, *19*, 1183–1186.
203. Aoba, T. *Crit. Rev. Oral Biol. Med*. **1997**, *8*, 136–153.
204. Fathi, M. H.; Zahrani, E. M. *J. Alloy. Comp*. **2009**, *475*, 408–414.
205. Chen, Y.; Miao, X. *Biomaterials* **2005**, *26*, 1205–1210.
206. Rodriguez-Lorenzo, L. M.; Hart, J. N.; Gross, K. A. *Biomaterials* **2003**, *24*, 3777–3785.

207. Cheng, K.; Weng, W.; Wang, H.; Zhang, S. *Biomaterials* **2005**, *26*, 6288–6295.
208. Wang, Y.; Zhang, S.; Zeng, X.; *et al*. *Acta Biomater*. **2007**, *3*, 191–197.
209. Kay, M. I.; Young, R. A.; Posner, A. S. *Nature* **1964**, *204*, 1050–1052.
210. Harrison, J.; Melville, A. J.; Forsythe, J. S.; *et al*. *Biomaterials* **2004**, *25*, 4977–4986.
211. Legeros, R. *Prog. Cryst. Growth Charact.* **1981**, *4*, 1–45.
212. Baig, A. A.; Fox, J. L.; Young, R. A.; Wang, Z.; Hsu, J. *Calcif. Tissue Int.* **1998**, *64*, 437–449.
213. Tas, A. C.; Bhaduri, S. B.; Jalota, S. *Mater. Sci. Eng. C* **2007**, *27*, 394–401.
214. Webster, T. J.; Ergun, C.; Doremus, R. H.; Bizios, R. *J. Biomed. Mater. Res.* **2002**, *59*, 312–317.
215. Sogo, Y.; Sakurai, T.; Onuma, K.; Ito, A. *J. Biomed. Mater. Res.* **2002**, *62*, 457–463.
216. Ikeuchi, M.; Ito, A.; Dohi, Y.; *et al*. *J. Biomed. Mater. Res. A* **2003**, *67*, 1115–1122.
217. Yamada, Y.; Ito, A.; Sakane, M.; Miyakawa, S.; Uemura, T. *Mater. Sci. Eng.* **2007**, *27*, 762–766.
218. Yamada, Y.; Ito, A.; Kojima, H.; *et al*. *J. Biomed. Mater. Res.* **2007**, *84*, 344–352.
219. Kawamura, H.; Ito, A.; Miyakawa, S.; *et al*. *J. Biomed. Mater. Res.* **2000**, *50*, 184–190.
220. Barralet, J.; Gbureck, U.; Habibovic, P.; Vorndran, E.; Gerard, C.; Doillon, C. J. *Tissue Eng. A* **2009**, *15*(7), 1601–1609.
221. Gerard, C.; Bordeleau, L. J.; Barralet, J.; Doillon, C. J. *Biomaterials* **2010**, *31*, 824–831.
222. Xue, W.; Moore, J. L.; Hosick, H. L.; *et al*. *J. Biomed. Mater. Res. A* **2006**, *79*, 804–814.
223. Kim, H. W.; Koh, Y. H.; Kong, Y. M.; Kang, J. G.; Kim, H. E. *J. Mater. Sci. Mater. Med.* **2004**, *15*, 1129–1134.
224. Capuccini, C.; Torricelli, P.; Sima, F.; *et al*. *Acta Biomater.* **2008**, *4*, 1885–1893.
225. Wong, C. T.; Lu, W. W.; Chan, W. K.; *et al*. *J. Biomed. Mater. Res. A* **2004**, *68*, 513–521.
226. Qu, H.; Wei, M. *Acta Biomater.* **2006**, *2*, 113–119.
227. Inoue, M.; Nagatsuka, H.; Tsujigiwa, H.; Legeros, R. Z.; Yamamoto, T.; Nagai, N. *Dent. Mater. J.* **2005**, *24*, 398–402.
228. Redey, S. A.; Nardin, M.; Bernache-Assolant, D.; *et al*. *J. Biomed. Mater. Res.* **2000**, *50*, 353–364.
229. Dekker, A.; Reitsma, K.; Beugeling, T.; Bantjes, A.; Feijen, J.; Van Aken, W. G. *Biomaterials* **1991**, *12*, 130–138.
230. Schakenraad, J. M.; Busscher, H. J.; Wildevuur, C. R.; Arends, J. *Cell Biophys.* **1988**, *13*, 75–91.
231. Van Kooten, T. G.; Schakenraad, J. M.; Van De Rmei, H. C.; Busscher, H. J. *Biomaterials* **1992**, *13*, 897–904.
232. Redey, S. A.; Razzouk, S.; Rey, C.; *et al*. *J. Biomed. Mater. Res.* **1999**, *45*, 140–147.
233. Doi, Y.; Iwanaga, H.; Shibutani, T.; Moriwaki, Y.; Iwayama, Y. *J. Biomed. Mater. Res.* **1999**, *47*, 424–433.
234. Hasegawa, M.; Doi, Y.; Uchida, A. *J. Bone Joint Surg. Br.* **2003**, *85*, 142–147.
235. Anderson, R. E.; Jee, W. S.; Woodbury, D. M. *Calcif. Tissue Int.* **1985**, *37*, 646–650.
236. Spence, G.; Patel, N.; Brooks, R.; Bonfield, W.; Rushton, N. *J. Biomed. Mater. Res. A* **2009**, *92*(4), 1292–1300.
237. Landi, E.; Celotti, G.; Logroscino, G.; Tampieri, A. *J. Eur. Ceram. Soc.* **2003**, *23*, 2931–2937.
238. Ellies, L. G.; Carter, J. M.; Natiella, J. R.; Featherstone, J. D.; Nelson, D. G. *J. Biomed. Mater. Res.* **1988**, *22*, 137–148.
239. Yao, F.; Legeros, J. P.; Legeros, R. Z. *Acta Biomater.* **2009**, *5*, 2169–2177.

1.120. Synthetic Bone Grafts: Clinical Use

C Nich, Faculté de Médecine – Université de Paris, Paris, France; European Hospital of Paris, Paris, France
M Hamadouche, Faculté de Médecine – Université de Paris, Paris, France; Hôpital Cochin – Université de Paris, Paris, France

© 2011 Elsevier Ltd. All rights reserved.

1.120.1.	**Introduction**	335
1.120.2.	**A Brief History of Bone Grafts**	336
1.120.3.	**Synthetic Bone Graft Substitutes**	337
1.120.3.1.	Calcium Sulfate (Plaster of Paris)	337
1.120.3.2.	Calcium Phosphate Ceramics	337
1.120.3.3.	Calcium Phosphate Cements	342
1.120.3.4.	Bioactive Glasses and Ceramics	343
1.120.3.5.	Glass Ionomer Cements	344
1.120.3.6.	Biomimetic Nanocomposites and Nanopolymers	345
1.120.4.	**Conclusion**	346
References		346

Abbreviations

ACP	Amorphous calcium phosphate	**GIC**	Glass ionomer cements
AW	Apatite/wollastonite	**HA or HAP**	Hydroxyapatite
BCP	Biphasic calcium phosphate	**hBMSC**	Human bone marrow-derived stromal cells
BMP	Bone morphogenetic protein	**MBCP**	Macroporous biphasic calcium phosphate
CP ceramics or CPC	Calcium phosphate ceramics	**PHA**	Precipitated hydroxyapatite
		PMMA	Polymethyl metacrylate
DBM	Demineralized bone matrix	**rhBMP-2**	Recombinant human bone morphogenetic protein-2
DCPD	Dicalcium phosphate dihydrate	**SBF**	Simulated body fluid
ECM	Extracellular bone matrix	**TCP**	Tricalcium phosphate

1.120.1. Introduction

Bone tissue has a remarkable ability for regeneration and repair. However, in some situations, bone repair cannot occur spontaneously because the bone defect has reached a critical size. These so-called *critical defects*, defined as defects of a size that will not heal during the lifetime of the patient/animal, are encountered in various conditions, including trauma, infection, congenital disease or surgical resection for tumor, or in association with failed joint replacements. Various procedures have been described to solve these often complex issues. Most of them imply the use of a bone graft, either natural or synthetic. Natural bone graft can be obtained from a genetically nonidentical donor of the same species as the recipient (allograft or homograft or allogenic bone transplant) or from the patient himself (autograft). Allografts circumvent some of the issues relative to autograft, such as donor site morbidity and limited supply. However, there are concerns associated with their use, including the risk of transmission of infectious disease, immunological reactions in the recipient, loss of biologic and mechanical properties due to their processing, increased costs, and availability. The gold standard of bone grafts remains autogenous bone graft or autograft. The latter is usually harvested from the iliac crest, but other donor sites are possible. Properties of autogenous bone graft include *osteointegration*, *osteoconduction*, *osteoinduction*, and *osteogenesis*. *Osteointegration* is considered the ability of achieving a bone-implant interface without an intervening fibrous layer. *Osteoconduction* refers to the ability of supporting the growth of bone over the surface of the graft. The graft supports the proliferation of new osteoblasts and osteoprogenitor cells, providing a matrix through which new cells can migrate and new vessels can form. When materials are porous, the requisite pore size for bone ingrowth into porous implants is 100–500 μm, and the interconnections typically exceed 100 μm. *Osteoinduction* refers to the ability of a graft to induce differentiation of pluripotential stem cells or osteoprogenitor cells to an osteoblastic phenotype. Finally, *osteogenesis* is defined as the property of a graft to form new bone from osteoblastic cells present within the material (Figure 1).

Only autogenous bone graft satisfies all these requirements. However, the limited quantity of bone autograft considerably limits its clinical use. Moreover, bone autografting implies the need for an additional surgical site, limited quantity, inappropriate form, and donor site morbidity (hematoma, infection, nerve damage, and chronic pain). In addition, the mechanical properties of the iliac bone are often poor, especially in postmenopausal women.

The disadvantages and potential complications related to the use of allo- and autograft have dictated the progress toward synthetic bone grafts and/or a biologic alternative, because

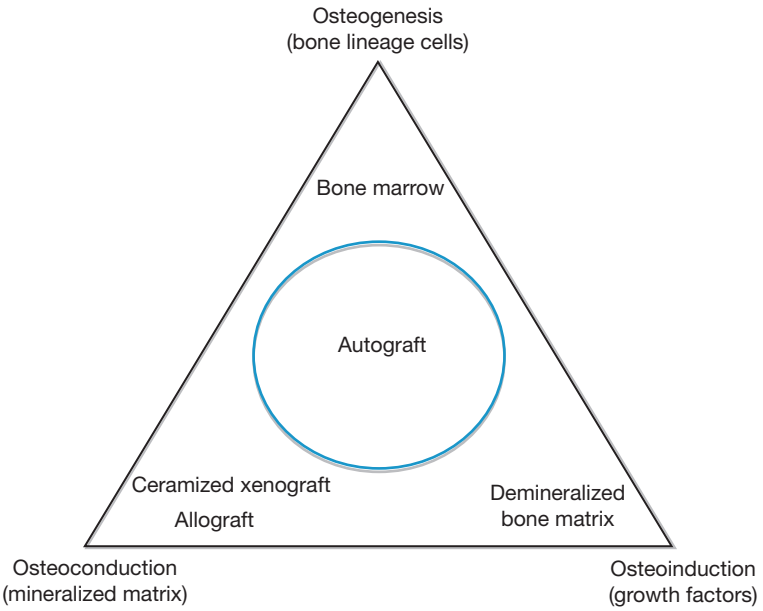

Figure 1 Bone autograft still represents the gold standard for bone grafting. As shown in the diagram, it combines the three most desirable properties of a bone graft material, namely ostoconduction, osteoinduction, and osteogenesis. Main families of bone substitutes are presented in the diagram with regard to their respective biological activity.

they circumvent all the risks related to the substitute procured from living tissue. There is no consensus definition of a synthetic bone graft substitute. One should consider a synthetic bone grafting material as a synthetically derived device, intended to fill, augment, or reconstruct bone defects of the skeleton. Also, recent generations of bone substitutes have introduced and increased the potential of synthetic bone grafts to promote biologic repair, to provide support for treatment, that is, antibiotics or bone morphogenetic proteins (BMPs), and to enhance osseointegration of orthopedic implants.

Today, current indications for bone substitutes are in spinal fusion, bone defects, osteoporotic fractures, revision prosthetic surgery, and vertebroplasty. Theoretically, a given synthetic bone graft should be biocompatible and well tolerated by the recipient, bioresorbable in the mid-term, easy to handle and store, and available at a reasonable cost; it should enhance bone repair and provide satisfying mechanical support. This chapter focuses on conventional synthetic bone grafts, with the exclusion of growth factors and gene- and cell-based strategies, proposed in the orthopedic field.

1.120.2. A Brief History of Bone Grafts

Original attempts at bone reconstruction were made using allogafts or xenografts. Cosmas and Damian, twin physiotherapists and surgeons, described a limb reconstruction with an heterologous graft in the fourth century AD. Hence, their most famous, miraculous, and legendary exploit was the grafting of a leg from a recently deceased Ethiopian to replace the leg of a patient who suffered from a bone tumor. Surgical repair of deformities or defects of the skull with varied materials (such as precious metals and gourds), a procedure currently named cranioplasty, was performed by many ancient civilizations, and a number of these procedures date back to 3000 BC, especially to the Inca period in Peru. There is strong evidence that this practice continued all around the world during the following centuries until the introduction of modern medicine by Hippocrates in Ancient Greece. Interestingly, it was not until the late sixteenth century, in 1565, that true cranioplasty in the form of a gold plate was described by the Italian anatomist and physiotherapist Fallopius (1523–1562) and Petronius. Later, the first bone graft was officially recorded by Job Janszoon van Meekeren (1611–1666), a Dutch surgeon, who reported (not performed!), in a posthumous publication in 1668, the repair of a cranial defect in a Russian soldier with a piece of bone from a dog's skull. Although healing was obtained, the Church ordered the removal of the graft. Recent researches have revealed that the description of the technique of cranioplasty could be attributed to a Turkish surgeon, Ibrahim bin Abdullah, who originally reported repair of skull defects with xenograft in AD 1505.[1] In the twentieth century, polymeric materials have largely replaced metallic bone substitutes in this indication. Polymethyl metacrylate (PMMA) was introduced in 1940 and is currently the most common material used in cranial bone defects, although its nature does not make it a true bone substitute.

In the nineteenth century, techniques of bone replacement became more common after the original publication of autologous bone graft by Van Merren d'Amsterdam in 1810. The safe use of materials of human or synthetic origin to replace bony segments did not come into practice until the advance of aseptic surgical techniques at the end of the nineteenth century. Thus, Ollier established the basic science of bone banking. During the same period, the first attempts to reconstruct long bone defects by nonosseous materials were reported. Among several materials, such as ivory, gold, or wood, only plaster of Paris, which is still employed, fulfilled some of the requirements of a true bone substitute. In 1892, Dressman from the Trendelenburg Clinic[2] first reported on the

clinical results of eight cases of bone filling with plaster of Paris. Subsequently, L.F. Peltier of the United States regularly reported clinical experience from the 1950s to the 1970s.[3–5]

The use of ceramic calcium phosphate materials to promote bone formation was reported close to a century ago. In 1920, Albee and Morrison[6] described the use of 'triple calcium phosphate' to promote bone ingrowth. Their results indicated that bone fractures associated with a bone defect, showed a more rapid bone ingrowth and healing when triple calcium phosphate was injected into the gap between the bone ends than did controls. In 1952, Ray and Ward[7] evaluated the effectiveness of synthetic hydroxyapatite (HA) granules in the reconstruction of experimental defects in the long bones and iliac wings of dogs and bur holes in cats' crania. They observed that synthetic hydroxyapatite graft could be replaced by new bone, but they concluded that HA was not as effective as autologous bone graft. Self-hardening calcium phosphate (CP) cements were developed in the late 1980s. Marshall Urist found in the early 1960s that the demineralized bone matrix (DBM) had the capability of inducing bone formation in an ectopic site.[8] This property was named osteoinductivity several years later, and the agent responsible for it was found to be a protein named BMP.

1.120.3. Synthetic Bone Graft Substitutes

Approximately, 60% of the synthetic bone graft substitutes currently available involve ceramics, either alone or in combination with another material. Ceramic bone substitutes include by calcium sulfate, CPs, and bioactive glasses and glass ceramics.

1.120.3.1. Calcium Sulfate (Plaster of Paris) (Table 1)

Plaster of Paris is a mineral bone substitute, composed of dihydrated calcium sulfate ($CaSO_4 + 2H_2O$), that has been employed since the end of the nineteenth century. Currently, calcium sulfate is obtained either by chemical synthesis or by a gypsum calcinating process. Sterilization is obtained by γ-radiation (min 25 kGy). Calcium sulfate is characterized by an absence of macroporosity, as a result of its industrial production process employing powder compression. Therefore, no osteoconduction can be allowed with this material. Compressive strength of calcium sulfate appears greater than cancellous bone, although tensile strength appears slightly inferior. It is noteworthy that plaster of Paris tends to soften and fragment if exposed to moisture, which results in a significant loss of mechanical properties upon its degradation in bony environment. Compression stress has been evaluated to 23 028 KPa in a dry sample, as compared to 10 342 KPa in a wet sample.

Calcium sulfate is biocompatible and bioactive, and biodegrades experimentally after 2–5 weeks. In clinical applications, a complete resorption of the material is usually observed 4–8 weeks after implantation. In a bone tissue environment, calcium sulfate degrades progressively in a centripetal pattern following a process of dissolution, in parallel with bone ingrowth. In an experimental model, it has been reported that the osteoblastic repair process was enhanced in the presence of calcium sulfate in critical bone defects without evidence of a foreign body reaction.[9–11]

Calcium sulfate has been used for over a century in clinical practice, mainly as a bone void filler. Current applications concern spine fusion, used alone or in combination with bone autograft, packing of benign tumors or cysts after resection or curettage, and trauma. It is noteworthy that indications for plaster of Paris should be limited to non-load-bearing bony voids or gaps, or should always be employed in association with a rigid internal fixation. Calcium sulfate appears as a viable option in filling bone cavities, and is not contraindicated in the presence of infection. Osteoset™ with or without DBM was used in 23 patients with bone cysts or benign bone tumors. Healing was observed in all patients and the rate and amount of bone regeneration was not dependent on the addition of DBM to the calcium sulfate granules. Osseous repair of the lesions was considered complete by 6 months, and all but one patient resumed normal functional activities in 12 months.[12] In a multicenter trial, Osteoset™ pellets were used in 46 patients with benign bone tumors. In 36 of 42 patients, a mixture of additional graft materials including DBM, bone marrow aspirate, and autograft were used. Results showed 100% pellet resorption and 96% bone ingrowth at 12 months, with no significant difference between patients receiving Osteoset alone or in combination with other graft material.[13]

Calcium sulfate is commercially available as small pellets ranging from 3 to 4.8 mm in diameter for implantation (Osteoset™, Wright Medical Technology, Arlington, TN). Calcium sulfate also comes impregnated with tobramycin (Osteoset™ T) (4% weight). Osteoset™ T comes in the form of 4.8 mm pellets and is indicated in the treatment of osteomyelitic bone defects, or during revision arthroplasties. Boneplast™ (Biomet Osteobiologics, Warsaw, IN) comes in the form of a mixing kit, composed of a calcium sulfate powder and saline. It is moldable to fit any shape defect up to 8 min after mixing. It begins hardening in 10 min. Calcium sulfate is also commercially presented as a carrier of DBM, which has been proved to stimulate osteoinduction (Allomatrix™ Injectable DBM Biocomposite, Wright Medical Technology).

1.120.3.2. Calcium Phosphate Ceramics (Table 1)

CP materials account for most of the ceramic-based bone graft substitutes currently available. They have been employed in clinical practice for over 20 years. The most desirable property of CPCs is their ability to form a direct bond with host bone, resulting in a strong interface as compared to bioinert or biotolerant materials, which form a fibrous interface. Numerous experimental and clinical reports since the 1970s have shown their applicability in filling bone defects in various fields such as periodontics, oral and maxillofacial surgeries, neurosurgery, and orthopedics.

The primary inorganic component of bone is a nonstoichiometric carbonated apatite, namely calcium HA. CPCs are characterized by their chemical composition similar to that of the mineral phase of calcified tissue.

The CP family includes numerous members, characterized by their chemical formula, and their calcium to phosphate ratio (Ca/P). It is possible to control the composition of the untreated product by adjusting the Ca/P ratio of the starting material to obtain a product as desired. This procedure allows the production of the four main CPCs, designed as

Table 1 Presentation of commercially available calcium-based ceramics currently employed as bone graft substitutes

	Ca sulfate	*Ca phosphate ceramics*							
		β-TCP				*Silicon-substituted synthetic HAP*	*Biologic HAP*	*Biphasic CaP ceramics (HAP + β-TCP)*	
Commercial presentation (manufacturer)	Osteoset™ BVF (Wright Medical Technology, Arlington, TN) Boneplast™ (Biomet Osteobiologics, Warsaw, IN), Cem-ostetic™ (Berkeley Advanced Biomaterials, Inc., San Leandro, CA)	Bio 1™-kit Biosorb™ (Science for Biomaterials, Lourdes, France)	Synthes ChronOS™ tcp (Synthes, Paoli, PA)	Vitoss™ (Orthovita Co, Malvern, PA)	Conduit™ TCP Granules (DePuy Acromed Inc., Raynham, MA)	Actifuse™ family bone graft substitute (Apatech Ltd, Oregon city, OR)	Pro Osteon™ 200R, Pro Osteon™ 500R (Interpore Cross Intl, Irvine, CA)	MBCP™, MBCP+™, Tribone 80™ (Biomatlante, Vigneux de Bretagne, France), HATriC™ (Arthrex, Inc., Naples, FL)	Ceraform™ (Teknimed sa, Round Rock, TX)
Form	Pellets, putty	Granules, cylinders, wedges	Granules, blocks, cylinders, wedges	Granules, blocks	Granules	Putty	Blocks, granules	Granules, disks, wedges, cylinders, sticks	Granules, sticks
Chemical formula	$[CaSO_4 + 2H_2O]$	$[Ca_3(PO_4)_2]$	$[Ca_3(PO_4)_2]$	$[Ca_3(PO_4)_2]$	$[Ca_3(PO_4)_2]$	$[Ca_{10}(PO_4)_{(6-x)}(SiO_4)_{(x)}(OH)_{(2-x)}]$	NA	60% HA, 40% β-TCP (MBCP™, HATriC™) 20% $[Ca_{10}(PO_4)_6(OH)_2]$/ 80% $[Ca_3(PO_4)_2]$ (MBCP+™, Tribone 80™)	65% $[Ca_{10}(PO_4)_6(OH)_2]$/ 35% $[Ca_3(PO_4)_2]$
Purity	>98%	>95%	>95%	>95%	>99%	96%	>90% (HA)		
Ratio Ca/P	NA	1.5	NA		1.5	NA	NA	1.6	1.63<Ca/P<1.67
Porosity	No	0–70%	60% (granules), 72% (blocks)	90%	60–80%	80%	65% (Pro Osteon 500)	70%	– 60–85%
– Macropore volume		– >80%	– 100–500 μm	– 1–1000 μm	– 200–500 μm		– 260–600 μm (Pro Osteon 500)	– 300–600 μm	– 150–400 μm
– Macropore size		– 150–400 μm			– <5 μm			– <10 μm	
– Micropore size		– <10 μm							
Mechanical resistance	– Compression: 23 028 kPa (dry), 10 342 kPa (wet) – Traction: 4136 kPa (dry), 2068 kPa (wet)	Compr: from 1 to >120 Mpa	Compression: 10–20 MPa (granules), 7.5 MPa (blocks)	Compression: 1–2 MPa	Compression: 1–5 MPa	NA	2–4 MPa (Pro Osteon 500)	<10 MPa	<5 MPa
Bioresorption (delay)	4–8 weeks (2–5 weeks experimentally)	>12 weeks (complete from 1 to 2 years)	6–12 months	6 months (80% is resorbed within 12 weeks)	6–10 months	NA	Slow	NA	Partial
Historic	– 1894 (animal)	– 1986	– 1979	– 1996	– 1988	– 2005, 2006	– 1970 (animal)	– 1985	– 1990
– First studies	– 1892, 1925	– 1992	– 1980	– 1998	– 1990	– 2007	– 1981	– 1985	– 1994

– Animal exp – Clin. exp. – FDA approval	– 1996 (Osteoset™) – 2007 (Boneplast™) – 2003 (Cem-ostetic™)	– 1993 – 2006 (Bio 1), 2003 (Biosorb)	– 1982 – 2002	– NA – 2000	– 2002 – 2002		– 1998 (Pro osteon 500R)	– 1986 – 2003 (MBCP™), 2007 (MBCP+™, Tribone 80™), 2004 (HATriC™)	– 1996 – 2004
Comments			Available since 2007 in the form of a composite (Synthes ChronOS™ Composite), combining ChronOS™ tcp and a matrix of poly (lactide-*co*-ε-caprolactone)	Available since 2008 in combination with purified type I bovine collagen (Vitoss™ Foam Bone Graft Substitute)		Actifuse™ ABX is phase-pure silicon-substituted HA. Substitution of CaP by silicate ions results in an enhancement of bone ingrowth	Trabecular calcium carbonate covered with a 2–10 μm layer of hydroxyapatite Obtained by thermo chemical process from coral Goniopora (Pro Osteon 500)		

Ca phosphate ceramics

Biphasic CaP ceramics (HAP + β-TCP)

Commercial presentation (manufacturer)	Bi-ostetic™, Bi-ostetic™ foam (Berkeley Advanced Biomaterials, Inc., San Leandro, CA)	Atlantik™, (Medical Biomat, Inc., Vaulx-en-Velin, France)	BoneSave™ (Stryker Corp., Kalamazoo, MI)	Osmosys™ (Medicrea, Round Rock, TX)	Mastergraft™ BVF, (Medtronic Sofamor Danek USA, Inc., Memphis, TN)	Duowedge™ (Kasios, Round Rock, TX)
Form	Granules, blocks, injectable putty	Granules, blocks	Granules	Granules, sticks	Granules, putty	Wedges
Chemical formula	60% $[Ca_{10}(PO_4)_6(OH)_2]$/40% $[Ca_3(PO_4)_2]$	70% $[Ca_{10}(PO_4)_6(OH)_2]$/ 30% $[Ca_3(PO_4)_2]$	20% $[Ca_{10}(PO_4)_6(OH)_2]$/ 80% $[Ca_3(PO_4)_2]$	60% $[Ca_{10}(PO_4)_6(OH)_2]$/ 40% $[Ca_3(PO_4)_2]$	60% or 85% $[Ca_{10}(PO_4)_6(OH)_2]$/ 40% or 15% $[Ca_3(PO_4)_2]$	60% $[Ca_{10}(PO_4)_6(OH)_2]$/ 40% $[Ca_3(PO_4)_2]$
Purity	NA	>99%	NA	NA	NA	NA
Ratio Ca/P	NA	1.62	NA	1.60	NA	NA
Porosity	50%	70%	50%	60–80%	80%	– 300–700 μm
– Macrop vol	– 260 μm	– 60%	– 400–600 μm	– 300–500 μm	– 400–600 μm	
– Macrop size	– <10 μm	– 50–1500 μm		– <5 μm	– 100–150 μm	
– Microp size		– 1–2 μm				
Mechanical resistance	NA	10 MPa (blocks)	105–120 MPa	1–5 MPa	NA	>40 MPa
Bioresorption (delay)	NA	NA	NA	6–10 months	NA	>6 months
Historic	– 1995	– 1998	– 1987	– 1990	– 1998	– 1990
– First studies	– 2000	– 2001	– 2004	– 1992	– 1999	– 1992
– Animal exp.	– 2001	– 2007		– 2003	– 2000	– 2006
– Clin. exp.	– 2003	– 2007		– 2005	– 2002	– 2009
– FDA approval						
Comments			Combined with bone allograft to improve reproducibility of the reconstruction		Available since 2007 in combination with type I bovine collagen (Mastergraft™ Putty)	Designed for valgus tibial osteotomy

Sterilization is obtained by γ-radiation (25 kGy) in all substitutes. exp, experiments; clin, clinical; NA, not available.

calcium tetraphosphate ($Ca_4P_2O_9$), characterized by a Ca/P ratio equal to 2, hydroxyapatite or hydroxylapatite (HA) [$Ca_{10}(PO_4)_6(OH_2)$] (Ca/P = 1.67), tricalcium phosphate (TCP) [$Ca_3(PO_4)_2$] (Ca/P = 1.5), and dicalcium phosphate dihydrate (DCPD or brushite) [$CaHPO_4 \cdot 2(H_2O)$] (Ca/P = 1). Among these compounds, HA and β-TCP are the most widely used (**Table 1**), mainly in combination in variable proportion in so-called biphasic calcium phosphate (BCP) ceramic. Of note is the fact that β-TCP ceramics are much more soluble and biodegradable compared to HA.[14,15] In addition, Becker *et al.*[16] showed that Chronos used in combination with autologous bone marrow (Chronos Perfusion Concept) could be almost entirely replaced by host bone 12 weeks after implantation. There is no report of systemic toxicity or immunologic or foreign body reaction, nor infectious disease transmission with these materials.

CPC biocompatibility has been shown to be excellent in *in vitro* and *in vivo* settings. For a given chemical composition, ceramics with lower Ca/P ratios resorb more rapidly, giving rise to unpredictable biodegradation profiles, which may result in undesirable loss of strength. On the other side, those with greater Ca/P ratios degrade more slowly but may give rise to remnants that may induce inflammation. Lower degradation rates usually result in less new bone formation around the scaffold. For instance, when dense HA ceramics are used as bone implants, they are almost nonresorbable and remain bioinert. The combination of different CP compounds can be used as a manufacturing strategy to control bioresorption rates of the ceramics. Under physiological conditions, material characteristics such as crystallinity, crystal size, particle size and size distribution, porosity and surface roughness also have been reported to influence biological performance.[15,17] Among these parameters, pore interconnectivity seems to be one of the most important parameters for bone ingrowth.[18–20]

CPCs may be prepared by several synthetic routes, which include hydrolysis, hydrothermal synthesis, hydrothermal exchange (coral-derived ceramics), solid process from bovine bone (ceramized xenograft), sol–gel processes, spray pyrolysis from natural coralline, and wet chemical methods. Conventional CPCs are usually prepared from highly purified precursor powders. The powders are calcined at temperatures below 900 °C. The mono- or multiphasic powders are then compacted at high pressure, and fired to high temperatures (1100–1300 °C), this step being termed 'sintering.' Once recrystallization and grain growth of the original powder has occurred after cooling, a material characterized by a mosaic pattern of aggregated crystals is obtained. These procedures result in a dense ceramic material. Its porosity is in the micrometric range, with the pore size always <100 μm in diameter. However, to favor bone ingrowth, a ceramic material should have an open macropore structure that enables cell migration. This is obtained at the step of sintering with the addition of pores and canal structure-forming agents in the form of porogen particles, such as naphthalene. The porogen compound is finally eliminated during the sintering phase. Another method relies on the decomposition of hydrogen peroxide to generate the desired porous structure. This manufacturing process should be stringently controlled as it dictates the mechanical, physical, chemical, and biological properties of the final ceramic product. Hence, the macrostructure of the material is determined by the particles size of the porogen compound. Macroporosity is defined by a pore size higher than 100 μm. Experimental studies have shown that optimal bone tissue ingrowth was observed in porous ceramics with macropores diameter ranging from 100 to 500 μm, combined with high interconnectivity. The overall porosity of the material corresponds to all pores and connective canals between pores in the material, which is equivalent to the ratio of the volume of void in the ceramic to the volume of the whole. It averages 30–45% in commercially available products.

These synthetic ceramic products differ substantially from ceramics produced from coral. Hence, HA can be manufactured from natural reef building coral skeleton by a hydrothermal exchange reaction. This procedure drives the conversion of the calcium carbonate skeleton to CP, the main component of hydroxyapatite. This concept is based on the finding that the structure of certain reef-building coral species resembles the trabecular structure of bone. Specifically, with pore diameters ranging from 140 to 160 μm, *Porites* and *Goniopora* coralline species meet satisfying criteria for bone substitution, and are employed in commercialized bone substitutes.[21–24]

Studies have shown that porous CPCs were osteoconductive, biocompatible, and bioactive.[16,18,19] Porosity of the ceramic promotes biological and cellular events, leading to bone tissue ingrowth. Schematically, chemical events take place in micropores within the hours following implantation of the bone substitute. They include the recruitment of Ca^{2+} and PO_4^{2-} ions from both implant and surrounding bony environment, to form a biological apatite layer, similar to the crystalline phase of bone. Apatite crystals unite with local proteins, such as growth factors and collagen. In parallel, cell attachment, proliferation and differentiation, and also vascular invasion, occur in the macropores. These steps result in a direct contact between host bone tissue and the ceramic, without interposition of a fibrous layer, and, further on, in osteointegration.

Pure HA resorbs with time but its degradation rate is very low, as a result of its limited solubility in biological fluids. Solubility is increased in biphasic materials, which combine hydroxyapatite and TCP in variable proportion. Currently, most of the biphasic ceramics are composed of 60–65% HA and 35–40% β-TCP. The replacement of β-TCP by bone does not occur in an equitable way. There is always less bone volume produced than the volume of β-TCP reabsorbed. Bioresorption of the bone graft ceramic depends on different parameters, including chemical structure, shape, overall porosity, interconnectivity, pore size, crystallinity, and specific surface. *In vivo* resorption of porous CP ceramics begins with the dissolution of ionic precursors in the extracellular environment. Chemotactic agents included in the apatite HA layer stimulate giant cells and macrophages which participate in the resorption of the material. Also, the material is resorbed as part of the physiological Haversian remodeling process, driven by osteoclasts. Then, new lamellar bone produced by osteoblasts forms in place of the artificial material.

There is a growing interest in developing HA/β-TCP BCP ceramics as scaffold materials because they are more effective in bone repair or regeneration than each of its components taken separately, and their degradation rate is controllable to a certain degree.[25,26]

CPCs are brittle and weak under tension and shear, and resistant to compressive loads. Their mechanical resistance has been evaluated from 10 to 15 MPa for current products. The compressive and tensile strengths of β-TCP are very similar to those of cancellous bone, whereas dense ceramics such as HA can resist in compression up to 100 MPa and have a much higher modulus of elasticity than bone. Therefore, CPC are not indicated in constrained or load-bearing areas, and should be employed in conjunction with an osteosynthesis. Mechanical resistance improves in parallel with osseointegration and ceramic remodeling.

CPCs are considered as reference bone substitutes, provided that indications and handling are in line with their properties. They have been demonstrated to bond to bone tissue under optimal conditions, including close contact between synthetic graft and host, achievement of primary stability, and a well-vascularized environment. These ceramics are indicated in a wide variety of fields, specifically in orthopedics, including prosthetic hip revision surgery, spine surgery, trauma, benign bone tumor filling, and high tibial valgus osteotomy. A few studies reported the use of bone substitutes in hip replacement revision. Historically, CPCs were employed to fill cavitary defects in acetabular reconstructions during hip revision surgery. Oonishi *et al.*[27] presented encouraging results of impaction technique with HA granules applied to acetabular reconstruction during revision in total hip replacement. The series included 40 hips, with a follow-up ranging from 4 to 10 years. Postoperatively, load bearing was restricted for 10–12 weeks. Socket migration occurred in five hips with severe segmental and cavitary defects. The authors concluded that socket loosening and migration could be reduced when major peripheral segmental defects were stabilized by structural allografts, allowing firm packing of the HA granules. Furthermore, histological analysis of HA granules retrieved from filled-in acetabular bone defects 1–10 years after surgery suggested that bone ingrowth into spaces between HA could be expected.[28] In a series of 32 acetabular reconstructions with a mean follow up of 5 years, Schwartz and Bordel[29] showed that a BCP ceramic employed as granules or blocks could result in satisfying bone stock restoration in a vast majority of hips.

During the past years, authors have reported successful results of femoral reconstruction with a morsellised impacted bone allograft technique.[30–33] Limited aseptic failure rates have been observed in the mid- to long term,[34,35] with a 90.5% global survival rate at 10–11 years reported by the Exeter group.[36] However, initial stability of the stem–graft composite was still far from optimal. Subsidence of the stem is a common finding that is considered as a positive event.[30,31,37,38] In parallel, CPCs have been shown to exhibit both much greater mechanical stability and reproducibility than pure allograft in experimental tests.[39] This has led one of us to investigate the use of a macroporous CPC in femoral reconstruction in revision hip surgery.[40] The bone graft substitute was employed as porous granules of macroporous biphasic calcium phosphate (MBCP), consisting of 75% hydroxyapatite (HA) and 25% β-TCP (Biosel®, Depuy Bioland, France). HA granules were irregular in shape and size (2–3 mm). Macropores ranged from 200 to 500 µm in diameter, resulting in a 70% overall porosity of the material. We retrospectively reviewed 21 femoral reconstructions with impacted CPC in 20 patients, at a mean of 36 months. Femoral cavitary defects were reconstructed according to a firm impaction of ceramic granules, followed by a cementing of the stem. At follow-up, we observed a satisfying bone reconstruction in all femurs but two, which required rerevision (one septic recurrence and one aseptic failure), and a limited rate of subsidence. Functional improvement was noted in all non-rerevised cases. We concluded that femoral reconstruction with an impacted bone graft BCP substitute was safe and reliable (Figure 2). These results were

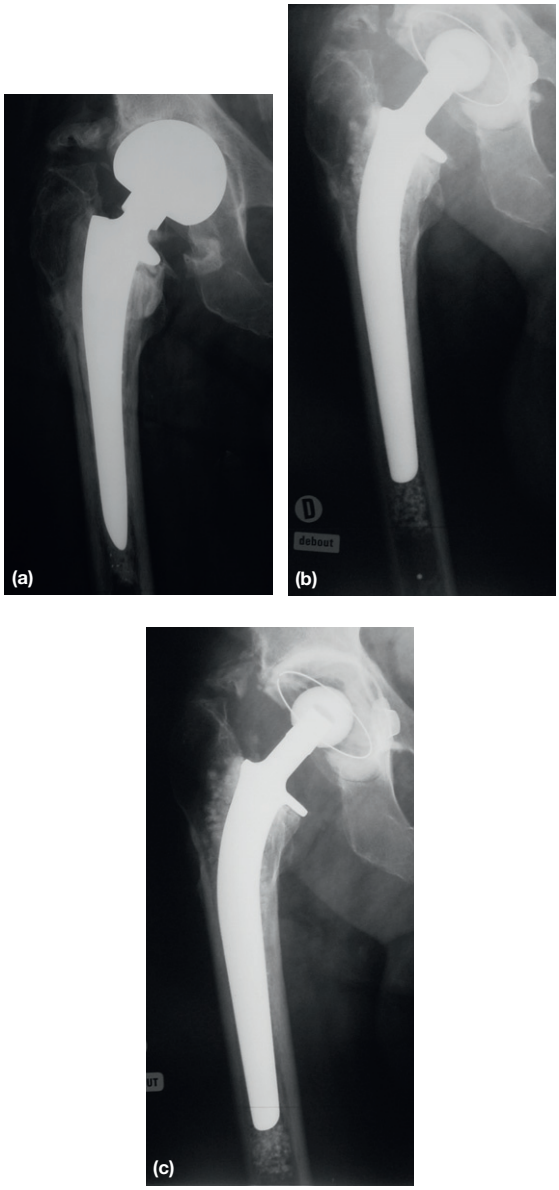

Figure 2 First hip revision in a 74-year-old active man. (a) Preoperative radiographs showing aseptic loosening of a bipolar hemiarthroplasty performed for femoral neck fracture. (b) Immediate postoperative anteroposterior view showing conversion to a total hip replacement and femoral reconstruction with hydroxyapatite/β-tricalcium phosphate granules. The graft–cement packing was considered complete and homogenous. (c) Radiographs taken 34 months postoperatively exhibit a good bone reconstruction and a satisfying synthetic graft incorporation. There is no evidence of stem subsidence and no radiolucent lines at the cement–bone interface. Functional score was rated excellent.

similar to those recently reported by Aulakh *et al.*[41] in terms of functional outcome and graft incorporation.

CPCs have also been proven to be an effective promoter of fusion in spine arthrodesis,[42,43] with radiological results similar to that obtained with autograft alone. A few studies reported on the use of CPCs in high tibial open-wedge osteotomy in the treatment of medial compartment osteoarthritis of varus knee.[44,45] These conditions are theoretically favorable, as the bone graft implantation is performed in a cancellous bone environment, well vascularized, and mechanically stable. Authors reported that signs of fusion and good integration of the implanted wedges were regularly observed, with no inflammatory reaction. Macroporous ceramics have been employed successfully in the treatment of acute fractures, including metaphyseal long bones fractures,[46] calcaneal fractures,[47] and in trauma sequelae.[48] Also, CPCs are indicated as void fillers after benign bone tumors curettage, either under the form of pure HA,[49,50] or as β-TCP,[51] but a combination of both is also a suitable option (**Figure 3**). Authors reported satisfying osseointegration of the graft substitute with no specific complication related to the bone substitute. Several authors have reported the lack of complete resorption of HA,[52] but it is probable that clinical implications of this phenomenon are moderate. An effort has been made to solve the problem of CP brittleness without reducing bone-bonding properties, by employing a hybrid composite of CP and a polysaccharide such as chitosan.[53–56] Ito *et al.*[55] demonstrated that subperiosteal implantation of HA/chitosan composite membranes over rat calvaria were biologically well tolerated, with occasional osteogenesis. Also, Zhang and Zhang[53] have shown that the addition of β-TCP to flexible chitosan resulted in an improvement in the compressive modulus and yield strength of the composite scaffolds. Recently, Ding[56] demonstrated that a CaP/chitosan ratio of 5% by mass to volume in the composite achieved the significantly higher bending strength, but a higher CaP content adversely affected mechanical properties of the hybrid composite.

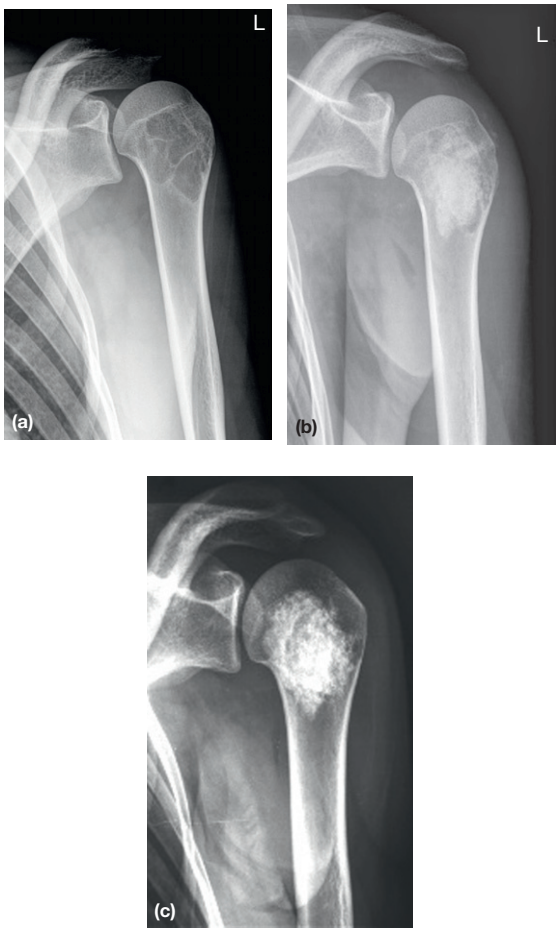

Figure 3 (a) A preoperative X-ray of left humerus shows a cavitary lesion (fibrous dysplasia) of proximal metaphysis in a 22-year-old woman. (b) A curettage followed by a filling of the cavity with hydroxyapatite/β-tricalcium phosphate (HA/β-TCP) (60/40) granules were performed. Immediate postoperative X-ray shows the cavity filled with granules of HA/β-TCP. (c) Eighteen months after surgery, the cavity has been remodeled and HA/β-TCP granules are considered osseointegrated.

1.120.3.3. Calcium Phosphate Cements

The first self-hardening calcium phosphate cements were introduced in the late 1980s by Brown and Chow.[57] The first CP composition received approval from the US FDA in 1996. The term *calcium phosphate cement* is synonymous with *apatitic cement, ionic cement, or hydraulic cement*. Despite the large number of formulations, CP cements can only have three different end products, namely apatite (PHA) (neutral), brushite (DCPD) (acid), and amorphous calcium phosphate (ACP) (basic). With the exception of several CP cements that form brushite as the product, most CaP cements form apatitic or carbonato-apatitic products, such as Norian™ SRS (Synthes USA, West Chester, PA). Apatitic CaP cements are viscous and easily moldable, but usually difficult to inject. In contrast, brushite CaP cements can be initially very liquid and still set within a short period of time. Data in the literature indicate that cementation can occur in mixtures containing a wide variety of CP compounds. The cement setting reaction determines the intermediate and the final products that will be formed in the CaP cement, and, consequently, its mechanical and biological properties. For brushite cements, setting time depends on the solubility of the basic phase (the higher the solubility of the basic phase, the faster the setting time), and ranges from a few seconds to several minutes.

Cement hardening is the result of three theoretical mechanisms, described as (1) reactions among calcium products in an aqueous environment (dissolution/reprecipitation reactions), (2) reaction between calcium and a carboxylic acid, and (3) reaction between CP and an aqueous polymer solution (acid–base reaction between the carboxyl groups of the polymer and the alkaline CP).[58] All brushite CaP cements are obtained by an acid–base reaction. Brushite can only precipitate at a pH value lower than 6. After setting, the pH of the cement paste slowly changes toward the equilibrium pH, and is dependent on the basic phase content.

The volume of CaP cements stays almost constant during the setting reaction. Unlike PMMA cements, CaP cements do not harden through a polymerization reaction and only a small amount of heat is released. CP cement is a microporous solid consisting of nanometer-sized HA or micrometer-sized DCPD

crystals. Therefore, the microporosity of the material, and its subsequent specific surface, are very high. Ionic exchanges between crystal surface and extracellular environment are very important. CaP cements can slowly degrade in a bony environment, without the need for a macroporous interconnected structure. Thus, CP cements degrade layer by layer, but this may be viewed as a drawback when compared to open macroporous CaP blocks. Sometimes, bone ingrowth is observed inside the cement, within a crack. However, the presence of macropores can facilitate ingrowth of bone and the overall process of cement replacement by newly formed bone.[58]

The biocompatibility of apatitic CaP cements is excellent, and their biodegradation is much larger than that of HA, but still very slow. HA-forming and DCPD-forming CP cements do not dissolve spontaneously in a normal physiological fluid environment, but are resorbable under cell-mediated acidic conditions. Being more soluble, the DCPD-forming CP cements resorb more rapidly than HA-forming CP cements. Frayssinet *et al.*[59] reported a 25% resoprtion of a brushite CP cement after 18 weeks implantation in a rabbit femur. This feature should help in making a choice between CP cements, in order to achieve optimum clinical results.

Once hardening has occurred, CP cements are brittle and have relatively low bending/flexural strengths. Mechanical properties of CaP cements depend on their composition, with brushite cements being slightly weaker than apatitic CaP cements. The main determining factor is the ratio of cement powder to the amount of mixing liquid: the higher the powder/liquid ratio, the lower the porosity of the cement. Hence, most CP cements have a tensile strength ranging from 1 to 10 MPa, whereas the compression strength varies in the range of 10–100 MPa. Therefore, CaP cements can only be used in combination with metal implants or in low or non-load-bearing applications as CPCs blocks. Significant increases in the mechanical properties of CaP cements have been achieved by incorporating biocompatible and bioresorbable reinforcement additives, such as Vicryl meshes,[60] or chitosan.[61] Moreover, the mechanical properties of the apatitic CaP cement may vary with implantation time. The mechanical properties of apatitic CaP cements tend to increase with time, in contrast to those of brushite CP cements, which decrease initially and increase after a few weeks of implantation when bone grows, explained by the higher solubility of DCPD compared with that of HA. Compression strengths and setting times have been evaluated for several CP cements[62]:

- Norian™ SRS (Synthes USA): 33 ± 5 MPa and 8.5 ± 5 min (= 50% porosity)
- Cementek™ LV (Teknimed SA, L'Union, France): 8 ± 2 MPa and 17 ± 1 min
- α-BSM™ (Etex Corporation, Cambridge, MA): 4 ± 1 MPa and 19 ± 1 min (= 80% porosity)
- ChronOS™ Inject (Synthes USA): 5–8 MPa and 11 ± 2 min (50% porosity)
- Bonesource™ BVF (Styker): 65 MPa and 7–10 min

In vivo, CP cements are injected as a liquid or as a paste. Injectability of CP cements is influenced by various intrinsic parameters including particle size and shape, particle size distribution, powder/liquid ratio, liquid viscosity and also by an extrinsic parameter, that is, the delay between mixing and implantation of the cement. Cement cohesion may be altered during this phase, resulting in a demixing of the cement: the liquid is expelled without the CaP particles. Decohesion of the cement during mixing can lead to inflammatory reactions.

Among the various products, Norian™ SRS has been widely studied. Its mechanical properties allow for rapid load bearing and/or provide good additional stabilization in unstable fractures of the distal radius,[63,64] tibial plateau,[65] and calcaneus.[66–68] CaP cements have also been proposed as bone void filler in acetabular defects in revision hip replacements.[69] Of note are the potential adverse effects of apatitic cements, described as soft-tissues reactions induced by cement.[70] CaP cement can be used as a delivery system for therapeutic peptides, antibiotics, anticancer drugs, anti-inflammatory drugs, or growth factors.[71]

1.120.3.4. Bioactive Glasses and Ceramics

Bioactive glasses and ceramics have been studied for almost four decades. They constitute a group of synthetic silicate-based materials, characterized by their bioactivity and their unique bone bonding properties, related to their surface reactivity, via hydroxylation and dissolution reactions.[72–75] In addition, most of these materials degrade naturally: similarly to other synthetic substitutes such as CP compounds, the degradation products are entirely metabolized by the body. Bioactive glasses consist of silica, that forms the main component, as well as sodium oxide (Na_2O), calcium oxide (CaO), and phosphorus pentoxide (P_2O_5). Conventional bioactive glass and glass ceramic are obtained by melting the glass phase at high temperatures followed by casting of bulk implants or quenching of powders. In 1991, Li *et al.*[76] showed that a bioactive glass could be made by sol–gel processing. This finding offered a potential method for using this new generation of bioactive materials in porous scaffolds and coatings.[77]

By varying the content of sodium oxide, calcium oxide, and silicon dioxide in the glass, a full range of biological stability, from soluble to nonresorbable, can be produced. Bioactivity is dependent on chemical composition, with a maximal content of SiO_2 in the cast glass being equal to 60% in weight. Compositions for most rapid bonding not only to bone tissue, but also to soft tissues, range from 45% to 52% in weight of SiO_2. Glasses with a SiO_2 content ranging from 55% to 60% in weight react more slowly, and do not bind soft tissues. Compositions with >60% SiO_2 do not bond bone and are considered as bioinert. One of the most studied bioactive glasses is glass 45S5, which was developed at the University of Florida in the late 1960s.[78] The key composition features of 45S5 are that it contains <60% SiO_2, high Na_2O and CaO contents, and a high CaO/P_2O_5 ratio, which make it highly reactive to aqueous medium and bioactive. Thus, bone bonding occurs as a result of a rapid sequence of chemical, cellular, and tissue reactions on the surface of the implant after contact of the glass with the biological milieu. A rapid ions exchange of Na^+ and K^+ released from the glass with H^+ and H_3O^+ present in the extracellular fluids occurs. Bioactive glasses have been demonstrated to stimulate the growth and maturation of osteoblasts, and to promote the expression and maintenance of the osteoblastic phenotype through a direct control over genes that regulate cell cycle induction and progression.[79–85]

An important modification of bioactive glasses was the development of apatite/wollastonite (A/W) bioactive glass-ceramic at Kyoto University, Kyoto, Japan, in the mid 1980s.[86] A unique processing method produced a very fine-grained glass-ceramic composed of very small apatite (A) and wollastonite ($W = CaSiO_3$) crystals, bonded by a bioactive glass interface. This process resulted in a consistent improvement of the component with regard to mechanical strength, toughness, stability, and bone bonding.[87–89] Clinical success in spine surgery has been documented.[90]

The first bioactive glass device cleared for marketing used in the United States was a device used to treat conductive hearing loss by replacing the bones of the middle ear, in 1985. It was a solid, cast bioactive glass structure that acted to conduct sound from the tympanic membrane to the cochlea due to its unique property to bond to soft tissue as well as to bone tissue. More recently, particulate glass materials have been employed to restore bone loss resulting from periodontal disease.[91,92] It has been clinically used from 1993 onward. 45S5 bioactive glass was cleared for general orthopedic bone grafting in non-load-bearing sites in 2000 (Figure 4).

Some of the difficulties associated with the use of bioactive glasses in biomedical applications are related to their brittle behavior and weak mechanical properties. However, bioactive glass blocks resist drilling and shaping. As a consequence, they are difficult to fix to the skeleton. The bending strength of most bioactive glasses is in the range of 40–60 MPa, which is not enough for load-bearing applications, while their Young's modulus is 30–35 GPa, very close to that of cortical bone. To improve the mechanical properties of bioactive glasses, the authors have developed glass materials reinforced with stainless steel fibers (bioactive glass), or zirconia particles (A/W glass ceramic).[93]

The combination of biodegradable polymers with bioactive glasses has been proposed to produce biodegradable products that display high levels of bioactivity and also improved mechanical properties as compared to conventional glasses. Among the various polymers such as poly(lactic acid), poly (caprolactone), and natural polymers (collagen, starch, and chitosan), polysulfone has been demonstrated to yield mechanical characteristics that are comparable to cortical bone and represents, therefore, a promising material.[94]

1.120.3.5. Glass Ionomer Cements

In the early 1970s, glass ionomer cements (GICs) were suggested as materials of choice for tooth restoration because they bond chemically to dental hard tissues and release useful amounts of fluoride ions over a relatively long period. They have the additional advantage of being aesthetic in that they match the natural color of the tooth. Their properties have initiated their development in medical applications, mainly in the field of ear, nose, and throat surgery (bone cements, auditory ossicular reconstructions, and craniofacial implants).

Conventional GIC are derived from aqueous polyalkenoic acid such as polyacrylic acid and an ion-leachable silicate glass,

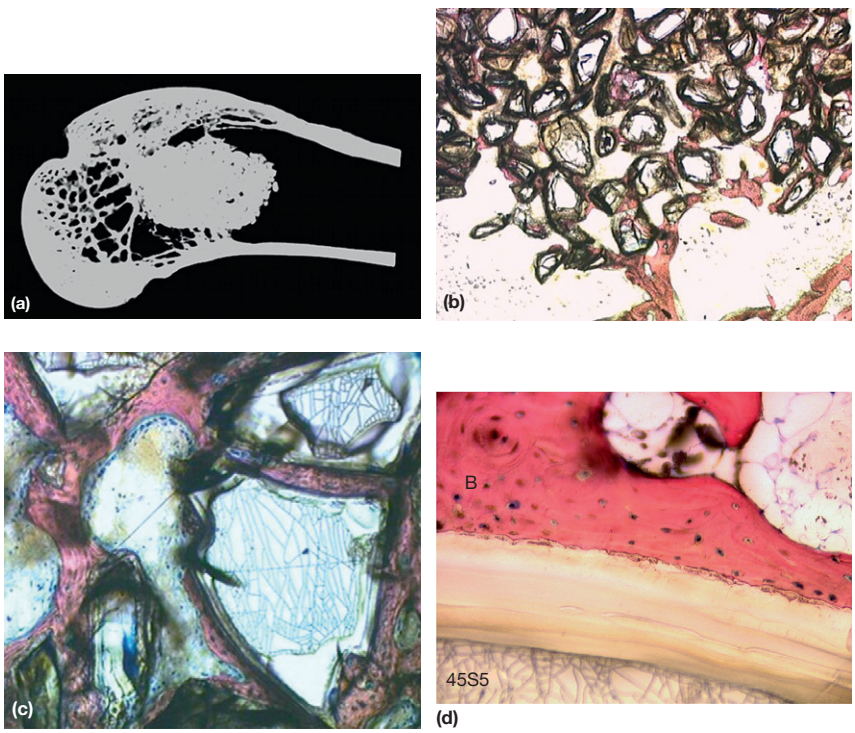

Figure 4 Bioactive glasses interact with surrounding bone tissue. (a) A figure shows a microradiograph of the distal femur of an adult rabbit 28 days after implantation of 45S5 Bioglass™ in particulate form: osseointegration is obtained, trabecular bone has reached the implant in a centripetal pattern. (b) Nondecalcified histology of the same implant showing that 45S5 particles are surrounded by newly formed bone (Magnification × 100, staining picrofuschine, Stevenel Blue). (c, d) Histological sections illustrating direct bone bonding to Bioglass™ particles, with no intermediate fibrous layer (Magnification × 200 and × 400 respectively, staining picrofuschine, Stevenel Blue). B = bone.

usually a fluoroaluminosilicate. When the powder and liquid are mixed together, an acid–base reaction occurs. As the metallic polyalkenoate salt begins to precipitate, gelation occurs and a porous cement paste is obtained.[95,96] Once the cement has hardened, maturation processes take place over several weeks. The final product is a rigid material with a porecelain-like appearance.

In the 1990s, several faster setting, high viscosity conventional GIC were developed.[97–99] Important modifications of GIC were developed to improve mechanical strength, such as the addition of silver-amalgam alloy powder to conventional GIC. Resin-modified GICs have been introduced more recently.[100] In these materials, the acid–base reaction is supplemented by a second resin polymerization usually initiated by a light-curing process, which requires the presence of photoinitiators within the formulation. Resin-modified GIC have been used in bone augmentation.[101] Advantages of GIC include their ability to bond directly to the surface of the tooth through an ionic exchange at the interface,[102] the progressive release of fluoride being potentially cariostatic, their color that is very close from that of tooth, and their biocompatibility. GIC have a number of advantages over acrylic bone cements, including lack of exothermic reaction during setting, and, therefore, absence of heat-labile protein damage, absence of monomer, and an improved release of therapeutic agents, such as antibiotics. One of the main drawbacks of GIC is their relative lack of flexural strength and low resistance to abrasion and wear. Although their compressive strength (180–220 MPa) and modulus of elasticity are comparable to cortical bone after 24 h, GIC remain very brittle and prone to bulk fracture,[103] and therefore should not be employed in load-bearing applications. In addition, early release of fluoride and aluminium ions and release of polyacids have been implicated in tissue compatibility, specifically neurotoxicity. Thus, GIC are contraindicated in contact with neural tissue or cerebrospinal fluid.

1.120.3.6. Biomimetic Nanocomposites and Nanopolymers

Conventional materials implanted today to regenerate tissues may be rough at the macro/microscale but are usually smooth at the nanoscale, and therefore, provide inadequate surface roughness value to cells. Since surface properties of a material vary with grain/particle size, there is a growing interest in nanomaterials in bone regeneration, as they enhance interaction of protein with implant surface, and subsequent cell function. Hence, bone tissue may be viewed as a nanocomposite system with a complex hierarchical structure, composed of biological entities such as collagen type I, and hydroxyapatite crystals. Cells are naturally accustomed to interact with nanostructured surface roughness in physiological environment. Such a roughness can be mimicked in polymers through the use of nanophase materials.

Cellular response to a biomaterial may be enhanced in synthetic polymer formulations by mimicking the surface roughness of natural bone tissue in the nanoscale range. Nanotechnology allows for the production of materials and systems whose structures and components exhibit novel and significantly changed properties that are controlled at the atomic, molecular, and supramolecular levels. HA nanocrystals are prepared by a wet chemical method that can control the fiber size, shape, and composition. A synthetic material characterized by a high surface area to volume ratio and an ultrafine structure, similar to biological apatite, is obtained. A nanocomposite includes a hydrogel and synthetic HA nanocrystals. They are characterized by their high specific surface, over $100\,m^2\,g^{-1}$, compared to that of CP sulfates, which is about $2\,m^2\,g^{-1}$.

It is now believed that cell responses might be more sensitive to changes in surface roughness in the nanometer scale (<100 nm) as compared with conventional regimes (>100 nm) and also that sensitivity may vary with cell type.[104] Recent studies have demonstrated that the adsorption and bioactivity of biomolecules (specifically, proteins such as fibronectin and vitronectin) were enhanced in terms of mediating osteoblast adhesion on nanophase materials.[105] Of note is the influence of the nanometer surface structure in controlling cell functions, as demonstrated by Dalby *et al.*[106]

Ramay and Zhang[107] first introduced the concept of nanocomposites to porous scaffolds for bone tissue engineering. Nanocomposites made of β-TCP as a matrix and HA nanofibers were used to produce porous scaffolds through a technique that integrated the gel casting with polymer sponge methods. These authors showed that inclusion of HA nanofibers as a second phase in β-TCP porous ceramic matrix significantly improved the mechanical properties of the porous scaffold. With a porosity of ≈73% and containing 5% in weight of HA nanofibers, the porous scaffold attained a compressive strength of 9.8 ± 0.3 MPa, which is comparable to the high-end value of the compressive strength of cancellous bone. The toughness, that is, the material's resistivity to crack propagation, of BCP ceramics correlated with HA fiber concentration in the scaffolds, and increased up to $1.72 \pm 0.02\,kN\,m^{-1}$ with the incorporation of 5 wt% HA nanofibers. The authors concluded that these porous scaffolds reinforced with nanofibers had better mechanical properties than the scaffolds of single-phase calcium prepared previously. In addition, it was shown that an electrospun nanocomposite containing amorphous TCP exhibited high *in vitro* bioactivity, cell proliferation, and osteogenic differentiation of human mesenchymal stem cells.[108]

The authors have also shown that some of the drawbacks of nano HA, such as bioresorption and particle migration in surrounding tissues, could be alleviated by using composites of HA nanocrystals in conjugation with polymers, such as the polysaccharides, chitosan,[56,109] polysulfone, polyhydroxybutyrate, collagen,[110] and polylactide acid. In parallel, Itoh *et al.*[111] reported that the use of a hydroxyapatite/collagen (HA/Col) nanocomposite as a carrier for the delivery of rhBMP-2 was effective in controlling both the mechanical strength and bioresorbability of the material, and was suitable for promoting anterior fusion of the cervical spine in a dog model. The beneficial use of ceramics in a nanoparticulate form as fillers in biopolymers has been demonstrated in numerous investigations. The bioactivity of nano biocomposite was evaluated in an *in vitro* and *in vivo* study by Jie *et al.*[112] A composite of nano HA and polyamide was evaluated after immersion in simulated body fluid (SBF) solution and after implantation in the muscles or femorae of rabbits. These authors confirmed that an apatite-like layer formed *in vitro* on the surface of the biocomposite and that a direct bonding between the composite and bone was present after implantation in a bony environment.

The conjunction of HA and collagen may be considered as an attempt to mimic composition and structure of the extracellular bone matrix (ECM), which mainly consists of collagen type I fibrils, mineralized with HA nanocrystals. Bernhardt *et al.*[110] observed an increased activity of alkaline phosphatase in human bone marrow-derived stromal cells (hBMSCs) cultured on membranes of biomimetically mineralized collagen. These results indicated a promoting effect of mineralized collagen on the osteogenic differentiation of hBMSC. Also, studies have suggested that osteoblast and osteoclast activity could be increased, while at the same time fibroblast function decreased on materials with nanostructured features, which may lead to improve osseointegrative potentials. Furthermore, these materials combine favorable properties such as ductility/flexibility of polymer fibers with the stability and bioactivity of CPC.

1.120.4. Conclusion

Considerable improvements have been realized with regard to synthetic bone grafting in recent years, due to a better understanding of biological events leading to bone repair. These recent developments are mainly due to the fusion of several research fields, such as chemistry, molecular and cell biology, medicine, and tissue/bioengineering. This has resulted in an exponential increase of graft materials that have to be tested and clinically validated. However, it implies that not all bone substitutes will perform the same way and that the orthopedic surgeon has therefore to face the dilemma of graft choice. The surgeon is asked to carefully match the clinical problem with the capabilities/properties of the graft material, having in mind that the gold standard remains the autograft. Although bone repair and bone regeneration are dependent on osteoblastic response, the development and/or preservation of an adequate vascular environment and the ability to maintain stability constitute crucial parameters in the technical choice.

With the exception of growth factors, that were not described here, most synthetic bone grafts available are osteointegrative and osteoconductive. They are currently employed as bone void fillers, and are indicated in non-load-bearing situations, with numerous clinical successes reported. Production of biodegradable and osteoconductive scaffolds with a 3D interconnected porous structure and adequate mechanical strength and toughness represent a formidable challenge. Further advances will result in new carrier constructs, characterized by the association of adequate biological scaffolds and growth factors and/or mesenchymal stem cells.

References

1. Aciduman, A.; Belen, D. *Surg. Neurol.* **2007**, *68*, 349–352.
2. Dressman, H. *Klin. Chir.* **1892**, *9*, 461–464.
3. Peltier, L. F.; Bickel, E. Y.; Lillo, R.; Thein, M. S. *Ann. Surg.* **1957**, *146*, 61–69.
4. Peltier, L. F. *Clin. Orthop. Relat. Res.* **1961**, *21*, 1–31.
5. Peltier, L. F.; Jones, R. H. *J. Bone Joint Surg. Am.* **1978**, *60*, 820–822.
6. Albee, F. H.; Morrison, H. F. *Ann. Surg.* **1920**, *71*, 32–39.
7. Ray, D. R.; Ward, A. A. *Surg. Forum* **1952**, *51*, 429.
8. Urist, M. R. *Science* **1965**, *12*(150), 893–899.
9. Ljubovic, E.; Nikulin, A. *Acta Med. Iugosl.* **1956**, *10*, 1–36.
10. Edberg, E. *Acta Chir. Scand.* **1930**, *67*, 313–319.
11. Turner, T. M.; Urban, R. M.; Gitelis, S.; Kuo, K. N.; Andersson, G. B. *J. Bone Joint Surg. Am.* **2001**, *83*(Suppl. 2), 8–18.
12. Gitelis, S.; Piasecki, P.; Turner, T.; Haggard, W.; Charters, J.; Urban, R. *Orthopedics* **2001**, *24*, 162–166.
13. Kelly, C. M.; Wilkins, R. M.; Gitelis, S.; Hartjen, C.; Watson, J. T.; Kim, P. T. *Clin. Orthop. Relat. Res.* **2001**, *382*, 42–50.
14. Le Huec, J. C.; Clément, D.; Brouillaud, B.; *et al*. *Biomaterials* **1998**, *19*, 733–738.
15. Le Huec, J. C.; Schaeverbeke, T.; Clement, D.; Faber, J.; Le Rebeller, A. *Biomaterials* **1995**, *16*, 113–118.
16. Becker, S.; Maissen, O.; Ponomarev, I.; Stoll, T.; Rahn, B.; Wilke, I. *Spine* **2006**, *31*, 11–17.
17. Bohner, M.; Baumgart, F. *Biomaterials* **2004**, *25*, 3569–3582.
18. Eggli, P. S.; Müller, W.; Schenk, R. K. *Clin. Orthop. Relat. Res.* **1988**, *232*, 127–138.
19. Holmes, R. E.; Bucholz, R. W.; Mooney, V. *J. Orthop. Res.* **1987**, *5*, 114–121.
20. Braye, F.; Weber, G.; Irigaray, J. L.; Frayssinet, P. *J. Biomed. Mater. Res.* **1997**, *36*, 315–324.
21. Sartoris, D. J.; Holmes, R. E.; Bucholz, R. W.; Mooney, V.; Resnick, D. *Invest. Radiol.* **1987**, *22*, 590–596.
22. Bucholz, R. W.; Carlton, A.; Holmes, R. *Clin. Orthop. Relat. Res.* **1989**, *240*, 53–62.
23. Guillemin, G.; Patat, J. L.; Fournie, J.; Chetail, M. *J. Biomed. Mater. Res.* **1987**, *21*, 557–567.
24. Guillemin, G.; Meunier, A.; Dallant, P.; Christel, P.; Pouliquen, J. C.; Sedel, L. *J. Biomed. Mater. Res.* **1989**, *23*, 765–779.
25. Ryu, H. S.; Youn, H. J.; Hong, K. S.; Chang, B. S.; Lee, C. K.; Chung, S. S. *Biomaterials* **2002**, *23*, 909–914.
26. Kohri, M.; Miki, K.; Waite, D. E.; Nakajima, H.; Okabe, T. *Biomaterials* **1993**, *14*, 299–304.
27. Oonishi, H.; Iwaki, Y.; Kin, N.; *et al*. *J. Bone Joint Surg. Br.* **1997**, *79*, 87–92.
28. Oonishi, H.; Kadoya, Y.; Iwaki, H.; Kin, N. *J. Biomed. Mater. Res.* **2000**, *53*, 174–180.
29. Schwartz, C.; Bordel, R. *Eur. J. Orthop. Surg. Traumatol.* **2005**, *15*, 191–196.
30. Gie, G. A.; Linder, L.; Ling, R. S.; Simon, J. P.; Slooff, T. J.; Timperley, A. J. *J. Bone Joint Surg. Br.* **1993**, *75*, 14–21.
31. Karrholm, J.; Hultmark, P.; Carlsson, L.; Malchau, H. *J. Bone Joint Surg. Br.* **1999**, *81*, 135–142.
32. Meding, J. B.; Ritter, M. A.; Keating, E. M.; Faris, P. M. *J. Bone Joint Surg. Am.* **1997**, *79*, 1834–1841.
33. Ornstein, E.; Atroshi, I.; Franzen, H.; Johnsson, R.; Sandquist, P.; Sundberg, M. *Clin. Orthop. Relat. Res.* **2001**, *389*, 126–133.
34. Fetzer, G. B.; Callaghan, J. J.; Templeton, J. E.; Goetz, D. D.; Sullivan, P. M.; Johnston, R. C. *J. Arthroplasty* **2001**, *16*, 195–202.
35. Mikhail, W. E.; Wretenberg, P. F.; Weidenhielm, L. R.; Mikhail, M. N. *Arch. Orthop. Trauma. Surg.* **1999**, *119*, 288–291.
36. Halliday, B. R.; English, H. W.; Timperley, A. J.; Gie, G. A.; Ling, R. S. *J. Bone Joint Surg. Br.* **2003**, *85*, 809–817.
37. Eldridge, J. D.; Smith, E. J.; Hubble, M. J.; Whitehouse, S. L.; Learmonth, I. D. *J. Arthroplasty* **1997**, *12*, 535–540.
38. Franzen, H.; Toksvig-Larsen, S.; Lidgren, L.; Onnerfalt, R. *J. Bone Joint Surg. Br.* **1995**, *77*, 862–864.
39. Grimm, B.; Blom, A. W.; Miles, A. W.; Turner, I. G. In *Bioceramics*; Trans tech: Zurich, 2002; Vol. 14, pp 375–378.
40. Nich, C.; Sedel, L. *Int. Orthop.* **2006**, *30*, 525–531.
41. Aulakh, T. S.; Jayasekera, N.; Kuiper, J. H.; Richardson, J. B. *Biomaterials* **2009**, *30*, 1732–1738.
42. Daculsi, G.; Passuti, N.; Martin, S.; Deudon, C.; Legeros, R. Z.; Raher, S. *J. Biomed. Mater. Res.* **1990**, *24*, 379–396.
43. Passuti, N.; Daculsi, G.; Rogez, J. M.; Martin, S.; Bainvel, J. V. *Clin. Orthop. Relat. Res.* **1989**, *248*, 169–176.
44. Gaasbeek, R. D.; Toonen, H. G.; Van Heerwarden, R. J.; Buma, P. *Biomaterials* **2005**, *26*, 6713–6719.
45. Van Hemert, W. L.; Willems, K.; Anderson, P. G.; Van Heerwaarden, R. J.; Wymenga, A. B. *Knee* **2004**, *11*, 451–456.
46. Schwartz, C.; Liss, P.; Jacquemaire, B.; Lecestre, P.; Frayssinet, P. *J. Mater. Sci. Mater. Med.* **1999**, *10*, 821–824.
47. Jiang, S. D.; Jiang, L. S.; Dai, L. Y. *Foot Ankle Int.* **2008**, *29*, 1015–1019.
48. Scheer, J. H.; Adolfsson, L. E. *Injury* **2009**, *40*, 262–267.
49. Uchida, A.; Araki, N.; Shinto, Y.; Yoshikawa, H.; Kurisaki, E.; Ono, K. *J. Bone Joint Surg. Br.* **1990**, *72*, 298–302.
50. Yamamoto, T.; Onga, T.; Marui, T.; Mizuno, K. *J. Bone Joint Surg. Br.* **2000**, *82*, 1117–1120.

51. Galois, L.; Mainard, D.; Delagoutte, J. P. *Int. Orthop.* **2002**, *26*, 109–115.
52. Schindler, O. S.; Cannon, S. R.; Briggs, T. W.; Blunn, G. W. *J. Orthop. Surg.* **2008**, *16*, 66–74.
53. Zhang, Y.; Zhang, M. *J. Biomed. Mater. Res.* **2001**, *55*, 304–312.
54. Yin, Y.; Ye, F.; Cui, J.; Zhang, F.; Li, X.; Yao, K. *J. Biomed. Mater. Res.* **2003**, *67*, 844–855.
55. Ito, M.; Hidaka, Y.; Nakajima, M.; Yagasaki, H.; Kafrawy, A. H. *J. Biomed. Mater. Res.* **1999**, *45*, 204–208.
56. Ding, S. J. *Dent. Mater. J.* **2006**, *25*, 706–712.
57. Brown, W. E.; Chow, L. C. In *Cements Research Progress 1986*; Brown, P. W., Ed.; American Ceramic Society: Westerville, OH, 1987; pp 352–379.
58. Chow, L. C. *Dent. Mater. J.* **2009**, *28*, 1–10.
59. Frayssinet, P.; Gineste, L.; Conte, P.; Fages, J.; Rouquet, N. *Biomaterials* **1998**, *19*, 971–977.
60. Xu, H. H.; Quinn, J. B.; Takagi, S.; Chow, L. C. *Biomaterials* **2004**, *25*, 1029–1037.
61. Xu, H. H.; Quinn, J. B.; Takagi, S.; Chow, L. C. *J. Dent. Res.* **2002**, *81*, 219–224.
62. Driessens, F. C.; Boltong, M. G.; De Maeyer, E. A.; Verbeeck, R. M.; Wenz, R. *J. Mater. Sci. Mater. Med.* **2000**, *11*, 453–457.
63. Sanchez-Sotelo, J.; Munuera, L.; Madero, R. *J. Bone Joint Surg. Br.* **2000**, *82*, 856–863.
64. Cassidy, C.; Jupiter, J. B.; Cohen, M.; *et al*. *J. Bone Joint Surg. Am.* **2003**, *85*, 2127–2137.
65. Lobenhoffer, P.; Gerich, T.; Witte, F.; Tscherne, H. *J. Orthop. Trauma* **2002**, *16*, 143–149.
66. Thordarson, D. B.; Hedman, T. P.; Yetkinler, D. N.; Eskander, E.; Lawrence, T. N.; Poser, R. D. *J. Bone Joint Surg. Am.* **1999**, *81*, 239–246.
67. Schildhauer, T. A.; Bauer, T. W.; Josten, C.; Muhr, G. *J. Orthop. Trauma* **2000**, *14*, 309–317.
68. Wee, A. T.; Wong, Y. S. *Foot Ankle Spec.* **2009**, *2*, 98–106.
69. Speirs, A. D.; Oxland, T. R.; Masri, B. A.; Poursartip, A.; Duncan, C. P. *Biomaterials* **2005**, *26*, 7310–7318.
70. Welkerling, H.; Raith, J.; Kastner, N.; Marschall, C.; Windhager, R. *J. Bone Joint Surg. Br.* **2003**, *85*, 238–239.
71. Maus, U.; Andereya, S.; Gravius, S.; Ohnsorge, J. A.; Niedhart, C.; Siebert, C. H. *J. Biomater. Appl.* **2008**, *22*, 559–576.
72. Hench, L. L.; Paschall, H. A. *J. Biomed. Mater. Res.* **1973**, *7*, 25–42.
73. Ogino, M.; Ohuchi, F.; Hench, L. L. *J. Biomed. Mater. Res.* **1980**, *14*, 55–64.
74. Hench, L. L.; Wilson, J. *Science* **1984**, *226*, 630–636.
75. Hench, L. L. In *Bioceramics, Material Characteristics vs in vivo Behavior*; Ducheyne, P., Lemons, J., Eds.; New York Acadamy of Sciences: New York, 1988; pp 54–71.
76. Li, R.; Clark, A. E.; Hench, L. L. *J. Appl. Biomater.* **1991**, *2*, 231–239.
77. Hamadouche, M.; Meunier, A.; Greenspan, D. C.; *et al*. *J. Biomed. Mater. Res.* **2000**, *52*, 422–429.
78. Hench, L. L. *J. Mater. Sci. Mater. Med.* **2006**, *17*, 967–978.
79. Xynos, I. D.; Edgar, A. J.; Buttery, L. D.; Hench, L. L.; Polak, J. M. *J. Biomed. Mater. Res.* **2001**, *55*, 151–157.
80. Dieudonné, S. C.; van den Dolder, J.; de Ruijter, J. E.; *et al*. *Biomaterials* **2002**, *23*, 3041–3051.
81. Loty, C.; Sautier, J. M.; Tan, M. T.; *et al*. *J. Bone Miner. Res.* **2001**, *16*, 231–239.
82. Kaufmann, E. A.; Ducheyne, P.; Shapiro, I. M. *J. Biomed. Mater. Res.* **2000**, *52*, 783–796.
83. Xynos, I. D.; Hukkanen, M. V.; Batten, J. J.; Buttery, L. D.; Hench, L. L.; Polak, J. M. *Calcif. Tissue Int.* **2000**, *67*, 321–329.
84. Bosetti, M.; Zanardi, L.; Hench, L.; Cannas, M. *J. Biomed. Mater. Res.* **2003**, *64*, 189–195.
85. Hattar, S.; Berdal, A.; Asselin, A.; Loty, S.; Greenspan, D. C.; Sautier, J. M. *Eur. Cell Mater.* **2002**, *4*, 61–69.
86. Nakamura, T.; Yamamuro, T.; Higashi, S.; Kokubo, T.; Itoo, S. *J. Biomed. Mater. Res.* **1985**, *19*, 685–698.
87. Kitsugi, T.; Yamamuro, T.; Nakamura, T.; *et al*. *J. Biomed. Mater. Res.* **1987**, *21*, 467–484.
88. Ono, K.; Yamamuro, T.; Nakamura, T.; Kokubo, T. *Biomaterials* **1990**, *11*, 265–271.
89. Ono, K.; Yamamuro, T.; Nakamura, T.; Kokubo, T. *J. Biomed. Mater. Res.* **1990**, *24*, 47–63.
90. Kasai, Y.; Takegami, K.; Uchida, A. *J. Spinal Disord. Tech.* **2003**, *16*, 31–37.
91. Schepers, E.; de Clercq, M.; Ducheyne, P.; Kempeneers, R. *J. Oral Rehabil.* **1991**, *18*, 439–452.
92. Wilson, J.; Low, S. B. *J. Appl. Biomater.* **1992**, *3*, 123–129.
93. Seghi, R. R.; Denry, I. L.; Rosenstiel, S. F. *J. Prosthet. Dent.* **1995**, *74*, 145–150.
94. Oréfice, R.; West, J.; Latorre, G.; Hench, L.; Brennan, A. *Biomacromolecules* **2010**, *11*, 657–665.
95. Wilson, A. D.; Kent, B. E. *Br. Dent. J.* **1972**, *132*, 133–135.
96. Mount, G. *Dent. Update* **1991**, *18*, 276–279.
97. Frankenberger, R.; Sindel, J.; Krämer, N. *Quintessence Int.* **1997**, *28*, 667–676.
98. Berg, J. H. *Pediatr. Dent.* **1998**, *20*, 93–100.
99. Berg, J. H. *Pediatr. Dent.* **2002**, *24*, 430–438.
100. Wilson, A. D. *Int. J. Prosthodont.* **1990**, *3*, 425–429.
101. Ramsden, R. T.; Herdman, R. C.; Lye, R. H. *J. Laryngol. Otol.* **1992**, *106*, 949–953.
102. Wilson, A. D.; Groffman, D. M.; Kuhn, A. T. *Biomaterials* **1985**, *6*, 431–433.
103. Williams, J. A.; Billington, R. W.; Pearson, G. J. *Br. Dent. J.* **1992**, *172*, 279–282.
104. Balasundaram, G.; Webster, T. J. *Macromol. Biosci.* **2007**, *7*, 635–642.
105. Webster, T. J.; Ergun, C.; Doremus, R. H.; Siegel, R. W.; Bizios, R. *J. Biomed. Mater. Res.* **2000**, *51*, 475–483.
106. Dalby, M. J.; Riehle, M. O.; Johnstone, H.; Affrossman, S.; Curtis, A. S. *Biomaterials* **2002**, *23*, 2945–2954.
107. Ramay, H. R.; Zhang, M. *Biomaterials* **2004**, *25*, 5171–5180.
108. Schneider, O. D.; Loher, S.; Brunner, T. J.; *et al*. *J. Biomed. Mater. Res. B Appl. Biomater.* **2008**, *84*, 350–362.
109. Murugan, R.; Ramakrishna, S. *Biomaterials* **2004**, *25*, 3829–3835.
110. Bernhardt, A.; Lode, A.; Boxberger, S.; Pompe, W.; Gelinsky, M. *J. Mater. Sci. Mater. Med.* **2008**, *19*, 269–275.
111. Itoh, S.; Kikuchi, M.; Koyama, Y.; Takakuda, K.; Shinomiya, K.; Tanaka, J. *Cell Transplant.* **2004**, *13*, 451–461.
112. Jie, W.; Hua, H.; Lan, W.; Yi, H.; Yubao, L. *J. Mater. Sci. Mater. Med.* **2007**, *18*, 529–533.

1.121. Polymer Fundamentals: Polymer Synthesis

V Hasirci, P Yilgor, T Endogan, G Eke, and N Hasirci, Middle East Technical University, Ankara, Turkey

© 2011 Elsevier Ltd. All rights reserved.

1.121.1.	**Introduction to Polymer Science**	350
1.121.1.1.	Classification of Polymers	351
1.121.1.2.	Polymerization Systems	352
1.121.2.	**Polycondensation**	353
1.121.2.1.	Characteristics of Condensation Polymerization	353
1.121.2.2.	Kinetics of Linear Polycondensation	354
1.121.2.2.1.	Molecular weight control in linear polycondensation	355
1.121.2.3.	Nonlinear Polycondensation and Its Kinetics	356
1.121.2.3.1.	Prediction of the gel point	356
1.121.2.4.	Mechanisms of Polycondensation	356
1.121.2.4.1.	Carbonyl addition–elimination mechanism	356
1.121.2.4.2.	Other mechanisms	356
1.121.2.5.	Typical Condensation Polymers and Their Biomedical Applications	357
1.121.3.	**Addition Polymerization**	357
1.121.3.1.	Free Radical Polymerization	358
1.121.3.1.1.	Initiation	358
1.121.3.1.2.	Propagation	358
1.121.3.1.3.	Termination	359
1.121.3.1.4.	Kinetics of radical polymerization	359
1.121.3.1.5.	Degree of polymerization	359
1.121.3.1.6.	Thermodynamics of polymerization	360
1.121.3.2.	Ionic Polymerization	360
1.121.3.2.1.	Cationic polymerization	360
1.121.3.2.2.	Anionic polymerization	360
1.121.3.3.	Coordination Polymerization	360
1.121.3.4.	Typical Addition Polymers and Their Biomedical Applications	361
1.121.3.5.	Comparison of Addition and Condensation Polymerization	361
1.121.3.6.	New Polymerization Mechanisms	361
1.121.3.6.1.	Atom transfer radical polymerization	361
1.121.3.6.2.	Nitroxide-mediated polymerization	362
1.121.3.6.3.	Reversible addition–fragmentation chain transfer polymerization	362
1.121.4.	**Polymer Reactions**	363
1.121.4.1.	Copolymerization	363
1.121.4.1.1.	Types of copolymerization	364
1.121.4.1.2.	Effects of copolymerization on properties	365
1.121.4.1.3.	Kinetics of copolymerization	365
1.121.4.2.	Cross-Linking Reactions	367
1.121.4.2.1.	Effect of cross-linking on properties	367
1.121.4.2.2.	Cross-linking of biological polymers	367
1.121.4.2.3.	Cross-linking agents	368
1.121.5.	**Conclusion**	369
References		370

Glossary

Addition polymerization Rapid polymerization based on initiation, propagation, and termination of double bonded monomers and no small molecules are eliminated.

Anionic polymerization Polymerization initiated by a anion.

Cationic polymerization Polymerization initiated by cation and propagated by a carbonium ion.

Condensation polymerization Polymerization in which polyfunctional reactants produce larger units in a continuous, stepwise manner.

Coordination polymers Polymers based on coordination complexes.

Copolymer Polymers composed of chains containing more than one monomer unit.
Degree of polymerization Average number of repeating units in main chains.
Gel point Point at which cross-linking begins to produce polymer insolubility.
Glass transition temperature (T_g) Temperature at which a polymer gains local or segmental mobility.
Initiation Start of polymerization.
Kinetic chain length Average length of the polymer chain initiated by one free radical.
Propagation Continuous successive chain extension in a chain reaction.
Repeating unit Basic molecular unit that can represent a polymer backbone chain.
Tacticity Arrangement of the pendant groups in space; that is, isotactic, syndotactic, atactic.
Termination Destruction of active growing chains in a chain reaction.

1.121.1. Introduction to Polymer Science

A polymer is a macromolecule composed of a combination of many small units that repeat themselves along the long molecule. The small starting molecules are called monomers, and the unit which repeats itself along the chain is called the repeating unit. In general, polymer chains have several thousand repeat units. The length of the polymer chain is specified by the number of repeating units in the chains and this number is called the degree of polymerization. Most of the monomers are composed of carbon, hydrogen, oxygen, and nitrogen. Few other elements such as fluorine, chlorine, sulfur, etc. may also exist. Syntheses of polymers are carried out in vessels or large reactors, sometimes with application of heat and pressure, and the small monomeric units connect to each other through the chemical reactions. The chemical process used for the synthesis of polymers is called the polymerization process.

Polymers which have the ability to melt and flow are used in manufacturing and are generally identified with the common name, plastics. In general, plastic products contain other added ingredients such as antioxidants and lubricants to give the desired properties to the object produced.

Most of the macrochains obtained in polymerization reactions are linear polymers and are formed by the reactions of monomers containing either carbon–carbon double bonds or have two active functional groups or difunctionality. Many monomers have different active groups on the same molecule such as one end of the monomer contains a carboxylic acid and the other end contains an alcohol, and the reaction of the acid group of one molecule with the alcohol group of the other forms polyesters. Polymerization reactions also take place when one of the monomers contains two acid groups and the other contains two alcohol or two amine groups. If there are some monomers which have more than two functionalities (e.g., 3- or 4-functionality), their presence in the chain cause the formation of extra chains linked to the main backbone. In this case, branched polymers are obtained. If the extent of branching is very high and all the macrochains are connected to each other, then they form a highly cross-linked, three-dimensional structure which is called a network. These networks have infinite molecular weights since all chains are connected to each other. In a polymer structure, all chains are tangled around each other forming the bulk structure. At low temperatures they are solid, but in a good solvent, the chains start to separate from each other and for linear and branched polymers this separation leads to complete solubility. The cross-linked network polymers, however, cannot dissolve in a solvent; they swell, forming gels.

The process of creating macromolecules from monomers is called polymerization. If only one type of monomer is used in polymerization, there will be only one type of repeating unit in the chain. In this case, the macromolecule is a homopolymer. If the polymer is formed from two different monomers (have two different repeating units), it is known as a copolymer. If a chain is formed from only ethylene, the polymer is a homopolymer and named as polyethylene. On the other hand, the copolymer of ethylene and vinyl acetate has two monomers and, therefore, has two different repeating units. If three different monomers are used to produce a polymer, the product is a terpolymer. Biological polymers, such as enzymes, are formed from many different amino acids, and therefore, their structures contain a variety of repeating units.

Since a large number of combinations of these molecules are available, it becomes possible to design and synthesize polymers with the desired properties ranging from fibers to films, sponges to elastomers. This versatility makes them essential materials to be used in various applications ranging from macro-sized products used in the households to nanoscale devices used in nanotechnological and biomedical applications.

Polymers such as cellulose, silk, and chitin can be obtained from natural sources and polymers such as polyethylene, polystyrene, and polyurethanes can be synthesized in the laboratories and plants. The macrochains such as DNA, RNA, and enzymes have biological importance and are crucial for life. In general, the backbone of a polymer is formed mainly of carbon atoms. These are called the organic polymers. There are also a few inorganic polymers, and the atoms in their backbones are different than carbon. An example is silicone, the backbone of which is constituted of silicon and oxygen.

One very important property which strongly influences the mechanical strength of the polymer is its molecular weight. Hydrocarbon molecules with increasing number of carbons are methane, ethane, propane, etc. The ones containing up to five carbons are in the gaseous state. As the number of carbons, and therefore, the molecular weight increases, they become liquids, wax type solids, and eventually hard solids. The ones called polymers contain more than 100 carbons along the chain. Most polymers which are useful as plastics, rubbers,

fibers, etc. have at least 50 repeating units and have molecular weights between 10^4 and $10^6\,g\,mol^{-1}$. Most of the properties of the polymers (plastics) are dependent on the chain length. As it increases, the softening point, melting point, or mechanical strength of the polymers also increase. Molecular weights of polymers are defined with average molecular weight values since there is always a distribution in chain lengths and no constant length for chains during the polymerization process. Although there are various averaging approaches, the most commonly used ones are the number average molecular weight (M_n) and the weight average molecular weight (M_w). The equations for these parameters are given below:

$$M_n = \frac{\sum M_i N_i}{\sum N_i} \quad [1]$$

$$M_w = \frac{\sum M_i^2 N_i}{\sum M_i N_i} \quad [2]$$

where N_i is the number of moles of molecules with a molecular weight of M_i.

The simplest polymer is polyethylene which has the repeating unit of $(-CH_2-CH_2-)$. The repeating units of polyethylene have high regularity and the chains come close to each other and cause high intermolecular interactions. If one of the hydrogen atoms of polyethylene repeating unit is changed with a different atom or molecule such as a halogen atom or R group, the arrangement of the chain may have different possibilities. The arrangement of atoms or groups fixed by chemical bonding in a molecule is called the configuration. Some examples are cis and trans isomers, and D and L forms of molecules. Chains may have different orientations arising from rotation of the chain about single bonds. These types of arrangements which are continuously changing are called conformations. A chain can have many different conformations.

In vinyl polymers isomerism is also defined with head-to-tail configuration. If there is a substitute attached to one carbon atom of the double bond, this carbon side can be named as the head, and the other carbon will then be the tail. During polymerization, the carbon atoms containing a substitute come together in either head-to-tail configuration or head-to-head and tail-to-tail configurations.

Carbon atoms make four bonds in a tetrahedral geometry. If the –C–C– main backbone which forms a zigzag structure is assumed to be on a plane, the other two bonds of each carbon, linked to an atom or a group, are either on one side or the other side of this plane. Depending on the organization of the side groups linked to the adjacent chiral center carbons, a stereochemistry is created and this is named tacticity. If the polymer is isotactic, it means that all the substituted side groups on each successive chiral center are on the same side of the backbone plane and have the same stereochemical configuration. For syndiotactic polymers, the side groups take place alternatingly on opposite sides of the backbone plane, and each successive chiral center has the alternating stereochemical configuration. There is no regular arrangement of the subgroups in atactic polymers. The substituents are placed randomly along the chain. Different placements of substituent group R in vinyl polymers are shown in Figure 1. Since tacticity

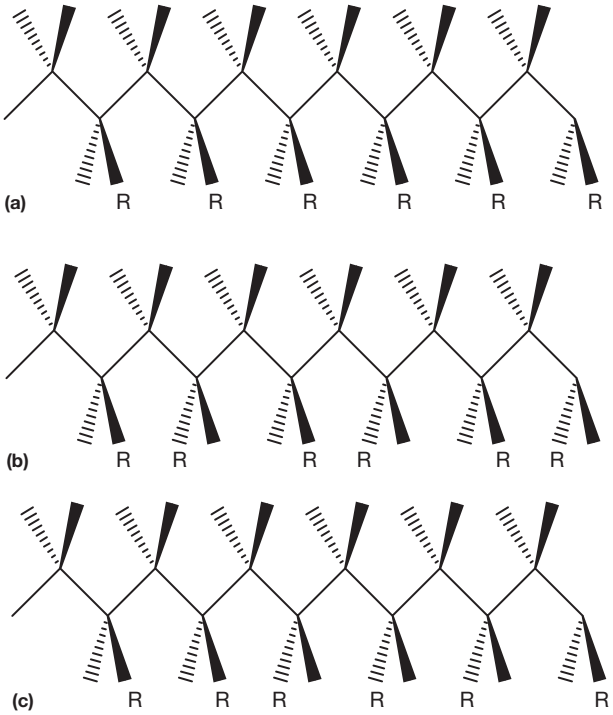

Figure 1 Tacticity of vinyl polymers: (a) isotactic, (b) syndiotactic, and (c) atactic.

creates highly ordered organization of repeating units along the chains, those polymers are more rigid with higher crystallinity and strength compared to atactic ones. Although this is the case in the industry for most of the processes, atactic polymers are preferred because of their ease of processing.

As defined previously, long chains are entangled with each other and stay together in a polymer structure forming a solid mass. This type of polymers have no ordered intermolecular arrangements and are called amorphous polymers. The vinyl polymers which contain bulky substitutes such as poly(methyl methacrylate) or polystyrene are amorphous polymers. On the other hand, in some polymers, intermolecular attractions are very strong and many backbone chains form closely packed structure as a result of these strong intermolecular forces. In these cases, they form crystalline polymers. Some polymers are partially crystalline, and some regions of the different or the same chains are closely packed and have strong attractions. These highly ordered domains are distributed in the amorphous matrix. In this case, the material is a semicrystalline polymer. Since crystallinity indicates highly ordered arrangement of macrochains with strong intermolecular forces, these polymers are stronger and have higher mechanical and thermal properties compared to their amorphous counterparts.

1.121.1.1. Classification of Polymers

During the early years of polymer science, two types of classifications have come into use. One was based on polymer structure (backbone) and divided polymers into Condensation and Addition polymers[1] and the other was based on

polymerization kinetics and mechanism and divided polymerizations into Step and Chain polymerizations.[2] Although these terms are often used interchangeably, because most condensation polymers are produced by step polymerizations and most addition polymers are produced by chain polymerizations, this is not always the case.

Polymers can be synthesized from hundreds of monomers in numerous combinations in very different forms ranging from solid elastomers to fibers, from films to sponges, from tubes to gels. Therefore, they are very important in our daily life. Polymers can be classified in many different ways depending on their various properties. Some of them are given below.

Polymer classification according to:

1. The origin
   a. *Natural polymers*: Proteins, starch, cellulose, natural rubber, etc. are of natural origin.
   b. *Synthetic polymers*: These are man-made polymers synthesized in the laboratories.
2. The polymerization process
   a. *Condensation polymers*: These polymers are formed when two di- or polyfunctional molecules react and condense forming macromolecules and with the possible elimination of a small molecule such as water in the case of polyester formation. All the natural polymers are condensation polymers.
   b. *Addition polymers*: These polymers are produced by chain reactions of double-bonded monomers in which the chain carrier can be a radical or an ion. Free radicals are usually formed by the decomposition of a relatively unstable compound, called the initiator.
3. The structural forms of the chains
   a. *Linear polymers*: These polymers are composed of long chains and their monomers have only two functional groups if the polymer is a condensation polymer or a single double bond if it is an addition polymer.
   b. *Branched polymers*: Similar to linear polymers, but they have long chains with shorter side chains (branches) caused by the presence of small amounts of trifunctional monomers for condensation or two unsaturations for addition polymers.
   c. *Network polymers*: These are cross-linked three-dimensional polymers. They consist of long chains connected to each other with multifunctional units and form a network.
4. The composition of the main backbone of the polymers
   a. *Homopolymers*: These polymers contain only carbon–carbon bonds in their backbone.
   b. *Heteropolymers*: These polymers contain atoms other than carbon in their main chain. The most common noncarbon atoms are oxygen and nitrogen.
5. The structure
   a. *Organic polymers*: These polymers contain mainly carbon atoms in their main chain.
   b. *Inorganic polymers*: The main chain of these polymers is not composed of carbon but mainly of inorganic atoms such as silicon in silicone rubbers.
   c. *Coordination (chelate) polymers*: In this type of polymers, a chelate ring is formed from an ion or metal and different organic ligands which have donor–acceptor bonds between.
6. The molecular weight
   a. *Oligomers*: These are the polymers with a molecular weight in the range of 500–5000 g mol^{-1}.
   b. *High polymers*: These are the polymers used in the industry in the production of materials and have a molecular weight in the range of 10^4–10^6 g mol^{-1}.
7. The thermal behavior
   a. *Thermoplastics*: These are linear or slightly branched chains containing polymers and they soften and flow when the temperature is increased. If they are loaded in a mold in this soft form and cooled, they solidify forming the product. Since there is no new chemical bond formation during the heating and cooling, they can be reshaped with further application of heat and pressure.
   b. *Thermoset polymers*: During the processing of these polymers, cross-linking reactions take place upon increase of temperature and they set in the shape of the mold they are in. Therefore, they cannot be melted and reshaped with the application of heat. At high temperatures, they decompose.
8. The arrangement of the repeating units
   a. *Homopolymers*: They are formed from single type of monomers.
   b. *Copolymers*: They are made of two or more types of monomers. The arrangements of the different repeating units in the chain can be different, and therefore, copolymers can be further divided into groups as given below.
      i. *Alternating copolymers*: the repeating groups of two different monomers alternatingly follow each other along the macrochain.
      ii. *Random copolymers*: there is no order in the positions of the repeating units of different monomers.
      iii. *Block copolymers*: in these polymers, one type of the monomer reacts and forms a long chain (a block) and then reacts with the other type of monomer forming a different block. These block copolymers can be diblock copolymers which are formed as AB type blocks, three-block copolymers which are formed as ABA type blocks, or graft copolymers in which the main chain is one type of block and the other type is attached to the main chain as side chains.
9. *The linkages repeating in the chains*: These polymers are classified according to the chemical linkages between the monomeric units which repeat along the chain. For example, polyethers have ether linkages, polyesters have ester linkages, polyurethanes have urethane linkages, etc.

1.121.1.2. Polymerization Systems

Polymerization reactions are carried out in vessels or reactors generally with application of heat and with the addition of different substituents. Depending on the phases that exist and the forms of the medium, the polymerization processes are classified as homogeneous and heterogeneous systems, which include different techniques as given below:

1. *Homogeneous polymerization systems*: All chemicals added into the reaction medium create a homogeneous mixture in which polymer formation occurs. These processes are either bulk or solution polymerization processes.

a. *Bulk polymerization*: In these polymerizations, there are only monomers and initiators in the reaction medium. These processes are generally used in the production of condensation polymers in which the reactions are mildly exothermic, less viscous, and therefore, mixing, heat transfer, and control of the process is easier compared to chain polymerization of vinyl polymers.
b. *Solution polymerization*: A monomer and a initiator are added in a solvent and the reaction takes place in this solution medium. This approach can be used for addition or condensation polymerizations since the medium does not get too viscous which makes mixing, heat transfer, and control of the process easy. On the other hand, it requires purification and removal of the solvent.

2. *Heterogeneous polymerization systems*: In these systems there are more than one phase creating heterogeneous media for the monomer, polymer, and initiator.
a. *Gas phase polymerization*: In these systems, the monomer is in gaseous form and the polymer formed is either in liquid or solid form. Ethylene polymerization is an example (Figure 2).
b. *Precipitation polymerization*: This is similar to bulk or solution polymerization, but the polymer formed precipitates as soon as it forms. This polymer is not soluble in its monomer and the solvent of the monomer is also not a solvent for the polymer (Figure 3).
c. *Solid phase polymerization*: Some solid crystalline olefins or cyclic monomers polymerize by solid state polymerization. In these systems, polymerization generally starts with radiation such as X-rays or γ-rays (Figure 4).
d. *Suspension polymerization*: In these systems, organic phase containing monomer and initiator is dispersed as droplets in the aqueous phase containing the stabilizers such as cellulose or polyvinyl alcohol. Initiator is soluble in the monomer phase, and therefore, in the droplet the mechanism is very similar to bulk polymerization. Size of the droplets is in the range of 0.01–0.50 cm and the polymer forms as dispersed solid particles of this size (Figure 5).
e. *Emulsion polymerization*: This system is similar to suspension system, but the initiator is soluble in the aqueous phase. As the polymerization starts in the aqueous phase, emulsifier molecules surround the growing chain forming micelles. As the polymerization proceeds, chains in the micelles elongate to get the monomer from the organic phase. Therefore, the monomer droplets get smaller and polymer micelles get larger. Still, these particles are very small (about 0.1 μm) (Figure 6).

There are numerous types of synthetic polymers or copolymers which are produced in the laboratories and every year new ones are added to the list. In addition, some new biological polymers are also added to the list obtained by some novel molecular techniques. These can be derived from renewable biomass sources, such as vegetable oil, corn starch, or microbiota. Some examples for these polymers are starch-based polymers (used for the production of drug capsules in the pharmaceutical sector), polylactic acid (PLA; produced from cane sugar or glucose, and used in the production of foil, molds, tins, cups, bottles, and as bone plates in the medical sector), poly(3-hydroxybutyrate) (PHB; is biodegradable and produced by certain bacteria), polyamide-11 (PA11; is derived from natural oil and not biodegradable), bioderived polyethylene (can be produced by fermentation of agricultural feed stocks such as sugar cane or corn, and is chemically and physically identical to traditional polyethylene), and bioplastics (produced by genetically modified organisms such as GM crops).

1.121.2. Polycondensation

1.121.2.1. Characteristics of Condensation Polymerization

Condensation polymerization is used for polymerization of monomers with functional groups and involves a series of

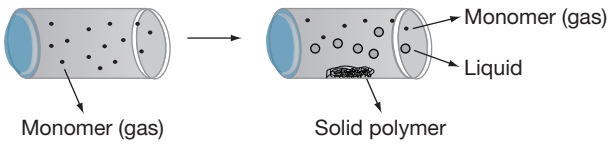

Figure 2 Gas phase polymerization.

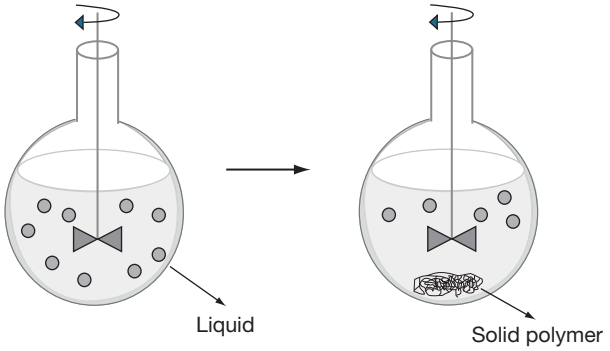

Figure 3 Precipitation polymerization.

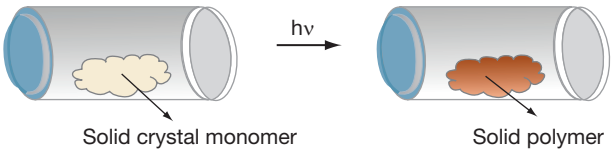

Figure 4 Solid phase polymerization.

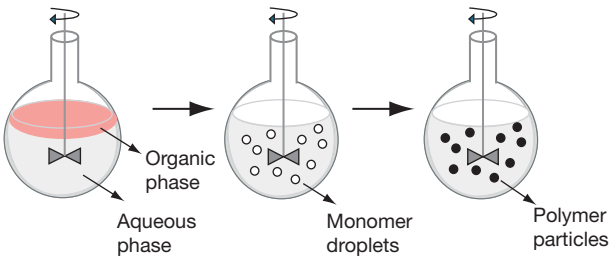

Figure 5 Suspension polymerization.

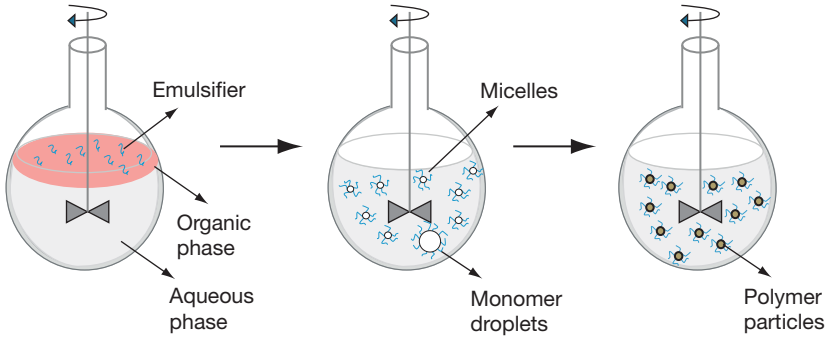

Figure 6 Emulsion polymerization.

chemical condensation reactions progressing generally with the elimination of side products with low molar weight, such as water, alcohol, or hydrogen.

In condensation polymers, the elemental composition of the repeating unit differs from that of the two monomers by the elements of the eliminated small molecule. Condensation polymers can, therefore, be degraded to their monomers upon the addition of the eliminated small molecules.

1.121.2.2. Kinetics of Linear Polycondensation

The type of product formed in a condensation reaction is determined by the functionality of the monomers, that is, by the number of reactive functional groups per monomer. Bifunctional monomers form long linear polymers but monofunctional monomers when used with bifunctional monomers form only low molecular weight products.

The monomers can have the same type or different type of functional groups, and in the former case, two different difunctional monomer types are necessary for product formation. Polyesters are formed by typical condensation reactions with the elimination of water. If a polyester is synthesized from a diol and a diacid, the first step is the reaction of the diol and diacid monomers to form a dimer:

$$\mathrm{HO{-}R{-}OH + HOOC{-}R^1{-}COOH \rightarrow}$$
$$\mathrm{HO{-}R{-}OCO{-}R^1{-}COOH + H_2O} \qquad [\mathrm{I}]$$

The dimer then might form a trimer by reaction with a diol monomer:

$$\mathrm{HO{-}R{-}OCO{-}R^1{-}COOH + HO{-}R{-}OH \rightarrow}$$
$$\mathrm{HO{-}R{-}OCO{-}R^1{-}COO{-}R{-}OH + H_2O} \qquad [\mathrm{II}]$$

or with a diacid monomer:

$$\mathrm{HO{-}R{-}OCO{-}R^1{-}COOH + HOOC{-}R^1{-}COOH \rightarrow}$$
$$\mathrm{HOOC{-}R^1{-}COO{-}R{-}OCO{-}R^1{-}COOH + H_2O} \qquad [\mathrm{III}]$$

Dimer could also react with itself to form a tetramer:

$$\mathrm{2HO{-}R{-}OCO{-}R^1{-}COOH \rightarrow HO{-}R{-}OCO{-}R^1{-}}$$
$$\mathrm{COO{-}R{-}OCO{-}R^1{-}COOH + H_2O} \qquad [\mathrm{IV}]$$

The tetramer and trimer proceed to react with themselves, with each other, with the monomer and the dimer.[3] The polymerization proceeds in this stepwise manner with the molecular weight of the polymer gradually increasing with time. Condensation polymerizations are characterized by the disappearance of monomer early in the reaction for before the production of any polymer of sufficiently high molecular weight to be of practical use.

The rate of a condensation polymerization is the sum of the rates of reactions between molecules of various sizes. The kinetics of such a situation with innumerable separate reactions is normally very difficult to analyze. However, it is generally assumed that the rate of reaction of a group is independent of the size of the molecule to which it is attached; in other words, the functional group reactivity is assumed to be independent of the molecular weight. These simplifying assumptions, often referred to as the concept of equal reactivity of functional groups, make the kinetics of condensation polymerization identical to those for the analogous small molecule reaction. There is both theoretical[4] and experimental[2] justification of these simplifying assumptions.

The kinetics of condensation polymerization can be explained by taking the formation of a polyester from a diol and a diacid as a model system. Condensation polymerization typically involves equilibrium reactions of the type

$$\mathrm{A + B} \underset{k_r}{\overset{k_f}{\rightleftarrows}} \mathrm{C + D} \qquad [\mathrm{V}]$$

and the rates of the forward and reverse reactions are $k_f[A][B]$ and $k_r[C][D]$, respectively. At equilibrium these rates are equal, therefore

$$K = \frac{k_f}{k_r} = \frac{[C][D]}{[A][B]} \qquad [3]$$

If the system is not at equilibrium, as in the initial stages of polymerization, the reverse reaction is negligibly slow and changes in the concentrations of the reactants may be considered to result from the forward reaction alone. This reaction is normally catalyzed by acids, however, in the absence of a strong acid, the diacid monomer acts as its own catalyst for the esterification reaction and the reaction is followed by measuring the rate of disappearance of carboxyl groups:

$$-\frac{d[COOH]}{dt} = k[COOH]^2[OH] \qquad [4]$$

where one of [COOH] represent the catalysis phenomenon.

If the starting concentrations of carboxyl and hydroxyl groups are equal

$$-\frac{d[COOH]}{dt} = k[COOH]^3 \quad [5]$$

rearrangement and integration gives:

$$2kt = \frac{1}{[COOH]_t^2} + \text{constant} \quad [6]$$

The extent of reaction, p, is defined as the fraction of functional groups that has reacted at time t. Therefore,

$$p = \frac{[COOH]_o - [COOH]_t}{[COOH]_o} \quad [7]$$

Substitution of p into eqn [6] and rearrangement gives:

$$\frac{1}{(1-p)^2} = 2k[COOH]_o^2 t + \text{constant} \quad [8]$$

or a plot of $1/(1-p)^2$ versus t should be linear with a slope of $2k[COOH]_o^2$ from which k can be determined (**Figure 7**).[3]

It was shown with experimentation that uncatalyzed esterifications require quite long times to reach high degrees of polymerization. Greater success is achieved by adding a small amount of acid catalyst to the system, whose concentration is constant throughout the reaction. In this case, the concentration of the catalyst has to be included in the rate constant (k'):

$$-\frac{d[COOH]}{dt} = k'[COOH][OH] \quad [9]$$

If the initial concentrations of carboxyl and hydroxyl groups are equal,

$$-\frac{d[COOH]}{dt} = k'[COOH]^2 \quad [10]$$

$$[COOH_o]k't = \frac{1}{(1-p)} + \text{constant} \quad [11]$$

If only bifunctional reactants are present in the reaction system and no side reactions occur, the number of unreacted carboxyl groups equals the total number of molecules (N) in the system. If acid or glycol groups separately (not in pairs) are defined as structural units, the initial number of carboxyls present is equal to the total number of structural units present N_0. The number average degree of polymerization, $\bar{X}_n$, is:

$$\bar{X}_n = \frac{\text{Number of original molecules}}{\text{Number of molecules at time } t} = \frac{N_0}{N} = \frac{[COOH]_o}{[COOH]_t} = \frac{1}{1-p} \quad [12]$$

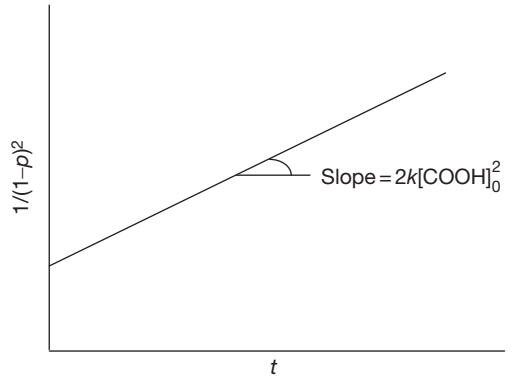

Figure 7 Plot of $1/(1-p)^2$ versus t in the determination of rate constant of linear polycondensation.

1.121.2.2.1. Molecular weight control in linear polycondensation

It is important to control the change in polymer molecular weight with reaction time since molecular weight determines the properties of the polymer. One method of stopping the reaction at the desired molecular weight is cooling. But, this is not preferable since the polymer could restart growing upon subsequent heating because the ends of the polymer molecules contain unused functional groups.

The easiest way to avoid this situation is to adjust the starting composition of the reaction mixture slightly away from stoichiometric equivalence, by adding either a slight excess of one bifunctional reactant or by introducing a small amount of a monofunctional reagent. Eventually, the monomer which is low in amount is completely used up and all chain ends consist of the excess group. If only bifunctional reactants are present and the two types of groups are initially present in numbers N_A and N_B with a ratio $r = N_A/N_B$, the total number of monomers present is

$$\frac{N_A + N_B}{2} = \frac{N_A(1 + 1/r)}{2} \quad [13]$$

At a given time, if p is the extent of reaction defining the fraction of reacted groups, $(1-p)$ will show the fraction of unreacted groups. Therefore, the total number of chain ends will be

$$N_A(1-p) + N_B(1-rp) = N_A\left[1 - p + \frac{1-rp}{r}\right] \quad [14]$$

Since each monomer is difunctional, the number of groups is twice the number of molecules present. Therefore, $\bar{X}_n$ will be

$$\overline{X}_n = \frac{N_A\frac{\left(1+\frac{1}{r}\right)}{2}}{N_A\frac{\left(1-p+\frac{1-rp}{r}\right)}{2}} = \frac{1+r}{1+r-2p} \quad [15]$$

This equation shows the variation of the degree of polymerization with the stoichiometric imbalance r and the extent of reaction p. When the two bifunctional monomers are present in equal amounts ($r = 1$), the equation reduces to

$$\overline{X}_n = \frac{1}{(1-p)} \quad [16]$$

On the other hand, for 100% conversion the $\bar{X}_n$ becomes

$$\overline{X}_n = \frac{1+r}{1+r-2} = \frac{1+r}{r-1} \quad [17]$$

In actual practice, p may approach but never becomes equal to unity. This means there are always some functional groups that are left unreacted.[5]

Stoichiometric balance should be precisely maintained in order to obtain high degrees of polymerization. Loss of one ingredient, side reactions, or the presence of monofunctional impurities may severely limit the degree of polymerization.[6]

1.121.2.3. Nonlinear Polycondensation and Its Kinetics

Polyfunctional monomers with more than two functional groups per molecule yield branched or hyperbranched condensation polymers. With certain monomers, cross-linking will also take place with the formation of network structures in which branches from one polymer molecule become attached to other molecules and eventually yield insoluble molecules.

The structures of these nonlinear condensation polymers are more complex than those of linear ones. Nonlinear polycondensation occurs with gelation, the formation of essentially infinitely large polymer networks. The sudden onset of gelation marks the division of the mixture into two parts: the gel, which is insoluble in all nondegrading solvents; and the sol, which remains soluble and can be extracted from the gel. As the polymerization proceeds beyond the gel point, the amount of gel increases at the expense of sol and the mixture rapidly transforms from a viscous liquid to an elastic material of infinite viscosity. An important feature of the onset of gelation is that the number average molecular weight stays very low while the weight average molecular weight becomes infinite.[7]

1.121.2.3.1. Prediction of the gel point

In order to calculate the point in the reaction at which gelation takes place, a branching coefficient (α) is defined as the probability that a given functional group on a branch unit to connect to another branch unit. In the case where polyfunctional A_f units are present with functionality f, the criterion for gel formation is that at least one of the $f-1$ segments radiating from the end of a segment is in turn connected to another branch unit. Therefore, the critical value of α for gelation (α_c) is given as:

$$\alpha_c = \frac{1}{f-1} \qquad [18]$$

The gel point can also be observed experimentally when the polymerizing mixture suddenly loses fluidity. If the extent of reaction is followed as a function of time by determining the number of functional groups present, the value of p (extent of reaction) at the gel point can be experimentally determined.[8]

1.121.2.4. Mechanisms of Polycondensation

As was stated earlier, all condensation polymerizations take place either by using a monomer with two unlike groups suitable for polycondensation (AB type, e.g., polycondensation of hydroxycarboxylic acids) or two different monomers, each possessing a pair of identical reactive groups that can react with each other (AA and BB type, e.g., polycondensation of diols with dicarboxylic acids).

These monomers polymerize following different routes such as carbonyl addition–elimination, carbonyl addition–substitution, nucleophilic substitution, double bond addition, or free radical coupling.[5]

1.121.2.4.1. Carbonyl addition–elimination mechanism

Carbonyl addition–elimination is the most important reaction which has been used for the preparation of polyamides, polyacetals, phenol–, urea–, and melamine–formaldehyde polymers. Some typical examples of this reaction include:

Direct reaction: The reaction of a dibasic acid and a glycol (to form a polyester) or a dibasic acid and a diamine (to form a polyamide) are some examples of direct reaction. A strong acid or acidic salt often serves as a catalyst. The reaction may be carried out by heating the reactants together and removing water (to draw the reaction toward product formation) usually by applying vacuum in the later stages.

Interchange: The reaction between a glycol and an ester yields polyesters and is preferred especially when the dibasic acid has low solubility. Frequently the methyl ester is used, as in the production of poly(ethylene terephthalate) from ethylene glycol and dimethyl terephthalate. The reaction between a carboxyl and an ester is much slower, but other interchange reactions, such as amine–amide, amine–ester, and acetal–alcohol are well known.

Acid chloride or anhydride: Either of these can be reacted with a glycol or an amine. Polyamides are prepared by the reaction of an acid chloride with a diamine.

Interfacial condensation: The reaction of an acid halide with a glycol or a diamine proceeds rapidly to high molecular weight polymer if carried out at the interface between two immiscible liquid phases each containing one of the reactants. Very high molecular weight polymers can be prepared. Typically, an aqueous phase containing the diamine or glycol and an acid acceptor is layered at room temperature over an organic phase containing the acid chloride. The polymer formed at the interface can be pulled off as a continuous film or filament. The method is applied to the formation of polyamides, polyurethanes, and polyureas. It is particularly useful for preparing polymers which are unstable at the higher temperatures.

Ring versus chain formation: Bifunctional monomers may react intramolecularly to produce a cyclic product. Thus, hydroxyacids may give either lactones or polymers on heating and amino acids may give lactams or linear polyamides. The type of the product is generally dependent on the size of the ring that can be formed.

1.121.2.4.2. Other mechanisms

Carbonyl addition–substitution reactions: The reaction of aldehydes with alcohols involving addition followed by substitution at the carbonyl group leads to the formation of polyacetals.

Nucleophilic substitution reactions: Nucleophilic substitution is the reaction of an electron pair donor (the nucleophile) with an electron pair acceptor (the electrophile). These reactions are used in the polymerization of epoxides. Nucleophiles attack the electrophilic C of the C–O bond causing it to break, resulting in ring opening. Opening the ring relieves the ring strain and epoxides can react with a large range of nucleophiles (such as H_2O, ROH, R–NH_2). Nucleophilic substitution reactions are also the basis for the formation of natural polysaccharides and polynucleotides.

Double bond addition reactions: Although addition reactions at double bonds are often associated with addition

polymerization, this is not always the case. The ionic addition of diols to diisocyanates in the production of polyurethanes is an example of condensation polymerization.

Free radical coupling: These reactions are used in the preparation of arylene ether polymers, polymers containing acetylene units, and arylenealkylidene polymers.

Aromatic electrophilic substitution reactions: This type of reactions including the use of Friedel–Crafts catalysts produces polymers by condensation polymerization.

1.121.2.5. Typical Condensation Polymers and Their Biomedical Applications

Polyesters, polyurethanes, polyamides, polyanhydrides, polycarbonates, and polyureas are among the condensation polymers that find broad use in medical applications in various forms. Some naturally occurring polymers such as proteins (collagen) and polysaccharides (hyaluronic acid) as well as bacterial polyesters (polyhydroxyalkanoates) are classified as condensation polymers, since their synthesis from their reactants are achieved by the elimination of water.[3,9] Some typical examples of condensation polymers and their biomedical applications are listed in Table 1.

1.121.3. Addition Polymerization

Polymerization in which the polymer forms by addition of monomeric unit to the growing chain is called as addition polymerization. Generally, a monomer containing double bond and an initiator creates the first active unit; they are needed to start the chain growth. The active group, which is the chain carrier group, may be a free radical, an anion, or a cation.

In addition polymerization reaction takes place by opening of the double bond and the created active group adds the monomer at a very high rate so that immediately high molecular-weight polymer chains form. Therefore, the reaction medium consists of large polymers and monomers unlike in condensation polymerization. Depending on the type of initiator a radical, anion, or cation is created and depending on the chemistry, adds monomers and eventually form a large molecule. The molecular weight of the polymer chains is practically unchanged during polymerization, but in time more of the monomer is converted into polymers and monomer concentration decreases.[3]

Monomers show varying degrees of selectivity with regard to the type of reactive center that will lead to polymerization. Most monomers are polymerized by free radicals, but they are more selective to the ionic mechanisms. For example, acrylamide polymerizes anionically but not cationically, whereas *N*-vinyl pyrrolidone polymerizes by cationic but not anionic route.[6] For both monomers, free radical polymerization is possible. Another type of polymerization is coordination polymerization in which special catalysts are used and highly ordered polymers with stereospecific properties are obtained.

Table 2 shows the types of initiation that polymerize various monomers. Although the polymerization of the monomers in Table 2 is thermodynamically feasible by having $\Delta G < 0$, practically polymerization is achieved only with a certain type of initiator.[3] The key to this phenomenon lies in the polarity of the monomer and the strength of the ion formed. Monomers with electron-donating groups (alkoxy, alkyl, alkenyl, and phenyl) attached the carbons of the unsaturation, increase the electron density on the carbon–carbon double bond and when these electrons react with a cationic initiator, a stable carbenium ion forms on the growing unit. In this case, chain polymerizes with cationic catalysts. On the other hand, monomers with electron-withdrawing substituents (aldehyde, ketone, acid, ester) decrease the electron density on the double bond and facilitate the attack of anionic catalysts leading to anionic polymerization. Free radical polymerization takes place in most cases but may be considered to be an intermediate case and a radical created on the growing chain leads to the formation of macromolecules. Many

Table 1 Typical condensation polymers and their biomedical applications

Type	*Characteristic linkage*	*Sample polymer*	*Biomedical application*
Polyacetal		Poly(ethyl glyoxylate)	Hard tissue replacement
Polyamide		Nylon	Intracardiac catheters, sutures, dialysis device components, heart mitral valves, hypodermic syringes
Polycarbonate		Bisphenol-A polycarbonate	Intraocular lenses, dialysis device components, heart/lung assist devices, blood collection, arterial tubules
Polyester		Poly(lactic acid-*co*-glycolic acid)	Grafts, sutures, implants, prosthetic devices, micro and nanoparticles
Polypeptides		Proteins, enzymes	Tissue engineering scaffolds, wound dressings
Polyurea		Polyisobutylene-based polyurea	Blood contacting surfaces
Polyurethane		Poly(ether urethane)	Aortic patches, heart assist devices, adhesives, dental materials, blood pumps, artificial heart and skin

Table 2 Types of addition polymerization suitable for common monomers

	Polymerization mechanism			
Monomer	*Radical*	*Cationic*	*Anionic*	*Coordination*
Ethylene	+	+	−	+
Propylene and α-olefins	−	−	−	+
Styrene	+	+	+	+
Vinyl chloride	+	−	−	+
Tetrafluoroethylene	+	−	−	+
Acrylic and methacrylic esters	+	−	+	+
Acrylonitrile	+	−	+	+

+, high polymer formed; −, no reaction or oligomers only.
Modified from Billmeyer, F.W. *Textbook of Polymer Science*, Wiley: New York, 1984.

monomers can polymerize by free radical mechanism in addition to an ionic mechanism.[3,5]

1.121.3.1. Free Radical Polymerization

Free radicals are unpaired electrons that are highly reactive and have short lifetimes. In free radical polymerizations, each polymer chain grows by addition of monomer to the free radical of the growing chain. Upon addition of the monomer, the free radical is transferred to the new chain end. Free radical polymerization has three stages: initiation, propagation, and termination.

1.121.3.1.1. Initiation

In the initiation step free radicals are formed from an initiator and then these free radicals bind to a monomer. Initiators can be peroxides or azo compounds in which scission of a single bond creates radicals, or a redox reaction in which radicals are created by an electron transfer to or from an ion or molecule.

Dissociation can be affected by the application of heat or electromagnetic radiation (e.g., UV, γ). Peroxides and hydroperoxides are frequently used as initiators because of the instability of the O–O bond. In the case of azo compounds, the process is driven by the release of N_2. Redox reactions are preferred especially when the polymerization is needed to be carried out at low temperatures.[6,10] Heat and electromagnetic radiations can also start polymerization by breaking the double bond of the monomeric units and creating two active radicals. In this case, the chain adds to monomeric units from both ends. Some of the most widely used initiator systems are given in Table 3.

The free radical initiation step can be shown as follows:

Dissociation of an initiator (I) such as benzoyl peroxide yields two radicals (R•) with a dissociation rate constant k_d:

$$I \xrightarrow{k_d} 2R\bullet \qquad [VI]$$

This radical then attacks to a monomer molecule to create the first radical M•.

$$R\bullet + M \xrightarrow{k_i} RM\bullet \qquad [VII]$$

where k_i is the rate constant of initiation.

Table 3 Free radical initiation reactions

1. Acyl peroxides, alkyl peroxides or hydroperoxides
Benzoyl peroxide:

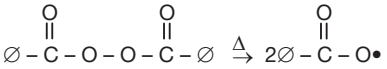

t-butyl peroxide:

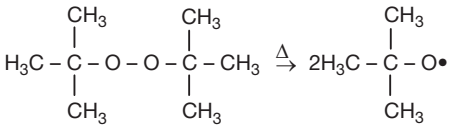

Cumyl hydroperoxide:

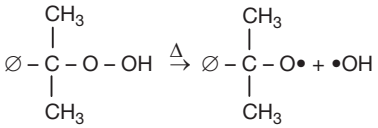

2. Azo compounds
2,2′-Azobisisobutyronitrile (AIBN):

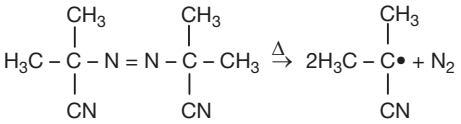

3. Redox systems

$H_2O_2 + Fe^{2+} \rightarrow OH^- + Fe^{3+} + \bullet OH$

$S_2O_8^{2-} + Fe^{2+} \rightarrow SO_4^{2-} + Fe^{3+} + SO_4^{-\bullet}$

4. Electromagnetic radiation (photoinitiation)
Styrene, Benzoin:

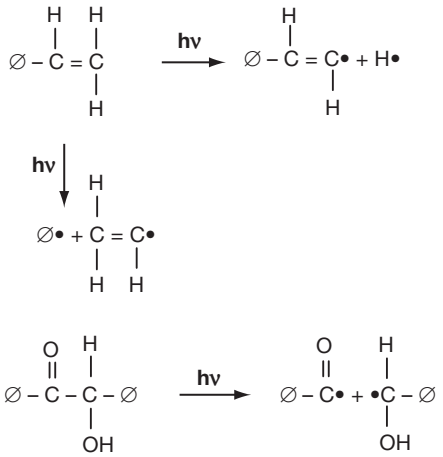

1.121.3.1.2. Propagation

The free radicals formed are very active and immediately add on monomer molecules leading to growing macroradicals. Each addition creates a new radical that has the same identity as the previous one, except that it is larger by one monomer

unit. In the polymerization mechanism, it is assumed that all growing chains have the same propagation constant (k_p). The successive additions may be represented by:

$$M_n^{\bullet} + M \xrightarrow{k_p} M_{n+1}^{\bullet} \qquad [VIII]$$

Propagation with growth of the chain takes place in milliseconds and k_p for most monomers is in the range of 10^2–$10^4\,l\,mol^{-1}\,s^{-1}$.[3]

1.121.3.1.3. Termination

Termination usually occurs by combination or disproportionation reactions. Combination is coupling of two growing chains to form a single polymer molecule.

$$M_n^{\bullet} + M_m^{\bullet} \xrightarrow{k_{tc}} M_{n+m} \qquad [IX]$$

where k_{tc} is the rate constant for termination by combination.

In disproportionation reaction, a hydrogen atom is abstracted and exchanged between the growing chains leaving behind two terminated chains:

$$M_n^{\bullet} + M_m^{\bullet} \xrightarrow{k_{td}} M_n + M_m \qquad [X]$$

where k_{td} is the rate constant for termination by disproportionation.

Termination by disproportionation forms one polymer molecule with a saturated end-group and another with an unsaturated end-group. Type of termination affects the molecular weight. If it is through combination, average molecular weight will be two times higher than that of polymers terminated by disproportionation. In general, both types of termination reactions take place in different proportions depending upon the monomer and the polymerization condition. For example, polystyrene chains terminate by combination whereas poly(methyl methacrylate) chains terminate by disproportionation, especially at temperatures above 60 °C.[10]

1.121.3.1.4. Kinetics of radical polymerization

In radical polymerization reactions, decomposition of the initiator (such as peroxides and azo compounds) proceeds much more slowly than the reaction of the free radical with the monomer. This step is therefore the rate-determining step. The rate of initiation (R_i) is

$$R_i = \left(\frac{d[M^{\bullet}]}{dt}\right)_i = 2fk_d[I] \qquad [19]$$

where f is the initiator efficiency, the fraction of the radicals successful in initiating chains, k_d is the rate constant for initiator dissociation, and [I] is the concentration of the initiator. The constant 2 defines that two radicals are formed from one initiator molecule. The initiator efficiency is in the range of 0.3–0.8 due to side reactions. The initiator efficiency decreases when side reactions terminates the radicals.[6]

For a redox initiation system, rate of initiation is given as

$$R_i = \left(\frac{d[M^{\bullet}]}{dt}\right)_i = f\,k[Ox][Red] \qquad [20]$$

where [Ox] and [Red] are the concentrations of oxidizing and reducing agents and k is the rate constant.

For photochemical initiation, intensity of light affects the rate and equation is given as

$$R_i = \left(\frac{d[M^{\bullet}]}{dt}\right)_i = 2\Phi I_{abs} \qquad [21]$$

where I_{abs} is the intensity of the light absorbed and the constant Φ is called quantum yield.

The rate of termination is represented as

$$R_t = -\left(\frac{d[M^{\bullet}]}{dt}\right)_i = 2k_t[M^{\bullet}]^2 \qquad [22]$$

where k_t is the overall rate constant for termination. The constant 2 shows that the two growing chains are terminated by each termination reaction.

At the start of the polymerization, the rate of formation of radicals greatly exceeds the rate of termination. As the reaction proceeds, the rate of formation and the rate of loss of radicals by termination becomes equal and it can be stated that there is no change in the concentration of M•. This is the steady state ($d[M^{\bullet}]/dt = 0$). At steady state, the rates of initiation (R_i) and termination (R_t) are equal, leading to

$$[M^{\bullet}] = \left(\frac{f\,k_d[I]}{k_t}\right)^{1/2} \qquad [23]$$

The rate of propagation is represented as

$$R_p = -\left(\frac{d[M]}{dt}\right)_t = k_p[M][M^{\bullet}] \qquad [24]$$

so using eqn [23], R_p can be obtained as

$$R_p = k_p\left(\frac{f\,k_d[I]}{k_t}\right)^{1/2}[M] \qquad [25]$$

If the initiator efficiency is high (close to 1) and if f is independent of monomer, rate of polymerization is proportional to the first power of the monomer concentration.

In chain polymerization, one important phenomenon is 'gel effect' or 'Trommsdorff – Norrish effect' which is autoacceleration of the polymerization. In these cases, viscosity of the reaction medium increases and the mobility of the growing chains are restricted. Chains continue to grow with addition of monomers, but they cannot terminate. Therefore, the system is no longer in steady state. Fast polymerization causes heat evolution and local hot spots, leading to cross-linking and gel formation.[11]

1.121.3.1.5. Degree of polymerization

Kinetic chain length v is defined as the number of monomer molecules used per active center. It is, therefore, represented as $R_p/R_i = R_p/R_t$. Therefore,

$$v = \frac{k_p[M]}{2k_t[M^{\bullet}]} \qquad [26]$$

using eqn [24],

$$v = \frac{k_p^2[M]^2}{2k_tR_p} \qquad [27]$$

The number average degree of polymerization, $\bar{X}_n$, is the average number of monomer molecules added to the polymer

molecule. If the propagating radicals terminate by combination $\bar{X}_n = 2\nu$, and if termination is by disproportionation $\bar{X}_n = \nu$.

Chain transfer is the reaction of a growing chain with an inactive molecule to produce a dead polymer chain and a molecule with a radical. The transfer agent may be the initiator, monomer, polymer, solvent, or an impurity. When the transfer does not lead to new chain growth, it is called inhibition. If the newly formed radical is less reactive than the propagating radical, then it is called retardation.[3]

1.121.3.1.6. Thermodynamics of polymerization

Addition polymerizations of olefinic monomers have negative ΔH and ΔS. The exothermic nature of polymerization arises because the process involves the formation of new bonds and the negative ΔS arises from the decreased degree of freedom of the polymer compared to the monomer. ΔG depends on both parameters and is given by

$$\Delta G = \Delta H - T\Delta S \qquad [28]$$

The numerical value of ΔS is much smaller than ΔH. Therefore ΔG is negative under ambient T conditions since $|\Delta H| > |T\Delta S|$. Polymerization is thermodynamically favorable. However, thermodynamic feasibility does not mean that the reaction is practically feasible. For the polymerization reaction to take place at appreciable rates, it may require specific catalyst systems. This is the case with the α-olefins, which require Ziegler–Natta or coordination-type initiators.[3]

1.121.3.2. Ionic Polymerization

Addition polymerization of olefinic monomers can also be achieved with active centers possessing ionic charges. These can be either cationic polymerizations or anionic polymerizations depending on the type of the chain carrier ion. The ionic charge of the active center causes these polymerizations to be more selective unlike free radical polymerization. They proceed only with monomers that have appropriate substituent groups which can stabilize the active center. Since the required activation energy for ionic polymerization is small, these reactions may occur at very low temperatures. High rate of polymerization at low temperatures is a characteristic of ionic polymerizations. For cationic active centers, electron-donating substituent groups are needed. For anionic polymerization, the substituent group must be electron withdrawing to stabilize the negative charge. Thus, most monomers can be polymerized either by cationic or by anionic polymerization but not by both. Only when the substituent group has a weak inductive effect and is capable of delocalizing both positive and negative charges (e.g., styrene and 1,3-dienes) both cationic and anionic polymerization can be achieved.

Another important difference between free radicalic and ionic polymerizations is that many ionic polymerizations proceed at much higher rates than free radical polymerization, mainly because the concentration of propagating chains is much higher (by a factor of 10^4–10^6). Another difference is that an ionic active center is accompanied by a counter ion of opposite charge. Both the rate and stereochemistry of propagation are influenced by the counter ion and the strength of interaction with the active center. Finally, termination does not occur by a reaction between two ionic active centers because they are of similar charge.[10]

1.121.3.2.1. Cationic polymerization

Typical catalysts for cationic polymerization are strong electron acceptors and include Lewis acids, Friedel–Crafts halides, Brönsted acids, and stable carbenium-ion salts. Many of them require a cocatalyst, usually a proton donor, to initiate polymerization. Those monomers with electron donating 1-1-substituents that can form stable carbenium ions are polymerized by cationic mechanisms. For these systems, the polymerization rate is very high; for isobutylene initiated by $AlCl_3$ or BF_3, in few seconds at $-100\,^{\circ}C$, chains of several million daltons can form. Both the rate and the molecular weight decrease with temperature and are much lower at room temperature.[5]

In certain cationic polymerizations, a distinct termination step may not take place; therefore 'living' cationic polymers are formed. However, chain transfer to a monomer, polymer, solvent, or counterion can terminate the growth of chains. Cationic polymerizations are usually conducted in solution, at low temperature, typically -80 to $-100\,^{\circ}C$. The solvent is important because it determines the activity of the ion at the end of the growing chain. There is a linear increase in polymer chain length and an exponential increase in polymerization rate as the dielectric strength of the solvent increases.[12]

1.121.3.2.2. Anionic polymerization

The initiator in an anionic polymerization needs to be a strong nucleophile, including Grignard reagents and other organometallic compounds like *n*-butyl (n-C_4H_9) lithium. When the starting reagents are pure and the polymerization reactor is free of traces of oxygen and water, the chain can grow until all the monomer is consumed. For this reason, anionic polymerization is sometimes called 'living' polymerization. Termination occurs only by the deliberate introduction of oxygen, carbon dioxide, methanol, or water. In the absence of a termination mechanism, the number average degree of polymerization, $\bar{X}_n$, is

$$\bar{X}_n = \frac{[M]_o}{[I]_o} \qquad [29]$$

where $[M]_o$ and $[I]_o$ are the initial concentrations of the monomer and the initiator, respectively.

The absence of termination during a living polymerization leads to a very narrow molecular weight distribution with a heterogeneity index (HI) as low as 1.06, whereas for free radical polymerization polydispersities as high as 2 were reported.[12]

1.121.3.3. Coordination Polymerization

Use of some special catalysts may lead to the formation of very orderly structured polymers with high stereospecificity. For example, the processes used in the polymerization of both isotactic polypropylene (*i*-PP) and high density polyethylene (HDPE) employ transition-metal catalysts called Ziegler–Natta catalysts, which utilize a coordination type mechanism during polymerization. In general, a Ziegler–Natta catalyst is an

organometallic complex with the cation from Groups I to III in the Periodic Table, (e.g., $Al(C_2H_5)_3$), a hallide of transition metal from Groups IV to VIII, (e.g., $TiCl_4$). HDPE can be prepared by bubbling ethylene gas into a suspension of $Al(C_2H_5)_3$ and $TiCl_4$ in hexane at room temperature. Although the exact mechanism is still unclear, it is proposed that the growing polymer chain is bound to the metal atom of the catalyst and that monomer insertion involves a coordination of the monomer with the atom. It is this coordination of the monomer that results in the stereospecificity of the polymer. Coordination polymerizations can be terminated by introduction of water, hydrogen, aromatic alcohol, or metals.[12]

1.121.3.4. Typical Addition Polymers and Their Biomedical Applications

Addition polymers such as polyethylene, polypropylene, polystyrene, polyacrylates can be easily fabricated in many forms such as fibers, textiles, films, rods, and viscous liquids and they are used in a variety of biomedical applications. Some are given in Table 4.[13,14]

1.121.3.5. Comparison of Addition and Condensation Polymerization

The main characteristic of step polymerization that distinguishes it from chain polymerization is that the reaction occurs between any of the different sized species present in the reaction system. In step polymerization, the size of the polymer molecules increases at a relatively slow pace and the monomers disappear early in the reaction unlike chain polymerization where the monomer concentration decreases gradually (medium generally contains long and dead chains and monomers) and growth occurs very rapidly by addition of one unit at a time to the end of the growing chain. Longer polymerization durations are essential in obtaining high molecular weight condensation polymers whereas with chain polymers long reaction times give high yields but do not affect the molecular weight significantly.

The typical step and chain polymerizations differ significantly in the relationship between polymer molecular weight and the percent conversion of monomer. The chain polymerization will show the presence of high molecular weight polymer molecules at all percent of conversions. There are no intermediate sized molecules in the reaction mixture (only monomer and high polymer). The only change that occurs with conversion is the continuous increase in the number of polymer molecules. On the other hand, high molecular weight polymer is obtained in step polymerizations only near the very end of the reaction (at 98% conversion).[3,15,16]

1.121.3.6. New Polymerization Mechanisms

1.121.3.6.1. Atom transfer radical polymerization

Atom transfer radical polymerization (ATRP) is a controlled/living polymerization technique which is highly effective in obtaining well-defined polymers or copolymers with predetermined molecular weight, narrow molecular weight distribution, and a high degree of chain end functionality. ATRP has been used in the preparation of polymers with precisely controlled functionalities, topologies (linear, star/multiarmed,

Table 4 Some additional polymers used in biomedical applications

Synthetic polymers	*Monomeric unit*	*Applications*
Polyethylene (PE)	$\{CH_2–CH_2\}_n$	Pharmaceutical bottles, nonwoven fabrics, catheters, pouches, flexible containers, orthopedic implants (e.g., hip implants)
Poly(2-hydroxyethyl methacrylate) (PHEMA)	$\{CH_2–C(CH_3)(COOCH_2CH_2OH)\}_n$	Contact lenses, surface coatings, drug delivery systems
Poly(methyl 2-cyanoacrylate)	$\{CH_2–C(CN)(COOCH_3)\}_n$	Surgical adhesive
Poly(methyl methacrylate) (PMMA)	$\{CH_2–C(CH_3)(COOCH_3)\}_n$	Blood pumps and reservoirs, membranes for dialyzers, intraocular lenses, bone cement, drug delivery systems
Polypropylene (PP)	$\{CH_2–CH(CH_3)\}_n$	Disposable syringes, blood oxygenator membranes, sutures, nonwoven fabrics, artificial vascular grafts, reinforcing meshes, catheters
Polystyrene (PS)	$\{CH_2–CH(C_6H_5)\}_n$	Tissue culture flasks, roller bottles, filterwares
Poly(tetrafluoro ethylene) (PTFE)	$\{CF_2–CF_2\}_n$	Catheters, artificial vascular grafts, various separator sheets
Poly(vinyl chloride) (PVC)	$\{CH_2–CH(Cl)\}_n$	Blood bags, surgical packaging, i.v. sets, dialysis devices, catheter bottles, connectors, and cannulae

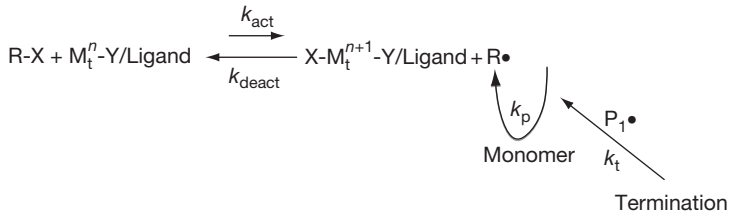

Figure 8 General mechanism of ATRP.

comb, hyperbranched, and network polymers), and compositions (homopolymers, block copolymers, statistical copolymers, gradient copolymers, graft copolymers).

Monomer, initiator with a transferable atom (halogen), and catalyst (transition metal with suitable ligands) are the main components of ATRP. In some cases, an additive (metal salt in a higher oxidation state) may be used. Type of solvent and level of temperature are important parameters for a successful ATRP. The most commonly used monomers are styrenes, methacrylates, methacrylamides, dienes, and acrylonitriles.

Atom transfer step is the key elementary reaction leading to the uniform growth of the polymeric chains. In ATRP, radicals are formed by a reversible redox reaction of a transition metal complex, M_t^n-Y/ligand, where M_t is transition metal and Y may be another ligand or a counterion. Transfer of an X atom (usually halogen) from a dormant species to the metal results in an oxidized metal complex (X-M_t^{n+1}-Y/ligand which is the persistent species) and a free radical (R•). Activation and deactivation processes occur with rate constants of k_{act} and k_{deact}, respectively (**Figure 8**).

Even when the same ATRP conditions (same catalyst and initiator) are used, each monomer has its own unique atom transfer equilibrium constants for its active and dormant species. The rate of polymerization depends on K_{eq} ($K_{eq} = k_{act}/k_{deact}$). If it is too small, polymerization reaction will occur slowly, and if it is too large, due to the high radical concentration, termination will occur and polymerization will be uncontrolled.

The new radical can initiate the polymerization by addition to a monomer with the rate constant of propagation k_p. Termination reactions (rate constant is k_t) also occur in ATRP, by combination or disproportionation, or the active species is reversibly deactivated by the higher oxidation state metal complex. In a well-controlled ATRP, no more than a few percent of the polymer chains undergo termination. During the initial, short, nonstationary stage of the polymerization, the concentration of radicals decays by the unavoidable irreversible self termination, whereas, the oxidized metal complexes increase steadily as the persistent species. As the reaction proceeds, the decreasing concentration of radicals causes a decrease in self-termination and cross-reaction with persistent species toward the dormant species. The decrease in the stationary concentration of growing radicals minimizes the rate of termination which has a key role in the first-order kinetic.

The stabilizing group (e.g., phenyl or carbonyl) on the monomers produces a sufficiently large atom transfer equilibrium constant. Typically, alkyl halides (RX) are used as the initiator. The halide group (X) must rapidly and selectively migrate between the growing chain and the transition-metal complex to form polymers with narrow molecular weight distributions. Catalyst is an important component of ATRP since it determines the position of the atom transfer equilibrium and the dynamics of exchange between the dormant and active species. A variety of transition metal complexes have been used as ATRP catalysts such as transition metal complexes of copper, ruthenium, palladium, nickel, and iron. Polymerization is conducted either in bulk or in solvents (benzene, water, etc.) at moderate temperatures (70–130 °C).[17–21]

1.121.3.6.2. Nitroxide-mediated polymerization

Nitroxide-mediated polymerization (NMP) is another controlled radical polymerization method. NMP allows the preparation of very well-defined polymers with controlled molecular weight and narrow molecular weight distribution and to extend chains with different monomers to obtain multiblock copolymers. Combination of a nitroxide and a free radical initiator or alkoxyamines serving as both initiators and controlling agents are used in this technique.

NMP is based on a reversible recombination between propagating species (P•) and nitroxide (R_2NO•, R = alkyl group) with the formation of alkoxyamine (R_2NOP), resulting in a low radical concentration and decreases the irreversible termination reactions. Polymer chains with equal chain lengths and reactive chain ends can be obtained because a majority of dormant living chains can grow until the monomer is fully consumed.

NMP is metal free and not colored, and polymer does not require any purification after synthesis. The main limitation of NMP is the range of monomers that can be effectively controlled. Some efficient alkoxyamines and nitroxides are able to control most of the conjugated vinyl monomers such as styrene and derivatives, acrylates (including some functional acrylates), acrylamides, acrylonitrile, and methacrylates (with some limitations) and also some dienes such as isoprene.[22,23]

1.121.3.6.3. Reversible addition–fragmentation chain transfer polymerization

Reversible addition–fragmentation chain transfer polymerization (RAFT) is one of the most versatile methods of controlled radical polymerization because it allows a wide range of functionalities in the monomers and solvents, including aqueous solutions. The method is relatively new for the synthesis of living radical polymers and may be more versatile than ATRP or NMP. RAFT polymerization uses thiocarbonylthio compounds, such as dithioesters, dithiocarbamates, trithiocarbonates, and xanthates in order to mediate the polymerization via a reversible chain-transfer process. The technique is applicable to a wide range of monomers including methacrylates, methacrylamides, acrylonitrile, styrene and derivatives, butadiene,

vinyl acetate, and *N*-vinyl pyrrolidone. As a result of its exceptional effectiveness and the wide range of monomers and solvents, RAFT polymerization has developed into an extremely versatile polymerization technique. Especially, the molecular weight of the polymer can be predetermined and the molecular weight distribution can be controlled fairly well.

Typically, a RAFT polymerization system consists of an initiator, monomer, chain transfer agent, and solvent. The control of temperature is crucial. It can be performed by simply adding a certain quantity of an appropriate RAFT agent (i.e., a thiocarbonylthio compound) to a conventional free radical polymerization medium. Radical initiators such as azobisisobutyronitrile (AIBN) and 4,4′-azobis(4-cyanovaleric acid) (ACVA) are widely used as initiators in RAFT polymerizations. RAFT agents (also called chain transfer agents) must be thiocarbonylthio compounds where the Z and R groups perform different functions (Figure 9). The Z group primarily controls the effectiveness with which radical species can add to the C=S bond. The R group must be a good homolytic leaving group which is able to initiate new polymer chains.

There are four steps in a typical RAFT polymerization: initiation, addition–fragmentation, reinitiation, and equilibration (Figure 10).

In the initiation step, the reaction is started using radical initators (I) such as AIBN. The initiator reacts with a monomer to create a radical species which starts an actively polymerizing chain. During addition–fragmentation step, the active chain (P_n) reacts with the dithioester, which releases the homolytic leaving group (R•). This is a reversible step, with an intermediate species capable of losing either the leaving group (R•) or the active species (P_n•). Reinitiation occurs with the reaction between the leaving group radical and another monomer species, starting another active polymer chain. This active chain (P_m•) then goes through the addition–fragmentation or equilibration steps. Equilibration is a fundamental step in the RAFT process which traps the majority of the active propagating species into the dormant thiocarbonyl compound. This limits the possibility of chain termination. Active polymer chains (P_m• and P_n•) are in an equilibrium between the active and dormant stages. While one polymer chain is in the dormant stage (bound to the thiocarbonyl compound), the other is active in polymerization.[24–28]

RAFT process allows the synthesis of polymers with specific macromolecular architectures such as block, gradient, statistical, linear block, comb/brush, star, hyperbranched, and network copolymers and dendrimers. Examples of architectures that can be synthesized by RAFT are given in Figure 11.

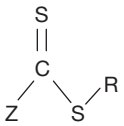

Figure 9 General structure of RAFT agents.

1.121.4. Polymer Reactions

1.121.4.1. Copolymerization

Copolymers are polymers formed from two or more monomeric units. The arrangement of repeating units can be in various ways along the chain. Some copolymers are very similar to homopolymers, because they have one type of repeating units. But proteins and some polysaccharides are copolymers of a number of different monomers.

Copolymers constitute the vast majority of commercially important polymers. Compositions of copolymers may vary from only a small percentage of one component to comparable proportions of both monomers. Such a wide variation in composition permits the production of polymer products with vastly different properties for a variety of end uses. The minor constituent of the copolymer may, for example, be a diene introduced into the polymer structure to provide sites for such polymerization reaction as vulcanization; it may also be a trifunctional monomer incorporated into the polymer to

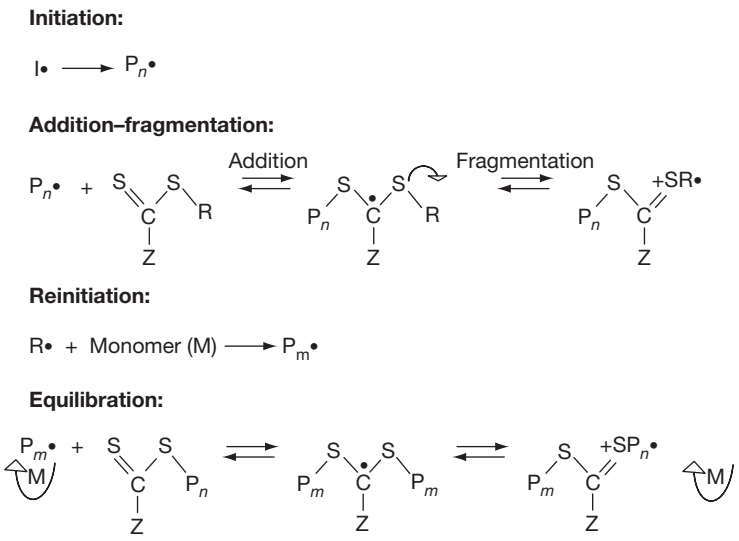

Figure 10 RAFT mechanism.

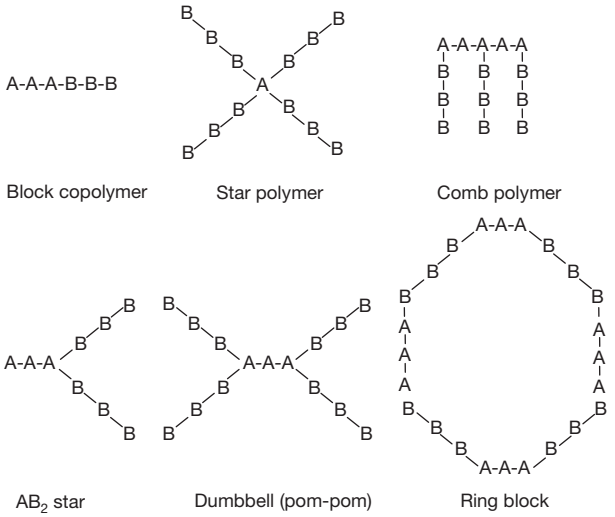

Figure 11 Examples of complex architectures prepared by RAFT.

ensure cross-linking, or possibly it may be a monomer containing carboxyl groups to enhance product solubility, dyeability, or some other desired properties.[12]

1.121.4.1.1. Types of copolymerization

In free radical polymerization, reactivity ratios of the monomers, r_1 and r_2, should be considered. Reactivity ratios represent the relative preference of a given radical that is adding its own monomer to the other monomer.

$$r_1 = \frac{k_{11}}{k_{12}} \qquad [30]$$

where k_{11} and k_{22} are the rate constants for radicals adding their own type of monomer and k_{12} and k_{21} are the rate constants for adding the opposite kind.

$$r_2 = \frac{k_{22}}{k_{21}} \qquad [31]$$

Depending on the r values, copolymerization reaction can form ideal, random, alternating, or block copolymers. Another type is graft copolymers.

In ideal copolymerization ($r_1 r_2 = 1$), the growing chain end reacts with one of the monomeric unit with a statistically possible preference. The multiplication of reactivity ratios should be equal to 1.

When $r_1 r_2 = 1$ then,

$$r_1 = \frac{1}{r_2} \quad \text{or} \quad \frac{k_{11}}{k_{12}} = \frac{k_{21}}{k_{22}} \qquad [32]$$

The relative amounts of the monomer units in the chain are determined by the reactivities of the monomer and the feed composition of the reaction medium.

$r_1 r_2 = 1$ occurs under two conditions:

1. $r_1 > 1$ and $r_2 < 1$ or $r_1 < 1$ and $r_2 > 1$.

   One of the monomers is more reactive than the other. The copolymer will contain a greater proportion of the more reactive monomer in the random sequence of monomer units. In this case, production of copolymers with significant quantities of both monomers will be more difficult as the difference in reactivities of the two monomers increases.
2. $r_1 = r_2 = 1$.

   Under these conditions, the growing radicals cannot distinguish between the two monomers. The composition of the copolymer is the same as that of the input concentrations and the monomers are arranged randomly along the chain. These copolymers show properties of both homopolymers of its constituents.

Random copolymers are formed when r values of both monomers are close to each other. A mixture of two or more monomers is polymerized in one process and where the arrangement of the monomers within the chains is determined by kinetic factors. If the reacting monomers are shown as A and B, the sequence will have no order in the chain, such as –AABBAAABABAA–.

Random copolymers tend to average the properties of the constituent monomers in the proportion to the relative abundance of the comonomers.

In the alternating copolymerization, r values of both monomers are equal to zero. When $r_1 = r_2 = 0$ (or $r_1 r_2 = 0$), each radical reacts exclusively with the other monomer; that is, neither radical can regenerate itself. Consequently, the monomer units are arranged alternately along the chain. These are called alternating copolymers and can be shown as –ABABAB–.

Polymerization continues until one of the monomers is used up and then it stops. Perfect alternation occurs when both r_1 and r_2 are zero. As the quantity $r_1 r_2$ approaches zero, there is an increasing tendency toward alternation. This has practical significance because it enhances the possibility of producing polymers with appreciable amounts of both monomers from a wider range of feed compositions.[12] Alternating copolymers, while relatively rare, are characterized by combining the properties of the two monomers along with structural regularity. Crystalline polymers can be obtained if a very high degree of regularity (stereoregularity extending along the all configuration of the repeat units) exists.

Block or segmented copolymers are usually prepared by multistep processes. The blocks may be a homopolymer or may themselves be copolymers. Diblock can be shown as –AAAABBB– and triblock can be shown as –AAABBBBAAAA–. In multiblock copolymers, the A and B segments repeat themselves many times along the chain.

Block copolymers are generally prepared by sequential addition of monomers to living polymers, rather than by depending on the improbable $r_1 r_2 > 1$ criterion in monomers.[6]

Graft copolymers and branched copolymers are formed by copolymerization of macromonomers and can form as a consequence of intramolecular rearrangement. In general, the backbone and the chain is formed from one type of monomer, and the chains of other type are attached as branches. This can be shown as

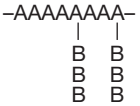

Special classes of branched copolymers are star polymers, dendrimers, hyperbranched copolymers, and microgels.[29]

1.121.4.1.2. Effects of copolymerization on properties

Copolymer synthesis offers the ability to alter the properties of homopolymer in the desired direction by the introduction of an appropriately chosen second repeating unit. Since the homopolymers are combined in the same molecule, copolymer demonstrates the properties of both homopolymers. Properties, such as crystallinity, flexibility, T_m, T_g can be altered by forming copolymers. The magnitudes and sometimes even the directions of the property alteration differ depending on whether random, alternating, or block copolymer is involved. The crystallinity of a random copolymer is lower than that of either of the respective homopolymers (i.e., the homopolymers corresponding to the two different units) because of the decrease in structural regularity. The melting temperature of any crystalline material formed is usually lower than that of either homopolymer. The T_g value will be in between those for the two homopolymers.

Alternating copolymers have a regular structure, and their crystallinity may not be significantly affected unless one of the repeating units contains rigid, bulky, or excessively flexible chain segments. The T_m and T_g values of an alternating copolymer are in between the corresponding values for the homopolymers. Block copolymers show the properties (e.g., crystallinity, T_m, T_g) present in the corresponding homopolymer as long as the block lengths are not too short. This behavior is typical since A blocks from different polymer molecules aggregate with each other and separately, B blocks from different polymer molecules aggregate with each other. This offers the ability to combine the properties of two very different polymers into the one block copolymer. The exception to this behavior occurs infrequently when the tendency for cross-aggregation between A and B blocks is the same as for self-aggregation of A blocks with A blocks and B blocks with B blocks.

Most commercial utilization of copolymerization falls into one of the two groups. One group consist of various random copolymers in which the two repeating units posses the same functional groups. The other groups of commercial copolymers consist of block copolymers in which two repeating units have different functional groups although only few commercial random copolymers in which the two repeating units have different functional groups exist. The reason for the situation probably lies in the difficulty of finding one set of reaction condition for simultaneously performing two different reactions.[30]

1.121.4.1.3. Kinetics of copolymerization

1.121.4.1.3.1. Kinetics of addition copolymerization

Kinetics of copolymerization reactions are very complicated. The copolymerization between two different monomers can be described using four reactions, two homopolymerizations and two cross-polymerization additions. Reaction mechanism is given in **Table 5**. The specific rate constants for the different reaction steps described are assumed to be independent of chain length.[11]

At steady state, the concentrations of $M_1^{\bullet}$ and $M_2^{\bullet}$ are assumed to remain constant. Therefore the rate of conversion of $M_1^{\bullet}$ to $M_2^{\bullet}$ necessarily equals that of conversion of $M_2^{\bullet}$ to $M_1^{\bullet}$. Thus,

Table 5 Reaction mechanism, rate constants, and rate equation or copolymerization

Reaction	*Rate constant*	*Rate equation*
$M_1^{\bullet} + M_1 \rightarrow M_1M_1^{\bullet}$	k_{11}	$k_{11}[M_1^{\bullet}][M_1]$
$M_1^{\bullet} + M_2 \rightarrow M_1M_2^{\bullet}$	k_{12}	$k_{12}[M_1^{\bullet}][M_2]$
$M_2^{\bullet} + M_2 \rightarrow M_2M_2^{\bullet}$	k_{22}	$k_{22}[M_2^{\bullet}][M_2]$
$M_2^{\bullet} + M_1 \rightarrow M_2M_1^{\bullet}$	k_{21}	$k_{21}[M_2^{\bullet}][M_1]$

$$k_{21}[M_2^{\bullet}][M_1] = k_{12}[M_1^{\bullet}][M_2] \quad [33]$$

The rate of polymerization can be given with the rates of disappearance of monomers M_1 and M_2 as shown below:

$$\frac{-d[M_1]}{dt} = k_{11}[M_1^{\bullet}][M_1] + k_{21}[M_2^{\bullet}][M_1] \quad [34]$$

$$\frac{-d[M_2]}{dt} = k_{11}[M_1^{\bullet}][M_2] + k_{22}[M_2^{\bullet}][M_1] \quad [35]$$

From the division of the two equations, the copolymer equation is obtained. The ratio of $d[M_1]/d[M_2]$ gives the monomer ratios present in the polymer chain.

$$\frac{d[M_1]}{d[M_2]} = \frac{[M_1]r_1[M_2] + [M_2]}{[M_2][M_1] + r_2[M_2]} \quad [36]$$

Here, r_1 and r_2 are monomer reactivity ratios and are defined by

$$r_1 = \frac{k_{11}}{k_{12}} \quad [37]$$

and,

$$r_2 = \frac{k_{22}}{k_{21}} \quad [38]$$

Monomer-radical reaction rates are also affected by steric hindrance. The role of steric hindrance in the reduction of the reactivity of 1,2-disubstituted vinyl monomers can be illustrated by the fact that while these monomers undergo copolymerization with other monomers (e.g., styrene), they do not tend to homopolymerize. Homopolymerization is prevented because of the steric effect of the 2-substituent on the attacking radical and the monomer. On the other hand, there is no 2- or β-substituent when the attacking radical is styrene; consequently, copolymerization is possible.[12]

The effect of steric hindrance in reducing reactivity may also be demonstrated by comparing the reactivities of 1,1- and 1,2 disubstituted olefins with reference radicals. The addition of a second 1-substituent usually increases reactivity three to ten-fold; however, the same substituent in the 2-position usually decreases reactivity 2- or 20-fold. The extent of reduction in reactivity also depends on the energy differences between *cis* and *trans* forms.[5]

1.121.4.1.3.2. Kinetics of condensation copolymerization:

- *Random copolymers:* The copolymerization of a mixture of monomers offers a route to random copolymers; for instance, a copolymer of overall composition XWYV is synthesized by copolymerizing a mixture of the four monomers.

(X) HOOC–R–COOH
(Y) HOOC–R_2–COOH
(W) H_2N–R_1–NH_2
(V) H_2N–R_3–NH_2

→ HOOC–CONH–R_1–NHCO–R_2–CONH–R_3–NH_2
Copolymer of XWYV

It is highly unlikely that the reactivities of the various monomers would be such that block or alternating copolymers are formed. The overall composition of the copolymer obtained in a step polymerization will almost always be the same as the composition of the monomer mixture since these reactions are carried out to essentially 100% conversion (a necessity for obtaining high molecular weight polymer). In the step copolymerization of monomer mixtures, one often observes the formation of random copolymers. This occurs either because there are no differences in the reactivities of the functional groups existing on different monomers or the polymerization under reaction conditions where there is extensive interchange. The use of only one diacid or diamine would produce a variation on the copolymer structure with either R=R_2 or R_1=R_3.[31]

Statistical copolymers containing repeating units each with a different functional group can be obtained using appropriate mixture of monomers. For example, a polyesteramide can be synthesized from a ternary mixture of a diol, diamine, and diacid or binary mixture of a diacid and amine–alcohol.

- *Alternating copolymers*: It is possible to synthesize an alternating copolymer in which R=R_2 by using a two-stage process. In the first stage, a diamine is reacted with an excess of diacid to form a trimer:

$$n\text{HOOC–R–COOH} + m\text{H}_2\text{N–R}_1\text{–NH}_2 \rightarrow m\text{HOOC–R–CONH–R}_1\text{–NHCO–R–COOH} \quad \text{[XI]}$$

The trimer is then reacted with an equamolar amount of a second diamine in the second stage:

$$n\text{HOOC–R–CONH–R}_1\text{–NHCO–R–COOH} + n\text{H}_2\text{N–R}_3\text{–NH}_2 \rightarrow \text{HO(–CO–R–CONH–R}_1\text{–NHCO–R–CONH–R}_3\text{–NH)}_n\text{–H} + (2n-1)\text{H}_2\text{O} \quad \text{[XII]}$$

Alternating copolymers with two different functional groups are similarly synthesized by using preformed reactants.[32–35]

$$n\text{OCN–R–CONH–R}_1\text{–OSi(CH}_3)_3 \xrightarrow[-(\text{CH}_3)_3\text{SiF}]{\text{HF}} \text{HF–(CH}_3)_3\text{SiF(CO–NH–R–CO–NH–R}_1\text{–O)}_n \quad \text{[XIII]}$$

$$n\text{OCN–R–CONH–R}_1\text{–NHCO–R–NCO} + \text{HO–R}_2\text{–OH} \xrightarrow{\text{HF}} \text{HF–(CONH–R–CONH–R}_1\text{–NHCO–R–NHCOO–R}_2\text{–O)}_n \quad \text{[XIV]}$$

The silyl ether derivative of the alcohol is used in reaction [XIII]. The corresponding alcohol OCN–R–CONH–R_1–OH cannot be isolated because of the high degree of reactivity of isocyanate and alcohol groups toward each other.

- *Block copolymers*: There are two general methods for synthesizing block copolymers. These two methods, the one prepolymer and the two prepolymer methods, are described below for block copolymers containing different functional groups in the repeating units. They are equally applicable to block copolymers containing the same functional groups in the two repeating units. The two prepolymer method involves the separate synthesis of two different prepolymers, each containing appropriate end groups, followed by the polymerization of two polymers via reaction of their end groups. Consider the synthesis of a polyester-block-polyurethane. A isocyanate-terminated polyester prepolymer is synthesized from HO–R_3–OH and HOOC–R_1–COOH using an excess of diol reactant. An isocyannate-terminated polyurethane prepolymer is synthesized from OCN–R_2–NCO and HO–R_3–OH using an excess of the diisocyanate reactant. The α,ω-dihydroxypolyester and α,ω-diisocyanatapolyurethane prepolymers, referred to as macrodiol and macrodiisocyanate, respectively, are subsequently polymerized with each other to form the block copolymer:

$$\text{H–(–O–R–OCC–R}_1\text{–CO–)}_n\text{–O–ROH} + \text{OCN–(–R}_2\text{–NHCOO–R}_3\text{–OOCNH)}_m\text{–R}_2\text{–NCO} \rightarrow \text{H–(–O–R–OOC–R}_1\text{–CO–)}_n\text{–O–RO–OCNH–R}_2\text{–(NHCOO–R}_3\text{–OOCNH–R}_2\text{–)}_m\text{–NCO} \quad \text{[XV]}$$

The block lengths n and m can be varied by adjusting the stoichiometric ratio r of reactants and conversion in each prepolymer synthesis. In typical systems, the prepolymers have molecular weights in the range of 500–6000 Da. A variation of the two-prepolymer method involves the use of a coupling agent to join the prepolymers. For example, a diacyl chloride could be used to join together two different macrodiols or two different macrodiamines or a two different macrodiamines or a macrodiol with a macrodiamine.

The one-prepolymer method involves one of the above prepolymers with two 'small' reactants. The macrodiol is reacted with a diol and diisocyanate

$$\text{H–(–O–R–OOC–R}_1\text{–CO)}_n\text{OR–OH} + (m+1)\text{OCN–R}_2\text{–NCO} + m\text{HO–R}_3\text{–OH} \rightarrow \text{H–(O–R–OOC–R}_1\text{–CO)}_n\text{OR–OOCNH–(–R}_2\text{–NHCOO–R}_3\text{–OOCNH)}_m\text{–R}_2\text{–NCO} \quad \text{[XVI]}$$

The block lengths and the final polymer molecular weights are again determined by the details of the prepolymer synthesis and its subsequent polymerization. An often-used variation of the one-prepolymer method is to react the macrodiol with excess diisocyanate to form an isocyanate-terminated prepolymer. The latter is then chain-extended (i.e., increased in molecular weight) by reaction with a diol.

The one- and two-prepolymer methods can in principle yield exactly by the same final block copolymer. However, the dispersity of the polyurethane block length is usually narrower when the two-prepolymer method is used.[32,35]

1.121.4.2. Cross-Linking Reactions

Cross-linking is the predominant reaction upon irradiation of many polymers. It involves attachment of polymeric chains to each other. When each molecule is bonded at least once, then the whole sample becomes insoluble. It is accompanied by the formation of a gel and ultimately by the insolubilization of the specimen. Cross-linking has a beneficial effect on the mechanical properties of polymers.

In commercial practice, cross-linking reactions take place during the fabrication of articles made with thermosetting resins. The cross-linked network is stable against heat and does not flow or melt. Most linear polymers are thermoplastic. They soften and take on new shapes upon the application of heat and pressure.[5]

Cross-linking can be achieved by the action of electromagnetic radiation, heat, or catalysts and results in opening of unsaturated groups on chains and reaction of multifunctional (>2) groups. Control of cross-linking is critical for processing. The period after the gel point, when all the chains are bonded at least to one other chain is usually referred to as the curing period.

1.121.4.2.1. Effect of cross-linking on properties

The change in properties is determined by the extent of cross-linking. Lightly cross-linked polymers swell extensively in solvents in which the uncross-linked material dissolves, but covalently (irreversibly) cross-linked polymers cannot dissolve but only swell in the solvent of the uncross-linked form. Upon extensive cross-linking, the sample may even not swell appreciably in any solvent.

Cross-linking has a significant effect on viscosity; it becomes essentially infinite at the onset of gelation. The effect of chain branching and cross-linking on T_g are explained in terms of free volume. A high amount of branches increase the free volume and lower the T_g, whereas cross-linking lowers the free volume and raises the T_g.

The addition of cross-links leads to stiffer, stronger, tougher products, usually with enhanced tear and abrasion resistance. However, extensive cross-linking of a crystalline polymer leads to a loss of crystallinity, and this might decrease mechanical properties. When this occurs, the initial trend of properties may be toward either enhancement or deterioration, depending on the degree of crystallinity of the unmodified polymer and the method of formation and location (crystalline or amorphous regions) of the cross-links.[5]

1.121.4.2.2. Cross-linking of biological polymers

1.121.4.2.2.1. Cross-linking of proteins

Proteins are found to be chemically (permanent) or physically (reversibly) cross-linked. These cross-links can be intra or intermolecular. For example the triple helix of collagen is intermolecularly cross-linked whereas many reversible cross-links are observed in the secondary and tertiary structure of the proteins. Proteins are also cross-linked for various applications (biotechnological, biomedical, etc.).

Physical cross-linking methods include drying, heating, or exposure to γ or UV radiation. The primary advantage of physical methods is that they do not cause harm. However, the limitation of such methods is that obtaining the desired amount of cross-linking is difficult. In chemical cross-linking methods, cross-linkers are generally used to bond the functional groups of amino acids. In recent years, there has been an increase in interest in physical cross-linking methods. The main reason is that use of cross-linking agents is avoided because most cause some toxic effects. However, the degree of cross-linking is considerably lower and cross-links are weaker than obtained by chemical methods.

Collagen is the major protein component of bone, cartilage, skin, and connective tissue and also the major constituent of all extracellular matrices in animals. Collagen can be chemically cross-linked by various compounds including glutaraldeyde, carbodiimide, genipin, and transglutaminase. 1-Ethyl-3-diaminopropyl carbodiimide (EDC) and *N*-hydroxysuccinimide (NHS) catalyze covalent bindings between carboxylic acid and amino groups; thus, cross-linking between collagen structures is possible (**Figure 12**). Furthermore, other extracellular matrix components containing carboxyl groups, such as glycosaminoglycans, can also be cross-linked with this approach.[36,37]

1.121.4.2.2.2. Cross-linking of polysaccharides

Chemical and physical methods are used for cross-linking of polysaccharides. Physical cross-linking is achieved by physical interaction between different polymer chains.

In physical cross-linking, polysaccharides form cross-linked networks with the counterions on the surface. High counterion concentration requires long exposure times to achieve complete cross-linking of the polysaccharides. Chemical cross-linking of polysaccharides leads to products with good mechanical stability. During cross-linking, counterions diffuse into the polymer and reacts with polysaccharides forming intermolecular or intramolecular linkages. Factors which affect chemical cross-linking are the concentration of the cross-linking agents and the cross-linking duration. High concentration of cross-linking agent induces rapid cross-linking. Like physical cross-linking, high counterion concentration require longer exposure times to achieve complete cross-linking of the polysaccharides.

Polysaccharides can be chemically cross-linked with either addition or condensation cross-linking mechanism. For addition polymerization, the network properties can be easily tailored by the concentration of the dissolved polysaccharide and the amount of cross-linking agent. These reactions are preferably carried out in organic solvents because water can also react with the cross-linking agent.

Polysaccharides can be cross-linked through condensation using 1,6-hexamethylene diisocyanate or 1,6-hexanedibromide or other reagents. Condensation cross-linking can also be done by carbodiimide which induces cross-links between carboxylic acid and amine groups without itself being incorporated. The commonly used carbodiimide is a water-soluble

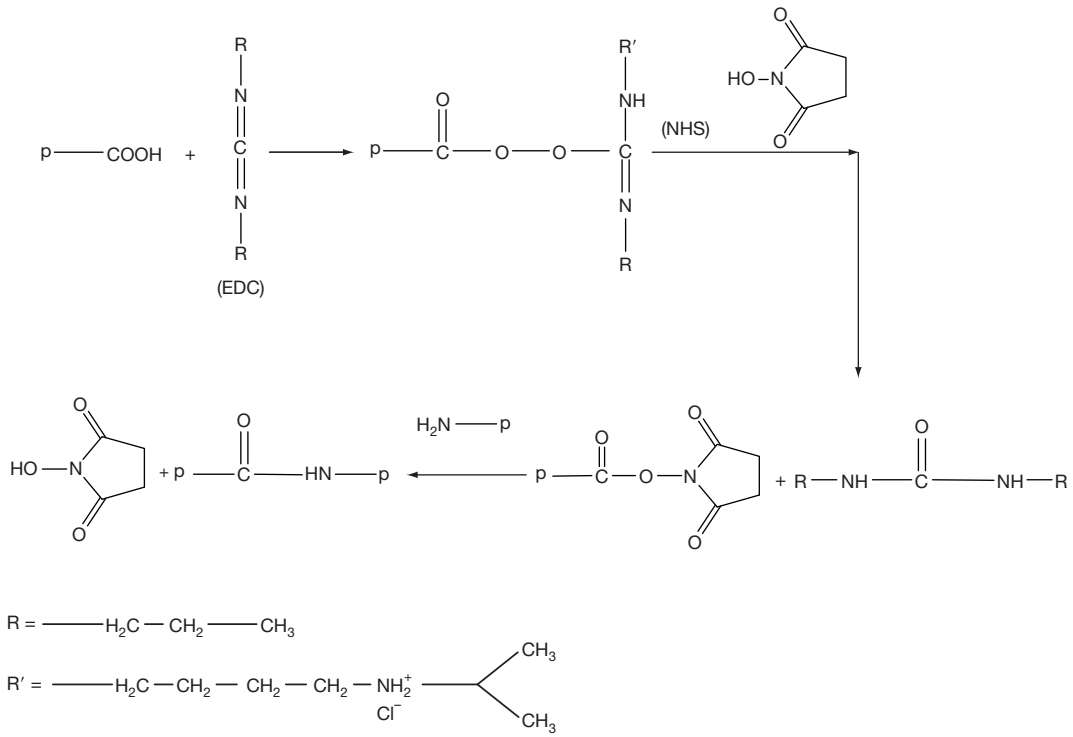

Figure 12 Mechanism of protein cross-linking using carbodiimide (EDC).

carbodiimide called 1-ethyl-3-(3-dimethyl aminopropyl) carbodiimide (EDC). EDC cross-linking involves the activation of the carboxylic acid groups of aspartic acid (Asp) or glutamic acid (Glu) residues by EDC to give *O*-acylisourea groups. Besides EDC, another reagent, *N*-hydroxysuccinimide (NHS) is used in the reaction for the purpose of suppressing side reactions of *O*-acylisourea groups such as hydrolysis and the *N*-acyl shift. NHS can convert the *O*-acylisourea group into a NHS activated carboxylic acid group, which is very reactive toward amine groups of hydroxy lysine, yielding a so called zero length cross-link. In this cross-linking process, neither EDC nor NHS is incorporated in the matrix.

1.121.4.2.3. Cross-linking agents

Cross-linkers (CL) are either homo- or hetero-bifunctional reagents permitting the establishment of inter- as well as intramolecular cross-linkages. Homo-bifunctional reagents, specifically reacting with primary amine groups (i.e., ε-amino groups of lysine residues) have been used extensively as they are soluble in aqueous solvents and can form stable inter- and intrasubunit covalent bonds.

Genipin is a naturally occurring cross-linking agent that has significantly low toxicity. It can form stable cross-linked products with resistance against enzymatic degradation that is comparable to that of glutaraldehyde-fixed tissue. Genipin reacts in a similar manner to glutaraldehyde, but can only bind to one other genipin molecule.

Even though the definite cross-linking mechanism of genipin is not known some mechanisms are proposed as presented in Figure 13(a) and 13(b). In scheme (a) NH_2 group of the protein binds to the ester group (outside the ring structure) which then reorganizes by releasing a methanol group and achieves the binding. Then two protein-bound genipins interact to create the cross-linkage. In scheme (b), the reaction begins with an initial nucleophilic attack of a primary amine group of the protein on the C3 carbon atom of genipin to form an intermediate aldehyde group. Opening of the dihydropyran ring is then followed by an attack on the resulting aldehyde group by the secondary amine formed in the first step of the reaction.

The predominant chemical agent that has been investigated for the treatment of collageneous tissues is glutaraldehyde, which yields a high degree of cross-linking when compared to formaldehyde, epoxy compounds, cyanamide, and the acylazide method. Glutaraldehyde, a popular reagent, has been used in a variety of applications where maintenance of structural rigidity of protein is important. It covalently binds to amino groups, but can also bind to other glutaraldehyde molecules.

The glutaraldehyde cross-linking reactions have been extensively studied (Figure 14). In general, it is believed that aldehydes react with the amine groups of proteins, yielding a Schiff base. However, the exact cross-linking structure is still not clear because a mixture of free aldehyde and mono- and dehydrated glutaraldehyde and monomeric and polymeric hemiacetals is always present in a glutaraldehyde aqueous solution. However, depolymerization of polymeric glutaraldehyde cross-links has been reported. This depolymerization leads to the release monomeric glutaraldehyde and subsequent toxicity.

Calcium ions may also be used as a cross-linker for alginates which are water soluble polymers. When a sodium alginate

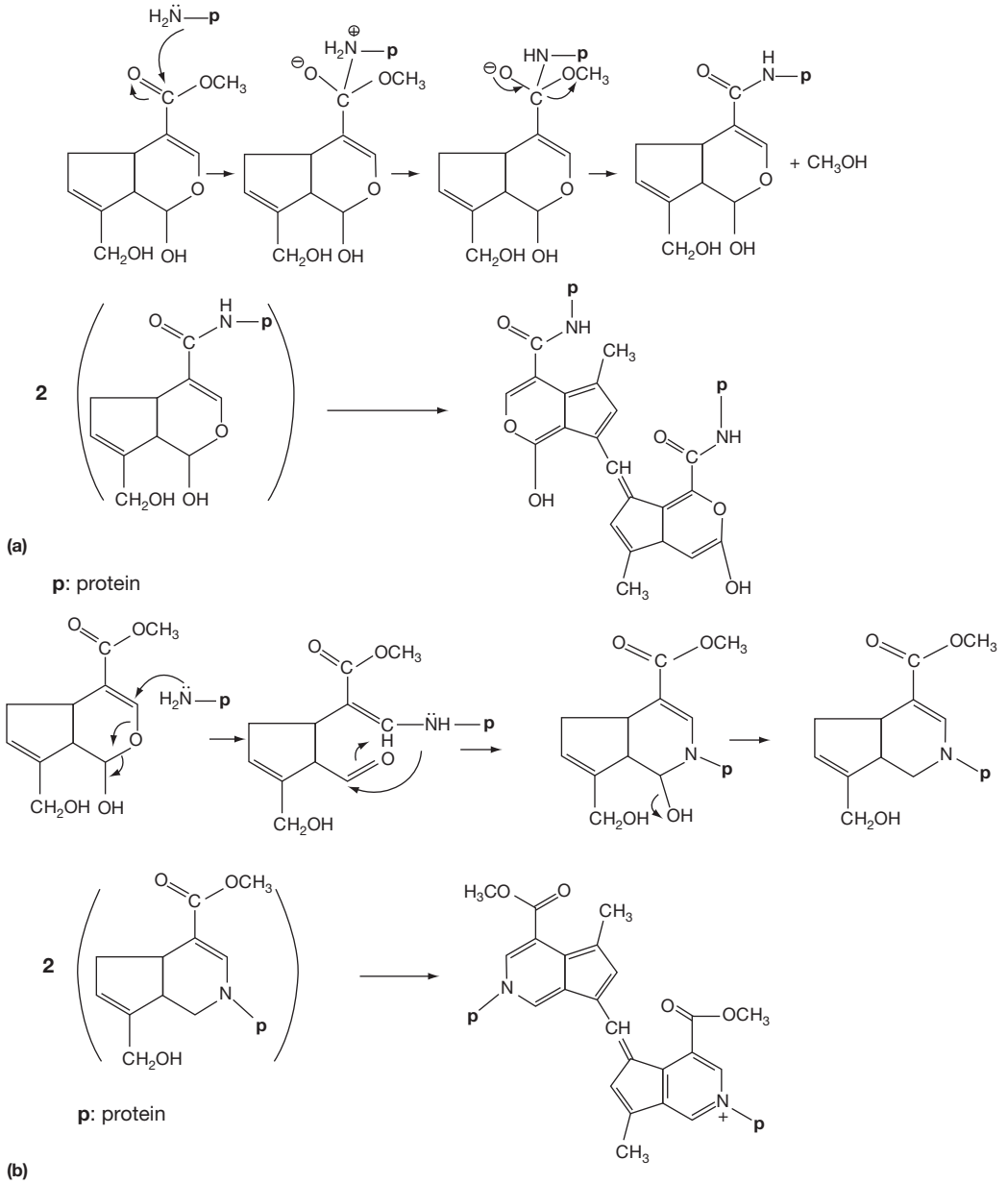

Figure 13 Mechanism of protein cross-linking using Genipin. a) Protein binding to ester group (outside the ring structre) of genipin and crosslinking, b) Protein binding to ring structure of genipin and crosslinking.

$$RNH_2 + HOC\text{-}CH_2\text{-}CH_2\text{-}CH_2\text{-}CHO \longrightarrow R\text{-}N{=}CH\text{-}CH_2\text{-}CH_2\text{-}CH_2\text{-}CHO$$

(a) Glutaraldehyde

$$2RNH_2 + HOC\text{-}CH_2\text{-}CH_2\text{-}CH_2\text{-}CHO \longrightarrow R\text{-}N{=}CH\text{-}CH_2\text{-}CH_2\text{-}CH_2\text{-}CH{=}N\text{-}RNH_2$$

Glutaraldehyde

RNH_2 : Chitosan

(b)

Figure 14 Cross-linking mechanism with glutaraldehyde. (a) Glutaraldehyde activated chitosan and (b) Glutaraldehyde cross-linked chitosan.

solution is dipped into a solution containing calcium ions, each calcium ion replaces two sodium ions. The alginate molecule contains plenty of hydroxyl groups that can be coordinated to cations (Figure 15).[3,11]

1.121.5. Conclusion

In brief, polymers are very complex molecules owing to the large variety of initiators, catalysts, monomers, and mechanisms

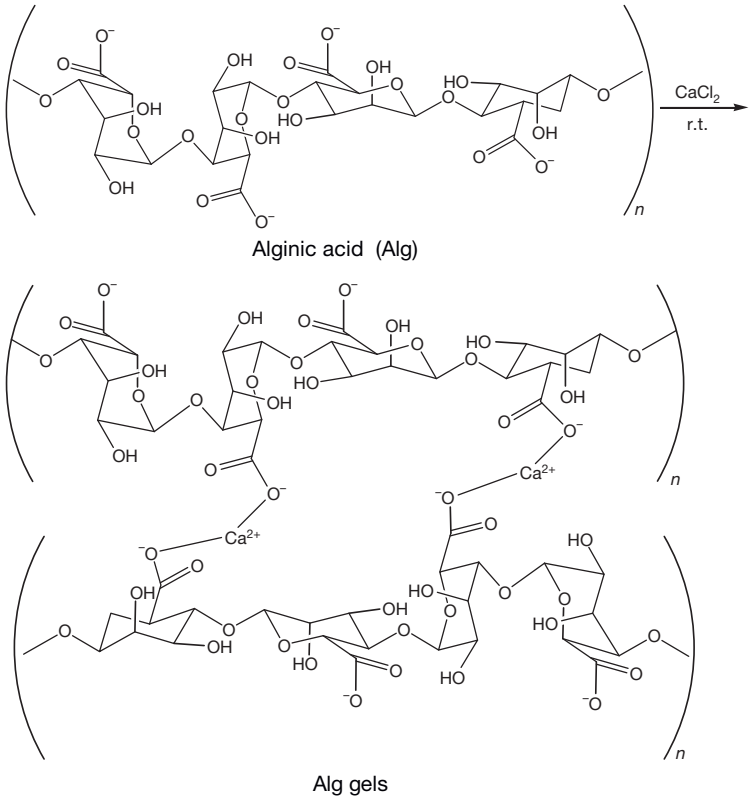

Figure 15 Cross-linking of alginic acid with calcium ions.

available. This enables us to produce very large numbers of different polymers with very diverse properties and this is precisely why polymers play a very important role as a source for materials needed to satisfy human needs. They can be made flame retardant, conductive, bio- or hemocompatible, inert or reactive, stable or degradable at a controlled rate, very tough or soft as gelly. The biomedical field benefits from this diversity immensely since the physical and chemical properties of polymers resemble that of the tissues of the human body more than any other material type such as metals or ceramics. With the developments in biotechnology, nanotechnology, and nanomedicine polymers will keep getting better and more useful for human well-being.

References

1. Carothers, W. H. *J. Am. Chem. Soc.* **1929**, *51*, 2548.
2. Flory, P. J. *Principles of Polymer Chemistry*. Cornell University Press: Ithaca, NY, 1953.
3. Odian, G. *Principles of Polymerization*, 4th ed.; Wiley-Interscience: New York, 2004.
4. Rabinowitch, E. *Trans. Faraday Soc.* **1937**, *33*, 1225–1233.
5. Billmeyer, F. W. *Textbook of Polymer Science*. Wiley: New York, NY, 1984.
6. Hiemenz, P. C.; Lodge, T. P. *Polymer Chemistry*, 2nd ed.; CRC Press: Boca Raton, FL, 2007.
7. Chanda, M. *Introduction to Polymer Science and Chemistry*. CRC Press: Boca Raton, FL, 2006.
8. Ebewele, R. O. *Polymer Science and Technology*. CRC Press: Boca Raton, FL, 2000.
9. Park, J. B.; Lakes, R. S. *Biomaterials: An Introduction*, 3rd ed.; Springer: New York, 2007.
10. Young, R. J.; Lovell, P. A. *Introduction to Polymers*, 2nd ed.; Chapman & Hall: London, 1995.
11. Carraher, C. E. *Polymer Chemistry*, 7th ed.; CRC Press: Boca Raton, FL, 2008.
12. Fried, J. R. *Polymer Science and Technology*. Prentice Hall: Englewood Cliffs, NJ, 1995.
13. Park, J. B.; Bronzino, J. D. *Biomaterials: Principles and Applications*. CRC Press: Boca Raton, FL, 2003.
14. Shi, D. *Introduction to Biomaterials*. Tsinghua University Press: Beijing, 2006.
15. Braun, D.; Cherdron, H.; Rehahn, M.; Ritter, H.; Voit, B. *Polymer Synthesis: Theory and Practice, Fundamentals, Methods, Experiments*, 4th ed.; Springer: Berlin, Heidelberg, New York, 2005.
16. Moad, G.; Solomon, D. H. *The Chemistry of Radical Polymerization*, 2nd ed.; Elsevier: Oxford, 2006.
17. Fischer, H. *Macromolecules* **1997**, *30*(19), 5666–5762.
18. Matyjaszewski, K.; Xia, J. *Chem. Rev.* **2001**, *101*, 2921–2990.
19. Matyjaszewski, K.; Davis, T. P. *Handbook of Radical Polymerization*. Wiley: Hoboken, NJ, 2002.
20. Matyjaszewski, K.; Tsarevsky, N. V. *Nat. Chem.* **2009**, *1*, 276–288.
21. Tsarevsky, N. V.; Matyjaszewski, K. *Chem. Rev.* **2007**, *107*, 2270–2299.
22. Detrembleur, C.; Debuigne, A.; Jerome, C.; Phan, T. N. T.; Bertin, D.; Gigmes, D. *Macromolecules* **2009**, *42*, 8604–8607.
23. Guillaneuf, Y.; Gigmes, D.; Marque, S. R. A.; Tordo, P.; Bertin, D. *Macromol. Chem. Phys.* **2006**, *207*, 1278–1288.
24. Lubnin, A.; O'Malley, K.; Hanshumaker, D.; Lai, J. *Eur. Polym. J.* **2010**, *46*(7), 1563–1575.
25. Moad, G.; Rizzardo, E.; Thang, S. H. *Polymer* **2008**, *49*(5), 1079–1131.
26. Mya, K. Y.; Lin, E. M. J.; Gudipati, C. S.; Gose, H. B. A. S.; He, C. *J. Phys. Chem. B* **2010**, *114*(28), 9128–9134.
27. Ozturk, T.; Goktas, M.; Hazer, B. *J. Appl. Polym. Sci.* **2010**, *117*(3), 1638–1645.
28. West, A. G.; Barner-Kowollik, C.; Perrier, S. *Polymer* **2010**, *51*(17), 3836–3842.

29. Herman, F. M.; Alfrey, T. *Annu. Rev. Phy. Chem.* **1950**, *1*, 337–346.
30. Ahluwalia, V. K.; Mishra, A. *Polymer Science: A Textbook*. CRC Press: Boca Raton, FL, 2007.
31. Jackson, W. J.; Morris, J. C. *J. Polym. Sci. Polym. Chem. Ed.* **1988**, *26*, 835 –835.
32. Gopal, J.; Srinivasan, M. *Makromol. Chem.* **1986**, *187*(1), 1–7.
33. Adduci, J. M.; Amone, M. J. *J. Polym. Sci. Polym. Chem. Ed.* **1989**, *27*, 1115–1123.
34. Mormann, W. N.; Tiemann, N.; Turuskan, E. *Polymer* **1989**, *30*, 1127–1132.
35. Liou, G. S.; Hsiao, S. H. *J. Polym. Sci. Polym. Chem. Ed.* **2001**, *39*(10), 1786–1799.
36. Ber, S.; Kose, G. T.; Hasirci, V. *Biomaterials* **2005**, *26*(14), 1977–1986.
37. Ulubayram, K.; Aksu, E.; Gurhan, S.; Deliloglu, I.; Serbetci, K.; Hasirci, N. *J. Biomaterials Sci. Polym. Ed.* **2002**, *13*(11), 1203–1219.

1.122. Structural Biomedical Polymers (Nondegradable)

L A Pruitt, University of California, Berkeley, CA, USA

© 2011 Published by Elsevier Ltd.

1.122.1.	**Historical Overview**	373
1.122.2.	**Classifications of Medical Polymers and Their Applications**	374
1.122.2.1.	Polyethylene	375
1.122.2.2.	Acrylates	376
1.122.2.3.	Fluorocarbon Polymers	376
1.122.2.4.	Polypropylene	377
1.122.2.5.	Polyester	377
1.122.2.6.	Polyamide	377
1.122.2.7.	Polyurethane	378
1.122.2.8.	Polyetheretherketone	378
1.122.2.9.	Silicone	378
1.122.3.	**Designing Structural Implants with Polymers**	379
1.122.4.	**Summary**	379
References		379

Glossary

Acetabulum The cup-shaped socket in the hip that receives the head of the thigh bone (femur).
Amorphous Unorganized or random arrangement of molecules (no long-range order).
Biocompatibility The ability of a material to function properly in the body without eliciting any undesirable local or systemic effects in the patient or beneficiary of the medical device/implant.
Biomimetic The ability to replicate something found in nature or the body.
Femoral Relating to the thigh bone or femur.
Glass transition temperature The temperature at which the amorphous phase of a polymer begins to show large segmental motion. It often represents the transition from glassy to rubbery behavior.
Mer The basic molecular unit that comprises a collection of atoms. This unit is continuously repeated in macromolecular structures.
Neovascularization Formation of new blood vessels.
Polymer Macromolecules that contain thousands of repeating mers bonded to form a long chain.
Stent A load-bearing tube, usually in mesh form, that restores blood flow to an occluded artery or other blood conduit in the body.
Young's modulus The material property that linearly relates stress and strain up until the point of permanent (plastic) deformation. The modulus is found by taking the slope of the stress versus strain plot in the linear elastic regime.

1.122.1. Historical Overview

Polymers have been utilized in medical implants for nearly 80 years. Polymethylmethacrylate (PMMA) was first used in the body in the 1930s and was initially chosen for its biocompatibility, stiffness, and optical properties. Today, PMMA is widely used as a medical implant in applications such as bone cement for dental and orthopedic applications.[1] For the next 20 years, polymers expanded their use in the body with a diverse range of applications including blood pumps, heart–lung machines, vascular grafts, angioplasty catheters, dental and orthopedic implants, and mammary prosthetics.[2] Materials such as rubbers, silicones, polyurethanes (PU), and cyanoacrylate adhesives were employed during this time; however, there were no stringent FDA regulations in place, and many of the earlier plastic components suffered from *in vivo* degradation and stress cracking. In the 1960s and 1970s, developments in heart valve technology, orthopedics, sutures, dental materials, and soft-tissue reconstruction prevailed. Early heart valve cages made of silicones fared poorly due to lipid adsorption; urethane foam surfaces and silicone mammary prosthetics were suspected of causing chronic inflammatory response; and Teflon utilized in the bearing surfaces of both dental and orthopedic implants was complicated by high wear rates and premature device failure.[3,4] By 1976, medical devices were subject to premarket approval by the FDA. Over the decades that followed, certain materials such as the original silicone breast implants and Teflon materials were removed from the market, while other polymers became the mainstay of certain device applications. During the past 20 years, attention has focused on the improvement of medical polymers known to fare well in the body.

Polymers are now widely used in biomaterial applications, with diverse applications in vascular grafts, balloon catheters, stent coatings, orthopedic bearings, screws, suture anchors,

bone cement, sutures, and soft-tissue reconstruction. One primary advantage of polymeric materials is that their macromolecular structure provides many biomimetic properties that can be utilized in the body. The elastic modulus and strength of a polymer can be tailored through chemistry and processing to provide values that are bounded by those of biological materials. A comparison of elastic modulus values for metals, ceramics, and polymers, as well as hard and soft tissues is given in Figure 1. The modulus can be extended to lower values by reducing the molecular weight or expanding the polymer so that it is porous. This controlled variability of polymer properties enables these medical materials to be utilized in a way that optimizes compliance match with structural tissues, ranging from blood vessels to bone. This is a great advantage of polymers over metals and ceramics, which are often much stiffer than adjacent tissues. A compliance mismatch can result in clinical complications such as stress shielding in bone; in total hip replacements, for example, if a femoral stem is too stiff, then the stress is not sufficiently carried by the neighboring bone and the tissue resorbs around the implant, resulting in loosening of the device.

One of the most important structural polymers used in the body is ultra-high-molecular-weight polyethylene (UHMWPE). This material has been employed in the body since the early 1960s and remains the gold standard as a bearing material in total joint replacements.[5] High-density polyethylene (HDPE) is used in tendon reconstruction and catheter tubes. Ligaments can be reconstructed with braided forms of expanded polytetrafluoroethylene (e-PTFE) that offer both strength and stability.[6–8] This same polymer, e-PTFE, is most successful not only in vascular applications,[9,10] where its porous structure offers tissue integration and opportunity for neovascularization (growth of new blood vessels), but also in facial reconstruction, where the open pore structure facilitates tissue ingrowth and fixation of the implant.[11–13] Nylon and polyester polymers have good tensile strength and are often employed in applications such as sutures[14] and in vascular devices such as balloon catheters.[15] PUs have shown excellent promise as bearing materials and are being utilized in orthopedic applications.[16] Bioresorbable polymers are used where structural properties are temporarily needed and where tissue integration and resorption are required in a medical device; degradable polymers are used in applications such as resorbable sutures,[17] suture anchors,[18] bone screws,[19] and drug delivery devices.[20] Polymeric coatings can also be used to obtain desired surface properties, such as the use of a fluorinated surface treatment for improved lubricity[21] of catheters or for improved biocompatibility of a device.[22] A summary of the primary medical polymers used today in orthopedics, dentistry, and cardiovascular and soft-tissue implants is given in Table 1.

1.122.2. Classifications of Medical Polymers and Their Applications

Medical polymers are used in a wide range of medical devices including restorative dentistry, soft-tissue reconstruction, orthopedic implants, and vascular structures. The most commonly used inert medical polymers include polyethylenes (low-density polyethylene (LDPE), HDPE, and UHMWPE), PMMA, fluoropolymers such as e-PTFE, polypropylenes (PP), polyesters, polyamides (nylons), PU, siloxanes (silicone), and polyetheretherketones (PEEK). Nondegradable polymers are used where long-term structural stability and biocompatibility are needed and are utilized in applications such as bearing surfaces in hip, knee, or shoulder implants; vascular grafts or

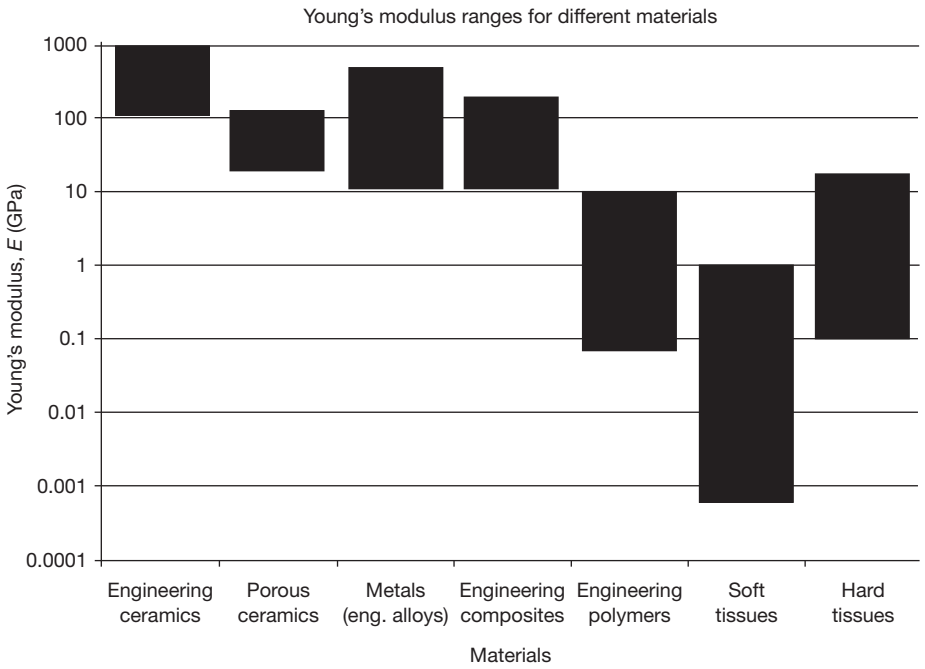

Figure 1 Elastic modulus values are compared for engineering materials and tissues. Polymers offer the greatest overlap with both hard and soft tissues.

Table 1 Examples of polymers used in load-bearing medical devices

Application	*Devices*	*Polymers*	*Performance requirements*
Vascular	Balloons/catheters	Nylon, polyester/LDPE, LLDPE, HDPE	Rupture, flexibility, friction
			Compliance, tissue integration
	Grafts	E-PTFE, polyester	Compliance, tissue integration
Soft tissues	Suture anchors	PEEK	Resilience, strength
	Sutures	Polyester, nylon	Tensile strength
	Breast implants	Silicone	Burst strength
Dental	Crown/filling	Acrylic resins	Wear, fatigue, thermal expansion
	Cements	PMMA	Adhesive strength, interface fracture
Orthopedics	Joint replacements	UHMWPE	Fracture, wear, fatigue, creep
	Spinal implants	Polyurethanes	Fatigue, creep, fracture, wear
	Tendons/ligaments	HDPE, e-PTFE	Strength, wear, creep
	Bone cement	PMMA/PS	Interface fracture
	Spinal fusion	PEEK	Fracture, wear, fatigue

Table 2 Summary of commonly used medical polymers with their structural properties

Polymer	*Linkage*	*Morphology*	T_g *(C)*	T_m *(C)*
Polyethylene (PE)	$-(C_2H_4)-$	Semicrystalline	−80	125–135
Polypropylene (PP)	$-(CH_2CH{\cdot}CH_3)-$	Semicrystalline	−10	125–167
Polytetrafluoroethylene (PTFE)	$-(C_2F_4)-$	Semicrystalline	−70	340
Polyester (PET)	$-(RC{=}OOR')-$	Semicrystalline	50–70	250–265
Polymethylmethacrylate (PMMA)	$-(C_5O_2H_8)-$	Amorphous	118	–
Polyurethane (PU)	$-(R_1{-}O{-}C{=}ONR_2R_3)-$	Amorphous–semicrystalline	−80 to 140	240
Polyamide (nylon)	$-(NHCO(CH_2)_4CONH(CH_2)_6)$	Amorphous or semicrystalline	45	190–350
Silicone	$-(OSiR_2)-$	Amorphous	−127	300
PEEK	$-C_6H_4-O-C_6H_4-O-C_6H_4-CO-$	Semicrystalline	140	340

Table 3 Range of properties in polyethylene polymers

Polyethylene	*Molecular weight (g mol^{-1})*	*Crystallinity (%)*	*Density (g cm^{-3})*	*Applications*
LDPE	30 000–50 000	30–40	0.910–0.925	Medical packaging, catheters
MDPE	60 000–100 000	50–60	0.926–0.940	Facial implants
HDPE	200 000–500 000	70–90	0.941–0.980	Tendons, catheters
UHMWPE	4–6 million	45–60	0.925–0.935	Orthopedic bearings

catheters; fillings and resins for teeth; nose, chin, and cheek implants; and ocular implants. Polymers that are porous by design can facilitate tissue ingrowth and enable long-term stability. A summary of commonly used medical polymers along with their structural properties is provided in Table 2.

1.122.2.1. Polyethylene

Polyethylene polymers are commonly employed as biomaterials and, depending on the specific structure, they can be employed as catheter tubes, facial implants, artificial tendons, or bearing components in total joint replacements. Polyethylene is made through an addition polymerization reaction that utilizes an ethylene monomer ($-C_2H_4-$) repeated along the chain. Process time, temperature, and pressure conditions enable a broad range in degree of branching, molecular weight, crystallinity, entanglements, and cross-linking to be obtained in polyethylene polymers (Table 3). The molecular weight of polyethylene can vary from 30 000 to 6 000 000 g mol^{-1}, density can range from 0.91 to 0.98 g cm^{-3}, and crystallinity can span 30–90%. The melting temperature is typically in the range of 120–147 °C and the glass transition temperature is on the order of −80 °C. Additionally, the polymer can be cross-linked through either chemical or energetic means. This provides an enormous range of structural and mechanical properties within the category of polyethylene. For this reason, polyethylene is generally subcategorized as LDPE, medium-density polyethylene (MDPE), HDPE, or UHMWPE. Thus, it is imperative that the details of the processing, structure, and mechanical properties are well characterized when using polyethylene in medical implants.

The branched form of polyethylene (LDPE) minimizes the packing efficiency of chains, resulting in lower crystallinity and density. The linear form of polyethylene (HDPE) facilitates efficient packing of chains and concomitantly has high crystallinity (70–90%) and density (0.96–0.98 g cm^{-3}). If the polymerization is allowed to continue, the linear chains get very long and a UHMWPE is achieved (4–6 million g mol^{-1}). The very high molecular weight enhances the propensity for entanglement, limits the ability to crystallize (50%), and

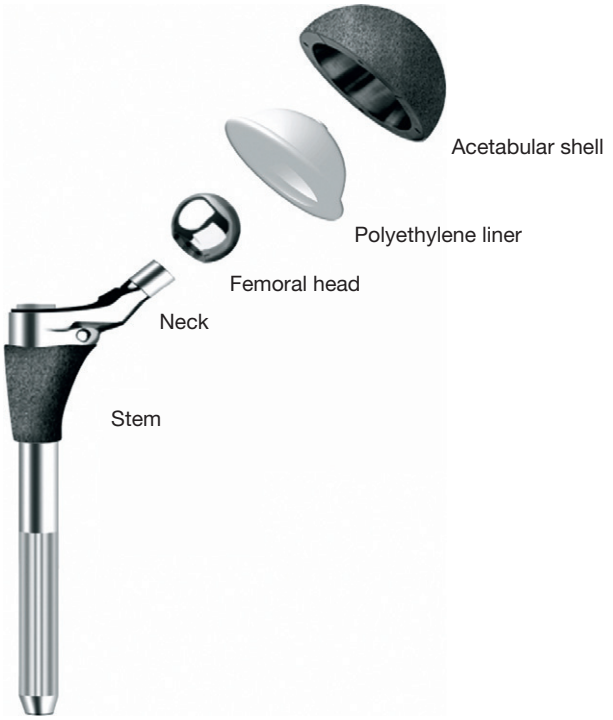

Figure 2 A typical total hip replacement utilizing a UHMWPE acetabular cup that articulates against a Co–Cr femoral head.

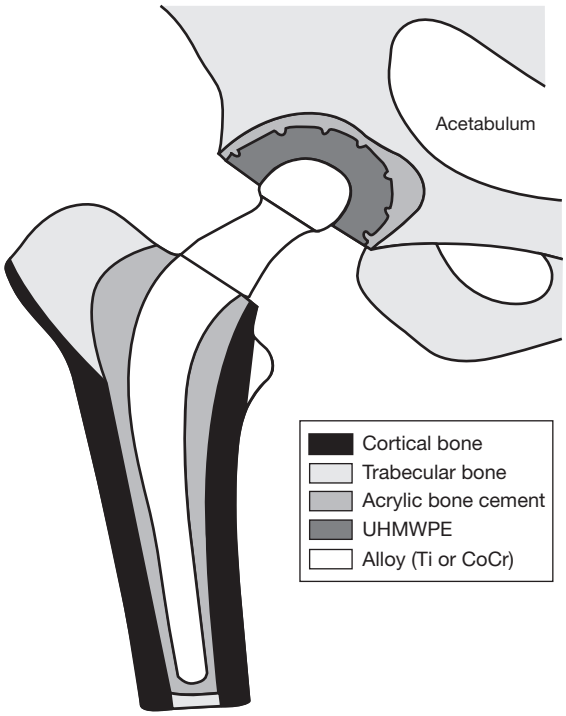

Figure 3 Illustration depicting the use of acrylic bone cement as a bonding agent between the implant and adjacent bone.

results in lower density (0.935 g cm^{-3}). The unique properties of UHMWPE provide it with exceptional energetic toughness, low coefficient of friction, and good wear resistance. UHMWPE can also be cross-linked to further minimize wear in this polymer.[23] UHMWPE is a widely studied medical polymer, especially in the domain of orthopedic bearings, and decades of research have been devoted to the characterization of microstructure, processing, sterilization, oxidation, mechanical behavior, fatigue behavior, and wear behavior of this material.[5,24] UHMWPE remains the gold standard as a bearing material in total joint replacements for hips, knees, shoulders, and elbows. A typical total hip replacement utilizing an UHMWPE acetabular cup that articulates against a Co–Cr femoral head is shown in Figure 2. Such implant designs can have survivorship rates of up to 90% after two decades of *in vivo* service.

1.122.2.2. Acrylates

Acrylate polymers are widely used in dentistry and in bone cements. PMMA polymers are also made through an addition polymerization reaction; the chemical formulation of PMMA is –($C_5O_2H_8$)–. The bulky side groups on this backbone chain limit its ability to crystallize and to have high ductility. In general, this PMMA is amorphous, with a relatively high elastic modulus (3–4 GPa) and glass transition temperature (118 °C). The molecular weight can vary widely (200 000–700 000 g mol^{-1}), depending on processing conditions. Without any additives, this material is known to have excellent transparency. For this reason, it can be used in ocular implants. With additive or copolymerization, this material is commonly used as a grouting agent to secure implants to bone, and it may be best known for its application as bone cement, used in orthopedics and dentistry. There is an abundance of literature devoted to the structure and properties of PMMA, and its use as a bone cement.[1] The greatest challenge for PMMA as a bone cement is that it is mixed at the time of surgery and is prone to porosity and void entrapment that can affect its mechanical performance *in vivo*.[25] One of its primary benefits is that, when it is first mixed, the bone cement is doughy for several minutes and is able to penetrate the pores and open spaces of the adjacent bone tissue. In fact, more cement penetration is achieved in porous bone; this bone cement serves as an excellent fixation medium for patients with osteoporotic bone.[26] The bone cement sets within about 10 min, and, from that point onward, it provides a secure interface and load transfer mechanism between the implant and the bone tissue. Figure 3 shows the use of bone cement as a bonding interface in a total hip replacement.

1.122.2.3. Fluorocarbon Polymers

Fluorocarbon polymers are addition-reacted polymers that are fully or partially fluorinated along the carbon backbone. Polytetrafluoroethylene, commonly known as Teflon®, is a fully fluorinated form with a chemical formulation –(CF_2–CF_2)–. These polyolefins (flexible polymer chains) possess exceptional properties such as chemical inertness, mechanical integrity, and lubricity that are due to the highly electronegative fluorine sheath that protects the carbon backbone from chemical attack and results in a hydrophobic polymer with low surface energy. Most fluorocarbon polymers are semicrystalline

and have a low glass transition temperature (−70 °C) that enables exceptional resilience. The primary fluoropolymer used in biomedical applications is based on e-PTFE. The success of this biomaterial has resulted from its microporous structure, which allows biointegration for fixation and provides structural integrity (Figure 4). The first successful medical applications of e-PTFE were initiated with vascular grafts and then evolved to soft-tissue reconstruction.[27] The mechanical properties of e-PTFE depend strongly on the porosity and microstructure of the polymer as well as strain rate.[11] However, the predominant success of e-PTFE as a biomaterial is due to its microporous structure, which allows biointegration for fixation and long-term stability *in vivo*.[12]

1.122.2.4. Polypropylene

PP polymers are also generated through addition polymerization and have structural properties similar to polyethylene due to their close chemical formulation, –(CH_2CHCH_3)–. This polymer has a methyl side group that can affect the crystallinity of the polymer, depending on its arrangement on the backbone. Typically, the molecular weight spans 200 000–700 000 g mol^{-1} and the density spans 0.85–0.98 g cm^{-3}. Its melting temperature spans 125–167 °C and its glass transition temperature is on the order of −10 °C. This material has exceptional fatigue life in flexion and is commonly used in finger joint prostheses, grafts, and nondegradable sutures (Figure 5).

1.122.2.5. Polyester

Polyester polymers are generated through condensation reactions. A polyester has a characteristic ester linkage, –(RC=OOR′)–, in its backbone chain and includes materials such as polyethylene terephthalate (PET) and Dacron® fibers. Polyesters typically have a high melting temperature (250–265 °C) and high crystallinity. PET is known to be hydrophobic and nonthrombogenic and is commonly employed as a vascular graft or as a suture material. The most widely known polyester is marketed under the trade name Dacron® and is utilized in fabric form as a graft material.

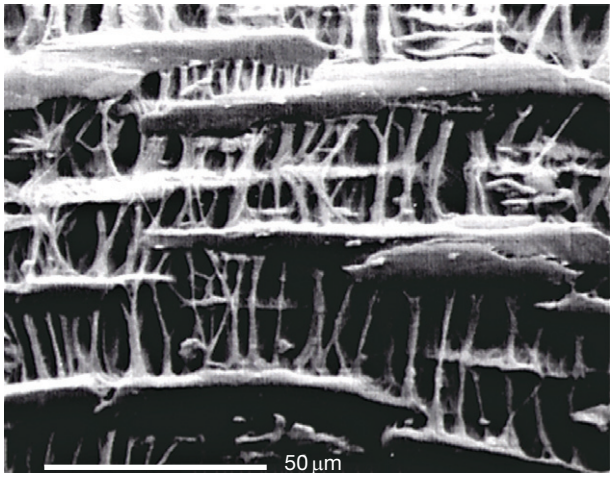

Figure 4 Microstructure of expanded polytetrafluoroethylene used in vascular grafts.

1.122.2.6. Polyamide

Another group of condensation polymers are the polyamides or nylons. These materials have a common amide linkage, –(RCONH–R′)–. Polyamides have a broad range of properties, depending on the specific chemistry and processing, and may be amorphous or semicrystalline. The melting temperature spans 190–350 °C, and the glass transition temperature is on the order of 45 °C. These polymers are susceptible to swelling in aqueous solutions but are often employed in short-term applications such as catheters and catheter balloons in angioplasty procedures or stent deployment. Nylons are a classification of polymer fibers within polyamides, and the most commonly used forms are nylon 6 and nylon 6,6. The general chemical form for the latter is –$(NHCO(CH_2)_4CONH(CH_2)_6)$–. Nylon is commonly used as the outer layer of balloon angioplasty catheters and also as the balloon used for deployment of a stent or the expansion of an occluded artery. Nylons offer strength and stiffness to balloon angioplasty systems; an example of a nylon balloon used in the deployment of a stent is illustrated in Figure 6.

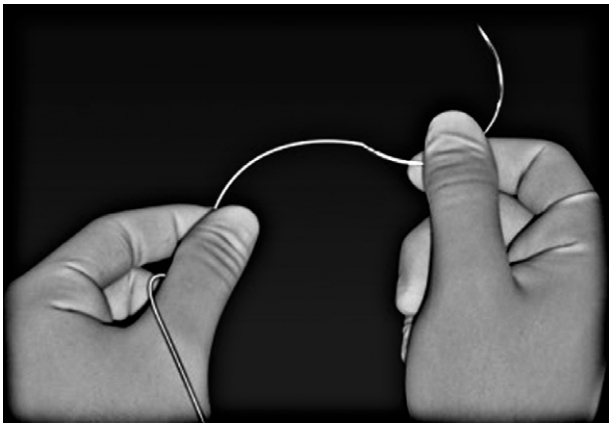

Figure 5 Polypropylene has good tensile strength and is commonly employed as a nondegradable suture.

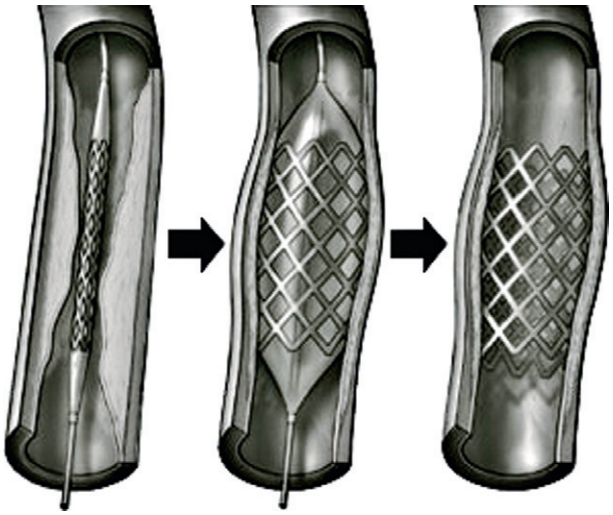

Figure 6 Schematic of nylon balloon that is expanded to deploy a stent in an artery.

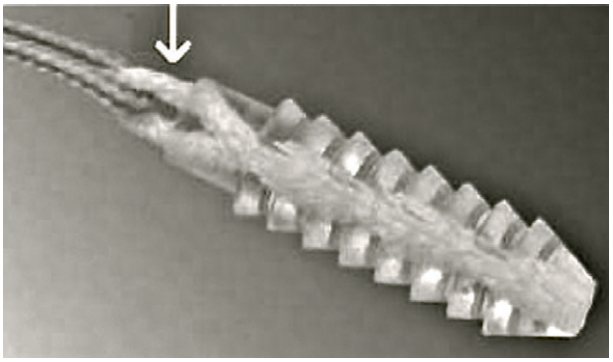

Figure 7 Illustration of a suture anchor and the anchoring point (arrow) used to securely fasten a suture in soft-tissue repair.



Figure 8 Early silicone breast implants were susceptible to rupture and leaking.

1.122.2.7. Polyurethane

PUs are generated through a step-growth polymerization that combines a monomer comprising at least two isocyanate functional groups with another mer containing at least two hydroxyl (alcohol) groups. The urethane links that build the polymer chains have the chemical formulation (R_1–O–C=ONR_2R_3). PUs can be processed to have hard and soft segments of varying glass transition temperatures and can span a full range of structural properties, ranging from elastomeric (rubber-like) to glassy. Thus, all its properties are highly dependent upon its backbone chemistry. As a biomaterial, PUs can be used as bearing materials in orthopedics or spinal implants, and, in elastomeric form, they can be used for soft-tissue reconstruction.

1.122.2.8. Polyetheretherketone

PEEK is a thermoplastic that offers exceptional mechanical properties. The backbone structure of PEEK is $(–C_6H_4–O–C_6H_4–O–C_6H_4–CO–)_n$, and this structure provides strength and resistance to deformation. PEEK is used in spinal cages and is also used in suture anchors in soft-tissue repair. Suture anchors must maintain an anchoring point to fasten a suture securely and are often employed in shoulder arthroplasty (Figure 7).

1.122.2.9. Silicone

Silicones are a broad class of polymers also known as siloxanes. These polymers comprise –($OSiR_2$)– on their backbones and are known best for their elastomeric–viscoelastic properties. A well-known subclassification of silicone is

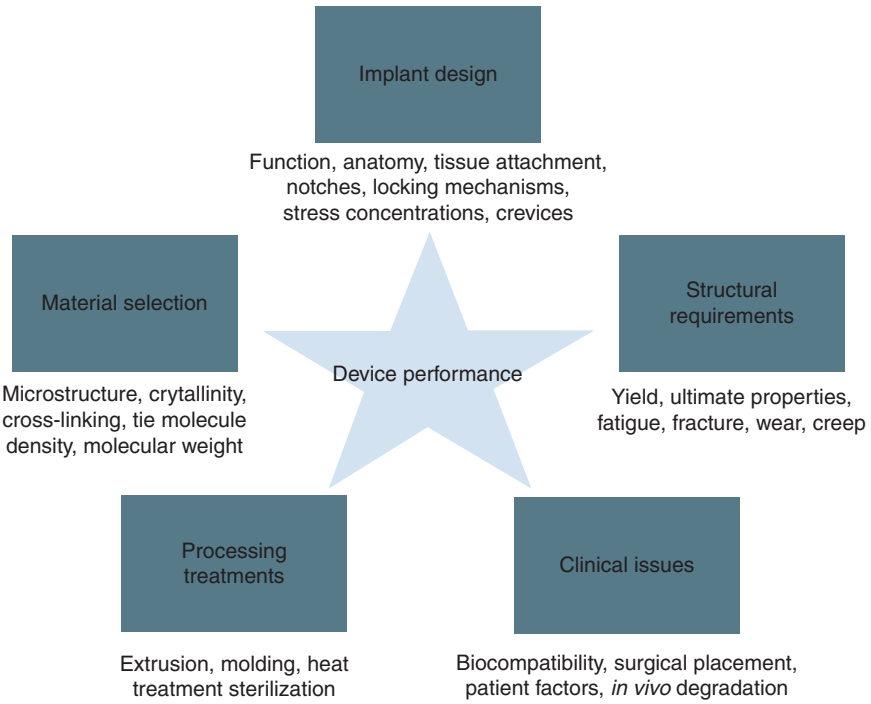

Figure 9 Schematic showing the factors that contribute to device performance.

polydimethylsiloxane (PDMS), which was once used as the fluid filler in silicone breast implants, but this technology was terminated due to concern about leaking (Figure 8); modern breast implants utilize a cross-linked form of silicone that is a soft solid and elastomeric in nature.

1.122.3. Designing Structural Implants with Polymers

Structural implants made with medical polymers are susceptible to failures *in vivo*. The functional demands placed on a polymer implant may result in damage that is sufficient to cause clinical failure of the implant. The performance of a medical device is quite complicated as there are several contributing and related factors, including the implant design, material selection, the structural requirements of the device, the processing or manufacturing modality of the implant, and clinical issues. Figure 9 schematically illustrates the contributing factors that affect device performance.

1.122.4. Summary

Polymeric materials provide a broad range of structural properties and offer numerous benefits as biomaterials. Polymers can be tailored to have high toughness, resilience, wear resistance, compliance match to tissue, and controlled resorption in the body. Medical polymers are commonly employed as bearing materials in total joint replacements, artificial tendons and ligaments, vascular grafts, catheter balloons, bone and device fixation, and soft-tissue repair.

References

1. Kühn, K. D. *Bone Cements: Up-to-Date Comparison of Physical and Chemical Properties of Commercial Materials*; Springer: Berlin, New York, 2000.
2. American Society of Metals (ASM). In *Handbook of Materials for Medical Devices*; Davis, J. R., Ed.; ASM International: Materials Park, OH, 2003.
3. Feinerman, D. M.; Piecuch, J. F. *Int. J. Oral Maxillofac. Surg.* **1993**, *22*(1), 11–16.
4. Zardenta, G.; Mukai, H.; Marker, V.; Milam, S. B. *J. Oral Maxillofacial Surg.* **1996**, *54*, 873–878.
5. Kurtz, S. M. *The UHMWPE Handbook: Principles and Clinical Applications in Total Joint Replacement*; Elsevier Academic Press: New York, 2004.
6. Hanff, G.; Dahlin, L. B.; Ludborg, G. *Scand. J. Plast. Reconstr. Surg. Hand Surg.* **1992**, *26*(1), 43–49.
7. Paavolainen, P.; Makisalo, S.; Skutnabb, K.; Holmstrom, T. *Acta Orthop. Scand.* **1993**, *64*, 323–328.
8. Bolton and Bruchman (1983).
9. Campbell, C. D.; Goldfarb, D.; Roe, R. *Ann. Surg.* **1975**, *18*, 138–143.
10. Watanabe, T. *J. Jpn Surg. Soc.* **1984**, *85*, 580–591.
11. Catanese, J.; Cooke, D.; Maas, C.; Pruitt, L. *Appl. Biomat.* **1999**, *48*, 187–192.
12. Greene, D.; Pruitt, L.; Maas, C. *Laryngoscope* **1997**, *107*, 957–962.
13. Maas, C. S.; Gnepp, D. R.; Bumpous, J. *Arch. Otolaryngol Head Neck Surg.* **1993**, *90*, 1008–1015.
14. Lawrence, T.; Davis, R. C. *J. Hand Surg.* **2005**, *30*(4), 836–841.
15. Wheatley, G. H.; McNutt, R. T.; Diethrich, E. B. *Ann. Thorac. Surg.* **2007**, *83*(1).
16. Geary, C.; Birkinshaw, C.; Jones, E. *J. Mater. Sci. Mater. Med.* **2008**, *19*, 3355–3363.
17. Amass, W.; Amass, A.; Tighe, B. *Polym. Int.* **1998**, *47*(2), 89–144.
18. Stanford, R. *J. Shoulder Elbow Surg.* **2001**, *10*(3), 286–291.
19. Bailey, C. A.; Kuiper, J. H.; Kelly, C. P. *J. Hand Surg. (British and European Volume)* **2006**, *31*(2), 208–212.
20. Arosio, P.; Busini, V.; Perale, G.; Moscatelli, D.; Masi, M. *Polym. Int.* **2008**, *57*(7), 912–920.
21. Klapperich, C.; Pruitt, L.; Komvopoulos, K. *J. Mater. Sci. Mater. Med.* **2001**, *12*, 549–556.
22. Ratner, B. D.; Hoffman, A. S.; Schoen, F. J.; Lemons, J. E. *Biomaterials Science: An Introduction to Materials in Medicine*; Academic Press: London, 1996.
23. Muratoglu, O. K. *J. Arthroplasty* **2001**, *16*(2), 149–160.
24. Kurtz (2009).
25. Graham, J.; Ries, M.; Pruitt, L.; Gundiah, N. *J. Arthroplasty* **2000**, *15*(8), 1028–1035.
26. Graham, J.; Ries, M.; Pruitt, L. *J. Bone Joint Surg.* **2003**, *85A*(10), 1901–1908.
27. Pruitt, L. In *Advances in Polymer Science: Encyclopedia of Materials: Science and Technology*; Williams, D. F., Ed.; Elsevier Science Limited: Oxford, 2001.
28. Charnley, J. *Lancet* **1963**, *II*, 1379.
29. Hughes, K.; Ries, M. D.; Pruitt, L. *J. Biomed. Mater. Res.* **2003**, *65A*, 126–135.
30. Rosen, S. L. *Fundamental Principles of Polymeric Materials*, 2nd ed.; Wiley: New York, 1993.

1.123. Degradable Polymers

K K L Phua, E R H Roberts, and K W Leong, Duke University, Durham, NC, USA

© 2011 Elsevier Ltd. All rights reserved.

1.123.1.	**Introduction**	382
1.123.2.	**Overview of PLGA Copolymers**	383
1.123.2.1.	PLGA History and Uses	383
1.123.2.2.	Common Manufacturing Techniques	384
1.123.3.	**Parameters Affecting Degradation Rate of PLGA**	384
1.123.3.1.	Copolymer Ratio	384
1.123.3.2.	Molecular Weight	384
1.123.3.3.	Crystallinity and Glass Transition Temperature	384
1.123.3.4.	Heterogeneous Degradation	385
1.123.3.5.	Degradation and Length Scale	385
1.123.3.6.	Environmental Factors Affecting Degradation	387
1.123.4.	**Biocompatibility of PLGA**	387
1.123.4.1.	*In Vivo* Biocompatibility of Implants	387
1.123.4.2.	*In Vivo* Biocompatibility of Microspheres	387
1.123.4.3.	*In Vivo* Biocompatibility of Nanoparticles	387
1.123.4.4.	Bioavailability: Damage to Encapsulated Payload	388
1.123.5.	**Applications of PLGA Across Length Scales**	388
1.123.5.1.	Nanoscale Particles	388
1.123.5.1.1.	Drug delivery	388
1.123.5.1.2.	Gene delivery	389
1.123.5.2.	Nanoscale Fibers	390
1.123.5.3.	Microscale Particles	391
1.123.5.3.1.	Vaccines	391
1.123.5.3.2.	Contrast agent for ultrasound	392
1.123.5.3.3.	Tissue engineering	393
1.123.5.4.	Macroscale Hydrogel	393
1.123.5.5.	Macroscale Foams	394
1.123.6.	**Rationale for Development of PPEs**	394
1.123.7.	**Structure–Function Relationships of PPEs**	394
1.123.7.1.	Material Properties of PPE Films	394
1.123.7.2.	Degradation	398
1.123.7.3.	Structure–Degradation and Length Scale–Degradation Relationship	399
1.123.8.	**Toxicity and Biocompatibility of PPEs**	401
1.123.9.	**Design of PPE Drug Carriers**	403
1.123.9.1.	Amphiphilic PPE Copolymers as Drug Carriers	403
1.123.9.2.	Drug-Loading Index	404
1.123.9.3.	Effect of Molecular Structure on Critical Micelle Concentration	404
1.123.9.4.	Drug Release Kinetics	405
1.123.10.	**Design of Thermoresponsive PPEs**	406
1.123.10.1.	Molecular Structures of Thermoresponsive PPEs	407
1.123.10.2.	Effects of Solution Properties on Thermal Transition	408
1.123.10.3.	Thermoresponsive PPEs Conjugated to PEG, Gold Nanoparticles, and Enzyme-Cleavable Side Chains	408
1.123.11.	**Design of PPE and PPA Gene Carriers**	409
1.123.11.1.	Molecular Structures of PPE and PPAs Gene Carriers	409
1.123.11.2.	Effect of Polymer Backbone on Gene Delivery Applications	409
1.123.11.3.	PPE/DNA Gene Delivery System	410
1.123.11.4.	PPA–DNA Gene Delivery System: DNA Compaction Capacity of PPAs	410
1.123.11.5.	Effect of N/P Ratio and Cell Culture Conditions on Transfection Efficiency of PPA–DNA Particles	411
1.123.11.6.	Effect of Charged Groups on Transfection Efficiency of PPA–DNA Particles	411
1.123.11.7.	Effect of PPA Side-Chain Structure on Transfection Efficiency	411
1.123.11.8.	Combinatorial Approach Nanoparticle Formulated with PPAs Bearing Different Charge Groups	411

1.123.11.9. PPA with Imidazole Moiety: Improving Buffering Capacity 412
1.123.11.10. Effect of on Transfection Efficiency by Ligand-Modified and PEG-Modified PPA 413
1.123.12. Conclusion 414
References 414

Glossary

Critical aggregation temperature Refers to a change in hydrodynamic radius of a particle when subjected to temperature variations.
Drug-loading capacity (DLC) Weight of drug loaded in carrier/weight of drug-loaded carriers × 100%.
Drug-loading efficiency (DLE) Weight of drug loaded in carrier/weight of drug used for loading × 100%.
Drug-loading index A parameter used to quantify the overall effectiveness of drug carrier (DLC usually varies inversely with DLE). Calculated using the formula: DLC × DLE.
Glass transition Is the reversible transition (of amorphous materials) from a hard and relatively brittle state into a molten or rubber-like state.
IC_{50} Half maximal inhibitory concentration, usually in microgram per milliliter, a quantitative measure that indicates how much of a particular substance is needed to inhibit proliferation of cells by 50% relative to controls.
Length scale A term used to describe the physical size of biomaterials (length, width, or depth).
Macroscale Describes biomaterials with length scales above 1 mm.
Microscale Describes biomaterials with length scales between 1 μm to 1 mm.
Nanoscale Describes biomaterials with length scales below 1 μm.
Polymer backbone Refers to the longest continuous molecular sequence of a polymer molecule.

Abbreviation

PCL Polycaprolactone
PEEP Poly(ethyl ethylene) phosphase
PEG Poly(ethylene glycol)
PGA Poly(glycolide)
PLA Poly(lactide)
PLGA Poly(lactide-*co*-glycolide)
PPA Polyphthalamide
PPE Poly(phosphoester)
PVA Poly(vinyl alcohol)

1.123.1. Introduction

Degradable polymers find their biomedical applications mostly as devices that provide temporary structure support or deliver therapeutics.[1] They have also been intensively studied and developed for environmental applications as recyclable materials, the importance of which will undoubtedly grow with time. The focus of this review will, however, be on medical applications of biodegradable polymers. Biodegradable sutures composed of polyesters represent early examples of commercial success of biodegradable polymers in the 1960s. Advance of drug delivery in the 1970s saw the appeal of using biodegradable polymeric carriers to provide a local and sustained release of drugs. Controlled drug delivery can offer tremendous benefits including maximization of drug efficacy, minimization of side effects, and improvement of patient compliance.[2] The idea of a carrier breaking down into harmless products to be cleared from the body after release of the embedded drug has captured the imagination of the scientists and public alike. This stimulated the remarkable growth of biodegradable polymer research and development, sustained by emergence of the fields of gene therapy and tissue engineering two decades later. As an alternative to viral vectors, biodegradable and cationic polymers can condense nucleic acids into nanoparticles for intracellular delivery. Although highly inefficient compared to viral delivery, nonviral gene transfer compensates with potential long-term safety and less demanding manufacturing hurdles. Biodegradable gene carriers can play a significant role in advancing nonviral gene transfer by satisfying the conflicting requirements of binding the nucleic acid tightly in the extracellular space and releasing it intracellularly.[3] As scaffolding material to support tissue growth *in vitro* and *in vivo*, biodegradable polymers offer the advantage of gradual disappearance to free up space for cellular infiltration and tissue development. Many other medical devices, such as a stent for percutaneous transluminal angioplasty or bone cement for spinal fusion, can also benefit from a biodegradable polymeric design.

A vast array of biodegradable polymers, ranging from synthetic to natural and to hybrid, have been studied and developed. It would be impossible to provide a comprehensive review on these different types of polymers. Readers are referred to other reviews on this topic.[4–17] This review will instead focus on the poly(lactide-*co*-glycolide) (PLGA) copolymers and poly (phosphoester)s (PPEs). Enjoying the favorable status of the U.S. Food and Drug Administration (FDA) approval, PLGAs are the obvious choice for the development of many biodegradable medical devices. Since numerous reviews have already covered this class of polymers, we will concentrate on its degradation behavior, its influence of drug release kinetics, and its dependence on the length scale. As the

device shrinks from the macro- to micro- and then to the nanoscale, the structure–property relationship of PLGAs may differ, which may impact their applications. After a brief review of the PLGAs, we will discuss PPEs in comparison. PPEs were developed with the rationale of versatility and potential biocompatibility. Due to the pentavalency of phosphorous, the physicochemical properties of PPEs can be independently varied with respect to their backbone or side-chain structure. This affords a wealth of chemical structures that can be applied to drug and gene delivery and tissue engineering. We will again concentrate on the structure–property relationship of these polymers and their performance across different length scales. It is our hope that this focused review can offer a glimpse of the working principles and vast potential of biodegradable polymers in medicine.

1.123.2. Overview of PLGA Copolymers

Approved by the FDA for some human uses since the 1970s, PLGA polymers are being used in a growing array of applications. This chapter explores the degradation behavior of PLGA in applications in length scales from nano to macro. PLGA is a synthetic polymer made from monomers of lactide and glycolide. Poly(lactide) (PLA), poly(glycolide) (PGA), and their copolymer PLGA are aliphatic polyesters. PLGA is synthesized by ring-opening reactions of glycolic and lactic acid and linked linearly through ester bonds (**Figure 1**).[18] Polymers made of only L-lactide are crystalline, but generally both the D- and L-stereoisomers of lactide are used so that the polymer is more amorphous. To change the properties of the polymer, the molar ratio of lactide to glycolide and the molecular weight of the polymer can be varied; the molar ratio is the most important parameter influencing degradation rate.[19,20]

The polymer degrades by hydrolysis of the ester bonds. PLGA causes low levels of toxicity and immunogenicity when implanted in the body, which is why it is considered biocompatible. The FDA has approved the human use of PLGA for several applications, which makes it an attractive choice for future biodegradable polymer uses. This chapter focuses on the biodegradation of PLGA and highlights some of its applications from each length scale: nano, micro, and macro.

1.123.2.1. PLGA History and Uses

PGA was used in the first totally biodegradable sutures developed in the 1960s and marketed in the 1970s under the name Dexon. However, the tension in the sutures decreased by half 2 weeks post implantation because of PGA's hydrophobic nature and relatively fast degradation.[21] To lengthen the degradation time of these sutures, PLA/PGA copolymers were developed. The sutures, which had a lactide-to-glycolide ratio of 10:90, were marketed as Vicryl and Polyglactin 910.[21,22] The sutures had good mechanical properties and biocompatibility as well as predictable degradation rates, so the applications of PLA/PGA copolymers expanded to tissue engineering and drug delivery.[23]

Devices and therapies made with PLGA have garnered FDA approval over the last several decades, making the route to FDA approval transverse to attain by other proposed PLGA therapies. Some of the applications PLGA devices have been marketed for are sutures, bone fixatives, suturing reinforcements,

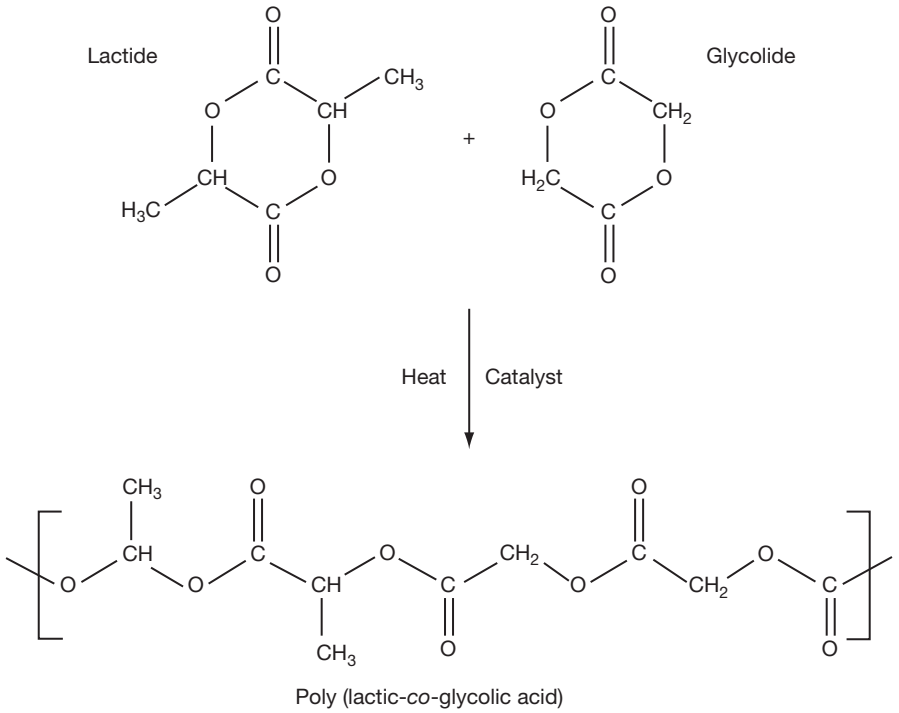

Figure 1 The basic structures of lactide, glycolide, and PLGA. Reproduced from Uchegbu, I. F.; Schatzlein, A. G. *Polymers in Drug Delivery*; CRC Press: Boca Raton, FL, 2006.

artificial skin, dental materials, bone regeneration, artificial blood vessels, as well as protein, nucleic acid, and small molecule delivery.[21] PLGA therapies of various types have been so successful that PLGA is often used as a standard for comparison with other polymers, both in efficacy and biocompatibility.

1.123.2.2. Common Manufacturing Techniques

One of the most common ways to generate PLGA micro- or nanoparticles is by the solvent evaporation method, either by a single or double emulsion. With a single emulsion (O/W), the polymer is dissolved in a volatile organic solvent (the oil phase), which is then dispersed into a large volume of aqueous solvent (the water phase) so that small droplets are formed. An emulsifier such as poly(vinyl alcohol) (PVA) is typically used in the water phase. Dispersion is generally accomplished by stirring, homogenization, or sonication. The mixture is placed under reduced pressure or is vigorously stirred at atmospheric pressure to evaporate the organic solvent. Another method of removing the oil phase is by extraction, where the emulsion is placed in a larger volume of water into which the organic solvent diffuses. The particles that remain are then washed, collected, and dried. Lipophilic drugs can be loaded into the particles by dissolving them with the polymer in the organic solvent (**Figure 2**).[23]

A double emulsion (W/O/W) is appropriate for loading micro- or nanoparticles with water-soluble drugs or genes. An aqueous solution of drug, possibly with a stabilizer such as gelatin, is dispersed into an organic phase with PLGA (W/O). This solution is added into a larger volume of the second aqueous phase with stirring. The solvent evaporation or solvent extraction method is employed, leaving PLGA particles encapsulating drugs.[23]

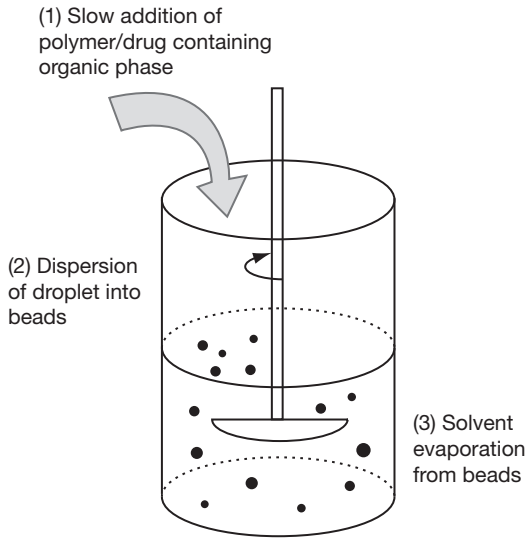

Figure 2 Oil-in-water solvent evaporation steps. The organic phase is dispersed in the aqueous phase, forming droplets. The solvent is evaporated from the organic phase under stirring or low pressure, leaving polymer beads, which are then collected, washed, and dried. Reproduced from Freiberg, S.; Zhu, X. X. *Int. J. Pharm.* **2004**, *282*, 1–18, with permission from Elsevier.

1.123.3. Parameters Affecting Degradation Rate of PLGA

The mechanism of degradation of PLGA is nearly always by simple hydrolysis of the ester bonds in the chain backbone. The degradation process occurs by random scission wherever water is able to penetrate into the polymer structure. The degradation rate of the PLGA structure depends on the monomer ratio, the molecular weight of the polymer, the crystallinity, the glass transition temperature, the size of the device, and environmental factors such as temperature and pH, among others.

1.123.3.1. Copolymer Ratio

The copolymer ratio (lactide-to-glycolide) determines the hydrophilicity of the polymer matrix; lactide is more hydrophobic and glycolide is more hydrophilic. There is more water penetration with an increased fraction of glycolide because glycolide–glycolide and glycolide–lactide bonds are preferentially hydrolyzed.[24] An increasing fraction of glycolide increases the weight loss from degradation.[19] The fastest-degrading PLGA polymers have a 50:50 lactide-to-glycolide ratio, with the degradation rate increasing with higher glycolide or lactide content.[23] However, it is not common to use polymers with more than 50% glycolide composition.

1.123.3.2. Molecular Weight

PLGA with a lower molecular weight degrades faster and has a larger burst release of its payload, when a burst release is present. Heya *et al.* created microspheres loaded with the thyrotropin-releasing hormone from a double emulsion method from PLGA with a lactide-to-glycolide ratio 75:25 and molecular weights of 6, 8, and 11 kDa. The observed drug release *in vitro* for all polymer molecular weights at low drug loading levels had two parts: an initial burst release followed by a slower release over a longer time. The initial burst was larger for microspheres made with lower molecular weight PLGA. The researchers measured the decrease in molecular weight and polymer weight over the long term and found that all the polymers' molecular weights decreased at about the same rate but the weight loss was much faster from the lower molecular weight polymers. Drug release rate and polymer erosion rate were correlated. The drug release rate was faster than the polymer weight loss, so the authors concluded that the drug diffuses out from the polymer matrix as the matrix degrades. The *in vivo* release rate results correlated with those of the *in vitro* release rate.[25]

1.123.3.3. Crystallinity and Glass Transition Temperature

The crystallinity of PLGA depends on the type of its component PLA and PGA, the molar ratio of the two, and the molecular weight of the polymer. The crystallinity affects the mechanical strength, swelling behavior, and capacity to undergo hydrolysis of the polymer, which influence the biodegradation rate.[23]

Lactic acid is a chiral molecule and exists in the D- and L-forms; L-lactic acid is the naturally occurring stereoisomer. D-PLA and L-PLA are both semicrystalline polymers but the

racemic mixture of the two with less than 85% PGA is amorphous.[20] L-PLA and D,L-PLA are much more commonly used than D-PLA.[22]

It has been reported that in some cases more crystalline PLGA degrades and releases drug faster than the less crystalline variety, and in some cases the opposite effect has been observed. The release rates may be affected by drug loading and drug portioning.[19] During the degradation of a semicrystalline device, the amorphous portions degrade first, so over time the crystallinity of the device increases.[26]

Because the glass transition temperature (T_g) of PLGA is above 37 °C, at physiological temperature the polymer has a rigid-chain structure and significant mechanical strength.[23] T_g increases with increasing molecular weight and increasing lactide content of the polymer. As water penetrates a PLGA device, the T_g decreases, which increases chain mobility and drug release.[20]

1.123.3.4. Heterogeneous Degradation

Though initially thought otherwise, careful study by several groups has shown that PLGA undergoes a heterogeneous degradation. By hydrolysis, PLGA ester bonds are broken throughout an initially homogenous macro- or microscale bulk device. A small amount of monomer is lost into solution from the outside of the device, but the monomers in the interior are unable to diffuse away, become trapped, and begin to accumulate. The carboxylic acid end groups of the degradation products lower the pH inside the device and catalyze further degradation in the interior. The device develops two speeds of degradation: a fast-hydrolyzing interior and a slow-hydrolyzing exterior that acts as a one-way membrane to allow water to penetrate the device while keeping the degradation products in the interior from escaping into solution. Vert *et al.*, speaking of macroscale PLGA devices, propose that the outer section finally becomes thin enough that it degrades and releases the degradation products from the interior, followed by slow degradation of the whole device. Park *et al.*, speaking of PLGA microparticles, propose that the osmotic pressure increases inside the microparticles due to the reduced pH until the capsule bursts.[24,27]

1.123.3.5. Degradation and Length Scale

The size of the PLGA device itself impacts the degradation rate of the polymer. Two studies by Lee *et al.* and Dunne *et al.* investigated the release mechanism of model drugs from PLGA nano- and microparticles. Both determined that diffusion plays the dominant role and the length scale influences the rate, at least until mass loss changes the porosity of the particles.

Lee *et al.* studied the *in vitro* cyclosporin A release rate of three particle size regimes ('nanoparticles,' 'small microparticles,' and 'large microparticles') made of PLA, PLGA 50:50, and PLGA 85:15. The authors found that the release mechanism was predominantly by diffusion over matrix erosion and that release occurred more quickly with smaller particles. They postulated that the faster release was due to the larger surface area to volume ratio and the smaller diffusion length of the nanoparticles.[28]

Dunne *et al.* studied *in vitro* the degradation of PLGA 50:50 nanoparticles and microparticles and found that the molecular weight of the larger particles decreased faster than that of the smaller particles (**Figure 3**). While molecular weight starts to decrease immediately, no mass loss is observed for some time, indicating that the degradation products must diffuse to the surface to escape, and that process is slower for larger particles. These trapped degradation products will begin to catalyze the remaining hydrolytic reactions to speed the PLGA degradation. Once mass loss begins, the particles become so porous that the differences due to length scale become negligible and the rate of degradation is similar among all of them.[29]

Another study considered how PVA may affect drug release rates for different sized particles. Panyam *et al.* found that for

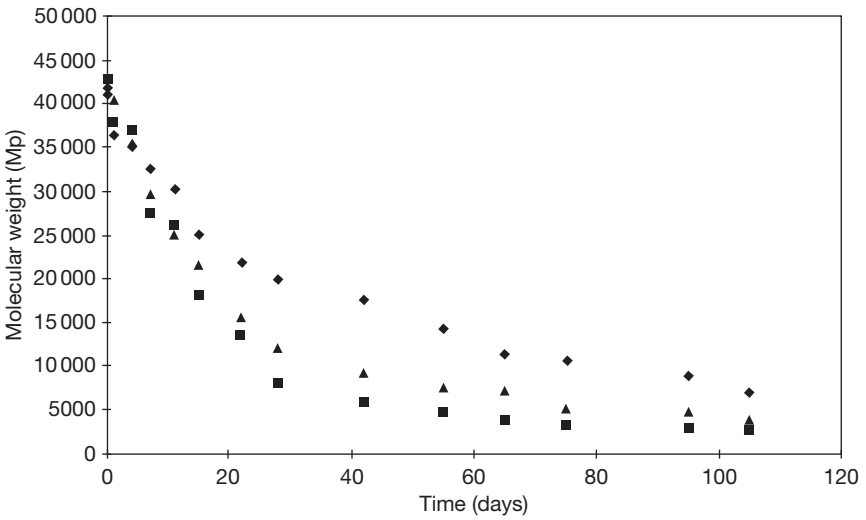

Figure 3 The molecular weight degradation profiles of several PLGA microparticles over time. Average diameters are 530 nm for solid diamonds, 6.87 μm for solid triangles, and 22.5 μm for solid squares. Reproduced from Dunne, M.; Corrigan, O. I.; Ramtoola, Z. *Biomaterials* **2000**, *21*, 1659–1668, with permission from Elsevier.

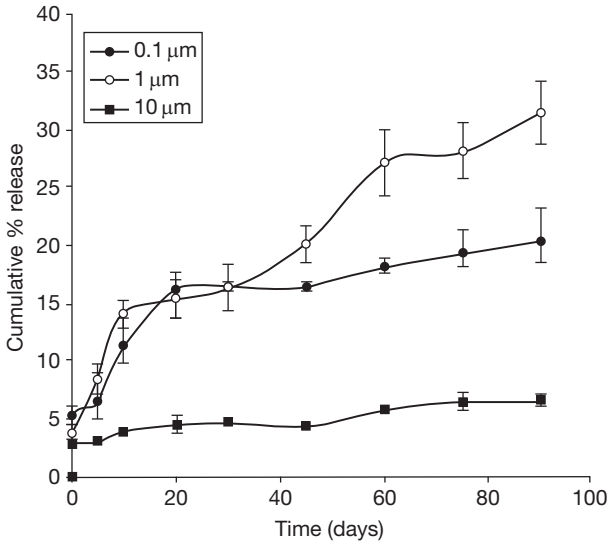

Figure 4 The cumulative BSA release from PLGA micro- and nanoparticles. Reproduced from Panyam, J.; Dali, M. A.; Sahoo, S. K.; *et al. J. Control. Release* **2003**, *92*, 173–187, with permission from Elsevier.

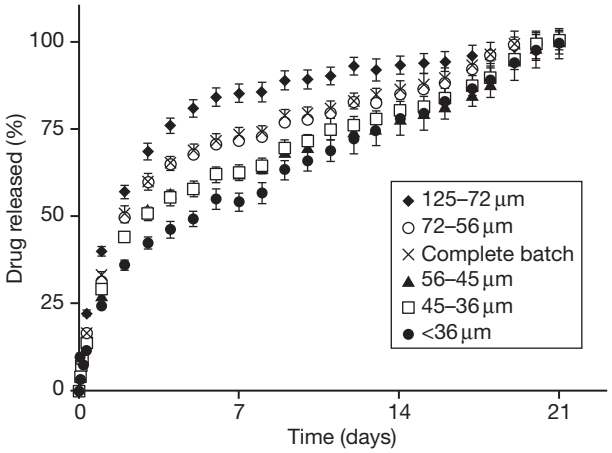

Figure 5 Percentage of drug released from PLGA microparticles of various size ranges. Reproduced from Siepmann, J.; Faisant, N.; Akiki, J.; Richard, J.; Benoit, J. P. *J. Control. Release* **2004**, *96*, 123–134, with permission from Elsevier.

120 kDa 50:50 PLGA, particles in the size range of 1 μm released bovine serum albumin (BSA) the fastest, followed by 100 nm particles, followed by 10 μm particles (Figure 4). Degradation for particles in all size ranges occurred in two distinct steps: a rapid degradation in the first 20–30 days and then a slower degradation over 60–70 days. The first stage of degradation involves fast molecular weight loss and autocatalytic acceleration of the degradation due to the slow escape of the degradation products. The second phase occurs when the particles have become more porous so that the degradation products can escape more easily. Degradation occurred fastest for the nanoparticles but there was no significant difference between the rates for the microparticles.[30]

The authors believe that PVA might be confounding the more straightforward relationship between drug release and particle size found by other researchers. The 100 nm particles had more PVA associated with them than did the larger particles. The authors hypothesize that, during the initial degradation phase, the relatively high amount of PVA on the 100 nm particles formed a barrier to outward diffusion of the degradation products, leading to faster degradation. In the second phase of degradation, the PVA had been mostly lost so it did not play a significant role.[30]

Siepmann *et al.* came to a conclusion opposite to those of Lee *et al.* and Dunne *et al.*, arguing that the drug release rate increased with the particle diameter. Microspheres were manufactured with 104 kDa 50:50 PLGA by the double emulsion solvent evaporation method and loaded with 5-fluorouracil. The microspheres were grouped into five size ranges between <36 and 125 μm for analysis with a mathematical model that took into account both diffusion and polymer degradation. The authors found that drug release rate increased with particle diameter and that there was no significant contribution from the polymer degradation due to trapped degradation products (Figure 5). Instead, they concluded for their system that the increased rate for larger microspheres was due to higher initial drug loading, which after leaching out would leave the larger microspheres more porous than the smaller microspheres.[31]

Berkland *et al.* went a step further to consider how the type of drug loaded into the PLGA particles might affect drug loading and therefore release. The authors made monodispersed, drug-loaded microparticles in a range of sizes to investigate the effect of particle diameter on drug release and polymer degradation. They used 15 kDa 50:50 PLGA to create microspheres with diameters 10, 20, 40, 50, 65, and 100 nm encapsulating rhodamine, and microparticles with diameters 10, 50, and 100 nm encapsulating prioxicam. Small microspheres rapidly released the drug while larger microspheres followed a sigmoidal drug release profile, and the type of drug loaded had an effect on the release profile. Rhodamine-loaded particles lost polymer molecular weight faster than piroxicam-loaded particles. Rhodamine is much more soluble in water than prioxicam at neutral pH, which likely facilitates water penetration into the microsphere for the rhodamine-loaded microparticles. Increasing rhodamine loading in microspheres sped up degradation, while increasing prioxicam loading decreased the degradation rate. Through SEM (scanning electron microscopy), the authors observed that in larger microparticles rhodamine preferentially distributes uniformly at the surface of the microparticles while piroxicam partitions to the interior of the particle and forms large crystals. In the smaller particles, the drug distributions were more uniform. Larger particles, particularly rhodamine-loaded particles, had faster degradation rates, likely due to trapping degradation particles within the matrix. Smaller microparticles had higher drug encapsulation efficiency and, as the diameter increased, the differences between rhodamine and piroxicam distributions became more evident. The authors concluded that this was due to the differences in polymer phase-inversion rate between the two drugs.[32]

It is apparent that there is a complex relationship between PLGA particle length scale and degradation and drug release. Most papers indirectly evaluate PLGA degradation by measuring drug release rates, which can be dominated by diffusion

instead of matrix erosion. The drug loading, drug type, and manufacturing parameters affect how the polymer matrix erodes.

1.123.3.6. Environmental Factors Affecting Degradation

Alexis reports, based on *in vitro* tests in the literature, that extreme pH environments can accelerate the degradation of PLGA. The ester bonds can be cleaved by acid- or base-catalyzed reactions.[19]

Dunne *et al.* charted the effect of temperature on the molecular weight of PLGA 50:50 for microspheres incubated *in vitro*. There was no observed loss of molecular weight or shape of the particles over 175 days for particles incubated at 5 °C. For microspheres incubated at 25, 37, and 45 °C, however, there was increasing molecular weight loss with increasing temperature, according to the Arrhenius equation (**Figure 6**).[29]

1.123.4. Biocompatibility of PLGA

The monomeric products of PLGA degradation are lactic acid and glycolic acid. Lactic acid is metabolized by the body and is expired as CO_2 and H_2O. Glycolic acid is excreted through the kidneys or metabolized as CO_2 and H_2O.[23] Because these monomeric products are naturally handled by the body, the biocompatibility of PLGA is very good, and this property has contributed to it becoming such a popular choice of polymer.

1.123.4.1. *In Vivo* Biocompatibility of Implants

Kou *et al.* examined the biocompatibility of PLGA implants in the rat brain for use in a future drug delivery application. They implanted 50:50 PLGA rods (no loaded drug) 1 cm long with diameter 300 μm into the right lateral ventricles of 24 rats. The rats were sacrificed on days 3, 7, 14, and 28 for histological analysis; direct comparison was made to the contralateral side of each animal's brain. The authors observed that the implants were well tolerated and that PLGA was a suitable material for brain implants. On days 3 and 7, the brain showed signs of a reaction typical after a foreign body invasion – mild gliosis and moderate inflammation with mineralized deposit. At day 14, the authors observed mild gliosis, mineralized debris attributed to bone fragments from the implantation, and minimal early neuronal degeneration. At day 28, the gliosis and inflammation were greatly reduced and there was no sign of neuronal degeneration, and the polymer was nearly completely eroded. The authors classified PLGA to be somewhere between 'nonreactive' and 'reactive' on the scale proposed by Stensaas *et al.*, similar to platinum and Teflon.[33]

1.123.4.2. *In Vivo* Biocompatibility of Microspheres

Visscher *et al.* completed a detailed study of the biocompatibility of 15.5 kDa 50:50 PLGA microspheres (average diameter 30 μm) injected intramuscularly into Sprague–Dawley rats. Tissues were examined using light microscopy, transmission electron microscopy (TEM), and SEM. On days 1 and 4 after injection, a slight inflammatory response was observed and the microspheres were thinly walled off. By day 12, fibroblasts, macrophages, and foreign body giant cells were present. After 35 days, the outer part of the microspheres appeared intact but the inner part had started eroding, and by day 42 the outer shells had eroded as well. By day 63, only fragments of the microspheres remained and the inflammatory response was almost completely resolved. The tissue response observed was consistent with previous observations of foreign bodies in muscle tissue and was considered minimal.[34]

1.123.4.3. *In Vivo* Biocompatibility of Nanoparticles

Kumar and colleagues studied the *in vivo* biocompatibility of estradiol-loaded PLGA nanoparticles in rats. PLGA nanoparticles were made using the solvent evaporation method from low- and high-molecular-weight PLGA with lactide-to-glycolide ratios of 50:50 and 65:35. The authors carried out histopathological analysis for the presence of inflammation of the liver, spleen, duodenum, jejunum, and ileum of the rats and compared them with untreated controls. In the liver, the

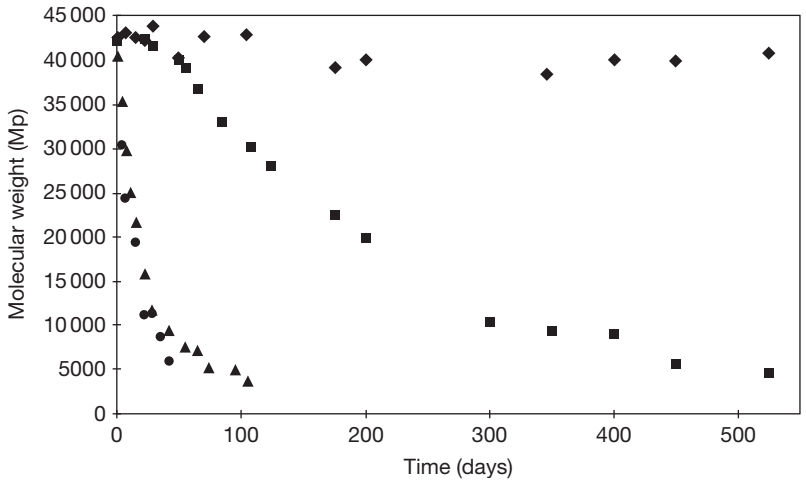

Figure 6 The molecular weight decrease of PLGA when incubated at various temperatures. Diamonds are 5 °C, squares are 25 °C, triangles are 37 °C, and circles are 45 °C. Reproduced from Dunne, M.; Corrigan, O. I.; Ramtoola, Z. *Biomaterials* **2000**, *21*, 1659–1668, with permission from Elsevier.

authors found no difference in the number, arrangement, and appearance of Kupffer's cells, hepatocytes, and sinusoids. The spleens of treated rats were no different from those of untreated controls in the lymphoid tissue mass, sinusoids, and number and appearance of red blood cells (RBCs). The treated animals' intestines showed no difference in the number or distribution of the lymphocytes in the lamina propria region of the intestinal mucosal layer, and the authors observed no evidence of inflammation in the mucosa, submucosa, and muscularis. The authors found no significant increase in white blood cell count during the study for the low-molecular-weight 50:50 PLGA (not reported for other PLGA formulations). It was concluded that the nanoparticles showed good biocompatibility and would be appropriate as an oral drug delivery system for estradiol.[35,36]

1.123.4.4. Bioavailability: Damage to Encapsulated Payload

The degradation of PLGA and particularly the drop in pH in the center of microspheres due to the presence of degradation products can damage the encapsulated payload. The drop in pH in the center of PLGA microspheres was studied by Fu *et al.* using pH-sensitive fluorescent dyes. The authors used a double emulsion technique with 25 kDa 50:50 PLGA to create dye-loaded microspheres of varying diameters. They used the emission ratio of carboxyl SNARF-1 to C1-NERF, both conjugated to dextran, to determine the pH inside the microspheres in the range of 1.5–3.5. The study was unique in that the distribution of the pH within the microspheres could be assessed, and not just the average. Pockets of extreme pH within a microsphere could damage encapsulated drugs even if the average pH would not. Microspheres were incubated in phosphate-buffered saline (PBS) for 15 days and imaged periodically. The pH inside the microsphere dropped over time, reaching 1.5 in the center of the microspheres, and there was a gradient of pH along the radius of the microsphere, with the lowest pH in the center and the higher pH near the outer edge. The diameter of the microspheres affected the pH gradient within the microspheres; the smaller diameter microspheres had smaller pockets of low pH. This is likely because clearance of the products of degradation from the microsphere interior is faster for smaller microparticles. (**Figure 7**).[37]

The low-pH interior of the microspheres should be taken into account when designing a delivery vehicle for proteins or nucleic acids that may be sensitive to low-pH environments, either by a different choice of agent to be delivered or by encapsulating additional compounds that can buffer the interior. It is possible that certain encapsulated proteins could buffer the interior of the microsphere so that the pH is partially neutralized.[37]

1.123.5. Applications of PLGA Across Length Scales

PLGA has been used in many different devices and therapies from nano- through macro-length scales. In this section, we highlight certain applications in each of the length regimes, from nanoparticles to tissue engineering scaffolds, focusing on the degradation kinetics of the applications.

1.123.5.1. Nanoscale Particles

PLGA nanoparticles have been widely applied and are being used in several clinical trials and products on the market. They are typically created by the double emulsion solvent evaporation method using PVA as the emulsifier.[15] The nanoparticles are most often used for cytoplasmic delivery of drugs, proteins, and nucleic acids because of their comparatively high efficiency of uptake into cells.[10] In this section, we will look at a few examples of loading and release studies for PLGA nanoparticles.

1.123.5.1.1. Drug delivery

The detailed study by Mittal *et al.* demonstrates how the parameters of molecular weight and copolymer ratio affect particle size, loading efficiency, and release rates for estradiol. The authors used mathematical models to conclude which nanoparticles' release kinetics was dominated by diffusion of the drug out of the matrix and which was dominated by polymer degradation. The authors determined that the bioavailability of the drug was prolonged by using PLGA nanoparticles in comparison with administering the pure drug.[36]

Mittal *et al.* completed both *in vitro* and *in vivo* drug loading and release studies for estradiol delivery using PLGA nanoparticles of various molecular weights (14.5, 45, 85, 137, and 213 kDa) and copolymer ratios (50:50 with 85 kDa, 65:35 with

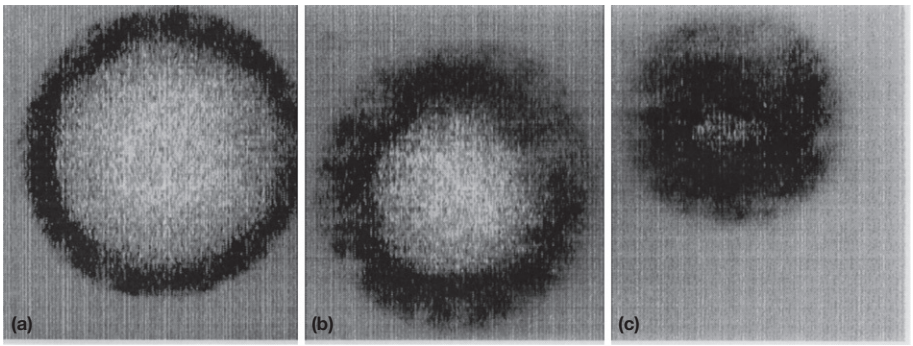

Figure 7 The pH difference in the centers of different sized microspheres. Microsphere diameters are (a) 38 μm, (b) 24 μm, and (c) 14 μm. Color scale: black pH 3.5 or higher, white pH 1.5. Reproduced from Fu, K.; Pack, D. W.; Klibanov, A. M.; Langer, R. *Pharm. Res.* **2000**, *17*, 100–106, with permission from Springer.

97 kDa, 85:15 with 87 kDa) prepared by a double emulsion solvent evaporation method. Nanoparticle diameter increased with increasing molecular weight, probably due to the polymer solution's increased viscosity that makes larger emulsified droplets for the same stirring speed, but the diameter did not change significantly for different copolymer ratios.[36]

The *in vitro* drug release studies were performed by dispersing nanoparticles in pH 7.4 phosphate buffer in dialysis membranes and suspending the bags in pH 7.4 ionic strength 10 mM phosphate buffer; the release medium was replaced completely at 6 and 12 h on the first day and then sampled every 24 h. Increasing the molecular weight significantly decreased the release rate of estradiol from the PLGA nanoparticles (**Figure 8(a)**). The 14.5 kDa PLGA released 94.7% of the estradiol within 18 days, while the 213 kDa PLGA released 26.6% of the estradiol within 19 days. The authors fitted the release profiles and concluded that the two lower molecular weight polymers released the drug at zero order and the two higher molecular weight polymers released the drug consistent with Higuchi's square root relation. This indicates that for lower molecular weight polymers, drug release is dominated by degradation, which increases with time because of autocatalysis and lowering the glass transition temperature. For higher molecular weight polymers, drug release is mediated by diffusion with little contribution from degradation.[36]

The authors also examined release rate from nanoparticles made with different copolymer ratios but all with high-molecular-weight polymers. There was a decrease in release rate with increasing glycolide content (up to 50:50), but the release was still dominated by diffusion, not degradation (**Figure 8(b)**). The authors state that the decrease in release rate is due to the increase of hydrophobicity of the polymer which has increased affinity with the drug. The authors note that they did not observe a burst release of drug from the nanoparticles as is typical for most particle formulations, perhaps because there was no unbound drug associated with the particles.[36]

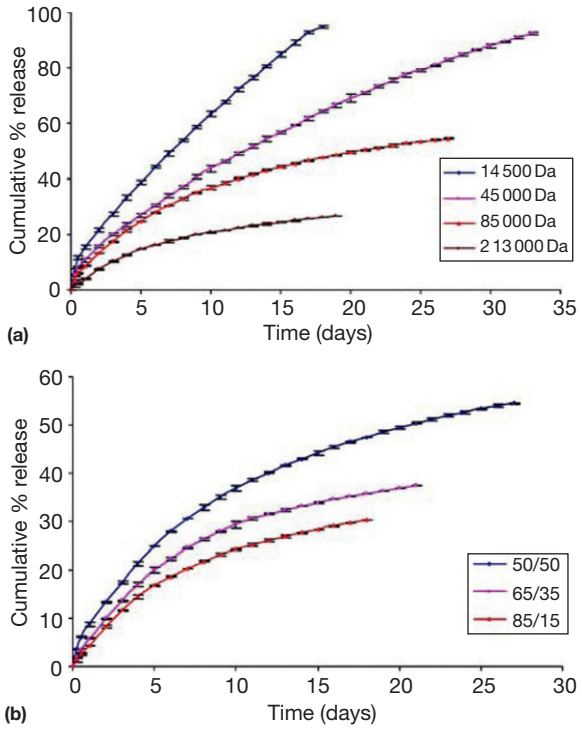

Figure 8 *In vitro* cumulative estradiol release from (a) PLGA nanoparticles with 50:50 copolymer ratio and varying molecular weights and (b) PLGA nanoparticles with average molecular weight 85–97 kDa with varying copolymer ratios. Reproduced from Mittal, G.; Sahana, D. K.; Bhardwaj, V.; Kumar, M. *J. Control. Release* **2007**, *119*, 77–85, with permission from Elsevier.

Mittal *et al.* administered estradiol-loaded nanoparticles orally to rats and included oral and intravenous delivery of pure estradiol and measured the resulting blood estradiol levels. The nanoparticles were made of 50:50 PLGA at molecular weights 14.5, 45, and 213 kDa and 65:35 PLGA at 97 kDa. The *in vivo* studies show that increasing the molecular weight of PLGA or increasing the lactide content decreases the drug release rate (**Figure 9**). Particle size was also found to strongly influence the release rate because the 65:35 97 kDa PLGA (diameter 126 nm) showed a much more sustained release than the 50:50 213 kDa PLGA (diameter 155 nm). The studies show improved bioavailability of estradiol loaded into nanoparticles versus delivered as pure drug.[36]

1.123.5.1.2. Gene delivery

Kang *et al.* compared the transfection, cytotoxicity, and efficacy *in vitro* and *in vivo* of DNA-loaded PLGA nanoparticles, DNA-loaded polyethyleneimine (PEI) nanoparticles, and naked DNA delivering the gene for the vascular endothelial growth factor (VEGF). PLGA nanoparticles were found to sustain VEGF transfection levels better than naked VEGF DNA and DNA-loaded PEI nanoparticles. VEGF will promote vascular growth in the mouse ischemic limb model.[38] Biocompatibility was tested *in vivo* with TUNEL (Terminal Deoxynucleotidyl Transferase Mediated dUTP Nick End Labeling) staining for apoptosis of skeletal muscle tissue in normal mice one day after injection of naked VEGF pDNA, PEI nanoparticles containing VEGF pDNA, and PLGA nanoparticles containing VEGF pDNA. The apoptosis level in tissue transplanted with PLGA nanoparticles was significantly less than for tissue injected with PEI nanoparticles. The naked VEGF pDNA produced the highest transfection levels six days after administration, but the PLGA nanoparticles with VEGF pDNA produced the highest levels 12 days after administration, and the VEGF level in the PLGA group increased with time while all other groups' VEGF levels decreased.[38]

The authors used the mouse ischemic limb model to determine the therapeutic potential of each delivery system, measuring neovascularization and capillary density (**Figure 10**). PLGA/VEGF pDNA nanoparticles produced the most extensive neovasuclarization, highest capillary density, and highest growing capillary density of the three groups. This is because the PLGA nanoparticles were able to sustain the VEGF pDNA delivery and were less cytotoxic in comparison with PEI.[38]

Prabha and Labhasetwar studied how the PLGA and PVA formulation parameters in a double emulsion solvent evaporation method could influence DNA delivery to human breast carcinoma and human prostate cancer cells. PVA was included in the study because it had been previously found that the hydrophobic segment of PVA anchors into the polymer matrix

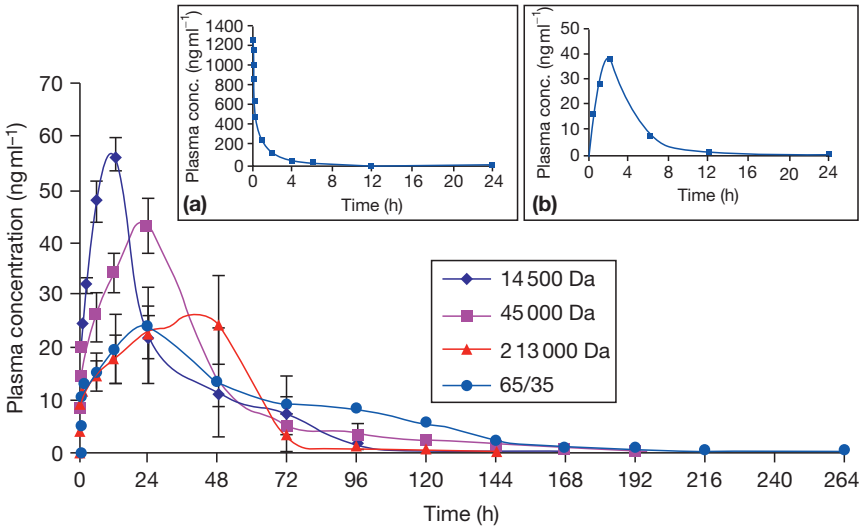

Figure 9 Blood plasma concentration following administration of PLGA nanoparticles of varying molecular weights for 50:50 PLGA as well as molecular weight 65:35 PLGA 97 kDa. Inset is plasma concentration of pure estradiol administered (a) intravenously and (b) orally. Reproduced from Mittal, G.; Sahana, D. K.; Bhardwaj, V.; Kumar, M. *J. Control. Release* **2007**, *119*, 77–85, with permission from Elsevier.

of the nanoparticle and remains associated with the surface. PLGA molecular weight was found to affect particle size; nanoparticles made with higher molecular weight PLGA (143 kDa) were smaller and more uniform in size than those made with lower molecular weight PLGA (12 and 53 kDa). The efficiency of encapsulation, the total amount of DNA released, and the transfection levels were also higher for higher molecular weight PLGA in both cell types.[39]

The authors also compared PLA to 75:25 and 50:50 PLGA (all 53 kDa) and found that DNA release and transfection were highest for 75:25 PLGA. PVA concentration, molecular weight, and the degree of hydrolysis were also studied for their effect on gene transfection. DNA loading was higher for nanoparticles made with 2 and 5% PVA than for those made with 0.5% PVA. The highest gene transfection levels were observed for 2% PVA, and 0.5% PVA had higher transfection than 5% PVA despite lower DNA loading. The authors propose that a higher amount of surface-associated PVA could shield the surface charge reversal necessary for nanoparticles to escape the acidic endolysosomes, based on previous studies and the observation that there are more nanoparticles in the cytoplasmic fraction formed with lower concentrations of PVA than those formed with higher concentrations of PVA. With increased PVA hydrolyzation (89 vs. 80%), DNA loading and release increased, surface-associated PVA decreased, and transfection increased. Nanoparticles made with lower molecular weight PVA were smaller and had higher DNA loading, but had lower transfection than those made with higher molecular weight PVA. Transfection was greater from nanoparticles with higher molecular weight PVA and higher hydrolyzation levels because those nanoparticles had less surface-associated PVA. All of these parameters were studied *in vitro*, but the authors believe that these parameters will have a similar influence over nanoparticles applied *in vivo*.[39] This study makes a valuable contribution to the body of knowledge on PLGA formulation parameters, as PVA is such a popular emulsifier in the creation of micro- and nanoparticles.

1.123.5.2. Nanoscale Fibers

Nanofibers are attractive candidates as scaffold components for tissue-engineering applications because of their porous nature, which facilitates mass transport, high surface area for attachment, and possibility of providing topographical cues. PLGA for these reasons has been used extensively in fiber fabrication. The degradation rate of fibers in these scaffolds needs to be optimized so that cells produce their own extracellular matrix (ECM) at approximately the same rate as scaffold degradation. Shin *et al.* studied how the copolymer ratio in PLGA nanofibers affected degradation time and the suitability of PLGA nanofibers as a scaffold for tissue-engineered cartilage (Figure 11). The PLGA tested had a lactide-to-glycolide ratio of 50:50, 75:25, and a 1:1 blend of the two. The authors made electrospun fibers that averaged 550 ± 150 nm for the 75:25 PLGA and with 80.68% porosity in the scaffolds.

The Young's modulus of the scaffolds was 66 MPa for 50:50 PLGA and 111 MPa for 75:25 with the blend intermediates; the ultimate tensile stress had a similar pattern and ranged from 1.8 to 4.7 MPa. The mechanical properties were greater for 30% PLGA solution than 25% PLGA solution and for aligned over nonaligned fibers architecture. By comparing their work with work from another group that measured the mechanical properties of 85:15 PLGA, the authors estimated that a polymer with a lactide-to-glycolide ratio of between 85:15 and 75:25 would be optimal to mimic the mechanical properties of cartilage. *In vitro* fiber degradation was also more rapid with higher glycolide content, as measured by mass, molecular weight, and pH changes, likely because of the greater hydrophilic character and lower crystallization rate of the polymer that would facilitate water absorption and diffusion.

The architecture of the scaffold also affects the degradation time. Shin *et al.* cited a study of 50:50 PLGA block-like scaffolds with similar molecular weight that degraded more slowly than the nanofiber scaffolds in their study. While a block-like scaffold would experience autocatalytic acceleration of

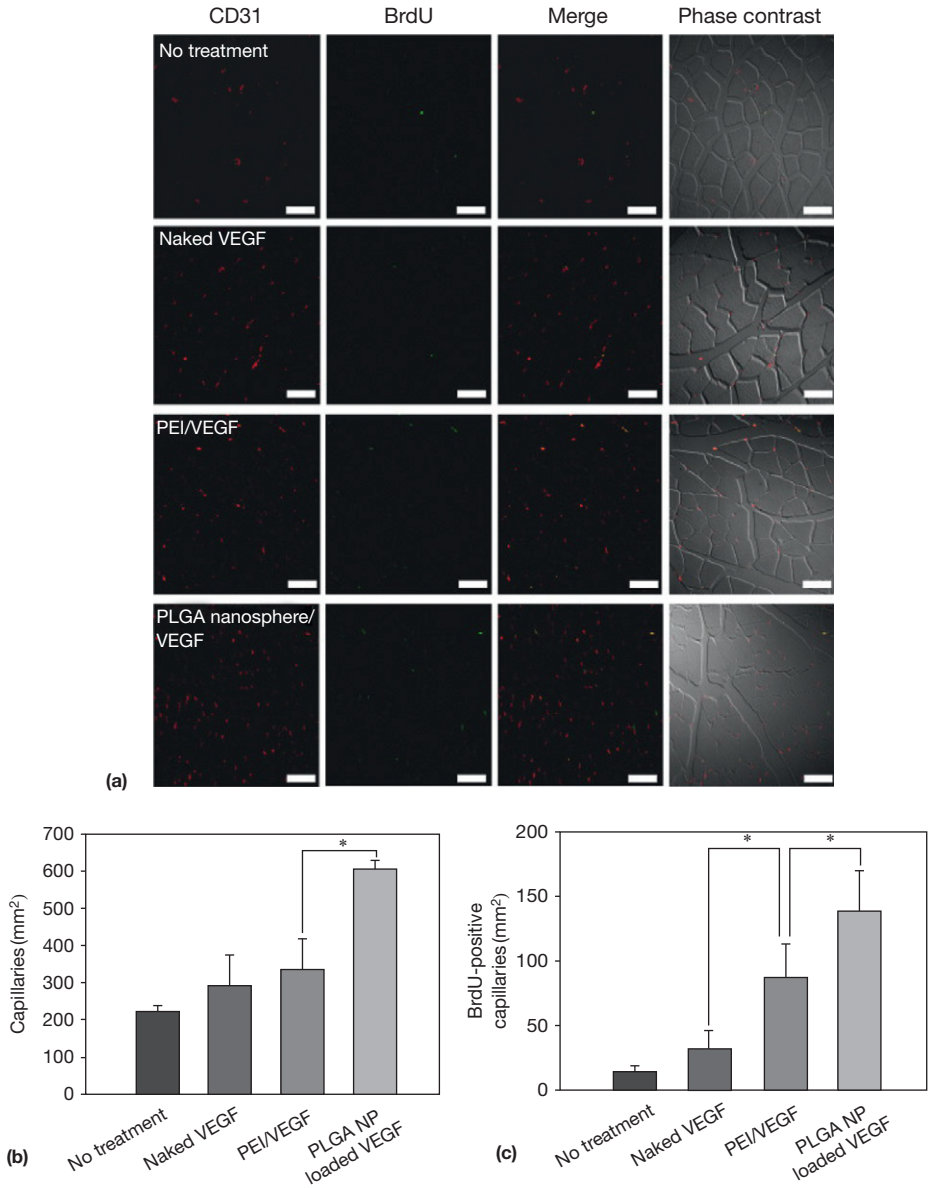

Figure 10 (a) Immunofluorescent staining of CD31 and BrdU of mouse ischemic limb model for PLGA nanoparticles delivering VEGF and controls. Scale bars are 50 μm. (b) Capillary density and (c) BrdU-positive capillary density in mouse ischemic limb model. BrdU-positive cells signify growing capillaries $*p < 0.05$. Reproduced from Kang, S. W.; Lim, H. W.; Seo, S. W.; Jeon, O.; Lee, M.; Kim, B. S. *Biomaterials* **2008**, *29*, 1109–1117, with permission from Elsevier.

degradation due to the lack of clearance of the degradation products, nanofibers are more susceptible to hydrolysis because of the high surface area to volume ratio of the fibers and scaffold. The PLGA nanofibers also had good biocompatibility with chondrocytes as measured by cell proliferation and morphology despite concerns about the solvents used in the electrospinning process.[40]

1.123.5.3. Microscale Particles

Microparticles are well sized to be taken up by antigen-presenting cells and are therefore ideal for delivering DNA vaccines.[13] Also discussed in this section are microparticles used for a contrast agent in ultrasound and to construct macroscale scaffolds for tissue engineering. Most microparticles are made by the emulsion solvent evaporation process or spray-drying.

1.123.5.3.1. Vaccines

In developing a single-administration human immunodeficiency virus (HIV) vaccine using the gp120 subunit, Cleland *et al.* capitalize on the presence of an initial burst release from their PLGA microspheres and design their delivery vehicle to produce a second delayed burst instead of a continuous release. Ideal for vaccination situations where a follow-up visit to a physician may not be possible, the initial burst release

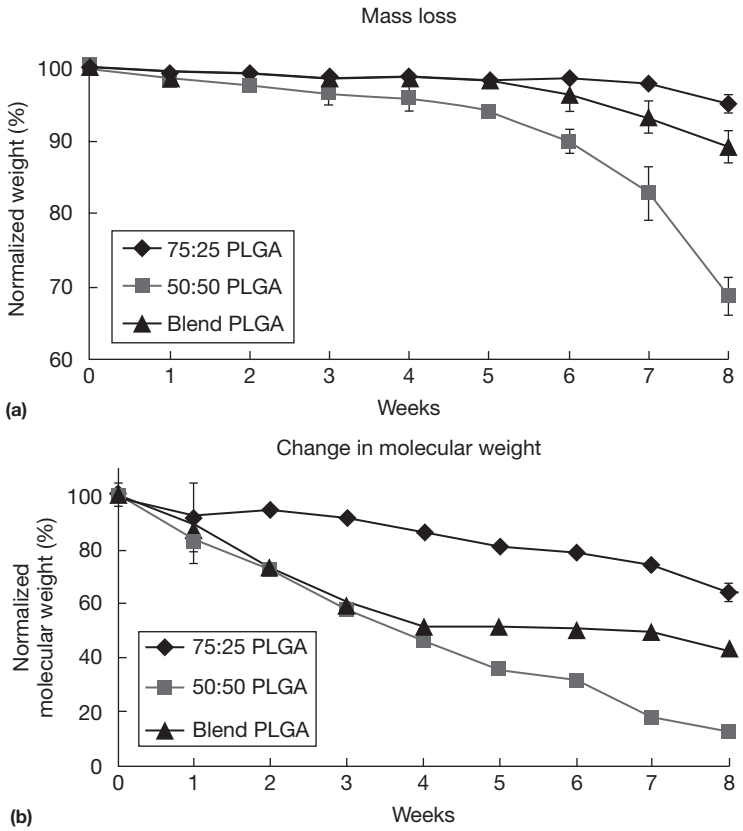

Figure 11 The degradation of nanoscale PLGA fibers in terms of (a) weight and (b) molecular weight. Reproduced from Shin, H. J.; Lee, C. H.; Cho, I. H.; *et al. J. Biomater. Sci. Polym. Ed.* **2006**, *17*, 103–119, with permission from Brill.

of gp120 serves as the priming vaccination and the second release serves as the booster. This is a more effective immunization strategy than a continuous release of gp120. The authors formed microspheres using a double emulsion method with low aqueous volume in comparison with the mass of polymer so that the pore structure in the microsphere would be discontinuous. This made for very low rates of release of gp120 until the matrix was nearly fully degraded, at which point the second burst release of gp120 occurred. The authors tuned the polymer properties to dictate when the second burst release occurred (1, 2, 3, or 4 months after the initial burst). To decrease the rate of degradation, the authors changed the lactide-to-glycolide ratio away from 50:50, increased the molecular weight of the polymer, and increased the degree of crystallinity.[41]

Jaganathan *et al.* developed and tested *in vitro* and *in vivo* a vaccine against hepatitis B virus (HBV) using PLGA microspheres modified with the natural biodegradable polymer chitosan. Vaccines available on the market at the time of publication were successful in generating humoral immune responses, but not the necessary cellular immune response. Mucosal immunization and the generation of secretory IgA were determined to be the most effective first line of defense as most HBV infections occur through the mucus membranes, so the authors studied the effectiveness of PLGA microparticles as a nasal vaccine. W/O/W microparticles 1–10 μm in diameter and with 80% loading efficiency were created with recombinant hepatitis B surface protein (HBsAg) in the inner aqueous phase, 50:50 PLGA (MW 30–70 kDa) in the oil phase, and chitosan and PVA in the outer aqueous phase. Chitosan was added to the surface of the PLGA microspheres to promote mucoadhesion. The particles were kept below 10 μm in diameter to more effectively target the antigen-presenting cells in the mucous membranes. Nasal clearance time of the microparticles in rabbits increased from 30 to 180 min. *In vitro* testing showed that $\geq$90% of loaded HBsAg had been released from the microspheres by day 42 and that the stability of the HBsAg in the PLGA microspheres was similar to the control, which was alum-absorbed HBsAg. The authors studied the antibody response in mice after intranasal administration of the modified PLGA microspheres and controls. They found that modified PLGA microspheres delivering HBsAg induced a mucosal immune response more effectively than unmodified PLGA microspheres and a control alum vaccine, particularly when a booster dose of the microspheres was administered.[42]

1.123.5.3.2. Contrast agent for ultrasound

AI-700 is a gas-filled PLGA microparticle technology used as an ultrasound contrast agent for echocardiography and has been taken through Phase III clinical trials. The biocompatibility of PLGA made it an attractive candidate for this application. The microparticles are prepared using an emulsion and spray-drying method. Ammonium bicarbonate is in the

inner aqueous phase to give the microparticles a porous, honeycomb-like structure. The polymer layer also contains 1,2-diarachidoyl-*sn*-glycero-3-phosphocholine (DAPC), which helps to trap the gas in the microparticle following reconstitution. The AI-700 microparticles were directly compared with Optison™, a commercially available contrast agent for ultrasound. In the functional assay, the backscatter generated at 2.25 MHz from the AI-700 was stable at around 60 dB for 10 min, while the backscatter from Optison dropped to less than 40 dB in the same period. The microparticles were not destroyed even under extreme ultrasound conditions, showing them to be more stable than many currently used ultrasound contrast agents.[43]

1.123.5.3.3. Tissue engineering

Jaklenec *et al.* fused PLGA microspheres to create a porous scaffold appropriate for cell seeding and flexible for many different tissue-engineering applications. The microspheres were less than 20 μm in diameter and had up to 4.3% BSA loading to add a drug delivery function to the scaffold. To make the scaffold, microspheres were added to a disk mold 6 mm in diameter and 1–2 mm high and placed in a chamber with dichloromethane. The dichloromethane diffused into the microspheres and lowered the T_g of the microspheres, softening the polymers and allowing them to fuse. The scaffolds were removed to air for 10 min, where the T_g rose and the scaffold hardened, and then taken out of the mold and dried under vacuum. During the fusion experiments, the authors found that higher BSA content and larger microsphere mass required increased time for fusion. The scaffolds and control loose microspheres were subjected to an *in vitro* BSA release study over 20 days. Two scaffolds, fused for 10 and 10.5 min, were found to have statistically identical release rates. The loose microspheres released BSA faster in the first week of incubation, but overall they released the same amount of BSA as the scaffolds. The authors proposed that the scaffolds have a slower BSA release rate because of their lower surface area in comparison with the loose microspheres.

The authors created two sizes of microspheres averaging 11 and 113 μm, which resulted in scaffolds with pore sizes of 20 and 200 μm (Figure 12). The scaffolds with the larger pore sizes were used in a cell attachment study. The authors were able to seed fibroblasts into their prewet scaffolds, and the cells attached to the surface and in the pores of the scaffold, demonstrating biocompatibility of their scaffolds.[44]

1.123.5.4. Macroscale Hydrogel

Thermosensitive hydrogels of poly(ethylene glycol) (PEG)–PLGA–PEG block copolymers have been developed and used for *in vivo* drug delivery applications. Jeong *et al.* characterized the sol–gel transition ranges of PEG–PLGA–PEG with molecular weights from 3.5 to 4.5 kDa and various PLGA lengths. The PLGA polymer block forms the hydrophobic core of a micelle, and the PEG block forms the corona. At room temperature, the solution is free-flowing, but with increasing temperature the PEG and PLGA partially phase-mix and the micelles become close-packed and overlapping, and at body temperature the polymer is a gel.[45]

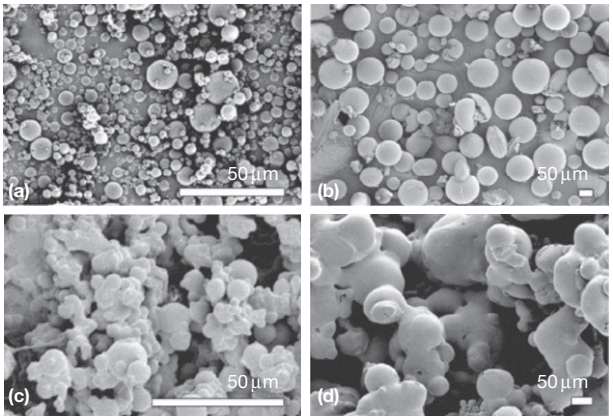

Figure 12 SEM images of (a and b) loose microspheres and (c and d) scaffolds made from (a and c) small and (b and d) large microspheres. Scale bars are 50 μm. Reproduced from Jaklenec, A.; Wan, E.; Murray, M. E.; Mathiowitz, E. *Biomaterials* **2008**, *29*, 185–192, with permission from Elsevier.

Jeong *et al.* tracked the *in vitro* release rates of ketoprofen and spironolactone from two PEG–PLGA–PEG copolymers, one with block lengths 550–2810–550 and molecular weight 4.27 kDa and the other with block lengths 550–2320–550 and molecular weight 3.56 kDa. Ketoprofen is more hydrophilic and spironolactone is more hydrophobic, so under the micelle model they should partition differently within the gel and exhibit different release profiles. Ketoprofen's release was almost complete after about 5 days and obeyed the Higuchi equation, showing it was diffusion-dominated. The authors concluded that ketoprofen partitions more in the PEG domain of the gel so that the continuous repartitioning of the drug between the polymer phases results in easier diffusion out of the gel. Spironolactone's drug release profile was S-shaped, indicating two mechanisms of release. The authors concluded that spironolactone partitions more in the hydrophobic PLGA core. The initial diffusion release is probably from the drug partitioned in the hydrophilic regions, and the later drug release is due to degradation of the PLGA. Increasing the hydrophobic PLGA domain lowers the water content in the gel, slowing PLGA degradation and spironolactone release.[46] Changing the lactide-to-glycolide ratio greatly changed drug release when controlled by degradation and diffusion but had little influence on the rate of diffusion-controlled release.[47]

Li *et al.* delivered pDNA from a thermosensitive 12.8 kDa PEG–PLGA–PEG copolymer. Incubating for 48 h with HEK293 cells showed that the hydrogel persisted for about 30 days and produced no change in cell morphology and 98% cell viability, with pDNA release occurring over about 15 days. The authors applied the luciferase pDNA-loaded hydrogel to a skin wound on mice, where it gelled in about 45 min. Biopsied tissue showed that luciferase expression peaked after about 24 h and was at 6.4% of the peak at 72 h.[48]

PLGA–PEG–PLGA thermosensitive hydrogels have been commercialized under the name ReGel®. *In vivo* paclitaxel release from ReGel was diffusion-controlled for about 2 weeks and then degradation- and diffusion-controlled for about 5 weeks. Subcutaneous injection of insulin in ReGel maintained insulin levels for 15 days.[47]

1.123.5.5. Macroscale Foams

Lu *et al.* studied the degradation processes of PLGA foams (diameter 13.45 mm, thickness 350–800 μm) and compared them with the degradation processes undergone by PLGA microparticles and films. Tailoring the degradation rate of these foams is crucial for tissue-engineering applications. The authors created six types of foams using the solvent-casting, particulate-leaching technique. One-half of the foams used 50:50 PLGA (MW 94.5 kDa) and the other half used 85:15 PLGA (MW 140.4 kDa), each with varying fabrication conditions such as NaCl crystal size and NaCl % weight. The degradation was studied *in vitro* and *in vivo*, where the *in vitro* system was a shaking, 37 °C PBS bath where the PBS was replaced once per week and the *in vivo* system was implantation into the mesentery of rats.

The *in vitro* and *in vivo* results for the PLGA 85:15 foams were similar; the weight remained relatively constant over 20 weeks and there was little change in the porosity, median pore diameter, and surface-to-volume ratio but the molecular weights decreased exponentially, with half-lives between 9.4 and 14.3 weeks. The 50:50 PLGA foams degraded faster *in vitro* than the 85:15 foams, with dramatic weight loss occurring after about 6 weeks. The pore distribution changed over time and the porosity and surface-to-volume ratio decreased and the pore size increased after about 8 weeks. Molecular weight also decreased exponentially but the half-lives were between 3.0 and 3.3 weeks *in vitro*. *In vivo* the degradation of the 50:50 PLGA foams was even faster, with half-lives of molecular weight degradation between 1.9 and 2.4 weeks. The longer degradation time of the 85:15 PLGA is consistent with previous research that showed decreased water penetration into the more hydrophobic 85:15 PLGA due to the higher lactide content. The authors determined that the shorter degradation time of the 50:50 PLGA foams *in vitro* was due to the autocatalytic acceleration of degradation inside the foams because of the accumulation of degradation products near the foams *in vivo*. The degradation times of these porous PLGA foams were similar to those previously reported for PLGA films and microparticles.[49]

1.123.6. Rationale for Development of PPEs

PPEs represent a class of biodegradable polymers having a phosphoester linkage in the backbone, which would include polyphosphates, polyphosphonates, and polyphosphites.[50] Much of the research into the basic science of these polymers has been pioneered by Penczek and his colleagues.[51–53] Here, we highlight the characteristics of PPEs that will repeatedly manifest in various biomedical applications discussed in this chapter. The pentavalency of phosphorus in the backbone of PPEs makes it possible to conjugate functional groups. Starting from the parent polyphosphite, the P–H bonds can be readily converted for conjugation of different chemical structures, including charged groups through a phosphate (P–O) or a phosphoramide (P–N) bond as side chains. These are tabulated on the basis of their applications in Table 1 (biodegradation (1-1 to 1-3), drug and gene carriers (2-1 to 2-5), and thermoresponsive PPEs (3-1 to 3-6)). The phosphorus-containing backbone confers versatility and tunability in PPE-based material design as the physicochemical and degradation properties can be adjusted by changing the backbone and the side-chain structures. Secondly, the flexible phosphoester bond in the backbone also provides the plasticizing effect to lower the glass transition temperature and improve solvent solubility and processibility of polymers with otherwise unfavorable physical and colligative properties. Thirdly, the intermediate and ultimate hydrolytic breakdown products of PPEs are innocuous, conferring PPEs excellent toxicity and biocompatibility profiles. This section will closely examine the structure–property relationships of PPEs by drawing upon data published in the last 10 years. Discussions will highlight the application of the unique characteristics of PPEs (mentioned above) over a wide range of biomedical applications.

1.123.7. Structure–Function Relationships of PPEs

1.123.7.1. Material Properties of PPE Films

Many biomedical applications involve the use of scaffold materials to provide mechanical support or to deliver therapeutic agents (drugs, cells, etc.). As different parts of the body experience different types, patterns, and ranges of mechanical stress, scaffold requirements inevitably depend on the site of application.

Dacron (poly(ethylene terephthalate), PET)) is a highly crystalline, nondegradable polymer ($T_m = 265$ °C, $T_g = 69$ °C). Introduction of the ethyl phosphate bond into the backbone not only introduces degradable characteristics but also significantly changes the bulk properties of the polymer. An initial attempt to synthesize a PPE P(BHET-EOP) by polycondensing 1,4-bis(hydroxyethyl) terephthalate (BHET) with ethyl phosphorodichloridate (EOP) at stoichiometric ratios resulted in a very viscous semisolid at room temperature ($T_g = 19$ °C, water-in-air contact angle = 8°), which was not suitable for tissue engineering. To raise the T_g and improve the mechanical properties of the polymer, a two-step polymerization scheme was applied to synthesize a series of poly(terephthalate-*co*-phosphate)s with different contents of the phosphoester component (EOP).[54] When the EOP/TC (terephthaloyl chloride) ratio is higher than 1 (i.e., 50:50), the PPEs are amorphous; no melting point (T_m) is observed in differential scanning calorimetry (DSC) analysis and the copolymers begin to soften at around 150 °C. As expected, the glass transition temperature (T_g) increases as the EOP/TC ratio decreases. Nevertheless, the T_g increment is minor until the EOP/TC ratio decreases to below 3 (i.e., 75: 25). There is a dramatic increase of T_g from P(BHET-EOP/TC, 80:20) ($T_g = 25$ °C) to P(BHET-EOP/TC, 50:50) ($T_g = 64$ °C). At the EOP/TC ratio of 1, DSC shows a melting peak at 201 °C, indicating the presence of a crystalline phase. The T_g values of a series of other P(BHET-EOP/TC) copolymers of differing EOP/TC ratios are shown in Table 2.

Introducing sterically hindered diol to the polymer backbone, by substituting ethylene glycol with 2-methylpropylene diol (MPD) or 2,2-dimethylpropylene diol (DMPD) residues, reduces its glass transition temperature (Table 2). The T_g values of the copolymers with DMPD and MPD residues are

Table 1 Structures of polyphosphoester family of degradable polymers

Structures of copolymers of polyphosphoesters as degradable polymers

1-1 LDI-based poly(phosphoester-urethanes)
Polymer composition:
PLU-1:
–[0–1–0½–4½–0½–6½]–
PLU-2:
–[0–3–0½–4½–0½–6½]–
PLU-4:
–[0–2–0½–5½–0½–6½]–
PLU-5:
–[0–2–0½–4½–0½–6½]–

[0]

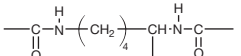

Ethyl 2,6-diisocynatohexanoate (LDI)

[1]

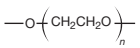

Poly(ethylene oxide)

[2]

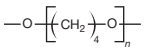

Poly(tetramethylene oxide)

[3]

Polycaprolactone

[4]

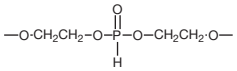

Bis(2-hydroxyethyl)phosphite

[5]

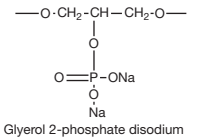

Glyerol 2-phosphate disodium

[6]

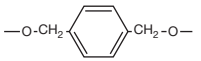

1,4-Benzenedimethanol

1-2 Poly(terephthalate-*co*-phosphate)s
Monomeric units:
BHET:
1,4-bis(2-hydroxyethyl) terephthalate
EOP:
Ethyl phosphorodichloridate
TC:
Terephthaloyl chloride
MOP:
Methyl phosphorodichloridate

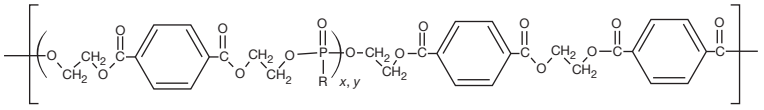

P[BHET-EOP/MOP/TC, x/y/(100-x-y)]

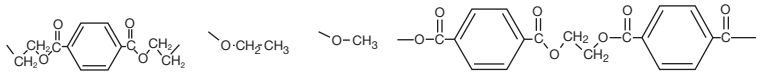

BHET EOP MOP TC

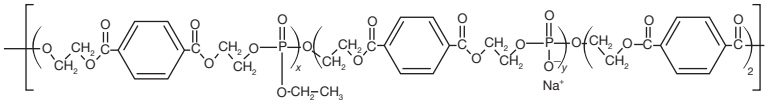

P[BHET-EOP/NaOP/TC, *x*/*y*/(100-*x*-*y*)]

1-3 PEEP–PDL

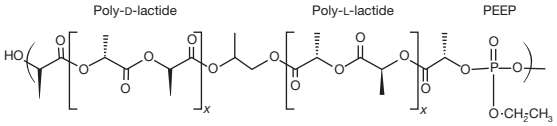

(*Continued*)

Table 1 (Continued)

Structures of amphiphilic degradable polyphosphoester-based drug carriers

2-1 $PLLA_x$–$PEEP_y$

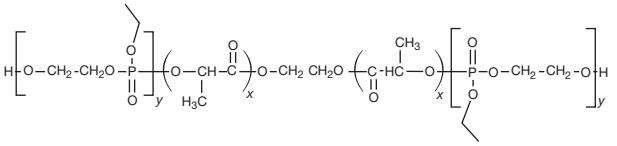

2-2 PCL_x–$PEEP_y$

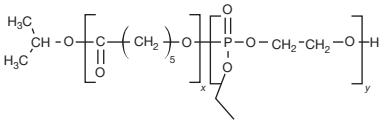

2-3 $PEEP_y$–PCL_x–$PEEP_y$

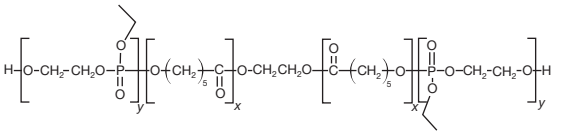

2-4 Star-shaped (ss) PCL-PEEP

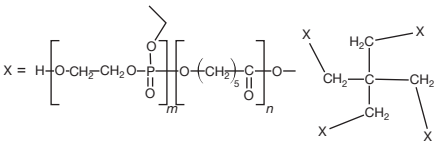

2-5 PEG-TEGP

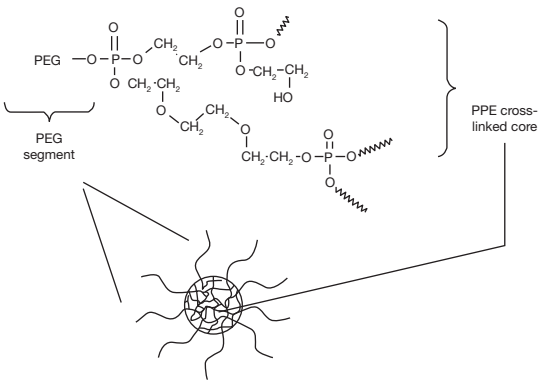

Structures of thermoresponsive degradable polyphosphoester

3-1 PEHA
$a = 0.92$
$x = 0.02$
$y = 0.06$

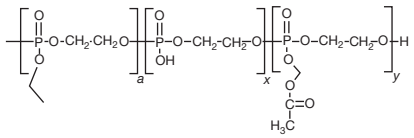

3-2 PIPP

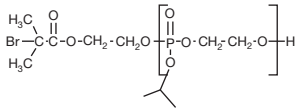

3-3 PI_xE_yP

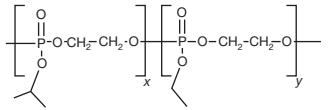

3-4 PCL_x-*b*-P(EEP_Y-*co*-MEP_Z)*
PCL_x-*b*-P(EEP_Y-*co*-PEP_Z)#

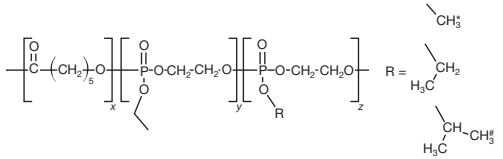

3-5 $mPEG_x$-*b*-P(EEP_Y-*co*-PEP_Z)

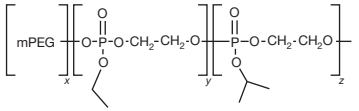

3-6 Thioctate Ester of
$mPEG_x$-*b*-P(EEP_Y-co-PEP_Z)

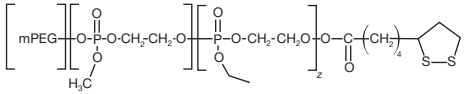

Table 2 Physical properties of P(BHET-EOP/TC) copolymers

Copolymer type	T_g	*Water-in-air contact (°)*	*Solubility*				T_g *of P(BHET-EOP/TC) with different diol backbone*			*Tensile stress @ yield (MPa)*	*Elongation @ break (%)*	*Young's modulus (MPa)*
			$CHCl_3$	*CH_2Cl_2*	*NMP*	*DMF*	*MPD*	*DMPD*	*EG*			
P(BHET-EOP/TC, 100:0)	19	8	+++	+++	++	++	11.8	14.7	19.7			
P(BHET-EOP/TC, 95:5)	21	10	+++	+++	++	++	–	–	21.9			
P(BHET-EOP/TC, 90:10)	21	ND	+++	+++	++	++	–	16.6	22.8			
P(BHET-EOP/TC, 85:15)	28	54	++	++	++	++	24.7	20.4	30.5			
P(BHET-EOP/TC, 80:20)	25	65	++	++	++	++	–	23.5	25.7	1.47	86.6	13.8
P(BHET-EOP/TC, 50:50)	64	ND	Insoluble	Insoluble	+/Δ	+/Δ	44	–	62.7			
P(BHET-EOP/MOP/TC, 60:20:20)	32	14								2.55	74.6	26.8
P(BHET-EOP/MOP/TC, 40:40:20	39	9								2.79	48.6	27.6
P(BHET-NaOP/TC, 80:20)	58 ($T_m = 180$)	ND										
P(BHET-EOP/NaOP/TC, 60:20:20)	52	ND										
P(BHET-EOP/NaOP/TC, 40:40:20)	63	ND										

+++ = readily soluble; ++ = soluble; +/Δ = soluble upon heating; MPD = 2-methylpropylene diol; DMPD = 2,2 dimethylpropylene diol; EG = ethylene diol; T_g = glass transition temperature; T_m = melting temperature.

lower than that of ethylene glycol EG residues. Results demonstrate that polymer chains with extra pendant methyl groups are not only more rigid but also more amorphous (packed less closely and orderly).

The solubility of the copolymers also decreases as the phosphate content decreases (Table 2). When the EOP/TC ratio is 1, the resulting copolymer P(BHET-EOP/TC, 50:50) becomes insoluble in chloroform. The relative hydrophobicity of the P(BHET-EOP/TC) series is also determined by measuring the water-in-air contact angle (Table 2). The contact angle decreases dramatically from 65° for P(BHET-EOP/TC, 80:20) to 8° for P(BHET-EOP/TC, 100:0). Substituting the ethoxy side chain with methoxy side chain (MOP) also markedly increases the hydrophilicity (Table 4). At the ratio of EOP/MOP/TC of 40:40:20, the contact angle decreases to a value close to that of P(BHET-EOP/TC:100:0). Furthermore, introducing negative charges to the phosphate side chains by converting the methoxy groups into sodium salt renders the polymer less soluble in chloroform and methylene chloride. The negatively charged P(BHET-ENaOP/TC)s become hydrophilic by gross observation. As expected, the methoxy group-substituted P(BHET-EOP/TC) and the negatively charged poly(terephthalate-*co*-phosphate)s have much higher T_g values than their parent polymers (Table 2). P(BHET-NaOP/TC, 80:20) has a clear, sharp melting peak at 180 °C as determined by DSC.[54] Poly(terephthalate-*co*-phosphate)s show typical tensile properties of amorphous or low-crystalline thermoplastics. At an EOP/TC ratio higher than 90:10, the film becomes weak and difficult to handle. The P(BHET-EOP/TC, 80:20) film yields at 86.6% elongation (Table 2), with a modulus of elasticity of 13.8 MPa. Substituting EOP with MOP partially (40:40 or 60:20) does not affect the film-forming property significantly, except that the film becomes more brittle and less ductile. P(BHET-EOP/MOP/TC)s have nearly 100% higher moduli of elasticity than P(BHET-EOP/TC, 80:20). In addition, fibers could be drawn from copolymer melts at 160–180 °C from all three copolymers (i.e., P(BHET-EOP/TC, 80:20), P(BHET-EOP/MOP/TC,60:20:20), and P(BHET-EOP/MOP/TC,40:40:20)).[54]

1.123.7.2. Degradation

PPEs can be degraded both enzymatically and chemically. Enzymatic degradation can be mediated by endogeneous phosphodiesterases and phosphotriesterases commonly involved in cellular metabolism.[55] Although enzymes are known to be highly specific, drug-loaded PPE coblock polymers are more rapidly degraded in the presence of phosphoesterases,[56,57] suggesting that enzymatic degradation is a valid mode of polymer degradation even when they are not endogeneous metabolic substrates. As phosphoesterases are not ubiquitous in the body, it is important from an application standpoint that degradable polymers can also be chemically broken down. Indeed, the hydrolysis of the phosphoester bond can occur,[58] and the rate of degradation increases with pH because of a higher concentration of hydroxide ions, which are strong nucleophiles.[59]

1.123.7.3. Structure–Degradation and Length Scale–Degradation Relationship

As degradation of PPEs is dependent on the presence of water, the rate of degradation can be controlled by controlling the rate of water penetration. Hydrophobic segments can be introduced into the PPE backbone in a controlled way to yield predictable degradation profiles.[54,60] These structures are shown in Table 1 (1-1 to 1-4). In the former,[60] PLU-4 contains no degradable linkage in the backbone and is expected to be stable (Figure 13). The modest weight loss is possibly caused by the cleavage of the disodium phosphate in the side chain. PLU-5 shows a mass loss because of the presence of the biodegradable BEP. PLU-2 shows a higher mass loss than PLU-5 because of the substitution of poly(tetramethylene oxide) (PTMO) with polycaprolactone (PCL) which is degradable by itself. Finally, when PTMO is replaced by a more hydrophilic poly(ethylene oxide) (PEO), an even higher mass loss is observed in PLU-1.

Similar structure-dependent degradation profile is observed in poly(terephthalate-*co*-phosphate) copolymer.[54] As mentioned in previous sections, changing the side chains of PPE can further modify its structure–function relationship. In the P(BHET-EOP/TC, 80:20) series, substituting the ethoxy with a methoxy group yields copolymers with increased hydrophilicity, which in turn accelerates the *in vitro* degradation as demonstrated in Figure 13. Furthermore, converting the methoxy group to a sodium salt dramatically increases the degradation rate. Taken together, these data demonstrate the feasibility of tuning the degradation rates of the phosphoester-based polymers by adjusting the backbone structure (e.g., EOP/TC ratio) and changing the side-chain structure (ethyl group vs. methyl group). The resultant copolymers become more hydrolytically labile as the phosphate component (EOP) is increased and as the side chains are switched from the ethoxy to the methoxy group, which allows a higher rate of water penetration.

Figure 14 shows the SEM images of the cross-sections of degrading samples of P(BHET-EOP/TC, 80:20) and P(BHET-EOP/TC, 85:15) disks immersed in 0.1 M PBS at 37 °C for 18 days. P(BHET-EOP/TC, 80:20) disks (Figure 14 left) swell much less than P(BHET-EOP/TC, 85:15) disks (Figure 14 right). The latter has a more porous and coarser texture at the edge compared to its interior, indicating a greater extent of degradation, while the texture of P(BHET-EOP/TC, 80:20) disks is still relatively uniform throughout the disks even when imaged at a higher magnification. P(BHET-EOP/TC, 80:20) degrades at a slower rate than P(BHET-EOP/TC, 85:15), reflecting the influence of the phosphoester backbone in accelerating the rate of degradation. The former shows a gradual decrease in mass over time, losing more than 20% in total mass after 18 days of incubation (75–80% mass remaining), while the latter has 57% (mass remaining) on day 18.

The length scale of degradable polymers is expected to affect the rate of degradation. Degradation profiles of PPEs in different length scales are collated in Figure 15.[61–63] Their molecular structures are shown in Table 1(1-2). As the degradation rate depends on the rate of water penetration, macro-scale constructs are expected to degrade at a lower rate due to lower surface to volume ratio. Consequently, degradation of micrometer-scale constructs takes weeks to reach 50% of their original mass, and the same takes significantly longer for macroscale constructs. However, on the nanoscale, measuring the percentage of mass remaining may not be practical because the amount of polymers applied on a nanoscale is usually very low (in micrograms) and difficult to recover. Therefore, rate of degradation on a nanoscale is usually monitored via the percentage reduction of

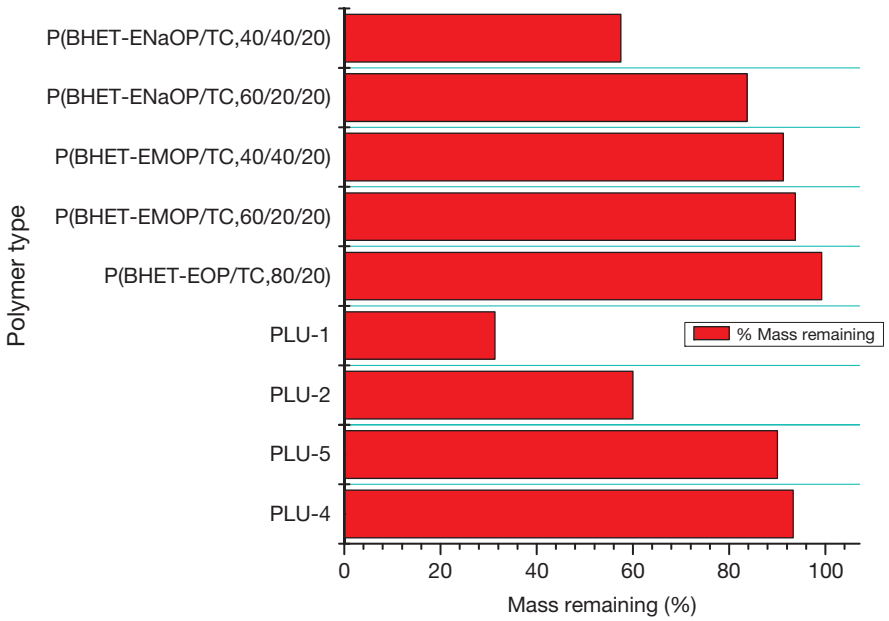

Figure 13 Structure–degradation relationship of polyphosphoesters. Replotted from Shi, F. Y.; Wang, L. F.; Tashev, E.; Leong, K. W. In *Polymeric Drugs and Drug Delivery Systems*; American Chemical Society: Washington, DC, 1991; pp 141–154; Mao, H.; Leong, K. W.; Leaf Huang, M.-C. H.; Ernst, W. *Adv. Genet.* **2005**, *53*, 275–306.

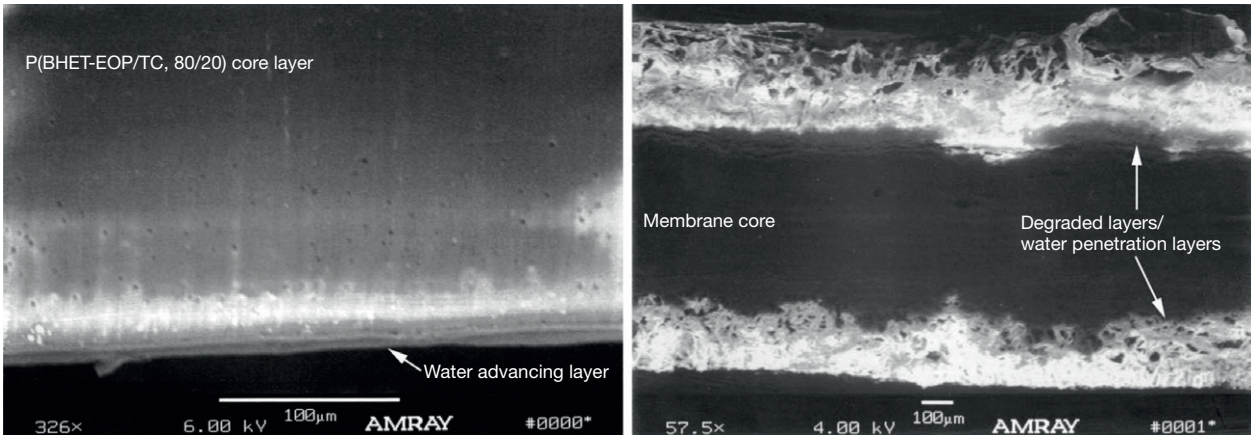

Figure 14 SEM images of degrading P(BHET-EOP/TC, 80:20) and P(BHET-EOP/TC, 80:15) disks. Reproduced from Mao, H. Q.; Shipanova-Kadiyala, I.; Zhao, Z.; Dang, W. B.; Brown, A.; Leong, K. W. *J. Biomater. Sci. Polym. Ed.* **2005**, *16*, 135–161, with permission from Brill.

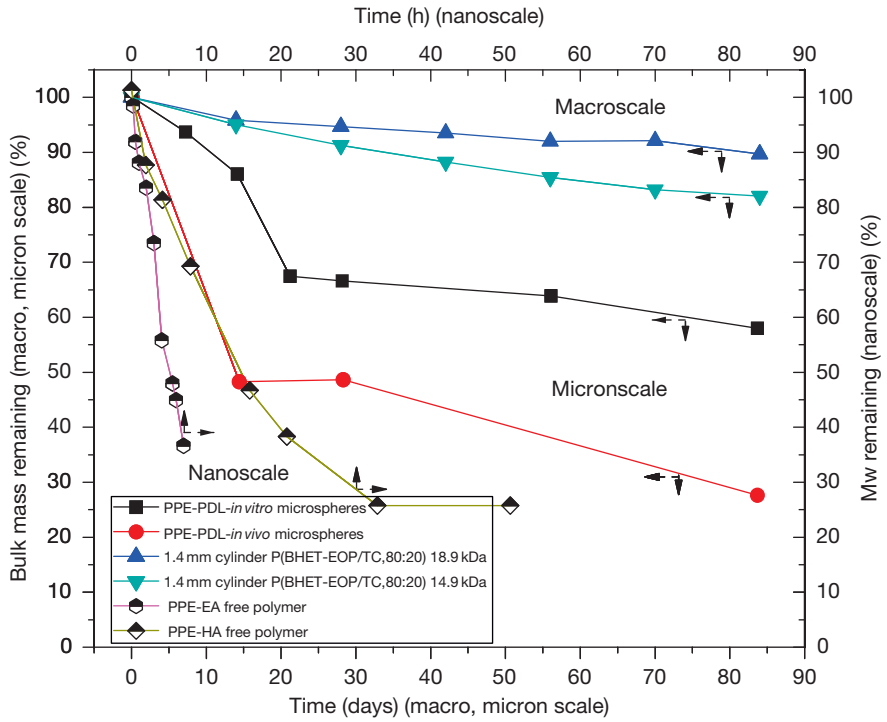

Figure 15 Rate of bulk degradation as a function of length scales (macro, micro, nano). Replotted from Chaubal, M. V.; Su, G.; *et al. J. Biomater. Sci. Polymer Ed.* **2003**, *14*(1), 45–61; Wang, J.; Mao, H. Q.; Leong, K. W. *J. Am. Chem. Soc.* **2001**, *123*, 9480–9481; Wang, S.; Wan, A. C. A.; *et al. Biomaterials* **2001**, *22*(10), 1157–1169.

molecular weight (Figure 15, top and right axes) using sensitive analytical techniques such as gel permeation chromatography (GPC), nuclear magnetic resonance (NMR), or matrix-assisted laser desorption/ionization (MALDI).

Molecular weight also plays a role in the rate of degradation of macroscale constructs. The total surface area of the 6 mm OD disk (263 mm^2) is similar to that of 1.4 mm OD hollow cylinders (both cylinders are reported to be identical in size: 258 mm^2; wall thickness = 0.17 mm) and thus the rate of degradation is expected to be similar despite differences in geometry.[61,64] The molecular weight of P(BHET-EOP,TC, 80/20) disk is 7.9 K compared to those of the cylinders which are 14.9 and 18.9 K, respectively.[64] The rate of degradation correlates with the molecular weights: the 7.9 K disk degrades much faster than the cylinders, and the 14.9 K cylinder slightly faster than the 18.9 K cylinder (Figure 16). The reason for an increased rate of degradation can be attributed to a higher degree of water penetration in the lower molecular weight constructs as seen on the graph inset in Figure 16. At all time points, the percentage weight increase

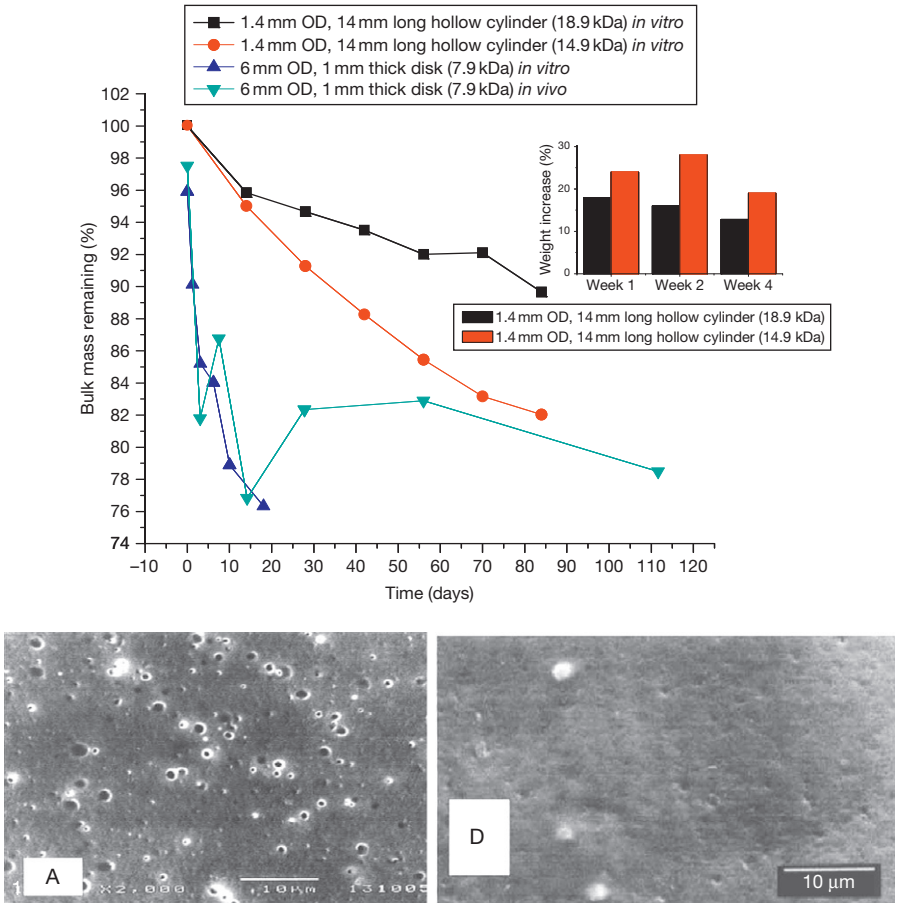

Figure 16 Rate of bulk degradation as a function of molecular weight. Bottom: SEM images of P(BHET-EOP/TC, 80:20) hollow cylinders (left: 14.9 kDa, right: 18.9 kDa). Reproduced from Wang, S.; Wan, A. C. A.; *et al*. *Biomaterials* **2001**, *22*(10), 1157–1169; Mao, H.; Leong, K. W.; Leaf Huang, M.-C. H.; Ernst, W. *Adv. Genet*. **2005**, *53*, 275–306, with permission from Elsevier.

of the 14.9 K cylinder is always higher than its 18.9 K counterpart. While one could attribute a higher degree of water penetration to a more amorphous morphology in the lower molecular weight construct, that may not be the critical factor. SEM images show that cylinders made of lower molecular weight P(BHET-EOP,TC, 80/20) (Figure 16, left) are more porous than their higher molecular weight counterparts (Figure 16, right). This might more likely be the explanation for the higher rate of water penetration and consequently the higher rate of degradation.

Figure 17 shows the correlation between the length scale and the rate of degradation measured in terms of molecular weight (MW) reduction under both *in vitro* and *in vivo* conditions. These data are collated from Mao *et al.*[64] and Chaubal *et al.*[63] There is better agreement between *in vitro* and *in vivo* results on a micrometer scale than on the macroscale. The rate of MW reduction is much faster on a micrometer scale than on the macroscale. Cylinders of 14.9 kDa P(BHET-EOP/TC, 80:20) correlate with a higher rate of MW reduction both *in vitro* and *in vivo*. Together with Figure 16, it can be inferred that lower MW leads to an increase in both the rate of bulk degradation as well as molecular weight reduction. Interestingly, as shown on Figure 18, the positive correlation between bulk degradation and molecular weight reduction differs across length scales. Bulk mass and MW losses on the macroscale correlates linearly, but not so on the micrometer scale, where initial degradation is characterized by a rapid decrease in MW (from 100 to 70%) while bulk mass remains relatively constant (100%).

In summary, the degradation behavior of PPEs is determined by the rate of water penetration into the polymer. Although the polymer can be enzymatically hydrolyzed, for practical applications the rate of degradation can be assumed to be a direct function of water penetration. The latter can be systematically controlled via the backbone structure by copolymerizing PPE with a hydrophobic residue, via the side-chain structure by substituting ethoxy groups with methoxy groups, and via length scale as well as the molecular weight of the polymer.

1.123.8. Toxicity and Biocompatibility of PPEs

The cytotoxicity of a biomaterial is important for practical reasons. Over time, biomaterials break down and release oligomers (partial breakdown) and monomers (complete breakdown). These degradation products are taken up by cells and exert a range of biological effects on them. The culmination of such effects may lead to cell death, which is undesirable in

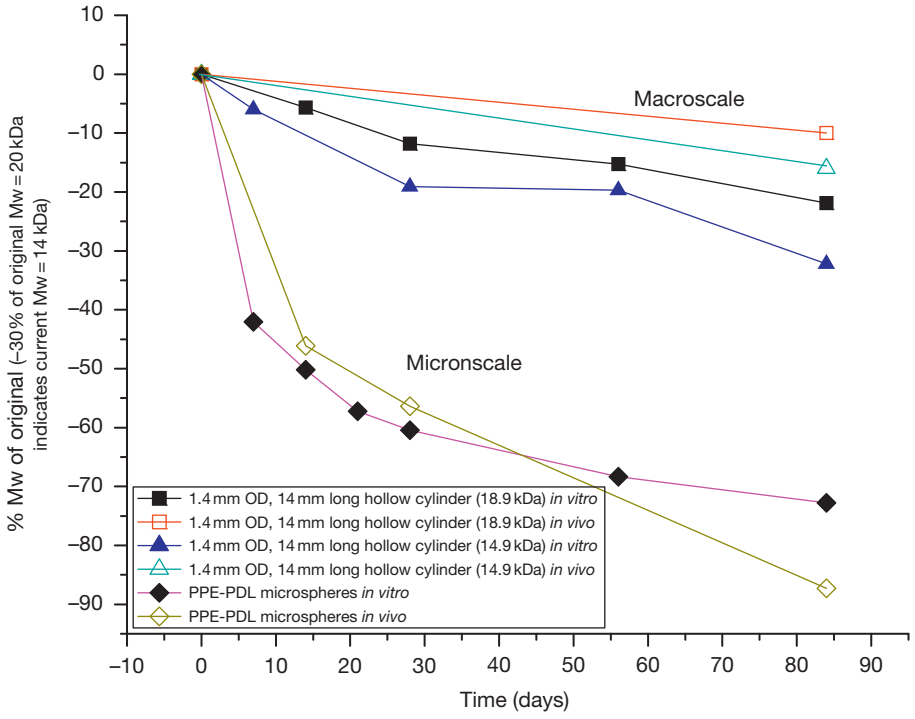

Figure 17 Rate of molecular weight reduction on macro and micro scales. Replotted from Wang, S.; Wan, A. C. A.; *et al*. *Biomaterials* **2001**, *22*(10), 1157–1169; Chaubal, M. V.; Su, G.; *et al*. *J. Biomater. Sci. Polymer Ed*. **2003**, *14*(1), 45–61.

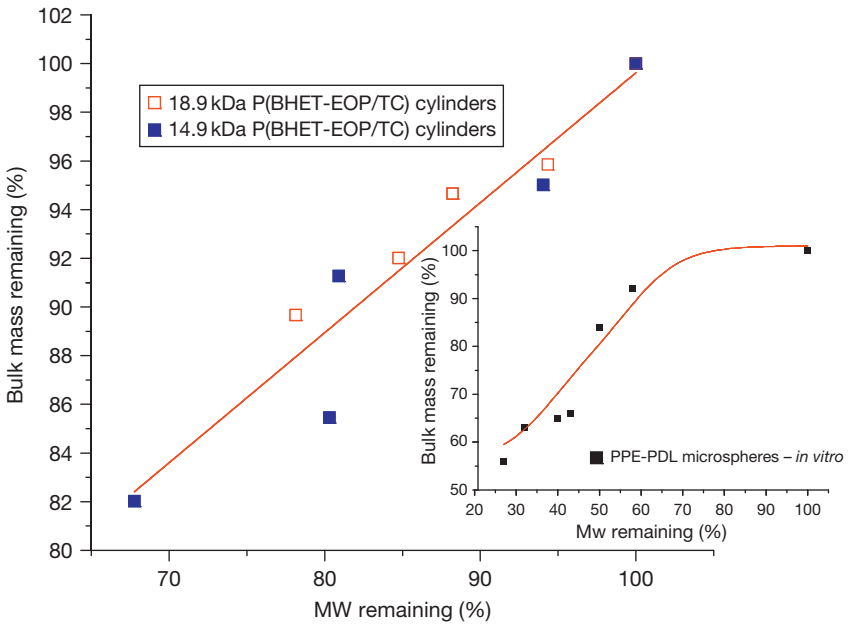

Figure 18 Correlation of mass loss and MW loss. Replotted from Wang, S.; Wan, A. C. A.; *et al*. *Biomaterials* **2001**, *22*(10), 1157–1169; Chaubal, M. V.; Su, G.; *et al*. *J. Biomater. Sci. Polymer Ed*. **2003**, *14*(1), 45–61.

biomedical applications. For PPEs, the major degradation products include aliphatic diols, phosphates, phosphoramides (PPAs), aliphatic amines, and alcohols. Thus by carefully choosing the building blocks of PPEs, the degradation products of PPEs can be biocompatible. The backbones of most PPEs contain α-propylene glycol, which has a favorable safety profile compared to other diols. When PPEs are applied in gene delivery applications, cationic moieties (which are necessary to complex with anionic DNA) are introduced by linking residues containing amino groups to the phosphoryl side chain via

either phosphorous–ester or phosphorous–amide bonds. These amines have also been carefully selected to minimize toxicity.[65]

Cytotoxicity assays for PPEs and PPAs have mostly been assessed using the 3-(4,5-Dimethylthiazol-2-yl)-2,5-diphenyl-tetrazolium bromide (MTT) assay. A compendium of toxicity data of PPEs and PPAs is given in **Table 3**. As cytotoxicity is cell type dependent, we have also included the cell types in both tables. PPEs in general possess excellent toxicity and biocompatibility profiles and have been evaluated over a wide range of applications. The IC_{50} is commonly used as an indicator of *in vitro* toxicity, and materials with IC_{50} between 500 and 1000 $\mu g\,ml^{-1}$ can be considered excellent. All PPEs (except PPE-HA and PCEP) listed in **Table 3** are reported to have an IC_{50} far greater than 500 $\mu g\,ml^{-1}$. With recently reported PPEs having IC_{50} values greater than 10 $mg\,ml^{-1}$, the safety profile of PPE as a class of polymer is indeed encouraging.

Although the IC_{50} values of PPAs ($>100\,\mu g\,ml^{-1}$) are at least four times higher than that of PEI ($\sim 25\,\mu g\,ml^{-1}$), they are still significantly lower than those of PPEs. PPAs are mostly applied as gene carriers, as they mediate higher transfection efficiencies ($\sim$1 order of magnitude) than their PPE counterparts. Due to this reason, applications of PPA might be limited to gene delivery.

1.123.9. Design of PPE Drug Carriers

1.123.9.1. Amphiphilic PPE Copolymers as Drug Carriers

Biodegradable nanoparticles such as micelles and liposomes have been widely studied as chemotherapeutic drug carriers. The most basic characteristics of amphiphilic copolymers include the ability to self-assemble into a core–shell structure

Table 3 Toxicity profiles of PPEs and PPAs

	Application	*Cell type*	*Assay*	*References*
PPEs				
$IC_{50} \sim 1\ mg\,ml^{-1}$				
ssPCL–PEEP	Drug carrier	HEK-293	MTT	Cheng *et al.*[69]
mPEG-TEGP[a]	Drug carrier	A549	MTT	Xiong *et al.*[57]
PPE-EA[a]	Gene carrier	COS-7	MTT	Wang *et al.*[61]
PPE-HA-ACRL[a]	Hydrogels	Primary goat mesenchymal stem cells	WST-1	Li[89]
POPEMA–PEG–POPEMA[a]	Hydrogels	Primary ICR mice osteoblast	MTT	Du[90]
PIOP[a]	Hydrogels	Chinese hamster fibroblast V-79	Cell colonies were counted	Iwasaki[91]
PEEP–PCL–PEEP[a]	Drug carrier	HEK-293	MTT	Wang *et al.*[67,68]
PEEP–PLLA–PEEP[a]	Drug carrier	HEK-293	MTT	Yang *et al.*[66]
$IC_{50} \sim$ indicated values ($\mu g\,ml^{-1}$)				
PCEP (90 $\mu g\,ml^{-1}$)	Drug carrier			
PEEP–PEG–PEEP (345 $\mu g\,ml^{-1}$)[a]	Drug carrier	A549	MTT	Wu *et al.*[75]
Poly(BHET-EOP/TC,80:20) microspheres (500 $\mu g\,ml^{-1}$)[a]	Nerve guide conduit, drug carrier	GT3TKB	MTT	Mao *et al.*[54,64]
Degraded products from poly(BHET-EOP/TC,80:20) (500 $\mu g\,ml^{-1}$)	Nerve guide conduit, drug carrier	GT3TKB	MTT	Mao *et al.*[54,64]
PPE–MEA(500 $\mu g\,ml^{-1}$)	Gene carrier	COS-7	MTT	Wang *et al.*[62]
PPE-HA (200 $\mu g\,ml^{-1}$)	Gene carrier	COS-7	MTT	Wang *et al.*[62]
$IC_{50} \sim 10\ mg\,ml^{-1}$				
PCL-PEEP[a]	Thermoresponsive	HEK-293	MTT	Wang *et al.*[56,74,92]
PCL-P(EEP-MEP)[a]	Thermoresponsive	HEK-293	MTT	
PCL-P(EEP-PEP)[a]	Thermoresponsive	HEK-293	MTT	
mPEG-PEEP[a]	Thermoresponsive	HEK-293	MTT	Wang *et al.*[56,74,92]
mPEG-P(EEP-PEP)[a]	Thermoresponsive	HEK-293	MTT	Yuan *et al.*[76]
AU-mPEG-P(EEP-PEP)[a]	Thermoresponsive	HEK-293	MTT	Yuan *et al.*[76]
PPE-HE	Gene carrier	COS-7	MTT	Huang[93]
PPAs				
PPAs with different types of charge groups, tested in COS-7 cells	PPA-EA	PPA-MEA	PPA-DMA	PPA-TMA
IC_{50}	100	100	>500	>500
PPAs with primary amine charge groups but different lengths of linear side chains, tested in HeLa cells	PPA-EA	PPA-PA	PPA-BA	
IC_{50}	104	117	110	
PPAs with primary amine charge groups but different lengths of branching side chains, tested in HeLa cells	PPA-DEA	PPA-EPA	PPA-DPA	PPA-BPA
IC_{50}	122	96	103	105

[a]Cell viability was $>80\%$ at indicated value, higher concentrations were not assayed.

where the hydrophobic core encapsulates lipophilic drugs and the hydrophilic shell stabilizes the particles and prevents the drug from precipitating out of water. The range of sizes in which these particles form allows passive accumulation via the enhanced permeation and retention (EPR) effect in tumor tissues. As these drug-loaded particles degrade, the hydrophobic drugs can be released in a controlled manner. This basic design has been greatly improved in the recent years to improve circulation time (via pegylation), drug targeting (via ligand conjugation), and environmental responsiveness for payload release (pH, heat, magnetic, light, electricity, etc.). Table 1 (2-1 to 2-5) shows the list of PPE-based drug carriers. The hydrophobic segments are provided by poly-L-lactide (PLLA) or PCL, while the hydrophilic segments are provided by poly(ethyl ethylene) phosphate (PEEP). Structures 2-1 to 2-3 are linear di- or triblock copolymers, while Structure 2-4 (ssPCL-PEEP) is a star-shaped copolymer synthesized starting with a branched polyalcohol. Structure 2-5 (PEG–TEGP), however, does not have any hydrophobic PCL or PLLA segments. Instead, it is synthesized starting with a PEG molecule (as macroinitiator) and extending it with difunctional phosphate monomers, which eventually forms a nanogel with a cross-linked core.

1.123.9.2. Drug-Loading Index

Drug carriers are also characterized by their ability to encapsulate drugs. This is commonly measured using two different parameters: drug-loading capacity (DLC) and drug-loading efficiency (DLE), as defined in Table 4. If a given amount of the drug carrier is unable to fully encapsulate a fixed quantity of the drugs, one would increase the amount of drug carrier to soak up the remainder. At such time, as DLE increases, DLC drops. This inverse relationship is well illustrated by paclitaxel-loaded PCL_x–$PEEP_y$ diblock copolymer (Table 4). For ease of discussion, we define a useful parameter: DLI defined in Table 4 to quantify the overall efficacy of drug loading while factoring in the inverse relationship between DLC and DLE. For example, the DLI of PCL_x–$PEEP_y$ diblock copolymer decreases by almost one-third when polymer/drug ratio is increased from 50 to 200. Even though DLE increases from 77 to 90%, DLC dives from 1.55 to 0.47%. At such time, DLI can be a good indicator of drug-loading characteristics.

Although one would expect a more hydrophobic copolymer to have a higher DLE, there seems to be no apparent structure–DLI relationship for PPE-based block copolymers. The highest DLI for a diblock copolymer is seen for both PCL_{67}–$PEEP_{36}$ and PCL_{150}–$PEEP_{30}$ at 195 and 192, respectively. The highest DLI for a star-shaped diblock copolymer is for $ssPCL_{33}$–$PEEP_{53}$, while that for a triblock copolymer is for $PEEP_{48}$–PCL_{94}–$PEEP_{48}$ without an apparent trend correlating hydrophobic/hydrophilic ratio. PEG–TEGP has the highest DLI due to a heavily cross-linked PEEP core. Moreover, each PEEP repeat unit contains a hydrophobic ethyl side chain, and the combination of both factors could have greatly increased the hydrophobicity and therefore the partition coefficient of doxorubicin into its nanogel interior.

1.123.9.3. Effect of Molecular Structure on Critical Micelle Concentration

Carrier properties can be tuned in a predictable manner by varying the chain lengths of the hydrophobic and/or hydrophilic segments. For triblock copolymers, the critical micelle concentration (CMC) can be systematically adjusted by varying the chain length (i.e., degree of polymerization, DP) of the hydrophilic segment (PEEP). Data obtained from two different triblock copolymers (PEEP–PLLA–PEEP by Yang *et al.*[66] and PEEP–PCL–PEEP[67]) are collated and analyzed.

Table 4 Drug-loading characteristics of polyphosphoester-based drug carriers

No.		x	y	*Carrier:drug ratio*	*DLC (%)*	*DLE (%)*	*DLI (%)*
1	PCL_x–$PEEP_y$ diblock copolymer (paclitaxel) micelles	67	36	10	4.42	44.2	195
				20	2.87	57.5	165
				50	1.55	77.4	120
				200	0.47	92.9	44
2	PCL_x–$PEEP_y$ (doxorubicin) micelles	150	30	10	4.38	43.8	192
3	$ssPCL_x$–$PEEP_y$ star-shaped diblock copolymer (paclitaxel) micelles	33	25	10	1.62	16.19	26
		33	35	10	2.64	26.38	70
		33	53	10	3.46	34.59	120
		33	69	10	2.09	20.88	44
		44	32	10	2.79	27.86	78
		69	35	10	2.52	25.08	63
		69	56	10	2.63	26.28	69
4	$PEEP_y$–PCL_x–$PEEP_y$ triblock copolymer (paclitaxel) micelles	27	44	10	0.56	5.6	3
		36	7	10	0.92	9.2	8
		36	21	10	1.56	15.6	24
		36	49	10	1.32	13.2	17
		63	45	10	2.46	24.6	61
		94	48	10	3.16	31.6	100
		186	49	10	1.81	18.1	33
5	$[PEG_{5kDa}]_x$–$[TEGP]_y$ nanogel	1	5	10	9.10	91.0	828

Drug-loading capacity (DLC) = Weight of drug loaded in carrier/weight of drug-loaded carriers × 100%; Drug-loading efficiency (DLE) = Weight of drug loaded in carrier/weight of drug used for loading × 100%; Drug-loading index (DLI) = DLC × DLE.

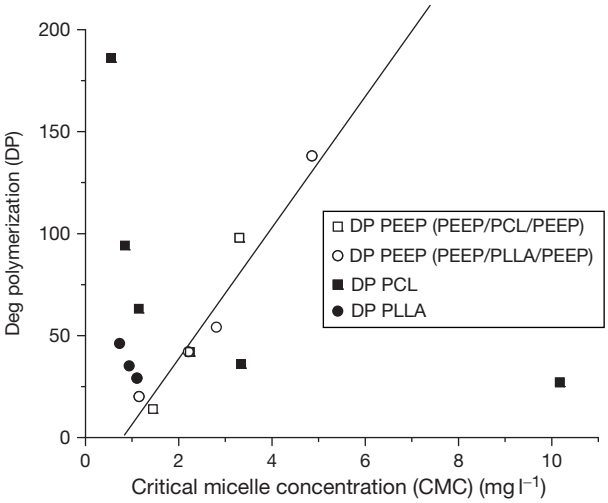

Figure 19 Linearity between degree of polymerization of PEEP (empty symbols) and critical micelle concentration. Replotted from Wang, F.; Wang, Y.-C.; Yan, L.-F.; Wang, J. *Polymer* **2009**, *50*, 5048–5054; Yang, X. Z.; Wang, Y. C.; Tang, L. Y.; Xia, H.; Wang, J. *J. Polym. Sci. A Polym. Chem.* **2008**, *46*, 6425–6434.

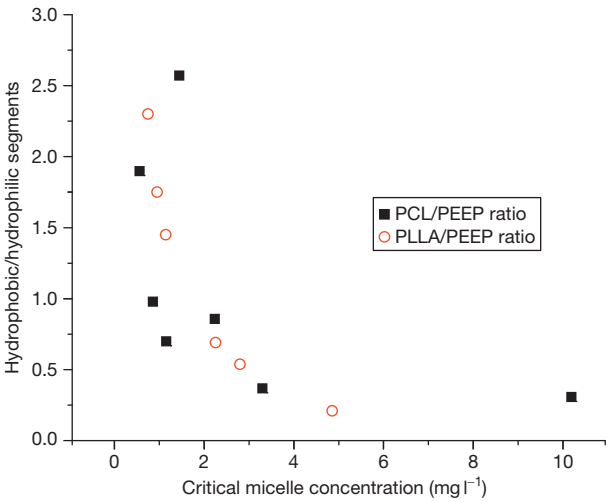

Figure 20 Effects of polymer backbone on critical micelle concentration. Replotted from Yang, X. Z.; Wang, Y. C.; Tang, L. Y.; Xia, H.; Wang, J. *J. Polym. Sci. A Polym. Chem.* **2008**, *46*, 6425–6434; Wang, Y. C.; Tang, L. Y.; Sun, T. M.; Li, C. H.; Xiong, M. H.; Wang, J. *Biomacromolecules* **2008**, *9*, 388–395; Wang, Y. C.; Liu, X. Q.; Sun, T. M.; Xiong, M. H.; Wang, J. *J. Control. Release* **2008**, *128*, 32–40.

When DP is plotted against CMC, some results are highly consistent and collapsed into a straight line as shown in Figure 19. The empty symbols plotted for PEEP–PLLA–PEEP and PEEP–PCL–PEEP are obtained by varying the chain length (i.e., DP) of the PEEP segment while keeping, respectively, PLLA (DP = 29) and PCL (DP = 36) segments constant. Linearity is not observed when PLLA and PCL segments are varied while keeping PEEP segment constant. Instead, only a general trend is observed describing a decrease in CMC when PLLA and PCL segment lengths are increased. This is expected because the molecular structures of PLLA and PCL are inherently different. Figure 19 points to the possibility of varying the physicochemical properties of drug carriers in a predictable manner by adjusting the length of the PPE backbone. Also, an inverse relationship ($y = 1/x$) exists between the CMC and the hydrophobic/hydrophilic ratio (Figure 20). The CMC approaches asymptotically to about 0.6 mg l^{-1} while the hydrophobic/hydrophilic ratio approaches 0.25. As the final drug carrier design is almost always a compromise among various factors, from a rational design standpoint these values provide useful guidance in drug carrier design and optimization.

1.123.9.4. Drug Release Kinetics

As drug carriers degrade over time, hydrophobic drugs are released from its core. At such time, the rate of drug release is a function of rate of degradation of the drug-loaded carrier. As the rate of degradation for PPE is dependent on water penetration, a carrier with a longer hydrophobic segment is expected to have a slower rate of drug release as water penetration is impeded. The drug release characteristics of diblock copolymers are collated and replotted on Figure 21. The rate of doxorubicin release by PCL_{150}–$PEEP_{30}$[56] is much slower than that of paclitaxel by PCL_{67}–$PEEP_{36}$[68] even though doxorubicin itself is more soluble than paclitaxel. This can be attributed to a more hydrophobic core that impedes water penetration needed for the degradation of both phosphoester (in PEEP) and polyester bonds (in PCL). These structures are listed in Table 1 (2-2, 2-3).

The same phenomenon is observed in the star-shaped PCL–PEEP copolymer,[69] with $ssPCL_{33}$–$PEEP_{69}$ having the highest PEEP content and hence the highest drug release rates (Figure 21). This is followed by $ssPCL_{69}$–$PEEP_{56}$ (PCL:PEEP = 1.23) and $ssPCL_{44}$–$PEEP_{32}$ (PCL:PEEP = 1.38), respectively, with the former having a slightly higher rate of release due to a slightly lower PCL:PEEP content in the copolymer backbone. When seen over a time scale of days, it can be observed that all copolymers, despite differences in molecular structures and segment lengths, have similar burst release characteristic, diverging after about 20% of it payload is released. At such, the graph at the early time points are expanded (inset of Figure 21) and further analyzed. In time scales of hours, there are differences in rate of drug release; however, 20% of total payload is released after 18 h of incubation in PBS (experimental conditions used for various drug release studies). Therefore, it is also important to consider the time scale of the intended drug delivery application. If the time scale is in the order of days, one may assume a burst release characteristic of 20% for all copolymers and focus on the drug release rate after 18 h, using the molecular structure of the drug carrier to design a desired rate of release. On the other hand, if the intended application requires drug release rates over a short period of 18 h, direct infusion might be a simpler and more reliable alternative. Similar trends are observed in triblock copolymers[67] in Figure 22. As the PCL segment is increased, the rate of drug release drops correspondingly.

Structure 3-5 (PEG–TEGP) is a nanogel with PEG arm and a cross-linked PEEP core.[57] The PEG arm is expected to increase the circulation time of the nanogel in the body, while the heavily cross-linked PEEP core provides the

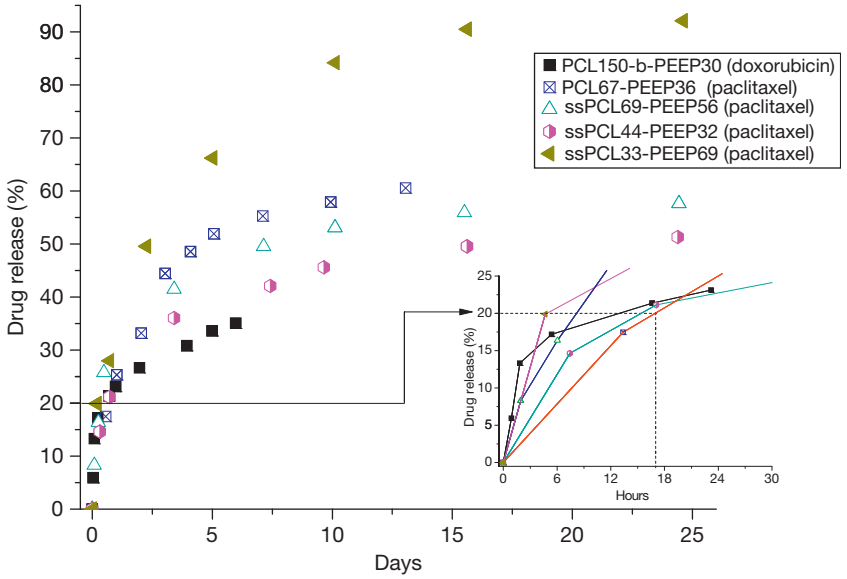

Figure 21 Cumulative drug release of diblock copolymers. Replotted from Cheng, J.; Ding, J. X.; Wang, Y. C.; Wang, J. *Polymer* **2008**, *49*, 4784–4790; Wang, Y. C.; Tang, L. Y.; Sun, T. M.; Li, C. H.; Xiong, M. H.; Wang, J. *Biomacromolecules* **2008**, *9*, 388–395; Wang, Y. C.; Liu, X. Q.; Sun, T. M.; Xiong, M. H.; Wang, J. *J. Control. Release* **2008**, *128*, 32–40; Wang, F.; Wang, Y.-C.; Yan, L.-F.; Wang, J. *Polymer* **2009**, *50*, 5048–5054.

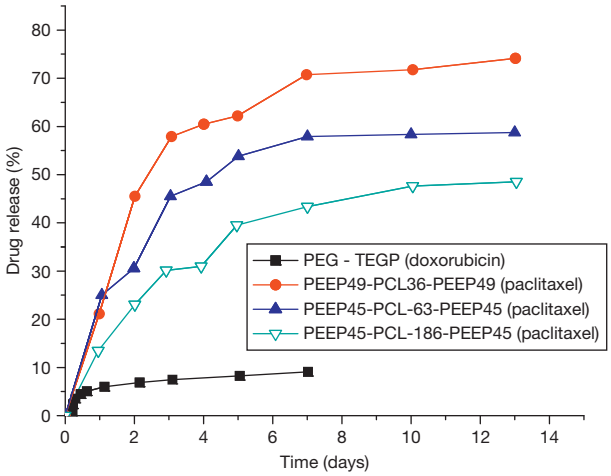

Figure 22 Cumulative drug release of triblock copolymers and PEG-TEGP nanogel. Replotted from Wang, Y. C.; Tang, L. Y.; Sun, T. M.; Li, C. H.; Xiong, M. H.; Wang, J. *Biomacromolecules* **2008**, *9*, 388–395; Wang, Y. C.; Liu, X. Q.; Sun, T. M.; Xiong, M. H.; Wang, J. *J. Control. Release* **2008**, *128*, 32–40.

hydrophobic core needed for drug encapsulation. PEG–TEGP has a high DLI contributed by both a higher DLC (9.1%) and DLE (91%) (Table 4). However, the heavily cross-linked PEEP core might not have allowed sufficient water to penetrate into its interior. Therefore, the drug is released at a very slow rate after the initial burst.

In summary, the molecular structure of PPE-based amphiphilic block copolymers can predict its properties as a drug carrier. By varying the DP of the hydrophilic PEEP residues in triblock copolymers, the CMC can be varied. The ratio of hydrophobic to hydrophilic segments in the copolymer also varies asymptotically to CMC. The rate of drug release from diblock copolymers increases with increasing hydrophilic chain lengths, with at least 20% of drugs released within the first 18 h. There is no apparent impact of structure on drug-loading characteristics for the carriers discussed in this section.

1.123.10. Design of Thermoresponsive PPEs

Thermoresponsive biodegradable materials have attracted great attention because of their unique properties for a variety of biomedical applications. These amphiphilic materials are water soluble, but phase separates when heated above their lower critical solution temperature (LCST). This is attributed to the operation of a two-stage mechanism: a coil-to-globule transition, followed by aggregation of the resultant globules. Support for this proposition has been furnished by light scattering, fluorescence energy transfer, and time-resolved fluorescence anisotropy measurements (TRAMS).[70] There is a general consensus that rapid thermoreversibility of phase separation is effected by the collapse of polymer chains in aqueous solution, but opinions differ as to how to explain this phenomenon. Some favor the idea of a breakdown of polymer–water hydrogen-bonding interactions needed to maintain a coiled polymer conformation, whereas others attribute the polymer chain collapse to changes in the 'hydrophobic effect.' It is likely that both mechanisms occur, but one could dominate the other under varying circumstances. The thermodynamics of hydrophobic hydration on a molecular basis was comprehensively reported for PEO–water system.[71] As the mechanism of thermoresponsiveness in PPEs is likely the latter, we will provide a simplified summary below.

In a soluble (amphiphilic) polymer–water system, the polymer molecules (solute) are 'caged' within a dynamic three-dimensional (3D) network of water (solvent) as water molecules interact with hydrophilic moieties of the polymer, while the hydrophobic moieties of the polymer occupy the interstitial spaces of water network (this dissolution model is also called hydrophobic hydration). As the hydration shell forms around the caged polymer, the water molecules in the vicinity of the polymer chains are more restricted than their counterparts in the bulk region. This enhanced water structure around the polymer is energetically unfavorable ($\Delta S < 0$, hence $-T\Delta S$ is positive). However, the system remains soluble ($\Delta G = \Delta H - T\Delta S$, $\Delta G < 0$) because of a more favorable enthalpy term (ΔH). As temperature reaches the LCST, to continue to maintain a caged structure will require a significant gain of entropy relative to the bulk water molecules (which is now at a higher temperature). Now, the entropy term outweighs enthalpy, causing $\Delta G > 0$, and consequently phase separation ensues. The phase separation behavior is commonly known as the 'salting out' effect and can be metaphorically described as the polymer 'falling out of the cage' when the LCST is exceeded.

1.123.10.1. Molecular Structures of Thermoresponsive PPEs

The molecular structures of thermoresponsive PPEs reported are shown in Table 1(3-1 to 3-6). The thermal responsive behavior of PEEP was first reported by Iwasaki,[72] as shown in Figure 23. $PEEP_{100}$ has a thermal transition (indicated by the presence of an LCST) at 38 °C, indicating that this polymer may be dissolved in water primarily via hydrophobic hydration mechanism described earlier. Thermoresponsiveness is enhanced when a portion of the ethyl side chains is substituted by propyl groups (Figure 23). This enhancement is manifested by a sharper transition. As the proportion of isopropyl ethylene phosphate (IPP) is increased, thermal transition is shifted downward. It was also reported that the hydrodynamic size of $P(I_{24}E_{76})P$ increases from 6 nm at 20 °C to about 6 μm at 50 °C.

A systematic investigation was then conducted on the thermal responsive property of PEEP via PCL–PEEP diblock copolymers.[57] The LCST in the PCL–PEEP diblock copolymer exists if there is a high enough DP of PEEP. The $PCL_{25}PEEP_{42}$ diblock copolymer does not have an LCST. However, as the DP (PEEP) is increased to 103, incomplete transition, measured in terms of the percentage light transmittance, occurs. Full thermal transition is seen at DP (PEEP) 217 and 329. It can also be observed that with a higher DP (PEEP), the cloud point (temperature at which thermal transition occurs) is lower, indicating a downward shift of the LCST. The establishment of LCST in the PCL–PEEP diblock copolymer is attributed to the hydrophobicity of the PEEP side chains. PCL-P(EEP-MEP) is obtained when a portion of ethyl ethylene phosphoester (EEP) residues is replaced with less the hydrophobic methyl ethylene (MEP) residues. As the DP (MEP) increases, transitions are not only incomplete but also shift to higher temperatures until they are totally abolished, indicating abrogation of LCST in a DP (MEP)-dependent manner. On the other hand, the LCST is enhanced in PCL-P(EEP-PEP), where a portion of EEP phosphoester residues is replaced with more hydrophobic isopropyl ethylene residues (PEP) shown in Table 1 (3-4). Compared to the PCL–PEEP diblock copolymer, the LCST of PCL-P(EEP-PEP) is not only shifted lower, but the transition is also sharper. These data demonstrate a well-defined structure–LCST relationship. By tuning the side chains with the right hydrophobicity–hydrophilicity using appropriate proportions of ethyl and propyl groups, PPEs can be designed for a user-defined LCST with the desired sharpness of thermal transition.

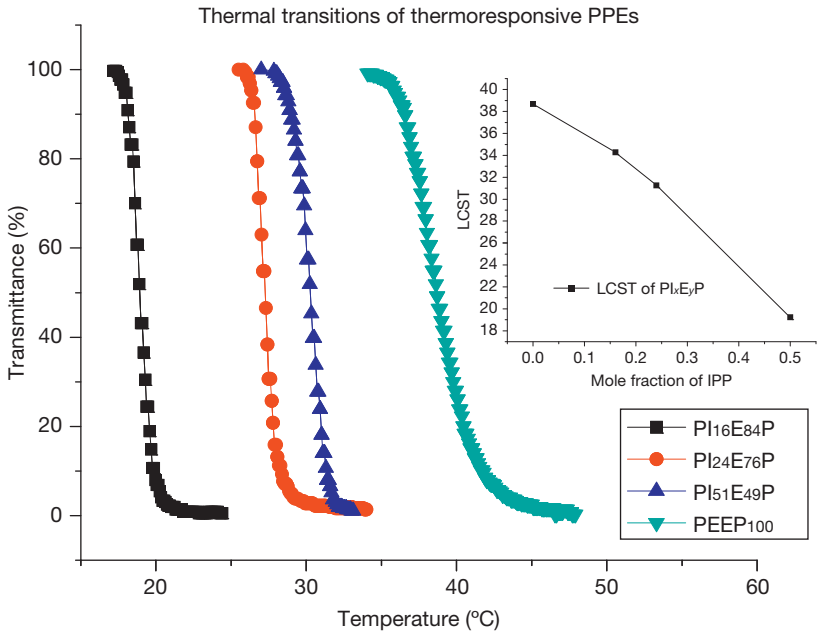

Figure 23 Thermal transitions of thermoresponsive PPEs. Replotted from Wang, Y. C.; Yuan, Y. Y.; Du, J. Z.; Yang, X. Z.; Wang, J. *Macromol. Biosci.* **2009**, *9*, 1154–1164; Wang, Y. C.; Tang, L. Y.; Li, Y.; Wang, J. *Biomacromolecules* **2009**, *10*, 66–73.

1.123.10.2. Effects of Solution Properties on Thermal Transition

For biomedical applications, it is crucial for polymers to retain functionality under physiological conditions. Thermal transitions of thermoresponsive PPEs discussed so far pertained to those dissolved in pure water. As thermoresponsive PPEs have been discovered only very recently, limited data is available on the effects of solution properties on the thermal transition of these PPEs. Such solution properties may include salt concentration, type of salts (mono- or divalent), pH, and the presence of other polyelectrolytes. Nevertheless, the effects of NaCl[57] and PBS[73] have been reported. Wang *et al.* reported that minute amounts of salt cause a downward shift in the LCST and also decrease the sharpness of the thermal transition. Increasing the NaCl concentration from 17 to 154 mM (isotonic saline) shifts the LCST toward lower temperatures but does not further deteriorate the sharpness of transition. As mentioned in an earlier section, phase transition occurs in two consecutive phases: coil-to-globule transition, followed by aggregation of newly formed globules. Iwasaki *et al.* reported that under favorable salt conditions (150 mM NaCl), globules once formed do not further aggregate. But when dissolved in PBS, globules continue to aggregate and eventually precipitate out of the solution. Thus, more work needs to be done to resolve the 'salting out' phenomenon.

1.123.10.3. Thermoresponsive PPEs Conjugated to PEG, Gold Nanoparticles, and Enzyme-Cleavable Side Chains

As mentioned earlier, a prominent advantage of PPEs is structural versatility, which can be translated to functional outcomes. Instead of PCL, PEG is conjugated to thermosensitive P(EEP-PEP) to form PEG-P(EEP-PEP) block copolymers for potential drug delivery applications.[74] The PEG moiety is desirous because of its ability to increase systemic circulation time by avoiding clearance via the reticuloendothelial system. The optimal hydrophobic/hydrophilic ratio needed for thermoresponsiveness can additionally be tuned by varying the segment lengths of P(EEP-PEP) and PEG, respectively. This is an added design flexibility compared to PCL-P(EEP*x*-PEP*y*) and PI*x*E*y*P, where this ratio is tuned by varying only the side chains of the PPE. The critical aggregation temperature (CAT), characterized by a rapid increase in hydrodynamic particle size (above 1 μm), increases with increasing PEG chain length but decreases with increasing PEP segment in the PPE backbone. The CAT is not the LCST, but correlates positively with it.

However, in drug delivery applications, particle size plays a significant role in the effectiveness of the drug delivery system. The CAT is useful as a heat trigger, but it would also be necessary to control the size of the final particle aggregates to achieve drug delivery efficacy. In a further investigation, the desired sizes of the $PEEP_{151}$–PEG_{2000}–$PEEP_{151}$ diacrylate micelle particles are first tuned via temperature and polymer concentration[75] (Figure 24). Diacrylate moieties are then activated to cross-link the core of the swollen particles (at high T) before allowing it to shrink (at lower T). These particles can later be mixed with drug molecules, swollen again at high temperature and cooled rapidly to encapsulate drugs in the interior.

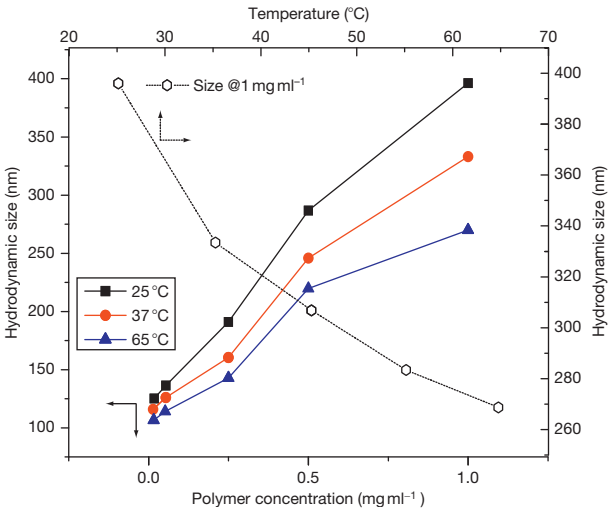

Figure 24 Effects of polymer concentration and temperature on particle sizes of $PEEP_{151}$–PEG_{2k}–$PEEP_{151}$. Replotted from Wu, J.; Liu, X. Q.; Wang, Y. C.; Wang, J. *J. Mater. Chem.* **2009**, *19*, 7856–7863.

Thermoresponsive PPEs modified at both terminal ends have also been reported,[76] as shown in Table 1 (3-6). In this case, one end of P(EEP–PEP) is capped by a PEG segment while the other end is capped by a thioctic acid. The resultant thioctate group can be reduced to release thiol groups, which are known to self-assemble into a monolayer on a gold surface. As a result, the thermoresponsive PPE is conjugated onto surfaces of gold nanoparticles, forming a heat-sensitive corona that extends itself below the LCST and collapses above the LCST. The sharpness of thermal transition of the thermoresponsive PPE–gold nanoparticle is not affected by the presence of gold, but the cloud point is shifted down slightly toward lower temperature, probably due to the thermal conductivity of gold.

A thermoresponsive PPE whose thermal transition can be abrogated by enzymes has also been reported.[73] A very small portion (~6%) of ethyl side chains of PEEP is substituted by acetoxymethyl ester groups, which can be cleaved by esterases. As a result, the thermal responsiveness is muted after 6 h and completely abrogated after 24 h. This is another example of how the chemical versatility of PPE facilitates functionalization and how slight changes to the polymer structure may mediate significant functional consequences.

In summary, thermoresponsive PPEs represent a recent development that should find many interesting biomedical applications. Starting from PEEP, which already has the right ratio of hydrophilic/hydrophobic ratio in its molecular structure for thermoresponsiveness, thermal transitions can be fine-tuned by modifying the main chain (using PEG) or the side chains (isopropyl groups). The polymer can further be modified at the side chains to become enzyme-sensitive or at its ends for conjugation onto gold nanoparticles. These thermoresponsive properties are sensitive to salt concentrations, while the interplay with other desirable PPE properties such as biodegradability and biocompatibility has yet to be investigated. Given these unknowns, more work on thermoresponsive PPEs is expected in the near future.

1.123.11. Design of PPE and PPA Gene Carriers

Polycationic polymers have been increasingly proposed as potential vectors because of their versatility. Rigidity, hydrophobicity/hydrophilicity, charge density, biodegradability, and molecular weight of the polymer chain are all parameters that in principle can be adjusted to achieve an optimal complexation with DNA. As the required characteristics of the DNA nanoparticles, or polyplexes, would differ on the basis of different cells or tissues, or different routes of administration *in vivo*, polymeric carriers with their versatility are well positioned to meet the challenges. Hence, the design of new polymeric gene carriers has been an intensively pursued research area in recent years. Polymers spanning the spectrum of biodegradable, biostable, linear, branched, dendrimeric, and cross-linked have all been investigated. This section concentrates on a series of PPEs and PPAs containing different charge groups in the side chain connected to the backbone through a phosphate (P–O) or a phosphoramide (P–N) bond, respectively. It highlights a systematic design of gene carriers with different strategies for dealing with the barriers of nonviral gene delivery. These PPA- and PPE-based gene carriers have different charge groups, side-chain lengths, and branching structures, but they are structurally related to allow a systematic investigation of the structure–property relationship, including DNA-binding capacity and protection, biodegradability, DNA release kinetics, and transfection efficiency.

1.123.11.1. Molecular Structures of PPE and PPAs Gene Carriers

The pentavalency of a phosphorus atom in the backbone of PPEs makes it possible to conjugate functional groups, including charged groups through a phosphate (P–O) or a phosphoramide (P–N) bond as side chains. Starting from the parent polyphosphite, the P–H bonds can be readily converted for conjugation of different chemical structures. Consequently, it is possible to synthesize a series of cationic PPEs and PPAs from the precursor polymer poly(1,2-propylene-*H*-phosphonate) shown in Table 5. This backbone structure is chosen with consideration of biocompatibility. Comprising propylene oxide in the backbone, the potential breakdown products should be relatively innocuous as α-propylene glycol has a favorable safety profile compared to other diols. Conjugation of amino groups to this parent polymer produces water-soluble PPEs or PPAs that can complex efficiently with DNA. In keeping the chemical structure of the backbone and the molecular weight constant, effects of the charge groups on toxicity and transfection efficiency can be systematically studied to establish the structure–transfection efficiency relationship.

As the gene carrier design is centered on overcoming the various barriers to gene delivery, it would be useful to know these barriers to gene delivery and readers are referred to Mao *et al.*[54] for details. The transfection efficiencies of PPE/DNA complexes vary with a multitude of factors that fall into two categories. The first consists of extrinsic factors such as the nanoparticle composition (e.g., N/P ratio), the ζ potential of the nanoparticles, as well as the cell culture conditions. The second consists of intrinsic factors related to polymer structure, namely, the type of charged groups, length of the spacer, charge density, molecular weight, as well as the backbone structure.

1.123.11.2. Effect of Polymer Backbone on Gene Delivery Applications

For applications that require more stable nanoparticles and/or intracellular delivery, PPA carriers are more suitable than PPEs because the latter degrades at a much faster rate (because of the P–O bond). As such, applications of PPE/DNA particles are limited to local DNA delivery at the sites of injection, acting as a depot to prolong the gene expression in the muscle.[17,61,62,77]

Table 5 Structure of polyphosphoester and polyphosphoramide degradable gene carriers

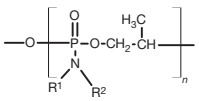

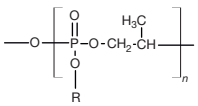

PPA with different types of charged groups	R1	R2
PPA-EA	–H	$-CH_2-CH_2-NH_2$
PPA-MEA	–H	$-CH_2-CH_2-NH-(CH_3)$
PPA-DMA	–H	$-CH_2-CH_2-N-(CH_3)_2$
PPA-TMA	–H	$-CH_2-CH_2-N^+-(CH_3)_3$
PPA with linear side chains		
PPA-EA	–H	$-CH_2-CH_2-NH_2$
PPA-PA	–H	$-CH_2-CH_2-CH_2-NH_2$
PPA-BA	–H	$-CH_2-CH_2-CH_2-CH_2-NH_2$
PPA with branching side chains (different lengths)		
PPA-DEA	$-CH_2-CH_2-NH_2$	$-CH_2-CH_2-NH_2$
PPA-EPA	$-CH_2-CH_2-NH_2$	$-CH_2-CH_2-CH_2-NH_2$
PPA-DPA	$-CH_2-CH_2-CH_2-NH_2$	$-CH_2-CH_2-CH_2-NH_2$
PPA-BPA	$-CH_2-CH_2-CH_2-NH_2$	$-CH_2-CH_2-CH_2-NH_2$

PPE with linear side chains

PPE-EA	$-CH_2-CH_2-NH_2$
PPE-MEA	$-CH_2-CH_2-NH-(CH_3)$
PPE-HA	$-CH_2-CH_2-CH_2-CH_2-CH_2-CH_2-NH_2$
PPE-HE	$-CH_2-CH_2-OH$

PPA with imidazole moiety

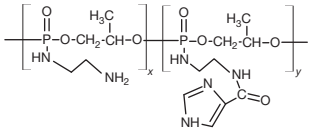

PEG-*b*-PPA

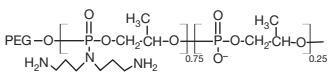

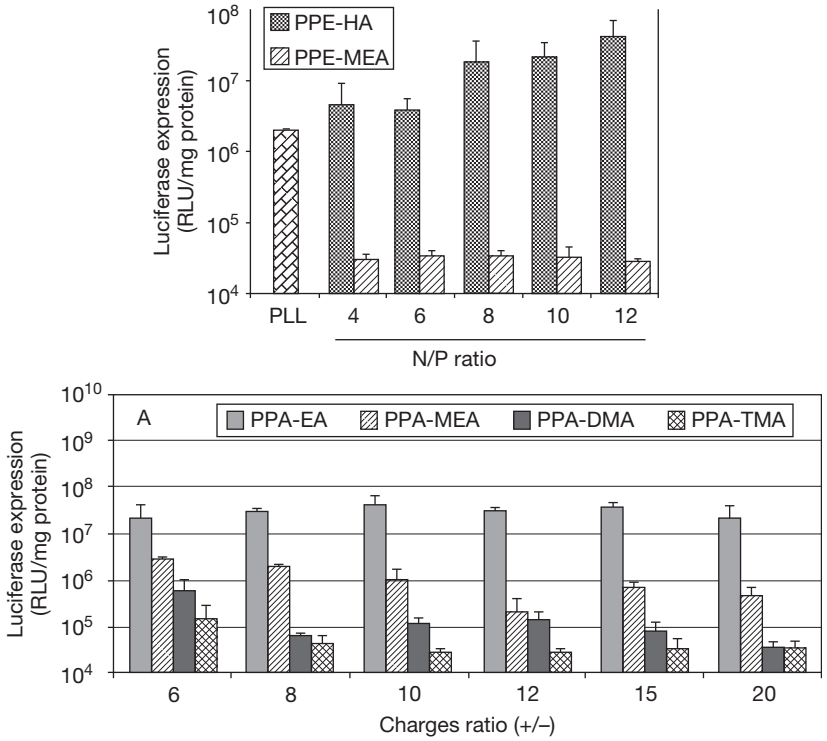

Figure 25 Effects of side chains on the transfection efficiency of PPE and PPA gene carriers. Reproduced from Wang, J.; Huang, S. W.; Zhang, P. C.; Mao, H. Q.; Leong, K. W. *Int. J. Pharm.* **2003**, *265*, 75–84, with permission from Elsevier; Wang, J.; Gao, S. J.; Zhang, P. C.; Wang, S.; Mao, H. Q.; Leong, K. W. *Gene Ther.* **2004**, *11*, 1001–1010.

On the other hand, applications of PPA–DNA particles may be more versatile and can be applied in systemic or oral delivery applications,[78,79] which require the carrier to be stable over longer periods of time. As shown in Figure 25, PPE/DNA particles generally mediate lower transfection efficiencies compared to their PPA–DNA counterparts, resulting in a dearth of information on PPE-based gene delivery system.

1.123.11.3. PPE/DNA Gene Delivery System

Among the three cationic PPEs studied, that is, poly(phosphoester)-ethylamine (PPE-EA), poly(phosphoester)-hexylamine (PPE-HA), and poly(phosphoester)-(methyl)-ehtylamine (PPE-MEA), DNA compaction capacity decreases in the sequence PPE-EA (highest) > PPE-HA > PPE-MEA (lowest).[62,80] PPE-EA, PPE-HA, and PPE-MEA can compact DNA completely at an N/P ratio of 1.0, 1.5, and 4, respectively. Based on gel electrophoresis DNA-retardation assays, the poor DNA compaction of PPE-MEA is due to the rapid degradation of PPE-MEA. GPC analysis further reveals that the side chains of PPE-MEA responsible for compacting DNA are rapidly cleaved during the degradation process. Of the three carriers, PPE-MEA releases DNA too fast to provide a meaningful depot, whereas PPE-HA degrades too slowly. The PPE-EA/DNA particle system is able to release DNA over a few days depending on the formulation, which is subsequently applied as a DNA depot for sustained release in a murine model following intramuscular and intracisternal injections. The success of this strategy is largely dependent upon the N/P ratio. Intramuscular injection of PPE-EA/DNA complexes at N/P ratios of 0.5 and 1 leads to a higher transgene expression than naked DNA injection for both a β-galactosidase expression model (in anterior tibialis muscle) and a systemic delivery model (interferon α2b expression in blood circulation) in Balb/c mice.[77] As the PPE-EA/DNA particles are prepared at higher N/P ratios, the enhancement effect is less pronounced but still higher than that of naked DNA control. However, the enhancement effect decreases (below naked DNA control) when the dosage of PPE/DNA nanoparticles exceeds a threshold value. In a central nervous system (CNS) delivery model,[81] PPE-EA/DNA complexes at an N/P ratio of 2, when injected intracisternally into the mouse cerebrospinal fluid, mediate a persistent level of transgene expression in the brain (mostly in cerebral cortex, basal ganglia, and diencephalons) for at least 4 weeks. At week 4, PPE-EA/DNA complexes maintain a 15-fold higher luciferase expression than naked DNA and about 3-fold higher than PEI/DNA complexes. The difference in optimal N/P ratio observed in these *in vivo* models demonstrates that the optimal carrier–DNA electrostatic interaction is different in different tissues. There can be no one-size-fit-all nanoparticle formulation.

1.123.11.4. PPA–DNA Gene Delivery System: DNA Compaction Capacity of PPAs

All PPAs listed in Table 5 exhibit high DNA compaction capability.[77,79,82] Plasmid DNA in these complexes is partially protected from enzyme degradation, as demonstrated using

DNase I as a model enzyme. The PPAs, except PPA-BA, are able to condense plasmid DNA completely at an N/P ratio of less than or equal to 1, suggesting that these cationic PPA carriers have a high DNA compaction capacity. Among them, PPAs with tertiary amino groups, quaternary amino groups, and those have branching side chains have a slightly higher DNA compaction capacity. At near neutral surface charge (N/P ratio ~1), PPA–DNA nanoparticles tend to aggregate severely in an effort to decrease the surface area to volume ratio. In addition, the average particle size also decreases as the N/P ratio increases because excess positive charges facilitate higher DNA condensation efficiencies. However, particle sizes hit a plateau at an N/P ratio of 8, beyond which excess polymers would not be incorporated into the nanoparticle and remain in the solution as free polymers. All PPA–DNA particles show similar average size ranging from 120 to 140 nm at high N/P ratios (>8). Under these N/P ratios, the surfaces of these particles are positively charged with a ζ potential of about 20–30 mV.

1.123.11.5. Effect of N/P Ratio and Cell Culture Conditions on Transfection Efficiency of PPA–DNA Particles

Similar to those of the other polycationic gene carriers, transfection efficiencies of PPA–DNA complexes are dependent on the charge ratio (N/P) of the carrier to DNA. For example, the transfection efficiency of PPA-BPA/DNA complexes in HEK 293 cells increases with N/P ratio, reaching a maximum at N/P ratios between 15 and 20.[80] In the presence of 100 μM of chloroquine (CQ), the optimal N/P ratios of PPA-BPA/DNA complexes shift to 5–10. Under these conditions, PPA-BPA/DNA nanoparticles transfect cells nearly as efficiently as PEI/DNA and transfast/DNA complexes in HEK 293 cells. As mentioned in an earlier section, PPA forms more stable nanoparticles suitable for delivery over longer durations. One such example is to deliver genes to the CNS through a retrograde transport model. This is a noninvasive approach to deliver genes to the brain by injecting polycation/DNA complexes to the peripheral muscle. Following intramuscular injection of PPA-BPA/DNA nanoparticles (formulated at a sufficient N/P ratio required for particle stability) to the mouse tongue where the hypoglossal motor neurons locate, bcl-2- expression is detected on day 2 in the brain stem of the injected mouse at a level similar to that obtained with PEI/DNA complexes. The nanoparticles are thought to be transported to the neuron body by the motor neuron in the injected muscle via a retrograde transport mechanism.[77]

1.123.11.6. Effect of Charged Groups on Transfection Efficiency of PPA–DNA Particles

PPA-mediated transfection is charge-group dependent, as illustrated in a series of four PPA carriers with an identical backbone, same side-chain spacer, similar molecular weights, but different charge groups containing primary to quaternary amino groups[82] (PPA-EA, PPA-MEA, PPA-DMA, and PPA-TMA, see Table 5). Although the DNA compaction capacities of these PPAs increase in the order PPA-EA (lowest) < PPA-MEA < PPA-DMA < PPA-TMA (highest), their transfection efficiencies decrease in the same order (highest for PPA-EA, lowest for PPA-TMA). PPA-EA/DNA complexes gave the highest transfection efficiency in cell lines at N/P ratios from 6 to 20 (Figure 25). The *in vivo* transfection efficiency of this series of PPA–DNA nanoparticles is evaluated in a rat spinal cord gene expression model following intrathecal injection of PPA–DNA nanoparticles at a charge ratio of 10.[82] Matching the trend of transfection efficiency observed *in vitro*, gene expression level in the spinal cord is dependent upon the type of charge group. At a DNA dose of 4 μg, PPA-EA mediates the highest transgene expression among all four carriers. The luciferase expression activity is comparable to that of PEI, but with lower tissue toxicity. PPA-MEA with secondary amino group side chain follows with a 3.5-fold lower luciferase expression. PPA-DMA and PPA-TMA are not effective in this model, giving only a background level of gene expression. At such, one aspect of structure–transfection relationship can be established. PPA carriers bearing primary amino groups mediate the highest transfection efficiency.

1.123.11.7. Effect of PPA Side-Chain Structure on Transfection Efficiency

The side-chain structure (length and branching of PPA side chains bearing the terminal primary amino groups) is also a factor,[83] as illustrated in a series of seven PPA carriers: PPA-EA, PPA-PA, PPA-BA, PPA-DEA, PPA-EPA, PPA-DPA, and PPA-BPA (Table 5). These gene carriers fall into two groups based on their branching structure of side chains: those with linear side chains and those with branching side chains. Those with branching side chains consequently possess a higher charge density (two positive charges per repeating unit). When PPA–DNA complexes are used to transfect HeLa cells, transfection efficiency correlates strongly with the branching structure of the side chain rather than the length of the side chain. Transgene expression by PPAs with branching side chains generally show about tenfold higher efficiency than those with linear side chains (Figure 26). However, transfection efficiencies are not sensitive to the length of the PPA side chains. The same trend is also observed in transgene expression in primary rat hepatocytes.[79]

1.123.11.8. Combinatorial Approach Nanoparticle Formulated with PPAs Bearing Different Charge Groups

As mentioned in an earlier section, the type of charge group significantly influences the transfection efficiency of the gene carrier. PPAs with primary amino group side chains show high transfection efficiency in culture, whereas PPAs with secondary, tertiary, and quaternary amino groups are significantly less efficient.[82] But it has been speculated that the high transfection efficiency of PEI is a result of the coexistence of primary, secondary, and tertiary amino groups in the PEI structure.[84] Reschel *et al.* also showed that, of all the polymethacrylamide carriers they synthesized, the highest transfection activity was found for a copolymer carrier containing both primary and tertiary amines.[85] Polyamidoamine (PAMAM) dendrimer is a class of polymer that comprises a mixture of primary amino groups (on the surface) and tertiary amino groups (in the interior). Tang *et al.* reported that the fractured dendrimers (by partial hydrolysis to expose the tertiary amino groups) show 50-fold higher transfection efficiency than the

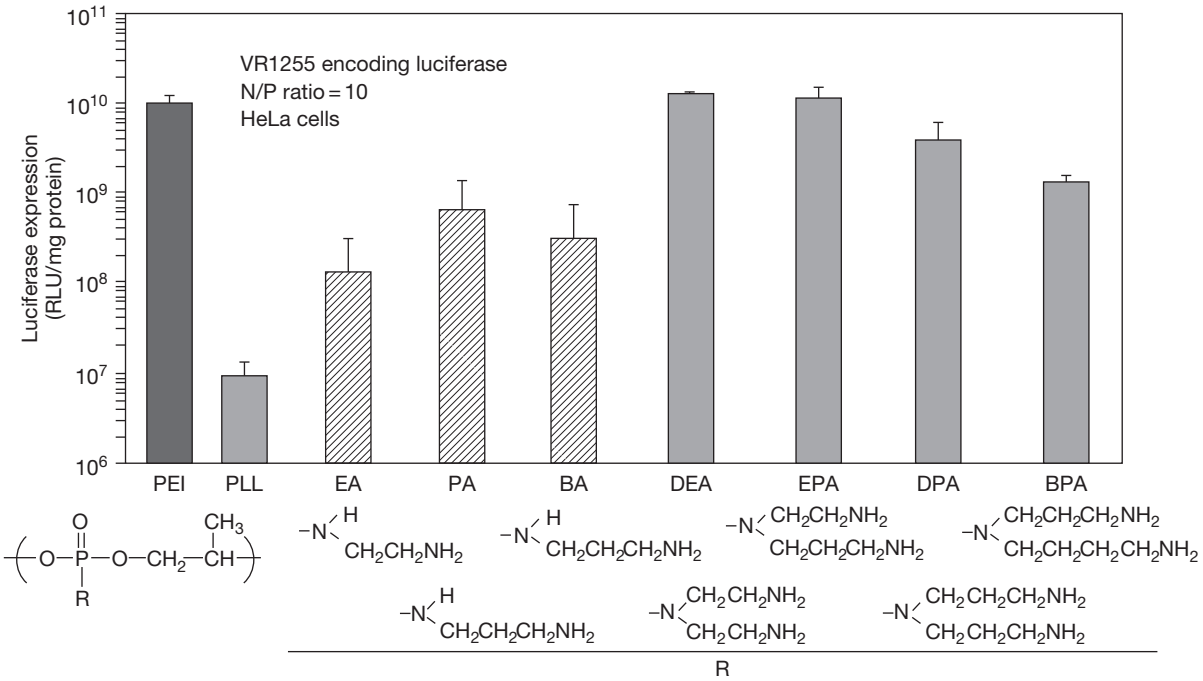

Figure 26 Transfection efficiencies of PPA with different side-chain lengths. Reproduced from Mao, H.; Leong, K. W.; Leaf Huang, M.-C. H.; Ernst, W. *Adv. Genet.* **2005**, *53*, 275–306, with permission from Elsevier.

intact dendrimers.[86] These results suggest that a combination of amino groups, other than primary amines, could enhance the transfection efficiency. However, the mechanism of enhancement is not clear at the current stage. Some groups claim that coexistence of different amine classes in the same polymer molecule enhances transfection efficiencies via proton-sponge effect (PEI) due to favorable apparent pK_a's.[87] However, this buffering effect occurs above physiological pH (8–10) and only a modest buffering effect is observed between pH 4 and 6[88] regardless of the amine class. Despite controversies surrounding the proton-sponge effect, it is certain that coexistence of different amine classes can enhance transfection efficiencies. Our work in PPAs also confirms this observation and will now be discussed.

Synthesizing PPAs with different amino groups in their side chains on the same polymer backbone in a controlled manner is challenging. Instead of synthesizing such a polymer, effects of different amine classes on transfection efficiency can be mimicked by formulating multicomponent complexes (e.g., formulating DNA with a mixture of two types of PPA: one containing 100% primary amino groups and another containing 100% tertiary amino groups). Such a ternary particle system containing DNA and PPAs with primary amino groups (PPA-SP, named as PPA-BPA in **Table 5**) and tertiary amino groups (PPA-DMA) was evaluated.[83] Transfection of COS-7 cells using the ternary complexes (PPA-SP/PPA-DMA/DNA) mediates significantly higher levels of gene expression than PPA-SP or PPA-DMA carrier alone, and the transfection efficiency is dependent on the ratio of the two carriers (**Figure 27**). Under optimal conditions (at a PPA-SP/PPA-DMA molar ratio of 4), the transfection efficiency achieved by the PPA-SP/PPA-DMA mixture is 20 and 160 times higher than PPA-SP and PPA-DMA-mediated transfection, respectively (**Figure 27**). Characterization of the nanoparticles and cellular uptake studies indicate that the enhancement in transfection efficiency by these ternary and quaternary systems appears to be unrelated to their particle size, zeta potential, or DNA uptake. In addition, the titration assay and the transfection experiment using a proton pump inhibitor suggest that the enhancement effect is unlikely due to the slightly improved buffering capacity of the mixture over PPA-BPA. Although the mechanism remains unclear, this study illustrates, from a different approach, that the charge group in the gene carrier, and in a general sense charge group in the nanoparticle formulation, is a crucial parameter determining the transfection efficiency of nanoparticles. This formulation method represents an alternative strategy to modulate the transfection efficiency of DNA nanoparticles.

1.123.11.9. PPA with Imidazole Moiety: Improving Buffering Capacity

All PPA and PPE carriers show a significant enhancement of gene expression in cell culture when chloroquine diphosphate (CQ) is present. This implies that these gene carriers have a low buffering capacity, a property that can facilitate endosomal escape of DNA or complexes into the cytosol. Imidazole moieties possess high buffering capacities. As the side chains of PPAs can be chemically modified, the buffering capacity of PPA carriers can be increased if imidazole groups are conjugated to the side chains of PPAs. As imidazolyl acetic acid is grafted on PPA-EA (two grafting densities were applied: 11 and 43%), the DNA-binding affinity of imPPA-EA (imidazole-modified PPA-EA) decreases as the imidazolyl conjugation degree

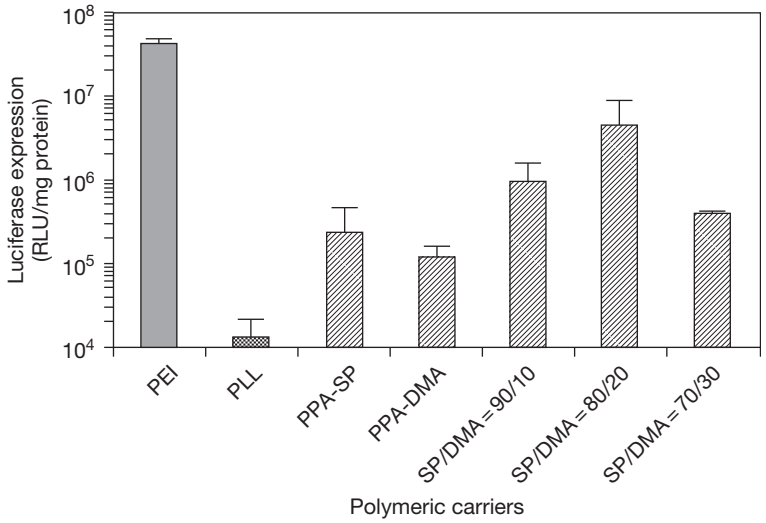

Figure 27 Transfection efficiencies of tenary PPA–DNA particles. Reproduced from Zhang, P.-C.; Wang, J.; *et al*. *Biomacromolecules* **2004**, *6*(1), 54–60, with permission from American Chemical Society.

increases. The minimum N/P ratios to completely complex plasmid DNA for imPPA-EA-11% and imPPA-EA-43% are 1.5 and 6.0, respectively. The ζ-potential of complexes at an N/P ratio of 8 decreases significantly from 34 mV to about 4 mV. Conjugated imidazole groups markedly increase the buffering capacity of imPPA-EA-43% above that of PEI. However, this does not translate into enhancement in gene expression. The transfection efficiency decreases as the imidazole content increases. This is most likely due to the reduced DNA compaction capacity of imPPA-EA, leading to a 'loose' complex. The average diameter of the complexes also increases substantially (from 78 nm for PPA-EA/ DNA to 746 nm for imPPA-EA-43%). These data indicate that DNA compaction capacity is crucial in maintaining the nanoparticle integrity and transfection efficiency.

1.123.11.10. Effect of on Transfection Efficiency by Ligand-Modified and PEG-Modified PPA

Transfection efficiencies may be increased by higher cellular uptake via receptor-mediated endocytosis. One such ligand–receptor pair is galactose and asialoglycoprotein found on hepatocytes. Effect of ligand modification on transfection efficiency is investigated by grafting galactose onto side chains of PPA-DPA with different degrees of ligand conjugation (6.5, 12.5, and 21.8%).[79] Due to multivalency effects, the affinity of Gal-PPA–DNA nanoparticles to galactose-recognizing lectin increases with increasing degree of galactose substitution. However, transfection efficiency for these galactosylated PPAs is decreased in HepG2 cells. This is due to the decreased DNA-binding capacity and decreased particle stability (similar to the observation of reduced transfection efficiency for imPPA-EA carriers discussed earlier). In order to overcome this reduced stability, DNA was precondensed with PPA at a charge ratio of 0.5, yielding nanoparticles with negative surface charge, followed by adding Gal-PPA to the required N/P ratio, resulting in a Gal-PPA–DNA–PPA ternary complex. Such a ternary nanoparticle formulation leads to significant size reduction compared to binary nanoparticles, particularly at low N/P ratios (2–5). In HepG2 cells and primary rat hepatocytes, and at low N/P ratios (2–5), transfection efficiency mediated by ternary nanoparticles prepared with 6.5% Gal-PPA is 6–7200 times higher than that of PPA-DPA/DNA nanoparticles.[79] Such an enhancement effect is not observed in HeLa cells that lack the asialoglycoprotein receptor (ASGPR). The improvement in transgene expression is most prominent at lower N/P ratios. Nevertheless, increasing the galactosylation degree of PPA carrier (higher than 12.5%) significantly reduces the stability of ternary particles, as well as the transfection efficiency. This study demonstrates that ligand conjugation (in this case galactosylation) of PPA carrier significantly affects the physiochemical properties of PPA–DNA nanoparticles as a result of the lowered DNA compaction capacity, reduced stability, and increased particle size. This is so despite the fact that galactosylated nanoparticles can efficiently recognize and bind to galactose-recognizing lectin moieties.

Pegylation is another common strategy in nanomedicine used to increase the transfection efficiency of nanoparticles via avoidance of the reticuloendothelial system and increased colloidal stability. PPA-DPA is pegylated by using PEG as the macroinitiator during the synthesis of PPA-DPA, resulting in the PEG-*b*-PPA copolymer.[78] When compared to PPA-DPA/DNA nanoparticles, PEG-*b*-PPA–DNA nanoparticles are slightly smaller (~100 nm) and possess a lower zeta potential (~+10 mV). Although the *in vitro* transfection efficiency of PEG-*b*-PPA–DNA particles (in primary rat hepatocytes) is lower than its unpegylated counterparts, the *in vivo* efficiency (via intrabilliary infusion of nanoparticles into bile duct, which eventually reaches the liver) is significantly higher. This study demonstrates that PEG is able to increase the transfection efficiency *in vivo* by preventing aggregation of PEG-*b*-PPA–DNA nanoparticles. However, no transfection is detected in lung, kidney, heart, and spleen. Given the fact PEG-*b*-PPA–DNA particles still possess a positive zeta potential, the degree of pegylation might not have been sufficient to avoid clearance by reticuloendothelial system.

In summary, this section highlights a systematic approach to the design of PPE and PPA gene carriers. PPA forms more stable DNA nanoparticles than PPE, leading to higher transfection efficiencies. Effects of charge groups, segment length, side-chain branching, and N/P ratios on the physiochemical properties of PPA–DNA nanoparticles and transfection efficiencies have been investigated. Effort to increase the buffering capacity and cellular uptake of the gene carriers has also been successful by conjugating imidazole moieties and galactose ligand, respectively, but produces overall disappointing results because of the offsetting factors of poorer DNA protection and larger particle size. Combinatorial approach of formulating particles with different classes of amines has proved to be moderately effective in increasing transfection efficiencies. PEG-modified PPA has been effective in reducing incidences of particle aggregation, leading to higher transfection efficiencies *in vivo*. Our investigations hitherto reinforce the notion that an integrative approach addressing all the barriers of the delivery process is crucial to the success of gene carrier development. Along this line, the versatility of the PPE gene carriers offers excellent opportunities for optimization.

1.123.12. Conclusion

In this chapter, we provided an overview of the basics of PLGAs and how they are applied in the context of drug and gene delivery as well as tissue engineering. In particular, different length scales of similar PLGAs differ widely in bulk properties and are consequently applied in different ways. Additionally, we also rigorously reviewed PPEs on how changes in molecular structure not only affect material properties at different length scales but also give rise to novel material properties. We also reviewed that it is possible to tune the material properties of PPE-based biomaterials by changing the molecular compositions of the PPE backbone or the side chains. As medical technologies increasingly demand more complex functions, the call for more sophisticated biodegradable polymers will correspondingly increase. Opportunities abound, for example, to innovate with more sensitive stimulus–responsiveness or shape memory to accentuate the dynamic properties of degradable biomaterials. The best days of biodegradable polymers are still ahead of us.

References

1. Williams, D. F. *Biomaterials* **2009**, *30*, 5897–5909.
2. Langer, R. *Science* **2001**, *293*, 58–59.
3. Grigsby, C. L.; Leong, K. W. *J. R. Soc. Interface* **2010**, *7*(Suppl. 1), S67–S82.
4. Bowman, K.; Leong, K. W. *Int. J. Nanomedicine* **2006**, *1*, 117–128.
5. Chakraborty, S.; Liao, I. C.; Adler, A.; Leong, K. W. *Adv. Drug Deliv. Rev.* **2009**, *61*, 1043–1054.
6. Dang, J. M.; Leong, K. W. *Adv. Drug Deliv. Rev.* **2006**, *58*, 487–499.
7. Gunatillake, P.; Mayadunne, R.; Adhikari, R. *Biotechnol. Annu. Rev.* **2006**, *12*, 301–347.
8. Ifkovits, J. L.; Burdick, J. A. *Tissue Eng.* **2007**, *13*, 2369–2385.
9. Luten, J.; van Nostrum, C. F.; De Smedt, S. C.; Hennink, W. E. *J. Control. Release* **2008**, *126*, 97–110.
10. Panyam, J.; Labhasetwar, V. *Adv. Drug Deliv. Rev.* **2003**, *55*, 329–347.
11. Park, J. H.; Ye, M.; Park, K. *Molecules* **2005**, *10*, 146–161.
12. Pridgen, E. M.; Langer, R.; Farokhzad, O. C. *Nanomedicine (Lond)* **2007**, *2*, 669–680.
13. Putnam, D. *Nat. Mater.* **2006**, *5*, 439–451.
14. Saito, N.; Murakami, N.; Takahashi, J.; *et al. Adv. Drug Deliv. Rev.* **2005**, *57*, 1037–1048.
15. Vasir, J. K.; Labhasetwar, V. *Adv. Drug Deliv. Rev.* **2007**, *59*, 718–728.
16. Yamanaka, Y. J.; Leong, K. W. *J. Biomater. Sci. Polym. Ed.* **2008**, *19*, 1549–1570.
17. Zhao, Z.; Wang, J.; Mao, H. Q.; Leong, K. W. *Adv. Drug Deliv. Rev.* **2003**, *55*, 483–499.
18. Lu, J. M.; Wang, X. W.; Marin-Muller, C.; *et al. Expert Rev. Mol. Diagn.* **2009**, *9*, 325–341.
19. Alexis, F. *Polym. Int.* **2005**, *54*, 36–46.
20. Uchegbu, I. F.; Schatzlein, A. G. *Polymers in Drug Delivery*. CRC Press: Boca Raton, FL, 2006.
21. Ueda, H.; Tabata, Y. *Adv. Drug Deliv. Rev.* **2003**, *55*, 501–518.
22. Engelberg, I.; Kohn, J. *Biomaterials* **1991**, *12*, 292–304.
23. Jain, R. A. *Biomaterials* **2000**, *21*, 2475–2490.
24. Park, T. G. *Biomaterials* **1995**, *16*, 1123–1130.
25. Heya, T.; Okada, H.; Ogawa, Y.; Toguchi, H. *Int. J. Pharm.* **1991**, *72*, 199–205.
26. Anderson, J. M.; Shive, M. S. *Adv. Drug Deliv. Rev.* **1997**, *28*, 5–24.
27. Li, S. M.; Garreau, H.; Vert, M. *J. Mater. Sci. Mater. Med.* **1990**, *1*, 131–139.
28. Lee, W. K.; Park, J. Y.; Yang, E. H.; *et al. J. Control. Release* **2002**, *84*, 115–123.
29. Dunne, M.; Corrigan, O. I.; Ramtoola, Z. *Biomaterials* **2000**, *21*, 1659–1668.
30. Panyam, J.; Dali, M. A.; Sahoo, S. K.; *et al. J. Control. Release* **2003**, *92*, 173–187.
31. Siepmann, J.; Faisant, N.; Akiki, J.; Richard, J.; Benoit, J. P. *J. Control. Release* **2004**, *96*, 123–134.
32. Berkland, C.; Kim, K.; Pack, D. W. *Pharm. Res.* **2003**, *20*, 1055–1062.
33. Kou, J. H.; Emmett, C.; Shen, P.; *et al. J. Control. Release* **1997**, *43*, 123–130.
34. Visscher, G. E.; Robison, R. L.; Maulding, H. V.; Fong, J. W.; Pearson, J. E.; Argentieri, G. J. *J. Biomed. Mater. Res.* **1985**, *19*, 349–365.
35. Hariharan, S.; Bhardwaj, V.; Bala, I.; Sitterberg, J.; Bakowsky, U.; Kumar, M. *Pharm. Res.* **2006**, *23*, 184–195.
36. Mittal, G.; Sahana, D. K.; Bhardwaj, V.; Kumar, M. *J. Control. Release* **2007**, *119*, 77–85.
37. Fu, K.; Pack, D. W.; Klibanov, A. M.; Langer, R. *Pharm. Res.* **2000**, *17*, 100–106.
38. Kang, S. W.; Lim, H. W.; Seo, S. W.; Jeon, O.; Lee, M.; Kim, B. S. *Biomaterials* **2008**, *29*, 1109–1117.
39. Prabha, S.; Labhasetwar, V. *Pharm. Res.* **2004**, *21*, 354–364.
40. Shin, H. J.; Lee, C. H.; Cho, I. H.; *et al. J. Biomater. Sci. Polym. Ed.* **2006**, *17*, 103–119.
41. Cleland, J. L.; Lim, A.; Barron, L.; Duenas, E. T.; Powell, M. F. *J. Control. Release* **1997**, *47*, 135–150.
42. Jaganathan, K. S.; Vyas, S. P. *Vaccine* **2006**, *24*, 4201–4211.
43. Straub, J. A.; Chickering, D. E.; Church, C. C.; Shah, B.; Hanlon, T.; Bernstein, H. *J. Control. Release* **2005**, *108*, 21–32.
44. Jaklenec, A.; Wan, E.; Murray, M. E.; Mathiowitz, E. *Biomaterials* **2008**, *29*, 185–192.
45. Jeong, B.; Bae, Y. H.; Kim, S. W. *Macromolecules* **1999**, *32*, 7064–7069.
46. Jeong, B.; Bae, Y. H.; Kim, S. W. *J. Control. Release* **2000**, *63*, 155–163.
47. He, C. L.; Kim, S. W.; Lee, D. S. *J. Control. Release* **2008**, *127*, 189–207.
48. Li, Z. H.; Ning, W.; Wang, J. M.; *et al. Pharm. Res.* **2003**, *20*, 884–888.
49. Lu, L.; Peter, S. J.; Lyman, M. D.; *et al. Biomaterials* **2000**, *21*, 1837–1845.
50. Richards, M.; Dahiyat, B. I.; Arm, D. M.; Brown, P. R.; Leong, K. W. *J. Biomed. Mater. Res.* **1991**, *25*, 1151–1167.
51. Penczek, S.; Lapienis, G.; Kaluzynski, K.; Nyk, A. *Pol. J. Chem.* **1994**, *68*, 2129.
52. Baran, J.; Penczek, S. *Macromolecules* **1995**, *28*, 5167–5176.
53. Penczek, S.; Pretula, J.; *et al. Pol. J. Chem.* **2001**, *75*(8), 1087–1194.
54. Mao, H.; Leong, K. W.; Leaf Huang, M.-C. H.; Ernst, W. *Adv. Genet.* **2005**, *53*, 275–306.
55. Cleland, W. W.; Hengge, A. C. *Chem. Rev.* **2006**, *106*, 3252–3278.
56. Wang, F.; Wang, Y.-C.; Yan, L.-F.; Wang, J. *Polymer* **2009**, *50*, 5048–5054.
57. Xiong, M. H.; Wu, J.; Wang, Y. C.; *et al. Macromolecules* **2009**, *42*, 893–896.
58. Baran, J.; Penczek, S. *Macromolecules* **1995**, *28*, 5167–5176.
59. Cassano, A. G.; Anderson, V. E.; Harris, M. E. *J. Am. Chem. Soc.* **2002**, *124*, 10964–10965.
60. Shi, F. Y.; Wang, L. F.; Tashev, E.; Leong, K. W. In *Polymeric Drugs and Drug Delivery Systems*; Dunn, R. L., Ottenbrite, R. M., Eds.; American Chemical Society: Washington, DC, 1991; pp 141–154.
61. Wang, J.; Mao, H. Q.; Leong, K. W. *J. Am. Chem. Soc.* **2001**, *123*, 9480–9481.
62. Wang, J.; Huang, S. W.; Zhang, P. C.; Mao, H. Q.; Leong, K. W. *Int. J. Pharm.* **2003**, *265*, 75–84.
63. Chaubal, M. V.; Su, G.; *et al. J. Biomater. Sci. Polymer Ed.* **2003**, *14*(1), 45–61.
64. Mao, H. Q.; Shipanova-Kadiyala, I.; Zhao, Z.; Dang, W. B.; Brown, A.; Leong, K. W. *J. Biomater. Sci. Polym. Ed.* **2005**, *16*, 135–161.
65. Tabor, C. W.; Tabor, H. *Annu. Rev. Biochem.* **1984**, *53*, 749–790.

66. Yang, X. Z.; Wang, Y. C.; Tang, L. Y.; Xia, H.; Wang, J. *J. Polym. Sci. A Polym. Chem.* **2008**, *46*, 6425–6434.
67. Wang, Y. C.; Tang, L. Y.; Sun, T. M.; Li, C. H.; Xiong, M. H.; Wang, J. *Biomacromolecules* **2008**, *9*, 388–395.
68. Wang, Y. C.; Liu, X. Q.; Sun, T. M.; Xiong, M. H.; Wang, J. *J. Control. Release* **2008**, *128*, 32–40.
69. Cheng, J.; Ding, J. X.; Wang, Y. C.; Wang, J. *Polymer* **2008**, *49*, 4784–4790.
70. Barker, I. C.; Cowie, J. M. G.; Huckerby, T. N.; Shaw, D. A.; Soutar, I.; Swanson, L. *Macromolecules* **2003**, *36*, 7765–7770.
71. Kjellander, R.; Florin, E. *J. Chem. Soc. Faraday Trans. I* **1981**, *77*, 2053–2077.
72. Iwasaki, Y.; Wachiralarpphaithoon, C.; *et al*. *Macromolecules* **2007**, *40*(23), 8136–8138.
73. Iwasaki, Y.; Kawakita, T.; Yusa, S. *Chem. Lett.* **2009**, *38*, 1054–1055.
74. Wang, Y. C.; Yuan, Y. Y.; Du, J. Z.; Yang, X. Z.; Wang, J. *Macromol. Biosci.* **2009**, *9*, 1154–1164.
75. Wu, J.; Liu, X. Q.; Wang, Y. C.; Wang, J. *J. Mater. Chem.* **2009**, *19*, 7856–7863.
76. Yuan, Y. Y.; Liu, X. Q.; Wang, Y. C.; Wang, J. *Langmuir* **2009**, *25*, 10298–10304.
77. Wang, J.; Zhang, P. C.; Mao, H. Q.; Leong, K. W. *Gene Ther.* **2002**, *9*, 1254–1261.
78. Jiang, X.; Dai, H.; Ke, C.-Y.; *et al*. *J. Control. Release* **2007**, *122*, 297–304.
79. Zhang, X. Q.; Wang, X. L.; Zhang, P. C.; *et al*. *J. Control. Release* **2005**, *102*, 749–763.
80. Wang, J.; Zhang, P. C.; Lu, H. F.; *et al*. *J. Control. Release* **2002**, *83*, 157–168.
81. Li, Y.; Wang, J.; Lee, C. G. L.; *et al*. *Gene Ther.* **2004**, *11*, 109–114.
82. Wang, J.; Gao, S. J.; Zhang, P. C.; Wang, S.; Mao, H. Q.; Leong, K. W. *Gene Ther.* **2004**, *11*, 1001–1010.
83. Zhang, P.-C.; Wang, J.; Leong, K. W.; Mao, H.-Q. *Biomacromolecules* **2004**, *6*, 54–60.
84. Thomas, M.; Klibanov, A. M. *Proc. Natl. Acad. Sci. USA* **2002**, *99*, 14640–14645.
85. Reschel, T.; Konák, C.; Oupický, D.; Seymour, L. W.; Ulbrich, K. *J. Control. Release* **2002**, *81*, 201–217.
86. Tang, M. X.; Redemann, C. T.; Szoka, F. C. *Bioconjug. Chem.* **1996**, *7*, 703–714.
87. Suh, J.; Paik, H. J.; Hwang, B. K. *Bioorg. Chem.* **1994**, *22*, 318–327.
88. von Harpe, A.; Petersen, H.; Li, Y.; Kissel, T. *J. Control. Release* **2000**, *69*, 309–322.
89. Li, Q.; Wang, J.; *et al*. *Biomaterials* **2006**, *27*(7), 1027–1034.
90. Du, J. Z.; Sun, T. M.; *et al*. *Biomacromolecules* **2007**, *8*(11), 3375–3381.
91. Iwasaki, Y.; Nakagawa, C.; *et al*. *Biomacromolecules* **2004**, *5*(3), 1110–1115.
92. Wang, Y. C.; Tang, L. Y.; Li, Y.; Wang, J. *Biomacromolecules* **2009**, *10*, 66–73.
93. Huang, S. W.; Wang, J.; *et al*. *Biomacromolecules* **2004**, *5*(2), 306–311.

1.124. Polymer Films Using LbL Self-Assembly

V Kozlovskaya and E Kharlampieva, University of Alabama at Birmingham, Birmingham, AL, USA
S A Sukhishvili, Stevens Institute of Technology, Hoboken, NJ, USA

© 2011 Elsevier Ltd. All rights reserved.

1.124.1.	**Introduction: Strategies for Surface Modification with Polymers**	418
1.124.2.	**Fundamentals of Multilayer Formation: LbL Thin Films**	419
1.124.2.1.	Electrostatic Self-Assembly of Polymers from Aqueous Solutions	419
1.124.2.1.1.	Equilibrium and dynamics in PEMs: lessons from PECs	419
1.124.2.1.2.	Internal structure of electrostatically assembled multilayers	421
1.124.2.2.	Hydrogen-Bonded Self-Assembly of Polymers from Aqueous Solutions	422
1.124.2.2.1.	Assembly, internal structure, and properties of HB films	423
1.124.2.2.2.	Temperature-controlled HB release films	424
1.124.2.3.	LbL-Derived Hydrogels	425
1.124.2.3.1.	Hydrogels derived from electrostatically assembled multilayers	425
1.124.2.3.2.	Hydrogels derived from HB multilayers	426
1.124.2.3.3.	LbL-derived hydrogels via click chemistry	427
1.124.2.3.4.	Mechanical properties of the LbL-derived hydrogel films	427
1.124.2.3.5.	Applications of LbL hydrogels to controlled release of bioactive molecules	427
1.124.2.3.6.	Nanoparticle-containing layered hydrogel films	428
1.124.3.	**Conclusions**	428
References		429

Abbreviations

AFM	Atomic force microscopy
ATR-FTIR	Attenuated total reflection–Fourier transform infrared spectroscopy
DP	Degree of polymerization
dPMAA	Deuterated poly(methacrylic acid)
EDA	Ethylenediamine
EDC	1-Ethyl-3-(3-dimethylaminopropyl) carbodiimide hydrochloride
FITC	Fluorescein isothiocyanate
FTIR	Fourier transform infrared spectroscopy
GA	Glutaraldehyde
HA	Hyaluronic acid
HB	Hydrogen-bonded
HPC	Hydroxypropylcellulose
LbL	Layer-by-layer
LCST	Lower critical solution temperature
Lys	Lysozyme
MC	Methylcellulose
NHS	*N*-hydroxysulfosuccinimide
PAA	Poly(acrylic acid)
PAAM	Poly(acrylamide)
PAH	Poly(allylamine hydrochloride)
PAMA	Poly(dimethylaminoethyl methacrylate)
PE	Polyelectrolyte
PEAA	Poly(ethacrylic acid)
PEC	Polyelectrolyte complex
PEI	Poly(ethylene imine)
PEM	Polyelectrolyte multilayers
PEO	Poly(ethylene oxide)
pH_{crit}	Critical pH value
PHEA	Poly(2-hydroxyethyl acrylate)
PLL	Poly(L-lysine)
PMAA	Poly(methacrylic acid)
PMAA-SH	Cysteamine-modified poly(methacrylic acid)
PNIPAM	Poly(isopropylacrylamide)
PSMA	Poly(styrene-alt-(maleic acid))
PSS	Poly(styrene sulfonate)
PVA	Poly(vinyl alcohol)
PVCL	Poly(vinylcaprolactam)
PVME	Poly(vinyl methyl ether)
PVPON	Poly(vinylpyrrolidone)
Q20	20%-quaternized poly(*N*-ethyl-4-vinylpyridinium bromide)
QPVP	Quaternized poly(*N*-ethyl-4-vinylpyridinium bromide)
SA LbL	Spin-assisted layer-by-layer assembly
SAM	Self-assembled monolayer
TEM	Transmission electron microscopy
UCST	Upper critical solution temperature
WPEC	Water-soluble polyelectrolyte complex
wPEM	Weak polyelectrolyte multilayer

Symbols

b	Scattering length
d_{bl}	Bilayer thickness
f^+	Fraction of positively charged units
K	KiloDalton
Q	Wavevector

V	Volume	σ	Interlayer roughness
z	Distance from Si template	Σ	Scattering density

1.124.1. Introduction: Strategies for Surface Modification with Polymers

Along with the bulk properties of biomaterials, the chemistry and structure of biomaterial surfaces are critically important to assure desired biocompatibility, wear resistance, adherence or antifouling properties. Controlled surface modification is therefore the key to developing advanced materials with rationally designed biological responses. Polymer coatings can be deposited at surfaces using traditional techniques established for depositing inorganic materials in semiconductor and microelectronics industries, which include spin-coating, physical and chemical vapor deposition, sputtering, or anodic polymerization[1,2] (Scheme 1). Two other groups of techniques – chemical grafting and molecular self-assembly – include bottom–up approaches with significantly better molecular-level control of surface architectures (Scheme 1). For example, polymer brushes of various chemistry and grafting density can be fabricated at surfaces using a chemical grafting approach which can be subdivided into growing polymer brushes via surface-initiated polymerization or grafting presynthesized polymer chains to surfaces ('grafting from' and 'grafting to' approaches, respectively).[3] Another group of surface modification techniques includes molecular self-assembly which is represented by deposition of self-assembled monolayers (SAMs)[4] and layer-by-layer (LbL) polymer films[5,6] (Scheme 1). In the SAM approach, organic molecules are deposited at the substrate driven by the interaction between the head group of self-assembling molecules and surface-binding sites, while the choice of chemistry of molecular end-group affords great flexibility in decorating substrate surfaces with specific chemical functionalities. A similar advantage of molecular control of surface chemistry is also afforded by the chemical grafting approach. However, while both chemical grafting and SAM approaches are advantageous over more traditional polymer film deposition techniques, they are both significantly limited by the requirement of specific chemistry of the substrate surface. In particular, grafting approaches require decoration of surfaces with specific functional groups or initiators capable of supporting polymerization or grafting chemical reactions. The SAM approach is even more restrictive as it involves formation of covalent Si–O or strong thiol–metal bonds between organic molecules and the surface, and usually can only be applied to a limited number of surfaces, such as silicon, aluminum oxide, or noble metals.

Compared to the above surface-modification techniques, deposition of polymer films at surfaces using LbL self-assembly has emerged as a promising and versatile surface modification technique.[7–12] The LbL procedure is all-aqueous based, and is not restricted by specific chemistry of substrates or depositing polymers. Indeed, conformal LbL films can be produced on substrates of virtually any shape or chemistry. Film growth occurs as polymer molecules sequentially adsorb at a surface driven by a variety of interactions in aqueous environment, for example, through electrostatic interactions, hydrogen bonding, and hydrophobic forces, or even specific 'key-lock' type binding between biological molecules.[8,13] Recently, the versatility of the LbL technique was further extended by the demonstration that LbL films of noninteracting polymers can also be fabricated at surfaces by chemically reacting polymers using 'click chemistry.'[14] Besides earlier reported use of 'as-is' self-assembled multilayers, recent studies showed several promising opportunities in converting self-assembled LbL films into surface-bound functional hydrogels using postdeposition cross-linking followed by release of film components[15] (Scheme 2). Such soft, functional surface coatings have a multilayer-templated, nanoscopic level of control of film thickness, and are attractive for biomedical applications such as soft hydrogel coatings, which can also serve as 'depots' for controlled delivery of bioactive molecules from biomaterial surfaces. In addition, LbL films can also be used as base layers for further decorations of biomaterial surfaces with polymer brushes when one needs to achieve better

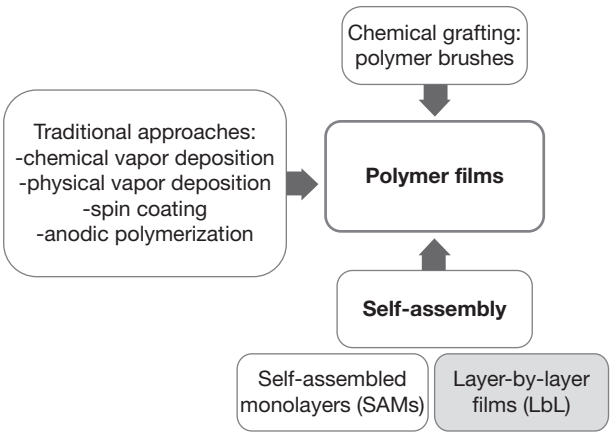

Scheme 1 Various techniques for depositing polymer films at surfaces.

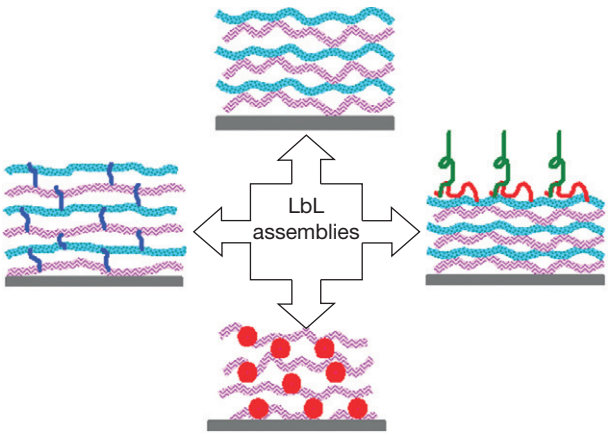

Scheme 2 Possible ways of functionalizing surfaces using LbL self-assembly.

lubrication, biocompatibility or antifouling properties of polymer coatings. While the LbL approach has not yet made a strong appearance in everyday applications in practical biomaterials science, we believe that the technique will become a universal tool for engineering multifunctional coatings of next generation biomaterials. Therefore, in this chapter we will discuss fundamentals of depositing macromolecules at surfaces using the LbL technique, internal structure of LbL films, and postassembly modification of polyelectrolyte multilayers (PEMs) into responsive surface hydrogels, all with the central focus on understanding structure–property relationships of such coatings.

1.124.2. Fundamentals of Multilayer Formation: LbL Thin Films

The fundamentals and applications of LbL films as novel types of nanoscopically structured materials are summarized in several recent reviews.[13,16–19] The deposition procedure is temptingly simple and is often viewed as being applicable to virtually any pair of synthetic polyelectrolytes (PEs) or biological macromolecules such as proteins, enzymes, or nucleic acids. Indeed, a variety of interacting macromolecules have been successfully used for multilayer construction. However, here we would like to first focus on the fundamental correlation between the formation of polyelectrolyte complexes (PECs) in solutions and deposition of PEMs at surfaces, and discuss the rarely mentioned cases when such coatings cannot be constructed.

1.124.2.1. Electrostatic Self-Assembly of Polymers from Aqueous Solutions

1.124.2.1.1. Equilibrium and dynamics in PEMs: lessons from PECs

Cohen Stuart and coworkers[20] have clearly emphasized the correlation between the phase behavior of PECs in solution and the deposition of PEMs. Specifically, using a PE pair of poly(dimethylaminoethyl methacrylate) (PAMA) and poly (acrylic acid) (PAA), the authors observed overshoots in the total amount of polymers within a film at the step of the polycation addition. Kovačević *et al.*[21] found that erosion of PAMA/PAA PEMs at ionic strength of 5 mM was explained by the formation of a negatively charged water-soluble PE complex (WPEC) or positively charged WPECs during the deposition of polyanion or polycation, respectively. Because of the interrelationships in behavior of PEMs and PECs, understanding occurrences of PEM erosion is very important as it will eventually provide materials scientists with a 'map' of PEM growth enabling them to rationally avoid unstable regimes during film deposition.[22]

Limitations of the LbL technique were recognized in cases when no interpolyelectrolyte binding occurred, such as for polymers whose charge density is lower than critical.[23,24] Disruption of interpolyelectrolyte binding can also be salt-induced[25] and or pH-induced.[26–28] Other observations, however, were also made of removal of PE chains from the PEM when the substrate is brought in contact with PE solutions. Such chain removal has been reported by several authors[29–31] and is usually related to solubilization of adsorbed chains through formation of WPECs.[32] Competitive removal of PE chains from PEM to WPEC implies that chains remain strongly associated both in the PEM and WPEC, but redistribution of chains occurs, favoring WPECs and resulting in PEM erosion. One then concludes that strong intermolecular association between a pair of PE chains is not the only prerequisite for successful film deposition.

Indeed, when a PEM is brought in contact with a solution of free PE chains (a situation routinely occurring during PEM buildup), erosion of multilayers can occur. Under these conditions, one usually finds a large excess of PE in solution compared to an oppositely charged polymer within the film. For PE systems in which chain exchange occurs at the experimental time scale, such excess of charged chains in solution is most favorable for the formation of WPECs.[33]

Detailed understanding of competition between surface and solution as applied to PEMs requires either selective labeling of polymers and/or the application of techniques which allow chemically specific monitoring of film components, such as *in situ* attenuated total reflection–Fourier transform infrared (ATR-FTIR) spectroscopy. Using this technique, effects of a number of parameters, such as the type of interacting PE chains, the ratio of their lengths, as well as ionic strength and pH of deposition solutions, can be considered to determine the likelihood of multilayer stability or erosion.[22] **Figure 1**, top panel, shows data where 98% quaternized poly-*N*-ethyl-4-vinylpyridinium bromide (QPVP, M_w of 330 K, a polymerization degree DP_{QPVP} of 1600) was assembled with poly (methacrylic acid) (PMAA, M_w of 150 K, DP_{PMAA} of 1700) at pH 8.4, when both components are strongly charged.

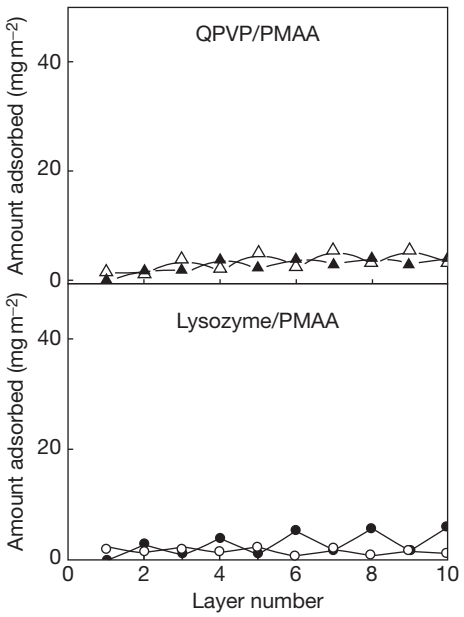

Figure 1 LbL deposition of ten layers in QPVP/PMAA (top panel) and lysozyme/PMAA systems (bottom panel). Assembly of PMAA (open symbols) and QPVP or lysozyme (filled symbols) were performed for 30 min from 0.1 mg ml^{-1} solution in 0.01 M phosphate buffer at pH 8. Reprinted with permission from Sukhishvili, S. A.; Kharlampieva, E.; Izumrudov, V. A. *Macromolecules* **2006**, *39*, 8873–8881. Copyright 2006 American Chemical Society.

A similar failure in film deposition occurs when one tries to self-assemble a globular protein, lysozyme (Lys, M_w 14 600, p*I* 11.0), with PMAA at pH 8.4 where PMAA is fully ionized and Lys carries overall positive charge. As shown in Figure 1, bottom panel, Lys is completely removed from the surface to solution at the step of polyacid deposition, and adsorbed polyacid is, in turn, solubilized by Lys. In solution, strong binding between a positively charged protein and charged polycarboxylic acids was found, with formation of WPECs in excess PMAA.[34] Also, solubilization of PE chains by proteins of opposite charge has been observed earlier.[35,36]

In contrast, enhanced deposition of polymer layers, illustrated in Figure 2 (bottom panel), is dictated by the phase diagrams of WPECs (Figure 2, top panel), which shows that formation of water-insoluble complexes is thermodynamically favorable at relatively high salt concentrations. The equilibrated amounts adsorbed depend on phase diagrams for a particular polycation/polyanion pair and may vary greatly between systems. Interestingly, while multilayer formation is prohibited in 0.01 M phosphate buffer solutions, films exhibit significant growth when the concentration of counter ions becomes very low (less than 0.003 M buffer or salt solutions).

The type of PE has been shown to critically affect the binding energy and equilibration time of interacting PEs in solution. In general, polycations with high density of primary amino groups and polyanions with sulfate or sulfonate groups

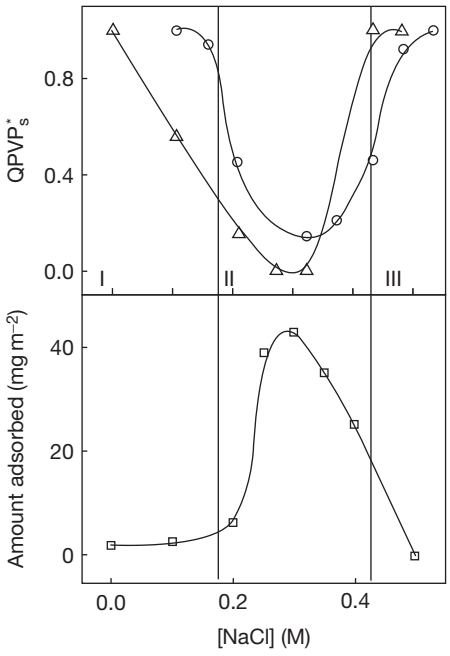

Figure 2 Top panel: Fraction of QPVP remaining in supernatants (QPVP*$_s$) of QPVP/PMAA mixtures for PMAA (M_w 350 K, DP 4000) in excess of PMAA, $f^+ = 0.167$ (circles) and in excess of QPVP (M_w 330 K, DP 1600), $f^+ = 0.833$ (triangles) plotted against concentration of added salt. Bottom panel: Total amount adsorbed of nine-layer QPVP/PMAA films deposited from solution with various salt concentrations. Concentrations of polymers were 0.04 M (in monomer units) in top panel, and 0.1 mg ml^{-1} in bottom panel. In all experiments, 0.01 M phosphate buffer at pH 8.4 was used. Reprinted with permission from Sukhishvili, S. A.; Kharlampieva, E.; Izumrudov, V. A. *Macromolecules* **2006**, *39*, 8873–8881. Copyright 2006 American Chemical Society.

show the strongest interpolyelectrolyte binding, resulting in inhibited chain exchange within PECs and/or PEMs. With weakly bound PE pairs – polycations containing quaternary ammonium groups and carboxylate polyanions – WPECs are easily formed, often resulting in erosion of PEMs.

For easily equilibrating PEC systems consisting of polyamines with tertiary or quaternary amino groups and polyacids with carboxylate or phosphate groups, it was shown that WPECs are thermodynamically stable structures, with a measurable chain transfer rate between molecularly dispersed complexes.[37] Here, we consider cases where all participating polymers are highly charged, that is, either the case of strong polyacids and polybases, or weak polyacids/polybases exposed to pH values significantly higher/lower than their pK_a so that macromolecules can be considered strong PEs under these conditions. Binding of two oppositely charged PE chains results in formation of multiple polymer–polymer contacts. The multiplicity of polymer–polymer contacts within polymer complexes has major consequences for PE interactions. Therefore, the observation of chain removal during deposition of strongly charged PEs within PEMs is a common phenomenon when polycations with tertiary or quaternary amino groups and polycarboxylic acid chains are used.

Recently, a quantitative approach to evaluate the binding constants K_1 and K_n, where K_1 is the binding constant of the interacting monomeric units, and K_n is the binding constant between two interacting chains having n polymer–polymer contacts, was proposed based on studies of competitive reactions in three-component PE solutions. Interestingly, for 3,3-ionene/DNA and 3,3-ionene/PAA systems, K_1 values showed only a small difference (1.012 and 1.024 for 3,3-ionene/DNA and 3,3-ionene/PAA, respectively). However, for systems with polystyrene sulfonate (PSS), much larger K_1 values were found. Specifically, for PSS/poly-L-histidine systems K_1 was ~2, that is, twice that of DNA/poly-L-histidine[38] or DNA/3,3-ionene[39] complexes. The large difference reflected irreversible binding of PSS with the polycation in the presence of DNA. This finding is consistent with other reports that in mixtures of polyanions, a polycation preferentially binds with macromolecules with sulfonate and/or sulfate groups such as, poly (vinylsulfonate),[40] PSS,[41–43] or poly(vinylsulfate).[44] The presence of a small number of sulfate or sulfonate groups in the polycarboxylate polymer chains provides strong selective binding with a polycation in polyanion mixtures, even though the mixture contained polycarboxylate polyanions of much higher charge density.[45,46]

Strong binding of sulfate- and sulfonate-based polyanions with polycations also has a profound impact on kinetics of interpolyelectrolyte chain exchange. The first striking observation is a significant acceleration of the substitution reactions, that is, an increase in the transfer rate of polycations from carboxylate to sulfate- and sulfonate-based polyanions. The rate of chain exchange in PECs is enhanced in the presence of low molecular weight electrolytes due to screening and weakening of interpolymer electrostatic interactions.[37] For example, while transfer of QPVP from QPVP/PMAA WPEC to free PMAA chains occurred at a measurable rate in 0.05 M NaCl solution, the competitive displacement of PMAA from WPEC by incoming PSS chains required one order of magnitude lower concentration of salt.[42] Just as PSS is one of the strongest competitors

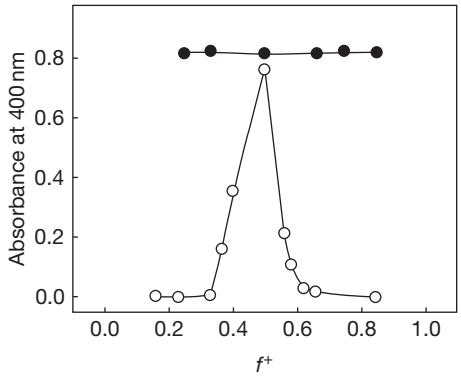

Figure 3 Turbidity of QPVP/PMAA (open circles) and PAH/PMAA (filled circles) mixtures measured as the absorbance of 0.04 M (repeat units) solutions at 400 nm as a function of the mole fraction of positively charged units f^+. The pH of 8.4 was supported by 0.01 M Trizma buffer. PMAA, QPVP and PAH with M_w of 72, 200, and 70 K, respectively, were used for the experiment. Reprinted with permission from Sukhishvili, S. A.; Kharlampieva, E.; Izumrudov, V. A. *Macromolecules* **2006**, *39*, 8873–8881. Copyright 2006 American Chemical Society.

for binding with polycations, polyamines containing primary amino groups are the strongest binders among polycations. When various polyamines were investigated for their binding with DNA, their association strength with DNA increased from quaternary to tertiary-, secondary-, and primary-amine polycations as amino groups became more sterically accessible. In addition, significant contribution of nonelectrostatic dispersive interactions to the binding energy is likely to occur in the case of PSS and/or primary-amine polycations.

Figure 3 contrasts phase behavior of polycation/polyanion mixtures in solution for strongly bound and weakly bound PE pairs. In mixtures of PMAA with the primary-amine polycation, poly(allylamine hydrochloride) (PAH), insoluble complexes are formed in a wide range of polycation-to-polyanion ratios, even when the excess of PMAA or PAH units is large. In contrast, solubility behavior of PMAA mixtures with the quaternized polyamine QPVP is drastically different: precipitation occurs only when f^+ is close to 0.5, that is, close to the equimolar charge ratio. Excess of PMAA or QPVP (at $f^+ < 0.35$ and >0.6, respectively) results in WPECs solubilized by either negative or positive charge in unpaired polymer units.

In contrast to QPVP/PMAA films whose deposition at a surface is greatly inhibited by exchange with solution (see Figure 1, top panel), the irreversible deposition of polymer chains at surfaces occurs under the same conditions for strongly interacting systems such as PAH/PMAA or PAH/PSS. Specifically, formation of very strong and irreversible ionic pairs affords high stability to PAH/PSS films and makes this system a favorite choice for multilayer buildup. Thus, as described above, the trends observed with multilayers directly correlate with properties of PECs in solution.

1.124.2.1.2. Internal structure of electrostatically assembled multilayers

Neutron reflectometry was first utilized to study the internal structure of dip-coated strong PE LbL films containing deuterated PE marker layers.[47–50] In PAH/PSS films, the intensity, width, and wavevector (Q) dependence of the superlattice reflectivity peaks produced by deuterated marker layers provides a wealth of information about the quality of layering within the LbL films. Polymer cationic or anionic components with individual layer thicknesses of several nanometers were partially intermixed, but strong evidence of internal layering was also observed. For example, in PAH/PSS films assembled at high salt concentration (>0.5 M) the interlayer roughness between adjacent PE layers was found to be on the order of 1.2–1.6 nm, comprising ~0.4 d_{bl}, where d_{bl} is the PAH/PSS bilayer thickness, indicating a well-defined layer structure with intermixing between adjacent layers of the same order as the layer thickness.[49,50]

Using neutron reflectometry, well-ordered layered structures were also found in the case of lipid layers[51] or multilayer films made of alternating sheets of rigid cellulose crystals and flexible PAH.[52] Internal layer ordering was shown to be influenced by external parameters such as pH, ionic strength, temperature, and humidity both during deposition and after postassembly treatment.[6,53–56] For example, increasing ionic strength or temperature during deposition resulted in increased interfacial mixing of PAH/PSS films.[57,58] Schlenoff and coworkers demonstrated that postassembly exposure of PEMs to high concentrations of salt (0.8–1.0 M NaCl) induces a significant increase in polymer interlayer mixing.[59]

Neutron reflectometry was also employed to resolve the structure of multilayers composed of weak PEs, which exhibit more diffuse polymer layering as compared to strong PEs.[60] As-assembled films show Bragg peaks characteristic of substrate-mediated layering within the film, as shown in Figure 4(a), with typical 'fussiness' found earlier for different electrostatically self-assembled films.[59,61] Neutron reflectometry applied together with *in situ* ATR–FTIR was used to study postassembly pH treatment of LbL films composed of weak PEs.[60] When a multilayer made of PMAA and a polycation with 20% of charged units (Q20) was deposited at pH 5 and then exposed to pH 7.2, about half the PMAA amount is released, while no mass loss is observed for Q20. The mechanism of response of weak polyelectrolyte multilayers (wPEMs) to pH variation involves pH-induced accumulation of excess charge within wPEMs, when the pH changes are in the region close to the apparent pK_a of a weak PE. *In situ* ATR–FTIR allows quantification of the pH-induced imbalance of negative to positive charges, which correlates with a rapid increase in ionization of self-assembled PMAA upon pH variations. When negative charges accumulate within the film as a result of pH variation, PMAA chains with excess charge are released into solution to bring the film charge ratio back to its original value close to unity.[60]

Importantly, multilayer structure of the weak PE films completely disappeared after pH-induced release of polyacid. The absence of periodic Bragg peaks in the reflectivity profile revealed mixing of the Q20 and PMAA layers, and the reduction of the total polymer layer thickness from 56 to 47 nm implies release of 35–38% of the PMAA originally present in the film (Figure 4(b)). However, after changing the solution pH back to its deposition value (pH 5) in the presence of deuterated PMAA (dPMAA), films recovered 95 ± 5% of their original thickness, implying complete reabsorption of dPMAA (Figure 4(c)). The constant scattering-length-density profile of

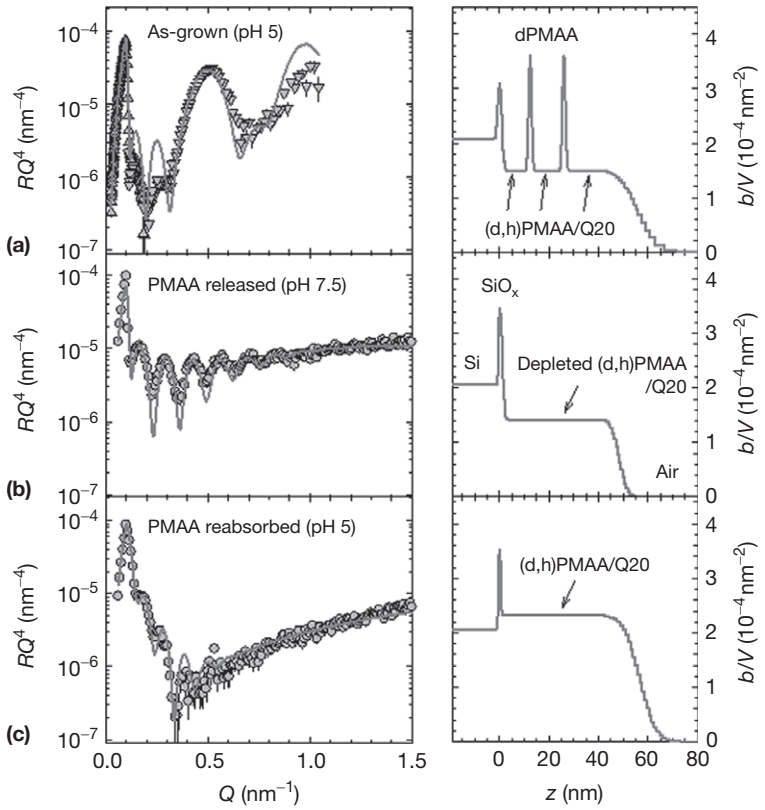

Figure 4 Neutron reflectivity data (left) for air-dried $((PMAA/Q20)_4/(dPMAA/Q20))_4$ films after deposition at pH 5 (a), after exposure to pH 7.5 (b) and after return to pH 5 (c) and fitted scattering-length-density profiles (right) obtained experimentally. Every fifth PMAA ($M_w = 22$ kDa) layer is deuterated to enhance neutron contrast. Reprinted with permission from Kharlampieva, E.; Ankner, J. F.; Rubinstein, M.; Sukhishvili, S. A. *Phys. Rev. Lett.* **2008**, *100*, 128303. Copyright 2008 by the American Physical Society.

the film after reabsorption suggests a uniform distribution of this material throughout the film.

Besides studies of conventional LbL films (obtained by alternating dipping from polymer solutions), neutron reflectometry was also applied to LbL multilayers constructed by spraying.[62,63] It was shown that spraying does not dramatically affect layering quality. However, the sprayed layers were 30% thinner than conventional dipped LbL films obtained under the same conditions.[63]

Neutron reflectometry was also applied to probe the internal structure of spin-assisted layer-by-layer (SA LbL) films composed of electrostatically assembled PEs.[64] SA LbL assembly has been introduced by Char and Wang as a combination of conventional LbL growth with spin coating and was shown to have several advantages over the conventional assembly.[65,66] First, it enables much faster film construction as compared to dipping assembly, and thus is considered to be more 'technologically friendly.' Second, SA LbL films have been found to possess remarkable physical properties, such as high mechanical robustness and strength. Based on this technique, a method to obtain flexible free-standing membranes with thicknesses down to 30 nm and lateral dimensions of several centimeters was developed.[67–69] Finally, SA LbL technique enables deposition of nonpolar hydrophobic moieties not possible using conventional LbL assembly.[70]

Application of neutron reflectometry uncovered distinct layering in SA LbL films when deposited from salt-free solutions and showed that the degree of molecular intermixing of film components could be controlled by varying the type and concentration of salt in the deposition solutions.[64] The addition of 10 mM phosphate buffer induced intermixing. The enhanced layer intermixing was explained as a result of weakening chain-to-chain interactions induced by phosphate buffer caused by an ability of phosphate ions to specifically interact with primary amino groups.[21,71] Indeed, the phosphate–PAH interaction results in partial neutralization of positively charged PAH segments and the formation of a loopy structure upon chain adsorption. However, the presence of 0.1 M NaCl in the phosphate buffer restored layer stratification. In addition, conventional dipped LbL films prepared under identical conditions from buffer solution displayed a more intermixed internal structure as compared to those made by SA LbL assembly.

1.124.2.2. Hydrogen-Bonded Self-Assembly of Polymers from Aqueous Solutions

Apart from LbL assembly of oppositely charged polymers, deposition of polymer films driven by the formation of hydrogen bonds has strongly emerged as a powerful technique. Hydrogen bonding is the key to defining the secondary structure and behavior of many biological molecules, including proteins and poly(nucleic acids). Synthetic chemists mimic approaches existing in nature when producing supramolecular polymeric

structures from short nonpolymeric building blocks.[72,73] In the case of synthetic polymers, multiple hydrogen bonding between polymer components was demonstrated to lead to deposition of LbL films. Since the discovery of such assembly more than a decade ago,[74,75] a great deal of research has been focused on the development of hydrogen-bonded (HB) films as promising surface coatings. This interest stems from the fact that HB LbL materials open new opportunities in LbL films which are harder to achieve with electrostatically assembled components. Specifically, the new attractive features of HB assembly include: (1) the possibility to include polymers which carry no charge; (2) the ease of producing films at mild pH responsive to environmental temperature and/or pH changes; (3) wide possibilities in converting HB films into single- or multiple-component ultrathin hydrogel materials. The above features enable future application of such assemblies as pH- and/or temperature-responsive drug delivery materials or release films compatible with biological tissues, as well as materials with tunable mechanical properties.

In aqueous solutions, the first example of HB assembly involved polyaniline self-assembled with a number of nonionic polymers, such as poly(vinylpyrrolidone) (PVPON), poly(vinyl alchohol) (PVA), poly(acrylamide) (PAAM) and poly(ethylene oxide) (PEO)[74] and a conjugated copolymer of the poly(phenylenevinylene) type containing hydroxyl groups which were capable of hydrogen bonding with amine groups of a co-self-assembled poly(ethyleneimine).[76] The use of aqueous solutions for HB assembly is, however, more attractive[77] as water is a friendly environment for biological and drug delivery applications. HB self-assembly of water-soluble polymers often involves a weak PE, such as a polycarboxylic acid, and a neutral polymer.[78–80] The inclusion of polycarboxylic acids allows for tuning the growth of HB films via variations of film constituents and deposition conditions. Because the HB assembly involves polymers which are electrically neutral, deposition is performed at acidic pH when polyacids are fully protonated.

1.124.2.2.1. Assembly, internal structure, and properties of HB films

As with other materials, HB films exhibit a close correlation between their structure and properties. Although in earlier studies HB multilayers have been assumed to be strongly intermixed,[81] the first direct observation of internal layering within HB LbL was studied using neutron reflectometry.[82] By applying this technique, it was shown that polymer layering deviated significantly from the ideal stratification of polymers within dense polymer layers (**Figure 5(a)**), and the degree of interpenetration of polymer layers, expressed as interlayer roughness, σ, strongly correlates with strength of intermolecular interactions between the adjacent layers. For the dPMAA layer closest to the substrate, the value of σ ranged from 35 to 60 Å for PVPON/PMAA, poly(*N*-vinylcaprolactam) (PVCL)/PMAA, and poly(*N*-isopropylacrylamide) (PNIPAM)/PMAA films. A new and interesting observation was that the polymer layers became more diffuse with increasing distance from the surface and as polymers deposited within the film were found in more random conformations (**Figure 5(b)**). For the PEO/PMAA system, films were completely interdiffused (**Figure 5(c)**), in agreement with weak intermolecular binding and exponential growth of PEO/PMAA films.

The key property of HB multilayers composed of neutral hydrogen-bonding polymers and polycarboxylic acids is that they can be erased by an increase in pH.[80] When carboxylic groups involved in hydrogen bonding become ionized, interpolymer hydrogen bonds are disrupted, eventually causing film dissolution at a critical value of pH (pH_{crit}). Extreme pH variations are not required to erase these films, and film dissolution occurs at slightly acidic or neutral pH values. With weaker hydrogen-bonding systems, films dissolve at a lower pH than that for stronger bound systems. The bilayer thickness of HB films correlates with the number of interpolymer binding points, determined by the intrinsic strength of interpolymer binding. For neutral polymers of comparable length, films

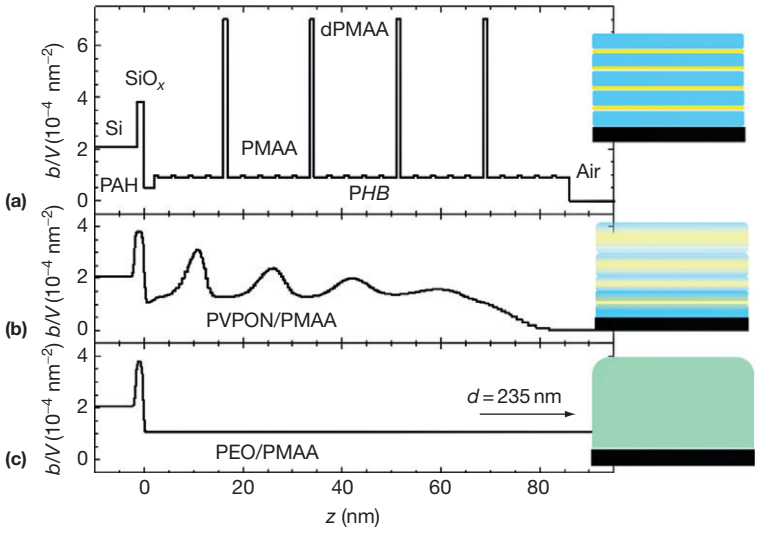

Figure 5 Hydrogen-bonded (HB) layers assuming perfect layering (a) and actual structure of HB LbL PVPON/PMAA (b) and PEO/PMAA (c) films. Scattering density Σ (defined as $\Sigma = b/V$, where b is a scattering length and V is a volume) is plotted against distance from Si template (z). PAH and PHB stands for poly(allylamine hydrochloride) and hydrogen-bonding polymers (PVPON or PEO), respectively. Reprinted with permission from Kharlampieva, E.; Kozlovskaya, V.; Ankner, J. F.; Sukhishvili, S. A. *Langmuir* **2008**, *24*, 11346–11349. Copyright 2008 American Chemical Society.

of PMAA with PEO, poly(vinyl methyl ether) (PVME), PAAM, or poly(2-hydroxyethyl acrylate) (PHEA) show higher bilayer thicknesses than strongly bound systems, such as PMAA assembled with PVPON, PNIPAM or PVCL.[77] Thicker bilayers in the case of PEO/PMAA and PVME/PMAA films are a result of more loopy conformations of self-assembled polymer chains. An analogy can be drawn with electrostatically assembled films where thicker layers are also reported for PEs with lower charge density. The morphology of HB films is also greatly affected by the type of polymer used in self-assembly. Hammond, Char and coworkers included a micelle-forming hydrophobically-modified PEO (HM-PEO) within HM-PEO/PAA HB LbL films and demonstrated that multilayers developed grainy morphologies.[83]

The dependence of bilayer thickness on molecular weight is strikingly different for strongly and weakly bound polymer systems. For example, the weakly bound PEO/PAA system exhibits an approximately sevenfold increase in bilayer thickness when PEO M_w was increased from 1.5 to 20 kDa.[84]

1.124.2.2.1.1. Effect of polymer solution pH

For both weakly bound and strongly bound HB films, bilayer thickness drastically decreased as deposition pH approached pH_{crit}. The effect of the deposition pH is very strong, allowing construction of HB films with bilayer thickness varying from several angstroms to hundreds of nanometers. For example, for PEO/PAA system, film thickness sharply decreased in a range of deposition pH from ~2.8 to 3.5, and films could not be deposited at pH 3.5 or higher. With PEO/PMAA films, this 'modulation window' of film growth inhibition was shifted to slightly higher pH values.[84] For stronger associated PVPON/PAA and PVPON/PMAA polymer pairs, films could not be deposited at a pH higher than 4.0[85] and 4.5, respectively.[77]

The effect of extremely low deposition pH on PVPON/PAA film thickness has also been studied. Films deposited from solution at pH 0.2–1.0 were very rough and unusually thick, with bilayer thickness around 48 nm. These large bilayer thicknesses were explained by the collapse of PAA chains into denser and less soluble globules at the extreme pH values where PAA becomes completely uncharged.[85]

1.124.2.2.1.2. Ionic strength of polymer solutions

There are many effects of salts on the growth of HB films. First, ions screen electrostatic charge within the film and, therefore, increase ionization of weak PEs. Secondly, they may interact with polymers in highly specific ways. Finally, the presence of salts might affect solubility of polymers. All these factors affect the individual layer thicknesses of polymers deposited within HB LbL films. In one example, the addition of monovalent and divalent salts in higher concentrations (higher than 0.5 M) during assembly of PEO/PAA systems resulted in inhibition of film growth[84] probably due to increased ionization of PAA. If both polymers remain uncharged, the effects of moderate concentrations of salts on the growth of HB films include dehydration and ion–dipole interactions and are usually smaller than those in electrostatically assembled systems. For example, in the case of strongly associated PVPON/PMAA films, film thickness increased by only ~10% when self-assembly was performed in 0.5 M NaCl solution.[77] Finally, salt can dramatically decrease the solubility of hydrophobic polymers resulting in thicker layers within the film, as in the case of deposition of a relatively hydrophobic poly(styrene-alt-(maleic acid))[86] within PEO/PSMA films, which gave layers twice as thick in 0.2 M NaCl as compared to those in 0.02 M NaCl solutions.

1.124.2.2.1.3. Temperature of polymer solutions

Caruso and coworkers demonstrated that PNIPAM/PAA films deposited from PNIPAM solutions[86] at 30 °C were of higher thickness and much lower roughness compared to films prepared at 10 or 21 °C.[86] Larger amounts of PNIPAM were deposited within the films when the lower critical solution temperature (LCST) of PNIPAM (32 °C) was approached and PNIPAM became less soluble in water. The behavior of other temperature-responsive polymers, PVME (LCST ~36 °C[87]) and PVCL (LCST ~35 °C),[88] was similar.[77] Bilayer film thickness increased with temperature even for films composed of PEO or PVPON and PAA[77] whose LCST is significantly higher than the temperature of deposition solutions (e.g., LCST of PEO is 100–150 °C depending on molecular weight).[89] Such an increase is due to a positive entropy of binding PEO with polycarboxylic acids,[90] which leads to a stabilization of HB multilayers at high temperatures.

However, if HB films contain a polymer pair with upper critical solution temperature (UCST), thinner layers are deposited within LbL films at higher temperatures.[91] One example is the PAAM/PAA system, for which the UCST of 20–25 °C was reported in the case of PAAM/PAA interpenetrated networks.[92] As temperature is raised above UCST, intermolecular hydrogen bonds between the polyacid and PAAM dissociate, resulting in thinner polymer layers within HB LbL films.

1.124.2.2.1.4. Concentration of polymer solutions

In addition to all the parameters listed above, thickness of HB films is also affected by the concentration of assembly solutions.[93] Similar to electrostatically assembled films, deposition of HB PVPON/PAA films at higher concentrations of assembly solutions resulted in larger amounts of polymer adsorbed at each deposition cycle.[93]

1.124.2.2.2. Temperature-controlled HB release films

Along with pH responsiveness, temperature can be used as an important trigger in manipulating properties of HB films containing temperature-responsive components. Application of HB PNIPAM/PMAA films as temperature-triggered platforms for releasing biological materials from surfaces has been explored.[94] Specifically, cells with attached patches (or 'backpacks') of electrostatically assembled LbL films were harvested from the substrate as a result of lowering the solution temperature to selectively dissolve the PNIPAM/PMAA surface stack and to release cellular backpacks from surfaces. Generality and the mechanism of such temperature-triggered release were studied.[95] Specifically, it was shown that deposition temperature of HB films containing PNIPAM, PVCL, or PVME as a temperature-sensitive neutral component plays a crucial role in pH-triggered dissolution of the films. For example, the critical pH of $(PNIPAM/PMAA)_5$ film disintegration shifted from 5.5 to 5.8 and to 6.1 when films were constructed at 10, 23, and 30 °C, respectively. Such drastic effect of assembly temperature on pH-stability of multilayer HB films of temperature-responsive polymers indicates stronger binding

of PNIPAM segments with PMAA at higher temperatures due to increased hydrophobic interactions.[82] This also correlated with the almost doubled bilayer thickness of PNIPAM/PMAA films deposited at 30 °C compared to that at 10 °C (8.7 nm vs. 4.4 nm, respectively). Importantly, temperature of postassembly solutions also critically affects the pH-stability of HB LbL films. For example, when PNIPAM/PMAA films built at pH 2 and 23 °C were immersed in solutions with increasingly high pH values at 10, 23, and 37 °C, the stability of the films went up from pH 5.2 to 5.8 and to 5.9, respectively. The increased film stability at temperatures close to the LCST is correlated with decreased solubility of PNIPAM and also with the hydrophobic stabilization of hydrogen bonding between PNIPAM and PAA. When poly(carboxylic acid)s were assembled with PAAM, a polymer with a UCST, the opposite effect of temperature on multilayer stability was observed. For example, the value of pH_{crit} decreased when temperature was raised from 10 to 37 °C due to the increased solubility of PAAM at a higher temperature which resulted in weakening intermolecular hydrogen bonds within the film. No such temperature-triggered change in the film pH stability was observed for HB films which did not contain temperature-responsive polymers. Importantly, by selecting different pairs of hydrogen-bonding polymers from a pool of neutral polymers and polycarboxylic acids, the working pH range for such temperature-triggered release films can be controlled and adjusted to neutral and slightly basic pH values. Specifically, the use of poly(ethacrylic acid) (PEAA) instead of PAA or PMAA in film assembly enabled construction of HB LbL films which can be released by applying temperature as a trigger at a near-physiologic pH. This feature makes this approach promising for future biomedical and tissue engineering applications.

1.124.2.3. LbL-Derived Hydrogels

Hydrogel matrix provides an ideal environment for hosting a variety of functional molecules such as drugs or proteins. Unlike macroscopic slab hydrogels, thin hydrogels (<100 nm) enable fast response to external stimuli.[96–98] At the same time, in contrast to polymer brushes,[99–101] SAMs or monolayers of adsorbed polymers, surface hydrogels possess high loading capacity to functional compounds. Such a combination of desirable properties is particularly valuable for applications in biotechnology.

Electrostatic interactions between polymer layers in a multilayer assembly are often used in fabrication of ionic LbL-derived ultrathin hydrogel films and membranes. Although highly swollen hydrogel-like structures can be fabricated using postassembly pH variations of non-cross-linked wPEM,[91] such films often lose their structure and rearrange after long-term exposure to extreme pH environments. HB multilayers, on the other hand, often readily dissolve at neutral and slightly basic pH values. Therefore, cross-linking is usually applied to convert LbL films to surface hydrogels.

The LbL-type surface hydrogels can be fabricated using sequential chemical cross-linking during self-assembly,[102,103] co-self-assembly of linear polymers with microgel particles,[104,105] or postassembly treatment of preconstructed LbL films via thermal-, photo-, or chemical cross-linking.[106,107] Conventionally assembled electrostatic or HB LbL films are converted into ultrathin hydrogels via cross-linking between self-assembled polymer chains of the same type, or between the two different types of polymers. The use of weak PEs for LbL hydrogel fabrication enables the use of pH to control loading and to trigger release of functional molecules from such matrices.

1.124.2.3.1. Hydrogels derived from electrostatically assembled multilayers

Glutaraldehyde (GA) is often used as a cross-linking agent in fabricating LbL-derived ultrathin hydrogels films because of its high solubility in water.[108] Cationic single-component LbL hydrogel films and capsules were initially synthesized by using selective cross-linking of chitosan by GA within chitosan/PAA multilayers.[109] The GA-treated chitosan/PAA films were exposed to carbonate buffer at pH 9 overnight to induce the pH-dependent swelling of the chitosan/PAA membranes as ionization of the polyacid increased. Such a treatment resulted in complete PAA removal from the cross-linked films leaving behind chitosan hydrogel LbL-derived films or hollow capsules. Swelling of the capsules was observed when the pH was changed from the neutral to acidic with a transition at pH ~5.5. By simply changing the cross-linking time, a different degree of cross-linking was achieved. A similar strategy was applied to various multilayer systems of electrostatically interacted weak PEs. For example, GA was also used to selectively cross-link PAH within PAH/PSS capsules via formation of a Schiff base between the aldehyde and the amine groups in PAH.[110] After cross-linking and exposure to pH = 12, the capsules slowly released PSS molecules from the cross-linked networks. After a 2-h cross-linking with GA and partial release of PSS, the permeation coefficient of these films to dextran molecules of M_w ~250 kDa decreased threefold as compared to the initial PAH/PSS capsules, probably due to partial polymerization of GA. In another work, a similar strategy was applied to selectively cross-link branched poly(ethylene imine) (PEI) within PEI/PAA LbL capsule membrane.[93] The resultant cross-linked PEI capsule walls contained physically trapped PAA chains.

Two-component LbL hydrogels can also be fabricated if both film constituents contain reactive functional groups. Carbodiimide chemistry is generally exploited for covalent cross-linking between amine or hydroxyl and carboxylic group-containing moieties of the PE components. For instance, the chemical cross-linking of hyaluronic acid/PAH (HA/PAH) multilayer films and capsules with a mixture of water-soluble carbodiimide, 1-ethyl-3-(3-dimethylaminopropyl) carbodiimide hydrochloride (EDC), and *N*-hydroxysulfosuccinimide (NHS) produced biocompatible and noncytotoxic LbL-derived HA–PAH assemblies stable under low and high pH conditions.[111] If non-cross-linked, these HA–PAH assemblies dissolved due to ionization-induced swelling at pH <2 or >7.2. Biocompatible chitosan–alginate LbL capsules assembled from natural polysaccharides on calcium carbonate particles were also chemically stabilized with the GA treatment.[112] Both components, chitosan and alginate, were present in the capsule wall after GA cross-linking as confirmed by the FTIR. Along with the GA cross-linking, carbodiimide chemistry was applied to directly cross-link neighboring layers of chitosan and alginate to increase stability of the films toward

enzymatic erosion and to reduce the release rate of encapsulated indomethacin.[113]

Apart from chemical cross-linking, thermal treatment of electrostatically assembled LbL films and capsules has been applied as a way to stabilize LbL systems against pH-induced dissolution.[114] One example is thermal cross-linking of $CaCO_3$-deposited $(PAH/PAA)_4$ microcapsules at 180 °C for 2 h.[114] The thermal treatment stabilized the polymer network through the formation of PAH–PAA amide linkages. Interestingly, the capsules kept their shape even when severely swollen in highly acidic solutions. Under these low pH conditions, electrostatic pairing between PAH and PAA was disrupted, and the capsule walls were converted to positively charged ultrathin hydrogels capable of binding polyanions, such as PSS.[114]

1.124.2.3.2. Hydrogels derived from HB multilayers

HB LbL assembly of neutral polymers and poly(carboxylic acids) is another route of fabrication for ultrathin hydrogels. HB multilayers are uniquely suited for constructing responsive hydrogel films since polymer–polymer hydrogen bonds can be easily dissociated by exposure to mild values of pH. In contrast, in electrostatically assembled films, dissociation of ionic pairs is more problematic and, if possible, requires exposure to extreme values of solution pH. Therefore, stabilization of HB multilayers through covalent bonds has been recently developing as a novel technique in building ultrathin LbL hydrogel materials with unique properties.[115] The approach extended the use of HB films to neutral and basic range of pH, making such materials promising candidates for biomedical or biosensing applications.

Several cross-linking strategies have been explored to produce stable hydrogels from HB films, including chemical,[116] thermal,[107] or photo-cross-linking.[107] Carbodiimide chemistry has been widely applied to selectively cross-link poly(carboxylic acids) with ethylenediamine (EDA) within polyacid/nonionic polymer HB films or capsules.[117–119] The use of nonfunctionalized PVPON, PVCL, or PEO in the HB LbL assembly resulted in complete release of nonionic polymer from the cross-linked films upon exposure to high pH, yielding single-component polyacid hydrogel films or capsules. Using this route, single-component PAA, PMAA, or PEAA hydrogel membranes were derived from the corresponding HB LbL assemblies. An astounding feature of these membranes is that in a wide range of pH values there is no extensive noncovalent binding between units of poly(carboxylic acid), and that capsule walls, or the surface-attached LbL films exist as highly hydrated (up to 300% swellable at pH 7.5) ultrathin hydrogels.

Also, cross-links were introduced between both components within HB multilayer films and capsules. Rubner and coworkers have reported on PAAM/PAA or PAAM/PMAA hydrogel-like films and capsules fabricated via thermal, photo- or carbodiimide-facilitated formation of amide links between polymer counterparts.[120–122] Hydrogels with strongly enhanced swelling at high pH values were also produced using PVPON- and PVCL-based copolymers. To that end, PVPON- or PVCL-based copolymers with a fraction of units containing amino groups (PVPON-*co*-NH_2 or PVCL-*co*-NH_2, respectively)[123] were assembled with poly(carboxylic acids) through hydrogen bonding. Following exposure to solutions of water-soluble carbodiimide, amide links formed between PVPON-*co*-NH_2 (or PVCL-*co*-NH_2) and polyacid chains, resulting in two-component hydrogel-like films and capsules.[119,123]

Significant differences were found between single- and two-component hydrogel capsules derived from HB assemblies.[119,123] In the case of two-component capsules, when the pH was decreased below the critical value, hydrogen bonds between a neutral counterpart and poly(carboxylic acid) units were reformed. In the case of a single-component hydrogel system, lowering the pH-induced deswelling of such hydrogel capsule walls as a consequence of decreased polyacid ionization. Remarkably, both types of capsules reversibly changed their size in response to variations in pH and/or ionic strength (Figure 6). At the same time, distinct swelling hysteresis occurred in the case of two-component capsules (inset in Figure 6). In particular, larger capsule sizes were detected when the pH was lowered compared to those when the pH was increased. Significantly, at basic pH values, both types of hydrogel capsule walls did not contain HB polymers and were highly swollen.

Recently, hydrogen bonding between PAA and methylcellulose (MC) has also been successfully used as a platform for preparation of thin hydrogel films of 600 nm thickness.[124] Advantageously, these films could be cross-linked by heating at 120 °C for 2–6 h, and swelled at high pH producing freely floating films. HB capsules of hydroxypropylcellulose/PAA (HPC/PAA)[125] dissolved at pH higher than 3.3, and were converted into the pH-stable capsules with hydrogel-like walls through carbodiimide cross-linking between hydroxyl groups of HPC and carboxylic groups in PAA. These two-component LbL-derived hydrogels continuously swelled in the pH range

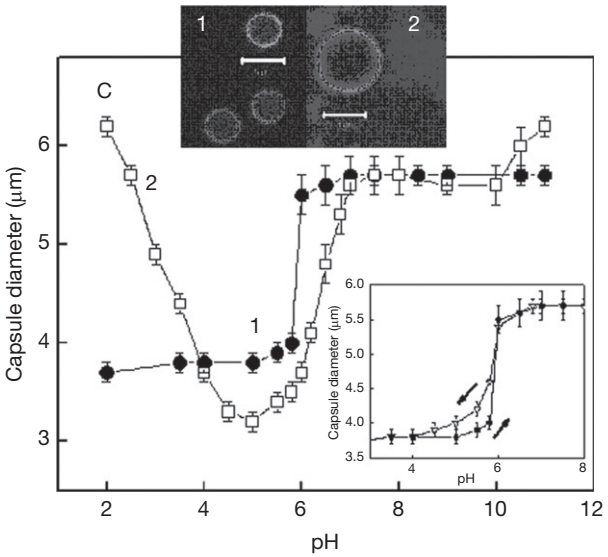

Figure 6 Confocal laser scanning microscopy (CLSM) images of $(PVPON\text{-}co\text{-}NH_2\text{-}20/PMAA)_7$ (1) and $(PMAA)_7$ (2) capsules at pH 2, scale bar is 1 μm; pH dependence of the diameter of $(PVPON\text{-}NH_2\text{-}20/PMAA)_7$ (curve 1, filled circles) and $(PMAA)_7$ capsules (curve 2, open squares) cross-linked for 18 h. The inset shows hysteresis of $(PVPON\text{-}NH_2\text{-}20/PMAA)_7$ capsule size upon increasing (filled circles) and decreasing (open triangles) pH. Reprinted with permission from Kozlovskaya, V.; Sukhishvili, S. A. *Macromolecules* **2006**, *39*, 5569–5572. Copyright 2006 American Chemical Society.

from 3 to 5 due to deprotonation of the carboxylic groups. The HPC/PAA cross-linked hydrogels required 5–15 days to reach the swelling equilibrium. The prolonged swelling kinetics observed for both lightly and heavily cross-linked HPC/PAA capsules was due to the hydrophobic nature and significant rigidity of the HPC chains.

1.124.2.3.3. LbL-derived hydrogels via click chemistry

An elegant approach to prepare single-component ultrathin LbL films and capsules of PAA via click chemistry was introduced by Caruso and coworkers.[14,126] In click chemistry, covalent reactions with high yields can be performed under mild conditions. Using azide- or alkyne-modified PAA polymers, stepwise growth of LbL films was demonstrated in the presence of copper(I) and sodium ascorbate in aqueous solution.[14] The deposition was promoted by the formation of 1,2,3-triazole cross-links.[126] However, the requirement for the use of copper in the azide–alkyne click chemistry reaction prevents the use of this approach for biological applications. Thiol–ene reaction was also explored for the fabrication of LbL hydrogels.[127] First, thiol-PMAA and ene-PMAA were LbL-assembled with PVPON and the PMAA layers were then cross-linked via thiol–ene reaction initiated by UV-light. The release of PVPON from the film at pH 7 resulted in layered PMAA hydrogel films.

1.124.2.3.4. Mechanical properties of the LbL-derived hydrogel films

Mechanical properties of pH-responsive hydrogel-like capsules were investigated using atomic force microscopy (AFM) single capsule force spectroscopy measurements.[128] The microcapsule stiffness of one- and two-component hydrogel capsules was dramatically pH-dependent. In the case of cross-linked PVPON-*co*-NH_2/PMAA capsules at pH 2, intermolecular hydrogen-bonding interactions of the hydrogel network dominated, and the capsule walls were rigid. Dramatic softening of (PVPON-*co*-NH_2/PMAA)$_7$ capsules occurred in a narrow range of pH between 5.4 and 6, as intermolecular hydrogen bonds dissociated at higher pH values (Figure 7). The corresponding decrease in stiffness of the walls was from 18 ± 9 to 1.4 ± 0.5 mN m^{-1} for pH 5.4 and 6, respectively. A decrease in stiffness from 550 ± 150 to less than 1 mN m^{-1} also occurred for single-component (PMAA)$_{10}$ hydrogel capsules. The large difference between the systems was due to the different capsule wall thickness of 20 and 7 nm for (PMAA)$_{10}$ and (PVPON-*co*-NH_2/PMAA)$_7$, respectively. The important finding was made that mechanical properties of LbL-derived hydrogels can be designed as switchable in response to environmental stimuli, with the switch triggered at mild pH conditions. This possibility of switching mechanical properties holds a significant potential for designing future-generation controlled delivery membranes and containers.

In a different system, a nanoindentation approach employing colloidal probe AFM was used to study the effect of cross-linking on the elastic properties of cross-linked poly(L-lysine)/hyaluronan (PLL/HA) films.[129] Higher concentrations of carbodiimide resulted in a larger number of cross-links within the film and enhanced film stiffness. Similar modulation of stiffness was used to tune cell adhesion properties of cross-linked films of a poly(carboxylic acid) and PAAM.[130] Highly swellable, with a swelling degree of more than 300%, low Young's modulus cross-linked films of PAAM/PAA and PAAM/PMAA were resistant to cell adhesion.

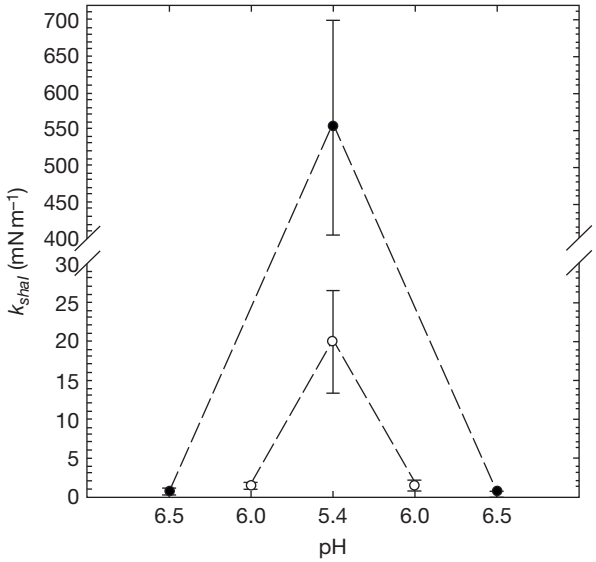

Figure 7 Reversibility of the softening process for cross-linked (PVPON-*co*-NH_2-20/PMAA)$_7$ (open circles) and cross-linked (PMAA)$_{10}$ (filled circles) microcapsules for pH changes from 5.4 to 6 or 6.5, respectively. Reproduced from Elsner, N.; Kozlovskaya, V.; Sukhishvili, S. A.; Fery, A. *Soft Matter* **2006**, *2*, 971, with permission from The Royal Society of Chemistry.

1.124.2.3.5. Applications of LbL hydrogels to controlled release of bioactive molecules

Hydrogels derived from HB LbL films are promising materials capable of pH-controlled loading and release of functional compounds. Specifically, loading of proteins and heparin within LbL-derived surface-attached PMAA hydrogels was studied *in situ* using ATR–FTIR and ellipsometry.[15] The loading of Lys, a protein with an isoelectric point of 11.5, within the PMAA hydrogels was fast and saturated after ~15 min when 0.1 mg ml^{-1} protein solutions were used. Almost 98% of Lys loaded at pH 7.5 released when the gel was exposed to pH 4 and carboxylic groups became completely protonated. Excellent correlation of the amount of Lys loaded within the film with the charge density of the PMAA hydrogels points to an essentially electrostatic nature of protein interactions with the hydrogel matrix. A similar trend of reversible binding of positively charged protein within PMAA hydrogels was obtained with another protein, ribonuclease. The hydrogel mesh size was large enough to allow transport of Lys globules through the hydrogel matrix. Negatively charged macromolecules such as heparin could also be included within the amphoteric hydrogels. The amount of heparin loaded at pH 3 was proportional to PMAA hydrogel thickness. Figure 8 contrasts the inclusion of heparin and Lys within surface hydrogels at various pH values. As in the case of Lys, heparin adsorption was irreversible towards dilution with buffer solutions at a constant pH. However, heparin was effectively released from the PMAA hydrogel upon an increase in pH, when the hydrogel carboxylic groups deprotonated and acquired negative charge.

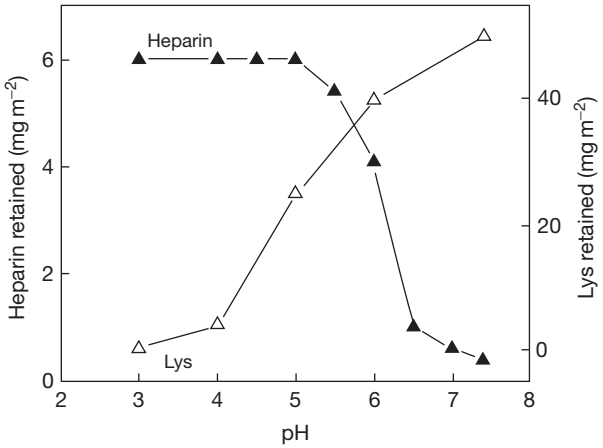

Figure 8 pH dependence of amounts of Lys (open triangles) and heparin (filled triangles) absorbed within $(PMAA)_5$ hydrogel as inferred from *in situ* ATR–FTIR and confirmed with ellipsometry. pH values were supported by 0.01 M phosphate buffer solutions. Reprinted with permission from Kharlampieva, E.; Erel-Unal, I.; Sukhishvili, S. A. *Langmuir* **2007**, *23*, 175–181. Copyright 2007 American Chemical Society.

In a similar way, at physiologic pH values of 7.5, the most abundant plasma protein, albumin, could not be included into the PMAA matrix due to size and charge considerations.

A possibility of constructing functional containers with biodegradable hydrogel walls has also been explored. The walls of such containers consisted of single-component PMAA hydrogel cross-linked via biodegradable disulfide links,[131] produced by treatment of HB multilayers of PVPON and cysteamine-modified PMAA (PMAA-SH) with hydrogen peroxide.[132] The PMAA capsules stabilized with disulfide bonds were able to load proteins, oligonucleotides, or DNA and then to release their cargo under reducing conditions.[133,134] For example, encapsulated fluorescently labeled protein, FITC-transferrin was released after deconstruction of the capsules in the presence of thiol–disulfide exchange reagent – dithiothreitol.

1.124.2.3.6. Nanoparticle-containing layered hydrogel films

The LbL-derived hydrogel matrices in their swollen states possess large number of functional groups able to attract various metal or metal-containing ions. This advantage can be successfully used for the creation of nanoparticle-loaded thin hydrogel coatings by incorporating presynthesized nanoparticles within such hydrogels, or by using the hydrogels as templates for *in situ* synthesis of nanoparticles.

In situ synthesis of nanoparticles has been applied to carbodiimide-cross-linked PAAM/PAA HB precursor matrices to fabricate silver-loaded ultrathin hydrogel films and capsules.[120,121] Metal ions were bound to the carboxylic acid groups when the films were suspended in aqueous solutions of silver acetate and Ag was reduced in the presence of borohydride. Multiple ion loading and reduction cycles were performed to increase nanoparticle size. While the above approach of using carboxylic groups of the hydrogel as binding sites for metal precursor ions is useful for the synthesis of Ag/hydrogel composites, it cannot be used for *in situ* synthesis of gold nanoparticles, as hydrogel

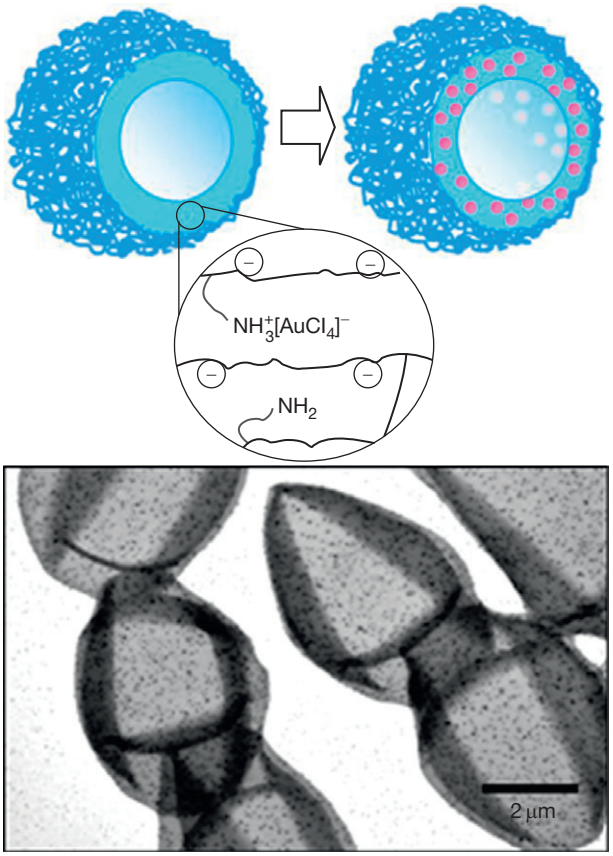

Figure 9 Top: *In situ* synthesis of gold nanoparticles within PMAA hydrogel capsules derived from PVPON/PMAA hydrogen-bonded capsules through cross-linking with ethylenediamine. Bottom: Transmission electron microscopy (TEM) Images of cross-linked hydrogel capsules after gold reduction within the shell. Reprinted with permission from Kozlovskaya, V.; Kharlampieva, E.; Chang, S.; Muhlbauer, R.; Tsukruk, V. V. *Chem. Mater.* **2009**, *21*, 2158–2167. Copyright 2009 American Chemical Society.

carboxylate groups and $[AuCl_4]^-$ ions are both anionic. The direct synthesis of gold nanoparticles within layered PMAA hydrogel capsules was demonstrated for hydrogels cross-linked with EDA.[135] The $[AuCl_4]^-$ ions were bound with a fraction of amino groups of one-end-tethered EDA cross-linker within the hydrogel. Well-dispersed gold nanoparticles of 10 ± 2 nm were obtained within PMAA hydrogels (Figure 9). Importantly, the pH-responsive properties of the PMAA hydrogel capsules were preserved after the formation of gold nanoparticles. Combining unique properties of metal nanoparticles (localized surface plasmons, thiol-based tethering of biomolecules to nanoparticle surfaces, or antibacterial properties in case of silver nanoparticles, enhancement of mechanical rigidity, biocompatibility and nontoxicity of gold nanoparticles) with responsive behavior of ultrathin LbL-derived hydrogels can result in materials crucially important in biosensing and delivery of functional cargo.

1.124.3. Conclusions

Recent developments in LbL-based surface modifications demonstrate the power of this technique in engineering surface

coatings with controlled thickness, architecture, nanoscopic structure, and mechanical properties. The technique is applicable to the deposition of a broad range of functional polymers at a variety of surfaces including biomaterials, and the deposition procedures for LbL coatings may be varied from sequential dipping to spin-coating[66] or spraying.[136,137] The use of chemical approaches to LbL films, such as postassembly cross-linking, or chemical reactions during polymer assembly, enables fabrication of soft hydrogel surface coatings with controlled thickness and swelling capabilities. Such highly swollen surface coatings are excellent candidates for controlling cellular adhesion and spreading, or endowing surfaces with antifouling properties. Furthermore, LbL hydrogels can be used as versatile matrices for loading and controlled release of bioactive molecules. Versatility of the LbL approach and its value to modification of biomaterial surfaces can be further enhanced by combining the LbL technique with chemical grafting of polymer chains, including polypeptide sequences, to the LbL matrix. Such surface constructs will be capable of dual control of biomaterial interaction with biological tissues by delivering bioactive compounds from the bulk of the film, while additionally controlling cellular adhesion through grafted chemical moieties. These opportunities make LbL films promising candidates for modification of biomaterial surfaces.

References

1. Brodie, I.; Muray, J. J. *The Physics of Micro/Nano-Fabrication*; Plenum: New York, 1992.
2. Petty, M. C. In *Surfaces and Interfaces for Biomaterials*; Vadgama, P., Ed.; Woodhead: Cambridge, 2005; p 61.
3. Ducker, R.; Garcia, A.; Zhang, J.; Chen, T.; Zauscher, S. *Soft Matter* **2008**, *4*, 1774–1786.
4. Mrksich, M. *Acta Biomater.* **2009**, *5*, 832–884.
5. Decher, G. *Science* **1997**, *277*, 1232–1242.
6. Decher, G.; Eckle, M.; Schmitt, J.; Struth, B. *Curr. Opin. Colloid Interface Sci.* **1998**, *3*, 32–39.
7. Dubas, S. T.; Schlenoff, J. B. *Macromolecules* **1999**, *32*, 8153–8160.
8. Fisher, P.; Laschewsky, A.; Wischerhoff, E.; Arys, X.; Jonas, A.; Legras, R. *Macromol. Symp.* **1999**, *137*, 1–24.
9. Graul, W. G.; Li, M.; Schlenoff, J. B. *J. Phys. Chem. B* **1999**, *103*, 2718–2723.
10. Kotov, N. A.; Magonov, S.; Tropsha, E. *Chem. Mater.* **1998**, *10*, 886–895.
11. Schlenoff, J. B.; Dubas, S. T. *Macromolecules* **2001**, *34*, 592–598.
12. Sukhorukov, G. B.; Möhwald, H.; Decher, G.; Lvov, Y. M. *Thin Solid Films* **1996**, *440*, 220–223.
13. Sukhishvili, S. A. *Curr. Opin. Colloid Interface Sci.* **2005**, *10*, 37–44.
14. Such, G. K.; Quinn, J. F.; Quinn, A.; Tjipto, E.; Caruso, F. *J. Am. Chem. Soc.* **2006**, *128*, 9318–9319.
15. Kozlovskaya, V.; Kharlampieva, E.; Erel-Unal, I.; Sukhishvili, S. A. *Polym. Sci. Ser. A* **2009**, *51*, 719–729.
16. Bertrand, P.; Jonas, A.; Laschewsky, A.; Legras, R. *Macromol. Rapid Commun.* **2000**, *21*, 319–348.
17. Cooper, C. L.; Dubin, P. L.; Kayitmazer, A. B.; Turksen, S. *Curr. Opin. Colloid Interface Sci.* **2005**, *10*, 52–78.
18. Decher, G.; Schlenoff, J. B. *Multilayer Thin Films. Sequential Assembly of Nanocomposite Materials*; Wiley-VCH: Weinheim, 2003.
19. Hammond, P. *Curr. Opin. Colloid Interface Sci.* **1999**, *4*, 430–442.
20. Kovačević, D.; Van der Burgh, S.; de Keizer, A.; Cohen Stuart, M. A. *Langmuir* **2002**, *18*, 5607–5612.
21. Kovačević, D.; Van der Burgh, S.; de Keizer, A.; Cohen Stuart, M. A. *J. Phys. Chem. B* **2003**, *107*, 7998–8002.
22. Sukhishvili, S. A.; Kharlampieva, E.; Izumrudov, V. A. *Macromolecules* **2006**, *39*, 8873–8881.
23. Glinel, K.; Moussa, A.; Jonas, A. M.; Laschewsky, A. *Langmuir* **2002**, *18*, 1408–1412.
24. Steitz, R.; Jaeger, W.; Klitzing, R. *Langmuir* **2001**, *17*, 4471–4474.
25. Dubas, S. T.; Schlenoff, J. B. *Macromolecules* **2001**, *34*, 3736–3740.
26. Kharlampieva, E.; Kozlovskaya, V.; Tyutina, J.; Sukhishvili, S. A. *Macromolecules* **2005**, *38*, 10523–10531.
27. Kharlampieva, E.; Sukhishvili, S. A. *Langmuir* **2003**, *19*, 1235–1243.
28. Mendelsohn, J. D.; Barrett, C. J.; Chan, V. V.; Pal, A. J.; Mayes, A. M.; Rubner, M. F. *Langmuir* **2000**, *16*, 5017–5023.
29. Hoogeveen, N. G.; Cohen Stuart, M. A.; Fleer, G. J.; Böhmer, M. R. *Langmuir* **1996**, *12*, 3675–3681.
30. Schoeler, B.; Kumaraswamy, G.; Caruso, F. *Macromolecules* **2002**, *35*, 889–897.
31. Sui, Z.; Salloum, D.; Schlenoff, J. B. *Langmuir* **2003**, *19*, 2491–2495.
32. Kabanov, V. A.; Zezin, A. B. *Pure Appl. Chem.* **1984**, *56*, 343–354.
33. Kabanov, V. A. In *Macromolecular Complexes in Chemistry and Biology*; Dubin, P. L., Bock, J., Davis, R. M., Schulz, D. N., Thies, C., Eds.; Springer: Berlin, 1994; p 151.
34. Izumrudov, V. A.; Lim, S. H. *Polym. Sci.* **2002**, *A44*, 484–490.
35. Kabanov, V. A.; Yaroslavov, A. A.; Sukhishvili, S. A. *J. Control. Release* **1996**, *39*, 173–189.
36. Zaitsev, V. S.; Izumrudov, V. A.; Zezin, A. B. *Polym. Sci. USSR* **1992**, *34*, 54 (translated from Vysokomolekulyarniye Soyedineniya Seriya A, *34*, 138–139).
37. Bakeev, K. N.; Izumrudov, V. A.; Kuchanov, S. I.; Zezin, A. B.; Kabanov, V. A. *Macromolecules* **1992**, *25*, 4249–4254.
38. Trukhanova, E. S.; Izumrudov, V. A.; Litmanovich, A. A.; Zelikin, A. N. *Biomacromolecules* **2005**, *6*, 3198–3201.
39. Zelikin, A. N.; Trukhanova, E. S.; Putnam, D. A.; Izumrudov, V. A.; Litmanovich, A. A. *J. Am. Chem. Soc.* **2003**, *125*, 13693–13699.
40. Patchornik, A.; Berger, A.; Katchalski, E. *J. Am. Chem. Soc.* **1957**, *79*, 5227–5230.
41. Izumrudov, V. A.; Bronich, T. K.; Zezin, A. B.; Kabanov, V. A. *J. Polym. Sci., Polym. Lett. Ed.* **1985**, *23*, 439–444.
42. Kabanov, V. A.; Zezin, A. B.; Izumrudov, V. A.; Bronich, T. K.; Bakeev, K. N. *Makromol. Chem. Suppl.* **1985**, *13*, 137–155.
43. Oupicky, D.; Konak, C.; Dash, P. R.; Seymour, L. W.; Ulbrich, K. *Bioconjug. Chem.* **1999**, *10*, 764–772.
44. Kakizawa, Y.; Harada, A.; Kataoka, K. *Biomacromolecules* **2001**, *2*, 491–497.
45. Izumrudov, V. A.; Chaubet, F.; Clairbois, A.-S.; Jozefonvicz, J. *Macromol. Chem. Phys.* **1999**, *200*, 1753–1763.
46. Izumrudov, V. A.; Zhiryakova, M. V.; Kudaibergenov, S. *Biopolymers* **1999**, *52*, 94–108.
47. Kellogg, G. J.; Mayes, A. M.; Stockton, W. B.; Ferreira, M.; Rubner, M. F.; Satija, S. K. *Langmuir* **1996**, *12*, 5109–5113.
48. Korneev, D.; Lvov, Y.; Decher, G.; Schmitt, J.; Yaradaikin, S. *Phys. B Conden. Matter* **1995**, *213*, 954–956.
49. Lösche, M.; Schmitt, J.; Decher, G.; Bouwman, W. G.; Kjaer, K. *Macromolecules* **1998**, *31*, 8893–8906.
50. Schmitt, J.; Grünewald, T.; Decher, G.; Pershan, P. S.; Kjaer, K.; Lösche, M. *Macromolecules* **1993**, *26*, 7058–7063.
51. Delajon, C.; Gutberlet, T.; Steitz, R.; Möhwald, H.; Krastev, R. *Langmuir* **2005**, *21*, 8509–8514.
52. Jean, B.; Dubreuil, F.; Heux, L.; Cousin, F. *Langmuir* **2008**, *24*, 3452–3458.
53. Carrière, D.; Krastev, R.; Schönhoff, M. *Langmuir* **2004**, *20*, 11456–11472.
54. Glinel, K.; Prevot, M.; Krustev, R.; Sukhorukov, G. B.; Jonas, A. M.; Möhwald, H. *Langmuir* **2004**, *20*, 4898–4902.
55. Kügler, R.; Schmitt, J.; Knoll, W. *Macromol. Chem. Phys.* **2002**, *203*, 413–419.
56. Tanchak, O. M.; Yager, K. G.; Fritzsche, H.; Harroun, T.; Katsaras, J.; Barrett, C. J. *Langmuir* **2006**, *22*, 5137–5143.
57. Gopinadhan, M.; Ivanova, O.; Ahrens, H.; Günther, J.-U.; Steitz, R.; Helm, C. A. *Macromolecules* **2005**, *38*, 5228–5235.
58. Gopinadhan, M.; Ivanova, O.; Ahrens, H.; Günther, J.-U.; Steitz, R.; Helm, C. A. *J. Phys. Chem. B* **2007**, *111*, 8426–8434.
59. Jomaa, H. W.; Schlenoff, J. B. *Macromolecules* **2005**, *38*, 8473–8480.
60. Kharlampieva, E.; Ankner, J. F.; Rubinstein, M.; Sukhishvili, S. A. *Phys. Rev. Lett.* **2008**, *100*, 128303.
61. Decher, G.; Eckle, M.; Schmitt, J.; Struth, B. *Curr. Opin. Colloid Interface Sci.* **1998**, *3*, 32–39.
62. Félix, O.; Zheng, Z.; Cousin, F.; Decher, G. *C. R. Chim.* **2009**, *12*, 225–234.
63. Kolasinska, M.; Krastev, R.; Gutberlet, T.; Warszynski, P. *Langmuir* **2009**, *25*, 1224–1232.
64. Kharlampieva, E.; Kozlovskaya, V.; Sukhishvili, S. A. *Adv. Mater.* **2009**, *21*, 3053–3065.

65. Chiarelli, P. A.; Johal, M. S.; Casson, J. L.; Roberts, J. B.; Robinson, J. M.; Wang, H.-L. *Adv. Mater.* **2001**, *13*, 1167–1171.
66. Cho, J.; Char, K.; Hong, J.-D.; Lee, K.-B. *Adv. Mater.* **2001**, *13*, 1076–1078.
67. Jiang, C.; Markutsya, S.; Tsukruk, V. V. *Adv. Mater.* **2004**, *16*, 157–161.
68. Lin, Y. H.; Jiang, C.; Xu, J.; Lin, Z.; Tsukruk, V. V. *Soft Matter* **2007**, *3*, 432–436.
69. Zimnitsky, D.; Shevchenko, V. V.; Tsukruk, V. V. *Langmuir* **2008**, *24*, 5996–6006.
70. Lee, S.; Lee, B.; Kim, B. J.; *et al*. *J. Am. Chem. Soc.* **2009**, *131*, 2579–2587.
71. Irigoyen, J.; Moya, S. E.; Iturri, J. J.; Llarena, I.; Azzarony, O.; Donath, E. *Langmuir* **2009**, *25*, 3374–3380.
72. Binder, W. H. *Monatsh. Chem.* **2005**, *136*, 1–19.
73. Bosman, A. W.; Sijbesma, R. P.; Meijer, E. W. *Mater. Today* **2004**, *7*, 34–39.
74. Stockton, W.; Rubner, M. F. *Macromolecules* **1997**, *30*, 2717–2725.
75. Wang, L.; Wang, Z. Q.; Zhang, X.; Shen, J. C.; Chi, L. F.; Fucks, H. *Macromol. Rapid Commun.* **1997**, *18*, 509–514.
76. Benjamin, I.; Hong, H.; Avny, Y.; Davidov, D.; Neumann, R. *J. Mater. Chem.* **1998**, *8*, 919–924.
77. Kharlampieva, E.; Sukhishvili, S. A. *J. Macromol. Sci. Part C: Polym. Rev.* **2006**, *46*, 377–395.
78. Quinn, J. F.; Johnston, A. P. R.; Such, G. K.; Zelikin, A. N.; Caruso, F. *Chem. Soc. Rev.* **2007**, *36*, 707–718.
79. Sukhishvili, S. A.; Granick, S. *J. Am. Chem. Soc.* **2000**, *122*, 9550–9551.
80. Sukhishvili, S. A.; Granick, S. *Macromolecules* **2002**, *35*, 301–310.
81. Guan, Y.; Yang, S.; Zhang, Y.; Xu, J.; Han, C.; Kotov, N. A. *J. Phys. Chem. B* **2006**, *110*, 13484–13490.
82. Kharlampieva, E.; Kozlovskaya, V.; Ankner, J. F.; Sukhishvili, S. A. *Langmuir* **2008**, *24*, 11346–11349.
83. Seo, J.; Lutkenhaus, J. L.; Kim, J.; Hammond, P. T.; Char, K. *Macromolecules* **2007**, *40*, 4028–4036.
84. DeLongchamp, D.; Hammond, P. *Langmuir* **2004**, *20*, 5403–5411.
85. Yang, S.; Zhang, Y.; Zhang, X.; Xu, J. *Soft Matter* **2007**, *3*, 463–469.
86. Quinn, J. F.; Caruso, F. *Langmuir* **2004**, *20*, 20–22.
87. Yanul, N.; Kirsh, Y.; Anufrieva, E. V. *J. Therm. Anal. Calorim.* **2000**, *62*, 7–14.
88. Maeda, Y. *Langmuir* **2001**, *17*, 1737–1742.
89. Rackaitis, M.; Strawhecker, K.; Manias, E. *J. Polym. Sci. B Polym. Phys.* **2002**, *40*, 2339–2342.
90. Khutoryanskiy, V.; Nurkeeva, Z.; Mun, G.; Dubolazov, A. *J. Appl. Polym. Sci.* **2004**, *93*, 1946–1950.
91. Hiller, J.; Rubner, M. F. *Macromolecules* **2003**, *36*, 4078–4083.
92. Chu, L.-Y.; Li, Y.; Zhu, J.-H.; Chen, W.-M. *Angew. Chem. Int. Ed.* **2005**, *44*, 2124–2127.
93. Tong, W.; Gao, C.; Möhwald, H. *Macromolecules* **2006**, *39*, 335–340.
94. Swiston, A.; Cheng, C.; Um, S.; Irvine, D.; Cohen, R.; Rubner, M. *Nano Lett.* **2008**, *8*, 4446–4453.
95. Zhuk, A.; Pavlukhina, S.; Sukhishvili, S. A. *Langmuir* **2009**, *25*, 14025–14029.
96. Am Ende, M. T.; Hariharan, D.; Peppas, N. A. *React. Polym.* **1995**, *25*, 127–137.
97. Osada, Y.; Gong, J. P.; Tanaka, Y. *J. Macromol. Sci. C Polym. Rev.* **2004**, *C44*, 87–112.
98. Peppas, N.; Leobandung, W. *J. Biomater. Sci. Polym. Ed.* **2004**, *15*, 125–144.
99. Luzinov, I.; Minko, S.; Tsukruk, V. V. *Prog. Polym. Sci.* **2004**, *29*, 635–698.
100. Minko, S.; Muller, M.; Luchnikov, V.; *et al*. In *Polymer Brushes*; Advincula, R. C., Brittain, W. J., Caster, K. C., Ruehe, J., Eds.; Wiley-VCH: Weinheim, 2004; p 403.
101. Uhlmann, P.; Ionov, L.; Houbenov, N.; *et al*. *Prog. Org. Coat.* **2006**, *55*, 168–174.
102. Serizawa, T.; Matsukuma, D.; Nanameki, K.; Uemura, M.; Kurusu, F.; Akashi, M. *Macromolecules* **2004**, *37*, 6531–6536.
103. Serizawa, T.; Nakashima, Y.; Akashi, M. *Macromolecules* **2003**, *36*, 2072–2078.
104. Serpe, M. J.; Lyon, L. A. *Chem. Mater.* **2004**, *16*, 4373–4380.
105. Serpe, M. J.; Yarmey, K. A.; Nolan, Ch.M.; Lyon, L. A. *Biomacromolecules* **2005**, *6*, 408–413.
106. Kozlovskaya, V.; Ok, S.; Sousa, A.; Libera, M.; Sukhishvili, S. A. *Macromolecules* **2003**, *36*, 8590–8592.
107. Yang, S. Y.; Rubner, M. *J. Am. Chem. Soc.* **2002**, *124*, 2100–2101.
108. Kurita, K. *Prog. Polym. Sci.* **2001**, *26*, 1921–1971.
109. Zhang, Y.; Guan, Y.; Zhou, S. *Biomacromolecules* **2005**, *6*, 2365–2369.
110. Tong, W.; Gao, C.; Möhwald, H. *Chem. Mater.* **2005**, *17*, 4610–4616.
111. Szarpak, A.; Pignot-Paintrand, I.; Nicolas, C.; Picart, C.; Auzély-Velty, R. *Langmuir* **2008**, *24*, 9767–9774.
112. Zhao, Q.; Mao, Z.; Gao, C.; Shen, J. *J. Biomater. Sci. Polym. Ed.* **2006**, *17*, 997–1014.
113. Wang, C.; Ye, S.; Dai, L.; Liu, X.; Tong, Z. *Biomacromolecules* **2007**, *8*, 1739–1744.
114. Tong, W.; Gao, C. *Polym. Adv. Technol.* **2005**, *6*, 827–833.
115. Kharlampieva, E.; Kozlovskaya, V.; Chan, J.; Ankner, J. F.; Tsukruk, V. V. *Langmuir* **2009**, *25*(24), 14017–14024.
116. Yang, S. Y.; Lee, D.; Cohen, R. E.; Rubner, M. *Langmuir* **2004**, *20*, 5978–5981.
117. Kharlampieva, E.; Erel-Unal, I.; Sukhishvili, S. A. *Langmuir* **2007**, *23*, 175–181.
118. Kozlovskaya, V.; Kharlampieva, E.; Mansfield, M. L.; Sukhishvili, S. A. *Chem. Mater.* **2006**, *18*, 328–336.
119. Kozlovskaya, V.; Shamaev, A.; Sukhishvili, S. A. *Soft Matter* **2008**, *4*, 1499–1507.
120. Lee, D.; Cohen, R. E.; Rubner, M. F. *Langmuir* **2005**, *21*, 9651–9659.
121. Lee, D.; Rubner, M. F.; Cohen, R. E. *Chem. Mater.* **2005**, *17*, 1099–1105.
122. Yang, S. Y.; Mendelsohn, J. D.; Rubner, M. F. *Biomacromolecules* **2003**, *4*, 987–994.
123. Kozlovskaya, V.; Sukhishvili, S. A. *Macromolecules* **2006**, *39*, 5569–5572.
124. Khutoryanskaya, O. V.; Williams, A. C.; Khutoryanskiy, V. V. *Macromolecules* **2007**, *40*, 7707–7713.
125. Guan, Y.; Zhang, Y.; Zhou, T.; Zhou, S. *Soft Matter* **2009**, *5*, 842–849.
126. Such, G. K.; Tjipto, E.; Postma, A.; Johnston, A. P. R.; Caruso, F. *Nano Lett.* **2007**, *7*, 1706–1710.
127. Connal, L. A.; Kinnane, C. R.; Zelikin, A. N.; Caruso, F. *Chem. Mater.* **2009**, *21*, 576–578.
128. Elsner, N.; Kozlovskaya, V.; Sukhishvili, S. A.; Fery, A. *Soft Matter* **2006**, *2*, 966–972.
129. Francius, G.; Hemmerle, J.; Ohayon, J.; *et al*. *Microsc. Res. Tech.* **2006**, *69*, 84–92.
130. Mendelsohn, J. D.; Yang, S. Y.; Hiller, J.; Hochbaum, A. I.; Rubner, M. F. *Biomacromolecules* **2003**, *4*, 96–106.
131. Zelikin, A. N.; Li, Q.; Caruso, F. *Chem. Mater.* **2008**, *20*, 2655–2661.
132. Zelikin, A. N.; Quinn, J. F.; Caruso, F. *Biomacromolecules* **2006**, *7*, 27–30.
133. Zelikin, A. N.; Becker, A. L.; Johnston, A. P. R.; Wark, K. L.; Turatti, F.; Caruso, F. *ACS Nano* **2007**, *1*, 63–69.
134. Zelikin, A. N.; Li, Q.; Caruso, F. *Angew. Chem. Int. Ed.* **2006**, *45*, 7743–7745.
135. Kozlovskaya, V.; Kharlampieva, E.; Chang, S.; Muhlbauer, R.; Tsukruk, V. V. *Chem. Mater.* **2009**, *21*, 2158–2167.
136. Izquierdo, A.; Ono, S. S.; Voegel, J.-C.; Schaaf, P.; Decher, G. *Langmuir* **2005**, *21*, 7558–7567.
137. Schlenoff, J. B.; Dubas, S. T.; Farhat, T. *Langmuir* **2000**, *16*, 9968–9969.

1.125. Polyurethanes and Silicone Polyurethane Copolymers

R S Ward, Emergence Venture Partners, LLC., Berkeley, CA, USA
R L Jones, DSM Biomedical, Berkeley, CA, USA

© 2011 Elsevier Ltd. All rights reserved.

1.125.1.	**Introduction**	432
1.125.1.1.	The Polyurethanes and Polyurethane-Ureas	432
1.125.1.2.	World's Largest Class of Polymers	435
1.125.1.2.1.	Chemistry and synthetic methods	436
1.125.1.2.2.	The urethane and urea bonds	436
1.125.2.	**Commercially important PUs and PUUs**	437
1.125.2.1.	Range of Chemical Compositions and Structure Possibilities	438
1.125.2.2.	Lab and Commercial Synthetic Methods	444
1.125.2.2.1.	Thermoplastic pellets for extrusion and molding	444
1.125.2.2.2.	Solution synthesis for coating and dipping	445
1.125.2.2.3.	100% solids curable prepolymer systems for potting and encapsulation	447
1.125.2.2.4.	Water-borne dispersions for coatings	447
1.125.3.	**Utility of PUs and PUUs as Biomaterials**	448
1.125.3.1.	Biostable PUs and PUUs	448
1.125.3.1.1.	Structure and composition: soft-segment chemistry	448
1.125.3.1.2.	Importance of block and segmented PUs in long-term implants	449
1.125.4.	**Composition of Important biostable PU and PUUs**	450
1.125.4.1.	Chain Extenders	450
1.125.4.1.1.	Diols	451
1.125.4.1.2.	Diamines	451
1.125.4.2.	Soft Segments	451
1.125.4.2.1.	Polyester	451
1.125.4.2.2.	Polyethers	452
1.125.4.2.3.	Other polyalkylene oxides (also known as polyethers)	452
1.125.4.2.4.	Aliphatic polycarbonates	452
1.125.4.3.	General Properties of Polymers with a Single Soft Segment Chemistry	453
1.125.4.3.1.	Effect of alkylene chain length	453
1.125.4.4.	Mixed Soft Segments	453
1.125.4.5.	Hydrophobic and Hydrophilic Polyethers	453
1.125.4.6.	Silicone and Polyether and Silicone and Polycarbonate	454
1.125.4.7.	Silicone and Aliphatic Polycarbonate	455
1.125.4.7.1.	Polydimethylsiloxane (silicone)	455
1.125.4.7.2.	History of silicone–urethane development	456
1.125.4.7.3.	Benefits of silicone modification of PU and PUU	458
1.125.4.7.4.	Effect on surface chemistry and biological interactions	459
1.125.5.	**Composition of Some Bioresorbable Polyurethanes**	460
1.125.5.1.	Comparison to Biostable Analogues	460
1.125.5.1.1.	Degradable soft segments	460
1.125.5.1.2.	Degradable hard segments	461
1.125.6.	**Basic Structure–Property Relationships in Block and Segmented PUs and PUUs**	461
1.125.6.1.	Effect of Hard-Segment Chemistry and Content	461
1.125.6.1.1.	Importance of hydrogen bonding	461
1.125.6.1.2.	Effect of soft-segment chemistry and content	462
1.125.6.1.3.	Effect of end groups on surface chemistry	462
1.125.6.1.4.	Optimizing polyurethanes for specific biomedical applications	464
1.125.7.	**Fabrication of Medical Device Components from PUs and PUUs**	465
1.125.7.1.	Solution Processing: Dipping, Spraying, Solvent Bonding, and Web Coating	465
1.125.7.2.	Thermoplastic Processing	468
1.125.7.3.	Other Fabrication Methods	468
1.125.8.	**Sterilization of Segmented and Block Copolymer PUs and PUUs**	469
1.125.8.1.	Ethylene Oxide	469
1.125.8.2.	Radiation	470
1.125.8.2.1.	Gamma irradiation	470

1.125.8.2.2. Electron beam 470
1.125.8.3. Autoclaving 470
1.125.8.4. Other Methods 471
1.125.9. The Issue of MDA Formation in Aromatic Polyurethanes 471
1.125.9.1. Extreme Conditions Required to Produce MDA 471
1.125.9.2. The Need for Aromatic Hard Segments in Biostable PUs and PUUs 471
1.125.9.3. History of the Issue 472
1.125.9.4. The Epping Bakery Incident 472
1.125.10. Future of Biomedical Polyurethanes and Silicone Polyurethanes 472
References 474

Abbreviations

APPJ	Atmospheric pressure plasma jet
DBD	Dielectric barrier discharge
DMAc	Dimethylacetamide
DMBA	Dimethylol butyric acid
DMF	Dimethylformamide
DMPA	Dimethylol propionic acid
DSC	Differential scanning calorimetry
EB	Electron beam (radiation)
EO, EtO	Ethylene oxide
ESC	Environmental stress cracking
ESCR	Environmental stress cracking resistance
HALS	Hindered-light amine stabilizers
HEMA	Hydroxyl-ethyl methacrylate (2-Hydroxyethyl 2-methylprop-2-enoate)
HEPA	High efficiency particulate air (filter)
HMD	Hexamethylene diamine
HMDI	Hexamethylene diisocyanate (1,6-diisocyanatohexane)
IAB	Intraaortic balloon
IARC	International Agency for Research on Cancer
IM	Interfacial modification
IPDI	Isophorone diisocyanate
LDI	L-Lysine methyl ester diisocyanate
LEE	Lysine ethyl ester
LMED	Lysine methyl ester diisocyanate
MDCI	Dicyclohexylmethane 4,4′-diisocyanate
MDI	Methylene diphenyl diisocyanate isomers
MIDE	2,2′-(methylimino)Diethanol (2-[2-hydroxyethyl(methyl)amino]ethanol)
MIO	Metal-oxide-induced oxidation
PAEK	Polyaryletherketone
PBA	Poly(butyleneadipate)
PCL diol	Poly(ε-caprolactone) diol
PDMS	Polydimethylsiloxane (also PSX)
PEEK	Polyether ether ketone
PEU	Poly(ether urethane)
PHB–PHV	Poly(hydroxybutyrate)–poly(hydroxvalerate)
PHMC	Polyhexamethylene carbonate
PHMO	Polyhexamethylene oxide
PIB	Polyisobutylene
PIBd	Polyisobutylene diol
PO	Propylene oxide; epoxypropane
PPG	Polypropylene glycol
PSX	Polydimethylsiloxane (also PDMS)
PTG	The Polymer Technology Group (now DSM Biomedical)
PTMO	Polytetramethyleneoxide (varying molecular weight)
PUs	Polyurethanes
PUT	Putrescine; 1,4-diaminobutane
PUU	Polyurethane urea
RBD	Resistive barrier discharge
RIM	Reactive injection molding
RTV	Room temperature vulcanizing (silicone adhesive)
SAM	Self-assembling monolayer
SAME	Self-assembling monolayer end groups™
SME	Surface-modifying end groups™
SPU	Segmented polyurethane
TAH	Total artificial heart
THF	Tetrahydrofuran
TMP	Trimethoylpropane; 2-(hydroxymethyl)-2-ethylpropane-1,3-diol
TPCU	Thermoplastic polycarbonate-urethane (e.g., Bionate®)
TPU	Thermoplastic polyurethane
TSPU	Thermoplastic segmented polyurethane, also thermoplastic silicone-polyurethane
VAD	Ventricular assist device

1.125.1. Introduction

1.125.1.1. The Polyurethanes and Polyurethane-Ureas

Since the 1960s, polyurethanes (PUs) have been used in the most demanding medical devices and prostheses. As blood- and tissue-contacting components of well-designed chronic implants, they can maintain a function for years while continuously flexing, bearing high loads, or maintaining electrical insulation. With improvements in biostability and the control of bulk and surface properties occurring at a rapid pace, polyurethanes are likely to remain important biomaterials for many years to come.

Macromolecules that contain urethane and/or urea linkages constitute one of the largest classes of industrial polymers – not in volume produced, but in terms of possible structures and compositions. In the 1960s and 1970s, a few members of this

huge family of materials were successfully adopted as biomaterials and continue to be used today. These early polyurethanes with trade names like Lycra®, Adiprene®, Estane®, Pellethane®, and Q-Thane®, were industrial polymers originally developed for a variety of nonmedical applications ranging from shoe soles to textile fibers. Given that they were used with little or no modification, it was serendipitous that they had properties useful to medical device designers. A few false starts in early medical applications did occur, however, when certain compositions now known to degrade in the body were used in chronic implants in which biostable materials were needed. Unfortunately, these exceptions have persisted in the public and scientific consciousness, perpetuating numerous myths and inaccuracies about the suitability of polyurethanes as biomaterials. In addition, the almost limitless variety of polymers commonly referred to as 'urethanes' contribute to the confusion about their suitability as biomaterials. A few commercial suppliers took advantage of this to promote their own polymers in medical applications, adding still more confusion.

The most successful early 'urethane' biomaterials were rubbery polyether-containing elastomers that were found to perform well, particularly when used in contact with blood. One of the most important early uses was as the material of construction of total artificial hearts, ventricular assist devices, intraaortic balloons, and pacemaker leads. The availability of tough, flexible polyurethanes made possible a sea change in the options for treating heart disease. This is especially true in the case of early balloon-, sac-, and diaphragm-type cardiac assist devices, which required thromboresistant materials with outstanding flex life. Certain 'segmented' polyether-urethanes, for example, Biomer™ and BioSpan®, adopted from early DuPont spandex fiber chemistry, provided a unique combination of these two properties that was unavailable in any other elastomer (Figure 1).

Forty years after their initial use in cardiovascular implants, polyurethanes have become important materials in many other biomedical applications, including orthopedic implants, neurostimulation devices, and selectively permeable dense membranes for *in vivo* sensors and drug delivery. This has occurred because new compositions have been developed *specifically* for biomedical use, supported by structure–property relationships elucidated by a number of academic and industrial researchers. The tailoring of physical–mechanical properties is now very straightforward, at least within the narrow group of so-called segmented or block copolymers that have become platform biomaterials. Likewise, the control of permeability is fairly well understood. However, the study of how structure and composition affect biostability has probably had the biggest influence on the growth of polyurethanes as biomaterials. This understanding has supported the continual improvement of the *in vivo* stability of polyurethane biomaterials, driven by the clinical demand for longer service life of prosthetic implants and life-supporting devices.

Among the earliest biomedical polyurethanes was a solvent-cast silicone–urethane 'hybrid' (actually a copolymer-stabilized pseudo-interpenetrating network) known as Avcothane™-51, and later Cardiothane®-51. The suffix '51' was shorthand for the 510th formulation evaluated by its inventor Emory Nyilas, revealing the empirical approach that was used, by necessity, in the late 1960s.[1–3] Until *c.*1975 it was synthesized in fairly crude equipment (Figure 2), until it was scaled up in support of the growing demand for sale of intraaortic balloons, and interest from designers of other blood-contacting devices (Figure 3).

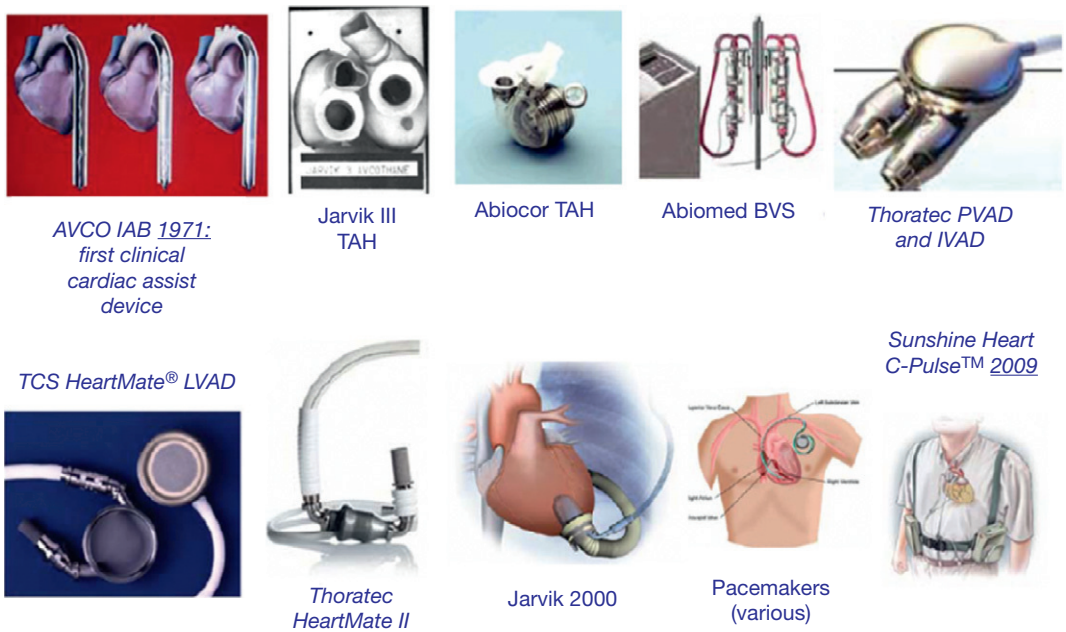

Figure 1 Polyurethanes and silicone–urethanes have been used successfully in clinical cardiac assist devices even before 1971. Balloon-, sac-, and diaphragm-type devices need the flex-life and thromboresistance of polyurethanes and silicone-polyurethanes. A new blood pump (C-Pulse) with no blood-contacting surfaces requires good flex life and abrasion resistance. Even axial flow devices like the HearMate II and Jarvik 2000 use polyurethanes as tough, biostable electrical insulation.

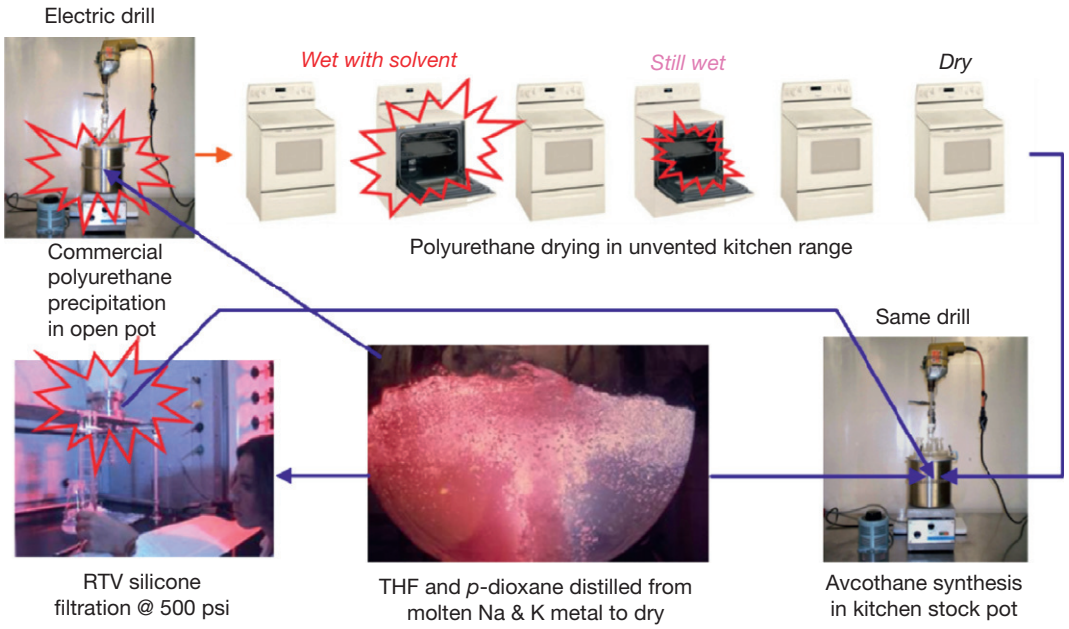

Figure 2 The original manufacturing process for one of the first high-performance biomedical polyurethanes: Avcothane-51 also known as Cardiothane: thermoplastic polyurethane was dissolved in THF and precipitated in methanol. After drying the purified PU was dissolved in anhydrous THF/*p*-dioxane solvent and combined with acetoxy-functional RTV silicone medical adhesive, prefiltered to remove silica filler. The small amount of silicone–urethane copolymer formed by co-condensation of silanol (–Si–OH) and carbinols (–C–OH) apparently stabilized the remaining silicone until device fabrication, drying and cross-linking could occur.

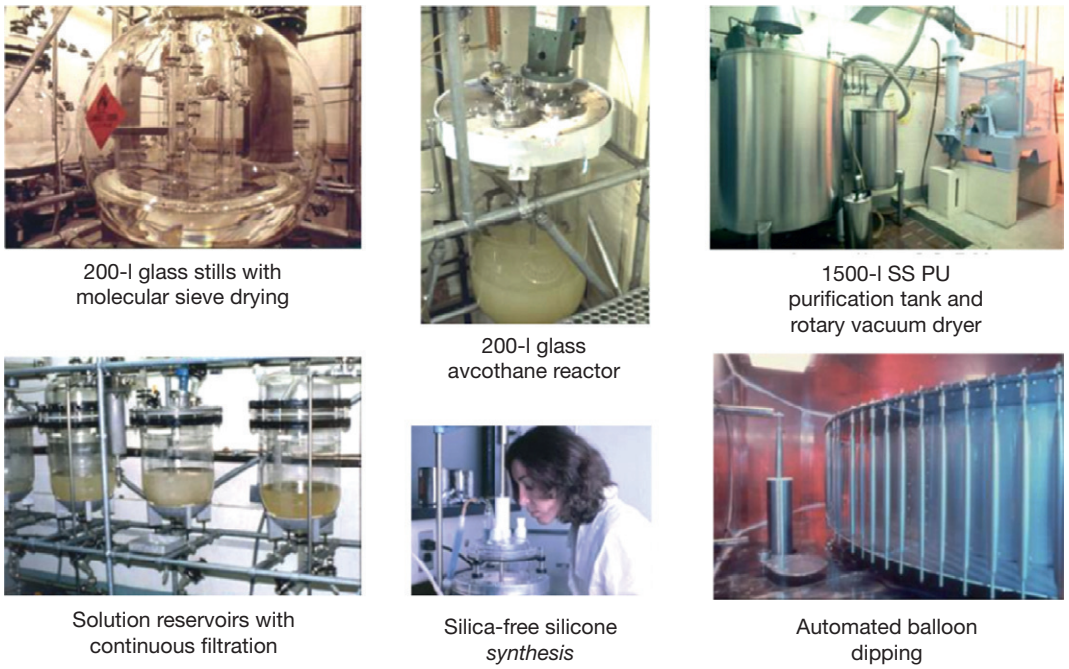

Figure 3 Avcothane/cardiothane production *c*.1976. In addition to improved polymer synthesis, automated balloon dipping within a clean room environment replaced labor-intensive 'candle' dipping techniques used in early IAB manufacturing. Note white color of Avothane solution caused by gross phase separation of the silicone (**Figure 4**) and resulting light scattering.

Although 'Avcothane' was moisture sensitive and difficult to process during device manufacturing, its successful clinical use in intraaortic balloons (IAB) represented an important step forward that demonstrated the benefits of combining polyurethanes with another very useful biomedical polymer: polydimethylsiloxane, also known as silicone (**Figure 4**). By design, the passive *thromboresistance* of Avcothane-51 was excellent relative to peroxide-cured silicone rubber and other

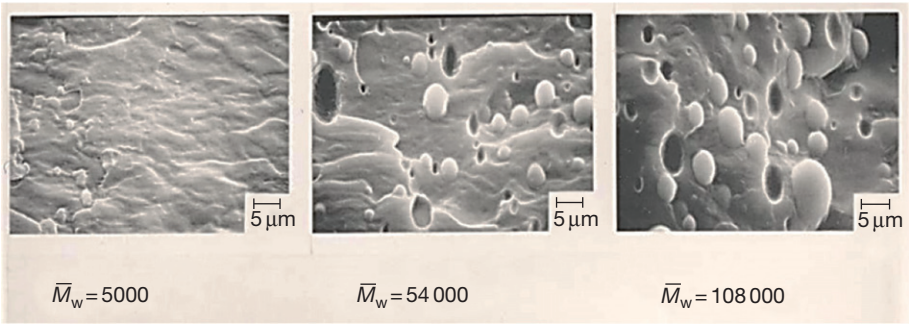

Figure 4 Liquid N_2 fractured Avothane films made with polydimethylsiloxane (PSX) of three different molecular weights: all at 10 wt% silicone. The extremely large silicone domains in the center photo are typical of the standard material. Their size and difference in refractive index from the polyurethane-rich continuous phase cause light scattering and gives this and other admixed silicone–urethane systems their characteristic opacity. Most modern silicone–urethane copolymers are phase mixed, or phase separated on a scale too fine to scatter light, and are, therefore, optically transparent. Covalent bonding within the backbone and much lower silicone molecular weight both contribute to optical clarity.

elastomers available at that time. The *biostability* of Avcothane-51 was also tested with encouraging results, albeit inadvertently, by those occasional IAB patients who could not be weaned from the pump. Based on this anecdotal data, and the known *in vivo* stability of silicones, it was later hypothesized that silicone could enhance the biostability of polyurethanes when copolymerized within the polymer backbone, or used as covalently bonded end groups.[4] This was later confirmed with *in vitro* and *in vivo* experiments that led to new families of highly biostable thermoplastic silicone–urethane *copolymers*, with improved processability. Whereas Avcothane-51 required solvent casting, dipping or spraying within a moisture-controlled (clean-room) environment, the thermoplastic silicone-polyurethanes (TSPUs) can also be injection molded, extruded, and heat sealed.

The development of well-defined silicone–urethane copolymers occurred slowly because the immiscible reactants required modified synthetic procedures. Backward integration to the scale up of stable, high-purity, *difunctional* silicone oligomers (e.g., carbinols) suitable for step growth polymerization was also required. Today, thermoplastic silicone–urethane copolymers belong to a growing class of urethane biomaterials that combine the biostability of silicone with the superior physical properties of segmented urethanes in roughly inverse proportion to their silicone content. They will, therefore, be a major topic within this chapter.

The use of silicone and a second, so-called soft block (e.g., polyalkylene-ether or polyalkylene-carbonate) is a specific example of the use of two or more soft blocks in the same polyurethane. This is an important aspect of a very useful polyurethane structure that serves as a 'biomaterials toolkit' for tailoring bulk and surface properties for specific, and seemingly unrelated, medical devices.

This chapter is based on one author's 40-year experience in the development and application of biomedical polyurethanes. It is intended to be a practical reference for scientists and engineers developing or using polyurethanes in clinical devices and prosthetic implants. Because material performance depends on handling, fabrication, and sterilization, processing methods used in the R&D/manufacturing of medical devices are included. Due to space limitations, only clinically relevant biostable polyurethanes will be covered in detail.

1.125.1.2. World's Largest Class of Polymers

The range of compositions and polymer structures within the class of polymers commonly referred to as polyurethanes is almost unlimited. Even if this long list of materials is abbreviated to include only those polymers synthesized from commercially available reactants, the category is still enormous. By comparison, the list of polyurethane compositions that have been used successfully in prosthetic devices is small. By far the most common polyurethane biomaterials are block or segmented polymers. These are actually *co*polymers containing oligomeric soft blocks and short hard segments along the main polymer chain. Most of the urethane or urea groups are found in the glassy or semicrystalline hard segments, with few, if any, present in the liquid-like soft segment.

Under typical service conditions, the useful properties of these PU and polyurethane-urea (PUU) copolymers are related to the incompatibility of different regions within these composite molecules. At body temperature, soft segments are thermodynamically incompatible with hard segments and have a lower degree of intermolecular attraction. In many linear and branched co-polyurethanes the bonds that hold the hard segments together and provide strength to the polymer are thermolabile, dissociating at melt processing temperatures or in solution to form viscous liquids that can be shaped into device components. Ease of processing requires a degree of phase mixing in the melt or in solution, followed by phase separation, also known as soft-segment/hard-segment 'demixing' after fabrication.[5–7] That is, after cooling from the melt, or evaporation of solvent from a polyurethane solution, the hard segment intermolecular bonds re-form to recreate discrete nanoscale domains. The ability of the hard segments to remain intact under stress, while the attached soft segments deform reversibly gives PU device components their useful properties in the warm, aqueous environment of the body.

Hard segments are literally hard: structural rigidity and isomeric purity increase the efficiency of packing and promote the formation of hydrogen bonds among like segments on adjacent chains. When present at sufficient concentration within the polyurethane backbone, these crystalline or glassy domains retain measurable melting points and/or glass transition temperatures that are well above body temperature.

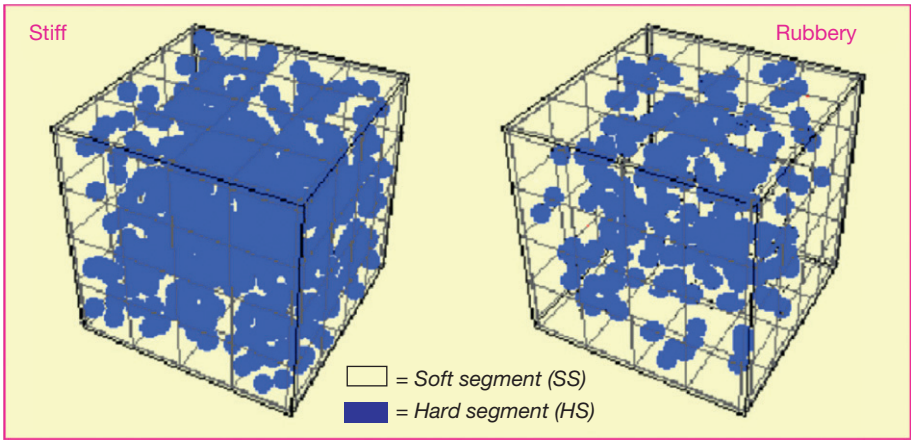

Figure 5 Many useful biomedical polyurethanes are phase separated copolymers at body temperature. Hard segment domains ~100 Å in diameter may be dispersed within a continuous phase of soft segment in elastomeric (rubbery) homologues. If hard segment is increased during synthesis, the hard segment can become the continuous phase in which the soft segments are dispersed. At intermediate compositions both hard and soft segments may form co-continuous phases. Many bulk properties depend on the ratio of soft-to-hard segment in the polymer. In addition to modulus/stiffness, permeability is strongly influenced by the chemistry and concentration of the liquid-like soft segment, as most hard segments are essentially impermeable.

If prepared as high molecular weight homopolymers instead of being used as segments within copolymers, many urethane hard segments would be rigid plastics. In fact, the earliest polyurethane homopolymers made by Otto Bayer in Germany were developed to compete with nylon fibers (Figure 5).

Unlike urethane hard segments, most useful soft segments, for example, dienes, silicones, and aliphatic polyethers and polycarbonates, are viscous liquids at body temperature. Even at high molecular weight, most would be too weak as linear homopolymers to be useful biomaterials. Certain soft segments that are capable of hydrogen bonding with hard segments can produce polyurethanes with improved properties and processability. Polytetramethyleneoxide (PTMO), for example, produces better 'physicals' than silicone (PDMS) or polyisobutylene (PIB), in part because the ether group within the PTMO repeat unit is a hydrogen bond acceptor, absent in both PDMS and PIB: ethers enhance phase mixing in the melt and lower melt viscosities during extrusion and injection molding. Flex life appears to be best in those soft segments that undergo reversible (strain-induced) crystallization during stretching. PTMO is superior in this way to many other soft segments, including other polyethers (e.g., polypropyleneoxide) that do not crystallize when elongated.

Currently, important polyurethanes, polyurethane-ureas and silicone-containing analogues used in medical devices are strong, biostable materials designed (or empirically determined) to be resistant to enzymatic, hydrolytic or oxidative degradation *in vivo*. Early review articles on polyurethane biomaterials are available including those by Lyman *et al.*[8], and the CRC Press, *Polyurethanes in Biomedical Applications* by Lamba *et al.*[9] Later articles on more-recent developments were covered by Zdrahala and Zdrahala.[10] More comprehensive reviews are also available.[11,12] A 2001 review[13] emphasizes specific silicone–polyetherurethane copolymers[14]. It also includes a useful description of the synthesis and processing of biomedical polyurethanes.

A general overview of the chemistry and technology involved in polyurethane synthesis is provided here to orient the reader, but much more detail can be found in the cited references.

1.125.1.2.1. Chemistry and synthetic methods

Although the urethane bond may constitute only a small fraction of the covalent bonds in polyurethane biomaterials, it is an important characteristic of this polymer family. Two main reactions are used to produce the urethane bond: the reaction between bischloroformate and a diamine (releasing hydrogen chloride, Figure 6) or the more commercially useful reaction between a diisocyanate and a diol (Figure 7).

In the presence of hydroxyls or amines in the bulk, or in solution, isocyanates can be very reactive, providing nearly quantitative conversion into urethane or urea groups respectively. Figure 7 illustrates bond formation via the attack of the nucleophilic oxygen of the alcohol on the electrophilic carbon of the isocyanate; this shows a base-catalyzed reaction where the base increases the nucleophilicity of the oxygen through hydrogen-bonding to the adjacent proton.[15] The exact mechanisms are still unclear due to side reactions, the existence of coordination complexes, and the poorly understood role of the optional solvent.

1.125.1.2.2. The urethane and urea bonds

The most important side reactions during urethane synthesis are allophanate formation, which occurs when isocyanate reacts with a preformed urethane group, and biuret formation, in which isocyanate reacts with a urea group. Either side reaction can produce branching or cross-linking, and so must be controlled during synthesis. Polyurethane-ureas are most commonly made by reacting diisocyanates with short-chain diamines instead of diols, together with the hydroxyl-terminated polyols that become the soft segments. The resulting polyurea hard segments are capable of forming twice as many hydrogen bonds as the equivalent urethane hard segment. This structural difference, and the resulting improvement in phase separation, produces polymers with useful properties at much lower



Figure 6 Reaction between bischloroformate and diamine to form a urethane bond.

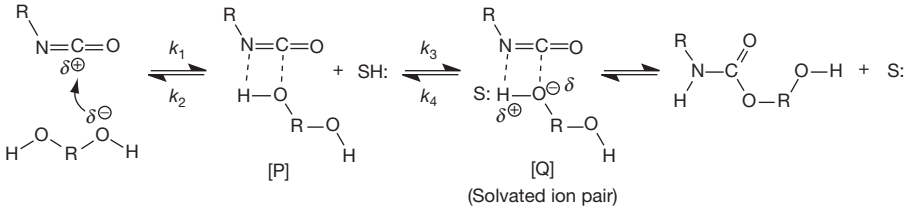

Figure 7 Reaction between isocyanate and diol to form a urethane bond.

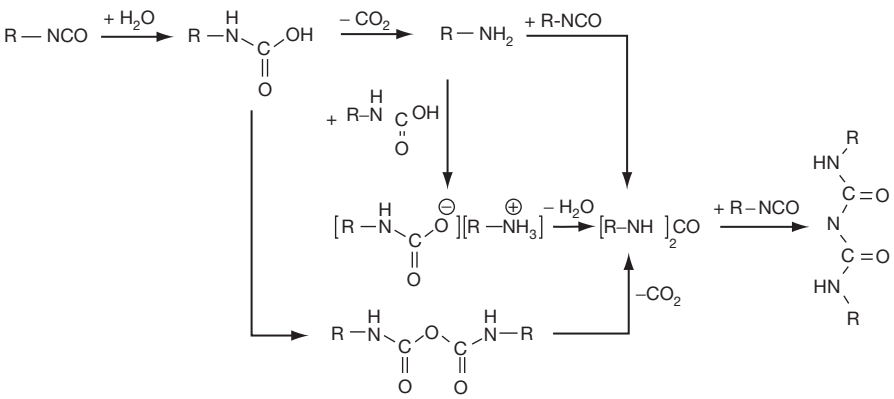

Figure 8 Reaction between isocyanate and water. Reproduced from Shkapenko, G.; Gmitter, G. T.; Gruber, E. E. *Ind. Eng. Chem.* **1960**, *52*(7), 605–608.

hard-segment contents than the corresponding urethanes. Elastomers with excellent flex life and rubber-like elasticity are synthesized in solution using certain diamine chain extenders at only ~15–25 wt% hard segment. An analogous polymer with only urethane groups might require >35% hard segment to achieve comparable strength, but would therefore have a higher modulus and indentation hardness.

Water can also be used as a chain extender yielding only half the urea content of a diamine while evolving CO_2 (Figure 8).

Depending on relative concentration, the reaction of isocyanate groups with water can result in the formation of large amounts of carbon dioxide which can be entrained during the formation of the polymer. The reaction mechanism has been proposed and studied by a number of authors and the kinetics described in detail[16]. With stabilization provided by included surfactants this reaction can produce a foamed product with many industrial and commercial applications.

If thermally stable cross-linking is avoided, water-extended polyurea-urethanes can be melt-processed due to their reduced urea content.[17] However, as TPUs they provide little advantage over diol-extended analogues which are easier to synthesize in bulk. The already enhanced phase separation of polyurea hard segments can be further increased with certain highly incompatible soft segments that do not form hydrogen bonds. Amine-terminated silicone and polyisobutylene oligomers both give processable, albeit relatively weak, thermoplastic polyurea elastomers at hard-segment content as low as 10 wt%.[18–20] In general, however, too high a polyurea content gives polymers that cannot be melt-processed or even dissolved in common organic solvents.

1.125.2. Commercially important PUs and PUUs

Macromolecules containing urea or urethane-rich hard segments covalently bonded to soft segments constitute an important family of industrial polymers. Many contain rigid aromatic or cyclic aliphatic groups in their hard segments, and polyester, polyether, polydiene or aliphatic polycarbonate soft segments. Silicone soft segments are still the exception in commercial urethanes, although relatively large quantities of silicone-ureas are consumed as release coatings for pressure sensitive adhesive and encapsulants for solar cells.[21,22]

An extensive property map can be generated by combining various hard segments, soft segments and chain extenders in different proportions as described in the preceding sections. Polymer hardness ranges from soft sticky gels, to rubber-like elastomers, to flexible 'leathery' polymers, to very rigid homologues that resemble impact-modified plastics. Nonmedical

uses include paints and varnishes, safety glass laminates, skateboard wheels, waterproof moisture-vapor-permeable textile coatings, abrasion-resistant tubing and hose, plasticizer-free cable insulaton, dent-resistant automobile facia, puncture-resistant extruded film, mattress foam, shoe soles and laundry-stable spandex fibers that mimic natural rubber.

Although polyurethanes can be formed from an almost unlimited combination of reactants, in practice, commercial urethanes are only synthesized from raw materials that are readily available at attractive prices. The main synthetic route to commercial thermoplastic PU (TPU) copolymers is step-growth polymerization of a mixture of difunctional reactants including diisocyanates, short-chain diol chain extenders and oligomeric glycols or diamines that comprise the soft segments. Although the range of possible compositions is wide and the synthesis is straightforward, it requires high-purity reactants and precise control of stoichiometry to obtain high molecular weight. Lot-to-lot consistency requires tight controls of these variables, as well as the order of addition, mixing efficiency, reaction time/temperature, pH and the concentration of optional catalyst (e.g., organotin compounds or amines). Another important variable is the concentration of ever-present trace water in the reaction mixture, due to its ability to react with isocyante groups.

The versatility of polyurethanes is due to the many possible combinations of reactants, and their easily varied concentrations and arrangements within the polymer's molecular structure. In the simplest thermoplastic polyurethane, the ratio of the concentration of soft-segment polyol to the diisocyanate-diol reaction product that becomes the hard segments can be used to vary properties significantly. Soft segment molecular weight can also be varied over the range of a few hundred to a few thousand Daltons, to affect changes in rheology and other properties. In addition, intermediate physical properties can be obtained by physically blending members of a single family of polyurethanes that differ in hard segment content. However, even polyurethanes with identical hard segment composition made with different soft segments may be thermodynamically incompatible. This can lead to eventual separation of blends, particularly in solution where stratification may occur on standing.

The manufacture of polyurethanes is a well-developed, commercially mature industry and has been studied and reviewed by a number of authors. There exists a very large body of information on polyurethanes in the patent literature and there are many reviews and journal articles, which provide excellent background and overview.[23] The invention and early developments in the field, including accounts of historical nature, are well described and are referenced widely. The *Polyurethane Handbook*[24] remains a valuable resource that provides an overview of the early literature and a lot of practical information for manufacturers.

In the synthesis of (biostable) biomaterials, the range of raw materials employed is not nearly as large as in the commercial polyurethanes. This is due, in part, to the combination of surface *and* bulk properties required in biomedical applications. It is also due to slow acceptance of completely new compositions by risk-averse device manufacturers who naturally demand extensive testing and documentation before adopting new biomaterials. It is also worth noting that the volume of polyurethanes produced as biomaterials is a tiny fraction of what is sold for nonmedical uses, providing little incentive for manufacturers to create new reactants specifically for high-risk biomedical polymers. Reviews of biomedical polyurethanes by Woods[25] and later by Scycher[26] are noteworthy. Less comprehensive, but equally important, are the review articles by Petrovic and Ferguson[27] and, more recently, Król[28] that provide a detailed review of the catalytic and kinetic processes.

1.125.2.1. Range of Chemical Compositions and Structure Possibilities

Many properties of commonly used biomedical polyurethanes are determined by soft-segment chemistry and concentration. Within the polyurethane backbone, soft segments typically have their dominant thermal transitions below body temperature, making them amorphous liquids at 37 °C. Candidates for the soft segments include polyesters, polylactones, polydienes, polyethers and aliphatic polycarbonates. Currently, polyethers or polycarbonates are used in most biostable polyurethanes (see **Table 1**). Polyesters and polylactones are subject to hydrolytic degradation and are generally unsuitable for biostable compositions. More recently polydimethylsiloxane, also known as silicone, has become an important co-segment for enhancing long-term biostability and/or tailoring permeability. Depending on cost and availability, highly stable polyisobutylene, like silicone, may also become an important soft segment. It is likely to be used in combination with polycarbonate, polyether or other biostable co-soft segments for improved physical–mechanical properties.

Thus, the major polyurethane soft segments that have been used as biomedical polyurethanes are:

1. Polyester (soft segment) containing polyurethanes: although now known to be hydrolytically unstable, they were used in a few early implants. Compositions containing these soft segments are typically made by (co)polymerizing monomeric diols such as ethylene glycol, 1,3-propanediol, and 1,4-butanediol with dicarboxylic acids such as adipic acid, succinic acid, maleic acid, or acid anhydrides. Typical molecular weight range is from 300 to 2000 Da. Polyesterdiols having an even number of carbons in the soft-segment backbone are able to crystallize and phase-separate less than those containing an odd number (e.g., pentane diols vs. hexane diols). Such 'irregular structures' create poor packing of adjacent chains. This discourages hydrogen bonding so intermolecular attractions are weakened and melting points are reduced.[29]

   A number of studies report the effects of synthesis and post processing conditions on mechanical properties of the poly(ester-urethane) polymers, including curing temperatures during and after formation.[30] Poly(ester-urethane)s synthesized from poly(ethylene glycol adipate) (PEG) and 2,4-toluene diisocyanate (TDI) with PEG as soft-segment films and cured above 60 °C possess higher tensile strength and elongation at break, showing that reaction temperature and cure temperature play an important role in structure development, and the resulting mechanical properties, of semicrystalline PU.

Table 1 Commonly used components of biomedical polyurethanes

Reactants/(common name)(a)	*Abb.*	*Structure/IUPAC*	*Comments*
● Methylene diphenyl diisocyanate, ● Methylenebis(phenyl isocyanate), ● 4,4'-Methylenediphenyl diisocyanate	MDI	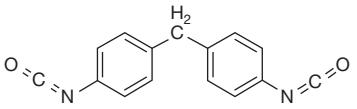 1-isocyanato-4-[(4-isocyanatophenyl) methyl] benzene CAS Number: 101-68-8	Pure isomer gives the best physicals and biostability
● 2,4-Tolylene diisocyanate ● 4-Methyl-1,3-phenylene diisocyanate ● 4-Methyl-meta-phenylene diisocyanate	TDI	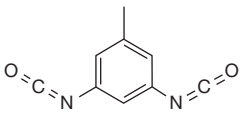 2,4-diisocyanato-1-methyl-benzene CAS Number: 584-84-9	Less used in biomaterials; second most produced diisocyanate for PU use
● Methylenedicyclohexyl diisocyanate	HMDI, H12MDI H_{12}MDI	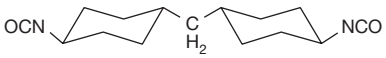 1-isocyanato-4-[(4-isocyanatocyclohexyl) methyl]cyclohexan CAS Number: 5124-30-1	Mixture of three isomers. Nonyellowing cycloaliphatic structure Biostability and flex life is < with MDI
● Hexamethylene diisocyanate ● 1,6-hexane diisocyanate	HDI	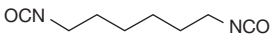 1,6-diisocyanatohexane CAS Number: 822-06-0	Used in biodegradables to avoid possible toxic degradation products Gives lower strength PUs
Isophorone diisocyanate ● 1-(Isocyanatomethyl)-5-isocyanato-1,3,3-trimethylcyclohexane ● 1,3,3-Trimethyl-1-(isocyanatomethyl)-5-isocyanatocyclohexane ● 1-Isocyanato-3-(isocyanatomethyl)-3,5,5-trimethylcyclohexane	IPDI	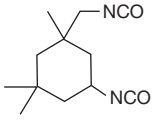 5-isocyanato-1-(isocyanatomethyl)-1,3,3-trimethyl- cyclohexane CAS Number: 4098-71-9	High-strength aliphatic PUs The two isocyanate groups have different reactivities.
Butane diol ● 1,4-Butanediol ● 1,4-Butanediol 1,4-butylene glycol butylene glycol ● 1,4-Butylene glycol	BD	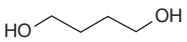 Butan-1,4-diol CAS Number: 110-63-4	Most commonly used diol in thermoplastics
Ethylene glycol ● 1,2-Dihydroxyethane ● 1,2-Ethanediol ● 1,2-Ethanediol ● 1,2-Ethylene glycol	EG	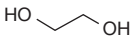 Ethane-1,2-diol CAS Number: 107-21-1	
Ethylene diamine ● 1,2-Diaminoethane ● 1,2-Ethanediamine ● 1,2-Ethylenediamine	ED	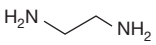 1,2-diaminoethane CAS Number: 107-15-3	Main chain extender in polyurethane-urea elastomers, for example, BioSpan® SPU
● 1,3-Cyclohexane diamine	1,3-CHD	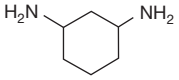 Cyclohexane-1,3-diamine 3385-21-5	Minor chain extender in polyurethane-urea elastomers. Improves fiber spinning from solution
● 1,4-Cyclohexane diamine	1,4-CHD	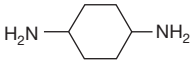 Cyclohexane-1,4-diamine CAS Number: 3114-70-3	Has been used in place of 1,3-CHD due to commercial availability

(*Continued*)

Table 1 (Continued)

Reactants/(common name)(a)	*Abb.*	*Structure/IUPAC*	*Comments*
Polyethyleneglycol ● 1,2-Ethanediol, homopolymer ● Carbowax ● Ethylene glycol polymer ● Macrogol ● Oxirane, homopolymer	PEG, PEO	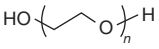 poly(oxyethylene) {structure-based}, poly(ethylene oxide) {source-based} CAS Number: 25322-68-3	Oxidatively unstable, hydrophilic soft segment. Increases water permeability and water absorption
Polypropyleneglycol ● 2-Methyloxirane; oxirane	PPO	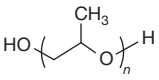 2-methyloxirane; oxirane CAS Number: 9003-11-6	Stable against hydrolysis, but does not strain crystallize. Elastomers are inferior to PTMO-containing analogues
Polytetramethylene glycol ● Poly(tetramethylene ether) glycol ● Polytetrahydrofuran ● Terathane ● PolyTHF	PTMO, PTMEG, PolyTHF	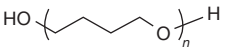 butane-1,4-diol CAS Number: 732189-03-6	Best overall polyether polyol in many *in vivo* applications. Subject to (cobalt-catalyzed) oxidative degradation especially when strained
Polyhexamethylene oxide	PHMO	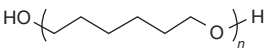	Oxidatively unstable when strained but has less ether contant than PTMO. H-Bond donor 'compatiblizing' polyol used at low concentration in some silicone–urethanes.
Polyhexamethylene carbonate ● poly(hexamethylene carbonate) diol	PHMC PHMCD	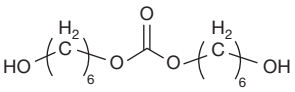	Oxidatively and hydrolytically stable *in vivo* especially when ether free. Gives highest strength TPUs.
Silanol-terminated polydimethylsiloxane ● Dimethyl siloxanes and silicones ● Dimethylpolysiloxane ● Polydimethylsiloxane ● Siloxanes and silicones, dimethyl	PDMS, PSX	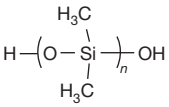 poly(dimethylsiloxane) CAS Number: 63148-62-9	Does not from silicone–urethanes when reacted with diisocyantes. May co-condense with carbinols under certain condtions
Polybutadiene	PBD	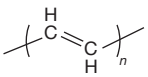	Oxidatively and hydrolytically stable *in vivo*. Useful in ultrasonic probes.
Polyisobutylene ● Butyl rubber	PIB	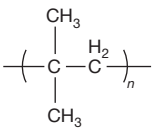	Oxidatively and hydrolytically very stable *in vivo*. Gives low-strength TPUs when used without H-bonding co-blocks.
Octodecanol ● 1-Octadecanol Stearyl alcohol ● 1-Hydroxyoctadecane ● Octadecyl alcohol		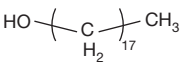 1-Octadecanol CAS Number: 112-92-5	
Carbinol-terminated polydimethylsiloxane ● Dimethyl siloxanes and silicones ● Dimethylpolysiloxane ● Polydimethylsiloxane ● Siloxanes and silicones, dimethyl	PDMS	poly(dimethylsiloxane) CAS Number: 63148-62-9	Silicon-carbon bonds join hydroxy-functional organic group to terminal silicon atoms. Forms silicone–urethanes in reactions with (di)isocanates
Perflourinated octadecanol $C_{18}F_{37}OH$:			Surface-modifying end group self assembles in surface of formed articles US 5929290 Issued Jul 1999
Monofunctional HO-PEO		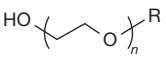 R = CH_3, CH_2CH_3, PDMS, etc.,	Surface-modifying end group self assembles in surface of formed articles

(*Continued*)

Table 1 (Continued)

Reactants/(common name)(a)	*Abb.*	*Structure/IUPAC*	*Comments*
Sulphonated alcohol Isethionic acid ● 2-hydroxyethanesulphonic acid ● Ethanolsulfonic acid		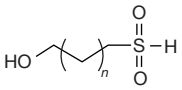 When n = 1: 2-hydroxyethanesulfonic acid CAS Number: 107-36-8	Surface-modifying end group self assembles in surface of formed articles
Ethylene bis-stearamide ● 1,2-Bis(octadecanamido)ethane ● 1,2-Ethylenebis(stearamide)		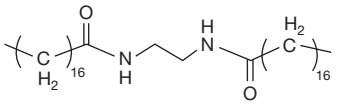 *N*-[2-(octadecanoylamino)ethyl] octadecanamide CAS Number: 110-30-5	Leachable, low-molecular weight, waxy processing aid used in many TPUs. Affects surface properties and melt viscosity. Major determinant of surface chemistry when present.
Calcium stearate		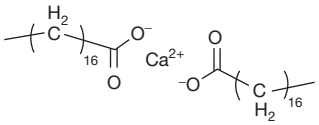 Calcium octadecanoate CAS Number: 1592-23-0	Alternative to ethylenebis(stearamide)
Hindered phenolics, antioxidants Butylated hydroxyanisole ● tert-Butyl-4-hydroxyanisole ● tert-Butyl-4-methoxyphenol	BHA	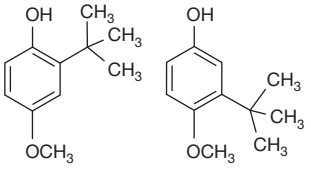 2-tert-butyl-4-hydroxyanisole and 3-tert-butyl-4-hydroxyanisole (mixture) 25013-16-5, 8003-24-5, 9009-68-1, 121-00-6, 88-32-4	Stabilizer
Butylated hydroxytoluene ● Butylhydroxytoluene ● 2,6-Di-t-butyl-4-methylphenol	BHT	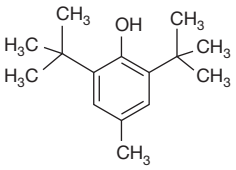 2,6-bis(1,1-dimethylethyl)-4-methylphenol CAS Number: 128-37-0	
Free radical traps		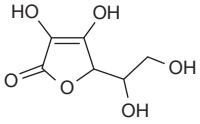 Ascorbic acid 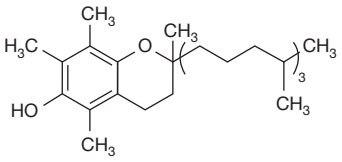 α-tocopoherol	

(*Continued*)

Table 1 (Continued)

Reactants/(common name)(a)	*Abb.*	*Structure/IUPAC*	*Comments*
Stannous octoate ● Hexanoic acid, 2-ethyl-, tin(2+) salt		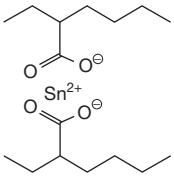 2-ethylhexanoate; tin(2+) CAS Registry Number: 301-10-0	Catalyzes urethane formation. Less cytotoxic, but less effective than DBT
Dibutyltin dilaurate ● Stannane, dibutylbis(lauroloxy)-		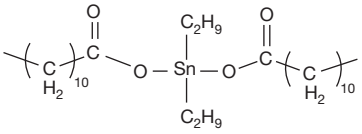 [dibutyl(dodecanoyloxy)stannyl] dodecanoate CAS Number: 77-58-7	Catalyzes urethane formation. Low concentrations required, but highly cytotoxic

References/Sources: (a) American Chemical Society 2010. Common Chemistry from CAS. (www.commonchemistry.org. *last accessed* 5/ 2010).

As conventional polyester polyurethanes are subject to hydrolytic degradation they are of little use in long-term implantable devices.[31] A more stable polyester soft segment is polycaprolactone (PCL) diol. Unlike esters prepared from diacids and diols, PCL it is synthesized by ring opening of cyclic caprolactone monomer. Although it is hydrolytically unstable, it degrades slowly *without* releasing autocatalytic acidic byproducts, which are *also* undesirable because they can elicit an inflammatory response in the surrounding tissues. Polycaprolactone is, therefore, a preferred component of *intentionally* biodegradable polymers, although unsuitable for use in implanted biostable polyurethanes, despite its advantages over common polyadipate ester diols.

Compositions containing both polyesters and polyether diols (polycaprolactone as a polyester diol, and polyethyleneoxide (PEO) capped PEO/PO polyether diol containing less than 20% ethylene oxide, EO) with a diisocyanate and butanediol as chain extender, have been described as transparent thermoplastic polyurethanes that have good combinations of clarity, tensile strength, hydrolytic stability and processability compared to TPUs prepared using either polyester or polyether diols alone, or similar combinations with a higher EO polyether diol.[32] In general, however, the use of hydrophilic moieties like PEO together with hydrolytically unstable soft segments like PCL or polyadipate-esters *increases* degradation rate. The *in vivo* water absorption of the bulk polymer is increased by the presence of the hydrophilic PEO, which exposes the hydrolytically unstable segments to a higher average water concentration while increasing the polymer's permeability. This results in faster cleavage of unstable ester bonds.

Recent developments with cross-linked, dual soft-segment poly(ester urethane urea) prepared by extending poly(propylene oxide)-based triisocyanate-terminated prepolymer with a polycaprolactone diol (PCL) have shown promising results in nonhemolytic membrane applications.[33] Such compositions may be suitable in short-term or disposable device applications, but are unlikely to have good long-term biostability for the reasons stated above. In general, polyesters are finding renewed interest in the field of tissue engineering and bioresorbable materials such as stents and sutures (*vida infra*).

2. Polyether (soft segment) containing polyurethanes: generally are much more hydrolytically stable than the polyester-containing polyurethanes, although *oxidative* stability can be lower in softer grades, particularly in the presence of certain metal ions such as cobalt.[34] Examples include PEO (also known as PEG), polypropyleneoxide (PPO) and polytetramethyleneoxide (PTMO). As alkylene chain length within the repeat unit increases the polyethers become more hydrophobic: PEG is water soluble, PTMO is not. Methylene groups adjacent to the ether oxygens are susceptible to oxidation, particularly when the polymer is stretched in use, or compressed, for example, by ligating sutures. In PEO, *all* of the methylenes are adjacent to ether oxygens, making it the least oxidatively stable polyether polyol. Of these three commercially available polyethers polyols, PTMO gives the best balance of physical–mechanical properties and biostability. Unlike PPO, PTMO soft segments undergo reversible strain-induced crystallization, giving elastomers with low tensile hyteresis and good flex life. Attempts to increase the methyelene chain length to six carbons in order to *significantly* enhance biostability were unsuccessful until a high concentration of silicone was included as a co-soft segment at the expense of the PHMO concentration[35,36] (**Figure 9**).

Chang and Wilkes[37] reported the structure property relationship of a variety of hard segments combined with oligomeric PEO, poly(propylene oxide) (PPO), or both PEO and PPO soft segments. They showed copolymers of both PEO and PPO display enhanced domain and anisotropic superstructures and attributed this phenomenon to polymer soft segment incompatibility. The effects on morphology and the effectiveness of different diamines as chain extenders were accounted for by the symmetry, hydrogen bonding and rigidity of the hard segments as well as

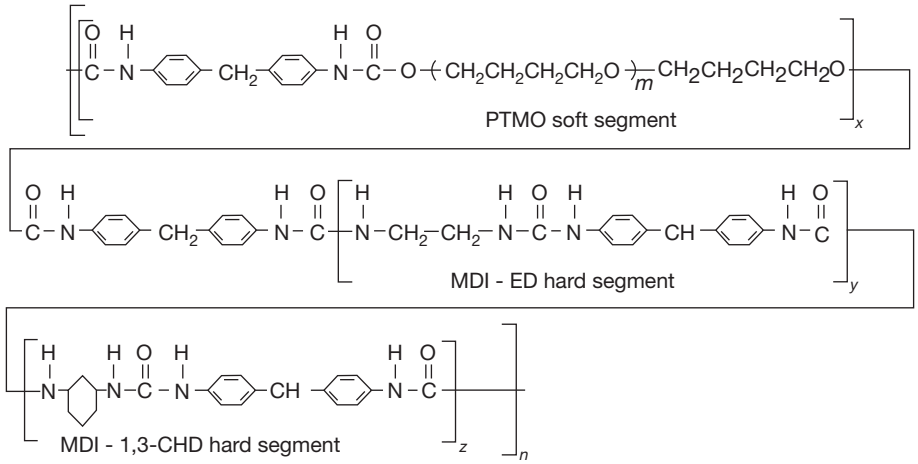

Figure 9 Idealized repeat structure of a so-called segmented polyurethane, for example, BioSpan® and Biomer™ segmented polyurethanes. Prepolymers prepared from polytetramethyleneoxide (PTMO) diols and methylene diisocyanate are chain extended in dimethylacetamide solution with two different diamines:ethylene diamine and 1.3-cyclohexane diamine. They therefore have urea hard segments bonded to the soft segment PTMO chains via urethane groups. At hard segment content of 20–25 wt% these polymers are among the best man-made elastomers ever developed. They were originally developed to replace natural rubber in textile applications and are similar to the structure of commercial Lycra Spandex *c.*1968. In addition to the base polymer the casting solutions contain a complex additive package designed to protect spandex thread *in the laundry cycle*! This composition, which has exceptional flex life, continues to be used in certain sac and diaphragm-type blood pumps primarily for historical/regulatory reasons. Thoralon SPU has similar but not identical structure with a simpler additive package. Thoralon also contains a silicone–polyetherurethane surface modifying additive (SMA) that improves thromboresistance and which may also enhance biostability.

incompatibility with the soft segments. The formation and deformation of superstructures led to a model to account for the formation of the resultant anisotropic structure and mechanical properties.

Materials with equivalent stoichiometries but different hard segment length distributions were prepared by Miller *et al.*[38] in either a one-step polymerization or by the multistep, so-called prepolymer method. Polyurethane block polymers based on poly(tetramethylene oxide) (PTMO), MDI and butanediol (BD) were prepared and evaluated. The single-step polymers were shown to have *fewer* hard segments containing a single MDI unit compared to the corresponding multistep samples. This is counterintuitive as the rationale for the two-step process is often to *discourage* the chain extension/coupling of polyols by maintaining excess diiocyanate during formation of the isocyanate-terminated prepolymer. However, in this study the multistep materials exhibited a *greater* degree of phase mixing, as the very short chain-extending MDI segments were more likely to be dissolved in the soft phase than were the longer hard segments. Another interpretation is that chain extension of soft segment by a single diisocyante introduces hydrogen-bonding urethane groups into the middle of the soft segment, increasing its compatibility with the hard segment, albeit while doubling its molecular weight. The hard phase volume fraction and crystallinity were found to be greater in the single-step materials due to the lower degree of phase mixing in these polymers (and presumably their higher average hard-segment molecular weight).

3. Polyurethanes with polycarbonate soft segments are much more oxidatively stable than polyether-containing polyurethanes, although the inclusion of ether groups into the polycarbonate under certain conditions of polyol synthesis *may* reduce oxidative stability somewhat. It should be noted that the *aliphatic* polyalkylenecarbonate diols used as soft segments in (biomedical) polyurethanes are distinctly different from the rigid *aromatic* bisphenol-A plastic commonly referred to as 'polycarbonate.' Aliphatic polycarbonate polyols contain no bisphenol-A. They can be produced by several methods, most often by ester interchange reaction using an alkane diol and a dialkyl carbonate.[39] An important example includes the tin-catalyzed electrophilic attack of aliphatic hexane diol on the methine carbon of ethylene or propylene carbonate to form polyhexamethylene carbonate diol.[40] Temperature control is essential in the case of ethylene carbonate, because side products resulting in the formation of oxidatively unstable ether linkages in the polymerized polycarbonate diol are possible. Understanding and control of this side reaction has led to the availability of improved ether-free polycarbonate-urethane biomaterials, for example, Bionate® II polycarbonate-urethane. The lack of 'contamination' by hydrogen-bonding ether groups increases toughness but appears to reduce phase mixing in the melt, giving some neat polymers a higher melt viscosity at equivalent molecular weight. This has been overcome with molecular weight control using surface-active, self-assembling octodecyl end groups created from the corresponding alcohol. The resulting C_{18} end groups are surface-active, which improves mold release, and they 'lubricate' the molten chains to improve melt processing. As a monofuntional reactant in the formation of urethane groups, octodecanol conveniently provides molecular weight control by acting as chain stoppers during synthesis.[41–43]

Thermoplastic polyurethane elastomers based on polyhexamethylene carbonate diol and polyhexamethylene–pentamethylene carbonate diol of different molecular weights

and hard segments and consisting of varying ratios of diphenylmethane diisocyanate and 1,4-butanediol have been synthesized in bulk, and the effects on thermal and mechanical properties investigated.[44] As seen in many polyurethanes, increasing soft-segment length, via polyol molecular weight, or increasing the hard-segment content, gives increased microphase separation, more hard-domain order/crystallinity, and higher stiffness. In phase-separated systems better development of the reinforcing hard-domain structure was observed. The 'physical cross-link sites' provided by the hard-segments and the elastic nature of soft segments, make softer homologues elastomeric.

With increasing hard-segment concentration at constant polycarbonate diol molecular weight, properties such as rubbery plateau, modulus, solvent resistance, melting point, hardness, tensile strength and hard-segment run length all 'improve.'[45] Note that in studies of homologous co-polyurethanes with varying block lengths, the soft segment molecular weight actually *determines* hard-segment molecular weight. In a simple linear copolymer of fixed composition, as soft segment molecular weight increases so does the hard-segment molecular weight, because the hard segments are positioned between the soft-segment chains along the linear polymer backbone. In the study by Harris, increasing hard-segment concentration at fixed polycarbonate block length caused an increase in hard-segment molecular weight *and* concentration. It is likely that phase separation increased for both reasons.

In general, the useful properties and processability of PU and PUU block copolymers are related to the relative thermodynamic incompatibility of the different regions within these composite molecules. Depending on molecular weight, soft segments are usually incompatible with hard segments, in part because hard-segment domains have higher cohesive density and the related property of higher solubility parameters. The hydrogen bonds that hold the hard segments together and provide strength to the polyurethane dissociate at melt processing temperatures or in solution in organic solvents. The resulting liquids can be formed into useful device components by a number of different conversion methods. Ease of processing requires a degree of phase mixing in the melt or in solution followed by phase separation, also known as soft-segment/hard-segment demixing after fabrication.[5–7,46] After cooling from the melt or during solvent evaporation, the hard-segment hydrogen bonds reform to recreate separate domains. In use, the ability of certain soft segments to reversibly orient or strain crystallize when stretched, and the ability of hard segments to remain hydrogen-bonded under stress are responsible for many of the desirable properties of polyurethane biomaterials.

1.125.2.2. Lab and Commercial Synthetic Methods

Batch-type laboratory methods for synthesizing polyurethanes generally provide good control of temperature and mixing. However, the control of the stoichiometry necessary in step-growth polymerization can become more precise as reaction scale increases. This consideration and manageable reaction exotherms facilitate scale-up to manufacturing. Synthesis can include bulk, solution, and even emulsion methods (e.g., in water-borne systems using aliphatic diisocyantates).

In bulk and solution synthesis, all the reactants can be combined in a 'single-shot' procedure with intensive mixing, or in the 'prepolymer' or two-step (or even three-step) method mentioned above. The prepolymer technique involves prereacting the soft-segment polyol(s) with excess diisocyanate followed by chain extension with short-chain diols or diamaines. Despite the effect on phase separation mentioned above, it is often more convenient to handle a prepolymer than the more volatile diisocyanate, from which it is made. Less volatile diisocyantes that are solids at room temperature require heated piping and vessels to prevent crystallization. Prepolymers however, are often viscous liquids at or slightly above room temperature and are more easily handled by oven preheating. As already mentioned, mixing intensity, pH, the order and rate of addition, the concentration of optional catalysts, and the concentration of the inevitable traces of water are all determinants of the lot-to-lot consistency of the final polymer.

1.125.2.2.1. Thermoplastic pellets for extrusion and molding

In the batch-type bulk (i.e., solvent-free) synthesis of thermoplastics, the reacting mixture is quickly removed from the reactor prior to solidification, while still exotherming. It is often cast into Teflon-lined pans or polypropylene molds and heated in an oven for several hours to continue the polymerization. During solidification the resulting slab shrinks and can be demolded. Grinding and subsequent melting and pelletization or dicing on a thermoplastic extrusion line is done to complete the reaction and produce pellets for characterization and processing. A major drawback of batch-type bulk synthesis is that the grinding step and added handling may increase particulate contamination in the final polyurethane. Furthermore, little or no feedback of final polymer molecular weight is available to the operator during synthesis (**Figure 10**).

For the manufacturing volumes typical of implantable thermoplastic polyurethanes, an excellent, but capital-intensive method is continuous synthesis on a small twin-screw extruder. In one example, reactants are accurately metered to an injection port on the extruder barrel. The barrel is maintained at melt processing temperatures, usually 190 ± 25 °C, and the screw design and speed of rotation assure good mixing and adequate residence time. Torque, back pressure, and/or electrical current drawn by the constant-speed extruder motor provide continuous feedback dependent on melt viscosity. As melt viscosity increases with chain length, the approximate molecular weight of the product can be predicted and controlled via the stoichiometry determined by individual reactant feed rates. The fully reacted molten polymer may emerge from the extruder through an underwater pelletizer where it forms spherical pellets while cooling. The pellet slurry is dewatered and collected inside a HEPA-filtered enclosure. Later, desiccant hopper driers are used at atmospheric pressure just prior to processing the pellets. Directly after drying, free-flowing pellets are fed to injection molding machines and extruders during the fabrication of device components. 'Pelletized' polymers are also more easily dissolved in solvents for dipping, casting or spraying, or for use as an adhesive in device assembly. This is especially true for recently (re)pelletized polyurethanes, apparently due to the slow reformation of intermolecular allophonate bonds broken in the melt.

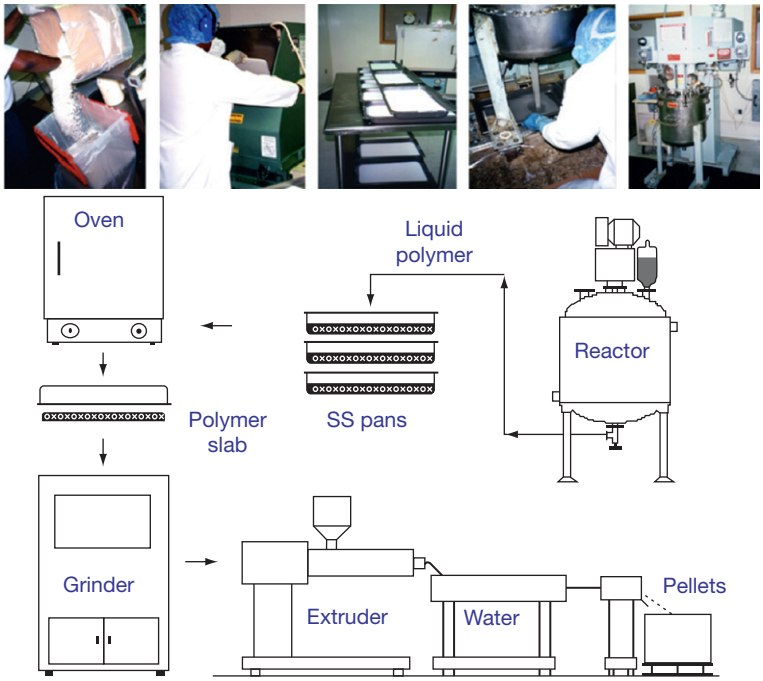

Figure 10 Batch-type synthesis of thermoplastic polyurethanes. From right to left the reaction mixture is chain extended in a batch 'kettle' with intensive mixing. During the resulting exotherm, but before solidification, the reacting mixture is discharged from the reactor into pans for further reaction in an oven. The slabs cure for several hours and shrink enough to allow de-molding and grinding. Roughly shaped ground polymer shown in the photo at extreme left is dried and fed to a thermoplastic extruder to complete the reaction and to form smooth, free-flowing pellets for subsequent processing, for example, molding or extrusion.

Using a 27 mm continuous reactor/twin-screw extruder, an output of 10–40 lbs h^{-1} is achievable and several developmental materials can be produced in a single day. Promising candidates can easily be scaled up by reproducing the reaction conditions used in development runs. These benefits, and the improved cleanliness it provides, make continuous reactive extrusion nearly ideal for manufacturing thermoplastic biomaterials. Scale up is straightforward but expensive, as output and equipment cost increases considerably with the diameter and length of the extruder. The continuous process using an endless belt shown in Figure 11 is capable of producing hundreds of pound per hour of pelletized polyurethane, but it is less versatile during development than the twin-screw reactive extruder.

During melt processing, thermal history and the extent of drying are determinants of polyurethane viscosity and therefore ease of extrusion and molding. As thermal history increases and/or water content is reduced, melt viscosity increases making processing more difficult. For this reason, over-drying must be avoided, and measurement and control of trace water level can greatly facilitate control of extrusion and molding operations.

1.125.2.2.2. Solution synthesis for coating and dipping

A typical two-step solution synthesis begins with the addition of pure diisocyante to the reactor, followed by slow addition of polyol to maintain an excess of diisocyante throughout the reaction. The final *prepolymer* is an isocyanate end-capped oligomer admixed with excess diisocyanate monomer. In addition, a fraction of the polyol may become chain extended, forming dimers or trimers, for example, when one mole of diisocyanate reacts with two moles of polyol, etc. At this stage a dry polar, aprotic organic solvent such as DMF or DMAc is added to the reactor to form a prepolymer solution. The reactive solution is chain extended via addition of a near stoichiometric amount of diamine or diol to form the product polymer solution, at a final concentration of ~5–40 wt%. Concentrated solutions of amine-extended polymers may become very viscous as the reaction proceeds and require dilution before being filtered for use in device fabrication. High-purity, glass-distilled chromatographic-grade solvents are preferred as any nonvolatile solvent impurity will be left behind on the part being dipped, coated, or cast (Figure 12).

Solution synthesis and fabrication is often the only practical method for polymers with aromatic polyurea hard segments which generally cannot be melt-processed. Solution synthesis is used in the preparation of high-flex-life PUU, currently the preferred elastomers for sac- and diaphragm-type cardiac assist devices. However, recovery of neat thermoplastics from a solution synthesis is usually impractical except at laboratory scale. This is due to lower polymer yield per unit of reactor volume, and the need to precipitate in a nonsolvent, rinse, and thoroughly dry the reaction product. This process also requires solvent recovery or licensed waste disposal.

New methods of polyurethane synthesis continue to be developed. Well-defined polyurethane-polydimethylsiloxane particles of tunable diameter in the range of 0.5–20 mμm were synthesized in a 'one-shot' step-growth polymerization using supercritical carbon dioxide as a solvent.[47] This method has the potential to produce very-high-purity polymers as



Figure 11 Top: continuous synthesis of biomedical polyurethanes and silicone polyurethanes with optional Surface Modifying End Groups (SME™) or Self-Assembling Monolayer End Groups (SAME™) is easily accomplished on this reactive extruder with downstream pelletizer and high-efficiency particulate air (HEPA)-filtered collection area. Reactants are metered to a feed port on the extruder barrel (right). The polymer is synthesized within the barrel of the twin-screw extruder/reactor while being mixed and conveyed by the rotating screws. The fully reacted polymer exits through a die into a stream of water where surface tension creates spherical pellets which quickly cool in the flowing water. The slurry is dewatered and pellets are collected in the soft-wall enclosure at the left of the photo. Bottom: an older alternative method of continuous synthesis deposits the molten polymer or reaction mixture on a moving belt. Reaction is completed inside a heated tunnel that is temperature controlled and HEPA filtered. A solid ribbon of polymer emerges from the tunnel and passes through a dicer to produce, hexagonal pellets.

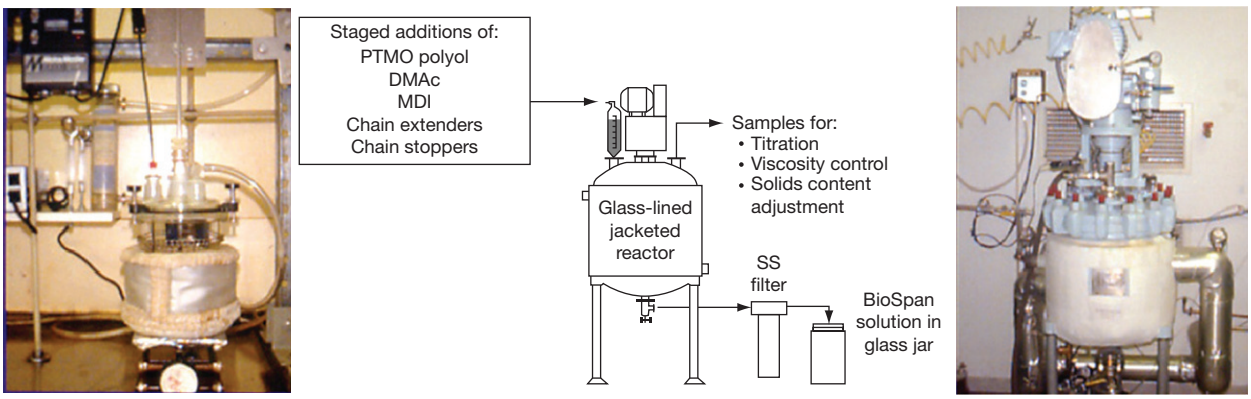

Figure 12 Batch-type solution synthesis of polyurethane-urea of the structure shown in **Figure 9**. A 2-l lab-scale reactor is shown on the left. The 10 gallon glass-lined Pfaudler-type reactor on the right is used in manufacturing the relatively small volumes needed for implantable applications.

product recovery involves simply reducing the pressure of the reaction mixture to allow polymer precipitation and recovery of carbon dioxide gas. Of course, solubility in super critical CO_2 is required, so the method may not work for all (e.g., silicone-free) polyurethanes.

1.125.2.2.3. 100% solids curable prepolymer systems for potting and encapsulation

Two-component polyurethane liquid systems capable of rapid curing are often referred to as potting compounds.[48] Bulk-synthesized reactive liquid prepolymers can be stored in dry containers at reduced pH to extend shelf life. When mixed with a chain extending diol or triol, or analogous amines, polymerization takes place. The pot life is also controlled via pH and catalyst concentration, to allow time to for mixing, degassing and transfer of the reacting mixture into molds. In this way potting resembles batch-type bulk synthesis of thermoplastics, without the grinding and pelletizing steps. This technique can be used to encapsulate electrical coils and circuits, and to make cast parts. If mixing and mold filling are done on a specially designed injection molding machine, it is called reactive injection molding (RIM) and is capable of making large complex parts. However, the advantages of slow-speed *hand* casting are low equipment cost and the ability to encapsulate delicate parts due to the low viscosity and flow rate of the reacting mixture. The use of polyfunctional reactants to make cross-linked parts with improved thermal and chemical resistance is also possible. The amount of unreacted diisocyanate present in the prepolymer determines the amount of chain extender/cross-linker required and therefore the resulting hardness of the polymer. By varying soft-segment composition and concentration, a wide range of physical properties can be obtained. In this way, electrical properties including dielectric strength, arc/trac resistance and dissipation factor, along with properties such as coefficient of thermal expansion, elasticity and speed of sound can be optimized. Biomedical applications include insulation (for electrical circuits and transcutaneous power transmission coils), ultrasonic probes and vascular access ports. Due to the absence of a melt-processing step following chain extension, mechanical properties of un-cross-linked cast parts may be inferior to thermoplastics of identical composition.

As mentioned in Section 1.125.1.2.2 neat prepolymers can be chain extended with water and the CO_2 generated can foam the reaction mixture. In the presence of an optional foam-stabilizing surfactant (e.g., a silicone–polyether copolymer) a porous construct will result. Open-cell or 'reticulated' versions have application as tissue engineering scaffolds, wound dressings, and sponges. Closed-cell foams can be used in sewing cuffs and vascular grafts with tailored compliance that minimize bleeding when stuck with a needle. A more controlled approach in device fabrication is to include a pore former like sodium chloride, sugar, or soluble polymer particles in the urethane, which is leached out after device fabrication to produce pores (Figure 13).

1.125.2.2.4. Water-borne dispersions for coatings

The manufacture of polyurethane dispersions generally involves synthesis of polyurethanes having carboxylic acid or nonionic hydrophiles like PEG incorporated into, or pendant from, the polymer backbone. Carboxylic acids are usually neutralized with a tertiary amine, which creates an ionic center enabling the pre-polymer to be dispersed in water as emulsions.[49] The much faster amine–isocyanate reaction relative to the water–isocyanate reaction is used to convert the prepolymer emulsion to a fully reacted polyurethane emulsion or dispersion upon the addition of amine.

Recently, aqueous polyurethane dispersions derived from various polycarbonate-diols, di(4-isocyanatocyclohexyl) methane (HMDI) and various carboxylic diols, including dimethylol propionic acid (DMPA), dimethylol butyric acid (DMBA) and a carboxylic polycaprolactone-diol have been prepared and shown to exhibit higher temperature resistance when compared with those derived from isophorone diisocyanate (IPDI).[50] Biodegradable and biocompatible poly(ester-urethane)s have been synthesized by *in situ* homogeneous solution polymerization of poly(ε-caprolactone) diol, dimethylolpropionic acid (DMPA) and methylene diphenyl diisocyanate in acetone followed by solvent exchange with water.[51]

Certain water-borne polyurethanes are useful as coatings over a variety of substrates including preformed polyurethanes, particularly when a solvent-based coating would damage thin underlying layers, for example, in sensors. However, some water-borne polyurethanes do require 'coalescing solvents' to facilitate fusion of polymer micelles into a dense film during drying. Biostable water-borne polyurethane coatings may be candidates for use in subchronic implantable devices, for

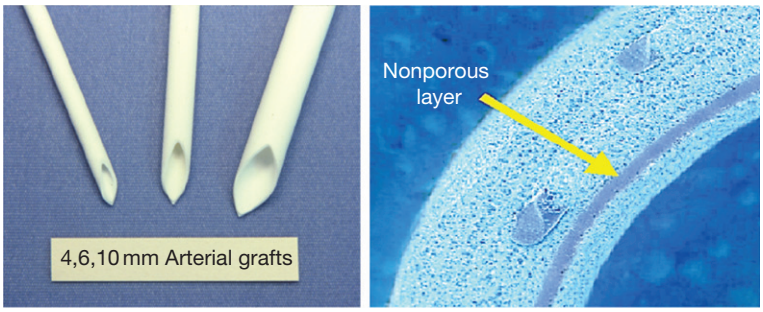

Figure 13 Prototypes of the Thoratec Vectra vascular graft fabricated from segmented polyurethane. The cross section shown at right reveals alternating layers of porous and nonporous polymer, and a fiber reinforcement that prevents kinking. Varying the pore size and void volume allow tailoring the radial compliance in an attempt to match natural arteries. The dense layer close to the luminal surface prevents seromas and helps seal after needle sticks when the graft is used for blood access (in dialysis).

example, as antimicrobial or lubricious coatings. However, the wet strength and biostability of the final coating may be lowered by residual hydrophilic moities.

1.125.3. Utility of PUs and PUUs as Biomaterials

The selection of a biomaterial for a critical device invariably requires specifying both bulk and surface property requirements. Bulk properties include hardness, modulus, tensile and compressive properties, flex life, permeability, water absorption, dielectric strength, optical clarity, density, leachable fraction and biostability. Surface properties include thromboresistance, wettability, (non)specific protein adsorption, abrasion resistance, coefficient of friction and cell and protein interactions. The wide range of reactants available for use in polyurethane synthesis provides the raw materials for tailoring *bulk* properties, and many useful structure-versus-bulk property relationships are reported in the literature. Even when limiting the choice of reactants to those already known to be safe and biostable, the material scientist has a lot to work with. On the other hand, less is known about the relationship between the bulk composition and structure and their effect on the chemistry and nanostructure of the surface region that comprises the biological interface. This complicates the understanding of how the polyurethane surface affects biological interactions, and favors the use of research techniques such as self-assembling monomers adsorbed on gold, in place of actual biomaterials. New methods have been developed that promise similar control of the surface region of actual polyurethane biomaterials (see Section 1.125.6.1.3).

1.125.3.1. Biostable PUs and PUUs

The long-term stability of segmented/block polyurethanes in the body depends on a number of factors including structure and composition, the presence of optional stabilizing additives, the chosen implant site and the sample's purity and processing history. Fabrication, handling, residual solvent, sterilization method and device design are also important factors. These will be discussed separately.

1.125.3.1.1. Structure and composition: soft-segment chemistry

Various researchers recognized early on that differences in soft-segment chemistry affect biostability: polyester soft segments were found to be much more susceptible to hydrolytic degradation and attack by microorganisms than were polyethers.[52] Work that began in the 1970s after some failures of first-generation polyurethane pacemaker leads has been continued to elucidate failure modes and to screen new candidate polymers. Much of this work was done using protocols that greatly accelerate degradation rate, either through the use of highly oxidizing and hydrolyzing conditions, elevated temperature, use of intramuscular implant sites, and/or the practice of stretching the test sample to several times its initial length. Those polymers that degrade predominantly by chain scission and molecular weight reduction often show early signs of *environmental stress cracking* (ESC) under microscopic examination. These highly strained samples, often in the form of thin-walled tubing or film, may ultimately fail catastrophically as these cracks propagate under the atypical static elongation superimposed on them during the test. Soft poly*ether* urethanes degrade even faster in these accelerated *in vitro* and *in vivo* tests if they are exposed to certain metal oxides during the test. Cobalt, a commonly used metal in alloys for high-flex-life pacemaker wire and orthopedic implants is known to accelerate polyether oxidation. This has been termed *metal-oxide-induced oxidation* (MIO). As cobalt-containing metal alloys are often used in chronic implants, the use of softer grades of polyether-urethanes in close proximity to these alloys should be avoided. Even when covered by biostable, yet permeable silicone elastomer, degradation of a polyetherurethane having a durometer hardness of 80A has been observed when in contact with cobalt alloys.[53,54]

The reader should note that, the above consideration notwithstanding, with well-designed medical devices it is rare to see the extent of *in vivo* degradation that occurs in accelerated *in vitro* degradation testing. Furthermore, materials used as positive controls in these accelerated degradation tests are *softer* homologues of polyurethane that are successfully used in pacemaker leads, and many other implants. Even softer polyetherurethane-ureas can be very stable in blood pumps and vascular grafts in which MIO is not a factor.

Whereas softer (e.g., 80 Shore A) polyalkylether-urethanes are hydrolytically stable, they *are* susceptible to oxidation in accelerated testing when attacked by macrophages and foreign body giant cells *in vivo*. Analogous polyalkylenecarbonate, first thought to undergo minor surface hydrolytic degradation *in vivo*, may actually be susceptible to some surface oxidation particularly when it contains trace ether linkages introduced during polyol synthesis. Exclusion of ether linkages in the polymer appears to improve surface biostability in preliminary accelerated degradation testing. The presence of hydrophobic hexamethylene chains shielding the polycarbonate linkages protects this specific polycarbonate, in part by reducing permeability. A similar effect *may* slightly improve oxidative stability of polyhexamethyleneoxide relative to polytetramethyleneoxide, which has two less methylene groups in its repeat unit, and therefore, a higher bulk concentration of ether groups per unit volume.

As previously discussed, the *concentration* of the soft segment(s) is a major determinant of polyurethane biostability. Assuming a stable hard segment is chosen (e.g., MDI+BD or MDI+ED) the harder homologues, that is, those with the least soft segment, have the best biostability in virtually all of the polymer families studied to date. Soft segments that give tough polyurethanes but which are inherently susceptible to significant degradation by hydrolysis and/or oxidation are unsuitable for use in biostable formulations: polyadipate esters and polylactones are examples. At the other end of the spectrum are candidates that are oxidatively and hydrolytically much more stable but which give relatively weak polymers: single-soft-segment PUs and PUUs based on polydimethylsiloxane or polyisobutylene are included in this group. The most commonly used organic soft segments in biostable polyurethane(urea)s are currently aliphatic polycarbonates and aliphatic polyethers, wherein the length of the repeating alkyl chain is either four or six carbon atoms. These provide polymers having excellent initial physical–mechanical properties

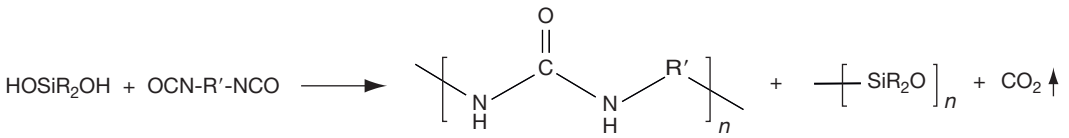

Figure 14 Reaction of isocyanate with silanol. Reproduced from Sheludyakov, V. D.; Kozyukov, V. P.; Mironov, V. F. *Russ. Chem. Rev.* **1976**, *45*(3), 227–245.

and *in vivo* stability that is more than adequate for many implant applications.

In fact, the long-term performance of biomaterials depends on both the *initial* properties of the polymer and the extent to which the initial bulk and surface properties are retained during implantation. Inherent oxidative biostability of commonly used soft segments in polyurethanes of nominal 80 Shore A indentation hardness, in decreasing order of inherent stability during accelerated testing *i*, in the author's experience is:

polyisobutylene > polydimethylsiloxane
> poly (hexamethylenecarbonate)
> polyoxyalkylene (polyether)

However, this is *not* the same order of the initial toughness of the resulting polymers, which is roughly the reverse, except that polycarbonate polyols of equivalent concentration and molecular weight often give tougher polymers than polyethers.

Studies that consider various aspects of stability continue: cross-linked poly(ether polyurethanes) based on poly (1,4-butane diol), and 4,4′-diphenylmethane diisocyanate having varied aliphatic hard segments consisting of 1,6-hexamethylene diisocyanate have been prepared having diols and triols which hydrolytically degraded in distilled water at 37 °C. The degree of degradation is dependent on the degree of cross-linking and nature of the diisocyanates and chain extenders.[55] The polyether polyurethane Elasthane 80A has been evaluated for *in vivo* cellular responses including foreign body reaction cytokines release at the site of the material implant,[56] and in T-cell-deficient mice.[57]

Specific surface modifications to polyether polyurethanes have been made via the use of *surface-modifying end groups* to modify biological response. The role of serum proteins and material surface chemistry in the formation of *Staphylococcus epidermidis* biofilm on polyurethanes (Elasthane 80A, hydrophobic) modified with polyethylene oxide (Elasthane 80A-6PEO, hydrophilic) and fluorocarbon (Elasthane 80A-6F, hydrophobic) was reported by Patel *et al.*[58]. On the hydrophilic Elasthane 80A-6PEO surface, bacterial adhesion decreased steadily over 24 h and, most notably, the polyethylene oxide surface was found to significantly inhibit *S. epidermidis* biofilm formation over 48 h *in vitro*.

Polyether urethanes based on poly(tetramethylene oxide) (PTMO, MW 2000), chain extended with butenediol and having silanol-terminated polydimethylsiloxane (PDMS, MW 2000) blocks exhibit various degrees of microphase separation that influenced their stability and biological performances *in vitro*. The combination of enhanced mechanical properties, biostability, cellular affinity as well as platelet nonadherence was improved with PDMS.[59] However, we note that the authors of this study may have unknowingly prepared an admixture of silicone fluid in polyurethane rather than the intended

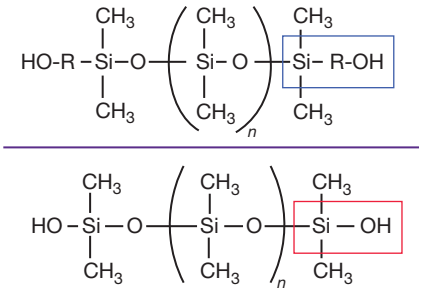

Figure 15 The synthesis of well-defined, high-molecular weight silicone–urethane(urea) copolymers requires oligomeric diols (or diamines) with the top structure. The organic R group can be a short-alkyl chain, but often includes an ether oxygen that may improve compatibility. Silanol-terminated fluids are readily available reactants used in the manufacture of RTV silicones, but they do not form silicone–urethanes in reactions with (di)isocyanates as discussed above.

silicone–urethane copolymer: hydroxyl groups bonded to silicon: also known as *silanols*, generally do not react with isocyanates to form urethane groups. Instead, isocyanates abstract water from silanols creating new siloxane bonds (–O–Si–O–) that increase silicone chain length. The condensed water *can* react with –NCO to form unstable carbamates that decompose to release CO_2 and form amines that produce *ureas* by reacting with –NCO. For example, the reaction of model monofunctional organic isocyanates with silanediols and oligosiloxanes containing terminal hydroxyls proceeds with the isocyanate acting as a dehydrating agent (Figure 14).

The polycondensation of dialkylsilanediols or polyalkylsiloxanediols with hexamethylene or tolylene diisocyanates, oligourethanes with terminal isocyanato-groups, yields insignificant amounts of organosilicon polyurethanes: these reactions result mainly in the evolution of CO_2 and water and the formation of organic polyureas in admixture with polysiloxanes (Figure 15).

1.125.3.1.2. Importance of block and segmented PUs in long-term implants

During more than 40 years of polyurethane use in chronic implants, our knowledge of polymeric biomaterials has evolved from an empirical approach to more systematic macromolecular design. The advancement of biomaterials science and the introduction of new bulk and surface analytical techniques and instrumentation have facilitated the development of biomaterials for specific applications, gradually replacing the older process of adopting commercial polymers for use in device manufacturing. The relative ease with which polyurethane bulk and surface properties can now be tailored during synthesis makes them one of the best platforms for the development of advanced biomaterials.

As previously mentioned an early and notable success with polyurethane biomaterials was in the fabrication of cardiac assist devices including balloon, sac, and diaphragm types in which available silicone homopolymers lacked sufficient flex life, toughness and thromboresistance. This remains an important application considering that these life-supporting devices must flex with the beating heart about 750 000 times per week. Federal Drug Administration (FDA) approval of sac- and diaphragm-type devices as alternatives to heart transplantation indicates the importance and reliability of certain block and segmented polyurethanes in such 'destination devices.' The earliest cardiovascular applications all used solvent-based fabrication methods including dipping, casting, spraying, and even labor-intensive pouring of viscous polymer solutions with hand manipulation of molds. This limited their early use to less cost-sensitive devices in which the material itself was 'enabling technology.'

In the mid 1970s, in response to the success of the early solvent-based polyurethanes (Biomer and Avothane-51), Upjohn Corporation offered a series of experimental thermoplastic polyether-urethanes: the Pellethane 2363X series. The first clinical use may have been an extruded catheter for AVCO's intraaortic balloon pump, followed soon after by pacemaker lead insulation from Medtronic. This pioneering development work with thermoplastic PUs led to the introduction of commercially available 'medical grade' thermoplastic Pellethanes® by Upjohn. The Pellethane 2363 Series was later acquired by Dow Chemical. Implantable applications continued to be developed until *c.*1989 when, during the so-called biomaterials crisis, Dow announced that Pellethane would no longer be sold for use in chronic implants, at the same time DuPont and Ethicon established the same policy for Biomer™ Segmented Polyurethane. At the urging of National Institute of Health (NIH), The Polymer Technology Group in Berkeley, CA (now DSM Biomedical) developed replacements for both polymers (Elasthane™ TPU and BioSpan® SPU), which became platform biomaterials for a number of more advanced biomedical polyurethanes and silicone–polyurethane copolymers (see **Figure 5**). Although the *current* trend in mechanical cardiac assistance is toward the use of 'axial flow' devices that do not use flexing polymeric components to pump blood, thermoplastic polycarbonate-urethane (e.g., Bionate® TPCU) is being used in another critical component of these devices: the insulation of electrical leads that transmit power and information to and from the implanted device.

At present the role of a small number of polyurethanes in long-term cardiovascular implants is unique and still required due to an unmatched combination of physical–mechanical properties, biostability and processability. The latter is related to the many fabrication methods available to the device manufacturer – an important consideration when specifying biomaterials during device design.

1.125.4. Composition of Important biostable PU and PUUs

Virtually all high-strength, biostable polyurethanes and silicone–polyurethane copolymers used in chronic implants are synthesized from the components listed in **Table 2**. In most polymers, the aromatic diisocyanate (MDI) is used to form the hard segments. Although they may be more easily extruded and molded, polymers based on the cycloaliphatic analogue, HMDI generally have inferior long-term biostability, reduced heat and solvent resistance and lower physical–mechanical properties at equal hard segment concentration. Biodegradable polyurethanes, on the other hand, often use aliphatic or cycloaliphatic diisocyantes to avoid aromatic degradation products resulting from their intended decomposition *in vivo*.

1.125.4.1. Chain Extenders

Commonly used chain extenders include butanediol (BD), and ethylene diamine (ED). Even-numbered chain extenders are often preferred because they can improve efficiency in hydrogen bonding and resulting physical–mechanical properties.

Sanchez-Adsuar and Martín-Martínez[60] studied the influence of the length of the chain extender using three linear chain extenders: ethylene glycol, 1,4-butanediol, and 1,6-hexanediol. Short-chain extenders produced phase separation, higher crystallinity and adequate rheological properties but did not affect

Table 2 Polyurethane and silicone–polyurethane copolymers used in chronic implants

Type	*Tradename*	*Manufacturer*	*Difunctional Isocyanate*	*Chain Extender*	*Polyol(s)*	*End Groups*
Poly-carbonate TPU	Bionate®	DSM Biomedical	MDI	BD	PHMC	NA
Surface-modified polycarbonate TPU	Bionate® II	DSM Biomedical	MDI	BD	PHMC	C_{18} alkyl
Silicone-polycarbonate TPU	CarboSil®	DSM Biomedical	MDI	BD	PHMC PDMS	PDMS
Polyether TPU	Pellethane®	Lubrizol	MDI	BD	PTMO	NA
Polyether TPU	Elasthane™	DSM Biomedical	MDI	BD	PTMO	NA
Silicone-polyether TPU	PurSil®	DSM Biomedical	MDI	BD	PTMO PDMS	PDMS
Solution-type polyether SPU	BioSpan®	DSM Biomedical	MDI	ED 1,3-CHD	PTMO	Dialkyl
Solution-type polyether SPU	Biomer™	World Heart	MDI	ED 1,3-CHD	PTMO	Dialkyl
Surface-modified solution-type polyether SPU	BioSpan®-S	DSM Biomedical	MDI	ED 1,3-CHD	PTMO	PDMS
High silicone-polyether TPU	Elasteon™	Aortech	MDI	BD	PHMO PDMS	NA

the surface properties. Improved crystallinity and a high degree of phase separation were created in the PUs by the decrease in the length of the chain extender. In addition, Bae *et al.*[61] compared dynamic mechanical behaviors of polyurethanes with different types of linear and nonlinear chain extenders and showed the T_g of the soft-segment matrix varying with the type of chain extenders.

The effects of butanediol (BD) or 2,2′-(methylimino) diethanol (MIDE) as chain extenders on the degradation, mechanical properties, hydrophilicity, and cytophilicity of polyurethanes containing (MDI) and polycaprolactone diol (PCL-diol) have been evaluated. *In vitro* degradation studies showed that PU containing MIDE has a higher degradation rate than PU synthesized using BD.[62] Adhikarir *et al.*[63] used silicone chain extenders and showed improved compatibility in PDMS soft-segment phase with the hard segment in mixed macrodiols.

Yoon and Ratner[64] used various perfluoro chain extenders in making polyurethanes. They found the perfluoro chain-extended polymers had more soft segments at the material surface than those at the same hard-segment content. Decreasing the soft-segment molecular weight increased fluorine content or hard-segment concentration in the surface region. The same fluorine content was found uniformly distributed throughout the surface region and in the bulk. Symmetric fluorine substitution in the chain-extender region generally enhances the mixing of hard and soft segments.[65]

Aromatic diamines have been used as chain extenders in reactive injection molding (RIM) for polyurethane elastomers.[66] Heterocyclic polyurethanes synthesized by the extension reaction of macrodiisocyanates with heterocyclic diamines have been shown to increase the decomposition temperature of the polyurethanes.[67] Colored or transparent materials were made elastic (based on polyethylene glycol adipate) or brittle (low molecular glycols) depending on the nature of the heterocyclic unit.

1.125.4.1.1. Diols

Linear and branched chain extenders are used (see **Table 1**). Important considerations include the molecular weight of the diol or polyol. Diols used as chain extenders are subject to similar requirements as found in those used as soft-segments: uniformity and purity, and especially batch-to-batch consistency are important parameters in maintaining reproducible consistent properties and quality of the final polyurethane product.

Aliphatic diols of varying lengths including up to and beyond C_{12} have been developed.[68] In addition, branched structures, such as 2-methyl-1,3-propane diol, and triols (glycerine (1,2,3-propane diol), trimethoylpropane (TMP)) are commonly used. The ability to bind functional organics such as heparin has also been developed using specially designed diols.[69] The trend towards developing biodegradable or resorbable diol chain extenders having multiple ester or ether linkages with applications in tissue engineering scaffolds and bioresorbables is also seen.

1.125.4.1.2. Diamines

Diamines are useful as chain extenders in polyurethane-ureas. The hydrogen-bonding ability of the resulting polyurea hard segments provides exceptional tensile strength at low hardness. Compared to low molecular weight diol chain extenders, diamines provide twice the hydrogen bonding capacity per reacted isocyanate group. Phase separation is excellent even at low hard segment content, making tough rubber-like elastomers possible. These elastomers can have extremely good flex life in blood-contacting applications in VADs and TAHs. Examples include Biomer™ and BioSpan® SPUs.

Common diamine chain extenders include ethylene diamine, and the cyclo-aliphatic primary diamine 1,3-cyclohexanediamine (Table XX) which may be used in the same polymer, and aliphatic and aromatic secondary diamines.[70] Slower reacting secondary aliphatic diamines have been studied as chain extenders in aliphatic polyurea spray applications.[71] Polyether-based polyurethane membranes have been made and characterized with chain extenders having varying lengths.[72] Permeability and diffusivity of gases increased with the increasing length of the chain extenders, as did the extent of microdomain phase separation.

Diamine chain extenders having *biodegradable* properties have been developed in tissue engineering applications. Bioresorbable components including putrescine (PUT) or branched lysine ethyl ester (LEE) diamines have been reported.[73] The products from their decomposition are seen as being more biocompatible while the polymers have properties approaching typical diamine chain extended materials.

1.125.4.2. Soft Segments

Study of polyurethane soft segments and the variety of diols available for consideration is extensive and has been recently reviewed.[74] Because it is one of the major components responsible for final material properties, selection of the soft-segment component is a critical aspect in the design of biomedical polyurethanes. The soft-segment molecular weight, distribution, (di)functionality, solubility with other reactants during synthesis, and compatibility with the hard segment are all important considerations, as is the ability to crystallize during elongation in the product polymer. Decomposition mechanisms and degradation pathways leading to bioabsorption or biostability make for tunable soft segment and provide factors that receive additional consideration in tissue scaffold and bioresorbables engineering.[75]

1.125.4.2.1. Polyester

Polyester-based polyurethanes degrade by hydrolytic degradation of ester functional groups.[76] These polyester-based urethane elastomers degrade even in moist air via acid-catalyzed hydrolysis of the ester group, and sometimes revert to viscous liquids.[77] The reaction is autocatalytic, with one acid group being generated per $-CO_2-$ group. Appreciable loss in mechanical properties can occur with only a small number of $-CO_2-$ linkages being reacted due to appreciable loss in molecular weight: each reaction of a carboxyl group generates one new molecule containing an acid group which can further react. Melting points and densities of the poly(ester polyurethanes) are strongly dependent on soft-segment (polyester) concentration.[78]

1.125.4.2.1.1. Adipate esters

Adipates are saturated polyesters that exhibit strength and durability, excellent tear and abrasion resistance, resistance to

solvents and resistance to oxidation and UV light degradation. Depending on the hard-segment content and other substitutions, hydrolytic stability can vary from good to marginal: microorganisms have been isolated that can use adipic acid-based PUs as their sole source of carbon and nitrogen.[79]

An Estane polyurethane, is a commercially available random copolymer consisting of poly(butyleneadipate) (PBA) and butane diol soft segments formed from adipic acid and MDI and BDO hard segments.[80] It has been used in a number of biomedical applications and has been evaluated for orthoplastic applications.[81] Polymers including PBA soft segments are clearly not suitable as biostable polyurethanes due to the hydrolytic instability of the soft segment. They may be candidates of use in bioresorbable polymers but appear to be less desirable than polylactones (see **Section 1.125.4.2.1.2**).

Recently, Pierce *et al.*[82] designed a series of completely amorphous poly(ester urethane) based on adipic acid and β-hydromuconic acid that has a wide range of mechanical properties. In kinetic analyses these materials were found to have extremely fast linear degradation profiles with little or no cytotoxic response.

For improving surface properties, Ming and Ping[83] treated biomedical poly(ester)urethanes based on polyester adipate soft segments with low-powered gaseous CO_2, O_2, NH_3, and SO_2 plasmas, which resulted in the incorporation of oxygen-containing groups, nitrogen-containing groups and sulfur-containing groups. They found an increase in the polar character resulting from increased wettability for all the treated surfaces.

1.125.4.2.1.2. Lactones

Lactones comprise a large portion of potential soft-segment candidates and homo- and copolymers of lactone-containing soft segments have been prepared.[84] From this class of candidates, caprolactone has been used in polyurethane-containing biomaterials, especially for biodegradation and bioresorbable properties. Polycaprolactone PUs have been extensively studied for tissue engineering and scaffolding applications.[85–87] Saccharic acid dilactones prepared from D-glucose and D-mannitol, D-glucaro- and D-mannaro-dilactones decompose easily in phosphate buffers under neutral or slightly basic conditions (pH 7 or 8), and are additional examples of novel degradable polymeric materials containing lactone soft segments.[88]

1.125.4.2.2. Polyethers

A number of different polyethers have been used[89]: segmented polyurethanes (SPUs) based on polyethylene glycol (PEG), polypropylene glycol (PPG) and a series of pluronics with different ethylene oxide/propylene oxide ratios (EO/PO) and molecular weights have been prepared.[90] Segmented polyurethanes (SPUs) based on polyethylene glycol (PEG), polypropylene glycol (PPG) and a series of Pluronics with different ethylene oxide/propylene oxide ratios (EO/PO) and molecular weights were prepared. Different diisocyanates were used for making SPUs: 4,4-diphenylmethane diisocyanate (MDI), 4,4-dicyclohexylmethane diisocyanate (MDCI), hexamethylene diisocyanate (HMDI) and isophorone diisocyanate (IPDI). Butane diol (BD) and ethylene diamine (ED) were used as chain extenders. The polymers obtained were characterized by infrared spectroscopy (IR), nuclear magnetic resonance (NMR) and differential scanning calorimetry (DSC). The microphase morphology (phase separation and phase mixing) was discussed in detail.

Grasel *et al.*[91] made a series of PTMO polyurethane block copolymers with varying levels of propyl sulfonate groups incorporated into the hard segment block. The highly sulfonated materials were found to rearrange to minimize their interfacial tension, depending on the contacting environment. They also looked at platelet deposition which was found to decrease as the level of sulfonation increased: highly sulfonated polymer showing substantially less platelet spreading and activation. Inclusion of the sulfonate in the backbone, however, increased hydrophilicity and apparently reduced interchain hydrogen bonding compared to controls. The result was a significant reduction of physical–mechanical properties.

1.125.4.2.3. Other polyalkylene oxides (also known as polyethers)

Other polyalkylene oxides such as polyethylene glycol have been extensively used and studies in polyurethanes and early reviews exist.[92] Although PEG often imparts favorable surface properties including reduced protein adsorption and enhanced thromboresistance, incorporation of PEG soft segments into the backbone greatly reduces resistance to *in vivo* oxidative degradation of polyurethanes. For this reason, it is best used in short-term implants of $\sim\leq$6 month duration, for example, for sensors or immunoisolation devices.

1.125.4.2.4. Aliphatic polycarbonates

One of the most effective methods of improving oxidative stability in polyurethanes currently used in clinical applications has come with the development of polycarbonate soft-segment chemistry: enhanced biocompatibility and biostability for poly(carbonate)urethane has been reported by a number of authors (e.g., see Shan-hui *et al.*[93]).

Synthesis of polycarbonate diols (PCD) useful for soft segments has been described by Pawlowski and Rokicki[94] and synthesis, characterization and structure property relationship of poly(carbonate polyurethanes) has been reviewed.[44,95,96] In preparing polyurethanes, the influence of molecular weight and chemical structure of several polycarbonate diols on the kinetics of condensation reaction with *p*-tolyl isocyanate was also reported.[97]

Ahn *et al.*[98] prepared a series of polyurethane elastomers varying the composition of hard-segments chain extenders (BD and Isophrone, IPDA) and similarly controlling the ratio of soft segments (poly(tetramethylene ether) glycol and poly (hexamethylene carbonate) glycol). In his study, he was able to show that most of the urea carbonyl groups were associated in hydrogen bonding, while urethane carbonyls were only partially associated, depending on the hard-segment composition. They further reported that when the composition of soft segments was varied by partially exchanging PTMO with PHC, the polar properties of carbonate groups in the PHC seemed to increase the phase mixing of hard and soft segments.

The microphase separation between hard and soft segments in segments was observed to influence protein adsorption, platelet activation, and cellular attachment and growth. In a

series of poly(carbonate) MDI-based urethanes, Hsu and Lin[99] synthesized polyurethanes having four different soft segments: two aliphatic macrodiols (poly(hexyl, ethyl)carbonate diols, and two aromatic macrodiols in different molar ratios to MDI. Higher M_w poly(carbonate) macrodiols resulted in more phase-separated structure: aromatic macrodiols had better mechanical strength and biostability. Polyurethanes synthesized with poly(ethyl-hexyl)carbonate diol in a molar ratio MDI/macrodiol/chain extender of either 3/2/1 or 4/3/1 resulted in greater microphase separation and was found to have superior biocompatibility and biostability. In this fashion, control over the different aspects of the macrodiol such as molecular weight and ratio to other components have a tunable effect on final properties.

1.125.4.2.4.1. Potential importance of purity/lack of ether contaminants

In the synthesis of polycarbonate diols from ethylene carbonate at higher temperatures, the formation of oxyethylene group incorporation is possible[94]: polycarbonate polyurethanes having such ether linkages as 'impurities' can affect physical properties and thermoplastic processing. When the polycarbonate diol having these oxyethylene groups is incorporated into polyurethane, the expectation would be a decrease in hardness, a difference in modulus at equivalent hard-segment content, and a possible decrease in biostability (oxidative stability). However, depending on the amount of oxyethylene content, these groups having ethereal linkages can be effective in modulating polyurethane properties.

1.125.4.3. General Properties of Polymers with a Single Soft Segment Chemistry

General trends exist among the different classes of polyurethane copolymers. The contributions from the hard and soft segments can be easily adjusted via compositional changes during synthesis and often vary monotonically until a *phase inversion* point is encountered. In polymers with only one soft segment chemistry and one hard segment chemistry, composition affects many bulk properties including modulus, hardness, toughness and even permeability, albeit without much control of selectivity or molecular weight cutoff. At high soft-segment concentration, for example, 60–80 wt% in TPUs and ~70–90 wt% in solution PUUs, in which the soft segment is the *continuous phase*, polymers vary from soft, sticky gels, to rubber-like elastomers, to 'snappy' elastomers (i.e., with a tensile modulus > natural rubber). As soft segment ratio is decreased to the point that it is no longer the phase with highest volume fraction, the slope of a graph of a given property versus composition may change. Polymers with intermediate composition can have co-continuous phases and may be leathery but still flexible within the body, particularly in constructs with thin cross sections. As soft segment is reduced to the point that it becomes a minor, dispersed/noncontinuous volume fraction, polyurethanes may resemble impact-modified plastics, depending on composition and soft segment molecular weight. Decreasing soft segment concentration generally *increases* biostability, tensile strength, indentation hardness, and compressive, tensile and flexural moduli. It *decreases* ultimate elongation and permeability, the latter due to the glassy or semicrystalline nature of the hard segment. In the harder grades of thermoplastic polyurethanes in which hard segment concentration *and* molecular weight are high, phase compatibility is increased by reducing soft-segment molecular weight.

1.125.4.3.1. Effect of alkylene chain length

Martin *et al.*[36] compared the effect of average soft-segment length on morphology and properties of a series of poly(hexamethylene oxide) (PHMO) MDI/ BDO elastomers. Consistent with the above discussions, they reported that as soft-segment length was increased there was an increase in microphase separation, average interdomain spacing, hard-domain order, hardness, stiffness and opacity.

1.125.4.4. Mixed Soft Segments

When tailoring PU properties for a specific application, a valuable tool for extending the property range is the use of two or more soft segments in the same polymer. This approach is particularly effective when the two soft segments possess some thermodynamic compatibility with each other. In this case properties like permeability and absorption are more likely to vary systematically with soft segment composition. For example, power law relationships often give good fits to permeability versus composition data.[100]

Mixed polyisobutylene (PIB)/poly(tetramethylene oxide) (PTMO) soft-segment polyureas containing conventional hard segments were prepared by Jewrajka *et al.*[18,19]. The PIB-containing polymers had improved hydrolytic and oxidative stability. The authors believe that the PTMO segments were better able to transfer stress from continuous mixed soft phases to the dispersed hard phase, which strengthened and made these PIB-based polyureas flexible. It was reported that this significantly improved elastomeric properties without compromising oxidative and hydrolytic stability.

1.125.4.5. Hydrophobic and Hydrophilic Polyethers

One useful example of polyurethanes having mixed soft segments is polyethyleneoxide + polytetramethylene oxide. This combination of hydrophilic and hydrophobic polyethers permits close control of the permeability of dense polyurethane membranes to gases, vapors, and many solutes, which depend on the ratio of PEG to PTMO in the soft segment. However, this approach is only effective when the (swollen) soft segment comprises the major volume fraction of the polymer; for example, when the volume fraction of the soft segments in the dry polymer, plus the water (or other permeant) it absorbs brings the soft segment to a *volume* fraction of >~50% or preferably ≫ 50%. Note that the typically higher density of hard segments means that at 50 wt% the less dense soft segment is likely to be the continuous phase. In permeability optimizations the hard segments can be considered impermeable, acting like a filler that increases the diffusion path of permeants while reducing the cross-sectional area and volume of the polymer available for transport. Keeping hard segment domains low in concentration and therefore dispersed in a permeable continuous soft segment phase permits control of overall permeability via soft segment chemical composition *and* molecular weight.[100–102]

This provides a continuous diffusion path from one surface of the membrane to the other. It may also provide a 'reservoir phase' in drug delivery applications in which the drug is dispersed within a polymer matrix optionally tailored to maximize drug solubility.

Other hydrophilic polyether copolymer mixtures such as those having PEO and PPO soft segments also have the ability to absorb water, which can be similarly adjusted by changing the soft-segment composition and thereby attenuating the physical properties. Polymers have been compared at fixed or variable MDI/butanediol compositions.[103] At constant hard-segment ratios, increasing the amount of PPO over PEO decreases water uptake as expected, however saturation water concentrations were not related in a simple manner. (This is likely to be related to the *incompatibility* of PPO with PEO.) Similarly, at constant soft-segment ratios and composition, water uptake decreases with increasing hard-segment composition, although less dramatically.

1.125.4.6. Silicone and Polyether and Silicone and Polycarbonate

Silicone polymers have a long history in biomedical applications, especially in cardiovascular applications. Pure silicone polymers in general can be hemocompatible and relatively nonthrombogenic; however, they lack mechanical integrity and physical properties such as tear and cut growth propagation, and the higher modulus required in some critical applications. Polyurethanes containing silicones have been developed as a method for enhancing not only the physical properties of the silicone polymer, but also the surface and bulk properties of silicone-free polyurethanes.

Useful combinations of soft segments include polyalkylenecarbonate + polydimethylsiloxane or polyalkyleneoxide + polydimethylsiloxane. Increasing silicone content increases biostability and (oxygen) permeability, but quickly decreases toughness. Polyurethanes with these mixed soft segments can be optimized via soft segment composition, for example, for biostability and/or permeability while maximizing physical–mechanical properties. Figure 16 demonstrates the effect of silicone content on oxygen permeability in nine polymers, including those made with mixed PTMO+PSX soft segment combinations. When the graph is extrapolated to an 'imaginary polyurethane' with 100% silicone, the literature value of oxygen permeability for pure PSX is obtained (Figure 17).

In mixed soft segments it is also possible to take advantage of synergies unavailable through the use of single soft segment. The synergistic combination of silicone and organic soft segments in enhancing biostability was first reported in 1978, and again in 1988. This led to the commercial introduction or captive use of silicone urethane copolymers by several firms who all claimed novelty for their specific compositions.

Mixing PDMS and polyether (also known as polyalkylenoxide) soft segments in PUUs, Park *et al.*[104] created selective gas permeability and diffusion in membranes. They noted that the microstructure of polyether-based PU membranes transformed into a more polyphasic structure by an incorporation of the PDMS phase.

Early on, Nyilas *et al.*[1] had shown that eliminating various impurities and surface inhomogeneities in peroxide-cured silicone rubber (Silastic 372) greatly influenced *in vitro* clotting characteristics in cardiovascular applications. Processing methods, catalyst contaminants and molding conditions were found, in addition to reinforcing silica particles in submicroscopic domains, to affect clotting. Lim *et al.*[105] reported physical properties of segmented poly(dimethylsiloxane) polyurea-urethanes and the extent of phase separation in relation to blood-contacting properties. Whereas the physical properties (tensile strength and modulus) of these materials were not significantly lower compared to polymer without PDMS, the surface properties of the materials were more hydrophobic when measured by contact angle. The key

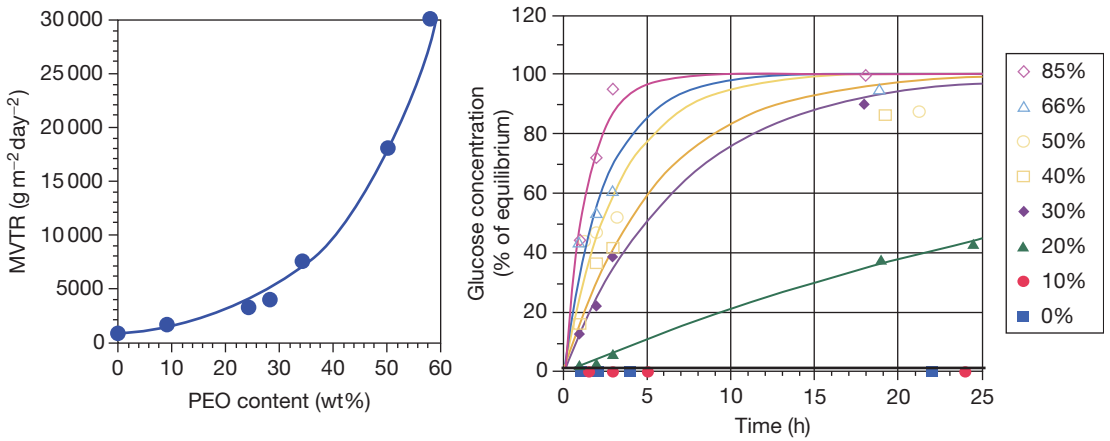

Figure 16 Permeability can be precisely controlled in nonporous polyurethane(urea)s having two soft segments, one of which is hydrophilic. Here increasing the polyethyleneoxide (PEO) content in a PEO+PTMO (polytetramethyleneoxide) polyetherurethane-urea yields increasing 'inverted-cup' moisture–vapor transmission rate (MVTR) measured according ASTM E 96-BW for 0.001 inch film thickness left. Among all classes of polymers MVTR values vary over five orders of magnitude. Hydrophilic polyurethanes are among the most moisture-permeable, high-strength polymers known. Applications include membranes, wound dressings and (biodegradable) films for postsurgical adhesion prevention. Tailoring glucose permeability (measured in diffusion cells) is also possible as shown in the right hand graph. Glucose permeability coefficients were immeasurable below about 10% PEO in this series of polymers, but increased rapidly with PEO content above that concentration.

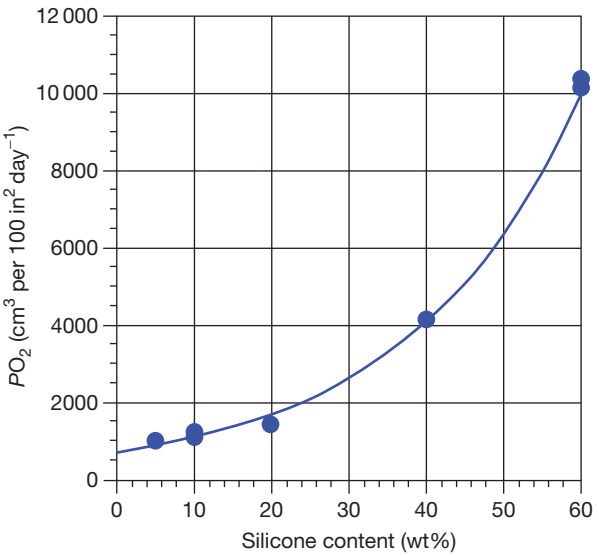

Figure 17 Oxygen permeability (Mocon) versus silicone content in a series of aliphatic and aromatic silicone-polyetherurethane: PurSil and PurSil-AL TSPUs.

realization from these findings was that surface interactions play a critical role in biointeraction and stability.[91,106]

Polydimethylsiloxane (PDMS) polyurea-urethanes based on hexane diisocyanate modified polyether-PDMS soft segments show three distinct phases: a PDMS-rich phase, a polyether soft-segment-rich phase and a hard-segment-rich phase. When evaluated for their blood-contacting properties in a canine *ex vivo* model, they had lower adherent platelet and fibrinogen deposition when compared to a polymer without PDMS in the soft segment. Varying the amount of PDMS in the soft segment of these polymers did not reveal significant differences in their blood-contacting properties.[105] PDMS incorporated into polyurethanes (as end groups, backbone or pendant groups or by admixture) is extremely surface active. The air-facing surface of configured articles may become saturated with PDMS at a bulk concentration of $\ll 1$ wt% silicone. This may explain the insensitivity of platelet and fibrinogen deposition to bulk silicone concentration in the study by Lim.

The biostability of soft-segment poly(ether urethane) (PEU) and poly(carbonate urethane) (PCU), and a material in which the soft segment was partially replaced with poly(dimethylsiloxane) (PDMS), have been compared *in vitro* using an oxidative solution of $H_2O_2/CoCl_2$.[107] Oxidative degradation of the polyether soft segment results in chain scission and cross-linking and pitting of the material surface. In addition, biaxial fatigue accelerated chemical degradation of PEU and eventually caused brittle stress cracking. Partial substitution of the polyether soft segment with PDMS enhanced oxidative stability. TPU containing polycarbonate soft segments was found to be more stable to oxidation with minimal chemical or physical degradation, even in biaxial fatigue.

Commercially, biomedical-grade thermoplastic silicone polyether urethanes such as PurSil® and Elasteon® are true thermoplastic urethane copolymers containing varying amounts of silicone as a soft segment. PurSil is manufactured using a continuous synthesis process in which polydimethylsiloxane (PDMS) comprises one of the soft segments along with polytetramethyleneoxide (PTMO). During prepolymer synthesis, intensive mixing and other conditions that favor compatibilizing the two normally immisible polyols facilitate the synthesis of polymers of any desired soft segment ratio. The hard segment of PurSil TSPU consists of an aromatic diisocyanate, MDI, with a low molecular weight diol chain extender. The copolymer chains are also terminated with silicone (or other) Surface-Modifying End Groups™ (SME). This polymer is noncytoxic, nonhemolytic, nongenotoxic, nonmutagenic, nonpyrogenic, and is the subject of an extensive FDA master file. PurSil has been shown[108,109] to have significantly better biostability than polymers with only PTMO as soft segment. However, during the development of PurSil[110] it was reported that soft homologues with only PTMO *decreased* in MW in intramuscular implants of (strained) film specimens, whereas homologues with only PDMS as soft segment *embrittled* due to apparent *cross-linking* of the polymer. This led to the conclusion that optimum silicone content existed at $\ll 100\%$ silicone soft segment. This is especially true in applications in which maximum physical–mechanical properties are required as high silicone levels generally reduce toughness, cut growth propagation, etc.

Poly(hexamethylene oxide) (PHMO) and poly(dimethylsiloxane) (PDMS)-based macrodiols and mixtures have recently been made and characterized, and they exhibit predictable hard- and soft-segment mixing characteristics.[111]

1.125.4.7. Silicone and Aliphatic Polycarbonate

In addition to the polyether polyol + PDMS soft segment combination described above, even tougher and possibly more biostable polyurethane(ureas) have been prepared in a similar manner, by combining silicone and polyalkylenecarbonate polyols as mixed soft segments, for example, CarboSil® thermoplastic silicone–urethane copolymer.

1.125.4.7.1. Polydimethylsiloxane (silicone)

Silicon-containing polymers and the science and technology of their synthesis have been reviewed by a number of authors (see, e.g., Jones *et al.*[112]). In addition, Yilgör and McGrath,[113] have surveyed polysiloxane containing copolymers and their applications.

As a biomaterial, silicones are frequently identified as one of the few materials having the low hardness and low modulus that is useful in many device applications.[114] Conventional silicone elastomers can have fairly high ultimate elongation, but only low-to-moderate tensile strengths. Consequently, as measured by the area under their stress–strain curves, the toughness of most biomedical (homopolymer) silicone elastomers is not particularly high. In addition, poor cut-growth propagation (e.g., when nicked by a scalpel) and the universal need for reinforcing fillers can also be considered as minor disadvantages in the use of silicones as biomaterials.

One of the least attractive properties of conventional silicone elastomers in device manufacturing is that the materials require covalent cross-linking *and* the inclusion of reinforcing (silica) fillers to develop useful properties. Linear or branched silicone (polydimethylsiloxane (PSX)) homopolymers are viscous liquids or gums at room temperature. Fabrication of device components must include, or be immediately followed by,

cross-linking to form chemical bonds among adjacent polymer chains. The infinite network thus formed gives the polymer its excellent rubber elasticity and characteristic physical–mechanical properties. Cross-linking of extrudable and moldable silicone stock is done via peroxide-generated free radicals adding to vinyl groups incorporated along the polymer backbone, or, more commonly, by the platinum-catalyzed addition of silane (–Si–H) to terminal vinyl groups in so-called LIM systems. Certain low-strength (RTV) silicone adhesives vulcanize at room temperature by *condensation* reactions, eliminating an acid or alcohol to generate –Si–$(OH)_2$ or silanols. This is followed by the elimination of water as silanols condense to form –Si–O–Si– (siloxane) bonds and create a three-dimensional network. Regardless of how the cross-linking or vulcanization is affected, the resulting thermoset silicone cannot be redissolved or remelted. This reduces the number of post-fabrication operations that can be used in device manufacturing with conventional silicones, relative to those possible with thermoplastic biomaterials. For instance, thermal forming, tipping, and tapering; radio-frequency welding; heat-sealing; and solvent-bonding are all useful postfabrication methods that are essentially unavailable when building devices from conventional silicone elastomers.

1.125.4.7.2. History of silicone–urethane development

Even though silicone polymer use preceded polyurethanes as biomaterials by several years, investigators recognized early on the possible advantages of combining silicone and polyurethane in a single biomaterial.[115] Since *c.*1968, combination materials have been prepared as coatings, blends, interpenetrating networks, surface-modifying additives in urethane base polymers, and, most recently, high-strength 'structural' copolymers of silicone and polyurethane.

Before 1970, polyether-based urethanes incorporating polytertramethylene oxide (PTMO) soft segments were known to be inherently stable to hydrolysis and for having excellent flex life. In the late 1970s, development continued with manufacture of segmented and thermoplastic multipolymers having two or more of these types of soft segments along the polymer backbone. The use of more than one soft segment allowed polymer properties to be optimized by controlling the concentration of each soft segment, and the total soft-segment to hard-segment ratio. The series of polymers resulting from thermodynamically compatible mixtures of the polyalkyleneoxides PTMO and PEO have a huge range of permeabilities to water, gases and solutes depending on the ratio of hydrophilic PEO to hydrophobic PTMO. These are currently used as membranes and occlusive dressings. As films or coatings they provide high moisture vapor permeability combined with liquid- and microbial-barrier properties.

In polyurethane–silicone copolymers, the silicone may be present along the polymer backbone and/or in the form of covalently bonded end groups or grafts. Because of the surface activity of silicones in organic base polymers (even when copolymerized), it is relatively easy to obtain silicone-like surface properties on polyurethanes at very low silicone content. This is particularly true when the silicone is present in the copolymer as mobile end groups that can easily 'self-assemble' at the copolymer surface. A bigger challenge has been to obtain some of the other desirable silicone properties – for example, biostability or low modulus – while preserving the bulk properties of polyurethanes such as optical clarity, thermoplastic processability, and extreme toughness (**Figure 18**).

In 1970, the solvent-cast silicone-polyurethane Avcothane-51 was specifically developed as a biomaterial and introduced by Avco Everett Research Laboratory (Everett, MA) for the first clinical intraaortic balloon. This material consisted of a hybrid/psuedo-interpenetrating network of linear polyether urethanes modified with silicone cross-linked after device fabrication (Avcothane-51 later renamed Cardiothane-51 continued to be used in IABs until about 2000). The material is best characterized as a hybrid in which a silicone–urethane copolymer (with Si–O–C bonds) formed *in situ* during solution synthesis stabilizes a blend of a larger amount of moisture-curing silicone homopolymer in a polyurethane-rich solution During fabrication, for example, by dipping, the organic solvent, a 2/1 mixture of THF and *p*-dioxane, evaporates. Atmospheric moisture then condenses on the surface and diffuses into the bulk to hydrolyze terminal diacetoxy groups on the silicone chains. This condenses acetic acid that catalyzes the next step: loss of acetic acid generating, end groups with two hydroxyl groups on each terminal silicon atom. These very reactive 'silanols' condense water to form siloxane cross-links by the same room-temperature vulcanization reaction used in bathtub caulking and silicone medical adhesives. Anhydrous conditions during processing are critical however, because moisture intrusion into the Avcothane dipping solution causes premature cross-linking of the silicone and gel formation in the liquid system, rendering it unusable (**Figure 19**).

The combination of silicone and polyurethane was first proposed to improve the thromboresistance of early cardiac-assist devices, which at the time were plagued by gross thrombogenicity. Cardiothane-51 has since been reported to have good thromboresistance, flex life, abrasion resistance and biostability. Despite excellent *in vivo* results, the Avcothane/Cardiothane system had several disadvantages that limited its use as a biomaterial. These include the need for solution processing, the tendency of the solution to prematurely react with water and coagulate, and the dependence of polymer surface properties on reaction and fabrication conditions. In addition, the polyblend nature of Cardiothane and the thermodynamic incompatibility in the high molecular weight silicone with the preformed polyurethane reactant led to the formation of silicone macrodomains large enough to scatter light. This causes Cardiothane and other hybrid systems to be opaque or translucent to visible light, depending on the actual size of the domains (e.g., see RimPlast™, a family of curable silicone containing thermoplastic compositions for injection molding produced by Huls America, Inc.).

Since the introduction of Avcothane-51, many investigators have sought to develop high-strength, *thermoplastic* silicone-polyurethane (TSPU) copolymers. The prospect of combining the biocompatibility and biostability of conventional silicone elastomers with the processability and toughness of TPUs is an attractive approach to what would appear to be a nearly ideal biomaterial. For instance, it has been firmly established that silicone acts synergistically with both polycarbonate and polyether-based polyurethanes to improve *in vivo* and *in vitro* stability – as, for example, when covalently bonded to the

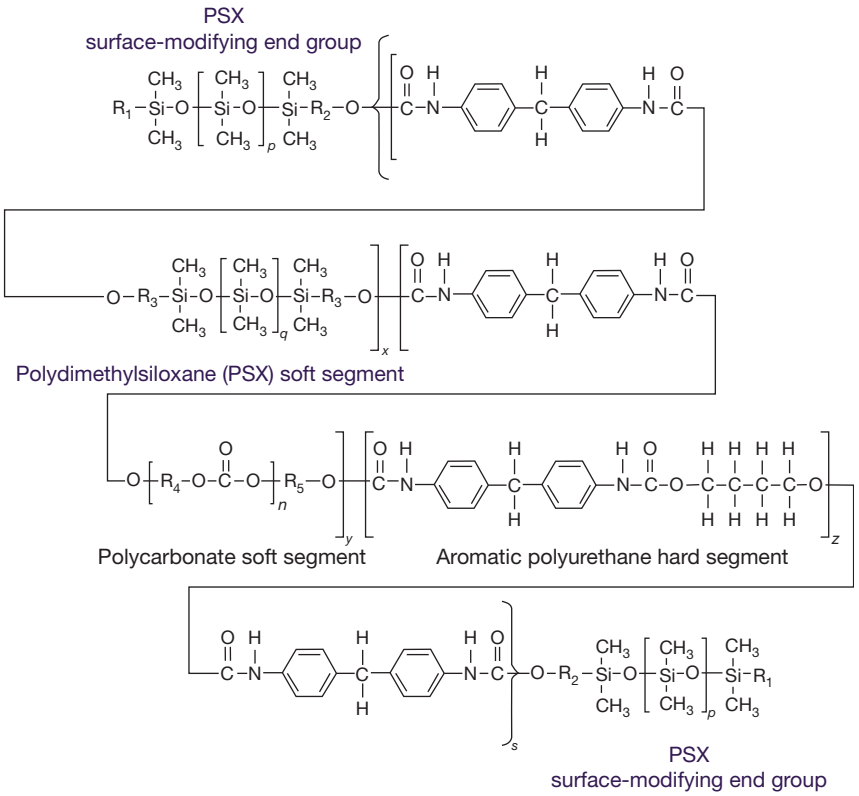

Figure 18 Structure of a thermoplastic silicone–polycarbonate–urethane copolymer with silicone surface modifying end groups. Silicone content, hard segment concentration, and end group chemistry may be easily varied during synthesis to produce a wide range of surface and bulk properties. Fluorocarbon end groups may be used, for example.

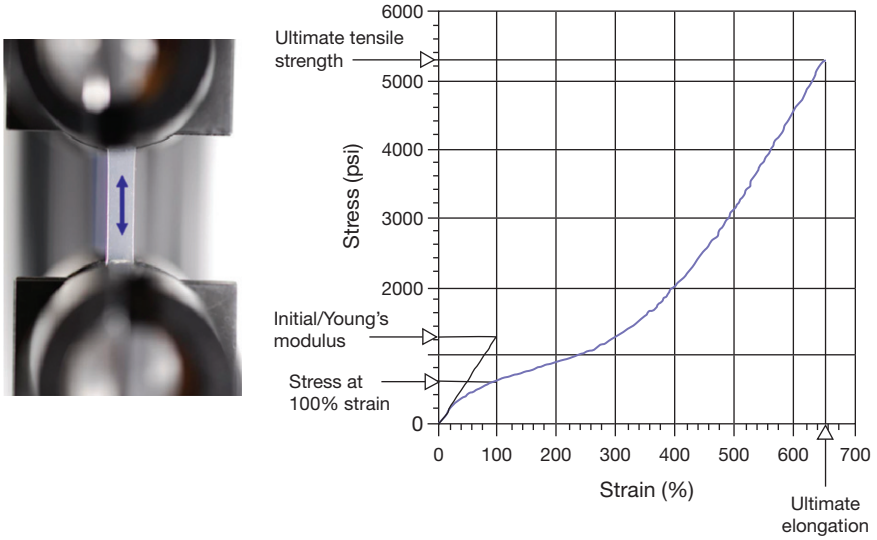

Figure 19 Typical stress versus (engineering) strain curve of a low- to medium-modulus polyurethane elastomer. It is measured in uniaxial tension on a tensile testing instrument (left). Various properties used in device design are labeled. Note the increasing slope in the upper elongation range. This is often caused by strain-induced crystallization, for example, with PTMO soft segments. The area under the stress–strain curve is the energy-to-break the sample, a measure of toughness. Except for very low strain, the nonlinear stress–strain behavior must be considered in device design, for example, when using finite element analysis (FEA).

urethane during synthesis.[109] Several copolymers have shown increased resistance to metal ion-induced oxidation and environmental stress-cracking,[43] both of which have been identified as modes of polyurethane failure in applications such as some early polyurethane pacemaker leads. In polycarbonate-based polyurethanes, silicone copolymerization has been shown to reduce degradation of the carbonate linkage (**Figure 20**), whereas in polyether urethanes, the covalently

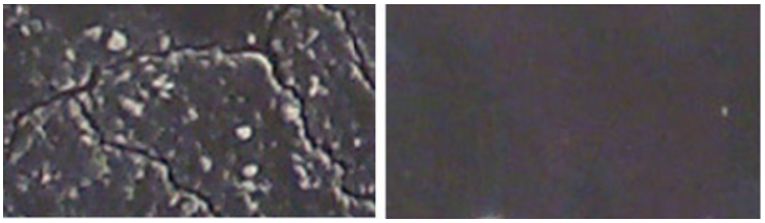

Figure 20 Scanning electron micrograph of early explants (*c*.1991) of low hardness (65A) segmented polycarbonate-urethane-ureas after 12-month intramuscular implantation in rabbits showing enhanced biostability via silicone copolymerization: (left) neat polycarbonate–urethane with environmental stress cracking; (right) silicone–polycarbonate–polyurethane copolymer with no stress cracking.

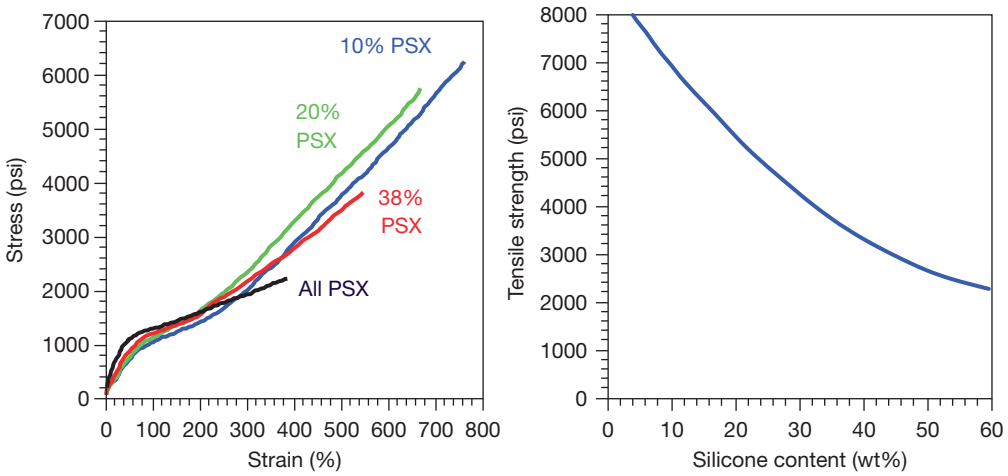

Figure 21 The relationship between tensile properties and silicone content in a series of aromatic thermoplastic silicone–urethane copolymers. Increasing silicone decreases ultimate tensile strength and energy to break, also known as toughness. Optimum silicone content for a soft elastomer often lies between 20% and 35% silicone by weight. In harder versions only 5–20% may be needed. Even at the higher silicone contents these silicone–urethanes have about 3 times the ultimate tensile strength of silicone rubber.

bonded silicone seems to protect the polyether soft segment from oxidative degradation *in vivo*.

1.125.4.7.3. Benefits of silicone modification of PU and PUU

Many of these silicone–urethane copolymers demonstrated previously unavailable combinations of properties. Aromatic silicone-polyether urethanes have a *higher* modulus at a given Shore hardness than do conventional polyether urethanes. Aliphatic silicone-polyether urethanes on the other hand, have a very low modulus and high ultimate elongation, which is typical of silicone homopolymers or even natural rubber. PTMO and polycarbonate soft segment containing polyurethanes polymers however, maintain tensile strengths 3–5 times higher than those of conventional typical silicone biomaterials.

Although less than 1% silicone can give silicone-like surface properties, higher silicone content is required to obtain silicone-like bulk properties such as biostability, permeability, or reduced water absorption. Not all the bulk properties of silicone are desirable in every application (low tensile strength is seldom desirable applications.) Thus, the more silicone that is used to replace the organic soft segment, the lower the tensile strength becomes (Figures 8 and 9). For many biomedical applications 5–25% by weight is an optimum concentration. If high permeability is required – for example, in membranes – higher silicone content may be required. The graph indicates that even when silicone content is as high as 60 wt% the thermoplastics can have tensile strength exceeding most conventional silicone elastomers at 1000–2000 psi. In addition, higher silicone content increases the ultimate raw materials cost of the polymers. Clearly, there is an incentive to determine the minimum silicone concentration that will produce a desired balance of properties (Figure 21).

1.125.4.7.3.1. Improvements in biocompatibility

Early realization that improved thromboresistance and biostability could also be achieved by combinations of soft-segment components (e.g., replacing portions of polyether with PDMS) led to studies directed towards finding this optimum level.[114,116,117] In addition, extending polyether soft segments with polysiloxane was proven to reduce corrosion of metallic parts and reduce the susceptibility to metal ion oxidation (MIO) in implanted devices such as pacemakers or neurostimulator leads.[43] In many applications polyurethanes containing 20–35% polysiloxane (PS-20 and PS-35) were found to be optimum *in vitro*. For implanted tubing samples on cobalt mandrels only traces of microscopic cracks (indicating degradation) were seen after 2 years. *In vivo* polysiloxane-polyether urethanes have also been shown to have higher resistance to biologic oxidation and stress-cracking.[42] PDMS significantly delayed MIO, while the polysiloxane-free controls were severely degraded (Figure 22).

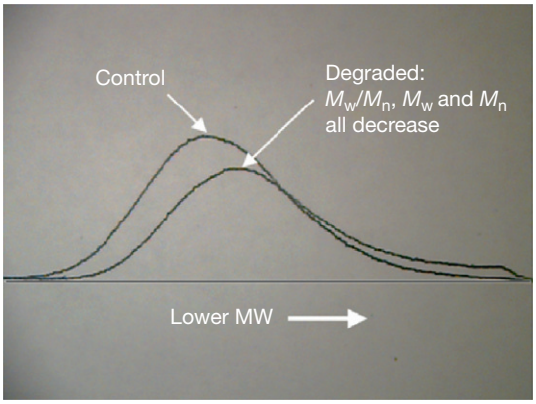

Figure 22 Environmental stress cracking and metal-ion induced oxidation of polyurethanes under accelerated conditions initially results in only surface damage. If the degradation penetrates the bulk significantly and/or if the sample has a very high surface-to-volume ratio, bulk changes may be measurable. Size exclusion chromatography of thin thermoplastic polyurethane films intentionally degraded *in vitro* reveals a reduction in both the number average and weight average molecular weights, and a narrowing of the molecular weight distribution as measured by the polydispersity index M_w/M_n consistent with chain scission.

There is a trade-off between biostability and flexibility, especially for the polyether containing polyurethanes as previously pointed out.[118] In addition, because the (oxidative degradation) reaction is initiated at the soft-segment carbons α to the ether oxygens, the softer the polymer, the more polyether is present and the more susceptible it is to degradation.[119] The harder, more rigid materials, containing the lowest percentage of polyether, are, therefore, more biostable. These have been used with success in cardiac pacing leads and in neurostimulation. The lack of very soft, highly-biostable, polyurethane based on a single soft segment chemistry has 'limits options' in the design of chronically implanted devices.

1.125.4.7.3.2. Improved processing of softer elastomers

Increasing the ratio of soft to hard segment increases the flexibility and lowers the modulus of TPUs while lowering the melt processing temperatures. However, as hardness is decreased polyurethanes derived from a single organic soft segment get increasingly sticky, particularly directly after thermoplastic extrusion or molding. Soft TPUs with some silicone in the backbone and/or as end groups are less prone to self-adhesion when processed, and therefore permit practical processing of softer grades. This allows silicone–urethane copolymers to approach the softness of cross-linked silicone homopolymers, particularly when cycloaliphatic diisocyanates are used, albeit at the possible expense of biostability in long-term implants.

In some cases, end groups have been extended to include alkane chains without the use of backbone silicone. Certain end groups' structures are capable of self-assembling into well organized monolayers which exhibit good stability once formed while also improving processability.[120] The effect of end groups on properties, M_w, and processability has been described in a number of articles.[121–123]

End groups may be incorporated during prepolymer synthesis and optimum amounts are generally determined empirically, with consideration for their effect on molecular weight.

1.125.4.7.3.3. Additives

The ability to thermally and mechanically process polyurethanes while maintaining physical and chemical properties can be improved by the addition of a variety of stabilizers, fillers, pigments, plasticizers, antioxidants and processing aids.[124] Environmental stability can also be improved with stabilizing additives, many of which are compounds with low or medium molecular weight. These additives must be used with caution in biomedical applications because of their potential for diffusion and leaching from the material *in vivo*. In some cases however, such chemicals are required for ease of processing, and their ability to leach out of the material has been tolerated. Perhaps the best example is ethylenebisstearamide wax (MW 580 Da), a multipurpose additive typically used at ~0.2–0.5 wt% to lower melt viscosity, reduce melt fracture, improve mold release, and reduce blocking (stickiness) of extruded parts. This material is extremely surface active and produces a surface layer of low-energy, close-packed C_{18} (stearyl) groups whatever is made from the polymer. As such is a determinant of biological interactions with the modified polyurethanes. However, it *may* contribute to environmental stress cracking if lost from the surface *in vivo*, and it certainly can interfere with the bonding of parts during device assembly.

Inorganic particulate fillers are used to render polyurethanes radiopaque and/or to pigment them. Barium sulphate and titanium dioxide are two examples. Their use requires attention to the quality of the compounding process that disperses them in the polymer. Good dispersion and wet out of the filler is important in minimizing exposed filler at the biological interface: silicone–urethane copolymers appear to evenly incorporate fillers better than silicone-free polymers, apparently due to improved wetting of the filler by the silicone-containing polymer. Often a pelletized concentrate of the filler is prepared on a twin-screw extruder and 'let down' with neat polymer by dry blending pellets in the feed hopper of the molding machine or extruder. Pigments and dyes are occasionally used in implantable biomedical polymers to create a contrast between the material and the surgical field or for cosmetic reasons.

When exposed to radiation, polyurethane, polyurea and polyurethane-polyurea polymers degrade at varying rates depending on temperature, structure and light intensity. Typically, stabilizers are added to preserve the useful lifetime of the materials. Hindered-light amine stabilizers (HALS) have been shown to be effective light stabilizers particularly when used with other stabilizers, such as UV absorbers: early contributions to polymer stabilization using HALS where those that had the ability to form peroxy radicals have been studied.[125] In general, radicals can be oxidized by HALS to produce nitroxides, which forms a cycle.[126]

1.125.4.7.4. Effect on surface chemistry and biological interactions

It is a fundamental assumption of biomaterials science that the chemical composition and (nano)structure of a surface are determinants of the biological interactions with that surface. In the case of tissue-contacting devices and prostheses, responses can range from passive integration with new blood vessel formation adjacent to the surface, to strong avascular fibrous tissue encapsulation or 'walling-off' of the implant.

Attack by macrophages and foreign body giant cells can degrade susceptible materials, and that degradation may produce byproducts that elicit still more inflammatory reaction, fibrous tissue formation, and/or material degradation leading to failure. Avoiding fibrous encapsulation, for example, is particularly important in implanted devices in which efficacy requires mass transport. These include drug delivery devices, sensors and (hybrid) artificial organs. Where direct blood contact is required, foreign surfaces may activate complement, bind proteins, generate microemboli or even gross thrombogenisis without some modification of the surface region and/or administration of systemic anticoagulants. Device-centered infection can also cause early device failure and/or increase patient morbidity or mortality.

For the polyurethanes, surface properties and biocompatibility have been studied by a number of authors.[127] showed that in a series of biocompatibility tests where polyether polyurethanes (chain extended by ethylene glycol) were compared with poly(tetramethylene) polyurethanes, no detectable differences were found although surface compositions varied. The polytetramethylene polyurethanes were similar to Biomer™ in biocompatibility.

1.125.5. Composition of Some Bioresorbable Polyurethanes

Biostable versus biodegradable polyurethanes are at opposite ends of the polyurethane spectrum and demonstrate the versatility of this large class of materials. The amount of work underway directed toward biodegradable polyurethane, tissue scaffolds is one notable example. A number of recent reviews are available (see, e.g., Holland *et al.*,[128] Howard,[129] Santerre *et al.*,[130] Guelcher[131]).

1.125.5.1. Comparison to Biostable Analogues

Improvements in the biostability of polyurethanes have focused on soft segments having reduced or eliminated reactive sites which are predominately ester or ether linkages. In this vein, the polycarbonate diols have exhibited notable stability over these predecessors and have demonstrated oxidative as well as hydrolytic stability in accelerated tests. Figure 23 compares loss in polymer molecular weight with time for commercially available biomedical grade polyurethanes having either polyether (Elasthane™) or polycarbonate (Bionate®) or Bionate II® (polycarbonate with octadecyl-SAM end groups) soft segments at increasing hard-segment concentrations. As pointed out previously, increasing the hard-segment concentration decreases the number of sites available for reactive degradation and increases the hydrophobicity of the polymer. Comparing the polyether-polyurethane (PEU) Elasthane™ 80A, which has a lower hardness value than Elasthane™ 55D, the oxidative stability is predictably less for the 80A sample. Predictably, both PEU's have lower oxidative stability than the polycarbonate containing polyurethanes.

Further improvements in stability have targeted complete elimination of oxygen in the soft segments by creating polyols resistant of both oxidation and hydrolysis. Polyisobutylene diol (PIBd),[132] and methods for preparing polyurethanes

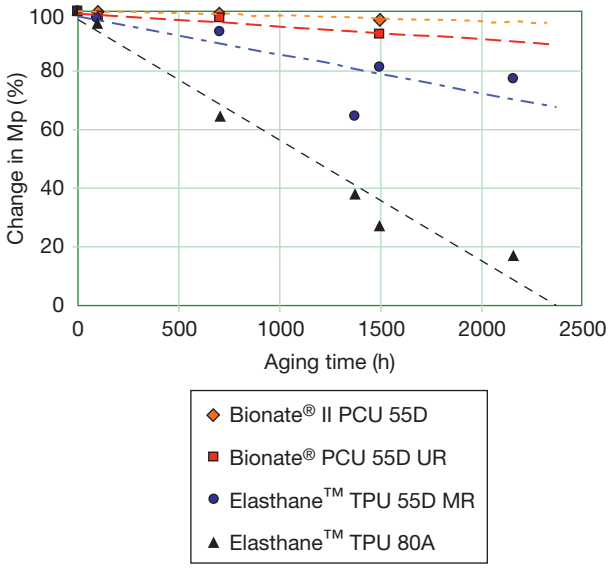

Figure 23 Accelerated *in vitro* oxidative stability of polyurethane elastomers: peak (size-exclusion) molecular weight versus time exposed to 20% hydrogen peroxide + 0.1 M cobalt chloride at 37 °C. The Elasthanes are aromatic polyether-urethanes and the Bionates have similar hard segments but use polyhexamethylene carbonate soft segments. Bionate II uses an ether-free polyol and ocatadecyl ($-C_{18}$) self-assembling monolayer end groups for improved molding and extrusion (without a leachable wax additive).

containing soft segments and multiblocks of this prepolymer[133] have been extensively studied by the Kennedy group (for additional examples see Erdodi *et al.*[134]). Polyurethanes having soft segments made using dihydroxy-polyisobutylene have been compared to polyurethanes containing polyether, polycarbonate, and silicon polycarbonate polyurethane elastomers.[134] Mechanical properties, hydrolytic, and oxidative stability have been reported as being better than comparative materials. Use in biomedical applications have been repeatedly indicated.[135] To date, only lack of a supplier of urethane-grade PIB polyols has limited use in biomedical polyurethanes applications.

1.125.5.1.1. Degradable soft segments

Due to polyurethanes ester linkages being hydrolytically unstable, (oxygen in ester linkages along the soft segment/polymer chain are sources of reactive initiations), polymeric molecules containing such linkages have been identified as suitable candidates for degradable polymers. Polymers for biodegradable medical devices have been made from poly(hydroxybutyrate)–poly(hydroxvalerate) (PHB–PHV), and copolymers of hydroxyvalerate were studied early on as candidates for biodegradable systems.[128] Many studies have included the lactones such as poly(ε-caprolactone) incorporated into polyurethane ureas.[136]

Amino acid-based polyesters have been prepared for use as biodegradable soft segments. Caracciolo *et al.*[137] compared the structure–property relationships for a series of biomedical segmented polyurethanes based on poly(ε-caprolactone) diol (PCL diol), 1,6-hexamethylene diisocyanate or L-lysine methyl

ester diisocyanate (LDI). Chain extenders containing urea groups or an aromatic amino acid derivative were used to strengthen hard-segment through either bidentate hydrogen bonding or π-stacking interactions. Although polyurethanes synthesized using hexamethylene diisocyanate (with the aromatic chain extender) exhibited the higher elongation, tear energy, and lower strain at break, and in general were stronger than those obtained using lysine methyl ester diisocyanate (LMED), the LMED containing polymers were shown to be biodegradable and possessed a range of sufficient thermal and mechanical properties.

Biodegradable polymers including polyglycolides and polylactides have been studied as tissue engineering prototypes by Gunatillake *et al.*[76]. They noted some disadvantages of these polymers including poor biocompatibility, release of acidic degradation products, along with poor processability and loss of mechanical properties during degradation.

Aliphatic diisocyantes have been used to couple lactide–PEG–lactide polyols in the synthesis of degradable polyurethanes (Cohn U.S. Patent 4,826,945). PEG-to-lactide ratio is easily changed to tailor degradation rate, which at high PEG concentration can be very rapid, giving water-soluble degradation products. Constructs using high-PEG homologues have high water absorption and need to be protected from atmospheric moisture to avoid premature degradation of the hydrolytically unstable lactide blocks.

1.125.5.1.2. Degradable hard segments

Biodegradable hard segments have been prepared by a number of methods. Diisocyanate amino acid analogs have been prepared having degradable segments,[138] and degradable ester linkages in the hard-segment and cross-linking interchanges have been prepared.[139] Methods to accelerate hard-segment degradation via degradable chain extender based on DL-lactic acid and ethylene glycol have been reported by Tatai *et al.*[140] In each of these cases, maintaining mechanical integrity and loss of material properties is always an issue when deviating from standard materials.[268–271]

1.125.6. Basic Structure–Property Relationships in Block and Segmented PUs and PUUs

A comprehensive review of the structure–morphology–property relations in segmented thermoplastic elastomers, including polyurethanes has recently been prepared.[141] Stoichiometric reactions of soft-segment oligomers and hard-segment precursors and the influence of soft-segment structure and molecular weight, hard-segment symmetry and crystallinity, and the strength of the hydrogen bonding on the morphology and properties of segmented, nonchain extended thermoplastic elastomers are key factors affecting 'physicals.' As previously discussed, the ratio of soft segment to hard segment and degree of hydrogen bonding plays a critical part of the overall development of polymer properties. The type of soft segment and the uniformity in the soft-segment distribution and the amount, type and distribution of the hard segment dictate the quantity and quality of hydrogen-bonding present in the material and allowed to form yielding ultimate structure–property relationships.

1.125.6.1. Effect of Hard-Segment Chemistry and Content

The concentration of hard-segment in PU block copolymers affects physical properties: barrier properties, indentation hardness, melt rheology, ultimate tensile properties, modulus and many other properties and processing-related variables. Control during synthesis of molecular weight and molecular weight distribution of the hard-segment component is a key factor in designing polyurethane elastomers and is crucial in producing consistent material. Elastomers having uniform hard segments are generally prepared by carefully ordered addition of components, and the resulting hard-segment chemical composition and distribution, as well as cross-linking reactions, are well controlled. As an example, lower reaction temperatures and simultaneous mixing of all reactants give the preferred size distribution of hard segments in reactions derived from an aliphatic diisocyanate when dealing with wide variations in reactivity between two isocyanate groups on the same molecule.[142]

Hard-segment composition and the effect of hard-segment segment size and molecular weight distribution have been related using dynamic-mechanical and thermal scanning behavior.[143] Detailed analysis of specific molecular motions can be explained in terms of domain perfection. Judicious ordering of the ratio of molecular weight of the soft segment and keeping hard segments crystallized and surrounded by uncrystallized soft segments has been used to produce highly efficient impact-resistant polyurethanes suitable for body armor applications.[144]

The level of phase segregation between hard and soft segments has been measured by several authors and found to depend especially upon the nature of the soft sequence and its average molecular weight, the nature of the hard sequence, and the number of hydrogen bonds established in the matrix (see, e.g., Elidrissi *et al.*[145]). In addition, for shape memory, polyurethane (PU) block copolymers composed of poly(tetramethylene glycol)/MDI/BD, 80−95% of shape recovery was obtained at 30−45 wt% of hard segment content.[146]

1.125.6.1.1. Importance of hydrogen bonding

The physical properties of polyurethanes are a result of the quality and quantity of association between the polymer chains which are chiefly developed as a result of hydrogen bonding. Early on Seymour[147] *et al.* (1970) made infrared studies of hydrogen bonding in polyether and polyester SPU elastomers and reported NH stretching vibration indicating almost all of the active NH groups form hydrogen bonds between the urethane nitrogen-hydrogen and the urethane carbonyl linkages in ester or ether prepolymer linkages. Furthermore the extent of hydrogen bonding did not change in samples stretched to over 300%. Quantifying this, Brunette[148] reported hydrogen-bonding spectral properties of polyurethane block copolymers comparing a variety of hard-segment components. He pointed out that the shift in the stretching frequency of the hydrogen-bonded X–H group (X–H. . .Y) could be used as a measure of the strength of the hydrogen bonding and that with increasing hydrogen bond strength, the X–Y distance (R) decreases and is usually accompanied by an increase in the difference between the associated X–H stretching frequency and nonassociated X–H stretching frequency.

Yilgör *et al.*,[149] compared hydrogen bonding in polydimethylsiloxane and polyether-based urethane and urea

copolymers using a variety of methods. The extent of interaction and resulting phase mixing between hard and soft segments in these copolymers was determined. Quantum mechanical calculations showed substantial hydrogen bonding between urea groups and the oxygen in the ether-type soft segments, but absence of any interaction between silicones and urea groups. Calculations were in agreement with thermomechanical behavior and mechanical properties of these copolymers.

1.125.6.1.2. Effect of soft-segment chemistry and content

The elastomeric nature of polyurethanes is due to the mobile amorphous soft-segment components in which the crystalline or glassy hard segments are dispersed. Several factors play a part in the expression of physical properties arising from this component. The molecular weight of the soft segment and the uniformity in molecular weight distribution are factors: chemical make-up, the amount and type of bonding present and compositional distribution in these long chain amorphous segments also play a critical role. These factors have been alluded to earlier and extensively studied by a number of authors (for early examples, see Takahara *et al.*[150–152]).

The three main general classes of soft-segment polyols currently used in commercial biomedical applications are (1) polyester soft segments (not susceptible to oxidation but readily undergo hydrolytic degradation); (2) polyether soft segments (oxidatively degrade under certain conditions) or (3) polycarbonate soft segments (more biostable than polyether soft segments).[153] Combinations of materials within these classes (e.g., lactones and adipates in the polyester class, polytetramethylene oxide/polyethylene glycol in the polyether class or combinations of poly(oligocarbonate diols),[154] can be mixed and matched to provide extended properties and improve biocompatibility.

Depending on the chemical composition under stress, there is a tendency in these soft segments to align. Rate-dependent stiffening and strain-hardening behavior of the microstructure can be tailored by increasing the hard-segment content resulting in improvement in barrier properties, increased stiffness and flow-stress levels.

1.125.6.1.2.1. Single soft segment

Single soft segment components can be selected over multiple segmented components to provide uniformity in compositional distribution. Single-component soft segments having narrow molecular weight distributions (i.e., a narrow molecular weight distribution in the polyol starting material depending on the method of synthesis), can produce a tailored polymer having uniform properties. Reproducibility in batch-to-batch is increased, and properties may be more consistent. However, polymers with single soft segments do not provide as much versatility in tailoring properties for specific applications as polymers having two or more soft segments in the backbone.

1.125.6.1.2.2. Mixed soft segments

Variations in composition made by including, both hydrophobic and hydrophilic prepolymers as soft-segments, are useful in tailoring permeation and absorption. Stepwise variation in average soft segment concentration gives systematic changes in the solubility and diffusivity of a wide range of permeants including gases, condensable vapors, proteins and other solutes. The hard segments can be chosen to meet specific physical–mechanical requirements but ideally constitute a minor volume fraction of the total polymer. Silicone containing prepolymers such as PDMS diol are copolymerized with 'organic' prepolymers based on polyether- or polycarbonate-diols to provide synergistic properties including controlled gas permeability and enhanced biostability.

1.125.6.1.3. Effect of end groups on surface chemistry

The surface that comprises the biological interface is often very important to implant performance. Unmodified surface may activate complement, initiate thrombosis, degrade and crack, adsorb fluids and biomolecules, bind cells, wear, and/or damage tissue. Surface properties are, therefore, equally as important as bulk properties when specifying a material for devices or prosthetic implants.

A variety of materials have been *applied* to polyurethane surfaces in order to modify biological interactions. Posttreatment of devices using a variety of techniques including plasma irradiation and deposition (see, e.g., Dejun *et al.*[155]), chemical ionization, ultraviolet irradiation (UV), gamma irradiation (GI), and interfacial modification (IM) followed by surface treatment with poly(ethylene glycol) (PEG), hydroxyl-ethyl methacrylate (HEMA) hexamethylene diamine (HMD), or chitosan (CT), have been developed, to mention a few. Alves *et al.*[156] showed that modification by GI gives high values of grafting yield and has the advantage of providing a clean modification without requiring initiators.

In modifying surface properties Takahara *et al.*[150,152] looked at MDI/BD polyurethanes having poly(ethylene oxide), poly(tetramethylene oxide), hydrogenated poly(butadiene), poly(butadiene) and poly(dimethylsiloxane) soft segments in relation to surface, bulk and *ex vivo* blood-contacting properties. Hydrophobic polyols poly(dimethylsiloxane) and hydrogenated poly(butadiene) showed distinct microphase separation between hard and soft segments with 'surface enrichment of the hydrophobic component at the air–solid interface.' This poly(dimethylsiloxane)-based segmented polyurethane had the lowest platelet adhesion among the segmented polyurethanes investigated in the study, while the platelet deposition on the poly(ethylene oxide)-based polymer increased with time. In addition, Bernacca *et al.*[157] studied parameters of blood compatibility to the response of two polyurethanes of differing primary structures and having a variety of surface modifications. Covalent attachment of heparin, taurine, a platelet membrane glycoprotein fragment, PEO, 3-aminopropyltriethoxysilane, and glucose or glucosamine were added to effect material thrombogenicity. While unmodified control polyurethanes caused platelet release and complement activation, high molecular weight (2000 Da) polyethylene oxide reduced platelet release slightly. Glucose attachment to the surface produced a significant reduction in platelet activation and was found to be the least activating. In both of these cases it was the surfaces and surface interactions that provided property improvements and increased biocompatibility.

In an additional selected example we note that Freij-Larsson *et al.*,[158] reported that hydrophilic surfaces prepared by grafting

polymer surfaces with hydrophilic polymers such as PEO lowered interfacial tension towards aqueous solutions which are known to adsorb very low amounts of proteins. They prepared and studied a number of amphiphilic polymers having backbones consisting of poly(methyl methacrylate-*co*-ethylhexyl acrylate) and poly(styrene-*co*-acrylamide), respectively, and PEO 2000 grafts combined with polyurethane and found that the modified surfaces had generally lower adsorption of blood proteins with the poly(methyl methacrylate-*co*-ethylhexyl acrylate) backbone blend modified surfaces having the lowest adsorption.

Topical treatments of preformed PU surface can certainly be effective, but they add one or more steps to device manufacturing, lowering yield and increasing cost. Modifying the polymer before component fabrication has several advantages including the seamless integration into device manufacturing. The use of covalently bonded surface-active end groups appended to the polymer during synthesis has proven to be an effective method of surface modification of polyurethanes and other step growth polymers (*vide infra*).

As the safety, effectiveness, and useful life of implants are often affected by surface properties, it follows that technology for controlling surface chemistry and structure can be useful in improving device performance. However, experimental investigations designed to determine the effect of systematic variations in surface properties on biological response do not always result in clear conclusions. In the case of polymers this may result from inaccurate assumptions about the resulting change in the surface produced by a change in the bulk. It may also be due to the lack of knowledge about the surface restructuring or relaxation that occurs upon a change in environment, or under adsorbates that interact with the surface. The use of sensitive, surface-specific methods of characterization, especially those that work within an environment relevant to the use of biomaterials is needed when developing reliable surface-structure-versus-property relationships.[272–275] Our understanding of how surfaces affect biologic interactions is far from complete, in part because of our inability to adequately characterize the surfaces before, during and after contact. On some surfaces the effect of the initial device surface chemistry and nanostructure on biological response may be blunted by the inevitable adsorption of proteins that occurs directly upon contact. However, this does not detract from the need for surface modification technology, particularly those that can be easily integrated into the routine manufacturing of medical devices (**Figure 24**).

In most condensed phases of matter (and polymers in particular) the surface is not merely a continuation or projection of the bulk onto the outer monolayer. The surface is usually very different from the bulk, and minor changes in the bulk may cause large changes at the surface. Liquids and solids spontaneously minimize their interfacial energy by a number of mechanisms including migration of species from the bulk to the surface region. Polymers with 'mobile' surfaces can also rearrange to minimize total surface area *and* their interfacial energy per unit area according to the environment in which they are immersed. They do this, by 'presenting' available chemical groups that minimize the energy gradient across the interfacial region. This can involve diffusion from the bulk, or flipping of polymer chains to expose different backbone or pendant groups, and/or by changes in packing density. These surface relaxations are favored in amorphous

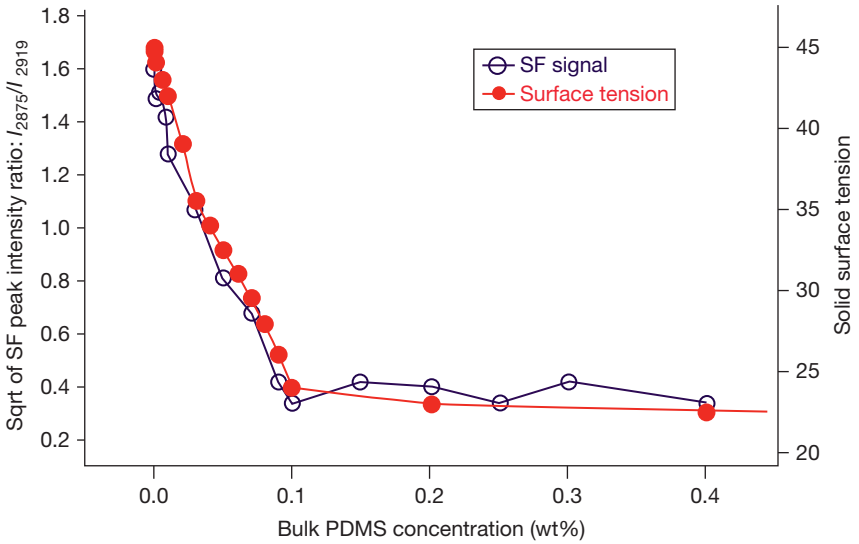

Figure 24 Surface concentration measured by sum frequency generation spectroscopy (SFG) versus bulk concentration in solid films made from a blend of silicone–urethane copolymer in high-molecular weight phenoxy resin. The base phenoxy was chosen for its high-solid surface tension and compatibility with polyurethanes. As small amounts of the PSX copolymer are added to the bulk polymer, the surface phenoxy concentration is reduced as silicone populates the surface. This decrease in surface phenoxy (and increase in surface silicone) is exactly mirrored in the reduction in solid surface tension (calculated from water and methylene iodide contact angle measurements) caused by the low-energy silicone. Only ~0.1 wt% bulk silicone is required to saturate the surface. Similar results are obtained with silicone end groups covalently bonded to polyurethanes during synthesis, making end groups useful for polymer surface modification. This behavior is quantitatively similar to conventional surfactants in liquid systems.

polymers above T_g that are free of cross-links and which are optionally plasticized by water. In softer polyurethane copolymers with soft segments that are above T_g at 37 °C, rearrangement may occur fairly rapidly. For this reason very minor amounts of *surface active* additives or impurities may produce a pronounced change in surface composition.

In addition to substances admixed with the neat polymer, polymer end groups can also be highly surface active, even though they are covalently bonded to the polymer backbone. Furthermore mobile end groups can be designed to spontaneously self assemble at high density in the surface region during and after device fabrication. Thus end groups can be designed which are chemically different from the backbone polymer and which act as permanent, built-in surface modifiers (see Section 1.125.6.1.4.1).

1.125.6.1.4. Optimizing polyurethanes for specific biomedical applications

Polyurethanes for implantable devices can be selected from commercially available biomedical polymers, that is, catalog items, or they may be custom synthesized for use in specific applications. The latter may be necessary when a complex, highly constrained property specification must be met.

Even when investigating available polymers there are considerations beyond the polymer properties listed on the data sheet, which are often measured dry at room temperature. These include immediate property changes upon implantation caused by heating to body temperature, and the absorption of water in the body. The role of water as a solvent/plasticizer is one important consideration in material selection, particularly in hydrogen bonded polymers such as PU and PUU. For example, oxidative stability of poly(carbonate urethanes) and their silicone-containing copolymers have caused them to be evaluated as a replacement for poly(ether urethanes) (PEUs) in a number of medical devices (see, e.g., Christenson *et al.*[159]). The ether groups increase equilibrium water content during implantation resulting in a different degree of softening, creep and permanent set in the polyetherurethane relative to the polycarbonate-containing analogue.

1.125.6.1.4.1. Satisfying bulk and surface property requirements

Soft-segment composition and concentration affect not only the bulk properties, but also the surface due to their ability to migrate and concentrate in the surface region. Movement from the bulk to the surface is 'surface activity.' The spontaneous ordering of like molecules in the surface is known as self assembly. In using surface activity and self assembly to modify polymer surfaces even the less restricted mobility of polymer end groups can be very useful.

Surface-modifying end groups (SMEs) add another dimension when tailoring (biomedical) base polymers and they can produce a desired surface chemistry without the use of additives. Some surface-active oligomers that have been covalently bonded to base polyurethanes during synthesis include: silicone (S), sulfonate (SO), fluorocarbon (F), polyethyleneoxide (P), hydrocarbon (H) groups, and quaternary ammonium halides. Often, very low bulk concentrations control the surface chemistry without compromising the bulk properties of the polymer (see Table 3). The result may improve a variety of surface properties, such as thromboresistance, biostability, abrasion resistance and antimicrobial properties. Surfaces of configured articles develop spontaneously once the surface is formed so the base polymer is permanently enhanced without the additional step of post-fabrication treatments or topical coatings.

Table 3 History of commercially-available silicone–urethane biomaterials

Trade name, patent date	*First soft segment*	*Second soft segment*	*Desired enhancement*
Avcothane-51 Cardiothane-51 PIPN, 1969	PTMO polyether	PSX blend	Thromboresistance biostability (1978)
Thoralon™ SPU & TPU, 1983	PTMO polyether	PSX	Thromboresistance biostability
PurSil™ w. SME TSPU, 1994	PTMO polyether	PSX	Biostability
CarboSil® w. SME TSPU, 1994	PHMC polycarbonate	PSX	Biostability
Elasteon™ TSPU, 1997	PHMO polyether	PSX	Biostability

Similar polymers with different trade names may have been used captively by device manufacturers. Avothane/Cardiothane demonstrated the benefits of combining silicone with polyurethane, albeit in an optically opaque material that was difficult to process. Progress in silicone chemistry and the availability of oligomeric silicone (PSX) diols and diamines made the manufacture of thermoplastic silicone–urethane copolymers possible.

The added mobility of end groups relative to the polyurethane backbone has been shown to facilitate the formation of uniform overlayers by the surface-active (end) blocks. The use of the surface-active end groups leaves the original polymer backbone intact so the polymer retains strength and processability. Surface-modified polymers have been made with tensile strengths exceeding 5000 psi containing only 0.5 wt% or less of end groups. This novel technology is applicable to a wide range of polymers. However, modification with highly surface-active end groups is particularly adapted to the synthesis of polymers that may incorporate low molecular weight monofunctional end-groups for molecular weight control: for example, polyurethanes and other step-growth polymers. The SME approach also allows the incorporation of mixed end groups on a single polymer. For example, the combination of hydrophobic and hydrophilic end groups gives the polymer 'amphipathic' surface characteristics in which the hydrophobic-to-hydrophilic balance may be controlled.

Self-assembling monolayer end groups (SAME®) is a related technology utilizing, second-generation surface-modifying end groups (SMEs). SAMEs are modeled after well-known SAMs, for example, alkane thiols. That is they have a self assembling alkane spacer chain and head group. Instead of a terminal thiol group used to chemisorb to a gold substrate from solution, the SAME typically has a hydroxyl or amine group which is reacted with isocyanate during polyurethane synthesis. Monofunctional SAME reactants are chain stoppers for step growth reaction so they automatically become end groups (Table 4).

Traditional SAM technology (e.g., thiols on gold or silanes on silica) has clearly demonstrated that bioactive 'head groups' can be appended to alkane chains as a method of creating model surfaces for *in vitro* research. Ideally, the chemistry used during such model studies could then be applied to actual medical devices to further improve clinical outcomes. However, SAM technologies are not easily transferred to medical device applications due to the fragility of such systems including the oxidative instability of the gold-thiol bond.[276]

SAME® technology, on the other hand, is capable of providing polymers with 'SAM-like' engineered surfaces.

Table 4 Surface-Modifying End Groups maintain bulk polymer properties while controlling surface chemistry

Surface-Modifying End Group (SME®)	*Advantages*
Silicone	Hydrophobic, nonadhesive surface, lubricious, may increase biostability under certain conditions, may increase infection resistance
Flurocarbon	Hydrophobic, nonadhesive surface, chemically-stable surface, may increase biostability under certain conditions, may increase infection resistance
Polyethylene Oxide	Hydrophilic, affects material permeability, reduces protein adsorption
Sulfonate	Hydrophilic, may be thromboresistant, can react or bind to proteins and peptides
Hydrocarbon)	Hydrophobic, may increase biostability under certain conditions, may bind albumin
Mixed SMEs	Example: Silicone (S) and PEO (P) – amphipathic structure: hydrophilic and hydrophobic polymer depending on the surrounding environment

Relative to backbone chains, polymer end groups are more mobile, in part because they are often tethered to the backbone by a single, flexible covalent bond (see Figure 3). End group mobility allows them to diffuse from the bulk and assemble in the polymer surface to affect surface composition. This occurs spontaneously if the presence of the end groups in the surface reduces system interfacial energy. Simple hydrophobic end groups may diffuse to an air interface, while purely hydrophilic end groups may enrich a polymer surface when exposed to aqueous body fluids. The self assembly of endgroups into monolayers using the SAME technology utilizes very specific hydrophobic or hydrophilic spacer groups, and a head group chemistry chosen for the particular application. The spacer groups will 'self-assemble' at the surface through either hydrophobic or hydrophilic interactions, and thus present the head group as the outermost monolayer of the polymer. One or more surface-modifying end groups give independent control of surface and bulk properties, where control of bulk properties can be extended via hard-segment composition and concentration. A variety of SME and SAME compositions have been used to modify surface properties such as antimicrobial and lubricous combinations (Figure 25).

1.125.7. Fabrication of Medical Device Components from PUs and PUUs

1.125.7.1. Solution Processing: Dipping, Spraying, Solvent Bonding, and Web Coating

Polyurethaneureas have hard segments with very high cohesive energy density and therefore may not be thermally processable. Such a high temperature may be required to liquefy the polymer so that soft segment degradation occurs. In cases where the polymer is solvent soluble, solution-processing methods can

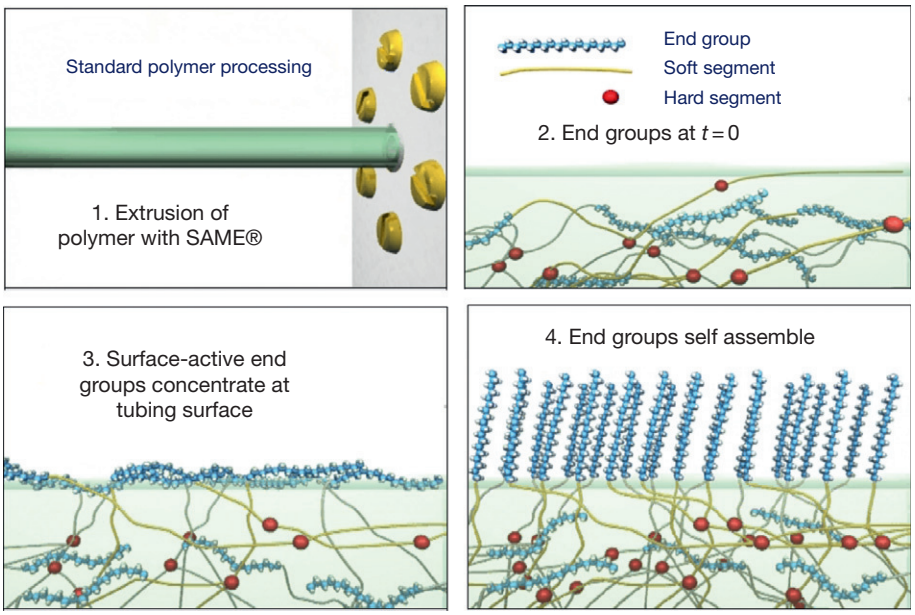

Figure 25 Self Assembling End Groups (SAME™): surface activity and self assembly produce and organized layer of close-packed end group in the surface of extruded biomedical tubing without any postfabrication coatings or surface treatments (schematic, not to scale).



Figure 26 Many sac- and diaphragm-type cardiac assist device are fabricated by solution processing. This can range from simple pouring with hand manipulation, of male or female molds, to robotic dipping. Environmental conditions must be controlled and worker safety must be considered given the evolution of toxic and flammable solvent vapors. It is vitally important to remove residual solvent from cast part to avoid negative effects on hemolysis, cytotoxicity and other biocompatibility tests.

be used. However, solution processing may also be attractive in some cases, even for linear or branched thermoplastics that can easily be molded or extruded. Use of solvent-based glues in device assembly is one example (Figure 26).

Solution processing begins with solution preparation and filtration. In solution synthesis of polyurethaneurea elastomers the *product* is often a concentrated solution, requiring dilution before use. Flammable, toxic, aprotic solvents with high boiling points are commonly used: dimethylacetamide (DMAc), dimethylformamide (DMF), dimethylsulfoxide (DMSO), and *n*-methylpyrolidone (NMP) are candidates. DMAc and DMF are commonly used in synthesis of PUUs, but the low-boiling (highly-flammable) solvent tetrahydrofuran (THF) may be used as a diluent, or even as the main solvent for more soluble TPUs. Very high-purity solvents are needed to avoid leaving nonvolatile impurities in or on the fabricated part. Prefiltered, chromatographic-grade, glass-distilled solvents are preferred. Suitable solvents are often hygroscopic and need to be protected from moisture before and after solution preparation.

Dissolution of prereacted, pelletized TPUs should be done in a fume hood in a covered vessel fitted with a high shear mixer. Safety procedures for the handling of toxic and flammable chemicals should be followed. It is best to slowly add free-flowing pellets to the stirring solvent to prevent agglomeration, which can greatly lengthen the solvent diffusion path and therefore the dissolution time. Gentle heat may be applied with a heat lamp while keeping the temperature well below the boiling point. This is difficult with THF as it boils at 66 °C, and shear heating from the mixer will raise solution temperature. The entire process of preparing a solution from pelletized TPU may take several hours, and is usually complete when the solution is clear and no undissolved polymer remains. Harder grades are much slower to dissolve than softer grades.

The starting solution *must* be filtered before device or component fabrication. Suitable filters are depth type that can remove undissolved gels *and* particulates while not sloughing off filter material into the filtrate stream. Suitable filters use sintered stainless steel fiber or polyproplylene media which have been thoroughly cleaned before use and flushed with pure solvent to prewet the pores. Absolute pore size ratings, measured by bubble point, ranging from ~<1 to 20 μM are used, but smaller pore size greatly increases pressure drop and the filtration time of viscous solutions. Filtrate is collected in precleaned glass vessels and covered using cap liners or other closures that are not attacked by the solvent. Any additional dilution required after filtration, for example, due to solvent evaporation, should be done with high-purity, prefiltered solvents (Figure 27).

Solutions may be used to fabricate device components by a number of methods. The most primitive involves simply pouring the solution over a male or female mold while manually manipulating the mold to achieve even solution coverage. Ultrasonic spraying of dilute solutions represents the other extreme, and may be useful when dimensional control of small parts is required, such as when coating stents. Other methods include dipping male mandrels into baths containing the polymer solution, or casting a solution onto a permanent substrate or a release surface. When roll goods are coated continuously in the manufacture of films or membranes the process is known as web coating and uses equipment that resembles a printing press. The delivery rate of the solution to the coating head, solids content, and web speed determine final thickness (Figures 28 and 29).

In order to produce consistent product free of pinholes and impurities, environmental controls are a necessity. Temperature and humidity controlled clean rooms *without* air recirculation are preferred as controlled evaporation rate, low particle count, dew point control and removal of toxic and flammable solvents are all required within the work space. Appropriate electrical service and environmental monitoring are important safety requirements for which professional help should be sought.

Ambient water concentration is a big determinant of the quality of solvent cast or dipped coatings and parts. Evaporative cooling during the process may condense atmospheric moisture on the drying part which mixes with the remaining solvent. As water is a nonsolvent for most polyurethanes the condensed water may act to coagulate the polymer rather than allowing it to dry to a dense film. This problem is particularly important when processing with high boiling solvents which may require either elevated temperature (ca. 35 °C) in the work space, or the use of industrial dehumidifiers capable or reducing dew point to very low levels. Note that very dry



Figure 27 Clean room dipping of simple tubes for use in a hybrid artificial pancreas. The membrane polymer in solution in DMAc is slowly pumped through a SS depth filter into the bottom of a dipping tube fitted with an overflow sump. It then returns by gravity to the reservoir tank that feeds the pump. This continuously supplies the dipping tube with particulate-free homogeneous polymer solution while 'sweeping' the surface clean.

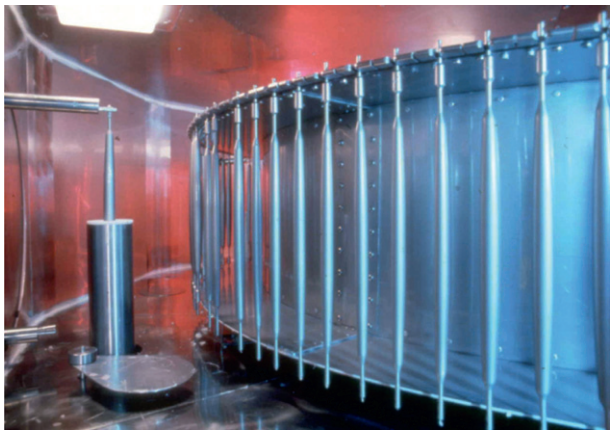

Figure 28 Automated dipping of intraaortic balloons on stainless steel mandrels *c*.1976. Dipping solution is continuously circulated and refiltered by pumps and filters located on the floor below the dipping machine. The internal environment is high efficiency particulate air (HEPA)-filtered air with controlled temperature and humidity. Mandrels are held stationary while the dipping tube moves up and down to coat the mandrel. Two dips in each direction are required per balloon.

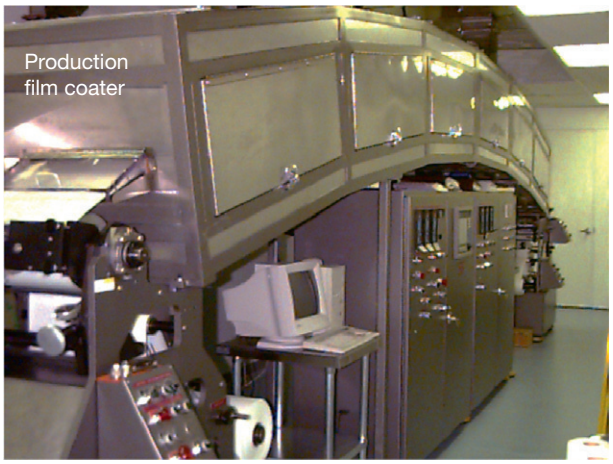

Figure 29 Continuous web coater for casting polymer films and coatings. A N_2-purged pressure pot containing the liquid coating feeds a gear pump the speed of which is automatically controlled using a noncontacting thickness gauge. Substrate roll goods ('webs') pass under the coating head enter the oven at left and emerge coated onto a take-up spool at far right. This equipment can produce large quantities of film, membranes, transdermal devices and coated fabric. Often the product is die cut prior to device assembly and packaging.

environments may increase static discharge caused by moving air, which can create a fire hazard.

Removal of trace quantities of solvent is a necessary part of all solution processing and can have a dramatic effect on the biocompatibility of the final product. Cytotoxicity and hemolysis can have consequences that are not related to the polyurethane material itself, but are only due to the residual solvent leaching out during testing or use. Thus, the removal of even trace quantities of residual solvent is important. Drying at elevated temperature ($\leq 60\,^{\circ}C$) in flowing air is often more effective than vacuum drying, as the main resistance to solvent loss at this stage may be diffusion within the polymer, not desorption from the surface. In order to reduce the residual solvent level in thick parts, water extraction may be required, for example, at 60 °C, followed by air or oven drying to remove absorbed water. Clean room particle count and inclusions in the finished device are additional issues that need to be considered when setting specifications for solvent-based processing.

As mentioned above, resolving the safety issues associated with solvent-based processes is of utmost importance. Professional engineering design input is highly advisable. Organic solvent vapors can exceed flammable limits without adequate exhaust and controls, and any sources of ignition from open flames, electrical equipment, static discharge, etc., can cause fires or explosions. Fire suppression equipment and proper grounding is vital, as is worker protective equipment including gas/vapor masks. All precautions and standard guidelines for handling flammable solvents and vapors must be rigorously followed and environmental monitoring must be routinely performed.

1.125.7.2. Thermoplastic Processing

Melt processing of the final polymer product is an engineering discipline which in itself has been extensively studied (see, e.g., Throne,[160] Lu *et al.*,[161] Erol and Kalyon[162]). It involves heating the polymer to reduce its viscosity to the point that it can be extruded or molded into a final shape followed by cooling to room temperature to 'lock in' the shape. Automated and/or continuous thermoplastic processes are capital intensive, but capable of high throughput and low cost of goods. Extrusion, injection molding, compression molding and thermal forming of polyurethanes are all standard, commercially developed methods for thermoplastic polyurethanes. Optimizing melt processing conditions for polyurethanes involves consideration of melt rheology as affected by temperature and shear rate, and the water content of the polymer fed to the process. The presence of allophonate cross-links can complicate processing due to their thermolabile nature. If present they can break during processing and reform slowly thereafter (**Figure 30**).

By using the intensive mixing and controlled temperature profiles offered in twin-screw extruders, the synthesis of pelletized TPUs can be achieved by further reacting a prepolymer with chain extender[163,164] or by metering all reactants to the throat of the extruder in the 'single shot' method. Although it is typical to collect a pelletized product for subsequent processing, it is possible to extrude tubing and profile from the extrudate of the reactor/extruder. This type of processing has also been termed reactive extrusion and is a well-studied and expanding field (see, e.g., Semsarzadeh *et al.*[165]).

For optimal results control of trace water in thermoplastic PUs prior to any melt processing is required.[166] The effect of water on the melt viscosity of certain TPUs can be dramatic: at high concentrations; foaming and thermal–hydrolytic degradation can occur. With trace amounts of moisture melt viscosities can actually be lower than for bone-dry polymer. Over drying can increase melt viscosity apparently by promoting allophonate cross-link (re)formation and/or by reducing the plasticizing effect of water. The effect of increased melt viscosity can be measured in, amperage draw on the extrusion equipment, and pressure drop across screen packs.

Drying is often done using dehumidifying hopper dryers in which air passes through one of two dessicant beds before entering the bin or hopper holding the polymer. As one bed is being used the other is regenerated with heat and the two are switched frequently. A dew point meter may be fitted to the hopper outlet to measure the approximate extent of drying via the moisture content of the exiting air stream.

Drying of TPUs can produce unwanted side effects so over drying is to be avoided to prevent yellowing of aromatic TPUs and the increased melt viscosity (decreased melt flow index) mentioned above. In all thermoplastic processing of thermoplastic polyurethane, attention to trace water levels and thermal history is advisable.

Despite the considerations unique to polyurethane chemistry, TPUs may be processed by virtually all thermoplastic processing methods used in the creation of semiconfigured like film and tubing, in the postconversion shaping of semiconfigured goods, and in the assembly of components into complete devices. Methods include rotational casting, thermoforming, vacuum forming, heat sealing, ultrasonic and RF welding, laser ablation, die cutting, and machining. Processors familiar with thermoplastic polyurethanes should be used whenever possible.

1.125.7.3. Other Fabrication Methods

In a typical reactive fabrication process, the use of solvents is unnecessary and the reacting liquid prepolymer plus chain extender and/or cross-linker is delivered to a mold before it solidifies. This can also be done on a batch or semicontinuous scale in which the reactants are hand mixed and the reaction

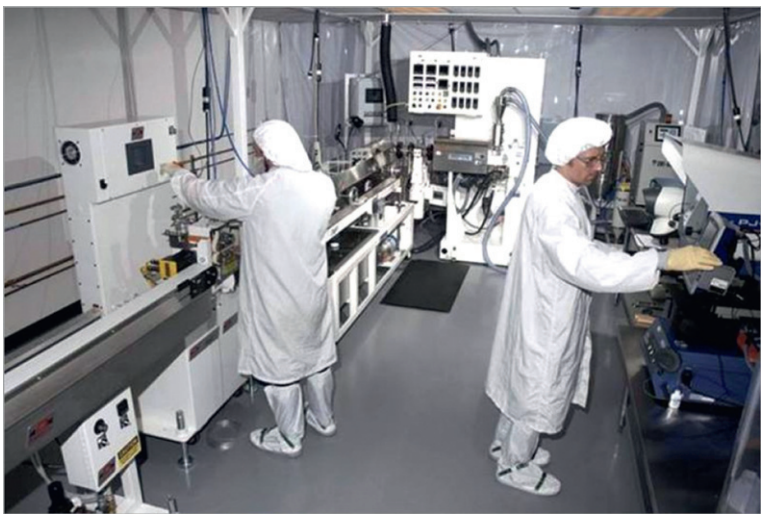

Figure 30 Clean room thermoplastic tubing extrusion line. The extruder is located at the rear at right angles to a metering pump, die, water bath, tractor-cutter and collection equipment. Predried polyurethane pellets are fed to the hopper of the extruder and are melted and conveyed by a screw within the heated extruder barrel. The homogeneous molten polymer emerges from the die inflated by air and enters a water bath. The chilled tubing is cut to size and collected.

mixture is poured or injected into a mold before it solidifies (also known as RIM). With slow reacting, hand cast systems the operator may outgas the mixture under vacuum to eliminate voids in the molded part. Reaction of the degassed liquid produces solidification in the mold. One and two-component reactive urethane systems can be useful in device prototyping or potting electrical components. They are generally referred to as '100%-solids' processes. By adjusting the stoichiometry and including water and a stabilizing surfactant in the reaction mixture CO_2 can be generated during solidification resulting in a foamed product. Additional post-foaming processing can convert closed-cell foams to open cell, so-called reticulated structures that may be useful as tissue scaffolds, filters and wound dressings.

Waterborne dispersions, mentioned previously, depend on polymer (or added surfactant) hydrophilic/lipophilic balance and its effect on the stability of the emulsion. Often the difference in reaction rates of the water–isocyanate and water–amine reactions are used to advantage in the synthesis of waterborne polyurethanes. One attractive feature is the potential to eliminate solvents that may attack substrates being *coated*, as waterbornes are seldom used to make thick monolithic components. Potential applications include multilayer sensor membranes.

1.125.8. Sterilization of Segmented and Block Copolymer PUs and PUUs

Terminal sterilization is routinely applied to virtually all implantable and extracorporeal devices made from polyurethanes, but it is not without consequences. The sterilization method chosen and the process conditions used can have a significant influence on the properties of the final device. If subjected to repeated sterilization cycles the effect on the polymer may be cumulative. Subtle, barely measurable changes may become more pronounced after multiple exposures to the same sterilization process/conditions. In rare cases the resulting change may improve certain properties: increasing cross-linking density via radiation sterilization may be useful in some applications. In others, creation of free radicals and chain scission can lead to immediate molecular weight reduction, increased extractables, and possible oxidative instabilities later. The ability of a sterilization method to induce changes in a specific material depends on process conditions, the specific polymer composition, the presence of added stabilizers, the packaging gas, and the number of cycles to which the polymer is exposed. Commonly used aromatic block and segmented biomedical polyurethanes sterilized by exposure to ionizing radiation will often appear virtually unchanged after a single cycle, but will discolor or embrittle slightly after repeated cycles, resulting in increased tensile strength and somewhat reduced elongation at break. This appears to be the result of cross-linking, although the remaining soluble phase may show a *reduction* in GPC-molecular weight and narrowing of the molecular weight distribution.

In general, sterilization by ethylene oxide and low dose, single cycle gamma radiation are the least problematic and most often used. Autoclaving is to be avoided. D*evices* that include polyurethane components can be exposed to multiple sterilization cycles to exaggerate and elucidate the effect on the polymer, and then be subjected to functional and biocompatibility testing after a more typical dose history, which is usually assumed to include at least one resterilization.

The effectiveness of sterilization techniques has been determined by a number of investigators.[167,168] In general, attention was given to perceived and measurable side reactions originating from the variety of sterilization methods. Hirata *et al.*[169] looked at the relationship between urethane components on polymer characteristics and formation of by-products such as MDA (*vida infra*). In sterilizing commercially-available dialyzers fabricated using different combinations of isocyanate and polyol, they confirmed earlier reports showing that the molecular weight of polyol (castor oil polyols were used in this study) influenced the production of MDA treated with either gamma or EtO sterilization regiments.

A number of studies have looked at changes in the physical and chemical properties before and after sterilization. For example, Abraham *et al.*[170] looked at changes in the physical and mechanical behavior induced by gamma irradiation or ethylene oxide sterilization in medical-grade segmented polyurethanes BioSpan® (a segmented poly(ether urethane urea) derived from a linear block copolymer of 4,4*-diphenylmethane diisocyanate (MDI) extended with a mixture of ethylene diamine (ED) and 1,3-cyclohexanediamine, and poly (tetramethylene oxide) glycol (PTMO), and the aliphatic ether-free polyurethane Chronoflex (a polyurethane-polycarbonate of 4,4*-dicyclohexylmethane diisocyanate (HMDI) chain extended with 1,4-butane-diol (BD) and polycarbonate-diol). Sterilized BioSpan® samples showed a decrease in the soft-segment glass transition temperature and an increase in the soft-segment crystallization heat along the quenching process. Sterilized Chronoflex materials showed the opposite behavior. Hysteresis and residual strain percent increased after sterilization and with irradiation dose and strain level. Surface analysis performed by scanning electron microscopy showed magnification of original surface defects after sterilization.

Correlations between the chemical and physical compositions of a silicone and a polyurethane and beta irradiation, ethylene oxide sterilization and steam sterilization were evaluated on polymer samples implanted in rats for 10 and 90 days.[171] Differences in the biological responses were small and independent of the sterilization method. After 10 days of implantation, the capsule thickness and the amounts of cell material adhering at the surfaces were different, and it appears that the silicone rubber induces more tissue response than the polyurethanes. The differences in the early tissue response evened out after 90 days implantation time and a steady-state situation evolved, which was found to be similar for the silicone and the polyurethane.

1.125.8.1. Ethylene Oxide

The use of ethylene oxide (EO) for sterilizing medical devices has been recently reviewed.[172] This review included EO mechanism of action and toxicity and offered a critical analysis on how it is possible to use EO sterilization for medical devices, emphasizing cycle design and validation. EO diffusion in different substrates (taking into account different environmental conditions both for sterilization and aeration), was also considered. Of the techniques that can be considered, EO

sterilization produces the least amount of MDA and other compounds. There have been studies concluding that risk posed by the amounts of MDA extracted were not significant[173] however, and residual EO gas may itself be more problematic.

1.125.8.2. Radiation

Radiation effectively interacts with biological systems in a number of ways, and only small amounts are generally required to affect sterility. The primary goal in achieving sterility should not interfere with the material properties, as is often the case. Cross-linking and oxidation due to the creation and persistence of free radicals due to radiation is/ can be problematic, but can be addressed – and in some cases used to an advantage – if cross-linking or some other property that improves device design is achieved through the radiation.

1.125.8.2.1. Gamma irradiation

The change in molecular weight, tensile strength, absorbance, and residual amount of radicals as a result of GI has been reported on Pellethane-type materials by Shintani *et al.*[174]). They observed no significant difference in molecular weight; however, the polymer chain extended with 1,4-butanediol (BU) showed degradation while linear chain extended PU showed mainly cross-linking. A linear relationship between the irradiation dose and the residual radical amount was found, but the amount of residual radical on the characteristics of the material was not significant. Elution of PU oligomers was confirmed from the GPC pattern of methanol extracts. Methanol extract at an early stage is more toxic due to abundant elution of lower molecular weight compound. Cytotoxicity of a 25 kGy sterilized polyurethane film tested for *in vitro* interaction of fibroblast cells in a culture medium containing serum samples showed no signs of cell toxicity when evaluated in comparison with control groups.[175]

Zhang *et al.*[176]) compared tensile dynamic mechanical properties and the tensile short-term static creep of five medical-grade gamma-sterilized polyurethane elastomers: (Elast-Eon E2A from AorTech, Pellethane 2363 80A from Dow Chemical, Bionate 80A UR, Bionate 90A S and Carbosil 20 90A – all from Polymer Technology Group). Results showed that (1) both the storage moduli and the damping (tan delta) of the five PU increase with the frequency; (2) gamma sterilization increases the storage moduli and decreases the creep-strain of the five PU; (3) among the five PU samples, Elast-Eon E2A has the highest storage modulus, and the lowest creep-strain under a load of 0.1 MPa; and (4) the T_g of the five PU can be determined by the peak temperature of the loss modulus curve.

Haugen *et al*[177]07) found no differences in attenuated total reflectance Fourier transform infrared spectroscopy (ATR-FTIR) analysis of thermoplastic polyether-urethane (TPU) when comparing steam with different gamma-radiation sterilization methods. The molecular weight (M_w) had a net increase by gamma-sterilization and the samples that were irradiated also had an increase in polydispersity index in comparison, which indicate branching. Liquid chromatography/mass spectroscopy (LC/MS) analysis showed that there was a correlation between the concentration of the breakdown product, methyl dianiline, and cytotoxicity. The concentration of this compound was found to be four times higher in the steam-sterilized sample compared with that of the polymer sample that was gamma-sterilized. The cytotoxicity of TPU was found to decrease with higher radiation doses, and was significantly higher for the steam-sterilized samples.

Citing hydrolytic instability of poly(ether)urethanes [sic] versus the stability but insufficient mechanical properties of polysiloxanes, Briganti, like others before him,[178] sought to combine these materials in the form of poly(ether)urethane-PDMS grafts for use as microfibrillar vascular grafts and porous membranes. In his study, he optimized 25 kGy of GI on these materials and found no significant changes in physical–chemical and mechanical properties of the material. Where results previously obtained with cell cultures showed material preparation and manufacturing procedures not introducing any toxicity in the products at each PDMS concentration investigated[179]; cytotoxicity evaluations performed on L929 fibroblasts showed no signs of cytotoxicity after sterilization.

Hsu *et al.*[180]6) fabricated small diameter polyurethane (Pellethane 2363-80A) vascular grafts modified by epoxy-cross-linked gelatin and an RGD-containing protein to facilitate the endothelial cell seeding on the surface. After GI, the contact angle of the irradiated PU dropped a little and the environmental stress cracking resistance (ESCR) spectra revealed oxygen bonding. There were observed increases in extractables and molecular weight distribution with only slight decreases in mechanical properties. They concluded that freeze-drying followed by GI at 2.5 Mrad was the proper way to process and store vascular grafts made from these materials.

1.125.8.2.2. Electron beam

All[181] looked at the electrical and structural properties of electron-beam irradiated 'polyurethane' films in the range 90–300 kGy. He reported an increase in electrical conductivity due to degradation products with large variations in spectral composition. Irradiation doses in the range 200–300 kGy caused branching, which reduced crystallinity and created lattice defects with significant changes in melting behavior.

Thin films of Tecoflex® (an *aliphatic* polyether PU) prepared by Guignot *et al.*[182] were irradiated under a dose-rate of 5 MGy h^{-1}, with doses varying from 25 to 1000 kGy under O_2. Chain scission and cross-linking were both found to increase with the irradiation dose. FTIR spectra showed the appearance of oxidation groups (formates, esters and carboxylic acids) with scission of chains in soft (SS) and hard (HS) segments as noted by decrease of both urethane and aliphatic ether absorbance. Coupled TG-FTIR analysis indicated the degraded molecules consisted of (i) oxidized SS fragments, (ii) long SS slightly oxidized and (iii) HS accompanied by SS.

1.125.8.3. Autoclaving

Sterilizing polyurethane using pressurized steam (autoclaving) is typically *not* recommended as many types of polyurethane can degrade under these combined thermal/hydrolytic conditions. Autoclave sterilization elutes more hydrophilic compounds when compared to sterilization using γ-ray irradiation and ethylene oxide gas (EOG). This has been shown to be especially significant for PUs produced from smaller-molecular-weight polyols.[173] Softer aliphatic polyurethanes soften and distort at the typical autoclaving temperature of

121 °C. Aromatic analogues are thermoformed in autclaves in the manufacture of some cardiac assist devices, for example, to produce precise dimensions for interfacing with metal components.

Recently, Terheyden *et al.*[183] compared sterilizing methods on dental ligatures made from polyurethane, silicone and natural rubber using an autoclave, ethylene oxide, irradiation, plasma sterilization, povidone-iodine or 70% isopropyl alcohol (for 24 h). In these tests polyurethane was most resistant to mechanical fatigue but became sticky after autoclaving. Ethylene oxide, irradiation, and plasma were also found to be better than autoclaving and disinfecting solutions. In this study, polyurethane sterilized with ethylene oxide was the material of choice.

1.125.8.4. Other Methods

A number of alternatives to the above sterilization methods have been developed, especially in light of such infectious agents as prions and viruses, which may require more rigorous treatment than steam or radiation. Surface ionization methods such as atmospheric pressure cold plasmas can be generated by various methods including dielectric barrier discharge (DBD), resistive barrier discharge (RBD), and atmospheric pressure plasma jet (APPJ).[184]

Concerned with the reuse electrophysiology catheters, Lerouge *et al.*[185,186]) compared plasma-based and ethylene oxide (EO) sterilization methods in terms of material damage and effectiveness. Using two different plasma-generating devices, they described oxidation from plasma as being limited to the near-surface layers whereas EO-induced slight but deeper alkylation. Hydrolytic stability of catheters was slightly changed by plasma-based sterilization, and they noted a small increase in released oligomers. The two different plasma-generating devices they tested had different impacts on catheters, such as the degradation of an additive and a clear difference in coloration.

1.125.9. The Issue of MDA Formation in Aromatic Polyurethanes

There has been some concern over methylene dianiline (4,4′-diaminodiphenylmethane, also 4,4′-methylenedianiline) or MDA which can possibly be found in polyurethanes made with methylene diisocyanate as a hard segment component. MDA has structural similarities to benzidine and 4-aminobiphenyl, two known human carcinogens and this may be a reason for concern; however, the carcinogenicity of MDA in humans is not clearly established. Human exposures to MDA have been covered in detail, both in the workplace and otherwise (*vida infra*), but, as we shall see, no increase in cancer or tumors have been reported.[187]

The EPA has not classified MDA for carcinogenicity although statistically significant increases in the incidence of several types of tumors, including liver and thyroid tumors have been reported in *lower* animals (rats and mice exposed to large amounts of the *dihydrochloride salt of MDA* in their drinking water). The International Agency for Research on Cancer (IARC) has classified MDA as a Group 2B, possible human carcinogen.[188]

1.125.9.1. Extreme Conditions Required to Produce MDA

In early studies, a number of authors attempted to extract or create MDA-production conditions in polyurethanes, possibly as a way of advancing polyurethanes containing nonaromatic hard-segment components.[189] Notably, after prolonged and extensive digestion with chloestrolase (enzymes) and using radio-labeled compounds to effectively enhance detection, MDA was characterized as one of the isolates from polymer decomposition.

Mazzu and Smith[190] were not able to find MDA in the aqueous extracts of polyurethane except in the case of prolonged steam autoclaving. The appearance of 3–5 ppb MDA in extracts under autoclaving conditions was attributed to hydrolysis of the polymer. They concluded that the stability of the polyurethanes under most conditions renders these materials useful in biomedical applications.

Early studies on δ-irradiation-sterilized thermoset 'potting' polyurethane materials extracted with methanol or serum led to the detection of MDA around a few parts per million in the original sample. The production of MDA increased with increasing irradiation doses and was related to the irradiation dose by a second-order equation. Interestingly, in these studies MDA was not found in autoclave sterilization materials,[191,192] and no traces of MDA could be detected in the aqueous extracts from methylene diphenyl diisocyanate (MDI) based hydroxyl-terminated polydimethyl siloxane type polyurethanes.[193]

The long-term (1- and 2-year) adverse tissue response including tumor formation by subcutaneous implantation of poly(ether urethanes) and silicone films into rats was compared by Nakamura *et al.*[194]2). In both implantation periods, the polyether urethanes gave higher incidents of the adverse responses including tumor formation when compared to silicone. No significant molecular-weight-dependent trend was found in a 1-year study; however, significant PU-dose-dependent trends were found in a 2-year study. More important, no detectable amounts of 4,4′-methylenedianiline (MDA) was found in the polyether urethanes and methanol extracts from the PUs were negative in the mutagenicity tests. The conclusion was that no relationship between the tumor formation by the polyether urethane films and the mutagenicities of the chemicals (mainly oligomers) leached from the PUs.

Polycarbonate polyurethanes synthesized with aromatic diisocyanates (MDI) are more (bio)stable than the materials synthesized with aliphatic diisocyanates. Structurally, it has been shown that the MDI molecules shield the polycarbonate segments from hydrolysis via hydrogen bonding at the carbonate sites.[195] MDA is not readily soluble in aqueous systems: it has been demonstrated to be a tremendous challenge to extract MDA for analysis in such environments (e.g., see Shintani[196]).

1.125.9.2. The Need for Aromatic Hard Segments in Biostable PUs and PUUs

In designing biomedical polyurethanes for critical applications the phase separation of the hard and soft segments provides many desirable properties of the resulting polymers. Phase separation is highly dependent on the extent of

hydrogen bonding among hard segments on adjacent polymer chains and, at this time, the properties obtained from aromatic hard segments cannot be duplicated with aliphatic or cycloaliphatic diisocyanates. The increased cohesive energy density provided by high-purity aromatic diisocyanates, and MDI in particular, gives improved chemical and solvent resistance, better flex life, creep resistance, and biostability. For example, without MDI it is very likely that the use of sac and diaphragm-type cardiac assist devices as 'destination devices' would not be possible. Here, as in many other critical device applications, the risk versus benefit analysis clearly favors the use of aromatic polyurethanes in chronic implants.

1.125.9.3. History of the Issue

Business considerations and junk science have influenced the history of MDA and biomedical polyurethanes. MDA in polyurethanes was also well addressed in an early review.[197]

1.125.9.4. The Epping Bakery Incident

In February 1965, 84 residents in the town of Epping, Essex, UK, ingested MDA-contaminated bread as a result of "a bag of flour being taken to the bakery in a van had split and mixed with the dangerous chemical diaminodiphenylmethane".[198] The case was detailed,[199] and extensively followed up at varying intervals throughout subsequent decades.

At the time of the incident, description of the presenting symptoms from ingestion included rigors, limb pains, malaise and obstructive jaundice which in some cases lasted for months. Differential diagnosis included cholelithiasis. Serum bilirubin, serum alkaline phosphatase and serum aspartate transaminase were raised to a varying and generally moderate degree. In a few cases there was blood eosinophilia. Seven patients had liver biopsies. These patients reportedly showed portal inflammation, eosinophil infiltration, cholangitis, cholestasis, and hepatocellular damage at different stages. Fibrosis appeared to be slight. Following the incident, and within 2 years afterward all patients made 'good clinical recoveries'.[200–202]

The incident is a classic example of public exposure to industrial chemicals and as a result has received extensive review. At 24 years follow-up, Hall *et al.*[203]) reported the health status of 68 (81%) of the group. The causes of death were unremarkable: there was one case of carcinoma of the biliary tract, two surviving cases had suffered retinal pathology, four surviving cases had a further episode of jaundice, including food intolerance, gastrointestinal disturbances, fatigue, and visual disturbances.[201,202] At 24 years the conclusions was that although the dose and route of administration in the epidemic differed from occupational exposure, this follow up study showed no evidence of long-term health effects. Thirty-eight-year follow up showed that mortality from all causes was close to expectation among females, and below expectation among males. Additionally, there were no observed deaths from cancer of the liver or from nonmalignant liver disease. The 38-year follow-up found no evidence to suggest that the ingestion of MDA had adversely affected mortality.[204]

Additional reports on MDA exposure, although not as dramatic, have followed similar etiology.[187] Between 1967 and 1976, 10 workers at a plant in Ontario that used MDA as an epoxy hardener developed acute jaundice. The group was followed from the date of exposure through to the end of 1991 looking specifically at cancer incidence. Remarkably, only one pathologically confirmed bladder cancer had developed, which was just above the expected number of cases predicted in the normal population.[205]

In 1997, a group of six techno-party-goers in Hanover Germany were admitted to the hospital with severe colicky abdominal pain and subsequently developed symptoms of hepatotoxicity.[206] They had ingested an alcoholic beverage that had been spiked with a powdery substance they dubbed MDA: they had mistakenly ingested MDA instead of the psychometric 'Ecstasy' drug: methylendioxyamphetamine (MDMA, *N*,α-dimethyl-1,3-benzodioxole-5-ethanamine; CAS 42542-10-9). As a result, clinical symptoms including acute jaundice developed within two days after ingestion. Enzymes indicating cholestasis increased steadily and transaminases remained moderately elevated. Between days 5 and 7, all patients became febrile for 1 day, their body temperatures rising up to 40 °C, thereafter the clinical status of all patients normalized. Laboratory values for enzymes and liver function returned to normal within 6 weeks, except for one patient, whose GGT value remained elevated due to the chronic consumption of alcohol. The long-term prognosis appeared favorable. All patients with 'Epping Jaundice' recovered and there were no further reports of recurring illnesses attributable to the 4,4′-diaminodiphenylmethane intoxication.

Additional cases of accidental and occupational exposure[207–210] can be found in the literature. Recent government publications from the State of California Office of Environmental Health Hazard Assessment (OEHHA) have extensively reviewed the literature on human and animal studies, evaluation and testing done with MDA.[211]

The possible metabolic pathways for metabolic processing of MDA have been proposed by Cocker.[212] The various metabolites included in the reaction scheme are potential candidates for monitoring exposure. Work on metabolic processes is continuing: vascular smooth muscle cells have recently been shown to be capable of converting MDA to *N*-acetyl methylenedianiline (*N*-acetyl-DAPM) and *N*,*N*′-diacetyl methylenedianiline (*N*,*N*′-diacetyl-DAPM).[213]

In addition to MDA, alternative diisocyanates and diamines such as toluene-diamine potentially formed from polyurethanes have been considered.[214] The metabolism of MDA in biological systems has been proposed by Cocker,[212] and is presented as a graphic in **Figure 31**.

1.125.10. Future of Biomedical Polyurethanes and Silicone Polyurethanes

In the immediate future perhaps the biggest growth area for implantable polyurethanes is in orthopedic implants in which polyurethanes and silicone-polyurethanes are used to create so-called compliant bearings for hip, knee, shoulder, spine and finger joint prostheses and resurfacing devices. This trend started in the mid-1990s with the successful use of polycarbonate urethane in a dynamic spinal fixation device, an application that has grown rapidly ever since.

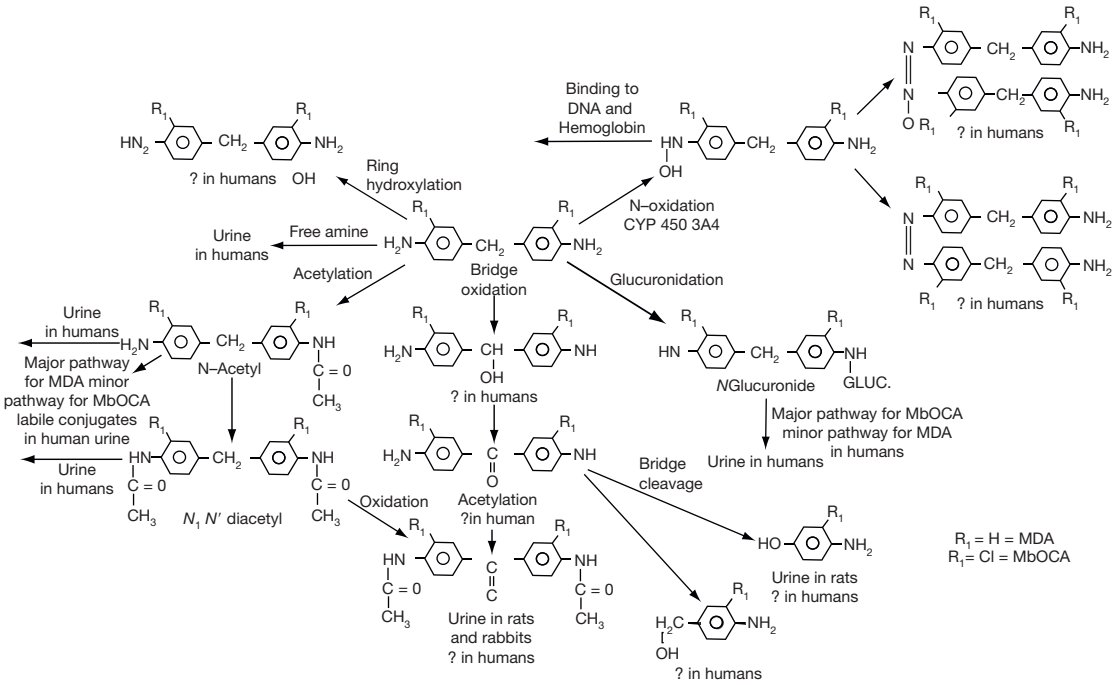

Figure 31 Metabolism of MbOCA or 4,4′-diaminodiphenylmethane in humans. Reproduced from Cocker, J. In *Biological Monitoring of Chemical Exposure in the Workplace*; Lehtinen, S., Ed.; World Health Organization: Geneva, 1996; Vol. 2, Chapter 4, pp 166–189.



Zimmer Dynesys® dynamic spinal stabilization system	Medtronic BRYAN® cervical disc	AxioMed Freedom® lumbar disc	Active Implants TriboFit® hip
• Over 14 years global experience • Over 40 thousand procedures	• 15 000 cases implanted without fracture • 3–6-year explants showed no trend of degradation	• CE Mark received • IDE pivotal study initiated	• CE Mark received • Several hundred implantations

Figure 32 Use of polyurethanes in orthopedic applications (selected examples).

As discussed in this chapter, however, polyurethanes constitute a huge class of polymers that are well suited to continued development of evermore sophisticated biomaterials. The very wide range of surface and bulk properties obtainable with the straightforward synthetic methods discussed here should maintain interest in these materials for many years. Economical, high-volume manufacturing methods, *and* easy fabrication techniques for prototyping make them attractive to device engineers, as does the ease with which custom materials can be prepared for the most materials-intensive applications (Figure 32).

The largely successful 40-year history of certain biostable polyurethanes in critical medical devices and prostheses supports the belief that they can be inherently safe, and unique in their combination of physical–mechanical properties and biostability. Continued improvements in biostability, for example, via novel combinations of polyols and/or new stabilization methods, should increase the useful life of polyurethanes in the body. This is important given the trend of implanting orthopedic implants in younger patients, and the increased prevalence of diabetes requiring sensors and artificial organs, to name just two examples.

The concept of a biomaterials toolkit based on polyurethanes has already proven to increase development efficiency by decoupling bulk and surface properties. The recognition that self assembly of polymer end groups can create the 'same' surfaces as fragile SAM thiols on gold, should allow the translation of research results to practical and stable *structural* materials. The range of surface modifications possible with end groups includes biologically active head groups

useful in diagnostic and therapeutic applications, as well as so-called passive chemistries.

More mundane developments will also increase the utility of polyurethane biomaterials including widening the property map of easily-processed thermoplastics to include materials that can replace soft thermosets like silicone, and hard engineering plastics including PAEK and PEEK. Control of macro- and micro-porosity of both biostable and bioresorbable 'urethanes' should help the development of tissue scaffolds for a number of uses, and composite biomaterials that use polyurethanes together with high-strength fibers can lead to high-performance orthopedic implants.

Considering the range of chemical compositions and physical–mechanical properties possible with polyurethanes, and their straightforward synthesis, and ease of processing, they are the most versatile biomaterials available today. This is likely to continue well into the future.

References

1. Nyilas, E.; Kupski, E. L.; Burnett, P.; Haag, R. M. *J. Biomed. Mater. Res.* **1970**, *4*, 369–432.
2. Nyilas, E. *J. Biomed. Mater. Res.* **1972**, *6*(4), 97–127.
3. Nyilas, E. *J. Biomed. Mater. Res.* **1972**, *6*(4), 97–127.
4. Ward, R. S., Jr.; Nyilas, E. In *Organometallic Polymers*; Carraher, C. E., Ed.; Academic Press: New York, 1978; pp 219–229.
5. Assink, R.; Wilkes, G. L. *Polym. Eng. Sci.* **1977**, *17*(8), 606.
6. Sheth, J. P.; Wilkes, G. L.; Fornof, A. R.; Long, T. E.; Yilgor, I. *Macromolecules* **2005**, *38*(13), 5681–5685.
7. Yilgor, I.; Yilgor, E.; Das, S.; Wilkes, G. L. *J. Polym. Sci. B Polym. Phys.* **2009**, *47*(5), 471–483.
8. Lyman, D. J.; Seare, W., Jr.; Albo, D., Jr.; *et al. Int. J. Polym. Mater.* **1977**, *5*(3), 211–229.
9. Lamba, N. M. K.; Woodhouse, K. A.; Cooper, S. L. *Polyurethanes in Biomedical Applications*. CRC Press/Taylor and Francis Group: Boca Raton, FL, 1997; p 288.
10. Zdrahala, R. J.; Zdrahala, I. J. *J. Biomater. Appl.* **1999**, *14*(1), 67–90.
11. Bergeron, M., Lévesque, S., Guidoin, R., Eds.; *Biomedical Applications of Polyurethanes*; Landes Bioscience: Georgetown, TX, 2001; p 272; ISBN 978-1-58706-023-6.
12. Planck, H. In *Proceedings of the 2nd International Conference on Polyurethanes in Biomedical Engineering*, Fellbach/Stuttgart, 18–19 June, 1986; ISBN 0444423982, 9780444423986.
13. Vermette, P.; Griesser, H. J.; Laroche, G.; Guidoin, R. *Biomedical Applications of Polyurethanes*. Landes Bioscience Georgetown: TX, 2001; 273 p, ISBN: 1-58706-023-X.
14. Ward, R. U.S. Pat. 4,675,361, 1983.
15. Chang, M.-C.; Chen, S.-A. *J. Polym. Sci. A Polym. Chem.* **1987**, *25*, 2543–2559.
16. Saunders, J. H.; Dobson, F. In *Non-Radical Polymerisation*; Bamford, C. H., Tipper, C. F. H., Eds.; *Comprehensive Chemical Kinetics*; Elsevier Science, 1976; Vol. 15, pp 473–582.
17. Gilding, D. K.; Taylor, J. A. U.S. Pat. 4,062,834, 1977.
18. Jewrajka, S. K.; Yilgor, E.; Yilgor, I.; Kennedy, J. P. *J. Polym. Sci. A Polym. Chem.* **2009**, *47*(1), 38–48.
19. Jewrajka, S. K.; Kang, J.; Erdodi, G.; Kennedy, J. P.; Yilgor, E.; Yilgor, I. *J. Polym. Sci. A Polym. Chem.* **2009**, *47*(11), 2787–2797.
20. Yilgor, E.; Atilla, G. E.; Ekin, A.; Kurt, P.; Yilgor, I. *Polymer* **2003**, *44*(26), 7787–7793.
21. Cray, S. In *Inorganic Polymers: Silicones in Industrial Applications*; DeJaeger, R., Ed.; Nova Science: Hauppauge, NY, 2007; 100 p, ISBN: 1-60021-656-0.
22. Jones, L. A.; Schmidt, R. G. In *Technology of Pressure-Sensitive Adhesives and Products (Handbook of Pressure-Sensitive Adhesives and Products)*; Benedek, I., Feldstein, M. M., Eds.; CRC Press/Taylor and Francis: Boca Raton, FL, 2009; p 568 ISBN: 978-1-4200-5939-7.
23. Ulrich, H. In *Encyclopedia of Polymer Science and Technology*; Wiley: New York, 2001; Vol. 4, pp 26–72; doi:10.1002/0471440264.
24. Oertel, G. *Polyurethane Handbook*. Macmillan: New York, 1985; ISBN 0-02-948920-2.
25. Woods, G. *The ICI Polyurethanes Book*. Wiley: New York, 1990; ISBN 0-471-92658-2.
26. Scycher, M. *Scycher's Handbook of Polyurethane*. CRC Press: Boca Raton, FL, 1999; ISBN-10: 0-8493-0602-7; ISBN-13: 978-0-8493-0602-0.
27. Petrovic, Z. S.; Ferguson, J. *Prog. Polym. Sci.* **1991**, *16*(5), 695–836.
28. Król, P. *Prog. Mater. Sci.* **2007**, *52*(6), 915–1015.
29. Chen, K.-S.; Yu, T. L.; Chen, Y.-S.; Lin, T.-L.; Liu, W.-J. *J. Polym. Res.* **2001**, *8*(2), 99–109.
30. Ming, Z.; Lina, Z. *J. Appl. Polym. Sci.* **2006**, *100*(1), 708–714.
31. Stokes, K.; McVenes, R.; Anderson, J. M. *J. Biomater. Appl.* **1995**, *9*(4), 321–354.
32. Sonnenschein, M. F.; Cox, J. M.; Van der Wal, H. R.; Wendt, B. L. U.S. Pat. 20,090,149,622, 2009.
33. Mónic, C. B.; Guiomar, A. J.; Carlo, A. G.; Bairos, V. A.; de Pinho, M. N.; Gil, M. H. *J. Biomed. Mater. Res. A* **2010**, *93*(3), 954–964.
34. Pachulski, R.; Zasadil, M.; Adkins, D.; Hanif, B. *Europace* **2002**, *4*, 45–47 and references therein.
35. Gunatillake, P. A.; Meijs, G. F.; McCarthy, S. J.; Adhikari, R.; Sherriff, N. *J. Appl. Polym. Sci.* **1998**, *69*(8), 1621–1633.
36. Martin, D. J.; Meijs, G. F.; Renwick, G. M.; Mccarthy, S. J.; Gunatillake, P. A. *J. Appl. Polym. Sci.* **1996**, *62*(9), 1377–1386.
37. Chang, Y.-J. P.; Wilkes, G. L. *J. Polym. Sci. Polym. Phys. Ed.* **1975**, *13*(3), 455–476.
38. Miller, J. A.; Lin, S. B.; Hwang, K. K. S.; Wu, K. S.; Gibson, P. E.; Cooper, S. L. *Macromolecules* **1985**, *18*(1), 32–44.
39. Harris, R. F. *J. Appl. Polym. Sci.* **1989**, *38*(3), 463–476.
40. Rokicki, G.; Kowalczyk, T. *Polymer* **2000**, *41*(26), 9013–9031.
41. Ward, B.; Anderson, J.; Ebert, M.; McVenes, R.; Stokes, K. *J. Biomed. Mater. Res. A* **2006**, *77*(2), 380–389.
42. Ward, R.; Anderson, J.; McVenes, R.; Stokes, K. *J. Biomed. Mater. Res. A* **2006**, *77*(3), 580–589.
43. Ward, B.; McCrea, K.; Tian, Y.; *et al.* Self assembly of end group modifications in polyurethanes. In *BioInterface Conference*, Excellence in Surface Science Award, San Mateo, CA, 4–6 Dec, 2006.
44. Eceiza, A.; Martin, M. D.; de la Caba, K.; *et al. Polym. Eng. Sci.* **2008**, *48*(2), 297–306.
45. Harris, R. F.; Joseph, M. D.; Davidson, C.; Deporter, C. D.; Dais, V. A. *J. Appl. Polym. Sci.* **1990**, *411*(3–4), 509–525.
46. Aneja, A.; Wilkes, G. L. *J. Appl. Polym. Sci.* **2002**, *85*, 2956–2967.
47. Renault, B.; Tassaing, T.; Cloutet, E.; Cramail, H. *J. Polym. Sci. A Polym. Chem.* **2007**, *45*(23), 5649–5661.
48. Clemitson, I. *Castable Polyurethane Elastomers*. CRC Press/Taylor and Francis: Boca Raton, FL, 2008; 272 p.
49. Howarth, G.; Manock, H. *Surf. Coat. Int. B Coat. Trans.* **1997**, *80*(7), 324–328.
50. Lee, D.-K.; Tsai, H.-B.; Tsai, R.-S. *Polym. Eng. Sci.* **2006**, *46*(5), 588–593.
51. Wang, W.; Guo, Y.; Otaigbe, J. U. *Polymer* **2008**, *49*(20), 4393–4398.
52. Darby, R. T.; Kaplan, A. M. *Appl. Microbiol.* **1968**, *16*(6), 900–905.
53. Stokes, K. In *Clinical Evaluation of Medical Devices, Principles and Case Studies*, 2nd ed.; Becker, K. M., Whyte, J. J., Eds.; Humana Press: Totowa, NJ, 2006; pp 285–304 Chapter 17.
54. Wiggins, M. J.; Wilkoff, B.; Anderson, J. M.; Hiltner, A. *J. Biomed. Mater. Res. B Appl. Biomater.* **2001**, *58*, 302–307.
55. Oprea, S. *J. Elastomers Plast.* **2010**, *42*(2), 163–179.
56. Rodriguez, A.; Meyerson, H.; Anderson, J. M. *J. Biomed. Mater. Res. A* **2009**, *89*(1), 152–159.
57. Rodriguez, A.; MacEwan, S. R.; Meyerson, H.; Kirk, J. T.; Anderson, J. M. *J. Biomed. Mater. Res. A* **2009**, *90*(1), 106–113.
58. Patel, J. D.; Ebert, M.; Ward, R.; Anderson, J. M. *J. Biomed. Mater. Res. A* **2007**, *80*(3), 742–751.
59. Hsu, S.-H.; Tseng, H.-J. *J. Biomater. Appl.* **2004**, *19*(2), 135–146.
60. Sanchez-Adsuar, M. S.; Martín-Martínez, J. M. *J. Adhes. Sci. Technol.* **1997**, *11*(8), 1077–1087.
61. Bae, J. Y.; Chung, D. J.; An, J. H.; Shin, D. H. *J. Mater. Sci.* **1999**, *34*(11), 2523–2527.
62. Zhang, C.; Zhang, N.; Wen, X. *J. Biomed. Mater. Res. B Appl. Biomater.* **2006**, *79*(2), 335–344.
63. Adhikarir, R.; Gunatillake, P. A.; McCarthy, S. J.; Meijs, G. F. *J. Appl. Polym. Sci.* **1999**, *74*(12), 2979–2989.
64. Yoon, S. C.; Ratner, B. D. *Macromolecules* **1986**, *19*(4), 1068–1079.
65. Yoon, S. C.; Sung, Y. K.; Ratner, B. D. *Macromolecules* **1990**, *23*(20), 4351–4356.
66. Nissen, D.; Markovs, R. A. *J. Elastomers Plast.* **1983**, *15*(2), 96–112.
67. Caraculacu, G.; Caraculacu, A.; Scoranu, E.; Brum, M.; Mandric, G. *Angew. Makromol. Chem.* **1983**, *116*(1), 1–11.

68. Kob, N.; Novak, B. In C12™: A new unique building block for polyurethanes. Poster presentation at Polyurethanes Technical Conference, 2003.
69. Tanzi, C. M. U.S. Pat. 6,143,893, 2000.
70. Posey, M. L.; Hillman, K. M.; Klein, H. P. New secondary amine chain extenders for aliphatic polyurea materials. Prepared for presentation at The Polyurea Development Association 2003 Annual Conference, Reno, NV, 2003 12p.
71. Perez, A.; Hillman, K. M.; House, D. W.; Ilijevski, D.; Scott, R. V. Secondary aliphatic diamine chain extenders in aliphatic polyurea spray applications. In *UTECH 2000: International Polyurethane Industry Conference*, The Hague, 28–30 March 2000, Rapra Technology: Shawbury, ROYAUME-UNI, 2000; pp P8.1–P8.10.
72. Semsarzadeh, M. A.; Sadeghi, M.; Barikani, M. *Iran. Polym. J.* **2008**, *17*(6), 431–440.
73. Guan, J.; Sacks, M. S.; Beckman, E. J.; Wagner, W. R. *J. Biomed. Mater. Res. A* **2002**, *61*(3), 493–503.
74. Ionescu, M. *Chemistry and Technology of Polyols for Polyurethanes*. Rapra Technology: England, 2005; p 586, ISBN 1-85957-2.
75. Jones, R. L. In *Advances in Tissue Engineering 18th Annual Short Course*, Rice University, Houston, TX, 11–14 Aug, 2010.
76. Gunatillake, P. A.; Martin, D. J.; Meijs, G. F.; McCarthy, S. J.; Adhikari, R. *Aust. J. Chem.* **2003**, *56*(6), 545–557.
77. Brown, D. W.; Lowry, R. E.; Smith, L. E. *Macromolecules* **1980**, *13*, 248–252.
78. Ferguson, J.; Ahmad, N. *Eur. Polym. J.* **1977**, *13*(11), 859–864.
79. Ibrahim *et al*., 2009.
80. Smith *et al*. 2003.
81. Quigley, F. P.; Buggy, M.; Birkinshaw, C. *J. Proc. Inst. Mech. Eng. H J. Eng. Med.* **2002**, *216*(1), 77–83.
82. Pierce *et al*., 2006.
83. Ming, J.; Ping, H. *J. Appl. Polym. Sci.* **2006**, *101*(3), 1273–1282.
84. Kim, Ha.-C.; El-Naggar, A. M.; Wilkes, G. L.; Yoo, Y.; McGrath, J. E. In *Radiation Curing of Polymeric Materials*; Hoyle, C. E., Kinstle, J. F., Eds.; ACS Symposium Series 417; American Chemical Society: Washington, DC, 1990; pp 474–497.
85. Gorna, K.; Gogolewski, S. *J. Biomed. Mater. Res. A* **2006**, *79*(1), 128–138.
86. Gogolewski, S. *Eur. Cells Mater.* **2004**, *7*(Suppl. 1), 32.
87. Guan, J.; Fujimoto, K. L.; Sacks, M. S.; Wagner, W. R. *Biomaterials* **2005**, *26*(18), 3961–3971.
88. Hashimoto, K.; Wibullcksanakul, S.; Okada, M. *J. Polym. Sci. A Polym. Chem.* **1995**, *33*(9), 1495–1503.
89. Zdrahala, R. J.; Critchfield, F. E. U.S. Pat. 4,190,711, 1980.
90. Lan, P. N.; Corneillie, S.; Schacht, E.; Davies, M.; Shard, A. *Biomaterials* **1996**, *17*(23), 2273–2280.
91. Grasel, T. G.; Lee, D. C.; Okkema, A. Z.; Slowinski, T. J.; Cooper, S. L. *Biomaterials* **1988**, *9*(5), 383–392.
92. Gurgiolo, A. E. *Polym. Rev.* **1966**, *1*(1), 39–190.
93. Shan-hui, H.; Yu-Chih, K.; Zu-Chang, L. *Macromol. Biosci.* **2004**, *4*(4), 464–470.
94. Pawlowski, P.; Rokicki, G. *Polymer* **2004**, *45*(10), 3125–3137.
95. Eceiza, A.; Larrañaga, M.; de la Caba, K.; *et al*. *J. Appl. Polym. Sci.* **2008**, *108*(5), 3092–3103.
96. Pudleiner, H.; Hoppe, H.-g.; Onig, K. K. U.S. Pat. 5,621,065, 1997.
97. Eceiza, A.; de la Caba, K.; Gascón, V.; Corcuera, M. A.; Mondragon, I. *Eur. Polym. J.* **2001**, *37*(8), 1685–1693.
98. Ahn, T. O.; Jung, S.-U.; Jeong, H. M.; Lee, S. W. *J. Appl. Polym. Sci.* **1994**, *51*(1), 43–49.
99. Hsu, S.-H.; Lin, Z.-C. *Colloids Surf., B* **2004**, *36*(1), 1–12.
100. Ward, R. S.; White, K. A.; Wolcott, C. A.; *et al*. *ASAIO J.* **1993**, *39*(3).
101. Ward, R. S.; White, K. A. *Chem. Tech.* **1991**, *21*(11), 670–676.
102. Ward, R. S.; White, K. A.; Gill, R. S.; Wolcott, C. A. In *The 21st Meeting of the Society for Biomaterials*, San Francisco, CA, 18–22 March, 1995.
103. Illinger, J. L. Interactions of water with hydrophilic polyether polyurethanes. Army Materials and Mechanics Research Center Report, Jun 1982; p 132.
104. Park, H. B.; Kim, C. K.; Lee, Y. M. *J. Membr. Sci.* **2002**, *204*(1–2), 257–269.
105. Lim, F.; Yang, C. Z.; Cooper, S. L. *Biomaterials* **1994**, *15*(6), 408–416.
106. Okkema, A. Z.; Fabrizius, D. J.; Grasel, T. G.; Cooper, S. L.; Zdrahala, R. J. *Biomaterials* **1989**, *10*(1), 23–32.
107. Wiggins, M. J.; MacEwan, M.; Anderson, J. M.; Hiltner, A. *J. Biomed. Mater. Res. A* **2004**, *68*(4), 668–683.
108. Ward, R.; Anderson, J.; Ebert, M.; McVenes, R.; Stokes, K. *J. Biomed. Mater. Res.* **2005**, *77*(2), 380–389.
109. Ward, R.; Tian, Y.; White, K.; *et al*. In *Society for Biomaterials 30th Annual Meeting*, Memphis, TN, 27–30 April, 2005.
110. Ward, R. S.; White, K. A.; Yilgor, I. In *Transactions of The Third World Congress of Biomaterials*, Kyoto, Japan, 21–25 April, 1988.
111. Choi, T.; Weksler, J.; Padsalgikar, A.; Runt, J. *Polymer* **2009**, *50*(10), 2320–2327.
112. Jones, R. G.; Andō, W.; Chojnowski, J. *Silicon-Containing Polymers: The Science and Technology of Their Synthesis*. Kluwer Academic: Norwell, MA, 2000; 768 pgs. ISBN: 0-412-83110-4.
113. Yilgör, İ.; McGrath, J. In *Polysiloxane Copolymers/Anionic Polymerization*; Springer: Berlin, 1988; Vol. 86, pp 1–86 ISBN 978-3-540-18506-2, ISSN 0065-3195 (Print) 1436-5030 (Online).
114. Ward, R. S. *Med. Device Diagn. Ind. Mag.* **2000**, *22*(4), 68–77.
115. Ward, 1978.
116. Ward, 2000.
117. Ward, 2000.
118. Ward, R. Biomedical polymers with controlled surface properties: synthesis, characterization and device fabrication. In *2006 PSE Symposium Polymers in Biomedicine & Pharmaceuticals*, Amherst, MA, 3–4 Oct, 2006.
119. Schubert, M. A.; Wiggins, M. J.; Defife, K. M.; Hiltner, A.; Anderson, J. M. *J. Biomed. Mater. Res.* **1996**, *32*, 493–504.
120. Ward, 2008.
121. Ebert, M.; Stokes, K.; McVenes, R.; Ward, R. S.; Anderson, J. M. In *The 28th Annual Meeting of the Society for Biomaterials*, 24–27 April, Tampa, FL., 2002.
122. Jones, J. A.; Soranno, D. E.; Collier, T. O.; *et al*. In *The 28th Annual Meeting of the Society for Biomaterials*, 24–27 April, Tampa, FL, 2002.
123. Patel, J. D.; Ebert, M.; Ward, R. S.; Anderson, J. M. *Effects of SME™ surface chemistry and shear stress on bacterial and neutrophil adhesion*. In *The 28th Annual Meeting of the Society for Biomaterials*, 24–27 April, Tampa, FL., 2002.
124. Flick, E. W. *Plastics Additives: An Industrial Guide*. Noyes Publication: Park Ridge, NJ, 1993; 1098 p, ISBN 0-8155-1313-5.
125. Capocci, G. *Plastics Compounding* **1987**, 13–14 16, 18, 25–27.
126. Step, E. N.; Turro, N. J.; Gande, M. E.; Klemchuk, P. P. *Macromolecules* **1994**, *27*(9), 2529–2539.
127. Affrossman, S.; Barbenel, J. C.; Forbes, C. D.; *et al*. *Clin. Mater.* **1991**, *8*(1–2), 25–31.
128. Holland, S. J.; Jolly, A. M.; Yasin, M.; Tighe, B. J. *Biomaterials* **1987**, *8*, 289–295.
129. Howard, G. T. *Int. Biodeterior. Biodegradation* **2002**, *49*(4), 245–252.
130. Santerre, J. P.; Woodhouse, K.; Laroche, G.; Labow, R. S. *Biomaterials* **2005**, *26*(35), 7457–7470.
131. Guelcher, S. A. *Tissue Eng. B Rev.* **2008**, *14*(1), 3–17.
132. Kennedy, J. P.; Kwon, Y. Polyisobutylenes and process for making the same. WO 2008 066914 A1, International Filing Date 30 Nov, 2007.
133. Kurian, P.; Zschoche, S.; Kennedy, J. P. *J. Polym. Sci. A Polym. Chem.* **2000**, *38*, 3200–3209.
134. Erdodi, G.; Kang, J.; Kennedy, J. P. *J. Polym. Sci. A Polym. Chem.* **2010**, *48*(11), 2361–2371.
135. Johan *et al*., 2009.
136. de Groot *et al*., 1997.
137. Caracciolo, P.; Buffa, F.; Abraham, G. *J. Mater. Sci. Mater. Med.* **2009**, *20*(1), 145–155.
138. Hettrich, W.; Becker, R. *Polymer* **1997**, *38*(10), 2437–2445.
139. Parakka, J. P.; Iyer, A.; Chau, W.; *et al*. Bioresorbable polyurethanes with degradable hard segments. In *Society for Biomaterials Meeting*, San Antonio, TX, 22–25 April, 2009 poster #616.
140. Tatai, L.; Moore, T. G.; Adhikari, R.; *et al*. *Biomaterials* **2007**, *28*, 5407–5417.
141. Yilgor, I.; Yilgor, E. *Polym. Rev.* **2007**, *47*(4), 487–510.
142. Lai, Y.-C.; Quinn, E. T.; Valint, P. L., Jr. *J. Polym. Sci. A Polym. Chem.* **1995**, *33*(11), 1767–1772.
143. Ng, H. N.; Allegrezza, A. E.; Seymour, R. W.; Cooper, S. L. *Polymer* **1973**, *14*(6), 255–261.
144. Hood, M.; Wang, B.; LaScala, J.; *et al*. *Bull. Am. Phys. Soc.* **2008**, *53*(2, APS March Meeting).
145. Elidrissi, A.; Krim, O.; Ousslimane, S. *Pigm. Resin Technol.* **2008**, *37*(2), 73–79.
146. Lee, B. S.; Chun, B. C.; Chung, Y.-C.; Sul, K. I.; Cho, J. W. *Macromolecules* **2001**, *34*(18), 6431–6437.
147. Seymour, R. W.; Estes, G. M.; Cooper, S. L. *Macromolecules* **1970**, *3*(5), 579–583.
148. Brunette, 1982.
149. Yilgör, E.; Burgaz, E.; Yurtsever, E.; Yilgör, I. *Polymer* **2000**, *41*(3), 849–857.
150. Takahara, A.; Coury, A. J.; Hergenrother, R. W.; Cooper, S. L. *J. Biomed. Mater. Res.* **1991**, *25*(3), 341–356.
151. Takahara, A.; Hergenrother, R. W.; Coury, A. J.; Cooper, S. L. *J. Biomed. Mater. Res.* **1992**, *26*(6), 801–818.

152. Takahara, A.; Okkema, A. Z.; Cooper, S. L.; Coury, A. J. *Biomaterials* **1991**, *12*(3), 324–334.
153. Chandy, T.; Hee, J. V.; Nettekoven, W.; Johnson, J. *J. Biomed. Mater. Res. B Appl. Biomater.* **2009**, *89*(2), 314–324.
154. Harris, R. F.; McDonald, L. A. *J. Appl. Polym. Sci.* **1989**, *37*(6), 1491–1511.
155. Dejun, L.; Jie, Z.; Hanqing, G.; Mozhu, L.; Fuqing, D.; Jianfang, H. *Phys. Lett.* **1992**, *9*(2), 79.
156. Alves *et al*., 2009.
157. Bernacca, G. M.; Gulbransen, M. J.; Wilkinson, R.; Wheatley, D. J. *Biomaterials* **1998**, *19*, 1151–1165.
158. Freij-Larsson, C.; Jannasch, P.; Wesslén, B. *Biomaterials* **2000**, *21*(3), 307–315.
159. Christenson, E. M.; Dadsetan, M.; Wiggins, M.; Anderson, J. M.; Hiltner, A. *J. Biomed. Mater. Res. A* **2004**, *69*(3), 407–416.
160. Throne, J. L. *Technology of Thermoforming*. Hanser: Cincinnati, OH, 1996; p 882, ISBN 3-446-17812-0.
161. Lu, G.; Yilgor, I.; Yilgor, E. *Polym. Eng. Sci.* **2003**, *43*, 1863–1877.
162. Erol, M.; Kalyon, D. *Int. Polym. Proc.* **2005**, *20*, 228–237.
163. Ward, R. S.; Tian, Y.; Wang, S.; *et al*. In *Society for Biomaterials 29th Annual Meeting Transactions*, Reno NV, 30 April–3 May, 2003.
164. White, K. A.; Ward, R. S.; Tian, Y.; Stanciu, V.; Wang, S.; Serpilio, J. In *Society for Biomaterials 29th Annual Meeting Transactions*, Reno, NV, 30 April–3 May, 2003.
165. Semsarzadeh, M. A.; Navarchian, A. H.; Morshedian, J. *Adv. Polym. Tech.* **2004**, *23*(3), 239–255.
166. White, K. A.; Ward, R. S.; Prewett, D.; Serpilio, J.; Ascano, P.; Le, H. In *The 27th Annual Meeting of the Society for Biomaterials*, St. Paul, MN, 25–29 April, 2001.
167. Massey, L. K. *The Effect of Sterilization Methods on Plastics and Elastomers*, 2nd ed.; Plastics Design Library/William Andrew: Norwich, NY, 2006; p 413; ISBN-10: 0815515057; ISBN-13: 978-0815515050.
168. Matthews, I. P.; Gibson, C.; Samuel, A. H. *Clin. Mater.* **1994**, *15*(3), 191–215 and references therein.
169. Hirata *et al*., 1995.
170. Abraham, G. A.; Frontini, P. M.; Cuadrado, T. R. *J. Appl. Polym. Sci.* **1999**, *65*(6), 1193–1203.
171. Zhang, Y. Z.; Bjursten, L. M.; Freij-Larsson, C.; Kober, M.; Wesslén, B. *Biomaterials* **1996**, *17*(23), 2265–2272.
172. Mendes, G. C. C.; Brandão, T. R. S.; Silva, C. L. M. *Am. J. Infect. Control* **2007**, *35*(9), 574–581.
173. Shintani, H. *Biomed. Instrum. Technol.* **1995**, *29*(6), 513–519.
174. Shintani, H.; Kikuchi, H.; Nakamura, A. *J. Appl. Polym. Sci.* **1990**, *41*, 661–675.
175. Sheikh, N. *Nucl. Instrum. Meth. Phys. Res. Sect. B* **2003**, *208*, 215–219.
176. Zhang, K.; Wallick, M.; Brinkerhuff, H. In *Materials and Processes for Medical Devices*, Desert Springs/Spa: Palm Desert, CA, 2007.
177. Haugen, H. J.; Brunner, M.; Pellkofer, F.; Aigner, J.; Will, J.; Wintermantel, E. *J. Biomed. Mater. Res. B Appl. Biomater.* **2007**, *80*(2), 415–423.
178. Briganti *et al*., 2009.
179. Briganti *et al*., 2006.
180. Hsu, S.-H.; Chuang, S.-C.; Chen, C.-H.; Chen, D. C. *Biomed. Mater. Eng.* **2006**, *16*(6), 397–404.
181. All, S. A. E. *J. Phys. D Appl. Phys.* **2007**, *40*, 6014–6019.
182. Guignot, C.; Betz, N.; Legendre, B.; LeMoel, A.; Yagoubi, N. *Nucl. Instrum. Meth. Phys. Res. Sect. B* **2001**, *185*(1–4), 100–107.
183. Terheyden, H.; Lee, U.; Ludwig, K.; Kreusch, T.; Hedderich, J. *Br. J. Oral Maxillofac. Surg.* **2000**, *38*, 299–304.
184. Laroussi, M. *Plasma-based sterilization*. In *International Conference on Phenomena in Ionized Gases*, Conference Proceedings, Greifswald, Germany, 15–20 July, 2003.
185. Lerouge, S.; Guignot, C.; Tabrizian, M.; Ferrier, D.; Yagoubi, N.; Yahia, L'.H. *J. Biomed. Mater. Res. A* **2000**, *52*(4), 774–782.
186. Lerouge, S.; Tabrizian, M.; Wertheimer, M. R.; Marchand, R.; Yahia, L. H. *Biomed. Mater. Eng.* **2002**, *12*(1), 3–13.
187. Schütze, D.; Sepai, O.; Lewalter, J.; Miksche, L.; Henschler, D.; Sabbioni, G. *Carcinogenesis* **1995**, *16*(3), 573–582.
188. Rosemond, Z. A.; Llados, F. Toxiological profile for methylenedianiline. In *U.S. Department of Health and Human Services, Public Health Service Agency for Toxic Substances and Disease Registry, Agency for Toxic Substances and Disease Registry*, 1998; p 194.
189. Tang, Y. W.; Labow, R. S.; Santerre, J. P. *Biomaterials* **2003**, *24*, 2805–2819.
190. Mazzu, A. L.; Smith, C. P. *J. Biomed. Mater. Res.* **1984**, *18*(8), 961–968.
191. Shintani, H.; Nakamura, A. *J. Anal. Toxicol.* **1989**, *13*(6), 354–357.
192. Shintani, H.; Nakamura, A. *Fresenius J. Anal. Chem.* **1989**, *333*(6), 637–640.
193. Mudumba *et al*., 2005.
194. Nakamura, A.; Kawasaki, Y.; Takada, K.; *et al*. *J. Biomed. Mater. Res.* **1992**, *26*(5), 631–650.
195. Tang, Y. W.; Santerre, J. P.; Labow, R. S. *J. Biomed. Mater. Res.* **2001**, *57*, 597–611.
196. Shintani, H. *J. Anal. Toxicol.* **1991**, *15*(4), 198–201.
197. Pinchuk, L. *J. Biomater. Sci. Polym. Ed.* **1994**, *6*(3), 225–267.
198. Binns, D. Tributes paid to respected doctor and solver of great jaundice mystery. *Guardian, Epping Forest News*. 2009.
199. Kopelman, H.; Robertson, M. H.; Sanders, P. G.; Ash, I. *Br. Med. J.* **1966**, *26*, 514–516.
200. Kopelman, H.; Scheuer, P. J.; Williams, R. *Q. J. Med.* **1966**, *35*(4), 553–564.
201. Kopelman, H. *Ann. Intern. Med.* **1968**, *68*(5), 1148.
202. Kopelman, H. *Postgrad. Med. J.* **1968**, *44*(507), 78–81.
203. Hall, A. J.; Harrington, J. M.; Waterhouse, J. A. H. *J. Epidemiol. Commun. Health UK* **1992**, *46*(4), 327–328.
204. Nichols, L. *Int. Arch. Occup. Environ. Health* **2004**, *77*(8), 592–594.
205. Liss, G. M.; Guirguis, S. S. *Am. J. Ind. Med.* **1994**, *26*(1), 117–124.
206. Tillmann, H. L.; Van Pelt, F. N. A. M.; Martz, W.; *et al*. *Clin. Toxicol.* **1997**, *35*(1), 35–40.
207. Cohen, S. R. *Arch. Dermatol.* **1985**, *121*, 1022–1027.
208. Emmett, E. A. *J. Occup. Environ. Med.* **1976**, *18*(12), 802–804.
209. Lewandowski, T. A.; Hayes, A. W.; Beck, B. D. *Hum. Exp. Toxicol.* **2005**, *24*, 655–662.
210. Roy, C. W.; McSorley, P. D.; Syme, I. G. *Hum. Toxicol.* **1985**, *4*, 61–66.
211. Office of Environmental Health Hazard Assessment. 4,4′-Methylene Dianiline. Office of Environment Health Hazard Assessment, USA CA.gov, 2001; Vol. A-87, 8 p.
212. Cocker, J. In Lehtinen, S., Ed.; *Biological Monitoring of Chemical Exposure in the Workplace*; World Health Organization: Geneva, 1996; Vol. 2, Chapter 4, pp 166–189.
213. Chen, K.; Dugas, T. R.; Cole, R. B. *J. Mass Spectrom.* **2006**, *41*(6), 728–734.
214. Szycher, M.; Siciliano, A. A. *J. Biomater. Appl.* **1991**, *5*, 323–336.
215. Adhikaria, R.; Gunatillake, P. A.; Griffiths, I.; *et al*. *Biomaterials* **2008**, *29*(28), 3762–3770.
216. Affatato, S.; Spinelli, M.; Zavalloni, M.; Mazzega-Fabbro, C.; Viceconti, M. *Med. Eng. Phys.* **2008**, *30*(10), 1305–1317.
217. Alferiev, I.; Stachelek, S. J.; Lu, Z.; *et al*. *J. Biomed. Mater. Res. A* **2003**, *66*(2), 385–395.
218. Bezuidenhout, D.; Davies, N.; Black, M.; Schmidt, C.; Oosthuysen, A.; Zilla, P. *J. Biomater. Appl.* **2010**, *24*(5), 401–418.
219. Borda, J.; Bodnár, I.; Ráthy, I.; Zsuga, M. *Polym. Adv. Technol.* **2003**, *14*(11–12), 813–819.
220. Cao, N.; Pegoraro, M.; Severini, F.; Landro, L. D.; Zoia, G.; Greco, A. *Polymer* **1992**, *33*(7), 1384–1390.
221. de Vrijer, R.; Wildeboer, B.; Spaans, C.; Pennings, A. *Polym. Bull.* **1997**, *38*(2), 211–218.
222. Eloy, R.; Belleville, J.; Rissoan, M. C.; Baguet, J. *J. Biomater. Appl.* **1987**, *1987*(2), 475–519.
223. Engel, J. M.; Chen, J.; Liu, C.; Bullen, D. *J. Microelectromechanical Systems* **2006**, *15*(4), 729–736.
224. Field, K. J.; Lang, C. M. *Lab. Anim.* **1988**, *22*, 255–262.
225. Flory, P. J. *Principles of Polymer Chemistry*. Cornell University Press: Ithaca, NY, 1969; p 323.
226. Ghaill, N. A.; Little, E. G. *Proc. Inst. Mech. Eng. H J. Eng. Med.* **2008**, *222*(5), 683–694.
227. Geary, C.; Birkinshaw, C.; Jones, E. *J. Mater. Sci. Mater. Med.* **2008**, *19*(11), 3355–3363.
228. Ghanbari, H.; Viatge, H.; Kidane, A. G.; Burriesci, G.; Tavakoli, M.; Seifalian, A. M. *Trends Biotechnol.* **2009**, *27*(6), 359–367.
229. Grasel, T. G.; Cooper, S. L. *Biomaterials* **1986**, *7*(5), 315–328.
230. Grasel, T. G.; Pitt, W. G.; Murthy, K. D.; McCoy, T. J.; Cooper, S. L. *Biomaterials* **1987**, *8*(5), 329–340.
231. Gunatillake, P. A.; Adhikari, R. *Eur. Cells Mater.* **2003**, *5*, 1–16.
232. Haschke, E.; Sendijarevic, V.; Wong, S.; Frisch, K. C.; Hill, G. *J. Elastomers Plast.* **1994**, *26*(1), 41–57.
233. Hsieh, T.-T.; Hsieh, K.-H.; Simon, G. P.; Tiu, C. *Polymer* **1999**, *40*, 3153–3163.
234. Jana, R. N.; Bhunia, H. *High Perform. Polym.* **2010**, *22*(1), 3–15.
235. Jolly, A. M.; Yasin, M.; Tighe, B. J. *Biomaterials* **1987**, *8*, 289–295.
236. Khan, I.; Smith, N.; Jones, E.; Finch, D. S.; Cameron, R. E. *Biomaterials* **2005**, *26*(6), 621–631.
237. Khan, I.; Smith, N.; Jones, E.; Finch, D. S.; Cameron, R. E. *Biomaterials* **2005**, *26*(6), 633–643.

238. Kazama, H.; Tezuka, Y.; Imai, K. *Polym. Plast. Technol. Eng.* **1989**, *28*(2), 109–121.
239. Kim, J.-Y.; Suh, K.-D. *Polym. Bull.* **1996**, *36*(6), 737–744.
240. Lai, Y.-C. *J. Appl. Polym. Sci.* **1995**, *56*(3), 301–310.
241. Lai, Y.-C.; Quinn, E. T. *J. Polym. Sci. A Polym. Chem.* **1995**, *33*(11), 1783–1793.
242. Lu, H.; Nguyen, B.; Powers, J. M. *J. Prosthet. Dent.* **2004**, *92*(2), 151–154.
243. Luo, J.; Deng, Y.; Sun, Y. *J. Bioactive Compatible Polym.* **2010**, *25*(2), 185–206.
244. Marcos-Fernández, A.; Abraham, G. A.; Valentín, J. L.; San Román, J. *Polymer* **2006**, *47*(3), 785–798.
245. Nair, L. S.; Laurencin, C. T. *Prog. Polym. Sci.* **2007**, *32*(8–9), 762–798.
246. Nyilas, E.; Ward, R. S., Jr. *J. Biomed. Mater. Res. Symp.* **1977**, *8*, 69–84.
247. Ojha, U.; Kulkarni, P.; Faust, R. *Polymer* **2009**, *50*(15), 3448–3457.
248. Oprea, S.; Vlad, S.; Stanciu, A.; Ciobanu, C.; Macoveanu, M. *Eur. Polym. J.* **1999**, *35*(7), 1269–1277.
249. Oprea, S.; Vlad, S.; Stanciu, A. *Polymer* **2001**, *42*(17), 7257–7266.
250. Pierce, B. F.; Brown, A. H.; Sheares, V. V. *Macromolecules* **2008**, *41*(11), 3866–3873.
251. Prisacariu, C.; Scortanu, E.; Buckley, C. P. *Int. J. Polym. Anal. Charact.* **2009**, *14*(6), 527–539.
252. Qi, H. J.; Boyce, M. C. *Mech. Mater.* **2005**, *36*, 817–839.
253. Rui, W.; Lian-meng, Z.; Chong-hui, W.; Shui-ping, W. In *3rd International Conference on Bioinformatics and Biomedical Engineering*, 11–13 June, 2009; pp 1–4.
254. Scholes, S. C.; Burgess, I. C.; Marsden, H. R.; Unsworth, A.; Jones, E.; Smith, N. *J. Proc. Inst. Mech. Eng. H J. Eng. Med.* **2006**, *220*(5), 583–596.
255. Shkapenko, G.; Gmitter, G. T.; Gruber, E. E. *Ind. Eng. Chem.* **1960**, *52*(7), 605–608.
256. Sheludyakov, V. D.; Kozyukov, V. P.; Mironov, V. F. *Russ. Chem. Rev.* **1976**, *45*(3), 227–245.
257. Wanamaker, C. L.; Bluemle, M. J.; Pitet, L. M.; O'Leary, L. E.; Tolma, W. B.; Hillmyer, M. A. *Biomacromolecules* **2009**, *10*(10), 2904–2911.
258. Wang, W.; Ping, P.; Yu, H.; Chen, X.; Jing, X. *J. Polym. Sci. A Polym. Chem.* **2006**, *44*(19), 5505–5512.
259. Ward, R. S.; White, K. A.; Hu, C. B. In *Polyurethane in Biomedical Engineering*; Planck, H., Egbers, G., Syre, I., Eds.; Elsevier: Amsterdam, 1984; pp 181–200.
260. Ward, R. S.; White, K. A.; Wolcott, C. A. In *Transactions of the 20th Annual Meeting of the Society for Biomaterials*, Boston, MA, 5–9 April, 1994.
261. Ward, R. S.; White, K. A. U.S. Pat. 5,428,123, 1995.
262. Ward, R. S. *The chemistry and technology of biomedical polyurethanes: Past, present and future*. In *Frontiers in Biomedical Polymers Symposium*, Granada, Spain, 16–19 June, 2005.
263. Ward, R.; McCrea, K. In *20th European Conference on Biomaterials*, Nantes, France, 27 Sept–1 Oct, 2006.
264. Welch, W. C.; Boyle, C.; Cheng, B. C.; *et al*. *Neurosurg. Focus* **2007**, *22*(1), E8.
265. Ward, R. S.; McCrea, K.; Tian, Y.; Parakka, J. U.S. Pat. 200,500,282,997, 2005.
266. Weng, R.; Wang, C.; Zhang, L.; Wang, S. *Mater. Sci. Forum* **2009**, *620–22*, 741–744.
267. Wu, X. S. In *Encyclopedic Handbook of Biomaterials and Bioengineering*; Wise, D. L., Ed.; Marcel Dekker: New York, 1995; pp 1015–1054.
268. Bezwada, R. S. *Polym. Mater. Sci. Eng.* **2009**, *101*, 1007–1008.
269. Parakka, J. P.; Iyer, A.; Chau, W.; *et al*. In *Society for Biomaterials Meeting*, San Antonio, TX, 22–25 April, 2009, poster #616.
270. Bezwada, R. S. U.S. Patent Publication 2006/0188547.
271. Bezwada, R. S. U.S. Patent Publication 2006/0172983.
272. Chen, Z.; Shen, Y. R.; Somorjai, G. A. *Annu. Rev. Phys. Chem.* **2002**, *53*, 437–465.
273. Chen, Z.; Ward, R.; Tian, Y.; Eppler, A. S.; Shen, Y. R.; Somorjai, G. A. *J. Phys. Chem. B.* **1999**, *103*(15), 2935–2942.
274. Chen, Z.; Ward, R.; Tian, Y.; *et al*. *J. Am. Chem. Soc.* **2000**, *122*(43), 10615–10620.
275. Zhang, D.; Gracias, D. H.; Ward, R.; *et al*. *J. Phys. Chem. B* **1998**, *102*, 6225–6230.
276. Jones, J. A.; Qin, L. A.; Meyerson, H.; Kwon, I. K.; Matsuda, T.; Anderson, J. M. *J. Biomed. Mater. Res. A* **2008**, *86A*, 261–268.

1.126. Shape-Memory Polymers

A Lendlein, C Wischke, K Kratz, M Heuchel, J Zotzmann, B Hiebl, A T Neffe, and M Behl, Center for Biomaterial Development and Berlin-Brandenburg Center for Regenerative Therapies, Institute of Polymer Research, Helmholtz-Zentrum Geesthacht, Teltow, Germany

© 2011 Elsevier Ltd. All rights reserved.

1.126.1.	Fundamental Principles of Shape-Memory Polymers and of the Quantification of Shape-Memory Properties	480
1.126.2.	Synthesis and Properties of Selected Examples of SMP Intended for Biomedical Applications	485
1.126.3.	Multifunctional SMPs by Integrating Hydrolytic Degradability or Controlled Drug Release Capability	487
1.126.4.	Biomedical Applications of SMPs	492
References		495

Glossary

Drug delivery system Drug delivery systems are used to control the release rate and timeframe, in which drugs become available for pharmacological effects in the body of a patient.

Implant Any medical device made from one or more materials that is intentionally placed within the body, either totally or partially buried beneath an epithelial surface.

Medical devices Products to be used with human beings for the purpose such as for diagnosis, prevention, monitoring, or treatment of diseases, injuries, or disabilities with the intended principal action being achieved by means other than pharmacological, immunological, or metabolic mechanisms; for example, by a supportive function; Council Directive 93/42/EEC Helmholtz-Zentrum Geesthacht.

Methacrylate Salts or esters from the methacrylic acid ($C H_2{=}CHCOOH$), containing reactive vinyl ($CH_2{=}CHR$) groups, which can polymerize.

Minimally invasive surgery Surgical technique which is less invasive than open surgery employed for the same clinical purpose and often involves small keyhole incisions only.

Polyurethane/polyetherurethane/ polyesterurethane A polymer consisting of polyether/ polyester units joined by urethane units.

Thermoplast A polymer which turns into liquid when heated above the highest thermal transition temperature (T_{perm}). Unlike thermosetting polymers, thermoplasts can be remelted and remolded. In general, thermoplasts are high-molecular-weight polymers.

Abbreviations

BA	*n*-Butyl acrylate
DSCP	Dual-shape creation proceure
EO	Ethylene oxide
FDA	United States Food and Drug Administration
ΔH_m	Melting enthalpy
MDI	Methylene diphenylene diisocyante
MIS	Minimally invasive surgey
NIR	Near infrared
NMRI	Naval Medical Research Institute
N-PCGDMA	Networks for poly(ε-caprolactone-*co*-glycolide) dimethacrylates
PCG	Poly(ε-caprolactone-*co*-glycolide)
PCGDMA	Poly(ε-caprolactone-*co*-glycolide) dimethacrylate
PCL	Poly(ε-caprolactone)
PCLDMA	Poly(ε-caprolactone)dimethacrylate
PDC	Multi block copolymer of PPDO and PCL
PEGMA	Poly(ethylene glycol) dimethacrylate
PEU	Poly(ether urethane)
PLG	Poly[(*rac*-lactide)-*co*-glycolide]
PPDO	Poly(*p*-dioxanone)
PTMO	Poly(tetramethylene oxide)
R_f	Shape fixity ratio
RH	Relative humidity
R_r	Shape recovery ratio
σ_{max}	Recovery stress
SMCP	Shape-memory creation process
SME	Shape-memory effect
SMP	Shape-memory polymer
T_{deform}	Deformation temperature
T_g	Glass transition temperature
T_{high}	Highest temperature in the course of SMCP
T_{low}	Lowest temperature in the course of SMCP
T_m	Melting transition temperature
TMDI	Trimethyl hexamethylene diisocyanate (isomeric mixture of 1,6-diisocyanato 2,2,4-trimethylhexane and 1,6-diisocyanato-2,4,4-trimethylhexane)
T_{perm}	Highest thermal transition temperature of a thermoplastic material at which the domains acting as physical cross links melt
T_{sw}	Switching temperature
TSCP	Triple-shape creation procedures
$T_{\sigma,\ max}$	Temperature determined at the maximum of recovery stress
T_{trans}	Thermal transition temperature

1.126.1. Fundamental Principles of Shape-Memory Polymers and of the Quantification of Shape-Memory Properties

Each biomedical application such as implants, surgical instruments, extracorporal devices, wound covers, or controlled drug delivery systems requires a specific combination of material properties and functions. Polymeric biomaterials are of high relevance for such applications, as the functions and properties can be tuned in a wide range by only small variations of their chemical structure. An important function, which, for example, implants such as hernia meshes or wound clips have to fulfill, is a function on the macroscopic level such as the mechanical function. In addition, biofunctionality is required, especially when a polymer-based device should guide a regeneration process. For medical devices that will be in contact with blood, such as artificial heart valves and tubes used in extracorporal devices, hemocompatible surfaces play a key role. Although the number of fields of applications for polymeric biomaterials is increasing steadily, the number of materials, which are applied in the clinics, is very limited. Hurdles in the development of novel biomaterials are long development times connected with financial risks, regulatory aspects, and uncertainties in the reimbursement. The rapid progress in the development of surgical techniques, especially in minimally invasive surgery (MIS) as an example, is leading to more complex requirements for modern implants. How can a bulky implant be placed in the body through a small keyhole incision or how can an implant be adapted to the individual geometry of a patient? How can a second surgery for implant removal be avoided?

The challenge associated with the first question can be addressed by smart materials, which are capable of an active on-demand movement.[1–6] In this chapter, we describe the shape-memory effect (SME) of polymers, which enables polymers to change their shape in a predefined way on demand when exposed to a suitable stimulus. At present, most investigated shape-memory polymers (SMPs) are thermally-induced SMPs, which are triggered by heat. A bulky implant having a switching temperature (T_{sw}) between room temperature and body temperature could be inserted into the body through a small incision in a compressed or elongated temporary shape. As soon as the implant is placed in the body, it is heated to body temperature and changes into its bulky application-relevant shape. The temporary shape is created by a thermomechanical process and can be adjusted to the individual needs of a patient.

A strategy to address the question of implant removal will be the introduction of hydrolytically degradable bonds into the implant material.[7] In the design of such materials, it has to be considered that the degradation products should be either fully metabolized or excretable as polymer fragments. Furthermore, degradable polymeric biomaterials enable the application of polymeric biomaterials as matrix materials for controlled drug release systems. This requires the characterization of the drug diffusion characteristics or the polymer's erosion behavior.

In the following, the fundamental principles of the thermally-induced SME as well as its characterization are discussed. Afterward, the basics of additional functionalities such as hydrolytical degradability, biofunctionality, and drug release are introduced and combinations of these functions are described as examples for multifunctional SMPs. Selected biomaterials with SME are presented, including data of the biocompatibility, whenever available. The application potential of SMP in medical devices is sketched by an overview on SMP-based medical devices being developed with a focus on general surgery, the cardiovascular system, and urogenital application. Here, a special emphasis is given on the potential use of SMPs as matrix materials in controlled drug release systems.

SMPs are different from shape-changing materials as they are able to change their shape in a predefined way on demand when exposed to a suitable stimulus, which can be heat or light.[1,8] By application of external stress, such SMPs can be deformed and temporarily fixed in a second, temporary shape. In Figure 1, a thermally-induced SMP is shown in its temporary shape. When the material is heated above a certain switching temperature (T_{sw}), the SMP recovers its original, permanent shape. The movement during recovery is predefined as it reverses the mechanical deformation which was applied for the creation of the temporary shape.

Besides this tailored thermomechanical procedure, which is also referred to as programming or shape-memory creation procedure (SMCP), the SME requires a suitable molecular

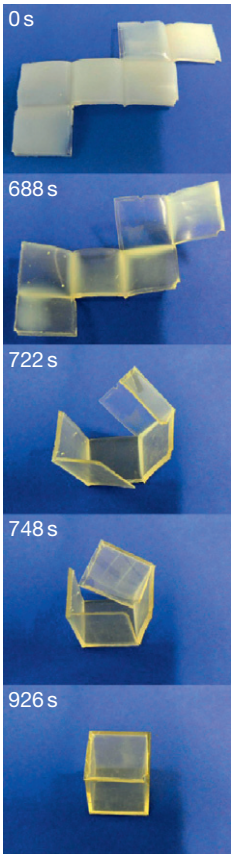

Figure 1 Time series of photographs showing recovery of a shape-memory cube when heated with an IR-lamp. Total time from start to finish of the process was 926 s. The tube was made of a poly(ε-caprolactone)dimethacrylate polymer network (the M_n of the network's switching segments was 10^4) that had been programmed to form a flat cube. Reproduced from Behl, M.; Razzaq, M. Y.; Lendlein, A. Adv. Mater. **2010**, *22*, 3388–3410. Copyright Wiley-VCH-Verlag GmbH & Co KGaA.

architecture/morphology. Suitable polymeric materials that are capable of an SME provide a polymer network architecture consisting of netpoints, chain segments, and molecular switches, with the latter being sensitive to an external stimulus. The netpoints, interconnected by the chain segments, determine the permanent shape of the SMP. They can be of chemical (covalent bonds) or physical (intermolecular interactions) nature. While the creation of covalent bonds requires suitable crosslinking chemistry, the formation of netpoints by intermolecular interactions demands a morphology consisting of at least two segregated domains, for example, a crystalline and an amorphous phase. In such multiphase polymers, the polymer chain segments form domains. The domains that are related to the highest thermal transition temperature (T_{perm}) are called hard domains and they act as physical netpoints.

During the deformation applied when creating the temporary shape in the course of SMCP, a sufficient elastic deformability of the polymer network is required. This deformability can be reached by the chain segments, which must be capable of sustaining a certain orientation. The extent of the deformability increases with growing length and flexibility of these chain segments. Furthermore, the recoiling of the chain segments, which is entropically driven, enables the recovery of the permanent shape.

Stimuli-sensitive switches that form additional reversible crosslinks, which can be established and cleaved on demand, enable a reversible fixation of the temporary shape and prevent in this way the recoiling of the chain segments. Like the permanent netpoints, these additional crosslinks can be built by the formation of chemical (covalent) reversible bonds, intermolecular interactions of side groups, or by the solidification of domains formed by these polymer chain segments upon cooling below their correlated thermal transition temperatures T_{trans}. That is why such polymer chain segments are called switching segments; the associated domains are named switching domains. As this solidification is triggered by heat in such a thermosensitive SMP, which presently is the most prominent class of SMP, an additional classification can be performed according to the thermal transitions related to the solidification of the polymer chain segments. T_{trans} can be a glass transition temperature (T_g), a melting transition temperature (T_m), or a liquid crystalline transition. While T_gs span over a broad temperature interval, the latter ones can show a transition in a relatively small temperature interval. Melting transitions mostly extend over a temperature range between 15 and 20 K, while liquid crystalline transitions can even occur in a temperature interval between 1 and 5 K. In all cases, heating of the thermally-induced SMP above the thermal transition causes melting of the crystallites or regain of flexibility of the vitrified switching domains so that the viscous state is reached again. In a thermoplastic SMP, only the domains associated to the polymer chain segments with the second highest T_{trans} act as switching domains. Chemical crosslinks as stimuli-sensitive switches can be realized by the reaction of two functional groups under formation of a reversible chemical bond. The application of a suitable stimulus enables cleavage of these bonds on demand.

On the macroscopic level, shape-memory properties of polymers are characterized by the extent to which the temporary shape can be fixed (shape fixity ratio R_f) and the permanent shape is recovered (shape recovery ratio R_r). Further characteristic measures of SMP properties are the switching temperature (T_{sw}) obtained under stress-free recovery conditions or the temperature $T_{\sigma,max}$, determined at the maximum of the recovery stress (σ_{max}) under constant strain conditions. These shape-memory characteristics strongly depend on the polymer's structural design as well as on the parameters (e.g., heating or cooling rates or the type of mechanical deformation) applied during the SMCP.

Various different test procedures have been applied for SME quantification (e.g., determination of the material's shrinkage[9–11] or application bending tests[12] as well as three-point flexural tests[13,14]) of which cyclic, thermomechanical tensile tests[3,15,16] are the most common method for quantification of macroscopic shape-memory properties. Moreover, for biomaterials it is essential to explore the shape-memory behavior in aqueous environments similar to physiological conditions.

Cyclic, thermomechanical tensile experiments are typically performed with a tensile testing machine equipped with a thermo chamber that enables an accurate temperature control during mechanical deformation. In such experiments, the specimen is typically uniaxially deformed (e.g., elongated or compressed). In general, such test protocols or cycles consist of a SMCP where the temporary shape is generated and a recovery module where either the recovery of the original shape or the generated recovery stress is analyzed. The programming module SMCP as well as the recovery module can both be performed under stress-controlled or strain-controlled conditions. While strain-controlled procedures allow measurement of the stress on the specimen at defined thermal conditions, the change in strain is obtained in stress-controlled tests. The cyclic test protocols can be further differentiated according to the applied deformation temperature T_{deform}. In cold drawing protocols, the deformation to the temporary shape takes place at the fixation temperature $T_{low} = T_{deform}$, which is below T_{trans} of the switching domains. In a conventional heating–stretching–cooling protocol, the deformation is performed at the recovery temperature $T_{high} = T_{deform}$, which is above T_{trans}.

A strain-controlled SMCP typically consists of three steps: (1) heating of the sample to the upper working temperature $T_{high} > T_{trans}$, for elongation to a certain extension ε_m with a defined strain rate $\dot{\varepsilon}$ for a fixed time period at $T_{high} = T_{deform}$; (2) cooling to the lower working temperature $T_{low} < T_{trans}$ with a certain cooling rate β_c while ε_m is kept constant for fixation of the temporary shape; (3) unloading of the specimen to zero stress at T_{low} resulting in the fixed shape ε_u. From a σ–ε diagram as displayed in **Figure 2(a)**, the Young modulus $E(T_{high})$ at T_{high} which is also called rubber modulus E_{rubber} can be determined from the initial slope of the σ–ε curve in step (1). The corresponding Young's modulus $E(T_{low})$ at T_{low} also named E_{unload} can be obtained from the slope of the unloading path in step (3).[17] After the temporary shape is fixed, the recovery process can be initialized (step 4) as discussed below.

In the equivalent stress-controlled SMCP, the programming steps (1) and (3) remain unchanged while step (2) is adapted. After ε_m is reached, the sample is allowed to relax to a stress σ_m, which is then kept constant during cooling to T_{low}, whereby the deformation of the sample to ε_l is monitored during cooling. If the sample is cooled under constant stress σ_m, different effects have to be considered, for example, changes

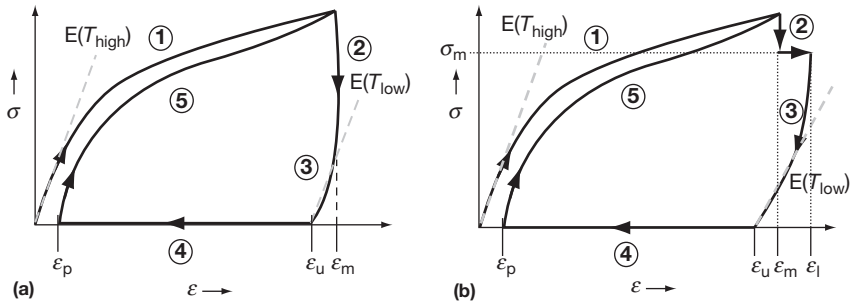

Figure 2 Schematic representation of stress–strain curve as a result of the cyclic, thermomechanical tensile tests for two different cycle types. (a) Strain-controlled programming with stress-free recovery ($\sigma-\varepsilon$ diagram) cycle type A.3: ①, stretching to ε_m at T_{high}; ②, cooling to T_{low} with constant cooling rate β_c while ε_m is kept constant; ③, unloading to zero stress while reaching ε_u; ④, heating up to T_{high} under stress-free conditions, while keeping $\sigma = 0$ MPa and ε_p is recovered; ⑤, start of the second cycle. (b) Stress-controlled programming with stress-free recovery ($\sigma-\varepsilon$ diagram): ①, stretching to ε_m at T_{high} while relaxation to σ_m is allowed; ②, cooling down to T_{low} with constant cooling rate β_c while σ_m is kept constant and ε_l is reached; ③, unloading to zero stress while reaching ε_u; ④, heating up to T_{high} under stress-free conditions, while keeping $\sigma = 0$ MPa and ε_p is recovered; ⑤, start of the second cycle. In both $\sigma-\varepsilon$ diagrams the gray dashed lines represent Young's modulus which can be determined either at T_{high} in step ① or at T_{low} during unloading in step ③. Modified from Lendlein, A.; Kelch, S. *Angew. Chem. Int. Ed.* **2002**, *41*, 2034–2057. Copyright Wiley-VCH-Verlag GmbH & Co KGaA, reproduced with permission.

of the expansion coefficient of the stretched specimen at temperatures above and below T_{trans} as well as volume changes arising from vitrification ($T_{trans} = T_g$) or crystallization ($T_{trans} = T_m$) of the switching domains. Finally, in step (3) the specimen is unloaded to zero stress at T_{low} whereby ε_u is reached (see **Figure 2(b)**).

For quantification of the applied programming, R_f is determined which describes the ability to fix the mechanical deformation ε_m. R_f is calculated by the amplitude ratio of ε_m to the total deformation ε_u. In a strain-controlled programming protocol, R_f is given by the ratio of the strain in the stress-free state after the withdrawal of the tensile stress in the Nth cycle $\varepsilon_u(N)$ and the maximum strain ε_m (eqn [1]). In the stress-controlled programming protocol, R_f is given by the ratio of the tensile strain after unloading, $\varepsilon_u(N)$, to the maximum strain $\varepsilon_l(N)$ at $\sigma = \sigma_m$ after cooling to T_{low}, $\varepsilon_l(N)$ (eqn [2]).[3]

$$\text{Strain-controlled: } R_f(N) = \frac{\varepsilon_u(N)}{\varepsilon_m} \quad [1]$$

$$\text{Stress-controlled: } R_f(N) = \frac{\varepsilon_u(N)}{\varepsilon_l(N)} \quad [2]$$

After the SMCP is finished and ε_u is fixed, the next step in a cyclic, thermomechanical test is heating from T_{low} to T_{high} with a constant heating rate β_h ((4) as in **Figure 2(a)**), allowing the recovery of the original permanent shape when performed under stress-free conditions (at $\sigma = 0$ MPa). After T_{high} is reached, a recovered shape ε_p is achieved as displayed in a strain-stress-recovery diagram (**Figure 2(a)**).

For quantification of the recovery in dual-shape tests, the R_r is calculated, depending on the applied SMCP type (stress-controlled or strain-controlled).

$$\text{Strain-controlled SMCP: } R_r(N) = \frac{\varepsilon_m - \varepsilon_p(N)}{\varepsilon_m - \varepsilon_p(N-1)} \quad [3]$$

$$\text{Stress-controlled SMCP: } R_r(N) = \frac{\varepsilon_l(N) - \varepsilon_p(N)}{\varepsilon_l(N) - \varepsilon_p(N-1)} \quad [4]$$

In a strain-controlled protocol, the change in strain obtained during the programming step in the previous cycle ($\varepsilon_m - \varepsilon_p(N-1)$) is related to the change in strain that occurs during the present cycle $\varepsilon_m - \varepsilon_p(N)$ (eqn [3]). The recovered strain in two successively passed cycles in the stress-free state before application of yield stress is represented by $\varepsilon_p(N-1)$ and $\varepsilon_p(N)$. In the case of a stress-controlled programming and stress-free recovery after cooling to T_{low} during the Nth cycle $\varepsilon_l(N)$, the shape recovery ratio R_r quantifies the ability of the material to memorize its permanent shape. For this purpose, the change in strain which occurs during the programming step in the $(N-1)$th cycle $\varepsilon_l - \varepsilon_p(N-1)$ is compared to the change in strain which occurs as a result of the following cycle $\varepsilon_l - \varepsilon_p(N)$ (eqn [4]).[3]

Further characteristic values that can be determined from recovery under stress-free conditions are the switching temperature (T_{sw}), the temperature interval of recovery ΔT_{rec}, and the recovery rate $v_{rec.}$[16] ΔT_{rec} is defined as the difference between the temperature T_{end} where the transition from the temporary to the original shape ends and the temperature T_{start} where the recovery process begins (eqn [5] and **Figure 3(a)**). The recovery rate v_{rec} is given as the ratio of the strain recovery ratio R_r over the temperature interval ΔT_{rec} (eqn [6]). T_{sw} can be determined as inflection point of the ε–T diagram representing the peak of $v_{rec.}$[15,18]

$$\Delta T_{rec} = T_{end} - T_{start} \quad [5]$$

$$v_{rec} = \frac{R_r}{\Delta T_{rec}} \quad [6]$$

If recovery takes place under constant strain conditions ($\varepsilon = \varepsilon_m =$ constant), the generation of the recovery stress can be monitored in a stress–temperature recovery σ–T diagram (see **Figure 3(b)**). For dual-shape SMPs (especially thermoplastics) in the σ–T diagram, typically a stress maximum σ_{max} is observed at a characteristic temperature $T_{\sigma,max}$ when heating to $T_{high.}$[15,16] Here, σ_{max} represents an equilibrium state between the stored forces applied during deformation and the retracting forces, driven by the entropy elasticity, which is a result of the softening of the polymer caused by the decrease in Youngs's modulus. The latter effect dominates the behavior at temperatures above $T_{\sigma,max}$.

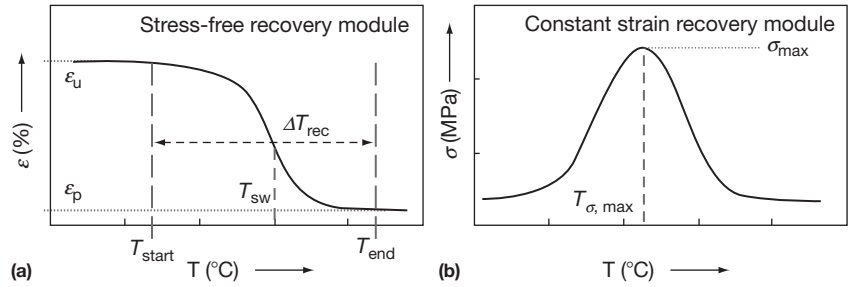

Figure 3 Schematic representation of recovery curves for thermoplastic SMPs. (a) ε–T diagram of a thermoplastic SMP recovered under stress-free conditions. (b) σ–T diagram of a thermoplastic SMP, recovered under constant strain conditions. Reproduced from Wagermaier, W.; Kratz, K.; Heuchel, M.; Lendlein, A. *Adv. Polym. Sci.* **2010**, *226*, 97–145, with permission from Springer Science+Business Media.

Several model approaches have been developed to analyze and simulate the shape-memory behavior of SMPs. Viscoelastic models, which are based on the structural concept of SMPs consisting of at least two phases (switching domains and hard domains) with different transition temperatures, considered two Maxwell models (spring and dashpot) connected in parallel.[19,20] According to a recently introduced phenomenologically thermomechanical model for SMP by Liu *et al.*,[21] the structural conformation of an amorphous SMP at a certain temperature could be described as coexistence of frozen and active volume fractions. A central assumption of this model is that only the active volume fractions were elongated in the rubbery state at $T > T_g$ and the applied deformation was fixed during cooling. In addition, specific models for crystallizable SMPs have been reported, which consider that during cooling from a melt (at T_{high}), newly formed crystals stabilize the SMP and act as physical crosslinks. Barot *et al.*[22] developed a model for the thermomechanical behavior of crystallizable SMPs within a thermodynamic framework for homogenous and inhomogeneous deformation in different geometries. In this model, four different polymer-related processes and states of the SMP are theoretically described: (i) the rubbery, totally amorphous state at $T > T_m$ of the switching segments, (ii) the semicrystalline phase at temperatures $T < T_m$, (iii) the crystallization process on cooling below T_m, and (iv) the melting process caused by heating again above T_m.

When, on the molecular level, a second switching segment is integrated into the polymer network which enables a morphology of at least two segregated domains and results in two transition temperatures $T_{trans,A}$ and $T_{trans,B}$, the capability of two subsequent shape changes can be implemented in a polymeric material.[23–29] The original shape (C) is defined by the netpoints resulting from the crosslinking reaction, while shapes (A) and (B) are created in a two-step thermomechanical programming process. The physical crosslinks associated to the highest transition temperature $T_{trans,B}$ are associated to shape (B), while shape (A) relates to the second highest transition temperature $T_{trans,A}$. Various triple-shape creation procedures (TSCP) have been investigated; the most obvious method is a twofold dual-shape creation procedure (DSCP). In this type of a TSCP, named TSCP-1, the triple-shape material of a permanent shape (C) is first heated to T_{high} where the polymer network is in the elastic state and then a deformation is applied. The cooling under external stress to T_{mid} ($T_{trans,A} < T_{mid} < T_{trans,B}$) results in formation of physical crosslinks related to $T_{trans,B}$. Shape (B) is obtained after release of the external stress. Subsequent deformation of this shape at T_{mid} and cooling to T_{low} under external stress creates shape (A). When the material is heated to T_{mid}, shape (B) is recovered; subsequent heating to T_{high} results in shape (C). In the following, a typical cyclic, thermomechanical triple-shape test consisting of a TSCP-1 programming module followed by recovery under stress-free conditions is described for an AB multiphase polymer network named MACL composed of crystallizable poly(ε-caprolactone) (PCL) segments and amorphous poly (cyclohexyl methacrylate) (PCHMA) segments (see **Figure 4**). In the first step, the specimen is heated to $T_{high} > T_{trans,B} = T_{g,PCHMA}$ where the material is in a rubber-elastic state. After equilibration at T_{high}, the sample was deformed to ε_B^0. Then, the material is cooled to a temperature T_{mid} which is in between $T_{trans,A} = T_{m,PCL}$ and $T_{g,PCHMA}$ and external stress is maintained until the physical crosslinks fixing shape (B) are established (ε_B^{load}). After releasing the external stress, shape (B), ε_B is obtained. In the second step, shape (A) is created. The sample, which presently is in shape stress, (B), is further deformed at T_{mid} to ε_A^0 (shape A). Cooling under external stress to $T_{low} < (T_{trans,A} - 20\,K)$ leads to a second set of physical netpoints related to $T_{trans,A}$ stabilizing ε_A^{load}. These new physical crosslinks fix shape (A) (ε_A), which is obtained when the external stress is released. Finally, the sequential recovery of the shapes (B) (ε_B^{rec}) and (C) (ε_C^{rec}) is triggered by reheating to T_{high} as shown in **Figure 4**.

In addition, in a procedure named TSCP-2, the material can be deformed at T_{high}, and subsequently cooled to T_{low} to fix the shape (B). Afterward, the material is heated to T_{mid} where a second deformation is applied. After cooling to T_{low}, the shape (A) is created. The recovery sequence by heating is the same as that for TSCP-1.[30] Besides three individual shapes, such triple-shape materials allow by individual choice of the transition temperatures two dual-shape effects.[26]

Indirect actuation of the thermally-induced SME broadens the applicability of SMP. Two different strategies enable the indirect actuation of the SME: the first strategy involves heating of the SMP indirectly, for example, by exposure to energy transporting radiation. Lowering of T_{trans} so that the SME is triggered while the sample temperature remains constant is the second strategy and can be realized by diffusion of a plasticizer into the polymer. Here, we will focus on the first strategy.

In a medical device based on polyurethane, the SME could be induced by illumination with light of an IR laser.[31,32]

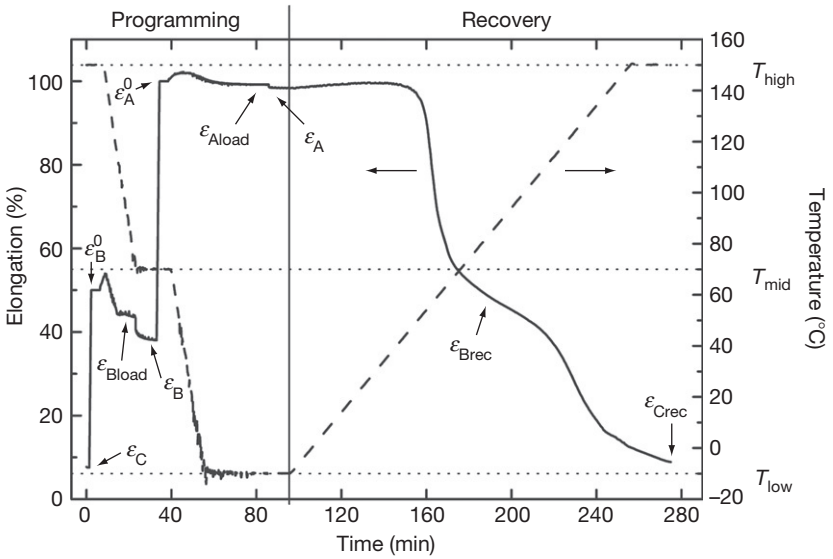

Figure 4 Cyclic, thermomechanical tensile test for quantification of triple-shape effect. Strain and temperature as a function of time taken from the fifth cycle for MACL(45) multiphase network composed of crystallizable PCL segments and amorphous poly(cyclohexyl methacrylate) segments with 45 wt% PCL content ($T_{trans,A} = T_{m,PCL} = 50\,^{\circ}C$ and $T_{trans,B} = T_g = T_{g,PCHMA} = 140\,^{\circ}C$). The solid line indicates strain; the dashed line indicates temperature. In this triple-shape experiment, the sample first is stretched from ε_C to ε_B^0 at $T_{high} = 150\,^{\circ}C$, then cooled to T_{mid} with a cooling rate of $\beta_c = 5\,K\,min^{-1}$ to under stress-control results in ε_B^{load} and after unloading ε_B is fixed. Then the sample is further elongated at T_{mid} to ε_A^0 and subsequently cooled to T_{low} under stress-control with $\beta_c = 5\,K\,min^{-1}$ whereas the elongation decreases to ε_A^{load}. Shape (A), corresponding to ε_A, is obtained by unloading. The recovery process of the sample is monitored by reheating with a heating rate of $\beta_h = 1\,K\,min^{-1}$ from T_{low} to T_{high} while the stress is kept at 0 MPa and the sample contracts to recovered shape (B) at ε_B^{rec} and finally shape (C) at ε_C^{rec} is recovered. Reprinted from Bellin, I.; Kelch, S.; Langer, R.; Lendlein, A. *Proc. Natl. Acad. Sci. USA* **2006**, *103*(48), 18043–18047. Copyright 2006 National Academy of Sciences, USA.

The principle could be extended to laser-activated shape-memory vascular stents and SMP foams for aneurysm treatment,[33,34] both of which require a light diffuser for the uniform application of light.[35] In all cases, energy absorption by the polymer for actuation is quite low.

An increase in the absorbed energy can be reached by the incorporation of conductive fillers such as heat-conductive ceramics, carbon black, and carbon nanotubes resulting in a better interconnection between the heat source and the shape-memory devices.[14,36,37] Here, it needs to be considered that besides a better heat transfer, the incorporation of particles also influences the mechanical properties.

The incorporation of carbon nanotubes into shape-memory polyurethanes enables a certain level of conductivity to be reached. Upon application of an electrical current, the sample temperature is increased as a result of the high ohmic resistance of the composite, so that electrical energy is converted into heat.[38–41] This warming can be used to trigger the SME. The addition of other conducting materials such as polypyrrole, short carbon fibers, and nickel particles increased conductivity, in case the conductivity of carbon nanotubes was not sufficiently high enough.[40–44] The addition of 2.5 wt% carbon nanotubes increased the modulus from 12 to 148 MPa, and addition of 5 wt% polypyrrole results in a modulus of 112 MPa. A composite having 2.5 wt% carbon nanotubes and 2.5 wt% polypyrrole featured a modulus of 112 MPa. The composites having nickel particles arranged in chains were prepared by curing the SMP resin containing small amounts of Ni powder in a weak magnetic field.[43,44] While the ohmic resistance is reduced so that a voltage of 20 V is sufficient for actuation, the storage modulus is increased compared to pure SMP resin or randomly distributed Ni.

A remote actuation of the thermally-induced SME in alternating magnetic fields had been realized by the incorporation of magnetic nanoparticles of iron(III) oxide cores in a silica matrix into SMP.[45–47] The sample temperature is increased by inductive heating of the nanoparticles as soon as the nanocomposite is placed in the alternating magnetic field ($f = 258$ kHz, $H = 7$–$30\,kA\,m^{-1}$). Thermoplastic materials as well as covalent polymer networks were selected as the matrix. A first material was a thermoplastic, biodegradable multiblock copolymer named PDC having poly(*p*-dioxanone) (PPDO) hard and PCL switching segments. A second thermoplastic multiblock copolymer was an aliphatic PEU from methylene bis(*p*-cyclohexyl isocyanate), butanediol (BD), and polytetrahydrofuran named TFX. In TFX, the switching domains are amorphous compared to PDC which has crystalline switching domains. Incorporation of the nanoparticles into PCL dimethacrylates and their subsequent polymerization yielded nanoparticle composite networks. The energy spectrum for the indirect actuation could be shifted to radio frequency when a near single crystal metal alloy comprising terbium, iron, and dysprosium-d of nominal composition $Tb_{0.3}Dy_{0.7}Fe_{1.92}$ was embedded in an epoxy thermoset. Here, the radio frequency triggers the magnetoelectroelastic effect, which generates the indirect heating.[48] In composites based on a matrix from thermoplastic polyurethanes derived from diphenylmethane-4,4′-diidocyanate, adipic acid, ethylene oxide, propylene oxide, 1,4-BD, and bisphenol A with $T_{trans} = T_g$, a reduction in the frequency and the magnetic field required for triggering the

SME of composites could be achieved by using magnetite particles in the range of 9 μm.[49] In addition, the indirect magnetic actuation of thermosets could be achieved by the incorporation of nickel zinc ferrite particles into a commercial ester-based thermoset polyurethane.[50]

When a second phase capable of providing domains having an additional transition temperature is introduced, a remotely actuated triple-shape effect is enabled (Figure 5).[46] This system consisted of silica-coated iron(III) oxide nanoparticles incorporated into a polymer network matrix similar to the above described MACL networks. When stimulated by increasing the magnetic field strength stepwise, a two-step recovery of shapes B and C could be obtained, whereby the best triple-shape properties were achieved for nanocomposites containing 40 wt% of PCL. In this way, the triple-shape effect could be characterized by two distinct switching magnetic strengths $H_{sw,1}(A \rightarrow B)$ and $H_{sw,2}(B \rightarrow C)$ corresponding to the switching temperatures determined in cyclic, thermomechanical tensile tests for thermally-induced triple-shape polymers.

SMPs, which can be controlled independently from heat, were obtained by incorporating light-sensitive reversibly reacting molecular switches into polymer networks resulting in the light-induced SME.[51] Suitable light-triggered molecular switches are cinnamic acid (CA) or cinnamyliden acetic acid (CAA). A 2 + 2 cycloaddition reaction occurs between two of these light-sensitive moieties, forming covalent crosslinks by formation of cyclobutane rings upon irradiation with UV light of $\lambda > 260$ nm. When irradiated with UV light of $\lambda < 260$ nm, these crosslinks can be cleaved again. The permanent shape of these photoresponsive SMPs is determined by the amorphous permanent polymer network.

The light-induced SME could be realized in two kinds of polymer structures: a grafted polymer and an interpenetrating polymer. In the first one, the CA molecules were grafted onto the permanent polymer network by copolymerization of *n*-butylacrylate, hydroxyethyl methacrylate, and ethyleneglycol-1-acrylate-2-CA using poly(propylene glycol)-dimethacrylate ($M_n = 560\ g\ mol^{-1}$) as a crosslinker. The interpenetrating polymer network was formed by loading a permanent polymer network consisting of *n*-butylacrylate with 3 wt% poly(propylene glycol)-dimethacrylate ($M_n = 1000\ g\ mol^{-1}$) as the crosslinker with 20 wt% star-poly(ethylene glycol) endcapped with CAA terminal groups (SCAA). The loading of the polymer was achieved by swelling in a 10 wt% SCAA chloroform solution, obtained as an opaque yellow film after removal of the solvent. The permanent shape of both light-sensitive SMPs, the grafted and the interpenetrating polymer networks, is determined by the permanent network (Figure 6).

In the DSCP, the polymer network is stretched first, resulting in a strain of the coiled polymer segments. Afterward, the polymer network is irradiated with UV light $\lambda > 260$ nm, whereby additional crosslinks are created, which fix the elongated form in a temporary shape. When irradiated with UV light of $\lambda < 260$ nm, the crosslinks are reversibly cleaved and the permanent shape is recovered. The grafted polymer featured in the fifth cycle R_fs of max. 52% and R_rs of max. 95%. The interpenetrating network showed in the third cycle 33% R_f and 98% R_r. As light-induced SMPs circumvent the constraints of external heating, they have a high application potential in the medical field.

1.126.2. Synthesis and Properties of Selected Examples of SMP Intended for Biomedical Applications

In covalently crosslinked polymer networks, the general parameters for controlling the shape-memory behavior are the nature of the switching segments influencing the characteristics of the SME such as T_{sw} and the crosslink density influencing the mechanical properties.

A common strategy for the synthesis of SMP networks with covalent crosslinks is subsequent crosslinking of linear

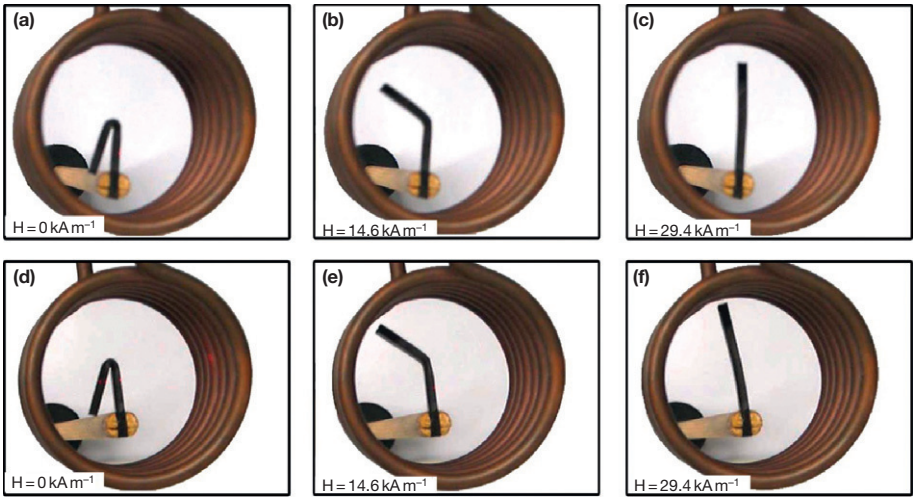

Figure 5 Images obtained for a triple-shape composite polymer network obtained from cyclohexylmethacrylate, poly(ε-caprolactone) dimethacrylate, and 12.5 wt% silica-coated iron(III) oxide nanoparticles during recovery at magnetic field strength *H* of 0, 14.6, and 29.4 kA m^{-1}. (a-c) TSCP-1: (a) shape A at 0 kA m^{-1}, (b) shape B at 14.6 kA m^{-1}, and (c) shape C at 29.4 kA m^{-1}. (d-f) TSCP-2s-II: (d) shape A at 0 kA m^{-1}, (e) shape B at 14.6 kA m^{-1}, and (f) shape C at 29.4 kA m^{-1}. Reproduced from Narendra Kumar, U.; Kratz, K.; Wagermaier, W.; Behl, M.; Lendlein, A. *J. Mater. Chem.* **2010**, *20*, 3404–3415, with permission from Royal Society of Chemistry.

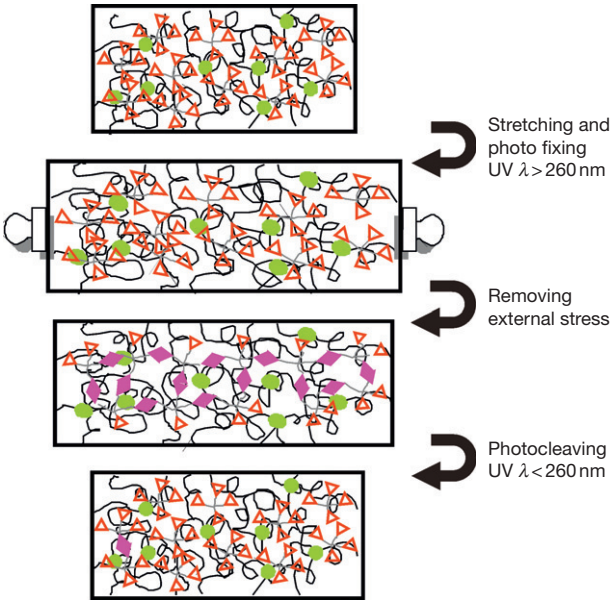

Figure 6 Molecular mechanism of shape-memory effect of the interpenetrating polymer network: the chromophores (open triangles) are covalently connected to star-shaped oligomers, which are loaded into the permanent polymer network (filled circles, permanent crosslinks), forming photoreversible crosslinks (filled diamonds); fixation and recovery of the temporary shape are realized by UV light irradiation of suitable wavelengths.

polymers by postprocessing methods. Crosslinked poly(ethylene-*co*-(vinyl acetate)) (PEVA) is produced by curing linear PEVA with the radical initiator dicumyl peroxide, enabling a thermally-induced crosslinking reaction.[52] A second strategy comprises the one-step synthesis of polymer networks by (co) polymerization of monomers or oligomers with monomers having three or more reactive groups. Examples for this synthesis strategy are SMPs based on polyesters, which are obtained from ring-opening polymerization with the addition of crosslinking dilactone.[53,54] The most important approach to covalently crosslinked SMP networks involves the crosslinking of linear or branched polymeric precursors in a second step either by crosslinking precursors having three or more reactive groups ('star-shaped' precursors) with a crosslinker having two reactive groups or by crosslinking linear precursors with crosslinkers having three or more reactive groups. The shape-memory characteristics of these polymer networks can be controlled by parameters such as the number of polymer chain segments originating from netpoints (arms), the length of the chain segments, the thermal transition of the domains provided by the switching segments, and the number of phases. The mechanical properties are determined by the crosslink density, which is controlled by the chain segment length and the functionality of crosslinks as predefined in the polymeric precursors and the crosslinker. Switching segments can be amorphous or crystallizable. In addition, the nature of the switching segment influences the hydrolytic degradation and determines the trigger of the SME.

The copolymerization of diethylene glycol dimethacrylate (DEGMA) or poly(ethylene glycol) dimethacrylate (PEGMA) with low-molecular-weight acrylates yielded AB copolymer networks with $T_{trans} = T_g$ having covalent crosslinks. The choice of the acrylate enabled control of the elastic properties as well as T_{trans}. Furthermore, the elastic properties could be controlled by the molecular length and by the weight amount of the crosslinker.[13] When *t*-butyl acrylate (tBA) was copolymerized with DEGMA, AB copolymers with T_g around 55 °C were obtained. The rubbery modulus of the SMP networks could be adjusted between 1.5 and 11.5 MPa by the variation of the crosslinker content which was varied between 0 and 40 wt%. When methacrylate was used in such AB copolymer networks instead of tBA, the T_g could be varied between 56 and 92 °C while values of the rubbery modulus between 9.3 and 23.0 MPa were obtained.[55] *In vitro* biocompatibility tests are published for a PEGMA-*co*-methyl methacrylate SMP including tests for cytotoxicity, sensitization, irritation, acute and subchronic toxicity, and genotoxicity of sample extracts according to the 10993 GLP guidelines and have shown highest passing scores possible for all tests.[56]

Covalently crosslinked SMPs with $T_{trans} = T_m$ were created from semicrystalline polycyclooctene having unsaturated carbon bonds by ring-opening methathesis and which was subsequently crosslinked by the addition of dicumyl peroxide.[57]

Linear multiblock copolymers enable SMPs, in which the permanent crosslinks are replaced by physical crosslinks, to allow reshaping of the permanent shape when necessary. A necessity in these thermoplastic SMPs is the formation of at least two segregated phases forming hard domains and switching domains, respectively. The hard domains determine the permanent shape by physical crosslinks, which can be removed only by overstepping the thermal transition of the hard domains. T_{trans} of the switching domains is related to T_{sw} and therefore is applied to trigger the SME. Thermoplastic SMP can be synthesized by direct coupling of presynthesized polymer blocks with a linker, by applying the prepolymer method, or by melt blending.

A widely used method for the synthesis of multiblock copolymers is the coupling of the different oligomeric building blocks with a reactive linker.[4,58–60] A straightforward coupling method of hydroxytelechelic polymer blocks (diols) is the application of diisocyanates. The polyaddition reaction leads to urethane bonds without other reaction products. Frequently used diisocyanates are 2,4-diisocyanatotoluene (TDI), 1,6-diisocyanatohexane (HDI), and 1,6-diisocyanato-2,2(4),4-trimethylhexane (TMDI).

In the process called the prepolymer method, isocyanate-terminated prepolymers are obtained by reaction of hydroxytelechelic oligoesters or -ethers with an excess of a low-molecular-weight diisocyanate. Low-molecular-weight diols or diamines are added as so-called chain extenders to further couple these prepolymers. In this way, shape-memory polyurethanes or polyureas can be obtained as phase-segregated block copolymers having the prepolymer as switching domains. The hard domains contain highly polar urethane and urea bonds exhibiting high values of T_{trans}. The length of the hard segment blocks can be adjusted by the ratio of the prepolymer to diisocyanate/chain extender.[61]

Blending is a way to obtain thermoplastic SMP rather by processing than by synthesis. In this type of thermoplastic SMP, the component providing the hard segment and the component forming the switching segment are located in different linear multiblock copolymers.[62] While the mechanical properties could be varied systematically by the blend

composition, T_{sw} was nearly constant. The principle of shape-memory blends is of high interest as the segments in general can be selected according to the requirements of specific applications.

The polyaddition of polytetramethyleneoxide (PTMO) precursors with HMDI and 1,4-BD by the prepolymer method leads to phase-segregated PEUs with $T_{trans} = T_g$.[45,61,63] Here, the polyaddition of the HMDI with 1,4-BD forms the segment providing the hard domains, while the PTMO segment provides the switching domains. In a commercially available PEU synthesized from methylene bis(*p*-cyclohexyl isocyanate) (H12 MDI), BD, and PTMO diol T_g is at 74 °C. Determination of shape-memory properties revealed R_f of 100% and R_r of 80% after the third cycle at ε_m 50%. Remote actuation of the thermally-induced SME in alternating magnetic fields was realized by the incorporation of silica-coated magnetic nanoparticles of iron(III) oxide core into a polymer matrix of the described polymer.[45]

A polyether-based SMP with a T_{trans} of about 55 °C exhibited no cytotoxic effects on the adhesion and proliferation of human skin fibroblasts and gingival fibroblasts. In addition this PEU limited the adhesion of platelets.[64] The cytocompatibility and hemocompatibility made this PEU useful for artificial hearts, wound dressings, and pacemaker leads.[61] Plasma sterilized noncytotoxic PEU foams with T_gs of 35 and 55 °C could be used as a material for endovascular procedures.[65,66] In dogs with lateral aneurysms on both carotid arteries, the PEU-based SMP foams were able to occlude the aneurysms (test period: for 3 weeks) and to cause neointima formation at the neck of the aneurysm.[66] However, variations in PEU blood compatibility have been observed, with improved thromboresistance correlating to more alkylated soft segments,[67] higher soft-segment content on the surface,[68] well-developed microphase separation, and surface treatments such as grafted sulfonate groups.[69,70] On polyurethane-derived SMPs based on methylene diphenylene diisocyanate (MDI), PTMO, and *N*,*N*-bis(2-hydroxyethyl)isonicotinamide, effective nonleaching biocidal properties could be shown.[71] It was found that this polyurethane SMP possessed good bactericidal activity against *Staphylococcus aureus* and bacteriostatic activity against *Escherichia coli*. Also PCL-based shape-memory polyurethane ionomers with quaternarized pyridine moieties proved to be suited to reduce the bacterial activity of *Klebsiella pneumoniae* (− 96.2%) and *S. aureus* (−100%). Cytotoxicity testing by use of the agarose overlay assay with L929 mouse fibroblasts revealed no adverse effects of the materials on these cells.[72]

Polyurethane-based shape-memory block copolymers having $T_{trans} = T_m$ are synthesized by coupling of crystallizable hydroxytelechelic precursors with diisocyanates. Switching segments can be polyethers such as PTMO or polyesters such as PCL exhibiting a T_m near body temperature. A polyesterurethane consisting of hard segments based on 4,4′-MDI and 1,4-BDO and soft segments of PCL (PU/PCL, 70/30) and with T_{trans} at body temperature was blended with the PCL, which provided the switching segment. The blended SMP supported adhesion and proliferation of human bone marrow mesenchymal stem cells (MSCs). This gives the possibility to use the material for cardiovascular stents with an MSC coating on the blend for possibly better tissue compatibility.

1.126.3. Multifunctional SMPs by Integrating Hydrolytic Degradability or Controlled Drug Release Capability

Besides different ways of stimulation and the application driven adjustment of thermal and mechanical properties, a challenge in the development of SMP is the addition of novel functions resulting in multifunctional materials. Multifunctionality is the targeted combination of material functions, which are not linked with each other.[73,74] Multifunctional materials can be created by the integration of various functions in multimaterial systems on the nano- or micro-level. Single material systems combining the different functions on the molecular level[73] were reached as well, for example, by combining the shape-memory capability with hydrolytical degradability. This combination of functions is advantageous when devices or implants are only temporarily required, as a second surgery for the removal of the implant can be avoided. Another function that can be created in SMP is the controlled release of drugs. This function aims at ensuring constant levels of a drug over an extended period of time by simultaneously reducing the frequency of administration of the drug.[75] Often lower dosages of drug are effective in this way compared to oral administration, thereby possibly leading to reduction of drug side effects. SMP matrices as drug carrier would allow implanting of bulky devices by MIS and fixation of such devices in the body, combined with the above-mentioned advantages. Such a combination of functions is demanded by biomaterial-assisted therapies, for example, for vascular and urinary stents or as scaffold material for reconstructive or esthetic surgery (e.g., breast remodeling), and in tissue engineering applications (e.g., bone regeneration).

Degradation of SMP devices *in vivo* involving breakdown of macromolecules is mainly designed to utilize hydrolytic bond cleavage. However, it needs to be considered that breakage of bonds *in vivo* can be enhanced by enzymatic processes. The hydrolytic degradation rate is determined by the hydrolysis rate of the cleavable bonds and by diffusion processes: the diffusion of water into and of small degradation products out of the polymer matrix. In general, two mechanisms of hydrolytic degradation can be differentiated, which are determined by the relation between hydrolysis rate and diffusion rate.[76] If the hydrolysis rate is high compared to the diffusion rate, the degradation is confined to a thin layer on the surface. This 'surface erosion' (**Figure 7(a)**) is directed from the surface to

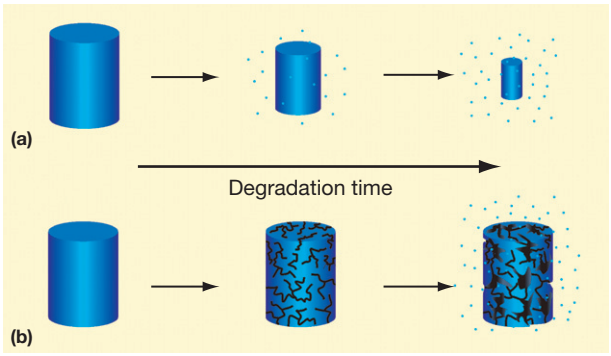

Figure 7 Mechanisms of hydrolytic degradation: (a) surface erosion; (b) bulk degradation.

the center of the polymeric implant reducing it permanently in size and mass, while the material which is distant from the surface sustains its original properties. On the other hand, 'bulk degradation' (**Figure 7(b)**) is a nondirected process. Here, diffusion is fast compared to the hydrolysis and allows degradation to take place all over the polymer matrix. First, mechanical properties change without size reduction of the polymer matrix. Randomly distributed bond breaks lead to the generation of larger degradation products. After a material-specific induction time, the degradation products become soluble and small enough to diffuse out of the matrix and the implant disintegrates with a fast mass loss. Depending on diffusion rate, hydrophilicity, and homogeneity of the implant material, the effective degradation behavior often shows characteristic elements from both degradation mechanisms.[77,78]

Biodegradability of SMP was realized by the introduction of hydrolyzable bonds, which could be easily cleaved under physiological conditions.[79] However, if biodegradable polymers are used in medical devices, the compatibility of the polymer and its degradation products to the surrounding tissue has to be considered.[80] In polymers, the chemical nature of the polymer itself determines the hydrolyzation rate: orthoesters hydrolyze faster than ester bonds, which in turn hydrolyze faster than amide bonds. Another influencing factor is the steric accessibility of the hydrolyzable bonds. The degradation is slower if bulky substituents hinder the access of the medium to the cleavable bonds and in this way the hydrolysis. The diffusion rate of water and water-soluble degradation products within the material depends on hydrophilicity and morphology of the polymer. When the hydrophilicity is comparable, the hydrolyzation of amorphous polymers is favored compared to semicrystalline polymers. Unlike semicrystalline polymers, they show a more homogeneous degradation which is advantageous for application in implants as the diffusion processes are significantly reduced in crystalline domains resulting in slow surface erosion on the microscopic level. Furthermore, the macroscopic shape of a material needs to be considered. Porous materials degrade faster than solid materials because of the higher surface/volume ratio as well as the shorter distances for diffusion within the polymer matrix.

The most widely applied class of biodegradable SMP is the class of aliphatic (co)polyesters. The ester bond is a suitable target for hydrolytic cleavage. In general, the more an ester bond is activated by electron-accepting substituents, the faster it is hydrolyzed. In polyesters from monomers with long aliphatic hydrocarbon chains, the ester bond is not activated. Therefore, hydrolyzation of these polymers is slower than of that of polyesters based on hydrophilic monomers with short hydrocarbon chains and acceptor substituents (**Figure 8**).

In aliphatic (co)polyesters from lactone monomers such as the cyclic diesters diglycolide and dilactide resulting in poly(α-hydroxy acids), bulk degradation could be observed. Polyglycolide (PGA), polylactide (PLA), and copolymers are established biomaterials in clinical application. But hydrophilic (co)polyesters incorporating poly(ethylene oxide) (PEO) or PPDO also showed bulk degradation.[81] Here, ether bonds enhanced the hydrophilicity and could activate adjacent ester bonds for hydrolyzation. A frequently applied method to increase the rate of degradation of polyesters exhibiting a slow degradability was the introduction of easily hydrolyzable ester bonds by copolymerization. Here, the incorporation of glycolide units, especially glycolide–glycolide diads, leads to copolymers with enhanced degradability, whereas the rate of the hydrolytic degradation could be controlled by the glycolide content and distribution in the polymer chain.[82–86]

Hydrolyzable polymer chain segments retained their biodegradability when they were incorporated into multiblock copolymers or copolymer networks by coupling thermally with short linkers or photochemically with unsaturated end groups. In polymer networks, the degradation properties could be

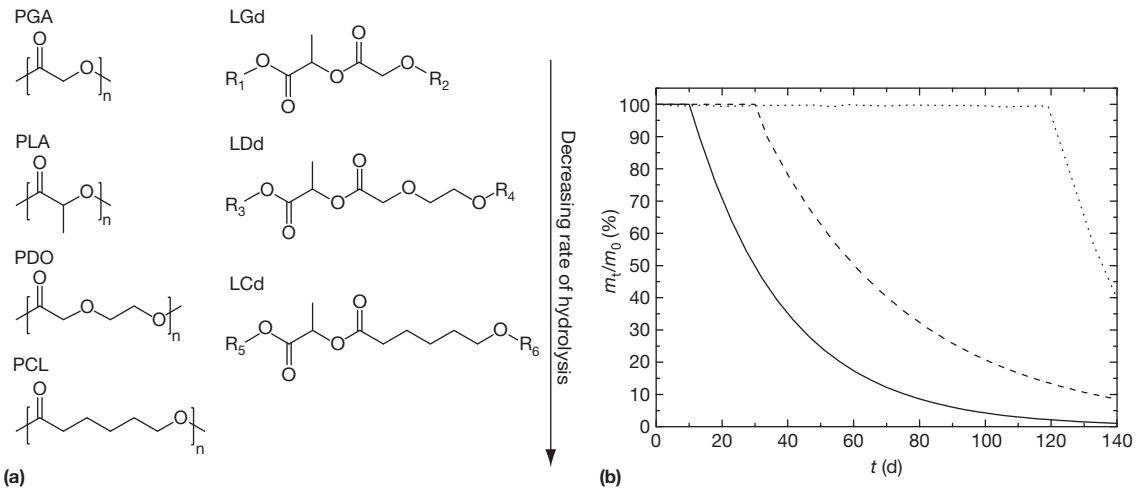

Figure 8 Comparison of the rate of hydrolysis of polyesters applied in SMP. (a) Influence of the chemical structure in polyesters and diads of copolyesters ordered according to their rate of hydrolysis. PGA, polyglycolide; PLA, poly(*rac*-lactide); PDO, poly(*p*-dioxanone); PCL, poly (ε-caprolactone); LGd, lactide–glycolide diad; LDd, lactide–dioxanone diad; LCd, lactide–caprolactone diad. (b) Influence of the copolymer content in networks based on poly((*rac*-lactide)-*co*-glycolide), mass fraction of the networks relative to the original mass as function of the degradation time, solid line: 52 wt% glycolide, dashed line: 30 wt% glycolide, dotted line: 20 wt% glycolide. In part with permission from Lendlein, A.; Zotzmann, J.; Feng, Y.; Alteheld, A.; Kelch, S. *Biomacromolecules* **2009**, *10*, 975–982. Copyright 2009 American Chemical Society.

influenced by the crosslink density. Most SMPs were phase-segregated block copolymers or copolymer networks being composed of two or more different polymer segments. These segments differed substantially in their rate of hydrolysis leading to a faster degrading part and a residual part, which remained in the body until fully degraded (enzymatically or by slow hydrolysis) or eliminated by other physiological mechanisms.

In the following, specific approaches will be discussed, which led to hydrolyzable SMPs. Hydrolyzability was realized, for example, in thermoplastic SMPs, which have been obtained as linear multiblock copolymers with PCL blocks, PPDO blocks, and diisocyanate as junction unit.[81,87] The M_n of the switching segment as well as the composition of the SMP have an influence on T_m of the switching domains and consequently on T_{sw}.[88,91] These multiblock copolymers named PDC displayed a linear mass loss *in vitro*, resulting in continuous release of degradation products. In contrast to the hydrophilic PPDO, the PCL exhibited a very slow degradation rate. In *in vivo* and *in vitro* experiments, the degradation behavior of biodegradable multiblock copolymer SMPs, PDC containing PPDO hard segments, and crystallizable PCL switching segments, which were synthesized via cocondensation of two oligomeric macrodiols with an aliphatic diisocyanate as junction unit,[89,90] was tested.[81,91] The study showed that the *in vivo* degradation process of PDC is characterized by a release of microparticles, which were supposed to primarily consist of PPDO, and which did not negatively affect a strong integration of the SMP in the subcutis of rats[89] and mice.[92] This might be explained by the angiogenic effect of the PDC, which was shown in the hen's egg chorioallantoic membrane test (HET-CAM test)[93] and also after subcutaneous implantation in rats[89] (**Figure 9**) and mice.[92]

In multiblock copolymers having a PCL switching segment and a polyurethane hard segment, an increased elasticity above T_{trans} could be achieved by incorporating polyhedral oligosilsesquioxane (POSS) sequences.[94]

Another example of biodegradable SMP is multiblock copolymers containing poly(L-lactide) (PLLA) and poly(glycolide-*co*-(ε-caprolactone)) (PGCL).[95] The degradability of the PGCL segment was improved by incorporation of easily hydrolyzable glycolic acid ester bonds. The change of shape-memory properties during hydrolytical degradation was investigated in a biodegradable shape-memory polyesterurethane from poly (adipate)diol. The poly(adipate)diol provided the segments forming the domains acting as switching domains while hard domains were built by the reaction between MDI and BD using the applied prepolymer method.[96] The degradation process could be divided into three phases: an induction phase, a phase of continuous degradation, and a phase of accelerated degradation. R_r remained fairly constant during phase one and decreased slowly during phase two. The increase in crystallinity in phase two was accompanied by an increase in R_f.

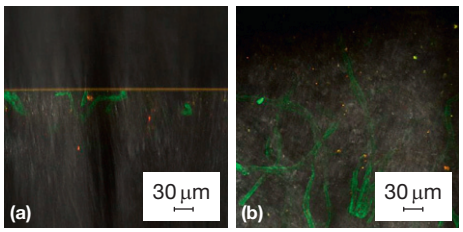

Figure 9 (a) Newly formed microvessels 10 µm above a PDC implant. (b) Three weeks after subcutaneous implantation in the rat neck; nonsoluble degradation products yellow stained; micro-blood vessels visualized by fibronectin staining in green; (a): cross-section, PDC red. Reproduced from Lendlein, A.; Behl, M.; Hiebl, B.; Wischke, C. *Expert Rev. Med. Devices* **2010**, *7*(3), 357–379, with permission from Expert Reviews Ltd.

In addition to the polyesters, other classes of hydrolyzable polymers were used to combine shape-memory capability with biodegradability, including polydepsipeptides which are alternating copolymers of α-amino acids and α-hydroxy acids and are known to be nontoxic and degradable. Biodegradable SMPs were obtained as thermoplastic multiblock copolymers by coupling of oligodepsipeptide diols and PCL diols using TMDI.[97,98] The PCL domains had the function of the switching domains, while the polydepsipeptide segments provided the hard domains.

Glassy switching domains based on a copolymer segment are frequently utilized for the adjustment of T_{sw} to a specific temperature as it is necessary for SMPs in medical applications. Depending on the ratio of the comonomers during polymerization of the copolymer block, the T_g can be altered within the temperature range defined by the T_gs of the two related homopolymers. An example is a polyesterurethane having switching domains based on copolymers from L-lactide and ε-caprolactone, and polyurethane hard domains from BD and TDI.[99] In this thermoplastic SMP, T_{sw} could be adjusted between 28 and 53 °C. It was shown that the degradation rate of the copoly(ether)esterurethanes depended not only on the hydrolysis rate of their ester bonds, but also on the materials' hydrophilicity and on the molecular mobility, which was significantly different at temperatures above or below T_g.

SMP networks with a certain degradability having $T_{trans} = T_m$ could be obtained by initiator-free photopolymerization of PCL-based macrodimethacrylates, which were created by an esterification reaction of PCL macrodiols with methacryloyl chloride. The shape-memory properties of the polymer networks, named N-PCLDMA, were excellent, with R_r between 92 and 97% and R_f between 86 and 97% after five cycles. Recently, the *in vitro* degradation of SMP network nanocomposites consisting of crosslinked PCL and Fe_3O_4 nanoparticles had been investigated.[100]

AB polymer networks with $T_{trans} = T_m$ were prepared from linear PCL or PGCL which were functionalized with methacrylate end groups and were copolymerized with *n*-butyl acrylate (BA), yielding the polymer networks N-PCLDMA-BA or N-PCGDMA-BA. The networks with BA as comonomer contain an amorphous poly(*n*-butyl acrylate) phase exhibiting a very low glass transition temperature ($T_g = -55$ °C) and provide additional elasticity to the polymer network.[101] Molecular parameter for controlling T_{sw} was the molecular weight of the used macrodimethacrylate crosslinker while the mechanical properties were a function of the BA comonomer content. With increasing BA content, the values of the elastic modulus, the tensile strength ε_m, and the tensile stress at break σ_R decrease by approximately an order of magnitude. In biocompatibility tests, the SMP N-PCLDMA-BA, which was made sterile using ethylene oxide,[102] was able to induce angiogenesis and strong tissue integration in male Naval Medical Research

Institute (NMRI) mice already one week after subcutaneous implantation.[92] The same SMP also proved its capability for auto-induced regeneration of a radical stomach wall defect in rats.[103,104] No gas leakage after gas insufflation could be detected and fast and unfavorable degradation of the polymer did not occur. A tight connection between the polymer and the adjacent stomach was found, resulting in adequate mechanical stability under the extreme pathophysical conditions of the stomach milieu (**Figure 10**).

Incorporation of additional easily cleavable ester bonds increases hydrolytic degradability of polyester-based SMP networks substantially.[105] By UV-curing of poly((ε-caprolactone)-*co*-glycolide)-dimethacrylates (PCGDMA), crystalline, hydrolytically degradable, covalently crosslinked SMP networks (N-PCGDMA) with an increased hydrolytical degradation were obtained. The precursors had a glycolide content of 14 mol% and M_n of 4900 or 12 800 g mol^{-1}. While T_{sw} of N-PCGDMA using PCGDMA of 4900 g mol^{-1} was at 30 °C, N-PCGDMA built from PCGDMA of 12 800 g mol^{-1} had a T_{sw} at 38 °C. N-PCGDMA using PCGDMA of 4900 g mol^{-1} displayed R_r of 86% and $R_f > 96\%$ after five cycles with $\varepsilon_m = 150\%$. With increasing molecular weight of the precursors, R_r and R_f increased, so that R_f of >97% and R_r of >99% were obtained.

ABA triblock polymers with hydrolytically degradable switching segments and with $T_{trans} = T_g$ were prepared by a ROP of *rac*-dilactide with poly(propylene oxide) (PPO)-diol as macroinitiator in the presence of dibutyltin oxide (DBTO) as catalyst. Here, the poly(*rac*-lactide) (PLA) block represents the switching segment in the polymer network. The PPO B-blocks exhibit a T_g well below ambient temperature, which cannot be used as T_{trans} but provided additional elasticity to the SMP networks. The ABA triblock copolymer diols with a middle block of PPO were end-group functionalized with methacrylate groups and photochemically crosslinked using UV light to obtain polymer networks.[101]

However, methacrylate networks were relatively brittle and therefore difficult to handle. Copolyesterurethane networks prepared from star-shaped macrotriols or macrotetrols and a diisocyanate as a junction unit resulted in well-defined SMP networks. These precursors were synthesized by ROP utilizing initiators having more than two initiating reactive groups. ROP of *rac*-dilactide and diglycolide with a hydroxytelechelic three-armed PPO macroinitiator led to diblock star-shaped precursors, which were crosslinked in a second step with TMDI. The tailored crosslink density led to amorphous polymer networks containing poly((*rac*-lactide)-*co*-glycolide) (PLG) switching segments with more favorable elastic properties.[106] The elastic properties in such PLG-derived polymer networks could be further improved by the incorporation of a PPO segment contributing to the elasticity.[107] However, these PLG-derived polymer networks with a glycolide content between 15 and 18 wt% are limited in their applicability because of their relatively high T_{sw} between 48 and 66 °C. The synthesis of star-shaped macrotetrols by copolymerization of *rac*-lactide with *p*-dioxanone (PLD), or ε-caprolactone (PLC), or glycolide (PLG) yielded SMP networks, in which T_{sw} could be varied between 14 and 56 °C (**Figure 8**).[88]

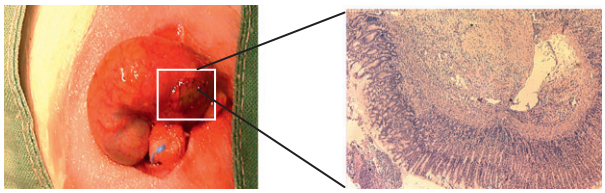

Figure 10 Left: Radical defect (diameter: 100 mm) in a rat stomach wall 4 weeks after defect closure with a PCL/BA-based SMP disk (diameter: 10 mm, thickness: 200 μm[136]); the implant was fixed by conventional suturing. Adapted from Rickert, D.; Lendlein, A.; Kelch, S.; Franke, R. P.; Moses, M. A. *Biomed. Tech. (Berl.)* **2005**, *50*, 92–99. Right: Hematoxylin–eosin stained histological section of the defect zone: the critical stomach wall defect was completely regenerated 4 weeks after defect closure with the SMP. Reproduced from Lendlein, A.; Behl, M.; Hiebl, B.; Wischke, C. *Expert Rev. Med. Devices* **2010**, *7*(3), 357–379, with permission from Expert Reviews Ltd.

Biodegradability involves hydrolytic degradability as well as enzymatically supported degradability. Enzymatic degradation becomes more important when slowly or nonhydrolyzable polymer segments are incorporated into biodegradable SMPs.[108] In contrast to water, the availability of specific enzymes can differ locally in the body and their diffusion capabilities are limited. However, in some cases the degradation of hydrolyzable bonds can be substantially accelerated by enzymes. Hydrolytic degradation of polymer monolayers by Langmuir—Blodgett techniques was shown to be a useful tool for the investigation of enzymatic degradation processes.[109] The enzymatic degradation of PCL and PCL-diol monolayers displayed degradation by random chain scission, which could be fitted by computer models.[110] In multiblock copolymers from PCL and PPDO, the enzymatic degradation rate decreased with increasing content of PPDO blocks, which was in contrast to hydrolytic degradation.[111] Furthermore, it was shown that the enzymes could penetrate into the PCL domains of thin films of this multiblock copolymer, whereby the penetration depth was a function of the PCL content resulting in a selective degradation of PCL blocks.[112]

Conclusively, a possible contribution to degradation by enzymatic processes is hardly predictable without *in vivo* tests and depends on several factors specific for the respective application. Biodegradability of SMP is mainly determined *in vitro* by exposure to aqueous buffer solutions under physiological conditions. The time dependence and extent of deterioration of the characteristic properties can be determined as well as the identity and quantity of degradation products. Within the SMP class of polyesters, degradation products are mainly the hydroxycarboxylic acids or oligomers thereof, which are expected to have no physiologically harmful influence, as long as their concentration is low enough to avoid a significant decrease in pH.

In multifunctional SMPs that involve controlled drug release, specific processes in synthesis, processing, and programming have to be applied to enable each of the functionalities. Key for a release of bioactive molecules is their incorporation into the polymer matrix. Drug incorporation into the matrix can principally be achieved by soaking of the synthesized matrix in a drug solution and a subsequent drying step, or alternatively by mixing of defined amounts of drug with polymer network precursors and subsequent crosslinking. The latter method often allows higher drug loading but is limited by the chemical stability of the drug under

the crosslinking conditions.[113,114] Drug release from polymer matrices is most often ruled either by diffusion or by degradation of the matrix. Although these mechanisms can occur at the same time, it is advisable to design the polymer matrix in a way that one mechanism predominates in order to better control the release pattern. Diffusion-controlled release from a degradable matrix can, for example, be achieved for small water-soluble molecules from bulk-degrading materials (such as polyesters, e.g., PLG),[115–117] in which monomer composition and polymer architecture can be used to prolong the induction time for degradation of the matrix till the time point when basically all of the drug has been released.[118] Alternatively, the use of surface-eroding materials such as polyanhydrides[119] or poly (orthoesters)[120] allows an erosion-controlled drug release.

Figure 11 depicts three functions of a multifunctional implant, that is, the SME, drug release by diffusion, and degradation of the polymer matrix. In the given example, these three independent functionalities are given in the consecutive order which is likely to be important for applications. After implantation of a medical device, the SME can allow a fixation of the device at the site of implantation. Subsequently, a diffusion-controlled drug release for treating infections, reducing inflammatory responses, or, potentially, supporting regeneration processes, takes place. Finally, the degradation of the matrix after completed drug release can avoid a second surgery for removal of the implant.

One of the biggest challenges in the design and formation of a multifunctional polymer is to ensure that the different steps in the formation or recall of the functionality do not erase one of the other functions. For the drug releasing, degradable SMPs, it is important that (i) the incorporation of hydrophilic or hydrophobic drugs does not influence the shape-memory functionality, (ii) an either diffusion- or degradation-controlled release is enabled, and (iii) the programming process and shape recovery, which a device experiences during implantation, do not change the drug release kinetics. Therefore, an evaluation strategy for drug releasing, biodegradable SMPs was introduced.[113,121] Four steps were identified, which need to be analyzed for usage of drug-loaded SMPs in a physiological environment, which include traditional assessments of drug release matrices such as the determination of the drug loading and release profile as well as the interdependence of matrix functionalities. Drug-loaded implants for long-term treatments contain a large amount of drug compared to the daily dose. Therefore, it is an important safety aspect to ensure that no dose dumping, that is, an uncontrolled fast release of possibly toxic drug levels occurs.

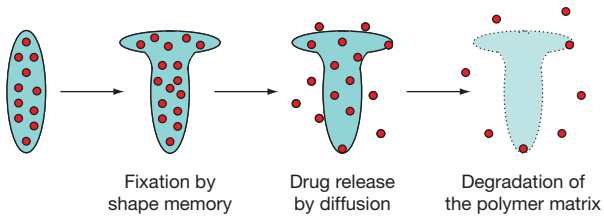

Figure 11 Consecutively initiated functionalities of a multifunctional material: SME for fixation of the device, diffusion-controlled drug release, and degradation of the matrix.

So far, only a few systems representative for triple functional materials combining biodegradability, SME, and controlled drug release have been published. All of them belong to the bulk-degrading polyesters with a diffusion-controlled release. However, monomer type and ratio as well as network architectures resulted in quite different capabilities of the networks which will be discussed in more detail to highlight common characteristics and individual advantages and shortcomings. In the following, several semicrystalline matrices and an amorphous matrix will be compared regarding drug loading, thermomechanical and shape-memory properties, and release profiles.

The first example for triple functional SMPs was N-PCGDMA polymer networks. In these semicrystalline networks, hydrophobic and hydrophilic drugs could be incorporated either by swelling (up to 0.72 wt%) of the final networks in an organic solvent saturated with the respective drug, or by mixing defined amounts of the drug (in this case, 0.2–5.7 wt%) with the network precursors followed by irradiation (*in situ* incorporation).[114,122] A semicrystalline polymer network was chosen so that the crystalline phases of the networks were used for fixation of the temporary shape, while drug molecules should predominantly be incorporated in the amorphous phases without having a too strong influence on the melting point of the polymer crystallites or the shape fixation and recovery.[113] Drug incorporation did have some influence on crystallite formation and, therefore, on T_m and T_{sw}. However, this was only the case in networks with a high glycolide content (>14 mol%) or small precursor M_n (<6900 g mol^{-1}), as these networks only form crystallites to a small extent even in the drug-free state. The same was observed when large amounts of drug were incorporated by *in situ* loading (>4.8 wt%). In these cases, the formation of crystallites was inhibited leading to a decrease of T_{sw} and/or low shape fixity. Large amounts of drug furthermore decreased the elongation at break of the networks, which reduced their programmability. In materials with high crystallinity, in the drug-free state (i.e., glycolide contents ≤14 mol% and precursor $M_n \geq 6900$ g mol^{-1}), no effect of drug loading on the thermomechanical properties and shape-memory functionality was observed.

Drugs loaded by swelling were released from the selected materials in three phases, that is, an initial burst release (34–39 wt%), a diffusion-controlled subsequent release (cumulative release >80 wt%, over 120–140 days) that linearly correlated with the square root of time,[123] and a final nonlinear phase. Drug-loaded networks which were shown to have high shape fixity and shape recovery were subjected to hydrolytic degradation and compared with drug-free samples. The induction time for erosion as observed by the onset of mass loss of the matrix was about 120 days. This illustrates that a diffusion-controlled release was realized before erosion of the matrix would have led to changes in drug release. Furthermore, independence of polymer functionalities could be demonstrated. However, alterations in polymer network composition are typically limited for semicrystalline SMPs by the need to form crystallites for shape fixation. In addition, only limited amounts of drug could be incorporated by swelling (<1 wt%), which was theoretically high enough to ensure pharmacological efficiency of the model drugs, but might be necessary to be increased for other drugs.

By introducing an additional amorphous phase by incorporation of 60 wt% *n*-butyl acrylate, AB polymer networks were obtained in which the PCGDMA copolyester chains served as degradable crosslinkers.[101] With increasing glycolide molar content χ_G, that is, increasing hydrophilicity of the material, more of a hydrophilic model drug could be incorporated by the swelling technique. At the same time, larger hydrophilicity of the polymer networks also favors water uptake and rapid initial drug release. Therefore, tailoring the material's hydrophilicity by adjusting χ_G is suitable to control the drug release rates from the AB networks.[124]

Oligo(ε-caprolactone)octols crosslinked by low-molecular-weight aliphatic diisocyanates also form degradable semicrystalline SMPs.[125] Defined amounts (10 and 20 wt%) of theophylline as model drug were mixed with the oligomers followed by crosslinking, a methodology which potentially could result in drug modification. Drug incorporation increased T_m and ΔH_m, which indicated improved crystallization of ε-caprolactone segments. Drug loading did not affect shape fixity. Remarkably, the temperature interval for shape recovery was very small for this network, in both the drug-free and drug-loaded materials. No major burst release was found in this system, and a complete linear release was achieved within 35 days.

It was assumed that a higher drug loading by swelling can be achieved in fully amorphous SMPs such as the star-shaped PLG networks described above. In contrast to semicrystalline materials, the entire matrix is amorphous and therefore accessible to drug.[121] Furthermore, crystallization is not required for shape fixation thus allowing a wider variability for network composition (monomer type and ratio) and network architecture.[113] Also, loading may not impact shape fixation. However, drug molecules may act as softeners and reduce the T_g of amorphous SMPs which could result in an unwanted shift in T_{sw}.

The star-shaped PLG networks loaded by swelling showed loading levels up to 2.6 wt%. Drug loading did not impede the thermomechanical properties or the shape-memory functionality after synthesis. Interestingly, it could be demonstrated that the uptake of water as a softener reduced the T_g from 54 to 36 °C, that is, into a physiologically relevant temperature range. Depending on the type of drug, different phases of drug release were observed to be present at different levels, that is, a burst release of up to 25 wt% of the drug, a linear diffusion-controlled release, and a final nonlinear release that timely overlaps with erosion. Drug release was completed after 4 months. During degradation, drug-loaded polymer networks exhibited lower Young's moduli than the drug-free network. However, the rate of degradation was not influenced by the incorporation of drugs.[121] On the basis of that, it may be expected that future work on drug-loaded SMPs will explore, for instance, in larger detail (i) alterations in the SMP structure to obtain higher drug loadings by swelling; (ii) the effect of the drug loading methodology on release, SME, and biodegradation; (iii) the extent of possible changes in covalent SMP network architecture to control release rates without impairing the SME; (iv) the types of drugs, which can be released from SMPs, and whether the programming technology for thermosensitive SMPs is compatible with thermal stability of therapeutic peptides and proteins; or (v) important issues of prototype development and translation into clinical use including aspects like sterilization, shelf-life, etc.[126]

1.126.4. Biomedical Applications of SMPs

The trend in the clinics toward MIS[127] will allow complicated treatment procedures with a strongly reduced risk of iatrogenic infections. This is because MIS in contrast to open surgery avoids major incisions in the body. Also, patients often recover faster from MIS interventions compared to open surgery and hospitalization costs may be significantly reduced. At the same time, MIS sets new requirements for materials to be used as matrix of medical devices, that is, the capability to be inserted through keyhole incisions and afterward gain full functionality. The advantages of SMPs as candidate matrices rely on two unique properties to fulfill these requirements, that is, their capability to undergo controlled, predefined changes in shape and to generate forces during shape recovery. Both are required to allow adoption of the functional implant shape in a tissue environment.

Depending on the respective application, implants should provide a supportive function and mechanical strength over a long period of time (e.g., stents[55,128]) while for other tasks mechanical forces may only be required initially for deploying the implant (e.g., neuronal electrodes[129]). Furthermore, there are suggested applications where mechanical forces are temporarily useful, but the material should then biodegrade and disappear from the site of application, for example, for self-tightening suture materials.[81] Such specific requirements can be fulfilled by selecting a material from the growing number of different SMP platforms (see **Section 1.126.3**). So far, the suggested SMP medical devices only base on thermosensitive SMPs. Besides triggering the shape recovery by direct exposure to heat (e.g., body temperature; flushing with warm water), indirect heating by light absorption of near infrared (NIR) dyes loaded into the material[31] is an intensively evaluated approach particularly for intravascular applications.

Grouping of medical devices from SMPs may be conducted based on the aspects of (i) the involved material (polymer macromolecular chemistry, degradable, nondegradable); (ii) the engineered implant shapes (e.g., threads for sutures, rods for fixation plugs, hollow fibers for stents, foams for aneurysm closure); or (iii) their indication. In order to illustrate the variety of targeted clinical applications, the latter approach was used in **Figure 12** for a graphical summary of the so far suggested SMP devices as recently discussed in more detail.[130]

According to the trend to MIS and the requirements for new materials, SMP devices for intravascular interventions represent the most intensively studied application. However, it should be noted that device failure in such indication can be of life-threatening consequences. In addition, the induction of shape recovery by local intravascular hyperthermia is a complex and challenging procedure. Therefore, a significant amount of research may still need to be conducted to further improve the set-ups and rule out safety concerns associated with SMP-based medical devices for intravascular applications. However, other applications, for example, as ureteral stents, suture material, or devices for soft tissue fixation to bones,

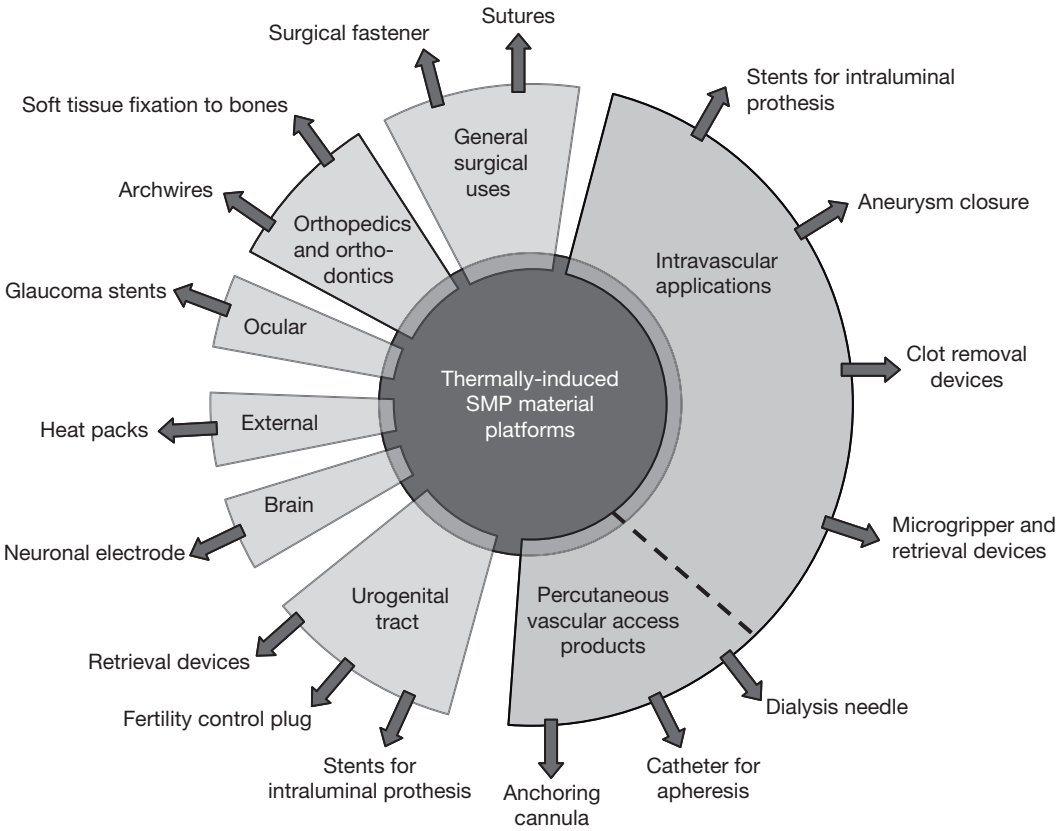

Figure 12 Summary of suggested clinical applications of SMP-based medical devices as published in the scientific and patent literature. A comprehensive list of references as well as a more detailed description of the involved principles can be found in. Lendlein *et al*.[130]

may not be associated with such risks and thus be accepted by clinicians for clinical evaluation. Therefore, such applications may possibly be the first fields of SMP usage in the clinics.

For optimal healing with minimal scar formation, wounds have to be closed by applying a defined pressure to the wound lips. This can be realized by shape recovery of SMPs whose thermomechanical properties have been tailored to the clinical need. Moreover, since biodegradability of sutures is generally well accepted by patients, efforts were made to design biodegradable SMPs. Such polymers have first been described by Lendlein *et al.* and were suggested as suture materials.[81] As illustrated in **Figure 13**, loops of suture threads first loosely connect the wound lips, which subsequently are closed upon heating to moderate temperature.

Stents are used to eventually keep open the internal lumen of flow pathways where local flow constrictions were removed by cardiovascular intervention. Stents have to be inserted in a shape with a small outer diameter, to subsequently expand and apply pressure against the surrounding tissue. In the United States, coronary stents cover about two-thirds of an expected revenue of $5 billion solely for stent devices in 2010, but peripheral applications including renal and biliary stents are also of high relevance.[127] Despite the clinical need and intensive usage, stent technology requires further improvement. This is clearly shown by common restenosis of bare-metal stents, and, in the case of drug eluting stents, by safety concerns due to, for example, late thrombosis with a mortality rate of up



Figure 13 Degradable SMP suture for wound closure that shrinks upon heating in order to bring together the edges of the wound with a defined pressure for optimal healing. Reproduced from Lendlein, A.; Langer, R. *Science* **2002**, *296*, 1673–1676, with permission from AAAS.

to 45% as recently summarized.[131] Therefore, fully degradable stents are believed to be the future in stent technology.[132] However, so far most studies on SMPs as stent matrices have been conducted with nondegradable SMPs. For example, often materials based on acrylate chemistry with polyethylene glycole dimethacrylate crosslinkers[55] or polyurethanes[33] were used. Only in some cases, partially degradable materials employing degradable polyester segments were evaluated.[25]

SMP matrices were shown to be feasible for the required expansion of polymeric stents in vessels and resistance against intravascular pressure.[133] It has been suggested that suitable expansion sizes can be achieved by unrolling and unfurling from a compact shape which can by administered by a 18 Fr. catheter (**Figure 14**).[55] Formerly suggested concepts that involve changes in implant length upon shape recovery have not been followed any further, possibly because of lower feasibility for intravascular placement.[128,134] As shape recovery of

the thermosensitive SMP matrix must be avoided before proper adjustment of the stent, the T_{sw} of the employed materials was typically up to 20 °C above body temperature. Local heating was achieved by loading the SMP with an NIR absorbing dye and heating by laser light with an optical fiber.[33] This technique is challenging at least at flow rates relevant for intravascular conditions because of cooling of the device down to body temperature by the blood stream.

As mentioned before, because of possible interoperative or postoperative risks from potential stent failure in cardiovascular applications, the field of renal or biliary stent applications might be easier to be entered by novel SMP devices. Recently, a demonstrator of a ureteral stent has been designed from a biodegradable material. As illustrated in a model set-up in Figure 15,[122] the device can be anchored at elevated temperatures, for example, as a result of flushing with warm water.

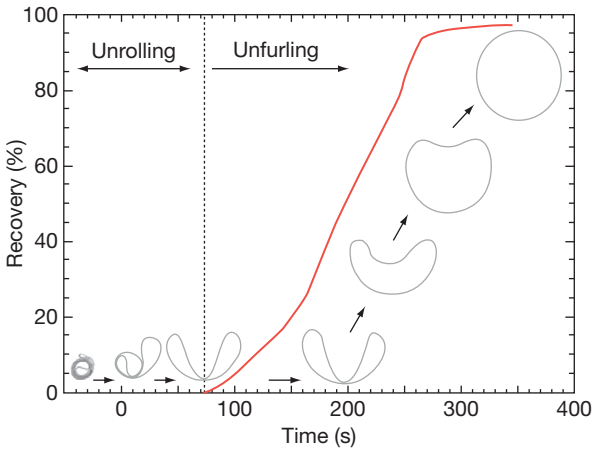

Figure 14 Example of a stent's shape recovery from a furled and rolled temporary shape. Reproduced from Yakacki, C. M.; Shandas, R.; Lanning, C.; Rech, B.; Eckstein, A.; Gall, K. *Biomaterials* **2007**, *28*, 2255–2263. Copyright 2007, with permission from Elsevier.

Moreover, as a controlled drug release could be established from the polymer matrix used in this study, and generally is advantageous for ureteral stents to avoid infections, this stent exemplarily illustrates the advantageous combination of three functionalities in one device – shape-memory, controlled drug release, and biodegradability.

Fixation of ruptured tendons or ligaments to bones is conventionally done with the help of metal screws that are drilled into the bone, possibly damaging the ligament or getting loose over time. On the contrary, cylindrical SMP plugs that are inserted into predrilled cavities together with the end of a ruptured ligament or ligament graft may transfer the mechanical load more homogeneously against the wall of the bone tunnel. The principle of such SMP plugs is shown in Figure 16.[56]

In the literature, a brief report can be found on a successful functional evaluation *in vivo* of an SMP plug in the reconstruction of knee ligaments (anterior cruciate ligament) in a sheep model.[135] Moreover, an FDA clearance was recently obtained for an SMP anchor with attached suture material for ligament fixation to the bone.[136] This strongly shows that the SMP technology is moving forward toward biomedical applications and that some products may be launched in the near future.

Overall, SMPs as a technology platform can be envisaged to have a high potential for transfer into biomedical applications requiring biodegradable, multifunctional materials because of the generality of the underlying fundamental principles of the SME and the synthetic preparation of SMP network architectures as polymer systems, in which functions and properties can be tuned in a wide range by only small variations of their chemical structure. While basic research in SMPs is progressing rapidly, broadening the application potential of the SMP platform besides biomedical applications, the polymer system approach enables existing SMPs to be tailored to the challenging demands of the medicinal sector. This included the investigation of suitable sterilization techniques as well as their interaction with the SMPs. In the last few years, these efforts have been crowned with success when first pilot trials toward a

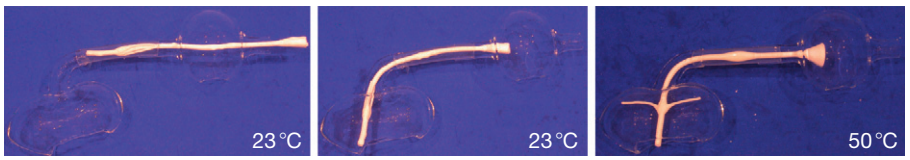

Figure 15 Demonstrator for an ureteral stent from oligo((ε-caprolactone)-*co*-glycolide)dimethacrylate-based polymer network. Reproduced from Neffe, A. T.; Hanh, B. D.; Steuer, S.; Lendlein, A. *Adv. Mater.* **2009**, *21*, 3394–3398. Copyright Wiley-VCH Verlag GmbH & Co KGaA.

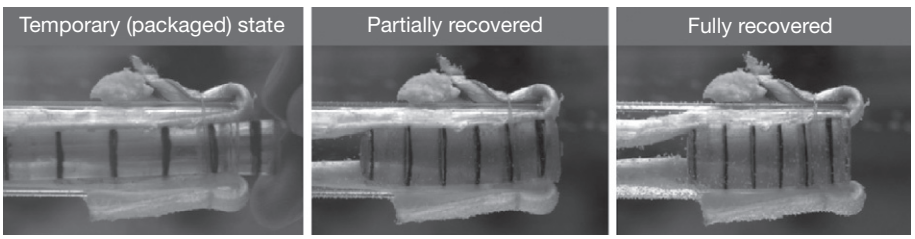

Figure 16 Illustration of a suggested principle of ligament fixation in bone tunnels by SMP plugs (black rings were drawn on the outer surface for better visualization). Reproduced from Yakacki, C. M.; Shandas, R.; Safranski, D.; Ortega, A. M.; Sassaman, K.; Gall, K. *Adv. Funct. Mater.* **2008**, *18*, 2428–2435. Copyright 2008, with permission from Elsevier.

future translation of the materials into clinical applications have been conducted. SMP devices that progressed farthest toward an FDA clearance are for nonintravascular use. Stent technology as one of the most intensively studied fields of SMP applications will certainly remain a major focus of research because of the enormous revenues in this medical field. Although several challenges of SMP stents for intravascular applications will still have to be addressed, biodegradability as one feature of stents from multifunctional SMPs might advantageously overcome clinical complications like late thrombosis. Furthermore, controlled drug release capability as another feature of multifunctional SMPs may open up new opportunities for SMP applications beyond the medical device act.

References

1. Behl, M.; Lendlein, A. *Soft Matter* **2007**, *3*, 58–67.
2. Gunes, I. S.; Jana, S. C. *J. Nanosci. Nanotechnol.* **2008**, *8*, 1616–1637.
3. Lendlein, A.; Kelch, S. *Angew. Chem. Int. Ed.* **2002**, *41*, 2034–2057.
4. Liu, C.; Qin, H.; Mather, P. T. *J. Mater. Chem.* **2007**, *17*, 1543–1558.
5. Liu, Y. J.; Lv, H. B.; Lan, X.; Leng, J. S.; Du, S. Y. *Compos. Sci. Technol.* **2009**, *69*, 2064–2068.
6. Mondal, S. *Mini-Rev. Org. Chem.* **2009**, *6*, 114–119.
7. Weigel, T.; Schinkel, G.; Lendlein, A. *Expert Rev. Med. Devices* **2006**, *3*, 835–851.
8. Behl, M.; Zotzmann, J.; Lendlein, A. In *Shape-Memory Polymers, Vol.: Advances in Polymer Sciences*; Lendlein, A., Ed.; Springer, Berlin, 2010; Vol. 226, pp 1–40.
9. Capaccio, G.; Ward, I. M. *Colloid Polym. Sci.* **1982**, *260*, 46–55.
10. Chowdhury, S. R.; Das, C. K. *J. Appl. Polym. Sci.* **2000**, *77*, 2088–2095.
11. Chowdhury, S. R.; Mishra, J. K.; Das, C. K. *Polym. Degrad. Stab.* **2000**, *70*, 199–204.
12. Lin, J. R.; Chen, L. W. *J. Appl. Polym. Sci.* **1998**, *69*, 1575–1586.
13. Gall, K.; Yakacki, C. M.; Liu, Y. P.; Shandas, R.; Willett, N.; Anseth, K. S. *J. Biomed. Mater. Res. A* **2005**, *73A*, 339–348.
14. Liu, C. D.; Mather, P. T. *Proceedings of the Annual Technical Conference - Society of Plastics Engineers, 61st (Vol. 2), Society of Plastics Engineers*; Brookfield: CT, USA, **2003**; 1962–1966.
15. Cui, J.; Kratz, K.; Lendlein, A. *Mater. Res. Soc. Symp. Proc.* **2009**, *1190*, 93–98.
16. Wagermaier, W.; Kratz, K.; Heuchel, M.; Lendlein, A. *Adv. Polym. Sci.* **2010**, *226*, 97–145.
17. Atli, B.; Gandhi, F.; Karst, G. *J. Intell. Mater. Syst. Struct.* **2009**, *20*, 87–95.
18. Kolesov, I. S.; Kratz, K.; Lendlein, A.; Radusch, H.-J. *Polymer* **2009**, *50*, 5490–5498.
19. Lin, J. R.; Chen, L. W. *J. Appl. Polym. Sci.* **1999**, *73*, 1305–1319.
20. Lin, J. R.; Chen, L. W. *J. Polym. Res. (Taiwan)* **1999**, *6*, 35–40.
21. Liu, Y. P.; Gall, K.; Dunn, M. L.; Greenberg, A. R.; Diani, J. *Int. J. Plast.* **2006**, *22*, 279–313.
22. Barot, G.; Rao, I. J.; Rajagopal, K. R. *Int. J. Eng. Sci.* **2008**, *46*, 325–351.
23. Behl, M.; Bellin, I.; Kelch, S.; Lendlein, A. *Adv. Funct. Mater.* **2009**, *19*, 102–108.
24. Behl, M.; Lendlein, A. *J. Mater. Chem.* **2010**, *20*, 3335–3345.
25. Bellin, I.; Kelch, S.; Langer, R.; Lendlein, A. *Proc. Natl. Acad. Sci. USA* **2006**, *103*, 18043–18047.
26. Bellin, I.; Kelch, S.; Lendlein, A. *J. Mater. Chem.* **2007**, *17*, 2885–2891.
27. Wagermaier, W.; Zander, T.; Hofmann, D.; Kratz, K.; Narendra Kumar, U.; Lendlein, A. *Macomol. Rapid Commun.* **2010**, *31*(17), 1546–1553.
28. Zotzmann, J.; Behl, M.; Feng, Y.; Lendlein, A. *Adv. Funct. Mater.* **2010**, *20*(20), 3583–3594.
29. Zotzmann, J.; Behl, M.; Hofmann, D.; Lendlein, A. *Adv. Mater.* **2010**, *22*, 3424–3429.
30. Behl, M.; Bellin, I.; Kelch, S.; Wagermaier, W.; Lendlein, A. *Mater. Res. Soc. Symp. Proc.* **2009**, *1140*, 3–8.
31. Maitland, D. J.; Metzger, M. F.; Schumann, D.; Lee, A.; Wilson, T. S. *Lasers Surg. Med.* **2002**, *30*, 1–11.
32. Small, W.; Wilson, T. S.; Benett, W. J.; Loge, J. M.; Maitland, D. J. *Opt. Express* **2005**, *13*, 8204–8213.
33. Baer, G. M.; Small, W.; Wilson, T. S.; *et al. Biomed. Eng. Online* **2007**, *6*, 8.
34. Maitland, D. J.; Small, W.; Ortega, J. M.; *et al. J. Biomed. Opt.* **2007**, *12*, 030504.
35. Small, W. I. V.; Buckley, P. R.; Wilson, T. S.; Loge, J. M.; Maitland, K. D.; Maitland, D. J. *J. Biomed. Opt.* **2008**, *13,* 024018/024011–024018/024017.
36. Biercuk, M. J.; Llaguno, M. C.; Radosavljevic, M.; Hyun, J. K.; Johnson, A. T.; Fischer, J. E. *Appl. Phys. Lett.* **2002**, *80*, 2767–2769.
37. Li, F. K.; Qi, L. Y.; Yang, J. P.; Xu, M.; Luo, X. L.; Ma, D. Z. *J. Appl. Polym. Sci.* **2000**, *75*, 68–77.
38. Cho, J. W.; Kim, J. W.; Jung, Y. C.; Goo, N. S. *Macromol. Rapid Commun.* **2005**, *26*, 412–416.
39. Gunes, I. S.; Cao, F.; Jana, S. C. *Polymer* **2008**, *49*, 2223–2234.
40. Sahoo, N. G.; Jung, Y. C.; Cho, J. W. *Mater. Manuf. Processes* **2007**, *22*, 419–423.
41. Sahoo, N. G.; Jung, Y. C.; Yoo, H. J.; Cho, J. W. *Compos. Sci. Technol.* **2007**, *67*, 1920–1929.
42. Leng, J. S.; Lv, H. B.; Liu, Y. J.; Du, S. Y. *Appl. Phys. Lett.* **2007**, *91*, 144105.
43. Leng, J. S.; Huang, W. M.; Lan, X.; Liu, Y. J.; Du, S. Y. *Appl. Phys. Lett.* **2008**, *92*, 204101.
44. Leng, J. S.; Lan, X.; Liu, Y. J.; *et al. Appl. Phys. Lett.* **2008**, *92*, 014104.
45. Mohr, R.; Kratz, K.; Weigel, T.; Lucka-Gabor, M.; Moneke, M.; Lendlein, A. *Proc. Natl. Acad. Sci. USA* **2006**, *103*, 3540–3545.
46. Narendra Kumar, U.; Kratz, K.; Wagermaier, W.; Behl, M.; Lendlein, A. *J. Mater. Chem.* **2010**, *20*, 3404–3415.
47. Razzaq, M. Y.; Behl, M.; Kratz, K.; Lendlein, A. *Mater. Res. Soc. Symp. Proc.* **2009**, *1140*, 185–190.
48. Hazelton, C. S.; Arzberger, S. C.; Lake, M. S.; Munshi, N. A. *J. Adv. Mater. (Covina, CA, USA)* **2007**, *39*, 35–39.
49. Razzaq, M. Y.; Anhalt, M.; Frormann, L.; Weidenfeller, B. *Mater. Sci. Eng. A* **2007**, *444*, 227–235.
50. Buckley, C. P.; Prisacariu, C.; Caraculacu, A. *Polymer* **2007**, *48*, 1388–1396.
51. Lendlein, A.; Jiang, H. Y.; Jünger, O.; Langer, R. *Nature* **2005**, *434*, 879–882.
52. Li, F. K.; Zhu, W.; Zhang, X.; Zhao, C. T.; Xu, M. *J. Appl. Polym. Sci.* **1999**, *71*, 1063–1070.
53. Palmgreen, R.; Karlsson, S.; Albertsson, A.-C. *J. Polym. Sci. A* **1997**, *35*, 1635–1649.
54. Pitt, C. G.; Hendren, R. W.; Schindler, A.; Woodward, S. C. *J. Control. Release* **1984**, *1*, 3–14.
55. Yakacki, C. M.; Shandas, R.; Lanning, C.; Rech, B.; Eckstein, A.; Gall, K. *Biomaterials* **2007**, *28*, 2255–2263.
56. Yakacki, C. M.; Shandas, R.; Safranski, D.; Ortega, A. M.; Sassaman, K.; Gall, K. *Adv. Funct. Mater.* **2008**, *18*, 2428–2435.
57. Liu, C. D.; Chun, S. B.; Mather, P. T.; Zheng, L.; Haley, E. H.; Coughlin, E. B. *Macromolecules* **2002**, *35*, 9868–9874.
58. Behl, M.; Lendlein, A. *Mater. Today* **2007**, *10*, 20–28.
59. Beloshenko, V. A.; Varyukhin, V. N.; Voznyak, Y. V. *Russ. Chem. Rev.* **2005**, *74*, 265–283.
60. Ratna, D.; Karger-Kocsis, J. *J. Mater. Sci.* **2008**, *43*, 254–269.
61. Guignot, C.; Betz, N.; Legendre, B.; Le Moel, A.; Yagoubi, N. *Nucl. Instrum. Meth. B* **2001**, *185*, 100–107.
62. Behl, M.; Ridder, U.; Feng, Y.; Kelch, S.; Lendlein, A. *Soft Matter* **2009**, *5*, 676–684.
63. Lamba, N. M. K.; Woodhouse, K. A.; Cooper, S. L. *Polyurethanes in Biomedical Applications*. CRC Press: Boca Raton, FL, 1997.
64. Silvia, F.; Viviana, V.; Paola, P.; *et al. J. Biomed. Mater. Res. A* **2005**, *73A*, 1–11.
65. De Nardo, L.; Alberti, R.; Cigada, A.; Yahia, L.; Tanzi, M. C.; Fare, S. *Acta Biomater.* **2009**, *5*, 1508–1518.
66. Metcalfe, A.; Desfaits, A. C.; Salazkin, I.; Yahia, L.; Sokolowski, W. M.; Raymond, J. *Biomaterials* **2003**, *24*, 491–497.
67. Coury, A. J.; Levy, C. R.; McMillin, Y.; *et al.* In *Biomaterials Science: An Introduction to Materials in Medicine*; Ratner, B. D., Hoffman, A. S., Schoen, F. J., Lemons, J. E., Eds.; Academic Press, Elsevier Science: New York, **1996**; 243.
68. Silver, J. H.; Myers, C. W.; Lim, F.; Cooper, S. L. *Biomaterials* **1994**, *15*, 695–704.
69. Lelah, M. D.; Lambrecht, L. K.; Young, B. R.; Cooper, S. L. *J. Biomed. Mater. Res.* **1983**, *17*, 1–22.
70. Lelah, M. D.; Grasel, T. G.; Pierce, J. A.; Cooper, S. L. *J. Biomed. Mater. Res.* **1985**, *19*, 1011–1015.
71. Grapski, J. A.; Cooper, S. L. *Biomaterials* **2001**, *22*, 2239–2246.
72. Meng, Q.; Hu, J.; Liu, B.; Zhu, Y. *J. Biomater. Sci. Polym. Ed.* **2009**, *20*, 199–218.
73. Behl, M.; Razzaq, M. Y.; Lendlein, A. *Adv. Mater.* **2010**, *22*, 3388–3410.

74. Lendlein, A.; Kelch, S. *Mater. Sci. Forum* **2005**, *492–493*, 219–223.
75. Langer, R.; Peppas, N. *J. Macromol. Sci., Rev. Macromol. Chem. Phys.* **1983**, *C23*, 61–126.
76. Tamada, J. A.; Langer, R. *Proc. Natl. Acad. Sci. USA* **1993**, *90*, 552–556.
77. Hofmann, D.; Entrialgo-Castaño, M.; Kratz, K.; Lendlein, A. *Adv. Mater.* **2009**, *21*, 3237–3245.
78. Neffe, A. T.; Tronci, G.; Alteheld, A.; Lendlein, A. *Macromol. Chem. Phys.* **2010**, *211*, 182–194.
79. Lendlein, A.; Neuenschwander, P.; Suter, U. W. *Macromol. Chem. Phys.* **1998**, *199*, 2785–2796.
80. Zange, R.; Li, Y. X.; Kissel, T. *J. Control. Release* **1998**, *56*, 249–258.
81. Lendlein, A.; Langer, R. *Science* **2002**, *296*, 1673–1676.
82. Edelman, E. R.; Nathan, A.; Katada, M.; Gates, J.; Karnovsky, M. J. *Biomaterials* **2000**, *21*, 2279–2286.
83. Jabbal-Gill, I.; Lin, W.; Kistner, O.; Davis, S. S.; Illum, L. *Adv. Drug Deliv. Rev.* **2001**, *51*, 97–111.
84. Lendlein, A.; Colussi, M.; Neuenschwander, P.; Suter, U. W. *Macromol. Chem. Phys.* **2001**, *202*, 2702–2711.
85. Li, S. M. *J. Biomed. Mater. Res.* **1999**, *48*, 342–353.
86. Witschi, C.; Doelker, E. *J. Control. Release* **1998**, *51*, 327–341.
87. Grablowitz, H.; Lendlein, A. *J. Mater. Chem.* **2007**, *17*, 4050–4056.
88. Lendlein, A.; Zotzmann, J.; Feng, Y.; Alteheld, A.; Kelch, S. *Biomacromolecules* **2009**, *10*, 975–982.
89. Hiebl, B.; Kratz, K.; Fuhrmann, R.; Jung, F.; Lendlein, A.; Franke, R. *Mater. Res. Soc. Symp. Proc.* **2009**, *1190*, 113–118.
90. Hiebl, B.; Rickert, D.; Fuhrmann, R.; Jung, F.; Lendlein, A.; Franke, R. *Mater. Res. Soc. Symp. Proc.* **2009**, *1140*, 143–149.
91. Tzoneva, R.; Weckwerth, C.; Seifert, B.; *et al. J. Biomat. Sci-Polym. E* **2010**, [E-pub ahead of print on November 11 (2010)] DOI: 10.1163/092050610X537147.
92. Binzen, E.; Rickert, D.; Kelch, S.; Fuhrmann, R. *Clin. Hemorheol. Microcirc.* **2003**, *28*, 183–188.
93. Rickert, D.; Lendlein, A.; Peters, I.; Moses, M. A.; Franke, R. P. *Eur. Arch. Otorhinolaryngol.* **2006**, *263*, 215–222.
94. Knight, P. T.; Lee, K. M.; Chung, T.; Mather, P. T. *Macromolecules* **2009**, *42*, 6596–6605.
95. Min, C.; Cui, W.; Bei, J.; Wang, S. *Polym. Adv. Technol.* **2005**, *16*, 608–615.
96. Pretsch, T.; Jakob, I.; Müller, W. *Polym. Degrad. Stab.* **2009**, *94*, 61–73.
97. Feng, Y.; Behl, M.; Kelch, S.; Lendlein, A. *Macromol. Biosci.* **2009**, *9*, 45–54.
98. Feng, Y.; Lu, J.; Behl, M.; Lendlein, A. *Macomol. Biosci.* **2010**, *10*(9), 1008–1021.
99. Wang, W.; Ping, P.; Chen, X.; Jing, X. *J. Appl. Polym. Sci.* **2007**, *104*, 4182–4187.
100. Yu, X. J.; Zhou, S. B.; Zheng, X. T.; Xiao, Y.; Guo, T. *J. Phys. Chem. C* **2009**, *113*, 17630–17635.
101. Choi, N. Y.; Kelch, S.; Lendlein, A. *Adv. Eng. Mater.* **2006**, *8*, 439–445.
102. Rickert, D.; Lendlein, A.; Schmidt, A. M.; *et al. J. Biomed. Mater. Res. B Appl. Biomater.* **2003**, *67B*, 722–731.
103. Rickert, D.; Lendlein, A.; Kelch, S.; Franke, R. P.; Moses, M. A. *Biomed. Tech. (Berl.)* **2005**, *50*, 92–99.
104. Rickert, D.; Lendlein, A.; Kelch, S.; Moses, M. A.; Franke, R. P. *Clin. Hemorheol. Microcirc.* **2005**, *32*, 117–128.
105. Choi, N. Y.; Lendlein, A. *Soft Matter* **2007**, *3*, 901–909.
106. Alteheld, A.; Feng, Y.; Kelch, S.; Lendlein, A. *Angew. Chem. Int. Ed.* **2005**, *44*, 1188–1192.
107. Zotzmann, J.; Alteheld, A.; Behl, M.; Lendlein, A. *J. Mater. Sci. Mater. Med.* **2009**, *20*, 1815–1824.
108. Vert, M. *J. Mater. Sci. Mater. Med.* **2009**, *20*, 437–446.
109. Kulkarni, A.; Reiche, J.; Lendlein, A. *Surf. Interface Anal.* **2007**, *39*, 740–746.
110. Kulkarni, A.; Reiche, J.; Kratz, K.; Kamusewitz, H.; Sokolov, I. M.; Lendlein, A. *Langmuir* **2007**, *23*, 12202–12207.
111. Reiche, J.; Kulkarni, A.; Kratz, K.; Lendlein, A. *Thin Solid Films* **2008**, *516*, 8821–8823.
112. Kulkarni, A.; Reiche, J.; Hartmann, J.; Kratz, K.; Lendlein, A. *Eur. J. Pharm. Biopharm.* **2008**, *68*, 46–56.
113. Wischke, C.; Neffe, A. T.; Lendlein, A. *Adv. Polym. Sci.* **2010**, *226*, 177–205.
114. Wischke, C.; Neffe, A. T.; Steuer, S.; Lendlein, A. *Eur. J. Pharm. Sci.* **2010**, *41*, 136–147.
115. Duvvuri, S.; Janoria, K. G.; Mitra, A. K. *Pharm. Res.* **2006**, *23*, 215–223.
116. Liu, H.; Finn, N.; Yates, M. Z. *Langmuir* **2005**, *21*, 379–385.
117. Wischke, C.; Schwendeman, S. P. *Int. J. Pharm.* **2008**, *364*, 298–327.
118. Breitenbach, A.; Li, Y. X.; Kissel, T. *J. Control. Release* **2000**, *64*, 167–178.
119. Göpferich, A.; Tessmar, J. *Adv. Drug Deliv. Rev.* **2002**, *54*, 911–931.
120. Heller, J.; Barr, J.; Ng, S. Y.; Schwach Abdellauoi, K. R. G. *Adv. Drug Deliv. Rev.* **2002**, *54*, 1015–1039.
121. Wischke, C.; Neffe, A. T.; Steuer, S.; Lendlein, A. *J. Control. Release* **2009**, *138*, 243–250.
122. Neffe, A. T.; Hanh, B. D.; Steuer, S.; Lendlein, A. *Adv. Mater.* **2009**, *21*, 3394–3398.
123. Wada, R.; Hyon, S. H.; Nakamura, T.; Ikada, Y. *Pharm. Res.* **1991**, *8*, 1292–1296.
124. Wischke, C.; Neffe, A. T.; Steuer, S.; Engelhardt, E.; Lendlein, A. *Macromol. Biosci.* **2010**, *10*(9), 1063–1072.
125. Nagahama, K.; Ueda, Y.; Ouchi, T.; Ohya, Y. *Biomacromolecules* **2009**, *10*, 1789–1794.
126. Wischke, C.; Lendlein, A. *Pharm. Res.* **2010**, *27*(4), 527.
127. N39F-54: 20 *Medical Device Technologies Changing Healthcare*. **2008**, Frost & Sullivan, TX, USA.
128. Wache, H. M.; Tartakowska, D. J.; Hentrich, A.; Wagner, M. H. *J. Mater. Sci. Mater. Med.* **2003**, *14*, 109–112.
129. Sharp, A. A.; Panchawagh, H. V.; Ortega, A.; *et al. J. Neural Eng.* **2006**, *3*, L23–L30.
130. Lendlein, A.; Behl, M.; Hiebl, B.; Wischke, C. *Expert Rev. Med. Devices* **2010**, *7*(3), 357–379.
131. Newsome, L. T.; Kutcher, M. A.; Royster, R. L. *Anesth. Analg.* **2008**, *107*, 552–569.
132. Wykrzykowska, J. J.; Onuma, Y.; Serruys, P. W. *Expert Opin. Drug Deliv.* **2009**, *6*, 113–126.
133. Baer, G. M.; Wilson, T. S.; Small, W.; *et al. J. Biomed. Mater. Res. B Appl. Biomater.* **2009**, *90B*, 421–429.
134. Hildebrand, G.; Tack, J.; Käufer, H.; Wache, H. M.; Müller, T.; Ewert, P. Eur. Patent EP1 335 760 B1, **2006**.
135. Yakacki, C. M.; Gall, K. In *Shape-Memory Polymers*; Lendlein, A., Ed.; Advances in Polymer Sciences; Heidelberg, Germany: Springer, **2010**, Vol. 226, 147–175.
136. FDA. Clearance of Section 510(k) premarket notification for WedgeLoc™ 180x Suture Anchor and Opti-Fiber™ Sutures (K091202); 510(k) Clearances from U.S. Food and Drug Administration (FDA), **2009**.
137. Lendlein, A.; Schmidt, A. M.; Langer, R. *Proc. Natl. Acad. Sci. USA* **2001**, *98*, 842–847.

1.127. Electrospinning and Polymer Nanofibers: Process Fundamentals

P K Bhattacharjee, Monash University, Clayton, VIC, Australia
G C Rutledge, Massachusetts Institute of Technology, Cambridge, MA, USA

© 2011 Elsevier Ltd. All rights reserved.

1.127.1.	**Introduction**	498
1.127.2.	**Process Description**	499
1.127.3.	**Mechanics: Electrostatics and Hydrodynamics**	501
1.127.3.1.	The Leaky Dielectric Model	501
1.127.3.2.	Governing Equations and Major Results	501
1.127.3.3.	Electrospinning Zones	504
1.127.3.3.1.	The conical meniscus	504
1.127.3.3.2.	The thinning jet	506
1.127.3.3.3.	The whipping jet	506
1.127.3.4.	Discussion on Current Carried by Electrospinning Jet	507
1.127.4.	**Products of Electrospinning**	508
1.127.4.1.	Electrospun Fibers: Diameter and Morphology	508
1.127.4.2.	Properties of the Electrospun Mat	510
1.127.5.	**Summary and Conclusion**	511
References		511

Glossary

Advection A mechanism of transport with the net flow of the fluid.
Constitutive equation An equation relating the stress accumulated in a material to the history of deformation that the material experiences.
Debye length The length scale over which mobile charge carriers screen out the effect of electric fields.
Elastic modulus The tendency of an object to deform elastically with applied force.
Electrohydrodynamics Study of the dynamics of electrically charged fluids.
Electrostatics A branch of science that deals with stationary or slow-moving charges.
Extensional viscosity The resistance provided by a fluid to extensional deformation (like stretching). Typically measured as a ratio of the stress to the strain rate experienced in extensional flow.
Inviscid Devoid of viscosity. Typically pertains to material with very low viscosity.
Metastability A system is considered metastable when it is susceptible to fall into a lower energy state by the slightest interaction, although it experiences a condition of equilibrium in its present state
Newtonian and non-Newtonian fluids A fluid is said to be Newtonian when the stress in the fluid scales linearly with the strain rate. The proportionality constant is called the viscosity of the fluid. Fluids that deviate from this simple relationship between stress and strain rate are called non-Newtonian fluids.
Phenomenological model A mathematical model that expresses the results of observed phenomena without detailing their fundamental significance
Rheology Study of deformation and flow of matter
Strain hardening A condition where the extensional viscosity of a fluid increases with increasing strain.
Viscoelasticity A phenomenon by which a material demonstrates both viscous and elastic characters when deformed.
Zero-shear-rate viscosity The constant viscosity of a fluid measured at vanishingly small shear rates.

Abbreviations

De Deborah number
Fr Froude number
Oh Ohnesorge number
Pe Electric Peclet number
TR Trouton ratio
We Weber number

Symbols

a	Tube diameter (m)
b	Kuhn step length (m)
b_{max}	Finite extensibility parameter in the FENE-P model
c	Concentration of polymer in solution ($kg\,m^{-3}$)
D	Radius of curvature of the jet (m)
D_c	Curvilinear diffusion coefficient ($m^2\,s^{-1}$)
d_g	Distance between the electrodes (m)
E	Local electric field ($V\,m^{-1}$)
E_∞	Applied electric field strength ($V\,m^{-1}$)
h	Instantaneous jet diameter (m)
h_0	Nozzle diameter (m)
h_t	Terminal diameter of the jet (m)
I	Current flowing through the jet ($C\,s^{-1}$)
I_0, I_1	Modified Bessel functions
K	Conductivity of the solution ($\mu S\,cm^{-1}$)
k_B	Boltzmann constant ($J\,K^{-1}\,mol^{-1}$)
L_c	Characteristic length scale of flow in the conical meniscus (m)
l_{cap}	Capillary length (m)
L_N	Characteristic length scale at which transition from charge conduction to charge advection occurs (m)
M_c	Critical molecular weight for entanglements ($g\,mol^{-1}$)
M_e	Molecular weight between entanglements ($g\,mol^{-1}$)
M_w	Molecular weight ($g\,mol^{-1}$)
N_e	Number of Kuhn monomers between entanglements
N_K	Number of Kuhn monomers per chain
Q	Flow rate ($m^3\,s^{-1}$)
s	Separation distance between fibers (m)
T	Absolute temperature (K)
t_e	Charge relaxation time (s)
t_f	Characteristic times of fluid flow (s)
u, v	Velocity ($m\,s^{-1}$)
V	Voltage (V)
z	Distance along the direction of propagation of the jet (m)
Z	Number of entanglements per chain
δ	Kronecker delta function
ε	Dielectric constant of the fluid
$\bar{\varepsilon}$	Dielectric permittivity of vacuum ($C^2\,N^{-1}\,m^{-2}$)
$\dot{\varepsilon}$	Strain rate (s^{-1})
γ	Surface tension coefficient ($N\,m^{-1}$)
$\dot{\gamma}$	Shear rate (s^{-1})
$[\eta]$	Intrinsic viscosity ($m^3\,kg^{-1}$)
η_0	Zero-shear-rate viscosity (Pa s)
η_E	Extensional viscosity (Pa s)
λ_{max}	Stretch ratio
η	Viscosity of a Newtonian fluid (Pa s)
ν	Solvent quality parameter
ρ	Density of the fluid ($kg\,m^{-3}$)
σ	Surface charge density ($C\,m^{-2}$)
ζ	Monomeric friction coefficient
Σ	Volumetric charge density (Cm^{-3})
τ	Relaxation time of polymeric fluid (s)
τ_d	Reptation time (s)
τ_e	Entanglement relaxation time (s)
τ_p	Polymeric stress (Pa)
τ_R	Rouse relaxation time (s)
χ	Aspect ratio
ω_{max}	Growth rate of the fastest-growing mode of the surface-tension-driven Rayleigh instability (s^{-1})

1.127.1. Introduction

The electrospinning process has been extensively used in recent times for producing very fine fibers from a wide variety of materials, easily and inexpensively. The fibers that are produced through electrospinning span almost 4 orders of magnitude in their diameters, ranging from tens of micrometers down to only a few nanometers, and are essentially unlimited in length. Thus, the process has generated much interest among scientists and engineers. Electrospun fibers are finding widespread application in the emerging areas of nanotechnology.[1–3] The technique also holds much promise in enriching biomedical research and industry through contributions to biomaterials,[4,5] drug encapsulation and delivery,[6–8] tissue engineering,[9–13] etc. Thus, there is much to be gained by understanding the underlying physical principles that allow control of various aspects of the process by which such novel materials can be fabricated. Uncovering the physics that govern electrospinning is a formidable task, however. The technique presents a rich variety of challenges that arise from the interactions among a large number of physical processes acting in tandem. However, concerted effort on the part of the scientific community has succeeded in generating robust understanding of some critical aspects of the process. Our aim here is to outline these so that engineers and scientists can find some assistance in designing electrospinning processes. In this chapter, we start by discussing the electrospinning process in general and also discuss the problems associated with scaling up the process. A discussion on the electrostatic, hydrodynamical, and rheological aspects associated with electrospinning is provided next. In this part we also provide an overview of the leaky dielectric model that is used to describe the electrical properties of the fluids used in electrospinning. Furthermore, we summarize major concepts associated with the mechanics in various regions of the electrospinning jet and review the physics that eventually lead to the formation of fibers. Thereafter, we consider the morphologies of the fibers formed in electrospinning and also review some properties of the electrospun fabrics, especially those associated with porosity, which is of particular relevance in the consideration of many biomaterials. The scope of the chapter restricts our discussion to major concepts and results only. Readers are, nevertheless, encouraged to consult the many references that are listed for further information on the details of the subjects of their interest.

1.127.2. Process Description

A schematic of the electrospinning process is shown in Figure 1. In the laboratory, typically a small amount of fluid is extruded out of a capillary using a syringe pump and is subjected to a high potential difference with respect to a grounded counter electrode. As a result of electrification, charge accumulates on the surface of the fluid, subsequent repulsion among the charges leads to the destabilization of the meniscus, and a jet ensues. The electrified jet accelerates downfield, usually more or less in a straight line at first, but eventually this steady jet becomes unstable with respect to transverse bending perturbations, and takes on a whipping-like motion. The instability is hence called the 'whipping instability.' It is believed that the whipping instability imposes the final drawdown usually responsible for the formation of the very small diameter fibers in electrospinning. The fluids used in electrospinning typically contain a volatile solvent that evaporates as the jet propagates downstream, leading to the formation of solid fibers that are eventually deposited on the counter electrode in the form of a nonwoven mat. The morphologies of the fibers formed in electrospinning vary, depending on the processing conditions and fluid properties. The most common occurrences are those of homogeneous uniform fibers and morphologies that resemble beads on strings. However, other morphologies, such as flat ribbons,[14] fibers with wrinkled surfaces,[15,16] porous fibers, etc., have also been reported. Some examples of these structures are shown in Figure 1.

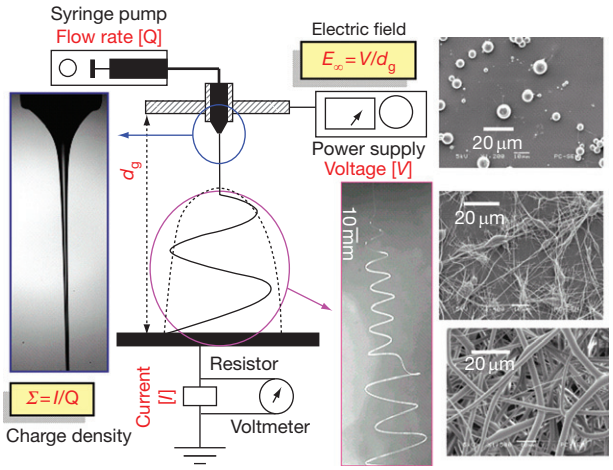

Figure 1 Schematic diagram of electrospinning showing details of the jetting processes, the whipping instability, as well as the fiber morphologies that can be obtained. The flow rate (Q), the voltage (V) and the distance between the electrodes (d_g) are set, and the current (I) flowing through the jet is measured. The electric field strength is calculated as $E_\infty = V/d_g$. The quantity $\Sigma = (I/Q)$ is the volumetric charge density. The photograph on the left hand side shows the straight section of the steady jet immediately after it ejects from the conical meniscus. The photograph on the right shows the whipping instability, where the centerline of the jet bends at a characteristic wavelength. These photographs were obtained using a digital SLR camera (Nikon D60) and by backlighting the jet. The micrographs on the extreme right show products that can be obtained by electrospinning the same polymer (a polyurethane) at different concentrations. As the concentration is increased, the product changes from drops to beads-on-string morphologies and finally to homogeneous fibers (top to bottom).

The controlling variables in electrospinning are the infusion rate Q, the applied accelerating voltage V, and the distance between the electrodes d_g. Also important are the properties of the fluid, most notably the electrical conductivity (K), dielectric constant (ε), surface tension (γ), and the viscoelastic properties (e.g., viscosity η and relaxation time τ, or storage modulus G' and loss modulus G''). Each of these quantities has to be adjusted, either individually or in tandem, to obtain desirable results. The electrospinning process constitutes an electrical circuit, and the current flowing though this 'circuit' is significantly influenced by the control parameters, the flow rate for instance. This makes electrospinning a challenging problem to analyze. The extent of the challenge can be appreciated by studying Figure 2, which shows the different ways in which the fiber size can be manipulated empirically in electrospinning.

Electrospinning, however, is simple to set up. Therefore, a variety of configurations have been reported. These can be broadly categorized into two groups: (a) those using a spinneret (capillary tubes/nozzles/emitters) and (b) those that use 'nozzleless' configurations, based mainly on the electrification of free surfaces of fluids. In most laboratory experiments, however, a configuration using a single needle is used for simplicity, and the apparatus resembles the one shown in Figure 1, sometimes referred to as a 'parallel-plate' configuration. More commonly, the plate on the high voltage electrode is discarded, in what is then referred to as a 'point-plate' configuration. Gravitational forces are relatively weak compared to the electrical ones, so different orientations of the nozzle and collectors (vertical, horizontal, and at a specific angle) have also been reported, with similar results. Variations in nozzle design, for example, nozzles having a coaxial structure for fabricating compound core–shell electrospun fibers[18,19] or nozzles that allow fluids to flow side by side during electrospinning,[20] have also been incorporated within the process. Even scanning probe tips have been used to serve as emitters of jets in electrospinning.[21] An early example of a nozzleless configuration is that reported by Yarin and Zussman.[22]

The practicality of scale-up for industrial production is a persistent concern in electrospinning, because the production rate of fibers from a single spinneret is often very low, and the smallest fibers are frequently obtained using the lowest flow rates. To increase production rate, multiple emitters/nozzles have been introduced in electrospinning.[23] The latter arrangements not only increase the overall production rate significantly, but also allow the production of multicomponent mats of fibers. However, the arrangement of nozzles is complicated by the electrostatic interactions between neighboring charged jets. Scale-up has also been achieved using the free surface configuration.[22] One advantage of using this configuration is that the difficulties associated with pumping of viscous fluids can be mitigated. Furthermore, maintenance aspects associated with large-scale production involving multiple jets are simplified. Figure 3(a) shows a photograph of an arrangement that uses a rotating cylinder or mandrel as the source of the electrospinning jets. In Figure 3(b), the rotating cylinder is replaced by a pair of wheels with wires strung

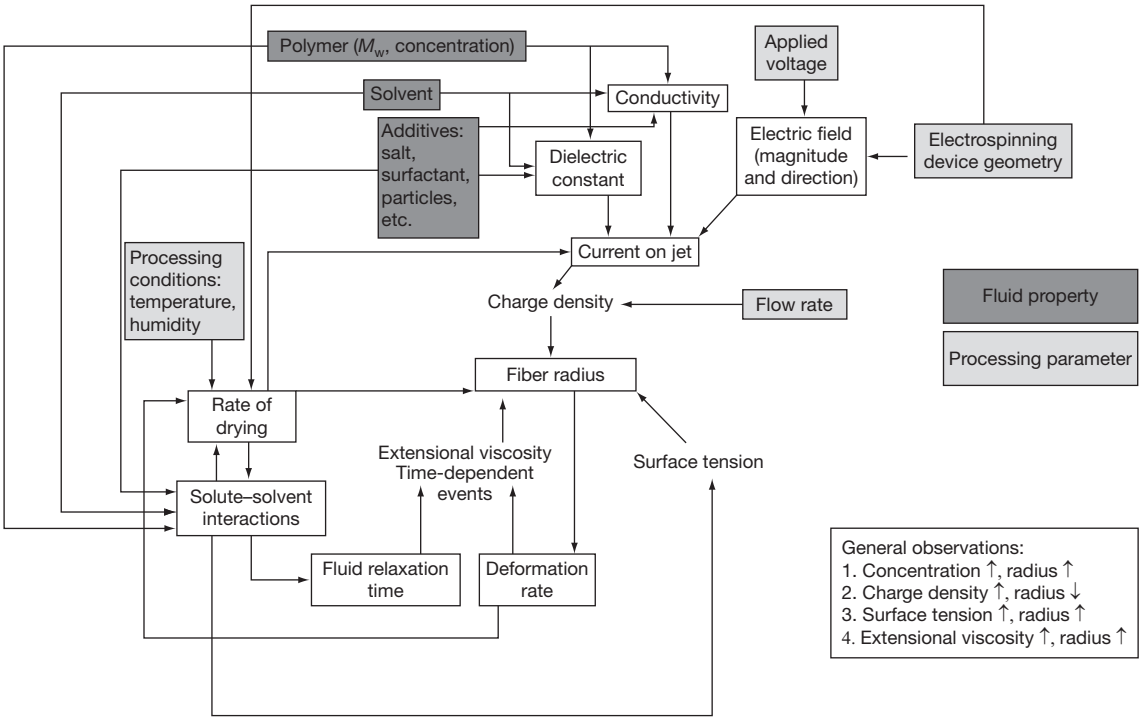

Figure 2 Flow diagram demonstrating the manner in which the properties of the fluid and process variables affect the diameter of the fibers obtained from electrospinning. Diagram from Yu and Rutledge.[17]

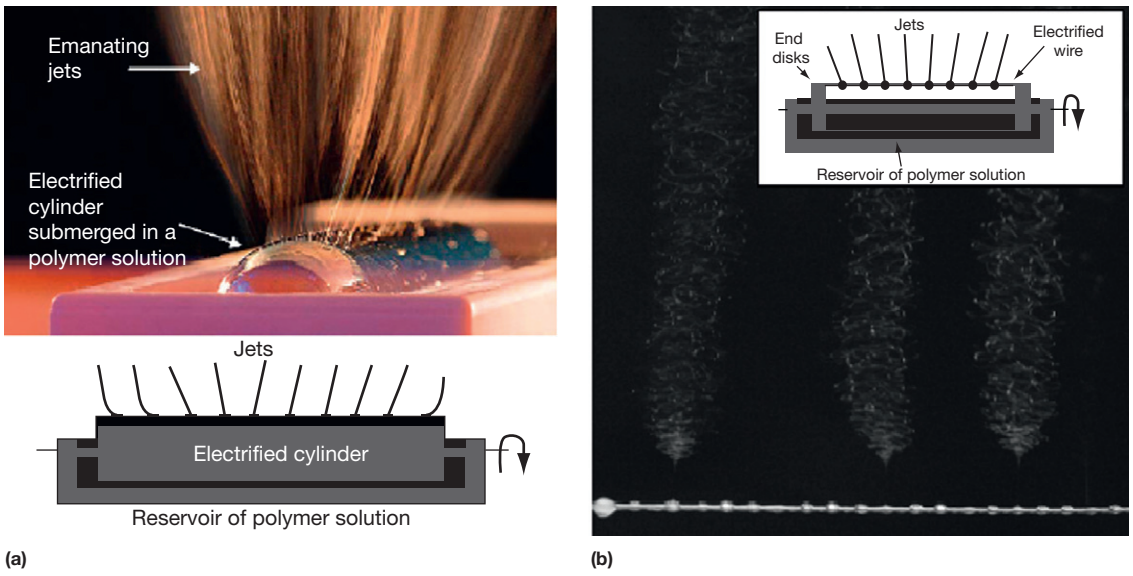

Figure 3 Examples of nozzle-free configurations used in electrospinning. (a) Jets arising from an electrified cylinder immersed in a polymer solution. Image courtesy Elmarco Company, Liberec, Czech Republic. A schematic is shown in the bottom panel. (b) Multiple jets arising from liquid drops on an electrified wire as shown in the schematic diagram in the inset. The wire periodically dips into a polymer solution, which then breaks up into droplets that serve as sites for the eventual jetting process. Image courtesy of Dr. R. M. Hill, Institute for Soldier Nanotechnologies, MIT Cambridge, USA.

between them; in this case, the jets arise from droplets on the electrified metallic wire, which form as the wire dips into and rises out of a solution bath. Both arrangements shown in Figure 3(a) and 3(b) allow for reasonably easy scale-up, with the additional advantage that the spacing among the jets is chosen naturally rather than imposed, as in the case of arrangements using multiple nozzles. The electrical interactions between jets results in repulsion among the jets and affects the deposition density of the fibers on the substrate.[24] On the other hand, with the rotating cylinder source the jets

are no longer truly continuous, resulting in fibers of finite (albeit quite long) length. Nonetheless, these arrangements demonstrate the ease with which electrospinning can be set up to generate nanofibers. Some of these configurations now serve as the basis for commercial electrospinning equipment designed for manufacture of nanofibers. However, control of the process is commensurately challenging. In the following sections, we discuss some aspects of the process that are fairly well studied and understood.

1.127.3. Mechanics: Electrostatics and Hydrodynamics

1.127.3.1. The Leaky Dielectric Model

Two advantages of electrospinning are that it is very easy to implement, and a wide variety of materials can be processed through the technique. Since electrospinning is predominantly an electrically driven process, it is important to consider the electrical characteristics of the fluids used. The dynamics of the fluids under the influence of an external electric field are generally discussed in the framework of the leaky dielectric model, which was first proposed by Melcher and Taylor.[25] A leaky dielectric differs from a perfect conductor or a dielectric material in that free charges accumulate on the surface of the material in the presence of an external electric field and modify the local field. Under these conditions, two components of the electrical field develop, one tangential to the interface and another normal to it. The presence of a tangential component on the surface prevents the interface from being in an equilibrium condition and provokes it to deform. In contrast, the electrical stress in perfect dielectrics and conductors is always perpendicular to the interface. Electromechanical coupling occurs at the fluid-fluid interface alone; forces resulting from charges in the bulk are negligibly small. As the fluid accelerates, the tangential component of the electrical stress is largely balanced by the viscous, or viscoelastic, response of the fluid. Thus, both the constitutive behavior and the electrical properties of the fluid determine the condition of the process. It is common practice in electrospinning to include ionic salts that increase the conductivity of the fluid or surfactants that decrease its intrinsic surface tension. However, it is important to bear in mind that if the changes in conductivity resulting from these additions are large enough to alter the behavior of the fluid from that of a leaky dielectric to that resembling a conductor, then the tangential component of the electrical stress that accelerates the fluid is likely to diminish and the flow process be stopped. In this limit the electrical stress will be balanced by the alteration of the shape of the interface and surface tension only. These aspects are discussed in detail in a separate review.[26]

Electrohydrodynamic processes, including electrospinning, are often discussed in the 'quasi-electrostatic' limit, in which the charge distribution on the surface is unaffected by translocation or alteration of the shape of the interface. For a fluid of large enough electrical conductivity there is a layer of charge carriers on the surface, of thickness on the order of the Debye length, that is in a perfect equilibrium state. This charge layer is described by the well-known Poisson–Boltzman equation. When the liquid moves, it disturbs the equilibrium charge distribution on the surface as some of the charges are swept away by flow. However, the surface layer is maintained if the charges are replenished faster than the rate at which they are removed. The 'quasi-electrostatic' condition is valid in this limit. It is realized when $t_f \gg t_e$, where t_f and t_e are the characteristic times of fluid flow and charge relaxation, respectively. The latter is given by $t_e = \varepsilon\bar{\varepsilon}/4\pi K$, where ε is the dielectric constant of the fluid, $\bar{\varepsilon}$ is the dielectric permittivity of vacuum, and K is the conductivity of the solution. In general, the choice of t_f depends on the process of interest. For momentum transfer to a viscous fluid, for instance, the hydrodynamic time $t_f = (\rho h_0^2/\eta)$ can be considered. For polymeric fluids the viscoelastic relaxation time might be more relevant. It has been observed for fluids where these time constants become comparable that the jetting process becomes unstable and chaotic. However, for cases where $t_f \gg t_e$, stable flow conditions are obtained.[27]

1.127.3.2. Governing Equations and Major Results

The equations that describe the dynamics in electrospinning constitute, at a minimum, those describing the conservation of mass, momentum and charge, and the electric field equation. Additionally a constitutive equation for the fluid behavior is also required. Assuming the simplest Newtonian fluid properties, the governing equations take the following form:

$$h^2 v = 1 \quad [1]$$

$$Eh^2 + Pehv\sigma = 1 \quad [2]$$

$$vv' = \frac{1}{Fr} + \frac{3}{Re}\frac{1}{h^2}\left(\eta h^2 v'\right)' + \frac{1}{We}\frac{h'}{h^2} + \Omega\left(\sigma\sigma' + \beta EE' + \frac{2E\sigma}{h}\right) \quad [3]$$

$$E = E_\infty - \ln\chi\left[(\sigma h)' - \frac{\beta}{2}\left(Eh^2\right)''\right] \quad [4]$$

The above equations were invoked originally in Hohman *et al.*[28] within the Slender Thinning Jet approximation and describe the steady-state conditions of the jet. These were subsequently put in the nondimensional form shown above by Feng.[29] Similar derivations are also available in other reports.[30] In the above equation, the primed quantities signify spatial derivatives. The variables v, h, σ, and E signify the velocity, the radius of the jet, the surface charge density, and the local electric field, respectively. The variable $E_\infty = V/d_g$, where V is the imposed driving potential, and d_g is the distance between the electrodes. Nondimensionalization is carried out based on characteristic values at the nozzle: the radius of the nozzle, h_0, for length, $v_0 = Q/\pi h_0^2$ for velocity, $E_0 = I/\pi h_0^2 K$ for electric field, and $\sigma_0 = \bar{\varepsilon}E_0$ for surface charge density. The dimensionless groups that represent the comparative strength of various forces are as follows:

Electric Peclet Number: (charge convection/conduction) $Pe = 2\bar{\varepsilon}v_0/Kh_0$
Froude Number: (inertia/gravity) $Fr = v_0^2/gh_0$
Reynolds number: (inertial force/viscous force) $Re = \rho v_0 h_0/\eta$
Weber number: (inertia/surface tension) $We = \rho v_0 h_0/\gamma h$
The charge induction parameter: $\beta = (\varepsilon/\bar{\varepsilon}) - 1$
Aspect ratio: $\chi = D/h_0$
Electrostatic force parameter: $\Omega = \bar{\varepsilon}E_0^2/\rho v_0^2$

The subscript '0' in these equations signifies the relevant quantity at the nozzle. Reneker *et al.*[31] also considered the gravitational and aerodynamic conditions and concluded that these are inconsequential to the electrospinning process.

The equations listed above assume that the fluid involved is Newtonian. Newtonian fluids exhibit a linear relationship between the applied stress and the rate of deformation, characterized by a constant viscosity. However, in most electrospinning experiments polymeric fluids are used, and these demonstrate significantly nonlinear behavior. In these fluids, the viscosity remains constant only up to deformation rates that are of the order of the inverse of the longest relaxation time (τ_d) of the fluid. In shear flows, this feature of polymeric fluids leads to a definition of the zero-shear-rate viscosity (η_0), which essentially is the constant viscosity observed in polymeric fluids at low shear rates ($\dot{\gamma}$). At high shear rates, the shear viscosity (η) typically decreases rapidly. This phenomenon is commonly known as shear thinning. In extensional flows such as that observed in electrospinning, the 'extensional' viscosity (η_E) becomes important. In Newtonian fluids, $\eta_E = 3\eta_0$. In viscoelastic fluids, the extensional viscosity also remains constant at a value of $3\eta_0$ up to the point where the imposed extensional strain rate ($\dot{\varepsilon}$) is of the order of the inverse of the longest relaxation time of the fluid. Higher extensional strain rates elicit a response where η_E may increase over 2–3 orders of magnitude above the base value of $3\eta_0$, a phenomenon known as extensional strain hardening. This response is generally observed in solutions having low concentration of polymers and where the polymer coils are isolated from each other.[32] For polymer melts or concentrated solutions, where significant overlap among polymer chains occur, η_E first decreases for $\dot{\varepsilon} \geq 1/\tau_d$, and again starts to increase when $\dot{\varepsilon} \geq 1/\tau_R$, where τ_R is the Rouse relaxation time of the polymer chains in the fluid.[33] For systems where the overlap is significant, τ_d and τ_R are related through the equation $\tau_d = 3Z\tau_R$, where Z is the average number of entanglements per chain. Z is dependent on the concentration (number of chains per unit volume, c) and the length of the chains (molecular weight M_w). Procedures for estimating the number of entanglements and time constants are available.[34]

Since the flow properties of polymer solutions vary dramatically with changes in solution concentration and molecular weight, it is useful to review briefly some of the relevant methods that are used to characterize polymer solutions. It is well known[35,36] that there exists, for a given molecular weight, a critical concentration, c^*, below which the polymer coils do not overlap each other. A polymer solution is considered dilute when the $c < c^*$. In this regime the characteristic properties of the polymer solutions are significantly influenced by the interaction of the polymer with the solvent. For instance the intrinsic viscosity, defined as $[\eta] = (\eta - \eta_s)/(c\eta_s)$, where η and η_s are the solution and the solvent viscosities respectively, and c is the polymer concentration, scales with molecular weight, M_w, as $[\eta] \sim M_W^{(3\nu-1)}$. Similarly, there exists another concentration c^{**} above which the solvent ceases to affect the properties of the solution. For $c > c^{**}$, the solution is considered concentrated. For entanglements to occur in these solutions, the molecular weight of the chains should typically be about twice a critical molecular weight, M_c. Thus, it is possible to have a concentrated but unentangled solution if the molecular weight is small enough, even though the concentration in solution is large. For unentangled, concentrated solutions, $\eta_0 \sim cM_w$. For those solutions where entanglements dominate, $\eta_0 \sim c^4 M_w^{3.4}$.[37] In between these two regions, there are zones denoted 'semidilute,' where both solvent effects and the effects of entanglement density become important. The quantities c^*, c^{**}, and M_c can be established using theoretical arguments, and polymer solutions can be effectively classified into regimes based on the concentration of the polymer in solution and its molecular weight. A plot showing these regimes is known as the Graessley diagram, named after W. W. Graessley who first introduced it.[38] An example is shown in Figure 4, along with data from a group of representative solutions of poly(ethylene oxide) in water (PEO–water) that have been used in electrospinning.

In Figure 4, the line demarcating the limits of the dilute region is obtained from the relationship $c^* \approx 1/[\eta]$, where the intrinsic viscosity is given as $[\eta] \propto M_w^{\alpha}$ and $\alpha = 3\nu - 1$. Here ν is the solvent quality parameter, which ranges from 0.5 to 0.7, approximately. For the current purpose, we follow the experimental work of Daga and Wagner[48] and use $\alpha = 0.67$ for demarcating this limit. The above dependence of the $[\eta]$ on M_w holds at low concentrations ($c < c^*$) and at low values of M_w. As M_w is increased, there exists a value of c at which the dependence of $[\eta]$ on M_w deviates significantly from that noticed at low concentrations. The concentration at which the crossover from the dilute solution to the concentrated solution occurs is theoretically given by $c^{**} = 0.77/[\eta^{**}]$, where $[\eta^{**}]$ is the value of the intrinsic viscosity at which the first deviation from the dilute solution behavior of the intrinsic viscosity is observed.[38] For purposes of illustration in Figure 4, we again follow Daga and Wagner[48] and estimate

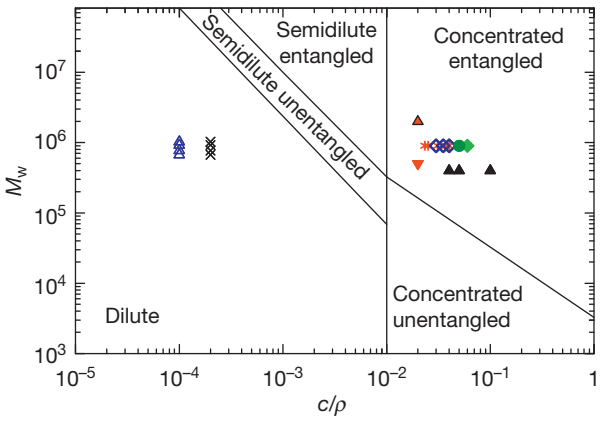

Figure 4 The Graessley diagram showing the various regimes for PEO–water solutions. The markers correspond to systems reported in the literature that have been used for electrospinning and yielded uniform fibers. The dilute solutions shown are those reported in Yu *et al.*[39] These correspond to PEO–water solutions having two different concentrations whose background viscosities are increased by addition of polyethylene glycol having shorter length of chains. Other markers correspond to PEO–water solutions used in Shin *et al.*[40,41] (red up triangle), Daga *et al.*[42] (red star), Zhou *et al.*[43] (green diamond), Deitzel *et al.*[44] (black up-triangle), Uyar and Besenbacher[45] (blue open diamonds), Liu and He[46] (red down triangle), and Panda and Ramakrishna[47] (green circle).

c^{**} as $c^{**} \approx 8c^*$. The line demarcating the semidilute unentangled and semidilute entangled solutions is given by $M_w = (c^{**}/c)^{1/\alpha}(\rho/c^{**})M_{c,melt}$, where $M_{c,melt}$ is the critical molecular weight for onset of entanglements in a melt.[37,49] Typically, $2 \le M_{c,melt}/M_{e,melt} \le 5$, where $M_{e,melt}$ is the entanglement molecular weight, defined below. For the current calculations we have taken the lower bound, so that $M_{c,melt} = 2M_{e,melt}$. $M_{e,melt} = 1624\ g\ mol^{-1}$ for PEO.[50] In the concentrated region the decrease in the number of entanglements per chain with decreasing concentration leads to a linear variation of the critical molecular weight for entanglements. The line demarcating the crossover from unentangled to entangled in the concentrated solution region ($c^{**} \le c \le \rho$) is given by $M_{c,soln} = (\rho/c)M_{c,melt}$.[33,37] It is immediately apparent that most experiments with PEO–water systems have been conducted in the concentrated entangled region; the work of Yu *et al.*[39] is a notable exception. All these experiments resulted in homogeneous fibrous products. The diagram is unique to a given polymer–solvent system and provides a valuable aid to the design of solutions used in electrospinning and rheology.

In general, the constitutive behaviors of polymer solutions vary with the concentration and the molecular weight. A large number of models are available for describing these. Excellent texts are now available that provide details of the models.[36,51] However, since concentrated entangled solutions are frequently used in electrospinning, a brief description of the behavior of these solutions in extensional flow fields is warranted here.

The dynamics of entangled polymeric fluids are usually studied within the framework of the Doi–Edwards theory.[35] The theory envisages an isolated chain in a concentrated entangled solution to be confined within a 'tube of constraints' set by its neighboring chains. The average diameter of the tube 'a' is determined by the average amplitude of fluctuation of the position of a chain segment between entanglement points separated by a number of Kuhn monomers (N_e). For melts and concentrated solutions $a \approx b\sqrt{N_e}$, where b is the Kuhn step length of the chains concerned. For a chain containing N monomers, the tube can be thought of as being composed of N/N_e segments of diameter a. Lateral motion of the chain beyond the 'walls' of the tube is energetically unfavorable. However, within the tube itself (i.e., on a length scale smaller than a), the dynamics of the chain is governed by the monomeric friction coefficient ζ, which arises due to thermodynamic interactions between chains. The time taken for N_e monomers to move a distance of the order of the tube diameter is $\tau_e = (a^2/D_c) = (b^2N_e)/(k_BT/\zeta N_e) = (\zeta b^2/k_BT)N_e^2$. Here D_c is the curvilinear diffusion coefficient along the chain contour, k_B is the Boltzman constant and T is the absolute temperature. One can also write $\tau_e = (\zeta b^2 N_K^2/k_BT)(N_e/N_K)^2 = \tau_R/Z^2$, where $\tau_R = (\zeta b^2 N_K^2/k_BT)$ is the Rouse time for a chain containing N_K monomers, and $Z = (N_K/N_e)$, is the number of entanglements per chain. Following deformation, the entire chain relaxes stress through a snake-like motion along its backbone, called 'reptation.' The reptation process is completed in a timescale τ_d, which constitutes the longest relaxation time of the chain. In entangled melts, the longest relaxation time of the chains is related to the timescale of segmental motion (τ_e), through the relationship $\tau_d = 3Z^3\tau_e = 3Z\tau_R$.[34] In general, the dynamics of entangled solutions are also governed by these timescales. The relevant length scale is the equilibrium length of the tube, which is related to the radius of gyration of the chain. Watanabe provides an excellent review on the subject.[52]

The original Doi–Edwards model has been subsequently modified and extended. Ianniruberto and Marrucci[53] have suggested a relatively simple model, popularly known as the 'double constraint release with chain stretch' (DCR-CS) model, that is capable of capturing qualitatively the important dynamical features associated with flow of entangled solutions. In Figure 5, predictions of the model in extensional flows are provided to illustrate the influence of polymer molecular weight and the number of entanglements per chain on the extensional viscosity. The figures are plotted in terms of Trouton ratio, $TR = \eta_E/\eta_0$, and Deborah number, $De = \dot{\varepsilon}\tau_d$. Figure 5 illustrates the universal behavior that the Trouton ratio remains constant at a value of 3 for $De < 1$ and starts to decrease rapidly between $1 \le De \le (\tau_d/\tau_R)$, due to orientation of the molecular coils in the direction of flow.

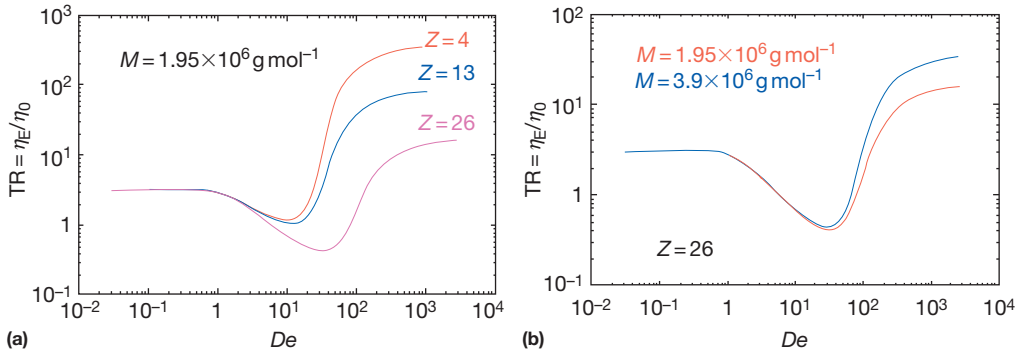

Figure 5 Theoretical predictions of the DCR-CS model for the extensional flow behavior of an entangled polymer solution, plotted as the steady-state Trouton ratio, $TR = (\eta_E/\eta_0)$ versus Deborah number (De) based on the longest relaxation time (τ_d). $De = \dot{\varepsilon}\tau_d$, where $\dot{\varepsilon}$ is the imposed strain rate. The predictions are based on polystyrene ($M_{e,melt} = 13\,300\ g\ mol^{-1}$) in diethyl phthalate. (a) Predictions of extensional flow behavior for solutions having the same molecular weight (M_w) but different entanglement numbers (Z). As the entanglement number increases, the upturn in the TR is delayed to higher values of De. Also the maximum achievable TR, shown by the dotted lines, decreases with increasing values of Z. (b) Predictions of extensional flow behavior for solutions having the same Z but different values of M_w. The maximum achievable TR increases as M_w increases. Also, the rate of increase of the TR is greater for longer lengths of chains.

For $De \geq (\tau_d/\tau_R)$, however, the Trouton ratio increases rapidly due to the onset of stretching of the chains and reaches a value much larger than the Newtonian limit of TR = 3. The Trouton ratio ultimately saturates at very large values of *De*, when the finite extensibility limit is reached and the polymer chains are completely stretched out.

Figure 5(a) illustrates the effect of the number of entanglements per chain, $Z = N_K/N_e$, on the Trouton ratio. In the melt phase, each polymer is characterized by a number of Kuhn segments between entanglements, $N_{e,melt}$, or equivalently the entanglement molecular weight $M_{e,melt} = M_w\ (N_{e,melt}/N_K)$. Fetters *et al.*[50] have tabulated these values for a large number of polymeric species. In concentrated solution, as the concentration of the polymer is decreased, Z also decreases since the degree of overlap among the chains goes down. In the concentrated, entangled region, the M_e of the solution can be related to $M_{e,melt}$ through the relationship $M_e = M_{e,melt}(c/\rho)^{-1}$, where c is the concentration of the polymer in solution and ρ is the bulk polymer density; this assumes that the solvent is approximately a θ-solvent for the polymer. The maximum Trouton ratio achievable by a given polymer solution can be derived using asymptotic analysis of the equations of the DCR-CS model. When $De \to \infty$, $TR \to 6\lambda_{max}^2/(1 + 1.5Z)$, where $\lambda_{max} = \sqrt{N_K/Z}$ is the stretch ratio and $N_K \sim M_w$, the molecular weight of the polymer. Thus, as concentration in solution decreases (for a given molecular weight of polymer), Z decreases and λ_{max} increases so that the limiting Trouton ratio at high strain rate becomes larger. Also as M_e decreases, the λ_{max} decreases concomitantly (since N_K is directly proportional to M_w). Consequently, the maximum Trouton ratio also decreases. In effect, the chains become 'stiffer' and 'less extensible' with respect to flow. **Figure 5(b)** illustrates the same effect arising from a change of molecular weight: as M_w decreases (at constant Z), λ_{max} decreases, resulting in a decrease in the limiting Trouton ratio.

Meanwhile, **Figure 5(a)** also shows that the solutions with larger concentrations (larger Z) demonstrate an upturn in the Trouton ratio at a larger Deborah number. The upturn in the extensional viscosity is expected to occur for $\dot{\varepsilon} \approx 1/\tau_R$. For Deborah number based on the longest relaxation time, this criterion translates to $De = \dot{\varepsilon}\tau_d \approx \tau_d/\tau_R = 3Z$. Thus, the critical Deborah number at which the upturn in the Trouton ratio occurs shifts to the right. However, since τ_R is also larger, the critical strain rate at the upturn, $\dot{\varepsilon}_c$, is actually lower. Further details of this analysis can be found elsewhere.[54]

In the context of electrospinning, several models have also been used to describe the non-Newtonian behavior of the fluid. In one such model, called FENE-P (finitely extensible nonlinear elastic dumbbell model with Peterlin's approximation), the polymeric stress contribution depends on the average of the polymer configuration tensor and the finite extensibility of the polymer chain. For the FENE-P model, the polymeric stress can be obtained as follows:

$$\tau_p = nk_BT\left(\delta - \frac{\langle QQ\rangle}{1 - \mathrm{tr}\langle QQ\rangle/b_{max}}\right) \qquad [5]$$

In the equation above, $\langle QQ\rangle$ is the polymer chain configuration tensor and b_{max} is the finite extensibility parameter. The term δ is the Kronecker delta function. Also, n is the monomer density, k_B is the Boltzmann constant, and T is the absolute temperature. The details of the physics leading to the FENE-P model are available elsewhere[51] and are not discussed here. For the purposes of this review, it suffices to state that this model has been successful in predicting the rheological behavior of polymer solutions. Other models that have been used in the study of electrospinning include the linear Maxwell,[55] the Oldroyd-B,[30] and the neo-Hookean[56] models. In addition, Feng[29] has used an empirical nonlinear model representing fluid behavior in his work. Apart from FENE-P, the other models that have been used are 'phenomenological' in nature. One shortcoming of phenomenological models is that their predictions depend strongly on the numerical values of certain 'adjustable' model parameters. The adjustable parameters might or might not have a physical or molecular significance. The accuracy of the predictions of these models depends on how good the estimates of the parameters are. The parameters are often estimated by elaborate 'fitting' procedures over a limited range of experimental rheological data. Extrapolating the predictions beyond the range of conditions used to estimate the parameters can become problematic. On the contrary, the molecular models, like DCR-CS or FENE-P, relate rheological phenomena to the dynamics of the polymer chain and its interactions with the surroundings (solvents, for instance). This is advantageous because flow properties of the fluids can be designed by suitably tailoring the polymer chain architecture or the properties of the solvent. For this reason, we have chosen to illustrate the behavior of entangled fluids using the DCR-CS model in this section. However, such models have not, thus far, been widely used in the electrospinning literature.

1.127.3.3. Electrospinning Zones

The electrospinning process has been studied in terms of three distinct zones: namely, the conical meniscus region, the straight thinning jet region, and the 'whipping jet' region, which constitutes the zone where the jet bends and a nonaxisymmetric convective instability sets in. In the following sections, we discuss each of these regions briefly.

1.127.3.3.1. The conical meniscus

As the fluid exits from the spinneret and enters the electric field, it assumes a conical (or nearly conical) shape, from the apex of which a thin jet emerges. In inviscid fluids, the shape that the meniscus attains depends on the interplay between the electric field and the surface tension and has been studied extensively since the early 1900s. Zeleny first demonstrated that a drop of liquid having surface tension γ, held at the end of a capillary tube of radius r_0, and raised to a potential difference of V disintegrates into a spray. He also demonstrated that at the point of disintegration the ratio $V^2/r_0\gamma$ remained approximately constant.[57,58] Taylor[57] elaborated upon this analysis and suggested that the critical half angle of the meniscus approaches a value of 49.3° close to the disintegration event. This condition of the meniscus is well known as the 'Taylor cone.' However, Yarin *et al.*[59,60] showed that the Taylor cone represents a specific self-similar solution, whereas there exist other, non-self-similar solutions that do not tend to the semivertical angle of 49.3° near criticality. In this way, Yarin *et al.*



Figure 6 Various shapes of the meniscus observed for three solutions of poly(methyl methacrylate) ($M_w = 540$ kDa), having different concentrations (10, 12, 15 wt% in dimethyl formamide), and hence, different zero-shear-rate viscosities (0.5, 1.1, and 10 Pa s respectively). The solutions were subjected to conditions where the electric field and infusion rates are identical.

demonstrated that the electrified meniscus can assume a wide variety of shapes that are different from that of the Taylor cone. Figure 6 shows some examples of such shapes. Here, three solutions of polymethyl methacrylate having identical polymer molecular weights but at different concentrations in dimethylformamide and also differing in the zero-shear-rate viscosity are considered. The solutions were subjected to identical electric field strengths and infusion rates during electrospinning. Clearly, the shape of the meniscus changes as the concentration of the polymer in solution and the solution viscosity increases. Collins *et al.*[61] have shown that such changes in the shape of the meniscus can be brought about by altering the conductivity of the fluid. In the limit of high fluid conductivity, the Taylor cone shape is dominant. As mentioned previously, tangential stresses are generally insignificant in highly conducting fluids. Typically, in fluids with high conductivity, the charge relaxation time is small, and charges are made available instantaneously to the surface. In this way, the capillary pressure that continually rises in a sharpening meniscus is always balanced by the electrostatic pressure. Also, as a consequence of high conductivity, the electric field in the fluid vanishes. The lack of an internal electric field prevents the development of significant tangential (or shear) components along the surface. These conditions preserve the spherical symmetry of the flow and lead to the Taylor cone geometry in conducting fluids. However, as conductivity of the fluid decreases and the dielectric character increases, a deviation from the conical shape predicted by Taylor's theory is observed. The change in the shape is attributed to the development of tangential (shear) stresses on the surface of the meniscus in fluids with low conductivity. These tangential stresses couple with the viscous nature of the fluid to accelerate the fluid near the apex, deforming the meniscus and causing its shape to deviate from that of a perfect Taylor cone. This process is reflected in the menisci shown in Figure 6. Since the mobility of the charges in a fluid scales approximately inversely with viscosity,[26] higher-viscosity fluids are likely to be less conductive (more dielectric) and thus deviate from the Taylor cone shape the most. From left to right in Figure 6, a change in behavior is observed from that characteristic of fluids with low viscosity and high conductivity, where a jet appears abruptly from the apex of a conical meniscus, to that typical of viscous, dielectric fluids, where a more gradual transition from the conical meniscus to a steady jet occurs.

The motion of the fluid within the conical meniscus can also be quite complicated. For liquids of low conductivity and viscosity, Hayati *et al.*[62] discovered intense meridional circulation of liquid toward the apex along the surface of the conical meniscus and away from the apex along the axis of symmetry within the conical meniscus. The motion inside the conical meniscus occurs due to the existence of the tangential component of electrical stress on the surface of the meniscus. The stable jet is essentially maintained by the shearing flow on the surface of the cone that supplies material to the jet. The balance of the viscous and electrical forces on the surface of the meniscus establishes a velocity scale for flow into the jetting region.[63] Recirculation within the meniscus occurs when $u \geq Q/L_c^2$ approximately.[63] The meridional circulation decreases with increasing conductivity of the solution, as the tangential electric stress diminishes in magnitude. For sufficiently high conductivity, the flow within the fluid is not much different from a sink flow corresponding to the imposed flow rate Q. In a sink flow, the fluid moves radially inward to a point where it disappears at a constant rate. As mentioned earlier, in this limit, the meniscus approaches the shape of the Taylor cone.

While the work of Collins *et al.* provides some qualitative insight into how the viscosity and conductivity can affect the shape of the meniscus, it does not explain how the viscoelasticity of the fluid is likely to affect these shapes. Using the neo-Hooken model[56] for a purely elastic fluid, Yarin *et al.*[59,60] showed that the critical angle at the apex of the cone decreases from the value predicted by Taylor's theory as the influence of elastic forces increases. By contrast, using numerical simulations with the FENE-P constitutive model, Carroll and Joo[30] demonstrated that fluids with increasing elastic character adopt larger critical apex angles, even when possessing the same viscosity and conductivity and subjected to the same electric field. Around the same time, Yu *et al.*[39] reported similar trends, observed experimentally. Both the FENE-P model and the results of Yu *et al.* apply to dilute polymer solutions, where the isolated polymer molecules remain in a coiled state for strain rates that are less than the inverse of the longest relaxation time of the polymer. In this limit the stress accumulated in the fluid is borne mostly by the solvent and is directly proportional to rate of strain imposed by flow. However, at higher strain rates, the polymer chains unravel, and the subsequent loss in entropy manifests as an elastic stress in the fluid. In effect, a single time constant, the polymer relaxation time, governs the separation between regions of linear (viscous) and nonlinear (viscoelastic) fluid behavior. Ultimately, at very large strain rates, the elastic stress saturates as the polymer molecule is stretched to its maximum length. Meanwhile, the solutions represented in Figure 6 fall in the category of semidilute or entangled polymer solutions. These fluids are typically much less extensible than dilute polymer solutions. Thus, the complexities arising from elastic effects are less evident in these experiments than in the work of Yu *et al.* Moreover, the slow motion near the nozzle is likely to be dominated by the viscous response of the fluid, which explains why a qualitative explanation of the shape of the meniscus can be provided following the arguments of Collins *et al.* These complexities arising from the rheological behavior of the fluid thus make the prediction of the shape of the meniscus in electrospinning an ongoing challenge. Further attention to these aspects is warranted.

1.127.3.3.2. The thinning jet

The conical meniscus eventually gives rise to a slender jet that emerges from the apex of the meniscus and propagates downstream. An example of the jet emanating from a conical meniscus region is shown in Figure 7. The jetting process can be studied using the mathematical framework described in Section 1.127.3.2. Hohman *et al.*[28] first reported this approach for the relatively simple case of Newtonian fluids. This suggests that the shape of the thinning jet depends significantly on the evolution of the surface charge density and the local electric field. As the jet thins down and the charges relax to the surface of the jet, the charge density and local field quickly pass through a maximum, and the current due to advection of surface charge begins to dominate over that due to bulk conduction. The crossover occurs on the length scale given by eqn [6][64]:

$$L_N = \left[K^4 Q^7 \rho^3 (\ln \chi)^2 / 8\pi^2 E_\infty I^5 \bar{\varepsilon}^2\right]^{1/5} \quad [6]$$

This length scale defines the 'nozzle regime' over which the transition from the meniscus to the steady jet occurs. Sufficiently far from the nozzle regime, the jet thins less rapidly and finally enters the asymptotic regime, where all forces except inertial and electrostatic forces cease to influence the jet. In this regime, the radius of the jet decreases as follows:

$$h = \left(\frac{Q^3 \rho}{2\pi^2 E_\infty I}\right)^{1/4} z^{-1/4} \quad [7]$$

Here z is the distance along the centerline of the jet. This equation was first derived by Kirichenko *et al.*[65] and was later verified experimentally by Shin *et al.*[40,41] Between the 'nozzle regime' and the 'asymptotic regime,' the evolution of the diameter of the thinning jet can be affected by the viscous response of the fluid. Indeed by balancing the viscous and the electrostatic terms in the force balance equation it can be shown that the diameter of the jet decreases as $h = (6\mu Q^2 / \pi E_\infty I)^{1/2} z^{-1}$.

The mathematical framework of Section 1.127.3.2 has also been used to study the effect of nonlinear (e.g., viscoelastic) fluid behavior on the thinning that takes place in the straight section of the electrospinning jet, as represented by the works of Feng[29] and Carroll and Joo.[30] In fact, the straight jet section has been studied extensively to understand the influence of viscoelastic behavior on the axisymmetric instabilities[28,66] and crystallization[67] and has even been used to extract extensional viscosity of polymeric fluids at very high strain rates.[68] For highly strain-hardening fluids, Yu *et al.*[39] demonstrated that the diameter of the jet decreased with a power-law exponent of $-1/2$, rather than $-1/4$ or -1, as discussed earlier for Newtonian fluids. This $-1/2$ power-law scaling for jet thinning in viscoelastic fluids has been explained in terms of a balance between electromechanical stresses acting at the surface of the jet and the viscoelastic stress associated with extensional strain hardening of the fluid.[69] Additionally, theoretical studies of viscoelastic fluids predict a change in the shape of the jet due to non-Newtonian fluid behavior. Both Yu *et al.*[39] and Han *et al.*[68] have demonstrated that substantial elastic stresses can be accumulated in the fluid as a result of the high strain rate in the transition from the meniscus into the jetting region. This elastic stress stabilizes the jet against external perturbations. Further downstream the rate of stretching slows down, and the longitudinal stresses relax through viscoelastic processes. The relaxation of stresses following an extensional deformation, such as those encountered in electrospinning, has been studied in isolation for viscoelastic fluids.[54,70] Interestingly, Yu *et al.*[39] also observed that, elastic behavior notwithstanding, the straight jet transitions into the whipping region when the jet diameter becomes of the order of 10 μm.

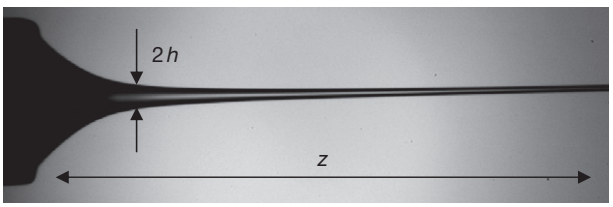

Figure 7 The jet that emerges from the meniscus steadily tapers down at a rate that is dependent on the properties of the fluid. The strain rate in the tapering jet is given by $\dot{\varepsilon} = -(2Q/h^3)(dh/dz)$.

1.127.3.3.3. The whipping jet

While it is in principle possible to draw out fibers of small diameter by electrospinning in the cone-jet mode alone, the jet does not typically solidify enough *en route* to the collector and succumbs to the effect of force imbalances that lead to one or more types of instability. These instabilities distort the jet as they grow. A family of these instabilities exists, and can be analyzed in the context of various symmetries (axisymmetric or nonaxisymmetric) of the growing perturbation to the jet. Some of the lower modes of this instability observed in electrospinning have been discussed in a separate review.[64] The 'whipping instability' occurs when the jet becomes convectively unstable and its centerline bends. In this region, small perturbations grow exponentially, and the jet is stretched out laterally. Shin *et al.*,[40,41] Fridrikh *et al.*,[71] and Fridrikh *et al.*[72] have demonstrated how the whipping instability can be largely responsible for the formation of solid fiber in electrospinning. This is significant, since as recently as the late 1990s the bifurcation of the jet into two more or less equal parts (also called 'splitting' or 'splaying') was thought to be the mechanism through which the diameter of jet is reduced, leading to the fine fibers formed in electrospinning. Despite some evidence of the splitting of the jet in 'postmortem' micrographs of fibers, it has been demonstrated that conditions that lead to the splitting of the jet are difficult to sustain in ordinary electrospinning experiments.[73] Thus, these events are in fact quite rare. Nevertheless, diagrams that suggest this relatively rare form of instability to be operative during electrospinning continue to appear in the literature. In contrast to 'splitting' or 'splaying,' the appearance of secondary, smaller jets from the primary jet have been observed more frequently and in situ.[59,60,73] These secondary jets occur when the conditions on the surface of the jet are such that perturbations in the local field, for example, due to the onset of the slightest bending of the jet, is enough to overcome the surface tension forces and invoke a local jetting phenomenon. Figure 8(a) shows the whipping event observed in a polymer solution. Figure 8(b) demonstrates the growth of the amplitude attained during whipping in a series of time-lapse traces.

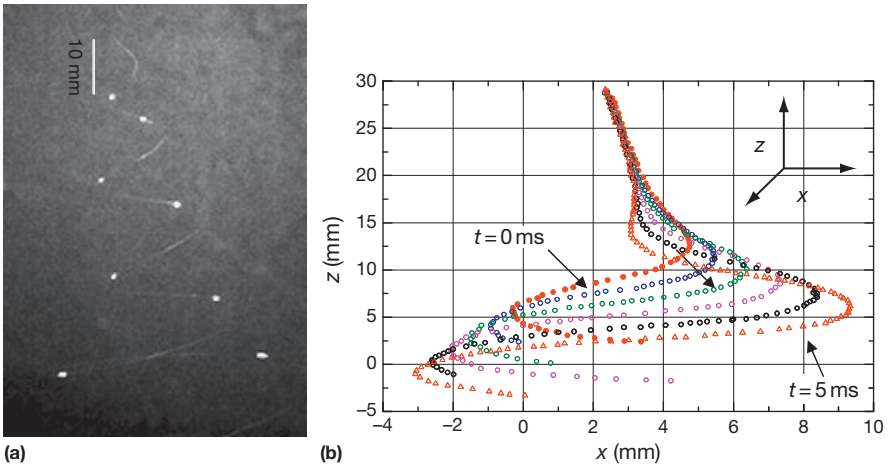

Figure 8 The whipping motion observed in a jet of a 2% (w/w) solution of polyethylene oxide ($M_w = 1.25 \times 10^6$ g mol^{-1}) in water. (a) Photograph shows the convective nature of the whipping instability that propagates downstream with an approximately constant wavelength. The growth in the amplitude of the instability with distance can also be observed from the photograph. The photograph was taken using a digital SLR, which was backlit by a flash that could be remotely triggered. The flash was triggered once with the shutter speed held at 1/100 s. (b) Traces of the growing amplitude observed through time-lapse photography performed using a high-speed camera (Phantom V5, Vision Research) at 1000 frames per second. Traces were extracted from individual images using digitization software. A calibrated grid placed in the plane of focus provided the spatial reference. The evolution of the jet immediately following the onset of the whipping instability is shown.

The conditions necessary for the transition of the straight jet to the whipping jet has been discussed in the works of Gañán-Calvo,[74] Yarin *et al.*,[59,60] Reneker *et al.*,[31] and Hohman *et al.*[28] Gañán-Calvo has analyzed the transition in terms of propagation speeds of surface disturbances, the upstream component of which is delayed by convection of surface charge. His analysis reveals that the transition occurs at a point where the net propagation speed (downstream) of surface perturbations becomes imaginary, and the straight jet ceases to be convectively stable. Yarin *et al.*,[59,60] Reneker *et al.*,[31] and Hohman *et al.*[28] however, adopt a more microscopic viewpoint and conjecture that charges arranged in a straight line and interacting with each other through Coulomb's forces are intrinsically unstable, and that the perturbation caused by these interactions leads to the bending of the jet.

Following the onset of the whipping instability, small perturbations grow exponentially, and the amplitude of the instability increases convectively as the jet thins down. Hohman *et al.*[28] and Fridrikh *et al.*[72] have calculated the growth rates and the wave numbers associated with the jet undergoing a whipping instability by extending the equations of motion (eqns [1]–[4]), which have also been derived for curvilinear jets,[28] into the nonlinear regime. In developing the dispersion relationship, the surface charge repulsion, surface tension, and inertia were considered more important than the effects of Maxwell's stress, which arises due to the electric field and finite conductivity of the fluid. Using the equations reported by Hohman *et al.*, and under similar restrictions, Fridrikh *et al.*[72] obtained an equation for the lateral growth of the jet excursions arising from the whipping instability far from the onset and deep into the nonlinear regime. These developments have been summarized in the review article of Rutledge and Fridrikh.[64]

The whipping instability is postulated to impose the stretch necessary to draw out the jet into fine fibers. As discussed previously, the stretch imposed can invoke an elastic response in the fluid, especially if the fluid is polymeric in nature. An empirical rheological model was used to explore the consequences of nonlinear behavior of the fluid on the growth of the amplitude of the whipping instability in numerical calculations.[72] There it was observed that the elasticity of the fluid significantly damps the amplitude of oscillation of the whipping jet. The elastic response also stabilizes the jet against the effect of surface tension. This effect is well known and is a topic of current research in nonelectrified viscoelastic jets. In the absence of any elasticity, the jet eventually breaks up and forms an aerosol. However, the presence of a polymer in the fluid can arrest this breakup if the factor $\tau/(\rho h^3/\gamma)^{1/2} \gg 1$, where τ is the relaxation time of the polymer, ρ is the density of the fluid, h is a characteristic radius, and γ is the surface tension of the fluid.

1.127.3.4. Discussion on Current Carried by Electrospinning Jet

The current carried by the jet plays a critical role in various aspects of electrospinning. The current in the jet consists of two contributions, one due to Ohmic conduction and another due to the advection of the surface charge with the flow. Rewriting eqn [2], the current can be expressed as follows:

$$I = \pi h^2 K E_z + 2\sigma Q/h \qquad [8]$$

As before, I is the current carried by the jet of radius h subjected to an electrical field with an axial component E_z. The variables Q and σ represent the flow rate and the surface charge density, respectively. The first term in the above equation is due to the conduction current, and the second is due to advection of surface charge. As the jet thins down, the conduction component becomes smaller and the advection component dominates. The electrospinning process is in

large part driven by electrostatic interactions among the charges that appear on the surface of the fluid following electrification. Since it is difficult to determine directly the surface charge density on the thinning jet in experiments, the current is usually measured instead. Numerous investigations have reported the nonlinear dependence of the current on the applied driving voltage and fluid flow rates. Demir *et al.*[76] and Theron *et al.*[77] determined a power-law dependence of the current on the applied voltage, V, with exponents of 2.17 and 2.7 respectively. Similarly, a power-law dependence of the measured current on the flow rate, Q, has also been reported,[71,76,77] with the exponent ranging from −1.04 to +1. The nonlinear behavior of the current has been difficult to rationalize analytically. The observed nonlinear behaviors have been attributed to the onset of fluid instabilities[40,41,44] as well as to the limitation on the mobility of charge in the equipment concerned.[77] Recent measurements have shown that $I \sim E(QK)^{0.5}$ for a large number of experimental systems reported in the literature.[78] This compares with the power-law behavior observed in electrospray systems, where the current scales as $I \sim (QK)^{0.5}$ but does not depend on electric field, E.[79] The similarity between the two systems is conspicuous. A careful study of the jet current has led to the proposal that secondary electrosprays may form on the whipping jet in some cases.[78]

Having measured the current carried by the jet, the surface charge density is then estimated using the relation $\sigma = (h/2)(I/Q)$, which follows from eqn [8] in the limit where the radius of the jet is small enough to neglect the contribution from Ohmic conduction (the first term in eqn [8]). However, other sources of current may interfere with such measurements unless appropriate precautions are taken. One of these is the plasma current, which is most noticeable at high voltages and in equipment configurations of the point-plate type. The secondary jetting processes previously mentioned[78,80] lead to aerosols that also carry a measurable current not associated with the main jet; in such cases, the existence of the aerosol contribution makes it difficult to estimate the amount of charge that is carried by the main jet. A third source of current can arise from the partial ionization of the surroundings (particularly when the humidity is high) near the surface of the electrified jet, leading to free ions that also discharge on the grounded counter electrode.[81] These processes can make the measurement of the actual current carried by the main jet extremely complicated, and prone to overestimation. These complications have impeded efforts to accurately measure current and the surface charge density. Better methods to make such measurements are certainly needed.

1.127.4. Products of Electrospinning

1.127.4.1. Electrospun Fibers: Diameter and Morphology

As mentioned in the introduction, the electrospinning technology is capable of generating fibers with diameters spanning about 4 orders of magnitude, from tens of microns down to tens of nanometers. Much effort has gone into determining to what extent the morphology and the size of the fibers in this range influence the properties of the products formed. For instance, Ma *et al.*[82] and Tuteja *et al.*[83] have shown that the capacity of electrospun mats to repel oil or water strongly depends on the fiber size, the spacing between the fibers, and the morphology of the fibrous products. Ma first showed that the apparent contact angle, θ^*, of a fluid with an electrospun mat increased with decreasing fiber diameter, and that the introduction of the beads-on-string morphology provided a significant enhancement in liquid repellency over the simple, uniform fiber morphology; these results were understood in terms of relative spacing between fibers or beads, s/d, where s is the separation distance between fibers (or beads) and d is the diameter of fibers (or beads).[82] Tuteja *et al.*[83] subsequently proposed two dimensionless design parameters by which to understand the repellency of fluids on various surfaces: the spacing ratio, $D^* = (1+s/d)$, and the robustness $H^* = 2(1-\cos\theta)\, dl_{cap}/s^2$, where $l_{cap} = (\gamma/\rho g)^{0.5}$. Here, θ is the intrinsic contact angle that the liquid forms on a smooth flat film of the same material. The robustness parameter in particular introduces for the first time a length scale, l_{cap}, and provides insight into the significance of small fiber size to enhance the metastability of a liquid drop on a mat of fibers comprised of material with an intrinsic contact angle less than 90°. It was demonstrated that for conditions where $D^* \gg 1$ and $H^* \gg 1$, wettable surfaces can be made repellant to a given liquid. The robustness concept was later embellished to include both a robustness height, H^* and a robustness angle, T^*; both robustness parameters quantify the sagging of the vapor–liquid interface between fibers (or beads) as a result of a pressure difference across the interface.[84] In short, these works demonstrated that with the control of the fiber size, fiber spacing, morphology, and chemical composition, it is possible to tailor repellency of electrospun surfaces to organic and inorganic fluids. These aspects have been highlighted in a recent review.[85] The mechanical modulus of electrospun fibers has also been shown to deviate from the bulk value of the polymer as a consequence of fiber size in a number of instances. Arinstein *et al.*[86] reported an increase in the elastic modulus of individual electrospun fibers with decreasing diameter, and argued that the enhancement of the modulus results from confinement effects arising from the decreasing lateral dimension of the fibers. These aspects have generated substantial interest in understanding the physics that govern the morphologies and diameters of the fibers obtained via electrospinning.

Predicting the morphologies and diameters of electrospun fibers has been a challenge, however. The difficulties arise because the hydrodynamic, viscoelastic and electrical stresses cannot be directly measured in an electrospinning jet. The rapid evaporation of the volatile solvent further complicates the analysis. Nevertheless, neglecting the effects of evaporation during jet thinning, Fridrikh *et al.*[71] proposed a relation for fiber diameter by balancing the surface charge repulsion force acting on the jet with surface tension, in the limit where gradients in the velocity subside and the effects of viscosity are unimportant. This so-called 'terminal' diameter (h_t) of the jet can be expressed as follows:

$$h_t = \left(\frac{2\gamma\bar{\varepsilon}}{\pi(2\ln\chi - 3)}\right)^{1/3}\left(\frac{I}{Q}\right)^{-2/3} \qquad [9]$$

In the above equation, $\chi \sim D/h$ is a dimensionless measure of the wavelength of the instability, D being the radius of

curvature of the jet. The final solid fiber diameter is then determined from h_t through an appropriate volume correction for solvent removal. These assumptions were tested and found to be valid for a number of polymer solutions.[71] However, many studies in the literature[69,87] highlight the apparent correlation of fiber diameter with solution viscosity, which is not captured by eqn [9]; presumably, under many conditions of electrospinning, the assumptions behind eqn [9] are not met before the jet solidifies, either due to premature solvent removal or viscoelastic hardening of the jet. Thus, while eqn [9] may be viewed as a valuable lower bound, the quantitative prediction of fiber diameter in general remains a substantial challenge.

Besides fiber diameter, the fiber morphology can vary from smooth fibers with near-uniform diameter to those resembling 'beads on a string,' depending on the fluid properties and processing conditions. Even droplets can be obtained under suitable conditions. A large body of work that discusses these effects (occurrences of droplets, beaded fibers, or smooth fibers) in terms of the nonlinear viscoelastic behavior of polymeric fluids exists.[44,88] Shenoy *et al.*[89] offered an appealing physical interpretation, in terms of entanglements between polymer molecules in solution required to obtain smooth, uniform fibers. Helgeson and Wagner,[87] on the other hand, emphasized the role of shear viscosity, through the use of the Ohnesorge number $Oh = \mu/(\rho\gamma r_0)^{0.5}$. However, using a set of well-characterized fluids, Yu *et al.*[39] demonstrated that neither the entanglement density nor the Ohnesorge number provide a reliable predictor of uniform fiber formation. Instead, they argued that the elastic stress invoked in the fluid during electrospinning is of fundamental importance. Such elastic stresses can be induced through increased entanglement density in the solution or by the more efficient transfer of stress from the surface of the jet to the jet interior, as a consequence of viscosity, but they can be induced by other mechanisms as well. For the formation of fibers with a uniform morphology, sometimes referred to as 'electrospinnability,' it suffices that the elastic stress generated during processing is much greater than the capillary pressure that would cause breakup of the fluid filament. Yu *et al.* provided a criterion based on the Deborah number (De), which relates the characteristic process timescale to the relaxation time of the fluid, to predict the formation of uniform fibers. According to this criterion, the relevant Deborah number is given by $De = \tau\omega_{max}$, where τ is the relaxation time of the polymeric fluid and ω_{max} is the growth rate of the fastest-growing mode of the surface-tension-driven Rayleigh instability; to a good approximation, ω_{max} can often be estimated using the conventional formula for an uncharged, Newtonian fluid filament, $\omega_{max} = \left[\rho R_0^3 I_0(x_R)/\gamma I_1(x_R)\left(1 - x_R^2\right)x_R\right]^{-1/2}$, where ρ is density, R_0 is the initial radius of the jet, γ is the surface tension, and $x_R = 0.697$ is the reduced wave number of the fastest-growing mode; I_0 and I_1 are modified Bessel functions. When $De < 1$, breakup of the jet into a spray of droplets results; for $De > 1$, beaded fibers are obtained. For $De > 6$, uniform fibers are routinely observed. Significantly, Yu *et al.* used experimental measurements of extensional viscosities and strain hardening of the fluids to explain the influence of elastic stresses on electrospun products. Prior to this, explanations had depended largely on measurements of rheological response in shear flow, which frequently becomes weaker with increasing shear rate. However, their experiments were restricted to a rather narrow range of field strength, and it was not clear whether significantly higher electric fields could also serve to retard the development of the Rayleigh instability, as suggested by the work of Hohman *et al.* (cf. equation [20] in Hohman *et al.*[28]).

In addition to beading along the fiber, the morphology of electrospun fibers can be varied, for example, in the shape of their cross-section. For example, electrospun fibers with wrinkled surfaces[16,90] and those resembling flat ribbons[14] have been reported. In these cases, the effect of the skin that forms due to rapid evaporation of the solvent from the surface has been emphasized. This phenomenon can be understood as arising from the formation of a skin layer on the surface of the fiber, which subsequently buckles as the core of the fiber continues to shrink. In order to explain these observations qualitatively, Wang *et al.*[90] and Pai *et al.*[16] correlated the observed wrinkled and porous morphologies with the ratio of a drying time, $t_D = R_0/2W_{E0}$, which gives an order of magnitude of time for the drop to solidify by evaporation, and a buckling time, $t_B = D_2(\phi_{pg} - \phi_{p0})^2/W_{E0}^2$, which characterizes the onset of the buckling instability, as proposed previously by Pauchard and Allain[91,92] and Pauchard and Couder[93] for liquid drops. Here, W_{E0} is the initial evaporation rate, R_0 is the radius of the drop or jet, D_2 is the mutual diffusion coefficient of the solvent–polymer system, ϕ_{pg} is the volume fraction of polymer undergoing vitrification at the surface of the jet, and ϕ_{p0} is the initial volume fraction of the polymer in the solvent. Using these characteristic times, qualitative predictions for the fiber morphologies could be obtained. In general, it was observed that larger fibers tend to buckle due to the larger drying time associated with the reduced surface area (relative to volume) for evaporation; polymer solutions made from higher-molecular-weight polymer tend to buckle due to a shorter buckling time associated with the smaller mutual diffusion coefficient; and polymer solutions with larger concentration tend to collapse due to the smaller difference between the polymer concentration at the fiber surface and at the core.

In addition to the competition between drying and buckling, many electrospun fibers exhibit either superficial or internal porosity, which arises due to a temperature- or nonsolvent-induced liquid–liquid phase separation prior to solidification of the fiber. The works of Casper *et al.*[15] and Megelski *et al.*[94] provide some excellent examples of the wide variety of porous surface morphologies that can be obtained by varying the solvent, humidity, and polymer molecular weight. Surface pores are typically obtained when processing from highly volatile solvents. The evaporation of the volatile solvent can lead to a significant decrease in the surface temperature. The lowering of temperature induces phase separation at the surface of the jet or condensation of liquid from the ambient air, through a mechanism discussed by Srinivasarao *et al.*[95] By contrast, processing from less volatile solvents in the presence of a nonsolvent vapor typically allows for internal phase separation and the formation of pores internally or throughout the fibers. Pai *et al.*[16] demonstrated that electrospun fibers obtained by electrospinning a solution of a polymer in a hygroscopic solvent and in a humid atmosphere contain internal pores or

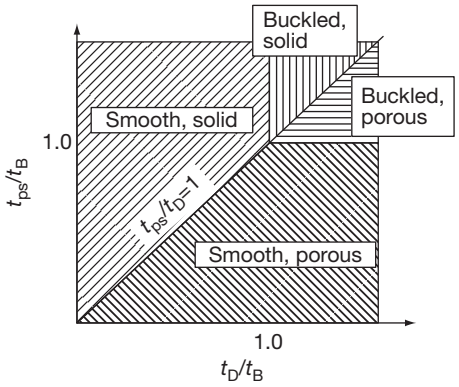

Figure 9 Phase diagram demarcating areas where fibers with different surface morphologies and internal structures can be expected. See Pai *et al.*[16] for details.

voids. In their case, the water vapor from the ambient permeated into the hygroscopic solvent and acted as a nonsolvent for the polymer. This caused the polymer to phase separate during processing and led to the formation of voids within the fiber, which amounted to as much as 30% of the volume of the fiber, depending on the molecular weight of the polymer used. This phase-separation process competes with the buckling and drying processes mentioned earlier. To understand this new competition, one can introduce a phase-separation time, t_{PS}, corresponding to the time required for sufficient cooling or exchange of solvent and nonsolvent to induce phase separation within the jet, as described by Dayal and Kyu[96] or by Pai *et al.*[16] For processes that satisfy the conditions where the $t_D/t_B > 1$ and $t_{PS}/t_B < 1$, fibers with smooth external morphologies can be expected. Based on the competition between the several processes of drying, buckling, and phase separation, one can construct a diagram such as that shown in **Figure 9**, demarcating regions where the various fiber morphologies can be expected. Lastly, hollow fibers or those having a core–shell morphology can be obtained by electrospinning two fluids simultaneously in a coaxial configuration.[18,19,97,98] Similar core–shell morphologies have also been obtained by spinning from an emulsion.[99] Such morphologies are thought to be promising for a variety of applications, including drug delivery.[100,101] Coaxial electrospinning can also be used to encapsulate a block copolymer as the core within a more thermally stable outer shell; upon subsequent annealing of these fibers, novel ordered morphologies are found to occur.[102–105] These ordered morphologies are significantly different from those that are observed in the same copolymers in bulk. For example, copolymers that are known to form lamellar morphologies in the bulk are prone to form a novel, 'concentric lamellar' morphology under confinement within a fiber whose diameter is on the order of 1–10 periods of the bulk lamellar morphology. Radial confinement also leads to novel defect structures, such as the recently identified radial edge dislocation loop.[105]

1.127.4.2. Properties of the Electrospun Mat

In addition to the liquid repellency and mechanical properties of the mats, discussed earlier in the context of fiber size, two other properties of the electrospun mat probably deserve mention in the context of biomaterials applications. These are (1) the organization of fibers within the mat and (2) the porous structure of the mat. In the absence of special efforts to control the deposition of fibers on the grounded electrode, the dynamics of the whipping process are responsible for the formation of the seemingly random array of fibers within a two-dimensional (2D) network that is usually observed in scanning electron micrographs. The deposition area can be controlled somewhat, through the use of focusing rings[106] or environmental conditions.[81] Rotors,[107,108] patterned electrodes,[109] parallel bars,[110] and disks[12,13] have all been used to alter the deposition, fiber alignment, and collection of electrospun mats. Liquids have also been used as collectors.[111–114] The fibers can also 'weld' at points of contact between fibers, depending on the amount of solvent remaining in the fiber at deposition, or by subsequent thermal or chemical treatment[115,116]; such welding has been shown to improve electrical properties of the mat.

While much attention has been devoted to the characterization of fiber diameters, far less attention has been directed to the characterization of the porous structure of the fibrous mat. Nevertheless, the overall porosity and the distribution of void space within an electrospun mat are crucially important for applications such as composites and tissue engineering. Characterization of the void space, however, is problematic. The overall pore volume fraction, or porosity, can be measured gravimetrically, for sufficiently thick samples. However, characterizing the distribution of the void volume within the mat, and the interconnectivity of these pores, remains a challenge. Eichhorn and Sampson[117] have developed models that relate the characteristic pore size and the available surface area to the length, width, and linear density (mass per unit length) of fibers, the porosity, and the mean coverage of the network; the mean coverage corresponds to the mean number of fibers that would project down onto a common point in the 2D plane of the mat. The fiber diameter plays an important role in determining the pore dimensions in the network. Interestingly, these models indicate that the available surface fraction for a given value of porosity does not strongly depend on the mean coverage.

On the experimental side, a number of techniques have been used to characterize the porosity of the electrospun mats.[118–120] Most popular among these are mercury intrusion porosimetry, liquid extrusion porosimetry, and capillary flow porosimetry. Recently microcomputed tomography has been utilized to characterize electrospun mats.[121] Scanning electron microscopy (SEM) is also routinely used for the purpose. However, SEM provides only qualitative information of pore structure, unless appropriate image analysis techniques are employed to account for the 2D projection of 3D structure. Of these techniques, perhaps the most common method of characterization is mercury porosimetry. However, this method is known to introduce artifacts, such as the 'ink-bottle effect,' in the characterization of complex porous geometries. For compliant materials like aerogels and electrospun mats, deformation of the sample under measurement conditions also leads to systematic errors in the characterization of pore sizes. Recently, a method for correcting such liquid intrusion data for deformation of the sample, by either buckling or elastic compression, has been reported, and the method

has been applied to several materials used for cultivation of human dermal fibroblasts.[122,123] These and other studies[11] confirm the nearly linear correlation between fiber diameter and characteristic void size in electrospun mats. Several empirical efforts to exert some control over the packing density and patterning of the mat have been reported. These include the use of special collectors, for example, coated vitreous enamel substrates with tailored dielectric properties and coating thicknesses,[124,125] the variation of composition of mixed solvents,[126] and the introduction of sacrificial components such as salts, ice crystals, beads, an extractable blend component, or a second extractable fiber type.[122,127,128] The results of such methods are mixed, however. Removal of sacrificial components has been reported to either decrease or increase porosity and pore size, depending on such factors as capillarity and the thermal transitions of the polymer component left behind.

1.127.5. Summary and Conclusion

In this review, we have attempted to summarize some of the important results from ongoing research into the fundamental physics that govern the electrospinning process. The idea has been to provide a few guiding principles for those who would use electrospinning to fabricate materials for biological or biomedical applications, and to instill an appreciation for the richness and complexity of the phenomena that are responsible for the formation of such materials. We have outlined the flow processes involved in the electrified meniscus and those associated with the jetting process. The relevant processes are the steady thinning jet, whose behavior can be understood quantitatively using continuum equations of electrohydrodynamics, and the ensuing fluid dynamical instabilities that give rise to whipping of the jet. The current carried by the jet is of critical importance to the process, and some scaling aspects concerning the total measured current have been discussed. The resulting materials are equally rich in their diversity of structure and morphology. Solvent evaporation and solidification of the jet into a fiber, and arrest of the filament-stretching process, are areas that merit further attention. These processes play a role in setting both the diameters and the textures of the ensuing material. Since electrospun materials are frequently used as scaffolds in biomedical applications, a discussion of some aspects of the electrospun mats thought to be particularly relevant to such applications, such as fluid repellency, mechanical properties, and pore size distribution, has been included. We hope that, armed with such guiding principles, the biomaterials community may be better prepared to advance the applications of electrospun material in this field.

References

1. Huang, Z.-M.; Zhang, Y. Z.; Kotaki, M.; Ramakrishna, S. *Compos. Sci. Technol.* **2003**, *63*(15), 2223–2253.
2. Ramakrishna, S.; Fujihara, K.; Teo, W. E.; Yong, T.; Ma, Z.; Ramasheshan, R. *Mater. Today* **2006**, *9*, 40–50.
3. Reneker, D. H.; Chun, I. *Nanotechnology* **1996**, *7*(3), 216–223.
4. Altman, G. H.; Diaz, F.; Jakuba, C.; *et al*. *Biomaterials* **2002**, *24*(3), 401–416.
5. Keun Kwon, I.; Kidoaki, S.; Matsuda, T. *Biomaterials* **2005**, *26*(18), 3929–3939.
6. Sill, T. J.; von Recum, H. A. *Biomaterials* **2008**, *29*(13), 1989–2006.
7. Wang, X.; Wenk, E.; Matsumoto, A.; Meinel, L.; Li, C.; Kaplan, D. L. *J. Control. Release* **2007**, *117*(3), 360–370.
8. Zeng, J.; Xu, X.; Chen, X.; *et al*. *J. Control. Release* **2003**, *92*(3), 227–231.
9. Barnes, C. P.; Sell, S. A.; Boland, E. D.; Simpson, D. G.; Bowlin, G. L. *Adv. Drug Deliv. Rev.* **2007**, *59*(14), 1413–1433.
10. Laurencin, C. T.; Ambrosio, A. M. A.; Borden, M. D.; Cooper, J. A. *Annu. Rev. Biomed. Eng.* **1999**, *1*(1), 19–46.
11. Pham, Q. P.; Sharma, U.; Mikos, A. G. *Tissue Eng.* **2006**, *12*(5), 1197–1211.
12. Xu, C.; Inai, R.; Kotaki, M.; Ramakrishna, S. *Tissue Eng.* **2004**, *10*(7–8), 1160–1168.
13. Xu, C. Y.; Inai, R.; Kotaki, M.; Ramakrishna, S. *Biomaterials* **2004**, *25*(5), 877–886.
14. Koombhongse, S.; Liu, W.; Reneker, D. H. *J. Polym. Sci. B Polym. Phys.* **2001**, *39*(21), 2598–2606.
15. Casper, C.-L.; Stephens, J. S.; Tassi, N. G.; Chase, D. B.; Rabolt, J. F. *Macromolecules* **2003**, *37*(2), 573–578.
16. Pai, C.-L.; Boyce, M. C.; Rutledge, G. C. *Macromolecules* **2009**, *42*(6), 2102–2114.
17. Yu, J. H.; Rutledge, G. C. In *Encyclopedia of Polymer Science and Technology*, Wiley: New Jersey, 2007.
18. Sun, Z.; Zussman, E.; Yarin, A. L.; Wendorff, J. H.; Greiner, A. *Adv. Mater.* **2003**, *15*(22), 1929–1932.
19. Yu, J. H.; Fridrikh, S. V.; Rutledge, G. C. *Adv. Mater.* **2004**, *16*(17), 1562–1566.
20. Gupta, P.; Wilkes, G. L. *Polymer* **2003**, *44*(20), 6353–6359.
21. Kameoka, J.; Orth, R.; Yang, Y.; *et al*. *Nanotechnology* **2003**, *14*(10), 1124–1129.
22. Yarin, A. L.; Zussman, E. *Polymer* **2004**, *45*, 2977–2980.
23. Fang, D.; Chang, C.; Hsiao, B. S.; Chu, B. In *Polymeric Nanofibers*; Reneker, D. H., Fong, H., Eds.; American Chemical Society: Washington, DC, 2006; pp 91–105.
24. Theron, S. A.; Yarin, A. L.; Zussman, E.; Kroll, E. *Polymer* **2005**, *46*(9), 2889–2899.
25. Melcher, J. R.; Taylor, G. I. *Annu. Rev. Fluid Mech.* **1969**, *1*(1), 111–146.
26. Saville, D. A. *Annu. Rev. Fluid Mech.* **1997**, *29*, 27–64.
27. Marginean, I.; Nemes, P.; Vertes, A. *Phys. Rev. Lett.* **2006**, *97*(6), 064502–064504.
28. Hohman, M. M.; Shin, M.; Rutledge, G.; Brenner, M. P. *Phys. Fluids* **2001**, *13*(8), 2201–2220.
29. Feng, J. J. *Phys. Fluids* **2002**, *14*, 3912.
30. Carroll, C. P.; Joo, Y. L. *Phys. Fluids* **2006**, *18*.
31. Reneker, D. H.; Yarin, A. L.; Fong, H.; Koombhongse, S. *J. Appl. Phys.* **2000**, *87*(9), 4531–4547.
32. Gupta, R. K.; Nguyen, D. A.; Sridhar, T. *Phys. Fluids* **2000**, *12*(6), 1296–1318.
33. Bhattacharjee, P. K.; Oberhauser, J. P.; McKinley, G. H.; Leal, L. G.; Sridhar, T. *Macromolecules* **2002**, *35*(27), 10131–10148.
34. Larson, R. G.; Sridhar, T.; Leal, L. G.; McKinley, G. H.; Likhtman, A. E.; McLeish, T. C. B. *J. Rheol.* **2003**, *47*(3), 809–818.
35. Doi, M.; Edwards, S. F. *The Theory of Polymer Dynamics*; Oxford University Press: Oxford, 1986.
36. Strobl, G. R. *The Physics of Polymers: Concepts for Understanding Their Structures and Behavior*; Springer: Berlin, 1997.
37. McKinley, G. H.; Sridhar, T. *Annu. Rev. Fluid Mech.* **2002**, *34*(1), 375–415.
38. Graessley, W. W. *Polymer* **1980**, *21*, 258–262.
39. Yu, J. H.; Fridrikh, S. V.; Rutledge, G. C. *Polymer* **2006**, *47*(13), 4789–4797.
40. Shin, Y. M.; Hohman, M. M.; Brenner, M. P.; Rutledge, G. C. *Appl. Phys. Lett.* **2001**, *78*(8), 1149–1151.
41. Shin, Y. M.; Hohman, M. M.; Brenner, M. P.; Rutledge, G. C. *Polymer* **2001**, *42*(25), 09955–09967.
42. Daga, V. K.; Helgeson, M. E.; Wagner, N. J. *J. Polym. Sci. B Polym. Phys.* **2006**, *44*(11), 1608–1617.
43. Zhou, F.-L.; Gong, R.-H.; Porat, I. *J. Mater. Sci.* **2009**, *44*(20), 5501–5508.
44. Deitzel, J. M.; Kleinmeyer, J.; Harris, D.; Beck Tan, N. C. *Polymer* **2001**, *42*(1), 261–272.
45. Uyar, T.; Besenbacher, F. *Eur. Polym. J.* **2009**, *45*(4), 1032–1037.
46. Liu, Y.; He, J.-H. *Int. J. Nonlinear Sci. Numer. Simul.* **2007**, *8*, 393–396.
47. Panda, P.; Ramakrishna, S. *J. Mater. Sci.* **2007**, *42*(6), 2189–2193.
48. Daga, V. K.; Wagner, N. J. *Rheol. Acta* **2006**, *45*, 813–824.
49. Osaki, K.; Nishimura, Y.; Kurata, M. *Macromolecules* **1985**, *18*, 1153–1157.
50. Fetters, L. J.; Lohse, D. J.; Richter, D.; Witten, T. A.; Zirkel, A. *Macromolecules* **1994**, *27*(17), 4639–4647.
51. Bird, R. B.; Armstrong, R. C.; Hassager, O. *Dynamics of Polymeric Liquids*. Wiley: New York, 1987.
52. Watanabe, H. *Prog. Polym. Sci.* **1999**, *24*, 1253–1403.
53. Ianniruberto, G.; Marrucci, G. *J. Rheol.* **2001**, *45*, 1305–1318.

54. Bhattacharjee, P. K.; Nguyen, D. A.; McKinley, G. H.; Sridhar, T. *J. Rheol*. **2003**, *47*(1), 269–290.
55. Spivak, A. F.; Dzenis, Y. A.; Reneker, D. H. *Mech. Res. Commun.* **2000**, *27*(1), 37–42.
56. Treolar, L. R. *Physics of Rubber Elasticity*; Oxford University Press: Oxford, 1958.
57. Taylor, G. I. *Proc. R. Soc. Lond. A Math. Phys. Sci*. **1964**, *280*(1382), 383–397.
58. Zeleny, J. *Phys. Rev*. **1917**, *10*, 1.
59. Yarin, A. L.; Koombhongse, S.; Reneker, D. H. *J. Appl. Phys*. **2001**, *89*(5), 3018–3026.
60. Yarin, A. L.; Koombhongse, S.; Reneker, D. H. *J. Appl. Phys*. **2001**, *90*, 4836–4846.
61. Collins, R. T.; Jones, J. J.; Harris, M. T.; Basaran, O. A. *Nat. Phys*. **2008**, *4*(2), 149–154.
62. Hayati, I.; Bailey, A. I.; Thadros, T. F. *Nature* **1986**, *319*, 41–43.
63. Barrero, A.; Gañán-Calvo, A. M.; Fernandez-Feria, R. *J. Aerosol Sci*. **1996**, *27*, S175–S176.
64. Rutledge, G. C.; Fridrikh, S. V. *Adv. Drug Deliv. Rev*. **2007**, *59*(14), 1384–1391.
65. Kirichenko, V. N.; Petryanov-Sokolov, I. V.; Suprun, N. N.; Shutov, A. A. *Sov. Phys. Dokl* **1986**, *31*, 611.
66. Carroll, C. P.; Joo, Y.-L. *J. Non-Newtonian Fluid Mech*. **2008**, *153*(2–3), 130–148.
67. Zhmayev, E.; Joo, Y. L. In *The XV International Congress on Rheology: The Society of Rheology 80th Annual Meeting, Monterey, California*; American Institute of Physics: College Park, MD, 2008.
68. Han, T.; Yarin, A. L.; Reneker, D. H. *Polymer* **2008**, *49*(6), 1651–1658.
69. Helgeson, M. E.; Grammatikos, K. N.; Deitzel, J. M.; Wagner, N. J. *Polymer* **2008**, *49*(12), 2924–2936.
70. Orr, N. V.; Sridhar, T. *J. Non-Newtonian Fluid Mech*. **1996**, *67*, 77–108.
71. Fridrikh, S. V.; Yu, J. H.; Brenner, M. P.; Rutledge, G. C. *Phys. Rev. Lett*. **2003**, *90*(14), 144502.
72. Fridrikh, S. V.; Yu, J. H.; Brenner, M. P.; Rutledge, G. In *Polymeric Nanofibers*; Reneker, D. H., Fong, H., Eds.; American Chemical Society: Washington, DC, 2006; Vol. 918, pp 36–55.
73. Paruchuri, S.; Brenner, M. P. *Phys. Rev. Lett*. **2007**, *98*(13), 134502–134504.
74. Gañán-Calvo, A. M. *J. Fluid Mech*. **1997**, *335*, 165–188.
75. Reneker, D. H.; Yarin, A. L. *Polymer* **2008**, *49*(10), 2387–2425.
76. Demir, M. M.; Yilgor, I.; Yilgor, E.; Erman, B. *Polymer* **2002**, *43*(11), 3303–3309.
77. Theron, S. A.; Zussman, E.; Yarin, A. L. *Polymer* **2004**, *45*(6), 2017–2030.
78. Bhattacharjee, P. K.; Schnieder, T.; Brenner, M. P.; McKinley, G. H.; Rutledge, G. C. *J. Appl. Phys*. **2008**, *107*, 044306–044313.
79. De La Mora, J. F.; Loscertales, I. G. *J. Fluid Mech*. **1994**, *260*(1), 155–184.
80. Yarin, A. L.; Kataphinan, W.; Reneker, D. H. *J. Appl. Phys*. **2005**, *98*(6), 064501–064512.
81. Korkut, S.; Saville, D. A.; Aksay, I. A. *Phys. Rev. Lett*. **2008**, *100*(3), 034503–034504.
82. Ma, M.; Gupta, M.; Li, Z.; *et al*. *Adv. Mater*. **2007**, *19*(2), 255–259.
83. Tuteja, A.; Choi, W.; Ma, M.; *et al*. *Science* **2007**, *318*(5856), 1618–1622.
84. Tuteja, A.; Choi, W.; Mabry, J. M.; McKinley, G. H.; Cohen, R. E. *Proc. Natl. Acad. Sci. USA* **2008**, *105*(47), 18200–18205.
85. Ma, M.; Hill, R. M.; Rutledge, G. C. *J. Adhesion Sci. Technol*. **2008**, *22*(15), 1799–1817.
86. Arinstein, A.; Burman, M.; Gendelman, O.; Zussman, E. *Nat. Nano* **2007**, *2*(1), 59–62.
87. Helgeson, M. E.; Wagner, N. J. *AIChE J*. **2007**, *53*(1), 51–55.
88. Barrero, A.; Loscertales, I. G. *Annu. Rev. Fluid Mech*. **2007**, *39*, 89–109.
89. Shenoy, S. L.; Bates, W. D.; Frisch, H. L.; Wnek, G. E. *Polymer* **2005**, *46*(10), 3372–3384.
90. Wang, L.; Pai, C.-L.; Boyce, M. C.; Rutledge, G. C. *Appl. Phys. Lett*. **2009**, *94*(15), 151916-3.
91. Pauchard, L.; Allain, C. *Europhys. Lett*. **2003**, *62*(6), 897–903.
92. Pauchard, L.; Allain, C. *Phys. Rev. E* **2003**, *68*(5), 052801.
93. Pauchard, L.; Couder, Y. *Europhys. Lett*. **2004**, *66*(5), 667–673.
94. Megelski, S.; Stephens, J. S.; Chase, D. B.; Rabolt, J. F. *Macromolecules* **2002**, *35*(22), 8456–8466.
95. Srinivasarao, M.; Collings, D.; Philips, A.; Patel, S. *Science* **2001**, *292*(5514), 79–83.
96. Dayal, P.; Kyu, T. *J. Appl. Phys*. **2006**, *100*(4), 043512–043516.
97. Li, D.; Xia, Y. *Nano Lett*. **2004**, *4*(5), 933–938.
98. Zhang, Y.; Huang, Z.-M.; Xu, X.; Lim, C. T.; Ramakrishna, S. *Chem. Mater*. **2004**, *16*(18), 3406–3409.
99. Reznik, S. N.; Yarin, A. L.; Zussman, E.; Bercovici, L. *Phys. Fluids* **2006**, *18*(6), 062101–062113.
100. Qi, H.; Hu, P.; Xu, J.; Wang, A. *Biomacromolecules* **2006**, *7*(8), 2327–2330.
101. Sanders, E. H.; Kloefkorn, R.; Bowlin, G. L.; Simpson, D. G.; Wnek, G. E. *Macromolecules* **2003**, *36*(11), 3803–3805.
102. Kalra, V.; Lee, J. H.; Park, J. H.; Marquez, M.; Joo, Y.-L. *Small* **2009**, *5*(20), 2323–2332.
103. Kalra, V.; Mendez, S.; Lee, J. H.; Nguyen, H.; Marquez, M.; Joo, Y. L. *Adv. Mater*. **2006**, *18*(24), 3299–3303.
104. Ma, M.; Krikorian, V.; Yu, J. H.; Thomas, E. L.; Rutledge, G. C. *Nano Lett*. **2006**, *6*(12), 2969–2972.
105. Ma, M.; Titievsky, K.; Thomas, E. L.; Rutledge, G. C. *Nano Lett*. **2009**, *9*(4), 1678–1683.
106. Deitzel, J. M.; Kleinmeyer, J. D.; Hirvonen, J. K.; Beck Tan, N. C. *Polymer* **2001**, *42*(19), 8163–8170.
107. Bhattarai, N.; Edmondson, D.; Veiseh, O.; Matsen, F. A.; Zhang, M. *Biomaterials* **2005**, *26*(31), 6176–6184.
108. Sundaray, B.; Subramanian, V.; Natarajan, T. S.; Xiang, R.-Z.; Chang, C.-C.; Fann, W.-S. *Appl. Phys. Lett*. **2004**, *84*(7), 1222–1224.
109. Li, D.; Ouyang, G.; McCann, J. T.; Xia, Y. *Nano Lett*. **2005**, *5*(5), 913–916.
110. Li, D.; Wang, Y.; Xia, Y. *Adv. Mater*. **2004**, *16*, 361–366.
111. Bazbouz, M. B.; Stylios, G. K. *Eur. Polym. J*. **2008**, *44*(1), 1–12.
112. Gokul, S.; Darrell, H. R. *Polym. Int*. **1995**, *36*(2), 195–201.
113. Myung-Seob, K.; Shanta Raj, B.; Hak-Yong, K.; Sung-Zoo, K.; Keun-Hyung, L. *J. Biomed. Mater. Res*. **2005**, *72B*(1), 117–124.
114. Teo, W.-E.; Gopal, R.; Ramaseshan, R.; Fujihara, K.; Ramakrishna, S. *Polymer* **2007**, *48*(12), 3400–3405.
115. Anzenbacher, P.; Palacios, M. A. *Nat. Chem*. **2009**, *1*(1), 80–86.
116. Jang, S. Y.; Seshadri, V.; Khil, M. S.; *et al*. *Adv. Mater*. **2005**, *17*(18), 2177–2180.
117. Eichhorn, S. J.; Sampson, W. W. *J. R. Soc. Interface* **2005**, *2*, 309–318.
118. Ko, J.-B.; Lee, S.; Kim, D.; *et al*. *J. Porous Mater*. **2006**, *13*, 325–330.
119. Li, D.; Frey, M. W.; Joo, Y. L. *J. Membr. Sci*. **2006**, *286*, 104–114.
120. Ryu, Y. J.; Kim, H. Y.; Lee, H. K.; Park, H. C.; Lee, R. D. *Eur. Polym. J*. **2003**, *39*, 1883–1889.
121. Ho, S. T.; Hutmacher, D. W. *Biomaterials* **2006**, *27*(8), 1362–1376.
122. Lowery, J. L.; Datta, N.; Rutledge, G. C. *Biomaterials* **2010**, *31*(3), 491–504.
123. Rutledge, G. C.; Lowery, J. L.; Pai, C.-L. *J. Eng. Fibers Fabrics* **2009**, *4*(3), 1–13.
124. Mitchell, S. B.; Sanders, J. E. *J. Biomed. Mater. Res. A* **2006**, *78A*(1), 110–120.
125. Zucchelli, A.; Fabiani, D.; Gualandi, C.; Focarete, M. *J. Mater. Sci*. **2009**, *44*(18), 4969–4975.
126. Kidoaki, S.; Kwon, I. K.; Matsuda, T. *J. Biomed. Mater. Res. B Appl. Biomater*. **2006**, *76B*(1), 219–229.
127. Lee, Y. H.; Lee, J. H.; An, I.-G.; *et al*. *Biomaterials* **2005**, *26*(16), 3165–3172.
128. Simonet, M.; Schneider, O.; Neuenschwander, P.; Stark, W. *Polym. Eng. Sci*. **2007**, *47*, 2020–2026.

1.128. Fluorinated Biomaterials

F Liu and D W Grainger, University of Utah, Salt Lake City, UT, USA

© 2011 Elsevier Ltd. All rights reserved.

1.128.1.	**Introduction**	514
1.128.2.	**Fluorinated Polymer Chemical and Physical Properties**	515
1.128.2.1.	Fluoropolymer Properties Derived from Chemistry, Molecular Structure, and Bonding	515
1.128.2.2.	Perfluorinated Surfaces	515
1.128.3.	**Fluoropolymers**	516
1.128.3.1.	Polytetrafluoroethylene	516
1.128.3.2.	ePTFE (Gore-Tex™)	518
1.128.3.3.	Fluorinated Ethylene Propylene	518
1.128.3.4.	Other Fluoropolymers	518
1.128.3.5.	Fluoropolymer Processing	519
1.128.3.6.	Fluorinated Coatings	519
1.128.4.	**Biomedical Applications of Fluorinated Biomaterials**	519
1.128.4.1.	PTFE (Teflon™) and ePTFE (Gore-Tex™) Vascular Implants	520
1.128.4.2.	ePTFE and Teflon™ Tissue Meshes	522
1.128.4.3.	Arteteriovenous ePTFE Grafts for Dialysis Access	522
1.128.4.4.	Multilumen Catheters	522
1.128.4.5.	Guiding Catheters	522
1.128.4.6.	PTFE Introducer	522
1.128.4.7.	Perfluorocarbon Liquids, Surfactants, and Emulsions as Oxygen-Carrying Blood Substitutes	522
1.128.4.8.	Other Fluorinated Material Biomedical Applications	523
1.128.4.8.1.	Fluorinated (meth)acrylates and (meth)acrylated perfluoroalkylated silicones as cross-linked polymer cores for soft contact lenses	523
1.128.4.8.2.	Fluorinated coatings as antifouling coatings for IOLs	524
1.128.4.8.3.	PTFE paste injectable bulking agent	524
1.128.4.8.4.	Ligament replacement	524
1.128.4.8.5.	Sutures	524
1.128.5.	**Conclusion and Perspectives**	524
References		525

Glossary

Catheter An intraluminal medical device, typically tubular in design, inserted to gain transient access (minutes–days) to tissues, blood, or organs within the human body; can be single or multiple lumen.

Emulsion A dispersion of one immiscible liquid phase within another, stabilized by interfacial surfactants; microdroplet suspensions.

Fluoridated Ionic or electrostatic association of fluoride anion with a cation in a metal or ceramic salt or material.

Fluorinated Covalent attachment of fluorine to another element (e.g., C, S, P) in a molecule or material.

Microporous Open pore structure within a bulk solid of a scale of one to several hundred microns in pore diameter.

Perfluorinated Complete replacement of C–H bonds with C–F bonds.

Perfluoropolymer A polymer where hydrogen has been replaced completely by fluorine (e.g., PTFE).

Plasma Two very distinct meanings with contextual differentiation: (1) the complete milieu of blood but without the cellular fraction (i.e., all soluble, noncellular components), or (2) a highly excited and extremely reactive gaseous phase containing many reactive species used for cleaning or etching surfaces, or depositing chemical coatings, depending on the chemistry and excitation energies.

Plasma expander A therapeutic nontoxic material with high intrinsic oxygen-carrying capacity used to supplement blood volume and function *in vivo* in cases of acute blood loss.

Surface energy The free energy resident at a solid surface or liquid interface (typically with gas or air) that drives adsorption events, surface rearrangement of molecules, and physical and chemical reactions at this surface.

Abbreviations

ACL	Anterior cruciate knee ligament
A-V	Arteriovenous
CTFE	Chlorotrifluoroethylene (monomer or repeat unit)
ECM	Extracellular matrix
ePTFE	Mechanically expanded, porous PTFE
ETFE	Ethylene tetrafluoroethylene, a copolymer of non-fluorinated ethylene monomer and perfluorinated ethylene monomer
FDA	US Food and Drug Administration
FEP	Fluorinated ethylene propylene, a copolymer of tetrafluoroethylene (TFE) and hexafluoropropylene (HFP)
HDPE	High density poyethylene
HFP	Hexafluoropropylene
IOLs	Intraocular lenses
MRI	Magnetic resonance imaging
PCTFE	Polychlorotrifluoroethylene polymer homopolymerized from the chlorine-fluorine-containing CTFE monomer
PE	Polyethylene
PET	Poly(ethylene terephthalate) polyester
PFA	Perfluoroalkoxy
PTFE	Poly(tetrafluoroethylene)
PVDF	Poly(vinylidene fluoride)
RGDS, PHSRN, YIGSR, IKVAV	Cell adhesion peptide motifs
RGPs	Rigid gas permeable contact lenses
TIPS	Trans-jugular intra-hepatic porto-systemic shunt
TMJ	Temporomandibular joint

1.128.1. Introduction

Materials that contain substantial amounts of covalently attached fluorine are classed as fluorinated or perfluorinated materials. These fluorinated liquids and solids are chemically and physically distinct from fluoridated hydroxyapatites, bioactive glasses and ceramics, dentifrice compounds, cements, and other ceramics where fluoride ion (F^-) is complexed into the material using salt or ionic formulations. Fluorinated biomaterials have a substantial history in various medical device applications and their use and development is important currently. As with other materials, structure–property relationships are critical to why fluorinated biomaterials offer distinct properties of interest to medical device applications. Understanding these properties requires some introduction to the chemistry of fluorinated compounds and why chemical attachment of high amounts of fluorine atoms produces beneficial biomaterials properties. As primary materials of biomedical interest, fluoropolymers comprise a family of highly fluorinated thermoplastic carbon-based polymers analogous to polyethylene (PE) in which some or all of the hydrogen atoms attached to the carbon polymer chain are replaced by fluorine or pendant fluorinated alkyl groups. Other halogen atoms such as chlorine are also included in some polymers.[1] Interests in and applications for fluorinated materials have increased significantly as DuPont scientist, Roy Plunkett, first serendipitously discovered polytetrafluoroethylene (PTFE) in 1938 as a pioneering perfluorinated polymer: a slippery white powder inside a canister of tetrafluoroethylene (TFE) gas, now well-recognized as Teflon™. Prior to 1937, only three pure perfluorocarbons were known, and none was solid: carbon tetrafluoride, hexafluoroethane, and TFE. However, numerous fluorochemicals and fluoropolymers have since been invented and commercialized, and now used in excess of 90 kt annually: primarily PTFE, but also poly(vinylidene fluoride) (PVDF) and other minority fluoropolymer chemistries. Notably, fluoropolymers show unique properties distinct from other polymeric materials, including chemical inertness, extreme hydrophobicity and solvent resistance, low coefficients of friction, and temperature resistance.[1] These properties facilitate their wide use in certain biomedical applications where most hydrocarbon-based materials fail. However, fluoropolymers are often considerably more expensive.

In 1949, shortly after PTFE's commercial launch as DuPont's Teflon™ product, fine Teflon™ shavings were implanted into the canine peritoneal cavity and found to produce no observable acute inflammatory changes or overt tissue reactions in the peritoneum.[2] Thin fibrous sheaths containing fibroblasts were observed to surround the plastic pieces, but the Teflon™ surface was apparently not biologically reactive to their eyes. On the basis of this initial promising outcome, the first practical biomedical applications for Teflon™ mesh were proposed.[2] However, fabrication processes to alter this material proved (and continue to prove) challenging and limiting to its use. In 1963, Oshige (Sumitoma Electric Industries, Osaka, Japan), discovered a process for expanding PTFE films to produce highly uniform, continuous fibrous porous structures. These materials retained their microstructure but with vastly improved mechanical strength after thermal processing.[3] In 1972, this expanded fibrous material was first used experimentally as a venous graft substitute[4] and as an arterial bypass implant 1 year later.[5] In 1976, expanded PTFE (now generally referred to as ePTFE) was refined to production scales by Gore (USA), allowing expanded access and clinical use in commercialized biomedical products.[6] This allowed this interesting, unique fluorinated biomaterial to be developed for many biomedical applications, both inside and outside the living host. While fluorinated polymers are expensive raw materials and often exhibit challenging processing conditions, their device fabrication properties, namely, intrinsic lubricity and broadly observed biocompatibility in certain conditions, resulting from fluorinated chemistry, are two key properties sought in their biomedical technologies. Understanding certain aspects of fluorinated chemistry is important to appreciate their value to biomedical products.

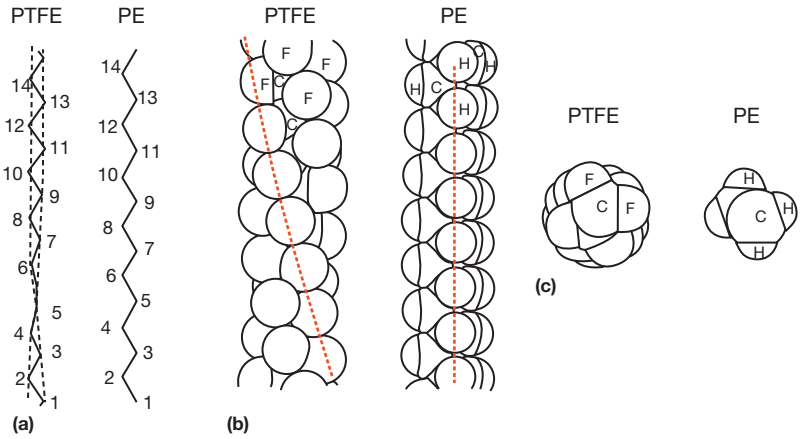

Figure 1 (a) Polytetrafluoroethylene (PTFE) twisted zig-zag chain compared to polyethylene (PE) molecular zig-zag chain; (b) side space-filling views, and (c) top views of PTFE chain versus hydrocarbon chain (PE). Adapted from Bunn, C. W.; Howells, E. R. *Nature* **1954**, *174*, 549–551, with permission from Macmillan.

1.128.2. Fluorinated Polymer Chemical and Physical Properties

1.128.2.1. Fluoropolymer Properties Derived from Chemistry, Molecular Structure, and Bonding

Replacing large amounts of hydrogen in C–H bonded materials with fluorine to create C–F chemistry produces dramatic changes to the material's physical and chemical properties. Fluorine's highest electronegativity polarizes the C–F bond, facilitating irregular hydrogen bonding patterns with other materials. The C–F bond is the strongest carbon bond, some 25 kcal mol^{-1} stronger than C–Cl.[7] This, with fluorine's intrinsically poor leaving group ability, makes alkyl fluorides 10^2–10^6 times less reactive than the corresponding alkylchlorides in certain solvolysis and displacement reactions, improving chemical stability.[7] Adjacent aliphatic bonds are also strengthened by fluorination (the CF_3–CF_3 bond is 10 kcal mol^{-1} stronger than the CH_3–CH_3 bond).[7] Extraordinary thermal and chemical stabilities of perfluorinated materials result from this chemistry. Fluorine's high ionization potential and low polarizability support a tendency for relatively weak intermolecular forces, low interfacial energies, and low refractive indices in fluorinated materials. Partially fluorinated commercial polymers, polyvinylidene difluoride (PVDF) and ethylene tetrafluoroethylene copolymer (ETFE), have zig-zag polymer chain conformations with different C–F dipole alignments along the chain,[7] while perfluorocarbons with only C–F bonds assume helical chains orientations with C–F dipoles distributed axially around the backbone helix.[8–14] PTFE, for example, as a model of very high molecular weight perfluorocarbon chain, is known to have a rich phase diagram of several distinct helical chain solid phases (Figures 1 and 2).[15]

1.128.2.2. Perfluorinated Surfaces

High levels of materials fluorination from this same C–F bonding chemistry presented at surfaces show unique molecular structure–property relationships, imparting specific, technologically attractive interfacial properties. Perfluorinated surfaces

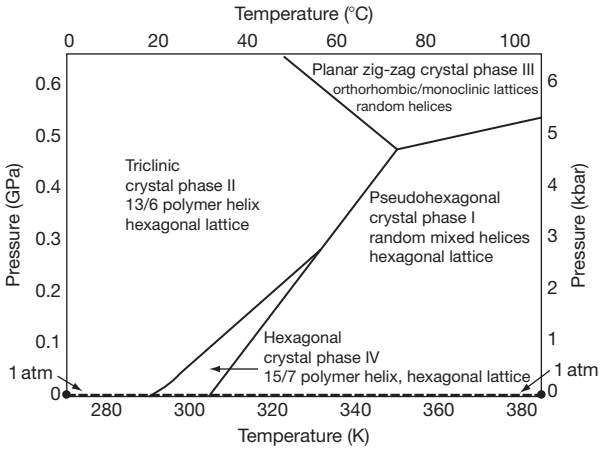

Figure 2 Polytetrafluoroethylene (PTFE) pressure–temperature solid phase diagram. PTFE's phase behavior first reported in 1954 and further refined exhibits two crystalline transitions at 19 °C (phase II) and 30 °C (phase IV) at atmospheric pressure (dashed line indicated as 1 atm). Substantial polymer chain molecular motion within these crystals is observed in this temperature range far below PTFE's melting point (~340 °C). A first-order phase transition at 19 °C between phases II and IV unravels the polymer crystal helical conformation from a well-ordered triclinic structure with 13 atoms/180° turn to a partially ordered hexagonal phase with 15 atoms/turn. Heating phases II and IV above 30 °C produces further rotational helical disordering and untwisting to yield a pseudo-hexagonal structure I with dynamic conformational disorder but retaining long-range positional and orientational order. These phase changes in PTFE solid structure affect PTFE's mechanical stability and use at body temperature (37 °C), particularly under pressure or stress in device applications. Three unique PTFE crystalline phases possible at ambient pressure near both room and body temperature influence PTFE's solid properties, relevant to many applications dependent on its solid-state phase mechanics under those conditions. Adapted from Brown, E. N.; Dattelbaum, D. M.; Brown, D. W.; Rae, P. J.; Clausen, B. *Polymer* **2007**, *48*, 2531–2536; Bunn, C.W.; Howells, E. R. *Nature* **1954**, *174*, 549–551; Clark, E.S. *Polymer* **1999**, *40*(16), 4659–4665; Wu, C. K.; Nicol, M. *Chem. Phys. Lett.* **1973**, *21*, 53–156.

Table 1 Interfacial free energies for perfluorocarbon versus analogous hydrocarbon materials

Material		*Solid interfacial free energy ($mN\,m^{-1}$)*[a]
PTFE		17
PVDF		30
HDPE		40
ETFE		22
Liquid interfacial free energy ($\gamma_{l/v}$)[b]	*Perfluorocarbon*	*Hydrocarbon*
n-Pentane	9.4	15.2
n-Hexane	11.4	17.9
n-Octane	13.6	21.1
Decalin	17.6	29.9
Benzene	22.6	28.5

[a]Values taken from Fraunhofer IGB website, accessed January, 2011 (http://www.igb.fraunhofer.de/www/gf/grenzflmem/gf-physik/en/GFphys-PolymOberfl.en.html).
[b]$mN\,m^{-1}$, from Smart, B. E. In *Organofluorine Chemistry: Principles and Commericial Applications*; Banks, R. E., Tatlow, J. C., Smart, B. E., Eds.; Plenum: New York, 1994 ($\gamma_{l/v}$ values).

often demonstrate low solid-state surface free energy (or surface tension), lubricity, and chemical resistance and durability. Perfluorocarbon liquids exhibit the lowest interfacial free energies, designated $\gamma_{l/v}$, (also known as surface tension[7]) – see values comparing hydrocarbon and perfluorocarbon liquids, **Table 1** – spreading spontaneously ('wetting') over nearly all solid surfaces, a result of perfluorocarbons' intrinsically low intermolecular forces. **Table 1** also shows that fluorinated liquids always exhibit lower surface free energies than their hydrocarbon (shown) or partially fluorinated liquid analogs (data not shown). **Table 1** data evidence solid perfluorinated PTFE exhibiting lower interfacial free energy (consistent with its Zisman critical surface tension γ_c values)[7,8,15] than its PE analog or partially fluorinated copolymers (e.g., PVDF, ETFE), correlating directly with PTFE's recognized utility as a low energy, low adhesion, low friction surface. Substituting either hydrogen or another halogen for fluorine along the polymer backbone results in significant increases in solid-state interfacial free energy values (as seen by comparing PTFE with high density polyethylene (HDPE), PVDF, and ETFE in **Table 1**). For further details, please refer to **Chapter 6.603, Ultrahigh Molecular Weight Polyethylene Total Joint Implants**.

Lowest solid surface free energies[1] are generally attributed to ambient, organized exposure of $-CF_3$ groups: a very low γ_c or $\gamma_{s/v}$ value is measured for close-packed, organized monolayers of nearly vertically aligned $CF_3(CF_2)_{10}COOH$ molecules coated on a solid, closely packing the ambient-exposed terminal CF_3 groups.[16,17] Substituting only one hydrogen for one fluorine in this terminal, exposed CF_3 group increases the surface free energy to a less impressive value of $15\,mN\,m^{-1}$.[17] Maximizing the surface density of exposed CF_3 groups reduces solid surface tension by exploiting CF_3 group orientation/organization/presentation. In fact, several coating strategies have sought to place and then orient CF_3 groups on surfaces using various means without a perfluorinated base material or perfluoropolymer matrix. Because adjustments of the surface density and organization of these groups are necessary to achieve low surface tensions, presenting the CF_3 group alone at surfaces is insufficient to reduce solid surface free energies to useful levels. Alignment of alkyl chains terminating in this perfluorochemistry at the surface is required: surface tension reduction proceeds to a minimum as chain length approaches $n = 8–10$.[18] Coupling this with surface chain organization can often change this requirement: organized monolayers comprising long-chain surfactant $CF_3(CF_2)_n(CH_2)_{16}COOH$ reduce surface free energy over that observed for oriented monolayers of shorter $CF_3(CF_2)_nCOOH$ when $n{\sim}6$.[17] Additionally, orienting side chains in polymer films comprising perfluoroalkyl side-chain acrylates and methacrylates to enrich surfaces with side-chain terminal CF_3 groups[17,19–21] achieves low interfacial energies. Perfluoroalkyl-grafted polysiloxanes also exhibit side-chain orientation to reduce surface tension via presentation of their perfluorinated chemistry, sometimes with spontaneous perfluorinated group organization.[22–26]

1.128.3. Fluoropolymers

Fluoropolymers can be classified into homopolymers and copolymers on the basis of the monomer(s) used in their respective polymerizations. These can be either completely (perfluorinated) or partially fluorinated on the basis of the amount of fluorine in the main chain. **Table 2** lists some currently available commercial fluoropolymers and manufacturers. Although most fluoropolymers share general properties (e.g., thermal and chemical stability, lubricity), their mechanical properties are slightly different, depending on whether they are fully fluorinated or contain fractional hydrogenation. Generally, fully (per)fluorinated polymers exhibit greater elongation and higher maximum service temperatures than partially hydrogenated fluoropolymers, with latter also exhibiting higher stiffness. **Figure 3** compares some mechanical properties for different fluoropolymers.[15]

1.128.3.1. Polytetrafluoroethylene

PTFE (DuPont trade-name Teflon™) is perhaps the most typically cited fluoropolymer. As described for its chemistry above, size and mutual repulsion of adjacent fluorine atoms, PTFE macromolecular chains exhibit a twisting helix comprising 13 CF_2 groups per 180° turn, distinct from the classic PE hydrocarbon's planar zig-zag chain.[21] **Figure 1** shows this important chain conformational distinction that imparts certain fluoropolymer physical properties. Helical PTFE chains (often of very high molecular weight from the polymerization of the gaseous monomer TFE) pack into solid crystallites (see phase diagram, **Figure 2**) comprising long parallel rods where individual molecules can slip over each other as quasicylindrical masses under shear stress. Mutually repulsive forces of adjacent fluorine atoms keep the PTFE chain backbone rigid, with low energy barriers to chain slip events due to low chain–chain cohesive energies. Tight helical presentation of fluorine atoms in highly crystalline PTFE polymers (**Figures 1** and **2**) lowers the surface free energy, giving PTFE a low coefficient of friction and low adhesion properties.[1,7,15] Its very high bulk solid

Table 2 Abbreviations, molecular structures, compositions, and suppliers for commercial fluorinated polymers

Abbreviation		*Repeat unit structure*	*Polymer name*	*Manufacturer*	*Product trade name*
Homopolymers	PTFE	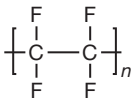	Poly(tetrafluoro ethylene)	DuPont ICI Hoechst Montefluos Asahi-ICI fluoropolymers Daikin Industries Ltd	Teflon® Fluon Hostaflon TFE Algoflon Fluon Polyflon
	PVDF	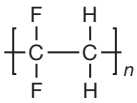	Poly(vinylidene fluoride)	Atochem USA Atochem Solvay Daikin Industries Kureha chemical	Kynar Foraflon Solef Neoflon KF
	PCTFE	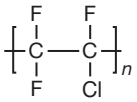	Poly(chlorotrifluoro-ethylene)	3 M Allied-signal Atochem Daikin Industries	Kel-F Aclon Voltalef Daiflon
Copolymers	FEP	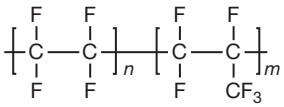	Fluorinated ethylene-propylene	DuPont Hoechst Montefluos Daikin Industries Ltd	Teflon® FEP Hostaflon Algoflon Neoflon
	PFA	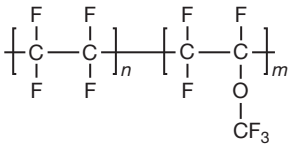	Perfluoroalkoxy- copolymer	DuPont Hoechst Daikin	Teflon®PFA Hostaflon PFA Neoflon
	ECTFE	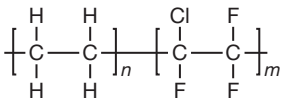	Ethylene chlorotrifluoro ethlyene	Allied chemical	Halar®
	ETFE	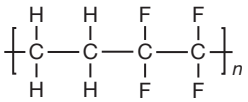	Ethylene tetrafluoroethylene	DuPont	Tefzel®

fractional crystallinity in all solid state phases, means that the PTFE polymer scatters light of most visible wavelengths, resulting in PTFE's characteristic opaque white color. Importantly, Figure 2 also indicates that solid PTFE exhibits two crystalline helix-based transitions at 19 °C (phase II) and 30 °C (phase IV) at atmospheric pressure, altering the polymer crystal's helical conformation from a well-ordered triclinic structure with 13 atoms/180° turn[21] to a partially ordered hexagonal phase with 15 atoms/turn between 19 and 30 °C. Heating both phases II and IV above 30 °C produces further helical disordering and untwisting, producing a pseudohexagonal structure I. These changes in PTFE solid structure alter PTFE's solid-state mechanics. Three unique PTFE crystalline phases possible at ambient pressure near both room and body temperature indicate that PTFE's mechanical properties, including cold creep, in many applications depend on its phase transitions under those conditions.

As a result, PTFE is the most lubricious polymer available, with a low coefficient of friction (0.1). This property is a major selection criterion for manufacturing fluoropolymer tubing used in medical devices. Unfortunately, this also makes PTFE solids very susceptible to cold flow (creep) under stress – a major reason for their poor performance in mechanical and repetitive wearing applications (i.e., poor bearing and joint surfaces). For examples, the original Teflon hip prosthesis cup developed by Sir John Charnley in 1956,[27] and the proplast-Teflon temporomandibular joint (TMJ) implant, developed formerly and sold by Vitek (USA) more recently, represent such failed biomedical mechanical PTFE applications. Furthermore, mechanical failure and tribological wear can break down PTFE into particles that can induce intense foreign-body reactions and also prompt bone resorption around the implant. Because of the increasing number of clinical reports of implant failure of Vitek's devices, the US Food and Drug Administration issued a nation-wide safety alert in 1990, and subsequently recalled Vitek's devices. Even after Vitek declared bankruptcy from rising litigation costs, it continued to market the TMJ implants, and surgeons still used them, until eventually the FDA seized all products from Vitek as well as its subsidiaries.[28,29] For further details, please refer to **Chapter 5.517, Tissue Engineering of the Temporomandibular Joint**.

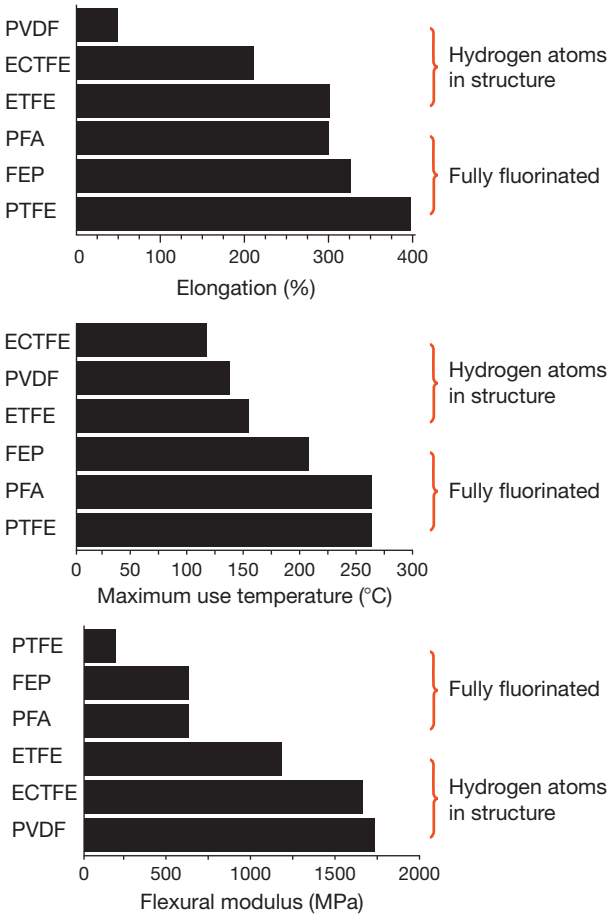

Figure 3 Comparison of mechanical properties for select fluoropolymers. Reprinted with permission from Scheirs, J. *Modern Fluoropolymers*; Wiley series in polymer science; Wiley: New York, 1997; p xx, 637.

Lastly, PTFE's extremely high molecular weights (e.g., $>10^6$) and rigid helical chain conformation manifest themselves in PTFE's high melt viscosities (e.g., 10^{12}–10^{12} Pa s^{-1}) that are ~6 times higher than that for most thermoplastic polymers. This is excessive for conventional melt processing methods used to fabricate thermoplastic medical devices (e.g., extrusion and injection molding). PTFE's high melt viscosity requires a high continuous service temperature (i.e., ~260 °C) for its processing into devices. Processing technologies for PTFE are similar to those of powder metallurgy, involving form-casting of prepolymerized PTFE granulated powders or latex formulations, followed by compression and sintering. PTFE's high thermal stability is key to success in processing under these conditions.[1,7]

1.128.3.2. ePTFE (Gore-Tex™)

When extruded under conditions of anisotropic loading, PTFE solids can be fabricated into highly porous solids with fabric-like properties. Using a series of mechanical operations – extrusion, rolling, and stretching – a biaxially stretched PTFE microporous membrane is produced, first by stretching in the longitudinal direction parallel to the rolling direction, and second by stretching perpendicular to the axis of the initial

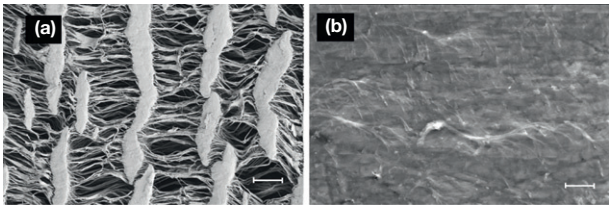

Figure 4 (a) Scanning electron micrograph (SEM) of expanded PTFE (ePTFE) showing regular node-fiber open materials structure (scale bar, lower right corner = 10 μm; we kindly acknowledge B. Wagner, W. L. Gore & Associates, Flagstaff, AZ, USA, for the ePTFE micrograph). (b) SEM of solid surface of Teflon™ (P. Hogrebe is acknowledged for these SEM micrographs) showing the cross-sectional porous structure from the compressed sintering of PTFE particles and dense continuous top surface (scale bar = 10 μm).

stretch. The resulting expanded Teflon™ microarchitecture (called ePTFE) exhibits pores axially aligned along the direction of stretch, resulting in a unique material with an oriented microporous architecture, eventually commercialized as Gore-Tex™.[6] ePTFE (initially Gore-Tex) is a porous structural material characterized by consistent PTFE nodes interconnected by PTFE fibrils (**Figure 4(a)**). The morphological characteristics of ePTFE compared to solid PTFE are contrasted in **Figure 4(a)** versus **4(b)**, respectively. ePTFE internodal spacing or distance (i.e., PTFE fibril length between solid PTFE nodes) is often used to describe and control biological behavior.[30] ePTFE exhibits high strength, a smooth external surface, and billions of continuous superfine interconnected fibrils per square centimeter. Pore size can be controlled by mechanical processing from 1 to 100 μm[31] while retaining properties similar to PTFE, for example, biological adsorption, low tensile strength, low modulus of elasticity, chemical stability, and ready sterilizability. Porous ePTFE structures also provide versatile options to mechanically modulus-match this material to tissue sites better than other polymers for many soft biological tissue applications.[32] Porosity also importantly encourages in-growth of tissue and hence moderate levels of tissue fixation, even when bulk PTFE does not exhibit this property.

1.128.3.3. Fluorinated Ethylene Propylene

Fluorinated ethylene propylene (FEP) is a copolymer of TFE and hexafluoropropylene (HFP), first produced by DuPont in 1956 (Teflon™ FEP) to reduce PTFE's high crystallinity and melt viscosity, and thereby improve its processing characteristics. Bulky FEP perfluoromethyl groups produce defects in solid polymer FEP crystallites, reducing the polymer melting point, impeding chain slip, and reducing solid cold flow.[33] FEP combines the unique mechanical and chemical properties of PTFE with the melt-processability of more conventional polymers. FEP has a maximum service temperature of 204 °C and a slightly higher coefficient of friction.

1.128.3.4. Other Fluoropolymers

Besides PTFE, ePTFE, and FEP, other fluoropolymers have not been commonly accepted for use as biomedical materials. They are more typically used in nonmedical industry. ETFE is a copolymer of monomers TFE and ethylene, first produced by

DuPont in 1970 (Tefzel™), with a higher tensile strength and lower creep than PTFE, FEP, or perfluoroalkoxy (PFA) as a result of ETFE's planar zig-zag chain configuration and strong electronic interactions between the bulky CF_2 units on one chain and smaller CH_2 groups of adjacent chains.[1,15] PVDF is a homopolymer of vinylidene monomer (CH_2CF_2), and sold as Kynar™. PVDF has the highest flexural modulus of all fluoropolymers because of interpenetration of larger CF_2 groups crystallizing with adjacent smaller CH_2 groups on adjacent chains. Unlike other fluoropolymers, PVDF is soluble in highly polar solvents (e.g., dimethylformamide, tetrahydrofuran), acetone, and esters.[1] PVDF's high dielectric constant, high dielectric loss factor, and interesting piezoelectric behavior under certain conditions result from this chemistry and resulting solid state structures. Fluorine' shielding effects to all neighboring CH_2 groups provide PVDF with good chemical resistance and thermal stability[15,33] PCTFE (polychlorotrifluoroethylene) is homopolymerized from the chlorine-fluorine-containing chlorotrifluoroethylene (CTFE) monomer. Regular introduction of Cl atoms along the polymer chain promotes chain–chain attractive forces. This lowers PCTFE's melting point and reduces its electrical and chemical resistance properties.[34] Removal of chlorine is more facile than fluorine, leading to some chemical, thermal, and photo-stability issues. PCTFE is melt-processed with difficulty because of its high melt viscosity but has improved mechanical properties with greater hardness, tensile strength, and better resistance to cold flow compared to PTFE.

1.128.3.5. Fluoropolymer Processing

Fluoropolymers are commonly processed into products by solid melt extrusion, where polymers develop flow upon melting in normal extrusion equipment. This technique exposes fluoropolymers to very high temperatures in order to reduce viscosity and improve flow characteristics for extended production runs and product lengths. Owing to its high crystallinity and processing problems, PTFE is often processed by a more complex, multistep treatment termed 'paste extrusion.' Fluoropolymers such as FEP, PFA, and PVDF will readily melt-flow when heated, typically above 260 °C. This permits uninterrupted feed of polymer resin into the extruder to produce long continuous lengths of product (i.e., tubing). By contrast, PTFE extrusion is limited by the requirements for its paste handling, size of the polymer stock preform, and tubing. Nonetheless, because PTFE is not melt-processable like other polymers, this presents an important opportunity: PTFE tubing important for several biomedical applications can be manufactured to tighter size tolerances, with wall thicknesses as small as 25 μm and tolerances of ±10 μm. This benefit is largely due to PTFE's inability to melt flow, allowing more precise control over its use in extrusion forms. This property is essential for producing medical products requiring tight tolerances such as small-diameter and multilumen tubing with multiple precision passages (i.e., for advanced catheters). Because fluorinated polymers are generally expensive, their appropriate or unique properties must justify their applications for biomedical use over less expensive materials. For further details, please refer to **Chapter 4.406, Protein Interactions with Biomaterials** and **Chapter 1.122, Structural Biomedical Polymers (Nondegradable)**.

1.128.3.6. Fluorinated Coatings[35]

In many fluid matrices, low interfacial energies for most perfluorinated liquids and solids drive partitioning of this material to interfaces with air to minimize surface energies, a process commonly called 'blooming' in the coatings industry. This means that desirable low surface tension, lubricity, durability, and chemical inertness associated with perfluorinated species might be imparted to surfaces selectively without requiring the entire bulk material (where such properties may not be needed) to be fluorinated. This reduces the expense of using perfluorinated materials, exploits the intrinsic fluid properties for many lower molecular weight fluorinated precursors for coating applications, and allows many modes of application (i.e., dipping, coating, spraying, painting) over prefabricated components of complex shape. Perfluorinated chemistry is known to migrate to surfaces spontaneously if permitted kinetically (i.e., in liquid coatings that are cured into films).[35] Film formation and coatings from perfluorinated components take place readily, both as applied over layers as well as when bloomed from bulk liquid mixtures, because of their surface energy-lowering properties. This has significant cost advantages as materials bulk fluorination costs and associated processing are quite expensive. Additionally, coatings-only properties are often preferred as bulk fluorinated materials mechanical properties are less than ideal (e.g., creep and flow in PTFE), despite intrinsic interfacial mechanical and wear limitations in these coatings. Emphasis on surface-fluorinated coatings and films has therefore increased as technological drivers provide impetus for new, improved, and less expensive methods to put this value-added chemistry on surfaces. Plasma-deposited fluorinated coatings (i.e., from gaseous precursors reacted under high energy excitation) are well developed for this purpose as well,[36] representing a mature industry and biomedically relevant materials treatment (e.g., for intraocular lenses, IOLs).[37] Lastly, while several different methods are reported to deposit PTFE-like thin overlayers onto surfaces as coatings (i.e., e-beam/laser sputtering from solid PTFE targets, vacuum evaporation) pulsed laser deposition of fluorinated chemistry has been shown to yield higher quality PTFE-like coatings.[38]

1.128.4. Biomedical Applications of Fluorinated Biomaterials

Table 3 provides a list of fluoropolymers applied as biomedical materials. Fluorinated solids, liquids, and coatings find widespread biomedical applications, particularly popular as transient clinical interventional and luminal access devices (i.e., catheters in many forms), more permanent implants (cardiovascular,[39] dental,[40] ocular,[41] craniofacial,[42] urological,[43] and abdominal[44] applications), and in biotechnology *in vitro* components (reagent dispensing tubing, protein blotting and filtration membranes). Annually, millions of perfluorinated polymer components are used worldwide in biological milieu both *in vitro* and *in vivo*. PTFE (e.g., Teflon™) and ePTFE (e.g., Gore-Tex™) are widely used in medical tubing, advanced catheters, vascular grafts, meshes, sutures, and other medical implants. For further details, please refer to **Chapter 1.122, Structural Biomedical Polymers (Nondegradable)**. PVDF is used for biotechnology blotting/separation membranes.

Table 3 Fluoropolymer biomedical application chronology

Decade	*Fluorinated materials medical applications*
1970s	Implantable vascular grafts, peripheral catheters, and introducers
1980s	Guiding catheters, protein blotting membranes, tissue meshes, dialysis shunts
1990s	Stents, perfluorinated oxygen carriers, lens cores, IOL coatings
2000s	Perfluorinated imaging/targeting microparticles, combination drug delivery

Fluoropolymer surface properties desired in these biomedical applications appear to be divided into two distinct behaviors, specifically seeking to exploit claims that fluoropolymer surfaces (1) resist microbial colonization and cell attachment, and (2) readily adsorb, transfer, and filter proteins from aqueous-based gels and milieu for bio-separations and analysis. Both biomedical performance goals result from common inseparable consequences of the strong interactions of low-energy fluoropolymer surfaces with soluble proteins in physiological systems. While fluoropolymers are often regarded as chemically inert, their surfaces are not inert to protein adsorption, either *in vitro* or *in vivo*. In fact, extremely tight binding of serum albumin to fluoroplasma-deposited surfaces,[45] high levels of fibronectin and hemoglobin on PVDF,[46] various serum proteins,[47] significantly adsorbed fibrinogen,[48] and high levels of both fibronectin and albumin[49] on PTFE are observed *in vitro*. Importantly, protein adsorption to fluoropolymers is also observed *in vivo*[50,51] and correlated with platelet activation responses often observed on ePTFE vascular graft materials *in vivo*.[50,52,53] Importantly, nonspecific serum protein adsorption is significant and often irreversible on fluoropolymer surfaces, leading to their utility as blotting membranes, deliberately protein-masked assay components, and chemically cleanable surfaces in biotechnology batch reactors. For further information, please refer to **Chapter 4.406, Protein Interactions with Biomaterials**.

Nonetheless, because of high uptake of proteins not conducive to engaging most cell receptors, general cell attachment for numerous cell types and clinically observed host endothelialization are recognized as poor on *nonporous* solid fluoropolymer chemistries[41,47,50,53–55] with the apparent exception of macrophages[56] and neural cells seeded onto preadsorbed albumin on chemically modified patterns on PTFE.[57] In contrast, porous fluoropolymers with 60–80 μm voids, including ePTFE, promote cell and bacterial in-growth by porous, physical integration and infiltration despite protein adsorption.[58,59] While adsorbing proteins and activating platelets in blood, fluoropolymer's plasma protein conditioning film[60] does not support ready cell attachment, mandating preclotting with fibrin, or treatment with an adhesive over layer of protein matrix (e.g., collagen or fibronectin) to promote reliable cell adhesion.[61,62] For further details, please refer to **Chapter 2.207, Extracellular Matrix: Inspired Biomaterials** and **Chapter 4.411, Peptide- and Protein-Modified Surfaces**.

Serum albumin, the largest mass fractional protein component in blood, is known to hinder cell attachment and block nonspecific binding,[63,64] while fibronectin, collagens, and other subtle trace matricellular proteins (e.g., osteopontin, laminin, vitronectin) – as important components of extracellular matrix (ECM) – enable integrin receptor-based cell attachment and proliferation on surfaces. Hence, observed fluoropolymer inability to support cell attachment is plausibly related to ratios of nonadhesive (e.g., albumin) to adhesive (e.g., fibronectin) proteins selectively adsorbed to fluoropolymer surfaces from multicomponent solution (e.g., plasma or serum).[49] A critical adsorbed density of ECM proteins in a mixed adsorbed protein layer must be readily recognized by cell-resident adhesion receptors (e.g., integrins). For further details, please refer to **Chapter 2.207, Extracellular Matrix: Inspired Biomaterials**; **Chapter 4.411, Peptide- and Protein-Modified Surfaces**; and **Chapter 4.414, Molecular Biomimetic Designs for Controlling Surface Interactions**.

In addition to surface *density*, adsorbed ECM protein structural *conformation* on surfaces must also permit cell receptor access to putative cell binding motifs on these surface-adsorbed proteins (e.g., RGDS, PHSRN, YIGSR, IKVAV peptide motifs)[65,66] *in situ* in order to facilitate ready cell attachment and spreading. For further details, please refer to **Chapter 4.414, Molecular Biomimetic Designs for Controlling Surface Interactions**. Commercial bioadhesive cell culture protein formulations (e.g., Pronectin™, Biocoat™, or Matrigel™) artificially bias these ECM density requirements for adhesive proteins in order to overcome deficiencies in surface chemistry to successfully adhere cells independent of surface chemistry. However, direct fluoropolymer *in vivo* exposure to blood plasma containing thousands of soluble proteins simultaneously cannot ensure such cell-adhesive protein adsorption bias. Because all fluoropolymer surfaces adsorb substantial amounts of these proteins irreversibly, both amounts and conformations of adsorbed ECM proteins (e.g., collagens, fibronectin), competing with the majority nonadhesive serum proteins, determine subsequent cell attachment behavior on fluoropolymer surfaces. Therefore, while fluoropolymers can become 'passivated' by non-ECM protein coating, there is little evidence showing that fluoropolymers are intrinsically 'biologically inert' or passive to classical biological reactions (i.e., adsorption, blood activation, microbial attachment). In fact, the opposite is true: fluoropolymers are intrinsically reactive and adsorptive to almost every protein studied. Implanted device interfacial response to fluoropolymers is then a product of its adsorbed protein conditioning film. As most host protein content comprises albumin – a non-ECM plasma protein with little intrinsic cell interaction capability – under most serum- or blood-contact conditions, fluoropolymers are rapidly coated with a matrix mostly comprising albumin. This is then modified over time with continuous host protein and cell exposure, producing the clinical performance observed and attributed to fluoropolymers. As albumin often passivates surfaces against blood contact activation, highly stable adsorbed albumin correlates with some nonthrombogenic interfacial properties attributed to ePTFE *in vivo*. For further details, please refer to **Chapter 4.406, Protein Interactions with Biomaterials** and **Chapter 4.411, Peptide- and Protein-Modified Surfaces**.

1.128.4.1. PTFE (Teflon™) and ePTFE (Gore-Tex™) Vascular Implants

A 1951 innovation facilitated the spinning of PTFE paste into PTFE fibers for weaving or knitting into fabrics or meshes.[67]

Attracted by PTFE's alleged consistent nonthrombogenicity demonstrated in early animal studies, PTFE weaves were applied in vascular grafts.[68] However, these early woven vascular grafts exhibited both high early failure rates and substantial late failure rates. Graft thrombosis was the most frequent early complication, accompanied by a high mortality rate.[69] ePTFE vascular graft designs supplanted these early PTFE weaves in blood-contacting applications (initially as Gore-Tex™ ePTFE), now with over 40 years of innovation in medical implants. An interesting long-standing legal controversy over the original inventorship of and rights to patent privileges for the synthetic vascular graft, centered largely on Gore's marketing of Gore-Tex for this application, is only recently settled in court.[70]

Microporous ePTFE graft prostheses were used initially for major thoracic venous and abdominal vein repair in 1972,[4] and shortly followed for use in arterial bypass.[5] The first commercial ePTFE vascular graft device (e.g., first as Gore-Tex™ and later as Impra™ brands) was clinically approved in the 1970s for vascular grafting and has since become a major device application for fluoropolymers in medicine. ePTFE fabrics have been used in tens of millions of implants in cardiac, vascular, and endovascular surgeries, neurosurgery, hernia repair, and thoracic reconstruction. Hemodialysis access and vascular by-pass and replacement applications represent the major ePTFE applications (detailed in **Section 1.128.4.3**). Implant performance is highly variable compared to other prosthetics and autologous vascular grafts, depending on many factors, including patient co-morbidities, anatomical site of placement, the surgical team and medical center, and human versus animal model.[71] For further details, please refer to **Chapter 6.628, Vascular Grafts**.

ePTFE's porous inner surface is often proposed as essential to promote formation of a beneficial host 'pseudo-intimal lining' that is thought to passivate the graft material against extended host thrombosis and inflammatory responses. Its porous outer surface promotes perigraft tissue infiltration that stabilizes the prosthesis in place, preventing kinking.[72] Another important role advocated for ePTFE's porous structure is natural promotion of transmural endothelialization (e.g., implant cell colonization and growth) by encouraging angiogenesis, first demonstrated in a nonhuman primate model[58] decades ago. This cell colonization strategy is also reported effective in rats,[73] sheep,[74] and dogs,[75,76] but with very limited success to date in humans.[77] Unlike most animal models, humans do not readily form neointimal endothelium in these grafts. However, host cell–ePTFE responses can be enhanced, at least *in vitro*, by introducing exogenous protein growth factors (e.g., fibroblast growth factor) to the graft surface.[73,78,79] Additionally, microporosity geometries can influence results: Higher graft patency rates were achieved for ePTFE prostheses with internodal distances below 22 μm placed in both canine carotid and femoral sites. Patency rates for prostheses with average microfiber lengths of 34 μm or longer were lower. In animal models, ePTFE prostheses with a microfiber length of 30 μm improved fibroblastic in-growth producing a thinner neointima than 90-μm long fibrial ePTFE prostheses, showing substantial host fibrotic response.[4] More recent studies of ePTFE vascular grafts of different internodal porosities (i.e., 10–90 μm) showed optimal intermodal distances of ~60 μm: the 10–30 μm fibril grafts failed to achieve luminal endothelial cell coverage, and 90 μm grafts showed pseudointimal endothelial cell loss in animals.[80–82]

Improving ePTFE vascular graft endothelialization remains a major strategy to improve ePTFE vascular device implant performance both *in vivo* and *in vitro*.[83–85] Host native endothelium plays a major role in inhibiting thrombosis and controlling intimal hyperplasia. Various strategies therefore seek to induce and retain host endothelialization of ePTFE graft surfaces either prior to implantation (preseeding with cells *in vitro*) or by accelerating host *in situ* graft endothelialization *in vivo*. Early clinical trials using ePTFE preseeding were disappointing and remain controversial. Limitations for graft preendothelialization methods are long recognized and challenging, specifically as they (1) are not practical for acute or emergency interventions, and (2) require preharvest of host venous endothelial cells to obtain sufficient endothelial cells to completely cover the graft luminal surface prior to implantation. The approach currently requires a two-stage procedure with technical skills and facilities for patient cell harvest, cell expansion, and cell seeding on-graft: an initial surgical intervention before cell-seeded graft placement by a second surgical procedure. Most importantly, while animal studies demonstrate efficacy of this method, human seeding does not yet result in a reliable neointima on vascular grafts. Human performance is distinct from animal models in this regard.[83]

To overcome these issues, *in vivo* endothelialization of the implanted graft *in situ* in the host is sought.[85] To facilitate host endothelial cell colonization of the implanted ePTFE surface, grafts must rapidly and reliably select host endothelial cells (and not, e.g., host macrophages or other leukocyte cells) from circulating blood. To encourage host cell adhesion, ePTFE surfaces are chemically modified prior to implantation with cell-specific adhesion synthetic peptides[85] to attract and engage circulating endothelial cells, endothelial progenitor cells,[86] and other less well-defined progenitor cells.[87] Endovascular PTFE-covered stents are reported to reduce in-stent restenosis – a major drawback of bare metal stents.[88,89] PTFE coating also improves trans-jugular intrahepatic porto-systemic shunt (TIPS) patency and decreases clinical failures for TIPS use.[90] Nonetheless, these PTFE-covered grafts still report high incidences of hepatic or portal vein stenosis.[91,92] PTFE-coating alone cannot improve this device: further improvements in stent design and insertion techniques are necessary.[93] For further details, please refer to **Chapter 4.411, Peptide- and Protein-Modified Surfaces** and **Chapter 6.628, Vascular Grafts**.

ePTFE (Gore-Tex) is currently used most widely to fabricate medium-size (4–10 μm internode) vascular grafts for use when autogenous saphenous vein grafting is not possible, or to replace damaged vessels,[94] bypass blocked arteries and veins,[95] and for vascular access in hemodialysis.[96,97] ePTFE vascular prostheses are most clinically successful in high blood flow, low resistance conditions (i.e., large peripheral arteries $>5\sim6$ mm diameters). However, to date ePTFE is not suitable for smaller arterial reconstructions (e.g., coronary circulation and peripheral vascular placements) under high-resistance, low-flow conditions. Typical ePTFE suffers from thrombosis, poor healing, lack of compliance, and excessive intimal hyperplasia leading to stenosis.[83] Surface biofunctionalization of ePTFE (and PTFE) seeks to improve ePTFE graft *in vivo* behavior by modifying the ePTFE surface with

diverse chemistry such as coatings, plasma treatments, and immobilization. For further details, please refer to **Chapter 4.414, Molecular Biomimetic Designs for Controlling Surface Interactions**

Anticoagulant (e.g., heparinized) coatings,[98,99] or local antiplatelet drug release or systemic therapy (e.g., platelet surface glycoprotein IIb/IIa inhibitors) and locally delivered antiproliferative agents (e.g., rapamycin) attempt to overcome intrinsic materials performance issues with varying success.[100,101] These modifications improve thrombosis and healing, and prolong graft patency in short-term animal studies.[85,102] Efficacy in human patients is not clear to date. For further details, please refer to **Chapter 4.411, Peptide- and Protein-Modified Surfaces** and **Chapter 6.628, Vascular Grafts**.

1.128.4.2. ePTFE and Teflon™ Tissue Meshes

Teflon meshes have been used to repair abdominal wall defects[103] and hernias.[104–106] Despite some success, original Teflon™ mesh does not reliably integrate into body tissues, is not infection-resistant, and manifests a rate of wound complications too high for routine use in hernia or abdominal repair. Early clinical failure of PTFE meshes in hernial applications prompted a switch to ePTFE meshes that remain the primary material clinically used to repair ventral hernia, incisional hernia, laparoscopic inguinal hernia, and other laparoscopic hernia repairs.[107] These mesh materials minimize risks of postoperative intestinal obstruction and bowel fistula.[108,109] As in the case of PTFE meshes in these applications, infection complications and intestinal obstructions remain for ePTFE mesh. However, they are better controlled with systemic antibiotic therapies without mesh removal. ePTFE meshes have also been used as abdominal surgery barriers against adhesions.[110,111] For further details, please refer to **Chapter 6.638, Biomaterials for Hernia Repair**.

ePTFE has been FDA-approved for use in facial plastic surgery for facial defect reconstruction and augmentation, including rhinoplasty,[112] mentoplasty, forehead defects, auriculoplasty, reconstructive lip augmentation, orbital repair, facial folds, for facial slings, and for cosmetic reconstruction in the nasolabia folds and glabellar creases. It is contraindicated in cosmetic lip augmentation, temporomandibular joint reconstruction, cardiovascular defects, and dermal placement.[113] Nonetheless, Gore and Advanta have discontinued marketing of their products for plastic surgery.

1.128.4.3. Arteteriovenous ePTFE Grafts for Dialysis Access

Hemodialysis – essential for patients with end-stage renal disease – often requires regular, repeated (weekly) access to large blood vessels capable of producing high flow rates through an external artificial kidney device. Hemodialysis patients typically undergo cannula puncture of skin, underlying tissue, and vasculature to provide this access to the external artificial kidney. Repeated trauma to patient skin, tissue, and blood vessels from 13- to 17-gauge access needles produces notable complications including hyperplasia, thrombosis, hematoma, occlusion, infection, and other morbidities. Vascular access complications remain the main reason for hemodialysis patient hospitalization. Synthetic ePTFE arteriovenous (A–V) grafts are surgically placed across the basilic vein and brachial artery to permit cannula access and reduce tissue trauma complications. A–V prosthetic graft failure rates are substantial (>50%), leading to increasing use of native fistulas and catheters.[93,114] However, synthetic grafts reliably provide high blood flow rates shortly after placement, as they do not require maturation before use. In A–V ePTFE grafts, stenosis occurs most commonly at the graft-venous anastomosis. Histologically, macrophages are seen in large numbers in the adventitial and medial layers in the anastomotic tissues from AV ePTFE grafts.[86,114] For further details, please refer to **Chapter 6.628, Vascular Grafts**.

1.128.4.4. Multilumen Catheters

Fluoropolymer multilumen medical-grade tubing is central to many new minimally invasive catheters that permit surgeons to perform several different invasive procedures through several lumens offered in a single inserted catheter device without removing one entire catheter to insert another. These *in vivo* exposures are short term, typically using endo-luminal femoral access, and increasingly minimally invasive. PTFE's unique processing properties facilitate multilumen precision manufacture, offsetting their higher materials expense.

1.128.4.5. Guiding Catheters

A work-horse interventional tool with a well-established history, the guiding catheter is used to deliver stents and other devices endoluminally. Central to the guiding catheter is a PTFE inner liner with its superior lubricity and low friction coefficient that slides within an outer lumen. Lubricity is so critical to this device function that FEP as the second-most lubricious (and perfluorinated) material available is insufficient as a catheter liner. During catheter construction, PTFE is chemically etched onto the tube's outer diameter to promote PTFE bonding to the outer diameter of the liner and enable slip. Bonding is accomplished by using an FEP heat-shrinkable fusing sleeve. The FEP mold can then be removed from the device, leaving a smooth outer PTFE jacket.

1.128.4.6. PTFE Introducer

With over 30 years of use, the PTFE introducer facilitates catheter clinical insertion into a patient's vein, taking advantage of PTFE's endo-luminal lubricity and precision tubing processing. Once the catheter is inserted, the PTFE sheath can be removed from the patient. The introducer exploits PTFE processing that molecularly orients the fluoropolymer material in the tubing-based sleeve over the device. When this is used, PTFE tubing can be readily split and torn longitudinally from the catheter *in situ*. This allows a surgeon to remove a PTFE introducer from a patient while the primary device remains in place.

1.128.4.7. Perfluorocarbon Liquids, Surfactants, and Emulsions as Oxygen-Carrying Blood Substitutes

Perfluorofluid and/or fluorinated surfactant properties valuable for biomedical applications include high specific gravity, spreading coefficient, high contact angle and low solubility with water, low refractive index, absence of protons, and

concentration of sufficient ^{19}F nuclei useful in magnetic resonance imaging (MRI). Low molecular weight perfluorinated fluids can be aspirated into the lungs directly or injected as submicron-sized emulsion droplets into the blood to facilitate oxygen transport, exploiting their high oxygen-carrying capacities.[87,115] Liquid perfluorocarbons in the lung eliminate the gas–lung interface, acting to reduce tension in the lung alveolus and reducing mechanical work required to breathe during respiratory distress and pathologies involving lung surfactant deficiency. Liquid perfluorofluids can be inspired into the lung in large volumes (i.e., filling the lungs) without adverse effects.[115] Dispersion of perfluorofluids in aqueous media using surfactants creates submicron emulsified perfluorodroplets much smaller than red blood cells. These liquid carriers provide enormous additional oxygen carrying capacity in blood supplementing normal oxygenation in microcirculation. Several clinical trials on various perfluorinated fluid oxygen carriers as 'plasma expanders' have been conducted, most recently on Oxygent™ (Alliance Pharmaceuticals, USA), but none has been approved for human use. This microemulsion formulation comprises two different perfluorocarbon fluids stabilized with egg phospholipids. Figure 5 compares the distinct oxygen carrying capacity of this perfluorinated fluid micronized emulsion versus whole blood.

Fluorocarbon emulsion-based injectable image contrast agents to enhance ultrasound *in vivo* imaging are already commercialized (e.g., Optison®, Definity®).[116–120] Perfluorinated emulsions are eliminated from blood after parenteral injection by macrophage/monocyte clearance and exhaled eventually from the lung largely unchanged chemically. Fluorinated surfactants, while generally much more surface-active than their hydrogenated analogs, are generally much less hemolytic.[115] As a testament to their relative safety, the US Food and Drug Administration has approved the ingestion of liquid perfluorinated octyl bromide ($C_8F_{17}Br$) in large volumes (l) as a contrast agent for intestinal imaging by ^{19}F-MRI.

1.128.4.8. Other Fluorinated Material Biomedical Applications

1.128.4.8.1. Fluorinated (meth)acrylates and (meth) acrylated perfluoroalkylated silicones as cross-linked polymer cores for soft contact lenses

Exploiting the intrinsic high oxygen permeability well known for perfluorinated materials, rigid gas permeable contact lenses (RGPs) have used many variations of cross-linked perfluorinated acrylates and perfluorinated silicone gels as lens cores to improve extended-wear lens' on-eye performance. Multiple patents describe diverse materials in this regard, with several major lens manufacturers developing these lens materials. For further details, please refer to **Chapter 6.633, Development of Contact Lenses from a Biomaterial Point of View – Materials, Manufacture, and Clinical Application**.

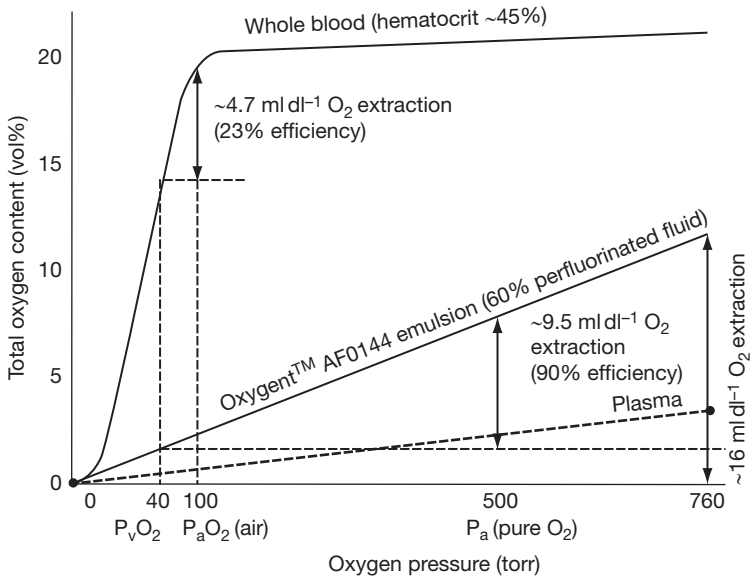

Figure 5 Comparison of efficiency of oxygen transport by a commercial emulsified fluorocarbon liquid (Oxygent™, phase III clinical trials) versus hemoglobin (Hb) in whole blood, and intrinsic oxygen solubility in plasma. In perfluorocarbon liquid dispersions, oxygen solubility is characterized by van der Waals interactions, following Henry's Law: oxygen solubility is linearly and directly proportional to oxygen's partial pressure. Oxygent™ is a 60 w/v% concentrated submicron perfluorofluid emulsion comprising primarily F-octyl bromide ($C_8F_{17}Br$, *perflubron*) with a small mass fraction of longer chain F-decyl bromide ($C_{10}F_{21}Br$). F-octyl bromide used as the perfluorofluid bulk phase is the empirical compromise between required emulsion stability in blood and a clinically acceptable physiological excretion rate. Emulsion stability increases with decreasing perfluorofluid water solubility (i.e., increasing molecular weight), while excretion diminishes exponentially with increasing molecular weight. By contrast, Hb as the oxygen carrier in blood exhibits specific coordinate bonding into the heme porphyrin iron atom and associated Hb amino acid stabilizing ligands as is well established. Successive binding of four oxygen molecules to all four hemes in each Hb is cooperative, and Hb saturation occurs when all four iron atoms bind oxygen. This results in the well-known sigmoidal shape of the oxygen saturation curve for blood that plateaus when the oxygen partial pressure in the atmosphere is attained. Lower total oxygen carrying capacity observed for perfluorinated fluid emulsions is balanced by their much higher oxygen extraction efficiencies. Adapted from Krafft, M. P.; Riess, J. G. *J. Polym. Sci. A Polym. Chem.* **2007**, *45*(7), 1185–1198.

1.128.4.8.2. Fluorinated coatings as antifouling coatings for IOLs

Cell adhesion to implanted polymer IOLs can produce complications with optical visual interference. To prevent occular cells from migrating onto and coating the implanted IOL device optical surface, thin optically transparent plasma-deposited fluorocarbon films, or layers of other fluorinated polymers are deposited on the IOL back surface. Several patents describe this approach and the IOL application. For further details, please refer to **Chapters 4.406, Protein Interactions with Biomaterials**.

1.128.4.8.3. PTFE paste injectable bulking agent

Teflon™ particles formulated into an injectable paste are reported for urological treatment of vesico-ureteric reflux (VUR)[121] in a large animal model, as it is corrected by subureteric injection of a PTFE paste.[122] Subureteric paste injection by endoscopy has successfully addressed primary and secondary VUR in children for nearly two decades.[123–125]

Similarly, PTFE paste is also used for decades to treat female stress urinary incontinence[126–128] with promising short-term results. However, this treatment does not have regulatory approval because of the associated high risk of PTFE microparticle migration and granuloma induction, especially in lymph nodes, kidneys, lungs, and brain.[129] Teflon™ paste injection nonetheless remains clinically effective and convenient in this application,[130–132] but its side effects concerns limit clinical use.[126]

1.128.4.8.4. Ligament replacement

The Gore-Tex™ ligament prosthesis comprises a single long fiber of ePTFE woven into multiple loops. Mechanical testing shows that the resulting ultimate tensile strength is ~3 times that of the human anterior cruciate knee ligament (ACL). Creep and bending fatigue testing validate this ePTFE device as a strong synthetic ACL replacement material.[133] *In vivo* in humans, 129 out of 130 patients implanted with a high strength ePTFE ACL ligament devices exhibited improved knee stability up to 15 months.[133] But initial improvements were followed by progressive prosthetic loosening.[134] Longer term follow-up of Gore-Tex ACL implant reconstructions showed a similar pattern of early improvement postoperatively with deterioration over time. Clinical failure rates of 33% were reported at 3-year follow-up.[135] Another study showed a 90% success rate at 2 years versus only a 76% success rate at 3 years or more.[136] The Gore-Tex ACL prosthesis is currently FDA-approved for use in patients with failed autogenous intraarticular graft procedures.[137]

1.128.4.8.5. Sutures

PTFE is also applied in suture fibers in various forms. Both PTFE monofilament and ePTFE fibers are surgically proven with desirable surgeon handling and lubricity properties. Additionally, PTFE is blended into other common surgical sutures used for myocardial heart valve prostheses fixation. Poly(ethylene terephthalate) (PET polyester) braided sutures are impregnated with PTFE polymer to limit wrinkling of the braid and consequent swelling. PTFE hydrophobic properties likely limit water uptake by the polyester braid, slowing its degradation by hydrolysis.[138]

1.128.5. Conclusion and Perspectives

Perfluoropolymers as solid and liquids, and perfluorinated coatings and films all offer unique properties to benefit certain biomedical devices and applications. High degrees of material fluorination produce unique chemical and thermal stability, very low interfacial energies and hydrophobicity, and low chain cohesion energies not only facilitating surface lubrication but also producing cold flow and poor solid mechanical properties. They also produce physical solid state properties that, while intractable for typical device processing applications, can be exploited using specialized approaches to yield very unique materials forms and dimensions benefiting catheters and tubing. Some of these properties are interesting and beneficial for biomaterials, both *in vitro* and *in vivo*. Fluorinated materials' reputation for 'biological inertness' is not supported by many *in vitro* assays that show substantial irreversible protein adhesion to surfaces of several perfluorinated materials chemistries. Poor cell adhesion generally characteristic of perfluorinated surfaces is instead attributed to surface binding of proteins nonadhesive to cells (e.g., albumin, lipoproteins) from blood, serum, plasma, and biological fluids that hinder cell–surface interactions. This 'tight' protein-surface adhesion is an important property for molecular biology's *in vitro* PVDF blotting membranes and other surface-protein 'masking' techniques. PTFE has played an important role in many minimally invasive medical devices, mostly intended for interventional luminal access (e.g., multilumen catheter fabrication) because of its high viscosity/high temperature paste extrusion requirements that impart high size/design tolerances in small dimensions with long production runs. Permanent *in vivo* fluorinated materials use is dominated by ePTFE in most implant applications, primarily in cardiovascular and hemodialysis. ePTFE's unique, variable expanded node-fibrillar microporous morphology permits mechanical control, processing, tissue integration, and clinically accepted biocompatibility in certain applications. Despite a rich history of biomedical development and practical utility, fluoropolymers are still developed for new biomedical opportunities. *In vivo* implant cell endothelialization within the host (discussed in **Section 1.128.4.1**) is a critical area for performance breakthroughs for implanted vascular graft fluorinated materials. Imaging and drug delivery are other areas of opportunity that extend fluorinated materials' previous extensive development as microparticle-based blood oxygen carriers. Both ultrasound contrast imaging and ^{19}F-MRI exploit perfluorofluid emulsions in tissue and will see continued development. As exploited in current imaging emulsions, fluorinated amphiphiles also produce highly stable colloids and particles capable of surface modification for utility as drug carriers.[139–143] While fluorocarbon-based targeted drug delivery vehicles are only in limited preclinical clinical testing, recent progress in DNA,[144] cytolytic peptide,[145] and pulmonary drug delivery[146] shows promise for modifying such vehicles to provide a 'see-and-treat' therapeutic modality where both fluorinated agent-based imaging and triggered drug release can be combined in a single vehicle.[116,141] Lastly, a new everolimus-releasing cardiovascular endoluminal drug-eluting stent (Xience V®, Abbott Vascular, USA) is reportedly designed to overcome some limitations of

first-generation drug-eluting stents. This design uses a thin fluoropolymer coating over the metallic stent struts to elute the antirestenotic drug, everolimus, to effectively suppress neointimal tissue and promote rapid reendothelialization above and between stent struts, as shown in preclinical studies.[70] For further details, please refer to **Chapter 4.406, Protein Interactions with Biomaterials**.

Acknowledgments

D.W. Grainger gratefully acknowledges NIH grants EB-00894 and EB-001473 for support during the preparation of this manuscript as well as for some of the experiments described herein. F. Liu acknowledges scholarship support from the Chinese Scholarship Council.

References

1. Drobny, J. G. *Fluoroplastics (Rapra Review Report 184)*. Smithers Rapra: Boca Raton, FL, 2005.
2. Leveen, H. H.; Barberio, J. R. *Ann. Surg.* **1949**, *129*(1), 74–84.
3. Oshige, S. Japanese Patent 42-13560(67/13560), Aug 1967.
4. Soyer, T.; Lempinen, M.; Cooper, P.; Norton, L.; Eiseman, B. *Surgery* **1972**, *72*(6), 864–872.
5. Matsumoto, H.; Hasegawa, T.; Fuse, K.; Yamamoto, M.; Saigusa, M. *Surgery* **1973**, *74*(4), 519–523.
6. Gore, R. W. *Process for Producing Porous Products*. W. L. Gore & Associates: Newark, DE, 1976.
7. Smart, B. E. In *Organofluorine Chemistry: Principles and Commercial Applications*; Banks, R. E., Tatlow, J. C., Smart, B. E., Eds.; Plenum: New York, 1994; pp 57–82.
8. Stone, M.; Nevell, T. G.; Tsibouklis, J. *Mater. Lett.* **1998**, *37*(1–2), 102–105.
9. Kobayashi, H.; Owen, M. J. *Trends Polym. Sci.* **1995**, *3*(10), 330–335.
10. Zhang, Y. X.; Da, A. H.; Hogen-Esch, T. E.; Butler, G. B. *J. Polym. Sci. C Polym. Lett. Ed.* **1989**, *28*(7), 213–218.
11. Bar, G.; Thomann, Y.; Brandsch, R.; Cantow, H. J.; Whangbo, M. H. *Langmuir* **1997**, *13*(14), 3807–3812.
12. Doeff, M. M.; Lindner, E. *Macromolecules* **1989**, *22*(7), 2951–2957.
13. Sun, F.; Mao, G.; Grainger, D. W.; Castner, D. G. *Thin Solid Films* **1994**, *242*(1–2), 106–111.
14. Sun, F.; Grainger, D. W.; Castner, D. G.; Leach-Scampavia, D. K. *Macromolecules* **1994**, *27*(11), 3053–3062.
15. Scheirs, J. *Modern Fluoropolymers*; *Wiley Series in Polymer Science* Wiley: New York, 1997; xx, 637 p.
16. Twieg, R. J.; Russell, T. P.; Siemens, R.; Rabolt, J. F. *Macromolecules* **1985**, *18*(6), 1361–1362.
17. Russell, T. P.; Rabolt, J. F.; Twieg, R. J.; Siemens, R. L.; Farmer, B. L. *Macromolecules* **1986**, *19*(4), 1135–1143.
18. Dorset, D. L.; Zhang, W. P. *Biochim. Biophys. Acta* **1990**, *1028*(3), 299–303.
19. Clark, E. S.; Muus, L. T. *Z. Kristallogr.* **1962**, *117*, 119–127.
20. Naselli, C.; Swalen, J. D.; Rabolt, J. F. *J. Chem. Phys.* **1989**, *90*(7), 3855–3860.
21. Bunn, C. W.; Howells, E. R. *Nature* **1954**, *174*, 549–551.
22. Schneider, J.; Erdelen, C.; Ringsdorf, H.; Rabolt, J. F. *Macromolecules* **1989**, *22*(8), 3475–3480.
23. Tsao, M. W.; Hoffmann, C. L.; Rabolt, J. F.; *et al*. *Langmuir* **1997**, *13*(16), 4317–4322.
24. Clark, E. S. *Polymer* **1999**, *40*(16), 4659–4665.
25. Pittman, A. G. In *Fluoropolymers*; Wall, L. A., Ed.; Wiley: New York, 1972; pp 419–449.
26. Hare, E. F.; Shafrin, E. G.; Zisman, W. A. *J. Chem. Phys.* **1954**, *58*(3), 236–239.
27. Charnley, J. *Low Friction Arthroplasty of the Hip: Theory and Practice*. Springer: Berlin, 1979.
28. Abramowicz, S.; Dolwick, M. F.; Lewis, S. B.; Dolce, C. *Int. J. Oral Maxillofac. Surg.* **2008**, *37*(8), 763–767.
29. Driemel, O.; Braun, S.; Muller-Richter, U. D.; *et al*. *Int. J. Oral Maxillofac. Surg.* **2009**, *38*(9), 909–920.
30. McClurken, M. E.; McHaney, J. M.; Colone, W. M. In *Vascular Graft Update: Safety and Performance*; Kombic, H. E., Katrowitz, A., Sung, P., Eds.; ASTM: Philadelphia, PA, 1986; pp 82–94.
31. Santiago, E. J.; Chatamra, K.; Taylor, D. E. *Ann. R. Coll. Surg. Engl.* **1981**, *63*(4), 253–256.
32. Mole, B. *Plast. Reconstr. Surg.* **1992**, *90*(2), 200–206.
33. Drobny, J. G. *Technology of Fluoropolymers*. CRC Press: Boca Raton, FL, 2001; p 172.
34. Saunders, K. J. *Organic Polymer Chemistry: An Introduction to the Organic Chemistry of Adhesives, Fibres, Paints, Plastics and Rubbers*, 2nd ed.; Chapman & Hall: London, 1988.
35. Frankel, A. *Blood money. Lawyer* **2009**, 1–7 November.
36. Yasuda, H.; Gazicki, M. *Biomaterials* **1982**, *3*(2), 68–77.
37. Koziol, J. E.; Peyman, G. A.; Yasuda, H. *Arch. Ophthalmol.* **1983**, *101*(11), 1779–1781.
38. Chrisey, D. B.; Pique, A.; McGill, R. A.; *et al*. *Chem. Rev.* **2003**, *103*(2), 553–576.
39. Stanley, J. C. *Biologic and Synthetic Vascular Prostheses*. Grune & Stratton: New York, 1982; p xxi, 681.
40. Ratner, B. D. *J. Biomed. Mater. Res.* **1993**, *27*(7), 837–850.
41. Legeais, J. M.; Werner, L. P.; Legeay, G.; Briat, B.; Renard, G. *J. Cataract Refract. Surg.* **1998**, *24*(3), 371–379.
42. Valdevit, A.; Turegun, M.; Kambic, H.; Siemionow, M.; Zins, J. *J. Biomed. Mater. Res.* **2000**, *53*(1), 62–66.
43. Reid, G.; Busscher, H. J.; Sharma, S.; Mittelman, M. W.; McIntyre, S. *Surf. Sci. Rep.* **1995**, *21*(7), 251–273.
44. Grannis, F. W., Jr. *Ann. Thorac. Surg.* **1995**, *60*(1), 197–199.
45. Kiaei, D.; Hoffman, A. S.; Horbett, T. A. *J. Biomater. Sci. Polym. Ed.* **1992**, *4*(1), 35–44.
46. Paynter, R. W.; Rutner, B. D. In *Surface and Interfacial Aspects of Biomedical Polymers*, 2nd ed.; Andrade, J. D., Ed.; Springer: New York, 1985; pp 189–210.
47. Dekker, A.; Reitsma, K.; Beugeling, T.; Bantjes, A.; Feijen, J.; van Aken, W. G. *Biomaterials* **1991**, *12*(2), 130–138.
48. Chandy, T.; Das, G. S.; Wilson, R. F.; Rao, G. H. *Biomaterials* **2000**, *21*(7), 699–712.
49. Grainger, D. W.; Pavon-Djavid, G.; Migonney, V.; Josefowicz, M. *J. Biomater. Sci. Polym. Ed.* **2003**, *14*(9), 973–988.
50. Roald, H. E.; Barstad, R. M.; Bakken, I. J.; Roald, B.; Lyberg, T.; Sakariassen, K. S. *Blood Coagul. Fibrinolysis* **1994**, *5*(3), 355–363.
51. van Wachem, P. B.; Beugeling, T.; Feijen, J.; Bantjes, A.; Detmers, J. P.; van Aken, W. G. *Biomaterials* **1985**, *6*(6), 403–408.
52. Hoffman, A. S.; Ratner, B. D.; Garfinkle, A. M.; Horbett, T. A.; Reynolds, L. O.; Hanson, S. R. In *MRS Symposium Proceedings*; Williams, J. M., Nichols, M. F., Zingg, W. Eds.; 1986; Vol. 55, p 3.
53. Callow, A. D. *Int. Angiol.* **1988**, *7*(3), 246–253.
54. Kempczinski, R. F.; Rosenman, J. E.; Pearce, W. H.; Roedersheimer, L. R.; Berlatzky, Y.; Ramalanjaona, G. *J. Vasc. Surg.* **1985**, *2*(3), 424–429.
55. Schmidt, S.; Decleer, W.; Wagner, U.; Kindermann, D.; Pringle, K.; Krebs, D. *Eur. J. Obstet. Gynecol. Reprod. Biol.* **1991**, *42*(Suppl.), S84–S86.
56. Godek, M. L.; Michel, R.; Chamberlain, L. M.; Castner, D. G.; Grainger, D. W. *J. Biomed. Mater. Res. A* **2009**, *88*(2), 503–519.
57. Ranieri, J. P.; Bellamkonda, R.; Jacob, J.; Vargo, T. G.; Gardella, J. A.; Aebischer, P. *J. Biomed. Mater. Res.* **1993**, *27*(7), 917–925.
58. Clowes, A. W.; Kirkman, T. R.; Reidy, M. A. *Am. J. Pathol.* **1986**, *123*(2), 220–230.
59. Clark, R. E.; Boyd, J. C.; Moran, J. F. *J. Surg. Res.* **1974**, *16*(5), 510–522.
60. Baier, R. E.; Meyer, A. E.; Natiella, J. R.; Natiella, R. R.; Carter, J. M. *J. Biomed. Mater. Res.* **1984**, *18*(4), 327–355.
61. Zilla, P.; Fasol, R.; Preiss, P.; *et al*. *Surgery* **1989**, *105*(4), 515–522.
62. Kesler, K. A.; Herring, M. B.; Arnold, M. P.; *et al*. *J. Vasc. Surg.* **1986**, *3*(1), 58–64.
63. Koenig, A. L.; Gambillara, V.; Grainger, D. W. *J. Biomed. Mater. Res. A* **2003**, *64*(1), 20–37.
64. McClary, K. B.; Ugarova, T.; Grainger, D. W. *J. Biomed. Mater. Res.* **2000**, *50*(3), 428–439.
65. Healy, K. E. *Curr. Opin. Solid State Mater. Sci.* **1999**, *4*(4), 381–387.
66. Koenig, A. L.; Grainger, D. W. In *Biomimetic Materials and Design: Interactive Biointerfacial Strategies, Tissue Engineering and Targeted Drug Delivery*; Lowman, A., Dillow, A., Eds.; Marcel-Dekker: New York, 2002; pp 154–206.
67. Berry, K. L. DuPont, U.S. Patent SN 214, 223, 1951.
68. Edwards, W. S. *Surgery* **1959**, *45*(2), 298–309.
69. Boyd, D. P.; Midell, A. I. *Vasc. Surg.* **1971**, *5*(3), 148–153.
70. Claessen, B. E.; Caixeta, A.; Henriques, J. P.; Piek, J. J. *Expert Rev. Cardiovasc. Ther.* **2010**, *8*(10), 1363–1374.

71. W.L. Gore & Associates, Inc. *Literature Summary for Vascular Access*. W.L. Gore & Associates: Flagstaff, AZ, 2004; pp AH1313-EN1.
72. White, R. A. *ASAIO Trans*. **1988**, *34*(2), 95–100.
73. Masuda, S.; Doi, K.; Satoh, S.; Oka, T.; Matsuda, T. *ASAIO J*. **1997**, *43*(5), M530–M534.
74. Grabenwoger, M.; Fitzal, F.; Sider, J.; *et al*. *Ann. Thorac. Surg.* **1998**, *66*(Suppl. 6), S110–S114.
75. Wu, M. H. D.; Shi, Q.; Onuki, Y.; Kouchi, Y.; Sauvage, L. R. *Ann. Vasc. Surg.* **1996**, *10*(1), 11–15.
76. Hazama, K.; Nishibe, T.; Shimada, T.; *et al*. *J. Surg. Res.* **1999**, *81*(2), 174–180.
77. Tomizawa, Y.; Takanashi, Y.; Noishiki, Y.; Nishida, H.; Endo, M.; Koyanagi, H. *ASAIO J*. **1998**, *44*(5), M496–M500.
78. Gray, J. L.; Kang, S. S.; Zenni, G. C.; Dae, K. *J. Surg. Res.* **1994**, *57*(5), 596–612.
79. Miura, H.; Nishibe, T.; Yasuda, K.; *et al*. *Eur. Surg. Res.* **2002**, *34*(3), 224–231.
80. Golden, M. A.; Hanson, S. R.; Kirkman, T. R.; Schneider, P. A.; Clowes, A. W. *J. Vasc. Surg*. **1990**, *11*(6), 838–844; discussion 845.
81. Nagae, T.; Tsuchida, H.; Peng, S. K.; Furukawa, K.; Wilson, S. E. *Cardiovasc. Surg*. **1995**, *3*(5), 479–484.
82. Hirabayashi, K.; Saitoh, E.; Ijima, H.; Takenaka, T.; Kodama, M.; Hori, M. *J. Biomed. Mater. Res.* **1992**, *26*(11), 1433–1447.
83. Bordenave, L.; Fernandez, P.; Remy-Zolghadri, M.; Villars, S.; Daculsi, R.; Midy, D. *Clin. Hemorheol. Microcirc.* **2005**, *33*(3), 227–234.
84. Campbell, G. R.; Campbell, J. H. *Curr. Pharm. Biotechnol*. **2007**, *8*(1), 43–50.
85. de Mel, A.; Jell, G.; Stevens, M. M.; Seifalian, A. M. *Biomacromolecules* **2008**, *9*(11), 2969–2979.
86. Melero-Martin, J. M.; Khan, Z. A.; Picard, A.; Wu, X.; Paruchuri, S.; Bischoff, J. *Blood* **2007**, *109*(11), 4761–4768.
87. Aoki, J.; Serruys, P. W.; van Beusekom, H.; *et al*. *J. Am. Coll. Cardiol*. **2005**, *45*(10), 1574–1579.
88. Bureau, C.; Garcia-Pagan, J. C.; Otal, P.; *et al*. *Gastroenterology* **2004**, *126*(2), 469–475.
89. Hernandez-Guerra, M.; Turnes, J.; Rubinstein, P.; *et al*. *Hepatology* **2004**, *40*(5), 1197–1202.
90. Haskal, Z. J. *Radiology* **1999**, *213*(3), 759–766.
91. Riggio, O.; Angeloni, S.; Salvatori, F. M.; *et al*. *Am. J. Gastroenterol*. **2008**, *103*(11), 2738–2746.
92. Vizzutti, F.; Arena, U.; Rega, L.; *et al*. *Gut* **2009**, *58*(4), 582–584.
93. Angeloni, S.; Merli, M.; Salvatori, F. M.; *et al*. *Am. J. Gastroenterol*. **2004**, *99*(2), 280–285.
94. Hanel, K. C.; McCabe, C.; Abbott, W. M.; Fallon, J.; Megerman, J. *Ann. Surg.* **1982**, *195*(4), 456–463.
95. Kannan, R. Y.; Salacinski, H. J.; Butler, P. E.; Hamilton, G.; Seifalian, A. M. *J. Biomed. Mater. Res. B Appl. Biomater.* **2005**, *74*(1), 570–581.
96. Jenkins, A. *Br. Med. J.* **1976**, *2*(6030), 280.
97. Konner, K. *Nephrol. Dial. Transplant.* **2005**, *20*(12), 2629–2635.
98. Engbers, G. H.; Feijen, J. *Int. J. Artif. Organs* **1991**, *14*(4), 199–215.
99. Walluscheck, K. P. *Ital. J. Vasc. Endovasc. Surg.* **2006**, *13*(3), 137–147.
100. Cagiannos, C.; Abul-Khoudoud, O. R.; DeRijk, W. *J. Vasc. Surg.* **2005**, *42*(5), 980–988.
101. Kidane, A. G.; Salacinski, H.; Tiwari, A.; Bruckdorfer, K. R.; Seifalian, A. M. *Biomacromolecules* **2004**, *5*(3), 798–813.
102. Sarkar, S.; Sales, K. M.; Hamilton, G.; Seifalian, A. M. *J. Biomed. Mater. Res. B Appl. Biomater.* **2007**, *82*(1), 100–108.
103. Ludington, L. G.; Woodward, E. R. *Surgery* **1959**, *46*(2), 364–373.
104. Gibson, L. D.; Stafford, C. E. *Am. Surg.* **1964**, *30*, 481–486.
105. Snijders, H. *Arch. Chir. Neerl*. **1969**, *21*(3), 199–202.
106. Kalsbeek, H. L. *Arch. Chir. Neerl*. **1974**, *26*, 71–75.
107. DeBord, J. R. *Surg. Clin. North Am.* **1998**, *78*(6), 973–1006; vi.
108. DeGuzman, L. J.; Nyhus, L. M.; Yared, G.; Schlesinger, P. K. *Endoscopy* **1995**, *27*(6), 459–461.
109. Lo Monte, A. I.; Damiano, G.; Maione, C.; *et al*. *Transplant. Proc.* **2009**, *41*(4), 1398–1401.
110. Tulandi, T. *Curr. Opin. Obstet. Gynecol*. **1997**, *9*(4), 239–243.
111. Morris-Stiff, G. J.; Hughes, L. E. *J. Am. Coll. Surg.* **1998**, *186*(3), 352–367.
112. Rothstein, S. G.; Jacobs, J. B. *Entechnology* **1989**, *42*, 44–45; Sep 40.
113. Levine, B.; Berman, W. E. *Ear Nose Throat J*. **1995**, *74*(10), 681–682; 684.
114. Haruguchi, H.; Teraoka, S. *J. Artif. Organs* **2003**, *6*(4), 227–235.
115. Krafft, M. P.; Riess, J. G. *J. Polym. Sci. A Polym. Chem.* **2007**, *45*(7), 1185–1198.
116. Srinivas, M.; Cruz, L. J.; Bonetto, F.; Heerschap, A.; Figdor, C. G.; de Vries, I. J. *Biomaterials* **2010**, *31*(27), 7070–7077.
117. Riess, J. G. *Curr. Opin. Colloid Interface Sci*. **2003**, *8*(3), 259–266.
118. Schutt, E. G.; Klein, D. H.; Mattrey, R. M.; Riess, J. G. *Angew. Chem. Int. Ed. Engl*. **2003**, *42*(28), 3218–3235.
119. Klibanov, A. L. *Ernst Schering Res. Found. Workshop* **2005**, *49*, 171–191.
120. Liu, Y.; Miyoshi, H.; Nakamura, M. *J. Control. Release* **2006**, *114*(1), 89–99.
121. Puri, P. *Br. J. Urol*. **1995**, *75*(2), 126–131.
122. Puri, P.; O'Donnell, B. *Br. Med. J. (Clin. Res. Ed.)* **1984**, *289*(6436), 5–7.
123. Le Guillou, M.; Ferriere, J. M.; Pourquie, J.; Barthaburu, D.; Amory, J. P.; Nony, P. *Ann. Urol. (Paris)* **1984**, *18*(2), 121–123.
124. Dodat, H.; Paulhac, J. B. *Pediatrie* **1987**, *42*(3), 211–214.
125. Puri, P. *Curr. Opin. Urol*. **2000**, *10*(6), 593–597.
126. Meschia, M.; Pifarotti, P.; Gattei, U.; Crosignani, P. G. *Gynecol. Obstet. Invest*. **2002**, *54*(2), 67–72.
127. Beckingham, I. J.; Wemyss-Holden, G.; Lawrence, W. T. *Br. J. Urol*. **1992**, *69*(6), 580–583.
128. Politano, V. A. *Br. J. Urol*. **1992**, *69*(1), 26–28.
129. Aaronson, I. A.; Rames, R. A.; Greene, W. B.; Walsh, L. G.; Hasal, U. A.; Garen, P. D. *Eur. Urol*. **1993**, *23*(3), 394–399.
130. Herschorn, S.; Glazer, A. A. *J. Urol*. **2000**, *163*(6), 1838–1842.
131. Harrison, S. C.; Brown, C.; O'Boyle, P. J. *Br. J. Urol*. **1993**, *71*(1), 25–27.
132. Lopez, A. E.; Padron, O. F.; Patsias, G.; Politano, V. A. *J. Urol*. **1993**, *150*(3), 856–858.
133. Bolton, C. W.; Bruchman, W. C. *Clin. Orthop. Relat. Res.* **1985**, *196*, 202–213.
134. Glousman, R.; Shields, C., Jr.; Kerlan, R.; *et al*. *Am. J. Sports Med*. **1988**, *16*(4), 321–326.
135. Woods, G. A.; Indelicato, P. A.; Prevot, T. J. *Am. J. Sports Med*. **1991**, *19*(1), 48–55.
136. Indelicato, P. A.; Pascale, M. S.; Huegel, M. O. *Am. J. Sports Med*. **1989**, *17*(1), 55–62.
137. Mascarenhas, R.; Macdonald, P. B. *Mcgill. J. Med*. **2008**, *11*(1), 29–37.
138. Bhat, S. V. *Biomaterials*. Kluwer: Boston, MA, 2002; p xii, 265.
139. Rogueda, P. G. *Drug Dev. Ind. Pharm.* **2003**, *29*(1), 39–49.
140. Selvam, P.; Peguin, R. P.; Chokshi, U.; da Rocha, S. R. *Langmuir* **2006**, *22*(21), 8675–8683.
141. Marsh, J. N.; Partlow, K. C.; Abendschein, D. R.; Scott, M. J.; Lanza, G. M.; Wickline, S. A. *Ultrasound Med. Biol*. **2007**, *33*(6), 950–958.
142. Riess, J. G. *Curr. Opin. Colloid Interface Sci*. **2009**, *14*(5), 294–304.
143. Krafft, M. P. *Adv. Drug Deliv. Rev.* **2001**, *47*(2–3), 209–228.
144. Xiong, S. D.; Li, L.; Jiang, J.; *et al*. *Biomaterials* **2010**, *31*(9), 2673–2685.
145. Soman, N. R.; Lanza, G. M.; Heuser, J. M.; Schlesinger, P. H.; Wickline, S. A. *Nano Lett*. **2008**, *8*(4), 1131–1136.
146. Tsagogiorgas, C.; Krebs, J.; Pukelsheim, M.; *et al*. *Eur. J. Pharm. Biopharm.* **2010**, *76*(1), 75–82.

1.129. Engineering the Biophysical Properties of Basement Membranes into Biomaterials: Fabrication and Effects on Cell Behavior

E J Tocce, S J Liliensiek, M J Wilson, B Yanez-Soto, and P F Nealey, University of Wisconsin, Madison, WI, USA
C J Murphy, University of California, Davis, CA, USA

© 2011 Elsevier Ltd. All rights reserved.

1.129.1.	**Introduction**	528
1.129.2.	**Basement Membrane**	528
1.129.2.1.	Biochemical Composition of BMs	528
1.129.2.2.	Cellular Adhesion via Macromolecules of BMs	529
1.129.2.3.	Diseases Associated with BMs	529
1.129.2.4.	Biophysical Cues of BMs: Elastic Modulus	531
1.129.2.5.	Biophysical Cues of BMs: Topography	532
1.129.3.	**Nanostructure Fabrication**	533
1.129.3.1.	Design Parameters	534
1.129.3.2.	Classical Lithography	535
1.129.3.2.1.	Electron-beam lithography	535
1.129.3.2.2.	Photolithography	535
1.129.3.3.	Next Generation Lithography	535
1.129.3.3.1.	Nanoimprint lithography	535
1.129.3.3.2.	Soft lithography	535
1.129.3.3.3.	Colloidal lithography	535
1.129.3.4.	Other Methods	536
1.129.4.	**Cellular Response to Topographic Cues with Dimensions from Nano- to Micron-Scales**	537
1.129.4.1.	Micron Range (>1000 nm Widths)	538
1.129.4.2.	Submicron (400–1000 nm Widths)	539
1.129.4.3.	Upper BM Range (100–400 nm Widths)	539
1.129.4.4.	Lower BM Range (10–100 nm Widths)	541
1.129.4.5.	Importance of Depth	542
1.129.4.6.	Overview	543
References		543

Glossary

Basement membrane Specialized extracellular matrix that separates the basal layer of epithelial or endothelial cells from the stroma.

Biochemical cues Specific biochemical motifs of the soluble and/or extracellular matrix that are presented to cell-surface receptors which induce intracellular signaling pathways.

Biophysical cues Specific characteristics of the physical extracellular matrix (ECM), such as ECM stiffness, topographical structure, and applied mechanical force, which induce intracellular signaling pathways.

Compliance A measure of the ability of a material to yield to an applied force.

Contact guidance The elongation or morphological alteration of a cell in response to physical structures of the extracellular environment.

Elastic modulus Ratio of stress to strain that relates to the relative stiffness of an elastic material.

Nanofabrication The practice of making nanometer scale features and patterns on a substrate.

Topography Description of the features of the surface of a substrate, both in scale and geometry.

Abbreviations

AFM	Atomic force microscopy
BHK	Baby hamster kidney
BM	Basement membrane
DNA	Deoxyribonucleic acid
E	Young's elastic modulus
EBL	Electron-beam lithography
ECM	Extracellular matrix
EUV	Extreme ultraviolet
FGF	Fibroblast growth factor

GLAD	Glancing angle deposition
HCEC	Human corneal epithelial cell
HUVEC	Human umbilical vein endothelial cell
IL	Interference lithography
LADI	Laser-assisted direct imprint
MDCK	Madin–Darby canine kidney
NGF	Nerve growth factor
NGL	Next generation lithography
NIL	Nanoimprint lithography
PC12 cells	Pheochromocytoma (tumor) of the rat adrenal medulla
PLLA	Poly(L-lactic acid)
RGD	Arginine-glycine-aspartic acid
RIE	Reactive ion etching
RNA	Ribonucleic acid
SCC	Squamous cell carcinomas
SV40-HCEC	Simian virus 40-transformed human corneal epithelial cell
TCPS	Tissue culture polystyrene
THF	Tetrahydrofuran
UV	Ultraviolet
VEGF	Vascular endothelial growth factor

1.129.1. Introduction

Great effort is being expended in the design and fabrication of biomaterials for tissue engineering aimed at best approximating the chemical and biophysical cues provided by the native extracellular matrix (ECM). A growing number of reports have focused on characterizing the extracellular environment and elucidating the specific elements that have the greatest impact on cell behavior. These elements are then incorporated into the design and fabrication of synthetic biomaterials with the hope that they will provide biomimetic cues to support formation and maintenance of fully functional self-regenerating healthy tissue.

Cells receive cues from their extracellular environment from multiple sources which include soluble factors in the extracellular milieu as well as the protein matrix in which they reside. It is well recognized that the biochemical components of the soluble factors and ECM have a substantial impact on cell behavior. Recent reports have now demonstrated that the biophysical attributes of the ECM, which include both nanotopography and elastic modulus, are also key regulators of cell behavior. Understanding how these biophysical cues affect cellular behavior will directly impact *in vitro* cell culture methods, the design of materials for tissue-engineering applications, and the development of improved prosthetics.

To understand and exploit the influence of biophysical cues, we must first determine the biophysical attributes of the native ECM. The focus of this chapter is on epithelial and vascular endothelial cells that are basally anchored to the ECM through a highly organized specialization of the ECM known as the basement membrane (BM). Because of its essential function within tissues throughout the body, several groups have investigated and quantified the biophysical attributes of BMs from different species and anatomic locations.

1.129.2. Basement Membrane

The BM serves as structural support as well as an interface through which cells that line organs, cavities (epithelium), and the interior of blood vessels (endothelium) interact with the underlying stroma.[1,2] BMs have also been found to line muscle and fat cells and are associated with Schwann cells surrounding peripheral nerve axons.[3,4] This specialized structure supports the overlying cells and demarcates tissue compartmentalization between the connective tissue and the epithelium or endothelium.[5] Among the primary and most studied functions of the BM are serving as the structural interface for the attachment of the overlying epithelium or endothelium, provision of ligands for binding of cell membrane-associated integrins, and serving as a reservoir for soluble cytoactive factors such as polypeptide growth factors.

Cell–substrate adhesion provides strength and integrity and is critical in the formation and maintenance of the overlying epithelial or endothelial tissue. The adhesion of cells through the underlying BM is a dynamic process *in vivo*. For example, in many epithelial-lined structures such as the skin and the cornea, a population of basal epithelial cells within the stratified squamous epithelium will undergo differentiation wherein cells will lose their cell–substrate attachment in order to physically migrate toward the surface. This continuous movement and reorganization of cells requires dynamic but regulated changes that will allow for the normal homeostasis of the tissue.

Other functional attributes of the BMs include their ability to provide a source or 'trap' for growth factors, hormones, and ions that are essential for cell function.[5–8] For example, vascular endothelial growth factor (VEGF) is released during vascular BM remodeling and is sequestered by heparin-binding proteoglycans in the BM. The sequestered VEGF is 'stored' for use in blood vessel formation at the site of injury.[9] In some cases, the BM acts as a semipermeable barrier for blood filtration, specifically in mammalian kidneys.[7] These examples, among others, demonstrate that BMs and their components play essential roles in normal organ development and function.

1.129.2.1. Biochemical Composition of BMs

The complex meshwork of proteins that comprises BMs includes glycoproteins and proteoglycans.[10–12] Type IV collagen, laminin, nidogen/enactin, and perlecan are ubiquitously expressed in all BMs.[10,12] Other minor components of the BM include agrin, type XVII and XV collagen, fibulin, and BM-40 Sparc.[13] These macromolecules are excreted from cells and subsequently self-assemble into a dense heterogeneous matrix. Although the four main constituents are present in all BMs, it is the unique combination of the macromolecular isoforms that distinguishes, for example, a corneal BM from a

glomerular BM.[10] In addition, differences in the concentrations of each biochemical component may account for biophysical differences including those in thickness, stiffness, and topography that have been reported between BMs of different tissues.[14] For example, the thickness of the BM can range from 50 nm to tens of micrometers depending on anatomic location within the tissue, age, and pathological conditions.[14–22] The macromolecular composition provides specific and necessary environmental cues for epithelial and endothelial cells in close proximity to the BM, which consequently lead to proper cell function and homeostasis within the tissue.

The most abundant macromolecule within the BM is type IV collagen, typically making up about half of the total protein composition. Type IV collagen is a nonfibrillar collagen that confers structural integrity[23] and flexibility to the BM network. It is excreted from cells as protomers (protomers are composed of three alpha chains) and a total of six protomers of type IV collagen have been identified.[24] Collagen 1V combined with the other main component laminin provides the structural mesh-like framework which allows for binding of other protein components.[2,11]

Laminin, another major constituent of the BM, has been shown to influence fundamental cell behaviors including attachment,[25,26] proliferation, and differentiation.[27] Two distinct areas of the laminin molecule have a high affinity for cell binding. Laminin molecules are heterotrimers assembled from alpha, beta, and gamma chain subunits with a semblance of a three pronged fork. Different combinations of various alpha, beta, and gamma subunits define a laminin isoform. In total, 15 isoforms of laminin have now been identified.

Nidogen (also known as enactin) stabilizes the BM as it binds to and bridges laminin and type IV collagen.[23,28,29] Nidogen has also been shown to recruit collagen into the assembly of the BM. Two isoforms of nidogen have been identified, and it has been shown that at least one of the isoforms must be present for proper BM development and function.[30] Results from these studies indicate that nidogen is essential for development, maintenance, and function of the BM.

The fourth main constituent of the BM, perlecan, is a heparan sulfate proteoglycan. The presence of heparan sulfate allows these molecules to aid in charge-dependent filtration[31] through the membrane as well as to sequester growth factors.[32,33] Similar to nidogen, perlecan also binds laminin and type IV collagen in the ultrastructure of the BM.

The coordination of the assembly of these four macromolecules, in addition to other minor components, is a complex combination of intermolecular self-assembly and network bonds, which ultimately results in the formation of the BM. Type IV collagen self-assembles into a flexible, highly cross-linked network stabilized by covalent, noncovalent, and disulfide interactions.[34] Similarly, laminin self-assembles into a honeycomb-like structure in the presence of calcium.[35] Laminin, disparate from the other major BM macromolecules, is necessary for initial basement formation.[23,36,37] Perlecan and nidogen are secreted and incorporated into the BM network individually. They bridge the two suprastructure networks of laminin and type IV collagen[10,38] (**Figure 1**).

1.129.2.2. Cellular Adhesion via Macromolecules of BMs

Cells attach to the underlying substrate through adhesion complexes which include focal adhesions. Focal adhesions were first identified as electron dense areas localized to areas of cell attachment to the BM.[39] These complexes are composed of transmembrane glycoproteins that link the cytoskeleton of the overlying cell to the extracellular environment through the BM components. Each type of adhesion involves its own set of interacting proteins and molecules to achieve adhesion to the BM and allow for cell mobility. Both mechanical and key cellular signals are transmitted through the focal adhesion complex, which ultimately impact essential cell behaviors.

Focal adhesions provide a link from the cell to the external ECM and recruit and concentrate signaling receptor molecules at integrin-binding sites. The transmembrane glycoproteins known as integrins have been characterized as one of the main family of receptor molecules involved in formation of adhesion complexes with the BM.[40] Integrins are heterodimers that can bind to several BM proteins, including collagen, laminin, vitronectin, and fibronectin.[41] Integrins are expressed most intensely in basal cells that lay adjacent to BMs.[42–44]

Cell-surface receptors, such as integrins, have two distinct roles: (1) anchor cells to the extracellular environment and (2) activate signal transduction pathways. For example, upon anchoring to the components of the BM, integrins on the cell-surface cluster and signal for the assembly of actin filaments; this suggests a close link between integrin activation and cytoskeleton assembly. This clustering and rearrangement of the cytoskeleton is evident in the formation of focal adhesions.[40] The second role of the cell-surface receptor, namely the activation of signal transduction pathways, occurs from outside-in signaling where a cell-surface receptor binds to a ligand. These signaling events ultimately regulate gene expression and phenotypical responses, such as proliferation or differentiation.[40,45]

Cell-surface receptors interact with well-defined binding sites of the ECM proteins. These specific interactions can be mimicked by fabricating small oligopeptides derivatives of the original protein sequence that are recognized by cell-surface receptors. The tripeptide arginine-glycine-aspartic acid (RGD) has been used widely as an adhesive motif to mediate cell adhesion to synthetic materials (for complete reviews, please refer to Hersel *et al.*[46] and Shin *et al.*[47]). Although it is an oversimplification of the dynamic interface provided by the combination of the BM proteins, RGD can encourage cell adhesion,[48] spreading, and migration.[49] Synthetic incorporation of adhesive ligands with subsequent study of cell behaviors can provide useful information including minimum required ligand density,[50] the relationship between cell–substratum adhesion strength and cell motility,[51] and spatial organization of ligands[49] that encourage desired cell phenotypes (for further review, see Lutolf and Hubbell[52]). In addition, integration of ligands into synthetic matrices enables researchers to understand synergistic interactions between the biochemical and biophysical attributes of the BM.

1.129.2.3. Diseases Associated with BMs

Deviations from normal BM thickness and composition have proven to be important indicators of several disease states.

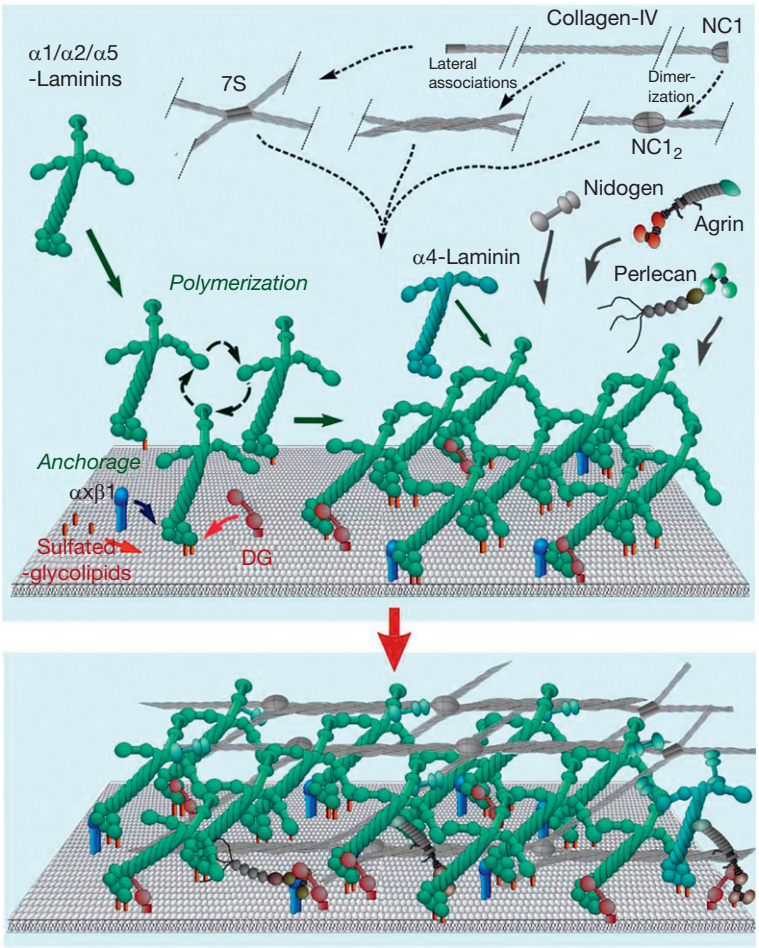

Figure 1 Assembly of basement membrane components. Laminin and type IV collagen self-assemble into covalently cross-linked networks. Nidogen and perlecan incorporate into the networks and provide stability to the matrix. The basement membrane matrix presents specific ligands that interact with cell-surface receptors, such as integrins ($\alpha \times \beta 1$) and dytroglycans (DS), and anchor cells to the BM. Reproduced from Yurchenco, P. D.; Patton, B. L. *Curr. Pharm. Des.* **2009**, *15*, 1277–1294.

Alterations in the BM component amounts and mutations within BM components have been associated with many different diseases including diabetes mellitus,[19,53–56] hyperlipemia, hyperglycemia and other vascular diseases,[57,58] corneal epithelial BM dystrophy,[59] keratoconus,[60–62] autoimmune disorders affecting the epidermal surface, cancer, and many others. Several examples of the importance of the homeostasis of the BM tissue are illustrated below.

Diabetic patients have provided one of the most studied examples in the published literature demonstrating significant alterations of BMs in a wide range of epithelial and endothelial tissues. A thickened endothelial BM in the kidney glomerulus was originally reported in diabetic patients as early as the 1960s[19,63] measuring up to 5 μm in width.[64,65] The increased thickness of BM has now been reported in many different tissues, including cornea (see **Figure 2**). Changes in levels of specific BM components including nidogen and laminin have also been observed when compared to the BM of healthy corneal membranes.[53,66] Disruption of the normal homeostasis of the BM leads to pathogenesis related to cardiovascular and microvascular complications and the development of corneal defects due to retinopathy in the microvasculature of the eye, resulting in blindness.

Mutations in specific BM components have also been shown to disrupt BM function leading to diseased states. One example is Alport syndrome which is a genetic disease that can affect multiple tissues including the kidney, inner ear, and eye. The syndrome is characterized by mutations in the collagen synthesis genes including *COL4A3*, *COL4A4*, and *Col4A5*, which ultimately result in the improper production and assembly of type IV collagen.[67–69] Mutations in the production of type IV collagen eventually result in defects in the normal filtration process of the BM. Further progression of the disease results in a thickened BM that can eventually lead to kidney failure, hearing loss, deterioration of vision, and development of corneal erosions.

The biophysical attributes of the BM and other extracellular matrices have recently been shown to play a direct role in tumor development. Early studies on the role of the microenvironment and tumors focused on specific structural alterations in BMs and how they correlate with tumor growth and prognosis.[70] For example, differentiated squamous cell carcinomas (SCC) retain the ability to deposit BM, whereas

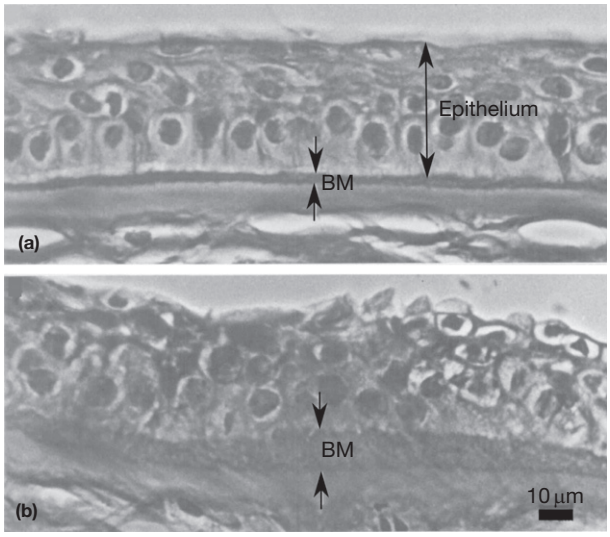

Figure 2 Diabetic cornea exhibits thickened basement membrane. Light micrographs of (a) the basement membrane of normal thickness and (b) thickened basement membrane of a diabetic patient. Tissues were stained with periodic acid-Schiff (PAS). Adapted from Taylor, H. R.; Kimsey, R. A. *Invest. Ophthalmol. Vis. Sci.* **1981**, *20*, 548–553, with permission from IVOS.

undifferentiated SCC have only minimal BM deposition.[71] Tumors exhibiting changes in the protein composition, organization, and integrity of their associated BMs ultimately may lead to alterations in the biophysical properties including topography and stiffness. This has been demonstrated in several different cancers, such as breast cancer, where there is a stiffening of matrix by an increase in collagen deposition and ECM cross-linking.[72–74] Even so, each type of tumor will need to be analyzed individually to determine the optimal biophysical properties to inhibit the tumorigenic phenotype. Neuroblastoma cells cultured on ECM of increasing stiffness exhibited decreased proliferation as well as inhibition of transcription factors involved in oncogenic proliferation.[75] These and other reports have now demonstrated that changes in the biophysical properties of the tumor microenvironment can inhibit or induce the formation of tumors and even impact the response to treatment.[76–79]

In summary, changes in the thickness and composition of the BM most likely impact the physical attributes including topography and stiffness, which then in turn impact the behavior of the overlying cells. On the basis of these observations, recent reports have sought to characterize the normal biophysical attributes of both epithelial and endothelial BMs in order to better understand how these properties influence cell function. Characterization of the biophysical attributes of normal BM is therefore essential to begin to elucidate the impact of changes in the BM as it is related to normal tissue homeostasis for both tissue-engineering applications and the development of novel therapeutic strategies.

1.129.2.4. Biophysical Cues of BMs: Elastic Modulus

As previously described, the extracellular microenvironment including the BM provides essential cues that impact cell behavior. Recent developments have now emphasized the importance of examining the biophysical cues and the impact on essential cell behaviors. Biophysical cues include mechanical forces, electrical stimuli, and other physical properties including topography and elastic modulus.[80] Although each of these parameters is important, the elastic modulus and topographic features of the BM and ECM are the focus of many ongoing studies in the field because they are definable biomaterial properties.

The elastic modulus is a measure of the relative stiffness of a material. One commonly reported elastic modulus is Young's modulus which measures the tensile elasticity of a material. Young's modulus (E) is calculated as the extent of deformation, or relative change in length (strain) for an imposed stress (force/area). Elastic moduli, including Young's modulus, can be measured using macroscopic methods (disk rheometer, tensile testing, bulge testing, ultrasonic elastography, and tomography), or microscopic methods (atomic force microscopy (AFM), microindentation, and nanoindentation).[81–83] With increasing frequency, especially in biology, the relative stiffness of a material is described in terms of compliance rather than elastic modulus. Compliance is the degree to which an elastic body is deformed by an applied force and is inversely proportional to the elastic modulus. Soft, or compliant, materials have low modulus values. For example, gelatin has a reported range of moduli of 15–20 kPa.[84] Hard or stiff materials have higher modulus values, such as high-density polyethylene, which has a modulus of about 7 MPa.[85] Some representative elastic modulus values for tissues are brain (500 Pa), muscle (10 kPa), collagenous bone (100 kPa),[86] and trabecular bone (5–15 GPa).[87] See **Table 1** for more examples.

Much of the literature has focused on 'bulk' modulus measurements of whole tissues as opposed to local modulus of individual layers within the tissue. Although the modulus of whole tissues provides information that aids in understanding how mechanical properties affect cell behavior, it does not necessarily represent the local mechanical cues presented to epithelial or endothelial cells. Therefore, current studies have examined and characterized the local elastic modulus of the supporting BMs in order to provide a biologically relevant range of modulus values that can be incorporated into synthetic matrix design. For example, in the human cornea, a bulk modulus of 0.2–1 MPa has been reported.[93] However, local modulus measurements using AFM have demonstrated that each layer within the cornea has a unique modulus value. Specifically, the human anterior corneal BM has a modulus of 7.5 kPa.[100] Studies have also incorporated *in vivo*-like conditions during measurement of the elastic modulus to more closely replicate the natural cellular environment. Using a bulge test, which applies pressure to the cornea, Danielsen[92] reported the modulus of human Descemet's membrane as 2.57 MPa. Other reported BM modulus measurements highlight the range of modulus values associated with BMs spanning tissue and species: chick inner limiting membrane 1–3 MPa,[15] mouse retinal inner limiting membrane 3.8–4.1 MPa,[15] and tectorial membrane 24–210 kPa.[97] These values indicate the heterogeneity of elastic modulus values between species and tissues indicating that the biophysical features may be involved in extracellular signaling cues to the cells which ultimately lead to downstream signaling events.

Table 1 Compilation of measured elastic modulus for various tissues

Species	*Tissue*	*Method*	*Modulus (kPa)*	*References*
Chick	Chick inner limiting membrane	AFM	950–3300	15
Fish	Lamellipodia of fish epidermal keratocytes	AFM	10–55	88
Human	Platelets	AFM	1–50	89
Human	Endothelial cells	AFM	1.4–7	90
Human	Normal breast tissue	Indentation	3.25	91
Human	Fibrodenoma breast tissue	Indentation	6.4	91
Human	Descemet's membrane	Bulge test	2570	92
Human	High-grade IDC tumor breast tissue	Indentation	42.5	91
Human	Cornea	Bulge test	200–1000	93
Human	Normal trabecular meshwork	AFM	1–34	94
Human	Glaucoma trabecular meshwork	AFM	110	94
Monkey	Monkey lens	AFM	0.4–3.2	95
Mouse	Skeletal muscle cells	AFM	25	90
Mouse	Edges of motile 3T3 fibroblasts	AFM	12	96
Mouse	Retinal inner limiting membrane	AFM	3810–4070	15
Mouse	Tectorial membrane	AFM	24–210	97
Porcine	Gelatin (pork skin)	AFM	20 in water 1800 in 85% propanol	84
Porcine	Cartilage	AFM	2600	98
Rabbit	Cardiac cells	AFM	100	90
Rat	Hippocampus	AFM	0.137–0.308	99

Pelham and Wang are the first known group to initiate studies incorporating varying modulus substrates (10–80 Pa) and their impact on cell behavior. Significant differences in cell spreading motility and phosphorylation pathways were observed with murine fibroblasts and rat kidney epithelial cultures on substrates with varied elasticity. They observed significant differences in cell spreading, motility, and phosphorylation pathways.[101] Since then, the effects of elastic modulus on different cellular fates, such as cytoskeletal organization, differentiation, migration, and proliferation, have been demonstrated. In general, cells show increased adhesion, spreading, and cytoskeletal organization when the stiffness of the substrate is increased. This behavior has been observed with various cell types, such as fibroblasts,[102–104] smooth muscle cells,[105–108] endothelial cells,[109] and chondrocytes.[110] Maximized spreading and adhesion may not be the desired cell behavior depending on the application. For example, Engler *et al.* hypothesize that cell spreading equal to half of the maximum spreading is optimal for cell attachment and migration. They demonstrated that the half-maximum spreading of smooth muscle cells occurs when the modulus of the substrate mimics the native tissue,[111] further signifying the importance of the native mechanical properties of tissues.

Cell differentiation has been reported to be directly affected by modulating the elastic modulus of the substrate on which the cells reside. Working with mesenchymal stem cells (MSCs), Engler *et al.*[86] showed that MSCs' ability to differentiate is highly dependent on the stiffness of the substrate: on soft matrices with modulus close to brain tissue cells differentiated into neural lines, on stiffer surfaces that mimic muscle tissue cells differentiated into muscle lines, and on rigid matrices that mimic bone cells differentiated into osteoblasts. Georges *et al.*[112] tested the influence of stiffness *in vivo*, by showing the differentiation of MSCs into fibrogenic myofibroblasts when the stiffness of the liver is altered after injury. Other examples that demonstrate how differentiation is modulated by the stiffness of the substrata include neurogenesis,[113] tubulogenesis,[111,114,115] angiogenesis,[116,117] and spheroid formation.[118]

The modulus of the substrata has also been reported to influence cellular migration.[119] Experiments with neutrophils demonstrated that their migration is optimal on substrates of biologically relevant stiffness of 4 kPa.[120] They hypothesized that, on softer surfaces, the low level of cellular adhesion prevents traction forces, and on stiffer substrates, the adhesion is stronger and more established, preventing migration.[120] Cell directed migration through durotaxis has also been observed toward areas of increased stiffness.[121,122] In addition, remote cell–cell sensing of the underlying substrate has been reported in response to the strain created by migrating neighboring cells when cultured on soft substrates.[123]

Proliferation of the cells is also influenced by the modulus of the matrix.[124] Experimenting with neuron–astrocyte cocultures, Georges *et al.*[125] observed that, on stiff substrates, astrocytes significantly outnumber neurons, overtaking the culture, while neurons exhibited enhanced growth when cultured on softer substrates with a modulus within the range reported for brain tissue (several hundred Pascals). These studies provide evidence to support the importance of elastic modulus as an essential component in the design of biomimetic artificial BMs for the design of prosthetics, wound healing applications, and the creation of improved *in vitro* culture models.

1.129.2.5. Biophysical Cues of BMs: Topography

In addition to the elastic modulus of the BM and ECM, cells also receive biophysical cues from the topographic features, or structure, on which the cells reside. The BM has a three-dimensional (3D) topography composed of fibers, pores, and elevations on the order of tens to hundreds of nanometers.[126]

Table 2 Compilation of basement membrane feature dimensions for various tissues

Species	*Tissue BM*	*Mean feature height (nm)*	*Mean fiber diameter (nm)*	*Mean pore diameter (nm)*	*References*
Bovine	Glomerulus	–	3–15	9.8 ± 3	127
Bovine	Tubular	–	3–15	11.4 ± 4	127
Canine	Cornea	150 ± 41	18 ± 9	32 ± 18	126
Canine	Descemet's	115 ± 30	15 ± 7	24 ± 8	126
Human	Cornea	182 ± 49	46 ± 16	92 ± 34	129
Human	Descemet's	131 ± 41	31 ± 9	38 ± 15	129
Human	Foreskin	–	24 ± 8	40 ± 17	130
Human	Amniotic	–	9–11	45 ± 33[a]	131
Human	Bronchial epithelium	–	–	1500 ± 80[b]	132
Mouse	Oral mucosa, gingiva, and tongue	–	30	–	133
Porcine	Aortic valve	–	27 ± 12	38 ± 24	134
Rat	Glomerulus	–	6.4	9.7	135
Rat	Renal Bowman's capsule	–	7	14.1	135
Rat	Renal tubular	–	6.8	13.1	135
Rhesus	Cornea	190 ± 72	77 ± 39	71 ± 44	136
Rhesus	Aorta	506 ± 119	30 ± 11	62 ± 37	14
Rhesus	Carotid	319 ± 149	31 ± 11	60 ± 42	14
Rhesus	Saphenous	112 ± 31	27 ± 8	38 ± 16	14
Rhesus	Bladder	178 ± 57	52 ± 28	82 ± 49	137
Synthetic	Matrigel	162 ± 52	69 ± 35	105 ± 70	136

[a]Distance between branch points of globular collagen domains. Not exactly pore diameters, but on the same scale.
[b]Values reported as 95% confidence interval rather than standard deviation.

In comparison, a single cell can average 10–100 μm in length depending on the cell type. Thus, a cell is approximately two to four orders of magnitude larger than the topographic features on which the cell resides *in vivo*. This size difference enables a single cell to interact with hundreds to thousands of individual nano- and submicron-scale features.

Across different species, tissues, and anatomic locations, the scale of features of the BM is relatively consistent with a few notable exceptions (Table 2). The BM of the bovine glomerulus has significantly smaller fiber and pore sizes (3–11 nm fiber diameters[7,135]), which are most likely involved in the specific function of the tissue which involves filtration. Also, in both porcine[134] and rhesus[14] blood vessels, the pore and fiber diameters (~24–63 nm) are significantly less than pore and fiber diameters found in BMs of the bladder, foreskin, and anterior BM of the cornea. Differences have also been reported within a tissue. The human cornea topographic features vary in scale between the anterior BM and Descemet's membrane. On average, Descemet's membrane has smaller average pore (38 nm) and fiber (31 nm) diameters than the anterior BM (92 nm pore and 44 nm fiber diameters).[129] These structural differences may have important effects on the ultimate function of the overlying epithelium and endothelial cells in the human cornea.

Understanding the impact of this range of topographical features on cellular behavior has the potential to impact many biological applications within tissue engineering. It is critical to first examine how a wide range of topographic feature sizes modulate cell behavior. Initial steps have been taken to examine how BM range topography to micron-scale topography affects cellular behavior. Examples highlighted in Section 1.129.4 are categorized by the scale of the topography which accentuates the differences in cell behavior depending on the scale of the underlying topography. To fully appreciate how the scale of the topography influences cell behavior, we must first understand how topographical features are fabricated and the advantages and limitations associated with different fabrication techniques. In the following section, we highlight some of the main nanofabrication methods used in bioengineering and briefly discuss current methods under development that will contribute to advancements in the field of tissue engineering.

1.129.3. Nanostructure Fabrication

Nanofabrication processes have historically taken cues from the microelectronics industry. From classical processes such as photolithography and electron-beam lithography (EBL) to next generation lithography (NGL) such as nanoimprint lithography (NIL), the bioengineering field has exploited a multitude of fabrication techniques to develop topographically patterned substrates for cell studies.[138–140] A spectrum of topographical patterns with a wide range of lateral dimensions, from tens of nanometers to hundreds of micrometers, and various geometries, such as pores and fibers, have been successfully fabricated. Although the microelectronics industry has the capability to produce nano- to micron-scale features over very large areas (several square centimeters and larger), the availability of current industrial lithographic techniques are not accessible to most bioengineering research groups. Bioengineering research is limited to more modest nanofabrication methods that require researchers to use some creativity in the design of nanopatterned substrates. Depending on the substrate design needs, one fabrication technique may produce samples faster or have more flexibility in the composition compared to another technique. In addition to patterning processes, steps are often taken to transfer the pattern into the underlying substrate or into an alternative material. Pattern

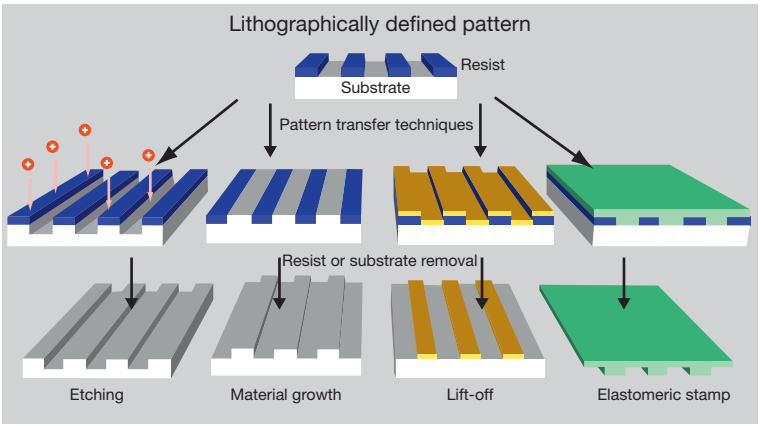

Figure 3 Schematic highlighting some of the options in pattern transfer using lithography. The pattern can be directly etched into the underlying substrate, or used as a mask for substrate regrowth, or used as a template for metal deposition and subsequent lift-off, or used as a master for fabrication of elastomeric stamps. Adapted from Chen, Y.; Pepin, A. *Electrophoresis* **2001**, *22*, 187–207.

transfer can be achieved through different processes including etching, substrate material regrowth, inorganic deposition and lift-off, and elastomeric molding (Figure 3).

Choosing the lithography and pattern transfer techniques from among the many options available is dependent on the biological application and available resources to produce the substrates. Each cell study may require different substrate design criteria in order to confirm a hypothesis. Additionally, there are a number of different nanofabrication options available to meet those design parameters. Some general design parameters and an array of nanofabrication processes are discussed below.

1.129.3.1. Design Parameters

One quality of nanofabrication that makes it useful for cell studies is its high fidelity and reproducibility for making nano- to micron-scale patterns. How best to take advantage of this quality depends on the intended bioengineering application. A few simple guidelines in substrate design can eliminate or reduce uncertainty in cell data due to uncertainty in the substrate itself.

First, the substrates must have controlled topographic feature dimensions, such that the resulting cellular observation can be attributed to a narrow range of sizes within a low percentage of error (<10%). For example, SV40-transformed human corneal epithelial cells (SV40-HCECs) demonstrate increased adhesion when cultured on 220 ± 21 and 453 ± 18 nm ridges (400 and 800 nm in pitch) compared to 680–2150 nm ridges (1200–4000 nm in pitch).[141] This observation was elucidated by using well-defined topography. In contrast, a substrate with large variations in feature dimensions, on the order of several hundred nanometers, would not have allowed for the observed quantifiable differences in adhesion. There is some criticism in using well-defined and ordered structures, mainly because this does not necessarily mirror the biophysical attributes of the native BM. *In vivo*, cells encounter a wide range of topographic length scales; however, by using a reductionist approach, we can better understand how each topographic length scale individually and in combination affects cellular response. Understanding how a specific lateral dimension modulates cell behavior will prove useful in design of improved cell culture environments and ultimately design of improved prosthetics.

In addition to well-defined lateral dimensions, the vertical dimension (or depth) of the topography needs to be well defined, with enough depth to optimally elicit a cellular response. Several studies have indicated the importance of depth on contact guidance and how this acts to amplify the cellular response to lateral dimensions.[142–147] In contrast, shallow features with limited depth can inhibit cellular response to topography.[144] Fabricating features with small lateral dimensions (replicating the range of nanoscale features quantified from BMs) with appreciable depths has been logistically difficult to obtain. As the lateral scale decreases and the aspect-ratio increases, problems occur with patterning (such as collapsing of features), etching, speed of production, and overall cost. In some cases, compromising on the overall design or substrate throughput is necessary in order to produce usable topographically patterned substrates for thorough cell studies. To address some of these problems, techniques are being used to easily produce nanotopography with more structurally reliable geometries, such as wave-like structures and 3D porous scaffolds.

The third critical design parameter is presenting large enough patterned areas to include a robust number of cells within each study. For example, surface area of the topographic patterns must be large enough to collect data from thousands to millions of cells for protein or RNA studies. Other phenotypical responses such as migration and morphology do not require as many cells, and therefore do not require as large a patterned surface area. As a cell is typically on the order of 10–100 μm, well-defined topographic features must cover a range from a square millimeter to several square centimeters, depending on the intended application. Patterning large areas can limit the fabrication techniques used for substrate production as several processes including EBL and AFM direct write are time consuming when fabricating at the multiple square millimeter scale. In addition, facile and rapid fabrication processes are desirable in order to produce many substrates for large-scale cell experiments.

As nanolithographic techniques improve (mainly driven by the microelectronics industry's objective to produce smaller transistors), so do the techniques for production of nanobiomaterials. Discussed below are some traditional lithographic fabrication processes and some techniques devised specifically for tissue-engineering applications.

1.129.3.2. Classical Lithography

Two types of classical exposure methods are commonly used for patterning of nano- to micron-scale structures and determining which method to use is dependent on production speed and expense. The first method is a serial method where a scanning focused beam patterns individual 'pixels' and is typically used in making masters and masks for other lithographic techniques. The slow speed of the serial method limits the productivity of the process and makes it cost prohibitive for mass production purposes.[148] On the other hand, serial methods typically can produce smaller feature dimensions and allow for patterning of complex designs. A second type of exposure process is a parallel replication method where substrates are exposed to irradiation through a mask. This method has increased throughput and is routinely used for mass production. One disadvantage to the parallel lithographic techniques involves the high cost of the equipment (such as radiation sources).[149]

1.129.3.2.1. Electron-beam lithography

EBL was first reported as a technique for patterning substrate materials as early as the 1960s[150,151] and has been used for patterning nano- to micron-scale features for cell studies for the past 20 years.[145,152–154] Pattern transfer using EBL is achieved through a focused electron beam which serially exposes a polymeric resist pixel-by-pixel to form a custom pattern.

The advantages of EBL include precise control over lateral dimensions down to the 5–7 nm level,[155–157] and flexibility in patterning of complex geometries. However, with a patterning speed of approximately 10^7 pixels s^{-1},[158] EBL is a very slow process making it too expensive for mass production. Additionally, stitching errors (discontinuities) can create problems when patterning large areas.[159] With its ability for precise control of patterning nanometer length scales, EBL is a principal technique used for producing master templates that are subsequently used in higher-throughput nanofabrication processes, such as photolithography and NIL.

1.129.3.2.2. Photolithography

Similar to EBL, photolithography includes identical fabrication steps with one important difference: instead of an electron beam 'writing' a pattern, in photolithography, a mask is used to expose a polymeric resist to light in specific areas simultaneously. Early applications of photolithography were limited by the wavelength of the light used for exposure: several hundreds of nanometers. In order to fabricate substrates with topographic features in the nanometer range, new techniques that parallel traditional photolithography have been developed. Extreme ultraviolet (EUV) lithography uses radiation with wavelengths of 10–120 nm (typically around 13.4 nm,[160]) to pattern sub-100 nm features.[161,162] Combining EUV with interference lithography (IL) can achieve even smaller line widths (38 nm and below,[163] see review Solak[164]). X-ray lithography also uses small (0.5–4 nm) wavelength radiation from synchrotron radiation or laser-induced plasma sources to pattern high aspect-ratio structures into resists.[149,165]

Photolithography has been used since the 1980s[166] to define micron-scale topographically patterned substrates for cell studies. It is still used today as one of many techniques that can fabricate nano- and micron-scale features. The major advantage of photolithography is the rapid substrate production (great for producing many substrates for cell studies). However, the expensive equipment including masks are drawbacks to these processes which have pushed the development of new, inexpensive lithographic techniques.

1.129.3.3. Next Generation Lithography

In order to circumvent some of the cost and production speed problems associated with classical lithographic processes, a number of 'NGL' processes are in development to provide inexpensive alternatives while maintaining the high rate of substrate fabrication.[149] A few examples of NGL approaches are NIL, soft lithography, and self-assembly of biological, organic, and inorganic molecules. Many of these approaches are already being used for fabrication of nano- to micron-scale topography for biological applications.

1.129.3.3.1. Nanoimprint lithography

NIL is a nanoscale analog of micron-scale compression molding (used in industries such as compact disc manufacturing,[167]). Briefly, NIL is a high-throughput process whereby a polymeric resist layer is patterned using a master template as a stamp. The master is commonly fabricated by EBL or other high resolution processes. The master is then used to imprint under conditions such as (1) elevated temperatures and pressures (so that the resist can flow into the spaces of the master) or (2) UV light (to photo-activate polymerization of the resist). In some cases, the molded resist or polymer can be used directly for cell studies.

Chou *et al.* were pioneers of NIL, demonstrating dot and line arrays down to tens of nanometers in dimension.[167,168] They continue to make strides in production of high-throughput NIL techniques such as laser-assisted direct imprint (LADI) where no resist is needed to directly pattern silicon substrates.[169]

1.129.3.3.2. Soft lithography

Soft lithography (also known as micro-contact printing) uses an elastomeric stamping technique to print an 'ink' onto either a surface or a mold and shape a polymeric film. Replica molding using a silicone-based stamp has been used to fabricate submicron features[170] and sub-100 nm features (using a composite stamp).[171] Recently, perfluoropolyethers, an alternative to silicone, have been used to create sub-200 nm features with higher aspect ratios than conventional silicone.[172] These soft lithography systems show promise in producing inexpensive nanostructures of high quality with speed.

1.129.3.3.3. Colloidal lithography

Colloidal lithography is a type of 'bottom-up' approach to patterning nano-, submicron-, and micron-scale arrays. Colloidal crystals are assembled through many different processes

including sonication,[173] spin coating,[16,174] and epitaxial growth.[175] The colloidal templates are then used for metal deposition,[16] or used as masks for etching into substrate materials such as silicon. Facile fabrication of sub-500 nm 3D patterns can be done using polystyrene colloids.[176,177]

1.129.3.3.3.1. Electrospun fibers

Electrospinning of collagen or other polymeric materials is a useful process to fabricate nano- to micron-scale fibers for cell culture. This method has recently gained prominence, as biologists are investigating methods to incorporate topography or biophysical cues and may not have access to alternative nanofabrication processes. The common electrospinning fabrication technique includes a syringe from which a polymeric base material is secreted, a collector onto which the fibers are spun, and a bias voltage that attracts the polymeric stream to the collector. By varying solution concentration, flow rate, applied voltage, needle size, distance between needle and collector, and collector rotation speed, the fiber size and orientation can easily be manipulated (**Figures 4** and **5**).

Electrospinning is a simple, cost-effective process that can produce fibers with diameters from tens of nanometers to several microns. Calfskin type I collagen has been electrospun into fibers with diameters of 100 ± 40 nm and been used to show that smooth muscle cells can fully infiltrate the porous scaffold. The orientation, either random or ordered, can be controlled with an array of biocompatible polymers.[178] In addition, many biologists argue that electrospun fibers more closely mimic the natural topography of the ECM to which cells are exposed, making this nanofabrication technique widely used and accepted.

1.129.3.3.3.2. Molecular self-assembly

Molecular self-assembly is the spontaneous arrangement of molecules into well-defined nanostructures that are stabilized by noncovalent interactions.[179] In nature, DNA alpha helixes and protein crystal structures are just some examples. For instance, type I collagen forms fibrils with diameters on the order of 5–500 nm.[180,181] Organic compounds, such as block copolymers, will also self-assemble into nanostructures such as lamellae, spheres, or cylinders depending on the composition of each block and the interactions between blocks. Self-assembled molecules can be used on an as is basis, or modified to be used as masks or templates for further fabrication processing (**Figure 6**).

1.129.3.3.3.3. Phase separation

Phase separation uses the temperature-sensitive nature of dissolved polymers to form polymer rich and pore phases. Removal of solvent solidifies the polymer into polymeric islands or fibrils.[140] Different morphologies and porosities can be produced by varying the polymer concentration, types of polymers and solvents, and phase separation temperature.[140] For example, poly(L-lactic acid) (PLLA) dissolved in tetrahydrofuran (THF) was phase separated, solvent exchanged with water, then freeze-dried to yield a highly porous material with fibers on the order of 50–500 nm in diameter.[182] In some cases, pH can induce phase separation and form nano- to micron-scale topography.[183] Hajicharalambous *et al.*[184] used pH-induced phase separation to form nano- and submicron porous structures for cell migration and proliferation studies.

1.129.3.4. Other Methods

There are many additional methods that are used or are in development for use in tissue engineering. Some examples include sub-100 nm wave-like features called wave-ordered structures (WOS) that are formed by low-energy ion bombardment. The method is a simple and rapid parallel process that can pattern large areas for statistically robust cell

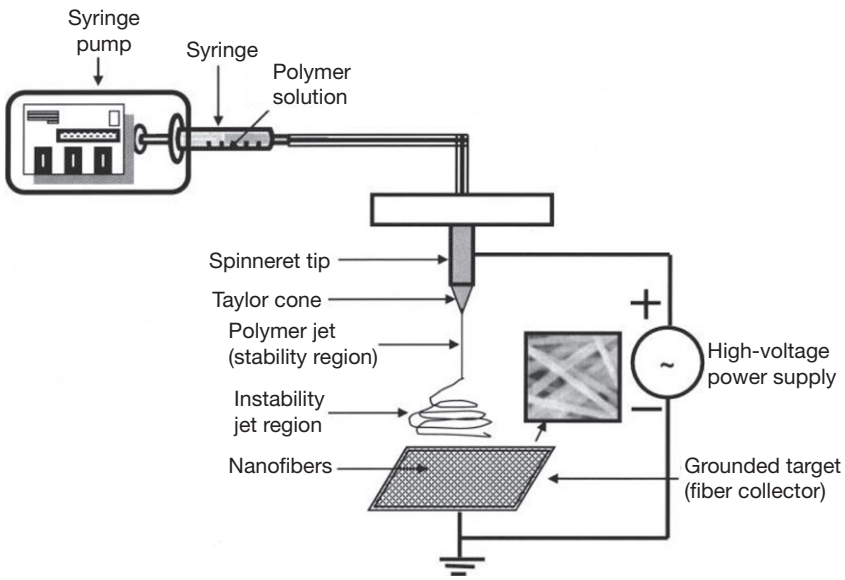

Figure 4 Schematic of the electrospinning process for making fibers. A syringe extrudes a polymer dissolved in a solvent through a tip. The voltage applied across the tip and target helps to produce a jet stream of polymer. While the polymer jet is stretched, the solvent evaporates quickly and forms the ultrafine fibers. Reproduced from Murugan, R.; Ramakrishna, S. *Tissue Eng.* **2006**, *12*, 435–447.

experiments[185–187] (Figure 7). Physical vapor deposition, specifically glancing angle deposition (GLAD), can produce nanocolumn arrays.[188] Direct writing techniques (such as with an AFM) of polymeric materials can form well-defined micron-scale features with irregular and/or custom geometries.[189] Even techniques using native tissues can produce nanotopography. Soft tissue protein extraction and gelation (pH-induced or temperature-induced gelation) show topographical features similar to dimensions found in ECMs of multiple tissues.[190]

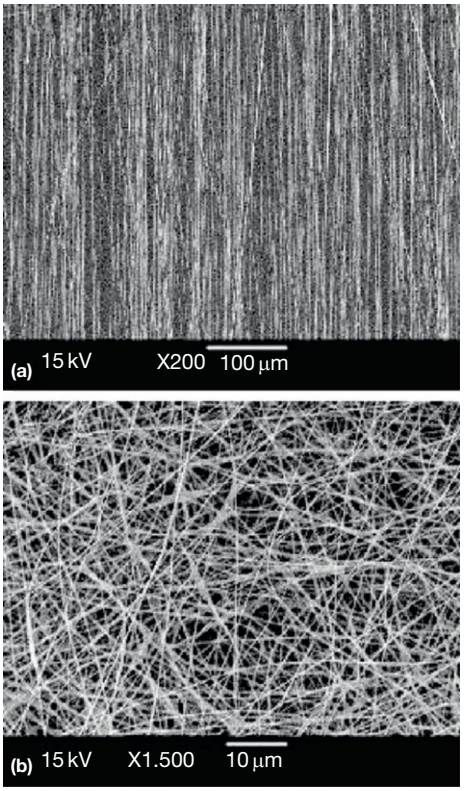

Figure 5 Both (a) ordered nanofibers and (b) random nanofibers can be produced using electrospinning techniques as shown above in these SEMs. Reproduced from Yang, F.; Murugan, R.; Wang, S.; Ramakrishna, S. *Biomaterials* **2005**, *26*, 2603–2610, with permission from Elsevier.

1.129.4. Cellular Response to Topographic Cues with Dimensions from Nano- to Micron-Scales

It has been well established over the past 100 years that cells exhibit contact guidance to structural and topographic elements in their environment. Contact guidance is defined as the elongation or morphological alteration of a cell in response to physical cues. This response is typically measured in the total number or percentage of cells elongated and aligned in a defined direction with respect to the underlying topography.[191,192] Cell guidance by substrate features has been studied as far back as the early 1900s when Harrison[193] reported cells aligning along spider web fibers. In the past 20 years, the impacts of both the shape and scale of topographic cues have been more closely examined.[143,194–204] As fabrication and substrate design techniques have improved, researchers have developed surfaces ranging from micron down to the nanoscale with the goal of more closely mimicking the biophysical environment that the cells are exposed to *in vivo*. One particular area of intense interest for both epithelial and endothelial tissues is the characterization and replication of the topographic features of the BM.

Several groups have successfully characterized and measured the topographic features of the BM from different species, tissues, and even different locations within the same tissue.[11,14,128,129,131,134,136,137,205,206] Using techniques such as transmission electron microscopy (TEM), scanning electron microscopy (SEM), and AFM, it has been observed that the BM is composed of a complex 3D environment consisting of both pores and fibers. Overall, the average dimensions of the topographic features of the native BM are similar in that they encompass both the nano- and submicron-scale range. However, in some tissues, significant variations occur, such as the pore size in both porcine heart valve and rhesus macaque vascular tissue.[14,134]

These small but significant differences in BM topography may have a profound impact on the phenotypic response of the overlying cells and may account for variations observed between or within the same tissue *in vivo*. For example, the differences in pore and fiber size reported in vascular tissues may partially account for the heterogeneity in endothelial cell function. Other significant findings include the variations observed in pore size within the two BMs in the human cornea.

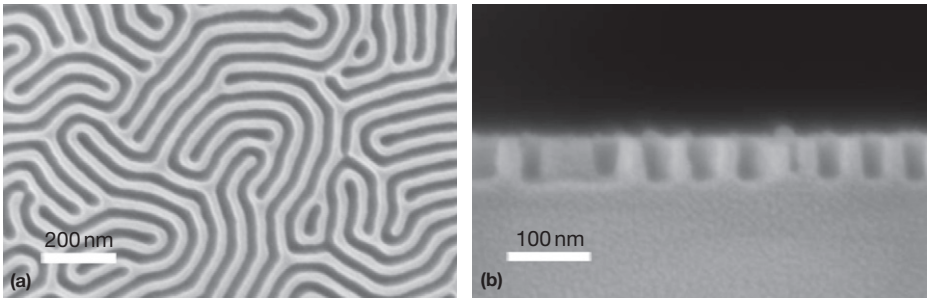

Figure 6 Self-assembly of block copolymers can be used to fabricate nanoscale structures over larger areas. In this example, the block copolymer poly (styrene)-*block*-poly(methylmethacrylate) (PS-*b*-PMMA) self-assembles into lamellae structures with a pitch of 48 nm. The PMMA block can be selectively removed to leave the PS block behind, which can be used as a mask to etch into the silicon substrate. SEMs show the top-down (a) and cross-sectional views (b) of the resulting lamellae pattern in silicon.

The average anterior BM (epithelial cells) contains pores with an average size that is double than that of the Descemet's BM (endothelial cells), which also suggests that topographic cues from the BM may be involved in guidance of cell function. These *in vivo* BM measurements have allowed the measured features to be incorporated into substrates to further examine specific cell behaviors.

Although early work focused on large micron-scale topography, recent studies have investigated smaller topography that falls into the range of measured features within the BM. A wide range of reports in the literature have observed that modulation of fundamental cell behaviors including proliferation, adhesion, morphology, and differentiation is subject to the dimensions, geometry and feature size of the topographical cues. Historically, studies involving substrates with micron size features were reported first, and as fabrication techniques have improved, more recent studies have focused on impact of cell behavior at the nanoscale.



Figure 7 Nanofeatures known as wave-ordered structures (WOS) can be fabricated with dimensions in the range of the smallest features measured in the basement membrane. WOS are formed by low-energy ion bombardment and can be patterned over large areas. Surfaces were kindly provided by Wostec, Inc. (Moscow, Russia).

To examine the impact of topographical cues, we have described in detail how the scale of topographic features can significantly modulate cell phenotype. Additionally, we consider the possible impact that the incorporation of relevant biophysical cues may have on the future design of improved tissue-engineering scaffolds.

In addition to the scale of topographic cues, the shape or geometry of the topography is also presented to the overlying cell. Although relevant, only limited studies have specifically investigated the impact of the geometry on cellular behavior. Notably, HCEC adhesion strength was tested by applying a shear force to cells that were seeded on topographically patterned ridge–groove features and pores of similar pitch. Cells on anisotropic ridges and grooves compared to cells cultured on pores with the same size pitch demonstrated similar adhesion strength.[141,207] Human umbilical vein endothelial cells (HUVECs) have also been utilized in studies investigating whether the shape or scale of features is relevant for changes in proliferation rates. HUVEC proliferation is significantly decreased on substrates containing features 800 nm or smaller regardless of the geometry,[208] suggesting that the scale rather than the geometry of the underlying topography is the most influential factor on cell behavior. On the basis of these observations, we have focused on the scale (lateral and vertical dimensions) rather than the geometry (**Figure 8**).

1.129.4.1. Micron Range (>1000 nm Widths)

There are some notable examples of micron-scale topography significantly influencing cellular function in comparison to flat controls. Some of the earliest work looking at micron-scale topographical effects on cellular behavior examined fibroblasts,[209] neuroblastoma cells,[210] and neutrophil leukocytes.[211] Brunette *et al.* began investigations into how epithelial cells would be affected by micron-scale ridge–groove features. They observed cell contact guidance along ridges and outgrowth of human gingival explants in the direction of the long axis of the topography.[166] Other studies have used similar

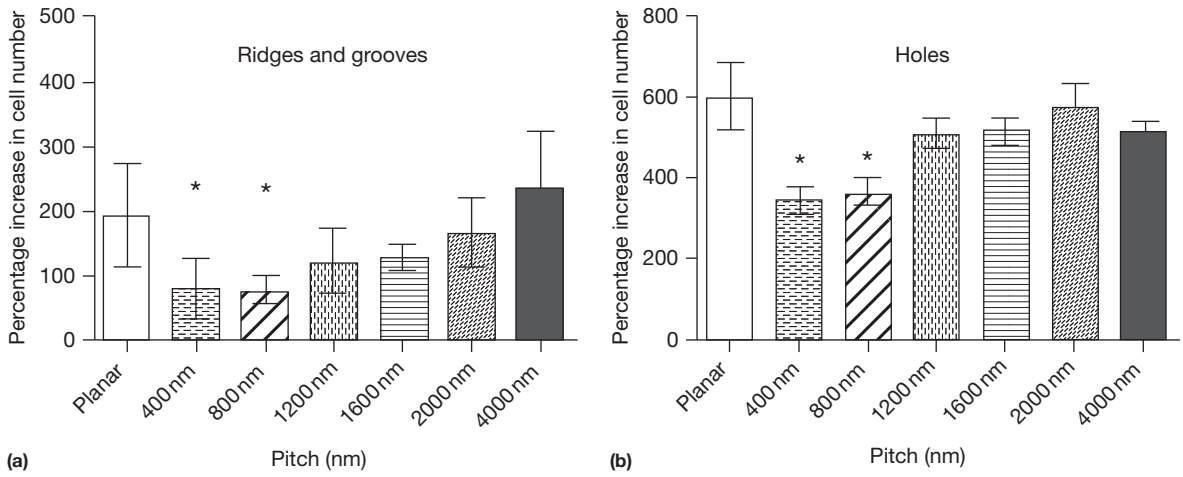

Figure 8 HUVECs demonstrate reduced proliferation rates on sub-1200 nm pitch features compared to micron-scale features and flat controls. The proliferation response was only dependent on the scale of the features: similar proliferation rates were observed for cells cultured on both ridge–groove (a) and pore (b) structures of the same pitch. Reproduced from Liliensiek, S. J.; Wood, J. A.; Yong, J.; Auerbach, R.; Nealey, P. F.; Murphy, C. J. *Biomaterials* **2010**, *31*, 5418–5426, with permission from Elsevier.

micron-scale ridge–groove features, including investigation into proper functioning macrophages, which are white blood cells that encapsulate (phagocytose) and digest debris and pathogens.[212] P388D1-macrophages showed increased cell attachment and phagocytosis when cultured on micro-grooved silicon surfaces (2–10 μm widths) compared to flat controls. In addition, as depth increased, so did phagocytosis.[212] This suggests that the addition of topographical cues aids in proper cell function of macrophages and by controlling the scale of the features (in this example, depth), the cell response can be modulated.

Other cell types cultured on micron-scale topographically patterned substrates also have demonstrated improved cell function and expression of characteristic protein markers. For example, osteoblasts, like many cell types, exhibit increased cell attachment to micron-scale topography (pores of 10–100 μm in diameter) compared to flat controls.[213] Osteoblasts also express increased levels of osteocalcin and alkaline phosphatase, two indicators of normal osteoblast phenotype, when cultured on micron-scale pores with submicron roughness compared to smooth micron pores and flat controls. This suggests that the submicron scale has an important role in proper osteoblast phenotype, and the combination of micron and submicron-scale topography has synergistic effects on cell behavior.[213] These studies show the impact that substrate topography can have on cell behavior and have encouraged researchers to probe the effects of even smaller feature sizes.

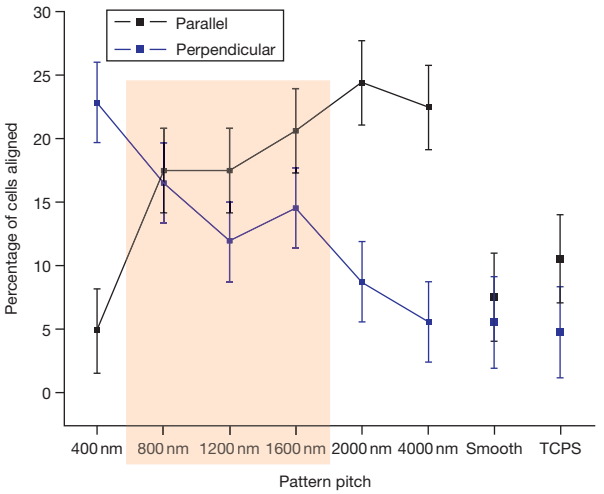

Figure 9 Human corneal epithelial cells in EpiLife® basal medium demonstrate transitional response to the underlying topographically patterned substrate when the feature dimensions increase from the submicron scale to the micron scale. HCECs align preferentially perpendicular to the 400 nm pitch groove–ridge features but prefer to align parallel to 2000 and 4000 nm pitch features. Cells align both parallel and perpendicularly on intermediate features of 800–1600 nm pitch. Adapted from Teixeira, A. I.; McKie, G. A.; Foley, J. D.; Bertics, P. J.; Nealey, P. F.; Murphy, C. J. *Biomaterials* **2006**, *27*, 3945–3954, with permission from Elsevier.

1.129.4.2. Submicron (400–1000 nm Widths)

With an abundance of data showing the impact of micron-scale topography on cellular behavior, numerous studies have taken one step closer to BM scale topography and have explored the effects of submicron features. Although these substrates do not directly mimic the scale of topographical features measured within the normal BM, they do provide insight into the importance and possible function of other topographic cues presented to the cell *in vivo*. For example, the BM can have a different topographical make-up during states such as wound healing or as a result of disease. Recent studies that use submicron and micron features have observed a transition zone in the range of 600–800 nm where differences in fundamental cell behaviors are observed. For example, HCECs cultured in media without serum have a significant population of cells that align perpendicular to ridge topography with widths of 70–400 nm. HCECs on substrates with ridge widths of 1–2 μm orient preferentially in the direction of the topographic cues. On topography with ridge widths in between the two ranges noted above (i.e., 600–800 nm), HCECs demonstrate populations of cells that align both parallel and perpendicular to the underlying ridge–groove structures[214] (**Figure 9**). It should be noted that this 'transition' in cell behavior from nano- to micron-scale may be cell-type specific and dependent on the culture environment. When a transition in cell behavior is observed, understanding how the behavior changes as a result of changes in the scale of topography may help in identifying the mechanistic pathways behind cell response to topography.

Other fundamental cell behaviors including proliferation, adhesion, and migration of HCEC cells also demonstrate a significant transitional response from the submicron to micron range. HCECs on submicron topography exhibit reduced rates of proliferation below submicron wide ridges compared to cells on micron and planar control.[215] Transformed SV40-HCECs also demonstrate modulation of cell adhesion strength in the submicron-scale range. On both 222–453 nm wide ridge structures (400–800 nm pitch) and 255 and 455 nm pores (400 and 800 nm pitch), SV40-HCECs demonstrate increased adhesion and resistance to shear flow compared to that on micron-scale topography.[141,207]

Cell migration rates are dependent on the scale of the topography and show significant differences between the submicron and micron ranges. Migration rates were high for SV40-HCECs on topography around the transition zone of 600–1000 nm wide ridges. Reduced rates were observed for cells on substrates with topography of 200–400 nm ridges (400–800 nm pitch) and on 2 μm ridges.[216] In a similar study, SV40-HCECs showed increased migration rates on 600 nm porous surfaces compared to nonporous controls.[184] What these and other reports have shown is that the submicron-scale topography can elicit a markedly different cell response compared to both micron-scale topography and flat controls. These findings provide more incentive to continue probing smaller and smaller features, specifically, feature sizes that better represent the scale of topography found in normal BMs (**Figure 10**).

1.129.4.3. Upper BM Range (100–400 nm Widths)

The upper range of topographical features, including elevations and diameters of fibers and pores, found in native BMs is 100–400 nm. Fabrication techniques to produce well-defined

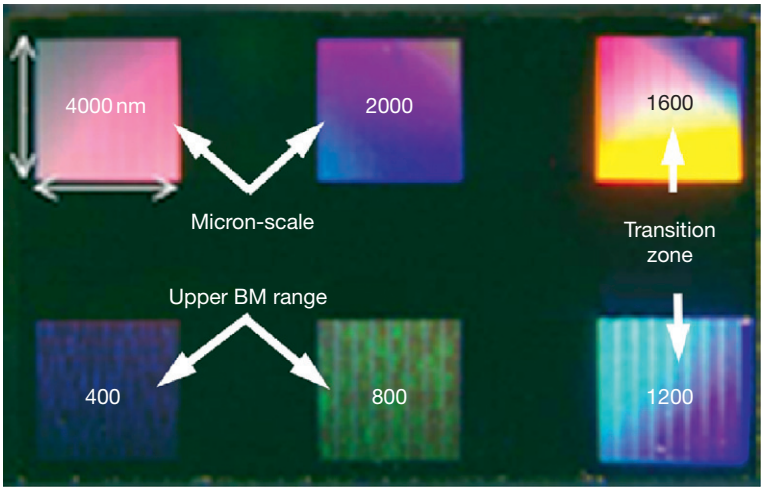

Figure 10 Three significant ranges of lateral dimensions, micron-scale, micron 'transition zone,' and submicron, are all represented on one silicon chip for cell studies. Studies have shown that certain cells exhibit different response (such as contact guidance, proliferation, and adhesion) to each scale. Adapted from Foley, J. D.; Grunwald, E. W.; Nealey, P. F.; Murphy, C. J. *Biomaterials* **2005**, *26*, 3639–3644, with permission from Elsevier.

topography in the upper BM range (in comparison to the lower BM range) are more advanced and highly employed in academia. The ease by which large patterned areas can be fabricated has created a wide breadth of research focusing on this range of topography. Examples of different cells and their characteristic responses to upper BM topography are presented below.

Topography in the range of 100–400 nm features influences cellular behaviors, such as adhesion,[141,207] contact guidance,[214] proliferation,[208,215] and migration[216] differently than submicron and micron features. HCECs have demonstrated increased adhesion when cultured on BM range topography compared to submicron, micron, and flat controls.[141] This finding suggests that the scale of the normal BM topography may play a role in cell adhesive strength and resistance to shear forces that may arise (as in blinking, blood flow, etc.). The strength of adhesion of corneal epithelial cells to 200–400 nm wide topography most likely directly impacts the ability of the cell to migrate. HCECs migrate along 200–400 nm ridges (400–800 nm pitches) at slower rates than cells on larger topography and flat controls.[216] In contrast, bovine corneal epithelial cells showed increased migration (as observed by cell outgrowth from a central button) on 100–800 nm pore substrates compared to micron-scale pores.[217] Together, these observations highlight the differences that arise between different cell types and their responses to topographical cues.

Cell protein expression and secretion are affected by topography with dimensions in the upper BM range and ranges found in other extracellular matrices. In bone, collagen fibers are organized in alternating parallel orientation with feature dimensions spanning from nano- to micron-scale.[218,219] Many studies have looked at the impact of nano- and submicron-scale topography on bone-specific cell types. For example, osteoblasts align and secrete collagen matrix parallel to 150 nm grooved (300 nm pitch and 60–70 nm deep) surfaces.[220] In addition, calvarial osteoblastic cells demonstrate increased proliferation rates and alkaline phosphatase activity on submicron rough surfaces compared to flat controls.[221] This range of topographic features may be essential for proper osteoblast phenotype.

Neurons are another example of cells that preferentially elongate in a particular direction in their native state. When cultured on topographical ridge features with submicron and micron-scale widths, PC12 (neuron) cells will align and elongate in the direction of the topography. When nerve growth factor (NGF) is present in high concentrations (50 ng ml^{-1}), PC12 cells will form neurites (a projection from a neuron cell body).[222] In the presence of both topography and NGF, PC12 cells demonstrate a threefold enhanced neurite formation on 200–400 nm (400 and 800 nm pitch) grooved surfaces compared to micron-scale grooved and flat surfaces when cultured in suboptimal concentration of NGF (5 ng ml^{-1} compared to 50 nm ml^{-1}).[223] Fibril topography with diameters in the range of 100–300 nm also elicits significantly longer neurite length and fibroblast growth factor (FGF-2) production from astrocytes.[224]

Topographic features in the upper BM range may also inhibit cell proliferation. On 200–400 nm ridge features (400–800 nm pitches), HCECs show decreased proliferation rates compared to larger topography and flat controls.[215,225] When taken collectively, the data presented for HCECs suggest that topography in the upper range of dimensions found in the BM have markedly different effects on cell phenotype than topography with larger dimensions and, most important, flat surfaces. One application for upper BM range topography is for improved *in vitro* cell culture systems. Most *in vitro* studies use tissue culture polystyrene (TCPS) for basic biological experimentation and development of therapeutics. The smooth surface of TCPS that does not replicate the native physical environment to which these cells are exposed could play a critical role in how cells respond to different chemical inputs, and possibly be a major contributor to inconsistencies between *in vitro* and *in vivo* studies.

1.129.4.4. Lower BM Range (10–100 nm Widths)

One of the major challenges researchers have faced when examining the effects of BM size topography on cellular behavior is the fabrication of nanometer (sub-100 nm wide) features. With the advancements of lithographic techniques designed primarily for the semiconductor industry, it is possible to produce surfaces with nanoscale features over large enough areas on which to culture cells. In general, most BMs have pore and fiber diameters ranging from 10 to 100 nm.[14,127–129,131,133–137,205,226] These dimensions constitute the lower size scale of topographical cues to which the basal layers of epithelial cells or endothelial cells are exposed.

To successfully mimic the smaller dimensions found in the BM, several studies have fabricated substrates with wave-like structures, lines, nanowires, fibers, islands, and pores with sub-100 nm features. These substrates have been used to determine the smallest feature width to which cells will exhibit a morphological response. Measured endpoints of the response have included both contact guidance and degree of filopodia extension. For example, Loesberg *et al.* investigated the lower topographic size range that would elicit cell contact guidance. They reported that rat dermal fibroblasts align to shallow 100 nm ridges (200 nm pitch, 77.4 nm depths), but do not significantly align to ridge widths below 100 nm.[145] In another study, immortalized human fibroblasts demonstrated a decrease in cell area and an increase in total number of filopodia when seeded on pit-defined topography with 75 nm pits (200 nm pitch and 100 nm depth) in comparison to flat controls. However, human fibroblasts did not exhibit significant differences on 35 nm pits (100 nm pitch, 50 nm depth) compared to flat controls.[227] These two studies suggest that fibroblast cells cannot sense topographic cues below a range of 75–100 nm features (or about 200 nm in pitch). In contrast, HCECs have been shown to increase alignment in response to wave-like structures with widths down to 30 nm (60 nm pitch and 200 nm depth)[187] (**Figure 11**). There are several differences between the studies including those in cell type, depth, and geometry of features, and the materials of substrates. These differences can contribute significantly to the responsiveness of the cells to topographical cues and may account for dissimilarities in a cell's ability to recognize sub-100 nm features. What all of these studies show is that there is a minimum feature dimension (given a specific depth and cell type) that will elicit a macroscopic cell response. This can be viewed as a given cell's tactile acuity limit. Understanding this lower scale of topographic features (in comparison to larger features and flat controls) will ultimately be beneficial in the design of improved prosthetics.

Other essential cell behaviors including adhesion, migration, and proliferation of cells in the presence of the smallest nanotopography fabricated have also been investigated. HUVECs

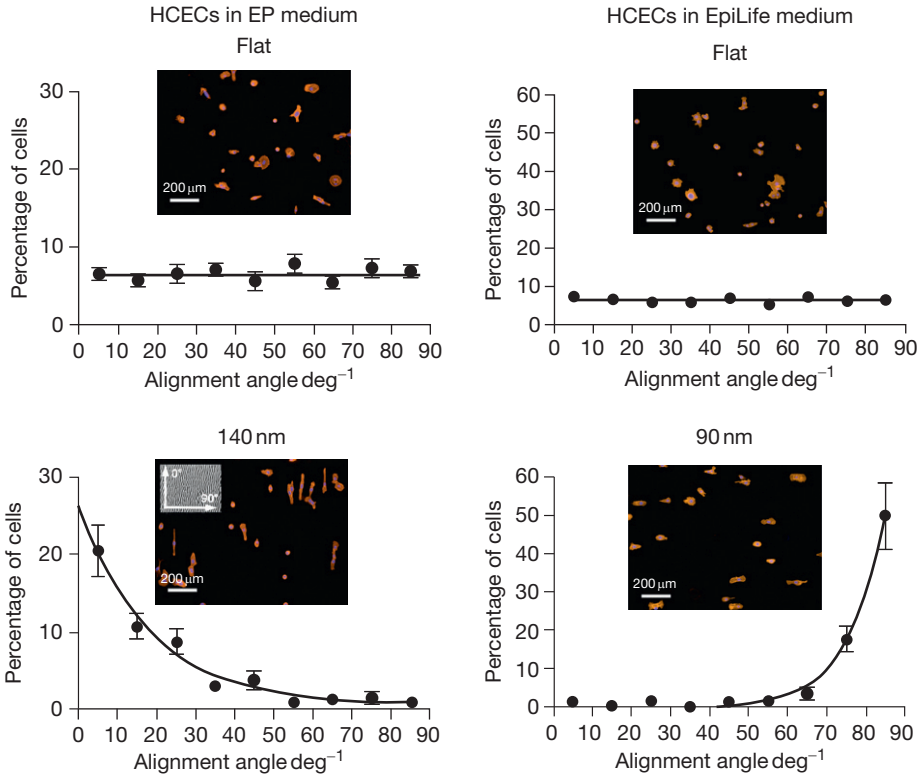

Figure 11 Human corneal epithelial cells demonstrate contact guidance to features with dimensions in the lower range of those characterized in basement membranes. HCECs in epithelial (EP) medium preferentially align parallel to 70 nm ridges (140 nm pitch), while cells in EpiLife® medium preferentially align perpendicularly to features as small as 45 nm (90 nm pitch). This example highlights the synergistic effects of topographical and soluble cues on cellular behavior. Adapted from Tocce, E. J.; Smirnov, V. K.; Kibalov, D. S.; Liliensiek, S. J.; Murphy, C. J.; Nealey, P. F. *Biomaterials* **2010**, *31*, 4064–4072, with permission from Elsevier.

exhibit enhanced adhesion and proliferation rates when seeded onto rough ($R_a = 30–40$ nm) surfaces compared to smooth controls.[228] Likewise, Hajicharalambous *et al.*[184] report increased SV40-HCEC attachment and migration on 100 nm porous surfaces compared to 600 nm porous and nonporous surfaces. In contrast, human fibroblasts demonstrate decreased attachment to 100, 200, and 300 nm pitch pits (35, 75, and 120 nm hole diameters) compared to flat controls.[229] These studies highlight the importance that experimental conditions (cell type, topographic scale and geometry, chemical make-up of the substrates, and method for collecting adhesion data) can have on observed cell outputs.

Most reports investigating how the range of topographical cues of the BM affects cellular behavior analyze cells in an undifferentiated single monolayer state. While results from these experiments are extremely insightful, they do not always represent how the cells will respond to similar cues *in vivo*. *In vivo*, epithelial cells are not organized into a single monolayer, but form multiple differentiated layers of cells. For example, the corneal epithelium is composed of several layers which include a basal layer of proliferating cells that adhere to the BM and six to eight layers of stratified superficial cells that have been induced to undergo differentiation. To investigate whether topographical cues impact the differentiation process, Evans *et al.*[230] observed bovine corneal epithelial cell proliferation and differentiation on substrates with pores ranging from 100 to 3000 nm in diameter. They observed the formation of a continuous basal lamina and a regular pattern of hemidesmosomes, similar to those observed in intact tissue, when cells were cultured on 100 nm pore surfaces. This indicates that BM relevant scale topography is possibly important for native basal lamina formation. In comparison, discontinuous basal lamina and interrupted hemidesmosome patterns were observed on 400–2000 nm pores, while neither a basal lamina nor hemidesmosomes were observed on 3000 nm pores.[230] Also, bovine CECs showed more stratified layers when cultured on 100 and 400 nm pore surfaces compared to 800–2000 nm pores and flat controls.[231] These observations reemphasize that the scale of topographical cues is important in eliciting cellular response and that topography with dimensions in the range of those found in the BM may play an important role in proper tissue development.

There are limited studies looking specifically at topographical cues with dimensions in the range of the smallest dimensions quantified in the BM (10–100 nm). However, the observations that have been reported are exciting and help us narrow down the range of sizes that should be tested. It is also critical to acknowledge that a 'one size fits all' approach is not going to work. Small changes to the environment to which the cells are exposed can have huge impacts on the cell response. Therefore, careful investigation of each cell type will be necessary to determine the best attributes to incorporate into substrate design.

1.129.4.5. Importance of Depth

For several cell types investigated, the depth is a critical factor involved in the cell's ability to respond to the lateral topographic features. In a study examining the influence of depth on HCEC contact guidance to 200–2000 nm ridges (400–4000 nm pitch), HCECs did not show significant levels of cellular alignment until the depth of the features exceeded 150 nm.[144] In another study, HCECs significantly aligned to 150 nm deep features compared to flat controls, but showed an increased percentage of cellular alignment when the depth was increased to 600 nm.[146] Together, these studies imply that the minimum depth needed to elicit HCEC contact guidance on 400 nm pitch features and larger is around 150 nm (Figure 12).

Research has also shown that the minimum depth necessary to elicit contact guidance is cell-type dependent. In a parallel study with HCECs, human stromal fibroblasts were examined to determine if depth played a significant role in eliciting contact guidance on 200–2000 nm ridged (400–4000 nm pitch) features. The stromal fibroblasts showed alignment to features with depths as low as 75 nm, which is significantly less than the depth needed to elicit contact guidance from HCECs.[144] Another study showed fibroblasts aligned to 2000 nm wide features with depth down to 50 nm depth.[142] In the same study, human endothelial cells and smooth muscle cells did not show significant alignment to 50 nm deep features. A minimum depth of 100 nm was necessary to elicit contact

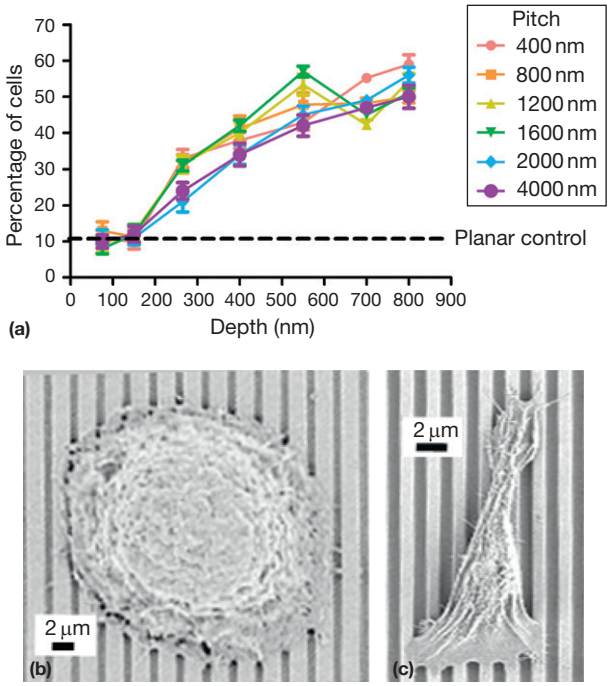

Figure 12 Cell contact guidance increases as depth of features increases. (a) Primary human corneal epithelial cells demonstrated increased alignment and elongation response when the depth of groove–ridge features increased from 70 to 900 nm. Similar cell response was observed for all groove and ridge features with pitches from 400 to 4000 nm. (b) If the depth was too shallow, cells did not show preferred elongation and alignment to the underlying topography, as represented by this cell on 4000 nm pitch features with a depth of 75 nm. (c) With depths of 265 nm and greater, cells elongated and aligned to all lateral pitches, including this cell on features with 1600 nm pitch and a depth of 265 nm. Adapted from Fraser, S. A.; Ting, Y. H.; Mallon, K. S.; Wendt, A. E.; Murphy, C. J.; Nealey, P. F. *J. Biomed. Mater. Res. A* **2008**, *86*, 725–735, copyright Wiley Periodicals, Inc., 2007.

guidance of endothelial and smooth muscle cells. Both studies highlight that cell response to topographical features is both depth and cell type-dependent. These are critical parameters to take into consideration when designing topographically patterned substrates for cell phenotype regulation.

Depth is not an 'on–off' switch for cellular response to lateral dimensions; rather, it is a factor that controls the extent to which cells respond to the lateral dimension. The fraction of baby hamster kidney (BHK) and Madin–Darby canine kidney (MDCK) cells aligning parallel to micron-scale grooved substrates increased as the depth increased (from 0.2 to 1.9 μm). The fraction of cells aligning was less affected by the lateral pitch (from 4 to 24 μm), showing similar fractions across all pitches for a given feature depth.[143] Similarly, incremental changes in depth from 75 to 800 nm resulted in gradual increases in aligned HCECs and stromal fibroblasts to 200–2000 nm ridge features. Other studies also have demonstrated that increasing depth of nano- and micron-scale lateral features significantly increases contact guidance of bovine aortic endothelial cells,[147] rat dermal fibroblasts,[145] and human fibroblasts.[142] Depth is a major factor in controlling cell response to topographical features and should play a role in the design of biomaterials.

1.129.4.6. Overview

The BM constitutes the native physical environment on which epithelial and endothelial cells reside and is composed of a compliant protein fibrous network that provides specific cues to the cells. A variety of BMs, across tissues and species, have been well characterized in terms of their protein composition, degree of stiffness (i.e., elastic modulus), and size of fibril features (i.e., topography). These biophysical cues help to regulate cell phenotype *in vivo*, but the mechanisms behind the regulation are largely unknown.

To answer some of the questions about how biophysical cues, specifically topography and elastic modulus, affect cell behaviors, researchers have fabricated an array of materials for *in vitro* cell culture. Many studies have shown that biomimetic elastic modulus alone can regulate cell behaviors and expression. Additionally, with the use of substrates containing nano- to micron-scale features, researchers have shown the impact that topography has on cell response. The nano- and microfabrication techniques used for these purposes have been widely employed in the semiconductor industries and adapted for cell culture. With the improvement of nanofabrication techniques over the past 50 years, it is now possible to produce small enough features to mimic those found in the native BM.

Topographical cues have been shown to have a significant impact on a variety of cell behaviors. Proliferation, differentiation, protein expression, migration, and cell morphology are affected by micron, submicron, or nanoscale features. Researchers have used a wide range of lateral dimensions, from tens of nanometers to hundreds of micrometers, to show that (1) topography plays an important role in cell function, (2) the scale of topography can modulate cell response to the topographical cues, (3) topographical cues work synergistically with other environmental factors (such as the soluble composition) to elicit controlled cell responses, and (4) cell responses to topographical cues are cell-type dependent.

The next step is to understand how biophysical cues regulate cell behaviors and to examine combinatorial effects of substrate topography and elastic modulus. By modulating these two substrate parameters, a clearer picture of how these specific biophysical attributes of the native BM influence cell behaviors can be drawn. In conclusion, the ultimate goal is to provide the necessary extracellular cues, through the incorporation of both biochemical and biophysical cues into the design of biomaterials, to initiate and maintain healthy tissue regeneration, create improved cell cultures systems that better approximate the *in vivo* environment, and inform the design and fabrication of improved prosthetics.

Acknowledgments

The authors would like to thank Julie Last and Jennifer Brockman for their helpful discussions. This work is supported in part by the NIH-National Eye Institute (1RO1EY017367-01A and 1RO1EY016134-01A2) and the Heart Lung and Blood Institute (R01HL079012-01A), and its contents are solely the responsibility of the authors and do not necessarily represent the official views of the National Eye Institute or the NIH.

References

1. Ekblom, E.; Timpl, R. *Curr. Opin. Cell Biol*. **1996**, *8*, 599–601.
2. Timpl, R. *Curr. Opin. Cell Biol*. **1996**, *8*, 618–624.
3. Sasaki, T.; Fassler, R.; Hohenester, E. *J. Cell Biol*. **2004**, *164*, 959–963.
4. Chen, C. H.; Hansma, H. G. *J. Struct. Biol*. **2000**, *131*, 44–55.
5. Merker, H. J. *Microsc. Res. Tech*. **1994**, *28*, 95–124.
6. Farquhar, M. G. *J. Clin. Invest*. **2006**, *116*, 2090–2093.
7. Farquhar, M. G.; Wissig, S. L.; Palade, G. E. *J. Exp. Med*. **1961**, *113*, 47–66.
8. LeBleu, V. S.; MacDonald, B.; Kalluri, R. *Exp. Biol. Med*. **2007**, *232*, 1121–1129.
9. Kalluri, R. *Nat. Rev. Cancer* **2003**, *3*, 422–433.
10. Paulsson, M. *Crit. Rev. Biochem. Mol. Biol*. **1992**, *27*, 93–127.
11. Yurchenco, P. D.; O'Rear, J. In *Molecular and Cellular Aspects of Basement Membranes*; Rohrbach, D. H., Timpl, R., Eds.; Academic Press: San Digeo, 1993; pp 19–47.
12. Yurchenco, P. D.; Schittny, J. C. *FASEB J*. **1990**, *4*, 1577–1590.
13. Sasaki, T.; Fassler, R.; Hohenester, E. *J. Cell Biol*. **2004**, *164*, 959–963.
14. Liliensiek, S. J.; Nealey, P.; Murphy, C. J. *Tissue Eng. A* **2009**, *15*, 2643–2651.
15. Candiello, J.; Balasubramani, M.; Schreiber, E. M.; *et al*. *FEBS J*. **2007**, *274*, 2897–2908.
16. Fischer, U. C.; Zingsheim, H. P. *J. Vac. Sci. Technol*. **1981**, *19*, 881–885.
17. Osawa, T.; Onodera, M.; Feng, X. Y.; Nozaka, Y. *J. Electron Microsc. (Tokyo)* **2003**, *52*, 435–440.
18. Prince, J.; Diesem, C.; Eglitis, I.; Ruskell, G. *Anatomy and Histology of the Eye and Orbit in Domestic Animals*. Charles C Thomas: Springfield, IL, 1960.
19. Siperstein, M. D.; Unger, R. H.; Madison, L. L. *J. Clin. Invest*. **1968**, *47*, 1973–1999.
20. Williamson, J. R.; Vogler, N. J.; Kilo, C. *Diabetes* **1969**, *18*, 567–578.
21. Williamson, J. R.; Vogler, N. J.; Kilo, C. *Am. J. Pathol*. **1971**, *63*, 359–370.
22. Wu, H. S.; Dikman, S.; Gil, J. *Comput. Methods Programs Biomed*. **2010**, *97*, 223–231.
23. Poschl, E.; Schlotzer-Schrehardt, U.; Brachvogel, B.; Saito, K.; Ninomiya, Y.; Mayer, U. *Development* **2004**, *131*, 1619–1628.
24. Kalluri, R.; Cosgrove, D. *J. Biol. Chem*. **2000**, *275*, 12719–12724.
25. Aumailley, M.; Nurcombe, V.; Edgar, D.; Paulsson, M.; Timpl, R. *J. Biol. Chem*. **1987**, *262*, 11532–11538.
26. Carlsson, R.; Engvall, E.; Freeman, A.; Ruoslahti, E. *Proc. Natl. Acad. Sci. USA – Biol. Sci*. **1981**, *78*, 2403–2406.
27. Drago, J.; Nurcombe, V.; Bartlett, P. F. *Exp. Cell Res*. **1991**, *192*, 256–265.
28. Chung, A. E.; Dong, L. J.; Wu, C. Y.; Durkin, M. E. *Kidney Int*. **1993**, *43*, 13–19.

29. Erickson, A. C.; Couchman, J. R. *J. Histochem. Cytochem.* **2000**, *48*, 1291–1306.
30. Bader, B. L.; Smyth, N.; Nedbal, S.; *et al. Mol. Cell. Biol.* **2005**, *25*, 6846–6856.
31. Miettinen, A.; Stow, J. L.; Mentone, S.; Farquhar, M. G. *J. Exp. Med.* **1986**, *163*, 1064–1084.
32. Folkman, J.; Klagsbrun, M.; Sasse, J.; Wadzinski, M.; Ingber, D.; Vlodavsky, I. *Am. J. Pathol.* **1988**, *130*, 393–400.
33. Vigny, M.; Ollier-Hartmann, M. P.; Lavigne, M.; *et al. J. Cell. Physiol.* **1988**, *137*, 321–328.
34. Yurchenco, P. D.; Smirnov, S.; Mathus, T. *Meth. Cell Biol.* **2002**, *69*, 111–144.
35. Yurchenco, P. D.; Tsilibary, E. C.; Charonis, A. S.; Furthmayr, H. *J. Biol. Chem.* **1985**, *260*, 7636–7644.
36. Miner, J. H.; Li, C.; Mudd, J. L.; Go, G.; Sutherland, A. E. *Development* **2004**, *131*, 2247–2256.
37. Smyth, N.; Vatansever, H. S.; Murray, P.; *et al. J. Cell Biol.* **1999**, *144*, 151–160.
38. Yurchenco, P. D.; O'Rear, J. J. *Curr. Opin. Cell Biol.* **1994**, *6*, 674–681.
39. Otey, C. A.; Burridge, K. *Semin. Cell Biol.* **1990**, *1*, 391–399.
40. Giancotti, F. G.; Ruoslahti, E. *Science* **1999**, *285*, 1028–1032.
41. Hynes, R. O. *Cell* **1987**, *48*, 549–554.
42. De Luca, M.; Tamura, R. N.; Kajiji, S.; *et al. Proc. Natl. Acad. Sci. USA* **1990**, *87*, 6888–6892.
43. Giancotti, F. G.; Stepp, M. A.; Suzuki, S.; Engvall, E.; Ruoslahti, E. *J. Cell Biol.* **1992**, *118*, 951–959.
44. Stepp, M. A. *Exp. Eye Res.* **2006**, *83*, 3–15.
45. Howe, A.; Aplin, A. E.; Alahari, S. K.; Juliano, R. L. *Curr. Opin. Cell Biol.* **1998**, *10*, 220–231.
46. Hersel, U.; Dahmen, C.; Kessler, H. *Biomaterials* **2003**, *24*, 4385–4415.
47. Shin, H.; Jo, S.; Mikos, A. G. *Biomaterials* **2003**, *24*, 4353–4364.
48. Massia, S. P.; Hubbell, J. A. *Anal. Biochem.* **1990**, *187*, 292–301.
49. Maheshwari, G.; Brown, G.; Lauffenburger, D. A.; Wells, A.; Griffith, L. G. *J. Cell Sci.* **2000**, *113*, 1677–1686.
50. Massia, S. P.; Hubbell, J. A. *J. Cell Biol.* **1991**, *114*, 1089–1100.
51. Palecek, S. P.; Loftus, J. C.; Ginsberg, M. H.; Lauffenburger, D. A.; Horwitz, A. F. *Nature* **1997**, *385*, 537–540.
52. Lutolf, M. P.; Hubbell, J. A. *Nat. Biotechnol.* **2005**, *23*, 47–55.
53. Ljubimov, A. V.; Huang, Z. S.; Huang, G. H.; *et al. J. Histochem. Cytochem.* **1998**, *46*, 1033–1041.
54. Rehany, U.; Ishii, Y.; Lahav, M.; Rumelt, S. *Cornea* **2000**, *19*, 534–538.
55. Tsilibary, E. C. *J. Pathol.* **2003**, *200*, 537–546.
56. Williamson, J. R.; Vogler, N. J.; Kilo, C. *Acta Diabetol. Lat.* **1971**, *8*(Suppl. 1), 117–134.
57. Pieraggi, M. T.; Bouissou, H. *Ann. Pathol.* **1981**, *1*, 271–279.
58. Simionescu, M. *Arterioscler. Thromb. Vasc. Biol.* **2007**, *27*, 266–274.
59. Labbe, A.; De Nicola, R.; Dupas, B.; Auclin, F.; Baudouin, C. *Ophthalmology* **2006**, *113*, 1301–1308.
60. Bystrom, B.; Virtanen, I.; Rousselle, P.; Miyazaki, K.; Linden, C.; Pedrosa Domellof, F. *Histochem. Cell Biol.* **2007**, *127*, 657–667.
61. Saghizadeh, M.; Brown, D. J.; Castellon, R.; *et al. Am. J. Pathol.* **2001**, *158*, 723–734.
62. Tuori, A. J.; Virtanen, I.; Aine, E.; Kalluri, R.; Miner, J. H.; Uusitalo, H. M. *Curr. Eye Res.* **1997**, *16*, 792–801.
63. Hayden, M. R.; Sowers, J. R.; Tyagi, S. C. *Cardiovasc. Diabetol.* **2005**, *4*, 9.
64. Asmussen, I.; Kjeldsen, K. *Circ. Res.* **1975**, *36*, 579–589.
65. Zweifach, B. W. In *Vascular Endothelium and Basement Membrane*; Altura, B. M., Ed.; Karger: New York, 1980; pp 206–225.
66. Carter, R. T. *Vet. Ophthalmol.* **2009**, *12*(Suppl. 1), 2–9.
67. Dendrou, C. A.; Plagnol, V.; Fung, E.; *et al. Nat. Genet.* **2009**, *41*, 1011–1015.
68. Devuyst, O.; Dahan, K.; Pirson, Y. *Nephrol. Dial. Transplant.* **2005**, *20*, 1290–1294.
69. Saemann, M. D.; Weichhart, T.; Horl, W. H.; Zlabinger, G. J. *Eur. J. Clin. Invest.* **2005**, *35*, 227–235.
70. Liotta, L. A.; Rao, C. N.; Barsky, S. H. *Lab. Invest.* **1983**, *49*, 636–649.
71. Oguro, K.; Kazama, T.; Isemura, M.; Nakamura, T.; Akai, S.; Sato, Y. *J. Invest. Dermatol.* **1991**, *96*, 250–254.
72. Erler, J. T.; Weaver, V. M. *Clin. Exp. Metastasis* **2009**, *26*, 35–49.
73. Kass, L.; Erler, J. T.; Dembo, M.; Weaver, V. M. *Int. J. Biochem. Cell Biol.* **2007**, *39*, 1987–1994.
74. Levental, K. R.; Yu, H.; Kass, L.; *et al. Cell* **2009**, *139*, 891–906.
75. Lam, W. A.; Cao, L.; Umesh, V.; Keung, A. J.; Sen, S.; Kumar, S. *Mol. Cancer* **2010**, *9*, 35.
76. Beinke, C.; Van Beuningen, D.; Cordes, N. *Int. J. Radiat. Biol.* **2003**, *79*, 721–731.
77. Cordes, N.; Beinke, C. *Cancer Biol. Ther.* **2004**, *3*, 47–53.
78. Cordes, N.; Beinke, C.; Plasswilm, L.; van Beuningen, D. *Strahlenther. Onkol.* **2004**, *180*, 157–164.
79. Kenny, P. A.; Bissell, M. J. *Int. J. Cancer* **2003**, *107*, 688–695.
80. Farach-Carson, M. C.; Wagner, R. C.; Kiick, K. L. In *Tissue Engineering and Artificial Organs*; Bronzino, J. D., Ed.; CRC Press/Taylor and Francis: Boca Raton, FL, 2006; pp 1–22.
81. Butt, H. J.; Cappella, B.; Kappl, M. *Surf. Sci. Rep.* **2005**, *59*, 1–152.
82. Hansma, H.; Clegg, D. O.; Kokkoli, E.; Oroudjev, E.; Tirrel, M. *Meth. Cell Biol.* **2002**, *69*, 163–193.
83. Sarvazyan, A. In *Handbook of Elastic Properties of Solids, Liquids and Gases*; Levy, M., Bass, H., Stern, R. R., Eds.; Academic Press: New York, 2001; pp 107–127.
84. Domke, J.; Radmacher, M. *Langmuir* **1998**, *14*, 3320–3325.
85. Kalay, G.; Sousa, R. A.; Reis, R. L.; Cunha, A. M.; Bevis, M. J. *J. Appl. Polym. Sci.* **1999**, *73*, 2473–2483.
86. Engler, A. J.; Sen, S.; Sweeney, H. L.; Discher, D. E. *Cell* **2006**, *126*, 677–689.
87. Zysset, P. K.; Guo, X. E.; Hoffler, C. E.; Moore, K. E.; Goldstein, S. A. *J. Biomech.* **1999**, *32*, 1005–1012.
88. Laurent, V. M.; Kasas, S.; Yersin, A.; *et al. Biophys. J.* **2005**, *89*, 667–675.
89. Radmacher, M.; Fritz, M.; Kacher, C. M.; Cleveland, J. P.; Hansma, P. K. *Biophys. J.* **1996**, *70*, 556–567.
90. Mathur, A. B.; Collinsworth, A. M.; Reichert, W. M.; Kraus, W. E.; Truskey, G. A. *J. Biomech.* **2001**, *34*, 1545–1553.
91. Samani, A.; Zubovits, J.; Plewes, D. *Phys. Med. Biol.* **2007**, *52*, 1565.
92. Danielsen, C. C. *Exp. Eye Res.* **2004**, *79*, 343–350.
93. Elsheikh, A.; Wang, D.; Pye, D. *J. Refract. Surg.* **2007**, *23*, 808–818.
94. Russell, P.; Last, J.; Ding, Y.; *et al.* Compliance and the human trabecular meshwork: Implications about glaucoma. In *Association for Research in Vision and Ophthalmology Annual Meeting*, Fort Lauderdale, FL, 2010.
95. Ziebarth, N. M.; Wojcikiewicz, E. P.; Manns, F.; Moy, V. T.; Parel, J. M. *Mol. Vis.* **2007**, *13*, 504.
96. Rotsch, C.; Jacobson, K.; Radmacher, M. *Proc. Natl. Acad. Sci. USA* **1999**, *96*, 921.
97. Gueta, R.; Barlam, D.; Shneck, R. Z.; Rousso, I. *Proc. Natl. Acad. Sci. USA* **2006**, *103*, 14790.
98. Stolz, M.; Raiteri, R.; Daniels, A. U.; VanLandingham, M. R.; Baschong, W.; Aebi, U. *Biophys. J.* **2004**, *86*, 3269–3283.
99. Elkin, B. S.; Azeloglu, E. U.; Costa, K. D.; Morrison Iii, B. *J. Neurotrauma* **2007**, *24*, 812–822.
100. Last, J. A.; Liliensiek, S. J.; Nealey, P. F.; Murphy, C. J. *J. Struct. Biol.* **2009**, *167*, 19–24.
101. Pelham, R. J., Jr.; Wang, Y. *Proc. Natl. Acad. Sci. USA* **1997**, *94*, 13661–13665.
102. Chou, S.-Y.; Cheng, C.-M.; LeDuc, P. R. *Biomaterials* **2009**, *30*, 3136–3142.
103. Ghosh, K.; Pan, Z.; Guan, E.; *et al. Biomaterials* **2007**, *28*, 671–679.
104. Solon, J.; Levental, I.; Sengupta, K.; Georges, P. C.; Janmey, P. A. *Biophys. J.* **2007**, *93*, 4453–4461.
105. Engler, A.; Bacakova, L.; Newman, C.; Hategan, A.; Griffin, M.; Discher, D. *Biophys. J.* **2004**, *86*, 617–628.
106. Peyton, S. R.; Raub, C. B.; Keschrumrus, V. P.; Putnam, A. J. *Biomaterials* **2006**, *27*, 4881–4893.
107. Polte, T. R.; Eichler, G. S.; Wang, N.; Ingber, D. E. *Am. J. Physiol. Cell Physiol.* **2004**, *286*, C518–C528.
108. Zaari, N.; Rajagopalan, P.; Kim, S. K.; Engler, A. J.; Wong, J. Y. *Adv. Mater.* **2004**, *16*, 2133.
109. Thompson, M. T.; Berg, M. C.; Tobias, I. S.; Rubner, M. F.; Van Vliet, K. J. *Biomaterials* **2005**, *26*, 6836–6845.
110. Genes, N. G.; Rowley, J. A.; Mooney, D. J.; Bonassar, L. J. *Arch. Biochem. Biophys.* **2004**, *422*, 161–167.
111. Engler, A. J.; Griffin, M. A.; Sen, S.; Bonnemann, C. G.; Sweeney, H. L.; Discher, D. E. *J. Cell Biol.* **2004**, *166*, 877–887.
112. Georges, P. C.; Hui, J. J.; Gombos, Z.; *et al. Am. J. Physiol. Gastrointest. Liver Physiol.* **2007**, *293*, G1147–G1154.
113. Gunn, J. W.; Turner, S. D.; Mann, B. K. *J. Biomed. Mater. Res. A* **2005**, *72A*, 91–97.
114. Deroanne, C. F.; Lapiere, C. M.; Nusgens, B. V. *Cardiovasc. Res.* **2001**, *49*, 647–658.
115. Wozniak, M. A.; Desai, R.; Solski, P. A.; Der, C. J.; Keely, P. J. *J. Cell Biol.* **2003**, *163*, 583–595.
116. Califano, J. P.; Reinhart-King, C. A. *Cell. Mol. Bioeng.* **2008**, *1*, 122–132.
117. Yamamura, N.; Sudo, R.; Ikeda, M.; Tanishita, K. *Tissue Eng.* **2007**, *13*, 1443–1453.

118. Semler, E. J.; Lancin, P. A.; Dasgupta, A.; Moghe, P. V. *Biotechnol. Bioeng.* **2005**, *89*, 296–307.
119. Zaman, M. H.; Trapani, L. M.; Siemeski, A.; *et al. Proc. Natl. Acad. Sci. USA* **2006**, *103*, 10889–10894.
120. Stroka, K. M.; Aranda-Espinoza, H. *Cell Motil. Cytoskeleton* **2009**, *66*, 328–341.
121. Isenberg, B. C.; DiMilla, P. A.; Walker, M.; Kim, S.; Wong, J. Y. *Biophys. J.* **2009**, *97*, 1313–1322.
122. Lo, C. M.; Wang, H. B.; Dembo, M.; Wang, Y. L. *Biophys. J.* **2000**, *79*, 144–152.
123. Winer, J. P.; Oake, S.; Janmey, P. A. *Plos One* **2009**, *4*, e6382.
124. Banerjee, A.; Arha, M.; Choudhary, S.; *et al. Biomaterials* **2009**, *30*, 4695–4699.
125. Georges, P. C.; Miller, W. J.; Meaney, D. F.; Sawyer, E. S.; Janmey, P. A. *Biophys. J.* **2006**, *90*, 3012–3018.
126. Abrams, G. A.; Bentley, E.; Nealey, P. F.; Murphy, C. J. *Cells Tissues Organs* **2002**, *170*, 251–257.
127. Yamasaki, Y.; Makino, H.; Ota, Z. *Nephron* **1994**, *66*, 189–199.
128. Abrams, G.; Teixeira, A.; Nealey, P.; Murphy, C. In *Biomimetic Materials and Design: Biointerfacial Strategies, Tissue Engineering, and Targeted Drug Delivery*; Dillow, A., Lowman, A., Eds.; Marcel Dekker: New York, 2002; pp 91–136.
129. Abrams, G. A.; Schaus, S. S.; Goodman, S. L.; Nealey, P. F.; Murphy, C. J. *Cornea* **2000**, *19*, 57–64.
130. Liliensiek, S. J.; Nealey, P. F.; Murphy, C. J. Primary keratinocytes, sik immortalized keratinocytes and transformed scc4 cells respond differently to topographic cues. In *Timberline Symposium*, Mt. Hood: Oregon, USA, 2006.
131. Yurchenco, P. D.; Ruben, G. C. *J. Cell Biol.* **1987**, *105*, 2559–2568.
132. Howat, W. J.; Barabás, T.; Holmes, J. A.; Holgate, S. T.; Lackie, P. M. *J. Struct. Biol.* **2002**, *139*, 137–145.
133. Abe, M.; Osawa, T. *Arch. Oral Biol.* **1999**, *44*, 587–594.
134. Brody, S.; Anilkumar, T.; Liliensiek, S.; Last, J. A.; Murphy, C. J.; Pandit, A. *Tissue Eng.* **2006**, *12*, 413–421.
135. Hironaka, K.; Makino, H.; Yamsaki, Y.; Ota, Z. *Kidney Int.* **1993**, *43*, 334–345.
136. Abrams, G. A.; Goodman, S. L.; Nealey, P. F.; Franco, M.; Murphy, C. J. *Cell Tissue Res.* **2000**, *299*, 39–46.
137. Abrams, G. A.; Murphy, C. J.; Wang, Z. Y.; Nealey, P. F. *Urol. Res.* **2003**, *31*, 341–346.
138. Lu, Y.; Chen, S. C. *Adv. Drug Deliv. Rev.* **2004**, *56*, 1621–1633.
139. Mitragotri, S.; Lahann, J. *Nat. Mater.* **2009**, *8*, 15–23.
140. Smith, L. A.; Liu, X.; Ma, P. X. *Soft Matter* **2008**, *4*, 2144–2149.
141. Karuri, N. W.; Liliensiek, S.; Teixeira, A. I.; *et al. J. Cell Sci.* **2004**, *117*, 3153–3164.
142. Biela, S. A.; Su, Y.; Spatz, J. P.; Kemkemer, R. *Acta Biomater.* **2009**, *5*, 2460–2466.
143. Clark, P.; Connolly, P.; Curtis, A. S. G.; Dow, J. A. T.; Wilkinsin, C. D. W. *Development* **1990**, *108*, 635–644.
144. Fraser, S. A.; Ting, Y. H.; Mallon, K. S.; Wendt, A. E.; Murphy, C. J.; Nealey, P. F. *J. Biomed. Mater. Res. A* **2008**, *86*, 725–735.
145. Loesberg, W. A.; te Riet, J.; van Delft, F. C.; *et al. Biomaterials* **2007**, *28*, 3944–3951.
146. Teixeira, A. I.; Abrams, G. A.; Bertics, P. J.; Murphy, C. J.; Nealey, P. F. *J. Cell Sci.* **2003**, *116*, 1881–1892.
147. Uttayarat, P.; Toworfe, G. K.; Dietrich, F.; Lelkes, P. I.; Composto, R. J. *J. Biomed. Mater. Res. A* **2005**, *75*, 668–680.
148. Yang, L. X.; Akhatov, I.; Mahinfalah, M.; Jang, B. Z. *J. Chin. Inst. Eng.* **2007**, *30*, 441–446.
149. Chen, Y.; Pepin, A. *Electrophoresis* **2001**, *22*, 187–207.
150. Ku, H. Y.; Scala, L. C. *J. Electrochem. Soc.* **1969**, *116*, 980–985.
151. Larkin, M. W.; Matta, R. K. *Solid State Electron.* **1967**, *10*, 491–494.
152. Meyle, J.; Gultig, K.; Brich, M.; Hammerle, H.; Nisch, W. *J. Mater. Sci. Mater. Med.* **1994**, *5*, 463–466.
153. Rajnicek, A. M.; Britland, S.; McCaig, C. D. *J. Cell Sci.* **1997**, *110*, 2905–2913.
154. Rajnicek, A. M.; McCaig, C. D. *J. Cell Sci.* **1997**, *110*, 2915–2924.
155. Chen, W.; Ahmed, H. *Appl. Phys. Lett.* **1993**, *62*, 1499–1501.
156. Chen, W.; Ahmed, H. *Appl. Phys. Lett.* **1993**, *63*, 1116–1118.
157. Craighead, H. G.; Howard, R. E.; Jackel, L. D.; Mankiewich, P. M. *Appl. Phys. Lett.* **1983**, *42*, 38–40.
158. Grigorescu, A. E.; Hagen, C. W. *Nanotechnology* **2009**, *20*, 292001.
159. Luttge, R. *J. Phys. D Appl. Phys.* **2009**, *42*, 123001.
160. Chen, Y.; Pepin, A. *Electrophoresis* **2001**, *22*, 187–207.
161. Cardinale, G. F.; Henderson, C. C.; Goldsmith, J. E. M.; Mangat, P. J. S.; Cobb, J.; Hector, S. D. *J. Vac. Sci. Technol. B* **1999**, *17*, 2970–2974.
162. Gwyn, C. W.; Stulen, R.; Sweeney, D.; Attwood, D. *J. Vac. Sci. Technol. B* **1998**, *16*, 3142–3149.
163. Solak, H. H.; He, D.; Li, W.; *et al. Appl. Phys. Lett.* **1999**, *75*, 2328–2330.
164. Solak, H. H. *J. Phys. D Appl. Phys.* **2006**, *39*, R171–R188.
165. Simon, G.; Haghiri-Gosnet, A. M.; Bourneix, J.; *et al. J. Vac. Sci. Technol. B* **1997**, *15*, 2489–2494.
166. Brunette, D. M.; Kenner, G. S.; Gould, T. R. L. *J. Dent. Res.* **1983**, *62*, 1045–1048.
167. Chou, S. Y.; Krauss, P. R.; Renstrom, P. J. *Science* **1996**, *272*, 85–87.
168. Chou, S. Y.; Krauss, P. R.; Renstrom, P. J. *Appl. Phys. Lett.* **1995**, *67*, 3114–3116.
169. Chou, S. Y.; Keimel, C.; Gu, J. *Nature* **2002**, *417*, 835–837.
170. Xia, Y.; Kim, E.; Zhao, X. M.; Rogers, J. A.; Prentiss, M.; Whitesides, G. M. *Science* **1996**, *273*, 347–349.
171. Odom, T. W.; Love, J. C.; Wolfe, D. B.; Paul, K. E.; Whitesides, G. M. *Langmuir* **2002**, *18*, 5314–5320.
172. Truong, T. T.; Lin, R.; Jeon, S.; *et al. Langmuir* **2007**, *23*, 2898–2905.
173. Park, S. H.; Qin, D.; Xia, Y. *Adv. Mater.* **1998**, *10*, 1028.
174. Wang, D. Y.; Mohwald, H. *Adv. Mater.* **2004**, *16*, 244.
175. vanBlaaderen, A.; Ruel, R.; Wiltzius, P. *Nature* **1997**, *385*, 321–324.
176. Lee, Y. J.; Braun, P. V. *Adv. Mater.* **2003**, *15*, 563–566.
177. Liu, L.; Li, P.; Asher, S. A. *Nature* **1999**, *397*, 141–144.
178. Murugan, R.; Ramakrishna, S. *Tissue Eng.* **2006**, *12*, 435–447.
179. Whitesides, G. M.; Mathias, J. P.; Seto, C. T. *Science* **1991**, *254*, 1312–1319.
180. Kadler, K. E.; Holmes, D. F.; Trotter, J. A.; Chapman, J. A. *Biochem. J.* **1996**, *316*, 1–11.
181. Zhang, S. *Nat. Biotechnol.* **2003**, *21*, 1171–1178.
182. Ma, P. X.; Zhang, R. *J. Biomed. Mater. Res.* **1999**, *46*, 60–72.
183. Mendelsohn, J. D.; Barrett, C. J.; Chan, V. V.; Pal, A. J.; Mayes, A. M.; Rubner, M. F. *Langmuir* **2000**, *16*, 5017–5023.
184. Hajicharalambous, C. S.; Lichter, J.; Hix, W. T.; Swierczewska, M.; Rubner, M. F.; Rajagopalan, P. *Biomaterials* **2009**, *30*, 4029–4036.
185. Smirnov, V. K.; Kibalov, D. S.; Krivelevich, S. A.; *et al. Nucl. Instrum. Meth. B* **1999**, *147*, 310–315.
186. Smirnov, V. K.; Kibalov, D. S.; Orlov, O. M.; Graboshnikov, V. V. *Nanotechnology* **2003**, *14*, 709–715.
187. Tocce, E. J.; Smirnov, V. K.; Kibalov, D. S.; Liliensiek, S. J.; Murphy, C. J.; Nealey, P. F. *Biomaterials* **2010**, *31*, 4064–4072.
188. Gish, D. A.; Summers, M. A.; Brett, N. *Photonics Nanostruct. Fundam. Appl.* **2006**, *4*, 23–29.
189. Barry, R. A.; Shepherd, R. F.; Hanson, J. N.; Nuzzo, R. G.; Wiltzius, P.; Lewis, J. A. *Adv. Mater.* **2009**, *21*, 2407.
190. Uriel, S.; Labay, E.; Francis-Sedlak, M.; *et al. Tissue Eng. C* **2009**, *15*, 309–321.
191. Rosenberg, M. D. *Science* **1963**, *139*, 411–412.
192. Weiss, P.; Garber, B. *Proc. Natl. Acad. Sci. USA* **1952**, *38*, 264–280.
193. Harrison, R. G. *Science* **1911**, *34*, 279–281.
194. Chehroudi, B.; Gould, T. R.; Brunette, D. M. *J. Biomed. Mater. Res.* **1988**, *22*, 459–473.
195. Chehroudi, B.; McDonnell, D.; Brunette, D. M. *J. Biomed. Mater. Res.* **1997**, *34*, 279–290.
196. den Braber, E. T.; de Ruijter, J. E.; Smits, H. T. J.; Ginsel, L. A.; von Recum, A. F.; Jansen, J. A. *J. Biomed. Mater. Res.* **1995**, *29*, 511–518.
197. den Braber, E. T.; de Ruijter, J. E.; Smits, H. T. J.; Ginsel, L. A.; von Recum, A. F.; Jansen, J. A. *Biomaterials* **1996**, *17*, 1093–1099.
198. den Braber, E. T.; de Ruijter, J. E.; Smits, H. T. J.; Ginsel, L. A.; von Recum, A. F.; Jansen, J. A. *Biomaterials* **1996**, *17*, 2037–2044.
199. den Braber, E. T.; de Ruitjer, J. E.; Ginsel, L. A.; von Recum, A. F.; Jansen, J. A. *J. Biomed. Mater. Res.* **1998**, *40*, 291–300.
200. Fewster, S. D.; Coombs, R. R. H.; Kitson, J.; Zhou, S. *Nanobiology* **1994**, *3*, 201–214.
201. Green, A. M.; Jansen, J. A.; ven der Waerden, J. P. C. M.; von Recum, A. F. *J. Biomed. Mater. Res.* **1994**, *28*, 647–653.
202. Hoch, H.; Staples, R.; Whitehead, B.; Comeau, J.; Wolf, E. *Science* **1997**, *235*, 1659–1662.
203. Wojciak-Stothard, B.; Curtis, A. S. G.; Monaghan, W.; McGrath, M.; Sommer, I.; Wilkinson, C. D. W. *Cell Motil. Cytoskeleton* **1995**, *31*, 147–158.
204. Wojciak-Stothard, B.; Madeja, Z.; Korohoda, W.; Curtis, A.; Wilkinson, C. *Cell Biol. Int.* **1995**, *19*, 485–490.
205. Abrams, G. A.; Goodman, S. L.; Nealey, P. F.; Murphy, C. J. *Invest. Ophthalmol. Vis. Sci.* **1998**, *39*, s760.
206. Yamasake, Y.; Makino, H.; Ota, Z. *Nephron* **1994**, *66*, 189–199.
207. Karuri, N. W.; Porri, T. J.; Albrecht, R. M.; Murphy, C. J.; Nealey, P. F. *IEEE Trans. Nanobioscience* **2006**, *5*, 273–280.
208. Liliensiek, S. J.; Wood, J. A.; Yong, J.; Auerbach, R.; Nealey, P. F.; Murphy, C. J. *Biomaterials* **2010**, *31*, 5418–5426.
209. Ohara, P. T.; Buck, R. C. *Exp. Cell Res.* **1979**, *121*, 235–249.
210. Cooper, A.; Munden, H. R.; Brown, G. L. *Exp. Cell Res.* **1976**, *103*, 435–439.
211. Wilkinson, P. C.; Shields, J. M.; Haston, W. S. *Exp. Cell Res.* **1982**, *140*, 55–62.

212. Wojciak-Stothard, B.; Curtis, A.; Monaghan, W.; MacDonald, K.; Wilkinson, C. *Exp. Cell Res.* **1996**, *223*, 426–435.
213. Zinger, O.; Zhao, G.; Schwartz, Z.; *et al*. *Biomaterials* **2005**, *26*, 1837–1847.
214. Teixeira, A. I.; McKie, G. A.; Foley, J. D.; Bertics, P. J.; Nealey, P. F.; Murphy, C. J. *Biomaterials* **2006**, *27*, 3945–3954.
215. Liliensiek, S. J.; Campbell, S.; Nealey, P. F.; Murphy, C. J. *J. Biomed. Mater. Res. A* **2006**, *79*, 185–192.
216. Diehl, K. A.; Foley, J. D.; Nealey, P. F.; Murphy, C. J. *J. Biomed. Mater. Res. A* **2005**, *75*, 603–611.
217. Fitton, J. H.; Dalton, B. A.; Beumer, G. J.; Johnson, G.; Griesser, H. J.; Steele, J. G. *J. Biomed. Mater. Res.* **1998**, *42*, 245–257.
218. Robinson, R. A. *J. Bone Joint Surg. Am.* **1952**, *34A*, 389–435.
219. Weiner, S.; Traub, W. *FASEB J.* **1992**, *6*, 879–885.
220. Zhu, B.; Lu, Q.; Yin, J.; Hu, J.; Wang, Z. *Tissue Eng.* **2005**, *11*, 825–834.
221. Hatano, K.; Inoue, M.; Matsunaga, T.; Tsujisawa, C.; Uchiyama, C.; Uchida, Y. *Bone* **1999**, *25*, 439–445.
222. Green, S.; Dobrjansky, A.; Carswell, E. A.; *et al*. *Proc. Natl. Acad. Sci. USA* **1976**, *73*, 381–385.
223. Foley, J. D.; Grunwald, E. W.; Nealey, P. F.; Murphy, C. J. *Biomaterials* **2005**, *26*, 3639–3644.
224. Delgado-Rivera, R.; Harris, S. L.; Ahmed, I.; *et al*. *Matrix Biol.* **2009**, *28*, 137–147.
225. Martin, J. Y.; Schwartz, Z.; Hummert, T. W.; *et al*. *J. Biomed. Mater. Res.* **1995**, *29*, 389–401.
226. Abrams, G. A.; Goodman, S. L.; Nealey, P. F.; Murphy, C. J. *Invest. Ophthalmol. Vis. Sci.* **1997**, *38*, s505.
227. Dalby, M. J.; Gadegaard, N.; Riehle, M. O.; Wilkinson, C. D. W.; Curtis, A. S. G. *Int. J. Biochem. Cell Biol.* **2004**, *36*, 2005–2015.
228. Chung, T. W.; Liu, D. Z.; Wang, S. Y.; Wang, S. S. *Biomaterials* **2003**, *24*, 4655–4661.
229. Curtis, A. S.; Gadegaard, N.; Dalby, M. J.; Riehle, M. O.; Wilkinson, C. D.; Aitchison, G. *IEEE Trans. Nanobioscience* **2004**, *3*, 61–65.
230. Evans, M. D.; Dalton, B. A.; Steele, J. G. *J. Biomed. Mater. Res.* **1999**, *46*, 485–493.
231. Dalton, B. A.; Evans, M. D.; McFarland, G. A.; Steele, J. G. *J. Biomed. Mater. Res.* **1999**, *45*, 384–394.

1.130. Electroactive Polymeric Biomaterials

L K Povlich, University of Michigan, Ann Arbor, MI, USA; University of Delaware, Newark, DE, USA
K E Feldman and B S Shim, University of Delaware, Newark, DE, USA
D C Martin, University of Michigan, Ann Arbor, MI, USA; University of Delaware, Newark, DE, USA

© 2011 Elsevier Ltd. All rights reserved.

1.130.1.	**Introduction**	547
1.130.2.	**Conjugated Polymer Electrode Coatings**	548
1.130.2.1.	Polypyrrole	548
1.130.2.2.	Poly(3,4-ethylenedioxythiophene)	549
1.130.2.3.	PPy and PEDOT Derivatives and Copolymers	550
1.130.2.4.	Melanin	550
1.130.3.	**Conjugated Polymers on Devices**	551
1.130.3.1.	Conjugated Polymers for Living Tissue Interfaces	551
1.130.3.2.	Neural Electrodes for Recording and Stimulating	551
1.130.3.3.	Nerve Regeneration Guidance Channels and Bionic Interfaces	552
1.130.3.4.	Neural Communication Through Ionic Stimulation	553
1.130.4.	**Implantable Modification of Conjugated Polymers**	553
1.130.4.1.	Conjugated Polymer/Hydrogel Composites	553
1.130.5.	**Conjugated Polymer-Based Drug Delivery**	556
1.130.6.	**Synthesis of Conducting Polymers *In Vivo***	557
1.130.7.	**Summary and Future Outlook**	559
References		560

Abbreviations

a-MSH	A-melanocyte-stimulating hormone
ATP	Adenosine 5′-triphosphate
BDNF	Brain-derived neurotrophic factor
CS	Chondroitin sulfate A
DS	Dextran sulfate
DRG	Dorsal root ganglia
EDOT	3,4-Ethylenedioxythiophene
EDOT-COOH	Carboxylic acid-functionalized 3,4-ethyelenedioxythiophene
EDOT-N_3	Azide-functionalized 3,4-ethylenedioxythiophene
EDOT-NHS	*N*-hydroxysuccinimide-functionalized EDOT
EDOT-OH	Hydroxymethyl-functionalized 3,4-ethyelenedioxythiophene
EPR	Enhanced permeation and retention
HA	Hyaluronic acid
ITO	Indium tin oxide
NGF	Nerve growth factor
NT-3	Neurotrophin-3 growth factor
PAA	Poly(acrylic acid)
PBS	Phosphate buffered saline
PEDOT	Poly(3,4-ethylenedioxythiophene)
PEG	Poly(ethylene glycol)
PEPOP	Poly(3,4-etheylenedioxypyrrole)
PLA	Poly(lactic acid)
PLGA	Poly(lactic-*co*-glycolic acid)
PMAS	Poly(2-methoxyaniline-5-sulfonic acid)
PPy	Polypyrrole
PS	Polystyrene
PSS	Poly(styrene sulfonate)
pTS	*para*-toluene sulfonate
S-EDOT	Sulfonatoalkoxy-3,4-ethylenedioxythiophene

1.130.1. Introduction

The development of conjugated polymers, also referred to as π-conjugated or semiconducting polymers, has established a new class of materials that can interface electrically active devices with living tissue. These devices include neural probes for recording[1,2] and stimulating neurons,[3,4] prosthetic devices that can record from or stimulate peripheral nerves,[5,6] cochlear implants,[7] retinal implants,[8] and cardiac pacemakers.[9] Typical device electrodes are made from electrically conductive materials such as gold, platinum, stainless steel, and iridium oxide. These materials produce flat, hard electrodes that do not integrate well with soft, ionically conducting tissue. In addition, there is an increasing need for smaller electrodes in order to record or stimulate localized areas of tissue for greater device specificity. Reducing a metal electrode surface area will result in an increase in electrical impedance and will produce a device with decreased recording and stimulating capabilities. On the other hand, conjugated polymers are a softer class of organic materials that can be synthesized with much higher surface

area and drastically reduced impedance compared to metal electrodes. Also, conjugated polymers can be chemically tailored with specific functional groups and can incorporate biological molecules either through covalent modification or entrapment during polymerization. These biological molecules could help reduce the inflammatory response and scar formation that occur upon implantation of a device in living tissue.[10] Consequently, the development and optimization of conjugated polymers for interfacing devices with biological tissue has been the focus of research groups around the world.[11–16]

Conjugated polymers have π-conjugated backbones that facilitate the movement of electrons or holes when the polymers are reduced or oxidized, resulting in conductivity.[17,18] The types of conjugated polymers used for electrode coatings have monomers with low oxidation potentials and include polypyrrole, polythiophenes, polyanilines, and derivatives of these polymers (Figure 1). An especially important derivative of polythiophene is poly(3,4-ethylenedioxythiophene) (PEDOT). This polymer and its derivatives have produced promising bioelectrode materials and will be discussed in depth in this article. Many other types of conjugated polymers exist, but they cannot all be easily synthesized as films on electrodes via electrochemical oxidation of the monomer. Electrochemical polymerization is the most common method for preparing conjugated polymer electrode coatings since it produces films grown directly off an electrode surface. In this synthesis route, a monomer and electrolyte solution are placed in a cell with a working electrode, a counter-electrode, and a reference electrode. Upon application of an electric potential or current, the monomer is oxidized and forms radical cations at the electrode surface (Figure 1). If conditions are suitable, the radical cations react to form polymer chains that precipitate onto the electrode surface.[19] As-polymerized polymer chains have charged backbones and thus must incorporate counterions from the electrolyte in order to create a neutral, stable film. Doping with counterions allows the positive charge or hole to move throughout the conjugated backbone and provides substantial charge capacity to the material. In addition, if the polymer films are oxidized or reduced, mobile anions or cations can move in and out of the film to compensate for changes in backbone charge. Many different types of anions have been used as dopants including small molecules, such as perchlorates, chlorides, and sulfonates, polymers with anionic pendant groups, and anionic biological molecules.

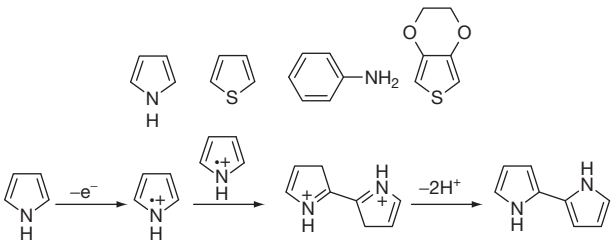

Figure 1 Monomer structures for commonly electrochemically polymerized polymers (top): pyrrole, thiophene, aniline, and 3,4-ethylenedioxythiophene. Electrochemical dimerization scheme for pyrrole (bottom). The same radical cation process continues until precipitation of the polymer.

In this chapter, we will discuss the different types of conjugated polymers used to interface devices with tissue. The material properties and biological interactions of polypyrrole and PEDOT will be discussed in detail, along with novel derivatives of these polymers and the potential use of a natural conjugated polymer, melanin. Also, other material processing techniques including gel encapsulation and nanotube formation will be included. In addition, we will review *in vivo* testing of conjugated polymers on devices, drug delivery through conjugated polymer actuation, and the possibility for *in situ* polymerization of conjugated polymer in living tissue.

1.130.2. Conjugated Polymer Electrode Coatings

1.130.2.1. Polypyrrole

The extensive study of electrochemically polymerized polypyrrole (PPy) films began in the 1980s, although there are reports of chemically polymerized PPy as early as 1963.[20–22] Since it was demonstrated that PPy could be easily deposited on metal electrodes,[23] its chemical, electrical, mechanical, and structural properties have been studied in detail. These properties, however, are highly dependent on the conditions during electrochemical polymerization, including the solvent, dopant, pH, current or voltage, and temperature.[24,25] Most importantly, it has been shown that the dopant used can affect the morphology of PPy films and, consequently, the electrical impedance of the material.[26,27] Cui *et al.* demonstrated that PPy films doped with small peptide fragments have fuzzy morphologies with high surface area.[28] As a result, the films have impedance magnitudes that are 1–2 orders of magnitude lower than bare gold at a frequency range from 10 to 10^4 Hz.

The interactions between PPy and living cells have also been examined, along with any potential toxicity. Williams and Doherty showed that electrochemically polymerized PPy doped with p-toluene sulfonate and washed with methanol is not cytotoxic to 929 mouse fibroblast and neuro2a neuroblastoma cells.[29] Additionally, a small current was applied through the PPy films and the cells continued to proliferate. Other studies using primary neural cells and tissue explants have shown similar results and indicate that unfunctionalized PPy is biopassive *in vitro*, meaning the polymer does not influence cell behavior.[30] However, the ability of PPy to facilitate electrical current has been used to change cellular morphology. Schmidt *et al.* subjected primed PC-12 cells to electrical stimulation on PPy and the cells produced longer neurites and spread out more on the substrate compared to control samples.[31] Although the cells could be electrically stimulated using the bare indium tin oxide (ITO) electrode, the cells did not adhere well to ITO, demonstrating that the cells prefer the rough, organic surface of PPy. Numerous *in vivo* studies have been performed using PPy as well. These studies are discussed in detail in the device section since most of the studies performed have implanted electrode-coated devices in animals.

Shimidzu *et al.* established that PPy can be doped with polyanions such as sodium poly(styrene sulfonate) (PSS).[32] These negatively charged polymers become entangled with PPy as electrochemical polymerization occurs and provide additional mechanical integrity to the films. Since the anionic polymer is trapped in the conducting polymer film, the cation,

sodium, is the mobile species. PPy has also been polymerized with polyanions that are biologically active such as growth factors,[33] polymers with extracellular matrix protein fragments,[28] enzymes,[34] peptide fragments,[28] heparin,[35] and hyaluronic acid.[34,36] Biological molecules can be incorporated with a co-dopant to improve the quality of the conjugated polymer films. In addition, these molecules may be physically trapped by the growing PPy film, rather than simply acting as the dopant. Unlike the passive nature of polypyrrole, the addition of bioactive molecules to electrode films can provide a means for directing cellular behavior. Importantly, it has been shown that biological molecules retain their biological activity after being trapped in conducting polymer. Kim *et al.* demonstrated that nerve growth factor (NGF) can be incorporated in PPy through electrochemical polymerization and the resulting films promote neurite outgrowth in PC-12 cells.[33] Also, the conducting polymer still has low impedance and high charge capacity. Interestingly, it has also been shown that live cells can be trapped in conducting polymer during electrochemical polymerization. Campbell *et al*. incorporated erythrocytes into PPy to create immunosensors. The erythrocytes can bind to specific antibodies, which changes the electrical resistance of PPy, thus providing a sensing mechanism.[37]

The main problem with using PPy for biomedical applications is its chemical and electrical instability.[38,39] Since pyrrole is unfunctionalized at both its α and β carbon positions, it has four available reactive sites during electrochemical polymerization. In an oxidative environment α–β′ coupling can occur and water or other nucleophilic compounds can react at the β carbon, creating defects in the polymer backbone. This type of reaction can also occur in the polymer during electrical stimulation. Yamato *et al*. compared the electrical stability of PPy and PEDOT, both with PSS counterion.[39] After holding the polymers at a constant potential in phosphate buffered saline for 16 h, the authors found that PPy lost 95% of its original electrochemical activity, whereas PEDOT only lost 11% of its original activity. It was predicted, based on previous literature, that hydroxide ions attack the β-position on the pyrrole repeat unit and break the conjugation of the polymer backbone (**Figure 2**). PEDOT, on the other hand, does not react with hydroxide ions since it has diethoxy functionalization at the β position. This study and other similar results have demonstrated that PEDOT is more suitable than PPy for devices that require long-term implantation and consistent electrical activity.

1.130.2.2. Poly(3,4-ethylenedioxythiophene)

The electrochemical polymerization of EDOT was first published in 1992 and the polymer PEDOT quickly became of interest as an electrode coating for its low oxidation potential and high chemical and electrical stability.[40,41] Similar to polpyrrole, it was shown that PEDOT has a high charge capacity and low impedance compared to the electrodes used for deposition. High surface area morphologies and tailored microstructures have been created that lower the impedance even further, making the polymer even more suitable for small bioelectrode coatings.[42–44] Although not necessarily an important property for biological applications, PEDOT films are also electrochromic, changing from dark blue to sky blue as the polymer is oxidized.[45]

In vitro toxicity and biocompatibility experiments have demonstrated that PEDOT, like PPy, is not cytotoxic to cells. Hep-2 human epithelial cells were shown to adhere better to PEDOT doped with perchlorate counterion than stainless steel electrodes and exhibited normal morphology and proliferation.[46] When treated with bovine serum albumin and other cell culture medium proteins the PEDOT samples adsorbed quantities of protein similar to polystyrene cell culture wells and stainless steel. Extracellular matrix protein adsorption allows cells to adhere to substrates *in vitro* but protein adsorption *in vivo* may result in foreign body recognition followed by an inflammatory response. To further examine the cytotoxicity of EDOT and PEDOT and to create hybrid conducting polymer-live cell electrodes, Richardson-Burns *et al*. polymerized EDOT around living SH-SY5Y neuroblastoma cells.[47] EDOT monomer was not significantly toxic to the cells over the time period needed for polymerization and the cells were able to survive the polymerization process. This finding has led to the polymerization of EDOT in tissue and the possibility of *in vivo* polymerization,[48] which is discussed at the end of this article.

Like other electrochemically polymerized conjugated polymers, PEDOT can incorporate anionic polymers and biomolecules as dopants, including peptides,[49] hyaluronic acid (HA), heparin, fibrinogen,[50] collagen,[33] and adenosine 5′-triphosphate (ATP).[51] Asplund *et al.* incorporated HA, heparin and fibrinogen into PEDOT as dopants and investigated the electrical and surface properties of the films.[50] These biomolecules are abundant in the human body and may be more suitable counterions for *in vivo* applications when compared to PSS. HA is a glycosaminoglycan found in the extracellular matrix of neural tissue, heparin is a polysaccharide anticoagulant, and fibrinogen is a glycoprotein involved in coagulation and thrombosis. PEDOT:HA and PEDOT:heparin films polymerized in a manner similar to PEDOT:PSS. On the other hand, PEDOT:fibrinogen was difficult to polymerize due to adherence of fibrinogen on the metal electrode surface prior to polymerization. In order to overcome this problem, a layer of PEDOT was deposited first, followed by PEDOT:fibrinogen. PEDOT:HA and PEDOT:heparin films have impedance and capacitance behavior similar to PEDOT:PSS, but PEDOT:fibrinogen did not produce films with adequate electrical and ionic conductivity. Additionally, it has been shown that PEDOT:heparin and PEDOT:HA films are not cytotoxic to L929 fibroblasts and SH-SY5Y neuroblastoma cells.[52] The incorporation of ATP, a nucleotide

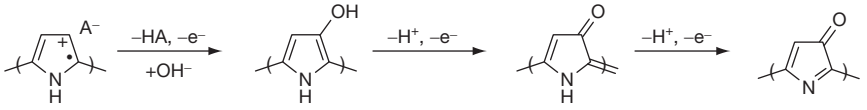

Figure 2 Side reactions during electrochemical stimulation of PPy. Hydroxide ions react at the β position and break the conjugation in the polymer.[39]

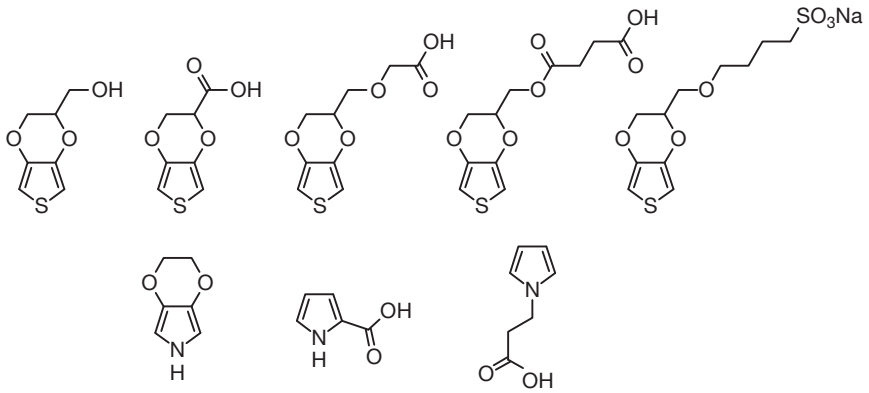

Figure 3 Example functionalized monomers for conjugated polymer electrode coatings (from top left): EDOT-OH,[54] EDOT-COOH,[55,56] C_2-EDOT-COOH, C_4-EDOT-COOH,[54] S-EDOT,[57] EDOP,[58] Py-α-COOH,[59] and PyCOOH.[60]

involved in multiple cellular functions including neural communication, also has interesting implications.[51] PEDOT:ATP films have a rough morphology, low impedance and promote adhesion of PC-12 cells. In addition, ATP is small enough to be released from conducting polymer films through electrical stimulation, resulting in an ATP delivery system.[53]

1.130.2.3. PPy and PEDOT Derivatives and Copolymers

Derivatives of PPy and PEDOT have been synthesized to produce conducting polymer films with additional chemical or biological functionality (**Figure 3**). Monomers with charged functional groups such as sulfonatoalkoxy-EDOT (S-EDOT) have been synthesized and can be used as self-dopants during electrochemical polymerization.[57] Another EDOT derivative that has been synthesized incorporates the hydroxymethyl functional group, which improves the solubility of EDOT in water. Additional functionality can also be added through reactions with hydroxy groups. Luo *et al.* used hydroxymethyl-functionalized EDOT (EDOT-OH) to create pendant carboxylic acid (EDOT-COOH), azide (EDOT-N_3) and *N*-hydroxysuccinimide groups (EDOT-NHS) on the EDOT monomers.[54] The films produced by microemulsion electrochemical polymerization of these monomers are ultra-smooth and have low cytotoxicity. In addition, the carboxylic acid can then be further functionalized with peptides or proteins through carbodiimide chemistry. Carboxylic acid functionalization has also been added to EDOT directly off of the diethoxy ring, producing the simplest possible EDOT-COOH.[55,56] Carboxylic acid-functionalized pyrroles have also been synthesized both as a pendant off of the pyrrole nitrogen and as an end-cap off of the α-position on the pyrrole ring.[59,60] RGD peptide-functionalized PPy made from these monomers have been used to increase cellular adhesion in human umbilical vascular endothelial cells compared to regular PPy. Derivatives of PPy based on poly(3,4-alkylenedioxypyrrole)s such as poly(3,4-etheylenedioxypyrrole) (PEDOP) also show potential for bioelectrode coatings. These polymers have better chemical and electrical stability than PPy and also very low oxidation potentials.[58] Many other EDOT derivatives have also been synthesized for nonbiological applications and have been reviewed in detail by the Reynolds group.[61,62]

The chemical functionality and material properties of conjugated polymer films can also be tailored through the process of electrochemical copolymerization. Monomers with similar oxidation potentials can be simultaneously polymerized to make random copolymer films. Block copolymer films can be formed by sequential polymerization of monomers. With this method, however, it is unclear whether the second polymer is covalently bonded to the first polymer or if they form two unbonded layers. Commonly, functionalized monomers are copolymerized with unfunctionalized monomers to create films with optimized functionality and stability. Biotin-functionalized pyrrole has been copolymerized with pyrrole in order to create stable, conducting films that can react with the protein avidin.[63] Biotin-functionalized enzyme or other protein can then bind to another avidin reactive site, thus producing biomolecule immobilized films.[64] Copolymerization is also advantageous in the formation of films with S-EDOT. Since this monomer is charged, the electrochemical polymerization of pure S-EDOT forms water-soluble oligomers.[65] Incorporation of unfunctionalized EDOT increases the hydrophobicity of the polymer and allows precipitation of the copolymer onto an electrode surface. Other copolymers have been formed including PEDOT/PPy,[66] PEDOT/PEDOT-OH,[67] PEDOT/polyindole,[68] and PPy/polyindole.[69]

1.130.2.4. Melanin

PPy and PEDOT can be biofunctionalized in order to reduce inflammation upon implantation and control cellular behavior, but using a natural conducting polymer may result in a more desirable biological response. The conducting polymer melanin is found in pigmented tissue such as hair, skin and eyes. Interestingly, it is also found in the inner ear and substania nigra of the brain.[70] Although the function of melanin in these areas is not known, it is speculated that it could be involved in ion binding and transport.[71] Eumelanin, a specific type of melanin, has been electrochemically polymerized, often using the monomer L-dopa and counterion sodium tetraborate to produce dark brown films with broadband absorption.[72] However, these films have not been used as biomaterials, possibly due to the toxicity of the tetraborate counterion and, therefore, lack of biocompatibility. Melanin

electrode films have been made using other precursors but most have not been investigated for their ability to interface with biological tissue. However, it has been shown that chemically polymerized eumelanin is not cytotoxic to PC-12 cells nor primary Schwann cells.[73] Recently, 5,6-dimethoxyindole-2-carboxylic acid, a methoxy derivative of a melanin repeat unit, was electrochemically polymerized to produce green films that are also electrochromic, unlike typical eumelanin.[74] The ability to tailor the chemical structure and properties of melanin may result in well-designed melanin films that can be used to interface electrodes with biological tissue; however, this has not yet been obtained.

1.130.3. Conjugated Polymers on Devices

1.130.3.1. Conjugated Polymers for Living Tissue Interfaces

Currently, one of the most successful biomedical applications of conducting polymers is the coating of neural implants to form efficient bioactive interfaces between living tissues and electronic devices. In a living body, this neural electrode works as an electrochemical transducer of electronic to ionic signal and, more specifically, to neuronal signals. The neuronal signal, or action potential, is regulated by ion flux across the cell membrane through ion channel proteins. These ion channels are gated by electromotive potential (voltage-gated), chemical transmitters (ligand-gated) and other activation mechanisms such as pressure (mechanically gated). Each ion channel responds only to its specific gate stimuli.[75] Furthermore, ionic transport through the ion channels is only $\sim 10^8$ ions per second, which is considerably slower than electronic charge carrier mobility ($1\,A \sim 10^{18}$ electrons per second). Thus, if an electrode is designed to interact with cells by effectively providing a gating stimulus, then milder stimuli can be employed to overcome any bottleneck effect of the signal transduction at the interface, which will minimize tissue damage.

Conjugated polymers can provide several gating signals to cells, including charge conduction, storage/release of neurotransmitters and mechanical swelling or contraction. For practical reasons, the conventional neural electrode studies utilized electrochemical potential mechanisms.[76,77] At the interface of electrochemical cells, charge exchange occurs between ions and electrons by capacitive (nonfaradaic), pseudocapacitive (reversible faradaic), and irreversible faradaic charge transfers. Merrill *et al.* reviewed the details of these charge injection mechanisms and safe stimulation protocols of neural electrodes.[77] Among these, the desirable charge transfer mechanism is reversible faradaic charge injection/reception at the interface because both electrodes and living tissues are less damaged by harmful irreversible reactions and corrosion. In polymer electrodes, this pseudocapacitive charge can be significantly increased by ion exchange in the polymer chains, micro-/nanopores affecting ionic boundary layers,[78] and ion pools controlled by a Donnan potential equilibrium (**Figure 4**).[79] One note here is that charge exchange sites can exist not just at the surface but also throughout the whole volume of conducting polymer, unlike metallic and ceramic electrodes. Furthermore, these reversible faradaic transfers are relatively slow to reconcile fast electronic injection to the slow biological ion channel gating at cell surfaces. Thus, conjugated polymers work more efficiently as electrochemical transducers and are superior to conventional electrode materials in living tissue applications. In addition, polymers are easily tailored to mimic the chemical structures, morphologies, and functions of living tissues so that their material properties become more chemically and mechanically similar to living tissues.

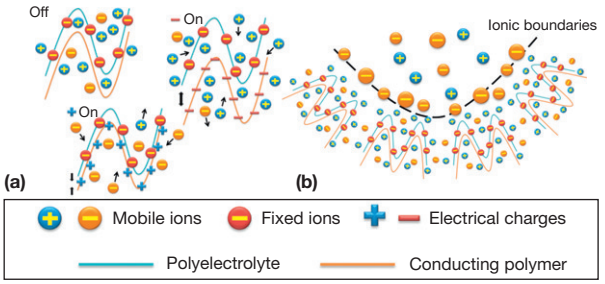

Figure 4 (a) Charge balancing between mobile cations and anions depending on the net potential of the molecular backbone and (b) Donnan equilibrium across an interface where the local concentration is balanced by a net ionic charge.

1.130.3.2. Neural Electrodes for Recording and Stimulating

Early studies of neural stimulation through conjugated polymers were performed by the Langer group. As mentioned previously, Schmidt *et al.* demonstrated that electrical stimulation of PC-12 neural cells on PPy:PSS results in enhanced neurite outgrowth.[31] This work ignited the applications of electrically conducting polymers toward living tissue interfaces with two ramifications: coatings on neural electrodes and nerve regeneration guidance channels. Soon after, Cui *et al.* reported that PPy:PSS could be selectively coated on multichannel microelectrodes, often called the 'Michigan Probe,' which are designed for single cell neural stimulation and recording. Compared to bare Au, this PPy:PSS coating can reduce the impedance of a microelectrode site by more than two orders of magnitude. *In vivo* guinea pig tests demonstrated that PPy:PSS coatings improved acute neural recordings dramatically compared to bare metal electrodes.[80] In order to mimic extracellular matrix, the same group mixed extracellular matrix components such as fibronectin and laminin fragments with the PPy coating.[28] Human neuroblastoma cells showed a greater affinity for these PPy/peptide coatings than Au electrodes *in vitro*. Furthermore, this polymeric electrode coating has shown great potential for *in vivo* and possibly chronic neural communication. Demonstration of longevity upon implantation is one of the ultimate challenges in neural probe research. Both low impedance of implanted electrodes and close proximity of neurons are required for effective neural signal recording. The latter can be potentially accomplished by recruiting a high population of neurons to the surface and by minimizing glial scarring at the interface. Migration of neurons away from electrodes is typical with implanted devices, especially hard materials. The PPy/peptide interface promotes the adhesion of living neural cells, demonstrated by *in vivo* guinea pig implantation and histology experiments. Although inflammatory gliosis still

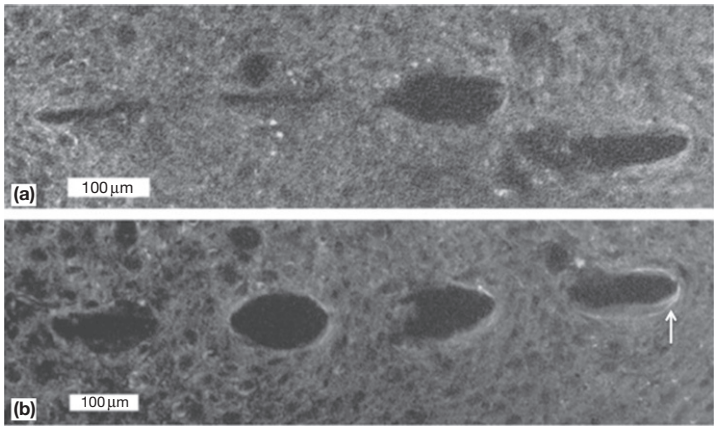

Figure 5 Immunostaining of neurofilaments around (a) uncoated bare Au electrode and (b) PPy/peptide coated electrode probes after 2 weeks of implantation. Higher densities of neurofilaments are shown around the coated than the uncoated probes. A representative neurofilament is highlighted with an arrow. This result explains why the coated probes have more neural signal recordable sites. Reprinted from Cui, X. Y.; Wiler, J.; Dzaman, M.; Altschuler, R. A.; Martin, D. C. *Biomaterials* **2003**, *24*, 777–787, with permission from Elsevier.

proceeds over time, the PPy/peptide certainly improved recording over a 3 weeks period by recruiting neural cells to the electrode interface (Figure 5).[38] In later studies, it was shown that PEDOT on neural probe electrodes is more chemically and electrically stable than PPy (Figure 6),[49] as initially indicated by Yamato *et al.*,[39] while sharing the advantages of PPy such as biocompatibility and the ability to be doped with biomolecules. In a report by Nyberg *et al.*, PEDOT:PSS coated microelectrodes demonstrated more sensitive and stable recordings of cortical cell neural networks compared to ITO electrodes.[81] In addition, Ludwig *et al.* demonstrated the *in vivo* biocompatibility of PEDOT by implanting PEDOT: perchlorate coated 'Michigan Probes' in the motor cortexes of eight rats.[82] PEDOT lowered the impedance of the electrodes and increased the signal-to-noise ratio for 6 weeks after implantation. However, after 6 weeks scar formation around the implant created an increase in impedance for both the PEDOT-coated and control neural probes.

The diverse morphologies of conjugated polymers have been utilized to improve the physical properties of neural electrodes. Given the softness and slow charge transport of cells, efforts have been made to create porous and soft polymers. Yang *et al.*, demonstrated that the porosity could be controlled both in PPy and PEDOT polymers by polystyrene (PS) microsphere templating techniques.[83] It has also been found that PEDOT forms nanofibrillar structures when mixed with poly(acrylic acid) (PAA) and lithium perchlorate.[43] The mechanical properties of PEDOT coatings with different morphologies have been tested, with the lowest modulus of PEDOT reported to be around 10 MPa.[44] The lowest impedances were also obtained with the softest, roughest coatings. This pattern implies that ionic transport in and out of the polymer is facilitated with fuzzier PEDOT morphologies (Figure 7). In a study by Gelmi *et al.*, the stiffness of PPy was adjusted through the use of different counterions.[84] When PPy is electrochemically polymerized with *para*-toluenesulfonic acid (pTS), hyaluronic acid (HA), dextran sulfate (DS), chondroitin sulfate A (CS), and poly(2-methoxyaniline-5-sulfonic acid) (PMAS), the Young's moduli were 1000, 706, 660, 290, and 30 MPa, respectively. This controllability of stiffness may be useful for applications at harder tissue interfaces such as muscle.

1.130.3.3. Nerve Regeneration Guidance Channels and Bionic Interfaces

The full function of injured or severed nerves can be recovered only if properly treated. Clinically, the gold standard of peripheral nerve regeneration is utilization of autologous nerve grafts, which are taken from the injured patient, as guidance conduits. However, autologous nerve grafts are not always available. Thus, foreign or synthetic materials should be adopted for clinical applications. The ideal nerve guidance conduits may require durability, flexibility, biodegradability, supply of bioactive substances such as growth factors and support cells, oriented intraluminal channels, and electrical activity.[85,86] Many studies have been performed, but so far no synthetic material meets all of these conditions. Instead, acellular nerve tissue grafts from human tissue donors are commercialized and expected to fulfill the clinical needs. The past research efforts on creating synthetic guidance channels may not be applicable directly to neural regeneration, but the research findings are still beneficial for chronic bionic interfaces that are now emerging.

The key difference between peripheral nerve guidance channels and central nervous system electrodes is that guidance channels aim to promote axonal outgrowth and alignment so that the channels interface mostly with axons rather than cell bodies. This interaction has been demonstrated by Corey *et al.* in the use of aligned electrospun nanofibers made out of poly-L-lactate, which influence the directionality of neurite growth in dorsal root ganglia (DRG) explants.[87] The Wallace group combined biodegradable fibers with a PPy conducting polymer platform to stimulate aligned axonal growth.[88] Electrical stimulation through the conducting polymer enhanced both axonal growth and migration of Schwann cells from DRG explants (Figure 8). Furthermore, the axonal growth and migration of Schwann cells were aligned along the uniaxial poly(lactic acid)

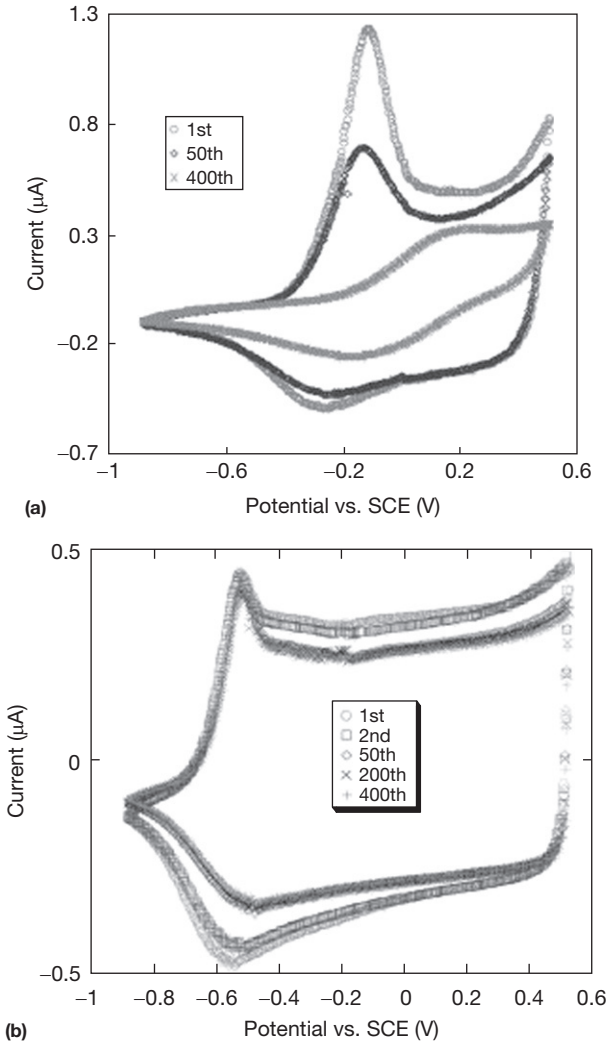

Figure 6 Electrochemical stability by cyclic voltammetry of (a) PPy:PSS and (b) PEDOT:PSS with scan rate 0.1 V s^{-1}. While PPy:PSS loses its charge storage capacity with repeated cycles, PEDOT:PSS maintains a relatively large storage capacity. Reprinted from Cui, X. Y.; Martin, D. C. *Sensors Actuat. B Chem.* **2003**, *89*, 92–102, with permission from Elsevier.

(PLA) and poly(lactic-*co*-glycolide) (PLGA) fibers. In another similar study, Lee *et al.* demonstrated that PC-12 cells could be aligned on PPy coated PLGA nanofibers.[89] With electrical stimulation and fiber alignment, the cells had 40–90% more neurites than control samples and the neurites were also 40–50% longer.

Certainly, electrical stimulation of neural cells on conducting polymers facilitates neurite outgrowth, which has been confirmed by many other reports. One addition to this principle is that conducting polymers with bioactive molecules such as growth factors enhance the length of neurites synergistically with electrical stimulation. Richardson *et al.* and Thompson *et al.* reported that both electrical stimulation through PPy:pTS and delivery of neurotrophin-3 (NT-3) growth factor affect the length and the number of neurites on cells in cochlear explants.[90,91]

1.130.3.4. Neural Communication Through Ionic Stimulation

One of the most unique applications for conjugated polymers is a static ion pump with selective ion flux controls. Conventional neural electrode concepts involve charge transduction between electrons and ions at cellular interfaces. However, ion pumps made using PEDOT:PSS can directly inject ions to communicate with cells, even without creating fluid flow or pressure build-up. Isaksson *et al.* created microfabricated PEDOT:PSS patches that can selectively drive cellular signaling ions, such as Ca^{2+} and K^{+}, to microchannels containing individual neural cells.[92] It was shown that stimulation with ions could affect the behavior of cells in the microchannel without influencing cells 500 μm away. This ion pump was further developed to deliver selective neurotransmitters *in vivo* to guinea pig cochlea through a syringe-like pump design.[93] This direct ion-injecting paradigm has advantages in establishing communication between living tissues and devices including the safety of avoiding electrical shock, the versatility in delivering bioactive ions, and direct controllability by electrophoretic modulation. Thus, it is expected that new neural electrode designs following this ion pump concept will be actively researched in the future. A similar concept utilizes the fact that conjugated polymers can accept various quantities of electrons or ions, which can be described as different electrochemical states. The varying electrochemical redox states of PEDOT have been used to influence cellular behavior.[94] Epithelial cells were tested on PEDOT:pTS surfaces *in vitro*. Interestingly, the cells proliferated selectively on reduced PEDOT surfaces, not on the oxidized material. The cause, as the authors suggested, may be the conformational changes of fibronectin on oxidized PEDOT:pTS, and the resulting inability for cellular adhesion. This electrochemical modulation technique may be used as an on/off type tool for manipulating living tissues.

1.130.4. Implantable Modification of Conjugated Polymers

1.130.4.1. Conjugated Polymer/Hydrogel Composites

Conducting polymers can be modified with hydrogels, which improve small molecule transport, the degree of hydration, and the mechanical flexibility of the composite. As a result, these conjugated polymers composites become even more similar to the extracellular matrix. Conducting hydrogels are used in various applications such as biosensors and drug delivery, which were discussed in recent reviews.[95,96] Our discussion here will be limited to neural electrode applications of conjugated polymer hydrogels. The most important features of hydrogels are their mechanical softness and flexibility. Thus, conducting polymer hydrogels can provide a mechanical buffer layer between the rigid electrodes and living tissues. The brain, whose elastic and shear moduli are the orders of 1[97] and 10 kPa,[98] respectively, is one of the softest tissues in the body. Furthermore, regeneration of nervous systems,[99] rate of neurite extension,[100] and neuronal differentiation of stem cells[101] all exhibit a preference for soft, elastic culture matrices.

Secondly, hydrogels contain structures that function well as electrochemical transducers. While conducting polymers

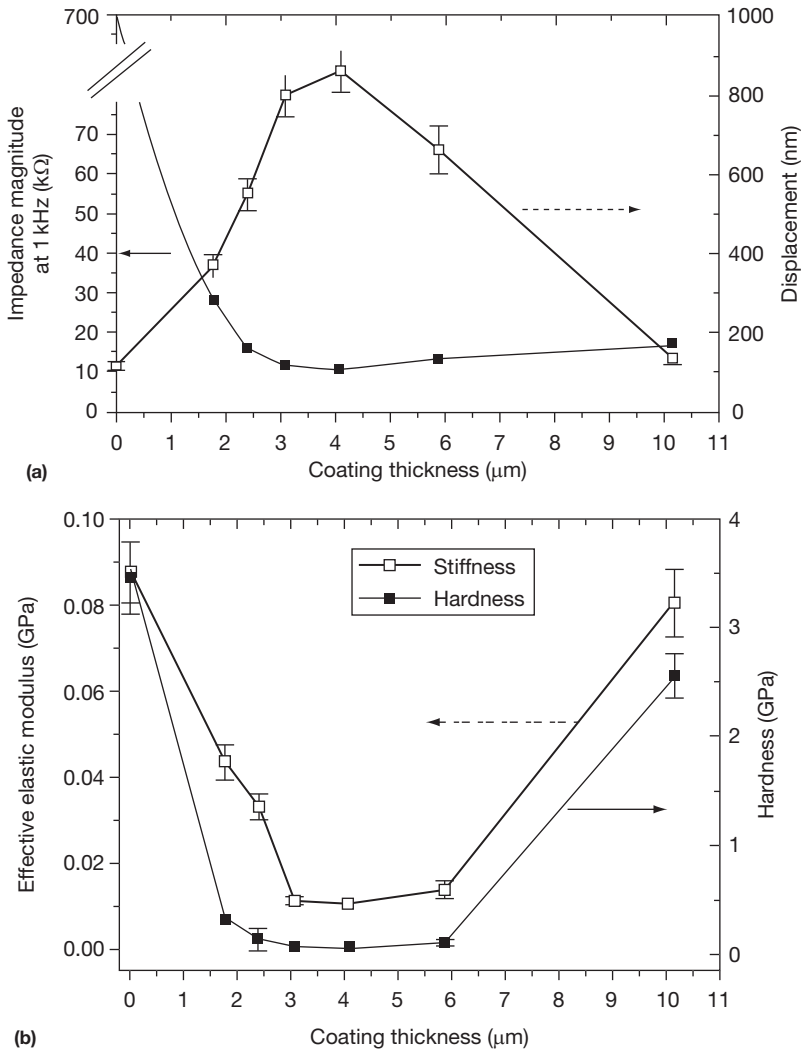

Figure 7 (a) Impedances and displacement of nanoindentation and (b) modulus and hardness as a function of PEDOT thickness. Reprinted from Yang, J. Y.; Martin, D. C. *J. Mater. Res.* **2006**, *21*, 1124–1132, with permission from Material Research Society.

provide delocalized electromigration pathways through the conjugated backbone, electrical field-mediated ion movement can occur from the polymeric chains to fluid media and vice versa. In a conducting polymer gel, the capacity of this ion flux is even further expanded by the elevated porosity and hydration. Thus, the merits of employing conducting gel bioelectrodes cover not only mechanical and biological properties, such as low interfacial tension and the promotion of cell adhesion, but also improvement of electrochemical efficiency and electrode safety by reducing possible tissue damage through irreversible faradaic reactions.

Charge transfer efficiency studies were performed in the early works on conjugated polymer hydrogels, following the technical demonstration of electrochemical polymerization through hydrogel networks.[102] Kim *et al.* introduced biocompatible conducting composite hydrogels with natural alginate and PPy on neural microelectrodes.[103] After alginate gels containing pyrrole monomer were formed by $CaCl_2$ cross-linking, PPy/PSS was vertically grown from the microelectrode along the gel by galvanostatic deposition. This vertical polymerization through a gel is a general process of conducting polymer growth and has been shown in other materials like PEDOT (**Figure 9**).[104] Also, the polymerization pattern corroborates the theory that electrical charges are locally injected by ion flux out of alginate chains and long distance electro-migrations are only guided by conducting polymer chains inside the hydrogel (**Figure 4**). Thus, these expanded ion migration pools in the PPy/PSS/alginate conducting hydrogels are reflected by the exceptionally high charge storage capacity, 560 mC cm^{-2}[103] which can be compared to 186 mC cm^{-2} for a PPy/PSS only coating.[80]

Neural electrodes with conducting polymer/hydrogel composites have been tested to establish stable recording performances with hopes of chronic recording in the future. Kim *et al.*, found that alginate hydrogel with PEDOT grown through it can relay stable neural recordings to microelectrodes in a guinea pig animal model.[105] PEDOT-hydrogel coatings perform better than hydrogel coatings alone. Since PEDOT is

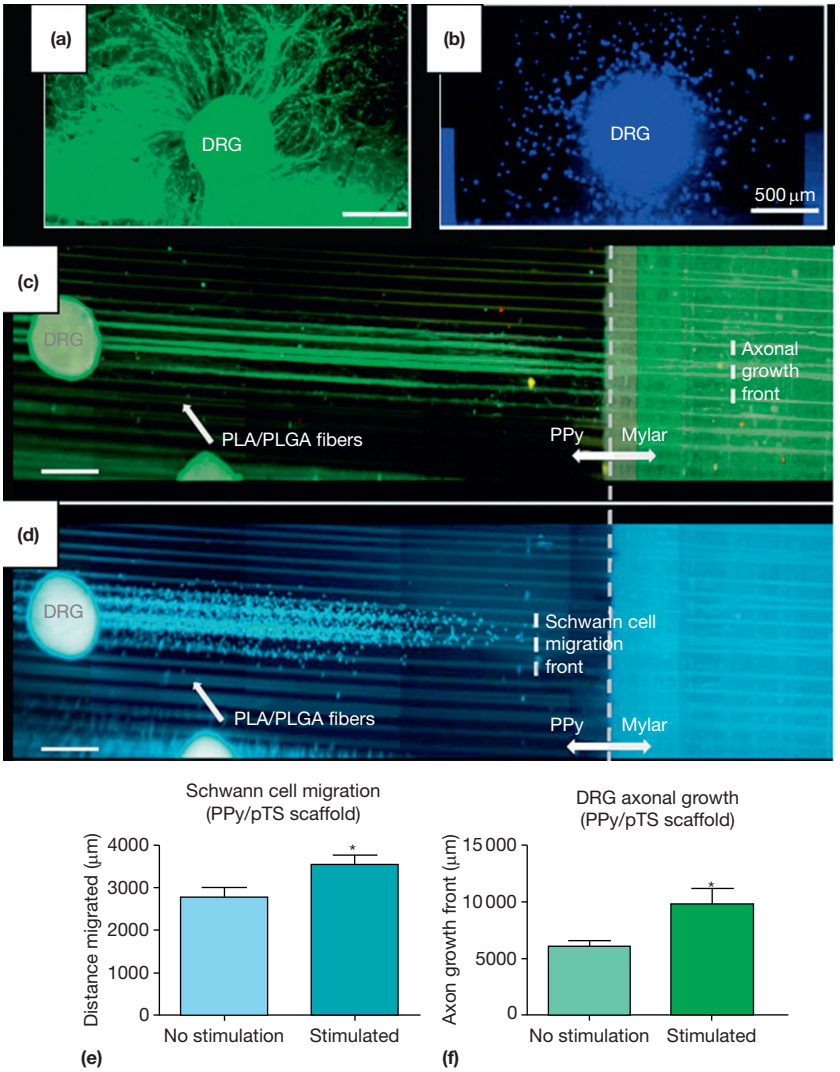

Figure 8 DRG grown on laminin coated PPy/pTS substrate. (a, c) DRG and (b, d) Schwann cells (c, d) with and (a, b) without aligned fibers. Biphasic electrical stimulation effects on (e) Schwann cell migration and (f) DRG axonal growth. Reprinted from Quigley, A. F.; Razal, J. M.; Thompson, B. C.; *et al*. *Adv. Mater.* **2009**, *21*, 4393–4397, with permission from Wiley.

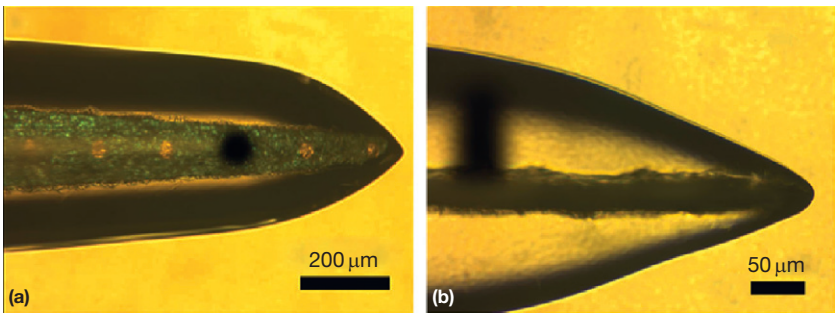

Figure 9 Optical micrographs of vertical growth of conjugated polymer, PEDOT (black color), through the alginate hydrogel. (a) Top view and (b) side view of the coated electrode. Reprinted from Abidian, M. R.; Martin, D. C. *Adv. Funct. Mater.* **2009**, *19*, 573–585, with permission from Wiley.

grown through the hydrogel, a better electrical connection is maintained with the surrounding neurons. Currently, long-term electrochemical stability of a conducting hydrogel coating has not yet been obtained. Meanwhile, several other techniques such as conducting elastomers and conducting polymer nanotubes have been employed to reduce the mechanical modulus while preserving electrochemical durability. Keohan *et al.* used PPy conductive elastomer to soften the

interfaces of cuff electrodes.[106] PPy-siloxane copolymers showed electrochemical stability over more than 10 days of stimulation *in vitro*. Another way to buffer the mechanical stiffness of metallic electrodes is to form conducting polymer nanotubes. In a recent report by Abidian *et al.* it was demonstrated that PEDOT nanotube coatings on a neural microelectrode could enhance *in vivo* signal-to-noise ratio significantly. Furthermore, these enhancements were translated to the chronic performance stability of PEDOT nanotube-coated neural electrodes, which lasted up to 49 days.[107]

Although some long-term *in vivo* studies have been reported, the ultimate challenge in neural electrodes is creating an interface that is stable and robust for years. Generally, the communication breakup of neural electrodes may be caused, not by the failure or degradation of materials, but by inflammation such as implantation trauma, Wallerian degeneration, and glial scar formation (gliosis). The insulating scars, which are gradually thickened, isolate electrodes from tissues, similar to body piercing effects, thereby disrupting communication signals. Therefore, a chronic interface may be possible by quenching the inflammation response toward implanted electrodes. A new approach has been demonstrated involving anti-inflammatory drugs that can quench gliosis and thus extend the life of the neural electrodes. Demonstrating that hydrogels are excellent biomolecule carriers, Kim *et al.* showed that PLGA nanoparticles with dexamethasone, which is an anti-inflammatory and immune-suppressive steroid, could be mixed into an alginate hydrogel coating on neural electrodes.[108] *In vivo* Guinea pig studies revealed that the impedances of the coated electrodes were stable for more than three weeks while noncoated metal electrodes lost their functionality in 16 days. Similarly, Zhong *et al.* showed that the anti-inflammatory neuropeptide α-melanocyte stimulating hormone (α-MSH) can be used in coating neural electrodes.[109]

1.130.5. Conjugated Polymer-Based Drug Delivery

The delivery of drugs to targeted locations in the body in a controlled way is a significant technical challenge. Traditional oral- or injection-based delivery relies on maintaining a high systemic drug concentration; this consequently requires multiple doses, and a large fraction of the delivered drug is often cleared from the body before performing its therapeutic function. Particularly in the case of highly toxic drugs, local, targeted delivery is critical as high systemic concentrations could lead to undesirable side effects. In other instances, sensitive compounds must be protected from enzymatic or hydrolytic degradation before reaching the target site.

Many strategies have been recently developed to overcome such limitations. Drugs have been conjugated to synthetic polymers such as poly(ethylene glycol) (PEG) to provide enhanced water solubility and circulation times, while helping prevent uptake by the spleen, liver, and kidneys.[110] Conjugation with linear polymers is typically through one or both chain ends, which limits loading capacity. As an alternative, several groups have begun using dendrimers,[111] which present many surface functional groups in a compact macromolecular architecture. Liposome and micelle-based carriers can also provide a protected environment for the drug to circulate and allow for very high loading.[112] Targeting of specific delivery sites has been attempted through the use of recognition elements such as peptides,[113] or in the case of cancer treatment through the enhanced permeation and retention (EPR) effect.[114] When systemic circulation is especially undesirable, drugs have been encapsulated within hydrogels[115] or biodegradable polymers,[116] allowing for much slower release and localized delivery through implantation of the conjugate at the site of interest.

In contrast to such passive strategies, conducting polymers have provided a means for targeted, triggered delivery through electrical or electrochemical actuation. PPy and PEDOT in particular have proven to be highly biocompatible, both *in vitro* and *in vivo*. Thin films can be electrochemically deposited on conducting substrates or cast from solutions of chemically synthesized polymers, and many unique geometries have been demonstrated such as porous sponges,[117] nanotubes,[107,118–120] and coated acellularized scaffolds.[121]

The use of conducting polymers for drug delivery is based on actuation through reversible oxidation and reduction of the polymer backbone. In the fully oxidized state, the polymer is positively charged and has anions associated for charge neutrality. The actuation mechanism depends in part on the nature of the counterion, whether large and bulky or small and mobile. As the polymer is biased and reduced, the overall cationic charge density decreases, and in the case of small anions this change is accompanied by the expulsion of counterions and a decrease in the polymer volume. In the case of large, immobile counterions such as PSS, anion expulsion is not possible and so cations in the surrounding solution diffuse into the film and increase its volume. This effect has been utilized in macroscopic soft actuators[122] as well as microscopic drug delivery vectors.

Triggered drug delivery using conducting polymers can be achieved in several ways, but the most common strategy is to directly incorporate the drug of interest as the counterion during polymer synthesis. Because electrochemical polymerization results in cationic polymer chains, anionic drugs are the primary targets. When a particular anionic species cannot be directly incorporated during deposition, ion exchange via electrochemical cycling in the presence of the desired compound is used to 'load' the film. Cationic drugs are less common but can be incorporated when the primary counterion is bulky, such as PSS. Glutamate,[123] dopamine,[123] adenosine 5′-triphosphate (ATP),[124,125] salicylate,[126] naproxen,[126] and neurotrophin-3[127,128] have all been incorporated into conducting polymer layers as counterions and subsequently released electrochemically.

Much more challenging, however, is the delivery of neutral drugs. Because conducting polymer actuation is based on charging and discharging of the polymer backbone and the associated release of counterions, no driving force exists for the movement of neutral species. Early attempts involved doping the conducting polymer film with an ionic cyclodextrin followed by loading with a neutral guest, but its release still relied on a redox reaction of the guest molecule.[129] In neural applications, inflammation and scar tissue formation are highly undesirable and so the delivery of anti-inflammatory drugs, such as dexamethasone, is an important target. Several strategies have been developed to overcome this limitation; the

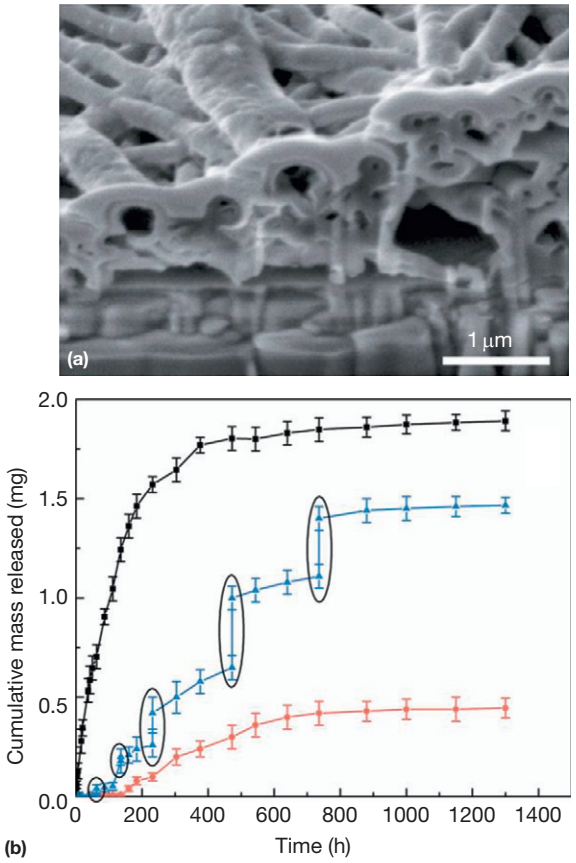

Figure 10 Electrically stimulated release of dexamethasone from PEDOT nanotubes (top) and SEM micrograph showing the size and morphology of the nanotubes. Reprinted from Abidian, M. R.; Kim, D. H.; Martin, D. C. *Adv. Mater* **2006**, *18*, 405–409, with permission from Wiley.

pro-drug dexamethasone disodium phosphate can be converted *in vivo* into an active drug and has been incorporated into PPy as a counterion during deposition.[117,130,131] More recently, triggered release of neutral dexamethasone has been achieved through its incorporation in PEDOT nanotubes.[119] Fibers of a degradable polymer containing the drug were electrospun, then coated with PEDOT via electrochemical deposition (Figure 10). Degradation of the fibers resulted in hollow nanotubes containing the drug, which could be compressed and released using an applied bias. On actuation via an externally applied voltage bias, dexamethasone was shown to be released into the solution, either through cracks and pores in the tube walls or out the ends of the tubes.

Beyond delivering a single drug, it is desirable to trigger the release of multiple different drugs at defined time points. To demonstrate this, a microchip has been developed with addressable microelectrodes onto which PPy can be deposited electrochemically. The electrically triggered release of two different drugs, ATP and sulfosalicylic acid, was achieved.[132] Chemical triggers can also be utilized for drug release. Reduction of PPy/ATP films by either hydrazine or the bioreductant dithiothreitol resulted in the release of ATP and a decrease in the film conductivity.[53]

1.130.6. Synthesis of Conducting Polymers *In Vivo*

Conducting polymers, in particular PPy and PEDOT, are demonstrably biocompatible and have been utilized in implantable devices as electrically active coatings, sensors, and actuators. It is presumed, however, that even more effective electrical connectivity with living tissue would be achieved through one of several routes, including seeding of the device with neural progenitor cells or electrochemical polymerization directly within the tissue itself (rather than by implantation of a pre-formed device). The former strategy attempts to minimize the formation of the reactive scar around the implant through the secretion of neuroprotective and neurotrophic factors and consequently allow the signaling neurons to remain closer to the electrode. This strategy has shown some success over the short term in neural probes, with an initial reduction in nonneuronal encapsulation, but over long-term implantation a greater concentration of nonneuronal cells compared to nonseeded probes was observed.[133] Similarly, cochlear implants seeded with brain derived neurotrophic factor (BDNF)-secreting fibroblasts yielded a significant improvement in spinal ganglion cell survival for several weeks post-implantation.[134]

In contrast, electrochemical deposition of conducting polymer within living tissue has been proposed as a strategy to effectively extend the electrode past the glial scar by the formation of conductive filaments through the interstitial spaces. This strategy provides several potential benefits. First, the natural immune response could be allowed to proceed unhindered, after which electrochemical polymerization would be performed to extend the electrical connection past the scar layer. Additionally, signal transport between the electronically conductive metal electrode and ionically conductive neurons could be facilitated through intimate contact of each with the conducting polymer.

Initial studies have demonstrated the feasibility of this approach. Both erythrocytes[37] and neural cells[47] have been shown to maintain reasonable viability upon exposure to low concentrations of monomer (0.001–0.01 M) as well as low electrical current (0.5–5 mA mm^{-2}). After culturing cells on electrodes and allowing for attachment to the substrate, PEDOT can be grown around the cells to yield a thin, nodular coating that reflects the cell morphology (Figure 11). Removal of the cells using trypsin results in a cell-templated PEDOT film containing holes and caves, and repopulation with new cells demonstrated their enhanced affinity toward the templated regions. Although cell viability could be maintained for up to a week after PEDOT deposition, apoptosis was induced as long as 24–72 h after deposition. Additionally, disruption of the cytoskeleton was observed through a reduction in F-actin stress fibers, reflecting a lack of focal adhesions and possibly contributing to apoptosis. Interaction between PEDOT and neural cells could potentially be improved by the incorporation of cell adhesive peptides or extracellular matrix components either as dopants or via chemical attachment to the polymer backbone, and both strategies are being actively researched by a number of groups.

With the demonstration that cell viability can be maintained after electrochemical polymerization, experiments were undertaken to show that such polymerizations could be

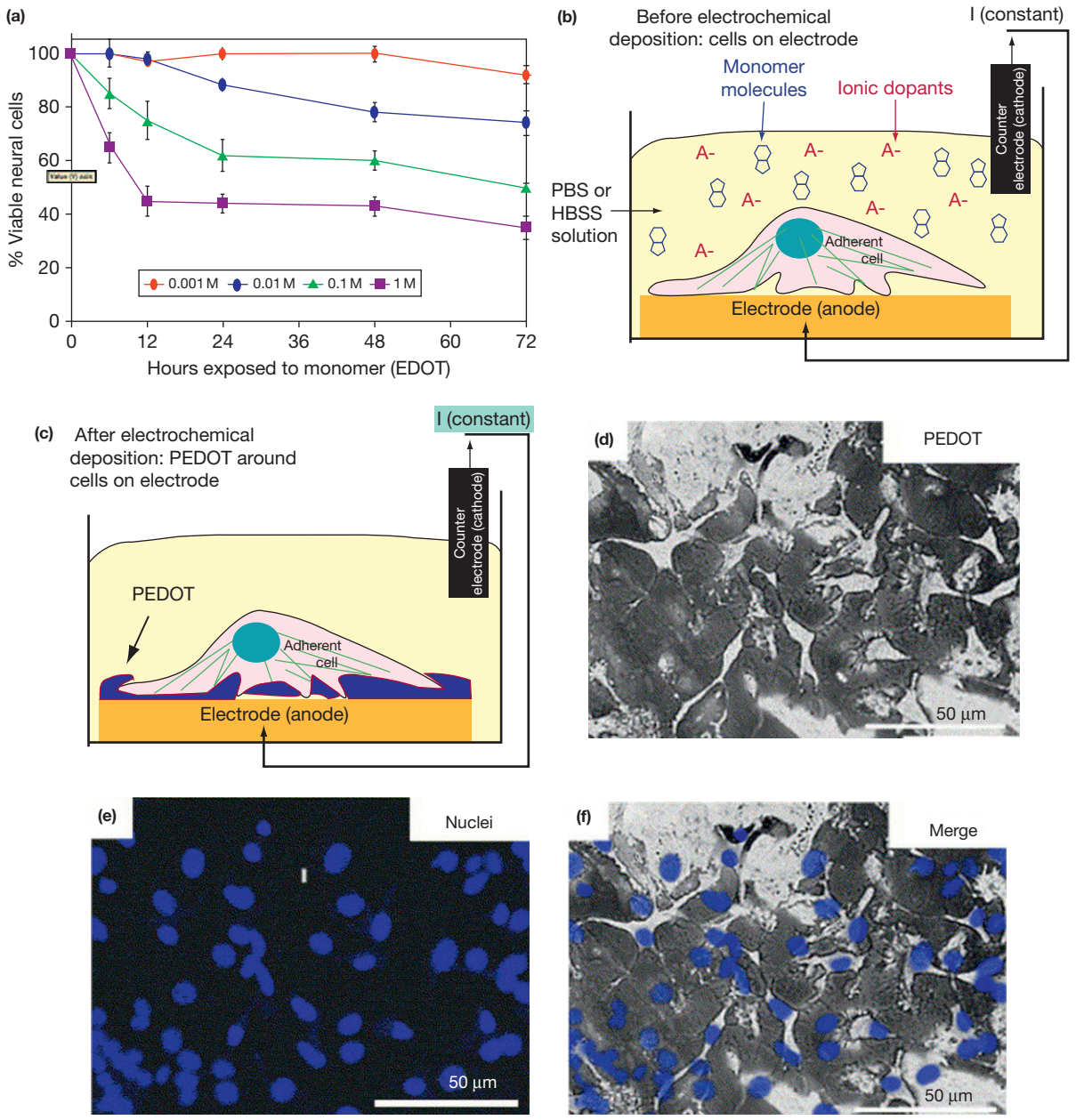

Figure 11 (a) MTT cytotoxicity assay for exposure of SY5Y neural cells to increasing concentrations of EDOT in monomer solution (all with 0.02 M PSS) for 0–72 h. (b) Diagram representing the electrochemical deposition cell and the neural cell monolayer cultured on the surface of the metal electrode prior to polymerization. (c) Diagram representing PEDOT polymerized around living cells. (d) PEDOT (dark substance) polymerized in the presence of a monolayer of SY5Y neural cells cultured on an Au/Pd electrode. (e) Nuclei of SY5Y cells stained with Hoechst 33342 (blue florescence). (f) Merged image showing nuclei of cells around which PEDOT is polymerized. Reprinted from Richardson-Burns, S. M.; Hendricks, J. L.; Foster, B.; Povlich, L. K.; Kim, D. H.; Martin, D. C. *Biomaterials* **2007**, *28*, 1539–1552, with permission from Elsevier.

done directly within living tissue, allowing for intimate contact between implanted electrodes and electrically active cells such as neurons, cardiac cells, or skeletal muscle cells. Electrochemical polymerization of EDOT was demonstrated in rat brain slice cultures by embedding the slice in gelatin, exposing the entire slice to dilute monomer solution, and applying current to a gold wire working electrode implanted in the tissue (Figure 12).[48] PEDOT was grown as micro and nano filaments through the extracellular space, and with an even modest total polymerization charge (90 mC) the PEDOT cloud extended nearly 1 mm away from the electrode. The presence of the PEDOT cloud drastically improved the electrical properties of the electrode, reducing the impedance by 1–2 orders of magnitude primarily through an increase in the effective electrode surface area due to the filamentous structure. Exposing a large volume of tissue to EDOT monomer is unfeasible and undesirable, so new strategies are being developed to locally deliver both the monomer solution and

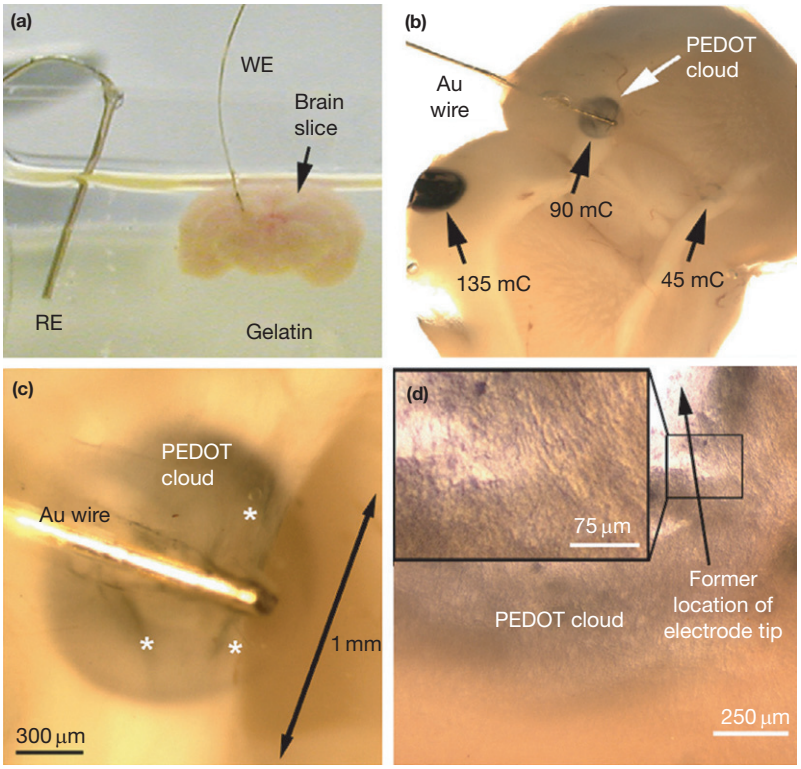

Figure 12 A network of conducting PEDOT filaments can be polymerized directly within brain tissue from an implanted electrode. (a) An image of the set-up used to polymerize PEDOT directly within a mouse brain slice. The tissue slice is physically stabilized within gelatin then a microwire electrode is inserted into the tissue and a platinum wire reference/counter electrode is inserted into the gelatin. (b) A mouse brain slice (2 mm thick) within which three distinct PEDOT networks were polymerized from a Au microwire using increasing polymer deposition charges of 45, 90, and 135 mC. (c) A higher magnification image reveals that the PEDOT cloud integrates directly within the tissue and appears to intensify near and follow white matter fiber tracts (see white stars). (d) High magnification optical micrograph reveals the microscale structure of the PEDOT filaments within the network and suggests that tissue and extracellular matrix structures were used as a scaffold for polymerization. These data are representative of similar findings in roughly 20 brain slices in which PEDOT was polymerized using similar deposition conditions. Reprinted from Richardson-Burns, S. M.; Hendricks, J. L.; Martin, D. C. *J. Neural Eng.* **2007**, *4*, L6–L13, with permission from IOPP.

polymerization current and extend this technology to the direct polymerization of EDOT *in vivo*.

Given that the counterion incorporated during electrochemical polymerization can have a significant effect on the electrical, structural, and mechanical properties of conducting polymers, an important question is what anions would be incorporated during *in vivo* polymerization within the complex ionic environment of living tissue. Recent studies have shown that in mixtures of ions (such as PBS), Cl^- is preferentially incorporated over $H_2PO_4^-$, HPO_4^{-2}, and $LiClO^{4-}$.[135] When PSS is present, however, its polyanionic character leads to a high preference for incorporation since association of a chain with one $PEDOT^+$ site allows for association and quenching of many more neighboring sites. It is therefore possible that during *in vivo* electrochemical polymerization, extracellular matrix components or proteins could serve as counterions.

1.130.7. Summary and Future Outlook

Conjugated polymers such as PPy and PEDOT have shown tremendous potential as materials for interfacing electrically conducting devices with biological tissue. Besides being semi-conducting, these polymers are organic, relatively soft, ionically conductive, have low cytotoxity and have the ability to be morphologically and chemically tailored. These properties and the low electrical impedance of conjugated polymer films make them suitable for neural microelectrode coatings and nerve regeneration fibers. PEDOT and its derivatives have proven to be the most promising of these polymers for their chemical and electrically stability. In addition, composites of conjugated polymers with hydrogels are softer, even more tissue-like materials. The actuation ability of conjugated polymers also enables the release of ions for ionic stimulation of cells, or drugs to manipulate cellular behavior. The current state of development for biologically interfacing conjugated polymers requires further investigation into *in vivo* interactions. For chronic cortical neural probes, it is necessary to maintain a long-term electrical connection between electrodes and neurons. Currently, this is impeded by the formation of insulating glial scars around implanted probes. Therefore, methods such as anti-inflammatory drug delivery, *in vivo* polymerization or other techniques that reduce or work around the scarring should be optimized and tested in animal models to demonstrate their effectiveness. Conjugated polymer constructs have also shown promise as nerve guidance fibers, but

these also need to demonstrate regenerative capabilities *in vivo*. As biofunctionalized conjugated polymers, drug-loaded constructs or techniques such as *in vivo* polymerization are shown to work successfully, conjugated polymers may prove to be an essential component for stable, permanent connections between electronic devices and biological tissue.

Acknowledgments

Research in the Martin group has been supported in part by the National Institutes of Health, the US Army Multidisciplinary University Research Initiative, the National Science Foundation, Biotectix LLC, the Michigan University Commercialization Initiative, the University of Michigan College of Engineering Translational Research (GAP) funding, and the University of Delaware. DCM is a cofounder and Chief Scientific Officer for Biotectix LLC (www.biotectix.com) an Allied Minds (www.alliedminds.com), University of Michigan spin-off company that is investigating the use of conducting polymers on a variety of biomedical devices.

References

1. Hoogerwerf, A. C.; Wise, K. D. *IEEE Trans. Biomed. Eng.* **1994**, *41*, 1136–1146.
2. Nordhausen, C. T.; Maynard, E. M.; Normann, R. A. *Brain Res.* **1996**, *726*, 129–140.
3. Campbell, P. K.; Jones, K. E.; Huber, R. J.; Horch, K. W.; Normann, R. A. *IEEE Trans. Biomed. Eng.* **1991**, *38*, 758–768.
4. Tehovnik, E. J. *J. Neurosci. Meth.* **1996**, *65*, 1–17.
5. Akin, T.; Najafi, K.; Smoke, R. H.; Bradley, R. M. *IEEE Trans. Biomed. Eng.* **1994**, *41*, 305–313.
6. Navarro, X.; Krueger, T. B.; Lago, N.; Micera, S.; Stieglitz, T.; Dario, P. *J. Peripher. Nerv. Syst.* **2005**, *10*, 229–258.
7. Wilson, B. S.; Dorman, M. F. *Hear. Res.* **2008**, *242*, 3–21.
8. Margalit, E.; Maia, M.; Weiland, J. D.; *et al. Surv. Ophthalmol.* **2002**, *47*, 335–356.
9. Trohman, R. G.; Kim, M. H.; Pinski, S. L. *Lancet* **2004**, *364*, 1701–1719.
10. Polikov, V. S.; Tresco, P. A.; Reichert, W. M. *J. Neurosci. Meth.* **2005**, *148*, 1–18.
11. Berggren, M.; Richter-Dahlfors, A. *Adv. Mater.* **2007**, *19*, 3201–3213.
12. Guimard, N. K.; Gomez, N.; Schmidt, C. E. *Prog. Polym. Sci.* **2007**, *32*, 876–921.
13. Kotov, N. A.; Winter, J. O.; Clements, I. P.; *et al. Adv. Mater.* **2009**, *21*, 3970–4004.
14. Owens, R. M.; Malliaras, G. G. *MRS Bull.* **2010**, *35*, 449–456.
15. Poole-Warren, L.; Lovell, N.; Baek, S.; Green, R. *Expert Rev. Med. Devices* **2010**, *7*, 35–49.
16. Wallace, G. G.; Spinks, G. M. *Chem. Eng. Prog.* **2007**, *103*, S18–S24.
17. Chiang, C. K.; Fincher, C. R.; Park, Y. W.; *et al. Phys. Rev. Lett.* **1977**, *39*, 1098–1101.
18. Kumar, D.; Sharma, R. C. *Eur. Polym. J.* **1998**, *34*, 1053–1060.
19. Sadki, S.; Schottland, P.; Brodie, N.; Sabouraud, G. *Chem. Soc. Rev.* **2000**, *29*, 283–293.
20. Asavapiriyanont, S.; Chandler, G. K.; Gunawardena, G. A.; Pletcher, D. *J. Electroanal. Chem.* **1984**, *177*, 229–244.
21. McNeill, R.; Weiss, D. E.; Wardlaw, J. H.; Siudak, R. *Aust. J. Chem.* **1963**, *16*, 1056–1075.
22. Street, G. B.; Lindsey, S. E.; Nazzal, A. I.; Wynne, K. J. *Mol. Cryst. Liq. Cryst.* **1985**, *118*, 137–148.
23. Diaz, A. F.; Kanazawa, K. K.; Gardini, G. P. *J. Chem. Soc. Chem. Commun.* **1979**, 635–636.
24. Imisides, M. D.; John, R.; Riley, P. J.; Wallace, G. G. *Electroanalysis* **1991**, *3*, 879–889.
25. Satoh, M.; Kaneto, K.; Yoshino, K. *Synthetic Met.* **1986**, *14*, 289–296.
26. Silk, T.; Hong, Q.; Tamm, J.; Compton, R. G. *Synthetic Met.* **1998**, *93*, 59–64.
27. Silk, T.; Hong, Q.; Tamm, J.; Compton, R. G. *Synthetic Met.* **1998**, *93*, 65–71.
28. Cui, X. Y.; Lee, V. A.; Raphael, Y.; *et al. J. Biomed. Mater. Res.* **2001**, *56*, 261–272.
29. Williams, R. L.; Doherty, P. J. *J. Mater. Sci. Mater.* **1994**, *5*, 429–433.
30. George, P. M.; Lyckman, A. W.; Lavan, D. A.; *et al. Biomaterials* **2005**, *26*, 3511–3519.
31. Schmidt, C. E.; Shastri, V. R.; Vacanti, J. P.; Langer, R. *Proc. Natl. Acad. Sci. USA* **1997**, *94*, 8948–8953.
32. Shimidzu, T.; Ohtani, A.; Iyoda, T.; Honda, K. *J. Electroanal. Chem.* **1987**, *224*, 123–135.
33. Kim, D. H.; Richardson-Burns, S. M.; Hendricks, J. L.; Sequera, C.; Martin, D. C. *Adv. Funct. Mater.* **2007**, *17*, 79–86.
34. Foulds, N. C.; Lowe, C. R. *J. Chem. Soc. Faraday Trans. I* **1986**, *82*, 1259–1264.
35. Garner, B.; Georgevich, A.; Hodgson, A. J.; Liu, L.; Wallace, G. G. *J. Biomed. Mater. Res.* **1999**, *44*, 121–129.
36. Collier, J. H.; Camp, J. P.; Hudson, T. W.; Schmidt, C. E. *J. Biomed. Mater. Res.* **2000**, *50*, 574–584.
37. Campbell, T. E.; Hodgson, A. J.; Wallace, G. G. *Electroanalysis* **1999**, *11*, 215–222.
38. Cui, X. Y.; Wiler, J.; Dzaman, M.; Altschuler, R. A.; Martin, D. C. *Biomaterials* **2003**, *24*, 777–787.
39. Yamato, H.; Ohwa, M.; Wernet, W. *J. Electroanal. Chem.* **1995**, *397*, 163–170.
40. Dietrich, M.; Heinze, J.; Heywang, G.; Jonas, F. *J. Electroanal. Chem.* **1994**, *369*, 87–92.
41. Heywang, G.; Jonas, F. *Adv. Mater.* **1992**, *4*, 116–118.
42. Yang, J. Y.; Kim, D. H.; Hendricks, J. L.; Leach, M.; Northey, R.; Martin, D. C. *Acta Biomater.* **2005**, *1*, 125–136.
43. Yang, J. Y.; Lipkin, K.; Martin, D. C. *J. Biomater. Sci. Polym. Ed.* **2007**, *18*, 1075–1089.
44. Yang, J. Y.; Martin, D. C. *J. Mater. Res.* **2006**, *21*, 1124–1132.
45. Pei, Q. B.; Zuccarello, G.; Ahlskog, M.; Inganas, O. *Polymer* **1994**, *35*, 1347–1351.
46. Del Valle, L. J.; Aradilla, D.; Oliver, R.; *et al. Eur. Polym. J.* **2007**, *43*, 2342–2349.
47. Richardson-Burns, S. M.; Hendricks, J. L.; Foster, B.; Povlich, L. K.; Kim, D. H.; Martin, D. C. *Biomaterials* **2007**, *28*, 1539–1552.
48. Richardson-Burns, S. M.; Hendricks, J. L.; Martin, D. C. *J. Neural Eng.* **2007**, *4*, L6–L13.
49. Cui, X. Y.; Martin, D. C. *Sensor. Actuator. B Chem.* **2003**, *89*, 92–102.
50. Asplund, M.; Von Holst, H.; Inganas, O. *Biointerphases* **2008**, *3*, 83–93.
51. Xiao, Y. H.; Li, C. M.; Toh, M. L.; Xue, R. *J. Appl. Electrochem.* **2008**, *38*, 1735–1741.
52. Asplund, M.; Thaning, E.; Lundberg, J.; *et al. Biomed. Mater.* **2009**, *4*, 045009.
53. Pernaut, J. M.; Reynolds, J. R. *J. Phys. Chem. B* **2000**, *104*, 4080–4090.
54. Luo, S. C.; Ali, E. M.; Tansil, N. C.; *et al. Langmuir* **2008**, *24*, 8071–8077.
55. Kim, J.; Cho, J. C.; Povlich, L. K.; Martin, D. C. U.S. Pat. 7,708,908 B2, 2010.
56. Povlich, L. K.; Cho, J. C.; Spanninga, S.; Martin, D. C.; Kim, J. *Polym. Preprint.* **2007**, *48*, 7–8.
57. Xiao, Y. H.; Cui, X. Y.; Martin, D. C. *J. Electroanal. Chem.* **2004**, *573*, 43–48.
58. Schottland, P.; Zong, K.; Gaupp, C. L.; *et al. Macromolecules* **2000**, *33*, 7051–7061.
59. Lee, J. W.; Serna, F.; Schmidt, C. E. *Langmuir* **2006**, *22*, 9816–9819.
60. Lee, J. W.; Serna, F.; Nickels, J.; Schmidt, C. E. *Biomacromolecules* **2006**, *7*, 1692–1695.
61. Groenendaal, B. L.; Jonas, F.; Freitag, D.; Pielartzik, H.; Reynolds, J. R. *Adv. Mater.* **2000**, *12*, 481–494.
62. Kumar, A.; Welsh, D. M.; Morvant, M. C.; Piroux, F.; Abboud, K. A.; Reynolds, J. R. *Chem. Mater.* **1998**, *10*, 896–902.
63. Torres-Rodriguez, L. M.; Roget, A.; Billon, M.; Bidan, G. *Chem. Commun.* **1998**, 1993–1994.
64. Cosnier, S.; Galland, B.; Gondran, C.; Le Pellec, A. *Electroanalysis* **1998**, *10*, 808–813.
65. Stephan, O.; Schottland, P.; Le Gall, P. Y.; Chevrot, C.; Mariet, C.; Carrier, M. *J. Electroanal. Chem.* **1998**, *443*, 217–226.
66. Sonmez, G.; Sarac, A. S. *Synthetic Met.* **2003**, *135*, 459–460.
67. Doherty, W. J.; Wysocki, R. J.; Armstrong, N. R.; Saavedra, S. S. *Macromolecules* **2006**, *39*, 4418–4424.
68. Xu, J. K.; Nie, G. M.; Zhang, S. S.; Han, X. J.; Hou, J.; Pu, S. Z. *J. Mater. Sci.* **2005**, *40*, 2867–2873.
69. Wan, F.; Liang, L.; Wan, X. B.; Xue, G. *J. Appl. Polym. Sci.* **2002**, *85*, 814–820.
70. Fedorow, H.; Tribl, F.; Halliday, G.; Gerlach, A.; Riederer, P.; Double, K. L. *Prog. Neurobiol.* **2005**, *75*, 109–124.
71. Hong, L.; Simon, J. D. *J. Phys. Chem. B* **2007**, *111*, 7938–7947.
72. Subianto, S.; Will, G.; Meredith, P. *Polymer* **2005**, *46*, 11505–11509.
73. Bettinger, C. J.; Bruggeman, P. P.; Misra, A.; Borenstein, J. T.; Langer, R. *Biomaterials* **2009**, *30*, 3050–3057.

74. Povlich, L. K.; Le, J.; Kim, J.; Martin, D. C. *Macromolecules* **2010**, *43*, 3770–3774.
75. Kandel, E. R.; Schwartz, J. H.; Jessel, T. M. *Principles of Neural Science*, 4th edn.; McGraw-Hill: New York, 2000.
76. Cogan, S. F. *Annu. Rev. Biomed. Eng.* **2008**, *10*, 275–309.
77. Merrill, D. R.; Bikson, M.; Jefferys, J. G. R. *J. Neurosci. Meth.* **2005**, *141*, 171–198.
78. Majumdar, S.; Ray, P. S.; Kargupta, K.; Ganguly, S. *ChemPhysChem* **2010**, *11*, 211–219.
79. Lonergan, M. C.; Cheng, C. H.; Langsdorf, B. L.; Zhou, X. *J. Am. Chem. Soc.* **2002**, *124*, 690–701.
80. Cui, X. Y.; Hetke, J. F.; Wiler, J. A.; Anderson, D. J.; Martin, D. C. *Sensor. Actuator. A Phys.* **2001**, *93*, 8–18.
81. Nyberg, T.; Shimada, A.; Torimitsu, K. *J. Neurosci. Meth.* **2007**, *160*, 16–25.
82. Ludwig, K. A.; Uram, J. D.; Yang, J. Y.; Martin, D. C.; Kipke, D. R. *J. Neural Eng.* **2006**, *3*, 59–70.
83. Yang, J. Y.; Martin, D. C. *Sensor. Actuator. B Chem.* **2004**, *101*, 133–142.
84. Gelmi, A.; Higgins, M. J.; Wallace, G. G. *Biomaterials* **2010**, *31*, 1974–1983.
85. Hudson, T. W.; Evans, G. R. D.; Schmidt, C. E. *Clin. Plast. Surg.* **1999**, *26*, 617–628.
86. Schmidt, C. E.; Leach, J. B. *Annu. Rev. Biomed. Eng.* **2003**, *5*, 293–347.
87. Corey, J. M.; Lin, D. Y.; Mycek, K. B.; *et al*. *J. Biomed. Mater. Res.* **2007**, *83A*, 636–645.
88. Quigley, A. F.; Razal, J. M.; Thompson, B. C.; *et al*. *Adv. Mater.* **2009**, *21*, 4393–4397.
89. Lee, J. Y.; Bashur, C. A.; Goldstein, A. S.; Schmidt, C. E. *Biomaterials* **2009**, *30*, 4325–4335.
90. Richardson, R. T.; Thompson, B.; Moulton, S.; *et al*. *Biomaterials* **2007**, *28*, 513–523.
91. Thompson, B. C.; Richardson, R. T.; Moulton, S. E.; *et al*. *J. Control. Release* **2010**, *141*, 161–167.
92. Isaksson, J.; Kjall, P.; Nilsson, D.; Robinson, N. D.; Berggren, M.; Richter-Dahlfors, A. *Nat. Mater.* **2007**, *6*, 673–679.
93. Simon, D. T.; Kurup, S.; Larsson, K. C.; *et al*. *Nat. Mater.* **2009**, *8*, 742–746.
94. Svennersten, K.; Bolin, M. H.; Jager, E. W. H.; Berggren, M.; Richter-Dahlfors, A. *Biomaterials* **2009**, *30*, 6257–6264.
95. Green, R. A.; Baek, S.; Poole-Warren, L. A.; Martens, P. J. *Sci. Technol. Adv. Mater.* **2010**, *11*, 014107.
96. Guiseppi-Elie, A. *Biomaterials* **2010**, *31*, 2701–2716.
97. Taylor, Z.; Miller, K. *J. Biomech.* **2004**, *37*, 1263–1269.
98. Atay, S. M.; Kroenke, C. D.; Sabet, A.; Bayly, P. V. *J. Biomech. Eng. Trans. ASME* **2008**, *130*, 021013.
99. Georges, P. C.; Miller, W. J.; Meaney, D. F.; Sawyer, E. S.; Janmey, P. A. *Biophys. J.* **2006**, *90*, 3012–3018.
100. Balgude, A. P.; Yu, X.; Szymanski, A.; Bellamkonda, R. V. *Biomaterials* **2001**, *22*, 1077–1084.
101. Engler, A. J.; Sen, S.; Sweeney, H. L.; Discher, D. E. *Cell* **2006**, *126*, 677–689.
102. Kim, B. C.; Spinks, G. M.; Wallace, G. G.; John, R. *Polymer* **2000**, *41*, 1783–1790.
103. Kim, D. H.; Abidian, M.; Martin, D. C. *J. Biomed. Mater. Res.* **2004**, *71A*, 577–585.
104. Abidian, M. R.; Martin, D. C. *Adv. Funct. Mater.* **2009**, *19*, 573–585.
105. Kim, D. H.; Wiler, J. A.; Anderson, D. J.; Kipke, D. R.; Martin, D. C. *Acta Biomater.* **2010**, *6*, 57–62.
106. Keohan, F.; Wei, X. F. F.; Wongsarnpigoon, A.; Lazaro, E.; Darga, J. E.; Grill, W. M. *J. Biomater. Sci. Polym. Ed.* **2007**, *18*, 1057–1073.
107. Abidian, M. R.; Ludwig, K. A.; Marzullo, T. C.; Martin, D. C.; Kipke, D. R. *Adv. Mater.* **2009**, *21*, 3764–3770.
108. Kim, D. H.; Martin, D. C. *Biomaterials* **2006**, *27*, 3031–3037.
109. Zhong, Y. H.; Bellamkonda, R. V. *J. Control. Release* **2005**, *106*, 309–318.
110. Greenwald, R. B.; Choe, Y. H.; McGuire, J.; Conover, C. D. *Adv. Drug Deliv. Rev.* **2003**, *55*, 217–250.
111. Boas, U.; Heegaard, P. M. H. *Chem. Soc. Rev.* **2004**, *33*, 43–63.
112. Allen, C.; Maysinger, D.; Eisenberg, A. *Colloid. Surface B* **1999**, *16*, 3–27.
113. Arap, W.; Pasqualini, R.; Ruoslahti, E. *Science* **1998**, *279*, 377–380.
114. Seymour, L. W. *Crit. Rev. Ther. Drug* **1992**, *9*, 135–187.
115. Qiu, Y.; Park, K. *Adv. Drug Deliv. Rev.* **2001**, *53*, 321–339.
116. Panyam, J.; Labhasetwar, V. *Adv. Drug Deliv. Rev.* **2003**, *55*, 329–347.
117. Luo, X. L.; Cui, X. T. *Electrochem. Commun.* **2009**, *11*, 1956–1959.
118. Abidian, M. R.; Corey, J. M.; Kipke, D. R.; Martin, D. C. *Small* **2010**, *6*, 421–429.
119. Abidian, M. R.; Kim, D. H.; Martin, D. C. *Adv. Mater.* **2006**, *18*, 405–409.
120. Abidian, M. R.; Martin, D. C. *Biomaterials* **2008**, *29*, 1273–1283.
121. Peramo, A.; Urbanchek, M. G.; Spanninga, S. A.; Povlich, L. K.; Cederna, P.; Martin, D. C. *Tissue Eng. A* **2008**, *14*, 423–432.
122. Okuzaki, H.; Suzuki, H.; Ito, T. *Synthetic Met.* **2009**, *159*, 2233–2236.
123. Che, J. F.; Xiao, Y. H.; Zhu, X. F.; Sun, X. J. *Polym. Int.* **2008**, *57*, 750–755.
124. Li, L. D.; Huang, C. B. *J. Am. Soc. Mass Spectr.* **2007**, *18*, 919–926.
125. Xiao, Y. H.; Che, J. F.; Li, C. M.; *et al*. *J. Biomed. Mater. Res.* **2007**, *80A*, 925–931.
126. Kontturi, K.; Pentti, P.; Sundholm, G. *J. Electroanal. Chem.* **1998**, *453*, 231–238.
127. Richardson, R. T.; Wise, A. K.; Thompson, B. C.; *et al*. *Biomaterials* **2009**, *30*, 2614–2624.
128. Thompson, B. C.; Moulton, S. E.; Ding, J.; *et al*. *J. Control. Release* **2006**, *116*, 285–294.
129. Bidan, G.; Lopez, C.; Mendesviegas, F.; Vieil, E.; Gadelle, A. *Biosens. Bioelectron.* **1995**, *10*, 219–229.
130. Luo, X. L.; Cui, X. T. *Electrochem. Commun.* **2009**, *11*, 402–404.
131. Wadhwa, R.; Lagenaur, C. F.; Cui, X. T. *J. Control. Release* **2006**, *110*, 531–541.
132. Ge, D. T.; Tian, X. D.; Qi, R.; *et al*. *Electrochim. Acta* **2009**, *55*, 271–275.
133. Purcell, E. K.; Seymour, J. P.; Yandamuri, S.; Kipke, D. R. *J. Neural Eng.* **2009**, *6*, 026005.
134. Rejali, D.; Lee, V. A.; Abrashkin, K. A.; Humayun, N.; Swiderski, D. L.; Raphael, Y. *Hear. Res.* **2007**, *228*, 180–187.
135. Spanninga, S. A.; Martin, D. C.; Chen, Z. *J. Phys. Chem. C* **2009**, *113*, 5585–5592.

1.131. Superporous Hydrogels for Drug Delivery Systems

H Omidian, Nova Southeastern University, Fort Lauderdale, FL, USA
K Park, Purdue University, West Lafayette, IN, USA

© 2011 Elsevier Ltd. All rights reserved.

1.131.1.	**Introduction**	563
1.131.2.	**Hydrogels in Drug Delivery**	564
1.131.3.	**Superporous Hydrogels**	564
1.131.4.	**SPH Synthesis**	565
1.131.5.	**SPH Properties**	565
1.131.5.1.	Swelling Capacity	565
1.131.5.2.	Swelling Rate	566
1.131.5.3.	Mechanical Strength	566
1.131.6.	**SPH Generations**	566
1.131.6.1.	The First SPH Generation	567
1.131.6.2.	The Second SPH Generation	567
1.131.6.3.	The Third SPH Generation	567
1.131.6.4.	Research on SPHs	568
1.131.7.	**SPH Scale Up**	569
1.131.8.	**SPH Stability**	570
1.131.8.1.	SPH Identity	570
1.131.8.2.	SPH Purity	570
1.131.8.3.	SPH Potency	571
1.131.9.	**SPH Safety**	571
1.131.10.	**SPH Platform Design for Drug Delivery**	571
1.131.11.	**SPH in Drug Delivery and Other Areas**	572
1.131.11.1.	Gastric Retention	572
1.131.11.2.	Peroral Intestinal Delivery	574
1.131.11.3.	SPHs as Diet Aid	574
1.131.11.4.	SPHs as Superdisintegrant	574
1.131.11.5.	Other Applications	574
1.131.12.	**Conclusions**	575
References		575

Abbreviations

aq	Aqueous
CD	Circular dichroism
CMC	Carboxymethylcellulose
CSPHs	Conventional superporous hydrogels
DDS	Drug delivery system
DSC	Differential scanning calorimetry
EDX	Energy-dispersive X-ray spectroscopy
FDA	Food and Drug Administration
FTIR	Fourier transform infrared
HEMA	Hydroxyethyl methacrylate
HPMC	Hydroxypropyl methylcellulose
NIPAM	N-isopropyl acrylamide
NMR	Nuclear magnetic resonance
PEG	Polyethylene glycol
PVP	Poly(vinyl pyrrolidone)
s	Solid
SEM	Scanning electron microscope
SPH	Superporous hydrogel
SPHCs	Superporous hydrogel composites
SPHHs	Superporous hydrogel hybrids
TGA	Thermogravimetric analysis
UV/VIS	Ultraviolet/visible

1.131.1. Introduction

Regardless of the payload (drug, solvent, fertilizer, pesticide, etc.), a delivery system should possess two major tools to function. It should accommodate the payload and release it later on at a controlled rate. Novel delivery systems possess an extra tool to deliver the load to a desirable site, and are intended for targeting delivery. Hydrogels have long been known for their ability to house drugs and to prevent drug release by a simple diffusion process. Due to their long polymeric chains, they provide a physical barrier to drug transport, as a result of which a drug needs to take a longer path to

diffuse out of the delivery system. The barrier properties of the polymer chains become more significant when the chains are hydrated in an aqueous medium. Although these features are attractive in controlled drug delivery, some applications require a faster transport kinetic. The presence of pores within a hydrogel structure, through which the drug can be released at a faster rate, adds another dimension to the transport process.

Pores inside a hydrogel structure are generally closed, although populated. Porous hydrogels in general have a closed pore structure, with no well-tailored size or distribution. Superporous hydrogels (SPHs), on the other hand, are hydrogels with an interconnected structure with a relatively narrow pore size and distribution. The predecessor of SPHs, that is, superabsorbent polymers, are for instance found in ultrathin or ultra-absorbent baby diapers and feminine incontinence products due to their outstanding urine or blood absorption capability. These are made of a very hydrophilic but cross-linked structure (mostly based on acrylic acid and its sodium salt) with the ability to absorb 500–1000 $g\,g^{-1}$ of distilled water and 40–70 $g\,g^{-1}$ of saline (an aqueous solution containing 0.9 wt% sodium chloride). These structures are very sensitive to pH, nonsolvents, and ionic strength of the swelling medium. Since this product is supplied in granule and particle form, its swelling rate can be adjusted by the particle size, which significantly affects the particle surface area and hence its absorption ability. In other words, the larger particles absorb aqueous fluids at a slower rate than their smaller counterparts. Superporous hydrogels with the same swelling capacity, on the other hand, absorb aqueous fluids at almost the same rate, irrespective of their size in a dry state. Increased surface area in superporous hydrogels is provided by pores inside their structure. With an increase in their pore content and decrease in pore size, more hydrogel surface would be exposed to the swelling environment, which makes the swelling kinetic faster.

1.131.2. Hydrogels in Drug Delivery

There are more than 100 prescription drugs in the US market, in which one excipient is commonly used, that is, hydroxypropyl methylcellulose (HPMC). Although this polymer is water soluble, it provides gelling properties when exposed to an aqueous environment. HPMC with different degrees of substitutions is used in tablet form to control the release of the drug over a longer period of time. Apparently, there are two features that enable the HPMC to function as a controlled delivery system. First, it is very hydrophilic due to its hydroxypropyl contents. Second, the HPMC chains are in a very compressed form in a tablet, which prevents them from a fast dissolution in the aqueous environment. These two features provide gelling properties such as those found in a chemically cross-linked hydrogel. Although there is no chemical cross-linker in the HPMC structure, the applied pressure during tablet preparation supplies enough entanglement and barrier for the retarded dissolution of the polymer.

1.131.3. Superporous Hydrogels

A superporous hydrogel is a composite polymer made of a solid hydrogel and air. The SPH is a unique class of porous

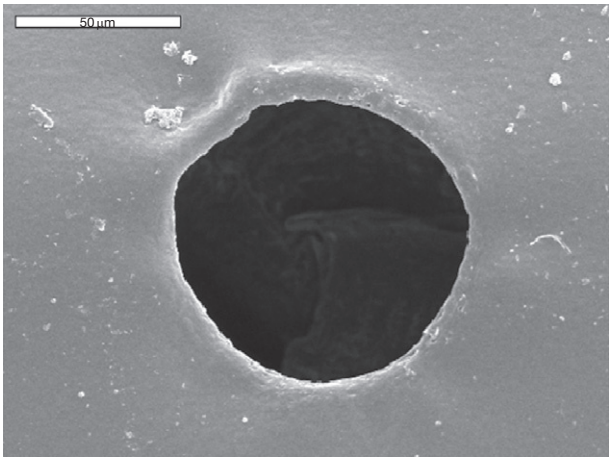

Figure 1 A typical superporous hydrogel with an average pore size of 50 µm.

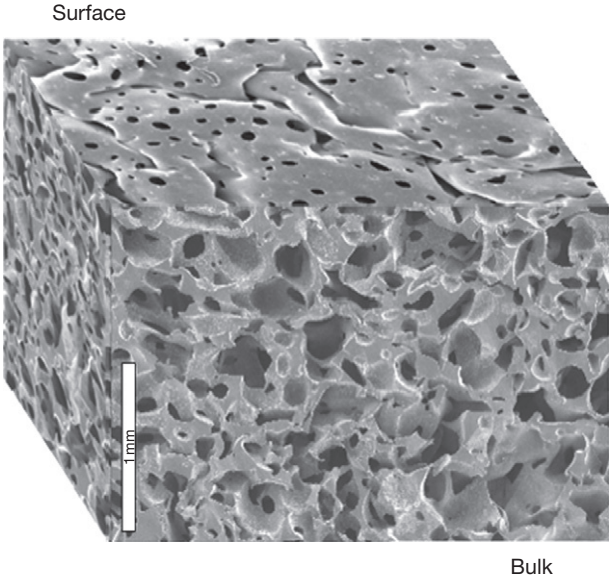

Figure 2 A three-dimensional porous structure of a typical superporous hydrogel.

hydrogels with an average pore size of 50–100 µm (Figure 1) and an interconnected pore structure (Figure 2).[1] As its pores are open, the fluid can travel in a three-dimensional path, as a result of which the swelling rate of a typical SPH becomes independent of the SPH size in its dry state.[2] While in nonporous hydrogels the solid part is responsible for the swelling and mechanical property, the air portion of the SPH structure plays a vital role in determining the final SPH properties. Generally speaking, properties such as density, swelling capacity, and mechanical strength are improved by solid content, while the swelling rate increases as the SPH air content increases. The pore content, size, morphology, and isotropicity are all pore features of the SPH, which could potentially affect SPH stability and function to a lesser or greater extent.

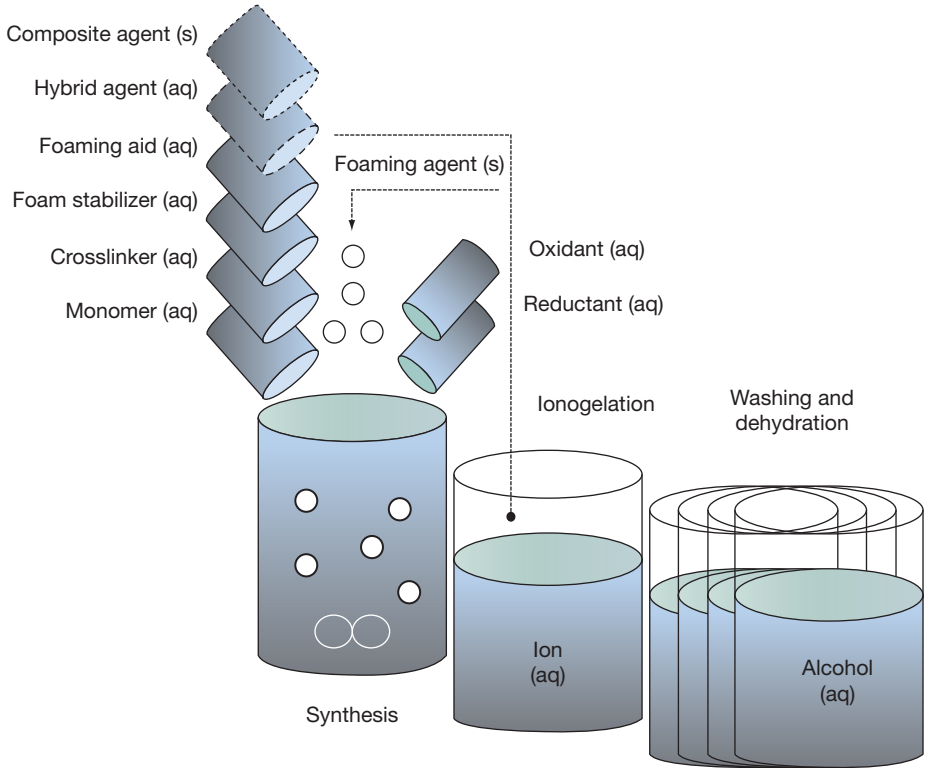

Figure 3 Synthesis, treatment, and purification of a typical superporous hydrogel.

1.131.4. SPH Synthesis

In the preparation of SPHs, a bicarbonate foaming agent is used, which is water soluble and becomes active in an acidic aqueous medium. So a solution polymerization is a preferred method of SPH synthesis. Aqueous solutions of monomer, cross-linker, foam stabilizer, and foaming aid are added in turn to the reacting mixture under very mild mixing. Following a complete homogenization, the reductant and oxidant are added consecutively and are mixed quickly with the reacting mixture. In a very short period of time, the solid foaming agent (e.g., bicarbonate) is effectively dispersed and mixed throughout the reacting solution. The bicarbonate reacts with the foaming aid (e.g., an organic acid) to generate carbon dioxide gases; this reaction in turn increases the pH of the reacting solution, which favors the decomposition of the initiator. Due to the retarding effect of the oxygen, there is an induction, or lag period, which is followed by a fast exothermic polymerization reaction.[3] The foaming and gelling reactions occur almost simultaneously and proceed to their maximum extent at the polymerization temperature, which is determined by the type of monomer, its concentration in the solution, and initiator concentration. A successful SPH is synthesized if the chemical gelation and physical foaming happen in a synchronized way.[4,5] The formation of the SPH foam requires the CO_2 gases to be entrapped within the hydrogel matrix, and this would be possible if the reacting hydrogel mass reaches a certain viscosity, μ_f. The foaming viscosity is determined by the rate at which the gelling reaction happens. At viscosities well below and beyond the μ_f, the efficiency of the foaming process would be decreased significantly and no SPH would actually be formed.



Figure 4 Steps in producing a superporous hydrogel foam.

With no increase in the foam height and no increase in the reaction temperature, both gelling and foaming reactions are slowed down and the SPH foam is then relaxed for further treatment, purification, and drying. The overall procedure of SPH synthesis is shown in Figures 3 and 4 (see Chapter 1.121, Polymer Fundamentals: Polymer Synthesis).

1.131.5. SPH Properties

1.131.5.1. Swelling Capacity

Swelling capacity in hydrogels and SPH polymers in particular is defined by the structural hunger for an aqueous fluid. Apparently, the more hydrophilic the structure of the hydrogel, the stronger the intermolecular interactions that can be built by the hydrogel with its surrounding aqueous medium. A stronger polymer–water interaction would be established if the hydrogel structure contains ionizable groups such as carboxyl or its salt derivatives such as potassium or sodium carboxylate. These hydrophilic and ionic functional groups are responsible for the polymer–water interaction, electrostatic forces, and osmotic forces, which are the driving forces for the swelling process to occur. By far the most important consideration in hydrogel

swelling is the status of water with respect to the hydrogel core. Like the electronic layers surrounding the nucleus of an atom, several layers of water are built up around the hydrophilic and ionic groups. An electron is separated with more ease in the presence of electron-loving atoms if it is located in the outermost electronic layers. Likewise, water molecules within the hydrogel located at the outermost layers, far from the hydrophilic or ionic groups, can be separated with ease. As a result, the status of water in hydrogels is generally defined as free and bound water, which reflects the extent of polymer and water interaction within a hydrogel.

Swelling capacity in hydrogels is generally measured under free and loaded conditions. A hydrogel is simply placed in water or an aqueous solution with a little or no pressure applied on the hydrogel. The hydrogel begins the process of water absorption via its functional groups and continues to absorb water until all the functional groups receive the same amount of water. The amount of water absorbed can simply be calculated by measuring the hydrogel weight before and after the swelling.

1.131.5.2. Swelling Rate

The rate at which water or an aqueous medium is absorbed into the hydrogel structure depends on the hydrogel's chemical and physical structure. As far as the chemistry is concerned, the hydrogels containing more hydrophilic and ionic groups offer a faster swelling process. At the same chemical composition, hydrogels small in size or thin (film), and having a porous structure, can swell faster in an aqueous medium than nonporous, large in size, and thick (sheet) hydrogels. A nonporous hydrogel structure absorbs water at its surface layer by layer. In other words, the water is absorbed into the structure of such hydrogels following a two-dimensional path. Then, the first partially swollen layer acts as a water reservoir for the lower layers. With a porous structure, on the other hand, the whole hydrogel mass could have the same access to the water, and hence water can penetrate into the hydrogel structure following a three-dimensional path. To measure the swelling rate or the swelling kinetic, the amount of water absorbed into the hydrogel structure is measured versus time. While the amount of water absorbed at times zero and infinite reflect the weight of the hydrogel in its dry and fully swollen states, respectively, the hydrogel behavior within this time period reflects the mechanism of the swelling kinetic. For instance, the swelling kinetic would be zero order if the absorption is linear. On the other hand, the absorption occurs as a first-order kinetic if the behavior is exponential. Generally, the absorption mechanism changes with the cross-link content of the hydrogel. A zero-order kinetic is favored at higher cross-link content.

1.131.5.3. Mechanical Strength

A hydrogel in its swollen state is a composite material composed of solid, liquid, and air. Apparently, the extent of intermolecular forces within a solid is more extensive than in the other two. Therefore, a hydrogel with more solid properties (less water and air content) is considered stronger in its swollen state. To measure the mechanical properties, a hydrogel is stressed under static or dynamic loads until it fails.[6,7] The testing force should be selected on the basis of actual service conditions. For example, if the SPH is required to resist the compressive forces, a compression test should be designed accordingly. Similarly, if the SPH is expected to resist a dynamic compression (compression–decompression cycles) force, an appropriate dynamic test should be designed to evaluate the SPH for such an application.[7] For gastric retention studies, the SPH for instance is required to not only resist the combined forces of compression, tension, and bending altogether, but also serve in a very harsh acidic condition. A gastric simulator, which examines the mechanical strength of the SPH by mimicking the real gastric conditions, has been reported.[8–10] The SPHs for such application should quickly swell up in the acidic medium of the stomach juice to a size larger than the pyloric sphincter. The SPH is assumed to resist the mechanical pressures inside the stomach while it is saturated with the stomach fluid. Evaluating and screening hydrogels that resist the real stomach pressures have always been challenging. A texture analyzer and compressive or tensile mechanical tester are normally used to evaluate the mechanical properties of hydrogels. Although such equipment can predict the comparative properties of hydrogels, they fail to predict real mechanical properties. The simulator generates mixed forces of compression, tension, bending, and twisting, based on a water-hammer effect. The sample under test will receive almost the same amount of forces throughout its body. Finally, the stress concentrated on the weakest part of the SPH body would result in the formation of craze, crack, and finally disintegration of the whole platform. The simulator can practically measure the amount of work needed to break the hydrogel apart under real service conditions.

The swelling capacity, swelling rate, and hydrogel strength are all ultimately dependent on the bound water and free water within the hydrogel. Due to the lack of accuracy in measuring the amount of water in each status, all measurements would face a larger standard deviation. Therefore, any measuring procedure or instrument needs to be validated to obtain more accurate and reliable data.

1.131.6. SPH Generations

Hydrogels with fast swelling and superabsorbent properties, different from conventional superabsorbent polymers, were first reported by Chen *et al.*[11] Fundamental structural and property differences between the superabsorbent hydrogels and superporous hydrogels have been reviewed, with an emphasis on the evolution of SPHs and different generations of SPHs.[12] Superporous hydrogels were evolved about a decade ago, and their introduction was triggered by a need strongly felt in the pharmaceutical area.[13] There are dozens of drugs with a limited absorption across the gastrointestinal tract, which are extensively absorbed at certain areas of the GI tract such as the upper intestine. These are called drugs with a narrow absorption window. To increase their absorption and hence their bioavailability, these drugs need to be retained in the stomach (gastric) area for an extended period of time. There are currently a few technologies available to increase the retention of such drugs in the gastric medium; among them the floatable, mucoadhesive, and swellable delivery systems have been studied extensively. With the swellable delivery system, the drug would be

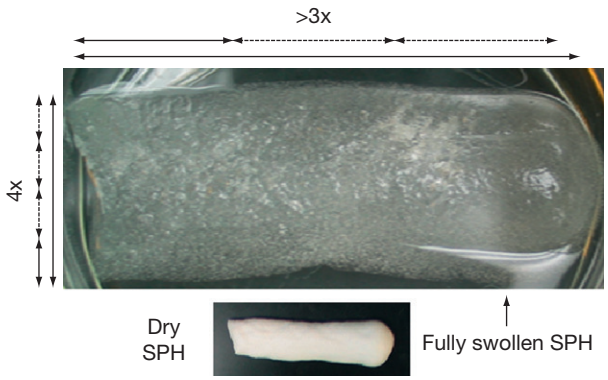

Figure 5 Unique swelling feature of a superporous hydrogel polymer.

accommodated in the swellable hydrogel structure and take a very rough path to release itself from the platform by diffusion. In this way, the drug can stay longer in the area of interest and release itself in a more controlled manner. The early superporous hydrogels, like their superabsorbent predecessor, possessed a very high absorption capacity and a very fast swelling rate. These features were attractive enough for their development in this area of application. Figure 5 shows a typical SPH, in which its dimensions are increased to about four times the original length in about a minute after complete swelling in water.

1.131.6.1. The First SPH Generation

A variety of monomers and polymers, as well as approaches, have been exploited to make SPHs with different structures and properties.[11,14] Among monomers, those with very hydrophilic (e.g., carboxyl or amide in acrylic acid and acrylamide respectively) or ionic (e.g., carboxylate in sodium or potassium acrylate) functions could offer superior swelling properties. These hydrogels are generally prepared in solution by incorporating monomers, initiators, and cross-linkers, as well as foaming agents, into the reaction. The final product is a superporous hydrogel with an interconnected pore structure, which could absorb great amounts of water in a few minutes. However, these hydrogels do not possess any mechanical strength due to the vast number of water layers around their hydrophilic cores. In other words, such hydrogels contain a high proportion of free or semibound water in their swollen state, which make them weak under mechanical pressures. As there is no provision to increase their mechanical strength, these hydrogels are called conventional superporous hydrogels. Figure 6 shows a typical synthetic procedure and structure of the first SPH generation.

1.131.6.2. The Second SPH Generation

The need for better mechanical property triggered the development of the second generation of SPHs or the SPH composites.[15–17] These SPHs are prepared by adding a swellable filler to the original formulation of the conventional SPHs. The swellable filler is selected among pharmaceutically acceptable cross-linked and hydrophilic polymers, including cross-linked sodium carboxymethylcellulose (CMC), cross-linked poly(vinyl pyrrolidone), and cross-linked sodium starch glycolate. These are

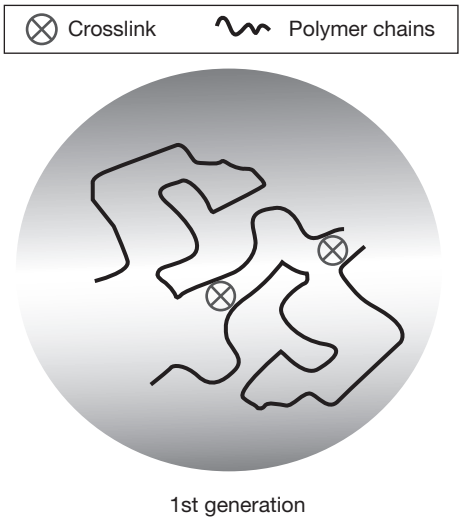

Figure 6 A conventional superporous hydrogel.

commonly used as a superdisintegrant in the preparation of tablets and other solid doses. The use of these in hydrogel formulation could positively affect the SPH strength, presumably due to the strength nods or the physical cross-links built into the hydrogel structure (see **Chapter 4.423, Polymeric Drug Conjugates by Controlled Radical Polymerization**).

1.131.6.3. The Third SPH Generation

Although the SPHs of the second generation could provide a hydrogel with a better strength, much higher strength was felt to be needed, for the gastric retention application in particular. This triggered the development of the third SPH generation, also called superporous hydrogel hybrids (SPHHs), with superior mechanical properties. The primary, secondary, and tertiary approaches have so far been disclosed. The SPH is prepared in a conventional way, but an active material is added during SPH synthesis, which is then treated in the ion solutions. While the primary approach is particularly useful in making SPHs with rubbery properties, SPHs with good mechanical strength can be obtained by adopting the secondary approach.[3] Although the mechanical properties of SPHs can be significantly enhanced after an ion treatment, the ion composition was found to be a useful tool for better controlling the swelling and mechanical properties. Depending on the activity of the ion (sodium, calcium, aluminum, and iron in particular), any ion composition can be used to modify and modulate SPH properties.[4] Figure 7 displays the fundamental structural differences between the second, the third, and the modified SPH generations.

SPH hybrids are prepared according to conventional SPH formulations but a water soluble and ionogelling polymer (synthetic or natural) is added during hydrogel preparation. After preparation, the SPH is treated in an ion solution to become strong and elastic.[3,18] A dried SPH hybrid possesses a folded surface morphology as shown in Figure 8. Utilizing an ionogelling monomer in the basic monomer solution has also been practiced to obtain improved SPH structures. For example, a hydroxyethyl methacrylate (HEMA)-based SPH with modulated swelling and mechanical property has been prepared by

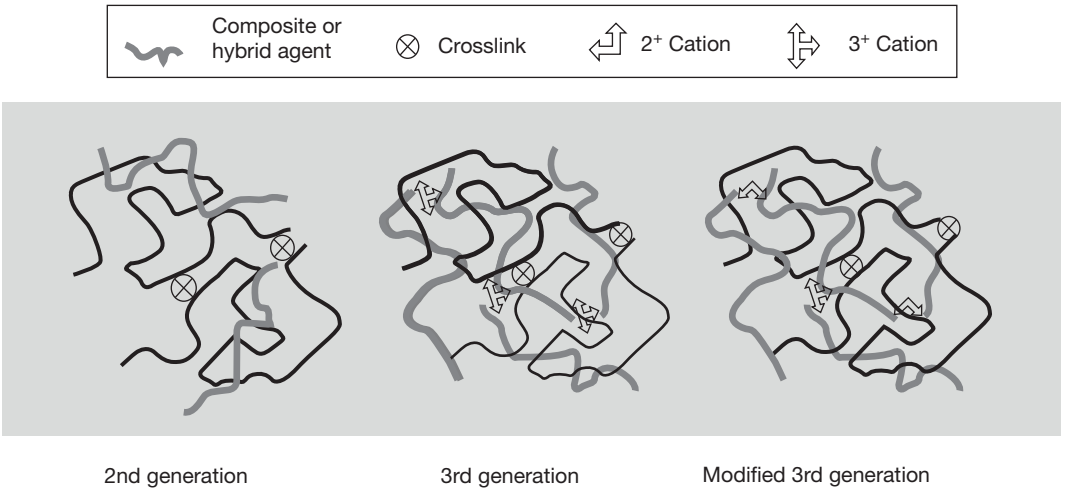

Figure 7 Different superporous hydrogel generations.

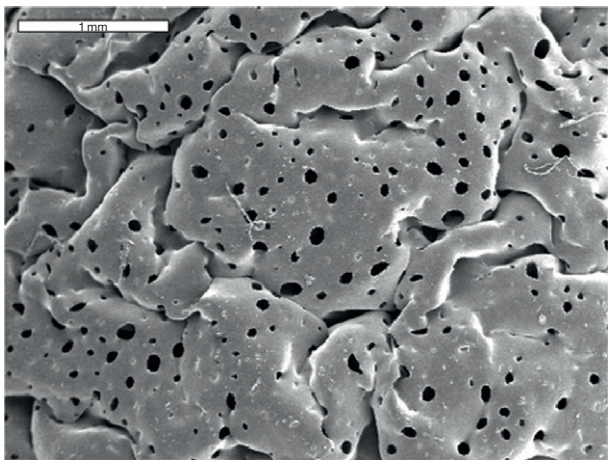

Figure 8 The surface morphology of a typical superporous hydrogel hybrid.

adding acrylic acid into the HEMA formulation containing a cross-linker. After formation, the SPH foam is treated in calcium or aluminum ions to improve the SPH strength and swelling. It then displays stable swelling and mechanical properties in a very harsh service environment such as gastric medium.[5]

1.131.6.4. Research on SPHs

By far the most common monomers used in the preparation of SPHs are acrylic acid and acrylamide. The swelling response of SPHs based on acrylamide and acrylic acid has been studied with the change in the pH of the swelling medium and pressure.[19,20] Solid-state NMR, swelling, density, and scanning electron microscopy were utilized to characterize the SPH composites of acrylamide and acrylic acid polymers cross-linked with *N*,*N*′-methylenebisacrylamide. Apparent density and SEM measurements showed that the SPH composites are more porous than conventional SPHs, which results in hydrogels with superior swelling but weaker mechanical properties.[21] Due to their ionic structures, the swelling property of the poly(acrylamide-*co*-acrylic acid) copolymeric SPHs are dependent on the pH and ionic strength of the solution. These SPH structures display a fast 'on–off' shrinking–swelling cycle in the pH range of 1.2 and 7.5, respectively.[19] Floatable SPHs loaded with vitamin B12 were prepared via copolymerization of acrylamide and acrylic acid in the presence of a porogen and a catalyst.[22] The increased surface area of SPHs has been utilized for grafting purposes. Acrylic acid could be grafted at a high grafting efficiency on polyacrylamide gels using potassium diperiodatocuprate. This feature also helps with the purification process by facilitating the mass transfer process as well as the adsorption of ligands.[23] The PEG-grafted superporous hydrogels based on acrylic acid and acrylamide are prepared in the presence of PEG acrylate and a foaming agent. This modification has caused about sixfold increase in the swelling rate.[24] An amphiphilic coating based on poly(ethylene glycol–tetramethyleneoxide) has been used to improve the swelling kinetics of SPHs.[25] The effect of acidification has been examined on the swelling and mechanical properties of poly(acrylamide-*co*-acrylic acid) SPHs. SPH swells much less in acidic water than in distilled water. Acidification reduces the swelling ratio but improves the mechanical properties.[26] The interpenetrating network of cross-linked poly(acrylamide-*co*-acrylic acid) with polyethyleneimine has also been examined.[27] The effect of synthetic factors on the swelling of superabsorbent hydrogels based on neutralized acrylic acid and methylenebisacrylamide has been studied. The swelling was interpreted by a Voigt-based viscoelastic model, and the hydrogel kinetic and thermodynamic parameters were found accordingly.[28] A partially neutralized acrylic based superabsorbent hydrogel has been studied using different water-soluble and oil-soluble cross-linkers and a combined porogen system of bicarbonate/acetone system. Highly porous gels were obtained under conditions where the gelation period was short. Highly cross-linked hydrogels showed almost no swelling dependence on salt.[29] SEM morphological studies and swelling studies show the synergistic effect of the combined porogen system compared to the use of individual gas blowing systems.[30] Porous polyacrylamide has been synthesized using calcium carbonate microparticles, followed by an acid treatment. The hydrogel

swelling is adversely affected by the calcium microparticles and the chemical cross-linker.[31] In another study, a Taguchi experimental design was used to evaluate the effect of the synthetic variables on the gel strength of the acrylamide-based hydrogels and superporous hydrogels.[32] Poly(vinyl alcohol) has been used to improve the strength of the SPHs based on potassium salt of sulfopropyl acrylate, acrylic acid, and PEG diacrylate. The SPH is intended for gastric retention application.[33] An SPH hybrid of acrylamide and sodium alginate has been prepared via a two-step polymerization and treatment. The process involves polymerization and cross-linking of acrylamide in the presence of alginate, followed by treating the prepared SPH in an ion solution. The SPH prepared via this approach possesses superior mechanical and elastic properties.[18] The mechanical property of the conventional SPH polymers has been improved via network-in-network formation by including polyacrylonitrile in the reaction.[34] In another study, the gel strength of the superabsorbent hydrogel was increased via addition of kaolin during the hydrogel synthesis. FT-IR study confirmed the existence of acrylic grafts on the kaolin surface. Despite an increase in gel strength, the swelling property of the hydrogel was reduced to a great extent. The thermal property of the prepared hydrogels has been characterized using thermal analysis including DSC and TGA.[35] Interpenetrated SPH network of poly(acrylamide-*co*-acrylic acid) with chitosan and glycol chitosan was prepared. In distilled water, both systems behave similarly but swelling increases in acidic medium with increase in chitosan concentration. Since glycol chitosan is more hydrophilic than chitosan, a significant increase in swelling rate was observed[36] (see **Chapter 2.213, Chitosan**).

N-isopropyl acrylamide (NIPAM) and acrylamide have been used to prepare thermosensitive SPHs with pore size of about 100 μm. An on–off swelling–shrinking cycle is obtained if a certain composition of the thermosensitive superabsorbent SPH is heated up from a low (e.g., 10 °C) to a high (e.g., 65 °C) temperature.[14] A higher temperature favors the hydrophobic interactions and the polymer loses its water affinity due to a weaker hydrophilic interaction. A temperature-sensitive poly (NIPAM) hydrogel was prepared in an aqueous sodium chloride solution. This technique resulted in a hydrogel with significantly higher swelling and swelling response due to the effect of salt, which was claimed to be responsible for phase separation and heterogeneity of the structure. These porous hydrogels are characterized by a larger pore and smaller pore at low and high temperature respectively, which result in complete and no release of the bovine serum albumin, respectively.[37] Superporous hydrogel of CMC–NIPAM hydrogel was attained via simultaneous irradiation cross-linking and addition of a foaming agent.[38] Sucrose-based hydrogels and their SPH counterparts were prepared by reacting sucrose with glycidyl acrylate, followed by its polymerization. The superporous sucrogels showed faster swelling and degradation in both acidic and basic media.[39]

A combined gas-foaming and freeze-drying technique has been used to prepare interpenetrated SPHs based on glycol chitosan and poly(vinyl alcohol). It was shown that the number of freezing–thawing cycles has a more significant effect on the hydrogel strength than the freezing time. A differential scanning calorimetry was used to evaluate the thermal behavior associated with the hydrogen bond-induced crystalline structure of the hydrogel.[40] Highly porous poly(2-hydroxyethyl methacrylate) slabs were prepared by a simultaneous polymerization and cross-linking of the HEMA monomer and ethylene dimethacrylate. Porosity was achieved using porogens such as cyclohexanol, dodecan-1-ol, and saccharose. Low density values for these hydrogels indicate a closed cell rather than an interconnected structure. Mercury porosimetry was used to evaluate the superporosity and microporosity status of the gels.[41] Hydrofluoric acid (HF) treatment was also used to extract nanosized silica particles from a hydrogel matrix to make a porous hydrogel.[42]

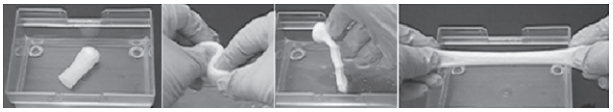

Figure 9 Mechanical property of a typical superporous hydrogel hybrid under various forces.

Superporous hydrogels interpenetrated with sodium alginate have displayed pH- and salt-responsive swelling properties. Moreover, the alginate-modified SPH shows no significant cell or mucosal damage based on thiazolyl blue, lactate dehydrogenase assays, as well as rat's intestine morphology.[43] A fully interpenetrated superporous hydrogel with superior mechanical and elastic properties is obtained when a synthetic monomer is polymerized and cross-linked in the presence of a hydrocolloid with ionogelling ability. A fully interpenetrated network is obtained when the hydrogel is treated in an ion solution containing calcium, iron, or aluminum.[18] **Figure 9** shows a typical acrylamide–alginate-based SPH hybrid in its fully swollen state, which resists compression, bending and tensile forces for a long period of time before it breaks apart. Pectin has been used as a base for an intelligent superabsorbent polymer with pH and thermosensitive swelling properties, which can potentially be used for controlled delivery of nonsteroidal anti-flammatory drugs. Results have shown that the drug could be delivered to the intestine without being lost in the stomach.[44]

1.131.7. SPH Scale Up

Scale up is the process of preparing the SPH on a large scale. A larger scale means an increase in the starting materials, an increase in the container size, and dealing with a very exothermic reaction on a large scale. If the synthesis of an SPH is successful in a container with a certain geometry, it does not necessarily mean a successful synthesis on a larger scale. During the SPH polymerization, heat is released, which is entrapped in the reacting mix due to the insulation property of the pores inside the forming SPH structure. The heat buildup can increase the rate at which normal polymerization happens, the rate of gas formation, and also the chance of popcorn polymerization by which cross-link density of the SPH increases to a great extent. To release the heat from the reacting mixture, an adequate surface should be provided, which is determined by the aspect ratio of the container (diameter/height ratio).

Dispersion of the foaming agent into the SPH formulation during the synthesis is a typical active suspension process. There are generally three types of suspension processes: dispersion of a nonreactive filler into a nonreactive medium (e.g., paint formulation), dispersion of a nonreactive filler into a reacting medium (e.g., kaolin in hydrogel synthesis), and finally, dispersion of a reactive filler into a reactive medium (e.g., bicarbonate in SPH synthesis). Once dispersed, the bicarbonate particles can increase the pH by consuming the acid component of the formulation, which in turn increases the rate at which the redox couple would react. This in turn increases the magnitude of the polymerization reaction and its exothermicity. In other words, the extent of the gelling reaction would critically depend on the amount of the bicarbonate in the system. If not well-dispersed, a so-called 'local hot spot' is produced around which a polymerization to a very high extent is expected. This causes an undesirable heterogeneity in the SPH structure. By far the most challenging aspect of the manufacture of SPHs on a large scale is the dispersion of bicarbonate into an ongoing reaction. An SPH with a uniform pore size and distribution is achieved if the bicarbonate is evenly dispersed into the gelling mass. In general, the bicarbonate dispersion within the reacting mass should be completed in a few seconds. If not, the gelling and foaming reactions would become closely dependent on each other and would affect progress to a great extent. The bicarbonate can effectively be dispersed if a high-pressure gun powder is used.[45] Moreover, the mixing agitator should have a very specific function, to be able to sweep the bottom part of the reaction very effectively to avoid the formation of a nonporous hydrogel at the bottom of the container. Heat buildup, and hence a faster hydrogel formation, may be observed in areas where mixing is not effective. Another important operational factor is the size of the bicarbonate particles. As these particles are reactive, their reactivity would be dependent on their size. As bicarbonate size decreases, its surface area increases. This in turn increases the rate at which pH increases, the rate at which CO_2 gases are formed, and the rate of both chemical gelling and physical foaming reactions. The corresponding rates of these two critical reactions can be controlled by selecting appropriate bicarbonate or mixing bicarbonates of different sizes.

1.131.8. SPH Stability

In determining the stability of a given drug, adequate documentation is provided to the FDA or similar organizations to prove the identity, purity, and potency of the drug. For a superporous hydrogel product, the same procedure should be followed.

1.131.8.1. SPH Identity

There are certain instances in which the identity of an SPH product may change. Moisture, oxygen, ultraviolet light, and heat are potentially the most important factors. The moisture originates from two sources, the moisture retained in the product, and environmental moisture. The product moisture can be minimized by freeze drying, while the environmental moisture is minimized by storing the SPH product under a dry condition using silica gel. Although the SPH itself is also hygroscopic, a silica gel is more effective and faster in moisture absorption. As far as the chemical structure is concerned, an SPH containing, for example, ester (–COO), amide (–NHCO), and anhydride (–COOC) groups would be more susceptible to hydrolysis.

If the SPH contains groups such as ethers (ROR′), and aldehyde (–RCHO), it needs to be protected from oxidative reactions. The most common way to protect the SPH from oxygen invasion is to use different primary, secondary, and tertiary antioxidants. Primary antioxidants such as butylated hydroxyl anisol (BHA), butylated hydroxyl toluene (BHT), tocopherol (vitamin E), and propyl gallate can provide electrons to free radicals and act as free radical scavengers. Compounds such as ascorbic acid and sodium bisulfite are secondary antioxidants and can consume oxygen through autooxidation. The last group of antioxidants, that is, tertiary antioxidants, can react with the ions responsible for initiating the oxidation reactions. The ion scavengers include citric acid, tartaric acid, and ethylenediamine tetraacetic acid.

Functional groups including carbonyl (–CO–) and the C=C bond make a superporous hydrogel sensitive to ultraviolet light. Theoretically, these groups may absorb light at or greater than 280 nm. Photolysis can be prevented by storing the SPHs in an opaque or a dark-colored container. Heat can also change the SPH identity by expediting the hydrolytic, oxidative, and photolytic reactions.

1.131.8.2. SPH Purity

The SPH impurities can be classified as primary, secondary, and tertiary. Primary impurities are residual monomer, initiator, and cross-linker left from the polymerization and cross-linking reaction. Due to incomplete conversion of the monomer to polymer, and incomplete inclusion of the cross-linker into the polymer structure, unreacted monomers and cross-linkers need to be removed after SPH synthesis. Many researchers attempt to find ways to reduce residual monomers, but reducing the residual initiators is also a very important consideration. Following monomer removal, the SPH is generally washed with water and alcohol solutions for complete purification. These two are considered secondary impurities. More water will be removed by adding more alcohol and alcohol itself is removed by low pressure drying. One of the very major challenges regarding SPHs for pharmaceutical applications is that they must be reasonably pure. Different methods have been proposed to make a pure SPH. These include the use of low and high glass transition monomers during the SPH synthesis and the use of physically induced expansion and contraction in a solvent–nonsolvent system, as well as the use of mechanical processes such as filtration, rubbing, and centrifugation.[45] The last type of impurities originate from two sources, that is, during SPH storage and SPH service. Since water exists in the SPH even at a very low concentration, this may result in a long-term hydrolysis. Oxidative reactions may also proceed in a given SPH as moisture can act as a plasticizer and facilitate the inclusion of oxygen into the SPH structure. Generally speaking, these reactions are associated with a change in the SPH appearance and color, from snow-white to off-white or pale yellow. During service, the SPH may face a harsh environment such as

very low acidic conditions, and so on, so its structure may be changed or degraded, which is associated with the generation of impurities. Appropriate analytical tests and methods should be developed for a complete characterization of all types of impurities within the SPH product.

1.131.8.3. SPH Potency

The SPH potency can be defined as its swelling power, which depends on the exact amounts of the SPH and its chemical structure. For instance, the SPH potency for a typical gastric retention application may be defined as the amount of HCl solution that one gram of the SPH can absorb over a certain period of time, that is, $g\,g^{-1}\,s^{-1}$ or $ml\,g^{-1}\,s^{-1}$. The cross-link density and the pore structure of the SPH can affect this factor significantly. Although complete care needs to be taken to purify the SPH product, increased cross-link density (physical or chemical) may arise from other sources including polymer crystallization, polymorph formation, entanglement, and complexation. Polymer chains can adopt different conformations during long-term storage, which might affect their swelling ability. Since the SPH is required to be compressed for proper encapsulation, this partial pressure would increase the intermolecular forces between the chains, by which the swelling rate would be affected. The most common sources of increased cross-link density are the SPH interaction with the oppositely charged species such as calcium, aluminum, iron, sulfate, and phosphate ions. The SPH as a final product when it is encapsulated in an orally administrable capsule may face another instability due to the SPH–capsule interaction either directly or indirectly. For instance, this may happen due to a charge difference between the SPH structure and the structure of the capsule or due to the interaction between the ions within the SPH structure and the capsule material, which results in polymer–polymer interchain complexation and ion–polymer complexation, respectively.

Although the SPH potency should not theoretically be correlated to the amount of pore, the pore can affect both the SPH swelling capacity and its rate. Since the SPH product is soft in general, and the pores are embedded into a soft SPH matrix, their shape and size can be changed upon application of minor pressures. Pores not only provide capillary action to the water diffusion process, but they also increase the contact surface area with the aqueous medium. Any change in the shape and size of the pores would imbalance the swelling–pore correlation. As SPHs for oral delivery are required to be encapsulated, the original size of the SPH needs to be reduced in order to fit the capsule size. This compression effect apparently affects the SPH pore structure, which might affect the ultimate swelling property of the SPH. A swelling–compression correlation has been found, whose magnitude depends on the orientation of the SPH during compression. In other words, the original noncompressed SPH swelling is preserved if the SPH is compressed along the gas movement line which is from the bottom to the top. Compression force applied in the opposite direction severely affects the swelling kinetic of an SPH.[20] The SEM and swelling studies displayed that the swelling kinetics of the SPH is not affected by the surface morphology and surface porosity measured via mercury porositometry. Studies show that SPH swelling is predominantly determined by the internal SPH structure.[1]

From the biopharmaceutics perspective, the SPH may lose its potency due to interaction with foods or beverages. Fatty foods, oils, and materials of such nature may reduce the SPH potency by making the swelling environment more lypophilic. On the other hand, more basic or more acidic juices as well as salts may also affect the SPH potency to a lesser or greater extent. If the SPH is ionic in nature, its potency would dramatically be reduced by increasing the ionic strength of the swelling medium. The effect of different beverages on the swelling behavior of multiple SPH formulations has been studied for gastric retention applications.[46]

1.131.9. SPH Safety

The SPH may be considered safe if it does not affect the human body either chemically or physically. To be considered chemically safe, the SPH should contain less than tolerated amounts of residual materials. This requires developing a very effective purification process and very accurate analytical methods. The SPH is considered physically safe if its administration does not pose any threat to the human body. One of the most serious concerns in administrating a swellable material is esophagus obstruction. Due to its rapid water absorption, a naked SPH may absorb water in the esophagus area, become expanded and hence obstruct the area. This can be avoided by using proper encapsulation materials and methods. Multiple SPH doses may be administered to ensure that esophagus obstruction does not occur under severe and aggressive conditions.

Another aspect of an SPH dosage form is its chemical interaction with the stomach acids. For instance, an ester-based superporous hydrogel is susceptible to ester hydrolysis under severe acidic conditions in the stomach, in particular under long-fasting gastric conditions. An adequate number of studies should be conducted to ensure that there are no, or only safe, by products of such a reaction. In the preparation of SPHs and their dosage form for human clinical studies, care must be taken to use materials with nonanimal origin, which require a TSE (transmissible spongiform encephalopathy) certificate for every starting material.

1.131.10. SPH Platform Design for Drug Delivery

To deliver a drug via a swellable platform, the drug needs to be incorporated into the SPH platform. The drug is first formulated into a drug delivery system (DDS) and the DDS is then incorporated into the SPH platform. Although many designs are possible, two designs have been practiced for gastric retention and peroral intestinal delivery of different drugs. Depending on the position of the DDS with respect to the SPH platform, these may be called internal DDS and external DDS designs as shown in Figure 10. In the former, the DDS is placed in the center of the SPH platform and is held in place using an SPH plug. The SPH plug is also held in place by gluing it onto the SPH body from the top. The whole platform is then encapsulated inside an orally administrable capsule.

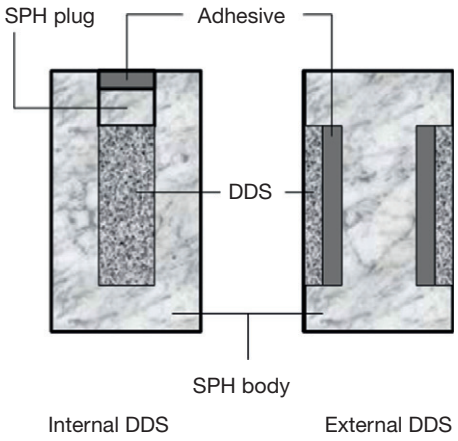

Figure 10 Different platform designs for the superporous-hydrogel-based drug delivery.

Upon administration and the exposure of the capsule to the stomach acid (for gastric retention), the capsule is dissolved and the SPH platform would be exposed to the gastric contents. This results in an immediate expansion of the SPH to its full extent, which is followed by drug release by diffusion.[47–50] In the external DDS approach, the SPH is attached externally to the SPH body using biocompatible glue, and the platform is then encapsulated in an oral capsule. For peroral intestinal delivery, the capsule itself is enterically coated to prevent the capsule and the SPH from premature dissolution or swelling in the gastric medium. Upon entering the intestine area, the higher pH favors capsule dissolution, which is followed by SPH expansion. The SPH would expand to a size large enough to dock itself into the intestinal wall. The drug is then released directly through the intestinal cells.[51–53]

1.131.11. SPH in Drug Delivery and Other Areas

SPHs were originally intended for prolonging retention of drugs with a narrow window of absorption. In designing a superporous hydrogel for such applications, one needs to consider the drug–SPH interaction, which is caused by interaction of their functional groups. Drugs such as acetohydroxamic acid (AHA),[54] repaglinide,[56] metoclopramide,[57,58] and amoxicillin[59,60] contain amide groups. Amine groups can be found in drugs such as acyclovir,[61] amoxicillin, cefuroxime axetil,[62] furosemide,[63] gabapentin,[64] levodopa,[65–67] metformin HCl,[68] metoclopramide, ranitidine HCl,[69] and famotidine.[70] The carboxyl groups are part of amoxicillin, ciprofloxacin,[71] furosemide, gabapentin, ibuprofen,[57] levodopa, and repaglinide-can structures. All these drugs have been examined for gastric retention applications via different methods. From a compatibility perspective, SPHs containing ion may not be a good choice to prolong the gastric retention of levodopa or gabapentine, which contain carboxyl groups. SPHs containing carboxyl groups may interact via hydrogen bonding with the drugs containing carboxyl and amine groups. SPHs, due to their moisture content, may expedite the hydrolysis of amide-containing drugs during storage. SPH compatibility with other excipients used to make the DDS also requires careful evaluation.

1.131.11.1. Gastric Retention

A holy grail in oral drug delivery is to develop a dosage form with the ability to control drug release for a relatively long period of time. Besides floating and mucoadhesion concepts, a swelling concept has also been exploited to extend the residence time of the drugs with a narrow absorption window.[47,49,72–75] Following the discovery of *Helicobacter pylori*, a need for an efficient dosage form with the ability to remain in the gastric medium was also felt. A gastroretentive platform needs to be designed based on a good knowledge of physiological factors and biopharmaceutical aspects of the gastric medium.[76] The SPH design for gastric retention applications has been the subject of several articles.[15,77,78]

Gastric retention requires the swellable platform to stay in the gastric medium for a reasonable period of time, that is, a few hours after dose administration. The mechanism by which a platform would stay in the gastric medium is by swelling, and this requires the SPH to swell to a size larger than the pylorus diameter. Assuming an average pylorus diameter of 1.5–2 cm, at least two out of three dimensions of the hydrogel should be larger than 2 cm. On the other hand, the platform needs to be administered orally using a conventional capsule for human administration. Generally, a 00 gelatin or HPMC capsule with an outer diameter of 8.53 mm, height of 23.30 mm, and volume of 0.95 ml is used. A simple calculation shows that a swellable hydrogel for such an application should expand in the gastric medium to at least 2.3 times its original dimension, or to at least 12 times its original volume. The required rate at which a swellable hydrogel should expand is dependent on many factors, which affect gastric emptying. For example, if the stomach contains only water, it takes about 25 min to have half of the consumed water depleted from the stomach. This is a good assumption to design a platform with a desirable swellability. The hydrogel would face a premature depletion from the stomach if it cannot swell to its maximum size in less than 25 min. In order to stay integrated in the gastric medium for a desirable period of time, the SPH should resist gastric contraction and expansion forces, which are maximized during the housekeeping period of the phase III stomach motility. By far, this is the most challenging part in designing SPHs for such applications. The maximum volume that the SPH can acquire in its dry state is about 0.95 ml for encapsulation into, for example, a 00 gelatin capsule. Depending on the drug loading capacity, a certain volume of the SPH is occupied by the drug or the DDS. In other words, the effective capsule volume occupied by the SPH would be around 0.6 ml. With the SPH having a density of 1 g ml^{-1}, the maximum feasible weight of the SPH inside the capsule would be around 0.6 g. The calculation shows that the SPH in its fully swollen state would contain about 95 wt% of water. Ironically, a hydrogel which contains 5% of solid and 95% of water should resist the very aggressive stomach forces, which requires significant intermolecular forces within the swollen SPH structure to preserve the SPH integrity in such conditions. Moreover, the SPH needs to possess all these required properties under a very low pH condition of the stomach. The SPH screened for such application also requires to be very safe chemically and physically, and this needs to be proved first in animals. As far as its efficacy is concerned, the proof of gastric retention can be first conducted

in animal models, but for many reasons the results would not necessarily prove the concept in humans. Since no animal has proved to be a reliable model for such studies, the proof of gastric retention would at best be confirmed by conducting a small-scale study in humans.

One of the most important considerations in using swellable platforms for gastric retention is the SPH–DDS interaction. Two studies have been conducted in which the drug model was formulated into a wax and a solid based delivery system. In both studies, the dissolution was performed in a USPII paddle type apparatus using 900 ml of 0.01 N HCl (pH 2.0) at $37 \pm 0.2\,^{\circ}C$ and 100 rpm. An HP8453 UV/VIS was used to measure the absorbance of the drug model at 280 nm. Different formulations were prepared by including a model drug into a low (Gelucire) and high (Compritol) molecular weight wax.[50,79] The amount of drug loaded into the wax system was about 20 wt%. An HPMC capsule was used to encapsulate both the wax and the wax-loaded SPH. The study showed that the same amount of drug is released from the wax system and the SPH–wax system when a low melting wax was used as the delivery system. On the other hand, a prolonged release was observed over a much longer period of time for the higher melting wax system. Apparently, as shown in Figure 11, the low melting wax is removed from the SPH system at the dissolution temperature of 37 °C, while the majority of the high melting wax still remains over the same retention time (i.e., 48 h) in the dissolution medium. With the latter, the SPH pores are presumably blocked by the wax, which results in a much slower drug release.

In another study, a delivery system with a drug loading of 75 wt% was designed using the combination of a fast dissolving polymer (polyvinyl pyrrolidone) and a slow dissolving polymer (hydroxypropyl methylcellulose) at different ratios.[80] While the pure drug model was released from the SPH in less than 30 min, the delivery system containing higher HPMC contents showed an extended release over a much longer period of time resembling a zero-order kinetic at the highest HPMC/PVP ratio as shown in Figure 12. These observations may be accounted for in terms of the solubility behavior of the two polymers. As the PVP is very water soluble, it can be dissolved in water even when only a small amount of water is available. On the other hand, a complete dissolution of HPMC requires much more water to be freely available to the polymer. When a tablet containing HPMC is enclosed within the SPH platform, the HPMC, due to the lack of water availability, produces a very thick gelatinous mass inside the SPH. This causes the drug to experience a much longer path for its complete release from the platform.

The proof of the gastric retention principle for various SPH hybrids has been studied in swine. The study showed that an acrylate–chitosan hybrid could provide a minimum of 24 h retention in the swine stomach under different fed and fasted conditions.[81,82] The safety and toxicity of different hydrogel formulations have been studied for gastric retention applications.[83] SPH retention in man has been studied using scintigraphy. SPHs radiolabeled with ^{99}Tc were encapsulated in an enteric-coated gelatin capsule and administered orally.[84] In a study on SPHs based on chitosan and glycol chitosan for gastric retention application, it was found that the swelling property of the glycol chitosan is superior to that of chitosan alone.[85] Superporous hydrogel of (acrylic acid-*co*-acrylamide)/*O*-carboxymethyl chitosan has been evaluated for oral insulin delivery. Followed by insulin loading and release, the circular dichroism (CD) spectra indicated a stable insulin conformation as well as its bioactivity according to hypoglycemic effect in mice. The hydrogel could bind to Ca^{2+} and entrap enzymes, which resulted in inactivation of trypsin and α-chymotrypsin. Results of this study showed a significant hypoglycemic effect for insulin loaded into the SPH and better bioavailability compared to subcutaneous insulin injection.[86] Another study with the same polymer indicated a physical interaction between the polymer and insulin.[87] The polymer was also examined for its cytotoxicity and genotoxicity. The study showed that the SPH caused minimal damage to cell viability, lysosomal activity, and metabolic activity. A study on mice showed that the SPH which contains minute amounts of monomer and cross-linker, is truly biocompatible and can be considered a safe carrier for protein delivery.[88] Glycol chitosan SPHs were prepared and loaded with dispersed and conjugated amoxicillin to treat the

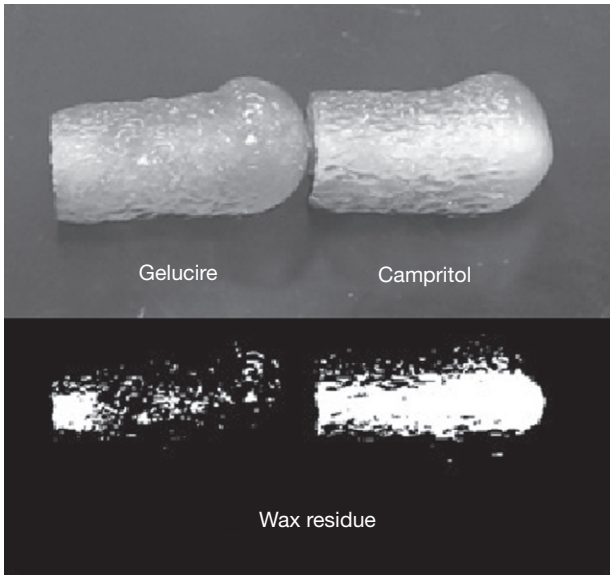

Figure 11 Superporous hydrogel with wax-based delivery systems.

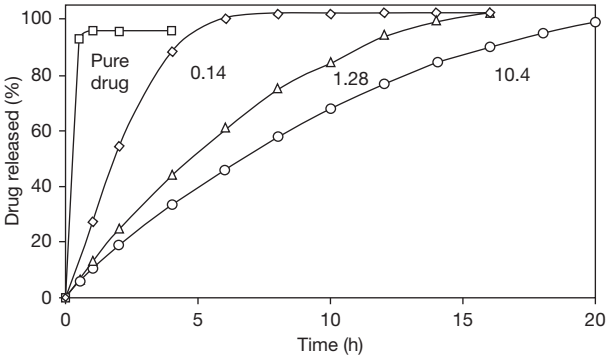

Figure 12 Drug release from superporous hydrogel with solid-based delivery systems.

H. pylori. A prolonged drug delivery effect was observed for the conjugated system whose release mechanism was due to hydrolysis as opposed to diffusion for the dispersed drug.[89]

1.131.11.2. Peroral Intestinal Delivery

Conventional and composite generations of SPHs have been widely studied for peroral peptide and protein administration.[90] The CSPHs and SPHCs were evaluated for enhancing the drug transport (different molecular weights) across the porcine intestine (*in vitro* study).[51] Among the factors studied were the possible damage to intestinal cells, the ability of SPH for mechanical fixation, the SPH effect on paracellular drug permeability, and cytotoxicity in Caco-2 monolayers.[91] The release behavior of peptides such as buserelin, octreotide, and insulin,[92] the intestinal *in vitro* absorption of desmopressin,[93] and the mechanism of paracellular tight junction opening in the Caco-2 cells[94] have also been studied. Due to improved mechanical properties, *in vitro* mucoadhesion forces and loading capability, hydrogels based on acrylic acid-*co*-acrylamide and *O*-carboxymethyl chitosan have been proposed as a potential mucoadhesive system for peroral delivery of proteins and peptides.[95]

1.131.11.3. SPHs as Diet Aid

A highly swelling SPH with gastric retention ability can be designed to occupy a large portion of the stomach volume to induce fullness in humans. To achieve a sense of fullness, a minimum of 400 ml of the stomach volume should presumably be occupied by the SPH. If a pure SPH with no drug or DDS is used for this application, around 0.6 g of the SPH can be housed in a 00 capsule as mentioned before. To be effective in such application, a single 0.6 g dose of SPH should have a potency of at least 650 ml g^{-1}. Using conventional materials and techniques, this potency can hardly be achieved under very low acidic conditions of the stomach. Therefore, the application requires the use of multiple doses of SPH to achieve adequate volume, which brings more safety risks as related to the impurities and physical esophagus obstruction. Moreover, water itself due to the high concentration (minimum of 650 ml) should also be studied as a control to see if it can induce any fullness effect at such concentration. Potentially, an SPH platform as a diet aid may be formulated with other excipients to achieve its maximum potency. These may include excipients to adjust stomach pH or relax stomach motility.

1.131.11.4. SPHs as Superdisintegrant

Superdisintegrants are pharmaceutically acceptable polymers based on cellulose, poly(vinyl pyrrolidone), and starch derivatives, which have a tailor-made swelling property. These are supplied in particle form and mixed into a solid dosage formulation to offer a desirable disintegration. The SPHs are also cross-linked hydrophilic polymers, whose swelling capacity and rate can be tailored for such applications. Nonetheless, there are issues that need to be addressed before the use of SPH particles can be justified. For gastric retention, intestinal retention, and diet application, the SPH is produced and used as a single platform, generally in a cylindrical shape as shown in

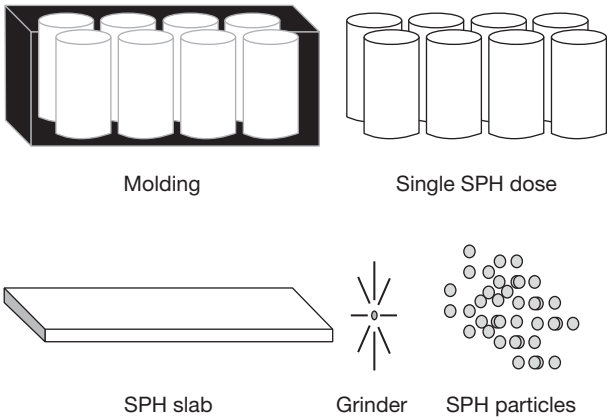

Figure 13 Manufacturing superporous hydrogels for various applications.

Figure 13. The SPH particulates on the other hand can be produced in powder form by grinding the SPH slabs using appropriate equipment or can be produced directly in particle form by an inverse dispersion technique. With the grinding technique, which is cost effective and commercially more attractive, the most challenging issue would be to keep the production environment as dry as possible. The SPH dust can sit and make a gel coat on almost any piece of equipment during processing. A major difference between the SPH superdisintegrant and conventional superdisintegrants is that the former can provide a much larger surface due to its size and its pore content. In one study, the SPH particles, in particular those based on poly(acrylic acid) were used as a wicking agent in the formulation of fast-disintegrating tablets.[96]

1.131.11.5. Other Applications

Sodium CMC and hydroxyethyl cellulose cross-linked with divinyl sulphone have been used to remove body fluids during surgery and to collect body fluids in the treatment of edema. The polymer biocompatibility is also promising in diuretic therapy.[97,98] Sodium CMC and hydroxyethyl cellulose as well as poly(ethylene glycols) of different molecular weights have been used in developing orally administrable hydrogels for water absorption.[98] High capacity super water absorbents were injected intracerebrally for studying hypothalamic areas in controlling the female production cycle.[99] The SPH microspheres were used in the clinical evaluation of transcatheter arterial embolization for hypervascular metastatic bone tumor.[100] In another biomedical application, freeze-dried water absorbents were used to design plugs and haemostatic and other medical devices.[101] These were also used in compact and light-weight bags[102] and in surgical drapes[103] to manage body fluids. As the core for wound dressing, the polyacrylate water absorbents could retain microorganisms and reduce the number of viable germs.[104] Hydrogels based on sodium acrylate, *N*-vinyl pyrrolidone, and silver were also studied for their antibacterial activity[105] (see **Chapter 1.122, Structural Biomedical Polymers (Nondegradable)**).

In cell scaffolding, PEG diacrylate has been studied for cell infiltration and vascularization.[106] To be used as a support for

cell cultivation, an SPH based on HEMA and ethylene dimethacrylate has been prepared. The porosity of the structure was achieved via a salt-leaching technique using sodium chloride and ammonium persulfate. Different techniques including SEM, mercury porositometry, and dynamic desorption of nitrogen were used to characterize the hydrogels.[107] A hydrogel with good mechanical properties to function with a healthy cartilage, yet porous to allow tissue integration, is very much needed for articular cartilage repair. Such a potential material has been prepared using poly(vinyl alcohol) and poly(vinyl pyrrolidone) through a double emulsion process followed by a freezing–thawing process.[108] Superporous hydrogels have the potential to be used as scaffold for cell transplantation. A highly interconnected poly(ethylene glycol) diacrylate with macropores in the range of 100–600 μm has shown a rapid cell uptake and cell seeding.[109] The SPH formulation containing hydroxyapatite as filler can potentially be used as scaffold in bone tissue engineering due to improved mechanical strength.[110] Different techniques including FTIR, SEM/EDX, and cytocompatibility using L929 fibroblasts were utilized to characterize the prepared SPHs. A photo-cross-linking reaction and a foaming process have been utilized in developing a PEG-based superporous hydrogel with high pore interconnectivity. This feature is essential for applications such as tissue engineering where tissue invasion and nutrient transport are basic requirements.[111] Kroupova *et al.* have shown that SPHs have the potential to initiate the differentiation of embryonic stein (ES) cells[112] (see **Chapter 1.132, Dynamic Hydrogels**).

1.131.12. Conclusions

Due to their hydrophilic, cross-linked, and porous structure, SPH polymers display a swelling behavior different from that of conventional water swelling hydrogels. This feature has been utilized in developing swellable platforms for drug delivery applications. SPHs have been studied for prolonging the retention of drugs with a narrow window of absorption, and for peroral intestinal absorption of peptide and protein drugs. The feasibility of SPHs in pharmaceutical applications relies on many factors, including its scale up, safety, and stability. This chapter discusses the basic concepts in developing a synthetic swellable platform for certain pharmaceutical and biomedical applications.

References

1. Gemeinhart, R. A.; Park, H.; Park, K. *Polym. Adv. Technol*. **2000**, *11*, 617–625.
2. Chaterjia, S.; Kwon, K.; Park, K. *Prog. Polym. Sci*. **2007**, *32*, 1083–1122.
3. Omidian, H.; Qiu, Y.; Yang, S. C.; Kim, D.; Park, H.; Park, K. U.S. Pat. 6,960,617, 2005.
4. Omidian, H.; Rocca, J. G. U.S. Pat. 7,056,957, 2006.
5. Omidian, H.; Rocca, J. G. U.S. Pat. Applic. 20080089940, 2008.
6. Omidian, H.; Park, K.; Rocca, J. G. *J. Pharm. Pharmacol*. **2007**, *59*, 317–327.
7. Han, W.; Omidian, H.; Rocca, J. G. *Dynamic Swelling of Superporous Hydrogels Under Compression*; American Association of Pharmaceutical Scientists (AAPS): Tennessee, USA, 2005.
8. Gavrilas, C.; Omidian, H.; Rocca, J. G. Dynamic mechanical properties of superporous hydrogels. In *8th US–Japan Symposium on Drug Delivery Systems*, HI, 2005.
9. Gavrilas, C.; Omidian, H.; Rocca, J. G. A novel gastric simulator. In *The 32nd Annual Meeting of the Controlled Release Society (CRS)*, Miami, FL, 2005.
10. Gavrilas, C.; Omidian, H.; Rocca, J. G. A novel simulator to evaluate fatigue properties of superporous hydrogels. In *8th US–Japan Symposium on Drug Delivery Systems*, HI, 2005.
11. Chen, J.; Park, H.; Park, K. *J. Biomed. Mater. Res*. **1999**, *44*, 53–62.
12. Omidian, H.; Rocca, J. G.; Park, K. *J. Control. Release* **2005**, *102*, 3–12.
13. Park, K.; Park, H. U.S. Pat. 5,750,585, 1998.
14. Chen, J.; Park, K. *J. Macromol. Sci. Pure Appl. Chem*. **1999**, *A36*, 917–930.
15. Chen, J.; Park, K. *J. Control. Release* **2000**, *65*, 73–82.
16. Park, K.; Chen, J.; Park, H. U.S. Pat. 6,271,278, 2001.
17. Park, K.; Chen, J.; Park, H. Superporous hydrogel composites: A new generation of hydrogels with fast swelling kinetics, high swelling ratio and high mechanical strength. In *Polymeric Drugs and Drug Delivery systems*; Ottenbrite, R., Kim, S. W., Eds.; CRC Press: Boca Raton, FL, 2001.
18. Omidian, H.; Rocca, J. G.; Park, K. *Macromol. Biosci*. **2006**, *6*, 703–710.
19. Gemeinhart, R. A.; Chen, J.; Park, H.; Park, K. *J. Biomater. Sci. Polym. Ed*. **2000**, *11*, 1371–1380.
20. Gemeinhart, R. A.; Park, H.; Park, K. *J. Biomed. Mater. Res*. **2001**, *55*, 54–62.
21. Dorkoosh, F. A.; Brussee, J.; Verhoef, J. C.; Borchard, G.; Rafiee-Tehrani, M.; Junginger, H. E. *Polymer* **2000**, *41*, 8213–8220.
22. Bajpai, S. K.; Bajpai, M.; Sharma, L. *Iran. Polym. J*. **2007**, *16*, 521–527.
23. Savina, I. N.; Mattiasson, B.; Galaev, I. Y. *Polymer* **2005**, *46*, 9596–9603.
24. Huh, K. M.; Baek, N.; Park, K. *J. Bioact. Compat. Polym*. **2005**, *20*, 231–243.
25. Baek, N.; Park, K.; Park, J. H.; Bae, Y. H. *J. Bioact. Compat. Polym*. **2001**, *16*, 47–57.
26. Kim, D.; Seo, K.; Park, K. *J. Biomater. Sci. Polym. Ed*. **2004**, *15*, 189–199.
27. Kim, D.; Park, K. *Polymer* **2004**, *45*, 189–196.
28. Kabiri, K.; Omidian, H.; Hashemi, S. A.; Zohuriaan-Mehr, M. J. *J. Polym. Mater*. **2003**, *20*, 17–22.
29. Kabiri, K.; Omidian, H.; Hashemi, S. A.; Zohuriaan-Mehr, M. J. *Eur. Polym. J*. **2003**, *39*, 1341–1348.
30. Kabiri, K.; Omidian, H.; Zohuriaan-Mehr, M. J. *Polym. Int*. **2003**, *52*, 1158–1164.
31. Mahdavinia, G. R.; Mousavi, S. B.; Karimi, F.; Marandi, G. B.; Garabaghi, H.; Shahabvand, S. *Express Polym. Lett*. **2009**, *3*, 279–285.
32. Omidian, H.; Park, K. *J. Bioact. Compat. Polym*. **2002**, *17*(6), 433–450.
33. Yang, S.; Park, K.; Rocca, J. G. *J. Bioact. Compat. Polym*. **2004**, *19*, 81–100.
34. Qiu, Y.; Park, K. *AAPS Pharm. Sci. Tech*. **2003**, *4*, E51.
35. Kabiri, K.; Zohuriaan-Mehr, M. J. *Polym. Adv. Technol*. **2003**, *14*, 438–444.
36. Seo, K. W.; Kim, D. J.; Park, K. N. *J. Ind. Eng. Chem*. **2004**, *10*, 794–800.
37. Cheng, S. X.; Zhang, J. T.; Zhuo, R. X. *J. Biomed. Mater. Res. A* **2003**, *67A*, 96–103.
38. Abd El-Rehim, H. A.; Hegazy, E. S. A.; Diaa, D. A. *J. Macromol. Sci. Pure Appl. Chem*. **2006**, *A43*, 101–113.
39. Chen, J.; Park, K. *Carbohydr. Polym*. **2000**, *41*, 259–268.
40. Park, H.; Kim, D. *J. Biomed. Mater. Res. A* **2006**, *78A*, 662–667.
41. Hradil, J.; Horak, D. *React. Funct. Polym*. **2005**, *62*, 1–9.
42. Kaneko, T.; Asoh, T. A.; Akashi, M. *Macromol. Chem. Phys*. **2005**, *206*, 566–574.
43. Yin, L. C.; Fei, L. K.; Tang, C.; Yin, C. H. *Polym. Int*. **2007**, *56*, 1563–1571.
44. Pourjavadi, A.; Barzegar, S. *Starch-Starke* **2009**, *61*, 161–172.
45. Omidian, H.; Gavrilas, C.; Han, W.; Li, G.; Rocca, J. G. U.S. Pat. Applic. 20080206339, 2008.
46. Li, G.; Omidian, H.; Rocca, J. G. *Solvent Effects on the Swelling Properties of Superporous Hydrogels*; American Association of Pharmaceutical Scientists (AAPS): Tennessee, USA, 2005.
47. Rocca, J. G.; Omidian, H.; Shah, K. Controlled release of compounds mediated by retention in the upper part of the GI tract. In *The 30th Annual Meeting and Exposition of the Controlled Release Society (CRS)*, Glasgow, Scotland, 2003.
48. Rocca, J. G.; Omidian, H.; Shah, K. *Business Briefing Pharmatech*. 2003, 152–156.
49. Rocca, J. G.; Omidian, H.; Shah, K. *Drug Deliv. Technol*. **2005**, *5*, 40–46.
50. Rocca, J. G.; Shah, K.; Omidian, H. *Gattefosse Tech. Bull*. **2004**, *97*, 73–84.
51. Dorkoosh, F. A.; Borchard, G.; Refiee-Tehrani, M.; Verhoef, J. C.; Junginger, H. E. *Eur. J. Pharm. Biopharm*. **2002**, *53*, 161–166.
52. Dorkoosh, F. A.; Verhoef, J. C.; Borchard, G.; Rafiee-Tehrani, M.; Junginger, H. E. *J. Control. Release* **2001**, *71*, 307–318.
53. Dorkoosh, F. A.; Verhoef, J. C.; Verheijden, J. H. M.; Refiee-Tehrani, M.; Borchard, G.; Junginger, H. E. *Pharm. Res*. **2002**, *19*, 1532.
54. Umamaheswari, R. B.; Jain, S.; Tripathi, P. K.; Agrawal, G. P.; Jain, N. K. *Drug Deliv*. **2002**, *9*, 223–231.
55. Fukuda, M.; Peppas, N. A.; Mcginity, J. W. *J. Control. Release* **2006**, *115*, 121–129.

56. Rokhade, A. P.; Patil, S. A.; Belhekar, A. A.; Halligudi, S. B.; Aminabhavi, T. M. *J. Appl. Polym. Sci.* **2007**, *105*, 2764–2771.
57. Tang, Y. D.; Venkatraman, S. S.; Boey, F. Y. C.; Wang, L. W. *Int. J. Pharm.* **2007**, *336*, 159–165.
58. Singh, S.; Singh, J.; Muthu, M. S.; Balasubramaniam, J.; Mishra, B. *Curr. Drug. Deliv.* **2007**, *4*, 269–275.
59. Torrado, S.; Prada, P.; de la Torre, P. M.; Torrado, S. *Biomaterials* **2004**, *25*, 917–923.
60. Rajinikanth, P. S.; Balasubramaniam, J.; Mishra, B. *Int. J. Pharm.* **2007**, *335*, 114–122.
61. Groning, R.; Berntgen, M.; Georgarakis, M. *Eur. J. Pharm. Biopharm.* **1998**, *46*, 285–291.
62. Dhumal, R. S.; Rajmane, S. T.; Dhumal, S. T.; Pawar, A. P. *J. Sci. Ind. Res.* **2006**, *65*, 812–816.
63. Sakkinen, M.; Tuononen, T.; Jurjenson, H.; Veski, P.; Marvola, M. *Eur. J. Pharm. Sci.* **2003**, *19*, 345–353.
64. Gabapentin extended-release – Depomed: Gabapentin ER, gabapentin gastric retention, gapapentin GR. *Drugs R D* **2007**, *8*(5), 317–320.
65. Goole, J.; Deleuze, P.; Vanderbist, F.; Amighi, K. *Eur. J. Pharm. Biopharm.* **2008**, *68*, 310–318.
66. Klausner, E. A.; Eyal, S.; Lavy, E.; Friedman, M.; Hoffman, A. *J. Control. Release* **2003**, *88*, 117–126.
67. Hoffman, A.; Stepensky, D.; Lavy, E.; Eyal, S.; Klausner, E.; Friedman, M. *Int. J. Pharm.* **2004**, *277*, 141–153.
68. Metformin extended release – DepoMed: Metformin, metformin gastric retention, metformin GR. *Drugs R D* **2004**, *5*(4), 231–233.
69. Hassan, M. A. *J. Drug Deliv. Sci. Technol.* **2007**, *17*, 125–128.
70. Jaimini, M.; Rana, A. C.; Tanwar, Y. S. *Curr. Drug Deliv.* **2007**, *4*, 51–55.
71. Varshosaz, J.; Tavakoli, N.; Roozbahani, F. *Drug Deliv.* **2006**, *13*, 277–285.
72. Davis, S. S. *Drug Discov. Today* **2005**, *10*, 249–257.
73. Davis, S. S.; Wilding, E. A.; Wilding, I. R. *Int. J. Pharm.* **1993**, *94*, 235–238.
74. Hwang, S. J.; Park, H.; Park, K. *Crit. Rev. Ther. Drug Carrier Syst.* **1998**, *15*, 243–284.
75. Streubel, A.; Siepmann, J.; Bodmeier, R. *Curr. Opin. Pharmacol.* **2006**, *6*, 501–508.
76. Bardonnet, P. L.; Faivre, V.; Pugh, W. J.; Piffaretti, J. C.; Falson, F. *J. Control. Release* **2006**, *111*, 1–18.
77. Chen, J.; Blevins, W. E.; Park, H.; Park, K. *J. Control. Release* **2000**, *64*, 39–51.
78. Bajpai, S. K.; Bajpai, M.; Sharma, L. *J. Macromol. Sci. Pure Appl. Chem.* **2006**, *A43*, 507–524.
79. Li, G.; Omidian, H.; Rocca, J. G. Wax-loaded superporous hydrogel platforms. In *The 32nd Annual Meeting of the Controlled Release Society (CRS),* Miami, FL, 2005.
80. Han, W.; Omidian, H.; Rocca, J. G. A novel acrylate ester-based superporous hydrogel. In *The 32nd Annual Meeting of the Controlled Release Society (CRS),* Miami, FL, 2005.
81. Han, W.; Omidian, H.; Rocca, J. G. *In Vivo and In Vitro Studies on Novel Gastroretentive Superporous Hydrogel (SPH) Platforms*; American Association of Pharmaceutical Scientists (AAPS): Salt Lake City, Utah, USA, 2003.
82. Han, W.; Omidian, H.; Rocca, J. G. Evaluation of gastroretentive superporous hydrogel platforms using swine model. In *The 31st Annual Meeting of the Controlled Release Society (CRS),* Honolulu, HI, 2004.
83. Townsend, R.; Rocca, J. G.; Omidian, H. Safety and toxicity studies of a novel gastroretentive platform administered orally in a swine emesis model. In *The 32nd Annual Meeting of the Controlled Release Society (CRS),* Miami, FL, 2005.
84. Dorkoosh, F. A.; Stokkel, M. P. M.; Blok, D.; *et al. J. Control. Release* **2004**, *99*, 199–206.
85. Park, H.; Park, K.; Kim, D. *J. Biomed. Mater. Res.* **2006**, *76A*, 144–150.
86. Yin, L. C.; Ding, J. Y.; Fei, L. K.; *et al. Int. J. Pharm.* **2008**, *350*, 220–229.
87. Yin, L. C.; Zhao, Z. M.; Hu, Y. Z.; *et al. J. Appl. Polym. Sci.* **2008**, *108*, 1238–1248.
88. Yin, L.; Zhao, X.; Cui, L.; *et al. Food Chem. Toxicol.* **2009**, *47*, 1139–1145.
89. Park, J.; Kim, D. *J. Biomater. Sci. Polym. Ed.* **2009**, *20*, 853–862.
90. Dorkoosh, F. A.; Verhoef, J. C.; Borchard, G.; Refiee-Tehrani, M.; Junginger, H. E. *J. Control. Release* **2001**, *71*, 307–318.
91. Dorkoosh, F. A.; Setyaningsih, D.; Borchard, G.; Refiee-Tehrani, M.; Verhoef, J. C.; Junginger, H. E. *Int. J. Pharm.* **2002**, *241*, 35–45.
92. Dorkoosh, F. A.; Verhoef, J. C.; Ambagts, M. H. C.; Refiee-Tehrani, M.; Borchard, G.; Junginger, H. E. *Eur. J. Pharm. Sci.* **2002**, *15*, 433–439.
93. Polnok, A.; Verhoef, J. C.; Borchard, G.; Sarisuta, N.; Junginger, H. E. *Int. J. Pharm.* **2004**, *269*, 303–310.
94. Dorkoosh, F. A.; Broekhuizen, C. A. N.; Borchard, G.; Rafiee-Tehrani, M.; Verhoef, J. C.; Junginger, H. E. *J. Pharm. Sci.* **2004**, *93*, 743–752.
95. Yin, L. C.; Fei, L. K.; Cui, F. Y.; Tang, C.; Yin, C. H. *Biomaterials* **2007**, *28*, 1258–1266.
96. Yang, S. C.; Fu, Y. R.; Hoon, S.; Park, J. K.; Park, K. *J. Pharm. Pharmacol.* **2004**, *56*, 429–436.
97. Sannino, A.; Esposito, A.; de Rosa, A.; Cozzolino, A.; Ambrosio, L.; Nicolais, L. *J. Biomed. Mater. Res. A* **2003**, *67A*, 1016–1024.
98. Esposito, A.; Sannino, A.; Cozzolino, A.; *et al. Biomaterials* **2005**, *26*, 4101–4110.
99. Ohta, M.; Homma, K. *Gen. Comp. Endocrinol.* **1988**, *72*, 424–430.
100. Ken'ichiro, H.; Katsuyuki, N.; Munehito, S.; *et al. Clin. Orthop. Surg.* **2004**, *39*(10), 1307–1314.
101. Sawhney, A. S.; Bennett, S. L.; Pai, S. S.; Sershen, S. R.; Co, F. H. U.S. Pat. Applic. 2007/0231366, 2007.
102. Ohta, T.; Kuroiwa, T. *Surg. Neurol.* **1999**, *51*, 464–465.
103. Tankerseley, T. N. U.S. Pat. 2007/0135784, 2007.
104. Bruggisser, R. *J. Wound Care* **2005**, *14*, 438–442.
105. Lee, W. F.; Huang, Y. C. *J. Appl. Polym. Sci.* **2007**, *106*, 1992–1999.
106. Keskar, V.; Gandhi, M.; Gemeinhart, E. J.; Gemeinhart, R. A.; Keskar, V. *J. Tissue Eng. Regen. Med.* **2009**, *3*, 486–490.
107. Horak, D.; Hlidkova, H.; Hradil, J.; Lapcikova, M.; Slouf, M. *Polymer* **2008**, *49*, 2046–2054.
108. Spiller, K. L.; Laurencin, S. J.; Charlton, D.; Maher, S. A.; Lowman, A. M. *Acta Biomater.* **2008**, *4*, 17–25.
109. Keskar, V.; Marion, N. W.; Mao, J. J.; Gemeinhart, R. A. *Tissue Eng. Part A* **2009**, *15*, 1695–1707.
110. Tolga Demirtas, T.; Karakecili, A. G.; Gumusderelioglu, M. *J. Mater. Sci. Mater. Med.* **2008**, *19*, 729–735.
111. Sannino, A.; Netti, P. A.; Madaghiele, M.; *et al. J. Biomed. Mater. Res. A* **2006**, *79A*, 229–236.
112. Kroupova, J.; Horak, D.; Pachernik, J.; Dvorak, P.; Slouf, M. *J. Biomed. Mater. Res. B Appl. Biomater.* **2006**, *76B*, 315–325.

1.132. Dynamic Hydrogels

M W Toepke and W L Murphy, University of Wisconsin, Madison, WI, USA

© 2011 Elsevier Ltd. All rights reserved.

1.132.1.	**Introduction**	578
1.132.1.1.	Motivation: Utility of Dynamic Hydrogels	578
1.132.1.2.	Historical Context: Development of Dynamic Hydrogels	578
1.132.2.	**Functional Modes/General Dynamic Mechanisms**	579
1.132.2.1.	Hydrogen Bonding and Hydrophobic Interactions	579
1.132.2.2.	Electrostatic Interactions and Donnan Equilibrium	579
1.132.2.3.	Competitive Binding	579
1.132.2.4.	Covalent Bonding and Bond Cleavage	580
1.132.3.	**Specific Stimuli and Response Mechanisms**	580
1.132.3.1.	Physical Stimulus	580
1.132.3.1.1.	Temperature	581
1.132.3.1.2.	Electrical, magnetic, and electromagnetic fields	582
1.132.3.1.3.	Pressure	584
1.132.3.2.	Chemical Stimulus	585
1.132.3.2.1.	pH	585
1.132.3.2.2.	Ionic strength	585
1.132.3.2.3.	Ligand binding and ion-specific interactions	586
1.132.3.3.	Biochemical Stimulus	586
1.132.3.3.1.	Competitive ligand binding	586
1.132.3.3.2.	Enzyme catalysis	587
1.132.3.3.3.	Conformational shifts	587
1.132.4.	**Biomedical Applications**	588
1.132.4.1.	Controlled Release of Soluble Factors	588
1.132.4.1.1.	Step function release	588
1.132.4.1.2.	Rate modification	588
1.132.4.1.3.	Switchable surface	590
1.132.4.2.	Sensing and Detection	590
1.132.4.3.	Mechanical Actuation: Artificial Muscles, Robotics, and Microfluidics	591
1.132.4.3.1.	Artificial muscles and robotics	591
1.132.4.3.2.	Microfluidics	591
1.132.5.	**Future Directions**	592
References		592

Glossary

Donnan equilibrium An unequal distribution of diffusible ions between two solutions that are in contact due to a physical restraint preventing one or more ionic species from passing freely between the two solutions.

Interpenetrating polymer networks (IPN) A structure containing two or more interlocking polymer networks that are not covalently bonded to one another.

Lower critical solution temperature (LCST) The temperature below which the polymer is miscible with a solvent phase in all proportions.

Upper critical solution temperature (UCST) The temperature above which the polymer is miscible with a solvent phase in all proportions.

Abbreviations

AAPBA	3–Acrylamidophenylborionic acid
AFP	Alpha fetoprotein
BCAm	Benzo-18-crown-6-acrylamide
BMA	Butyl methacrylate
bR	Bacteriorhodopsin
BZ	Belousov–Zhabotinsky
DAMA	*N*-(*N*′,*N*′-dicarboxymethylaminopropyl) methacrylamide
DMAA	*N*,*N*′ -dimethylacrylamide
ELP	Elastin-like peptide
GEMA	2-Glucosyloxyethyl methacrylate
HPMA	*N*-(2-hydroxypropyl)-methacrylamide
IEP	Isoelectric point

IPN	Interpenetrating polymer networks	**SP**	Spirobenzopyran
LCST	Lower critical solution temperature	**UCST**	Upper critical solution temperature
MIP	Molecularly imprinted polymer	**VBC**	Viscosity B coefficient
NiPAAm	*N*-isopropylacrylamide	**VEGF**	Vascular epithelial growth factor
RGD	Arginine-glycine-aspartic acid	**VPTT**	Volume phase transition temperature

1.132.1. Introduction

Also referred to as smart, intelligent, environmentally sensitive, or responsive, dynamic hydrogels are hydrophilic polymer networks that undergo a structural modification in response to specific environmental stimuli. The stimulus acts by altering the balance of molecular forces within the hydrogel–solvent system, which causes the hydrogel structure to rearrange to achieve the lowest possible free energy state. The structural change is accompanied by alterations in the chemical and mechanical properties of the hydrogel. It is the ability to change these properties in a controllable manner that has made dynamic hydrogels an enabling technology in biomedical applications ranging from drug delivery to chemical analysis.

The materials used to create dynamic hydrogels, along with their corresponding activating stimuli, are as diverse as the potential applications. Neutral and ionic polymers, enzymes, and nanoparticles have all been incorporated into dynamic hydrogels in order to create structures that are sensitive to stimuli such as temperature, pH, ligands, and light. Hydrogels formed with multiple materials via copolymerization, formation of interpenetrating polymer networks (IPNs), and particle entrapment can be made to respond to several distinct stimuli. Regardless of the material and stimulus used, the structure of the network at any given time is a thermodynamic balance between (a) covalent forces holding the polymer backbone together; (b) noncovalent intramolecular and intermolecular interactions between polymer chains and the solvent; and (c) entropy acting to minimize the free energy of the system. Herein, we describe the historical development of dynamic synthetic hydrogels, discuss the forces and stimuli used to achieve dynamic structural changes, and review applications of dynamic hydrogels.

The scope of this chapter is limited primarily to chemically cross-linked hydrogels that are made via synthetic processes. Several aspects make synthetic hydrogels an attractive alternative to materials derived from natural sources, such as Matrigel. For example, the use of high purity monomers makes the chemistry in synthetic hydrogels relatively well defined in comparison to materials such as Matrigel, which has been found to contain over 300 different proteins.[1] In addition, batch-to-batch variability in properties of naturally derived hydrogels limits their utility as a class of robust, dynamic hydrogels. Because the focus of the chapter is on biomaterials, dynamic hydrogel behavior in aqueous solutions will be emphasized.

1.132.1.1. Motivation: Utility of Dynamic Hydrogels

Hydrogels have been used extensively in applications requiring stable, biocompatible materials, dating back to the introduction of the first soft contact lenses by Wichterle and Lim.[2] While static and slowly degradable hydrogel structures are effective in uses such as contact lenses and burn dressings,[3] the ability to change the physical and chemical properties of hydrogels on demand leads to a wider array of potential biomedical applications. Specifically, dynamic hydrogels can be used to address applications related to artificial muscles, memory and switching elements, sensors, detectors, and separations tools that would otherwise not be possible with static hydrogels. For example, a hydrogel that can be made to expand and contract based on an electrical or chemical signal would be able to mimic natural muscles for prosthetic devices.

In addition to enabling new utilities, dynamic hydrogels can also provide more flexibility in areas where fixed hydrogels were previously employed. One area of particular interest is controlled release drug delivery. The first hydrogels used in drug delivery typically depended upon diffusion and erosion mechanisms to achieve sustained release. While these approaches can be tailored to achieve a variety of dosing regimens, they are not necessarily the most efficient means of accomplishing the desired release profile. In particular, these approaches make it difficult to alter the release profile once the treatment has been administered. Such a predetermined release profile works well in applications where a constant concentration in the blood stream is required; however, these approaches are ill-equipped to address dosing applications where the appropriate release rate changes in time based on the physiological conditions.

One of the great appeals of dynamic hydrogels is their ability to sense conditions in their local environment and respond in a controllable manner. For example, a dynamic hydrogel might be designed to undergo a structural change based on the concentration of glucose in solution, and the structural change could then be used to release insulin, which would be of interest in managing type I diabetes. The power of such a system is that the hydrogel acts on a continuous and autonomous basis to both monitor a parameter of interest (glucose level) and act in a predetermined manner based on that reading (e.g., increase insulin release if the sugar level is too high), creating a simple control loop. In contrast, traditional treatment requires patients to make the conscious effort to periodically measure blood glucose levels and administer the necessary insulin dose.

1.132.1.2. Historical Context: Development of Dynamic Hydrogels

In 1948, Kuhn and Katchalsky reported that solutions containing poly(methacrylic acid) showed a marked increase in viscosity when titrated with a basic solution.[4] The change in physical properties of poly(methacrylic acid) during titration

was attributed to the elongation of the polymer chain due to ionic interactions between the charged carboxylic acid groups. Soon thereafter, the two groups developed polyionic hydrogels to test their hypothesis that molecular scale conformational changes could be translated into macroscopic motion.[5,6] Their effort was successful in demonstrating that a hydrogel fiber could elongate and contract when exposed to various pH conditions. In a later work, they demonstrated that the hydrogel could be put through several expansion–contraction cycles and showed that the contractions could perform work on a load, indicating that the materials might be used as artificial muscles.[7] It was noted that the hydrogel underwent continuous swelling upon titration with a base until the solution pH approached the pK_a of the acid groups in the hydrogel. Partial collapse of the hydrogel began to occur when titration continued beyond the pK_a, which they attributed to charge shielding from the neutralization salts in solution. The observed behavior made it clear that the physical state of the hydrogel depended upon molecular forces that could be manipulated with different stimuli.

The concept of using dynamic hydrogels to transform chemical potential into mechanical work was further refined to create an engine driven by hydrogels that alternated between swollen and collapse states based on the solution conditions.[8,9] The extensive theoretical and experimental work that followed found that in addition to pH, hydrogel conformational changes could be induced by changes in parameters such as solvent composition,[10–13] temperature,[14] and solution ionic strength.[15,16] The kinetics of these transitions and the corresponding water transport in hydrogels have also received considerable attention,[17–21] with interesting transient effects having been observed in some instances.[22,23]

1.132.2. Functional Modes/General Dynamic Mechanisms

Dynamic hydrogel networks are held together via chemical bonds or physical interactions. These cross-links tend to reduce the dynamic behavior of the hydrogel by physically restricting the range of motion of the polymer chains within the network.[24] Nevertheless, cross-linked hydrogels can swell to several times their original volume when exposed to the appropriate environmental conditions. The polymer chains that make up hydrogels interact with both themselves and their environment to form structures that achieve the lowest possible free energy state of the system. Consequently, the degree of swelling in the network is determined in large part by the cumulative effect of hydrophobic interactions and other relatively weak molecular forces, much like the tertiary structure of proteins. As is the case with some proteins, a slight perturbation in the balance of these molecular interactions can result in large conformational changes within the molecular structure. The following sections review the forces that are frequently involved in dynamic changes in hydrogel structures.

1.132.2.1. Hydrogen Bonding and Hydrophobic Interactions

Hydrogen bonding, the force that is largely responsible for the unique properties of water, plays a crucial role in determining the structure of hydrogels. Hydrogen bonding can occur between polymer chains and water molecules as well as between two chains within the polymer network. The most common hydrogen bonding sites within hydrogels are amine, amide, alcohol, and carboxylic acid groups. The dipole–dipole interaction in hydrogen bonds is relatively weak (10–30 kJ mol^{-1}) in comparison to covalent bonds (~350 kJ mol^{-1} for a typical carbon–carbon bond); the energy required to break a hydrogen bond is on the order of the kinetic energy of a water molecule at room temperature. Increasing the temperature above room temperature further weakens the extent of these interactions. Nevertheless, the cumulative force of many of these interactions acting in concert can be significant.

In comparison, hydrophobic interactions are even weaker than hydrogen bonds (<10 kJ mol^{-1}), so much so that it has only been recently that the strength of these interactions could be measured.[25] Previously, it was a matter of debate whether the interactions between nonpolar groups in aqueous solution was due solely to entropic exclusion of water. In contrast to hydrogen bonds, hydrophobic interactions are generally enhanced by increasing temperatures. In hydrogels with both hydrophobic and hydrophilic groups, hydrogen bonding acts to solvate the hydrophilic regions of the polymer while hydrophobic interactions and entropy favor polymer–polymer interactions. Given that these molecular interactions are dependent upon temperature and pressure, the balance between hydrogen bonding and hydrophobic interactions can be shifted by changes in thermodynamic parameters.

1.132.2.2. Electrostatic Interactions and Donnan Equilibrium

The structure of hydrogels containing ionizable groups is largely dependent upon the degree of ionization of the polymer chains. In an uncharged state, ionic hydrogels behave in a manner similar to hydrogels containing polar groups and the chains in the hydrogel can participate in hydrogen bonding. Hydrogen bonding is gradually disrupted as functional groups become ionized and coulombic forces act to separate the like-charged groups on the polymer chains, resulting in hydrogel swelling. The repulsive force can be overcome to a certain extent by shielding effects from soluble counter ions, as observed previously.[7]

In addition to electrostatic interactions, the immobilized charge of the ionizable groups on the polymer chains has the effect of increasing the internal osmotic pressure of the hydrogel due to a Donnan equilibrium partitioning of counter ions between the hydrogel and the bulk solution. The increased internal osmotic pressure contributes to the swelling of the hydrogel.

1.132.2.3. Competitive Binding

Individual polymer chains within a hydrogel can also associate with one another through noncovalent interactions.[26] For example, a hydrogel containing a protein and its ligand covalently attached to the polymer backbone in their active states will form dynamic cross-links due to the protein–ligand binding interactions.[75] The interactions are in a dynamic equilibrium, making the associations reversible in nature. Introduction of soluble

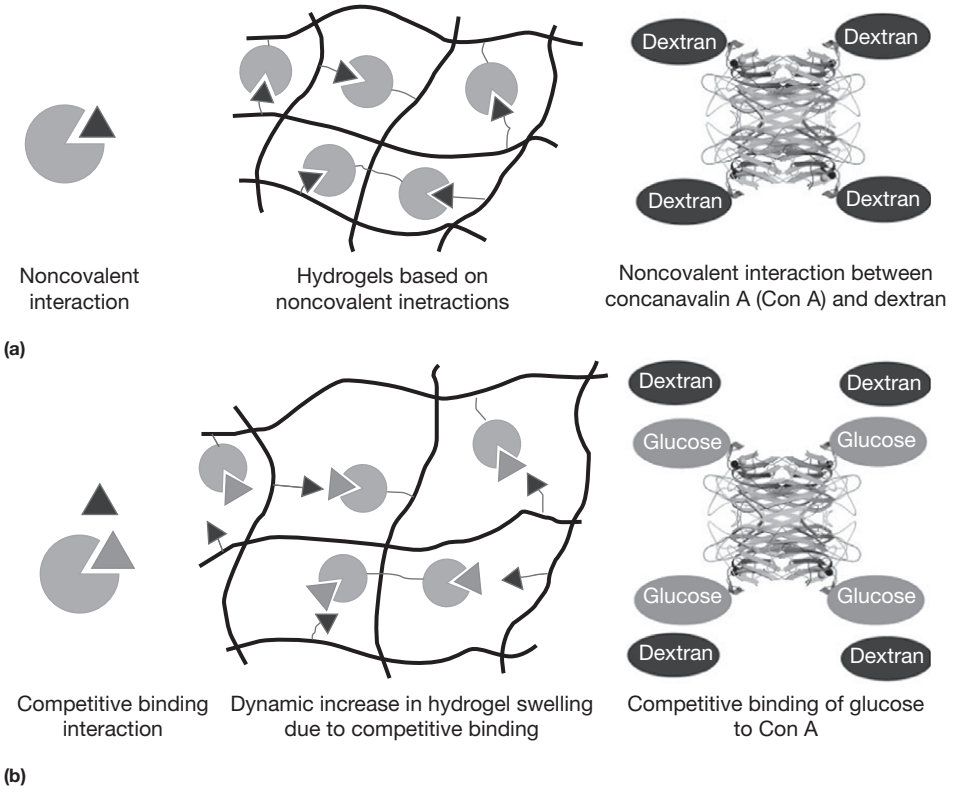

Figure 1 Swelling of a dynamic hydrogel via competitive ligand binding. The hydrogel structure swells as the interactions with immobilized ligands are displaced by soluble ligand, reducing the effective cross-linking density in the hydrogel. Reproduced from Mohammed, J. S.; Murphy, W. L. *Adv. Mater.* **2009**, *21*, 2361–2374, with permission from Copyright Wiley-VCH Verlag GmbH & Co., KGaA.

ligand into the solution will compete for binding sites and a new equilibrium will be established based on the binding constants and concentrations of the ligand in solution and those bound to the hydrogel. Thus, the degree of swelling in the hydrogel will increase as soluble ligand displaces the hydrogel immobilized ligand. The hydrogel swelling can be gradually reversed by exchanging the solution with solution that does not contain soluble ligand. The concept of using competitive binding to create dynamic hydrogels is shown schematically in Figure 1.

1.132.2.4. Covalent Bonding and Bond Cleavage

Many hydrogels are covalently bonded networks of water-soluble polymers. The covalent bonds in the network act to maintain a network structure that would otherwise be dispersed due to entropy and forces such as osmotic pressure. Covalent bonds are significantly stronger than other intermolecular forces and are therefore generally stable, even if they are not thermodynamically favorable. However, these bonds can be dissociated in catalyzed reactions, causing the hydrogel structure to swell or even dissolve. For example, poly(lactic acid) has been used extensively as a component of hydrogel networks because it is degraded by acid-catalyzed hydrolysis. Similarly, certain cells excrete proteases to remodel the local extracellular matrix. Hydrogels that have cross-links containing protease-specific peptide sequences can be created to develop materials that respond to a particular protease, the presence of which may be associated with tissue development or a disease state.

1.132.3. Specific Stimuli and Response Mechanisms

Given the variety of mechanisms by which structural changes can be brought about and the wide range of applications for which they are being developed, it is reasonable to expect that there would be a diverse set of stimuli used to trigger dynamic responses in hydrogels. In many cases, the most appropriate triggering mechanism is dictated by the application in which the hydrogel is to be used. For example, a hydrogel that is impervious under low pH conditions and permeable under neutral or basic pH conditions might be the most appropriate means of oral administration of a drug that is both acid labile and readily absorbed in the more neutral pH of the intestine. The following section reviews some of the more common stimuli that have been used to trigger dynamic responses from hydrogels. There are many instances where the activating mechanism involves a cascade effect where the stimulus acts indirectly to achieve a dynamic hydrogel response. For example, the absorbance of light might be used to increase the temperature within a hydrogel and the change in temperature could then be used to cause a structural change in the hydrogel. In such an instance, the mechanism is listed by the initial stimulus (i.e., light).

1.132.3.1. Physical Stimulus

One attractive feature of using physical stimuli (e.g., temperature, pressure, electromagnetic forces) to initiate a dynamic

response from hydrogels is that they can be applied to closed systems, which may be advantageous for several reasons. In a case where the hydrogel needs to be rapidly switched back and forth between states, it would be easier to cycle the temperature of the sample than it would be to remove chemicals from the hydrogel structure. Physical stimuli can also reduce response times in thick hydrogels by eliminating mass transfer limitations that are present when chemicals are used as stimuli.

1.132.3.1.1. Temperature

Temperature-sensitive structures are prevalent throughout materials science and the field of dynamic hydrogels is no exception. Hydrogels can be made to either collapse or swell upon heating, depending on the monomers used to form the hydrogel. Lower critical solution temperature (LCST) hydrogels, occasionally referred to as volume phase transition temperature (VPTT) hydrogels, exhibit a decrease in volume when heated above their critical temperature. LCST hydrogels contain both hydrophobic and hydrophilic regions, which can be accomplished either with a pure monomer or a copolymer blend. Hydrogels made of *N*-isopropylacrylamide (NiPAAm) demonstrate LCST behavior and have been studied extensively, in large part because the hydrogels undergo a phase transition near *in vivo* temperatures.[27] The reader is referred to a review by Schild for further reading on the history and early uses of NiPAAm hydrogels.[28] In addition to NiPAAm, many other *N*,*N*′-alkyl substituted acrylamide monomers have various swelling behaviors upon heating, ranging from continuous swelling to discontinuous collapse.[29] The diverse swelling behavior observed in the series of analogs was due to both the hydrophobicity and size of the pendant groups. LCST hydrogels based on temperature-sensitive amino acid sequences have also been demonstrated using elastin-like peptides (ELP).[30,31] ELP offer the advantage of precise molecular weights and can be incorporated into fusion proteins to create dual functional materials.[32] Even with the wide selection of materials that display LCST behavior, NiPAAm continues to be the most widely used monomer for creating temperature-dependent hydrogels.

NiPAAm monomers contain a hydrophilic amide group and a hydrophobic isopropyl pendant group. At lower temperatures, the free energy of the system is dominated by enthalpic gains from hydrogen bonding between the water molecules and the hydrophilic regions of the hydrogel network. As the polymer is heated, the free energy balance shifts toward favoring hydrophobic interactions and entropic gains, leading to the aggregation of the hydrophobic regions of the polymer and collapse of the hydrogel network.[33] The transition of the hydrogel from a swollen to a collapsed state has been shown to be an endothermic process, demonstrating the importance of the entropic contribution to the phase transition.[33] The increase in polymer–polymer interactions and reduction in water content of hydrogels above the LCST have been verified using gravimetric, NMR, and small angle neutron scattering methods,[18,34,35] and a number of theoretical models have been developed to describe the phase transition.[36]

Nonuniform collapse has been observed in larger hydrogel structures when heated above the LCST.[37] Rapid heat transfer and fewer chain entanglements at the surface cause a dense skin to form at the surface of the hydrogel while the inner structure remains in a uncollapsed state that contains entrapped water. The interior of the hydrogel eventually collapses, but the transition can take an extended period of time and the change can be pulsating in nature.[38] Further, it was observed that the rate of transition of a thermoresponsive hydrogel was a function of the temperature, with the rate of change being essentially zero at the critical temperature and increasing as the temperature is increased beyond the critical temperature.[39] The slow transition time demonstrated by these hydrogels near their LCST could be a drawback in certain applications where are rapid response is required. Using a comb polymer architecture, Yoshida and coworkers demonstrated that response times for NiPAAm hydrogels could be decreased to as little as 20 min versus more than a month for a NiPAAm network without grafted groups.[40] The comb regions of the polymer network, which had a greater degree of freedom because their movement was restricted on only one end by the network, rapidly formed nucleation sites for the network portion of the polymer to aggregate around.

The volume transition at the LCST is sharp for homogenuous hydrogels made with a single monomer and becomes more gradual as the hydrogel structure becomes less homogeneous. For example, the average molecular weight of the polymer chains in a homopolymer network has been shown to impact the LCST.[41] Different oligomers can be grafted into a single hydrogel to produce multiple phase transitions in a single material.[41] Multiple phase transitions have also been demonstrated in core–shell nanoparticles, where the LCST of the core was lower than that of the outer shell.[42] It was shown that the particles could exist in three states: (a) collapsed core–collapsed shell; (b) collapsed core–expanded shell; and (c) expanded core and shell. The collapsed core–expanded shell state contained a transition region between the two domains that had an intermediate density between the two regions. The transition temperature of NiPAAm was found to be unchanged when it was incorporated into an IPN with poly(tetramethylene ether glycol) (PTMEG); however, the swollen volume was decreased proportionally with the amount of PTMEG used in the formulation.[37] A hydrogel made with NiPAAm and poly(acrylamide), which was heterogeneously distributed throughout the structure, was shown to exhibit temperature-sensitive shape memory.[43] In addition to bending, it was shown that the hydrogel could be used to grasp particles and fold the hydrogel into predetermined geometries.

In addition to making the phase transition more gradual, copolymerization also shifts the LCST of the hydrogel. Incorporation of hydrophobic monomers into the polymer network via copolymerization tends to decrease the transition temperature.[44] Conversely, copolymerization with hydrophilic monomers leads to an increase in the LCST and can even eliminate the discontinuous phase transition entirely.[45] The number of ionizable groups in the network and the pH of the solution have been found to play a key role in the temperature dependence of the phase transition.[46] A network made up of poly(*N*,*N*-diethylacrylamide) in water showed a continuous volume change upon heating, whereas a similar network containing 3 mol% sodium methacrylate showed a discontinuous phase transition at 51 °C.[47] Studies with hydrogels containing cationic functional groups showed a similar dependence on the concentration of the ionic groups.[48,49]

Kokufuta observed that the addition of surfactants to the solution containing a NiPAAm hydrogel increased the phase transition temperature and the degree of swelling when the transition occurred.[50] The effect varied by concentration and type of surfactant, with sodium dodecyl sulfate (SDS) having the greatest impact. The long alkyl chains of the surfactant molecules were thought to have associated with the isopropyl groups of NiPAAm through hydrophobic interactions, which would essentially fix the ionic charge of the surfactant to the hydrogel.

In contrast to LCST hydrogels, upper critical solution temperature (UCST) materials expand as the material is heated past the critical temperature and their behavior can be characterized using a thermal mixing model.[12,13,27] These hydrogels are typically composed of hydrophilic monomers, such as acrylamide and acrylic acid. Ilmain demonstrated a UCST IPN hydrogel that demonstrated a volume change that was dominated by hydrogen bonding interactions.[51] The hydrogel contained acrylamide and acrylic acid networks that formed hydrogen bonding pairs, akin to the pairing that occurs in DNA. Heating of the network led to the disruption of the hydrogen bonds and allowed the hydrogel to swell. Bae and coworkers demonstrated a similar IPN made with *N*-acryloylpyrrolidine and poly(oxyethylene) that exhibited a greater degree of maximal swelling when the network consisted of a 50–50% mixture of the two polymers than when either monomer was in excess.[52] The authors attributed the increased swelling of the 50–50% blend to enthalpically unfavorable mixing between the two monomers, which would lead to a repulsive force.

Katono found that incorporating butyl methacrylate (BMA) into an IPN of BMA/acrylamide and acrylic acid decreased the degree of swelling when the network was heated.[53] Addition of BMA also changed the swelling from a discontinuous to a continuous transition as a function of temperature. Hydrogels that did not contain BMA did not have reproducible swelling volumes when the temperature was cycled above and below the UCST. The swelling ratio became more reproducible as the BMA content was increased to 30% of the BMA–acrylamide copolymer portion of the IPN. These effects were thought to have been the result of the increased hydrophobic nature of the hydrogel. The hydrophobic effect is enhanced when the temperature is increased, which led to the suppression in swollen volume. The lower swelling volume in turn kept the hydrogen bonding pairs of the two polymer networks in close proximity, where they could more easily recombine when the temperature was reduced.

Demonstrating an alternative approach, Wang and coworkers demonstrated the use of a coiled-coil protein motif as a way to create a temperature-sensitive hydrogel.[54] The histidine-tagged protein was coordinated to an *N*-(2-hydroxypropyl)-methacrylamide (HPMA) backbone that contained the metal chelating monomer *N*-(*N*′,*N*′-dicarboxymethylaminopropyl) methacrylamide (DAMA). The protein chains were attached to the main polymer backbone through transition metal complexes between the polyhistidine tail of the polymer and the DAMA groups. The coils unraveled above the melting temperature of the protein and collapsed upon cooling below the melting.

1.132.3.1.2. Electrical, magnetic, and electromagnetic fields

1.132.3.1.2.1. Electric field

The ease with which electrical fields can be controlled with modern electronics has enabled extensive studies of hydrogels that are sensitive to electric fields. One of the first demonstrations of coupling electronic input to dynamic hydrogel action was demonstrated using a poly(vinyl alcohol)–poly(acrylic acid) copolymer fiber impregnated with platinum particles.[55] When the fiber was held at a negative potential, the polymer acted as the cathode in the electrolysis of water and the local proton concentration was depleted as hydrogen gas was formed. As a result, the acidic groups in the polymer dissociated and the fiber subsequently swelled due to the buildup of charge within the network. When the hydrogel was held at a positive potential, the electrolysis reaction was reversed and the hydrogel contracted as the acidic groups in the polymer were protonated.

Further extending this concept, Fragala and coworkers isolated a weak acid hydrogel between two electrodes by placing it between anion and cation ion exchange membranes.[56] The selective nature of the ion exchange membranes allowed protons to preferentially diffuse into or out of the central chamber, depending on the direction of the current. Passive diffusion across the membrane was minimal, so the pH in the central chamber could be held for an extended period of time after the applied voltage was removed. The design had the additional benefit that the overall chemical composition of the system was not changed, so the fiber could be repeatedly actuated without adding additional chemicals. Grodzinsky and coworkers were able to demonstrate that both static[57] and oscillating[58] tensile forces could be generated in a collagen membrane by altering the intramembrane ionic strength with an electric field applied transversely to the length of the cylindrical membrane.

Tanaka and coworkers developed a partially hydrolyzed acrylamide hydrogel that collapsed when exposed to electric field strengths of less than $2\,V\,cm^{-1}$.[59] In a 50% acetone–water mixture, the rod-shaped hydrogels first showed tapering toward the anode, and this effect became more pronounced as the field strength was increased. Eventually, uniform collapse across the length of the hydrogel was observed. In pure water, the samples demonstrated uniform collapse along the length of the hydrogel, regardless of the field strength. The collapse was attributed to stresses built up in the hydrogel due to the electric field acting on the charged groups of the polymer and the ions in solution. In a later study, the authors found that the change was actually due to a pH gradient that had formed within the hydrogel.[60] A study using poly (2-acrylamido-2-methyl-1-1-propanesulfonic acid) found that organic solvents, such as acetone and ethanol, reduced the rate and the magnitude of the hydrogel collapse for a given applied electrical field.[61] It was also shown that water permeation through the hydrogel could be increased by applying an electric field while the edges of the hydrogel were immobilized to prevent collapse of the bulk structure.

Shiga found that an acrylic acid-*co*-acrylamide hydrogel underwent similar behavior in a DC electric field.[62] The study found that hydrogels with a low concentration of carboxylic acid groups shrank in a DC electric field, but hydrogels with a high concentration of the acid groups swelled. Further, it was noted that the ends of long, thin hydrogels could be bent

toward the cathode. A net weight gain was associated with the deflection, indicating that asymmetric swelling was occurring on the anode side of the hydrogel due to osmotic pressure.

Bending toward the anode was observed in a composite hydrogel rod that had a core made out of a poly(vinyl alcohol)–poly(sodium acrylate) copolymer and an outer shell made out of poly(vinyl alcohol).[63] Cross sections of the hydrogel immediately after having been exposed to an electric field indicated that the region near the anode had a lower pH and the region near the cathode had an increased pH. Swelling on the cathode side of the hydrogel was due to osmotic pressure caused by the higher pH in the region. Polyampholytic hydrogels containing both anionic and cationic functional groups behaved similar to an anionic hydrogel when the pH was above the isoelectric point (IEP) and acted as a cationic hydrogel when the pH was below the IEP when exposed to an electric field.[64] Addition of a cationic surfactant to a solution containing an anionic hydrogel was shown to change the direction of bending in an electric field toward the anode.[65] The surfactant neutralized surface charges on the anode side of the poly (2-acrylamido-2-methyl propane) sulfonic acid hydrogel, which reduced the osmotic pressure at the hydrogel–solution interface. Association between the hydrocarbon tails of the surfactants further stabilized the bent conformation of the hydrogel.

An interpenetrating network of chitosan and poly(aniline) showed bending and oscillatory motions in an electric field.[66] At neutral pH, periodic swelling and contraction on the anode side of the hydrogel were observed. The hydrogel had a partial positive charge at the neutral pH, which caused the hydrogel to initially deflect toward the anode due to charge shielding resulting from the migrating counter ions. Hydrolysis near the anode led to protonation of the aniline groups, which made them susceptible to oxidation. The protonation had the added effect of causing the hydrogel to bend back toward the cathode. The subsequent oxidation caused shrinkage on the anode side, causing the hydrogel to bend toward the anode.

In studies using isopropylacrylamide beads, Hirotsu found that ionic hydrogels contracted when an electric field was applied, but neutral hydrogels did not.[67] The effect was observed for DC fields but not AC fields in the 10–100 Hz frequency range. Further, it was noted that the electrodes had to be submerged in the fluid containing the hydrogel for the field to have an effect. The collapse occurred on the positive electrode side first, and beads nearest the anode had the quickest response time, the lag time being nearly proportional to the square of the distance from the electrode, indicating that the kinetics were controlled by diffusion. Under large applied fields, it was noted that the hydrogel volume oscillated wildly for several hours. The oscillatory motion of hydrogels in an AC field was later modeled as a mechanical vibration in a cantilever beam made with poly(vinyl alcohol)–poly(sodium acrylate) hydrogel.[68] The resonance frequency was found to be proportional to the hydrogel thickness for hydrogels less than 1 mm thick, with the resonance frequency being on the order of 1–2 Hz. It was also noted that the number of nodes in the oscillating hydrogel increased as the frequency of the field increased.

Suleimenov and coworkers found that the initial rate of shrinkage of a hydrogel in an electric field was initially increased in the presence of an orthogonal magnetic field, eventually achieving the same rate as without a magnetic field.[69] The effect was attributed to segregation of charge carriers within the hydrogel due to the Hall effect. The postulated increase in charge density at the surface of the hydrogel would then be more strongly attracted to the oppositely charged electrodes used to establish the electric field.

1.132.3.1.2.2. Magnetic field

Incorporation of superparamagnetic materials can lead to hydrogels that are sensitive to magnetic fields.[70] Termed ferrohydrogels, these materials can be elongated, compacted, or bent when exposed to a nonuniform magnetic field.[71] The response times for magnetic field-actuated hydrogels are generally not rate limited by polymer chain diffusion or relaxation times, so they can be cycled between states faster than hydrogels that are actuated by many other forms of stimulus. The degree of deformation of ferrohydrogels is proportional to both the field strength and the volume of ferromagnetic material incorporated into the hydrogel, allowing for a continuum of deformation states. The brittleness of the hydrogel construct usually increases as the superparamagnetic loading increases. Fuhrer and coworkers overcame this limitation by creating a hydrogel with magnetic pendant groups.[72] The backbone consisted of poly(2-hydroxyethyl methacrylate) to which composite cobalt–carbon nanoparticles were attached using vinyl modification of the carbon portion of the particle with a vinyl biphenyl linker. Covalent attachment of the nanoparticles also prevented them from being leached into solution over time.

Hydrogels containing superparamagnetic materials can retain sensitivity to other stimuli, such as temperature and pH.[73] Takahashi demonstrated that temperature-sensitive NiPAAm-*co*-acrylamide hydrogels containing iron(III) oxide particles could be made to collapse by applying an alternating magnetic field, which heated the hydrogel due to magnetic hysteresis.[74] It was noted that the hydrogel experience uniform shrinking because heating was more evenly dispersed throughout the hydrogel than is the case when the trigger is introduced by conductive heat transfer.

1.132.3.1.2.3. Electromagnetic field

Light has been used to induce a phase transition in hydrogels via several different mechanisms. Many early efforts incorporated dyes into the network structure of temperature-sensitive hydrogels. Absorption of light by dye molecules leads to heating of the local hydrogel structure, which in turn causes the temperature-sensitive hydrogels to collapse.[75] Suzuki demonstrated such a system using a NiPAAm hydrogel that contained copper chlorophyllin cross-linked into the hydrogel structure.[76] A portion of the hydrogel was then selectively illuminated with a focused laser beam that heated the exposed region due to absorbance by the chromophore, resulting in shrinkage of the hydrogel only in the immediate area of illumination. Rapid heat transfer to the bulk solution surrounding the hydrogel played a critical role in ensuring that only the illuminated region collapsed. Gold nanoparticles have also been imbedded into NiPAAm hydrogels to achieve IR light-triggered collapse.[77,78]

A similar approach has been used to create pH-sensitive hydrogels that respond to light. Saaem developed photoresponsive hydrogels by coupling bacteriorhodopsin (bR), a

photoactuated proton pump, to poly(acrylic acid).[79] The bR molecules were oriented on the polymer backbone such that protons were pumped toward the polymer chain, decreasing the local pH. When exposed to green light, the low pH in proximity to the polymer chain caused the acrylic acid groups to become protonated and allowed the hydrogel to collapse.

Light sensitivity can also be conferred upon hydrogels by incorporating compounds that dissociate or change conformation upon exposure to light. Irie demonstrated just such an approach by cross-linking the photodissociating compound leucocyanide into a poly(acrylamide) hydrogel.[80] The leucocyanide groups dissociated when exposed to ultraviolet (UV) light and created a higher osmotic pressure within the hydrogel, which in turn caused the hydrogel to swell. The degree of swelling was found to be proportional to the concentration of the immobilized leucocyanide at low concentrations due to the increased osmotic pressure; however, higher concentrations were found to be less effective due to hydrophobic interactions between the leucocyanide groups. Following up on this work, the group later created hydrogels using NiPAAm instead of acrylamide, conferring both temperature and light sensitivity on the hydrogel.[81] Irie observed that hydrogels containing leucocyanide groups could also be made to selectively respond to electric fields.[82] The leucocyanide groups were ionized by UV light, making the hydrogels susceptible to electric fields; the electric field response was lost after the UV illumination was removed.

Szilagyi and coworkers incorporated an acrylated chromophore, spirobenzopyran (SP), into a NiPAAm hydrogel network and showed that photoisomerization could be used to induce a structural change.[83] Upon illumination with blue light, the protonated open ring structure of the chromophore transitioned to a deprotonated, closed ring. This transition led to a significant increase in the hydrophobicity of the pendant group and resulted in the collapse of the hydrogel. To verify that the collapse was due to a change in hydrophobicity and not heating, the material was shown to preferentially capture negatively charged polystyrene beads when in the dark state versus the illuminated state where the chromophore was in the hydrophobic state.

Juodkazis and coworkers demonstrated that optical pressure could be used to cause the collapse of hydrogels.[84] A NiPAAm hydrogel was shown to reversibly collapse when illuminated with an infrared laser, as shown in Figure 2. The radiation force from the laser promoted the interaction between hydrophobic regions of the hydrogel, causing the hydrogel within the laser spot to collapse. Evaluation of the local temperature profile using a thermosensitive dye indicated that heating was not a significant factor in the collapse of the hydrogel.

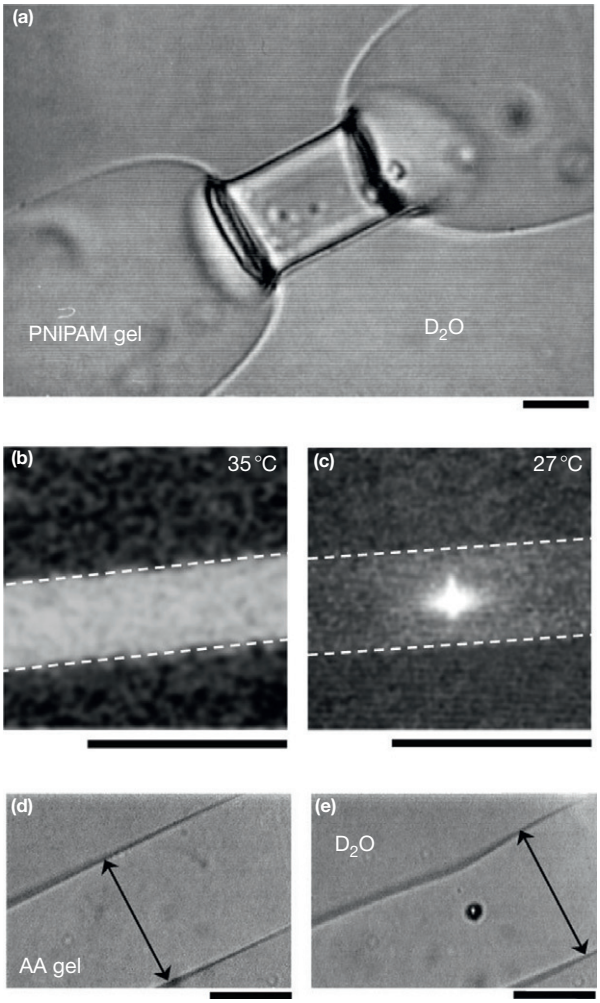

Figure 2 (a) Collapse of a portion of an *N*-isopropylacrylamide (NiPAAm) hydrogel rod using a focused laser to apply radiation force. The radiation force promoted chain–chain interactions within the hydrogel, leading to the collapse of the network. Deuterated water was used to minimize absorbance-based heating in the system. (b) Photoluminescence of 8-anilino-1-naphthalene-sulfonic acid sodium salt (ANS-Na), which is enhanced in hydrophobic environments, in a NiPAAm gel heated above the lower critical solution temperature (LCST) temperature. (c) ANS-Na luminescence in a NiPAAm gel below the LCST is enhanced in the region exposed to the radiation force of a laser spot. (d and e) Compaction of an acrylamide gel with radiation forces. The scale bars are equal to 20 μm. Reprinted from Juodkazis, S.; Mukai, N.; Wakaki, R.; Yamaguchi, A.; Matsuo, S.; Misawa, H. *Nature* **2000**, *408*, 178–181, with permission from Macmillan Publishers Ltd., Copyright 2000.

1.132.3.1.3. Pressure

The application of isotropic pressure has been shown to cause NiPAAm hydrogels to swell from their collapsed state when the samples were held under isothermal conditions.[85,86] The increase in pressure reduced the free volume of the system, which led to a reduction in the entropy of the system. The reduction in the free volume of the system also causes the internal energy of the system to increase through enhanced polymer–polymer and water–water interactions. The swelling of the hydrogel in response to the increase in pressure results in additional polymer–water interactions, which helps to reduce the free energy of the system.

The net effect of the pressure dependence is an observed shift in the LCST of the hydrogel to higher temperatures.[87] The phenomenon of pressure dependence appeared to have a critical value range above which the effect was no longer observed in NiPAAm hydrogels. The pressure-induced swelling was discontinuous in nature at 35 °C and gradually became continuous as the temperature was increased to 38 °C. NiPAAm hydrogels containing ionized functional groups showed pressure-induced swelling behavior between 37 and 42 °C.

Upon further increasing the pressure, the ionized hydrogels began to return to the collapsed state due to the pressure dependence of the hydrophilic interactions between the water molecules and the polymer chains.

1.132.3.2. Chemical Stimulus

While there are many advantages to using physical stimuli to trigger dynamic hydrogel response, the use of chemical responsive hydrogels would enable more intricate interaction with biological systems. For example, a hydrogel might be developed to release medication in response to a specific antigen. The ability for hydrogels to respond to specific molecules would also allow them to be used in applications that require feedback control mechanisms. The following sections discuss methods that are commonly used to create chemically responsive hydrogel structures.

1.132.3.2.1. pH

As was observed by Katchalsky and Kuhn, hydrogels containing acidic moieties swell when the pH of the solution is increased and the acid groups become deprotonated.[5,6] Conversely, hydrogels containing cationic groups tend to swell under low pH conditions. The swelling in both cases is due to an increase in electrostatic repulsion and internal osmotic pressure, which result from the increase in fixed charges in the polymer network. The effect becomes particularly noticeable near the pK_a of the functional groups in the hydrogel.

Firestone observed that the rate of swelling in a pH-sensitive hydrogel containing amine groups increased as the degree of ionization of the functional groups increased.[88] Conversely, the rate of deswelling in the hydrogel became slower as the pH was increased, possibly due to reduced proton mobility in the hydrogels resulting from interactions with the deprotonated amine groups at more basic pH conditions. In studying the pH dependence of *n*-alkyl methacrylate esters copolymerized with (dimethylamino)ethyl methacrylate, Siegel found that increasing the length of the alkyl chain on the methacrylate esters reduced the degree of swelling upon phase transition and shifted the phase transition to a lower pH for methyl, ethyl, and propyl groups.[89] Additionally, the discontinuous phase transition became more gradual with increased side chain length. These effects were attributed to the reduction in the concentration of charged groups within the hydrogel, which reduced the osmotic pressure, and the increased hydrophobic nature of the polymer, which made water uptake less favorable. However, the trend did not hold for butyl and hexyl groups, which they attributed in part to the increased stiffness of the polymer chain.

Luo and coworkers developed a poly(silamine) hydrogel that showed swelling in low pH conditions due to the protonation of the amine groups.[90] Unlike many hydrogels, the poly (silamine) hydrogels became more rigid in the swollen state. The increased rigidity of the swollen hydrogel was thought to be a result of a coordination of the protonated amine group, the counter ion, and the silicon atoms in the backbone. The coordination of the four atoms would then restrict the rotational freedom of the hydrogel chains.

A systematic study of acrylic acid hydrogel derivatives with varying amounts of *n*-alkyl acrylates ($n = 8$, 12, 18) determined that the transition pH became more basic as the length of the alkyl chain became longer and as the hydrophobic monomer content was increased in the hydrogel.[91] Further, the rate and degree of swelling did not seem to be impacted by chain length in the hydrogel samples that were tested. A potentiometric titration of the hydrogels found that the addition of alkyl groups had shifted the apparent pK_a of the acid groups in the hydrogels.

Nishi developed an IPN hydrogel membrane made with poly(oxyethylene) and poly(acrylic acid) and demonstrated that the flux and molecular weight selectivity of molecules passing through the membrane could be altered by varying the pH of the solution.[92] The hydrogel membrane swelled and the flux dropped off significantly at higher pH values due to the deprotonation of the acrylic acid groups. In the uncharged state, chains of poly(oxyethylene) and poly(acrylic acid) are known to associate.[93] Since the membrane was fixed in place by the test housing, the association of the two polymer networks was thought to enlarge the pores within the membrane to compensate for the inability of the membrane to contract to relieve the contractile stress. In the charged state, the hydrogel chains would no longer associate and the pores could relax back to their naturally smaller size.

The swelling volume of amphoteric hydrogels made with the copolymers trimethyl(*N*-acryloyl-3-aminopropyl)ammonium chloride–sodium acrylate–acrylamide–*N*,*N*′-methylenebisacrylamide has been shown to vary depending on the ratio of cationic groups to anionic groups, with the least amount of swelling for an equimolar composition and increased swelling for increasingly disproportionate ratios.[94] The reduced swelling with equimolar composition was likely due to hydrogen bonding within the gel while the increased swelling for disproportionate concentrations was due to an increase in the concentration of osmotic pressure-inducing ions in the hydrogel.

1.132.3.2.2. Ionic strength

Tanaka noted that the collapse of a partially hydrolyzed acrylamide hydrogel could be induced by increasing the salinity of the solution surrounding the hydrogel.[95,96] The report noted that the transition occurred at a much lower salt concentration when divalent magnesium cations replaced monovalent sodium. The swelling in weakly charged ionic hydrogels in the presence of monovalent ions was found to be in good agreement with Donnan equilibrium theory; however, the theory did not fully explain the behavior of the hydrogels in the presence of divalent ions.[97] A discontinuous phase transition was noted in an acrylic acid acrylamide copolymer hydrogel when the concentration of copper ions reached a certain threshold, which was found to be inversely related to the concentration of acidic groups in the polymer.[98] The authors did not observe the discontinuous phase transition for nickel ions. The varying behavior for the two divalent cations was attributed to the formation of coordination complexes between the copper ions and acid groups in the hydrogel, which acted as weak cross-links within the hydrogel.

Ampholytic hydrogels made with the copolymers acrylamido methyl propylsulfonic acid, methacryl-amido propyl trimethyl ammonium chloride, and dimethyl acrylamide that had equal amounts of cationic and anionic groups were shown

to swell in cesium salt solutions with concentrations above 10 mM.[99] The effect became more pronounced as the number of charged species in the hydrogel backbone increased. Polymers with a 1.4% excess of basic groups showed a rather complex response to varying solution concentrations of salt. The swelling ratio was steady below 10 μM and then increased slightly up to a salt concentration of 100 μM. The swelling then decreased as the concentration was increased from 100 μM to 10 mM and then steadily increased for salt concentrations up to 1 M. The multiple inflection points were attributed to changes in the relative importance of dissociation, polyampholytic, and polyelectrolyte effects. Ampholytic hydrogel response to salinity has also been studied as a function of the net charge of the hydrogel.[64] The hydrogels were found to swell to a greater degree in a 0.1 M KCl solution than when they were in distilled water when the pH was near the IEP of the hydrogel. Conversely, the presence of salt suppressed the level of swelling as the solution pH deviated from the IEP.

The salt concentration in solution can also impact the degree of swelling in nonionic hydrogels. Sodium chloride was also found to induce a phase transition in NiPAAm.[100] Sodium salts of phosphate and sulfate showed a gradual reduction in the degree of swelling in the hydrogel; however, they did not result in a phase transition. Inomata found that the phase transition temperature of NiPAAm could be reduced by adding KCl to the solution surrounding the hydrogel.[101] A 0.1 mM solution of KCl reduced the transition temperature from 33.8 to 20.6 °C. Other anions showed a less pronounced effect and the cation did not appear to play a role in the phenomenon. The reduction in transition temperature and the viscosity B coefficient (VBC), which depends in part on the interaction between the solvent and the polymer chains, showed a linear correlation for the monovalent anions tested. The authors attributed the observed relationship to the tendency of ions with a more positive VBC to promote hydrophobic interactions, which would cause the collapsed NiPAAm state to be favorable at a lower temperature. The work also investigated the impact of adding tetra alkylammonium bromides with various alkyl chain lengths to the solution and observed that the transition temperature was lowered in some instances while in others it was increased.

1.132.3.2.3. Ligand binding and ion-specific interactions

Crown ethers can be incorporated into hydrogel networks to confer cation-specific shifts in the LCST of hydrogel networks.[102] One particular hydrogel consisted of a copolymer of NiPAAm and benzo-18-crown-6-acrylamide (BCAm). The LCST of the polymer increased due to higher osmotic pressure when barium ions were captured by the crown ether structures and no change was observed when potassium ions replaced the barium ions in solution. The LCST was decreased when cesium ions were introduced into the solution, most likely due to a coordination effect in which the cesium ions became sandwiched between two crown ether structures. A similar study using a benzo-15-crown-acrylamide unit found that the LCST was preferentially reduced by potassium ions.[103]

Molecularly imprinted polymers (MIPs), also referred to as molecular recognition polymers, are an emerging method for developing molecular-specific responses from hydrogels.[104–106] The technique incorporates the specific guest molecule into the polymer blend before polymerization. Polymerization with the molecule in the hydrogel is thought to create a binding pocket in the hydrogel that will be able to preferentially interact with the molecule of interest. The templating molecule can then be rinsed out, leaving the binding pocket available for interactions when the appropriate molecule is present in solution.

Watanabe demonstrated molecular recognition hydrogels formed with NiPAAm and acrylic acid that demonstrated selective swelling from the collapsed state when specific molecular recognition molecules were introduced into solution.[107] Hydrogels were prepared in the presence of norephedrine or adrenaline. The NiPAAm monomers caused the hydrogels to be in a collapsed state at 50 °C. The hydrogel prepared with norephedrine showed concentration-dependent swelling in the presence of norephedrine, but did not swell when exposed to adrenaline. The opposite response was observed in the hydrogel prepared in the presence of adrenaline. Miyata and coworkers used molecular imprinting to create a hydrogel that would contract when exposed to the glycoprotein α fetoprotein (AFP), a tumor-specific marker.[108] To prepare the responsive hydrogel, lectin specific to the glycoprotein (Con A) and a polyclonal antibody (anti-AFP) were conjugated with *N*-succinimidylacrylate. The monomers were reacted with acrylamide and *N*,*N*′-methylenebisacrylamide in the presence of AFP. The hydrogel was then soaked in buffer to remove the AFP. A control hydrogel was prepared without AFP present. The AFP-templated hydrogel contracted when AFP was introduced into the solution, whereas the control hydrogel swelled slightly. Both hydrogels swelled to a small extent when exposed to ovalbumin, indicating that the templating process conferred a degree of specificity for AFP binding upon the hydrogel.

1.132.3.3. Biochemical Stimulus

Several mechanisms for achieving dynamic hydrogel response based on biochemical recognition have also been developed. These approaches take advantage of the high binding affinity and selective nature of biomolecular interactions. The ability to recognize and respond to specific molecules would enable dynamic hydrogels to be used in feedback loops and other complex behavior that occurs in biological systems. The following sections review some of the means by which biological molecular recognition has been translated into dynamic hydrogel behavior.

1.132.3.3.1. Competitive ligand binding

Miyata created a hydrogel with 2-glucosyloxyethyl methacrylate (GEMA) which was able to differentiate between mannose, glucose, and galactose.[109] Entrapped in the hydrogel was the lectin concanavalin A, a protein which binds to carbohydrates. The lectin had four binding sites that allowed it to associate with the glucose pendant groups of the GEMA polymer, creating physical cross-links in the hydrogel. These cross-links could then be competitively dissociated with free glucose and mannose, allowing the hydrogel to swell. The degree of swelling in the hydrogel was related both to the concentration of the free sugar in solution and the affinity of the lectin for the particular sugar. The hydrogel showed the greatest response for mannose, followed by glucose, and showed little response for galactose. The system was later improved by chemically cross-linking the

lectin into the hydrogel structure so that the swelling process could be reversible.[110] Kokufata covalently cross-linked concanavalin A into a NiPAAm hydrogel and showed that a phase transition could be induced when the cross-linked lectin associated with specific sugars.[111] The hydrogel swelled in the presence of the charged species dextran sulfate and collapsed back to its previous volume when an uncharged carbohydrate was introduced into the solution.

Miyata and coworkers demonstrated an antigen-sensitive hydrogel by covalently cross-linking antigen into the hydrogel and forming cross-links with free antibody.[112] The cross-links were disrupted when free antigen was introduced into the system and began to displace the interactions between the immobilized antigen and the antibody molecules, which allowed the hydrogel to swell. The interaction was shown to be antigen specific, but the process was not reversible. Later, they demonstrated a reversible system by immobilizing both the antibody and antigen in the hydrogel.[113]

1.132.3.3.2. Enzyme catalysis

Hydrogel swelling can also be initiated by enzyme-catalyzed reactions. An enzyme can be incorporated into the hydrogel structure and then catalyze a reaction, with the byproduct leading to a conformational change by one of the mechanisms listed above. For example, glucose oxidase has been incorporated into pH-responsive hydrogels to convert glucose into gluconic acid; the gluconic acid reduces the pH within the hydrogel, which in turn causes the pH-sensitive hydrogel to swell.[114] Similarly, rabbit liver esterase and urease have been immobilized to create hydrogels that were responsive to the presence of ethyl butyrate and urea, respectively.[115,116] The phase transitions were rapid and did not require the buildup of product in the bulk solution.

Alternatively, hydrogel cross-links have been designed so that they can be degraded by specific proteases. Unlike many of the systems discussed previously, this means of activation is not typically reversible. Hydrogels formed from albumin-cross-linked poly(vinylpyrrolidine) were shown to degrade in the presence of pepsin.[117] A phosphoester–poly(ethylene glycol) (PEG) hydrogel that was prepared as a matrix for bone tissue engineering was shown to undergo faster degradation in the presence of alkaline phosphatase.[118] A PEG hydrogel was synthesized with peptide cross-links that were susceptible to cleavage by matrix metalloprotease, and it was shown that metalloproteases released during cell culture enabled the artificial matrix to be remodeled.[119]

The need for two stimuli to achieve hydrogel activation may be of interest in some applications to provide an additional level of control. Yamamoto demonstrated an IPN hydrogel made with gelatin and dextran that required the presence of both dextranase and α-chymotrypsin to degrade the hydrogel.[120] Steric hindrance effects were believed to limit the enzymatic activity unless both of the enzymes were acting in concert. A degradable hydrogel requiring both the presence of the enzyme papain and a temperature below 35 °C has also been developed.[121] The hydrogel was readily degraded below the LCST, but the degradation could be stopped by increasing the temperature above the LCST, which was thought to limit the papain activity through steric hindrance.

1.132.3.3.3. Conformational shifts

Proteins that undergo dynamic conformational changes in response to specific ligands have also been incorporated into hydrogels to create dynamic structures. Several different approaches have been taken to translate conformational shifts in the structure of calmodulin into macroscopic changes in hydrogels. In one approach, the calmodullin molecule was tethered to the backbone of the hydrogel, along with a small molecule ligand.[122] The hydrogel showed reversible collapse upon the introduction of calcium ions, which caused a conformational change in the protein. The hydrogel also showed the properties of a competitive binding mechanism when free ligand was introduced into the system. In an alternative approach, double cysteine-substituted calmodulin was incorporated into a PEG tetraacrylate hydrogel backbone using Michael addition chemistry.[123] Introduction of the free ligand into solution caused calmodulin to transform from an open dumbbell conformation to a collapsed conformation. The collapse of the calmodulin molecules essentially shortened the average chain length in the hydrogel network (see Figure 3) and resulted in an approximate 15% reduction in the total volume of the hydrogel. A later work using PEG diacrylate instead of tetraacrylate demonstrated that the network volume could be reduced to 35% of the original volume.[124]

Yuan and coworkers demonstrated a hydrogel containing adenylate kinase that was able to undergo contraction when exposed to its substrate, ATP.[125] The polymer consisted of HPMA backbone with maleimide pendant groups. A mutated adenylate kinase, which had the native cysteine group substituted out and two cysteine groups added, was then attached to the maleimide groups via thiol–maleimide coupling reaction. The hydrogel reswelled when washed with ATP-free buffer for 30 min.

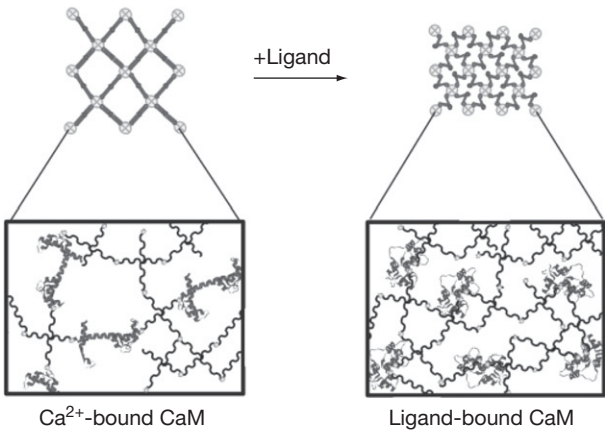

Figure 3 Collapse of a dynamic hydrogel brought about by the conformational change of a cross-linked protein. The ends of the protein molecule are cross-linked into the hydrogel structure. The two ends of the protein are brought closer together after the ligand binds to the protein, resulting in a reduction in the effective distance between polymer chains in the hydrogel. Reproduced from Murphy, W. L.; Dillmore, W. S.; Modica, J.; Mrksich, M. *Angew. Chem. Int. Ed.* **2007**, *46*, 3066–3069, with permission from Copyright Wiley-VCH Verlag GmbH & Co., KGaA.

1.132.4. Biomedical Applications

The diverse chemistries and trigger methods used to create dynamic hydrogels enable their properties to be tailored for specific applications. Further, the utility of dynamic hydrogels is not limited to applications such as artificial muscles that require macroscopic changes in size. For instance, the pore size of hydrogel networks can be altered by dynamic changes in hydrogel structure, which can have a profound effect on mass transfer within hydrogels.[126] For example, the tunable pore size was shown to be an effective means of optimizing the separation in a size exclusion chromatography column. In another example, Dong and Hoffman showed that enzymatic activity could be reversibly regulated by immobilizing an enzyme in a dynamic hydrogel.[127] The immobilized enzyme showed an increase in kinetics with increasing temperature due to Arrhenius effect up to the LCST temperature of the hydrogel, but showed a sharp reduction thereafter. The system was cycled several times to demonstrate that the reduced kinetics were due to the phase transition of the hydrogel and not due to enzyme deactivation. Similarly, the rate of enzymatic conversion has also been controlled using pressure sensitive hydrogels.[128]

Combining the high water capacity of hydrogels along with tunable pore size has led to their use as selective absorbent to take up low molecular weight solutes, leaving a solution enriched in higher molecular weight molecules.[129–131] Upon reversing the swelling of the hydrogels in fresh water, a portion of the solute molecules were rapidly expelled from the hydrogel along with water as the hydrogels collapsed. Solute continued to be released from the hydrogel via diffusion, which was considerably slower than the initial release. The selectivity of the process was reduced somewhat by the random nature of the polymerization process, which resulted in nonhomogeneous pore size throughout the hydrogel. We conclude the chapter by reviewing some of the other applications where the micro- and macroscopic properties of dynamic hydrogels have been used to create unique solutions to biomedical engineering problems.

1.132.4.1. Controlled Release of Soluble Factors

Self-regulation is vital to many biological systems. For example, blood sugar levels in humans must be maintained in a narrow range to prevent severe physiological damage. The body has a feedback system that (a) senses the concentration of glucose and (b) reacts by releasing the appropriate hormones (i.e., glucagon or insulin), which correct perturbations. The ability to both measure a parameter and selectively take action based upon its value is essential for creating self-regulating systems. In the case of type 1 diabetes, the body loses its ability to self-regulate because it is unable to release insulin. Currently, treatment for the condition requires electric monitoring of blood sugar levels followed by an insulin injection, if needed. Conversely, antibiotic treatments for infections are most effective when there is a constant concentration of the antibiotic in the circulatory system. Although these two instances represent two very different dosing profiles, dynamic hydrogels can potentially be tailored to meet the needs of both applications. The following sections discuss how dynamic hydrogels can be used to achieve various controlled release profiles.

1.132.4.1.1. Step function release

Bae and coworkers demonstrated a thermally responsive hydrogel that was able to switch between a constant release rate and a zero release rate.[44] The copolymer hydrogel utilized NiPAAm for its temperature sensitivity and BMA to improve the mechanical properties of the hydrogel. The hydrogel showed sustained release below the LCST, and the release stopped abruptly when the hydrogel was heated above the LCST. An IPN of NiPAAm and polytetramethylene ether glycol was shown to have a similar on–off release profile as a function of temperature.[132] The phase transition temperature for the hydrogel loaded with the drug indomethacin was lower than that for the hydrogel without the drug. The presence of the hydrophobic drug was thought to reduce the transition temperature by participating in hydrophobic interactions with the polymer chains. The authors also noted that they could reduce the amount of time it took to transition from the on release state to the off state by increasing the transition temperature.

Temperature-responsive hydrogels capable of releasing insulin have also been developed.[133] The IPN network of NiPAAm and poly(tetramethylene ether glycol) was permeable to both glucose and insulin below the LCST. Increasing the temperature above the LCST immediately stopped diffusion of both species out of the hydrogel due to a dense outer skin on the surface of the hydrogel. Diffusion of glucose through the hydrogel was quickly reestablished when the hydrogel was cooled back below the LCST, but there was a lag time of several hours before insulin diffusion rates were restored.

Kiser and coworkers demonstrated a novel hydrogel–lipid construct that mimicked the structure of secretory granules, the inert lipid-coated particles used to direct intra and extracellular transport of proteases and other molecules.[134] The particles consisted of a pH-sensitive methacrylic acid hydrogel core coated with a lipid bilayer. The lipid coating served as a barrier that isolated the hydrogel from the surrounding solution. The hydrogel then showed rapid swelling when the lipid bilayer was electroporated, achieving maximum swelling in 4 s (see **Figure 4**). The particles showed a burst release of the drug doxorubicin, with most of the drug being released within 13 min.

The use of pH-sensitive hydrogels has enabled the targeting of drug release to specific regions of the digestive system to maximize uptake efficiencies. Certain therapeutics, such as proteins, are easily hydrolyzed in the harsh conditions of the stomach. To protect them, they can be placed in an acidic hydrogel, which remains in the collapsed form when exposed to the acidic conditions of the stomach. The hydrogel then swells as it passes into the higher pH conditions of the intestine, enabling the drug molecules to diffuse out of the hydrogel. For example, a study of oral insulin treatment found that delivery via a pH-sensitive hydrogel was a more effective means of reducing serum glucose levels in rats than an oral dose of insulin solution.[135]

1.132.4.1.2. Rate modification

Aoki and coworkers created a thermally responsive IPN that showed an increase in the rate of release of ketoprofen when the hydrogel was heated from 20 to 40 °C.[136] The release rate from two different hydrogels was evaluated in the study. Both hydrogels contained an IPN of acrylic acid and

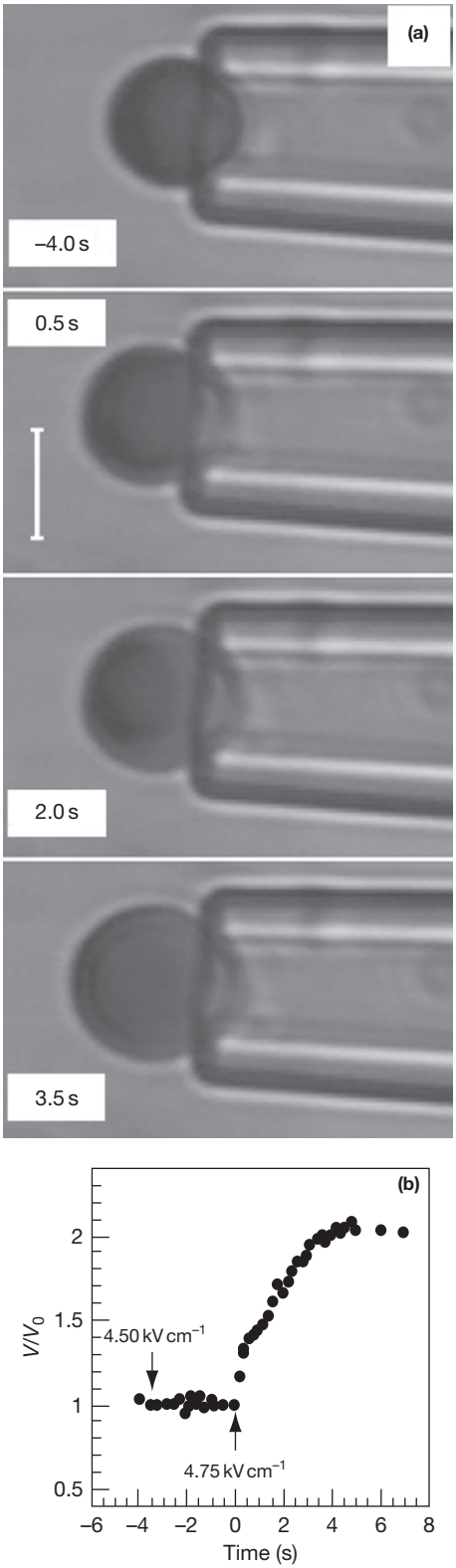

Figure 4 Rapid swelling of a pH-sensitive hydrogel after electroporation of the lipid bilayer surrounding the particle. The images show the hydrogel before being exposed to the critical electric field strength, 0.5, 2.0, and 3.5 s after exposure. The scale bar is equal to 4 μm. Reprinted from Kiser, P. F.; Wilson, G.; Needham, D. *Nature* **1998**, *394*, 459–462, with permission from Macmillan Publishers Ltd., Copyright 1998.

butylmethacrylate. In addition to these two components, one of the hydrogels also contained *N*,*N*′-dimethylacrylamide (DMAA). The release rate from the hydrogel containing DMAA doubled upon heating and was consistent through several heating cycles. The hydrogel without DMAA showed over a threefold increase in release rate on the first heating cycle, but showed steady decay in subsequent heating cycles. The difference in performance between the two hydrogels was attributed to the intermolecular bonding within the two hydrogels. The hydrogel without DMAA had a large degree of intramolecular hydrogen bonding between acrylic acid residues; these interactions were disrupted at 40 °C, which caused the hydrogel to undergo a large degree of swelling. In contrast, the hydrogel containing DMAA contained more stable intermolecular hydrogen bonding which was not disrupted at 40 °C, which limited the swelling in the hydrogel and consequently resulted in a lower rate of diffusion out of the hydrogel.

Controlled release has also been achieved using UCST hydrogels made with acrylic acid and acrylamide-*co*-butylmethacrylate.[53] The hydrogel showed a 20-fold increase in release rate of ketoprofen when it was heated from 10 to 30 °C. A twofold increase in diffusion would be expected due to Arrhenius kinetics, indicating that the primary cause for the increased release rate was due to the conformational change in the hydrogel structure rather than a temperature-dependent increase in ketoprofen transport.

A dextran hydrogel was developed for targeted drug release in the colon.[137] The hydrogel showed diffusion-limited release of hydrocortisone under normal conditions and showed much faster erosion-limited conditions in the presence of dextranase, an enzyme secreted by intestinal bacteria. Similarly, Kopecek developed hydrogels containing azoaromatic bonds that could be cleaved by the intestinal enzyme azoreductase.[138]

Siegel showed that the rate of caffeine release from a pH-sensitive hydrogel was related to the rate of water absorption by the hydrogel during the swelling process.[139] The methyl methacrylate/*N*,*N*-dimethylaminoethyl methacrylate hydrogel showed minimal release at neutral pH and zero order release for pH 5 and 3 solutions, with the pH 3 solution showing a faster release rate. Ishihara used a pH-sensitive hydrogel to develop a compound membrane system that showed glucose-sensitive release of insulin.[114] The system consisted of a hydrogel membrane containing immobilized glucose oxidase and a second membrane containing polyamine groups. The glucose oxidase converted glucose into gluconic acid, which dropped the local pH and protonated the amino groups on the second membrane. Protonation of the amino groups caused the membrane to take up additional water, which in turn increased the permeability of the membrane to insulin. Membranes containing both the amine functionality and glucose oxidase were developed shortly thereafter and were shown to swell and have higher insulin permeability in the presence of glucose.[140,141] Glucose oxidase was later incorporated into a pH-sensitive capsule to demonstrate controlled release of insulin.[142]

In an alternative approach, Hassan and coworkers incorporated glucose oxidase into a hydrogel containing methacrylic acid that collapsed in the presence of glucose.[143] The hydrogel was designed to oxidize glucose and lower the

pH, which would protonate the methacrylic acid and allow the hydrogel structure to collapse. The collapse of the hydrogel would then squeeze insulin out of the polymer network. The hydrogel also incorporated a catalase to eliminate the byproduct hydrogen peroxide that would otherwise inhibit the conversion of glucose to gluconic acid. Collapse-mediated release was also shown to be an effective means of modulating the release rate of vascular epithelial growth factor (VEGF) from a dynamic hydrogel.[144] The dynamic hydrogel contained calmodulin molecules cross-linked into the polymer backbone. The release rate of VEGF significantly increased when the calmodulin ligand trifluoperazine was introduced into solution, causing the hydrogel network to collapse.

While the previous examples illustrated glucose-sensitive hydrogels that required biochemical recognition, chemical methods have also been explored. Kataoka utilized the fact that glucose molecules stabilized the ionic form of 3-acrylamidophenylborionic acid (AAPBA).[145] The stabilization of the anionic form of the acid groups led to an equilibrium shift in the dissociation of the acid groups. The increase in fixed charge on the NiPAAm network led to increased swelling of the hydrogel, which was proportional to the solution concentration of glucose. Insulin release from the hydrogel was found to be proportional to the solution concentration of glucose.

Siegel proposed using hydrogel swelling to act as a mechanical actuator for insulin dosing.[146] The design consisted of a glucose-sensitive hydrogel and a chamber containing insulin separated by a movable partition. Swelling of the hydrogel would then act as a piston to compress the partition separating it from the insulin, which would in turn force insulin out of the device and into the surrounding tissue.

1.132.4.1.3. Switchable surface

Hydrogel surface properties are often altered when the hydrogel network undergoes a dynamic restructuring. Switchable NiPAAm hydrogels have been used to selectively attach and detach cells from surfaces.[147] At higher temperatures, the material presents a hydrophobic surface that is comparable to traditional cell culture plastic and cells can be grown to confluence. The cells can then be harvested by reducing the temperature below the LCST of the hydrogel, which results in an increase in surface hydrophilicity and lift-off of the attached cells. This approach is advantageous because it does not disrupt the cell–cell interactions as is the case with traditional trypsin treatments.[148] Ulijn and coworkers demonstrated an alternative approach to selective cell capture using Fmoc-F chemistry to prevent cells from adhering to a surface functionalized with the integrin binding peptide arginine–glycine–aspartic acid (RGD). Upon treatment with chymotrypsin, the surface was activated and allowed osteoblasts to adhere to the surface.[149] NiPAAm switchable films have shown to be similarly effective in controlling the adhesion of proteins onto surfaces.[150] The film presented a hydrophilic surface below the LCST, which prevented myoglobin adsorption. The film could then be turned hydrophobic by heating the hydrogel above the LCST, which led to protein adsorption on the surface. The protein was then released from the surface after the film temperature fell below the LCST.

The ability to switch the surface properties of NiPAAm between hydrophobic and hydrophilic has also been used to enable directional movement on surfaces. Kim and coworkers showed that the frictional force of NiPAAm on glass and pig intestine changed when the hydrogel switched from the collapsed state to the swollen state and vice versa.[151] They found that the frictional force required to move a NiPAAm test piece increased by 80% when the polymer was in the hydrophobic state. They then showed that this difference in frictional force was sufficient enough to allow one end of an inchworm-like device to be anchored to a pig intestine surface while the other end, in the hydrophobic state, was allowed to freely slide along the surface. They proposed that alternating the properties of the two ends would then allow directional motion to take place.

1.132.4.2. Sensing and Detection

The ability to respond to a specific stimulus with a dramatic structural change makes dynamic hydrogels an attractive class of materials for creating sensors. A wide variety of mechanisms have been used to translate dynamic hydrogel response into molecular sensors. A CO_2 sensor was created by measuring the swelling of a pH-sensitive hydrogel that was held in a confined space.[152] The CO_2 in the gas sample reached a vapor–liquid equilibrium with the solution in the hydrogel. The dissolved CO_2 formed carboxylic acid, which altered the pH of solution and caused the hydrogel to swell. Hydrogel swelling within a confined space was also used to develop an ionic strength sensor.[153]

Sharma and coworkers developed a creatine sensor by integrating polystyrene latex particles into a polyacrylamide hydrogel.[154] Creatinine deiminase was incorporated into the hydrogel to hydrolyze any creatine in solution to form a hydroxyl ion, and 2-nitrophenol was incorporated as a proton donor. Hydroxyl atoms produced in the presence of creatine led to deprotonation of the 2-nitrophenol groups in the hydrogel, and the fixed charges on the polymer backbone caused the hydrogel to swell. The concentration of creatine in solution could then be measured by measuring the shift in the light diffraction pattern of the styrene latex particles in the hydrogel.

Dong and coworkers demonstrated dynamic hydrogel lenses made out of NiPAAm and acrylic acid that were able to change their focal lengths based on temperature and pH stimuli.[155] A similar tunable focal length lens system was developed using a hydrogel made with immobilized calmodulin and phenothiazine, a calmodulin ligand.[156] Introduction of another calmodulin ligand, chloropromazine, disrupted the calmodulin–phenothiazine interactions that acted as cross-links and allowed the hydrogel to swell. The swelling, which was proportional to the amount of chloropromazine in solution, changed the focal length of the lens. Similar lens systems were demonstrated for protein and antigen detection.[157,158] A hydrogel with cross-links formed by complementary oligonucleotide pendant groups was coupled to an interferometer to create a label-free oligonucleotide sensor.[159] Competitive binding between the immobilized strands and free oligonucleotide in the sample solution led to hydrogel swelling, which was measured by the interferometer.

1.132.4.3. Mechanical Actuation: Artificial Muscles, Robotics, and Microfluidics

1.132.4.3.1. Artificial muscles and robotics

Many aspects of dynamic hydrogels closely mimic natural muscle functions. For example, both systems can be made to bend, relax, contract, and exert force based on chemical signals. A variety of hydrogel analogs have been developed to mimic muscles actions that occur in nature. In a series of works, Yoshida and coworkers demonstrated hydrogels systems that oscillated between swollen and shrunken states, akin to a beating heart. The first demonstration used a NiPAAm–acrylic acid copolymer suspended in a stirred tank reactor that was continuously replenished with chemicals to run a hydrogen peroxide–hydrogen sulfite–hexacyanoferrate (II) reaction that produced an oscillating pH.[160] The idea was further advanced when a ruthenium catalyst was cross-linked in a NiPAAm hydrogel to drive an oscillating Belousov–Zhabotinsky (BZ) reaction.[161] Changes in the redox state of the catalyst caused a shift in the transition temperature of the hydrogel, which in turn caused swelling/shrinking when the hydrogel was near the critical temperature. This demonstration was a great advancement over the previous system because the stimulus for the oscillation was generated internally. Yoshida and Uesusuki demonstrated an oscillating system that was activated by ATP.[162] The anionic poly(NiPAAm-*co*-2-(methacryloyl-oxy) ethyl phosphate) hydrogel contained immobilized creatine kinase, which generated an oscillating calcium concentration as it reacted with the ATP. The divalent Ca^{2+} ions served as physical cross-links between the phosphate groups in the anionic hydrogel. When calcium levels were low, the hydrogel swelled, and the hydrogel contracted when the calcium concentration was higher.

Kurauchi and coworkers demonstrated a grasping hand made out of electric field-sensitive poly(vinyl alcohol)-*co*-poly (acrylic acid).[163] The hand was able to pick up an egg in solution. The work also demonstrated that the electric field-responsive polymer could be used to create an artificial fish that could swim in solution using a flapping tail. Similarly, a thin polyanion hydrogel was attached to a polystyrene body to create a hydrogel that moved with an eel-like motion in an alternating electric field in the presence of a cationic surfactant.[164] The hydrogel bent in the cycling electric field due to preferential surfactant accumulation on the side of the hydrogel nearest the anode, thereby displacing water. Electric-field-sensitive PEG hydrogels have also been shown to achieve locomotion through other methods, one of which mimicked the swimming motion of an octopus.[165] Glucose sensing and delivery of beads from the body of these swimming structures were also demonstrated. Hydrogel locomotion has also been achieved by inducing collapse and expansion of select regions of a poly(NiPAAm) hydrogel confined in a tube, generating earthworm-like motion that resulted in the net displacement of the hydrogel.[166]

1.132.4.3.2. Microfluidics

Dynamic hydrogels have been incorporated into microfluidic devices for a number of applications, including sensing and autonomous control. The small dimensions and high surface area-to-volume ratios characteristic of microfluidic devices offer rapid mass transfer and, therefore, faster hydrogel response times than are seen in many applications. Beebe and coworkers were the first to take advantage of responsive hydrogels in microfluidic applications when they demonstrated hydrogel valves that could be opened and closed based on solution pH and showed that the valves could be used to route liquid through the device based on pH (see **Figure 5**).[167] Autonomous pH control was later demonstrated using a similar system.[168] At a near neutral pH, the pH-sensitive valve was in a swollen form and isolated the channel from a stream of high pH solution. The hydrogel became protonated and shrank when the solution pH dropped, allowing high pH solution to mix in with the main stream. As the pH increased, the hydrogel began to reswell and close off the valve. Changes in hydrogel chemistry and channel geometries could be used to adjust the set point of the pH control loop. A similar valving concept actuated by electrical signal was developed by creating a hydrogel containing poly(aniline), a redox-sensitive polymer.[169] Activation using redox chemistry helped the valves to actuate quickly, and the use of the hydrogel structure allowed the valves to achieve a greater degree of swelling than could be achieved with the redox polymer alone.

Hydrogel swelling within the confined space of a microchannel has also been used to drive fluid flow.[170,171] The basic design involves isolating a responsive hydrogel from a fluid reservoir by placing a flexible membrane between the two volumes. Swelling of the hydrogel causes a displacement of the membrane into the fluid reservoir, providing an increase of pressure that in turn drives fluid flow through a channel that is attached to the fluid reservoir.

Several microfluidic chemical sensors have been developed that rely on the degradation of a dynamic hydrogels to identify the presence of specific species. For example, a microfluidic chymotrypsin sensor was formed by fabricating hydrogel posts

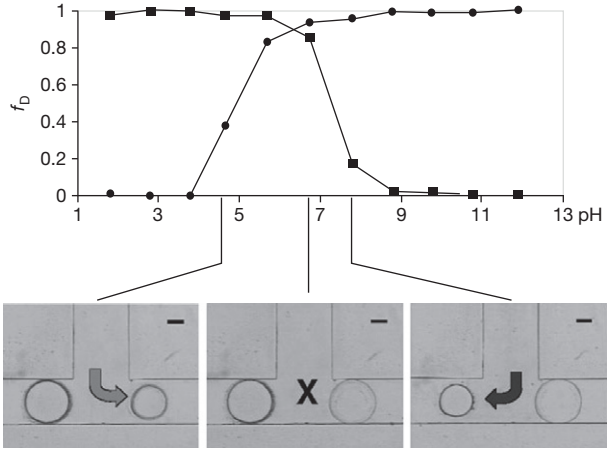

Figure 5 A microfluidic device for directing fluid based on pH. The valve on the right (circles) swells in basic conditions and contracts in acidic conditions, while the valve on the left (squares) swells in acidic conditions and contracts in basic conditions. The scale bar is equal to 300 μm. Reprinted from Beebe, D. J.; Moore, J. S.; Bauer, J. M.; *et al. Nature* **2000**, *404*, 588–590, with permission from Macmillan Publishers Ltd., Copyright 2000.

that contained a chymotrypsin recognition peptide sequence in the hydrogel backbone.[172] The post dissolved in the presence of chymotrypsin, but a control post made with a scrambled peptide sequence remained intact. Frisk used a similar approach to develop a peptide–hydrogel construct that dissolved upon exposure to Botulinum neurotoxin A.[173]

1.132.5. Future Directions

Dynamic hydrogels are being developed for a wide range of applications and a diverse set of synthetic materials can be used to tailor hydrogel performance to fit the need of a particular application. New materials and molecular triggers will continue to be a point of interest in dynamic hydrogel development. Creating hydrogels that can respond to specific diseases or infections will be a particular point of emphasis. For example, compound hydrogel systems with surface labeling that can attach to specific cell types will be useful for targeting imaging and therapeutic agents. Indeed, NiPAAm particles with folate groups attached to the surface were shown to be taken up preferentially by KB cells.[174]

One emerging area is the creation of hydrogels that can play an active role in tissue development. Hydrogels that can selectively display or release growth factors, sequester soluble signals, and change mechanical properties on demand would be of great value in tissue development. The ability to control the cellular microenvironment using hydrogels would also be an invaluable tool for elucidating fundamental signaling events in tissue development.

Many of these applications will require monodisperse micro- and nanoparticles with small feature sizes.[175] Smaller particles are more easily injected into the body, more mobile, and faster responding than larger hydrogels due to their smaller size. Nanoscale hydrogels could potentially be used to perform intracellular delivery via endocytosis. Methods such as precipitation polymerization[176,177] and nanoimprint lithography[178] will continue to be developed to allow ever smaller hydrogels to be formed with a variety of geometries.

References

1. Hansen, K. C.; Kiemele, L.; Maller, O.; *et al*. *Mol. Cell. Proteomics* **2009**, *8*, 1648–1657.
2. Wichterle, O.; Lim, D. *Nature* **1960**, *185*, 117–118.
3. Yannas, I. V.; Lee, E.; Orgill, D. P.; Skrabut, E. M.; Murphy, G. F. *Proc. Natl. Acad. Sci. USA* **1989**, *86*, 933–937.
4. Katchalsky, A.; Kunzle, O.; Kuhn, W. *J. Polym. Sci.* **1948**, *5*, 283–300.
5. Katchalsky, A. *Experientia* **1949**, *8*, 319–320.
6. Kuhn, W. *Experientia* **1949**, *8*, 318–319.
7. Kuhn, W.; Hargitay, B.; Katchalsky, A.; Eisenberg, H. *Nature* **1950**, *165*, 514–516.
8. Steinberg, I.; Oplatka, A.; Katchalsky, A. *Nature* **1966**, *210*, 568–571.
9. Sussman, M.; Katchalsky, A. *Science* **1970**, *167*, 45–47.
10. Amiya, T.; Hirokawa, Y.; Hirose, Y.; Li, Y.; Tanaka, T. *J. Chem. Phys.* **1987**, *86*, 2375–2379.
11. Ilavsky, M. *Macromolecules* **1982**, *15*, 782–788.
12. Katayama, S.; Hirokawa, Y.; Tanaka, T. *Macromolecules* **1984**, *17*, 2641–2643.
13. Tanaka, T. *Phys. Rev. Lett.* **1978**, *40*, 820–823.
14. Khokhlov, A. R. *Polymer* **1980**, *21*, 376–380.
15. Ilavsky, M. *Polymer* **1981**, *22*, 1687–1691.
16. Stejskal, J.; Gordon, M.; Torkington, J. A. *Polym. Bull.* **1980**, *3*, 621–625.
17. Matsuo, E. S.; Tanaka, T. *J. Chem. Phys.* **1988**, *89*, 1695–1703.
18. Park, T. G.; Hoffman, A. S. *J. Appl. Polym. Sci.* **1994**, *52*, 85–89.
19. Peters, A.; Candau, S. J. *Macromolecules* **1986**, *19*, 1952–1955.
20. Singh, J.; Weber, M. E. *Chem. Eng. Sci.* **1996**, *51*, 4499–4508.
21. Tanaka, T.; Fillmore, D. J. *J. Chem. Phys.* **1979**, *70*, 1214–1218.
22. Matsuo, E. S.; Tanaka, T. *Nature* **1992**, *358*, 482–485.
23. Tanaka, T.; Sun, S. T.; Hirokawa, Y.; *et al*. *Nature* **1987**, *325*, 796–798.
24. Ilavsky, M.; Hrouz, J. *Polym. Bull.* **1982**, *8*, 387–394.
25. Meyer, E. E.; Rosenberg, K. J.; Israelachvili, J. *Proc. Natl. Acad. Sci. USA* **2006**, *103*, 15739–15746.
26. Mohammed, J. S.; Murphy, W. L. *Adv. Mater.* **2009**, *21*, 2361–2374.
27. Hirokawa, Y.; Tanaka, T. *J. Chem. Phys.* **1984**, *81*, 6379–6380.
28. Schild, H. G. *Prog. Polym. Sci.* **1992**, *17*, 163–249.
29. Bae, Y. H.; Okano, T.; Kim, S. W. *J. Polym. Sci. B Polym. Phys.* **1990**, *28*, 923–936.
30. Nowatzki, P. J.; Tirrell, D. A. *Biomaterials* **2004**, *25*, 1261–1267.
31. Trabbic-Carlson, K.; Setton, L. A.; Chilkoti, A. *Biomacromolecules* **2003**, *4*, 572–580.
32. Kim, B.; Chilkoti, A. *J. Am. Chem. Soc.* **2008**, *130*, 17867–17873.
33. Otake, K.; Inomata, H.; Konno, M.; Saito, S. *Macromolecules* **1990**, *23*, 283–289.
34. Badiger, M. V.; Rajamohanan, P. R.; Kulkarni, M. G.; Ganapathy, S.; Mashelkar, R. A. *Macromolecules* **1991**, *24*, 106–111.
35. Plestil, J.; Ostanevich, Y. M.; Borbely, S.; Stejskal, J.; Ilavsky, M. *Polym. Bull.* **1987**, *17*, 465–472.
36. Otake, K.; Inomata, H.; Konno, M.; Saito, S. *J. Chem. Phys.* **1989**, *91*, 1345–1350.
37. Bae, Y. H.; Okano, T.; Kim, S. W. *Pharm. Res.* **1991**, *8*, 531–537.
38. Yoshida, R.; Sakai, K.; Okano, T.; Sakurai, Y. *Ind. Eng. Chem. Res.* **1992**, *31*, 2339–2345.
39. Tanaka, T.; Sato, E.; Hirokawa, Y.; Hirotsu, S.; Peetermans, J. *Phys. Rev. Lett.* **1985**, *55*, 2455–2458.
40. Yoshida, R.; Uchida, K.; Kaneko, Y.; *et al*. *Nature* **1995**, *374*, 240–242.
41. Inoue, T.; Chen, G. H.; Nakamae, K.; Hoffman, A. S. *Polym. Gels Networks* **1997**, *5*, 561–575.
42. Berndt, I.; Pedersen, J. S.; Lindner, P.; Richtering, W. *Langmuir* **2006**, *22*, 459–468.
43. Hu, Z. B.; Zhang, X. M.; Li, Y. *Science* **1995**, *269*, 525–527.
44. Bae, Y. H.; Okano, T.; Hsu, R.; Kim, S. W. *Makromol. Chem. Rapid Commun.* **1987**, *8*, 481–485.
45. Hirotsu, S.; Hirokawa, Y.; Tanaka, T. *J. Chem. Phys.* **1987**, *87*, 1392–1395.
46. Tanaka, T.; Fillmore, D.; Sun, S. T.; Nishio, I.; Swislow, G.; Shah, A. *Phys. Rev. Lett.* **1980**, *45*, 1636–1639.
47. Ilavsky, M.; Hrouz, J.; Ulbrich, K. *Polym. Bull.* **1982**, *7*, 107–113.
48. Hirokawa, Y.; Tanaka, T.; Sato, E. *Macromolecules* **1985**, *18*, 2782–2784.
49. Katayama, S.; Ohata, A. *Macromolecules* **1985**, *18*, 2781–2782.
50. Kokufuta, E.; Zhang, Y. Q.; Tanaka, T.; Mamada, A. *Macromolecules* **1993**, *26*, 1053–1059.
51. Ilmain, F.; Tanaka, T.; Kokufuta, E. *Nature* **1991**, *349*, 400–401.
52. Bae, Y. H.; Okano, T.; Kim, S. W. *Makromol. Chem. Rapid Commun.* **1988**, *9*, 185–189.
53. Katono, H.; Maruyama, A.; Sanui, K.; Ogata, N.; Okano, T.; Sakurai, Y. *J. Control. Release* **1991**, *16*, 215–228.
54. Wang, C.; Stewart, R. J.; Kopecek, J. *Nature* **1999**, *397*, 417–420.
55. Hamlen, R. P.; Kent, C. E.; Shafer, S. N. *Nature* **1965**, *206*, 1149–1150.
56. Fragala, A.; Enos, J.; Boyack, J.; Laconti, A. *Electrochim. Acta* **1972**, *17*, 1507–1522.
57. Grodzinsky, A. J.; Shoenfeld, N. A. *Polymer* **1977**, *18*, 435–443.
58. Shoenfeld, N. A.; Grodzinsky, A. J. *Biopolymers* **1980**, *19*, 241–262.
59. Tanaka, T.; Nishio, I.; Sun, S. T.; Uenonishio, S. *Science* **1982**, *218*, 467–469.
60. Hirose, Y.; Giannetti, G.; Marquardt, J.; Tanaka, T. *J. Phys. Soc. Jpn.* **1992**, *61*, 4085–4097.
61. Osada, Y.; Hasebe, M. *Chem. Lett.* **1985**, (9), 1285–1288.
62. Shiga, T.; Kurauchi, T. *J. Appl. Polym. Sci.* **1990**, *39*, 2305–2320.
63. Shiga, T.; Hirose, Y.; Okada, A.; Kurauchi, T. *J. Intell. Mater. Syst. Struct.* **1993**, *4*, 553–557.
64. Kudaibergenov, S. E.; Sigitov, V. B. *Langmuir* **1999**, *15*, 4230–4235.
65. Osada, Y.; Okuzaki, H.; Hori, H. *Nature* **1992**, *355*, 242–244.
66. Kim, S. J.; Kim, M. S.; Kim, S. I.; Spinks, G. M.; Kim, B. C.; Wallace, G. G. *Chem. Mater.* **2006**, *18*, 5805–5809.
67. Hirotsu, S. *Jpn. J. Appl. Phys. Suppl.* **1985**, *24*, 388–396.
68. Shiga, T.; Hirose, Y.; Okada, A.; Kurauchi, T. *J. Mater. Sci.* **1994**, *29*, 5715–5718.
69. Suleimenov, I. E.; Sigitov, V. B.; Kudaibergenov, S. E.; Didukh, A. G.; Fryasinova, T. S.; Bekturov, E. A. *Polym. Int.* **2001**, *50*, 194–196.

70. Zrinyi, M.; Barsi, L.; Szabo, D.; Kilian, H. G. *J. Chem. Phys.* **1997**, *106*, 5685–5692.
71. Zrinyi, M.; Szabo, D.; Kilian, H. G. *Polym. Gels Networks* **1998**, *6*, 441–454.
72. Fuhrer, R.; Athanassiou, E. K.; Luechinger, N. A.; Stark, W. J. *Small* **2009**, *5*, 383–388.
73. Bhattacharya, S.; Eckert, F.; Boyko, V.; Pich, A. *Small* **2007**, *3*, 650–657.
74. Takahashi, F.; Sakai, Y.; Mizutani, Y. *J. Ferment. Bioeng.* **1997**, *83*, 152–156.
75. Irie, M. *Adv. Polym. Sci.* **1990**, *94*, 27–67.
76. Suzuki, A.; Tanaka, T. *Nature* **1990**, *346*, 345–347.
77. Sershen, S. R.; Westcott, S. L.; Halas, N. J.; West, J. L. *J. Biomed. Mater. Res.* **2000**, *51*, 293–298.
78. Zeng, X. F.; Jiang, H. R. *Appl. Phys. Lett.* **2008**, *93*, 151101.
79. Saaem, I.; Tian, J. *Adv. Mater.* **2007**, *19*, 4268–4271.
80. Irie, M.; Kunwatchakun, D. *Macromolecules* **1986**, *19*, 2476–2480.
81. Mamada, A.; Tanaka, T.; Kungwatchakun, D.; Irie, M. *Macromolecules* **1990**, *23*, 1517–1519.
82. Irie, M. *Macromolecules* **1986**, *19*, 2890–2892.
83. Szilagyi, A.; Sumaru, K.; Sugiura, S.; *et al. Chem. Mater.* **2007**, *19*, 2730–2732.
84. Juodkazis, S.; Mukai, N.; Wakaki, R.; Yamaguchi, A.; Matsuo, S.; Misawa, H. *Nature* **2000**, *408*, 178–181.
85. Lee, K. K.; Cussler, E. L.; Marchetti, M.; Mchugh, M. A. *Chem. Eng. Sci.* **1990**, *45*, 766–767.
86. Zhong, X.; Wang, Y. X.; Wang, S. C. *Chem. Eng. Sci.* **1996**, *51*, 3235–3239.
87. Kato, E. *J. Chem. Phys.* **1997**, *106*, 3792–3797.
88. Firestone, B. A.; Siegel, R. A. *Polym. Commun.* **1988**, *29*, 204–208.
89. Siegel, R. A.; Firestone, B. A. *Macromolecules* **1988**, *21*, 3254–3259.
90. Luo, L. B.; Kato, M.; Tsuruta, T.; Kataoka, K.; Nagasaki, Y. *Macromolecules* **2000**, *33*, 4992–4994.
91. Philippova, O. E.; Hourdet, D.; Audebert, R.; Khokhlov, A. R. *Macromolecules* **1997**, *30*, 8278–8285.
92. Nishi, S.; Kotaka, T. *Macromolecules* **1986**, *19*, 978–984.
93. Smith, K. L.; Winslow, A. E.; Petersen, D. E. *Ind. Eng. Chem.* **1959**, *51*, 1361–1364.
94. Katayama, S.; Myoga, A.; Akahori, Y. *J. Phys. Chem.* **1992**, *96*, 4698–4701.
95. Ohmine, I.; Tanaka, T. *J. Chem. Phys.* **1982**, *77*, 5725–5729.
96. Tanaka, T. *Sci. Am.* **1981**, *244*, 124–138.
97. Ricka, J.; Tanaka, T. *Macromolecules* **1984**, *17*, 2916–2921.
98. Ricka, J.; Tanaka, T. *Macromolecules* **1985**, *18*, 83–85.
99. English, A. E.; Tanaka, T.; Edelman, E. R. *Polymer* **1998**, *39*, 5893–5897.
100. Park, T. G.; Hoffman, A. S. *Macromolecules* **1993**, *26*, 5045–5048.
101. Inomata, H.; Goto, S.; Otake, K.; Saito, S. *Langmuir* **1992**, *8*, 687–690.
102. Ju, X. J.; Chu, L. Y.; Liu, L.; Mi, P.; Lee, Y. M. *J. Phys. Chem. B* **2008**, *112*, 1112–1118.
103. Mi, P.; Chu, L. Y.; Ju, X. J.; Niu, C. H. *Macromol. Rapid Commun.* **2008**, *29*, 27–32.
104. Byrne, M. E.; Park, K.; Peppas, N. A. *Adv. Drug Deliv. Rev.* **2002**, *54*, 149–161.
105. Kryscio, D. R.; Peppas, N. A. *AIChE J.* **2009**, *55*, 1311–1324.
106. Wulff, G. *Angew. Chem. Int. Ed. Engl.* **1995**, *34*, 1812–1832.
107. Watanabe, M.; Akahoshi, T.; Tabata, Y.; Nakayama, D. *J. Am. Chem. Soc.* **1998**, *120*, 5577–5578.
108. Miyata, T.; Jige, M.; Nakaminami, T.; Uragami, T. *Proc. Natl. Acad. Sci. USA* **2006**, *103*, 1190–1193.
109. Miyata, T.; Jikihara, A.; Nakamae, K.; Hoffman, A. S. *Macromol. Chem. Phys.* **1996**, *197*, 1135–1146.
110. Miyata, T.; Jikihara, A.; Nakamae, K.; Hoffman, A. S. *J. Biomater. Sci. Polym. Ed.* **2004**, *15*, 1085–1098.
111. Kokufata, E.; Zhang, Y. Q.; Tanaka, T. *Nature* **1991**, *351*, 302–304.
112. Miyata, T.; Asami, N.; Uragami, T. *Macromolecules* **1999**, *32*, 2082–2084.
113. Miyata, T.; Asami, N.; Uragami, T. *Nature* **1999**, *399*, 766–769.
114. Ishihara, K.; Kobayashi, M.; Ishimaru, N.; Shinohara, I. *Polym. J.* **1984**, *16*, 625–631.
115. Kokufuta, E.; Tanaka, T. *Macromolecules* **1991**, *24*, 1605–1607.
116. Kokufuta, E.; Zhang, Y. Q.; Tanaka, T. *J. Biomater. Sci. Polym. Ed.* **1994**, *6*, 35–40.
117. Shalaby, W. S. W.; Peck, G. E.; Park, K. *J. Control. Release* **1991**, *16*, 355–364.
118. Wang, D. A.; Williams, C. G.; Yang, F.; Cher, N.; Lee, H.; Elisseeff, J. H. *Tissue Eng.* **2005**, *11*, 201–213.
119. Kraehenbuehl, T. P.; Zammaretti, P.; Van Der Vlies, A. J.; *et al. Biomaterials* **2008**, *29*, 2757–2766.
120. Yamamoto, N.; Kurisawa, M.; Yui, N. *Macromol. Rapid Commun.* **1996**, *17*, 313–318.
121. Kurisawa, M.; Matsuo, Y.; Yui, N. *Macromol. Chem. Phys.* **1998**, *199*, 705–709.
122. Ehrick, J. D.; Deo, S. K.; Browning, T. W.; Bachas, L. G.; Madou, M. J.; Daunert, S. *Nat. Mater.* **2005**, *4*, 298–302.
123. Murphy, W. L.; Dillmore, W. S.; Modica, J.; Mrksich, M. *Angew. Chem. Int. Ed.* **2007**, *46*, 3066–3069.
124. Sui, Z. J.; King, W. J.; Murphy, W. L. *Adv. Mater.* **2007**, *19*, 3377–3380.
125. Yuan, W. W.; Yang, J. Y.; Kopeckova, P.; Kopecek, J. *J. Am. Chem. Soc.* **2008**, *130*, 15760–15761.
126. Park, T. G.; Hoffman, A. S. *Biotechnol. Prog.* **1994**, *10*, 82–86.
127. Dong, L. C.; Hoffman, A. S. *J. Control. Release* **1986**, *4*, 223–227.
128. Wang, Y. X.; Zhong, X.; Wang, S. H. *J. Chem. Technol. Biotechnol.* **1996**, *67*, 243–247.
129. Cussler, E. L.; Stokar, M. R.; Varberg, J. E. *AIChE J.* **1984**, *30*, 578–582.
130. Freitas, R. F. S.; Cussler, E. L. *Sep. Sci. Technol.* **1987**, *22*, 911–919.
131. Hoffman, A. S.; Afrassiabi, A.; Dong, L. C. *J. Control. Release* **1986**, *4*, 213–222.
132. Bae, Y. H.; Okano, T.; Kim, S. W. *Pharm. Res.* **1991**, *8*, 624–628.
133. Okano, T.; Bae, Y. H.; Jacobs, H.; Kim, S. W. *J. Control. Release* **1990**, *11*, 255–265.
134. Kiser, P. F.; Wilson, G.; Needham, D. *Nature* **1998**, *394*, 459–462.
135. Lowman, A. M.; Morishita, M.; Kajita, M.; Nagai, T.; Peppas, N. A. *J. Pharm. Sci.* **1999**, *88*, 933–937.
136. Aoki, T.; Kawashima, M.; Katono, H.; *et al. Macromolecules* **1994**, *27*, 947–952.
137. Hovgaard, L.; Brondsted, H. *J. Control. Release* **1995**, *36*, 159–166.
138. Brondsted, H.; Kopecek, J. *Biomaterials* **1991**, *12*, 584–592.
139. Siegel, R. A.; Falamarzian, M.; Firestone, B. A.; Moxley, B. C. *J. Control. Release* **1988**, *8*, 179–182.
140. Albin, G.; Hrbett, T. A.; Ratner, B. D. *J. Control. Release* **1985**, *2*, 153–164.
141. Kost, J.; Horbett, T. A.; Ratner, B. D.; Singh, M. *J. Biomed. Mater. Res.* **1985**, *19*, 1117–1133.
142. Ishihara, K.; Matsui, K. *J. Polym. Sci. C Polym. Lett.* **1986**, *24*, 413–417.
143. Hassan, C. M.; Doyle, F. J.; Peppas, N. A. *Macromolecules* **1997**, *30*, 6166–6173.
144. King, W. J.; Mohammed, J. S.; Murphy, W. L. *Soft Matter* **2009**, *5*, 2399–2406.
145. Kataoka, K.; Miyazaki, H.; Bunya, M.; Okano, T.; Sakurai, Y. *J. Am. Chem. Soc.* **1998**, *120*, 12694–12695.
146. Siegel, R. A.; Firestone, B. A. *J. Control. Release* **1990**, *11*, 181–192.
147. von Recum, H. A.; Kim, S. W.; Kikuchi, A.; Okuhara, M.; Sakurai, Y.; Okano, T. *J. Biomed. Mater. Res.* **1998**, *40*, 631–639.
148. Yamada, N.; Okano, T.; Sakai, H.; Karikusa, F.; Sawasaki, Y.; Sakurai, Y. *Makromol. Chem. Rapid Commun.* **1990**, *11*, 571–576.
149. Todd, S. J.; Farrar, D.; Gough, J. E.; Ulijn, R. V. *Soft Matter* **2007**, *3*, 547–550.
150. Huber, D. L.; Manginell, R. P.; Samara, M. A.; Kim, B. I.; Bunker, B. C. *Science* **2003**, *301*, 352–354.
151. Kim, J.; Kim, B.; Ryu, J.; *et al. Jpn. J. Appl. Phys.* **2005**, *44*, 5764–5768.
152. Herber, S.; Bomer, J.; Olthuis, W.; Bergveld, P.; Van Den Berg, A. *Biomed. Microdevices* **2005**, *7*, 197–204.
153. Lin, G.; Chang, S.; Kuo, C. H.; Magda, J.; Solzbacher, F. *Sens. Actuat. B* **2009**, *136*, 186–195.
154. Sharma, A. C.; Jana, T.; Kesavamoorthy, R.; *et al. J. Am. Chem. Soc.* **2004**, *126*, 2971–2977.
155. Dong, L.; Agarwal, A. K.; Beebe, D. J.; Jiang, H. R. *Nature* **2006**, *442*, 551–554.
156. Ehrick, J. D.; Stokes, S.; Bachas-Daunert, S.; *et al. Adv. Mater.* **2007**, *19*, 4024–4027.
157. Kim, J.; Nayak, S.; Lyon, L. A. *J. Am. Chem. Soc.* **2005**, *127*, 9588–9592.
158. Kim, J. S.; Singh, N.; Lyon, L. A. *Angew. Chem. Int. Ed.* **2006**, *45*, 1446–1449.
159. Tierney, S.; Hjelme, D. R.; Stokke, B. T. *Anal. Chem.* **2008**, *80*, 5086–5093.
160. Yoshida, R.; Ichijo, H.; Hakuta, T.; Yamaguchi, T. *Macromol. Rapid Commun.* **1995**, *16*, 305–310.
161. Yoshida, R.; Takahashi, T.; Yamaguchi, T.; Ichijo, H. *J. Am. Chem. Soc.* **1996**, *118*, 5134–5135.
162. Yoshida, R.; Uesusuki, Y. *Biomacromolecules* **2005**, *6*, 2923–2926.
163. Kurauchi, T.; Shiga, T.; Hirose, Y.; Okada, A. *Mater. Res. Soc. Symp. Proc.* **1990**, *171*, 389–394.
164. Kim, B.; Gong, J. P.; Osada, Y. *Polym. Int.* **1999**, *48*, 691–698.
165. Kwon, G. H.; Park, J. Y.; Kim, J. Y.; Frisk, M. L.; Beebe, D. J.; Lee, S. H. *Small* **2008**, *4*, 2148–2153.
166. Yeghiazarian, L.; Mahajan, S.; Montemagno, C.; Cohen, C.; Wiesner, U. *Adv. Mater.* **2005**, *17*, 1869–1873.
167. Beebe, D. J.; Moore, J. S.; Bauer, J. M.; *et al. Nature* **2000**, *404*, 588–590.
168. Eddington, D. T.; Liu, R. H.; Moore, J. S.; Beebe, D. J. *Lab Chip* **2001**, *1*, 96–99.
169. Low, L. M.; Seetharaman, S.; He, K. Q.; Madou, M. J. *Sens. Actuat. B* **2000**, *67*, 149–160.

170. Eddington, D. T.; Beebe, D. J. *J. Microelectromech. Syst.* **2004**, *13*, 586–593.
171. Richter, A.; Klatt, S.; Paschew, G.; Klenke, C. *Lab Chip* **2009**, *9*, 613–618.
172. Plunkett, K. N.; Berkowski, K. L.; Moore, J. S. *Biomacromolecules* **2005**, *6*, 632–637.
173. Frisk, M. L.; Tepp, W. H.; Lin, G.; Johnson, E. A.; Beebe, D. J. *Chem. Mater.* **2007**, *19*, 5842–5844.
174. Nayak, S.; Lee, H.; Chmielewski, J.; Lyon, L. A. *J. Am. Chem. Soc.* **2004**, *126*, 10258–10259.
175. Raemdonck, K.; Demeester, J.; De Smedt, S. *Soft Matter* **2009**, *5*, 707–715.
176. Blackburn, W. H.; Lyon, L. A. *Colloid Polym. Sci.* **2008**, *286*, 563–569.
177. Singh, N.; Lyon, L. A. *Colloid Polym. Sci.* **2008**, *286*, 1061–1069.
178. Rolland, J. P.; Maynor, B. W.; Euliss, L. E.; Exner, A. E.; Denison, G. M.; Desimone, J. M. *J. Am. Chem. Soc.* **2005**, *127*, 10096–10100.

2.201. Bio-inspired Silica Nanomaterials for Biomedical Applications

T Ould-Ely, L A Bawazer, and D E Morse, University of California, Santa Barbara, CA, USA

© 2011 Elsevier Ltd. All rights reserved.

2.201.1.	**Introduction**	2
2.201.2.	**Biosilicification**	2
2.201.2.1.	Introduction	2
2.201.2.2.	Natural Biomolecules Directing Silicification in Sponges and Diatoms	3
2.201.2.2.1.	Sponge-derived biomolecules: silicateins	3
2.201.2.2.2.	Diatom-derived molecules: silaffins and long-chain polyamines	4
2.201.2.3.	Bio-inspired Silica Synthesis	6
2.201.3.	**Bio-inspired Silica Synthesis for Biomedical Applications**	7
2.201.3.1.	Introduction	7
2.201.3.2.	Silica Nanoparticles for Medical Imaging	7
2.201.3.3.	Silica-Based Nanomaterials for Biosensors	8
2.201.3.4.	Silica Nanoparticles for Drug Encapsulation and Delivery	10
2.201.3.5.	Silica-Based Nanomaterials for Implants and Tissue Engineering	10
2.201.4.	**Perspectives and Challenges**	11
2.201.4.1.	Silica Biocompatibility	12
2.201.4.2.	Novel Bio-inspired Silica Synthesis	12
2.201.4.3.	Genetically Engineering Silica Biomaterials	12
2.201.4.4.	Hierarchical Design of Silica-Based Next Generation Implants	13
2.201.5.	**Conclusion**	13
References		14

Abbreviations

C-dots	Core– shell fluorescent silica nanoparticles comprised of dye-rich core with a pure silica shell
CoCr	Cobalt–chromium alloys
DNA	Deoxyribonucleic acid
FAD	Flavin adenine dinucleotide (FAD), its reduced form is $FADH_2$
GaOOH(s)	Gallium hydroxides
GFP	Green fluorescent protein is a protein composed of 238 amino acid residues (26.9 kDa) that exhibits bright green fluorescence when exposed to blue light. The blue fluorescent protein is color mutant of GFP protein family
GOx	Glucose oxidase enzyme
HF	Hydrofluoric acid
His165	His is an abbreviation of histidine amino acid, also known as 2-Amino-3-(1H-imidazol-4-yl) propanoic acid; 165 refer to its position in the polypeptide chain, forming silica proteins filament (silicateins)
MSN	Mesoporous silica nanoparticles
NAD[H]	Nacotinamide adenine dinucleotide, abbreviated NAD^+, is a coenzyme found in all living cells. [H] suffix refers to hydrogenase [P] refer to phospahte
NIR	Near infrared
OPTA	*O*–phthalic hemithioacetal
Q	Quaternary sites
R5-	A synthetic peptide derived from Sil 1 proteins and composed of 19 amino acid sequence [H2NSSKKSGSYSGSKGSKRRIL–COOH]
RGD	A peptide sequence composed of arginine-glycine-aspartate
[Ru (phen)$_3$] Cl$_2$	Tris-(1,10-Phenanthroline) ruthenium (II) chloride
SAMs	Self-assembled Monolayer
Ser26	Ser is an abbreviation of serine amino acid, also known as 2-amino-3-hydroxypropionic acid; 26 refer to its position in the polypeptide chain, forming silica proteins filament (silicateins)
S_N^2-type	Nucleophilic substitution-type 2
TEM	Transmission electron microscopy
TEOS	Tetraethyl orthosilicate; also named tetraethoxysilane

2.201.1. Introduction

The mechanisms underlying biomineralization, which produce mineral-based components that form the shells, skeletons, and teeth of diverse organisms, are inspiring examples of Nature's ability to genetically control the growth of intricate macroscopic forms.[1] The decryption of these genetically encoded mechanisms is poised to revolutionize nanotechnology, especially nanomedical technology, as it affords us unprecedented ability to engineer therapeutic and bio-analytical systems that are on the same size-scale as biological molecules (at the nanoscale) and biological cells (at the microscale). To realize this potential, the scientific community must be able to exploit Nature's genetically encoded mechanisms governing materials synthesis and functionality at the nano- and microscales and develop novel functional materials based on these concepts. In particular, the developing understanding of biomineralization, and the subsequent translation of its mechanisms to new synthetic approaches for mineral synthesis, has significant implications for drug delivery, bone repair, biosensing, and many other medical technologies.

Biomineralization methods differ dramatically from anthropogenic solution-based methods for growing minerals in several important ways. They are produced in highly dynamic nonequilibrium systems that precisely organize the placement of metal or metalloid atoms or ions into (oftentimes crystalline) inorganic structures and, additionally, they are produced in very mild conditions (ambient pressure, temperature, and near neutral pH). The mild and dynamic conditions of biomineralization facilitate a variety of biomolecule–mineral interactions that lead to extraordinary and distinctive architectures.[2,3] While many of the mechanistic details of biomineralization remain to be elucidated, some general principles are understood.[4–7] Biological molecules participate as regulatory elements during mineralization, influencing kinetic and thermodynamic variables that govern mineral nucleation and growth; this influence may be exerted through surface recognition, templating, or dimensional constraint; through regulation of local pH levels and the concentrations of metal ions or other chemical species; or through more complex interactions.[8]

The major classes of minerals upon which most biological hard materials are based include calcium and magnesium carbonates,[4,9,10] calcium phosphate,[4,11] iron oxide,[4,12] and silica.[13–15] Owing to studies conducted over the past 10 years on marine sponge and diatom mineral structures, biosilica is arguably the most well-understood biomineral material in terms of the known biochemical and molecular mechanisms that contribute to the mineral's nucleation and directed growth. As a result of this understanding, a variety of new synthetic approaches toward silica materials have been developed that, through the use of appropriately selected catalysts and precipitation-accelerating agents, can produce structures at much milder and more biologically relevant conditions than the conventional industrial approaches for silica synthesis.

Silica is widely considered to have excellent biocompatibility and provides an advantageous balance between stability and degradability.[16,17] Silica biocompatibility can be tuned by controlling the structural and compositional material features (such as particle size, porosity, dopant chemistry, and surface coatings), and differences in these features can dramatically affect material toxicity.[18] Owing to the potential therapeutic and analytical utility of silica-based materials for a wide range of nanomedical applications,[19,20] there is an increased demand for well-defined biocompatible silica-based composites from cheap starting materials produced under mild conditions. Nature has developed a wide variety of mechanisms for successfully integrating silica structures within biological systems; it should thus provide valuable lessons for designing more biocompatible and functional silica structures. This chapter focuses on bio-inspired routes to silica synthesis and the potential applications of the synthesized materials in medical technologies. The chapter is developed in three main sections. In Section 2.201.2, we describe the natural biomineral components and associated mineral-synthesizing molecules that have served as models for bio-inspired silica syntheses, and the novel anthropogenic routes to silica synthesis that have been derived from these models. In Section 2.201.3, we review studies that establish the utility of silica in four unique biomedical applications – imaging, sensing, drug delivery, and tissue and implant engineering – and we discuss initial studies utilizing bio-inspired silica syntheses for these applications. In Section 2.201.4, we address the issue of toxicity and discuss a number of future prospects for productively merging bio-inspired silica syntheses with medicine.

2.201.2. Biosilicification

2.201.2.1. Introduction

The major current strategies for synthesizing silica for biomedical applications include variations of the Stöber process[21] and microemulsion techniques.[22] Both of these solution-based strategies rely on the controlled hydrolysis and subsequent condensation of silicon alkoxide precursors in ethanol–water mixtures with high concentrations of ammonium hydroxide as the hydrolytic catalyst.[17] These strategies are attractive because they are industrially scalable and yield highly uniform, chemically stable silica nanoparticles that can be functionalized in a variety of ways for use in specific applications,[17] as highlighted in Section 2.201.3. While these widely used synthetic approaches have demonstrated the promise of silica-based materials for biomedical applications, they also have disadvantages that must be addressed through further research. These procedures typically employ extreme pH or hydrothermal processing steps that are incompatible with DNA and protein stability, imposing procedural limitations that require silica synthesis to precede biological integration; further, resultant morphologies are limited to spherical configurations from 10 nm to 2 μm; and the silica chemistry – such as the extent of hydration or condensation – while influential on the resultant oxide properties, is poorly controlled.[17]

There is a need for fundamentally new, biologically compatible synthetic approaches to design silica-based materials with defined compositions, morphologies, and ultrastructures, and with consequently tailored stability and dissolution, mechanical, immunological, and fluorescent properties. Such approaches should further allow complex silica structures to be synthesized under environmentally benign conditions with high reproducibility. These latter features are, in fact, already exhibited in natural biomineralizing systems. Thus natural

biosilicification serves as an attractive model on which new synthetic approaches could be based. Indeed, the extent to which biology has evolved silica-based materials with tailored properties, spanning multiple phyla and length-scales,[23–25] demonstrates an intimate and robust relationship at the metabolic level between the synthesis and structure of silica-based materials and their physiological performance.

The natural evidence demonstrating feasibility that facile synthesis of silica occurs in biological systems with a level of complexity unmatched by current technologies is persuasive: biosilica is produced at a rate of gigatons per year. Silica synthesis is found in algae, protozoa, sponges, and higher plants; in diatoms alone – unicellular algae with a biosilica outer wall – there are more than 100 000 distinct species, each exhibiting unique silica architectures with intricate nano- and microscale designs.[26] Evolutionarily selected functions for natural biosilica continue to be discovered. For example, biosilica skeletons of marine sponges have recently been shown to exhibit sophisticated hierarchical architecture from the nanoscale to the macroscale that endow the support structure with robust mechanical properties (**Figure 1**).[27–30]

In other sponges, silica skeletal elements have been suggested to act as light waveguides, perhaps to harvest light under deep sea conditions to attract sponge larvae or symbiotic shrimp, or promote survival of symbiotic algae.[31,32]

Sponges and diatoms are relatively simple organisms, but their ancient evolutionary history has endowed them with a complex ensemble of molecular and biochemical specializations – including the ability to produce silica from the silicic acid dissolved in fresh or salt water. The cellular processes that contribute to the growth of these organisms and govern biosilicification have not yet been fully deciphered and remain the subject of current investigations.[33,34] A wide range of cellular functions contribute to biosilica formation, including (but not limited to) cell differentiation, protein signaling, gene regulation, and microtubule permutations.[33,35] For each skeletal component, a host of genetically encoded, mineral-associated biomolecules and cellular regulatory programs contribute to its genesis, growth, maintenance, and directed dissolution; and govern environmental silicon sequestration and internal transport, storage, and site-specific incorporation in mineral nucleation or growth.[36,37] The complexity of these dynamic interactions complicates efforts to elucidate the process of mineral synthesis in its entirety. However, studies of sponge and diatom biosilica, as well as related bio-inspired materials investigations, have demonstrated that by reducing the initially extensive mineral complex down to a few functional components, it is possible to extract, from simplified model systems, the salient features that can be used to create new materials synthesis strategies.

A variety of biomolecules have been identified as key regulators in the process of natural silicification; these include silicon transport proteins in both diatoms[38–40] and sponges,[41] protein networks that direct silica growth[39,42] and specialized mineralization compartments.[43–46] Each identified regulatory element represents a potential model for new bio-inspired strategies for synthesis under mild conditions, provided the mechanistic details of its *in vivo* activity can be elucidated. To date the most informative models for natural silica synthesis have been biopolymers found occluded within the encasing silica of sponges and diatoms: silicateins from sponges, and silaffins and polyamines from diatoms, both initially isolated by hydrofluoric acid (HF) dissolution of the oxide material. The first evidence of biocatalytic silica formation was advanced through the discovery of silicatein, when DNA sequence analysis revealed that the structure of this protein is related to a well-known family of enzymatic hydrolases.[13,14] Subsequent identification of silaffins and polyamines showed these diatom-derived molecules accelerate silica precipitation from silicic acid.[47] Thus, a variety of in-depth biochemical studies were focused on the silicateins, silaffins, and polyamines, to illuminate their mechanisms of silica formation. These studies included site-directed genetic mutational analysis;[48] mass spectrometry analysis for identification of posttranslational modifications[47]; and characterization of a number of *in vitro* mineralization reactions and the corresponding mineral products from near-neutral aqueous conditions with soluble mineral precursors using either natively extracted proteins,[13,49–53] recombinantly expressed proteins,[48] or a variety of bio-inspired *in vitro* biomolecular analogues.[49,51,54] As the details of these studies are reviewed extensively elsewhere,[23–25,55] here, we briefly review the most salient lessons learned from silicateins, silaffins, and polyamines, and show how these lessons inspired novel approaches for silica synthesis with relevance to biomedical applications.

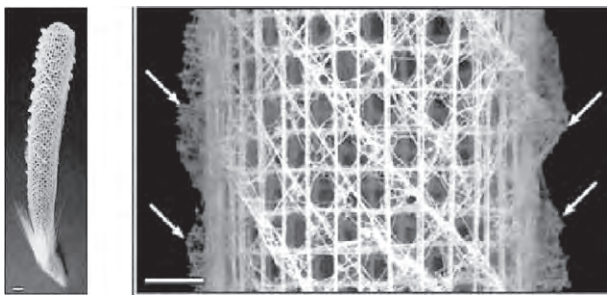

Figure 1 Structure of the intricate mineralized skeletal system of *Euplectella sp*. (a) Photograph of the entire skeleton, showing cylindrical glass cage. Scale bar = 1 cm. (b) Close-up of the cage structure showing the square-grid lattice of vertical and horizontal struts with diagonal elements arranged in a chessboard manner. Orthogonal ridges on the cylinder surface are indicated by arrows. Scale bar = 5 mm. Reproduced with permission from Aizenberg, J.; Weaver, J. C.; Thanawala, M. S.; Sundar, V. C.; Morse, D. E.; Fratzl, P. *Science (Washington, DC)* **2005**, *309*, 275–278. Copyright (2005) National Academy of Sciences, USA.

2.201.2.2. Natural Biomolecules Directing Silicification in Sponges and Diatoms

2.201.2.2.1. Sponge-derived biomolecules: silicateins

Silicateins are biomineralizing enzymes that self-assemble into polymeric filaments that present catalytically active and templating surfaces to initiate biosilica polycondensation from molecular precursors in a variety of marine sponges. First identified in the marine sponge *Tethya aurantia*, the silicatein filaments were found axially occluded within needle-like biosilica skeletal elements (known as spicules) microns in diameter and up to millimeters in length.[14] Three distinct

silicatein monomers were found to compose the polymeric filament; these monomers were found to be highly homologous to a well-known family of hydrolytic enzymes. Homology modeling led to an energy-minimized folded silicatein structure[56] and, combined with *in vitro* mineralization studies,[13,48,49,51,52,54,57,58] a proposed mechanism for silicatein activity. Purified native filaments were found to catalyze silica polycondensation at near-nuetral pH using TEOS (tetraethyl orthosilicate) as a precursor molecule, while heat denatured filaments lacked this activity.[13] The silica synthesized was found to deposit on the filament surface. In the proposed mechanism, the TEOS precursor molecule is hydrolyzed through enzymatic catalysis involving key amino acid residues, Ser26 and His165, at the putative enzyme active site. The released, reactive silanol species then undergoes subsequent polycondensation with other precursor molecules. As condensation proceeds, unique chemical and atomic topological features of the protein surface guide the deposition of the forming mineral onto the macroscopic protein template.

The mechanisms of both catalysis and templating have been substantiated in a number of ways, including site-directed mutagenesis of recombinant silicatein. When the key active site residues were knocked out, the ability of recombinant silicatein to catalyze silica polycondensation was dramatically reduced.[48] In addition to these requisite chemical interactions involving active site residues, the size and configuration of the active site pocket also appears to be important for catalysis. In a mutagenic study on cathepsin L, an enzyme that was initially found to have no silica condensing activity, investigators were able to introduce silicification activity by introducing silicatein-like character into the residues flanking the active site.[59] However, even with these modifications, reengineered cathepsin L enzymes were reactive only with prehydrolyzed silicic acid and not TEOS. These results suggest that both the chemical environment of the active site and other features governing the interactions with metal- or metalloid-bearing precursors are important for catalytic mineralization. Moving beyond the active site pocket and considering the solution-exposed surface of the folded protein, silicatein has been shown to be serine-rich, leading to the proposal that an array of hydroxyl moieties on the protein surface act as oxide condensation sites to guide mineral deposition.[14] This proposal was supported through the development of silicatein-mimetic surfaces constructed on gold using self-assembled monolayers (SAMs) of alkane-thiols terminated with either hydroxyl or imidizole groups (the functionalities identified by site-directed mutagenesis as essential for catalysis in the native enzyme) exposed to the solution. Using a planar substrate with alternating stripes of hydroxyl-terminated and imidazole-terminated alkane thiols, when the surface was reacted with a gallium nitrate precursor, GaOOH(s) synthesis was catalyzed initially at the interface between the two chemical groups, and subsequent deposition occurred preferentially on the hydroxyl-terminated strips (**Figure 2**).[58]

This result confirmed the role of hydroxyl moieties as oxide (or oxo-hydroxide) deposition sites when arranged adjacent to a catalytic site. In a previous study, cellulose fibers rich in hydroxyl groups (but lacking the critical amine functionality) were shown to be incapable of initiating silica deposition when reacted with TEOS.[13] An intimate temporal and spatial link between the dual functionalities of catalysis and templating thus seems important for the biogenic formation of higher-order silica structures. Another level of control exhibited by silicatein in such biogenic mineralization is afforded through the protein's self-assembly into filaments, a process shown to be driven by the interaction of hydrophobic patches on the protein surface and not present in related hydrolases.[56] The assembly process was further shown to proceed through fractal intermediates.[56,60]

In summary, silicatein initiates silica synthesis through catalytic hydrolysis of molecular precursors in the vicinity of condensation sites to promote local deposition, and these deposition events are collectively guided into structures of higher-order length-scales in part through geometric ordering of the polymerized protein template. The membrane surrounding the silicatein filament is presumed to provide additional structure-directing information. As illustrated by the SAM-based silicatein-mimetic surface described above, *in vitro* silicatein analogues have been used to substantiate the proposed model of silicatein activity. Other silicatein-analogue systems have been based on block copolypeptides,[54] other block copolymers,[61] catalytic small molecules,[51] and SAMs arranged on gold nanoparticles.[49] These experimental systems not only represent simplified *in vitro* models for studying silicatein activity, they also serve as valuable translational steps for engineering bio-inspired methods for silica synthesis under mild conditions. Such bio-inspired routes are attractive because they should afford the mechanistic control that underlies growth of sponge skeleton biosilica yet provide design strategies tractable enough to be merged with current industrial and laboratory synthetic approaches. In **Section 2.201.2.3**, we highlight the silicatein-mimetic systems based on block copolypeptides and small molecules.

2.201.2.2.2. Diatom-derived molecules: silaffins and long-chain polyamines

Diatomaceous earth is a widely available natural resource and has several industrial uses (such as a filtration material, an abrasive, a mechanical insecticide, an absorbent for liquids, and an activator for blood clotting). The detailed nanoscale architectures of the diatom cell frustules (i.e., silica cell-walls) that constitute this natural material are exquisite.[62–64] Considering the mild conditions under which they are synthesized, these frustules outstrip in complexity the material products of even the most skilled human engineers. The opportunity to design new industrial applications for such nano-architectured composite materials is highly appealing. The physical mechanisms affording this opportunity are becoming elucidated through identification of the biomolecules physically associated with diatom biosilica; several classes have been identified to date, including two subfamilies of 'silaffins' (named for biomolecules with 'silica affinity'), 'silacidins' (acidic silica-associated biomolecules), and long-chain polyamines.[47,50,65–69]

The activity of these biomolecules are investigated through *in vitro* mineralization studies which have mainly focused on the use of silicic acid as a mineral precursor under acidic conditions (pH ~5, intended to replicate the suspected *in vivo* environment).[24,47] The precipitation of silica from silicic acid is accelerated under these conditions by some of the identified molecules (the 'natSil 1' family of silaffins and long-chain polyamines) but not others (the 'natSil 2' family of silaffins and silacidins).

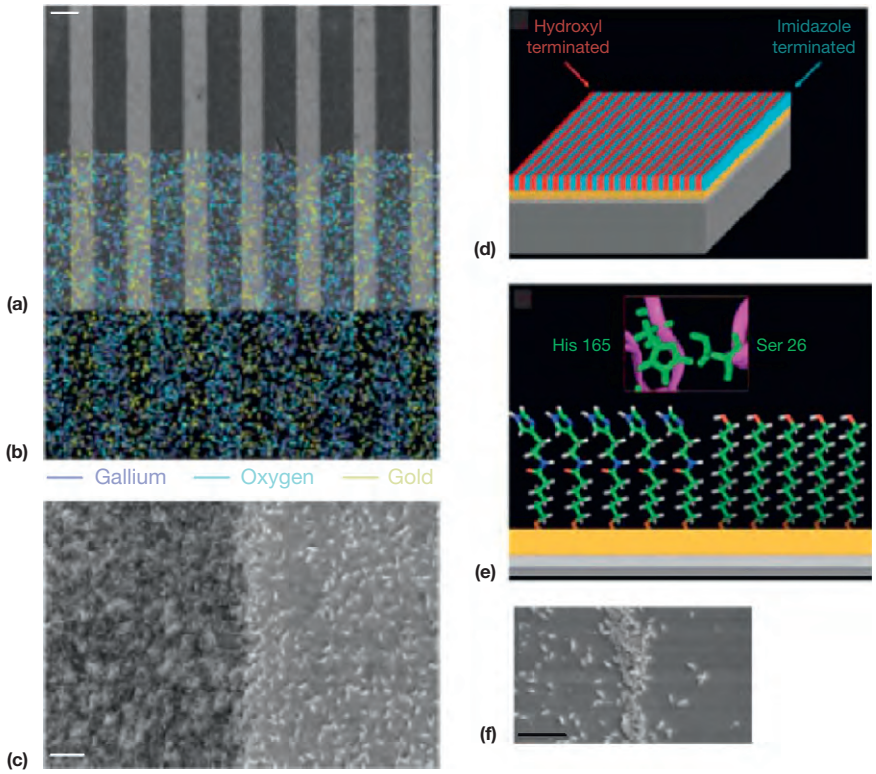

Figure 2 Products formed via catalytic templating from a biomimetic surface. The surface consists of a gold surface patterned with alternating stripes of self-assembled monolayers (SAMs) using hydroxyl- and imidazole-terminated alkane thiols that mimic the catalytic functionalities identified by genetic engineering of the silica-synthesizing enzyme, silicatein. (a) Scanning electron micrograph (SEM) depicting the product formed from the low-temperature hydrolysis and polycondensation of gallium nitrate (scale bar = 10 μm). (b) Energy dispersive X-ray spectroscopy elemental mapping demonstrating that gallium-rich products condensed on the hydroxyl stripes. (c) Higher magnification SEM image showing higher inorganic particle density on the hydroxyl bands, confirming the role of the hydroxyl groups in templating the mineral product. (d) Schematic depiction of the bifunctional SAM geometry. To produce the bifunctionalized SAM surface, a poly(dimethylsiloxane) stamp inked with an alkane thiole (either hydroxyl- or imidazole-terminated) is brought into contact with a gold surface, facilitating transfer by bonding of the thiol to the gold. After the initial printing of the first alkane thiol, the wafer is then immersed in the second alkane thiol solution to form stripes of the second monolayer. (e) Presentation of the essential functionalities required for hydrolysis, similar to those found in silicatein: an imidizole and hydroxyl hydrogen bonding pair. (f) Sample removed after a short reaction time with gallium nitrate demonstrates significantly more condensed product (gallium oxohydroxide) at the hydroxyl-imidiazole interface, with substantially less product away from the interface, supporting the mechanism of catalysis as proposed for the silicatein enzyme. Scale bar = 1 μm. Reprinted with permission from Kisailus, D.; Truong, Q.; Amemiya, Y.; Weaver, J. C.; Morse, D. E. *Proc. Natl. Acad. Sci. USA* **2006**, *103*, 5652–5657. Copyright (2006) National Academy of Sciences, USA.

Certain reaction conditions, including combinations of the different biomolecules or adjustments in the ionic strength of the solution, strengthen or attenuate the efficiency of silicification in a concentration-dependent manner. The first of the identified molecules, natSil 1[47] is rich in glycine, serine, and lysine and decorated with posttranslational modifications that endow the molecule with strongly zwitterionic character, mainly via serine phosphorylation and novel polyalkylamine modification of lysine residues. These posttranslationally modified natSil 1 molecules accelerate silica precipitation from silicic acid whereas analogous nonmodified polypeptides lack this activity under the same conditions.[47] This points to the importance of (bio-) polymer-directed electrostatic interactions in the precipitation of silica from silicic acid. Polyamine units provide multiple positive charges that are thought to act by stabilizing negatively charged prenucleation silica clusters. This proposed biological activity follows a previous investigation where synthetic polyamines were shown to accelerate silicic acid polymerization at neutral pH leading to hybrid organic–inorganic gel network formation.[70] While polyamines are found as posttranslational modifications of natSil 1, other free long-chain polyamines have also been identified in the diatom system, and shown to play an important independent role in accelerating silica precipitation as well.[67] The demonstration that zwitterionic salts facilitate this activity[71] further supports the importance of electrostatic interactions in this process. The additional finding of the natSil 2 class of silaffins[50] and silacidins,[69] which are polyanionic molecules that interact with natSil-1A and long-chain polyamines to form a silica-precipitating organic matrix, further highlighted the role of electrostatically driven interactions in biosilicification. NatSil 2 and silacidins are posttranslationally modified with phosphates, sulfates, or polysaccharides, and do not induce silica precipitation independently; rather, they act to modulate silicification by natSil 1 and long-chain polyamines in a concentration-dependent manner, yielding either enhanced silica yield[69] or unique silica microstructures at different mixture ratios,[50] presumably through controlling the self-assembled structure of the biomolecular matrix.

To begin translating these concepts to bio-inspired strategies, it is beneficial to explore the use of simplified functional elements from this complex system. These have initially been found through the use of the natSil-1-mimetic polypeptide R5[72] and polylysine.[70] Bio-inspired use of the R5 polypeptide is described in more detail in the following section.

2.201.2.3. Bio-inspired Silica Synthesis

Here we briefly describe three precedent-forming biomimetic systems that were further developed for medical applications (detailed in Section 2.201.3). Just as biological systems utilize a wide variety of molecular species in growth and development, from small molecules to extended macromolecular scaffolds, the three systems described here also utilize molecular agents for silicification of disparate sizes and structures: block co-polypeptides,[54] short polypeptides,[47] and small molecules.[51] This molecular diversity indicates that a variety of engineering strategies are available for creating new bio-inspired methods for silica synthesis.

Cha *et al.*[54] studied reactions of homopolypeptides and block co-polypeptides with TEOS, demonstrating that the catalytic, structure-directing and templating features of silicatein could be mimicked in a synthetic system. Scanning different homopolymer compositions for the TEOS reaction confirmed that amino-acid nucleophilicity promoted silica polycondensation: more nucleophilic constituent amino acids tended to produce more mineral silica product. This feature of biocatalytic silicification was suggested by earlier studies of silicatein. Of all the synthetic polypeptides studied, cysteine-lysine block co-polypeptides (closely corresponding to the amino acids identified by genetic engineering as essential constituents of the native enzyme's catalytic active site) produced the most silica, and provided several features of biomimetic control, for both silica yield and structure. Hydrogen bonding between the lysine amine and cysteine sulfhydryl served to increase the nucleophilicity of the TEOS-attacking nucleophile (the sulfhydryl group), just as was proposed to occur at the active site of silicatein (with the hydroxyl of serine serving as the nucleophile).[13,48] The polyamine domains of the copolymer structure also may act to promote clustering between negatively charged hydrolyzed silanol species by reducing electrostatic repulsion and stabilizing prenucleation clusters; this mechanism also has been proposed for polyamine-promoted synthesis of silica from silicic acid in diatoms.[47] It was further found that disulfide-mediated concatenation of the catalytic and structure-directing silicatein-mimetic peptides led to the catalytic synthesis and templating of long fibrilar bundles of silica, whereas blocking this concatenation led to the production of transparent, glassy silica spheres.[54] This co-polypeptide system thus provided structure-directing control of catalytically synthesized silica structures at neutral pH through both chemical and structural engineering of the biomimetic catalytic template. Interestingly, in cysteine-glutamate copolymers, the negatively charged glutamate residues abolished the silica-condensing activity of cysteine, a phenomenon ostensibly similar to the mitigation of natSil 1 silica-condensing activity by negatively charged natSil 2 molecules from diatoms.[50] While only a limited number of biomedical related studies have utilized block co-polypeptide systems directly (see Section 2.201.4.4), this system represents the first bio-inspired silica synthesis study. The results may still provide useful design lessons for the future development of silica structures for applications such as restorative bone, tooth, or other tissue engineering.

Much bio-inspired silica synthesis work stemming from diatom studies has focused on the use of the R5 peptide – a commercially available 19-mer polypeptide that represents a basic repeat-domain of natSil 1.[47] The demonstration of its utility in bio-inspired silica synthesis coincided with the development of related polypeptide-based selection strategies for synthesis of nonoxide material systems,[73–75] substantiating the utility of short polypeptides for biomimetic mineral engineering efforts. The R5 polypeptide is an unmodified version of a sequence that is naturally posttranslationally modified (by serine phosphorylation and lysine polyamination). This peptide has been shown to exhibit silica-condensing activity when reacted with monosilicic acid in phosphate buffer at pH 5.[47] One such use of this peptide involved the production of a holographically patterned polymeric-silica composite structure for photonic applications.[72] Silica- and silicon-based photonic materials synthesized with pulsed HF-etching have found a variety of novel uses in biomedical applications,[76–78] suggesting that there may be future potential for integrating bio-inspired synthetic silica approaches for the development of photonic materials for new therapeutic strategies.

In a later study, R5-accelerated silicification was used to encapsulate enzymes in a solid silica matrix under mild conditions that conserved enzyme function.[79] This approach is characterized by several advantages over alternative strategies for enzyme encapsulation,[80] especially over approaches using traditional silica synthesis strategies, which involve harsh conditions detrimental to the stability and activity of enzymes. Furthermore, this route for enzyme encapsulation in many cases leads to higher enzyme turnover and more stable enzymes that can operate over extended times and temperatures relative to the same enzymes free in solution.[80] Excellent reviews are available detailing developments of enzyme encapsulation via bio-inspired silicification.[24,80] We describe this technology further in Section 2.201.3.3.

The use of small molecules for bio-inspired silica synthesis may provide the most direct link between activity of natural polymers and current industrial systems. Inspired by the genetic engineering that identified the catalytic moieties of the silicatein active site as a nucleophilic group and a hydrogen-bonding amine,[48] the initial block co-polypeptide silicatein-mimetic investigations[54] and the studies of the biomimetic SAMs consistent with these results,[57,58] Roth *et al.*[51] demonstrated that small bifunctional molecules containing both such groups also act as mimics of the enzyme's catalytic site, producing silica from TEOS at neutral pH and low temperature. The most successful of these small bifunctional catalysts, cysteamine, presents a nucleophilic sulfhydryl group and an amine group linked and sterically constrained by a short carbon chain that spaces the two functional groups at a distance apparently optimal for hydrogen bonding. Shorter and longer terminally bifunctional analogs were progressively less active. This sterically determined positioning apparently facilitates catalysis of the alkoxide hydrolysis by a mechanism similar to that proposed for silicatein (and proven for certain homologous hydrolases), in which the nucleophilicity of the active group (oxygen or sulfur) is enhanced by hydrogen bonding to its partner amine.[13] This enhancement is

thought to facilitate nucleophilic attack at precursor silicon centers, facilitating hydrolysis of the alkoxide and subsequent polycondensation. Comparison of the activity of cysteamine to that of other small homologs showed that the immediate chemical environment of the functional moieties had a large impact on the ability to catalyze silica formation from silicon alkoxide precursors; small molecules with more highly substituted amines or weaker nucleophilic groups were less effective than cysteamine. The simple structures and ready availabilities of these small molecules promote their facile integration into applications for bio-inspired silica synthesis. For example, as described in **Section 2.201.3.2**, in the same study demonstrating its catalytic activity, Roth *et al.* demonstrated that cysteamine could be reacted with TMOS (tetramethyl orthosilicate) at neutral pH and low temperature to encapsulate proteins, enzymes, and live cells in silica with micropatterned features – avoiding the exposure to strongly acid or alkaline catalysts typically used for such encapsulations.[51]

We review a selected number of studies demonstrating mild, bio-inspired variations of the Stöber and microemulsion processes in **Section 2.201.4**. Cysteamine itself, while perhaps a strong candidate as a catalyst that can further develop such work, has not yet been used in this capacity. However, the copolymer, polypeptide, and small molecule catalytic systems that have been described in this section represent the kinds of biomimetic studies that will continue to further reveal underlying mechanisms of natural silicification while opening new routes for biocompatible synthetic silica production.

2.201.3. Bio-inspired Silica Synthesis for Biomedical Applications

2.201.3.1. Introduction

Silica-based nanomaterials exhibit high chemical and thermal stability, are easily solubilized in aqueous media, are nontoxic, and are readily synthesized with mesoporous structures or as capsules. Silica nanoparticles are optically transparent, making them highly attractive for encapsulating dyes and contrast agents.[17,81] The presence of a high surface density of silanol groups on silica nanoparticles facilitates their surface functionalization with a number of biologically active molecules, such as peptides, proteins, DNA, linking agents such as biotin and avidin, antigens, and antibodies.[82] These attributes make silica potentially useful for a wide number of medical applications such as drug encapsulation and delivery, biocompatible coatings (such as for implants), sensing, bioassays, and scaffolds for tissue engineering. However, while current silica synthesis procedures allow versatile control of silica nanoparticles, production of silica structures at higher-order length-scales or of more complex morphologies is limited. Thus, recent research to develop silica for medical uses has mainly utilized engineered silica nanoparticles. In this section we review key application areas where the use of silica nanomaterials for medicine has been demonstrated, and we describe relevant nascent efforts to harness bio-inspired silica synthesis methods for these applications. Rather than being exhaustive, we limit our review to four types of biomedical applications: (1) medical imaging, (2) biosensing, (3) drug delivery, and (4) tissue and implant engineering.

2.201.3.2. Silica Nanoparticles for Medical Imaging

In 2009 the U.S. medical-imaging market was worth more than 2 billion dollars,[83] but new report by BCC Research, forecast exponential growth by 2012 reaching $11.4 billion http://www.bccresearch.com/. In such a demanding market, new contrast agents must meet strict performance requirements. An ideal contrast agent must be highly efficient such that its signal resolution is maximized while dosage is minimized; it must be specific, nontoxic, sufficiently stable *in vivo* to avoid too rapid metabolic breakdown, yet its clearance from the body must be rapid after useful labeling has been achieved.

Organic dyes have been the most widely used materials for optical imaging. However, these contrast agents suffer from rapid photobleaching; also, their emission spectra often overlap with autofluorescence from tissues in which fluorophores such as nicotinamide (NAD[H]), flavins, collagen, and elastin are present. Furthermore, numerous photochemical reactions occur in the cellular environment that can lead to photodegradation of the dye. The encapsulation of dyes in an inert and transparent matrix such as silica is the most practical methodology presently in use to maximize both their *in vitro* and *in vivo* stability.[84–86] The fabrication of fluorescent silica nanoparticles with multifunctional features, strong resistance to photobleaching, high quantum yield, high absorbency, emission in the near infrared (NIR) 700–900 nm window, and adequate dispersibility in biological environments are highly useful for medical imaging technologies.[83] The ability of silica to encapsulate optically active molecules and dyes minimizes oxygen access, increases chemical stability, and allows surface modification of the shell to enhance hydrophilic character and cellular uptake. One further advantage of dye encapsulation in silica is the possibility of tuning the luminescence intensity of dye-doped silica nanoparticles as a function of the number of dye molecules doped in the silica matrix. Higher numbers of dye molecules usually lead to a stronger emission signal except at the concentration limit where self-quenching occurs. Luminescence intensity can also be improved by changing the quantum yield or the nanoparticle size.[87]

Wiesner and coworkers[88] have injected dye-doped 30-nm-diameter silica nanoparticles via the mouse tail-vein and monitored the fluorescence signal from the injected nanoparticles over the course of several weeks. No toxicity or abnormalities were evident over the course of the experiments and the particles were excreted via the reticuloendothelial system over the experimental time period. Furthermore, the particles were applied to *in vivo* vascular imaging via multiphoton microscopy (**Figure 3(b)**) and as probes for sentinel lymph node mapping as a demonstration of their applicability to clinically relevant procedures.

As mentioned in the previous section, the most common methods for encapsulating dyes use either the Stöber method[21] or reverse micelle techniques.[82] The Stöber method is often used to synthesize pure silica nanoparticles, and variations of this method have been used to encapsulate dyes within silica nanoparticles.[89] The traditional Stöber method involves the hydrolysis of a silicon alkoxide precursor (such as TEOS) in a mixture of ethanol and aqueous ammonium hydroxide. Silanol and silicic acid species are generated during hydrolysis, and condensation can proceed through

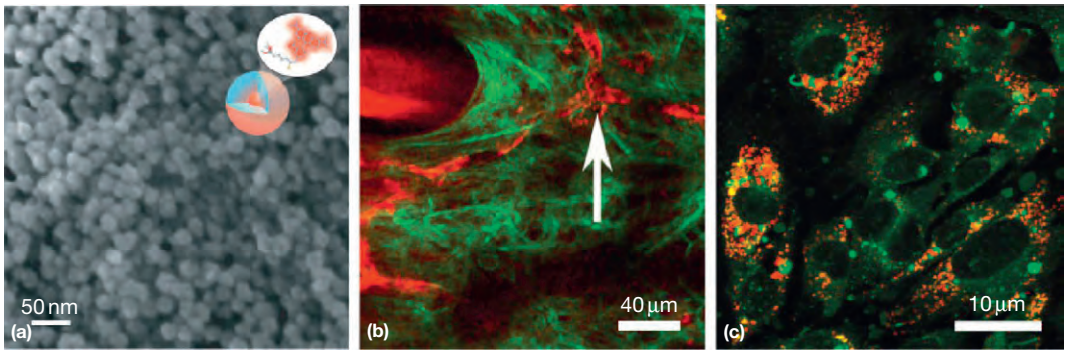

Figure 3 (a) A scanning electron microscopy image of 30-nm-diameter core–shell fluorescent silica nanoparticles comprised of a tetramethylrhodamine dye-rich core with a pure silica shell ('C-dots'), shown schematically in the upper right inset. (b) Intravenous injection of C-dots in mouse shows appreciable fluorescence. *In vivo* multiphoton microscopy of C-dots (red) overlaid on the second harmonic image from collagen autofluorescence (green). Arrow highlights C-dot fluorescence from capillaries. (The red structure in the upper-left is an autofluorescent hair follical.) (c) C-dots surface-functionalized with the TAT-peptide sequence showing significant uptake into mouse prostate carcinoma cells under physiological conditions. Reproduced by permission from Choi, J.; Burns, A. A.; Williams, R. M.; *et al. J. Biomed. Opt.* **2007**, *12*, 064007/1–064007/11. Copyright (2007) SPIE, Bellingham, WA, USA.

either S_N2-type attack of silanol species with prehydrolyzed precursors, or through precipitation of silica from silicic acid when its concentration exceeds its solubility in the ethanol-based solution. The particles obtained using this approach have a diameter between <10 nm and ~1 μm, and are generally nonuniform in size.[82]

Reverse micelle methods represent an alternative yet related approach allowing the synthesis of more monodisperse populations of particles. Reverse micelles, also known as water-in-oil (W/O) microemulsion systems, create thermodynamically stable aggregates of amphiphilic surfactants whose polar head-groups surround nanometer-sized water cores; the hydrophobic tails of the surfactant extend into an apolar continuous phase. The nanodroplets of water in the bulk oil phase act as nanoreactors in which particles form from the hydrolysis and subsequent polycondensation of silane precursors. The diameter of the prepared particles is controlled by the size of the water cores and the water-to-surfactant molar ratio, since the reaction is restricted to the water core. The microemulsion method is usually slower than the Stöber approach (2 days vs. few hours).[82] A basic pH is typically required for the Stöber method; this can interfere with the chemistry of some organic dyes, affecting their luminescence. The Stöber method and its variants have been used successfully to prepare fluorescent silica particles that contain the inorganic dye $[Ru(phen)_3]Cl_2$ yielding mono-dispersed silica nanoparticles; their derivatization with trialkoxysilane and their application as signal amplifiers in bioassays performed on glass slides was reported.[89]

The encapsulation of organic dyes is in some cases complicated due to the high hydrophilicity of the silica matrix and the relatively high hydrophobicity of the dye molecules to be encapsulated. Even after successful loading, dyes tend to leak out of the matrix; this effect can be ameliorated by chemical modification of the dye through covalent linkages to partner molecules or adjustments in the pH of encapsulation.[90] However, at neutral pH generally required for bioanalytical applications, acid-stabilized dyes can readily leak from the silica matrix. Another limitation of synthetic methods commonly used to prepare luminescent silica particles has been the use of large amounts of surfactants in microemulsions, requiring extensive washing for removal from the solid products, and the difficulty in scaling-up this synthesis method to suite industrial needs.[89]

As an alternative method, bio-inspired silica synthesis for dye-encapsulation offers the advantages of being scalable and operable at neutral pH. Roth *et al.*[51] showed the silicatein-mimetic small molecule cysteamine was particularly successful in encapsulating firefly luciferase, green and blue fluorescent proteins (GFPs, BFPs), and *E. coli* cells expressing GFP in silica matrices. The benign conditions used for catalytic synthesis of these silica composites conserved the activities of the encapsulated enzyme, fluorescent proteins, and live cells as shown by fluorescence measurements (**Figure 4**).

In conjunction with microcontact printing, this biomimetically catalyzed encapsulation method was used to produce patterned functional arrays of silica nanoparticulate composite materials.[51] Such an approach may find future application in development of chip implants that change their spectral properties as they degrade or as they release a loaded drug, or that could be imaged using visible light if implanted in transparent media such as the vitreous body of the eye.[91] Alternatively, if NIR, tissue-penetrating spectral features were encapsulated into such a chip, the fixture conceivably could be probed through the skin or through several millimeters of visibly opaque tissue. In an analogous fashion, Li *et al.*[92] demonstrated a drug delivery matrix that could be read through the skin by positioning the main spectral feature of the poly-lactide imprint within the low absorbance, NIR window of human tissue.

2.201.3.3. Silica-Based Nanomaterials for Biosensors

The market for biosensors is reaching $7 billion and the trend is showing constant increase.[93] Large shares of this market are devoted to home-use health monitoring devices (e.g., glucose biosensors and pregnancy test strips), while a number of other applications are growing rapidly; these include food quality assurance, environmental monitoring, industrial process control, and the detection and identification of infectious agents.

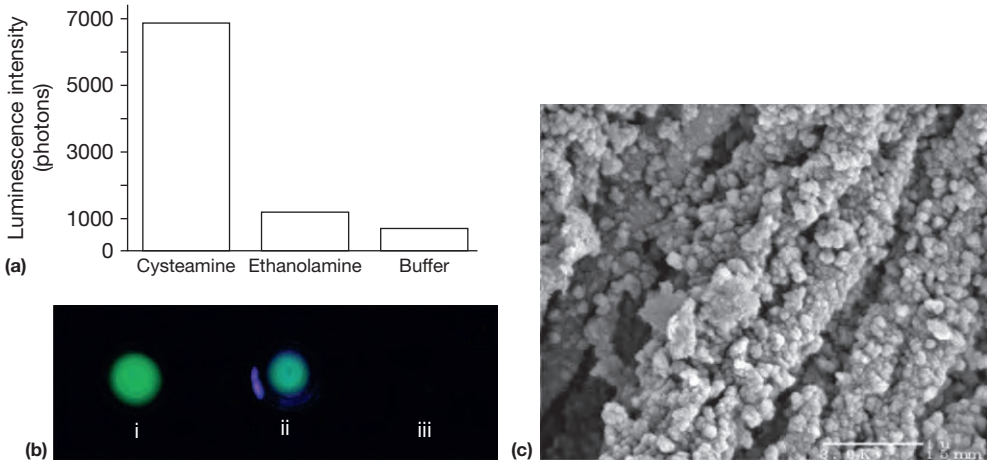

Figure 4 (a) Luminescence intensity produced by silica encapsulated luciferase (enzyme) after addition of luciferin reagent. Silica matrices formed by hydrolysis and polycondensation from silicon alkoxide catalyzed by cysteamine, ethanolamine, or buffer alone. (b) Fluorescent images of green fluorescent protein (GFP) entrapped within silica matrixes formed with (i) cysteamine, (ii) ethanolamine, and (iii) buffer only. (c) Scanning electron micrograph of silica obtained from polycondensation of tetraethyl orthosilicate catalyzed by 10 mM cysteamine. Scale bar = 1 μm. Reproduced by permission from Roth, K. M.; Zhou, Y.; Yang, W.; Morse, D. E. *J. Am. Chem. Soc.* **2005**, *127*, 325–330. Copyright (2005) American Chemical Society, USA.

Like contrast agents, ideal biosensors should be highly sensitive, specific, rapid, and inexpensive. Biosensors usually consist of two components: a highly specific recognition element and a transducer that converts the molecular recognition event into a quantifiable signal.[94] A variety of processes have been investigated to achieve signal transduction including electrochemical processes,[95–98] field-effect transistor processes,[99] and optical processes (absorption, fluorescence, interference).[100–102]

Porous silica-based materials have been employed for building a variety of biosensors using drugs, enzymes, antibodies, and DNA aptamers as recognition elements.[103–105] In such biosensors it is ideal to have well-formed regular pores to ensure quick diffusion of the analytes to the sensing sites. In addition, it is ideal to have a means of control over the rate of diffusion. Radu *et al.*[106] developed an optical biosensor based on mesoporous silica nanoparticles (MSNs). Utilizing a poly(lactic acid) layer as a semipermeable membrane, they spectrophotometrically characterized molecular recognition events between several structurally simple neurotransmitters (dopamine, tyrosine, and glutamic acid) and a pore surface-anchored *o*-phthalic hemithioacetal (OPTA) group that functions as a fluorescence-responsive recognition element that can react with the neurotransmitters through primary amine groups to form the corresponding fluorescent isoindole products. The poly(lactic acid) layer coated on MSNs introduced a unique 'sieving' effect that regulated the rates of diffusion of the amino acid-based neurotransmitters into the sensor mesopores of the silica material.[106]

Glucose biosensors are traditionally comprised of an oxygen electrode, an inner oxygen semipermeable membrane, a thin layer of glucose oxidase (GOx), and an outer dialysis membrane.[107] The outer membrane keeps the enzyme in close proximity to the electrode surface and controls the diffusion of glucose as well as oxygen; the inner membrane allows oxygen to pass while blocking some electroactive interferents from reaching the electrode.[93] GOx catalyzes the oxidation of glucose to gluconolactone while a redox cofactor (e.g., flavin adenine dinucleotide, FAD) is reduced to FADH2. A GOx- and horseradish peroxidase-loaded mesoporous silica material has been used as a selective sensor for glucose detection.[108,109] Myoglobin and hemoglobin were also immobilized in mesoporous silica-modified electrodes for use as sensors for H_2O_2 and NO_2.[110,111] Ren *et al.*[112] described an amperometric glucose biosensor fabricated by the immobilization of GOx in a platinum and silica sol.

As discussed above, bio-inspired silicification reactions recently have been shown to provide a useful tool for the construction of inorganic matrix structures capable of achieving high levels enzyme entrapment without the adverse effects on catalytic activity of the entrapped protein that previously were seen with conventional procedures.[113] Specifically, R5-mediated silica synthesis has been used to encapsulate butyryl cholinesterase,[79] catalase and horseradish peroxidase[114] without any loss of the enzymatic activity. Immobilization of nitrobenzene nitroreductase in silica produced by polyethyleneimine-accelerated silica synthesis[115] and butyryl cholinesterase in silica produced by lysozyme-mediated synthesis[116] has also been reported. (Lysozyme is a member of the hydrolase superfamily of enzymes, and thus related to silicatein.) Recently, a biosensor for organophosphates was created by encapsulating organophosphate hydrolase in a silica matrix directly on a waveguide surface, using surface-bound lysozyme as the biomolecular catalyst for silicification.[117] Due to the neutral pH at which the enzyme-silica layer was synthesized and the enhanced enzyme stability imparted by the encapsulating silica matrix, the resulting biosensor remained active for 60 days. As a wide variety of enzymes have been shown to be amenable to similar stabilizing silica encapsulation,[80] this bio-inspired strategy for developing biosensors may have wide applicability. Further, the catalytic or synthesis accelerating agents for bio-inspired silicification are diverse and amenable to directed modifications (see **Section 2.201.2.3**); such versatility may provide novel routes for integrating silica–enzyme analyte-recognition layers with the signal transduction

components of new biosensors, just as a (transducing-) surface-immobilized biocatalytic element was utilized in the work of Ramanathan *et al.*[117]

2.201.3.4. Silica Nanoparticles for Drug Encapsulation and Delivery

In 2007, the drug delivery market in the United States alone reached $82 billion.[118] With an annual growth rate of 10% the worldwide drug delivery market is expected to garner $700–$800 billion by 2015.[119] Nanomaterial-based drug delivery will play essential roles in site-directed or targeted drug release, to improve therapeutic efficacy and minimize toxicity,[120] and in novel delivery technologies for protein and peptide therapeutics. Any future drug delivery system must provide[121]: (1) *in vitro* and *in vivo* stability, (2) optimized physiological availability, specificity, and efficacy, (3) optimized biological half life, (4) patient convenience facilitating compliance, (5) low dosing frequency, (6) minimal toxicity, (7) minimal unwanted systemic exposure, and (8) optimized product life cycle management.

Advanced drug delivery systems such as micelles, liposomes, and polymeric nanoparticles have been designed over the past four decades that enable more effective drug administration.[118] The major limitation of these systems is their weak thermal and chemical stability and rapid elimination by the immune system.[118] In contrast, silica nanomaterials are potentially convenient drug delivery systems that are nontoxic (depending on size and conditions; see **Section 2.201.4.1**), highly soluble, relatively stable, and capable of encapsulating and transporting the desired guest molecules without significant loss before reaching the targeted location. Various schemes also have been engineered for their release of cargo in a controlled manner.[20,78] These characteristics, in addition to their biocompatibility, make them highly desirable as drug vectors, especially for toxic drugs that require low release before reaching the targeted cells or tissues. Furthermore, silica displays an advantageous balance between stability and degradability that makes it a useful drug delivery vector.

As an example of the utility of silica for drug delivery, MSNs surface functionalized with amino groups were used for *in vivo* gene delivery to the brain of a mouse.[29,122] Furthermore, *in vitro* cell targeting drug delivery studies using silica nanoparticles as carrier systems have been reported recently where the nanoparticles were conjugated to site-specific recognition element such as folic acid (targeting folate receptors)[123] and RGD (arginine-glycine-aspartate) peptides (which target integrin cell adhesion molecules displayed from cellular membranes).[124] Monoclonal antibody-functionalized MSNs for selective targeting of breast cancer cells have also been reported.[125] Novel organic–inorganic nanospheres formed by a hybrid organosilica shell and an internal liposomal core containing bioactive molecules such as doxorubicin have been successfully synthesized.[126] The external shell includes labile silsesquioxane linkers containing ester functional groups and provides stability to the system at the typical pH value of the blood stream (pH 7.5), but the ester groups are broken within the glioma cells, thereby liberating the drug.[126]

The above examples demonstrate that surface functionalized mesoporous silica materials provide an improved capacity for site-specific targeting of drug cargo. Release can be controlled either by physical (e.g., the size and morphology of the pores) or chemical means (such as disulfide-reduction, photochemical, or redox reactions).[20] External stimuli such as magnetic fields have also been used to release the drug cargo from mesoporous silica previously embedded with superparamagnetic nanoparticles. Macromolecules such as low generation polyamidoamine (PAMAM) dendrimers have also been used to cap the pores of mesoporous silica, providing a double drug delivery system (where both PAMAM and silica can carry and release distinct drug cargos).[20] One of the most commonly used approaches to release drug cargo is based on differential pH. Sailor and coworker[78] recently used chitosan hydrogel-capped porous SiO_2 as a pH responsive nano-valve for triggered release of insulin. In another recent example, investigators loaded small cargo molecules into hollow silica nanoparticles with mesoporous walls and sealed the pore openings with chemical nanovalves constructed on the nanoparticle surfaces.[127] Nanovalve design was based on cyclodextrin capping agents that were complexed to surface-anchored anilinoalkane stalks that disassembled in a pH-triggered manner.

The hollow, MSNs in the study of Du *et al.*[127] were synthesized using an alkaneamine template that is proposed to self-assemble around cotemplates of spherical micelles formed from poly(vinylpyrrolidone). This strategy suggests a general synergistic and sometimes subtle relationship between conventional silica syntheses and bio-inspired approaches. The alkaneamine template molecule closely mimics the alkylamine backbone of long-chain polyamines found in diatoms[53]; its use thus obviates the need for acid or base accelerators of silica precipitation. In fact, mesoporous silica has been produced in a wide variety of structures and morphologies, using many unique organic-molecule templating strategies,[54,128,129] many of which are biomimetic strategies.[130–132] It is not surprising that similarity emerges between synthetic and biological methods of silicification as new synthetic approaches begin to permit construction of more complex silica structures. The parallel progress in conventional and bio-inspired silica synthesis strategies will presumably continue to reveal further complementary principles as increasingly complex silica structures become achievable. To specifically design these structures for biomedical applications, there is strong incentive to remain aware of progressive research elucidating natural silicification so that the most biologically compatible synthetic strategies can be developed. For example, mesoporous silica structures have recently been identified in marine sponges.[133] Subsequent mechanistic investigations on the formation of this natural mesoporous silica might inform and inspire the development of novel, biocompatible synthetic approaches for constructing mesoporous silica for drug delivery applications. We further discuss the complementary relationship between conventional and bio-inspired silica syntheses in **Section 2.201.4.2**.

2.201.3.5. Silica-Based Nanomaterials for Implants and Tissue Engineering

Current demand for tissue engineering therapy is staggering both in scope and cost. By one estimate Americans spend ~$400 billion a year on treating some type of tissue loss or end-stage organ failure.[134] Each year 20 000 organ transplants, 500 000 joint replacements, and millions of dental and oral

craniofacial procedures, ranging from tooth restorations to major reconstruction of facial soft and mineralized tissues take place in the United States alone.[134]

Incorporation of biomimetic concepts with the methods of nanotechnology will enable the development of materials that mimic structural components of biological tissues in synthetic materials needed for various implant applications. In comparison to smooth surfaces, those with nanoscale features have been shown to promote better adsorption of proteins that are necessary to mediate cell adhesion and subsequent tissue regrowth.[135] But more than the surface topology alone, surface chemistry has been shown to be equally important.[136] Combining both of these advantageous features, surfaces and coatings that incorporate features resembling those made by biomineralization show great potential for implant and tissue repair – in part because these biomimetic substrates and surfaces can be quickly integrated and remodeled by cells *in vivo*.[135] Silica has been used successfully as an osteogenic scaffold material in tissue engineering of bone and cartilage; efficacious forms include bioactive glasses and composite materials.[137–142] Of equal importance to the biocompatibility of silica for these applications is the fact that it is progressively dissolved and replaced by the body's own biominerals, providing temporary stability while serving as a sacrificial osteogenic template.[141,143–145] Building on the promising results thus far, there is an increasing demand to improve these materials for their use in bone replacement and tissue engineering.

A high-performing implant material should be lightweight, reliable, durable, mechanically robust, and biologically responsive. Biological tissues possess hierarchically organized structures that facilitate optimum fluid transfer and healing, and exhibit remarkable biomechanical properties that are difficult to replicate. Bio-inspired approaches are thus of interest for producing materials to mimic, match, and be effectively integrated with natural systems without inducing the rejection or toxicity currently encountered with many implants. Living tissues usually display several types of responses to traditional implants[146]: (1) if the material is toxic, the surrounding tissue dies; (2) if the material is nontoxic and dissolves, the surrounding tissue replaces it; (3) if the material is nontoxic and biologically inactive, a fibrous tissue capsule of variable thickness forms; and (4) if the material is nontoxic and biologically 'active,' interfacial bonds may form.

The use of biomimetically formed silica can provide suitable coatings on metal implants to increase their biocompatibility and to provide reactive surfaces for the conjugation of specific molecules (oligopeptides, etc.) that act as potent recognition signals governing the deposition and attachment of extracellular matrix glycoproteins and the attachment of specific cell types.[147,148] Similar approaches may be advantageous for bone and dental tissue replacements as such strategies that allow the formation of bioactive coatings under mild *in vivo* conditions.[149–151] Thus, Schröder *et al.*[152] reported that mineralization (formation of calcium phosphate) by human osteosarcoma (bone tumor) cells is markedly increased when grown on culture plates precoated with silicatein and type 1 collagen and subsequently modified with biosilica via reaction with the silica precursor, TEOS (**Figure 5**).

Silicatein or its biomimetics also may provide a promising approach for producing silica coatings on titanium, titanium alloys, and CoCr implants used in surgery.[152] These results indicate that surfaces modified by silicatein-catalyzed silica formation are bioactive and enhance osteoblast function. Such surfaces may be of interest for tissue engineering or coatings of medical implants to promote new bone formation, as suggested in **Figure 5**.[152,193] In dentistry, silica-based bioactive coatings may open new possibilities for novel restorative materials, sealing of dentin tubules, controlling material–tooth interphases, and promoting mineralization along implant surfaces.[151,153]

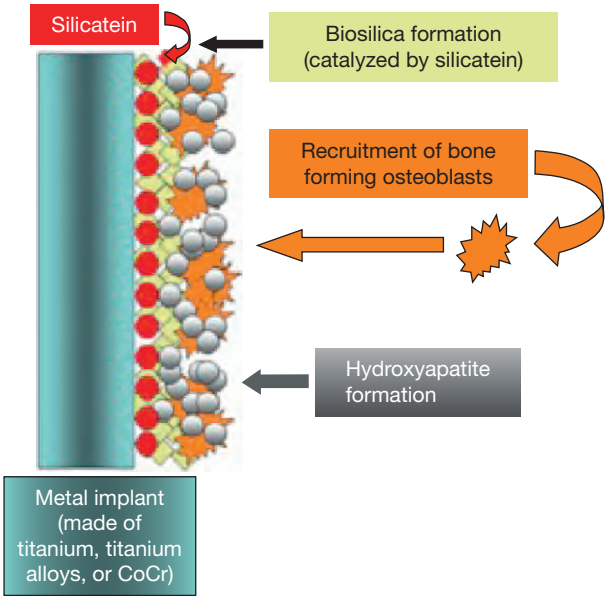

Figure 5 Scheme showing recruitment of bone-forming cells (osteoblasts) and formation of hydroxyapatite on a metal surface activated by the silicatein-catalyzed formation of a silica coating. Reproduced from Schröder, H. C.; Schlossmache, U.; Boreiko, A.; *et al.* In *Progress in Molecular and Subcellular Biology*; Müller, W. E. G., Grachev, M. A., Eds.; Springer: Berlin, 2009; Vol. 47, pp 251–273, DOI: 10.1007/978-3-540-88552-8, with kind permission of Springer Science+Business Media.

While silicatein-catalyzed silica formation has been used to demonstrate the utility of biocatalytic silica synthesis for implant coatings, the diversity of bio-inspired and biomimetic strategies available for silica synthesis can be expected to lead to additional and more readily controlled routes for producing silica-based bioactive implant coatings. Furthermore, many natural biosilica structures display impressive examples of hierarchical structure with unique mechanical advantages.[27] In the following section we review a number of studies that have begun to mimic natural design features that allow such higher-order mineral structures to be fabricated, and that have implications for the future development of more sophisticated biocompatible mineral implant materials.

2.201.4. Perspectives and Challenges

One of the ultimate goals of using bio-inspired synthesis for nanomaterials is to open new biomedical pathways while

improving existing ones. As the ability to control formation of silica structures under mild conditions continues to develop, considering the ease of integration of silica into composite structures, and its amenability to surface functionalization and its biocompatibility, we anticipate that more areas of medicine will be impacted by bio-inspired silica synthesis-based nanotechnology. However, paths to innovation will require concerted interdisciplinary research efforts. Here we describe challenges and opportunities in the following four areas: (1) biocompatibility, (2) new synthesis strategies, (3) genetic engineering, and (4) hierarchical design.

2.201.4.1. Silica Biocompatibility

Although silica is widely considered to have excellent biocompatibility, and has been 'generally recognized as safe' by the US Food and Drug Administration,[17] recent studies revealed evidence of toxicity in some nonoptimally designed cases.[18,154–156,192] Toxicity effects in these studies were found to depend on a number of parameters, including the size, morphology, porosity, surface chemistry, and dosage of the silica particles, and (in mice or rats) the location and manner of their physiological introduction. Studies showing desirable biocompatibility and nontoxicity of functional silica nanoparticles[157–160] indicate that it is possible to optimize these parameters for silica materials and thus avoid the calamitous lessons of asbestosis and silicosis. Bio-inspired silica synthesis routes can be used advantageously to reduce human cytotoxicity and improve biocompatibility both through implementation of benign synthetic conditions and through the resulting enhanced control over composite silica structure.

2.201.4.2. Novel Bio-inspired Silica Synthesis

Efforts to introduce bio-inspired modifications to the Stöber and microemulsion synthesis methods have already begun. For example, several studies have produced uniform silica nanoparticles (<12 nm) employing basic amino acids (lysine and arginine) in place of ammonia as the catalyst.[161,162] These syntheses did not require an alcohol solvent and were performed in the relatively mild pH range of 9–10 (vs. the conventional pH range for Stöber silica synthesis, 11–12). Using a cyclic amine as a bio-inspired catalyst, Masse *et al.*[163] produced unique core-shell silica nanoparticle structures with a granular core (templated onto the molecular catalyst) and a surrounding smooth silica outer layer, though this work was done at pH 12. Employing a microemulsion approach, Jin *et al.*[87] showed that silica nanoparticle sizes could be adjusted in the size range of 20–100 nm by varying the alkane chain length of the alcohol solvent phase. Such efforts may be interpreted as providing a controllable *in vitro* analogue to biomembrane permutations in compartmentalized biomineralization. In a related study, Bauer *et al.*[164] used a branched polyamine as a silicification accelerator from silicic acid in reverse micelles to obtain microscale silica particles at a range of pHs from neutral to basic. By changing the surfactant concentrations, they were able to produce hollow silica spheres up to several microns in size.

In addition to such studies developing milder conditions or better structural control, related chemical and physical investigations are further elucidating the basic mechanism of silica formation. For example, in their study showing the synthesis and stabilization of silica in organic nonalcoholic media using primary amines as catalysts, El Hawi *et al.*[165] used NMR to elucidate the molecular configuration of the coordination sphere of silica nuclei at early times during condensation. Their results showed that the relative physical proximity between the solvent, catalyst, and silicon Q sites are solvent-dependent and help determine the resulting nanoparticle sizes. Exploring another silica growth parameter with implications for both biomineralization and new bio-inspired synthetic strategies, Nozawa *et al.*[166] adjusted the conventional Stöber process by progressively adding TEOS to the solution during the reaction, in a manner that may be analogous to the controlled entry of silica precursors into biological silica mineralization vesicles. This progressive introduction of precursor led to the formation of monodisperse silica spheres up to 2 μm, significantly extending the size-limit of particles that can be synthesized with the Stöber method. As these and new bio-inspired silica synthesis strategies are further developed, and as the field of nanomedicine grows, there is a strong likelihood that one or more facile, biocompatible, and industrially scalable processes will emerge as a drivers for the development of next-generation biomedical devices, just as lessons from silicatein have led to the bio-inspired development of a new low-temperature synthesis method for a variety of nanostructured inorganics with applications ranging from batteries to infrared devices.[23,167–169]

2.201.4.3. Genetically Engineering Silica Biomaterials

Future genetic work with biomolecular catalysts of silicification is also likely to open the door to exciting new technologies for nanomedicine. The discovery that the interface between the inorganic world of silicon and the biopolymers that control siloxane polycondensation includes dynamic catalysts related to well-known and readily cloned enzymes offers prospects for biotechnological control that were previously unimagined. The importance of enzymes for the production of pharmaceutical, biotechnological, and industrial products,[170] their unique chemical versatility, and their relevance for understanding disease and developing novel therapeutics have driven the creation of a variety of enzyme engineering methodologies.[171–178] The possibility for reengineering silicatein or related enzymes for biomedical applications is highly appealing. Novel enzyme engineering methodologies might be advanced to screen libraries of genetically encoded, combinatorially altered silica-synthesizing enzymes for variants with specialized activities, such as the ability to synthesize silica-drug composites with defined sizes, dissolution rates and surface features, for example. While realization of such enzyme-enabled genetic tuning of biosilica properties will require significant advances in several fields, work showing that short polypeptides can be evolutionarily selected *in vitro* for mineral binding[179] and synthesis[10,74,75] (including silica synthesis[180]) suggests that such developments may be imminent. The opportunity to genetically evolve different mineral systems in this way could enable application in each of the four areas reviewed in Section 2.201.3 (imaging, biosensing, drug delivery, and tissue and implant engineering). Of these, one of the most dramatic new applications would be in the area of tissue and implant

engineering. *In vivo* mineralization catalyzed by appropriately engineered enzymes could stimulate bone or tooth growth in a site-specific, directed manner.

2.201.4.4. Hierarchical Design of Silica-Based Next Generation Implants

Shape-engineered nanomaterials are highly desirable for numerous biomedical applications.[181] New synthetic strategies are now being developed that move in this direction. Studies using either a ternary surfactant[182] or a self-assembling polypeptide[183] as the molecular templating element showed that silica helices[182] or centimeter-long, double-walled silica nanotubes could be synthesized by this approach.[183] Pouget *et al.* proposed a synthesis mechanism whereby polypeptide template self-assembly and mineralization proceed in a synergistic manner, driven by electrostatic interactions between the polypeptide monomers and the silica monomers. In related work employing a variety of biomimetic strategies, complex hierarchical silica-polymer composite mesostructures were produced using a shape-directing block copolymers system to assemble silica nanoparticles, followed by selected disassembly of the nanoparticles induced through swelling of one of the polymer phases.[184] These examples illustrate work that begins to mimic the multi-length-scale structural complexity observed in natural biosilica components, and thus may provide a starting point for designing more complex tissue scaffolds and silica implant materials (**Figure 6**).

While lessons learned from natural biominerals are likely to lead to advances in bone and dental tissue engineering, biomimetic strategies for engineering silica- and silicon-based materials may also contribute to engineering soft tissues. The medical device industry is moving from permanently implanted prostheses (based largely on metals and commonly used engineering plastics) to the development of a wide range of safe and effective biocompatible and biodegradable tissue scaffolds.[185] Thus, silicone polymers, elastomers, oligomers, and gels have been utilized in various biomedical applications including implants over the past several decades.[186] The finding that the silicateins can be harnessed to produce synthetic silsesquioxane (silicone) polymer networks *in vitro*[13,48] suggests there may be promise for adapting biomolecular mechanisms to develop new, environmentally benign routes for the synthesis of high-performance biocompatible polymeric implants materials. The demonstration that silicatein can also be used to catalyze polymerization of completely organic materials such as polylactides[187,188] further supports the prospect that new routes for synthesizing soft tissue biomaterials, such as function-specific, tailored, and biodegradable lactide-silicone and related complex polymer scaffolds, may be accessible through enzymatic strategies.

2.201.5. Conclusion

Technologies based on inorganic nanomaterials will increasingly become integrated with human health through devices implanted or circulating in the body to boost health and performance, to treat disease and to repair tissues and organs. By some estimates this merging will be seen to accelerate over the next two decades.[189] This vision, and the related revolution in nanomedicine, will require biocompatible, cheap, and scalable materials such as the silica-based nanomaterials discussed here. Silicon biotechnology has begun to reveal the proteins, genes, and molecular mechanisms controlling the biological

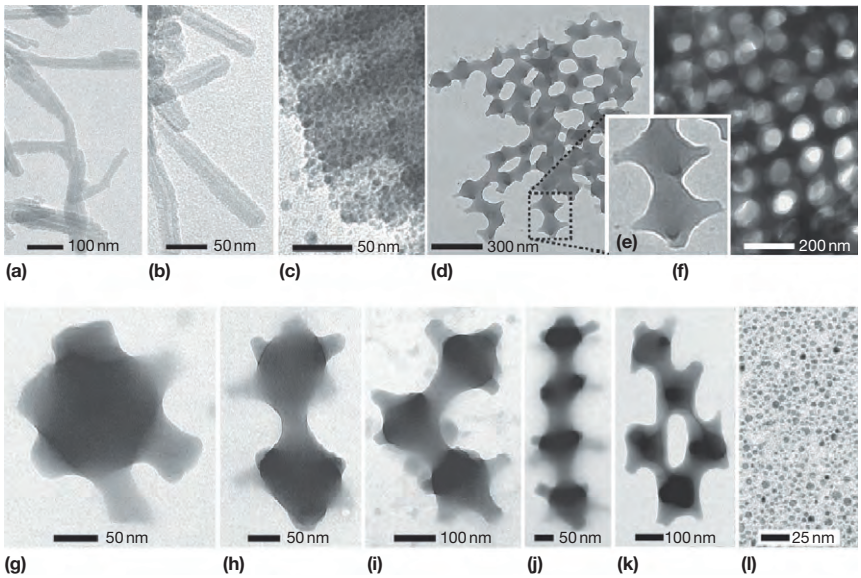

Figure 6 TEM images of a complex hybrid mesoporous silica mimicking features of natural biosilica structures, synthesized by assembly of silica nanoparticles on a shape-directing block co-polypeptide template with subsequent selected disassembly of silica nanoparticles. (a, b) Nanotubes formed during disassembly in toluene. (c) A partially disassembled mesostructure formed during disassembly in pentane in which the nanoparticles within the silica-rich walls are visible. (d–l) A structure consisting of silica-rich channels connected by sixfold nodes (d–f) and the subsequent disassembly into structural building units (g–l). The structural building units include monomers (g), dimers (h), trimers (i), tetramers (j), and pentamers (k), as well as individual nanoparticles (l). Reproduced with permission from Warren, S. C.; Disalvo, J. F.; Wiesner, U. *Nat. Mater.* **2007**, *6*, 156–161. Copyright (2007) Nature Publishing Group, USA.

nanofabrication of silicon-based materials.[190,191] The ability to translate these insights to new bio-inspired approaches for synthesizing silica-based composites holds large promise for advancing capabilities in medical diagnostics and therapeutics. Silica nanostructures created via current industrial strategies have already constructively impacted medical imaging, biosensing, drug delivery, and implant engineering. Further developments in each of these areas may be significantly accelerated by genetically engineered routes for silica synthesis. Collectively these advances will allow us to emulate nature by successfully integrating important biomolecular and pharmaceutical agents with functional silica structures in living systems.

Acknowledgment

This work was supported in part by grants from the US Army Research Office (through contract no. W911NF-09-D-0001 to the Institute for Collaborative Biotechnologies) and the US Department of Energy (grant # DE-FG02-02ER46006). L. Bawazer was supported by University of California Biotechnology Research and Education Program GREAT (Graduate Research and Education in Adaptive Bio-Technology) training grant #2007-17.

References

1. Niemeyer, C. M. *Angew. Chem. Int. Ed.* **2001**, *40*, 4128–4158.
2. De Yoreo, J. J.; Dove, P. M. *Science (Washington, DC)* **2004**, *306*, 1301–1302.
3. De Yoreo, J. J.; Wierzbicki, A.; Dove, P. M. *CrystEngComm* **2007**, *9*, 1144–1152.
4. Mann, S. In *Biomineralization: Principles and Concepts in Bioinorganic Materials Chemistry*, Oxford University Press: Oxford, 2001; p 240.
5. Sigel, A.; Sigel, H.; Sigel, R. K. O. *Biomineralization: From Nature to Application*. Wiley: New York, 2008.
6. Weiner, S.; Addadi, L. *J. Mater. Chem.* **1997**, *7*, 689–702.
7. Weiner, S.; Sagi, I.; Addadi, L. *Science (Washington, DC)* **2005**, *309*, 1027–1028.
8. Fu, G.; Valiyaveetil, S.; Wopenka, B.; Morse, D. E. *Biomacromolecules* **2005**, *6*(3), 1289–1298.
9. Aizenberg, J.; Muller, D. A.; Grazul, J. L.; Hamann, D. R. *Science (Washington, DC)* **2003**, *299*, 1205–1208.
10. Belcher, A. M.; Wu, X. H.; Christensen, R. J.; Hansma, P. K.; Stucky, G. D.; Morse, D. E. *Nature (London)* **1996**, *381*, 56–58.
11. Fantner, G. E.; Hassenkam, T.; Kindt, J. H.; *et al. Nat. Mater.* **2005**, *4*, 612–616.
12. Mandernack, K. W.; Bazylinski, D. A.; Shanks, W. C., III; Bullen, T. D. *Science (Washington, DC)* **1999**, *285*, 1892–1896.
13. Cha, J. N.; Shimizu, K.; Zhou, Y.; *et al. Proc. Natl. Acad. Sci. USA* **1999**, *96*, 361–365.
14. Shimizu, K.; Cha, J.; Stucky, G. D.; Morse, D. E. *Proc. Natl. Acad. Sci. USA* **1998**, *95*, 6234–6238.
15. Weaver, J. C.; Morse, D. E. *Microsc. Res. Tech.* **2003**, *62*, 356–367.
16. Lin Victor, S. Y. *Nat. Mater.* **2009**, *8*, 252–253.
17. Piao, Y.; Burns, A.; Kim, J.; Wiesner, U.; Hyeon, T. *Adv. Funct. Mater.* **2008**, *18*, 3745–3758.
18. Hudson, S. P.; Padera, R. F.; Langer, R.; Kohane, D. S. *Biomaterials* **2008**, *29*, 4045–4055.
19. Giri, S.; Trewyn, B. G.; Lin, V. S. Y. *Nanomedicine (London, UK)* **2007**, *2*, 99–111.
20. Slowing, I. I.; Trewyn, B. G.; Giri, S.; Lin, V. S. Y. *Adv. Funct. Mater.* **2007**, *17*, 1225–1236.
21. Stoeber, W.; Fink, A.; Bohn, E. *J. Colloid Interface Sci.* **1968**, *26*, 62–69.
22. Osseo-Asare, K.; Arriagada, F. J. *Colloids Surf.* **1990**, *50*, 321–339.
23. Brutchey, R. L.; Morse, D. E. *Chem. Rev. (Washington, DC)* **2008**, *108*, 4915–4934.
24. Dickerson, M. B.; Sandhage, K. H.; Naik, R. R. *Chem. Rev. (Washington, DC)* **2008**, *108*, 4935–4978.
25. Meldrum, F. C.; Colfen, H. *Chem. Rev.* **2008**, *108*, 4332–4432.
26. Currie, H. A.; Perry, C. C. *Ann. Bot. (Oxford, UK)* **2007**, *100*, 1383–1389.
27. Aizenberg, J.; Weaver, J. C.; Thanawala, M. S.; Sundar, V. C.; Morse, D. E.; Fratzl, P. *Science (Washington, DC)* **2005**, *309*, 275–278.
28. Miserez, A.; Weaver, J. C.; Thurner, P. J.; *et al. Adv. Funct. Mater.* **2008**, *18*, 1241–1248.
29. Walter, S. L.; Flinn, B. D.; Mayer, G. *Acta Biomater.* **2007**, *3*, 377–382.
30. Walter, S. L.; Flinn, B. D.; Mayer, G. *Mater. Sci. Eng. C* **2007**, *27*, 570–574.
31. Cattaneo-Vietti, R.; Bavestrello, G.; Cerrano, C.; *et al. Nature (London)* **1996**, *383*, 397–398.
32. Sundar, V. C.; Yablon, A. D.; Grazul, J. L.; Ilan, M.; Aizenberg, J. *Nature* **2003**, *424*, 899–900.
33. Müller, W. E. G.; Wang, X.; Kropf, K.; *et al. Cell Tissue Res.* **2008**, *333*, 339–351.
34. Wang, X.; Boreiko, A.; Schlossmacher, U.; *et al. J. Struct. Biol.* **2008**, *164*, 270–280.
35. Davis, A. K.; Hildebrand, M. *Met. Ions Life Sci.* **2008**, *4*, 255–294.
36. Leys, S. P.; Mackie, G. O.; Reiswig, H. M. *Adv. Mar. Biol.* **2007**, *52*, 1–145.
37. Simpson, T. L.; Vaccaro, C. A. *J. Ultrastruct. Res.* **1974**, *47*, 296–309.
38. Hildebrand, M.; Dahlin, K.; Volcani, B. E. *Mol. Gen. Genet.* **1998**, *260*, 480–486.
39. Martin-Jezequel, V.; Hildebrand, M.; Brzezinski, M. A. *J. Phycol.* **2000**, *36*, 821–840.
40. Thamatrakoln, K.; Alverson, A. J.; Hildebrand, M. *J. Phycol.* **2006**, *42*, 822–834.
41. Schroder, H. C.; Perovic-Ottstadt, S.; Wiens, M.; Batel, R.; Muller Isabel, M.; Muller Werner, E. G. *Cell Tissue Res.* **2004**, *316*, 271–280.
42. Schröder, H. C.; Natalio, F.; Shukoor, I.; *et al. J. Struct. Biol.* **2007**, *159*, 325–334.
43. Lopez, P. J.; Descles, J.; Allen, A. E.; Bowler, C. *Curr. Opin. Biotechnol.* **2005**, *16*, 180–186.
44. Lopez, P. J.; Gautier, C.; Livage, J.; Coradin, T. *Curr. Nanosci.* **2005**, *1*, 73–83.
45. Mugnaioli, E.; Natalio, F.; Schlossmacher, U.; Wang, X.; Müller, W. E. G.; Kolb, U. *ChemBioChem* **2009**, *10*, 683–689.
46. Reimann, B. E. F. *Exp. Cell Res.* **1964**, *34*, 605–608.
47. Kroger, N.; Deutzmann, R.; Sumper, M. *Science (Washington, DC)* **1999**, *286*, 1129–1132.
48. Zhou, Y.; Shimizu, K.; Cha, J. N.; Stucky, G. D.; Morse, D. E. *Angew. Chem. Int. Ed.* **1999**, *38*, 780–782.
49. Kisailus, D.; Choi, J. H.; Weaver, J. C.; Yang, W.; Morse, D. E. *Adv. Mater. (Weinheim, Ger.)* **2005**, *17*, 314–318.
50. Poulsen, N.; Sumper, M.; Kröger, N. *Proc. Natl. Acad. Sci. USA* **2003**, *100*, 12075–12080.
51. Roth, K. M.; Zhou, Y.; Yang, W.; Morse, D. E. *J. Am. Chem. Soc.* **2005**, *127*, 325–330.
52. Sumerel, J. L.; Morse, D. E. *Prog. Mol. Subcell. Biol.* **2003**, *33*, 223–247.
53. Sumper, M.; Kröger, N. *J. Mater. Chem.* **2004**, *14*, 2059–2065.
54. Cha, J. N.; Stucky, G. D.; Morse, D. E.; Deming, T. J. *Nature (London)* **2000**, *403*, 289–292.
55. Schröder, H. C.; Wang, X.; Tremel, W.; Ushijima, H.; Müller, W. E. G. *Nat. Prod. Rep.* **2008**, *25*, 455–474.
56. Murr, M. M.; Morse, D. E. *Proc. Natl. Acad. Sci. USA* **2005**, *102*, 11657–11662.
57. Kisailus, D.; Najarian, M.; Weaver, J. C.; Morse, D. E. *Adv. Mater. (Weinheim, Ger.)* **2005**, *17*, 1234–1239.
58. Kisailus, D.; Truong, Q.; Amemiya, Y.; Weaver, J. C.; Morse, D. E. *Proc. Natl. Acad. Sci. USA* **2006**, *103*, 5652–5657.
59. Fairhead, M.; Johnson, K. A.; Kowatz, T.; *et al. Chem. Commun. (Cambridge, UK)* **2008**, 1765–1767.
60. Murr, M. M.; Thakurb, G. S.; Li, Y.; Tsurutad, H.; Mezic, I.; Morse, D. E. *Nanotoday* **2009**, *4*, 116–124.
61. Adamson, D. H.; Dabbs, D. M.; Pacheco, C. R.; Giotto, M. V.; Morse, D. E.; Aksay, I. A. *Macromolecules (Washington, DC)* **2007**, *40*, 5710–5717.
62. Reimann, B. E.; Volcani, B. E. *J. Ultrastruct. Res.* **1967**, *21*, 182–193.
63. Reimann, B. E. F.; Lewin, J. C.; Volcani, B. E. *J. Cell Biol.* **1965**, *24*, 39–55.
64. Simpson, T. L., Volcani, B. E., Eds. In *Silicon and Siliceous Structures in Biological Systems*; Springer: New York, 1981; p 587.
65. Armbrust, E. V.; Berges, J. A.; Bowler, C.; *et al. Science (Washington, DC)* **2004**, *306*, 79–86.
66. Kröger, N.; Lorenz, S.; Brunner, E.; Sumper, M. *Science (Washington, DC)* **2002**, *298*, 584–586.
67. Kroger, N.; Deutzmann, R.; Bergsdorf, C.; Sumper, M. *Proc. Natl. Acad. Sci. USA* **2000**, *97*, 14133–14138.
68. Kroger, N.; Deutzmann, R.; Sumper, M. *J. Biol. Chem.* **2001**, *276*, 26066–26070.
69. Wenzl, S.; Hett, R.; Richthammer, P.; Sumper, M. *Angew. Chem.* **2008**, *47*, 1729–1732.

70. Mizutani, T.; Nagase, H.; Fujiwara, N.; Ogoshi, H. *Bull. Chem. Soc. Jpn.* **1998**, *71*, 2017–2022.
71. Sumper, M.; Lorenz, S.; Brunner, E. *Angew. Chem. Int. Ed.* **2003**, *42*, 5192–5195.
72. Brott, L. L.; Naik, R. R.; Pikas, D. J.; *et al. Nature* **2001**, *413*, 291–293.
73. Lee, S.-W.; Mao, C.; Flynn Christine, E.; Belcher Angela, M. *Science* **2002**, *296*, 892–895.
74. Mao, C.; Solis, D. J.; Reiss, B. D.; *et al. Science (Washington, DC)* **2004**, *303*, 213–217.
75. Whaley, S. R.; English, D. S.; Hu, E. L.; Barbara, P. F.; Belcher, A. M. *Nature* **2000**, *405*, 665–668.
76. Alvarez, S. D.; Derfus, A. M.; Schwartz, M. P.; Bhatia, S. N.; Sailor, M. J. *Biomaterials* **2008**, *30*, 26–34.
77. Alvarez, S. D.; Schwartz, M. P.; Migliori, B.; Rang, C. U.; Chao, L.; Sailor, M. J. *Phys. Status Solidi A* **2007**, *204*, 1439–1443.
78. Wu, J.; Sailor, M. J. *Adv. Funct. Mater.* **2009**, *19*, 733–741.
79. Luckarift, H. R.; Spain, J. C.; Naik, R. R.; Stone, M. O. *Nat. Biotechnol.* **2004**, *22*, 211–213.
80. Betancor, L.; Luckarift, H. R. *Trends Biotechnol.* **2008**, *26*, 566–572.
81. Corr, S. A.; Rakovich, Y. P.; Gun'ko, Y. K. *Nanoscale Res. Lett.* **2008**, *3*, 87–104.
82. Knopp, D.; Tang, D.; Niessner, R. *Anal. Chim. Acta* **2009**, *647*, 14–30.
83. Sharma, P.; Brown, S.; Walter, G.; Santra, S.; Moudgil, B. *Adv. Colloid Interface Sci.* **2006**, *123–126*, 471–485.
84. Bagwe, R. P.; Yang, C.; Hilliard, L. R.; Tan, W. *Langmuir* **2004**, *20*, 8336–8342.
85. Santra, S.; Bagwe, R. P.; Dutta, D.; *et al. Adv. Mater. (Weinheim, Ger.)* **2005**, *17*, 2165–2169.
86. Tapec, R.; Zhao, X. J.; Tan, W. *J. Nanosci. Nanotechnol.* **2002**, *2*, 405–409.
87. Jin, Y.; Lohstreter, S.; Pierce, D. T.; *et al. Chem. Mater.* **2008**, *20*, 4411–4419.
88. Choi, J.; Burns, A. A.; Williams, R. M.; *et al. J. Biomed. Opt.* **2007**, *12*, 064007/1–064007/11.
89. Rossi, L. M.; Shi, L.; Rosenzweig, N.; Rosenzweig, Z. *Biosens. Bioelectron.* **2006**, *21*, 1900–1906.
90. Zhao, X.; Bagwe, R. P.; Tan, W. *Adv. Mater. (Weinheim, Ger.)* **2004**, *16*, 173–176.
91. Cunin, F.; Li, Y. Y.; Sailor, M. J. *BioMEMS Biomed. Nanotechnol.* **2006**, *3*, 213–222.
92. Li, Y. Y.; Cunin, F.; Link, J. R.; *et al. Science (Washington, DC)* **2003**, *299*, 2045–2047.
93. Lee, T. M.-H. *Sensors* **2008**, *8*, 5535–5559.
94. Lin, V. S.; Motesharei, K.; Dancil, K. P.; Sailor, M. J.; Ghadiri, M. R. *Science* **1997**, *278*, 840–843.
95. Cash, K. J.; Ricci, F.; Plaxco, K. W. *Chem. Commun. (Cambridge, UK)* **2009**, 6222–6224.
96. Cash, K. J.; Ricci, F.; Plaxco, K. W. *J. Am. Chem. Soc.* **2009**, *131*, 6955–6957.
97. Hickman, J. J.; Ofer, D.; Laibinis, P. E.; Whitesides, G. M.; Wrighton, M. S. *Science (Washington, DC)* **1991**, *252*, 688–691.
98. Sumner, J. J.; Plaxco, K. W.; Meinhart, C. D.; Soh, H. *Proc. SPIE Int. Soc. Opt. Eng.* **2005**, *6007*, 600706/1–600706/6.
99. Poghossian, A.; Schoening, M. J. *Encycl. Sens.* **2006**, *9*, 463–533.
100. Brecht, A.; Gauglitz, G. *Biosens. Bioelectron.* **1995**, *10*, 923–936.
101. Li, H.; Bazan, G. C. *Adv. Mater. (Weinheim, Ger.)* **2009**, *21*, 964–967.
102. Wang, D.; Gong, X.; Heeger, P. S.; Rininsland, F.; Bazan, G. C.; Heeger, A. J. *Proc. Natl. Acad. Sci. USA* **2002**, *99*, 49–53.
103. Cha, B. H.; Lee, S.-M.; Park, J. C.; *et al. Biosens. Bioelectron.* **2009**, *25*, 130–135.
104. Crumbliss, A. L.; Stonehuerner, J.; Henkens, R. W.; O'Daly, J. P.; Zhao, J. *New J. Chem.* **1994**, *18*, 327–339.
105. De Stefano, L.; Rotiroti, L.; De Stefano, M.; *et al. Biosens. Bioelectron.* **2009**, *24*, 1580–1584.
106. Radu, D. R.; Lai, C.-Y.; Wiench, J. W.; Pruski, M.; Lin, V. S. Y. *J. Am. Chem. Soc.* **2004**, *126*, 1640–1641.
107. Clark, L. C., Jr.; Lyons, C. *Ann. N. Y. Acad. Sci.* **1962**, *102*, 29–45.
108. Dai, Z.; Bao, J.; Yang, X.; Ju, H. *Biosens. Bioelectron.* **2008**, *23*, 1070–1076.
109. Wei, Y.; Qiu, K.-Y. *Ser. Chem. Eng.* **2004**, *4*, 873–892.
110. Dai, Z.; Liu, S.; Ju, H.; Chen, H. *Biosens. Bioelectron.* **2004**, *19*, 861–867.
111. Teng, Y.; Wu, X.; Zhou, Q.; Chen, C.; Zhao, H.; Lan, M. *Sens. Actuators B* **2009**, *142*, 267–272.
112. Ren, X.; Meng, X.; Tang, F.; Zhang, L. *Mater. Sci. Eng. C* **2009**, *29*, 2234–2238.
113. Hatzimarinaki, M.; Vamvakaki, V.; Chaniotakis, N. *J. Mater. Chem.* **2009**, *19*, 428–433.
114. Naik, R. R.; Tomczak, M. M.; Luckarift, H. R.; Spain, J. C.; Stone, M. O. *Chem. Commun. (Cambridge, UK)* **2004**, 1684–1685.
115. Berne, C.; Betancor, L.; Luckarift, H. R.; Spain, J. C. *Biomacromolecules* **2006**, *7*, 2631–2636.
116. Luckarift, H. R.; Dickerson, M. B.; Sandhage, K. H.; Spain, J. C. *Small* **2006**, *2*, 640–643.
117. Ramanathan, M.; Luckarift, H. R.; Sarsenova, A.; *et al. Colloids Surf. B* **2009**, *73*, 58–64.
118. Barbe, C.; Bartlett, J.; Kong, L.; *et al. Adv. Mater. (Weinheim, Ger.)* **2004**, *16*, 1959–1966.
119. Findlay, S. http://www.azonano.com/news.asp?newsID=7721; 2008.
120. Rigby, S. P.; Fairhead, M.; Van Der Walle, C. F. *Curr. Pharm. Des.* **2008**, *14*, 1821–1831.
121. Kumar, T. R. S.; Soppimath, K.; Nachaegari, S. K. *Curr. Pharm. Biotechnol.* **2006**, *7*, 261–276.
122. Wang, L.; Zhao, W.; Tan, W. *Nano Res.* **2008**, *1*, 99–115.
123. Liong, M.; Lu, J.; Kovochich, M.; *et al. ACS Nano* **2008**, *2*, 889–896.
124. Wu, P.; He, X.; Wang, K.; *et al. J. Nanosci. Nanotechnol.* **2008**, *8*, 2483–2487.
125. Tsai, C.-P.; Chen, C.-Y.; Hung, Y.; Chang, F.-H.; Mou, C.-Y. *J. Mater. Chem.* **2009**, *19*, 5737–5743.
126. Corma, A.; Diaz, U.; Arrica, M.; Fernandez, E.; Ortega, I. *Angew. Chem. Int. Ed.* **2009**, *48*, 6247–6250; S6247/1–S6247/17.
127. Du, L.; Song, H.; Liao, S. *Appl. Surf. Sci.* **2009**, *255*, 9365–9370.
128. Schacht, S.; Huo, Q.; Voigt-Martin, I. G.; Stucky, G. D.; Schuth, F. *Science (Washington, DC)* **1996**, *273*, 768–771.
129. Wan, Y.; Zhao, D. *Chem. Rev.* **2007**, *107*, 2821–2860.
130. Li, X.; Yang, T.; Gao, Q.; Yuan, J.; Cheng, S. *J. Colloid Interface Sci.* **2009**, *338*, 99–104.
131. Sun, Q.; Vrieling, E. G.; Van Santen, R. A.; Sommerdijk, N. A. J. M. *Curr. Opin. Solid State Mater. Sci.* **2004**, *8*, 111–120.
132. Zhou, F.; Li, S.; Vo, C. D.; *et al. Langmuir* **2007**, *23*, 9737–9744.
133. Jensen, M.; Keding, R.; Hoche, T.; Yue, Y. *J. Am. Chem. Soc.* **2009**, *131*, 2717–2721.
134. Murray, P. E.; Garcia-Godoy, F.; Hargreaves Kenneth, M. *J. Endod.* **2007**, *33*, 377–390.
135. Webster, T. J. *Mater. Sci. Forum* **2007**, *539–543*, 511–516.
136. Liu, H.; Webster, T. J. *Biomaterials* **2006**, *28*, 354–369.
137. Hench, L. L.; Wilson, J. *Science (Washington, DC)* **1984**, *226*, 630–636.
138. Chen, S.; Osaka, A.; Hayakawa, S.; Tsuru, K.; Fujii, E.; Kawabata, K. *J. Sol-Gel Sci. Technol.* **2008**, *48*, 322–335.
139. Ehrlich, H.; Janussen, D.; Simon, P.; *et al. J. Nanomater.* **2008**.
140. Heinemann, S.; Heinemann, C.; Bernhardt, R.; *et al. Acta Biomater.* **2009**, *5*, 1979–1990.
141. Karpov, M.; Laczka, M.; Leboy, P. S.; Osyczka, A. M. *J. Biomed. Mater. Res. A* **2008**, *84*, 718–726.
142. Thimm, B. W.; Unger, R. E.; Neumann, H.-G.; Kirkpatrick, C. J. *Biomed. Mater. (Bristol, UK)* **2008**, *3*, 015007/1–015007/10.
143. Gao, T.; Aro, H. T.; Ylanen, H.; Vuorio, E. *Biomaterials* **2001**, *22*, 1475–1483.
144. Tian, D.; Dubois, P.; Jerome, R. *J. Polym. Sci. A Polym. Chem.* **1997**, *35*, 2295–2309.
145. Vitale-Brovarone, C.; Baino, F.; Miola, M.; Mortera, R.; Onida, B.; Verne, E. *J. Mater. Sci. Mater. Med.* **2009**, *20*, 809–820.
146. Hench, L. L. *Science* **1980**, *208*, 826–831.
147. Ruoslahti, E. *Annu. Rev. Cell Dev. Biol.* **1996**, *12*, 697–715.
148. Ruoslahti, E. *Nat. Rev. Cancer* **2002**, *2*(2), 83–90.
149. Balasundaram, G.; Webster, T. J. *J. Mater. Chem.* **2006**, *16*, 3737–3745.
150. Kim, T.-I.; Jang, J.-H.; Kim, H.-W.; Knowles, J. C.; Ku, Y. *Curr. Pharm. Des.* **2008**, *14*, 2201–2211.
151. Müller, W. E. G.; Boreiko, A.; Wang, X.; *et al. Calcif. Tissue Int.* **2007**, *81*, 382–393.
152. Schröder, H. C.; Boreiko, O.; Krasko, A.; Reiber, A.; Schwertner, H.; Müller, W. E. G. *J. Biomed. Mater. Res. B* **2005**, *75B*, 387–392.
153. Advincula, M. C.; Patel, P.; Mather, P. T.; Mattson, T.; Goldberg, A. J. *J. Biomed. Mater. Res. B* **2009**, *88*, 321–331.
154. Blumen, S. R.; Cheng, K.; Ramos-Nino, M. E.; *et al. Am. J. Respir. Cell Mol. Biol.* **2007**, *36*, 333–342.
155. Di Pasqua, A. J.; Sharma, K. K.; Shi, Y.-L.; *et al. J. Inorg. Biochem.* **2008**, *102*, 1416–1423.
156. Vallhov, H.; Gabrielsson, S.; Stromme, M.; Scheynius, A.; Garcia-Bennett, A. E. *Nano Lett.* **2007**, *7*, 3576–3582.
157. Burns, A. A.; Vider, J.; Ow, H.; *et al. Nano Lett.* **2009**, *9*, 442–448.
158. Lopez, T.; Basaldella, E. I.; Ojeda, M. L.; Manjarrez, J.; Alexander-Katz, R. *Opt. Mater. (Amsterdam, Neth.)* **2006**, *29*, 75–81.
159. Witasp, E.; Kupferschmidt, N.; Bengtsson, L.; *et al. Toxicol. Appl. Pharmacol.* **2009**, *239*, 306–319.
160. Wu, S.-H.; Lin, Y.-S.; Hung, Y.; *et al. ChemBioChem* **2008**, *9*, 53–57.
161. Davis, T. M.; Snyder, M. A.; Krohn, J. E.; Tsapatsis, M. *Chem. Mater.* **2006**, *18*, 5814–5816.

162. Yokoi, T.; Wakabayashi, J.; Otsuka, Y.; *et al*. *Chem. Mater*. **2009**, *21*, 3719–3729.
163. Masse, S.; Laurent, G.; Chuburu, F.; Cadiou, C.; Dechamps, I.; Coradin, T. *Langmuir* **2008**, *24*, 4026–4031.
164. Bauer, C. A.; Robinson, D. B.; Simmons, B. A. *Small* **2007**, *3*, 58–62.
165. El Hawi, N.; Nayral, C.; Delpech, F.; *et al*. *Langmuir* **2009**, *25*, 7540–7546.
166. Nozawa, K.; Gailhanou, H.; Raison, L.; *et al*. *Langmuir* **2005**, *21*, 1516–1523.
167. Brutchey, R. L.; Cheng, G.; Gu, Q.; Morse, D. E. *Adv. Mater. (Weinheim, Ger.)* **2008**, *20*, 1029–1033.
168. Livingston, F. E.; Sarney, W. L.; Niesz, K.; Ould-Ely, T.; Tao, A. R.; Morse, D. E. *Proc. SPIE* **2009**, *7321*, 73210I/1–73210I/13.
169. Zhang, H. M.; Morse, D. E. *J. Mater. Chem.* **2009**, *19*(47), 9006–9011.
170. Knowles, J. R. *Nature* **1991**, *350*, 121–124.
171. Arnold, F. H., Georgiou, G., Eds. In *Directed Evolution Library Creation. Methods in Molecular Biology*; Humana Press: Totowa, NJ, 2003; Vol. 231, p 224.
172. Arnold, F. H., Georgiou, G., Eds. In *Directed Enzyme Evolution: Screening and Selection Methods. Methods in Molecular Biology*; Humana Press: Totowa, NJ, 2003; Vol. 230, p 383.
173. Chen, K.; Arnold, F. H. *Proc. Natl. Acad. Sci. USA* **1993**, *90*, 5618–5622.
174. Gerlt, J. A.; Babbitt, P. C. *Curr. Opin. Chem. Biol*. **2009**, *13*, 10–18.
175. Giver, L.; Gershenson, A.; Freskgard, P.-O.; Arnold, F. H. *Proc. Natl. Acad. Sci. USA* **1998**, *95*, 12809–12813.
176. Macbeath, G.; Kast, P.; Hilvert, D. *Science* **1998**, *279*, 1958–1961.
177. Miller, O. J.; Bernath, K.; Agresti Jeremy, J.; *et al*. *Nat. Methods* **2006**, *3*, 561–570.
178. Zhang, J.-H.; Dawes, G.; Stemmer, W. P. C. *Proc. Natl. Acad. Sci. USA* **1997**, *94*, 4504–4509.
179. Brown, S. *Nat. Biotechnol*. **1997**, *15*, 269–272.
180. Naik, R. R.; Brott, L. L.; Clarson, S. J.; Stone, M. O. *J. Nanosci. Nanotechnol*. **2002**, *2*, 95–100.
181. Balogh, L. P.; Ould-Ely, T.; Lesniak, G. W. In *Nanomedicine; Design of Particles, Sensors, Motors, Implants, Robots, and Devices*; Mark, S. J., Shanov, V. N., Yun, Y., Eds.; Artech House, 2009; Chapter 4.
182. Lin, G.-L.; Tsai, Y.-H.; Lin, H.-P.; Tang, C.-Y.; Lin, C.-Y. *Langmuir* **2007**, *23*, 4115–4119.
183. Pouget, E.; Dujardin, E.; Cavalier, A.; *et al*. *Nat. Mater*. **2007**, *6*, 434–439.
184. Warren, S. C.; Disalvo, J. F.; Wiesner, U. *Nat. Mater*. **2007**, *6*, 156–161.
185. Kohn, J. *Nat. Mater*. **2004**, *3*, 745–747.
186. Colas, A.; Curtis, J. In *Biomaterials Science*, 2nd ed.; Elsevier: San Diego, CA, 2004; pp 80–86.
187. Curnow, P.; Bessette, P. H.; Kisailus, D.; Murr, M. M.; Daugherty, P. S.; Morse, D. E. *J. Am. Chem. Soc*. **2005**, *127*, 15749–15755.
188. Curnow, P.; Kisailus, D.; Morse, D. E. *Angew. Chem. Int. Ed*. **2006**, *45*, 613–616.
189. Schulz, J., Mark, S., Vesselin, N., Yun, Y., Eds.; In *Nanomedicine: Design of Particles, Sensors, Motors, Implants, Robots, and Devices*; Artech House: Boston, 2009.
190. Morse, D. E. *Trends Biotechnol*. **1999**, *17*(6), 230–232.
191. Morse, D. E. In *Organosilicon Chemistry IV: Form Molecules to Materials* (Lectures and Poster Contributions presented at the Muechner Silicontage), Muechen, Apr. 4, 1998; Auner, N., Weis, J., Eds.; Wiley-VCH Verlag, Weinheim, Germany, 2000; pp 5–16.
192. Lin, W.; Huang, Y.-W.; Zhou, X.-D.; Ma, Y. *Toxicol. Appl. Pharmacol*. **2006**, *217*, 252–259.
193. Schröder, H. C.; Schlossmache, U.; Boreiko, A.; *et al*. In: Müller, W. E. G., Grachev, M. A., Eds.; *Progress in Molecular and Subcellular Biology*; Springer: Berlin, 2009; Vol. 47, pp 251–273. DOI: 10.1007/978-3-540-88552-8.

2.202. Engineering Viruses For Gene Therapy

J Bergen and D Schaffer, University of California, Berkeley, CA, USA

© 2011 Elsevier Ltd. All rights reserved.

2.202.1.	**Introduction**	18
2.202.1.1.	Defining Gene Therapy	18
2.202.1.2.	Prospects and Challenges of Gene Therapy	18
2.202.1.3.	Design Requirements for Therapeutic Gene Vectors	19
2.202.1.4.	Techniques for Evaluating Gene Delivery Vectors	20
2.202.1.4.1.	Reporter genes	20
2.202.1.4.2.	Gene expression assays	21
2.202.2.	**Viral Engineering**	22
2.202.2.1.	Viruses as Gene Delivery Vectors	22
2.202.2.2.	Rational Approaches to Vector Design	23
2.202.2.2.1.	Retargeting	23
2.202.2.2.2.	Immune evasion	23
2.202.2.3.	Library Approaches to Vector Design	24
2.202.2.3.1.	Library selection	24
2.202.2.3.2.	Directed evolution	26
2.202.3.	**Design of Artificial Viruses**	26
2.202.3.1.	Materials for Gene Delivery	26
2.202.3.2.	Functionalization of Synthetic Gene Delivery Vectors	26
2.202.3.2.1.	Ligands for cell binding and internalization	28
2.202.3.2.2.	Endosomal escape ligands	28
2.202.3.2.3.	Ligands for cytosolic trafficking	28
2.202.3.2.4.	Nuclear entry ligands	29
2.202.4.	**Conclusions and Future Work**	29
2.202.4.1.	Future Directions	29
2.202.4.1.1.	Engineering control systems for gene expression	29
2.202.4.1.2.	Integration of gene delivery systems with biomaterials	30
2.202.4.1.3.	Alternative gene delivery systems	31
2.202.4.2.	Safety Considerations	31
2.202.4.3.	Summary	31
References		31

Glossary

Adeno-associated virus A nonenveloped, single-stranded DNA virus that is nonpathogenic in humans and can be engineered to deliver transgenes up to 4.9 kilobases.

Adenovirus A nonenveloped, double-stranded DNA virus that naturally infects the upper respiratory tract and can be engineered to deliver transgenes up to 36 kilobases.

Artificial virus A nonviral vector that has been functionalized to mimic the gene delivery properties displayed by viruses for efficient gene delivery to cells.

Directed evolution The process of performing iterative rounds of genetic diversification (e.g., mutation) and selection in order to improve the fitness of selected mutants toward specified selection criteria.

Gene therapy The introduction of genetic material into cells as a means to manipulate gene expression profiles to achieve a favorable clinical outcome.

Gene vector A delivery system, viral or nonviral, used to introduce exogenous nucleic acids into cells.

Library selection The process of applying selective pressures to a genetically diverse library in order to identify mutants with a desired characteristic.

Lipoplex A lipid/nucleic acid complex used to deliver DNA into cells.

Monogenetic disease An inherited disease caused by mutation of a single gene, resulting in either a loss of gene function or a pathogenic gain of function, such as the production of a toxic mutant protein.

Nonviral vector A system or construct that relies on synthetic or natural materials, such as lipids, polymers, peptides, and small molecules, to accomplish nucleic acid delivery to cells.

Nucleic acid delivery The process of introducing exogenous nucleic acids into cells in such a way that the nucleic acids become available or bioactive to the appropriate intracellular compartments and machinery.

Plasmid For gene delivery to mammalian cells, a circular DNA construct encoding a mammalian expression cassette as well as elements for propagation in bacteria.
Polyplex A polymer/nucleic acid complex used to deliver DNA into cells.
Reporter gene An exogenous gene used to obtain information about the quality and/or quantity of gene expression afforded by a gene delivery system.
Retroviruses A family of enveloped viruses that integrate into the host genome and can be engineered to deliver transgenes up to ~10 kilobases.
Transduction The process of introducing nucleic acids into cells using viral vectors.
Transfection The process of introducing nucleic acids into cells using nonviral vectors.
Transgene A gene that is transferred from an exogenous source to a recipient cell.

Abbreviations

AAV	Adeno-associated virus
Ad	Adenovirus
DOPE	Dioleoylphosphatidylethanolamine
DOTAP	1,2-Dioleoyl-3-trimethylammonium propane
FISH	Fluorescence *in situ* hybridization
GFP	Green fluorescent protein
GMP	Good Manufacturing Practice
ICC	Immunocytochemistry
miRNA	MicroRNA
MLV	Murine leukemia virus
NLS	Nuclear localization signal
PEG	Poly(ethylene glycol)
PEI	Poly(ethylenimine)
PLL	Poly-L-lysine
RT-qPCR	Reverse transcription-quantitative polymerase chain reaction
SCID-X1	X-linked severe combined immunodeficiency
siRNA	Short interfering RNA
VAPs	Viral attachment proteins

2.202.1. Introduction

Gene therapy offers a promising future treatment approach for myriad diseases and disorders, many of which are intractable using the current tools of clinical medicine. Section 2.202.1 introduces the concept of gene therapy as a means of treating disease at the genetic level and discusses the prospects and challenges of the gene therapy field. It also provides an introduction to traditional gene delivery methods and techniques for evaluating the performance of gene delivery vectors. Ultimately, several challenges that currently hinder the clinical translation of gene delivery vectors must be overcome. Consequently, Sections 2.202.2 and 2.202.3 describe strategies to engineer improved gene delivery vectors. Specifically, Section 2.202.2 discusses approaches to modify viruses in order to improve and/or tune their properties for gene delivery applications, while Section 2.202.3 describes the approach of designing biologically inspired 'artificial viruses' by functionalizing nonviral gene delivery vectors. The final section summarizes the current status of gene therapy as a field and suggest future directions for engineering improved gene delivery systems for gene therapy applications.

2.202.1.1. Defining Gene Therapy

The concept of a 'magic bullet' that selectively eliminates disease while avoiding healthy tissues, postulated by Paul Ehrlich in the early 1900s, has inspired a century-long quest to design targeted medicines. Although originally conceived as small molecule chemotherapeutics or antibodies that target disease-causing cells associated with cancer or bacterial infections,[1] the magic bullet concept has since become the paradigm of targeted medicine for the treatment of myriad human diseases. With recent scientific and technological advances, this bullet is materializing in forms far beyond what may have been conceivable a century ago. The integration of various fields – including biomaterials, tissue engineering, and molecular therapies – has opened doors toward revolutionary disease treatments. An exceptionally promising avenue in modern targeted medicine is gene therapy. In a broad sense, gene therapy encompasses strategies to replace, repair, or modify the expression levels of specific genes.[2–4] The traditional concept of gene therapy involves introducing a therapeutic gene into a patient's cells to correct a disease caused by a genetic mutation and/or by the lack of a necessary gene product. In the case of a monogenetic disease, this approach can be curative because it directly addresses the genetic cause of the disease. Even in cases where the genetic cause of a disease is unknown, genes encoding therapeutic proteins can be delivered as an alternative to protein therapy. More recently, insight into the mechanisms of RNA interference via short interfering RNA (siRNA) and microRNA (miRNA) has opened the possibility of manipulating gene expression profiles at the level of transcription, thereby expanding the types of diseases that can be treated by gene therapy.[5,6] Yet another approach involves *in situ* gene repair, where synthetic DNA molecules that target the disease-causing mutation are introduced to the cell in such a way as to trigger the cell's endogenous DNA repair mechanisms.[7] The genetic manipulation strategies that encompass the current field of gene therapy are illustrated in Figure 1.

2.202.1.2. Prospects and Challenges of Gene Therapy

A progressively increasing understanding of the genetic basis of disease has facilitated the identification of therapeutic targets, leading to the development of strategies and genetic cargos to

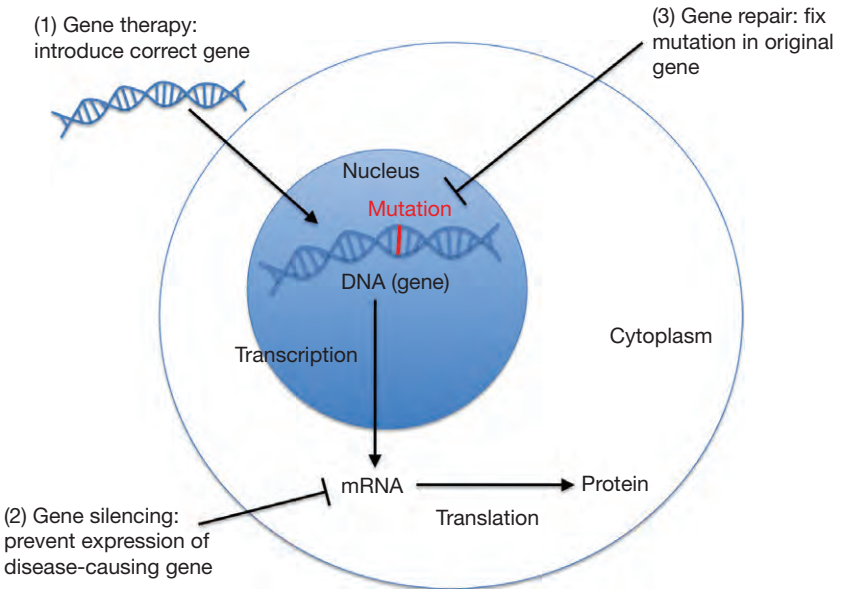

Figure 1 Gene therapy: strategies for correcting disease at the genetic level. Gene therapy encompasses strategies to replace, repair, or modify the expression levels of specific genes. (1) The traditional concept of gene therapy involves introducing a corrective gene to the cell nucleus so that it can express the nonmutated form of a protein. The therapeutic gene can also encode a therapeutic protein that treats a disease for which the genetic basis is not yet understood (not pictured). (2) Gene silencing strategies involve silencing the expression of disease-causing genes by targeting mRNA transcripts for destruction. (3) *In situ* gene repair can be employed to fix disease-causing genetic mutations using the cell's endogenous DNA repair mechanisms.

treat monogenetic diseases such as hemophilia and cystic fibrosis, as well as genetically complex disorders such as cancer, neurological disease, and viral infectious disease.[8] Even when the genetic basis of a disease is unclear, genes whose protein products are known to have a therapeutic effect can be delivered (e.g., neurotrophins to protect diseased neurons in neurogenerative disease and suicide genes or cytokines to promote tumor regression in cancer). Given its potential to address myriad diseases at the molecular level, gene therapy represents a therapeutic modality capable of achieving the specificity and efficacy required of an ideal magic bullet.

There are, however, many clear challenges in the development of such genetic medicines. Foremost is the design of delivery vectors that safely and efficiently deliver their genetic cargo to targeted cells. Although various physical and chemical methods of gene delivery have been explored (see Al-Dosari and Gao[9] for a recent review), viruses are natural candidates as gene delivery vectors because of their innate ability to deliver genetic material to host cells. Indeed, preliminary success has been achieved in clinical trials using viral vectors such as adenovirus (Ad), adeno-associated virus (AAV), and retrovirus (primarily murine leukemia virus (MLV)). These vectors are naturally occurring viruses that have been genetically modified to package therapeutic genes. Notably, a clinical trial evaluating MLV-based retroviral delivery of a cytokine receptor subunit to the hematopoietic stem cells of patients with X-linked severe combined immunodeficiency (SCID-X1) resulted in full correction of the disease phenotype.[10] Additional early phase clinical trials have yielded encouraging results in the treatment of hemophilia B,[11] cancer,[12] cystic fibrosis,[13] and X-linked adrenoleukodystrophy.[14] Recently, very promising results have been achieved in phase I clinical trials employing adeno-associated viral vectors carrying therapeutic genes designed to treat Parkinson's disease[15] and the blinding disease, Leber's congenital amaurosis.[16–20]

Despite encouraging results from these gene therapy trials, a number of setbacks in the field have slowed progress toward clinical approval of gene therapies. In 1999, a severe adverse event involved a fatal immune reaction to an adenoviral vector carrying a gene intended to treat a metabolic deficiency,[21] underscoring the need to better understand the interactions between viruses and the immune system. In addition, 3 years after the apparently successful SCID-X1 gene therapy trial, 3 of the 15 treated patients developed T cell leukemia as a result of retroviral insertion near an oncogene promoter[22,23] (though it should be noted that 12 patients were fully cured of an otherwise fatal disorder). Importantly, these failures were not caused by the therapeutic transgene itself, but were instead due to unfavorable interactions between the vector and its host. Thus, in order to realize the remarkable potential of gene therapy to treat human disease, intelligent vector design is critical.

2.202.1.3. Design Requirements for Therapeutic Gene Vectors

The design requirements for ideal gene transfer vectors can be understood in the context of the gene delivery pathway. Effective gene vectors are macromolecular assemblies that must integrate a set of complex biological 'activities' that enable them to overcome a series of barriers encountered along the delivery pathway, including (i) navigation through the extracellular space and arrival at targeted cells, (ii) passage through cellular membranes, (iii) intracellular trafficking toward the nucleus, and (iv) unpackaging and nuclear delivery

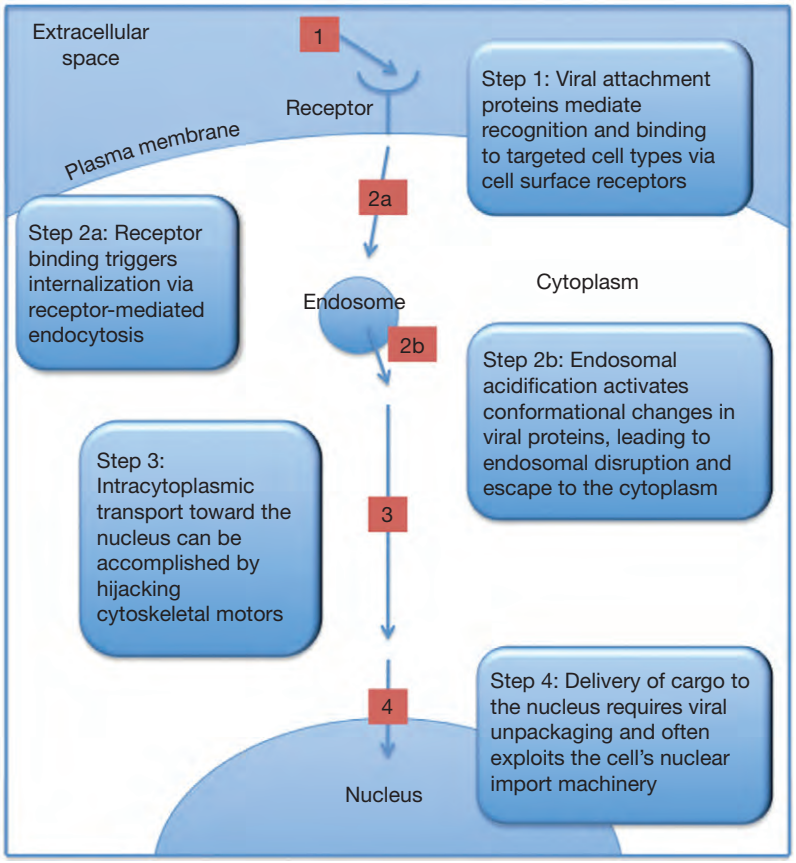

Figure 2 The multistep gene delivery pathway. The ability of viruses to efficiently infect cells relies on their deployment of various molecular mechanisms to overcome a series of intracellular barriers, from cellular binding to nuclear entry. Mechanisms commonly employed by viruses in their cellular entry programs include (1) recognition and binding to specific cellular receptors by viral attachment proteins, (2) entry via endocytosis and acid-triggered endosomal escape from early endosomes (pH ~6.0), (3) intracellular transport on cytoskeletal motor proteins, and (4) unpackaging and nuclear entry via the cell's nuclear import machinery.

of the genetic cargo. As natural gene vectors, viruses employ various mechanisms to overcome these intracellular barriers, as illustrated in Figure 2. However, additional criteria must be met as well. Specifically, a vehicle should ideally deliver therapeutic genetic material with high specificity and efficacy while avoiding toxicity or immunogenicity. Additionally, for viral vectors that integrate their transgene into the host chromosome, the position of insertion must be controlled such that insertion does not lead to oncogenesis. Further, gene delivery systems must be economically produced, must comply with Good Manufacturing Practice (GMP) guidelines,[24–26] and should ideally be amenable to controllable expression levels of the therapeutic transgene.

The challenge of designing this ideal vector has stimulated numerous and diverse research efforts. Both natural viruses and synthetic materials have been studied as platforms for gene delivery vectors, and progress has been made through both rational design and library selection approaches. Efforts to address the complexity of the gene delivery problem are necessarily multidisciplinary, synthesizing insights and tools from virology, cell biology, immunology, medicine, engineering, and chemistry. The development of delivery systems that satisfy the design requirements for gene therapy applications is currently pursued through two major research efforts: (i) viral engineering, which seeks to reengineer natural viruses for use as therapeutic delivery vectors and (ii) the development of 'artificial viruses,' which is concerned with designing synthetic materials endowed with gene delivery capabilities (Figure 3). These strategies will be described in detail in Sections 2.202.2 and 2.202.3, respectively.

2.202.1.4. Techniques for Evaluating Gene Delivery Vectors

The ultimate measure of successful gene transfer is the correction of a disease phenotype by the delivery of a therapeutic gene. However, the development of vectors for gene delivery applications necessitates techniques capable of qualitatively and quantitatively characterizing gene expression in model systems, such as cells, tissues, and organisms. This section will introduce methods for evaluating the performance of gene delivery vectors. Vectors that perform well in these assays would then advance to preclinical studies using a therapeutic gene in a relevant disease model.

2.202.1.4.1. Reporter genes

Reporter genes are exogenous genes used to detect and measure gene expression achieved by a gene delivery system. Early studies employed reporter genes such as chloramphenicol

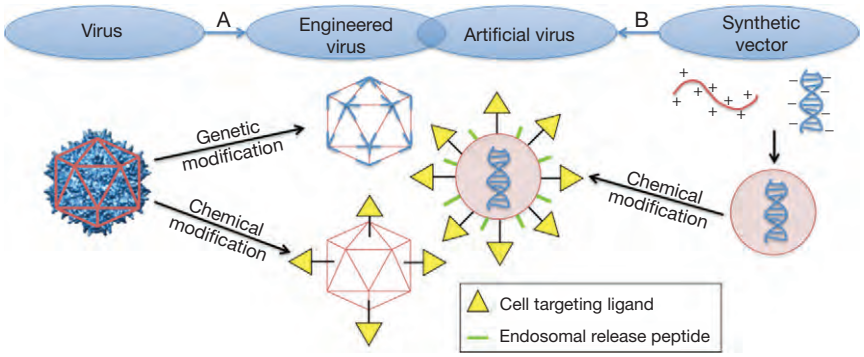

Figure 3 Design strategies for gene delivery vectors. (a) Viral engineering involves chemically and/or genetically modifying the viral capsid. Modifications can be introduced to the viral capsid through rational design or library screening and directed evolution. (Three-dimensional reconstruction of AAV capsid from VIPER database (http://viperdb.scripps.edu).) (b) Artificial viruses are generated by introducing functional modular elements, such as targeting ligands and endosomal release peptides, to synthetic vectors composed of DNA condensed by cationic lipids or polymers. The design of increasingly sophisticated artificial viruses may lead to the generation of systems that resemble engineered viruses.

acetyltransferase and β-galactosidase, enzymes that convert their corresponding substrate to a compound that is detectable via its radioactivity or optical absorbance, respectively. More recently, reporters that are fluorescent or luminescent have been adopted because of their more sensitive and facile detection and quantification. An important fluorescent reporter is the green fluorescent protein (GFP), which was originally isolated from the jellyfish *Aequorea victoria*,[27] while the most common luminescent reporter is firefly luciferase from *Photinus pyralis*.[28]

In order for transgenes to be expressed in mammalian cells, they must be delivered as part of an expression cassette consisting of three major elements: (i) a promoter/enhancer element that serves as a docking site for transcription factors, (ii) the transgene coding region itself flanked by start and stop codons, and (iii) a polyadenylation signal, which plays an important role in mRNA processing in the cell. The promoter is typically a constitutively active, strong promoter, although tissue-specific or inducible promoters can be used to tune a gene delivery system for controlled expression in a particular cell or tissue type or for tunable expression levels. This expression cassette can be packaged as part of a recombinant viral genome or can be inserted into a plasmid and delivered using nonviral gene delivery agents such as polymers or lipids.

Several considerations should be made in selecting a reporter gene. GFP is a robust marker for both qualitative and quantitative determination of gene expression in live cell populations, and it is suitable for histology (see **Section 2.202.1.4.2** for assays).[29] Luciferase might be selected if highly sensitive detection is required because of its extremely low background, but it typically requires cell or tissue lysis for detection in the luminescence reaction.[30] Another consideration is the reporter gene size. Certain viruses have a limited genome capacity, such as AAV with a ~4.9 kilobase genome, which excludes the use of expression cassettes much larger than this size. (Most other viruses studied for gene therapy applications have larger genome capacities.) Also, it is important to consider the half-life of the reporter gene in cells. For example, the half-life of GFP is over 24 h, which enables robust detection of gene expression in individual cells but complicates analysis of gene expression dynamics. On the other hand, the relatively short half-life of luciferase enables kinetic analysis of gene expression on short timescales.[31]

2.202.1.4.2. Gene expression assays

Gene expression assays are important tools used to study the ability of a gene vector to deliver its genetic cargo to a population of cells where it will have its therapeutic effect. In an experimental design, the type of reporter gene and gene expression assay employed are dependent on the specific therapeutic goal. Gene expression assays can be performed in both *in vitro* and *in vivo* models, as described in the following sections.

2.202.1.4.2.1. In vitro *assays*

Cell-based (*in vitro*) assays are an important tool to study gene expression mediated by a gene delivery vector of interest. The particular cell culture model selected depends on the therapeutic application. Often, a vector is initially tested in an immortalized cell line, which is readily available from a cell bank and easily cultured. (It should be noted, however, that the cell line selected must express the appropriate receptors in the case of a delivery vector that relies on particular surface receptors for cellular entry and intracellular processing.) Later, the vector can be further tested and optimized using a more relevant cell type (such as primary cells isolated from the tissue or organ of interest) and/or a more sophisticated culture system that mimics the physiological characteristics of the target tissue or organ (e.g., a specialized culture system that enables localized delivery to polarized cells or a coculture system that replicates the cellular organization of an organ).

A variety of assays can be performed to evaluate gene delivery to an *in vitro* system. Commonly, gene expression is detected by the presence of the protein that is produced by successful nuclear delivery and processing of the transgene expression cassette. The appropriate detection method is determined by the nature of the reporter gene. In the case of GFP or other fluorescent proteins, fluorescence can be detected and measured in live or fixed cells by any of a number of

techniques, including fluorescence microscopy, flow cytometry, or fluorescence spectrophotometry. Enzymatic reporter gene products, such as the luciferase and β-galactosidase proteins, produce detectable signals upon exposure to their respective substrates. Luciferase, for example, catalyzes a reaction that emits light in the presence of its cell membrane-permeable substrate, luciferin. A more general technique to detect virtually any expressed gene is immunocytochemistry (ICC), which utilizes antibodies that specifically recognize the protein of interest and can be detected using labeled primary or secondary antibodies. Another antibody-based technique that can be used to detect reporter proteins is the Western blot. Quantification of the signals produced by reporter genes can provide information about the efficiency of transfection or transduction by a particular vector as well as the dynamics and duration of gene expression. Accurate quantification of gene expression must take into account the number of cells transfected as well as the half-life of the reporter protein.

An alternative *in vitro* assay for gene delivery is the detection of mRNA produced by the transcription of the delivered transgene. Established techniques such as the Northern blot, fluorescence *in situ* hybridization (FISH), and reverse transcription-quantitative polymerase chain reaction (RT-qPCR) enable the detection of mRNA transcripts. Not only are such assays highly specific and sensitive, but they also enable detection of expression earlier than a protein reporter can be detected. Additionally, the short half-lives of mRNA transcripts facilitate detailed analysis of gene expression dynamics.

If *in vitro* assays reveal that gene delivery is inefficient, limitations of the delivery system can be diagnosed by studying its intracellular trafficking in cells. Techniques have been developed to fluorescently label gene delivery vectors and/or their enclosed nucleic acid cargo and track their intracellular path.[32–35] Information pertaining to the internalization and intracellular trafficking of the gene delivery vector can inform rational design efforts to improve the delivery efficiency. Finally, it is important to determine whether the gene delivery vector or its expression product is toxic to cells. Cytotoxicity assays, such as those that assess cell membrane integrity or measure the reducing potential of the cell, and even more complex assays like microarray analysis are relatively straightforward to perform and may accompany gene expression assays in the full characterization of a gene delivery vector.

2.202.1.4.2.2. In vivo *assays*

Although *in vitro* assays are an important system to begin evaluating new gene delivery vectors, it is impossible to recapitulate the complexity of a whole organism in an *in vitro* system. Consequently, in cases where a gene delivery vector is intended for *in vivo* administration, it is important to perform studies that evaluate the tolerable dosage for a given administration route, the biodistribution profile of the vector and transgene product, and the dynamics of expression in a relevant model organism. One option for studying gene delivery *in vivo* is to isolate selected organs or tissues at a specified timepoint after administration and assay for reporter gene expression by one of the techniques described above for *in vitro* assays. Such techniques are useful to sensitively detect gene expression in a tissue of interest and to characterize the biodistribution of the gene product among major tissues and organs. However, the destructive nature of these assays limits the acquisition of data pertaining to the expression dynamics of the reporter gene.

More recently, noninvasive imaging techniques have been developed that enable the acquisition of dynamic, whole-body biodistribution information while minimizing the number of animals required. *In vivo* bioluminescence imaging, which utilizes a light-emitting reporter (typically firefly luciferase), is a common technique for imaging gene expression in small laboratory animals, including mice and rats.[36] At a selected timepoint after gene vector administration, the animals are injected with the luciferase substrate, luciferin, and imaged using a charge-coupled device (CCD) camera to examine profile of gene expression. Using this technique, data can be obtained regarding the magnitude and location of gene expression. The same animals can then be reimaged at later timepoints to follow the expression dynamics of the luciferase reporter gene. A limitation of *in vivo* bioluminescence imaging is that the imaging depth is small (in the range of a few centimeters), restricting studies to small animals or superficial tissues in larger animals. To overcome this limitation, Gambhir *et al.* introduced a technique that utilizes positron emission tomography (PET) in combination with a reporter gene that sequesters a positron-labeled compound in the cell as a detectable marker of gene expression.[37,38] As this modality affords a large imaging depth, it could be readily translated to larger animals and humans.

2.202.2. Viral Engineering

Viruses possess the ability to efficiently deliver genes to cells. As such, they have been utilized as gene delivery vectors in numerous preclinical and clinical studies with increasing levels of success. Nevertheless, complications have arisen due to adverse reactions to viral gene vectors, some of which evolved in nature as human pathogens. It would be beneficial to modify viruses to minimize their immunostimulatory or pathogenic properties while retaining their efficient gene delivery abilities. Such efforts have become increasingly possible with an improved understanding of molecular virology. Two major approaches that have been employed to modify viral properties are rational design and library selection, which can be coupled with directed evolution. Because viruses are multiprotein assemblies with a high density of molecular contacts between interfacing proteins, unique challenges including inherent limitations in modularity arise in attempts to predictably engineer their properties. The design strategies employed in viral engineering, as well as unique challenges posed by attempts to engineer a biological system with a low degree of modularity, are discussed in the following sections.

2.202.2.1. Viruses as Gene Delivery Vectors

Given their natural gene delivery capabilities, it is obvious why viruses were selected as prototypical therapeutic gene delivery vectors. In addition, advances in virology and viral structural biology have progressively elucidated basic mechanisms responsible for this efficient viral gene delivery. Although viruses exist in diverse forms, they share common features (**Figure 4**).

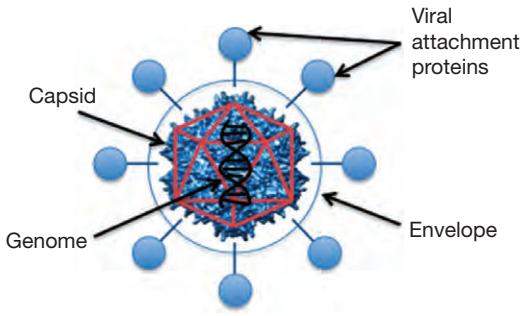

Figure 4 Schematic of a generalized virus. The viral capsid is a multiprotein assembly that surrounds the viral genome and, in some cases, viral accessory proteins. Viral attachment proteins are displayed from the viral surface, either the viral capsid or envelope.

The viral genome consists of either DNA or RNA that encodes the viral capsid, a protein shell that surrounds the genome, as well as accessory proteins necessary to support the viral infection cycle. Some viral capsids, including those of simple retroviruses and lentiviruses, are further enveloped by a lipid bilayer. Viral attachment proteins (VAPs) displayed on the viral surface interact with cellular receptors to mediate binding and entry as the first step in viral infection. Subsequently, viruses deploy specific functionalities encoded in their proteome in overcoming intracellular barriers. In many cases, viral proteins contain functional domains that mediate escape from the degradative endolysosomal pathway,[39] that interact with the intracellular transport machinery for assisted transport through the cytosol,[40] and that exploit the cell's endogenous nuclear import machinery to accomplish nuclear entry.[41] Interestingly, while simple retroviruses such as MLV rely on nuclear envelope breakdown during cell division to accomplish nuclear delivery of their genomes, other viruses such as lentivirus, AAV, and Ad are capable of introducing their genetic material into the intact nuclei of nondividing cells.

Although viruses have evolved mechanisms to accomplish efficient gene delivery to host cells as part of their natural infection process, viral evolution does not necessarily favor specific, important properties that would be beneficial for human therapeutic applications. Some viruses, including certain retroviruses, are natural pathogens and, even when attenuated to reduce replication and pathogenicity, pose inherent safety risks ranging from inflammatory responses to insertional oncogenesis, which was encountered in the SCID-X1 clinical trials.[22,23] Even viruses considered nonpathogenic, such as AAV, elicit adaptive immune responses that do not necessarily pose a risk to patients but whose memory (i.e., the generation of antibodies that neutralize the infectivity of the viral vector or memory T cells that can respond to eliminate the transduced cells) poses major challenges for vector administration and readministration. Consequently, valid concerns with the immunogenicity and toxicity of viral vectors used for gene therapy have been raised.[4,8] There have therefore been efforts to attenuate viral vector interactions with the immune system. Another limitation posed by the use of viruses as delivery vectors is that the natural tropism of the virus may not match the desired biodistribution profile of a therapeutic gene vector. For example, AAV transduces a broad range of tissues to enhance its ability to replicate,[42] whereas HIV infects only a small set of cells as part of its life cycle.[43] Therefore, the development of vehicles that target specific cells of therapeutic value is challenging. The following sections will discuss strategies to overcome the limitations of using viral vectors for gene therapy.

2.202.2.2. Rational Approaches to Vector Design

Increasing insights into fundamental virology have fostered the possibility to manipulate viral properties on the basis of a rational understanding of structure–function relationships. Rational design strategies have predominantly focused on modifying the molecular recognition characteristics of the viral shell to introduce several key properties, including tissue- or cell-specific targeting and evasion of unwanted host immune responses. Various approaches for modifying the viral shell are illustrated in **Figure 5**.

2.202.2.2.1. Retargeting

Given our basic understanding of the role that VAPs play in viral recognition and binding to cell surface receptors, the retargeting of viruses toward clinically relevant cells or tissues has been the primary focus of efforts to reengineer viruses for gene delivery applications. As different viral strains and families exhibit distinct tissue transduction patterns, a common means to redirect viruses is by vector pseudotyping, which involves the modular swapping of VAPs between viral strains. Pseudotyping has been routinely applied to modify the tropism of retroviral vectors[44,45] and has become common for nonenveloped vectors including Ad[46] and AAV.[47,48] It is also possible to generate mosaic particles that combine VAPs from multiple sources into the same virion particle, highlighting a certain extent of modularity in the assembly properties of these proteins.[49] Efforts to identify additional natural virus variants may offer a more extensive collection of viral proteins from which to build novel vectors.[48,50,51]

Although some success has been achieved using pseudotyping to retarget viral vectors, this approach is largely restricted to the natural transduction repertoires of existing viruses. Therefore, in cases where the desired tissue transduction profile cannot be achieved using targeting modules derived from natural viruses, chemical and genetic modifications of viral capsids are complementary approaches. For example, cell-specific targeting ligands, receptors, or antibodies can be attached to the viral 'chassis' via chemical conjugation[52,53] or using biomolecular adaptors such as bispecific antibodies[54,55] or avidin/biotin.[56,57] Alternatively, exogenous targeting ligands, such as peptides or antibody fragments, can be genetically incorporated into capsid proteins. For example, insertion of peptides bearing the integrin-binding RGD motif or the polycation oligolysine into Ad capsid proteins has achieved successful vector retargeting, although other peptide motifs tested were unable to redirect Ad tropism.[58]

2.202.2.2.2. Immune evasion

By employing similar approaches to those used for vector retargeting, progress has been made in modifying vectors to avoid the host immune response. A problem commonly encountered when using human viruses for therapeutic applications is preexisting immunity, as many of us have been

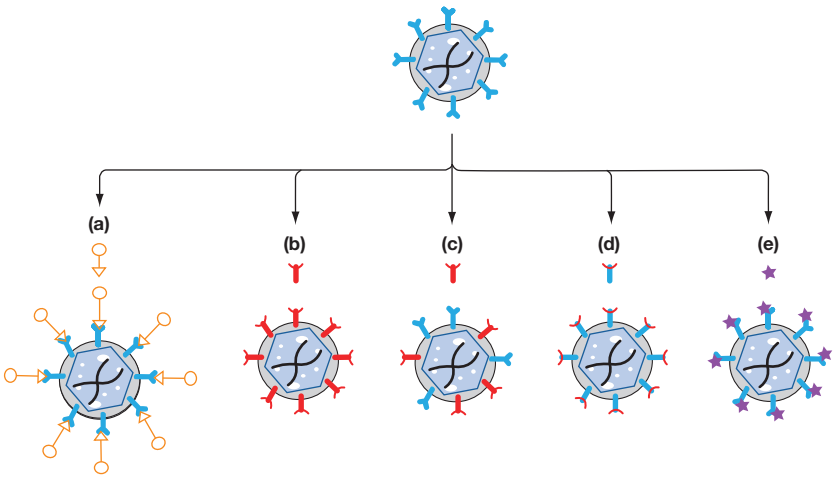

Figure 5 Rational design strategies for engineered viruses. Various modifications can be made to the viral surface, including (a) ligand display by attachment via a bispecific adaptor, (b) pseudotyping with viral attachment proteins (VAPs) from another viral strain, (c and d) creating mosaic or chimeric viral particles that incorporate VAPs from multiple sources, and (e) introducing genetically engineered VAPs bearing mutations and/or peptide insertions. Reproduced from Schaffer, D. V.; *et al. Annu. Rev. Biomed. Eng.* **2008**, *10*, 169–194, with permission from Annual Reviews, Inc.

exposed to and thereby 'naturally vaccinated' against a number of viruses. Consequently, upon systemic delivery of viral vectors based on human viruses or animal viruses with sufficient amino acid sequence similarity to related human viruses, their surface proteins may be recognized by neutralizing antibodies that bind and block viral infection. To avoid this outcome, that is, to protect the virus from the immune system, pseudotyped or chimeric vectors can be employed to take advantage of VAPs from natural variants that are not recognized by host immunity. This strategy has been successfully demonstrated for Ad[59] and AAV.[60,61] Another approach is to chemically modify the viral surface with polymers to sterically shield it from immune recognition. Poly(ethylene glycol) (PEG) is a hydrophilic polymer commonly employed for this purpose, and successful immune evasion has been achieved by PEGylation of both lentiviral[62] and adenoviral vectors,[63] although it has been only moderately successful for AAV.[64] As PEGylation has been shown to ablate native viral tropism in some instances, strategies are being pursued to conjugate targeting ligands to the distal ends of PEG chains to simultaneously achieve immune evasion and vector retargeting.[52,65,66] A more detailed discussion and additional examples of rational vector design are provided in recent reviews.[67,68]

2.202.2.3. Library Approaches to Vector Design

Despite selected examples where it has been possible to successfully manipulate the properties of natural viruses via rational design, efforts to modify viruses often result in a loss of innate function rather than a gain in novel function. There are numerous reasons underlying this problem, many of which are related to the inherent biological complexity of viruses. First, there is a low degree of modularity in a self-assembled viral capsid with many intersubunit contacts, such that swapping pieces of viral proteins responsible for distinct activities to achieve novel functions is challenging (refer to **Figure 2** for a summary of viral activities). In addition, viral capsids most often do not follow a one domain, one function design, as certain viral properties are distributed across nonadjacent protein domains in the viral capsid.[69,70] It is therefore extremely challenging first to identify which regions underlie specific functions, and second to reengineer those distributed functions. In some cases, attempts to introduce novel properties by swapping domains among viral serotypes have instead resulted in unintended inactivation of viral infectivity,[71] suggesting that rational domain swapping may be on the basis of a model of the viral capsid that underestimates its structural and functional complexity. As a related problem, insertion of an exogenous sequence, such as a targeting peptide, into the viral capsid can often disrupt one or more capsid functions and thereby reduce infectivity.

An additional challenge at the genome level is that viral evolution has favored an economical use of their genomes such that a high density of biological functions are often encoded in overlapping open reading frames in the viral genome. Given the high degree of functional overlap in both viral nucleic acids and proteins, it can be difficult to deconvolve and modularize viral sequence–function relationships to aid in design. Finally, even if structure–function relationships can be elucidated in certain cases, it can be difficult to predict and control the emergent properties of complex biological systems. Library selection and directed evolution offer an opportunity to overcome these challenges, as discussed in the following sections.

2.202.2.3.1. Library selection

Library selection approaches offer an invaluable tool for viral engineering as they obviate the need for detailed knowledge of structure–function relationships. This approach, which involves a single round generation of large libraries of genetic mutants and selection of variants based on novel phenotypes (**Figure 6**), is particularly well suited for viruses because of the fact that the viral genotype and phenotype are physically linked. Consequently, libraries can be selected or screened, and the genomes of variants with the desired properties can be isolated and characterized.

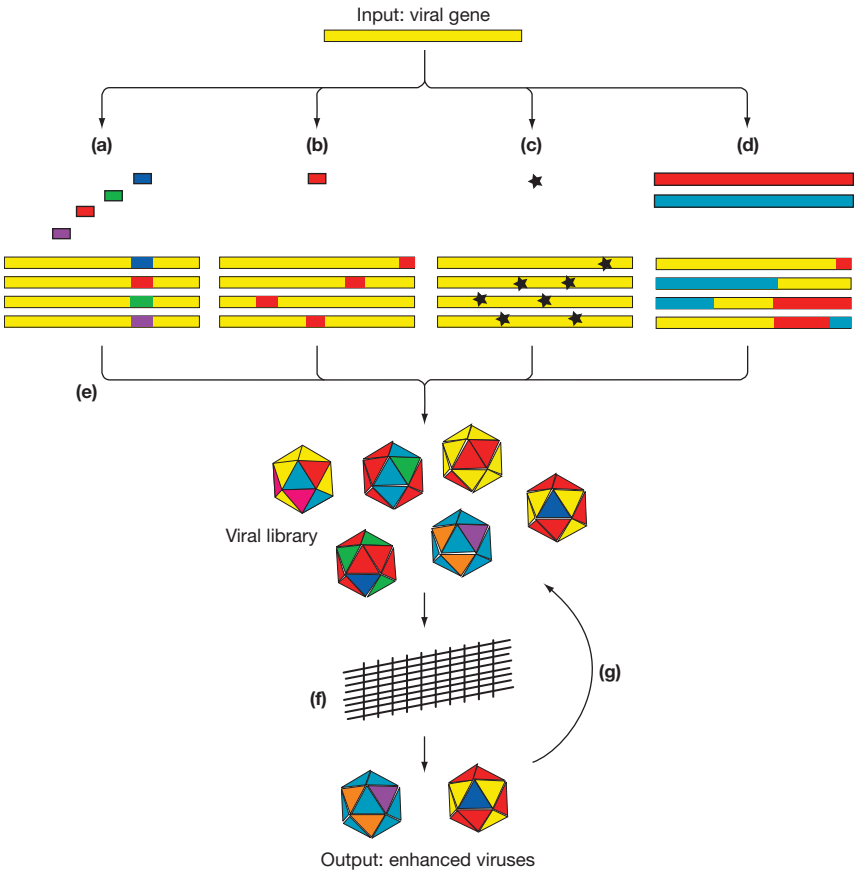

Figure 6 The viral library selection process. Libraries of viral mutants can be generated by (a) insertion of random peptides at a single, defined location, (b) the insertion of a peptide at multiple, random locations, (c) random point mutagenesis accomplished through error-prone PCR, and (d) DNA shuffling. A highly diverse library is then packaged (e) and subjected to selective pressures (f). Successful mutants are collected and can be subjected to additional rounds of selection (g). Reprinted from Schaffer, D. V.; *et al. Annu. Rev. Biomed. Eng.* **2008**, *10*, 169–194, with permission from Annual Reviews, Inc.

Several classes of viral libraries have been constructed using various strategies to generate genetic diversity, including random peptide display, random insertional mutagenesis, and random point mutagenesis (reviewed in Schaffer *et al.*[68]). Additionally, recombination-based strategies can be applied to pools of related viral genes or repeat regions to generate highly diverse chimeric libraries.[72–74] Library selection has been applied to several viral vectors that are candidates for therapeutic gene delivery and, in many cases, has led to the identification of variants with superior gene delivery efficiency and specificity. As one example, an AAV library was generated by random peptide insertion at a permissive site in the viral capsid and subjected to a selection protocol to identify variants capable of infecting a nonpermissive cell line.[75] Following multiple rounds of selection for AAV capsids capable of binding to receptors on a cell line that could not be infected with wild-type AAV, a consensus peptide sequence that endowed AAV with the ability to infect a selected cell line was identified. Library selection has also been employed to modify the transduction characteristics of retroviruses. While gamma retroviruses such as MLV have shown promise as human gene therapy vectors, they suffer from an inability to undergo nuclear entry and are therefore unable to infect nondividing cells, such as neurons. To overcome this limitation, Yu *et al.* generated a library of MLV variants with randomly inserted nuclear localization sequence peptides and, from this library, identified MLV variants capable of infecting neurons.[76]

In addition to generating a wide array of engineered viruses with novel properties that could be beneficial for gene delivery applications, library selection strategies can also contribute toward increasing elucidation of structure–function relationships underlying the mechanisms of viral infection. Notably, the selection of random viral chimeras incorporating fragments of capsid proteins from various serotypes can yield insights into the locations of modular functional domains that would not have been predicted *a priori*.[73] As illustrated in Figure 7, functional domains are often distributed across the viral capsid in exposed surface loops, and viral properties could be altered considerably by loop swapping, where surface loops from one serotype were modularly transplanted onto the chassis of another serotype. This random chimera approach can therefore take steps toward learning how to 'modularize' viruses, yielding basic information that can be applied toward future rational design.

In addition to identifying functional capsid domains in viral chimeras, libraries can be studied to map viral functional

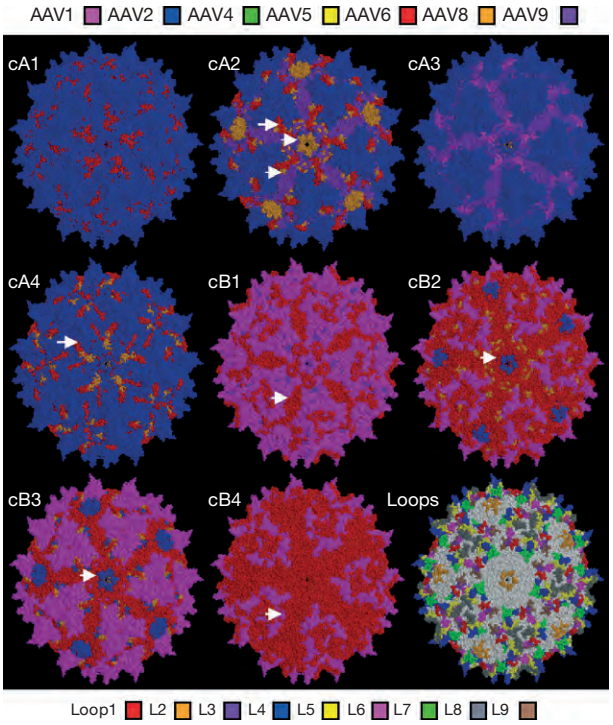

Figure 7 Capsid structure representations of AAV chimeras. AAV chimeras were generated by *in vitro* recombination of seven serotypes. Eight variants were selected for further study, four with substantial sequence similarity to AAV2 (cA1-4) and four with similarity to AAV1/6 (cB1-4). The resulting chimeras displayed strikingly different properties from the parent serotypes with respect to cell tropism and resistance to antibody neutralization. Molecular models of the capsids of the selected AAV chimeras reveal that contributions from multiple serotypes, often distributed across the capsid in surface loops, account for functional diversity among variants. Reprinted from Koerber, J. T., *et al. Mol. Ther.* **2008**, *16*, 1703–1709, with permission from Nature Publishing Group.

domains using a forward genetics approach employing random mutant pools of a single serotype. This approach has recently been employed to map the capsid regions of AAV5 and AAV6 responsible for their distinct cell-binding profiles (Koerber *et al.*, submitted). Such efforts enhance our basic knowledge of virology and can aid future design efforts.

2.202.2.3.2. Directed evolution

Viruses are highly adaptable biological entities, as readily apparent in their ability to undergo repeated rounds of mutagenesis and selection as part of the natural evolution process. Directed evolution, which mimics natural evolution by employing iterative rounds of mutation and selection, in contrast to the single round of genetic diversification and selection discussed in library selection, represents a powerful technique for rapidly and progressively improving viral vectors for gene delivery applications. By allowing for the accumulation of multiple beneficial mutations through iterative rounds of mutagenesis and selection, this process offers the potential to introduce synergistic mutations that confer entirely novel properties on the viral capsid. This accumulation of multiple beneficial mutations can be achieved by selecting promising mutants from the original library and subsequently performing additional mutagenesis and selection to further hone the properties of the selected mutants. As an example, Maheshri *et al.*[70] employed PCR-based mutagenesis and directed evolution of the AAV capsid to introduce novel properties such as resistance to neutralizing antibodies and altered heparin affinity. Recently, our group has demonstrated the utility of directed evolution approaches to target therapeutically attractive cell types – such as human airway epithelia,[77] glial cells in the central nervous system,[78] Muller cells in the retina,[79] and stem cells (Jang *et al.*, submitted) – as well as to target specific organs through *in vivo* panning (Kwon *et al.*, unpublished work). In these examples, additional rounds of mutagenesis and selection afforded further enhancement of the selected properties, thus supporting the value of this iterative approach for generating vectors capable of overcoming a variety of gene delivery challenges.

2.202.3. Design of Artificial Viruses

Rather than attempting to manipulate the highly complex viral architecture from the top down, a number of parallel efforts have focused on a 'bottom-up' approach that involves synthesizing an artificial virus from individual chemical or biological elements. The design of artificial viruses based on synthetic gene vectors may give rise to modular gene delivery systems that are easily manipulated and tuned. This section will describe efforts toward this goal.

2.202.3.1. Materials for Gene Delivery

Synthetic gene vectors are based on materials, such as cationic lipids or polymers, capable of condensing nucleic acids into nanoparticulate complexes that can be taken up by cells.[80–83] Common materials used for nonviral gene delivery, as well as a schematic of polyplex formation, are illustrated in **Figure 8**. Synthetic vectors address many of the limitations posed by the use of viral vectors, offering minimal or reduced toxicity and immunogenicity, greater flexibility in the genetic payload, the potential for straightforward and economical scale-up and production, and the possibility of modular design. However, with a few notable exceptions, current synthetic vectors are plagued by inefficiency compared to their viral counterparts. For example, whereas viral vectors have evolved cunning strategies to efficiently enter host cells, navigate through the intracellular milieu, and deliver their genetic cargo to the nucleus,[84] synthetic vectors passively rely on natural intracellular transport processes and mass action to achieve nuclear delivery.[85,86] Therefore, even in cases where synthetic vectors mediate gene expression levels equivalent to viral vectors, they require uptake of several orders of magnitude more gene copies to compensate for their intracellular trafficking inefficiencies.[87,88]

2.202.3.2. Functionalization of Synthetic Gene Delivery Vectors

As we elucidate the mechanisms underlying viral infection, it is becoming increasingly possible to apply this information and explore biomimetic strategies to enhance the efficiencies of synthetic delivery systems.[89] Toward this end, one could envision using virus-derived or virus-mimetic modules to functionalize

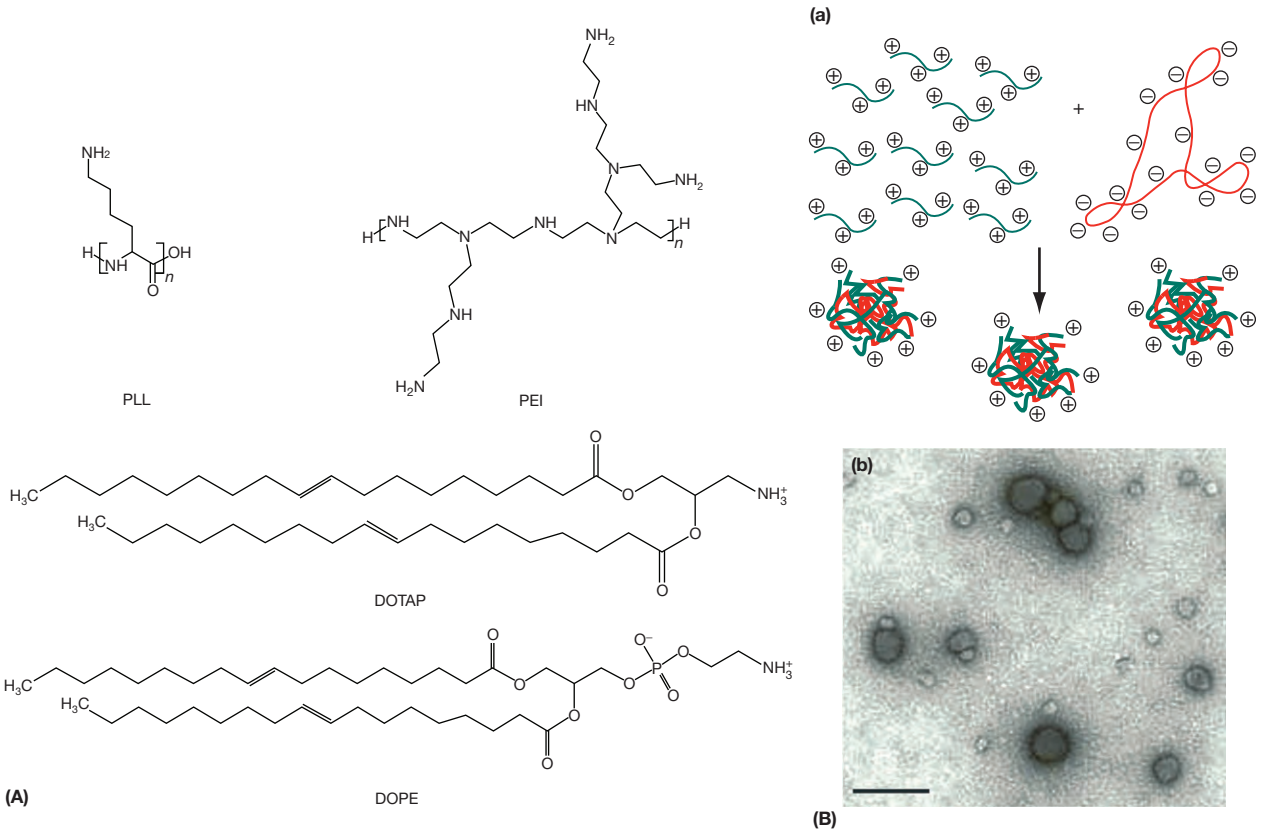

Figure 8 Materials for nonviral gene delivery. (A) The chemical structures of common polymers and lipids used as synthetic gene vectors are illustrated. Common cationic polymers include poly-L-lysine (PLL) and poly(ethylenimine) (PEI). A cationic lipid commonly used for gene delivery is 1,2-dioleoyl-3-trimethylammonium propane (DOTAP), while dioleoylphosphatidylethanolamine (DOPE) is a neutral 'helper' lipid often found in cationic lipid formulations. Reprinted from Bergen, J. M.; *et al. Pharm. Res*. **2008**, *25*, 983–998, with permission from Springer. (B) Polyplexes are formed in aqueous solutions by the electrostatic interactions between positively charged polymers and negatively charged DNA (a), resulting in the formation of nanoparticles (scale bar = 200 nm; image is a transmission electron micrograph). Reprinted Pack, D. W.; *et al. Nat. Rev. Drug Discov.* **2005**, *4*, 581–593, with permission from Nature Publishing Group.

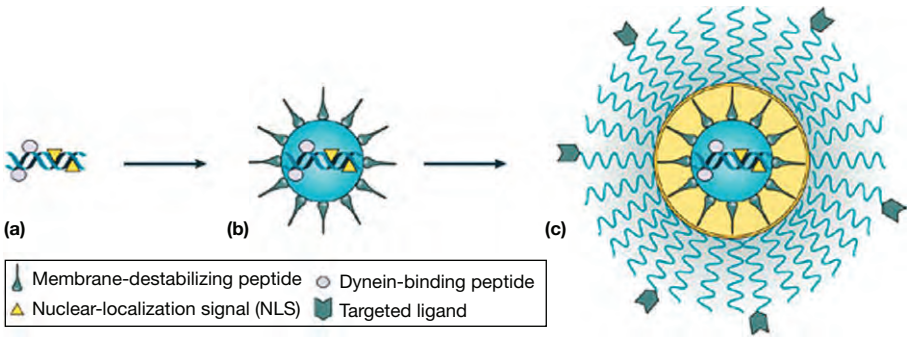

Figure 9 Conceptual model of a multifunctional 'artificial virus.' A multifunctional artificial virus may be assembled as three layers. (a) The core consists of plasmid DNA encoding the therapeutic gene. The plasmid has been modified with functional elements like dynein-binding peptides and nuclear localization signals (NLS) that promote intracellular trafficking toward the nucleus and entry of the gene into the nucleus through nuclear pores, respectively. (b) The functionalized plasmid DNA is condensed with a cationic material, such as a cationic polymer, which is then decorated with membrane-destabilizing peptides, which will function to release the particle from the cell's endosome. (c) The outer layer consists of a shell of polymers or peptides that prevents the particles from aggregating and binding to off-target cells. Binding to targeted cells is mediated through the targeting ligands displayed on the outside of the shell. Reproduced from Mastrobattista, E.; *et al. Nat. Rev. Drug Discov.* **2006**, *5*, 115–121, with permission from Nature Publishing Group.

synthetic vectors with elements to enhance their intracellular delivery efficiencies. This could give rise to 'artificial viruses' built from the minimal essential elements necessary for efficient transfection of targeted cells. A conceptual model of an 'artificial virus' is illustrated in Figure 9. Fueled by insights into molecular virology and studies of viral trafficking, considerable progress has been made toward improving the efficiency of synthetic gene delivery vectors by adding modular, functional parts. Ultimately,

integrating multiple functional modules into multicomponent assemblies has the potential to generate artificial viruses capable of efficient and specific gene delivery. Lessons learned from attempts to mimic essential viral properties are also likely to generate further insights into molecular virology.

2.202.3.2.1. Ligands for cell binding and internalization

Just as viruses display attachment proteins on their capsid or envelope to mediate cellular recognition and binding,[90] artificial viruses must be designed to incorporate modules that direct cellular binding and internalization. An obvious strategy is to attach recombinant VAPs to the surface of synthetic vectors as targeting components. This approach was attempted by Medina-Kauwe *et al.*[91] by incorporating adenoviral penton base proteins into a synthetic vector, although the resulting targeted vector mediated significantly lower transfection efficiencies than the parent virus. These results were partially explained by the internalization of the recombinant penton base proteins via routes that differed from those of Ad itself, highlighting the need to account for context-dependent functionalities of VAPs and providing another example of challenges with viral protein modularity.[92] Aside from VAPs, various biological molecules – including antibodies, growth factors, transferrin, carbohydrates, small molecules, and peptides – have been explored as potential targeting ligands for synthetic vectors.[93,94] In order to maximize the efficacy of targeting strategies, design parameters such as the surface properties of the complex, the length of the spacer between the ligand and complex, and ligand valency should be considered,[95] as these parameters can profoundly influence the ability of the targeting ligand to perform as a modular component of the system.

2.202.3.2.2. Endosomal escape ligands

Both viruses and synthetic vectors must overcome formidable cellular membranes to gain entry into the host cell. While certain enveloped viruses undergo fusion with the plasma membrane concomitant to receptor binding, most nonenveloped viruses and synthetic vectors, as well as some types of enveloped viruses, undergo cellular internalization via endocytosis and must subsequently escape endocytic vesicles to avoid degradation in the endo-lysosomal pathway. Viruses have evolved mechanisms to evade this degradative pathway, some of which rely on acid-induced conformational changes in viral capsid or envelope proteins that lead to exposure of fusogenic domains that mediate endosomal disruption or membrane fusion.[39,96] For example, it has been demonstrated that endosomal acidification triggers disassembly of the Ad capsid, releasing protein VI to lyse the endosomal membrane.[97] Enveloped viruses that undergo endocytosis, such as influenza virus, enter the cytoplasm following fusion events mediated by acid-triggered conformational changes in viral envelope proteins.[98,99]

The ability of viruses to efficiently escape endosomes contributes significantly to their superior gene delivery efficiencies compared to synthetic vectors. In several cases, it has been possible to improve the delivery efficiencies of synthetic vectors by incorporating virus-derived fusogenic peptides. For example, attachment of a peptide derived from the N-terminus of the influenza virus hemagglutinin subunit HA-2 to both polymer- and lipid-based synthetic vectors has resulted in enhanced gene transfer.[100,101] More recently, a peptide derived from the endodomain of HIV gp41, which is involved in membrane fusion between the virus and the cell membrane, was shown to enhance gene delivery by a polymeric synthetic vector.[102] Additional fusogenic peptides identified from natural sources or designed with properties that mimic fusogenic domains have also been shown to be effective enhancers of synthetic gene delivery (see Wagner,[103] Bergen and Pun,[104] and Martin and Rice[105] for reviews).

Finally, certain synthetic polymers and lipids used to deliver genes have themselves been shown or even designed to incorporate endosomolytic properties.[106–110] Of particular interest is a class of 'smart' polymers designed to disrupt biological membranes in a pH-dependent manner.[111] These polymers incorporate pH-responsive functionalities such that they undergo a hydrophilic-to-hydrophobic conversion in the acidifying endosome. At endosomal pH (~6.0), the hydrophobic polymer is believed to partition into the endosomal membrane, mediating disruption. By attaching cell targeting motifs and therapeutic nucleic acids to the polymer backbone, these pH-responsive, 'smart' polymers are capable of enhancing nucleic acid delivery to the cell cytosol. Additional polymeric gene delivery systems designed for enhanced endosomal escape are discussed elsewhere.[81] Despite significant progress designing nonviral nucleic acid carriers that overcome the endosomal barrier, increases in transfection afforded by these strategies are unable to rival the gene transfer efficiencies of viruses, suggesting that additional functionalities are necessary to achieve highly efficient gene delivery.

2.202.3.2.3. Ligands for cytosolic trafficking

A potentially major, but often overlooked, barrier to intracellular trafficking is the limited cytoplasmic mobility of nanoparticulate gene carriers. Recent studies have established that the translational diffusion of macromolecules and nanoparticles in the cytoplasm is severely restricted, primarily due to molecular crowding.[112–114] To facilitate efficient intracellular transport of macromolecules, cells have developed a highly complex active transport infrastructure that conveys cargo along cytoskeletal filaments. For retrograde transport toward the nucleus, dynein is the primary minus end-directed motor.[115,116] Several viruses – including Ad, influenza virus, herpes simplex virus, HIV, and human papillomavirus – have been shown to recruit the dynein motor for assisted transport toward the host cell nucleus.[40,117–121] The ability to harness a motor complex for assisted transport toward the nucleus is a desirable attribute for synthetic gene carriers.[122–125] It has been demonstrated that synthetic gene delivery systems can undergo motor-mediated transport along microtubules following entry into cells.[32,126–129] However, as synthetic systems are believed to rely on either transport within vesicles or the ability of specific plasmid sequences to access dynein-associated protein complexes in the cell, a need remains to identify strategies to improve intracellular transport efficiencies of vectors following their release from endosomes. Despite attempts to identify virus-mimetic ligands capable of mediating attachment of synthetic vectors to the dynein motor complex,[123] successful dynein recruitment by synthetic vectors following endosomal escape remains a challenge.

2.202.3.2.4. Nuclear entry ligands

The nuclear envelope presents a final barrier that must be overcome to achieve successful nuclear gene delivery. While synthetic vectors and simple retroviruses typically rely on nuclear envelope breakdown during cell division for delivery of exogenous DNA,[130] many viruses have been shown to exploit the cell's nuclear import machinery to achieve efficient nuclear delivery to interphase cells. Nuclear import of the viral genome can be accomplished through the recognition of a viral nuclear localization signal (NLS) by the cell's nuclear import machinery.[99] The attachment of synthetic peptides bearing an NLS motif to synthetic vectors has been explored as a biomimetic strategy to enhance their gene delivery efficiencies (see Cartier and Reszka[131] for a review). However, NLS-bearing synthetic vectors have often failed to achieve nuclear delivery of their cargo,[132,133] presumably because of a size limitation for nuclear import dictated by the diameter of the nuclear pore complex.[134,135] Consequently, size is a critical parameter that should be considered when designing artificial viruses.

2.202.4. Conclusions and Future Work

Gene therapy offers remarkable potential as a future therapeutic modality. The previous sections have described the current challenges facing the field as well as efforts to engineer improved gene delivery vectors to overcome these challenges. Beyond current efforts at designing engineered viruses, there are various additional research endeavors that could contribute greatly toward therapeutic translation, including the engineering of the genetic cargo to be delivered. This section will describe future directions for this field.

2.202.4.1. Future Directions

Viral engineering is a multidisciplinary field that draws from a variety of disciplines, including virology, cell biology, immunology, medicine, engineering, and chemistry. Additional advances may be achieved by merging gene delivery with other cutting-edge fields such as synthetic biology and tissue engineering, as described in the following sections.

2.202.4.1.1. Engineering control systems for gene expression

Designing vectors that accomplish efficient gene delivery to targeted cells is a major step toward achieving therapeutic gene delivery. However, as with any drug-based therapy, the levels of the expressed protein must be maintained within an optimal dosage range, that is, the therapeutic window. Inefficient delivery systems may result in the production of subtherapeutic levels of transgene product. However, both viral and synthetic gene delivery systems typically employ strong, constitutive viral or endogenous promoters capable of driving the expression of large amounts of the therapeutic transgene, which can exceed therapeutic dosages for some cargos and thus pose toxicity problems if delivery is efficient. Success to date has largely relied on the treatment of disease conditions that can benefit from relatively low amounts of secreted transgene product or that can tolerate uncontrolled expression levels. However, the unregulated expression of certain transgenes can severely limit their therapeutic efficacy. For example, expression of neurotrophic factors in the brain has been shown to alleviate the clinical symptoms of certain neurodegenerative diseases;[136,137] however, overexpression of these factors can negate the clinical benefits and can even lead to deleterious side effects such as sensory neurite ingrowth[138] and aberrant fiber sprouting.[139] In another cautionary example, it was demonstrated that overexpression of certain short hairpin RNA constructs led to liver toxicity and morbidity in mice via competitive inhibition of endogenous miRNA processing.[140] To avoid potential adverse effects caused by the unregulated expression of therapeutic genes, the ideal gene delivery system would be subject to expression control to maintain therapeutic levels of the transgene product.

The majority of systems currently studied to control expression levels in gene delivery applications function at the transcriptional level by employing inducible promoters controlled by small molecules such as tetracycline, rapamycin, progesterone, or ecdysone.[141–145] However, although improved variants of these systems are being developed, the original systems can sometimes exhibit relatively high basal expression levels because of leaky promoters and relatively low levels of expression upon induction, limiting the possible dosage range.[142,146] With the development of increasingly sophisticated gene regulatory elements that function in mammalian cells, there is opportunity to integrate these elements with therapeutic gene delivery systems. The growing field of synthetic biology already offers a number of expression control options that function at the transcriptional and/or posttranscriptional levels. An elegant example of an efficient, tunable transcriptional switch that functions in mammalian cells was recently presented by Deans *et al.*[147] (**Figure 10**). Their switch, which included modules that responded to repressor proteins as well as RNAi-mediated knockdown of the transcript, was tunable on the basis of the amount of inducer and achieved >99% repression in the absence of inducer.

At the posttranscriptional level, synthetic biology offers RNA-based regulatory elements capable of controlling gene expression. Bayer *et al.* designed ligand-controlled riboregulators containing an antisense domain to target mRNA transcripts as well as an aptamer domain that was susceptible to allosteric control by an exogenous ligand[148] (**Figure 11**). Switching was reversible and tunable on the basis of the concentration of the ligand. Integrating improved gene delivery vectors with gene expression control elements has the potential to generate superior and safe delivery and expression systems for gene therapy applications. Further sophistication may be achieved by designing systems that respond to physiological cues rather than external stimuli.[149] Just as beta cells in the pancreas rely on natural biofeedback mechanisms to regulate blood insulin levels, fully integrated control systems could be engineered to sense levels of a therapeutic gene product in the body and implement control algorithms to maintain expression levels within the therapeutic window. While challenging, the application of sophisticated control systems toward therapeutic gene expression will benefit from continued efforts by synthetic biologists to design novel gene regulatory networks.

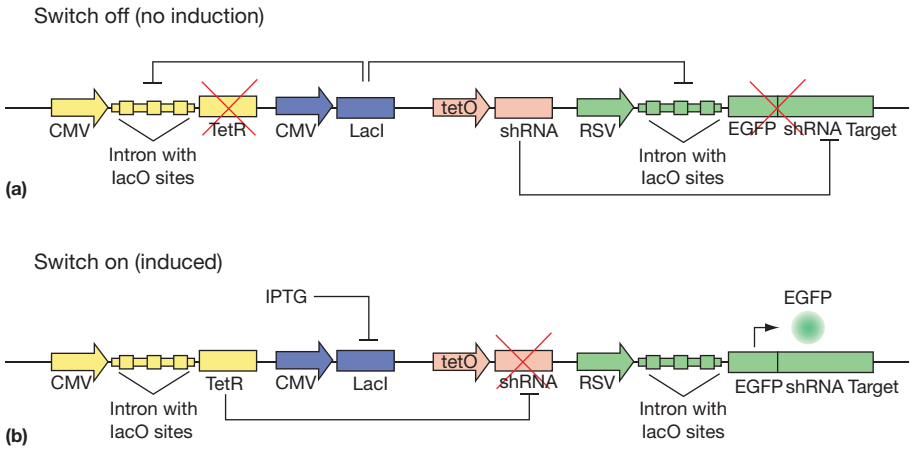

Figure 10 Gene expression control using a synthetic gene network. (a) In the uninduced state, constitutive expression of LacI directly inhibits the expression of the EGFP reporter gene by binding to *lac* operator sites upstream of the EGFP gene. Leaky expression of the EGFP reporter is prevented by the expression of short hairpin RNA (shRNA) designed to destroy any mRNA transcript that may be produced. Consequently, GFP expression is maintained at undetectable levels. (b) Upon induction with isopropyl-β-thiogalactopyranoside (IPTG), LacI activity is suppressed, releasing its inhibition of EGFP expression and simultaneously preventing the expression of the shRNA that blocks the EGFP mRNA transcript. In this state, GFP expression is robust. Reprinted from Deans, T. L.; *et al*. *Cell* **2007**, *130*, 363–372. Copyright (2007), with permission from Elsevier.

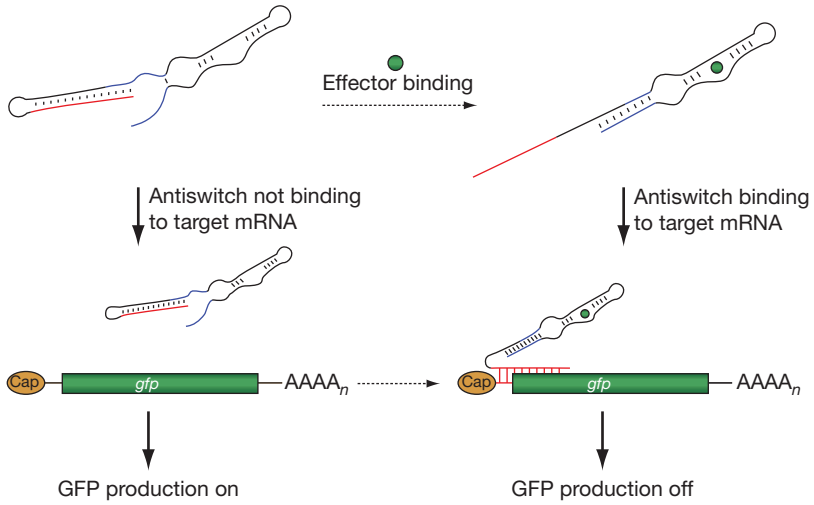

Figure 11 Posttranscriptional control via the antiswitch regulator. In the absence of an exogenous ligand, the antiswitch does not bind to its target mRNA and translation occurs. Once introduced, the ligand binds to the antiswitch, inducing a conformational change in the regulator and exposing the antisense domain, which silences gene expression. Removal of the ligand reverses this inhibition. Reprinted from Bayer, T. S.; Smolke, C. D. *Nat. Biotechnol*. **2005**, *23*, 337–343, with permission from Nature Publishing Group.

2.202.4.1.2. Integration of gene delivery systems with biomaterials

The convergence of gene therapy with tissue engineering has opened up exciting opportunities for regenerative medicine (see Bleiziffer *et al.*[150] and De Laporte and Shea[151] for recent reviews). Already, there has been significant work toward integrating gene delivery systems into biomaterial scaffolds with the idea that cells infiltrating the scaffold and taking up genes available on the scaffold's surface will express factors that promote tissue healing and/or regeneration. Both viral and nonviral gene delivery vectors have been incorporated into scaffolds made from both natural and synthetic materials. Applications utilizing gene delivery from biomaterial scaffolds have already focused on regenerating tissues such as skin, bone, cartilage, nerve, liver, pancreas, and blood vessels.[150] The numerous examples of successful gene integration into biomaterial scaffolds highlight the potential for this technology.

Despite its therapeutic potential, much of the preliminary work demonstrating that genes can be integrated into biomaterial scaffolds relies on nonspecific interactions between the gene delivery system and the scaffold, with limited control on the spatial patterning of genes in the matrix or the temporal release profile of the adsorbed genes. Advances in vector engineering may lead to improved strategies to more precisely integrate gene delivery systems into biomaterial scaffolds. For example, gene delivery vectors could be engineered to

display ligands on their surface that bind to a patterned receptor on the surface of the scaffold. (The feasibility of this concept has already been demonstrated in an *in vitro* system,[152] although additional development is required to translate this technology to a three-dimensional scaffold.) Using multiple ligand–receptor pairs, various genes could be patterned onto a scaffold to direct tissue organization. Additionally, specific ligand/receptor pairs with known binding affinity or specific linkage chemistries could be selected to tune the temporal release profile of genes. Finally, the delivered gene expression cassettes could also be engineered for controlled expression, further tuning the expression of the therapeutic gene.

2.202.4.1.3. Alternative gene delivery systems

Although most current gene delivery systems are on the basis of mammalian viruses or synthetic materials designed to mimic the gene delivery properties of viruses, there remains the possibility of utilizing alternative biological systems as gene delivery vectors. One potential alternative delivery vehicle is the bacteriophage. Although natural bacteriophages are prokaryotic viruses, several groups have demonstrated the feasibility of engineering phage to deliver genes to mammalian cells.[153,154] In these studies, filamentous phage genetically engineered to display targeting ligands on their surface were demonstrated to mediate gene delivery to mammalian cells in culture. While gene transfer efficiencies were low, and considerable improvements are needed, gains may conceivably be achieved by building further modifications onto the phage-based 'scaffold' in modular fashion. However, as with mammalian viruses, manipulation of phage is challenged by the lack of modularity in its compact capsid and genome. One approach to address this may be to employ a 'simplified' phage. It was demonstrated by Chan *et al.*[155] that, by removing elements of overlap in the natural phage genome, the redesigned phage could be more easily studied and manipulated because of its increased modularity. One could envision the extension of this system into 'plug-and-play' phage, with new modules being introduced to specify novel properties, such as those required for efficient gene delivery.

Engineered cells are another system that could potentially fulfill the requirements of a gene delivery vehicle. Extensive work by synthetic biologists to engineer bacterial cells that perform novel functions may also lead to the use of engineered bacteria as 'machines' that perform functions such as (i) homing to the target tissue in the body, (ii) sensing levels of endogenous proteins, and (iii) secreting the necessary transgene products.[156–158] These functions might also be performed by engineered eukaryotic cells, from yeast to stem cells, in what could be considered an extension of *ex vivo* gene therapy. Increasingly sophisticated engineered genetic circuits will support the development of cellular machines that can function as highly effective gene and drug delivery systems.

2.202.4.2. Safety Considerations

Although efforts to engineer improved gene delivery vectors hold tremendous potential for the future of gene therapy, it is extremely important to implement measures to prevent unintended consequences of these technologies. Engineering entities that are capable of infecting humans carries risks that must be mitigated through the implementation of safety measures, including the use of nonpathogenic viruses, the utilization of replication-incompetent viral systems, and the development of systems that prevent recombination to create replication-competent virus. In addition, it is well recognized that new capabilities in DNA synthesis raise the potential for misuse of viral engineering technologies. A potentially alarming example of the safety risks posed by increasingly accessible technology to manipulate or build biological systems was the synthesis of an infectious poliovirus on the basis of a published sequence of its genome.[159] However, with thoughtful vector design, rigorous testing to confirm vector safety and efficacy, and appropriate oversight, it will be possible to engineer improved gene delivery systems that can be translated safely from the bench to the bedside.

2.202.4.3. Summary

The field of gene therapy holds remarkable potential to treat previously intractable diseases. A number of recent clinical successes drive further progress in the field, and additional success is likely to result from the development of improved gene delivery systems. This chapter has described two major approaches for engineering next-generation 'magic bullet' gene delivery systems: (i) reengineering natural viruses using rational design and/or library selection approaches and (ii) designing 'artificial viruses' based on synthetic gene delivery systems. Improved gene delivery systems generated using these approaches are likely to fuel continued progress in the field.

References

1. Strebhardt, K.; Ullrich, A. *Nat. Rev. Cancer* **2008**, *8*, 473–480.
2. Morgan, R. A.; Anderson, W. F. *Annu. Rev. Biochem.* **1993**, *62*, 191–217.
3. Mulligan, R. C. *Science* **1993**, *260*, 926–932.
4. Verma, I. M.; Weitzman, M. D. *Annu. Rev. Biochem.* **2005**, *74*, 711–738.
5. Lopez-Fraga, M.; Martinez, T.; Jimenez, A. *BioDrugs* **2009**, *23*, 305–332.
6. Marquez, R. T.; McCaffrey, A. P. *Hum. Gene Ther.* **2008**, *19*, 27–38.
7. Kmiec, E. B. *J. Clin. Invest.* **2003**, *112*, 632–636.
8. Verma, I. M.; Somia, N. *Nature* **1997**, *389*, 239–242.
9. Al-Dosari, M. S.; Gao, X. *AAPS J.* **2009**, *11*, 671–681.
10. Cavazzana-Calvo, M.; Hacein-Bey, S.; de Saint, Basile, G.; *et al. Science* **2000**, *288*, 669–672.
11. Kay, M. A.; Manno, C. S.; Ragni, M. V.; *et al. Nat. Genet.* **2000**, *24*, 257–261.
12. Khuri, F. R.; Nemunaitis, J.; Ganly, I.; *et al. Nat. Med.* **2000**, *6*, 879–885.
13. Moss, R. B.; Rodman, D.; Spencer, L. T.; *et al. Chest* **2004**, *125*, 509–521.
14. Cartier, N.; Hacein-Bey-Abina, S.; Bartholomae, C. C.; *et al. Science* **2009**, *326*, 818–823.
15. Kaplitt, M. G.; Feigin, A.; Tang, C.; *et al. Lancet* **2007**, *369*, 2097–2105.
16. Bainbridge, J. W.; Smith, A. J.; Barker, S. S.; *et al. N. Engl. J. Med.* **2008**, *358*, 2231–2239.
17. Cideciyan, A. V.; Aleman, T. S.; Boye, S. L.; *et al. Proc. Natl. Acad. Sci. USA* **2008**, *105*, 15112–15117.
18. Hauswirth, W. W.; Aleman, T. S.; Kaushal, S.; *et al. Hum. Gene Ther.* **2008**, *19*, 979–990.
19. Maguire, A. M.; Simonelli, F.; Pierce, E. A.; *et al. N. Engl. J. Med.* **2008**, *358*, 2240–2248.
20. Simonelli, F.; Maguire, A. M.; Testa, F.; *et al. Mol. Ther.* **2010**, *18*, 643–650.
21. Raper, S. E.; Chirmule, N.; Lee, F. S.; *et al. Mol. Genet. Metab.* **2003**, *80*, 148–158.
22. Hacein-Bey-Abina, S.; von Kalle, C.; Schmidt, M.; *et al. N. Engl. J. Med.* **2003**, *348*, 255–256.
23. Hacein-Bey-Abina, S.; Von Kalle, C.; Schmidt, M.; *et al. Science* **2003**, *302*, 415–419.
24. Cornetta, K.; Reeves, L.; Cross, S. *Meth. Mol. Biol.* **2008**, *433*, 17–32.

25. Smith, K. T.; Shepherd, A. J.; Boyd, J. E.; Lees, G. M. *Gene Ther.* **1996**, *3*, 190–200.
26. Wikstrom, K.; Blomberg, P.; Islam, K. B. *Biotechnol. Prog.* **2004**, *20*, 1198–1203.
27. Tsien, R. Y. *Annu. Rev. Biochem.* **1998**, *67*, 509–544.
28. Wilson, T.; Hastings, J. W. *Annu. Rev. Cell Dev. Biol.* **1998**, *14*, 197–230.
29. Chalfie, M.; Tu, Y.; Euskirchen, G.; Ward, W. W.; Prasher, D. C. *Science* **1994**, *263*, 802–805.
30. Gould, S. J.; Subramani, S. *Anal. Biochem.* **1988**, *175*, 5–13.
31. Ignowski, J. M.; Schaffer, D. V. *Biotechnol. Bioeng.* **2004**, *86*, 827–834.
32. Bergen, J. M.; Pun, S. H. *J. Gene Med.* **2008**, *10*, 187–197.
33. Lai, S. K.; Hanes, J. *Meth. Mol. Biol.* **2008**, *434*, 81–97.
34. Medina-Kauwe, L. K.; Xie, J.; Hamm-Alvarez, S. *Gene Ther.* **2005**, *12*, 1734–1751.
35. Suk, J. S.; Suh, J.; Lai, S. K.; Hanes, J. *Exp. Biol. Med. (Maywood)* **2007**, *232*, 461–469.
36. Rice, B. W.; Cable, M. D.; Nelson, M. B. *J. Biomed. Opt.* **2001**, *6*, 432–440.
37. Gambhir, S. S.; Barrio, J. R.; Wu, L.; *et al. J. Nucl. Med.* **1998**, *39*, 2003–2011.
38. Yu, Y.; Annala, A. J.; Barrio, J. R.; *et al. Nat. Med.* **2000**, *6*, 933–937.
39. Gruenberg, J.; van der Goot, F. G. *Nat. Rev. Mol. Cell Biol.* **2006**, *7*, 495–504.
40. Smith, G. A.; Enquist, L. W. *Annu. Rev. Cell Dev. Biol.* **2002**, *18*, 135–161.
41. Whittaker, G. R.; Kann, M.; Helenius, A. *Annu. Rev. Cell Dev. Biol.* **2000**, *16*, 627–651.
42. Summerford, C.; Samulski, R. J. *J. Virol.* **1998**, *72*, 1438–1445.
43. Sattentau, Q. J.; Weiss, R. A. *Cell* **1988**, *52*, 631–633.
44. Cronin, J.; Zhang, X. Y.; Reiser, J. *Curr. Gene Ther.* **2005**, *5*, 387–398.
45. Schnierle, B. S.; Stitz, J.; Bosch, V.; *et al. Proc. Natl. Acad. Sci. USA* **1997**, *94*, 8640–8645.
46. Von Seggern, D. J.; Huang, S.; Fleck, S. K.; Stevenson, S. C.; Nemerow, G. R. *J. Virol.* **2000**, *74*, 354–362.
47. Grimm, D.; Kay, M. A. *Curr. Gene Ther.* **2003**, *3*, 281–304.
48. Wu, Z.; Asokan, A.; Samulski, R. J. *Mol. Ther.* **2006**, *14*, 316–327.
49. Rabinowitz, J. E.; Bowles, D. E.; Faust, S. M.; Ledford, J. G.; Cunningham, S. E.; Samulski, R. J. *J. Virol.* **2004**, *78*, 4421–4432.
50. Gao, G.; Vandenberghe, L. H.; Wilson, J. M. *Curr. Gene Ther.* **2005**, *5*, 285–297.
51. Gao, G. P.; Alvira, M. R.; Wang, L.; Calcedo, R.; Johnston, J.; Wilson, J. M. *Proc. Natl. Acad. Sci. USA* **2002**, *99*, 11854–11859.
52. Eto, Y.; Gao, J. Q.; Sekiguchi, F.; *et al. J. Gene Med.* **2005**, *7*, 604–612.
53. Kreppel, F.; Gackowski, J.; Schmidt, E.; Kochanek, S. *Mol. Ther.* **2005**, *12*, 107–117.
54. Bartlett, J. S.; Kleinschmidt, J.; Boucher, R. C.; Samulski, R. J. *Nat. Biotechnol.* **1999**, *17*, 181–186.
55. Wurdinger, T.; Verheije, M. H.; Raaben, M.; *et al. Gene Ther.* **2005**, *12*, 1394–1404.
56. Etienne-Julan, M.; Roux, P.; Carillo, S.; Jeanteur, P.; Piechaczyk, M. *J. Gen. Virol.* **1992**, *73*(Pt 12), 3251–3255.
57. Pereboeva, L.; Komarova, S.; Roth, J.; Ponnazhagan, S.; Curiel, D. T. *Gene Ther.* **2007**, *14*, 627–637.
58. Wickham, T. J.; Tzeng, E.; Shears, L. L., II; *et al. J. Virol.* **1997**, *71*, 8221–8229.
59. Roberts, D. M.; Nanda, A.; Havenga, M. J.; *et al. Nature* **2006**, *441*, 239–243.
60. Grimm, D.; Zhou, S.; Nakai, H.; *et al. Blood* **2003**, *102*, 2412–2419.
61. Peden, C. S.; Burger, C.; Muzyczka, N.; Mandel, R. J. *J. Virol.* **2004**, *78*, 6344–6359.
62. Croyle, M. A.; Callahan, S. M.; Auricchio, A.; *et al. J. Virol.* **2004**, *78*, 912–921.
63. Mok, H.; Palmer, D. J.; Ng, P.; Barry, M. A. *Mol. Ther.* **2005**, *11*, 66–79.
64. Lee, G. K.; Maheshri, N.; Kaspar, B.; Schaffer, D. V. *Biotechnol. Bioeng.* **2005**, *92*, 24–34.
65. Lanciotti, J.; Song, A.; Doukas, J.; *et al. Mol. Ther.* **2003**, *8*, 99–107.
66. Ogawara, K.; Rots, M. G.; Kok, R. J.; *et al. Hum. Gene Ther.* **2004**, *15*, 433–443.
67. Kwon, I.; Schaffer, D. V. *Pharm. Res.* **2008**, *25*, 489–499.
68. Schaffer, D. V.; Koerber, J. T.; Lim, K. I. *Annu. Rev. Biomed. Eng.* **2008**, *10*, 169–194.
69. Lochrie, M. A.; Tatsuno, G. P.; Christie, B.; *et al. J. Virol.* **2006**, *80*, 821–834.
70. Maheshri, N.; Koerber, J. T.; Kaspar, B. K.; Schaffer, D. V. *Nat. Biotechnol.* **2006**, *24*, 198–204.
71. Shen, X.; Storm, T.; Kay, M. A. *Mol. Ther.* **2007**, *15*, 1955–1962.
72. Grimm, D.; Lee, J. S.; Wang, L.; *et al. J. Virol.* **2008**, *82*, 5887–5911.
73. Koerber, J. T.; Jang, J. H.; Schaffer, D. V. *Mol. Ther.* **2008**, *16*, 1703–1709.
74. Li, W.; Asokan, A.; Wu, Z.; *et al. Mol. Ther.* **2008**, *16*, 1252–1260.
75. Perabo, L.; Buning, H.; Kofler, D. M.; *et al. Mol. Ther.* **2003**, *8*, 151–157.
76. Yu, J. H.; Schaffer, D. V. *J. Virol.* **2006**, *80*, 8981–8988.
77. Excoffon, K. J.; Koerber, J. T.; Dickey, D. D.; *et al. Proc. Natl. Acad. Sci. USA* **2009**, *106*, 3865–3870.
78. Koerber, J. T.; Klimczak, R.; Jang, J. H.; Dalkara, D.; Flannery, J. G.; Schaffer, D. V. *Mol. Ther.* **2009**, *17*, 2088–2095.
79. Klimczak, R. R.; Koerber, J. T.; Dalkara, D.; Flannery, J. G.; Schaffer, D. V. *PLoS ONE* **2009**, *4*, e7467.
80. Gao, X.; Kim, K. S.; Liu, D. *AAPS J.* **2007**, *9*, E92–E104.
81. Pack, D. W.; Hoffman, A. S.; Pun, S.; Stayton, P. S. *Nat. Rev. Drug Discov.* **2005**, *4*, 581–593.
82. Schaffert, D.; Wagner, E. *Gene Ther.* **2008**, *15*, 1131–1138.
83. Segura, T.; Shea, L. D. *Annu. Rev. Mater. Res.* **2001**, *31*, 25–46.
84. Campbell, E. M.; Hope, T. J. *Gene Ther.* **2005**, *12*, 1353–1359.
85. Dean, D. A.; Strong, D. D.; Zimmer, W. E. *Gene Ther.* **2005**, *12*, 881–890.
86. Dinh, A. T.; Pangarkar, C.; Theofanous, T.; Mitragotri, S. *Biophys. J.* **2007**, *92*, 831–846.
87. Hama, S.; Akita, H.; Ito, R.; Mizuguchi, H.; Hayakawa, T.; Harashima, H. *Mol. Ther.* **2006**, *13*, 786–794.
88. Varga, C. M.; Tedford, N. C.; Thomas, M.; Klibanov, A. M.; Griffith, L. G.; Lauffenburger, D. A. *Gene Ther.* **2005**, *12*, 1023–1032.
89. Wagner, E. *Mol. Ther.* **2008**, *16*, 1–2.
90. Waehler, R.; Russell, S. J.; Curiel, D. T. *Nat. Rev. Genet.* **2007**, *8*, 573–587.
91. Medina-Kauwe, L. K.; Kasahara, N.; Kedes, L.; *et al. Gene Ther.* **2001**, *8*, 795–803.
92. Rentsendorj, A.; Xie, J.; MacVeigh, M.; *et al. Gene Ther.* **2006**, *13*, 821–836.
93. Schaffer, D. V.; Lauffenburger, D. A. *Curr. Opin. Mol. Ther.* **2000**, *2*, 155–161.
94. Wagner, E.; Culmsee, C.; Boeckle, S. *Adv. Genet.* **2005**, *53*, 333–354.
95. Schaffer, D. V.; Lauffenburger, D. A. *J. Biol. Chem.* **1998**, *273*, 28004–28009.
96. Marsh, M.; Helenius, A. *Cell* **2006**, *124*, 729–740.
97. Wiethoff, C. M.; Wodrich, H.; Gerace, L.; Nemerow, G. R. *J. Virol.* **2005**, *79*, 1992–2000.
98. Skehel, J. J.; Wiley, D. C. *Vaccine* **2002**, *20*(Suppl. 2), S51–S54.
99. Smith, A. E.; Helenius, A. *Science* **2004**, *304*, 237–242.
100. Wagner, E.; Plank, C.; Zatloukal, K.; Cotten, M.; Birnstiel, M. L. *Proc. Natl. Acad. Sci. USA* **1992**, *89*, 7934–7938.
101. Zhang, X.; Collins, L.; Fabre, J. W. *J. Gene Med.* **2001**, *3*, 560–568.
102. Kwon, E. J.; Bergen, J. M.; Pun, S. H. *Bioconjug. Chem.* **2008**, *19*, 920–927.
103. Wagner, E. *Adv. Drug Deliv. Rev.* **1999**, *38*, 279–289.
104. Bergen, J. M.; Pun, S. H. *MRS Bull.* **2005**, *30*, 663–667.
105. Martin, M. E.; Rice, K. G. *AAPS J.* **2007**, *9*, E18–E29.
106. Boussif, O.; Lezoualc'h, F.; Zanta, M. A.; *et al. Proc. Natl. Acad. Sci. USA* **1995**, *92*, 7297–7301.
107. Cheung, C. Y.; Murthy, N.; Stayton, P. S.; Hoffman, A. S. *Bioconjug. Chem.* **2001**, *12*, 906–910.
108. Mui, B.; Ahkong, Q. F.; Chow, L.; Hope, M. J. *Biochim. Biophys. Acta* **2000**, *1467*, 281–292.
109. Pack, D. W.; Putnam, D.; Langer, R. *Biotechnol. Bioeng.* **2000**, *67*, 217–223.
110. Putnam, D.; Gentry, C. A.; Pack, D. W.; Langer, R. *Proc. Natl. Acad. Sci. USA* **2001**, *98*, 1200–1205.
111. Murthy, N.; Campbell, J.; Fausto, N.; Hoffman, A. S.; Stayton, P. S. *Bioconjug. Chem.* **2003**, *14*, 412–419.
112. Dauty, E.; Verkman, A. S. *J. Biol. Chem.* **2005**, *280*, 7823–7828.
113. Lukacs, G. L.; Haggie, P.; Seksek, O.; Lechardeur, D.; Freedman, N.; Verkman, A. S. *J. Biol. Chem.* **2000**, *275*, 1625–1629.
114. Verkman, A. S. *Trends Biochem. Sci.* **2002**, *27*, 27–33.
115. King, S. M. *Biochim. Biophys. Acta* **2000**, *1496*, 60–75.
116. Vallee, R. B.; Williams, J. C.; Varma, D.; Barnhart, L. E. *J. Neurobiol.* **2004**, *58*, 189–200.
117. Dohner, K.; Wolfstein, A.; Prank, U.; *et al. Mol. Biol. Cell* **2002**, *13*, 2795–2809.
118. Florin, L.; Becker, K. A.; Lambert, C.; *et al. J. Virol.* **2006**, *80*, 6691–6696.
119. Lakadamyali, M.; Rust, M. J.; Babcock, H. P.; Zhuang, X. *Proc. Natl. Acad. Sci. USA* **2003**, *100*, 9280–9285.
120. Leopold, P. L.; Kreitzer, G.; Miyazawa, N.; *et al. Hum. Gene Ther.* **2000**, *11*, 151–165.
121. McDonald, D.; Vodicka, M. A.; Lucero, G.; *et al. J. Cell Biol.* **2002**, *159*, 441–452.
122. Bergen, J. M.; Park, I. K.; Horner, P. J.; Pun, S. H. *Pharm. Res.* **2008**, *25*, 983–998.
123. Bergen, J. M.; Pun, S. H. *Mol. Pharm.* **2007**, *4*, 119–128.
124. Cohen, R. N.; Rashkin, M. J.; Wen, X.; Szoka, F. C. *Drug Discov. Today Technol.* **2005**, *2*, 111–118.
125. Mastrobattista, E.; van der Aa, M. A.; Hennink, W. E.; Crommelin, D. J. *Nat. Rev. Drug Discov.* **2006**, *5*, 115–121.
126. Kulkarni, R. P.; Castelino, K.; Majumdar, A.; Fraser, S. E. *Biophys. J.* **2006**, *90*, L42–L44.
127. Mesika, A.; Kiss, V.; Brumfeld, V.; Ghosh, G.; Reich, Z. *Hum. Gene Ther.* **2005**, *16*, 200–208.

128. Suh, J.; Wirtz, D.; Hanes, J. *Proc. Natl. Acad. Sci. USA* **2003**, *100*, 3878–3882.
129. Vaughan, E. E.; Dean, D. A. *Mol. Ther.* **2006**, *13*, 422–428.
130. Brunner, S.; Sauer, T.; Carotta, S.; Cotten, M.; Saltik, M.; Wagner, E. *Gene Ther.* **2000**, *7*, 401–407.
131. Cartier, R.; Reszka, R. *Gene Ther.* **2002**, *9*, 157–167.
132. Nagasaki, T.; Myohoji, T.; Tachibana, T.; Futaki, S.; Tamagaki, S. *Bioconjug. Chem.* **2003**, *14*, 282–286.
133. van der Aa, M. A.; Koning, G. A.; d'Oliveira, C.; *et al. J. Gene Med.* **2005**, *7*, 208–217.
134. Ludtke, J. J.; Zhang, G.; Sebestyen, M. G.; Wolff, J. A. *J. Cell Sci.* **1999**, *112*(Pt 12), 2033–2041.
135. Pante, N.; Kann, M. *Mol. Biol. Cell* **2002**, *13*, 425–434.
136. Bowers, W. J.; Howard, D. F.; Federoff, H. J. *Exp. Neurol.* **1997**, *144*, 58–68.
137. Tinsley, R.; Eriksson, P. S. *Acta Neurol. Scand.* **2004**, *109*, 1–8.
138. Levi-Montalcini, R.; Angeletti, P. U. *Physiol. Rev.* **1968**, *48*, 534–569.
139. Georgievska, B.; Kirik, D.; Bjorklund, A. *Exp. Neurol.* **2002**, *177*, 461–474.
140. Grimm, D.; Streetz, K. L.; Jopling, C. L.; *et al. Nature* **2006**, *441*, 537–541.
141. Gossen, M.; Bujard, H. *Proc. Natl. Acad. Sci. USA* **1992**, *89*, 5547–5551.
142. Goverdhana, S.; Puntel, M.; Xiong, W.; *et al. Mol. Ther.* **2005**, *12*, 189–211.
143. No, D.; Yao, T. P.; Evans, R. M. *Proc. Natl. Acad. Sci. USA* **1996**, *93*, 3346–3351.
144. Rivera, V. M.; Clackson, T.; Natesan, S.; *et al. Nat. Med.* **1996**, *2*, 1028–1032.
145. Wang, Y.; DeMayo, F. J.; Tsai, S. Y.; O'Malley, B. W. *Nat. Biotechnol.* **1997**, *15*, 239–243.
146. Agha-Mohammadi, S.; Lotze, M. T. *J. Clin. Invest.* **2000**, *105*, 1177–1183.
147. Deans, T. L.; Cantor, C. R.; Collins, J. J. *Cell* **2007**, *130*, 363–372.
148. Bayer, T. S.; Smolke, C. D. *Nat. Biotechnol.* **2005**, *23*, 337–343.
149. Greber, D.; Fussenegger, M. *J. Biotechnol.* **2007**, *130*, 329–345.
150. Bleiziffer, O.; Eriksson, E.; Yao, F.; Horch, R. E.; Kneser, U. *J. Cell. Mol. Med.* **2007**, *11*, 206–223.
151. De Laporte, L.; Shea, L. D. *Adv. Drug Deliv. Rev.* **2007**, *59*, 292–307.
152. Park, I. K.; von Recum, H. A.; Jiang, S.; Pun, S. H. *Langmuir* **2006**, *22*, 8478–8484.
153. Larocca, D.; Kassner, P. D.; Witte, A.; Ladner, R. C.; Pierce, G. F.; Baird, A. *FASEB J.* **1999**, *13*, 727–734.
154. Poul, M. A.; Marks, J. D. *J. Mol. Biol.* **1999**, *288*, 203–211.
155. Chan, L. Y.; Kosuri, S.; Endy, D. *Mol. Syst. Biol.* **2005**, *1*, 0018.
156. Anderson, J. C.; Clarke, E. J.; Arkin, A. P.; Voigt, C. A. *J. Mol. Biol.* **2006**, *355*, 619–627.
157. Arkin, A. *Nat. Biotechnol.* **2008**, *26*, 771–774.
158. Voigt, C. A. *Curr. Opin. Biotechnol.* **2006**, *17*, 548–557.
159. Cello, J.; Paul, A. V.; Wimmer, E. *Science* **2002**, *297*, 1016–1018.

2.203. Protein-Engineered Biomaterials: Synthesis and Characterization

W Mulyasasmita and S C Heilshorn, Stanford University, Stanford, CA, USA

© 2011 Elsevier Ltd. All rights reserved.

2.203.1.	**Introduction**	36
2.203.2.	**Rational Design and Modular Building Blocks**	36
2.203.2.1.	Structural Domains	37
2.203.2.2.	Bioinstructive Domains	39
2.203.2.3.	Bioresponsive Domains	40
2.203.3.	**Synthesis and Purification**	40
2.203.3.1.	Recombinant DNA Technology and Protein Synthesis	40
2.203.3.2.	Purification of Recombinant Proteins	41
2.203.3.2.1.	Column chromatography	41
2.203.3.2.2.	Batch phase separation	42
2.203.3.2.3.	Lipopolysaccharide removal	43
2.203.4.	**Postsynthesis Materials Processing**	43
2.203.5.	**Characterization**	44
2.203.5.1.	Molecular Structure Details	44
2.203.5.1.1.	Protein sequence and composition	44
2.203.5.1.2.	Molecular mass and purity	45
2.203.5.1.3.	Protein conformation	46
2.203.5.1.4.	Domain association	47
2.203.5.2.	Material Bulk Properties	47
2.203.5.2.1.	Mechanical properties	47
2.203.5.2.2.	Morphological features	48
2.203.6.	**Biological Interactions and Immunogenicity**	49
2.203.7.	**Future Directions and Conclusions**	50
References		51

Glossary

Codon Three-nucleotide code in mRNA that basepairs with the anticodon of the corresponding tRNA to specify the identity of amino acid to be incorporated during translation. Since there are 64 possible codons and only 20 amino acids, multiple codons may encode for the same amino acid.

Column chromatography A molecular separation technique that employs physical methods to separate or analyze a mixture of compounds. Separation is achieved by exploiting different properties of the mixture's constituents, which facilitate differential retention times of individual compounds in the column.

Endotoxins Lipopolysaccharides found in the cell wall of Gram-negative bacteria that can elicit innate immune responses when introduced into the body.

Noncanonical amino acids Amino acids with side groups distinct from the 20 naturally existing amino acids found in most biosynthesized polypeptide chains. Noncanonical amino acids are engineered to carry novel functionalities such as photo-cross-linking or fluorescence.

Plasmid Circular piece of DNA that contains an origin of replication that enables self-replication to occur independently of genomic DNA.

Posttranslational modification Covalent modification and functionalization (e.g., phosphorylation and glycosylation) that are added to a polypeptide chain after its translation in a eukaryotic expression system.

Protein conformation A unique 3D configuration adopted by a polypeptide chain, usually essential for its function.

Protein domain Part of a protein that folds and functions properly by itself, independent of the rest of the protein. Multiple protein domains can be assembled together to form a multifunctional polypeptide chain.

Protein fusion tag Short peptide sequence that is usually appended 'in-frame' through the encoding DNA template at the N- or C-terminus of a protein. The short peptide sequence allows for the purification of any arbitrary protein by using resins that bind specifically to the peptide tag.

Recombinant expression The introduction of nonnative genes into a cellular host and their subsequent overexpression, usually for the purpose of protein production.

Transcription The process in which RNA polymerase uses a strand of DNA as a template to make complementary RNA molecules. The resulting RNA molecules are called messenger RNAs (mRNAs), which are subsequently used to guide protein translation.

Translation The process in which ribosomes read, one codon at a time, the information encoded in mRNA, and incorporate the corresponding amino acids into a peptide chain to synthesize a protein.

Abbreviations

AFM	Atomic force microscopy
CHO	Chinese hamster ovary
ECM	Extracellular matrix
ELP	Elastin-like polypeptide
FRET	Fluorescence resonance energy transfer
FTIR	Fourier transform infrared
HPLC	High-performance liquid chromatography
ITC	Isothermal titration calorimetry
LCST	Lower critical solution temperature
LPS	Lipopolysaccharides
MALDI-TOF	Matrix-assisted laser desorption ionization time-of-flight
MMPs	Matrix metalloproteinases
MS	Mass spectrometry
NMR	Nuclear magnetic resonance
PAGE	Polyacrylamide gel electrophoresis
SANS	Small-angle neutron scattering
SEM	Scanning electron microscopy
SPR	Surface plasmon resonance
TEM	Transmission electron microscopy
tPA	Tissue plasminogen activator
uPA	Urokinase plasminogen activator

2.203.1. Introduction

Both synthetic and biologically derived polymers have been broadly explored in the fabrication of biomaterials for tissue engineering applications. In an effort to recapitulate natural biological functions, the design criteria of biomaterials have witnessed a paradigm shift. The ideal biomaterial is no longer bioinert, but is one that seamlessly integrates both the structural and interactive elements of the native extracellular environment. By necessity, these criteria demand exquisite control over the material's blueprint. Owing to the statistical nature of synthetic polymerization reactions,[1] synthetic biomaterials generally suffer from a distribution of sequence and composition, which not only interferes with material tunability and reproducibility, but may also negatively affect postimplantation biodistribution and toxicity.[2] The advent of recombinant technology has ushered in a new class of biomaterials, consisting of protein polymers, which are made of repeating amino acid sequences. By virtue of high-fidelity translation, recombinant protein polymers exhibit monodispersity and precise biochemical compositions. Furthermore, genetic engineering techniques have imparted a high degree of modularity and combinatorial freedom during sequence design of the encoding DNA, thus giving birth to a myriad of novel protein-based biomaterials. Unlike many petroleum-based synthetic polymers, protein biomaterials are cytocompatible and biodegradable, upon cleavage of the peptide bonds, into resorbable degradation products. Coupled with large-scale production in microbial systems, engineered proteins thus provide a sustainable source of cytocompatible and bioresorbable materials for cell and tissue engineering.

Historically, many protein-based biomaterials such as Matrigel and collagen are being harvested from the natural extracellular matrix (ECM). However, since these materials are animal derived and subject to extensive *in vivo* posttranslational processing, they pose certain challenges, such as scarcity, immunogenicity, and batch-to-batch irreproducibility. Attempts to overcome these limitations, aided by the repertoire of genetic manipulation tools made available by recombinant technology, have precipitated the development of custom-engineered protein biomaterials. Reports on protein-engineered biomaterials first emerged in the late 1980s; they were built primarily upon motifs from naturally occurring structural proteins such as silk,[3] elastin,[4] and collagen[5] to create protein polymers with exact structural specifications. These early protein-engineered biomaterials were further investigated as potential cellular scaffolds, and the recent emphasis on dynamic cell–material interactions has led to the incorporation of those extracellular domains that are capable of triggering specific cellular responses or reacting to cell-mediated processes. Among the first nonstructural domains to decorate protein biomaterials were the arginine–glycine–aspartic acid (single letter code: RGD) tripeptide and cell-surface integrin-binding sequence which were incorporated to promote cellular adhesion and spreading.[6] Building upon these early successes and by utilizing the diversity of protein domain databases, a wide array of peptide modules, chosen on the basis of structural and biological functionalities, have been stitched together to create highly functional and dynamic biomaterials (Table 1).

Molecular engineering tools, which have been traditionally used in the development of globular proteins for many years, are increasingly becoming an integral aspect of biomaterials research. Underpinning the core of combinatorial design, domain modularity has enabled the assimilation of multiple peptide motifs to create highly functional biomaterials for *in vitro* cell culture, *in vivo* cell implantation, and drug-delivery applications. Advancing from the intersection of protein engineering and materials science, protein-engineered biomaterials require an interdisciplinary set of experimentation and characterization methods. In this chapter, we describe the various strategies employed in the *de novo* design, synthesis, and characterization of modular protein biomaterials, with an emphasis on recombinantly engineered polymers. Other routes leading to the fabrication of protein biomaterials include solid-phase peptide synthesis and the conjugation of peptide blocks by native chemical ligation.[41] For reports on peptide-based and -chemically synthesized protein biomaterials, the reader is referred to several excellent reviews[42,43] and **Chapter 4.411, Peptide- and Protein-Modified Surfaces** and **Chapter 4.415, Surface Engineering Using Peptide Amphiphiles** in this book.

2.203.2. Rational Design and Modular Building Blocks

Control over polymer compositions has been the holy grail of polymer chemistry for many years. While new chemical synthesis schemes, such as living polymerization and atom-transfer radical polymerization, have moved the field closer

to the realization of this goal,[44] synthetic polymers with strict compositional uniformity remain difficult to produce. In contrast, biopolymers such as DNA and proteins have exact composition because their synthesis is guided by molecular templates. In the case of proteins, specification of the primary amino acid sequence results in a unique three-dimensional (3D) dynamic structure that in turn dictates the protein's functions. Eclectic collections of peptide domains are available for incorporation into protein-engineered biomaterials, the most prevalent being those derived from naturally existing wild-type sequences. In addition, artificial domains, generated through computation and high-throughput screening methods, have more recently been utilized in newly developed biomaterials.

Table 1 Representative domains used in the modular design of engineered protein biomaterials

Function	*Representative domains*	*References*
Structural domains		
Elasticity	Elastin-like	3,7–12
	Silk–elastin-like	13
	Resilin	14–16
Fibrous	Spider dragline silk	17–20
	Silkworm silk	21,22
Physical self-assembly	Coiled coils	23–26
	WW domains/polyproline repeats	27
	Calmodulin	28–30
Flexibility	Amino acid sequence with random coil secondary structures	23,31
Bioinstructive domains		
Cell-binding	Cell–ECM: RGD, REDV, IKVAV	32,33
	Cell–cell: Cadherin	34
Growth factors	Vascular endothelial growth factor	35
Growth factor-binding	Heparin-binding domain	36
Bioresponsive domains		
Protease degradation sites	tPA and uPA sites	37
	Fibrin site	38
	Plasmin site	39
Inorganic-binding site	R5 peptide (silica mineralization)	40

The construction of protein-engineered biomaterials is based on the concept of modular domain design, with an underlying assumption that individual peptide building blocks retain their native functionalities when serially fused into a longer protein polymer. With such an assumption, different domains are mixed and matched to generate materials with systematically tunable, mechanical, biochemical, and biodegradation functionalities. As an added advantage over synthetic biomaterials, genetic engineering of protein biomaterials allows the native extracellular elements to be encoded directly into the material's primary amino acid sequence, thereby obviating the downstream peptide grafting steps. In broad terms, domains that constitute the protein-engineered biomaterials can be categorized into structural, bioinstructive, and bioresponsive (**Table 2** and **Figure 1**), all coming together to create highly functional mimics of the ECM.

2.203.2.1. Structural Domains

In contrast to other protein engineering areas, the use of proteins for bio-material applications faces a unique requirement: mechanical integrity. As tissue engineering platforms, biomaterials must accommodate cellular infiltration, in addition to providing structural reinforcement to the regenerating tissue.

Table 2 Commercially available peptide fusion tags for protein purification by affinity column chromatography

Tag	*Length (sequence)*	*Position*	*Binding partner*	*Elution*	*Additional use(s) of tag*
Biotin carboxyl carrier protein (BCCP)	100	N-terminal or C-terminal	Avidin or streptavidin	Biotin or denaturation	Detection, immobilization
FLAG	8 (DYKDDDK)	N-terminal or C-terminal	Monoclonal antibody	Low pH, EDTA, or FLAG peptide	Detection
Glutathione *S*-transferase (GST)	211	N-terminal or C-terminal	Glutathione	Reduced glutathione	Detection, increased expression, increased solubility, and immobilization
Maltose-binding protein	396	N-terminal or C-terminal	Cross-linked amylose	Maltose	Detection, increased expression, increased solubility
Polyhistidine (His-tag)	2–10 (usually 6: HHHHHH)	N-terminal or C-terminal	Divalent metal (e.g., Ni^{2+}, Co^{2+}, Cu^{2+}, Zn^{2+})	Imidazole or low pH	Detection, immobilization
S-tag	15 (KETAAAKFERQHMDS)	N-terminal, C-terminal, or internal	S-fragment of RNAse A	Low pH	Detection
T7	260	N-terminal	Monoclonal antibody	Low pH	Increased expression
Thioredoxin (Trx)	109	N-terminal or C-terminal	Phenylarsinine oxide	Thiol-containing reducing agent (e.g., Dithiothreitol, β-Mercapto ethanol)	Increased solubility

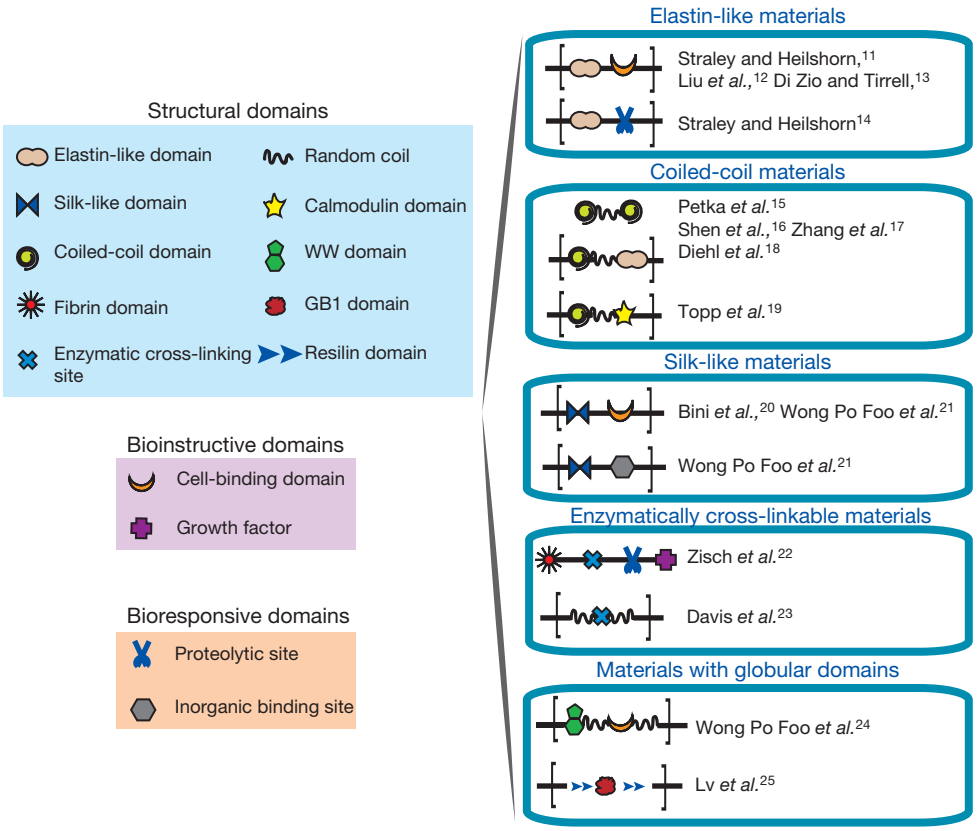

Figure 1 Schematic representation of selected modular protein-engineered biomaterials. Through recombinant technology, peptide domains with diverse structural, bioinstructive, and bioresponsive properties are fused together in the polypeptide chains to create a wide array of functional biomaterials.

Moreover, cell behaviors such as focal adhesion assembly, migration, gene expression, and differentiation are profoundly affected by the elasticity of the matrix,[45] which, in the body, ranges from around 100 Pa (brain) to 100 kPa (bone).[46] Consequently, the development of protein biomaterials for regenerative medicine applications often involves selecting a structural module as the first step in their design.

Logically, the majority of protein biomaterial designs utilize sequences derived from naturally existing structural proteins such as collagen,[47] elastin,[48] silk,[49] and resilin.[15] Materials based upon elastin-like polypeptides of repetitive amino acid sequence $(VPGZG)_n$, where Z is any amino acid except proline, have shown elastomeric properties similar to those of native elastin, prompting soft-tissue applications such as small-diameter vascular grafts[8] and spinal cord repair.[7] In a recent work, a fusion of resilin (an elastomeric protein derived from the wing-hinge of insects) and GB1 protein (a bacterial globular protein capable of rapid and reversible refolding) was designed to create serial molecular springs that mimic the properties of titin, a protein found in muscle.[14]

The mechanical integrity of the bulk material often stems from the physical association or hierarchical self-assembly of their structural modules into supramolecular architectures, as seen in the spontaneous organization of α-helical collagen-like modules into fibrillar architectures[50] or in the assembly of elastin-mimetic triblock copolymers into nanostructured hydrogels.[51] The formation of the desired microstructure is determined at the molecular level through specific interactions between the protein building blocks. Departing from ECM-derived components, material scientists have begun adopting the molecular-binding domains of globular proteins to impart novel properties, such as stimuli-responsiveness and self-assembly, to the structural components of protein biomaterials.

One pioneering example is the leucine zipper hydrogel[23] whose gelation is triggered by the association of coiled-coil domains. The leucine zipper is a naturally found DNA-binding domain of various transcriptional regulatory proteins.[52] A classical leucine zipper motif contains an amphiphilic α-helical structure that comprises six heptad repeats with leucine residues residing in the hydrophobic core of the helix. Driven by electrostatic and hydrophobic interactions, these motifs multimerize into coiled-coil structures that form junction points in the hydrogel network. Owing to the electrostatic nature of the coiled-coil interactions, the hydrogelation process is pH-dependent and pH-reversible. In addition to the interchain association junctions, chain flexibility and favorable chain interactions with the solvent are required for the formation of a swollen hydrogel network. To address these requirements, repeated hydrophilic, polyelectrolyte, random coils of sequence $((AG)_3PEG)_n$ are inserted between two flanking leucine zipper motifs to create triblock copolymers that self-assemble into a swollen, 3D, polymer network at near-neutral pH.

In a different modular design, the $((AG)_3PEG)_n$ spacer sequence has been used to link calmodulin (a Ca^{2+}-sensitive

globular protein) to a leucine zipper domain, to create smart materials whose self-assembly is predictably and reversibly dictated by both pH and Ca^{2+} concentration.[28] Another recent addition to the collection of novel protein-engineered biomaterials is the mixture-induced two-component hydrogel system,[27] where each component is a block copolymer containing multiple repeats of either WW or proline-rich peptide domains that are interspersed with $((AG)_3PEG)_n$ hydrophilic modules. Upon mixing, the WW and proline-rich domains in both the components form physical associations which initiate a sol–gel transition without the need for any external environmental triggers.

The stiffness of self-assembling physical hydrogels is positively correlated with the binding strength and the interval between the association domains. In instances where transient physical cross-linking is incapable of stabilizing a material with desired stiffness, reactive amino acid residues such as cysteine and lysine can be incorporated to mediate covalent cross-linking between the association modules.[53] As seen in synthetic hydrogels, small-molecule cross-linkers, such as bi- and trifunctional isocyanates,[54] *N*-hydroxysuccimidyl esters,[7] and hydroxymethylphosphines[55], have been used to form permanent cross-links in many chemical hydrogels. Other means of chemical cross-linking are catalytic in nature, and are mediated either by photoactivation[15] or by enzymes such as the transglutaminases.[31,56,57]

Cross-linked protein polymers can be viewed as typical amorphous polymeric networks. By stipulating both the intervals between cross-linking sites in the protein primary sequence and the extent of the cross-linking reaction, covalent cross-linking provides a predictive scheme for controlling the mechanical properties of the material such as viscoelasticity, network mesh size, and degree of swelling in water. The mathematical model for polymer elasticity, also known as the rubber elasticity theory, was originally developed by Flory.[1] By approximating each polymer segment as an entropic spring that is deformed in a theta solvent, this model shows the inverse dependence of elastic modulus on the average molecular weight between cross-links (M_c). Accounting for the high water content in hydrogels, the rubber elasticity theory was modified to derive the following relation between shear modulus (G) and M_c:

$$G = \frac{\rho RT}{M_c} Q^{1/3} \qquad [1]$$

where ρ is the polymer density, Q is the volumetric swelling ratio, R is the universal gas constant, and T is absolute temperature.[58] Furthermore, for a highly swollen hydrogel ($Q > 10$), the simplified form of the Flory–Rehner equilibrium swelling theory predicts that Q scales with M_c to the power 3/5.[1]

2.203.2.2. Bioinstructive Domains

Once the structural component has been established, the next step is to customize the scaffold with biofunctional peptide modules. These modules, selected, based on the intended tissue engineering application, can be encoded directly into the primary amino acid sequence as concatenations in the structural domain. One of the first nonstructural peptide motifs to be introduced into protein biomaterials was the (RGD) tripeptide,[6,59] naturally found in various ECM proteins, to promote cell adhesion and spreading by interacting with cell-surface integrins of many cell types.[60] To achieve preferential adhesion of specific cell types, nonintegrin peptide ligands such as the laminin-derived IKVAV sequence have been designed into protein-engineered biomaterials to promote neural cell adhesion and stimulate neurite outgrowth.[32] In another example, the extracellular domain of *N*-cadherin (a key cell–cell adhesion protein in neural development) was fused to the Fc region of the IgG antibody to create an artificial ECM surface that stably adsorbs onto neural stem cells so as to maintain their undifferentiated state and preserve their differentiation potential.[61]

In addition to cell-adhesion domains, other bioinstructive moieties such as growth factors and cell signaling components are being added to the protein-engineered biomaterials toolbox. Such modifications are particularly valuable in regenerative medicine, where protein-engineered ECM scaffolds can be tailored to artificially recapitulate the local *in vivo* niche signals that are thought to direct stem cell self-renewal and differentiation. One example is the incorporation of the active domains of the DSL ligand of the Notch receptor into an elastin-based backbone, for the purpose of modulating glial–neuronal differentiation fates of neural stem cells.[62]

Direct encoding of bioactive sequences into the protein backbone may be problematic in longer peptide sequences (>50 amino acids) whose complex folding may be abolished due to conjugation at the N- and/or C-termini. To eliminate this concern, fully folded soluble factors have been immobilized to the scaffold, either by covalent conjugation or affinity binding. Immobilization of soluble growth factors bestows the benefit of prolonged signal retention not only by dampening burst release, but also by preventing the internalization of the growth-factor–receptor complexes by cells. Covalent conjugation is commonly achieved by cross-linking reactive functional groups on both the growth factor and the biomaterial scaffold. Targets of protein bioconjugation include the terminal amine ($-NH_2$) and carboxyl (–COOH) groups that flank the N- and C-termini of each polypeptide, as well as the amine and sulfhydryl (–SH) groups in the side chains of lysine and cysteine, respectively. However, certain lysine and cysteine residues may play critical roles in maintaining the structural and functional integrity of the growth factor, such that promiscuous modifications at these sites may be deleterious. Problems of nonspecific bioconjugation can be overcome by employing an enzymatic route to cross-linking, as demonstrated by the transglutaminase-mediated conjugation of the vascular endothelial growth factor (VEGF) to a fibrin-based biomaterial. By recombinant DNA technology, a substrate for the transglutaminase factor XIIIa was expressed as an amino-terminal fusion to VEGF, to confer angiogenic activity on the fibrin scaffold.[35]

An alternative approach, which expands the potential of biomaterials as vehicles for controlled drug release, is to immobilize the bioactive signals by noncovalent, affinity-based interactions. One method is to fuse the bioactive factor to an ECM-binding domain. For example, transforming growth factor-beta (TGF-β) has been recombinantly engineered to contain a collagen-binding domain from von Willebrand's factor.[63] Similarly, the fusion of epidermal growth factor (EGF) and a fibronectin-derived collagen-binding domain has

been developed to impart growth factor activity to collagen gels.[64] A less direct approach is to exploit the protein–saccharide interactions that exist in the natural ECM. A particularly important mediator is heparin, a highly anionic, sulfated glycosaminoglycan in the ECM that binds to many proteins such as antithrombin III and various growth factors such as flibroblast growth factor (FGF).[65] Heparin-binding domains, either derived from antithrombin III[36] or from directed evolution by phage display[66], have been covalently incorporated into the biomaterial matrix to immobilize heparin, which in turn binds to the growth factor molecules to sequester them in the matrix.

2.203.2.3. Bioresponsive Domains

Biomaterials for regenerative medicine serve as provisional matrices that are capable of responding to changes in the local microenvironment, as cells migrate and secrete their own ECM. One of the key events in tissue remodeling is the cleaving of the ECM at specific sites by cell-secreted proteases to clear the path for cell migration.[67] Traditionally, biomaterial degradation has been achieved through nonspecific bulk or surface hydrolysis, which fails to recapitulate selective remodeling that is normally observed in the natural context. Cell-mediated degradation was first achieved in synthetic hydrogels by chemically introducing substrates for the matrix metalloproteinases (MMPs), which are enzymes capable of degrading structural ECM constituents such as collagen.[68] For protein-engineered biomaterials, recombinant DNA technology enables the modular integration of protease degradation sites directly into the primary amino acid sequence, which is an added advantage. This not only uncouples the cross-linking sites from the degradation sites, but also allows the scaffold degradation kinetics to be tailored according to specific cellular events. Using modular design, peptide sequences that are sensitive to degradation by neurite growth-cone-specific proteases tPA (tissue plasminogen activator) and uPA (urokinase plasminogen activator) have been encoded into elastin-based protein hydrogels to clear the path for elongating neurites. Minor amino acid sequence mutations in the putative proteolytic sites yield hydrogel variants with 97% sequence homology and identical initial mechanical properties but with degradation kinetics that span two orders of magnitude.[37]

Assisted by modular design principles and a better understanding of cellular behavior, the expanding repository of peptide modules discussed above have led to the development of protein biomaterials that not only present relevant matrix mechanics and bioinstructive chemical signals, but also dynamically respond to the remodeling activities of the local cells. While modular flexibilities constitute one of the most attractive features of protein-engineered biomaterials, the splicing of protein domains may unwittingly introduce secondary structures that in turn alter signal activity or scaffold mechanics. For instance, interspersing identical fibronectin-derived CS5 cell-binding domain sequences within two elastin-like sequences, differing only by 3.4% in amino acid content, significantly altered the cell adhesion properties of the peptide.[69] Furthermore, as a protein domain becomes larger, the fidelity of its tertiary folding may not be preserved when it is fused, in series, to other domains. The responsibility thus lies on the designer to perform theoretical and empirical analyses to verify that the new combination does not affect the preexisting material properties in any unintended manner.

2.203.3. Synthesis and Purification

Downstream of the design steps, recombinant production of the engineered protein polymers is realized through a series of genetic engineering steps, and begins with selecting a host organism whose cellular machinery is capable of producing the target protein. Next, the encoding DNA template is customized in a species-specific manner to optimize protein yield. Following expression, the recombinant protein is isolated from other endogenous host proteins and contaminants through a purification scheme that typically exploits differences in protein size, binding affinity, and other physicochemical properties. A flowchart outlining the production of protein-engineered biomaterial is given in **Figure 2**.

2.203.3.1. Recombinant DNA Technology and Protein Synthesis

The choice of host organism determines the quality and quantity of recombinant protein expression. As the outcome of protein biosynthesis is highly contingent upon cellular machinery, a wide array of recombinant proteins have been expressed in a range of host organisms including mammalian,[70] plant,[71] yeast,[72] and bacterial cells;[73] each selected to optimize the production of the desired protein product. Equipped with specialized organelles for folding and posttranslational modifications (i.e., the endoplasmic reticulum and the Golgi apparatus), eukaryotic cells are generally used for the expression of complex proteins. On the other hand, lower-level prokaryotes, while incapable of elaborate posttranslational processing, have lower technical and economical barriers to large-scale protein expression.

In cases where posttranslational modifications such as glycosylation are essential for protein function, expression in mammalian cells is usually the gold standard. A large sector of commercial recombinant protein production harnesses Chinese hamster ovary (CHO) cell lines as their expression factory.[70] Under optimal fermentation conditions, CHO cells can be cultured in bulk liquid with a doubling time of 15 h. Unfortunately, this rather slow growth rate imposes a prohibitive cost on production scale-ups. As an alternative, scientists have resorted to different strains of yeast such as *Saccharomyces cerevisiae* and *Pichia pastoris* as the expression host. As a eukaryote, yeast possesses dedicated organelles for proper protein folding and modification. Unlike CHO cells, however, yeast has a faster doubling time of 2 h and demands less intensive culture maintenance.

Discounting the need for posttranslational processing, *Escherichia coli* (*E. coli*), a prokaryotic organism, is the most attractive recombinant expression host.[73] The use of *E. coli* for heterologous expression is mainly motivated by its rapid growth rate, ease of culture, well-characterized genetics, and amenability to genetic modification and exogenous gene transformation. Many *E. coli* strains have been mutated to address specific aspects in the cloning and protein synthesis process. In addition, a myriad of plasmid vectors, each harboring

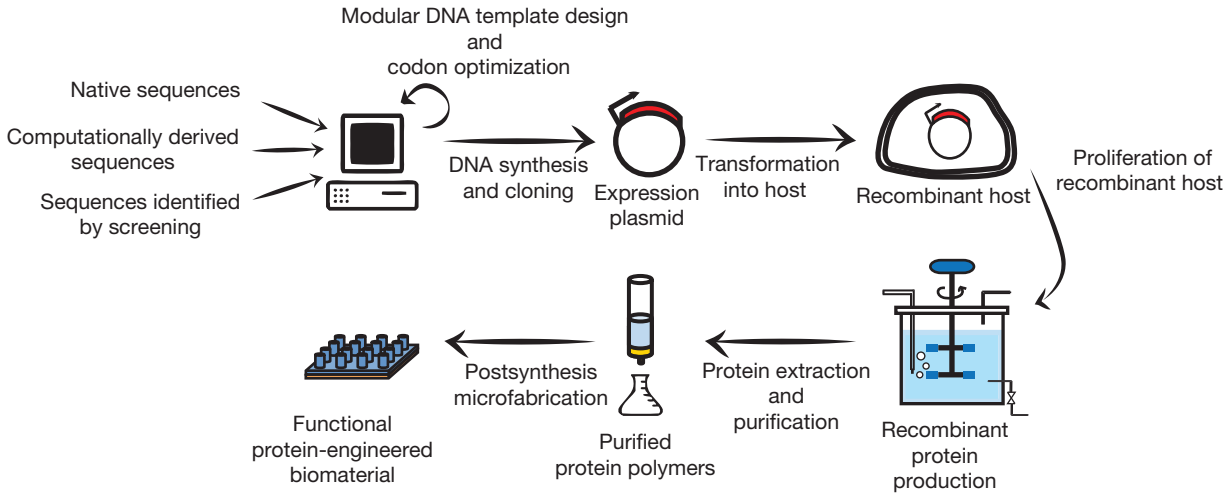

Figure 2 Design and synthesis scheme of recombinantly engineered protein biomaterials. Peptide domains used in the modular design can be derived from wild-type sequences, generated through computation, or identified by high-throughput screens. The modules are then concatenated and back-translated into a DNA template, which is then cloned into a recombinant plasmid and transformed into the host cell of choice, where overexpression of the engineered protein occurs. Following extraction and purification, the target protein is further processed into a biomaterial scaffold with specialized function and morphology.

specialized origins of replication, resistance markers, inducible promoters, and purification tags, are now commercially available for recombinant protein production in *E. coli*. Collectively, these attributes render *E. coli* a very desirable host expression system for the production of simple protein domains that do not require extensive modifications.

The choice of host organism bears a major significance in the subsequent cloning step, especially in the design of the DNA template. Conforming to the central dogma of molecular biology, heterologous proteins are produced via a residue-by-residue transfer of information by transcription (DNA → mRNA), followed by translation (mRNA → protein). During translation, mRNA is read as triplet codons by complementary transfer RNAs, which add amino acids to the growing peptide chain according to the codons they recognize. The genetic code is degenerate, meaning that several synonymous codons can be used to encode a single amino acid. Also, even though the genetic code is generally conserved, the relative abundance of each tRNA pool is species-specific, such that there exists among different host organisms a substantive variability in the frequency of codon usage. For example, though extensively used in humans, the AAG and AGA codons for arginine are scarce in the *E. coli* genome.[74] This phenomenon is referred to as codon bias.[75] The presence of rare codons can trigger translational stalling, leading to mRNA degradation and ultimately a decrease in translational efficiency.[76] By carefully selecting the DNA sequence, codon bias can be harnessed to maximize the yield of recombinant protein expression.

The past decade has witnessed a steep decline in the cost of DNA synthesis, thus allowing bottom-up construction of DNA to be performed routinely. Recombinant protein synthesis strategies derive many benefits from *de novo* DNA design, among which is the possibility of rational codon selection. Even though addressing codon bias can contribute to yield improvement, choosing the same high frequency codon for each amino acid in the protein polymer repeat units may be counterproductive. Highly repetitive DNA sequences are prone to recombination events that lead to undesired genetic mutation.[77] Thus, a degree of codon diversity must be included when designing the template for repetitive amino acid sequences. In addition to codon bias, optimal gene expression involves other factors such as strength of ribosome-binding site and mRNA structure and stability;[78] all of these together render codon optimization a nontrivial process. Algorithms, including publicly available software, are presently being developed and implemented to enhance translational efficiency and protein yield in specific expression systems.[79]

2.203.3.2. Purification of Recombinant Proteins

Purification of a target protein to a level that is necessary for reproducible biomaterial fabrication and cytocompatibility is typically one of the most laborious steps in recombinant protein production. For nonsecreted proteins, extraction begins with cell lysis by repeated freeze–thaw cycles, sonication, high-pressure homogenization, or permeabilization by organic solvents. Subsequently, soluble proteins are fractionated and isolated from the cell lysate by exploiting the differences in size, charge, hydrophobicity, or ligand interactions. In broad strokes, methods of purifying recombinantly engineered protein polymers are facilitated either by column chromatography or batch-phase separation.

2.203.3.2.1. Column chromatography

Column chromatography, in which a protein solution is flowed through a tube packed with a solid matrix, is one of the most routinely used laboratory techniques for the separation of protein mixtures. Depending on their interactions with the matrix, the individual protein species are subjected to different extents of retardation, and can thus be collected in separate fractions as they elute out of the column. The selection of matrix dictates the basis of separation, that is, charge

(ion-exchange chromatography), hydrophobicity (hydrophobic interaction chromatography), size (gel-filtration or size-exclusion chromatography), or the ability to bind to ligand (affinity chromatography).

Ion-exchange chromatography exploits the differential arrangement of charges on the surface of the proteins and is facilitated by a matrix of beads that carry either a positive or negative charge. Examples are diethylaminoethylcellulose (DEAE-cellulose) and caboxymethylcellulose (CM-cellulose), which are positively and negatively charged, respectively. In the column, the movement of proteins that have the opposite-charge with respect to the matrix will be retarded due to electrostatic attraction. As the strength of association is dictated by the ionic strength of the solution and the net charge on the proteins, effective fractionation is achieved by systematically feeding solutions of varying salt concentration and pH into the column. Generally, retention time is reduced either by increasing the counter ion (relative to the matrix) concentration, or by increasing and decreasing the pH in cation and anion exchange columns, respectively.[80,81]

In hydrophobic interaction chromatography, proteins are separated based on the favorability of their interaction with the hydrophobic side chains (phenyl, octyl, or butyl) that protrude from the stationary beads.[82] Exposure of the hydrophobic regions on the protein surface, for immobilization onto the matrix, is achieved by initially applying high-ionic-strength salts (e.g., ammonium sulfate) that promote the dissipation of water from the solvation layer around a protein. More hydrophobic proteins require less salt to promote binding. Therefore, the elution of proteins with increasing hydrophobicity is achieved by applying salt solutions of decreasing ionic strength or concentration.[83]

Size-based protein fractionation by size-exclusion chromatography utilizes an inert but porous matrix.[84,85] Smaller molecules infiltrate the pores more easily, and therefore have longer retention times in the column. Commercially available beads are commonly fabricated from polysaccharides (dextran, agarose, or acrylamide), with cross-linking densities tailored to produce pore sizes that are suitable for the fractionation of molecules of molecular weight ranging from a few to several thousand kilodaltons.

Ordinary column chromatography often suffers from matrix dyshomogeneities, causing uneven solvent flow which in turn limits the resolution of separation. Furthermore, flow rates are intentionally kept low (about one column volume per hour) to achieve sufficient equilibration between the protein solutes and the matrix. A newer chromatography technique, referred to as high-performance liquid chromatography (HPLC), affords much higher resolution by making use of smaller (3–10 μm in diameter) particles that are tightly packed, using a special apparatus, into a stainless steel column.[86] Aided by an elaborate system of pumps and valves, high external pressure is applied to the column to achieve rapid flow rates (about one column volume per minute). By virtue of the small matrix particle size, sufficient solute equilibration in an HPLC column is achievable in spite of the high flow rates. Depending on the nature of the matrix particles, HPLC can be categorized into three separation modes – adsorption chromatography (analogous to hydrophobic interaction chromatography), ion-exchange chromatography, and size-exclusion chromatography.

Common to all of the aforementioned chromatographic methods is an initial capture step which is followed by a gradual retention and elution of the target protein. Given the complex composition of the cell lysate, multiple passages through the column or serial purification through several column types may be necessary to achieve satisfactory purity. These time-intensive procedures typically recover only 50% of the starting material.[87] To sidestep this limitation, systems that take advantage of binding interactions to specific matrix-immobilized ligands have been developed, which give over 90% yield, in a few or even a single column passage. Collectively, these procedures are referred to as affinity chromatography.[88,89]

By recombinant DNA technology, molecular tags exhibiting affinity to their respective ligands can be directly encoded into the plasmid vector, as a fusion to the protein of interest. This way, virtually any recombinant protein can be purified without *a priori* knowledge of its physiochemical properties. Thanks to their size and proteolytic stability, several purification tags impart an additional benefit of increasing the solubility and/or expression of the heterologous protein.[90] Examples of commercially available affinity tags are maltose-binding protein,[91] glutathione *S*-transferase,[92] thioredoxin,[93] cellulose-binding domain, and biotin carboxyl carrier protein,[94] as well as shorter peptide tags such as polyhistidine,[95] S-peptide,[96] and FLAG™ peptide.[29]

For many clinical applications, it is imperative that the affinity tags be removed postpurification because they may prompt unwelcomed effects such as immune response activation. Tag removal is usually achieved by inserting a specific cleavage site between the target protein and the purification tag, and proteolysis is performed either enzymatically (e.g., enterokinase, thrombin)[87] or chemically (e.g., cyanogen bromide cleavage at methionine).[97] A brief summary of affinity chromatography purification tags and tag removal systems is given in **Table 2**.

Affinity chromatography generally allows efficient one-step isolation of a recombinant protein from the cell lysate. Performing orthogonal chromatography modes in succession can further increase purity, although, inevitably, at the expense of increased time and cost.

2.203.3.2.2. Batch phase separation

While invaluable for laboratory-scale purification, column chromatography techniques can rapidly become time- and cost-prohibitive at the final preparative scale-up stage. To facilitate economical and scalable purification, a common strategy is to exploit the differential dependence of the proteins' phase properties on controllable environmental parameters (e.g., temperature or solvent quality). One such example is the reversible lower critical solution temperature (LCST) transition, which is exploited in the purification of recombinant elastin-like polypeptides (ELPs).[48] Below their LCST, ELPs are soluble in water. Unlike most proteins, however, the hydrophobic nature of the ELP peptide sequence favors their desolvation as temperature increases above the LCST, resulting in the aggregation of the protein polymers into an insoluble phase.

This LCST transition of ELPs has made them useful as fusion tags for the purification of recombinant proteins. The exact length and composition of the ELP sequence can be tailored to yield an LCST of about 37 °C, such that the ELP

fusion protein would remain soluble during culture in *E. coli* but precipitate rapidly upon a mild temperature shift. Through alternating cycles of hot (35–45 °C) and cold (4 °C) centrifugation, as well as modulation of extrinsic solvent parameters such as ionic strength, the ELP fusion proteins have been successfully purified from the *E. coli* host contaminants in a scalable, completely nonchromatographic procedure.[9] Modifications to the procedure have allowed ELPs to be used as efficient purification tags for numerous target proteins. Recently, a self-cleaving element derived from the bacterial intein protein has been inserted between the ELP tag and the target protein to facilitate nonenzymatic tag removal.[98] Mild shifts in pH and temperature trigger a rapid C-terminal splicing of the intein element, upon which the tag can be removed by a final thermal precipitation step to yield a pure, unmodified target.

Apart from temperature cycling, ion-based precipitation cycles have also been explored for nonchromatographic protein purification. Such methods rely on the Ca^{2+}-binding affinity of the annexin B1 tag, which allows the annexin B1-intein-target fusion proteins to be selectively precipitated from the solution at 20 mM Ca^{2+}, and the tag subsequently removed by the self-catalytic cleavage of the intein moiety.[99]

2.203.3.2.3. Lipopolysaccharide removal

Other nonproteinaceous host contaminants that are toxic and immunogenic must be eliminated from recombinant protein preparations that are intended for implantable therapeutics. Used as a major workhorse in recombinant technology, *E. coli* provides an easy and economical means of protein production, but may also require an additional purification step due to the presence of lipopolysaccharides (LPS, also known as endotoxins). Common to all Gram-negative bacteria, LPS are an integral part of the outer cell membrane, and occupy up to three-quarters of the bacterial cell surface.[100] Hence, endotoxins are present at high levels in the crude cell lysate and remain a concern even after the removal of contaminating host proteins because even minute quantities in the bloodstream can be lethal.

An LPS molecule is composed of a hydrophilic polysaccharide moiety covalently linked to Lipid A, a hydrophobic moiety that is responsible for the biological toxicity of endotoxins. Individual LPS molecules carry a negative charge at neutral pH and have molecular weights ranging from 10 to 20 kDa, although they tend to self-assemble into 1000 kDa aggregates.[101] Relative to proteins, LPS are highly heat- and pH-stable, and thus cannot be inactivated without also inducing protein denaturation.

By taking advantage of the net negative charge on LPS, endotoxins can be eliminated by anionic-exchange chromatography, although only positively charged target proteins can be simultaneously purified without incurring significant material loss.[102] A more generic method is based on the binding affinity of lipid A to polymyxin B, a peptide antibiotic that can be immobilized on sepharose resin to facilitate endotoxin removal by affinity column chromatography.[103] The success of chromatographic methods relies not only upon the differential affinity between the endotoxin and the target protein for the chromatography matrix, but also on the affinity of the endotoxin for the protein. As a result, it is a common practice to dissociate LPS–protein complexes with surfactants (e.g., alkanediol) prior to chromatographic separation.[104] Pioneered by the pharmaceutical industry, other techniques, including ultrafiltration, phase separation, and adsorption, have been developed to remove endotoxins without compromising the properties of the target protein.[105]

2.203.4. Postsynthesis Materials Processing

Eliciting appropriate biological responses often serves as a yardstick by which the success of an engineered biomaterial scaffold is measured. In turn, signal transduction to cells is significantly influenced by the nano- and microscale scaffold architecture presented at the cell–material interface.[106] Following purification, the engineered proteins are then self-assembled or chemically cross-linked to create a bulk biomaterial scaffold. These straightforward processes have produced porous materials with robust mechanical properties, but they usually result in amorphous 3D morphologies. While a recapitulation of the natural structural hierarchy of the ECM can be achieved to a certain extent by the self-assembly of engineered polypeptides into fibrillar structures, these bottom-up supramolecular assembly strategies are only applicable to specific classes of polypeptides, (e.g., helical,[50] beta-structured,[107] and amphiphilic[108]), and are incapable of supporting complex structural specifications at a length or scale that is appropriate for tissue-level organization. Additionally, nutrient perfusion and mass transport limitations (especially oxygen diffusion) render constructs larger than a few hundred micrometers pragmatically ineffective.[109] In view of these considerations, postsynthesis processing of simple porous scaffolds into intricate micro- and nanoscale structures naturally becomes an integral part of the fabrication of protein-engineered biomaterials. Similar to other polymeric materials, protein-engineered biomaterials can be processed by methods such as electrospinning, nano- or micromolding, and photopatterning. However, owing to the sensitivity of proteins to heat and pH-induced denaturation, extreme processing parameters should be avoided when working with protein-based biomaterials.

Electrospinning is one of the most straightforward and versatile tools for processing a wide variety of polymeric materials (melts or solutions; natural or synthetic) into fibrillar threads.[110] The basic setup consists of a high voltage power supply, a spinneret (a polymer reservoir, usually assembled by fitting a blunt tip needle to a syringe), a syringe pump, and a grounded collector. The polymer sample is initially held by surface tension at the tip of the spinneret. Subsequent delivery of high electric potential induces a mutually repulsive charge on the chains, causing the hemispherical liquid meniscus to morph into a conical shape known as the Taylor cone. At a critical electric potential value, where the repulsive electric force exceeds the surface tension, a charged jet of polymer solution or melt is ejected from the tip of the spinneret toward a grounded target. During its flight, the jet undergoes a whipping process, where incipient fibers begin to elongate due to electrostatic repulsion between the fiber segments. Concomitant solvent evaporation results in deposits of dry polymer fibers that range from 50 nm to 10 μm in diameter. A plethora of protein polymers such as collagen,[111] tropoelastin,[112] and silk[113] have been electrospun into continuous, high

surface area-to-volume ratio, and porous, fibrillar, matrices reminiscent of natural ECM morphologies. By adjusting parameters such as polymer molecular weight, solution viscosity, electric potential, flow rate, and collection geometry, scaffolds of various shapes, fiber orientations, and mechanical properties have been created to meet the specifications for various soft-tissue engineering applications including skin, blood vessel, tendon/ligament, cardiac patch, nerve, and skeletal muscle.[114]

Borrowing concepts from microelectronics, rapid prototyping of various micro- and nanomolded biomaterials has been propelled by the advent of lithographic techniques, particularly soft lithography, which refers to the fabrication of patterned copies using a poly(dimethylsiloxane) (PDMS) device.[115] Since its inception, several variants of the soft lithography technique have been described. These include microcontact printing (μCP),[116] replica molding (REM),[117] microtransfer molding,[118] and solvent-assisted micromolding (SAMIM).[119] Without going into the operational details, the core of these techniques can be reduced to four general steps: (1) pattern design, (2) fabrication of a topologically patterned master, (3) high-fidelity pattern transfer from a master to an elastomeric device, and (4) pattern transfer from the device to a biomaterial by printing, molding, or embossing.[120] The utility of micro- and nanomolded surface patterns in tissue engineering has been demonstrated through, for instance, the ability to align cardiac myofibers[121] and to control stem cell morphology and differentiation.[122] Although current examples are historically dominated by synthetic biomaterials, micro- and nanomolding technologies are rapidly making headway into the burgeoning field of protein biomaterials.

Optical techniques such as surface photolithography and two-photon laser scanning lithography represent another emerging class of microfabrication technology. Photopatterning hinges upon the base material's intrinsic amenability to photopolymerization or photoablation, and the ability to incorporate noncanonical amino acids into recombinantly expressed proteins has enabled the introduction of photoreactivity into protein biomaterials. For example, *para*-azidophenylalanine ($p$$N_3$Phe), a photosensitive noncanonical amino acid, was engineered into elastin-like materials to create a family of photo-cross-linkable artificial ECM films that could be surface-patterned by photolithographic techniques.[24] Through surface patterning, researchers have gleaned tremendous insight into cellular behavior when grown on biomimetic substrates. However, a complete understanding of the cellular spatial sensitivity requires complex 3D geometry, which cannot be manufactured by conventional single-mask photolithography. Layer-by-layer fabrication, which forms the basis of stereolithography, is typically required to construct patterns in 3D. Recently, dynamic mask projection stereolithography has been used in conjunction with photoactive $p$$N_3$Phe amino acids to create 3D landscapes and user-defined curvatures on elastin-based cell culture substrates.[123]

The freedom to inscribe arbitrarily shaped microstructures within a bulk substrate is also possible through photo-cross-linking or photoablation by two-photon lithography, which capitalizes on a confocal laser scanning microscope being able to deliver finely focused photons onto micron-scale focal volumes. Along the optical path, the laser focal point is the only location where the two photons converge. Therefore, photoreactive processes that are energetically driven by the simultaneous absorption of two finely focused photons are confined to the focal volume, leaving the out-of-focus regions unaltered.[124] Benefiting from this strategy, complex nerve guidance microchannels have been successfully photoablated within PEGylated-fibrinogen hydrogels to direct the outgrowth of neurites from the dorsal root ganglia.[125] Supported by their compatibility with protein materials and the geometric flexibility they afford, two-photon lithography techniques are being foreseen to be powerful tools in the 3D patterning of new protein-engineered biomaterials.

The emergence of new micro- and nanofabrication technologies is continually offering exciting opportunities for the design of biomaterial scaffolds with increasing levels of geometric and functional intricacies. The brief descriptions outlined above are meant to briefly acquaint those who are new to the field. For in-depth discussion of how such fabrication technologies are applied in tissue engineering, the reader is encouraged to consult several excellent reviews.[126–128]

2.203.5. Characterization

In order to confirm the correct synthesis of the desired material, assure batch-to-batch consistency, and assess the performance of the material, which ultimately dictates the final biological outcome, the development of novel biomaterials has to culminate in a systematic characterization scheme. At the most fundamental level, the desired chemical composition and domain functionality of the protein, which originally motivated the design considerations, must be verified. Next, postfabrication material properties such as mechanical behavior and degradation profiles have to be characterized. In addition, since cell migration and nutrient diffusion through the material are paramount to successful engraftment, an investigation of the surface properties and morphological features is integral to the series of material characterization tests. Protein-engineered biomaterials are created through an interdisciplinary convergence of protein engineering and materials science. Consequently, characterization of these materials invokes a battery of tests commonly employed in biochemistry and polymer science. Discussed in detail below are assays that investigate the composition, purity, and molecular characteristics of the target proteins, as well as the mechanical properties and mesoscopic structures of the resulting bulk materials (**Figure 3**). Downstream biological responses such as cell adhesion, migration, proliferation, and gene expression, since cells are seeded upon or within protein-engineered biomaterials, are characterized using standard *in vitro* assays described elsewhere in this textbook.

2.203.5.1. Molecular Structure Details

2.203.5.1.1. Protein sequence and composition

DNA sequencing and amino acid analysis are two methods of confirming the proper oligonucleotide sequence of the DNA template and the chemical composition of the resulting target protein. For materials that have been rationally designed and built from ground up, confirming that the components have been created as they were designed is an essential first step in

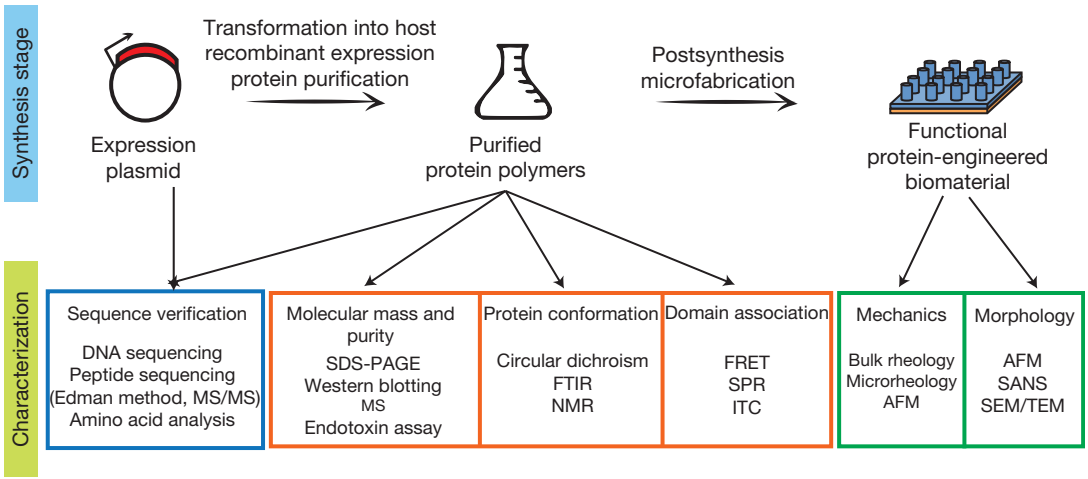

Figure 3 Flowchart for the analysis of protein-engineered biomaterials. Characterization tools are categorized according to the corresponding synthesis steps, beginning with verification of the chemical compositions, structural and functional analysis of the peptide modules, and finally mechanical and morphological characterizations of the fabricated biomaterial. This suite of material characterizations is followed by a series of *in vitro* and *in vivo* studies to determine the biological outcome of the engineered material.

their characterization. Today, DNA sequencing is performed routinely for a small fee by commercial companies, using a modified version of the chain-terminating DNA sequencing method developed in the 1970s.[129] In this technique, the DNA sample is replicated in the presence of standard nucleotides and a small amount of fluorescently labeled chain-terminating nucleotide analogs. Termination of DNA replication by the incorporation of these analogs produces new DNA fragments that are truncated at different points along the template. These fragments are subsequently size-separated by capillary electrophoresis, with the shortest sequence moving the fastest, and thus the furthest. By tracking the fluorescence signals as the DNA pieces migrate along the capillary, the sequence of the parent DNA can be deduced.

DNA sequencing is routinely coupled with amino acid analysis, which focuses on the downstream protein product. Unlike DNA sequencing, which reveals the exact nucleotide sequence, amino acid analysis gives the quantity of each amino acid that is incorporated into the full-length protein. In this process, the protein sample is first acid-hydrolyzed to release the individual amino acid residues, which are then derivatized with chromophores to facilitate their detection when subsequently separated in an HPLC system.[130] Buffers of increasing pH are fed into the HPLC column, and individual amino acids are eluted as the pH reaches their respective isoelectric points. The quantity of each eluted amino acid is determined either by comparing its average retention time and absorbance to that of an internal standard, or through the addition of a colorimetric reagent whose color change exhibits a dependence on the amino acid concentration.

Direct determination of the amino acid sequence of a protein is made possible without the knowledge of the encoding DNA through Edman degradation, and more recently, through mass spectrometry (MS). In Edman degradation, the polypeptide chain is recursively subjected to three chemical reactions. First, the N-terminal residue is reacted with phenylisothiocyanate (PITC) before it is cleaved from the polypeptide by acid hydrolysis in the second step. The resulting free amino acid residue, now existing as a cyclic phenylthiohydantoin (PTH) derivative, is then identified by chromatography or electrophoresis. The procedure is repeated with the shortened polypeptide to identify the next amino acid in the sequence.[131] Reliable sequence determination by Edman degradation can only be obtained with polypeptide chains shorter than 50 residues because such N-terminal cleavage is not 100% efficient. Thus, longer peptides are often first digested into shorter fragments using endopeptidases such as trypsin and pepsin, which cleave the proteins at distinct sites. Following sequencing by Edman degradation, the fragments are overlapped to reconstruct the full-length sequence.

Facilitated by increasing computing power and access to bioinformatics, MS has recently become the method of choice for rapid protein identification.[132] As discussed in the next section, MS analysis can be utilized to sequence amino acids under certain circumstances.[133]

2.203.5.1.2. Molecular mass and purity

Owing to the repetitive nature of engineered protein polymers, molecular weight characterization is often performed in conjunction with amino acid analysis to verify the correct length and composition of the engineered protein. The molecular weight of purified proteins is routinely characterized through polyacrylamide gel electrophoresis (PAGE), either under native or denaturing conditions.[134] Both methods rely on the electrophoretic mobility of proteins through a polyacrylamide gel as they are subjected to an electric field. Under denaturing conditions, the sample is first incubated with sodium dodecyl sulfate (SDS), an anionic detergent that disrupts noncovalently held secondary and tertiary structures, and imparts a negative charge to each protein with nearly identical charge to mass ratio. Reducing agents such as β-mercaptoethanol are often used in conjunction with SDS to eliminate disulfide linkages. In this protocol (also known as SDS-PAGE), proteins will migrate to the positive electrode at different rates and separate according to their molecular weights. In contrast, a native PAGE is run in the absence of SDS, which therefore retains protein structure. As the

individual protein conformation and charge are preserved, migration rates vary according to the hydrodynamic size and intrinsic charge of the protein at the pH of the running buffer. While not indicative of molecular weights, native PAGE is a valuable tool for studying conformation, self-association, and ligand binding. Following electrophoresis, the gel is treated with protein stains such as Coomassie Blue to identify the location of the resolved proteins. In the case of SDS-PAGE, the size of the target protein is determined by visual comparison to a protein ladder of known molecular weights.

Besides molecular weight, PAGE is often used detect protein impurities, which appear as extraneous bands on the gel. Furthermore, due to its resolving power, PAGE also constitutes the first step in immunoblotting (or western blotting), an assay that confirms a protein's identity through antibody detection.[134] For western blotting, following gel electrophoresis, proteins are transferred from the gel onto a nitrocellulose or polyvinylidene difluoride (PVDF) membrane, whereupon the membrane is treated with a dilute solution of inexpensive proteins such as bovine serum albumin (BSA) or skim milk to preemptively block nonspecific interactions between the membrane and the antibody. In the final step, the membrane is incubated with the respective antibody, which is typically linked to a reporter (e.g., a fluorescent label or an enzyme that catalyzes a colorimetric or chemiluminescent reaction) to allow detection.

More quantitative mass determination is usually achieved by MS, which begins with sample ionization, followed by acceleration and detection of the resulting ions. Matrix-assisted laser desorption ionization time-of-flight (MALDI-TOF) MS is commonly used for studying macromolecules such as proteins.[135] Here, the sample is mixed with an organic solvent and dried on a metal target, which is then blasted with a laser to ionize the constituent peptides into charged gas molecules. The charged molecules are then accelerated in an electric field to a speed that is proportional to their mass to charge ratio (m/z ratio). As a molecule moves through the flight column, its retention time is recorded and used to characterize the m/z ratio, from which the exact molecular weight of the corresponding protein can be calculated. In addition to molecular weight, amino acid sequences can be deduced from a technique called tandem mass spectrometry (MS/MS). Here, the parent protein is predigested using endopeptidases into shorter peptides before being subjected to MS. Selected peaks from the resulting mass spectrum are then further cleaved and analyzed in a second round of MS. As fragmentation occurs at the peptide bond, the peptide sequence can be deduced by scoring mass differences among the fragments to identify the respective amino acids residues.[133] Sample impurities,[136] posttranslational modifications,[137] and disulfide bridges,[138] identified by the presence of uncharacteristic peaks, are other pieces of information that can be obtained by MS.

Common nonproteinaceous impurities in proteins that are produced recombinantly in Gram-negative bacteria such as *E. coli* are LPS or endotoxins. Especially, for implantable protein biomaterials, endotoxin quantities must be determined and reduced to a level that is safe for *in vivo* applications. The ceiling for acceptable endotoxin levels for intravenously introduced biologics is currently set by the United States Food and Drug Administration (FDA) at 5.0 EU per kg of body weight per hour (EU = endotoxin unit; 1 EU = 100 pg of endotoxin). To account for product-to-product dose variability, the endotoxin limit in the product is calculated as K/M, where K is 5.0 EU kg^{-1}, and M is maximum dose per kilogram that would be administered within a duration of 1 h. For example, an injected, protein-engineered drug delivery biomaterial that has a dose of 20 mg kg^{-1} must contain at most $(5.0\ \text{EU kg}^{-1})/(20\ \text{mg kg}^{-1}) = 0.25\ \text{EU mg}^{-1}$ of endotoxin. For implantable biomaterials, the endotoxin level must be below the limit for biomedical devices, which is 0.5 EU ml^{-1} of rinse volume.[139] The most popular method of endotoxin detection is the Limulus Amoebocyte Lysate (LAL) assay. Derived from the blood of horseshoe crabs (Limulus polyphemus), LAL clots upon interacting with endotoxin. Several formats of the LAL assay are commercially available, the simplest being the gel-clot assay. Here, a gel will form if the endotoxin level in the sample is above the sensitivity limit of the assay. To quantify the endotoxin level, the sample is assayed at serial dilutions until no clot formation is observed. LAL assay is also available in turbidimetric and chromogenic formats, which monitor, over time, the appearance of turbidity and a yellow color, respectively. The kinetics of turbidity and color formations, which are dependent on the amount of endotoxin, are then compared to standard curves to give accurate values of endotoxin levels in the sample.

2.203.5.1.3. Protein conformation

Despite their advantages, the previously described techniques are performed in harsh, nonnative conditions, resulting in the loss of structural information, such as folding state, which prescribes eventual protein function. Accurate assessment of a protein's conformation warrants assay conditions that closely mimic the operational environment. One technique that probes protein confirmation in its native environment is circular dichroism,[140,141] which capitalizes on the chirality of proteins. As chiral molecules, proteins exhibit differential absorption of polarized light of different handedness. Classes of secondary structures such as α-helices, β-sheets, β-turns, and random coils possess distinct degrees of chirality and, consequently, interact differently with polarized light. By monitoring the spectral signatures of these interactions, probable secondary structures of a protein can be inferred. Such structural information can then be used to ascertain the correct folding state of a domain when synthesized as part of a fusion protein, thus verifying the core assumption that underlies modular protein design strategies.

The absorption of infrared light by amide bonds in the polypeptide backbone can also be used to probe the secondary structure of a protein. Characteristic amide bond absorption frequencies have been correlated with the presence of different secondary structures such as α-helices or β-sheets.[142] By mapping the absorbance spectra, as is usually done in a technique called Fourier transform infrared (FTIR) spectroscopy, one can deduce the secondary structure of a given protein. Used in combination, FTIR and circular dichroism complement each other and give more comprehensive secondary structure information.

Another native-condition structural characterization technique is nuclear magnetic resonance (NMR), which employs a strong magnetic field to induce synchronous precession of atoms in a molecule. The decay of this precession, following the removal of the magnetic field, can be measured to unveil

the molecular environment enshrouding each atom.[143] Traditionally, such information is used to sketch the identity of interatomic covalent bonds. More recently, real-time NMR techniques have also been developed which shed light on dynamic conformational changes within a protein.[144] Presently, protein tertiary structures can be elucidated directly in solution, thanks to the emergence of sophisticated 2D homonuclear and nuclear Overhauser effect NMR modalities.[145]

2.203.5.1.4. Domain association

The mechanical properties of several protein biomaterials – especially physically cross-linked materials – hinge on the association between multiple domains. For domains that are known to associate into complexes, it is important to characterize the strength of binding, the timescale of complex assembly and disassembly, as well as the influence of external factors on these associations.

Binding interactions can be characterized by using an optical technique called fluorescence resonance energy transfer (FRET),[146] where two fluorescent moieties (denoted as the donor and acceptor), with overlapping emission and excitation spectra, are attached to each of the interacting molecules. As the domains bind, the two fluorescence moieties are brought into close proximity, triggering an energy transfer from the donor to the acceptor. This energy transfer can then be detected by measuring a shift in the frequency of the fluorescence readout (i.e., from the donor to the acceptor emission wavelengths). One disadvantage of this technique is the necessity of tagging the domains of interest with fluorescent markers; this may confound the experimental results by altering domain structure or mechanism of the domain interactions.

Surface plasmon resonance (SPR) is another method of quantifying binding interactions. In an SPR experiment, the receptor protein is first immobilized onto a sensor chip (typically made of gold) that is attached to one side of a glass prism. When a beam of light strikes the prism at a certain angle, called the resonance angle, it interacts with the cloud of electrons in the metal film to generate surface plasmons, which are electromagnetic waves that propagate parallelly to the metal–glass interface. Surface plasmons are very sensitive to the environment that is proximal to the interface, such that any changes, such as the adsorption of molecules to the metal surface, would measurably affect the resonant angle. Binding measurements are performed by making the putative ligand solution flow past the sensor chip. The association of ligand molecules onto the immobilized receptor changes the resonance angle, which is monitored in real time to derive the association rate constant (k_{on}). In the subsequent buffer wash step, the dissociation rate constant (k_{off}) is measured according to how fast the ligand detaches from the receptor. The binding association constant (K_a) is calculated from the ratio of k_{on} to k_{off}. In addition, since the signal change is proportional to the mass of the immobilized complex, relative SPR readouts are indicative of binding stoichiometry. As the receptor is immobilized, however, SPR measurements may not be representative of binding interactions that occur in solution.

A more rigorous means of measuring the strength of molecular interactions, without derivatization, is isothermal titration calorimetry (ITC).[147] Unlike SPR, which is based on the kinetics of interactions, ITC measures the thermodynamic properties of binding. ITC is performed within an adiabatic system, where the putative ligand is titrated against the receptor contained within a reaction cell. As the binding event progresses, heat will be produced or absorbed, creating a temperature discrepancy between the reaction and the reference cells. The amount of energy used to equalize the temperature of the cells is directly proportional to the binding enthalpy of the reaction, which can then be used to evaluate the thermodynamics of the binding reaction. Using ITC, interaction stoichiometry (n), as well as the characteristic thermodynamic parameters such as the association constant (K_a), the binding free energy (ΔG_b), entropy (ΔS_b), and enthalpy (ΔH_b) can be determined in a single experiment.

2.203.5.2. Material Bulk Properties

2.203.5.2.1. Mechanical properties

Depending on the time scale of observation, biological polymers and hydrogels may exhibit viscous and/or elastic characteristics when undergoing deformation. This property is called viscoelasticity, and describes the time-dependent deformation response of a material to an applied load. The ideal viscoelastic properties of a biomaterial are often specified according to its intended use. For example, hydrogels used as carriers for noninvasive drug or cell delivery are tailored to be shear-thinning and self-healing in order to promote injectability. In contrast, mechanical integrity is required for materials that are to be used as scaffolds for cell culture or substrates for patterning. In addition to the end application, it is also important to consider the effects of material mechanics on cell behavior. Recent investigations have shown that scaffold stiffness is a vital determinant of gene expression, cell phenotype, and differentiation.[46,148] Mechanical-property investigations should therefore constitute an integral part of the characterization of biomaterials including, but not limited to, protein-engineered materials.

Protein-engineered viscoelasticity is most commonly explored by rheology. The theory and practical measurements of rheological properties are described in detail in several introductory books (see **Chapter 5.502, Engineering Scaffold Mechanical and Mass Transport Properties**).[149,150] In essence, rheological tests are conducted by subjecting the bulk material to deformation, and monitoring the resulting mechanical responses. Typical test modes include oscillatory shear measurement, creep, and creep recovery tests. In the oscillatory shear mode, sinusoidally oscillating shear strain (or shear stress) is applied, and the resulting shear stress (or shear strain) is measured. To ensure that the measured variables are independent of the magnitude of imposed strain or stress, deformation is generally exerted within the material's linear viscoelastic region. Critical output parameters are the shear storage modulus (G'), loss modulus (G''), and loss factor ($\tan\delta = G''/G'$), and are monitored as a function of time, frequency, temperature, or strain. G' and G'' correspondingly represent the stored and dissipated deformation energies, and are thus used to report material stiffness and flow characteristics, respectively. $G''<G'$ ($\tan\delta<1$) indicates an elastic, solid-like behavior, while $G''>G'$ ($\tan\delta>1$) indicates a liquid-like behavior. The storage modulus G' is also proportional to the hydrogel cross-linking density,[151] as discussed in **Section 2.203.2.1**. Hence, tracking G′ and G″ over time offers a convenient, nonchemical means of studying gelation and degradation kinetics.

To serve as an injectable delivery vehicle, a hydrogel must be reversibly thixotropic, that is, its viscosity must decrease under high shear and quickly rebound when the perturbation is removed. Thixotropic investigations on a rheometer typically consist of three oscillatory test intervals. The material, in its pristine state, is first measured at a small, fixed amplitude and frequency before its structure is destroyed in the second high-amplitude shear step. In the ensuing recuperation step, the recovery of the gel structure is monitored by once again measuring the sample at a small, fixed amplitude and frequency.

Viscoelastic properties can also be probed under tensile or compressive modes, in which the specimen undergoes uniaxial elongational or compressional deformation, rather than a displacement gradient across a shear gap. Operating in the tensile mode, creep and creep recovery tests are conducted in succession to unveil the long-term responses of the viscoelastic behavior of the hydrogel. Briefly, a constant stress is applied on the specimen for a stipulated duration and it is completely removed in the subsequent recovery phase. The temporal evolution of the resultant strain is recorded in both tests to gauge the permanence of the deformation.

In the field of cell biology, genetic and soluble factors are widely perceived to be the primary determinants of cell fate and function. However, a growing body of insightful research continues to shed light on the dynamic interplay among mechanics, ECM ligands, and cytoskeletal organization as being equally important regulators of cell behavior.[152] This dynamic interplay cannot be captured by the macroscopic characterization of passive scaffold properties such as stiffness and composition, because, owing to variations in cell cycle and local scaffold degradation, cellular responses to scaffold mechanics are heterogenous and are on the nanoscale. Newer methods such as tracer particle microrheology and atomic force microscopy (AFM) are now available for probing these mechanical properties at resolutions that are smaller than the size of a cell.[153]

Recent developments in particle tracking algorithms have enabled the development of a novel characterization method called microrheology, which computes rheological properties based on the measured trajectories of tracer particles.[154] In a typical setting, monodispersed, micron-sized particles are homogenously embedded and equilibrated in the test material and then tracked using video microscopy to quantify an ensemble of passive (thermally driven) particle trajectories. Local viscoelastic parameters, within the volume of interrogation, are then calculated from the power law dependence of the average particle mean-squared displacement in time:

$$\langle \Delta r^2(\tau) \rangle \sim \tau^n \qquad [2]$$

where $\langle \Delta r^2 \rangle$ is the thermal-averaged mean-squared displacement, τ is the time interval of observation, and n is a constant. By the generalized Stokes–Einstein relationship, the creep compliance of a purely elastic material ($n = 0$) can be calculated from the power law by the following relation:

$$J(\tau) = \frac{\pi a \langle r^2(\tau) \rangle}{k_B T} \qquad [3]$$

where J is creep compliance, a is particle radius, and $k_B T$ is the thermal energy. For a liquid exhibiting a purely diffusive trajectory ($n = 1$), its viscosity (η) is related to creep compliance by:

$$\eta = \frac{\tau}{J(\tau)} \qquad [4]$$

In passive microrheology, eqn [3] is used to determine the upper limit of the measurable storage modulus ($G_{max} = 1/J$) for a given particle size, microscope resolution, and camera frame rate. The observation of subdiffusive trajectories, where $0 < n < 1$ implies a viscoelastic network. Particle motion can also be driven in stiffer materials by applying external forces and is typically facilitated by a magnetic field[155] or optical tweezers.[156] These more sophisticated methods are collectively known as active microrheology.

AFM is another convenient tool for probing the local modulus with nanoscale resolution.[157] At the heart of the AFM is a cantilever equipped with a sharp tip that probes the sample surface topography. As this occurs, forces between the sample and the tip cause the cantilever to undergo deflection, which is usually detected either by laser reflection, optical interferometry, or piezoresistive sensing. Common probing modes, in decreasing order of invasiveness, are contact mode, noncontact mode, and tapping mode. Mechanical characterization is usually performed in contact mode, where the tip is in close contact with the surface. As the probe is indented into and retracted from the surface, the force versus deflection data are converted into the surface modulus by using Hooke's law and the cantilever's spring constant. Unlike microrheology, however, AFM is limited to surfaces and hence cannot be used for investigating mechanics within the interior of a material.

2.203.5.2.2. Morphological features

Properties of biomaterials, such as hydrogel swelling, mechanical stiffness, and permissivity to diffusion, are governed on the mesoscopic level by pore size and network morphology. Extending beyond these physical properties, mesoscopic structures also critically determine the ability of the construct to support cell growth and tissue integration following implantation. For example, a study with poly(2-hydroxyethyl methacrylate) (PHEMA) has shown that angiogenesis and the maintenance of vascular ingrowth requires interconnected pores with a diameter comparable to the size of a cell ($\sim$10 μm).[146] Interesting insights can therefore be extracted by visualizing and characterizing such mesoscopic structures.

AFM, as discussed above in the mechanical characterization section, can also be used to visualize local molecular structures with subnanometer resolution. During operation in the tapping mode, AFM produces high-resolution topographic imaging of soft materials whose structures are sensitive to mechanical disruption. In this mode, the cantilever probe tip comes in contact with the sample surface by vertically oscillating at frequency ranges that are high enough to make the viscoelastic sample behave elastically. Stiff and elastic surfaces prevent sample disruption by eliminating tip-sample adhesion. Also, a unique strength of AFM imaging is its ability to investigate the sample in ambient air or liquid environments without the need for special treatment protocols.[158] An example of the topographical characterization of protein biomaterials by AFM is shown in **Figure 4**, revealing degradation pits on surface-patterned silk films due to MMP-mediated cleavage by osteogenic cells.[159]

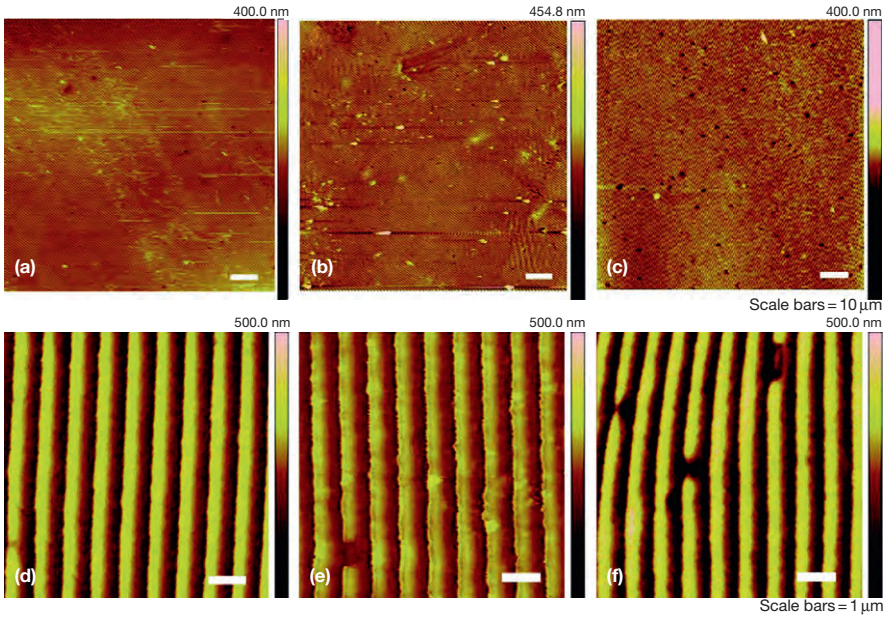

Figure 4 AFM images of degradation pits on patterned silk films caused by negative controls (a and d), osteoblasts (b and e), and osteoclasts (c and f). Scan size = 100 μm, scale bars = 10 μm (a to c); scan size = 10 μm, scale bars = 1 μm (d to f). Reprinted with permission from Sengupta, S.; Park, S. H.; Seok, G. E.; *et al*. *Biomacromolecules* **2010**, *11*, 3592–3599, with permission from ACS Publications.

Advanced scattering techniques such as small-angle neutron scattering (SANS) also provide structural information on scaffolds, from the near atomic scale (~1 nm) to the near micron scale.[160] Using Fourier transform, scattering information from the reciprocal space is fit, using different form factors, to give information on the morphology of the network. Particularly valuable for hydrogel characterization is the use of ultra-SANS (USANS), which extends the range of length scale to well beyond 10 μm.[161] Performed in ambient conditions, SANS measurements are capable of revealing real-time structure evolution, thus providing mechanistic insight into self-assembly processes. Despite its utility, SANS experiments are not as easily accessible as the other techniques because there are only a handful of neutron scattering facilities in the world.

A millimeter-scale field of view of biomaterial morphology is commonly acquired through scanning and transmission electron microscopy (SEM and TEM).[162] In a conventional setup, the biomaterial construct is mounted on a grid and dehydrated by air- or freeze-drying to accommodate the requirement for vacuum during image acquisition. In addition, contrast-enhancing agents are often deposited on the specimen to accentuate fine features. Owing to such sample preparation protocols, the utility of electron microscopy is limited to dense and fibrous protein-based materials. For biomaterials that are hydrogels, the hydrated state is a key determinant of nanostructural morphology, and electron microscopy images obtained from dehydrated samples are not representative of the true morphology. To partially circumvent this technical limitation, hydrogels are often imaged using cryoelectron microscopy, which studies the specimen at cryogenic temperatures.[163] Once secured on the grid, the hydrogel is submerged into liquid nitrogen or liquid ethylene, upon which water in the hydrogel undergoes vitrification. Another technique is environmental SEM (ESEM), which, by operating under a saturated environment, removes the high vacuum constraints and allows even fully hydrated samples to be analyzed.[164] While these process may preserve the nanostructure of some biomaterials,[165] images acquired from hydrogels must still be interpreted with caution, as the relation between the observed structure and the truly hydrated hydrogel network can be based only on educated inference.

When implemented together, the suite of characterization techniques mentioned above affords a means of analyzing the interdependence among domain sequences, structures, self-assembly, and ultimately, scaffold morphology and bulk material mechanics. This exercise not only reinforces the underlying design rationales, but is also instrumental in spawning future design iterations.

2.203.6. Biological Interactions and Immunogenicity

The design of a highly functional protein-engineered biomaterial may prove futile if it overlooks host responses subsequent to material implantation. Knowledge of how the biomaterial construct and its degradation products modulate the host immune system is critical for the safety, biocompatibility, and ultimate function of the biomaterial. Elicitation of the foreign body innate immune response by biomaterial scaffolds is relatively well known.[166] Recently, biomaterials have also been discovered to act as adjuvants for the adaptive immune response by activating antigen-presenting cells.[167]

Owing to the recombinant expression strategy, protein-engineered biomaterials carry a potential danger of exposing xenogenic contaminants to human patients. Eukaryotic hosts such as chinese hamster ovary (CHO) cells may mediate host-to-host pathogen transfer, while prokaryotic hosts may carry antigenic cellular components. Specific to the cell wall of Gram-negative bacteria such as *E. coli* is the presence of

lipopolisaccharides that are synonymously known as endotoxins. Several endotoxin removal and detection techniques, as well as acceptable FDA limits for gram-scale implantation have been described in previous sections in this chapter. Endotoxins act by activating the innate immune system, particularly the monocytes and macrophages, which in turn release a plethora of mediators including interleukins, prostaglandins, tumor necrosis factor, colony-stimulating factor, and free radicals. These factors can result in systemic inflammatory reactions, which ultimately lead to multiple pathophysiological effects such as endotoxin shock, tissue injury, and death.[168] In light of these biological hazards, recombinant synthesis schemes must satisfy stringent purification standards, and insights from the biotechnology industry may prove instrumental in developing safe and economical protein biomaterials production protocols.

As protein biomaterials are constructed from amino acid sequences, they have the potential to activate the adaptive immune response through unwelcome antigenic effects. As a preemptive measure, the domains used in the modular design of many recombinant protein polymers are constructed from amino acid sequences that either are of human origin (e.g., laminin, fibronectin, elastin), or whose biocompatibility has been established in human recipients (e.g., silk). As part of the rational design effort, spacer sequences used to stitch multiple domains together can be chosen to be nonimmunogenic. Motivated by the vaccine therapeutics field, computational algorithms now exist, which can predict epitope-free amino acid sequences that may evade recognition by the antigen-presenting cells.[169]

Ultimately, a comprehensive evaluation of material biocompatibility requires the empirical and systematic appraisal of both the innate and the adaptive immune reactions, which typically involves a battery of laboratory and preclinical tests, before taking the leap into human clinical trials. Initial stages of *in vitro* cytotoxicity and *in vivo* animal studies on elastin-like polymers and silk fibroin have shown encouraging outcomes.[170,171] Clinical trials are currently in progress to assess the compatibility of recombinant silk–elastin polymers as spinal disc replacements in patients with early-stage degenerative spinal disc disease.[172]

2.203.7. Future Directions and Conclusions

Scientists working under the rubric of recombinantly engineered biomaterials are being presented with a multitude of challenges and opportunities – some exclusive to protein-engineered biomaterials, and others more common to the larger biomaterials community – these are continually reshaping various research endeavors in the field. Particular to protein-engineered biomaterials is the call to expand the library of peptide modules that can be used to successfully design new protein-engineered materials. Despite the wealth of domains that exist in the proteomic databases, the majority of protein-engineered biomaterial designs mainly utilize short peptide modules (<50 amino acids) that exhibit spontaneous folding and robust expression in the recombinant host. Including additional peptide modules with new functionalities is a challenging task given the restrictions in both recombinant protein synthesis machinery and chemical diversity of the 20 natural amino acids. For example, the use of bacterial hosts limits domain selections to those requiring no posttranslational modifications. Major research thrusts in recombinant DNA technology and protein engineering currently seek to overcome some of these limitations.

To illustrate the above, efforts are being directed toward the bacterial recombinant production of collagen, whose post-translational hydroxylation of specific proline residues by the enzyme prolyl 4-hydroxylase (P4H) has made biosynthesis in prokaryotic hosts extremely challenging. In one approach, trans-4-hydroxyproline (Hyp) was cotranslationally incorporated in place of proline in *E. coli* by growing the culture in hyperosmotic media supplemented with Hyp.[173] Another potential scheme is to coexpress collagen precursors with the P4H enzyme within the same bacterial cell. The success of human recombinant P4H synthesis in *E. coli* is a major step forward in the realization of this strategy.[174]

In the protein engineering field, short peptide sequences have been identified and modified to recapitulate or even outperform the activity of the larger protein domains. For example, a 9-amino acid neuroprotective peptide called ADNF-9 has been identified and shown to be more potent than the parent 14 kDa ADNF (activity-dependent neurotrophic factor) protein.[175] Through combinatorial mutations and yeast surface display, 11-amino acid peptide sequences containing an RGD motif have been developed which bind to both $\alpha_v\beta_3$ and $\alpha_v\beta_5$ integrins with high affinity.[176] Thanks to such developments, it may no longer be necessary to include the full-length protein sequence in modular protein-engineered biomaterial design, thus circumventing the challenges associated with complicated folding requirements.

In recent years, the ability to genetically encode noncanonical amino acids has endowed recombinant proteins with functionalities that were previously unavailable in natural proteins. Nonbiological moieties such as halogenated, photoactive, and unsaturated amino acid analogs have been incorporated into recombinant proteins to stabilize collagen-[173] and ELP polymers,[177] enable photo-cross-linking of leucine zipper–elastin fusions,[178] and allow the orthogonal chemical tethering through copper-catalyzed click reactions.[179] The variety of noncanonical amino acids, methods for their incorporation, as well as examples in protein polymer design have been discussed in great depth in several review articles.[180,181]

As the field matures, creativity in modular protein design has spawned an array of novel recombinant protein-engineered biomaterials whose functions extend beyond just acting as ECM scaffold mimics. Fusing organophosphate hydrolase to the leucine zipper domain has produced self-assembling catalytic hydrogels, which are intended for the detection, bioremediation, and prophylactic decontamination of organophosphate neurotoxins, a potent class of chemical weapons.[182] In drug delivery, the fusion of a cell-penetrating peptide and a cell-cycle inhibitory domain was tagged with an elastin-like polypeptide (ELP) to create a thermally responsive drug that targeted solid tumors via localized hyperthermia.[182] These examples demonstrate the inherent value in continuing to expand the library of peptide domains that can be designed into functional biomaterials.

In a relatively brief span of two decades, protein-engineered biomaterials have emerged at the forefront of regenerative

medicine. Endowed with highly tunable mechanical properties, diverse biochemical functionalities, and controllable degradation profiles, this new class of biomaterials offers excellent scaffolds for tissue engineering, versatile platforms for studying cell–microenvironment interactions, and exciting opportunities to design functional biomaterials for complex medical and biotechnological applications.

References

1. Flory, P. J. *Principles of Polymer Chemistry*. Cornell University Press: Itacha, NY, 1953.
2. Seymour, L. W.; Duncan, R.; Strohalm, J.; Kopecek, J. *J. Biomed. Mater. Res.* **1987**, *21*, 1341–1358.
3. Cappello, J.; Crissman, J.; Dorman, M.; *et al*. *Biotechnol. Prog.* **1990**, *6*, 198–202.
4. Mcpherson, D. T.; Morrow, C.; Minehan, D. S.; Wu, J.; Hunter, E.; Urry, D. W. *Biotechnol. Prog.* **1992**, *8*, 347–352.
5. Goldberg, I.; Salerno, A. J.; Patterson, T.; Williams, J. I. *Gene* **1989**, *80*, 305–314.
6. Nicol, A.; Gowda, D. C.; Urry, D. W. *J. Biomed. Mater. Res.* **1992**, *26*, 393–413.
7. Straley, K. S.; Heilshorn, S. C. *Soft Matter* **2009**, *5*, 114–124.
8. Di Zio, K.; Tirrell, D. *Macromolecules* **2003**, *36*, 1553–1558.
9. Meyer, D. E.; Chilkoti, A. *Nat. Biotechnol.* **1999**, *17*, 1112–1115.
10. Betre, H.; Liu, W.; Zalutsky, M. R.; Chiilkoti, A.; Kraus, V. B.; Setton, L. A. *J. Control. Release* **2006**, *115*, 175–182.
11. Betre, H.; Setton, L. A.; Meyer, D. E.; Chilkoti, A. *Biomacromolecules* **2002**, *3*, 910–916.
12. Mie, M.; Mizushima, Y.; Kobatake, E. *J. Biomed. Mater. Res. B Appl. Biomater.* **2008**, *86*, 283–290.
13. Haider, M.; Cappello, J.; Ghandehari, H.; Leong, K. W. *Pharm. Res.* **2008**, *25*, 692–699.
14. Lv, S.; Dudek, D. M.; Cao, Y.; Balamurali, M. M.; Gosline, J.; Li, H. *Nature* **2010**, *465*, 69–73.
15. Elvin, C. M.; Carr, A. G.; Huson, M. G. *Nature* **2005**, *437*, 999–1002.
16. Charati, M. B.; Ifkovits, J. L.; Burdick, J. A.; Linhardt, J. G.; Kiick, K. L. *Soft Matter* **2009**, *5*, 3412–3416.
17. Bini, E.; Foo, C. W.; Huang, J.; Karageorgiou, V.; Kitchel, B.; Kaplan, D. L. *Biomacromolecules* **2006**, *7*, 3139–3145.
18. Fahnestock, S. R.; Bedzyk, L. A. *Appl. Microbiol. Biotechnol.* **1997**, *47*, 33–39.
19. Fahnestock, S. R.; Irwin, S. L. *Appl. Microbiol. Biotechnol.* **1997**, *47*, 23–32.
20. Lazaris, A.; Arcidiacono, S.; Huang, Y. *Science* **2002**, *295*, 472–476.
21. Asakura, T.; Nitta, K.; Yang, M.; Yao, J.; Nakazawa, Y.; Kaplan, D. L. *Biomacromolecules* **2003**, *4*, 815–820.
22. Tanaka, C.; Asakura, T. *Biomacromolecules* **2009**, *10*, 923–928.
23. Petka, W. A.; Harden, J. L.; Mcgrath, K. P.; Wirtz, D.; Tirrell, D. A. *Science* **1998**, *281*, 389–392.
24. Carrico, I. S.; Maskarinec, S. A.; Heilshorn, S. C. *J. Am. Chem. Soc.* **2007**, *129*, 4874–4875.
25. Liu, B.; Lewis, A. K.; Shen, W. *Biomacromolecules* **2009**, *10*, 3182–3187.
26. Stevens, M. M.; Allen, S.; Sakata, J. K. *Langmuir* **2004**, *20*, 7747–7752.
27. Wong Po Foo, C. T.; Lee, J. S.; Mulyasasmita, W.; Parisi-Amon, A.; Heilshorn, S. C. *Proc. Natl. Acad. Sci. USA* **2009**, *106*(52), 22067–22072.
28. Topp, S.; Prasad, V.; Cianci, G. C.; Weeks, E. R.; Gallivan, J. P. *J. Am. Chem. Soc.* **2006**, *128*, 13994–13995.
29. Porumb, T.; Yau, P.; Harvey, T. S.; Ikura, M. *Protein Eng.* **1994**, *7*, 109–115.
30. Murphy, W. L.; Dillmore, W. S.; Modica, J.; Mrksich, M. *Angew. Chem. Int. Ed. Engl.* **2007**, *46*, 3066–3069.
31. Davis, N. E.; Karfeld-Sulzer, L. S.; Ding, S.; Barron, A. E. *Biomacromolecules* **2009**, *10*, 1125–1134.
32. Nakamura, M.; Mie, M.; Mihara, H.; Kobatake, E. *J. Biomed. Mater. Res. B Appl. Biomater.* **2009**, *91*, 425–432.
33. Girotti, A.; Reguera, J.; Rodriguez-Cabello, J. C.; Arias, F. J.; Alonso, M.; Matestera, A. *J. Mater. Sci. Mater. Med.* **2004**, *15*, 479–484.
34. Nagaoka, M.; Si-Tayeb, K.; Akaike, T.; Duncan, S. A. *BMC Dev. Biol.* **2010**, *10*, 60.
35. Zisch, A. H.; Schenk, U.; Schense, J. C.; Sakiyama-Elbert, S. E.; Hubbell, J. A. *J. Control. Release* **2001**, *72*, 101–113.
36. Sakiyama-Elbert, S. E.; Hubbell, J. A. *J. Control. Release* **2000**, *65*, 389–402.
37. Straley, K. S.; Heilshorn, S. C. *Adv. Mater.* **2009**, *21*, 4148–4152.
38. Schense, J. C.; Bloch, J.; Aebischer, P.; Hubbell, J. A. *Nat. Biotechnol.* **2000**, *18*, 415–419.
39. Davis, N. E.; Ding, S.; Forster, R. E.; Pinkas, D. M.; Barron, A. E. *Biomaterials* **2010**, *31*, 7288–7297.
40. Wong Po Foo, C.; Patwardhan, S. V.; Belton, D. J. *Proc. Natl. Acad. Sci. USA* **2006**, *103*, 9428–9433.
41. Paramonov, S. E.; Gauba, V.; Hartgerink, J. D. *Macromolecules* **2005**, *38*, 7555–7561.
42. Holmes, T. C. *Trends Biotechnol.* **2002**, *20*, 16–21.
43. Woolfson, D. N.; Ryadnov, M. G. *Curr. Opin. Chem. Biol.* **2006**, *10*, 559–567.
44. Ali, M.; Brocchini, S. *Adv. Drug Deliv. Rev.* **2006**, *58*, 1671–1687.
45. Discher, D. E.; Janmey, P.; Wang, Y. L. *Science* **2005**, *310*, 1139–1143.
46. Engler, A. J.; Sen, S.; Sweeney, H. L.; Discher, D. E. *Cell* **2006**, *126*, 677–689.
47. Toman, P. D.; Chisholm, G.; Mcmullin, H. *J. Biol. Chem.* **2000**, *275*, 23303–23309.
48. Mcpherson, D. T.; Xu, J.; Urry, D. W. *Protein Expr. Purif.* **1996**, *7*, 51–57.
49. Prince, J. T.; Mcgrath, K. P.; Digirolamo, C. M.; Kaplan, D. L. *Biochemistry* **1995**, *34*, 10879–10885.
50. Woolfson, D. N. *Biopolymers* **2010**, *94*, 118–127.
51. Wright, E. R.; Conticello, V. P. *Adv. Drug Deliv. Rev.* **2002**, *54*, 1057–1073.
52. Landschulz, W. H.; Johnson, P. F.; Mcknight, S. L. *Science* **1988**, *240*, 1759–1764.
53. Shen, W.; Lammertink, R. G. H.; Sakata, J. K.; Kornfield, J. A.; Tirrell, D. A. *Macromolecules* **2005**, *38*, 3909–3916.
54. Nowatzki, P. J.; Tirrell, D. A. *Biomaterials* **2004**, *25*, 1261–1267.
55. Lim, D. W.; Nettles, D. L.; Setton, L. A.; Chilkoti, A. *Biomacromolecules* **2007**, *8*, 1463–1470.
56. Hu, B. H.; Messersmith, P. B. *J. Am. Chem. Soc.* **2003**, *125*, 14298–14299.
57. Mchale, M. K.; Setton, L. A.; Chilkoti, A. *Tissue Eng.* **2005**, *11*, 1768–1779.
58. Metters, A. T.; Anseth, K. S.; Bowman, C. N. *Polymer* **2000**, *41*, 3993–4004.
59. Liu, J. C.; Heilshorn, S. C.; Tirrell, D. A. *Biomacromolecules* **2004**, *5*, 497–504.
60. Ruoslahti, E.; Pierschbacher, M. D. *Science* **1987**, *238*, 491–497.
61. Yue, X. S.; Murakami, Y.; Tamai, T. *Biomaterials* **2010**, *31*, 5287–5296.
62. Liu, C. Y.; Westerlund, U.; Svensson, M. *J. Hematother. Stem Cell Res.* **2003**, *12*, 689–699.
63. Andrades, J. A.; Han, B.; Becerra, J.; Sorgente, N.; Hall, F. L.; Nimni, M. E. *Exp. Cell Res.* **1999**, *250*, 485–498.
64. Ishikawa, T.; Terai, H.; Yamamoto, T.; Harada, K.; Kitajima, T. *Artif. Organs* **2003**, *27*, 147–154.
65. Burgess, W. H.; Maciag, T. *Annu. Rev. Biochem.* **1989**, *58*, 575–606.
66. Maxwell, D. J.; Hicks, B. C.; Parsons, S.; Sakiyama-Elbert, S. E. *Acta Biomater.* **2005**, *1*, 101–113.
67. Werb, Z. *Cell* **1997**, *91*, 439–442.
68. West, J. L.; Hubbell, J. A. *Macromolecules* **1999**, *32*, 241–244.
69. Heilshorn, S. C.; Liu, J. C.; Tirrell, D. A. *Biomacromolecules* **2005**, *6*, 318–323.
70. Hossler, P.; Khattak, S. F.; Li, Z. J. *Glycobiology* **2009**, *19*, 936–949.
71. Karg, S. R.; Kallio, P. T. *Biotechnol. Adv.* **2009**, *27*, 879–894.
72. Graf, A.; Dragosits, M.; Gasser, B.; Mattanovich, D. *FEMS Yeast Res.* **2009**, *9*, 335–348.
73. Zerbs, S.; Frank, A. M.; Collart, F. R. *Meth. Enzymol.* **2009**, *463*, 149–168.
74. Gustafsson, C.; Govindarajan, S.; Minshull, J. *Trends Biotechnol.* **2004**, *22*, 346–353.
75. Hershberg, R.; Petrov, D. A. *Annu. Rev. Genet.* **2008**, *42*, 287–299.
76. Li, X.; Hirano, R.; Tagami, H.; Aiba, H. *RNA* **2006**, *12*, 248–255.
77. Bzymek, M.; Lovett, S. T. *Proc. Natl. Acad. Sci. USA* **2001**, *98*, 8319–8325.
78. Griswold, K. E.; Mahmood, N. A.; Iverson, B. L.; Georgiou, G. *Protein Expr. Purif.* **2003**, *27*, 134–142.
79. Gao, W.; Rzewski, A.; Sun, H.; Robbins, P. D.; Gambotto, A. *Biotechnol. Prog.* **2004**, *20*, 443–448.
80. Jungbauer, A.; Hahn, R. *Meth. Enzymol.* **2009**, *463*, 349–371.
81. Yigzaw, Y.; Hinckley, P.; Hewig, A.; Vedantham, G. *Curr. Pharm. Biotechnol.* **2009**, *10*, 421–426.
82. Mccue, J. T. *Meth. Enzymol.* **2009**, *463*, 405–414.
83. Mahn, A.; Asenjo, J. A. *Biotechnol. Adv.* **2005**, *23*, 359–368.
84. Berek, D. *J. Sep. Sci.* **2010**, *33*, 315–335.
85. Stulik, K.; Pacakova, V.; Ticha, M. *J. Biochem. Biophys. Meth.* **2003**, *56*, 1–13.
86. Snyder, L. R.; Glajch, J. L.; Kirkland, J. J. *Practical Hplc Method Development Chromatography Method Development*. Wiley: New York, 1998.
87. Arnau, J.; Lauritzen, C.; Petersen, G. E.; Pedersen, J. *Protein Expr. Purif.* **2006**, *48*, 1–13.
88. Terpe, K. *Appl. Microbiol. Biotechnol.* **2003**, *60*, 523–533.

89. Urh, M.; Simpson, D.; Zhao, K. *Meth. Enzymol.* **2009**, *463*, 417–438.
90. Lavallie, E. R.; Diblasio, E. A.; Kovacic, S.; Grant, K. L.; Schendel, P. F.; Mccoy, J. M. *Biotechnology NY* **1993**, *11*, 187–193.
91. Maina, C. V.; Riggs, P. D.; Grandea, A. G., III. *Gene* **1988**, *74*, 365–373.
92. Smith, D. B.; Johnson, K. S. *Gene* **1988**, *67*, 31–40.
93. Smith, P. A.; Tripp, B. C.; Diblasio-Smith, E. A.; Lu, Z.; Lavallie, E. R.; Mccoy, J. M. *Nucleic Acids Res.* **1998**, *26*, 1414–1420.
94. Tsao, K. L.; Debarbieri, B.; Michel, H.; Waugh, D. S. *Gene* **1996**, *169*, 59–64.
95. Smith, M. C.; Furman, T. C.; Ingolia, T. D.; Pidgeon, C. *J. Biol. Chem.* **1988**, *263*, 7211–7215.
96. Kim, J. S.; Raines, R. T. *Protein Sci.* **1993**, *2*, 348–356.
97. Rais-Beghdadi, C.; Roggero, M. A.; Fasel, N.; Reymond, C. D. *Appl. Biochem. Biotechnol.* **1998**, *74*, 95–103.
98. Banki, M. R.; Feng, L.; Wood, D. W. *Nat. Meth.* **2005**, *2*, 659–661.
99. Ding, F. X.; Yan, H. L.; Mei, Q. *Appl. Microbiol. Biotechnol.* **2007**, *77*, 483–488.
100. Rietschel, E. T.; Kirikae, T.; Schade, F. U.; *et al. FASEB J.* **1994**, *8*, 217–225.
101. Rietschel, E. T.; Brade, L.; Schade, F. U.; *et al. Immun. Infekt.* **1993**, *21*, 26–35.
102. Weber, C.; Henne, B.; Loth, F.; Schoenhofen, M.; Falkenhagen, D. *ASAIO J.* **1995**, *41*, M430–M434.
103. Issekutz, A. C. *J. Immunol. Meth.* **1983**, *61*, 275–281.
104. Lin, M. F.; Williams, C.; Murray, M. V.; Ropp, P. A. *J. Chromatogr. B Analyt. Technol. Biomed. Life Sci.* **2005**, *816*, 167–174.
105. Magalhaes, P. O.; Lopes, A. M.; Mazzola, P. G.; Rangel-Yagui, C.; Penna, T. C.; Pessoa, A., Jr. *J. Pharm. Pharm. Sci.* **2007**, *10*, 388–404.
106. Curtis, A.; Wilkinson, C. *Biomaterials* **1997**, *18*, 1573–1583.
107. Nagarkar, R. P.; Hule, R. A.; Pochan, D. J.; Schneider, J. P. *J. Am. Chem. Soc.* **2008**, *130*, 4466–4474.
108. Cui, H.; Webber, M. J.; Stupp, S. I. *Biopolymers* **2010**, *94*, 1–18.
109. Lovett, M.; Lee, K.; Edwards, A.; Kaplan, D. L. *Tissue Eng. B Rev.* **2009**, *15*, 353–370.
110. Reneker, D. H.; Chun, I. *Nanotechnology* **1996**, *7*, 216–223.
111. Mccullen, S. D.; Miller, P. R.; Gittard, S. D. *Tissue Eng. C Meth.* **2010**, *16*(5), 1095–1105.
112. Li, M.; Mondrinos, M. J.; Gandhi, M. R.; Ko, F. K.; Weiss, A. S.; Lelkes, P. I. *Biomaterials* **2005**, *26*, 5999–6008.
113. Zhang, X.; Reagan, M. R.; Kaplan, D. L. *Adv. Drug Deliv. Rev.* **2009**, *61*, 988–1006.
114. Kumbar, S. G.; James, R.; Nukavarapu, S. P.; Laurencin, C. T. *Biomed. Mater.* **2008**, *3*, 034002.
115. Wolfe, D. B.; Qin, D.; Whitesides, G. M. *Meth. Mol. Biol.* **2010**, *583*, 81–107.
116. Kumar, A.; Whitesides, G. M. *Appl. Phys. Lett.* **1993**, *63*, 2002–2004.
117. Xia, Y. N.; Mcclelland, J. J.; Gupta, R. *Adv. Mater.* **1997**, *9*, 147–149.
118. Zhao, X. M.; Xia, Y. N.; Whitesides, G. M. *Adv. Mater.* **1996**, *8*, 837–840.
119. Kim, E.; Xia, Y. N.; Zhao, X. M.; Whitesides, G. M. *Adv. Mater.* **1997**, *9*, 651–654.
120. Qin, D.; Xia, Y.; Whitesides, G. M. *Nat. Protoc.* **2010**, *5*, 491–502.
121. Cimetta, E.; Pizzato, S.; Bollini, S.; Serena, E.; De Coppi, P.; Elvassore, N. *Biomed. Microdevices* **2009**, *11*, 389–400.
122. Guvendiren, M.; Burdick, J. A. *Biomaterials* **2010**, *31*, 6511–6518.
123. Wang, S.; Wong Po Foo, C.; Warrier, A.; Poo, M. M.; Heilshorn, S. C.; Zhang, X. *Biomed. Microdevices* **2009**, *11*, 161–171.
124. Lafratta, C. N.; Fourkas, J. T.; Baldacchini, T.; Farrer, R. A. *Angew. Chem. Int. Ed. Engl.* **2007**, *46*, 6238–6258.
125. Sarig-Nadir, O.; Livnat, N.; Zajdman, R.; Shoham, S.; Seliktar, D. *Biophys. J.* **2009**, *96*, 4743–4752.
126. Borenstein, J. T.; Weinberg, E. J.; Orrick, B. K.; Sundback, C.; Kaazempur-Mofrad, M. R.; Vacanti, J. P. *Tissue Eng.* **2007**, *13*, 1837–1844.
127. Park, H.; Cannizzaro, C.; Vunjak-Novakovic, G.; Langer, R.; Vacanti, C. A.; Farokhzad, O. C. *Tissue Eng.* **2007**, *13*, 1867–1877.
128. Tsang, V. L.; Bhatia, S. N. *Adv. Biochem. Eng. Biotechnol.* **2007**, *103*, 189–205.
129. Sanger, F.; Nicklen, S.; Coulson, A. R. *Proc. Natl. Acad. Sci. USA* **1977**, *74*, 5463–5467.
130. Rutherfurd, S. M.; Gilani, G. S. *Curr. Protoc. Protein Sci.* **2009**, *58*, 11.9.1–11.9.37.
131. Lodish, H. F. *Molecular Cell Biology*. W.H. Freeman: New York, 2000.
132. Sadygov, R. G.; Cociorva, D.; Yates, J. R., III. *Nat. Meth.* **2004**, *1*, 195–202.
133. Kwon, I.; Kirshenbaum, K.; Tirrell, D. A. *J. Am. Chem. Soc.* **2003**, *125*, 7512–7513.
134. Creighton, T. E. *Protein Structure: A Practical Approach*. IRL Press at Oxford University Press: Oxford and New York, 1997.
135. Karas, M.; Hillenkamp, F. *Anal. Chem.* **1988**, *60*, 2299–2301.
136. Rhodes, D. G.; Laue, T. M. *Meth. Enzymol.* **2009**, *463*, 677–689.
137. Qin, J.; Chait, B. T. *Anal. Chem.* **1997**, *69*, 4002–4009.
138. Huwiler, K. G.; Mosher, D. F.; Vestling, M. M. *J. Biomol. Tech.* **2003**, *14*, 289–297.
139. FDA 1987. *Guideline on Validation of the Limulus Amebocyte Lysate Test as an End-Product Test for Human, Animal Parenteral Drugs, Biological Products, and Medical Devices*. Rockville, MD: US Department of Health and Human Services, Center for Drug Evaluation and Research.
140. Kelly, S. M.; Price, N. C. *Biochim. Biophys. Acta* **1997**, *1338*, 161–185.
141. Ranjbar, B.; Gill, P. *Chem. Biol. Drug Des.* **2009**, *74*, 101–120.
142. Byler, D. M.; Susi, H. *Biopolymers* **1986**, *25*, 469–487.
143. Wuthrich, K. *Nat. Struct. Biol.* **2001**, *8*, 923–925.
144. Dyson, H. J.; Wright, P. E. *Annu. Rev. Phys. Chem.* **1996**, *47*, 369–395.
145. Mulder, F. A.; Filatov, M. *Chem. Soc. Rev.* **2010**, *39*, 578–590.
146. Piston, D. W.; Kremers, G. J. *Trends Biochem. Sci.* **2007**, *32*, 407–414.
147. Velazquez-Campoy, A.; Leavitt, S. A.; Freire, E. *Meth. Mol. Biol.* **2004**, *261*, 35–54.
148. Saha, K.; Keung, A. J.; Irwin, E. F. *Biophys. J.* **2008**, *95*, 4426–4438.
149. Macosko, C. W. *Rheology: Principles, Measurements and Applications*. Wiley: New York, NY, 1994.
150. Mezger, T. G. *The Rheology Handbook: For Users of Rotational and Oscillatory Rheometers*. Vincentz Network GmbH and Co KG: Hannover, 2006.
151. Young, R. J.; Lovell, P. A. *Introduction to Polymers*. Chapman & Hall: London, 1991.
152. Keung, A. J.; Kumar, S.; Schaffer, D. V. *Annu. Rev. Cell Dev. Biol.* **2010**, *26*, 533–556.
153. Zhong, Q.; Inniss, D.; Kjoller, K.; Elings, V. B. *Surf. Sci.* **1993**, *290*, L688–L692.
154. Crocker, J. C.; Hoffman, B. D. *Meth. Cell. Biol.* **2007**, *83*, 141–178.
155. Bausch, A. R.; Ziemann, F.; Boulbitch, A. A.; Jacobson, K.; Sackmann, E. *Biophys. J.* **1998**, *75*, 2038–2049.
156. Yao, A.; Tassieri, M.; Padgett, M.; Cooper, J. *Lab Chip* **2009**, *9*, 2568–2575.
157. Francis, L. W.; Lewis, P. D.; Wright, C. J.; Conlan, R. S. *Biol. Cell* **2010**, *102*, 133–143.
158. Sitterberg, J.; Ozcetin, A.; Ehrhardt, C.; Bakowsky, U. *Eur. J. Pharm. Biopharm.* **2010**, *74*, 2–13.
159. Sengupta, S.; Park, S. H.; Seok, G. E. *Biomacromolecules* **2010**, *11*, 3592–3599.
160. Neylon, C. *Eur. Biophys. J.* **2008**, *37*, 531–541.
161. Reynolds, P. A.; Mcgillivray, D. J.; Jackson, A. J.; White, J. W. *Phys. Rev. E Stat. Nonlin. Soft Matter. Phys.* **2009**, *80*, 011301.
162. Andrade, J. D.; King, R. N.; Gregonis, D. E. In *ACS Symposium Series*, 1976, Washington: DC, pp 206–224.
163. Estroff, L. A.; Leiserowitz, L.; Addadi, L.; Weiner, S.; Hamilton, A. D. *Adv. Mater.* **2003**, *15*, 38–42.
164. Manero, J. M.; Gil, F. J.; Padros, E.; Planell, J. A. *Microsc. Res. Tech.* **2003**, *61*, 469–480.
165. Stuart, K.; Panitch, A. *Biomacromolecules* **2009**, *10*, 25–31.
166. Anderson, J. M.; Rodriguez, A.; Chang, D. T. *Semin. Immunol.* **2008**, *20*, 86–100.
167. Norton, L. W.; Park, J.; Babensee, J. E. *J. Control. Release* **2010**, *146*, 341–348.
168. Erridge, C.; Bennett-Guerrero, E.; Poxton, I. R. *Microbes Infect.* **2002**, *4*, 837–851.
169. Lee, Y.; Ferrari, G.; Lee, S. C. *Biomed. Microdevices* **2010**, *12*, 207–222.
170. Rincon, A. C.; Molina-Martinez, I. T.; De Las Heras, B. *J. Biomed. Mater. Res. A* **2006**, *78*, 343–351.
171. Wang, Y.; Rudym, D. D.; Walsh, A. *Biomaterials* **2008**, *29*, 3415–3428.
172. Boyd, L. M.; Carter, A. J. *Eur. Spine J.* **2006**, *15*(Suppl. 3), S414–S421.
173. Buechter, D. D.; Paolella, D. N.; Leslie, B. S.; Brown, M. S.; Mehos, K. A.; Gruskin, E. A. *J. Biol. Chem.* **2003**, *278*, 645–650.
174. Neubauer, A.; Soini, J.; Bollok, M. *J. Biotechnol.* **2007**, *128*, 308–321.
175. Brenneman, D. E.; Hauser, J.; Neale, E. *J. Pharmacol. Exp. Ther.* **1998**, *285*, 619–627.
176. Kimura, R. H.; Levin, A. M.; Cochran, F. V.; Cochran, J. R. *Proteins* **2009**, *77*, 359–369.
177. Kim, W.; Mcmillan, R. A.; Snyder, J. P.; Conticello, V. P. *J. Am. Chem. Soc.* **2005**, *127*, 18121–18132.
178. Zhang, K.; Diehl, M. R.; Tirrell, D. A. *J. Am. Chem. Soc.* **2005**, *127*, 10136–10137.
179. Kirshenbaum, K.; Carrico, I. S.; Tirrell, D. A. *ChemBioChem* **2002**, *3*, 235–237.
180. Connor, R. E.; Tirrell, D. A. *Polym. Rev.* **2007**, *47*, 9–28.
181. Young, T. S.; Schultz, P. G. *J. Biol. Chem.* **2010**, *285*, 11039–11044.
182. Lu, H. D.; Wheeldon, I. R.; Banta, S. *Protein Eng. Des. Sel.* **2010**, *23*(7), 559–566.

2.204. Peptoids: Synthesis, Characterization, and Nanostructures

J Seo, Gwangju Institute of Science and Technology, Gwangju, Republic of Korea
B-C Lee, Genentech Inc., South San Francisco, CA, USA
R N Zuckermann, Lawrence Berkeley National Laboratory, Berkeley, CA, USA

© 2011 Elsevier Ltd. All rights reserved.

2.204.1. Introduction 54
2.204.1.1. Bioinspired Polymers 54
2.204.1.2. Properties of Peptoids as Useful Biomaterials 55
2.204.2. Synthesis 55
2.204.2.1. Solid-Phase Synthesis 55
2.204.2.2. Solution-Phase Synthesis 56
2.204.2.3. Other Methods for Peptoid Synthesis 57
2.204.3. Peptoid Structure and Characterization 57
2.204.3.1. Peptoid Secondary Structures: Helices and Turns 57
2.204.3.2. Noncovalent Local Interactions in Peptoids 58
2.204.3.3. Cyclic Peptoids 58
2.204.3.4. Computational Modeling 58
2.204.3.5. Protein-Like Structures and Functions 58
2.204.3.6. Peptoid Self-Assembly: Nanostructures 60
2.204.4. Combinatorial Discovery of Peptoid Ligands 60
2.204.4.1. Synthesis Technologies 61
2.204.4.1.1. Automated synthesis 61
2.204.4.1.2. Parallel synthesis 61
2.204.4.1.3. SPOT synthesis 61
2.204.4.1.4. Split/mix synthesis 61
2.204.4.2. Analytical Methods 62
2.204.4.2.1. Separations 62
2.204.4.2.2. Characterization 62
2.204.4.3. Screening Methods 63
2.204.5. Drug Discovery 64
2.204.5.1. Protein Receptor Ligands 64
2.204.5.1.1. Protein–protein interaction inhibitors 64
2.204.5.1.2. Receptor ligands 65
2.204.5.2. Nucleic Acid Binders 66
2.204.5.3. Antimicrobial Agents 66
2.204.5.4. Lung Surfactants 68
2.204.5.5. Peptoid Pharmacology 69
2.204.6. Cellular Delivery/Uptake Vectors 70
2.204.6.1. Cell-Penetrating Peptoids 70
2.204.6.2. Lipitoids for Cellular Delivery of Nucleic Acids 71
2.204.7. Biomimetic Materials 71
2.204.7.1. Collagen Mimicry 71
2.204.7.2. Antifouling Agents 71
2.204.7.3. Glycopeptoids 73
2.204.7.4. Other Applications 73
2.204.7.4.1. Enantioselective catalysts 73
2.204.8. Summary and Future Directions 74
References 74

Glossary

Antifouling agent An antifouling agent prevents undesirable accumulation of microorganisms on wetted surfaces.

Antimicrobial peptoids Antimicrobial peptoids are designed to mimic antimicrobial peptides. Typical antimicrobial peptoids are cationic and facially amphipathic.

Chemoselectivity Chemoselectivity refers to the selective reactivity of one functional group in the presence of others.
Foldamer A polymer or an oligomer that adopts a secondary structure stabilized by noncovalent interactions.
Glycopeptoids Glycopeptoids are peptoids that contain carbohydrate moieties covalently attached to the side chains of the peptoid residues.
Heteropolymers A polymer comprising two or more monomers that are different from one another is called heteropolymer.
Lipitoids Conjugates of cationic lipids and peptoids are called lipitoids.
Peptidomimetics A peptidomimetic is a compound that is designed to mimic a biologically active peptide, but has structural differences that give advantages for its function.
Peptoid A class of peptidomimetic polymers, whose side chains are appended to the nitrogen atom of the peptide backbone rather than to the α-carbon. They are also called poly(*N*-substituted glycines).
Peptoid helix Peptoids fold into helical secondary structures by the incorporation of bulky chiral side chains. Unlike peptide helices, peptoid helices result from the repeating local steric influence of the side chain which restricts backbone rotation.
Peptoid nanosheet Amphiphilic periodic peptoids self-assemble to form well-defined 2D sheet architecture. The free-floating sheets have a thickness of 2.7 nm.
Submonomer synthesis An efficient solid-phase synthesis method to generate peptoids from simple starting materials. Instead of using monomers, two 'submonomers' are successively incorporated to form a monomer unit.

Abbreviation

AMP	Antimicrobial peptide
Apaf	Apoptotic protease activating factor
Boc	*N*-*tert*-butoxycarbonyl
BSL-2	Biosafety level 2
CD	Circular dichroism
CE	Capillary electrophoresis
CPP	Cell-penetrating peptides
DIC	*N*,*N*′-diisopropylcarbodiimide
DMF	*N*,*N*-dimethylformamide
DMPE	Dimyristoyl phosphatidyl-ethanolamine
DOPA	3,4-Dihydroxyphenylalanine
EPM	Equimolar peptide mixtures
Fmoc	Fluorenylmethyloxycarbonyl
GlcNAc	*N*-acetylglucosamine
GPCR	G-protein coupled receptor
HDM	Human double minute
HPLC	High performance liquid chromatography
HTS	High-throughput screening
Hyp	Hydroxyproline
IC_{50}	Half maximal inhibitory concentration
K_d	Dissociation constant
LC	Liquid chromatography
MAOS	Microwave-assisted organic synthesis
MBNL	Muscleblind protein
MeNPOC	(*R*,*S*)-1-[3,4-[methylene-dioxy]-6-nitrophenyl]ethyl chloroformate
MHC	Major histocompatibility complex
MIC	Minimal inhibitory concentration
MS	Mass spectrometry
NaOAc	Sodium acetate
NCA	*N*-substituted carboxyanhydrides
NHC	*N*-heterocyclic carbenes
NLeu	*N*-isobutylglycine
NLys	*N*-(4-aminobutyl)glycine
NMDA	*N*-methyl-D-aspartate
Nme (or Nmeg)	*N*-(2-methoxyethyl)glycine
NMR	Nuclear magnetic resonance spectroscopy
Nspe	(*S*)-*N*-(1-phenylethyl)glycine
OBOC	One-bead-one-compound
PITC	Phenylisothiocyanate
PMC	2,2,5,7,8-Pentamethylchromane-6-sulfonyl
PTC	Phenylisocyanate
PyBOP	Benzotriazol-1-yloxytris(pyrrolidino) phosphonium hexafluorophosphate
PyBrOP	Bromotris(pyrrolidino)phosphonium hexafluorophosphate
QD	Quantum dot
ROP	Ring opening polymerization
SDS	Sodium dodecyl sulfate
SH3	SRC (sarcoma) homology 3
SP	Surfactant proteins
TEMPO	2,2,6,6-Tetramethylpiperidine-1-oxyl
TM	Transmembrane
UPLC	Ultra performance liquid chromatography
VEGFR	Vascular endothelial growth factor receptor
VR	Vanilloid receptor

2.204.1. Introduction

2.204.1.1. Bioinspired Polymers

Sequence-specific heteropolymers are growing in importance as useful tools in chemical biology, drug discovery/delivery, and materials science. Recent advances in synthetic chemistry have made it possible to generate relatively simple protein-like structures and functions from nonbiological synthetic heteropolymers. Many of these synthetic heteropolymers are stable to biological proteases and extreme environments such as high temperatures and harsh chemical conditions. Further, they can be assembled in high yields from relatively cheap building blocks. Proteins are marginally stable; they are easily degraded by biological proteases and denatured by various chemicals

and high temperatures. Thus, there is a great opportunity to develop a new class of protein–mimetic polymers that are capable of molecular recognition and catalysis and yet are highly robust to the environment. The unusual stability properties and synthetic versatility of synthetic sequence-specific heteropolymers provide great promise for such materials and will have great impact in therapeutic, diagnostic, and materials science applications.

Researchers are making progress toward creating synthetic polymers that mimic the sophisticated structures and functions of proteins, although no synthetic polymer currently has the capacity to perform complex biological functions such as selective molecular recognition, catalysis, transport, energy conversion, etc. It has been difficult to find a single polymer system in which one can achieve stable secondary structures, sequence diversity, and long main chain lengths. It has been only the past decade since researchers have begun to mimic protein-like tertiary structures and functions.

The creation of new synthetic heteropolymers has been inspired and guided by protein folding and design principles. Advances in synthetic, combinatorial, and physical chemistry have provided a variety of useful tools to create folded protein–mimetic polymers where a variety of functionalized monomers can be arranged in a particular sequence. However, despite decades of study, the rules that govern the kinetics and thermodynamics of folding polymer chains into stable tertiary structures are not yet fully understood. Energetically, the dominant forces that drive folding of polymer chains in aqueous solution are well known,[1] and this has been useful for the design of new foldable polymer sequences. Still it has been difficult to understand the atomic structural details of the molecular interactions that drive unique and stable tertiary structures. Synthetic heteropolymers that allow detailed control of molecular interactions would help to understand folding principles on an entirely new level.

This chapter will focus on peptoids (*N*-substituted glycine polymers), one of several in the class of sequence-specific synthetic heteropolymers. Readers can find many comprehensive reviews regarding other synthetic heteropolymers.[2–4] Ever since peptoids first found utility in drug discovery,[5] many new areas of peptoid research have recently emerged as a result of their many useful properties. New structural motifs and design principles have emerged. Peptoids offer great new opportunities to create protein-like tertiary structures and functions. Peptoid polymers that spontaneously organize into well-defined supramolecular nanostructures are a promising new platform in materials science.

2.204.1.2. Properties of Peptoids as Useful Biomaterials

Peptoids are *N*-substituted glycine polymers in which the side chains are appended to the backbone nitrogen (**Figure 1**). This *N*-substitution in peptoids precludes the intra-backbone hydrogen bonding that is found in proteins, providing us the opportunity to explore polymer properties and chain folding in the absence of backbone hydrogen bonding.

Peptoids are efficiently synthesized using a solid-phase synthesis. Using the solid-phase submonomer method that we developed, 48-mer polypeptoids have been synthesized in excellent yields.[6] In terms of sequence diversity, over 300

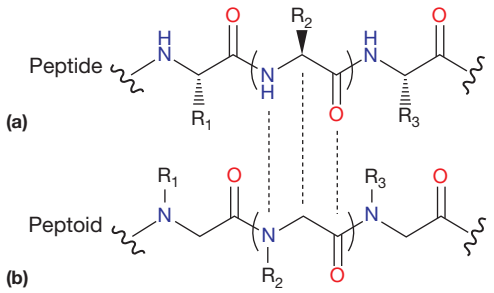

Figure 1 The comparision of (a) peptide and (b) peptoid.

primary amines are currently available that can be incorporated into peptoids as side chains. Thus, the diversity of peptoid side chains is much greater than that found in proteins.

Peptoids as short as 5-mers have been shown to adopt helical conformations when they contain chiral side chains adjacent to the main chain nitrogen.[7,8] These peptoid helical structures showed extreme stability to chemical denaturants and temperature.[9] The peptoids have been also shown to be stable to proteolysis,[10,11] opening the door to therapeutic, diagnostic, and biomaterials applications. Numerous short peptoid oligomers have been found that bind to therapeutically relevant proteins, acting as antagonists, inhibitors, or activators.[12] In this chapter, many of these useful features and examples will be discussed.

2.204.2. Synthesis

2.204.2.1. Solid-Phase Synthesis

Originally standard peptide solid-phase synthesis techniques were utilized for peptoid synthesis using Fmoc-protected *N*-substituted glycine monomers (**Figure 2(b)**).[5] This monomeric method involves tertiary amide bond formation between the existing secondary amine on the resin and the incoming monomer by the activation of carboxyl group in the monomer using benzotriazol-1-yloxytris(pyrrolidino) phosphonium hexafluorophosphate (PyBOP) or bromotris (pyrrolidino)phosphonium hexafluorophosphate (PyBroP). Then, the Fmoc group is deprotected with piperidine, generating a secondary amine for next amide coupling. This monomeric peptoid synthesis requires labor-intensive synthesis of Fmoc-protected *N*-substituted glycine monomers.

The invention of the submonomer solid-phase synthesis method for peptoids in 1992 was a major breakthrough because it greatly increased the synthetic efficiency, synthesis yields, and available side chain diversity, while also dramatically reducing time and costs.[6] As shown in **Figure 2(a)**, a secondary amine on the resin is first acylated by an activated haloacetic acid, such as bromoacetic acid, with *N*,*N*-diisopropylcarbodiimide (DIC). Then the bromine is displaced by a primary amine. In this S_N2 reaction, ~300 commercially available primary amines can be added, expanding the diversity and convenience of introducing side chains. Moreover, many new submonomers have been synthesized and incorporated into peptoids. These include *N*-BOC-tryptamine, *O*-*t*-butyl tyramine, and PMC-guanidino-propylamine to mimic natural amino acids tryptophan, tyrosine, and arginine.[13] In addition, carboxamide, carboxylic acid, and thiol derivatives of (*S*)-1-phenylethylamine

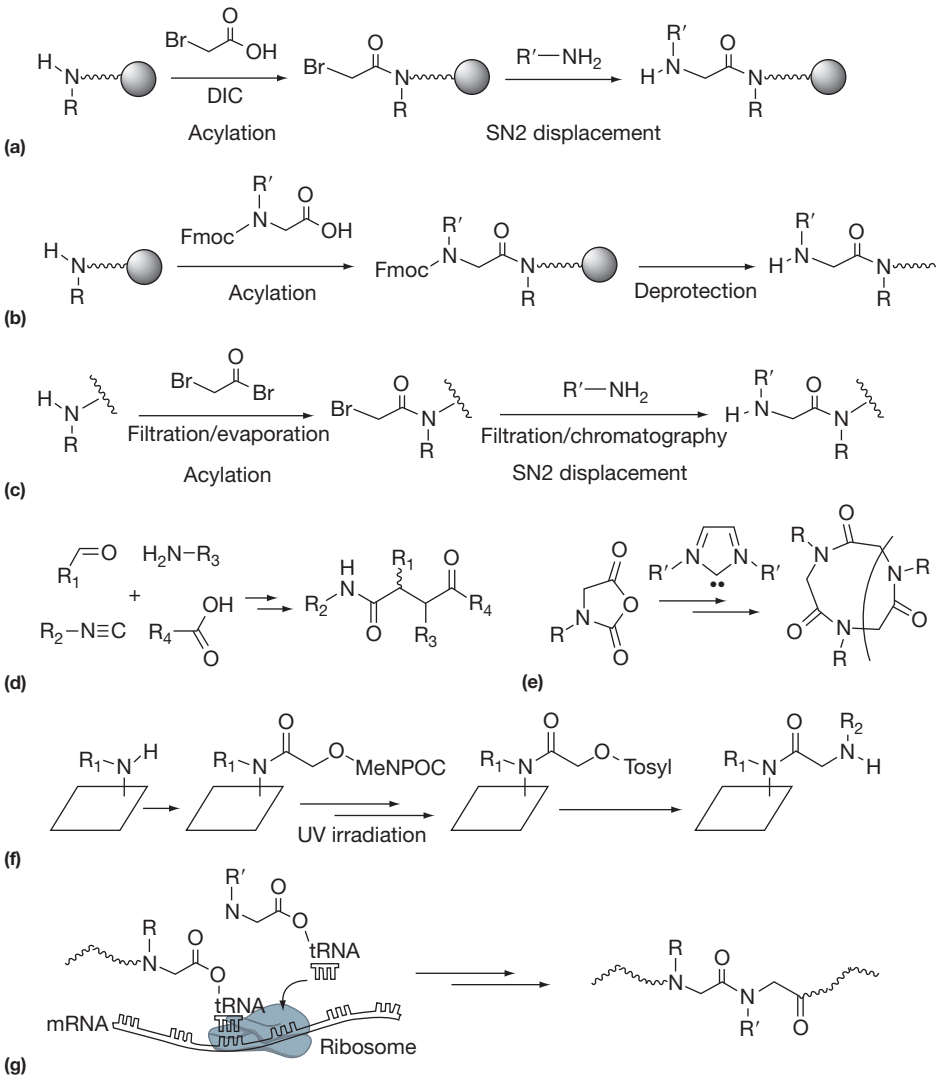

Figure 2 Methods for peptoid synthesis. (a) Solid-phase synthesis: submonomer method. (b) Solid-phase synthesis: Fmoc-method. (c) Solution-phase synthesis: bromoacetylbromide-method. (d) Solution-phase synthesis: Ugi four-component reaction. (e) Solution-phase synthesis: amine-initiated ring-opening polymerization. (f) Photolithographic synthesis. (g) *In vitro* ribosomal synthesis.

were synthesized to introduce a helical structure decorated with chemical functionalities.[14] A variety of chemoselective conjugation groups such as thiol, activated disulfides, aldehyde, aminooxy, and hydrazine groups have been also incorporated into peptoids via N- and C-terminal modification or the submonomer method that allowed an efficient ligation between peptoids.[15] Recently, amine derivatives of heterocycles such as histamine, pyridine and tryptamine were successfully incorporated into peptoids using chloroacetic acid in the acylation step.[16] Conformationally constrained cyclic peptoids can also be synthesized using the submonomer method, followed by solution-phase cyclization.[17] The submonomer synthesis is still widely used for peptoid synthesis.

2.204.2.2. Solution-Phase Synthesis

There are a couple of methods for making peptoids completely in solution as shown in **Figure 2(c)**. So far, the lengths of sequences made by this method are limited to <10 residues. One of the solution-phase peptoid syntheses is a submonomeric method using bromoacetylbromide.[18] The first step is the acylation reaction of the N-terminus of the existing peptoid chain with bromoacetylbromide. After filtration and evaporation, the crude bromoacetamide intermediate is then reacted with a primary amine. The newly formed peptoid is then isolated by flash chromatography before the next cycle of submonomer addition. Thus, this method requires labor-intensive filtration, evaporation, and chromatography, although it generates reasonably large quantities.

Another method for solution-phase synthesis is the Ugi four component reaction (4-CR) as shown in **Figure 2(d)**.[19] The Ugi-4CR is an efficient process in which a primary amine, an oxo compound, a carboxylic acid, and an isocyanide react in one pot to form a dipeptoid backbone. The Ugi-4CR has been combined with macrocyclization, generating many useful compounds such as functional macrocycles, cryptands, cages, etc.[20,21]

2.204.2.3. Other Methods for Peptoid Synthesis

Amine-initiated ring-opening polymerization (ROP) has been utilized to synthesize high molecular weight peptoid macrocycles (Figure 2(e)).[22] *N*-heterocyclic carbenes (NHCs) mediate ROP of cyclic substrates *N*-substituted carboxyanhydrides (N^R-NCA) through a zwitterionic propagating species and yield cyclic peptoid polymers in a controlled and efficient manner. This method is limited to single type of side chains in the peptoid polymers. In addition to this ROP, poly β-peptoids had been produced by the polymerization reaction of aziridines and carbon monoxide.[23,24]

The submonomer method of peptoid synthesis had been adapted for photolithographic application (Figure 2(f)).[25] A four-step monomer addition cycle was developed for the photolithographic synthesis of peptoids. Glycolic acid protected with a light-sensitive protecting group (MeNPOC) was first coupled to an amine-modified surface. The hydroxyl group was unmasked by UV irradiation and then activated with tosyl chloride. Finally, the tosylate was displaced with a primary amine to complete the construction of a monomer unit. This chemistry allows the spatially addressable synthesis of peptoids on an array by photolithography, since hydroxyl group unmasking, activation, and amine displacement will occur only at addresses that have been irradiated with UV light.

To our surprise, peptoid polymers have also been synthesized on a small scale using biosynthetic machinery. An *E. coli* cell-free translation system was used with genetically coded mRNA and artificial tRNAs charged with peptoid monomers as shown in Figure 2(g).[26] In this translation system, certain proteinogenic amino acids and/or cognate aminoacyl-tRNA synthetases are withdrawn (*withdrawn* PURE system; *w*PURE), diminishing the competing background incorporation of the proteinogenic amino acids in the translation elongation event. They prepared a wide variety of tRNAs charged with nonproteinogenic peptoid monomers using artificial tRNA acylation ribozymes. Using this method, six peptoid monomers were translated from the genetic code and purified.

2.204.3. Peptoid Structure and Characterization

2.204.3.1. Peptoid Secondary Structures: Helices and Turns

As we learned from biological polymers, efficient functions are derived from well-defined structures. One of the key strategies to forming well-defined, atomically ordered folded polypeptoids is to control the local secondary structure. Control over local and global molecular interactions can reduce the conformational freedom of the polymer chain resulting in ordered states in aqueous environment. Borrowing from nature's design principles found in proteins, many synthetic polymer systems have been developed to create protein–mimetic materials. However, most synthetic sequence-specific polymers are relatively short in main chain length, due to synthetic inefficiencies. Still, with relatively short chain lengths, many specific protein ligands have been developed. Longer sequences have been used for antifouling materials, antimicrobial agents, lung surfactant mimetics, drug delivery vehicles and protein mimicry. However, it is still in infancy to create protein-like structures and functions in purely nonbiological polymers.

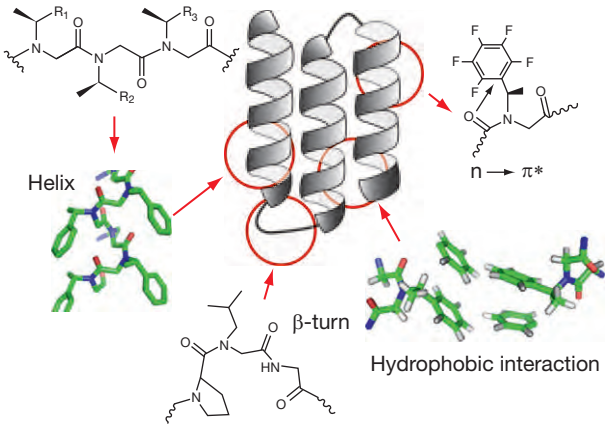

Figure 3 Schematic diagram for a hierarchical approach toward creating a tertiary structure in peptoids from local to global interactions. The local interactions include the formation of secondary structures such as helices and turns, and the tunable interactions such as n→π* interaction. The hydrophobic interaction has been utilized as a folding core of peptoid helix bundles.

A number of proteins fold up sequentially from initial secondary structures to well-defined tertiary structures. Thus, one of the methods toward unique tertiary structures in nonbiological polymers would be first to create secondary structures and then, engineer them further to assemble in three-dimension (3D). In peptoids, we have been using this sequential strategy, aiming toward unique 3D peptoid structures (Figure 3).

Like the secondary structures in proteins, helices and turns have been generated in peptoids. Peptoid helical structures are well established and exhibit extreme chemical and thermal stability.[9] Intrinsically, the peptoid backbone is more flexible than the peptide backbone due to the lack of hydrogen bond donors and main chain chirality. However, a bulky chiral side chain appended to the Nα position in peptoids significantly reduces the conformational freedom of the chain backbone and induced well-defined helical structures with three residues per turn (Figure 3).[7] The peptoid helical structures have been characterized by a range of high-resolution techniques, such as 2D-NMR, X-ray crystallography, and computational modeling.[27–29] The structural parameters including backbone ϕ and ψ angles and the distance between two helical pitches showed that the peptoid helical structures given by α-chiral steric bulk resemble the polyproline type-I helical structure in peptides. Because of the steric hindrance given by the bulky chirality at the Nα position, the backbone ϕ angle is limited to a certain range of angles to prevent the steric clash with nearby backbone carbonyl groups. This molecular steric hindrance in peptoids allows even small pentamer peptoids to form stable helical structures with extreme chemical and thermal stability. The peptoid helical structures were stable to 8 M urea and to 75 °C.[9]

The turn structures in peptoids are recently generated, but not well established comparing to the helices. A series of tripeptoids containing either *N*-methylglycine or *N*-isobutylglycine in position i + 1/i + 2 were synthesized and tested for intramolecularly H-bonded β-turn formation in chloroform solution.[30] The population of the type-II β-turn increased when they incorporated the achiral peptoids at the position $i+2$. Toward the β-turn mimic, geometrically constrained triazole ring had

been introduced into peptoids as a monomer unit, stabilizing a turn in the middle of linear peptoids. This triazole motif mimicked the β-hairpin structures in peptides.[31]

2.204.3.2. Noncovalent Local Interactions in Peptoids

Several types of noncovalent interactions have been found,[32–35] expanding significantly the scope of peptoid design and the utility of peptoids for a broad range of applications. These interactions stabilize peptoid secondary structures further and can even switch the conformation, depending on the environment such as pH and solvent.

Hydrophobic interactions and n→π* interactions have been shown to play a role in peptoid folding.[32,36,37] The conformation of the secondary structures could be tunable by these noncovalent interactions. For example, the rotameric *cis* to *trans* equilibria of the backbone amides could be controlled by n→π*, steric, and hydrogen bonding interactions (**Figure 3**).[32,34] Especially, *cis*-amides in the peptoid backbone could be exclusively formed by *N*-R-chiral acetanilide and *N*-1-naphthylethyl side chains, by $n\rightarrow\pi^*_{C=O}$/hydrogen bonding interactions and $n\rightarrow\pi^*_{Ar}$/steric interactions, respectively.[34] The pair interaction of fluoroaromatic and other electron-deficient aromatic side chain in pepoids could be an effective strategy for controlling peptoid structures.[33]

The rotameric *cis* to *trans* equilibrium of the backbone amides could be also dependent on the nearby amides in the backbone. Using NMR, the kinetics of *cis* to *trans* equilibrium of the backbone amides could be measured in monomers, di- and tri-peptoids[38] with a range of rate constants from 0.03 to 0.37 s^{-1}. These findings would be useful for understanding the transition between different conformations and developing an accurate force field in peptoids.

Previously, a threaded loop structure was found in peptoids by well-defined local interactions.[39] This structure is unique to peptoid nonamers with achiral side chains and was first identified in a homononamer of Nspe. The threaded loop structure is stabilized by three intramolecular hydrogen bonds from backbone carbonyl groups (residues 5, 7, and 9) to the N-terminal secondary ammonium, and one intramolecular hydrogen bond from a backbone carbonyl (residue 2) to the C-terminal primary amide. The peptoid threaded loop contains four *cis* and four *trans* amide bonds. Interestingly, methanol was able to disrupt the set of intramolecular hydrogen bonds, converting the threaded loop to helical structure.

L-phenylalanine *tert*-butyl ester had been utilized for the synthesis of (*S*)-*N*-(1-carboxy-2-phenylethyl)glycine oligomers.[35] These peptoids formed stable secondary structures in aqueous solution in which the conformation is dramatically responsive to variations in pH and solvent composition. The electrostatic interaction between monomer units was responsible for this pH-dependent conformational switch.

2.204.3.3. Cyclic Peptoids

Cyclization of the linear polymer chains has been developed over the past few decades as an effort to find an efficient method for conformational ordering.[40] This type of confined structures via cyclization provides a useful platform for high-affinity molecular recognition due to the gain of the entropic term in thermodynamic binding free energy. Head-to-tail macrocyclization was estabilished in peptoids, allowing the enhancement of the conformational ordering and the crystallization of cyclic peptoid hexamer and octamer.[17] The high-resolution crystal structures of these cyclic peptoids revealed that the peptoid backbone could accommodate tight turns via distorted *cis* and *trans* amide conformers in the solid state.[17] This head-to-tail macrocyclization have been utilized recently for useful alkali metal ion transporters.[41]

Another macrocyclization have been also established in peptoids via chemical linkages of side chains. Especially, the azide-alkyne cycloaddition was used widely in peptoids for macrocyclization.[42–44] Amide coupling through side chains was also developed[45,46] and employed further for cyclic peptoid arrays.[45]

2.204.3.4. Computational Modeling

Computational modeling of biological molecules has been advanced significantly in the past decade, providing a very useful tool for predicting secondary and tertiary structures in proteins and nucleic acids. This success was made possible due to the development of super-computing power and more accurate force fields in amino acids and nucleotides than ever, and the database of protein and nucleic acid structures. The computational tools are now being applied to many other nonbiological synthetic heteropolymers as an aid for the design of new molecules. However, accurate force fields are required for the success of design and understanding of synthetic heteropolymers. There are a number of computational studies in peptoids to guide us toward more accurate models of peptoid structures.[27,28,47–50] The recent high-level quantum mechanics simulation had a good agreement with available peptoid atomic-detail structures as shown in the Ramachandran plot of peptoid backbone ϕ versus ψ angle (**Figure 4**).[48] This simulation revealed that local energetics dictates the conformational preference in peptoids.[48]

Distance geometry and ensemble calculations have been carried out using the distance information from NMR data in order to refine the peptoid helical structures and understand the amide backbone *trans* to *cis* isomerism.[28,50] The *trans* conformation of the backbone amide is generally not preferred in peptoids due to the *N*-substitution.[38] Quantum mechanical *ab initio* calculations have been applied for this problem.[47,48] Although the angle of the amide backbone depends on the side chains, it is not fully understood yet about the determining factors of this amide backbone *trans* to *cis* isomerism. The accurate force field of peptoids is necessary for understanding this problem.

In order to understand the folding cooperativity in peptoid helix bundles, a dynamic programming approach was carried out using statistical mechanical partition functions of foldamer chain molecules.[51] This model showed that the peptoid three-helix bundle fold anticooperatively and predicts that two-helix bundles are unstable in proteins but stable in peptoids.

2.204.3.5. Protein-Like Structures and Functions

One of the ultimate goals in the area of bioinspired heteropolymers is to create precisely folded nanostructures with protein-like functions. There have been recent efforts to construct

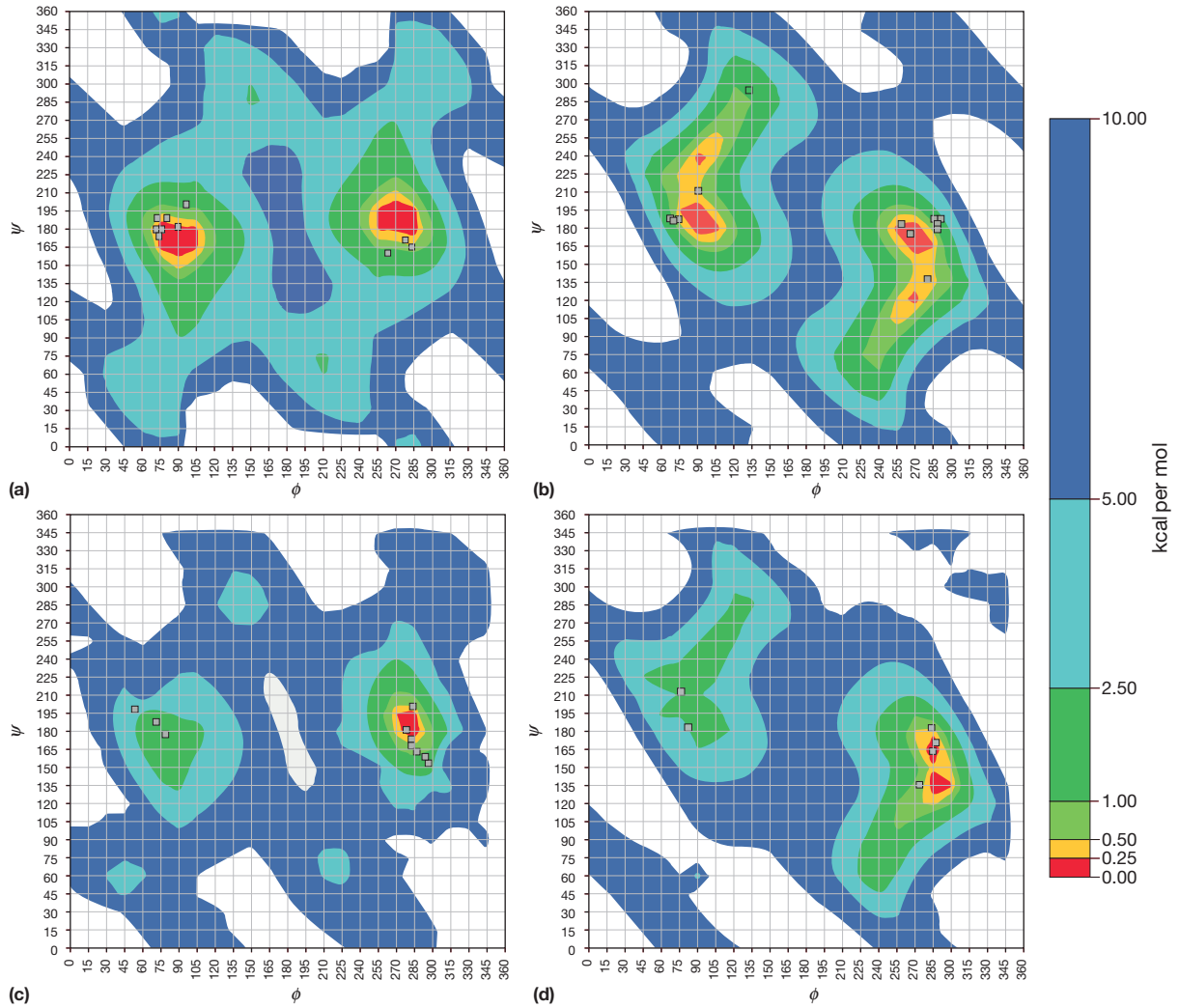

Figure 4 Ramachandran plot of peptoid backbone phi vs. psi angels revealed by a recent high-level quantum mechanical simulation. Monomeric peptoids, Ac-Nme-N(CH_3)$_2$ (a and b) and Ac-Nspe-N(CH_3)$_2$ (c and d) were calculated by the quantum mechanical calculation at the B3LYP/6-311+G(2d,p)//HF/6-31G* level. The backbone ω is *cis* at the left plots (a and c), and *trans* at the right plots (b, d). Squares are corresponding experimental residues from crystal structures. Nme and Nspe stand for *N*-(methoxyethyl)glycine and (S)-*N*-(1-phenylethyl)glycine, respectively. Adapted from Butterfoss, G. L.; Renfrew, P. D.; Kuhlman, B.; Kirshenbaum, K.; Bonneau, R. *J. Am. Chem. Soc.* **2009**, *131*, 16798–16807, with permission from American Chemical Society.

synthetic polymers that mimic protein properties. Although it has been difficult to achieve stable secondary structures, a multiletter alphabet, and long chain lengths within a single type of polymer, our group has been able to create helix bundle structures with hydrophobic folding cores and introduce one of the simplest biological functions such as high-affinity zinc binding into peptoid two-helix bundles.[36,37] The advancement of synthetic technologies and design principles would enable us to create more complicated protein-like structures and functions.

The helix bundle was the first target toward tertiary structures in peptoids because the helical secondary structures are well established in peptoids. One of the key strategies for generating protein-like helix bundles was utilizing amphiphilic self-assembled peptoid helical structures.[52] The hydrophobic groups at every third position allow the amphilicity of peptoid helices and provide a stable hydrophobic folding core inside self-assembled helix bundles. The combinatorial chemistry had been carried out to identify amphiphilic peptoid helices that have a well-defined hydrophobic core.[52] Using these peptoid helices, single-chain folded helix bundles had been created by orthogonal chemoselective conjugations between peptoid helices. By three consecutive conjugations, a 12 kDa peptoid four-helix bundle had been created previously.[37]

To mimic protein-like functions, our group was able to introduce high-affinity zinc-binding site into the peptoid two-helix bundles.[36] Borrowing from well-understood zinc-binding motifs in proteins, thiol and imidazole moieties were positioned within the peptoid two-helix bundles such that both helices must align in close proximity to form a binding site. Certain peptoid two-helix bundles bind zinc with nanomolar affinities and high selectivity compared to other divalent metal ions. This work is a significant step toward generating protein-like structures and functions.

2.204.3.6. Peptoid Self-Assembly: Nanostructures

Polypeptoids are a unique material that allows not only the mimicry of proteins, but the precise engineering of polymers. Sequence level control and the ability to synthesize relatively high molecular weights have resulted in a number of interesting applications. The nanoscale self-assembly of polymeric peptoid materials is an area of tremendous potential, as the fields of protein folding and polymer self-assembly become ever closer. Peptoid polymers have been studied as bulk solids and shown to have improved process ability over polypeptides. Recently, certain sequences of peptoids showed their ability to form nanoribbon/tapes and 2D floating sheets in aqueous solution,[53–55] gaining their potentials for useful nanostructured materials.

A series of peptoid homopolymers were studied with respect to their thermal properties as bulk solids.[56] Many of these sequences form crystalline phases with discrete melting temperatures. Interestingly, a comparison was made between a polypeptide and a perfectly analogous polypeptoid (i.e., everything in the structure was identical except for the point of side chain attachment). The peptoid was found to exhibit a reversible melting transition at modest temperatures, whereas the corresponding peptide did not melt all the way up to its decomposition temperature. This suggests that the lack of hydrogen bonding in polypeptoids is an important feature that may contribute to improved processability in the bulk.

During the development of a novel class of peptoid β-sheet breaker as amyloid inhibitors, a retro-peptoid sequence corresponding to the amyloidogenic peptide sequences amylin, SNNFGAILSS, was found to form the supramolecular nanoribbon/tape structures.[53] Due to the formation of this self-assembled peptoid nanostructures, this retro-peptoid was not efficient to inhibit the amyloid formation of amylin, but provided a useful nanostructure.

Recently, our group systematically explored the impact of amphiphilic sequence patterns in the self-assembly of peptoid polymers, and we discovered one of the largest 2D organic crystals known. Remarkably well-defined 2D free-floating peptoid nanosheets formed spontaneously in aqueous solution after mixing a 1:1 ratio of two oppositely charged peptoid 36-mers of a specific sequence.[54] A repeating, alternating sequence pattern of a polar ionic monomer followed by a nonpolar aromatic monomer was key to formation of the sheet architecture. These giant free-floating sheets were shown to have a bilayer structure (i.e., two molecules thick) and have a thickness of only 2.7 nm, yet a width and length of tens of microns (**Figure 5**). The unprecedented direct imaging of individual peptoid chains was made possible by the recent development of aberration-corrected transmission electron microscopy (TEAM 0.5) at the National Center for Electron Microscopy, Lawrence Berkeley National Laboratory. Direct observation of individual polymer chains revealed that the peptoid chains are fully extended in structure and run parallel to one of the sheet edges. Further, the chain–chain spacing of 4.5 Å could be directly imaged, which corresponded well to the spacings observed by X-ray and electron diffraction experiments. It was further demonstrated that the peptoid nanosheets could be functionalized with biologically active ligands and that they could specifically bind their protein target with high specificity.

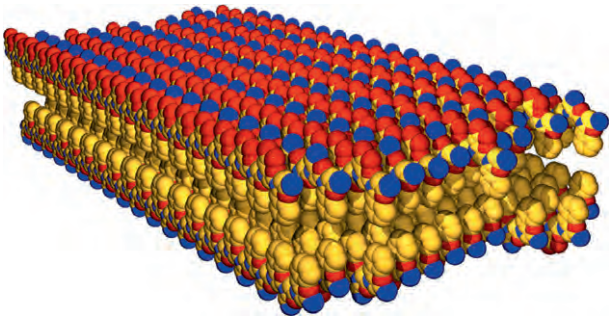

Figure 5 Free-floating nanosheets can be formed by the self-assembly of two oppositely charged peptoid 36-mers of a specific sequence pattern. The peptoid sequence is a repeat of an alternating sequence of a polar ionic monomer and a nonpolar aromatic monomer. The peptoid nanosheets consist of a bilayer, which is <3 nm in thickness, yet many tens of microns in length and width. Adapted from Nam, K. T.; Shelby, S. A.; Marciel, A. B.; *et al*. *Nat*. *Mater*. **2010**, *9*, 454–460.

Importantly, this is the first demonstration that biological sequence information (a beta-sheet-like alternating sequence) can be introduced into a synthetic polymer to generate an atomically defined biomimetic structure. Interestingly, because the peptoids are achiral, these peptoid nanosheets are completely flat, in contrast to peptidic beta sheets, which have an inherent twist in their structure that is a result of the amino acid chirality. Thus, the synthetic flexibility and biocompatibility of peptoids provide a flexible and robust platform for integrating functionality into defined nanostructures.

2.204.4. Combinatorial Discovery of Peptoid Ligands

Molecular diversity as a source of potential drug candidates, protein–mimetics, and various other functional materials has been of enormous interest. Combinatorial library synthesis provides an efficient route to achieve great molecular diversity and has been extensively used both in academic and industrial research.[12] Inspired by nature's intrinsic molecular diversity provided by biopolymers (i.e., proteins), researchers at Chiron Corp, now part of Novartis AG, pursued new drug discovery technologies employing a peptoid combinatorial library platform.[5] The invention of the solid-phase submonomer synthesis methods facilitated the library synthesis and enabled peptoids to be an ideal class of molecules for combinatorial library synthesis. First, the solid-phase peptoid synthesis allows the resin-splitting methods, which are crucial for mix-and-split type combinatorial library synthesis where equimolar compound mixtures can be synthesized. Second, each residue incorporation step is composed of highly efficient bromoacetylation and amine displacement reactions. These reactions provide high yields and are not sensitive to air and moisture; therefore, the chemistry is automatable. Third, due to the availability of a number of peptoid submonomers as primary amines, a wide variety of chemical functionalities can be incorporated. These favorable aspects of peptoids for combinatorial library synthesis along with the availability of state-of-the-art lab automation instruments, the synthesis of millions of peptoids now became a straightforward process. In addition, the ability to screen and analyze peptoids

rapidly and inexpensively from the libraries has been a primary tool in modern peptoid research.

2.204.4.1. Synthesis Technologies

2.204.4.1.1. Automated synthesis

Solid-phase synthesis techniques have been introduced in the early 1960s by Bruce Merrifield, a Nobel laureate in 1984, and have been applied to biopolymer synthesis including peptides, oligonucleotides, nonnatural peptides, and oligosaccharides. In the case of peptide synthesis, the key steps of the synthetic cycle, namely deprotection and coupling, are repeated until the complete sequence is assembled on the solid matrix. Afterward, the crude product is cleaved from the support, purified, and characterized.[57] Nowadays the synthesis of peptides is fully automated and routinely performed on automated synthesizers. Because the peptoid monomer addition cycle is also two steps, peptoid synthesis can be carried out by most commercial peptide synthesizers with only a few minor programming changes.[58] In the automated synthesis of peptoids, amine solutions are placed in the 'amino acid' reservoirs. Depending on the synthesizer's specification, (1) many samples are handled in parallel (up to ~30 wells) on a typical scale of 0.1 mmol per well; or (2) one-bead-one-compound (OBOC) peptoid libraries of tens to hundreds of thousands of compounds can be synthesized using an automated resin mix-and-split step.[59,60]

2.204.4.1.2. Parallel synthesis

In parallel synthesis, each library member is synthesized in a separate reaction vessel. For the synthesis of 16 peptoid dimers, 16×2 cycles of peptoid monomer unit incorporation is required. For the same number of peptoid dimer synthesis, a mix-and-split method needs only 8 cycles and is well suited for a large size library synthesis to cover larger chemical space.[61] However, the advantages of the parallel synthesis are that the entities in the library are known and that a large amount of peptoid can be prepared in each reaction vessel. A library prepared by the mix-and-split method often requires additional deconvolution or encoding steps to identify peptoid on a specific resin.

Microwave-assisted organic synthesis (MAOS) was originally developed for simple organic transformations such as hydrolysis. Then the technique has been successfully applied to the synthesis of peptides, peptidomimetics, and carbohydrates.[62] The microwave irradiation for peptoid library synthesis has been reported and has shown advantages in terms of both higher purity and dramatically shorter reaction time.[63,64] The optimal conditions for the bromoacetylation step involved irradiation for 30 s and heating to 35 °C using temperature control probe, and for the amine displacement, irradiation for 90s and heating to 95 °C again using the temperature control (at room temperature, typical reaction time for bromoacetylation is 20 min and for amine displacement is 60 min). The MAOS is being used actively in the preparation of peptoid library synthesis either in the parallel synthesis or in the mix-and-split library synthesis.

2.204.4.1.3. SPOT synthesis

The SPOT synthesis technique employs the parallel synthesis method mentioned above, but the difference is that the synthesis is carried out directly on a cellulose membrane rather than on resin beads in a reaction vessel.[65] The SPOT method follows the standard peptoid submonomer synthesis protocol: preparation and functionalization of the cellulose membrane, stepwise bromoacetylation and amine displacement, and cleavage of the side chain protecting groups. If necessary, peptoids can be cleaved from the cellulose membrane by the incorporation of appropriate linkers between the membrane and the peptoid. Peptoid synthesis on cellulose allows the parallel synthesis of large numbers of positionally addressable peptoids in small quantities, and the cost of SPOT synthesis is far cheaper than that of conventional resin-based synthesis.

Wenschuh *et al.* first reported the SPOT synthesis of peptomers (peptide–peptoid hybrids) and peptoids.[66–68] They used Whatman 50 cellulose membranes and modified by treatment with epibromohydrin and 4,7,10-trioxa-1,13-tridecanediamine to provide homogeneous terminal primary amines on the cellulose membrane. Slight modification on conventional peptoid submonomer protocol was employed by using bromoacetic acid 2,4-dinitrophenyl ester instead of commonly used bromoacetic acid/DIC, and selective bromoacetylation on the terminal secondary amines over residual hydroxyl groups on cellulose was achieved. For the dry state cleavage of peptoids, the authors used a photo-labile linker system to cleave membrane-bound peptoids via UV irradiation. The peptoid SPOT array consisting of 8000 peptoids and peptomers are screened for the monoclonal antibody Tab-2, and micromolar affinity ligands were identified demonstrating the potential utility of this method for the rapid identification of novel nonpeptidic protein ligands.

2.204.4.1.4. Split/mix synthesis

In the early 1990s, the OBOC combinatorial library method was first introduced by Lam and coworkers.[69,70] With the OBOC library technique, tens of thousands to millions of compound beads could be rapidly prepared and then screened for a specific biological activity. For the synthesis of OBOC libraries, a mix-and-split synthesis method is utilized such that each bead displays only one compound.[71] Originally, Lam *et al.* developed the OBOC library technique for the synthesis of short linear peptides. Afterwards, led by Zuckermann and Kodadek, the application of the technique was expanded to the preparation of the peptoid libraries.[58,72]

Prior to the library synthesis, the size of the library including the length of the oligomer and the number of amine submonomers must be considered. If nothing is known about the target protein, diverse sets of amines are used. However, the information about the target-binding site can help design the library and significantly reduce the number of amine submonomers to be used. Typically, 6–30 amine submonomers are used to conveniently prepare an OBOC library. The scale of the library synthesis depends on the amount of material needed for screening. Generally, for the synthesis of peptoid trimer library, 2.4 mmol of resin is used, yielding about 1 ml of each of 24 pools, each at a concentration of 100 μM per compound. This quantity is sufficient for hundreds of screens when screened at 1 μM per compound.

In 1992, Zuckermann and coworkers introduced a fully automated peptoid synthesis protocol that is capable of synthesizing equimolar peptide mixtures (EPM).[59] Equimolarity

was achieved by employing the resin-splitting method, namely isopycnic slurry method, where the resin was suspended as slurry in a solvent system that had a similar density to resin, causing the resin particles to settle very slowly. The authors suspended a polystyrene resin (100–200 mesh and 1% cross-link with divinylbenzene) as a 3% w/v free-flowing slurry in 65% 1,2-dichloroethane/DMF. The resin slurry was then transferred by a robotic pipet hand into separate reaction vessels (up to 36). When short peptides/peptoids were synthesized, the equimolarity of the library was well maintained after repeated split-and-pool processes. With the automated EPM synthesizer on hand, the authors prepared ~5000 peptoid dimers and trimers to identify high-affinity ligands for 7TM/GPCR (see Section 2.204.5.1 for further discussions).[73] In this work, iterative deconvolution method was successfully employed for the structural determination of the peptoid hits. This method is based on an iterative process of screening and resynthesis of smaller sublibraries in an attempt to fractionate a mixture into its most active constituents. Popularized by Houghten *et al.*,[71] iterative deconvolution has been used as a screening method to identify hits from non-OBOC libraries.

2.204.4.2. Analytical Methods

2.204.4.2.1. Separations

In combinatorial chemistry, a vast number of diverse compounds are generated by robotic instruments; for example, thousands of compounds can be synthesized daily. Due to the increase in the rate of compounds synthesized, the demand for rapid analysis and characterization of the library is high. For separation purposes, widely used analytical instruments are LC/MS (liquid chromatograpy/mass spectrometry), HPLC (high performance liquid chromatography), and more recently UPLC (ultra performance liquid chromatography). Typically, liquid chromatography separations are carried out on a reverse phase mode; C18 or C4 supports are used as stationary phase, and water/acetonitrile gradients are eluted as mobile phase. Technical advances in this field have enabled high-resolution separations of mixtures and high sensitivity detection of compounds in small quantity.

One active area of investigation is in the development of capillary electrophoresis (CE). CE is designed to separate species based on their size to charge ratio in the interior of a small capillary filled with a matrix. The advantages of CE are the requirement of small sample quantity and the wide variety of separation mechanisms modulated by types of matrices and by mobile phase solutions. The superior separation efficiency of CE makes it a powerful tool for many of the analytical challenges in biopharmaceutical research.

Lunte and coworkers evaluated the utility of the CE technique for the separation of a combinatorially synthesized peptoid mixture.[74,75] The mixture consisted of 24 trimeric peptoids that ranged in molar mass from 392 to 699 with pK_a values ranging from 3 to 10. With reverse phase HPLC, separation of this mixture posed a significant challenge. Hence, the authors used a fused-silica capillary electrophoresis and surveyed different types of mobile phase buffers and additives for efficient separation. Significantly enhanced separation was achieved when they used a combination of heptane sulfonic acid (25 mM) and methyl-β-cyclodextrin (40 mg ml^{-1}) in 250 mM sodium phosphate buffer at pH = 2.0. As for the additives, heptane sulfonic acid was used as an ion-pairing agent to reduce hydrophobic intramolecular interactions and to disrupt electrostatic interactions with the capillary wall, and methyl-β-cyclodextrin was used to provide host–guest interactions and resolve very hydrophobic components of the peptoid mixture. Later the authors reported the use of SDS micelles in conjunction with methyl-β-cyclodextrin, and the additives in the same sodium phosphate buffer (pH = 2.0) provided dramatic improvement in the separation of the peptoid mixture.

Lunte and coworkers demonstrated the potential advantages of CE over conventional HPLC for the analysis of complex peptoid mixtures. Only nanoliters of sample are injected for each analysis, and this offers tremendous benefit when extremely small amounts of sample are available as is typical with OBOC combinatorial chemistry.

2.204.4.2.2. Characterization

Numerous techniques have been applied for the characterization of combinatorial libraries. For libraries prepared by parallel synthesis, all compounds in the library are addressed individually, and characterization process is relatively straightforward. However, evaluation of libraries prepared by mix-and-split synthesis is much more challenging. Taking into account that an OBOC library is composed of individual beads containing unique chemical entities, the first approach to characterize the mix-and-split library is to analyze the individual beads. This approach is often limited because each bead contains only a picomolar quantity of a compound; therefore, highly sensitive analytical methods have to be used. Generally, the methods of choice are mass spectrometry, microsequencing and amino acid analysis. Sensitivity of modern automatic microsequencers is greatly improved and allows the characterization of the small quantity of compound on a single bead. Sequencing based on Edman degradation can be combined with mass spectrometry, and evaluation of mixtures generated by the degradation using mixture of phenylisothiocyanate (PITC) and phenylisocyanate (PTC) can be performed. The use of PTC does not cleave the N-terminal amino acid: this amino acid is capped and the resulting phenylcarbamoyl peptide (or peptoid) resists further degradation. Repeated cycles of this procedure provide a mixture of peptide (or peptoid) fragments differing by a single peptoid monomer unit, which can be characterized by mass spectrometry. For peptoid Edman degradation, Kodadek *et al.* noted the importance of a strong denaturing wash (with hot 1% SDS buffer) of peptoid beads prior to sequencing; this step eliminated any undesirable interference of bound proteins on sequencing reactions. With minor modifications, peptoid Edman sequencing protocol was well established using a standard peptide sequencer.[72,76]

Using the Edman degradation, peptide/peptoid structures can be determined directly on resin without being cleaved; however, only 3–4 peptides/peptoids can be sequenced each day with an automated sequencer.[69,77,78] Analysis of unnatural amino acids by Edman degradation is especially slow because it requires the synthesis and analysis of standards for each unnatural residue.[78] Mass spectrometry (MS) offers both high sensitivity and speed for characterizing peptoid combinatorial library. Tandem MS (or MS/MS) has been routinely used for

the sequence determination of peptides, and this technique was shown to be readily applicable to analyze peptoids.[79,80]

Zuckermann and coworkers developed a method for the rapid identification of sequence of hit compounds from OBOC peptoid libraries.[81] They used a cleavable hydrophilic linker to reduce nonspecific binding to biological samples and allows for the attachment of a halogen tag, which facilitates postscreening sequencing by tandem mass spectrometry (MS/MS). The linker is based on a tartaric acid unit and produces a C-terminal aldehyde upon cleavage from resin. Then the aldehyde can be derivatized with a bromine-containing aminooxy compound that serves as an isotope tag for subsequent MS/MS analysis. The authors showed a number of peptoids can by synthesized using the linker and demonstrated very low levels of nonspecific binding to proteins in a bead screening and sequencing step. Another strategy for rapid and robust sequencing of peptoids and peptomers from OBOC libraries was developed by Pei and coworkers.[82] In this strategy, beads were subjected to multiple cycles of partial Edman degradation by treatment with a 1:3 molar mixture of phenyl isothiocyanate (PITC) and 9-fluorenylmethyl chloroformate (Fmoc-Cl) to generate a series of N-terminal truncation pruducts for each resin-bound peptoids. After the partial Edman degradation step, the Fmoc groups were removed by piperidine treatment. The resulting mixture of the full-length peptoid and its truncation products was analyzed by mass spectrometry, and the full-length peptoid was sequenced. The authors showed this method was also readily applicable to peptomers (peptide–peptoid hybrids).

2.204.4.3. Screening Methods

A reliable high-throughput assay is essential to successfully screen a combinatorial library. A systematic screening of diverse compound collections has proved to be a fruitful source of a number of pharmaceutical lead compounds.[83] For combinatorial library screening, solid-phase and solution-phase assays have been developed. In the solid-phase assays, the ligands are still attached to the resin, and the assay involves either (1) direct binding of molecular target to the bead-attached ligand or (2) detection of functional properties of the bead-attached ligand such as identifying the activity of the ligand as a substrate to a protein. Solution-phase assays require cleavage of ligands from the beads, and the ligands have to be spatially separated such as in 96-well plates.

In peptoid research, major advances in screening technology have enabled combinatorial peptoid libraries to be mined quickly and inexpensively for specific protein binders.[76] Kodadek and colleagues focused on the discovery of peptoid binders for proteins, with the purpose of using the high-affinity binders for the construction of protein-detecting microarrays. The primary approach they used was the OBOC peptoid library screening. The screening was conducted by binding a fluorescently-labeled target protein to the OBOC peptoid library beads. After trial and error to find an optimal system for peptoid library screening, they found a Texas Red-labeled protein to a library of tens to hundreds of thousands of peptoids displayed on TentaGel beads worked well for their purpose.[77] A visual examination and identification of the beads that contained peptoids and the Texas Red-labeled protein were performed under a fluorescent microscope, and the fluorescent beads were isolated manually using a micropipette. Technical improvement was made to increase the visual contrast between hits and nonhits by employing a biotinylated protein and detecting its binding to the bead by subsequent hybridization with a streptavidin-coated quantum dot. The intense signal from the quantum dot made it easier to distinguish hits from nonhits (autofluorescent beads), and the sequence of the peptoid on the bead was determined by Edman degradation and mass spectrometry. For the sequencing step after this on-bead screening, bound proteins were stripped from the bead by the treatment of 1% SDS solution, and the bead was subjected to an automated Edman sequencer. If peptoids are not attached on beads, the sequence can be determined by tandem mass spectrometry[81] or partial Edman degradation and mass spectrometry.[82] Recently, Kodadek *et al.* reported a new bead screening technique for the identification of specific peptoid ligands for cell surface receptors.[84] Because of the difficulty of handling membrane receptors (i.e., poor solubility and/or lack of stability when isolated), the standard screening methods developed for soluble proteins could not be easily employed for membrane receptors. Therefore, cell-based assay techniques have been developed based on the use of live cells carrying target receptor.[85] Kodadek *et al.* used a two-color, cell-based screening method to isolate peptoid hits to exhibit specificity for a membrane protein, VEGFR-2 (vascular endothelial growth factor receptor-2). They labeled cells lacking VEGFR-2 with a green quantum dot (QD), and cells carrying VEGFR-2, but were otherwise identical, were labeled with a red QD. The QDs did not contaminate the cell surface because they were taken up into cells by endocytosis. The cells were then incubated with ~300 000 OBOC beads displaying nonameric peptoids under carefully controlled conditions to minimize nonspecific adhesion of cells to the beads. The binding of cells on beads were then inspected under fluorescent microscope. Hundreds of beads were observed to bind both red and green cells implying that the peptoids were not specific ligands for VEGFR-2. Five beads bound only red cells, meaning that the peptoids were likely to be specific VEGFR-2 ligands. Subsequent *in vitro* assay confirmed the five peptoids were specific ligands for VEGFR-2 with binding affinity of low-micromolar range. Later, the authors used the hits to develop peptoid 'antibody surrogate' with extremely high specificity toward VEGFR-2 (see **Section 2.204.5.1**). Solution-phase assays, usually in the 96-well plate format, have been used for synthetic compounds or natural products that are added as a soluble form into each individual well for biological testing. In principle, all solution-phase biological assays including competitive receptor-binding assays, antibacterial assays, and anticancer assays can be adapted to combinatorial library screening. Because the numbers of compounds are enormous, the current screening strategy is to use miniaturized and automated solution-phase assay set-ups. Ligands are attached to the beads via cleavable linkers; then the ligands are released from the each bead into solution phase, and the biological assays are carried out. The released compounds are subsequently identified (or sequenced).

Researchers have mimicked a biological event where the genetic material encoding molecules with superior functions survives natural selection and propagates to next generations. Harbury and colleagues utilized the concept of evolutionary mechanism and DNA-programmed combinatorial chemistry to

prepare a large library of peptoids individually associated with specific DNA sequences, enabling amplification of compound hits.[86] The authors adopted the bioinspired but completely abiotic approach to prepare a collection of 100 million distinct peptoids. The library was then subjected to a selection process for binding to the N-terminal SH3 domain of the proto-oncogene Crk, and novel ligands were discovered after six amplification steps. The hits bind to the protein tightly with affinities similar to those of peptide SH3 ligands discovered from phage display libraries.

2.204.5. Drug Discovery

In general, peptides possess distinctive advantages including (1) relatively straightforward synthesis and modification; (2) high affinity and specificity of peptides for different molecular targets such as receptors, antigens, and enzymes; and (3) low toxicity relative to synthetic small molecules. However, peptide drugs often exhibit poor oral bioavailability, a short plasma half-life, a potential for immunogenicity, and unfavorable pharmacokinetic profile; therefore, considerable effort has been directed to the design and development of nonnatural surrogates for peptides. Peptoids exhibit enhanced stability toward proteolysis relative to peptides,[10] significantly different lipophilicity and physicochemical properties, better cell penetration,[87] and low immunogenicity. Hence peptoids find interesting applications in biological probe development as well as in drug discovery.

2.204.5.1. Protein Receptor Ligands

2.204.5.1.1. Protein–protein interaction inhibitors

Protein–protein interactions play a crucial role in cellular and biological processes. Consequently, the chemical intervention of protein–protein interactions would enable new therapeutic possibilities. Targeting protein–protein interactions often can be a challenging task for small molecules that satisfy Lipinski's rules because of the large protein surface area to cover. High-throughput screening (HTS) programs can sometimes lead to the discovery of small molecules that are capable of disrupting certain protein–protein interactions; however, the eventual success of these compounds as drugs remains uncertain. Peptides and peptidomimetics, which are larger molecules than the small molecules, have been identified as high-affinity binders to protein–protein interaction surfaces and are currently being developed as drug candidates.

Apoptosis, a critical biological process that is strongly regulated by protein–protein complex formation, is implicated in human disease states such as cancer, ischemic injuries, and neurological disorders. Development of an apoptosis modulator through inhibition of apoptosome assembly formation has been reported by Pérez-Payá and coworkers.[88,89] Apoptosome, a multi-protein complex consisting of cytochrome c, apoptotic protease activating factor-1 (Apaf-1), procaspase 9, and dATP, mediate the caspase cascade and apoptosis. From the screening of a positional scanning diversity-oriented library (~5000 peptoids) and further chemical optimization process, Pérez-Payá and coworkers identified peptoid oligomers (**Figure 6, (1)** and **(2)**) that directly bind Apaf-1 and showed the decrease in the apoptotic phenotype in mitochondrial-mediated models of

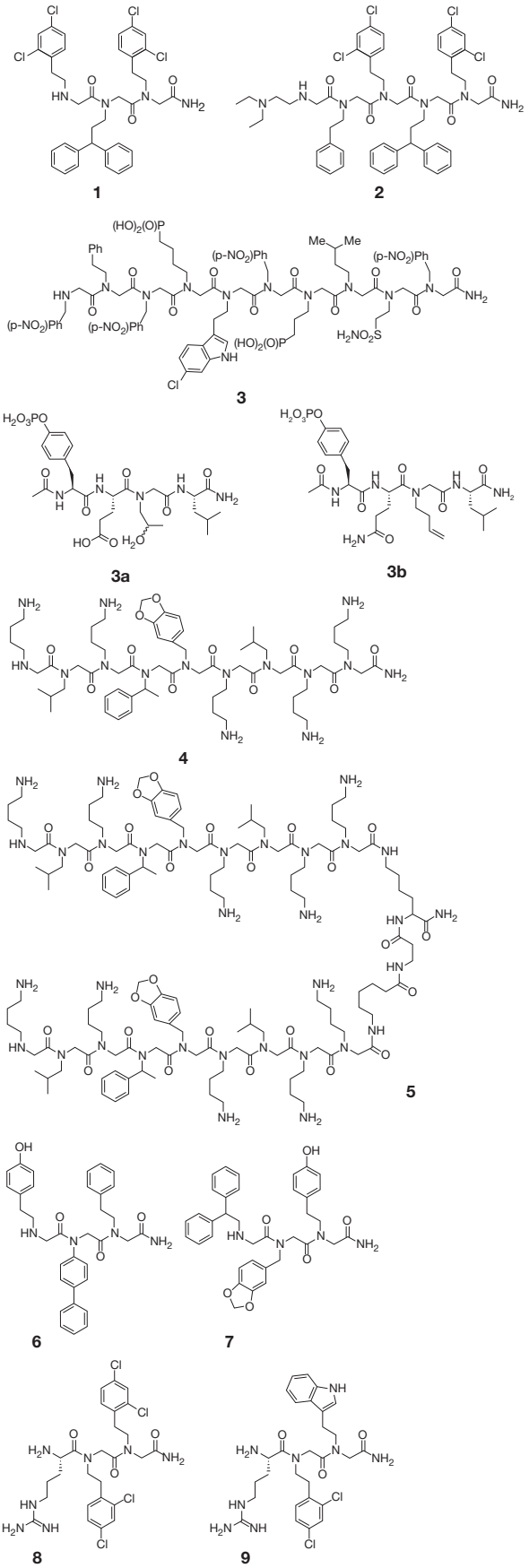

Figure 6 Peptoid ligands that bind to protein receptors.

cellular apoptosis. To increase antiapoptotic activity of **1**, the authors conjugated the peptoid trimer to poly-L-glutamic acid (pL-Glu), and the resulting peptoid-polymer conjugate not only enhanced the antiapoptotic activity but also lowered cytotoxicity of **1** in various cell lines. Further studies include conjugation of **1** to cell-penetrating peptides (i.e., penetratin and HIV-tat) and cyclization of **1**. Along with the pL-Glu-**1** conjugate, penetratin-**1** and cyclo-**1** indicated better cell permeability and efficacy in an *ex vivo* assay, and the authors are moving forward to examine the effectiveness of Apaf-1 inhibitors for *in vivo* myocardial infarction model.[90]

Connections between cancer and protein 53 (or p53) have been well established.[91] Protein 53 is a tumor suppressor protein that regulates the cell cycle and prevents cancer; therefore, when p53 is inactive, cells are able to grow and proliferate. Human double minute 2 (HDM2), which has emerged as an independent anticancer drug target, downregulates p53 function and inactivates the protein. Overexpression of HDM2 has been linked to tumor aggressiveness, and inhibition of HDM2 can restore p53 function and prevent tumor growth. The crystal structure of a p53 peptide bound to HDM2 provides useful information for the design of HDM2 inhibitors. Using structure-guided design, Appella and coworkers designed peptoid-based HDM2 inhibitors.[92] To mimic the p53 peptide fragment bound to HDM2, the authors initially prepared peptoid helices as HDM2 binders. However, their best inhibitor (**Figure 6**, **(3)**) lacked a helical structure but still maintained good binding affinity against HDM2 ($IC_{50} \approx 6.6\,\mu M$). Dissociation constants measured by isothermal titration calorimetry indicated that the binding affinity of **3** ($K_d \approx 1.23\,\mu M$) was about a half of the p53 (15–29) peptide fragment ($K_d \approx 0.62\,\mu M$). From their experience, the authors concluded that starting with rigid peptoid scaffold may not always be optimal to develop new inhibitors.

Alternatively, Kodadek and coworkers used peptoid combinatorial library screening to identify an inhibitor of HDM2 protein.[77] Constructed by standard mix-and-split synthesis on TentaGel, their peptoid libraries were composed of one- to five-hundred thousand peptoid hexamers. They used 13 peptoid submonomers with distinct functionalities, so their peptoid library was chemically diverse. On-bead screening using Texas Red-labeled HDM2 protein provided a peptoid octamer with $K_d \approx 37\,\mu M$.

Src homology 3 (SH3) and WW protein interaction domains participate in diverse signaling pathways, and their functional roles in cancer, osteoporosis, and inflammation are implicated. The SH3 protein domains recognize a specific proline-rich sequence motif, PXXP, where P is proline and X is any amino acid. In addition, it is known that these domains broadly accept amide N-substituted residues instead of recognizing only the critical prolines. In comparison to natural peptides which have proline as the only *N*-subsituted amino acid, peptoids provide enormous number of *N*-substituted nonnatural amino acids. Lim *et al*. exploited the diversity offered by peptoid residues, screened a series of ligands in which key prolines were replaced by nonnatural *N*-substituted residues, and discovered a ligand that selectively bound the Grb2 SH3 domain with 100 times greater affinity than natural peptide.[93] The authors carried out further variation of the peptoid residues and created highly domain-specific peptide–peptoid hybrids.[94] Members of the Src homology 2 (SH2) family have also been targeted with peptide–peptoid hybrids. The structures of the peptomer ligands for Syk[95] and Shc[96] domains are shown in **Figure 6** (**(3a)** and **(3b)**, respectively). The peptomer ligands were discovered by a peptoid scan which provided a useful method to examine to what extent a peptide sequence can be transformed into a peptoid (or a peptomer) while maintaining its binding affinity.

The binding of vascular endothelial growth factor (VEGF) to the receptor VEGFR is an important signaling event in angiogenesis, and inhibition of the hormone-receptor binding can lead to a possible treatment of cancer. Monoclonal antibodies such as Avastin® and Erbitux® have shown to block the VEGF signaling pathway; however, more effective VEGFR antagonists will help increase patients survival time significantly.

Employing mix-and-split combinatorial peptoid library as a source of receptor-binding ligands, Kodadek *et al*. screened on-bead peptoid oligomers for VEGFR2 using a two-color, cell-based screening technique.[84] From the screening of ~300 000 size peptoid library, they discovered peptoid nonamer **4** (**Figure 6**) with low-micromolar-binding affinity to VEGFR2 *in vitro* ($K_d = 2\,\mu M$). Because VEGFR2 functions as a homodimer, the authors envisioned that homodimer of **4** would increase the binding affinity and, indeed, found homodimer **5** had a binding affinity of $K_d = 30$ nM for VEGFR2. The peptoid antibody surrogate was proven to be active in a mouse model and inhibited tumor growth *in vivo*. In the following study, the authors identified three side chains in the peptoid nonamer as minimally required pharmacophore and found backbone amide atoms participated in the binding with VEGFR-2.[97] Interestingly, the peptoid ligand did not bind to the anticipated site and did not compete with VEGF for binding to VEGFR-2. The authors proposed an allosteric mechanism of the peptoid antagonist that might prevent the receptor from acquiring the proper conformation to propagate downstream signals.[98]

2.204.5.1.2. Receptor ligands

Highly potent peptoid ligands for 7-transmembrane G-protein-coupled receptors (7TM/GPCR) were identified from a peptoid combinatorial library.[73] Peptoid timers **6** and **7** (**Figure 6**) showed low-nanomolar-binding affinities for α_1-adrenergic receptor ($K_i = 5$ nM) and μ-opiate receptor ($K_i = 6$ nM), respectively. This study was the first demonstration of the generation of high-affinity ligands for a pharmaceutically relevant receptor from a synthetic combinatorial library. The peptoid library design was based on an analysis of known GPCR ligands, which revealed that each peptoid should contain at least one aromatic hydrophobic side chain and one hydrogen-bond donating side chain. This rational design strategy lowered total number of peptoids in the library (~5000 peptoids), and successfully provided tight binders to GPCR receptors.

Following the Zuckermann's discovery of the peptoid GPCR ligands, a vast number of peptoids or peptomers were reported as ligands for various receptors. Adan and coworkers reported discovery of peptomers targeting the melanocortin receptors.[99,100] The melanocortin receptors are G-protein-coupled receptors with five different isoforms, MC1R–MC5R. Particularly, MC4R are known to be an excellent drug target for the treatment of obesity. The authors used a peptoid scan to transform an MC4R selective peptide heptameric ligand into peptomers, assayed the 31 peptomers for binding toward melanocortin subtypes, and found that the peptomers generally

retained selectivity for MC4R. Although introduction of peptoid moieties resulted in a decrease of affinity, many of the peptomers were still active at submicromolar concentrations. In addition, the authors observed increased bioavilability of the peptomers when three or more of the seven peptide residues were substituted with peptoid residues.

The vanilloid receptor subunit 1 (VR1), also known as the capsaicin receptor, plays essential role in inflammatory pain in the peripheral nervous system. Ferrer-Montiel *et al*. synthesized and screened trimeric peptoid library to discover novel VR1 antagonists.[101] Compound **8** in Figure 6 showed submicromolar potency and *in vivo* analgesic and anti-inflammatory activities. Using the scaffold for further optimizatoin, Albericio *et al*. synthesized 20 indole-containing peptoids and evaluated the biological activity of the peptoids as novel VR1 antagonists.[102] In this series, compound **9** (Figure 6) showed the best potency and selectivity: ~4-fold stronger potency and 10-fold higher selectivity than the parent peptoid **8** was obtained.

Other than the peptoid or peptomer ligands introduced here, there are a vast number of peptoids or peptomers discovered as ligands for various receptors and proteins. Cholecystokinin receptor antagonists,[103] hsst2 receptor-binding somatostatin mimics,[104] Tachykinin NK_3 receptor antagonists,[105] concanavalin A-binding oligomannopeptoids,[106,107] P-glycoprotein-binding multi-drug resistance reversal peptoids,[108] NMDA (*N*-methyl-D-aspartate) receptor antagonists,[109] VLA-4 inhibitors,[110] MHC-II ligands,[111] maltose-binding protein ligands,[112] and urokinase plasminogen activator receptor ligands[113] are all included in this category. All these works demonstrated that peptoids were an excellent source of biologically active receptor ligands. Most of the compounds isolated in these efforts had potency in the low-micromolar range. But there are some lessons learned from the earlier works regarding peptoid ligand discovery: (1) Simple transformation of a known peptide ligand to a peptoid (or to a peptomer) may not always retain binding affinity of the parent peptide. Often a significant conformational change occurs upon single mutation of a peptide residue to a peptoid residue. In addition, the unavailability of backbone–NH proton in peptoid can lead to a loss of an existing hydrogen bonding interaction. (2) Peptoid ligands identified in library screening do not always bind to expected binding sites and may have different mechanism of action from that of natural ligands as was shown by Kodadek's VEGFR-2 ligand.[98] (3) Generally, peptoid library that is highly diverse, but modestly sized (i.e., 5000 ~ 10 000 compounds from 20 different amines), was sufficient to provide high-quality ligands.[12]

2.204.5.2. Nucleic Acid Binders

Antisense oligonucleotides have been used in biological studies for the determination of gene function and in medicine for the suppression of disease-related genes.[114] More recently, synthetic molecules are being used to target RNAs. Most of the RNA targeting synthetic molecules have been discovered by high-throughput screening of a library for binding therapeutically relevant RNAs. Disney *et al.* prepared peptoid microarrays that were composed of peptoid scaffolds with moieties known to bind RNA.[115] They screened the library for inhibiting the group I intron RNA from Canadida albicans, an opportunistic pathogen that kills immunocompromised host. Each peptoid ligand identified from the screening inhibited self-splicing in the presence of 1 mM nucleotide concentration of bulk yeast tRNA with IC_{50} values between 150 and 2200 μM. Based on the structural features of the peptoid binders, second generations of peptoids were designed and synthesized; all second generation peptoid inhibitors showed enhanced potencies with IC_{50} values lower than 100 μM. The best peptoid in this study had an IC_{50} of 31 μM and contained one phenylguanidino- and three indole-functionalities (**1** in Figure 7). Peptoid **1** was sixfold more tightly binding to the RNA than pentamidine, a clinically used drug that inhibits self-splicing. This study is a successful example of rational library design and screening to identify a synthetic RNA binder.

The same group reported the discovery of RNA binders through rational design of peptoid RNA binders solely based on the information about the ligand-binding site in RNA. They employed modularly assembled ligands targeting the RNA that causes myotonic dystrophy (DM), an inherited disease that is characterized by wasting of muscles.[116,117] 6′-*N*-5-Hexynoate kanamycin A is known to bind 2 × 2 nucleotide, pyrimidine-rich RNA internal loops. Multiple copies of such loops are found in the RNA hairpin that causes DM2. The authors displayed 6′-*N*-5-hexynoate kanamycin A on a peptoid scaffold with various degrees of multivalency and spacing to target several internal loops simultaneously. The multivalent display of 6′-*N*-5-hexynoate kanamycin A on a peptoid scaffold yielded a peptoid that inhibited the interaction of DM2 RNA and muscleblind protein (MBNL-1). The most potent binder displays three 6′-*N*-5-hexynoate kanamycin A modules, each separated by four spacer peptoid monomers (**2**, Figure 7). The peptoid showed an IC_{50} value of 25 nM for the inhibition of the RNA-protein complex formation, and binds the DM2 RNA at least 30 times more tightly than related RNAs and 15 times more tightly than MBNL-1. In addition, they showed peptoid **2** could penetrate cell membrane by an uptake study into a mouse myoblast cell line.

2.204.5.3. Antimicrobial Agents

Over the past decades, a broad class of antimicrobial peptides (AMPs) has been identified as an intrinsic defense in animals, plants, and in a wide variety of organisms. AMPs have been of great interest to researchers not only because AMPs belong to the innate host-defense immune system, but also because they are promising candidates for the development of antibiotics. The antimicrobial activity of AMPs encompasses diverse species including Gram-positive and Gram-negative bacteria, fungi, and virus. The mechanism of action for most AMPs is permeabilization of the bacterial cytoplasmic membrane, which is facilitated by their cationic amphipathic structure.[118,119] Another possible mechanism of AMPs is that the peptides penetrate cell membrane and target intracellular substances such as nucleic acids.[120] Both mechanisms do not necessarily involve specific receptors, so the chances for bacteria to develop resistance for AMPs are thought to be slim.

AMPs are typically short (10–50 amino acids) sequences with α-helical, β-hairpin, extended or loop structures and usually have a cationic amphipathicity. Bacterial membranes are composed of an excess of phosphatidylserine over phosphatidylcholine and are negatively charged; hence, the cationic

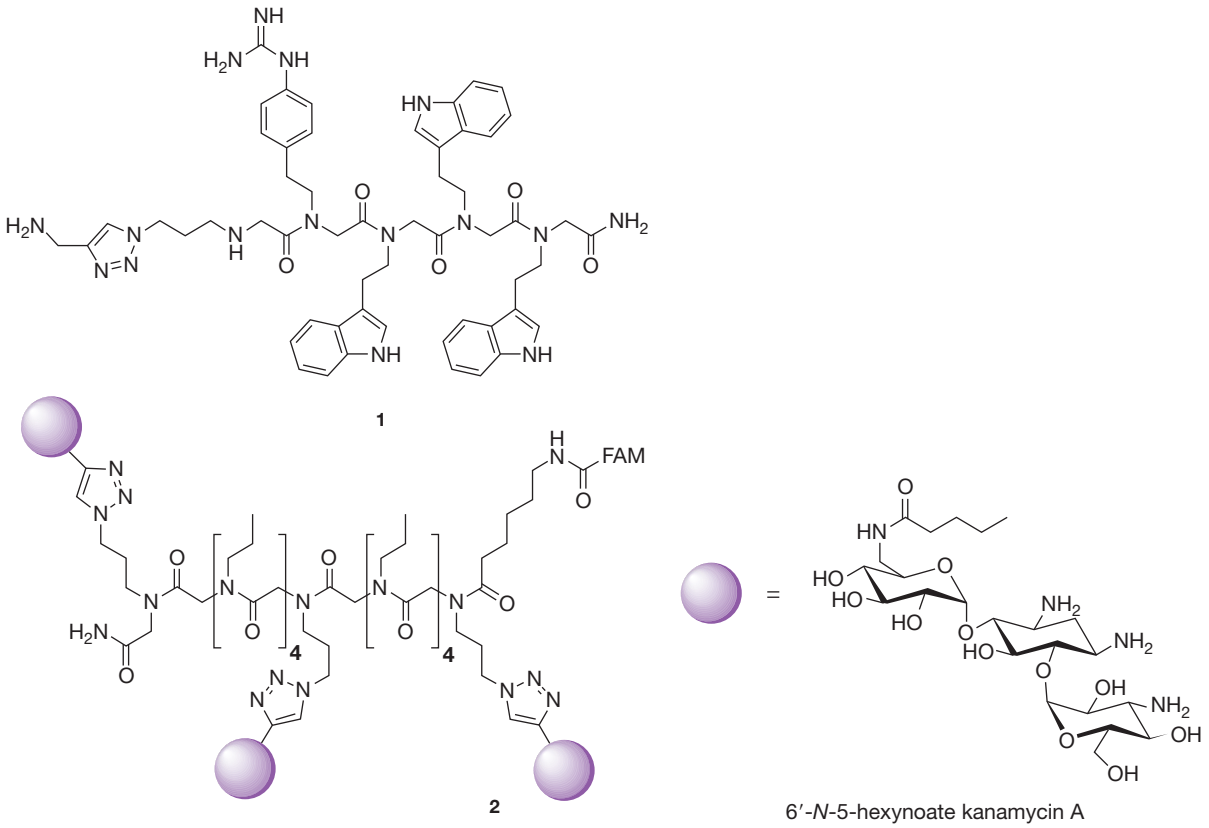

Figure 7 Peptoids that target nucleic acids.

region of AMPs provides a degree of selectivity toward the bacterial membranes over mammalian membranes. The hydrophobic portions of AMPs are believed to play a role for the insertion or penetration into the bacterial cell membrane.

Discovery of antimicrobial agents has been a very active area in peptoid research. Although AMPs possess a number of positive aspects, they have not been developed as drugs due to the poor pharmacokinetics. This problem motivates the effort to develop peptoid mimics of AMPs as antibiotics.

Magainin-2, a linear, cationic, facially amphipathic helical AMP, was successfully mimicked by Barron and coworkers using peptoid helices.[121–124] Several members of antimicrobial peptoids or ampetoids were discovered with low-micromolar MIC (minimal inhibitory concentration) value and relatively low toxicity (**1** and **2**, Figure 8). Peptoid **1** is composed of a helix-inducing and hydrophobic residue, Nspe, and a cationic residue NLys. The latter was incorporated every third position to create a cationic face on the helix (peptoid helix has a periodicity of three residues per turn). Peptoid **2**, a variant of peptoid **1**, was created by replacing the Nspe at position 6 with L-proline. Circular dichroism (CD) study indicated that L-proline is well accomodated in right-handed type-I polyproline-like peptoid helices, and **1** and **2** showed similar helical intensity. Compared to the parent peptoid, **2** exhibited similar antimicrobial activity while less hemolysis and less cytotoxicity were observed. Broad spectrum activities of these ampetoids against clinically relevant BSL-2 pathogens including *Staphylococcus aureus* were also shown in their study. Carefully designed structure–activity relationship study by Barron and coworkers provides some important information: (1) excessive hydrophobicity and helicity in a peptoid leads to greater hemolysis and toxicity; (2) number of cationic charges needs to be higher than +3; and (3) selective peptoids appear to have induced helicity increase upon interaction with negatively charged membrane. These design strategy will help the development of more selective antimicrobial peptoids in the future.

Earlier than Barron's work, Winter and coworkers used combinatorial library screening to discover peptoid trimers that inhibit bacterial growth.[125,126] The MIC of the representative peptoid (**3**, Figure 8) showed 5–40 μM. Excessive hydrophobicity, however, caused the peptoid to be hemolytic.

Mutations of AMPs with various peptoid residues generated selective AMP analogs.[127] Melittin (**4**), an active component of bee venom, is a highly potent AMP, but at the same time, it is nonselective. Melittin contains leucine zipper motif, two leucine residues and an isoleucine are positioned at 7-residue intervals, and the motif promotes dimerization of melittin. Shin and coworkers generated a series of melittin mutants by replacing Leu-6, Leu-13, and Ile-20 with Nala, Nleu, Nphe, or Nlys (**5**, **6**, **7**, **8**, respectively), and investigated their secondary structure, dimerization capability, antimicrobial activity, and cell selectivity.[128] CD study demonstrated that the substitutions disrupted the helical integrity of melittin, and Nleu, Nphe, or Nlys substitution disturbed the dimerization of melittin in an aqueous media. Compounds **5**–**8** maintained the interaction with negatively charged bacterial membrane but lost the interaction with

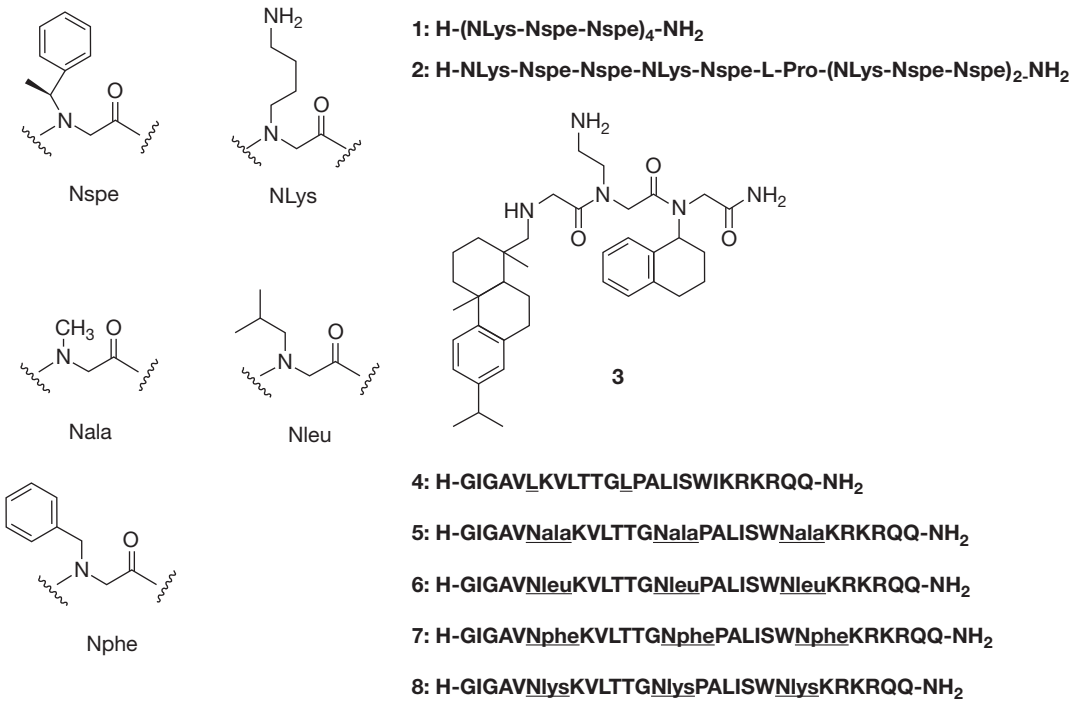

1: H-(NLys-Nspe-Nspe)$_4$-NH$_2$

2: H-NLys-Nspe-Nspe-NLys-Nspe-L-Pro-(NLys-Nspe-Nspe)$_2$-NH$_2$

4: H-GIGAVLKVLTTGLPALISWIKRKRQQ-NH$_2$

5: H-GIGAVNalaKVLTTGNalaPALISWNalaKRKRQQ-NH$_2$

6: H-GIGAVNleuKVLTTGNleuPALISWNleuKRKRQQ-NH$_2$

7: H-GIGAVNpheKVLTTGNphePALISWNpheKRKRQQ-NH$_2$

8: H-GIGAVNlysKVLTTGNlysPALISWNlysKRKRQQ-NH$_2$

Figure 8 Peptoids with antimicrobial activity.

zwitterionic mammalian cell membrane providing significant selectivity increase. In their study, melittin analogs **7** and **8** showed the best selectivity toward bacterial cells. The authors concluded that the peptoid substitution changed melittin's mode of action from membrane-targeting mechanism to possible intracellular component targeting mechanism.

2.204.5.4. Lung Surfactants

Surfactant proteins (SP) play an important role for innate host defense and are essential for physiological lung function. Four pulmonary SP have been identified so far, known as SP-A, -B, -C, and -D. SP-B and -C are small, hydrophobic proteins that function in conjunction with lipids to reduce surface tension at the air-liquid interface of the lung.[129] A deficiency of SP-B and -C, frequently observed in premature infants, results in impaired lung function and gas exchange known as infant respiratory distress syndrome (IRDS). SP-A and -D are hydrophilic collagen-like lectins that bind oligosaccharides on the surface of microorganisms.[130] As members of innate immune system, these two proteins opsonize and aggregate bacteria and viruses; therefore, SP-A and -D enhance uptake of pathogens by immune cells such as alveolar macrophages and neutrophils. Reduced levels of SP-A and -D make the host susceptible to bacterial and viral infections.

Surfactant replacement therapy (SRT) using exogenous lung surfactant (SP-B or SP-C) has been an effective treatment for IRDS, and premature infant survival has improved significantly. However, there are drawbacks regarding the usage of the current animal-derived surfactant proteins (SP-B and SP-C) such as high production costs, batch-to-batch variability, and possible transfer of cross-species infectious agents, which has prompted investigation into the discovery of synthetic SP preparations.

Development of synthetic and biomimetic surfactants utilizing peptoids has been actively investigated by Barron and colleagues.[129] First, sequence-specific peptoid analogs of SP-C (5-32) have been reported.[131–133] The sequences of the peptoid-based SP-C mimics were designed to adopt key structural features of the natural protein; (1) a helical and hydrophobic region and (2) an N-terminal amphipathic achiral region were incorporated. The peptoid comprising 22 monomers acted as an excellent mimic of SP-C protein (**1** and **2**, Figure 9). When integrated into a lipid film, the amphipathic helical peptoid SP-C mimic captures the essential biophysical surface-activity of the natural protein. The authors carried out a systematic structure–function relationship study and characterized the peptoid mimics using various biophysical characterizations including CD, Langmuir-Wilhelmy surface balance, fluorescence microscopy, and pulsating bubble surfactometry. They concluded that (1) the aromatic-based SP-C peptoids have superior surface activity and film morphology than the aliphatic-based peptoids and (2) increased activity was observed upon increasing helical length.

Along with the biomimetic SP-C, Barron group actively developed peptoid-based SP-B mimics.[134] Initially, they designed and synthesized simple amphipathic peptoid helices (**3** and **4**, Figure 9). Surface pressure-area isotherms, surfactant film phase morphology, and dynamic adsorption behavior indicated that the peptoids were promising mimics of SP-B$_{1\text{-}25}$. The helicity and lipophilicity of the peptoids were shown to be important in the activities of the SP-B mimics. Later, the authors attempted to mimic natural SP-B protein in a more precise way: (1) the incorporation of a hydrophobic, helical insertion region with aromatic side chains showed significantly improved *in vitro*



SP-C peptide (1):
Peptide mimic of surfactant protein C (Val –> Leu, Cys –> Ser)

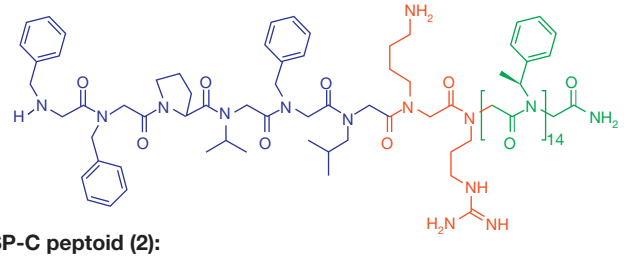

SP-C peptoid (2):
Peptoid mimic of surfactant protein C (5–32)

Phe Pro Ile Pro Leu Pro Tyr Ala Trp Leu Ala Arg Ala Leu Ile Lys Arg Ile Gln Ala Met Ile Pro Lys Gly

SP-B peptide 1–25 (3):
(Cys8 –> Ala, Cys11 –> Ala)

4: H-Nspe-Nspe-(Lys-Nspe-Nspe)$_5$-NH$_2$

5: H-Nspe$_8$-NLys-Nspe$_2$-NLys-NLys-Nspe$_4$-NLys-Nspe$_2$-NH$_2$

6: H-Nspe$_2$-(NLys-Nspe-Nspe)$_5$-Nmeg$_4$

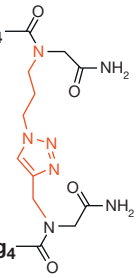

H-Nspe$_2$-(NLys-Nspe-Nspe)$_5$-Nmeg$_4$

Figure 9 Peptoids that act as lung surfactant mimetics.

surface activity (**5**, Figure 9)[135] and (2) dimerization of the peptoid SP-B mimics using click chemistry provided better mimicry of natural SP-B homodimeric protein, and enhanced surface activity was observed (**6**, Figure 9).[136]

2.204.5.5. Peptoid Pharmacology

As described earlier, peptoids differ from peptides only in that peptoid side chains are attached to the backbone amide nitrogen instead of the α-carbon. This unique structure of peptoids leads to quite different pharmacological properties from peptides: (1) they are highly stable against proteases or peptidase;[10,11] (2) they lack a backbone hydrogen-bonding donor, which prevents backbone-driven aggregation and thus increases bioavailability; and (3) they showed increased cell permeability over peptides.[87]

To assess the potential of peptoids as useful therapeutic agents, pharmacokinetic profile of small peptoid was investigated.[137] In this study, radiolabeled tripeptoid and tetrapeptide which had similar physicochemical properties (molecular weight, hydrogen-bonding capacity, and octanol–water partition coefficient) were compared for their *in vivo* pharmacokinetic behaviors. Both compounds showed similar adsorptive clearances, but different absorption and disposition characteristics in the rat. Their comparable intestinal permeability was likely from their similar physicochemical properties. However, the structural difference between peptide and peptoid appeared to be the reason for their dissimilarities in *in vivo* absorption and disposition. As was expected, it was observed that the tetrapeptides was rapidly metabolized, but the tripeptoid was stable in the body. The authors in this study concluded that the peptoid appeared to have advantages over the peptide in terms of metabolic stability, but its low oral absorption and rapid biliary excretion still present challenges.

Pharmacological study was carried out for the peptoid ligand of α_1-adrenergic receptor (compound **6** in Figure 6). The peptoid trimer was demonstrated to be soluble and metabolically stable *in vitro* and to have receptor antagonist activity in animals.[138] The intravenous administration of **6** to dogs antagonized the epinephrine-induced increase in intraurethal pressure. In both rats and guinea pigs, **6** antagonized the epinephrine-induced increase in mean arterial blood pressure

in a dose-dependent manner. The rates of systemic clearance of 6 following intravenous administration were 60 and 104 ml $min^{-1} kg^{-1}$ in rats and guinea pigs, respectively. Another peptoid trimer, CHIR-5585, which was discovered as a potent inhibitor of the urokinase plasminogen activator receptor, was also shown to be an active antagonist *in vivo*. Intranasal administration of the peptoid to rats and subsequent tissue distribution study demonstrated the significant delivery of the peptoid throughout the central nervous system and deep cervical lymph nodes.[113] The results suggest that intranasal administration of peptoids may provide a way to bypass the blood–brain barrier.

2.204.6. Cellular Delivery/Uptake Vectors

2.204.6.1. Cell-Penetrating Peptoids

In recent years, methods to enhance or control selective passage of therapeutics or diagnostics through cell membrane have been actively investigated. Research in this area introduced a variety of delivery vectors and enabled the intracellular uptake of various molecular cargoes (e.g., antisense oligonucleotides, plasmid DNA, siRNA, prodrugs, peptides, proteins, imaging agents, and nanomaterials). Cell-penetrating peptides (CPPs) have become widely used vectors for such delivery and hold great potential in basic and applied biomedical research.[139] Among many CPPs, HIV-tat is the most popular CPP; the sequence responsible for the cellular uptake of the HIV-tat peptide consists of the highly basic region, amino acid residues 49–57 (RKKRRQRRR). Poly-lysine, another effective cellular transporter, is also composed of highly basic amino acids.

Using the structure–function relationships obtained with CPPs, Wender and coworkers designed a series of polyguanidine peptoid derivatives.[140] Significantly enhanced cellular uptake was observed for guanidine peptoid 9-mer over R9 (L-Arg 9-mer) and r9 (D-Arg 9-mer), and the stability of peptoid could explain this result (peptoid > D-peptide > L-peptide). The authors also found both the number of guanidine residues and the length of side chain spacer affected the function of cell-penetrating peptoids; more number of guanidino groups and longer side chain spacer appeared to be beneficial for higher cellular uptake. The best cell-penetrating peptoid discovered in this study is shown in Figure 10 (compound **1**).

Instead of using guanidine-containing side chains, Bradley and coworkers focused on amine-containing side chains and evaluated the polylysine-like peptoids for cellular uptake.[141,142] A series of fluorescein-labeled polylysine-like peptoids were synthesized, and their uptakes into HeLa, L929, and K562 cell lines were examined via flow cytometry. As was observed in guanidino-peptoids, longer cationic peptoids showed greater cellular penetration.

Bräse and coworkers compared the two types of peptoids, one with guanidino-side chains and the other with amino-side chains, and compared their cellular uptake (**2** and **3**, Figure 10).[143,144] In this study, the authors found that amino-peptoid **2** required longer times to complete translocation into the cell, while the uptake rate for guanidino-peptoid **3** was much faster, and reasoned that different translocation mechanisms were involved for the two types of peptoids. Intracellular localization of the two peptoids was also different; amino-peptoid **2** resides in the cytosol, but guanidino-peptoid **3** accumulated preferentiallies in the nucleus. Hence, they showed the interesting possibility that the uptake rate and cellular localization of the peptoid transporter can be fine-tuned by simple modification on the peptoid side chain. Notably, no significant cytotoxicities of **2** and **3** were observed.

Membrane permeability of peptoids has led the design of peptoid-based transcription factor mimics, allowing for upregulation of targeted genes. Kodadek and coworkers screened a peptoid library to identify oligomers capable of binding a transcriptional co-activator. A peptoid hit sequence was conjugated to a polyamide to provide specific binding to a target region of DNA.[145,146] The biological activity of the conjugate was facilitated by the membrane permeability of cationic peptoid.

An elegant method to measure the relative cell permeability of synthetic compounds was reported by the Kodadek group.

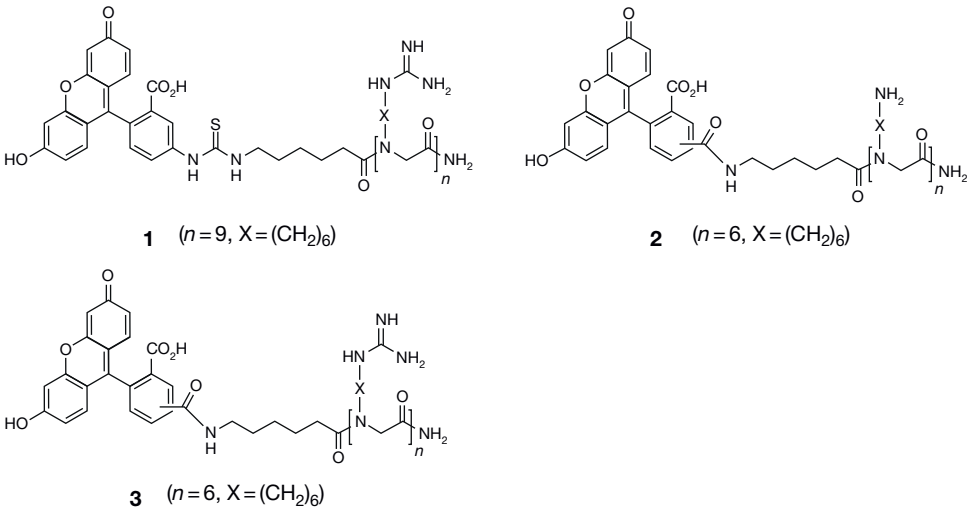

Figure 10 Peptoids with cell-penetrating activity.

The compound of interest was conjugated to a dexamethasone derivative. Upon entry of the conjugate into living cells, the Gal4-responsive luciferase gene was activated. The level of luciferase expression was therefore quantitatively proportional to the cell permeability of the conjugate. Using this reporter gene-based assay, the cell permeability of peptide and peptoid was compared,[87] and general trend showed superior cell permeability of peptoid over peptides. The authors reasoned the lack of backbone–NH protons in peptoids resulted in the increased lipophilicity and therefore membrane permeability. The authors also compared relative cell permeability of linear and cyclic peptides. Generally, cyclic peptides are thought to be more cell permeable than their linear counterparts due to the conformational rigidity. However, the authors proved that cyclic peptides were not generally more cell permeable than linear peptides.[147]

2.204.6.2. Lipitoids for Cellular Delivery of Nucleic Acids

Although synthetic nonviral vectors have shown promise for the delivery of plasmid DNA, their efficiencies in gene transfer have not matched those of viral vectors. Therefore, the need for developing a new class of synthetic nonviral vectors is high. Zuckermann and coworkers first showed the ability of peptoids to serve as nucleic acid delivery vector.[148] Simple mimicry of peptide transporters (e.g., poly-lysine) did not directly lead to active gene delivery peptoids. Employing a library screening method, they found 36-mer peptoids with a specific triplet motif was the most active transfection agent. The triplet motif was composed of two hydrophobic residues and a cationic (i.e., *N*-2-aminoethyl glycine) residue. The cationic peptoids were able to form complexes with DNA and facilitated cell transfection with efficiencies similar to that of commercial cationic lipids. After the discovery, Zuckermann *et al*. systematically investigated the structure–activity relationship of cationic peptoid–lipid conjugates (or lipitoids); they prepared a small library of lipitoids and evaluated their ability as gene transfer agents.[149] The authors showed that several lipitoids condensed plasmid DNA into very discrete and uniform 100-nm particles and protected DNA from nuclease digestion. The best lipitoid in the study was DMPE-(Nae-Nmpe-Nmpe)$_3$ (**1**, **Figure 11**). Lipitoid **1** was active in the presence of serum and exhibited remarkably low cellular toxicity, indicating its potential for *in vivo* studies. Further, **1** showed better efficiency than lipofectin or DMRIE-C, two commercial cationic lipid transfection reagents. Later, Kirshenbaum *et al*. demonstrated this reagent's effectiveness as an siRNA (short interfering RNA) transfection reagent.[150] The lipitoid proved to have remarkably low toxicity and be highly effective in specific siRNA-mediated gene silencing across several cell lines, including primary cells.

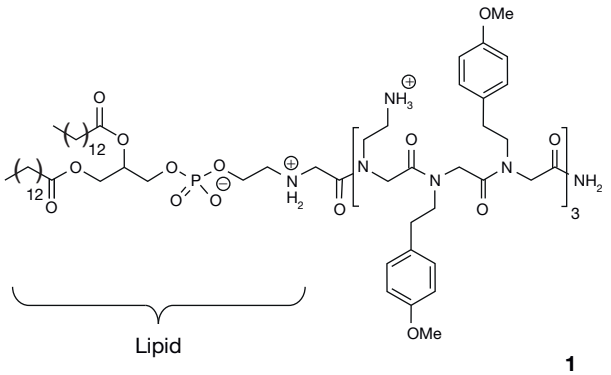

1

Dimyristoyl phosphatidyl-ethanolamine (DMPE)

Figure 11 Lipitoid reagent for intracellular delivery of nucleic acids.

2.204.7. Biomimetic Materials

2.204.7.1. Collagen Mimicry

Collagen is the most abundant fibrous protein in the body. It is responsible for providing the scaffolding matrix upon which complex biological structures are supported. So mimicry of collagen and pursuit of novel collagen-like materials has been a major area of biomimetic materials research. The collagen mimics have diverse potential applications in drug delivery, biomedical devices, and tissue engineering (i.e., wound healing); therefore, major research has been performed to understand how its conformation is controlled by its typical Gly-X-Y repeats.

Goodman *et al*. first reported the incorporation of peptoid residues into the collagen-like triple helical structures. Initially, they focused on a bulky hydrophobic peptoid residue *N*-isobutylglycine (or Nleu) and introduced the submonomer as a proline surrogate.[49,151,152] A series of peptide–peptoid hybrids were synthesized based on (Gly-Pro-Nleu), (Gly-Nleu-Pro) or (Gly-Nleu-Nleu) sequences, which were then coupled to KTA scaffold (cis, cis-1,3,5-trimethylcyclohexane-1,3,5-tricarboxylic acid, also known as the Kemp triacid).[153] Biophysical analysis revealed that the sequences $(\text{Gly-Pro-Nleu})_n$ and $(\text{Gly-Nleu-Pro})_n$ ($n \geq 9$ and $n \geq 6$, respectively) formed stable triple helices. Interestingly, $(\text{Gly-Nleu-Pro})_n$ formed more stable triple helices than $(\text{Gly-Pro-Nleu})_n$ did, and the authors explained with molecular modeling that the isobutyl side chain of Nleu could have more hydrophobic contact with Pro in triple helices composed of $(\text{Gly-Nleu-Pro})_n$ than in those composed of $(\text{Gly-Pro-Nleu})_n$.

Unlike the other two sequences, $(\text{Gly-Nleu-Nleu})_n$ did not form a triple helical conformation; it had to be included in a host–guest fashion within sequences such as $(\text{Gly-Pro-Hyp})_n$ to adopt the triple helix conformation.[154] An example of the sequence is Ac-$(\text{Gly-Pro-Hyp})_3$-$(\text{Gly-Nleu-Nleu})_3$-$(\text{Gly-Pro-Hyp})_3$-NH_2, and the guest–host structure reatined triple helicity. Another sequence that behaved like Gly-Nleu-Nleu was Gly-N_x-Pro sequences where N_x was composed of a variety of alkyl peptoid residues. Using these guest–host collagen mimetic structures as model systems, the authors elucidated the contributions of steric and hydrophobic effects that are important for the triple helix formation.

2.204.7.2. Antifouling Agents

Exposure of medical devices to biological fluids is often accompanied by undesirable accumulation of proteins, cells, and microorganisms on the surface. Biofouling of surfaces can result in compromised device performance and in some cases may be life threatening to the patient. Various antifouling polymers have been used as coating materials for such medical devices and have

proven to be efficient in preventing protein and cell adsorption; however, few are ideal for providing long-term biofouling resistance. In this regard, Messersmith and Barron introduced a novel strategy to develop an efficient biomimetic antifouling system that was composed of a water-soluble inert peptoid and an anchor derived from mussel adhesive proteins.[155] The methoxyethyl side chain (Nmeg) of the peptoid portion was chosen for its chemical resemblance to the repeat unit of the known antifouling polymer poly(ethylene glycol) (PEG), and the 5-mer anchoring peptide was chosen to mimic the DOPA- and Lys-rich sequence of a known mussel adhesive protein (**1** in **Figure 12**). Peptide–peptoid conjugate **1** was found to be highly soluble in aqueous solution and adsorbed strongly onto TiO_2 surfaces by simple immersion process. Both modified and unmodified TiO_2 surfaces were then exposed to whole human serum, and the modified surface showed dramatic reduction of protein adsorption and resistance to mammalian cell attachment for over 5 months. Hence, these new antifouling polymers showed potential as long-term control of surface biofouling in physiological environments.

Numerous pathogenic microorganisms are capable of attaching and aggregating themselves on a surface and forming

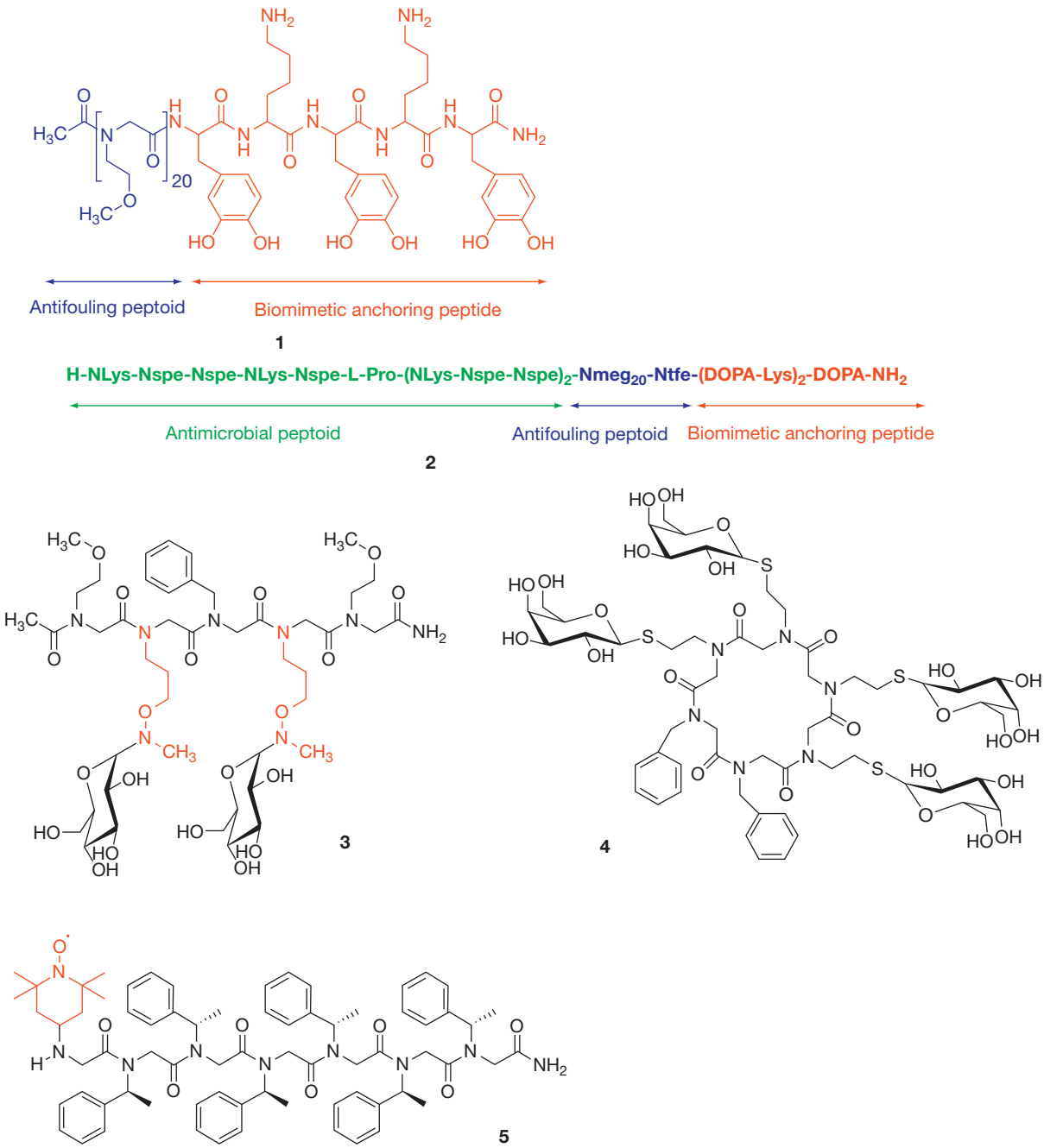

Figure 12 Peptoid-based biomaterials.

biofilm. Biofilms are known to be extremely difficult to eradicate and have been found to be involved in a wide variety of microbial infections in the body. Messersmith, Barron, and coworkers advanced their original antifouling peptide–peptoid hybrids by attaching antimicrobial peptoids at the N-terminus (**2** in **Figure 12**).[156,157] Surface modifications with this peptide–peptoid hybrid created a surface that was both antimicrobial (active) and antifouling (passive), and this material provided a promising solution to infections associated with implantable medical devices.

2.204.7.3. Glycopeptoids

Glycosylation, a ubiquitous posttranslational modification in proteins, plays critical roles in protein folding, stabilization, trafficking, and recognition. Owing to the inherent complexity of carbohydrates, glycosylation can produce enormous structural diversity in proteins and induce a variety of functional changes. In an attempt to decipher these structure–function relationships, protein and peptide chemists have developed various chemical and enzymatic methods for the synthesis of homogeneous and well-defined glycoconjugates. Among the glycosylation methods, the *N*-alkylaminooxy-strategy is attractive because it employs native, completely unprotected sugars to glycosylate *N*-alkylaminooxy-containing peptides.[158] Carrasco and coworkers synthesized an *N*-methylaminooxy-containing primary amine as a peptoid submonomer, incorporated the submonomer into various peptoid chains, and demonstrated glycosylation of the peptoids using native sugars (**Scheme 1**).[159] The authors optimized the glycosylation conditions: a mildly acidic aqueous solution (0.1 M NaOAc, pH = 4.0) and a gentle microwave heating at 40 °C for a short time (~10 min) worked well for D-glucose, D-maltose, D-melibiose, D-lactose, maltotriose, and GlcNAc. Carbohydrates that contain an axial hydroxyl group such as galactose (C4 position) or D-mannose (C2 position) did not provide pure glycopeptoid products; they contained a portion of furanose by-products. Next the authors showed a divalent glycopeptoid was readily prepared using microwave conditions (**3** in **Figure 12**). The chemoselectivity of the glycosylation was also demonstrated using a peptoid that contained hydroxyl, amino, sulfhydryl, and carboxamido functionalities in addition to the *N*-methylaminooxy group. This N-methoxyaminooxy-strategy provides an efficient way to generate an extensive range of biologically functional glycopeptoids and multivalent glycopeptoids.

Another strategy of preparing glycopeptoids is to use protected carbohydrate-containing monomer units[160,161] or submonomeric units[106,162] as building blocks. This strategy is amenable for the synthesis of glycopeptoids that contain more than two different types of sugars in a single peptoid chain. But the potential drawback of this strategy is that a large-scale preparation of the peptoid monomers (or submonomers) can sometimes be cumbersome. Several groups reported *O*-linked, *N*-linked or *C*-linked glycopeptoid synthesis using this strategy.[107,163–165] Also Comegna *et al.* recently reported a method for an inexpensive and rapid synthesis of linear and cyclic *S*-linked glycopeptoids (**4** in **Figure 12**).[162] These glycopeptoids provide well-defined glycopeptide or glycoprotein mimics and are useful in many applications such as lectin-binding ligands, glycopeptide antigen mimics, multivalent carbohydrate display, and antifreezing protein mimics.

2.204.7.4. Other Applications

2.204.7.4.1. Enantioselective catalysts

Proteins form tertiary structures and provide chiral microenvironments required for asymmetric catalysis. Since Whitesides pioneered the conversion of a protein to a homogeneous enantioselective hydrogenation catalyst, artificial enzymes have been developed for various asymmetric reactions.[166,167] Mimicry of this effect with peptoid polymers has been achieved by Kirshenbaum and coworkers by positioning a catalytic center in a chiral microenvironment using peptoid helices.[168] Substrates that meet the spatial arrangement can access the active site and are converted to desired products. They used TEMPO (2,2,6,6-tetramethylpiperidine-1-oxyl) as the catalytic center for the oxidation of secondary alcohols to ketones and incorporated this active site into either middle position or N-terminal position of various peptoid sequences. Interestingly, best result was obtained when TEMPO was positioned at the N-terminus of peptoid helix (**5** in **Figure 12**); 84% conversion with >99% ee was achieved when 1% peptoid catalyst **5** was loaded. The reaction was carried out at 0 °C for 2 h. When TEMPO was incorporated into peptoid helix with the opposite handedness, the catalyst exhibited the opposite enantioselectivity with similar reaction conversion. This work

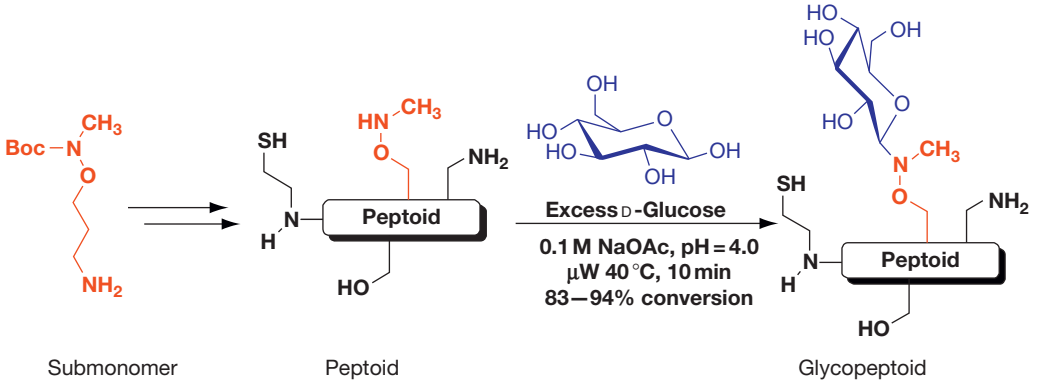

Scheme 1 General synthesis of glycopeptoids using *N*-methylaminooxy functionality.

provides a nice proof-of-concept study: a well-defined conformational ordering created by synthetic foldamers can mimic the asymmetric microenvironment produced by protein secondary or tertiary structures. This is an important step toward emulating protein function.

2.204.8. Summary and Future Directions

Peptoids are a bioinspired material whose properties lie in-between natural biopolymers and nonnatural synthetic polymers. Like biopolymers, they are information-rich polymers, offering precise control of main chain length, side chain functionality, and monomer sequence. Because peptoids are synthesized one monomer at a time from readily available building blocks, an almost infinite sequence-space awaits to be explored. The structural similarity to polypeptides has been responsible for the impressive diversity of biological activity observed for peptoids. The ability to precisely engineer polypeptoid structure is unprecedented for a synthetic polymer and will open up many fundamental studies in polymer physics and polymer self-assembly. The lack of a hydrogen-bond donor in the backbone holds great promise for polypeptoid-based self-assembly.

An impressive body of work on peptoids has been achieved in the past 20 years. Advances in the chemistry of peptoid synthesis have enabled a better understanding and control of peptoid secondary and tertiary structure. Computational methods to model and predict polypeptoid conformation are at an early stage, and improvements in these tools are greatly needed. Combinatorial synthesis and screening methods of peptoid libraries have been developed for a variety of functions, ranging from drug discovery and drug delivery to materials science.

Ultimately, as the understanding of peptoid conformational control, chain folding, and self-assembly continues to grow, we expect to be able to generate a new family of advanced materials that rival the structure and function of proteins. Such protein–mimetic materials would be capable of sophisticated functions like molecular recognition and catalysis, and yet would have enhanced stability to biological, chemical, and environmental stresses.

The accelerating efforts in peptoid research described in this chapter are a result of the practical nature of their synthesis, as well as in their intriguing properties. Yet the field is actually in an unusual situation; synthesis of polypeptoids is not limiting the field. These tools are well developed and easily adopted. The challenges are now centered on how to design molecules with the desired properties and activities. Combinatorial screening methods will continue to be important while the tools for prediction of peptoid structure and function catch up. It is a very exciting time for the field, as we see the immense gap between biopolymers and synthetic polymers begin to close.

References

1. Dill, K. A. *Biochemistry* **1990**, *29*, 7133–7155.
2. Gellman, S. H. *Acc. Chem. Res.* **1998**, *31*, 173–180.
3. Goodman, C. M.; Choi, S.; Shandler, S.; DeGrado, W. F. *Nat. Chem. Biol.* **2007**, *3*, 252–262.
4. Hill, D. J.; Mio, M. J.; Prince, R. B.; Hughes, T. S.; Moore, J. S. *Chem. Rev.* **2001**, *101*, 3893–4011.
5. Simon, R. J.; Kania, R. S.; Zuckermann, R. N.; *et al. Proc. Natl. Acad. Sci. USA* **1992**, *89*, 9367–9371.
6. Zuckermann, R. N.; Kerr, J. M.; Kent, S. B. H.; Moos, W. H. *J. Am. Chem. Soc.* **1992**, *114*, 10646–10647.
7. Kirshenbaum, K.; Barron, A. E.; Goldsmith, R. A.; *et al. Proc. Natl. Acad. Sci. USA* **1998**, *95*, 4303–4308.
8. Wu, C. W.; Sanborn, T. J.; Zuckermann, R. N.; Barron, A. E. *J. Am. Chem. Soc.* **2001**, *123*, 2958–2963.
9. Sanborn, T. J.; Wu, C. W.; Zuckerman, R. N.; Barron, A. E. *Biopolymers* **2002**, *63*, 12–20.
10. Miller, S. M.; Simon, R. J.; Ng, S.; Zuckermann, R. N.; Kerr, J. M.; Moos, W. H. *Bioorg. Med. Chem. Lett.* **1994**, *4*, 2657–2662.
11. Miller, S. M.; Simon, R. J.; Ng, S.; Zuckermann, R. N.; Kerr, J. M.; Moos, W. H. *Drug Dev. Res.* **1995**, *35*, 20–32.
12. Zuckermann, R. N.; Kodadek, T. *Curr. Opin. Mol. Ther.* **2009**, *11*, 299–307.
13. Uno, T.; Beausoleil, E.; Goldsmith, R. A.; Levine, B. H.; Zuckermann, R. N. *Tetrahedron Lett.* **1998**, *40*, 1475–1478.
14. Seo, J. W.; Barron, A. E.; Zuckermann, R. N. *Org. Lett.* **2010**, *12*, 492–495.
15. Horn, T.; Lee, B. C.; Dill, K. A.; Zuckermann, R. N. *Bioconjug. Chem.* **2004**, *15*, 428–435.
16. Burkoth, T. S.; Fafarman, A. T.; Charych, D. H.; Connolly, M. D.; Zuckermann, R. N. *J. Am. Chem. Soc.* **2003**, *125*, 8841–8845.
17. Shin, S. B. Y.; Yoo, B.; Todaro, L. J.; Kirshenbaum, K. *J. Am. Chem. Soc.* **2007**, *129*, 3218–3225.
18. Hjelmgaard, T.; Faure, S.; Caumes, C.; De Santis, E.; Edwards, A. A.; Taillefumier, C. *Org. Lett.* **2009**, *11*, 4100–4103.
19. Wessjohann, L. A.; Rivera, D. G.; Vercillo, O. E. *Chem. Rev.* **2009**, *109*, 796–814.
20. Rivera, D. G.; Wessjohann, L. A. *J. Am. Chem. Soc.* **2006**, *128*, 7122–7123.
21. Vercillo, O. E.; Andrade, C. K. Z.; Wessjohann, L. A. *Org. Lett.* **2008**, *10*, 205–208.
22. Guo, L.; Zhang, D. H. *J. Am. Chem. Soc.* **2009**, *131*, 18072–18074.
23. Darensbourg, D. J.; Phelps, A. L.; Le Gall, N.; Jia, L. *J. Am. Chem. Soc.* **2004**, *126*, 13808–13815.
24. Jia, L.; Sun, H. L.; Shay, J. T.; Allgeier, A. M.; Hanton, S. D. *J. Am. Chem. Soc.* **2002**, *124*, 7282–7283.
25. Li, S. W.; Bowerman, D.; Marthandan, N.; *et al. J. Am. Chem. Soc.* **2004**, *126*, 4088–4089.
26. Kawakami, T.; Murakami, H.; Suga, H. *J. Am. Chem. Soc.* **2008**, *130*, 16861–16863.
27. Armand, P.; Kirshenbaum, K.; Falicov, A.; *et al. Fold. Des.* **1997**, *2*, 369–375.
28. Armand, P.; Kirshenbaum, K.; Goldsmith, R. A.; *et al. Proc. Natl. Acad. Sci. USA* **1998**, *95*, 4309–4314.
29. Wu, C. W.; Kirshenbaum, K.; Sanborn, T. J.; *et al. J. Am. Chem. Soc.* **2003**, *125*, 13525–13530.
30. Rainaldi, M.; Moretto, V.; Crisma, M.; *et al. J. Pept. Sci.* **2002**, *8*, 241–252.
31. Pokorski, J. K.; Jenkins, L. M. M.; Feng, H. Q.; Durell, S. R.; Bai, Y. W.; Appella, D. H. *Org. Lett.* **2007**, *9*, 2381–2383.
32. Gorske, B. C.; Bastian, B. L.; Geske, G. D.; Blackwell, H. E. *J. Am. Chem. Soc.* **2007**, *129*, 8928–8929.
33. Gorske, B. C.; Blackwell, H. E. *J. Am. Chem. Soc.* **2006**, *128*, 14378–14387.
34. Gorske, B. C.; Stringer, J. R.; Bastian, B. L.; Fowler, S. A.; Blackwell, H. E. *J. Am. Chem. Soc.* **2009**, *131*, 16555–16567.
35. Shin, S. B. Y.; Kirshenbaum, K. *Org. Lett.* **2007**, *9*, 5003–5006.
36. Lee, B. C.; Chu, T. K.; Dill, K. A.; Zuckermann, R. N. *J. Am. Chem. Soc.* **2008**, *130*, 8847–8855.
37. Lee, B. C.; Zuckermann, R. N.; Dill, K. A. *J. Am. Chem. Soc.* **2005**, *127*, 10999–11009.
38. Sui, Q.; Borchardt, D.; Rabenstein, D. L. *J. Am. Chem. Soc.* **2007**, *129*, 12042–12048.
39. Huang, K.; Wu, C. W.; Sanborn, T. J.; *et al. J. Am. Chem. Soc.* **2006**, *128*, 1733–1738.
40. Wipf, P. *Chem. Rev.* **1995**, *95*, 2115–2134.
41. De Cola, C.; Licen, S.; Comegna, D.; *et al. Org. Biomol. Chem.* **2009**, *7*, 2851–2854.
42. Holub, J. M.; Jang, H. J.; Kirshenbaum, K. *Org. Lett.* **2007**, *9*, 3275–3278.
43. Jagasia, R.; Holub, J. M.; Bollinger, M.; Kirshenbaum, K.; Finn, M. G. *J. Org. Chem.* **2009**, *74*, 2964–2974.
44. Roy, O.; Faure, S.; Thery, V.; Didierjean, C.; Taillefumier, C. *Org. Lett.* **2008**, *10*, 921–924.
45. Kwon, Y. U.; Kodadek, T. *Chem. Commun.* **2008**, 5704–5706.
46. Vaz, B.; Brunsveld, L. *Org. Biomol. Chem.* **2008**, *6*, 2988–2994.
47. Baldauf, C.; Gunther, R.; Hofmann, H. J. *Phys. Biol.* **2006**, *3*, S1–S9.

48. Butterfoss, G. L.; Renfrew, P. D.; Kuhlman, B.; Kirshenbaum, K.; Bonneau, R. *J. Am. Chem. Soc.* **2009**, *131*, 16798–16807.
49. Melacini, G.; Feng, Y. B.; Goodman, M. *J. Am. Chem. Soc.* **1996**, *118*, 10725–10732.
50. Melacini, G.; Feng, Y. B.; Goodman, M. *Biochemistry* **1997**, *36*, 8725–8732.
51. Lucas, A.; Huang, L.; Joshi, A.; Dill, K. A. *J. Am. Chem. Soc.* **2007**, *129*, 4272–4281.
52. Burkoth, T. S.; Beausoleil, E.; Kaur, S.; Tang, D. Z.; Cohen, F. E.; Zuckermann, R. N. *Chem. Biol.* **2002**, *9*, 647–654.
53. Elgersma, R. C.; Mulder, G. E.; Kruijtzer, J. A. W.; Posthuma, G.; Rijkers, D. T. S.; Liskamp, R. M. J. *Bioorg. Med. Chem. Lett.* **2007**, *17*, 1837–1842.
54. Nam, K. T.; Shelby, S. A.; Choi, P. H.; *et al. Nat. Mater.* **2010**, *9*, 454–460.
55. Murnen, H. K.; Rosales, A. M.; Jaworski, J. N.; Segalman, R. A.; Zuckermann, R. N. *J. Am. Chem. Soc.* **2010**, *132*, 16112–16119.
56. Rosales, A. M.; Murnen, H. K.; Zuckermann, R. N.; Segalman, R. A. *Macromolecules* **2010**, *43*, 5627–5636.
57. Andrews, R. P. *Nature* **1986**, *319*, 429–430.
58. Figliozzi, G. M.; Goldsmith, R.; Ng, S. C.; Banville, S. C.; Zuckermann, R. N. *Comb. Chem.* **1996**, *267*, 437–447.
59. Zuckermann, R. N.; Kerr, J. M.; Siani, M. A.; Banville, S. C. *Int. J. Pept. Protein Res.* **1992**, *40*, 497–506.
60. Zuckermann, R. N.; Kerr, J. M.; Siani, M. A.; Banville, S. C.; Santi, D. V. *Proc. Natl. Acad. Sci. USA* **1992**, *89*, 4505–4509.
61. Tan, D. S. *Nat. Chem. Biol.* **2005**, *1*, 74–84.
62. Collins, J. M.; Leadbeater, N. E. *Org. Biomol. Chem.* **2007**, *5*, 1141–1150.
63. Gorske, B. C.; Jewell, S. A.; Guerard, E. J.; Blackwell, H. E. *Org. Lett.* **2005**, *7*, 1521–1524.
64. Olivos, H. J.; Alluri, P. G.; Reddy, M. M.; Salony, D.; Kodadek, T. *Org. Lett.* **2002**, *4*, 4057–4059.
65. Frank, R. *Tetrahedron* **1992**, *48*, 9217–9232.
66. Ast, T.; Heine, N.; Germeroth, L.; Schneider-Mergener, J.; Wenschuh, H. *Tetrahedron Lett.* **1999**, *40*, 4317–4318.
67. Heine, N.; Ast, T.; Schneider-Mergener, J.; Reineke, U.; Germeroth, L.; Wenschuh, H. *Tetrahedron* **2003**, *59*, 9919–9930.
68. Heine, N.; Germeroth, L.; Schneider-Mergener, J.; Wenschuh, H. *Tetrahedron Lett.* **2001**, *42*, 227–230.
69. Lam, K. S.; Lebl, M.; Krchnak, V. *Chem. Rev.* **1997**, *97*, 411–448.
70. Lam, K. S.; Salmon, S. E.; Hersh, E. M.; Hruby, V. J.; Kazmierski, W. M.; Knapp, R. J. *Nature* **1991**, *354*, 82–84.
71. Houghten, R. A.; Pinilla, C.; Blondelle, S. E.; Appel, J. R.; Dooley, C. T.; Cuervo, J. H. *Nature* **1991**, *354*, 84–86.
72. Reddy, M. M.; Bachhawat-Sikder, K.; Kodadek, T. *Chem. Biol.* **2004**, *11*, 1127–1137.
73. Zuckermann, R. N.; Martin, E. J.; Spellmeyer, D. C.; *et al. J. Med. Chem.* **1994**, *37*, 2678–2685.
74. Robinson, G. M.; Manica, D. P.; Taylor, E. W.; Smyth, M. R.; Lunte, C. E. *J. Chromatogr. B* **1998**, *707*, 247–255.
75. Robinson, G. M.; Taylor, E. W.; Smyth, M. R.; Lunte, C. E. *J. Chromatogr. B Analyt. Technol. Biomed. Life Sci.* **1998**, *705*, 341–350.
76. Kodadek, T.; Bachhawat-Sikder, K. *Mol. Biosyst.* **2006**, *2*, 25–35.
77. Alluri, P. G.; Reddy, M. M.; Bachhawat-Sikder, K.; Olivos, H. J.; Kodadek, T. *J. Am. Chem. Soc.* **2003**, *125*, 13995–14004.
78. Chen, J. K.; Lane, W. S.; Brauer, A. W.; Tanaka, A.; Schreiber, S. L. *J. Am. Chem. Soc.* **1993**, *115*, 12591–12592.
79. Heerma, W.; Boon, J.; Versluis, C.; Kruijtzer, J. A. W.; Hofmeyer, L. J. F.; Liskamp, R. M. J. *J. Mass Spectrom.* **1997**, *32*, 697–704.
80. Heerma, W.; Versluis, C.; deKoster, C. G.; Kruijtzer, J. A. W.; Zigrovic, I.; Liskamp, R. M. J. *Rapid Commun. Mass Spectrom.* **1996**, *10*, 459–464.
81. Paulick, M. G.; Hart, K. M.; Brinner, K. M.; Tjandra, M.; Charych, D. H.; Zuckermann, R. N. *J. Comb. Chem.* **2006**, *8*, 417–426.
82. Thakkar, A.; Cohen, A. S.; Connolly, M. D.; Zuckermann, R. N.; Pei, D. *J. Comb. Chem.* **2009**, *11*, 294–302.
83. Hirschman, R. *Angew. Chem.* **1991**, *30*, 1278–1301.
84. Udugamasooriya, D. G.; Dineen, S. P.; Brekken, R. A.; Kodadek, T. *J. Am. Chem. Soc.* **2008**, *130*, 5744–5752.
85. Peng, L.; Liu, R.; Marik, J.; Wang, X.; Takada, Y.; Lam, K. S. *Nat. Chem. Biol.* **2006**, *2*, 381–389.
86. Wrenn, S. J.; Weisinger, R. M.; Halpin, D. R.; Harbury, P. B. *J. Am. Chem. Soc.* **2007**, *129*, 13137–13143.
87. Kwon, Y. U.; Kodadek, T. *J. Am. Chem. Soc.* **2007**, *129*, 1508–1509.
88. Malet, G.; Martin, A. G.; Orzaez, M.; *et al. Cell Death Differ.* **2006**, *13*, 1523–1532.
89. Vicent, M. J.; Perez-Paya, E. *J. Med. Chem.* **2006**, *49*, 3763–3765.
90. Mondragon, L.; Orzaez, M.; Sanclimens, G.; *et al. J. Med. Chem.* **2008**, *51*, 521–529.
91. Toledo, F.; Wahl, G. M. *Nat. Rev. Cancer* **2006**, *6*, 909–923.
92. Hara, T.; Durell, S. R.; Myers, M. C.; Appella, D. H. *J. Am. Chem. Soc.* **2006**, *128*, 1995–2004.
93. Nguyen, J. T.; Turck, C. W.; Cohen, F. E.; Zuckermann, R. N.; Lim, W. A. *Science* **1998**, *282*, 2088–2092.
94. Nguyen, J. T.; Porter, M.; Amoui, M.; Miller, W. T.; Zuckermann, R. N.; Lim, W. A. *Chem. Biol.* **2000**, *7*, 463–473.
95. Ruijtenbeek, R.; Kruijtzer, J. A. W.; van de Wiel, W.; *et al. Chembiochem* **2001**, *2*, 171–179.
96. Choi, W. J.; Kim, S. E.; Stephen, A. G.; *et al. J. Med. Chem.* **2009**, *52*, 1612–1618.
97. Udugamasooriya, D. G.; Dunham, G.; Ritchie, C.; Brekken, R. A.; Kodadek, T. *Bioorg. Med. Chem. Lett.* **2008**, *18*, 5892–5894.
98. Udugamasooriya, D. G.; Ritchie, C.; Brekken, R. A.; Kodadek, T. *Bioorg. Med. Chem.* **2008**, *16*, 6338–6343.
99. Kruijtzer, J. A. W.; Nijenhuis, W. A. J.; Gispen, W. H.; Adan, R. A. H.; Liskamp, R. M. J. *Biopolymers* **2003**, *71*, P348.
100. Kruijtzer, J. A. W.; Nijenhuis, W. A. J.; Wanders, N.; Gispen, W. H.; Liskamp, R. M. J.; Adan, R. A. H. *J. Med. Chem.* **2005**, *48*, 4224–4230.
101. Garcia-Martinez, C.; Humet, M.; Planells-Cases, R.; *et al. Proc. Natl. Acad. Sci. USA* **2002**, *99*, 2374–2379.
102. Quintanar-Audelo, M.; Fernandez-Carvajal, A.; Van Den Nest, W.; Carreno, C.; Ferrer-Montiel, A.; Albericio, F. *J. Med. Chem.* **2007**, *50*, 6133–6143.
103. Low, C. M. R.; Black, J. W.; Broughton, H. B.; *et al. J. Med. Chem.* **2000**, *43*, 3505–3517.
104. Tran, T. A.; Mattern, R. H.; Afargan, M.; *et al. J. Med. Chem.* **1998**, *41*, 2679–2685.
105. Boden, P.; Eden, J. M.; Hodgson, J.; *et al. J. Med. Chem.* **1996**, *39*, 1664–1675.
106. Yuasa, H.; Honma, H.; Hashimoto, H.; Tsunooka, M.; Kojima-Aikawa, K. *Bioorg. Med. Chem. Lett.* **2007**, *17*, 5274–5278.
107. Yuasa, H.; Kamata, Y.; Kurono, S.; Hashimoto, H. *Bioorg. Med. Chem. Lett.* **1998**, *8*, 2139–2144.
108. Masip, I.; Cortes, N.; Abad, M. J.; *et al. Bioorg. Med. Chem.* **2005**, *13*, 1923–1929.
109. Planells-Cases, R.; Montoliu, C.; Humet, M.; *et al. J. Pharmacol. Exp. Ther.* **2002**, *302*, 163–173.
110. Lewis, I.; Rohde, B.; Mengus, M.; *et al. Mol. Divers.* **2000**, *5*, 61–73.
111. de Haan, E. C.; Wauben, M. H. M.; Grosfeld-Stulemeyer, M. C.; Kruijtzer, J. A. W.; Liskamp, R. M. J.; Moret, E. E. *Bioorg. Med. Chem.* **2002**, *10*, 1939–1945.
112. Reddy, M. M.; Kodadek, T. *Proc. Natl. Acad. Sci. USA* **2005**, *102*, 12672–12677.
113. Ross, T. M.; Zuckermann, R. N.; Reinhard, C.; Frey, W. H. *Neurosci. Lett.* **2008**, *439*, 30–33.
114. Wheeler, T. M.; Sobczak, K.; Lueck, J. D.; *et al. Science* **2009**, *325*, 336–339.
115. Labuda, L. P.; Pushechnikov, A.; Disney, M. D. *ACS Chem. Biol.* **2009**, *4*, 299–307.
116. Lee, M. M.; Childs-Disney, J. L.; Pushechnikov, A.; *et al. J. Am. Chem. Soc.* **2009**, *131*, 17464–17472.
117. Lee, M. M.; Pushechnikov, A.; Disney, M. D. *ACS Chem. Biol.* **2009**, *4*, 345–355.
118. Hancock, R. E.; Sahl, H. G. *Nat. Biotechnol.* **2006**, *24*, 1551–1557.
119. Zasloff, M. *Nature* **2002**, *415*, 389–395.
120. Park, C. B.; Yi, K. S.; Matsuzaki, K.; Kim, M. S.; Kim, S. C. *Proc. Natl. Acad. Sci. USA* **2000**, *97*, 8245–8250.
121. Chongsiriwatana, N. P.; Patch, J. A.; Czyzewski, A. M.; *et al. Proc. Natl. Acad. Sci. USA* **2008**, *105*, 2794–2799.
122. Patch, J. A.; Barron, A. E. *J. Am. Chem. Soc.* **2003**, *125*, 12092–12093.
123. Kapoor, R.; Eimerman, P. R.; Hardy, J. W.; Cirillo, J. D.; Contag, C. H.; Barron, A. E. *Antimicrob. Agents Chemother.* **2011**, *55*, 3058–3062.
124. Chongsiriwatana, N. P.; Miller, T. M.; Wetzler, M.; *et al. Antimicrob. Agents Chemother.* **2011**, *55*, 417–420.
125. Goodson, B.; Ehrhardt, A.; Ng, S.; *et al. Antimicrob. Agents Chemother.* **1999**, *43*, 1429–1434.
126. Ng, S.; Goodson, B.; Ehrhardt, A.; Moos, W. H.; Siani, M.; Winter, J. *Bioorg. Med. Chem.* **1999**, *7*, 1781–1785.
127. Song, Y. M.; Park, Y.; Lim, S. S.; *et al. Biochemistry* **2005**, *44*, 12094–12106.
128. Zhu, W. L.; Song, Y. M.; Park, Y.; *et al. Biochim. Biophys. Acta Biomembr.* **2007**, *1768*, 1506–1517.
129. Brown, N. J.; Johansson, J.; Barron, A. E. *Acc. Chem. Res.* **2008**, *41*, 1409–1417.
130. Eggleton, P.; Reid, K. B. *Curr. Opin. Immunol.* **1999**, *11*, 28–33.

131. Brown, N. J.; Seurynck, S. L.; Wu, C. W.; Johnson, M.; Barron, A. E. *Biophys. J.* **2005**, *88*, 576A–577A.
132. Brown, N. J.; Wu, C. W.; Seurynck-Servoss, S. L.; Barron, A. E. *Biochemistry* **2008**, *47*, 1808–1818.
133. Wu, C. W.; Seurynck, S. L.; Lee, K. Y. C.; Barron, A. E. *Chem. Biol.* **2003**, *10*, 1057–1063.
134. Seurynck, S. L.; Patch, J. A.; Barron, A. E. *Chem. Biol.* **2005**, *12*, 77–88.
135. Seurynck-Servoss, S. L.; Dohm, M. T.; Barron, A. E. *Biochemistry* **2006**, *45*, 11809–11818.
136. Dohm, M. T.; Seurynck-Servoss, S. L.; Seo, J.; Zuckermann, R. N.; Barron, A. E. *Biopolymers* **2009**, *92*, 538–553.
137. Wang, Y. F.; Lin, H.; Tullman, R.; Jewell, C. F.; Weetall, M. L.; Tse, F. L. S. *Biopharm. Drug Dispos.* **1999**, *20*, 69–75.
138. Gibbons, J. A.; Hancock, A. A.; Vitt, C. R.; *et al. J. Pharmacol. Exp. Ther.* **1996**, *277*, 885–899.
139. Fischer, R.; Fotin-Mleczek, M.; Hufnagel, H.; Brock, R. *ChemBioChem* **2005**, *6*, 2126–2142.
140. Wender, P. A.; Mitchell, D. J.; Pattabiraman, K.; Pelkey, E. T.; Steinman, L.; Rothbard, J. B. *Proc. Natl. Acad. Sci. USA* **2000**, *97*, 13003–13008.
141. Peretto, I.; Sanchez-Martin, R. M.; Wang, X. H.; Ellard, J.; Mittoo, S.; Bradley, M. *Chem. Commun.* **2003**, *9*, 2312–2313.
142. Unciti-Broceta, A.; Diezmann, F.; Ou-Yang, C. Y.; Fara, M. A.; Bradley, M. *Bioorg. Med. Chem.* **2009**, *17*, 959–966.
143. Schroder, T.; Niemeier, N.; Afonin, S.; Ulrich, A. S.; Krug, H. F.; Brase, S. *J. Med. Chem.* **2008**, *51*, 376–379.
144. Schroder, T.; Schmitz, K.; Niemeier, N.; *et al. Bioconjug. Chem.* **2007**, *18*, 342–354.
145. Xiao, X.; Yu, P.; Lim, H. S.; Sikder, D.; Kodadek, T. *Angew. Chem. Int. Ed. Engl.* **2007**, *46*, 2865–2868.
146. Xiao, X. S.; Yu, P.; Lim, H. S.; Sikder, D.; Kodadek, T. *J. Comb. Chem.* **2007**, *9*, 592–600.
147. Kwon, Y. U.; Kodadek, T. *Chem. Biol.* **2007**, *14*, 671–677.
148. Murphy, J. E.; Uno, T.; Hamer, J. D.; Cohen, F. E.; Dwarki, V.; Zuckermann, R. N. *Proc. Natl. Acad. Sci. USA* **1998**, *95*, 1517–1522.
149. Huang, C. Y.; Uno, T.; Murphy, J. E.; *et al. Chem. Biol.* **1998**, *5*, 345–354.
150. Utku, Y.; Dehan, E.; Ouerfelli, O.; *et al. Mol. Biosyst.* **2006**, *2*, 312–317.
151. Feng, Y. B.; Melacini, G.; Taulane, J. P.; Goodman, M. *Biopolymers* **1996**, *39*, 859–872.
152. Goodman, M.; Melacini, G.; Feng, Y. B. *J. Am. Chem. Soc.* **1996**, *118*, 10928–10929.
153. Goodman, M.; Feng, Y. B.; Melacini, G.; Taulane, J. P. *J. Am. Chem. Soc.* **1996**, *118*, 5156–5157.
154. Kwak, J.; Jefferson, E. A.; Bhumralkar, M.; Goodman, M. *Bioorg. Med. Chem.* **1999**, *7*, 153–160.
155. Statz, A. R.; Meagher, R. J.; Barron, A. E.; Messersmith, P. B. *J. Am. Chem. Soc.* **2005**, *127*, 7972–7973.
156. Statz, A. R.; Kuang, J. H.; Ren, C. L.; Barron, A. E.; Szleifer, I.; Messersmith, P. B. *Biointerphases* **2009**, *4*, 22–32.
157. Statz, A. R.; Park, J. P.; Chongsiriwatana, N. P.; Barron, A. E.; Messersmith, P. B. *Biofouling* **2008**, *24*, 439–448.
158. Peri, F.; Dumy, P.; Mutter, M. *Tetrahedron* **1998**, *54*, 12269–12278.
159. Seo, J.; Michaelian, N.; Owens, S. C.; *et al. Org. Lett.* **2009**, *11*, 5210–5213.
160. Kim, J. M.; Roy, R. *Carbohydr. Res.* **1997**, *298*, 173–179.
161. Kim, J. M.; Roy, R. *Tetrahedron Lett.* **1997**, *38*, 3487–3490.
162. Comegna, D.; De Riccardis, F. *Org. Lett.* **2009**, *11*, 3898–3901.
163. Burger, K.; Bottcher, C.; Radics, G.; Hennig, L. *Tetrahedron Lett.* **2001**, *42*, 3061–3063.
164. Dechantsreiter, M. A.; Burkhart, F.; Kessler, H. *Tetrahedron Lett.* **1998**, *39*, 253–254.
165. Norgren, A. S.; Budke, C.; Majer, Z.; Heggemann, C.; Koop, T.; Sewald, N. *Synthesis* **2009**, 488–494.
166. Letondor, C.; Humbert, N.; Ward, T. R. *Proc. Natl. Acad. Sci. USA* **2005**, *102*, 4683–4687.
167. Wilson, M. E.; Whitesides, G. M. *J. Am. Chem. Soc.* **1978**, *100*, 306–307.
168. Maayan, G.; Ward, M. D.; Kirshenbaum, K. *Proc. Natl. Acad. Sci. USA* **2009**, *106*, 13679–13684.

2.205. Self-Assembling Biomaterials

J S Rudra and J H Collier, University of Chicago, Chicago, IL, USA

© 2011 Elsevier Ltd. All rights reserved.

2.205.1.	**Introduction**	77
2.205.2.	**Planar Self-Assembling Systems**	78
2.205.2.1.	Self-Assembled Monolayers	78
2.205.2.2.	Functionalized SAMs for Modulating Cell Attachment	78
2.205.2.3.	Patterning and SAMs	79
2.205.2.4.	Responsive Elements and Dynamic SAMs	80
2.205.3.	**3D Self-Assembling Systems**	80
2.205.3.1.	Self-Assembling Peptides	81
2.205.3.2.	Coiled Coils	81
2.205.3.3.	Biomaterials from Coiled Coils	83
2.205.3.4.	Self-Assembling Peptides Based on β-Sheet Fibrils	84
2.205.3.5.	Self-Assembling Peptides Based on Collagens	85
2.205.3.6.	Self-Assembling Peptide Amphiphiles	86
2.205.3.7.	Self-Assembling Peptides with Aromatic Groups	87
2.205.3.8.	β-Hairpins	87
2.205.3.9.	Proteins	87
2.205.4.	**Modulating the Mechanics of Self-Assembling Systems**	88
2.205.5.	**Advantages Provided by Self-Assembled Systems for Biomaterials Applications**	89
2.205.6.	**Immune and Inflammatory Responses to Self-Assembling Materials**	89
2.205.7.	***In vivo* Applications of Self-Assembled Biomaterials**	90
2.205.8.	**Concluding Remarks**	92
References		92

Abbreviations

AFM	Atomic force microscopy
CFA	Complete Freund's adjuvant
ELISA	Enzyme-linked immunosorbent assay
HPMA	Hydroxypropyl methacrylate
ISCOMs	Immune-stimulating complexes
PAs	Peptide amphiphiles
PEG	Poly(ethylene glycol)
SAMs	Self-assembled monolayers
TEM	Transmission electron microscopy
μCP	Microcontact printing

2.205.1. Introduction

Molecular self-assembly can be defined as the spontaneous transition of initially disordered molecules into predictable supramolecular structures, usually driven by specific noncovalent interactions. Much of biology is a result of self-assembly, which taken to an extreme, produces the high molecular weight networks that constitute the cytoskeleton and the extracellular matrix. Self-assembling strategies in biomaterials can likewise produce highly structured, compositionally defined, multicomponent, multifunctional materials from a discrete set of molecular building blocks.

Self-assembly has become a prominent strategy in chemistry and materials science as a whole. It has become significant in highly diverse applications, in fields ranging across electronic materials, synthetic biology, structural materials, chemical biology, and biomaterials. The objective of this chapter is to generally outline several of the concepts and strategies based on molecular self-assembly that have received particular interest in the past several years for designing biomaterials. Specifically, the chapter focuses on biomaterials that self-assemble in two-dimensional (2D) structures, primarily self-assembled monolayers, and biomaterials that self-assemble in 3D structures, primarily those based on peptides and proteins. Bioconjugates of peptides and polymers are addressed, but purely polymeric self-assembling materials are outside the scope of the chapter and have been covered in several recent reviews.[1,2]

The forces that direct molecular self-assembly tend to be weak intermolecular interactions between molecules in solution. These include hydrogen bonding, hydrophobic interactions, Coulombic interactions, π-stacking, and van der Waals forces. Accordingly, self-assembling systems tend to be highly dependent on solution conditions such as pH, ionic strength, concentration, temperature, and solvent polarity, aspects that have been exploited to produce conditionally assembling or stimulus-sensitive materials. In addition to controllable stimulus-sensitivity, self-assembling approaches provide a set

of unique advantages that make them useful as biomaterials. First, large, relatively complex supramolecular structures and objects such as fibrils, networks, and membranes can be formed from synthetically accessible, small molecular weight components. In this way, the chemical definition of the material can be highly controlled, even when multiple co-assembling constituents are present. In comparison with structurally and compositionally heterogeneous biomaterials such as biologically sourced polymers, such definition is a significant advantage. Second, by identifying molecules that can self-assemble and be functionalized with ligands or chemical groups either postassembly or preassembly, materials displaying complex combinations of molecular features can be produced from an easy-to-synthesize initial set of molecules. In this way, multifunctional materials can be systematically produced and optimized. In the sections below, 2D and 3D biomaterials that take advantage of these properties are discussed.

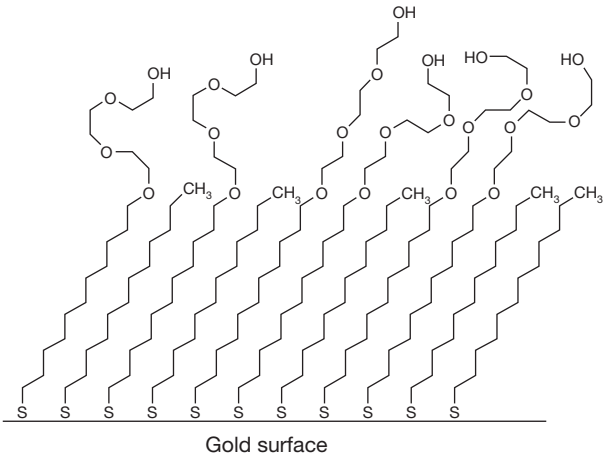

Figure 1 A self-assembled monolayer (SAM) displaying nonfouling oligo(ethylene glycol) terminal functionalities.

2.205.2. Planar Self-Assembling Systems

Although almost all physiological processes operate in three dimensions, planar surfaces have been the *de facto* substrate for adherent cells for most of the history of cell culture. Planar systems are useful because of their chemical definition, simplicity, cost-effectiveness, and compatibility with a wide range of imaging methods. However, traditional glass or polystyrene tissue culture surfaces mediate cell adhesion through an adsorbed layer of proteins. This layer can be derived from serum proteins in the culture medium, from proteins secreted by the cells themselves, or by purposefully precoating the surface with matrix proteins such as fibronectin or collagen. Such adsorbed layers are complex, presenting varied and dynamic mixtures of conformations for different proteins, making the precise engineering or study of cell–surface interactions challenging. Many 2D self-assembling biomaterials have been developed in order to improve upon these simple, poorly defined substrates. As described below, one of the main goals of 2D self-assembling biomaterials is to provide surfaces for which the identity, density, availability, spatial positioning, and dynamic properties of specific cell–surface interactions may be specified. Strategies that allow the lateral motion of surface functionalities, such as supported lipid bilayers, have been extremely useful for modeling cell–surface interactions, for studying proteins and structures associated with cell membranes, and for producing functionalized culture surfaces. However, this section focuses primarily on strategies for which lateral diffusion is minimal or nonexistent, owing to the robustness and applicability of such surfaces within many biomaterials contexts. Supported bilayers have been reviewed recently and are addressed in other chapters of this comprehensive volume as well.[3–5]

2.205.2.1. Self-Assembled Monolayers

Self-assembled monolayers (SAMs) are molecular layers that assemble on a surface by adsorption, usually from solution. Their formation is mediated by a specific functional group that has a strong affinity for a particular surface. Several different SAMs have been developed for a range of different materials including medically related metals such as titanium,[6] but the most extensively investigated have been SAMs utilizing alkanethiolates and gold.[7–9] When a gold surface is immersed in a solution of alkane thiolates, the sulfur atoms coordinate to the gold (111) surface in a densely packed array (Figure 1). The alkane portion extends from the surface, and it can be functionalized with a wide range of chemical modifications, either preassembly or postassembly, to provide surfaces with defined chemistries. Useful properties of SAMs include their optical transparency when applied to thin gold layers and their electrical conductivity, which makes them applicable to electrochemical modulation of surface properties. Mixed SAMs of multiple different alkane thiols may also be produced by incubating gold surfaces under mixed solutions of different alkanethiolates. In this way, ligands, chemical functionalities, or nonfouling alkane thiols can be applied to a surface in defined formulations, as described below. In this chapter, several overarching concepts in the development of SAMs will be discussed, citing relevant examples from the literature. For a more complete recent discussion of the various approaches used, the reader is referred to Robertus *et al.*[9]

2.205.2.2. Functionalized SAMs for Modulating Cell Attachment

As an alternative to the poorly controlled adsorbed layers of proteins that are a general feature of traditional cell culture systems, SAMs displaying precise combinations of biochemical features have been developed. One of the initial steps involved in creating such defined self-assembled surfaces has been to first reduce or eliminate the protein adsorption that naturally complicates traditional culture surfaces. In this regard, SAMs displaying terminal oligoethylene glycol groups have been the most thoroughly investigated, though SAMs terminated with other nonfouling groups such as oligosarcosines, permethylated sorbitol groups, or oligophosphorylcholines have also demonstrated good resistance to protein adsorption.[9–11] Such monolayers are stable in cell culture for several days.

Early work with functionalized SAMs utilized oligoethylene glycol monolayer backgrounds containing around 1 mol% or less of a functionalized alkane thiol. For example, a small amount of RGD peptide-terminated alkanethiolates was mixed

with triethylene glycol-terminated alkanethiolates to promote cell adhesion via integrin binding.[12] This system has also been used with other peptide ligands of interest, such as the PHSRN peptide from the ninth type-III domain of fibronectin.[13] The ability to adjust the relative amounts of each ligand on the surface has been utilized to study the mechanism of integrin binding to these fibronectin fragments. Mixed SAMs have also been employed to produce gradients of cell adhesion molecules for investigating cell adhesion and migration.[14,15] One potential concern, however, is that it is possible that phase-separated domains may form in such mixed monolayers, but it has been found that such phase separation can usually be avoided if the density of the functionalized alkanethiolate is kept below 1% of the total alkanethiolate.[8]

2.205.2.3. Patterning and SAMs

SAMs are natural complements to surface patterning techniques such as microcontact printing (μCP), which uses an elastomeric stamp to transfer 'ink' to defined patterns of a planar surface.[16] Stamps are produced by casting an elastomer, typically polydimethylsiloxane, onto a high-aspect-ratio topographical pattern fabricated via photolithography. The stamp is then inked with an alkane thiol of choice and placed in contact with a gold surface, whereby the alkanethiol is transferred to the gold. A second alkane thiol can then be applied to nonstamped regions by immersing the surface in a solution containing the second alkane thiol. In a foundational report of using this technique to control cell behavior, Chen and coworkers produced cell-adhesive islands with varying sizes surrounded by a nonadhesive background. Cells restricted to small islands became apoptotic, whereas apoptosis was progressively diminished as island size increased.[17] μCP and SAMs have since been utilized to explore a wide range of cell behaviors, including differentiation, cell division axis orientation, epithelial monolayer growth, proliferation, and others (for review see Ruiz and Chen[16]). In more recent work, μCP has been used to control the subcellular shape of the cytoskeleton, which in turn exerts strong influences on cell contractility and differentiation.[18–20] For example, Mrksich and coworkers developed pentagonal patterns on which single cells could be maintained, where the concavity of the pentagonal features were modulated (Figure 2).[18] They found that rounded features (producing a flower-like pattern) promoted the differentiation of mesenchymal stem cells into adipocytes, whereas pointed features (a star pattern) promoted osteoblastic differentiation. One of the critical features of the highly defined SAM substrates used in this study was the reproducibility of both the pattern and the surface chemistry supporting each individual cell. Owing to these features, the cytoskeletal organization of dozens of cells exposed to extremely similar microenvironments could be overlaid so as to statistically compare them and generate averaged structures of their cytoskeletons (Figure 2). It is anticipated that these and similar methods of reducing population heterogeneity in biological samples will prove to be powerful techniques in fields ranging from cell biology to drug discovery in the coming years.

In addition to sharply defined patterns such as those produced with techniques like μCP, gradated patterns on SAMs are also of significant interest, especially for studies of cell migration. Methods for producing gradients include electrochemical desorption of alkanethiolates from SAMs,[21] photochemistry,[22] and microfluidic manipulation. In an example combining microfluidics with SAMs displaying short chemically defined peptide ligands, one recent approach created patterns of 33-μm squares containing gradients of cell-adhesive peptide ligands within each square. The squares were placed within a background of a nonfouling tri(ethylene glycol)-terminated SAM. Gradients of RGD ligands were produced by flowing gradated mixtures of functional RGD peptides and nonfunctional scrambled RDG peptides onto patterns of maleimide-terminated SAMs using a microfluidic system. The gradient produced within the solution phase of the microfluidic system was reflected by a similar gradient immobilized to the maleimide-terminated SAMs, and the total peptide immobilized to the surfaces was kept constant.[23] When cultures of mouse melanoma cells were seeded onto these substrates, the RGD gradients were reflected in a proportional distribution of the focal adhesion protein vinculin, demonstrating that the gradients influenced the spatial organization of cellular adhesive complexes.

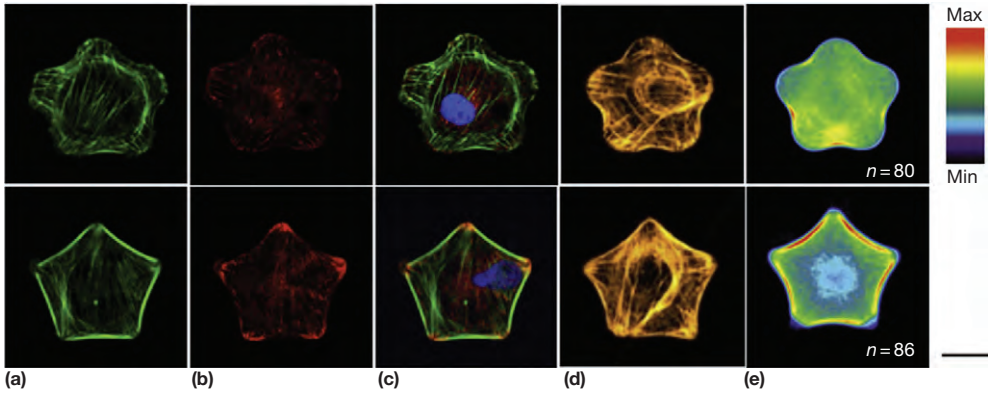

Figure 2 Defined two-dimensional self-assemblies such as self-assembled monolayers provide the opportunity to place individual cells in highly repeatable chemical and geometric environments. Shown are immunofluorescent images of human mesenchymal stem cells in flower and star shapes stained for F-actin (green), vinculin (red), nuclei (blue), and myosin IIa (orange) (a–d). Heat maps of >80 different overlaid images of myosin IIa can be used as a quantitative measure of contractility (e). Scale bar = 20 μm. Reproduced with permission from Kilian, K. A., Bugarija, B., Lahn, B. T., Mrksich, M. *Proc. Natl. Acad. Sci. USA* **2010**, *107*, 4872–4877, with permission from Mrksich.

Further, although micropatterning approaches have significantly utilized SAMs, micropatterned culture surfaces have also been explored using a wide range of other patterning approaches, including those based on photolithography,[24,25] photolithographically patterned polymer coatings,[26] anisotropic surfaces,[27,28] and microfluidics.[29]

2.205.2.4. Responsive Elements and Dynamic SAMs

Planar self-assembled biomaterials such as SAMs are amenable to modification with a range of chemical approaches, including oxidation, electrochemistry, photochemistry, and other regio- or chemoselective techniques. Either singly or in combination, such strategies have been utilized to produce biomaterials with dynamic control over their interactions with cells. A goal of these techniques is to produce surfaces for which a specific biological activity, such as engagement of a specific cell or receptor, can be turned 'off' or 'on.' Such 'switchable' surfaces are valuable in applications ranging from basic biological investigations to cell-based devices and sensors. They have been particularly useful in combination with patterning techniques, which allow the switching of spatially resolved areas of culture surfaces.

Owing to the inherent electrical conductivity of the gold layers on which SAMs are immobilized, electrochemical approaches in particular have been exploited to develop switching strategies. In one example, nonfouling SAM constituents were desorbed by application of a reductive potential, switching the surface from one that resisted protein and cell adhesion to one that supported cell adhesion and migration.[30] By initially confining cells within micropatterned areas of cell adhesiveness and then rendering the entire surface adhesive by desorbing the nonfouling triethylene glycol SAM regions, a useful migration assay was produced. Electrochemical desorption has also been utilized to release cells captured to the SAM via SAM-linked antibodies. In a recent example, T cells were captured on a SAM presenting anti-CD4 antibodies. Subsequently, an applied reductive potential could be used to trigger detachment of the SAM and a corresponding cell detachment.[31] Such processes could be useful for capturing, concentrating, and releasing specific cells from heterogeneous mixtures. Another example of switching a SAM surface from displaying a ligand to releasing it focused on SAMs displaying biotin tethered via a quinone propionic ester, which upon application of a reductive potential released the biotin into the solution.[32] A similar approach was later applied to SAMs displaying RGD peptides instead of biotin. This chemistry was patterned into circular regions using μCP and displayed on the same surface as other regions displaying RGD peptides tethered to the SAM via an *O*-silyl hydroquinone, which could release the ligand under oxidative potentials instead of reductive ones.[33] By patterning the two different chemistries into different regions of the surface, and by also including a third nonelectroactive RGD-bearing SAM, cells could be selectively released in one region by application of a reductive potential, in a second region by application of an oxidizing potential, or maintained on the surface within the nonelectroactive regions. Other means for switching cytophobic surfaces to cell-adhesive surfaces have included the use of microelectrodes to locally generate Br_2 to degrade oligoethylene glycol-terminated SAMs, leaving alkyl-terminated SAMs.[34] In this work, the local degradation of the otherwise protein- and cell-resistant oligoethylene glycol termini of the SAM rendered the remaining alkyl-terminated SAMs able to adsorb proteins.[34,35] By using a microelectrode as a 'pen,' patterns could be drawn on culture surfaces in a customizable manner. Surfaces switchable via UV illumination have also been developed for silane-based monolayers on glass, in which SAMs terminated with photocleavable 2-nitrobenzyl groups were employed.[36,37] When these SAMs were coated with Pluronic block copolymers, they were non-cell-adhesive, but irradiation by UV light resulted in the development of a carboxy-terminus on the SAM. This switch desorbed the Pluronic coating, allowing subsequent fibronectin adsorption and the rendering of the surface cell-adhesive. This chemistry has been utilized to study the process of cell migration in single-cell microarray formats.[37]

Techniques for selectively attaching ligands to SAM surfaces have also been developed using both electrochemical and photochemical approaches. In an early example of an electrochemical strategy for doing so, monolayers presenting hydroquinone groups against a background of triethylene glycol groups could be switched with an oxidizing potential to present benzoquinone groups, which could subsequenty be reacted with cyclopentadiene-terminated peptides via a Diels–Alder reaction to afford peptide-terminated SAMs.[38] In this way, surfaces could be switched from being nonadhesive to being cell-adhesive (**Figure 3(a)–3(c)**). This approach has been useful in constructing migration assays and spatially organized co-cultures. In the fabrication of co-cultures, one cell type was allowed to attach to a specific pattern, after which the remaining surface was rendered cell-adhesive to support the attachment of a second cell type. In an example of a photochemical approach for creating switchable surfaces, monolayers presenting NVOC-protected hydroquinone groups were developed (**Figure 3(d)**). Deprotection of the hydroquinone could be achieved by illumination with 370 nm light. Conversion of the hydroquinone groups to quinones via chemical oxidation and subsequent conjugation of cyclopentadiene-terminated RGD peptides then produced the RGD-terminated SAMs in photopatterned arrays.[39] An exhaustive discussion of the strategies developed to date for designing switchable SAMs is beyond the scope of this chapter; for a more extensive review, the reader is referred to Robertus *et al.*[9]

Collectively, SAMs and other planar self-assembling systems provide surfaces that are highly defined chemically. This precise definition enables a wide range of electrochemical, photochemical, microstamp-based, or microfluidic manipulations that can be used to position specific functionalities and to switch them dynamically.

2.205.3. 3D Self-Assembling Systems

Molecular self-assembly into 3D structures has become an increasingly common synthetic route in applications ranging from electronics to 'smart' materials to composites. Self-assembling approaches can employ aqueous conditions, organic solvents, inorganic materials, organic compounds, or even macroscopic objects. Despite this wide range of strategies available, within the biomaterials field a subset of self-assembling materials has received the most intense interest: those that assemble in aqueous solutions, and those that are

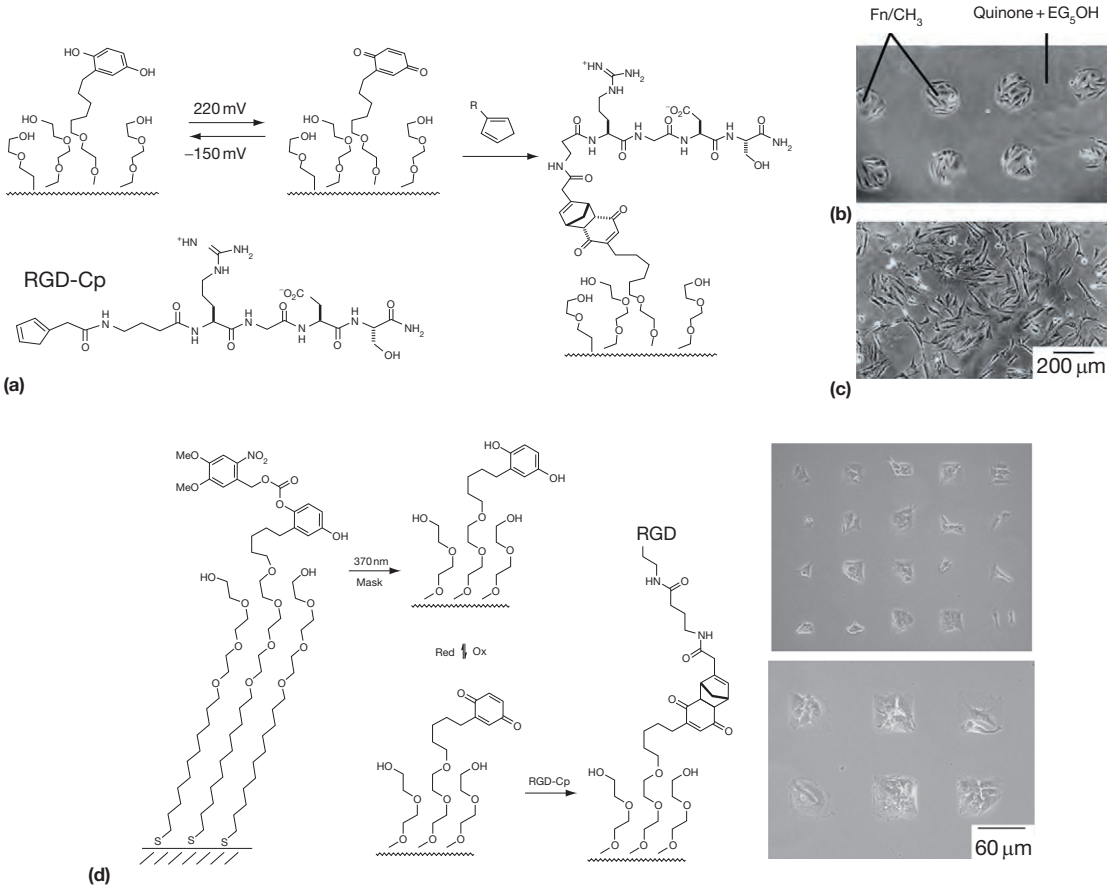

Figure 3 Self-assembled monolayers (SAMs) presenting electrically active groups (a–c) and photoreactive groups (d). In electrically switchable SAMs (a), inert monolayers presenting hydroquinone groups mixed with penta(ethylene glycol) groups were converted to monolayers that support cell attachment and spreading by application of a positive potential, which converted the hydroquinone groups to quinone groups. The quinone groups then underwent a Diels–Alder reaction with RGD–cyclopentadiene (RGD–Cp) to conjugate the peptide onto the surface. Fibronectin was adsorbed on to the methyl-terminated regions and initially cells attached only to the fibronectin-coated regions (b), but after oxidation of the substrate in the presence of RGD–Cp, cells were able to migrate and then grow to fill the entire monolayer (c). Photoreactive SAMs have included those presenting photosensitive NV OC-protected hydroquinone groups in a background of oligoethylene glycol groups (d). Illumination by 370 nm light revealed hydroquinone groups, which could be converted to quinones by applying tetramethylbenzoquinone and functionalized further with RGD-Cp (left, d). 3T3 fibroblasts could be patterned on RGD-functionalized islands of the substrate (right, d). Reproduced with permission from Mrksich, M. *Acta Biomater.* **2009**, *5*, 832–841, with permission from Elsevier.

based on native biopolymers, especially peptides and proteins. Aqueous conditions are required for interfacing with biological processes, and polyamino acids afford bioactive structures that can, in principle, approach the functionality of native proteins.

2.205.3.1. Self-Assembling Peptides

Peptides have been extensively employed in self-assembling biomaterials strategies owing to their native biofunctionality, their ease of synthesis, and their chemical definition. Standard synthesis and purification techniques allow for significant control over structure and purity, and they provide opportunities for chemically modifying the peptide termini, for chemically modifying side chains, for conjugating peptides to other macromolecules such as polymers, or for incorporating any number of commercially available nonnative amino acids. The construction of supramolecular structures from peptides has also been enhanced by the elucidation of design rules that can be exploited to direct peptide folding into several useful secondary and tertiary structures, including coiled coils, β-sheet fibrils, collagen triple helices, and other more specifically folded domains. Each of these structures is stabilized by multiple noncovalent forces that act in concert, including hydrogen bonds, hydrophobic interactions, van der Waals forces, or the stacking of aromatic groups. The following sections will discuss these structures in greater detail.

2.205.3.2. Coiled Coils

As one of the fundamental secondary structures in nature, the α-helix is a useful building block for self-assembling biomaterials. However, α-helices tend not to be stable as monomers in solution owing to the ability of water to interact with their backbone N–H and C=O groups, providing an entropic cost for helix formation. This entropic penalty can be overcome by designing peptides where multiple noncovalent intermolecular

interactions are used to stabilize helical folding. To accomplish this in biomaterials strategies, the coiled coil has been the most heavily investigated structure. Coiled coils (Figure 4(a) and 4(b)) are common motifs found in a wide range of proteins,[40,41] including fibrous proteins,[42] transcription factors,[43] extracellular matrix proteins,[44] load-bearing proteins,[45] and membrane spanning proteins.[46,47] Most coiled coils exist as a supercoil of 2–5 helices,[41] and their primary structures tend to possess a regular pattern of polar and nonpolar residues in a well-known heptad repeat denoted by $(abcdefg)_n$, where residues in the *a* and *d* positions are nonpolar, and the other positions are polar (Figure 5). The average spacing between nonpolar residues is thus 3.5 residues, and the 3.6-residue pitch of the α-helix leads to the formation of a hydrophobic stripe that spirals around the helix. Burial of this hydrophobic stripe by oligomerization with other helices then forms a supercoil with a left-handed twist. While residues in the *a* and *d* positions form the hydrophobic contacts between different coils, residues in the *b*, *c*, and *f* positions are exposed to the solvent, and residues in the *e* and *g* positions can participate in interhelical electrostatic interactions that modify the topology or oligomerization state of the helices (Figure 5).

Coiled coils can be parallel or antiparallel, and the packing of *a* and *d* residues differs between the two topologies. In parallel coiled-coil dimers, residues in *a* positions form close contacts with *a* residues of the second helix, whereas in antiparallel dimers, residues from *a* positions pair most closely with residues in *d* positions of the second helix (Figure 5(a)). Likewise, the pattern of electrostatic interactions between *e* and *g* residues differs with antiparallel versus parallel topology. In parallel coiled-coil dimers, electrostatic interactions exist between *e* residues on one helix and *g* residues on the other, whereas in antiparallel coiled coils, interhelical interactions occur between *g*–*g* pairs and *e*–*e* pairs (Figure 5(b)). Knowledge of these intermolecular interactions between residues in the $(abcdefg)_n$ heptad repeat are the basis of many design strategies that have been utilized to construct coiled-coil self-assembling biomaterials.

Additional levels of design rules have also been developed for specifying coiled-coil assembly. First, the identity and packing of the *a* and *d* residues in the hydrophobic core can be tuned to specify oligomerization state. In general, aliphatic residues have been the most heavily utilized in this regard owing to the steric constraints of aromatic residues. Aromatic residues are relatively uncommon in *a* and *d* positions of natural coiled-coil structures, although Trp zippers and Phe zippers have been designed and produced.[48,49] For the formation of dimers, *a* positions containing β-branched residues (Ile and Val) and *d* positions containing Leu have been found to be particularly stabilizing.[50,51] This is thought to be a result of the ability of these branched residues to pack appropriately to fill the space between the two helices. In contrast, it has been shown in some models that if all *a* and *d* residues are Ile, trimers are favored, whereas Leu in *a* positions and Ile in *d* positions favors tetramers.[52,53] Electrostatic pairing between *e* and *g* residues can also influence the oligomerization state, especially when used in conjunction with strategies for packing residues in the hydrophobic core.[54] Studies of amino acids in

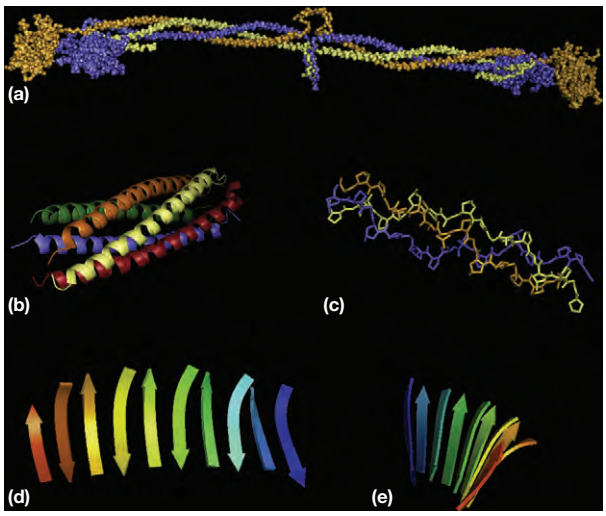

Figure 4 Peptide folding that has been utilized in self-assembling biomaterials. Networks of extracellular matrix proteins are constructed through hierarchical levels of self-assembly. As an example, the symmetrical dimer of trimers forming the protein fibrinogen (a, chicken fibrinogen shown) forms a long fibrous protein in part by the oligomerization of long stretches of triple-helical coiled coils. A pentameric coiled-coil bundle (b). Self-assembled synthetic collagen triple helices (c) have been utilized for producing collagen-mimetic biomaterials. β-sheet fibrillization ((d) side view; (e) axial view illustrating twist) has been a heavily investigated mechanism of self-assembly for peptide biomaterials. Figures created using PyMOL, Delano Scientific.

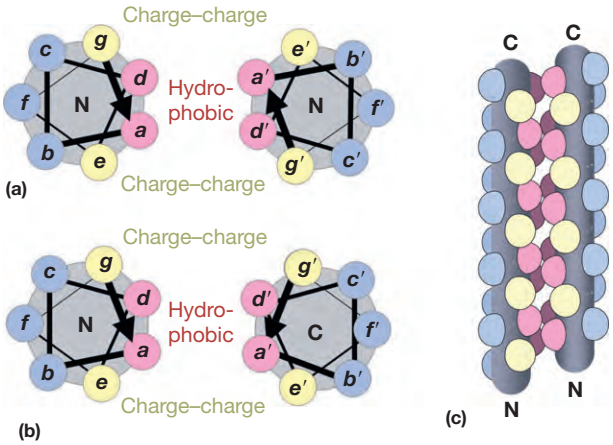

Figure 5 Coiled-coil helical wheel projections (a, b). Residues in *a* and *d* positions form hydrophobic contacts between helices. In parallel coiled-coil dimers (a), residues in *d* positions make closest contacts with those in *d*′ positions, located diagonally across the hydrophobic interface when depicted in helical wheel diagrams (the prime denotes the second helix). Residues in *a* positions make closest contacts with residues in *a*′ positions. Conversely, in antiparallel coiled-coil dimers (b), residues in *d* positions make close contact with residues in *a*′ positions (again located diagonally across the hydrophobic interface in helical wheel projections), and vice versa. Residues in *g* and *e* positions participate in Coulombic interactions to stabilize coiled-coil folding, with residues in *g* positions interacting with residues in *e*′ positions in parallel bundles (a). In antiparallel bundles, *g*–*g*′ contacts and *e*–*e*′ contacts are made. Part (c) adapted from Arndt, K. M.; Pelletier, J. N.; Müller, K. M.; Alber, T.; Michnick, S. W.; Plückthun, A. *J. Mol. Biol.* **2000**, *295*, 27–639, with permission from Elsevier.

the ***e*** and ***g*** positions have shown that a Lys-Glu pair is more stabilizing in the E***e***–K***g*** position as compared to K***e***–E***g*** position,[55] and amino acids in ***b***, ***c***, and ***f*** positions can be specified to guide lateral assembly into higher-order coiled-coil structures.[56–58]

To specify the alignment of helices with respect to each other axially, one strategy has been to place polar residues, such as Asn, in putative nonpolar ***a*** or ***d*** positions. Alignments between multiple helices that position two or more of these nonpolar residues together in the hydrophobic core are then less destabilizing than independently acting buried polar residues.[53,59] Even when buried polar residues are paired, however, some degree of destabilization results, so a compromise must be made between coiled-coil stability and registration in this design strategy. Peptide length is also a factor that impacts coiled-coil stability, and it is generally challenging to produce stable coiled-coil bundles with fewer than three complete heptads.[60] Peptides as short as fourteen amino acids have been designed de novo, however, and in some cases lengthening a coiled-coil peptide can destabilize it if it is only moderately stable to begin with, illustrating some exceptions to this rule.[61,62] For a more extensive discussion of coiled-coil folding and design in the context of biomaterials construction, see Apostolovic *et al.*[63]

2.205.3.3. Biomaterials from Coiled Coils

The relative simplicity of coiled-coil structures compared to more complex folding of proteins has led to extensive use of coiled coils as components of self-assembling biomaterials. Several computational programs like 'COILS,'[64] 'PAIRCOIL,'[65] and 'MULTICOIL'[66] have been developed that aid in the selection and design of such peptides. For biomaterials, one of the critical issues regarding the use of coiled coils as oligomerization domains is how to connect them into extended networks. To this end, several strategies have been developed for producing fibers, fibrils, or cross-linked structures capable of behaving as gels. These approaches can be categorized into several groups, including expressed proteins, peptide–polymer conjugates, and short peptides that form coiled-coil fibers (**Figure 6**). In high enough concentrations, each of these types of molecules is capable of forming gels that can be used as biomaterials.

Peptide–polymer conjugates and proteins capable of forming gels through coiled-coil assembly have been based significantly on designs having terminal helical peptide sequences flanking a central hydrophilic and disordered sequence (**Figure 6(b)**). Oligomerizaiton of the helical portion of such proteins into coiled coils in water produces viscoelastic materials.[68] Hydrophilic polymers with side chain helical peptides have also been developed (**Figure 6(a)**), and assembly of the helical peptides into coiled coils likewise can produce hydrogels.[67] Combining peptide sequences with polymers not only provides control over structure but also allows the incorporation of biologically interactive materials. In tissue engineering applications, hydrogels based on the coiled-coil peptide motif conjugated to HPMA[67,71,72] and PEG[69] have been reported by Kopecek and coworkers and Collier and coworkers, respectively. Properties such as temperature responsiveness, swelling behavior, and viscoelasticity can be tuned on the basis of peptide design and the number of peptide grafts on each polymer chain.[71–74] Since their introduction in the late 1990s, the designs of both protein-based and peptide–polymer coiled-coil biomaterials have been systematically improved.[73] Recent advances have included strategies for regulating the interconnectivity between the coiled-coil domains, including minimizing the formation of short loops or intramolecular helical bundles. Both intramolecular assembly and loops can

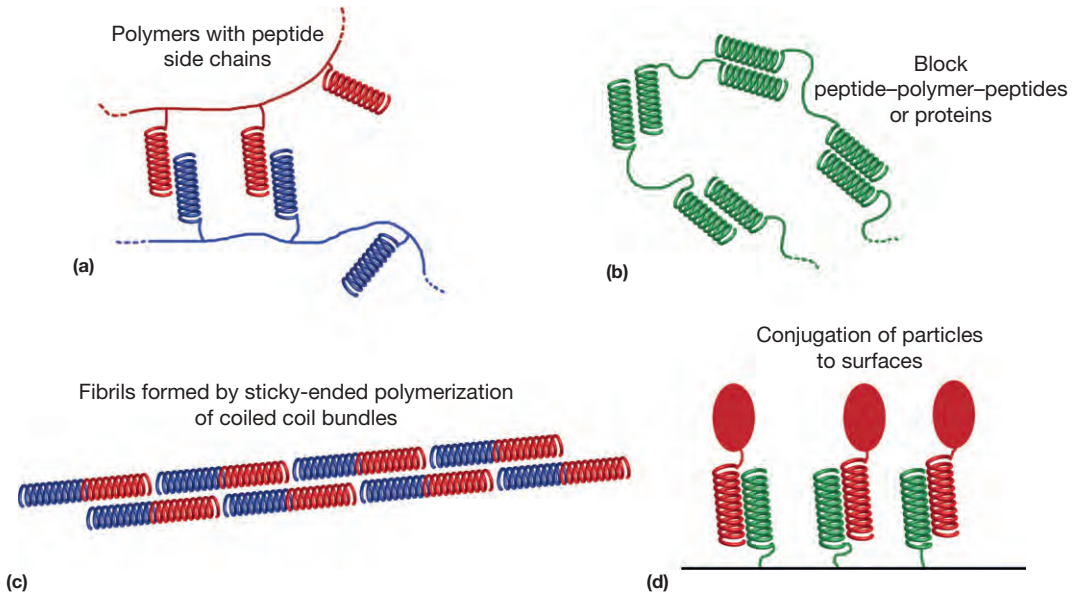

Figure 6 Coiled coils as oligomerizing domains for self-assembled biomaterials. Strategies that are capable of forming biomaterials and gels include polymers with side chain helical peptides that cross-link via coiled-coil oligomerization (a),[67] peptide–polymers or expressed proteins that have terminal helical peptides separated by a random-coil central domain (b),[68,69] and long fibrous bundles formed by the 'sticky-ended' noncovalent polymerization of coiled-coil bundles (c).[56] Coiled coils may also be used to attach proteins or particles to surfaces (d).[70]

compromise the gels' mechanical properties, so strategies for reducing them have been important for enhancing the robustness and lifetime of coiled-coil materials.[75] Also, covalent cross-linking has been employed to minimize any rearrangements in the supramolecular assemblies that could cause individual molecules to pull out of the extended network. Such covalently linked coiled-coil assemblies have been used to generate stable coatings for biomaterials.[76]

Although most approaches for producing gels have utilized polymers or randomly structured protein chains to link coiled coils together into extended networks, a recent strategy utilized coiled-coil peptides as the sole structural components (**Figure 6(c)**). Peptides were designed that polymerized via coiled-coil bundles with 'sticky ends,' or single-helix overhangs, and the fibrils themselves further assembled to form fibers and other laterally entangled networks.[56,77] By specifying the extent of lateral assembly through the selection of appropriate ***b***, ***c***, and ***f*** residues, hydrogels could be produced that were amenable to cell culture. Variants of this strategy have also been developed for introducing kinks,[78] branches,[79] and fiber-recruiting peptides into these scaffolds,[80] illustrating the diverse topologies that may be possible in this system. Beyond their use as gel materials, coiled coils have also been used for the controlled oligomerization of nanoparticles[70] and proteins,[81] for the attachment of proteins onto surfaces,[82] and the binding of nonbiological cofactors.[83]

2.205.3.4. Self-Assembling Peptides Based on β-Sheet Fibrils

The β-sheet fibril has received considerable attention as an engineered biomaterial. β-sheets are formed by adjacent parallel or antiparallel peptide strands that are hydrogen bonded in a 'pleated' conformation.[84,85] In β-sheets, the backbone N–H and C=O of one strand hydrogen bond with the C=O and N–H of an adjacent strand, respectively, and the side chains project alternatively above and below the plane of the sheet. Although this hydrogen bonding pattern between peptide backbones is the defining characteristic of β-sheets, the structure is also reinforced by hydrophobic interactions, van der Waals forces, and electrostatic interactions that occur between the side chains and between the side chains and backbone. Most sheets also have a twist of 0–30° between consecutive strands.

It is known that certain patterns of polar and nonpolar amino acids favor the formation of β-sheet structures.[86] Peptides with strictly alternating polar and nonpolar residues, for example, can produce β-sheet fibrils, and many such peptides have been utilized in the construction of self-assembling biomaterials.[87] In a β-sheet with alternating polar/nonpolar sequences, all hydrophobic residues are placed on one side of the sheet, and all hydrophilic residues are placed on the opposite side, providing an amphiphilic surface that drives assembly into tertiary structures such as fibrils. However, alternating sequences do not always result in well-defined sheets,[88] and many β-sheet fibrillizing peptide sequences that do not strictly adhere to the alternating polar/nonpolar design have been described.[3,4,89–97] Despite the wide range of primary sequences that can form β-sheet fibrils, once they are fibrillized, they can be very difficult to distinguish on the basis of their morphology. β-sheet fibrils are highly consistent in their morphology, even when constructed from unrelated peptides or proteins. The fact that there exist so many peptides of varying sequences, lengths, and patterning of polar and nonpolar residues that form β-sheet fibrils suggests that β-sheet assemblies can tolerate a variety of appended sequences or other modifications. This property has been capitalized on in recent years to produce functionalized β-sheet fibrillar biomaterials, as described below. β-sheet fibrils tend to be relatively unbranched, laterally entangled, about 8–15 nm wide, and up to several microns long. Individual peptide strands run perpendicular to the fibril axis, although the parallel-versus-antiparallel topography can vary, as can the presence of turns or hairpins at the fibril edge. In millimolar concentrations, such peptides tend to form gels in water.

One of the most useful features of β-sheet fibrillizing peptides is that their assembly is highly dependent on solution conditions, including ionic strength and pH. This sensitivity can in turn be used to design systems that assemble under defined stimuli or triggers.[98] Salt-sensitive assembly was systematically studied for the peptide $(FKFE)_3$. For this peptide, it was found that the critical salt concentration for inducing assembly was highly dependent on the salt's valency, with higher valencies inducing assembly at lower concentrations.[99] These findings were in agreement with the Derjaguin–Landau–Verwey–Overbeek (DLVO) theory and the Schultz–Hardy rule. It was also found that increasing the hydrophobicity of the residues in the nonpolar amino acid positions decreased the critical salt concentration, also consistent with DLVO theory.[99] Such salt sensitivity also has a unique advantage with regard to β-sheet peptide use as biomaterial scaffolds, as it enables *in situ* gelation when injected into the body. For example, Lee and coworkers utilized the conditional gelation of RADA-16 peptides to deliver injectable peptide scaffolds to the myocardium in small animal models.[100,101]

Early work developing β-sheet fibrillar biomaterials was conducted in the 1990s based on peptides having strictly alternating polar/nonpolar sequences and electrostatic complimentarity between residues in the polar positions.[87,102] These materials produced hydrogels, which in subsequent years have been explored in many different contexts and with many different modifications. Among these materials has been the commercially available PuraMatrix™. β-sheet fibrillizing peptides can be extended at either the C-terminus or the N-terminus with a variety of ligand sequences (e.g., RGD, IKVAV) so as to integrate specific functionality into the scaffold. Successful applications of such ligand-decorated fibrils include their use to specify the adhesion and proliferation of fibroblasts[92]; the proliferation of endothelial cells[3,4,103]; the proliferation, differentiation, and migration of osteoblasts[104]; or the adhesion and differentiation of neural cells.[105,106] Currently, it is not precisely known in detail what structural impact such terminal decoration of β-sheet fibillizing peptides may have on their topology, strand orientation, and lateral aggregation, but in many cases any disruption of fibrillization appears to be minimal. As an example, the self-assembly of the peptide Q11 (QQKFQFQFEQQ) appears to tolerate the inclusion of N-terminal ligand sequences without significant disruption of fibrillization (**Figure 7**). Co-assembly of ligand-bearing Q11 peptides (e.g., GGRGDSGGG-Q11 or GGIKVAVGGG-Q11)

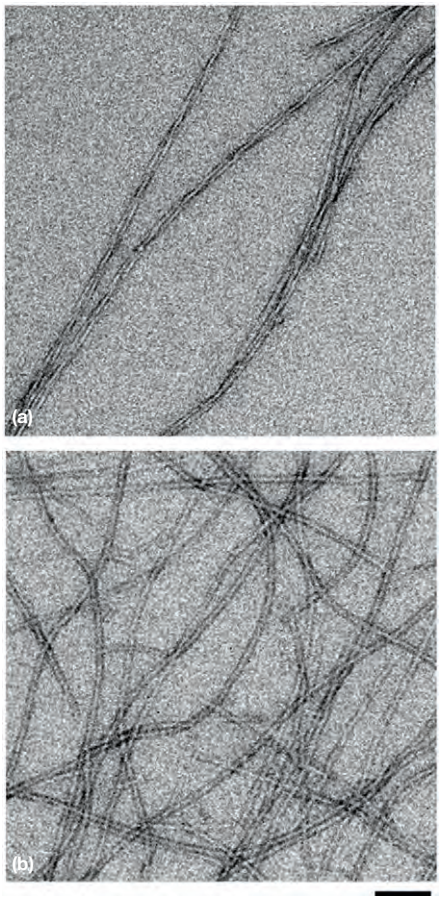

Figure 7 TEM images of β-sheet fibrillar peptide assemblies. Shown are Q11 (a), and OVA-Q11 (b). Scale bar = 100 nm. Reproduced with permission from Rudra, J. S., Tian, Y., Jung, J. P., Collier, J. H. *Proc. Natl. Acad. Sci. USA* **2010**, *107*(2), 622–627.

into backgrounds of unmodified Q11 in ratios of up to at least 10% afforded mixed fibrils with similar secondary structure by CD, similar mechanical properties by oscillating rheometry, and similar nanostructure by TEM compared to 100% unmodified Q11 fibrils.[3,4] The fibrillization of Q11 is also tolerant to the inclusion of N-terminal Cys residues and C-terminal thioesters for covalent stabilization via native chemical ligation,[93] or even 17-residue immune epitopes (Figure 7).[97] In all of these cases, nanofibers are formed in physiological buffers that are morphologically similar to those of unmodified Q11. As discussed below, this enables the production of multipeptide materials with modular construction via noncovalent coassembly.[107] There is also strong evidence that Q11 sequences bearing N-terminal ligands or epitopes display a significant proportion of the epitope sequence on the surface of the fibrils, confirmed with ELISA[97] and immunogold labeling[3,4,97] (Figure 8). For these reasons, β-sheet fibrillizing peptides appear to be a versatile system for the display of a multitude of ligands or chemical functionalities on nanofibers. Other self-assembling biomaterials employing β-structure have included peptide–polymers such as tetraphenylalanine–PEG conjugates.[108,109] Such materials assemble into fibrils, nanotubes, and hydrogels via the formation of antiparallel β-sheets

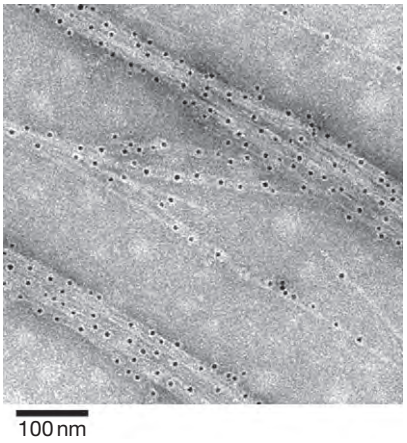

Figure 8 β-sheet fibrillizing peptides bearing functional amino acid ligands on their termini are capable of displaying those ligands on the surface of the self-assembled fibrils. Shown is biotinylated GGRGDSGGG-(Q11), labeled with avidin-conjugated gold particles in a TEM image.

and π–π interactions. Superstructures of hybrid copolymers containing β-strand peptides and PEG in alternating blocks have also been investigated by Klok and coworkers.[110]

2.205.3.5. Self-Assembling Peptides Based on Collagens

Although β-sheet fibrils and α-helical coiled-coil materials have been two of the most intensively investigated peptide-based self-assembling biomaterials, other peptide folds have been employed, including collagen-like folding. Collagens are defined by their characteristic triple helix structure, in which three peptide strands form left-handed polyproline II-type helices that coil around each other to form a right-handed triple helix (Figure 4(c)). Collagens have a primary structure of XaaYaaGly tandem repeats, Gly being required in every third position owing to the tight packing between the helices. Amino acids in the Xaa positions tend to be proline, and amino acids in the Yaa positions tend to be hydroxyproline, with Pro-Hyp-Gly being the most common XaaYaaGly repeat in fibrillar collagens (Figure 4(c)). In contrast to β-sheet fibrils and coiled coils, which are substantially reinforced by hydrogen bonding and hydrophobic interactions, collagen triple helices are noncovalently stabilized by stereoelectronic effects and by only one interstrand hydrogen bond per triplet (for review, see Shoulders, and Raines[111]). Self-assembly of triple helices during natural collagen production in tissues is initiated intracellularly by the binding of the C-terminal regions of the collagen propeptides, which brings the three chains in proximity and templates the coiling and winding of the triple helix towards the N-terminus. During this process, prolyl hydroxylases and lysyl hydroxylases modify proline and lysine residues, respectively, producing hydroxyproline and sites for glycosylation. Once the trimer is folded, it is exported to the extracellular space, where the globular domains of the N- and C-termini are cleaved, an event that enables the fibrillization of the collagen into the classic banded structure observable by transmission electron microscopy (TEM), atomic force microscopy (AFM), and other techniques. Owing to the involved

process by which collagen is synthesized naturally and the relative inability of small collagen-like peptides to template their own self-assembly in the absence of such processes, it has been somewhat challenging to produce gelled self-assemblies of short peptides based entirely on the folding of the collagen triple helix. Strategies to provide additional structure stabilization are necessary to assemble short collagen-like peptides into network-forming biomaterials.[112] This is reflected by the relatively fewer examples of successfully synthesized collagen peptide-based gels in comparison to those based on β-sheet fibrillar peptides or coiled-coil peptides. Nevertheless, the centrality of collagens as the most abundant protein in animals, their usefulness in tissue engineering applications, and the difficulty of producing them recombinantly make collagen-mimicking peptide biomaterials extremely attractive targets for synthesis. One early example of synthetic peptide-based collagen-like fibrils utilized native chemical ligation to polymerize collagen-related peptides into long polymers, which formed fibers (Figure 9(d)).[116] In another approach analogous in some ways to the production of sticky-ended coiled-coil bundles described above, Raines and coworkers designed trimers of collagen-related peptides linked by a disulfide knot such that they contained single-helix overhangs (Figure 9(a)).[113] This covalent preorganization of the collagen peptide trimers enabled the assembly of fibers over 400 nm long. Similar sticky-ended disulfide-linked trimers have been utilized recently to produce hydrogels,[117] and to host the integrin-binding, collagen-derived sequence GFOGER for improved cell attachment.[118] Other strategies for stabilizing the folding and assembly of short collagen peptides have included the use of electron-poor pentafluorophenyl groups and electron-rich phenyl groups at either terminus of the peptide to promote assembly via π-stacking (Figure 9(c)),[114] or the inclusion of charged residues at the peptide termini to similarly promote assembly through electrostatic interactions (Figure 9(b)).[115] In another strategy that combined the chemical definition of synthetic peptides with the mechanical stability of full-length collagen, functionalized collagen-mimetic peptides were intercalated into collagen fibers by thermally unfolding the collagen and cooling it in the presence of the peptides. In this way, the peptides co-assembled into the full-length protein to provide decorated collagen fibrils.[119,120]

2.205.3.6. Self-Assembling Peptide Amphiphiles

Peptide amphiphiles (PAs) are molecules that contain a hydrophilic peptide head group and one or more hydrophobic alkyl tails. They can self-assemble into a variety of nanostructures including micelles, vesicles, bilayers, and nanofibers.[121] Fibrillizing systems in particular have received the most interest as biomaterials, owing to their ability to form gels by fibril entanglement at low millimolar concentrations. Such materials have been extensively studied as 3D substrates for cell culture and as matrices for regenerative medicine.[122–126] Several features of PAs have been shown to be important in their assembly.

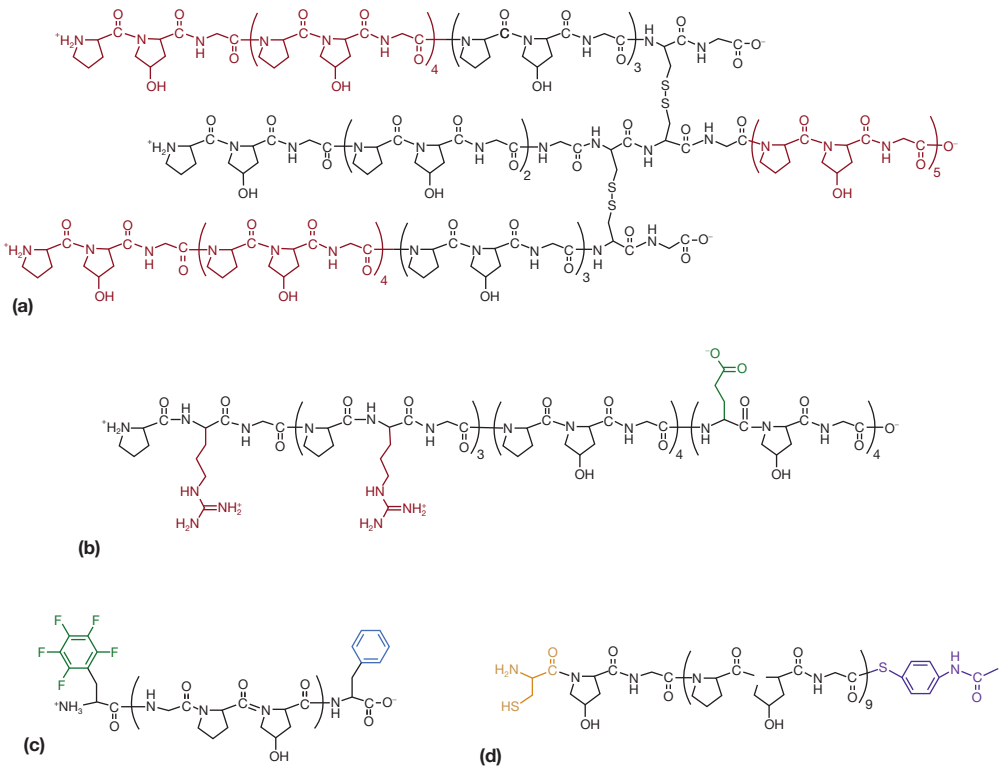

Figure 9 Strategies for producing biomaterials from synthetic collagen-mimetic peptides. Long fibrils can be produced via the sticky-ended assembly of disulfide-linked trimers with staggered single helix overhangs (a).[113] Peptide alignment and templating of triple helix formation can be achieved for collagen-mimetic peptides with charged residues placed at the peptide termini (b)[114] or through π-stacking between electron-poor pentafluorophenyl groups and electron-rich phenyl groups (c).[115] Long polymers of collagen-mimetic peptides have been obtained through the polymerization of such peptides by native chemical ligation (d).[116]

First, clustering of the hydrophobic tails of peptide amphiphiles stabilizes the 3D structure of the peptide head group, and an overall conical shape of the molecule favors fibrillization rather than membrane or micelle formation.[127–129] At the same time, recent studies have shown that the secondary structure of the peptide domains also plays an essential role in PA self-assembly.[130] Residues closest to the hydrocarbon tail, and thus closest to the nanofiber core, are involved in hydrogen bonding similar to β-sheets. By investigating peptide amphiphiles with N-methylated amino acids, it was shown that disruption of hydrogen bonding in this region resulted in spherical micelle formation rather than fibrillar assembly.[131] In addition, the morphologies of the fibrils produced by both PAs and by β-sheet fibrillizing peptides lacking hydrocarbon tails are similar when viewed with AFM or TEM.[107]

One of PAs' most useful features has been their demonstrated amenability to terminal functionalization with a wide variety of ligands and chemical groups. For example, several different cell-binding peptide ligands such as RGDS and IKVAV have been incorporated into the head groups of peptide amphiphiles and have been shown to promote cell adhesion and differentiation.[123,125,132] More recently, PAs displaying peptide sequences having cytotoxic characteristics have been investigated as cancer therapeutics,[133] and PAs with other terminal functionalities including heparin-binding peptides, growth factor-binding peptides, and hydroxyapatite-nucleating peptides have been explored in a variety of applications within regenerative medicine.[124,126,134–136] Within these investigations, one particularly useful modification of the basic PA design has been to incorporate enzyme substrates that allow them to be degraded by matrix metalloproteinases *in vivo*.[137] Given the generally slow degradability of β-rich assemblies, this is a significant advancement.

2.205.3.7. Self-Assembling Peptides with Aromatic Groups

Short peptides containing aromatic groups have been shown to assemble into fibrils. For example, diphenylalanine can self-assemble to form peptide nanotubes through a combination of hydrogen bonding and π-stacking.[138–141] Because of the combined effects of these noncovalent forces, at sufficient concentrations aromatic short peptides can form gels having storage moduli between 2 and 10 kPa.[142] The fibrillar morphology of these types of materials can be variable with pH[138,142] and solvent polarity,[139,143] and their assembly can be triggered through stimuli such as enzymatic action.[144] Xu and coworkers have utilized a complementary pair of kinase/phosphatase enzymes to assemble and dissemble Fmoc-tyrosine and napthyl-pentapetides.[71,72,140] The tyrosine residues can be dephosphorylated by a phosphatase to induce gelation, and a kinase can be used to reverse the process. The structures obtained through enzyme-mediated assembly were found to be more uniform than those obtained with pH switching.[71,72] In another work, enzyme substrate activity was provided for self-assembling Fmoc-peptides using the thermolysin substrate Gly-Phe-Cys. In this work, the Fmoc-peptides were conjugated to gold particles to produce optical enzyme sensors.[145] For biomaterials applications, short peptides with aromatic groups form gels capable of supporting cell culture. Gels of Fmoc-FF supported the growth of chondrocytes in 2D and 3D cell cultures.[138] These systems, like longer β-sheet fibrillizing peptides, are also amenable to modification, as shown by the fact that mixtures of Fmoc-FF peptides and Fmoc-RGD peptides could be co-assembled in order to present the RGD ligand on the surface of the fibrils. Such fibrils were competent for modulating the adhesion of dermal fibroblasts through specific RGD-integrin binding, with subsequent cell spreading and proliferation.[146] Short dipeptides that self-assemble through aromatic interactions are attractive alternatives to longer peptides and folding motifs, as the small size of the molecules can reduce synthesis costs while still providing for mechanisms of stimulus-responsiveness, bioactivity, and gel formation.

2.205.3.8. β-Hairpins

β-Hairpins are secondary structures formed by two antiparallel β-sheet strands with only 2–5 intervening residues forming a turn between them. Schneider, Pochan, and coworkers have designed and investigated MAX1, a peptide containing alternating lysine and valine residues on either side of a β-turn on the basis of a D-Pro-L-Pro sequence.[88,147] Other variations of the MAX1 peptide include MAX2/MAX3[148] and photocaged MAX7,[149] whose gelation properties can be triggered by heat and light, respectively. Gelation of these β-hairpins can be induced by the addition of cell culture media, and rheological studies have shown that under various conditions they possess storage moduli in the 1–10 kPa range or greater, making them attractive as tissue engineering scaffolds.[150] β-Hairpins are noncytotoxic and biocompatible with mammalian cells, but some have been shown to be selectively toxic to gram-positive and gram-negative bacteria, making them attractive candidates for regenerative medicine applications under conditions that may not be entirely sterile.[151] Mesenchymal stem cells have also been encapsulated within β-hairpin hydrogel networks, which were then shear-thinned and delivered to target sites via a syringe. After injection, the cells remained viable and the resolidified construct remained intact.[152] To achieve stiffening of β-hairpin networks in a reversible fashion, borate ion complexation has been employed to form physical cross-links between lysine residues.[153] Other means to modulate the materials' viscoelasticity has included substitution of lysine residues with negatively charged glutamic acid residues, which has led to faster gelation and stiffer gels.[152] Controlling the gelation rate in this way enabled cell encapsulation without cell aggregation or sedimentation. In sum, β-hairpins have proven to be a flexible, modifiable platform for producing chemically defined self-assembled biomaterials.

2.205.3.9. Proteins

Although the bulk of self-assembling biomaterials to date have focused on synthetic molecules such as peptides and peptide–polymers, or proteins that oligomerize through discrete peptide folds such as coiled coils, these materials fall short of biological supramolecular assemblies in terms of complexity and exquisite control over folding and specificity. In contrast, biological assemblies such as viral capsids (see Chapter by Schaffer *et al.*), extracellular matrices, and the cytoskeleton are formed by the self-assembly of multiple protein constituents with highly specific affinities for each other.

Inspired by these natural protein networks, a number of strategies have been developed to induce or control self-assembly into materials using designed proteins. A few examples will be provided here. For a more detailed review, see Papapostolou and Howorka.[154] One approach has been to place cysteine residues on opposing sides of a protein, which can be further functionalized with specific ligands such as biotin. This bivalent unit can then be self-assembled with tetravalent streptavidin to form a network of proteins.[155] Another approach has been to remodel patches on protein surfaces into contact sites. Using site-directed mutagenesis, the contact sites for the naturally occurring octamer Rua-B were engineered to assemble into fibers of associated octamers.[156] In other approaches, self-assembling proteins with different oligomerization valencies were fused recombinantly, and the resultant fusion proteins could be self-assembled into geometrically defined nanoscale polyhedra.[157] In biomedical applications, self-assembled proteins have been useful as epitope carriers for vaccine development. As an alternative to inactive viruses, noninfectious adenoviruses,[158,159] tobacco mosaic virus capsids,[160] and planar S layer lattices[161] have been used as carrier proteins for pathogen-specific epitopes. The spatial repetition of the epitope is known to enhance immune responses relative to the free antigen.[162] Self-assembling proteins have been exploited in variety of other biologically relevant applications, including biotemplating of nanoparticles,[163] selective removal or concentration of ions,[164] and templates for metallic nanotubes.[165,166]

2.205.4. Modulating the Mechanics of Self-Assembling Systems

It is increasingly appreciated that viscoelasticity can play a fundamental role in the behavior of cells in contact with materials.[167,168] In 3D self-assemblies, recent work has focused on modulating viscoelasticity so as to provide a means, along with ligand presentation, for directing cell behavior. One challenge associated with self-assemblies is that they are constructed predominantly with noncovalent bonds, so their strength, elasticity, and moduli tend to be somewhat lower than those of gels or materials made from higher molecular weight polymers. This poses a practical problem for creating devices that can mechanically withstand the forces involved in their placement and operation within specific tissue sites, and it also reduces the ability to adjust stiffness to favor particular cell behaviors.

In 3D self-assemblies, viscoelasticity can be controlled through several routes, including modulating the stiffness of individual self-assembled components (e.g., fibrils), controlling the strength and degree of lateral interactions of these fibrils, and establishing covalent cross-linking between fibrillar elements. Before such strategies are employed, however, often an initial goal is to render the mechanical properties of a self-assembly consistent, regardless of the types of ligands or functionalities co-assembled into it. To accomplish this, the most common approach has been to dope ligand-bearing or otherwise functional peptides into a background of nonfunctionalized base material. Ligand-bearing β-sheet peptides or peptide amphiphiles can be co-assembled with unfunctionalized β-sheet peptides or peptide amphiphiles to entrap the ligands within the self-assembles while minimally perturbing gel mechanics.[3,4,146,169] Such a strategy has been applied to β-sheet peptides,[3,4] peptide amphiphiles,[169] and short peptides with aromatic sequences.[146] For example, the β-sheet fibrillizing peptide Q11 can tolerate the inclusion of N-terminal cell binding peptide ligands such as RGDS or IKVAV in concentrations that significantly modulate cell attachment and growth without influencing storage modulus.[3,4] An analogous approach in SAMs is to dope a ligand-bearing alkanethiol into a background of nonfouling oligo(ethylene glycol)-terminated alkane thiol, but in this case the goal is to minimally perturb the SAM's nonfouling character, not its mechanics.[8]

Once a reproducibly stiff matrix has been established, modulation of its viscoelastic properties can be achieved either by adjusting the noncovalent lateral associations of self-assembled elements, or by establishing covalent bonds within the network. One of the simplest ways to increase the stiffness of self-assembled matrices is to increase the peptide or protein concentration.[93,146,169] The mechanics of most fibrillar self-assemblies are significantly dependent on total peptide concentration, although the topographical details of fibril entanglement as a function of concentration have not yet been worked out for most systems. Although concentration modulation can be an effective way of specifying mechanics, an upper limit of stiffness is reached at the point where the peptides are no longer soluble. Large changes in total peptide concentration are also undesirable if there is a need to control matrix stiffness without affecting other parameters such as network topology or porosity.

Efforts to specify the lateral aggregation of self-assembled fibrillar elements have included work with the MAX1 β-hairpin system, in which single amino acid substitutions have been employed to modulate the Coulombic interactions involved in intramolecular folding and fibrillization.[152,153,170] By installing a Glu residue at a previous Lys position in the $(Lys\text{-}Val)_2$ β-strand portion of the molecule, intramolecular folding could be significantly accelerated, leading to faster gelation kinetics and stiffer gels. Overall, the morphology of the β-sheet fibril did not change with this Lys→Glu substitution, indicating that the number of physical cross-links may have been increased owing to the faster gelation kinetics. Importantly, the speed with which the modified hairpin gelled and the ultimately stiffer material enabled cell encapsulation in 3D. In contrast, the unmodified MAX1 hairpin gelled so slowly that cells sedimented before they could be encapsulated.[152] In an example of modulating lateral assembly in self-assembled gels based on coiled coils, Woolfson and colleagues modified the charged and polar residues found in ***b***, ***c***, and ***f*** helix positions so as to avoid fiber coarsening.[56] The resultant materials formed hydrogels with rapid enough gelation kinetics to allow 3D cell encapsulation. Viscoelasticity can also be modulated through ion complexation, as has been demonstrated with MAX1 β-hairpins and borate complexation[153] as well as with β-sheet fibrillizing peptides and the complexation of phosphate or magnesium ions.[171]

Several covalent strategies have been reported for stiffening self-assembling biomaterials, including disulfide bond formation[171] and native chemical ligation.[93] In the native chemical ligation strategy, matrix stiffening was achieved by engineering a C-terminal thioester and an N-terminal cysteine into the

self-assembling peptide Q11. Ligated Q11 gels showed a five-fold increase in storage modulus and were able to support significantly enhanced endothelial cell proliferation compared to less stiff gels. The chemistry was also orthogonal to the inclusion of ligand-bearing Q11 derivatives, and gels doped with RGD-Q11 showed even greater endothelial cell proliferation and CD31 expression compared to those with RGD or ligation alone.[93] Such a co-assembling strategy enables increasingly systematic fine-tuning of scaffolds for applications ranging from 2D cell culture scaffolds to tissue engineering, and the degree of functionalization that can be incorporated into these materials has only begun to be exploited.

2.205.5. Advantages Provided by Self-Assembled Systems for Biomaterials Applications

One of the most significant advantages of self-assembling strategies is that they can lead to complex, multicomponent materials starting with a discrete, chemically defined set of molecules. Chemical definition in turn enables precise investigation, experimentation, and optimization in applications ranging from cell culture to *in vivo* cell therapies. Contrasting with the chemical definition of self-assemblies, the most utilized materials for providing multicomponent scaffolds for cells have traditionally been biologically derived biopolymers. For cell culture, such materials include collagens, alginates, and the mixture of proteins that constitutes Matrigel. Matrigel is a heterogeneous mixture of glycoproteins secreted by Engelbreth–Holm–Swarm mouse sarcomas.[172,173] It is rich in laminins and other basement-membrane proteins, and it has been a centrally important material for the development of 3D cell culture models and cell–matrix investigations. Its usefulness in these contexts cannot be overstated, but at the same time, Matrigel's compositional heterogeneity, its incomplete definition, and its batch-to-batch variability have made it a challenging material for engineering applications. Moreover, its xenogeneic nature makes it problematic for use in humans. Self-assembling materials contrast with the heterogeneity of such naturally derived biopolymer matrices. What chemical definition affords is the ability to choose to include, at a predetermined dose, any number of therapeutic or biologically active ligands or chemical groups of interest, while at the same time definitively excluding any other molecules that may confound investigation of the biological process of interest. Small molecular weight contaminants, opsonins, residual growth factors, cytokines, and unknown low-concentration matrix components are all possible constituents in naturally derived biopolymers that can significantly derail or complicate both basic investigations and development efforts. Further, given that biological processes occur in an extremely complex milieu of soluble and insoluble factors, any opportunity to reduce or specify such complexity facilitates the engineering of these systems. For both 2D and 3D self-assembled biomaterials, such considerations have been a major driving force behind their development. As one example, SAMs with chemically and spatially defined regions of cell adhesiveness allow one to force a population of cells to assume nearly identical geometries, so that statistical distributions in the precise arrangement of multiple cells' cytoskeletons can be revealed.[18] In unpatterned substrates, such analyses cannot be accomplished in a straightforward manner.

On the other hand, instead of rendering culture surfaces highly uniform, the modularity of many 3D self-assembling systems can also enable combinatorial or high-throughput analyses of multicomponent matrices. The noncovalent construction of scaffolds that are created from the co-assembly of more than one molecular constituent enables the production of a limitless range of different ratios of assembled ligands or chemical features, simply by mixing and inducing co-assembly. For ligand-bearing β-sheet peptides, this can be achieved by dissolving them in water, mixing them in specified ratios, and gelling the mixture with buffers or culture media.[3,4] Many other 3D cell culture matrices currently used or under development such as polymer hydrogels are produced as integrated, covalently connected materials, so production of a range of formulations would be less straightforward than in co-assembling systems. In addition, many advantages of synthetic systems, including the possibility for incorporating nonnative amino acids or chemical modifications, are retained in self-assembling biomaterials.

Noncovalent interactions are sensitive to solution conditions, including pH, temperature, ionic strength, and others, providing opportunities for rendering self-assembling biomaterials stimulus-sensitive. As an example, β-sheet fibrillar self-assembly could be rapidly triggered under the stimulus of warming from room temperature to body temperature, or by near-infrared light.[98] In this approach, calcium ions capable of inducing self-assembly were sequestered away from the peptide within liposomes that had been engineered to be either light- or temperature-sensitive. Application of the relevant stimulus initiated the release of the ions into the extravesicular space, leading to rapid gelation. Triggered gelation through the addition of salt-containing buffers has also been widely used to produce 3D cell culture matrices.[3,4,88,93,106,125,137] Similarly, delivery of unassembled peptides to tissue sites can induce gelation upon contact with the high osmolarity and neutral pH of the physiological milieu.[100,101,126] Stimulus-sensitive peptide self-assembly has been reviewed recently.[174]

A final advantage of self-assembled biomaterials is that they are highly multivalent. This can be used to enhance the activity of ligands or peptides that have relatively low affinities. For example, high epitope density has been utilized to promote neuron regeneration using peptide amphiphiles bearing the laminin-derived IKVAV sequence.[124,126] It is also likely that the antibody production elicited by OVA323-339-conjugated Q11 peptides was a result of the materials' high degree of multivalency.[97] As another example in α-helical designed proteins, multivalency and control over the precise distance between charged groups or saccharides have been utilized to significantly increase affinities for biological toxins, such as the cholera toxin.[175,176] Highly multivalent materials have also been reviewed for targeted delivery recently.[177]

2.205.6. Immune and Inflammatory Responses to Self-Assembling Materials

All biomaterials have a potential to interact with inflammatory or immune processes, and such interactions will be decisive factors regarding their clinical usefulness.[107,178] Initial

investigations of self-assembled biomaterials *in vivo* have been encouraging as almost all reported studies have found them to be minimally immunogenic.[3,4,100,101,106] RAD16-II peptide fibrils injected within rat[101] or mouse[100] myocardium have been found to elicit negligible immune or inflammatory responses. Low antibody titers have also been reported for RAD16 peptides in rabbits and goats,[106] and nitric oxide-releasing peptide amphiphiles were well tolerated in rats.[179] Both the self-assembling peptide Q11 and the RGD-bearing variant GGRGDSGGG-Q11 were nonimmunogenic when delivered to mice subcutaneously.[3,4] In sum, almost all reports of self-assembled peptide biomaterials *in vivo* have indicated minimal or negligible responses. These findings prompted a study to test the extent to which even known T and B cell epitopes presented on self-assembled peptide fibrils could be tolerated (**Figure 10**). This series of experiments sought to clarify whether or not the minimal immunogenicity of self-assembled fibrils was a general property. Interestingly, when a peptide from chicken egg ovalbumin ($OVA_{323–339}$) containing known B and T cell determinants was fused to Q11 and delivered subcutaneously to mice, strong antibody responses were observed without any adjuvant.[97] The anti-OVA titers were comparable to the free peptide administered in complete Freund's adjuvant (CFA), one of the strongest adjuvants known. In contrast, the unmodified self-assembling peptide Q11 was nonimmunogenic by itself, even when administered in CFA, illustrating that Q11 was a very poor immunogen without an attached epitope. Furthermore, these high antibody titers were completely abrogated when mice were immunized with mixtures of free OVA peptide and Q11, suggesting that self-assembly and fibrillization were critical to the observed antibody responses. No cytokine production was detected in peptide-challenged cultures of splenocytes of mice immunized with OVA-Q11, which might have indicated that T cells were not significantly involved in the response, but this mechanism continues to be under investigation.

In the absence of strong epitopes, self-assembled peptides are useful as scaffolds for regenerative medicine, as has been demonstrated in several animal models.[100,101,126,179] As these efforts move forward, continued avoidance of strong epitopes may be a significant factor to consider, and it may even be possible that a mild antibody response could be acceptable in the context of the regenerative processes that many of these materials seek to promote. At the same time, owing to their ability to act as adjuvants for strong epitopes, self-assembled peptides may also be useful in immunotherapies or for raising antibodies in animals. Currently, the development of peptide-based vaccines is complicated by the heterogeneous nature of currently available adjuvants. The mechanism of action of even clinically approved adjuvants such as alum is still not well understood.[180] Several other adjuvants like oil-in-water emulsions, toll-like receptor agonists, and immunostimulating complexes have been investigated for adjuvanting peptide immunotherapies, but their molecular heterogeneity makes it challenging to fully understand or modulate their mechanism of action.[181] In contrast, self-assembling peptides may be produced with more precise chemical definition.[3,4] Taken together, the picture that is emerging is that self-assembling peptides may be engineered for nonimmunogenicity or targeted immunogenicity, depending on the nature of the epitope conjugated to them, and this distinction may be exploited for applications in both regenerative medicine and immunotherapies.

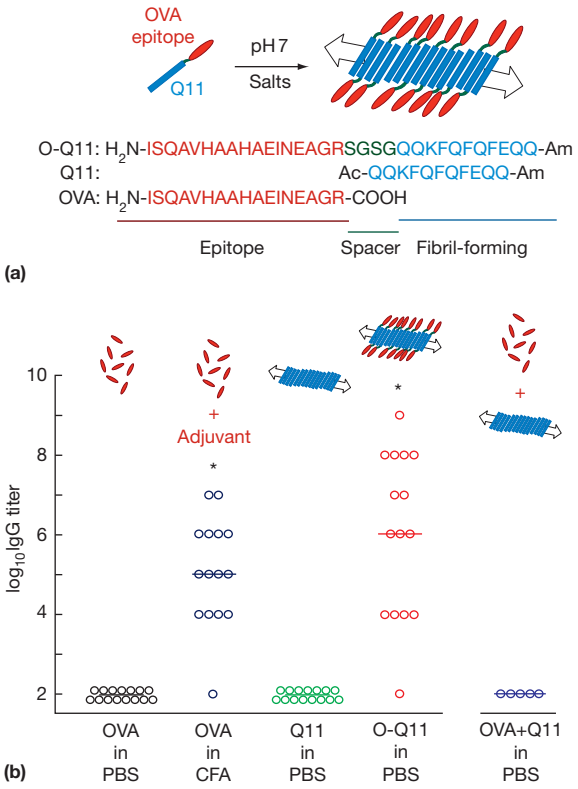

Figure 10 Self-assembling peptides can be well tolerated immunologically or can elicit antibody responses, depending on the epitope peptide attached to them. The peptide Q11 was nonimmunogenic by itself or when conjugated to RGD peptides.[3,4] However, when it was placed in tandem with a peptide from the protein ovalbumin (OVA) containing known T and B cell epitopes (O-Q11, a), it elicited the production of high titers of specific antibodies in mice without the co-administration of any adjuvant (b). Total IgG titers determined by ELISA; groups correspond to peptides shown in (a), delivered to mice either in PBS or in complete Freund's adjuvant (CFA), as indicated. The OVA+Q11 group corresponds to mice that received a mixture of soluble OVA peptide and unmodified Q11 in PBS. Adapted with from Rudra, J. S., Tian, Y., Jung, J. P., Collier, J. H. *Proc. Natl. Acad. Sci. USA* **2010**, *107*(2), 622–627.

2.205.7. *In vivo* Applications of Self-Assembled Biomaterials

Throughout the preceding sections, a few examples of clinical uses of self-assembled biomaterials have been touched upon to illustrate chemical or structural aspects of the materials. In this section, these efforts will be discussed in terms of their promise for tissue engineering and regenerative medicine (**Figure 11**). One of the most common uses of self-assembled biomaterials in regenerative medicine approaches has been to employ them as relatively inert carriers for injected cells in various tissues. As mentioned above, Lee and coworkers have investigated RADA16 peptides as carriers for cardiomyocytes or embryonic stem cells delivered to damaged myocardium. In these studies,

suspension of the cells in soluble peptide prior to injection allowed delivery via a needle, after which gelation (triggered by the physiological environment) entrapped the cells at the tissue site.[100,182] Delivery of the cells in this way promoted cell survival or the recruitment of progenitor cells from the nearby tissues. Transplanted embryonic stem cells also showed signs of differentiation into cardiomyocytes when injected with the fibrillizing peptides. The full range of functions that the peptides may be performing as carriers for cells is not completely known, and the critical interactions that ultimately lead to improved regeneration are also not entirely clear. Possible mechanisms include retaining cells at the injection site, providing an open network that facilitates cellular infiltration and angiogenesis, eliciting a mild inflammatory response that aids in regeneration, or some other mechanism. Other studies have investigated acellular injections of self-assembled materials designed specifically to promote the infiltration of regenerating tissues, for example, peptide amphiphiles bearing IKVAV ligands for use in neural regeneration applications.[124,126] In this study, evidence of healing in spinal cord compression injuries was observed for rats in which ligand-bearing peptide amphiphiles were delivered to the injury site, but the specific processes responsible for such observations have not yet been clarified. The potential tissue responses to self-assembled biomaterials may be complex and dependent on the species, tissue site, inflammatory responses, or other parameters. Beneficial tissue responses have been reported in several cases, however, making them interesting and highly useful to clarify these materials' mechanism of action in the coming years.

Self-assemblies that release drugs have a conceptually more direct mechanism of action, although some of the other possible mechanisms listed above may also play roles as well. Using nitric oxide-releasing gels of peptide amphiphiles, neointimal hyperplasia could be diminished in a rat carotid artery insult model.[179] In this study, nitric oxide-releasing peptide amphiphile gels were applied around the adventitia of arteries that had been damaged by balloon angioplasty. The most successful formulation tested reduced neointimal hyperplasia by over 70% compared to untreated controls, and led to a reduction in smooth muscle cell proliferation and an increase in endothelialization. In another example of a combination therapy, peptide amphiphiles have been utilized in the pores of titanium foams in order to improve bone integration within orthopedic implants.[135,136] Combining soft self-assemblies as coatings or

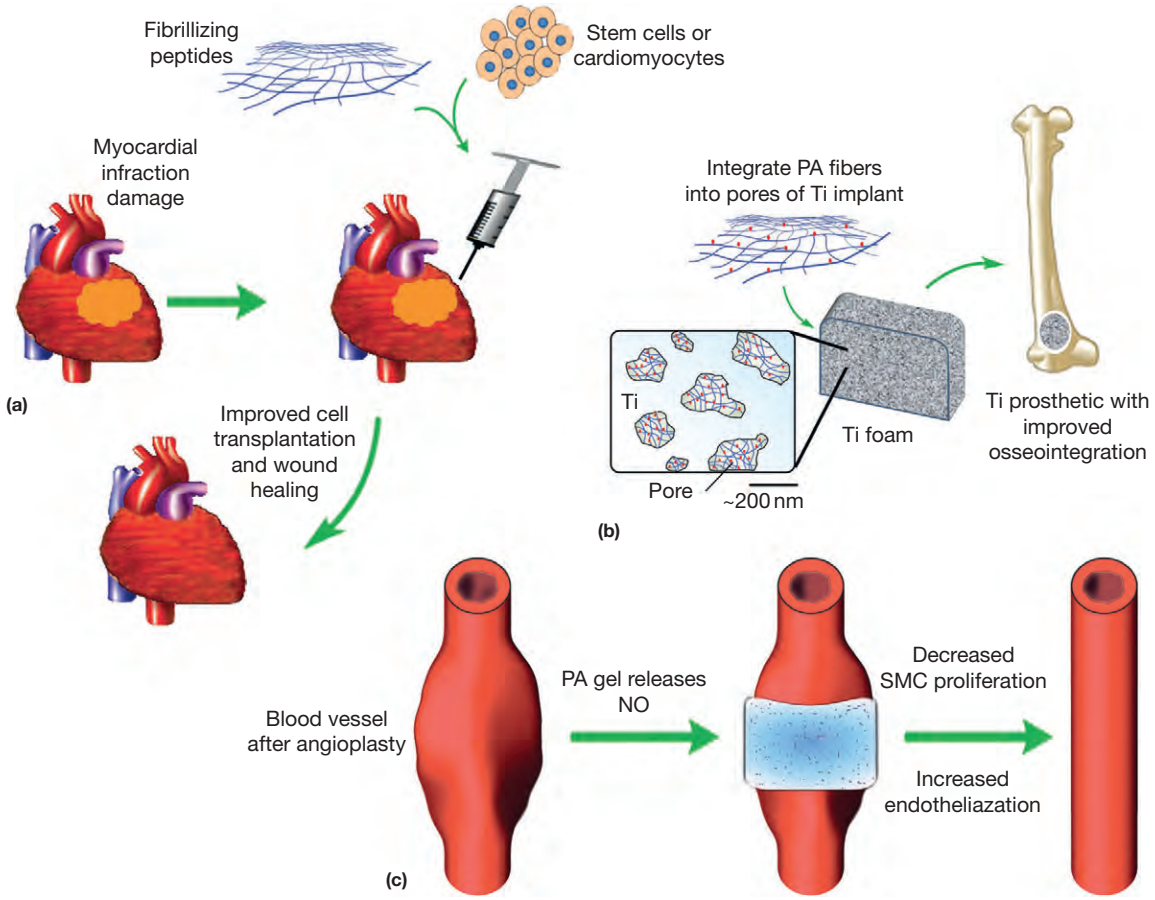

Figure 11 Potential clinical applications of fibrillar peptide gels. (a) Cell-based therapies. Fibrillizing peptides were mixed with cardiomyocytes or undifferentiated stem cells and injected into damaged myocardium.[100,182] (b) Improvement of prosthetics. PAs were integrated into the pores of titanium foam to create bioactive composites that induced mineralization and vascularization around and within orthopedic implants.[135,136] (c) Direct application of a therapeutic-releasing gel. Following angioplasty, a nitric oxide-releasing PA gel was applied directly to the exterior of the vessel at the site of injury, reducing smooth muscle cell proliferation and increasing endothelialization compared with untreated controls.[179] Reproduced with permission from Jung, J. P., Gasiorowski, J., Collier, J. H. *Biopolymers* **2010**, *94*, 49–59, with permission from Wiley.

pore-filling matrices on stiff materials may be a simple and useful way of improving the mechanics of self-assemblies while still retaining their biological activity. In addition, modifying existing devices and biomaterials may be a useful platform for gaining more mechanistic insight into the biological activity of some self-assemblies by virtue of being able to build from models and devices that already benefit from some mechanistic understanding.

2.205.8. Concluding Remarks

The use of noncovalent self-assembly has been a significant trend in the development of many classes of materials, including electronic materials, environmental materials, structural materials, and biomaterials. Their modularity, ability to mimic native structures, ability to assemble multiple components into defined matrices, and ability to create complex structures from comparatively simple starting compounds all make them exciting materials to be used in biological contexts. These properties, along with their multivalency and stimulus-sensitivity, provide opportunities and experimental systems for understanding how materials interact with physiology. It is anticipated that the both these materials' biotechnological development and their use as defined model systems will continue to be interesting and productive research areas in the coming years.

References

1. Blanazs, A.; Armes, S. P.; Ryan, A. J. *Macromol. Rapid Commun.* **2009**, *30*, 267–277.
2. Kuo, S. W. *Polym. Int.* **2009**, *58*, 455–464.
3. Jung, J. P.; Nagaraj, A. K.; Fox, E. K.; Rudra, J. S.; Devgun, J. M.; Collier, J. H. *Biomaterials* **2009**, *30*, 2400–2410.
4. Jung, H. A.; Robison, D.; Cremer, P. S. *J. Struct. Biol.* **2009**, *168*, 90–94.
5. Tanaka, M.; Sackmann, E. *Nature* **2005**, *437*, 656–663.
6. Schuler, M.; Trentin, D.; Textor, M.; Tosatti, S. G. P. *Nanomedicine* **2006**, *1*, 449–463.
7. Love, J. C.; Estroff, L. A.; Kriebel, J. K.; Nuzzo, R. G.; Whitesides, G. M. *Chem. Rev.* **2005**, *105*, 1103–1169.
8. Mrksich, M. *Acta Biomater.* **2009**, *5*, 832–841.
9. Robertus, J.; Browne, W. R.; Feringa, B. L. *Chem. Soc. Rev.* **2010**, *39*, 354–378.
10. Chen, S. F.; Lui, L. Y.; Jiang, S. Y. *Langmuir* **2006**, *22*, 2418–2421.
11. Ostuni, E.; Chapman, R. G.; HOlmlin, R. E.; Takayama, S.; Whitesides, G. M. *Langmuir* **2001**, *17*, 5606–5620.
12. Houseman, B. T.; Mrksich, M. *Biomaterials* **2001**, *22*, 943–955.
13. Feng, Y. Z.; Mrksich, M. *Biochemistry* **2004**, *43*, 15811–15821.
14. Burton, E. A.; Sirnon, K. A.; Hou, S. Y.; Ren, D. C.; Luk, Y. Y. *Langmuir* **2009**, *25*, 1547–1553.
15. Lamb, B. M.; Barrett, D. G.; Westeott, N. P.; Yousaf, M. N. *Langmuir* **2008**, *24*, 8885–8889.
16. Ruiz, S. A.; Chen, C. *Soft Matter* **2007**, *3*, 168–177.
17. Chen, C. S.; Mrksich, M.; Huang, S.; Whitesides, G. M.; Ingber, D. E. *Science* **1997**, *297*, 1425–1428.
18. Kilian, K. A.; Bugarija, B.; Lahn, B. T.; Mrksich, M. *Proc. Natl. Acad. Sci. USA* **2010**, *107*, 4872–4877.
19. Thery, M.; Pepin, A.; Dressaire, E.; Chen, Y.; Bornens, M. *Cell Motil. Cytoskeleton* **2006**, *63*, 341–355.
20. Xia, N.; Thodeti, C. K.; Hunt, T. P.; *et al. FASEB J.* **2008**, *22*, 1649–1659.
21. Plummer, S. T.; Wang, Q.; Bohn, P. W.; Stockton, R.; Schwartz, M. A. *Langmuir* **2003**, *19*, 7528–7536.
22. Ryan, D.; Parviz, B. A.; Linder, V.; *et al. Langmuir* **2004**, *20*, 9080–9088.
23. Petty, R. T.; Li, H. W.; Maduram, J. H.; Ismagilov, R.; Mrksich, M. *J. Am. Chem. Soc.* **2007**, *129*, 8966–8967.
24. Derda, R.; Li, L.; Orner, B. P.; Lewis, R. L.; Thomson, J. A.; Kiessling, L. L. *ACS Chem. Biol.* **2007**, *2*, 347–355.
25. Hui, E. E.; Bhatia, S. N. *Langmuir* **2007**, *23*, 4103–4108.
26. Thomas, C. H.; Collier, J. H.; Sfeir, C. S.; Healy, K. E. *Proc. Natl. Acad. Sci. USA* **2002**, *99*, 1972–1977.
27. Jeon, H.; Hidai, H.; Hwang, D. J.; Healy, K. E.; Grigoropoulos, C. P. *Biomaterials* **2010**, *31*, 4286–4295.
28. Saez, A.; Ghibaudo, M.; Buguin, A.; Silberzan, P.; Ladoux, B. *Proc. Natl. Acad. Sci. USA* **2007**, *104*, 8281–8286.
29. Koepsel, J. T.; Murphy, W. L. *Langmuir* **2009**, *25*, 12825–12834.
30. Jiang, X. Y.; Ferrigno, R.; Mrksich, M.; Whitesides, G. M. *J. Am. Chem. Soc.* **2003**, *125*, 2366–2367.
31. Zhu, H.; Yan, J.; Revzin, A. *Collioids Surf. B Biointerfaces* **2008**, *64*, 260–268.
32. Hodneland, C. D.; Mrksich, M. *J. Am. Chem. Soc.* **2000**, *122*, 4235–4236.
33. Yeo, W. S.; Mrksich, M. *Langmuir* **2006**, *22*, 10816–10820.
34. Zhao, C.; Witte, I.; Wittstock, G. *Angew. Chem. Intl. Ed.* **2006**, *45*, 5469–5471.
35. Zhao, C.; Zawisza, I.; Nullmeier, M.; *et al. Langmuir* **2008**, *24*, 7605–7613.
36. Nakanishi, J.; Kikuchi, Y.; Takarada, T.; Nakayama, H.; Yamaguchi, K.; Maeda, M. *J. Am. Chem. Soc.* **2004**, *126*, 16314–16315.
37. Nakanishi, J.; Kikuchi, Y.; Inoue, S.; Yamaguchi, K.; Takarada, T.; Maeda, M. *J. Am. Chem. Soc.* **2007**, *129*, 6694–6695.
38. Yousaf, M. N.; Houseman, B. T.; Mrksich, M. *Proc. Natl. Acad. Sci. USA* **2001**, *98*, 5992–5996.
39. Dillmore, W. S.; Yousaf, M. N.; Mrksich, M. *Langmuir* **2004**, *20*, 7223–7231.
40. Lupas, A. *Trends Biochem. Sci.* **1996**, *21*, 375–382.
41. Mason, J. M.; Arndt, K. M. *Chembiochem* **2004**, *5*, 170–176.
42. Cohen, C.; Parry, D. A. D. *Trends Biochem. Sci.* **1986**, *11*, 245–248.
43. Glover, J. N. M.; Harrison, S. C. *Nature* **1995**, *373*, 257–261.
44. Hohenester, E.; Engel, J. *Matrix Biol.* **2002**, *21*, 115–128.
45. Frank, S.; Schulthess, T.; Landwehr, R.; *et al. J. Biol. Chem.* **2002**, *277*, 19071–19079.
46. Harbury, P. B. *Structure* **1998**, *6*, 1487–1491.
47. Skehel, J. J.; Wiley, D. C. *Cell* **1998**, *95*, 871–874.
48. Liu, J.; Yong, W.; Deng, Y. Q.; Kallenbach, N. R.; Lu, M. *Proc. Natl. Acad. Sci. USA* **2004**, *101*, 16156–16161.
49. Liu, J.; Zheng, Q.; Deng, Y. Q.; Kallenbach, N. R.; Lu, M. *J. Mol. Biol.* **2006**, *361*, 168–179.
50. Tripet, B.; Wagschal, K.; Lavigne, P.; Mant, C. T.; Hodges, R. S. *J. Mol. Biol.* **2000**, *300*, 377–402.
51. Wagschal, K.; Tripet, B.; Lavigne, P.; Mant, T.; Hodges, R. S. *Protein Sci.* **1999**, *8*, 2312–2329.
52. Harbury, P. B.; Kim, P. S.; Alber, T. *Nature* **1994**, *371*, 80–83.
53. Harbury, P. B.; Zhang, T.; Kim, P. S.; Alber, T. *Science* **1993**, *262*, 1401–1407.
54. Schnarr, N. A.; Kennan, A. J. *J. Am. Chem. Soc.* **2003**, *125*, 667–671.
55. Kohn, W. D.; Kay, C. M.; Hodges, R. S. *J. Mol. Biol.* **1998**, *283*, 993–1012.
56. Banwell, E. F.; Abelardo, E. S.; Adams, D. J.; *et al. Nat. Mater.* **2009**, *8*, 596–600.
57. Papapostolou, D.; Smith, A. M.; Atkins, E. D. T.; *et al. Proc. Natl. Acad. Sci. USA* **2007**, *104*, 10853–10858.
58. Zhou, M.; Bentley, D.; Ghosh, I. *J. Am. Chem. Soc.* **2004**, *126*, 734–735.
59. Akey, D. L.; Malashkevich, V.; Kim, P. S. *Biochemistry* **2001**, *40*, 6352–6360.
60. Su, J. Y.; Hodges, R. S.; Kay, C. M. *Biochemistry* **1994**, *33*, 15501–15510.
61. Dong, H.; Hartgerink, J. D. *Biomacromolecules* **2006**, *7*, 691–695.
62. Kwok, S. C.; Hodges, R. S. *Biopolymers* **2004**, *76*, 378–390.
63. Apostolovic, B.; Danial, M.; Klok, H. A. *Chem. Soc. Rev.* **2010**, *39*, 3541–3575.
64. Lupas, A.; Vandyke, M.; Stock, J. *Science* **1991**, *252*, 1162–1164.
65. Berger, B.; Wilson, D. B.; Wolf, E.; Tonchev, T.; Milla, M.; Kim, P. S. *Proc. Natl. Acad. Sci. USA* **1995**, *92*, 8259–8263.
66. Wolf, E.; Kim, P. S.; Berger, B. *Protein Sci.* **1997**, *6*, 1179–1189.
67. Wang, C.; Stewart, R. J.; Kopecek, J. *Nature* **1999**, *397*, 417–420.
68. Petka, W. A.; Harden, J. L.; McGrath, K. P.; Wirtz, D.; Tirrell, D. A. *Science* **1998**, *281*, 389–392.
69. Jing, P.; Rudra, J. S.; Herr, A. B.; Collier, J. H. *Biomacromolecules* **2008**, *9*, 2438–2446.
70. Stevens, M. M.; Flynn, N. T.; Wang, C.; Tirrell, D. A.; Langer, A. *Adv. Mater.* **2004**, *16*, 915–918.
71. Yang, Z. M.; Liang, G. L.; Wang, L.; Xu, B. *J. Am. Chem. Soc.* **2006**, *128*, 3038–3043.
72. Yang, J. Y.; Xu, C. Y.; Wang, C.; Kopecek, J. *Biomacromolecules* **2006**, *7*, 1187–1195.
73. Kopecek, J.; Yang, J. Y. *Acta Biomater.* **2009**, *5*, 805–816.
74. Xu, C. Y.; Joss, L.; Wang, C.; Pechar, M.; Kopecek, J. *Macromol. Biosci.* **2002**, *2*, 395–401.
75. Shen, W.; Zhang, K. C.; Kornfield, J. A.; Tirrell, D. A. *Nat. Mater.* **2006**, *5*, 153–158.

76. Fischer, S. E.; Mi, L. X.; Mao, H. Q.; Harden, J. L. *Biomacromolecules* **2009**, *10*, 2408–2417.
77. Pandya, M. J.; Spooner, G. M.; Sunde, M.; Thorpe, J. R.; Rodger, A.; Woolfson, D. N. *Biochemistry* **2000**, *39*, 8728–8734.
78. Ryadnov, M. G.; Woolfson, D. N. *Nat. Mater.* **2003**, *2*, 329–332.
79. Ryadnov, M. G.; Woolfson, D. N. *Angew. Chem. Int. Ed.* **2003**, *42*, 3021–3023.
80. Ryadnov, M. G.; Woolfson, D. N. *J. Am. Chem. Soc.* **2004**, *126*, 7454–7455.
81. Pack, P.; Pluckthun, A. *Biochemistry* **1992**, *31*, 1579–1584.
82. Willcox, P. J.; Reinhart-King, C. A.; Lahr, S. J.; DeGrado, W. F.; Hammer, D. A. *Biomaterials* **2005**, *26*, 4757–4766.
83. Xu, T.; Shu, J. *Soft Matter* **2009**, *6*, 212–217.
84. Pauling, L.; Corey, R. B. *J. Am. Chem. Soc.* **1950**, *72*, 5349.
85. Pauling, L.; Corey, R. B.; Branson, H. R. *Proc. Natl. Acad. Sci. USA* **1951**, *37*, 205–211.
86. Brack, A.; Orgel, L. E. *Nature* **1975**, *256*, 383–387.
87. Zhao, X. J.; Zhang, S. G. *Chem. Soc. Rev.* **2006**, *35*, 1105–1110.
88. Schneider, J. P.; Pochan, D. J.; Ozbas, B.; Rajagopal, K.; Pakstis, L.; Kretsinger, J. *J. Am. Chem. Soc.* **2002**, *124*, 15030–15037.
89. Aggeli, A.; Bell, M.; Boden, N.; *et al*. *Nature* **1997**, *386*, 259–262.
90. Collier, J. H.; Messersmith, P. B. *Bioconjug. Chem.* **2003**, *14*, 748–755.
91. Collier, J. H.; Messersmith, P. B. *Adv. Mater.* **2004**, *16*, 907–910.
92. Gras, S. L.; Tickler, A. K.; Squires, A. M.; *et al*. *Biomaterials* **2008**, *29*, 1553–1562.
93. Jung, J. P.; Jones, J. L.; Cronier, S. A.; Collier, J. H. *Biomaterials* **2008**, *29*, 2143–2151.
94. Kasai, S.; Ohga, Y.; Mochizuki, M.; Nishi, N.; Kadoya, Y.; Nomizu, M. *Biopolymers* **2004**, *76*, 27–33.
95. Kasai, S.; Urushibata, S.; Hozumi, K.; *et al*. *Biochemistry* **2007**, *46*, 3966–3974.
96. Riley, J. M.; Aggeli, A.; Koopmans, R. J.; McPherson, M. J. *Biotechnol. Bioeng.* **2009**, *103*, 241–251.
97. Rudra, J. S.; Tian, Y.; Jung, J. P.; Collier, J. H. *Proc. Natl. Acad. Sci. USA* **2010**, *107*, 622–627.
98. Collier, J. H.; Hu, B. H.; Ruberti, J. W.; *et al*. *J. Am. Chem. Soc.* **2001**, *123*, 9463–9464.
99. Caplan, M. R.; Moore, P. N.; Zhang, S. G.; Kamm, R. D.; Lauffenburger, D. A. *Biomacromolecules* **2000**, *1*, 627–631.
100. Davis, M. E.; Motion, J. P. M.; Narmoneva, D. A.; *et al*. *Circulation* **2005**, *111*, 442–450.
101. Hsieh, P. C. H.; Davis, M. E.; Gannon, J.; MacGillivray, C.; Lee, R. T. *J. Clin. Invest.* **2006**, *116*, 237–248.
102. Zhang, S.; Holmes, T.; Lockshin, C.; Rich, A. *Proc. Natl. Acad. Sci. USA* **1993**, *90*, 3334–3338.
103. Genove, E.; Shen, C.; Zhang, S.; Semino, C. E. *Biomaterials* **2005**, *26*, 3341–3351.
104. Horii, A.; Wang, X.; Gelain, F.; Zhang, S. *PLoS One* **2007**, *2*, e190.
105. Gelain, F.; Bottai, D.; Vescovi, A.; Zhang, S. G. *PLoS One* **2006**, *1*, e119.
106. Holmes, T. C.; de Lacalle, S.; Su, X.; Liu, G.; Rich, A.; Zhang, S. *Proc. Natl. Acad. Sci. USA* **2000**, *97*, 6728–6733.
107. Jung, J. P.; Gasiorowski, J.; Collier, J. H. *Biopolymers* **2010**, *94*, 49–59.
108. Castelletto, V.; Hamley, I. W. *Biophys. Chem.* **2009**, *141*, 169–174.
109. Tzokova, N.; Fernyhough, C. M.; Topham, P. D.; *et al*. *Langmuir* **2009**, *25*, 2479–2485.
110. Rosler, A.; Klok, H. A.; Hamley, I. W.; Castelletto, V.; Mykhaylyk, O. O. *Biomacromolecules* **2003**, *4*, 859–863.
111. Shoulders, M. D.; Raines, R. *Annu. Rev. Biochem.* **2009**, *78*, 929–958.
112. Koide, T. *Connect. Tissue Res.* **2005**, *46*, 131–141.
113. Kotch, F. W.; Raines, R. T. *Proc. Natl. Acad. Sci. USA* **2006**, *103*, 3028–3033.
114. Cejas, M. A.; Kinney, W. A.; Chen, C.; *et al*. *J. Am. Chem. Soc.* **2007**, *129*, 2202–2203.
115. Rele, S.; Song, H. Y.; Apkarian, R. P.; Qu, Z.; Conticello, V. P.; Chaikof, E. L. *J. Am. Chem. Soc.* **2007**, *129*, 14780–14787.
116. Paramonov, S. E.; Gauba, V.; Hartgerink, J. D. *Macromolecules* **2005**, *38*, 7555–7561.
117. Yamazaki, C. M.; Asada, S.; Kitagawa, K.; Koide, T. *Biopolymers* **2008**, *90*, 816–823.
118. Yamazaki, C. M.; Kadoya, Y.; Hozumi, K.; *et al*. *Biomaterials* **2010**, *31*, 1925–1934.
119. Mo, X.; An, Y. J.; Yun, C. S.; Yu, S. M. *Angew. Chem. Int. Ed.* **2006**, *45*, 2267–2270.
120. Wang, A. Y.; Mo, X.; Chen, C. S.; Yu, S. M. *J. Am. Chem. Soc.* **2005**, *127*, 4130–4131.
121. Kunitake, T. *Angew. Chem. Int. Ed.* **1992**, *31*, 709–726.
122. Behanna, H.; Rajangam, A. K.; Stupp, S. I. *J. Am. Chem. Soc.* **2007**, *129*, 321–327.
123. Hartgerink, J. D.; Beniash, E.; Stupp, S. I. *Science* **2001**, *294*, 1684–1688.
124. Silva, G. A.; Czeisler, C.; Niece, K. L.; *et al*. *Science* **2004**, *303*, 1352–1355.
125. Storrie, H.; Guler, M. O.; Abu-Amara, S. N.; *et al*. *Biomaterials* **2007**, *28*, 4608–4618.
126. Tysseling-Mattiace, V. M.; Sahni, V.; Niece, K. L.; *et al*. *J. Neurosci.* **2008**, *28*, 3814–3823.
127. Yu, Y. C.; Berndt, P.; Tirrell, M.; Fields, G. B. *J. Am. Chem. Soc.* **1996**, *118*, 12515–12520.
128. Yu, Y. C.; Roontga, V.; Daragan, V. A.; Mayo, K. H.; Tirrell, M.; Fields, G. B. *Biochemistry* **1999**, *38*, 1659–1668.
129. Yu, Y. C.; Tirrell, M.; Fields, G. B. *J. Am. Chem. Soc.* **1998**, *120*, 9979–9987.
130. Bitton, R.; Schmidt, J.; Biesalski, M.; Tu, R.; Tirrell, M.; Bianco-Peled, H. *Langmuir* **2005**, *21*, 11888–11895.
131. Paramonov, S. E.; Jun, H. W.; Hartgerink, J. D. *J. Am. Chem. Soc.* **2006**, *128*, 7291–7298.
132. Niece, K. L.; Hartgerink, J. D.; Donners, J. J. J. M.; Stupp, S. I. *J. Am. Chem. Soc.* **2003**, *125*, 7146–7147.
133. Standley, S. M.; Cheng, T. D.; Soukasene, H.; *et al*. *Cancer Res.* **2010**, *70*, OF1–OF7.
134. Guler, M. O.; Hsu, L.; Soukasene, S.; Harrington, D. A.; Hulvat, J. F.; Stupp, S. I. *Biomacromolecules* **2006**, *7*, 1855–1863.
135. Sargeant, T. D.; Guler, M. O.; Oppenheimer, S. M.; *et al*. *Biomaterials* **2008**, *29*, 161–171.
136. Sargeant, T. D.; Oppenheimer, S. M.; Dunand, D. C.; Stupp, S. I. *J. Tissue Eng. Regen. Med.* **2008**, *2*, 455–462.
137. Galler, K. M.; Aulisa, L.; Regan, K. R.; D'Souza, R. N.; Hartgerink, J. D. *J. Am. Chem. Soc.* **2010**, *132*, 3217–3223.
138. Jayawarna, V.; Ali, M.; Jowitt, T. A.; *et al*. *Adv. Mater.* **2006**, *18*, 611–614.
139. Reches, M.; Gazit, E. *Science* **2003**, *300*, 625–627.
140. Yang, Z. M.; Gu, H. W.; Fu, D. G.; Gao, P.; Lam, J. K.; Xu, B. *Adv. Mater.* **2004**, *16*, 1440–1444.
141. Yang, Z. M.; Xu, B. *Chem. Commun.* **2004**, 2424–2425.
142. Smith, A. M.; Williams, R. J.; Tang, C.; *et al*. *Adv. Mater.* **2008**, *20*, 37–41.
143. Reches, M.; Gazit, E. *Nat. Nanotechnol.* **2006**, *1*, 195–200.
144. Toledano, S. R.; Williams, J.; Jayawarna, V.; Ulijn, R. V. *J. Am. Chem. Soc.* **2006**, *128*, 1070–1071.
145. Laromaine, A.; Koh, L. L.; Murugesan, M.; Ulijn, R. V.; Stevens, M. M. *J. Am. Chem. Soc.* **2007**, *129*, 4156–4157.
146. Zhou, M.; Smith, A. M.; Das, A. K.; *et al*. *Biomaterials* **2009**, *30*, 2523–2530.
147. Lamm, M. S.; Rajagopal, K.; Schneider, J. P.; Pochan, D. J. *J. Am. Chem. Soc.* **2005**, *127*, 16692–16700.
148. Pochan, D. J.; Schneider, J. P.; Kretsinger, L.; Ozbas, B.; Rajagopal, K.; Haines, L. *J. Am. Chem. Soc.* **2003**, *125*, 11802–11803.
149. Haines, L. A.; Rajagopal, K.; Ozbas, B.; Salick, D. A.; Pochan, D. J.; Schneider, J. P. *J. Am. Chem. Soc.* **2005**, *127*, 17025–17029.
150. Kretsinger, J. K.; Haines, L. A.; Ozbas, B.; Pochan, D. J.; Schneider, J. P. *Biomaterials* **2005**, *26*, 5177–5186.
151. Salick, D. A.; Kretsinger, J. K.; Pochan, D. J.; Schneider, J. P. *J. Am. Chem. Soc.* **2007**, *129*, 14793–14799.
152. Haines-Butterick, L.; Rajagopal, K.; Branco, M.; *et al*. *Proc. Natl. Acad. Sci. USA* **2007**, *104*, 7791–7796.
153. Ozbas, B.; Rajagopal, K.; Haines-Butterick, L.; Schneider, J. P.; Pochan, D. J. *J. Phys. Chem. B* **2007**, *111*, 13901–13908.
154. Papapostolou, D.; Howorka, S. *Mol. Biosyst.* **2009**, *5*, 723–732.
155. Ringler, P.; Schulz, G. E. *Science* **2003**, *302*, 106–109.
156. Grueninger, D. N.; Treiber, M.; Ziegler, O. P.; Koetter, J. W. A.; Schulze, M. S.; Schulz, G. E. *Science* **2008**, *319*, 206–209.
157. Padilla, J.; Colovos, E. C.; Yeates, T. O. *Proc. Natl. Acad. Sci. USA* **2001**, *98*, 2217–2221.
158. Matthews, Q. L.; Yang, P.; Wu, Q.; *et al*. *Virol. J.* **2008**, *5*, 98.
159. Roberts, D. M.; Nanda, A.; Havenga, M. J. E.; *et al*. *Nature* **2006**, *441*, 239–243.
160. Smith, M. L.; Lindbo, J. A.; Dillard-Telm, S.; *et al*. *Virology* **2006**, *348*, 475–488.
161. Gerstmayr, M.; Ilk, N.; Schabussova, I.; *et al*. *J. Immunol.* **2007**, *179*, 7270–7275.
162. Bachmann, M.; Rohrer, U. H.; Kundigk, T. M.; Burki, K.; Hengartner, H.; Zinkernagel, R. M. *Science* **1993**, *262*, 1448–1451.
163. Sadasivan, S.; Patil, A. J.; Bromley, K. M.; Hastie, P. G. R.; Banting, G.; Mann, S. *Soft Matter* **2008**, *4*, 2054–2058.
164. Douglas, T.; Young, M. *Nature* **1998**, *393*, 152–155.

165. Fowler, C. E.; Shenton, W.; Stubbs, G.; Mann, S. *Adv. Mater.* **2001**, *13*, 1266–1269.
166. Shenton, W. T.; Douglas, M.; Young, M.; Stubbs, G.; Mann, S. *Adv. Mater.* **1999**, *11*, 253–256.
167. Discher, D. E.; Janmey, P.; Wang, Y. L. *Science* **2005**, *310*, 1139–1143.
168. Engler, A. J.; Sen, S.; Sweeney, H. L.; Discher, D. E. *Cell* **2006**, *126*, 677–689.
169. Webber, M.; Tongers, J. J.; Renault, M. A.; Roncalli, J. G.; Losordo, D. W.; Stupp, S. I. *Acta Biomater.* **2010**, *6*, 3–11.
170. Karthikan, R.; Lamm, M. S.; Haines-Butterick, L. A.; *et al. Biomacromolecules* **2009**, *10*, 2619–2625.
171. Aulisa, L.; Dong, H.; Hartgerink, J. D. *Biomacromolecules* **2009**, *10*, 2694–2698.
172. Hansen, K. C.; Kiemele, L.; Maller, O.; *et al. Mol. Cell. Proteomics* **2009**, *8*, 1648–1657.
173. Hassell, J. R.; Robey, P. G.; Barrach, H. J.; Wilczek, J.; Rennard, S. I.; Martin, G. R. *Proc. Natl. Acad. Sci. USA* **1980**, *77*, 4494–4498.
174. Smith, A. M.; Ulijn, R. V. *Chem. Soc. Rev.* **2008**, *37*, 664–675.
175. Liu, S.; Kiick, K. L. *Macromolecules* **2008**, *41*, 764–772.
176. Polizzotti, B. D.; Maheshwari, R.; Vinkenborg, J.; Kiick, K. L. *Macromolecules* **2007**, *40*, 7103–7110.
177. Vance, D.; Martin, J.; Patke, S.; Kane, R. S. *Adv. Drug Deliv. Rev.* **2009**, *61*, 931–939.
178. Collier, J. H. *Soft Matter* **2008**, *4*, 2310–2315.
179. Kapadia, M. R.; Chow, L. W.; Tsihlis, N. D.; *et al. J. Vasc. Surg.* **2008**, *47*, 173–182.
180. Marrack, P.; McKee, A. S.; Munks, M. W. *Nat. Rev. Immunol.* **2009**, *9*, 287–293.
181. Lambrecht, B. N.; Kool, M.; Willart, M. A. M.; Hammad, H. *Curr. Opin. Immunol.* **2009**, *21*, 23–29.
182. Davis, M. E.; Hsieh, P. C. H.; Takahashi, T.; *et al. Proc. Natl. Acad. Sci. USA* **2006**, *103*, 8155–8160.

2.206. Phages as Tools for Functional Nanomaterials Development

W-J Chung, M Sena, A Merzlyak, and S-W Lee, University of California, Berkeley, CA, USA

© 2011 Elsevier Ltd. All rights reserved.

2.206.1.	**Introduction**	96
2.206.1.1.	Introduction of Bacteriophage	96
2.206.1.2.	Structure of M13 Phage	96
2.206.1.3.	Directed Evolution of Phage	97
2.206.2.	**Phages for Inorganic–Organic Hybrid Materials**	98
2.206.2.1.	Self-Assembly of Inorganic Materials using Phage	100
2.206.3.	**Phage for Energy Materials**	101
2.206.3.1.	Phage for Energy Storage Materials	101
2.206.3.2.	Phage for Energy Producing Materials	101
2.206.4.	**Phage for Sensing Materials**	103
2.206.4.1.	Phage-Based Molecular Recognition	103
2.206.4.2.	Phage for a Sensing Platform	104
2.206.4.3.	Micro- and Nanomechanical Sensing	104
2.206.4.4.	Electrochemical Sensing	105
2.206.4.5.	Optical Sensing	106
2.206.5.	**Phage for Biomedical Application**	107
2.206.5.1.	Phage Therapy	107
2.206.5.2.	Phage for Drug and Gene Delivery	107
2.206.5.3.	Phage for Tissue-Engineering Materials	108
2.206.6.	**Summary and Future Perspectives**	108
References		110

Glossary

Bacteriophage Bacteriophage (phage) is a prokaryotic virus that can infect bacterial host cells. The name 'bacteriophage' can be translated as 'bacteria eater' in Greek.

Directed evolution Directed evolution is a method of utilizing the power of natural selection at the molecular level to evolve proteins or RNA that are customized to meet desired specifications.

Molecular recognition element The molecular recognition element is a specific amino acid sequence that binds to a particular molecular target which can be discovered through directed evolution processes.

Nanobot The nanobot is a new future machinery concept proposed by Dr. Eric Drexler in his book *Engines of Creation* in 1983. He coined the term 'Nanobot (Nanoscale Robot)' for systems that can self-assemble, self-evolve, and self-replicate – serving as fabricators of the next generation of improved future machine systems.

Phage display Phage display is an accelerated evolutionary screening process that allows one to isolate peptides that bind specifically to a particular target material.

Phage therapy Phage therapy is the therapeutic use of bacteriophage to treat bacteria-related disease.

Phagemid The phagemid is a hybrid cloning vector from the filamentous phage M13 and plasmids. The vector can grow into a plasmid and also can be packaged as a single-stranded DNA in viral capsids. In order to enable single-stranded DNA replication and packaging of the phagemid DNA into phage particles, bacterial host containing phagemid is subjected to infection with a helper phage to provide the viral components.

Virotronics The Virotronics is a novel virus-based material design technology that can be used to create novel functional materials with precise molecular-level structural and functional control using unique biological advantages of viruses, such as specific molecular recognition, evolution, and self-replication.

Abbreviations

AAV	Adeno-associated virus
DNT	1,3-Dinitrotoluene
EGF	Epidermal growth factors
ELISA	Enzyme-linked immunosorbent assay
FACS	Fluorescence-activated cell sorting
FDA	Food and drug administration
FGF	Fibroblast growth factors
HER2	Human epidermal growth factor receptor
HPQ	Histidine-proline-glutamine tripeptide
IKVAV	Isolucine-lysine-valine-alanine-valine tetrapeptide
ITR	Inverted terminal repeat
LAPS	Light-addressable potentiometric sensors
LC	Liquid crystal

ME	Magnetoelastic	**QCM**	Quartz crystal microbalance
MEMS	Microelectromechanical system	**RES**	Reticuloendothelial system
MREs	Molecular recognition elements	**RGD**	Arginine-glycine-aspartate tripeptide
PEG	Polyethylene glycol	**SPR**	Surface plasmon resonance
PSMA	Prostate-specific membrane antigen	**TNT**	1,3,5-Trinitrotoluene

2.206.1. Introduction

Nanotechnology is an interdisciplinary science and engineering field that enables us to observe, measure, and control matters at the molecular level. Its development has allowed us to envision clean and efficient energy conversion devices,[1,2] super-computers operated by light,[3] and tissues and organs regenerated by smart tissue scaffolding.[4] Despite the existence of various methodologies to manipulate atoms and molecules into exquisite new functional materials, designing new materials with well-defined structures and desired functions is still a challenge in materials science.[5] Conventional materials are developed through rational design and intensive characterization. Based on the results, new materials with improved physical and chemical properties can be designed. Many new materials are generated by this iterative design and performance characterization process. Nature, however, solves such material design issues using an evolutionary approach. Nature prepares a diversified set of candidates and tests them in a given environment through mutation. The best candidates are then selected and propagated through generations over the course of millions of years. Examples of advanced biological materials with well-defined structures and functions include glass sponges (optical fibers),[6] brittle stars (optical lens array),[7] diatoms (sophisticated periodic structures), abalone shells (fracture-resistance materials),[8] bones (support structure for vertebrates),[9] and cells (exquisite self-replicating biomachines).[10] Efforts to mimic the unique biological structures in nature have provided a variety of tools and resources that are useful to scientists and engineers.[11,12] However, whole organisms have complex functions and self-templated hierarchical structures that cannot be easily mimicked. These unique characteristics, which have accumulated through evolution, are inherited genetically. Genetic information is translated into proteins, which work as molecular machines to control precisely programmed processes in biosystems. Although protein-based 'bottom-up' synthesis of nanoscale functional materials and devices is one of the most promising areas in the newly emerging field of nanotechnology,[13] identifying active basic building blocks from biological examples is still a challenge because of their complex and encrypted sequence structure. Genetic engineering of phage viruses provides opportunities for building novel bio-nanomaterials by integrating biology, chemistry, physics, materials science, electric engineering, and other disciplines. By mimicking the evolutionary process in nature, phages can be used as an information-mining tool to identify functional peptide (or protein) sequences that can specifically recognize desired materials at the molecular level.[14,15] These recognition elements can be used to guide the design of unprecedented materials such as semiconductor and metallic materials. Additionally, because of their well-defined shape, viral particles can be used to catalyze self-assembly of ordered nanostructures, which is useful in applications including energy,[16–18] biosensors,[19] electronics,[14] and tissue regenerating materials.[20,21] In this chapter, we introduce the unique features of viruses, recent accomplishments in the development of virus-based materials for use as tools to fabricate functional nanomaterials, and review the potential future applications of this emerging technology.

2.206.1.1. Introduction of Bacteriophage

Bacteriophage (phage) is a prokaryotic virus that can infect bacterial host cells.[22] The name 'bacteriophage' can be translated as 'bacteria eater.' As its name implies, once a bacteriophage infects the bacterial host, the virus exploits the host's biosynthetic machinery in order to produce many identical copies of itself. Phages are some of the most common organisms on earth.[23] Phages are commonly composed of a protein capsid, or shell, which encapsulates and protects the virus's genomic material (DNA or RNA) (**Figure 1**).[24] There are many types of phages, each having differing genomic materials, replication processes, and shapes. Genomic materials can be either DNA or RNA in a single-stranded or double-stranded form.[25] With regard to the replication processes, phages can be lysogenic or lytic.[25] Lysogenic phages infect the host cells by injecting their genomic materials. The genetic materials uptake the host cell metabolisms and reproduce the same genetic materials and corresponding proteins. These protein products are delivered to the host cell membranes, where new phages are packaged and released without disruption of the host cell walls. On the other hand, lytic phages are replicated and accumulate inside the host cells rather than at the cell membrane. Following replication, the newly amplified phages destroy the host cell wall and can infect other host cells. There are many different shapes of phages such as linear (M13, Fd, F1)[26] or spherical (MS2)[27] (**Figure 1**). Some shapes are quite sophisticated. For example, T4 and T7 phages possess an icosahedral head and a long tail connected through a cylindrical body. Regardless of differences in shape, composition, and life cycle, all phages share the capacity to make exact copies of themselves with incredible structural precision. Because of this property, phages are great candidates to aid the development of novel bio-nanomaterials. Thanks to the commercially available genetic tool kits, M13 phage, in particular, has been extensively used as evolvable nanoscale material. Therefore, we discuss mainly M13 phage and introduce other phages whenever applicable.

2.206.1.2. Structure of M13 Phage

M13 phage is a bacterial virus that comprises a single-stranded DNA encapsulated by several major and minor coat proteins.

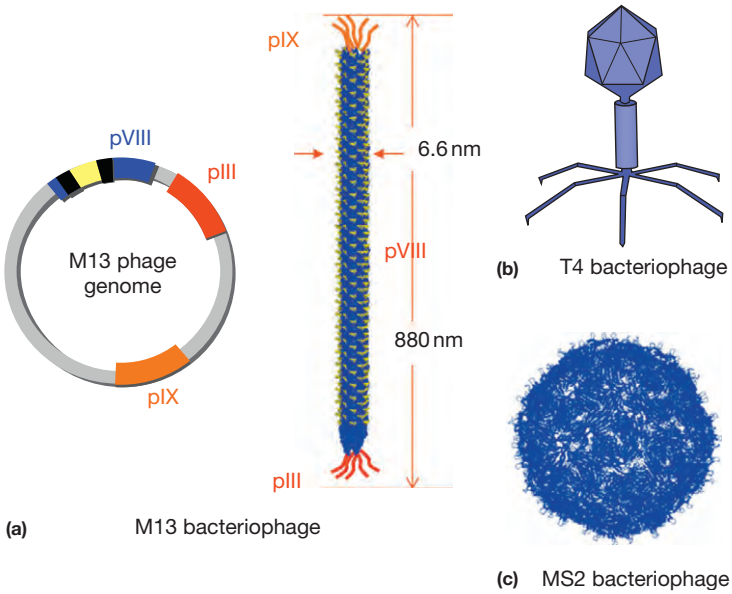

Figure 1 Schematic diagram of various distinct structures of various phages. (a) Long-rod structure of M13 bacteriophage with genomic schematic diagrams to show the each protein expressed on the M13 phage surfaces. (b) Structure of T4 bacteriophage with icosahedral head and long tail connected through cylindrical body. (c) Sphere structure of MS2 bacteriophage.

It has a long-rod filament shape that is approximately 880 nm in length and 6.6 nm in diameter (**Figure 1(a)**).[28,29] The viral capsid is composed of 2700 copies of helically arranged major coat protein, pVIII, and 5–7 copies of the minor coat proteins, pIII, pVI, pIX, and pVII, located at either of its ends.[28,29] M13 phage can only infect and propagate within bacteria displaying F-pili, such as *Escherichia coli*.[30] It is a nonlytic bacterial virus, meaning that it does not break the bacterial cell membrane upon exit, but instead is secreted through a protein pore channel in the bacterial membrane.[28,31,32] Bacterial host growth is slowed down because of the increased metabolic demands of phage production, but continues after infection.[33] These qualities allow for easy mass amplification of the bacteriophage in bacterial culture. Over the past 2 decades, the biochemical landscape of the phage structure has been greatly expanded through genetic engineering of the phage[21,34–36] and site-specific organic synthesis approaches.[37–40] Through genetic engineering, many foreign or synthetic DNA have been integrated into phage genome and expressed at various sites of the phage body.[36,41] Nonnatural amino acids have been expressed on the phage surfaces using amber codon tRNA approaches.[42,43] In addition, reactions have been developed that enable site-specific modification of phage surfaces with chemicals such as fluorescent dyes or chromophores for various applications including biochemical imaging and energy harvesting.[38–40]

2.206.1.3. Directed Evolution of Phage

One of the most remarkable features of phage-based materials, which distinguishes them from traditional engineering materials, is their ability to be chemically evolved in a directed fashion. Evolution mainly consists of genetic diversification, functional selection, and replication processes. In nature, mutation can occur during gene replication, resulting in diversified species with various new functions. By mimicking this natural process, phage can be used as a template to perform directed evolution through a technique called phage display.[36,41] Phage display is an accelerated evolutionary screening process that allows one to isolate peptides that bind specifically to a particular target material. All the phage coat proteins can be genetically modified to display relatively short (<8–20 amino acid) peptide sequences. Insertion of randomized DNA sequences at specific locations within the phage genome enables one to generate a highly diverse library of peptides (up to 10^{11} random sequences) expressed on the viral particle surface.[36,44]

To select the functional peptide sequence for a given target material, the engineered phage library pool goes through several rounds of selection, which is typically based on affinity for the target material (**Figure 2**). As for the affinity selection, the phages are first allowed to bind to the target. The nonbound phages are then washed away, and the bound ones are eluted separately. The eluted phages are then amplified through *E. coli* bacterial host infection. This is repeated for several rounds with increasingly stringent binding conditions in order to enrich the phage pool with high-affinity peptides. Finally, the dominant binding peptides emerge and are identified through DNA analysis of the phage genome. Phage display on pIII is most often utilized, as it is the biggest phage coat protein and allows for greater peptide sequence variability. pIII is also conducive for display of constrained libraries.[36,45] The lower valency of the protein (only 5 copies as opposed to 2700 for pVIII) allows for the selection of peptides with higher affinity toward the target, because of the lack of avidity effects.[35] Recently, major coat engineered libraries have been developed and used for inorganic material syntheses involving semiconductors, metallic materials, and conjugation of phage with carbon nanotubes.[14–16,18,46] By applying microelectromechanical system (MEMS) techniques, Liu *et al.* have recently developed a microfluidic device that performs phage display in an automated manner on a microliter scale.[47]

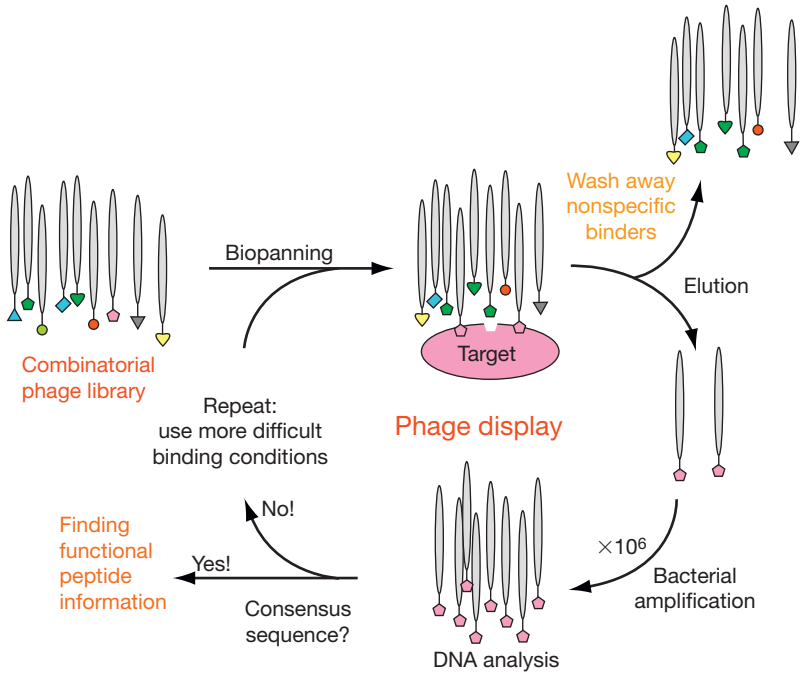

Figure 2 Schematic diagram of the phage display processes to identify the functional recognition peptide motifs.

The phage display technique was originally developed for small peptides and antibodies and for identifying epitope-like ligands. The main advantage of this approach is that the use of an amino acid library allows for identification of an epitope sequence from a protein that is not necessarily in sequential order, but could assemble and become functional through protein folding.[35] Further, presentation of such a library on a phage protein allows for a direct connection between the peptide identified and its encoding genetic sequence.[34,35] Since the inception of this method, a variety of peptide ligands have been discovered that are involved in interactions including specific protein binding,[48–50] DNA binding,[51] receptor binding,[52,53] and cell and tissue binding.[53] Further, through the use of phage-display, short peptide motifs can be further matured for enhanced binding against the target of interest.[54,55] For example, phage display was instrumental in determining the best binding conformation for the well-known RGD motif, as well as elucidating the different sequences of RGD flanking residues which confer binding specificity for certain classes of integrins.[53] However, identified peptide sequences should be carefully confirmed with appropriate binding assays. Results from nonspecific binding can mislead the interpretation, particularly when panning phage libraries against cell surfaces, which include many of their molecules as well as the target receptor.

2.206.2. Phages for Inorganic–Organic Hybrid Materials

Phage display has also been utilized to identify affinity peptide sequences for a variety of inorganic substances, such as semiconductor and magnetic and metallic materials.[14,46,55–57] Specific binding peptide sequences identified through such directed evolution screening methods have been summarized in recent reviews.[58–60] Phage display performed with inorganic substrates can uncover novel information about the particular binding interaction between inorganic crystals and organic peptides. Belcher and coworkers have demonstrated that a genetically engineered phage can specifically recognize inorganic semiconductor substrates. For example, Whaley *et al.* demonstrated that the phage could be selected for binding to GaAs (III–V semiconductor) (Figure 3).[15] The resulting phages and corresponding peptide sequences exhibit remarkable specificity in their binding to different crystallographic orientations, such as (100) and (111), and similar surface structures,

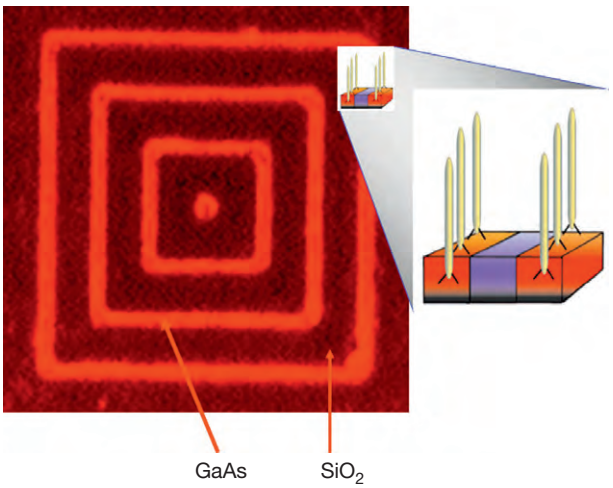

Figure 3 Specific recognition of phage onto semiconductor surfaces. Fluorescence image of the phage can bind to square patterned GaAs semiconductor surfaces. Reproduced from Whaley, S. R.; English, D. S.; Hu, E. L.; Barbara, P. F.; Belcher, A. M. *Nature* **2000**, *405*, 665–668, with permission from Nature. © 2000 Macmillian Publishing Ltd.

such as (111)A (gallium-terminated) or (111)B (arsenic-terminated) face of GaAs.[15] Another study of phage display screening using carbon nanotubes and graphite surfaces showed that selective binding of sequences with multiple tryptophan residues could be attributed to aromatic ring interaction between the peptides and nanotubes.[57,61] Recently, similar display screening methods, such as bacterial cell surface display[60,62] and yeast display,[63] have also been applied to identify the specific binding peptide against the various inorganic seminconductor and metallic materials and uncover the specific binding peptides and proteins.

By mimicking the biomineralization processes in nature, the phages and their peptides discovered from phage display can also be used for the synthesis of inorganic materials. In nature, specific binding proteins against various inorganic crystals, such as silica in diatoms,[64,65] iron oxide in magnetotetic bacteria,[66] calcium carbonate in abalone shells,[67] or calcium phosphate in bones and teeth,[68,69] play a critical role in the synthesis of hybrid organic–inorganic materials.[70] Similarly, specific recognition peptides identified through phage display for desired crystal surfaces can be exploited in order to template the growth of various target inorganic crystals. Flynn *et al.* identified specific binding peptide motifs with high affinity for II–VI semiconductor materials (ZnS, CdS, PbS, etc.) and used them to direct mineralization of different phases of the inorganic crystals in controlled shape and morphology.[55] The researchers showed, for example, that linear and constrained binding peptides selected for zinc sulfide crystal surfaces are capable of nucleating cubic (zinc blende) and hexagonal (wurtzite) phases of ZnS nanocrystals, respectively.

Genetic engineering of functional peptides with crystal-nucleating or recognition capabilities on multiple phage coat proteins has allowed for construction of many interesting functional nanomaterials and nanostructures. Single or multiple genetic modification schemes are depicted in **Figure 4**. Single modification of pIII minor coat protein was used to synthesize ZnS and CdS nanoparticles at the terminus of the phage.[14,55] Nam *et al.* modified both the end minor coat proteins (pIII and pIX) with six histidines and HPQ (His-Pro-Gln) streptavidin-binding peptide motifs. These phages were then used to construct nanoscale viral ring structures through specific binding of chemically conjugated streptavidin and Ni-NTA linkers.[71] By incorporating complementary leucine zipper sequences on both ends of the phage, Sweeney *et al.* programmed phage to self-assemble into linear structures.[72] By expressing the semiconductor- and metal-binding peptides on the major coat proteins using phagemid vectors, one-dimensional polycrystalline semiconductor and magnetic and metallic nanowires can be synthesized on viral templates.[46] After high-temperature annealing processes, high-quality single-crystal ZnS or CdS nanowires with uniform size and shape could be fabricated on the templated phage

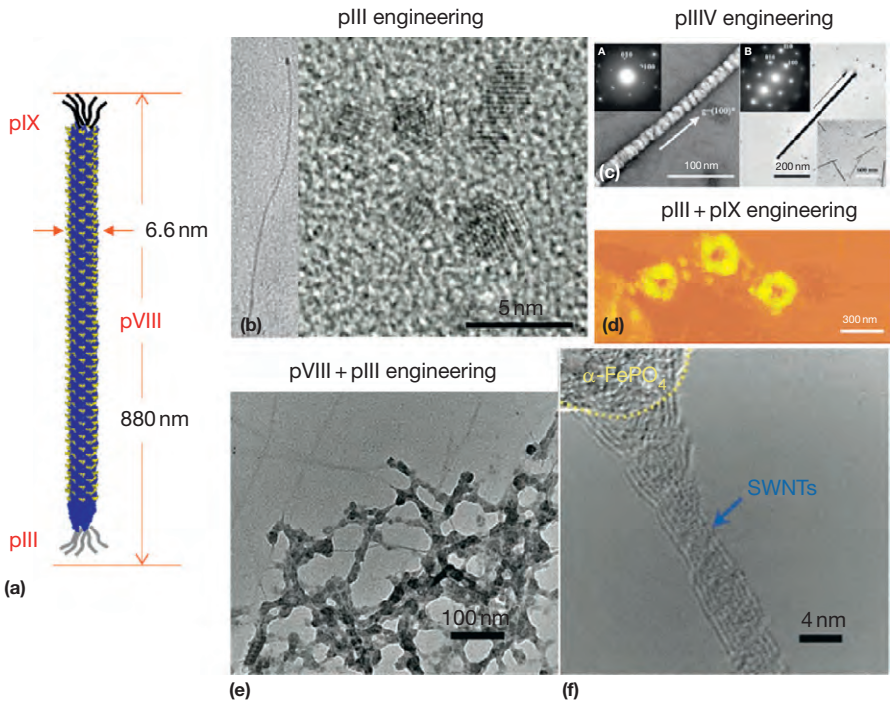

Figure 4 Engineering of M13 phage for programmed functionalization from material synthesis to specific conjugation. (a) Schematic diagram of M13 phage. Single engineering: (i) pIII engineering: specific nanoparticle synthesis on minor coat proteins (b); (ii) pVIII engineering: major coat protein engineering for the synthesis of ZnS nanowires which can be used for the semiconductor synthesis or energy producing nanoscale nanowired materials (c). Multiple gene engineering: (i) pIII and pIX engineering to construct ring structures using fillamentous phage (d) and (ii) pIII and pVIII engineering to synthesize energy storing phage for battery materials synthesis and wiring to SWNT (e, f). (b, c, e, f) Reproduced from Lee, S. W.; Mao, C. B.; Flynn, C. E.; Belcher, A. M. *Science* **2002**, *296*, 892–895; Mao, C. B.; Solis, D. J.; Reiss, B. D.; *et al*. *Science* **2004**, *303*, 213–217; Lee, Y. J.; Yi, H.; Kim, W.-J.; *et al*. *Science* **2009**, *324*, 1051–1055, with permission from Science. © 2002, 2004, and 2009 American Association for the Advancement of Science. (d) Reproduced from Nam, K.; Beau, R. P.; Lee, S. W.; Belcher, A. M. *Nano Lett*. **2004**, *4*, 23–27, with permission from American Chemical Society. © 2004 American Chemical Society.

structures. These nanowires exhibited promising electrooptical and magnetic properties.[46] By inserting multiple major coat protein genes in the phage genome, Nam *et al.* demonstrated that the phage can nucleate gold and metal oxides simultaneously.[17] A variety of architectures of phage-templated nanostructures have been successfully demonstrated using concurrent modification of pIII and pVIII coat proteins.[73] Both ends and major coat protein-engineered phage might conduct multiple programmed operations. Such engineered phages are expected to be able to serve as electronic components and wires, potentially resulting in self-assembled, self-interconnected, self-fabricated electronic devices. As a proof of concept, Huang *et al.* showed that exquisitely programmed materials can perform electronic functions.[73] They fabricated two terminal electrodes, which were interconnected by virus-based conductive gold nanowire, and measured *I*–*V* behaviors, which exhibited ohmic behaviors of the viral nanowires.

2.206.2.1. Self-Assembly of Inorganic Materials using Phage

Because of their monodispersity and long-rod shape, many filamentous viruses have been extensively studied as liquid crystalline model systems.[74,75] By changing variables such as concentrations, ionic strength, and external fields, viruses are able to form ordered liquid crystalline structures (Figure 5). At a low concentration range (below 5 mg ml^{-1}), phages are randomly ordered in an isotropic liquid crystalline phase. With increasing concentration (10–20 mg ml^{-1}), the distance between neighboring viral particles becomes smaller than their length. The virus particles begin to sterically hinder each other and align into orientationally ordered configurations called nematic phase liquid crystals. In the nematic concentration range, the helicity exhibited by viral particles such as M13, F1, and Ff phages is conserved in the nematically ordered phage layer. Therefore, each nematic layer becomes twisted about the normal axis of the layer below it. In the concentration range between 20 and 80 mg ml^{-1} (cholesteric phase), the rotation of nematic layers generates optically distinguishable periodic structures, which may resemble finger print textures in the optical micrographs (Figure 5). Finally, above 100 mg ml^{-1}, the viral particles acquire both positional and orientational order (smectic phase).[74] Some viral particles such as M13 viruses have been studied at much higher concentration ranges as solid phase two-dimensional thin films[14,75] and one-dimensional fibers.[76] Two-dimensional viral liquid crystalline films grown at the air–liquid–solid interfaces of a meniscus have been shown to exhibit a chiral smectic C structure (Figure 5).[75]

The use of polymeric templates and surface patterning tools has greatly expanded the self-assembly capabilities of phages. Yoo *et al.* developed a novel M13 phage patterning methodology by combining M13 phages with polyelectrolytes such as polyethyleneimine and poly acrylic acid.[77] In this approach, M13 phages were segregated from the bulk charged polymers when deposited on the surface of a suitable substrate. The resulting aligned films exhibited a high degree of positional and orientational order and could be further modified with inorganic nanomaterials such as cobalt and gallium nitride thin films. Using solvent-assisted capillary molding methods, Yoo *et al.* showed that phage can be densely packed atop micropatterned surfaces. Surface feature size was dependent on phage length as well as the swelling properties of the underlying electrolyte polymers.[78] Solis *et al.* also showed that, by combining soft-lithography techniques with phage antibodies, they could first pattern phage antibodies on the gold substrates. By tuning the concentration of the phage solution, they could immobilize phages on the gold substrates on a large scale in a controllable manner.[79] In the future, these

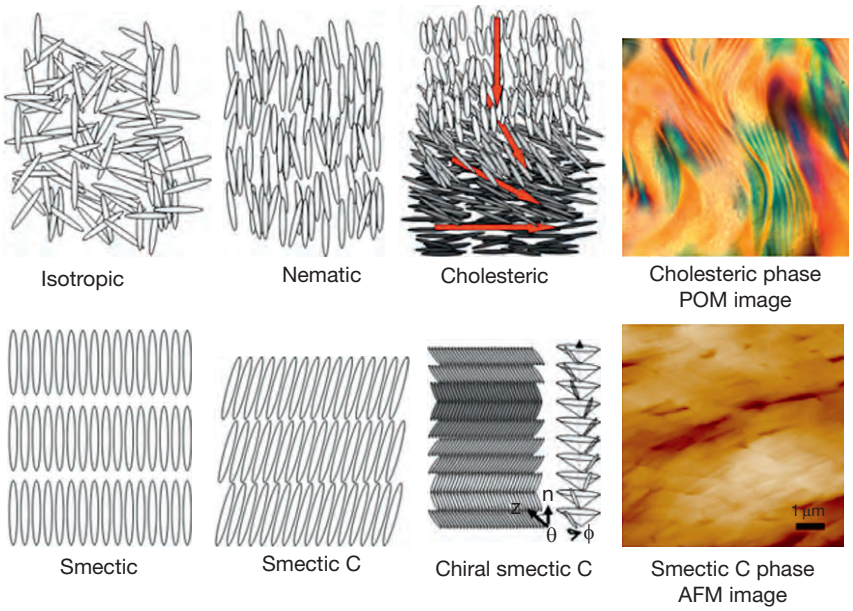

Figure 5 Schematic diagram of the M13 bacteriophage in a various liquid crystalline ordered structures and their microscopy image. Reproduced from Lee, S. W.; Wood, B. M.; Belcher, A. M. *Langmuir* **2003**, *19*, 1592–1598, with permission from American Chemical Society. © 2003 American Chemical Society.

surface patterning techniques may be useful for biosensor development, semiconductor fabrication, and energy storage and conversion devices.

Phage self-assembly combined with peptide display via genetic modification has been exploited to organize a variety of nanocomponents into periodically ordered films and fibers.[14,55,76] After the identification of ZnS-specific binding peptides through phage display, ZnS nanoparticles were self-assembled into periodically ordered film structures. Similarly, anti-streptavidin viruses were used to align gold nanoparticles, organic dyes, and biological molecules.[80] Magnetic nanoparticle–virus composite films (FePt, CoPt, etc.) were constructed using both phagemid and pVIII engineering of viruses.[81] Finally, spontaneously ordered virus-based thin films integrated with semiconductor (GaN) and metallic (Au) nanoparticles have been fabricated on multilayered electrolyte polymer films using layer-by-layer deposition.[17]

Besides electronic and magnetic particles, viruses can also be used for the assembly of biological tissues. Merzlyak *et al.* engineered M13 phage with RGD (integrin-binding peptide) and IKVAV (neural cell stimulating peptides) displayed on the major coat proteins.[21] Following formation of the liquid crystalline suspensions, these phages were spun along with target cells using a micropipette. The resulting microfiber structures contained aligned phages, which served as scaffolds for the controlled growth of fibroblasts and neural stem cells. Mechanically sheared thin films composed of liquid crystalline phages can also exhibit directional organization and serve as substrates that direct cell growth processes.[20]

2.206.3. Phage for Energy Materials

In recent times, there has been a rising demand for novel materials that can generate, store, and utilize energy with performance levels exceeding those of current technologies. In this research area, the ability to nucleate nanocrystals and self-assemble long-range ordered phage structures has attracted much attention.

2.206.3.1. Phage for Energy Storage Materials

One of the advantages of the use of engineered viruses as molecular templates is the fact that they permit nanomaterial synthesis and assembly in an energy-efficient and environmentally friendly manner. Nam *et al.* demonstrated that engineered M13 phages can be used to synthesize and assemble nanowires of cobalt oxide at room temperature, which can then be used as materials in lithium-ion batteries.[17] In this work, tetraglutamate (EEEE-, 4E) was first inserted into the N-terminus of the pVIII major coat protein. This phage was further engineered to express gold-binding peptide motifs. Both gold and cobalt oxide nanoparticles nucleated on the major coat protein, which resulted in hybrid nanowire structures composed of cobalt oxide with spatially interspersed gold nanoparticles (**Figure 6(a)**). These cobalt oxide nanowires mineralized by the M13 virus in aqueous condition at room temperature exhibited a high degree of crystallinity that was comparable to that of cobalt oxide nanoparticles prepared using conventional high-temperature (>500 °C) methods. When these virus-based hybrid composite Au–Co_3O_4 nanowires were applied to lithium battery electrode materials, the resulting electrodes showed improved energy storage capacity compared to the pure Co_3O_4 nanowires (>30% greater). This was mainly because of the enhanced conductivity and catalytic activity of the gold nanoparticles that participated in the redox reaction of Li with cobalt oxide. In order to integrate these hybrid nanomaterials into a thin and flexible energy storage system, M13 viruses (4E) were assembled in a two-dimensional polyelectrolyte using layer-by-layer assembly (linear poly(ethyleneimine)/poly(acrylic acid)). Spontaneously assembled viruses were then transformed to cobalt oxide nanowires in a similar fashion, enabling fabrication of lightweight, flexible, and transparent anode electrode films. The resulting self-assembled virus-based lithium-ion battery film exhibited enhanced battery performance in comparison to commercial batteries and displayed a cycling rate remarkably close to the theoretical limits. The main reason for the improved performance of novel virus-based battery materials is that the monodisperse nanowires templated by engineered viruses enable assembly of close-packed layered structures with a high surface area to volume ratio, and thus charge carrying capacity. The Belcher group has also developed a method for spatial positioning of virus-based electrodes using microcontact printing.[18] After coating a PDMS template (4-μm diameter circular patterns) with alternating layers of positive and negative polyelectrolytes, the engineered virus (4E) solution was dropcasted on the multilayers. The whole assembly was dipped into the cobalt oxide precursor solution and cobalt oxide nanowires formed on the micropatterned regions. Stamping the template onto a platinum microband current collector (cobalt oxide side down) produced a patterned array that served as the anode electrode component of an effective battery. In order to fabricate cathode materials needed for a full virus-based battery system, Lee *et al.* developed a novel multigene engineered virus.[16] The new cathode-fabricating viruses were engineered to nucleate iron phosphate on the pVIII major coat protein and to bind to carbon nanotubes on pIII minor coat proteins. The resulting viral particles successfully mineralized iron phosphate and interconnected the conductive carbon nanotubes, forming a conductive network cathode material (**Figure 6(b)**). It was found that incorporating carbon nanotubes increases the cathode's conductivity without adding much weight to the battery. By combining virus-based cathodes and anodes (viral silver Ag nanowires), the Belcher group has demonstrated complete virus-based 3-V batteries that can be used to power light-emitting diodes (LEDs).

2.206.3.2. Phage for Energy Producing Materials

Inspired by the natural photosynthetic systems, the well-defined structure of viral protein shells has also been used to develop biomimetic photosynthetic materials. In natural photosynthetic systems, several types of chromophores are spaced precisely so that the resulting structures can transfer absorbed solar energy in a highly efficient manner.[81] Thus, in manmade systems, the spacing between individual energy transferring components should be regulated with nanometer precision. In order to accomplish this, the well-defined structure of viral particles such as MS2 phage has been taken advantage of for precise spatial tuning of self-assembled structures that mimic

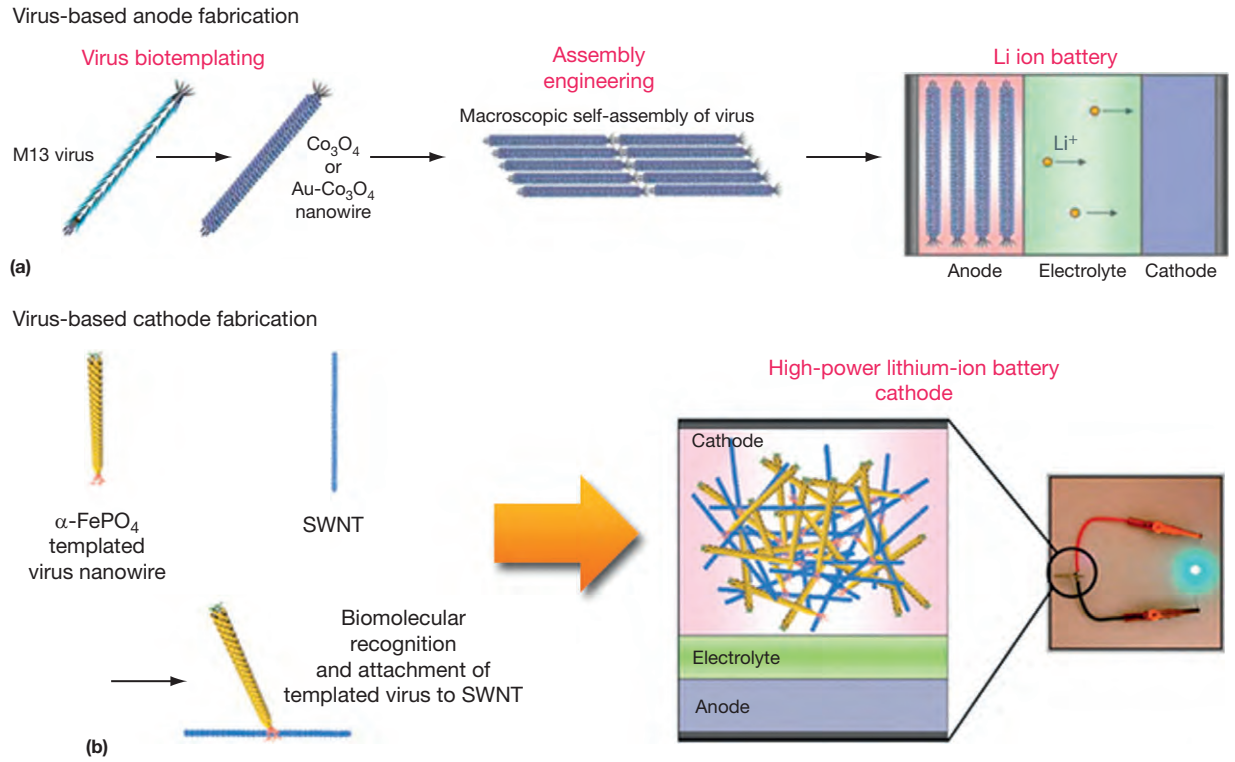

Figure 6 Schematic diagram of the virus-enabled synthesis and assembly of nanowires as negative and positive electrode materials for Li-ion batteries. (a) Rationally designed peptides were expressed on the major coat p8 proteins of M13 viruses to grow Co_3O_4 and Au–Co_3O_4 nanowires. Macroscopic ordering of the viruses was used to fabricate an assembled monolayer of Co_3O_4 nanowires for flexible, lightweight Li-ion batteries. Reproduced from Nam, K. T.; Kim, D.-W.; Yoo, P. J.; *et al*. *Science* **2006**, *312*, 885–888, with permission from Science. © 2006 American Association for the Advancement of Science. (b) Fabrication of genetically engineered li-ion battery cathodes using multifunctional viruses and a photograph of the battery used to power a green LED. Reproduced from Lee, Y. J.; Yi, H.; Kim, W.-J.; *et al*. *Science* **2009**, *324*, 1051–1055, with permission from Science. © 2009 American Association for the Advancement of Science.

natural energy transfer systems.[38,83] The protein structure of viral particles can be modified by genetic engineering or chemoselective bioconjugation approaches for incorporating specific functional groups at desired locations.[21,40] Using such techniques, photocatalytic materials such as porphyrins can be conjugated to genetically engineered M13 bacteriophage for investigation of virus-based energy transfer reactions.[84] Scolaro *et al.*, for example, have genetically modified M13 phage to express inserted peptides containing tryptophan (Trp) residues at the exposed N-terminal region of the pVIII major coat protein. Cationic porphyrin derivatives were then electrostatically immobilized to the negatively charged M13 phage surface. Fluorescence quantum yields of the resulting porphyrin–virus hybrid structures were examined at three different wavelengths (295, 400, and 438 nm) in order to observe energy transfer events from the external tryptophan residues of M13 to the contiguous porphyrins. In the presence of M13 with Trp residues, fluorescence quantum yields at 295 nm were found to be approximately two times higher than those observed with wild-type M13 phage. This only happened at 295 nm, which indicated that Trp residues were actively involved in the donor–acceptor coupling and energy transfer processes.

Site-specific chemical reactions have also been developed to precisely control the protein shell structure for design of well-defined multifunctional viral particles used in photosynthetic systems. Stephanopoulos *et al.* used viral capsids of sphere-shaped MS2 viral particles, which can be assembled in a hollow 27-nm diameter shell, to arrange fluorescent dyes (Oregon green) and zinc-porphyrin through chemoselective reactions (**Figure 7(a)**).[39] The maleimide-containing donor dyes were targeted to the interior surface of MS2 phage, which was modified with cysteine residues. The dyes were chosen to have emission spectra that overlapped with the porphyrin absorbance band. The exterior of the capsid was modified through an oxidative coupling reaction on the aniline residue[37] to introduce an aldehyde functional group, which was further modified with the aminooxy-containing derivative of Zn-porphyrin to form an oxime linkage. This arrangement enables fluorescence resonance energy transfer from the dyes inside to the porphyrin on the outside through the 2-nm-thick protein shell. The electron-transfer ability of the complex was monitored by photoreduction of methyl viologen by excited-state Zn-porphyrins (**Figure 7(b)**). The addition of 2-mercaptoethanol completed the catalytic cycle by reducing the porphyrin cations. Viral capsids with both fluorophore donors and porphyrin acceptors showed a 3.5-fold increase in the photoreduction of methyl viologen upon illumination at 505 nm for 15 min in comparison to the capsids without donor (**Figure 7(c)**). The results indicate that well-designed nanostructures incorporating donor dyes and porphyrins at

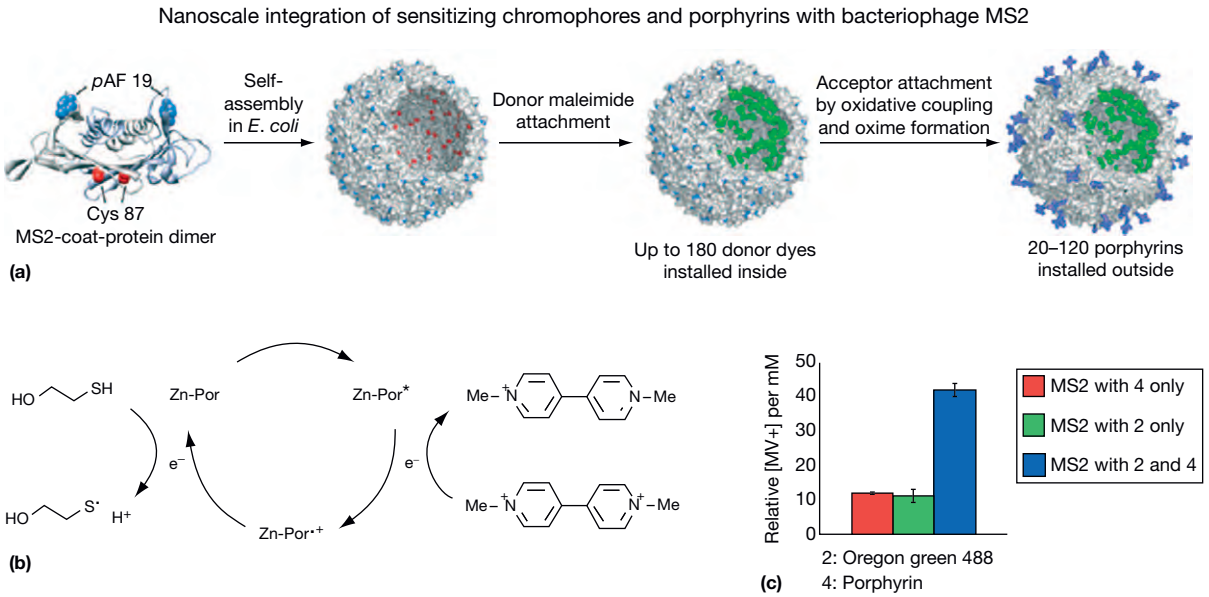

Figure 7 Integration of sensitizing chromophores and porphyrins into subunits of bacteriophage MS2 and photoreduction of methyl viologen by a sensitized porphyrin system. (a) Two mutations were introduced into subunits of the MS2 coat protein. After capsid formation in *E. coli*, the interior and exterior surfaces were differentially modified in a multistep sequence. (b) Catalytic cycle of photoreduction. (c) Relative efficiency of the photoreduction with different systems upon illumination at 505 nm for 15 min. Reproduced from Nicholas, S.; Carrico. Z. M. C.; Francis, M. B. *Angew. Chem. Int. Ed.* **2009**, *48*, 9498–9502, with permission from Wiley-VCH Verlag GmbH & Co. KGaA © 2009 Wiley-VCH Verlag GmbH & Co. KGaA.

specific locations can perform energy transfer from the inside to the outside of the capsids.

2.206.4. Phage for Sensing Materials

Phages have been used extensively in sensing applications over the course of the past 2 decades. Because of their genetically tunable chemical surface properties, self-assembling capabilities, and biological activity, phages have emerged as valuable tools for detection of various targets including small molecules,[85–87] biomolecules,[88–93] and whole cells.[94–104] Phages have been applied to biological and chemical sensor development in three fundamental ways[19]: First, phage display techniques have been used for rapid evolutionary screening of peptide molecular recognition elements (MREs) capable of binding to a particular target of interest. Once their sequence is identified, these MREs can be chemically synthesized and applied to assays for further development of integrated sensor systems. Second, engineered target-binding phages can be mass produced using a bacterial host and used, intact, as a sensing probe. Serving as a nanometer-scale scaffold, a phage probe is capable of displaying MREs in high copy numbers with controlled orientation. Finally, the biological activity of lytic phages can be utilized for detection of host bacteria. In this case, high phage replication rates and unique phage–host interactions enable rapid and specific sensing of microorganisms.

2.206.4.1. Phage-Based Molecular Recognition

The success of the use of phages for chemical and biological sensing can be attributed to their broad adaptability and ease of genetic manipulation as a molecular recognition agent; capacity to enhance target binding by serving as multivalent scaffolds for MREs; and natural ability to recognize, replicate inside of, and sometimes destroy microorganisms. Phages are thus versatile sensing probes with incredible chemical diversity and structural complexity. They can be applied for chemical and biological sensing much in the same way as antibody,[105] peptide,[106] aptamer,[107] or imprinted polymers.[108]

Both phage display and rationale modification have emerged as convenient tools for the development of sensing probes. As discussed in the previous chapter, by insertion of the randomized gene sequences into phage genome, it is possible to express billions of peptide-based receptor candidates. These peptide libraries enable rapid evolutionary screening for receptors. There are many reviews related to receptor development using phage display.[19,36,109–112] As an illustration, we briefly introduce one example of rapid receptor discovery performed using trinitrotoluene (TNT) explosive as a molecular target. Jaworski *et al.* identified TNT- and DNT-binding peptide motifs using phage display processes.[86,113] These two explosive molecules possess very similar chemical structures with one nitro functional group difference. After four rounds of TNT screening using phage display, the researchers identified TNT-binding sequences with the consensus motif of Trp-His-Trp-X (X: hydroxylated, amine, or positively charged side chain) at the N terminus of the receptor (**Figure 8**).[86] From competitive screening experiments, 95% of the strong binding phage exhibited the same tetrapeptide motif: Trp-His-Trp-X. The most abundant sequence was assigned as the best TNT-binding peptide candidate (Trp-His-Trp-Gln-Arg-Pro-Leu-Met-Pro-Val-Ser-Ile: TNT-binding peptide (TNT-BP)). Similarly, consensus DNT-binding motifs were identified after five rounds of screening (**Figure 8(a)**). Among the subset

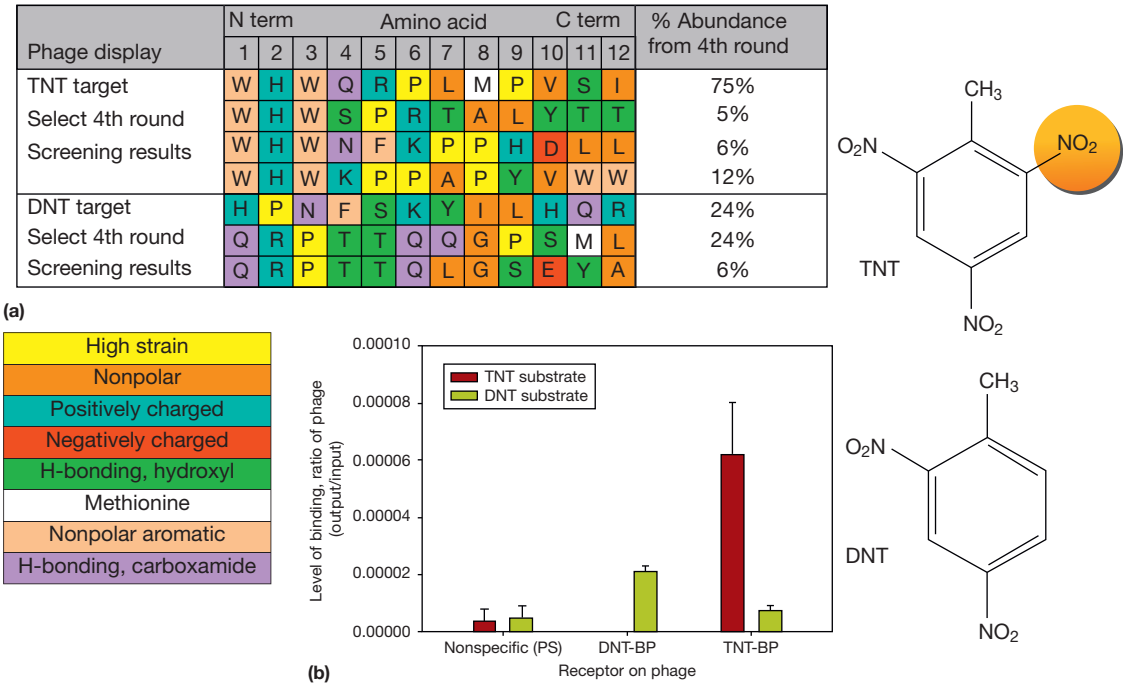

Figure 8 Phage display screening against TNT and DNT explosives: (a) Converged amino acid sequences from fourth round of phage display screening with noted percentage abundance obtained from sequencing results. (b) Selectivity screening of DNT receptor and TNT receptor against DNT substrates and TNT substrates with level of binding quantified from phage titration. Nonspecific binding levels are identified by polystyrene (PS) binding phage against TNT and DNT substrate. All data presented as mean ± standard deviation. Reproduced from Jaworski, J. W.; Raorane, D.; Huh, J. H.; Majumdar, A.; Lee, S. W. *Langmuir* **2008**, *24*, 4938–4943, with permission from American Chemical Society. © 2008 American Chemical Society.

of TNT-binding sequences, several exhibited varying affinity for DNT. In order to enhance the selectivity between TNT and DNT targets, negative screening was performed for the DNT molecules using the isolated TNT-binding peptides. The TNT-binding peptides with the lowest affinity for DNT exhibited remarkable selectivity for the TNT target (Figure 8(b)). This result demonstrates that M13-linked receptor sequences identified from phage display can selectively bind a predetermined target. Through investigation using fluorescent binding assays and peptides with alanine substitutions in the N-terminal region, it was shown that the conserved tryptophan and histidine residues are critical for effective TNT binding. The tryptophan replacement resulted in a 58% decrease in affinity, while the histidine replacement reduced binding by 48%. By comparing the identified TNT-binding sequence, scrambled sequence, histidine substitute, and tryptophan substitute for different substrates, the investigators provided evidence of substrate selectivity through multivalent binding. Cerruti *et al.* later demonstrated that these TNT receptor peptides have a remarkable selectivity for target TNT molecules following immobilization on quartz crystal microbalance (QCM) liquid sensing platforms.[113] The rapid receptor discovery technique for the TNT and DNT explosive introduced here is one of many examples of the application of the phage display for molecular sensing. With its evolutionary capabilities, phages can be generalized as tools for the discovery of novel molecular receptors for environment-, terrorism-, and health-related target toxicants in a rapid and convenient manner.

2.206.4.2. Phage for a Sensing Platform

Phages have been used in combination with many transducing modalities not only for the discovery of receptors for various target analytes but also as functional sensor components. In order to generate an observable output signal as a result of a specific molecular recognition event, phage particles have been coupled with nano- or micromechanical, electrochemical, and optical sensing platforms, which have recently been reviewed.[19] Using many of the self-assembly approaches discussed in the previous section, it can be convenient to fabricate phage-based sensor systems with highly dense and customizable molecular recognition elements. Both whole-phage and phage-derived probes can be implemented in several sensing formats, for example, as alternatives to antibodies in solution-based and surface-based assays,[109,110] or as a biochemical signal amplifier in bacterial culture-based assays.[100,101,114] A variety of useful sensing systems and devices that utilize phage have emerged since the development of phage display for molecular biopanning.[86,113] These can be based on the measurement of mechanical, electrical, or optical signals in response to the presence of molecular or cellular targets (Table 1).

2.206.4.3. Micro- and Nanomechanical Sensing

Phages have been used to coat materials for various micro- and nanomechanical sensing platforms. Since their original development for microweighing applications,[118] quartz crystal microbalances (QCMs), nano-cantilevers, and magnetoelastic

Table 1 Classes of phage-based sensing systems

Mechanism	*Platform*	*Probe*	*Target*	*References*
Nano/ micromechanical	Quartz crystal microbalance	pVIII-engineered Fd phage	*S. typhimurium*, β-galactosidase, prostate-specific membrane antigen (PSMA)	89,91,98,101,114
	Magnetoelastic resonator	pVIII-engineered Fd phage	*S. typhimurium*, *B. anthracis*	95–97
Electrochemical	Amperometric sensor	Phage λ; M13 phagemid/ALP	*E. coli* K12 (MG1655); *E. coli* TG-1	99,100
	Impedance sensor	T4 phage, λ phage, pVIII-engineered M13 phage	*E. coli*, *Salmonella* spp., anti-M13 IgG, PSMA	91,93,102,115
	Light-addressable potentiometric sensor	pIII-engineered M13 phage	Human phosphatase of regenerating liver-3 (hPRL-3) marker carcinoma cell (MDAMB231)	87,103
Optical	Fluorescence, ELISA	pVIII-engineered Fd phage, pIII-engineered M13 phage	*B. anthracis*, staphylococcal enterotoxin B 2,4,6-trinitrotoluene, *S. typhimurium*, hepatitis B surface antigen	84,88,90,94,116
	Surface plasmon resonance	pVIII-engineered M13 phage, pVIII-engineered M13 phage	β-Galactosidase, L-monocytogenes	89,98
	Opto-fluidic ring resonator	Bifunctional (pVIII and pIII-engineered) Fd phage (RGD and HPQ)	Streptavidin	92

resonators have been used widely for real-time, label-free studies of biomolecular interactions and cellular adhesion.[119,120] Detection is typically based on the accumulation of mass at the sensor surface and a corresponding shift in the vibrational resonance of the transducer.

Commercially available piezoelectric transducers such as QCMs are commonly functionalized with target-binding receptors such as engineered phage and implemented for sensing.[92,102,115] On the application of an alternating electric field, coated QCMs undergo mechanical vibrations at a frequency that is dependent on the amount of accumulated target. In one comparative study of label-free QCM and standard ELISA-based molecular sensing,[115] Nanduri *et al.* demonstrated the efficacy of physically adsorbed pVIII-engineered Fd phage as a target-binding agent against a model protein, β-galactosidase. They found that, while immobilized phage performed similarly to monoclonal antibodies in a standard ELISA format, QCM-based measurements yielded a fundamentally different dose–response curve (~12-fold lower K_d value and a ~3-fold lower Hill coefficient), perhaps indicating a relative improvement in target accessibility and thus sensing capability.

Another means of inducing vibrational resonance in a mechanical sensing platform is through the use of magnetoelastic (ME) materials. When subjected to megahertz-range oscillating magnetic fields, submillimeter ME 'ribbons' oscillate, generating a corresponding alternating current in a remote pickup coil. This technique allows for wireless measurement of frequency shifts and thus remote sensing.[96–98] In a recent demonstration of multiplexed detection of pathogenic organisms,[97] Huang *et al.* determined the concentrations of pathogenic *Salmonella typhimurium* and *Bacillus anthracis* simultaneously using phage-functionalized ME ribbons with two different resonance frequencies (**Figure 9**). Separately functionalized ME platforms were highly specific with no detectable cross talk between frequency channels.

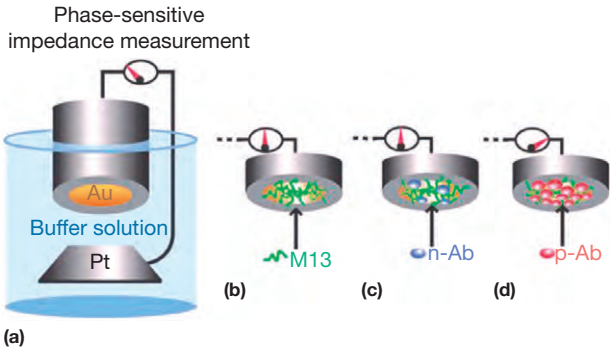

Figure 9 Phages as sensor coating materials. Schematic diagram of virus-based impedance measurement setup. (b) A dense virus layer was covalently bonded to the gold surface that produces a dense phage layer that completely electrically insulates the gold surface from contact with the buffer solution. (c) Exposure of this virus electrode to a 'negative' antibody (n-Ab, blue) causes no change to either the imaginary component of impedance, Z_{Im} or to $Z_{Re.}$ (d) Exposure to a 'positive' antibody (p-Ab, red) that is selectively recognized and bound by the phage causes a significant increase in the high-frequency Z_{Re}. Reproduced from Yang, L.-M. C.; Tam, P. Y.; Murray, B. J.; *et al. Anal. Chem.* **2006**, *78*, 3265–3270, with permission from American Chemical Society. © 2006 American Chemical Society.

2.206.4.4. Electrochemical Sensing

Molecular recognition of specific targets by phage peptide receptors can be detected using electrochemical sensors. Electrochemical sensing systems are useful because they allow for direct interrogation of the sample on a compact, integrated platform. Detection is typically based on the simple readout of changes in currents, impedances, and potentials associated with the presence of target species. Amperometric sensing systems measure current flow in a solution undergoing an oxidation–reduction reaction. In conjunction with such

systems, phages can be utilized for highly specific detection of their bacterial host (target) on generation of an electrochemically active reporter. In one example, phage λ was used as a lysing agent for a specific strain of *E. coli*. Release of β-D-galactosidase enzyme and subsequent conversion of an added substrate (*p*-aminophenyl-β-D-galactopyranoside) to an electroactive product allowed for detection of cells at concentrations as low as 0.01 colony-forming units per milliliter.[101] Detection without lysis of the target microorganism has also been demonstrated using a phagemid system to express alkaline phosphatase as a reporter.[99]

Impedance spectroscopy is one of the most well-developed electrochemical techniques used in combination with engineered phage for sensing applications.[92,94,103,116,121] Impedance measurements are easy to conduct over a range of frequencies and are highly sensitive to perturbations (e.g., target binding) at the surface of the sensing electrode. In one example of such a sensor,[92] Yang *et al.* covalently attached a dense layer of pVIII-engineered M13 phage to a gold electrode, which was then immersed in a test solution. Measuring time-dependent changes in electrical impedance of the circuit at the kHz frequency range resulted in a target (PSMA) detection limit of ~120 nM and signal to noise ratios greater than 10. More recently, the authors used the same technique to thoroughly characterize binding of anti-M13 antibodies to the phage-coated electrode and determined 4–140 kHz as an optimal driving frequency for the sensing circuit.[116] Additional examples of impedance sensing involve detection of *E. coli* on screen-printed carbon electrode arrays functionalized with T4 bacteriophage,[103] and real-time observation of salmonella infection and lysis by bacteriophage.[94]

Phages have also been used as a bioresponsive coating for light-addressable potentiometric sensors (LAPS).[88,104] Composed of a semiconductor–insulator base (e.g., $Si–Si_3N_4$), which can be activated by directed light pulses, these devices allow for interrogation of surface potentials generated as a result of ion gradients, redox reactions, or pH changes.[122] Such devices have been coated with engineered phage for label-free detection of human phosphatase marker and cancer cells.[88] More recently, LAPS were covalently modified with four different phages selected against metastatic SW620 cells.[104] When tested with other highly metastatic lines (e.g., MDAMB231) added to a plasma sample, the system was able to detect as few as 100 cancer cells with almost no background from healthy leukocytes.

2.206.4.5. Optical Sensing

Employing phenomena such as colorimetric amplification, fluorescence, and photonic resonance, optical sensing modalities are quite versatile. Detection can be based either on signals associated with optical labels or on changes in the optical properties of a sensor–sample interface.[19] In either case, optical systems are extremely sensitive, with high signal-to-noise ratios and, sometimes, single-molecule resolution.

ELISA-like assays are commonly carried out on microtiter plates using engineered phage or phage-derived affinity peptides.[85,89,91,95,117] This allows for rapid assay development and the use of standard absorbance or fluorescence-based plate readers. For example, Sorokulova *et al.* performed intensive landscape phage screening against *S. typhimurium* using both phage-capture and target bacteria-capture sandwich ELISAs.[117] Secondary labeling of captured target with alkaline phosphatase-conjugated antibodies allowed for colorimetric measurements of binding affinities. Fluorescently labeled phage can also serve as the reporter in these assays.[85,123] In addition, fluorescent labels allow for microscopy, FACS analysis,[117] and Förster resonance energy transfer assays, whereby distance-dependent, nonradiative energy transfer from a donor fluorophore to an acceptor allows for the detection of highly specific biomolecular interactions (e.g., between phage-derived antibody fragments and morphine[124]). Fluorescent quantum dot labels have been used in conjunction with engineered phage in order to carry out detection of host bacteria.[114] Here, phages were engineered to display a peptide tag, which could be biotinylated by the host's biotin ligase protein. After being released into solution, biotinylated phage progenies were then labeled by streptavidin-conjugated quantum dots. Viral infection thus served as a means of signal amplification, as quantum dot fluorescence was directly correlated with phage infectivity. Because of rapid replication, a 100-fold amplification was observed within 1 h, allowing for a detection limit of 10 bacterial cells per milliliter of sample.

Label-free optical sensing platforms that employ surface plasmon resonance (SPR), waveguides, interferometers, and ring resonators allow for real-time detection of target-binding events.[125] These systems measure refractive index changes at a surface functionalized with MREs. For example, pVIII-engineered phage can be used for highly sensitive SPR detection of β-galactosidase, a model protein,[90] or for kinetic binding analysis of *Listeria monocytogenes*, a pathogenic bacterium.[99] In these studies, this technique was easily adaptable, as engineered phages specific to the target of choice were simply adsorbed onto a commercial SPR chip. Whispering gallery mode resonators represent another class of versatile optical biosensors that have been implemented on microspheres, microtoroids, planar ring waveguides, and cylindrical optofluidic devices.[126] Because of recirculation of resonant light modes, these systems are extremely sensitive. In one example,[93] Zhu *et al.* developed a phage-based optofluidic microring resonator by depositing streptavidin-binding phage on the interior of a pulled microcapillary tube. The resonator was coupled to a light source and photodetector via a tapered optical fiber. Shifts in the resonant frequency peak of circulating whispering gallery modes corresponded linearly to both phage deposition and target binding, and allowed for a streptavidin detection limit of 100 pM.

Each of the sensing modalities described above exists because of a unique combination of sensitivity, specificity, speed, cost, and adaptability. No single system is 'best' overall – optimality depends on the particular sensing application of interest. However, at least for the purpose of sensor development, an engineered phage may be advantageous over other probes because of its broad adaptability. The ability to develop MREs specific to almost any molecular or cellular target of interest is extremely powerful, as it allows investigators to focus on the detection systems rather than the probe, alone.

2.206.5. Phage for Biomedical Application

Over the past century, phages have been used in biomedical applications including antibiotics, drug delivery, gene therapy, and tissue engineering. As mentioned, the word 'bacteriophage' (directly translated from Greek as 'bacteria eater') implies that we can use it as an antibacterial drug. The first description of bacteriophages in scientific literature originated from a British bacteriologist, Ernest Hankin, in 1896, when he observed that a substance present in the waters of the Ganges and Jumna rivers in India significantly reduced the titer of *Vibrio cholerae* bacteria when grown in culture.[127,128] Twenty years later, two independent scientists, Fredrick Twort in 1915 and Felix d'Herelle in 1917, conducted more conclusive studies to characterize such bactericidal effects. It was at that time that d'Herelle reported that they were caused by a bacteria-infecting virus and coined the term 'bacteriophage.' Soon after this discovery, d'Herelle and his contemporaries began using bacteriophage preparations as a medical therapy against the bacteria that caused diseases such as dysentery and cholera.[128,129] Despite early clinical success and even commercialization by several well-known companies including Eli Lilly[128,129] phage therapy failed to take off. Several factors led to its early demise, including lack of in-depth knowledge of phage–bacteria interactions, failure to efficiently purify the phage from lysed bacterial solution, and rapid clearance of the phage from the body's circulation.[128,129] Another factor that led most Western researchers to abandon the advancement of phage therapy was the coming of an antibiotic era. While most phage-bacteria interactions are species specific, antibiotics can have a blanketing bacteriocidal effect on bacterial populations. Thus, at the time, they were more effective and attractive for eliminating bacteria.

2.206.5.1. Phage Therapy

During the past 60 years, phage therapy investigations continued in centers across Eastern Europe and the former Soviet Union. Today, with the rise of antibiotic-resistant bacteria[130] and further developments in molecular and microbiology, the idea of phage therapy is becoming more popular among the scientific[127,128,131] as well as business communities. Previous problems associated with phage therapy are now being addressed, and scientists are expanding on molecular biology knowledge of phage–host interactions and infective mechanisms. For example, it has been shown that M13 bacteriophage are only able to infect Gram-negative bacterial cells that display the F pilus protein on the outer membrane, such as *E. coli*. Specific interactions between the TolQRA bacterial receptor and the pIII and pVIII proteins facilitate virus penetration and DNA transfer.[132–134] This specificity allows for the use of *E. coli* for effective replication and amplification of the virus but ensures that M13 will not infect or replicate within a human patient's indigenous bacterial population or eukaryotic cells, which lack the necessary tropism. Another major problem that previously led to failure of administered phage therapy was contamination of phage mixtures with either bacterial particles or endotoxins, which can incite potentially harmful immunogenic reactions.[135] At present, advanced purification methods including ultracentrifugation, precipitation, and ion chromatography allow for solutions of phage to be prepared that are free of bacteria and related particles.[128,129,136]

Phages can be cleared from the body through two pathways. Composed of proteins foreign to the body, a virus may evoke an immune system response that would inactivate and destroy it. Alternatively, phage particles may be rapidly cleared by the reticuloendothelial system (RES), which includes filtering organs such as the liver, spleen, kidneys, and cells therein that are responsible for phagocytosis of bacteriophages and other foreign particles.[137] The RES may be the more prominent mechanism for phage clearance. For example, when mice or rats were injected with phages, neutralizing antibodies could not be detected in the animal's blood,[137,138] suggesting that phages were removed from the circulation before an immune response could be initiated. To allow the virus to perform its designated function and remain in the circulation longer, directed evolution approaches have proven effective for bypassing neutralizing antibodies[138] as well as reducing RES clearance.[140] In these cases, the virus coat protein was either allowed to mutate during the selection process[140] or chosen from a recombinant virus library.[139] The fittest candidate after several rounds of stringent selection had only a few amino acid differences in its coat protein. However, it was either 96 times more resistant to antibody opsonization[139] or was able to avoid RES entrapment 16 000 times better 24 h after injection.[140]

Several recent articles have reviewed the potential of medicinal phage therapy along with the obstacles that still need to be overcome before widespread use.[127–129,131] One challenge is the intensive regulatory approval process that any phage-based application will have to face.[131] A step in this direction is the FDA's recent approval of the use of a phage mixture to combat *Listeria* bacterial growth on meat and cold cuts. The first of its kind, this approval was granted in August 2006 to Intralytix, Inc. based in Maryland[141] and may pave the way for future human-based phage applications.

2.206.5.2. Phage for Drug and Gene Delivery

In addition to therapies centered on bacterial lysis, medical applications that harness the ability to alter phage surface proteins through either genetic engineering or chemical conjugation are also being developed. Several groups are investigating engineered filamentous bacteriophage for *in vivo* screening via phage display within organs[53] or cancerous tissue,[142,143] for targeted drug delivery,[138,144] or as an imaging agent.[145] At this time, behavioral and histological evaluations of animals post-therapy, as well as previous reports of humans treated for infection with phage solutions, have not indicated the existence of any harmful side effects of phage therapy.[128,138,143,145]

For gene delivery applications, therapeutic genetic material can be incorporated into phage DNA and carried into cells following receptor uptake.[146] Phage can be locally targeted to cell receptors (i.e., via RGD or other ligands) by incorporation of specific targeting and/or internalization peptides. To make phage even more effective as DNA delivery vehicles, they can be further decorated with peptides that facilitate endosomal escape or nuclear localization motifs that target the nuclear envelope.[147] The most widely used bacteriophages for gene

delivery are M13 filamentous phages[148–150] and lambda phages.[151] In general, these can be engineered to incorporate targeting ligands without undergoing significant structural change. To enhance gene delivery efficiency, phage with multifunctional peptides can be produced using a phagemid system, which facilitates manipulation of expressed proteins on the viral vectors.[149] Phage display technology has allowed for identification of novel homing peptides that target unknown cell surface proteins. The targeting peptides can be incorporated into bacteriophage coat proteins through the genetic engineering techniques described previously.[146] These include peptides (RGD, glioma-binding peptide),[149,152] HER2 receptor targeting antibody,[150] growth factors (EGF, FGF2),[148,153,154] and the penton base of adenovirus.[151]

Eukaryotic viruses such as adeno-associated virus (AAV) have fantastic transgene delivery capabilities, but they require elimination of native tropism for mammalian cells. In contrast, M13 bacteriophages have no tropism for mammalian cells; however, their gene delivery efficiency is poor. Thus, there has been an effort to combine the advantageous aspects of AAV and M13 bacteriophages into a single system.[146] Hajitou *et al.* constructed hybrid phage with two genes from phage and nucleus integrating gene from AAV, called inverted terminal repeats. Additionally, these phages were engineered integrin-binding peptides on minor coat proteins. Therefore, the RGD peptide-induced internalization of the phage through integrin-mediated endocytosis process and the inverted terminal repeats (ITR) led to improved transgene delivery in the cytoplasm. The resulting AAV/phage system provided superior tumor transduction over phage alone. Nucleic acid cargo can also be incorporated into scaffolding materials for delivery to cells. It has been shown that DNA materials that are tethered to a matrix, rather than simply encapsulated, are more effectively transferred to the cell.[155]

2.206.5.3. Phage for Tissue-Engineering Materials

The unique biochemical and structural features of genetically engineered phage can be also used in the context of tissue engineering in order to control cellular growth (**Figure 10**). Merzlyak *et al.*, for example, have explored the use of genetically modified M13 phage as a novel building block for tissue engineering materials.[21] This was accomplished by engineering the phage to display specific cell signaling motifs and then assembling the viral particles into a macroscopic scaffolding material.[21] Many peptide expression systems have previously been demonstrated on the various capsid proteins of the phage through creation of peptide libraries.[36,44,156] However, as biological particles for peptide display, phages possess the inherent limitation of having to be successfully expressed and assembled within the *E. coli* bacteria host, which restricts the type and number of peptides that can be displayed.[45,157–159] In order to expand the utility of M13 for phage display, Merzlyak *et al.* developed a novel cloning approach for display of an integrin-binding RGD motif on every copy of the pVIII major coat protein. The researchers constructed the phage using a partial library, in which an engineered octamer insert for pVIII included a constrained RGD group that was surrounded by flanking degenerate residues.[21] This allowed for expression of inserts that retained the desired function of the RGD motif and yet were biologically compatible with *E. coli* during the intricate phage replication process. After construction of engineered phage that stably displayed either RGD- or IKVAV-peptide groups on every copy of the pVIII protein, Merzlyak *et al.* constructed aligned two- and three-dimensional scaffolding materials containing phages and tested their applicability for tissue engineering. First, the investigators verified the biocompatibility of the materials by growing NIH-3T3 fibroblast and neural progenitor cells on phage films and in phage containing media. Both cell types showed normal morphology and proliferation when in direct contact with phage materials. Neural progenitor cells either retained their progenitor state or differentiated toward the neural cell phenotype depending on media conditions. It was then demonstrated that three-dimensional phage materials could support proliferation and differentiation of neural progenitor cells. Both RGD- and IKVAV-phage matrices facilitated colony formation of neural progenitor cells, which sustained a viability of over 85% during the 7-day observation period. In comparison to RGE and wild-type phage controls, RGD and IKVAV phage resulted in enhanced binding and spreading of neural progenitor cells with high specificity. Finally, by simple extrusion or spinning of phage solution, the researchers constructed aligned three-dimensional phage fiber matrices with embedded neural progenitor cells. The resulting phage fibers encouraged neural cell differentiation and directed cell growth parallel to the long axis of the fibers.[21] Mechanical shearing of phage solution on a glass substrate resulted in two-dimensional directionally oriented films. These oriented films were shown to direct the alignment and morphology of fibroblasts, osteoblasts, and neural cells.[20] The Grinstaff group has worked in panning phage-displayed combinatorial peptide libraries against biomaterials[160] and implantable biomedical devices[161,162] to identify binding peptides usable in surface modification. They have synthesized heterobifunctional peptides which include a cell-adhesion promoting sequence (RGD) along with an identified binding sequence for the target surfaces. The interfacial biomaterial coating for polymers (polyglycolic acid, polystyrene)[160,163] and the metal surface (titanium)[162] using as-prepared peptides enabled the material to guide endothelialization on the coated surface. In the same groups, the HKH tripeptide motif was identified as the titanium-binding contributor using a phage display screening process.[161] A synthetic peptide containing three repeats of HKH was conjugated with PEG. The pegylated analogue of the peptide was shown to adsorb to the titanium surface, preventing nonspecific protein adsorption and bacterial colonization which can cause orthopedic implant failure.

2.206.6. Summary and Future Perspectives

Viruses are unique in their intrinsic ability to self-replicate within a cellular host and self-assemble into highly ordered two- and three-dimensional nanostructures. By combining these self-replicating and self-assembling functions, virus-based materials can be used to construct nanomaterials and devices with novel structure and function. Moreover, in order to improve the performance of the desired function, it is possible either to evolve these materials toward a directed endpoint or to incorporate rational design modifications

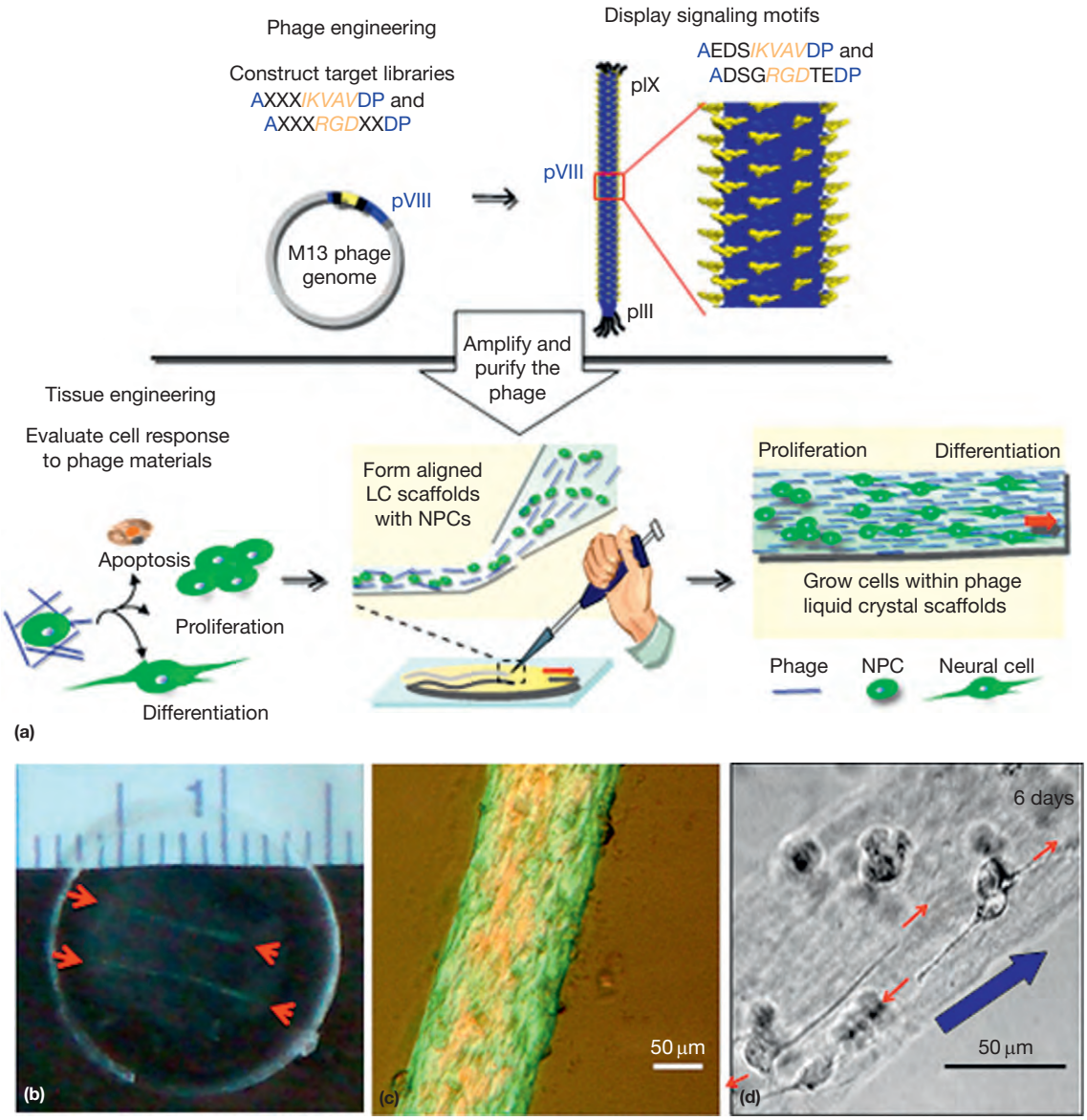

Figure 10 Phage-based tissue engineering materials. (a) Schematic diagram of developing M13 phage tissue engineering process to depict phage engineering, cell response characterization, and aligned fiber matrix fabrication. Directional guidance of neural cells using the liquid crystalline phage matrices. (b) Photograph of the phage microfiber (1 cm in length) spun in agarose, shown with a centimeter scale ruler. (c) POM image shows nematic liquid crystalline structure of the phage microfiber, scale bar = 50 μm. (d) Polarized optical microscopy images of the differentiated neural cells within aligned RGD-phage matrices after 6 days. Reproduced from Merzlyak, A.; Indrakanti, S.; Lee, S. W. *Nano Lett*. **2009**, *9*, 846–852, with permission from American Chemical Society. © 2009 American Chemical Society.

through genetic engineering. Over the past couple of decades, we have witnessed the emergence of a new class of virus-based nanomaterials and nanotechnologies. As discussed in this chapter, viruses have been developed as templates for fabrication of exquisite nanostructures including electronic or semiconductor materials, energy storage materials, sensors, and biomedical materials. They can be deposited as functional coatings for existing devices used for applications such as biological and chemical sensing. The resulting novel materials and devices benefit from the unique biological, physiochemical, and structural features of viruses such as self-replication, self-assembly, directed-evolution, and target recognition.[14,21,55,76,86]

Through eons of evolution, nature has arguably mastered the process of biosynthesis. There are several reasons for this: First, biological systems can replicate with remarkable precision at molecular, cellular, and macroscopic scales. Second, these systems can self-organize in a hierarchical fashion, generating structures and exhibiting behaviors that extend beyond the capabilities of a single subunit. Third, through diversification (mutation) and selection processes, these systems progressively evolve and adapt in order to maintain fitness in the presence of environmental pressures. This information is recorded genetically and passed to future generations. Inspired by these exquisite biological systems and their apparent ability

to self 'design,' Dr. Eric Drexler proposed several characteristics of future materials and machinery in his book *Engines of Creation* in 1983.[164] He coined the term 'Nanobot (Nanoscale Robot)' for systems that can self-assemble, self-evolve, and self-replicate – serving as fabricators of the next generation of improved nanobots. To our knowledge, synthetic systems that exhibit these behaviors do not currently exist, and it is difficult to imagine them in the near future. Virus-based materials and devices, on the other hand, may be the best representations of the nanobot concept proposed by Dr. Drexler. Through the application of techniques described in this chapter, along with methodologies that have not yet been developed, we might witness a real nanoscale 'robot' that is capable of performing intricate programmable tasks. We have termed this emerging science and engineering field '*virotronics*' because it seeks to exploit the unique properties of viruses for human benefit.[59] *Virotronics* represents a novel virus-based design technology that can be used to create new materials with precise molecular-level structural and functional control. As we described throughout this chapter, *virotronics* incorporates the unique biological advantages of viruses, such as specific molecular recognition, evolution, and self-replication with engineering principles including information mining, data storage and processing, as well as structural self-assembly, self-templating, and organization of various materials into functional devices at multiple length scales. In the near future, we strongly believe that products derived from *virotronics* will be used regularly for data mining, storage, and computation, for generation of clean and green energy, for sensing of chemical toxicants and biological pathogens, for regeneration of damaged tissues, and for other unforeseen applications which will have an impact on human health and quality of life.

References

1. Huynh, W. U.; Dittmer, J. J.; Alivisatos, A. P. *Science* **2002**, *295*, 2425–2427.
2. Kim, J. Y.; Lee, K.; Coates, N. E.; *et al*. *Science* **2007**, *317*, 222–225.
3. Sirringhaus, H.; Tessler, N.; Friend, R. H. *Science* **1998**, *280*, 1741–1744.
4. Silva, G. A.; Czeisler, C.; Niece, K. L.; *et al*. *Science* **2004**, *303*, 1352–1355.
5. Alivisatos, P.; Majumdar, A.; Cummings, P.; *et al*. *Nanoscience Research for Energy Needs; Report of the March 2004 NNI Grand Challenge Workshop*; DOE 2004: Washington, DC, 2004.
6. Sundar, V. C.; Yablon, A. D.; Grazul, J. L.; Ilan, M.; Aizenberg, J. *Nature* **2003**, *424*, 899–900.
7. Aizenberg, J.; Weaver, J. C.; Thanawala, M. S.; Sundar, V. C.; Morse, D. E.; Fratzl, P. *Science* **2005**, *309*, 275–278.
8. Cha, J. N.; Stucky, G. D.; Morse, D. E.; Deming, T. J. *Nature* **2000**, *403*, 289–292.
9. Weiner, S.; Traub, W.; Wagner, H. D. *J. Struct. Biol*. **1999**, *126*, 241–255.
10. Lodish, H. F.; Berk, A.; Kaiser, C. A. *Molecular Cell Biology*. St. Martin's Press: New York, 2008.
11. Dolphin, D., McKenna, C., Murakami, Y., Tabushi, I., Eds.; In *Biomimetic Chemistry*; American Chemical Society: Washington, DC, 1980.
12. Mann, S. *Biomineralization: Principles and Concepts in Bioinorganic Materials Chemistry*. Oxford University Press: Oxford, UK, 2001.
13. Seeman, N. C.; Belcher, A. M. *Proc. Natl. Acad. Sci. USA* **2002**, *99*, 6451–6455.
14. Lee, S.-W.; Mao, C.; Flynn, C. E.; Belcher, A. M. *Science* **2002**, *296*, 892–895.
15. Whaley, S. R.; English, D. S.; Hu, E. L.; Barbara, P. F.; Belcher, A. M. *Nature* **2000**, *405*, 665–668.
16. Lee, Y. J.; Yi, H.; Kim, W.-J.; *et al*. *Science* **2009**, *324*, 1051–1055.
17. Nam, K. T.; Kim, D.-W.; Yoo, P. J.; *et al*. *Science* **2006**, *312*, 885–888.
18. Nam, K. T.; Wartena, R.; Yoo, P. J.; *et al*. *Proc. Natl. Acad. Sci. USA* **2008**, *105*, 17227–17231.
19. Mao, C.; Liu, A.; Cao, B. *Angew. Chem. Int. Ed. Engl*. **2009**, *48*, 6790–6810.
20. Chung, W.-J.; Merzlyak, A.; Yoo, S.-Y.; Lee, S.-W. *Langmuir* **2010**, *26*, 9885–9890.
21. Merzlyak, A.; Indrakanti, S.; Lee, S.-W. *Nano Lett*. **2009**, *9*, 846–852.
22. Luria, S. E. *Science* **1950**, *111*, 507–511.
23. Lawrence, C. M.; Menon, S.; Eilers, B. J.; *et al*. *J. Biol. Chem*. **2009**, *284*, 12599–12603.
24. Trevor, M.; Richard, S. *J. Chem. Technol. Biotechnol*. **2000**, *75*, 6–17.
25. Flint, S. J.; Enquist, L. W.; Racaniello, V. R.; Skalka, A. M. *Principles of Virology: Molecular Biology, Pathogenesis, and Control of Animal Viruses*. ASM Press: Washington, DC, 2000.
26. Straus, S.; Scott, W.; Symmons, M.; Marvin, D. *Eur. Biophys. J*. **2008**, *37*, 521–527.
27. Valegard, K.; Liljas, L.; Fridborg, K.; Unge, T. *Nature* **1990**, *345*, 36–41.
28. Marvin, D. A.; Welsh, L. C.; Symmons, M. F.; Scott, W. R.; Straus, S. K. *J. Mol. Biol*. **2006**, *355*, 294–309.
29. Rodi, D. J.; Mandova, S.; Makowski, L. In *Phage Display in Biotechnology and Drug Discovery*; Sidhu, S. S., Ed.; CRC Press/Taylor & Francis: Boca Raton, FL, 2005.
30. Jacobson, A. *J. Virol*. **1972**, *10*, 835–843.
31. Opalka, N.; Beckmann, R.; Boisset, N.; Simon, M. N.; Russel, M.; Darst, S. A. *J. Mol. Biol*. **2003**, *325*, 461–470.
32. Russel, M.; Linderoth, N. A.; Sali, A. *Gene* **1997**, *192*, 23–32.
33. Hohn, B.; Lechner, H.; Marvin, D. A. *J. Mol. Biol*. **1971**, *56*, 143.
34. Parmley, S. F.; Smith, G. P. *Gene* **1988**, *73*, 305–318.
35. Scott, J. K.; Smith, G. P. *Science* **1990**, *249*, 386–390.
36. Smith, G. P.; Petrenko, V. A. *Chem. Rev*. **1997**, *97*, 391–410.
37. Carrico, Z. M.; Romanini, D. W.; Mehl, R. A.; Francis, M. B. *Chem. Commun*. **2008**, 1205–1207.
38. Miller, R. A.; Presley, A. D.; Francis, M. B. *J. Am. Chem. Soc*. **2007**, *129*, 3104–3109.
39. Nicholas, S.; Carrico, Z. M. C.; Francis, M. B. *Angew. Chem. Int. Ed*. **2009**, *48*, 9498–9502.
40. Schlick, T. L.; Ding, Z.; Kovacs, E. W.; Francis, M. B. *J. Am. Chem. Soc*. **2005**, *127*, 3718–3723.
41. Smith, G. P. *Science* **1985**, *228*, 1315–1317.
42. Feng, T.; Tsao, M. L.; Schultz, P. G. *J. Am. Chem. Soc*. **2004**, *126*, 15962–15963.
43. Liu, C. C.; Mack, A. V.; Tsao, M. L.; *et al*. *Proc. Natl. Acad. Sci. USA* **2008**, *105*, 17688–17693.
44. Petrenko, V. A.; Smith, G. P.; Gong, X.; Quinn, T. *Protein Eng*. **1996**, *9*, 797–801.
45. Rodi, D. J.; Soares, A. S.; Makowski, L. *J. Mol. Biol*. **2002**, *322*, 1039–1052.
46. Mao, C. B.; Solis, D. J.; Reiss, B. D.; *et al*. *Science* **2004**, *303*, 213–217.
47. Liu, Y. L.; Adams, J. D.; Turner, K.; Cochran, F. V.; Gambhir, S. S.; Soh, H. T. *Lab Chip* **2009**, *9*, 3604.
48. Cao, B.; Mao, C. *Biomacromolecules* **2009**, *10*(3), 555–564.
49. Chen, Y.; Wiesmann, C.; Fuh, G.; *et al*. *J. Mol. Biol*. **1999**, *293*, 865–881.
50. Devlin, J. J.; Panganiban, L. C.; Devlin, P. E. *Science* **1990**, *249*, 404–406.
51. Cheng, X.; Kay, B. K.; Juliano, R. L. *Gene* **1996**, *171*, 1–8.
52. Giordano, R. J.; Vila, M.; Ahdenranta, J. L.; Apasqualini, R.; Arap, W. *Nat. Med*. **2001**, *7*, 1249–1253.
53. Pasqualini, R.; Ruoslahti, E. *Nature* **1996**, *380*, 364–366.
54. Brissette, R.; Goldstein, N. I. In *Methods in Molecular Biology*; Fisher, P., Ed.; Humana: Totowa, NJ, 2007.
55. Flynn, C. E.; Lee, S. W.; Peelle, B. R.; Belcher, A. M. *Acta Mater*. **2003**, *51*, 5867–5880.
56. Naik, R. R.; Stringer, S. J.; Agarwal, G.; Jones, S. E.; Stone, M. O. *Nat. Biotechnol*. **2002**, *1*, 169–172.
57. Wang, S.; Humphreys, E. S.; Chung, S.; *et al*. *Nat. Mater*. **2003**, *2*, 196–200.
58. Kriplani, U.; Kay, B. K. *Curr. Opin. Biotechnol*. **2005**, *16*, 470–475.
59. Merzlyak, A.; Lee, S.-W. *Curr. Opin. Chem. Biol*. **2006**, *10*, 246–252.
60. Sarikaya, M.; Tamerler, C.; Jen, A. K. Y.; Schulten, K.; Baneyx, F. *Nat. Mater*. **2003**, *2*, 577–585.
61. Pender, M. J.; Sowards, L. A.; Hartgerink, J. D.; Stone, M. O.; Naik, R. R. *Nano Lett*. **2005**, *6*, 40–44.
62. Brown, S. *Nat. Biotechnol*. **1997**, *15*, 269–272.
63. Peelle, B. R.; Krauland, E. M.; Wittrup, K. D.; Belcher, A. M. *Acta Biomater*. **2005**, *1*, 145–154.
64. Brutchey, R. L.; Morse, D. E. *Chem. Rev*. **2008**, *108*, 4915–4934.
65. Kroger, N.; Lorenz, S.; Brunner, E.; Sumper, M. *Science* **2002**, *298*, 584–586.
66. Komeili, A. *Ann. Rev. Biochem*. **2007**, *76*, 351–366.
67. Belcher, A. M.; Wu, X. H.; Christensen, R. J.; Hansma, P. K.; Stucky, G. D.; Morse, D. E. *Nature* **1996**, *381*, 56–58.
68. Du, C.; Falini, G.; Fermani, S.; Abbott, C.; Moradian-Oldak, J. *Science* **2005**, *307*, 1450–1454.

69. Hoang, Q. Q.; Sicheri, F.; Howard, A. J.; Yang, D. S. C. *Nature* **2003**, *425*, 977–980.
70. Estroff, L. A. *Chem. Rev.* **2008**, *108*, 4329–4331.
71. Nam, K.; Beau, R. P.; Lee, S. W.; Belcher, A. M. *Nano Lett.* **2004**, *4*, 23–27.
72. Sweeney, R. Y.; Park, E. Y.; Iverson, B. L.; Georgiou, G. *Biotechnol. Bioeng.* **2006**, *95*, 539–545.
73. Huang, Y.; Chiang, C. Y.; Lee, S. K.; *et al. Nano Lett.* **2005**, *5*, 1429–1434.
74. Dogic, Z.; Fraden, S. *Curr. Opin. Colloid Interf. Sci.* **2006**, *11*, 47–55.
75. Lee, S. W.; Wood, B. M.; Belcher, A. M. *Langmuir* **2003**, *19*, 1592–1598.
76. Lee, S. W.; Belcher, A. M. *Nano Lett.* **2004**, *4*, 387–390.
77. Yoo, P. J.; Nam, K. T.; Qi, J.; *et al. Nat. Mater.* **2006**, *5*, 234–240.
78. Yoo, P. J.; Nam, K. T.; Belcher, A. M.; Hammond, P. T. *Nano Lett.* **2008**, *8*, 1081–1089.
79. Daniel, J. S.; Sean, R. C.; Andrès, J. G.; Emmanuel, D. *Adv. Mater.* **2009**, *22*, 111–114.
80. Lee, S.-W.; Lee, S. K.; Belcher, A. M. *Adv. Mater. (Weinheim, Germany)* **2003**, *15*, 689–692.
81. Lee, S. K.; Yun, D. S.; Belcher, A. M. *Biomacromolecules* **2006**, *7*, 14–17.
82. Ahn, T. K.; Avenson, T. J.; Ballottari, M.; *et al. Science* **2008**, *320*, 794–797.
83. Gust, D.; Moore, T. A.; Moore, A. L. *Acc. Chem. Res.* **2000**, *34*, 40–48.
84. Scolaro, L. M.; Castriciano, M. A.; Romeo, A.; *et al. J. Am. Chem. Soc.* **2006**, *128*, 7446–7447.
85. Goldman, E. R.; Pazirandeh, M. P.; Charles, P. T.; Balighian, E. D.; Anderson, G. P. *Anal. Chim. Acta* **2002**, *457*, 13–19.
86. Jaworski, J. W.; Raorane, D.; Huh, J. H.; Majumdar, A.; Lee, S. W. *Langmuir* **2008**, *24*, 4938–4943.
87. Marks, K. M.; Rosinov, M.; Nolan, G. P. *Chem. Biol.* **2004**, *11*, 347–356.
88. Jia, Y.; Qin, M.; Zhang, H.; *et al. Biosens. Bioelectron.* **2007**, *22*, 3261–3266.
89. Lu, X. Y.; Weiss, P.; Block, T. *J. Virol. Methods* **2004**, *119*, 51–54.
90. Nanduri, V.; Balasubramanian, S.; Sista, S.; Vodyanoy, V. J.; Simonian, A. L. *Anal. Chim. Acta* **2007**, *589*, 166–172.
91. Tan, W. S.; Tan, G. H.; Yusoff, K.; Seow, H. F. *J. Clin. Virol.* **2005**, *34*, 35–41.
92. Yang, L.-M. C.; Tam, P. Y.; Murray, B. J.; *et al. Anal. Chem.* **2006**, *78*, 3265–3270.
93. Zhu, H.; White, I. M.; Suter, J. D.; Fan, X. *Biosens. Bioelectron.* **2008**, *24*, 461–466.
94. Amorim, L. R.; Silva, J. G.; Gibbs, P. A.; Teixeira, P. C. *Int. J. Microbiol.* **2009**, *2009*, 259456.
95. Brigati, J.; Williams, D. D.; Sorokulova, I. B.; *et al. Clin. Chem.* **2004**, *50*, 1899–1906.
96. Huang, S.; Yang, H.; Lakshmanan, R. S.; *et al. Biotechnol. Bioeng.* **2008**, *101*, 1014–1021.
97. Huang, S.; Yang, H.; Lakshmanan, R. S.; *et al. Biosens. Bioelectron.* **2009**, *24*, 1730–1736.
98. Lakshmanan, R. S.; Guntupalli, R.; Hu, J.; *et al. J. Microbiol. Methods* **2007**, *71*, 55–60.
99. Nanduri, V.; Bhunia, A. K.; Tu, S. I.; Paoli, G. C.; Brewster, J. D. *Biosens. Bioelectron.* **2007**, *23*, 248–252.
100. Neufeld, T.; Mittelman, A. S.; Buchner, V.; Rishpon, J. *Anal. Chem.* **2005**, *77*, 652–657.
101. Neufeld, T.; Schwartz-Mittelmann, A.; Biran, D.; Ron, E. Z.; Rishpon, J. *Anal. Chem.* **2002**, *75*, 580–585.
102. Olsen, E. V.; Sorokulova, I. B.; Petrenko, V. A.; Chen, I. H.; Barbaree, J. M.; Vodyanoy, V. J. *Biosens. Bioelectron.* **2006**, *21*, 1434–1442.
103. Shabani, A.; Zourob, M.; Allain, B.; Marquette, C. A.; Lawrence, M. F.; Mandeville, R. *Anal. Chem.* **2008**, *80*, 9475–9482.
104. Zhang, H.; Li, X.; Bai, Y.; *et al. Biotechnol. Appl. Biochem.* **2009**.
105. Conroy, P. J.; Hearty, S.; Leonard, P.; O'Kennedy, R. J. *Semin. Cell Dev. Biol.* **2009**, *20*, 10–26.
106. Dover, J. E.; Hwang, G. M.; Mullen, E. H.; Prorok, B. C.; Suh, S. J. *J. Microbiol. Methods* **2009**, *78*, 10–19.
107. Cheng, A. K.; Sen, D.; Yu, H. Z. *Bioelectrochemistry* **2009**, *77*, 1–12.
108. Ye, L.; Mosbach, K. *Chem. Mater.* **2008**, *20*, 859–868.
109. Petrenko, V. A. *Microelectron. J.* **2008**, *39*, 202–207.
110. Petrenko, V. A.; Smith, G. P. *Protein Eng.* **2000**, *13*, 589–592.
111. Petrenko, V. A.; Sorokulova, I. B. *J. Microbiol. Methods* **2004**, *58*, 147–168.
112. Petrenko, V. A.; Vodyanoy, V. J. *J. Microbiol. Methods* **2003**, *53*, 253–262.
113. Cerruti, M.; Jaworski, J.; Raorane, D.; *et al. Anal. Chem.* **2009**, *81*, 4192–4199.
114. Edgar, R.; Mckinstry, M.; Hwang, J.; *et al. Proc. Natl. Acad. Sci. USA* **2006**, *103*, 4841–4845.
115. Nanduri, V.; Sorokulova, I. B.; Samoylov, A. M.; Simonian, A. L.; Petrenko, V. A.; Vodyanoy, V. *Biosens. Bioelectron.* **2007**, *22*, 986–992.
116. Yang, L. M.; Diaz, J. E.; Mcintire, T. M.; Weiss, G. A.; Penner, R. M. *Anal. Chem.* **2008**, *80*, 5695–5705.
117. Sorokulova, I. B.; Olsen, E. V.; Chen, I. H.; *et al. J. Microbiol. Methods* **2005**, *63*, 55–72.
118. Sauerbrey, G. *Z. Phys.* **1959**, *155*, 206–222.
119. Arnau, A. *Sensors* **2008**, *8*, 370–411.
120. Waggoner, P. S.; Craighead, H. G. *Lab Chip* **2007**, *7*, 1238–1255.
121. Diaz, J. E.; Yang, L. M.; Lamboy, J. A.; Penner, R. M.; Weiss, G. A. *Methods Mol. Biol.* **2009**, *504*, 255–274.
122. Owicki, J. C.; Bousse, L. J.; Hafeman, D. G.; *et al. Ann. Rev. Biophy. Biomol. Struct.* **1994**, *23*, 87–113.
123. Goldman, E. R.; Pazirandeh, M. P.; Mauro, J. M.; King, K. D.; Frey, J. C.; Anderson, G. P. *J. Mol. Recognit.* **2000**, *13*, 382–387.
124. Pulli, T.; Hoyhtya, M.; Soderlund, H.; Takkinen, K. *Anal. Chem.* **2005**, *77*, 2637–2642.
125. Fan, X.; White, I. M.; Shopova, S. I.; Zhu, H.; Suter, J. D.; Sun, Y. *Anal. Chim. Acta* **2008**, *620*, 8–26.
126. Vollmer, F.; Arnold, S. *Nat. Methods* **2008**, *5*, 591–596.
127. Adhya, S.; Merril, C. *Nature* **2006**, 754–755.
128. Sulakvelidze, A.; Alavidze, Z.; Morris, J. G., Jr. *Antimicrob. Agents Chemother.* **2001**, *45*, 649–659.
129. Carlton, R. M. *Arch. Immunol. Ther. Exp. (Warsz)* **1999**, *47*, 267–274.
130. The Interagency Task Force on Antimicrobial Resistance; A Public Health Action Plan to Combat Antimicrobial Resistance, National Center for Preparedness, Detection, and Control of Infectious Diseases (NCPDCID), 2009.
131. Thiel, K. *Nat. Biotechnol.* **2004**, *22*, 31–36.
132. Bennett, N. J.; Rakonjac, J. *J. Mol. Biol.* **2006**, *356*, 266–273.
133. Click, E. M.; Webster, R. E. *J. Bacteriol.* **1998**, *180*, 1723–1728.
134. Riechmann, L.; Holliger, P. *Cell* **1997**, *90*, 351–360.
135. Stone, R. *Science* **2002**, *298*, 728–731.
136. Yamamoto, K. R.; Alberts, B. M.; Benzinger, R.; Lawhorne, L.; Treiber, G. *Virology* **1970**, *40*, 734–744.
137. Geier, M. R.; Trigg, M. E.; Merril, C. R. *Nature* **1973**, *246*, 221–223.
138. Dickerson, T. J.; Janda, K. D. *AAPS J.* **2005**, *7*, E579–E586.
139. Maheshri, N.; Koerber, J. T.; Kaspar, B. K.; Schaffer, D. V. *Nat. Biotechnol.* **2006**, *24*, 198–204.
140. Merril, C. R.; Biswas, B.; Carlton, R.; *et al. Proc. Natl. Acad. Sci. USA* **1996**, *93*, 3188–3192.
141. Lavecchia, M.; Waldron, E. *FDA Approval of Listeria-Specific Bacteriophage Preparation on Ready-to-Eat (RTE) Meat and Poultry Products*. US FDA/Center for Food Safety and Applied Nutrition, 2006.
142. Arap, W.; Pasqualini, R.; Ruoslahti, E. *Science* **1998**, *279*, 377–380.
143. Krag, D. N.; Shukla, G. S.; Shen, G. P.; *et al. Cancer Res.* **2006**, *66*, 8925.
144. Bar, H.; Yacoby, I.; Benhar, I. *BMC Biotechnol.* **2008**, *8*, 37.
145. Frenkel, D.; Solomon, B. *Proc. Natl. Acad. Sci. USA* **2002**, *99*, 5675–5679.
146. Hajitou, A.; Trepel, M.; Lilley, C. E.; *et al. Cell* **2006**, *125*, 385–398.
147. Martin, M. E.; Rice, K. G. *AAPS J.* **2007**, *9*, E18–E29.
148. Larocca, D.; Witte, A.; Johnson, W.; Pierce, G. F.; Baird, A. *Human Gene Ther.* **1998**, *9*, 2393–2399.
149. Mount, J. D.; Samoylova, T. I.; Morrison, N. E.; Cox, N. R.; Baker, H. J.; Petrenko, V. A. *Gene* **2004**, *341*, 59–65.
150. Poul, M.-A.; Marks, J. D. *J. Mol. Biol.* **1999**, *288*, 203–211.
151. Piersanti, S.; Cherubini, G.; Martina, Y.; *et al. J. Mol. Med.* **2004**, *82*, 467–476.
152. Hart, S. L.; Knight, A. M.; Harbottle, R. P.; *et al. J. Biol. Chem.* **1994**, *269*, 12468–12474.
153. Burg, M. A.; Jensen-Pergakes, K.; Gonzalez, A. M.; Ravey, P.; Baird, A.; Larocca, D. *Cancer Res.* **2002**, *62*, 977–981.
154. Seow, Y.; Wood, M. J. *Mol. Ther.* **2009**, *17*, 767–777.
155. Segura, T.; Shea, L. D. *Bioconj. Chem.* **2002**, *13*, 621–629.
156. Petrenko, V. A.; Smith, G. P.; Mazooji, M. M.; Quinn, T. *Protein Eng.* **2002**, *15*, 943–950.
157. Iannolo, G.; Minenkova, O.; Petruzzelli, R.; Cesareni, G. *J. Mol. Biol.* **1995**, *248*, 835–844.
158. Kuzmicheva, G. A.; Jayanna, P. K.; Sorokulova, I. B.; Petrenko, V. A. *Protein Eng. Des. Selection* **2009**, *22*, 9–18.
159. Makowski, L. *Gene* **1993**, *128*, 5–11.
160. Huang, X.; Zauscher, S.; Klitzman, B.; *et al. Ann. Biomed. Eng.* **2010**, *38*, 1965–1976.
161. Khoo, X.; Hamilton, P.; O'Toole, G. A.; Snyder, B. D.; Kenan, D. J.; Grinstaff, M. W. *J. Am. Chem. Soc.* **2009**, *131*, 10992–10997.
162. Meyers, S.; Hamilton, P.; Walsh, E.; Kenan, D. J.; Grinstaff, M. W. *Adv. Mater.* **2007**, *19*, 2492–2498.
163. Kenan, D. J.; Walsh, E. B.; Meyers, S. R.; *et al. Chem. Biol.* **2006**, *13*, 695–700.
164. Drexler, K. E. *Engines of Creation: The Coming Era of Nanotechnology*. Anchor Books: New York, NY, 1986.

2.207. Extracellular Matrix: Inspired Biomaterials

H M Waldeck and W J Kao, University of Wisconsin-Madison, Madison, WI, USA

© 2011 Elsevier Ltd. All rights reserved.

2.207.1.	**Introduction**	114
2.207.2.	**Overview of ECM Structure and Function**	115
2.207.3.	**Types of ECM Mimicry**	116
2.207.3.1.	Mimicking ECM Functions by Using ECM Components	116
2.207.3.1.1.	Full/direct copy	116
2.207.3.1.2.	Partial copy	119
2.207.3.2.	Mimicking ECM Function Through ECM Architecture and Topography	121
2.207.3.2.1.	Hierarchical microstructure and porosity	121
2.207.3.2.2.	Topographical features and patterning	122
2.207.3.3.	Mimicking ECM Protein Design and Assembly	125
2.207.4.	**Future Directions**	126
References		126

Glossary

Affinity (protein-ligand) Characteristic binding strength between a single protein and ligand; commonly described by the dissociation constant.

Allogeneic immunologic response Immune response to cells or other materials derived from a genetically nonidentical donor of the same species (allograft).

Angiogenesis The process by which new blood vessels are grown from preexisting vessels.

Anisotropy A property of a material having directional dependence.

Avidity (protein-ligand) Strength of binding derived from multiple bond interactions.

Basement lamina Characteristic extracellular matrix found under epithelial or endothelial cells consisting of the fusion of two distinct layers: the basal lamina and the reticular lamina.

Bioderivation Extracting certain components/information from the biological system and then applying that to a different area of use.

Bioinspiration Deriving strategies different from that employed by nature to achieve the same function and properties.

Biomimicry Learning the principles governing the function of a biological system and then using that same strategy to create a synthetic system that functions with a similar precision.

Bioresorption A form of resorption in which materials degrade when they come into contact with one or more specific biological molecules.

Cell differentiation Process by which a cell becomes more specialized through modifications in gene expression that can lead to alteration in morphology and activity.

Collagen Primary structural ECM protein family. All collagen subunits initially organize into triple-helical fibers and then these fibers associate further to form fibrillar, sheet-like, or fibril-associated structures.

Cytokine Small cell-signaling proteins, peptides, or glycoproteins which are released into the extracellular environment by various cell types for intercellular communication.

Cytoskeleton Intracellular protein scaffolding which plays important roles in cell morphology, cellular mobility, intracellular transport, and cellular division.

Denaturation The process through which proteins or nucleic acids lose either tertiary or secondary structure due to the application of an external stress. A loss of function is typically seen in conjunction with this loss of structure.

Electrospinning Process by which continuous nano- to microscale fibers are formed by using electric forces to overcome surface tension and thereby elongate droplets of polymer melt or solution into a stream.

Excitation threshold Minimum amount of stimulus necessary to create an action potential in a nerve cell.

Extracellular matrix (ECM) The native cell microenvironment composed of specific proteins, proteoglycans, small molecules, water, etc. depending on the cell type and resident tissue. Through adhesion to the ECM, cells are exposed to physical, mechanical, and biochemical cues capable of altering cell differentiation, activation, migration, and adhesion strength.

Fibrillogenesis Creation of thin fibril structures present in the collagen fiber architecture.

Filopedia Nanoscale cellular extensions capable of interacting with nanoscale physical cues.

Glycoprotein Proteins which contain covalently attached oligosaccharide chains.

Glycosaminoglycan (GAG) Long, unbranched polysaccharides consisting of repeating disaccharide units.

Hydrogel Water-swollen, polymeric structures containing either covalent or physical cross-links. Hydrogels are highly varied in composition, construction method, and the resulting chemical and physical characteristics.

Hydrolysis A chemical process in which a molecule, such as a polymer, is split into two parts through the addition of a molecule of water.
Hydrophobicity/hydrophilicity A physical property which characterizes the ability of a molecule to repel/attract water molecules.
Hydroxyapatite The naturally occurring mineral form of calcium apatite. A modified form of this substance is a primary component of bone tissue.
Integrins A large family of heterodimeric transmembrane proteins which serve as the primary receptors between cells and ECM proteins.
Isotropy A property of a material being homogeneous in all directions.
Ligand Substance capable of forming a complex through binding to another molecule or binding site. Typically in biology, ligands are small molecules or functional groups which are able to bind to specific sites on proteins.
Mechanotransduction Mechanism though which cells convert mechanical stimuli into chemical activity.
Microablation Microscale removal of material from a surface.
Microstructure Structural features of a material which can be visualized using a microscope at 25× magnification.
Morphogenesis The process by which an organism, tissue, or cell develops its shape and/or structure.
Morphology Form or structure of an organism including shape, size, and structural features.
Motif Characteristic sequence or structure found in a protein which performs a biological function or results in specific higher-order structures, respectively.
Nanocomposite A solid multiphase material in which the size of the phases, the distance between the phases, or the structural repeats have nanoscale dimensions.
Nanopatterning Fabrication of a nanoscale pattern on a surface.
Nanostructure Structural features which range in size between molecular and micrometer dimensions.
Osteogenesis The process by which new bone tissue is developed through the laying down of new bone material by osteoblasts.
Phenotype Observable physical, biochemical, or behavioral characteristics of an organism.
Porosity A measure of the void spaces within a material.
Protease An enzyme which can catalyze the breakdown of peptide bonds within the primary protein structure.
Proteoglycans A diverse family of molecules whose structure consists of a core protein covalently attached to multiple glycosaminoglycan chains.
Recombinant DNA/recombinant protein Engineered DNA which is developed by combining sequences which would not normally occur in nature. Often this process is accomplished by introducing foreign DNA into an existing organismal DNA, such as the plasmids of bacteria. Recombinant DNA technology is used to manufacture recombinant proteins.
Tangent modulus The slope of the compression stress–strain curve as a specified stress or strain. Typically, the tangent modulus is used to describe the behavior of materials beyond their elastic regions.
Topography The composition and configuration of physical features on a surface.
Ultimate strength Maximum load or stress a material can withstand before necking of the material occurs.
Ultrastructure Detailed biological structure of a specimen not able to be visualized using a light microscope.
Viscoelasticity A property of materials that demonstrate both viscous and elastic characteristics when undergoing deformation.
Xenogeneic immunologic response Immune response to cells or other material derived from a donor of a different species (xenograft).

Abbreviations

3D	Three-dimensional
DNA	Deoxyribonucleic acid
DRG	Dorsal root ganglia
ECM	Extracellular matrix
FAK	Focal adhesion kinase
GAG	Glycosaminoglycan
HAp/Col	Hydroxyapitite/collagen nanocomposite
hMSC	Human mesenchymal stem cell
MCL	Medial collateral ligament
MMP	Matrix metalloproteinase
PCL	Poly(ε-caprolactone)
PEG	Poly(ethylene glycol)
PGS	Poly(glycerol sebacte)
PLGA	Poly(DL-lactic-*co*-glycolide)
rhBMP	Recombinant human bone morphogenetic protein
RT-PCR	Reverse transcriptase polymerase chain reaction
SIS	Small intestinal submucosa
SLRP	Small leucine-rich proteoglycan

2.207.1. Introduction

Of all the advances in science, technology, and engineering in the past few decades, the deeper understanding of biological systems has led to an ever more intimate contact between individuals and technology. This personal impact of biology-based technologies has been demonstrated to be a very powerful force in shaping the scientific community. The creation of biology-centered enablers is the result of the pursuit of three general research paradigms: biomimicry, bioinspiration,

and bioderivation. *Biomimicry* is defined as "learning the principles governing the function of a biological system and then using that same strategy to create a synthetic system that functions with similar precisions." Examples of this are protein/cell-based biosensors for detecting (bio)hazards and self-assembled materials with unprecedented responsiveness, complexity, and ability to interact and evolve. *Bioinspiration* is defined as "devising strategies different from that employed by nature to achieve the same function and properties." Examples of this are novel light harvesting methods based on nanotechnology and microorganism-based air/water filtration systems to control pollution including greenhouse gases. *Bioderivation* is viewed as extracting certain components/information from the biological system and then applying that to a different area of use. Examples of this are also plentiful: alternative fuel sources, incorporation of biologically derived molecules for targeted drug delivery, and biofunctionalized materials for advanced cellular and molecular medicine such as stem cell and gene therapies.

Earlier biomaterial research has mainly focused on biocompatibility and application-specific macroscale requirements such as mechanical, adhesive, or optical properties. The design constraints were therefore primarily concerned with preventing adverse effects on the body caused by a foreign material. Although these subjects remain to be critical issues in biomedical research with incomplete mechanistic insights, the advancement in biological sciences have influenced and expanded current biomaterial research and design. By applying biological principles through biomimicry, bioinspiration, or bioderivation to material design, the overall rationale and motivation is to expand the property and to improve the biological interaction of these materials. This chapter focuses on how the structural and functional principles derived from the native cell microenvironment, the extracellular matrix (ECM), have been applied to biomaterial design and construction. By mimicking the ECM, researchers are able to take inspiration from defined cell–matrix interfaces to subsequently control cell–biomaterial interactions. Furthermore, the hierarchical structure of ECM architecture is a desirable characteristic to incorporate into material design. Several methodologies are covered ranging from directly incorporating ECM proteins to utilizing self-assembly principles to construct materials. An overview of basic ECM structural and functional features is given followed by selected examples throughout the chapter that illustrate how these bioactive attributes are incorporated into biomaterials.

2.207.2. Overview of ECM Structure and Function

The interplay between cells and the surrounding ECM establishes a dynamic tissue microenvironment capable of performing the varied functions seen in biological systems. Cells secrete ECM molecules and maintain the matrix through continuous remodeling of the structure. The ECM, in turn, supports and maintains the cells by providing nutrition and indirectly mediating cell–cell communication. Furthermore, in some tissues, the ECM also acts as the structure responsible for carrying out the central function of a tissue. The organization and composition operate cooperatively to balance strength, flexibility, and complexity to establish specific tissue properties. ECM-inspired biomaterials attempt to mimic the bioactive and bioresponsive relationship between cells and ECM as well as the ECM's hierarchical structure through the incorporation of ECM-derived biochemical and structural components. This section focuses on the basis for such mimicry by providing an overview of how the main constituents and structural characteristics of native ECM contribute to overall tissue function (for a more in-depth examination of the ECM structure–function relationship, see Plopper[1]).

The tissue-specific ECM is composed of a unique combination of water, glycoproteins, proteoglycans, and sequestered signaling molecules integrated into a highly complex three-dimensional (3D) cell scaffold. The individual properties and subsequent configuration of these components play multiple roles in the tissue hierarchy. Proteoglycans are a diverse family of molecules whose structure consists of a core protein covalently attached to one or more glycosaminoglycan (GAG) chains. The anionic nature of the GAG leads to electrically driven association with cations and these, in turn, attract water molecules. The association of a large amount of water with the GAG chains causes overall structural rigidity as well as hydration. As such, large interstitial proteoglycans, for example, aggrecan, are able to maintain tissue hydration and establish tissue structure. Proteoglycan-mediated hydration allows diffusion of small molecules and increases the tissue's ability to resist compression forces. The relatively rigid and large structure helps define ECM architecture and can also act to prevent bacterial infiltration. Additionally, the ability of proteoglycans to bind other components facilitates organization of the ECM into functional structures. For example, binding of small leucine-rich proteoglycans (SLRPs) to collagen helps stabilize and align fibers leading to mechanical anisotropy. Soluble factors, such as cytokines or proteases, are sequestered through interactions with proteoglycans creating depots or gradients of these regulatory molecules throughout the ECM. Subsequent cell-mediated degradation of the matrix results in liberation and/or activation of these soluble proteins, enabling bioresponsive cell signaling.

The principal structural ECM proteins, collagens, are organized into a variety of functionally relevant configurations. All collagen subunits initially organize into approximately 1.5-nm triple-helical fibers and then these fibers associate further to form fibrillar, sheet-like, or fibril-associated structures. Fibrillar collagens are formed through bundling of progressively larger fibers along a single axis till eventually fibers with diameters up to approximately 3 μm are achieved. The final structure displays directionally dependent mechanical properties, for example, increased strength in the direction of alignment. Sheet-like collagens, on the other hand, are organized into defined planar networks and are better able to withstand forces in multiple directions. Collagen is often paired with elastin in tissues requiring flexibility, because of collagen's strength and elastin's ability to resist structural deformation. Alternating regions of hydrophobic and hydrophilic peptide sequences in the structure of elastin's subunit allow it to return to its original coil shape without any loss of energy. This property is advantageous for tissues undergoing constant deformation, such as blood vessels and skin because the tissue superstructure is maintained without excessive expenditure of energy. Similar association of collagens with other cell-adhesive ECM proteins, such as the bifunctional

glycoproteins, fibronectin, and laminin, may also influence mechanical properties of tissues by defining the arrangement of mechanically active cells.

Through adhesion to the ECM, cells are exposed to physical, mechanical, and biochemical cues capable of altering cell differentiation, activation, migration, and adhesion strength. Collagen, fibronectin, laminin, and other ECM proteins contain adhesive motifs within their structure to which cells can bind through transmembrane integrin receptors (Figure 1). Integrin activation through binding can in itself trigger a variety of downstream effects through intracellular signaling pathways. Increased understanding of cell–ECM interactions, however, has revealed a more complex relationship with spatial, temporal, and multisignal components. The spatial arrangement of the ECM components leads to cell interaction with differential densities and types of adhesive motifs, 3D constructs, and micro- and nanoscale topographical features. Furthermore, mechanical characteristics of the ECM are able to alter cell behavior to a similar degree as biochemical signals.[2] This concept is true not only for the overall mechanics of the tissue but also for the mechanical differences established by cellular and subcellular scale ECM structural features such as fibers or pores. All of these different types of signals coalesce to create a niche with the ability to control the adhesion strength, rate of proliferation, differentiation state, migration, and morphology of cells.

Cells, in turn, are able to manipulate and remodel the ECM environment. For example, after injury, through complex, yet coordinated, phases of healing, a temporary fibrin scaffold must be established and then quickly degraded to be replaced by fibrous tissue consisting mainly of loose bundles of type III collagen as well as new vascularization. To fully regain tissue function, this fibrous tissue must be remodeled into the native ECM of the injured tissue. Throughout these phases, a continuous progression of cell-mediated degradation, synthesis, and organization of ECM molecules occurs. Degradation is mediated by recognition of cleavable peptide sequences contained within the ECM molecules by proteases released from or located within the membrane of cells. Assembly of ECM structures is primarily driven through extracellular protein–protein interactions; however, cells participate by drawing together and orienting higher-order ECM structures through application of traction forces to the networks to which they are bound. For example, mechanical loading of collagen scaffolds stimulates cells to align collagen fibers in the direction of tension. The ECM's ability to influence and respond to the cellular environment makes it a crucial factor in important biological processes such as tissue development, blood clotting, wound healing, and cancer metastasis, all of which are targets for biomaterial applications.

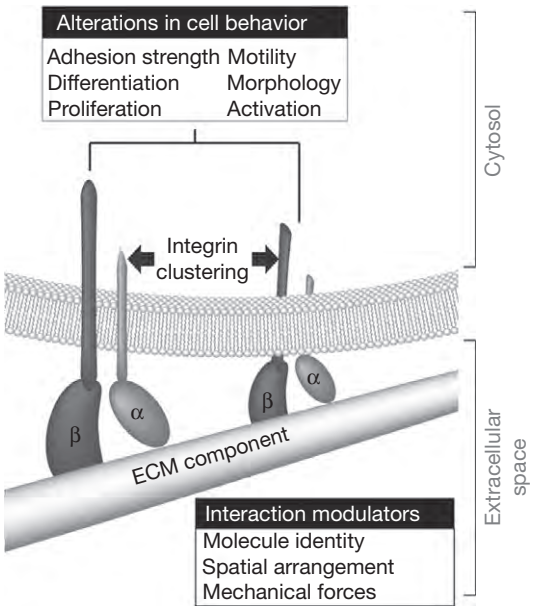

Figure 1 Integrin binding to the extracellular matrix (ECM) and subsequent extra- and intracellular clustering can lead to a variety of downstream effects causing changes in cell behavior. The ECM properties participate in the determination of cellular responses.

2.207.3. Types of ECM Mimicry

In order to take advantage of both the structural and biological functions of ECM, material design has drawn inspiration from the structure–function principles of ECM. There are various approaches in which both natural and synthetic materials can be formulated to mimic either the function and/or structure of the ECM (Figure 2). In this section, an overview of main methods of mimicry is given and selected case studies are presented to demonstrate different methods of incorporating ECM-derived biological principles (for an excellent review of tissue engineering focused ECM mimicry, see Place *et al.*[3]).

2.207.3.1. Mimicking ECM Functions by Using ECM Components

2.207.3.1.1. Full/direct copy

The most straightforward methods to achieve ECM mimicry involve incorporating native ECM components into biomaterials as structural and/or functional factors. The vast array of both

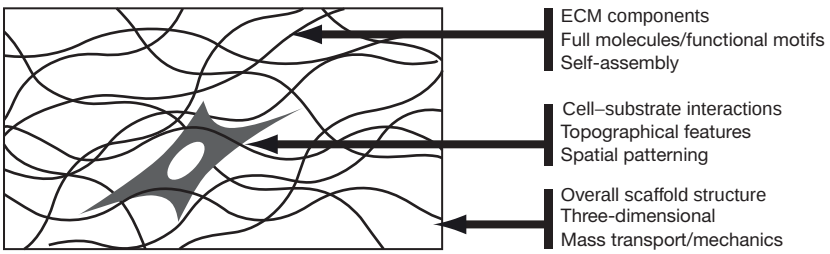

Figure 2 Extracellular matrix properties targeted for mimicry.

the types of ECM components and methods of incorporation provides a flexible and relatively controllable platform to incorporate bioactivity into material design. For example, structural proteins, mainly collagen type I or III, may be manipulated to form 3D matrices or combined with synthetic materials as a bioactive component. Soluble factors, such as growth factors, are often sequestered into a matrix, to be delivered to the surrounding tissue upon implantation or to cells encapsulated within or adhered to the biomaterial. Full versions of the molecules have the potential to retain complete functionality in terms of physical properties and/or the ability to interact with the cellular environment. By controlling the presentation of these molecules, the correct cues for various cell processes, for example, differentiation, may be accomplished through biomaterial applications (reviewed in Abraham *et al*.[4]). ECM molecules for use in biomaterial production are derived from a variety of harvested tissues, typically from animal sources, or through chemical synthesis or biosynthesis using recombinant DNA technology. The primary challenge of this methodology is maintaining the bioactivity of full copies of ECM components, in particular proteins, during material construction or processing where denaturation and loss of higher-order structures are common. Additionally, simply incorporating individual native ECM components may not fully represent the complexities of the ECM to the extent needed for certain cell interactive applications.

The multicomponent, hierarchical structure of the ECM can be more closely mimicked by decellularized ECM scaffold material derived from intact mammalian tissue (see Badylak *et al*.[5] for a more in-depth review). A variety of tissues can be used as source material including small intestinal submucosa (SIS), heart valves, blood vessels, ligaments, nerves, and tendons. After removing the cellular material to avoid adverse allogeneic or xenogeneic immunologic responses, what remains is a scaffold consisting of a preformed 3D matrix composed of the necessary ECM molecules and architecture appropriate for a particular tissue. Despite their xenogeneic source, decellularized ECM scaffolds stimulate a minimal inflammatory response[6] and demonstrate prominent host cell infiltration leading to successful engraftment and resolution of the inflammatory response. Facilitation of tissue reconstruction in both animal and preclinical models occurs though the scaffold's ability to affect cell proliferation, migration, and differentiation as well as stimulating angiogenesis. These effects are attributed to the presence of a combination of different types of collagen, sequestered growth factors, bifunctional glycoproteins, and other soluble and insoluble bioactive molecules. Additionally, the degradation products of these scaffolds have also been shown to stimulate cell proliferation and cell migration. However, the decellularization process can lead to alterations in the structure, composition, and type of host response that these materials elicit.[7] For example, the loss of water may lead to changes in the scaffold's mechanical properties caused by alterations to collagen fiber morphology or creation of physical bonds between proteins. Lack of proper hydration may also lead to reduced bioactivity because of protein denaturation or the aforementioned creation of physical bonds. Conversely, maintaining the ECM scaffolds in a hydrated state could lead to other consequences including the loss of proteoglycans or other sequestered soluble factors. A few options exist to manipulate the ECM scaffolds' mechanical and functional properties including introducing cross-links between proteins within the matrix, creating multilaminate constructs from several ECM scaffold sheets, preloading the tissue to cause collagen fiber alignment, or combining powdered (50–200 μm particles) or gel forms of the ECM scaffold material with synthetic materials with the appropriate mechanical and/or degradation properties. These methods, however, may also lead to changes in the bioactivity of the material and alter the host immunological response.

2.207.3.1.1.1. Case study: hydroxyapatite/collagen nanocomposite based material for bone regeneration

Skeletal bones consist of a complex hierarchical porous structure comprised of mainly collagen type I and hydroxyapatite crystals ranging in size from 30 to 120 nm. Bone defects resulting from injury or disease have the ability to self-repair due to the osteoconductive nature of the native ECM components. When the defect size is large, however, the tissue framework is too damaged to effectively support the regrowth of bone tissue. Tissue engineering strategies to induce bone formation often incorporate native ECM components in order to take advantage of their ability to stimulate osteogenesis as well as for their natural biocompatibility. For example, collagen I isolated from xenogenic tissues such as skin, bone, tendons, ligaments, and cornea are able to be employed after undergoing a purification process to remove a majority of the antigenic components such as the telopeptide regions. Hydroxyapatite can also be derived from xenogenic tissues, but is more commonly obtained through direct precipitation of calcium and phosphate ions. Chemical methods, however, may result in an impure product or nonmimetic crystal sizes. Third, the delivery of recombinant bone morphogenic proteins (BMPs) has been shown to stimulate complete bone morphogenesis and has been approved by the USDA for clinical applications. The success of these individual native ECM components in supporting and enhancing repair of large bone defects has prompted creation of scaffolds containing various combinations and arrangements of these molecules to more closely mimic native bone ECM.

In a study by Sotome *et al.*,[8] a hydroxyapatite/collagen nanocomposite (HAp/Col) and alginate hybrid material was investigated as a bone filler and BMP delivery system using a rat model. Previous work had demonstrated the bone-like nanostructure of the HAp/Col composite with hydroxyapatite crystals of up to 50 nm aligned along the collagen fibers. However, the density of the blocks of the HAp/Col composite prohibited tissue invasion and thus, limited its efficacy. By combining a powder form of the HAp/Col nanocomposite with alginate, they were able to create an injectable, porous scaffold. Application of this scaffold to holes in a rat femur demonstrated enhanced proximal bone formation and tissue ingrowth over 8 weeks compared to both porous HAp scaffold and alginate gels. Additionally, recombinant human BMP-2 (rhBMP-2)-induced ectopic bone formation showed dose dependent amounts of bone growth throughout almost the entire matrix as compared to the isolated small area of bone growth seen with rhBMP-2 loaded collagen scaffolds. Coupled with the scaffold's ability to maintain its shape in the compressive environment of bone tissue, the results

suggest that the HAp/Col-alginate scaffold would be a more effective BMP delivery vehicle in bone tissue than traditionally employed collagen matrices.

By incorporating multiple native components, the material more closely mimicked the native structure of bone ECM in both structural features and the ability to direct cell behavior *in vivo*. The results of this study, however, represent preliminary comparisons of feasibility and do not examine the quality of the regenerated tissue. While the material may have been able to stimulate cellular ingrowth and some bone formation, the ideal outcome of scaffold replacement with functional bone tissue was not demonstrated within the time frame or with the materials employed. The dependence of tissue ingrowth on swelling limits the possible applications of this material and may lead to an eventual lower rate of healing. Thus, while the use of ECM molecules provides advantageous bioactivity through stimulation of osteogenesis, further consideration must be given to mimic the mechanical and cell permissive properties of native ECM to achieve optimal tissue regeneration.

2.207.3.1.1.2. Case study: use of ECM scaffolds to repair ligaments

Ligaments are highly hydrated tissues featuring closely packed fibers composed of mainly collagen type I as well as collagen types III, V, and SLRPs. Type I collagen dominates the structure and is the main component responsible for the tissue's mechanical properties. Variations in the relative quantities or organization of these components can lead to significant differences in the mechanical properties of the tissue. Injuries to ligament tissue in the form of ruptures or tears usually result in regenerated tissue with significantly inferior mechanical properties to normal ligaments because of alterations in composition and ultrastructure even after years of remodeling. In particular, increases in the relative concentration of collagen type V and the amount of proteoglycans as well as a decrease in fiber diameter are commonly seen in the healed tissue.[9]

One strategy employed to improve healing efficacy is surgically implanting a SIS-derived biological scaffold into the site of ligament injury. In a series of investigations, a single layer of SIS was sutured into a 6 mm gap medial collateral ligament (MCL) injury in a rabbit model and compared to nontreated injuries and a sham control of undermined, but not injured, ligament.[10,11] After 12 weeks, SIS-treated MCL had greater collagen density, cellularity, overall collagen fiber diameter (**Figure 3**), and fiber alignment than nontreated controls. Additionally, RT-PCR investigations of the healed tissues demonstrated lower relative concentrations of collagen type V and certain SLRPs in SIS-treated conditions than in nontreated conditions. These compositional differences corresponded to at least 50% increases in the stiffness, tangent modulus, and ultimate strength of the SIS-treated healing tissue compared to nontreated controls. Such effects are attributed to cell signaling through the presence of growth factors and the degradable collagenous cell scaffold material as well as to the SIS scaffold's ability to maintain hydration within the wound environment.

Despite the improvements seen in SIS-treated healing tissue as compared to nontreated tissue, the composition and mechanical properties of the healed tissue from each condition were still vastly different from those of the sham controls even after 26 weeks. One important requirement of scaffolds

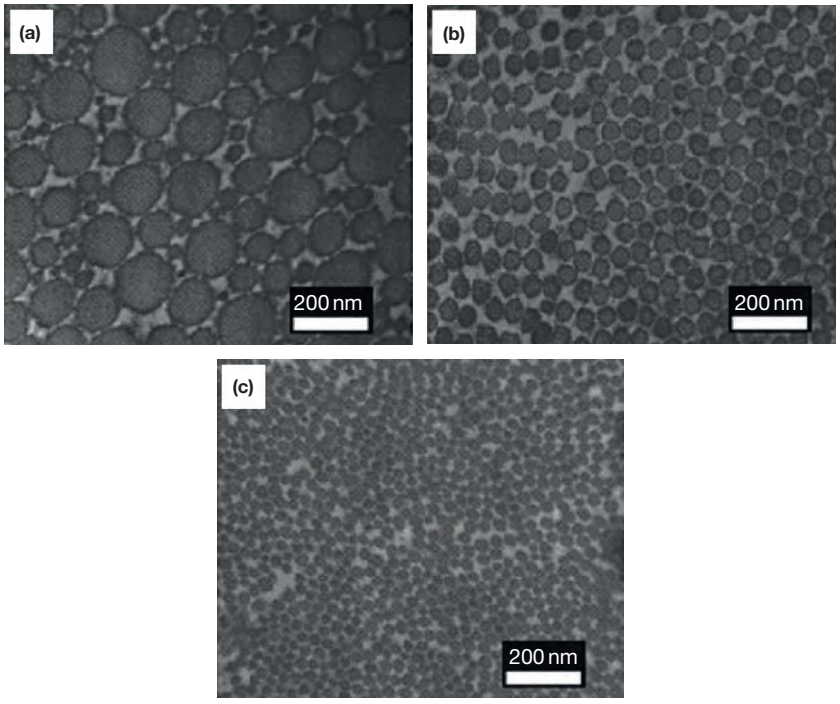

Figure 3 Transmission electron micrographs (70 000×) of cross-sectional collagen fibrils in (a) sham-operated medial collateral ligament (MCL), (b) small intestinal submucosa-treated MCL, and (c) nontreated MCL at 12 weeks post-6-mm gap injury. Adapted from Woo, S. L. Y.; Abramowitch, S. D.; Kilger, R.; Liang, R. *J. Biomech.* **2006**, *39*, 1–20.

employed to regenerate tissue is to be able to transmit the mechanical forces across the injury. This requisite not only provides the replacement of lost function but also allows for mechanical conditioning of the regenerating tissue. As ECM scaffolds, including SIS, reflect the composition and architecture of the source tissue, application of these materials to different types of allogenic or xenogenic tissue may not fully replicate the environment necessary to restore functioning tissue. In this case, SIS lacking some crucial characteristics of ligaments, such as collagen fiber orientation in space, may have limited its ability to fully stimulate remodeling of the healing tissue despite containing many of the same structural molecules. Some current research focuses on mechanically preconditioning cell-seeded ECM scaffolds that reorient fibers and increase mechanical properties.[12] Such steps may allow ECM scaffolds from more accessible tissues to be more effective in mimicking the properties of ECM from different tissues.

2.207.3.1.2. Partial copy

Using full-length copies of proteins is not always feasible or appropriate for certain biomaterial applications. ECM scaffolds may not fulfill either the required mechanical or bioactive role or the rapid degradation may compromise the material efficacy. Individual ECM proteins are often not sufficiently stable to successfully retain bioactivity after incorporation into the biomaterial and the amount of source material or the cost of production to achieve the required bioactive concentration can be prohibitory. Additionally, full proteins may stimulate undesired cell responses, especially in cases where certain cell differentiation states must be maintained (reviewed in Carson and Barker[13]). As mentioned previously, ECM–cell interactions and interactions between ECM proteins are mediated by recognition of small peptide sequences contained within ECM proteins. Exploiting this relationship provides an alternative method to attaining the desired protein–protein interaction though incorporating a fraction of the native ECM protein in the form of a functional motif. Through these protein–protein interactions, changes in cell behavior and ECM structure can be stimulated through alterations of protein configuration, formation of membrane-proximinal protein clusters, transmission of mechanical forces between cells and ECM, and organization or enzymatic cleavage of ECM proteins. By taking advantage of the relatively low complexity of these recognition motifs, bioactivity and bioresponsiveness can be incorporated and controlled in synthetic or natural biomaterials.

The techniques used to modify biomaterials with these functional peptide motifs generally fall into two categories: 'surface modification' and 'incorporation' into the scaffold structure. Surface modification methods, as opposed to bulk material modification, are typically employed with materials having a lower surface to volume ratio where cell–material interactions occur within a limited surface area. This approach is also advantageous in *in vivo* settings as it allows the material to maintain its bulk mechanical properties while adding surface bioactivity. The major methods of immobilizing peptides to the biomaterial surface include electrostatic interaction (e.g., adsorption, self-assembled monolayers), ligand–receptor interactions (e.g., biotin–avidin, antibody–antigen), and covalent attachment (e.g., silanization, polymer tethering; see Garcia,[14] Goddard and Hotchkiss,[15] Raynor *et al.*[16] for more detailed reviews). Limited availability of the ligand due to surface rearrangement, nonspecific adsorption of proteins, and changes in ligand conformation is a common challenge that reduces the efficacy of these techniques. To overcome some of these limitations, one common strategy is to introduce a spacer group, typically in the form of a hydrophilic polymer, between the surface and the bioactive molecule to increase availability, prevent denaturation, and reduce nonspecific protein adsorption. For highly porous materials, typically hydrogels or other polymeric scaffolds, ECM mimetic ligands are often incorporated directly into the polymeric structure. Peptide sequences can be covalently attached to polymer chains prior to formation of the scaffold or a peptide sequence can be incorporated on formation of the scaffold through the attachment of cross-link-susceptible chemical groups or interactions with proteins. For example, SLRP-mediated collagen fibrillogenesis has been mimicked in collagen scaffolds by incorporating a small peptidoglycan containing collagen-binding peptide sequences derived from these SLRPs.[17] In this way, functional peptide sequences are presented throughout the scaffold in a similar manner, as seen with surface modification, or as an integral, bioresponsive segment of the polymeric chains.

2.207.3.1.2.1. Case study: multiple ligand–integrin interactions alter intracellular signaling

Integrin binding to adhesive motifs that are present in a variety of ECM proteins may direct cell phenotypes and guide various cell processes such as adhesion, intra- and intercellular signaling, and cell death. Affinity between the ligand and integrin, avidity of the ligand, and integrin specificity are all influential factors in the subsequent downstream cellular effects. One of the first and most commonly employed peptide motifs in biomaterial design is the ECM ubiquitous integrin-binding tripeptide sequence arginine-glycine-aspartic acid (RGD). RGD was first employed to increase or control adhesion to materials which normally may not support adhesion, but has been found to influence a variety of cell behaviors including cell phenotype. For example, variations in monocyte behavior seeded onto poly(ethylene glycol) (PEG)-based hydrogels with or without incorporation of a tethered RGD motif demonstrate possible implications toward modifying the host response using functional motifs.[18] Both adhesion of and inflammatory cytokine and protease release from primary monocytes were shown to be modulated by the presence and density of RGD within the scaffold. While the ability of simple peptide sequences, such as RGD, to bind multiple integrin pairs is advantageous for increasing cell adhesion, in cases where unambiguous downstream outcomes are desired, integrin-specific binding is necessary. Moreover, additional complexity present in the native protein may provide further bioactivity than is seen with binding to just a simple, small peptide sequence. For example, presentation of the collagen I derived adhesive motif, GFOGER, in a triple-helical conformation similar to that of native collagen is critical for $\alpha_2\beta_1$ integrin binding. By incorporating integrin-specific protein fragments into biomaterials, researchers hope to exploit individual integrin-mediated bidirectional transfer of biochemical signals.

Both $\alpha_2\beta_1$ and $\alpha_5\beta_1$ integrin pairs have been shown to play integral roles in mediating the interaction of several cell types,

for example osteoblasts, fibroblasts, and chondrocytes, with their native ECM. Most studies, however, deviate from what is seen in the ECM by incorporating only a single adhesive motif. In a study by Reyes *et al.*,[19] surfaces combining two specific integrin-binding motifs were employed to elucidate possible synergistic effects on fibrosarcoma cell adhesion, integrin binding, and integrin-mediated signaling responses. Biotinylated triple-helical GFOGER and a fibronectin fragment (FNIII7-10) were attached in various ratios to avidin-adsorbed tissue culture polystyrene surfaces using the well-known high-affinity interaction between avidin and biotin. The fibronectin fragment spanned the 7th–10th type III repeats containing the adhesive motif RGD and its synergistic binding domain PHSRN. Previous work had demonstrated the increase in $\alpha_5\beta_1$ binding specificity of this fragment as compared to that of the linear RGDS peptide. The presentation of both GFOGER and FNIII7-10 demonstrated synergistic enhancement of cell adhesion, FAK activation (implicated in integrin-mediated intracellular signaling), and cell proliferation as compared to single ligand or no ligand surfaces (**Figure 4**). The use of ligand mimics providing specific integrin binding as well as antiintegrin antibody controls point to specific coordinated integrin binding of the adhesion motifs leading to membrane-proximal clustering of the two integrin types and possible further downstream interaction between signaling pathways.

The results of these studies demonstrated intracellular convergence of integrin-activated signaling pathways through use of fibronectin and collagen mimetic ligands presented on a material surface. Such synergistic effects demonstrate some of the complexity involved in mimicking cell–ECM adhesive interactions. While there are prevalent examples of incorporation of the single ECM mimetic ligands into biomaterial scaffolds, cell-responsive benefits may be gained by expanding the number and types of motifs. However, further material development and cell-based studies are needed to determine if multiligand materials could be employed to improve material efficacy in an *in vivo* or in a clinical setting.

2.207.3.1.2.2. Case study: enhancement of chrondrogenic differentiation by MMP-13 degradable hydrogels

Differentiation of stem cells to dedicated cell types requires highly coordinated processes integrating multiple types of signals derived from growth factor–receptor binding to mechanotransduction. An additional level of complexity is also presented in the form of temporal synchronization of these varied signals. As such, while stem cells hold much promise as a tool for research and clinical purposes, many challenges remain concerning both stimulating and inhibiting differentiation. Designing and constructing biomaterials to act as platforms for controlling differentiation states will require a similar level of complexity as seen in the native ECM environment which normally mediates stem cell fate. While research into this field is still in its infancy, several promising bioactive materials have been developed by incorporating ECM functional motifs.

Temporal principles of chondrogenesis were applied to enhance human mesenchymal stem cells (hMSC) differentiation seeded on an enzymatically responsive PEG hydrogel.[20,21] Differentiation of hMSC into chrondrocytes has been shown to require an increase in fibronectin, specifically the RGD adhesive motif, during preliminary phases of chondrogenesis, likely to stimulate cell–cell interactions. A subsequent decrease in fibronectin is then seen as differentiation proceeds and cells adapt a more spherical shape. In fact, the persistent presence of fibronectin may be inhibitive to chondrocyte function as was seen in *in vitro* work from another group using RGD-conjugated alginate gels. Incorporation of RGD into a PEG hydrogel was shown to support hMSC viability and initiate chondrogenic differentiation; however, results also demonstrated that extended incubation of the hMSC reduced the percent differentiation. On the basis of studies which demonstrated matrix metalloprotease-13 (MMP-13) upregulation at 7–12 days of hMSC chondrogenesis, a MMP-13 cleavage site, derived from the cartilage ECM component aggrecan, was incorporated into the PEG hydrogel. By integrating a 12-mer peptide containing both

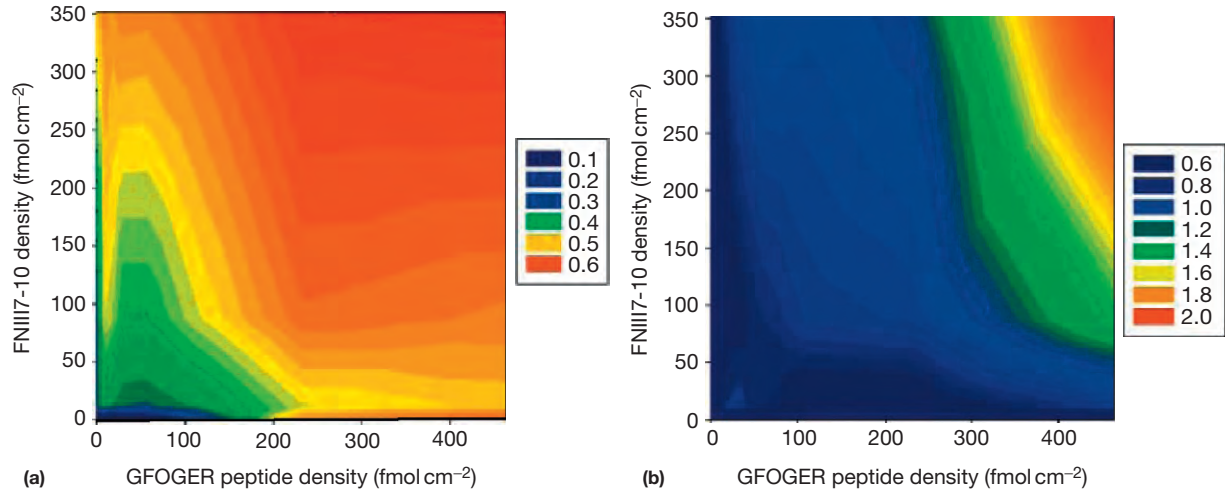

Figure 4 Contour plots displaying the effect of the GFOGER and fibronectin fragment mixed densities on adhesion ligands on fibrosarcoma; (a) adhesion and (b) FAK phosphorylation. Results are presented as (a) postcentrifugation calcein-AM signal normalized to the precentrifugation signal and (b) activated FAK normalized to total FAK detected for those conditions. Adapted from Reyes, C. D.; Petrie, T. A.; Garcia, A. J. *J. Cell Physiol*. **2008**, *217*, 450–458.

the cleavage site, PENFF (proline-glutamic acid-asparagine-phenylalanine-phenylalanine), and RGD into the PEG hydrogel, bioresponsive enzymatic cleavage of the RGD sequence was achieved. While there was a loss of viability of hMSC encapsulated in hydrogels containing the cleavage site after 11 days, likely because of the loss of adhesion sites, there was a dramatic increase in glycosaminoglycan deposition, an indicator of chondrogenesis, compared to RGD-only controls.

These studies demonstrated effective temporal and bioresponsive presentation of ECM cues to modulate differentiation of hMSC through incorporation of biological principals to material design. While these studies address mimicking down-regulation of signals in the extracellular environment, one important function of native ECM, maintenance of cell viability, was not achieved, and it demonstrates the need for further material development to fully realize how materials can control cell fate. Furthermore, additional levels complexity must be considered for possible future *in vivo* applications of bioresponsive materials. For example, levels of MMP-13 may be altered in an inflammatory environment as compared to an *in vitro* hMSC culture system leading to possible incorrect timing of RGD cleavage.

2.207.3.2. Mimicking ECM Function Through ECM Architecture and Topography

While specific ligand–receptor interactions between ECM components and the cellular environment are the primary interface responsible for mediating ECM functions, the way in which these components are organized play a major role in controlling both the downstream cellular effects and overall function of the tissue. The hierarchical configurations of the ECM ultrastructure establish macrolevel mechanical and mass-transport properties in a tissue. Well-defined nanostructural topographical and mechanical cues are able to influence cell–material interaction by promoting cell proliferation, differentiation, adhesion, and migration. Additionally, nanopatterning of cell-adhesive motifs provides a secondary level of cell behavioral control. In this section, an overview of how these ECM features are replicated and employed in material design is discussed.

2.207.3.2.1. Hierarchical microstructure and porosity

The core structure of the ECM across tissues consists of a 3D, highly hydrated, porous matrix. This configuration allows for water retention, mass transport of nutrients such as glucose and oxygen, as well as directed cell migration and soluble factor storage. For example, cell migration efficiency has been found to be optimal at pore diameters that are the same or slightly smaller than the diameter of polarized cells (reviewed in Friedl and Wolf[22]). Larger and smaller pore sizes lead to reduced cell migration rates because of decreased amounts of cell–ECM contacts and steric hindrance, respectively. Also, the additional complexity incorporated into the porous structure of the ECM creates differential physical properties of a tissue. Simple architectural features, such as fibers (see **Section 2.207.3.2.2**), are able to undergo further organization to form multifunctional lattice structures with specific densities and spatial arrangements. Developing these hierarchical arrangements establishes tissue-specific directionally dependent mechanical properties and cell arrangement (see Isenberg and Wong[23] for further review). For example, helical arrangement of successive layers of collagen- and elastin-embedded smooth muscle cells provides enhanced circumferential load-bearing properties and high torsional stability in arterial walls. Another widespread example is the organization of the basement membrane in a variety of endothelial tissues: the high density of structural ECM components forms nearly a 2D platform for cell attachment and organization through steric- and adhesion-based inhibition of endothelial cell migration. Mimicking the structural properties of the ECM in biomaterial design can range from simply imitating the properties of the core structure to incorporating mechanically effective higher-order lattice construction.

A major biomaterial application requirement is to support cell viability and growth, particularly in tissue engineering and wound healing applications. Hydrogels composed of both hydrophilic synthetic polymers (e.g., PEG) and natural macromolecules (e.g., collagen) have garnered attention for their similarity to the ECM core structure in terms of possessing basic cell-supportive properties including providing hydration, mass transport, and a 3D environment. This broad class of materials is highly varied in terms of polymer chemistry, construction methods, and types of functional modifications (see Andriola Silva *et al.*,[24] Jia and Kiick,[25] and Tibbett and Anseth[26] for relevant reviews) allowing extensive customization of hydrogels for different applications. By controlling the material chemistry and the porosity, specific mechanical properties and transport characteristics can be achieved. For example, hydrogels or similar systems can act as local reservoirs for soluble proteins where diffusion of soluble factors can be controlled, in part, by pore size and interactions with the polymer backbone similar to what is seen in native ECM. Additionally, controlling the density of physical or chemical cross-links will alter mechanical properties of the hydrogel. However, highly porous materials are traditionally limited in both the strength and complexity of the mechanical characteristics they can achieve. Additionally, pore size is typically heterogeneous and not able to be precisely controlled using simpler scaffold construction techniques. Therefore, while the core structural characteristics of the ECM are able to be mimicked with relative ease, achieving coordinated mass transport and mechanical properties requires adaptation of more complex architectural features.

Approaches in scaffold design are able to mimic higher-order ECM architecture through creation of hierarchical or micropatterned porous structures that provide the desired mechanical and mass-transport properties. Possibly the simplest methodology to achieve porous structures with anisotropic mechanical properties is through the mechanical conditioning of existing porous scaffolds. For example, scaffold alignment can be achieved through cell- or temperature-mediated mechanical cycling of collagen or synthetic polymer hydrogels, respectively.[12,27] Alignment of electrospun fibers can also be employed to create anisotropic materials while at the same time presenting important topographical cues to cells (see **Section 2.207.3.2.2**). These techniques, however, often do not achieve cell permissive pore sizes or physiological mimetic mechanical properties. More complex techniques are available to create 3D structures with defined pore size and shape

ranging from microablation of pores into polymer membranes to computational-driven layer by layer manufacturing of complex 3D scaffolds from polymer, hydrogel, ceramic, and metal materials (see Hollister[28] for in-depth review). The latter technique provides rigorous control of the scaffold architecture, allowing construction of materials with a single pore size or wavy fibers, for example. By varying the shape, orientation, and distribution of the pores, porosity can thereby be used to create direction-dependent mechanical properties instead of relying solely on material chemistry.

2.207.3.2.1.1. Case study: anisotropic honeycomb structure for ventricular myocardium repair

Ventricular myocardium is structurally highly complex, requiring directionally dependent mechanical and electrical properties for its proper function. In native tissue, cardiomyocytes are interwoven into a multifaceted network of collagen fibers which display honeycomb-like organization. This type of organization produces mechanical and electrical anisotropy. Damage to the ventricular myocardium, typically as a result of a cardiac infarction, leads to cardiomyocyte death and replacement of native tissue with nonfunctional fibrous tissue. Previous attempts to repair myocardial tissue using 3D scaffolds has failed to effectively regenerate functional tissue due to structural and mechanical variances from native tissue. For example, scaffolds were unable to promote more than isolated regions of cardiomyocyte alignment or effectively transmit physiological mechanical forces. More recent efforts borrow from native ECM collagen fiber orientation to more closely mimic directionally dependent myocardial structural and mechanical characteristics.

In a study by Engelmayr *et al.*,[29] a polymeric scaffold exhibiting anisotropic characteristics was designed and evaluated for use in cardiac tissue engineering. An accordion-like honeycomb structure was created by laser microablating two overlapping $200 \times 200\,\mu m$ square pores oriented at 45° into approximately 250-μm-thick poly(glycerol sebacte) (PGS) wafers. The resulting accordion-like scaffold exhibited anisotropic mechanical properties more closely mimicking that of right ventricular myocardium than scaffolds constructed with square or rectangular pores. Further manipulation of the mechanical characteristics could be achieved by reducing the polymer curing time, cyclic loading, and culture with heart cells. While in some cases, this modulation helped to achieve better-matched properties, cell interaction reduced the stiffness of the scaffold to levels below what is seen in native tissue after one week. Cardiomyocytes and cardiac fibroblasts cocultured on the accordion-like scaffolds demonstrated cell alignment and slightly lower excitation thresholds in the preferred direction than more isotropic materials. Additionally, an initial attempt to create a bilayer structure by combining a partially and a fully excised PGS wafer resulted in cell penetration and interpore connectivity.

Mimicry of mechanical properties in tissue engineering scaffolds is important for correct transmission of mechanical forces across repairing tissues. This study demonstrates that use of a geometrically controlled porous structure can better match the mechanical characteristics of native tissues than heterogeneous or isotropic scaffolds. Creation of directionally dependent mechanical properties also provided cues that were able to partially guide cell alignment and thereby, cell-mediated electrical properties. The authors also attempted to address *in vitro* to *in vivo* scaling issues by layering the PGS wafers to create additional thickness. Scaling is a major hurdle to translating these types of precise material construction techniques from the miniature *in vitro* cell culture environment to implants used in considerably larger areas of tissue in *in vivo* environments. For scaffolds to successfully function at the tissue level, materials must be able to be constructed with a variety of shapes and sizes, typically much larger than what is used *in vitro*.

2.207.3.2.2. Topographical features and patterning

The ECM contains a considerable amount of cell-instructional information within micro- and nanometer scale topographical and biochemical details. In native ECM, these features are established through the arrangement and configuration of ECM components creating geometric cues or differential densities of functional motifs. Cells interact with simple physical cues, such as varying elevations or nanoscale pores, through nanoscale cellular extensions, known as filopedia. Although the mechanism by which these physical cues influence cell behavior is not completely understood, one contributing factor is the significant increase in the surface area-to-volume ratio and overall complexity of the surface. These features facilitate contact guidance phenomena and subsequent changes in cell morphology and migration. Concentration gradients of growth factors or proteins containing adhesive motifs also function to direct cell migration and alignment along the gradient. Additionally, specific ligand clustering or patterning of dissimilar motifs or signaling proteins can lead to alterations in cell behavior beyond what is seen for disorganized ligand–integrin binding. Although the exact mechanism by which adhesive ligand clustering affects intracellular signaling is unknown, it is generally thought that subsequent spatial proximity of integrins leads to further intracellular protein interaction, particularly with various cytoskeleton proteins. The addition of nanometer scale details in biomaterials can be accomplished by mimicking native ECM structures or can be imitated using surface modification techniques to add topological or patterned biochemical cues.

One of the most common methods to replicate micro- and nanoscale structural features of the ECM is to mimic the fibrillar construction of the ECM scaffold. In addition to influencing cell behavior through topological details, interactions between cells and ECM nanofibers also play an important role in mechanotransduction through viscoelastic deformation of the fibers in response to external and internal stresses. Nanofiber-based biomaterials can be manufactured using several different techniques, the most commonly employed being phase separation, self-assembly, and electrospinning (see Nisbet *et al.*[30] and Madurantakam *et al.*[31] for relevant reviews). Thermally induced phase separation involves partitioning of a polymer phase from a solvent phase through controlled or, more frequently for nanofiber formation, rapid cooling. Self-assembly of nanofibers can be accomplished by driving assembly of carefully designed monomers using hydrophobic or ionic interaction. For example, Hartgerink *et al.*[32] constructed a biofunctional nanofibrillar network containing fibers with an average diameter of 7.1 nm on the basis of hydrophobic interactions between akyl chains linked to

functional polypeptides (for more examples of self-assembled structures, see **Section 2.207.3.3**). The more common current approach for forming fibrous scaffolds because of its relative ease of use, versatility, and scalability, is electrospinning. Electrospinning involves forming continuous fibers by using electric forces to overcome surface tension and thereby elongate droplets of polymer melt or solution into a stream. Using this technique, natural or synthetic polymers can be employed as substrates for fiber formation and by varying process, environmental, and substrate parameters, fibers with a vast diversity of properties can be constructed. For example, while traditional methods produce nonwoven, randomly oriented fiber mats, using a rotating, electrified collector results in fiber alignment and thereby improved mechanical and cell-guidance properties. Recent work has also explored increasing the fiber's bioactivity by incorporating the delivery of drugs or growth factors and even cell encapsulation within the fiber structure.[33]

While electrospinning provides a versatile construction method for mimicking ECM architecture, several limiting design constraints remain. Processing conditions, in particular the use of volatile solvents, have been shown to cause denaturation of the native protein structure. For example, collagen type I-based nanofibers demonstrated a loss of triple-helical structure, lack of crystallinity, and lower denaturation temperature suggesting that the collagen had been reverted to a gelatin-like state.[34] Moreover, the resulting pore sizes of the 3D fibrous scaffold often prohibit cell migration into the matrix. Steps can be taken to increase porosity such as the addition of easily removable components to the structure, for example, salts or highly degradable polymers. Finally, while electrospinning is typically associated with production of nanofibers able to mimic the fibers of the ECM, most current production methods achieve fibers with larger diameters than native tissue. Typical electrospun fiber diameters are >500 nm; however, several methods do exist to achieve dimensions closer to native ECM. Furthermore, increases in the understanding of parameters relevant to fiber diameter coupled with technological advances promise closer ECM fiber mimics.

Using ECM structural mimics, such as nanofibers, to construct biomaterials currently does not provide the level of control or bioactivity needed to fully investigate and/or exploit microscale or nanoscale cell–material interactions. To accomplish these goals, the material design parameters are commonly focused to the area of cell–material interface through use of surface modification techniques. Methods to incorporate nanoscale features onto the surface can be categorized on the basis of the level of user-specific control of the resulting patterns they provide. Unordered topographies can be manufactured using techniques such as polymer demixing, colloidal lithography, and chemical etching (see Norman and Desai[35] for a more detailed review). These methods allow a small amount of user control over the type and number of nanofeatures obtained through variations in processing parameters, but cannot create structures with complex prescribed geometries or organization. In exchange, these methods are capable of rapid coverage of large substrate surfaces. The resulting unordered surface topographies are able to mimic the nanoscale features of the ECM but may not present the same amount of complexity and therefore cell-instructional information of native tissue.

Ordered topographies can be developed using laser ablation, microfluidics, or a variety of lithographical techniques (for more extensive reviews, see Christman *et al.*,[36] Hook *et al.*,[37] Mrksich,[38] and Schmidt and Healy[39]). Through molecule removal from the surface, molecule addition to the surface, or surface group modification, organized nanopatterns can be attained. Both physical and biochemical cues can be patterned by adding motifs directly to the surface or manipulating the chemical composition of the surface to prevent or accept biofunctional molecules through adsorption or covalent binding. Alternatively, imprint lithography and microcontact printing use nanopatterned rigid masters, manufactured using the previously mentioned techniques, to topographically mold surfaces or stamp proteins onto surfaces. However, the relatively high cost, low throughput, and lack of available equipment needed to employ these techniques limit the application of ordered nanopatterning to biomaterial design. All of these methodologies are able to spatially control molecule placement on biomaterial surfaces allowing creation of more complex biomaterials. Yet, currently, the main advantage of being able to define surface nanopatterns is derived from the ability to gain a better understanding of how individual nanoscale topographical and biological patterns affect cell behavior and phenotype at an *in vitro* level.

Patterning of functional motifs onto biomaterial surfaces has been used extensively to study how engineering material surfaces can be used to alter cell adhesion strength, spreading, migration, and differentiation. Initial and continuing work in this area involved micropatterning of proteins, such as fibronectin, through preferential adsorption to certain chemical domains patterned onto the substrate or lithographic printing methods.[40,41] Cell morphology and adhesion strength, for example, were shown to be controlled by modulating the area of cell–material contact.[14] Development of more sophisticated nanopatterning techniques has shifted the focus to creating subcellular arrangements of proteins or, more commonly, functional motifs. For example, a density gradient of RGD causes preferential migration and alignment of cells.[42] Additionally, the density and spatial proximity of nanoscale RGD clusters can modulate differentiation, spreading, proliferation, and motility of cells.[43,44] One reason for the observed variations was demonstrated by a series of studies where a spatial limit between RGD clusters was established for the formation of focal adhesions.[45] The limitations of these techniques revolve around the 2D system necessary for the creation of these nanoscale patterns. Therefore, while the existence of nanoscale features in the ECM is known, the level of knowledge and technology needed to mimic these aspects to control cell–biomaterial interactions in a more clinical setting has not yet been achieved.

2.207.3.2.2.1. Case study: electrospun nanofibers for repair of peripheral nerves

The peripheral nervous system consists of bundles of neuronal axons (nerve fibers) typically surrounded by a myelin sheath formed by layers of Schwann cells, a type of glial cell. Damage to peripheral nerves usually presents as a severance of an axon and can be repairable without intervention with significant restoration of function. In cases where there is extensive loss of tissue, however, random nerve sprouting at the site of injury because of a lack of directional cues is insufficient to effectively

regenerate the lost tissue. Infiltration of inflammatory cells and eventual establishment of granulation tissue at the site of injury create an inhibitory microenvironment for nerve regeneration. Several different types of tissue engineering approaches have been attempted to create a more permissive environment for nerve regeneration.[46] Conventional treatment involves insertion of nerve autografts or allografts; however, autograft material is limited and allografts may lead to immunological rejection. Polymer nanofiber-based biomaterials are promising for neural cell–material applications because of their resemblance to native ECM and ability to directionally guide neurite outgrowth. Of particular interest are nanofibers constructed out of poly(α-hydroxy esters) because of their bioresorbable and biocompatible nature.

Poly(DL-lactic-*co*-glycolide) (PLGA) and poly(ε-caprolactone) (PCL) nanofibers have been used for *in vitro* and *in vivo* neural tissue engineering applications concerning neurite outgrowth for damaged peripheral nerve reconstruction. When whole dorsal root ganglia (DRG), dissociated DRG cells, Schwann cells, and fibroblasts were seeded on aligned PCL and PCL/collagen blend nanofibers (500–600 nm diameter), greater alignment of neurite growth parallel to the fiber orientation was demonstrated as compared to nonfibrous poly-D-lysine surfaces (**Figure 5**).[47] The addition of collagen to the nanofiber composition led to an increased fiber orientation, glial cell migration, and elongation of fibroblasts, but decreased rate of neurite elongation, likely attributed to stronger cell–material interactions due to the presence of collagen. Furthermore, on PCL/collagen nanofibers, there was evidence of neurite growth on top of Schwann cells suggesting indirect directionality conveyed by the nanofibers to the extending neurites. In a separate *in vivo* study, tubes constructed with both PCL microfibers (2.5–8 μm diameter) and PCL/PLGA blend nanofiber tubes (140–500 nm diameter) were used to treat a 10-mm gap wound in the sciatic nerve in a rat model.[48] Improved rat sciatic nerve regeneration was achieved as compared to both transected nerve and nontreated 10-mm gap injury controls. After 4 months, regenerated tissue consisting of neural fibers, glial cells, fibroblasts, and ECM consistent with regenerating basal lumina was observed throughout the length of the scaffold. Meanwhile, the nerve stumps never reconnected in the case of the two controls; instead, random neurite sprouting led to attachment to the surrounding muscle tissue. Evidence of partial reinnervation was seen on the basis of transmission of neural tracers across the regenerated tissue as well as behavioral and neurophysiological tests. The success of the scaffold was attributed to increased cell adhesion and directional migration across the fibrous structure as well as a lack of excess inflammatory response. The fibrous structure provided high flexibility, porosity, and surface-to-volume ratio allowing higher levels of protein adsorption and an absence of mechanical microinjury as seen with stiff continuous tubes. In addition to serving as a guide for the regenerating nervous tissue, the relatively close-knit structure of the fibers prevented unwanted tissue infiltration while still allowing passage of nutrients.

Despite the success of the employment of nanofibrous tubes over nontreated controls, full function was not restored to the tissue. Myelination was not seen throughout the regenerated nervous tissue and the restored basement lamina was disorganized compared to uninjured tissue. In this *in vivo* study, the

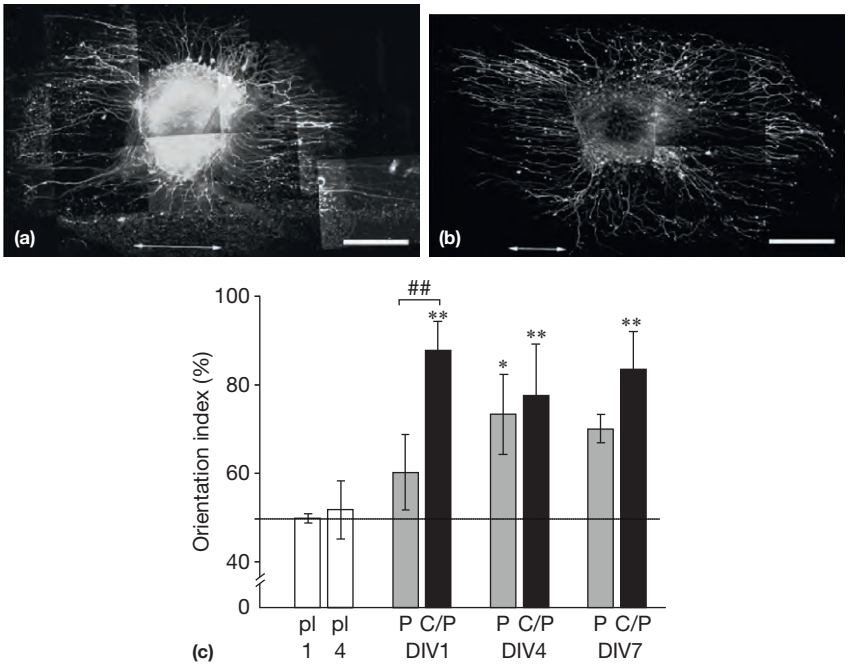

Figure 5 Orientation of neurite growth from dorsal root ganglia explants. (a,b) Neurofilament staining at 4 days on (a) poly(ε-caprolactone) (PCL) nanofibers and (b) PCL/collagen blend nanofibers; scale bar = 500 μm. Arrows indicate direction of nanofibers. (c) Comparison of axon orientation on poly(lysine)-coated coverslips at 1 and 4 days *in vitro* (DIV) and on PCL and PCL/collagen nanofibers at 1, 4, and 7 DIV; orientation index of 50% indicates random orientation of neuritess, 100% complete alignment with nanofibers, 0% orientation perpendicular to nanofibers. Significantly different than 50% $*p < 0.01$, $**p < 0.05$; $\#\#p < 0.01$. Adapted from Schnell, E.; *et al*. *Biomaterials* **2007**, *28*, 3012–3025.

fibers were randomly oriented and relied on the tube structure to direct longitudinal growth of the neurites. Improvements may be seen by applying the *in vitro* results discussed previously by increasing geometric directional cues and incorporating native ECM components into the material. In either case, however, tissue engineering approaches incorporating ECM architectural principles to peripheral nerve regeneration are relatively novel and further development will be needed before clinically efficient demonstrations can be achieved.

2.207.3.3. Mimicking ECM Protein Design and Assembly

Biological polypeptides are, in essence, complex copolymers which derive their properties from the precisely organized sequences and compositions of the basic amino acid monomers. Depending on the properties of the amino acid side chains, proteins will adapt various secondary, tertiary, and quaternary assemblies. Furthermore, through controlled associations between motifs incorporated into different polypeptide molecules, ECM proteins have the ability to self-assemble into complex 3D scaffolds. The design versatility, synthetic homogeneity, and biocatalytic assembly of biopolymers are attractive attributes to incorporate into material design and construction. In this section, a brief overview of how concepts of ECM protein design and self-assembly are both mimicked by and incorporated into biomaterials is provided (for more in-depth reviews, see Deming[49] and Maskarinec and Tirrell[50]).

Advances in recombinant DNA technology and chemical peptide synthesis techniques have stimulated interest and provided the necessary tools to explore *de novo* designed polypeptide sequences with material application potential. Designing proteins which assemble into higher-order structures using recombinant DNA technology is the most complex adaptation of mimicking protein assembly into material design. By designing novel polypeptide sequences from first principles utilizing sequence-based structural elements, researchers hope to be able to control higher-order structures or interactions between proteins. Successful cases of achieving functional tertiary structures are rare; however, greater progress has been made utilizing sequence-to-structure concepts on a smaller scale. Artificially created amino acids can be substituted to change the overall properties of the polypeptide. Incorporation of fluorine-containing amino acid analogues, for example, has been used to integrate properties seen in fluorinated synthetic polymers, such as low surface energy, low friction coefficient, and good hydrolytic stability, into polypeptides. Thus, multi-monomer, well-defined polypeptides can assimilate desirable chemical properties normally seen in polymers with heterogeneous molecular weight distribution and less complex chemical composition. The configuration of small polypeptide sequences has also been altered to perform a non-native function. For example, introducing different sequence mutations into functional domains has been used to artificially confer specificity. Richards *et al.*[51] produced a FNIII10 fragment with an RGDWXE sequence that demonstrated enhanced affinity and specificity to the $\alpha_v\beta_3$ rather than the $\alpha_5\beta_1$ integrin. Finally, controlled periodicity of sequence structure can stimulate thermodynamic folding into higher-order structures such as fibers or sheets. By exploiting structural and ionic characteristics of amino acids, peptide sequences without chemical modification have been designed to fold into β-sheets or α-helical structures. Further modification of the peptide sequence can lead to systematic interactions between polypeptide chains leading to the formation of coiled-coil or stacked structures. For example, in a study by Banwell *et al.*,[52] modifications to a repeating heptad peptide sequence capable of self-assembling into α-helical structures were able to control the formation of higher-order materials (Figure 6). That is, more specific

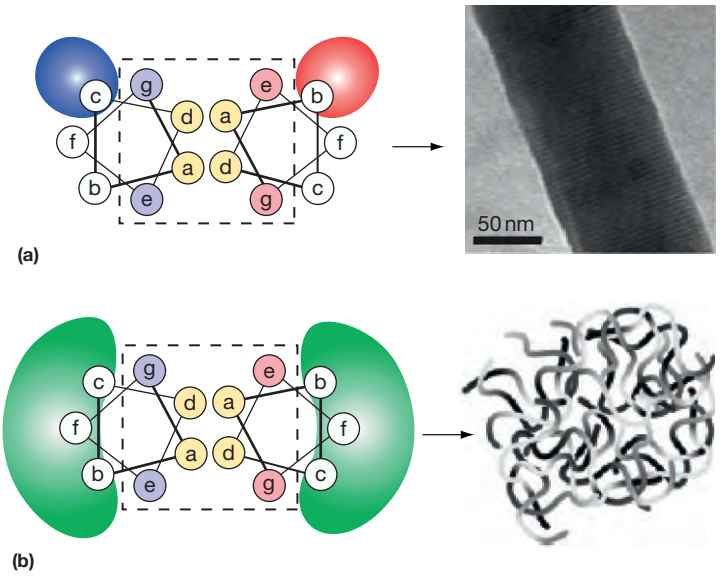

Figure 6 Schematic representation of design principles behind the hierarchical assembly of polypeptide chains containing the coiled-coil heptad sequence repeat, abcdefg. By incorporating specific interactions between amino acids at positions b and c, the α-helical structures further organized to form thicker fibrils. Alternatively, incorporation of more general, weaker interactions at positions b, c, and f led to the formation of thinner, more flexible fibers which could form hydrogels based on physical interactions between chains. Adapted from Banwell, E. F.; *et al*. *Nat*. *Mater*. **2009**, *8*, 596–600.

interactions between chains led to α-helical dimer association to form larger fibrils or more general interactions led to hydrogel formation containing more flexible chains. Such a work exhibits potential for creating highly controllable and biocompatible materials by translating nanoscale structural principles.

2.207.4. Future Directions

The merging of material and biological principles allows for the creation of materials that function as cooperative parts of the biological environment. As shown in this chapter, particular promise lies in incorporating principles derived from the native ECM into biomaterial design. Contained within the ECM is a complex regimen of spatial and temporally controlled cellular cues and structural elements responsible for maintaining and adapting to changes in the biological environment. In addition to multiple biomaterial applications benefiting from the addition of structural and functional ECM-derived principles, this design approach can also provide new insights into biological mechanisms that are not fully understood. While many strategies exist for incorporating these features, mimicry of the complex multicomponent, spatially and temporally controlled system has not been truly achieved in biomaterial design. The future lies in increasing the specificity and control of the presentation of multiple types of signals and structures. However, incorporating this type of complexity into biomaterials requires an additional level of inquiry into scalability issues and possible host modification once the material is applied to *in vivo* clinical settings. Furthermore, when nanoscaled or technologically complicated techniques are used to construct the materials, additional consideration must be paid toward the long-term efficacy and impact versus 'traditional' biomaterial in the face or regulatory hurdles, clinical availability concerns, and potentially high costs of production. Nonetheless, ECM mimicry holds much promise in advancing biomaterial research into controlling host–biomaterial interactions and creating new ways to construct materials.

References

1. Plopper, G. In *Cells*; Lewin, B., Cassimeris, L., Lingappa, V. R., Plopper, G., Eds.; Jones and Bartlett, 2007; p 645.
2. Fredberg, J. J.; Discher, D.; Dong, C.; *et al*. *Ann. Biomed. Eng.* **2009**, *37*(5), 847–859.
3. Place, E. S.; Evans, N. D.; Stevens, M. M. *Nat. Mater.* **2009**, *8*, 457–470.
4. Abraham, S.; Eroshenko, N.; Rao, R. R. *Regen. Med.* **2009**, *4*(4), 561–578.
5. Badylak, S. F.; Freytes, D. O.; Gilbert, T. W. *Acta Biomater.* **2009**, *5*, 1–13.
6. Kim, M. S.; Ahn, H. H.; Shin, Y. N.; Cho, M. H.; Khang, G.; Lee, H. B. *Biomaterials* **2007**, *28*, 5137–5143.
7. Brown, B.; Lindberg, K.; Reing, J.; Beer Stolz, D.; Badylak, S. F. *Tissue Eng.* **2006**, *12*(3), 519–526.
8. Sotome, S.; Uemura, T.; Kikuchi, M.; *et al*. *Mater. Sci. Eng.* **2004**, *24*, 341–347.
9. Woo, S. L. Y.; Abramowitch, S. D.; Kilger, R.; Liang, R. *J. Biomech.* **2006**, *39*, 1–20.
10. Liang, R.; Woo, S. L.; Nguyen, T. D.; Liu, P.; Almarza, A. *J. Orthop. Res.* **2008**, *26*(8), 1098–1104.
11. Woo, S. L.; Takakura, Y.; Liang, R.; Jia, F.; Moon, D. K. *Tissue Eng.* **2006**, *12*(1), 159–166.
12. Androjna, C.; Spragg, R. K.; Derwin, K. A. *Tissue Eng.* **2007**, *13*(2), 233–243.
13. Carson, A. E.; Barker, T. H. *Regen. Med.* **2009**, *4*(4), 593–600.
14. Garcia, A. J. *Adv. Polym. Sci.* **2006**, *203*, 171–190.
15. Goddard, J. M.; Hotchkiss, J. H. *Prog. Polym. Sci.* **2007**, *32*, 698–725.
16. Raynor, J. E.; Capadona, J. R.; Collard, D.M; Petrie, T. A.; Garcia, A. J. *Biointerphases* **2009**, *4*(2), FA3–FA16.
17. Paderi, J. E.; Sistiabudi, R.; Ivanisevic, A.; Panitch, A. *Tissue Eng.* **2009**, *15*(10), 2991–2999.
18. Chung, A. S.; Waldeck, H. M.; Schmidt, D. R.; Kao, W. J. *J. Biomed. Mater. Res.* **2009**, *91A*(3), 742–752.
19. Reyes, C. D.; Petrie, T. A.; Garcia, A. J. *J. Cell Physiol.* **2008**, *217*, 450–458.
20. Salinas, C. N.; Anseth, K. S. *Macromolecules* **2008**, *41*, 6019–6026.
21. Salinas, C. N.; Anseth, K. S. *Biomaterials* **2008**, *29*, 2370–2377.
22. Friedl, P.; Wolf, K. *J. Cell Biol.* **2009** [Online].
23. Isenberg, B. C.; Wong, J. Y. *Mater. Today* **2006**, *9*(12), 54–60.
24. Andriola Silva, A. K.; Richard, C.; Bessodes, M.; Scherman, D.; Merten, O.-W. *Biomacromolecules* **2009**, *10*, 9–18.
25. Jia, X.; Kiick, K. L. *Macromol. Biosci.* **2009**, *9*, 140–156.
26. Tibbett, M. W.; Anseth, K. S. *Biotechnol. Bioeng.* **2009**, *103*(4), 655–663.
27. Millon, L. E.; Mohammadi, H.; Wan, W. K. *J. Biomed. Mater. Res.* **2006**, *79B*, 305–311.
28. Hollister, S. J. *Nat. Mater.* **2005**, *4*, 518–525.
29. Engelmayr, G. C.; Cheng, M.; Bettinger, C. J.; Borenstein, J. T.; Langer, R.; Freed, L. E. *Nat. Mater.* **2009**, *7*, 1003–1010.
30. Nisbet, D. R.; Forsythe, J. S.; Shen, W.; Finkelstein, D. I.; Horne, M. K. *J. Biomater. Appl.* **2009**, *24*, 7–29.
31. Madurantakam, P. A.; Cost, C. P.; Simpson, D. G.; Bowlin, G. L. *Nanomedicine* **2009**, *4*(2), 193–206.
32. Hartgerink, J. D.; Beniash, E.; Stupp, S. I. *Science* **2001**, *294*, 1684–1688.
33. Ashammakhi, N.; Wimpenney, I.; Nikkola, L.; Yang, Y. *J. Biomed. Nanotechnol.* **2009**, *5*(1), 1–19.
34. Zeugolis, D. I.; Knew, S. T.; Yew, E. S. Y.; *et al*. *Biomaterials* **2008**, *29*, 2293–2305.
35. Norman, J. J.; Desai, T. A. *Ann. Biomed. Eng.* **2006**, *34*(1), 89–101.
36. Christman, K. L.; Enriquez-Rios, V. D.; Maynard, H. D. *Soft Matter* **2006**, *2*, 928–939.
37. Hook, A. L.; Voelcker, N. H.; Thissen, H. *Acta Biomater.* **2009**, *5*(7), 2350–2370.
38. Mrksich, M. *Acta Biomater.* **2009**, *5*, 832–841.
39. Schmidt, R. C.; Healy, K. E. *J. Biomed. Mater. Res.* **2009**, *90A*, 1252–1261.
40. Coyer, S. R.; Garcia, A. J.; Delamarche, E. *Angew. Chem. Int. Ed.* **2007**, *46*, 6837–6840.
41. Liu, L.; Ratner, B. D.; Sage, E. H.; *et al*. *Langmuir* **2007**, *23*, 11168–11173.
42. DeLong, S. A.; Gobin, A. S.; West, J. L. *J. Control. Release* **2005**, *109*, 139–148.
43. Comisar, W. A.; Kazmers, N. H.; Mooney, D. J.; Linderman, J. J. *Biomaterials* **2007**, *28*, 4409–4417.
44. Maheshwari, G.; Brown, G.; Lauffenburger, D. A.; Wells, A.; Griffith, L. G. *J. Cell Sci.* **2000**, *113*, 1677–1686.
45. Cavalcanti-Adam, E. A.; Volberg, T.; Micoulet, A.; Kessler, H.; Geiger, B.; Spatz, J. P. *Biophys. J.* **2007**, *92*, 2964–2974.
46. Subramanian, A.; Krishnan, U. M.; Sethuraman, S. *J. Biomed. Sci.* **2009**, *16*, 108–118.
47. Schnell, E.; Klinkhammer, K.; Balzer, S.; *et al*. *Biomaterials* **2007**, *28*, 3012–3025.
48. Panseri, S.; Cunha, C.; Lowery, J.; *et al*. *BMC Biotechnol.* **2008**, *8*, 39–50.
49. Deming, T. J. *Adv. Mater.* **1997**, *9*(4), 299–310.
50. Maskarinec, S. A.; Tirrell, D. A. *Curr. Opin. Biotechnol.* **2005**, *16*, 1–5.
51. Richards, J.; Miller, M.; Abend, J.; Koide, A.; Koide, S.; Dewhurst, S. *J. Mol. Biol.* **2003**, *326*, 1475–1488.
52. Banwell, E. F.; Abelardo, E. S.; Adams, D. J.; *et al*. *Nat. Mater.* **2009**, *8*, 596–600.

2.208. Artificial Extracellular Matrices to Functionalize Biomaterial Surfaces

S Bierbaum and D Scharnweber, Institute of Materials Science, Technische Universität Dresden, Dresden, Germany

© 2011 Elsevier Ltd. All rights reserved.

2.208.1.	**Introduction**	128
2.208.2.	**Components to Be Used for aECM**	129
2.208.2.1.	Collagens	129
2.208.2.2.	Noncollagenous Glycoproteins	131
2.208.2.2.1.	Elastin	132
2.208.2.2.2.	Fibronectin	132
2.208.2.2.3.	Laminin	132
2.208.2.2.4.	Vitronectin	132
2.208.2.2.5.	Tenascin, osteopontin, and thrombospondin	132
2.208.2.3.	Proteoglycans	132
2.208.2.3.1.	Small leucine-rich proteoglycans	132
2.208.2.3.2.	HyA-binding PGs (hyalectans)	133
2.208.2.3.3.	Non-HyA-binding PGs	133
2.208.2.4.	Glycosaminoglycans	133
2.208.2.4.1.	Hyaluronan	134
2.208.2.4.2.	Heparin/HS	134
2.208.2.4.3.	Chondroitin sulfate, dermatan sulfate, and keratan sulfate	134
2.208.3.	**Biological Interaction Profiles of aECM and Their Components**	135
2.208.3.1.	Direct	135
2.208.3.1.1.	Cell-surface receptors	135
2.208.3.1.2.	Collagen	135
2.208.3.1.3.	Glycoproteins	135
2.208.3.1.4.	Proteoglycans	136
2.208.3.1.5.	Glycosaminoglycans	136
2.208.3.2.	Indirect	136
2.208.3.2.1.	Collagens and glycoproteins	136
2.208.3.2.2.	Proteoglycans	137
2.208.3.2.3.	Glycosaminoglycans	137
2.208.4.	**Preparation and Structure of aECM**	139
2.208.4.1.	Heterotypic Fibrils	140
2.208.4.2.	Collagen Fibrils with Glycoproteins	140
2.208.4.3.	Collagen Fibrils with PGs	141
2.208.4.4.	Collagen Fibrils with Modified Proteins and/or Peptides	141
2.208.4.5.	Collagen Fibrils with GAGs	142
2.208.5.	**Biochemical Characterization of aECM**	143
2.208.5.1.	Glycoproteins and PGs	143
2.208.5.2.	Glycosaminoglycans	143
2.208.5.3.	Growth Factor Interactions	144
2.208.6.	**Immobilization of aECM**	144
2.208.7.	**Cell Biological Effects of aECM**	145
2.208.7.1.	Collagens	146
2.208.7.2.	Glycoproteins and PGs	147
2.208.7.3.	Glycosaminoglycans	147
2.208.8.	**Results from Animal Experiments**	148
2.208.8.1.	Collagens	148
2.208.8.2.	Glycoproteins and PGs	149
2.208.8.3.	Glycosaminoglycans	149
2.208.9.	**Conclusions and Outlook**	150
References		151

Abbreviations

aECM	Artificial extracellular matrix
ALP	Alkaline phosphatase
AT-III	Antithrombin III
BMP	Bone morphogenetic protein
C1q	Complement factor 1q
CAM	Cell adhesion molecule
CNS	Central nervous system
CS	Chondroitin sulfate
CS-PG	Chondroitin sulfate proteoglycans
DDR	Discoidin domain receptors
DG	Dystroglycan
DNA	Desoxyribonucleic acid
DPS	D-periodic symmetry
DS	Dermatan sulfate
ECM	Extracellular matrix
EDC	1-Ethyl-3-[3-dimethylaminopropyl] carbodiimide hydrochloride
EGF	Endothelial growth factor
EGF-R	EGF-receptor
ePTFE	Expanded polytetrafluoroethylene
ERK	Extracellular signal regulated kinase
FAC	Focal adhesion complex
FACITs	Fibril-associated collagens with interrupted triple helices
FAK	Focal adhesion kinase
FGF	Fibroblast growth factor
FGF-R	Fibroblast growth factor receptor
FN	Fibronectin
GAG	Glycosaminoglycan
GF	Growth factor
GM-CSF	Granulocyte macrophage colony stimulating factor
GPI	Glycosylphosphatidylinositol
GTP	Guanosine triphosphate
HARE	HyA receptor for endocytosis
HB-EGF	Heparin-binding EGF
hESC	Human embryonal stem cells
HGF	Hepatocyte growth factor
HGF-R	Hepatocyte growth factor receptor
hMSC	Human mesenchymal stem cells
HS	Heparan sulfate
HS-PG	Heparan sulfate proteoglycans
HyA	Hyaluronic acid, hyaluronan
IGF	Insulin like growth factor
IGF-R, IGF-IR	IGF receptor, IGF-I receptor
IL	Interleukine
KS	Keratan sulfate
LAIR	Leucocyte-associated immunoglobuline receptor
LRR	Leucine-rich repeats
LYVE-1	Lymphatic vessel endothelial HA receptor 1
MAPG-1	Microfibril-associated glycoprotein 1
MAPK	Mitogen-activated protein kinase
MCP-1	Monocyte chemoattractant protein
MIP2	Murine IL-8 analogon
MMP	Matrix metalloprotease
mRNA	Messenger ribonucleic acid
MSC	Mesenchymal stem cell
N-CAM	Neural cell adhesion molecule
NF-κB	Nuclear factor κ-light-chain-enhancer of activated B cells
NHS	*N*-hydroxysuccinimide ester
OB	Osteoblastic cells
OPN	Osteopontin
PAI-1	Type 1 plasminogen activator inhibitor
PDGF	Platelet-derived growth factor
PDGF-R	PDGF receptor
PECAM	Platelet/endothelial cell adhesion molecule 1
PG	Proteoglycan
PI3K	Phosphoinositide 3 kinase
RANTES	Regulated upon activation, normal T cell expressed and secreted
RHAMM	Receptor for hyaluronan-mediated motility
RPTG-γ	Signal transducing receptor-type tyrosine phosphatase
SLRPs	Small leucine-rich proteoglycans
TES	*N*-Tris(hydroxymethyl)methyl-2-aminoethanesulfonic acid
TGase	Transglutaminase
TGF-β	Transforming growth factor-β
TLR	Toll-like receptor
TN	Tenascin
TNFα	Tumor necrosis factor α
TSG	Twisted gastrulation
TSP	Thrombospondin
uPAR	Urokinase type plasminogen activator inhibitor
VCAM	Vascular cell adhesion molecule
VEGF	Vascular endothelial growth factor
VEGF-R	VEGF receptor
VN	Vitronectin
vWF	Von Willebrand factor
WISP-I	Wnt1 inducible signalling pathway protein

2.208.1. Introduction

A key process in the integration of implants and scaffolds into the host tissue is the interaction of the host tissue cells with the implant surface. Achieving a surface that guides these interactions is therefore a prime goal of biomaterial development.

Guiding cellular reactions is no trivial thing: *in vivo* cells exist in a highly complex environment, their fate being determined by information received from soluble factors, from other cells, and from the physical network they adhere to. This physical network that provides structure and support is the extracellular matrix (ECM), a viscoelastic milieu rich in biological information that plays an important role in guiding development, maintaining homeostasis, and directing regeneration, and thus constituting the gold standard for an environment that can steer and determine cellular reactions.

What is the ECM, and how does it achieve this? The term 'extracellular matrix' comprises a large and very heterogeneous set of components that are assembled locally into an ordered, highly site-specific network, and through the differences in composition the ECM takes an active part in regulating the cellular processes and responses in specific situations and tissues. ECM structure varies widely depending on the tissue and developmental stage of the collagen fibril as the central building block that is modified by other collagen types or noncollagenous components. The organic part of bone for instance consists to 90% of collagen type I, with small additions of type V and at times type III, as well as associated proteins such as decorin, osteopontin (OPN), and bone sialoprotein, which in mineralized tissues are also involved in the process of biomineralization. Cartilage, on the other hand, is made up largely of collagen type II and proteoglycans (PGs) (mainly aggrecan) that are responsible for osmotic swelling and elastic properties,[1] while blood vessel walls have to be elastic to support a pulsatile flow and consequently are made up of collagen I, type III, and elastin.

The mentioned proteins belong to certain component groups of the ECM (which will be discussed in detail in the following chapter): collagens, noncollagenous glycoproteins, PGs, and glycosaminoglycans (GAGs). Collagens are the most abundant proteins in the body, making up the lion's share of the structural network. They are modified in their structure and function by glycoproteins and PGs; these usually consist of a protein core to which one or more GAG chains are attached. GAGs are unbranched chains of repeating disaccharide units, and with few exceptions they occur only bound to the mentioned protein cores. Members of these different groups not only associate with each other in a defined manner but also specifically interact with cells and soluble proteins.

One very basic characteristic of the structural protein components of the ECM is that they confer cell adhesion, which is of vital importance for almost all cells, and the first use made of ECM components – mainly of collagen and fibronectin (FN) – was to increase cell adhesion to biomaterial surfaces not optimally suited to it. While a sound strategy, it does not do justice to the true functions and possibilities of the ECM. Cell adhesion to the ECM is a complex process and conveyed by specific adhesion receptors, enabling the cells to 'see' their surroundings and respond to them. Consequently, adhesion is intimately coupled to signal transduction, with most adhesion receptors functioning as signaling molecules. Engagement of these different receptors gives rise to a wide variety of intracellular signals that in turn influence proliferation, differentiation, and apoptosis (see Section 2.208.3 for details).

The direct interaction of the ECM with cellular receptors is by no means the only mechanism for influencing cells, as many of the structural components associate with growth factors and cytokines. These soluble factors are potent regulators of cell function, and the matrix components in turn regulate their functions: storing, activating, or inactivating them, protecting them from degradation, and retaining them at one place, thus generating gradients that cells can follow as in the case of vascular endothelial growth factor (VEGF). Without the matrix, there would be no gradient and therefore no ordered growth of blood vessels.

What now needs to be understood is the term 'artificial ECM' (aECM), which is the topic of this chapter? An aECM is a matrix consisting of isolated ECM components that have been reconstituted *in vitro* to construct a microenvironment that mimics the ECM in its ability to guide morphogenesis in tissue repair and engineering. It does not mean perfectly reconstructing the host tissue, a task that is beyond us as yet, but using those parts of the complex whole that elicit a specific response. This biomimicry may include, depending on the purpose, biochemical composition, fibrillar structure, and mechanical properties, as well as bioadhesive character, proteolytic susceptibility, and growth factor binding capacity.[2] Although both bioderived and biosynthetic materials can be applied, this chapter focuses mainly on the use of naturally derived materials (**Chapter 2.207, Extracellular Matrix: Inspired Biomaterials** and **Chapter 4.414, Molecular Biomimetic Designs for Controlling Surface Interactions**).

2.208.2. Components to Be Used for aECM

Some ECM components lend themselves more readily to use in artificial matrices than others. In this section, the main focus is placed on those proteins and polysaccharides that either have already been used in such a way, or are of potential interest; it does not constitute a comprehensive overview of the ECM. Materials which do not naturally occur but have been adapted to use in an artificial construct are included in a few exemplary cases only, for while of interest in this field, they are beyond the scope of this chapter (**Chapter 2.205, Self-Assembling Biomaterials** and **Chapter 2.203, Protein-Engineered Biomaterials: Synthesis and Characterization**).

2.208.2.1. Collagens

Collagens are the most abundant among the structural proteins. In humans, 28 collagens and collagen-like proteins have been identified so far,[3,4] although the defining line between collagen and collagen-like is blurred. In general, the term collagen encompasses all proteins containing regions characterized by the repeating amino acid motif (Gly-X-Y) that form a right-handed triple-helical structure and have a role in tissue assembly or maintenance. The collagen family can be subdivided into the following: fibrillar collagens, fibril-associated collagens (FACITs), beaded filament-forming collagens, basement membrane collagens, transmembrane collagens, collagens forming hexagonal networks and anchoring fibrils, and multiplexins (**Table 1**).[5] Among them, there is a considerable degree of complexity in structure, splice variants, presence of nonhelical domains, assembly, and function. The most abundant collagens are those of the fibril-forming subfamily with about 90% of the total collagen,[6] and these are the ones of the most interest for application in aECM (**Chapter 2.215, Collagen: Materials Analysis and Implant Uses**).

The fibril-forming collagens are I, II, III, V, XI, XXIV, and XXVII, and they are characterized by their ability to assemble into highly organized aggregates with a typical suprastructure, the quarter-staggered fibril-array with diameters between 25 and 400 nm. This results in a banding pattern with the so-called D-periodicity between 64 and 67 nm (depending on the tissue) on the basis of the staggered arrangement of the collagen monomers (for more detail see Section 2.208.4).

Table 1 Collagens and their receptors

Family	*Type*	*Receptors*	*Occurrence*
Fibril forming	I	Monomers: $\alpha2\beta1$, $\alpha1\beta1$, $\alpha10\beta1$, $\alpha11\beta1$ Fibrils: $\alpha2\beta1$, $\alpha11\beta1$ Denatured: $\alpha5\beta1$, $\alpha v\beta1$ DDR1, DDR2 Glycoprotein VI LAIR-1	Noncartilaginous tissues, bone, tendon, skin, ligaments, cornea, vasculature, interstitial connective tissues
Fibril forming	II	Monomers: $\alpha2\beta1$, $\alpha1\beta1$, $\alpha10\beta1$, $\alpha11\beta1$ DDR1, DDR2 Glycoprotein VI	Cartilage, vitreous body, nucleus pulposus, intervertebral disk
Fibril forming	III	Monomers: $\alpha2\beta1$, $\alpha1\beta1$, $\alpha10\beta1$, $\alpha11\beta1$ DDR1, DDR2 Glycoprotein VI LAIR-1	Embryonic skin, lung vasculature, vessel wall, elastic tissues
Network forming	IV	$\alpha1\beta1$, $\alpha10\beta1$, $\alpha2\beta1$, $\alpha11\beta1$ $\alpha1$(IV): $\alpha1\beta1$ $\alpha2$(IV): $\alpha v\beta3$, $\alpha v\beta5$ $\alpha3$(IV): $\alpha v\beta3$, $\alpha3\beta1$ DDR1	Basement membranes
Fibril forming	V	Monomers: $\alpha2\beta1$, $\alpha1\beta1$, $\alpha10\beta1$, $\alpha11\beta1$ DDR1, DDR2 Glycoprotein VI	Cornea, embryonic tissues, bone, interstitial matrix
Beaded filament forming	VI	$\alpha1\beta1$, $\alpha10\beta1$, $\alpha2\beta1$, $\alpha11\beta1$ DDR1	Muscle, dermis, cartilage, placenta, lung, vessel wall, invertebral disk
Anchoring fibrils	VII	$\alpha2\beta1$	Dermal–epidermal junction, skin, oral mucosa, cervix
Network forming	VIII	$\alpha1\beta1$, $\alpha2\beta1$ DDR1	Descement's membrane, endothelial cells
FACIT	IX	$\alpha1\beta1$, $\alpha2\beta1$, $\alpha10\beta1$, $\alpha11\beta1$	Cartilage, vitreous humous, cornea
Network forming	X	$\alpha2\beta1$ DDR2	Hypertrophic cartilage
Fibril forming	XI	Glycoprotein VI	Cartilage, vitreous body
FACIT	XII		Ligaments, tendon, perichondrium
Transmembrane	XIII	$\alpha1\beta1$	Neuromuscular junction, skin, epidermis, liver, lungs, chondrocytes
FACIT	XIV	$\alpha1\beta1$, $\alpha2\beta1$	Dermis, tendon, vessel wall, placenta, lungs, liver
Endostatins (multiplexins)	XV		Muscle, microvessels, eye, fibroblast, pancreas, kidney, smooth muscle cells
FACIT (multiplexins)	XVI		Fibroblasts, aminon, keratinocytes
Transmembrane	XVII	Denatured: $\alpha5\beta1$, $\alpha v\beta$ LAIR-1	Epithelia, dermal–epidermal junction
Endostatins (multiplexin)	XVIII	$\alpha5\beta1$, $\alpha v\beta3$, $\alpha v\beta5$	Basement membranes, lungs, liver
FACIT	XIX		Basement membranes
FACIT	XX		Corneal epithelium, embryonic skin, sternal cartilage, tendon
FACIT	XXI		Widespread distribution, vessel wall
FACIT	XXII		Tissue junctions, cartilage–synovial fluid
Transmembrane	XXIII		Limited distribution
Fibril forming	XXIV		Developing cornea and bone
Transmembrane	XXV		Collagenous Alzheimer amyloid plaque component
Beaded filament forming	XXVI		n.d.
Fibril forming	XXVII		Embryonic cartilage, developing dermis
Beaded filament forming	XXVIII		Basement membrane around Schwann cells
Transmembrane	Ectodysplasin A		Ectoderm
Transmembrane	Gliomedin		Myelinating Schwann cells

Source: Gelse, K.; Poschl, E.; Aigner, T. *Adv. Drug Deliv. Rev.* **2003**, *55*, 1531–1546; Heino, J. *Bioessays* **2007**, *29*, 1001–1010; Kadler, K. E.; Baldock, C.; Bella, J.; Boot-Handford, R. P. *J. Cell Sci.* **2007**, *120*, 1955–1958; Leitinger, B.; Hohenester, E. *Matrix Biol.* **2007**, *26*, 146–155.

Collagen type I is the most abundant as well as the best studied and is often viewed as the archetypical collagen. It is the major collagen of bone, tendons, skin, ligaments, cornea, vasculature, and many interstitial connective tissues with very few exceptions such as hyaline cartilage, brain, and vitreous body. Type II occurs mainly in cartilage where it accounts for 80% of the collagen content; it is also found in some other locations such as the vitreous body, the invertebral disk, and during embryonic epithelial–mesenchymal transitions.[7] Type III usually occurs associated with collagen type I, mainly in relatively elastic tissues such as embryonic skin, lung, and blood vessels; type V occurs with type I in bone, cornea, and the interstitial matrix, and is highly expressed during tissue development and wound repair. Type XI occurs with type II in cartilage, while type XXIV and XXVII associate with type I and type II, respectively.[6]

All fibril-forming collagens closely resemble each other. They are composed of three peptide chains called α-chains, forming triple-helical molecules of 300 nm length flanked by the telopeptides, nonhelical sequences about 20 amino acids in length. The larger N- and C-terminal propeptides are removed immediately before fibril formation. Type II and type III each has three identical α1(II) and α1(III) chains, respectively, and type I has two identical α1(I) and one α2(I) chain, while for collagen V and XI all three chains differ. Characteristic of type III is the higher degree of hydroxylation and two cystein residues, which allow this collagen type to rapidly form intramolecular cross-links, something of great advantage during embryogenesis and wound healing.[8]

Type I is dominant in most tissues, but there are a variety of ways to achieve the diversity needed in fibrillar architecture for different tissues and developmental stages. One is through the minor collagens, for which healing of fetal bone is an example. While in mature bone type I is predominant (90%) with small additions of type V, in fracture healing the type III expression rises in the initial phase, forming a scaffold for the migration of osteoprogenitor cells and capillary ingrowth. Only later it is replaced by collagen type I via an intermediate stage of heterotypic I and III fibrils.[8] Such copolymers are the norm in most tissues, with the minor collagens functioning both as initiators of fibril formation and as modulators of fibril morphology. To the latter is attributed the fact that for the collagens V and XI the propeptides can be incompletely removed, which is thought to control fibril assembly, growth, and diameter.[9]

Other regulators of fibril architecture are the so-called small leucine-rich proteoglycans (SLRPs), which have been shown to have a large effect on fibril assembly[10] and are discussed under Section 2.208.2.3.

2.208.2.2. Noncollagenous Glycoproteins

The proteins of this group are quite heterogenous, existing in several variant forms and possessing multiple binding domains capable of interacting with collagen and PGs as well as with the cell surface (Table 2). The binding domains contain specific amino acid sequences that interact with cell-surface receptors and serve as adhesion recognition signals. FN,

Table 2 Noncollagenous glycoproteins and their interactions

Name	*Structure*	*Interactions*	*Occurrence*
Elastin	72 kDa, closely resembles collagen		Elastic tissues
Fibronectin	500 kDa dimer	Collagens (I, II, III), CS, fibrinogen, heparin, α2β1, α3β1, α4β1, α4β7, α5β1, α8β1, αvβ1, αvβ3, αvβ5, αvβ6, αvβ8, αIIbβ3, cell-surface PGs	ECM and cell surface, soluble variant in plasma
Laminin	Heterotrimers in 18 isoforms	Heparin, collagen IV, agrin, α1β1, α2β2, α3β1, α4β1, α5β1 α6β1, α7β1, α9β1, αvβ3, α6β4, syndecans, dystroglycans, perlecan	Basement membranes, epithelial and endothelial tissues
Vitronectin	75 kDa	Heparin, AT-III, PGs, collagens, αvβ3, αvβ5, avβ1, αIIbβ3, urokinase receptor, PAI-1, uPAR	Circulates in blood stream, loose connective tissues, blood vessel walls, lymph nodes
Tenascin (-C, -X, -R, -W)	Multimeric, subunits 190–300 kDa	Heparin, FN, aggrecan, versican, brevican, neurocan, syndecan, glypican, αvβ3, αxβ1, α8β1, α9β1, αvβ6, α2β1, CAM, phosphacan/RPTP ζ/β, annexin II, EGF-R	Connective tissue, dermis, tendons, near kidney, vascular smooth muscle, CNS, lung, skin kidney, bone, muscle
Osteopontin	Phosphoprotein, 264–301 amino acids	Collagen, FN, αvβ1, αvβ3, αvβ5, αvβ6, α5β1, α8β1, α9β1, CD44 variants	Bone, blood vessels, kidney, brain, smooth muscle, immune organs, body fluids
Thrombospondin-1 to -5		PGs, decorin, FN, laminin, collagen (I, II, IX), aggrecan, heparin, HS, DS, CS, matrilin-2, -3, fibrinogen, α5β3, syndecan-1, -3, -4, cell-surface PGs, integrins, perlecan, versican, VEGF	Lung, cartilage, brain, bone, tendon, CNS

Brunner, A.; Tzankov, A. *Biomark Insights* **2007**, *2*, 418–427; Durbeej, M. *Cell Tissue Res.* **2009**; Jones, F. S.; Jones, P. L. *Dev. Dyn.* **2000**, *218*, 235–259; Kazanecki, C. C.; Uzwiak, D. J.; Denhardt, D. T. *J. Cell. Biochem.* **2007**, *102*, 912–924; Liu, L.; Qin, C.; Butler, W. T.; Ratner, B. D.; Jiang, S. *J. Biomed. Mater. Res. A* **2007**, *80*, 102–110; Madsen, C. D.; Sidenius, N. *Eur. J. Cell Biol.* **2008**, *87*, 617–629; Pankov, R.; Yamada, K. M. *J. Cell Sci.* **2002**, *115*, 3861–3863; Plow, E. F.; Haas, T. A.; Zhang, L.; Loftus, J.; Smith, J. W. *J. Biol. Chem.* **2000**, *275*, 21785–21788; Ruoslahti, E. *Annu. Rev. Biochem.* **1988**, *57*, 375–413; Sano, K.; Asanuma-Date, K.; Arisaka, F.; Hattori, S.; Ogawa, H. *Glycobiology* **2007**, *17*, 784–794; Schvartz, I.; Seger, D.; Shaltiel, S. *Int. J. Biochem. Cell Biol.* **1999**, *31*, 539–544; Tan, K.; Lawler, J. *J. Cell Commun. Signal.* **2009**; Tucker, R. P.; Chiquet-Ehrismann, R. *Biochim. Biophys. Acta* **2009**, *1793*, 888–892.

laminin, vitronectin (VN), thrombospondin (TSP), and tenascin (TN) are members of this class of ECM proteins.

2.208.2.2.1. Elastin

Although not a collagen, this elastic 72 kDa protein resembles collagen closely, the main difference being that, unlike collagen, it contains only little proline and much lysine. It is the major insoluble protein in elastic tissues, where it contributes to their elasticity and influences cell migration, proliferation, and elastin synthesis.[11]

2.208.2.2.2. Fibronectin

FN is a multifunctional adhesive glycoprotein that plays an important role in tissue repair, in regulating cell attachment and motility, and in embryogenesis. It is a dimeric, disulfide-bonded glycoprotein of 500 kDa with a multimodular structure, comprising repeats of three distinct types of motifs called FN I–III. The protein occurs in the ECM and on the cell surface; the plasma variant does not polymerize into superstructures, but can be integrated into FN fibrils.[12]

The protein interacts with many macromolecules such as collagens, GAGs, and fibrinogen and mediates cell attachment via various sequence domains (RGD, RGDS, LDV, REDV),[13] of which especially the RGD peptide is widely used as a cell adhesion motif. FN is known to bind several types of collagen, with the binding site localized to a 30–40 kDa domain near the N-terminus of each FN chain. FN interacts with the α-chains of collagen I–III through a binding domain approximately two-thirds from the N-terminus of the α-chains, although there may be at least one more binding site of a different affinity along the α1(I) chain.[14]

2.208.2.2.3. Laminin

Laminin is found mainly associated with basement membranes and consists of three disulfide-linked chains that form a cross-shaped structure. There are 18 isoforms, all the products of closely related genes,[15] all of which contain cell adhesion sequences (RGD, PDSGR, YIGSR, IKVAV) and have a high binding affinity for heparin and type IV collagen. Cell adhesion peptides based on laminin sequences that bind α3β1 integrin have been used comparably to the FN-based RGD peptide in matrix engineering.[16]

Laminin also associates with cell-surface receptors, such as through an endothelial growth factor (EGF)-like sequence that becomes available only after degradation and can stimulate cell proliferation and differentiation. Both laminin and FN are reported to promote neurite extension and are thus critical in neural development.[17,18]

2.208.2.2.4. Vitronectin

VN is a multifunctional glycoprotein of 75 kDa that binds to various biological ligands and plays a key role in tissue remodeling by regulating cell adhesion through binding to different types of integrins, mainly via the RGD sequence. VN also regulates blood-system-related protease cascades such as coagulation and fibrinolysis through interaction with heparin and thrombin–antithrombin III complexes. Tissue VN interacts with PGs and collagens, but plasma VN is believed to be in the inactive monomer form that does not bind, requiring activation through urea, heat, or certain ligands like heparin.[19]

2.208.2.2.5. Tenascin, osteopontin, and thrombospondin

TN, OPN, and TSP are glycoproteins that also convey a multitude of functions and might thus be of interest for aECM. Even though no use has been made of them so far, they are shortly mentioned here for this reason.

The TNs are a family of large multimeric, six-armed molecules that are widely expressed: TN-X, -R, and -W, as well as the best described TN-C. They are found during organogenesis and inflammation, in muscle, connective tissue, developing bone, and the nervous system,[20] and contain multiple functional domains including EGF-like and FN III repeats.[21]

OPN is present mainly in mineralized tissues, where it is one of the most abundant noncollagenous proteins. It can bind to collagen and FN, and regulates bone formation and remodeling, the inflammatory response, wound healing, and foreign body response. The protein interacts with the αvβ3 integrin via an RGD sequence and is critical in osteoblast and osteoclast function.[22,23]

The TSPs are a protein family that guides ECM synthesis and is essential for dynamic tissues remodeling, being involved in angiogenesis, matrix assembly, transforming growth factor (TGF) activation, and neurite outgrowth. They bind cell adhesion receptors as well as a multitude of other ECM components: PGs, FN, laminin, matrilin, collagen I, II, and IX, fibrin, aggrecan, heparin, heparan sulfate (HS), dermatan sulfate (DS), and chondroitin sulfate (CS). This may allow them to play a role in forming a molecular bridge between matrix components or components and the cell surface[24] (**Table 2**).

2.208.2.3. Proteoglycans

PGs are molecules composed of a core protein substituted with covalently linked sulfated GAG chains covalently linked to the core protein via serine residues. They can be subdivided into the SLRPs and those PGs of a large molecular weight. These include the hyaluronic acid (HyA)-binding hyalectans, and non-HyA-binding PGs, among which are basement membrane and cell-surface PGs (**Table 3**).

2.208.2.3.1. Small leucine-rich proteoglycans

SLRPs are a large family of proteins characterized by core proteins with leucine-rich repeats (LRR), which are believed to be important for the protein–protein interactions, and at least one GAG side chain.[25] Additional diversity can be achieved by combinations with different GAGs: decorin and biglycan, for instance, are substituted mainly with DS in unmineralized tissues, gaining consecutively more CS as mineralization progresses.[26]

SLRPs are important regulators of various biological processes through their ability to interact with different cell-surface receptors, cytokines, and growth factors (for details see **Section 2.208.3**), while their interaction with the fibril-forming collagens regulates fibril assembly and diameter, something important for the proper assembly of tissues. Loss of decorin results in fused fibrils with irregular contours and an abnormal skin fragility,[27] loss of fibromodulin in thinner tendon fibrils, and loss of lumican in cornea fibrils without diameter control and organization. The interaction is mediated in most cases by the protein core, while the GAG chains maintain

Table 3 Examples for proteoglycans and their interactions

Family	*Name*	*GAG*	*Interactions*
SLRP	Decorin	CS/DS	Collagen, tenascin-X, fibrillin-1, tropoelastin, MAPG-1, EGF-R, IGF-IR, LRP-IR, TGF, PDGF, IGF-I, vWF, TNFα, WISP-I, C1q
	Biglycan	CS/DS	Collagen, tropoelastin, MAPG-1, TLR-2, -4, selectin-L, CD44, C1q, TGF, TNFα, WISP-I, BMP-2, -4
	Fibromodulin	KS	Collagen, C1q, TGF, BMP
	Lumican	KS	Collagen, FasL, CXC-chemokine KC
	Keratocan	KS	Collagen
	Osteoadherin	KS	C1q
	PRELP	KS	Collagen, HS, heparin
	Chondroadherin	KS	C1q
	Tuskushi	n.d.	BMP
Hyalectans	Versican	CS/DS	HyA, collagen I, fibrillin-1, FN, tenascin-R, CD44, P- and L-selectin, EGF-R, β1-integrin, TLR2
	Aggrecan	CS/KS	HyA, HS, heparin, tenascin-R
	Neurocan	CS	HyA, tenascin-R, tenascin-C, N-CAM
	Brevican	CS	HyA, tenascin-R
Basement membrane PGs	Agrin	HS	Laminin, dystroglycan, integrins
	Perlecan	HS	Laminin, collagen IV, FGF
	Collagen XVIII	HS	Basement membrane components
Cell-surface PGs	Syndecans	CS/HS	Collagen, FN, tenascin, laminin, VN, integrins, FGF-2, HGF, VEGF, midkine
	Glypicans	HS	FN, Wnt, TGF, FGF, VEGF, BMP, midkine, IGF
	Betaglycan	CS/HS	TGF, BMP, FGF

Merline, R.; Schaefer, R. M.; Schaefer, L. *J. Cell Commun. Signal*. **2009**; Schaefer, L.; Iozzo, R. V. *J. Biol. Chem.* **2008**, *283*, 21305–21309; Schaefer, L.; Schaefer, R. M. *Cell Tissue Res*. **2009**; Uitto, V. J.; Larjava, H. *Crit. Rev. Oral Biol. Med*. **1991**, *2*, 323–354; Mythreye, K.; Blobe, G. C. *Cell Signal* **2009**, *21*, 1548–1558; Kirn-Safran, C.; Farach-Carson, M. C.; Carson, D. D. *Cell. Mol. Life Sci*. **2009**, *66*, 3421–3434; Tillgren, V.; Onnerfjord, P.; Haglund, L.; Heinegard, D. *J. Biol. Chem.* **2009**, *284*, 28543–28553; Yamaguchi, Y. *Cell. Mol. Life Sci*. **2000**, *57*, 276–289.

interfibrillar space[10] and contribute to matrix integrity by binding other ECM components such as TN-X.[28] Collagen-binding SLRPs include decorin (DS/CS), fibromodulin (KS), lumican (KS), biglycan (CS/DS), keratocan (KS), and osteoglycan (KS), with decorin, biglycan, and lumican being the best characterized. The mechanism of action seems to be an interaction with collagen that leads to coating of the fibril with the PG, as has been shown for decorin. Low decorin concentrations at the fibril tip allow for an increase in length while maintaining a constant fibril diameter. Biglycan interacts with collagen without influencing fibril diameter, and may be involved in organizing assembly of type IV collagen into networks. Both SLRPs may also be involved in elastic fiber biology.[28]

SLRPs bind to a number of growth factors. Decorin, biglycan, asporin, and fibromodulin bind TGF-β, with the decorin–TGF interaction being the best studied. Decorin inactivates TGF-β signaling by forming a TGF–decorin complex and sequestering it into the ECM via binding to collagen. Conversely, this may also enhance TGF activity, as seen during bone formation in remodeling when the TGF is again released. Decorin also binds PDGF and IGF-I, but with a comparatively low affinity, and through its GAG chains it interacts with vWF. Decorin and biglycan are also able to immobilize the proinflammatory cytokine TNFα and interact with WISP-I, while biglycan and fibromodulin can modulate BMP activity.[28]

2.208.2.3.2. HyA-binding PGs (hyalectans)

Among the hyalectans are counted versican, aggrecan, neurocan, and brevican. They consist of three domains: a central one that carries most of the GAGs, flanked by N-terminal domains that bind to HyA and C-terminal domains that interact with lectins.

Versican (CS/DS) is a regulator of cell–matrix interactions through its ability to interact with a large number of ECM and cell proteins (HyA, collagen type I, fibrillin-1, FN, CD44, selectin, integrin β1). Aggrecan (CS/KS) is expressed mainly in cartilage and brain and exists exclusively in the form of HyA/aggrecan aggregates with up to 100 aggrecan molecules, while neurocan (CS) and brevican (CS) occur in the central nervous system.[25]

2.208.2.3.3. Non-HyA-binding PGs

The non-HyA-binding PGs are also often termed heparan sulfate proteoglycans (HSPGs), as they are, unlike the other PGs, often linked to HS. Among these are the PGs that are part of the basement membrane: agrin, perlecan, and collagen XVIII, the last one being considered to be a hybrid collagen–PG. Cell-surface PGs also belong to this group, but these are not part of the ECM, but serve as receptors on the cell surface.

2.208.2.4. Glycosaminoglycans

GAGs are linear polysaccharides able to interact with numerous proteins and modulate their activities. They fall into two classes: (1) sulfated GAGs comprising CS, DS, keratin sulfate, heparin, and HS; and (2) the nonsulfated GAG hyaluronan, which is the only one to occur without a core protein.

GAG chains are made up of repeating disaccharide units consisting mainly of acetylated amino sugars (*N*-acetyl-galactosamine or *N*-acetyl-glucosamine) and uronic acids (D-glucuronic acid or L-iduronic acid) (Table 4).

Table 4 Glycosaminoglycans and their interactions

Name	*Major disaccharide unit*	*Interactions*	*Occurrence*
Heparan sulfate	D-GlcA-β(1→4)-D-GlcNAc-α(1→4)	Laminin, FN, VN, TSP, CD44, P- and L-selectin, PECAM, FGF-R, N-CAM, BMP-R FGFs, HGF, BMP-2, -4, -7, Wnt, TGF-β, interleukines, TNFα, AT-III, EGFs, IGF-II, PDGF, VEGF, GM-CSF, RANTES	Extracellular on cell surface and in basement membrane
Heparin	L-IdoA2S-α(1→4)-D-GlcNS6S-α(1→4)	See heparan sulfate	Intracellular in mast cells
Chondroitin sulfate	D-GlcA-β(1→3)-D-GalNAc4S-β(1→4)	CD44, P- and L-selectin, Chemokines, FGF-2, -10, -16, -18, midkine, pleiotrophin, EGF	Cartilage, tendon, ligament, aorta
Dermatan sulfate	L-IdoA-β(1→3)-D-GalNAc4S-β(1→4)	CD44, P- and L-selectin, FGF-2, FGF-7, HGF/SF	Skin, blood vessels, heart valves
Keratan sulfate	D-Gal-β(1→4)-D-GalNAc6S-β(1→3)		Cornea, cartilage
Hyaluronic acid	D-GlcA-β(1→4)-D-GlcNAc-α(1→4)	Versican, aggrecan, neurocan, brevican, CD44, LYVE-1, HARE, RHAMM	Synovial fluid, vitreous humor, loose connective tissue

Cool, S. M.; Nurcombe, V. *Int. J. Biochem. Cell. Biol*. **2005**, *37*, 1739–1745; Gandhi, N. S.; Mancera, R. L. *Chem. Biol. Drug Des*. **2008**, *72*, 455–482; Lamanna, W. C.; Kalus, I.; Padva, M.; Baldwin, R. J.; Merry, C. L.; Dierks, T. *J. Biotechnol*. **2007**, *129*, 290–307; Schaefer, L.; Schaefer, R. M. *Cell Tissue Res*. **2009**; Sugahara, K.; Mikami, T.; Uyama, T.; Mizuguchi, S.; Nomura, K.; Kitagawa, H. *Curr. Opin. Struct. Biol*. **2003**, *13*, 612–620; Taylor, K. R.; Gallo, R. L. *FASEB J*. **2006**, *20*, 9–22.

2.208.2.4.1. Hyaluronan

Hyaluronan (HyA) is composed of repeating disaccharides in which *N*-acetylglucosamine and glucuronic acid are combined by β-1,3 and β-1,4 linkages. It is structurally the simplest GAG, as it is neither associated with a core protein nor sulfated, and it is also the largest with a mass up to 10^7 Da, which gives it unique viscoelastic properties.[29] HyA occurs primarily in the ECM and pericellular tissue, with half of the total amount being found in skin. Although it was first assumed to function only as an inert filling molecule in the connective tissue, it is now known that HyA binds to a variety of ECM proteins as well as interacts with several receptors (CD44, receptor for HyA-mediated motility-expressed protein, lymphatic vessel endothelia HyA receptor 1, HyA receptor for endocytosis), so that it may function as a signaling molecule. Nevertheless, the functions of HyA depend mainly on its molecular size: large polymers are space-filling, antiangiogenic, and immunosuppressive, and intermediate sizes (25–50 disaccharides) are inflammatory, immunostimulatory, and highly angiogenic, while still smaller oligosaccharides are antiapoptotic and induce heat shock proteins. Thus, HyA fragments which accumulate during injury may be involved in stimulating the healing response.[25]

2.208.2.4.2. Heparin/HS

Heparin is produced almost exclusively by mast cells, while HS is the most ubiquitous GAG and present on virtually every cell in the body. The differences between the two are quantitative, not qualitative. Both consist of repeating units of glucuronic acid 1,4-linked to glucosamine. Heparin undergoes extensive sulfation and uronic acid epimerization, so that more than 80% of the *N*-acetyl-glucosamine residues are N-deacetylated and N-sulfated, and more than 70% of the glucuronic acid is converted to iduronic acid. HS is similar to heparin in basic design, but with less epimerization to iduronate, lower density of N- and O-sulfation, higher N-acetylation, and greater asymmetry of sulfation and charge density along the polymer.[30]

The interaction of GAGs with proteins involves a variety of mechanisms, such as hydrogen bonds and hydrophobic interactions with the carbohydrate backbone, as well as van der Waals forces and electrostatic interactions, with the sulfation pattern being an important determinator. As the patterns are generated through a non-template-driven process, there is high diversity and tissue specificity. Specific patterns are also associated with various developmental events, such as brain and axon development, as well as angiogenesis. HS is known to interact with a number of proteins such as growth factors, morphogens, ECM molecules, cytokines, and enzymes (see Table 4). Through its associations with the cell membrane, it often plays a role as a coreceptor, binding and presenting solute factors.

2.208.2.4.3. Chondroitin sulfate, dermatan sulfate, and keratan sulfate

These GAGs occur mainly in the ECM. Like HS, they also display distinct sulfation patterns and are able to interact with a variety of proteins. Because of their location in the tissue, they can not only present but also bind and sequester solute factors, building gradients or protecting them from degradation.

CS consists of glucuronic acid and galactosamine [D-GlcA-β(1→3)-D-GalNAc4S-β(1→4)], where the galactosamine can be sulfated in the C4 (chondroitin-4-sulfate, CS A) or the C6 (chondroitin-6-sulfate, CS C) position. DS (also called CS B) consists of iduronic acid and galactosamine [L-IdoA-β(1→3)-D-GalNAc4S-β(1→4)], with galactosamine sulfated in the C4 or C6 and iduronic acid in the C4 position. Keratan sulfates (KS) are based on repeating disaccharides containing galactose [D-Gal-β(1→4)-D-GalNAc6S-β(1→3)].

Chondroitin and DS often exist in the form of hybrid chains that alternate between the two forms, which makes them, together with HS, the structurally most complex species. Like HS, they are biologically active as regulators of growth factors, cytokines, and adhesion molecules through a considerable number of unique oligosaccharide sequences.[31]

CS/DS interact with HS-binding proteins such as FGF and HGF, adhesion molecules, and chemokines, playing important roles in growth factor signaling, morphogenesis, and the development of the central nervous system. In cartilage, their effect is of a structural nature: PGs interact with collagen, and CS side chains provide electrostatic forces, enabling joints to function amid compressive, shear, and tensile forces. Differences in CS sulfation profiles have been observed in arthritic tissues; indeed it has been demonstrated that oversulfated structures of CS such as CS-D, CS-E, and CS-H are involved in various vertebrate tissues and have a strong affinity to heparin-binding growth factors.[32]

2.208.3. Biological Interaction Profiles of aECM and Their Components

2.208.3.1. Direct

All the ECM components described in the previous chapter are able to interact directly with cells. This interaction is conferred by cell adhesion receptors specific to the ECM proteins, and binding of these receptors to their ligands induces signal transduction pathways that in turn influence a wide range of cell and tissue events.[33]

2.208.3.1.1. Cell-surface receptors

Cell-surface receptors are usually transmembraneous proteins that can interact with specific ligands, and the interaction induces the activation of signal transduction pathways in the cell. There are numerous types of cell-surface receptors that can interact with ECM proteins: the membrane-spanning group that includes the PGs syndecan-1 to -4, betaglycan, CD44, neuroglycan C, and RPTG-ζ, as well as the GPI (glycosylphosphatidylinositol)-anchored PGs glypican-1 to -6 and a brevican variant. Syndecan and glypican are the major HSPGs on the cell surface and act as coreceptors, facilitating ligand encounters with signaling receptors via their GAG chains. They are involved in the regulation of various signaling pathways including that of Wnt, FGF, hedgehog, BMP, and IGF, regulating cell proliferation, differentiation, adhesion, and migration.

The largest as well as the best studied group of ECM adhesion receptors is the integrins. Integrins are heterodimeric, transmembrane proteins with 24α- and 18β-units known to date. These can dimerize to 24 different integrins, and they are unique in their bidirectional signaling capacity across the plasma membrane. Of the ECM proteins mentioned in Section 2.208.2, they recognize collagens, FN, laminin, VN, and OPN with a high redundancy in ligand specificity, but the affinities are varied through changes in integrin conformation and clustering, a process known as inside-out signaling.[34,35] For some integrins, interactions with the GAGs, CS, and heparin have also been described.[36,37] All adherent cells express integrins, but the pattern depends on cell type and differentiation state, allowing cells to sense their environment in this way, and making the construction of matrices targeted to specific cell types possible.

Integrin binding induces a wide array of intracellular signal transduction events.[33,34] It not only coordinates cytoskeletal polymerization, allowing integrins to form a physical link to the ECM, but also gives rise to the formation of signal transduction complexes that center around the integrins. These focal adhesion complexes (FACs) include the adhesion receptors, cytoskeletal elements, and a large spectrum of adaptor and signaling proteins (outside-in signaling).[38] The signal transduction pathways activated by integrins are often the same as those utilized by growth factors[34,39] and include influence on the cytoskeleton, serine/threonine phosphorylation, tyrosine phosphorylation, rho GTPase activation, lipid formation, and regulation of proteolytic activity.[38,40]

2.208.3.1.2. Collagen

Receptor-binding sites on collagen can be divided into four different categories: (i) specific motif in the triple-helical areas, (ii) common sequences such as GPO (glycine–proline–hydroxyproline), (iii) cryptic-binding sites that are recognized only after denaturation, and (iv) binding sites in noncollagenous domains. Many collagens seem to have more than one binding site, so that receptor clustering may be of biological significance. The diverse biological functions of collagen receptors include platelet activation, inflammation, angiogenesis, wound healing, proliferation of mesenchymal cells, matrix remodeling (collagen synthesis, matrix metalloproteinase (MMP) expression, collagen endocytosis/phagocytosis), and development (mammary gland, skeleton, periodontal ligament).[5]

Collagen is mainly recognized by integrins α1β1 and α2β1. Although these receptors have opposite effects on many signaling pathways, mesenchymal cells express them simultaneously, indicating that the cellular response may be determined by the dominance of one or the other of these receptors. α10β1 and α11β1 have a narrower tissue distribution, the first seemingly limited to cartilage, while the second is expressed in many mesenchymal tissues during development. The activation state of these collagen receptors can be regulated, which may affect binding specificity to the collagen types.[5]

Many other cell membrane proteins have also been reported to bind collagens. Among them are the discoidin domain receptors 1 and 2 (DDR1 and DDR2), and receptor tyrosine kinases that bind to the intact collagen triple helix in an integrin-independent manner. DDR1 is expressed mostly on epithelial cells and leukocytes, and DDR2 on mesenchymal cells. They control developmental processes, cell adhesion, migration, proliferation, and matrix remodeling.[41] Also mentioned should be syndecans and glypicans, glycoprotein VI that regulates platelet function during thrombosis, the leukocyte-associated immunoglobulin-like receptor-1 (LAIR-1) that is expressed on peripheral blood mononuclear cells, and annexin A5 (annexin V, anchorin II) which is expressed in cartilage and bone where it binds to collagen II and X and may regulate the influx of Ca^{2+} into matrix vesicles, thus playing a role in skeletal development.[5]

2.208.3.1.3. Glycoproteins

2.208.3.1.3.1. Fibronectin

FN is a widely expressed cell adhesion protein influencing cell adhesion, migration, and differentiation. Cells interact with it mainly via its integrin- and heparin-binding sites. The integrin interaction is determined by peptide sequences, with RGD being recognized by α5β1, LDV and REDV by α4β1 and

α4β7, and EDGIHEL by α4β1 and α9β1, while the heparin-binding site interacts primarily with cell-surface PGs.[42]

2.208.3.1.3.2. Laminin

Laminin is recognized by all four syndecans, α-dystroglycan and, depending on the isoform, by the integrins α1β1, α2β1, α3β1, α6β1, α7β1, α9β1, αvβ3, and α6β4,[15] the biological effects of laminin presumably mediated by linking laminin matrices via these receptors to intracellular signaling pathways.

2.208.3.1.3.3. Vitronectin

The main receptors for VN are integrins (αvβ3, αvβ5, avβ1, αIIbβ3) and the urokinase receptor.[43] VN mediates cell adhesion and spreading, cytoskeletal reorganization, intracellular ion transport, lipid metabolism, and gene expression, with protein phosphorylation being one of the earliest events detected in response to binding. This leads to the activation of mitogen-activated protein kinase signal transduction pathways, indicating that the pathways for VN and growth factor signaling may be linked, which may provide a mechanism for the synergistic action of growth factors and ECM proteins. Through the integrin αvβ3, which is involved in angiogenesis, VN may also play an important role in wound healing and tumor progression.[19]

2.208.3.1.3.4. Tenascin, osteopontin, and thrombospondin

Cell-surface receptors for TN include integrins, cell adhesion molecules (CAM) of the immunoglobulin superfamily, phosphacan/RPTP ζ/β, and annexin II. Binding to TN in the developing skeleton may be involved in regulating osteoblast differentiation,[21] as TN-W promotes osteoblast adhesion and inhibits differentiation, while the EGF-like repeats may bind and activate the EGF receptor (EGF-R).[44]

OPN binds via integrins that recognize the RGD motif. In general, OPN promotes cell adhesion, migration, and survival, with αvβ1 and αvβ3 interactions being essential for osteoclast migration and resorption. For smooth muscle cells, it is involved in adhesion and migration, its chemotactic function for these cells being in part mediated by the αvβ3 integrin. αvβ1, αvβ5, and αvβ6 also bind OPN, α5β1, and α9β1 only after a cryptic site on OPN is exposed after cleavage. The hyaluronan CD44 receptors also bind OPN, although for some isoforms this also requires the binding of β1 integrin in an RGD-independent manner. CD44 binding to OPN has been implicated in the migration of macrophages and tumor cells.[22]

The binding of TSPs to PG cell-surface receptors is mainly mediated through their GAG chains. An FN-induced conformational change in TSP-1 promotes the interaction of TSP-1 with α3β1,[24] and proangiogenic effects are mediated by syndecan-4 on endothelial cells. TSP-3 is expressed in osteoblasts and probably also binds to PG cell-surface receptors, affecting bone maturation.

2.208.3.1.4. Proteoglycans

There is little information in the literature on direct binding of PGs to adhesion receptors, as the majority of the interactions seem to be with cell signaling receptors. Versican has been described to bind P- and L-selectin, CD44, EGF-R, integrin β1, and TLR2,[25] and the SLRPs decorin, biglycan, fibromodulin, osteoadherin, and chondroadherine bind C1q, activating the classical complement pathway and leading to an enhanced inflammatory response. Lumican binds and signals via the Fas ligand FasL, enhancing secretion of proinflammatory cytokines and recruitment of macrophages and neutrophils.[28]

SLRPs are also involved in recruitment of immune cells to site of injury, by direct interaction with receptors, or by indirect mechanisms. Decorin stimulates production of MCP-1, a mononuclear cell recruiting chemokine, thereby sustaining the inflammatory state, while biglycan is directly involved in the recruitment of natural killer cells. In combination with VN, decorin can affect the remodeling of the ECM by inducing MMP-1, a scenario where multimeric interactions with integrins may play a role.[28]

2.208.3.1.5. Glycosaminoglycans

The role of HyA in cell motility, adhesion, and proliferation is mediated by cell-surface HyA receptors such as CD44 receptors or RHAMM (receptor for hyaluronan-mediated motility, which also acts as coreceptor modulating PDGF signaling).[45]

CD44 has also been described to recognize sulfated GAGs such as HS and CS, as have been P- and L-selectins. These receptors are expressed by a variety of cells such as neutrophils, endothelial cells, platelets, monocytes, and fibroblasts. Their adhesion to GAGs may play a role in leukocyte invasion, both through direct interactions as well as by binding and presenting chemokines.[46,47]

2.208.3.2. Indirect

The ECM influences biological processes not only by directly interacting with the cells. In addition, there are two major mechanisms which can be considered as indirect, with the dividing line between 'direct' and 'indirect' having been somewhat arbitrarily drawn at the direct interaction with specific receptors as described above. These indirect mechanisms are (i) interaction with growth factor receptors, and (ii) interactions with soluble factors such as growth factors, cytokines, and chemokines, as a large number of such factors can associate with ECM components to form functional units that modulate their biological activity.[48–50]

2.208.3.2.1. Collagens and glycoproteins

The ECM is regarded as a physiological depot for various mitogens. Although the structural proteins such as collagen and the glycoproteins make up the major part of the ECM, and especially collagen is commonly used as a carrier for growth factors such as BMP and TGF, very few specific interactions such as that for certain BMP-2 isoforms binding to collagen have been described.[51]

An indirect interaction according to the definition given above that does occur is the interplay of adhesion receptors with growth factor receptors. Adhesion receptors such as the integrins are able to modulate the function of growth factors,[52] so that the binding of the cell to the ECM influences its ability to respond to soluble mitogens,[53] and differences in matrix composition and consequently integrin-binding pattern can thus influence the activity of growth factors such as EGF, FGF, PDGF, VEGF, TGF-β, and IGF-I.[54–56] Binding of the α2β1 integrin by collagen thus acts synergistically with PDGF on the phosphorylation of the PDGF-receptor (PDGF-R) and the

subsequent ERK-2 activation,[39] while VN influences IGF-I activity via αVβ3 binding. β3 and β1 integrins control angiogenesis, α6β4 cooperates with tyrosine kinase in epithelial cells, and β1 with EGF.[57] The mechanism of these interactions is in most cases an association between integrins and growth factor receptors, such as EGF, bFGF, and PDGF, where both regulate the same receptor tyrosine kinase.[58]

2.208.3.2.2. Proteoglycans

In direct opposition to the situation for collagen and other glycoproteins, PGs interact with a host of different cell-surface receptors, cytokines, and growth factors. Indeed, the PGs, and especially the SLRPs, have been termed matricellular proteins because of their ability to modulate various biological processes,[28] and abundance of certain SLRPs at a specific site may switch on one pathway, whereas their absence is permissive for other pathways,[59] providing a mechanistic explanation for the growth and differentiation-promoting abilities of the ECM.

SLRPs are involved in the triggering of multiple cell responses. Decorin modulates receptor signaling pathways, and influences regulation at certain cell-cycle check points. It affects cell proliferation by binding to EGF-R and inducing dimerization and autophosphorylation of the receptor, which causes a sustained activation level that leads to an activation of the MAPK pathway, Ca^{2+} influx, and subsequent induction of p21, a cyclin-dependent kinase inhibitor. This in turn leads to cell-cycle arrest, and a decorin-induced growth arrest in tumor cells is indeed associated with this pathway.[28]

Decorin also binds to IGF-IR via the N-terminus of the core protein, resulting in phosphorylation, activation, and down-regulation of the receptor, and via the PI3K/Akt pathway leading to the inhibition of apoptosis in endothelial, epithelial, and bone marrow cells. Decorin may even compete with IGF-I for binding to the receptor and thus prevent IGF-I signaling, so that decorin and IGF-IR may cooperate *in vivo*,[59] and VEGF-R2 is another receptor that may be affected by decorin.[28]

Many members of the SLRP family are able to modulate BMP/TGF-β pathways. Decorin, biglycan, asporin, lumican, and fibromodulin all bind TGF-β, with decorin inhibiting TGF action and thus proliferation.[10]

Lumican is similar to decorin in being a negative regulator of cell proliferation, although the underlying mechanisms appear to be different. The infiltration of neutrophils is also regulated by lumican by binding of the core protein to the CXC-chemokine KC and thus establishing a chemokine gradient.[28] It has also been shown to interact with the TLR4 pathway by presenting lipopolysaccharide to CD14, a cell-surface-binding protein required for TLR4 activation.[59]

PDGF-induced proliferation is inhibited by biglycan, but proliferative phases of osteoblast development are associated with biglycan overexpression; perhaps the regulation is cell type specific, either directly via receptors or by contributing to cross talk. There is no biglycan signaling through the EGF-R, but rather Toll-like receptors-2 and -4 have been identified as signaling receptors for biglycan.[28] Biglycan also influences the response to TGF-β, as biglycan-deficient mice develop age-dependent osteopenia due to a decreased ability to make new bone because of a reduced response of bone marrow stromal cells to TGF-β, showing that biglycan is important in controlling skeletal cell differentiation. Biglycan may be important in regulating BMP signaling, too. Osteoblasts lacking biglycan display a defect in differentiation due to reduced BMP-4 binding, followed by lower BMP-4 sensitivity, less BMP-4 signal transduction, and decreased expression of core-binding factor α1, an essential transcription factor for osteoblast activation. Biglycan increases BMP-4 binding to chordin and TSG (twisted gastrulation), improving the complexes' efficiency in inactivating BMP-4.

Tukushi is also involved in BMP signaling, functioning as a BMP antagonist and binding both BMP and chordin. It regulates BMP transcription by directly binding to X-delta-1 and modulating notch signaling, thereby controlling ectodermal pattering and neural crest specification. It also seems to regulate FGF.[59]

Another function of SLRPs is as direct and indirect modulators of inflammation. Biglycan may be involved in the regulation of the inflammatory response by acting as a ligand of immunity receptors TLR4 and TLR2 in macrophages, inducing ERK (extracellular signal-related kinase), p38, and NF-κB, and stimulating expression of inflammatory cytokines TNFα and MIP2 (murine IL-8 analogon). For this activation, intact and soluble biglycan is required, suggesting that both the protein core and GAG side chains are required and that proteolytic release from the ECM is necessary to initiate the proinflammatory function.[59] Collagen XVIII, a hybrid collagen–PG, is also involved in inflammation by regulating the infiltration of inflammatory cells to the endothelium. It may provide a link between the initial rolling of inflammatory cells via L-selectin and the induction of chemokine-independent, integrin-dependent adhesion by enhancing α4β1 integrin binding to VCAM-1.[60]

2.208.3.2.3. Glycosaminoglycans

Although many SLPR functions are determined by the core protein, the GAG chains are at least as relevant, and for a number of growth factors such as BMP, FGF, TGF, and PDGF interactions with GAGs have been described.[61–65] GAGs present the largest diversity among biological macromolecules: They vary in basic saccharide composition, acetylation, and N- and O-sulfation, with respect to their linkage and chain length. A hexasaccharide can thus present 2 million times more variations than a 6-mer of DNA. They are known to interact with hundreds of proteins including proteases, cytokines, adhesion molecules, growth factors, and chemokines.

GAGs fulfill two different functions: they play a critical role in assembling protein–protein complexes such as growth factor–receptor or enzyme–inhibitor aggregates, both on the cell surface and in the ECM, and in this manner are directly involved in initiating cell signaling events. Furthermore, GAGs can potentially immobilize and sequester proteins or present them to the appropriate sites for activation. The positioning of the protein-binding oligosaccharide motif along the GAG chain determines if an active signaling complex is assembled at the cell surface, or an inactive complex is sequestered into the matrix. Such extracellular modulation of biological functions is an emerging paradigm in the postgenomics area,[66] and the chemical heterogeneity and polydispersity of GAG arising from their nontemplate-driven biosynthesis allow them to encode a large amount of information.

2.208.3.2.3.1. Mechanism of GAG–protein binding

The specificity of GAG–protein binding is defined by a number of parameters that are determined by the structural fit between GAG and protein based on the three-dimensional (3D) structure of the GAG. The most important are the ionic interactions of the sulfate and carboxylate groups of the GAG with the basic amino acids of the protein, although van der Waals contacts also play a role. They depend on the number, position, and distribution (O- or N-) of the sulfate groups, the length of the sugar chain,[61,67,68] as well as the 3D structure of the polysaccharide backbone and resultant orientation of the sulfate groups. Typically, tetra- to hexasaccharides are sufficient to bind with high affinity.[66]

GAGs characteristically adopt a linear extended conformation with different helical symmetries for different GAGs. The parameters associated with the different helical structures include bond length, bond angles, and torsion angles of the GAG backbone. Given that bond length and angles are mostly constant, the main parameters are glycosidic torsion angles and the hexapyranose ring conformation of the monosaccharides. Glucosamine and galactosamine adopt a $^4C_1$ (C-chair) conformation, and glucuronic acid favors a $^1C_4$ pyranose pucker. The iduronic acid ring can adopt multiple, equienergetic conformations: $^4C_1$, $^1C_4$, $^2S_0$ (S-skew boat), and $^0S_2$. The orientation and topological arrangement of specific sulfate groups, governed by the rotation about the glycosidic torsion angles and the ring conformation, play a key role in the specificity of GAG–protein interactions. The ability of the iduronic acid to adopt multiple conformations gives additional freedom for IdoA-containing GAG chains to form specific binding motifs.[66]

2.208.3.2.3.2. Physiological significance

On the basis of their importance in cell growth and development, the interaction of GAGs with growth factors is most extensively studied, and the majority of these studies focus on HS, as the HSPGs on the cell surface often work as cofactors for GF receptors. The best characterized interaction is between HS and FGF, both basic FGF-2 and acidic FGF-1. HS plays a critical role in FGF signaling by facilitating the formation of FGF–FGF-R complexes and enhancing/stabilizing FGF oligomerization.

Heparin-derived oligosaccharides contain predominant repeat units of $-[I_{2S}-H_{NS,6S}]_n-$, with n between 2 and 6. The 2-*O*-sulfate of the iduronate and the N-sulfate of the glucosamine are critical modifications that are required for FGF signaling, and while the 6-O-sulfation is critical for FGF-1, it is not completely necessary for FGF-2. As already mentioned, tetra- to hexasaccharides mediate GF binding; however, oligosaccharides or longer are required for bridging dimeric FGF-2 with the receptor to form a ternary signaling complex.[66]

One of the best known activities of GAGs, especially heparin, is the inhibition of coagulation cascade. Heparin prevents coagulation by forming a complex with thrombin and AT-III, a serine protease inhibitor. AT-III recognizes a specific pentasaccharide in heparin ($H_{NAc,6S}$-G-$H_{NS,3S,6S}$-I_{2S}-$H_{NS,6S}$), where a 3-*O*-sulfate group on the glucosamine $H_{NS,3S,6S}$ is absolutely necessary for the specific interaction. Not only sequence but also chain length is important: heparin binding to heparin cofactor II requires a minimal chain length of 13 monosaccharides, and the complete inhibition of thrombin a chain length of 26 monosaccharides.[66]

The specificity of GAG–protein interactions goes beyond the GAG primary sequence. In the case of AT-III, binding induces a conformational change in the protein, and the specificity is precisely defined at the pentasaccharide sequence, where the conformation of IdoA is important. In the case of FGF, there is no conformational change, and there seems to be a significant overlap of sequence specificities for different FGFs. This may be due to the biological interactions involved: the coagulation cascade has to be quickly and tightly regulated, while growth factor interactions require some degeneracy in the GAG sequence to accommodate longer time frames for the signaling events as well as to maintain the graded affinities necessary for generating morphogen gradients.[66] This is of special interest for chemokines, and chemotactic cytokines are a large family of small proteins distinguished from all other cytokines by being the only ones that act on the receptor superfamily of G-protein-coupled receptors. In their case, interaction with GAGs is thought to play a role in the sequestration of chemokines and subsequent presentation to receptors.[69]

Less work than with HS and heparin has been done in the field of CS/DS. CS and DS, like HS, are found on the cell surface and in the ECM. Similar to HS, highly sulfated DS chains have been shown to bind FGF-2 and -7, impacting cell growth and wound repair, and to activate HGF signaling pathways through the c-met receptor. Binding tends to be of a slightly lower affinity, which is reflected in the minimal required length: a tetrasaccharide for HS and a hexasaccharide for DS. Oversulfated variations as for brain CS-PGs with specific sulfation patterns have been implicated in neural adhesion, migration, and neuritogenesis via their interaction with pleiotrophin and midkine, where two mechanisms apply: while cell-surface CS and pleiotropin complexes are involved in signaling, CS in the ECM sequesters this protein instead.[66] CS-E, an oversulfated CS variant, has also been shown to bind several heparin-binding growth factors, including midkine, pleiotropin, heparin-binding EGF (HB-EGF), FGF-16, and FGF-18.[60]

As with HS, CS and DS become soluble after injury and are a major component of wound fluid. Soluble DS activates FGF-2 and FGF-7, the minimum size for activation of FGF-2 being an octasaccharide; 4-O-sulfation is sufficient, and an increase to a 2/4-*O*-disulfide does not appear to increase activity. Hepatocyte growth factor/scatter factor also requires a DS octasaccharide, but with unsulfated IdoA and 4-*O*-sulfated GalNAc.[60]

2.208.3.2.3.3. Inflammation and injury

Recent data show that GAGs initiate and control events associated with inflammation. After injury, GAGs are enzymatically released from the PGs, and these soluble GAGs can be further modified by altering chain length or revealing specific, priorly masked domains, such as a pentasaccharide sequence from syndecan-HS that stimulates FGF-2. Another possible mechanism is the modification of receptor specificity, as for the hyaluronan receptor CD44, which can be modified by HS chain addition to bind FGF-2, VEGF, and HB-EGF, but not chemokines.[60]

The influence on inflammation can be conveyed by affecting the TLR-4 receptor: HyA, C4S, C6S, and HS all have been shown to reduce inflammatory events induced by LPS in this manner. The degrees vary, with C4S and HS being the most effective, followed by C6S, and HyA with a slight effect only.[70] Also, the recruitment of inflammatory cells such as leucocytes is influenced by generating chemokine and cytokine gradients, that is, for IL-2,3,4,5,7,8,10,12, GM-CSF, RANTES, IP-10, MCP-1, and MCP-4. The interaction with IL-8 and HS is especially well studied. The IL-8 is held at the cell surface by HSPGs (syndecan-2 or -1), creating a gradient for inflammatory cell recruitment.[60] Both DS and CS have also been shown to bind several molecules involved in the recruitment of leukocytes, as in the CSPG versican; the CS chain binds L-selectin and P-selectin at the same sites as HS. Binding of CS and DS to selectins is sulfation dependent, and oversulfated CS and DS are able to bind chemokines and inhibit their activity, possibly providing a reservoir.[9]

HyA functions are a special case as they depend mainly on size. HyA recruits leukocytes to sites of inflammation via CD44 interaction, and RHAMM appears to be involved in cellular motility and migration because of its interactions with the cytoskeleton.[9]

2.208.4. Preparation and Structure of aECM

Generating collagen-based scaffolds with noncollagenous components can be accomplished by two main methods. One utilizes the natural self-assembly potential of collagen that allows for an *in vitro* formation of fibrils, the other is on the basis of using insoluble collagen slurres or suspensions. Both can then be used to coat implants or scaffolds, or be freeze-dried and cross-linked into scaffolds with no additional superstructure. Both are discussed in the following, with the focus on the *in vitro* generation of fibrils, as this more controlled approach bears a closer relation to the assembly and resultant structure of the fibrils *in vivo*.

Not taken into account here is the use of gelatin as the denatured form of collagen.

The collagen used in the majority of both cases is extracted from tissues, although in a few instances, recombinant collagen has been utilized.[71] The latter circumvents some issues such as the risk of transmission of infectious agents, but the *in vitro* formation of fibrils from these monomers is often impaired as the posttranslational processing that is crucial for fibril assembly is not comparable to that of tissue-derived collagens.

Although collagen monomers are soluble in dilute acid, most collagen in tissues is enzymatically cross-linked via the telopeptides. Acid extraction yields the non-cross-linked portion with intact telopeptides. Another extraction method uses the protease pepsin, digesting the nonhelical telopeptides and thus breaking the link and giving higher yields. Although removal of the telopeptides reduces antigenicity, it also affects collagen self-assembly. The collagen fraction that is nonenzymatically cross-linked via the helical part is not accessible by either method, but can be used in the already mentioned insoluble slurries.

An often used method, especially for the construction of scaffolds, employs collagen preparations that contain both monomers and insoluble fibrils as extracted from tissues, forming a suspension or slurry, commonly in an acidic buffer. This suspension can be either freeze-dried to form scaffolds or adsorbed to biomaterial surfaces. Noncollagenous components are introduced either by adsorption to preformed fibrils or, if the soluble part is large enough, by coprecipitation in an acidic milieu. Especially, this last method has been used to generate collagen–GAG scaffolds.[72,73] While this results in a matrix consisting of both collagen and GAG, the morphology is that of an amorphous precipitate.

Preparing fibrils *in vitro* using the natural self-assembly potential of collagen allows the generation of a collagen matrix more defined with respect to components and structure, and thus ultimately of more defined properties. Resembling the *in vivo* process, fibrillogenesis can take place in the presence of collagen-binding and noncollagenous components, allowing not only component integration into the matrix but also alterations of collagen organization, controlling both structure and mechanical properties to an extent. The resultant fibril morphology represents a much closer analogy to the situation *in vivo*, for which the retention of the characteristic cross-striation pattern is an indication (**Figure 1**).[74] This may influence the adherent cells, as the supramolecular organization of the collagen matrix is of importance in cellular reactions.[75]

The self-assembly of monomers into fibrils is initiated by raising pH and temperature of the acidic solution into the physiological range. The assembly pattern is determined by the charge pattern on the monomer surface, but the fibril formation itself is an entropy-driven process, where surface-exposed hydrophobic residues are buried within the fibril, thereby increasing the entropy of the solvent. Fibril assembly proceeds via nucleation and growth, and classically shows three phases: an initial lag phase with no change in turbidity, a rapid growth phase, and a plateau region. During the lag phase, small numbers of molecules associate to form metastable nuclei, upon which further molecules accrete during the growth phase. The initial interaction seems to be of a pair of 4D staggered molecules with a short N- and C-terminal overlap, mediated by the telopeptides. Growth in fibril length then occurs via longitudinal and lateral interactions.[76]

In vitro fibrillogenesis was studied by a number of authors, most notably by Williams *et al.*,[77] who determined conditions under which the resultant fibril morphology was optimized, with a clear D-periodic banding pattern (mix on ice 1 mg collagen/ml 5 mM acetic acid with an equal volume of 60 mM TES, 60 mM sodium phosphate, and 270 mM NaCl, pH 7.3, then raise temperature to 30 °C). Most preparations of collagen fibrils are based on modifications of this method. The resulting collagen gel can be used as such, freeze-dried, or homogenized and treated like an insoluble collagen slurry.

The process of fibril formation and the structure of the resultant fibrils are influenced by a large number of parameters: *in vivo*, these include the collagen type or types, the extent of procollagen processing, and presence of noncollagenous components; *in vitro*, there are some additional parameters to be considered such as temperature, pH, and buffer composition.[78,79] In the buffer, pH, phosphate concentration, and ionic strength are deciding parameters. Depending on the pH, early/subfibrils are formed over a comparatively wide range, with low pH possibly stabilizing intermediate states.[80]

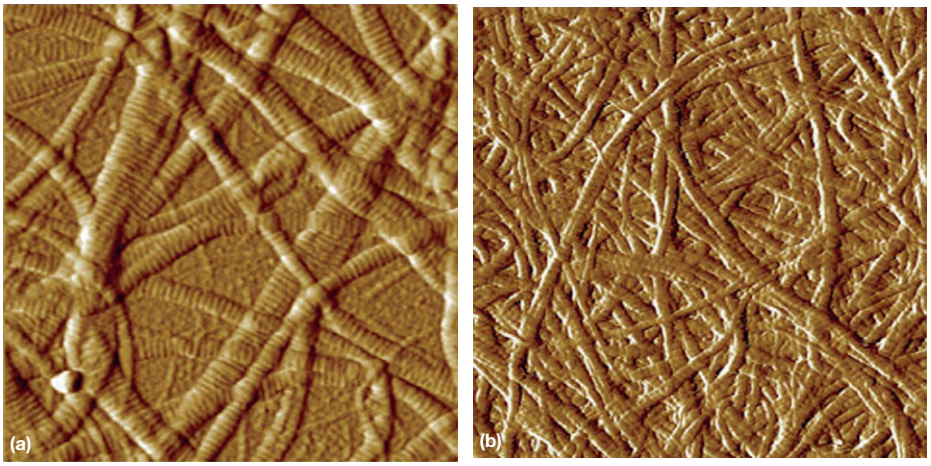

Figure 1 Collagen fibrils adsorbed to Ti6Al4V discs. Fibrils generated with 250 μg ml^{-1} collagen type I (IBFB) at 37 °C; AFM contact mode. (a) collagen buffer B and (b) collagen with 25 μg ml^{-1} decorin buffer B. Represented area 5 × 5 μm. Reproduced from Figure 3 from Bierbaum, S.; Douglas, T.; Hanke, T.; *et al*. *J*. *Biomed*. *Mater*. *Res*. *A* **2006**, *77*, 551–562.

The presence of phosphate is important for producing well-banded fibrils, but increasing phosphate over the optimum results in less and smaller fibrils of a different morphology. This effect is probably on the basis of phosphate binding to collagen; a fibril associated with phosphate may be hindered in the alignment of monomers, as the charge distribution of the monomer is changed, changing the nature of collagen molecular interactions.[81]

Ionic strength also influences the electrostatic interactions of the monomers, but in a way differing from phosphate, as an increase in ionic strength can – in the case of collagen type I – increase the size of the resultant fibrils. This is probably based in part on a facilitation of superfibrillar bundling, again because of changes in electrostatic interactions. Another part may be due to the slower growth rate, as this too gives rise to fibrils of increased diameter,[82] something that can also be achieved by lowering the formation temperature.[76]

The collagen preparation used also has a marked effect on fibrillogenesis. Intact telopeptides as in acid-extracted collagen help to initiate fibrillogenesis, producing long, cylindrical fibrils, while for collagen with degraded telopeptides self-assembly is slower, and the fibrils are slightly thicker and less stable. Selective removal of N-telopeptides results in a so-called D-periodic symmetry (DPS) fibrils, in which molecules assemble in an antiparallel manner, while loss of the D-telopeptides results in relatively short cigar-shaped D-periodic fibrils (**Chapter 2.205, Self-Assembling Biomaterials**; **Chapter 2.207, Extracellular Matrix: Inspired Biomaterials**; **Chapter 2.209, Materials as Artificial Stem Cell Microenvironments**; and **Chapter 2.220, Extracellular Matrix as Biomimetic Biomaterial: Biological Matrices for Tissue Regeneration**).[76]

2.208.4.1. Heterotypic Fibrils

One method employed *in vivo* to adapt the ECM to the specific tissue requirements is to modulate the architecture of the type I and type II fibrils by using minor collagens. The same principle can be applied for *in vitro* fibrillogenesis, where the collagens are mixed prior to the initiation of the fibril formation. *In vivo*, collagen type I and III form heterotypic fibrils;[8] *in vitro*, the inclusion of type III in the fibrillogenesis solution results in a decrease in fibril diameter (**Figure 2**). This reduction is probably due to lessening of fibril bundling, with collagen III inhibiting the interfibrillar interaction.[82,83] Type V also regulates the diameter of type I fibrils; in I–V cofibrils, the entire triple-helical domain of collagen V is buried within the fibril and type I molecules are present along the fibril surface, with the N-terminal domains of type V extending outward through the gap zones.[84]

2.208.4.2. Collagen Fibrils with Glycoproteins

Other ECM components such as glycoproteins or PGs can be included in the collagen matrix in the same manner as different collagen types. FN does not influence fibril morphology, but may accelerate assembly, and the amount integrated increased with an increase in ionic strength of the buffer system;[82,85] collagen–laminin gels can seemingly be prepared over a wide range of different ratios (10:1 to 1:1), both with and without the inclusion of other components such as FN and HyA, although no formation conditions and matrix characterization are given.[17,18]

Noncollagenous proteins can also be integrated into a collagen matrix by allowing them to bind to preformed fibrils. Such binding can be modulated by the conditions under which the fibrils were formed: collagen type I fibrils generated in buffers of high ionic strength bind about four times as much FN as fibrils generated in buffers of low ionic strength, reflecting the importance of structural parameters. Another modulating aspect that can be employed is the use of different collagen types: unlike type I, collagen type III binds large amounts of FN under all *in vitro* conditions studied, with heterotypic fibrils displaying intermediate binding profiles depending on the relative amounts of collagen types. This may be based on combination of the larger surface area of type III fibrils, changes in fibrillar architecture, and the fact that *in vivo* type III shows a higher affinity for FN in agreement with its function in the initial stages in wound repair.[82]

Using insoluble collagen instead of fibrils generated *in vitro* is a comparable process, although much less well defined.

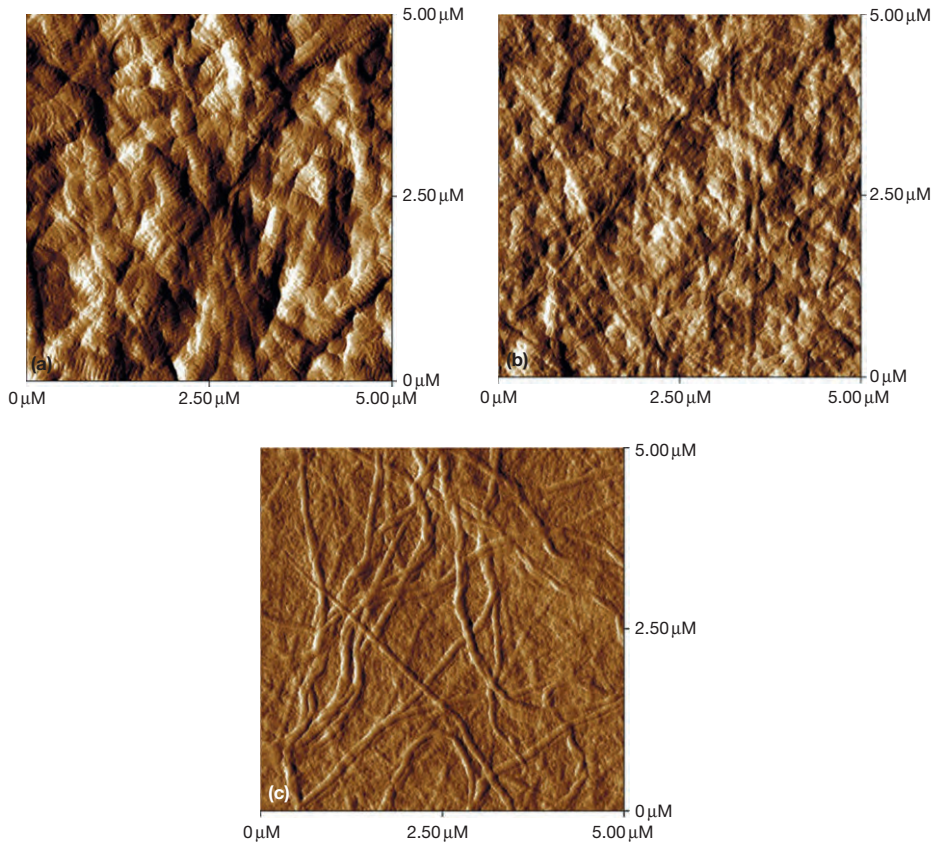

Figure 2 Collagen fibrils adsorbed to Ti6A14V disks. Fibrils generated in buffer B at 37 °C with 500 μg ml^{-1} collagen; AFM image, tapping mode. (a) collagen type I; (b) 50% collagen type I, 50% collagen type III; and (c) collagen type III. Reproduced from Figure 4 from Bierbaum, S.; Beutner, R.; Hanke, T.; Scharnweber, D.; Hempel, U.; Worch, H. *J. Biomed. Mater. Res. A* **2003**, *67*, 421–430.

Elastin/collagen scaffolds have been created in this manner with elastin/collagen ratios between 1:9 and 9:1; the components were mixed in acidic solution, freeze-dried, and EDC cross-linked to increase strength. Elastin and collagen interact with each other, although elastin tends to cluster and form spherical structures attached to collagen fibrils or sheets.[11]

2.208.4.3. Collagen Fibrils with PGs

Of special interest here are the collagen-binding SLRPs such as decorin, biglycan, fibromodulin, lumican, keratocan, and osteoglycin. Both *in vivo* and *in vitro*, decorin, osteoglycin, and fibromodulin interfere with fibril formation, resulting in a delayed assembly and signally reduced fibril diameters. Lumican also results in smaller fibrils, but accelerates fibril formation, while biglycan binds without affecting fibril assembly. In general, PG binding has the added effect of enhancing the thermal stability of collagen.[86] Removal of GAG chains generally does not abolish the described effects, demonstrating that they are due mainly to interactions of the core proteins with collagen, although GAG variations that are specific to tissues or developmental stages can modulate them.[26]

As most PGs inhibit fibril formation, there are limits to the applicable ratios of collagen to PG. In the case of decorin, a decorin/collagen ratio of 1:10 results in a strong decrease both in fibril diameter and the integration of collagen monomers into the fibrils.[74] The probable reason is that decorin binds to collagen closely via the core protein with the GAG chain extending outward,[87] inhibiting both the further association of monomers and the lateral fusion of fibrils. The binding of decorin to the fibrils is higher under conditions of low ionic strength, as they influence the electrostatic interactions of the collagen monomers and thus the resultant fibrils. The protein–protein interaction responsible for the binding of decorin may also be affected, as decorin associates with a polar region of collagen.[87] Still, the nature of the collagen–decorin interaction remains essentially the same as fibrillogenesis and monomer integration is affected similarly.[74]

Other factors influencing PG–collagen interaction are the collagen type, as collagen II binds more decorin and biglycan than type I and III,[88] and collagen preparation.[89]

2.208.4.4. Collagen Fibrils with Modified Proteins and/or Peptides

Instead of naturally occurring ECM components, engineered proteins or parts of proteins down to small peptide sequences may be used in the generation of aECM. This is useful if purification from tissues gives only low yield as it circumvents the question of the purity of the preparation. On the other hand,

using only parts of molecules will exclude a large and possible necessary part of their functions, as the actual principles of ECM tasks are complex and not fully understood yet.

Depending on their modification, these altered proteins can be included in the matrix analogously to naturally occurring ones. Synthetic peptidoglycans consisting of a collagen-binding peptide with an attached DS-chain modulate *in vitro* collagen fibrillogenesis similar to decorin[90] and give rise to D-banded fibrils. The same fibrils could be found if a laminin chain was present during fibrillogenesis, indicating that it did not significantly hinder the self-assembly process. If the fibrils were covalently cross-linked using transglutaminase (TGase), the banding pattern showed a slight shift from 64 and 78 nm to 73 and 94 nm, which can be attributed to changes in the spatial organization of fibrils due to the formation of cross-links within the collagen molecule.[91]

The most commonly used peptides are adhesion motifs for integrins, with RGD being the prime representative of this group. Because of their small size, peptides have to be covalently linked to the matrix to prevent desorption. Using TGase-linked laminin peptides in collagen gels, a peptide gradient could be established, although again there is no further matrix characterization (see **Chapter 4.411, Peptide- and Protein-Modified Surfaces**).[16]

2.208.4.5. Collagen Fibrils with GAGs

One of the most widely used combinations is that of collagen with GAGs, even though it must be considered as the most 'unphysiologic' one as with the exception of HyA, GAGs *in vivo* are usually bound to a core protein. Although no *in vivo* relevance for a GAG–collagen interaction has been described, it is possible that such interactions may occur as bound PGs can be deglycosilated *in situ*.[92]

As described above, the core protein of PGs mediates interactions with collagen, and removal of the GAG makes no significant difference. Removing the protein core and adding only the GAG, on the other hand, gives rise to some interesting results.

GAGs interact with collagens mainly because of their overall negative charge. Their effect on fibrillogenesis is heterogeneous: heparin induces a dose-dependent increase in fibril diameter[93] and gives rise to cigar-shaped fibrils, while addition of CS and HS increases both mean fibril diameters and heterogeneity of diameter distribution, which may be due to a promotion of lateral fusion of fibrils (**Figure 3**). The integration of monomers into fibrils is positively affected by CS below CS/collagen ratios of 1:10,[74] although the reason for this is unclear. Collagen/CS gels also contain larger void spaces, and the viscous gel component (loss modulus) is reduced.[94]

Because of the electrostatic nature of the interaction, ionic strength of the buffer systems has significant effects. In high ionic strength buffers, a characteristic fibrillogenesis curve can be seen over a wide range of GAG concentrations, but under conditions of low ionic strength, the higher GAG concentrations lead to very fast formation of aggregates with a more pronounced effect on fibril morphology. The effect appears to be common in the interaction of collagen and GAG, although the degree seems to vary depending on the collagens and GAGs used,[95] with an increase in sulfation of the GAG leading to a stronger interaction.[96]

Other methods of collagen–GAG matrix generation are precipitation from acidic solution, which has been used for collagen type I[97] and type III[98] with the GAGs CS,[74,98,99] HS,[100] and heparin,[101] or the cross-linking of preformed fibrils in the presence of GAGs.[102] The resultant matrices are cross-linked not only in this case but also as a rule, increasing stability and resistance against degradation.[100] The predominant method utilizes EDC, as glutaraldehyde has raised concerns about cytotoxicity and biocompatibility, with the cross-linking efficiency depending on the molar ratio of EDC to GAG carboxylic groups.[72] Other methods are dehydrothermal cross-linking,[99] where the matrix is heated under vacuum (i.e., 150 °C for 48 h) until the water content falls below 1% and the formation of interchain peptide bonds is possible, or using the enzyme transglutaminase, which cross-links via lysine and glutamine residues, resulting in the formation of ε(γ-glutamyl) lysine isopeptide bond (**Chapter 2.216, Collagen–GAG Materials**).[91]

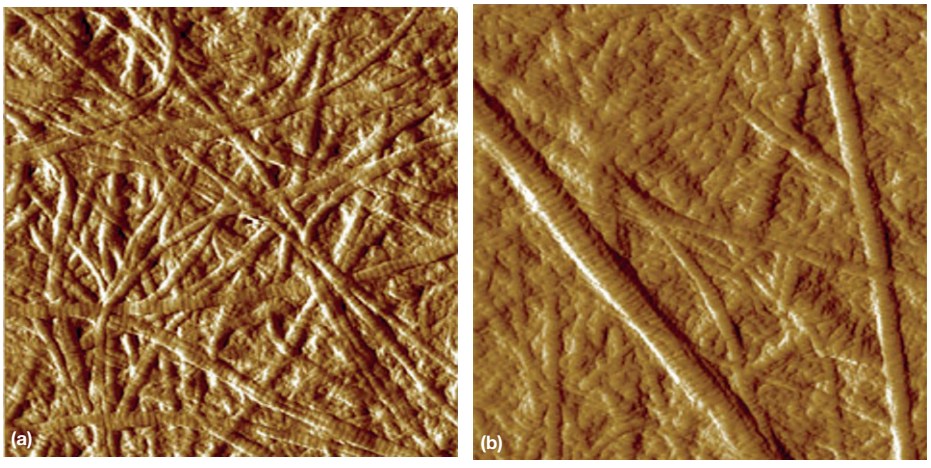

Figure 3 Collagen fibrils adsorbed to Ti6Al4V discs. Fibrils generated with 250 μg ml^{-1} collagen type I (IBFB) at 37 °C; AFM contact mode. (a) collagen buffer A; (b) collagen with 25 μg ml^{-1} chondroitin sulfate buffer A. Represented area 5 × 5 μm. Reproduced from Figure 3 from Bierbaum, S.; Douglas, T.; Hanke, T.; *et al. J. Biomed. Mater. Res. A* **2006**, *77*, 551–562.

2.208.5. Biochemical Characterization of aECM

The morphology of aECMs was described in the previous section. Here, some biochemical characteristics of differently prepared collagen matrices are reviewed, as matrix stability and desorption of components can be an issue. Collagen fibrils are stable under physiological conditions even if not cross-linked, but for noncollagenous components especially in non-cross-linked matrices, the question of stability and release is relevant. Cross-linked matrices, on the other hand, raise the question of bioavailability of their components, and whether their biological functions are still unimpaired. Although both aspects are important in matrix function, the characterization in many cases is only rudimentary and does not take them into account.

Another point that will be dealt with here is the ability of matrices to interact with soluble mediators such as growth factors and cytokines, as this should be impacted by the inclusion of noncollagenous components that possess affinities for such factors.

2.208.5.1. Glycoproteins and PGs

For both glycoprotein and PG-containing matrices, there is little information available. FN appears to be bound to collagen fibrils by two different mechanisms, one being a specific binding of high affinity, engendering only a negligible release of FN under physiologic conditions over 5 days. Any FN in excess of this amount is bound by unspecific adsorption and consequently released within the first 2 h.[82] For decorin that had associated with collagen during fibrillogenesis, only a very small amount desorbed in accordance with the strength of the specific interaction of the PG with collagen (dissociation constant 2.3×10^{-10} M).[103] A measurable desorption occurred only in the first hour, which was larger for conditions under which more decorin had bound to collagen,[74] indicating that here too, unspecific binding may play a role. It seems fair to assume that the mechanisms would be comparable for all collagen-binding proteins.

If higher amounts need to be immobilized, the matrices have to be cross-linked as in the case of collagen–elastin matrices with a ratio of 1:1. Although releasing 60% of the elastin within 24 h, EDC cross-linking practically abolished elastin desorption, after 7 days only 2% had been released. This effect depends on the cross-linking efficiency, which is higher for collagen than for elastin because of more available amine groups. As a result, the efficiency decreases with increasing amounts of elastin, resulting in a slightly higher release.[11]

2.208.5.2. Glycosaminoglycans

The interaction of GAGs with collagen is less specific and of a much lower affinity, for which reason a significant desorption can be detected if the GAG is not cross-linked to the collagen, amounting to a third of the bound amount within the first hour. If GAG is present during fibrillogenesis, the amount that associates with collagen fibrils depends on the GAG, the collagen, and the ionic strength of the buffer. As an example, collagen II binds more CS than collagen type I, and the affinity for different CSs is in the following order: CS C > CS B > CS A. In all cases, this was coupled to a reduction in fibril diameter as opposed to the increase usually seen with collagen type I (**Figure 4**).[104] The differences in affinity are probably based on the differences in CS sulfation, both in pattern and amount. This is supported by the fact that sulfated GAGs are integrated to a much higher degree than unsulfated ones.[94]

If the GAG was cross-linked to preformed fibrils, immobilization depended on available amino groups as well as on concentration of GAG and EDC.[101] The amounts of CS and HS that could be attached in this manner are in the region of 8% (w/w) for CS and 6% (w/w) for HS.[100,102]

Using coprecipitations from acidic solutions of collagen and CS, the immobilized amount was also in the region of 10% GAG in relation to the collagen amount,[99] and cross-linking reduced CS release almost completely; after 28 days in cell culture medium, 30 μg of the original 32 μg could still be found in the scaffolds.[98]

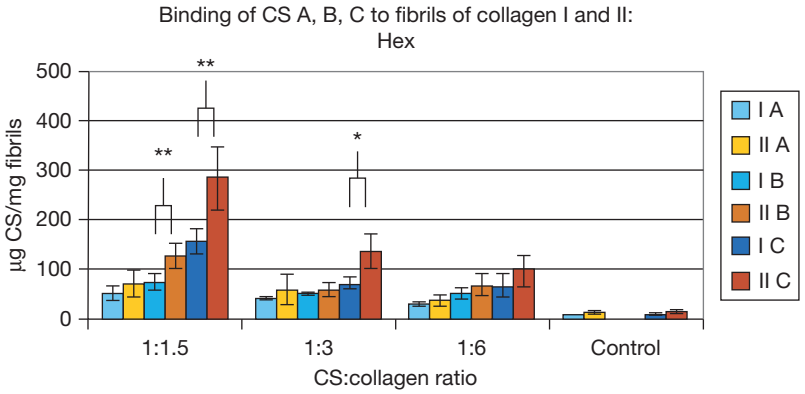

Figure 4 Comparison of amount of CS A–C bound by fibrils of collagen types I and II formed during fibrillogenesis by dimethylmethylene blue (DMMB) assay and hexosamine (hex) assay at differing CS: collagen ratios. A, CS A; B, CS B; C, CS C; I A, collagen I + CS A; I B, collagen I + CS B; I C, collagen I + CS C; II A, collagen II + CS A; II B, collagen II + CS B; II C, collagen II + CS C. All experiments were performed three times. Error bars show standard deviation. Significances: $*p < 0.05$, $**p < 0.01$, $***p < 0.001$. The absence of stars indicates no significant difference. Reproduced from Figure 2 from Douglas, T.; Heinemann, S.; Mietrach, C.; *et al*. *Biomacromolecules* **2007**, *8*, 1085–1092.

Another characteristic of matrices is their mechanical properties. These are not independent of the chemical ones, as not only cross-linking but also composition plays a role. Although for collagen matrices containing laminin, FN, or CS no obvious effects on the mechanical properties could be found,[17,105] this cannot be considered to be a general rule. Using collagen matrices to coat 3D polymeric scaffolds circumvents the problem of changes in the mechanical properties, as this will mainly change the biochemical characteristics.[106]

2.208.5.3. Growth Factor Interactions

An important aspect of aECM is its ability to bind growth factors and cytokines and the possibility to modulate it by adding components that are able to interact with such factors. Some work has been done on collagen scaffolds with no additives, and a certain interaction with growth factors can be observed. TGF-β has been shown to bind slightly faster to collagen fibrils than to uncoated titanium, with a slower release and a stabilizing effect on GF activity, indicating a protective effect of the collagen,[107] and the release of bFGF, HGF, and PDGF-BB is also retarded, most effectively for bFGF.[108] Still, the simple admixture of growth factors to matrices generally leads to a rapid clearance from the implant site because of their unspecific interactions with a low affinity.

Including other ECM components that bind both collagen and growth factors enhances the matrices ability to bind and deliver them, as could be shown for the domain I of perlecan. This domain binds collagen and bears HS and CS chains, and collagen/perlecan fibrils bound significantly more BMP-2 than collagen alone ($112 + 4$ ng vs. $49 + 3$ ng) and sustained a better release characteristic with 7% versus 47% of the initially bound amount after 3 days.[109]

More often, instead of the intact PG, only the GAG chain is used, as GAGs are more easily accessible, with less effect on immune response and inflammation, and have been shown to interact with a large number of growth factors. Collagen–HS matrices prepared by acid precipitation thus bind 1260 ± 207 ng FGF/mg matrix; the same matrices without HS bind only 372 ± 75 ng. Release kinetics were still characterized by an initial burst and following a more gradual release for collagen alone (23 ng followed by 3 ng day^{-1}), while the collagen–CS matrices sustained a more continuous release (13 ng followed by 12 ng day^{-1}).[102] A comparable change in release kinetics could be shown for collagen–heparin matrices;[110] here results suggest that three species populations of VEGF molecules are present in heparinized collagen matrices. The first species is about 15–25% of the total and comprises the nonbound VEGF molecules that are held responsible for the burst release characteristic, while the second group of 10–20% may be nonspecifically adsorbed to the collagen matrix. The third group is bound to the heparin molecule and is assumed to be released with it, and is held responsible for the enhanced angiogenic potential of heparinized collagen.[111] Sulfated GAGs such as heparin have also been shown to enhance the biological activity of BMP by retaining the growth factor in a soluble state (**Chapter 4.416, Growth Factors and Protein-Modified Surfaces and Interfaces**).[112]

2.208.6. Immobilization of aECM

The immobilization process of the aECM is an important aspect in creating surfaces with defined properties. Two basic methods are used: immobilization through adsorption, and through covalent cross-linking. Both have their benefits and their drawbacks. While covalent immobilization gives rise to a stably bound protein surface, it is also a sometimes complicated process, the chemistry of which is not always compatible with more labile molecules. Adsorptive immobilization, on the other hand, is a very simple process that can be conducted at physiological parameters, but the interaction is at least in parts reversible, and may also lead to conformational changes of less stable proteins.

There are a host of methods for the covalent linkage of proteins to surfaces; they vary depending on the surface chemistry and the protein in question. Common to all methods that can be considered as classical covalent linkages is the fact that the linkage is generally formed through reactions with functional groups present on the protein surface. These can be lysine residues, which readily form stable amine bonds with supports bearing active esters, the most common being *N*-hydroxysuccinimide (NHS) esters, a drawback being that NHS is unstable under aqueous conditions. Using protein amine groups is an alternative: they can be coupled with surface aldehydes to produce imines that can be reduced to form a stable secondary amine linkage, or react with epoxides. Cystein residues bearing the thiol group readily undergo conjugate addition with α, β-unsaturated carbonyls like maleimides to form stable thiolether bonds, and acidic residues such as aspartic and glutamic acid can be converted into active esters with a carbodiimide coupling agent (most commonly used is EDC, 1-ethyl-3-(3-dimethylaminopropyl) carbodiimide). These active esters can then react with amine-bearing supports.

With the exception of a few specific cases, conventional immobilization methods suffer from the general disadvantage of generating heterogenous populations of presented proteins because of the random orientation of the immobilized biomolecules, a significant number of which will be inactive. When exposed carboxy- or amino-bearing residues are used, another disadvantage is the coincidental alteration of protein stability, as their charges are important in maintaining proper protein folding; in the case of cystein residues, these are often involved in protein activity. To overcome these limitations, more complex, biologically mediated methods are being developed (the reader is referred to the review of Wong *et al.*[113]).

Covalent collagen immobilization has been performed by grafting of collagen on titanium using low-temperature glow discharge, followed by cross-linking with glutaraldehyde,[114] by deposition on reactive maleic anhydride copolymers that mediate covalent attachment,[115] or by carbodiimide cross-linking using aminopropyl triethoxysilane as coupling agent and the linker molecule *N*, *N*′-disulfosuccinimidyl suberate,[116] to name only a few.

In all cases, cell and animal experiments showed an improved biocompatibility, but the main question in the case of collagen is whether a covalent linkage is indeed necessary,

or if the alternative method of adsorptive immobilization is not sufficient.

Proteins tend to accrue at interfaces between solid and liquid phases; their interactions are determined by protein size, charge, hydrophobicity, and structure, by surface parameters such as roughness, hydrophilicity, and charge, and by the solvent and other solute components present.

Mechanisms which contribute to the adsorption of proteins to a surface are hydrophobic interactions, in which case parts of the protein and the sorbent surface dehydrate, electrostatic interactions, which depend on pH and ionic strength of the solvent, and van der Waals interactions and structural changes in the molecule, which may result in entropy or enthalpy changes. All of these interactions contribute in different parts, with the hydrophobic ones usually discussed to be the most important.[117] Protein adsorption will take place only if the basic criteria of a reduction of the free energy of the system is fulfilled, but because of the number of contributing interactions, no general rules can be established, and adsorption has to be tested for each protein/solvent/sorbent combination.

The kinetics of adsorption can be divided into three stages: a fast and reversible adsorption during the first few minutes, followed by a surface-induced conformational change of the protein that leads to an optimized protein–sorbent interaction, and complete protein denaturation after unlimited adsorption time.[118] The higher the free energy of the adsorption is, the less reversible will the process be. Conformational and orientational changes contribute to the free energy and reduce desorption, but these changes are comparatively slow, for which reason the desorption rate can be described as a function of the contact time. A desorption model that describes the times tending toward zero is a classical Langmuir situation, while the process becoming irreversible for infinitely long times is consistent with most literature data.[119]

For conformationally very stable molecules, there are little to no structural changes, and consequently no contributions to the free energy and no strong adsorptive interactions. Exceptions are large, fibrillar proteins: with their high surface area in relation to their molecular weight, they have a much higher number of potential binding sites than globular proteins of a comparable size, and can interact with the surface via several segments. Although the adsorption free energy of each segment may be small as no structural changes take place to contribute, engagement of many segments will increase the total adsorption free energy until the molecule does not readily desorb anymore.[120] In this case, there is no time dependency and adsorption is irreversible even after short times.

The irreversibility of adsorption refers to situations under buffer; if other molecules are present, the case is different, as the adsorbed proteins can be replaced by competing ones.[119] After longer time periods, only the proteins with the highest affinities will be found on the surface, a phenomenon well known as the Vroman effect.

Collagen fibrils have been successfully immobilized by a purely physisorptive process, with the resultant protein layer being stable against competitive adsorption of serum proteins.[121] The immobilization of the fibrils onto titanium depends to a certain degree on the buffer system used (between 40 and 60 $\mu g\,cm^{-2}$ at the extremes) as well as on the collagen type, but the differences in general tend to be small. For collagen I and III, the mean amount bound was similar despite the much finer type III fibrils. The buffer system used for immobilization had a certain effect, as buffers of high ionic strength tended to reduce immobilization by about 20% with the largest effect for collagen type III. This is probably due to their influence on electrostatic interactions; the increased sensitivity of type III may be on the basis of the higher surface area resulting from the finer fibrils. Heterotypic fibrils were found to take an intermediate position between the homotypic collagen ones, depending on the ratio of the collagen types used.[82] The addition of GAG or PG had no significant effect on the adsorbed collagen amount, the only exception being very thin fibrils as seen for high decorin concentrations.[74] Conclusively it can be said that as long as collagen fibrils can be generated, the adsorption behavior of the aECM will be determined by the collagen part, thus allowing for a stable immobilization by adsorption.

Which immobilization method is best suited obviously depends on the molecules used. For very small molecules such as peptides, the possible contribution of conformational changes is very small, and they do not have many adhesion points, so that adsorptive immobilization is not an option here and a method of covalent immobilization should be selected. For conformationally labile or structurally sensitive proteins, there is in both cases the danger of structural changes that will abolish protein activity. Here a more selective, possibly biologically mediated method is advisable, perhaps including spacers and enzymatic cross-linking, which depends very specifically on the protein in question and the application. Large and structurally extremely stable proteins like collagen fibrils, on the other hand, are optimally suited to adsorptive immobilization, as for them the process is fast, practically irreversible, and not associated with structural changes.

2.208.7. Cell Biological Effects of aECM

In vitro cell studies have addressed a vast number of questions concerning the influence of the ECM on cells, from adhesion and proliferation to signal transduction pathways and differentiation dependent gene and protein expression, using cell lines, tissue-specific primary cells, and stem cells. Consequently, this chapter can only focus on partial aspects, these being mainly studies involving cells relevant for bone, with only a few examples for other tissues.

Cell responses to the biomaterial surface are determined by a number of parameters; using aECM, the main mechanism is expected to be a biochemical one, but the morphological and mechanical aspects also have to be considered. Mechanical issues are of relevance primarily in 3D constructs, as the stiffness of the scaffold is sensed by the cells, and they are known to respond to this stimulus. For 2D coatings, this aspect holds less relevance, but cells also respond to morphological changes of their substrate, a fact that has led to sand-blasting and acid-etching of implant surfaces. As has been described in a previous section, using different components and formation conditions affects the morphology of the fibrils. This may in turn influence cells, but these effects are difficult to differentiate from biochemical ones, as composition and texture of the aECM

depend on each other. Using collagen fibrils as a base material, such effects are probably of secondary importance, as morphological changes of comparable magnitude, though not identical in nature, can be induced by varying the buffer system, and this does not affect cell response; neither does the use of different collagen preparations with obvious differences in fibril morphology.[74] However, the influence of structural changes in the matrix cannot be excluded at this point and may well act in conjunction with the biochemical alterations (**Chapters 2.207, Extracellular Matrix: Inspired Biomaterials** and **2.220, Extracellular Matrix as Biomimetic Biomaterial: Biological Matrices for Tissue Regeneration**).

2.208.7.1. Collagens

Collagen matrices have long been used as substrates for cell adhesion as either scaffolds or coatings on a variety of materials, and collagen type I fibrils on titanium were shown to promote adhesion of rat calvarial osteoblasts, although not differentiation,[121,122] and to prevent glyoxal-induced apoptosis.[123] Adding other ECM components, it should be possible to extend the influence exerted on the cells.

Variations of the collagen matrix by using different collagen types change mechanical and biochemical properties of the fibrils, influencing cellular responses. An increase in collagen type III in the matrix adsorbed to titanium for instance induced an increased collagen synthesis and a decrease in alkaline phosphatase (ALP) activity and Ca^{2+} deposition in primary osteoblastic cells from rat calvariae, while on collagen type I the situation was reversed (**Figure 5**).[85] This agrees with the fact that during intramembraneous fracture healing, collagen type III appears in the early phase associated with matrix production, and type I on the other hand in a later phase associated with matrix mineralization.[8] Cell morphology differed on gels of collagen I, I/III (a 1:1 mixture of I and III), and III, although this in all probability reflects mainly the changed mechanical properties of the gels, those consisting of type III being less stiff due to the finer fibrils.[85] On hard substrates,

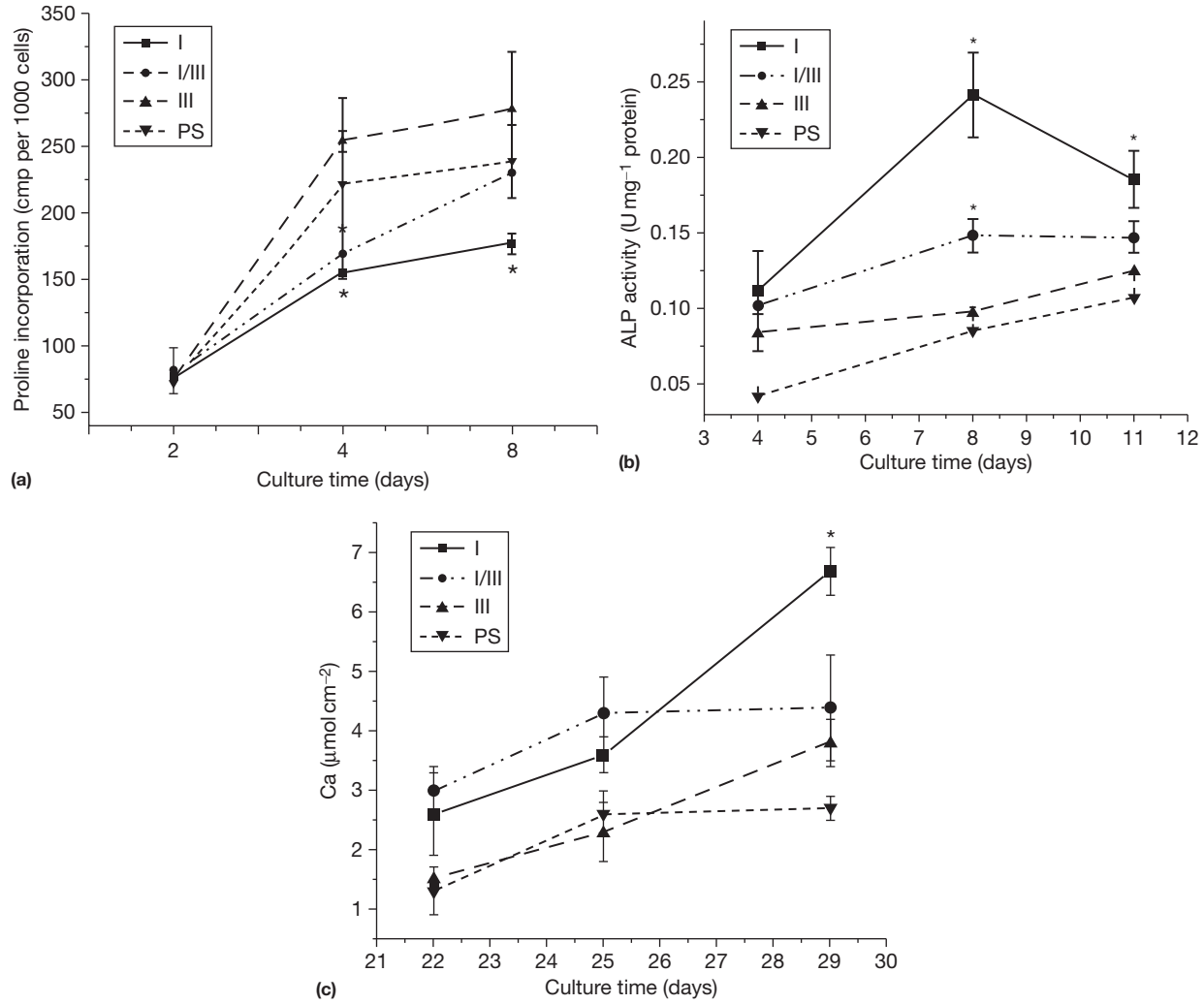

Figure 5 Collagen synthesis (a) alkaline phosphatase enzyme activity (b), and extracellular deposition of calcium (c) in osteoblasts on collagen-coated Ti6A14V disks. Osteoblasts were cultured on Ti6Al4V disks coated with either collagen type I, collagen type I/III cofibrils, or collagen type III with PS as control. At the indicated time points after analyses were performed. Asterisks indicate significant difference ($p < 0.05$) to control. Reproduced from Figures 4, 5, and 6 from Bierbaum, S.; Hempel, U.; Geissler, U.; *et al. J. Biomed. Mater. Res. A* **2003**, *67*, 431–438.

I, III, and V all promote attachment and spreading of fibroblasts, with I and III increasing DNA synthesis more than type V.[124] On soft substrates, on the other hand, collagen I/V coatings impair fibroblast spreading while type I supports it.[125]

The inclusion of growth factors is possible using plain collagen scaffolds, though there will in all probability be no synergistic interactions as the collagen serves only as a passive carrier. TGF-β adsorbed to collagen matrices immobilized on titanium, for instance, induced an increase in collagen synthesis in rat osteoblasts, and reduced mRNA and ALP activity as well as accumulation of Ca^{2+} and phosphate.[107]

2.208.7.2. Glycoproteins and PGs

Further variations include the addition of glycoproteins or PGs into collagenous matrices. The use of glycoproteins in aECM is not common; apart from FN, mainly laminin and, to some extent, elastin have been utilized. Glycoproteins such as FN are recognized by other cellular adhesion receptors rather than collagen, so that including them in the matrix changes the mechanism of cell adhesion. Depending on whether collagen or collagen/FN is used, different integrin receptors are engaged and activated,[85] which in turn can lead to the activation of different signaling pathways and thus ultimately to different cell responses (for details see **Section 2.208.3.1**). FN also interacts with cell-surface HS as part of a mechanism for triggering the signaling process that leads to cell adhesion.[126]

One glycoprotein that has been used in combination with collagen is laminin or laminin-derived peptide, mainly for the positive effect it has on neuronal cell growth. While collagen and HyA have no effect and FN negatively influences neurite growth, laminin has a dose-dependent positive effect, with neurites growing preferentially toward high laminin concentrations. As the gels in this study did not differ much in mechanical properties, the observed effects are on the basis of chemical interactions.[16,17] These interactions may involve α6β1-integrin binding to laminin, as this has been shown to play a role in the expansion and differentiation of human embryonal stem cells (hESC) into neurons.[127] The functions of laminin are not limited to neural cells: for swiss 3T3 fibroblasts, laminin peptides in collagen matrices resulted in a significant increase in cell proliferation,[91] and on human mesenchymal stem cells (hMSC) laminin has been reported to induce an osteogenic phenotype via an ERK-dependent pathway.[128] hMSCs respond similarily to other ECM proteins they adhere to through distinct integrins, although with varying affinities (FN > collagen I > collagen IV > vitronectin > laminin-1). The greatest osteogenic differentiation occurred on VN and collagen I, but almost none on FN.[129] The mechanisms by which collagen and VN support osteogenic differentiation differ: osteogenesis via VN is correlated with enhanced focal adhesion formation, the activation of FAK and paxillin, and the diminished activation of ERK and PI3K pathways. On collagen, hMSC exhibited reduced focal adhesion formation, reduced FAK and paxillin activation, and increased ERK and PI3K activation.[130] This may be on the basis of the fact that cells adhere to collagen mainly via β1-integrins, and to VN via αvβ3 and αvβ5 (**Chapter 2.209, Materials as Artificial Stem Cell Microenvironments**).[131]

Collagen type II, on the other hand, induces and supports chondrogenic over osteogenic differentiation of MSCs; the presence of TGF-β in the matrix enhances this process.[132]

Compared to glycoproteins and even more to GAGs, there are comparatively few studies concerning PGs. Unlike most of the glycoproteins, the largest part of PG influence on cells is probably not conveyed by direct interactions with cell adhesion receptors, but with other cell-surface receptors instead, and through the interactions of PGs with solute factors. Nonetheless, the addition of the PGs decorin and biglycan influences cell adhesion, accelerating and enhancing the formation of focal adhesions in osteoblastic cells.[74,88] Interestingly decorin and biglycan seem to play different roles in rats and humans: they promote the proliferation of humans but not of rat calvarial osteoblasts, collagen synthesis was inhibited by biglycan in rat but not in human osteoblasts, and decorin promoted proliferation slightly in humans but not in rat OB,[89] illustrating that aECM should be adapted carefully to the intended target cells.

Engineered proteins and protein fragments can also be used to modulate cell responses. Artificial peptides based on decorin glycosilated with DS increase the production of elastin, something that would be of interest in the tissue engineering of vascular constructs. The addition of DS without the attached protein core resulted in a decreased elastin production, indicating that presentation of GAG is important.[90]

The addition of growth factors can have different effects depending on the presenting matrices, making synergistic as well as antagonistic effects possible: in the case of adsorbed TGF-β, cell proliferation on collagen was reduced and collagen synthesis enhanced. If biglycan was present in the matrix, the reduction in proliferation was more marked, while decorin enhanced collagen synthesis.[88] Protein fragments can fulfill comparable functions, for example, the perlecan domain I which together with collagen and BMP-2 support chondrogenic differentiation in mouse embryonic mesenchymal cells;[109] peptides cannot be utilized this way, as they usually contain only one functional sequence and are not large enough to sustain additional effects.

2.208.7.3. Glycosaminoglycans

Unlike in the case of PGs, quite a number of studies have been performed using only the GAG part of these molecules, especially in conjunction with collagen. Collagen–GAG composites have been used in a number of applications such as skin, peripheral nerve, muscle, cartilage, and bone, and for the differently composed matrices effects on cytoskeletal organization, and protein expression and differentiation.

As CSs are synthesized by both chondrocytes and bone cells, they have often been used in applications concerning these tissues. In cartilage, CS stimulates PG production, inhibits cartilage cytokine production, and induces apoptosis of articular chondrocytes, while in bones, CS accelerates mineralization process and bone repair. In both tissues, CS has anti-inflammatory effects and inhibits extracellular proteases involved in the metabolism of connective tissues.[133] Matrices containing CS positively influenced adhesion of osteoblastic cells: the formation of focal adhesions was accelerated and enhanced if CS was present. As in case of the PGs, this is

probably not on the basis of specific ligand–receptor interactions, but because of the negatively charged sulfate groups of the GAG which have been shown to improve early cell adhesion.[134,135] The negative charge may accelerate integrin receptor binding via enhanced binding of Ca^{2+}, which has a higher binding affinity compared to monovalent or other divalent cations and is required for the formation of focal adhesions.[136] As about 90% of the cell-surface charges are negative at a physiological pH,[137] Ca^{2+} ions can also mediate cell adhesion by binding to both the negatively charged cell membrane and matrix. Interestingly, this depends on the CS type: in combination with collagen II, CS A and CS B, but not CS C, appeared to stimulate the formation of FACs by osteoblasts, indicating that other aspects may influence cell response over and above the overall charge effect.[104]

Collagen–GAG matrices generally increased proliferation, for example, for chondrocytes on collagen–CS,[97] and for endothelial cells on heparin-containing matrices, an effect that was increased by the addition of VEGF.[101,110]

Protein expression of osteoblastic cells on collagen–GAG matrices was usually slanted toward an osteogenic phenotype. Although calvarial osteoblasts grown on collagen-coated Ti6Al4V already expressed more OPN compared to the uncoated surface,[138] OPN expression was upregulated even more in cells cultured on collagen I–CS, suggesting that interaction with the GAG promotes osteoblastic differentiation.[74] For hMSC, a comparable effect of collagen–CS can be observed, as osteoblastic marker expression and calcium deposition are upregulated even without other differentiation additives.[106,139] Although matrix elasticity, cell shape, and cytoskeletal tension have also been shown to effect linage-specific osteogenic differentiation, many of the soluble growth and adhesive factors involved in osteogenic differentiation require GAG side chains to facilitate their interaction to their cell-surface receptors.[140] BMP has been shown to bind to cell-surface PGs such as perlecan and syndecan via their HS and CS chains; this modulates BMP osteogenic bioactivity by sequestering it at the cell surface where it is unable to bind BMP receptors.[141] GAG chains in the matrix can compete with the cell-surface GAGs for GF binding, thus making a larger part of GFs available. Oversulfated forms of CS have been shown to bind BMP-4 and stimulate osteoblastic differentiation in MC3T3 cells: heparin enhanced only mineralization and ALP activity, whereas CS-E enhanced ALP activity, collagen deposition, and mineralization, and the CS-E-induced mineralization was significantly inhibited by anti-BMP antibodies, demonstrating the interaction of the two factors.[32]

Chondrocytes grown on collagen II–CS scaffolds, on the other hand, show an increased expression of collagen II and PGs and form a denser cartilaginous layer,[97] although CS appears to influence the metabolic activity of chondrocytes seeded in a collagen I–CS matrix in a comparable manner.[142] The optimal ratio of collagen to GAG seems to depend on the cell type and the addressed tissue, and should be optimized in each case.[99,143]

Scaffolds containing HyA tend to behave slightly different, probably because fewer interactions are possible. In collagen–HyA scaffolds, small HyA quantities (2.5% wt) enhanced cell adhesion and growth, while larger ones (over 5% wt) inhibited it,[144] and migration rates of hematopoetic stem cells were reduced.[115] HyA did support chondrogenesis in eMSCs, but this effect was not enhanced by the addition of TGF-β,[145] probably because there was no interaction comparable to the sulfated GAGs possible.

2.208.8. Results from Animal Experiments

Much information exists concerning collagen, both as scaffold and coating for diverse applications in tissue engineering and as carrier for antibiotics and growth factors. Areas of use are in hard tissue, cartilage, and nerve regeneration as well as skin and soft tissue augmentation, and it can be used as lyophilized scaffold or coating of metals or polymers (i.e., silicone, polyurethane, polyethylene terephthalate, polylactic acid); this section will deal mainly with the use of collagen and other ECM molecules as coatings on bone implants. In many cases, for bone applications a mineral phase is included, both with and without organic components such as collagen. As the primary interest of this chapter is the use of aECM made up solely of organic components, such combinations with mineral phases have been specifically excluded here. Nevertheless, it should be kept in mind that they certainly are part of the ECM of bone, and using differently composed organic coatings may have relevance to mineralization processes, both *in vitro* and *in vivo*.

There are two drawbacks to the experiments discussed below. The first is of a general nature: the matrices used in such studies are often characterized only very insufficiently; the components are known, but the structure, the amount bound, or the release behavior is not known, which makes comparison and evaluation of results difficult. The second is more specific to the topic of this chapter: aECM has been defined as consisting of collagen with other ECM components modifying it, but such comparatively complex coatings have only very rarely been used for *in vivo* experiments up to now. For this reason many of the results presented below deal with single component coatings only (**Chapter 2.220, Extracellular Matrix as Biomimetic Biomaterial: Biological Matrices for Tissue Regeneration**).

2.208.8.1. Collagens

With very few exceptions, all studies using collagen make use of collagen type I. There are some instances where type II has been utilized, typically for cartilage applications in combination with GAGs,[97] but even here collagen type I has been employed. Type I is of course the most easily available collagen, but using the different types may still be of interest in specific situations. Collagen type III in a goat model appeared to be more effective in less dense bone after 4 and 12 weeks, which may be related to the fact that type III is associated with healing instead of mature bone.[146] This would agree with the fact that after longer time periods (6 months in the mandible of minipigs), collagen I and I/III showed higher bone–implant contact compared to uncoated, sandblasted implants, but no more differences between the collagens could be determined.[147]

Instead of the complete collagen molecule, several studies have used peptides based on the adhesive domains of collagen or, more often, FN. These peptides also convey effects in the *in vitro* studies that are comparable but not identical with those of the whole molecule, as they present only very specific aspects:

titanium coated with GFOGER, a collagen mimetic peptide, selectively promotes α2β1 integrin binding, triggering osteoblastic differentiation, and peri-implant bone regeneration and osseointegration.[148] Using peptides in combination with the larger, 3D molecular networks of ECM proteins is an intriguing aspect, as it allows further modification of aECM functions.

These larger structures of ECM proteins are necessary if growth factors are to be included in the matrix, as peptides cannot interact with them in addition to conveying adhesion. The use of growth factors in tissue regeneration has given rise to the development of a number of carriers, but a significant drawback that remains is that very high amounts of growth factor have to be used to achieve the desired effects. Smaller amounts as can be attained by adsorptively immobilizing, that is, BMP-2 to collagen coatings, often have no significant effect *in vivo*,[149] although cell culture results have been promising. This is certainly an aspect where the inclusion of matrix components that are known to interact with growth factors may be of use in the future.

2.208.8.2. Glycoproteins and PGs

On both glycoproteins and PGs, either alone or in combination with collagen, there is comparatively little *in vivo* data. For collagen and collagen–decorin matrices on acid etched titanium implants in the mandible of minipigs, both were better than uncoated implants, but no significant differences between them could be detected.[150] In experiments in rats, on the other hand, there are interesting results indicating that tissue responses to implants can be modulated by surface treatments using ECM proteins. On porous ePTFE disks implanted into the adipose tissue of rats, an FN coating resulted in an extensive inflammatory response with limited angiogenesis and neovascularization, and collagen IV in significant peri-implant angiogenic response but little neovascularization, while laminin-1 displayed both peri-implant angiogenesis and a coordinate neovascularization of the porous interstices of the biomaterial.[151] It seems that the major effect of FN is to stimulate a cytokine response that enhances monocyte/macrophage recruitment and the differentiation of cells into giant cells, while collagen IV appears as more of an angiostatic factor, supporting the maturation of blood vessels in the peri-implant region but not endothelial cell migration and neovascularization. Laminin, on the other hand, seems to both induce the production of angiogenic factors and support early and late events in the angiogenic process.[151] The mechanisms of these variable responses are still unclear, but they seem to involve the expression of various cytokines and growth factors by cells in the peri-implant region in response to the different matrices.

Laminin is of special interest in nerve cell regeneration: stem cell survival and improvement in cognitive functions in the mouse brain were better for scaffolds containing laminin or laminin peptides.[18] For collagen scaffolds implanted into the spinal cord of rats, a coating of a laminin peptide (YIGSR) enhanced more neurite growth than an FN coating,[152] illustrating that matrix composition affects all types of tissues, and that the most common choices, collagen type I and FN, are not necessarily the best in every case.

Not only the components included in a coating but also their physical presentation can influence cellular response. Collagen–elastin scaffolds that contain solubilized elastin induce angiogenesis and show no calcification in rats, in contrast to scaffolds containing elastin fibrils.[11] Although the mechanism is unclear, this indicates that structural aspects should not be ignored.

As in the case of collagen, peptides instead of the complete molecules can be used. Laminin peptides have already been mentioned, but the most commonly used peptide by far is the RGD sequence derived from FN. RGD and other adhesion peptides, when coated onto titanium, generally gave rise to greater bone–implant contact than uncoated, grid blasted implants,[153] although in comparison to collagen coatings in a goat model, the complete collagen induced more bone apposition than the peptide, indicating that mechanisms over and above adhesion via the integrin receptor targeted by RGD are responsible for tissue response.[146] Combining RGD with collagen, on the other hand, resulted for titanium implants in the dog mandible after 1 month in an enhanced bone–implant contact for collagen grafted with RGD peptide over unmodified collagen or RGD alone. The differences between coatings were no longer apparent after 3 months; interestingly, all coatings still displayed more bone–implant contact and bone volume density than uncoated, machined implants,[154] showing that both short- and long-term responses can be affected differently by the chosen coatings.

The use of an FN fragment such as the α5β1-specific FN fragment FNIII7-10 instead of just the integrin-binding sequence enhanced bone apposition not only over a peptide coating but also over the full-length FN in a rat model.[155] This may, like the use of RGD in combination with collagen, be due to the increased number of binding sites offered by the smaller peptide on the same area.

2.208.8.3. Glycosaminoglycans

Like collagen type I matrices, those consisting of collagen–glycosaminoglycans have been studied in a variety of experiments. Most matrices are cross-linked, which delays resorption and preserves scaffold integrity over a longer time.[100] Whether or not cross-linking is used thus depends on the application and the time that is considered necessary for the scaffold or coating to remain *in situ*. Especially for coatings, this reduces the necessity to cross-link, as the preservation of a 3D, porous structure is not an issue here, and most experiments indicate that the effect of coatings is a comparatively early one.

Among the GAGs, HyA occupies a somewhat separate position. Because of its unsulfated state, there is little interaction with growth factors or other ECM components; the main effect of HyA is via its size (see also **Section 2.208.3**). There are some applications as a dermal substitute, where collagen/HyA membranes were shown to have a good compatibility and low irritability,[144] but in the majority of the cases the sulfated GAGs were used.

Inclusion of GAGs into collagen matrices has a variety of effects, such as influencing the process of inflammation and foreign body response, an observation that has been reported repeatedly. In rats, both CS and HS in combination with collagen aid the generation of new host tissue with only a transient inflammatory response and a reduced foreign body

reaction,[100] and the activity of macrophages was reported to be markedly reduced around collagen–CS coating of titanium.[156]

More specifically, GAGs have been implicated in inducing and promoting angiogenesis, something of paramount importance especially in 3D constructs. Here biomaterials are of interest that can encode matricellular cues which regulate and enhance vascular progression by reproducing the natural interplay existing between matrix, cells, and angiogenic factors. In a rat model, collagen matrices with both HS and heparin showed improved angiogenesis over collagen alone,[100,101] the drawback being that this increase in vascularization was only in the periphery and probably transient.[102] This could be overcome by the addition of growth factors: VEGF further increased the angiogenic potential of collagen–heparin matrices,[101] and bFGF in combination with collagen/HS resulted in scaffolds that remained vascularized throughout the matrix during a 10-week implantation period. In addition, they revealed an intense and prolonged tissue response and considerably promoted the generation of new tissue.[102] The most interesting fact here is that adding bFGF to the collagen matrix had the same transient and peripheral effect as the collagen–HS matrix without the growth factor, indicating that not only does HS directly affect angiogenesis but also that it can work synergistically with bFGF. Including HyA in specific matrix location may be of further interest, as increasing HyA in collagen scaffolds works in a manner opposed to HS and heparin, inhibiting sprouting, and the combination might thus be utilized to direct vessel growth.[157]

In the osseous integration of implants, including GAGs has also led to positive results, although the mechanisms can be expected to be somewhat different. Collagen–CS coatings were consistently found to give higher bone volume and bone-implant contact than collagen alone for titanium implants in the minipig mandible;[158] again these effects were in the early phase and leveled off after 2 months.[150] Interestingly, the extraction torque of collagen–CS implants in the sheep tibia was in the region of hydroxyl apatite coatings (1153 N mm vs. 1088 N mm for collagen–CS) and higher than collagen (900 N mm) despite the fact that after 2 months the differences in bone apposition were no longer significant.[159]

On the cellular level, both for collagen and even more for collagen–CS there was a faster appearance of relevant cell types compared to uncoated, grid blasted implants, and osteoblast activity was increased around both collagen and collagen–CS.[156] This results in a significantly enhanced bone remodeling in the early stages of bone healing, which is reflected in the bone-implant contact after 4 weeks: 89% for collagen–CS, 76% for collagen, and 62% for uncoated implants.[160] In addition, macrophage and osteoclast activity were markedly reduced around collagen–CS coatings in a rat model, which agrees with the observations made in the angiogenic studies.[156] The impact of surface topography and animal model is illustrated by the fact that in the foxhound mandible, for machined and acid etched titanium samples, the bone-implant contact was enhanced by collagen–CS coatings in both cases, but the differences were significant only for the machined surfaces.[161]

GAGs have been described to interact with growth factors; using matrices that include these components to enhance the ability of aECM coatings to bind and deliver growth factors is thus a logical approach. For bone, most of the interest focuses on the BMPs; BMP-2 and BMP-4 are known to induce bone formation when released from carriers such as collagen fleeces *in vivo*. Using the high BMP amounts that are necessary to induce a response (these usually being in the microgram range), collagen–heparin matrices enhance BMP-induced osteoblast differentiation not only *in vitro* but also *in vivo*, the mechanism possibly being the protection of the growth factors from degradation, and an inhibition of BMP antagonists.[162] For lower BMP amounts as could be immobilized on 2D coatings of titanium implants, the situation is a different one. Here, either no BMP effect could be seen,[161] or a detrimental one. In the minipig mandible, the bone-implant contact for collagen–CS was 40%, but for collagen–CS–BMP-4 only 27% (**Figure 6**).[163,164] This indicates that, to utilize the complete range of potential that aECM can offer, still much needs to be learned about how ECM components and soluble factors interact with each other as well as with cells and proteins of the host tissue in the process of healing (**Chapter 5.522, Bone Tissue Engineering: Growth Factors and Cytokines**).

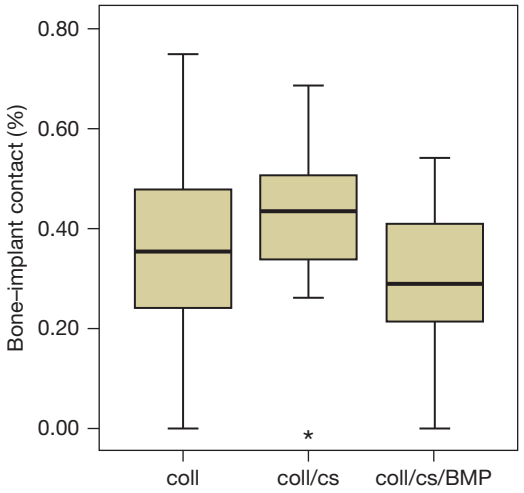

Figure 6 Percentage of implant surface in contact with bone. coll, coating from fibrillar collagen type I; coll/CS, coating from fibrillar collagen type I with chondroitinsulfate associated during fibrillogenesis; coll/CS/BMP4, coating Coll/CS loaded with 400 ng rhBMP4 per implant. Asterisk indicates significant difference ($p < 0.05$) to controls. Reproduced from Stadlinger, B.; Pilling, E.; Huhle, M.; *et al. Int. J. Oral Maxillofac. Surg.* **2008**, *37*, 54–59.

2.208.9. Conclusions and Outlook

Although the matrix has been recognized for a while now as being much more important in determining cell fate than previously thought, much still remains to be done in utilizing the possibilities it offers to construct defined microenvironments that can steer cellular responses. Only few of the components that make up the ECM *in vivo* have been utilized in the construction of aECM up to now; considering how specific the responses of cells and tissues can be, there is still much potential in this respect.

A promising approach is the use of engineered proteins and protein fragments, enhancing specific functionalities over

the naturally occurring levels by repeating the protein domains, or combining them with other functionalities. The ECM proteins themselves constructed in this manner consist of functional domains that occur in different proteins with varying combinations.

Using chemically modified GAGs is a related aspect, as changing the sulfation pattern impacts the interaction of the sugars with other proteins. Modified GAGs can be either sugars that are naturally not sulfated, such as chitosan, dextran, and hyaluronan,[165,166] or oversulfated forms of CS, DS, or HS.[32] It has been shown that such alterations influence the ability to bind growth factors as for HyA, where highly sulfated forms bind more BMP4 than those with low sulfate content.[167] Modified GAGs thus might be either used in GF carriers to immobilize higher amounts of growth factor, or can perhaps even be sufficiently engineered to exploit their ability to act synergistically with soluble factors.

Yet another aspect that has not received much attention is the influence of mechanical cues. Mechanical signals are as important for cells as biochemical ones; one example is the constant remodeling of bone on the basis of the mechanical load. The mechanical information is conveyed to the cells via the ECM, and specifically via the adhesion receptors, some of which also function as mechanoreceptors. Especially the integrins are probably involved in the whole plethora of mechanotransduction phenomenons.[168] Mechanical strain activates signal transduction pathways similar to growth factors;[169] indeed, sometimes mechanical stress activates growth factor receptors even in absence of the soluble ligand.[170] But this depends on the ECM composition: VN has been shown to be involved in the transduction of mechanical signals into the cells, OPN plays a major role in stress-induced bone remodeling,[22] and collagen–CS matrices enhance osteoblastic differentiation in combination with mechanical stress.[171]

Many aspects can thus potentially be addressed by differently composed aECM in healthy organisms and in those compromised by illness. A better understanding of the complex mechanism behind the observed effects of the ECM will be instrumental for significant progress in this field, and the developments in many areas of relevant research such as molecular medicine, cell–matrix interactions, and glycomics, to name only a few, hold much promise for the future.

References

1. Gentili, C.; Cancedda, R. *Curr. Pharm. Des.* **2009**, *15*, 1334–1348.
2. Hubbell, J. A. *Curr. Opin. Biotechnol.* **2003**, *14*, 551–558.
3. Kadler, K. E.; Baldock, C.; Bella, J.; Boot-Handford, R. P. *J. Cell Sci.* **2007**, *120*, 1955–1958.
4. Ricard-Blum, S.; Ruggiero, F. *Pathol. Biol. (Paris)* **2005**, *53*, 430–442.
5. Heino, J. *Bioessays* **2007**, *29*, 1001–1010.
6. Gelse, K.; Poschl, E.; Aigner, T. *Adv. Drug Deliv. Rev.* **2003**, *55*, 1531–1546.
7. Von Der Mark, K. *Structure, Biosynthesis and Gene Regulation of Collagens in Cartilage and Bone*. Academic Press: Orlando, 1999.
8. Kurdy, N. M.; Bowles, S.; Marsh, D. R.; Davies, A.; France, M. *J. Orthop. Trauma* **1998**, *12*, 122–126.
9. Fessler, J. H.; Shigaki, N.; Fessler, L. I. *Ann. N.Y. Acad. Sci.* **1985**, *460*, 181–186.
10. Iozzo, R. V. *J. Biol. Chem.* **1999**, *274*, 18843–18846.
11. Daamen, W. F.; Nillesen, S. T.; Wismans, R. G.; *et al. Tissue Eng. A* **2008**, *14*, 349–360.
12. Bruckner, P. *Cell Tissue Res.* **2009**, *339*, 7–18.
13. Pankov, R.; Yamada, K. M. *J. Cell Sci.* **2002**, *115*, 3861–3863.
14. Ruoslahti, E. *Annu. Rev. Biochem.* **1988**, *57*, 375–413.
15. Durbeej, M. *Cell Tissue Res.* **2010**, *339*, 259–268.
16. Yao, L.; Damodaran, G.; Nikolskaya, N.; Gorman, A. M.; Windebank, A.; Pandit, A. *J. Biomed. Mater. Res. A* **2010**, *92*, 484–492.
17. Deister, C.; Aljabari, S.; Schmidt, C. E. *J. Biomater. Sci. Polym. Ed.* **2007**, *18*, 983–997.
18. Tate, C. C.; Shear, D. A.; Tate, M. C.; Archer, D. R.; Stein, D. G.; Laplaca, M. C. *J. Tissue Eng. Regen. Med.* **2009**, *3*, 208–217.
19. Schvartz, I.; Seger, D.; Shaltiel, S. *Int. J. Biochem. Cell Biol.* **1999**, *31*, 539–544.
20. Tucker, R. P.; Chiquet-Ehrismann, R. *Biochim. Biophys. Acta* **2009**, *1793*, 888–892.
21. Jones, F. S.; Jones, P. L. *Dev. Dyn.* **2000**, *218*, 235–259.
22. Kazanecki, C. C.; Uzwiak, D. J.; Denhardt, D. T. *J. Cell. Biochem.* **2007**, *102*, 912–924.
23. Liu, L.; Qin, C.; Butler, W. T.; Ratner, B. D.; Jiang, S. *J. Biomed. Mater. Res. A* **2007**, *80*, 102–110.
24. Tan, K.; Lawler, J. *J. Cell Commun. Signal.* **2009**, *3*, 177–187.
25. Schaefer, L.; Schaefer, R. M. *Cell Tissue Res.* **2010**, *339*, 237–246.
26. Milan, A. M.; Sugars, R. V.; Embery, G.; Waddington, R. J. *Calcif. Tissue Int.* **2005**, *76*, 127–135.
27. Danielson, K. G.; Baribault, H.; Holmes, D. F.; Graham, H.; Kadler, K. E.; Iozzo, R. V. *J. Cell Biol.* **1997**, *136*, 729–743.
28. Merline, R.; Schaefer, R. M.; Schaefer, L. *J. Cell Commun. Signal.* **2009**, *3*(3–4), 323–335.
29. Kogan, G.; Soltes, L.; Stern, R.; Gemeiner, P. *Biotechnol. Lett.* **2007**, *29*, 17–25.
30. Gandhi, N. S.; Mancera, R. L. *Chem. Biol. Drug Des.* **2008**, *72*, 455–482.
31. Malavaki, C.; Mizumoto, S.; Karamanos, N.; Sugahara, K. *Connect. Tissue Res.* **2008**, *49*, 133–139.
32. Miyazaki, T.; Miyauchi, S.; Tawada, A.; Anada, T.; Matsuzaka, S.; Suzuki, O. *J. Cell. Physiol.* **2008**, *217*, 769–777.
33. Berrier, A. L.; Yamada, K. M. *J. Cell. Physiol.* **2007**, *213*, 565–573.
34. Eliceiri, B. P. *Circ. Res.* **2001**, *89*, 1104–1110.
35. Gahmberg, C. G.; Fagerholm, S. C.; Nurmi, S. M.; Chavakis, T.; Marchesan, S.; Gronholm, M. *Biochim. Biophys. Acta* **2009**, *1790*, 431–444.
36. Humphries, J. D.; Byron, A.; Humphries, M. J. *J. Cell Sci.* **2006**, *119*, 3901–3903.
37. Moyano, J. V.; Carnemolla, B.; Albar, J. P.; *et al. J. Biol. Chem.* **1999**, *274*, 135–142.
38. Zaidel-Bar, R.; Itzkovitz, S.; Ma'ayan, A.; Iyengar, R.; Geiger, B. *Nat. Cell Biol.* **2007**, *9*, 858–867.
39. Hollenbeck, S. T.; Itoh, H.; Louie, O.; Faries, P. L.; Liu, B.; Kent, K. C. *Biochem. Biophys. Res. Commun.* **2004**, *325*, 328–337.
40. Ruoslahti, E. *Annu. Rev. Cell Dev. Biol.* **1996**, *12*, 697–715.
41. Leitinger, B.; Hohenester, E. *Matrix Biol.* **2007**, *26*, 146–155.
42. Ruoslahti, E. *Cancer Metastasis Rev.* **1984**, *3*, 43–51.
43. Madsen, C. D.; Sidenius, N. *Eur. J. Cell Biol.* **2008**, *87*, 617–629.
44. Meloty-Kapella, C. V.; Degen, M.; Chiquet-Ehrismann, R.; Tucker, R. P. *Cell Tissue Res.* **2008**, *334*, 445–455.
45. Ziebell, M. R.; Zhao, Z. G.; Luo, B.; Luo, Y.; Turley, E. A.; Prestwich, G. D. *Chem. Biol.* **2001**, *8*, 1081–1094.
46. Kawashima, H.; Hirose, M.; Hirose, J.; Nagakubo, D.; Plaas, A. H.; Miyasaka, M. *J. Biol. Chem.* **2000**, *275*, 35448–35456.
47. Varki, A. *J. Clin. Invest.* **1997**, *99*, 158–162.
48. Barbero, A.; Benelli, R.; Minghelli, S.; *et al. J. Cell. Physiol.* **2001**, *186*, 183–192.
49. Ikuta, T.; Ariga, H.; Matsumoto, K. *Genes Cells* **2000**, *5*, 913–927.
50. Pouliot, N.; Connolly, L. M.; Moritz, R. L.; Simpson, R. J.; Burgess, A. W. *Exp. Cell Res.* **2000**, *261*, 360–371.
51. Uebersax, L.; Merkle, H. P.; Meinel, L. *Tissue Eng. B Rev.* **2009**, *15*, 263–289.
52. Chan, P. C.; Chen, S. Y.; Chen, C. H.; Chen, H. C. *J. Biomed. Sci.* **2006**, *13*, 215–223.
53. Juliano, R. *Bioessays* **1996**, *18*, 911–917.
54. Clemmons, D. R.; Maile, L. A. *Endocrinology* **2003**, *144*, 1664–1670.
55. Clemmons, D. R.; Maile, L. A. *Mol. Endocrinol.* **2005**, *19*, 1–11.
56. Wipff, P. J.; Hinz, B. *Eur. J. Cell Biol.* **2008**, *87*, 601–615.
57. Streuli, C. H.; Akhtar, N. *Biochem. J.* **2009**, *418*, 491–506.
58. Cabodi, S.; Moro, L.; Bergatto, E.; *et al. Biochem. Soc. Trans.* **2004**, *32*, 438–442.
59. Schaefer, L.; Iozzo, R. V. *J. Biol. Chem.* **2008**, *283*, 21305–21309.
60. Taylor, K. R.; Gallo, R. L. *FASEB J.* **2006**, *20*, 9–22.
61. Ashikari-Hada, S.; Habuchi, H.; Kariya, Y.; Itoh, N.; Reddi, A. H.; Kimata, K. *J. Biol. Chem.* **2004**, *279*, 12346–12354.
62. Huntington, J. A. *J. Thromb. Haemost.* **2003**, *1*, 1535–1549.
63. Iozzo, R. V. *Annu. Rev. Biochem.* **1998**, *67*, 609–652.

64. Vlodavsky, I.; Miao, H. Q.; Medalion, B.; Danagher, P.; Ron, D. *Cancer Metastasis Rev.* **1996**, *15*, 177–186.
65. Zafiropoulos, A.; Fthenou, E.; Chatzinikolaou, G.; Tzanakakis, G. N. *Connect. Tissue Res.* **2008**, *49*, 153–156.
66. Sasisekharan, R.; Raman, R.; Prabhakar, V. *Annu. Rev. Biomed. Eng.* **2006**, *8*, 181–231.
67. Blackhall, F. H.; Merry, C. L.; Lyon, M.; *et al. Biochem. J.* **2003**, *375*, 131–139.
68. Tapon-Bretaudiere, J.; Chabut, D.; Zierer, M.; *et al. Mol. Cancer Res.* **2002**, *1*, 96–102.
69. Proudfoot, A. E. *Biochem. Soc. Trans.* **2006**, *34*, 422–426.
70. Campo, G. M.; Avenoso, A.; Campo, S.; Traina, P.; D'Ascola, A.; Calatroni, A. *Arch. Biochem. Biophys.* **2009**, *491*, 7–15.
71. Yang, C.; Hillas, P. J.; Baez, J. A.; *et al. BioDrugs* **2004**, *18*, 103–119.
72. Pieper, J. S.; Hafmans, T.; Veerkamp, J. H.; Van Kuppevelt, T. H. *Biomaterials* **2000**, *21*, 581–593.
73. Pieper, J. S.; Oosterhof, A.; Dijkstra, P. J.; Veerkamp, J. H.; Van Kuppevelt, T. H. *Biomaterials* **1999**, *20*, 847–858.
74. Bierbaum, S.; Douglas, T.; Hanke, T.; *et al. J. Biomed. Mater. Res. A* **2006**, *77*, 551–562.
75. Mercier, I.; Lechaire, J. P.; Desmouliere, A.; Gaill, F.; Aumailley, M. *Exp. Cell Res.* **1996**, *225*, 245–256.
76. Hulmes, D. J. S. *Collagen Diversity, Synthesis and Assembly*; Springer Science+Business Media: New York, 2008.
77. Williams, B. R.; Gelman, R. A.; Poppke, D. C.; Piez, K. A. *J. Biol. Chem.* **1978**, *253*, 6578–6585.
78. Brightman, A. O.; Rajwa, B. P.; Sturgis, J. E.; Mccallister, M. E.; Robinson, J. P.; Voytik-Harbin, S. L. *Biopolymers* **2000**, *54*, 222–234.
79. Freudenberg, U.; Behrens, S. H.; Welzel, P. B.; *et al. Biophys. J.* **2007**, *92*, 2108–2119.
80. Harris, J. R.; Reiber, A. *Micron* **2007**, *38*, 513–521.
81. Mertz, E. L.; Leikin, S. *Biochemistry* **2004**, *43*, 14901–14912.
82. Bierbaum, S.; Beutner, R.; Hanke, T.; Scharnweber, D.; Hempel, U.; Worch, H. *J. Biomed. Mater. Res. A* **2003**, *67*, 421–430.
83. Stuart, K.; Panitch, A. *Biomacromolecules* **2009**, *10*, 25–31.
84. Birk, D. E. *Micron* **2001**, *32*, 223–237.
85. Bierbaum, S.; Hempel, U.; Geissler, U.; *et al. J. Biomed. Mater. Res. A* **2003**, *67*, 431–438.
86. Neame, P. J.; Kay, C. J.; Mcquillan, D. J.; Beales, M. P.; Hassell, J. R. *Cell. Mol. Life Sci.* **2000**, *57*, 859–863.
87. Weber, I. T.; Harrison, R. W.; Iozzo, R. V. *J. Biol. Chem.* **1996**, *271*, 31767–31770.
88. Douglas, T.; Hempel, U.; Mietrach, C.; Heinemann, S.; Scharnweber, D.; Worch, H. *Biomol. Eng.* **2007**, *24*, 455–458.
89. Douglas, T.; Heinemann, S.; Hempel, U.; *et al. J. Mater. Sci. Mater. Med.* **2008**, *19*, 1653–1660.
90. Paderi, J. E.; Sistiabudi, R.; Ivanisevic, A.; Panitch, A. *Tissue Eng. A* **2009**, *15*, 2991–2999.
91. Damodaran, G.; Collighan, R.; Griffin, M.; Navsaria, H.; Pandit, A. *Acta Biomater.* **2009**, *5*, 2441–2450.
92. Waddington, R. J.; Roberts, H. C.; Sugars, R. V.; Schonherr, E. *Eur. Cell Mater.* **2003**, *6*, 12–21; discussion 21.
93. Mcpherson, J. M.; Sawamura, S. J.; Condell, R. A.; Rhee, W.; Wallace, D. G. *Coll. Relat. Res.* **1988**, *8*, 65–82.
94. Stuart, K.; Panitch, A. *Biopolymers* **2008**, *89*, 841–851.
95. Smith, G. N., Jr.; Brandt, K. D. *Coll. Relat. Res.* **1987**, *7*, 315–321.
96. Lilja, S.; Barrach, H. J. *Exp. Pathol.* **1983**, *23*, 173–181.
97. Cao, H.; Xu, S. Y. *J. Mater. Sci. Mater. Med.* **2008**, *19*, 567–575.
98. Huang, B.; Li, C. Q.; Zhou, Y.; Luo, G.; Zhang, C. Z. *J. Biomed. Mater. Res. B Appl. Biomater.* **2010**, *92*, 322–331.
99. Tierney, C. M.; Haugh, M. G.; Liedl, J.; Mulcahy, F.; Hayes, B.; O'brien, F. J. *J. Mech. Behav. Biomed. Mater.* **2009**, *2*, 202–209.
100. Pieper, J. S.; Van Wachem, P. B.; Van Luyn, M. J. A.; *et al. Biomaterials* **2000**, *21*, 1689–1699.
101. Steffens, G. C.; Yao, C.; Prevel, P.; *et al. Tissue Eng.* **2004**, *10*, 1502–1509.
102. Pieper, J. S.; Hafmans, T.; Van Wachem, P. B.; *et al. J. Biomed. Mater. Res.* **2002**, *62*, 185–194.
103. Nareyeck, G.; Seidler, D. G.; Troyer, D.; Rauterberg, J.; Kresse, H.; Schonherr, E. *Eur. J. Biochem.* **2004**, *271*, 3389–3398.
104. Douglas, T.; Heinemann, S.; Mietrach, C.; *et al. Biomacromolecules* **2007**, *8*, 1085–1092.
105. Daamen, W. F.; Van Moerkerk, H. T.; Hafmans, T.; *et al. Biomaterials* **2003**, *24*, 4001–4009.
106. Rentsch, B.; Hofmann, A.; Breier, A.; Rentsch, C.; Scharnweber, D. *Ann. Biomed. Eng.* **2009**, *37*, 2118–2128.
107. Fischer, U.; Hempel, U.; Becker, D.; *et al. Biomaterials* **2003**, *24*, 2631–2641.
108. Kanematsu, A.; Yamamoto, S.; Ozeki, M.; *et al. Biomaterials* **2004**, *25*, 4513–4520.
109. Yang, W.; Gomes, R. R.; Brown, A. J.; *et al. Tissue Eng.* **2006**, *12*, 2009–2024.
110. Wolf-Brandstetter, C.; Lode, A.; Hanke, T.; Scharnweber, D.; Worch, H. *J. Biomed. Mater. Res. A* **2006**, *79*, 882–894.
111. Yao, C.; Roderfeld, M.; Rath, T.; Roeb, E.; Bernhagen, J.; Steffens, G. *Biomaterials* **2006**, *27*, 1608–1616.
112. Takada, T.; Katagiri, T.; Ifuku, M.; *et al. J. Biol. Chem.* **2003**, *278*, 43229–43235.
113. Wong, L. S.; Khan, F.; Micklefield, J. *Chem. Rev.* **2009**, *109*, 4025–4053.
114. Chang, W. J.; Ou, K. L.; Lee, S. Y.; *et al. Dent. Mater. J.* **2008**, *27*, 340–346.
115. Salchert, K.; Oswald, J.; Streller, U.; Grimmer, M.; Herold, N.; Werner, C. *J. Mater. Sci. Mater. Med.* **2005**, *16*, 581–585.
116. Muller, R.; Abke, J.; Schnell, E.; *et al. Biomaterials* **2005**, *26*, 6962–6972.
117. Norde, W.; Lyklema, J. *J. Biomater. Sci. Polym. Ed.* **1991**, *2*, 183–202.
118. Soderquist, M. E.; Gershman, H.; Anderson, J. M.; Walton, A. G. *J. Biomed. Mater. Res.* **1979**, *13*, 865–886.
119. Andrade, J. D.; Hlady, V. *Ann. NY Acad. Sci.* **1987**, *516*, 158–172.
120. Norde, W. *Adv. Colloid Interface Sci.* **1986**, *25*, 267–340.
121. Geissler, U.; Hempel, U.; Wolf, C.; Scharnweber, D.; Worch, H.; Wenzel, K. *J. Biomed. Mater. Res.* **2000**, *51*, 752–760.
122. Becker, D.; Geissler, U.; Hempel, U.; *et al. J. Biomed. Mater. Res.* **2002**, *59*, 516–527.
123. Tippelt, S.; Ma, C.; Witt, M.; Bierbaum, S.; Funk, R. H. *Cells Tissues Organs* **2004**, *177*, 29–36.
124. Kerkvliet, E. H.; Jansen, I. C.; Schoenmaker, T.; Beertsen, W.; Everts, V. *Matrix Biol.* **2003**, *22*, 217–227.
125. Breuls, R. G.; Klumpers, D. D.; Everts, V.; Smit, T. H. *Biochem. Biophys. Res. Commun.* **2009**, *380*, 425–429.
126. Sim, B.; Cladera, J.; O'shea, P. *J. Biomed. Mater. Res. A* **2004**, *68*, 352–359.
127. Ma, W.; Tavakoli, T.; Derby, E.; Serebryakova, Y.; Rao, M. S.; Mattson, M. P. *BMC Dev. Biol.* **2008**, *8*, 90.
128. Salasznyk, R. M.; Klees, R. F.; Boskey, A.; Plopper, G. E. *J. Cell. Biochem.* **2007**, *100*, 499–514.
129. Salasznyk, R. M.; Williams, W. A.; Boskey, A.; Batorsky, A.; Plopper, G. E. *J. Biomed. Biotechnol.* **2004**, *2004*, 24–34.
130. Kundu, A. K.; Putnam, A. J. *Biochem. Biophys. Res. Commun.* **2006**, *347*, 347–357.
131. Gronthos, S.; Simmons, P. J.; Graves, S. E.; Robey, P. G. *Bone* **2001**, *28*, 174–181.
132. Bosnakovski, D.; Mizuno, M.; Kim, G.; Takagi, S.; Okumura, M.; Fujinaga, T. *Biotechnol. Bioeng.* **2006**, *93*, 1152–1163.
133. Bali, J. P.; Cousse, H.; Neuzil, E. *Semin. Arthritis Rheum.* **2001**, *31*, 58–68.
134. Erskine, L.; Mccaig, C. D. *J. Cell Sci.* **1997**, *110*(Pt 16), 1957–1965.
135. Ohgaki, M.; Kizuki, T.; Katsura, M.; Yamashita, K. *J. Biomed. Mater. Res.* **2001**, *57*, 366–373.
136. D'souza, S. E.; Haas, T. A.; Piotrowicz, R. S.; *et al. Cell* **1994**, *79*, 659–667.
137. Rajnicek, A. M.; Robinson, K. R.; Mccaig, C. D. *Dev. Biol.* **1998**, *203*, 412–423.
138. Roehlecke, C.; Witt, M.; Kasper, M.; *et al. Cells Tissues Organs* **2001**, *168*, 178–187.
139. Wollenweber, M.; Domaschke, H.; Hanke, T.; *et al. Tissue Eng.* **2006**, *12*, 345–359.
140. Manton, K. J.; Leong, D. F.; Cool, S. M.; Nurcombe, V. *Stem Cells* **2007**, *25*, 2845–2854.
141. Jiao, X.; Billings, P. C.; O'connell, M. P.; Kaplan, F. S.; Shore, E. M.; Glaser, D. L. *J. Biol. Chem.* **2007**, *282*, 1080–1086.
142. Van Susante, J. L. C.; Pieper, J.; Buma, P.; *et al. Biomaterials* **2001**, *22*, 2359–2369.
143. Tierney, C. M.; Jaasma, M. J.; O'brien, F. J. *J. Biomed. Mater. Res. A* **2009**, *91*, 92–101.
144. Koller, J.; Bakos, D.; Sadlonova, I. I. *Cell Tissue Bank.* **2000**, *1*, 75–80.
145. Hegewald, A. A.; Ringe, J.; Bartel, J.; *et al. Tissue Cell* **2004**, *36*, 431–438.
146. Bernhardt, R.; Van Den Dolder, J.; Bierbaum, S.; *et al. Biomaterials* **2005**, *26*, 3009–3019.
147. Stadlinger, B.; Pilling, E.; Huhle, M.; *et al. J. Biomed. Mater. Res. B Appl. Biomater.* **2008**, *87*, 516–524.
148. Reyes, C. D.; Petrie, T. A.; Burns, K. L.; Schwartz, Z.; Garcia, A. J. *Biomaterials* **2007**, *28*, 3228–3235.
149. Schliephake, H.; Aref, A.; Scharnweber, D.; Bierbaum, S.; Roessler, S.; Sewing, A. *Clin. Oral Implants Res.* **2005**, *16*, 563–569.

150. Stadlinger, B.; Bierbaum, S.; Grimmer, S.; *et al*. *J*. *Clin*. *Periodontol*. **2009**, *36*, 698–704.
151. Williams, S. K.; Kleinert, L. B.; Hagen, K. M.; Clapper, D. L. *J*. *Biomed*. *Mater*. *Res*. *A* **2006**, *78*, 59–65.
152. Fukushima, K.; Enomoto, M.; Tomizawa, S.; *et al*. *J*. *Med*. *Dent*. *Sci*. **2008**, *55*, 71–79.
153. Park, J. W.; Lee, S. G.; Choi, B. J.; Suh, J. Y. *Int*. *J*. *Oral Maxillofac*. *Implants* **2007**, *22*, 533–541.
154. Schliephake, H.; Scharnweber, D.; Dard, M.; Sewing, A.; Aref, A.; Roessler, S. *J*. *Biomed*. *Mater*. *Res*. *B Appl*. *Biomater*. **2005**, *73*, 88–96.
155. Petrie, T. A.; Reyes, C. D.; Burns, K. L.; Garcia, A. J. *J*. *Cell Mol*. *Med*. **2009**, *13*, 2602–2612.
156. Rammelt, S.; Heck, C.; Bernhardt, R.; *et al*. *J*. *Orthop*. *Res*. **2007**, *25*, 1052–1061.
157. Borselli, C.; Oliviero, O.; Battista, S.; Ambrosio, L.; Netti, P. A. *J*. *Biomed*. *Mater*. *Res*. *A* **2007**, *80*, 297–305.
158. Stadlinger, B.; Pilling, E.; Mai, R.; *et al*. *J*. *Mater*. *Sci*. *Mater*. *Med*. **2008**, *19*, 1043–1049.
159. Ferguson, S. J.; Langhoff, J. D.; Voelter, K.; *et al*. *Int*. *J*. *Oral Maxillofac*. *Implants* **2008**, *23*, 1037–1046.
160. Rammelt, S.; Illert, T.; Bierbaum, S.; Scharnweber, D.; Zwipp, H.; Schneiders, W. *Biomaterials* **2006**, *27*, 5561–5571.
161. Schliephake, H.; Aref, A.; Scharnweber, D.; Bierbaum, S.; Sewing, A. *Clin*. *Oral Implants Res*. **2009**, *20*, 31–37.
162. Zhao, B.; Katagiri, T.; Toyoda, H.; *et al*. *J*. *Biol*. *Chem*. **2006**, *281*, 23246–23253.
163. Stadlinger, B.; Pilling, E.; Huhle, M.; *et al*. *J*. *Biomed*. *Mater*. *Res*. *B Appl*. *Biomater*. **2007**, *83*, 222–231.
164. Stadlinger, B.; Pilling, E.; Huhle, M.; *et al*. *Int*. *J*. *Oral Maxillofac*. *Surg*. **2008**, *37*, 54–59.
165. Degat, M. C.; Dubreucq, G.; Meunier, A.; *et al*. *J*. *Biomed*. *Mater*. *Res*. *A* **2009**, *88*, 174–183.
166. Zhou, H.; Qian, J.; Wang, J.; *et al*. *Biomaterials* **2009**, *30*, 1715–1724.
167. Hintze, V.; Möller, S.; Schnabelrauch, M.; *et al*. *Biomacromolecules* **2009**, *10*(12), 3290–3297.
168. Schwartz, M. A.; Desimone, D. W. *Curr*. *Opin*. *Cell Biol*. **2008**, *20*, 551–556.
169. Silver, F. H.; Devore, D.; Siperko, L. M. *J*. *Appl*. *Physiol*. **2003**, *95*, 2134–2141.
170. Silver, F. H.; Siperko, L. M. *Crit*. *Rev*. *Biomed*. *Eng*. **2003**, *31*, 255–331.
171. Hess, R.; Douglas, T.; Myers, K. A.; *et al*. *J*. *Biomech*. *Eng*. **2010**, *132*, 021001.

2.209. Materials as Artificial Stem Cell Microenvironments

S A Kobel and M P Lutolf, Ecole Polytechnique Fédérale de Lausanne (EPFL), Lausanne, Switzerland

© 2011 Elsevier Ltd. All rights reserved.

2.209.1.	**Introduction**	156
2.209.2.	**The Adult Stem Cell and Its Niche**	157
2.209.3.	**Naturally Derived ECM Components for *In Vitro* Stem Cell Manipulation**	158
2.209.4.	**Engineered Substrates as Artificial Stem Cell Niches**	158
2.209.4.1.	Control of Stem Cell Fate by Biomolecule-Functionalized Substrates	158
2.209.4.2.	Instructing Stem Cells via Engineered Substrates with Tailor-Made Biophysical Properties	159
2.209.4.3.	Instructing Stem Cells via Engineered Substrates with Controlled Spatial Properties	160
2.209.4.4.	High-Throughput Approaches to Identify Complex Artificial Niche Substrates	160
2.209.5.	**Topographically Patterned Substrates as Versatile Stem Cell Microenvironments**	162
2.209.6.	**Biomaterials Approaches to Emulate Stem Cell Niches in 3D**	163
2.209.6.1.	Building a Molecular Toolbox for 3D Artificial Niches	163
2.209.6.2.	Toward High-Throughput Screening of 3D Microenvironments	163
2.209.6.3.	3D-Micropatterning of Artificial Stem Cell Niches and Cells	164
2.209.6.4.	Toward Constructing Tissue Models	165
2.209.7.	**Conclusions**	166
References		166

Glossary

Adult stem cell A stem cell that is derived from an adult tissue. This stem cell is restricted to form the specialized cells of the tissue that it is derived from. These cells are responsible for tissue regeneration throughout life.
Asymmetric cell division Generation of two daughter cells with disparate function from a single stem cell division.
Embryonic stem cell Pluripotent stem cell lines derived from early embryo before formation of the tissue germ layers.
Hydrogel Water-swollen cross-linked polymer network.
Microfabrication Term to describe the fabrication and patterning of structures in the micrometer range. Adapted from the semiconductor industry, these methodologies are increasingly used for bioengineering applications.
Microfluidics Fluidics in micrometers-sized channels that are characterized by a laminar flow regime.
Multipotent Ability to form the types of differentiated cells of an entire tissue. Adult stem cells are considered multipotent.
Niche Stem cell-specific microenvironment regulating behavior of stem cells by niche-specific signaling factors.
Pluripotent Ability to form all types of differentiated cells of an organism, including germ cells. Embryonic stem cells are, for example, pluripotent.
Self-renewal Cell division leading to at least one daughter cell equivalent to the mother stem cell.

Abbreviations

ASC	Adult stem cell
BMP	Bone morphogenetic protein
CAD	Computer-assisted design
CAM	Cell adhesion molecule
DEP	Dielectrophoresis
DLL1	Delta-like 1
DTC	Distal tip cell
ECM	Extracellular matrix
ERK	Extracellular signal-regulated kinase
ESC	Embryonic stem cell
FGF	Fibroblast growth factor
FN	Fibronectin
GAG	Glycosaminoglycan
GSC	Germline stem cell
HSC	Hematopoietic stem cell
iPSC	Enduced pluripotent stem cell
LIF	Leukemia inhibitory factor
MAPK	Mitogen-activated protein kinase
MEF	Mouse embryonic fibroblast
MSC	Mesenchymal stem cells
MuSC	Muscle stem cell
NSC	Neural stem cell
PDFG	Platelet-derived growth factor
PEG	Poly(ethylene glycol)
VEGF	Vascular endothelial growth factor

2.209.1. Introduction

The ability of stem cells to produce more of themselves ('self-renewal') and to give rise to specialized progeny ('differentiation') that makes up a tissue has fueled hope for stem cell-based approaches in regenerative medicine.[1] The key paradigm currently under scrutiny is to implant stem cells or their progeny, possibly in combination with bioactive scaffolds, to the site of a damaged or genetically diseased tissue in order to facilitate regeneration. Alternatively, engineered tissues and organs generated from stem cell sources are sought to be applied in fundamental *in vitro* studies and for the next generation drug screening efforts. However, although significant progress has been made, we are still far away from realizing these appealing concepts, largely because of difficulties to grow stem cells *in vitro* without rapidly losing their characteristic functions. That is to say, pluripotent embryonic stem cells (ESC) or induced pluripotent stem cells (iPSC) can be readily expanded *in vitro*, but are difficult to differentiate in an efficient manner, whereas most adult stem cells types such as hematopoietic stem cells (HSC) or neural stem cells (NSC) can hardly be maintained in culture without loss of their multipotency (Figure 1). It has been hypothesized that the failure of these seemingly simple tasks is caused by the absence of a cell-instructive microenvironment in the currently applied cell culture systems.

In vivo, the delicate balance between stem cell self-renewal and differentiation is governed by tissue-specific niches that display

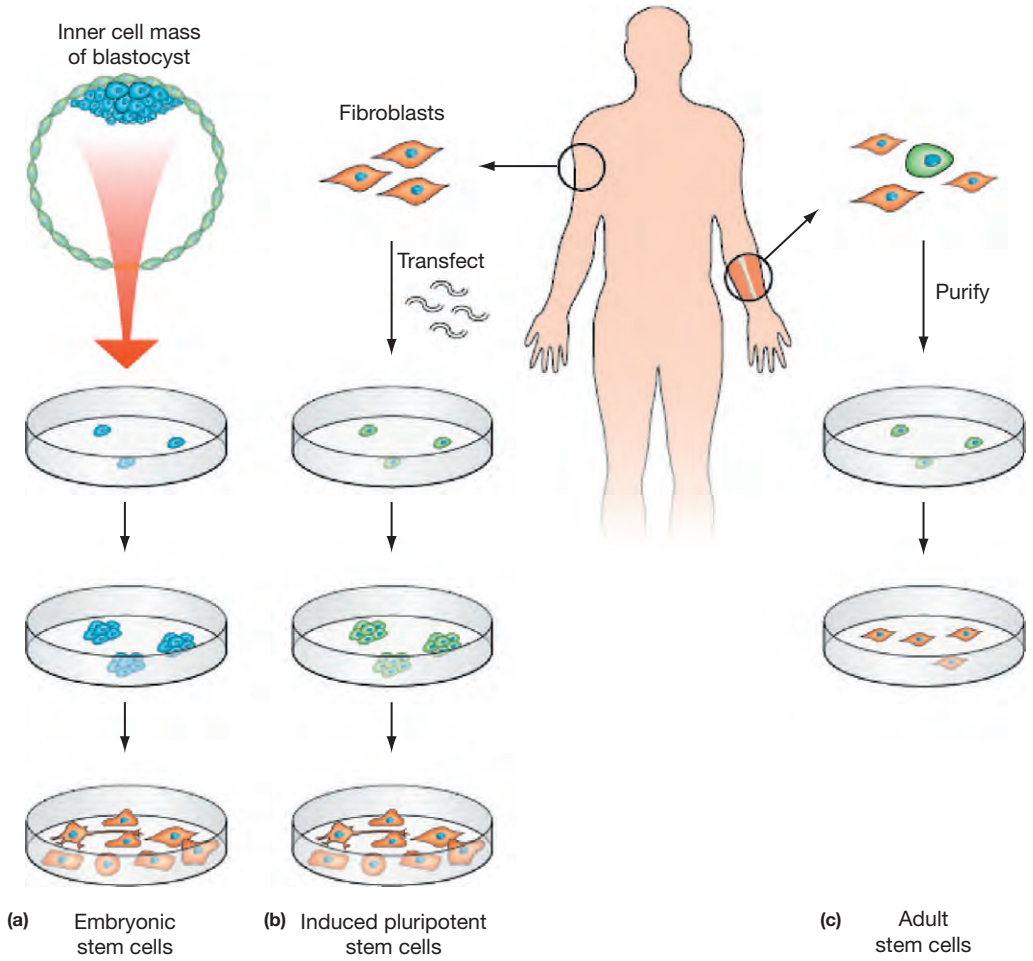

Figure 1 The main stem cell types: embryonic stem cells (ESC), induced pluripotent stem cells (iPSC), and adult stem cells (ASC). (a) ESC are derived from the inner cell mass of the early embryo (blastocyst) and provide a source for pluripotent stem cells that can differentiate into any cell type. (b) iPSC are generated by reprogramming somatic cells such as fibroblasts, with a few essential pluripotency transcription factors such as Oct4 and thus can overcome some ethical issues associated with embryonic stem cells.[2] Both, embryonic and iPSC can be propagated nearly infinitely in culture, which makes them a valuable source for stem cell-based therapy. However, the differentiation of these cells is cumbersome and often results in a heterogeneous mixture of multiple and only partially differentiated cell types, and hence there is a significant risk of tumor formation when transplanted into humans. (c) In contrast, adult stem cells can be found at low frequency in native tissues and hence have to be purified first; they efficiently differentiate into uniquely tissue-specific progenitors, alleviating the risk of tumors. Ironically, this differentiation cannot be halted *in vitro*, given the importance of the tissue-specific microenvironment that host these stem cells. For this reason, it is very difficult to obtain large numbers of these adult stem cells *in vitro* that would be required for clinical and pharmaceutical applications. Adapted from Lutolf, M. P.; Gilbert, P. M.; Blau, H. M. *Nature* **2009**, *462*, 433–441, with permission. © 2009 Nature Publishing Group.

complex, spatially and temporally modular mixtures of cell signaling cues. These signals can either be biochemical in nature, stemming from other cells (niche or support cells), the surrounding cross-linked extracellular matrix (ECM), and soluble biomolecules such as growth factors, or else biophysical, such as the elasticity or three-dimensional (3D) structure of the microenvironment.

The fact that many niches in mammals are poorly accessible and therefore difficult to directly study and manipulate *in vivo*, as well as an increasing awareness of the huge complexity of niches, has evoked the need to reconstruct this system *in vitro* in a much more simplified and better-controlled form. Indeed, important advances in biomaterials engineering have set the stage for the successful development of novel generations of such artificial niches with truly biomimetic functions. In combination with other techniques, such as microfabrication, microfluidics, or novel live-cell imaging modalities, these systems promise to offer novel insights into stem cell biology. This chapter summarizes some of the advances that have been made in the fabrication of artificial stem cell niches. We will focus on *selected* examples and limit our point of view on soft materials and *in vitro* applications, acknowledging that other types of biomaterials are successfully used in this context. For a more comprehensive understanding of the diverse types and applications of biomaterials in stem cell biology and bioengineering, we refer the reader to several reviews.[3–11]

2.209.2. The Adult Stem Cell and Its Niche

Stem cell niches are anatomically distinct, spatially restricted milieus that host and regulate stem cells. The niche concept was first postulated by Schofield on HSCs in the late 1970s.[12] However, experimental support came only 10 years later with the *in vivo* characterization of germline stem cells (GSCs) niches in *Drosophila*, demonstrating that short-range signals from niche cells are essential for stem cell maintenance.[13] Subsequently, mammalian niches were identified in almost all tissues including the skin (in the bulge region of the hair follicle), the brain (in the subventricular zone), bone marrow (on the endosteal surface and near blood vessels), or muscle (beneath the basal lamina of the muscle fiber). Some of these niches have been discussed in detail elsewhere.[14–19]

Although mammalian niches significantly vary in structure and composition, they share common features that are schematically depicted in **Figure 2(a)**. Stem cells in the niche are in close physical contact with niche cells and are either interacting with a basal lamina (e.g., in the muscle) or a highly hydrated, fibrillar network of ECM proteins and sugars (e.g., in bone marrow). By far, the best-studied types of niche signals are *soluble factors*. Niche cells secrete cytokines, growth factors, and developmental morphogen proteins such as Wnt proteins, hedgehog proteins, fibroblast growth factors (FGFs), or bone morphogenetic proteins (BMPs). Many of these proteins are believed to bind to the ECM by electrostatic interactions, in particular via heparan sulfate proteoglycans.[20,21] ECM-immobilization could thus prevent rapid degradation, localize growth factor distribution to the niche, and help establish stable gradients of signaling molecules that could define the size and polarity of a niche.

Another signal type emanating from the niche is the *cross-linked ECM*. Besides keeping stem cells at the right place, the ECM also directly interacts with stem cells which express ECM protein-binding receptors such as integrins. Indeed, most stem cell types express a well-defined set of integrins, and are therefore sensitive to composition of the niche ECM.[22] For example, apart from many other receptors, HSCs express the cell surface glycoprotein CD44 and the two integrins α4 and α5β1 that both bind to osteopontin, a glycoprotein specifically found in the ECM of the bone marrow.[23] The anchoring of stem cells to the ECM via integrins has a dual function. First, adhesion molecules transmit physical forces to the interior of the stem cell by linking the ECM with the cytoskeleton. Through this interaction, cells can sense external forces or mechanical properties of the niche.[24–26] Second, integrins act

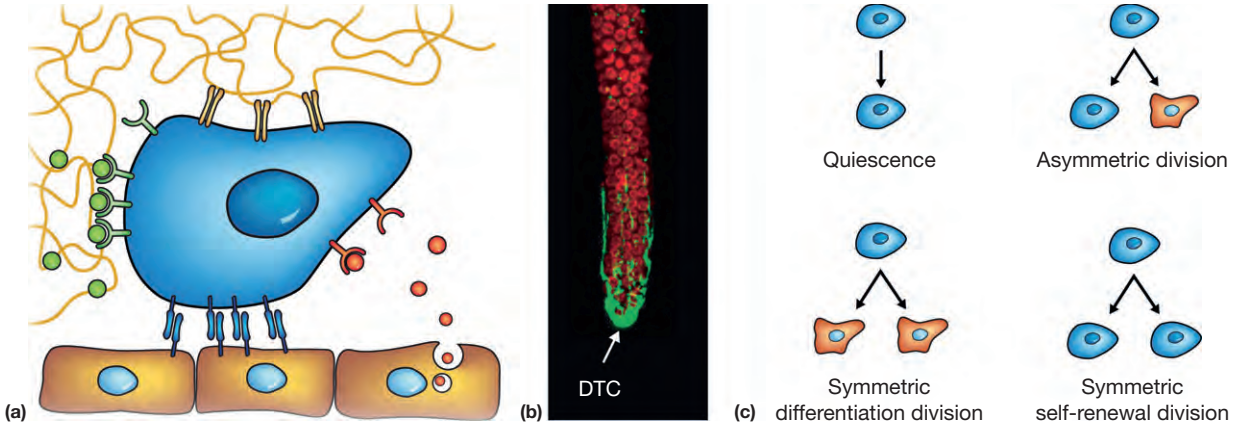

Figure 2 The niche of stem cells and its control of stem cell behavior. (a) *In vivo*, adult stem cells are located in tissue-specific microenvironments with well-defined architecture that protect and regulate stem cells. The niche is composed of extracellular matrix components and other niche (support) cells that present a complex mixture of extrinsic cues. (b) A well-characterized niche of the germline stem cells in the gonad of *Drosophila*, where distal tip cells (DTC, in green) are located at the bottom of an ECM-supported cavity and confine the stem cells through cell adhesion molecules to the niche. Loss of contact with the DTC will induce differentiation of stem cells (in red). (c) Accordingly, in the niche, cells can remain quiescent, proliferate, or differentiate. Adapted with permission from Kobel, S.; Lutolf, M. P. *BioTechniques* **2010**, *48*, IX–XXII; Morrison, S. J.; Kimble, J. *Nature* **2006**, *441*, 1068–1074. © 2006 Nature Publishing Group and 2010 BioTechniques.

as specific ECM protein receptors that upon binding induce intracellular signaling involved in regulating stem cell maintenance. Noteworthy, signals from growth factors and the ECM often synergistically regulate cell behavior, either by proximity effects on the cell membrane or by cross-talk in the downstream signal transduction pathways.[20,27]

A third class of niche cues worth mentioning are direct *cell–cell interactions* via cell adhesion molecules (CAMs) and other transmembrane receptors involved in juxtacrine signaling between adjacent cells. These proteins are either integrated into the cell membrane via transmembrane domains or covalently bound to its lipids and, by providing a very localized signal, prevent migration of stem cells.[22,28] The signaling via cell–cell interactions can be crucial for stem cell regulation as exemplified in the Drosophila gonads (**Figure 2(b)**). There, the niche cells express cadherins that tether the GSCs to the niche. As the niche is small and can host only few stem cells, some daughter cells generated via cell division quickly lose contact with the niche and initiate oogenesis.

Although the behavior of stem cells is not only influenced by the localized cues just described (the activation of HSCs is earlier for example, known to follow circadian rhythms[29]), the complex interplay of niche signals is key to the maintenance of stem cells. Best evidence for this is the loss of stem cell function due to stem cell removal from the niche. Arguably, the prime function of the niche is to retain stem cells in a quiescent state, as adult stem cells *in vivo* are believed to be mostly quiescent.[30] However, the niche presumably also regulates 'fate decisions' that can occur during cell division (**Figure 2(c)**). A self-renewing division of a stem cell can either result in two daughter cells acquiring equal stem cell fates, or in one daughter stem cell and one daughter that has started to undergo the first steps toward differentiation. These self-renewing divisions are either called symmetric (with respect to the potential of the two daughter cells) or asymmetric. Although concrete experimental proof for asymmetric divisions of mammalian adult stem cells is still missing, these divisions are assumed to be induced by an asymmetric distribution of cell-intrinsic, fate--determining proteins (such as Numb or Par proteins[31]), and/or by a polarized distribution of extrinsic cues which expose two equal daughter cells to a different cell-instructive microenvironment. Clearly, these cell fate decisions need to be tightly balanced in response to the physiological demands of a tissue, as insufficient self-renewal would deplete the stem cell pool over time, impairing tissue maintenance and regeneration, and an overproduction of stem cells could lead to cancer.

2.209.3. Naturally Derived ECM Components for *In Vitro* Stem Cell Manipulation

Mammalian ECMs are 3D networks made up of fibrillar proteins (e.g., collagens, fibronectin, elastin, laminin, vitronectin), glycosaminoglycans (GAGs) such as hyaluronan or heparin, and proteoglycans.[23,32] Many of these ECM components are commercially available, either as complex mixtures or as purified proteins, (see **Chapter 2.214, Hyaluronic Acid**; **Chapter 2.215, Collagen: Materials Analysis and Implant Uses**; **Chapter 2.216, Collagen–GAG Materials**; **Chapter 2.217, Fibrin**; and **Chapter 2.220, Extracellular Matrix as Biomimetic Biomaterial: Biological Matrices for Tissue Regeneration**) and have been extensively applied for stem cell culture. For example, Matrigel™, a reconstituted basement membrane hydrogel derived from the ECM-rich Engelbreth–Holm–Swarm sarcoma mainly composed of collagen IV, laminin, and heparan sulfate proteoglycans, is successfully used as substrate for many stem cells including human ESC, which classically rely on feeder layers of irradiated (i.e., nonproliferating) mouse embryonic fibroblasts (MEFs). However, these relatively ill-defined culture conditions are not acceptable for the clinical application of ESC. The application of Matrigel™ or purified laminin (in the case of human ESC) and collagen, gelatin, or fibronectin (in the case of mouse ESC) as substitutes for MEF-based cultures thus represents an important step toward the xeno-free culture of these pluripotent stem cells.[33] This example and a wealth of other studies reporting beneficial effects of adsorbed ECM proteins on directed stem cell differentiation[3,7,34] show that stem cell fate can be controlled *in vitro* by providing essential components of the natural ECM. In comparison to complex coculture conditions, these isolated ECM substrates are also well suited for systematically probing ECM regulation.

2.209.4. Engineered Substrates as Artificial Stem Cell Niches

Although natural ECM components are indispensable *in vitro* tools to further our understanding on how stem cells are regulated by extrinsic cues, the way by which these signals are currently applied in culture is arguably not ideal (see **Chapter 5.508, Scaffold Materials for hES Cell Culture and Differentiation**). In particular, many existing methods lack the possibility to tune the biochemical and biophysical properties of naturally derived ECMs to an extent similar to that observed *in vivo*.

2.209.4.1. Control of Stem Cell Fate by Biomolecule-Functionalized Substrates

Much can be learned on stem cell regulation from studies in which niche proteins are immobilized to biomaterial substrates (see **Chapter 4.411, Peptide- and Protein-Modified Surfaces**) mimicking their tethering to the ECM *in vivo* (**Figure 3(a)**). A logical way to do so is by using heparin, (see **Chapter 4.420, Drug Delivery via Heparin Conjugates**) the natural binding partner of many growth factors in the ECM. Heparin has, for example, been chemically modified in order to covalently incorporate it into a biomaterial scaffold.[35] This affinity-based binding strategy guarantees a good bioactivity and a physiological internalization of the growth factors. However, because affinity-based tethered growth factors are relatively quickly released and the decoration of biomaterials with heparin can be rather complicated and poorly controlled,[36,37] growth factors have been directly conjugated to a biomaterial using chemical linkers. For example, the covalent attachment of fibroblast growth factor 2 (FGF2) to polyamide nanofibers improved its stability in media as efficiently as heparin.[38] Importantly, compared to the soluble form, FGF2-immobilization led to a stronger activation of ERK/MAPK (extracellular signal-regulated kinase/mitogen-activated protein kinase) signaling and an increased proliferation of human ESC. Similar effects were observed in mesenchymal stem cells (MSCs) or

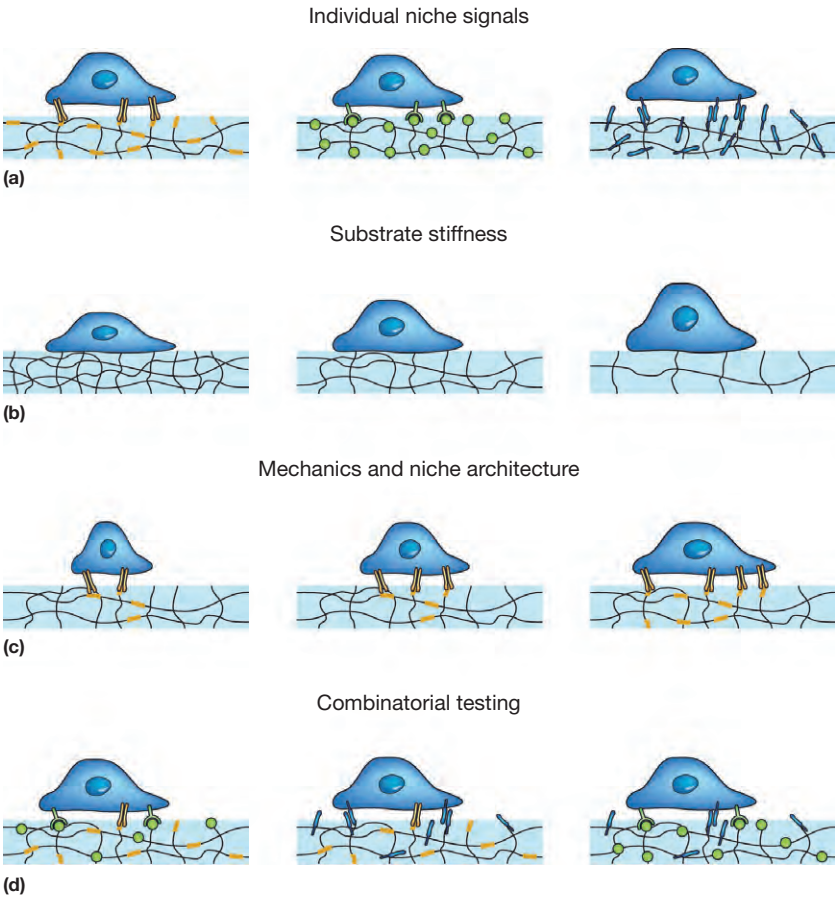

Figure 3 Materials engineering approaches to study stem cell regulation *in vitro*. Advanced biomaterial fabrication techniques enable (a) the decoration of biomaterials with defined biomolecules, such as ECM components, growth factors, or membrane-anchored proteins involved in cell–cell interactions, or (b) the modification of the elastic properties of the cell culture substrate. (c) Micropatterning techniques can be used to recapitulate spatial properties of niches and (d) robotic technology enables the fabrication of combinatorial protein mixtures to systematically screen putative niche signals. Adapted from Lutolf, M. P.; Gilbert, P. M.; Blau, H. M. *Nature* **2009**, *462*, 433–441, with permission. © 2009 Nature Publishing Group.

primary rat hepatocytes upon immobilization of epidermal growth factor (EGF) to a synthetic matrix[39,40] or in mouse ESC with bound leukemia inhibitory factor (LIF).[41] Importantly, it has recently been shown that many growth factors have strong interactions with nonproteoglycan ECM components. For example, the 12th to 14th type three repeats of fibronectin (FN III12–14) are a strong binding partner of most growth factors from the platelet-derived growth factor (PDGF), vascular endothelial growth factor (VEGF), and FGF families and some growth factors from the transforming growth factor beta (TGF-beta) and neurotrophin families.[42] This strategy was successfully explored to tether growth factors to and release them from fibrin hydrogels and will surely be a powerful means to augment to function of artificial niches.

The immobilization of proteins onto biomaterials can be used not only to recapitulate the tethering of growth factors to the native ECM, but also to mimic cell–cell communication via transmembrane proteins such as cadherins or Notch ligands (**Figure 3(a)**). For example, the immobilization of the Notch ligand Delta-like 1 (DLL1) or Jagged1 resulted in a strong proliferation of human cord-blood $CD133^+$ stem cells[43] or rat esophageal progenitor cells,[44] respectively. In another application, E-cadherin-coated surfaces enabled the retention of ESC pluripotency as was shown by immunostainings and teratoma assays, the gold standard to test the pluripotency of these cells. Concomitantly, ESC proliferated 50% faster on E-cadherin than on gelatin, indicating that cell–cell signals are a rate-limiting step in proliferation and that tethered E-cadherin can even replace the cell–cell signaling within mouse ESC colonies.[45,46]

The beneficial effect of tethered growth factors can probably be explained by a concentration effect, mimicking the aggregation of ligand–receptor complexes on the cell membrane and thus inducing increased signaling.[41] Further, the covalent growth factor immobilization to a surface can inhibit endocytosis of the growth factor and its receptor and consequently could prolong signaling.[27,40] We expect that the ability to precisely modulate the biomolecular properties of a cell culture substrate using smart bioconjugation strategies will be an important tool to further dissect the mechanisms of stem cell regulation and to manipulate stem cell fate in clinical settings.

2.209.4.2. Instructing Stem Cells via Engineered Substrates with Tailor-Made Biophysical Properties

Stem cells in developing and mature tissues are exposed to a wide range of biophysical stimuli, including, for example,

forces that act on cells during gastrulation, muscle movement, or blood flow (see **Chapter 5.504, Effect of Substrate Modulus on Cell Function and Differentiation**). Recent evidence suggests that the mechanical properties of the ECM, which naturally can span over four orders of magnitude, have an instructive role on stem cells independent of biochemical signals[25,47,48] (**Figure 3(b)**). A landmark study showed that the differentiation of human MSCs is strongly influenced by the elasticity of the cell culture substrate.[49] When cultured on soft, collagen I-modified poly(acrylamide) hydrogels in which stiffness was modulated by the concentration of a bisacrylamide cross-linker,[50] MSCs exposed to gels mimicking the elasticity of the brain differentiated into neurons, but acquired primarily a myoblast-like or osteoblast-like phenotype when seeded onto gels with similar mechanical properties as muscle tissues or the bone, respectively. This finding has inspired a wealth of studies in other stem cell systems and has motivated the development and application of engineered hydrogels with mechanical properties that can be independently tuned by the biochemical signals attached to their surface. For example, adhesion peptide-modified interpenetrating polymer networks were fabricated from variable ratios of acrylamide and bisacrylamide monomers having elastic moduli between 10 and 10 000 Pa. Adult NSC grown under differentiation conditions and exposed to these engineered gels were biased toward the neuronal lineage on softer gels (100–500 Pa, near the physiological stiffness of brain tissue) and glial lineage on stiffer gels (1000–10 000 Pa), independent of the cell adhesion ligand concentration.[51]

Not surprisingly, muscle stem cells (MuSCs), termed satellite cells, also respond to matrix elasticity.[52] Poly(ethylene glycol) (PEG) hydrogel substrates formed via Michael-type addition were engineered to recapitulate key biophysical and biochemical MuSC niche features. Unlike MuSCs on rigid plastic dishes ($\sim 10^6$ kPa), MuSCs cultured on laminin-functionalized gels that mimic the elasticity of muscle (12 000 Pa) were shown to self-renew *in vitro* and contribute extensively to regeneration when transplanted into damaged muscles of mice. Thus, the recapitulation of the physiological tissue rigidity in a stem cell culture environment appears to be important in the maintenance of stem cell function in culture, an aspect that will need to be taken into consideration in future stem cell-based therapies as well.

2.209.4.3. Instructing Stem Cells via Engineered Substrates with Controlled Spatial Properties

Apart from the stiffness of the microenvironment, spatial or geometrical inputs might play an important role (**Figure 3(c)**), as stem cells in their niche are also under spatial constraints (**Figure 2(b)**). In combination with biomaterials technologies, micropatterning techniques such as microcontact printing, photolithography, or microfluidics seem particularly well suited to recapitulate spatial niche characteristics, because of their ability to control the display of biomolecular signals *in vitro* at the cellular or even subcellular scale. The application of these techniques ranges from restricting the size of artificial niches and reconstruction of 'polarized' niche mimetics to the generation of gradients of biomolecules.[8,53,54] For instance, the fate of single human MSC grown under mixed adipogenic and osteogenic differentiation conditions was shown to be strongly responsive to the size of microcontact-printed fibronectin patterns.[55] When the cells were allowed to spread on larger patches, they preferentially differentiated into osteoblasts, whereas small features inhibited spreading-induced adipogenesis via a RhoA-dependent mechanism (**Figure 4(a)**). The same approach enabled identification of physical tension as a mechanism regulating MSCs, as well as the colony size-dependent paracrine signaling mechanism in ESC.[56,57] Along similar lines, the nanoscale topography has also been shown to influence stem cell behavior by perturbing the organization of integrins and the cytoskeleton.[58,59]

As stem cell niches are polarized structures with possibly a graded and overlapping distribution of multiple signaling cues, surface engineering efforts have also been dedicated to recapitulate spatial niche complexity. Building on the possibility of microfluidic technology to precisely position tiny amounts of liquids within microchannels, researchers have used microfluidic gradient makers to generate streams with a stepwise distribution or a gradient of adhesion molecules or growth factors.[54,60] Several successful examples of such microfluidic approaches to stem cell biology have been reported, for example the asymmetric stimulation of ESC colonies,[61] or the application of gradients of neurotrophic factors to neural progenitor cells.[62,63] Notably, most gradient systems thus far were applied to soluble rather than ECM-tethered stimuli. These shortcomings have spurred the integration of biomaterials technologies into micropatterning platforms to tether gradients onto substrates. Examples of these endeavors include adsorbed laminin gradients on plastic culture substrates[64] or the photopolymerization of peptide and protein gradients within hydrogels.[65,66] A recent study used PEG-based hydrogels decorated with NeutrAvidin and protein A to capture soluble gradients of biotinylated or Fc-tagged proteins on the gel surface (**Figure 4(b)**). Besides the rapid immobilization, the orthogonal binding scheme permitted to pattern multiple overlapping gradients of any shape on soft gels (**Figure 4(c)**).[67,68]

In summary, biomaterials technology can provide elegant means to precisely control selected biophysical substrate parameters relevant to stem cell biology. A further synergy of material science, microtechnology, and stem cell biology should help to accelerate the identification of new regulatory mechanisms in stem cells *in vitro*.

2.209.4.4. High-Throughput Approaches to Identify Complex Artificial Niche Substrates

As mentioned above, stem cells are influenced by a plethora of different extrinsic signaling cues acting in a spatially and temporally orchestrated manner to control fate. State-of-the-art experimental platforms described above allow modulating just a limited number of these interactions. To overcome this bottleneck in throughput, novel paradigms targeting a more comprehensive, system-level analysis have been conceived (**Figure 3(d)**). For example, robotic spotting technology, conventionally applied to the production of oligonucleotide microarrays, has been adapted to fabricate microarrays of biomaterials or biomolecules (see **Chapter 3.321, Microarrays in Biomaterials Research**). These libraries are arrayed on cell-repellent substrates such that seeded cells cannot migrate

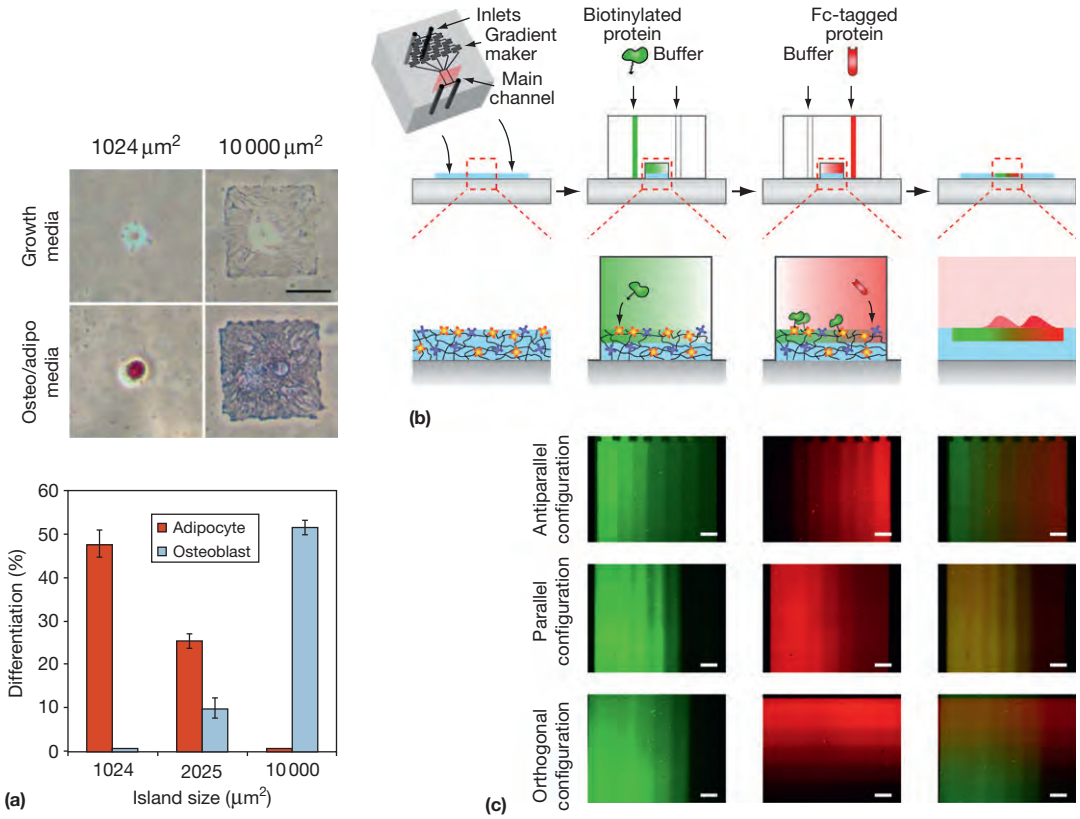

Figure 4 Micropatterning techniques to control the physical properties of the niche. (a) Cell spreading can efficiently be controlled by micropatterning cell adhesive substrates. This approach can confine size or shape of stem cell colonies down to a single-cell resolution. Notably, cell-spreading area can be an effective regulator of the differentiation of MSCs into adipocytes (visualized by a red oil stain) or osteocytes (in blue). Reprinted with permission from Mcbeath, R.; Pirone, D. M.; Nelson, C. M.; Bhadriraju, K.; Chen, C. S. *Dev. Cell* **2004**, *6*, 483–495. © 2004 Cell Press. (b) Because mixing is limited by diffusion in microfluidics, the merging of two streams, one with a protein and the other without, can yield a graded distribution of the biomolecules across the microchannel. (c) These gradients can be captured on hydrogel surfaces functionalized with capturing groups. Using orthogonal protein-binding systems, overlapping gradients can be produced as occurring during embryonic development. Reprinted with permission from Cosson, S.; Kobel, S. A.; Lutolf, M. P. *Adv. Funct. Mater.* **2009**, *19*, 3411–3419. © 2009 John Wiley and Sons.

between spots and are influenced only by the microenvironment to which they were initially exposed to (Figure 5(a)).

A pioneering study screened 32 combinations of the ECM proteins laminin, fibronectin, and collagen I–IV to induce differentiation of ESC toward an early hepatic fate and for the maintenance of primary rat hepatocytes. Using liver-specific marker genes, these authors observed a more than 100-fold change in gene expression between the least and most efficient protein combination, and identified protein combinations that were active in the regulation of primary hepatocytes and ESC fate.[69] The concept was later extended from ECM proteins to growth factors on arrays with up to hundreds of different microenvironments,[70,71] as well as combination of tethered and soluble regulatory cues.[72] By systematically pairing multiple putative niche signals, these high-throughput strategies allowed, for example, the identification of 'dominant' or 'additive' factors in niche signaling, and the dissection of the effects of growth factors and ECM components (Figure 5(b)).

Intriguingly, the possibility to screen for stem cell-relevant substrates is not restricted to natural niche components, but can be applied to synthetic biomaterials such as polymers. The latter are particularly appealing for the clinical application of stem cells where well-defined, animal product-free culture conditions are required. The robotic fabrication of synthetic polymer arrays, such as those based on acrylate monomers that can be easily polymerized using a light-induced radical initiator,[73] differs only marginally from protein microarrays. A wide range of commercially available monomers with different polarity, chain length, and number of the acrylate groups provides powerful means to diversify the chemical and mechanical properties of the library. Because automated and miniaturized analyses enable the characterization of the chemical and mechanical properties of these arrays in high-throughput, the amount of material can be reduced to a few nanoliters per experiment. The great potential of such a materials microarray approach was demonstrated in the context of maintenance of ECS and iPSC.[73,74] Cell attachment, spreading, and proliferation significantly depended on the chemical and mechanical properties of the substrate and multiple 'hit' polymers were identified that, when coated with human serum or ECM proteins, robustly supported stem cell growth in completely defined media. The ability to characterize the materials properties further allowed the correlation of the frequency of colony formation with the elastic modulus or the wettability of the substrate. For example, polymers with an elastic modulus below 0.2 GPa poorly supported stem cell growth whereas

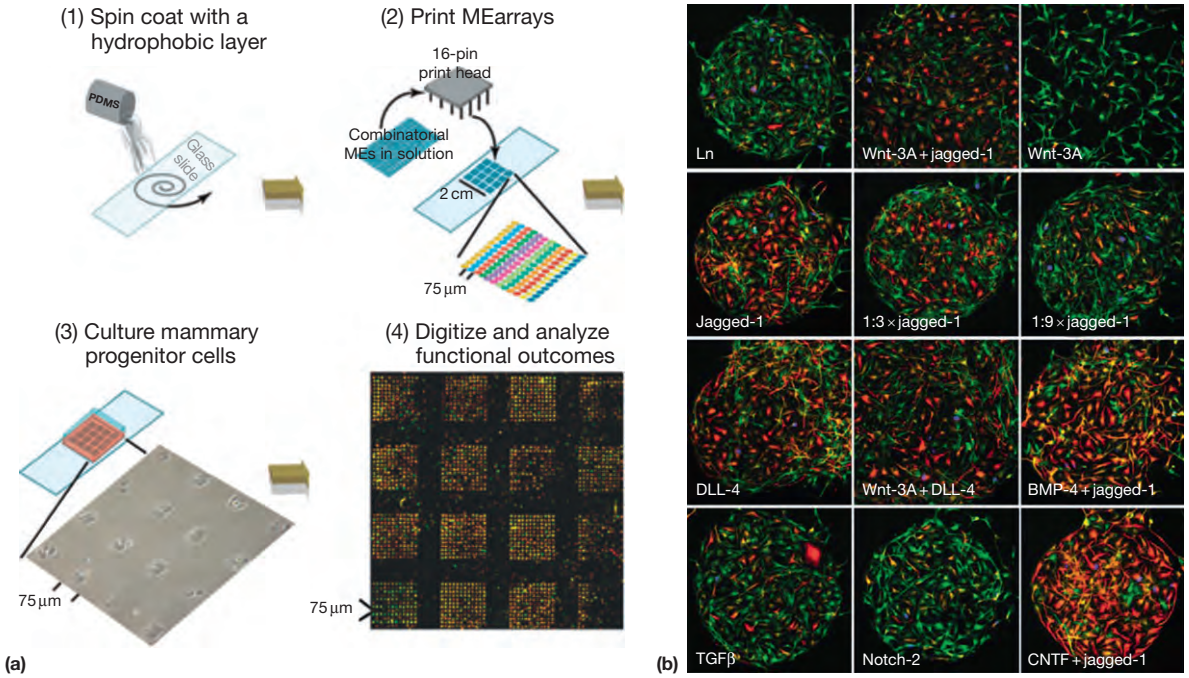

Figure 5 Robotically spotted microarrays for the high-throughput screening of putative niche factors. (a) Protein microarrays are typically fabricated on substrates rendered noncell adhesive with a layer of polydimethylsiloxane (PDMS) or by passivation of glass slides followed by the robotic dispensing of protein mixtures from libraries. The effect of protein combinations on the proliferation and differentiation of stem cells can then be determined by retrospective fate analysis such as immunostaining. Reprinted with permission from Labarge, M. A.; Nelson, C. M.; Villadsen, R.; *et al*. *Integr. Biol*. **2009**, *1*, 70–79. © 2009 Royal Society of Chemistry. (b) An example of primary human neural progenitors cultured on laminin (Ln) spots illustrating the strong influence of different growth factors combinations or concentrations on cell proliferation and the expression of neurogenic (TUJ1, in green) and glial (GFAP, in red) markers. Adapted with permission from Soen, Y.; Mori, A.; Palmer, T. D.; Brown, P. O. *Mol. Syst. Biol*. **2006**, *2*, 37. © 2005 Nature Publishing Group.

softer microenvironments did not significantly increase colony formation efficiency. In addition, a moderate wettability of the surface (contact angle of approximately 70°) was shown to be optimal for stem cell growth over a wide range of elastic moduli, indicating that the contact angle and the elastic properties did not directly correlate.[74] However, despite exciting progress in developing synthetic cell culture substrates by combinatorial chemistry, current biomaterial arrays still rely on a poorly defined coating of spots with proteins such as serum components or fibronectin. Here, the systematic screening of peptide or recombinantly expressed growth factors libraries coupled to materials could be an interesting avenue to move forward.

2.209.5. Topographically Patterned Substrates as Versatile Stem Cell Microenvironments

Most cell culture platforms described above are not amenable to dynamically investigating stem cells at the single-cell level. This could pose a significant problem, as many stem cell populations are highly heterogeneous and information on the behavior of rare stem cells can be masked in bulk cultures. This problem has been solved by the introduction of microwell array cultures for cell biology.[75–82] These modular platforms permit the analysis of a large number of individual, spatially confined cells. They have recently been successfully applied to stem cell biology, on both embryonic and adult stem cells.[77,78,80,81,86–89]

Polymer hydrogel networks such as those formed from PEG are well suited as microwell substrates and offer the advantage to simultaneously and independently assess the effects of biophysical and biochemical properties on stem cell fate at the clonal level, which is often necessary for inherently heterogeneous populations of enriched stem cell populations. Currently available hydrogel cross-linking chemistries and macromolecule architectures can generate a wide range of hydrogels with distinct and reproducible mechanical properties.[90,91] By employing a standard microfabrication technique using PDMS as a replica, it is possible to topographically structure hydrogel arrays to contain thousands of spatially segregated micropatterns such as round microwells with proteins printed specifically at the bottom of each structure.[88] For example, using a hydrogel microwell culture approach in conjunction with time-lapse microscopy, HSC division behavior in response to a panel of soluble and tethered molecules was assessed. Division patterns consistent with depletion (fast symmetric division), asymmetric (asymmetric cell division), and symmetric self-renewal (slow symmetric division) were observed and subsequently assayed *in vivo* with long-term blood reconstitution assays. This study showed that putative niche factors, such as Wnt3a and N-cadherin, could induce HSC self-renewal *in vitro*.[88] Additionally, it corroborates the idea that *in vitro* behaviors can be highly predictive of *in vivo* potential.[87] A similar approach could be applied to any number of stem cell types to identify novel physical and

chemical regulators and the relevant presentation of those molecules to elicit effects on single stem cell self-renewal or differentiation.

2.209.6. Biomaterials Approaches to Emulate Stem Cell Niches in 3D

So far, this chapter has focused on materials as cell culture platforms in which cells are grown on surfaces. This is of course an oversimplification of most native stem cell milieus, as *in vivo* most stem cell types are fully ensheathed within soft and highly hydrated cross-linked 3D networks of proteins and sugars. The exposure to a 2D environment, may – independent of the matrix biochemical features – result in the loss of stem cell functions because of a change in cell shape and polarity imposed by an aberrant substrate. 3D culture systems are believed to overcome this problem and are expected to increase the physiological relevance of artificial stem cell niches. Intriguingly, 3D approaches could allow going beyond the analysis of isolated cells toward a reconstruction and realization of the complexity of multicellular tissue-like constructs.

2.209.6.1. Building a Molecular Toolbox for 3D Artificial Niches

Not surprisingly, because of their inherent biological activity and mild cross-linking conditions, ECM protein-derived hydrogels such as Matrigel™, collagen, or fibrin have been extensively used for 3D stem cell cultures as reviewed elsewhere.[5] However, the biophysical and biochemical properties of these naturally derived matrices cannot be easily tuned and thus it is difficult to create microenvironments for specific stem cell types or to ask questions on the function of specific matrix components. In particular, currently used 3D models do not readily allow modulating matrix properties independently from each other.[92] For example, a change in collagen gel stiffness by increasing or decreasing the precursor content during gelation also alters adhesion ligand density, matrix porosity, degradablility, etc.

These shortcomings have led to the development of entirely synthetic microenvironments offering the intriguing possibility of constructing biophysical and biochemical matrix functionality 'from scratch.' The concept for a generic approach in the creation of such tailor-made 3D matrices is shown in Figure 6.[93] This toolbox concept is built on the mild cross-linking of biofunctional components from an entire array of synthetic building blocks. Proteins or oligopeptides derived from ECM proteins could serve as templates for chemically synthesized or genetically engineered biological building blocks that could be cross-linked via mild reactions using various approaches,[94,95] for example, hydrophilic and completely inert polymers or self-assembling building blocks such as peptides or peptide amphiphiles (see Chapter 2.205, Self-Assembling Biomaterials). Apart from mild reaction conditions for their formation, these 3D artificial niches must fulfill other physiological requirements. For example, dense or highly interconnected polymer scaffolds often suffer from limited nutrient exchange or pose physical constraints impeding cell proliferation, migration, and morphogenesis. To avoid these problems, hydrogel matrix porosity has been engineered in 3D biomaterials such as to allow cell migration.[10] Another approach consists in the design of degradable matrices, which can be achieved either by a chemical mechanism, such as ester hydrolysis, or a cell-controlled mechanism via proteolysis, that is, the incorporation of enzymatically cleavable peptide linkers (see Chapter 1.132, Dynamic Hydrogels). The latter approach is particularly appealing, as the peptide sequences can be engineered to be degradable by selected cell-secreted ECM-remodeling protease (e.g., matrix metalloproteases or plasmin), and thus the 3D matrix degradation becomes entirely controlled by cell-autonomous processes.[93]

The above molecular toolbox concept in synthetic ECM design is currently being exploited to create *in vitro* microenvironments for stem cells to identify the effects of biochemical and biophysical niche components. In an early example, PEG hydrogels were functionalized with adhesion peptide motifs to specifically activate integrins expressed by mouse ESC. In this model system, cells responded to different types and concentrations of adhesion peptides, and a combinatorial stimulation of the integrins $\alpha_5\beta_1$, $\alpha_v\beta_5$, $\alpha_6\beta_1$, and $\alpha_9\beta_1$ was sufficient to maintain ESC pluripotency.[96] By removing individual adhesion peptides, this molecularly well-defined system allow to dissect the influence of specific integrins and their downstream signaling pathways, and thus serves as a good example for this emerging toolbox approach.

2.209.6.2. Toward High-Throughput Screening of 3D Microenvironments

A truly fascinating question in stem cell biology and tissue engineering is just how the numerous signaling components of a stem cell niche could converge to govern cell fate decisions and tissue formation in 3D. This question is difficult to address *in vivo* or by any existing 2D *in vitro* approach, simply because of the complexity of a stem cell niche with the numerous physical, chemical, and mechanical effectors involved. Even if the specific nature of its components were known, testing them systematically would not be possible at the moment. Thus, developing new approaches aimed at high-throughput screening of combinations of 3D microenvironmental variables, in a manner analogous to 2D ECM protein or material microarrays described above, is a major goal.[10] In one of the early examples of this strategy, small-scale screening of cells encapsulated in hydrogels with well-controlled degradation kinetics, type, and concentration of adhesion ligands[97] revealed that MSCs survived and proliferated best in degradable hydrogels with a sufficiently high concentration of adhesion ligands. However, true 3D screening systems need to go beyond this first step of characterizing cell fate, and they also require further miniaturizing of the 3D assay. The latter has been achieved with human MCF7 breast cancer cells that were encapsulated in robotically spotted 20-nl drops of collagen or alginate, similar to 'classical' microarrays.[98] However, although the cells survived the spotting process and could be used for 3D drug testing applications, the spotting of cells is still challenging compared to spotting of biomaterials, because nanoliter samples with encapsulated cells are very sensitive to evaporation. Another challenge is the analysis of cellular responses such as self-renewal and differentiation in 3D, for which one focal plane in microscopic readouts is not sufficient and confocality is required.

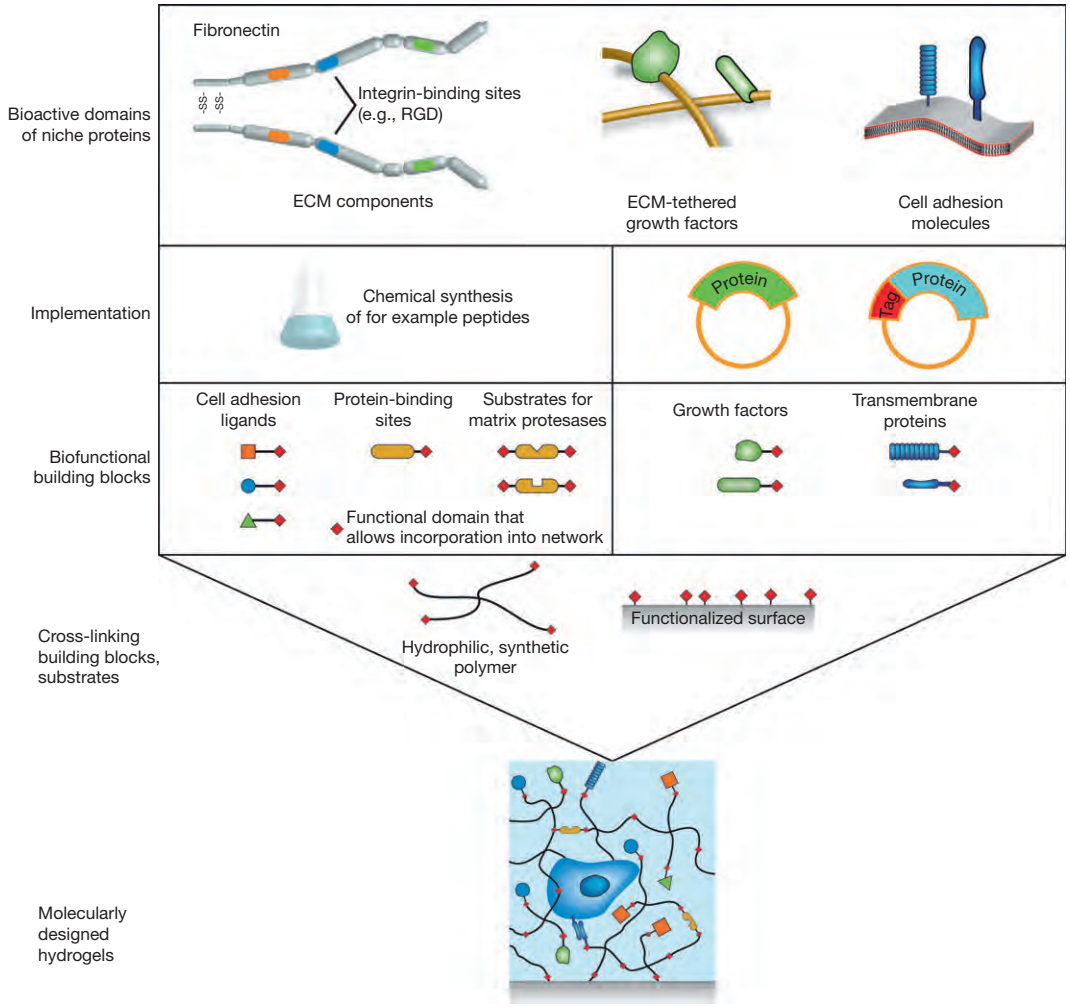

Figure 6 Design strategies for the fabrication of 3D matrices that can recapitulate key components of stem cell niches. Niche proteins or even single domains or peptide sequences thereof are fabricated as bioactive building blocks using chemical means or by recombinant protein expression. These building blocks ideally comprise cell adhesion ligands, proteins, or protein-binding sites such as heparin, and cleavage sites for matrix metalloproteases or other proteases. Synthetic hydrogels can be fabricated by cross-linking these building blocks into 3D hydrogels networks for stem cell culture. The modularity of this approach permits to molecularly engineer the properties of a desired cell culture substrate. Adapted from Lutolf, M. P.; Hubbell, J. A. *Nat. Biotechnol.* **2005**, *23*, 47–55, with permission. © 2006 Nature Publishing Group.

2.209.6.3. 3D-Micropatterning of Artificial Stem Cell Niches and Cells

Another formidable challenge in 3D stem cell culture is the recapitulation of the spatial architecture of niches, as randomly dispersed cells and biomolecules in a 3D matrix do not serve as a good model of native niches with their intricate spatial organization, even in tissues such as the skin or the intestine where stem cells grow on a sheet-like basal lamina providing crucial positional information on the stem cells.[14,16,17] Thus, there is an unmet need for tools to pattern artificial stem cell niches in 3D. The ideal approach should combine the construction of 3D hydrogel matrices with methods to precisely position multiple cell types and biomolecules with a high spatial resolution inside hydrogels (Figure 7).[10,99] This is currently not possible, but encouraging progress is being made.

For example, patterning approaches for biomolecular gradients have been adapted to 3D hydrogels integrated in microfluidic devices.[100,101] In one example, soluble protein gradients were established from microfluidics channels inside of a cell-laden alginate hydrogel, allowing to expose the cells to well-defined gradients of soluble molecules.[100] As proteins can be readily tethered to gel networks, it should be possible to combine tethered and soluble gradients of protein morphogens to mimic the exposure of cells to both ECM-bound and soluble biomolecule gradients, in order to more closely recreate a stem cell niche in 3D.

A powerful alternative to microfluidic technology for 3D hydrogel patterning is the light-controlled patterning of photoreactive moieties within synthetic gels. Using standard confocal laser scanning or two-photon microscopy, researchers have shown that virtually any 3D pattern can be generated in a

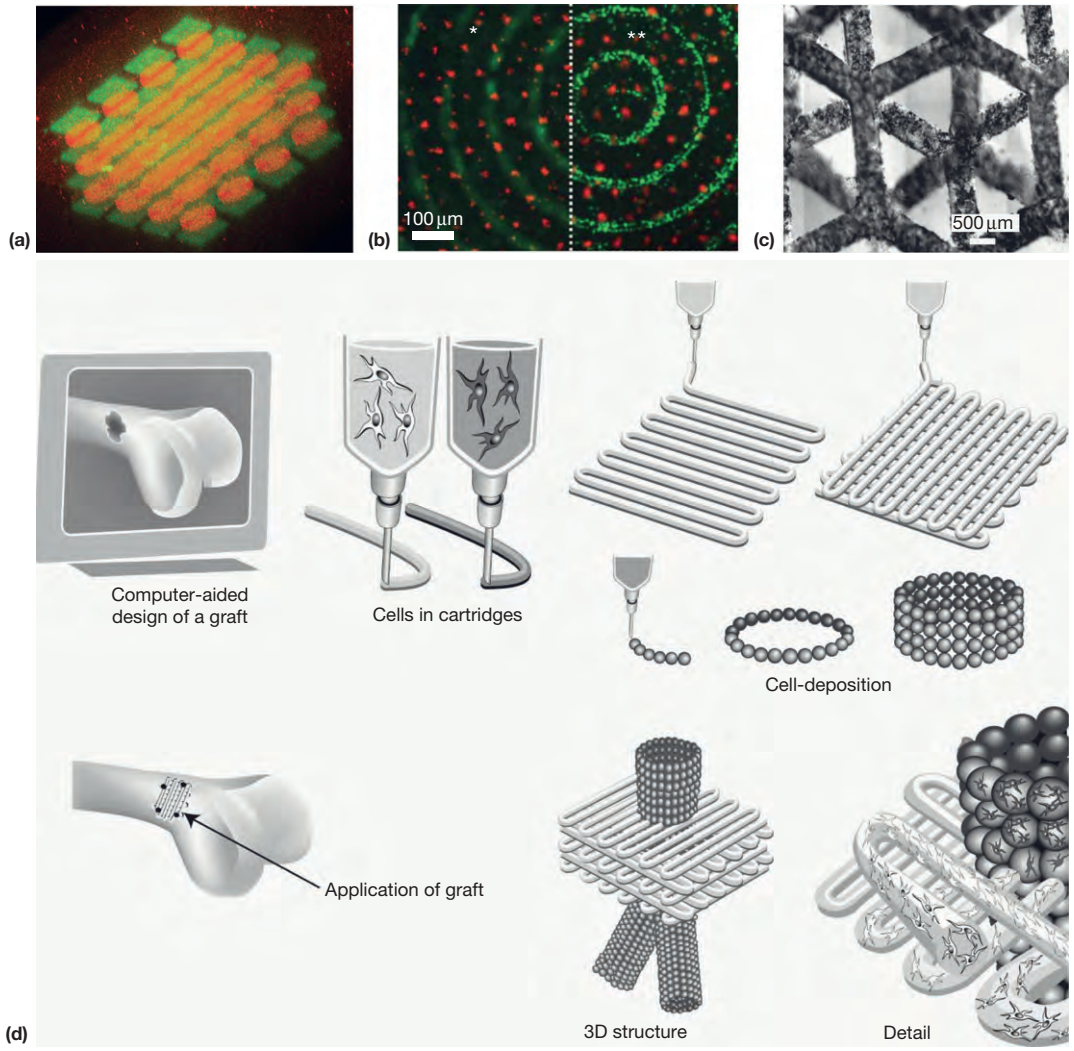

Figure 7 Promises and challenges of 3D micropatterning. Current biocompatible 3D patterning methods allow (a) the patterning of biomolecules with photolabile chemistries (reproduced from Wosnick, J. H.; Shoichet, M. S. *Chem. Mater.* **2008**, *20*, 55–60, with permission. © 2008 American Chemical Society), (b) the patterning of cells for example by using dielectrophoresis (reproduced from Albrecht, D. R.; Underhill, G. H.; Wassermann, T. B.; Sah, R. L.; Bhatia, S. N. *Nat. Methods* **2006**, *3*, 369–375, with permission. © 2006 Nature Publishing Group), or (c) the definition of complex 3D structures via photolithography (reproduced from Liu Tsang, V.; Chen, A. A.; Cho, L. M.; *et al. FASEB J.* **2007**, *21*, 790–801, with permission. © 2007 Federation of American Societies for Experimental Biology). (d) Bioprinting, the dispensing of miniature biological samples using ink-jet technology to assemble complex 3D tissue mimetics, could provide a valuable alternative in the future (reproduced from Fedorovich, N. E.; Alblas, J.; De Wijn, J. R.; Hennink, W. E.; Verbout, A. J.; Dhert, W. J. A. *Tissue Eng.* **2007**, *13*, 1905–1925. © 2007 Mary Ann Liebert, Inc.).

rapid-prototyping-like manner and with a very high spatial resolution (Figure 7(a)).[83,102,103] In addition, these systems permit to dynamically change the properties of a hydrogel, as photolabile groups can be cleaved within hydrogels, in the presence of cells and at any desired time point during an experiment. Accordingly, human MSCs were shown to respond to locally induced changes in matrix stiffness or availability of adhesion ligands. By cleaving a photolabile RGDS peptide, the change of the microenvironment of MSCs could be dynamically modulated and chondrogenic differentiation induced.[103]

The patterning of cells in 3D has also been achieved. For example, microfluidics was used to sandwich cells between two layers of hydrogel[104] or to create multiple hydrogel streams within microfluidic channels.[105,106] An alternative approach is the patterning of cells in hydrogels using dielectrophoresis (DEP) (Figure 7(b)). Cell handling and patterning via DEP is based on the fact that cells migrate when placed in nonhomogeneous electrical field. In combination with photopolymerization, DEP was used to construct gels with precisely 3D-patterned cells.[84,107] A caveat here could be the potential toxicity of some DEP buffers and the heat generated during DEP patterning, which would limit the use of this technique to relatively robust cells.[107,108]

2.209.6.4. Toward Constructing Tissue Models

3D hydrogel patterning has also been applied to fabricate artificial tissue models. For example, micromolding of collagen gels allows a precise control of the initial geometry of multicellular epithelial cell aggregates that have

morphogenetic potential.[109] These constructs can be induced to undergo a geometry-dependent epithelial-to-mesenchymal transition, occurring preferentially at the corner of the tissue mimetic. Using multilayered photolithography, another group fabricated artificial hepatic tissues that mimicked the 3D anatomy of the liver. The obtained mesh-like structure of the construct enhanced the performance of seeded cells, presumably by facilitating the perfusion and the nutrient exchange (**Figure 7 (c)**).[85] These are exciting advances, but the layer-by-layer assembly of hydrogel structures and cells is relatively complicated and has limited spatial resolution, problems that could potentially be overcome by the application of printing technologies of cells and soft biomaterials. Emerging 'bioprinting' approaches envision the application of custom-designed inkjet printers to deposit picoliter droplets of biomaterials precursors, containing cells and regulatory cues, into 3D constructs with high spatial resolution. Using computer-assisted designs (CAD) software, any type of cellular and materials architecture could in theory be assembled. Bioprinting is fast, as droplets can be printed at a frequency of several thousands of droplets per second, and allows to fabricate relatively large constructs (**Figure 7(d)**).[99,110] Although this technique has already been applied to a wide range of cell types and biomaterials,[110] only a few applications of bioprinting in stem cell biology have been reported.[111] One difficulty has been the lack of a 'bioink,' a hydrogel precursor which can rapidly polymerize and has cell-instructive characteristics to foster morphogenesis.[110] However, if these hurdles can be overcome, the *de novo* construction of complex artificial niches and tissue models with precisely patterned stem cells and their microenvironments should become possible.

2.209.7. Conclusions

The application of biomaterial engineering to stem cell biology offers many tantalizing possibilities to manipulate stem cell fate *in vitro* or *in vivo*. The rate at which biomaterial approaches are being applied to address questions in stem cell biology assures new insights into the mechanistic regulation of stem cell fate. In particular, much can be learned from studies using artificial niches that allow expansion of functional adult stem cells such as HSC as well as more efficient differentiation of ESC and iPSC toward specific lineages. However, although a plethora of ingenious biomaterial platforms to deconstruct the influence of stem cell niche biophysical and biochemical properties have been developed already, their application to direct stem cell fate remains in its infancy. True collaborative efforts between cell biologists and material scientists, as well as a new generation of bioengineers with in-depth training in both engineering and biological disciplines, are critical to move stem cell biology one step closer to the clinic.

References

1. Daley, G. Q.; Scadden, D. T. *Cell* **2008**, *132*, 544–548.
2. Takahashi, K.; Yamanaka, S. *Cell* **2006**, *126*, 663–676.
3. Burdick, J. A.; Vunjak-Novakovic, G. *Tissue Eng. A* **2009**, *15*, 205–219.
4. Chai, C.; Leong, K. W. *Mol. Ther.* **2007**, *15*, 467–480.
5. Dawson, E.; Mapili, G.; Erickson, K.; Taqvi, S.; Roy, K. *Adv. Drug Deliv. Rev.* **2007**, *60*, 215–228.
6. Dellatore, S. M.; Garcia, A. S.; Miller, W. M. *Curr. Opin. Biotechnol.* **2008**, *19*, 534–540.
7. Hwang, N. S.; Varghese, S.; Elisseeff, J. *Adv. Drug Deliv. Rev.* **2008**, *60*, 199–214.
8. Kobel, S.; Lutolf, M. P. *BioTechniques* **2010**, *48*, IX–XXII.
9. Little, L.; Healy, K. E.; Schaffer, D. V. *Chem. Rev.* **2008**, *108*, 1787–1796.
10. Lutolf, M. P.; Gilbert, P. M.; Blau, H. M. *Nature* **2009**, *462*, 433–441.
11. Saha, K.; Pollock, J. F.; Schaffer, D. V.; Healy, K. E. *Curr. Opin. Chem. Biol.* **2007**, *11*, 381–387.
12. Schofield, R. *Blood Cells* **1978**, *4*, 7–25.
13. Xie, T.; Spradling, A. C. *Science* **2000**, *290*, 328–330.
14. Fuchs, E.; Tumbar, T.; Guasch, G. *Cell* **2004**, *116*, 769–778.
15. Jones, D. L.; Wagers, A. J. *Nat. Rev. Mol. Cell Biol.* **2008**, *9*, 11–21.
16. Li, L.; Xie, T. *Annu. Rev. Cell Dev. Biol.* **2005**, *21*, 605–631.
17. Moore, K. A.; Lemischka, I. R. *Science* **2006**, *311*, 1880–1885.
18. Morrison, S. J.; Spradling, A. C. *Cell* **2008**, *132*, 598–611.
19. Scadden, D. T. *Nature* **2006**, *441*, 1075–1079.
20. Hynes, R. O. *Science* **2009**, *326*, 1216–1219.
21. Ramirez, F.; Rifkin, D. B. *Matrix Biol.* **2003**, *22*, 101–107.
22. Raymond, K.; Deugnier, M.-A.; Faraldo, M. M.; Glukhova, M. A. *Curr. Opin. Cell Biol.* **2009**, *21*, 623–629.
23. Daley, W. P.; Peters, S. B.; Larsen, M. *J. Cell Sci.* **2008**, *121*, 255–264.
24. Discher, D. E.; Mooney, D. J.; Zandstra, P. W. *Science* **2009**, *324*, 1673–1677.
25. Guilak, F.; Cohen, D. M.; Estes, B. T.; Gimble, J. M.; Liedtke, W.; Chen, C. S. *Cell Stem Cell* **2009**, *5*, 17–26.
26. Wozniak, M. A.; Chen, C. S. *Nat. Rev. Mol. Cell Biol.* **2009**, *10*, 34–43.
27. Keung, A. J.; Kumar, S.; Schaffer, D. V. *Annu. Rev. Cell Dev. Biol.* **2010**, *26*, 533–556.
28. Blank, U.; Karlsson, G.; Karlsson, S. *Blood* **2008**, *111*, 492–503.
29. Méndez-Ferrer, S.; Lucas, D.; Battista, M.; Frenette, P. S. *Nature* **2008**, *452*, 442–447.
30. Fuchs, E. *Cell* **2009**, *137*, 811–819.
31. Knoblich, J. A. *Cell* **2008**, *132*, 583–597.
32. Bishop, J. R.; Schuksz, M.; Esko, J. D. *Nature* **2007**, *446*, 1030–1037.
33. Xu, C.; Inokuma, M. S.; Denham, J.; *et al. Nat. Biotechnol.* **2001**, *19*, 971–974.
34. Dawson, E.; Mapili, G.; Erickson, K.; Taqvi, S.; Roy, K. *Adv. Drug Deliv. Rev.* **2008**, *60*, 215–228.
35. Sakiyama-Elbert, S. E.; Hubbell, J. A. *J. Control. Release* **2000**, *65*, 389–402.
36. Baldwin, A. D.; Kiick, K. L. *Biopolymers* **2010**, *94*, 128–140.
37. Willerth, S. M.; Rader, A.; Sakiyama-Elbert, S. E. *Stem Cell Res.* **2008**, *1*, 205–218.
38. Nur-E-Kamal, A.; Ahmed, I.; Kamal, J.; Babu, A. N.; Schindler, M.; Meiners, S. *Mol. Cell. Biochem.* **2008**, *309*, 157–166.
39. Fan, V. H.; Tamama, K.; Au, A.; *et al. Stem Cells* **2007**, *25*, 1241–1251.
40. Kuhl, P. R.; Griffith-Cima, L. G. *Nat. Med.* **1996**, *2*, 1022–1027.
41. Alberti, K.; Davey, R. E.; Onishi, K.; *et al. Nat. Methods* **2008**, *5*, 645–650.
42. Martino, M.; Hubbell, J. A. *FASEB J.* **2010**, *24*(12), 4711–4721.
43. Suzuki, T.; Yokoyama, Y.; Kumano, K.; *et al. Stem Cells* **2006**, *24*, 2456–2465.
44. Beckstead, B. L.; Santosa, D. M.; Giachelli, C. M. *J. Biomed. Mater. Res. A* **2006**, *79*, 94–103.
45. Nagaoka, M.; Koshimizu, U.; Yuasa, S.; *et al. PLoS ONE* **2006**, *1*, e15.
46. Nagaoka, M.; Si-Tayeb, K.; Akaike, T.; Duncan, S. A. *BMC Dev. Biol.* **2010**, *10*, 60.
47. Discher, D. E.; Janmey, P.; Wang, Y. L. *Science* **2005**, *310*, 1139–1143.
48. Keung, A.; Healy, K.; Kumar, S.; Schaffer, D. *WIREs Syst. Biol. Med.* **2010**, *2*, 49–64.
49. Engler, A. J.; Sen, S.; Sweeney, H. L.; Discher, D. E. *Cell* **2006**, *126*, 677–689.
50. Pelham, R. J.; Wang, Y. L. *Proc. Natl. Acad. Sci. USA* **1997**, *94*, 13661–13665.
51. Saha, K.; Keung, A. J.; Irwin, E. F.; *et al. Biophys. J.* **2008**, *95*, 4426–4438.
52. Gilbert, P. M.; Havenstrite, K. L.; Magnusson, K. E. G.; *et al. Science* **2010**, *329*(5995), 1078–1081.
53. Breslauer, D. N.; Lee, P. J.; Lee, L. P. *Mol. Biosyst.* **2006**, *2*, 97–112.
54. Paguirigan, A. L.; Beebe, D. J. *Bioessays* **2008**, *30*, 811–821.
55. Mcbeath, R.; Pirone, D. M.; Nelson, C. M.; Bhadriraju, K.; Chen, C. S. *Dev. Cell* **2004**, *6*, 483–495.
56. Bauwens, C. L.; Peerani, R.; Niebruegge, S.; *et al. Stem Cells* **2008**, *26*, 2300–2310.
57. Ruiz, S. A.; Chen, C. S. *Stem Cells* **2008**, *26*, 2921–2927.

58. Arnold, M.; Cavalcanti-Adam, E. A.; Glass, R.; *et al*. *Chemphyschem* **2004**, *5*, 383–388.
59. Gerecht, S.; Bettinger, C. J.; Zhang, Z.; Borenstein, J. T.; Vunjak-Novakovic, G.; Langer, R. *Biomaterials* **2007**, *28*, 4068–4077.
60. Jeon, N.; Dertinger, S.; Chiu, D.; Choi, I.; Stroock, A.; Whitesides, G. *Langmuir* **2000**, *16*, 8311–8316.
61. Fung, W.-T.; Beyzavi, A.; Abgrall, P.; Nguyen, N.-T.; Li, H.-Y. *Lab Chip* **2009**, *9*, 2591–2595.
62. Li Jeon, N.; Baskaran, H.; Dertinger, S. K. W.; Whitesides, G. M.; Van De Water, L.; Toner, M. *Nat. Biotechnol*. **2002**, *20*, 826–830.
63. Park, J. Y.; Kim, S.-K.; Woo, D.-H.; Lee, E.-J.; Kim, J.-H.; Lee, S.-H. *Stem Cells* **2009**, *27*, 2646–2654.
64. Gunawan, R. C.; Silvestre, J.; Gaskins, H. R.; Kenis, P. J. A.; Leckband, D. E. *Langmuir ACS J. Surfaces Colloids* **2006**, *22*, 4250–4258.
65. Burdick, J. A.; Khademhosseini, A.; Langer, R. *Langmuir ACS J. Surfaces Colloids* **2004**, *20*, 5153–5156.
66. Von Philipsborn, A. C.; Lang, S.; Jiang, Z.; Bonhoeffer, F.; Bastmeyer, M. *Sci. STKE* **2007**, *2007*, 16.
67. Allazetta, S.; Cosson, S.; Lutolf, M. P. *Chem. Commun. (Camb.)* **2011**, *47*(1), 191–193.
68. Cosson, S.; Kobel, S. A.; Lutolf, M. P. *Adv. Funct. Mater.* **2009**, *19*, 3411–3419.
69. Flaim, C. J.; Chien, S.; Bhatia, S. N. *Nat. Methods* **2005**, *2*, 119–125.
70. Labarge, M. A.; Nelson, C. M.; Villadsen, R.; *et al*. *Integr. Biol*. **2009**, *1*, 70–79.
71. Soen, Y.; Mori, A.; Palmer, T. D.; Brown, P. O. *Mol. Syst. Biol*. **2006**, *2*, 37.
72. Flaim, C. J.; Teng, D.; Chien, S.; Bhatia, S. N. *Stem Cells Dev*. **2008**, *17*, 29–39.
73. Anderson, D. G.; Levenberg, S.; Langer, R. *Nat. Biotechnol*. **2004**, *22*, 863–866.
74. Mei, Y.; Saha, K.; Bogatyrev, S. R.; *et al*. *Nat. Mater*. **2010**, *9*, 768–778.
75. Chin, V. I.; Taupin, P.; Sanga, S.; Scheel, J.; Gage, F. H.; Bhatia, S. N. *Biotechnol. Bioeng.* **2004**, *88*, 399–415.
76. Dusseiller, M. R.; Schlaepfer, D.; Koch, M.; Kroschewski, R.; Textor, M. *Biomaterials* **2005**, *26*, 5917–5925.
77. Karp, J. M.; Yeh, J.; Eng, G.; *et al*. *Lab Chip* **2007**, *7*, 786–794.
78. Khademhosseini, A.; Langer, R.; Borenstein, J.; Vacanti, J. P. *Proc. Natl. Acad. Sci. USA* **2006**, *103*, 2480–2487.
79. Koh, W.-G.; Itle, L. J.; Pishko, M. V. *Anal. Chem*. **2003**, *75*, 5783–5789.
80. Moeller, H.-C.; Mian, M. K.; Shrivastava, S.; Chung, B. G.; Khademhosseini, A. *Biomaterials* **2008**, *29*, 752–763.
81. Mohr, J. C.; De Pablo, J. J.; Palecek, S. P. *Biomaterials* **2006**, *27*, 6032–6042.
82. Revzin, A.; Russell, R.; Yadavalli, V.; *et al*. *Langmuir* **2001**, *17*, 5440–5447.
83. Wosnick, J. H.; Shoichet, M. S. *Chem. Mater*. **2008**, *20*, 55–60.
84. Albrecht, D. R.; Underhill, G. H.; Wassermann, T. B.; Sah, R. L.; Bhatia, S. N. *Nat. Methods* **2006**, *3*, 369–375.
85. Liu Tsang, V.; Chen, A. A.; Cho, L. M.; *et al*. *FASEB J*. **2007**, *21*, 790–801.
86. Cordey, M.; Limacher, M.; Kobel, S.; Taylor, V.; Lutolf, M. P. *Stem Cells* **2008**, *26*, 2586–2594.
87. Dykstra, B.; Ramunas, J.; Kent, D.; *et al*. *Proc. Natl. Acad. Sci. USA* **2006**, *103*, 8185–8190.
88. Lutolf, M. P.; Doyonnas, R.; Havenstrite, K.; Koleckar, K.; Blau, H. M. *Integr. Biol*. **2009**, *1*, 59–69.
89. Ungrin, M. D.; Joshi, C.; Nica, A.; Bauwens, C.; Zandstra, P. W. *PLoS ONE* **2008**, *3*, e1565.
90. Jia, X.; Kiick, K. L. *Macromol. Biosci*. **2009**, *9*, 140–156.
91. Lin, T.; Ambasudhan, R.; Yuan, X.; *et al*. *Nat. Methods* **2009**, *6*, 805–808.
92. Lutolf, M. P. *Integr. Biol*. **2009**, *1*, 235–241.
93. Lutolf, M. P.; Hubbell, J. A. *Nat. Biotechnol*. **2005**, *23*, 47–55.
94. Hennink, W. E.; Van Nostrum, C. F. *Adv. Drug Deliv. Rev*. **2002**, *54*, 13–36.
95. Kopeček, J.; Yang, J. *Polym. Int*. **2007**, *56*, 1078–1098.
96. Lee, S. T.; Yun, J. I.; Jo, Y. S.; *et al*. *Biomaterials* **2010**, *31*, 1219–1226.
97. Jongpaiboonkit, L.; King, W. J.; Murphy, W. L. *Tissue Eng. A* **2009**, *15*, 343–353.
98. Lee, M.-Y.; Kumar, R. A.; Sukumaran, S. M.; Hogg, M. G.; Clark, D. S.; Dordick, J. S. *Proc. Natl. Acad. Sci. USA* **2008**, *105*, 59–63.
99. Boland, T.; Xu, T.; Damon, B.; Cui, X. *Biotechnol. J*. **2006**, *1*, 910–917.
100. Choi, N. W.; Cabodi, M.; Held, B.; Gleghorn, J. P.; Bonassar, L. J.; Stroock, A. D. *Nat. Mater*. **2007**, *6*, 908–915.
101. Peret, B. J.; Murphy, W. L. *Adv. Funct. Mater*. **2008**, *18*, 3410–3417.
102. Hahn, M. S.; Miller, J. S.; West, J. L. *Adv. Mater*. **2006**, *18*, 2679–2684.
103. Kloxin, A. M.; Kasko, A. M.; Salinas, C. N.; Anseth, K. S. *Science* **2009**, *324*, 59–63.
104. Beningo, K. A.; Dembo, M.; Wang, Y.-L. *Proc. Natl. Acad. Sci. USA* **2004**, *101*, 18024–18029.
105. Braschler, T.; Johann, R.; Heule, M.; Metref, L.; Renaud, P. *Lab Chip* **2005**, *5*, 553–559.
106. Huang, C. P.; Lu, J.; Seon, H.; *et al*. *Lab Chip* **2009**, *9*, 1740–1748.
107. Mittal, N.; Rosenthal, A.; Voldman, J. *Lab Chip* **2007**, *7*, 1146–1153.
108. Seger-Sauli, U.; Panayiotou, M.; Schnydrig, S.; Jordan, M.; Renaud, P. *Electrophoresis* **2005**, *26*, 2239–2246.
109. Nelson, C. M.; Vanduijn, M. M.; Inman, J. L.; Fletcher, D. A.; Bissell, M. J. *Science* **2006**, *314*, 298–300.
110. Fedorovich, N. E.; Alblas, J.; De Wijn, J. R.; Hennink, W. E.; Verbout, A. J.; Dhert, W. J. A. *Tissue Eng.* **2007**, *13*, 1905–1925.
111. Lee, W.; Pinckney, J.; Lee, V.; *et al*. *NeuroReport* **2009**, *20*, 798–803.

2.210. Bone as a Material

L McNamara, National University of Ireland Galway, Galway, Ireland

© 2011 Elsevier Ltd. All rights reserved.

2.210.1.	**Introduction**	170
2.210.2.	**Bone Composition**	170
2.210.2.1.	Collagen	170
2.210.2.2.	Mineral	171
2.210.2.3.	Noncollagenous Proteins	172
2.210.2.4.	Bone Cells	173
2.210.2.4.1.	Mesenchymal stem cells and osteoprogenitors	173
2.210.2.4.2.	Osteoblasts and bone-lining cells	173
2.210.2.4.3.	Osteocytes	174
2.210.2.4.4.	Osteoclasts	174
2.210.3.	**Bone Formation**	175
2.210.3.1.	Endochondral Ossification	175
2.210.3.2.	Intramembranous Ossification	176
2.210.4.	**Bone Structure and Hierarchical Organization**	176
2.210.4.1.	Bone Tissue Structure and Organization	176
2.210.4.2.	Organ Level	177
2.210.5.	**Bone Mechanical Behavior**	177
2.210.5.1.	Structural Mechanical Behavior of Trabecular Bone	178
2.210.5.2.	Tissue Mechanical Behavior of Bone	178
2.210.5.3.	Fracture Behavior	179
2.210.6.	**Bone as a Dynamic Adaptive Material**	179
2.210.6.1.	Bone Modeling	179
2.210.6.2.	Bone Remodeling	180
2.210.6.3.	Fracture Healing	180
2.210.6.4.	Mechanosensation	180
2.210.7.	**Bone as a Material During Disease and Drug Treatment**	181
2.210.7.1.	Osteoporosis	182
2.210.7.1.1.	Bone cell biology during osteoporosis	182
2.210.7.1.2.	Mechanical behavior and structure during osteoporosis	182
2.210.7.1.3.	Approaches for treatment of osteoporosis	183
2.210.8.	**Conclusion**	184
References		184

Glossary

Angiogenesis The physiological process by which blood vessels are formed.

Apoptosis The process by which cells die in response to a variety of stimuli in a controlled, regulated fashion, and is often referred to as programmed cell death.

Cytokine A signaling molecule, such as a protein or peptide, which is secreted by immune cells to regulate the activity of other biological cells.

Differentiation The process by which a biological cell alters its size, shape, membrane potential, metabolic activity, and gene expression in response to signals to become a more specialized cell.

Hematoma A collection of blood within a body tissue in response to injury of a blood vessel.

Hematopoietic stem cell An unspecialized cell from the blood or bone marrow that can renew itself and differentiate to a variety of specialized cells.

Mesenchyme Mesenchyme is loose reticular connective tissue which is derived from all three germ layers and located within the embryo.

Morphogenesis A biological process that causes a tissue or organ to develop its shape by controlling the spatial distribution of cells during embryonic development.

Morphology The form or shape of an organism (i.e., cell, tissue, organ).

Osteogenesis The term used for the biological process by which osteoblasts produce bone tissue.

Abbreviations

BMD	Bone mineral density
BMU	Basic multicellular unit
ECM	Extracellular matrix
MSCs	Mesenchymal stem cells
NCPs	Noncollagenous proteins
OPG	Osteoprotegerin
OVX	Ovariectomized
PTH	Parathyroid hormone
RANK	Receptor for activation of nuclear factor kappa B
RANKL	Receptor for activation of nuclear factor kappa B ligand
μCT	Micro-computed tomography

2.210.1. Introduction

The skeletal system gives the body its structure, provides support for the heart and lungs, protects internal organs, such as the brain, kidneys, and uterus, and facilitates movement by acting as a system of kinematic links to which muscles can attach. Bone tissue is the primary structural element that forms the skeletal system. It is an exceptional material that is lightweight to allow efficient movement but also exhibits excellent strength and stiffness. This unique mechanical behavior is imparted by a composite material of organic proteins and mineral crystals, which are intricately organized on many scales to create the material properties that allow bone to serve these functions under the variety of loading conditions experienced during everyday activities.[1] Furthermore, healthy bone is a living, growing, dynamic material that has the capacity to renew itself, and adapt its architecture, so that it can maintain strength and continue to serve its functions throughout life. This adaptive behavior is facilitated by specialized biological cells from bone surfaces and marrow that continuously digest aged or damaged bone and reform new bone tissue in its place. During normal physiology, bone cells can also repair fractures that occur. Each of these characteristics is fundamental to the normal physiological function of bone tissue and is discussed in detail subsequently.

2.210.2. Bone Composition

Bone tissue is a porous composite material, consisting of a mineral phase and an organic phase. The organic phase comprises approximately 35% of the total mass of bone, of which 90% is a collagen matrix and the remainder is composed of other noncollagenous proteins (NCPs), water lipids, and cells. The mineral phase of bone is composed mainly of calcium and phosphorus in the form of hydroxyapatite crystals and accounts for approximately 25% of the total bone volume and 50% of the bone mass. The structure and mechanical behavior of bone is determined by the quantity and mechanical integrity of each of these phases, the structural organization of the different phases, and the physical interaction between them.

2.210.2.1. Collagen

Collagen is a ubiquitous constitutive protein that forms the fundamental matrix upon which all connective tissues are assembled. Its primary function is to provide structural integrity and shape to biological tissues. The tropocollagen molecule is the basic structural unit of collagen and comprises three polypeptide strands (α-chains), which are twisted together into a right-handed coiled coil known as a triple helix (Figure 1(d)). In bone tissue, tropocollagen molecules are synthesized by osteoblast cells during the initial phase of bone formation (Section 2.210.3). The formation of tropocollagen initiates when the polypeptide chains are produced by the nucleus of osteoblast cells (Figure 1(a)). Next, these chains are modified in the endoplasmic reticulum of the osteoblast when enzymes (proteases) break the peptide bonds between amino acid side chains (proline and lysine) of the polypeptide. This process is known as proteolytic cleavage (Figure 1(b)). These chains are

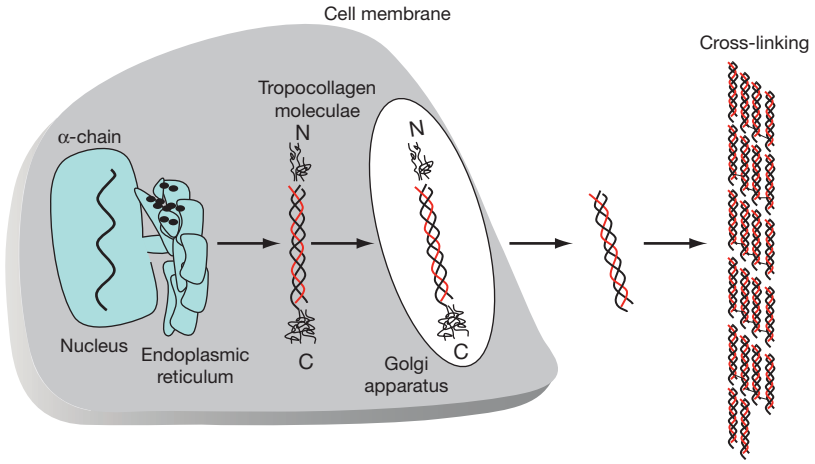

Figure 1 Intracellular synthesis and assembly of type I collagen in the osteoblast (a–c) and extracellular formation of collagen fibrils (d–e).

assembled into a triple-helix tropocollagen structure that is stabilized by hydrogen bonds. Within the space at the center of the triple helix, there is a repeating amino acid sequence consisting of glycine molecules and amino acids (e.g., proline and hydroxyproline). This process produces triple-helical collagen molecules that are approximately 1.5 nm in diameter and 300 nm long and have short nonhelical regions called telopeptides at each end, known as amino (N) and carboxyl (C) telopeptides, which facilitate later assembly into fibrils. The tropocollagen molecules are processed and packaged in the Golgi apparatus (**Figure 1(c)**) and then secreted to the extracellular matrix (ECM) in the form of soluble precursors called procollagens (**Figure 1(d)**). During secretion, the propeptides are removed by procollagen N and C proteinases, and this triggers these molecules to aggregate together extracellularly and assemble to form collagen fibrils (**Figure 1(e)**). Intermolecular cross-links are formed between the nonhelical domains and the helical domain of adjacent collagen molecules. These molecules are staggered from each other at a space of approximately 67 nm in fibrillar collagen.[2] The newly formed collagen fibers are stabilized by the formation of covalent cross-links between neighboring collagen molecules. Immature ketomine and aldimine cross-links are first formed, which contribute to the later formation of mature pyridinium or pyrrole cross-links. Together, these cross-links result in fibril formation, and these fibrils act as a scaffold for bone minerals and provide strength[3,4] and are responsible for the postyield behavior of bone tissue.[5]

There are more than 27 forms of collagen in biological tissues and each type is distinguished by roman numerals (e.g., Types I, II, III, V, and XI). The differences between each form of collagen lies in the manner in which the tropocollagen molecules and fibrils are arranged. Depending on the collagen type, the triple helix can be homotrimeric, that is, comprising three identical α-chains (e.g., type III collagen), or heterotrimeric, whereby at least one of the polypeptides is not identical to the others (e.g., type I collagen). The collagen in bone is primarily type I collagen ($[\alpha1(I)]_2\alpha2(I)$), which comprises 95% of the collagen content and 80% of the total proteins present in bone,[6] but types III, IV, and VI are also present.[7,8] In contrast to ligament and tendon, where fibrils are arranged in parallel bundles, the collagen fibrils in bone are arranged concentrically into packages known as lamellae (**Section 2.210.4.1**). Collagen fibers within the same lamella are parallel to one another (**Figure 2(a)**), whereas collagen fibers in adjacent lamellae may be oriented at an angle of up to 90° relative to each other (**Figure 2(b)**). It is through the intricate arrangement of collagen molecules at the nanoscale and fibrils at the microscale that collagen provides tensile strength, elasticity, and toughness (capacity to absorb energy) to bone.[9] Collagen forms the basis of immature bone tissue (osteoid) and acts as a template upon which proteins and mineral crystal are deposited[10] and are interspersed in the spaces between molecules and between adjacent fibrils (**Figure 3(a)**).

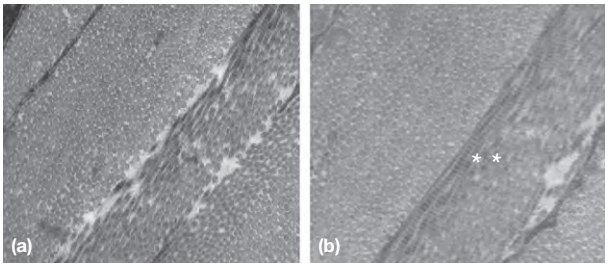

Figure 2 Transmission electron imaging of collagen fibrils in bone tissue: (a) collagen fibrils are oriented parallel to each other and (b) collagen fibrils in adjacent lamellae are oriented at an angle to each other (** indicates interface between lamellae).

2.210.2.2. Mineral

The mineral component of mature bone tissue consists of small crystals of impure hydroxyapatite ($Ca_{10}(PO_4)_6(OH)_2$) that are bound within and between the collagen fibrils in an ordered manner. This mineral is produced by osteoblast cells on the calcification front after the organic matrix is deposited, when calcium and phosphate ions bind in the presence of NCPs. These cells also regulate the binding of circulating calcium and phosphorus to the ECM. Over time, the size of the mineral particles increases slowly (secondary mineralization) so that within 5–10 days the matrix is 70% mineralized. Complete mineralization at any site takes between 3 and

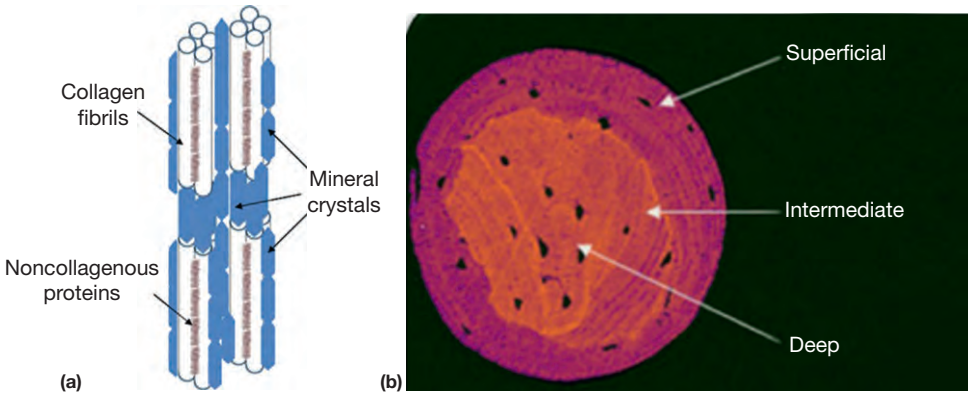

Figure 3 (a) Distribution of mineral and noncollagenous proteins within and between collagen fibrils and (b) color-enhanced image depicting variation in tissue mineral content with age; mineral content is lower in the superficial region.

5 months,[11] and mineralization of the entire skeleton does not occur for years. The mineral crystals are located within and between the spaces between collagen fibrils (**Figure 3(a)**) and are approximately 0.5 μm in length and have a thickness of 0.03 μm. The distribution and growth of these minerals, as well as their orientation, is governed by the structure and spatial limitations of the underlying collagen matrix,[12] which interacts with the mineral crystals.[13] Some proteins can inhibit crystal formation by binding to specific surfaces, blocking potential nucleation sites and thereby decrease crystal length.[14] Changes in local ionic concentration can also influence the rate of mineral deposition.[15] Together, these events regulate the formation of inorganic mineral crystals at distinct sites within bone tissue, which are aligned in the same orientation as the collagen fibrils.[11] The osteoid seam is a thin layer of unmineralized organic matrix that remains at the interface between newly formed osteoid and mineralized bone prior to mineralization of newly formed matrix.

The degree of bone tissue mineralization is vital for mechanical integrity of the skeleton, its load-bearing strength, and its stiffness.[1] The quantity of bone mineral varies considerably from different skeletal regions, within an individual, and from person to person; in particular sex, race and age-dependent differences have been reported.[16,17] The overall mineral content of bone tissue increases with age by an average of 5–10%,[18] but after 60 years of age, it has been shown to decrease again in males and females.[19] Such changes alter the stiffness and strength of bone tissue.[20] At high mineral contents, bone tissue becomes brittle and allows cracks to propagate easily, leading to a reduction in toughness and impact strength.[1,19] Genetic disorders that lead to defects in the underlying collagen structure can result in an altered mineral composition (**Section 2.210.7**).

2.210.2.3. Noncollagenous Proteins

There are many NCPs in the ECM of bone and these comprise approximately 10% of the entire bone by mass. The most prominent proteins are osteocalcin, osteopontin, alkaline phosphatase, fibronectin, bone sialoprotein, osteoprotegerin (OPG), osteonectin, and thrombospondin. These proteins fulfill numerous functions, including organizing the collagenous matrix, mediating cell attachment, regulating the rate of growth, and regulating the stability of the mineral phase crystals,[21] as is outlined in detail subsequently.

Osteocalcin, also known as bone gla protein (BGP), constitutes 20–25% of noncollagen bone protein and is ubiquitous in bone tissue. It is produced by osteoblast cells and binds to the calcium of hydroxyapatite to regulate the growth of mineral crystals in bone.[22] In particular, it is believed to be able to slow down the growth of HA crystals and thereby act as a mineralization inhibitor.[23] Other studies propose that osteopontin may act as a signal to osteoclast precursors to begin differentiating into mature osteoclasts and initiate the process of bone resorption.[23–25]

Osteopontin is a phosphorylated protein that is found in abundance in cement lines, in the spaces between mineralized collagen fibrils, and along the canalicular wall.[26–29] It mediates cell attachment by binding cell surface integrin receptors. Therefore, it is believed that osteopontin acts as a regulator of osteoclast activity during bone resorption.[25] It is able to influence cell dynamics, and it is proposed that it may also promote adhesion between opposing surfaces at cement lines in bone.[27] Furthermore, it has been proposed that osteopontin might facilitate osteocyte mechanical sensing[30,31] by binding the ECM to an integrin receptor ($\alpha_v\beta_3$) that is present along osteocyte cell processes.[30] In the absence of osteopontin, the response of bone to underloading is altered.[31] Osteopontin also plays an important role in the formation of new blood vessels (angiogenesis) and prevents apatite formation and growth because of its high affinity for apatite crystals.[14]

Thrombospondin is a protein that is synthesized by osteoblasts[32] during the early stages of bone formation and as such is ubiquitous in unmineralized osteoid.[25] Bone sialoprotein is a member of the small integrin-binding ligand, N-linked glycoproteins family (SIBLING proteins) that is produced by osteoblasts at a late stage of maturation. The protein codistributes with osteopontin and accumulates in cement lines and interfibrillar collagen spaces.[28] Fibronectin is an ECM glycoprotein that is relatively abundant in bone tissue. Thrombospondin, bone sialoprotein, and fibronectin – all mediate binding of osteoblasts to the collagen, mineral, and other proteoglycans in bone tissue.[22] Bone sialoprotein is also believed to act to promote the mineralization process,[25] whereas fibronectin regulates the differentiation of osteoblasts.[33]

Alkaline phosphatase is an enzyme glycoprotein that is produced by osteoblasts during the early stages of bone formation. It functions to remove phosphate groups (hydrolyze) from mineral deposition inhibitor proteins[34] and thereby provides an initial attachment site for mineral nucleation along the collagen fibrils and is vital for increasing local phosphate concentration.[15]

OPG, also known as osteoclastogenesis inhibitory factor (OCIF), is a cytokine that is a member of the tumor necrosis factor (TNF) receptor superfamily.[35,36] It is believed to play a role in inhibiting the formation of mature osteoclasts by blocking the binding of receptor for activation of nuclear factor kappa B ligand (RANKL) to RANK.[37] Therefore, the primary role of OPG is to act as a regulator of osteoclastic bone resorption.[36]

Osteonectin is the most abundant NCP in mineralized bone matrix. It contains calcium-binding domains and plays a role in regulating the bone mineralization process.[22] It also binds varyingly to collagen, and it has been shown to play roles in regulating the cell cycle, cell–matrix interactions, and cell morphology.[25]

It has long been established that many proteins regulate matrix organization by acting as mineral crystal nucleation sites that bind mineral crystals to the collagen matrix.[38–41] The proteoglycans have a high negative fixed charge density and readily bind to Ca^{2+} ions. They are also known to play an important role in facilitating cell attachment[42] and thereby regulate cellular activity and maintenance of the collagen–mineral interface. They are believed to be responsible for regulating the mechanical properties of the collagen–mineral interface between modulating the formation of bonds between collagen and mineral.[21] Recent studies now suggest that NCPs form tough bonds between the mineralized fibers[42,43] and that these bonds have molecular self-healing abilities.[44,45] Interestingly, *in vitro* studies have shown that these bonds may have both energy dissipation[42] and energy storage capabilities.[42,43] There are substantial local variations in the content and

distribution of bone proteins,[28] and it has been proposed that such compositional differences may influence cell dynamics and remodeling.[46] Therefore, collectively, the NCPs in the bone are important for regulating the mechanical strength of the bone by several different means.

2.210.2.4. Bone Cells

Bone tissue is made and maintained by cells of the osteogenic and phagocytic lineage. There are five main types of bone cells in bone tissue osteoprogenitors, osteoblasts, osteocytes, osteoclasts, and bone-lining cells, each of which are crucial for bone growth, healing, and remodeling. Osteoprogenitors, osteoblasts, and osteocytes are responsible for the production of bone matrix and mineral, whereas osteoclasts and bone-lining cells are fundamental for the maintenance of this tissue throughout life. Each cell type has a different internal structure, they interact varyingly with their external matrix, and these differences play a large role in dictating the different physiological functions of these bone cells and more importantly, the unique behavior of the bone as a material.

2.210.2.4.1. Mesenchymal stem cells and osteoprogenitors

Mesenchymal stem cells (MSCs) are unspecialized multipotent cells that have the potential to mature into various cell types. MCSs are present in the primary cells of the embryo (germ layers) and are responsible for early skeletal development, but they also persist in mature adult bones where they are found in the periosteum, endosteum, and bone marrow (**Figure 4(a)**). The MSC has a basic cell morphology characterized by a small cell body, comprising a large, round nucleus with a prominent nucleolus that is surrounded by finely dispersed chromatin particles, a Golgi apparatus, a rough endoplasmic reticulum, mitochondria, and polyribosomes. Within the cytoplasm, there is a three-dimensional (3D) network of proteins known as the cytoskeleton, which consists of microtubules, intermediate filaments, and actin filaments that extend across the entire cytoplasm and are oriented in parallel.[47] The cytoskeleton dictates the morphology and shape of cells, and MSCs extend their cytoplasm into the surrounding matrix in which they reside by means of cell processes. At the beginning of the bone formation process (osteogenesis), MSCs proliferate to form a dense nodule of cells and differentiate to become osteochondral progenitors (osteoprogenitors) under the influence of growth factors, cytokines, and physical stimuli. Osteoprogenitors are cells that have committed to differentiating along the osteochondral lineage, and from this stage onward, they only have the ability to differentiate into chondrogenic (cartilage) or osteogenic (bone) cells. Morphologically, osteoprogenitors have large cell bodies, with more Golgi apparatus and rough endoplasmic reticulum than MSCs and do not have cell processes. The question whether or not they ultimately become chondroblast or osteoblast cells is dependent on the presence of growth factors and the surrounding physical environment. Bone morphogenetic proteins (BMPs), fibroblast growth factor (FGF), platelet-derived growth factor (PDGF), and transforming growth factor beta (TGF-β) are believed to promote the division of osteoprogenitors and increase differentiation along the osteogenic lineage to become osteoblasts.

2.210.2.4.2. Osteoblasts and bone-lining cells

Osteoblasts are the bone cells that are primarily responsible for synthesizing bone matrix proteins and minerals during early bone formation in the embryo, but also control bone formation and mineralization throughout life. They are found in areas of high metabolism where new bone formation is occurring. They have differentiated from either osteoprogenitors in the mesenchyme of the embryo or osteoprogenitors near bone surfaces in mature bone to become cuboidal, columnar cells that have a large Golgi apparatus, a rough endoplasmic reticulum, and a central nucleus[50] (see **Figure 4(a)** and **4(b)**). During embryonic bone formation, osteoblasts secrete collagen and NCPs that act as a template for the bone, but also produce minerals and regulate the precipitation and binding of minerals from the blood to the newly formed osteoid to facilitate the formation of a mature mineralized bone tissue and regulate the flux of ions into the extracellular environment during mineralization. Osteoblasts also function throughout life to produce new bone that is required to replace aged or damaged bone (**Section 2.210.6.2**) or repair bone fractures (**Section 2.210.6.3**). The formation period typically persists for about 100–150 days.[49] Osteoblasts express a range of genetic markers and synthesize various proteins, including type I

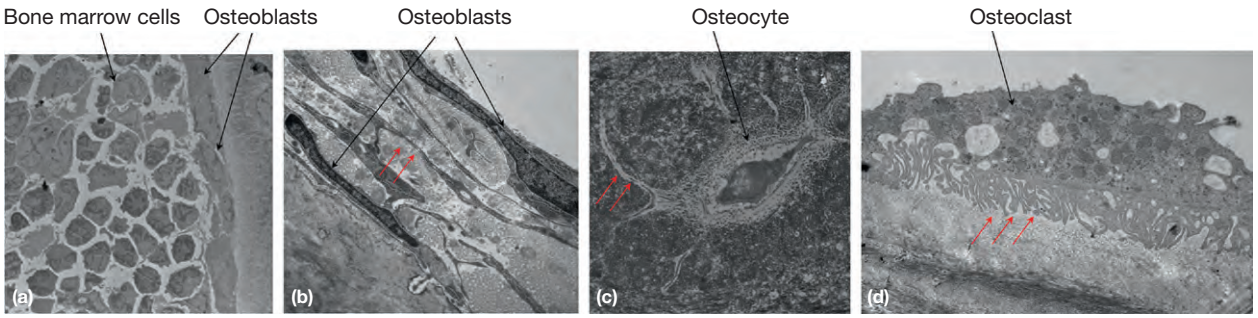

Figure 4 Transmission electron microscopy images of bone cells: (a) bone marrow cells containing blood cells, platelets, and progenitor cells and osteoblasts lining the bone surface; (b) osteoblasts on the surface become embedded in newly formed osteoid and develop cytoplasmic cell processes (↑↑) as they differentiate into osteocytes; (c) osteocyte embedded in bone cells with cytoplasmic cell processes encased in bone canaliculi (↑↑); and (d) osteoclast cells with ruffled border (↑↑↑) and multiple nuclei.

collagen, bone sialoprotein, macrophage colony-stimulating factor (M-CSF), RUNX2, alkaline phosphate, osteocalcin, osteopontin, and osteonectin. The mode of differentiation, recruitment, and inhibition of osteoblasts is controlled by numerous hormonal and growth factors,[48] including vitamin D, estrogen, and parathyroid hormone (PTH). Estrogens and PTH can increase the number of osteoblasts, which subsequently increases collagen production. Vitamin D also plays a part in the mineralization of bone matrix, and a lack of vitamin D results in osteomalacia (impaired mineralization). Osteoblasts have the ability to communicate with neighboring cells and osteocytes via gap junctions, and they secrete factors that activate osteoclasts (RANK ligand).

After osteoblasts have produced newly formed osteoid, a certain amount of the cells become encased in this matrix and differentiate to become osteocytes distributed throughout the bone matrix. Those that are not embedded remain on the new bone surface as quiescent osteoblasts, known as bone-lining cells, or undergo apoptosis (programmed cell death). Bone-lining cells have similar morphology to that of osteoblasts and serve to regulate the movement of calcium and phosphate into and out of the bone and provide access for osteoclasts during bone resorption.

2.210.2.4.3. Osteocytes

Osteocytes are the most mature and abundant cells in bone tissue and are formed when some osteoblasts become embedded in their secreted osteoid and begin to extend cytoplasmic cell processes to interconnect with each other (**Figure 4(b)**). During this time, the cells begin to differentiate into osteocytes and alter their morphology, their anabolic activity, and lose much of the organelle of osteoblasts. Mature osteocytes reside in a fluid-filled space in the ECM known as a lacuna and have a large nucleus, very little cytoplasm, and extend many elongated processes into their ECM (**Figure 4(c)**) to facilitate communication with other embedded osteocytes, bone-lining cells, and osteoblasts. These cell processes reside in fluid-filled channels known as canaliculi, which radiate from the osteocyte lacunae to the osteonic (haversian) canal to provide passageways for nutrient supply through the impermeable matrix.[11] The cell body and processes are surrounded by a glycocalyx,[50] and the cell processes are attached to the ECM by means of punctate integrin-based attachments.[30] The cells are distributed throughout the ECM at a spacing of approximately 1600 mm^2.

Osteocytes play an important role in controlling the extracellular concentration of calcium and phosphate in bone tissue over time, by means of a process known as secondary mineralization whereby they control the growth in the crystal size of mineral.[51–53] Some studies also suggest that osteocytes might be capable of controlling calcium release from the bone tissue to the blood in a process known as osteocyte osteolysis, although this theory remains contentious.[54] It is also believed that osteocytes play an integral role in sensing mechanical signals and transducing these into biochemical signals to osteoclasts and osteoblasts to alter bone mass.[55–57] Their ubiquitous spatial distribution throughout the bone and their extensive communication network is ideal to facilitate intercellular communication. It is by this mechanism that they communicate the requirements for adaptation of the skeleton under altered mechanical demands or repair due to damage. Osteocytes also have the ability to sense changes in interstitial fluid and the levels of hormones that circulate in it[58] and stabilize bone mineral by maintaining an appropriate local ionic environment.[11] It has been shown that osteocytes secrete large amounts of factors known to stimulate osteoclast resorption (M-CSF, RANKL) along their cell processes.[59] The activity of the cells is governed by estrogen, PTH, glucocorticoids, vitamin D, calcitonin, and prostaglandin.[60]

2.210.2.4.4. Osteoclasts

Osteoclasts are derived from precursor stem cells of the macrophage lineage, known as bone marrow stromal cells or monocytes, which reside in the hematopoietic bone marrow.[50] The primary function of the osteoclast is to digest aged, damaged, or disused bone during the physiological processes of modeling and remodeling. This process is known as bone resorption and begins when bone-lining cells degrade unmineralized osteoid and increase expression of growth factors to recruit preosteoclasts from the bone marrow. Under the influence of cytokine and growth factors, the monocytes fuse and differentiate to form mature active osteoclasts that have multiple nuclei and a large cytoplasm (**Figure 4(d)**) that has many vesicles and vacuoles.[61] The mature osteoclast attaches to bone surface via integrin-based attachment proteins, which involves binding of the integrin $\alpha_v\beta_3$ to vitronectin, to form a specialized cell membrane known as the ruffled border (**Figure 4(d)**). This membrane seals off the resorption site of the underlying matrix, and it is through this membrane that hydrogen ions and enzymes are secreted to acidify and dissolve the calcium and phosphate minerals in the matrix and thereby facilitate bone resorption. The function of the ruffled border is to maximize the surface through which hydrogen ions are released. The digested material is absorbed into small vesicles and these are released into the extracellular fluid as waste products. After resorption, osteoclasts undergo apoptosis.

Osteoclast differentiation and function is controlled primarily by three factors: M-CSF, RANKL, and OPG. M-CSF is produced by osteoblasts and is required for survival and differentiation of osteoclast precursors. RANK is a receptor that is present on the surface of osteoclast precursor cells. RANKL is expressed on the surface of osteoblasts and lining cells and binds to RANK, which leads to the differentiation and maturation of the osteoclast precursor into mature multinucleated osteoclasts. OPG is made by osteoblasts and blocks both osteoblasts formation and bone resorption. Osteoclast recruitment and differentiation is also governed by hormonal and growth factors[48] including estrogen, vitamin D, and PTH. Estrogen's effect on osteoclasts is inhibitory; estrogen activates osteoclast receptors to decrease formation of mature osteoclasts[62] and increases osteoclast apoptosis.[63] Vitamin D and PTH can increase the recruitment and activity of osteoclasts, stimulating bone resorption and resulting in an increase in blood calcium levels. Other growth factors and cytokines also regulate osteoclast activity: TNF-α, the interleukin cytokines (IL-1, IL-6, IL-7), TGF-β, vascular endothelial growth factor (VEGF), PDGF, and FGF.[64–66] As a result, the osteoclast resorption process is sensitive to hormonal status and drug treatments.

2.210.3. Bone Formation

During embryonic development, bone formation occurs by two distinct mechanisms; either endochondral ossification or intramembranous ossification. Bone formation also persists throughout life to alter the geometry of bones and provide larger bones that are sufficient to withstand changes in mechanical loading (modeling), or to replace aged or damaged bone (remodeling) or fill fracture gaps (Section 2.210.6). Bone formation is typically a two-step process whereby an organic matrix (osteoid/cartilage template) is initially laid down by osteoblasts, and then mineral crystals are precipitated and grow slowly over time to produce the composite material.

2.210.3.1. Endochondral Ossification

Endochondral ossification is the process by which bone tissue is formed in early fetal development. It begins when MSCs start to produce a cartilage template of long bones, such as the femur and the tibia, upon which bone morphogenesis occurs.[67] The process initiates when MSC cells differentiate to become chondroblast cells (Figure 5(a)) and form a membrane around the template known as the perichondrium. This template grows in length (interstitial growth) and thickness (appositional growth) when the chondroblasts proliferate or more chondroblasts are recruited from the perichondrium (Figure 5(b)). Together, these cells secrete an ECM comprised mainly of collagen and proteoglycans. Over time, these chondroblasts differentiate to become chondrocytes and begin to secrete alkaline phosphatase, which is an enzyme that acts as a nucleator for deposition of minerals on the template. They also secrete growth factors to promote the invasion of blood vessels into the perichondrium, which is known as vascularization. This process forms the outer membrane of the bone, which is primarily a dense irregular connective tissue known as the periosteum (Figure 5(c)). The periosteum is an important source for undifferentiated osteoprogenitor cells.[68] It is divided into an outer fibrous layer, which is a source for fibroblasts, and an inner osteogenic layer, which is a source for osteoprogenitor cells that develop into osteoblasts. The periosteum also provides sites for attachment for ligaments, tendons, and muscles. This process begins in the middle of the template, which is known as the primary center of ossification (Figure 5(c)). During mineralization, the chondrocytes undergo apoptosis and the cavities that remain are invaded by blood vessels from the perichondrium. These blood vessels are a source for hemopoietic cells that form the bone marrow and osteoprogenitor cells, which differentiate to become osteoblast cells and secrete bone proteins and minerals. Endothelial cells (ECs) on the lining of blood vessels produce essential growth factors that control the recruitment, proliferation, and differentiation of osteoblasts.[69] Therefore, vascularization is an essential requirement for bone formation.[68,70] A number of other factors regulate the formation of blood vessels, including oxygen tension, mechanical loading, nutrients, and growth factors.[71] Osteoclasts are also recruited during this time to remodel the template and form a cavity for bone marrow (medullary cavity), and together, these events provide the first bone tissue during fetal development. At birth, a secondary ossification center appears in the epiphyses of long bones, which is vascularized and forms a cartilage layer known as the growth plate (Figure 5(d)).

The formation and growth of bones is ongoing throughout childhood and is regulated by the epiphyseal or growth plate (Figure 5(d)), which continues to produce new cartilage, which is replaced by bone, and thereby facilitates lengthening of bones. In adults, lengthening of bones stops and the growth plate fuses and is replaced by bone, known as the epiphyseal line. Bones can continue to grow in diameter around the diaphysis by deposition of bone by osteoblasts beneath the periosteum, and simultaneously osteoclasts on the interior surface (endosteum) resorb bone to maintain a lightweight structure. The coordinated process of endochondral ossification is essential to the development and growth of long bones of the body, but also regulates fracture repair, as is discussed in Section 2.210.6.3.

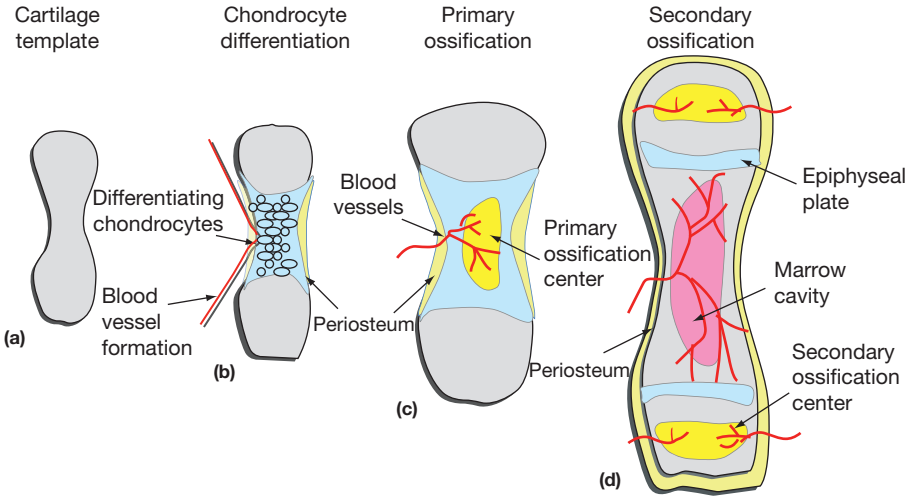

Figure 5 Schematic diagram of endochondral ossification.

2.210.3.2. Intramembranous Ossification

During embryonic development, bone formation also occurs by means of a process known as intramembranous ossification, which regulates the formation of nonlong bones such as the bones of the skull and clavicle. The primary difference between intramembranous and endochondral ossification is that the intramembranous process does not rely on the formation of a cartilage template. Instead, embryonic stem cells (MSCs) within mesenchymal tissue of the embryo, derived from primary tissue (germ layers), begin to proliferate and condense to form an aggregate of MSC cells. This nodule is surrounded by a membrane, and MSCs within the membrane begin to differentiate to first become osteoprogenitor cells and then osteoblasts. These osteoblasts line the nodule and secrete an ECM consisting of type I collagen fibrils within the center of the nodule. Some osteoblasts become embedded within the newly formed matrix, and in this environment, they differentiate and form interconnecting cytoplasmic processes to become osteocytes. The cells on the outer surface form a periosteum, and bone growth continues at the surface of the trabeculae. At this time, the nodule is mineralized to form rudimentary bone tissue that is populated by osteocytes and lined by active osteoblasts.[48] This tissue is known as a bone spicule and many spicules fuse to form trabeculae, known as primary spongiosa, which then fuse to form woven bone. Over time, this woven bone is remodeled to become lamellar bone, with concentric lamellae surrounding Haversian systems in what is known as an osteon.[48,72,73]

2.210.4. Bone Structure and Hierarchical Organization

Bone architecture is hierarchical and complex, consisting of component phases at different levels of structural organization,[74] and these can be classified from the organ level to the macrostructural, microstructural, and nanostructural level. This intricate and complex hierarchical organization of bone is fundamental to its function.

2.210.4.1. Bone Tissue Structure and Organization

The bone that comprises that adult skeleton is organized into two main types; approximately 80% of the mass is a bone tissue known as cortical bone and the remaining 20% is known as trabecular bone, which is also known as cancellous or spongy bone. The microstructure of the bone is organized differently depending on the anatomical location and the type of bone involved; however, the basis of the differences between bone types arises predominantly from the microstructural organization of layers, or lamellae, of bone tissue.

Cortical bone is a dense bone tissue that is characterized by a low porosity of approximately 5–10%. It is most commonly found in the shafts of long bones and also forms a shell around the ends of bones such as the vertebrae, scapula, and pelvis (Figure 6(d)). It serves to bear load, transmit mechanical forces from the musculature, and provide levers to facilitate movement. Cortical bone can be further classified into either woven or lamellar bone, and the tissue is organized into structural units known as lamellae and osteons. Woven bone is the term used for immature bone that has a highly irregular organization wherein there is no distinct organization of the collagen fiber bundles or osteocyte cells, but rather they are oriented at random in a meshwork. Owing to the lack of structural organization, woven bone exhibits low strength. Woven bone is present in newly formed bones and is gradually replaced by lamellar bone as growth continues by remodeling (Section 2.210.6.2), but is maintained at tendon insertions and tooth sockets. In lamellar bone, collagen fibrils and osteocyte lacunae are organized into parallel layers known as lamellae, and within each lamella, the collagen fibrils are oriented in the same direction, but collagen fibrils in adjacent lamellae are oriented by 90° relative to each other. This organization of lamellae differs in certain regions in the bone; lamellae that are organized parallel to periosteal and endosteal surfaces are known as circumferential lamellae, whereas in regions of bone tissue that contain blood vessels, lamellae are organized in concentric rings around a Haversian canal that contains a central vessel, and each structural unit is known as an osteon (Haversian system). These blood vessels are essential for providing a nutrient supply to the bone cells that reside in the impermeable bone matrix. The Haversian canal is approximately 70 μm in diameter and the blood vessel is 15 μm.[75] Primary osteons have few lamellae and small vascular channels and are formed in the embryo during mineralization of the cartilage template. Secondary osteons are formed by

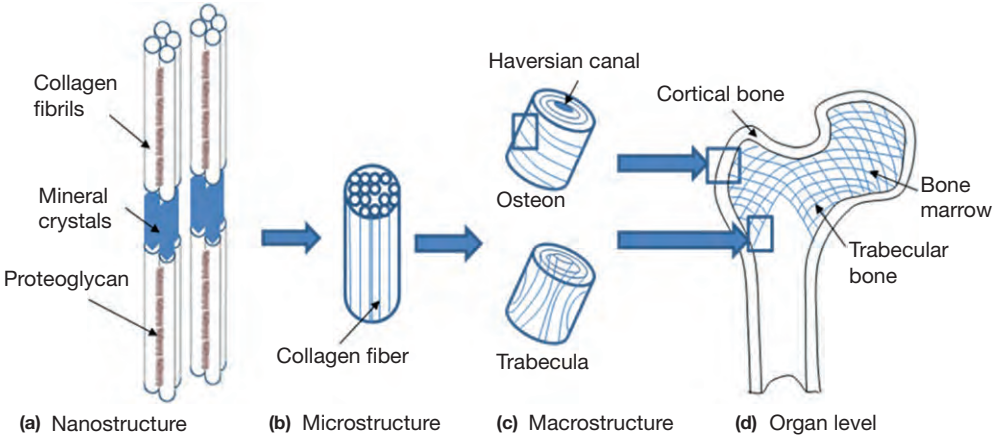

Figure 6 Schematic of bone tissue organization in the cortical and trabecular bone.

replacement of existing bone tissue during remodeling (Section 2.210.4) and are 200 μm in diameter. A significant feature of secondary osteons is the presence of cement lines that mark the interface between adjacent osteons. It is a matter of debate whether this material is less or more mineralized than the osteon,[76–78] and it has been proposed that the cement lines act as mechanical bonds between osteons or transfer energy between osteons to slow crack growth.[76] There are multiple types of microstructural pores within cortical bone tissue, vascular pores, lacunar–canalicular pores, and collagen–apatite pores.[74,79] These pores provide a network to transport nutrients, mineral ions, and waste products to and from the vascular system to bone cells. It is also believed that fluid flow, within these pores, provides essential mechanical stimulation to the cells.

The trabecular bone is a highly porous (typically 75–95%) form of bone tissue that is organized into a network of interconnected rods and plates called trabeculae which surround pores that are filled with bone marrow. This bone tissue is found at the ends of long bones such as the femur, and also in the vertebrae. In the trabecular bone, the lamellae are organized into single trabeculae, which are the structural units of the trabecular bone and are not vascularized. The intervening space between these trabeculae is filled with bone marrow. Human trabeculae are typically 150–300 μm in diameter and can be up to 2000 μm in length, and their shape is determined by their anatomical location and loading situation. It has been hypothesized that these trabeculae are directed along the force trajectories created by weight-bearing forces.[80] This highly specialized hierarchical organization lends bone its unique strength and stiffness to withstand the complex loading experienced during normal activities, but also ensures that bone is sufficiently lightweight to facilitate efficient movement in response to the forces generated by muscles. Extensive research has been carried out to characterize the exact morphology of the trabecular architecture.[81–83] Microarchitecture is a term which refers primarily to the microscopic morphology and organization of the trabecular bone. Bone microarchitecture is typically characterized using techniques such as micro-CT (μCT) scanning, which relies on exposing bone to an X-ray source, and using an X-ray detector to obtain 3D representations of the trabecular architecture at various resolutions. Such techniques have allowed the morphology of the trabecular bone to be analyzed at resolutions ranging from 14 to 250 μm. Quantitative parameters have been defined to characterize the structure of the trabecular bone, such as bone volume, trabecular thickness, trabecular separation, number of trabeculae/mm^2, and trabecular length.

It has been reported that more than 80% of the variance of trabecular bone strength and modulus can be explained by measures of density and trabecular orientation.[84] The degree of porosity of the trabecular bone varies with anatomical location. Besides the porosity associated with the marrow-filled cavities in the trabecular structure, trabecular bone tissue also has a lacunar–canalicular porosity and a collagen–apatite porosity.[79] These different levels of porosity serve to exchange bone fluid with the marrow, to provide mechanical stimuli for bone cells, and to transport nutrients and waste products to and from the marrow to the bone cells.

2.210.4.2. Organ Level

The skeleton consists of 206 bones, which are classified broadly into either the axial skeleton or the appendicular skeleton. The appendicular skeleton is composed of 126 bones, which are essential for locomotion and manipulation of objects in the environment. These bones include the long bones such as the femur, tibia, and fibula of the legs, and the humerus, ulna, and radius bones of the arm. Long bones are tubular in structure and have a shaft comprising dense cortical bone known as the diaphysis, which surrounds a medullary cavity filled with bone marrow. Porous trabecular bone is found in the extremities (epiphysis) and is covered by a thin shell of cortical bone. The epiphyseal plate is a hyaline cartilage plate in the metaphysis of long bones and is the site from where the bone grows in length. Hyaline cartilage covers the ends of bones and serves to prevent friction and absorb shock. Each of these bones is covered by vascular membranes known as the periosteum on the outside surface in regions where there is no hyaline cartilage, which attaches to ligaments and tendons, and an endosteum on the inner surface. Each of these linings is a source for bone cells that are essential for maintenance and remodeling.

The axial skeleton consists of 80 bones in the human skull, the rib cage, the vertebral column, the ossicles of the inner ear, and the hyoid bone of the throat. The vertebrae are primarily composed of the trabecular bone and are covered by a thin layer of cortical bone. In contrast to long bones, vertebrae have no medullar cavity. Short bones are comprised predominately of trabecular bone and have a thin shell of cortical bone surrounding. These bones include the bones of the wrist and ankle, such as the tarsal bones of the feet, the carpal and metacarpal bones of the hands, the phalanges, the pectoral girdles, clavicles, scapula, pelvis, and sesamoid bones.

2.210.5. Bone Mechanical Behavior

Bone is a highly specialized tissue that comprises a composite material which is organized in a complex hierarchical structure, and its biomechanical behavior is accordingly intricate and varies greatly depending on the length scale (i.e., tissue level, organ level) at which it is assessed. Given this complexity, the mechanical behavior has been investigated at different length scales and resolutions to provide a holistic understanding of the biomechanical behavior of the bone. In general, the mechanical behavior can be segregated into the whole bone mechanical behavior, the structural mechanical behavior, and the tissue-level mechanical behavior. The structural mechanical properties are determined by mechanical testing of samples that comprise multiple trabeculae and thereby the measured mechanical behavior encompasses the trabecular architecture and bone mass of the sample (Section 2.210.5.1). In contrast, the properties of the tissue itself are independent of bone mass and architecture and are typically characterized by testing single trabeculae or microscopic samples of bone tissue (Section 2.210.5.2). These studies have provided information regarding the complex hierarchical mechanical behavior of bone at the microscopic and nanoscopic levels. At each scale, bone can be classified as an anisotropic, heterogeneous,

nonlinear material, and the material properties of the trabecular bone vary considerably at different anatomical locations and the type and direction of loading that is applied.

2.210.5.1. Structural Mechanical Behavior of Trabecular Bone

The structural behavior (also known as the apparent behavior) is determined by the mechanical testing of cylinders (typically, 5 mm in diameter) or cubes (5 mm^3) of the trabecular bone. Samples of this size represent the continuum mechanical properties of the bone tissue but are sufficiently large to overcome limitations of the continuum assumption near biologic interfaces (within three to five trabeculae of an interface) and in areas of large stress gradients.[85] Mechanical testing of volumes of trabecular bone from the proximal and distal femur, the vertebral body, or the proximal tibia have provided an important understanding of the heterogeneous mechanical behavior of the trabecular bone.[82,86–88] At this scale, the heterogeneity is largely due to variations in the bone mass (volume fraction) and the 3D architecture of the trabeculae,[89] but variations in tissue composition and organization also contribute to this behavior (Section 2.210.5.2). The trabecular microarchitecture is an important determinant of bone strength and susceptibility to fracture.[90,91] The apparent elastic modulus of the trabecular bone varies considerably within a single vertebral bone, with modulus values ranging from 165 MPa in the superoinferior direction to 43 MPa in the lateral direction.[82] It has also been reported that the mean yield strength of the trabecular bone in tension is 15.6 MPa and that this is 30% lower than the yield strength under compressive loading.[92] The apparent yield strain of the trabecular bone is approximately 0.8%.[88] The fatigue failure criterion of the trabecular bone matrix has also been investigated by testing within normal physiological frequencies that range from 0.5 and 3 Hz, and it has been reported that the number of cycles to failure ranged from 20 cycles at 2.1% strain to 400 000 at 0.8% strain.[93]

The mechanical behavior of the trabecular bone varies across anatomical locations,[84,94,95] and further variations arise between different bones and species. The mechanical behavior of the trabecular bone deteriorates with the process of aging, and it has been reported that the ultimate stress of the trabecular bone from the human femur and spine is reduced by approximately 10% per decade in the adult skeleton.[96–98] Owing to the structure of the trabecular bone, the material properties obtained by testing volumes of the trabecular bone are highly dependent on the architecture of the matrix and do not represent the properties of the mineralized tissue itself.

2.210.5.2. Tissue Mechanical Behavior of Bone

As bone is a hierarchical material, the properties of the tissue must be known to fully understand the mechanical behavior of the bone. In particular, it is often widely assumed that the mechanical properties of the trabecular bone are the same as cortical bone at the tissue level, and that it is their architecture that distinguishes them. Mechanical testing of trabecular and cortical bone specimens has been carried out using a variety of methods such as 3/4-point bending,[99] buckling,[100,101] cantilever beam tests,[102] microtensile testing,[103–107] and ultrasonic measurement.[105] The details of these studies are summarized in Table 1. Reported values for the elastic modulus of trabecular tissue from these studies have conflicted, with values ranging from 0.75 to 20 GPa. One study applied both microtensile testing and an ultrasonic technique to compare the elastic modulus of individual trabeculae and microspecimens of the cortical bone[105] and reported that the elastic modulus of individual trabeculae (10.4 ± 3.5 GPa) is significantly lower ($p < 0.0001$) than that of cortical bone (18.6 ± 3.5 GPa). A system was designed to measure the tensile strength and elastic modulus of individual trabeculae, which overcame previous limitations by eliminating inaccuracies due to sample alignment, geometry, and gripping.[21] The results of this study indicated that the elastic modulus of the trabecular bone is

Table 1 Previous studies to determine the mechanical properties of bone tissue

Study	*Property*	*Mechanical test*	*Specimen origin*	*Elastic modulus (GPa) Mean (SD)*
McNamara *et al.*[103,172] and McNamara *et al.*[104]	Elastic modulus, yield strength, postyield strain	Tensile testing	Rat proximal tibia	2.81 ± 2.09
Townsend and Rose[241]	Elastic modulus	Buckling	Human medial tibia	14.1 (dry); 11.3 (wet)
Runkle and Pugh[100]	Elastic modulus	Buckling	Human subchondral bone	8.7 (3.2)
Mente and Lewis[102]	Elastic modulus	Cantilever beam	Dried human femur	6.2 (1.2)
			Fresh human tibia	11.2 (10.1)
Ryan and Williams[242]	Elastic modulus	Tensile	Bovine distal femurs	–
Ryan and Williams[106]	Elastic modulus	Compression	Bovine femora	0.8 (0.4)
Kuhn *et al.*[243]	Elastic modulus	Three-point bending	Human iliac crest	3.8
Choi and Goldstein[244]	Fatigue strength	Three-point bending	Proximal tibia	–
Choi *et al.*[99]	Elastic modulus	Three-point bending	Proximal tibia	4.6 (1.3)
Rho *et al.*[105]	Elastic modulus	Ultrasonic/microtensile	Proximal human tibia	10.4 (3.5)
Choi and Goldstein[108]	S–N curve	Four-point bending	Proximal tibia	–
Van Rietbergen *et al.*[245]	Elastic modulus	High-resolution FE modeling	Proximal human tibia	5.91
Rho *et al.*[112]	Elastic modulus	Nanoindentation	Human vertebrae	13.5 (2.0)
Turner *et al.*[116]	Elastic modulus	Nanoindentation	Human distal femur	18.14 (1.7)
		Acoustic microscopy		17.5 (1.12)

significantly lower than that of the cortical bone with an approximate elastic modulus of 2.8 GPa.[103,104] Three- and four-point bending tests of individual trabeculae have been applied to investigate the fatigue properties of individual trabeculae from the human proximal tibia and reported that the fatigue strength of trabecular bone tissue is 100–140 MPa and that at these stress levels, the number of cycles to failure is approximately 100 000.[108]

The tissue mechanical properties of the trabecular bone have also been assessed using the nanoindentation technique, which can characterize the submicrostructural (1–5 μm resolution) mechanical properties (elastic modulus, hardness) of bone tissue. Atomic force microscopy or scanning electron microscopy techniques can be used to image the indentation and accurately estimate the indent area. This technique has been extensively applied to compare the nanomechanical properties of bone tissue.[109–112] The stiffness calculated has ranged from 7 to 25 GPa for cortical, trabecular, and interstitial tissue.[109,112–114] The variability between different studies arises as a result of differences in the method of material preparation and degree of moisture of the sample.[112,115,116] Furthermore, nanoindentation systems are particularly sensitive to changes in temperature, humidity, and environmental vibrations.

Acoustic microscopy (30–60 μm resolution) can also be used to evaluate the microstructural elastic properties of the trabecular bone. This method involves producing an acoustic wave in a tiny area just in the vicinity of the surface (near-field area) through different interaction mechanisms. The acoustic properties of materials can be determined at a high resolution from the acoustic wave detected. Turner *et al.*[116] used both nanoindentation and acoustic microscopy to compare the Young's moduli of trabecular and cortical bone tissues from a common human donor.[116] They reported that the Young's modulus of the cortical bone in the longitudinal direction was about 40% greater than ($p < 0.01$) the Young's modulus in the transverse direction. The Young's modulus of trabecular bone tissue was slightly higher than the transverse Young's modulus of cortical bone, but substantially lower than the longitudinal Young's modulus of cortical bone. These findings were consistent for both measurement methods and suggest that elasticity of trabecular tissue is within the range of that of cortical bone tissue.

2.210.5.3. Fracture Behavior

Bone is a composite material, and as a result, its fracture behavior is intricate. Physiological bone fractures occur under creep, fatigue, and impact loading conditions. The fracture and damage occurring in the bone can be segregated into macro-level cracks and diffuse microdamage, which occur in the bone during both normal and extreme loading conditions. Studies have investigated the route of propagation of major cracks,[117–119] and it has been shown that for the most part, fracture occurs at the interfaces between separate bone tissue lamellae.[120] It is believed that this interface provides a toughening mechanism for the bone tissue by absorbing energy and resisting the growth of macro-level cracks. This energy is dissipated elastically to deform the collagen–mineral matrix, to deflect cracks along lamellar interfaces, or by the formation of microcracks prior to catastrophic fracture. In particular, it has been demonstrated that, in the presence of a large propagating cracks, smaller microcracks nucleate, grow, and coalesce to absorb energy from larger cracks in the bone.[121] Other studies have shown that toughening occurs in the bone when microcracks are bridged by collagen fibrils that span the width of the crack, and that this acts to increase fracture resistance in bone tissue.[122–124] The fracture behavior of the bone is anisotropic, and crack growth occurs by brittle mechanisms in the longitudinal direction, becomes deflected in the tangential direction, and is toughened by microcracking in the radial direction.[120] This is due to the organization of the collagen fibril matrix which resists cracks that attempt to drive across the grain, (fiber direction) that is, those that are oriented parallel to the collagen fibril axis.[120]

One of the most important features of the bone is that it has the ability to tolerate microdamage without causing macroscopic failure. Microdamage accumulates in bone tissue from the cyclic loading situations created by everyday activities such as walking and running throughout our lifetime.[125,126] Microcrack accumulation impairs the mechanical properties of the bone by reducing its elastic modulus.[127] The ability of the bone to renew is believed to be vital to remove this microdamage and maintain strength (**Section 2.210.6.2**). The fracture toughness of the bone gives a measure of the ability of the material to resist crack growth. It has been shown that young bone is tough under impact loading, which is less mineralized,[19] but the fracture toughness of the bone deteriorates significantly with age.[128,129] At high strain rates, the postyield region, the capacity for energy absorption, and the microcracking damage reduce significantly.[130,131]

2.210.6. Bone as a Dynamic Adaptive Material

Bone is a particularly fascinating dynamic material that has the capacity to adapt its shape, mass, and microstructural architecture throughout life by means of the physiological processes of bone modeling and remodeling. Bone modeling involves growth and adaptation of bones to produce a mechanically functional architecture,[48] whereas bone remodeling is a process whereby bone is renewed continuously so that it continues to maintain strength throughout life. Both processes are facilitated by the coupled action of osteoclast and osteoblast cells. Bone is also able to renew itself following fracture through a process known as fracture healing, which is regulated by stem cells, cartilage cells, and bone cells. These adaptive processes are fundamental to the normal physiological function of the skeleton as they allow bones to survive and adapt under the variety of loading conditions experienced.

2.210.6.1. Bone Modeling

Modeling is a process that facilitates the growth and change in shape of bones and predominantly occurs during childhood and adolescence. Modeling is defined as the process by which bone resorption by osteoclasts and bone formation by osteoblasts occur simultaneously, but on different surfaces of the bone, to alter the overall bone shape or dimensions.[132] For example, the cells operate to increase the diameter of long bones and develop a marrow cavity when osteoclasts resorb

the endosteum, while osteoblasts form a new bone at the periosteum. This process results in an overall change in the bone morphology and is distinct from bone remodeling.[132] Modeling also occurs in the adult skeleton and serves to regulate overall changes in bone morphology in response to altered mechanical loading. During unloading, bone resorption is not followed by formation and during overloading, bone formation occurs in the absence of bone resorption. Both processes result in changes in both the microarchitecture and whole bone shape.[133]

2.210.6.2. Bone Remodeling

Remodeling is a coordinated physiological process, which is regulated by osteoclast cells that digest aged or damaged bone tissue and osteoblasts that reform new bone tissue in its place. In contrast to modeling, osteoclasts and osteoblasts operate concurrently on the same surfaces and are known collectively as basic multicellular units (BMUs). The action of these cells appears to be coupled, with osteoclasts traveling along trabecular surfaces or tunneling into cortical bone resorbing unwanted or damage bone tissue and osteoblasts subsequently filling in the resorption cavity with new tissue,[134] see **Figure 7**. The process initiates when bone-lining cells degrade unmineralized osteoid and increase expression of growth factors to recruit bone resorbing osteoclasts from the bone marrow that attach to bone surfaces and secrete acids and enzymes to digest bone matrix. Osteoclasts resorb at a longitudinal rate of 40 μm per day, and a typical resorption cavity depth is 40–60 μm.[135,136] At any one spot on the surface, the resorption lasts approximately 2 weeks and the entire resorptive sequence lasts for 40–50 days.[49] After resorption, the osteoclasts undergo apoptosis, and additional growth factors are released which recruit osteoblasts to form layers of osteoid and slowly refill the cavity.[137] In normal remodeling, there is a small bone mass loss (−1 μm) with age, as osteoblasts deposit less bone tissue than the osteoclasts have resorbed.[49] These cells also produce growth factors that inhibit further resorption by osteoclasts. During normal physiology, this continuous cellular activity is coordinated so that bone mass and strength are maintained to allow bones to bear normal physiological loading.

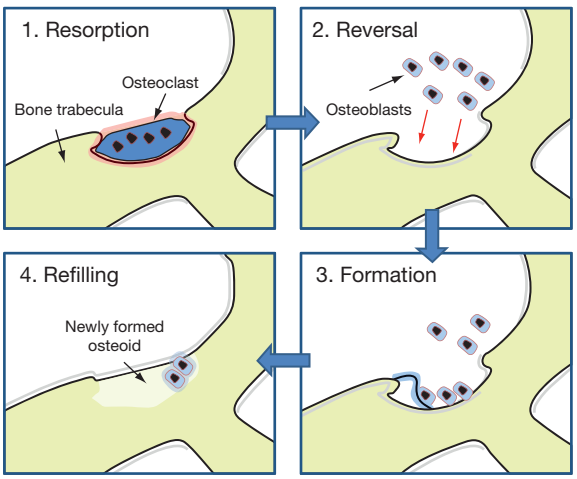

Figure 7 Schematic illustrating cellular activity during the bone remodeling process: (1 and 2) osteoclasts resorb damaged tissue and (3 and 4) osteoblasts refill the cavity with newly formed osteoid, which is subsequently mineralized.

2.210.6.3. Fracture Healing

Even though bone has the ability to repair and remodel itself continuously throughout life, certain traumatic injuries and various pathological diseases, such as osteoporosis, osteogenesis imperfecta, and Paget's disease, can impair these normal functions and lead to bone fractures (**Section 2.210.7**). Fracture healing is a physiological process by which bone fractures are repaired and occurs through the coordinated activity of osteoprogenitor, chondroblast, and osteoblast cells.[138] The process initiates when bleeding results in the formation of a hematoma and inflammatory cells are recruited to the fracture site. Next, cells within the bone and platelets within the hematoma produce cytokines that recruit fibroblasts and MSCs from the periosteum and marrow to the fracture site. These cells produce a granulation tissue, consisting of cells and blood vessels, at the site of fracture. Immune cells, known as macrophages, are also recruited to remove damaged tissues and other debris. The inflammatory period persists for 3–7 days and, after this initial period, the reparative phase begins whereby cells in the fracture site begin to differentiate into either osteoblasts or fibroblasts. Osteoblasts produce woven bone, which quickly forms a periosteal and marrow callus that fills the fracture gap, but has a low mechanical stiffness.[139] In sites of poor blood supply, fibroblasts within the granulation tissue differentiate to become chondrocytes and form hyaline cartilage.[139] The cartilage and woven bone together form the fracture callus. The callus has a larger cross-sectional area than the native fractured bone to compensate for the presence of fibrous tissue and woven bone, which reduce the callus stiffness. Over time, the woven bone is remodeled to become lamellar bone and the cartilage is replaced by means of endochondral ossification. The lamellar bone is vascularized by the invasion of vascular channels. This reparative phase lasts for approximately 1 month and produces new bone that has similar mechanical properties to that prior to fracture. However, the enlarged cross-sectional area at the site of the fracture callus has implications in the efficiency of movement. Therefore, the callus is continuously modeled and remodeled by osteoclasts and osteoblasts until the bone approaches its original geometry, strength, and stiffness. This remodeling process depends to a large extent on the mechanical forces applied to the bone. In some cases, for example, in excessively large fractures or during disease, fracture healing is not activated and as a result, bone fractures do not repair (nonunions).

2.210.6.4. Mechanosensation

It has long been established that the bone can adapt to its mechanical environment, and there is ample evidence of bone loss (atrophy) during disuse and bone formation (hypertrophy) during increased physical exercise.[140] The exact mechanical stimulus for such changes has been much debated, as has the mechanism by which the bone can detect and communicate the need for bone repair. It is most commonly

believed that bone adaptation in response to mechanical loading is regulated by mechanosensitive osteocyte cells that have the ability to direct osteoclasts and osteoblasts to alter bone mass and optimize strength.[55–57,141,142] It has been postulated that osteocytes are capable of sensing several stimuli; matrix strain, pericellular fluid flow, or physical damage.

In particular, it is believed that the bone adapts to changes in the matrix strain to optimize the bone mass and architecture so that the bone is sufficiently strong to bear the loads it experiences but has a minimal mass. Experimental evidence has demonstrated that, at low strains, net bone resorption occurs and that, at elevated strains, net bone formation occurs.[143] It has been shown that cells of the osteoblast lineage (osteoprogenitors, osteoblasts, osteocytes) are capable of transducing strain-based mechanical signals into biochemical stimuli.[141] Based on such experimental evidence, the theory of adaptive elasticity was proposed, which stated that the bone has the capacity to adapt its architecture to attain a remodeling equilibrium strain state.[144] When the loading conditions deviate from normal, the density and mechanical stiffness of the material or the geometry of the bone is adapted to return to the equilibrium strain state. This theory was capable of predicting net surface remodeling of the bone according to adaptive elasticity theory.[145] A number of strain-based mechanoregulation theories have been formulated upon the theory of adaptive elasticity to predict the adaptive behavior of the bone. These have been applied in computational simulations to successfully predict bone adaptation under various conditions.[146–151] This theory has also been used to test the hypothesis that the osteocyte network has a mechanosensory function and is capable of signaling bone cells to adapt trabecular architecture.[152,153]

Although osteocytes are regarded to be the primary mechanosensors in the bone, the precise mechanism by which they can sense mechanical strain is unknown. It has been hypothesized that deformation of the osteocyte lacuna, strain energy density in the bone tissue,[149,153] or strain-derived fluid flow in the osteocyte canalicular channels[154] might stimulate the cell membrane. Experiments have supported such theories by demonstrating that fluid flow[155–157] and matrix strain[158,159] activate an anabolic response by osteoblastic cells *in vitro*. Latest research found that osteocytes may sense matrix strain and fluid flow in bone canaliculi via integrin-based ($\alpha_v\beta_3$) focal attachments between their cell processes and the ECM.[30,160] Theoretical models have predicted that these attachments may participate in osteocyte mechanotransduction by amplifying fluid flow-induced and matrix stresses on osteocyte cell processes.[160] Another study identified cellular structures comprising microtubules known as primary cilia in bone tissue[161]; primary cilia are understood to act as fluid flow sensors in other tissues, in particular, the kidney.[162] Therefore, it has been proposed that primary cilia may facilitate bone cells to sense strain-derived fluid flow.[163,164] *In vitro* studies have supported this premise by identifying primary cilia on osteoblastic cell lines [MC3T3, MLYO4] in cell culture,[165,166] and one study has shown that these cilia play a role in production of proteins associated with osteogenic and bone resorptive responses under *in vitro* fluid flow.[165]

It is known that microdamage accumulates in the trabecular bone, from the cyclic loading situations created by everyday activities such as walking, running throughout our lifetime. *In vivo* microdamage has been identified in the bone by a number of researchers.[125,126] Microcrack accumulation impairs the mechanical properties of the bone by reducing its elastic modulus.[127] Therefore, it has been proposed that bone remodeling may be targeted to maintain bone strength by resorbing damaged bone and replacing it with new bone, thereby preventing accumulation of damage.[167–173] Experimental evidence has shown that resorption cavities occur preferentially in regions of microdamage,[167,174,175] which would suggest that resorption cavities might indeed be initiated in sites where microdamage is present. Studies observed that microcracks, resorption cavities, and osteon formation sites are located near the periosteal surface of the original cortex, but that there were no microcracks in new fibrolamellar bone at periosteal or endosteal surfaces.[176] In a later study, they observed that the average microcrack length is consistent between sites and across species, which supported the idea of a repair mechanism triggered beyond a critical crack length.[125]

Prendergast and Taylor[177] developed a damage-adaptive law for bone remodeling. They hypothesized that, even at remodeling equilibrium, there exists a homeostatic burden of microdamage in the form of microcracks within bone tissue. If the amount of damage changed from this equilibrium amount, then a stimulus for bone remodeling was generated. The repair rate for bone remodeling was determined from the homeostatic stress. Application of the theory was capable of giving physically reasonable predictions of the adaptive response of a bone diaphysis under a change in torsional load.

It has been proposed that physical damage acts as a stimulus to bone cells by rupturing cell processes and interrupting cell signaling,[167,174] by shearing osteocytes' cell processes,[178] or by causing apoptotic death of the osteocyte, which in turn signals for removal of the dead cell.[169,171–173,179]

It is likely that bone cells are responsive to both strain- and damage-based remodeling stimuli, in order to simultaneously maintain bone mass and prevent fracture. Recent models[171,179,180] have predicted that a regulatory system capable of responding to changes in *either* strain or microdamage, but which prioritizes removal of damaged bone, can successfully predict the bone remodeling process (resorption, reversal, refilling) at the cellular level. It was proposed that osteocyte processes can sense changes in strain and fluid flow, but when excessive microdamage occurs, this damage interferes with the signaling mechanism or causes osteocyte apoptosis so that a remodeling response occurs to remove the dead osteocytes.

2.210.7. Bone as a Material During Disease and Drug Treatment

The process of aging and various pathological diseases can impair the capacity of the bone to perform fundamental mechanical functions. The most prominent diseases affecting bone are osteoporosis, osteogenesis imperfecta, Paget's disease (osteitis deformans), osteomalacia, rickets (vitamin D deficiency), and cancer of the bone (osteosarcoma). Each of these conditions severely impairs the ability of the bone and leads to bone fractures, and often these fractures do not repair (nonunions) or cause immobility, severe pain, and deformity.

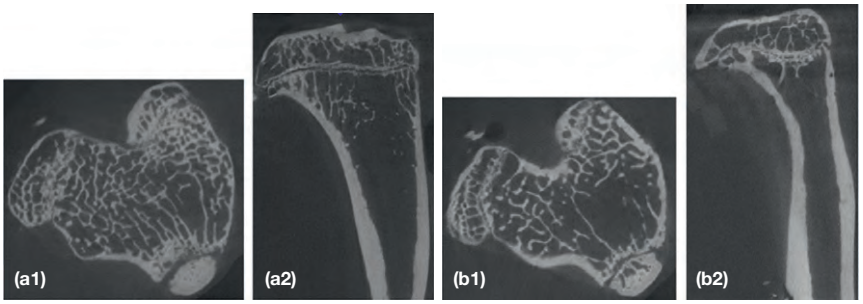

Figure 8 Micro-CT scanning image depicting the deterioration of bone microarchitecture during osteoporosis: (a1, a2) bone trabeculae are interconnected in normal bone tissue and (b1, b2) bone loss and microarchitectural deterioration (loss of connectivity, trabecular thinning) in osteoporotic bone.

2.210.7.1. Osteoporosis

Osteoporosis is a disease, which is most commonly manifested in postmenopausal women, that degrades bone mass and architecture. Physiologically, osteoporosis is manifested as an imbalance in bone cell activity during the remodeling process (Section 2.210.6.2) whereby excessive resorption occurs without adequate new bone formation. The basic bone units (trabeculae) become thin and eventually fracture and resorb altogether.[181] As a consequence, bone mass is reduced, the trabecular architecture is severely degraded (Figure 8), its mechanical strength is reduced, and bones become more susceptible to fracture. Fractures of the hip, wrist, or vertebra are most prevalent and lead to severe pain and spinal deformity.[182] Approximately 40% of women over 50 are at risk of developing the disease,[183] and the disease is the second most significant health threat to women, after breast cancer, with normal mortality rates increasing by 10–20% within a year of experiencing an osteoporotic fracture.[182,183]

2.210.7.1.1. Bone cell biology during osteoporosis

During menopause, the levels of circulating estrogen in the blood are deficient, and this deficiency is believed to play a role in the imbalance in the cellular activity during osteoporosis. Osteoclasts, osteoblasts, and osteocytes – all possess estrogen receptors (ERα, ERβ) that are activated to permit protein synthesis when they bind to estrogen.[184] The effect of estrogen deficiency on bone cell activity has been studied to identify pathways by which postmenopausal osteoporosis is manifested.

It has been found that osteoclastic activity is enhanced by estrogen deficiency, and that the reduced levels of circulating estrogen during osteoporosis are associated with increased rates of bone turnover and bone loss due. These changes occur as a result of an increase in the number and activity of osteoclasts.[185,186] The effect of estrogen deficiency on osteoclast behavior has been extensively characterized: (1) the activation frequency of BMUs and turnover rate is markedly increased,[187,188] (2) more osteoclasts are recruited,[186] (3) osteoclast apoptosis is inhibited,[63] and as a result, (4) the osteoclasts' resorption persists for a longer period, resulting in deeper resorption cavities and trabecular perforation.[189] The perforated trabeculae are removed by further remodeling, and this loss of bone mass, as is illustrated in Figure 8, increases the fragility of bones, resulting in a greater propensity for fracture.[90]

The effects of estrogen deficiency are not restricted to osteoclast activity as osteoblastogenesis also increases.[186,189] It has been suggested that estrogen allows the normal response of osteoblasts and osteocytes to loading.[190] As both cell types possess receptors for estrogen,[184] their function may be affected when estrogen production is deficient during postmenopausal osteoporosis. Previous findings regarding the effects of estrogen (E_2) on osteoblasts are inconsistent; E_2 enhances differentiation and mineralized bone nodule formation *in vitro*,[191] but alkaline phosphatase and osteocalcin expression are stimulated, inhibited, or unaffected.[192] Osteoblastic cells deprived of estrogen display deficient osteogenic responses to mechanical stimuli *in vitro*.[193,194] The osteoblasts may be no longer capable of completely refilling the resorbed space, resulting in irreversible bone loss. Estrogen deficiency induces osteocyte apoptosis,[195,196] which might result in hypermineralization of the surrounding tissue.[51,197,198] In addition, the organization of the osteocyte network is altered[199] and osteocyte density is reduced,[200] which may reduce the mechanoresponsiveness of the tissue.[201]

2.210.7.1.2. Mechanical behavior and structure during osteoporosis

The main concern with the disease of osteoporosis is that bone fractures occur unpredictably and with little force. For this reason, a number of studies have been carried out to characterize the biomechanical behavior of the bone during osteoporosis by assessing the structural degradation of the trabecular architecture and the mechanical consequences of bone loss.

At the onset of osteoporosis, an irreversible reduction in bone mass and volume occurs, leading to thinning and microfracture of trabecular struts and loss of trabecular connectivity.[181,202,203] Fractured trabeculae are eventually resorbed completely, resulting in an overall degradation in the trabecular network (see Figure 8(b)). Furthermore, the trabecular architecture of the osteoporotic bone is significantly more anisotropic than the normal bone, with fewer trabeculae transverse to the primary load axis.[204] Until recently, it was believed that bone loss occurred systemically, that is, bone resorption occurred throughout the trabecular architecture to the same extent, and that this loss was irreversible. However, recent studies have shown that, following an initial increase in bone loss and trabecular thinning in OVX rats, the few remaining trabeculae subsequently slowly increase in thickness.[205,206]

Assessment of the effects of osteoporosis on the mechanical behavior of the bone has been carried out previously using

whole bone testing of vertebrae and femora[207–211] or testing of volumes of cancellous bone[212–215] from rat and dog models. Using ovariectomy to induce osteoporosis in the rat, it has been found, for example, that the compressive strength of rat vertebral bodies and the bending strength of rat femora are significantly compared to the control bone.[208,210,211] In the human bone, it has been reported that the maximum modulus and ultimate stress is reduced in the femur following an osteoporotic fracture.[114,216] Such studies can explain the increase in fracture susceptibility at these sites. However, these observations were accompanied by significant decreases in trabecular bone volume and thus cannot discriminate whether changes were due only to the reduction in bone mass and loss of architecture, or whether a reduction in tissue strength also contributed.

It is essential to develop an understanding of the material behavior at the bone tissue level during osteoporosis to seek to fully address the issues of bone fracture during osteoporosis. It has been reported that trabecular bone tissue from osteoporotic patients had a lower apparent density, stiffness, and strength than age-matched patients with no evidence of disease.[217] In contrast, other studies have demonstrated that, while overall bone mass and bone mineral density are reduced, tissue (single trabeculae) stiffness and strength of ovariectomized rats are increased by 40–90%.[103,104] Despite the macrostructural and micromechanical changes in bone tissue during osteoporosis, to date no studies have confirmed that changes occur on the nanoscale.[218] In an ovine model of osteoporosis, the tissue modulus, as measured by nanoindentation, was significantly less than in the control bone.[219] While variations in experimental methods, animal model, or anatomical location might explain the discrepancies between previous studies, it is still unclear how bone mechanical properties are altered during osteoporosis. Such studies suggest that the primary constituents of bone tissue, namely, collagen, mineral, and NCPs, may be altered during osteoporosis.

A number of studies have been carried out that describe the effects of osteoporosis on the mineral content in the bone tissue with conflicting findings. Some studies report that the mineral content is unchanged or slightly lower in osteoporotic bone tissue,[217,220] and others reveal an increase in mineral content and a lack of collagen.[221–223] Variations in experimental methods, animal model, or anatomical location might explain this variability. The author undertook preliminary studies using a μCT system calibrated for bone mineral content assessment. Interestingly, a significant increase (11%) in mineral content of *remaining* tissue corroborated the unexpected changes in tissue properties.[103,104] Hence, these studies confirmed that, even though overall bone mass and strength are reduced during osteoporosis, the scarce tissue that remains is more mineralized, stiffer, and stronger.

Various changes in the compositional properties of the collagen have been reported at the onset of postmenopausal osteoporosis, in particular that changes in the amount of type I, VI, and III collagen occur.[224] The nature and quantity of the collagen cross-links that is altered,[225,226] in particular, the quantity of ketoimine, pyridinium,[227] aldimine,[224,228] and pyrrole cross-links, are decreased in osteoporotic bone.[229] Interestingly, these changes are more prevalent in the femoral neck, a site which is highly susceptible to fracture,[224] which indicates that such changes increase fracture susceptibility either by altering the strength of the collagen matrix or by secondary changes to the mineralization of this matrix.[224,230]

There is some evidence that the extent of microdamage is increased during estrogen deficiency,[231] which suggests that the tissue may be more brittle and less resistant to crack growth.[232–234] Alternatively, the remaining bone tissue may be more susceptible to damage following significant bone loss. Increased remodeling during osteoporosis has been proposed to be related to an accelerated removal of damaged tissue.[174]

2.210.7.1.3. Approaches for treatment of osteoporosis

The primary aim of drug treatments for osteoporosis is to reduce fracture incidence, and a variety of different treatments have been formulated which are based on the use of hormone replacement therapy, antiresorptive therapy, or anabolic agents. Hormone replacement therapy involves a pharmacological treatment with estrogen, which is often combined with progesterone, as a treatment for postmenopausal osteoporosis. This treatment has been shown to increase the bone mineral density of sufferers and thereby reduces the risk of hip and vertebral fractures in healthy postmenopausal women.[235] However, hormone therapy is no longer a popular choice of treatment, as it increases the risk of stroke, venous thromboembolism, coronary heart disease, and breast cancer. There is a wide range of antiresorptive therapies, such as bisphosphonates, selective tissue estrogenic activity regulators (STEARs), selective estrogen receptor modulators (SERMs), calcitonins, calcium, vitamin D, and metabolites and these represent a popular choice of treatment. While drugs of these types have different modes of operation, the common aim of antiresorptive drugs is to maintain bone mass and architecture by restoring the remodeling imbalance through inhibition of osteoclast activity and reducing bone resorption.[236] The efficacy of antiresorptive drug treatments has been assessed, and it has been found, for example, that treatment with tibolone[208,210,211] and other antiresorptive drugs such as risedronate,[213] etidronate,[209] alendronate,[212] pamidronate,[207] and incadronate[215] increases the structural or bulk trabecular bone strength[212,213,215] and the whole bone strength[207–211] compared to untreated osteoporotic bone by maintaining bone mass and trabecular architecture. PTH was shown to increase BMD and bone mineral content in ovariectomized monkeys.[237] PTH alone or in combination with antiresorptive medications reduces fracture risk of osteoporosis patients by increasing BMD.[238] While these drugs are capable of reducing the propensity to fracture by approximately 50%, even with continuous use of drug treatment fractures still arise.[239] It has been found that treatment with high doses of certain antiresorptive drugs is associated with an increase in the rate of spontaneous fractures of the thoracic spinous process, ribs, and pelvic fractures in animal models of osteoporosis.[209,240] A concern with some drugs for osteoporosis is that inhibiting the remodeling process prevents the necessary osteoclastic bone resorption, which serves as a repair mechanism to remove aged damaged bone tissue.[167,169,171–173,179] This may allow microdamage to accumulate in the bone tissue, so that, although bone mass and architecture are maintained, bone strength at the tissue level may be impaired.

2.210.8. Conclusion

Even with the vast amount of research, the complex biological and mechanical behavior of the bone is still intriguing, as the pathogenesis of bone disease is not fully understood and the occurrence of bone fractures remains a significant clinical issue. This fascinating material will continue to be studied until the normal physiological and mechanical function of the bone has been delineated and the pathogenesis of fracture is characterized.

References

1. Currey, J. D. *Philos. Trans. R. Soc. Lond. B Biol. Sci.* **1984**, *304*, 509–518.
2. Minary-Jolandan, M.; Yu, M. *Biomacromolecules* **2009**, *10*, 2565–2570.
3. Eyre, D. R.; Dickson, I. R.; Van.Ness, K. *Biochem. J.* **1988**, *252*, 495–500.
4. Viguet-Carrin, S.; Garnero, P.; Delmas, P. D. *Osteoporos. Int.* **2006**, *17*, 319–336.
5. Reilly, D.; Burstein, A. *J. Biomech.* **1975**, *8*, 393–405.
6. Niyibizi, C.; Eyre, D. *Eur. J. Biochem.* **1994**, *224*, 943–950.
7. Miller, A. *Philos. Trans. R. Soc. Lond. B Biol. Sci.* **1984**, *304*, 455–477.
8. Miller, E. J. *Fed. Proc.* **1969**, *28*, 1839–1845.
9. Ascenzi, A.; Bonucci, E. *Clin. Orthop. Relat. Res.* **1976**, *121*, 275–294.
10. Glimcher, M. *Rev. Mod. Phys.* **1959**, *31*, 359–393.
11. Cowin, S., Ed.; In *Bone Mechanics Handbook*; CRC: Boca Raton, FL, 2001.
12. Paschalis, E.; Dicarlo, E.; Betts, F.; Sherman, P.; Mendelsohn, R.; Boskey, A. *Calcif. Tissue Int.* **1996**, *59*, 480–487.
13. Landis, W.; Hodgens, K.; Arena, J.; Song, M.; McEwen, B. *Microsc. Res. Tech.* **1996**, *33*, 192–202.
14. Boskey, A.; Maressa, M.; Ulrich, W.; Boty, S.; Butler, W.; Prince, C. *Bone Miner.* **1993**, *22*, 147–159.
15. Boskey, A. L. In *Bone Biomechanics Handbook*; Cowin, S. C., Ed.; CRC: Boca Raton, FL, 2001.
16. Handschin, R.; Stern, W. *Clin. Rheumatol.* **1994**, *13*(Suppl. 1), 75–90.
17. Parfitt, A.; Han, Z.; Palnitkar, S.; Rao, D.; Shih, M.; Nelson, D. *J. Bone Miner. Res.* **1997**, *12*, 1864–1873.
18. Reid, S.; Boyde, A. *J. Bone Miner. Res.* **1987**, *2*, 13–22.
19. Currey, J. D.; Brear, K.; Zioupos, P. *J. Biomech.* **1996**, *29*, 257–260.
20. Currey, J. *J. Biomech.* **1988**, *21*, 131–139.
21. Luchinetti, E. In *Bone Mechanics Handbook*; Cowin, S., Ed.; CRC: Boca Raton, FL, 2001.
22. Heinegård, D.; Oldberg, A. *FASEB J.* **1989**, *3*, 2042–2051.
23. Roach, H. *Cell Biol. Int.* **1994**, *18*, 617–628.
24. Glowacki, J.; Rey, C.; Glimcher, M.; Cox, K.; Lian, J. *J. Cell. Biochem.* **1991**, *45*, 292–302.
25. Robey, P. *Connect. Tissue Res.* **1996**, *35*, 131–136.
26. Devoll, R.; Pinero, G.; Appelbaum, E.; *et al. Calcif. Tissue Int.* **1997**, *60*, 380–386.
27. McKee, M.; Nanci, A. *Connect. Tissue Res.* **1996**, *35*, 197–205.
28. Nanci, A. *J. Struct. Biol.* **1999**, *126*, 256–269.
29. Sodek, J.; McKee, M. *Periodontology 2000* **2000**, *24*, 99–126.
30. Mcnamara, L. M.; Majeska, R. J.; Weinbaum, S.; Friedrich, V.; Schaffler, M. B. *Anat. Rec. (Hoboken)* **2009**, *292*, 355–363.
31. Yoshitake, H.; Rittling, S.; Denhardt, D.; Noda, M. *Proc. Natl. Acad. Sci. USA* **1999**, *96*, 8156–8160.
32. Robey, P.; Young, M.; Fisher, L.; McClain, T. *J. Cell Biol.* **1989**, *108*, 719–727.
33. Moursi, A.; Globus, R.; Damsky, C. *J. Cell Sci.* **1997**, *110*(Pt 18), 2187–2196.
34. Clarke, B. *Clin. J. Am. Soc. Nephrol.* **2008**, *3*(Suppl. 3), S131–S139.
35. Feige, U. *Ann. Rheum. Dis.* **2001**, *60*, 81–84.
36. Kostenuik, P.; Shalhoub, V. *Curr. Pharm. Des.* **2001**, *7*, 613–635.
37. Boyle, W.; Simonet, W.; Lacey, D. *Nature* **2003**, *423*, 337–342.
38. Hunter, G. K.; Goldberg, H. A. *Proc. Natl. Acad. Sci. USA* **1993**, *90*, 8562–8565.
39. Qiu, S. R.; Wierzbicki, A.; Orme, C. A.; *et al. Proc. Natl. Acad. Sci. USA* **2004**, *101*, 1811–1815.
40. Tye, C. E.; Hunter, G. K.; Goldberg, H. A. *J. Biol. Chem.* **2005**, *280*, 13487–13492.
41. Tye, C. E.; Rattray, K. R.; Warner, K. J.; *et al. J. Biol. Chem.* **2003**, *278*, 7949–7955.
42. Fantner, G. E.; Hassenkam, T.; Kindt, J. H.; *et al. Nat. Mater.* **2005**, *4*, 612–616.
43. Zappone, B.; Thurner, P. J.; Adams, J.; Fantner, G. E.; Hansma, P. K. *Biophys. J.* **2008**, *95*, 2939–2950.
44. Fantner, G. E.; Adams, J.; Turner, P.; Thurner, P. J.; Fisher, L. W.; Hansma, P. K. *Nano Lett.* **2007**, *7*, 2491–2498.
45. Thurner, P. J.; Lam, S.; Weaver, J. C.; Morse, D. E.; Hansma, P. K. Localization of phosphorylated serine, osteopontin, and bone sialoprotein on mineralized collagen fibrils in bone. *J. Adhes.* **2008**, *85*, 526–545.
46. Ingram, R. T.; Clarke, B. L.; Fisher, L. W.; Fitzpatrick, L. A. *J. Bone Miner. Res.* **1993**, *8*(9), 1019–1029.
47. Rodríguez, J.; González, M.; Ríos, S.; Cambiazo, V. *J. Cell. Biochem.* **2004**, *93*, 721–731.
48. Jee, W. S. S. In *Bone Mechanics Handbook*; Cowin, S. C., Ed.; CRC: Boca Raton, 2001.
49. Eriksen, E. F.; Kassem, M. *Sandoz J. Med. Sci.* **1992**, *31*, 45–57.
50. You, L.; Cowin, S. C.; Schaffler, M. B.; Weinbaum, S. *J. Biomech.* **2001**, *34*, 1375–1386.
51. Frost, H. M. *Bull. Henry Ford Hosp.* **1960**, *8*, 27–35.
52. Gluhak-Heinrich, J.; Pavlin, D.; Yang, W.; MacDougall, M.; Harris, S. E. *Arch. Oral Biol.* **2007**, *52*, 684–690.
53. Inoue, K.; Mikuni-Takagaki, Y.; Oikawa, K.; *et al. J. Biol. Chem.* **2006**, *281*, 33814–33824.
54. Teti, A.; Zallone, A. *Bone* **2009**, *44*, 11–16.
55. Bonewald, L. *J. Musculoskelet. Neuronal Interact.* **2002**, *2*, 239–241.
56. Cowin, S. C.; Moss-Salentijn, L.; Moss, M. L. *J. Biomech. Eng.* **1991**, *113*, 191–197.
57. Lanyon, L. E. *Calcif. Tissue Int.* **1993**, *53*(Suppl. 1), S102–S106; discussion S106–S107.
58. Manolagas, S. C. *Endocr. Rev.* **2000**, *21*, 115–137.
59. Zhao, S.; Zhang, Y.; Harris, S.; Ahuja, S.; Bonewald, L. *J. Bone Miner. Res.* **2002**, *17*, 2068–2079.
60. Rodan, G. *Bone* **1992**, *13*(Suppl. 1), S3–S6.
61. Holtrop, M.; King, G. *Clin. Orthop. Relat. Res.* **1977**, *123*, 177–196.
62. Oursler, M. J.; Osdoby, P.; Pyfferoen, J.; Riggs, B. L.; Spelsberg, T. C. *Proc. Natl. Acad. Sci. USA* **1991**, *88*, 6613–6617.
63. Hughes, D. E.; Dai, A.; Tiffee, J. C.; Li, H. H.; Mundy, G. R.; Boyce, B. F. *Nat. Med.* **1996**, *2*, 1132–1136.
64. Lam, J.; Takeshita, S.; Barker, J. E.; Kanagawa, O.; Ross, F. P.; Teitelbaum, S. L. *J. Clin. Invest.* **2000**, *106*, 1481–1488.
65. Lerner, U. H. *J. Dent. Res.* **2006**, *85*, 584–595.
66. Teitelbaum, S. L. *Arthritis Res. Ther.* **2006**, *8*, 201.
67. Ortega, N.; Behonick, D.; Werb, Z. *Trends Cell Biol.* **2004**, *14*, 86–93.
68. Gerber, H.; Ferrara, N. *Trends Cardiovasc. Med.* **2000**, *10*, 223–228.
69. Sumpio, B.; Riley, J.; Dardik, A. *Int. J. Biochem. Cell Biol.* **2002**, *34*, 1508–1512.
70. Collin-Osdoby, P. *J. Cell. Biochem.* **1994**, *55*, 304–309.
71. Brandi, M.; Collin-Osdoby, P. *J. Bone Miner. Res.* **2006**, *21*, 183–192.
72. Chung, U.; Kawaguchi, H.; Takato, T.; Nakamura, K. *J. Orthop. Sci.* **2004**, *9*, 410–414.
73. Kanczler, J.; Oreffo, R. *Eur. Cell Mater.* **2008**, *15*, 100–114.
74. Rho, J.; Kuhn-Spearing, L.; Zioupos, P. *Med. Eng. Phys.* **1998**, *20*, 92–102.
75. Burr, D. B.; Martin, R. B. *Am. J. Anat.* **1989**, *186*(2), 186–216.
76. Burr, D.; Schaffler, M.; Frederickson, R. *J. Biomech.* **1988**, *21*, 939–945.
77. Schaffler, M.; Burr, D.; Frederickson, R. *Anat. Rec.* **1987**, *217*, 223–228.
78. Skedros, J.; Holmes, J.; Vajda, E.; Bloebaum, R. *Anat. Rec. A Discov. Mol. Cell. Evol. Biol.* **2005**, *286*, 781–803.
79. Cowin, S. *J. Biomech.* **1999**, *32*, 217–238.
80. Wolff, J. *Das Gesetz der Transformation der Knochen*. A. Hirschwald: Berlin, 1892.
81. Kothari, M.; Keaveny, T.; Lin, J.; Newitt, D.; Majumdar, S. *Bone* **1999**, *25*, 245–250.
82. Nicholson, P.; Cheng, X.; Lowet, G.; *et al. Med. Eng. Phys.* **1997**, *19*, 729–737.
83. Odgaard, A. *Bone* **1997**, *20*, 315–328.
84. Goldstein, S.; Goulet, R.; McCubbrey, D. *Calcif. Tissue Int.* **1993**, *53*(Suppl. 1), S127–S132; discussion S132–S133.
85. Harrigan, T.; Jasty, M.; Mann, R.; Harris, W. *J. Biomech.* **1988**, *21*, 269–275.
86. Keaveny, T.; Borchers, R.; Gibson, L.; Hayes, W. *J. Biomech.* **1993**, *26*, 991–1000.
87. Keaveny, T.; Pinilla, T.; Crawford, R.; Kopperdahl, D.; Lou, A. *J. Orthop. Res.* **1997**, *15*, 101–110.
88. Kopperdahl, D.; Keaveny, T. *J. Biomech.* **1998**, *31*, 601–608.
89. Keaveny, T.; Morgan, E.; Niebur, G.; Yeh, O. *Annu. Rev. Biomed. Eng.* **2001**, *3*, 307–333.
90. Dalle Carbonare, L.; Giannini, S. *J. Endocrinol. Invest.* **2004**, *27*, 99–105.
91. Recker, R. *Calcif. Tissue Int.* **1993**, *53*(Suppl. 1), S139–S142.

92. Keaveny, T.; Wachtel, E.; Ford, C.; Hayes, W. *J. Biomech.* **1994**, *27*, 1137–1146.
93. Michel, M.; Guo, X.; Gibson, L.; McMahon, T.; Hayes, W. *J. Biomech.* **1993**, *26*, 453–463.
94. Brown, T.; Ferguson, A. J. *Acta Orthop. Scand.* **1980**, *51*, 429–437.
95. Goldstein, S.; Wilson, D.; Sonstegard, D.; Matthews, L. *J. Biomech.* **1983**, *16*, 965–969.
96. Ding, M.; Odgaard, A.; Linde, F.; Hvid, I. *J. Orthop. Res.* **2002**, *20*, 615–621.
97. McCalden, R.; Mcgeough, J.; Court-Brown, C. *J. Bone Joint Surg. Am.* **1997**, *79*, 421–427.
98. Mosekilde, L.; Danielsen, C. *Bone* **1987**, *8*, 79–85.
99. Choi, K.; Kuhn, J.; Ciarelli, M.; Goldstein, S. *J. Biomech.* **1990**, *23*, 1103–1113.
100. Runkle, J.; Pugh, J. *Bull. Hosp. Joint Dis.* **1975**, *36*, 2–10.
101. Townsend, P.; Rose, R.; Radin, E. *J. Biomech.* **1975**, *8*, 199–201.
102. Mente, P.; Lewis, J. *J. Orthop. Res.* **1989**, *7*, 456–461.
103. Mcnamara, L. M.; Ederveen, A. G.; Lyons, C. G.; *et al. Bone* **2006**, *39*, 392–400.
104. Mcnamara, L. M.; Prendergast, P. J.; Schaffler, M. B. *J. Musculoskelet. Neuronal Interact.* **2005**, *5*, 342–343.
105. Rho, J.; Ashman, R.; Turner, C. *J. Biomech.* **1993**, *26*, 111–119.
106. Ryan, S.; Williams, J. *J. Biomech.* **1989**, *22*, 351–355.
107. Samelin, N.; Köller, W.; Ascherl, R.; Gradinger, R. *Biomed. Tech. (Berl.)* **1996**, *41*, 203–208.
108. Choi, K.; Goldstein, S. *J. Biomech.* **1992**, *25*, 1371–1381.
109. Ferguson, V.; Bushby, A.; Boyde, A. *J. Anat.* **2003**, *203*, 191–202.
110. Ozcivici, E.; Ferreri, S.; Qin, Y.; Judex, S. *Meth. Mol. Biol.* **2008**, *455*, 323–334.
111. Rho, J.; Roy, M. N.; Tsui, T.; Pharr, G. *J. Biomed. Mater. Res.* **1999**, *45*, 48–54.
112. Rho, J.; Tsui, T.; Pharr, G. *Biomaterials* **1997**, *18*, 1325–1330.
113. Hoffler, C.; Moore, K.; Kozloff, K.; Zysset, P.; Brown, M.; Goldstein, S. *Bone* **2000**, *26*, 603–609.
114. Zysset, P.; Guo, X.; Hoffler, C.; Moore, K.; Goldstein, S. *J. Biomech.* **1999**, *32*, 1005–1012.
115. Rho, J.; Pharr, G. *J. Mater. Sci. Mater. Med.* **1999**, *10*, 485–488.
116. Turner, C.; Rho, J.; Takano, Y.; Tsui, T.; Pharr, G. *J. Biomech.* **1999**, *32*, 437–441.
117. Koester, K.; Ager, J. R.; Ritchie, R. *Nat. Mater.* **2008**, *7*, 672–677.
118. Melvin, J. *J. Biomech. Eng.* **1993**, *115*, 549–554.
119. Robertson, D.; Robertson, D.; Barrett, C. *J. Biomech.* **1978**, *11*, 359–364.
120. Peterlik, H.; Roschger, P.; Klaushofer, K.; Fratzl, P. *Nat. Mater.* **2006**, *5*, 52–55.
121. Vashishth, D.; Behiri, J. C.; Tanner, K. E.; Bonfield, W. In *42nd Annual Meeting of the Orthopaedic Research Society*, Atlanta, GA, 1996.
122. Kruzic, J.; Scott, J.; Nalla, R.; Ritchie, R. *J. Biomech.* **2006**, *39*, 968–972.
123. Nalla, R.; Kruzic, J.; Ritchie, R. *Bone* **2004**, *34*, 790–798.
124. Nalla, R.; Stölken, J.; Kinney, J.; Ritchie, R. *J. Biomech.* **2005**, *38*, 1517–1525.
125. Lee, T.; Staines, A.; Taylor, D. *J. Anat.* **2002**, *201*, 437–446.
126. Vashishth, D.; Koontz, J.; Qiu, S.; *et al. Bone* **2000**, *26*, 147–152.
127. Burr, D. B.; Turner, C. H.; Naick, P.; *et al. J. Biomech.* **1998**, *31*, 337–345.
128. Nalla, R.; Kruzic, J.; Kinney, J.; Ritchie, R. *Bone* **2004**, *35*, 1240–1246.
129. Zioupos, P.; Currey, J. *Bone* **1998**, *22*, 57–66.
130. Hansen, U.; Zioupos, P.; Simpson, R.; Currey, J.; Hynd, D. *J. Biomech. Eng.* **2008**, *130*, 011011.
131. Zioupos, P.; Hansen, U.; Currey, J. *J. Biomech.* **2008**, *41*, 2932–2939.
132. Frost, H. *Anat. Rec.* **1990**, *226*, 403–413.
133. Mosekilde, L. *Bone Miner.* **1990**, *10*, 13–35.
134. Parfitt, A. *J. Cell. Biochem.* **1994**, *55*, 273–286.
135. Cohen-Solal, M.; Shih, M.; Lundy, M.; Parfitt, A. *J. Bone Miner. Res.* **1991**, *6*, 1331–1338.
136. Jaworski, Z.; Lok, E.; Wellington, J. *Clin. Orthop. Relat. Res.* **1975**, *107*, 298–310.
137. Parfitt, A. In *Vitamin D*, 2nd ed.; Feldman, D., Glorieux, F., Pike, W., Eds.; Elsevier Academic Press: New York, 2005.
138. Mckibbin, B. *J. Bone Joint Surg. Br.* **1978**, *60B*, 150–162.
139. Tsiridis, E.; Upadhyay, N.; Giannoudis, P. *Injury* **2007**, *38*(Suppl. 1), S11–S25.
140. Woo, S.; Kuei, S.; Amiel, D.; *et al. J. Bone Joint Surg. Am.* **1981**, *63*, 780–787.
141. El Haj, A. J.; Minter, S. L.; Rawlinson, S. C.; Suswillo, R.; Lanyon, L. E. *J. Bone Miner. Res.* **1990**, *5*, 923–932.
142. Klein-Nulend, J.; van der Plas, A.; Semeins, C. M.; *et al. FASEB J.* **1995**, *9*, 441–445.
143. Carter, D. *Calcif. Tissue Int.* **1984**, *36*(Suppl. 1), S19–S24.
144. Cowin, S. C.; Hegedus, D. H. *J. Elast.* **1976**, *6*, 313–326.
145. Cowin, S.; Van Buskirk, W. *J. Biomech.* **1979**, *12*, 269–276.
146. Beaupré, G.; Orr, T.; Carter, D. *J. Orthop. Res.* **1990**, *8*, 651–661.
147. Beaupré, G.; Orr, T.; Carter, D. *J. Orthop. Res.* **1990**, *8*, 662–670.
148. Carter, D.; Orr, T.; Fyhrie, D. *J. Biomech.* **1989**, *22*, 231–244.
149. Huiskes, R.; Ruimerman, R.; Van.Lenthe, G.; Janssen, J. *Nature* **2000**, *405*, 704–706.
150. Huiskes, R.; Weinans, H.; Grootenboer, H.; Dalstra, M.; Fudala, B.; Slooff, T. *J. Biomech.* **1987**, *20*, 1135–1150.
151. Weinans, H.; Huiskes, R.; Grootenboer, H. *J. Biomech.* **1992**, *25*, 1425–1441.
152. Mullender, M.; Huiskes, R. *Bone* **1997**, *20*, 527–532.
153. Mullender, M.; Huiskes, R.; Weinans, H. *J. Biomech.* **1994**, *27*, 1389–1394.
154. Cowin, S. C.; Weinbaum, S.; Zeng, Y. *J. Biomech.* **1995**, *28*, 1281–1297.
155. Bakker, A. D.; Soejima, K.; Klein-Nulend, J.; Burger, E. H. *J. Biomech.* **2001**, *34*, 671–677.
156. Mcgarry, J.; Klein-Nulend, J.; Prendergast, P. J. *Biochem. Biophys. Res. Commun.* **2005**, *330*, 341–348.
157. Mcgarry, J. G.; Klein-Nulend, J.; Mullender, M. G.; Prendergast, P. J. *FASEB J.* **2005**, *19*, 482–484.
158. Owan, I.; Burr, D.; Turner, C.; *et al. Am. J. Physiol.* **1997**, *273*, C810–C815.
159. You, J.; Yellowley, C.; Donahue, H.; Zhang, Y.; Chen, Q.; Jacobs, C. *J. Biomech. Eng.* **2000**, *122*, 387–393.
160. Wang, Y.; Mcnamara, L. M.; Schaffler, M. B.; Weinbaum, S. *Proc. Natl. Acad. Sci. USA* **2007**, *104*, 15941–15946.
161. Tonna, E. A.; Lampen, N. M. *J. Gerontol.* **1972**, *27*, 316–324.
162. Schwartz, E. A.; Leonard, M. L.; Bizios, R.; Bowser, S. S. *Am. J. Physiol.* **1997**, *272*, F132–F138.
163. Whitfield, J. F. *J. Cell. Biochem.* **2003**, *89*, 233–237.
164. Whitfield, J. F. *Cell. Signal.* **2008**, *20*, 1019–1024.
165. Malone, A. M.; Anderson, C. T.; Tummala, P.; *et al. Proc. Natl. Acad. Sci. USA* **2007**, *104*, 13325–13330.
166. Xiao, Z.; Zhang, S.; Mahlios, J.; *et al. J. Biol. Chem.* **2006**, *281*, 30884–30895.
167. Burr, D. B.; Martin, R. B.; Schaffler, M. B.; Radin, E. L. *J. Biomech.* **1985**, *18*, 189–200.
168. Frost, H. M. *J. Bone Joint Surg. Am.* **1960**, *42A*, 144–150.
169. Lee, T.; O'Brien, F.; Gunnlaugsson, T.; Parkesh, R.; Taylor, D. *Technol. Health Care* **2006**, *14*, 359–365.
170. Martin, R. *Bone* **2002**, *30*, 8–13.
171. Mcnamara, L. M.; Prendergast, P. J. *J. Biomech.* **2007**, *40*, 1381–1391.
172. McNamara, L. M.; van der Linden, J. C.; Weinans, H.; Prendergast, P. J. *J. Biomech.* **2006**, *39*, 734–741.
173. Prendergast, P.; Huiskes, R. *J. Biomech. Eng.* **1996**, *118*, 240–246.
174. Burr, D. B.; Forwood, M. R.; Fyhrie, D. P.; Martin, R. B.; Schaffler, M. B.; Turner, C. H. *J. Bone Miner. Res.* **1997**, *12*, 6–15.
175. Mori, S.; Burr, D. *Bone* **1993**, *14*, 103–109.
176. Lee, T. C.; O'Brien, F. J.; Taylor, D. *Int. J. Fatigue* **2000**, *22*, 847–853.
177. Prendergast, P. J.; Taylor, D. *J. Biomech.* **1994**, *27*(8), 1067–1076.
178. Hazenberg, J.; Freeley, M.; Foran, E.; Lee, T.; Taylor, D. *J. Biomech.* **2006**, *39*, 2096–2103.
179. Mcnamara, L. M.; Prendergast, P. J. *Eur. J. Morphol.* **2005**, *42*, 99–109.
180. Mulvihill, B. M.; Mcnamara, L. M.; Prendergast, P. J. *J. R. Soc. Interface* **2008**, *5*, 1243–1253.
181. Compston, J.; Mellish, R.; Croucher, P.; Newcombe, R.; Garrahan, N. *Bone Miner.* **1989**, *6*, 339–350.
182. Cummings, S. R.; Melton, L. J. *Lancet* **2002**, *359*, 1761–1767.
183. Melton, L. J., 3rd; Chrischilles, E. A.; Cooper, C.; Lane, A. W.; Riggs, B. L. *J. Bone Miner Res.* **2005**, *20*, 886–892.
184. Braidman, I. P.; Hainey, L.; Batra, G.; Selby, P. L.; Saunders, P. T.; Hoyland, J. A. *J. Bone Miner. Res.* **2001**, *16*, 214–220.
185. Bell, K.; Loveridge, N.; Lunt, M.; Lindsay, P. C.; Reeve, J. *Bone* **1996**, *19*, 131S.
186. Rosen, C. J. *Baillières Best Pract. Res. Clin. Endocrinol. Metab.* **2000**, *14*, 181–193.
187. Brockstedt, H.; Kassem, M.; Eriksen, E. F.; Mosekilde, L.; Melsen, F. *Bone* **1993**, *14*, 681–691.
188. Eriksen, E. F.; Langdahl, B.; Vesterby, A.; Rungby, J.; Kassem, M. *J. Bone Miner. Res.* **1999**, *14*, 1217–1221.
189. Bell, K. L.; Loveridge, N.; Lunt, M.; Lindsay, P. C.; Reeve, J. *Bone* **1996**, *19*(3, Supplement), 129–175.
190. Lanyon, L. E. *Bone* **1996**, *18*, S37–S43.
191. Rao, L. G.; Liu, L. J.; Murray, T. M.; McDermott, E.; Zhang, X. *Biol. Pharm. Bull.* **2003**, *26*, 936–945.
192. Rickard, D.; Harris, S. A.; Turner, R.; Khosla, S.; Spelsburg, T. C. In *Principles of Bone Biology*; Bilezikian, J. P., Raisz, L. G., Rodan, G. A., Eds.; Academic Press: San Diego, 2002.
193. Jessop, H. L.; Suswillo, R. F.; Rawlinson, S. C.; *et al. J. Bone Miner. Res.* **2004**, *19*, 938–946.
194. Sterck, J. G.; Klein-Nulend, J.; Lips, P.; Burger, E. H. *Am. J. Physiol.* **1998**, *274*, E1113–E1120.

195. Kousteni, S.; Bellido, T.; Plotkin, L. I.; *et al*. *Cell* **2001**, *104*, 719–730.
196. Tomkinson, A.; Reeve, J.; Shaw, R. W.; Noble, B. S. *J. Clin. Endocrinol. Metab.* **1997**, *82*, 3128–3135.
197. Boyde, A. *J. Anat.* **2003**, *203*, 173–189.
198. Kingsmill, V. J.; Boyde, A. *J. Anat.* **1998**, *192*(Pt 2), 245–256.
199. Knothe Tate, M. L.; Adamson, J. R.; Tami, A. E.; Bauer, T. W. *Int. J. Biochem. Cell Biol.* **2004**, *36*, 1–8.
200. Mullender, M. G.; Vandermeer, D. D.; Huiskes, R.; Lips, P. *Bone* **1996**, *18*, 109–113.
201. Tatsumi, S.; Ishii, K.; Amizuka, N.; *et al*. *Cell Metab.* **2007**, *5*, 464–475.
202. Lane, N. E.; Thompson, J. M.; Haupt, D.; Kimmel, D. B.; Modin, G.; Kinney, J. H. *J. Bone Miner. Res.* **1998**, *13*, 229–236.
203. Parfitt, A. M. *Am. J. Med.* **1987**, *82*, 68–72.
204. Ciarelli, T. E.; Fyhrie, D. P.; Schaffler, M. B.; Goldstein, S. A. *J. Bone Miner. Res.* **2000**, *15*, 32–40.
205. Waarsing, J. H.; Day, J. S.; van der Linden, J. C.; *et al*. *Bone* **2004**, *34*, 163–169.
206. Waarsing, J. H.; Day, J. S.; Verhaar, J. A.; Ederveen, A. G.; Weinans, H. *J. Orthop. Res.* **2006**, *24*, 926–935.
207. Bourrin, S.; Ammann, P.; Bonjour, J.; Rizzoli, R. *Bone* **2002**, *30*, 195–200.
208. Ederveen, A.; Spanjers, C.; Quaijtaal, J.; Kloosterboer, H. *J. Bone Miner. Res.* **2001**, *16*, 1674–1681.
209. Hirano, T.; Turner, C.; Forwood, M.; Johnston, C.; Burr, D. *Bone* **2000**, *27*, 13–20.
210. Kasugai, Y.; Ikegami, A.; Matsuo, K.; *et al*. *Bone* **1998**, *22*, 119–124.
211. Yoshitake, K.; Yokota, K.; Kasugai, Y.; Kagawa, M.; Sukamoto, T.; Nakamura, T. *Bone* **1999**, *25*, 311–319.
212. Hu, J.; Ding, M.; Søballe, K.; *et al*. *Bone* **2002**, *31*, 591–597.
213. Mosekilde, L.; Danielsen, C.; Søgaard, C.; Mcosker, J.; Wronski, T. *Bone* **1995**, *16*, 223–230.
214. Sugita, H.; Oka, M.; Toguchida, J.; Nakamura, T.; Ueo, T.; Hayami, T. *Bone* **1999**, *24*, 513–516.
215. Teramura, K.; Fukushima, S.; Iwai, T.; Nozaki, K.; Kokubo, S.; Takahashi, K. *Eur. J. Pharmacol.* **2002**, *457*, 51–56.
216. Hasegawa, K.; Takahashi, H.; Koga, Y.; *et al*. *Spine (Phila Pa 1976)* **1993**, *18*, 2314–2320.
217. Li, B.; Aspden, R. *Osteoporos. Int.* **1997**, *7*, 450–456.
218. Guo, X.; Goldstein, S. *J. Orthop. Res.* **2000**, *18*, 333–336.
219. Brennan, O.; Kennedy, O. D.; Lee, T. C.; Rackard, S. M.; O'Brien, F. J. *J. Biomech.* **2009**, *42*, 498–503.
220. Gadeleta, S. J.; Boskey, A. L.; Paschalis, E.; *et al*. *Bone* **2000**, *27*, 541–550.
221. Boyde, A.; Compston, J. E.; Reeve, J.; *et al*. *Bone* **1998**, *22*, 241–250.
222. Dickenson, R. P.; Hutton, W. C.; Stott, J. R. *J. Bone Joint Surg. Br.* **1981**, *63B*, 233–238.
223. Zioupos, P.; Aspden, R. M. In *Proceedings of the 12th Conference of the European Society of Biomechanics*, Dublin, Ireland; Prendergast, P. J., Lee, T. C., Carr, A. J., Eds.; 2000.
224. Bailey, A. J.; Wotton, S. F.; Sims, T. J.; Thompson, P. W. *Connect. Tissue Res.* **1993**, *29*, 119–132.
225. Batge, B.; Diebold, J.; Stein, H.; Bodo, M.; Muller, P. K. *Eur. J. Clin. Invest.* **1992**, *22*, 805–812.
226. Kowitz, J.; Knippel, M.; Schuhr, T.; Mach, J. *Calcif. Tissue Int.* **1997**, *60*, 501–505.
227. Mansell, J. P.; Bailey, A. J. *Int. J. Biochem. Cell Biol.* **2003**, *35*, 522–529.
228. Oxlund, H.; Mosekilde, L.; Ørtoft, G. *Bone* **1996**, *19*, 479–484.
229. Knott, L.; Whitehead, C. C.; Fleming, R. H.; Bailey, A. J. *Biochem. J.* **1995**, *310*, 1045–1051.
230. Bailey, A. J.; Knott, L. *Exp. Gerontol.* **1999**, *34*, 337–351.
231. Dai, R. C.; Liao, E. Y.; Yang, C.; Wu, X. P.; Jiang, Y. *J. Bone Miner. Metab.* **2004**, *22*, 215–223.
232. Burr, D. *Osteoporos. Int.* **2003**, *14*(Suppl. 5), S67–S72.
233. Mashiba, T.; Turner, C. H.; Hirano, T.; Forwood, M. R.; Johnston, C. C.; Burr, D. B. *Bone* **2001**, *28*, 524–531.
234. Schaffler, M. B. *Osteoporos. Int.* **2003**, *14*(Suppl. 5), S73–S77; discussion S77–S80.
235. Cauley, J.; Robbins, J.; Chen, Z.; *et al*. *JAMA* **2003**, *290*, 1729–1738.
236. Kloosterboer, H. J.; Ederveen, A. G. *J. Steroid Biochem. Mol. Biol.* **2002**, *83*, 157–165.
237. Brommage, R.; Hotchkiss, C.; Lees, C.; Stancill, M.; Hock, J.; Jerome, C. *J. Clin. Endocrinol. Metab.* **1999**, *84*, 3757–3763.
238. Vestgaard, P.; Jorgensen, N.; Mosekilde, L.; Schwarz, P. *Osteoporos. Int.* **2007**, *18*, 45–47.
239. Randell, K. M.; Honkanen, R. J.; Kroger, H.; Saarikoski, S. *J. Bone Miner. Res.* **2002**, *17*, 528–533.
240. Flora, L.; Hassing, G.; Cloyd, G.; Bevan, J.; Parfitt, A.; Villanueva, A. *Metab. Bone Dis. Relat. Res.* **1981**, *3*, 289–300.
241. Townsend, P. R.; Rose, R. M.; Radin, E. L. *J. Biomech.* **1975**, *8*, 99–201.
242. Ryan, S.; Williams, J. *J. Biomech.* **1989**, *22*, 351–355.
243. Kuhn, J. L.; Goldstein, S. A.; Choi, K.; London, M.; Feldkamp, L. A.; Matthews, L. S. *J. Orthop. Res.* **1989**, *7*, 876–884.
244. Choi, K.; Goldstein, S. *J. Biomech.* **1992**, *25*, 1371–1381.
245. van Rietbergen, B.; Weinans, H.; Huiskes, R.; Odgaard, A. *J. Biomech.* **1995**, *28*(1), 69–81.

2.211. Polymers of Biological Origin

S S Silva, J M Oliveira, H Sá-Lima, R A Sousa, J F Mano, and R L Reis, University of Minho, Taipas, Guimarães, Portugal; Institute for Biotechnology and Bioengineering (IBB), Guimarães, Portugal

© 2011 Elsevier Ltd. All rights reserved.

2.211.1.	**Introduction**	188
2.211.2.	**Natural-Based Polymeric Systems**	188
2.211.2.1.	Materials Inspired from the ECM	188
2.211.2.1.1.	Collagen	188
2.211.2.1.2.	Fibronectin	188
2.211.2.1.3.	Glycosaminoglycans	189
2.211.2.1.4.	Fibrin	189
2.211.2.2.	Other Peptide-Based Systems	189
2.211.2.2.1.	Hydrogels enabling enzymatically mediated cell migration	189
2.211.2.2.2.	Self-assembling materials	189
2.211.2.2.3.	Other protein-derived biomaterials	189
2.211.2.3.	Polysaccharides	189
2.211.2.3.1.	Plant polysaccharides	189
2.211.2.3.2.	Exudate gums	195
2.211.2.3.3.	Algal polysaccharides	195
2.211.2.3.4.	Animal polysaccharides	195
2.211.2.3.5.	Microbial polysaccharides	196
2.211.2.4.	Natural-Derived Polyesters	196
2.211.3.	**Processing of TE Scaffolds**	197
2.211.3.1.	Microspheres and Microparticles and Their Aggregation	198
2.211.3.2.	Fiber Meshes and Fiber Bonding	199
2.211.3.3.	Rapid Prototyping	200
2.211.4.	**Cell Encapsulation in Injectable Biodegradable Hydrogels for TE Applications**	200
2.211.4.1.	General Principles	200
2.211.4.2.	Selected Examples	201
2.211.5.	**Final Remarks**	201
References		202

Abbreviations

BC	Bacterial cellulose
CAD	Computer-assisted design
CATE	Computer-assisted tissue engineering
CHT	Chitosan
CO_2	Carbon dioxide
DA	Degree of acetylation
ECM	Extracellular matrix
FDM	Fused deposition modeling
FN	Fibronectin
GAG	Glycosaminoglycans
GlcNAc	*N*-acetyl-D-glucosamine
GP	Glycerophosphate
HA	Hyaluronic acid
HAp	Hydroxyapatite
HAp/CHT	Hydroxyapatite/chitosan
MMPs	Metalloproteinases
PAAm	Poly(*N*-isopropylacrylamide)
PCL	Polycaprolactone
PEG	Poly(ethylene glycol)
PEO	Poly(ethylene oxide)
PHA	Polyhydroxyalkanoates
PHB	Poly(hydroxybutyrate)
PHBV	Poly(hydroxybutyrate-*co*-valerate)
PPO	Poly(phenylene oxide)
RGD	Arginine–glycine–aspartic acid
RP	Rapid prototyping
SCF	Supercritical fluid technology
SFF	Solid free form
SLS	Selective laser sintering
SPCL	Starch and polycaprolactone
SPLA	Starch and poly(L-lactic acid)
TE	Tissue engineering

2.211.1. Introduction

In the new paradigms of regenerative medicine, the use of biomaterials in contact with biological material (e.g., cells, tissues/organs, physiological fluids, biomolecules) is a current illustration of the need of interdisciplinary scientific approaches that combine the most recent advances in materials science and technology, basic sciences, and life sciences. In tissue engineering (TE), matrices are developed to support cells, promoting their differentiation and proliferation toward the formation of new tissue. Such strategies allow the fabrication of hybrid constructs that can be implantable in patients to induce the regeneration of tissues or replace failing or malfunctioning organs. Different materials have been proposed to be used in the processing of scaffolds, namely biodegradable polymers. Natural-based polymers offer the advantage of being similar to biological macromolecules, which the biological environment is prepared to recognize and to deal with metabolically. Due to their similarity with the extracellular matrix (ECM), natural polymers may also avoid the stimulation of chronic inflammation or immunological reactions and toxicity, often detected with synthetic polymers. In this chapter, the different natural-based materials that have been proposed to be used in TE strategies will be overviewed. An important aspect, also addressed, is the processing of such kind of materials into porous matrices, a task that usually needs other technologies than those usually employed in the processing of conventional synthetic polymers. There is also a clinical need for processing biomaterials into other shapes, including nano-/microparticles (for control release application). Materials containing cells and bioactive agents that can be implanted in a noninvasive way are very attractive approaches in TE and regeneration contexts, which will be also discussed.

2.211.2. Natural-Based Polymeric Systems

The development of successful strategies for the design of biodegradable macromolecular systems for TE applications is directly related with the physicochemical and biological properties of the biomaterials. Thus, the creation and selection/modification of a certain biomaterial is a critical step in the fabrication of scaffolds for TE. Generally, the ideal biomaterial should be nontoxic and biocompatible and should promote favorable cellular interactions and tissue development, while possessing adequate mechanical and physical properties. In addition, it should be biodegradable and bioresorbable to support the reconstruction of a new tissue without inflammation.[1] On the other hand, novel concepts of TE are imposing new and more specific requirements on macromolecular components. Living organisms are able to synthesize a vast variety of polymers, which can be divided into major classes according to their chemical structure: (i) polysaccharides, (ii) proteins, and (iii) polyesters. Nowadays, with the advances in biotechnology, natural polymers can be obtained by fermentation of microorganisms[2] or produced *in vitro* by enzymatic processes.[3] However, the largest amount is still extracted from plants[4–6] and animal[7] sources or from algae.[8]

2.211.2.1. Materials Inspired from the ECM

ECM is the optimized milieu that Nature has been developing to maintain homeostasis and to direct tissue development. Therefore, a great effort has been spent in mimicking the ECM to guide morphogenesis in tissue repair and TE.[9,10] One strategy has been to isolate the main constituents of the ECM and directly use them after purification, with or without further modifications. As ECM plays an instructive role for cell activities, the hypothesis here is that such biomolecules would maintain the biological information and other physicochemical features that would preserve a potential space for new tissue development after cell seeding. This would overcome one of the main drawbacks in the use of synthetic materials, which lack cell-recognition signals. A description of some protein-based biomaterials isolated from ECM follows. These materials are typically extracted from blood plasma and from the skeleton. Other functional proteins, including growth factors, enzymes, and interleukins, used essentially as ingredients to be incorporated in biomaterials, will not be discussed here.

2.211.2.1.1. Collagen

Collagen is the most abundant protein present in mammalian tissues (cornea, blood vessels, skin, cartilage, bone, tendon, and ligament) and is also the main component of the ECM (see **Chapter 2.215, Collagen: Materials Analysis and Implant Uses**). More than 20 distinct forms have been identified, type I being the most abundant and most investigated for biomedical applications.[11] Properties such as high mechanical strength, good biocompatibility, low antigenicity, biodegradability, and the ability of cross-linking emphasize its value as a biomaterial, being currently used in a great number of TE applications.[12] Depending on the purpose, improvement of the physical, chemical, and biological properties of collagen-based materials can be necessary to address some of its drawbacks, for example, its high degradation rate, which leads rapidly to loss of mechanical properties. For example, matrices with adequate mechanical properties have been proposed after chemical glycation procedures or heat treatments.[9] Also, combinations of collagen with other materials have also been prepared. As an example, collagen microsponges may be easily impregnated into previously prepared synthetic polymeric scaffolds that will increase their mechanical performance.[13] On the other hand, growth factors and other active agents can be combined with collagen-based systems, including scaffolds and gels to prolong their release rate and increase their therapeutical effect in TE approaches.[14,15]

2.211.2.1.2. Fibronectin

Fibronectin (FN) is a multifunctional component of the ECM, known to induce cell attachment and spreading through its cell binding site and related synergy sites. It is also a paradigm adhesive protein, nonreactive with adhesion receptor in its soluble state but highly adhesive when insoluble.[16] Nevertheless, the ability of such glycoprotein (a disulfide-bonded dimmer of 220- to 250-kDa subunits) to serve as a substrate for cell adhesion is based on the biological activity of several modules: the arginine–glycine–aspartic acid (RGD) tripeptide in the tenth Fn3 module plays an important role here[17] and has been incorporated onto the surface of numerous biomaterials; several strategies have been summarized by Hubbell.[9] One of

the suggested strategies was to deposit layers of oriented FN in order to enhance the availability of its cell-binding site.[18] On an oriented FN layer, compared with an isotropic layer, human umbilical vein endothelial cells spread significantly faster and in a more spherical way.

2.211.2.1.3. Glycosaminoglycans

Glycosaminoglycans (GAGs) consist of linear chains of the repeating unit of a disaccharide, generically a hexosamine (glucosamine or galactosamine) and a uronic acid component.[19] The extracellular spaces, in particular those of connective tissues such as cartilage, tendon, skin, and blood vessel walls, contain collagen and other proteins embedded in a gel-like matrix that is composed largely of GAGs. Because of their ionic character, GAGs are able to absorb large quantities of water, and this osmotic swelling provides compressive strength.[9]

2.211.2.1.4. Fibrin

Fibrin plays an important role in hemostasis and spontaneous tissue repair (it naturally forms during blood coagulation). Fibrin is a complex network formed by polymerization of fibrinogen in the presence of the enzyme thrombin. Fibrinogen can be isolated from the blood plasma of the patient, limiting the potential for disease transmission and immunogenic reactions. Fibrin is not a regular component of the ECM, but is found as a temporary matrix that will be further replaced by the ECM, and is currently used as fibrin glue in clinical applications. It has excellent biocompatibility, biodegradability, and injectability.[20] Fibrin has been a useful cell delivery matrix for cartilage TE, especially in combination with other biodegradable substances, such as alginate,[21] or hyaluronic acid (HA).[22] It has been also utilized in the regeneration of skin, with considerable success, and even in the loading and posterior release of growth factors.[9]

2.211.2.2. Other Peptide-Based Systems

2.211.2.2.1. Hydrogels enabling enzymatically mediated cell migration

These systems are part of an interesting strategy to mimic the ECM, whose aim is to develop matrices that could promote cell-ingrowth through proteolytic degradation of the matrix, usually requiring the action of metalloproteinases (MMPs) which are secreted by cells. Very elegant works have reported the use of conjugates of poly(ethylene glycol) (PEG) and specific peptides that can be hydrolyzed in the presence of enzymes involved in cell migration.[23,24] Growth factors can be entrapped that can also promote mesenchymal stem cell infiltration and corresponding differentiation.[23,25] Instead of peptide segments, denaturated fibrinogen segments were combined with PEG to form biosynthetic hybrid hydrogels.[26]

2.211.2.2.2. Self-assembling materials

Inspired by Nature, self-assembling molecules have been used as building blocks for the construction of nano- and microscale structures or complex systems.[27] Molecular self-assembly is a process by which noncovalent, weak interactions formed between molecules drive their assembly and organization affording supramolecular structures that define the material.[27,28] Self-assembling materials also aimed at mimicking the ECM have been proposed as hydrogels for TE applications. Peptide amphiphilic-based nanostructured fibrous scaffolds were produced by pH-induced self-assembly that could also induce biomineralization.[29] Three-dimensional (3D) network based on nanofibers formed by self-assembly of peptide–amphiphilic molecules were also used to encapsulate neural progenitor cells, showing the ability to induce very rapid differentiation into neurons, while discouraging the development of astrocytes.[30] In fact, the self-assembling peptide nanofiber scaffolds have been shown a wide spectrum of uses with high potential for regenerative medicine and TE.[31]

2.211.2.2.3. Other protein-derived biomaterials

Animal- or vegetal-derived proteins have shown to have potential to be used as scaffolds for TE applications. Silk proteins, for example, contain a highly repetitive primary sequence that leads to a high content of β-sheets, responsible for the good mechanical properties of silk fibers (see **Chapter 2.212, Silk Biomaterials**). Moreover, silk fibroin can be processed in aqueous solutions into gels, sponges, and membranes, and easily modified due to the presence of amine and acid side chains[32,33] or by conjugation with polysaccharides.[34,35] It has been reported that silk fibroin may have the potential to be used in TE applications, where mechanically robust, long-term degradable materials are needed.[36] For example, porous silk scaffolds were combined with human articular chondrocytes for *in vitro* cartilage TE.[37] Additionally, casein and soybean protein-based materials were found to be promising materials to be used in different biomedical applications, including the production of composites for TE.[38] The major drawback of such materials is the possibility of eliciting some level of foreign body response following implantation *in vivo* that can be minimized, for instance, by purification.

2.211.2.3. Polysaccharides

Polysaccharides consist of monosaccharides linked together by O-glycosidic linkages. Differences in the monosaccharide composition, linkage types and patterns, chain shapes, and molecular weight, dictate their physical properties including solubility, flow behavior, gelling potential, and/or surface and interfacial properties. Polysaccharides are derived from renewable resources, namely from plants, animals, and microorganisms, and are therefore, widely distributed in nature. They perform different physiological functions and may offer a variety of potential applications in the fields of TE and regenerative medicine.

2.211.2.3.1. Plant polysaccharides

Starch is a mixture of glycans that plants synthesize as their principal food reserve. It is deposited in the chloroplasts of plant cells as insoluble granules composed of α-amylose (normally 20–30%) and amylopectin (normally 70–80%).[5] α-Amylose is a linear polymer of several thousands of glucose residues linked by $\alpha(1\rightarrow4)$ bonds. Amylopectin consists mainly of $\alpha(1\rightarrow4)$-linked glucose residues but it is a branched molecule with $\alpha(1\rightarrow6)$ branch points every 24–30 glucose residues in average (**Table 1**). Amylose forms a colloidal dispersion in hot water whereas amylopectin is completely insoluble. Starch has been converted into a thermoplastic[81] or blended with synthetic polymers[39] to enhance the strength of

Table 1 Examples of some polysaccharides available in nature, their relevant properties and examples of their applications in the fields of tissue engineering and regenerative medicine

Polysaccharide	*Source*	*Repeating unit*	*Relevant properties*	*Examples of proposed applications*
Starch	Plant (e.g., corn, rice, potato, wheat, tapioca, etc.)[5]	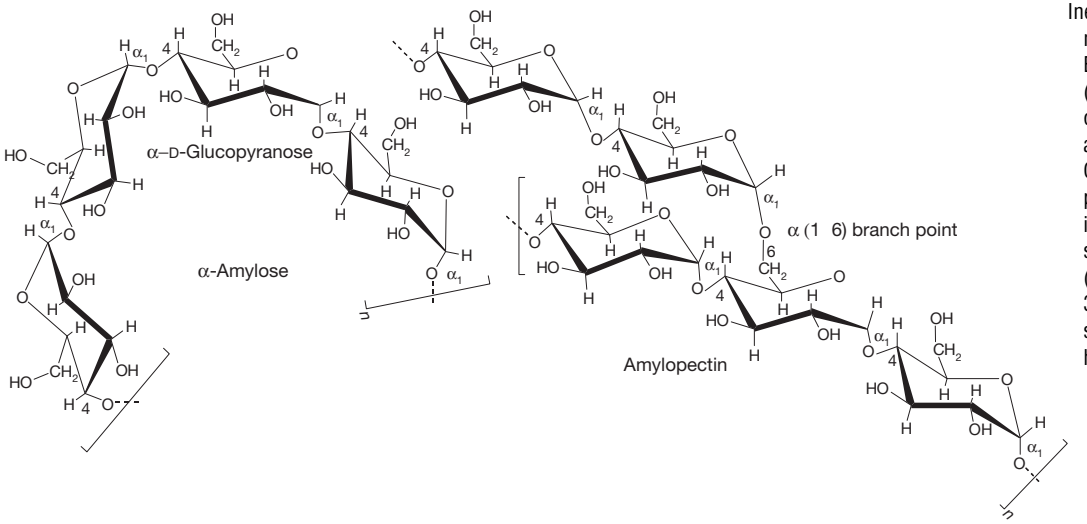	Inexpensive material Easily modified (cross-linked, oxidized, acetylated) Good processability into diverse shaped items (microspheres, 3D porous scaffolds, hydrogels)	3D scaffolds for bone TE[39–42] Microspheres as drug-delivery carriers, TE[43] Fiber mesh scaffolds for cartilage TE[44]
Cellulose	Plant (cotton, wood, straw, etc.)[4] Microbial (bacterial cellulose, *ex. Acetobacter xylinum*)[45]	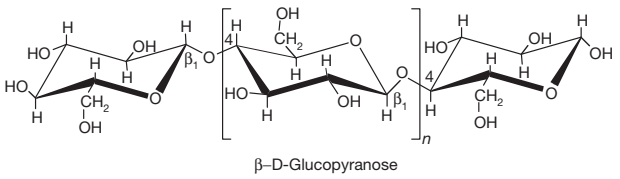	Resource available worldwide Insolubility in water Easily molded or drawn into fibers	Scaffolds for cardiac TE[46]; cartilage TE[45,47]; bone regeneration[48]

Arabinogalactan (larch gum)	Plant (extracted from the heartwood of the western larch *Larix occidentalis*)[49]	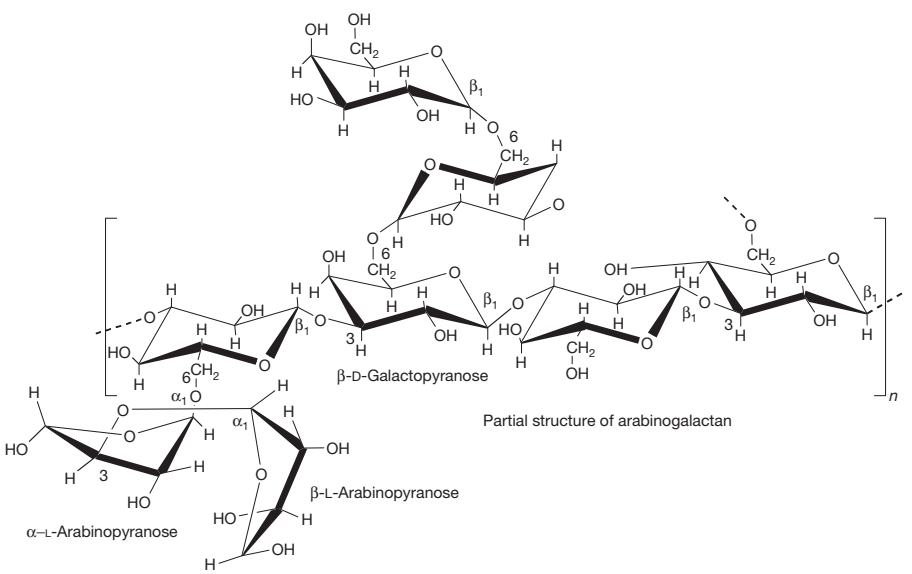	High water solubility (70% in water) Easy conjugation in aqueous medium	Sponges for TE[50]
Alginic acid	Brown algae (*Phaeophyceae*, mainly *Laminaria*) Microbial (bacteria *Pseudomonas mendocina*, *Azetobacter vinelandii*)[8]	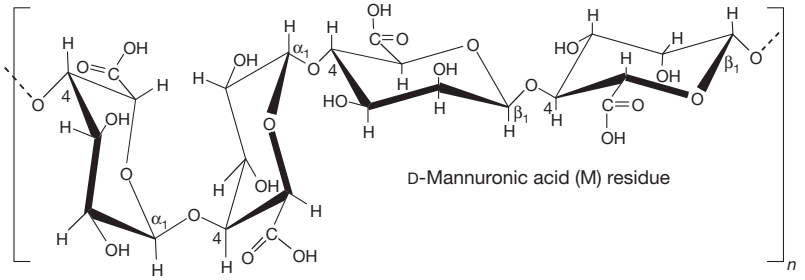	Simple gelation with divalent cations (e.g., Ca^{2+}, Mg^{2+}, Ba^{2+}, Sr^{2+})	Cell encapsulation matrix[51]; scaffolds for cancer gene therapy[52]; bone TE[53]; hepatic TE[54]; hydrogels for cartilage TE[55]
Agar	Red algae – *Rhodophycae* (*Gelidium and Gracilaria species*)[8]	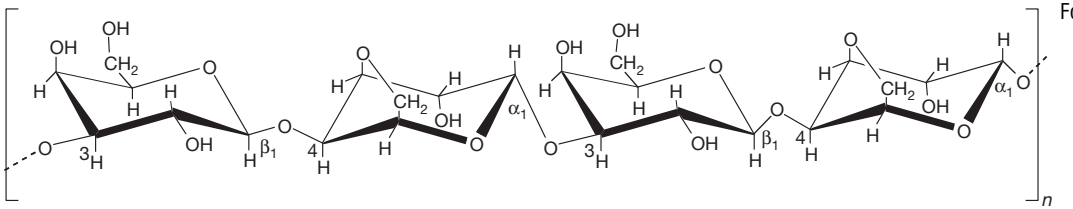	Formation of thermal reversible gels (cold setting gels at ~38 °C)	Gels/sponges for cartilage,[55,56] bone regeneration,[57] disk TE,[58] nerve regeneration[59]

(*Continued*)

Table 1 (Continued)

Polysaccharide	*Source*	*Repeating unit*	*Relevant properties*	*Examples of proposed applications*
Carrageenan	Red algae – *Rhodophycae* (*Chondrus crispus*, *Euchema cottonii*, *Euchema spinosum*)[8]	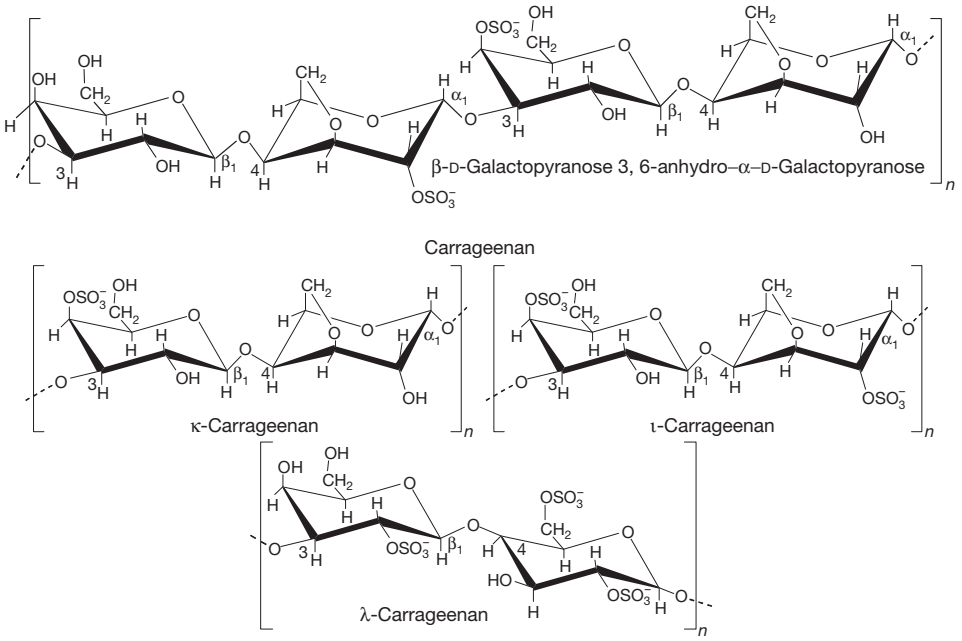	Thixotropic behavior Gel-forming ability	Nanoparticles for drug delivery[60]; polyelectrolyte for cell encapsulation[61]; hydrogels for bone TE[62]; injectable gel system for cartilage TE[63]
Chitin/chitosan	Animal (crustaceans shells, exoskeletons of insects, and other arthropods) Microbial (fungal cell walls)[64]	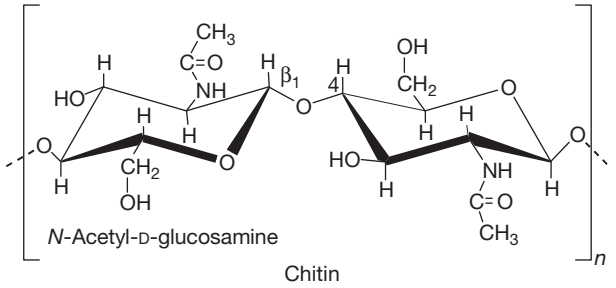	Enzymatic degradation by lysozyme Susceptibility to chemical modification Film-forming ability Hemostatic, bacteriostatic, and fungistatic activity Wound healing properties	Fiber mesh scaffolds for bone TE[65]; sponges (bone formation); tubes for nerve regeneration[66]; scaffolds for cartilage and osteochondral TE[67,68]

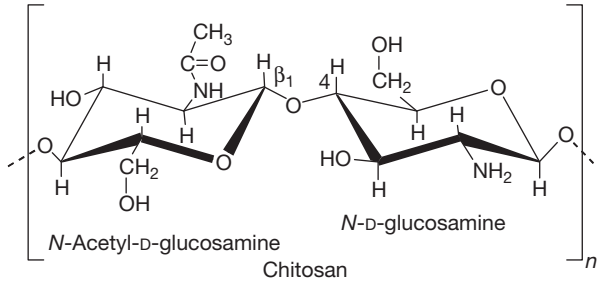

Chitosan

Hyaluronic acid	Animal (synovial fluid, vitreous humor of the eye, umbilical tissue)[69] Microbial (fermentation *Bacillus subtilis*[2,70])	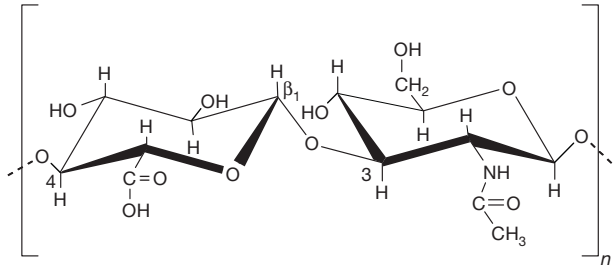	Solubility in water Viscoelasticity Hydrogel ability by covalent and photo-cross-linking Enzymatic degradation by hyaluronidase	Scaffolds for ligament TE[71]; sponges for the treatment of osteochondral defects[72]; photo-cross-linked hyaluronic acid hydrogels as TE scaffolds[70]
Dextran	Microbial (bacterium *Leuconostoc mesenteroides*[73])	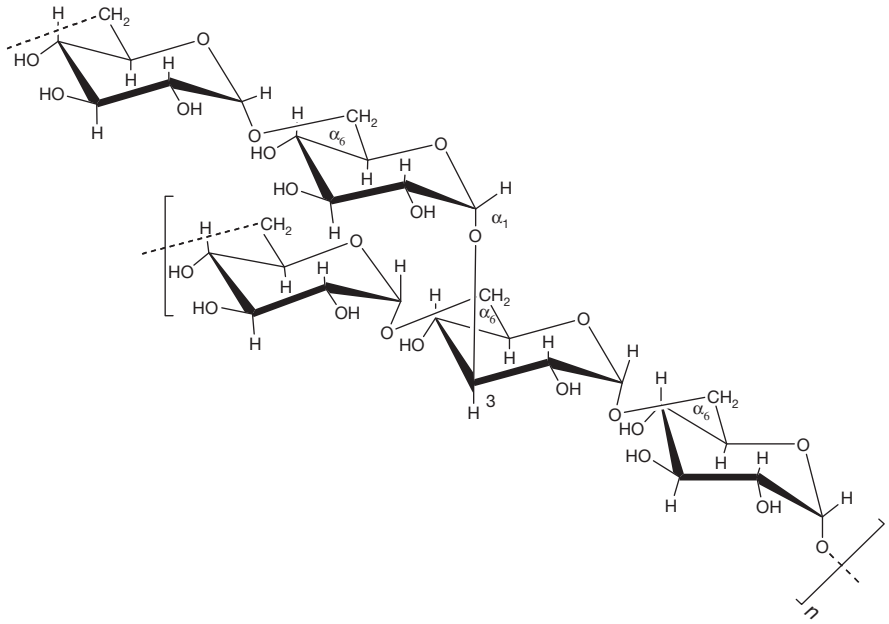	Solubility in both water and organic solvents (e.g., dimethyl sulfoxide) Stability under mild acidic and basic conditions Contains large number of hydroxyl groups available for modification/ conjugation with other molecules	Porous hydrogels as scaffolds for TE applications[74]; hydrogels for cartilage TE[75]

D-Glucuronic acid

N-Acetyl-D-glucosamine

(*Continued*)

Table 1 (Continued)

Polysaccharide	*Source*	*Repeating unit*	*Relevant properties*	*Examples of proposed applications*
Gellan gum	Microbial (bacterium *Sphingomonas elodea*[76])	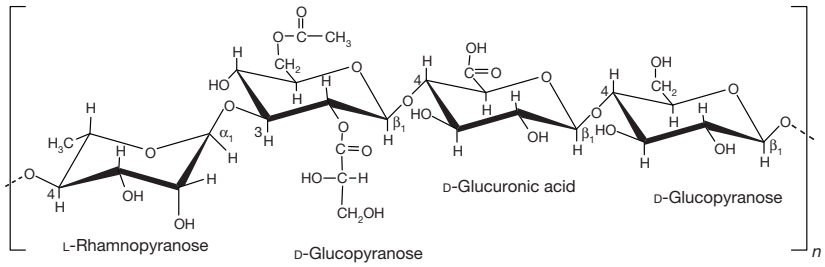 Native or high acyl gellan gum 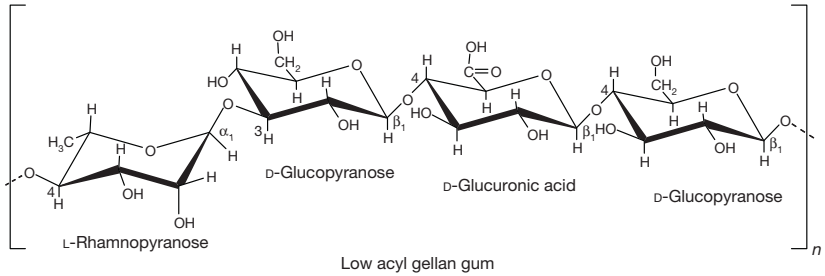 Low acyl gellan gum	High acyl gels set and melt at ~70–80 °C with no thermal hysteresis Low acyl gellan gum can form hard, nonelastic and brittle gels in the presence of cations, including Ca^{2+}, Mg^{2+}, Na^{+}, K^{+}, and H^{+}	Microparticles for nasal delivery system[77]; hydrogels for cartilage TE[78,79]
Pullulan	Microbial (fungus *Aureobasidium pullulans*[7])	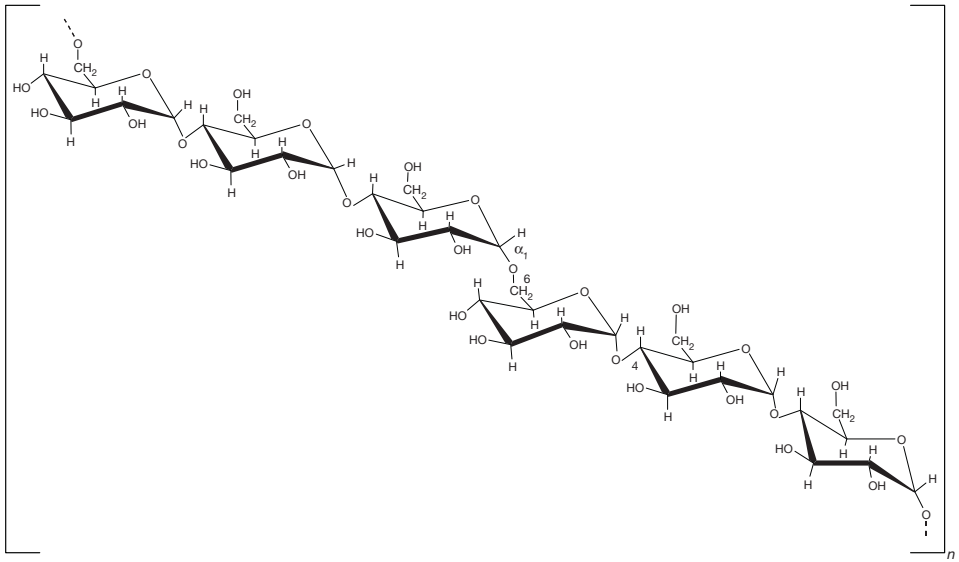	Dissolubility in water Ability to form a stable, viscous solution that does not gel Adhesive properties Easily derivatization	Carboxylated pullulan derivatives as extracellular matrix for TE applications (e.g., endothelial cells)[80]

starch and thus obtain better mechanical properties.[76] Starch-based materials are highly thermosensitive materials which easily degrade at high shear rates and with long residence times during processing. They can be processed by diverse techniques into different shaped items such as 3D porous scaffolds, microparticles, and hydrogels.[39,43,82]

Cellulose, the primary structural component of plant cell walls, is a linear polysaccharide of D-glucose units linked by β(1 → 4) glycosidic bonds (Table 1). The fully equatorial conformation of β-linked glucose residues stabilizes the chair structure, minimizing its flexibility. This highly cohesive, hydrogen-bonded structure gives cellulose fibers exceptional strength and makes them water insoluble despite their hydrophilicity. Cellulosic materials exhibit, however, poor degradation *in vivo*.[46] Moreover, cellulose can be converted into different derivatives (carboxymethylcellulose, cellulose nitrate, cellulose acetate, cellulose xanthate)[4] that can be easily molded or drawn into fibers.[46]

2.211.2.3.2. Exudate gums

Exudate gum polysaccharides are produced at the surface of a plant, usually as a result of trauma or stress (physical injury and/or fungal attack). These exudates are complex, uronic acid-containing polysaccharides, some even associated with proteins.[6] Most gums are soluble in water and have high viscosity. Major uses of gums are in the food and pharmaceutical industries, where their emulsifying, stabilizing, thickening, and gel-forming properties are the main physical requirements.[6]

Arabinogalactan is a major D-galactan obtained from soft woods such as larch (larch gum). It is composed of β(1 → 3)-linked D-galactose units, each containing a side chain at position C6. It is extracted from the *Larix* tree and it is available in 99.9% pure form with reproducible molecular weight and physicochemical properties. The high solubility in water, biocompatibility, biodegradability, and the ease of chemical modification in aqueous media makes it an attractive polymer for the production of scaffolds with application in TE.[50]

Gum arabic is an exudate gum obtained from *Acacia* trees and consists of a variable mixture of arabinogalactan oligosaccharides, polysaccharides, and glycoproteins. It is an acidic arabinogalactan with a complex structure. The main chain of this polysaccharide consists of β(1 → 3) and β(1 → 6)-linked D-galactose units along with β(1 → 6)-linked D-glucopyranosyl uronic acid units. Gum arabic has a high water solubility (up to 50% w/v) and relatively low viscosity[7] but it exhibits emulsification, encapsulation, and film-forming abilities.

2.211.2.3.3. Algal polysaccharides

Alginate, the monovalent form of alginic acid, is a linear polymer of β(1 → 4)-linked D-mannuronic acid and α(1 → 4)-linked L-guluronic acid, which occurs combined with calcium and other bases in the cell walls and intracellular matrix of brown seaweeds, constituting the main structural component.[8] The residues are present in blocks of each monomer, separated by regions in which they are randomly arranged or alternating. The proportions of mannuronic (M) and guluronic (G) residues (Table 1), and the lengths of the blocks, can vary considerably, depending on the source of the alginate. Furthermore, the properties of alginate depend on molecular weight, composition, and extent of the sequences. The polymer undergoes ionotrophic gelation in the presence of divalent cations and gelling depends on the ion binding ($Mg^{2+} << Ca^{2+} < Sr^{2+} < Ba^{2+}$).[7] One of the drawbacks of alginate hydrogels is that the degradation occurs via a slow and unpredictable dissolution process *in vivo*.[83,84]

Galactans, the major polysaccharides of the red algae *Rhodophyceae*, comprise agars, carrageenans, and related hybrid polysaccharides. *Agar* is made of two components, agarose – a nonsulphated fraction, and agaropectin – a mixture of various sulphated molecules. The separation of agarose from the polysaccharide mixture is based on the differences in solubility and chemical reactivity, which is associated with the anionic character of agaropectins.[8] *Agarose* is a linear polysaccharide based on the (1 → 3)-β-D-galactopyranose-(1 → 4)-3,6-anhydro-α-L-galactopyranose unit (Table 1). This arrangement allows the chains to join together and adopt a double helix. The two chains are wrapped together so tightly that any gaps are closed, trapping any water inside the helix.

Carrageenan polysaccharides are linear polymers consisting of chains of (1 → 3)-linked β-D-galactose and (1 → 4)-linked α-D-galactose units, which are variously substituted and modified to the 3,6-anhydro derivative, depending on the source and extraction conditions (Table 1).[85] Three major types of carrageenan are recognized on the basis of their patterns of sulphate esterification: κ (kappa), ι (iota), and λ (lambda). All carrageenans are highly flexible molecules, which, at higher concentrations, wind around each other to form double-helical structures. This gives them the ability to form a variety of different gels at room temperature. In fact, κ- and ι-carrageenans form thermoreversible gels on cooling in the presence of appropriate counterions. A particular advantage is that they are thixotropic,[61] that is, they thin under shear stress and recover their viscosity once the stress is removed.

2.211.2.3.4. Animal polysaccharides

Chitin is the principal structural component of the exoskeletons of invertebrates such as crustaceans, insects and is also present in the cell walls of most fungi and many algae. Basically, the chitin isolation from those sources consists of three important steps: demineralization (acid removal of calcium carbonate), deproteinization (removal of proteins), and depigmentation (removal of pigments), which involve the use of hydrochloric acid baths, alkaline treatment, and a mild oxidizing treatment, respectively.[64,86] Structurally, it is a homopolymer of β(1 → 4)-linked *N*-acetyl-D-glucosamine (GlcNAc) residues.[64] Chitin can be converted into soluble derivatives like chitosan (CHT), carboxymethylchitin, glycochitin, among others.[87] Chitin derivatives possess many unique properties such as biocompatibility, biodegradability, hydrophilicity, adsorption capability, and high reactivity. Moreover, chitin-based polymers are materials with great versatility to be processed in different forms (fibers, sponges, membranes, beads, hydrogels).[87–89] Water-soluble derivatives (e.g., carboxymethylchitin) can also be obtained, extending the domain of applications of chitin, especially in the biomedical field.

CHT is the *N*-deacetylation derivative of chitin; however, this *N*-deacetylation is almost never complete. The number fraction (%) of GlcNAc residues in the polymer chain is designated by degree of acetylation (DA) and influences the CHT physicochemical properties such as solubility, reactivity, biodegradability, and cell response.[64,88,90] This polymer has many

properties such as its polyelectrolyte and cationic nature, mucoadhesion, hemostatic action, film-forming ability, biodegradability, bacteriostatic and fungistatic activity, and the presence of reactive functional groups.[64,86,91] Because of the stable crystalline structure, CHT is normally insoluble in water, but soluble in dilute aqueous acidic solutions. Their solutions have been used in the production of gels, membranes, microparticles, fibers, porous structures, and tubes,[92,93] which combined with its pH sensitivity and high charge density (positive electrical charge) allows the development of drug-delivery devices, composites, and implants for TE.[94] On the other hand, the presence of functional groups (hydroxyl, amine) has been beneficial for chemical modifications to construct a wide range of useful derivatives with satisfactory mechanical, solubility, photoluminescent characteristics, and biological properties for specific use in diversified fields.[94–97]

HA, also known as hyaluronan or hyaluronate, is an important GAG component of connective tissue, synovial fluid, and the vitreous humor of the eye.[69] (see **Chapter 2.214, Hyaluronic Acid**) HA is a linear polysaccharide composed of 250–25 000 $\beta(1\rightarrow4)$-linked disaccharide units that consists of D-glucoronic acid and GlcNAc linked by $\beta(1\rightarrow3)$ bond (**Table 1**). The disaccharide units of HA are extended, forming a rigid molecule whose numerous repelling anionic groups bind cations and water molecules. In solution, hyaluronate occupies a volume ~1000 times that in its dry state. Hyaluronate solutions exhibit clear viscoelastic properties that make them excellent biological absorbers and lubrificants.[98] In addition, HA can be easily and controllably produced in large scales through microbial fermentation, enabling the scale-up of derived products and avoiding the risk of animal-derived pathogens. Owing to its good biocompatibility, widespread availability, and nonimmunogenic and viscoelasticity properties, hyaluronan has been extensively studied and employed as a delivery system, and for cell encapsulation.[98,99,100]

2.211.2.3.5. Microbial polysaccharides

Dextran is a branched bacterial polysaccharide, produced from sucrose via the action of dextransucrase enzyme,[73] consisting of $\alpha(1\rightarrow6)$-linked D-glucose residues with some degree of branching via $\alpha(1\rightarrow3)$ linkages (**Table 1**). The molecular weight and degree of branching is dependent on the source of dextrans and may vary from 0.5% to 60%. Both the degree of branching and molecular weight distribution affect its physicochemical properties. Characteristics as relatively low cost, availability, and hydroxyl functionality for chemical modification have increased the utilization of dextran for TE applications.[75,101,102]

Gellan gum is a high-molecular-weight bacterial exopolysaccharide. It is a linear anionic heteropolysaccharide composed of the tetrasaccharide $(1\rightarrow4)$-L-rhamnose-$\alpha(1\rightarrow3)$-D-glucose-$\beta(1\rightarrow4)$-D-glucuronic acid-$\beta(1\rightarrow4)$-D-glucose as repeating unit (**Table 1**). In its native or high acyl form, two acyl substituents D-acetate and D-glycerate are present. Both substituents are located in the same glucose residue. The high acyl form produces transparent, soft, elastic, and flexible gels which are resistant to heat and acid, whereas the low acyl form produces firm, nonelastic brittle gels. Gel formation is due to a conformational heat-reversible transition from a state of single random macromolecules to a more ordered state where macromolecules pair with each other to form double helixes.[103] In the context of biomedical applications, gellan gum has many advantages such as its lack of toxicity, processing under mild conditions, the ability to use it as an injectable system in a minimally invasive manner, and also the structural similarity it presents with native cartilage GAGs by the presence of glucuronic acid residues in their repeating unit.[78]

Pullulan is an extracellular microbial homopolysaccharide of glucose, produced from starch by fermentation, and consists of repeating units of maltotriose ($\alpha(1\rightarrow4)$-linked) joined by $\alpha(1\rightarrow6)$ linkages (**Table 1**). Some advantages of pullulan are its nontoxicity and lack of immunogenecity.[104]

Xanthan gum is an anionic polysaccharide produced from glucose via fermentation by the bacterium *Xanthomonas campestris*.[105] The structure of xanthan is based on a cellulosic backbone of $\beta(1\rightarrow4)$-linked glucose units which have a trisaccharide side chains of D-mannose-$\beta(1\rightarrow4)$-D-glucuronic acid-$\beta(1\rightarrow2)$-D-mannose linked to C3 every second glucose unit in the main chain. Some terminal mannose units can contain a pyruvate group and mannose residues attached to backbone units are variably acetylated. It has unique rheological properties (high viscosity even at low concentrations) and forms hydrogels by annealing the solution in sol state and subsequent cooling.[106]

Cellulose can be produced by the bacterium *Gluconacetobacter xylinus* (**Table 1**). Bacterial cellulose (BC) has unique properties, including biocompatibility, high water-holding capacity, high crystallinity, a fine fiber network, and high tensile strength in the wet state. In addition to its cost-efficient and relatively simple production, it has the advantage of *in situ* moldability.[45]

Table 1 summarizes the polysaccharides currently used in the field of TE and regenerative medicine. However, there is a wide variety of other potentially useful polysaccharides exhibiting diversity of structures and functions (e.g., pseudoplastic behavior, gelation, water binding, etc.), such as laminarin, gluco and galactomannans, exudate and mucilage gums, levan, curdlan, among others, which remain unexploited within the biomedical field. This situation may be associated with their current availability, difficulty on their isolation/purification and processing, and/or lack of information related with their biocompatibility and toxicity.

An important aspect to consider when using natural materials is that they can induce an undesirable immune response due to the presence of impurities and endotoxins, depending on the source of the material. Additionally, their properties may differ from batch to batch during large-scale isolation procedures due to inability to control the processing techniques. Nevertheless, as knowledge about these natural materials is being built, new approaches, including methods for production, purification, control of material properties (mechanical, degradation rate), and for enhancing material biocompatibility, are being developed for designing better scaffolding materials to support the development of more natural and functional tissues.

2.211.2.4. Natural-Derived Polyesters

Polyhydroxyalkanoates (PHAs) are degradable, biocompatible, thermoplastic polyesters derived from microorganisms, used

as a reserve of carbon and energy. A great variety of materials of this family can be produced, but the use of PHAs in TE has been mainly restricted to two polymers, namely poly(hydroxybutyrate) (PHB) and poly(hydroxybutyrate-*co*-valerate) (PHBV)[107,108]; the copolymerization produces less crystalline, more flexible, and more readily processable materials than pure PHB. Previous works have shown that such materials can be used as cell support for TE applications.[109–111]

2.211.3. Processing of TE Scaffolds

The several requirements that directly dictate the success of TE strategies are well reviewed in the literature. In all, the authors seem to agree that the selection of the appropriate biomaterial and the development of adequate scaffold architectures[112,113] play an important role in supporting the cells adhesion and tissue/organ repair/regeneration. As aforementioned, the scaffold is aimed at providing a temporary 3D structure and template upon which the tissue-specific cells can attach, proliferate, and produce ECM. In addition, the necessary diffusion of nutrients and metabolic wastes in a 3D environment demands highly porous scaffolds.[114] Consequently, we must choose a processing technique that allows for the preparation of scaffolds with controlled porosity, pore size, and interconnectivity, as well as tissue-matching mechanical properties. Of great importance as well, is the need to choose a biomaterial that degrades at a rate that matches with the deposition of ECM. Thus, the criteria for the selection of the best biomaterials and processing methods are of major importance. In this section, our attention is focused on the processing techniques available for the development of natural-origin scaffolds as the types of biomaterials have been reviewed in the previous sections.

Among the myriad processing methodologies, a wide range has been exploited by our group. *Conventional melt-based processing routes*, such as extrusion using blowing agents (which are responsible for inducing porosity), and other based on multistep processes such as compression molding followed by particulate leaching have attracted our research interest.[115,116] The nonthermoplastic behavior of natural polymers has limited their application, especially on the use of melt-based processing methods for the fabrication of TE scaffolds to these materials. For example, starch is a renewable and inherently biodegradable polymer[117] which has been successfully incorporated in many polymeric systems to develop partially or totally biodegradable plastics.[118] Thus, the use of starch materials has attracted great attention in TE applications, as it can allow the designing of scaffolds with an adequate degradation rate, that is, the degradation of the scaffold matching new tissue formation. Our group has been proposing the use of starch-based materials obtained from a blend of starch and polycaprolactone (SPCL) for bone TE applications. The advantages of starch-based materials are that they are biodegradable, present good mechanical properties, and can be processed by different methodologies.[119–123] TE scaffolds based on thermoplastic blends of starch with ethylene vinyl alcohol copolymer and cellulose acetate have also been produced by melt extrusion employing endothermic chemical blowing agents, based on mixtures of citric acid and sodium bicarbonate. Salgado *et al.*[124,125] demonstrated that these scaffolds are noncytotoxic, and exhibited adequate architecture for supporting *de novo* bone formation, *in vivo*. In other works,[39,126] the same approach was carried out to fabricate TE scaffolds based on injection molding. This technique differs from extrusion since it combines heat and shear effects to plasticize thermoplastic formulations. It is also worth to highlight that more recently, physical blowing agents such as supercritical CO_2 and water have been shown to be effective to injection mold polyether–urethane scaffolds[127,128] for TE applications.

Freeze-drying technique has also been widely used for the production of porous structures with different densities, shapes, porosities, and pore size distributions. By simply varying parameters such as polymer concentration,[129–132] type of solvent,[133] freezing temperature,[113,133–137] type of molds,[138,139] and incorporating porogens,[130,132,134,137] we may produce a wide variety of scaffolds. For example, Oliveira *et al.*[68] developed an innovative technique for obtaining bilayered structures with improved architecture, stability, and biological properties for osteochondral TE applications. Hydroxyapatite/chitosan (HAp/CHT) bilayered scaffolds were produced by adopting a two-step procedure. Firstly, HAp porous layer (bone-like layer) was obtained by the sponge burn-out method. Secondly, a 3 wt% CHT solution was prepared by dissolving CHT in 0.2 M acetic acid solution. The bilayered HAp/CHT scaffolds were fabricated by placing the HAp scaffolds into cylindrical silicon molds and transferring the 3 wt% CHT solution. Molds were frozen at $-80\,^{\circ}C$ and lyophilized to completely remove the frozen solvent, and allowed to obtain the 'cartilage-like layer' on the top of the 'bone-like layer.' This work illustrates that polymer solutions should be previously transferred into a mold and frozen before freeze-drying at temperatures typically ranging between -20 and $-80\,^{\circ}C$ to shape these scaffolds. Then, porosity and pore size can be obtained during freeze-drying as the space occupied by the frozen solvent will become empty after sublimation.[140] Interestingly, pore structure can also be tailored by simply varying the freezing rate.[141] However, when using this technique to produce scaffolds, a critical parameter to be controlled is related with the need of guarantee that the final freezing temperature is adequate to maintain all the molecules of solvent in the solid state.[142] Otherwise, the final structure will shrink during the drying process resulting in the formation of a dense external skin-like layer, which can be seen as a disadvantage from the scaffold biological performance point-of-view.

Supercritical fluid technology (SCF) is seen as a clean, inexpensive, and environmentally friendly technology that has also been proposed for developing[143] a wide range of particles and TE scaffolds. The main advantages of this technique are: (i) absence of organic solvents, (ii) ability to incorporate bioactive compounds and growth factors, and (iii) ability to control the architecture of the scaffold. The principle of this technique is based on the fact that supercritical fluids are gases and liquids at temperatures and pressures above their critical points (T_c, critical temperature, and P_c, critical pressure).[144] Of particular interest for supercritical fluids application are the ranges $1 < T/T_c < 1.1$ and $1 < P/P_c < 2$ as the supercritical fluids appear in single phase with several advantageous properties

of both liquids and gases. We will not pay special attention to this topic as several good reviews[145–148] have summarized not only the aspects dealing with the principle, but also those related to processing and applicability possibilities. An interesting review[143] focuses on the SCF-processing methods as a processing tool for incorporation of bioactive compounds into TE scaffolds.

Carbon dioxide is the most commonly used supercritical fluid since it requires less energy consumption, and it is nontoxic, nonflammable, and noncorrosive. Its elimination and the recovery of final products are simple, that is, no residue is left and a dry solid product can be obtained by controlling the pressure. Thus, supercritical carbon dioxide has been regarded as the main candidate to develop alternative clean processes for the preparation of drug-loaded polymeric matrices and foaming of hydrogels.[149] In this respect, our group has shown not only that it is possible to use SCF to impregnate CHT scaffolds[150] obtained by freeze-drying with a pharmacological drug, but we have also shown that using a supercritical phase inversion technique we were able to prepare composite scaffolds of dexamethasone and a polymeric blend of starch and poly(L-lactic acid) (SPLA) in a single step.[151] In another work,[152] we also investigated the possibility of the use of the supercritical immersion precipitation technique to to prepare highly porous and interconnected scaffolds of a polymeric blend of SPLA. Two organic solvents, dichloromethane and chloroform, were tested, and results have shown that chloroform was preferable for the process. This processing technique shows such versatility that also enabled us to prepare composite scaffolds of Bioglass® and SPLA blends in a one-step process.[153] Besides, as supercritical fluids are highly compressible (especially near the critical point), and their density can be carefully controlled by small changes in temperature and/or pressure, it has been shown to be possible the design of particles[144,154] namely, the particle size control or polymorphic purity.

Complexation of polymer of opposite charge, such as CHT and alginate or carrageenan, has been also attracting much attention.[155] When two polyelectrolytes of opposite charge are combined, the formation of a physical hydrogel might take place, the so-called ionotropic hydrogel. The main advantage of such a processing technique lies in the possibility of being able to process in aqueous solutions (possibly incorporate bioactive molecules in a one-step process) and under very mild conditions, thus avoiding the use of organic solvents or other aggressive methods. Thus, the physicochemical properties of these hydrogels depend on the type of forces that can be associated namely, molecular entanglements, ionic forces, hydrogen bonding, and hydrophobic forces. All these interactions are reversible and can be disrupted by changes in physical conditions such as ionic strength, pH, and temperature. By varying the concentration of the polyelectrolytes, different gel structures can be produced, such as beads, microparticles, and nanoparticles. For example, our group recently reported[60] the preparation and characterization of protein-loaded nanoparticles obtained by ionic complexation of CHT and carrageenan. These nanoparticles have been shown to be an interesting drug-delivery system which made possible the loading of albumin (from 4% to 17%) and demonstrated excellent capacity to provide a controlled release for up to 3 weeks. *In vitro* studies using L929 fibroblats revealed that the nanoparticles are noncytotoxic, which in turn are critical for allowing their use in TE and regenerative medicine strategies. Other interesting systems and formulations have been also reported. In a work reported by Wang *et al.*,[254] the spray-spinning technique was carried out to spray a CHT solution into a flowing sodium alginate solution and sheared into streamlines – the elongated streamlines subsequently transformed into alginate/CHT polyelectrolyte complexes fibers. The ability of certain polymers such as gellan gum or alginate to cross-link with cations, that is, to be ionically cross-linked, may also be used to produce scaffolds.[156–159] These polymers have been used in cartilage TE as hydrogels and besides showing appropriate mechanical properties they allow to encapsulate cells during processing and can be used in minimally invasive strategies.

Other interesting techniques used in TE scaffolding include *solvent casting and particle leaching*.[134,137] Particle leaching is widely used since it is a cheap, fast technique that easily allows us to tune the porosity and pore size/geometry of the scaffolds,[119,160] by simply varying the amount and size/shape of the porogen. Thus, the process is based on the dispersion of the porogen particles such as salt or others with a biomaterial, which in turn can be in a liquid or solid state.[134,137,161] After the shaping process using a mold, the porous structure is obtained by eliminating the porogen particles by soaking it in a specific solvent.[162] Despite these advantages, this technique presents a major drawback as it is difficult to control the pores interconnectivity.[163] However, Ghosh *et al.*[164] demonstrated that an increase of interconnectivity in SPLA-based scaffolds can be achieved using salt particles and poly(ethylene oxide) (PEO) as an additional polymeric porogen.

By means of using the previously described methodologies, it is possible to tailor the properties of the different scaffolds, namely their degradation, architecture, and mechanical properties, for several applications in TE scaffolding. In this section, we thought that the processing possibilities to obtain particles and fibers are worthy of special attention, and are therefore reviewed more extensively in the following sections.

2.211.3.1. Microspheres and Microparticles and Their Aggregation

Methods of relevance to TE and controlled release strategies that focus on the incorporation of bioactive molecules such as growth factors or cells within the scaffolds have attracted great deal of attention. For example, Kim *et al.*[165] reported the development of microspheres made of collagen–apatite nanocomposites mimicking the extracellular bone matrix. In this study, they developed microspheres constituted of collagen and apatite for the treatment of skeletal defects. A water-in-oil emulsion method was carried out for obtaining the microspheres starting from an apatite-precipitated collagen solution (30% apatite). Microspheres and microparticles have been used as supports for cell growth, proliferation, and differentiation. Thus, one can easily identify two different approaches: (i) the microspheres can be injected immediately mixed with cells or bioactive molecules[166–169] and (ii) the microspheres can act as a carrier for *in vitro* cell attachment

and injected at a later stage.[170] The example given for the second strategy makes use of poly(D,L-lactic-*co*-glycolic acid) which is a synthetic polymer. Despite many other examples, the use of natural-origin polymers is well reviewed elsewhere.[171] Alternatively, the aggregation of the microspheres/microparticles themselves can be used as a processing technique to produce TE scaffolds. The agglomeration step can be achieved using chemical, thermal, or physical processes. An interesting work has been reported by van Tomme *et al.*,[172] which produced a self-gelling hydrogel by simply mixing dispersions of oppositely charged cross-linked dextran microspheres. In addition, it is also possible the aggregation of dextran microspheres by seeding with cells in order to form a living tissue-engineered construct. Such type of strategies has been reported by our group.[173,174] In these studies, we have demonstrated the possibility of the development of several scaffolds based on CHT particles' aggregation, which were promising in the search for applications in cartilage, bone, and osteochondral TE. Another approach has been also proposed, consisting of a mixture of microspheres (loaded with bioactive molecules or cells) and hydrogels, which are then implanted into the defect area.[175,176] Finally, microspheres and particles can be combined with TE scaffolds either by direct combination, that is, by injecting them together with the TE scaffolds or by the infrequent method in which they are used as a coating for these scaffolds. Interestingly, Noritaka *et al.*[177] reported that the impregnation of the loaded microspheres into the scaffolds is much more effective when compared with the simultaneous injection of the loaded microspheres. Other examples[178] may be found in the literature. Thus, to conclude, we may state that the aforementioned strategies based on microsphere and microparticles showed to be promising adjuvant systems for delivering cells or bioactive agents for application in TE scaffolding strategies.

2.211.3.2. Fiber Meshes and Fiber Bonding

Fiber meshes are alternative structures that have been investigated as TE scaffolds. These can be produced from polymeric solution or melt-spun fibers. CHT alone or combined with other polymers has been wet-spun into fibers using acid solutions.[65,179] Our group has evaluated scaffolds based on starch[180,181] using a methodology based on melt spinning that avoids the use of hazardous solvents, in which fiber mesh scaffolds are produced through the application of a heat treatment to bond fiber bundles.[182,183] In this method, melt-spun fibers are cut to standard length and used in the production of fiber mesh scaffolds using a custom-designed mold. In order to control the final morphology, discrete amount of fibers are randomly placed into the mold cavities and subjected to thermal treatment before the application of predefined compression levels along the *z*-axis, in order to assure the bonding between fibers. Fiber mesh scaffolds such as those obtained by this method exhibited controlled porosity, pore interconnectivity, average pore size, and surface area. **Figure 1** presents the scanning electron micrographs for a scaffold based on a blend of starch with poly-ε-caprolactone (starch/PCL) produced by this method. These scaffolds present a large total surface area that promotes cell anchorage and high pore interconnectivity. Following the experiments-based study,[182] a significant correlation was found between porosity and pore interconnectivity, average pore size, and surface area. **Figure 2** presents the dependence of compression stiffness of scaffolds on the porosity. Porosity was found to be an important factor negatively affecting the compression stiffness of the scaffolds. The scaffolds produced by this method were found to exhibit adequate properties to be used in different TE contexts.[184–187] The control of scaffold morphology is a critical factor when optimizing the biological performance of these scaffolds. In this regard, it was found that intermediate values of porosity appear to be more adequate for enhancing cell seeding as opposed to very high porosities.[182] Inadequate scaffold morphologies can lead to uneven zonal distribution of cells. Upon longer times of culture, local variations in cell distribution are reduced, but partially reflect the initial zonal distribution of cells. There are several advantages for using this processing methodology such as: no use of solvent, attainment of high porosity and pore interconnectivity values and good overall control of scaffold morphology. Nevertheless, thermal-based methods like this one can only be effectively applied to polymers exhibiting thermoplastic-like behavior, which can hamper significantly its use with other natural-based polymers.

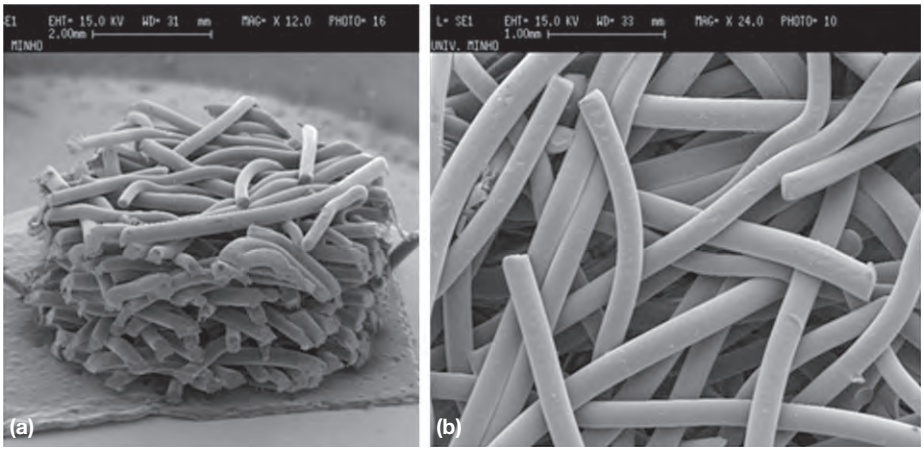

Figure 1 Scanning electron micrographs of a scaffold based on a blend of starch with poly-ε-caprolactone produced by fiber bonding: (a) 12x, and (b) 24x.

2.211.3.3. Rapid Prototyping

During the last few years, investigation has been carried out on the development of alternative processing methodologies based on rapid prototyping (RP). The use of RP allows the design and fabrication of anatomically adapted scaffolds, featuring customized internal architectures, through the integration of computer-assisted design (CAD) tool and medical imaging acquisition and processing techniques. The integration of these technologies into the production of TE scaffolds has been designated as computer-assisted TE (CATE).[188–192] Within the several RP technologies available, few have been applied to the fabrication of TE scaffolds using natural-based polymers. The nonfusible behavior of many natural-based polymers limits the application of many SFF techniques. Among the several available RP techniques, 3D printing is based on the selective bonding of powder particles via the deposition of a binder resin.[193] 3D printing has been originally adopted by Kim *et al.* for the fabrication of TE scaffolds.[194] In this context, starch[41,195] and alginate[196,197] have been used to process 3D scaffolds. Selective laser sintering (SLS) is an additive manufacturing technique that uses a high-power laser to fuse and bond particles into a 3D object. Blends of PCL with a starch, dextran, and gellan gum were processed into 3D scaffolds using SLS.[76] Among the several techniques, fused deposition modeling (FDM) applies heat to a filament of material, which is deposited layer by layer by an extrusion head, according to a programmable path. The temperature and flow of the material is controlled, while the scaffold construction in the *z*-axis is assured by the relative movement of the platform relatively to the extrusion head. Although the development of TE scaffolds by FDM has been reported,[198–203] its application to natural-derived polymers and blends is rather challenging. A possible alternative is the 3D deposition process, referred also as 3D bioplotting, in which the material in the powder or granular form is heated inside a barrel, being the respective molten materials displaced by a plunger or piston. Using this method, it is possible to process blends based on a starch base as they exhibit a thermoplastic behavior. Figure 3 presents, as an example, a scaffold geometry based on starch/PCL blend obtained by 3D bioplotting. Figure 3 presents examples of scaffold architectures obtained for a starch/PCL blend using bioplotting. Both architectures feature an orthogonal orientation pattern between consecutive layers and feature the same porosity. However, they differ relatively in terms of the *xy* positioning of equivalent layers. The main advantage of this RP method is related with the very high control of scaffold morphology, the achievement of fully interconnected pore structure and the use of mild processing conditions.

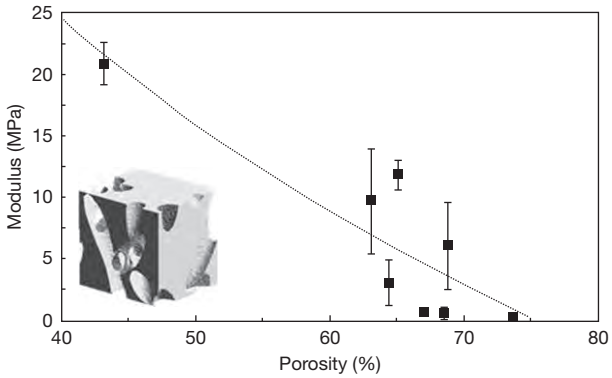

Figure 2 Dependence of compression stiffness from porosity: for scaffolds based on a blend of starch with poly-ε-caprolactone produced by hot fiber bonding. Inner figure: representative free volume for a cubic shape with 1 mm^3 obtained by microcomputed tomography.

2.211.4. Cell Encapsulation in Injectable Biodegradable Hydrogels for TE Applications

2.211.4.1. General Principles

Numerous investigations led to the development of varied and advanced tissue-engineered constructs with different architecture, and tailored material properties that guide and enhance the regeneration of target tissues. Most of the approaches involve the seeding of cells in 3D solid scaffolds exhibiting interconnected porosity.[204,205] Such solid-like structures comprise some advantages in sustaining the mechanical strength and structural shaping of the regenerated tissues; however, the downside within such structures is that cells attach to the walls of the materials' pores, but are not placed in 3D condition and may not exhibit the expected native phenotype.[206,207]

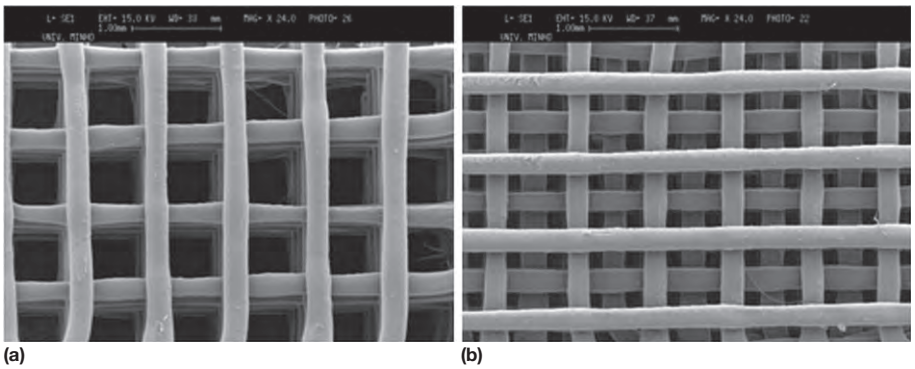

Figure 3 Scanning electron micrographs showing the top view of scaffolds based on blend of starch with poly-ε-caprolactone produced by 3D bioplotting featuring an orthogonal orientation pattern between consecutive layers (a) equivalent *xy* positioning between consecutive layers, and (b) offset positioning between consecutive layers.

Inspired by Nature, many researchers have thought to develop biomaterials that can mimic some essential biochemical and structural properties of the natural ECM of living tissues.[69,204] The morphological and biophysically similar structure of the hydrogels with soft biological tissues makes them attractive candidates as scaffolds for the delivery of cells in medical applications. Hydrogels are water swellable polymers with pore sizes that can be modulated, allowing the diffusion of nutrients and gas, while supporting the growth, differentiation, and enabling the embedded cell population to exhibit phenotypes more akin to those *in vivo*.[208,209]

Furthermore, recent advances in modern medicine and regenerative medicine are continuously driving toward minimally invasive trends, along with the development of improved and sophisticated injectable systems. Hydrogels, liquid precursor solutions where cells are suspended and then delivered to form a gel *in situ*, are used as 3D injectable TE devices that can be implanted without the need of invasive surgery. Many different hydrogel-based materials are available with contrasting properties which hold great promise in the TE field, both as drug delivery and cell encapsulated-based systems.[69,208–210]

Cell encapsulation is a technology, based on the immobilization of cells within a semipermeable biopolymeric membrane, which provides potential therapeutic treatments for a wide array of diseases.[207,211,212] The bioencapsulation within those membranes protects the transplanted cells from immune rejection, overcoming some of the current difficulties relating to whole graft rejection and potentially allowing allo- or xetransplantation without the need of administration of immunossupressants or immunomodulatory drugs.[211]

Many different natural origin-based materials are employed to encapsulate cells. Herein we present a basic overview of the recent advances in the selection of natural origin-based hydrogels used as cell delivery injectable systems for different TE applications.

2.211.4.2. Selected Examples

Collagen is the most widely used derived natural polymer. The ability of its fibers to self-aggregate and to form gels *in situ* is being used in many applications. Collagen gels can be easily manipulated and their mechanical and physical properties enhanced by chemical cross-linkers.

Gelatin is a derivative formed from the hydrolyzation of collagen that easily forms hydrogels by changing temperatures of solutions. Collagen and gelatin have been used to make hydrogels for cartilage regeneration as cell carrier for chondrocytes transplantation.[213] Cartilage constructs using composite HA/collagen I formulation also showed to increase the synthesis and deposition of ECM by chondrocytes.[214] Collagen hydrogels have also been employed in bone,[215] skin,[216] and liver regeneration,[217] as well as in injured spinal cord.[218]

HA is a glycosoaminoglycan present is ECM in a number of tissues that can form hydrogel by covalent cross-liking, and its can be properties tailored for desired applications. HA shows great potential for TE applications such as artificial skin,[216 219] tissue augmentation,[220] facial implants,[221] and wound healing.[222] Studies have also been conducted for cartilage-engineered products.[223]

Fibrin gels can be obtained as a result of the enzymatic polymerization of fibrinogen in the presence of thrombin forms and play an important role in natural wound healing. Fibrin has been used to encapsulate fibroblast[224] and keratinocytes[225] in order to develop skin substitutes, and also shown promising results in cartilage regeneration.[226,227] Fibrin has also been conjugated with other hydrogels such as HA to be used as cell delivery vehicle for chondrocytes.[228] Human mesenchymal stem cells were encapsulated within fibrin hydrogel toward osteogenic differentiation.[229,230] Considering the potential inherent features of fibrin gels, they have been employed in many other TE applications.[231]

Alginate is also versatile and widely used for cell encapsulation. Alginate gel was used as a filling scaffold for periosteum-derived chondrogenesis via minimally invasive procedure,[232] and also in the development of complex-shaped structures in animal models.[233] Alginate has found uses as wound dressing,[234] in the development of skin analogues,[235] and also in the transplantation of hepatocytes[236] and Langerhans islets for diabetes treatment.[237]

Ectopic reconstruction of bone and cartilage using bone marrow stromal cells encapsulated in alginate system was also demonstrated.[238] Alginate injectable systems are also under investigation for intervertebral disk regeneration.[239,240]

CHT and CHT-based hydrogel materials have been evaluated as injectable systems. One of the most interesting systems developed in the past decade is based on the neutralization of CHT with solutions of polyols salts, such as β-glycerophosphate (GP), leading to a temperature-responsive, pH-dependent gelation.[241] These systems are liquid at physiological pH and room temperature, solidifying when heated at body temperature. The CHT/GP formulation has been proposed for different biomedical application, and intensively for cartilage repair[242,243] and disc regeneration.[244] The incorporation of bioactive elements, such as bioactive glass–ceramic nanoparticles or osteoconductive elastin-like polymers may also open the potential of using such systems in bone regeneration.[245,246]

An alternative way to prepare CHT-based hydrogels is by grafting with synthetic polymers, which leads to the formation of thermosensitive formulations. Recently, CHT was grafted with Pluronic®, a family of PEO–PPO–PEO triblock copolymers, and proposed as an injectable cell delivery carrier for cartilage regeneration.[247] PEG was also incorporated into CHT and used as a therapeutic drug-delivery system.[248] A copolymer of poly(*N*-isopropylacrylamide) (PNIPAAm) and water-soluble CHT were evaluated for chondrogenic differentiation of human mesenchymal stem cells,[249] and also for chondrocytes and meniscus cells' encapsulation.[250]

Literature offers countless examples of natural-based materials used for cell encapsulation. Examples of those injectable systems are based on starch,[251] agarose,[252] and gellan gum,[78] among others.[69,205,206,208–210,253]

2.211.5. Final Remarks

In the field of TE, a great deal of effort has been taken to prepare different formulations based on natural polymers. However, and despite all the extensive literature containing

references to so-called 'natural-based' systems, it is the authors' opinion that much work is still needed in order to obtain clinically successful materials. Many improvements can be made in this context, as such systems offer a great versatility; they may be, for example, chemically modified, and combined with ceramics or other polymers (blends, copolymers, interpenetrated networks). Their interaction with cells and tissues may be improved or tuned, by adequate chemical modifications such as grafting with peptides (e.g., RGD) or by surface treatments (e.g., surface plasma modification, or modification of surface chemistry trough grafting with other polymers or functional groups or molecules). Many attempts have been made in order to produce smart natural-derived systems, that could be used in TE applications, including: (i) development of new injectable thermogelling materials, which could be used to deliver cells or growth factors through noninvasive routes; (ii) novel matrices that can be degraded by adequate cell signals; (iii) scaffolds or hydrogels that can deliver relevant bioactive agents in specific conditions (temperature, pH, ionic strength, or presence of specific enzymes); and (iv) self-assembling systems that can be tuned by external signals. Different processing routes have been proposed to produce scaffolds with a great variety of porous architectures. This is an especially delicate task as natural-derived macromolecules are typically nonmeltable (without degradation) and may be insoluble in many solvents. This compromises the use of many of the most traditional techniques to produce TE scaffolds. Efforts should, in fact, be made to develop or improve new or combined processing strategies in order to obtain repeatable porous constructs with controlled porous morphology, preferably at different scale levels (e.g., combination of nano- and microelements or pores), comprising different materials spatially organized and owing the capability to deliver relevant molecules, such as growth factors in a controlled way. Such new scaffolds should be designed for the different applications, addressing particular aspects, such as: to stimulate vascularization, facilitate the deposition of calcium phosphates in predefined regions, guide the regeneration of tissue in certain directions (trough gradient delivery of factors or anisotropic porous architecture), permit the development of different tissues (e.g., regeneration of osteochondral defects), or inhibit calcification and cell adhesion (e.g., in cardiovascular application), just to cite some examples. The field is widely open for new creative researchers to make some dreams come true and materialize in real clinical applications.

References

1. Kim, B. S.; Baez, C. E.; Atala, A. *World J. Urol*. **2000**, *18*, 2–9.
2. Widner, B.; Behr, R.; Von Dollen, S.; *et al*. *Appl. Environ. Microbiol*. **2005**, *71*, 3747–3752.
3. Kobayashi, S.; Fujikawa, S.-I.; Ohmae, M. *J. Am. Chem. Soc*. **2003**, *125*, 14357–14369.
4. Franz, G.; Blaschek, W. In *Methods in Plant Biochemistry*; Dey, P., Ed.; Academic Press: London, 1990.
5. Morrison, W. R.; Karkalas, J. In *Methods in Plant Biochemistry*; Dey, P., Ed.; Carbohydrates Academic Press: London, 1990.
6. Stephen, A. M.; Churms, S. C.; Vogt, D. C. In *Methods in Plant Biochemistry*; Dey, P., Ed.; Carbohydrates Academic Press: London, 1990.
7. Izydorczyk, M.; Cui, S. W.; Wang, Q. In *Food Carbohydrates: Chemistry, Physical Properties, and Applications*; Cui, S., Ed.; CRC Press Taylor & Francis Group: Boca Raton, 2005.
8. Percival, E.; Mcdowell, R. H. In *Methods in Plant Biochemistry*; Dey, P., Ed.; Academic Press: London, 1990.
9. Hubbell, J. A. *Curr. Opin. Biotechnol*. **2003**, *14*, 551–558.
10. Lutolf, M. P.; Hubbell, J. A. *Nat. Biotechnol*. **2005**, *23*, 47–55.
11. Lee, C. H.; Singla, A.; Lee, Y. *Int. J. Pharm*. **2001**, *221*, 1–22.
12. Glowacki, J.; Mizuno, S. *Biopolymers* **2008**, *89*, 338–344.
13. Chen, G.; Ushida, T.; Tateishi, T. *Adv. Mater*. **2000**, *12*, 455–457.
14. Lin, H.; Chen, B.; Sun, W. J.; Zhao, W. X.; Zhao, Y. N.; Dai, J. W. *Biomaterials* **2006**, *27*, 5708–5714.
15. Wallace, D. G.; Rosenblatt, J. *Adv. Drug Deliv. Rev*. **2003**, *55*, 1631–1649.
16. Magnusson, M. K.; Mosher, D. F. *Arterioscler. Thromb. Vasc. Biol*. **1998**, *18*, 1363–1370.
17. Ruoslahti, E.; Pierschbacher, M. D. *Science* **1987**, *238*, 491–497.
18. Calonder, C.; Matthew, H. W. T.; Van Tassel, P. R. *J. Biomed. Mater. Res*. **2005**, *75A*, 316–323.
19. Hayashi, T. *Prog. Polym. Sci*. **1994**, *19*, 663–702.
20. Nair, L. S.; Laurencin, C. T. *Prog. Polym. Sci*. **2007**, *32*, 762–798.
21. Perka, C.; Spitzer, R. S.; Lindenhayn, K.; Sittinger, M.; Schultz, O. *J. Biomed. Mater. Res. A* **2000**, *49*, 305–311.
22. Park, S. H.; Park, S. R.; Chung, S. I.; Pai, K. S.; Min, B. H. *Artif. Organs* **2005**, *29*, 838–845.
23. Lutolf, M. P.; Lauer-Fields, J. L.; Schmoekel, H. G.; *et al*. *Proc. Natl Acad. Sci. USA* **2003**, *100*, 5413–5418.
24. Mann, B. K.; Gobin, A. S.; Tsai, A. T.; Schmedlen, R. H.; West, J. L. *Biomaterials* **2001**, *22*, 3045–3051.
25. Lutolf, M. P.; Weber, F. E.; Schmoekel, H. G.; *et al*. *Nat. Biotechnol*. **2003**, *21*, 513–518.
26. Almany, L.; Seliktar, D. *Biomaterials* **2005**, *26*, 2467–2477.
27. Branco, M. C.; Schneider, J. P. *Acta Biomater*. **2009**, *5*, 817–831.
28. Whitesides, G.; Bartosz Grzybowski, B. *Science* **2002**, *295*, 2418–2421.
29. Hartgerink, J. D.; Beniash, E.; Stupp, S. I. *Science* **2001**, *294*, 1684–1688.
30. Silva, G. A.; Czeisler, C.; Niece, K. L.; *et al*. *Science* **2004**, *303*, 1352–1355.
31. Yang, Y. L.; Khoe, U.; Wang, X. M.; Horii, A.; Yokoi, H.; Zhang, S. G. *Nano Today* **2009**, *4*, 193–210.
32. Hardy, J. G.; Romer, L. M.; Scheibel, T. R. *Polymer* **2008**, *49*, 4309–4327.
33. Silva, S. S.; Maniglio, D.; Motta, A.; Mano, J. F.; Reis, R. L.; Migliaresi, C. *Macromol. Biosci*. **2008**, *8*, 766–774.
34. She, Z. D.; Liu, W. Q.; Feng, Q. L. *Polym. Int*. **2010**, *59*, 55–61.
35. Silva, S. S.; Motta, A.; Rodrigues, M. T.; *et al*. *Biomacromolecules* **2008**, *9*, 2764–2774.
36. Macintosh, A. C.; Kearns, V. R.; Crawford, A.; Hatton, P. V. *J. Tissue Eng. Regen. Med*. **2008**, *2*, 71–80.
37. Wang, Y. Z.; Blasioli, D. J.; Kim, H. J.; Kim, H. S.; Kaplan, D. L. *Biomaterials* **2006**, *27*, 4434–4442.
38. Vaz, C. M.; Fossen, M.; Van Tuil, R. F.; De Graaf, L. A.; Reis, R. L.; Cunha, A. M. *J. Biomed. Mater. Res*. **2003**, *65A*, 60–70.
39. Gomes, M. E.; Reis, R. L.; Cunha, A. M.; Blitterswijk, C. A.; De Bruijn, J. D. *Biomaterials* **2001**, *22*, 1911–1917.
40. Gomes, M. E.; Sikavitsas, V. I.; Behravesh, E.; Reis, R. L.; Mikos, A. G. *J. Biomed. Mater. Res*. **2003**, *67A*, 87–95.
41. Lam, C. X. F.; Mo, X. M.; Teoh, S. H.; Hutmacher, D. W. *Mater. Sci. Eng. C Biomimetic Supramol. Syst*. **2002**, *20*, 49–56.
42. Salgado, A. J.; Coutinho, O. P.; Reis, R. L.; Davies, J. E. *J. Biomed. Mater. Res*. **2007**, *80A*, 983–989.
43. Malafaya, P. B.; Stappers, F.; Reis, R. L. *J. Mater. Sci. Mater. Med*. **2006**, *17*, 371–377.
44. Oliveira, J. T.; Crawford, A.; Mundy, J. M.; *et al*. *J. Mater. Sci. Mater. Med*. **2007**, *18*, 295–302.
45. Svensson, A.; Nicklasson, E.; Harrah, T.; *et al*. *Biomaterials* **2005**, *26*, 419–431.
46. Entcheva, E.; Bien, H.; Yin, L.; Chung, C. Y. C.-Y.; Farrell, M.; Kostov, Y. *Biomaterials* **2004**, *25*, 5753–5762.
47. Müller, F. A.; Müller, L.; Hofmann, I.; Greil, P.; Wenzel, M. M.; Staudenmaier, R. *Biomaterials* **2006**, *27*, 3955–3963.
48. Zaborowska, M.; Bodin, A.; Bäckdahl, H.; Popp, J.; Goldstein, A.; Gatenholm, P. *Acta Biomater*. **2010**, *6*(7), 2540–2547.
49. Chandrasekaran, R.; Janaswamy, S. *Carbohydr. Res*. **2002**, *337*, 2211–2222.
50. Ehrenfreund-Kleinman, T.; Gazit, Z.; Gazit, D.; Azzam, T.; Golenser, J.; Domb, A. J. *Biomaterials* **2002**, *23*, 4621–4631.
51. Hunt, N. C.; Grover, L. M. *Biotechnol. Lett*. **2010**, *32*(6), 733–742.
52. Dvir-Ginzberg, M.; Konson, A.; Cohen, S.; Agbaria, R. *J. Biomed. Mater. Res. B Appl. Biomater*. **2007**, *80*, 59–66.
53. Bernhardt, A.; Despang, F.; Lode, A.; Demmler, A.; Hanke, T.; Gelinsky, M. *J. Tissue Eng. Regen. Med*. **2009**, *3*, 54–62.

54. Glicklis, R.; Shapiro, L.; Agbaria, R.; Merchuk, J. C.; Cohen, S. *Biotechnol. Bioeng.* **2000**, *67*, 344–353.
55. Awad, H. A.; Quinn Wickham, M.; Leddy, H. A.; Gimble, J. M.; Guilak, F. *Biomaterials* **2004**, *25*, 3211–3222.
56. Ng, K. W.; Wang, C. C.-B.; Mauck, R. L.; *et al*. *J. Orthop. Res*. **2005**, *23*, 134–141.
57. Watanabe, J.; Kashii, M.; Hirao, M.; *et al*. *J. Biomed. Mater. Res*. **2007**, *83A*, 845–852.
58. Gruber, H. E.; Hoelscher, G. L.; Leslie, K.; Ingram, J. A.; Hanley, E. N., Jr. *Biomaterials* **2006**, *27*, 371–376.
59. Balgude, A. P.; Yu, X.; Szymanski, A.; Bellamkonda, R. V. *Biomaterials* **2001**, *22*, 1077–1084.
60. Grenha, A.; Gomes, M. E.; Rodrigues, M. T.; *et al*. *J. Biomed. Mater. Res*. **2010**, *92A*, 1265–1272.
61. Bartkowiak, A.; Hunkeler, D. *Colloids Surf. B Biointerfaces* **2001**, *21*, 285–298.
62. Santo, V. E.; Frias, A. M.; Carida, M.; *et al*. *Biomacromolecules* **2009**, *10*, 1392–1401.
63. Pereira, R. C.; Scaranari, M.; Castagnola, P.; *et al*. *J. Tissue Eng. Regen. Med*. **2009**, *3*, 97–106.
64. Kumar, M. N. V. R. *React. Funct. Polym*. **2000**, *46*, 1–27.
65. Tuzlakoglu, K.; Alves, C. M.; Mano, J. F.; Reis, R. L. *Macromol. Biosci*. **2004**, *4*, 811–819.
66. Freier, T.; Montenegro, R.; Shan Koh, H.; Shoichet, M. S. *Biomaterials* **2005**, *26*, 4624–4632.
67. Malafaya, P. B.; Pedro, A. J.; Peterbauer, A.; Gabriel, C.; Redl, H.; Reis, R. L. *J. Mater. Sci. Mater. Med*. **2005**, *16*, 1077–1085.
68. Oliveira, J.; Rodrigues, M. T.; Silva, S. S.; *et al*. *Biomaterials* **2006**, *27*, 6123–6137.
69. Drury, J. L.; Mooney, D. J. *Biomaterials* **2003**, *24*, 4337–4351.
70. Leach, J. B.; Bivens, K. A.; Patrick, C. W.; Schmidt, C. E. *Biotechnol. Bioeng.* **2003**, *82*(5), 578–589.
71. Cristino, S.; Grassi, F.; Toneguzzi, S.; *et al*. *J. Biomed. Mater. Res*. **2005**, *73A*, 275–283.
72. Solchaga, L.; Gao, J.; Dennis, J.; *et al*. *Tissue Eng*. **2002**, *8*, 333–347.
73. Naessens, M.; Cerdobbel, A.; Soetaert, W.; Vandamme, E. J. *J. Chem. Technol. Biotechnol*. **2005**, *80*, 845–860.
74. Lévesque, S. G.; Lim, R. M.; Shoichet, M. S. *Biomaterials* **2005**, *26*, 7436–7446.
75. Jukes, J. M.; Van Der Aa, L. J.; Hiemstra, C.; *et al*. *Tissue Eng. A* **2010**, *16*, 565–573.
76. Ciardelli, G.; Chiono, V.; Vozzi, G.; *et al*. *Biomacromolecules* **2005**, *6*, 1961–1976.
77. Mahajan, H. S.; Gattani, S. G. *Chem. Pharm. Bull*. **2009**, *57*, 388–392.
78. Oliveira, J. T.; Martins, L.; Picciochi, R.; *et al*. *J. Biomed. Mater. Res. A* **2009**, *93*(3), 852–863.
79. Oliveira, J. T.; Santos, T. C.; Martins, L.; *et al*. *J. Tissue Eng. Regen. Med*. **2009**, *3*, 493–500.
80. Na, K.; Shin, D.; Yun, K.; Hong Park, K.; Lee, K. *Biotechnol. Lett*. **2003**, *25*, 381–385.
81. Rodriguez-Gonzalez, F. J.; Ramsay, B. A.; Favis, B. D. *Carbohydr. Polym*. **2004**, *58*, 139–147.
82. Boesel, L. F.; Mano, J. F.; Reis, R. L. *J. Mater. Sci. Mater. Med*. **2004**, *15*, 73–83.
83. Boontheekul, T.; Kong, H.-J.; Mooney, D. J. *Biomaterials* **2005**, *26*, 2455–2465.
84. Bouhadir, K. H.; Lee, K. Y.; Alsberg, E.; Damm, K. L.; Anderson, K. W.; Mooney, D. J. *Biotechnol. Prog*. **2001**, *17*, 945–950.
85. Thành, T. T. T.; Yuguchi, Y.; Mimura, M.; *et al*. *Macromol. Chem. Phys*. **2002**, *203*, 15–23.
86. Peniche, C.; Argüelles-Monal, W.; Goycoolea, F. In *Monomers, Polymers and Composites from Renewable Resources*; Belgacem, M., Gandini, A., Eds.; Elsevier, 2008.
87. Kurita, K. *Prog. Polym. Sci*. **2001**, *26*, 1921–1971.
88. Khor, E.; Lim, L. Y. *Biomaterials* **2003**, *24*, 2339–2349.
89. Madhumathia, K.; Sudheesh Kumar, P.; Kavyaa, K.; *et al*. *Int. J. Biol. Macromol*. **2009**, *45*, 289–292.
90. Freier, T.; Koh, H. S.; Kazazian, K.; Shoichet, M. S. *Biomaterials* **2005**, *26*, 5872–5878.
91. Pillai, C. K. S.; Paul, W.; Sharma, C. P. *Prog. Polym. Sci*. **2009**, *34*, 641–678.
92. Muzzarelli, R. A. A.; Muzzarelli, C. *Adv. Polym. Sci*. **2005**; Vol. 186, 151–209.
93. Silva, S. S.; Luna, S. M.; Gomes, M. E.; *et al*. *Macromol. Biosci*. **2008**, *8*, 568–576.
94. Muzzarelli, R. A. A. *Carbohydr. Polym*. **2009**, *76*, 167–182.
95. Alves, N. M.; Mano, J. F. *Int. J. Biol. Macromol*. **2008**, *43*, 401–414.
96. Mourya, V. K.; Inamdar, N. N. *React. Funct. Polym*. **2008**, *68*, 1013–1051.
97. Silva, S. S.; Ferreira, R. A. S.; Fu, L. S.; *et al*. *J. Mater. Chem*. **2005**, *15*, 3952–3961.
98. Hardingham, T. In *Chemistry and Biology of Hyaluronan*; Garg, H., Hales, C., Eds.; Elsevier, 2004; pp 1–19.
99. Kang, J. Y.; Chung, C. W.; Sung, J. H.; *et al*. *Int. J. Pharm*. **2009**, *369*, 114–120.
100. Wieland, J. A.; Houchin-Ray, T. L.; Shea, L. D. *J. Control. Release* **2007**, *120*, 233–241.
101. Liu, Y. X.; Chan-Park, M. B. *Biomaterials* **2010**, *31*, 1158–1170.
102. Mehvar, R. *J. Control. Release* **2000**, *69*, 1–25.
103. Cascone, M. G.; Barbani, N.; Cristallini, C.; Giusti, P.; Ciardelli, G.; Lazzeri, L. *J. Biomater. Sci. Polym. Ed*. **2001**, *12*, 267–281.
104. Gupta, M.; Gupta, A. *J. Pharm. Pharm. Sci*. **2004**, *7*, 38–46.
105. Rosalam, S.; England, R. *Enzyme Microb. Technol*. **2006**, *39*, 197–207.
106. Iseki, T.; Takahashi, M.; Hattori, H.; Hatakeyama, T.; Hatakeyama, H. *Food Hydrocolloids* **2001**, *15*, 503–506.
107. Chen, G.-Q.; Wu, Q. *Biomaterials* **2005**, *26*, 6565–6578.
108. Williams, S. F.; Martin, D. P.; Horowitz, D. M.; Peoples, O. P. *Int. J. Biol. Macromol*. **1999**, *25*, 111–121.
109. Deng, Y.; Zhao, K.; Zhang, X.-F.; Hu, P.; Chen, G.-Q. *Biomaterials* **2002**, *23*, 4049–4056.
110. Li, X.-T.; Zhang, Y.; Chen, G.-Q. *Biomaterials* **2008**, *29*, 3720–3728.
111. Ye, C.; Hu, P.; Ma, M.-X.; Xiang, Y.; Liu, R.-G.; Shang, X.-W. *Biomaterials* **2009**, *30*, 4401–4406.
112. Liu, C.; Xia, Z.; Czernuszka, J. T. *Chem. Eng. Res. Des*. **2007**, *85*, 1051–1064.
113. O'Brien, F. J.; Harley, B. A.; Yannas, I. V.; Gibson, L. J. *Biomaterials* **2005**, *26*, 433–441.
114. Karageorgiou, V.; Kaplan, D. *Biomaterials* **2005**, *26*, 5474–5491.
115. Correlo, V. M.; Gomes, M. E.; Tuzlakoglu, K.; *et al*. In *Biomedical Polymers*, Woodhead Publishing Ltd: Cambridge, 2007; pp 197–199.
116. Ghosh, S.; Viana, J. C.; Reis, R. L.; Mano, J. F. *Mater. Sci. Eng. C Biomimetic Supramol. Syst*. **2008**, *28*, 80–86.
117. Kaneko, T.; Ohno, T.; Ohisa, N. *Biosci. Biotechnol. Biochem*. **2005**, *69*, 1073–1081.
118. Gattin, R.; Copinet, A.; Bertrand, C.; Couturier, Y. *Int. Biodeterior. Biodegradation* **2002**, *50*, 25.
119. Ghosh, S.; Gutierrez, V.; Fernández, C.; *et al*. *Acta Biomater*. **2008**, *4*, 950–959.
120. Gomes, M. E.; Azevedo, H. S.; Moreira, A. R.; Ellä, V.; Kellomäki, M.; Reis, R. L. *J. Tissue Eng. Regen. Med*. **2008**, *2*, 243–252.
121. Gomes, M. E.; Godinho, J. S.; Tchalamov, D.; Cunha, A. M.; Reis, R. L. *Mater. Sci. Eng. C* **2002**, *20*, 19.
122. Gomes, M. E.; Ribeiro, A. S.; Malafaya, P. B.; Reis, R. L.; Cunha, A. M. *Biomaterials* **2001**, *22*, 883–889.
123. Oliveira, A. L.; Malafaya, P. B.; Costa, S. A.; Sousa, R. A.; Reis, R. L. *J. Mater. Sci. Mater. Med*. **2007**, *18*, 211–223.
124. Salgado, A. J.; Coutinho, O. P.; Reis, R. L.; Davies, J. E. (Eds) *Transactions – 7th World Biomaterials Congress*, Sydney, Australia, 2004, p 216.
125. Salgado, A. J.; Gomes, M. E.; Chou, A.; Coutinho, O. P.; Reis, R. L.; Hutmacher, D. W. *Mater. Sci. Eng. C* **2002**, *20*, 27–33.
126. Neves, N. M.; Kouyumdzhiev, A.; and Reis, R. L. *Mater. Sci. Eng. C* **2005**, *25*(2), 195–200.
127. Haugen, H.; Gerhardt, L. C.; Will, J.; Wintermantel, E. *J. Biomed. Mater. Res. B Appl. Biomater*. **2005**, *73*, 229–237.
128. Leicher, S.; Will, J.; Haugen, H.; Wintermantel, E. *J. Mater. Sci*. **2005**, *40*(17), 4613–4618.
129. Blacher, S.; Maquet, V.; Pirard, R.; Pirard, J.-P.; Jérôme, R. *Colloids Surf. A Physicochem. Eng. Asp*. **2001**, *187–188*, 375–383.
130. Chen, G.; Ushida, T.; Tateishi, T. *Mater. Sci. Eng. C* **2001**, *17*, 63–69.
131. Silva, S. S.; Oliveira, J. M.; Mano, J. F.; Reis, R. L. *Adv. Mater. Forum* **2006**, *514–516*, 1000–1004.
132. Weng, J.; Wang, M. *J. Mater. Sci. Lett*. **2001**, *20*, 1401–1403.
133. Madihally, S. V.; Matthew, H. W. T. *Biomaterials* **1999**, *20*, 1133–1142.
134. Hou, Q.; Grijpma, D. W.; Feijen, J. *Biomaterials* **2003**, *24*, 1937–1947.
135. Kang, H.-W.; Tabata, Y.; Ikada, Y. *Biomaterials* **1999**, *20*, 1339.
136. Mao, J. S.; Zhao, L. G.; Yin, Y. J.; Yao, K. D. *Biomaterials* **2003**, *24*, 1067.
137. Hou, Q.; Grijpma, D.; Feijen, J. *J. Biomed. Mater. Res. B Appl. Biomater*. **2003**, *67*, 732–740.
138. Ren, L.; Tsuru, K.; Hayakawa, S.; Osaka, A. *Biomaterials* **2002**, *23*, 4765.
139. Oliveira, J. M.; Silva, S.; Mano, J. F.; Reis, R. L. *Key Eng. Mater*. **2006**, *309–311*, 927–930.
140. Ho, M.-H.; Kuo, P.-Y.; Hsieh, H.-J.; *et al*. *Biomaterials* **2004**, *25*, 129–138.
141. O'brien, F. J.; Harley, B. A.; Yannas, I. V.; Gibson, L. *Biomaterials* **2004**, *25*, 1077–1086.
142. Mladenov, D.; Tsvetkov, T.; Vulchanov, N. *Cryobiology* **1993**, *30*, 335.
143. Quirk, R. A.; France, R. M.; Shakesheff, K. M.; Howdle, S. M. *Curr. Opin. Solid State Mater. Sci*. **2004**, *8*, 313–321.
144. York, P. *Pharm. Sci. Technol. Today* **1999**, *2*, 430–440.
145. Byrappa, K.; Ohara, S.; Adschiri, T. *Adv. Drug Deliv. Rev*. **2008**, *60*, 299–327.
146. Cansell, F.; Aymonier, C. *J. Supercrit. Fluids* **2009**, *47*, 508–516.

147. Pasquali, I.; Bettini, R.; Giordano, F. *Adv. Drug Deliv. Rev.* **2008**, *60*, 399–410.
148. Reverchon, E.; De Marco, I. *J. Supercrit. Fluids* **2006**, *38*, 146–166.
149. Tsioptsias, C.; Panayiotou, C. *J. Supercrit. Fluids* **2008**, *47*, 302–308.
150. Duarte, A. R. C.; Mano, J. F.; Reis, R. L. *Eur. Polym. J.* **2009**, *45*, 141–148.
151. Duarte, A. R. C.; Mano, J. F.; Reis, R. L. *Acta Biomater.* **2009**, *5*, 2054–2062.
152. Duarte, A. R. C.; Mano, J. F.; Reis, R. L. *J. Supercrit. Fluids* **2009**, *49*, 279–285.
153. Duarte, A. R. C.; Caridade, S. G.; Mano, J. F.; Reis, R. L. *Mater. Sci. Eng. C* **2009**, *29*, 2110–2115.
154. Fages, J.; Lochard, H.; Letourneau, J.-J.; Sauceau, M.; Rodier, E. *Powder Technol.* **2004**, *141*, 219–226.
155. Van Tomme, S. R.; Van Nostrum, C. F.; De Smedt, S. C.; Hennink, W. E. *Biomaterials* **2006**, *27*, 4141–4148.
156. Fan, J.; Gong, Y.; Ren, L.; Varshney, R. R.; Cai, D.; Wang, D.-A. *Acta Biomater.* **2010**, *6*, 1178–1185.
157. Kuo, C. K.; Ma, P. X. *Biomaterials* **2001**, *22*, 511–521.
158. Oliveira, J. O. T.; Santos, T. C.; Martins, L.; *et al. Tissue Eng. A* **2010**, *16*, 343–353.
159. Wang, C.; Gong, Y.; Lin, Y.; Shen, J.; Wang, D.-A. *Acta Biomater.* **2008**, *4*, 1226–1234.
160. Riddle, K. W.; Mooney, D. J. *J. Biomater. Sci. Polym. Ed.* **2004**, *15*, 1561–1570.
161. Lee, S. H.; Kim, B. S.; Kim, S. H.; Kang, S. W.; Kim, Y. H. *Macromol. Biosci.* **2004**, *4*(8), 802–810.
162. Lee, S. H.; Kim, B. S.; Kim, S. H.; *et al. J. Biomed. Mater. Res. A* **2003**, *66A*(1), 29–37.
163. Moore, M. J.; Jabbari, E.; Ritman, E. L.; Lu, L.; Currier, B. L.; Windebank, A. J.; Yaszemski, M. J. *J. Biomed. Mater. Res. A* **2004**, *71A*(2), 258–267.
164. Ghosh, S.; Viana, J. C.; Reis, R. L.; Mano, J. F. *J. Mater. Sci. Mater. Med.* **2007**, *18*, 185–193.
165. Kim, H.-W.; Gu, H.-J.; Lee, H.-H. *Tissue Eng.* **2007**, *13*, 965–973.
166. Chung, H. J.; Park, T. G. *Tissue Eng. A* **2009**, *15*, 1391–1400.
167. Kang, S.-W.; Jeon, O.; Kim, B.-S. *Tissue Eng.* **2005**, *11*, 438–447.
168. Nagae, M.; Ikeda, T.; Mikami, Y.; *et al. Tissue Eng.* **2007**, *13*, 147–158.
169. Silva, G. A.; Coutinho, O. P.; Ducheyne, P.; Shapiro, I. M.; Reis, R. L. *Tissue Eng.* **2007**, *13*, 1259–1268.
170. Newman, K. D.; Mcburney, M. W. M. W. *Biomaterials* **2004**, *25*, 5763–5771.
171. Malafaya, P. B.; Silva, G. A.; Reis, R. L. *Adv. Drug Deliv. Rev.* **2007**, *59*, 207–233.
172. Van Tomme, S. R.; Van Steenbergen, M. J.; De Smedt, S. C.; Van Nostrum, C. F.; Hennink, W. E. *Biomaterials* **2005**, *26*, 2129–2135.
173. Malafaya, P. B.; Reis, R. L. *Acta Biomater.* **2009**, *5*, 644–660.
174. Malafaya, P. B.; Santos, T. C.; Van Griensven, M.; Reis, R. L. *Biomaterials* **2008**, *29*, 3914–3926.
175. Ashton, R. S.; Banerjee, A.; Punyani, S.; Schaffer, D. V.; Kane, R. S. *Biomaterials* **2007**, *28*, 5518–5525.
176. Defail, A. J.; Chu, C. R.; Izzo, N.; Marra, K. G. *Biomaterials* **2006**, *27*, 1579–1585.
177. Noritaka, I.; Tadaaki, M.; Sumio, H.; *et al. J. Biomed. Mater. Res.* **2005**, *74A*, 408–418.
178. Cruz, D. M. G.; Ivirico, J. L. E.; Gomes, M. M.; *et al. J. Tissue Eng. Regen. Med.* **2008**, *2*, 378–380.
179. Malheiro, V. N.; Caridade, S. G.; Alves, N. M.; Mano, J. F. *Acta Biomater.* **2010**, *6*, 418–428.
180. Gomes, M. E.; Reis, R. L.; Behravesh, E.; Mikos, A. G.; Sikavitsas, V. I. *J. Biomed. Mater. Res. A* **2003**, *67*, 87–95.
181. Pavlov, M. P.; Mano, J. F.; Neves, N. M.; Reis, R. L. *Macromol. Biosci.* **2004**, *4*, 776–784.
182. Chung, S.; Martins, A.; Correlo, V. M.; *et al. Acta Biomater.* 2010.
183. Chung, S.; Martins, A.; Correlo, V. M.; *et al. Tissue Eng. A* **2008**, *14*, 718.
184. Martins, A. M.; Pham, Q. P.; Malafaya, P. B.; *et al. Tissue Eng. A* **2009**, *15*, 295–305.
185. Oliveira, A. L.; Costa, S. A.; Sousa, R. A.; Reis, R. L. *Acta Biomater.* **2009**, *5*, 1626–1638.
186. Oliveira, J. M.; Sousa, R. A.; Kotobuki, N.; *et al. Biomaterials* **2009**, *30*, 804–813.
187. Santos, M. I.; Unger, R. E.; Sousa, R. A.; Reis, R. L.; Kirkpatrick, C. J. *Biomaterials* **2009**, *30*, 4407–4415.
188. Sun, W.; Darling, A.; Starly, B.; Nam, J. *Biotechnol. Appl. Biochem.* **2004**, *39*, 29–47.
189. Sun, W.; Lal, P. *Comput. Meth. Programs Biomed.* **2002**, *67*, 85–103.
190. Sun, W.; Starly, B.; Darling, A.; Gomez, C. *Biotechnol. Appl. Biochem.* **2004**, *39*, 49–58.
191. Tuan, H. S.; Hutmacher, D. W. *Comput. Aided Des.* **2005**, *37*, 1151–1161.
192. Wettergreen, M. A.; Bucklen, B. S.; Starly, B.; Yuksel, E.; Sun, W.; Liebschner, M. A. K. *Comput. Aided Des.* **2005**, *37*, 1141–1149.
193. Wendel, B.; Rietzel, D.; Kuhnlein, F.; Feulner, R.; Hulder, G.; Schmachtenberg, E. *Macromol. Mater. Eng.* **2008**, *293*, 799–809.
194. Kim, S. S.; Utsunomiya, H.; Koski, J. A.; *et al. Ann. Surg.* **1998**, *228*, 8–13.
195. Pfister, A.; Landers, R.; Laib, A.; Hubner, U.; Schmelzeisen, R.; Mulhaupt, R. *J. Polym. Sci. A Polym. Chem.* **2004**, *42*, 624–638.
196. Cheng, J.; Lin, F.; Liu, H. X.; *et al. J. Manufact. Sci. Eng. Trans. ASME* **2008**, *130*, 021014–021019.
197. Nakamura, M.; Nishiyama, Y.; Henmi, C.; *et al. J. Imaging Sci. Technol.* **2008**, *52*, 060201–060206.
198. Chim, H.; Hutmacher, D. W.; Chou, A. M.; *et al. Int. J. Oral Maxillofac. Surg.* **2006**, *35*, 928–934.
199. Hsu, S. H.; Yen, H. J.; Tseng, C. S.; Cheng, C. S.; Tsai, C. L. *J. Biomed. Mater. Res. B Appl. Biomater.* **2007**, *80*, 519–527.
200. Hutmacher, D. W.; Schantz, T.; Zein, I.; Ng, K. W.; Teoh, S. H.; Tan, K. C. *J. Biomed. Mater. Res.* **2001**, *55*, 203–216.
201. Schantz, J. T.; Brandwood, A.; Hutmacher, D. W.; Khor, H. L.; Bittner, K. *J. Mater. Sci. Mater. Med.* **2005**, *16*, 807–819.
202. Schantz, J. T.; Ng, M. M. L.; Netto, P.; *et al. Mater. Sci. Eng. C Biomimetic Supramol. Syst.* **2002**, *20*, 9–17.
203. Zein, I.; Hutmacher, D. W.; Tan, K. C.; Teoh, S. H. *Biomaterials* **2002**, *23*, 1169–1185.
204. Mooney, D. J.; Vandenburgh, H. *Cell Stem Cell* **2008**, *2*, 205–213.
205. Tabata, Y. *J. R. Soc. Interface* **2009**, *6*(Suppl. 3), S311–S324.
206. Nicodemus, G. D.; Bryant, S. J. *Tissue Eng. B Rev.* **2008**, *14*, 149–165.
207. Wilson, J. T.; Chaikof, E. L. *Adv. Drug Deliv. Rev.* **2008**, *60*, 124–145.
208. Slaughter, B. V.; Khurshid, S. S.; Fisher, O. Z.; Khademhosseini, A.; Peppas, N. A. *Adv. Mater.* **2009**, *21*, 3307–3329.
209. Yu, L.; Ding, J. *Chem. Soc. Rev.* **2008**, *37*, 1473–1481.
210. Mano, J. F. *Adv. Eng. Mater.* **2008**, *10*, 515–527.
211. Orive, G.; Hernandez, R. M.; Gascon, A. R.; Igartua, M.; Pedraz, J. L. *Trends Biotechnol.* **2002**, *20*, 382–387.
212. Uludag, H.; De Vos, P.; Tresco, P. A. *Adv. Drug Deliv. Rev.* **2000**, *42*, 29–64.
213. Hoshikawa, A.; Nakayama, Y.; Matsuda, T.; Oda, H.; Nakamura, K.; Mabuchi, K. *Tissue Eng.* **2006**, *12*, 2333–2341.
214. Liao, E.; Yaszemski, M.; Krebsbach, P.; Hollister, S. *Tissue Eng.* **2007**, *13*, 537–550.
215. Bitar, M.; Salih, V.; Brown, R. A.; Nazhat, S. N. *J. Mater. Sci. Mater. Med.* **2007**, *18*, 237–244.
216. Auger, F. A.; Rouabhia, M.; Goulet, F.; Berthod, F.; Moulin, V.; Germain, L. *Med. Biol. Eng. Comput.* **1998**, *36*, 801–812.
217. Zhao, Y.; Xu, Y.; Zhang, B.; *et al. Tissue Eng. C Meth.* **2010**, *16*(4), 653–659.
218. Watanabe, K.; Nakamura, M.; Okano, H.; Toyama, Y. *Restor. Neurol. Neurosci.* **2007**, *25*, 109–117.
219. Metcalfe, A. D.; Ferguson, M. W. *J. R. Soc. Interface* **2007**, *4*, 413–437.
220. Duranti, F.; Salti, G.; Bovani, B.; Calandra, M.; Rosati, M. L. *Dermatol. Surg.* **1998**, *24*, 1317–1325.
221. Delorenzi, C.; Weinberg, M.; Solish, N.; Swift, A. *Dermatol. Surg.* **2009**, *35*(Suppl. 1), 313–321.
222. Dechert, T. A.; Ducale, A. E.; Ward, S. I.; Yager, D. R. *Wound Repair Regen.* **2006**, *14*, 252–258.
223. Chung, C.; Erickson, I. E.; Mauck, R. L.; Burdick, J. A. *Tissue Eng. A* **2008**, *14*, 1121–1131.
224. Cox, S.; Cole, M.; Tawil, B. *Tissue Eng.* **2004**, *10*, 942–954.
225. Meana, A.; Iglesias, J.; Del Rio, M.; *et al. Burns* **1998**, *24*, 621–630.
226. Eyrich, D.; Brandl, F.; Appel, B.; *et al. Biomaterials* **2007**, *28*, 55–65.
227. Eyrich, D.; Wiese, H.; Maier, G.; *et al. Tissue Eng.* **2007**, *13*, 2207–2218.
228. Park, S. H.; Cui, J. H.; Park, S. R.; Min, B. H. *Artif. Organs* **2009**, *33*, 439–447.
229. Catelas, I.; Sese, N.; Wu, B. M.; Dunn, J. C.; Helgerson, S.; Tawil, B. *Tissue Eng.* **2006**, *12*, 2385–2396.
230. Hou, T.; Xu, J.; Li, Q.; Feng, J.; Zen, L. *Tissue Eng. A* **2008**, *14*, 1173–1182.
231. Ahmed, T. A.; Dare, E. V.; Hincke, M. *Tissue Eng. Part B Rev.* **2008**, *14*(2), 199–215.
232. Stevens, M. M.; Qanadilo, H. F.; Langer, R.; Prasad Shastri, V. *Biomaterials* **2004**, *25*, 887–894.
233. Chang, S. C.; Tobias, G.; Roy, A. K.; Vacanti, C. A.; Bonassar, L. J. *Plast. Reconstr. Surg.* **2003**, *112*, 793–799; discussion 800-801.
234. Suzuki, Y.; Nishimura, Y.; Tanihara, M.; *et al. J. Biomed. Mater. Res.* **1998**, *39*, 317–322.
235. Hunt, N. C.; Shelton, R. M.; Grover, L. *Biotechnol. J.* **2009**, *4*, 730–737.
236. Chin, K.; Khattak, S. F.; Bhatia, S. R.; Roberts, S. C. *Biotechnol. Prog.* **2008**, *24*, 358–366.
237. De Vos, P.; Faas, M. M.; Strand, B.; Calafiore, R. *Biomaterials* **2006**, *27*, 5603–5617.

238. Cai, X.; Lin, Y.; Ou, G.; *et al*. *Cell Biol*. *Int*. **2007**, *31*, 776–783.
239. Gaetani, P.; Torre, M. L.; Klinger, M.; *et al*. *Tissue Eng*. *A* **2008**, *14*, 1415–1423.
240. Chou, A. I.; Nicoll, S. B. *J*. *Biomed*. *Mater*. *Res*. *A* **2009**, *91*, 187–194.
241. Chenite, A.; Chaput, C.; Wang, D.; *et al*. *Biomaterials* **2000**, *21*, 2155–2161.
242. Shive, M. S.; Hoemann, C. D.; Restrepo, A.; *et al*. *Oper*. *Tech*. *Orthop*. **2006**, *16*, 271–278.
243. Hoemann, C. D.; Sun, J.; Mckee, M. D.; *et al*. *Osteoarthr*. *Cartil*. **2007**, *15*, 78–89.
244. Richardson, S. M.; Hughes, N.; Hunt, J. A.; Freemont, A. J.; Hoyland, J. A. *Biomaterials* **2008**, *29*, 85–93.
245. Barbosa, J. S.; Ribeiro, A.; Testera, A. M.; *et al*. *Adv*. *Eng*. *Mater*. **2010**, *12*, B37–B44.
246. Couto, D. S.; Hong, Z. K.; Mano, J. F. *Acta Biomater*. **2009**, *5*, 115–123.
247. Park, K. M.; Lee, S. Y.; Joung, Y. K.; Na, J. S.; Lee, M. C.; Park, K. D. *Acta Biomater*. **2009**, *5*, 1956–1965.
248. Bhattarai, N.; Matsen, F. A.; Zhang, M. *Macromol*. *Biosci*. **2005**, *5*, 107–111.
249. Cho, J. H.; Kim, S. H.; Park, K. D.; *et al*. *Biomaterials* **2004**, *25*, 5743–5751.
250. Chen, J. P.; Cheng, T. H. *Macromol*. *Biosci*. **2006**, *6*, 1026–1039.
251. Balmayor, E. R.; Tuzlakoglu, K.; Marques, A. P.; Azevedo, H. S.; Reis, R. L. *J*. *Mater*. *Sci*. *Mater*. *Med*. **2008**, *19*, 1617–1623.
252. Mauck, R. L.; Yuan, X.; Tuan, R. S. *Osteoarthr*. *Cartil*. **2006**, *14*, 179–189.
253. Ruel-Gariepy, E.; Leroux, J. C. *Eur*. *J*. *Pharm*. *Biopharm*. **2004**, *58*, 409–426.
254. Wang, J.-Z.; Huang, X.-B.; Xiao, J. *et al*. *J*. *Mater*. *Sci*. **2010**, *21*(2), 497–506.

2.212. Silk Biomaterials

X Hu and D L Kaplan, Tufts University, Medford, MA, USA

© 2011 Elsevier Ltd. All rights reserved.

2.212.1.	**Overview**	207
2.212.2.	**Silk Film Biomaterials**	208
2.212.2.1.	Water Annealed and Slow Drying Silk Films	208
2.212.2.2.	Electric Field Aligned Silk Films	208
2.212.2.3.	Ultrathin Silk Films	208
2.212.3.	**Silk Sponge Scaffold Biomaterials**	210
2.212.4.	**Silk Nanofiber Biomaterials**	211
2.212.4.1.	Silk Nanofibers from Organic Solvent	211
2.212.4.2.	Silk Nanofibers from Aqueous Solvent	212
2.212.4.3.	Silk Nanofiber Composites	212
2.212.5.	**Silk Hydrogel Biomaterials**	212
2.212.5.1.	Natural Silk Hydrogel	213
2.212.5.2.	Ultrasound-Induced Silk Hydrogel	213
2.212.5.3.	Semi-interpenetrating Silk Hydrogels	213
2.212.5.4.	Injectable Silk Hydrogels	213
2.212.6.	**Silk Microsphere and Nanoparticle Biomaterials**	214
2.212.6.1.	Spray-Drying Silk Microspheres	214
2.212.6.2.	Silk Particles from Lipid–Aqueous Separation	215
2.212.6.3.	Silk Particles from Rapid Laminar Jet	215
2.212.6.4.	Silk Particles from Polymer Phase Separation	215
2.212.6.5.	Silk Particles from Organic–Aqueous Phase Separation	215
2.212.6.6.	Silk Particles from pH Variation	215
2.212.6.7.	Silk-Coated Polymer Particles	215
2.212.7.	**Silk Optical Biomaterials**	215
2.212.7.1.	Silk Nano- and Micropatterned Optical Materials	215
2.212.7.2.	Silk Optical Waveguides	216
2.212.7.3.	Color-Controllable Silk Materials	216
2.212.7.4.	Silk-Based Cornea Tissue Engineering	216
2.212.8.	**Other Silk Materials**	216
2.212.8.1.	Silk Microfluidic Devices	216
2.212.8.2.	Secondary Structure Micropatterned Silk Materials	216
2.212.8.3.	Direct-Write Silk Scaffolds	217
2.212.8.4.	Chemically Modified Silk Materials	217
2.212.9.	**Conclusions**	217
References		218

Glossary

Biological microelectromechanical systems (BioMEMS) A special class of microelectromechanical systems (MEMS) where biological matter is manipulated to analyze and measure its activity.

Electrospinning Electrospinning is a process that uses an electrical charge to draw very fine (typically on the micro or nano scale) fibers from a liquid.

Layer-by-Layer (LbL) A thin film fabrication technique: the films are formed by depositing alternating layers of oppositely charged materials with wash steps in between.

Spray drying A method of producing a dry powder from a liquid or slurry by rapidly drying with a hot gas.

Waveguide A waveguide is a process in which a light-transmitting material such as a glass or plastic fiber is used for transmitting information from point to point at wavelengths in the ultraviolet, visible-light or infrared portions of the spectrum. Also known as fiber waveguide/optical-fiber cable.

2.212.1. Overview

Silks are generally defined as protein polymers that are synthesized and spun into fibers by many organisms, including silkworms, spiders, scorpions, mites, and flies.[1–18] The more commonly utilized silk, such as from the silkworm, *Bombyx mori*, has been used in the textile industry for thousands of years due to its visual appeal and mechanical properties.[9,12]

Natural silks provide structural roles in cocoon structures, web formation, traps, nest building, safety lines, and egg protection.[9,12] Silks from silkworms can be obtained in significant quantities from naturally spun silk cocoons, and therefore, can be used as natural biomaterials.[9–12] Silks are intriguing materials due to their combination of high toughness and strength.[6,15,17] The toughness of some silks is higher than that of high-performance Kevlar fibers.[15] In addition to their impressive mechanical properties, silks offer a range of useful features, including environmental stability, biocompatibility, controllable biodegradability, and morphologic flexibility.[1,12,16] Thus, silks represent a unique family of structural proteins that are useful in the traditional textile industry, while also providing a wide range of properties for biomedical materials.

The highly repetitive primary sequence of silk proteins leads to significant homogeneity in their secondary structures related to structural material needs, in contrast to the less ordered globular proteins that provide catalytic and molecular recognition functions.[9–12] The secondary structure in silks permits tight packing of stacked beta sheets (crystalline domains) connected by hydrogen bonds between protein chains, generating hydrophobic regions with strength and resiliency.[1,19–23] Therefore, silk materials have significant crystallinity and are insoluble in most solvents, including water, dilute acids, and alkali.[11] The domesticated silkworm (*B. mori*) silk fibroin protein chain consists of two proteins: a heavy chain (~370 kDa) and a light chain (~26 kDa) which are present in a 1:1 ratio and linked by disulfide bond.[5] Compared with other proteins, silks fibroins have repetitive primary structures such as $(Gly\text{-}Ala\text{-}Gly\text{-}Ala\text{-}Gly\text{-}Ser)_n$, $(Gly\text{-}Ala\text{-}Gly\text{-}Ala\text{-}Gly\text{-}Tyr)_n$, or AGVGYGAG motifs.[5] The crystalline regions have been identified as rigid, tightly packed antiparallel beta-pleated sheets which exclude water, in part accounting for the remarkable stability of silk biomaterials.[8,9] Exposure of noncrystallized silk materials to organic solvents,[8,11] application of mechanical stress[15,17] or thermal treatments,[8,24–26] and the addition of metal ions[9,10,12] among other options, all induce the irreversible crystallization of silk proteins, which has become the foundation for processing silk into biomaterials.

In this chapter, we focus on recent progress in designing and producing new silk-based biomaterials, including silk film, sponges, nanofibers, hydrogels, microspheres and nanoparticles, optical biomaterials, and other systems (e.g., silk microfluidic devices, micropatterned materials, direct-write scaffolds, and chemically modified materials). The goal for this chapter is to convey the versatility and medical utility of silk-based systems to provide insight into recent silk material studies for tissue regeneration, controlled release, and biomedical optics applications and opportunities (**Figure 1**).

2.212.2. Silk Film Biomaterials

Silk film formation is an efficient way to mimic the natural process of silk self-assembly and to understand the role of water during structural transitions.[9,10,12,15,17] As a biomaterial, these films offer limited utility other than when used as coatings or perhaps as antiadhesion barriers. Exposure of silk films to organic acids or alcohols, applying physical stretching, or heat above the glass transition temperature induce beta-sheet (silk II structure) crystal formation (>35%) in silk films.[8,11] However, low beta-sheet content and aqueous insoluble silk films, such as alpha-helix-enriched (silk I structure) films, are difficult to produce. Therefore, many methods in the last few years have been developed to generate silk film biomaterials with low beta-sheet crystallinity for improved flexibility of films and for more rapid enzymatic degradation (**Figure 2**).

2.212.2.1. Water Annealed and Slow Drying Silk Films

A 'water annealing' technique was developed to produce the low beta-sheet content silk films.[27] The keys in this process are the preparation of silk films with a subsequent water-vapor annealing procedure. These films degraded more rapidly, as determined *in vitro* via enzymatic hydrolysis, yet supported human adult stem cell expansion *in vitro* in a similar or improved fashion to the high crystallinity films induced by organic solvents (e.g., methanol).[27] Furthermore, slow drying at room temperature also induced the formation of insoluble silk I films.[28–30] By controlling the drying rate, water-insoluble silk films can be prepared with a similar beta-sheet content as soluble silk films (~20%), versus the relatively high beta-sheet content in methanol- or water-annealed silk films (about 40 and 30%, respectively).[29] The high content of silk I structure in these films resulted in more rapid degradation compared with those generated by water annealing or methanol annealing, which leads to an extended range of biomedical material applications, such as where rapid degradation *in vivo* is desired.[29]

2.212.2.2. Electric Field Aligned Silk Films

Another example of new silk film biomaterials is based on the application of electric fields.[31,32] By casting silk solution under an alternating electric field (AC), dramatic changes in the alignment of molecular dipoles and the formation of oriented supramolecular assemblies were achieved.[32] Mechanical, thermal, and surface properties of the films were therefore changed compared to controls without this alignment process.[32] Cell responses were also affected; fibroblasts cultured on these anisotropic fibroin films preferentially spread parallel to the field direction 6 h after seeding.[32]

2.212.2.3. Ultrathin Silk Films

Compared with traditional bulk silk protein films, many advanced film techniques have been developed in recent years.[33–43] One of the examples is the layer-by-layer (LbL) nanoscale thin coating technique for silk fibroin studies.[33,37–43] Through an all aqueous step-wise deposition process, silk fibroin layers can be deposited on a substrate and monitored spectroscopically or with a quartz crystal microbalance.[33,37–43] The silk adsorption process generated stable and reproducible layers, with control of a single layer thickness ranging from a few to tens of nanometers, determined by the concentration of silk solution, salt concentration in the dipping solution, and the method of rinsing.[39–41] Compared with traditional polyelectrolyte LbL techniques, an intervening drying step is added to control the structure and stability of the self-assembled silk fibroin layers.[37,42] The drying process can be used to induce beta-sheet crystal formation in the films, similar to methanol

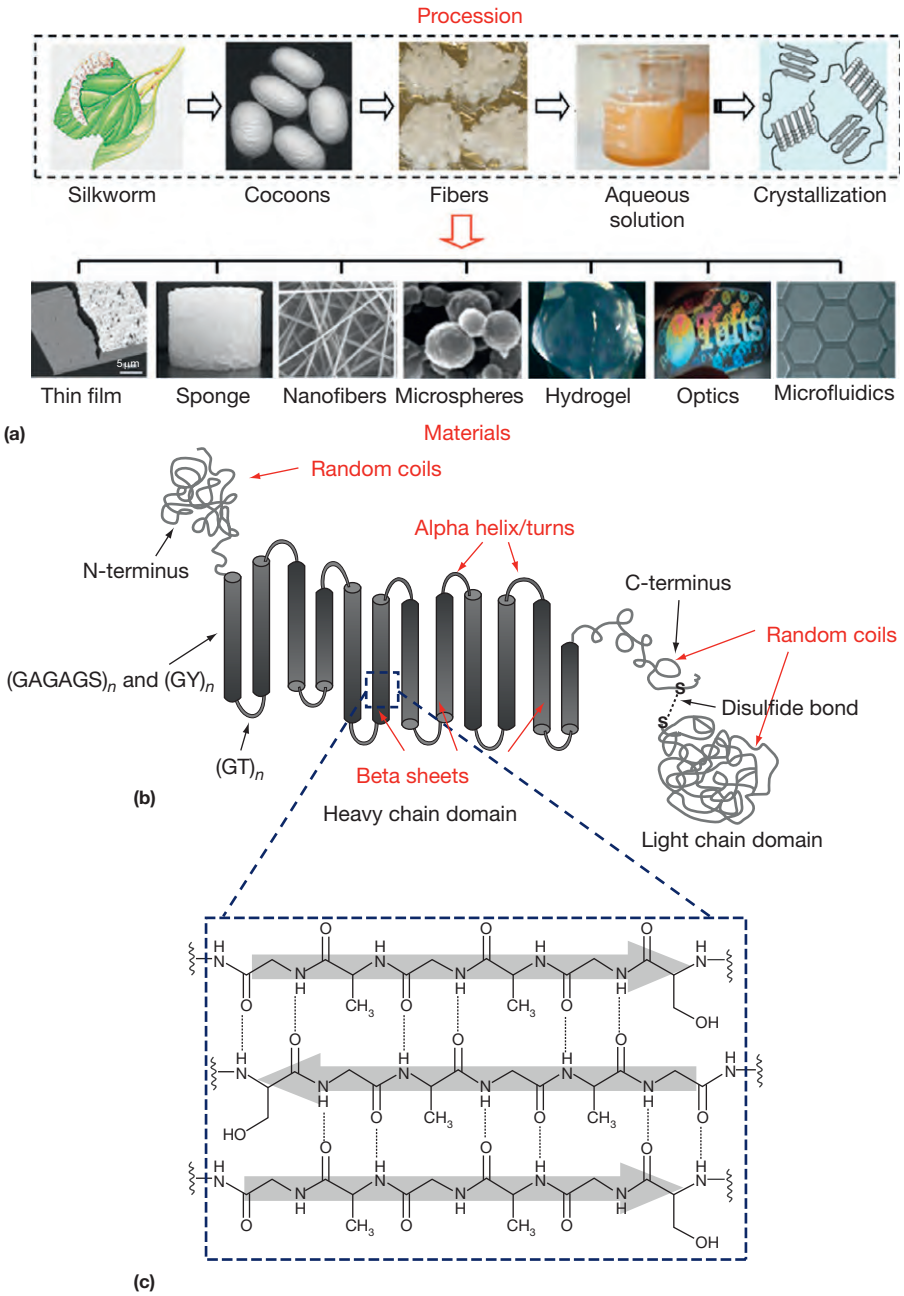

Figure 1 (a) Silk-based materials (*B. mori* silk fibroin protein); (b) secondary structure of one *B. mori* silk fibroin chain; (c) $(Gly\text{-}Ala\text{-}Gly\text{-}Ala\text{-}Gly\text{-}Ser)_n$ amino acid repeat units that self-assemble into antiparallel beta sheets. (b) Modified from Ha, S. W.; Gracz, H. S.; Tonelli, A. E.; Hudson, S. M. *Biomacromolecules* **2005**, *6*, 2563–2569. (c) Modified from Murphy, A. R.; John, P. S.; Kaplan, D. L. *Biomaterials* **2008**, *29*, 2829–2838.

treatment and thereby stabilizing the films to avoid dissolution in water.[37,42] The assembled films were stable under physiological conditions and supported stem cell adhesion, growth, and differentiation, providing new options for engineering biomaterial coatings in medical devices as well as controlling of interfacial properties conducive to specific cellular or tissue responses.[33,38,43]

These LbL nanocoatings were utilized as carriers to incorporate drugs.[38–41,43] Model small-molecule drugs, as well as large proteins such as azoalbumin, were incorporated into the LbL nanocoating process with ultrathin silk films. Control of beta-sheet crystal content and the multilayer structure of the silk coatings provide control of the release properties of these incorporated compounds during *in vitro* studies.[39–41] Higher crystallinity with thicker silk capping layers suppressed the initial burst release and prolonged the duration of release of the model drugs from the silk materials.[39–41] This approach provides an important option to regulate drug release kinetics from silk by controlling its structure and morphology, which is useful in surface engineering of biomaterials and medical devices for regulating the release of drugs.[39–41] The control of release kinetics of therapeutic drugs has also been validated

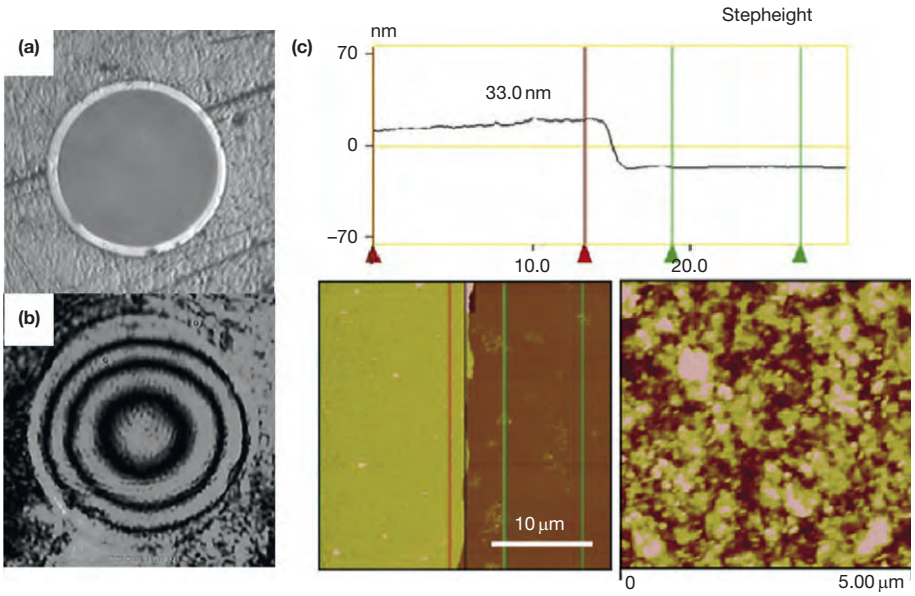

Figure 2 Image of a robust, uniform, and freely suspended silk fibroin layer-by-layer (LbL) film over a 150-μm opening: (a) Interference pattern without pressure and (b) deformed silk film under a pressure of 838 Pa. Reproduced from Jiang, C. Y.; Wang, X. Y.; Gunawidjaja, R.; *et al*. *Adv. Funct. Mater*. **2007**, *17*, 2229–2237. (c) AFM cross-section at the film edge area to obtain thickness of a rhodamine B model drug contained LbL silk ultrathin film. Reproduced from Wang, X. Q.; Wenk, E.; Hu, X.; *et al*. *Biomaterials* **2007**, *28*, 4161–4169; Wang, X. Q.; Wenk, E.; Matsumoto, A.; Meinel, L.; Li, C.; Kaplan, D. L. *J. Control. Release* **2007**, *117*, 360–370; Wang, X. Y.; Hu, X.; Daley, A.; Rabotyagova, O.; Cebe, P.; Kaplan, D. L. *J. Control. Release* **2007**, *121*, 190–199.

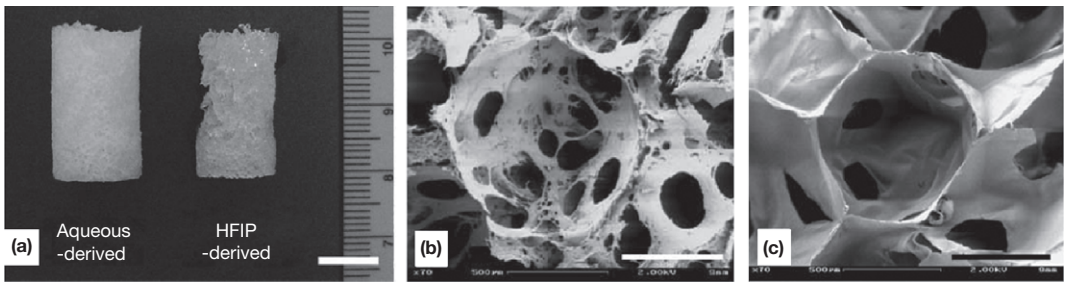

Figure 3 (a) Scaffolds prepared from silk fibroin in aqueous solution (8 wt%, pore size ~920 mm) or hexafluoroisopropanol (HFIP) solution (8 wt%, pore size ~890 mm). Scale bar = 1 cm. Scanning electron microscope (SEM) images of porous scaffolds (b) prepared from silk fibroin HFIP solution (8 wt%) with NaCl particles 850–1000 mm and (c) prepared from silk fibroin aqueous solutions (8 wt%) with NaCl particles 1000–1180 mm. Reproduced from Kim, U. J.; Park, J.; Kim, H. J.; Wada, M.; Kaplan, D. L. *Biomaterials* **2005**, *26*, 2775–2785.

in vivo in epilepsy animal models with silk-based brain implants.[38,43]

2.212.3. Silk Sponge Scaffold Biomaterials

Silk sponge scaffold biomaterials are frequently used systems for tissue engineering.[1,12,16,44] Silk sponge scaffolds for bone and organ regeneration provide useful features such as biocompatibility, impressive mechanical properties, versatility of chemistry, aqueous processing to entrain bioactive molecules, and cell-controlled degradability.[12,45] Generally, pore size and the porosity of the scaffolds are key factors to consider. Pore sizes larger than 100 μm in diameter are typically considered minimum for tissue scaffolds,[45] based on cell size and migration. Porosity determines how well the scaffold pores are interconnected, which directly controls the ability of the seeded cells to interact and signal one another.[45] Depending on the applications of the scaffolds, mechanical properties as well as degradation rate are also important for supporting tissue function, integration, and growth.[45] The core question during engineering silk scaffold systems is how to produce interconnected pores in a three-dimensional (3D) silk system. In addition, mechanisms to induce aqueous insolubility via beta-sheet crystallization are also required (Figure 3).

At least three methods have been reported to generate porous 3D sponge matrices from silk proteins[44–46]: salt leaching, gas forming, and lyophilization or freeze-drying. Salt leaching utilizes porogen leaching approaches, with granular salt particles (e.g., NaCl) in silk solutions.[44,45] The bulk of the silk particles are retained as solids because of saturation of the solution. Therefore, the sizes of salt particles can be used to control the pore sizes in scaffolds. Some salts (e.g., NaCl, KCl)

also induce beta-sheet crystals in silk protein during the process.[45] After 24 h at room temperature, the insoluble silk scaffolds are formed, and the salts can then be extracted by immersion of the scaffolds in water.[45] Gas forming uses bicarbonate salt (e.g., ammonium bicarbonate or sodium bicarbonate) as the porogen added to silk solution, with a porogen-to-silk weight ratio of 10:1∼20:1.[44] After drying and beta-sheet crystallization in alcohol, the scaffolds are immersed in 95 °C water to induce gas foaming and remove/dissolve the bicarbonate particles.[44] There are a variety of approaches to generate air bubbles in silk solution, after rapid crystallization by alcohol or freezing before crystallization, with the air bubbles used to generate the pores in the scaffolds.[44] The freeze-drying method utilizes ice particles as the source of pores.[44,46] By controlling freezing rate and freezing temperature, the size of the ice particles can be controlled. Therefore, gelation and crystallizing silk solution before freeze-drying, or crystallizing silk solid scaffolds after freeze-drying, can be used to obtain insoluble silk scaffolds for tissue engineering and other biomedical applications.[46] This method avoids organic solvents. Aside from the aforementioned pure silk approaches, additives such as gelatin to the silk fibroin solution can be used to control the conformation of silk with the formation of insoluble porous structures.[46] The pore sizes of scaffolds were controlled by adjusting the silk fibroin concentration.[46] The addition of the gelatin resulted in improved hydrophilicity and *in vitro* cell culture interactions compared to salt-leached silk fibroin scaffolds alone.[46]

2.212.4. Silk Nanofiber Biomaterials

Nanofiber scaffolds can mimic the nanoscale properties of fibrous components in the tissue native extracellular matrix (ECM), and have been broadly explored in tissue engineering, in wound healing, and related medical applications.[22,47–50] Compared with conventional fiber-processing techniques which produce fibers with tens of microns in diameter, nanofibers are at least two orders of magnitude smaller than the conventional fibers, but with similar geometry.[50] Self-assembly, phase separation, and electrospinning methods can be used to produce these types of nanofibers for different biomedical applications. Self-assembly and phase-separation techniques can generate fibers with diameters from 1 to 500 nm, but are effective with only a selected number of polymers.[50] Electrospinning is a versatile technique that enables the development of nanofiber-based silk biomaterial scaffolds.[50] A typical electrospinning setup usually contains three components: a high-voltage supplier, a capillary needle, and a grounded collector.[50] By applying an electric potential to the droplet of protein solution suspended on the needle, repulsive forces produced by charges in the solution and the attractive forces from the collector exert tensile forces on the protein solution. A nanofiber jet can then eject from the apex of the cone and accelerates toward the grounded collector.[50] Many factors can significantly affect the process of the formation of the electrospun nanofibers, including the solution conditions, such as viscosity, conductivity, concentration, surface tension, and molecular weight of the protein[50]; instrument impacts, such as applied electrical potential and morphology of the capillary tube[50]; or environmental parameters, such as temperature, humidity, and air velocity.[50] If the protein solution is too dilute, the fiber may break into microsize droplets before reaching the collector, which results in the phenomenon of 'electrospray.' If the protein solution is too concentrated, electrospinning solution may not produce fiber due to high viscosity (Figure 4).

2.212.4.1. Silk Nanofibers from Organic Solvent

Silk proteins have been widely utilized as electrospinning biomaterials. By choosing organic solvents, such as

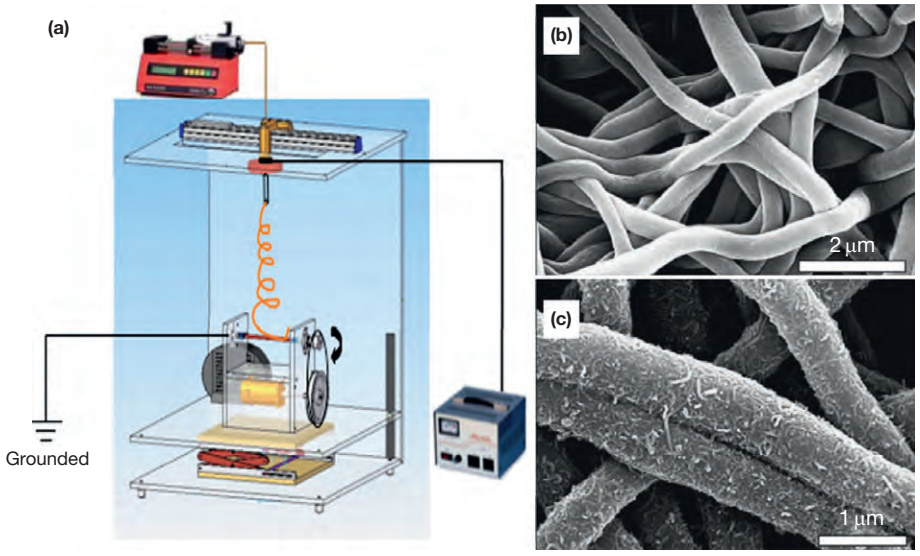

Figure 4 (a) Schematic of electrospinning setup; scanning electron microscope (SEM) images of crystallized and polyethylene-oxide (PEO)-extracted electrospun silk nanofibers, (b) unmodified, and (c) after adsorption of multi-wall carbon nanotubes (MWCNTs). (a) Reproduced from Zhang, X. H.; Reagan, M. R.; Kaplan, D. L. *Adv. Drug Deliv. Rev.* **2009**, *61*, 988–1006. (b and c) Reproduced from Kang, M.; Jin, H. J. *Colloid Polym. Sci.* **2007**, *285*, 1163–1167; Kang, M.; Jung, S.; Kim, H. S.; Youk, J. H.; Jin, H. J. *J. Nanosci. Nanotechnol.* **2007**, *7*, 3888–3891.

hexafluoroacetone (HFA), hexafluoroisopropanol (HFIP), or formic acid, continuous fibers were obtained with variable mean diameters and distributions.[50–52] It is believed that a faster evaporation rate of the solvent leads to the formation of thicker fibers with less elongation and lower beta-sheet crystal content. For example, the mean diameter of electrospun silk nanofibers dissolved in formic acid was smaller (80 nm) than those from rapidly evaporated HFIP solution (380 nm).[51]

2.212.4.2. Silk Nanofibers from Aqueous Solvent

Wang *et al.*[37,42,53,54] first electrospun *B. mori* silk fibroin using an aqueous solution, solving concerns of chemical residuals from organic solvents. Fibers formed when the aqueous silk solution reached 28% (w/v), with diameters from 400 to 800 nm.[37,42,53,54] However, when electrospinning 39% (w/v) silk solution, uneven and ribbon-shaped silk fibers were observed, due to the slow water evaporation from fiber surface.[37,42,53,54] Silk aqueous solutions with a viscosity lower than 40 mPa did not provide sufficient molecular chain entanglements for silk electrospinning.[37,42,53,54] The pH effects on electrospun fiber morphology and properties were investigated.[50] With the combined reduction in pH and concentration, the morphology of the electrospun silk fibers changed from ribbon-like to a uniform cylinder, from 265 nm in 25% (w/v) silk solution at a pH of 4.8 to 850 nm in 33% (w/v) silk solution at pH 6.9.[50] Fiber diameter dependence on electric potential was also observed by Meechaisue *et al.*[55] using 40% (w/v) silk fibroin solutions. The results indicated that when the electric field was doubled, the average diameter of electrospun silk fibers will also double.[55] The major conformations in electrospun silk fibroin nanofibers when spun from aqueous solution were random coil and alpha-helix (silk I), with a little beta sheet (silk II).[50]

However, it is challenging to obtain highly concentrated and stable silk aqueous solutions, as self-assembly leading to gelation can occur.[50,56] To solve this problem, Jin *et al.*[56] blended poly(ethylene oxide) (PEO) with a lower concentration of aqueous silk fibroin solution. From this blend, nanofibers (~750 nm) with comparable diameters to those from pure aqueous system were generated.[56] The water-soluble PEO was extracted out in distilled water after post-treatments of nanofibers to lock in the beta-sheet structure.[56] There are a number of treatments commonly performed to induce insolubility of electrospun fiber matrices. Kim *et al.*[52] used 50% (v/v) aqueous methanol for 10–60 min at room temperature. Conformational transitions of the unmodified silk fibroin nanofibers to crystalline structure were completed within 10 min.[51] Owing to brittle features of these methanol-treated silk fibroin matrices, alternate methods, such as water-vapor annealing, were also developed. Jeong *et al.*[51] reported differences in electrospun silk fibroin matrices after treatment with either aqueous methanol solution (50%) or water vapor. A longer time was required for water-vapor treatment at low temperatures, and different mechanical properties were found compared with MeOH-treated fiber mats, including better elasticity because of the lower beta-sheet content.[51] The efficiency of other solvents, such as ethanol, methanol, and propanol, temperature (25–55 °C) or treatment time was studied in detail.[51]

2.212.4.3. Silk Nanofiber Composites

In addition to pure silk nanofibers, many composite electrospun nanofibrous matrices based on silk, such as silk fibroin/chitin[57] or silk fibroin/collagen[58] mixtures, have been studied, using techniques such as a single-needle or side-by-side spinning approaches.[50] Wang *et al.* successfully encapsulated a silk fibroin core fiber within a PEO shell fiber.[53,54] After water-vapor treatment, PEO was extracted and the crystallized silk fibers with diameters, down to 170 nm, were obtained.[53,54]

Functionalized silk nanofibrous matrices have also been developed for release of molecules including antibiotics, proteins, small molecules, and DNA.[50,59–62] Drugs, enzymes, growth factors, various compounds, and conductive materials can be loaded via prespinning and mixing with silk solutions, and entrained in the fibers during coaxial electrospinning or postelectrospinning by covalently coating on nanofibers.[50] Lee *et al.* immobilized alpha-chymotrypsin (CT) on silk fibroin electrospun nanofibers with amino group preactivation with glutaraldehyde.[61] A significant increase in enzyme loading was observed and the activity of the immobilized CT was almost eight times greater than that on silk microfibers.[61] Li *et al.* incorporated bone morphogenetic protein-2 (BMP-2) into silk fibroin nanofibers in the spinning solution.[62] BMP-2 encapsulated silk fibroin matrices increased calcium deposition from human bone marrow-derived mesenchymal stem cells (hMSCs) when grown on the matrices, with enhanced transcript levels of bone-specific markers.[62] These BMP-2-loaded electrospun silk nanofibrous matrices were efficient delivery systems to improve bone formation.[62]

In addition to biological functionalization, electric property modifications have also been examined in silk electrospun matrices using multiwall carbon nanotubes (MWCNTs).[60,63] A significant amount of MWCNTs were retained on the surface of the nanofibers even after sonication, and the electrical conductivity of the MWCNT-absorbed silk matrices increased significantly at room temperature, compared with pure silk nanofibers.[63] Future research for electrospun silk fiber may focus on combining biological assays with silk nanofiber materials to assess cellular responses.

2.212.5. Silk Hydrogel Biomaterials

Hydrogels are insoluble 3D polymer chain networks that swell in aqueous solution and hold or entrap liquid components such as cells and drugs.[21,64–67] Hydrogels exhibit solid-like mechanical behavior, with high compliance and elastic strain, while consisting mostly of liquid.[21,65,66] The formation of hydrogels from solution is due to the connectivity of the protein chains as a result of 'cross-linking'.[64] Generally, there are two main types of cross-links in hydrogel systems: chemical and physical.[21,66] In chemically cross-linked hydrogels, networks are formed by chemical reactions or polymerization to stitch together the starting materials (such as monomers) via cross-linkers.[21,66] Physically cross-linked hydrogels can be obtained by crystallization, liquid–liquid phase separation, ionic interactions, or hydrogen bonding.[21,66] Silk fibroin aqueous solutions form hydrogels by physical cross-linking, with the rate of this sol–gel transition dependent on silk

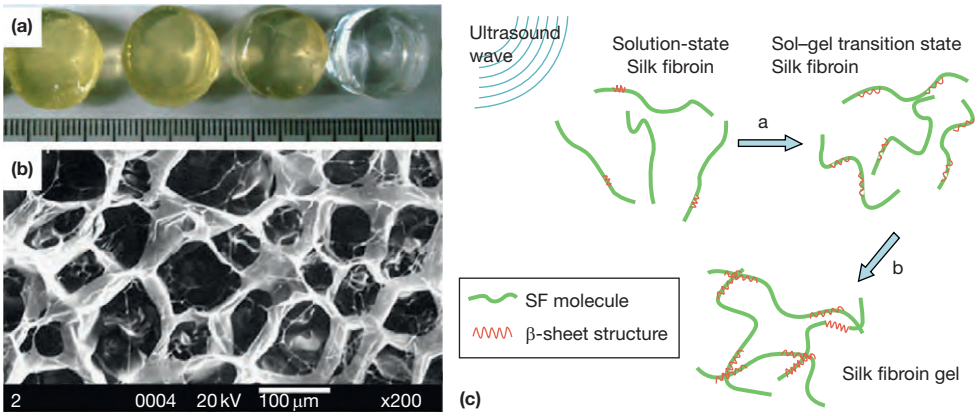

Figure 5 (a) Typical appearance of different silk/polyacrylamide semi-interpenetrating (semi-IPNs) hydrogels, (b) scanning electron microscope (SEM) image of silk/polyacrylamide semi-IPNs with composition ratios of 70/30, and (c) Schematic illustration of mechanism of silk gelation during ultrasonication. The gelation process contains two kinetic steps: (a) structural change from random coil to beta sheet with some interchain physical cross-links occurring in a short timeframe, and (b) beta-sheet structure-extended, large quantity of interchain beta-sheet cross-links, and molecules organized to gel network over a relatively long time frame. (a–b) Reproduced from Mandal, B. B.; Kapoor, S.; Kundu, S. C. *Biomaterials* **2009**, *30*, 2826–2836. (c) Reproduced from Wang, X. Q.; Kluge, J. A.; Leisk, G. G.; Kaplan, D. L. *Biomaterials* **2008**, *29*, 1054–1064; Wang, X. Y.; Zhang, X.; Castellot, J.; Herman, I.; Iafrati, M.; Kaplan, D. L. *Biomaterials* **2008**, *29*, 894–903.

concentration, temperature, metal ions, and pH.[38,43,68–70] The mechanism of gelation is self-assembly of the beta-sheet crystals.[69,70] Silk hydrogels have been used for biomedical applications because of their biocompatibility and adjustable mechanical properties (Figure 5).

2.212.5.1. Natural Silk Hydrogel

Early studies on the formation of silk hydrogels focused on the natural gelation process from silk fibroin aqueous solutions.[69,70] The gelation time of silk hydrogels decreased with increase in protein concentration and temperature, decrease in pH, and addition of PEO or Ca^{2+}.[69,70] However, other ions, such as K^{+}, did not have a significant impact on silk gelation time.[69] Freeze-dried silk hydrogel materials formed with Ca^{2+} exhibited larger pores than pure silk gels.[69] Mechanical compressive strength and modulus of silk hydrogels can be controlled by increasing the protein concentration and gelation temperature.[69] A conformational transition from random coil to beta-sheet structure promoted the formation, insolubility, and stability of silk hydrogels.[68–70] The impressive mechanical properties, biocompatibility, and biodegradability of silk hydrogels prompted additional studies to improve the gelation for different biomedical applications.

2.212.5.2. Ultrasound-Induced Silk Hydrogel

A novel method to accelerate the process and control silk fibroin gelation was reported through ultrasonication, as an energy input to the solution of silk to drive assembly and gel formation.[38,43] Power output and the time of sonication, along with silk fibroin concentration control gelation of silk from minutes to hours, allowing the addition of cells postsonication but prior to final gel formation.[38,43] hMSCs were successfully incorporated into these silk fibroin hydrogels after sonication and proliferated in the 4% silk hydrogels over 21 days.[38,43]

2.212.5.3. Semi-interpenetrating Silk Hydrogels

Other silk-based hydrogel studies focused on producing stimuli-responsive or semi-interpenetrating (semi-IPNs) hydrogel networks by blending silk with other polymers such as gelatin[71] and polyacrylamide.[72] For example, silk/gelatin hydrogel systems were formed with beta sheets formed via subsequent exposure to methanol, which entangled the gelatin molecular chains and stabilized the thermally responsive hydrogel network during the structural transition of gelatin.[71] Swelling and protein release kinetics of silk/gelatin hydrogels were controlled by varying composition. Through chemical cross-linking, silk/polyacrylamide hydrogels were synthesized using different ratios of silk fibroin/acrylamide mixtures.[72] The properties of these semi-IPNs depended on the ratio of two components.[72]

2.212.5.4. Injectable Silk Hydrogels

Injectable silk hydrogel systems have also been developed. By vortexing aqueous solutions of silk, a sol–gel transition was observed, with transition from random coil to beta-sheet structures, and orders of magnitude increase in shear modulus.[73] These vortex-induced silk hydrogels had permanent, physical, intermolecular cross-links, and the hydrogelation kinetics could be controlled by changing vortex time, assembly temperature, and/or protein concentration.[73] Such silk gel systems provide a useful time frame for cell encapsulation. The stiffness of preformed hydrogels recovered quickly, immediately after injection through a needle, enabling the use of these systems for injectable cell delivery systems.[73]

A gel-spinning method for silk tubes formation was developed for device formation.[74] By spinning an aqueous silk solution on a tube around a reciprocating rotating mandrel, the formed silk tube biomaterial exhibited specific winding patterns, porosity, and composite features.[74] Silk tube properties were further controlled via different postspinning

processing mechanisms, such as methanol treatment, air-drying, and lyophilization, which offered numerous tissue engineering applications such as biomaterial matrices useful for blood vessel grafts and nerve guides.[74]

Electrogelation, the application of a low-voltage electric field to an aqueous solution of silk fibroin, generated injectable silk hydrogels with adhesive properties.[75,76] This system demonstrated reversible adhesive properties and functioned on both hydrated and dry surfaces.[75] The structural transition of this silk gel was found to be reversible with random coil to alpha-helix transitions present.[75,76] This system utilizes all biocompatible components and functions in an all-aqueous process at ambient conditions, which provides potential applications in environmentally compatible material and medical device systems, including tissue adhesive functions.[76]

2.212.6. Silk Microsphere and Nanoparticle Biomaterials

Microspheres (1–1000 μm) and nanoparticles (1–1000 nm) are polymer particles used for biomedical applications such as controlled drug delivery and tissue engineering.[39,77–85] These structures can be used to incorporate drugs with controlled release kinetics, while retaining sufficient *in vivo* stability for function, biocompatibility, and degradability and the potential to target specific organs and tissues.[78,79,84] Microspheres are commonly used as depot drug carriers for long-acting delivery and usually administered intramuscularly or subcutaneously.[84] A depot delivery system requires particle sizes above 5 μm in order to remain at the injection site and slowly release drug contents.[84] Nanoparticles are usually designed as short-acting delivery vehicles (as a solid powder or with a liquid carrier) and administrated through intramuscular, intravenous, subcutaneous, oral, or transdermal routes.[84] With a smaller size, they can penetrate through small capillaries, across physiological barriers, and become incorporated into cells for treating various diseases such as cancers.[84]

Silk proteins have been used to produce micro- and nanospheres.[84] Compared with synthetic polymers and other natural degradable materials, silk proteins exhibit useful mechanical properties, tunable *in vivo* degradation rates, biocompatibility, and all aqueous material processing.[39,80,82–85] For drug delivery, small-molecule drugs or protein drugs can be incorporated with high efficiency, and drug release kinetics can be modulated through the control of crystalline beta-sheet content during processing.[84,86] Typical techniques available for the preparation of drug-loaded silk microsphere or nanoparticles are based on spray drying, emulsion-solvent evaporation/extraction, solvent displacement, phase separation, self-assembly, or rapid expansion of supercritical fluid solution. Silk fibroin has been fabricated into microspheres by many of these methods (Figure 6).

2.212.6.1. Spray-Drying Silk Microspheres

Silk microspheres were prepared by spray-drying an aqueous solution of silk, containing theophylline as a model drug with a small amount of ethanol.[87,88] The amorphous silk microspheres were then exposed to a humid atmosphere (89% relative humidity) to induce beta-sheet crystallization.[87] The mean diameter of the microspheres was around 5 μm.[87]

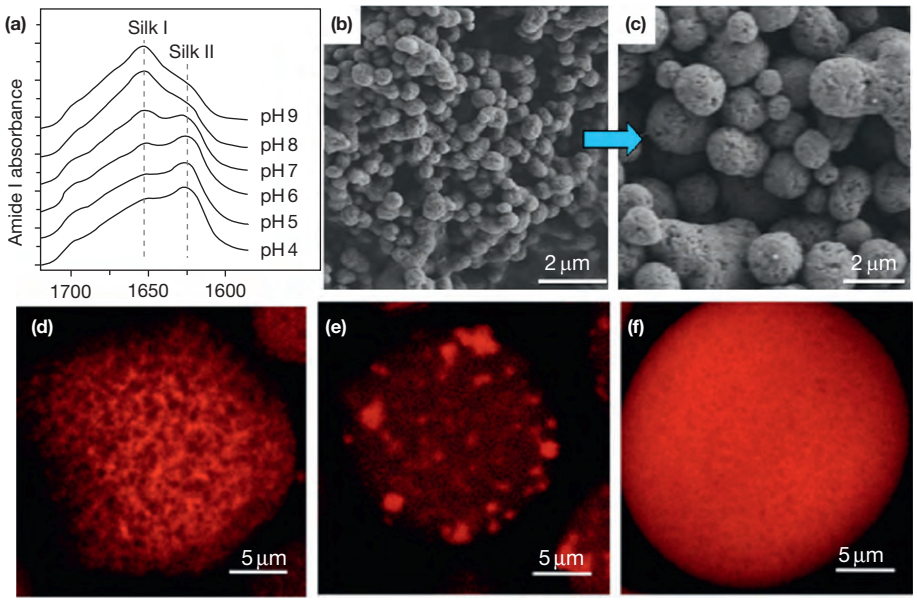

Figure 6 (A) FTIR spectra of silk fibroin particles produced by salting out with potassium phosphate at different pH values; (b and c) scanning electron microscope (SEM) of silk particles produced by salting out with potassium phosphate (pH 8) from a silk fibroin solution of (b) 0.25 mg ml^{-1} and (c) 20 mg ml^{-1}; (d–f) confocal images of loading and distribution of model drugs in silk fibroin spheres prepared from silk/PVA blend solution. Model drugs: (d) tetramethylrhodamine-conjugated bovine serum albumin (TMR-BSA, MW ~66 000 Da), (e) tetramethylrhodamine-conjugated dextran (TMR-dextran, MW ~10 000 Da), and (f) rhodamine B (RhB, MW ~479 Da) were premixed with silk solution. (a–c) Reproduced from Lammel, A. S.; Hu, X.; Park, S. H.; Kaplan, D. L.; Scheibel, T. R. *Biomaterials* **2010**, *31*, 4583–4591. (d–f) Reproduced from Wang, X. Q.; Yucel, T.; Lu, Q.; Hu, X.; Kaplan, D. L. *Biomaterials* **2010**, *31*, 1025–1035.

2.212.6.2. Silk Particles from Lipid–Aqueous Separation

Lipid vesicles were used to encapsulate protein drugs in silk protein to form microspheres under mild processing conditions.[40] Freeze-thaw treatments were applied to generate small vesicles with homogeneous size distributions.[40] After lyophilization, the lipid templates were removed by methanol or sodium chloride (NaCl), and the encapsulated silk microspheres were concurrently induced to form beta-sheet crystalline structures to promote the entrapment of the protein drugs.[40] The MeOH-based microspheres had an average size of 1.7 μm, while the average size of NaCl-based microspheres decreased with time of NaCl treatment, from 2.7 μm (1 h) to 1.6 μm (15 h).[40]

2.212.6.3. Silk Particles from Rapid Laminar Jet

Large microspheres for protein drug release were fabricated using a laminar jet with aqueous silk solution,[89] using a nozzle vibrating at controlled frequency and amplitude. The silk particles produced in the process had diameters in the range of 101–440 μm,[89] depending on the diameter of the nozzle and the treatment to induce water insolubility of silk fibroin.

2.212.6.4. Silk Particles from Polymer Phase Separation

Recently, silk microspheres and nanoparticles were produced by phase separation.[82,84] For example, polyvinyl alcohol (PVA) and silk solutions were mixed and subsequently cast into films. Varying the molecular weight of PVA and the ratio between PVA and silk changed the macro- and microphase separation.[84] After film dissolution in water and removal of residual PVA by subsequent centrifugation, silk spheres were recovered with a broad size distribution ranging from 300 nm up to 20 μm, with approximately 30% beta-sheet crystallinity.[84]

2.212.6.5. Silk Particles from Organic–Aqueous Phase Separation

Using 70% (v/v) water-miscible protonic and polar aprotonic organic solvents, silk protein can form nanospheres in a size range of 35–125 nm.[85,90] Silk microspheres can also be prepared via mild self-assembly of silk fibroin molecular chains by adding ethanol and quenching below the freezing point,[90] as ethanol is a poor solvent for silk fibroin, but miscible with water. When a small amount of ethanol was added into the silk aqueous solution, silk fibroin molecules first formed small beta-sheet microcrystals,[90] acting as a seed for the growth of silk fibroin aggregates with continuous stirring. During the freezing procedure, the amorphous phase attached or entrapped the crystalline phase to form spheres. The particles had sizes ranging from 0.2 to 1.5 μm,[90] and the distribution of these silk particles was affected by the amount of ethanol, the freezing temperature, and the concentration of silk fibroin.[90]

2.212.6.6. Silk Particles from pH Variation

For engineered spider silk proteins, microspheres were produced by salting out a high concentration of potassium phosphate at different pH.[91] Sphere size and growth were controlled by protein concentration and mixing rate. The resulting microspheres reached an average size less than 300 nm.[91] Incorporation of active ingredients into spider silk microspheres was obtained by adding a solution with the desired molecules before microsphere formation.[91] A similar method was also applied to silk fibroin to form controllably sized silk microspheres.[86] The engineered spider silk protein could be also assembled at an oil–water interface to form microcapsules.[92] Microcapsules with sizes between 1 and 30 μm were produced by emulsifying the spider silk aqueous solution into toluene.[92]

2.212.6.7. Silk-Coated Polymer Particles

Other than producing pure silk microspheres and nanospheres, silk proteins were also used to coat polymer particles[39,40,80] such as lipid, poly(lactic-*co*-glycolic acid) (PLGA), and alginate microspheres, using an LbL assembly technique.[39] Silk fibroin coatings stabilized microspheres from degradation, but also significantly sustained protein drug release by providing a diffusion barrier with improved mechanical strength.[39] Drug release can be retarded further by controlling coating thickness and crystalline content.[39]

2.212.7. Silk Optical Biomaterials

Silk is the strongest and toughest natural material known and has excellent surface flatness and optical transparency.[93] Free-standing silk films, as large as 40 cm^2, with a thickness between 40 and 100 μm, have excellent transparency across the visible spectrum.[93] These properties are useful to generate functionalized biophotonic components in contrast to inorganic glasses and semiconductors or synthetic organic polymers, which require either chemical postprocessing or high temperatures that negatively affect biological dopants.[93] Silk-based biophotonic materials have been produced recently in a variety of studies for biomedical optics. Silk-based optical elements, which offer biodegradability and biocompatibility, have led to a new class of new devices that could be used in the human body (**Figure 7**).[93]

2.212.7.1. Silk Nano- and Micropatterned Optical Materials

Methods have been developed for the construction of silk fibroin-based nano- and micropatterned optical materials.[93–95] This process included methods to produce optical-grade ultrapure silk fibroin solution, the casting process for patterning silk fibroin films, and the characterization of the smallest nanopatterns in silk fibroin films realized to date.[93] Diffraction gratings on silk films can be formed by replicating holographic gratings with features ranging from 600 to 3600 grooves per millimeter, resulting in optical elements such as lenses, microlens arrays, or 2D diffractive optics.[94] Mechanically robust, optically transparent silk films capable of sub-40 nm transverse pattern resolution were also obtained.[95] By employing this technique, high-quality optical films containing intricate 2D and 3D nano- and micropatterns were fabricated,[95] useful as optical elements in a range of biomedical applications. For example, silk optical elements were used as optical transducers to monitor the spectral response of the embedded biochemical compound.[93]

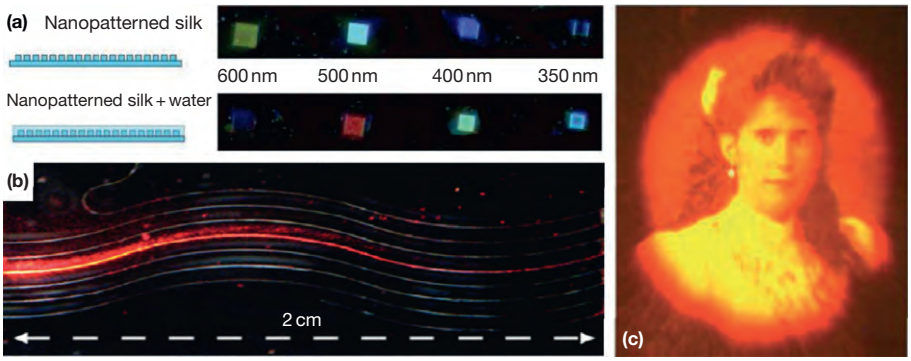

Figure 7 (a) Periodic imprinted nanoholes on silk films (200 nm in diameter and 30 nm deep), illuminated with a supercontinuum light source. The lattice constants vary as 600, 500, 400, and 350 nm. In the upper panel, the holes are in the air. In the bottom panel, the medium above the holes is water. Reproduced from Amsden, J. J.; Perry, H.; Boriskina, S. V.; *et al*. *Opt. Express* **2009**, *17*, 21271–21279. (b) Optical images of silk waveguides guiding light from a He:Ne laser source. Reproduced from Parker, S. T.; Domachuk, P.; Amsden, J.; *et al*. *Adv. Mater*. **2009**, *21*, 2411–2415. (c) High-quality projected image from a 3D diffraction pattern in silk fibroin film. Reproduced from Perry, H.; Gopinath, A.; Kaplan, D. L.; Negro, L. D.; Omenetto, F. G. *Adv. Mater*. **2008**, *20*, 3070–3072.

2.212.7.2. Silk Optical Waveguides

Silk protein was used to generate optical waveguides through direct ink writing of pure or doped silk fibroin solution.[96] The printed silk protein waveguides retain a rod-like morphology by crystallization in a methanol-rich reservoir.[96] Both straight and wavy architectures of silk fibers were produced and found to guide laser light. These printed silk waveguides have potential applications for many optical devices, including implantable medical biomaterials that would resorb over time.[96]

2.212.7.3. Color-Controllable Silk Materials

Color-controllable nanopatterns in pure silk fibroin protein films were also achieved.[20,97] Periodic 2D lattices in silk films with feature sizes of hundreds of nanometers exhibited different colors as a function of varying lattice spacing.[20] Further, when varying the index of refraction contrast between the nanopatterned lattice and the surrounding environment by applying liquids on top of the lattices, colorimetric shifts are observed. This feature enabled silk materials to form a new class of 'biologically active optics,' which can serve as a low-index biosensor platform for integration with microfluidics and other systems as biomaterials.[20,97]

2.212.7.4. Silk-Based Cornea Tissue Engineering

Based on the development of 'silk optics,' cornea tissue engineering with silk biomaterials was also studied.[98,99] Silk protein films were used to replicate corneal stromal tissue architecture. The films emulated corneal collagen lamellae dimensions and were surface-patterned to guide cell alignment.[98] Micropatterns with pores in 0.5–5.0 μm diameter range were introduced in the silk films to enhance translamellar diffusion of nutrients and to promote cell–cell interactions.[99] Human and rabbit corneal fibroblast proliferation, alignment, and corneal ECM expression on these films in both 2D and 3D cultures were successfully demonstrated.[98,99] The mechanical properties, optical clarity, and surface pattern features of these films, combined with their ability to support corneal cell functions, suggested that silk biomaterial systems offer important potential benefits for corneal tissue regeneration.

2.212.8. Other Silk Materials

With the studies and applications of silk-based biomaterials as outlined in the prior sections, many advanced techniques and methods have been introduced in recent years. In this section, we briefly focus on several trends in producing new silk-based biomaterials, which may help to continue to foster growth with these proteins and other polymer systems (**Figure 8**).

2.212.8.1. Silk Microfluidic Devices

Silk can be used as a biomaterial for biomicroelectrical mechanical systems (BioMEMS), due to its biocompatibility, toughness, and slow predictable biodegradation rate. Recently, techniques and materials processing strategies utilized in the fabrication of cell-seeded silk fibroin microfluidic devices were developed.[23,100] Silk-based microfluidic devices promoted adhesion and function of seeded cells, and facilitated protein or growth factor incorporation under mild conditions.[23] Through soft-lithographic techniques, silk microfluidic devices were fabricated. Biocompatibility and functionality of patent devices with cells was studied by seeding and perfusion with human hepatocarcinoma cells.[23]

2.212.8.2. Secondary Structure Micropatterned Silk Materials

A technique for patterning silk secondary structure at the microscale was recently developed utilizing capillary transfer lithography (CTL).[101] A sacrificial polystyrene (PS) mask was first deposited onto a flat silk film. The masked silk film was then briefly exposed to methanol vapor, which induced a localized transition to beta-sheet crystal in the exposed regions.[101] After dissolving away the PS mask, a flat silk film with silk I and silk II regions alternating at the micrometer scale can be fabricated, such as a line pattern with a spacing of 10 μm or a checkerboard pattern with a spacing of 3 μm.[101] The microscale silk I and silk II regions retained their intrinsic chemical and mechanical characteristics and showed well-developed modulation of localized properties, which have potential for tissue engineering, such as patterned silk scaffolds

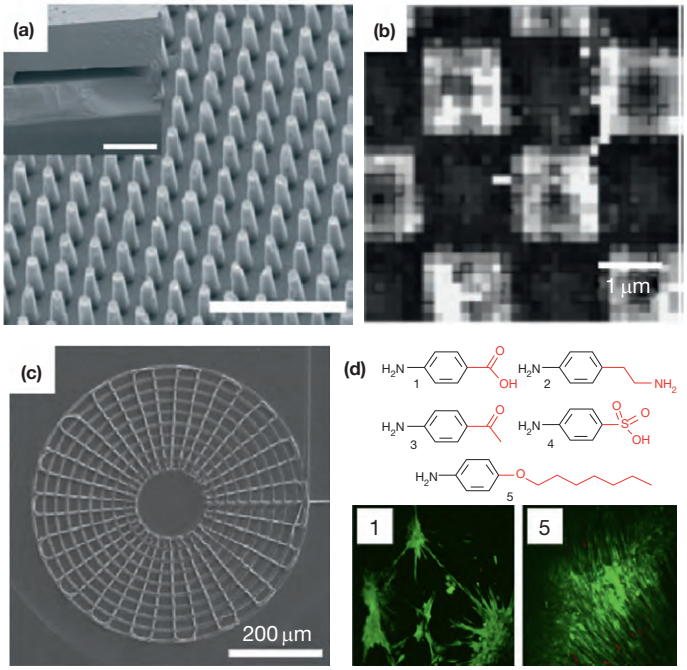

Figure 8 (a) Silk fibroin-based microfluidic devices (bar: 5 μm, insert picture bar: 200 μm). Reproduced from Bettinger, C. J.; Cyr, K. M.; Matsumoto, A.; Langer, R.; Borenstein, J. T.; Kaplan, D. L. *Adv. Mater.* **2007**, *19*, 2847–2850. (b) AFM force volume topography image of silk film patterned with a 3-mm checkerboard pattern. Reproduced from Gupta, M. K.; Singamaneni, S.; McConney, M.; Drummy, L. F.; Naik, R. R.; Tsukruk, V. V. *Adv. Mater.* **2010**, *22*, 115–119. (c) 3D direct ink writing of silk fibroin in liquid reservoir with a circular web shape. Reproduced from Ghosh, S.; Parker, S. T.; Wang, X. Y.; Kaplan, D. L.; Lewis, J. A. *Adv. Funct. Mater.* **2008**, *18*, 1883–1889. (d) Aniline derivatives used to modify silk (top), and live/dead fluorescent images of cells grown on carboxylic acid azosilk-1 and heptyl azosilk-5 (bottom). Reproduced from Murphy, A. R.; John, P. S.; Kaplan, D. L. *Biomaterials* **2008**, *29*, 2829–2838.

with uniform surface chemistry and variable mechanical properties or biodegradation.[101] Moreover, exposing the patterned silk I/silk II film to water resulted in selective dissolution of silk I regions, which can be extended to produce micropatterned silk materials in different geometries.[101] With the help of other microprinting techniques, such as inkjet printing, dip-pen lithography, nanosphere lithography, or photolithography, this method could be expanded to other surfaces with higher resolution and over larger areas.[101]

2.212.8.3. Direct-Write Silk Scaffolds

Direct ink-writing techniques were used to fabricate 3D, microperiodic scaffolds of regenerated silk fibroin.[102] Silk fibroin solution was treated as an 'ink' and deposited to become LbL 3D arrays of silk fibers, such as square lattice or circular webs, with diameters of individual fibers of 5 μm.[102] These scaffolds contained feature sizes that were significantly smaller than those produced by other rapid prototyping techniques.[102] Direct-write scaffolds used with hMSCs demonstrated support for cell adhesion and growth as well as enhanced chondrogenic differentiation.[102]

2.212.8.4. Chemically Modified Silk Materials

Although many attempts have been made for chemically modifying silk proteins, such as cyanuric chloride-activated coupling, enzyme-catalyzed reactions with tyrosinase, or sulfation of tyrosine residues with chlorosulfonic acid,[103,104] low reaction yield and a limited variety of functional groups for modification are challenging propositions. Recently, the chemical modification of silk chains using diazonium coupling chemistry was developed to tailor the structure and overall hydrophilicity of silk fibroin protein.[103,104] This reaction allows for the incorporation of a variety of functional groups using commercially available reagents. Five types of aniline derivatives, including carboxylic acid, amine, ketone, sulfonic acid, and alkyl functional groups, were used to modify the tyrosine side chains.[103] The introduction of hydrophobic functional groups promoted structural conversion of the protein from random coil to beta sheet, while the addition of hydrophilic groups inhibited this process.[103] When hydrophobic and hydrophilic silk derivatives were used as cell culture scaffolds, cells such as hMSCs displayed different growth rates and morphologies.[103] The cells were able to attach, proliferate-differentiate, and express osteogenic markers when subjected to osteogenic stimuli, regardless of the silk chemical modification.[103] These studies suggested that versatile chemistry could be widely useful for modifying silk structure and assembly, and providing new options of silk-based biomaterials.

2.212.9. Conclusions

Silk proteins have been exploited recently in a wide range of biomaterials. By processing into a diverse set of morphologies, such as films, nanofibers, microspheres, nanoparticles, hydrogels, or different micro-/nanopatterned devices, the potential

of silk-based biomaterials has expanded for potential biomedical applications. The versatility of silk proteins in terms of processing, including aqueous solutions, the biocompatibility, controllable *in vivo* biodegradation rate, along with the remarkably robust mechanical properties, prompt interest in the biomaterials generated from silk proteins. Further, the myriad of processing tools to control the structural state of silk proteins provide direct control over the mechanical properties and degradation lifetime of silk-based biomaterials. While we have emphasized more routine processing approaches, such as methanol and temperature treatments to crystallize silks, many other physical methods, such as electrical/dielectric field and electromagnetic fields, can induce beta-sheet crystallization in silk proteins, leading to new processing for silk--based biomaterials. We have also focused mainly on some of the more compelling biomaterial-related studies and applications with silk proteins, necessitating the omission of many studies and many areas of potential interest in the biomaterials field. For example, most studies on silk blending with other synthetic polymers and biomacromolecules have been omitted from this chapter.[105–107]

Acknowledgments

The authors thank the NIH P41 Tissue Engineering Resource Center, the NSF, and the AFOSR for support of this work.

References

1. Altman, G. H.; Diaz, F.; Jakuba, C.; *et al*. *Biomaterials* **2003**, *24*, 401–416.
2. Bini, E.; Knight, D. P.; Kaplan, D. L. *J. Mol. Biol*. **2004**, *335*, 27–40.
3. Foo, C. W. P.; Kaplan, D. L. *Adv. Drug Deliv. Rev*. **2002**, *54*, 1131–1143.
4. Fu, C. J.; Porter, D.; Shao, Z. Z. *Macromolecules* **2009**, *42*, 7877–7880.
5. Ha, S. W.; Gracz, H. S.; Tonelli, A. E.; Hudson, S. M. *Biomacromolecules* **2005**, *6*, 2563–2569.
6. Hardy, J. G.; Romer, L. M.; Scheibel, T. R. *Polymer* **2008**, *49*, 4309–4327.
7. Horan, R. L.; Antle, K.; Collette, A. L.; *et al*. *Biomaterials* **2005**, *26*, 3385–3393.
8. Hu, X.; Kaplan, D.; Cebe, P. *Macromolecules* **2006**, *39*, 6161–6170.
9. Jin, H. J.; Kaplan, D. L. *Nature* **2003**, *424*, 1057–1061.
10. Kaplan, D. L., Adams, W. W., Farmer, B., Viney, C., Eds.; In *Silk Polymers: Materials Science and Biotechnology*; ACS Symposium Series 544 American Chemical Society: Washington, DC, 1994.
11. McGrath, K., Kaplan, D. L., Eds.; In *Protein-Based Materials*; Birkhauser Press: Boston, 1996.
12. Omenetto, F. G.; Kaplan, D. L. *Science* **2010**, *329*, 528–531.
13. Porter, D.; Vollrath, F. *Soft Matter* **2008**, *4*, 328–336.
14. Pyda, M.; Hu, X.; Cebe, P. *Macromolecules* **2008**, *41*, 4786–4793.
15. Shao, Z.; Vollrath, F. *Nature* **2002**, *418*, 741.
16. Vepari, C.; Kaplan, D. L. *Prog. Polym. Sci*. **2007**, *32*, 991–1007.
17. Vollrath, F.; Knight, D. P. *Nature* **2001**, *410*, 541–548.
18. Zhao, C.; Asakura, T. *Prog. Nucl. Magn. Reson. Spectrosc*. **2001**, *39*, 301–352.
19. Amsden, J. J.; Domachuk, P.; Gopinath, A.; *et al*. *Adv. Mater*. **2010**, *22*, 1746–1749.
20. Amsden, J. J.; Perry, H.; Boriskina, S. V.; *et al*. *Opt. Express* **2009**, *17*, 21271–21279.
21. Barcili, B. *J. Pharm. Sci*. **2007**, *96*, 2197–2223.
22. Barnes, C. P.; Sell, S. A.; Boland, E. D.; Simpson, D. G.; Bowlin, G. L. *Adv. Drug Deliv. Rev*. **2007**, *59*, 1413–1433.
23. Bettinger, C. J.; Cyr, K. M.; Matsumoto, A.; Langer, R.; Borenstein, J. T.; Kaplan, D. L. *Adv. Mater*. **2007**, *19*, 2847–2850.
24. Hu, X.; Kaplan, D.; Cebe, P. *Thermochim. Acta* **2007**, *461*, 137–144.
25. Hu, X.; Kaplan, D.; Cebe, P. *Macromolecules* **2008**, *41*, 3939–3948.
26. Hu, X.; Lu, Q.; Kaplan, D. L.; Cebe, P. *Macromolecules* **2009**, *42*, 2079–2087.
27. Jin, H. J.; Park, J.; Karageorgiou, V.; *et al*. *Adv. Funct. Mater*. **2005**, *15*, 1241–1247.
28. Lawrence, B. D.; Omenetto, F.; Chui, K.; Kaplan, D. L. *J. Mater. Sci*. **2008**, *43*, 6967–6985.
29. Lu, Q.; Hu, X.; Wang, X. Q.; *et al*. *Acta Biomater*. **2010**, *6*, 1380–1387.
30. Tretinnikov, O. N.; Tamada, Y. *Langmuir* **2001**, *17*, 7406–7413.
31. Kim, D. H.; Viventi, J.; Amsden, J. J.; *et al*. *Nat. Mater*. **2010**, *9*, 511–517.
32. Servoli, E.; Maniglio, D.; Motta, A.; Migliaresi, C. *Macromol. Biosci*. **2008**, *8*, 827–835.
33. Jiang, C. Y.; Wang, X. Y.; Gunawidjaja, R.; *et al*. *Adv. Funct. Mater*. **2007**, *17*, 2229–2237.
34. Lu, Q.; Wang, X. Q.; Hu, X.; Cebe, P.; Omenetto, F.; Kaplan, D. L. *Macromol. Biosci*. **2010**, *10*, 359–368.
35. Lu, S.; Wang, X.; Lu, Q.; *et al*. *Biomacromolecules* **2010**, *11*, 143–150.
36. Motta, A.; Maniglio, D.; Migliaresi, C.; *et al*. *J. Biomater. Sci. Polym. Ed*. **2009**, *20*, 1875–1897.
37. Wang, H.; Zhang, Y.; Shao, H.; Hu, X. *J. Mater. Sci*. **2005**, *40*, 5359–5363.
38. Wang, X. Q.; Kluge, J. A.; Leisk, G. G.; Kaplan, D. L. *Biomaterials* **2008**, *29*, 1054–1064.
39. Wang, X. Q.; Wenk, E.; Hu, X.; *et al*. *Biomaterials* **2007**, *28*, 4161–4169.
40. Wang, X. Q.; Wenk, E.; Matsumoto, A.; Meinel, L.; Li, C.; Kaplan, D. L. *J. Control. Release* **2007**, *117*, 360–370.
41. Wang, X. Y.; Hu, X.; Daley, A.; Rabotyagova, O.; Cebe, P.; Kaplan, D. L. *J. Control. Release* **2007**, *121*, 190–199.
42. Wang, X. Y.; Kim, H. J.; Xu, P.; Matsumoto, A.; Kaplan, D. L. *Langmuir* **2005**, *21*, 11335–11341.
43. Wang, X. Y.; Zhang, X.; Castellot, J.; Herman, I.; Iafrati, M.; Kaplan, D. L. *Biomaterials* **2008**, *29*, 894–903.
44. Nazarov, R.; Jin, H. J.; Kaplan, D. L. *Biomacromolecules* **2004**, *5*, 718–726.
45. Kim, U. J.; Park, J.; Kim, H. J.; Wada, M.; Kaplan, D. L. *Biomaterials* **2005**, *26*, 2775–2785.
46. Lu, Q.; Zhang, X. H.; Hu, X.; Kaplan, D. L. *Macromol. Biosci*. **2010**, *10*, 289–298.
47. Kidoaki, S.; Kwon, I. K.; Matsuda, T. *Biomaterials* **2005**, *26*, 37–46.
48. Murugan, R.; Ramakrishna, S. *Tissue Eng*. **2006**, *12*, 435–447.
49. Murugan, R.; Ramakrishna, S. *Tissue Eng*. **2007**, *13*, 1845–1866.
50. Zhang, X. H.; Reagan, M. R.; Kaplan, D. L. *Adv. Drug Deliv. Rev*. **2009**, *61*, 988–1006.
51. Jeong, L.; Lee, K. Y.; Liu, J. W.; Park, W. H. *Int. J. Biol. Macromol*. **2006**, *38*, 140–144.
52. Kim, S. H.; Nam, Y. S.; Lee, T. S.; Park, W. H. *Polym. J*. **2003**, *35*, 185–190.
53. Wang, H.; Shao, H.; Hu, X. *J. Appl. Polym. Sci*. **2006**, *101*, 961–968.
54. Wang, M.; Yu, J. H.; Kaplan, D. L.; Rutledge, G. C. *Macromolecules* **2006**, *39*, 1102–1107.
55. Meechaisue, C.; Wutticharoenmongko, P.; Waraput, R.; *et al*. *Biomed. Mater*. **2007**, *2*, 181–188.
56. Jin, H. J.; Fridrikh, S. V.; Rutledge, G. C.; Kaplan, D. L. *Biomacromolecules* **2002**, *3*, 1233–1239.
57. Yoo, C. R.; Yeo, I. S.; Park, K. E.; *et al*. *Int. J. Biol. Macromol*. **2008**, *42*, 324–334.
58. Yeo, I. S.; Oh, J. E.; Jeong, L.; *et al*. *Biomacromolecules* **2008**, *9*, 1106–1116.
59. Jin, H. J.; Chen, J.; Karageorgiou, V.; Altman, G. H.; Kaplan, D. L. *Biomaterials* **2004**, *25*, 1039–1047.
60. Kang, M.; Jung, S.; Kim, H. S.; Youk, J. H.; Jin, H. J. *J. Nanosci. Nanotechnol*. **2007**, *7*, 3888–3891.
61. Lee, K. H.; Ki, C. S.; Baek, E. H.; Kang, G. D.; Ihm, D. W.; Park, Y. H. *Fibers Polym*. **2005**, *6*, 181–185.
62. Li, C.; Vepari, C.; Jin, H. J.; Kim, H. J.; Kaplan, D. L. *Biomaterials* **2006**, *27*, 3115–3124.
63. Kang, M.; Jin, H. J. *Colloid Polym. Sci*. **2007**, *285*, 1163–1167.
64. Flory, P. J. *Principles of Polymer Chemistry*. Cornell University Press: Ithaca, NY, 1953.
65. Hoffman, A. S. *Adv. Drug Deliv. Rev*. **2002**, *54*, 3–12.
66. Peppas, N. A.; Hilt, J. Z.; Khademhosseini, A.; Langer, R. *Adv. Mater*. **2006**, *18*, 1345–1360.
67. Peppas, N. A.; Huang, Y.; Torres-Lugo, M.; Ward, J. H.; Zhang, J. *Annu. Rev. Biomed. Eng*. **2000**, *2*, 9–29.
68. Fini, M.; Motta, A.; Torricelli, P.; *et al*. *Biomaterials* **2005**, *26*, 3527–3536.
69. Kim, U. J.; Park, J.; Li, C.; Jin, H. J.; Valluzzi, R.; Kaplan, D. L. *Biomacromolecules* **2004**, *5*, 786–792.
70. Matsumoto, A.; Chen, J.; Collette, A. L.; *et al*. *J. Phys. Chem. B* **2006**, *10*, 21630–21638.
71. Gil, E. S.; Frankowski, D. J.; Spontak, R. J.; Hudson, S. M. *Biomacromolecules* **2005**, *6*, 3079–3087.

72. Mandal, B. B.; Kapoor, S.; Kundu, S. C. *Biomaterials* **2009**, *30*, 2826–2836.
73. Yucel, T.; Cebe, P.; Kaplan, D. L. *Biophys. J.* **2009**, *97*, 2044–2050.
74. Lovett, M. L.; Cannizzaro, C. M.; Vunjak-Novakovic, G.; Kaplan, D. L. *Biomaterials* **2008**, *29*, 4650–4657.
75. Leisk, G. G.; Lo, T. J.; Yucel, T.; Lu, Q.; Kaplan, D. L. *Adv. Mater.* **2010**, *22*, 711–715.
76. Yucel, T.; Kojic, N.; Leisk, G. G.; Lo, T. J.; Kaplan, D. L. *J. Struct. Biol.* **2010**, *170*, 406–412.
77. Chen, R. R.; Mooney, D. J. *Pharm. Res.* **2003**, *20*, 1103–1112.
78. Chiellini, F.; Piras, A. M.; Errico, C.; Chiellini, E. *Nanomedicine* **2008**, *3*, 367–393.
79. Davis, M. E.; Chen, Z.; Shin, D. M. *Nat. Rev. Drug Discov.* **2008**, *7*, 771–782.
80. Gobin, A. S.; Rhea, R.; Newman, R. A.; Mathur, A. B. *Int. J. Nanomedicine* **2006**, *1*, 81–87.
81. Hofmann, S.; Foo, C. T.; Rossetti, F.; *et al. J. Control. Release* **2006**, *111*, 219–227.
82. Tanaka, T.; Tanigami, T.; Yamaura, K. *Polym. Int.* **1998**, *45*, 175–184.
83. Wang, X. Q.; Wenk, E.; Zhang, X.; Meinel, L.; Vunjak-Novakovic, G.; Kaplan, D. L. *J. Control. Release* **2009**, *134*, 81–90.
84. Wang, X. Q.; Yucel, T.; Lu, Q.; Hu, X.; Kaplan, D. L. *Biomaterials* **2010**, *31*, 1025–1035.
85. Zhang, Y. Q.; Shen, W. D.; Xiang, R. L.; Zhang, L. J.; Gao, W. J.; Wang, W. B. *J. Nanoparticle Res.* **2007**, *9*, 885–900.
86. Lammel, A. S.; Hu, X.; Park, S. H.; Kaplan, D. L.; Scheibel, T. R. *Biomaterials* **2010**, *31*, 4583–4591.
87. Hino, T.; Tanimoto, M.; Shimabayashi, S. *J. Colloid Interface Sci.* **2003**, *266*, 68–73.
88. Yeo, J. H.; Lee, K. G.; Lee, Y. W.; Kim, S. Y. *Eur. Polym. J.* **2003**, *39*, 1195–1199.
89. Wenk, E.; Wandrey, A. J.; Merkle, H. P.; Meinel, L. *J. Control. Release* **2008**, *132*, 26–34.
90. Cao, Z.; Chen, X.; Yao, J.; Huang, L.; Shao, Z. *Soft Matter* **2007**, *3*, 910–915.
91. Lammel, A.; Schwab, M.; Slotta, U.; Winter, G.; Scheibel, T. *ChemSusChem* **2008**, *1*, 413–416.
92. Hermanson, K. D.; Huemmerich, D.; Scheibel, T.; Bausch, A. R. *Adv. Mater.* **2007**, *19*, 1810–1815.
93. Omenetto, F. G.; KapLan, D. L. *Nat. Photonics* **2008**, *2*, 641–643.
94. Lawrence, B. D.; Cronin-Golomb, M.; Georgakoudi, I.; Kaplan, D. L.; Omenetto, F. G. *Biomacromolecules* **2008**, *9*, 1214–1220.
95. Perry, H.; Gopinath, A.; Kaplan, D. L.; Negro, L. D.; Omenetto, F. G. *Adv. Mater.* **2008**, *20*, 3070–3072.
96. Parker, S. T.; Domachuk, P.; Amsden, J.; *et al. Adv. Mater.* **2009**, *21*, 2411–2415.
97. Boriskina, S. V.; Lee, S. Y. K.; Amsden, J. J.; Omenetto, F. G.; Negro, L. D. *Opt. Express* **2010**, *18*, 14568–14576.
98. Gil, E. S.; Park, S. H.; Marchant, J.; Omenetto, F. G.; Kaplan, D. L. *Macromol. Biosci.* **2010**, *10*, 664–673.
99. Lawrence, B. D.; Marchant, J. K.; Pindrus, M. A.; Omenetto, F. G.; Kaplan, D. L. *Biomaterials* **2009**, *30*, 1299–1308.
100. Domachuk, P.; Tsioris, K.; Omenetto, F. G.; Kaplan, D. L. *Adv. Mater.* **2010**, *22*, 249–260.
101. Gupta, M. K.; Singamaneni, S.; McConney, M.; Drummy, L. F.; Naik, R. R.; Tsukruk, V. V. *Adv. Mater.* **2010**, *22*, 115–119.
102. Ghosh, S.; Parker, S. T.; Wang, X. Y.; Kaplan, D. L.; Lewis, J. A. *Adv. Funct. Mater.* **2008**, *18*, 1883–1889.
103. Murphy, A. R.; John, P. S.; Kaplan, D. L. *Biomaterials* **2008**, *29*, 2829–2838.
104. Murphy, A. R.; Kaplan, D. L. *J. Mater. Chem.* **2009**, *19*, 6443–6450.
105. Chen, H.; Hu, X.; Cebe, P. *J. Therm. Anal. Calorim.* **2008**, *93*, 201–206.
106. Hardy, J. G.; Scheibel, T. R. *Prog. Polym. Sci.* **2010**, *35*, 1093–1115.
107. Hu, X.; Wang, X.; Rnjak, J.; Weiss, A. S.; Kaplan, D. L. *Biomaterials* **2010**, *31*, 8121–8131.
108. Motta, A.; Migliaresi, C.; Faccioni, F.; Torricelli, P.; Fini, M.; Giardino, R. *J. Biomater. Sci. Polym. Ed.* **2004**, *15*, 851–864.

2.213. Chitosan

M A Barbosa, A P Pêgo, and I F Amaral, Universidade do Porto, Porto, Portugal

© 2011 Elsevier Ltd. All rights reserved.

2.213.1.	**Sources, Analysis, and Properties**	222
2.213.1.1.	Chemical Structure	222
2.213.1.2.	Solution Properties	222
2.213.1.3.	Chitosan Preparation: Chitin Isolation and *N*-deacetylation	223
2.213.1.4.	Chitosan Characterization	223
2.213.1.4.1.	Degree of acetylation	223
2.213.1.4.2.	Molecular weight	224
2.213.1.5.	General Aspects of Biological Behavior	225
2.213.1.5.1.	Biocompatibility	225
2.213.1.5.2.	Cytocompatibility	225
2.213.1.5.3.	Bacteriostatic and fungostatic properties	225
2.213.1.5.4.	Enzymatic degradation	226
2.213.1.5.5.	Immunoadjuvancy	226
2.213.1.5.6.	Hemostatic and blood clotting properties	226
2.213.1.5.7.	Cell-binding properties	226
2.213.1.5.8.	Wound-healing properties	226
2.213.1.5.9.	Bone-healing properties	226
2.213.1.6.	Chitosan Functionalization	227
2.213.2.	**Processing**	227
2.213.2.1.	Films and Porous Scaffolds (Freeze-Drying and Freeze-Gelling)	227
2.213.2.2.	Nanofibers	227
2.213.2.3.	Polyelectrolyte Complexes	228
2.213.2.4.	Micro- and Nanoparticles	229
2.213.2.5.	Cross-linking	229
2.213.3.	**Biomedical Applications**	229
2.213.3.1.	Wound Management	229
2.213.3.2.	Tissue Repair and Regeneration	230
2.213.3.3.	Delivery of Therapeutic Agents	232
2.213.3.4.	Other Applications	234
2.213.4.	**Future Prospects**	235
References		235

Glossary

Coacervation The process that results in the aggregation of molecules or colloidal particles under the action of electrostatic attractive forces.

Degree of acetylation (DA) Molar fraction of *N*-acetylated units in chitin/chitosan.

Electrospinning Technique used to produce nanofibers, based on the application of a sufficiently high voltage between a needle and a metallic collector, resulting in a very thin jet of fluid which is projected against a collector.

Endotoxin A toxin of internal origin. Endotoxins should be absent from chitosan used for biomedical applications.

Freeze-drying (of chitosan) Polymer solutions are frozen to temperatures that cause the formation of ice crystals, which are removed by sublimation under vacuum, producing a porous structure.

Freeze-gelling (of chitosan) A method alternative to freeze-drying to produce 3D-scaffolds. The method is based on freezing and subsequent extraction of the solution-rich phase by a nonsolvent for the polymer, while the polymer-rich phase is gelled under the action of a neutralizing agent.

Glycosaminoglycans A gel-forming repeating disaccharide units of the extracellular matrix.

Neuroma A growth or tumor of nerve tissue.

Polycation A macromolecule with many positively charged groups.

Polyelectrolyte complexes Self-assembled structures formed by reacting two oppositely charged polyelectrolytes in an aqueous solution.

Proteoglycans A constituent of the extracellular matrix resulting from the association of a protein and glycosaminoglycans.

Abbreviations

A	Absorbance
DA	Degree of acetylation
EC	Endothelial cells
ECM	Extracellular matrix
FN	Fibronectin
FT-IR	Fourier transform infrared spectroscopy
GAG	Glycosaminoglycan
H&E	Hematoxylin and Eosin
HA	Hyaluronic acid
HLC	Human-like collagen
IVD	Intervertebral disc
LbL	Layer-by-layer
M_n	Number average molecular weight
MSC	Mesenchymal stem cells
M_w	Weight average molecular weight
NMR	Nuclear magnetic resonance
PDGF	Platelet-derived growth factor
PECs	Polyelectrolyte complexes
PEO	Poly(ethylene oxide)
PLGA	Poly(lactic-*co*-glycolic acid)
PLLA	Poly(L-lactic acid)
SEC	Size exclusion chromatography
SEM	Scanning electron microscopy
TCP	Tricalcium phosphate
TGF-β1	Transforming growth factor beta 1
γ-PGA	Gamma-poly(glutamic acid)

2.213.1. Sources, Analysis, and Properties

2.213.1.1. Chemical Structure

Chitosan is a linear copolymer of D-glucosamine and *N*-acetyl-D-glucosamine in a β-(1–4) linkage, in which glucosamine is the predominant repeating unit (Figure 1). Chitosan itself may be found in the mycelia of certain fungi in association with other polysaccharides, but is mostly obtained by deacetylation of chitin. Chitin is the second most abundant polysaccharide in nature after cellulose, occurring in the cell walls of certain fungi[1] and yeasts, in plants as the equivalent to cellulose, and in many invertebrate groups such as mollusks and arthropods as the fibrous support of the inorganic mineral phase of their exoskeleton, as an alternative to collagen.[1] Chitin is a high molecular weight crystalline polysaccharide, which is theoretically comprised entirely of *N*-acetylated D-glucosamine units. Naturally occurring chitin, however, is mostly present as a copolymer, containing different proportions of *N*-glucosamine units, dependent on the source.[2] In chitin, the chains are arranged in sheets or stacks, the chains of each sheet having the same direction and being bonded through intrasheet hydrogen bonds between two adjacent chains. Naturally occurring chitins are found in three polymorphic forms, α-, β-, and γ-chitin, which differ in the arrangement of chains within the crystalline regions. In α-chitin, which is the one found in crab, lobster, and shrimp shells, adjacent sheets have opposite directions, and thus it has an antiparallel chain arrangement. In β-chitin, which is the form occurring in the pen of the squid genus *Loligo*, adjacent sheets have the same direction, and thus it has a parallel chain arrangement. In γ-chitin, every third sheet has the opposite direction to the previous two sheets. In addition to intrasheet interchain hydrogen bonds, α-chitin also presents hydrogen bonds between adjacent chains. These intersheet bondings are responsible for the lack of swelling in water of α-chitin, whereas β-chitin swells readily in water and forms hydrates.[2] Chitosan is also crystalline, but as compared to chitin, presents a longer distance between adjacent chains belonging to the same sheet, due to the removal of the *N*-acetyl groups during the conversion from chitin to chitosan, which hold together adjacent chains through C(2)N–H···O=C(7) hydrogen bonds.[2] Instant differentiation between chitin and chitosan can be made based on their solubility. While chitin is soluble in *N*,*N*-dimethylacetamide (DMAc) in the presence of 5–10% (w/v) lithium chloride and insoluble in dilute acid solutions, the reverse is true for chitosan.[2,3] In chitin/chitosan terminology, the molar fraction of *N*-acetylated units is termed the degree of acetylation (DA), expressed in percentage, or fraction of *N*-acetylated units (F_A).[4,5] Since a DA around or lower than 50% is usually required for chitosan solubility in dilute acidic solutions, the term chitosan is applied both to fully-deacetylated chitin and partially deacetylated chitin with DAs $\leq$ 50%.

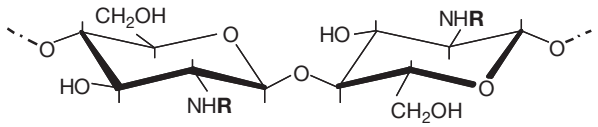

Figure 1 Chemical structure of chitosan, a linear copolymer of D-glucosamine (R=H) and *N*-acetyl D-glucosamine (R = $COCH_3$) in a β-(1–4) linkage. Glucosamine is the predominant repeating unit.

2.213.1.2. Solution Properties

Chitosan is neither soluble in water nor in organic solvents. However, after protonation of amine functionalities from glucosamine units by acid, the electrostatic repulsions between NH_3^+ groups lead to the destruction of interchain attractive interactions, such as hydrogen bonds and hydrophobic interactions, and consequently to chitosan solubility. At pH lower than its pK_a, which may range from ~6.5 to ~7, chitosan is a polycation and at pH 4.0 and below, it is completely protonated.[6] Chitosan solubility depends on chitosan charge density, which is tightly connected with structural parameters such as DA, chain length, and distribution of *N*-acetylated glucosamine units, as well as on environmental parameters, such as pH, ionic strength, and dielectric constant of the media.[7] The solubility range increases on increasing the DA, due to the increase of the steric hindrance related to the increase of the number of the acetyl groups, together with the increase of the intrinsic pK_a. According to Sorlier *et al.*,[6] the intrinsic pK_a of chitosan increases from 6.46 to 6.8 as the DA increases from 5% to 35%, respectively, revealing an increase of

cationicity of amine functionalities on increasing the DA. As a result, chitosans with DAs in the range of 45–55% are water-soluble, providing that the *N*-acetylated units are randomly distributed. In the presence of high ionic strengths, solubility is reduced. The high concentration of protons leads to the screening of the electrostatic interactions occurring between polymeric chains, with subsequent establishment of chain interactions and polymer precipitation. As a result, chitosan is not soluble in strong acids such as hydrochloric acid solutions with molarities higher than 0.1 M.[7]

2.213.1.3. Chitosan Preparation: Chitin Isolation and *N*-deacetylation

Commercially available chitin is most commonly prepared from the exoskeletons of crab, shrimp, and prawn, obtained as waste from the seafood processing industry. In these, chitin is tightly associated with proteins, inorganic material (mainly $CaCO_3$), pigments, and lipids. Deproteinization and demineralization are generally carried out by treatment with 1–2 M NaOH at 70 °C or higher temperature, and 1.25 M HCl at room temperature, respectively, deproteinization being usually done prior to demineralization. Both treatments may lead to the cleavage of chitin polymeric chains. In this sense, a number of alternative methods have been proposed in order to minimize the hydrolysis of glycosidic linkages during chitin extraction, including the use of proteolytic enzymes to remove protein and EDTA to remove mineral. Finally, the pigments present in the exoskeletons of crustaceans can be extracted with ethanol, acetone, or oxidizing agents such as $KMnO_4$.[2] The preparation of squid chitin, although similar, occurs under milder conditions, as β-chitin is composed exclusively of chitin and proteins, with only traces of metal salts.[8]

Deacetylation may be carried out under acid or basic conditions, but basic conditions are preferred, due to the susceptibility of chitin glycosidic linkages to acid hydrolysis. The deacetylation of α-chitin is usually carried out using strong aqueous bases at 90–150 °C for a few hours, to produce chitosan with a DA between 5% and 30%.[2,4,5,9] High reaction temperatures reduce the time required for deacetylation, but result in increased hydrolysis of polymeric chains. Deacetylation of chitin proceeds rapidly in 50% (w/v) aqueous NaOH at 100 °C during the first hour of alkali treatment, but extension of the reaction time results rather in chain hydrolysis than in significant deacetylation.[2] To obtain chitosans with low DAs (<15%), multistep alkali treatments with interspersed washing are required.[10] The washing with water in-between treatments induces the swelling of chitin chains, and increases the accessibility of chitin for subsequent deacetylation. In order to reduce chain cleavage during alkaline deacetylation, reactions are carried out at as low temperature as possible, under inert atmosphere, such as nitrogen or argon, or in the presence of oxygen scavengers or reducing agents, such as $NaBH_4$. As chitin is not soluble in such systems, deacetylation occurs under heterogeneous conditions. During deacetylation of α-chitin, NaOH acts initially on the amorphous regions of the polymer, and only afterwards on the crystalline regions. Heterogeneous deacetylation leads therefore to a block distribution of acetylated units, rather than a random distribution of the same. As a result, the characteristic infrared (IR) bands attributed to crystallinization of blocks of poly [β-(1→4) D-glucosamine] are only perceptible for DAs ≤ 9%, due to the later deacetylation of segments originally present in the crystalline region of chitin.[2,10] As compared to α-chitin, β-chitin present in squid pens is much easier to deacetylate, due to the absence of intersheet hydrogen bonding, which makes crystalline regions more accessible to reactives.[9] During deacetylation of β-chitin, the crystallinity decreases rapidly compared to that of α-chitin, and a completely amorphous product is obtained.[11]

Chitosan isolated from the cell walls of fungi have recently become commercially available.[12] As compared to chitosan obtained from marine animal resources, chitosan isolated from fungi cultured under controlled growing conditions presents higher reproducibility among batches and traceability, which makes its use in medical and pharmaceutical applications interesting.

'As received' chitosans are often subjected to purification steps, mainly to reduce the content of insoluble matter. The most frequently used method involves the filtration of chitosan acidic solutions to remove undissolved or gelatinous particles and the subsequent precipitation in an alkaline solution. The regenerated chitosan is then thoroughly washed in distilled water and finally freeze-dried. Precipitation by addition of NaOH under rapid stirring leads to a product with a high crystallinity index after drying, the so-called microcrystalline chitosan.[13]

Chitosans with specific DAs can be prepared by *N*-acetylation of almost fully-deacetylated chitosans.[9] Chitosan *N*-acetylation is usually carried out at room temperature and under homogeneous conditions, leading to the random introduction of acetyl groups with minimal hydrolysis of polymeric chains. This involves the dissolution of chitosan in a diluted acidic solution, prior to adding a cosolvent and a variable amount of the acetylating reactive, acetic anhydride.[14] The acetylation of chitosan under homogeneous conditions is also very useful to prepare water-soluble chitosans.

2.213.1.4. Chitosan Characterization

Regardless of the application envisaged, the degree of *N*-acetylation (DA) and the average molecular weight are the parameters most frequently assessed due to their impact on chitosan properties. Crystallinity, viscosity in aqueous solutions, dry matter content, amount of insoluble impurities, and ash content, are other parameters commonly analyzed. For the application of chitosan as a biomaterial, its characterization in terms of microbial contamination (bioburden), toxic heavy metals, protein content, and bacterial endotoxin levels is of crucial importance. For this purpose, the American Society for Testing and Materials (ASTM) has established standard guidelines for the characterization and testing of chitosan for use in biomedical and tissue-engineered medical product applications.[15] The two most important parameters affecting chitosan properties are discussed below.

2.213.1.4.1. Degree of acetylation

The DA is a structural parameter influencing charge density, crystallinity, solubility, as well as chitosan susceptibility to enzymatic degradability. Therefore, its accurate determination is of major importance. A number of methods have been developed for the determination of the DA of chitosan,

including elemental analysis, colloid titration with a polyanion, dye adsorption, and spectroscopies such as ultraviolet (UV), IR, and liquid/solid state nuclear magnetic resonance (NMR). The advantages and drawbacks of each technique have been discussed.[2,4,5] Among these, high-resolution proton NMR (^{1}H NMR) is considered the most accurate technique for the determination of the DA of chitosan. ^{1}H NMR is usually performed in D_2O containing DCl, the DA value being determined from the relative integrals of acetyl (*N*-acetyl and AcOH) and combined H2–H6 protons.[16,17] For chitosans with high acetyl contents, the use of solid state ^{13}C CP/MAS NMR is preferred to ^{1}H NMR, since complete dissolution of the sample prior to analysis is required for ^{1}H NMR. Because of its simplicity associated with accuracy, IR spectroscopy is the most frequently used technique. The use of FT-IR spectroscopy for the determination of the DA is based on the variation of an absorbance band characteristic of *N*-acetyl groups, as a function of an internal reference band. The DA value can be extrapolated from a calibration curve established using an absolute technique, such as NMR. A number of different methods have been proposed, differing in terms of the analytical and reference IR bands used, as well as in terms of the baselines used for the determination of the correspondent absorbance values.[18] One of the most frequently employed method is the one described by Baxter *et al.*[19] It uses the amide I band at 1655 cm^{-1} as the analytical band (the baseline is the one originally proposed for the A_{1655}/A_{2867} ratio) and the hydroxyl band at 3450 cm^{-1} as the internal reference band. The sample has, therefore, to be perfectly dry and the IR spectra immediately recorded. The DA is determined as follows:

$$DA(\%) = (A_{1655}/A_{3450}) \times 115$$

This relation was validated by dye adsorption, for DAs comprised between 0 and 55%. Later on, Brugnerotto *et al.*[20] proposed the use of the amide III band (C–N stretching coupled with N–H in plane deformation) at 1320 cm^{-1} as the analytical band and the band at 1420 cm^{-1} as the internal reference band. The authors analyzed chitin/chitosan samples covering the entire range of DAs, and used samples from different sources. A very good linear correlation between the ratio of absorbance bands (A_{1320}/A_{1420}) and the experimental values obtained from NMR was found in all the range of DA values, which could be expressed by the following relation:

$$A_{1320}/A_{1420} = 0.3822 + 0.03133 \times DA(\%)$$

Brugnerotto *et al.* found superior agreement between the experimental and estimated DA values using this ratio of absorbance bands than those involving the band at 3450 cm^{-1} (Figure 2).

2.213.1.4.2. Molecular weight

Depending on its source and preparation procedure, chitosan molecular weight may range from 300 to over than 1000 kD, squid pen chitosans presenting usually higher molecular weight, as compared to chitosans obtained from the exoskeletons of crustaceans.[21] Several techniques can be used to estimate the average molecular weight of chitosan. Among them are capillary viscometry, ultracentrifugation, and size exclusion chromatography (SEC) coupled with light scattering. Whatever the technique used, the tendency of the polymer chains to aggregate in solution constitutes a problem.[2,22] SEC is the most direct one, providing, in a single measurement, the weight-average molecular weight and the number-average molecular weight. From these two values, the polydispersity

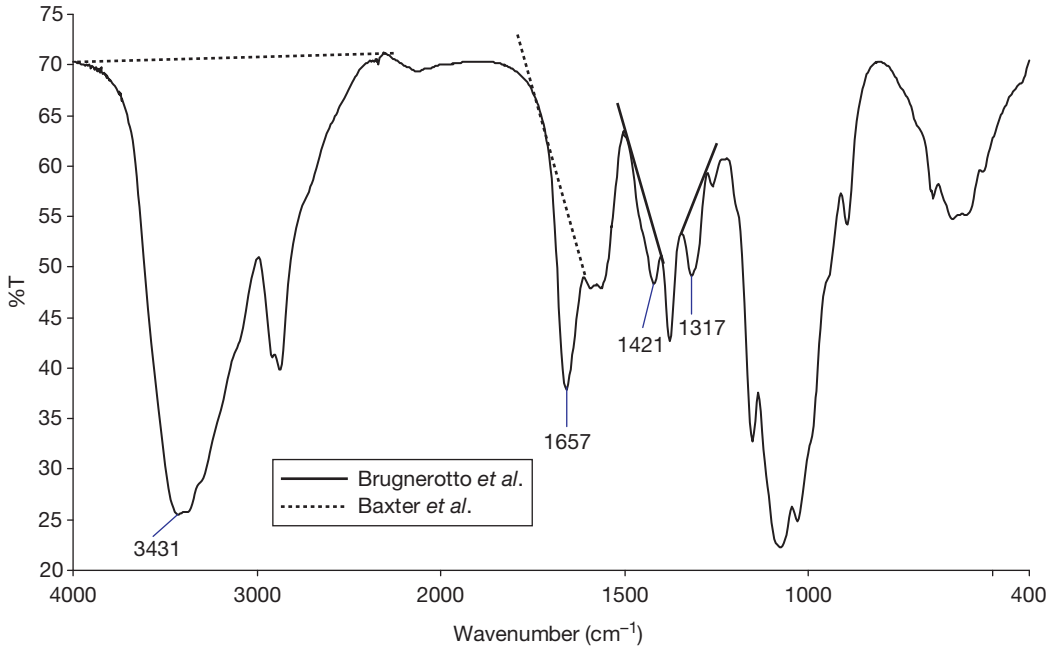

Figure 2 Squid pen chitosan infrared spectra, showing the baselines proposed by Brugnerotto *et al.*[20] and Baxter *et al.*[19] for the determination of the A_{1320}/A_{1420} and A_{1655}/A_{3450} ratio, respectively.

index Mw/Mn can be easily determined. Still, this technique requires previous calibration of the SEC system with narrow polydispersity standards of known molecular weight. The association of a light-scattering detector with SEC provides information on the absolute molecular weight as well as on molecular size parameters, such as the radius of gyration Rg. The analysis is usually performed using CH_3COOH/CH_3COONa buffers at pH near 4.5 as mobile phase, salt being added to screen electrostatic repulsion between protonated amine groups in chitosan.[23] For the analysis, the refractive index increment value (dn/dC) of chitosan in the CH_3COONa/CH_3COOH system used is required. The dn/dC values for chitosan may be found in literature, including some that are dependent on the DA.[24] In this case, previous characterization of the DA may be required. Alternatively and if possible, the dn/dC value can be measured using a differential refractometer. SEC coupled with light scattering is also the technique described in ASTM guidelines for the determination of chitosan molecular weight.

2.213.1.5. General Aspects of Biological Behavior

2.213.1.5.1. Biocompatibility

One of the major issues that have to be addressed while envisaging biomedical applications of a biomaterial is biocompatibility. The nontoxicity of chitosan films was initially showed by Rao and Sharma[25] using standard *in vivo* toxicological tests to evaluate chitosan safety and haemostatic potential. The biocompatibility of films with different DAs was examined by Tomihata and Ikada,[26] using a rat subcutaneous implant model. While chitosan films with DA 31% induced a relatively severe inflammatory reaction, with almost complete resorption after 4 weeks of implantation, films with lower DAs led to a lower inflammatory reaction and degraded at a slower rate. Films with DAs $\leq$ 16% showed a very mild tissue reaction. The biocompatibility of chitosan porous scaffolds (DA 8%) was addressed by VandeVord *et al.*,[27] using a mouse intraperitoneal and subcutaneous implant model. Histological assessment revealed an early migration of neutrophils into the implantation area, which resolved over implantation time. Besides this early accumulation of neutrophils, which are cells usually associated with acute inflammation, no evidence of other signs associated with an inflammatory response, such as erytema and edema, were found. A very low incidence of chitosan-specific immune reactions was observed and, with time, collagen deposition within and surrounding the implant, with capsule formation, was found. However, the capsule was always highly cellular and its thickness decreased over time. Angiogenic activity associated with the external implant surface was observed. Overall, chitosan with DA 8% was found to have a high degree of biocompatibility. Recently, we assessed the inflammatory response to chitosan porous scaffolds with two different DAs (DA 4% and DA 15%) using a subcutaneous air-pouch model of inflammation.[28] Implantation of chitosan scaffolds with DA 15% induced a higher recruitment of neutrophils and increased adhesion of inflammatory cells during the early phase of implantation, while DA 4% merely caused a slight increase in the number of leukocytes present in the inflammatory exudates. With time, chitosan scaffolds with DA 15% induced the formation of a thicker collagenous capsule and a high infiltration of inflammatory cells within the scaffold. Since inflammation and healing are interrelated, these results showed the importance of the careful selection of the DA while developing chitosan porous implants for tissue repair and regeneration.

2.213.1.5.2. Cytocompatibility

A wide number of cells have been successfully cultured on 2D and 3D chitosan matrices envisaging cell-based regenerative therapies, among them keratinocytes,[29] chondrocytes,[30,31] osteoblasts,[32–34] hepatocytes,[35] and Schwann cells.[36] The DA was found to be an important parameter affecting cell adhesion, lower DAs favoring cell adhesion. This effect was reported for a number of anchorage-dependent cells, such as keratinocytes,[29] fibroblasts,[29,37] dorsal root ganglion neurons,[38,39] and Schwann cells.[40] In our lab, we investigated the DA effect on the behavior of osteogenic cells on chitosan films and porous matrices, using DAs in the range of 4–49%.[32,33,41,42] These studies revealed a similar tendency to increased cell adhesion on decreasing the DA, and showed that differences in the DA as small as 9% can be critical in terms of osteoblastic response to chitosan.[41,42] For instance, in the case of rat bone marrow stromal cells, cell adhesion, cytoskeleton organization, proliferation, and osteogenic differentiation were only observed on chitosan with DA 4%, while the same were hampered on chitosans with higher DAs ($\geq$13%). We hypothesize that the DA could influence cell adhesion and osteoblast differentiation by influencing the adsorbed layer of adhesion proteins. For that, we performed protein adsorption studies using ^{125}I-fibronectin. In line with the higher cell adhesion levels found, chitosan with DA 4% showed the highest fibronectin (FN) adsorption both from a single FN protein solution and from diluted serum.[32,33] From these results we may speculate that protonated amine groups from glucosamine units in chitosan may modulate cell adhesion to chitosan by promoting the adsorption of cell adhesive proteins such as FN.

To improve cell behavior on chitosan matrices, several attempts have been made, including physiadsorption of adhesive proteins[43] and covalent binding of cell adhesion peptides.[44,45] For instance, endothelial cell (EC) adhesion to porous chitosan matrices is significantly enhanced upon previous incubation of chitosan matrices in an FN solution.[46] Interestingly, we found that EC adhesion to FN-coated chitosan matrices is also dependent on the DA. While cell adhesion was impaired on DA 15%, ECs were able to adhere, spread, and colonize chitosan matrices with DA 4%. Later on, protein adsorption studies on scaffolds with DA 4% revealed a higher number of exposed FN cell-binding domains, as well as greater ability to adsorb FN and to retain and exchange adsorbed FN in the presence of competitive proteins, in agreement with the higher cell numbers found.

2.213.1.5.3. Bacteriostatic and fungostatic properties

Chitosan exhibits an intrinsic antibacterial activity, inhibiting bacteria and fungi growth. As an example, in *Staphylococcus aureus* cultures, chitosan treatment promotes structural changes in the so-called membrane–wall complex leading to the impairment of surface cell structures and to bacterial

death.[47] The biological mechanisms underlying this property remain poorly understood. Bacterial growth inhibition is believed to be related to chitosan ability to establish electrostatic interactions between chitosan cationic amino groups and anions, such as *N*-acetylmuramic acid, sialic acid, and neuraminic acid, present on the bacterial cell wall. In addition to electrostatic interactions, hydrophobic interactions resultant from the presence of *N*-acetylated residues in chitosan are also thought to contribute to chitosan bacteriostatic properties, highly acetylated chitosans being reported to be excellent flocculants of *Escherichia coli* suspensions.[48]

2.213.1.5.4. Enzymatic degradation

In nature, chitosan can be hydrolysed by chitinases, chitosanases, and lysozymes, as well as by nonspecific hydrolases, such as α-amilases and lipases. In addition, like all polysaccharides, chitosan is vulnerable to acid hydrolysis and to oxidative–reductive depolymerization reactions.[49,50] In *vivo*, the human enzymes involved in chitosan hydrolysis are only partially known.

In human serum partially, *N*-acetylated chitosans are mainly depolymerized by lysozyme.[50] Lysozyme is normally present in the human serum, saliva, and other fluids, hydrolyzing preferentially the β-(1–4) glicosidic linkages between *N*-acetylglucosamine (NAGA) and *N*-acetylmuramic acid residues that occur in the cell walls of bacteria. Therefore, in addition to its natural substrate, lysozyme can hydrolyse partially *N*-acetylated chitosans. The active site of lysozyme binds six sugar rings, and three consecutive *N*-acetyl-D-glucosamine residues are required for lysozyme catalytic activity.[51] As a consequence, the susceptibility of chitosan to lysozyme depolymerization *in vitro* depends not only on the DA but also on the distribution of *N*-acetylated units along chitosan chains. The initial degradation rate increases with the DA, and this increase is more pronounced for *N*-acetylated chitosans prepared under homogeneous conditions than for chitosans obtained by heterogeneous deacetylation.[50,52] The same trend was observed *in vivo* upon subcutaneous implantation of chitosan films in a rat animal model.[26] Chitosans with low DAs may last several months *in vivo*.[27] Crystallinity is another parameter significantly influencing chitosan susceptibility to lysozyme hydrolysis, by reducing lysozyme accessibility to the substrate. For instance, the low degradation rates reported for chitosans with very low DAs have been frequently associated with the high levels of crystallinity and inter-molecular bindings present in these chitosans.[26,27] Finally, chitosan solubility may eventually shade the effect of lysozyme on chitosan degradation. This is the case of the accelerated mass loss observed for chitosans with DAs close to 50%, attributed to the enhanced solubility of chitosan molecules at physiologic pH.[38,39]

The enzymatic hydrolysis of chitosan in wound-healing process was addressed by Muzarelli.[49] Upon hydrolysis of chitosan by lysozyme, the oligomers released activate macrophages, inducing the production of diffusible molecules, such as interferon, tumor necrosis factor-α, and interleukin-1. Activated macrophages secrete more lysozyme as well as *N*-acetyl-β-D-glucosaminidase and chitinase, which further catalyze the depolymerization of chitosan into monomers. These become available for further incorporation into hyaluronate, keratan sulfate, and chondroitin sulfate.

2.213.1.5.5. Immunoadjuvancy

Chitosan is chemotactic for neutrophils, which has been attributed to specific interactions of chitosan or its oligosaccharides with neutrophils receptors, such as selectins.[27] In addition to being chemotactic to neutrophils, chitosan shows a biological aptitude for activating macrophages for tumoricidal activity and for production of interleukin-1,[53] as well as nitric oxide.[54] The immunoadjuvant properties of chitosan have been attributed to the NAGA units, rather than to the glucosamine units. Macrophage activation appears to be dependent on binding of NAGA to specific cell membrane receptors, namely involved in the binding of mannose- and NAGA-glycoproteins.[54]

2.213.1.5.6. Hemostatic and blood clotting properties

Chitosan is a powerful hemostatic agent[25] that induces blood clotting, even in the presence of extensive anticoagulation therapy.[55] Blood clotting was suggested to be related to the possible formation of polyelectrolyte complexes (PECs), involving chitosan amino functionalities and negatively charged acidic groups present at the surface of erytrocytes. Benesch and Tengvall[56] suggested that the procoagulant activity of chitosan could be related to the ability of chitosan to bind fibrinogen. In contrast, chitin displays anticoagulant properties, increasing upon *O*-sulfation,[57] which is attributed to its similarity to heparin, a naturally occurring sulfated glycosaminoglycan (GAG) used as anticoagulant agent in clinic.

2.213.1.5.7. Cell-binding properties

Chitosan is able to agglutinate a variety of mammalian cells in suspension. Cell adhesion to chitosan is attributed to nonspecific electrostatic interactions occurring directly between protonated amine groups from glucosamine units and negatively charged carboxylate and sulfate groups found in cell surface proteoglycans.[29,58] Close to the physiologic pH, the majority of chitosan ammonium groups are dissociated and subsequently uncharged. Still, the presence of a small amount of nondissociated ammonium groups in chitosan chains is sufficient to provide enough cationic sites and allow the establishment of electrostatic interactions.[30]

2.213.1.5.8. Wound-healing properties

Chitosan has been found to accelerate dermal wound healing and inhibit fibroplasia, showing a biological aptitude to stimulate cell proliferation and the deposition of an orderly organized connective tissue.[59] This behavior has been related to chitosan ability to activate macrophages for cytokine production (transforming growth factor beta 1 (TGF-β1) and platelet-derived growth factor (PDGF)), upon hydrolysis by lysozyme.[60,61] Moreover, Howling *et al.*[62] suggested that chitosan may interact with growth factors present in serum, potentiating their effect, as chitosan has a stimulatory effect on dermal fibroblast proliferation when added to serum-containing culture medium, highly deacetylated chitosans producing a stronger mitogenic response, as compared to samples with lower levels of deacetylation.

2.213.1.5.9. Bone-healing properties

The osteogenic potential of chitosan was first reported by Borah *et al.*[63] in 1992. In this study, chitosan was used to

treat bone defects, made in the endochondral long bones of the rabbit. Chitosan reportedly stimulated osteogenesis with closure of the critical size bone defects, as compared to controls, in 8–12 weeks. As time progressed, the possible osteogenic, osteoconducting, and osteoinducting properties became the subject of investigation. The most significant works demonstrating the osteoconductive properties of chitosan are possibly those carried out by Muzarelli *et al.*[64,65] In the first work, Muzzarelli *et al.*[65] treated bone defects made in the tibiae of rabbits with freeze-dried methyl pyrrolidinone chitosan. The experimental sites showed signs of neoformed bone tissue, as opposed to controls, originating from the preexisting bone, as well as from the periosteum. Subsequently, Muzzarelli *et al.* prepared a modified chitosan (DA 8%) carrying imidazole groups, to treat bone defects made in the femoral condyle of sheep. Within 40 days after surgery, the neoformed tissue occluded the surgical hole and assumed a trabecular structure in the peripheral area of the lesion. In the control group, no sign of ostegenesis or reparative process was observed and bone marrow was rich in adipocytes. The modified chitosan was reported to have a stimulatory effect on bone formation. Although several works have demonstrated the osteoconductive properties of chitosan, it was often combined with therapeutic molecules, growth factors, or calcium phosphates. The bone regenerative properties of unmodified chitosan are reported in a study of Park *et al.*[66] In this study, unmodified and PDGF-releasing chitosan sponges were applied to rat calvarial defects. Both matrices led to a significant increase in new bone formation, as compared to untreated defects, which became completely filled with fibrous connective tissue. In addition, a marked increase of bone formation and mineralization was observed in the presence of PDGF, as expected. The subsequent studies of Lee *et al.*[67] supported these results. The effect of the DA on osteogenesis was addressed by Hidaka *et al.*,[68] who implanted subperiosteally over the calvaria of rats membranes prepared from hydroxyapatite and chitosan. DAs of 0, 6, 20, 30, and 35% were used. The authors reported for DAs $\geq$ 20% a marked inflammatory reaction, followed by accumulation of osteocalcin positive cells at the site of implantation, while for lower DAs a mild inflammation with minimal osteogenesis was observed.

2.213.1.6. Chitosan Functionalization

Chitosan has both reactive amino or amido groups at C(2) positions, as well as primary and secondary hydroxyl groups at C(6) and C(3) positions which can be used to prepare derivatives with well-defined structures and biological properties under mild reaction conditions. Two modification reactions were already addressed in this chapter, namely deacetylation and *N*-acetylation. Other chemical modifications often explored to prepare versatile precursors and chitosan derivatives for biomedical applications include other acylation reactions, *N*-phthaloylation, Schiff's base formation, *N*,*O*-carboxymethylation, *N*-carboxyalkylation, and graft copolymerization.[2,9] Graft copolymerization, in particular, has been extensively used to introduce side chains onto chitosan, namely to obtain tailored hybrid materials composed of natural polysaccharides and synthetic polymers.

2.213.2. Processing

Chitosan is extremely versatile in terms of processing. Films, micro- and nanoparticles, porous scaffolds, micro- and nanofibers, and meshes can be produced with chitosan for a wide range of applications.

2.213.2.1. Films and Porous Scaffolds (Freeze-Drying and Freeze-Gelling)

Taking advantage of the solubility of chitosan in mildly acidic conditions, films can be produced by casting the resulting gel on a flat surface and then allowing the solvent to evaporate. Neutralization with an alkaline solution, washing, and drying are often employed to stabilize the films. These can then be used as substrates for cell culture experiments.

Porous scaffolds can be prepared by freeze-drying, also known as lyophilization. Acidic chitosan solutions are frozen to temperatures of −20 to −80 °C, which causes formation of ice crystals. The rate and temperature of freezing influence the size of the ice crystals and consequently the size of the pores formed during the sublimation phase. The latter is carried out in a vacuum at low temperature, in order to avoid melting of the chitosan-rich phase. After elimination of the ice crystals, drying can be continued to eliminate unfrozen water molecules. Pores with dimensions in the range 40–250 mm and porosities of 80% can be obtained. By applying a temperature gradient along a certain direction, preferential orientation of the pores can be obtained to produce structures with aligned porosity. **Figure 3** presents laser scanning confocal and scanning electron microscopy (SEM) images of chitosan sponges with two DAs (4% and 30%), which have been colonized by MG-63 cells.[42] It shows that a better spreading is reached with the lower DA.

In some cases, the freeze-drying method can damage the pore walls during evaporation of the solvent. Also, formation of skin can also occur. To avoid these problems, the method of freeze-gelling has been proposed for producing porous structures of poly(L-lactic acid) (PLLA), poly(lactic-*co*-glycolic acid) (PLGA), chitosan, and alginate.[69] The method is based on the extraction of the solution-rich phase by a nonsolvent for the polymer. Exemplifying for the case of chitosan, the procedure is the following. An acetic acid solution of chitosan is frozen to −20 °C, which causes the formation of ice crystals. To form the pores, the ice crystals are removed by immersing the frozen chitosan solution in an NaOH/ethanol solution at −20 °C. Neutralization of the acid by the sodium hydroxide causes the gelation of chitosan, whereas the ethanol dissolves the ice crystals. Subsequent evaporation of the ethanol at room temperature produces the pores. The method has also been applied to produce composite scaffolds of chitosan and gamma-poly (glutamic acid) (γ-PGA) for the delivery of rhBMP-2.[70] Concentrations of chitosan and γ-PGA were 4% and 1%, respectively, in a 0.2 M acetic acid solution. Freezing was done at −80 °C and gelation was achieved by immersing the frozen chitosan/γ-PGA in a 3-M NaOH/ethanol solution at −20 °C.

2.213.2.2. Nanofibers

Nanofibers of chitosan can be produced by electrospinning. This technique has become extremely useful for the

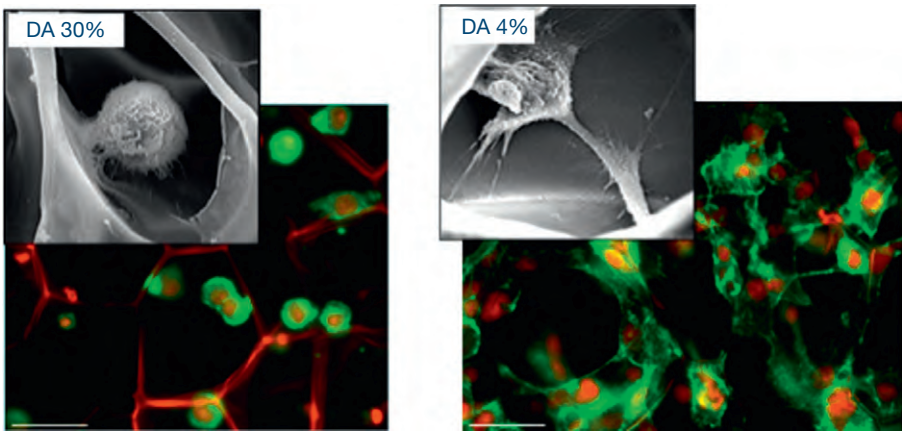

Figure 3 Fluorescence microscopy and scanning electron microscopic images of MG-63 cells cultured in chitosan sponges with different DAs. Red lines: chitosan walls of the pores; nuclei were stained with propidium iodide (red) and actin filaments with Alexa Fluor^{R} 488 phalloidin (green). Adapted from Amaral, I. F; Sampaio, P.; Barbosa, M. A. *J. Biomed. Mater. Res.* **2006**, *76A*(2), 335–346, with permission from Wiley.

preparation of nanofibers for tissue engineering, due to the wide range of polymers that can be processed to obtain nanofibers with diameters in the range 20–400 nm. Briefly, the application of a sufficiently high voltage between a needle and a metallic collector overcomes the surface tension holding a drop of liquid at the tip of the needle, resulting in a very thin jet of fluid being projected against the collector. The solvent is evaporated during the trajectory between needle and collector, resulting in a nonwoven structure. One of problems with electrospun meshes is the slow cell infiltration due to the high packing density of the nanofibers. To circumvent this problem fast degrading nanofibers can be combined with slow degrading fibers. This strategy has been developed by,[71] who have co-electrospun poly(epsilon-caprolactone) with poly(ethylene oxide) (PEO) from two separate spinnerets. The former polymer is slowly degradable, whereas the second one is water-soluble, acting as a sacrificial component of the scaffold. Seeding these scaffolds with mesenchymal stem cells (MSCs) has show that cell infiltration improved with the fraction of sacrificial polymer. High porosities (of the order of 95% to 97%) can be obtained also by coating microfibers with nanofibers, as demonstrated by.[72] Scaffolds made from polycaprolactone nanofibers electrospun onto polylactic acid microfibers supported infiltration of human chondrocytes, with higher porosities favoring cell infiltration.

2.213.2.3. Polyelectrolyte Complexes

The self-assembly of polymer chains due to electrostatic interactions is the basis for the formation of PECs. PECs are formed by reacting two oppositely charged polyelectrolytes in an aqueous solution. PECs are generally biocompatible networks and can be easily produced in the lab. PECs between chitosan and many polyanions have been described. Polysaccharides such as alginate, chondroitin sulfate, dextran sulfate and gellum gum form PECs with chitosan. Similarly, polyamino acids (e.g., poly-L-Lysine and poly(aspartic acid)), proteins (e.g., collagen), and glycosoaminoglycans (e.g., hyaluronic acid, HA) also bind electrostatically to chitosan, via anionic carboxylic or sulfate groups. The cationic amino groups of chitosan are responsible for the formation of electrostatic bonds with the anionic groups of the other polyelectrolyte. The formation of PEC hydrogels requires that the two polymers are oppositely charged. Since the pK_a of chitosan is in the vicinity of 6.5, the other polymer must have a lower pK_a for electrostatic aggregation to occur. If attraction is too strong, a precipitate, and not a hydrogel, will form. By modifying the ionic strength of the aqueous solution, for example, by addition of salts such as NaCl, the electrostatic interactions can be modulated so that a homogeneous hydrogel is formed. Functionalization of chitosan with positively charged (e.g., glycol–chitosan[73]), or negatively charged (e.g., sulfate[32,33]) groups expands the range of PECs that can be produced. Since no cross-linkers are required to form the hydrogel, these materials usually have excellent cytocompatibilty.

Using the principles that govern PEC formation, a film can be produced using the layer-by-layer (LbL) method, by alternate immersion of a substrate in solutions of positively and negatively charged polyelectrolytes. LbL films are usually very thin (typically $<1\mu m$). For larger thicknesses, the alternating layer structure becomes progressively disorganized due to interpenetration of the polymers chains. Polyelectrolyte multilayer (PEM) coatings of chitosan (Ch) and HA have shown varying degrees of resistance to enzymatic degradation, depending on whether they were used in the native state or cross-linked with 1-ethyl-3-(3-dimethylamino-propyl)carbodiimide (EDC).[74] The *in vitro* and *in vivo* degradation rate also depended on the molecular weight of chitosan, lower rates being obtained with the higher molecular weight chitosan. The same polymers have been used to produce self-assembled multilayers, by modifying them with DNA base pairs: chitosan with adenine and HA with thymine.[75] No cytotoxicity was reported. Stabilization of LbL films by cross-linking does not appear to always have the same effect on cells. Genipin, which is a nontoxic natural cross-linker, has been used in Ch/HA and Ch/alginate(Alg) films.[76] Cross-linking impaired the adhesion of MC3T3 preosteoblasts and rat fibroblast skin cells to Ch/HA multilayers (3, 5, and 10 bilayers), whereas for Ch/Alg substrates it caused the reverse effect. For high number of

bilayers and using higher concentrations of cross-linker, the effect on adhesion was more pronounced.

2.213.2.4. Micro- and Nanoparticles

Micro- and nanoparticles of chitosan can be prepared by various methods. The most common method consists in ionotropic gelation of chitosan molecules by anions, such as the polyanion tripolyphosphate (TPP)[77] and sulfate.[78] The experimental procedure involves drop-wise addition of the anion to a chitosan solution under agitation. Agitation can be performed mechanically, ultrasonically, or by a combination of both. The rate of agitation controls the size of the particles. Chitosan nanoparticles prepared by gelation with TPP were uptaken by A549 cells in percentages that depended on the molecular weight (M_w) and DA.[79] Uptake decreased by 26% when the M_w decreased from 213 000 to 10 000 and by 41% when the DA increased from 12% to 54%. The nanoparticles cytotoxicity was lower for the higher DA.

Nanoparticles have been produced for incorporating DNA, proteins and therapeutic agents. A complex coacervation method has been often used for incorporating DNA. In complex coacervation, separation of two oppositely charged colloids occurs. Normally, a chitosan solution (e.g., in sodium acetate buffer) and a DNA solution (e.g., in sodium sulfate) are preheated to ~50 °C and then quickly mixed and vortexed to form the chitosan/DNA complex nanoparticles.[80] Chitosan nanoparticles with various ratios of chitosan to plasmid OP-1 were used to transfect chondrocytes.[81] Nanoparticles with a chitosan/plasmid weight ratio of 10:1 entered the cells and resulted in the expression of the plasmid, which maintained its structural integrity. The size of the plasmid did, however, affect the efficiency of transfection to the cells.

2.213.2.5. Cross-linking

Like in other polymers, cross-linking of chitosan molecules is often used to increase the mechanical and chemical stability of chitosan. Cross-linking may involve covalent binding of chitosan molecules to chitosan molecules, or to other polymer chains. A hybrid polymer network is formed in this case. The covalent bonds are formed between the two different molecules, but they may also be established between molecules of the same polymer. Another possibility is to add to the chitosan solution a nonreacting polymer before cross-linking. The chains of this polymer become entangled in the structure of the cross-linked chitosan, contributing to its physical reinforcement. These are called semi-interpenetrating networks (semi-IPN). The reinforcing polymer can be subsequently cross-linked to form a full-IPN. The most common cross-linkers that have been used are dialdehydes, and particularly glutaraldhyde.[82] The aldehyde group forms imine bonds with the amino groups of chitosan and the reaction can be carried out in aqueous medium, without the need for other molecules to initiate the reaction. One of the disadvantages of the method is the toxicity of glutaraldhyde. Removal of residual glutaraldehyde molecules from the hydrogel cannot be guaranteed during washing, which has limited the use of this cross-linker. Genipin, which is a natural product used in traditional Chinese medicine and extracted from gardenia fruit,

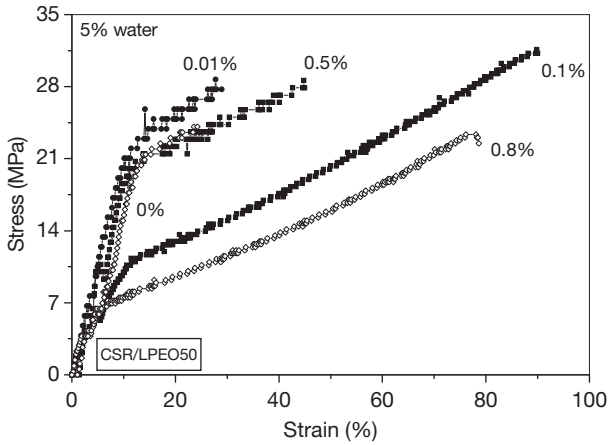

Figure 4 Stress–strain curves of chitosan/poly(ethylene oxide) (PEO) films cross-linked with genipin. The PEO used (LPEO) had a $M_w = 600$. Reproduced from Jin, J.; Song, M.; Hourston, D. J. *Biomacromolecules* **2004**, *5*(1), 162–168, with permission from Elsevier.

has been reported to have no such toxic effects. Cross-linking of chitosan/PEO blends with genipin resulted in more stable and elastic films.[83] Figure 4 shows the stress–strain curves of chitosan/PEO obtained with different concentrations of genipin. 0.1% genipin resulted in films that exhibited a strain to fracture of 90%. Genipin has also been used to stabilize polylectrolyte multilayers of chitosan/hyaluronan and chitosan/alginate.[76] Cell adhesion was markedly influenced by cross-linking. Water-soluble chitosan chlorides (low and high molecular weights) and chitosan glutamates (low and high molecular weights) were cross-linked using various concentrations (5% to 20%) of genipin, to encapsulate cells removed from bovine intervertebral discs.[84] A cell viability of 95% was obtained with the high molecular weight chitosan glutamate cross-linked with 5% genipin.

2.213.3. Biomedical Applications

Because of its well-known biocompability, chitosan is being widely explored for biomedical and pharmaceutical applications. In the following sections the main areas of application and research will be discussed.

2.213.3.1. Wound Management

Chitosan is referenced in the wound management field for its hemostatic properties[85] Furthermore, the biological properties including bacteriostatic and fungistatic[86] properties are particularly useful for wound treatment. It also affects inflammatory cell function that helps in faster wound healing, and has an aptitude to stimulate cell proliferation and histoarchitectural tissue organization.[87]

Chitosan has been explored as a topical hemostatic agent in a variety of forms,[88] reaching the market in recent years. Agents being commercialized include: (1) a dressing, which works by becoming extremely adherent when in contact with blood, sealing the wound and controlling bleeding (HemCon Medical

Technologies, Inc.); (2) high surface area flakes which, when in contact with blood, swell, gel, and stick together to make a gel-like clot (being commercialized by MedTrade Products Ltd.); and (3) a chitosan-coated nonwoven pad used in the management of bleeding wounds (Abbot Vascular, USA). The mechanisms underlying the action of chitosan are not completely understood, but it has been suggested to involve vasoconstriction, and the rapid mobilization of red blood cells, clotting factors and platelets to the site of the injury as a result of the positive charge on the chitosan molecule.[89] This action is reported to occur even in patients on anticoagulants.

Because of its high absorption capacity of fluids, wound-healing properties, adhesiveness, antibacterial activity, and film forming properties, chitosan has been explored for burn and wound dressings.[90] The modification of chitosan properties, either at the structural level or by association with other materials, has been explored[60,61] to potentially improve its biological performance. Despite these efforts, the commercial exploration of a wound dressing material based on chitosan is yet in its infancy.

Although the apparent potential of chitin and chitosan derivatives in the preparation of sutures have long been recognized, there is still no commercial production of chitin-based absorbable suture materials because of insufficient elasticity of chitin threads and certain limitations of their processability into the fiber form.[91,92] Strategies to overcome some of these hurdles have been thoroughly reviewed by Pillai and coworkers.[93]

2.213.3.2. Tissue Repair and Regeneration

Internal medical applications for tissue repair and regeneration include orthopedic implants, such as bone pins and plates, as well as bone fillers, such as cements, adhesives for tissue repair, and scaffolds for tissue engineering. Among the latter, skin, bone, cartilage, and nervous tissues are those where more investigation is taking place, involving the use of chitosan as a scaffolding material or as an extracellular matrix (ECM) analog.[94–96] The popularity of chitosan for tissue repair and regeneration is owing to the fact that it can be readily processed into a variety of forms that include fibers, films, sponges, or hydrogels. This provides the possibility to mimic the shape of target tissue or interfaces. Moreover, the similarity of its chemical structure to some polysaccharide constituents of the ECM and the possibility to chemically modify it to impart desired functionalities add to the great potential of chitosan as a biomaterial for tissue repair and regeneration.

In orthopedics, chitosan has been often used in combination with ceramics, such as hydroxiapatite and other calcium-containing ceramics to produce composites. These have been investigated as bone fillers, and many were found suitable as bone-filling materials.[97,98] The advantage of this approach is to develop bone substitute materials, which combine the biodegradability, strength, and flexibility of chitosan with the osteogenic potential and hardness of the mineral filler. In addition, the chitosan matrix acts as a binder, preventing postoperative migration of the mineral phase.[99] Chitosan has also been explored as an adjuvant additive, to render calcium phosphate cements injectable and to enable their use in minimally invasive surgical procedures.[100] Other bone cements combining chitosan, hydroxiapatite, and poly(methyl methacrylate) were also developed, and reported to provide porous spaces for osteoconduction, after chitosan degradation.[101] Finally, the association of growth factors with chitosan-based bone fillers has also been investigated, as a combinative strategy of controlled local drug delivery and bone regenerative therapy.[49] Besides being used as a filler material, chitosan has also been employed as a coating material, in order to improve titanium and hydroxyapatite implants osteointegration.[102–104] Envisaging to improve the biocompatibility of electrolytically deposited apatite coatings on Ti alloys, Wang *et al.*[105] prepared a hybrid calcium phosphate/chitosan coating. When compared to apatite coatings, this hybrid coating revealed to be more cytocompatible towards bone marrow stromal cells.

There are a wide variety of adhesives available for use in surgery, ranging from cyanoacrylates to fibrin-based mixtures. Chitosan use in the design of new tissue adhesives was motivated by the fact that it can bind to collagen due to hydrogen bonding and polyanionic–polycationic interactions. It is said to overcome some of the limitations of currently available materials. It is not blood-derived, and in light activated applications can be used without significant temperature raise. Lauto and coworkers[106,107] have developed flexible and insoluble strips of chitosan-based adhesives that incorporate indocyanin green dye, for use as a bandage to fix rectangular sections of sheep intestine using a diode laser. The chitosan bandage bonded effectively to tissue without sutures and preserved the ECM structure avoiding irreversible thermal denaturation of imbedded bioactive proteins. A photo-cross-linked chitosan hydrogel showed strong sealing ability when tested in a rabbit animal model of a punctured carotid artery and lung, stopping the bleeding and air leakage, respectively.[108] The sealing ability of the chitosan hydrogel was found to be similar or even stronger than that of fibrin.

Table 1 provides examples of works being developed in the field of tissue engineering using chitosan as a scaffold/matrix material.

Many studies have been reported on the use of chitosan as a scaffold in skin tissue engineering due to its many advantages for wound healing, such as hemostasis, accelerating tissue regeneration, and stimulating the fibroblast synthesis of collagen.[121] The use of chitosan for the preparation of skin substitutes was successfully explored in a blend with bovine collagen types I and III and GAGs, where fibroblast and keratinocytes have been cocultured. The blend-based porous substrate acts as a scaffold for fibroblasts, thereby producing a living dermal equivalent, which once epithelialized results in reconstructed skin.[122] The use of this skin substitute has been proven to lead not only to the reconstruction of surface epithelia for the treatment of pathological conditions of skin, but also as a testing platform for pharmatoxicologic studies, serving as a validated alternative to animal tests.

In articular cartilage tissue engineering, the ideal scaffold should mimic the natural environment in the articular cartilage matrix, which is highly hydrated and rich in ECM components, such as type II collagen and GAGs. These are known to play a key role in the expression of the chondrocytic phenotype and in supporting chondrogenesis *in vitro* as well as *in vivo*. Chitosan has been found particularly interesting for hyaline cartilage tissue engineering, due to its structural similarity with HA, a GAG abundant in the ECM of cartilage.[123] The

Table 1 Current applications of chitosan scaffolds in tissue engineering

Application	*Scaffold*	*DA (%)*	*Scaffold properties*	*Performed biological studies*	*References*
Skin	Asymmetric genepin-cross-linked chitosan membrane containing collagen I nanospheres	15	Asymmetric membrane (porosity 42–58%)	*In vitro* static primary culture of rat skin fibrobasts *In vivo* evaluation of skin regeneration in a rat animal model	109
Cartilage	Chitosan/β-chitin scaffolds	2	Porous (pore size 50–100 μm)	Rabbit chondrocytes (isolated from articular cartilage) culture and ECM production assessment	110
Cartilage	Temperature-responsive chitosan hydrogel (with β-sodium glycerophosphate and hydroxyethyl cellulose)	14	Hydrogel	*In vitro* cultures with adult sheep articular condrocytes *In vivo* implantation in articular cartilage defects in the sheep model	111
Nucleus pulposus of intervertebral discs (IVD)	Chitosan/glycerophosphate gels Chitosan/ glycerophosphate/ hydroxyethyl cellulose gels Chitosan/genipin gels	Chitosan: 5% and 21% Glutamate salt of chitosan: 15%	Hydrogel	*In vitro* primary cultures of peripheral annulus fibrosus and the central nucleus pulposus cells isolated from IVDs from the tails of bovine steers	112
Bone	Chitosan/TCP scaffolds	n.m.	Porous (pore size 100 μm)	Fetal rat calvarial osteoblastic cells proliferation, viability, and differentiation	113
Bone	Chitosan/nonsintered hydroxylapatite particles	12	Bilayered Porous layer (pore size 100–400 μm; porosity 30%)	Cytotoxicity of extracts (fibroblasts) Osteogenic and chondrogenic differentiation studies with mesenchymal stem cell (from human adipose tissue)	114
Bone	Chitosan and PDGF-BB loaded chitosan scaffolds	n.m.	Porous (pore size 100 μm)	Cytotoxicity tests: rat calvarial osteoblastic cells adhesion and proliferation Bone regeneration ability in a rat calvarial defect	66
Bone	Chitosan and chitosan/ chondroitin sulfate scaffolds Chitosan/PLLA scaffolds Chitosan coated PLLA scaffolds (all loaded or not with PDGF-BB)	30	Porous (pore size 100–150 μm) Porous (pore size 150–200 μm) Porous (pore size 100–150 μm)	Rat calvarial osteoblastic cells adhesion and proliferation Bone regeneration ability in a rat calvarial defect	67
Bone	Chitosan/gelatin and chitosan/gelatin/β-TCP macroporous scaffolds	~10	Porous (pore size 322 μm) Porous (pore size 185–420 μm)	Biocompatibility evaluation (subcutaneous implantation in a rabbit model)	115
Bone	Chitosan scaffolds and chitosan scaffolds modified with RGDS or RGES peptides	15	n. m.	Rat osteoblast-like cells (ROS 17/2.8) adhesion, proliferation, and differentiation	45
Nerve	Chitosan conduits containing oriented filaments of polyglycolic acid	7.7	Nonporous chitosan conduit containing oriented filaments of polyglycolic acid	Bridging sciatic nerve across a 30-mm defect in Beagle dogs	116
Nerve	Chitosan	8	Nonporous conduit	Implantation of extramedullary conduits seeded with neural stem and progenitor cells derived from transgenic green fluorescent protein rats after spinal cord transection	117
Ligament	Chitosan-based hyaluronan hybrid polymer fibers	19	Fibers	Rabbit fibroblast adhesion and proliferation; ECM production assessment	118

(*Continued*)

Table 1 (Continued)

Application	*Scaffold*	*DA (%)*	*Scaffold properties*	*Performed biological studies*	*References*
Liver	Galactosylated chitosan electrospun nanofibers	15	Fibers with an average diameter of ~160 nm	Attachment and culture of primary rat hepatocytes on the fibrous scaffolds and chitosan films Hepatocytes function assessment	119
Vascular	Human-like collagen (HLC, produced by recombinant *E. coli*)/chitosan tubular scaffolds	20–25	HLC/chitosan tubular scaffold (pore size $46 \pm 9\,\mu m$; porosity 85%)	*In vitro* human venous fibroblast culture *In vivo* biocompatability assessment in rabbits' livers	120

n. m. – not mentioned.

possibility of using chitosan in the hydrogel form is an added value in such application. In this form it may closely match the natural mechanical properties of hyaline cartilage. Furthermore, its application can be performed by a minimally invasive method. A number of in situ gelling chitosan-based hydrogels are currently under investigation for this purpose.[124,125]

In recent years, considerable attention has been given to the application of chitosan-based materials in the field of orthopedic tissue engineering. Interesting characteristics that render chitosan suitable for this purpose are its biocompatibility/biodegradability, structural similarity to ECM GAGs, intrinsic antibacterial nature, ability to bind anionic molecules such as growth factors, GAGs, and DNA, as well as its ability to be molded into porous structures suitable for cell ingrowth and osteoconduction.[126] In this sense, a wide number of support matrices in the form of injectable gels or porous scaffolds have been developed for bone tissue-engineering applications. Most often, chitosan is used in combination with a variety of materials, such as ceramics, PLLA, gelatin, GAGs, as well as growth factors, in an attempt to improve its mechanical properties, osteoconduction, and ability to induce bone regeneration (see **Table 1**). Binding with cell adhesive motifs has also been explored, in order to promote cell adhesion.

Although chitosan has been used as a scaffold for articular cartilage and bone formation by direct differentiation of mesenchymal cells into chondrocytes and osteoblast, respectively, only recently it has been used as a template for endochondral ossification.[31,127] The endochondral ossification pathway involves an intermediate cartilage stage and is responsible for the formation of long bones, vertebra, and the cranial base during development. Oliveira *et al.* have subcutaneously implanted a transient cartilage scaffold based on chitosan and a permanent cartilage scaffold in nude mice (see **Figure 5**). Only in the former, the deposition of ectopic bone was detected, as early as 1 month after implantation. After 3 months, bone trabeculae and bone marrow cavities were formed inside the scaffolds. The bone deposited was similar to the bone of the mice vertebra. Interestingly, no bone formation was observed in control implants, for the time span of the study.

When the extent of nerve damage prohibits the direct approximation of the two nerve stumps in peripheral nerve repair, autologous nerve grafting is considered the surgical treatment of choice. Artificial nerve guides, where a tube bridges the nerve gap, offer a promising alternative, preventing the sacrifice of a donor nerve and possible neuroma formation at the donor site. Furthermore, the use of synthetic nerve guides reduces operation time and prevents the mismatch between the damaged nerve and the graft. Peripheral nerve correction performed with chitosan-based nerve conduits has been explored with success.[116] Chitosan-based conduits present a number of advantages over other proposed guides, namely, the readiness of tuning their physical properties[38,39] and surface chemistry by changing the DA of chitosan, which in turn influences cell adhesion behavior of the key player cells in the nerve regeneration process.[40] The surface modification of chitosan scaffolds with cell adhesion proteins or motifs, such as the pentapeptides YIGSR and IKVAV, which bind to neural cell membrane receptors, has also been investigated either by physiadsorption[128] or chemical grafting.[129–131] The use of chitosan-based conduits for spinal cord injury treatment is also under study with the first *in vivo* studies showing promising results.[117,132,133] The incorporation into the scaffolds of proteins that can enhance nerve regeneration is being assessed as well.[134] Moreover, the possibility of culturing neural stem cells in these constructs also opens new avenues for addressing nerve lesion treatments.[135]

A transversal problem in the field of tissue engineering has been the vascularization of the tissue-engineered constructs postimplantation. The insufficient supply of oxygen and nutrients to the inner part of the cell–matrix constructs in the initial phases after implantation[136] was found to be contributing to the limited success of many of the proposed tissue regeneration strategies. To overcome this unsolved issue, a number of strategies are being developed to create a vascular network able to deliver oxygen and nutrients throughout an implanted cell–matrix construct. One of the promising approaches has been the precolonization of the scaffolds with vascular cell types, such as ECs or endothelial progenitor cells.[137,138] We have shown that the endothelization of chitosan scaffolds was found to be possible when these were precoated with the ECM protein FN.[46] However, as observed for other cell types, the DA was found to be a key parameter modulating EC adhesion to FN-coated chitosan scaffolds (see **Figure 6**) by influencing the adsorbed protein layer. The selection of suitable DAs will therefore be highly important for the design of new vascularization strategies.

2.213.3.3. Delivery of Therapeutic Agents

The use of chitosan in the pharmaceutical industry spans from its application as an excipient[139] to its application as a vehicle for the controlled delivery of therapeutic agents.

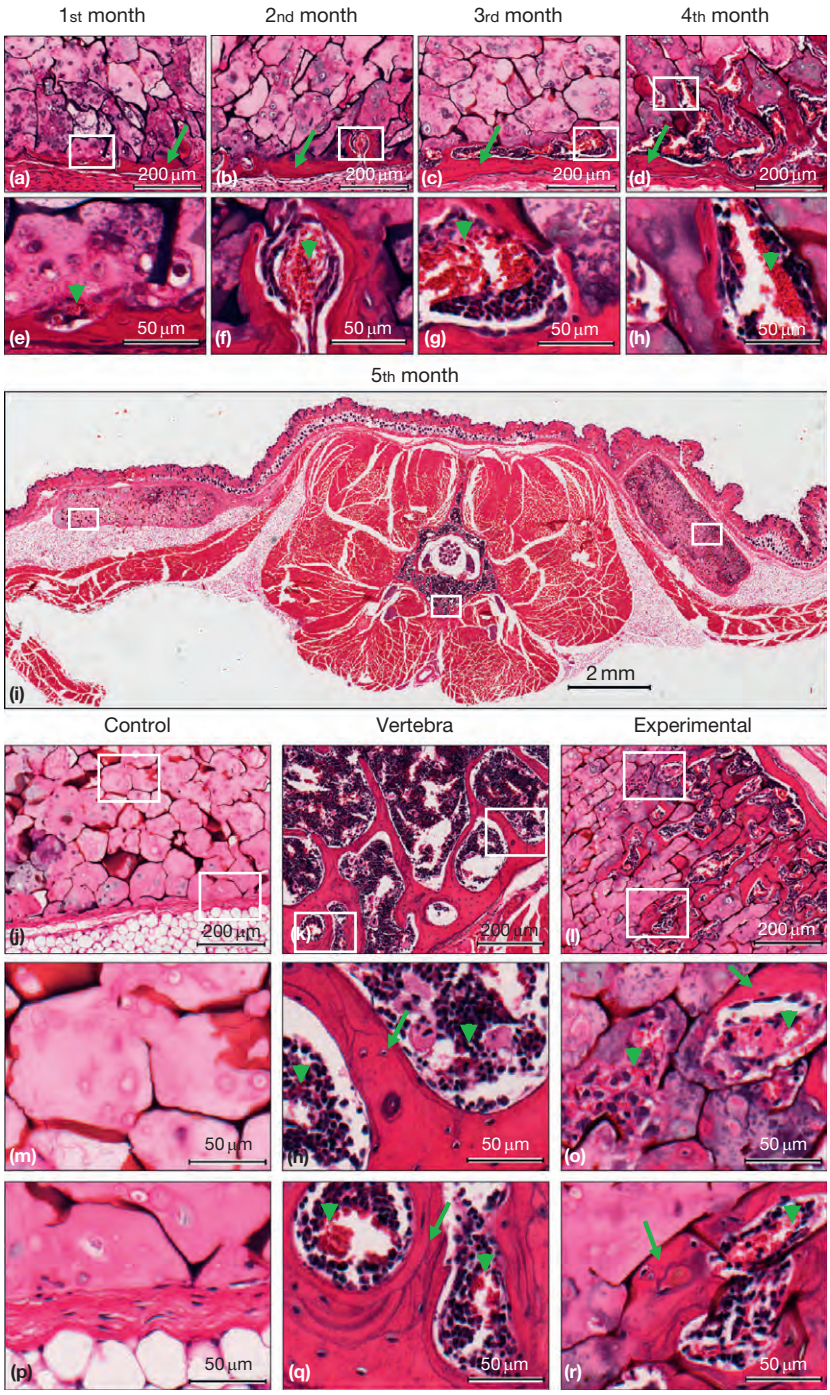

Figure 5 Histological analysis of chondrocyte/chitosan scaffolds implanted in the subcutaneous region of nude mice. Axial paraffin sections were cut through the body of the mouse (I, 5 month time point) to include the experimental and control scaffolds. Sections were stained with H&E and photographed. Details of bone forming in experimental scaffolds during the first 4 months of implantation are shown in images (a) through (d). Images (e), (f), (g), and (h) correspond to high magnifications of (a), (b), (c), and (d), respectively, showing the beginning of vascular invasion (arrow heads). The control scaffolds do not undergo visible changes during the first 5 months of implantation, and therefore only the 5th month is included in this figure. A complete section is shown after 5 months of implantation in image (i). Control scaffold is on the left and experimental is seen on the right side of the image. Details of control scaffold (j), vertebral body (k), and experimental scaffold (l) can be observed. Higher magnifications of control (m, p), mouse vertebra (n, q), and experimental scaffold (o, r) show tissue details. Deep in the control sample (m), only cartilage tissue can be observed. Vascular invasion of cartilage (arrow head in o) and bone deposition (arrow in o) can be observed in the experimental sample. Detail of vertebra (n, q) shows the presence of bone (arrow) and blood vessels (arrow head). Note bone formation deep in the experimental scaffold as well as the presence of blood vessels (r). Adapted from Oliveira, S. M.; Mijares, D. Q.; Turner, G.; Amaral, I. F.; Barbosa, M. A.; Teixeira, C. C. *Tissue Eng.* **2009**, *15*(3): 635–643, with permission from Liebert.

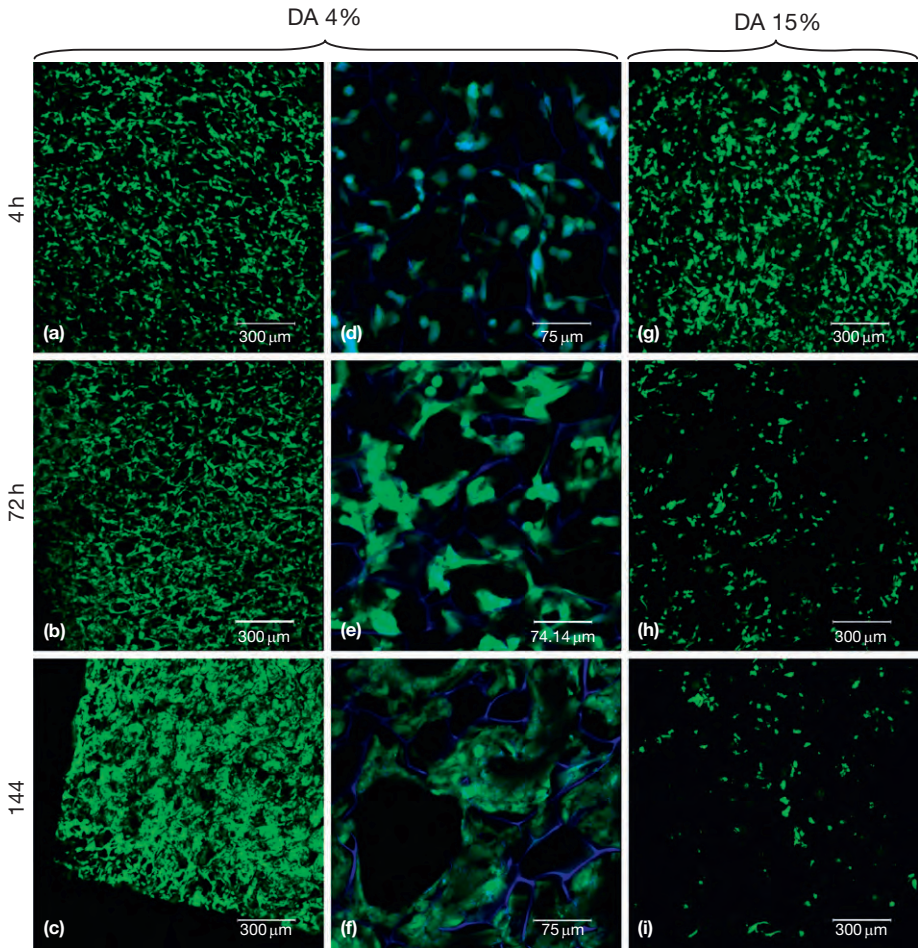

Figure 6 Confocal laser scanning microscopy of human pulmonary microvascular endothelial cells (HPMEC-ST1.6R cell line) grown on chitosan scaffolds previously incubated in a 40 μg ml^{-1} fibronectin solution. Cells were labeled with calcein AM resulting in green fluorescence of viable cells. Images were collected after 4, 72, and 144 h after cell seeding. HPMEC-ST1.6R cells seeded on scaffolds with DA 4% were able to spread and colonize the scaffolds (a) to (f). Cell spreading as well as the cellular layer covering the pore walls after 144 h of cell culture are shown in more detail in the higher magnification images (d) to (f). In these, the 3D scaffold is shown in blue due to chitosan autofluorescence upon excitation by the 405 nm laser. On chitosan scaffolds with DA 15%, very few cells were found after 72 and 144 h of cell culture (h) and (i). Scale bar is 300 μm except for images (d) to (f), for which the same bar corresponds to 75 μm. Adapted from Amaral, I. F.; Unger, R. E.; Fuchs, S. *et al*. *Biomaterials* **2009**, *30*(29), 5465–5475, with permission from Elseiver.

Taking advantage of the fact that positively charged chitosan can bind to negatively charged lipids and bile salt components, interfering with the lipid absorption process in the gut, chitosan has been introduced in the market as a weight and cholesterol control agent. However, the efficacy of its use has been questioned in the field.[140,141] Furthermore, chitosan has been used for the production of controlled release implant systems for delivery of hormones, proteins, and other peptides over extended periods of time.[142–144] The mucoadhesive properties and transmucosal absorption-promoting characteristics of chitosan have been exploited especially for nasal[145,146] and oral delivery[147–151] of polar drugs to include peptides, proteins, and nucleic acids and for vaccine development.[132,133,152] The immune adjuvant behavior of chitosan[153] has also been drawing the attention of the field to its application in vaccine development[154–156] and cancer treatment.[157–159]

Additionally, its cationic nature and high charge density in slightly acidic conditions allow chitosan to form PECs nucleic acids – both DNA and RNA.[94,95,160,161] Although chitosan is able to condense nucleic acids and protect them from nuclease degradation, its main advantage over other nonviral vectors relies on its low cytotoxicty and biodegradability. However, chitosan's poor solubility under physiological conditions and low transfection efficacy has impeded its use as a nucleic acid carrier. To overcome such limitations, a number of strategies for chitosan modification have been proposed by our group and others. These include the increase of chitosan overall positive charge by quaternization,[162] modification of its buffering capacity[163] and functionalization of chitosan with cell-binding molecules for receptor-mediated cell internalization.[164]

2.213.3.4. Other Applications

Other potential applications of chitosan include cosmetics, contact lenses, dialysis membranes, and coatings of the inner lumen of blood-contacting polymeric tubes, onto which an

antithrombotic agent is deposited. Comprehensive reading on these and other applications of chitosan in the biomedical field can be found in Dumitriu.[165]

2.213.4. Future Prospects

Chitosan cationicity and enzymatic degradability associated with structural analogy with ECM glycosaminoglicans (GAGs) contribute together to the increasing interest in its application as a biomaterial. A limitation to its use in clinics is related to the low reproductivity of chitosan physicochemical characteristics among batches as well as the presence of nonexpected contaminants. In this sense, chitosan obtained by biotechnology processes may constitute a better alternative to those presently obtained from marine animal sources. Furthermore, for the development of advanced chitosan-based biomaterials, international standards concerning the range of requirements for chitosan use in medical devices are still missing.

The possibility to covalently and ionically bound proteins and peptides to chitosan, combined with morphologically and mechanically tuned scaffolds for tissue repair/regeneration and targeted delivery of biologically-active entities for cell therapies are fields that remain vastly unexplored. The possibility of producing matrices with various degradation kinetics and inflammatory responses offers ample opportunities to expand the use of chitosan-based materials. In spite of the extensive research that has been carried out with these materials, a lot of clinically useful possibilities have not been tested in depth.

References

1. Rudall, K. M. *J. Polym. Sci. C Polym. Symp.* **1969**, *28PC*, 83.
2. Roberts, G. A. F. *Chitin Chemistry*. Macmillan: London, 1992.
3. Khor, E. *Chitin: Fulfilling a Biomaterials Promise*. Elsevier Science: Oxford, UK, 2001.
4. Roberts, G. A. F. In *Advances in Chitin Science*; Domard, A., Roberts, G. A. F., Varum, K. M., Eds.; Jacques André Publisher: Lyon, 1997; Vol. II, pp 22–31.
5. Roberts, G. A. F. In *Chitin Handbook*; Muzzarelli, R. A. A., Peter, M. G., Eds.; Atec: Grottammare, 1997; pp 127–132.
6. Sorlier, P.; Denuziere, A.; Viton, C.; Domard, A. *Biomacromolecules* **2001**, *2*(3), 765–772.
7. Cauchie, H.-M. In *Advances in Chitin Science*; Domard, A., Roberts, G. A. F., Varum, K. M., Eds.; Jacques André: Lyon, 1997; Vol. II, pp 32–39.
8. Kurita, K. In *Chitin Handbook*; Muzzarelli, R. A. A., Peter, M. G., Eds.; Atec: Grottammare, 1997; pp 491–493.
9. Kurita, K. *Prog. Polym. Sci.* **2001**, *26*(9), 1921–1971.
10. Mima, S.; Miya, M.; Iwamoto, R.; Yoshikawa, S. *J. Appl. Polym. Sci.* **1983**, *28*(6), 1909–1917.
11. Lamarque, G.; Viton, C.; Domard, A. *Biomacromolecules* **2004**, *5*(3), 992–1001.
12. Tchemtchoua, V. T.; Atanasova, G.; *et al*. *Anal. Biochem.* **2009**, *393*(1), 145–147.
13. Struszczyk, H. *J. Appl. Polym. Sci.* **1987**, *33*(1), 177–189.
14. Vachoud, L.; Zydowicz, N.; Domard, A. *Carbohydr. Res.* **1997**, *302*(3–4), 169–177.
15. ASTM International *Standard Guide for Characterization and Testing of Chitosan Salts as Starting Materials Intended for Use in Biomedical and Tissue-Engineered Medical Product Applications*. ASTM F 2103 – 01(2007)e2. ASTM International: West Conshohocken, PA, 2007.
16. Fernandez-Megia, E.; Novoa-Carballal, R.; Quinoa, E.; Riguera, R. *Carbohydr. Polym.* **2005**, *61*(2), 155–161.
17. Hirai, A.; Odani, H.; Nakajima, A. *Polym. Bull.* **1991**, *26*(1), 87–94.
18. Shigemasa, Y.; Matsuura, H.; Sashiwa, H.; Saimoto, H. *Int. J. Biol. Macromol.* **1996**, *18*(3), 237–242.
19. Baxter, A.; Dillon, M.; Taylor, K. D. A.; Roberts, G. A. F. *Int. J. Biol. Macromol.* **1992**, *14*(3), 166–169.
20. Brugnerotto, J.; Lizardi, J.; Goycoolea, F. M.; Arguelles-Monal, W.; Desbrieres, J.; Rinaudo, M. *Polymer* **2001**, *42*(8), 3569–3580.
21. Hudson, S. M.; Smith, C. In *Biopolymers from Renewable Resources*; Kaplan, D. L., Ed.; Springer-Verlag: Berlin, 1998; pp 96–118.
22. Anthonsen, M. W.; Varum, K. M.; Hermansson, A. M.; Smidsrod, O.; Brant, D. A. *Carbohydr. Polym.* **1994**, *25*(1), 13–23.
23. Terbojevich, M.; Cosani, A. In *Chitin Handbook*; Muzzarelli, R. A. A., Peter, M. G., Eds.; Atec: Grottammare, 1997; pp 87–101.
24. Schatz, C.; Viton, C.; Delair, T.; Pichot, C.; Domard, A. *Biomacromolecules* **2003**, *4*(3), 641–648.
25. Rao, S. B.; Sharma, C. P. *J. Biomed. Mater. Res.* **1997**, *34*(1), 21–28.
26. Tomihata, K.; Ikada, Y. *Biomaterials* **1997**, *18*(7), 567–575.
27. VandeVord, P. J.; Matthew, H. W. T.; DeSilva, S. P.; Mayton, L.; Wu, B.; Wooley, P. H. *J. Biomed. Mater. Res.* **2002**, *59*(3), 585–590.
28. Barbosa, J. N.; Amaral, I. F.; Aguas, A. P.; Barbosa, M. A. *J. Biomed. Mater. Res. A* **2010**, *93*(1), 20–28.
29. Chatelet, C.; Damour, O.; Domard, A. *Biomaterials* **2001**, *22*(3), 261–268.
30. Denuziere, A.; Ferrier, D.; Damour, O.; Domard, A. *Biomaterials* **1998**, *19*(14), 1275–1285.
31. Oliveira, S. M.; Amaral, I. F.; Barbosa, M. A.; Teixeira, C. C. *Tissue Eng.* **2009**, *15*(3), 625–634.
32. Amaral, I. F.; Granja, P. L.; Barbosa, M. A. *J. Biomater. Sci. Polym. Ed.* **2005**, *16*(12), 1575–1593.
33. Amaral, I. F.; Lamghari, M.; Sousa, S. R.; Sampaio, P.; Barbosa, M. A. *J. Biomed. Mater. Res.* **2005**, *75A*(2), 387–397.
34. Lahiji, A.; Sohrabi, A.; Hungerford, D. S.; Frondoza, C. G. *J. Biomed. Mater. Res.* **2000**, *51*(4), 586–595.
35. Elcin, Y. M.; Dixit, V.; Gitnick, G. *Artif. Organs* **1998**, *22*(10), 837–846.
36. Yuan, Y.; Zhang, P. Y.; Yang, Y. M.; Wang, X.; Gu, X. S. *Biomaterials* **2004**, *25*(18), 4273–4278.
37. Prasitsilp, M.; Jenwithisuk, R.; Kongsuwan, K.; Damrongchai, N.; Watts, P. *J. Mater. Sci. Mater. Med.* **2000**, *11*(12), 773–778.
38. Freier, T.; Koh, H. S.; Kazazian, K.; Shoichet, M. S. *Biomaterials* **2005**, *26*(29), 5872–5878.
39. Freier, T.; Montenegro, R.; Koh, H. S.; Shoichet, M. S. *Biomaterials* **2005**, *26*(22), 4624–4632.
40. Cao, W. L.; Jing, D. H.; Li, J. M.; Gong, Y. D.; Zhao, N. M.; Zhang, X. F. *J. Biomater. Applic.* **2005**, *20*(2), 157–177.
41. Amaral, I. F.; Cordeiro, A. L.; Sampaio, P.; Barbosa, M. A. *J. Biomater. Sci. Polym. Ed.* **2007**, *18*(4), 469–485.
42. Amaral, I. F.; Sampaio, P.; Barbosa, M. A. *J. Biomed. Mater. Res.* **2006**, *76A*(2), 335–346.
43. Cuy, J. L.; Beckstead, B. L.; Brown, C. D.; Hoffman, A. S.; Giachelli, C. M. *J. Biomed. Mater. Res.* **2003**, *67A*(2), 538–547.
44. Chung, T. W.; Lu, Y. F.; Wang, S. S.; Lin, Y. S.; Chu, S. H. *Biomaterials* **2002**, *23*(24), 4803–4809.
45. Ho, M. H.; Wang, D. M.; *et al*. *Biomaterials* **2005**, *26*(16), 3197–3206.
46. Amaral, I. F.; Unger, R. E.; *et al*. *Biomaterials* **2009**, *30*(29), 5465–5475.
47. Didenko, L. V.; Gerasimenko, D. V.; *et al*. *Bull. Exp. Biol. Med.* **2005**, *140*(3), 356–360.
48. Strand, S. P.; Vandvik, M. S.; Varum, K. M.; Ostgaard, K. *Biomacromolecules* **2001**, *2*(1), 126–133.
49. Muzzarelli, R. A. A. *Cell. Mol. Life Sci.* **1997**, *53*, 131–140.
50. Varum, K. M.; Myhr, M. M.; Hjerde, R. J.; Smidsrod, O. *Carbohydr. Res.* **1997**, *299*(1–2), 99–101.
51. Varum, K. M.; Holme, H. K.; Izume, M.; Stokke, B. T.; Smidsrod, O. *Biochim. Biophys. Acta Gen. Subj.* **1996**, *1291*(1), 5–15.
52. Nordtveit, R. J.; Varum, K. M.; Smidsrod, O. *Carbohydr. Polym.* **1994**, *23*(4), 253–260.
53. Nishimura, K.; Nishimura, S.; Seo, H.; Nishi, N.; Tokura, S.; Azuma, I. *J. Biomed. Mater. Res.* **1986**, *20*(9), 1359–1372.
54. Peluso, G.; Petillo, O.; *et al*. *Biomaterials* **1994**, *15*(15), 1215–1220.
55. Klokkevold, P. R.; Fukayama, H.; Sung, E. C.; Bertolami, C. N. *J. Oral Maxillofac. Surg.* **1999**, *57*(1), 49–52.
56. Benesch, J.; Tengvall, P. *Biomaterials* **2002**, *23*(12), 2561–2568.
57. Hagiwara, K.; Kuribayashi, Y.; *et al*. *Carbohydr. Polym.* **1999**, *39*(3), 245–248.
58. Henriksen, I.; Green, K. L.; Smart, J. D.; Smistad, G.; Karlsen, J. *Int. J. Pharm.* **1996**, *145*(1–2), 231–240.
59. Muzzarelli, R.; Baldassarre, V.; *et al*. *Biomaterials* **1988**, *9*(3), 247–252.
60. Ueno, H.; Mori, T.; Fujinaga, T. *Adv. Drug Deliv. Rev.* **2001**, *52*(2), 105–115.

61. Ueno, H.; Nakamura, F.; Murakami, M.; Okumura, M.; Kadosawa, T.; Fujinaga, T. *Biomaterials* **2001**, *22*(15), 2125–2130.
62. Howling, G. I.; Dettmar, P. W.; Goddard, P. A.; Hampson, F. C.; Dornish, M.; Wood, E. J. *Biomaterials* **2001**, *22*(22), 2959–2966.
63. Borah, G.; Scott, B.; Wortham, K. In *Advances in Chitin and Chitosan*; Brine, C. J., Sandford, P. A., Zikakis, J. P., Eds.; Elsevier: Amsterdam, 1992; pp 206–215.
64. Muzzarelli, R. A. A.; Mattiolibelmonte, M.; *et al*. *Biomaterials* **1994**, *15*(13), 1075–1081.
65. Muzzarelli, R. A. A.; Zucchini, C.; *et al*. *Biomaterials* **1993**, *14*(12), 925–929.
66. Park, Y. J.; Lee, Y. M.; Park, S. N.; Sheen, S. Y.; Chung, C. P.; Lee, S. J. *Biomaterials* **2000**, *21*(2), 153–159.
67. Lee, J. Y.; Nam, S. H.; *et al*. *J. Control. Release* **2002**, *78*(1–3), 187–197.
68. Hidaka, Y.; Ito, M.; Mori, K.; Yagasaki, H.; Kafrawy, A. H. *J. Biomed. Mater. Res.* **1999**, *46*(3), 418–423.
69. Ho, M. H.; Kuo, P. Y.; *et al*. *Biomaterials* **2004**, *25*(1), 129–138.
70. Hsieh, C. Y.; Hsieh, H. J.; Liu, H. C.; Wang, D. M.; Hou, L. T. *Dent. Mater.* **2006**, *22*(7), 622–629.
71. Baker, B. M.; Gee, A. O.; *et al*. *Biomaterials* **2008**, *29*(15), 2348–2358.
72. Thorvaldsson, A.; Stenhamre, H.; Gatenholm, P.; Walkenstrom, P. *Biomacromolecules* **2008**, *9*(3), 1044–1049.
73. Sakai, S.; Ono, T.; Ijima, H.; Kawakami, K. *J. Microencapsul.* **2000**, *17*(6), 691–699.
74. Picart, C.; Schneider, A.; *et al*. *Adv. Funct. Mater.* **2005**, *15*(11), 1771–1780.
75. Manna, U.; Bharani, S.; Patil, S. *Biomacromolecules* **2009**, *10*(9), 2632–2639.
76. Hillberg, A. L.; Holmes, C. A.; Tabrizian, M. *Biomaterials* **2009**, *30*(27), 4463–4470.
77. Calvo, P.; RemunanLopez, C.; VilaJato, J. L.; Alonso, M. J. *J. Appl. Polym. Sci.* **1997**, *63*(1), 125–132.
78. Berthold, A.; Cremer, K.; Kreuter, J. *J. Control. Release* **1996**, *39*(1), 17–25.
79. Huang, M.; Khor, E.; Lim, L. Y. *Pharm. Res.* **2004**, *21*(2), 344–353.
80. Mao, H. Q.; Roy, K.; *et al*. *J. Control. Release* **2001**, *70*(3), 399–421.
81. Xu, X.; Capito, R. M.; Spector, M. *J. Biomed. Mater. Res. A* **2008**, *84*(4), 1038–1048.
82. Schiffman, J. D.; Schauer, C. L. *Biomacromolecules* **2007**, *8*(2), 594–601.
83. Jin, J.; Song, M.; Hourston, D. J. *Biomacromolecules* **2004**, *5*(1), 162–168.
84. Mwale, F.; Iordanova, M.; Demers, C. N.; Steffen, T.; Roughley, P.; Antoniou, J. *Tissue Eng.* **2005**, *11*(1–2), 130–140.
85. Paul, W.; Sharma, C. P. *Trends Biomater. Artif. Organs* **2004**, *18*(1), 18–23.
86. Rinaudo, M. *Polym. Int.* **2008**, *57*(3), 397–430.
87. Park, C. J.; Gabrielson, N. P.; Pack, D. W.; Jamison, R. D.; Johnson, A. J. W. *Biomaterials* **2009**, *30*(4), 436–444.
88. Seyednejad, H.; Imani, M.; Jamieson, T.; Seifalian, A. M. *Br. J. Surg.* **2008**, *95* (10), 1197–1225.
89. Neuffer, M. C.; McDivitt, J.; Rose, D.; King, K.; Cloonan, C. C.; Vayer, J. S. *Mil. Med.* **2004**, *169*(9), 716–720.
90. Mi, F. L.; Shyu, S. S.; Wu, Y. B.; Lee, S. T.; Shyong, J. Y.; Huang, R. N. *Biomaterials* **2001**, *22*(2), 165–173.
91. Mikhailov, G. M.; Lebedeva, M. F. *Russ. J. Appl. Chem.* **2007**, *80*(5), 685–694.
92. Nakajima, M.; Atsumi, K.; Kifune, K.; Miura, K.; Kanamaru, H. *Jpn. J. Surg.* **1986**, *16*(6), 418–424.
93. Pillai, C. K. S.; Paul, W.; Sharma, C. P. *Prog. Polym. Sci.* **2009**, *34*(7), 641–678.
94. Dang, J. M.; Leong, K. W. *Adv. Drug Deliv. Rev.* **2006**, *58*(4), 487–499.
95. Kim, I. Y.; Seo, S. J.; *et al*. *Biotechnol. Adv.* **2008**, *26*(1), 1–21.
96. Muzzarelli, R. A. A. *Carbohydr. Polym.* **2009**, *76*(2), 167–182.
97. Cho, B. C.; Park, J. W.; Baik, B. S.; Kwon, I. C.; Kim, I. S. *J. Craniofac. Surg.* **2002**, *13*(6), 783–793.
98. Kawakami, T.; Antoh, M.; Hasegawa, H.; Yamagishi, T.; Ito, M.; Eda, S. *Biomaterials* **1992**, *13*(11), 759–763.
99. Khor, E.; Lim, L. Y. *Biomaterials* **2003**, *24*(13), 2339–2349.
100. Leroux, L.; Hatim, Z.; Freche, M.; Lacout, J. L. *Bone* **1999**, *25*(2), 31S–34S.
101. Kim, S. B.; Kim, Y. J.; *et al*. *Biomaterials* **2004**, *25*(26), 5715–5723.
102. Bumgardner, J. D.; Wiser, R.; Elder, S. H.; Jouett, R.; Yang, Y.; Ong, J. L. *J. Biomater. Sci. Polym. Ed.* **2003**, *14*(12), 1401–1409.
103. Bumgardner, J. D.; Wiser, R.; *et al*. *J. Biomater. Sci. Polym. Ed.* **2003**, *14*(5), 423–438.
104. Mattiolibelmonte, M.; Biagini, G.; *et al*. *J. Bioact. Compat. Polym.* **1995**, *10*(3), 249–257.
105. Wang, J.; de Boer, J.; de Groot, K. *J. Dent. Res.* **2004**, *83*(4), 296–301.
106. Lauto, A. *Lasers Surg. Med.* **2009**, *41*(5), 366–371.
107. Lauto, A.; Stoodley, M.; *et al*. *Lasers Surg. Med.* **2007**, *39*(1), 19–27.
108. Ishihara, M.; Ono, K.; *et al*. *New Dev. Glycomed.* **2001**, *1223*, 251–257.
109. Chen, K. Y.; Liao, W. J.; *et al*. *Biomacromolecules* **2009**, *10*(6), 1642–1649.
110. Suzuki, D.; Takahashi, M.; *et al*. *J. Mater. Sci. Mater. Med.* **2008**, *19*(3), 1307–1315.
111. Hao, T.; Wen, N.; Cao, J. K.; *et al*. *Osteoarthr. Cartil.* **2010**, *18*(2), 257–265.
112. Roughley, P.; Hoemann, C.; DesRosiers, E.; Mwale, F.; Antoniou, J.; Alini, M. *Biomaterials* **2006**, *27*(3), 388–396.
113. Lee, Y. M.; Park, Y. J. *J. Periodontol.* **2000**, *71*(3), 410–417.
114. Malafaya, P. B.; Pedro, A. J.; Peterbauer, A.; Gabriel, C.; Redl, H.; Reis, R. L. *J. Mater. Sci. Mater. Med.* **2005**, *16*(12), 1077–1085.
115. Yin, Y. J.; Ye, F.; Cui, J. F.; Zhang, F. J.; Li, X. L.; Yao, K. D. *J. Biomed. Mater. Res. A* **2003**, *67A*(3), 844–855.
116. Wang, X.; Hu, W.; Cao, Y.; Yao, J.; Wu, J.; Gu, X. *Brain* **2005**, *128*(Pt 8), 1897–1910.
117. Nomura, H.; Zahir, T.; *et al*. *Tissue Eng. A* **2008**, *14*(5), 649–665.
118. Funakoshi, T.; Majima, T.; *et al*. *J. Biomed. Mater. Res.* **2005**, *74A*(3), 338–346.
119. Feng, Z. Q.; Chu, X. H.; *et al*. *Biomaterials* **2009**, *30*(14), 2753–2763.
120. Zhu, C.; Fan, D.; *et al*. *J. Biomed. Mater. Res. A* **2009**, *89*(3), 829–840.
121. Muzzarelli, R. A.; Mattioli-Belmonte, M.; Pugnaloni, A.; Biagini, G. *Exs* **1999**, *87*, 251–264.
122. Auxenfans, C.; Builles, N.; *et al*. *Pathol. Biol.* **2009**, *57*(4), 290–298.
123. Suh, J. K. F.; Matthew, H. W. T. *Biomaterials* **2000**, *21*(24), 2589–2598.
124. Jin, R.; Moreira Teixeira, L. S.; *et al*. *Biomaterials* **2009**, *30*(13), 2544–2551.
125. Tan, H.; Chu, C. R.; Payne, K. A.; Marra, K. G. *Biomaterials* **2009**, *30*(13), 2499–2506.
126. Di Martino, A.; Sittinger, M.; Risbud, M. V. *Biomaterials* **2005**, *26*(30), 5983–5990.
127. Oliveira, S. M.; Mijares, D. Q.; Turner, G.; Amaral, I. F.; Barbosa, M. A.; Teixeira, C. C. *Tissue Eng.* **2009**, *15*(3), 635–643.
128. Itoh, S.; Yamaguchi, I.; *et al*. *Brain Res.* **2003**, *993*(1–2), 111–123.
129. Kato, K.; Utani, A.; *et al*. *Biochemistry* **2002**, *41*(35), 10747–10753.
130. Matsuda, A.; Kobayashi, H.; Itoh, S.; Kataoka, K.; Tanaka, J. *Biomaterials* **2005**, *26*(15), 2273–2279.
131. Wang, W.; Itoh, S.; *et al*. *J. Biomed. Mater. Res. A* **2008**, *85A*(4), 919–928.
132. Li, G. P.; Liu, Z. G.; Liao, B.; Zhong, N. S. *Cell Mol. Immunol.* **2009**, *6*(1), 45–50.
133. Li, X.; Yang, Z.; Zhang, A.; Wang, T.; Chen, W. *Biomaterials* **2009**, *30*(6), 1121–1132.
134. Chavez-Delgado, M. E.; Mora-Galindo, J.; *et al*. *J. Biomed. Mater. Res. B Appl. Biomater.* **2003**, *67B*(2), 702–711.
135. Wang, A.; Ao, Q.; *et al*. *Tsinghua Sci. Technol.* **2006**, *11*(4), 415–420.
136. Moon, J. J.; West, J. L. *Curr. Top. Med. Chem.* **2008**, *8*(4), 300–310.
137. Fuchs, S.; Motta, A.; Migliaresi, C.; Kirkpatrick, C. J. *Biomaterials* **2006**, *27*(31), 5399–5408.
138. Unger, R. E.; Peters, K.; Wolf, M.; Motta, A.; Migliaresi, C.; Kirkpatrick, C. J. *Biomaterials* **2004**, *25*(21), 5137–5146.
139. Illum, L. *Pharm. Res.* **1998**, *15*(9), 1326–1331.
140. Mhurchu, C. N.; Dunshea-Mooij, C.; Bennett, D.; Rodgers, A. *Obes. Rev.* **2005**, *6* (1), 35–42.
141. Pittler, M. H.; Ernst, E. *Am. J. Clin. Nutr.* **2004**, *79*(4), 529–536.
142. Janes, K. A.; Calvo, P.; Alonso, M. J. *Adv. Drug Deliv. Rev.* **2001**, *47*(1), 83–97.
143. Liu, Z. H.; Jiao, Y. P.; Wang, Y. F.; Zhou, C. R.; Zhang, Z. Y. *Adv. Drug Deliv. Rev.* **2008**, *60*(15), 1650–1662.
144. Prabaharan, M.; Mano, J. F. *Drug Deliv.* **2005**, *12*(1), 41–57.
145. Goycoolea, F. M.; Lollo, G.; Remunan-Lopez, C.; Quaglia, F.; Alonso, M. J. *Biomacromolecules* **2009**, *10*(7), 1736–1743.
146. Teijeiro-Osorio, D.; Remunan-Lopez, C.; Alonso, M. J. *Biomacromolecules* **2009**, *10*(2), 243–249.
147. Hejazi, R.; Amiji, M. *Int. J. Pharm.* **2002**, *235*(1–2), 87–94.
148. Hejazi, R.; Amiji, M. *J. Control. Release* **2003**, *89*(2), 151–165.
149. Hejazi, R.; Amiji, M. *Pharm. Dev. Technol.* **2003**, *8*(3), 253–262.
150. Hejazi, R.; Amiji, M. *Int. J. Pharm.* **2004**, *272*(1–2), 99–108.
151. Thanou, M.; Verhoef, J. C.; Junginger, H. E. *Adv. Drug Deliv. Rev.* **2001**, *50*, S91–S101.
152. Vila, A.; Sanchez, A.; *et al*. *Eur. J. Pharm. Biopharm.* **2004**, *57*(1), 123–131.
153. Nishimura, K.; Nishimura, S.; *et al*. *Vaccine* **1985**, *3*(5), 379–384.
154. Westerink, M. A. J.; Smithson, S. L.; *et al*. *Vaccine* **2001**, *20*(5–6), 711–723.
155. Yang, Y.; Chen, J.; *et al*. *Comp. Immunol. Microbiol. Infect. Dis.* **2007**, *30*(1), 19–32.
156. Zaharoff, D. A.; Rogers, C. J.; Hance, K. W.; Schlom, J.; Greiner, J. W. *Vaccine* **2007**, *25*(11), 2085–2094.
157. Chen, W. R.; Adams, R. L.; Carubelli, R.; Nordquist, R. E. *Cancer Lett.* **1997**, *115* (1), 25–30.
158. Chen, W. R.; Korbelik, M.; Bartels, K. E.; Liu, H.; Sun, J.; Nordquist, R. E. *Photochem. Photobiol.* **2005**, *81*(1), 190–195.

159. Seo, S. H.; Han, H. D.; Noh, K. H.; Kim, T. W.; Son, S. W. *Clin. Exp. Metastasis* **2009**, *26*(3), 179–187.
160. Borchard, G. *Adv. Drug Deliv. Rev.* **2001**, *52*(2), 145–150.
161. Lai, W. F.; Lin, M. C. *J. Control. Release* **2009**, *134*(3), 158–168.
162. Kean, T.; Roth, S.; Thanou, M. *J. Control. Release* **2005**, *103*(3), 643–653.
163. Moreira, C.; Oliveira, H.; Pires, L. R.; Simões, S.; Barbosa, M. A.; Pêgo, A. P. *Acta Biomater.* **2009**, *5*(8), 2995–3006.
164. Murata, J.-i.; Ohya, Y.; Ouchi, T. *Carbohydr. Polym.* **1996**, *29*(1), 69–74.
165. Dumitriu, S. *Polysaccharides in Medical Applications*. Marcel Dekker: New York, 1996.

Relevant Websites

http://www.euchis.org/ – European Chitin Society.
http://www.glycoforum.gr.jp/ – Glycoforum.

2.214. Hyaluronic Acid

J-W Kuo, HA Research, Wakefield, MA, USA
G D Prestwich, The University of Utah, Salt Lake City, UT, USA

© 2011 Elsevier Ltd. All rights reserved.

2.214.1. Introduction 240
2.214.1.1. Biological Origin and Primary Structure of Hyaluronic Acid 240
2.214.1.2. HA Structure of Higher Orders 241
2.214.1.3. Biophysical Function of HA 242
2.214.1.4. Influence of HA on Cell Behavior 242
2.214.2. Production of HA 242
2.214.2.1. Isolation of HA from Cock Combs 242
2.214.2.2. Bacterial Fermentation with Streptococci 243
2.214.2.3. Bacterial Fermentation with Recombinant *Bacillus subtilis* 243
2.214.2.4. Chemoenzymatic Synthesis 243
2.214.3. Analysis and Industry Standards 244
2.214.3.1. Qualitative Analysis 244
2.214.3.2. Quantitative Analysis 244
2.214.3.3. Absolute Viscosity 244
2.214.3.4. Pseudoplasticity 245
2.214.3.5. IV and Molecular Weight 245
2.214.3.6. Elasticity 245
2.214.3.7. Purity and Biocompatibility 246
2.214.4. Chemical Modification of HA 246
2.214.4.1. Rationale for HA Derivatization 246
2.214.4.2. Monolithic HA Derivatives 246
2.214.4.2.1. Carbodiimide-mediated reaction products 246
2.214.4.2.2. Divinylsulfone cross-linking 247
2.214.4.2.3. Esterification 247
2.214.4.2.4. Bis-epoxide cross-linked HA and epoxide-modified HA 247
2.214.4.2.5. Ionic cross-linking and polyelectrolyte complexes 248
2.214.4.2.6. Monolithic photocrosslinked hydrogels 248
2.214.4.3. Living HA Derivatives 248
2.214.4.3.1. Thiol-modified HA 248
2.214.4.3.2. Haloacetate-modified HA 249
2.214.4.3.3. Methacrylated HA 249
2.214.4.3.4. Tyramine-modified HA 249
2.214.4.3.5. Alkynylated and azidoalkylated HA 249
2.214.5. Medical Applications of HA 249
2.214.5.1. Ophthalmic Surgeries 249
2.214.5.1.1. Viscosity and lubricity 250
2.214.5.1.2. Thickness of coating and easiness of the removal of HA 250
2.214.5.1.3. Cohesiveness and dispersiveness 250
2.214.5.2. Injections for Osteoarthritic Joints 251
2.214.5.2.1. Effectiveness of HA injected in the knee 251
2.214.5.2.2. Clinical performance of native and chemically cross-linked HA 251
2.214.5.2.3. Mechanism of action for exogenous HA in the knee 251
2.214.5.3. Cosmetic Tissue Augmentation 252
2.214.5.3.1. Residence time 252
2.214.5.3.2. Elasticity 252
2.214.5.3.3. Safety and reversibility 252
2.214.5.4. Acute and Chronic Wound Healing 252
2.214.5.4.1. Acute cutaneous wounds 252
2.214.5.4.2. Acute surgical wounds 253
2.214.5.4.3. Chronic wounds 254
2.214.5.5. Selected Uses in Tissue Engineering and 3D Cell Culture 255
2.214.5.5.1. 3D cell culture 255
2.214.5.5.2. Cartilage and bone repair models 255

2.214.6.	**Future Perspectives and Conclusions**	256
2.214.6.1.	The Future of HA Science	256
2.214.6.2.	Concluding Remarks	257
References		257

Abbreviations

ACP	Autocrosslinked polymer
ACT	Autologous chondrocyte transplantation
AO	Aminooxy
AOP	Aminooxy-pluronic
BCDIs	Biscarbodiimides
bFGF	Basic fibroblast growth factor
CD	Circular dichroism
CMC	Carboxymethyl cellulose
CMHA-S	Thiol-modified HA
CMPI	2-Chloro-l-methylpyridinium iodide
cP	Centipose
CPC	Cetylpyridinium chloride
CS	Chondroitin sulfate
CS-ADH	Adipic hydrazide-modified CS
cSt	Centi-Stoke
DBM	Demineralized bone matrix
DEO	Diepoxyoctane
DMAB	Dimethylaminobenzaldehyde
DTPH	3,3′-Dithiolpropionyl bishydrazide
DVS	Divinyl sulfone
DXNs	Double-cross-linked networks
EDC, EDCI	*N*-ethyl, *N*, *N*-dimethylaminopropylcarbodiimide
EP	European Pharmacopoeia
FDA	Food and Drug Administration
GAGs	Glycosaminoglycans
GMA	Glycidylether methacrylate
Gtn-DTPH	Thiol-modified gelatin
HA	Hyaluronic acid
HA-ADH	Adipic hydrazide-modified HA
HABA	HA bromoacetate
HAIA	HA iodoacetate
HARE	HA receptor for endocytosis
***has*A**	Hyaluronan synthase gene A
HP-DTPH	Thiolated heparin
HP-DTPH	Thiol-modified heparin
HPLC	High-performance liquid chromatography
i.a.	Intraarticularly
i.v.	Intravenously
ID	Chemical identification
IOP	Intraocular pressure
IR	Infrared spectroscopy
ISHAS	International Society for Hyaluronan Research
IV	Intrinsic viscosity
KGF	Keratinocyte growth factor
LMW	Low molecular weight
MBI	Matrix Biology Institute
MDa	Megadaltons
MSC	Mesenchymal stem cell
MW	Molecular weight
NaHA	Sodium hyaluronate
NHS	*N*-hydroxysuccinimide
OA	Osteoarthritis
ORD	Optical rotary dispersion
OVD	Ophthalmic viscoelastic devices
PEG	Poly(ethylene glycol)
PEGDA	Poly(ethylene glycol) diacrylate
PEO	Polyethylene oxide
PEO-PPO-PEO	Polyethylene oxide–polypropropylene oxide–polyethylene oxide
pmHAS	*Pasteurella multocida* HA synthase
RGD	Arg-Gly-Asp
RHAMM	Receptor for HA-mediated motility
SD	Standard deviation
sECM	Synthetic extracellular matrix
SEM	Scanning electron microscope
STMP	Trisodium trimetaphosphate
TMJ	Temporal mandibular joint
TPP	Sodium tripolyphosphate
VEGF	Vascular endothelial growth factor

2.214.1. Introduction

2.214.1.1. Biological Origin and Primary Structure of Hyaluronic Acid

In 1934, Meyer and Palmer[1] reported a mucoid-like substance isolated from the bovine vitreous humor under acidic conditions, and it was identified as an acid polysaccharide containing uronic acid and amino sugar but no sulfate. This newly discovered naturally occurring polysaccharide was named hyaluronic acid (HA) after its biological origin, vitreous (hyaloid), and its major structural component, uronic acid. In the following years, HA was successfully isolated from other biological sources such as synovial fluid, skin, umbilical cord, cock's comb, and a bacterial source (streptococci).[2]

HA can be found extracellularly in most human tissues. Skin, lung, and intestine contain more than 50% of the HA in the body. Synovial fluid, skin, umbilical cord, and vitreous body of the eye are rich in HA content.[3] Under physiological conditions, virtually all HA molecules exist in the form of their salts – hyaluronate, such as sodium hyaluronate (NaHA). The generic term, hyaluronan, was introduced, to embrace the free acid and salts of HA, regardless of the degree of dissociation, or identity of the counterion (e.g., sodium, potassium, calcium). The acronym HA now stands for hyaluronic acid, hyaluronate, or hyaluronan, depending on the context in which it is mentioned.[4,5]

Historically, hyaluronidases played a critical role in establishing the structure of the repeating disaccharide units of HA.

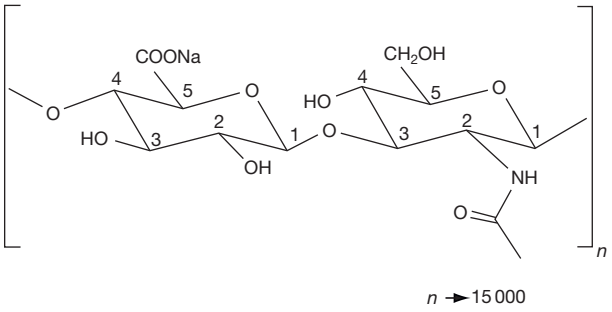

Figure 1 Structure of hyaluronic acid (HA). HA is a linear polysaccharide, with repeating disaccharide units of glucuronic acid–β-1,3-*N*-acetyl glucosamine linked by β-1,4-glycosidic bonds.

The actions of enzymes are specific, and the fragments created as products of hyaluronidase treatment retain the basic structural features. Both testicular and bacterial hyaluronidases hydrolyze only the *N*-acetylglucosaminidic bonds of HA from all sources. The degradation products of HA for both enzymes consistently demonstrated an equimolar ratio of glucuronic acid and *N*-acetylglucosamine. This strongly suggested a linear structure for HA with alternating arrangement of the two sugar units.[6–8]

Based on the study of the detailed structures of the disaccharide building blocks, scientists were able to draw conclusions that polymeric chain of HA is composed of repeat disaccharide units of glucuronic acid and *N*-acetylglucosamine. The linkage from glucuronic acid and *N*-acetylglucosamine is (1→3) and the linkage from *N*-acetylglucosamine to glucuronic acid is (1→4). HA has a wide range of molecular weight, up to several million Daltons (MDa) (**Figure 1**).

2.214.1.2. HA Structure of Higher Orders

The secondary structure of HA is mainly concerned with the spatial relationship of the neighboring functional groups.[9] An exhaustive review of the molecular structure studies of HA describes the history and complexities of this field of study in great detail.[10] Only the basic points will be summarized herein. The molecular structure of HA in **Figure 1** is represented by Haworth conformational formula, which allows visualization of the β-D-anomeric configuration of the C-1 atoms of glucuronic acid and *N*-acetylglucosamine units, as well as visualize the shape of the puckered ring conformations of the monosaccharide units such as the $^4C_1$ conformation of the β-D-glucopyranose.[11] This notation of $^4C_1$ defines a ring conformation with C-4 above the plane described by the oxygen atom and C-2, -3, and -5 carbon atoms; and with C-1 below the plane. The $^4C_1$ conformation of β-D-glucopyranose is favored, because it is more stable than the $^1C_4$ conformation. In the $^4C_1$ conformation, all substituents on the ring are equatorial; in the $^1C_4$ conformation, all substituents on the ring would be axial.[12]

The spatial relations of HA atoms and subunits have great impact on the rigidity of the polysaccharide chain. The degree of rigidity is largely determined by the restriction on the rotation of the glycosidic bonds by the geometry of sugar rings and, as in the case of HA, by the relatively bulky *N*-acetyl group adjacent to the glycosidic bond.

The tertiary structure of HA often refers to its chain conformation, which is partially helical. Such a tertiary structure of HA is possible because of certain characteristics of its primary and secondary structures. The repeating disaccharide building blocks in HA chains provide regularity in sequence and spacing of functional groups. The quaternary structure of a polysaccharide basically involves the aggregation of chains by noncovalent interactions.[11] For example, HA has been reported to form an antiparallel double helix and a honeycomb network at low concentrations of 0.5–1.0 mg ml^{-1}. The honeycomb-like structure of HA in aqueous solution was observed under rotary shadowing electron microscope.[13]

The evidence of ordered structures of HA in solutions first came from the studies of its optical properties using polarized light, providing data indicative of the presence of an ordered conformational structure. These optical properties include optical rotation, circular dichroism (CD),[14] and optical rotary dispersion (ORD).[15,16]

What are the microscopic aspects in solutions that actually cause an extended structure of HA molecules and their aggregation under certain conditions? The classic theory emphasizes the contribution of intramolecular hydrogen bonding, citing evidence from NMR studies that demonstrate the existence of the hydrogen bonding between the functional groups such as C=O, NH, and OH.[17,18] The hydrogen atoms directly involved in hydrogen bonding may show an increased value of chemical shift because of increased electron deficiency caused by such interactions. Furthermore, the NMR studies in aqueous solutions (deuterium oxide) also found that the spectrum of HA sharpens considerably under alkaline conditions. This suggested an enhanced segmental motion as a result of the breaking of hydrogen bonding under alkaline conditions.[18] It was also recognized that the possible hydrogen bonding could represent a fleeting association among the related atoms, that is, 'that the bonding may break and reform in a state of dynamic equilibrium.'[9] Another aspect of the classic theory is related to hydrophobic interaction. By examining the secondary structure of HA using space-filling molecular models, a 'hydrophobic patch' of eight C–H bonds was noticed that stretched across three sugar units. This putative hydrophobic region has been described as a driving force for the formation of the double helix mentioned above.[13,19]

More recently, molecular simulation studies have forced a reevaluation of the classical view. In the newer view, contribution of intrastrand hydrogen bonding is quite limited: 'if an intra-molecular hydrogen bond is present, it cannot exist for more than 5–15% of the time.'[20] It was, therefore, proposed that HA was 'a molecule that has an average local order in its 3D-structure, but with substantial dynamic flexing around this average structure.' The dynamic flexing can even be envisioned in an animation of a few nanoseconds movement of the HA hexa-saccharide model.[20] The dynamic nature appears to explain why even at very high concentrations HA cannot form the so called 'cuttable gels.' As to the driving force of an ordered HA structure in solution, theory supports the notion that this is more likely to be an entropy-driven phenomenon. The maximum entropy for HA plus water, as it so happens, is 'often observed to be consistent with the presence of intramolecular hydrogen bonds.'[21]

2.214.1.3. Biophysical Function of HA

As a major component of the extracellular matrix, biophysically HA serves as a packing material that fills organ space (vitreous, skin), as a biomechanical cushion that absorbs shock (cartilage), and as a lubricant between moving tissues (e.g., joints). Those functions of HA are based on the extraordinary ability of HA to retain water in the extracellular matrix.

The water retention property of HA is often described in terms of intrinsic viscosity (IV), which is a measure of hydrodynamic volume. IV is defined as the volume of water held by unit weight of the material of interest. HA has a very large hydrodynamic volume, which is made possible by the unique structural characteristics of HA and its very high molecular weight as mentioned above. For example, HA with a molecular weight of ~2 MDa has an IV of ~3000 ml g^{-1}.

2.214.1.4. Influence of HA on Cell Behavior

HA plays an important role in the regulation of cell behavior as well. A pattern of strong correlation between HA and the cell cycle has been demonstrated. Cells *in vivo* usually proliferate within an HA-rich extracellular matrix, and HA synthase activity usually peaks during mitosis and declines at confluence.[22,23]

The mechanism of action of HA on cell behavior can be twofold. On the one hand, it can be nonspecific, which is based on its space occupying capability. For cell migration, the presence of HA can create 'hydrated pathways separating cellular or fibrous barriers to penetration by migrating cells.'[22,23] For cell differentiation and morphogenesis, the condensation of mesenchymal cells occurs only after the removal of most of the intercellular HA and along with it the highly hydrated intercellular spaces.

On the other hand, there are specific interactions between HA and cells receptors. The HA receptor for endocytosis (HARE) is found in the liver and is the primary route of clearance of HA from the circulatory system. Blocking HARE with a specific antibody inhibits HA clearance in a perfused liver system.[24] The binding of HA to RHAMM (receptor for hyaluronan-mediated motility) can trigger signal transduction, which directs cell trafficking.[25] CD44, the principal HA receptor, is responsible for the internalization of HA during the development of bone, lung, and hair follicles.[22,23]

In addition to its function in the removal of HA, the cell receptor CD44 and its binding to HA play an intriguing role in maintaining the homeostasis of the cells. Under a relatively quiescent homeostatic state, cells divide only as much to compensate for normal cellular turnover. However, the receptor-mediated effects on cell behavior are molecular weight and viscosity dependent. Under inflammatory conditions, for example, in an arthritic synovium, this homeostasis is disrupted. Reactive oxygen species, particularly free radicals, degrade HA and reduce its molecular weight and viscosity. The binding of the lower viscosity HA with CD44 then sends out mitogenic signals to the mesenchymal cells, which then start the healing process. In this way, HA and CD44 complex regulates the cell behavior by acting as a biological rheostat, which would be a more sensitive and responsive regulatory mechanism than a simple on–off switch.[26]

2.214.2. Production of HA

To exploit the unique properties of HA, significant effort has been devoted to the development of medical products with HA as the major ingredient.[9] Four types of HA-based products are formally commercialized in the United States: (1) a surgical aid and tissue protective agent in ophthalmic surgery, (2) an injectable preparation to alleviate pain of knee osteoarthritis (OA), (3) a barrier in solid or solution form to prevent postsurgical adhesions, and (4) an injectable gel for cosmetic tissue augmentation. In addition, there are a growing number of new applications of HA derivatives and HA composites under development, including the use of HA and its derivatives for drug delivery and as clinical biomaterials. These compositions and uses will be addressed below in Sections 2.214.4 and 2.214.5.

HA can be used either in its native form or in its chemically modified form. In either case, the key step of manufacturing is the production of HA with high purity and a specific molecular weight range. There are three main methods for HA production: isolation from animal tissues, bacterial fermentation (homologous and heterologous), and chemoenzymatic synthesis.

2.214.2.1. Isolation of HA from Cock Combs

In 1949, Boas[27] first identified HA from rooster combs. It was known to stain with certain basic dyes, and therefore was believed to contain mucopolysaccharides. The rich content of HA contributes to the thick layer of connective tissue and the large size of the combs. The isolation and purification procedure can be summarized in the following steps: grinding freshly harvested combs, soaking comb material in acetone to remove fat, extracting HA using sodium acetate solution, adding ethanol to precipitate HA, adding chloroform, and shaking the mixture to remove protein. The final purified dried HA was white and fibrous, with a yield of ~0.1% weight of the combs processed.

Sevag[28] used ~20% chloroform to separate protein content from the carbohydrate content of the egg white. Blix and Snellman[29] adopted Sevag's method with some modifications, including increasing chloroform to 50% of the HA aqueous solution volume. Balazs increased the volume of chloroform to at least equal to the HA aqueous solution during the deproteinizing process.[30] Gently agitating this larger volume of chloroform with the HA solution denatured and separated proteins from HA, while preserving the high molecular weight of HA.

In the method of HA extraction and purification described by Swann,[31] pronase was used to remove protein and cetyl pyridinium chloride (CPC), a quaternary ammonium salt with a long lipophilic chain, was used to isolate the HA. CPC forms a complex with acidic polysaccharides, such as HA, as first described by Scott.[32] The HA-CPC complex precipitates in aqueous media and HA can be recovered in salt solution. In Swann's HA efficient purification method, chloroform was used mainly as a bacteriostatic agent. The amino acid content of the purified fraction of HA was only 0.35% (w/w). A reduction in HA viscosity, however, was observed along with the reduction of protein content.[33] The purified HA still maintained a molecular weight of 1.2 MDa.

2.214.2.2. Bacterial Fermentation with Streptococci

A number of bacterial strains are available to produce HA in good yield such as group A and C streptococci. The presence of HA is a common trait in streptococci,[34] which release cell wall components when grown in complex media. Pathogenic streptococci synthesize HA as the major capsular polysaccharide that serves to evade host defenses. Group A *Streptococcus pyogenes* is a human pathogen,[35] while the group C *Streptococcus* species *S. equi*, *S. equisimilis*, and *S. zooepidemicus* are animal pathogens.[36] Clearly, it makes sense to produce HA for use in human use from strains not related to human disease, and group C streptococci have become the most commonly used strain for HA production.

HA production by fermentation was first reported in 1937 by Kendall *et al.*[35] using group A streptococci. The polysaccharide appeared to be identical with that occurring in bovine vitreous humor. The method by Bracke and Thacker[37] produced HA from streptococcus by fermenting under anaerobic conditions. Glucose was used as the carbon source. Trichloroacetic acid was added to kill the bacteria after fermentation to facilitate the separation of the microorganisms from the HA. The HA prepared as described has an average molecular weight of about 55 000 Da within a range of 10 000 Da to 2 MDa.

Swann *et al.*[38] described an aerobic fermentation process with *S. zooepidemicus*, in which relatively high oxygen concentrations are made available during the initial exponential growth phase of the cultivated microorganism, until a predetermined growth has been reached. This improved overall yields of HA and the highest molecular weight of HA made by this process was slightly above 2.5 MDa. Later, Ellwood *et al.*[39] developed a continuous fermentation method using *S. equi* in a chemostat culture. This gave high yields of high MW HA uncontaminated by toxic impurities. The HA produced by this process had an average MW of 1–3 million.

Expression of the HA-degrading enzyme hyaluronidase and other extracellular protein is a drawback of wild-type streptococci. The application of chemical mutagenesis followed by a serial selection scheme has been exploited to obtain nonhemolytic and hyaluronidase negative mutants[40] and strains producing high MW HA.[36,41]

Nimrod *et al.*[42,43] treated *S. zooepidemicus* with a suitable mutagen, for example, nitrosoguanidine. The mutant derived did not have hemolytic activity and enhanced the HA yield. The method applies vigorous agitation and aeration to the medium. It was claimed to be the first fermentation method of producing HA with high molecular weight that exceeds 3.5 MDa.

Stahl[36,44] has claimed that by selecting supercapsulated mutants of strains of group A and C streptococci, particularly *S. equi* mutants (group C), HA with a molecular weight exceeding 6 MDa can be produced. The process avoided extensive turbulence and agitation and used the type of impeller able to achieve good mixing without generating excessive shear forces that could potentially degrad HA molecules.

2.214.2.3. Bacterial Fermentation with Recombinant *Bacillus subtilis*

In 1993, DeAngelis *et al.*[45] made a breakthrough in the molecular cloning and characterization of the streptococcal gene encoding the protein HasA, known to be in an operon required for bacterial HA synthesis.[46] The *hasA* gene was later used in the fermentation of HA by hosts from a different species (heterologous) such as *Bacillus subtilis*, as a useful alternative to the fermentation by streptococci.[47] *B. subtilis* offers a number of advantages (1) it is free of exotoxins and endotoxins, and therefore many products produced in this organism have been awarded a GRAS (generally recognized as safe) designation, (2) it does not produce hyaluronidase, (3) it is one of the best characterized Gram-positive microorganisms, and (4) its genome has been sequenced.[47,48]

The molecular weight of HA derived from *B. subtilis*-derived measured in the range of 1.1–1.2 MDa, with a polydispersity index of 1.5 (expressed as the ratio of weight/average molecular mass/number/average molecular mass, or M_w/M_n), comparable to what has been reported for commercially available sources.[49]

2.214.2.4. Chemoenzymatic Synthesis

Chemoenzymatic synthesis, a method where chemistry meets biology, combines the utilization of synthetic chemical tools and recombinant natural product enzymes. The chemoenzymatic synthesis of HA was developed by Jing and DeAngelis,[50] which involves an *in vitro* enzymatic reaction using the recombinant HA synthase pmHAS from Gram-negative *Pasteurella* species.

There are two classes of HA synthases. Gram-positive streptococcal, vertebrate, and viral HAS belong to Class I. In contrast, the class II enzyme has its only member, the Gram-negative *Pasteurella*[51] that contains a membrane bound, carboxy-terminal region. Deletion of this c-terminal region results in a soluble, cytoplasmic form of the enzyme.[52] Only the recombinant pmHAS, not streptococcal or vertebrate enzymes, has shown the ability to perform *in vitro* reactions to elongate HA-oligosaccharide acceptors exogenously supplied.

HA synthase pmHAS uses two separate glycosyltransferase sites to add GlcNAc and GlcUA monosaccharides to the nascent HA chain. Technologically, the reaction can be improved by the addition of HA oligosaccharide along with the UDP–sugar substrates, that is, UDP-GlcNAc and UDP-GlcA. The advantages of such methodologies are threefold. First, the rate of reaction can be accelerated 100-fold by the presence of HA oligosaccharide acceptor, which appears to be the result of bypassing the slow initiation stage and effecting the fast elongation from the very start of the reaction. Second, the molecular size of the HA polymer products can be controlled by the size of the added HA oligosaccharide acceptors. The larger the size of the HA oligosaccharides, the fewer reaction sites available, and the longer the final HA polymers become. Third, a narrow distribution of molecular weight of HA polymer product can be achieved by controlling the initial size of added HA acceptors and synchronizing the rapid elongation reactions. The chemoenzymatic method can produce HA polymers with MW of up to 2 MDa and very narrow size distributions with polydispersity value between 1.02 and 1.06.[53]

The dual-action HAS – glycosyltransferases rapidly adds two different sugars, GlcUA and GlcNAc. This would likely

result in long chain HA polymers, and are therefore unsuitable for production of short, defined oligosaccharides. To solve this problem, *Pasteurella multocida* HA synthase (pmHAS) was converted by mutation of one active site aspartate residue, affording two single-action glycosyltransferases (glucuronic acid transferase and *N*-acetylglucosamine transferase). A lesion in one active site leaves the activity of the other unmutated active site relatively unaffected.

When the two resulting transferases, a β-3GlcNAc-transferase and a β-4GlcUA-transferase, are purified and immobilized individually onto solid supports, the enzyme reactors used in an alternating fashion can produce an extremely pure, single-length HA oligosaccharide up to HA20, without purification of the intermediates.[54]

2.214.3. Analysis and Industry Standards

Numerous methods have been developed or adopted to analyze HA both qualitatively and quantitatively.[9] This chapter focuses on those most widely used in the tests of HA products for medical use in humans, especially those related to the chemical properties, rheological properties, and biocompatibility included in a variety of industry standards. Examples of those standards are the monograph of HA in European Pharmacopoeia (EP)[55] and two ISO (International Standards Organization) standards, ISO 15798 (Ophthalmic Implants – Ophthalmic Viscosurgical Devices, OVD[56]) and ISO 10993 (Biocompatibility).

2.214.3.1. Qualitative Analysis

Chemical identification (ID) is performed by infrared spectroscopy (IR) and Na tests as stipulated by EP. In IR analysis the partial assignments of absorptions are as follows: carboxylic acid 1736 cm^{-1} (main) and 1230 cm^{-1} (minor); carboxylate 1610 cm^{-1} (main) and 1410 cm^{-1} (minor); monosubstituted amide 1648, 1560, and 1315 cm^{-1}; and associated methyl group 1375 cm^{-1} (sharp). The IR method has evolved from conventional IR[57] to FTIR (Fourier transform IR),[58,59] from solid film samples[57,58] to HA aqueous solution.[59]

The carbazole assay, a classic, colorimetric assay, is often used as part of the HA identification.[60] The chromogenic reaction of the assay has two steps. The dehydration of hexuronic acid of HA with concentrated sulfuric acid forms a furfural derivative intermediate which reacts with carbazole to yield a distinct red color as an indication of the existence of a class of carbohydrates – uronic acid. Therefore, it is a semiqualitative test method.

Another classic colorimetric assay for HA is the Morgan and Elson[61] assay that measures *N*-acetyl hexosamine which is present at the reducing end of HA. Further studies of the assay by Kuhn and Krüger[62] and Beau *et al.*[63] have concluded that the chromogen generated when HA is treated under mild alkali conditions (Morgan–Elson reaction) was also a furan-type of compound which reacts with Ehrlich reagent DMAB (dimethylaminobenzaldehyde) to form a red color.

The applicability of the above identification tests is predicated on the high purity of the HA samples. Since HA routinely goes through lengthy isolation and purification processes, this level of purity is achieved. Impurities that could interfere with the ID tests of HA, for example, protein, are kept to a minimum (<0.3% of dry weight in EP). When the samples of HA contain significant amount of non-HA impurities, further purification would be necessary prior to ID analysis. If there is uncertainty regarding the nature of the material, additional analytical means such as the use of NMR may be necessary to verify its structure, as mentioned above.

2.214.3.2. Quantitative Analysis

The carbazole assay can also be used as a quantitative method to determine the concentration of HA. This is based on the improvement of carbazole assay by Bitter and Muir[64] using borate that enhances the red color formation and stability and decreases the sensitivity to salts. It also showed a better correlation between uronic acid and hexosamine contents. A solution containing 1 g ml^{-1} of uronic acid can show a positive color reaction. The absorbance at 530 nm is a linear function of concentration between 4 and 40 g ml^{-1}.

Another commonly used assay for HA concentration is the Reissig assay[65] which is a modified form of the Morgan–Elson assay. The Reissig method replaced the sodium carbonate with a concentrated borate buffer, improving the reproducibility of the assay even in the presence of protein or magnesium ions. The maximum absorbance of the red color produced is 520 and 550 nm.[66]

Alternatively, direct measurement of the UV absorbance as quantitative assay for HA concentration constitutes a simple, viable method that can replace or complement carbazole assay, as long as the HA sample is sufficiently pure. In practice, this method of detection is commonly used during high-performance liquid chromatography (HPLC) using an in-line UV detector.

2.214.3.3. Absolute Viscosity

Determination of the rheological properties of HA solutions assumes the utmost importance in the characterization of most HA-based products. At relatively high concentration where intermolecular action of HA becomes significant, its viscosity reflects its bulk properties, which affords HA its broad spectrum of medical uses that include lubrication, space filling, and tissue coating.

The viscosity of a fluid by definition is its resistance to flow. In one protocol, an HA solution is placed between the surfaces of two concentric cylinders of a viscometer. As one cylinder rotates, the ratio of the force per unit area (dyn cm^{-2}) to the velocity gradient (cm s^{-1} over cm = s^{-1}) gives the units of dynamic viscosity, which are expressed as poise (dyn s^{-1} cm^{-2}). Dynamic viscosity can also be expressed as Pascal-second (Pa s). One milli Pascal-second (mPa s) is equal to one centipose (cP). The viscosity of water is ~1 mPa s. A solution with a viscosity of 10 000 mPa s appears viscous, and a viscosity above 100 000 mPa s is characteristic of a gel.[67]

Both dynamic viscosity and kinematic viscosity belong to the category of absolute viscosity. Kinematic viscosity is defined as the quotient of the dynamic viscosity and the density. The numbers of the dynamic viscosity and kinematic viscosity of HA are practically the same as the density of HA solutions in low concentration is virtually one. The unit of kinematic viscosity is Stokes (cm^2 s^{-1}), and is often expressed

as centi-Stoke (cSt). Kinematic viscosity is one of those tests of HA required by ISO-OVD.

2.214.3.4. Pseudoplasticity

Velocity gradient is often referred to as shear rate. For many fluids such as water and mineral oil, viscosity is independent of the shear rate applied. These fluids are called Newtonian fluids. An aqueous solution of HA, however, is non-Newtonian; that is, the viscosity of an HA changes as the shear rate changes. Specifically, as the shear rate increases, the viscosity of an HA solution decreases. This phenomenon is called 'shear-thinning,' or pseudoplasticity (Figure 2).

To properly define the viscosity of HA, one should always cite the shear rate at which the viscosity is measured. A full scan of viscosities within a range of shear rates as show in Figure 2 is more informative of the rheological profile of HA products than a single-point viscosity measurement. For most practical purposes, however, a single low shear rate such as $1\,s^{-1}$ (1 Hz) is often used in comparing the viscosity of HA-based viscoelastic products.[68]

The pseudoplasticity of HA is customarily quantified as the quotient of the viscosity at rest over the viscosity at a shear rate of $100\,s^{-1}$. Note that pseudoplasticity merely reflects the relative effect of the shear force on the viscosity of a material. Pseudoplasticity by itself does not determine the absolute value of viscosity, and a higher pseudoplasticity does not necessarily mean a lower viscosity at the same shear rate. Taking the Healon family of OVD as an example,[69] Healon5 had a zero shear viscosity of 5525 Pa s, with a pseudoplasticity number of 591. This means that at shear rate of 100 Hz, the viscosity of Healon5 should be 9.36 Pa s (5525/591). Likewise, Healon has a viscosity of 243 Pa s at rest, and a pseudoplasticity number of 173, and therefore a viscosity of 1.40 Pa s (243/173) at a shear rate of 100 Hz. Even with a much higher pseudoplasticity, Healon5 is still more viscous than Healon at a shear rate of 100 Hz.

2.214.3.5. IV and Molecular Weight

While dynamic viscosity and kinematic viscosity are considered the physical property of a bulk material in its absolute physical sense, IV reveals many interesting chemical characteristics of the molecules in an isolated state. Measured at much diluted concentrations (normally <0.1%, w/v), IV leads to information related to the molecular weight of HA. IV $[\eta]$ is usually measured by a capillary viscometer, and a series of dilution of the polymer are allowed to pass through the capillary under gravity.

The ratio t/t_0, the efflux time t of the solution over the efflux time t_0 of the solvent, is defined as relative viscosity η_r. Specific viscosity is defined as $\eta_{sp} = \eta_r - 1$. Reduced viscosity η_{red} is η_{sp}/C, in which C is the concentration ($g\,ml^{-1}$). The extrapolation of reduced viscosity to zero concentration gives IV $[\eta]$. The unit of IV is ($ml\,g^{-1}$), the measure of the hydrodynamic volume of polymers (Figure 3).

Staudinger, winner of 1953 Nobel Prize in Chemistry, first proposed that the reduced viscosity of a polymer (η_{red}) is directly proportional to its molecular weight, hence the equation of $\eta_{red} = KM$. Later, Mark *et al.* modified this hypothesis by raising the molecular weight M to a power, and established the following equation $[\eta] = KM^{\alpha}$, where $[\eta]$ is IV and M is molecular weight.[70]

The exponent α and the factor K can be obtained by plotting the molecular weights (by light scattering analysis) and IV data of a certain polymer. Once α and K are established, the molecular weight of a polymer can be calculated by plugging in the measured IV number into Mark's equation.

For high molecular weight HA, the exponent α has been found around 0.8. The exponent α is a parameter that indicates the rigidity of polymer. The larger the exponent α, the more rigid the molecule is. Moreover, the rigidity (extendedness) contributes exponentially to the viscosity (dynamic volume, molecular size) of the molecule.

2.214.3.6. Elasticity

Elasticity goes hand in hand in hand with viscosity with all HA products, that is why HA is often called a viscoelastic fluid. For the use of HA or HA derivatives as dermal fillers (see Section 2.214.5.3), elasticity is especially important, because it is related to the essential feature of a cosmetic dermal filler – the firmness (hardness) of the gel, measured as the elastic modulus G'.

Consider the situation when a gel is placed between two plates. When the upper plate quickly moves horizontally a

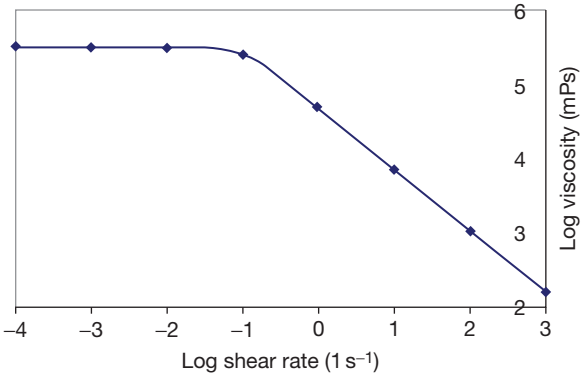

Figure 2 Shear thinning of hyaluronic acid (HA). HA exhibits pseudoplastic behavior, or shear thinning. As shear increases, viscosity decreases.

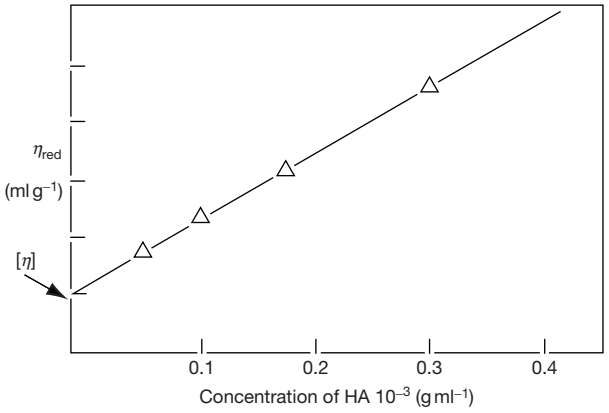

Figure 3 Intrinsic viscosity $[\eta]$ of hyaluronic acid (HA). The intrinsic viscosity of HA is measured by extrapolating reduced viscosity to zero concentration.

small distance, elastic gel tends to resist the change of form. G' is the elastic modulus, defined as the ratio of the shear stress to the shear strain. The unit of G' is (Pa).[71,72]

2.214.3.7. Purity and Biocompatibility

In addition to the qualitative and quantitative analysis mentioned above, for HA-based medical products the tests for purity and biocompatibility are essential for product characterization. HA is by nature compatible with human tissues, the potential toxicity usually come from the impurities. Protein, nucleic acid are routinely tested and their limits set for various applications.

Biocontamination is strictly controlled and closely monitored. During the product development stage, a battery of biocompatibility tests as stipulated by ISO 10993 is normally required by regulatory agencies in EU countries and the United States to establish the safety profile of the products. Examples of those tests are the guinea pig maximization method[73] for a sensitization study, the Ames mutagenicity assay,[74] the chromosomal aberration assay,[75] and the sister chromatid exchange assay[75] for genotoxicity (mutagenicity). For routine tests, sterility and endotoxin level are usually required. The endotoxin limits may vary, and for ophthalmic use ISO-OVD has set the limit at ≤ 0.5 EU ml^{-1}. This very low limit is justified by the highly sensitive nature of the eye tissues supported by the clinical data from the application of OVD.[76]

2.214.4. Chemical Modification of HA

2.214.4.1. Rationale for HA Derivatization

Native HA has several shortcomings for implementation in regenerative medicine, for applications that go beyond viscoelastic supplementation, and providing a moisturizing environment. These limitations include its relatively short residence time *in vivo*, its poor mechanical strength, the inability of most cells to attach to HA, and the inability to form stable structures. A vast array of chemical modifications of HA[77,78] have been developed to make materials more suited for regenerative and reparative medicine.[79] Many of these biomaterials have involved chemical cross-linking. Furthermore, chemical modification techniques have allowed the modification of the surfaces of implantable devices and biomaterials with HA.[80] In this section, we summarize the two main categories of HA modifications and list the principal modification employed. In the following section, we illustrate the use of HA and modified HA in human and veterinary medicine. The practical aspects of these HA-based medical products are the summary of a recent monograph.[9]

We recently categorized chemically modified HA derivatives into two major categories.[81] In *monolithic* derivatives, the modification results in a final form that cannot form new chemical bonds in the presence of cells or tissues, and can only be manipulated by fabrication into different physical forms. *In situ* cross-linking *in vivo* is not possible due to the harsh chemical conditions. However, in *living* derivatives, the modification permits the formation of new covalent bonds *in vivo* or *ex vivo*, enabling a change in physical form – from solution to hydrogel – during cell encapsulation or injection in a clinical procedure. This section presents the basic features of monolithic and living HA technologies and products, but earlier reviews should be consulted for details of using these materials for drug delivery,[82,83] for wound repair, and tissue engineering,[77,84] or for the production of clinically useful extracellular matrices.[85,86] The focus of this section is to highlight results since 2000 that are relevant to the preparation of monolithic and living HA derivatives.

2.214.4.2. Monolithic HA Derivatives

2.214.4.2.1. Carbodiimide-mediated reaction products

2.214.4.2.1.1. N-acylureas

The carboxylic acid moeities of the glucuronic acid units in HA readily react with water-soluble carbodiimides such as N-ethyl, N,N-dimethylaminopropylcarbodiimide (EDCI) to form an intermediate *O*-acylurea that can rearrange to produce the more stable *N*-acylurea adducts.[87,88] The interaction of the cationic acylurea moiety of the EDCI-modified HA and the remaining anionic carboxyl group forms an internal polyelectrolyte complex in the form of a water-insoluble gel. Seprafilm, a reaction product of EDCI with HA and carboxymethyl cellulose (CMC), is a bioabsorbable material used to prevent surgical adhesions that is an example of this type of modification. In addition, biscarbodiimides (BCDIs) can chemically cross-link HA to make bis-*N*-acylurea derivatives of HA which form stable hydrogels.[87]

2.214.4.2.1.2. Carbodiimide-mediated hydrazide chemistry

The reactive *O*-acylurea can undergo further reaction with nucleophiles. Because high molecular weight HA is viscous and diffusion in HA solutions is slow, reactions with amines are unpredictable, and often unproductive. [87] This problem is largely overcome by trapping the intermediate *O*-acylurea with *N*-hydroxysuccinimide, followed by subsequent reaction with the desired amine nucelophile.[89] Yet more efficient and versatile is the use of hydrazide chemistry. Hydrazides are effective nucleophiles at pH 4–6 because of the lower pK_a values (usually 2–4) rather than the higher values for simple amines (p$K_a \sim 12$).[90] The use of bishydrazide or polyvalent hydrazides can make cross-linked HA gels with a wide range of physicochemical properties, from being soft, pourable to more rigid and brittle, by varying reaction conditions and the molar ratios of the reagents.[91,92] Using multivalent hydrazides or hydrazides containing disulfide linkages, as discussed below, affords highly versatile living HA derivatives. One of these living thiolated HA derivatives, HA-DTPH(3,3′-dithiolpropionyl bishydrazide), has also been converted into a monolithic nanofibrous network by dual-syringe reactive electrospinning using polyethylene glycol dialdehyde as the cross-linker.[93] The cross-linking occurs rapidly during electrospinning, and polyethylene oxide (PEO) was present (and later dissolved out) to facilitate fiber formation. Fibroblasts migrated into HA nanomesh scaffolds coated with fibronectin.

The hydrazide chemistry has been adopted to make alkyl-modified HA. Thus, condensation of the adipic dihydrazide adduct of HA, HA-ADH, with aldehydes from octanal to hexadecanal afforded water-soluble but amphiphilic HA derivatives.[94] These alkylated HA-ADH derivatives self-assembled to form hydrophobic domains, affording viscous solutions that exhibited shear-thinning behavior. Compounds of this nature

have promise for viscosupplementation in medicine as discussed in more detail below.

HA-ADH has also been cross-linked into microgels with partially oxidized HA-dialdehyde. These microgels were further set into double-cross-linked networks (DXNs) to obtain an advanced biomaterial with properties desirable for restoring the viscoelastic properties of damaged vocal folds.[95] These HA-based DXNs were biocompatible and had elastic moduli similar to those of human vocal fold lamina propria. A second use of the partially oxidized HA dialdehyde involved forming a covalent network by condensation with gelatin in the presence of a pH 9.4 borax solution, giving, after removal of byproducts, a biocompatible hydrogel suitable for subsequent cell culture.[96]

2.214.4.2.1.3. Carbodiimide-mediated aminooxy chemistry

The reactive *O*-acylurea can also react with aminooxy compounds, which also retain their nucleophilicity at pH 4.75 used during carbodiimide coupling. Recently, aminooxy derivatives of the triblock polyethylene oxide–polypropylene oxide–polyethylene oxide (PEO–PPO–PEO) copolymers known as Pluronics were synthesized and coupled to HA carboxylates using EDCI.[97] Pluronics were prepared with a single AO group or with homobifunctional bis-AO groups. The bis-AOP-HA derivatives formed gels will all three Pluronics, regardless of the length of the hydrophobic segment, consistent with inter- and intramolecular gelation by both covalent cross-linking and noncovalent association of the hydrophobic PPO segments. The mono-AOP-HA also formed gels, but in this case the gelation was the result of hydrophobic–hydrophobic interactions driving self-assembly of the mono-AOP-HA derivatives.

2.214.4.2.2. Divinylsulfone cross-linking

Hylans[98] are chemically cross-linked through the hydroxyl groups of HA, leaving the carboxyl groups unchanged. Hylan A links the HA hydroxyl groups with residual protein by using formaldehyde, and the reaction product retains many of the bulk properties of linear HA, but with increased molecular weight. Hylan B is produced by the reaction of divinylsulfone with HA hydroxyl groups under alkaline conditions. This cross-linked HA network forms a highly swollen gel. The cross-linking and increased elasticity of Hylan B extend its half-life in the knee from 12 h for HA to 9 days for Hylan B. These properties make the Hylan A and B useful as injectable materials for OA, as dermal fillers, and as space-filling dressing in sinus surgery.

2.214.4.2.3. Esterification

2.214.4.2.3.1. Hydrophobic esters

A family of HA ester derivatives has been prepared by the reaction of a quaternary ammonium salt of HA and an alcohol in a polar aprotic solvent. These materials, known as HYAFFs, have increased hydrophobicity of esterified HA resulting from both masking the carboxyl as well as introduction of the hydrophobic side chains.[99] The HYAFFs can still absorb water as a function of degree of esterification. For example, the 100% benzyl ester (HYAFF 11) and 100% ethyl ester (HYAFF 7) hydrated in water at 37 °C by 48% and 259%, respectively; the 75% benzyl ester (HYAFF 11p75) was hydrated by 1250%. HYAFFs are only slowly degraded by hyaluronidases. Scaffolds made of the monolithic HYAFF 11 are cell adhesive and are sufficiently stable in aqueous solution to allow incubation with cells for over 3 weeks. A variety of cell types, including keratinocytes, fibroblasts, chondrocytes, and mesenchymal stem cells, can proliferate on the surface of a nonwoven HYAFF mesh. The monolithic HYAFF also has the potential as a drug delivery vehicle as described below.

2.214.4.2.3.2. Autocrosslinked HA

The HA carboxyl groups can be activated to form inter- and intrastrand esters with HA hydroxyl groups. An effective activating agent is 2-chloro-1-methylpyridinium iodide (CMPI).[100,101] autocrosslinked polymer (ACP) is the brand name of cross-linked HA products of Fidia based on such autocrosslinking technology. ACP gels have been used in preclinical studies for adhesion prevention.

2.214.4.2.3.3. Melt-processable esters

The cetyltrimethylammonium salts of HA containing different levels of silylation of the hydroxyl groups was reacted with acid chlorides to give are series of melt-processable HA esters.[102] Thermoplastic materials were obtained with multiple esters in which the alkyl chains were greater than ten atoms, with longer chains producing materials with lower melting points. These materials have medical applications in hot molding with thermoplastic ultra high molecular weight polyethylene for total joint replacements.

2.214.4.2.3.4. Physically and chemically cross-linked HA esters

The loose physically associated hydrogels arising from HA partially esterified with dodecyl chains were further cross-linked by a second partial esterification using tetraethylene glycol ditosylate.[103] Even at low levels of modification, the physically and chemically dual cross-linked gels would shear thin and showed potential utility for cartilage repair.

2.214.4.2.4. Bis-epoxide cross-linked HA and epoxide-modified HA

Under alkaline conditions, HA can be cross-linked by bisepoxides such as butane 1,4-diol diglycidyl ether or 1,2,7,8-diepoxyoctane (DEO).[78] Such hydrogels can be brittle, and may require reformulation with native HA as a carrier injection as cosmetic dermal fillers and in arthritic knees. Under acidic conditions, the reaction product of diepoxides with the carboxyl group of HA is an ester.[104] HA can be cross-linked twice with the same diepoxide, first under basic conditions and then under acidic conditions. Double cross-linking decreased the water absorbing capacity of the HA derivative and increased its resistance to hyaluronidase degradation when compared to the single cross-linked intermediate.[105]

Another type of bis-epoxide cross-linking was recently performed using polyethylene glycol bisepoxide.[106] Reaction with HA alone or HA plus collagen gave degradable HA hydrogels that were degradable by hyaluronidase and collagenase and had potential utility for tissue engineering.

The reactivity of HA with monoepoxides has been exploited to produce alkylated HA derivatives. Reaction of the primary 6-hydroxy group of the *N*-acetylglucosamine residue with glycidyl ethers (butyl, hexyl, octyl, decyl, and tetradecyl) under basic conditions afforded biocompatible amphiphilic derivatives.[107]

2.214.4.2.5. Ionic cross-linking and polyelectrolyte complexes

Several ionically gelled forms of HA have been produced. First, Intergel is a viscous formulation of HA formed by chelation with ferric chloride.[108] This reddish gel was approved for reduction of postsurgical adhesions in gynecological surgery, but was withdrawn from the market in 2003.

Second, HA can also be used to prepare multilayered polyelectrolyte films, such as the poly(L-lysine) (PLL)-HA films formed by an exponential growth regime.[109] Using fluorescently tagged polymers, it was found that PLL diffused throughout the film after each new PLL injection. As the PLL reached the outer layer of the film, it interacted with the incoming HA, forming the new HA-PLL layer, the thickness of which was proportional to the amount of PLL that diffused out of the film during the buildup step.

Third, HA has been combined with chitosan and ionically cross-linked with sodium tripolyphosphate (TPP) to give nanoparticles that could be loaded with proteins (albumin) or drugs (cyclosporine A).[110] The size and zeta potentials of these nanocarriers could be customized to a given need, and the nanoparticles were stable as freeze-dried powders and could be resuspended in biological media.

A fourth example that is related to ionic cross-linking, but which in fact likely includes covalent phosphate ester formation, involves the use of trisodium trimetaphosphate (STMP) to synthesize HA hydrogel particles.[111] The authors found a linear relationship between cross-linking density and methylene blue absorption.

2.214.4.2.6. Monolithic photocrosslinked hydrogels

There have been at least two reports of HA modified with photocrosslinkable groups, followed by high-energy irradiation to effect cross-linking (which would be incompatible with *in situ* cross-linking as discussed below). First, a postsurgical adhesion barrier was prepared by modification of HA first using EDCI and *N*-hydroxysuccinimide (NHS) chemistry as described above, followed by coupling with 3-aminopropyl cinnamate.[112] The resulting 20% modified compound was irradiated at 3000 W for 2 h to produce the cyclobutane-containing dimeric truxillic/truxinic acid derivatives. The degree of cross-linking was selected to obtain an injectable, biocompatible material. In a different study, styrenated HA was produced by coupling 4-vinylalanine under carbodiimide-coupling conditions.[113] Irradiation with other vinylated proteins and polysaccharides with initiators at 200 mW cm^{-2} produced hydrogels in a variety of physical forms for potential use as tissue engineering scaffolds.

2.214.4.3. Living HA Derivatives

2.214.4.3.1. Thiol-modified HA

The motivation to create living HA derivatives was the need to create an *in situ* cross-linkable equivalent of the extracellular matrix. HA was selected as the basic building block for this covalently cross-linked synthetic extracellular matrix (sECM).[86,114] To create a modular, clinically versatile and readily manufactured sECM, we developed a thiol-introduction chemistry[115] based upon the modification of the carboxylate groups of glycosaminoglycans (GAGs), proteins, and other synthetic polymers by hydrazide formation (**Figure 4**).[116] These mild aqueous conditions do not alter other chemical groups required for biological function of the GAG. Moreover, when the hydrazide reagent contains a disulfide bond,[91,115] thiol-modified HA, sulfated GAGs, even proteins such as gelatin[117,118] could be prepared and cross-linked into hydrogels

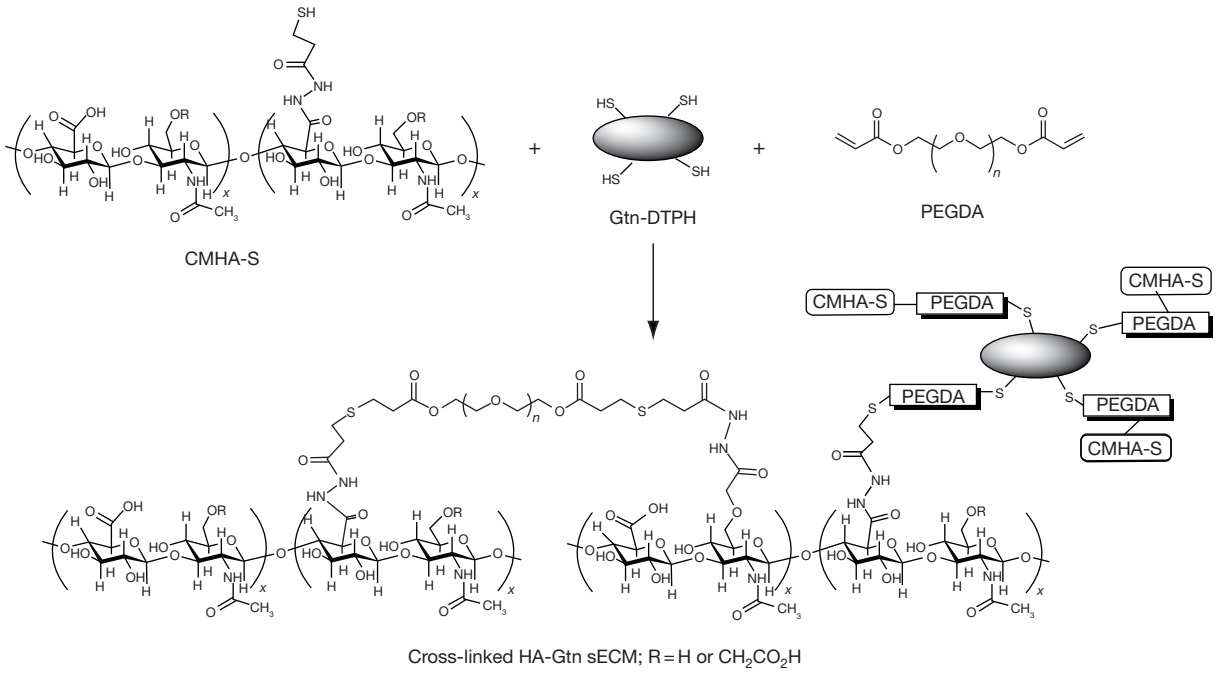

Figure 4 Chemical structure of CMHA-S and PEGDA-cross-linked synthetic extracellular matrix composed of CMHA-S and gelatin-DTPH.

under cytocompatible physiological conditions. For example, thiol-modified macromonomers spontaneously, but slowly, cross-linked in air only to a hydrogel; this gel could be dried to give a thin film or lyophilized to produce a porous sponge.[119] Alternatively, cross-linking with difunctional electrophiles can be accomplished, in the presence or absence of cells, to give injectable and biocompatible hydrogels.[114,118]

Different physical properties and rates of biodegradation can be obtained by controlling several parameters for the biocompatible HA hydrogels[119]: (1) molecular weight of starting HA employed; (2) percentage DTPH modification; (3) concentration of HA-DTPH; (4) molecular weight of poly(ethylene glycol) diacrylate (PEGDA); and (5) ratio of thiols to acrylates. We have also investigated polyfunctional acrylates, acrylamides, and additional thiol-reactive groups, for example, PEG divinyl sulfone, PEG bis-haloacetates, and PEG bis-haloamides.[120,121]

2.214.4.3.2. Haloacetate-modified HA

HA derivatives containing thiol-reactive electrophilic esters were prepared to react with thiol-modified macromolecules to give 'cross-linker-free' hydrogels. Specifically, an aqueous solution of HA was converted to HA bromoacetate (HABA) with a degree of substitution of 18% using ten equivalents of bromoacetic anhydride. Reaction occurs almost exclusively on the more reactive and less sterically hindered primary 6-hydroxy group of the *N*-acetylglucosamine residue. HA iodoacetate (HAIA) was prepared by displacement of bromide with excess iodide. Cross-linker-free hydrogels were then prepared by thiol alkylation using HAIA and HABA as polyvalent electrophiles and thiol-modified HA (CMHA-S) as the polyvalent nucleophiles.

2.214.4.3.3. Methacrylated HA

Photopolymerization offers many attractive opportunities for biocompatible hydrogel formation *in situ* with a range of natural and synthetic polymers, including HA.[122] Three methacrylate derivatized HA macromonomers have been prepared. This extremely useful living modification allows solutions to be seeded with cells and photocrosslinked into hydrogels using either UV or visible light in conjunction with a photoinitiator.[123] The most commonly used method involves the direct methyacrylation of HA with methacrylic anhydride in a pH 8.5 solution,[124] in analogy to the haloacetylation. Similarly, the methacrylation occurs on the primary 6-hydroxy group of the *N*-acetylglucosamine residue. Conditions can be adjusted to give low (~5%) to high (over 30%) modification.

Alternatively, several researchers have used the glycidyl ether methacrylate (GMA) method, which requires a stronger base.[125] The 6-hydroxyl group acts as a nucelophile to open the epoxide of the GMA, analogous to the diepoxide cross-linking described above. A large excess of GMA is required, because the basic conditions also lead to hydrolysis of GMA to glycidol, as well as hydrolysis of the methacrylated HA.

One problem with the photocrosslinked gels, as with the thioether cross-linked gels, was the inability to hydrolyze the gels and recover cells from culture. To solve this problem, a hydrolysable methacrylated HA was synthesized, in which a lactate spacer was introduced between the HA and the methacrylate group.[126]

2.214.4.3.4. Tyramine-modified HA

A new approach to creating a living hydrogel capable of *in situ* cross-linking was recently described, in which carbodiimide chemistry is used in step 1 to add controlled levels of tyramine to HA carboxylates, leaving most carboxylates unmodified.[127] In step 2, either in the presence or absence of cells, cross-linking is induced by the addition of small amounts of hydrogen peroxide to solutions of tyramine-based HA to which horseradish peroxidase has been added. The resulting peroxidase reaction forms phenolate radicals which isomerize and dimerize to form C–C bonded and fluorescent dityramine adducts.

2.214.4.3.5. Alkynylated and azidoalkylated HA

The now well-known Staudinger reaction of azides with alkynes to produce triazoles, or 'click chemistry,' has been applied in nearly every area of chemical biology. Recently, HA hydrogels were produced using this approach, and yeast cells were encapsulated during cross-linking.[128] Briefly, HA carboxylates were modified with proparygyl amine using carbodiimide chemistry to give the alkynyl HA component, and separately modified with 11-azido-triethyleneglycol amine linker to give the azido HA component. The hydrogel was formed at room temperature overnight in the presence of ~0.01% CuCl as a catalyst. While this is an interesting way to make an HA hydrogel, it is unlikely that such a protocol would be approvable or biologically robust in tissue engineering constructs either *ex vivo* or *in vivo*.

2.214.5. Medical Applications of HA

HA and its derivatives have an ever-expanding number of clinical and preclinical applications, including drug targeting and drug delivery.[82,129] Discussion of targeted drug delivery exceeds the scope of this chapter, and in the five sections below we summarize selected medical applications of HA in ophthalmic surgery, intraarticular injections in joints, dermal fillers, acute and chronic wound repair (including surgical adhesion prevention) and 3D cell culture and tissue engineering.

2.214.5.1. Ophthalmic Surgeries

The first HA-based medical products were developed for tissue protection for ophthalmic surgeries. Two rooster comb HA products, Healon (MW 3 MDa, HA 10 mg ml^{-1}) and Amvisc (MW 2 MDa, HA 12 mg ml^{-1}), received approval from the Food and Drug Administration (FDA) in 1983. Viscosity and transparency were critical characteristics for such applications, which included cataract extraction surgery. The viscosity of the HA products helped maintain a deep anterior chamber and retinal attachment surgery, and the HA aided in holding the retina against the sclera for reattachment. The transparency was critically important, since a material used as a surgical aid should neither obscure the vision of the ophthalmic surgeon during the surgery nor the patient postsurgery. The clearness of natural HA has rarely been a problem, unless contaminated by impurities, including particulates.

In the products as ophthalmic surgical aids, the HA ingredient normally has a molecular weight (MW) at or above

1 MDa, and a range of concentration around or above 1% (w/v). The viscous property of the products can be observed by the naked eye. Over the last three decades, HA-containing products have gained wide acceptance and even become a preferred choice for many ophthalmic applications especially in anterior segment surgeries. Here, we will use HA application in the procedures of cataract removal and insertion of intraocular lens as examples to explain the relationship between the product features and their functions.

2.214.5.1.1. Viscosity and lubricity

A certain degree of viscosity is required for HA to remain in the anterior chamber to prevent tissue–tissue contact. Lang *et al.* studied the viscosity of HA preparations under the shear rate of 10 Hz, a close approximation to the shear rate under many surgical conditions and concluded that a threshold of 80 P was needed for the surgery. Healon (1% w/v) has a viscosity of 270 P at such a shear rate. It is gel-like and remains in the eye even when external pressure is applied to the cornea. At rest, Healon's viscosity (zero shear rate viscosity) can reach 1000 P. This prevents the egress of HA from the surgically opened eye under the nonshear, compressive forces of the cornea and the iris–lens–vitreous diaphragm. The viscosity of the same HA material, however, can be reduced to 1 P when it passes through a thin cannula (e.g., 27-gauge) under a high shear rate of 1000 Hz. This is a typical example of shear-thinning phenomenon and the underlying pseudoplasticity of HA as discussed above.[67] This also explains why the same HA product can be both a good space filler and lubricant. Conceivably, pseudoplasticity enables the HA layer not in immediate contact with the tissue surface to move under shear force with less resistance than a Newtonian fluid such as a chondroitin sulfate (CS) solution. This reduces the abrasion such movement might impose on the tissue that the viscous material is supposed to protect.

2.214.5.1.2. Thickness of coating and easiness of the removal of HA

Cataract removal and the implantation of intraocular lens are the ophthalmic procedures where HA-based OVD is most widely used. Here, the viscosity and lubricity of the OVD only partially reflect the desired features of the OVD. The other important factors influencing product performance in such procedures are the thickness of the coating formed and the easiness of the removal of the OVD during postsurgical irrigation and aspiration.

First, the protective effect of a viscous layer depends in large part on the thickness of the layer present at the tissue surface. The bovine cornea abrasion studies by Hammer and Burch[130] indicated that an overly thin layer of high viscous material could cause damage to endothelial cells. This is consistent with the equation by which the viscosity η is defined ($\eta = f\, dy/A\, dv$). For a certain material with certain viscosity (η), the force f (so the damage to cells) is inversely proportional to the distance y (so the thickness).

The thickness of the HA layer that remains after cataract surgery (such as phacoemulsification) and during the insertion of intraocular lens is critical for the protection of cornea. Glasser *et al.*[131] found that a less viscous but more sticky Viscoat provided better corneal protection (~20% cell damage) than the more viscous but less sticky Healon (>40% cell damage) after the traumatic intraocular lens implantation. McDermott *et al.*[132] conducted a rabbit study to quantify the adherence of OVDs to the corneal endothelium after phacoemulsification, and found that the thickness of Viscoat was the highest among the group of Viscoat, Amvisc Plus, and Healon GV. This appears to support the notion that a thin layer of highly viscous material may be responsible for extra endothelial cell loss.

Second, the amount of the remaining HA residue postsurgery can affect the intraocular pressure (IOP), which is a safety related issue. The increase of IOP in the eye is caused by the net influx of the liquid and driven by osmotic pressure. A significant amount of exogenous HA residue in the eye can cause osmosis of liquid from outside, leading to the rise of IOP. Fry compared the IOP increase of four OVDs at 4 and 8 h after surgery.[133] The group of Viscoat without aspiration had the highest IOP increase, followed in decreasing order by the Viscoat group (with aspiration), the Amvisc group (with aspiration), and the Healon group (with aspiration). Viscoat contains HA and CS at high-concentrations (~30 mg NaHA per ml, 40 mg NaCS per ml) and low MW (HA >500 000, CS ~55 000). For the same amount of OVD, Viscoat has more molecules than any other OVDs in the study (Amvisc and Healon) and is therefore attributable to the larger increase of osmotic pressure.

2.214.5.1.3. Cohesiveness and dispersiveness

Another set of properties of OVDs related to the coating thickness during the phacoemulsification procedure: cohesiveness and dispersiveness. Arshinoff explained[134] that 'cohesion allows a viscoelastic to be removed as a single mass, by aspiration or irrigation at the end of the surgical procedure.' The opposite of cohesiveness is dispersiveness.

Cohesiveness can be measured by dynamic aspiration method[135] and the cornea retention method.[136] In the dynamic aspiration method, the percentage of viscoelastic samples aspirated was plotted against vacuum pressure. The slopes of these curves indicate the relative cohesion. The results of the cohesiveness were found in the following descending order: Healon GV (72.3), Provisc (46.0), Healon (31.2), Amvisc Plus (21.4), and Viscoat (3.4). It is noteworthy that the high cohesiveness of Healon GV is related to its very high MW (5 MDa) and medium HA concentration (10 mg ml^{-1}). Materials with higher cohesiveness are easier to remove than materials that are more dispersive.

The second method was the measurement of the retention of viscoelastic agents on corneal endothelial cells after the colored rabbit corneal endothelial cells covered with OVDs underwent irrigation and aspiration, with fluid turbulence similar to that encountered in phacoemulsification surgery.[136] The retention values (the percentage of cells with viscoelastic retained on the surface) were found as follows: Healon, 7; Provisc, 16; Amvisc Plus, 17; Formulation A (a synthetic dispersive preparation), 55; and Viscoat, 90. The results of this experiment also indicated that cohesive viscoelastics were readily removed from the cells, whereas dispersive viscoelastics were highly retained.

High MW contributes a great deal to the networking of HA, and therefore the cohesiveness of the viscoelastics, whereas low-MW materials such as Viscoat, composed of CS (55 kDa) and low-MW NaHA (0.5 MDa), have weaker intermolecular interactions. The lower MW polymer solutions have to be

more concentrated to be viscous. This is why dispersiveness of an OVD relates to its low MW and a high concentration.

The optimum function of an OVD should come from the careful design of its composition and formulation that strives to strike a proper balance between viscosity and ease of removal. There have been many different approaches toward this goal.

1. Amvisc Plus appears to be somewhere near the center in the full spectrum from being cohesive to dispersive, and related to that observation is the fact that Amvisc Plus also has both middle range of HA molecular weight ($1.5\,mg\,ml^{-1}$) and middle range of HA concentration ($\sim 16\,mg\,ml^{-1}$).
2. DuoVisc is an example of putting a typical dispersive product (Viscoat) and a typical cohesive product (ProVisc) in the same package. While Viscoat may provide better protection to the cornea during the cataract removal, Provisc (MW > 1 MDa, HA $10\,mg\,ml^{-1}$) can do a better job reducing the trauma during the insertion of the intraocular lens and is easier to remove afterwards.
3. DisCoVisc is an example of mixing a dispersive ingredient (high concentration of low molecular weight (LMW) OVD CS) and a more cohesive ingredient (an HA formulation very close to that of Amvisc Plus). The CDI (cohesive/dispersive index) of DisCoVisc is 12, as compared to the dispersive Viscoat (3.4) and cohesive Healon (40).
4. Healon5, a high molecular weight (4 MDa) and high concentration ($23\,mg\,ml^{-1}$) formulation of HA is highly viscoelastic and can become dispersive by being fragmented under high shear rates and turbulence generated during phacoemulsification. This property is called adaptiveness. In addition, the fragmentation of the OVD facilitates the forming of a cavity with an outer retentive shell, which is also protective.[69]

2.214.5.2. Injections for Osteoarthritic Joints

The effectiveness of injections of HA for the OA joints to alleviate local pain has been widely investigated. Reviews and analysis of human clinical trials of HA injections for the knee,[137] hip,[138] shoulder,[139] ankle,[140] and temporal mandibular joint (TMJ)[141] are available. However, to date only the knee indication has gained regulatory approval for marketing in the United States by the FDA after many controlled human clinical studies, and along with them a large body of data, which will be our focus in the following analysis.

2.214.5.2.1. Effectiveness of HA injected in the knee

As of the end of 2009, five HA-based injection products on the US market for the treatment of pain of OA of the knee were Hyalgan, Synvisc, Supartz, Orthovisc, and Nuflexxa (Euflexxa). Synvisc is the only chemically cross-linked HA product (cross-linked with divinylsulfone), and the others contain of native HA. Nuflexxa is the only product with HA from fermentation; the other four products use rooster comb HA. Unlike the use of HA in ophthalmic surgery, which has gained universal acceptance, the clinical value as well as the mechanism of action of HA-based formulations for the knee remain unclear.

How effective is HA as local injection into the OA knee? To answer the question objectively, one needs to examine the universe of clinical evidence in its entirety. A meta-analysis by Lo *et al.*[137] reviewed the data of the clinical studies of HA for knee injection from 1966 to 2003. The effectiveness data pertaining to pain relief were extracted from measures of change from baseline at 1–4 months after the first intraarticular injection. An analysis was considered intent-to-treat if there were no dropouts.

The key effectiveness parameter used by Lo *et al.* in their meta-analysis is *effect size*, defined as the pain improvement (Pain HA/Pain placebo) divided by the pooled standard deviation (SD). The effective size in the range of 0.2–0.5 was considered small, equivalent to the effect of nonsteroidal anti-inflammatory drugs.[142] A large effect size was deemed to be at or above 1.0, benchmarked against the effect of a total knee replacement.[143] The pooled effect size for the treatment of knee OA with HA injection versus buffered saline was 0.32, indicative of a small effect. In addition, the study has concluded that injection of saline control contributes ~80% of the treatment effect.

Another meta-analysis conducted by Arrich using data from inception to 2004 reached similar conclusion. Patients who received the HA injection experienced a reduction in pain during movement. The mean difference was from -3.8 to -7.1 mm on a 100-mm visual analogue scale and during the period from 2 to 30 weeks. However, a clinically meaningful difference would expected to be about 15 mm.[144]

As a whole, the intervention of knee OA by HA injection is only marginally effective. There may be subgroups of patients who react more favorably to the treatment than the population in general. But such particular subgroups, if they exist, have not been consistently identified across multiple trials.[137] In clinical practice, it is recommended only for those patients who have attempted other conservative therapies with no appreciable positive results.

2.214.5.2.2. Clinical performance of native and chemically cross-linked HA

To compare the effectiveness and safety of chemically cross-linked Hylan-based product (Synvisc) and native HA products for OA knee injection, Reichenbach *et al.*[145] performed a systematic review and meta-analysis of the pain related outcome of randomized controlled human clinical trials up till 2006. Thirteen trials with a pooled total of 2085 patients contributed to the meta-analysis.

The pooled effect size of all trials slightly favored Synvisc, but between-trial heterogeneity was high. For those trials with blinded patients and in an intent-to-treat analysis, the effect sizes were near zero. The meta-analyses on safety revealed an increased risk associated with the cross-linked Hylan product for any local adverse events including flares.

2.214.5.2.3. Mechanism of action for exogenous HA in the knee

There are two different schools of thought on the mechanism of action of exogenous HA in the OA knees. One theory (viscosupplementation) emphasizes local and physical effect, while the other maintains that the main effect is systemic. The local effect proponents argue that HA with high viscosity restores the physiological homeostasis of the joint characterized by the rheological property of healthy, viscous synovial fluid. Critics often point to the lack of strong clinical evidence of the efficacy of local

injection of HA over placebo, or the evidence of high viscosity formulations being superior to the lower viscosity ones. Proponents of systemic effect of HA on joints point to the fact that HA administered intravenously (i.v.) in horses actually works just as well as the HA injected intraarticularly (i.a.).

One of the products (Legend) for racehorses is approved for both i.v. and i.a. routes of administration. In the controlled trials, i.v. injection of Legend was shown to be as effective as i.a. injection, according to the Freedom of Information for Legend (NADA 140–883). The Legend injectable solution was 1% of sodium hyaluronate. In principle, a systemic effect can arise from either i.a. or i.v. injection. It is conceivable that a significant portion of the effect of locally injected HA may occur systemically.

What could be the scientific rationale behind such phenomena? Kawcak *et al.*[146] found that horses treated i.v. with HA had better (lower) lameness scores and synovial membrane histologic scores. In addition, the HA-treated group had a significantly lower concentration of total protein and prostaglandin E2 within synovial fluid 72 days after the surgery. It was postulated that i.v. administered HA may 'alleviate signs of lameness by interacting with synoviocytes, and by decreasing production and release of inflammatory mediators.'[146]

2.214.5.3. Cosmetic Tissue Augmentation

HA-based dermal fillers for cosmetic tissue augmentation are gaining increased popularity. The cross-linked HA products Restylane (cross-linked with BDDE, butanediol diglycidyl ether) and Hylaform (cross-linked with divinyl sulfone (DVS)) were first commercialized in the United States for the temporary correction of facial wrinkles in early 2000s. In the controlled clinical trials of Restylane (6 months) and Hylaform (12 weeks), both products were as effective as collagen-based product Zyplast in the correction of moderate to severe facial wrinkles and folds (such as nasolabial folds). In general, HA-based products offer more discernable results than facial creams and chemical peels, yet are less invasive than facial surgery. Since then, Juvederm (also BDDE cross-linked) and Elevess (BCDI cross-linked) also gained FDA approval and entered the US market. Puragen uses DEO as cross-linker and is often called double-cross-linked HA because epoxide can form an ether bond with the hydroxyl groups of HA under basic conditions, but form an ester bond under acidic conditions. FDA approval is pending as of 2009.[147]

2.214.5.3.1. Residence time

It is not accidental that all those HA dermal fillers use cross-linked HA as their major ingredients. In its native form, HA can only produce a cosmetic effect for the duration of only 1–2 days.[148] In contrast, cross-linked HA dermal fillers have residence time in skin from 4 months to a year.[149]

There is little doubt that the residence time of HA dermal fillers is a key parameter because HA has to be able to stay in the injected site long enough to be effective. This is unlike ophthalmic surgery, where HA is meant to be removed after its function as surgical aid is accomplished, or in the case of knee injection where the importance of residence time of exogenous HA has not been proven.

2.214.5.3.2. Elasticity

If viscosity is the predominant feature of HA products for ophthalmic use, elasticity may be considered as the most important parameter for HA-based dermal fillers. Elasticity is the resistance to deformation and in the case of a polymeric gel it is displayed and observed as its firmness. HA products with high elastic modulus G', such as Restylane and Perlane ($\sim$600 Pa) are more elastic than those with low G' values such as Hylaform (140–220 Pa) and Juvederm 30 HV (105 Pa).[72] In general, fillers with high G' can better resist forces during facial muscle movement and provide better lift for areas like nasolabial folds, whereas fillers with low G' are perhaps better suited to areas like lips where volume and softness of the filler are critical.[72]

The elasticity displayed by different HA fillers is determined by multiple factors. The degree of cross-linking is the first determinant for the firmness of an HA gel. The more the cross-linkers are chemically bonded to the HA molecules, the more structural support to the HA network and therefore the more physical force the gel can sustain. The second determinant has to do with HA concentration, which relates to the amount of HA that was cross-linked. Naturally, the more HA in the gel, the firmer the filler would become. Combining factors one and two can at least partially explain why Hylaform (5.5 mg ml^{-1} HA, 12% cross-linking) and Juvederm 30 HV (24 mg ml^{-1}, 2% cross-linking) have similar elasticity.

The third factor is the gel/sol ratio of the filler. Note that there is always a portion of the HA molecules in the filler that are either uncross-linked or very lightly cross-linked. That part of the filler is basically liquid in nature, which does not contribute to the firmness, but acts a lubricant to soften the gel. This soluble part of the filler is added by the manufacturer to improve injectability. The fourth factor is the post-cross-linking processing steps, such as sizing and homogenization. Sizing largely maintains the granular feature of the particles and elasticity, whereas homogenization reduces the particle sizes dramatically to make the filler smooth and in doing so also changes its elasticity.[71]

2.214.5.3.3. Safety and reversibility

As a biodegradable polymer, the safety profile of HA-based dermal fillers is generally acceptable, but serious adverse events do occur, whether the source of HA is avian or bacterial. Batch-to-batch quality consistency is also a challenge. Excessively large sizes of particles in the gel are the suspects for causing some granular tissue reactions. HA-based fillers, however, have the advantage of being reversible in the presence of its degrading enzyme hyaluronidase, which the clinicians may option to use if clinically necessary.[150]

2.214.5.4. Acute and Chronic Wound Healing

Modified HA products are used clinically in veterinary practice for wound healing and have potential for use in human patients as well. We present only a few highlights below and refer to web-based information and published literature for details.

2.214.5.4.1. Acute cutaneous wounds

Adipic hydrazide-modified HA and CS (HA-ADH and CS-ADH) were cross-linked with PEG-dialdehyde and the resulting

hydrogels were dried in air and sterilized with ethylene oxide.[151] The resulting films were used in two cutaneous injury models. First, full-thickness wounds were created on the dorsal side of Balb/c mice and were dressed with a GAG film plus Tegaderm or Tegaderm alone. A significant increase in reepithelialization was observed at day 5 and day 7 for the wounds treated with GAG films versus the controls. In addtion, wounds treated with either HA or CS films showed more fibro-vascular tissue by day 10. The GAG films, which rehydrated in the wound bed, provided a highly hydrated, pericellular environment in which assembly of other matrix components, presentation of growth and differentiation factors, and cell migration could occur.[151]

The second model for these GAG films was a pig model for the treatment of autograft sites of burn patients.[152] Multiple shallow (5 cm × 5 cm × 0.03 cm) wounds were created on the backs of pigs. Half of the wounds were treated with a GAG film (cross-linked CS-ADH or HA-ADH) plus an occlusive dressing (Tegaderm™), whereas the other half were treated with Tegaderm™ alone. At 3, 5, or 7 days after surgery, the partially healed wounds were excised and evaluated histologically for three animals at each time point. By day 3, epithelial cells had proliferated and migrated from wound edges and from epithelial islands associated with residual hair follicles to begin to cover the wound bed. A statistically significant increase in coverage was observed for GAG treated wounds over controls at day 3 and day 5 postsurgery. Both the HA and CS hydrogels accelerated wound healing by enhancing reepithelialization.[152]

Thiol modified HA (see **Section 2.214.4.3.1**), was first known as HA-DTPH, but was then replaced with an improved carboxymethylated HA derivative known as CMHA-S. The thiolated HA derivatives readily formed biocompatible hydrogels that did not support cell attachment and proliferation. Cross-linking was accomplished slowly via disulfide bond formation in air, or with better control of cross-linking time and hydrogel stiffness using cytocompatible bivalent cross-linkers. Using a murine full-thickness wound repair model, we evaluated the PEGDA-cross-linked CMHA-S derivative.[85] Bilateral injuries were formed on the flanks of each animal, allowing each animal to act as its own control. One site was left untreated, while a cross-linked HA film was applied to the contralateral wound; Tegaderm used for both sites to prevent dessication and reduce microbial invasion. After 6 days, the treated wounds were over 45% reepithelialized after 6 days, while the untreated wounds were only 12% healed. Moreover, wound filling, epidermal thickness, dermal thickness, and vascularization were also significantly enhanced in treated animals. Similarly, in a pilot study in horses, excisional wounds were more than 75% healed after 26 days without detectable proud flesh formation (**Figure 5**). These studies have now been repeated numerous times in clinical veterinary practice for dogs, cats, horses, ferrets, hawks, and other animals (www.sentrxanimalcare.com).

2.214.5.4.2. Acute surgical wounds

2.214.5.4.2.1. Seprafilm

Seprafilm was described above as a partially co-cross-linked formulation of HA and carboxymethylcellulose. It is indicated for use in abdominal surgery to reduce postsurgical adhesions (*Summary of Safety and Effectiveness Data of Seprafilm P950034*). Seprafilm can remain at surgical sites for up to a week, the critical time needed to prevent adhesion formation. However, it is brittle when dry and sticky when moist and is therefore difficult for surgeons to handle. A more pliable Seprafilm II has been developed which contains glycerol, in addition to the components of Seprafilm.[9] A BCDI cross-linked HA, Incert (Anika Therapeutics) was developed for the prevention of postsurgical adhesions.[87] Incert was effective in reducing tissue adhesions in a uterine horn model.[153]

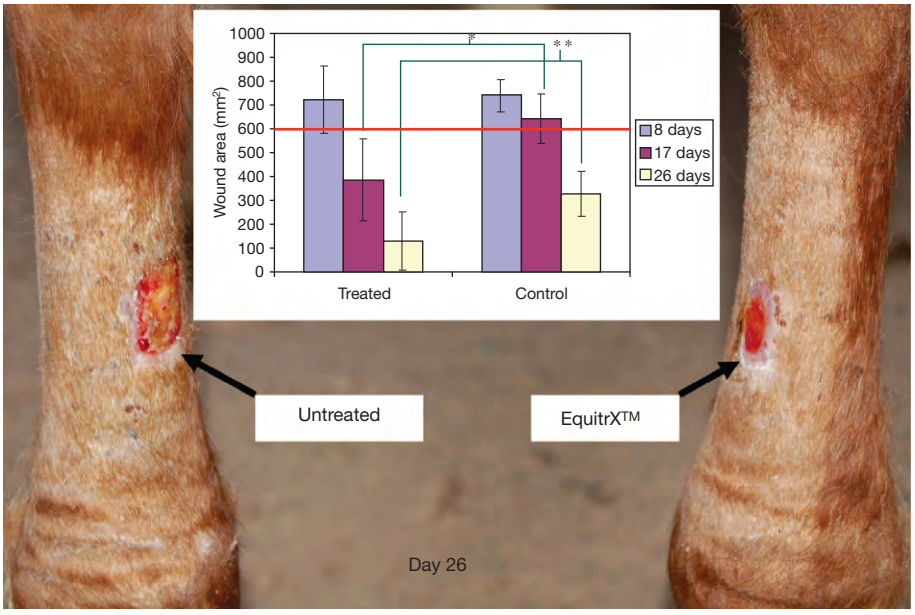

Figure 5 Pilot study for treatment of 1 × 2 cm excisional injuries in horses ($n = 8$) with cross-linked CMHA-S films (EquitrX) compared with untreated controls. Wounds were exposed and redressed at 8 and 17 days and photographed and quantified at 8, 17, and 26 days. The inset shows statistically significant healing at 17 days (*, $p < 0.004$) and 26 days (**, $p < 0.003$) and a complete lack of proud flesh formation.

2.214.5.4.2.2. Autocrosslinked HA products

Controlled human clinical studies have been conducted to investigate the effectiveness of internal ester cross-linked ACP gel (Hyalobarrier) in the prevention of intrauterine adhesions. Ultrasonographic data indicated that ACP gel kept uterine walls separated for at least 72 h. The group of patients receiving ACP gel during adhesiolysis showed significant decrease in incidence and severity of adhesion reformation than the control group (without gel) 3 months after the procedure.[154] Similarly, Hyalobarrier reduced *de-novo* adhesions after hysteroscopic surgical procedures to remove myomas and polyps.[155] An ACP formulation known as Hyaloglide also reduced adhesions after knee surgery in a rabbit model.[156]

2.214.5.4.2.3. Ionically cross-linked HA

The reddish ferric hydroxide cross-linked HA gel Intergel was approved by the FDA in 2001 to reduce postsurgical adhesions in patients undergoing open, conservative gynecological surgery (*Summary of Safety and Effectiveness Data of PMA P990015 of Intergel*). After about a week, the tissues absorbed the gel and the metabolites were excreted. However, in 2003, this product was withdrawn from the market, due to adverse events associated with off-label use in laparoscopy and nonconservative surgical procedures such as hysterectomy. A recent study documents the unacceptably high rates of postoperative morbidity following colorectal resection.[157]

2.214.5.4.2.4. Thiol-modified HA

The cross-linked thiol-modified CMHA-S and HA-DTPH materials have shown remarkable preclinical success in preclinical models for postsurgical adhesion prevention. Reduction of scarring following vocal fold injury *in vivo* was facilitated by the cross-linked HA-DTPH hydrogel[158] and the CMHA-S hydrogel.[159] Postoperative pericardial adhesions were dramatically reduced by the CMHA-S hydrogel in a rabbit cardiac abrasion model.[160] In rat uterine horn model, PEGDA-cross-linked HA-DTPH with or without mitomycin C as an antiproliferative agent significantly reduced the area and severity of adhesions.[161] Even more effective were the CMHA-S-PEGDA materials. In both a rat uterine horn model and a rat cecal abrasion model, the CMHA-S (Carbylan-SX) films were statistically superior to Seprafilm in reducing the extent and area of adhesions.[162] Importantly, the use of an *in-situ* gelling formulation of Carbylan-SX reduced adhesions to near zero in the cecal abrasion model.[162] In contrast, the Carbylan-SX films outperformed the hydrogels for the prevention of peritendinous adhesions following partial-thickness flexor tendon injury in rabbits.[163] Both treatments were superior to Seprafilm in reducing the severity of adhesions; the Carbylan-SX films actually reduced the force required to remove the tendon from the paw to the same value required for an unoperated control (**Figure 6**). The Carbylan-SX gels have also been used to reduce stenosis after tracheal injury,[164] to improve healing following endoscopic sinus surgery,[165] and to promote healing following middle ear injury.[166]

2.214.5.4.3. Chronic wounds

2.214.5.4.3.1. Esterified HA

The TissueTech autograft system comprises a dermal replacement (Hyalograft 3D) made of a 3D matrix of HYAFF 11 with autologous fibroblast *and* an epidermal replacement (Laserskin) made of a microperforated HYAFF 11 membrane containing autologous keratinocytes. A clinical study[167] of patients with chronic wounds such as diabetic or pressures

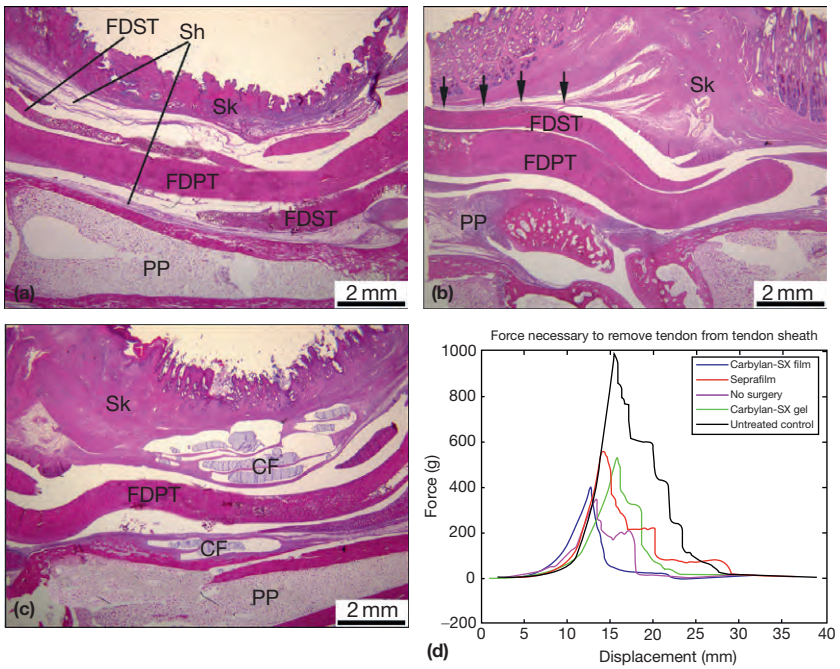

Figure 6 Tendon repair in rabbit flexor tendon model. (a) Unoperated tendon; (b) operated and untreated adhesion, with arrowheads showing adhesions; (c) CMHA-SX film wrapped tendon, showing absence of adhesions. H&E staining, scale bar = 2 mm. FDST, flexor digitorum superficialis tendon; FDPT, flexor digitorum profundus tendon; PP, proximal phalange; Sh, sheath; Sk, skin.

ulcers indicated that 59% of the treated ulcers reached complete closure in <4 months.

2.214.5.4.3.2. Thiol-modified GAGs and growth factors

Using a blend of HA-DTPH with a thiolated heparin (HP-DTPH) macromonomer, basic fibroblast growth factor (bFGF) was released from an HA-based sECM *in vitro* with a half-life of 1 month[168] when released from a CS-based sECM *in vivo*, bFGF showed dose-dependent acceleration of reepithelialization and improved formation of vascularized dermal tissue in the repair of large acute wounds in diabetic mice.[169]

2.214.5.5. Selected Uses in Tissue Engineering and 3D Cell Culture

2.214.5.5.1. 3D cell culture

2.214.5.5.1.1. Modular sECMs[170]

The use of modular sECMs for reparative medicine and for drug discovery in three dimensions[171] has been recently reviewed, with an emphasis on clinically useful materials.[85] Only illustrative examples are presented below. Incorporation of attachment factors to an HA-based hydrogel provides an sECM that supports cell attachment, growth, and proliferation in 3D. By co-cross-linking the thiol-modified gelatin (Gtn-DTPH) with HA-DTPH, we obtained materials to which cells readily attached and spread.[172] This can be accomplished with lyophilized macroporous sponges based on disulfide co-cross-linking, or with injectable materials using PEGDA cross-linking.[118] Alternatively, gelatin can be replaced by either an Arg-Gly-Asp (RGD) peptide[84] or selected domains of fibronectin.[173] These materials have been also be used centrifugal casting of endothelial cells[174] and have promise as biopaper in bioprinting strategies.[175] To further enhance cell growth and simultaneously enhance the rate of neovascularization, an HA-based sECM containing co-cross-linked thiol-modified heparin (HP-DTPH) was found to give a half-life for bFGF release of over 1 month *in vitro*.[168] Varying the GAG-DTPH composition regulates release of vascular endothelial growth factor (VEGF) and keratinocyte growth factor (KGF), with dual release[176] further enhancing vascularization and vascular maturation *in vivo*.[177]

2.214.5.5.1.2. Human embryonic stem cells (hESCs)

When encapsulated in a photocrosslinked HA methacrylate hydrogel, hESCs maintained their undifferentiated state, preserved their normal karyotype, and maintained their full differentiation capacity as indicated by embryoid body formation. Differentiation could be induced within the HA hydrogel by altering the soluble factors present in the medium. Living HA hydrogels, with their developmentally relevant composition and tunable physical properties, thus provide a unique microenvironment for the self-renewal and differentiation of hESCs.

2.214.5.5.2. Cartilage and bone repair models

2.214.5.5.2.1. Osteochondral defect repair with esterified HA

Two esterified HA products were tested for their ability to enhance the natural healing response in osteochondral defects on the femoral condyles of 4-month-old rabbits. Defects were filled with an autocrosslinked ACP sponge, or HYAFF-11 sponge, made of benzylated hyaluronan. While untreated defects filled with bone tissue up to or beyond the tidemark, at 12 weeks, the ACP-treated and HYAFF-11 treated defects had bone beyond the tidemark that was covered with a thin layer of hyaline cartilage. ACP-treated defects scored significantly higher than HYAFF-11-treated defects. The HA-based polymers provided an appropriate scaffolding and favorable microenvironment for the reparative process.[178]

More recently, this protocol has been translated to the clinic. Hyalograft C, consisting of autologous chondrocytes grown on a HYAFF 11 scaffold, used to treat cartilage defects of the knee. A clinical study[179] demonstrated that the functions and symptoms of the patients continued to improve for at least 3 years, suggesting that Hyalograft can be a valid alternative to autologous chondrocyte transplantation (ACT).

2.214.5.5.2.2. Defect repair with living HA

Chondrocytes encapsulated in photocrosslinkable HA methacrylate retained the chondrocytic phenotype and synthesized cartilage matrix *in vitro*, and accelerated healing in an osteochondral defect model *in vivo*.[180] The poor cell attachment to these *in situ* photopolymerized HA hydrogels can be significantly enhanced by RGD modification.[181] When human mesenchymal stem cells (MSCs) were encapsulated in the photocrosslinked HA methacrylate hydrogels, a significant upregulation in chondrogenic genes (type II collagen, aggrecan) was observed compared to MSCs in inert poly(ethylene glycol) (PEG) gels. Blocking CD44 receptors reduced the chondrogenic gene expression profile induced by HA gels, and microarray analysis identified a range of genes involved in this improved chondrogenesis, including specific matrix interactions that are only found with HA. This is an important example of biomaterial chemistry controlling stem cell differentiation and again emphasizes the importance of the microenvironment to provide cues to control MSC behavior.[182]

An sECM hydrogel using thiolated HA (CMHA-S) was also examined for repair of an osteochondral defect in a rabbit patellar groove.[183] In untreated control defects, extensive scar tissue accumulated after 12 weeks. However, simply filling the defect with the HA-gelatin-based sECM hydrogel resulted in regeneration of both new osteal and chondral tissues. More robust remodeling was accomplished by the addition of autologous MSCs to the sECM hydrogel, suggesting that localized cell delivery and retention can add an important dimension to the regenerative process. Nonetheless, the fundamental role of the sECM is to enhance the natural biological repair processes mediated by endogenous cells.

The stiffness and porosity of the ECM substitute were also important. In a rat femoral defect model, using either a hydrogel or a lyophilized sponge form of the cell-free two component sECM Extracel[184] to deliver human demineralized bone (DBM) enhanced bone repair (**Figure 7**). While untreated controls showed little new bone formation after 8 weeks, the sECM sponge treatments generated more new bone at all time points than the softer sECM hydrogels (**Figure 8**). In addition, the addition of DBM to either material gave a statistically significant improvement in healing, reaching over 85% repair at 4 weeks postinjury.

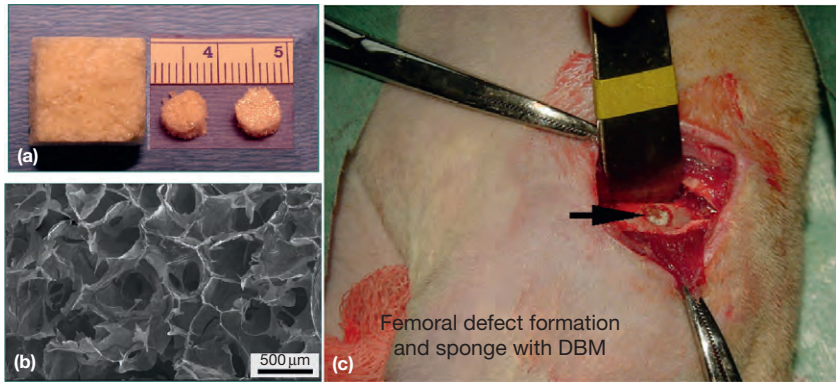

Figure 7 Paradigm for rat femoral defect model. (a) Lyophilized sponge block of PEGDA-cross-linked synthetic extracellular matrix composed of CMHA-S and gelatin-DTPH, and biopsy punch generated press-in cylinders. (b) Scanning electron microscope (SEM) of sponge containing 20% (w/w) demineralized bone matrix. (c) Insertion of sponge plug into defect site.

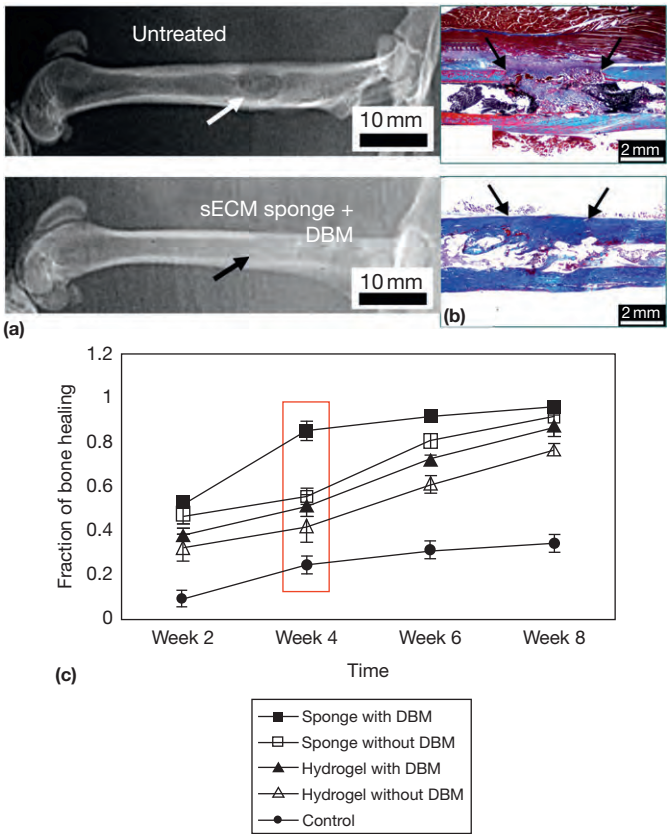

Figure 8 Bone repair in rat femoral defect model. (a) Radiology at 8 weeks for untreated and synthetic extracellular matrix (sECM) + demineralized bone matrix (DBM) treated bone. (b) Masson's Trichrome staining of same two conditions as panel A. (c) Time course of repair, showing highly significant acceleration of repair for DBM-containing sECM sponge.

2.214.6. Future Perspectives and Conclusions

2.214.6.1. The Future of HA Science

Three important resources exist for understanding both the historical perspectives and tracking the very dynamic research in hyaluronan science. The first is an online review series, entitled 'Hyaluronan Today,' which is hosted by the Seikagaku Company. This resource (http://www.glycoforum.gr.jp/science/hyaluronan/hyaluronanE.html) encompasses diverse subject areas, from the physical and synthetic chemistry of HA to HA–protein interactions and medical applications of HA.

The second is the International Society for Hyaluronan Research (ISHAS), which can be found at http://www.ishas.org/. The mission of ISHAS is to advance knowledge on the

structure, function, and therapeutic application of hyaluronan and its role in the structure and function of the extracellular matrix and cells. The ISHAS meets every 3–4 years and the proceedings are often published in monograph form.

The third is the Matrix Biology Institute (MBI) (http://www.matrixbiologyinstitute.org) which aims to further knowledge on the structure, function, and therapeutic applications of hyaluronan by supporting conferences with the primary objective of promoting communication between scientists and clinical investigators whose interest is hyaluronan or the intercellular matrix. MBI conducts and supports a project of collecting all scientific papers and books (basic research and clinically oriented) on hyaluronan since the late nineteenth century. This library is continually updated and references will be available at the website. In addition, since 2002 the MBI has been constructing an encyclopedia on hyaluronan. In 2010, MBI will post a definitive document for the characterization and analysis of HA from natural sources.

2.214.6.2. Concluding Remarks

Native HA has grown from laboratory curiosity to an essential player in clinical medicine over the past 40 years. In the last two decades, we have witnessed growing importance of the first generation of chemically modified HA derivatives, the so-called 'monolithic' materials, that can be injected, molded, shaped, spun, or woven for a variety of clinical uses. While these monolithic materials will continue to enjoy commercial and clinical success, the past 10 years has seen the emergence of an important second generation of 'living' HA derivatives. The living polymers offer many new opportunities for 3D cell culture, injectable tissue engineering, wound repair, scar-free healing, drug delivery, and toxicology testing. The applications of the living HA technology for therapeutic, veterinary, and laboratory research uses will continue to grow and mature during the decades to come.

Acknowledgments

The authors thank the NIH, the NSF, The Center for Biotechnology at the University at Stony Brook, Med Chem Products, Inc., Anika Therapeutics, Inc., Clear Solutions Biotech, Inc., Sentrx Surgical, Inc., the University of Utah, and The Center for Therapeutic Biomaterials, for financial funding over the past two decades that facilitated the author's activities with HA. Commercialization of the living sECM technology is currently pursued by Carbylan Biosurgery, Inc. (human therapeutics), Sentrx Animal Care, Inc. (veterinary products), and Glycosan BioSystems, Inc. (3D cell culture systems for research and toxicology).

References

1. Meyer, K.; Palmer, J. *J. Biol. Chem.* **1934**, *107*, 629–634.
2. Meyer, K. *Physiol. Rev.* **1947**, *27*, 335–359.
3. Laurent, T. C. In *Chemistry and Molecular Biology of the Intercellular Matrix*; Balazs, E. A., Ed.; Academic Press: London, 1970; Vol. 2, pp 703–732.
4. Laurent, T. *Ciba Found Symp.* **1989**, *143*, 1–20.
5. Balazs, E. A.; Laurent, T. C.; Jeanloz, R. W. *Biochem. J.* **1986**, *235*, 903.
6. Rapport, M. M.; Linker, A.; Meyer, K. *J. Biol. Chem.* **1951**, *192*, 283–291.
7. Rapport, M. M.; Meyer, K.; Linker, A. *J. Am. Chem. Soc.* **1951**, *73*, 2416–2420.
8. Weissman, B.; Meyer, K. *J. Am. Chem. Soc.* **1954**, *76*, 1753–1757.
9. Kuo, J. W. *Practical Aspects of Hyaluronan Based Medical Products*; CRC/Taylor & Francis: Boca Raton, FL, 2006; 217p.
10. Hargittai, I.; Hargittai, M. *Struct. Chem.* **2008**, *19*, 697–717.
11. Kennedy, J. F.; White, C. A. *Bioactive Carbohydrates in Chemistry, Biochemistry and Biology*; Ellis Horwood: New York, 1983.
12. *Eur. J. Biochem.* **1980**, *111*, 295–298.
13. Scott, J. E.; Cummings, C.; Brass, A.; Chen, Y. *Biochem. J.* **1991**, *274*(Pt 3), 699–705.
14. Hirano, S.; Kondo, S. *J. Biochem.* **1973**, *74*, 861–862.
15. Chakrabarti, B.; Balazs, E. A. *J. Mol. Biol.* **1973**, *78*, 135–141.
16. Stone, A. L. *Biopolymers* **1969**, *7*, 173–188.
17. Scott, J. E.; Heatley, F.; Hull, W. E. *Biochem. J.* **1984**, *220*(1), 197–205.
18. Welti, D.; Rees, D. A.; Welsh, E. J. *Eur. J. Biochem.* **1979**, *94*(2), 505–514.
19. Scott, J. E. In *The Chemistry, Biology and Medical Applications of Hyaluronan and its Derivatives*; Laurent, T. C., Ed.; Portland Press: London, 1998; Vol. 72, pp 7–15.
20. Almond, A.; Hardingham, T. E. *Hyaluronan: Current Macromolecular and Micromolecular Views*. http://www.glycoforum.gr.jp/science/hyaluronan/hyaluronanE.html; 2008.
21. Sheehan, J.; Almond, A. *Hyaluronan: Static, Hydrodynamic and Molecular Dynamic Views*. http://www.glycoforum.gr.jp/science/hyaluronan/hyaluronanE.html; 2001.
22. Toole, B. In *Cell Biology of Extracellular Matrix*, 2nd ed.; Hay, E. D., Ed.; Plenum: New York, 1991; pp 305–341.
23. Toole, B. In *The Chemistry, Biology and Medical Applications of Hyaluronan and its Derivatives*; Laurent, T. C., Ed.; Portland Press: London, 1998; Vol. 72, pp 155–160.
24. Weigel, J. A.; Raymond, R. C.; McGary, C.; Singh, A.; Weigel, P. H. *J. Biol. Chem.* **2003**, *278*(11), 9808–9812.
25. Entwistle, J.; Hall, C. L.; Turley, E. A. *J. Cell Biochem.* **1996**, *61*(4), 569–577.
26. Pure, E.; Assoian, R. K. *Cell Signal.* **2009**, *21*(5), 651–655.
27. Boas, N. *J. Biol. Chem.* **1949**, *181*, 573–575.
28. Sevag, M. G. *Biochem. Z.* **1934**, *273*, 419–429.
29. Blix, G.; Snellman, O. *Arkiv. Kemi.* **1945**, *19A*, 1–19.
30. Balazs, E. A. U.S. Pat. 4,141,973, 1979.
31. Swann, D. A. *Biochim. Biophys. Acta* **1968**, *156*(1), 17–30.
32. Scott, J. E. *Meth. Biochem. Anal.* **1960**, *8*, 145–197.
33. Swann, D. A. *Biochim. Biophys. Acta* **1968**, *160*(1), 96–105.
34. Ellwood, D. C. In *Hyaluronan*; Kennedy, J. F., Ed.; Woodhead: Cambridge, UK, 2002; Vol. 1, pp 221–226.
35. Kendall, F. E.; Heidelberger, M.; Dawson, M. H. *J. Biol. Chem.* **1937**, *118*, 61–69.
36. Stahl, S. U.S. Pat. 6,090,596, 2000.
37. Bracke, J. W.; Thacker, K. U.S. Pat. 4,517,295, 1985.
38. Swann, D. A.; Sullivan, B. P.; Jamieson, G.; Richardson, K. R.; Singh, T. U.S. Pat. 4,897,349, 1990.
39. Ellwood, D. C.; Evans, C. G. T.; Dunn, G. M.; McInnes, N.; Yeo, R. G.; Smith, K. J. U.S. Pat. 5,411,874, 1995.
40. Kim, J. H.; Yoo, S. J.; Oh, D. K.; *et al. Enzyme Microb. Technol.* **1996**, *19*, 440–445.
41. Chong, B. F.; Blank, L. M.; McLaughlin, R.; Nielsen, L. K. *Appl. Microbiol. Biotechnol.* **2005**, *66*(4), 341–351.
42. Nimrod, A.; Greenman, B.; Kanner, D.; Landsberg, M. U.S. Pat. 4,784,990, 1988.
43. Nimrod, A.; Greenman, B.; Kanner, D.; Landsberg, M.; Beck, Y. U.S. Pat. 4,780,414, 1988.
44. Stahl, S. U.S. Pat. 6,537,795, 2003.
45. DeAngelis, P. L.; Papaconstantinou, J.; Weigel, P. H. *J. Biol. Chem.* **1993**, *268*(20), 14568–14571.
46. Weigel, P. H.; Hascall, V. C.; Tammi, M. *J. Biol. Chem.* **1997**, *272*(22), 13997–14000.
47. Widner, B.; Behr, R.; Von Dollen, S.; *et al. Appl. Environ. Microbiol.* **2005**, *71*(7), 3747–3752.
48. Kunst, F.; Ogasawara, N.; Moszer, I.; *et al. Nature* **1997**, *390*(6657), 249–256.
49. Adam, N.; Ghosh, P. *Inflamm. Res.* **2001**, *50*(6), 294–299.
50. Jing, W.; DeAngelis, P. L. *J. Biol. Chem.* **2004**, *279*(40), 42345–42349.
51. DeAngelis, P. L. *Cell Mol. Life Sci.* **1999**, *56*(7–8), 670–682.
52. Jing, W.; DeAngelis, P. L. *Glycobiology* **2000**, *10*(9), 883–889.
53. Jing, W.; Haller, F. M.; Almond, A.; DeAngelis, P. L. *Anal. Biochem.* **2006**, *355*(2), 183–188.
54. DeAngelis, P. L.; Oatman, L. C.; Gay, D. F. *J. Biol. Chem.* **2003**, *278*(37), 35199–35203.

55. Sodium hyaluronate natrii hyaluronas. In *European Pharmacopoeia Supplement*. European Directorate for the Quality of Medicines of the Council of Europe: Strasbourg, 2000; p 1190–1193.
56. ISO 15798. *Ophthalmic Implants – Ophthalmic Viscosurgical Devices*; 2001.
57. Orr, S. F. D. *Biochim. Biophys. Acta* **1954**, *14*, 173–181.
58. Cael, J. J.; Isaac, D. H.; Blackwell, J.; Koenig, J. L. *Carbohydr. Res.* **1976**, *50*, 169–179.
59. Gilli, R.; Kacurakova, M.; Mathlouthi, M.; Navarini, L.; Paoletti, S. *Carbohydr. Res.* **1994**, *263*, 315–326.
60. Dische, Z. *J. Biol. Chem.* **1946**, *167*, 189–198.
61. Morgan, W. T. J.; Elson, L. A. *Biochem. J.* **1934**, *28*, 988–995.
62. Kuhn, R.; Krüger, R. *Chem. Ber.* **1957**, *90*, 264–277.
63. Beau, J.-M.; Rollin, P.; Sinay, P. *Carbohydr. Res.* **1977**, *53*, 187–195.
64. Bitter, T.; Muir, H. M. *Anal. Biochem.* **1962**, *4*, 330–334.
65. Reissig, J. L.; Strominger, J. L.; Leloir, L. F. *J. Biol. Chem.* **1955**, *217*, 959–966.
66. Muckenschnabel, I.; Bernhardt, G.; Spruss, T.; Dietl, B.; Buschauer, A. *Cancer Lett.* **1998**, *131*(1), 13–20.
67. Bothner, H.; Wik, O. *Acta Otolaryngol. Suppl.* **1987**, *442*, 25–30.
68. Leith, M. M.; Loftus, S. A.; Kuo, J. W.; DeVore, D. P.; Keates, E. U. *J. Cataract Refract. Surg.* **1987**, *13*(5), 534–536.
69. Dick, H. B.; Krummenauer, F.; Augustin, A. J.; Pakula, T.; Pfeiffer, N. *J. Cataract Refract. Surg.* **2001**, *27*(2), 320–326.
70. Billmeyer, F. W., Jr. *Synthetic Polymers – Building the Giant Molecule*; Doubleday: Garden City, NY, 1972.
71. Tezel, A.; Fredrickson, G. H. *J. Cosmet. Laser Ther.* **2008**, *10*(1), 35–42.
72. Kablik, J.; Monheit, G. D.; Yu, L.; Chang, G.; Gershkovich, J. *Dermatol. Surg.* **2009**, *35*(Suppl. 1), 302–312.
73. Magnusson, B.; Kligman, A. M. *J. Invest. Dermatol.* **1969**, *52*(3), 268–276.
74. Ames, B. N.; McCann, J.; Yamasaki, E. *Mutat. Res.* **1975**, *31*(6), 347–364.
75. Galloway, S. M.; Bloom, A. D.; Resnick, M.; *et al. Environ. Mutagen.* **1985**, *7*(1), 1–51.
76. Floren, I. *J. Cataract Refract. Surg.* **1998**, *24*(2), 145–146.
77. Prestwich, G. D. *Biomaterials from Chemically-Modified Hyaluronan*. http://glycoforum.gr.jp/science/hyaluronan/HA18/HA18E.html; Glycoforum 2001.
78. Shu, X. Z.; Prestwich, G. D. In *Chemistry and Biology of Hyaluronan*; Garg, H. G., Hales, C. A., Eds.; Elsevier: Amsterdam, 2004; pp 475–504.
79. Allison, D.; Grande-Allen, K. *Tissue Eng.* **2006**, *12*(8), 2131–2140.
80. Morra, M. *Biomacromolecules* **2005**, *6*(3), 1205–1223.
81. Prestwich, G. D.; Kuo, J.-W. *Curr. Pharm. Biotech.* **2008**, *9*, 242–245.
82. Vercruysse, K. P.; Prestwich, G. D. *Crit. Rev. Ther. Drug Carrier Syst.* **1998**, *15*(5), 513–555.
83. Luo, Y.; Prestwich, G. D. *Exp. Opin. Ther. Pat.* **2001**, *11*, 1395–1410.
84. Shu, X. Z.; Ghosh, K.; Liu, Y.; *et al. J. Biomed. Mater. Res.* **2004**, *68A*, 365–375.
85. Prestwich, G. D. *Organogenesis* **2008**, *4*, 42–47.
86. Prestwich, G. D. *J. Cell. Biochem.* **2007**, *101*, 1370–1383.
87. Kuo, J. W.; Swann, D. A.; Prestwich, G. D. *Bioconjug. Chem.* **1991**, *2*, 232–241.
88. Kuo, J. W.; Swann, D. A.; Prestwich, G. D. U.S. Pat. 5,356,883, 1994.
89. Bulpitt, P.; Aeschlimann, D. *J. Biomed. Mater. Res.* **1999**, *47*, 152–169.
90. Pouyani, T.; Harbison, G. S.; Prestwich, G. D. *J. Am. Chem. Soc.* **1994**, *116*, 7515–7522.
91. Vercruysse, K. P.; Marecak, D. M.; Marecek, J. F.; Prestwich, G. D. *Bioconjug. Chem.* **1997**, *8*, 686–694.
92. Prestwich, G. D.; Marecak, D. M.; Marecek, J. F.; Vercruysse, K. P.; Ziebell, M. R. *J. Control. Release* **1998**, *53*(1–3), 93–103.
93. Ji, Y.; Ghosh, K.; Li, B.; Sokolov, J.; Clark, R.; Rafailovich, M. *Macromol. Biosci.* **2006**, *6*, 811–817.
94. Creuzet, C.; Kadi, S.; Rinaudo, M.; Auzely-Velty, R. *Polymer* **2006**, *47*, 2706–2713.
95. Jia, X.; Yeo, Y.; Clifton, R.; *et al. Biomacromolecules* **2006**, *7*, 3336–3344.
96. Weng, L.; Pan, H.; Chen, W. *J. Biomed. Mater. Res.* **2008**, *85A*, 352–365.
97. Gajewiak, J.; Cai, S.; Shu, X. Z.; Prestwich, G. D. *Biomacromolecules* **2006**, *7*, 1781–1789.
98. Band, P. A. In *The Chemistry, Biology and Medical Applications of Hyaluronan and Its Derivatives*; Laurent, T. C., Ed.; Portland Press: London, 1998; Vol. 72, pp 33–42.
99. Campoccia, D.; Doherty, P.; Radice, M.; Brun, P.; Abatangelo, G.; Williams, D. F. *Biomaterials* **1998**, *19*(23), 2101–2127.
100. Della Valle, F.; Romeo, A. Eur. Pat. Applic. EP 265,116, 1988.
101. Young, J.; Cheng, K.; Tsou, T.; Liu, H.; Wang, H. *J. Biomater. Sci. Polym. Edn.* **2004**, *15*, 767–780.
102. Zhang, M.; James, S. *J. Mater. Sci.* **2005**, *40*, 2937–2943.
103. Huin-Amargier, C.; Marchal, P.; Payan, E.; Dellacherie, E. *J. Biomed. Mater. Res.* **2005**, *76A*, 416–424.
104. de Belder, A. N.; Malson, T. U.S. Pat. 4,886,787, 1989.
105. Zhao, X. B.; Fraser, J. E.; Alexander, C.; Lockett, C.; White, B. J. *J. Mater. Sci. Mater. Med.* **2002**, *13*(1), 11–16.
106. Segura, T.; Anderson, B.; Chung, P.; Webber, R.; Shull, K.; Shea, L. *Biomaterials* **2005**, *26*, 359–371.
107. Mlcochov, P.; Hajokova, V.; Steiner, B.; *et al. Carbohydr. Polym.* **2007**, *69*, 344–352.
108. Johns, D. B.; Rodgers, K. E.; Donahue, W. D. *Fertil. Steril.* **1997**, *68*, 37–42.
109. Picart, C.; Mutterer, J.; Richert, L.; *et al. Proc. Natl. Acad. Sci. USA* **2002**, *99*, 12531–12535.
110. Fuente, M.; Seijo, B.; Alonso, M. *Macromol. Biosci.* **2008**, *8*, 441–450.
111. Dulong, V.; Lack, S.; Le Cerf, D.; Picton, L.; Vannier, J.; Muller, G. *Carbohydr. Polym.* **2004**, *57*, 1–6.
112. Miyamoto, K.; Saski, M.; Minamisawa, Y.; Kurahashi, Y.; Kano, H.; Ishikawa, S. *J. Biomed Mater. Res.* **2004**, *70A*, 550–559.
113. Matsuda, T.; Magoshi, T. *Biomacromolecules* **2002**, *3*, 942–950.
114. Shu, X. Z.; Liu, Y.; Palumbo, F.; Luo, Y.; Prestwich, G. D. *Biomaterials* **2004**, *25*, 1339–1348.
115. Shu, X. Z.; Liu, Y.; Luo, Y.; Robert, M. C.; Prestwich, G. D. *Biomacromolecules* **2002**, *3*, 1304–1311.
116. Pouyani, T.; Prestwich, G. D. U.S. Pat. 5,652,347, 1997.
117. Shu, X. Z.; Liu, Y.; Palumbo, F. S.; Prestwich, G. D. *Biomaterials* **2003**, *24*, 3825–3834.
118. Shu, X. Z.; Ahmad, S.; Liu, Y.; Prestwich, G. D. *J. Biomed. Mater. Res.* **2006**, *79A*, 902–912.
119. Liu, Y.; Shu, X. Z.; Prestwich, G. D. *Biomaterials* **2005**, *26*, 4737–4746.
120. Ghosh, K.; Shu, X. Z.; Mou, R.; *et al. Biomacromolecules* **2005**, *6*, 2857–2865.
121. Vanderhooft, J. L.; Mann, B. K.; Prestwich, G. D. *Biomacromolecules* **2007**, *8*, 2883–2889.
122. Ifkovits, J.; Burdick, J. *Tissue Eng.* **2007**, *13*, 2369–2385.
123. Leach, J. B.; Bivens, K. A.; Patrick, C. W., Jr. *Biotechnol. Bioeng.* **2003**, *82*, 578–589.
124. Smeds, K. A.; Pfister-Serres, A.; Miki, D.; *et al. J. Biomed. Mater. Res.* **2001**, *54*(1), 115–121.
125. Leach, J. B.; Schmidt, C. E. *Biomaterials* **2005**, *26*(2), 125–135.
126. Sahoo, S.; Chung, C.; Khetan, S.; Burdick, J. *Biomacromolecules* **2008**, *9*, 1088–1092.
127. Darr, A.; Calabro, A. *J. Mater. Sci. Mater. Med.* **2009**, *20*, 33–44.
128. Crescenzi, V.; Cornelio, L.; Di Meo, C.; Nardecchia, S.; Lamanna, R. *Biomacromolecules* **2007**, *8*, 1844–1850.
129. Yadav, A.; Mishra, P.; Agrawal, G. *J. Drug Target.* **2008**, *16*, 91–107.
130. Hammer, M. E.; Burch, T. G. *Invest. Ophthalmol. Vis. Sci.* **1984**, *25*(11), 1329–1332.
131. Glasser, D. B.; Katz, H. R.; Boyd, J. E.; Langdon, J. D.; Shobe, S. L.; Peiffer, R. L. *Arch. Opththalmol.* **1989**, *107*, 1047–1051.
132. McDermott, M. L.; Hazlett, L. D.; Barrett, R. P.; Lambert, R. J. *J. Cataract Refract. Surg.* **1998**, *24*(5), 678–683.
133. Fry, L. L. *J. Cataract Surg.* **1989**, *15*, 415–420.
134. Arshinoff, S. A. *Ophthalmic Prac.* **1998**, *16*(1), 24–32.
135. Poyer, J. F.; Chan, K. Y.; Arshinoff, S. A. *J Cataract Refract. Surg.* **1998**, *24*(8), 1130–1135.
136. Poyer, J. F.; Chan, K. Y.; Arshinoff, S. A. *J Cataract Refract. Surg.* **1998**, *24*(1), 84–90.
137. Lo, G.; LaValley, M.; McAlindon, T.; Felson, D. *JAMA* **2003**, *290*(23), 3115–3121.
138. van den Bekerom, M. P.; Lamme, B.; Sermon, A.; Mulier, M. *Arch. Orthop. Trauma Surg.* **2008**, *128*(8), 815–823.
139. Blaine, T.; Moskowitz, R.; Udell, J.; *et al. J. Bone Joint Surg. Am.* **2008**, *90*(5), 970–979.
140. Sun, S. F.; Chou, Y. J.; Hsu, C. W.; Chen, W. L. *Curr. Rev. Musculoskelet. Med.* **2009**, *2*(2), 78–82.
141. Shi, Z.; Guo, C.; Awad, M. *Cochrane Database Syst. Rev.* **2003**, *1*, CD002970.
142. Felson, D. T. *Arthritis Rheum.* **2001**, *44*, 1477–1480.
143. Liang, M. H.; Larson, M. G.; Cullen, K. E.; Schwartz, J. A. *Arthritis Rheum.* **1985**, *28*, 542–547.
144. Arrich, J.; Piribauer, F.; Mad, P.; Schmid, D.; Klaushofer, K.; Mullner, M. *CMAJ* **2005**, *172*(8), 1039–1043.
145. Reichenbach, S.; Blank, S.; Rutjes, A. W.; *et al. Arthritis Rheum.* **2007**, *57*(8), 1410–1418.
146. Kawcak, C. E.; Frisbie, D. D.; Trotter, G. W.; *et al. Am. J. Vet. Res.* **1997**, *58*(10), 1132–1140.
147. Beasley, K. L.; Weiss, M. A.; Weiss, R. A. *Facial Plast. Surg.* **2009**, *25*(2), 86–94.
148. Kusin, S.; Lippitz, J. *Dis. Mon.* **2009**, *55*(4), 236–256.
149. Bogdan Allemann, I.; Baumann, L. *Clin. Interv. Aging* **2008**, *3*(4), 629–634.

150. Smith, K. C. *Dermatol. Online J.* **2008**, *14*(8), 3.
151. Kirker, K. R.; Luo, Y.; Nielson, J. H.; Shelby, J.; Prestwich, G. D. *Biomaterials* **2002**, *23*(17), 3661–3671.
152. Kirker, K. R.; Luo, Y.; Morris, S. E.; Shelby, J.; Prestwich, G. D. *J. Burn Care Rehabil.* **2004**, *25*, 276–286.
153. Haney, A. F.; Doty, E. *Fertil. Steril.* **1998**, *70*(1), 145–151.
154. Acunzo, G.; Guida, M.; Pellicano, M.; *et al. Hum. Reprod.* **2003**, *18*(9), 1918–1921.
155. Guida, M.; Acunzo, G.; Sardo, A. D.; *et al. Hum. Reprod.* **2004**, *19*(6), 1461–1464.
156. Brunelli, G.; Longinotti, C.; Bertazzo, C.; Pavesio, A.; Pressato, D. *J. Orthop. Res.* **2005**, *23*(6), 1377–1382.
157. Tang, C. L.; Jayne, D. G.; SeowChoen, F. A.; Ng, Y. Y.; Eu, K. W.; Mustapha, N. *Ann. Surg.* **2006**, *243*(4), 449–455.
158. Hansen, J. K.; Thibeault, S. L.; Walsh, J. F.; Shu, X. Z.; Prestwich, G. D. *Ann. Otol. Rhinol. Laryngol.* **2005**, *114*(9), 662–670.
159. Duflo, S.; Thibeault, S. L.; Li, W.; Shu, X. Z.; Prestwich, G. D. *Tissue Eng.* **2006**, *12*, 2171–2180.
160. Connors, R. C.; Muir, J. J.; Liu, Y.; *et al. J. Surg. Res.* **2007**, *140*(2), 237–242.
161. Liu, Y.; Li, H.; Shu, X. Z.; Gray, S. D.; Prestwich, G. D. *Fertil. Steril.* **2005**, *83*, 1275–1283.
162. Liu, Y.; Shu, X. Z.; Prestwich, G. D. *Fertil. Steril.* **2007**, *87*, 940–948.
163. Liu, Y.; Skardal, A.; Shu, X. Z.; Prestwich, G. D. *J. Orthop. Res.* **2008**, *26*(4), 562–569.
164. Sondrup, C.; Liu, Y.; Shu, X. Z.; Prestwich, G. D.; Smith, M. E. *Otolaryngol. Head Neck Surg.* **2006**, *135*(1), 28–35.
165. Orlandi, R. R.; Shu, X. Z.; McGill, L.; Petersen, E.; Prestwich, G. D. *Laryngoscope* **2007**, *117*, 1288–1295.
166. Park, A. H.; Jackson, A.; Hunter, L.; *et al. Otol. Neurotol.* **2006**, *27*, 1170–1175.
167. Uccioli, L. *Int. J. Low Extrem. Wounds* **2003**, *2*(3), 140–151.
168. Cai, S.; Liu, Y.; Zheng Shu, X.; Prestwich, G. D. *Biomaterials* **2005**, *26*(30), 6054–6067.
169. Liu, Y.; Cai, S.; Shu, X. Z.; Shelby, J.; Prestwich, G. D. *Wound Repair Regen.* **2007**, *15*, 245–251.
170. Serban, M. A.; Prestwich, G. D. *Methods* **2008**, *45*, 93–98.
171. Prestwich, G. D. *Acc. Chem. Res.* **2008**, *41*, 139–148.
172. Liu, Y.; Shu, X.; Gray, S.; Prestwich, G. *J. Biomed. Mater. Res.* **2004**, *68A*, 142–149.
173. Ghosh, K.; Ren, X.-D.; Shu, X. Z.; Prestwich, G. D.; Clark, R. A. F. *Tissue Eng.* **2006**, *12*, 601–613.
174. Mironov, V.; Kasyanov, V.; Zheng Shu, X.; *et al. Biomaterials* **2005**, *26*(36), 7628–7635.
175. Mironov, V.; Prestwich, G. D.; Forgacs, G. *J. Mater. Chem.* **2007**, *17*, 2054–2060.
176. Peattie, R. A.; Rieke, E. R.; Hewett, E. M.; Fisher, R. J.; Shu, X. Z.; Prestwich, G. D. *Biomaterials* **2006**, *27*(9), 1868–1875.
177. Hosack, L. W.; Firpo, M. A.; Scott, J. A.; Prestwich, G. D.; Peattie, R. A. *Biomaterials* **2008**, *29*(15), 2336–2347.
178. Solchaga, L. A.; Yoo, J.; Lundberg, M.; *et al. J. Orthop. Res.* **2000**, *18*, 773–780.
179. Nehrer, S.; Domayer, S.; Dorotka, R.; Schatz, K.; Bindreiter, U.; Kotz, R. *J. Radiol.* **2006**, *57*(1), 3–8.
180. Nettles, D. L.; Vail, T. P.; Morgan, M. T.; Grinstaff, M. W.; Setton, L. A. *Ann. Biomed. Eng.* **2004**, *32*(3), 391–397.
181. Park, Y. D.; Tirelli, N.; Hubbell, J. A. *Biomaterials* **2003**, *24*, 893–900.
182. Chung, C.; Burdick, J. *Tissue Eng. A* **2009**, *15*, 243–254.
183. Liu, Y.; Shu, X. Z.; Prestwich, G. D. *Tissue Eng.* **2006**, *12*(12), 3405–3416.
184. Liu, Y.; Ahmad, S.; Shu, X. Z.; Sanders, R. K.; Kopesec, S. A.; Prestwich, G. D. *J. Orthop. Res.* **2006**, *24*, 1454–1462.

2.215. Collagen: Materials Analysis and Implant Uses

D I Zeugolis, National University of Ireland, Galway, Ireland
M Raghunath, National University of Singapore, Singapore

© 2011 Elsevier Ltd. All rights reserved.

2.215.1.	**Origins of Collagen and Role in Animal Physiology**	262
2.215.1.1.	Collagen: A Component of the Extracellular Matrix	262
2.215.1.2.	General Characteristics of Collagen	262
2.215.1.3.	The Collagen Family: Types and Forms	264
2.215.2.	**The Biochemical Fingerprint of Collagen**	264
2.215.2.1.	Primary Structure	264
2.215.2.2.	Secondary to Quaternary Structure of Collagen	265
2.215.2.3.	Supramolecular Assembly of Collagen	265
2.215.2.4.	Natural Cross-Links of Collagen Aggregates	265
2.215.2.4.1.	Classical collagen cross-links	265
2.215.2.4.2.	Sugar-based collagen cross-links	267
2.215.2.4.3.	Other enzymatic cross-links	267
2.215.3.	**Sources of Collagen**	267
2.215.4.	**Collagen: Purification and Analysis**	268
2.215.5.	**Biomedical Applications of Collagen**	270
2.215.6.	**Outlook and Future for Collagen Materials**	273
References		274

Glossary

Collagen cross-links Covalent bond formation between α chains within a triple helix (intramolecular) or between α chains of neighboring triple helices (intermolecular). Cross-links are enzymatically initiated and are formed spontaneously over the lifetime of an organism. Cross-linking constitutes a crucial mechanism that stabilizes the tissues and provides resistance to wear and tear.

Collagen type Up to now, 29 different collagen types have been identified. All collagens are composed of polypeptide subunits called α chains. Three α chains make up each molecule (γ-component).

Collagen type I The most abundant collagen in mammalian body. It is used extensively for tissue-engineering applications.

Extracellular matrix (ECM) By definition, secreted molecules that become immobilized around a cell.

Gelatin Heat-denatured collagen whereby the α chains have been disassociated or separated from each other. In solution, these α chains do not come into proper register anymore and form random coil structures instead of triple helices.

Gly-X-Y repeat The classical amino acid sequence that characterizes the primary structure of collagen and represents it triple-helical domain. The X-position is often occupied by proline (Pro) while the Y-position is often occupied by hydroxyproline (Hyp).

Abbreviations

AGE	Advanced glycation endproduct
ECM	Extracellular matrix
FBS	Fetal bovine serum
Gly	Glycine
HFP	Hexafluoropropanol
HPLC	High performance liquid chromatography
Hyl	Hydroxylysine
Hyp	Hydroxyproline
kDa	Kilo Dalton
Lys	Lysine
mTGase	Microbial transglutaminase
PAGE	Polyacrylamide gel electrophoresis
PAMAM	Polyamidoamine
PEG	Polyethylene glycol
PEO	Polyethylene oxide
Pro	Proline
SCA	Sircol dye assay
SDS	Sodium dodecyl sulfate
SHG	Second harmonics generation
TGase	Transglutaminase

2.215.1. Origins of Collagen and Role in Animal Physiology

2.215.1.1. Collagen: A Component of the Extracellular Matrix

Collagen represents the major structural extracellular matrix (ECM) component of vertebrates. It is the most abundant mammalian protein accounting for about 20–30% of total body proteins.[1] About 700 My, collagen made its appearance in the oldest metazoan of the animal kingdom on earth, the sponges, and was found subsequently also in other invertebrates such as jellyfish, coral, and sea anemones (reviewed in Huxley-Jones *et al.*[2]). Starting from a prototypic collagen we now have evidence for an evolutionary branching into currently 29 different collagens in vertebrates.[3] Vertebrate ECM genes have mainly arisen through duplication of preexisting genes and modification of preexisting matrix molecules all of which were tested fiercely for their usefulness.[2] The collagen types that have survived the test of time are very sensitive to even point mutations. Single amino acid changes, mostly glycine substitutions in the collagenous or triple-helical region, lead to tissue pathology and disorder. Collagens, in particular the major class of fibrillar collagens, are often referred to scaffolds that hold cells in place and provide them with anchorage while lending tensile strength or stiffness to a tissue. Often overlooked are the ligands that bind to these collagenous aggregates and add function. Nonfibrillar collagens are to be mentioned here along with proteoglycans, growth factor-binding proteins, and growth factors themselves.[4] Cells therefore gather complex information from their microenvironment that induces them to spread, migrate, divide, regulate metabolic functions, or differentiate. This is accomplished not only via recognition of extracellular matrices with integrin receptors, but also via discoidin domain receptors that have recently emerged as nonintegrin-type receptors for collagen.[5] It is even speculated that cells can recognize a suprastructural collagen assembly as a whole, even different collagen types.[6] We have listed the currently known collagen types in **Table 1**. It is conspicuous from this table that dermis alone contains some ten different collagen types, and tendon at least eight. While collagen I amounts for roughly 70% of skin proteins, it is the almost, but not exclusive, component of tendons with 97–98%.[7] As animal dermis (e.g., bovine hides) and tendons (e.g., bovine or equine Achilles tendon) are a major source for acidic extracts and slurries for freeze-dried collagen sponges for biomedical uses, it becomes obvious that a substantial fraction of these biological functions that are created by the multitude of collagens and other ECM proteins might become lost during industrial processing, but some of them might be retained. It is therefore essential to know the basic composition of the connective tissue of the tissue unit used for manufacturing biomaterials and to envision the interaction of cells with it. This alone decides the fate integration, remodeling or inflammatory destruction of this biological biomaterial in a host.

2.215.1.2. General Characteristics of Collagen

Collagens are synthesized by a variety of mesenchymal and epithelial cells and details of their biosynthesis are reviewed extensively in Kielty and Grant.[8] All members of the collagen family have a common and unique signature, namely the [Gly-X-Y]*n* sequence in which the X- and Y-positions are frequently occupied by proline (Pro) and hydroxyproline (Hyp). The latter represents a significant posttranslational modification that occurs intracellular and is dependent on vitamin C. This unique primary structure translates into a unique secondary structure, the collagen α chain. It is not to be confused with the α-helix of a normal protein which is a right-handed structure stabilized by hydrogen bonds that bridge the turns of the helix. These hydrogen bonds –C=O:–H–N– occur between the α carbon atoms of the partnering amino acids. In contrast, the collagen α chain forms a left-handed helix that is stretched due to the abundance of prolyl residues acting as helix breakers. This increases the distance between turns (pitch) which precludes hydrogen bond formation. In addition, Pro is an unusual amino acid as the amino nitrogen is part of a secondary amino group (N–H) instead of the usual primary amino group ($-NH_2$). This means that after the dipeptide bond formation between Pro and another amino acid the α carbon atom of Pro has no further hydrogen to offer. Therefore, the collagen α chain is not stabilized by hydrogen bonds. Pro renders the collagen α chain stretched and stiff, therefore this secondary structure cannot fold into a superstructure. Thus, we have to consider secondary and tertiary structure of the collagen α chain as identical. (This aspect is often not discussed in textbooks. The triple helix is often given as the tertiary structure of collagen, which in fact it is not.) The quaternary structure, however, is unique again, represented by the association of three α chains forming a triple helix. The three pro-α chains are tightly wound around each other and form a three-stranded rod-like molecule with the glycyl residues representing the central core of this molecule. For this reason, Gly-X-Y repeats are also addressed as 'collagenous' or 'triple-helical' domains as they are a predictor for the formation of such a unique quaternary structure.

The Hyp residues are derived from posttranslational modification of a substantial number of abundant prolyl residues and they stabilize the triple-helical domain (not the single α chain) by interchain hydrogen bonding along the helix. Collagenous domains vary in length from as short as 30 to in excess of 1500 amino acid residues and are either uninterrupted or contain imperfections in the Gly-X-Y repeat that result in flexible regions within the relatively stiff, rod-like triple helix. With the exception of collagens XXIV and XXVII, the major triple-helical domain is slightly longer than 1000 amino acid residues and has a perfect Gly-X-Y triplet structure. All nonfibrillar collagens have at least one imperfection or interruption in their triple helices. The amino end of a fibrillar collagen, the *N*-propeptide, usually contains at least one small triple-helical domain, designated the minor helix. Once the major triple helix has formed, the amino and carboxyl ends are proteolytically removed from the central molecule by specialized enzymes in the extracellular space. These processed molecules align themselves in a quarter stagger arrangement in the growing fibril (reviewed in Kielty and Grant[8]). In transmission electron micrographs, collagen fibrils have an alternating light and dark pattern, which has led to them being termed 'banded' or 'cross-striated fibrils' – a typical signature feature shown in countless textbooks and publications, including this chapter. This banding pattern is also evident from

Table 1 The collagen family, types, forms, and tissue distribution

Collagen type	*Chains*	*Molecular assembly*	*Supramolecular structure*	*Mr × 10^{-3} α chain*	*Examples of tissue location*
I	$[\alpha1(I)]_2\alpha2(I)$	Monomers staggered by 67 nm	Large diameter 67 nm banded fibrils	95	Bone, cornea, dermis, tendon
I trimer	$[\alpha1(I)]_3$		67-nm banded fibrils		Tumors, dermis, bone
II	$[\alpha1(II)]_3$	Monomers staggered by 67 nm	67-nm banded fibrils	95	Cartilage, vitreous, cartilaginous zones of tendon
III	$[\alpha1(III)]_3$	Monomers staggered by 67 nm	Small-diameter, 67-nm banded fibrils	95	Dermis, aorta, uterus, admixture in tendon, intestine, blood vessels
IV	$[\alpha1(IV)]_2\alpha2(IV)$; also $\alpha3(IV)$, $\alpha4(IV)$, $\alpha5(IV)$, $\alpha6(IV)$	Association of 4N- and 2C-termini	Nonfibrillar meshwork	170–180	Basement membranes
V	$[\alpha1(V)]_2\alpha2(V)$ $[\alpha1(V)\alpha2(V)\alpha3(V)]$ $[\alpha1(V)]_3$	Monomers staggered by 67 nm	9-nm diameter banded fibrils	120–145	Placental/embryonic tissue dermis, bone, cornea
VI	$[\alpha1(VI)\alpha2(VI)\alpha3(VI)]$	Association into tetramers that aggregate end to end	5–10-nm diameter beaded microfibrils, 100-nm periodicity	$\alpha1(VI)$ 140 $\alpha2(VI)$ 140 $\alpha3(VI)$ 340	Uterus, dermis, cartilage Muscle
VII	$[\alpha1(VII)]_3$	Lateral aggregation of antiparallel dimers	Anchoring fibrils	170	Skin, amniotic membrane Cornea, mucosal epithelium
VIII	$[\alpha1(VIII)]_2\alpha2(VIII)$	?	Nonfibrillar, hexagonal lattice?	61	Descemet's membrane endothelial cells
IX	$[\alpha1(IX)\alpha2(IX)\alpha3(IX)]$	Covalently cross-linked to surface of collagen II fibrils	FACIT; nonfibrillar	68–115	Cartilage, vitreous, admixture in tendon
X	$[\alpha1(X)]_3$	?	Nonfibrillar, hexagonal lattice?	59	Calcifying cartilage (incl parts of tendons)
XI	$[\alpha1(XI)\alpha2(XI)\alpha3(XI)]$	Monomers staggered by 67 nm	Fine fibrils similar to those of collagen V	110–145	Cartilage, intervertebral disk
XII	$[\alpha1(XII)]_3$	Associates with surface of collagen fibrils?	FACIT; nonfibrillar	220, 340	Dermis, tendon, cartilage
XIII	$\alpha1(XIII)$	?	Membrane-intercalated	62–67	Endothelial cells, epidermis
XIV	$[\alpha1(XIV)]_3$	?	FACIT; nonfibrillar	220	Dermis, tendon, cartilage
XV	$\alpha1(XV)$	?	MULTIPLEXIN; nonfibrillar	125	Placenta, kidney, heart, ovary, testis
XVI	$\alpha1(XVI)$	?	FACIT; nonfibrillar	150–160	Heart, kidney, muscle
XVII	$[\alpha1\ (XVII)]_3$	?	Membrane-intercalated	180	Hemidesmosomes (skin) specialized epithelia
XVIII	$\alpha1(XVIII)$	?	MULTIPLEXIN; non fibrillar	200	Kidney, liver
XIX	$\alpha1(XIX)$	Aggregates	FACIT; nonfibrillar	165	Transitory embryonic expression, interneurons and formation of hippocampal synapses, basement membranes, muscle cell, rhabdomyosarcoma
XX	$\alpha1(XX)$	?	FACIT	185, 170, and 135	Corneal epithelium, embryonic skin, sternal cartilage, tendon
XXI	$\alpha1(XXI)$	?	FACIT	?	Blood vessel walls, secreted by smooth muscle cells
XXII	$\alpha1(XXII)$		FACIT	200	Tissue junctions
XXIII	$\alpha1(XXIII)$		Membrane-intercalated		Tumors (prostate)
XXIV	$\alpha1(XXIV)$		Fibrillar, fibril associated?		Regulation of collagen I fibrillogenesis, osteoblast differentiation marker
XXV	$\alpha1(XXV)$		Membrane-intercalated		Interaction with β amyloid plaques in Alzheimer's disease
XXVI	$\alpha1(XXVI)$		FACIT(?)	~80	Ovary and testis
XXVII	$\alpha1(XXVII)$	Network	Thin fibrils nonstriated		Hypertrophic cartilage
XXVIII	$\alpha1(XXVIII)$			~50	Basement membrane of Schwann cells
XXIX	$\alpha1(XXIX)$	?	Nonfibrillar?		Suprabasal cells in epidermis

images taken from the surface of fibrils as obtained via atomic force microscopy. What is not evident from these pictures is that these fibrils can be composed of a variety of collagen types and which isoform of a particular collagen type might be forming these fibrils.

2.215.1.3. The Collagen Family: Types and Forms

The difference between different pro-α chains within one collagen type allows compositional changes within one collagen type. For example, collagen I can exist as a heterotrimer of two α1 chains and one α2 chain, or as a homotrimer of three α1 chains. A series of collagens exist only as homotrimers (see Table 1). In contrast, six genes coding for six different α(4) chains create considerably diverse isoforms of collagen IV that have histologically distinct distribution in different types of basement membranes. Hence, different collagen types are necessary to confer distinct biological features to the various types of connective tissues in the body. For example, collagen type I is predominant in higher-order animals especially in the skin, tendon, and bone where extreme forces are transmitted. Type III is found in limited quantities (~10%) in association with type I. Thus, type III is a minor component of type I collagen from skin (reviewed in Friess[9]). In addition, blood vessels predominantly contain type III. This means that a typical cross-striated fiber in TEM might be in reality a heterotypic fiber, a composite of different collagen types.

Collagen III has been addressed previously as 'contaminant'[9] from the industrial point of view. We feel that with increasing knowledge about the diversity of the collagen family and the multiple collagenous composites found in vertebrate tissue it would be preferable to accept it as a given biological admixture that plays an important biological role (This explains the difficulty to obtain pure collagen III preparations. In several commercially available collagen III preparations we found mostly collagen I, truly much more than a mere contaminant in this case.) and to acknowledge that *in vivo* 'pure' collagen populations exist only on the microscale.

Currently, 29 collagen types have been identified, some of them with highly unique features, many with interrelated features, but often with specific localization in specific tissues. This variety points to crucial biological functions and is reflected by a multitude of physical structures. Currently, the collagen family falls into four divisions that are largely based on their primary structure and the respective sizes of their triple-helical domains.

Group 1 consists of the fibril-forming collagens I–III, V, XI, XXIV, and XXVII, as they have triple helices with uninterrupted Gly-X-Y stretches of approximately 300 nm in length. However, XXI and XXVII show imperfections in the triple-helical stretches as seen in invertebrates. The classical fibril-forming collagen triple helices act as monomers that form supramolecular assemblies by associating in parallel, but staggered by one-quarter of their length. This quarter staggered array leads to the typical cross-striation with a 67-nm banding pattern as seen after contrasting with heavy metals in transmission electron microscopy. This feature is absolutely typical for collagen. Collagen fibrils in the dermis, the source of leather and many types of collagen sponges, are often alloys of different collagen types, usually types I, III, and V. These fibers are referred to as heterotypic as opposed to homotypic fibrils that would be composed of only one collagen type, for example, collagen VII in anchoring fibrils of the dermoepidermal junction.

Group 2 hosts the basement membrane collagens IV, VII, and XXVIII. While collagen IV forms a fibrillar meshwork, collagen VII forms cross-striated fibrils, albeit with a different banding pattern and created by antiparallel dimer association.

Group 3 contains the short-chain collagens VI, VIII, and X. They are named after their triple-helical regions which extend to 100 and 150 nm, respectively. Collagen VI forms beaded microfilaments, while collagens VIII and X form most likely hexagonal lattices. The recently discovered collagen XXIX has a short uninterrupted triple-helical region that is flanked by several von Willebrand factor A domains.

Group 4 contains a collection of collagens that show multiple interruptions of the triple-helical Gly-X-Y stretches. These *f*ibril-*a*ssociated *c*ollagens with *i*nterrupted *t*riple helices are known as FACIT collagens and comprise types IX, XII, XIV, XVI, XIX–XXII. Taking the number of interruptions to the extreme are collagens XV and XVII which have been subsumed under the term MULTIPLEXINs. Finally, a remarkable subgroup are collagens XIII, XVII, XXIII, and XXV for they contain transmembrane domains that allow these molecules to be inserted in cell membranes while projecting the (interrupted) triple-helical domains outward into the extracellular space. A synopsis on current collagen types, their structure and tissue distribution are given in Table 1. The current collagens have been reviewed very recently,[3] further data on tissue distribution, and biochemical features of collagens I–XIX are discussed in Kielty and Grant,[8] while current references on collagens XX–XIX are given elsewhere.[10–19] Important to know is that the proteolytic breakdown products of collagens can have a biological life on their own. For example, the carboxyl terminal domains of collagens XV and XVIII can be cleaved to generate antiangiogenic peptides. These are called either endostatin and restin, or endostatin-XVIII and endostatin-XV.[20,21]

2.215.2. The Biochemical Fingerprint of Collagen

2.215.2.1. Primary Structure

Keeping in mind that any given tissue preparation can naturally contain half a dozen and more collagen types we can nevertheless focus on the most predominant collagen type, collagen I, as it presents the materials scientist with the typical analytical issues related to collagen and allows us to understand the biochemistry of all collagens in principle. Collagen I is a glycoprotein with a carbohydrate content of less than 1%. The sugar components are either a single galactose unit or a disaccharide of galactose and glucose *O*-glycosidically attached via hydroxylysine (Hyl) residues. The basic collagen I molecule contains three polypeptide pro-α chains, each consisting of more than 1000 amino acids. The triple-helical Gly-X-Y domain is uninterrupted. Thirty-three percent of the amino acids are Gly residues, 35% of the nonglycine positions are occupied by Pro, found almost exclusively in the X-position, and 4-Hyp, predominantly in the Y-position. Hyp and Pro account for approximately 22% of the total amino acid residues. Hyp is derived from Pro by catalytic activity of prolyl hydroxylase, an enzyme resident in the lumen of the

endoplasmic reticulum of fibrogenic cells. Limited amounts of Hyp can be found in elastin and collagen-like molecules, but their presence in any given tissue that is not extremely rich in elastic fibers is negligible. Hyp comprises approximately 10% of the amino acid composition of collagen and therefore is a molecular fingerprint for collagen or its breakdown products. Hyp can be quantified via HPLC or colorimetric assays after total hydrolysis (see Section 2.215.4). Collagen also contains the unusual amino acid Hyl, a posttranslational modification of lysine via lysyl hydroxylase. The formation of Hyl residues and subsequent attachment of sugar components appear to be important modulators of fibrillogenesis and further cross-linking and fibril stabilization.[8]

2.215.2.2. Secondary to Quaternary Structure of Collagen

Compared with most synthetic polymers, collagen shows considerable structural complexity. The α-chains form left-handed helices with 3.3 residues per turn and a pitch of 0.94 nm as identified by X-ray analysis. In comparison, common peptides form right-handed α-helices (or β-pleated sheets or mixtures of α-helices and β-sheets) with a pitch of 0.54 nm and 3.6 residues per turn. This means that the collagen α chain is stretched (larger pitch), but narrowly twisted (less amino residues per turn). The rod-shaped triple helix of collagen I has an average molecular weight of approximately 300 kDa, a length of 300 nm with a diameter of 1.5 nm. This extreme ratio of the dimensions gives rise to high viscosity in solutions and high mobility in electrical fields (reviewed in Friess[9]). Collagens are secreted as oversized molecules, procollagens. Specialized enzymes remove the N- and C-terminal propeptides leaving a triple helix with short nontriple helical stubs measuring 9–26 amino acids in length at the amino and carboxyl terminal chain ends. These nonhelical regions are denoted as telopeptides, they play a role in the registering of collagen α chains and cross-linking (see Section 2.215.2.4.1).[8]

2.215.2.3. Supramolecular Assembly of Collagen

Collagen triple helices are able to form supramolecular aggregates only after the enzymatic removal of the propeptides. The triple helices are staggered by 67 nm with an additional gap of 40 nm between succeeding molecules. The triple-helical molecules stagger longitudinally and bilaterally into fibrils with distinct periodicity. Fibrillogenesis starts with microfibrils consisting of four to eight collagen molecules that grow further into fibrils. Those fibrils reach from 10 to 500 nm in diameter depending on tissue type and stage of development. These collagen fibrils organize into fibers, which on their part can form even larger fiber bundles. Ultrastructurally, microfibrils, fibrils, and bundles exhibit the typical banding pattern; however, the absence of cross-striation does not signify absence of collagens, but merely absence of fibrillar collagens (see Table 1). Another particular physical feature of collagen fibers is their ability to be optically imaged in multiphoton microscopy through second harmonics generation (SHG).[22] The reason for this lies in the physical properties of the triple helix which – in crystallographic terms – is defined as a noncentrosymmetric structure, which after self-assembly into higher-order fibers provides an 'ordered nonlinear medium with a cross-sectional path length comparable to near infrared wavelengths.'[23] SHG has been used in multiphoton microscopy for specific optical imaging of collagen in tissues. In skin, the heterotypic interwoven collagen fibers and bundles (collagen types I≫III>V) give strong SHG signals, whereas the dermoepidermal junction (collagen IV, VII, XVII) does not. Thus, the SHG signal is strongly dependent on the material order, making it highly sensitive to structural changes such as go along with denaturation.[24]

2.215.2.4. Natural Cross-Links of Collagen Aggregates

2.215.2.4.1. Classical collagen cross-links

The systematic packaging of the triple helices lends strength and resilience to the collagen fibers. Additional mechanical and chemical stability is derived from intra- and intermolecular cross-links. The cross-linking occurs enzymatically and nonenzymatically. Initially, the formation of cross-links is initiated indirectly by lysyl oxidase during fibril formation (reviewed in Kielty and Grant[8]). The enzyme can only work on the surface of forming fibrils and paves the path for subsequent spontaneous cross-linking processes rather than creating the cross-linking itself. Its activity is limited to the nonhelical telopeptides and leads to the conversion of selective Lys and Hyl residues to the corresponding aldehydes allysine and hydroxylallysine. While the fibrils associate, these aldehydes can react spontaneously. Intramolecular cross-links form between two α chains in the nonhelical (telopeptide) section of the same molecule by aldol condensation of two aldehydes, for example, two allysines, resulting in α chain dimers that are evident in sodium dodecyl sulphate-polyacrylamide gel electrophoresis (SDS-PAGE) gels as β component (see Figures 1 and 2). Intermolecular cross-links occur between the telopeptides of one collagen molecule and the helical region of a quarterly staggered adjacent molecule. These bridges between two different triple helices result from aldimine between aldehyde residues and ε-amino groups presented by Lys and Hyl. The interchain bifunctional cross-links are still reactive and continue to form multifunctional cross-links through multiple condensations with His, Lys, or Hyl residues. These aldimine cross-links are acid labile and their detection depends on their prior reduction with sodium borohydride ($NaBH_4$), after which they can be recovered from acid hydrolysates of collagen and subsequent chromatography. Details of collagen cross-link formation are reviewed in Kielty and Grant.[8]

Quantification of the individual cross-links in collagen is performed currently in highly specialized laboratories and is complicated by the fact that in most tissues the number of borohydride-reducible cross-links decreases with age because they most probably mature into stable, nonreducible cross-links, the nature and number of which remain to be fully defined. In the case of the Hyl aldehyde pathway, the more mature cross-links appear to be based on trivalent 3-hydroxypyridinium residues – Hyl-pyridinoline (3Hyl) and Lys-pyridinoline (2Hyl and 1Lys). These two cross-links are naturally fluorescent and can be assayed directly in tissue hydrolysates (reviewed in Kielty and Grant[8]). The pyridinoline cross-links are stable and can be detected in urine by HPLC[25] or specific enzyme-linked immunosorbent assays.[26] Measurement of the excretion of these cross-links is gaining interest for the monitoring of osteoporosis and its treatment.

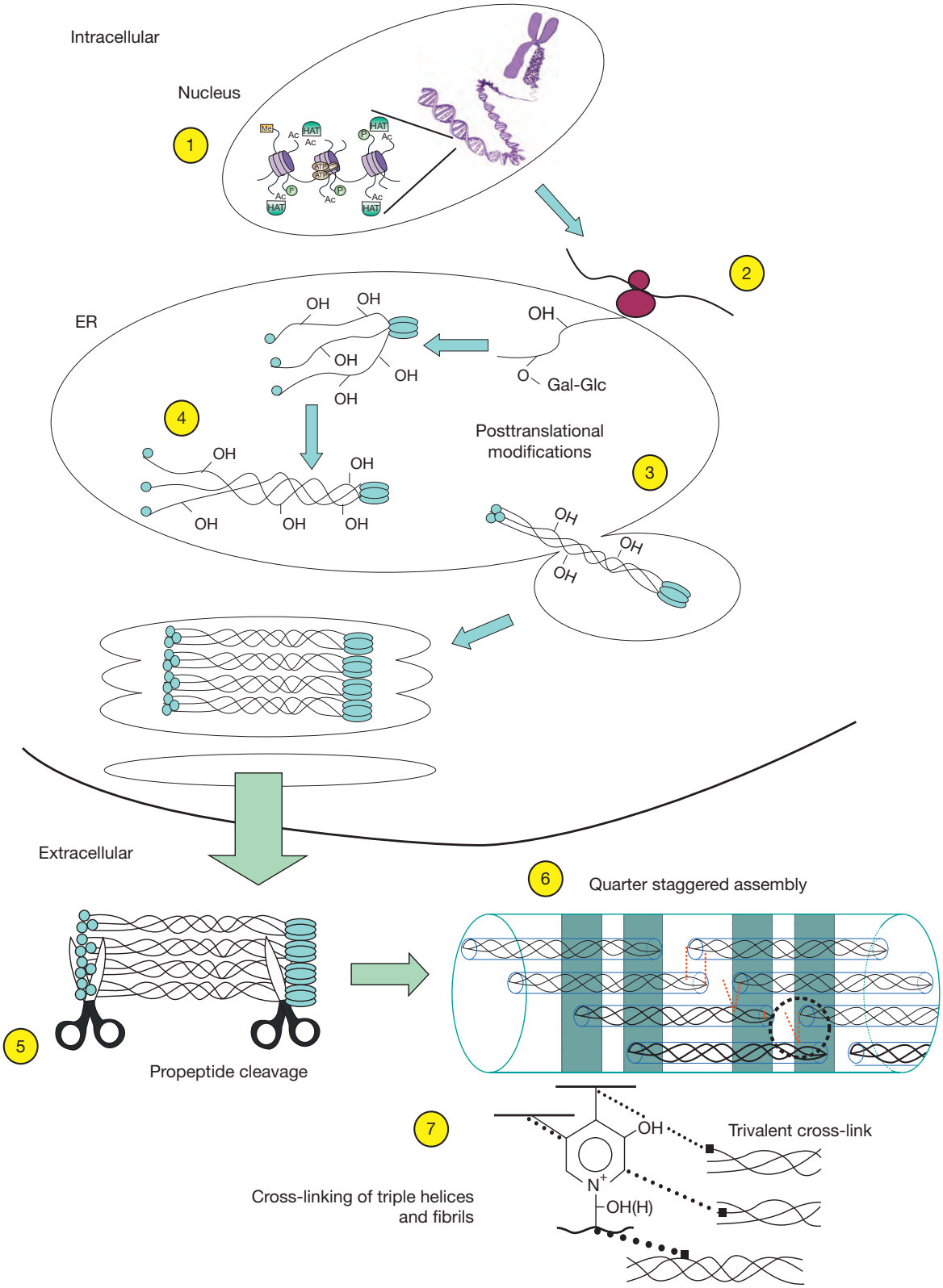

Figure 1 Cartoon of the intracellular and extracellular pathway of collagen biosynthesis, ranging from transcription/translation (1,2), posttranslational modification ((3) O-glycosylation. (4) hydroxylation), the extracellular trimming of procollagen to collagen (5) and its subsequent supramolecular assembly (6). The dotted lines in the quarter staggered assembly (6) represent di- and trivalent cross-links. The trivalent cross-link shown here (7) is a hydroxyl-pyridinoline cross-link. The position of the cross-links is given schematically and is not drawn to scale or in exact position. Adapted and modified from Chen, C.; Raghunath, M. *Fibrogenesis Tissue Repair* **2009**, *2*, 7.

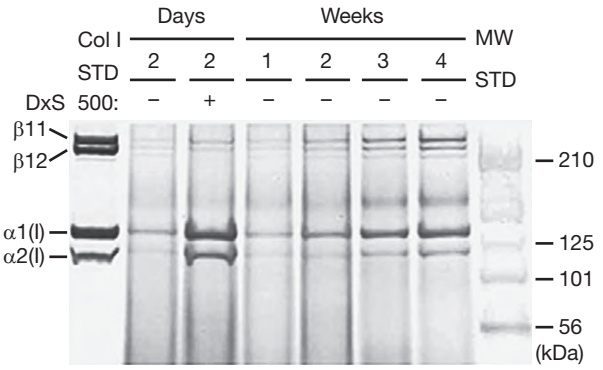

Figure 2 SDS-PAGE of collagen deposition after 2 days culturing in the presence (+) of dextran sulphate 500 kDa (100 μg ml^{-1}) and in its absence (–) for 2 days and up to 4 weeks. Adapted with modification from Lareu, R. R.; Subramhanya, K. H.; Peng, Y.; *et al*. *FEBS Lett*. **2007**, *581*, 2709–2714.

2.215.2.4.2. Sugar-based collagen cross-links

Collagen cross-links can also be formed by sugars. Since the discovery of nonenzymatic glycation of hemoglobin molecules in patients with diabetes mellitus, the role of sugars in modifying tissues has been of great interest. The prolonged exposure of collagens to reducing sugars produces glycation end-products that are implicated as factors in aging and diabetic complications. Indeed, glycation is a major cause of dysfunction of collagenous tissues in old age, and the process is accelerated in diabetic subjects due to the higher levels of glucose. Glycation can affect a number of properties of collagen including its biomechanical features and the formation of supramolecular aggregates. The most damaging effects, however, are caused by glucose-mediated intermolecular cross-links which decrease flexibility and permeability and reduce turnover. Almost all extracellular proteins can react nonenzymatically with a sugar group (frequently glucose) via a free ε-amino group of a Lys or Hyl. This form of glycation (Maillard reaction) involves the chemical reaction of a sugar aldehyde or ketone with a free amino group to form a Schiff base, which may undergo a rearrangement to form a fairly stable ketoimine (Amadori product). These structures go on to form advanced glycation end-products (AGEs) or are degraded into reactive α-dicarbonyl groups that react with other free amino groups to form cross-linked adducts. The occurrence and accumulation of these groups on stable low-turnover macromolecules such as collagen is receiving considerable attraction because these cross-links potentially influence the resistance of collagen to being broken down or remodeled[27–30] (reviewed in Kielty and Grant[8]).

2.215.2.4.3. Other enzymatic cross-links

The role of tissue-type transglutaminase (TGase 2) as a cross-linker of collagen matrices is not firmly anchored in textbooks on collagen and derived biomaterials yet. TGases belong to a family of enzymes that catalyze the formation of isodipeptide bonds between proteins (reviewed in Iismaa *et al.*[31]). The vertebrate TGases all require calcium for their catalytic activity. A few ECM targets of TGase 2 have been biochemically characterized. Fibronectin has been known for some time to be a target, but with regards to the collagens information exist only on collagen III, collagen V/XI in cell culture, and collagen VII in human skin. This has inspired us and other groups to explore the opportunities of enzymatic cross-linking of collagen-based biomaterials TGase 2 as the cross-links created would be biologically acceptable by the host organism (reviewed in Collighan and Griffin,[32] Zeugolis *et al.*,[33] and Orban *et al.*[34]). Data on TGase 2 treatment of collagen I derived from shark skin, gelatin from skin or bone suggests collagen I as a target; however, there is surprisingly little information as to the precise target sites. It cannot be ruled out that those reactive sites in collagen gels are provided by collagen III or V, which are, as mentioned above, admixtures of collagen preparations from skin. Microbial TGases (mTGases), in particular from *Streptoverticillium mobaraense* (also *Streptomyces mobaraensis*) are widely used in commercial food processing as glue for processed meat and fish products and to improve the texture of protein-rich foods. mTGases are ideal for industrial purposes since they do not require calcium and are active across a range of temperatures and pHs. In fact, mTGases have been used as cross-linkers for collagen type I gels,[35–38] but we would like to point out that this enzyme is biochemically very different from a mammalian protein. Our unpublished data suggest that TGase 2 is still present in considerable amounts after the cross-linking procedure. If the same holds true for mTGases, this might represent an immunogenic threat for implanted material. It might therefore be advisable to use mammalian, better even, human recombinant TGase 2 for cross-linked biomaterials that are to go into the body. Fingerprints of effected transamidation are the presence of ε-(glutamyl)-lysine isodipeptide that can be detected via specific antibodies or by HPLC.

2.215.3. Sources of Collagen

Although collagen is encountered almost everywhere in the mammalian body, skin and tendons are primarily used to extract collagen type I, and cartilaginous tissues are used to extract collagen type II due to their abundance in these tissues.[39–43] Fins, scales and bones, and waste materials of the fish industry have also been used to extract collagen for biomaterials applications.[44–47] Although different methods (neutral salt, alkali, acid, and enzyme) have been investigated over the years to isolate and purify different types and amounts of collagen from different tissues and species, the acid and enzyme extractions are the most preferred.[48–52] Dilute acidic solutions although effectively disassociate intermolecular cross-links of the aldimine type; they are ineffective against less labile cross-links such as ketoimine bonds. To this end, proteolytic enzymes-based approaches are used to cleave additional cross-links and to solubilize/extract more collagen.[9,40,42,48,49,53,54] The efficacy of enzymatic treatment arises from selective cleavage in the nonhelical N- and C-terminal telopeptides that allows dissection of essentially intact helices[55–57] unless the collagen molecule is partially unfolded, molten, or broken.[58] The resulting monomolecular collagen or atelocollagen benefits from the removal of the antigenic P-determinant located on the telopeptides and as a consequence the host immune response can be greatly reduced and a

more competitive biomaterial can be produced[59–67] that it is expected to become more widely used in clinical settings.[67–69]

Despite advances in extraction and purification procedures, collagen is a biopolymer derived from animals and thus there is the issue of interspecies transmission of disease.[70–75] For example, the recent concern about the transmission of bovine spongiform encephalopathy across species barriers has proven to be a significant drawback for manufacturing bovine-derived biomaterials despite reports stating that the transmission of this disease to humans, if it occurs at all, requires an effective dose for a sufficiently prolonged period of time.[76] For this reason, collagen-like synthetic peptides[77,78] and human recombinant collagens[79–81] have been investigated for scaffold fabrication.

Design and synthesis of synthetic peptides mimicking the structural, biological, and mechanical properties of native collagen has been the subject of research for several decades. The basic constituent of the collagen helix is the repeating triple-helical sequence of Glycine-X-Y, where X is often Pro and Y is frequently Hyp.[8,82–88] Data have revealed that five triplets are required to form a stable triple helix and for this reason 5–15 triplets are frequently used to mimic the primary and tertiary structures of collagen.[77,89] Several sequences have been investigated over the years,[90–95] including a synthetic peptide system able to self-assemble into a fibrous collagen-like homotrimeric helical structure with well-defined periodicity evident by transmission electron microscopy.[96] Studies using collagen-biomimetic peptides have provided invaluable insights into physiological[97,98] and pathophysiological[99] collagen-folding pathways as well as information about the triple helix stability[100–102] and biological functions including cell adhesion and cross-linking sites.[103–106] Despite the significant strides that have been achieved, the recent years in medicine, and nanotechnology using synthetic collagen-like peptides, it is still very difficult to mimic the higher-order supramolecular structures of native collagens.

The use of genetically engineered cells, microorganisms, animals, and plants appeared to be a cost-effective, scalable, and reproducible technology for the production of recombinant human collagens that avoids problems related with variations between batches, interspecies transmission of disease and possible xenogenic immuno-responses induced by animal-extracted collagens.[107–109] Several expression systems including transfected mammalian cells,[110,111] insect cells,[112,113] yeast,[114,115] bacteria,[116–118] transgenic mice,[119] transgenic plants such as tobacco,[120,121] corn,[122] and silkworms[123] have successfully been employed to produce human recombinant procollagens. However, expression of fully functional molecules has been difficult due to the complex nature of procollagen synthesis.[124] Moreover, in all cases, the procollagen expression levels have been low ranging from 15 mg ml^{-1} for mammalian cell culture[125] and yeast[126] to 60 mg ml^{-1} in baculovirus[113] and therefore limiting broad commercialization potential. Additionally, while recombinant collagens have been expressed in a thermostable triple-helical form, they lack specific domains otherwise present in native fibrillar collagens,[127,128] which further compromises their biological function and further reduce their use.

Recently, our laboratory has developed a novel biotechnological approach that involves the *in vitro* deposition of large amounts of collagen from fibrogenic human cell lines under conditions of macromolecular crowding which entails the addition of macromolecules >50 kDa in the culture media.[129–132] The principal of the approach is based on the fact that the deposition of a collagen matrix depends on the conversion of *de novo* synthesized procollagen to collagen in the extracellular space or immediately before its release into the same.[133] The rate-limiting step of collagen I deposition is the proteolytic conversion of procollagen to collagen. This step is catalyzed by procollagen C-proteinase and proteolytic modification of its allosteric regulator. We have recently demonstrated that this key step can be dramatically accelerated in the presence of high concentrations of macromolecules (e.g., polystyrene sulfonate, dextran sulphate, Ficoll) in the culture media.[134,135] In fact, under noncrowding conditions, lung fibroblasts produce approximately 6×10^5 collagen chains per hour per cell,[136] while the crowding system enables 10–30 times greater collagen deposition (**Figure 2**). To further increase the collagen production, transforming growth factor-β has been used, which has been shown to increase further collagen type I deposition *in vitro* under crowded and noncrowded conditions.[137,138] It has also been shown in cultured fibroblasts that the fibrogenic factor can cause a three- to sixfold increase of the rate of type I collagen synthesis by stimulating the transcription of type I procollagen genes.[139] It was postulated that this agent acts by modulating the synthesis of specific macromolecules rather than a general increase in cellular metabolism and proliferation.

2.215.4. Collagen: Purification and Analysis

Following collagen production, it is essential to purify the final collagen solution. All methods of purification are a compromise between removing as much impurity as possible without denaturating the collagen, particularly by heat, from its native form.[140] Soluble collagen is purified mainly by salt/polyelectrolyte precipitation, followed by centrifugation and dialysis. Precipitation has long been used as an early step in the process of purifying proteins from complex solutions.[141–146] Protein precipitation has been described as equilibrium between the protein phase (precipitate) and the saturated liquid phase (supernatant).[143] It has been reported that proteins precipitate through the formation of protein–polyelectrolyte complexes and the formation of particles from these complexes.[147] Electrostatic attraction and hydrogen and hydrophobic bonding have been recognized as the driving forces.[148] At low concentration of the additive, the protein solubility is increased and this is called the salting-in zone, while at higher concentrations, solubility decreases giving rise to the salting-out effect.[149] Different collagen types can be precipitated by differential salt/polyelectrolyte fractionation. Insoluble precipitates can be redissolved in dilute acidic solutions and proteolytic enzymes, followed by salt/polyelectrolyte fractionation. Collagen solutions contain varying proportions of monomer and higher molecular weight covalently linked aggregates, depending on the source and method of preparation and purification. It has been postulated that it is near impossible to obtain a truly monomeric collagen solution; however, pepsin-extracted collagen usually contains higher proportions of monomer than salt- or acid-extracted material.[9,56] Soluble collagen can be stored in solution, frozen or lyophilized. In any case, it is

essential to determine the level of purity of the collagen preparation as well as the collagen concentration.

The purity of collagen solutions has been evaluated over the years using numerous methods with variable level of complexity. Although mass spectroscopy has been used extensively in collagen research,[150–153] complication arising either due to the high molecular mass of collagen or due to the low molecular mass of collagen telopeptides, provide significant challenges in purity assessment of collagen with mass spectroscopy.[154] Amino acid analysis has also been employed as a very sensitive method to evaluate the collagen purity[155–162]; however the complexity of the method, the costs, and the requirement for specific columns limits its use. SDS-PAGE is the most commonly used method to assess the purity of collagen preparations as has been described previously.[163] The electrophoresis is based on the principle that charged molecules migrate through a semisolid medium (gel) when subjected to an electric field, during which proteins are separated from a complex mixture into distinct bands at a characteristic rate depending on charge, size, and other physical characteristics. Protein bands are customarily visualized by staining with Coomassie Brilliant Blue, although more sensitive stains (20–50-fold increased sensitivity) have been developed using silver for both proteins and carbohydrates. The heat-denaturated collagen sample binds to the SDS molecule that confers a net negative charge on each molecule and consequently the polypeptides migrate on the polyacrylamide gel proportionally to their molecular weight.[42,56,164] Delayed reduced electrophoresis has also been introduced to separate different collagen types from tissues; for example, the α1(III) chains can be resolved from the α1(I) chains by interrupted electrophoresis with delayed reduction of the disulfide bonds of the type III collagen.[165] **Figure 3** demonstrates that under nonreduced conditions, type I and III collagens comigrate, while under delayed reduction, separation of α1(III) and α1 (I) can be achieved. Subsequent densitometric analysis allows detection of samples on the nanogram scale,[40,166] while complementary Western blots can be used to assess the specificity of collagen type using monoclonal antibodies.[167,168]

To fabricate reproducible scaffolds with controllable properties, it is essential to be able to accurately determine the collagen concentration.[169–172] Moreover, collagen represents a crucial metabolic biomarker of cellular activity and phenotype, such as collagen type I and III production in dermal/keloid fibroblast culture[173] or the ratio of collagen type I and III to collagen II in chondrocyte culture, respectively.[167,174] Accurate determination of collagen content in pathophysiologies (e.g., fibrosis) is also crucial.[175–177] It is therefore essential to develop assays that will allow accurate determination of collagen synthesis or degradation. Collagen and elastin contain the unusual amino acids Hyl and Hyp.[178] Hyl is formed from lysine via enzymatic hydroxylation by lysyl hydroxylase, while Hyp is formed from Pro, by the enzyme 4-prolyl hydroxylase to form 4-Hyp in the endoplasmic reticulum.[9,179–181] Since the percentage of Hyp remains relatively constant throughout the various genetic forms, the amount of Hyp is used to calculate the total collagen content in collagen-based biomaterials, in tissue-engineering assays, and in tissue pathophysiologies with very little error.[56,182,183] Several methods have been introduced over the years to determine the collagen concentration through Hyp, but still there is no ideal one. Problems associated with endogenous synthesis and reutilization of Pro[184] have limited the use of the *in vivo* and metabolic labeling with radioactive amino acids.[185–189] High-performance liquid chromatography[187,190,191] and colorimetric assays based on the oxidation of free Hyp with chloramine-T reagent have been used for precise quantification of collagen to nanogram scale;[9,56,181–183,192–199] however, these approaches are time-consuming and not suitable for routine estimation of collagen content. Recently, the Sircol Collagen Assay (SCA; Biocolor Ltd., Northern Ireland) has been introduced as a more convenient colorimetric assay for the quantification of collagen in cell and tissue culture.[200–207] The SCA is based on the amino acid-binding property of sirius red (SR), an anionic dye with sulphonated acid side-chain groups that react with the side-chain groups of basic amino acids[208–212] and is also used as a selective histochemical stain for collagen in normal and pathological tissue.[213–219] During

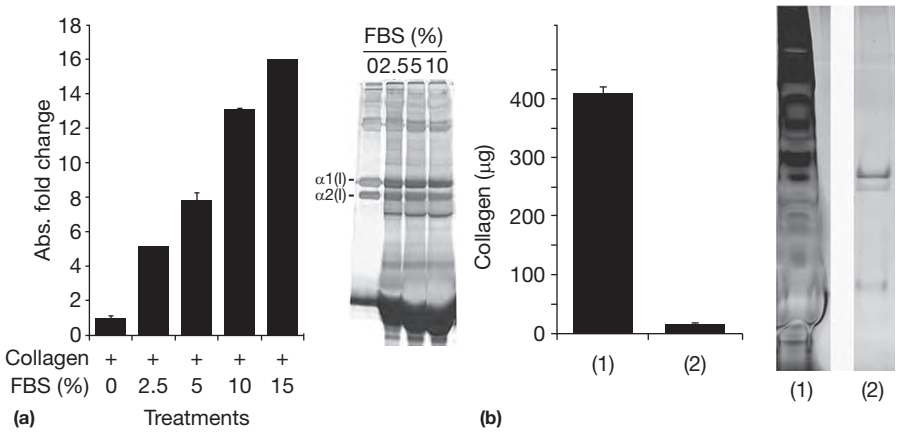

Figure 3 Using the SCA according to the manufacturer's protocol, the addition of increasing amounts of FBS into a collagen I solution (100 μg/ml^{-1}) lead to an erroneously increased apparent collagen content was detected (a, left). Large-format SDS-PAGE proves that all samples contain the same collagen concentration (a, right). Quantification of collagen using the unmodified SCA protocol (1) revealed a 24-fold overestimation of collagen content in culture media in comparison to the modified (2) protocol (b, left). Complementary SDS-PAGE demonstrates the low in collagen content culture media solution (b, right). Adapted with modification from Lareu, R.; Zeugolis, D. I.; Abu-Rub, M.; Pandit, A.; Raghunath, M. *Acta Biomater.* **2010**, *6*(8), 3146–3151.

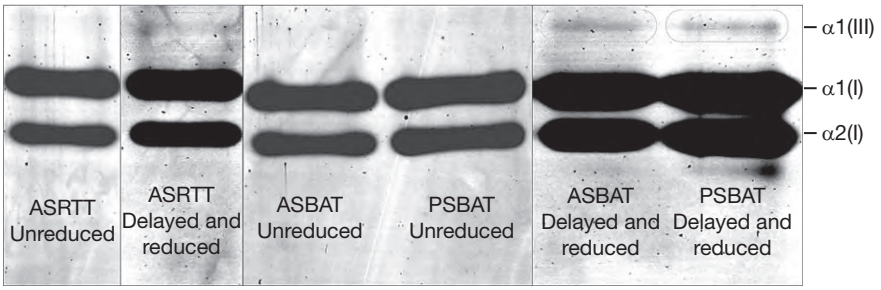

Figure 4 SDS-PAGE analysis of acid soluble rat tail tendon (ASRTT), acid-soluble bovine Achilles tendon (ASBAT), and pepsin-soluble bovine Achilles tendon (PSBAT) collagens. Reduction of disulfide bonds directly from the start of the gel electrophoretic run causes the single α1(III) chains to comigrate with the α1(I) chains. Delayed reduction disassembles the disulfide-linked collagen III trimer at a later stage of the run, so that they migrate above the α1 (I) chains and thus can be distinguished.

our attempts to quantify collagen content using SCA, we found that the presence of noncollagenous proteins in cell culture medium and tissue hydrolysates result in a dramatic overestimation of collagen content by 3–24-fold (Figure 4). To remedy this deficit, we have introduced a simple pepsin digestion followed by column ultrafiltration purification step that not only allows the removal of noncollagenous proteins, but also enables the accurate determination of collagen in complex protein solutions.[220]

If the collagen is to be freeze-dried, special attention should be paid during the process. Although it has been reported that the freeze-drying process does not alter the structure of the collagen molecule, at least with regard to its polypeptide composition,[221] incorrect application of heat could lead to irreversible dehydrothermal cross-linking and therefore increase the amount of insoluble collagen. We[166] and others[154] have recently evaluated a number of lyophilized collagen type I samples available from different commercial vendors and we found great variability in solubility among the samples (Figure 5). For this reason, we introduced a simple quality control step to evaluate the solubility of freeze-dried collagen preparations prior to use for biomedical applications.[166]

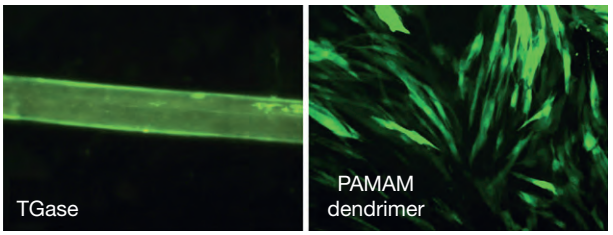

Figure 5 Using TGase, we have been able to incorporate fluorescent peptide in collagenous structures (left panel), while functionalization strategies based on PAMAM dendrimers allow transfection of cells (right panel). Left panel adapted with modification from Zeugolis, D. I.; Panengad, P. P.; Yew, E. S. Y. *et al. Journal of Biomed. Mat. Res. A* 2010, *92A*, 1310–1320.

2.215.5. Biomedical Applications of Collagen

Collagen-based materials have found applications in several aspects of our lives. Humans have been using skin from animals for several millennia. In Genesis (Genesis 3.21), it is mentioned that "the Lord God made garments of skin for Adam and his wife and clothed them." As early as 2000 BC animal sinew was used for suturing.[222,223] The Romans, as early as AD 1150, were using collagen to produce glue.[180] In the nineteenth century, collagen was used to describe 'the constituent of connective tissue that yields gelatin on boiling.'[86] Both collagen and gelatin have found numerous applications in the food industry (edible coatings, emulsifying, foaming, and gelling agents).[224] With the development of tissue engineering, several collagen-containing tissues have been used for biomedical applications.[225–228] Their use has been advocated because they closely match the tissue to be replaced. Early drawbacks of tissue grafts[229–232] have now been addressed[233,234] and recent data demonstrate normal tissue ingrowth in several animal models.[235–238] However, allografts and xenografts still face the risk of potential transmission of infectious diseases,[239–242] and autografts present the disadvantages of creating a donor site defect from harvesting. To this end, collagen-based biomaterials (fibers, films, sponges, hydrogels, and particles) have been developed for soft and hard tissue repair.[9,243–245] The attractiveness of collagen as a raw material for scaffold fabrication rests largely on its inherent properties such as cell recognition signals that promote cell attachment and growth and consequently tissue healing and regeneration, ability to form scaffolds of different conformation, high tensile strength, low antigenicity, and association with bioactive or therapeutic molecules.[8,246–252]

When designing a construct for tissue-engineering applications, it is essential for the scaffold material to provide mechanical stability, integrity, and thus a template for the three-dimensional organization for the developing tissue.[69,253–255] *In vivo*, native cross-linking takes place to impart desired mechanical stability and proteolytic resistance on collagen fibers in connective tissues.[9,88,179,256] As mentioned above, lysyl oxidase is secreted from fibrogenic cells as a 50-kDa proenzyme that is proteolytically processed to the mature enzyme in the extracellular space. Inhibition of lysyl oxidase action toward collagen molecules results in the accumulation and ultimate proteolytic degradation of soluble collagen monomers, thus preventing the formation of insoluble collagen fibers.[257] The participation of this enzyme is therefore critical to the development and repair of connective tissues.[258] However, the lysyl oxidase-mediated cross-linking does not

occur *in vitro*, and consequently, reconstituted forms of collagen lack sufficient strength and may disintegrate upon handling or collapse under the pressure from surrounding tissue *in vivo*. Thus, it is often necessary to introduce exogenous cross-links (chemical, biological, or physical) into the molecular structure, in order to control mechanical and thermal properties, biological stability, the residence time in the body and to some extent the immunogenicity and antigenicity of the device.[9,68,247,259–265]

However, biomaterials design has evolved from basic constructs that match the mechanical properties of the target body site, to biofunctional materials with incorporated instructive signals for the modulation of cellular functions such as proliferation, differentiation, and morphogenesis and therefore encourage functional tissue regeneration.[69,254,266–268] Indeed, biomaterials concepts provide the exciting possibility for the local and specific delivery of bioactive niche components that may inhibit or promote molecules or drugs that control biological functions. At present, there is no commonly accepted ideal cross-linking treatment for collagen-derived biomaterials and among them only TGase and polyamidoamine (PAMAM) dendrimeric systems offer opportunities of functionalization. Tissue TGase belongs to a family of enzymes that catalyze several posttranslational modifications of proteins by forming inter- and intramolecular bonds; the process results in the formation of stable covalently cross-linked proteins in the ECM in a Ca^{2+}-dependent manner.[269–273] We have recently demonstrated that TGase can be used to stabilize collagen scaffolds,[36,37] albeit limited.[33,265] We have, however, been able to use the resultant covalent γ-glutamyl-ε-lysine isopeptide bond to incorporate peptides into the molecular structure,[33] which indicates the functionalization potential of TGase in the biomaterials field (**Figure 6**, left panel). The limited stabilizing effect of TGase in addition to its single molecule functionality can limit its use in tissue-engineering applications. For these reasons, we[274,275] and others[276,277] have developed a multifunctional approach based on PAMAM dendrimers that not only enhance the mechanical properties of the produced scaffolds, but also offer multiple opportunities of functionalization (**Figure 6**, right panel). However, cytotoxicity complications of PAMAM dendrimers as a function of generation, independent of the surface charge, have caused concerns with regard to their use in the biomaterials field.[278–282] Polyethylene glycol (PEG) dendrimeric systems have been recently introduced as an alternative approach to PAMAM dendrimers. PEG-based polymers have a multifunctional dendrimeric core conjugated to PEG (or polyethylene oxide – PEO) chains. PEG has been shown to facilitate cell infiltration, tissue ingrowth, and enzyme degradation with improved blood compatibility and ability to resist protein adsorption.[283,284] Moreover, we have demonstrated that linear PEGs can significantly increase the mechanical stability of extruded collagen fibers[40,170,285] and collagen films. The use of PEG–dendrimer hybrids has been advocated due to the high ratio of multivalent surface moieties to molecular volume, low toxicity and haemolytic properties, long blood circulation times, low organ accumulation, and high accumulation in tumor tissue due to the enhanced permeation and retention effect.[286–295]

Many biological processes such as cell migration, axon extension, angiogenesis, bone formation, and development are regulated by the position and distribution of local signals.[296,297] Therefore, control of the spatial orientation of molecules on a surface or throughout a material using structural, biological, or biochemical cues is expected to imitate the native ECM environment and ultimately enhance functional neotissue formation. Numerous micro- and nanofabrication technologies have been developed over the years to achieve topographical, spatial, biochemical, biophysical, biological, and immunological control over cellular functions.[254,266,268,282,298–315] However, not all fabrication methods are applicable to natural biopolymers, such as collagen. For example, electrospinning has been recently introduced as the most promising technique to manufacture *in vitro* fibrous scaffolds for tissue-engineering application with fiber diameter ranging from less than 100 nm to a few microns.[316–320] Such materials mimic ECM components, such as collagen fibrils with an *in vivo* diameter range from 20 nm to 40 μm.[321–323] However, we[24] and others[324] have demonstrated that this nanofabrication process irreversibly denaturates collagen into gelatin and as such defeats its purpose, that is, to preserve the typical biological properties of collagen and imitate native ECM assemblies (**Figure 7**).

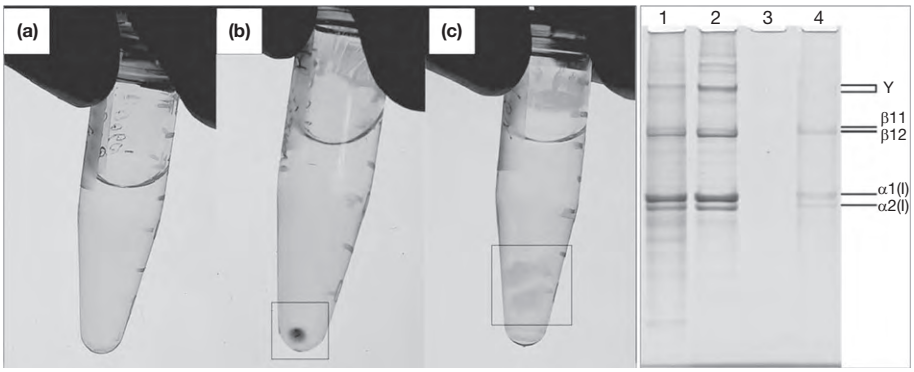

Figure 6 Visual impression of solubility in 0.5M acetic acid of 1mg ml^{-1} collagen suspensions from (a) Koken, (b) Sigma, and (c) Yi Erkang. Supplementary SDS-PAGE analyses of 1mg ml^{-1} in 0.5M acetic acid collagen samples from (1) Sigma, (2) Koken, (3) Yi Erkang, and (4) Fluka demonstrate that certain preparations are highly insoluble. Adapted with modification from Zeugolis, D. I.; Li, B.; Lareu, R. R.; Chan, C. K.; Raghunath, M. *J. Biomater. Sci. Polym. Ed.* **2008**, *19*, 1307–1317.

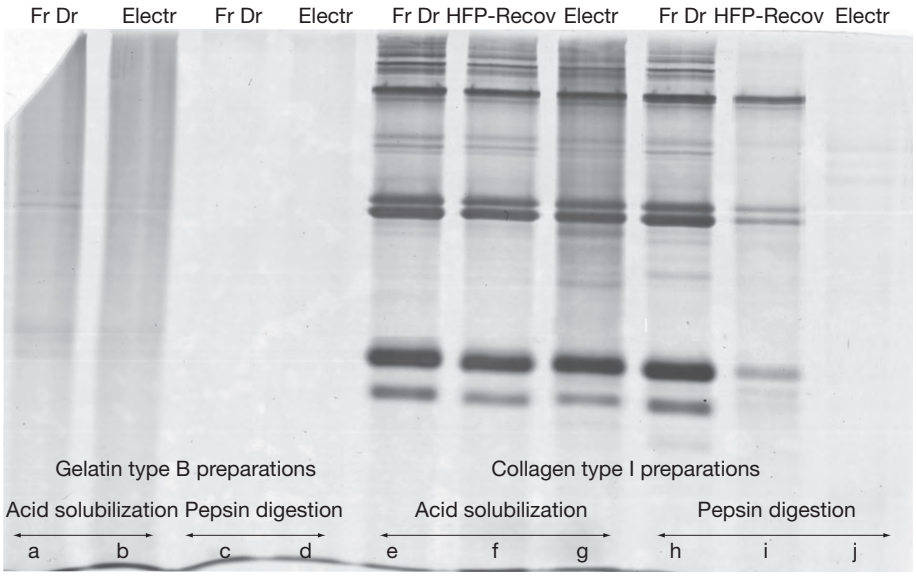

Figure 7 SDS-PAGE analysis of acid-solubilized and corresponding pepsin-digested materials: (a and c) freeze-dried Sigma gelatin type B; (b and d) Sigma gelatin type B electrospun nanofibers; (e and h) freeze-dried Symatese type I collagen; (f and i) Symatese type I collagen dissolved in hexafluoropropanol and subsequently freeze-dried (HFP-recovered); (g and j) Symatese collagen type I electrospun nanofibers. The results demonstrate reduction in collagen content after disassociation in HFP and even greater losses after electrospinning (up to 99%). Adapted with modification from Zeugolis, D. I.; Khew, S. T.; Yew, E. S. Y.; *et al*. *Biomaterials* **2008**, *29*, 2293–2305.

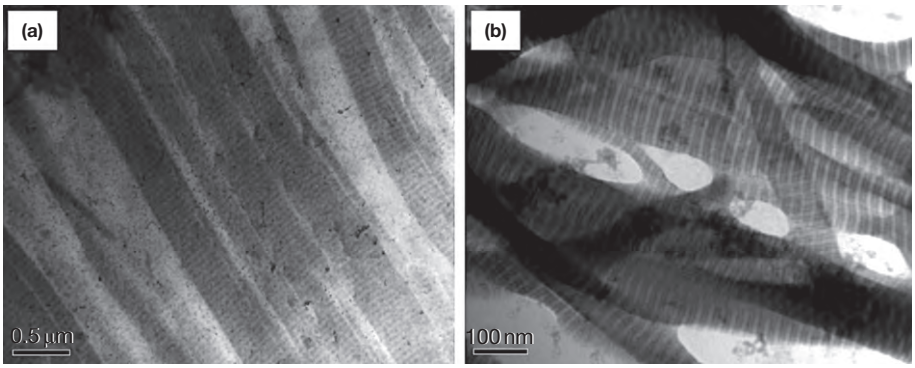

Figure 8 Cross-striated (a) native rat tail tendon collagen fiber and (b) self-assembled collagen fiber from pepsin-extracted rat tail tendon. Adapted with modification from Zeugolis, D. I.; Khew, S. T.; Yew, E. S. Y.; *et al*. *Biomaterials* **2008**, *29*, 2293–2305.

Despite the drawback of electrospun collagen-originated nanofibers, collagen-based biomaterials of different physical form have been used extensively for numerous tissue-engineering applications since they are closely imitating native ECM assemblies.[325,326] The use of collagen sponges has been proposed for the treatment of severe burns, drug-delivery and hemostatic applications, scaffold for tissue-guided regeneration, cerebral, peripheral nerve, pulmonary, vascular, and hepatic implants, and biodegradable composites.[261,327–335] Collagen films have been developed for clinical use as burn and wound dressings, abdominal wall repair, dura matter replacement, hemostatic/control bleeding agent, enhancer of healing of open dermal wounds, organ replacement, surgical tampons, and bone/skin reinforcements.[336–344] Collagen hydrogels have a long history in biomedical applications (corneal shields, hard and soft tissue implants, drug-delivery matrices, injectable suspensions).[65,345–351] Collagen fibers have been extensively used as substrate for several tissue regeneration applications due to their unique properties such as high surface area, softness, absorbency, and ease of fabrication into many product forms.[352–362] Collagen, under ideal conditions of concentration, temperature, pH, and ionic strength collagen solutions will spontaneously self-assemble *in vitro* into microscopic fibrils, fibril bundles, and macroscopic fibers that exhibit D periodic banding patterns and that are virtually indistinguishable from native fibers when examined by electron microscopy (**Figure 8**).[355,357,358,363–375]

The principle of self-assembly has been employed to fabricate collagen fibers with wet diameter range from 50 to 650 μm that have found great potential in tendon and nerve regeneration.[24,265,355,357,376–380] Furthermore, recent optical analysis using transmission electron microscopy and SHG microscopy demonstrated that such fibers possess high level of crystallinity and structural alignment that is characterized by

strong SHG signals in the presence of intense laser light.[24] In addition, the unique nanotextured surface topography of these fibers has been shown to facilitate directional cell migration and enhance spatially guided axonal growth that is essential for functional neotissue formation (Figure 9).[40,311,381]

One of the most interesting applications of collagen is the fabrication of hollow spheres.[309,382–384] The emerging field of tissue engineering requires accurate delivery of bioactive and/or therapeutic molecules to a specific location; this is a key issue in modern biotechnology and molecular biology. Glycosaminoglycans and proteoglycans[385–387] or bioactive molecules such as growth factors or hormones are traditionally used to enhance biological functions of biomaterials.[388–391] However, the biological half-life of growth factors is very limited; it is 2, 3, and 50 min for platelet-derived growth factor, basic fibroblast growth factor, and vascular endothelial growth factor, respectively.[392] As a result, the use of polymeric drug-delivery vehicles in the form of micro- or nanospheres to encapsulate the active molecules and maintain a sustained localized delivery to the target site is attractive (Figure 10).[292,389,393–400] This approach is benefited by tight regulation of release by controlling the shell material and protection of the active molecules until their delivery is required.[266,267] Moreover, loading hollow collagen microspheres with active molecules and embedding them within the fibrous structure would enable us to create gradients using the fibrous structure.[24] Gradients in the concentration of growth factors has been shown to enable directional cell migration, create patterns of cellular differentiation, and direct tissue organization into complex structures, such as branching networks of vascular or nervous systems.[298,342,401–403]

2.215.6. Outlook and Future for Collagen Materials

The existence of collagen as a biomaterial since the dawn of the animal kingdom commands respect as this implies that it has survived a fierce and rigorous material testing over the last 700 My. In fact the prototype not only survived but it flourished into the currently known successful 29 isoforms and

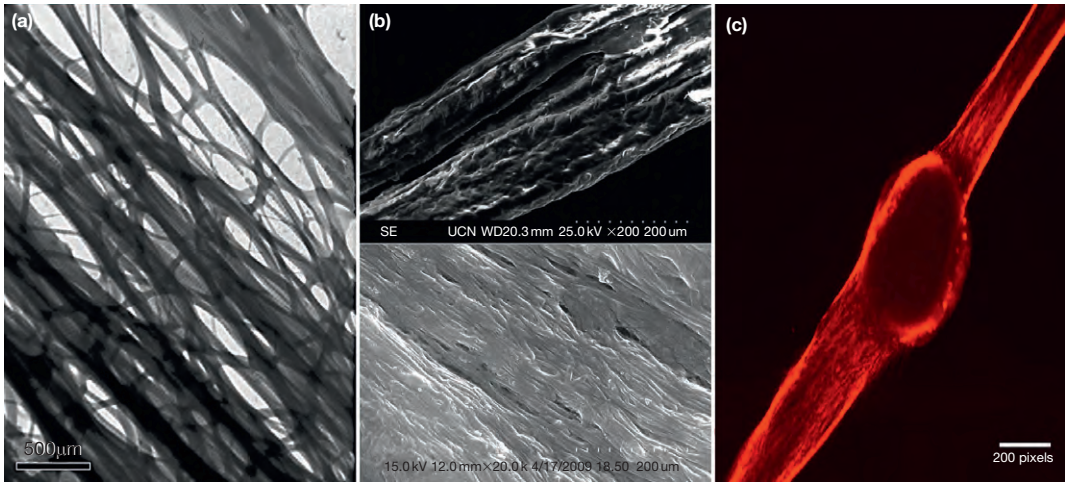

Figure 9 Transmission electron micrographs of self-assembled collagen fibers reveal an aligned collagen sub-fibrillar structure (a) that give rise to unique morphological features (e.g., grooves) apparent from scanning electron micrographs (b, top). Isoelectrically focused collagen solutions assemble into aligned supramolecular fibrillar hydrogels (b, bottom) that facilitate bidirectional neurite outgrowth along the axes of aligned hydrogels (c). (b, bottom) and (c) adapted with modification from Abu-Rub, M. T.; Billiar, K. L.; van Es, M. H.; *et al*. *Soft Matter*. **2011**, *7*, 2770–2781.

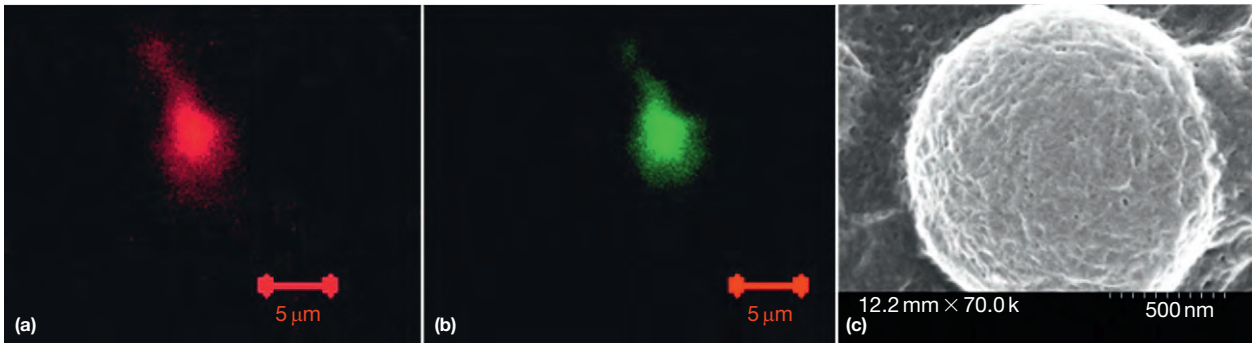

Figure 10 Encapsulation of therapeutic or bioactive molecules provides means of controlled delivery at the side of the injury. Confocal micrograph of ethidium-bromide-labeled pDNA (a) encapsulated into FITC-labeled shells (b). Hollow collagen spheres (c). Adapted with modification from Réthoré, G., Naik, H., Pandit, A. Hollow Biodegradable Nanospheres and Nanoshells for Delivery of Therapeutic and/or Imaging Molecules. (Preliminary US Continuation-in-part (CIP) Patent filed Mar 20, 2010 Patent 12/886492 (derived from PCT/EP2009/053258)).

variants as a major tissue constituent of the total protein in animals. This would predict that collagen-based materials will retain a firm place in consumer markets and biomedical applications. Driven by a strong interest in the food, leather, and pharmaceutical industry, six decades of modern research – not all of it published – have been dedicated to study the materials properties of collagen and ways to manufacture it into various biomedical products. The intrinsic task of all extracellular matrices is to be insoluble and cross-linked. This poses challenges in extracting and handling collagen and the subsequent manufacturing of biomaterials from it. It is comparably easy to completely denature collagen, melt its triple helices and thus to create gelatin, a product without which the food and pharmaceutical industry would be unthinkable today. But putting native collagen materials together again in the form of gels (from extracts derived from acidic or combined peptic/acidic extraction) or via freeze-drying from homogenized (as far as this is possible) slurry containing fibril fragments is much more demanding and complex. The intrinsic difficulty to work with collagen has spurned biomaterials scientists to search for synthetic materials that would be more amenable to handling, and pose less of a biohazard. This also is in keeping with an engineer's desire to control and to interfere. Materials were therefore sought that are better soluble, malleable, pure and defined, and can be subjected to a number of procedures. However, when we look at the implants and advanced wound care products in clinical use, we realize that this represents a very small selection of the vast number of novel biomaterials that have been developed and published in the last 30 years. This small selection represents that group of biomaterials that work within this group of collagen-based materials figure prominently. There is a good reason for this. Collagen has an undisputed excellent biocompatibility and a well-characterized low immunogenicity; it degrades into well-tolerated physiological compounds; it can be processed on an aqueous base; and enhances cellular penetration and wound repair.

Collagen is a very old biological component of animal tissues, and the over 213 cell types that build the human body are ancient biological entities that have coevolved with it and recognition systems for it. In contrast, cells have no receptors for polyethylene-based polymers or acrylic polymers, metals, ceramics, and the many more novel biomaterials that have been developed recently. Therefore, the best case scenario is often that these materials are ignored by the host tissue and do not elicit an attack by the immune system. Collagen therefore literally appears to be a natural choice. The uses of collagen biomaterials range from advanced wound care products to implantable drug-delivery devices and it is not difficult to see that this work will continue. Without any doubt, the recombinant expression of collagen represents a huge scientific feat that took some 15 years to come to fruition, but the amounts that can be produced to date are nowhere near the needs of the biomedical market, and it appears questionable whether the costs of recombinant human collagen will become cost-competitive in the near future. The reality of the market forces might defeat forecasts here. While fully synthetic collagen triple helices are technically not feasible currently, mini-triple helices can play a role in the creation of novel biomimetic biomaterials or at least surface modifications. However, looking into collagen from traditional sources, recent advances in wet spinning of collagen derived from tissue extract slurry look promising[404] for industrial scale and demonstrate that collagen-based biomaterials have not even reached their zenith.

Acknowledgments

DZ would like to acknowledge the Engineering and Physical Sciences Research Council, UK; the Faculty Research Committee of the Faculty of Engineering, NUS, Singapore; the Irish Research Council for Science Engineering and Technology, Ireland; the Science Foundation Ireland; the NUIG Millennium Research Fund; MR wishes to acknowledges the Raine Foundation (UWA, Western Australia), funding from the Faculty Research Committee, Faculty of Engineering, and the NUS Tissue Engineering Programme for financial and other support.

References

1. Harkness, R. D. *Biol. Rev.* **1961**, *36*, 399–463.
2. Huxley-Jones, J.; Robertson, D.; Boot-Handford, R. *Matrix Biol.* **2007**, *26*, 2–11.
3. Gordon, M.; Hahn, R. *Cell Tissue Res.* **2010**, *339*, 247–257.
4. Schultz, G.; Wysocki, A. *Wound Repair Regen.* **2009**, *17*, 153–162.
5. Vogel, W.; Abdulhussein, R.; Ford, C. *Cell. Signal.* **2006**, *18*, 1108–1116.
6. Farjanel, J.; Schürmann, G.; Bruckner, P. *Osteoarthr. Cartil.* **2001**, *9*, S55–S63.
7. Piez, K. A. In *Encyclopedia of Polymer Science and Engineering*; Kroschwitz, J. I., Ed.; Wiley: New York, 1985; pp 699–727.
8. Kielty, C. M.; Grant, M. E. In *Connective Tissue and Its Heritable Disorders: Molecular, Genetic and Medical Aspects*; Royce, P. M., Steinmann, B., Eds.; John Wiley Inc.: New York, 2002; pp 159–221.
9. Friess, W. *Eur. J. Pharm. Biopharm.* **1998**, *45*, 113–136.
10. Koch, M.; Foley, J.; Hahn, R.; *et al. J. Biol. Chem.* **2001**, *276*, 120–126.
11. Fitzgerald, J.; Bateman, J. *FEBS Lett.* **2001**, *505*, 275–280.
12. Koch, M.; Schulze, J.; Hansen, U.; *et al. J. Biol. Chem.* **2004**, *279*, 22514–22521.
13. Banyard, J.; Bao, L.; Zetter, B. *J. Biol. Chem.* **2003**, *278*, 20989–20994.
14. Matsuo, N.; Tanaka, S.; Hidekatsu, Y.; Koch, M.; Gordon, M.; Ramirez, F. *Connect. Tissue Res.* **2008**, *49*, 68–75.
15. Hashimoto, T.; Wakabayashi, T.; Watanabe, A.; *et al. EMBO J.* **2002**, *21*, 1524–1534.
16. Sato, K.; Yomogida, K.; Wada, T.; *et al. J. Biol. Chem.* **2002**, *277*, 37678–37684.
17. Plumb, D.; Dhir, V.; Mironov, A.; *et al. J. Biol. Chem.* **2007**, *2827*, 12791–12795.
18. Veit, G.; Kobbe, B.; Keene, D. R.; Paulsson, M.; Koch, M.; Wagener, R. *J. Biol. Chem.* **2006**, *281*, 3494–3504.
19. Söderhäll, C.; Marenholz, I.; Kerscher, T.; *et al. PLoS Biol.* **2007**, *5*, e242.
20. Sasaki, T.; Larsson, H.; Tisi, D.; Claesson-Welsh, L.; Hohenester, E.; Timpl, R. *J. Mol. Biol.* **2000**, *301*, 1179–1190.
21. Marneros, A.; Olsen, B. *FASEB J.* **2005**, *19*, 716–728.
22. Zipfel, W.; Williams, R.; Webb, W. *Nat. Biotechnol.* **2003**, *23*, 1369–1377.
23. Yeh, A.; Choi, B.; Nelson, S.; Tromberg, B. *J. Invest. Dermatol.* **2003**, *121*, 1332–1335.
24. Zeugolis, D. I.; Khew, S. T.; Yew, E. S. Y.; *et al. Biomaterials* **2008**, *29*, 2293–2305.
25. Ribel-Madsen, S.; Christgau, S.; Gronemann, S.; Bartels, E.; Danneskiold-Samsøe, B.; Bliddal, H. *Scand. J. Rheumatol.* **2007**, *36*, 470–477.
26. Chan, C.; Tang, O.; Lau, W.; Tang, G. *Eur. J. Obstet. Gynecol. Reprod. Biol.* **2006**, *124*, 204–206.
27. Paul, R. G.; Bailey, A. J. *Int. J. Biochem. Cell Biol.* **1999**, *31*, 653–660.
28. Mentink, C. J. A. L.; Hendriks, M.; Levels, A. A. G.; Wolffenbuttel, B. H. R. *Clin. Chim. Acta* **2002**, *321*, 69–76.
29. Monnier, V. M.; Sell, D. R.; Wu, X.; Rutter, K. *Int. Congr. Ser.* **2002**, *1245*, 9–19.
30. Monnier, V. M. *Arch. Biochem. Biophys.* **2003**, *419*, 1–15.
31. Iismaa, S.; Mearns, B.; Lorand, L.; Graham, R. *Physiol. Rev.* **2009**, *89*, 991–1023.
32. Collighan, R.; Griffin, M. *Amino Acids* **2009**, *36*, 659–670.
33. Zeugolis, D. I.; Panengad, P.; Yew, E. S. Y.; Sheppard, C.; Phan, T. T.; Raghunath, M. *J. Biomed. Mater. Res. A* **2010**, *92*(4), 1310–1320.

34. Orban, J. M.; Wilson, L. B.; Kofroth, J. A.; El-Kurdi, M. S.; Maul, T. M.; Vorp, D. A. *J. Biomed. Mater. Res.* **2004**, *68A*, 756–762.
35. Chen, R.-N.; Ho, H.-O.; Sheu, M.-T. *Biomaterials* **2005**, *26*, 4229–4235.
36. O Halloran, D. M.; Collighan, R. J.; Griffin, M.; Pandit, A. S. *Tissue Eng.* **2006**, *12*, 1467–1474.
37. Garcia, Y.; Wilkins, B.; Collighan, R. J.; Griffin, M.; Pandit, A. *Biomaterials* **2008**, *29*, 857–868.
38. Kuwahara, K.; Yang, Z.; Slack, G.; Nimni, M.; Han, B. *Tissue Eng. Part C Methods* **2010**, *16*(4), 609–618.
39. Gross, J.; Highberger, J. H.; Schmitt, F. O. *Proc. Natl. Acad. Sci. USA* **1955**, *41*, 1–7.
40. Zeugolis, D. I.; Paul, R. G.; Attenburrow, G. *J. Biomed. Mater. Res. A* **2008**, *86A*, 892–904.
41. Ahmed, I. M.; Lagopoulos, M.; McConnell, P.; Soames, R. W.; Sefton, G. K. *J. Orthop. Res.* **1998**, *16*, 591–596.
42. Bailey, A. J.; Light, N. D. *Connective Tissue in Meat and Meat Products*. Elsevier Applied Science: London/New York, 1989.
43. Herbage, D.; Bouillet, J.; Bernenco, J.-C. *Biochem. J.* **1977**, *161*, 303–312.
44. Nagai, T.; Suzuki, N. *Food Chem.* **2000**, *68*, 277–281.
45. Hwang, J.-H.; Mizuta, S.; Yokoyama, Y.; Yoshinaka, R. *Food Chem.* **2007**, *100*, 921–925.
46. Song, E.; Yeon Kim, S.; Chun, T.; Byun, H.-J.; Lee, Y. M. *Biomaterials* **2006**, *27*, 2951–2961.
47. Yunoki, S.; Nagai, N.; Suzuki, T.; Munekata, M. *J. Biosci. Bioeng.* **2004**, *98*, 40–47.
48. Nalinanon, S.; Benjakul, S.; Visessanguan, W.; Kishimura, H. *Food Chem.* **2007**, *104*, 593–601.
49. Skierka, E.; Sadowska, M. *Food Chem.* **2007**, *105*, 1302–1306.
50. Steven, F. S. *Biochim. Biophys. Acta* **1966**, *130*, 202–217.
51. Trelstad, R. L. *Biochem. Biophys. Res. Commun.* **1974**, *57*, 717–725.
52. Bannister, D. W.; Burns, A. B. *Biochem. J.* **1972**, *129*, 677–681.
53. Danielsen, C. C. *Mech. Aging Dev.* **1981**, *15*, 269–278.
54. Rigby, B. J. *Biochim. Biophys. Acta* **1967**, *133*, 272–277.
55. Na, G. C.; Butz, L. J.; Bailey, D. G.; Carroll, R. J. *Biochemistry* **1986**, *25*, 958–966.
56. Light, N. D. In *Methods in Skin Research*; Skerrow, D., Skerrow, C. J., Eds.; Wiley: New York, 1985; pp 559–586.
57. Gelman, R. A.; Poppke, D. C.; Piez, K. A. *J. Biol. Chem.* **1979**, *254*, 11741–11745.
58. Bruckner, P.; Prockop, D. J. *Anal. Biochem.* **1981**, *110*, 360–368.
59. Ishikawa, H.; Koshino, T.; Takeuchi, R.; Saito, T. *Biomaterials* **2001**, *22*, 1689–1694.
60. Alam, M. I.; Asahina, I.; Ohmamiuda, K.; Takahashi, K.; Yokota, S.; Enomoto, S. *Biomaterials* **2001**, *22*, 1643–1651.
61. Yamada, N.; Shioya, N.; Kuroyanagi, Y. *Scand. J. Plast. Reconstr. Surg. Hand Surg./Nordisk Plastikkirurgisk Forening [and] Nordisk Klubb For Handkirurgi* **1995**, *29*, 211–219.
62. Yin Hsu, F.; Chueh, S.-C.; Jiin Wang, Y. *Biomaterials* **1999**, *20*, 1931–1936.
63. Rodrigues, C. V. M.; Serricella, P.; Linhares, A. B. R.; *et al*. *Biomaterials* **2003**, *24*, 4987–4997.
64. Rosenblatt, J.; Rhee, W.; Wallace, D. *J. Control. Release* **1989**, *9*, 195–203.
65. Rosenblatt, J.; Devereux, B.; Wallace, D. G. *Biomaterials* **1994**, *15*, 985–995.
66. Wells, M. R.; Kraus, K.; Batter, D. K.; *et al*. *Exp. Neurol.* **1997**, *146*, 395–402.
67. Lynn, A. K.; Yannas, I. V.; Bonfield, W. *J. Biomed. Mater. Res. B Appl. Biomater.* **2004**, *71B*, 343–354.
68. Friess, W.; Lee, G. *Biomaterials* **1996**, *17*, 2289–2294.
69. Bonassar, L. J.; Vacanti, C. A. *J. Cell. Biochem. Suppl.* **1998**, *30–31*, 297–303.
70. Trentham, D. E.; Townes, A. S.; Kang, A. H. *J. Exp. Med.* **1977**, *146*, 857–868.
71. Rutala, W.; Weber, D. *Clin. Infect. Dis.* **2001**, *32*, 1348–1356.
72. Tiwari, A.; Patnayak, D.; Chander, Y.; Minakshi, P.; Goyal, S. *Avian Dis.* **2006**, *50*, 284–287.
73. Joly, J.; Nguyen, V.; Bourrat, F. *Prod. Anim.* **2001**, *14*, 91–96.
74. Louz, D.; Bergmans, H.; Loos, B.; Hoeben, R. *J. Gene Med.* **2005**, *7*, 1263–1274.
75. Louz, D.; Bergmans, H.; Loos, B.; Hoeben, R. *Rev. Med. Virol.* **2008**, *18*, 53–65.
76. Narotam, P. K.; Van Dellen, J. R.; Bhoola, K.; Raidoo, D. *Br. J. Neurosurg.* **1993**, *7*, 635–641.
77. Koide, T. *Philos. Trans. R. Soc. Lond. B Biol. Sci.* **2007**, *362*, 1281–1291.
78. Koide, T. *Connect. Tissue Res.* **2005**, *46*, 131–141.
79. Ito, H.; Steplewski, A.; Alabyeva, T.; Fertala, A. *J. Biomed. Mater. Res. A* **2006**, *76A*, 551–560.
80. Nokelainen, M. *Recombinant Human Collagens*. Medical Biochemistry, University of Oulu: Oulu, 2000.
81. Olsen, D.; Yang, C.; Bodo, M.; *et al*. *Adv. Drug Deliv. Rev.* **2003**, *55*, 1547–1567.
82. Melacini, G.; Bonvin, A. M. J. J.; Goodman, M.; Boelens, R.; Kaptein, R. *J. Mol. Biol.* **2000**, *300*, 1041–1049.
83. Madhan, B.; Thanikaivelan, P.; Subramanian, V.; Raghava Rao, J.; Unni Nair, B.; Ramasami, T. *Chem. Phys. Lett.* **2001**, *346*, 334–340.
84. Holmes, D. F.; Gilpin, C. J.; Baldock, C.; Ziese, U.; Koster, A. J.; Kadler, K. E. *Proc. Natl Acad. Sci. USA* **2001**, *98*, 7307–7312.
85. Wess, T. J.; Hammersley, A. P.; Wess, L.; Miller, A. *J. Struct. Biol.* **1998**, *122*, 92–100.
86. van der Rest, M.; Garrone, R.; Herbage, D. In *Advances in Molecular and Cell Biology*; Kleinman, H. K., Ed.; JAI Press: Stamford, CT, 1993; Vol. 6, pp 1–67.
87. Cotterill, G. F.; Fergusson, J. A. E.; Gani, J. S.; Burns, G. F. *Biochem. Biophys. Res. Commun.* **1993**, *194*, 973–977.
88. Bailey, A. J.; Paul, R. G.; Knott, L. *Mech. Ageing Dev.* **1998**, *106*, 1–56.
89. Raman, S.; Parthasarathi, R.; Subramanian, V.; Ramasami, T. *J. Phys. Chem. B* **2008**, *112*, 1533–1539.
90. Sakakibara, S.; Kishida, Y.; Kikuchi, Y.; Sakai, R.; Kakiuchi, K. *Bull. Chem. Soc. Jpn* **1968**, *41*, 1273.
91. Koide, T.; Homma, D.; Asada, S.; Kitagawa, K. *Bioorg. Med. Chem. Lett.* **2005**, *15*, 5230–5233.
92. Sakakibara, S.; Inouye, K.; Shudo, K.; Kishida, Y.; Kobayashi, Y.; Prockop, D. J. *Biochim. Biophys. Acta* **1973**, *303*, 198–202.
93. Heidemann, E.; Roth, W. *Adv. Polym. Sci.* **1982**, *43*, 143–203.
94. Fields, G. B.; Prockop, D. J. *Biopolymers* **1996**, *40*, 345–357.
95. Okuyama, K.; Hongo, C.; Wu, G.; *et al*. *Biopolymers* **2009**, *91*, 361–372.
96. Rele, S.; Song, Y.; Apkarian, R. P.; Qu, Z.; Conticello, V. P.; Chaikof, E. L. *J. Am. Chem. Soc.* **2007**, *129*, 14780–14787.
97. Stultz, C. *Protein Sci.* **2006**, *15*, 2166–2177.
98. Long, C.; Braswell, E.; Zhu, D.; Apigo, J.; Baum, J.; Brodsky, B. *Biochemistry* **1993**, *32*, 11688–11695.
99. Gauba, V.; Hartgerink, J. D. *J. Am. Chem. Soc.* **2008**, *130*, 7509–7515.
100. Miles, C. A.; Bailey, A. J. *J. Mol. Biol.* **2004**, *337*, 917–931.
101. Venugopal, M.; Ramshaw, J.; Braswell, E.; Zhu, D.; Brodsky, B. *Biochemistry* **1994**, *33*, 7948–7956.
102. Krishna, O.; Kiick, K. *Biomacromolecules* **2009**, *10*, 2626–2631.
103. Yao, J.; Yanagisawa, S.; Asakura, T. *J. Biochem.* **2004**, *136*, 643–649.
104. Khew, S. T.; Yang, Q. J.; Tong, Y. W. *Biomaterials* **2008**, *29*, 3034–3045.
105. Pêcher, J.; Pires, V.; Djaafri, I.; *et al*. *Eur. J. Med. Chem.* **2009**, *44*, 2643–2650.
106. Cejas, M.; Kinney, W.; Chen, C.; *et al*. *Proc. Natl Acad. Sci. USA* **2008**, *105*, 8513–8518.
107. Yang, C.; Hillas, P.; Báez, J.; *et al*. *BioDrugs* **2004**, *18*, 103–119.
108. Báez, J.; Olsen, D.; Polarek, J. *Appl. Microbiol. Biotechnol.* **2005**, *69*, 245–252.
109. Liu, W.; Merrett, K.; Griffith, M.; *et al*. *Biomaterials* **2008**, *29*, 1147–1158.
110. Geddis, A. E.; Prockop, D. J. *Matrix Biol.* **1993**, *13*, 399–405.
111. Fertala, A.; Sieron, A. L.; Ganguly, A.; *et al*. *Biochem. J.* **1994**, *298*, 31–37.
112. Lamberg, A.; Helaakoski, T.; Myllyharju, J.; *et al*. *J. Biol. Chem.* **1996**, *271*, 11988–11995.
113. Myllyharju, J.; Lamberg, A.; Notbohm, H.; Fietzek, P.; Pihlajaniemi, T.; Kivirikko, K. *J. Biol. Chem.* **1997**, *272*, 21824–21830.
114. Toman, P. D.; Chisholm, G.; McMullin, H.; *et al*. *J. Biol. Chem.* **2000**, *275*, 23303–23309.
115. Olsen, D. R.; Leigh, S. D.; Chang, R.; *et al*. *J. Biol. Chem.* **2001**, *276*, 24038–24043.
116. Buechter, D. D.; Paolella, D. N.; Lelie, B. S.; Brown, M. S.; Mehos, K. A.; Gruskin, E. A. *J. Biol. Chem.* **2003**, *278*, 645–650.
117. Xue, W.; Fan, D.; Shang, L.; Zhu, C.; Ma, X.; Yu, Y. *Biotechnol. Lett.* **2009**, *31*, 221–226.
118. Xu, C.; Yu, Z.; Inouye, M.; Brodsky, B.; Mirochnitchenko, O. *Biomacromolecules* **2010**, *11*(2), 348–356.
119. Toman, P. D.; Pieper, F.; Sakai, N.; *et al*. *Transgenic Res.* **1999**, *8*, 415–427.
120. Ruggiero, F.; Exposito, J. Y.; Bournat, P.; *et al*. *FEBS Lett.* **2000**, *469*, 132–136.
121. Stein, H.; Wilensky, M.; Tsafrir, Y.; *et al*. *Biomacromolecules* **2009**, *10*, 2640–2645.
122. Zhang, C.; Baez, J.; Pappu, K.; Glatz, C. *Biotechnol. Prog.* **2009**, *25*, 1660–1668.
123. Tomita, M.; Munetsuna, H.; Sato, T.; *et al*. *Nat. Biotechnol.* **2003**, *21*, 52–56.
124. Bulleid, N.; John, D.; Kadler, K. *Biochem. Soc. Trans.* **2000**, *28*, 350–353.
125. Fichard, A.; Tillet, E.; Delacoux, F.; Garrone, R.; Ruggiero, F. *J. Biol. Chem.* **1997**, *272*, 30083–30087.
126. Vuorela, A.; Myllyharju, J.; Nissi, R.; Pihlajaniemi, T.; Kivirikko, K. *EMBO J.* **1997**, *16*, 6702–6712.
127. Majsterek, I.; McAdams, E.; Adachi, E.; Dhuma, S. T.; Fertala, A. *Protein Sci.* **2003**, *12*, 2063–2072.
128. Ruggiero, F.; Koch, M. *Methods* **2008**, *45*, 75–85.

129. Zimmerman, S. B.; Minton, A. P. *Annu. Rev. Biophys. Biomol. Struct.* **1993**, *22*, 27–65.
130. Hall, D.; Minton, A. P. *Biochim. Biophys. Acta* **2003**, *1649*, 127–139.
131. Munishkina, L. A.; Cooper, E. M.; Uversky, V. N.; Fink, A. L. *J. Mol. Recognit.* **2004**, *17*, 456–464.
132. Harve, K.; Vigneshwar, R.; Rajagopalan, R.; Raghunath, M. *Proc. Natl Acad. Sci. USA* **2008**, *105*, 119.
133. Canty, E. G.; Kadler, K. E. *J. Cell Sci.* **2005**, *118*, 1341–1353.
134. Lareu, R. R.; Arsianti, I.; Subramhanya, H. K.; Yanxian, P.; Raghunath, M. *Tissue Eng.* **2007**, *13*, 385–391.
135. Lareu, R. R.; Subramhanya, K. H.; Peng, Y.; *et al. FEBS Lett.* **2007**, *581*, 2709–2714.
136. Breul, S.; Bradley, K.; Hance, A.; Schafer, M.; Berg, R.; Crystal, R. *J. Biol. Chem.* **1980**, *255*, 5250–5260.
137. Chen, C.; Peng, Y.; Wang, Z.; *et al. Br. J. Pharmacol.* **2009**, *158*, 1196–1209.
138. Hetzel, M.; Bachem, M.; Anders, D.; Trischler, G.; Faehling, M. *Lung* **2005**, *183*, 225–237.
139. Raghow, R.; Gossage, D.; Seyer, J. M.; Kang, A. H. *J. Biol. Chem.* **1984**, *259*, 12718–12723.
140. Eastoe, J. E.; Courts, A.; Ward, A. G. *Practical Analytical Methods for Connective Tissue proteins*. E. & F. N. Spon: London, 1963.
141. Polson, C.; Sarkar, P.; Incledon, B.; Raguvaran, V.; Grant, R. A. *J. Chromatogr. B* **2003**, *785*, 263–275.
142. Mahadevan, H.; Hall, C. K. *Fluid Phase Equilib.* **1992**, *78*, 297–321.
143. Kuehner, D. E.; Blanch, H. W.; Prausnitz, J. M. *Fluid Phase Equilib.* **1996**, *116*, 140–147.
144. Iyer, H. V.; Przybycien, T. M. *J. Colloid Interface Sci.* **1996**, *177*, 391–400.
145. Zeppezauer, M.; Brishammar, S. *Biochim. Biophys. Acta: Biophys. Incl. Photsynth.* **1965**, *94*, 581–583.
146. Yasueda, S.-I.; Inada, K.; Matsuhisa, K.; Terayama, H.; Ohtori, A. *Eur. J. Pharm. Biopharm.* **2004**, *57*, 377–388.
147. Kim, W.-S.; Hirasawa, I.; Kim, W.-S. *Chem. Eng. Sci.* **2001**, *56*, 6525–6534.
148. Chen, W.; Berg, J. C. *Chem. Eng. Sci.* **1993**, *48*, 1775–1784.
149. Timasheff, S. N.; Arakawa, T. *J. Cryst. Growth* **1988**, *90*, 39–46.
150. Vorm, O.; Reopstorff, P.; Mann, M. *Anal. Chem.* **1994**, *66*, 3281–3287.
151. Gusev, A.; Wilkinson, W.; Proctor, A.; Hercules, D. *Anal. Chem.* **1995**, *67*, 1034–1041.
152. Tyan, Y.-C.; Liao, J.-D.; Klauser, R.; Wu, I.-D.; Weng, C.-C. *Biomaterials* **2002**, *23*, 65–76.
153. Dreisewerd, K.; Rohlfing, A.; Spottke, B.; Urbanke, C.; Henkel, W. *Anal. Chem.* **2004**, *76*, 3482–3491.
154. Abraham, L. C.; Zuena, E.; Perez-Ramirez, B.; Kaplan, D. L. *J. Biomed. Mater. Res. B Appl. Biomater.* **2008**, *87B*, 264–285.
155. Neuman, R. E. *Arch. Biochem.* **1949**, *24*, 289–298.
156. Kang, A. H.; Bornstein, P.; Piez, K. A. *Biochemistry* **1967**, *6*, 788–795.
157. Piez, K. A.; Morris, L. *Anal. Biochem.* **1960**, *1*, 187–201.
158. Hulmes, D. J. S.; Miller, A.; Parry, D. A. D.; Piez, K. A.; Woodhead-Galloway, J. *J. Mol. Biol.* **1973**, *79*, 137–148.
159. Eastoe, J. E. *Biochemistry* **1955**, *61*, 589–600.
160. Miller, E.; Narkates, A.; Niemann, M. *Anal. Biochem.* **1990**, *190*, 92–97.
161. Osborne, R. M.; Longton, R. W.; Lamberts, B. L. *Anal. Biochem.* **1971**, *44*, 317–321.
162. Bailey, A. J. *Biochim. Biophys. Acta* **1968**, *160*, 447–453.
163. Laemmli, U. K. *Nature* **1970**, *227*, 680–685.
164. Smith, D. M. In *Food Analysis*; Nielsen, S. S., Ed.; Aspen: Springer, New York, 1998; pp 251–263.
165. Sykes, B.; Puddle, B.; Francis, M.; Smith, R. *Biochem. Biophys. Res. Commun.* **1976**, *72*, 1472–1480.
166. Zeugolis, D. I.; Li, B.; Lareu, R. R.; Chan, C. K.; Raghunath, M. *J. Biomater. Sci. Polym. Ed.* **2008**, *19*, 1307–1317.
167. Mallein-Gerin, F.; Ruggiero, F.; Quinn, T. M.; *et al. Exp. Cell Res.* **1995**, *219*, 257–265.
168. Deyl, Z.; Miksik, I. *J. Chromatogr. B Biomed. Sci. Appl.* **2000**, *739*, 3–31.
169. Zeugolis, D. I.; Paul, R. G.; Attenburrow, G. *J. Biomater. Sci. Polym. Ed.* **2009**, *20*, 219–234.
170. Zeugolis, D. I.; Paul, R. G.; Attenburrow, G. *J. Biomed. Mater. Res. B Appl. Biomater.* **2008**, *85B*, 343–352.
171. Friess, W.; Schlapp, M. *Eur. J. Pharm. Biopharm.* **2001**, *51*, 259–265.
172. Raspanti, M.; Viola, M.; Sonaggere, M.; Tira, M. E.; Tenni, R. *Biomacromolecules* **2007**, *8*, 2087–2091.
173. Lim, I. J.; Phan, T. T.; Bay, B. H.; *et al. Am. J. Physiol. Cell Physiol.* **2002**, *283*, C212–C222.
174. Benya, P. D.; Shaffer, J. D. *Cell* **1982**, *30*, 215–224.
175. Grenard, P.; Blanquier, B.; Ricard-Blum, S. *J. Hepatol.* **1997**, *26*, 1356–1362.
176. Takubo, Y.; Hirai, T.; Muro, S.; Kogishi, K.; Hosokawa, M.; Mishima, M. *Exp. Gerontol.* **1999**, *34*, 353–364.
177. Zhao, F.; Zhang, Y. F.; Liu, Y. G.; *et al. Transplant. Proc.* **2008**, *40*, 1700–1705.
178. Udenfriend, S. *Science* **1966**, *152*, 1335–1340.
179. Canty, E. G.; Kadler, K. E. *Comp. Biochem. Physiol. A Mol. Integr. Physiol.* **2002**, *133*, 979–985.
180. Gorham, S. D. In *Biomaterials. Novel Materials from Biological Sources*; Byrom, D., Ed.; Macmillan/ICI Biological Products Business: New York, 1991; pp 55–122.
181. Popenoe, E.; Aronson, R.; van Slyke, D. *Biochemistry* **1966**, *55*, 393–397.
182. Avery, N. C.; Sims, T. J.; Warkup, C.; Bailey, A. J. *Meat Sci.* **1996**, *42*, 355–369.
183. Komsa-Penkova, R.; Spirova, R.; Bechev, B. *J. Biochem. Biophys. Meth.* **1996**, *32*, 33–43.
184. Laurent, G. J. *Am. J. Physiol.* **1987**, *252*, C1–C9.
185. Raghunath, M.; Kielty, C. M.; Kainulainen, K.; Child, A.; Peltonen, L.; Steinmann, B. *Biochem. J.* **1994**, *302*, 889–896.
186. Raghunath, M.; Steinmann, B.; Delozierblanchet, C.; Extermann, P.; Supertifurga, A. *Pediatr. Res.* **1994**, *36*, 441–448.
187. McAnulty, R. J. In *Fibrosis Research*; Varga, J., Brenner, D. A., Phan, S. H., Eds.; Humana Press: Totowa, NJ, 2005; Vol. 117, pp 189–207.
188. Clark, J. G.; Hildebran, J. N. *Anal. Biochem.* **1984**, *140*, 478–485.
189. LeRoy, E. C.; Harris, E. D. J.; Sjoerdsma, A. *Anal. Biochem.* **1966**, *17*, 377–382.
190. Stimler, N. P. *Anal. Biochem.* **1984**, *142*, 103–108.
191. Sims, T. J.; Bailey, A. J. *J. Chromatogr. Biomed. Appl.* **1992**, *582*, 49–55.
192. Woessner, J. F. J. *Arch. Biochem. Biophys.* **1961**, *93*, 440–447.
193. Miyada, D. S.; Tappel, A. L. *Anal. Chem.* **1956**, *28*, 909–910.
194. Kolar, K. *J. Assoc. Off. Anal. Chem.* **1990**, *73*, 54–57.
195. Stegeman, H.; Stalder, K. *Clin. Chim. Acta* **1967**, *18*, 267–273.
196. Levine, R. *Microchim. Acta* **1973**, *61*, 797–800.
197. Jamall, I.; Finelli, V.; Que-Hee, S. *Anal. Biochem.* **1981**, *112*, 70–75.
198. Blumenkrantz, N.; Asboe-Hansen, G. *Anal. Biochem.* **1975**, *63*, 331–340.
199. Reddy, G. K.; Enwemeka, C. S. *Clin. Biochem.* **1996**, *29*, 225–229.
200. Ball, M. D.; O'Connor, D.; Pandit, A. *J. Mater. Sci. Mater. Med.* **2009**, *20*, 113–122.
201. Green, D. W.; Bolland, B. J. R. F.; Kanczler, J. M.; *et al. Biomaterials* **2009**, *30*, 1918–1927.
202. Henry, J. A.; Burugapalli, K.; Neuenschwander, P.; Pandit, A. *Acta Biomater.* **2009**, *5*, 29–42.
203. Almarza, A. J.; Yang, G.; Woo, S. L. Y.; Nguyen, T.; Abramowitch, S. D. *Tissue Eng.* **2008**, *14*, 1489–1495.
204. Fan, H.; Liu, H.; Toh, S. L.; Goh, J. C. H. *Biomaterials* **2008**, *29*, 1017–1027.
205. Gupta, V.; Werdenberg, J. A.; Mendez, J. S.; Grande-Allen, J. K. *Acta Biomater.* **2008**, *4*, 88–96.
206. Kanno, Y.; Kaneiwa, A.; Minamida, M.; *et al. J. Investig. Dermatol.* **2008**, *128*, 2792–2797.
207. Park, H. J.; Cho, D. H.; Kim, H. J.; *et al. J. Investig. Dermatol.* **2008**, *129*, 843–850.
208. Puchtler, H.; Sweat, F.; Gropp, S. *J. R. Microsc. Soc.* **1967**, *87*, 309–328.
209. Sweat, F.; Puchtler, H.; Rosenthal, S. I. *Arch. Pathol.* **1964**, *78*, 69–72.
210. Constantine, V. S. *J. Invest. Dermatol.* **1969**, *52*, 353–356.
211. Constantine, V. S.; Mowry, R. W. *J. Invest. Dermatol.* **1968**, *50*, 419–423.
212. Junqueira, L. C. U.; Bignolas, G.; Brentani, R. R. *Histochem. J.* **1979**, *11*, 447–455.
213. Whittaker, P.; Boughner, D. R.; Kloner, R. A. *Am. J. Pathol.* **1989**, *134*, 879–893.
214. Borges, L. F.; Gutierrez, P. S.; Cosiski-Marana, H. R.; Taboga, S. R. *Micron* **2007**, *38*, 580–583.
215. Puchtler, H.; Waldrop, F. S.; Valentine, L. S. *Beitr. Pathol.* **1973**, *150*, 174–187.
216. Whittaker, P.; Kloner, R. A.; Boughner, D. R.; Pickering, J. G. *Basic Res. Cardiol.* **1994**, *89*, 397–410.
217. Kratky, R. G.; Ivey, J.; Roach, M. R. *Matrix Biol.* **1996**, *15*, 141–144.
218. Dolber, P. C.; Spach, M. S. *J. Histochem. Cytochem.* **1993**, *41*, 465–469.
219. Brotchie, D.; Birch, M.; Roberts, N.; Howard, C. V.; Smith, V. A.; Grierson, I. *J. Neurosci. Methods* **1999**, *87*, 77–85.
220. Lareu, R.; Zeugolis, D. I.; Abu-Rub, M.; Pandit, A.; Raghunath, M. *Acta Biomater.* **2010**, *6*(8), 3146–3151.
221. Menicagli, C.; Giorgi, F. *Farmaco* **1990**, *45*, 93–99.
222. Blaker, J. J.; Nazhat, S. N.; Boccaccini, A. R. *Biomaterials* **2004**, *25*, 1319–1329.
223. Huber, C.; Eckstein, F. S.; Halbeisen, M.; Carrel, T. P. *Ann. Thorac. Surg.* **2003**, *75*, 1318–1321.
224. Montero, P.; Alvarez, C.; Marti, M. A.; Borderias, A. J. *J. Food Sci.* **1995**, *60*, 1–3.
225. Gammie, J. S.; Kaufman, C. L.; Michaels, M. G.; Ildstad, S. T. *Mol. Diagn.* **1996**, *1*, 219–224.

226. Halperin, E. C.; Knechtle, S. J.; Harland, R. C.; Yamaguchi, Y.; Sontag, M.; Randal Bollinger, R. *Radiother. Oncol.* **1990**, *18*, 29–37.
227. Squinto, S. P. *Curr. Opin. Biotechnol.* **1996**, *7*, 641–645.
228. Khor, E. *Biomaterials* **1997**, *16*, 95–105.
229. Milthorpe, B. K. *Biomaterials* **1994**, *15*, 745–752.
230. Roe, S. C.; Milthorpe, B. K.; True, K.; Rogers, G. J.; Schindhelm, K. *Clin. Mater.* **1992**, *9*, 149–154.
231. Madden, K. N.; Johnson, K. A.; Howlett, C. R.; *et al. Biomaterials* **1997**, *18*, 225–234.
232. van Steensel, C.; Schreuder, O.; van den Bosch, B.; *et al. J. Bone Joint Surg. Am.* **1987**, *69*, 860–864.
233. Badylak, S. F.; Tullius, R.; Kokini, K.; *et al. J. Biomed. Mater. Res.* **1995**, *29*, 977–985.
234. Johnson, K. A.; Rogers, G. J.; Roe, S. C.; *et al. Biomaterials* **1999**, *20*, 1003–1015.
235. Whitlock, P. W.; Smith, T. L.; Poehling, G. G.; Shilt, J. S.; Van Dyke, M. *Biomaterials* **2007**, *28*, 4321–4329.
236. Stone, K.; Walgenbach, A.; Turek, T.; Somers, D.; Wicomb, W.; Galili, U. *Arthroscopy* **2007**, *23*, 411–419.
237. Metcalf, M.; Savoie, F.; Kellum, B. *Oper. Tech. Orthop.* **2002**, *12*, 204–208.
238. Gilbert, T. W.; Stewart-Akers, A. M.; Simmons-Byrd, A.; Badylak, S. F. *J. Bone Joint Surg. Am.* **2007**, *89*, 621–630.
239. Evans, P.; Mackinnon, S.; Levi, A.; *et al. Muscle Nerve* **1998**, *21*, 1507–1522.
240. Conrad, E.; Gretch, D.; Obermeyer, K.; Moogk, M.; Sayers, M.; Wilson, J. *J. Bone Joint Surg. Am.* **1995**, *77A*, 214–224.
241. Asselmeier, M. A.; Caspari, R. B.; Bottenfield, S. *Am. J. Sports Med.* **1993**, *21*, 170–175.
242. Ireland, L.; Spelman, D. *Cell Tissue Bank.* **2005**, *6*, 181–189.
243. Lee, C. H.; Singla, A.; Lee, Y. *Int. J. Pharm.* **2001**, *221*, 1–22.
244. Ramshaw, J. A. M.; Werkmeister, J. A.; Glattauer, V. *Biotechnol. Genet. Eng. Rev.* **1995**, *13*, 335–382.
245. Ma, P. X. *Adv. Drug Deliv. Rev.* **2008**, *60*, 184–198.
246. Fratzl, P.; Weinkamer, R. *Prog. Mater. Sci.* **2007**, *52*, 1263–1334.
247. Paul, R. G.; Bailey, A. J. *ScientificWorldJournal* **2003**, *3*, 138–155.
248. Fujioka, K.; Maeda, M.; Hojo, T.; Sano, A. *Adv. Drug Deliv. Rev.* **1998**, *31*, 247–266.
249. Brown, R. A.; Phillips, J. B.; Kwang, W. J. *Int. Rev. Cytol.* **2007**, *262*, 75–150.
250. Spector, M. *Swiss Med. Wkly* **2006**, *136*, 293–301.
251. Emsley, J.; Knight, C. G.; Farndale, R. W.; Barnes, M. J. *J. Mol. Biol.* **2004**, *335*, 1019–1028.
252. White, D. J.; Puranen, S.; Johnson, M. S.; Heino, J. *Int. J. Biochem. Cell Biol.* **2004**, *36*, 1405–1410.
253. Heydarkhan-Hagvall, S.; Schenke-Layland, K.; Dhanasopon, A. P.; *et al. Biomaterials* **2008**, *29*(19), 2907–2914.
254. Hutmacher, D. W. *J. Biomater. Sci. Polym. Ed.* **2001**, *12*, 107–124.
255. Ker, R. F. *Int. J. Fatigue* **2007**, *29*, 1001–1009.
256. Miles, C. A.; Avery, N. C.; Rodin, V. V.; Bailey, A. J. *J. Mol. Biol.* **2005**, *346*, 551–556.
257. Vater, C. A.; Harris, E. D., Jr.; Siegel, R. C. *Biochem. J.* **1979**, *181*, 639–645.
258. Panchenko, M. V.; Stetler-Stevenson, W. G.; Trubetskoy, O. V.; Gacheru, S. N.; Kagan, H. M. *J. Biol. Chem.* **1996**, *271*, 7113–7119.
259. Koob, T. J.; Hernandez, D. J. *Biomaterials* **2002**, *23*, 203–212.
260. McKegney, M.; Taggart, I.; Grant, M. H. *J. Mater. Sci. Mater. Med.* **2001**, *12*, 833–844.
261. Cote, M. F.; Sirois, E.; Doillon, C. J. *J. Biomater. Sci. Polym. Ed.* **1992**, *3*, 301–313.
262. Rault, I.; Frei, V.; Herbage, D.; Abdul-Malak, N.; Huc, A. *J. Mater. Sci. Mater. Med.* **1996**, *7*, 215–221.
263. Chen, C. N.; Wu, C. C.; Tsai, C. C.; Sung, H. W.; Chang, Y. *J. Chin. Inst. Chem. Engrs.* **1997**, *28*, 389–397.
264. Osborne, C. S.; Barbenel, J. C.; Smith, D.; Savakis, M.; Grant, M. H. *Med. Biol. Eng. Comput.* **1998**, *36*, 129–134.
265. Zeugolis, D. I.; Paul, G. R.; Attenburrow, G. *J. Biomed. Mater. Res A* **2009**, *89*, 895–908.
266. Chai, C.; Leong, K. W. *Mol. Ther.* **2007**, *15*, 467–480.
267. Laporte, L. D.; Shea, L. D. *Adv. Drug Deliv. Rev.* **2007**, *59*, 292–307.
268. Lee, L. J. *Ann. Biomed. Eng.* **2006**, *34*, 75–88.
269. Bersten, A. M.; Ahkong, Q. F.; Hallinan, T.; Nelson, S. J.; Lucy, J. A. *Biochim. Biophys. Acta.* **1983**, *762*, 429–436.
270. Hevessy, Z.; Patthy, A.; Karpati, L.; Muszbek, L. *Thromb. Res.* **2000**, *99*, 399–406.
271. Case, A.; Ni, J.; Yeh, L.-A.; Stein, R. L. *Anal. Biochem.* **2005**, *338*, 237–244.
272. Lorand, L. *Neurochem. Int.* **2002**, *40*, 7–12.
273. Hucho, F.; Bandini, G. *FEBS Lett.* **1986**, *200*, 279–282.
274. Tiong, W. H. C.; Damodaran, G.; Naik, H.; Kelly, J. L.; Pandit, A. *Langmuir* **2008**, *24*, 11752–11761.
275. Chan, J. C.; Burugapalli, K.; Naik, H.; Kelly, J.; Pandit, A. *Biomacromolecules* **2008**, *9*, 528–536.
276. Kinberger, G. A.; Taulane, J. P.; Goodman, M. *Tetrahedron* **2006**, *62*, 5280–5286.
277. Yang, H.; Kao, W. J. *Encycl. Biomater. Biomed. Eng.* **2006**, 1–10.
278. Zinselmeyer, B. H.; Mackay, S. P.; Schatzlein, A. G.; Uchegbu, I. F. *Pharm. Res.* **2002**, *19*, 960–967.
279. Roberts, J. C.; Bhalgat, M. K.; Zera, R. T. *J. Biomed. Mater. Res.* **1996**, *30*, 53–65.
280. Jevprasesphant, R.; Penny, J.; Jalal, R.; Attwood, D.; McKeown, N. B.; D'Emanuele, A. *Int. J. Pharm.* **2003**, *252*, 263–266.
281. Jevprasesphant, R.; Penny, J.; Attwood, D.; McKeown, N. B.; D'Emanuele, A. *Pharm. Res.* **2003**, *20*, 1543–1550.
282. Dufes, C.; Uchegbu, I. F.; Schatzlein, A. G. *Adv. Drug Deliv. Rev.* **2005**, *57*, 2177–2202.
283. Deible, C. R.; Petrosko, P.; Johnson, P. C.; Beckman, E. J.; Russell, A. J.; Wagner, W. R. *Biomaterials* **1998**, *19*, 1885–1893.
284. Vasudev, S. C.; Chandy, T. *J. Biomed. Mater. Res.* **1997**, *35*, 357–369.
285. Zeugolis, D. I.; Paul, R. G.; Attenburrow, G. *J. Appl. Polym. Sci.* **2008**, *108*, 2886–2894.
286. Chen, H. T.; Neerman, M. F.; Parrish, A. R.; Simanek, E. E. *J. Am. Chem. Soc.* **2004**, *126*, 10044–10048.
287. Zhang, L.; Furst, E. M.; Kiick, K. L. *J. Control. Release* **2006**, *114*, 130–142.
288. Taguchi, T.; Xu, L.; Kobayashi, H.; Taniguchi, A.; Kataoka, K.; Tanaka, J. *Biomaterials* **2005**, *26*, 1247–1252.
289. Kim, M. S.; Hyun, H.; Kim, B. S.; Khang, G.; Lee, H. B. *Curr. Appl. Phys.* **2008**, *8*, 646–650.
290. Salaam, L. E.; Dean, D.; Bray, T. L. *Polymer* **2006**, *47*, 310–318.
291. Okuda, T.; Kawakami, S.; Akimoto, N.; Niidome, T.; Yamashita, F.; Hashida, M. *J. Control. Release* **2006**, *116*, 330–336.
292. Guillaudeu, S. J.; Fox, M. E.; Haidar, Y. M.; Dy, E. E.; Szoka, F. C.; Fréchet, J. M. J. *Bioconjug. Chem.* **2008**, *19*, 461–469.
293. Wechsler, S.; Fehr, D.; Molenberg, A.; Raeber, G.; Schense, J. C.; Weber, F. E. *J. Biomed. Mater. Res. A* **2008**, *85A*, 285–292.
294. Pasut, G.; Veronese, F. M. *Prog. Polym. Sci. Polym. Biomed. Appl.* **2007**, *32*, 933–961.
295. Raeber, G. P.; Lutolf, M. P.; Hubbell, J. A. *Biophys. J.* **2005**, *89*, 1374–1388.
296. Helmke, B. P.; Minerick, A. R. *Proc. Natl Acad. Sci. USA* **2006**, *103*, 6419–6424.
297. Oudega, M.; Gautier, S. E.; Chapon, P.; *et al. Biomaterials* **2001**, *22*, 1125–1136.
298. Khademhosseini, A.; Langer, R.; Borenstein, J.; Vacanti, J. P. *Proc. Natl Acad. Sci. USA* **2006**, *103*, 2480–2487.
299. Storrie, H.; Mooney, D. J. *Adv. Drug Deliv. Rev.* **2006**, *58*, 500–514.
300. Setton, L. *Nat. Mater.* **2008**, *7*, 172–174.
301. Ladet, S.; David, L.; Domard, A. *Nature* **2008**, *452*, 76–80.
302. Jiang, W.; Kim, B. Y. S.; Rutka, J. T.; Chan, W. C. W. *Nat. Nanotechnol.* **2008**, *3*, 145–150.
303. Xia, Y. *Nat. Mater.* **2008**, *7*, 758–760.
304. Kells, A. P.; Hadaczek, P.; Yin, D.; *et al. Proc. Natl Acad. Sci. USA* **2009**, *106*, 2407–2411.
305. Stitzel, J.; Liu, J.; Lee, S. J.; *et al. Biomaterials* **2006**, *27*, 1088–1094.
306. Hollister, S. J. *Nat. Mater.* **2005**, *4*, 518–524.
307. Salem, A. K.; Searson, P. C.; Leong, K. W. *Nat. Mater.* **2003**, *2*, 668–671.
308. Itoh, Y.; Matsusaki, M.; Kida, T.; Akashi, M. *Biomacromolecules* **2008**, *9*, 2202–2206.
309. Lee, M.; Lo, A. C.; Cheung, P. T.; Wong, D.; Chan, B. P. *Biomaterials* **2009**, *30*, 1214–1221.
310. Desai, T. A. *Med. Eng. Phys.* **2000**, *22*, 595–606.
311. Cornwell, K. G.; Downing, B.; Pins, G. D. *J. Biomed. Mater. Res. A* **2004**, *71A*, 55–62.
312. Zeltinger, J.; Sherwood, J. K.; Graham, D. A.; Mueller, R.; Griffith, L. G. *Tissue Eng.* **2001**, *7*, 557–572.
313. Carnell, L. S.; Siochi, E. J.; Holloway, N. M.; *et al. Macromolecules* **2008**, *41*, 5345–5349.
314. Zhong, S.; Teo, W. E.; Zhu, X.; Beuerman, R. W.; Ramakrishna, S.; Yung, L. Y. L. *J. Biomed. Mater. Res. A* **2006**, *79A*, 456–463.
315. Schnell, E.; Klinkhammer, K.; Balzer, S.; *et al. Biomaterials* **2007**, *28*, 3012–3025.
316. Vasita, R.; Katti, D. S. *Int. J. Nanomedicine* **2006**, *1*, 15–30.
317. Subbiah, T.; Bhat, G. S.; Tock, R. W.; Parameswaran, S.; Ramkumar, S. S. *J. Appl. Polym. Sci.* **2005**, *96*, 557–569.

318. Pham, Q. P.; Sharma, U.; Mikos, A. G. *Tissue Eng.* **2006**, *12*, 1197–1211.
319. Barnes, C. P.; Sell, S. A.; Boland, E. D.; Simpson, D. G.; Bowlin, G. L. *Adv. Drug Deliv. Rev.* **2007**, *59*, 1413–1433.
320. Chew, S.; Wen, Y.; Dzenis, Y.; Leong, K. *Curr. Pharm. Des.* **2006**, *12*, 4751–4770.
321. Jarvinen, T.; Jarvinen, T.; Kannus, P.; Jozsa, L.; Jarvinen, M. *J. Orthop. Res.* **2004**, *22*, 1303–1309.
322. Huang, Y.; Meek, K. M.; Ho, M.-W.; Paterson, C. A. *Exp. Eye Res.* **2001**, *73*, 521–532.
323. Silver, F. H.; Freeman, J. W.; Seehra, G. P. *J. Biomech.* **2003**, *36*, 1529–1553.
324. Yang, L.; Fitie, C. F. C.; van der Werf, K. O.; Bennink, M. L.; Dijkstra, P. J.; Feijen, J. *Biomaterials* **2008**, *29*, 955–962.
325. Hofman, S.; Sidqui, M.; Abensur, D.; Valentini, P.; Missika, P. *Biomaterials* **1999**, *20*, 1155–1166.
326. Schoof, H.; Apel, J.; Heschel, I.; Rau, G. *J. Biomed. Mater. Res.* **2001**, *58*, 352–357.
327. John, A.; Hong, L.; Ikada, Y.; Tabata, Y. *J. Biomater. Sci. Polym. Ed.* **2001**, *12*, 689–705.
328. Wallace, D. G.; Rosenblatt, J.; Ksander, G. A. *J. Biomed. Mater. Res.* **1992**, *26*, 1517–1534.
329. Yamamoto, Y.; Nakamura, T.; Shimizu, Y.; *et al. ASAIO J.* **1999**, *45*, 311–316.
330. Kawai, K.; Suzuki, S.; Tabata, Y.; Ikada, Y.; Nishimura, Y. *Biomaterials* **2000**, *21*, 489–499.
331. Ulubayram, K.; Nur Cakar, A.; Korkusuz, P.; Ertan, C.; Hasirci, N. *Biomaterials* **2001**, *22*, 1345–1356.
332. Ueda, H.; Hong, L.; Yamamoto, M.; *et al. Biomaterials* **2002**, *23*, 1003–1010.
333. Anselme, K.; Petite, H.; Herbage, D. *Matrix (Stuttgart, Germany)* **1992**, *12*, 264–273.
334. Yoshitani, M.; Fukuda, S.; Itoi, S.-I.; *et al. J. Thorac. Cardiovasc. Surg.* **2007**, *133*, 726–732; e723.
335. Hiraoka, Y.; Kimura, Y.; Ueda, H.; Tabata, Y. *Tissue Eng.* **2003**, *9*, 1101–1112.
336. Yarat, A.; Ozcelik, F.; Emekli, N. *J. Marmara Univ. Dent. Fac.* **1996**, *2*, 527–529.
337. Collins, R. L.; Christiansen, D.; Zazanis, G. A.; Silver, F. H. *J. Biomed. Mater. Res.* **1991**, *25*, 267–276.
338. Cote, M.-F.; Doillon, C. J. *Biomaterials* **1992**, *13*, 612–616.
339. Pachence, J. M. *J. Biomed. Mater. Res.* **1996**, *33*, 35–40.
340. Peterkova, P.; Lapcik, L. J. *Colloid Polym. Sci.* **2000**, *278*, 1014–1016.
341. Tiller, J. C.; Bonner, G.; Pan, L.-C.; Klibanov, A. M. *Biotechnol. Bioeng.* **2001**, *73*, 246–252.
342. Elliott, J. T.; Woodward, J. T.; Umarji, A.; Mei, Y.; Tona, A. *Biomaterials* **2007**, *28*, 576–585.
343. Lu, J. T.; Lee, C. J.; Bent, S. F.; Fishman, H. A.; Sabelman, E. E. *Biomaterials* **2007**, *28*, 1486–1494.
344. Liu, Y.; Gan, L.; Carlsson, D. J.; *et al. Invest. Ophthalmol. Vis. Sci.* **2006**, *47*, 1869–1875.
345. Blanco, M. D.; Bernardo, M. V.; Gomez, C.; Muniz, E.; Teijon, J. M. *Biomaterials* **1999**, *20*, 1919–1924.
346. Hutcheon, G. A.; Messiou, C.; Wyre, R. M.; Davies, M. C.; Downes, S. *Biomaterials* **2001**, *22*, 667–676.
347. Evans, M. D. M.; McLean, K. M.; Hughes, T. C.; Sweeney, D. F. *Biomaterials* **2001**, *22*, 3319–3328.
348. Hunter, C. J.; Imler, S. M.; Malaviya, P.; Nerem, R. M.; Levenston, M. E. *Biomaterials* **2002**, *23*, 1249–1259.
349. Haile, Y.; Berski, S.; Dräger, G.; *et al. Biomaterials* **2008**, *29*, 1880–1891.
350. Lee, C. S. D.; Gleghorn, J. P.; Won Choi, N.; Cabodi, M.; Stroock, A. D.; Bonassar, L. J. *Biomaterials* **2007**, *28*, 2987–2993.
351. Flanagan, T. C.; Wilkins, B.; Black, A.; Jockenhoevel, S.; Smith, T. J.; Pandit, A. S. *Biomaterials* **2006**, *27*, 2233–2246.
352. Knill, C. J.; Kennedy, J. F.; Mistry, J.; *et al. Carbohydr. Polym.* **2004**, *55*, 65–76.
353. Kojima, K.; Okamoto, Y.; Miyatake, K.; Kitamura, Y.; Minami, S. *Carbohydr. Polym.* **1998**, *37*, 109–113.
354. Ueno, H.; Yamada, H.; Tanaka, I.; *et al. Biomaterials* **1999**, *20*, 1407–1414.
355. Kato, Y. P.; Silver, F. H. *Biomaterials* **1990**, *11*, 169–175.
356. Wang, M. C.; Pins, G. D.; Silver, F. H. *Biomaterials* **1994**, *15*, 507–512.
357. Pins, G. D.; Silver, F. H. *Mater. Sci. Eng. C* **1995**, *3*, 101–107.
358. Cavallaro, J. F.; Kemp, P. D.; Kraus, K. H. *Biotechnol. Bioeng.* **1994**, *43*, 781–791.
359. Menard, C.; Mitchell, S.; Spector, M. *Biomaterials* **2000**, *21*, 1867–1877.
360. Rhee, S. H.; Suetsugu, Y.; Tanaka, J. *Biomaterials* **2001**, *22*, 2843–2847.
361. Yamada, K.; Imamura, K.; Itoh, H.; Iwata, H.; Maruno, S. *Biomaterials* **2001**, *22*, 2207–2214.
362. Comut, A. A.; Shortkroff, S.; Zhang, X.; Spector, M. *Biomaterials* **2000**, *21*, 1887–1896.
363. Delorenzi, N. J.; Gatti, C. A. *Matrix (Stuttgart, Germany)* **1993**, *13*, 407–413.
364. Hsu, S.; Jamieson, A. M.; Blackwell, J. *Biorheology* **1994**, *31*, 21–36.
365. Silver, F. H.; Trelstad, R. L. *J. Biol. Chem.* **1980**, *255*, 9427–9433.
366. Graham, H. K.; Holmes, D. F.; Watson, R. B.; Kadler, K. E. *J. Mol. Biol.* **2000**, *295*, 891–902.
367. Li, G. Y.; Fukunaga, S.; Takenouchi, K.; Nakamura, F. *J. Soc. Leather Technol. Chem.* **2004**, *88*, 66–71.
368. Farber, S.; Garg, A. K.; Birk, D. E.; Silver, F. H. *Int. J. Biol. Macromol.* **1986**, *8*, 37–42.
369. Brokaw, J. L.; Doillon, C. J.; Hahn, R. A.; Birk, D. E.; Berg, R. A.; Silver, F. H. *Int. J. Biol. Macromol.* **1985**, *7*, 135–140.
370. Silver, F. H.; Birk, D. E. *Int. J. Biol. Macromol.* **1984**, *6*, 125–132.
371. Ward, N. P.; Hulmes, D. J. S.; Chapman, J. A. *J. Mol. Biol.* **1986**, *190*, 107–112.
372. Birk, D. E.; Silver, F. H. *Arch. Biochem. Biophys.* **1984**, *235*, 178–185.
373. Helseth, D. L.; Veis, A. *J. Biol. Chem.* **1981**, *256*, 7118–7128.
374. Mould, A. P.; Hulmes, D. J. S.; Holmes, D. F.; Cummings, C.; Sear, C. H. J.; Chapman, J. A. *J. Mol. Biol.* **1990**, *211*, 581–594.
375. Berg, R. A.; Birk, D. E.; Silver, F. H. *Int. J. Biol. Macromol.* **1986**, *8*, 177–182.
376. Goldstein, J. D.; Tria, A. J.; Zawadsky, J. P.; Kato, K. Y.; Christiansen, D.; Silver, F. H. *J. Bone Joint Surg.* **1989**, *71A*, 1183–1191.
377. Kato, Y. P.; Christiansen, D. L.; Hahn, R. A.; Shieh, S.-J.; Goldstein, J. D.; Silver, F. H. *Biomaterials* **1989**, *10*, 38–42.
378. Wasserman, A. J.; Kato, Y. P.; Christiansen, D.; Dunn, M. G.; Silver, F. H. *Scanning Microsc.* **1989**, *3*, 1183–1197; discussion 1197–1200.
379. Rizvi, A. H.; Pins, G. D.; Silver, F. H. *Clin. Mater.* **1994**, *16*, 73–80.
380. Zeugolis, D. I.; Paul, G. R.; Attenburrow, G. *Acta Biomater.* **2008**, *4*, 1646–1656.
381. Zeugolis, D. I.; Paul, G. R.; Attenburrow, G. *J. Biomed. Mater. Res. A* **2009**, *89*, 895–908.
382. Liu, W.; Griffith, M.; Li, F. *J. Mater. Sci. Mater. Med.* **2008**, *19*, 3365–3371.
383. Wong, H.-L.; Wang, M.-X.; Cheung, P.-T.; Yao, K.-M.; Chan, B. P. *Biomaterials* **2007**, *28*, 5369–5380.
384. Thissen, H.; Chang, K.-Y.; Tebb, T. A.; *et al. J. Biomed. Mater. Res. A* **2006**, *77A*, 590–598.
385. Douglas, T.; Hempel, U.; Mietrach, C.; *et al. J. Biomed. Mater. Res. A* **2008**, *84A*, 805–816.
386. Cao, H.; Xu, S.-Y. *J. Mater. Sci. Mater. Med.* **2008**, *19*, 567–575.
387. Wright, K. T.; El Masri, W.; Osman, A.; *et al. Biochem. Biophys. Res. Commun.* **2007**, *354*, 559–566.
388. Yao, C.; Markowicz, M.; Pallua, N.; Magnus Noah, E.; Steffens, G. *Biomaterials* **2008**, *29*, 66–74.
389. Fontana, A.; Spolaore, B.; Mero, A.; Veronese, F. M. *Adv. Drug Deliv. Rev.* **2008**, *60*, 13–28.
390. Shen, Y. H.; Shoichet, M. S.; Radisic, M. *Acta Biomater.* **2008**, *4*, 477–489.
391. Liman, S. T.; Kara, C. O.; Bir, F.; Yildirim, B.; Topcu, S.; Sahin, B. *Int. J. Pediatr. Otorhinolaryngol.* **2005**, *69*, 1327–1331.
392. Chen, R.; Mooney, D. *Pharm. Res.* **2003**, *20*, 1103–1112.
393. Barras, F.; Pasche, P.; Bouche, N.; Aebischer, P.; Zurn, A. *J. Neurosci. Res.* **2002**, *70*, 746–755.
394. Tornqvist, N.; Bjorklund, L.; Almqvist, P.; Wahlberg, L.; Stromberg, I. *Exp. Neurol.* **2000**, *164*, 130–138.
395. Bensadoun, J.; Pereira de Almeida, L.; Fine, E.; Tseng, J.; Deglon, N.; Aebischer, P. *J. Control. Release* **2003**, *87*, 107–115.
396. Liang, D.; Luu, Y. K.; Kim, K.; Hsiao, B. S.; Hadjiargyrou, M.; Chu, B. *Nucleic Acids Res.* **2005**, *33*, 1–8.
397. Willerth, S. M.; Sakiyama-Elbert, S. E. *Adv. Drug Deliv. Rev.* **2007**, *59*, 325–338.
398. Zhang, X.; Pan, S.-R.; Hu, H.-M.; *et al. J. Biomed. Mater. Res. A* **2008**, *84A*, 795–804.
399. Réthoré, G.; Mathew, A.; Naik, H.; Pandit, A. *Tissue Eng. Part C Methods* **2009**, *15*(4), 605–613.
400. Réthoré, G.; Naik, H.; Pandit, A. Hollow Biodegradable Nanospheres and Nanoshells for Delivery of Therapeutic and/or Imaging Molecules. (Preliminary US Continuation-in-part (CIP) Patent filed March 20, 2010 patent 12/886492 (derived from PCT/EP2009/053258)).
401. Cheng, X.; Gurkan, U. A.; Dehen, C. J.; *et al. Biomaterials* **2008**, *29*, 3278–3288.
402. Kim, J. A.; Cho, K.; Shin, Y. S.; Jung, N.; Chung, C.; Chang, J. K. *Biosens. Bioelectron.* **2007**, *22*, 3273–3277.
403. Harley, B. A.; Hastings, A. Z.; Yannas, I. V.; Sannino, A. *Biomaterials* **2006**, *27*, 866–874.
404. Caves, J.; Kumar, V.; Wen, J.; *et al. J. Biomed. Mater. Res. B Appl. Biomater.* **2010**, *93*(1), 24–38.

2.216. Collagen–GAG Materials

S R Caliari and B A C Harley, University of Illinois at Urbana-Champaign, Urbana, IL, USA

© 2011 Elsevier Ltd. All rights reserved.

2.216.1.	**Introduction**	280
2.216.1.1.	Collagen	281
2.216.1.2.	Glycosaminoglycans	281
2.216.1.3.	Collagen–GAG Material Development	282
2.216.1.4.	Antigenicity and Immunogenicity of Collagen–GAG Materials	283
2.216.2.	**Fabrication of Collagen–GAG Materials**	283
2.216.2.1.	CG Scaffold Fabrication: Lyophilization	283
2.216.2.2.	Modifications to CG Scaffold During Fabrication	283
2.216.2.2.1.	Relative density	283
2.216.2.2.2.	Pore size and shape	283
2.216.2.2.3.	Crosslinking	284
2.216.2.3.	CGCaP Scaffold Fabrication	285
2.216.2.4.	Multicompartment CG Scaffold Fabrication	286
2.216.2.5.	CG Hydrogels	286
2.216.2.6.	CG Membranes	287
2.216.3.	**Characterization of Collagen–GAG Materials**	287
2.216.3.1.	Microstructure: Experimental Measurement and Modeling	287
2.216.3.2.	Permeability: Experimental Measurement and Modeling	288
2.216.3.3.	Mechanical Properties: Experimental Measurement and Modeling	288
2.216.3.4.	CG Scaffold Degradation Kinetics and Byproducts	291
2.216.4.	***In Vitro* Applications**	292
2.216.4.1.	Cell Attachment and Viability	292
2.216.4.2.	Cell Contraction	292
2.216.4.3.	Cell Motility	294
2.216.4.4.	Growth Factor and Gene Delivery	296
2.216.4.5.	Modifying Gene Expression	296
2.216.4.6.	Mechanical Stimulation	296
2.216.4.7.	Stem Cell Differentiation	297
2.216.5.	***In Vivo* Applications**	297
2.216.5.1.	Dermal Regeneration Applications	297
2.216.5.2.	Peripheral Nerve Regeneration Applications	298
2.216.5.3.	Conjunctiva and Corneal Regeneration Applications	298
2.216.5.4.	Cartilage and Fibrocartilage Disk Tissue Engineering Applications	298
2.216.5.5.	Bone, Osteochondral Regeneration Applications	299
2.216.5.6.	Brain Tissue Engineering Applications	300
2.216.5.7.	Lung Tissue Engineering Applications	300
2.216.6.	**Conclusions**	300
References		300

Abbreviations

CFD	Computational fluid dynamics
CFM	Culture force monitor
CG	Collagen–glycosaminoglycan coprecipitate
CGCaP	Collagen–glycosaminoglycan–calcium phosphate triple coprecipitate
COL*x*A*y*	Family of genes that encode for synthesizing distinct collagen subunit chains; *x*, *y* correspond to collagen type and subunit chain, respectively (e.g., COL1A2, COL3A2, COL2A1, COL4A4, COL4A5)
COX-2	Cyclooxygenase-2; key enzyme for the production of early bone formation marker prostaglandin E_2
DHT	Dehydrothermal crosslinking
DRT	Dermal regeneration template
ECM	Extracellular matrix
EDAC	1-Ethyl-3-(3-dimethylaminopropyl) carbodiimide hydrochloride
EDX	Energy-dispersive X-ray spectroscopy
ESEM	Environmental scanning electron microscopy
FGF	Fibroblast growth factor

GAGs	Glycosaminoglycans
GDNF	Glial cell line-derived neurotrophic factor
HA	Hyaluronic acid
HGF	Hepatocyte growth factor; a paracrine signaling factor involved in cellular growth, motility, morphogenesis, and angiogenesis
HMOX	Heme oxygenase; an enzyme that catalyzes the degradation of heme and is critically involved in angiogenesis
IPN	Interpenetrating network
MC3T3-E1	Mouse preosteoblast cell line
MMP	Matrix metalloproteinase; a family of enzymes that degrades extracellular matrix proteins. Key MMPs include: MMP-2, MMP-12, MMP-19
MSC	Mesenchymal stem cell or marrow stromal cell
NHS	*N*-Hydroxysulfosuccinimide
NRT	Nerve regeneration template
OPN	Osteopontin; late marker of bone formation
PGE_2	Prostaglandin E_2; early bone formation marker
SA/*V*	Specific surface area; total surface area per unit volume for a given unit cell
TC	Tropocollagen; the fundamental organizational unit of collagen
TGF-β1	Transforming growth factor-β1;
TIMP	Tissue inhibitor of metalloproteinase. Key MMP inhibitors include: TIMP1, TIMP3
UC	Unit cell
μCT	Microcomputed tomography
VEGF	Vascular endothelial growth factor; a chemical signal produced by cells that stimulates the growth of new blood vessels (angiogenesis)

Symbols

D_{jxn}	Strut junction spacing; defines the distance between points in the scaffold where multiple struts meet
d	Scaffold pore size
E_s	Elastic modulus of individual scaffold strut
E^*	Elastic modulus of the entire cellular material
E_sI	Scaffold strut flexural rigidity
ε	Compressive strain
F_c	Average contractile force generated by an individual cells within a 3D scaffold
I	Second moment of inertia
k	Scaffold permeability (m^2)
l	Edge length of unit cell
l_s	Scaffold strut length
σ^*_{el}	Compressive plateau stress
ρ_{jxn}	Strut junction density; the number of strut junctions per unit cell divided by the volume of the unit cell in a cellular material
ρ^*/ρ_s	Relative density (1 – porosity)

2.216.1. Introduction

The extracellular matrix (ECM) is a complex macromolecular structure composed of a fibrillar network of structural proteins (collagens, elastin, etc.), proteoglycans (polypeptide core with attached polysaccharide chains called glycosaminoglycans (GAGs)), specialized proteins for cell adhesion (fibronectin, laminin, etc.), and other tissue-specific materials such as apatite in bone. The ECM defines the physical morphology of tissues and the local environment in which cells reside. In addition to serving as a physical support structure and insoluble regulator of cell activity, the ECM is a reservoir of numerous soluble regulators of cell behavior.

Tissue engineering scaffolds are utilized as ECM analogs to heal or modify tissues in a defined manner. In order to be successful, these scaffolds must be able to mimic key aspects of the native ECM and support normal cell behaviors. As an analog of the native ECM, collagen–glycosaminoglycan (collagen–GAG) materials possess several vital characteristics that aid in the making of successful tissue engineering scaffolds, including three dimensionality with interconnected pores, tunable degradation and resorption rates, surface ligands for cell adhesion, and mechanical integrity.[1,2] Since their inception, these materials have been utilized in a variety of tissue engineering studies, both *in vivo* as regenerative templates for skin, peripheral nerves, conjunctiva, and cartilage[3–6] and *in vitro* as 3D microenvironments to probe more fundamental questions about cell behaviors and cell–matrix interactions. Scaffold microstructure characteristics, such as porosity, mean pore size, pore shape, interconnectivity, specific surface area,[4,5,7–15] and mechanical properties (Young's modulus, yield stress),[16–25] have been shown to be key factors that can influence cell behaviors such as adhesion, motility, contraction, stem cell differentiation, gene expression, and overall bioactivity.[4]

This chapter will provide an introduction to, and an overview of, the development and application of collagen–GAG (CG) materials. We begin with an overview of the structure and biochemistry of both collagen and GAGs and will consider questions concerning the immunogenicity, antigenicity, and regulatory compliance of CG biomaterials. We will continue with a summary of the fabrication techniques used to make a wide range of CG materials, including mineralized and nonmineralized (type I and II) scaffolds as well as membranes and hydrogels. Characterization of CG materials, notably microstructural, mechanical, and chemical properties, and the use of modeling approaches to describe these features will then be covered. We will detail *in vitro* applications of CG scaffolds for the investigation of cell adhesion, motility, contraction, stem cell differentiation, gene expression, and mechanotransduction. Finally, *in vivo* applications of CG materials as ECM

analogs for the regeneration of a wide variety of tissues, notably skin, peripheral nerves, conjunctiva, cartilage, and bone will be reviewed.

2.216.1.1. Collagen

Collagen is the major organic component of the natural ECM.[26–29] To date, 29 types of collagen have been identified,[26,28] although 90% of collagen in the human body is fibrillar (main types: I, II, III, and V). Type I collagen is the major structural component of the ECM in a wide variety of tissues such as skin, tendon, ligament, and bone. Type II collagen is found principally in cartilage; type III is found in skin, blood vessels, and intestines; and type V is a component of bone, skin, cornea, and other tissues.[28]

Like all biological proteins, collagen is defined by four levels of organization: primary, secondary, tertiary, and quaternary. The primary structure of the collagen is highly conserved among mammals and follows a Gly-X-Y pattern characterized by the presence of a glycine every third residue with X and Y representing other amino acids (**Figure 1(a)**). Common residues in these X and Y positions are proline (28% of total residues) and hydroxyproline (38%), respectively.[26–30] These amino acids form left-handed, polyproline II-type polypeptide chains that define the secondary structure. Three of these polypeptide chains come together in a coiled, helical manner to form a right-handed triple helix termed tropocollagen (TC). The TC molecule is the fundamental organizational unit of the collagen and defines its tertiary structure[26,28,30] (**Figure 1(b)**), with dimensions of approximately 280 nm in length and 1.5 nm in diameter.[28,30] Each of the three polypeptide units, or alpha units, contains 1050 amino acids.[27] Typically, two of these units have very similar sequences and are termed α1 chains while the dissimilar third chain is denoted as α2. Glycine is the only amino acid with a side group (single hydrogen) small enough to fit within the tight packing of the triple helix, thereby necessitating its presence at every third residue. While the glycines face inward because of steric constraints, the proline and hydroxyproline groups face outwards and help stabilize the overall triple helix structure via hydrogen bonding.[27,28]

For tissues composed of type I collagen (bone, tendon, ligament, etc.), TC molecules assemble into fibrils up to 500 nm in diameter and 1 cm in length (quaternary structure). Fibrillogenesis, and subsequent crosslinking, is aided by the presence of nonhelical residues on each end of the TC molecules called collagen telopeptides.[27,28] These ends contain lysyl residues that promote covalent crosslinking between opposing ends of adjacent TC molecules. This crosslinking insures the stability of the fibrillar structure. Each TC molecule is displaced from its laterally adjacent partner by 67 nm. This periodic organization is the key feature of the quaternary structure (**Figure 1(c)**).[27,28] Fibrils band together to form higher order fiber bundles that are tissue specific. For example, tendon is composed of uniaxially aligned, crimped fiber bundles. It is important to note that the banding (quaternary structure) of collagen is abolished as a result of acid coprecipitation during fabrication of CG materials, limiting platelet aggregation *in vivo*.[4,31] The destruction of the quaternary structure is accomplished without denaturing the collagen to gelatin. Gelatin is the amorphous form of collagen, having the same amino acid sequence but lacking the triple helical character of collagen. Gelatin can be formed by heating hydrated collagen past a critical temperature of 75–105 °C. The temperature varies according to collagen type, species, and hydration level. Dry collagen is denatured when heated over 150 °C.[30,31]

2.216.1.2. Glycosaminoglycans

GAGs are long, repeating disaccharide units that are linked to protein cores to form proteoglycans (**Figure 2**).[32] GAGs serve as

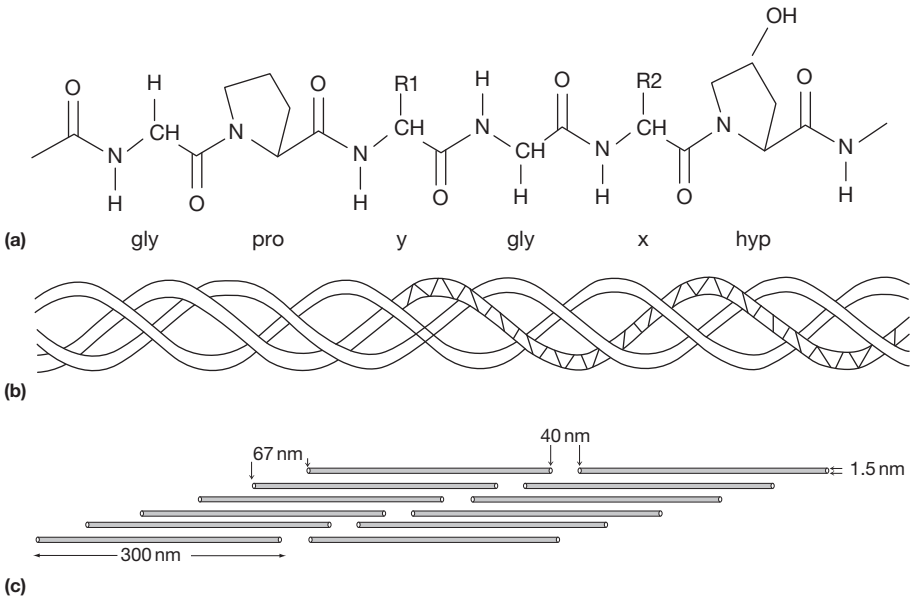

Figure 1 Structural and chemical overview of collagen type I. (a) Typical primary amino acid sequence. (b) Secondary left-handed helix and tertiary right-handed triple-helix structure. (c) Staggered quaternary structure displaying characteristic 67 nm lateral offset between fibrils. Reprinted with permission from Friess, W. *Eur. J. Pharm. Biopharm.* **1998**, *45*, 113–136.

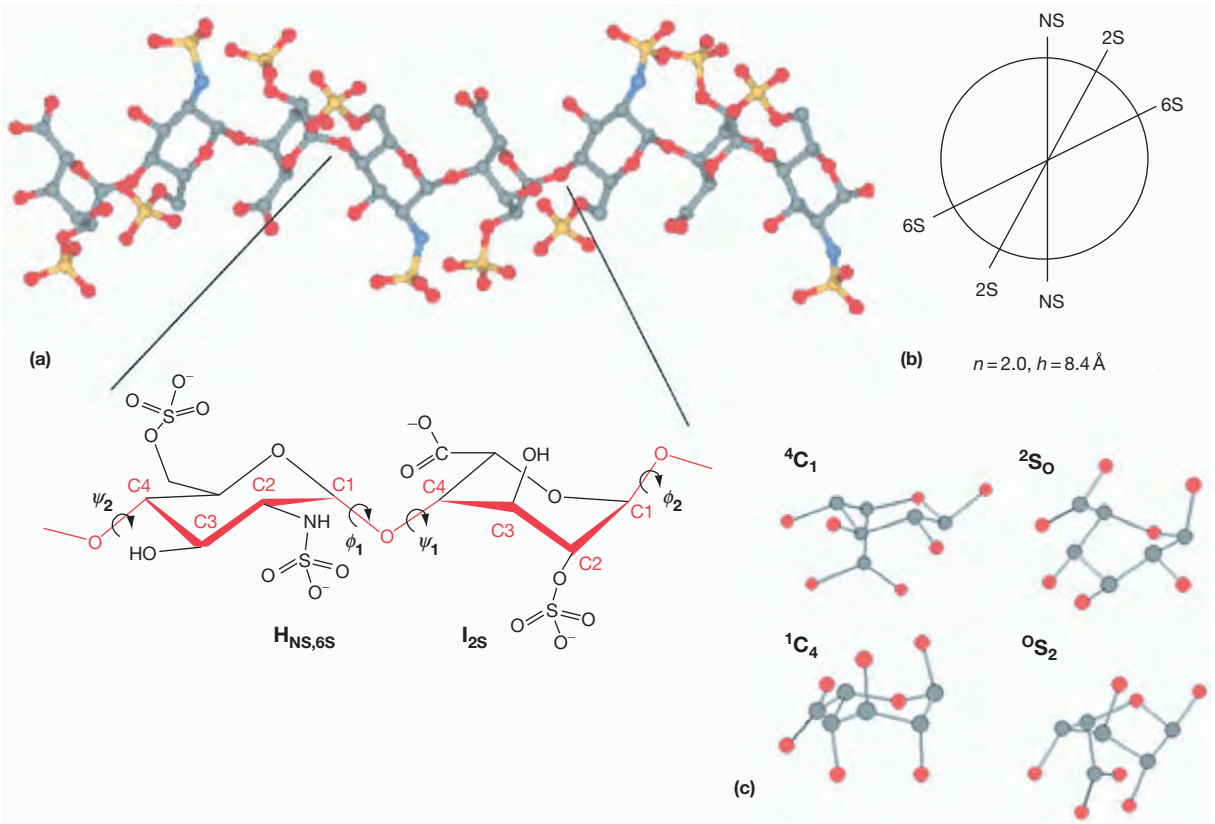

Figure 2 3D structure of GAG. (a) Top: ball-and-stick depiction of a heparin oligosaccharide with –[I_{2S}-$H_{NS,6S}$]– repeat unit (carbon, oxygen, nitrogen, and sulfur atoms are colored gray, red, blue, and yellow, respectively). Bottom: chair conformation of the expanded disaccharide unit showing backbone atoms (colored red) and glycosidic torsion angles (ϕ_1, ψ_1) and (ϕ_2, ψ_2). (b) Helical wheel projection of the sulfate groups of the structure shown in (a). (c) Commonly observed low-energy ring conformations of iduronic acid [atoms colored the same way as in (a)]. Reprinted with permission from Raman, R.; Sasisekharan, V.; Sasisekharan, R. *Chem. Biol.* **2005**, *12*, 267–277.

a crucial component of the native ECM and influence various biological functions including cell migration, division, angiogenesis, collagen fibrillogenesis, and the presentation of soluble factors.[27,32–34] These macromolecules are strongly negatively charged because of the presence of sulfate groups, resulting in large associated osmotic pressures and allowing them to significantly swell in water. These properties are responsible for the high compressive modulus and excellent resistance to repeated deformation seen in GAG-rich tissues such as articular cartilage.[35] The main GAG component of aggrecan, the chief proteoglycan in articular cartilage, is chondroitin sulfate, the most common GAG found in humans and also in CG materials.[27,31,36] Other common classes of GAGs include dermatan sulfate (a derivative of chondroitin sulfate), heparin sulfate and heparin, keratan sulfate, and hyaluronic acid (HA).[27,34,37] Chondroitin sulfate, like other GAGs, is composed of a disaccharide repeat unit consisting of a acidic sugar-like molecule and a sulfated amino sugar (the exception is HA, which is not sulfated).[32] For chondroitin sulfate, these sugars are D-glucuronic acid and *N*-acetyl galactosamine respectively.[27]

2.216.1.3. Collagen–GAG Material Development

CG materials were developed in the 1970s by a collaboration between Ioannis Yannas, a professor at Massachusetts Institute of Technology, and John F. Burke, a surgeon at Massachusetts General Hospital. Burke's search for a treatment for traumatic burns coupled with Yannas' background in collagen biochemistry led to the development of a CG membrane that was one of the first bioactive materials designed for a tissue engineering application, in this case the regeneration of full-thickness skin wounds. Collagen is a well characterized biopolymer and was chosen as a model material in part because of its controllable biodegradability, relative weak antigenicity/immunogenicity, and overall history in clinical applications (see **Chapter 2.215, Collagen: Materials Analysis and Implant Uses**).[31,38] GAGs were incorporated into the collagen material for several reasons beyond that of ECM chemistry and biomimicry. First, although the biodegradation rate of collagen can be adjusted over a wide range of values via crosslinking, heavy crosslinking leaves the material brittle and stiff. The copolymerization of collagen with GAG results in a material more resistant to degradation, thereby reducing the need for heavy crosslinking.[31] The addition of GAG was shown to significantly improve material mechanics, including elastic modulus and fracture energy.[31] SEM imaging also showed that scaffolds made with collagen and GAG exhibit a more open pore structure than scaffolds made from collagen alone, a critical design requirement to insure adequate cell migration and permeability throughout the entire construct. The addition

of GAG also gives CG materials their unique hemostatic properties discussed earlier, limiting platelet aggregation normally associated with collagen.[31]

2.216.1.4. Antigenicity and Immunogenicity of Collagen–GAG Materials

Collagen has been used in a variety of medical capacities, including sutures, skin and bone grafts, and for cosmetic purposes.[5,38–40] The collagen source for these applications as well as that used for CG biomaterials has typically been bovine skin or tendon. Collagens from these sources have consistently displayed low antigenicity (ability to interact with antibodies) and immunogenicity (ability to induce immune response), with adverse immune responses occurring even less frequently than nickel or latex allergies.[38] The majority of adverse responses arise from preexisting allergies (only 2–4% of population), but even in these cases, local inflammation and granulation subsides after several months to 1 year.[38,41,42] GAGs on their own have been utilized in orthopedic implants and more recently as dietary supplements to improve joint health. They are weak antigens and break down into oligosaccharides that can be cleared by native biological processes.[31] In addition, there is little evidence that the copolymerization of collagen and GAG increases antigenicity or immunogenicity of collagen on its own.[38] With over 1500 human cases, CG skin grafts have not had an adverse response to date.[5,38] With their long clinical history, CG materials are regulatory compliant in both the United States and Europe.

2.216.2. Fabrication of Collagen–GAG Materials

2.216.2.1. CG Scaffold Fabrication: Lyophilization

CG scaffolds are typically created via freeze-drying of a suspension consisting of coprecipitated type I collagen and the glycosaminoglycan chondroitin 6-sulfate in a solution of weak acetic acid.[4] HA has been used as an alternative to chondroitin 6-sulfate in CG scaffolds for cartilage tissue engineering.[43] Typical solids concentration for these suspensions are 0.5–1% (w/v) collagen and 0.05–0.1% (w/v) GAG. These values have been traditionally selected not only because the resultant scaffolds have high porosities to enable rapid cellular infiltration and diffusive transport processes, but also because of the inherent difficulty in processing CG suspensions with higher solids content without denaturing the collagen which occurs due to the increased temperature and shear stresses required for complete mixing of the CG content at high weight or volume percentages. The suspension is homogenized at 4 °C to prevent collagen gelatinization, degassed under vacuum to remove air bubbles introduced during mixing, and then freeze-dried to produce the porous CG scaffold.[1] During lyophilization, the CG suspension is frozen at a specified temperature,[44] resulting in a continuous, interpenetrating network of ice crystals intertwined with CG coprecipitate. Sublimation of the ice crystals produces a highly porous scaffold whose microstructure is formed by individual fibers of CG called struts (**Figure 3**). These scaffolds resemble low-density, open-cell foams, with an interconnected network of struts and relative densities (ρ^*/ρ_s) typically significantly less than 10%. Relative density is calculated as the ratio of the density of the porous material (ρ^*) to the density of the solid it is constructed from (ρ_s). Porosity, another key parameter used to describe porous biomaterials, can be calculated from scaffold relative density: porosity $= 1 - \rho^*/\rho_s$.

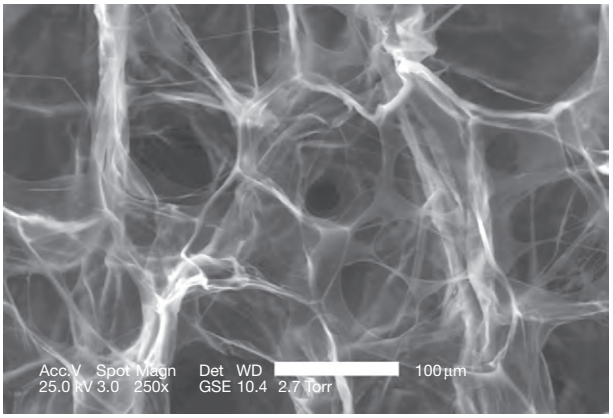

Figure 3 ESEM image of the pore structure of the CG scaffold ($T_f = -40$ °C). Scale bar: 100 µm. Reprinted with permission from Harley, B. A.; Leung, J. H.; Silva, E.; Gibson, L. J. *Acta Biomater.* **2007**, *3*, 463–474.

2.216.2.2. Modifications to CG Scaffold During Fabrication

2.216.2.2.1. Relative density

Scaffolds for certain applications, such as peripheral nerve and bone regeneration, have been created from CG suspension with considerably higher solids content (5–10%, w/v). Peripheral nerve scaffolds have been fabricated from high solids content CG suspension produced using plasticating extruders to homogenize the CG suspension.[3] Vacuum filtration has also been used to remove solvent from homogenized CG (both mineralized and nonmineralized) suspensions, thus increasing scaffold relative density. Nonmineralized CG suspensions were created with relative densities as high as 2.5% (w/v) while still enabling fabrication of bioactive, porous CG scaffold structure;[45] mineralized CG suspensions with relative densities as high as 18% (w/v) were also created in this manner.[46] These densified scaffolds have been created in order to improve mechanical properties and slow biodegradation rates relative to nondensified suspensions.[45,46]

2.216.2.2.2. Pore size and shape

During the freeze-drying process, modifying CG suspension thermal profiles enables fabrication of CG scaffolds with a wide range of pore sizes and shapes. Pore size is governed by the final freezing temperature, where lower temperatures lead to smaller pores.[44,47] Final freezing temperature and degree of undercooling control the rate of ice crystal nucleation in the suspension. Longer solidification times lead to more significant coarsening, where ice crystals aggregate to reduce their surface energy, resulting in larger pores.[9,10] Scaffolds with equiaxed pores can be fabricated using a constant cooling rate technique that results in homogenous cooling, solidification, and pore formation throughout the CG suspension.[44] Using this method in combination with final freezing temperatures ranging from −10 to −60 °C, CG scaffolds have been fabricated with pore sizes

from 85 to 325 μm but with constant relative density ($\rho^*/\rho_s = 0.006$) (Table 1).[9,10] More heterogeneous solidification processes at lower temperatures (−80 °C) have also been used to fabricate CG scaffolds with pore sizes as low as 10–20 μm.[5,47,48]

Scaffold microstructure can be further tuned by altering other aspects of the freezing profile. For example, the alignment and elongation of pores is controlled by the directionality of heat transfer during the freezing process. While the constant cooling method results in isotropic polyhedral pores by cooling the entire CG suspension homogenously, aligned tracks of ellipsoidal pores can be created using a thermally mismatched mold (polysulfone mold, copper base); the mismatch in thermal conductivity promotes unidirectional heat transfer through the copper bottom, resulting in aligned pores.[49] Forthcoming work modifying this technique has allowed fabrication of CG scaffolds with pore anisotropies as great as 1.5:1 (aligned:unaligned direction) (Caliari and Harley, unpublished). Aligned features are a critical design criterion for scaffolds aimed towards regenerating directional tissues such as peripheral nerves,[50] myocardium,[51] and tendon.[52] Rapid, unidirectional cooling has also been used to create aligned CG scaffolds for peripheral nerve regeneration.[47,48] CG scaffolds with pore size and alignment gradients have been used to entubulate the transected ends of peripheral nerves and induce regeneration.[3,48,53]

Tubular CG scaffolds with uniform pore microstructures have been fabricated by injecting high solids content CG suspension into a tubular mold with a rotating mandrel. Recently, a spinning technique to create radially patterned CG scaffold tubes has been developed.[54] The CG suspension is placed into a cylindrical copper mold and spun at high angular velocities (> 5000 rpm), resulting in radial sedimentation of the CG solids. The suspension is then flash frozen in liquid nitrogen, resulting in the creation of small ice crystals within the CG suspension that do not interrupt the sedimentation. By varying the angular velocity and spinning time, solid cylinders or hollow tubes of variable inner diameter and tube wall microstructure can be created. These tubes display a radially aligned pore structure and a gradient of porosity along the tube radius (Figure 4). A modeling framework that describes this sedimentation process using Lamm differential equations for collagen concentration and balances sedimentation and diffusion forces to determine scaffold tube geometry as a function of spinning conditions has also been recently developed.[55] These scaffolds are currently being investigated as substrates to limit the inward migration of exogenous contractile cells into and through the tube wall for a peripheral nerve regeneration application.

Table 1 Mean pore size of isotropic, equiaxed CG scaffolds produced using a variety of thermal treatments

Freezing temperature (°C)	*Mean pore size (μm)*	*References*
−10	325	9
−10	151	10
−20[a]	190	9
−20[b]	164	9
−20	121	10
−30	110	10
−40	120	9
−40	96	10
−60	85	9

[a]Initial freezing temperature followed by 48 h anneal at −10 °C.
[b]Initial freezing temperature followed by 24 h anneal at −10 °C.

2.216.2.2.3. Crosslinking

Crosslinking improves the mechanical competence (e.g., Young's modulus, yield stress) and decreases the degradation rate of CG scaffolds independent of the chemical and microstructural characteristics.[3,56,57] The three most common crosslinking techniques are the physically based dehydrothermal (DHT) and ultraviolet (UV) processes and the chemically based carbodiimide (EDAC) process. DHT and EDAC in particular have been used extensively for *in vitro* and *in vivo* applications.[5,56] DHT processing involves heating of the CG material under vacuum for a specified amount of time (typically 105–120 °C, <50 mTorr, 24–48 h) to remove residual moisture and introduce covalent crosslinks within the CG struts. Increasing the DHT crosslinking temperature and duration has been shown to increase compressive modulus by up to twofold and tensile modulus by up to 3.8-fold.[56,58] While increased crosslink density was correlated with increasing compressive modulus, higher denaturation levels led to higher tensile modulus, but also led to reduced ultimate stress and strain to failure.[58] EDAC processing utilizes carbodiimide chemistry to translate carboxyl (COOH) groups into unstable amine-reactive esters. This intermediate can be stabilized by *N*-hydroxysulfosuccinimide

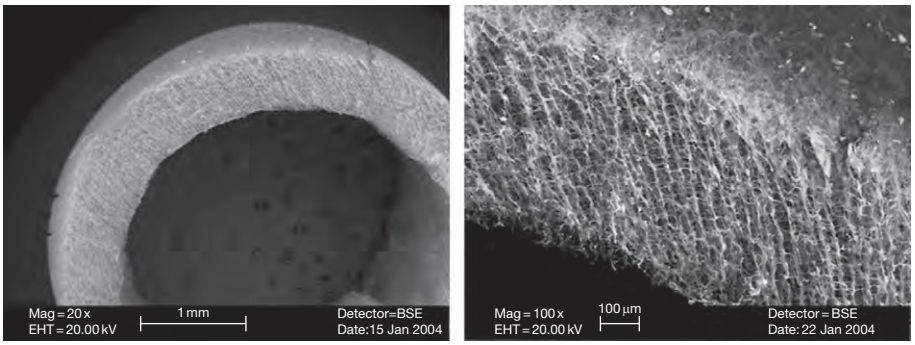

Figure 4 ESEM image of the pore structure of the tubular CG scaffold fabricated via spinning method. Scale bars: 1 mm (tube), 100 μm (wall). Reprinted with permission from Harley, B. A.; Hastings, A. Z.; Yannas, I. V.; Sannino, A. *Biomaterials* **2006**, *27*, 866–874.

(NHS), leading to the formation of stable amide crosslinks.[59] Increasing the ratio of EDAC and NHS to COOH increases the degree of crosslinking.[56,59] Both DHT and EDAC methods maintain the integrity of the open pore structure of the material by introducing crosslinks within the CG struts only.[56]

2.216.2.3. CGCaP Scaffold Fabrication

In addition to solidification-induced structural modifications, the CG construct can be chemically modified to create collagen composites for specific regenerative medicine applications. Mineralized CG scaffolds are of particular interest for orthopedic applications because of their potential to mimic the native biochemistry of bone: interpenetrating collagenous matrix (organic) and CaP (mineral) content. The addition of a mineral phase to the classic CG scaffold archetype allows for the development of materials with the requisite biochemical and biomechanical properties for bone and osteochondral tissue engineering. Mineralized CG scaffolds have been created via two distinct mechanisms: coating a fully formed CG scaffold with a mineral shell, or synthesizing a mineralized CG chemistry in liquid phase prior to freeze drying.

Mineralized CG materials have been fabricated via a surface coating process.[60] Here, CG scaffolds were initially synthesized using conventional freeze-drying and then sequentially soaked in phosphate ($NaNH_4HPO_4$) and calcium ($CaCl_2$) solutions. This treatment improved construct compressive modulus nearly 70-fold, from 0.3 to 31 kPa, while maintaining high porosity (95%).[60]

Mineralized CG (CGCaP) materials for bone and osteochondral tissue engineering can also be fabricated from a triple coprecipitate of collagen, GAG, and calcium phosphate (CaP). These scaffolds are synthesized from a suspension produced via a concurrent mapping technique that allows for simultaneous modulation of CG suspension pH as well as the CaP mass fraction (0–80 wt%), a range that covers a host of physiologically relevant tissues including subchondral bone (75%) and cartilage. This method is particularly powerful because it does not require the use of harmful titrants or additives that would be difficult to dissociate from the freeze-dried matrix.[61–63] Concurrent mapping uses 3D maps of pH and CaP mass yield derived from experimental data to determine the concentration of CaP needed to achieve a specific mass fraction, given the concentrations of collagen and GAG as well as the pH of the suspension.[62] This method yields nanocrystallite CaP content, precipitated within the CG struts, rather than coating the CaP on the CG content. This approach also enables the phase of the CaP mineral to be adjusted via hydrolytic conversion from the original brushite phase to either octacalcium phosphate or apatite, two biologically relevant CaP phases, without altering the pore structure of the scaffold.[61] Conversion from brushite to apatite results in a scaffold that is less soluble and has altered bone-bonding effectiveness.[64–66] Modified freeze-drying profiles have been developed to enable fabrication of CGCaP scaffolds with homogeneous microstructure (85 ± 3% porosity), highly interconnected pores, and tunable mean pore sizes from 56 to 1085 μm (**Figure 5**).[61] Mineralized CG scaffolds, produced by coating the CG scaffold with a mineral component or by precipitating nanocrystallites of CaP mineral into the CG content prior to fabrication, successfully mesh the advantageous microstructural and biochemical properties of standard CG scaffolds with the mechanical integrity and bone-bonding properties of calcium phosphate mineral in a manner reminiscent of the chemical composition of native bone[67] to produce a promising class of scaffolds for orthopedic application.

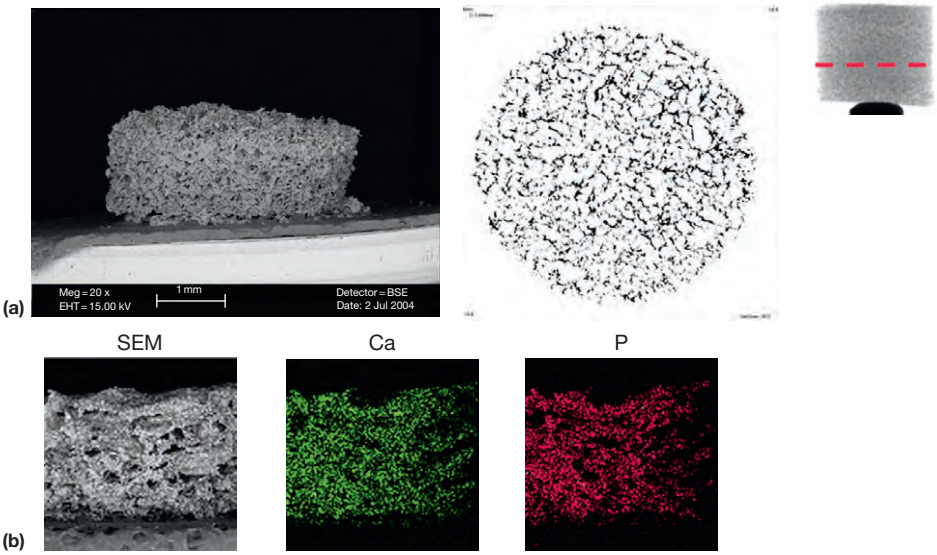

Figure 5 (a) SEM and μCT micrographs of CGCaP scaffold microstructure displaying an open pore structure with interconnected pores. (b) EDX analysis of CGCaP scaffold shows uniform distribution of both calcium (Ca) and phosphorous (P) throughout the scaffold. Scale bars: 1 mm. Reprinted with permission from Harley, B. A.; Lynn, A. K.; Wissner-Gross, Z.; Bonfield, W.; Yannas, I. V.; Gibson, L. J. *J. Biomed. Mater. Res. A* **2010**, *92*, 1066–1077.

2.216.2.4. Multicompartment CG Scaffold Fabrication

The CGCaP scaffold technology has been used as the basis for creating multiphase collagen scaffolds for the repair of interfacial tissues, notably osteochondral defects. A liquid phase cosynthesis method was created to fabricate multicompartment CG scaffolds. The multicompartment scaffold was designed to be a single biomaterial construct containing multiple regions ('compartments'), each with distinct microstructural, chemical, and mechanical properties that are connected via a continuous interface between regions. The initial multiphase scaffold developed via this approach contains an osseous compartment for subchondral bone regeneration (type I collagen, chondroitin 6-sulfate, and CaP) and a cartilagenous compartment for cartilage regeneration (type II collagen and chondroitin 6-sulfate). A key feature of this design is that by avoiding discrete interfaces between scaffold compartments that would require external fixation (sutures, glue, etc.) these materials reduce the potential for stress concentrations and resultant delamination at the interface.[68] The continuous interface is created by layering the cartilaginous compartment and the osseous compartment suspensions in a conventional freeze-drying mold, but then incorporating a processing step to enable partial diffusive mixing between the two suspensions near their interface. Once the region of interdiffusion was created between the suspension layers, freeze-drying was used to form the final multicompartment scaffold microstructure (Figure 6).[69] The continuous interface between scaffold regions is critical for the recapitulation of native interfacial physiology for tissues such as cartilage and tendon.[69] The differential chemistry, microstructure, and mechanics of the osseous and cartilaginous compartments enable these layered scaffolds to exhibit compressive deformation behavior that mimics behavior observed in natural articular joints.[69] These layered scaffolds are currently the subject of numerous *in vitro* and *in vivo* experiments for various orthopedic tissue engineering applications.

2.216.2.5. CG Hydrogels

CG hydrogels have been developed as alternative matrices for soft tissue engineering. CG hydrogels are typically composed of type I collagen, GAG, acetic acid, sodium hydroxide, and cell

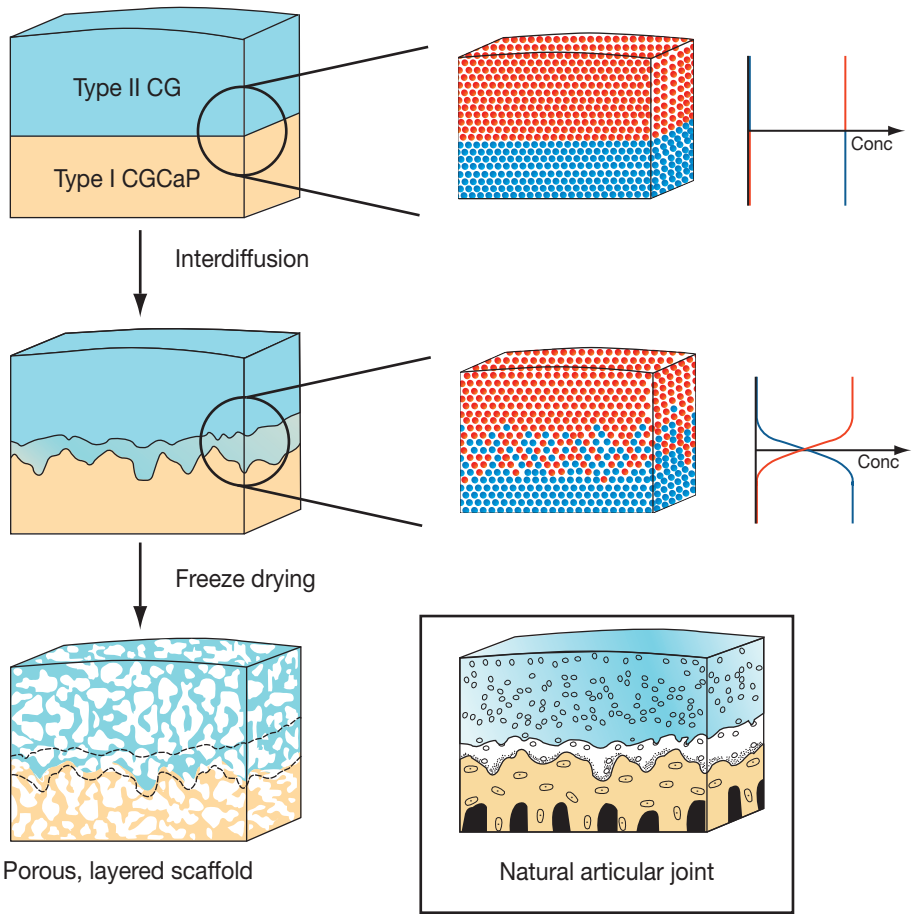

Figure 6 Schematic of liquid phase cosynthesis method used to produce layered osteochondral CG scaffold with soft, continuous interface. Nonmineralized, type II collagen–glycosaminoglycan (Type II CG) suspension is layered on top of mineralized, type I collagen–glycosaminoglycan (CGCaP) suspension, allowed to interdiffuse, and then freeze-dried to produce a porous, layered scaffold that mimics natural articular joint physiology. Reprinted with permission from Harley, B. A.; Lynn, A. K.; Wissner-Gross, Z.; Bonfield, W.; Yannas, I. V.; Gibson, L. J. *J. Biomed. Mater. Res. A* **2010**, *92*, 1078–1093.

culture media.[70,71] As collagen fibers are more dispersed within a gel compared to a porous scaffold, the addition of GAG imparts additional mechanical strength, significantly increasing tensile modulus (56 kPa vs. 40 kPa) and maximum stress (7 kPa vs. 5 kPa).[70] Other work has combined methacrylated HA hydrogels with semi-interpenetrating networks (semi-IPN) of collagen (see **Chapter 2.214, Hyaluronic Acid**).[72,73] Both methacrylation of HA and addition of collagen significantly improve mechanical properties (compressive modulus and fracture stress) and bioactivity (fibroblast adhesion). In addition, these hydrogels can be modified with microscale features using lithographic techniques, demonstrating their potential as tissue engineering constructs.[72] This type of hydrogel has also been explored as a neural tissue engineering template. Schwann cells remained viable in a collagen–HA hydrogel for 2 weeks and secreted nerve growth factor as well as brain-derived neurotrophic factor. The addition of laminin to the hydrogel increased secretion of these factors.[73]

2.216.2.6. CG Membranes

Nanoporous CG membranes have recently been developed as a bioactive, mechanically robust 2D substrate. CG membranes are synthesized by filtering and drying the classic type I CG suspension[74] (**Figure 7**). CG membranes have been created with a range of thicknesses (25–240 μm) but with relatively consistent relative densities (0.68 ± 0.06–0.91 ± 0.09). These membranes have been found to be mechanically isotropic (in plane) and have demonstrated tensile moduli as high as 47 MPa (hydrated) (Caliari, Ramirez, and Harley, Unpublished data). Ongoing work is looking to improve fabrication processes to enable enhanced control over membrane thickness, isotropy/anisotropy, relative density, mechanical properties, and metabolite permeability.

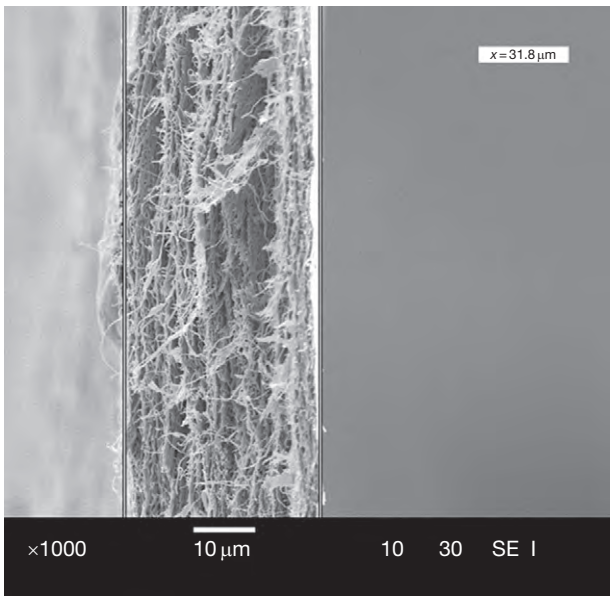

Figure 7 SEM of CG membrane microstructure. Mean thickness: 22.9 ± 2.6 μm; mean porosity: $32.1 \pm 5.9\%$. Scale bar: 10 μm.

2.216.3. Characterization of Collagen–GAG Materials

Experimental characterization of properties such as chemistry, pore morphology (size/shape), relative density, permeability, and mechanics of a number of CG scaffold variants has been undertaken; such experimental characterization has also been supplemented by modeling approaches allowing for a more complete understanding of the microenvironmental cues presented within the CG structure to distinct cells or populations of cells.

2.216.3.1. Microstructure: Experimental Measurement and Modeling

CG microstructure (pore size and morphology) is typically assessed using a stereological approach. Longitudinally and transversely oriented scaffold samples are embedded in glycol-methacrylate, sectioned, stained, and observed using optical microscopy. Using a linear intercept approach in any standard image analysis software package, a best-fit ellipse representative of the mean pore morphology is created. Dimensions of the ellipse (major and minor axis) are used to calculate an equivalent mean diameter and aspect ratio.[10,44,75] Microcomputed tomography (μCT) has also been utilized to analyze pore microstructure,[10,44,75] though often requires significant use of contrast agents to allow sufficient visualization of the nonmineralized CG content. Most recently, μCT analysis has been used to create a computational model of the CG microstructure for use in analysis of shear stresses on cells in dynamic culture conditions (**Figure 8**).[76]

Cellular solids modeling approaches have proven to be a useful tool in the description and characterization of CG scaffold pore geometry and microstructural properties (pore shape and specific surface area).[77] The complex geometry of foams (and scaffolds) is difficult to model exactly; instead, dimensional arguments can be used to model salient microstructural features without incorporating exact cell geometries using the cellular solids modeling framework. CG scaffolds have been primarily modeled as a low density, open-cell foam using a

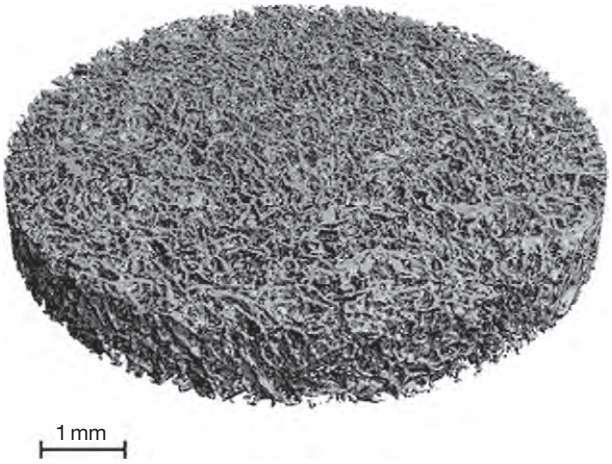

Figure 8 μCT scan of CG scaffold utilized in CFD simulations. Scale bar: 1 mm. Reprinted with permission from Jungreuthmayer, C.; Jaasma, M. J.; Al-Munajjed, A. A.; Zanghellini, J.; Kelly, D. J.; O'Brien, F. J. *Med. Eng. Phys.* **2009**, *31*, 420–427.

tetrakaidecahedral (14-sided polyhedron) unit cell. Modeling microstructural features of CG scaffolds in this manner is possible because the mean pore structure of it and a variety of other low-density, open-cell foams has been observed to have a number of consistent features, notably approximately 14 faces per unit cell, 5.1 edges per face, and vertices that are nearly tetrahedral.[77,78] The tetrakaidecahedron packs to fill space, nearly satisfies minimum surface energy requirements, and approximates the structural features of many experimentally characterized low density, open-cell foams (Figure 9).[77,79] Application of modeling approaches using the tetrakaidecahedral unit cell with CG scaffolds has led to estimations of a number of key microstructural features of the CG scaffolds, many of which will be discussed throughout this chapter. The first microstructural element described using cellular solids approaches was the scaffold specific surface area (SA/V), the total surface area divided by the volume of the scaffold. Specific surface area describes the relative amount of surface available for cells to attach, and has been shown to be an integral factor affecting overall scaffold bioactivity.[9,10] For a low density, open-cell foam with an interconnected pore structure and edges of circular cross-section modeled using the discussed approaches, specific surface area is related to the mean pore size (d) and the relative density (ρ^*/ρ_s):[10,77]

$$\frac{SA}{V} = \frac{10.15}{d}\left(\frac{\rho^*}{\rho_s}\right)^{1/2} \quad [1]$$

2.216.3.2. Permeability: Experimental Measurement and Modeling

Permeability of tissue engineering scaffolds is a critical design parameter to be controlled as it influences the diffusion of cytokines, nutrients, and waste throughout the scaffold prior to material vascularization; further, biomaterial permeability has also been shown to significant impact cell migration processes and scaffold biodegradation rates, among others.[80] Material permeability also affects fluid pressure fields and shear stresses within the construct, additional potential stimuli for functional adaptation.[81] Permeability of tissue engineering scaffolds is dictated by a variety of microstructural characteristics including porosity, pore size and orientation, pore interconnectivity, fenestration size and shape, specific surface area, and applied strain. Permeability of low porosity foams (porosity <90%) has previously been modeled and measured experimentally.[82] However, such models are not applicable to highly porous materials that are typically used in tissue engineering, such as CG scaffolds (porosity >99%); here, material permeability has been conventionally measured empirically with no associated modeling framework to describe the results. A series of CG scaffolds with constant relative density ($\rho^*/\rho_s = 0.006$) were used not only to characterize both CG scaffold permeability as a function of pore size (96–151 μm) and applied compressive strain (0–40%), but also to calibrate a cellular solids-based model of the permeability of low-density, open-cell foams. As with specific surface area, a low density, open-cell foam cellular solids model was successfully created to describe the permeability (k) of the entire class of CG scaffolds as a function of the scaffold mean pore size (d), percent compression (applied strain: ε), relative density (ρ^*/ρ_s), and a single dimensionless system constant (A'):[83]

$$k = A'\left(\frac{d}{2.785}\right)^2(1-\varepsilon)\left(\frac{1-\rho^*}{\rho_s}\right)^{3/2} \quad [2]$$

Experimental and modeling analyses showed that CG scaffold permeability increases with increasing pore size and decreases with increasing compressive strain (Figure 10). The experimentally measured and theoretically predicted scaffold permeability values showed excellent agreement with the need for only a single fitting constant (A') to describe the entire class of scaffolds, again validating the use of the model tetrakaidecahedral unit cell for describing microstructural features of CG scaffolds.[83] These results also suggested that cellular solids modeling techniques can be used to predict scaffold permeability under a wide range of physiological loading conditions and experimentally relevant pore microstructures (size and relative density).

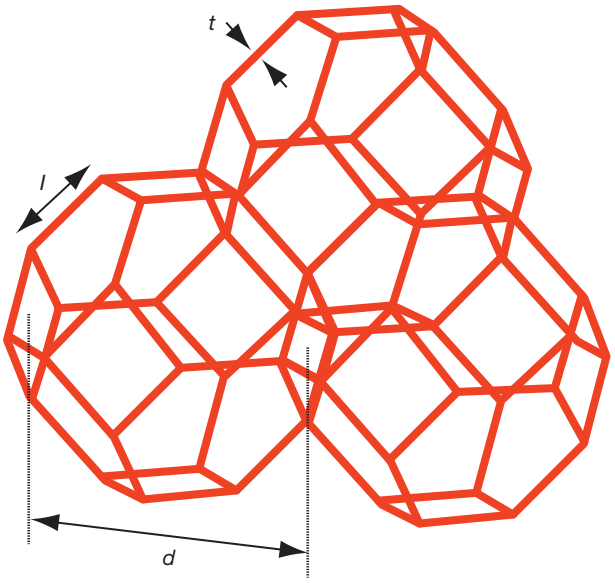

Figure 9 Tetrakaidecahedral unit cell. d, pore diameter; l, strut length; t, strut thickness. Reprinted with permission from Harley, B. A. C.; Kim, H. D.; Zaman, M. H.; Yannas, I. V.; Lauffenburger, D. A.; Gibson, L. J. *Biophys. J.* **2008**, *95*, 4013–4024.

2.216.3.3. Mechanical Properties: Experimental Measurement and Modeling

The mechanical properties of a range of biomaterials have been shown to significantly impact cell behaviors including adhesion, proliferation, differentiation, and overall bioactivity.[4,7,16–25] The mechanical properties of a number of CG scaffold variants have been tested in tension and compression; further, the elastic modulus of the individual struts that define the scaffold network has also been characterized[56] (Table 2). The mechanical behavior of CGCaP scaffolds under compression as well as the modulus of the individual mineralized struts has also been evaluated[61,84] (Tables 2 and 3). These results offer insight to the mechanical properties of a standardized set of CG materials.

Cellular solids modeling has been shown to be a powerful tool to aid the analysis of the mechanical properties of CG biomaterials. The cellular nature of CG scaffolds requires that

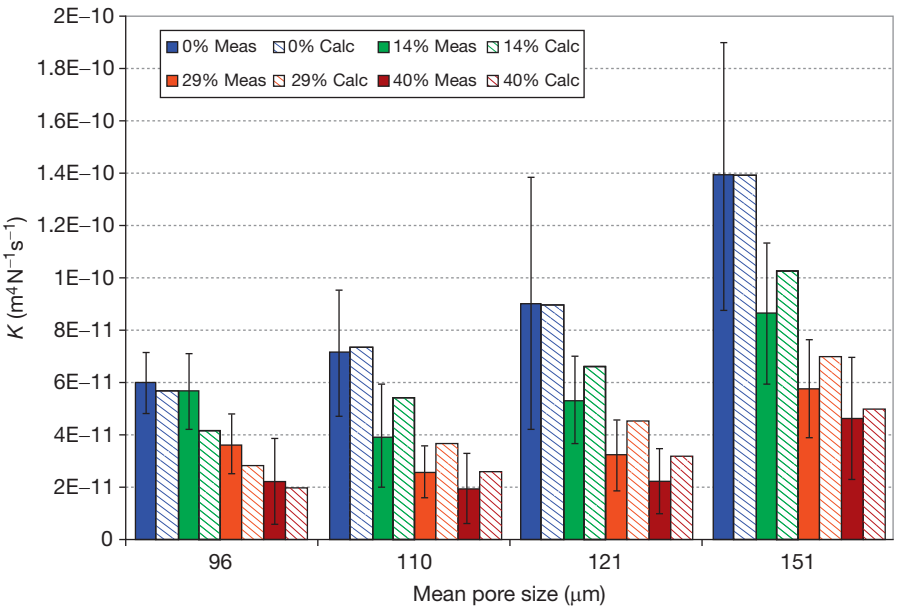

Figure 10 Comparison between experimental results (K_{meas}, solid bars) and the predicted values obtained from the mathematical model (K_{calc}, striped bars) for CG scaffold permeability under varying compressive strain (0, 14, 29, 40% strain, left to right for each pore size) for distinct pore sizes (96, 110, 121, 151 μm). Reprinted with permission from O'Brien, F. J.; Harley, B. A.; Waller, M. A.; Yannas, I. V.; Gibson, L. J.; Prendergast, P. J. *Technol. Health Care* **2007**, *15*, 3–17.

Table 2 Average (mean ± std. dev.) mechanical properties of the homogeneous CG scaffold variants (96–151 μm; 0.006 relative density; DHT crosslinking at 105 °C for 24 h; hydrated) and the mineralized CGCaP scaffold (202 μm; 0.038 relative density; DHT crosslinking at 105°C for 24 h; hydrated)

Property	*Hydrated CG scaffold*	*Hydrated mineralized (50%) CG scaffold*
E^*	0.208 ± 0.041 kPa	6.20 ± 1.51 kPa
σ^*_{el}	0.021 ± 0.008 kPa	0.547 ± 0.089 kPa
ε^*_{el}	0.10 ± 0.04	0.0960 ± 0.0302
$\Delta\sigma/\Delta\varepsilon$	0.092 ± 0.014 kPa	3.05 ± 0.392 kPa
E_s	5.28 ± 0.25 MPa	78.8 ± 8.5 MPa

Source: Harley, B. A.; Leung, J. H.; Silva, E.; Gibson, L. J. *Acta Biomater.* **2007**, *3*, 463–474; Kanungo, B. P.; Silva, E.; Van Vliet, K.; Gibson, L. J. *Acta Biomater.* **2008**, *4*, 490–503.

Table 3 Elastic moduli of individual scaffold struts within hydrated CG and CGCaP scaffolds crosslinked via DHT and EDAC/NHS techniques

Crosslinking treatment	*Scaffold strut elastic moduli (MPa)*	*Relative elastic modulus*	*Mineralized (50%) scaffold strut elastic moduli (MPa)*	*Relative elastic modulus*
Uncrosslinked	3.9 ± 0.20	0.74	49.1 ± 5.3	0.62
DHT105/24 (Standard)	5.28 ± 0.25	1.0	78.8 ± 8.5	1.0
DHT120/48	5.7 ± 0.30	1.08	No data	No data
EDAC1:1:5	10.6 ± 0.50	2.0	No data	No data
EDAC5:2:5	11.8 ± 0.56	2.24	No data	No data
EDAC5:2:1	38.0 ± 1.8	7.2	193.2 ± 20.7	2.45

Source: Harley, B. A.; Leung, J. H.; Silva, E.; Gibson, L. J. *Acta Biomater.* **2007**, *3*, 463–474; Kanungo, B. P., Silva, E., Van Vliet, K. & Gibson, L. J. *Acta Biomater.* **2008**, *4*, 490–503.

materials mechanical characterization must be performed at multiple scales: at the level of the whole material (macro) as well as at the level of the individual struts that define the scaffold structure (micro). The significant porosity of the CG scaffolds often results in multiple orders of magnitude difference in these mechanical properties. The theory predicts that stress–strain curves for low-density, elastomeric open cell foams in compression are characterized by three distinct regimes: a *linear elastic regime* (strut bending), a *collapse plateau regime* (struts buckling and pore collapse), and a *densification regime* (complete pore collapse) (Figure 11).[77] In tension, the initial linear elastic response is typically the same as is observed in compression for small strains; however, as the strain increases, the struts become increasingly oriented in the direction of applied tension, increasing the material stiffness until tensile failure.[77] Experimentally, the CG scaffold variants exhibited the theoretically predicted stress–strain behavior with distinct linear elastic, collapse plateau, and densification regimes (Figure 12). Experimental results show that CG scaffolds with equiaxed pores (mean pore sizes: 96–151 μm) as well as CGCaP scaffolds (50 wt% CaP) are microstructurally and mechanically isotropic.[56,84] CG materials demonstrated compressive moduli of order 30 kPa (dry) and 200 Pa (hydrated), independent of pore size, while CGCaP scaffold demonstrated compressive moduli of order 750 kPa (dry). The independent effects of variables including hydration level, pore size, and crosslink density on the mechanical properties were also determined (Tables 2 and 3).[56,84] The Young's modulus of the individual (CG and CGCaP) scaffold struts (E_s) that define the scaffold microstructure was measured via AFM (Figure 13).[56,84]

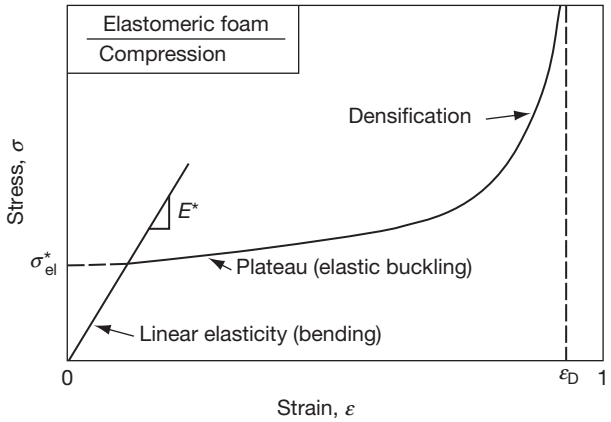

Figure 11 Uniaxial stress–strain curve for an elastomeric cellular solid in compression showing linear elastic, collapse plateau, and densification regions as well as the linear elastic modulus (E^*) and elastic collapse stress (σ^*_{el}). Reprinted with permission Gibson, L. J.; Ashby, M. F.; Harley, B. A. *Cellular Materials in Nature and in Medicine*; Cambridge University Press: Cambridge, 2010.

Using cellular solids theory, the Young's modulus (E^*) and elastic compressive strength (σ^*_{el}, also called the compressive plateau stress) of low density, open-cell foams such as CG scaffolds are predicted to depend on the foam relative density, ρ^*/ρ_s, the Young's modulus of the solid from which the foam is made, E_s (termed the strut modulus), and a constant of proportionality (C_1 and C_2) related to the cell geometry:[77] For elastomeric cellular solids, E^* and σ^*_{el} are

$$E^* = C_1 \left(\frac{\rho^*}{\rho_s}\right)^2 E_s \quad [3]$$

$$\sigma^*_{el} = C_2 \left(\frac{\rho^*}{\rho_s}\right)^2 E_s \quad [4]$$

Data for a wide variety of open-cell foams give approximate values as $C_1 \sim 1$ and $C_2 \sim 0.05$.[77] Interestingly, these equations show that the strain at which cell collapse by buckling occurs, ε^*_{el} is a constant value equal to $C_2/C_1 = 0.05$ and that both E^* and σ^*_{el} are expected to be independent of the pore size.[77]

Experimental results of scaffold mechanical characterization and low density, open-cell foam model predictions for the scaffold E^* and σ^*_{el} (eqns [3] and [4]) for the standard series of isotropic CG scaffold variants (ρ^*/ρ_s: 0.006; mean pore size: 96–151 μm) showed good agreement. Notably, CG scaffolds showed distinct *linear elastic*, *collapse plateau*, and *densification regimes*, and CG scaffold modulus was found to be independent of scaffold pore size, but highly dependent on scaffold ρ^*/ρ_s.[56] The effect of relative density on the mechanical properties of both mineralized and nonmineralized CG scaffolds has recently been evaluated.[45,46,56,84] Nonmineralized CG scaffolds over a range of relative densities (0.0062–0.0239) showed significant increases in compressive modulus and strength as well as tensile modulus with increasing relative density (Table 4).[45,56] While the model correctly predicted the relationship between E_s and E^*, it over-predicted E^* at higher relative densities. This is likely due to difficulties in fabricating CG scaffolds with high solids content, which often leads to areas of microstructural heterogeneities.[56]

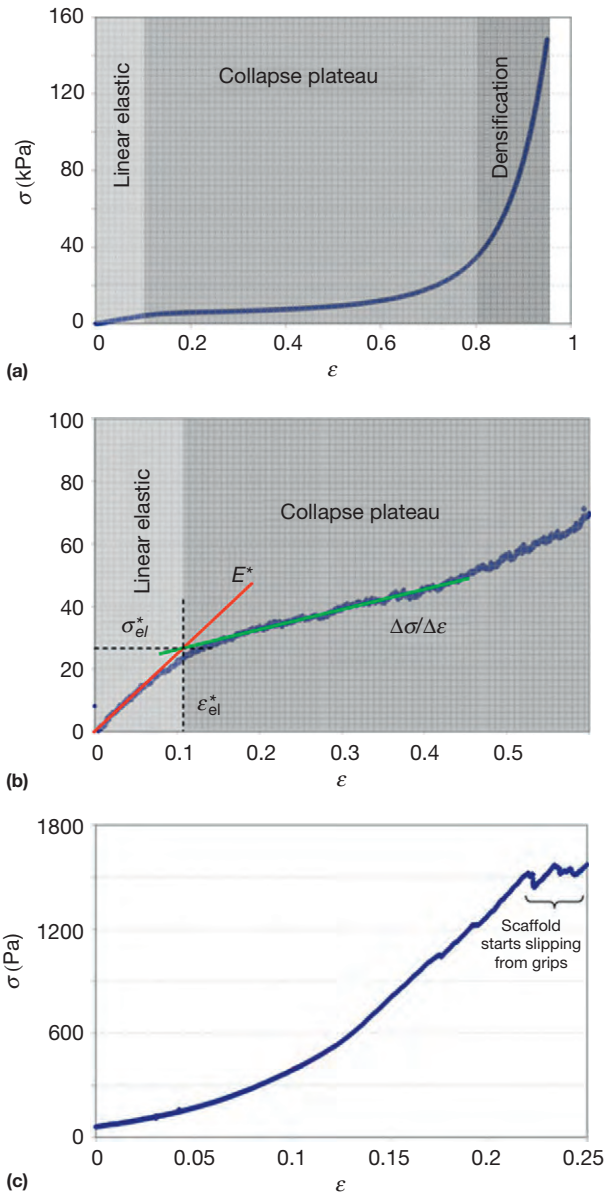

Figure 12 Characteristic stress–strain curves observed for the CG scaffold under compression for the entire tested strain range (a) ε: 0–0.95, and for a subregion of a hydrated CG scaffold (b) ε: 0–0.60. Linear regressions of the linear elastic and collapse plateau regimes are used to calculate the linear elastic modulus (E^*) and the collapse plateau modulus ($\Delta\sigma/\Delta\varepsilon$).The elastic collapse stress and strain are σ^*_{el}, ε^*_{el}. (c) Characteristic stress–strain curve observed for the (hydrated) CG scaffold variants under uniaxial tensile testing in the plane of the scaffold sheet. Reprinted with permission from Harley, B. A.; Leung, J. H.; Silva, E.; Gibson, L. J. *Acta Biomater.* **2007**, *3*, 463–474.

Likewise, mineralized CG scaffolds with relative densities from 0.045 to 0.187 had significantly increased compressive modulus and strength (both dry and hydrated) with increasing relative density (Table 4).[46] Meanwhile, modeling consistently over-predicted E^* and σ^*_{el} for the mineralized CG scaffolds. These discrepancies can be explained by the presence of voids, cracks, and disconnections within the scaffold microstructure.[84] Experimentally, CGCaP scaffolds with higher

Table 4 Mechanical properties (mean ± standard deviation) of CG (relative density 0.0062–0.0239) and CGCaP (0.045–0.187) scaffolds in the dry state

Scaffold	ρ^*/ρ_s	E* *(kPa)*	σ* *(kPa)*	ε* *(%)*	*Δσ/Δε (kPa)*
CG 1X	0.0062 ± 0.0008	32 ± 6	5.0 ± 1.1	15.8 ± 3.5	10.6 ± 1.0
CG 2X	0.0120 ± 0.0016	61 ± 5^{a}	11.8 ± 2.4^{a}	18.9 ± 2.5^{a}	43.6 ± 2.5^{a}
CG 3X	0.0198 ± 0.0014	97 ± 17^{aa}	15.6 ± 3.1^{aa}	15.9 ± 1.2	54.8 ± 9.3^{aa}
CG 4X	0.0239 ± 0.0021	127 ± 23^{aa}	19.0 ± 3.9^{a}	14.6 ± 3.5	43.3 ± 5.6^{aa}
CGCaP 1X	0.045 ± 0.002	780 ± 95	39 ± 10	5.00 ± 1.00	480 ± 35
CGCaP 2X	0.098 ± 0.004	3156 ± 760^{b}	132 ± 14^{b}	4.00 ± 1.41	1300 ± 200^{b}
CGCaP 3X	0.137 ± 0.002	6500 ± 1270^{bb}	242 ± 32^{bb}	4.00 ± 1.00	2680 ± 610^{bb}
CGCaP 4X	0.187 ± 0.027	3660 ± 820^{b}	275 ± 50^{bb}	4.38 ± 1.15	1875 ± 525^{bbb}

Superscripts $^{a, aa, aaa}$ (CG) and $^{b, bb, bbb}$ (CGCaP) denote statistically significant differences between groups. For example, *E** for the CG 1X, 2X, and 3X scaffolds are significantly different from each other while 3X and 4X are not.

Source: Kanungo, B. P.; Gibson, L. J. *Acta Biomater.* **2009**; Kanungo, B. P.; Gibson, L. J. *Acta Biomater.* **2009**, 5, 1006–1018

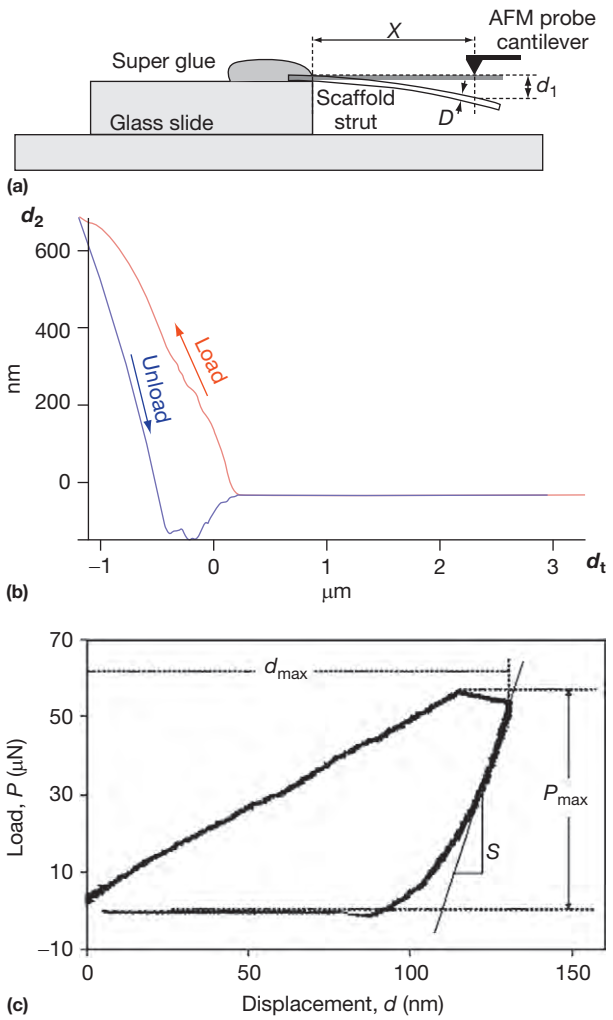

Figure 13 (a) AFM experimental setup to assess individual CG scaffold strut modulus. (b) Characteristic load–unload curve for bending tests performed via AFM on individual CG scaffold struts (nonmineralized variant) and (c) (mineralized variant). Reprinted with permission from Harley, B. A.; Leung, J. H.; Silva, E.; Gibson, L. J. *Acta Biomater.* **2007**, *3*, 463–474; Kanungo, B. P.; Silva, E.; Van Vliet, K.; Gibson, L. J. *Acta Biomater.* **2008**, *4*, 490–503.

mineral content (75 wt% CaP) displayed inferior mechanical properties to the 50 wt% CaP scaffolds.[84] This behavior is possibly caused by the retention of residual moisture, even after extensive freeze-drying, due to the dehydration of 33% of the CaP mineral content from brushite to monetite in the 75 wt% CaP scaffold.[84]

2.216.3.4. CG Scaffold Degradation Kinetics and Byproducts

The degradation kinetics of tissue engineering scaffolds must be carefully tuned so that the scaffold structure remains intact throughout the duration of the regenerative process to prevent wound contraction, while degrading rapidly enough so as not to impede the healing process.[1,2,4,85] This optimization has been termed the isomorphous tissue replacement model, where the biomaterial degradation half life of the scaffold (t_d) must equal the healing half life of the tissue (t_h) in which it is implanted. Scaffold degradation that happens too quickly ($t_d > t_h$) or too slowly ($t_d < t_h$) is detrimental to the tissue regeneration process.[4] In addition to degradation kinetics, byproducts must also be carefully considered in scaffold design. Many synthetic scaffolds degrade to cytotoxic byproducts, limiting their *in vivo* applicability.[1,2] However, CG scaffolds, like most scaffolds made of natural materials, break down into harmless byproducts already found in abundance in the body.[31]

The degradation kinetics of CG scaffolds can be tuned by altering chemical composition (collagen to GAG ratio), relative density, or most commonly through differential crosslinking (see previous section for more details), where increasing crosslinking densities are used to slow scaffold degradation.[1,86] Pek *et al.* have evaluated the degradative process of CG scaffolds treated with one of four conventional crosslinking techniques: noncrosslinked (Nx), DHT (Dx), EDAC (Ex), and DHT/EDAC (DEx) in real time.[86] Here, scaffolds displayed an inverse relationship between swelling ratio and crosslink density, as is characteristic of random polymeric materials. ESEM observation of Nx and Dx scaffolds degraded with collagenase showed micropitting and eventual collapse of scaffold struts, leading to complete loss of mechanical integrity after a week while Ex and DEx samples maintained their structure and showed only minor micropitting.[86] Degradation by chondroitinase led to distinct structural (but not mechanical) changes for the Nx and

Dx scaffolds that were predicted to be more prone to GAG removal: scaffold struts were observed to swell and thereby reduce the open pore interconnectivity of the microstructure. This effect was not nearly so pronounced for the Ex and DEx variants.[86]

2.216.4. *In Vitro* Applications

2.216.4.1. Cell Attachment and Viability

CG tissue engineering scaffolds must have a mean pore size that is large enough for efficient metabolite exchange and cell infiltration, but small enough to provide ample surface area (ligands) to achieve adequate cell attachment. Distinct optimal pore sizes have been hypothesized for different cells, biomaterial chemistries, and clinical applications. CG scaffolds with uniform, well characterized microstructures (pore sizes 85–325 μm) have been used as a platform to begin to investigate the relationship of pore microstructure and scaffold-specific surface area with cell attachment, viability, and the uniformity of their distribution throughout the material.[9,10,45] These scaffolds were seeded with MC3T3-E1 mouse clonal osteogenic cells and then cultured for anywhere between 1 and 7 days to determine viable cell number and distribution. Increased early cell adhesion (24–48 h) was correlated with increased scaffold specific surface area (**Figure 14**).[10] Modulating scaffold relative density (0.0062–0.0239) to alter scaffold SA/*V* also gave a linear relationship between scaffold specific area and MC3T3-E1 cell attachment ($R^2 = 0.97$ at 24 h).[45] These results indicate a strong correlation between specific surface area and early MC3T3-E1 cell attachment for this set of CG scaffolds. However, for longer culture periods (7 days), a higher number of cells are observed in scaffolds with larger pores (>300 μm). This result has been hypothesized to be due to the competing influence of scaffold proliferation and metabolic support via diffusion, both of which increase with increased scaffold pore size: larger pore sizes allow for easier cell proliferation and migration throughout the entire scaffold, especially at later time points (7 days). These results have helped confirm that scaffolds with larger pore sizes, 325 μm, may be more optimal for long-term bone tissue engineering applications.[9]

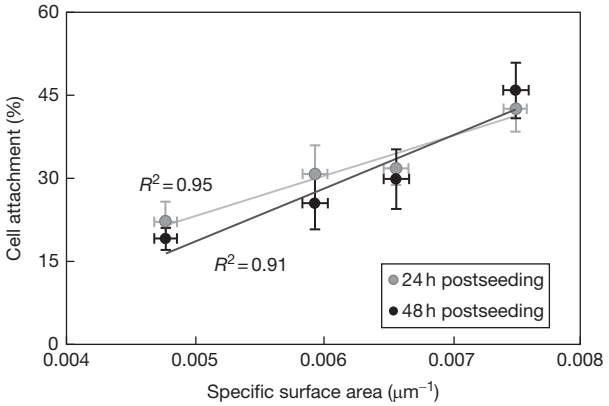

Figure 14 MC3T3-E1 cell attachment plotted against specific surface area showing a strong linear relationship at 24 (gray line) and 48 h (black line) postseeding. Reprinted with permission from O'Brien, F. J.; Harley, B. A.; Yannas, I. V.; Gibson, L. J. *Biomaterials* **2005**, *26*, 433–441.

Fabrication flexibility also has enabled investigation of the effect of CG scaffold chemical composition on initial cell attachment and viability. MC3T3-E1 attachment and viability have been shown to depend on scaffold chemical composition (collagen and GAG concentration)[12] and mechanical properties.[11] Here, scaffolds were fabricated over a range of concentrations of collagen (0.25–1%, w/v) and GAG (0–0.088%, w/v), seeded with cells, and cultured for 6 h to 7 days. Lower concentrations of collagen and GAG showed high initial cell attachment, likely because of a temporary increase in surface area due to loss of structural integrity (pore collapse).[12] However, the higher concentration of surface ligands on the 1% collagen scaffolds supported the highest cell attachment after 7 days; 0.088% GAG scaffolds also had better cell infiltration than their counterparts.

2.216.4.2. Cell Contraction

Cell-mediated contraction plays an integral role in many physiological and pathological processes, notably organized contraction and scar formation during wound healing. One of the key functions of CG and other tissue engineering scaffolds is to block wound contraction to prevent scar tissue proliferation, instead allowing for regeneration of functional tissue.[4] This objective requires a comprehensive understanding of the forces and kinetics associated with cell contractile processes within the scaffold microstructure so that scaffolds can be designed with the requisite mechanical integrity to withstand contraction for a critical period of time. Most studies of cell contraction *in vitro* have used 2D substrates. Here, contractile force is calculated as a function of substrate deformation due to a population of cells and the elastic modulus of the substrate.[87–93] This technique has been used to show that substrate elastic modulus significantly affects cell behaviors such as proliferation, differentiation, migration speed, directional persistence, and applied traction forces.[21,87,93–102] These methods yield estimates of fibroblast contractile forces on the order of hundreds of nanoNewtons.[90,93,95] However, these results are not likely comparable to *in vivo* contractile forces, given the fact that the shape and cytoskeletal organization of cells on these 2D substrates (amorphous, spread) are significantly different than that of fibroblasts observed in wound sites within the natural ECM (elongated spindle-shaped).[75,103–105]

CG scaffolds have been used in a number of investigations to quantify the macroscopic (bulk construct) and microscale (individual strut) contractile behavior of cell populations as well as the relationship between distinct integrin–ligand interactions, cytoskeletal organization, and cell contraction. Macroscopically, the average contractile force generated by a known cell population can be calculated as a function of the gross deformation of the CG scaffold by that cell population and the scaffold's elastic modulus. Total contractile force generated by a population of dermal fibroblasts within the CG scaffold was observed to reach an asymptote of 1.0 ± 0.2 nN, independent of the number of cells seeded, with an associated time constant of 5.2 ± 0.5 h.[17] When the stiffness of the scaffold system was changed, fibroblasts were observed to apply differential levels of strain but a constant average force to the CG scaffold, suggesting that dermal fibroblasts apply contractile forces independent of the local microenvironment (**Figure 15**).[106]

Similar analysis has been performed for chondrocytes[107] and Schwann cells.[108] Fibroblasts displayed significant cytoskeletal reorganization during contraction within the CG scaffold; initially rounded after seeding, they were observed to form attachments to single struts as well as between multiple CG struts and elongated over time into spindle-shaped cells. The average aspect ratio (maximal cell length/maximal cell thickness) of the cells increased asymptotically from 1.4 to 2.8 during the first 15 h in the scaffold (**Figure 15**) with a time constant similar to that observed for contractile force generation.[17,109] In addition, the role of integrin–ligand complexes in the contraction of CG scaffolds has been examined using a culture force monitor (CFM) via specific inhibition of integrins and distinct cell adhesion proteins (fibronectin, vitronectin, and collagen).[110] Initial dermal fibroblast attachment and force generation (0–5 h) was found to be sequentially mediated primarily by fibronectin followed by vitronectin. Attachment and force profiles at later time points (6–20 h) were shown to be dominated by cell–collagen interactions.[110]

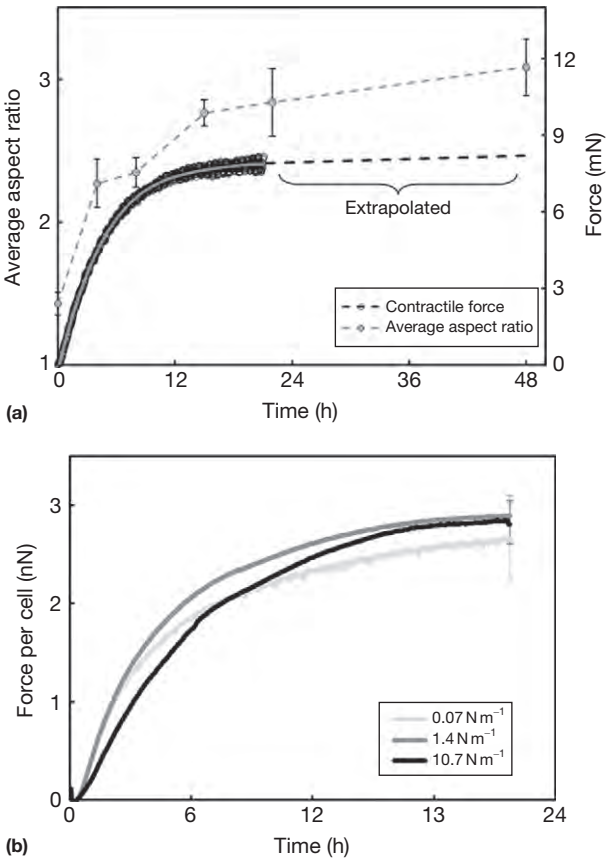

Figure 15 (a) Plot of the fibroblast aspect ratio and generated contractile force with time in the CG scaffold. The average cell aspect ratio increased up to 15 h postseeding in a manner similar to the total force generated by the cell population. (b) Plot of force per cell over time for different system stiffnesses. The displacement developed per cell increased as the system stiffness decreased but the force developed per cell was independent of the system stiffness. Reprinted with permission from Gibson, L. J.; Ashby, M. F.; Harley, B. A. *Cellular Materials in Nature and in Medicine*; Cambridge University Press: Cambridge, 2010.

However, two significant assumptions are made with this analysis. First, the deformation of the cell-seeded, rectangular CG scaffold sample was measured in only one direction. Second, the fraction of contractile cells versus the total cell population within the scaffold was not characterized. As the average force per cell was calculated using the assumptions that all cells were contracting in a single direction and that all cells were contracting at the same time, the calculated average contractile force of 1.0 ± 0.2 nN is a lower bound.

CG scaffolds have also been used to quantify the contractile forces generated by individual cells within a 3D ECM analog. Phase contrast microscopy has been used to generate time-lapse images of dermal fibroblasts differentially migrating through the scaffold, or contracting the local scaffold microstructure, resulting in buckling of the strut(s) to which the cell was attached (**Figure 16**).[17,106,109] Improved mechanical and

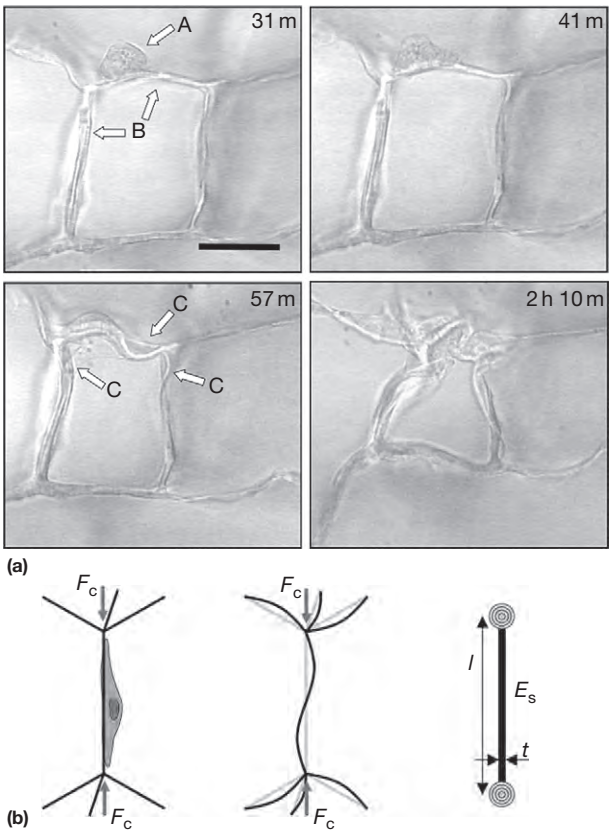

Figure 16 (a) Time lapse images of an individual dermal fibroblast within the CG scaffold. The sequence of images shows a dermal fibroblast (arrow A) elongating and deforming the surrounding scaffold struts (arrows B). Several struts are deformed over time (arrows C). Time, in hours and minutes, after cell seeding is indicated in the top right of corner of each image. Scale bar: 50 μm. (b) Schematic of a single cell applying a critical buckling load (F_c) to a scaffold strut within an idealized CG scaffold network (left). The surrounding struts inhibit rotation of the ends of the buckling strut (middle). A simplified model of CG scaffold strut buckling with the appropriate boundary conditions: the scaffold strut is restrained at its ends by a rotational spring that represents the surrounding strut network (right). Reprinted with permission from Harley, B. A.; Freyman, T. M.; Wong, M. Q.; Gibsony, L. J. *Biophys. J.* **2007**, *93*, 2911–2922.

microstructural characterization of the individual CG scaffold struts[75] and the application of cellular solids theory enabled the use of modified Euler column buckling relationships in order to quantify the magnitude of individual cell contractile forces within the CG scaffold.[75] The magnitude of the cell-mediated contraction forces generated by individual dermal fibroblasts within the CG scaffold was calculated from the observed strut deformation by individual dermal fibroblasts, strut dimensions and mechanical properties, and previous experimental and theoretical work describing the mechanics and collapse of open cell foams.[77] The critical load (F_c) at which a scaffold strut of length l_s, average pore size d, Young's modulus E_s, and second moment of area I (strut geometry was approximated as a cylindrical fiber, $I = \pi d^4/64$) buckles can be calculated by Euler's formula and the hydrostatic compression end restraint ($n^2 = 0.34$):[75,77,111]

$$F_c = \frac{n^2 \pi^2 E_s I}{l_s^2} \quad [5]$$

The contractile force generated by individual dermal fibroblasts that were able to buckle a CG scaffold strut was calculated to range between 11 and 41 nN, with an average contractile force (F_c) of 26 ± 13 nN.[75] The upper limit of fibroblast contractile capacity in CG scaffolds was established from data on a cell that was unable to buckle the strut it was attached to because that strut was significantly thicker than the average strut, thereby increasing its flexural rigidity (E_sI) and buckling load (F_c). Analysis of this strut's microstructure indicates that the force required to buckle the strut was approximately 450 nN. These results suggest that while dermal fibroblasts can easily develop the ~25 nN force required to buckle conventional CG scaffold struts, they are unable to develop contractile forces at the level of 450 nN.[75] While developed with a well-characterized CG scaffold system, this technique can be used to study individual cell contraction and cell–scaffold interactions within a wide variety of tissue engineering scaffolds.

2.216.4.3. Cell Motility

Cell motility plays an integral role in many physiologic and pathologic processes, notably organized wound contraction and fibroblast and vascular endothelial cell migration during wound healing,[4] metastatic tumor cell migration,[112] stem cell mobilization and homing,[113,114] and tissue remodeling.[4] Cell migration is a complex process modulated by a range of spatiotemporally presented biochemical and biophysical signals, both extracellular and intracellular.[115,116] Studies of cell motility on 2D substrates have led to an improved understanding of how surface features, particularly substrate stiffness, affect migration through changes in cytoskeletal organization and applied traction forces.[98–100] However, 3D biomaterials enable the investigation of the complex set of biophysical and biochemical signals that can affect motility in a 3D environment that better resembles physiologically and pathologically relevant conditions. Understanding of the microenvironmental factors that govern cell motility is also critical for acellular biomaterials (like CG scaffolds) because they must be able to induce rapid cellular invasion.

Cell motility in CG scaffolds relies on a phenomenon known as contact guidance. As CG scaffold pore sizes are significantly larger than the characteristic length of the fibroblasts, cells are forced to migrate along scaffold struts. External microstructural and mechanical stimuli from the scaffold provide physical cues (contact guidance) to regulate cell motility and other cell behaviors.[2] NR6 mouse fibroblasts were seeded into CG scaffolds with pore sizes ranging from 96 to 151 μm but with constant mechanical properties ($E^* = 208 \pm 41$ Pa), and single cell migration paths were tracked using 3D time-lapse confocal microscopy.[7] Cell dispersion (Wind-Rose plot, **Figure 17(a)**) and motile fraction (**Figure 17(b)**) significantly decrease with increasing pore size.[7] Cell speed was also shown to significantly decrease with increasing scaffold pore size (**Figure 17(b)**); cell speed is reduced almost by half over the range from 96 to 151 μm, from about 12 to 6 μm h^{-1}. Further, as cell speed was calculated for only the motile population, which also decreased significantly with mean pore size, scaffold pore size has an even more significant influence on overall cell motility than is suggested by **Figure 17(b)** alone. The effect of scaffold stiffness on NR6 fibroblast motility was assessed in a series of DHT- and EDAC-crosslinked CG scaffolds of constant pore size (96 μm) but variable strut modulus (E_s: 5.3–38 MPa). Cell migration speed exhibited a subtle biphasic behavior with strut modulus increasing (significantly) from 11 to 15 μm h^{-1} for strut moduli between 5 and 12 MPa and then decreasing (significantly) back to 12 μm h^{-1} for strut moduli of 38 MPa (**Figure 17(b)**). The effects of pore size and scaffold stiffness on cell migration speed correlated well with previous experimental and computational studies of cell motility in dense, 3D materials.[25,117] Unlike with the dense materials used in those studies, cells were not exposed to significant steric hindrances in these porous, CG scaffolds, so the strong dependence of cell motility on pore size was not expected.

In addition to satisfying the practical need to better understand cell motility in CG scaffolds to enable more efficient cellular invasion, the fabrication, characterization, and modeling tools recently developed for CG scaffolds enabled a rigorous analysis of the independent effect of microstructural and mechanical scaffold features on cell motility. Modeling techniques were then used in an attempt to better explain the initially inexplicable effect of pore size on cell motility. Cellular solids modeling suggested that while the strut moduli (E_s) and scaffold relative density (ρ^*/ρ_s) are constant for the scaffolds of different pore size, scaffolds with a larger pore size have longer and thicker struts (**Figure 9**). So, while the moduli (E_s) of these struts are identical, the second moment of inertia (I) increases with increasing pore size, translating to a larger strut flexural rigidity (E_sI) with increasing pore size. Cells are known to apply a constant contractile force to the CG scaffold regardless of the system stiffness[106] which suggests that cells probe their local mechanical environment by applying a constant traction force and measuring the resultant substrate deformation.[118] These results suggested that strut flexural rigidity, not stiffness, is the more relevant mechanical signal to cells. So even though the struts have a constant elastic modulus, they may 'feel' stiffer in scaffolds with larger pore sizes because of an increased resistance to buckling. The 'apparent' stiffness, or flexural rigidity (E_sI), of the scaffold with the largest pore size (151 μm) was calculated to be greater than that of the scaffold with the

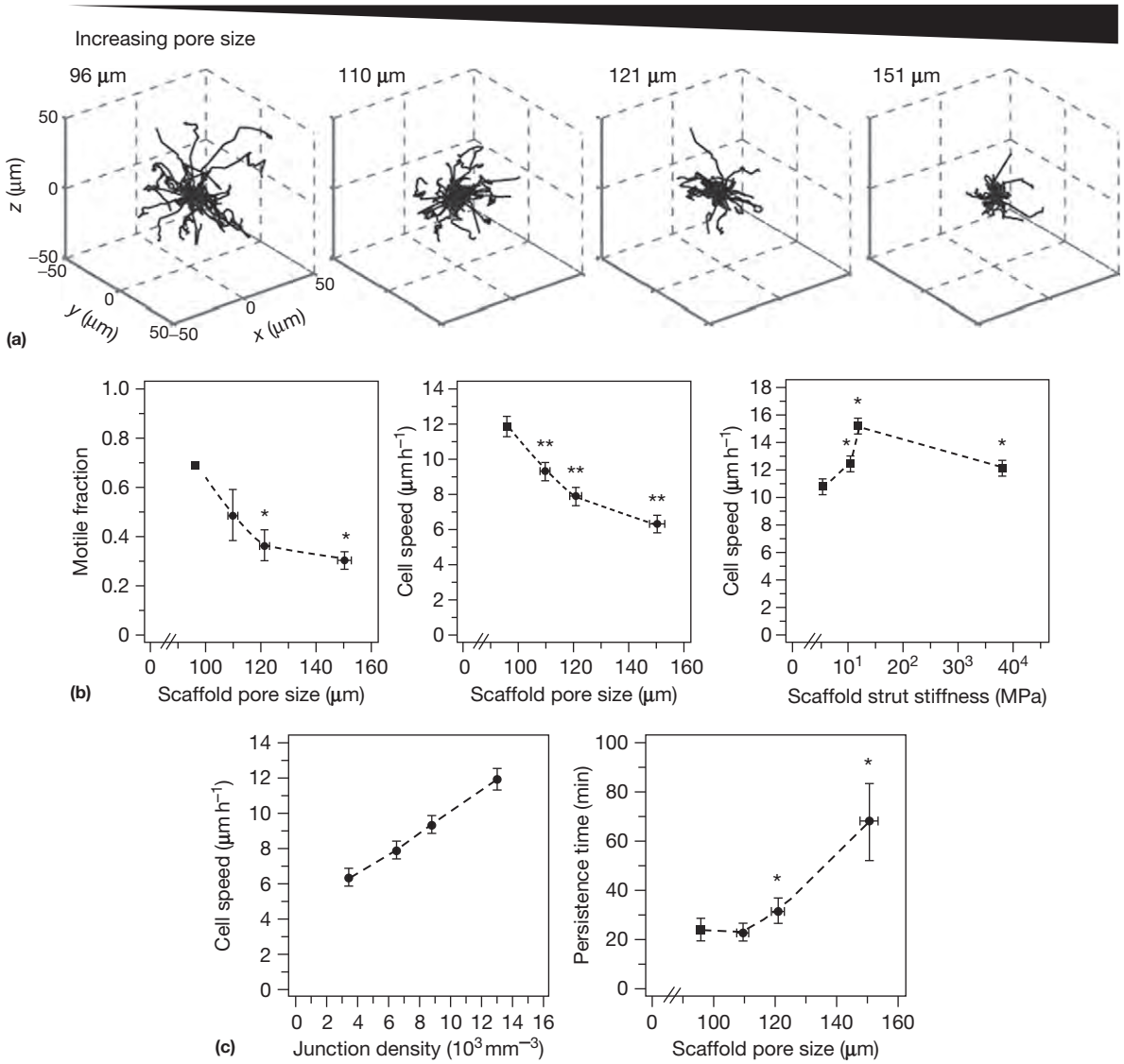

Figure 17 (a) 3D Wind-Rose plots of randomly chosen cell tracks showing cell dispersion; cell dispersion decreases as scaffold mean pore size increases. (b) Motile fraction and mean cell speed decrease as scaffold pore size increases. Cell speed shows a subtle biphasic relationship with scaffold strut modulus. (c) Cell speed increases proportionally with scaffold strut junction density. Cell persistence time increases with pore size (increasing distance between strut junctions). Reprinted with permission from Harley, B. A. C.; Kim, H. D.; Zaman, M. H.; Yannas, I. V.; Lauffenburger, D. A.; Gibson, L. J. *Biophys. J.* **2008**, *95*, 4013–4024.

smallest (96 μm) pore size by a factor of 6.1. Thus, if strut flexural rigidity was the mechanism by which pore size affected cell motility, cell motility would be expected to decrease for the series of scaffolds of constant pore size but increasing scaffold modulus (changing E_s in the flexural rigidity term (E_sI)). However, when strut modulus (E_s) was increased over a range (between 5.3 and 38.0 MPa; Factor: 7.2; Table 3) that closely approximated the change in strut flexural rigidity with mean pore size (Factor: 6.1), motility did not decrease but instead displayed subtle biphasic behavior (Figure 17(b)).[7]

After attempting to explain the significant influence of CG scaffold pore size on cell motility using predictions made by the cellular solids modeling regarding local scaffold mechanics, geometric insights from the cellular solids model regarding strut junctions (points in the scaffold where two or more struts meet) were investigated. The geometry of strut junctions within the scaffold was described as the mean spacing between junctions (D_{jxn}) or the mean junction density (ρ_{jxn}, the number of strut junctions per unit cell divided by the volume of a unit cell). D_{jxn} and ρ_{jxn} were calculated from the scaffold mean pore size (d) assuming a tetrakaidecahedral unit cell:[7]

$$D_{jxn} = \frac{d}{2.785} \quad [6]$$

$$\rho_{jxn} = \frac{11.459}{d^3} \quad [7]$$

Replotting the pore-size-dependent cell speed data against strut junction density, an exceptionally strong correlation

between cell speed and strut junction density was observed (Figure 17(c)). Further, cells migrating in scaffolds with larger pore sizes, and therefore larger D_{jxn} and lower ρ_{jxn}, were observed to exhibit greater persistence times, indicating more directional motion along a scaffold strut (Figure 17(c)). In contrast, persistence times of cells migrating in scaffolds with smaller pore sizes and greater ρ_{jxn} are significantly lower, representative of erratic movement (time turning) that likely occurs more often at junctions when cells encounter higher surface ligand densities and can therefore move with increased speed. These results provided a mechanistic explanation for the initially counter-intuitive observation that cell motility decreases as scaffold pore size increases,[7] as well as an excellent example of the types of mechanistic questions that can be answered using the CG scaffold system because of the capacity to create uniform scaffold variants with independently controlled microstructural and mechanical properties and to integrate rigorous characterization and modeling techniques.

2.216.4.4. Growth Factor and Gene Delivery

Tissue engineering scaffolds are frequently enhanced through the addition of exogenous factors including growth factors, drugs, and genes. CG scaffolds have been used as a platform to study the combined effects of the scaffold and delivery of growth factors and genes. Recently, marrow stromal cells (MSCs) were transfected with a plasmid encoding for glial cell line-derived neurotrophic factor (pGDNF) and seeded onto standard type I CG scaffolds.[119] For optimal plasmid loading, the level of GDNF remained six to seven times higher than a control after 2 weeks of culture, reaching previously described therapeutic levels.[120] These results show promise for future brain tissue engineering studies with CG scaffolds.

The potential for CG materials as cartilage and meniscus scaffolds has been enhanced using gene delivery. EDAC crosslinking of as little as 10 μg of IGF-1 plasmid to type II CG scaffolds resulted in sustained plasmid release that was controlled by the degradation rate of the scaffold. IGF-1 was overexpressed over a 2-week culture period, resulting in significantly higher amounts of chondrocyte-like cells, GAG, and type II collagen production compared to controls.[121] Another study transfected MSCs with a plasmid encoding endostatin, a potent antiangiogenic factor that could potentially prevent unwanted vascularization of cartilage, and cultured on CG scaffolds.[122] Endostatin levels, while negligible in control cultures, reached a peak of 13 ng ml^{-1} after 3 days and approached therapeutic levels after 2 weeks.[122] MSCs and meniscal cells have also been transfected with a vector for TGF-β1 and cultured *in vitro* on type I CG scaffolds. Implantation of transfected, cell-seeded constructs following culture led to increased matrix synthesis and meniscal gene expression over controls.[123]

2.216.4.5. Modifying Gene Expression

CG scaffolds have been used to compare gene expression profiles of fibroblasts cultured on 2D and 3D constructs. The gene expression profiles investigated focused on genes involved in angiogenesis (VEGF, HMOX, and HGF) and matrix remodeling (matrix metalloproteinases and their inhibitors, ECM components), two critical processes that must be understood for rational scaffold design. Genes for some matrix metalloproteinases (MMP-2, MMP-12, MMP-19), ECM protein synthesis (COL1A2, COL3A2, COL2A1, COL4A4, COL4A5), and proangiogenic factors were upregulated while some MMP inhibitors (TIMP1, TIMP3) were downregulated in the 3D CG scaffolds compared to the 2D CG surfaces.[8] These results indicate that the geometric and topographical differences between 2D and 3D CG substrates can critically affect gene expression and possibly matrix remodeling.

2.216.4.6. Mechanical Stimulation

Mechanical stimuli, derived from both physical extracellular binding sites and the movement of fluids within the ECM, is known to influence critical cell behaviors such as proliferation, differentiation, and gene expression.[124–126] Experimental, computational, and modeling techniques have all been used with the CG scaffold system to improve our understanding of how these mechanical forces affect cell behavior. For example, the effects of pore size and mechanical stimulation on gene expression profiles for MSCs in CG scaffolds have recently been evaluated. Osteogenic markers collagen type I, osteocalcin, and osteopatin were all upregulated in MSCs seeded into CG scaffolds with larger pores (151 μm vs. 96 μm),[127] indicating that larger pore sizes may be more optimal for bone tissue engineering. Also, scaffolds that were mechanically constrained to prevent contraction showed lower MSC RNA levels of osteocalcin, osteopatin, and bone sialoprotein, suggesting that prevention of cell-mediated contraction may be detrimental to osteogenesis.[127]

CG scaffolds have also been used to investigate the role of direct mechanical stimulation on osteoblastic activity. Mechanical loading of MC3T3-E1 cells in culture is known to improve bone morphogenic activity within scaffolds. In addition, mechanical stimulation during *in vitro* culture improves nutrient and waste transport within the scaffold while promoting cellular infiltration, which should lead to more uniform tissue engineering constructs compared to static culture. Dynamic culture was shown to upregulate the gene for cyclooxygenase-2 (COX-2), a key enzyme for the production of early bone formation marker prostaglandin E_2 (PGE_2). The gene for osteopontin (OPN), a later marker of bone formation, was also upregulated.[128] In addition, incorporation of rest periods during dynamic culture has been shown to significantly increase OPN expression over both static and dynamic conditions.[129] This suggests that mechanical stimulation via flow perfusion could be a useful technique for encouraging osteoblastic activity and bone formation in CG scaffolds (see **Chapter 5.501, Scaffolds: Flow Perfusion Bioreactor Design**).

3D computational fluid dynamics (CFD) modeling has further been utilized to estimate shear stress forces on cells seeded within CG scaffolds for bone tissue engineering during *in vitro* culture in perfusion bioreactors.[76,130] For bone, it is understood that applied wall shear stresses on cells are critical in activating matrix production and mineralization.[81] Accurate simulations of applied shear stresses on cells would allow the selection of an optimal perfusion rate that correlates to physiologic shear stress levels. CFD showed that cells in CG scaffolds were exposed to a wide range of shear stresses while conventional analytical methods to estimate shear stress report a mean shear stress value only. The analytical methods also

predicted shear stress values 10–20% higher than CFD and do not take into account the type of secondary cell deformation that can take place on the basis of cell orientation within the scaffold.[130] CFD analysis of fluid velocity, hydrostatic pressure, and wall shear stress on common cell attachment profiles within CG scaffolds (stretched along one strut or spread between two struts) shows that low wall shear stresses (~20 mPa) are sufficient to activate bone growth mechanisms.[76]

While computational methods can be useful, the above analysis focused on small scaffold sections only as it was impractical to analyze an entire scaffold area.[76,130,131] Recent work by Stops *et al.* has developed a finite element approach to predict cellular strains within CG scaffold systems (see **Chapter 3.307, Finite Element Analysis in Bone Research: A Computational Method Relating Structure to Mechanical Function**). Utilizing the tetrakaidecahedron unit cell and experimental data regarding scaffold deformation, cell attachment profiles, and cell sizes, a model was developed to predict individual cell strain as a function of pore size, cell length, and applied scaffold strain. This model correctly predicts individual cell strain within two standard deviations for 72% of cells.[131] This approach has also been applied to predict the differentiation of MSCs in CG scaffolds as a function of Young's modulus.[132] The model takes into account pore size, cell proliferation, angiogenesis, and shear stress/strain among other factors. Results over a range of 0.001–1000 MPa show that higher Young's modulus should lead to higher numbers of osteoblasts, indicating that stiffer CG scaffolds could be ideal for bone tissue engineering (**Figure 18**).[132] All of these tools highlight the multi-scale experimental and analytical tools available when utilizing the CG scaffold system for studies of cellular mechanotransduction.

2.216.4.7. Stem Cell Differentiation

CG scaffolds have recently been started to be used to explore extrinsic modulation of stem cell fate decisions (differentiation, quiescence, and self-renewal) (see **Chapter 2.209, Materials as Artificial Stem Cell Microenvironments**). Adult mesenchymal stem cells (MSCs) can differentiate into a myriad of tissues, including bone, cartilage, and tendon, making them a powerful tool for orthopedic tissue engineering. Farrell *et al.* has recently shown that adult MSCs in CG scaffolds could be induced to differentiate along osteogenic or chondrogenic lineages in the presence of osteogenic (dexamethasone, ascorbic acid, and β-glycerophosphate) and chondrogenic (dexamethasone and TGF-β1) factors, respectively.[133] The CG scaffold's demonstrated ability to support both bone and cartilage growth makes it a promising material for the treatment of osteochondral defects. Subsequent work has compared the osteogenic potential of MSCs on 2D substrates versus 3D CG constructs. While MSCs initially expressed collagen type I quicker on 3D substrates, the delayed expression of osteocalcin indicates that osteogenic differentiation is slower in CG scaffolds compared to that in 2D substrates.[134] MSCs cultured in CG materials have also shown variable differentiation and gene expression profiles under mechanical strain. High strains (15%) led to enhanced α-smooth muscle actin expression but poorer differentiation into type I collagen positive cells compared to lower strain levels (5%).[135] Ongoing work is examining the utility of CG scaffolds to influence fate decisions of hematopoietic and cardiac stem cells.

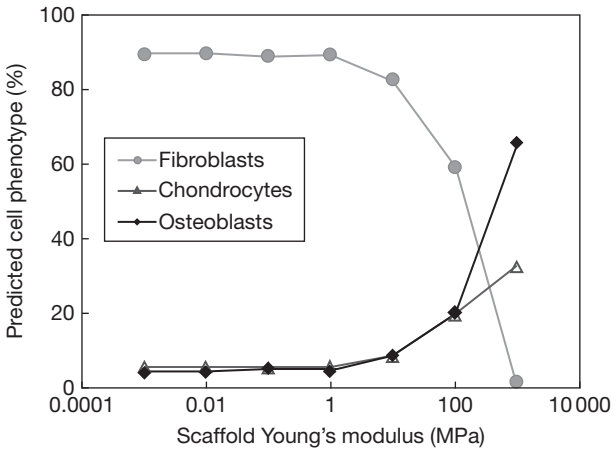

Figure 18 Percentage of MSC-derived cell phenotypes inside CG scaffold as a function of Young's modulus as predicted by finite element modeling. The fraction of osteoblasts compared to fibroblasts increases with increasing modulus, suggesting that stiffer CG scaffolds may be preferred for bone tissue engineering. Adapted from Khayyeri, H.; Checa, S.; Tagil, M.; O'Brien, F. J.; Prendergast, P. J. *J. Mater. Sci. Mater. Med.* **2010**, *21*, 2325–2330.

2.216.5. *In Vivo* Applications

Since the development of the first clinically viable artificial skin,[5] CG scaffolds have been used *in vivo* to regenerate a wide variety of chronic and acute injuries involving skin (see **Chapter 5.534, Skin Tissue Engineering**), peripheral nerves (see **Chapter 5.531, Peripheral Nerve Regeneration**), conjunctiva, cartilage (see **Chapter 5.515, Cartilage Tissue Engineering**), and other tissues.[4] CG scaffolds, like other tissue engineering scaffolds, serve a multitude of functions *in vivo* including physical inhibition of wound contraction, mechanical support for cells and neo-tissue growth, and carrier of biochemical ligands and signaling molecules. CG scaffold mechanical, chemical, and microstructural properties have been rigorously characterized *in vitro*, leading to independent control of pore size and shape, elastic moduli, biodegradation rate, chemical composition, and other scaffold parameters. These variables can be tuned to create scaffolds optimized for the regeneration of specific tissues.

2.216.5.1. Dermal Regeneration Applications

The CG scaffold is found to optimize skin regeneration as a monolithic, uniform structure (termed the dermal regeneration template (DRT)) that is fabricated from a CG copolymer with a 98:2 ratio of type I collagen to GAG (chondroitin 6-sulfate). This chemistry was developed in part because of the additional mechanical stability afforded by the GAG content as well as the processing to the collagen fibrils that allowed platelet attachment but prevented activation of platelet degranulation processes.[5,136] The DRT has isotropic pores with a 20–125 μm size range and a degradation time of 5–15 days. The DRT is typically implanted acellularly (without cells) along

with a thin silicone coating to control moisture loss and bacterial infection at the wound site. This bioactive scaffold recruits epidermal cells from the wound site and encourages spontaneous regeneration of skin tissue layer by layer. Sequential regeneration results in a mature epidermis and basement membrane as well as near physiologic dermis that lacks hair follicles. This scaffold has regenerated full-thickness skin wounds in animal models and human burn victims.[4,5]

2.216.5.2. Peripheral Nerve Regeneration Applications

Peripheral nerve injuries are typically treated by entubulating transected nerve ends. Tubes made of type I collagen have been the most successful as defined by morphological and electrophysiological methods.[3,4,48,137–139] While a tube is sufficient to induce regeneration across a gap of several millimeters, the addition of a porous material into the tube lumen can enhance the quality of regeneration and has been proven superior to other nonporous, nonpermeable lumen designs (**Figure 19**).[4,139] This porous core acts as a physical support for the growing nerve while allowing migration of cells and cytokines across the nerve gap. In addition, this central scaffold core has also been shown to organize wound contraction and scar proliferation.[54] The CG scaffold optimized for peripheral nerve regeneration, termed the nerve regeneration template (NRT), has axially elongated pores on the order of 10–20 μm that provide contact guidance for Schwann cell migration and axon formation between nerve stumps.[137] These scaffolds, with an optimal degradation half life of 6 weeks,[4,47] were found to regenerate peripheral nerves at the same level as autografts, the current gold standard in the industry.[137]

2.216.5.3. Conjunctiva and Corneal Regeneration Applications

CG scaffolds have demonstrated the ability to alter the typical contraction and scar synthesis healing mechanisms associated with full thickness lesions of the conjunctiva in a rabbit animal model. Scaffolds were able to significantly reduce wound contraction ($6.8 \pm 3.2\%$ fornix shortening vs. $26.4 \pm 5.0\%$ for ungrafted wound sites) and promote the synthesis of a nearly physiologic stroma layer.[140] CG scaffolds have also been shown to be promising substrates for the development of artificial corneas (see **Chapter 6.631, Keratoprostheses**). *In vitro* characterization of these scaffolds showed that stromal keratocytes, epithelial cells, and endothelial cells could be successively cocultured over a period of 12 weeks.[141] The cells produced a new ECM, complete with an epithelium, basement membrane, and endothelial cell monolayer.[141]

2.216.5.4. Cartilage and Fibrocartilage Disk Tissue Engineering Applications

CG scaffolds have been applied to the regeneration of a range of other orthopedic tissues including articular cartilage, meniscus, and the intervertebral disk (see **Chapters 5.524, Biomaterials for Replacement and Repair of the Meniscus and Annulus Fibrosus** and **6.615, Intervertebral Disc**). The effects of crosslinking density, chemical composition, and pore size of CG scaffolds, as well as the use of gene and growth factor seeded CG scaffolds, have been studied extensively in the context of articular cartilage regeneration.[121,142–146] Recently, CG scaffolds populated with TGF-β1 transfected meniscus cells

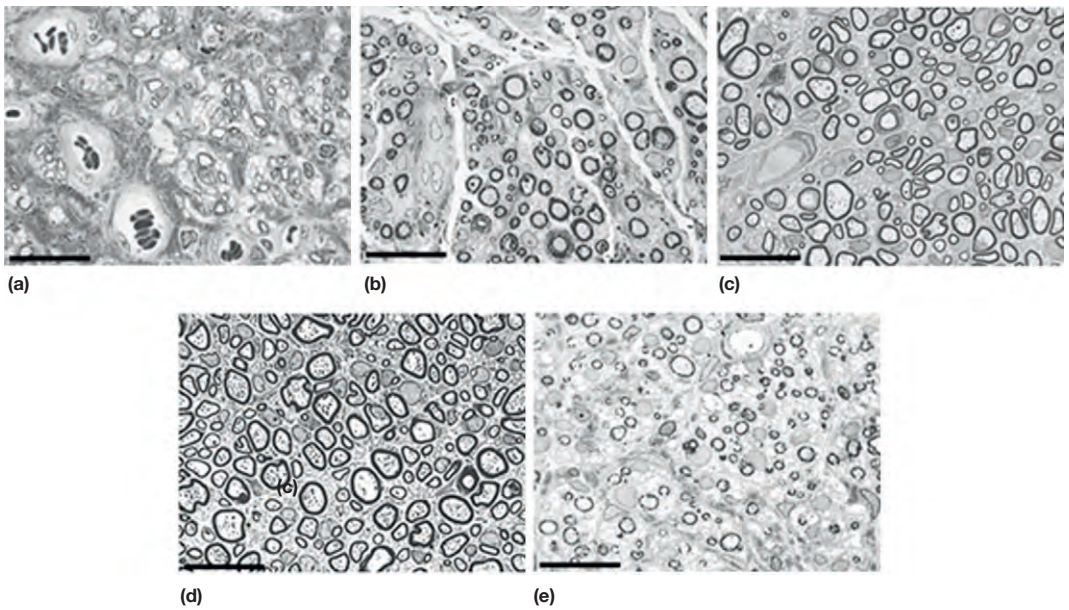

Figure 19 Histomorphometic, cross-sectional images of the nerve trunk regenerated using collagen tubes with tailored biodegradation rates. The images are arranged in order of lowest to highest crosslink density, or fastest to slowest degradation rate from (a) to (e). Nerves trunks regenerated in devices (c) and (d), characterized by intermediate levels of the crosslink density and degradation rate (device half life: 2–3 weeks), showed superior morphology, with significantly larger axons, a more well-defined myelin sheath, and a significantly larger *N* ratio. Scale bar: 25 μm. Reprinted with permission from Harley, B. A.; Spilker, M. H.; Wu, J. W.; *et al*. *Cells Tissues Organs* **2004**, *176*, 153–165, S. Karger AG, Basel, Switzerland.

were used to successfully fill avascular zone meniscus lesions with repair tissue.[123] Other work has compared type I and type II CG scaffolds for intervertebral disk tissue engineering applications, finding that type II CG scaffolds were preferential to type I on the basis of cell number as well as protein and GAG synthesis after 8 weeks.[147]

2.216.5.5. Bone, Osteochondral Regeneration Applications

Single phase and layered, multiphase CGCaP scaffolds have recently been developed for *in vivo* bone and osteochondral tissue engineering applications, respectively (see **Chapter 6.617, Bone Tissue Grafting and Tissue Engineering Concepts**).[61–63,69,148] These materials are currently undergoing *in vivo* examination as both bone scaffolds (single phase CGCaP form) and as full osteochondral scaffolds. CGCaP bone regeneration scaffolds are composed of type I collagen, chondroitin 6-sulfate, and calcium phosphate. Initial *in vitro* and *in vivo* experiments have demonstrated that these scaffolds can successfully integrate into bone defects and show preliminary bony substitution and mineralization as early as 6 weeks post implantation.[149]

The biphasic layered, gradient scaffold developed for the treatment of osteochondral defects has been shown to mimic aspects of the natural structure of articular joints,[69] notably a continuous boundary that should induce the formation of interfacial tissue as seen in healthy joints between articular cartilage and subchondral bone (**Figure 20**). Utilization of this fabrication method also prevents complications often observed in layered scaffolds with abrupt interfaces including delamination, foreign body contamination (from glue or other adhesives), and inefficient cellular transport between scaffold phases.[69] Under mechanical loading, the osteochondral scaffolds perform as expected for a biphasic material, with the

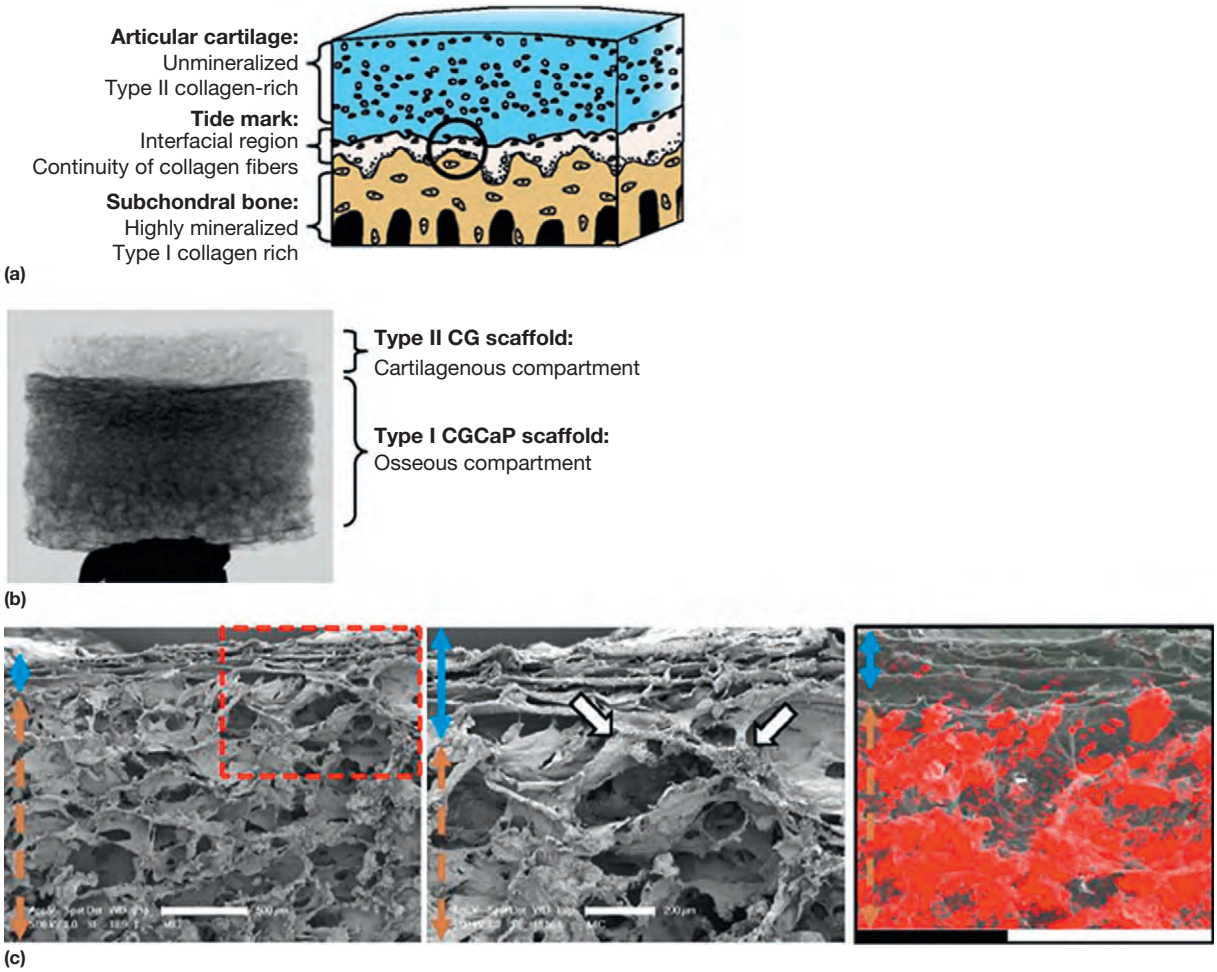

Figure 20 (a) Structure of the natural articular joint showing articular cartilage and subchondral bone joined by a continuous interfacial region. (b) X-ray μCT image of the layered osteochondral scaffold showing distinct cartilaginous and osseous compartments (scale bar 1 mm). (c) SEM images of the osteochondral scaffold showing the complete scaffold microstructure (left; scale bar 500 μm), and the interfacial region (middle; scale bar 200 μm) showing continuity between the osseous (tan dashed arrow) and cartilaginous (blue solid arrow) compartments including collagen struts extending across the transition (white arrows). No regional areas of delamination or debonding are observed between the compartments. Distribution of Ca mineral (P similar but not shown) content (red shading) superimposed over an SEM image of the osteochondral scaffold showed distinct mineralized (high CaP content, tan dashed arrow) and nonmineralized (low/zero CaP content, blue solid arrow) layers (right; black scale bar 400 μm). Reprinted with permission from Harley, B. A.; Lynn, A. K.; Wissner-Gross, Z.; Bonfield, W.; Yannas, I. V.; Gibson, L. J. *J. Biomed. Mater. Res. A* **2010**, *92*, 1078–1093.

majority of deformation confined to the cartilagenous compartment and no evidence of delamination between the scaffold compartments during or following loading.[69] This scaffold is currently being developed as a clinical product that can be implanted using a mosaicplasty approach without the use of sutures, glue, or screws.[69] This scaffold system is currently undergoing Phase I clinical trials for primary and secondary (backfill of traditional mosaicplasty harvest sites) osteochondral defects in the knee. The developed technologies and techniques hold promise for the regeneration of not only osteochondral defects, but also other physiological interfaces such as the tendon to bone insertion site.

2.216.5.6. Brain Tissue Engineering Applications

CG scaffolds are currently being explored as substrates for neural defects in the brain. These scaffolds are fabricated via the conventional freeze-drying approach from type I or type II collagen and HA, a GAG that is the chief component of the brain ECM.[150] Although the brain is almost entirely composed of HA, the collagen component of these CG scaffolds allows additional control of mechanical properties and biodegradation rates.[151] Altering the ratio of collagen to HA allowed manipulation of porosity over a wide range (75–91%, brain = 76%) and compressive modulus (1.33–6.31 kPa, brain = 1.06 kPa).[151] Neuronal stem cells showed the capacity to differentiate into neuronal cells in these HA–collagen scaffolds,[151] and ongoing studies are continuing to optimize scaffold properties via a series of *in vitro* and *in vivo* experiments.

2.216.5.7. Lung Tissue Engineering Applications

The cellular nature of CG scaffolds and the ability to modify scaffold porosity and pore size have made them candidate materials for regenerative medicine studies in the lung. CG scaffolds have been utilized as prospective materials to investigate design parameters for *in vivo* healing of lung tissue damage. Lung cells from Sprague-Dawley rats were seeded onto standard CG scaffolds (type I collagen and chondroitin 6-sulfate) and cultured for 2–21 days. This *in vitro* culture led to the development of alveolar-like structures as well as cell-mediated contraction, possibly as a result of expression of α-smooth muscle actin.[152] These results suggest that CG scaffolds hold promise as an *in vivo* treatment for lung defects and that they also might be interesting model systems for *ex vivo* culture of cells associated with a wide range of lung-tissue abnormalities and diseases.

2.216.6. Conclusions

Porous, 3D biomaterials have been used extensively for a variety of tissue engineering applications, primarily as analogs of the ECM capable of inducing regeneration of damaged tissues and organs. An important evolving application is their use as constructs to quantitatively study cell behavior and cell–scaffold interactions. Scaffold material, microstructural, and mechanical properties have all been observed to significantly affect individual cell behavior as well as overall scaffold bioactivity and regenerative capacity. CG scaffolds are comprised of naturally derived ECM and allow investigations of highly porous and fibrous ECM systems relevant to physiology and tissue engineering applications. Fabricating CG scaffolds via freeze-drying allows independent modulation of scaffold mean pore size, pore shape and orientation, relative density, mechanical properties, chemical composition, and available ligands. CG scaffolds and triple coprecipitated CGCaP nanocomposite scaffolds have been utilized as regenerative templates for a wide range of tissues following injury, notably of skin, peripheral nerves, brain, lung, cartilage, bone, fibrocartilage disks, and the conjunctiva. CG scaffolds have been shown to not only be a bioactive substrate for regenerative medicine applications, but are also well-suited to answer biologically relevant questions regarding cell–material interactions. As CG scaffolds as well as many other tissue engineering scaffolds resemble low-density, open-cell foams, with an interconnected network of struts, they can be modeled as cellular solids. Models for cellular solids contribute to our understanding of cell–scaffold interactions and hold promise for future studies of *in vitro* cell mechanobiology and *in vivo* tissue engineering.[153,154]

References

1. Harley, B. A. C.; Gibson, L. J. *Chem. Eng. J.* **2008**, *137*, 102–121.
2. Liu, Y.; Ramanath, H. S.; Wang, D. A. *Trends Biotechnol.* **2008**, *26*, 201–209.
3. Harley, B. A.; Spilker, M. H.; Wu, J. W.; *et al. Cells Tissues Organs* **2004**, *176*, 153–165.
4. Yannas, I. V. *Tissue and Organ Regeneration in Adults*; Springer: New York, 2001.
5. Yannas, I. V.; Lee, E.; Orgill, D. P.; Skrabut, E. M.; Murphy, G. F. *Proc. Natl. Acad. Sci. USA* **1989**, *86*, 933–937.
6. Yannas, I. V. *Angew. Chem. Int. Ed. Engl.* **1990**, *29*(1), 20–35.
7. Harley, B. A. C.; Kim, H. D.; Zaman, M. H.; Yannas, I. V.; Lauffenburger, D. A.; Gibson, L. J. *Biophys. J.* **2008**, *95*, 4013–4024.
8. Jaworski, J.; Klapperich, C. M. *Biomaterials* **2006**, *27*, 4212–4220.
9. Murphy, C. M.; Haugh, M. G.; O'Brien, F. J. *Biomaterials* **2010**, *31*, 461–466.
10. O'Brien, F. J.; Harley, B. A.; Yannas, I. V.; Gibson, L. J. *Biomaterials* **2005**, *26*, 433–441.
11. Tierney, C. M.; Haugh, M. G.; Liedl, J.; Mulcahy, F.; Hayes, B.; O'Brien, F. J. *J. Mech. Behav. Biomed. Mater.* **2009**, *2*, 202–209.
12. Tierney, C. M.; Jaasma, M. J.; O'Brien, F. J. *J. Biomed. Mater. Res. A* **2009**, *91*, 92–101.
13. Zeltinger, J.; Sherwood, J. K.; Graham, D. A.; Mueller, R.; Griffith, L. G. *Tissue Eng.* **2001**, *7*(5), 557–572.
14. Nehrer, S.; Breinan, H. A.; Ramappa, A.; *et al. Biomaterials* **1997**, *18*(11), 769–776.
15. Wake, M. C.; Patrick, C. W., Jr.; Mikos, A. G. *Cell Transplant.* **1994**, *3*(4), 339–343.
16. Engler, A.; Bacakova, L.; Newman, C.; Hategan, A.; Griffin, M.; Discher, D. *Biophys. J.* **2004**, *86*, 617–628.
17. Freyman, T. M.; Yannas, I. V.; Yokoo, R.; Gibson, L. J. *Biomaterials* **2001**, *22*, 2883–2891.
18. Grinnell, F.; Ho, C. H.; Lin, Y. C.; Skuta, G. *J. Biol. Chem.* **1999**, *274*, 918–923.
19. Grinnell, F.; Ho, C. H.; Tamariz, E.; Lee, D. J.; Skuta, G. *Mol. Biol. Cell* **2003**, *14*, 384–395.
20. Jiang, H.; Grinnell, F. *Mol. Biol. Cell* **2005**, *16*, 5070–5076.
21. Pelham, J.; Robert, J.; Wang, Y.-L. *Proc. Natl. Acad. Sci. USA* **1997**, *9*, 13661–13665.
22. Peyton, S. R.; Putnam, A. J. *J. Cell Physiol.* **2005**, *204*, 198–209.
23. Schulz-Torres, D.; Freyman, T. M.; Yannas, I. V.; Spector, M. *Biomaterials* **2000**, *21*, 1607–1619.
24. Yeung, T.; Georges, P. C.; Flanagan, L. A.; *et al. Cytoskeleton* **2005**, *60*, 24–34.
25. Zaman, M. H.; Trapani, L. M.; Sieminski, A. L.; *et al. Proc. Natl. Acad. Sci. USA* **2006**, *103*, 10889–10894.
26. Carter, E. M.; Raggio, C. L. *Curr. Opin. Pediatr.* **2009**, *21*, 46–54.
27. Lodish, H., Berk, A., Zipursky, S. L., Matsudaira, P., Baltimore, D., Darnell, J. E., Eds.; In *Molecular Cell Biology*; W.H. Freeman: New York, 2000.
28. Shoulders, M. D.; Raines, R. T. *Annu. Rev. Biochem.* **2009**, *78*, 929–958.

29. Berisio, R.; De Simone, A.; Ruggiero, A.; Improta, R.; Vitagliano, L. *J. Pept. Sci.* **2009**, *15*(3), 131–140.
30. Yannas, I. V. *J. Macromol. Sci. Rev. Macromol. Chem. Phys.* **1972**, *C7*, 49.
31. Yannas, I. V.; Burke, J. F. *J. Biomed. Mater. Res.* **1980**, *14*, 65–81.
32. Raman, R.; Sasisekharan, V.; Sasisekharan, R. *Chem. Biol.* **2005**, *12*, 267–277.
33. BI, Y. M.; Ehirchiou, D.; Kilts, T. M.; *et al. Nat. Med.* **2007**, *13*, 1219–1227.
34. Lamari, F. N.; Karamanos, N. K. *Adv. Pharmacol.* **2006**, *53*, 33–48.
35. Kiani, C.; Chen, L.; Wu, Y. J.; Yee, A. J.; Yang, B. B. *Cell Res.* **2002**, *12*, 19–32.
36. Roughley, P. J. *Eur. Cell Mater.* **2006**, *12*, 92–101.
37. Yoon, J. H.; Halper, J. *J. Musculoskelet. Neuronal. Interact* **2005**, *5*, 22–34.
38. Lynn, A. K.; Yannas, I. V.; Bonfield, W. *J. Biomed. Mater. Res. B Appl. Biomater.* **2004**, *71*, 343–354.
39. Mehlisch, D. R. *Oral Surg. Oral Med. Oral Pathol.* **1989**, *68*, 505–514; discussion 514–516.
40. Snyder, C. C. *Plast. Reconstr. Surg.* **1976**, *58*, 401–406.
41. Charriere, G.; Bejot, M.; Schnitzler, L.; Ville, G.; Hartmann, D. J. *J. Am. Acad. Dermatol.* **1989**, *21*, 1203–1208.
42. Cooperman, L.; Michaeli, D. *J. Am. Acad. Dermatol.* **1984**, *10*, 647–651.
43. Tang, S. Q.; Vickers, S. M.; Hsu, H. P.; Spector, M. *J. Biomed. Mater. Res. A* **2007**, *82A*, 323–335.
44. O'Brien, F. J.; Harley, B. A.; Yannas, I. V.; Gibson, L. *Biomaterials* **2004**, *25*, 1077–1086.
45. Kanungo, B. P.; Gibson, L. J. *Acta. Biomater.* **2009**, *5*, 1006–1018.
46. Kanungo, B. P.; Gibson, L. J. *Acta Biomater.* **2009**.
47. Chang, A. S.; Yannas, I. V.; Perutz, S.; *et al.* In *Progress in Biomedical Polymers*; Dunn, R. L., Ed.; Plenum Press: New York, 1990.
48. Chamberlain, L. J.; Yannas, I. V.; Hsu, H. P.; Strichartz, G.; Spector, M. *Exp. Neurol.* **1998**, *154*, 315–329.
49. Madaghiele, M.; Sannino, A.; Yannas, I. V.; Spector, M. *J. Biomed. Mater. Res. Part A* **2008**, *85A*, 757–767.
50. Kim, Y. T.; Haftel, V. K.; Kumar, S.; Bellamkonda, R. V. *Biomaterials* **2008**, *29*, 3117–3127.
51. Engelmayr, G. C.; Cheng, M.; Bettinger, C. J.; Borenstein, J. T.; Langer, R.; Freed, L. E. *Nat. Mater.* **2008**, *7*, 1003–1010.
52. Moffat, K. L.; Kwei, A. S.; Spalazzi, J. P.; Doty, S. B.; Levine, W. N.; Lu, H. H. *Tissue Eng. Part A* **2009**, *15*, 115–126.
53. Chamberlain, L. J.; Yannas, I. V. In *Methods of Molecular Medicine*; Morgan, J. R., Yarmush, M. L., Eds.; Humana Press: Totowa, NJ, 1998.
54. Harley, B. A.; Hastings, A. Z.; Yannas, I. V.; Sannino, A. *Biomaterials* **2006**, *27*, 866–874.
55. Sannino, A.; Silvestri, L.; Madaghiele, M.; Harley, B.; Yannas, I. V. *J. Appl. Polym. Sci.* **2010**, *116*(4), 1879–1888.
56. Harley, B. A.; Leung, J. H.; Silva, E.; Gibson, L. J. *Acta. Biomater.* **2007**, *3*, 463–474.
57. Yannas, I. V.; Tobolsky, A. V. *Nature* **1967**, *215*, 509–510.
58. Haugh, M. G.; Jaasma, M. J.; O'Brien, F. J. *J. Biomed. Mater. Res. A* **2009**, *89*, 363–369.
59. Olde Damink, L. H.; Dijkstra, P. J.; Van Luyn, M. J.; Van Wachem, P. B.; Nieuwenhuis, P.; Feijen, J. *Biomaterials* **1996**, *17*, 765–773.
60. Al-Munajjed, A. A.; O'Brien, F. J. *J. Mech. Behav. Biomed. Mater.* **2009**, *2*, 138–146.
61. Harley, B. A.; Lynn, A. K.; Wissner-Gross, Z.; Bonfield, W.; Yannas, I. V.; Gibson, L. J. *J. Biomed. Mater. Res. A* **2010**, *92*, 1066–1077.
62. Lynn, A. K.; Best, S. M.; Cameron, R. E.; *et al. J. Biomed. Mater. Res. A* **2010**, *92*, 1057–1065.
63. Lynn, A. K.; Bonfield, W. *Acc. Chem. Rev.* **2005**, *38*, 202–207.
64. Clarke, K. I.; Graves, S. E.; Wong, A. T. C.; Triffitt, J. T.; Francis, M. J. O.; Czernoszka, J. T. *J. Mater. Sci. Mater. Med.* **1993**, *4*, 107–110.
65. Itoh, S.; Kikuchi, M.; Takakuda, K.; *et al. J. Biomed. Mater. Res.* **2001**, *54*, 445–453.
66. Sasano, Y.; Kamakura, S.; Nakamura, M.; *et al. Anat. Rec.* **1995**, *242*, 40–46.
67. Kikuchi, M.; Itoh, S.; Ichinose, S.; Shinomiya, K.; Tanaka, J. *Biomaterials* **2001**, *22*, 1705–1711.
68. Genin, G. M.; Kent, A.; Birman, V.; *et al. Biophys. J.* **2009**, *97*, 976–985.
69. Harley, B. A.; Lynn, A. K.; Wissner-Gross, Z.; Bonfield, W.; Yannas, I. V.; Gibson, L. J. *J. Biomed. Mater. Res. A* **2010**, *92*, 1078–1093.
70. Osborne, C. S.; Barbenel, J. C.; Smith, D.; Savakis, M.; Grant, M. H. *Med. Biol. Eng. Comput.* **1998**, *36*, 129–134.
71. Saddiq, Z. A.; Barbenel, J. C.; Grant, M. H. *J. Biomed. Mater. Res. A* **2009**, *89*, 697–706.
72. Brigham, M. D.; Bick, A.; Lo, E.; Bendali, A.; Burdick, J. A.; Khademhosseini, A. *Tissue Eng. Part A* **2009**, *15*, 1645–1653.
73. Suri, S.; Schmidt, C. E. *Tissue Eng. A* **2010**, *16*, 1703–1716.
74. Green, J.; Kienitz, B.; Baskaran, H. In *AIChE Annual Meeting*, San Francisco, CA, 2006.
75. Harley, B. A.; Freyman, T. M.; Wong, M. Q.; Gibsony, L. J. *Biophys. J.* **2007**, *93*, 2911–2922.
76. Jungreuthmayer, C.; Jaasma, M. J.; Al-Munajjed, A. A.; Zanghellini, J.; Kelly, D. J.; O'Brien, F. J. *Med. Eng. Phys.* **2009**, *31*, 420–427.
77. Gibson, L. J.; Ashby, M. F. *Cellular Solids: Structure and Properties*; Cambridge University Press: Cambridge, UK, 1997.
78. Williams, R. E. *Science* **1968**, *161*, 276–277.
79. Thompson, W. *Philos. Mag.* **1887**, *24*, 503.
80. Agrawal, C. M.; Mckinney, J. S.; Lanctot, D.; Athanasiou, K. A. *Biomaterials* **2000**, *21*, 2443–2452.
81. Prendergast, P. J.; Huiskes, R.; Soballe, K. *J. Biomech.* **1997**, *30*, 539–548.
82. Levick, J. R. *Q. J. Exp. Physiol.* **1987**, *72*, 409–437.
83. O'Brien, F. J.; Harley, B. A.; Waller, M. A.; Yannas, I. V.; Gibson, L. J.; Prendergast, P. J. *Technol. Health Care* **2007**, *15*, 3–17.
84. Kanungo, B. P.; Silva, E.; Van Vliet, K.; Gibson, L. J. *Acta. Biomater.* **2008**, *4*, 490–503.
85. Hutmacher, D. W. *Biomaterials* **2000**, *21*, 2529–2543.
86. Pek, Y. S.; Spector, M.; Yannas, I. V.; Gibson, L. J. *Biomaterials* **2004**, *25*, 473–482.
87. Dembo, M.; Wang, Y.-L. *Biophys. J.* **1999**, *76*, 2307–2316.
88. Harris, *Science* **1980**, *208*, 177–179.
89. Lee, J.; Leonard, M.; Oliver, T.; Ishihara, A.; Jacobson, K. *J. Cell. Biol.* **1994**, *127*, 1957–1964.
90. Lemmon, C. A.; Sniadecki, N. J.; Ruiz, S. A.; Tan, J. L.; Romer, L. H.; Chen, C. S. *Mech. Chem. Biosyst.* **2005**, *2*, 1–16.
91. Oliver, T.; Dembo, M.; Jacobson, K. *Cytoskeleton* **1995**, *31*, 225–240.
92. Roy, P.; Petroll, W. M.; Chuong, C. J.; Cavanagh, H. D.; Jester, J. V. *Ann. Biomed. Eng.* **1999**, *27*, 721–730.
93. Tan, J. L.; Tien, J.; Pirone, D. M.; Gray, D. S.; Bhadriraju, K.; Chen, C. S. *Proc. Natl. Acad. Sci. USA* **2003**, *100*, 1484–1489.
94. Beningo, K. A.; Dembo, M.; Kaverina, I.; Small, J. V.; Wang, Y.-L. *J. Cell Biol.* **2001**, *153*, 881–887.
95. Beningo, K. A.; Wang, Y.-L. *Trends Cell Biol.* **2002**, *12*, 79–84.
96. Chen, C. S.; Ingber, D. E. *Osteoarthr. Cartil.* **1999**, *7*, 81–94.
97. Engler, A. J.; Sen, S.; Sweeney, H. L.; Discher, D. E. *Cell* **2006**, *126*, 677–689.
98. Lo, C.-M.; Wang, H.-B.; Dembo, M.; Wang, Y.-L. *Biophys. J.* **2000**, *79*, 144–152.
99. Munevar, S.; Wang, Y.-L.; Dembo, M. *Mol. Biol. Cell* **2001**, *12*, 3947–3954.
100. Wang, H.-B.; Dembo, M.; Hanks, S. K.; Wang, Y.-L. *Proc. Natl. Acad. Sci. USA* **2001**, *98*, 11295–11300.
101. Wang, H.-B.; Dembo, M.; Wang, Y.-L. *Am. J. Physiol. Cell Physiol.* **2000**, *279*, C1345–C1350.
102. Wang, N.; Butler, J. P.; Ingber, D. *Science* **1993**, *260*, 1124–1127.
103. Guilak, F.; Erickson, G. R.; Ting-Beall, H. P. *Biophys. J.* **2002**, *82*, 720–727.
104. Marquez, J. P.; Genin, G. M.; Zahalak, G. I.; Elson, E. L. *Biophys. J.* **2005**, *88*, 778–789.
105. Zahalak, G. I.; Wagenseil, J. E.; Wakatsuki, T.; Elson, E. L. *Biophys. J.* **2000**, *79*, 2369–2381.
106. Freyman, T. M.; Yannas, I. V.; Yokoo, R.; Gibson, L. J. *Exp. Cell Res.* **2002**, *272*, 153–162.
107. Zaleskas, J. M.; Kinner, B.; Freyman, T. M.; Yannas, I. V.; Gibson, L. J.; Spector, M. *Biomaterials* **2004**, *25*, 1299–1308.
108. Spilker, M. H.; Asano, K.; Yannas, I. V.; Spector, M. *Biomaterials* **2001**, *22*, 1085–1093.
109. Freyman, T. M.; Yannas, I. V.; Pek, Y.-S.; Yokoo, R.; Gibson, L. J. *Exp. Cell Res.* **2001**, *269*, 140–153.
110. Sethi, K. K.; Yannas, I. V.; Mudera, V.; Eastwood, M.; Mcfarland, C.; Brown, R. A. *Wound Repair Regen.* **2002**, *10*, 397–408.
111. Triantafillou, T. C.; Zhang, J.; Shercliff, T. L.; Gibson, L. J.; Ashby, M. F. *Int. J. Mech. Sci.* **1989**, *31*, 665–678.
112. Condeelis, J.; Segall, J. E. *Nat. Rev. Cancer* **2003**, *3*, 921–930.
113. Lapidot, T.; Dar, A.; Kollet, O. *Blood* **2005**, *106*, 1901–1910.
114. Wilson, A.; Trumpp, A. *Nat. Rev. Immunol.* **2006**, *6*, 93–106.
115. Friedl, P.; Zanker, K. S.; Brocker, E. B. *Microsc. Res. Tech.* **1998**, *43*, 369–378.
116. Lauffenburger, D. A.; Horwitz, A. F. *Cell* **1996**, *84*, 359–369.
117. Zaman, M. H.; Kamm, R. D.; Matsudaira, P.; Lauffenburger, D. A. *Biophys. J.* **2005**, *89*, 1389–1397.
118. Vogel, V.; Sheetz, M. *Nat. Rev. Mol. Cell. Biol.* **2006**, *7*, 265–275.
119. Bolliet, C.; Bohn, M. C.; Spector, M. *Tissue Eng. Part C Methods* **2008**, *14*, 207–219.
120. Price, T. J.; Louria, M. D.; Candelario-Soto, D.; *et al. BMC Neurosci.* **2005**, *6*, 4.
121. Capito, R. M.; Spector, M. *Gene Ther.* **2007**, *14*, 721–732.

122. Sun, X. D.; Jeng, L.; Bolliet, C.; Olsen, B. R.; Spector, M. *Biomaterials* **2009**, *30*, 1222–1231.
123. Steinert, A. F.; Palmer, G. D.; Capito, R.; *et al*. *Tissue Eng.* **2007**, *13*, 2227–2237.
124. Geris, L.; Vandamme, K.; Naert, I.; Vander Sloten, J.; Duyck, J.; Van Oosterwyck, H. *J. Biomech.* **2008**, *41*, 145–154.
125. Mcmahon, L. A.; Reid, A. J.; Campbell, V. A.; Prendergast, P. J. *Ann. Biomed. Eng.* **2008**, *36*, 185–194.
126. Wu, Q. Q.; Chen, Q. *Exp. Cell Res.* **2000**, *256*, 383–391.
127. Byrne, E. M.; Farrell, E.; Mcmahon, L. A.; *et al*. *J. Mater. Sci. Mater. Med.* **2008**, *19*, 3455–3463.
128. Jaasma, M. J.; O'Brien, F. J. *Tissue Eng. Part A* **2008**, *14*, 1213–1223.
129. Partap, S.; Plunkett, N. A.; Kelly, D. J.; O'Brien, F. J. *J. Mater. Sci. Mater. Med.* **2010**, *21*, 2325–2330.
130. Jungreuthmayer, C.; Donahue, S. W.; Jaasma, M. J.; *et al*. *Tissue Eng. Part A* **2009**, *15*, 1141–1149.
131. Stops, A. J.; Mcmahon, L. A.; O'mahoney, D.; Prendergast, P. J.; Mchugh, P. E. *J. Biomech. Eng.* **2008**, *130*, 061001.
132. Khayyeri, H.; Checa, S.; Tagil, M.; O'Brien, F. J.; Prendergast, P. J. *J. Mater. Sci. Mater. Med.* **2010**, *21*, 2331–2336.
133. Farrell, E.; O'Brien, F. J.; Doyle, P.; *et al*. *Tissue Eng.* **2006**, *12*, 459–468.
134. Farrell, E.; Byrne, E. M.; Fischer, J.; *et al*. *Technol. Health Care* **2007**, *15*, 19–31.
135. Kobayashi, M.; Spector, M. *Mol. Cell Biomech.* **2009**, *6*, 217–227.
136. Sylvester, M. F.; Yannas, I. V.; Salzman, E. W.; Forbes, M. J. *Thromb. Res.* **1989**, *55*, 135–148.
137. Chamberlain, L. J.; Yannas, I. V.; Arrizabalaga, A.; Hsu, H. P.; Norregaard, T. V.; Spector, M. *Biomaterials* **1998**, *19*, 1393–1403.
138. Chamberlain, L. J.; Yannas, I. V.; Hsu, H. P.; Strichartz, G. R.; Spector, M. *J. Neurosci. Res.* **2000**, *60*, 666–677.
139. Harley, B. A.; Yannas, I. V. *Minerva Biotecnologica* **2006**, *18*, 97–120.
140. Hsu, W. C.; Spilker, M. H.; Yannas, I. V.; Rubin, P. A. *Invest. Ophthalmol. Vis. Sci.* **2000**, *41*, 2404–2411.
141. Vrana, N. E.; Builles, N.; Justin, V.; *et al*. *Invest. Ophthalmol. Vis. Sci.* **2008**, *49*, 5325–5331.
142. Capito, R. M.; Spector, M. *IEEE Eng. Med. Biol. Mag.* **2003**, *22*, 42–50.
143. Kinner, B.; Capito, R. M.; Spector, M. *Adv. Biochem. Eng. Biotechnol.* **2005**, *94*, 91–123.
144. Lee, C. R.; Grodzinsky, A. J.; Hsu, H.-P.; Spector, M. *J. Orthop. Res.* **2003**, *21*, 272–281.
145. Samuel, R. E.; Lee, C. R.; Ghivizzani, S. C.; *et al*. *Hum. Gene Ther.* **2002**, *13*, 791–802.
146. Vickers, S. M.; Squitieri, L. S.; Spector, M. *Tissue Eng.* **2006**, *12*.
147. Saad, L.; Spector, M. *J. Biomed. Mater. Res. A* **2004**, *71*, 233–241.
148. Harley, B. A.; Lynn, A. K.; Wissner-Gross, Z.; Bonfield, W.; Yannas, I. V.; Gibson, L. J. In *Design and Fabrication of a Multiphase Osteochondral Scaffold*, Proceedings of the First International Conference on Mechanics of Biomaterials & Tissues, 2005.
149. Lynn, A. K.; Harley, B. A.; Wissner-Gross, Z.; Yannas, I. V.; Gibson, L. J.; Bonfield, W. In *Design and Fabrication of a Mineralized, Triple-co-Precipitate Collagen–Glycosaminoglycan Scaffold*, Proceedings of the First International Conference on Mechanics of Biomaterials & Tissues, 2005.
150. Bignami, A.; Hosley, M.; Dahl, D. *Anat. Embryol. (Berl)* **1993**, *188*, 419–433.
151. Wang, T. W.; Spector, M. *Acta Biomater.* **2009**, *5*, 2371–2384.
152. Chen, P.; Marsilio, E.; Goldstein, R. H.; Yannas, I. V.; Spector, M. *Tissue Eng.* **2005**, *11*, 1436–1448.

2.217. Fibrin

I Catelas, University of Ottawa, Ottawa, ON, Canada

© 2011 Elsevier Ltd. All rights reserved.

2.217.1.	**Historical Perspective**	304
2.217.2.	**Composition, Structure, and Properties**	304
2.217.2.1.	Composition and Polymerization	304
2.217.2.2.	Structure and Mechanical Properties	305
2.217.2.3.	Degradation Process: Fibrinolytic Properties	306
2.217.2.4.	Inherent Biological Properties	309
2.217.3.	**Fibrin Use as a Delivery System**	309
2.217.3.1.	Cell Delivery System	309
2.217.3.2.	Drug and Growth Factor Delivery System	311
2.217.3.2.1.	Drug delivery system	311
2.217.3.2.2.	Growth factor delivery system	312
2.217.3.3.	Gene Delivery System	314
2.217.3.3.1.	Viral delivery	314
2.217.3.3.2.	Nonviral delivery	315
2.217.4.	**Fibrin in Tissue Engineering Applications**	315
2.217.4.1.	Vascular Tissue Engineering	316
2.217.4.1.1.	Vascular grafts	316
2.217.4.1.2.	Engineered cardiovascular tissues	316
2.217.4.2.	Bone Tissue Engineering	317
2.217.4.3.	Cartilage Tissue Engineering	318
2.217.4.4.	Nervous Tissue Engineering	319
2.217.4.5.	Other Tissue Engineering Applications	319
2.217.4.5.1.	Skin	319
2.217.4.5.2.	Liver	320
2.217.4.5.3.	Skeletal muscles	320
2.217.4.5.4.	Tendons and ligaments	320
2.217.5.	**Fibrin in Clinical Practice**	321
2.217.5.1.	Commercially Available Fibrin Sealants	321
2.217.5.2.	Examples of Fibrin Uses in Clinical Practice	321
2.217.5.2.1.	Cardiovascular and thoracic surgeries	321
2.217.5.2.2.	Plastic and reconstructive surgeries	323
2.217.5.2.3.	Other clinical applications	324
2.217.6.	**Conclusion**	325
References		325

Glossary

Anastomosis Network of blood vessels that both branch out and reconnect.

Durotomy Incursion of the dura, especially during spinal surgery.

Ecchymosis Passage of blood from ruptured blood vessels into subcutaneous tissue, marked by a purple discoloration of the skin.

Electrocauterization Process of heating tissue with electricity. Procedure frequently used to stop bleeding.

Epididymis Narrow, tightly coiled tube connecting the efferent ducts from the rear of each testicle to its vas deferens (sperm 'carry-away vessel').

Fistula Abnormal connection or passageway between two epithelium-lined organs or vessels that normally do not connect.

Genitourinary injuries Injuries related to the genital organs.

Laparoscopic partial nephrectomy Procedure to remove a small renal tumor, while preserving the remainder of the kidney.

Necrosectomy Surgery excision of necrotic tissue.

Nephrectomy Surgical procedure to remove a kidney or a kidney section.

Oozing Exudation of fluid.

Rhynophyma Descriptive term for a large, bulbous, ruddy appearance of the nose caused by granulomatous infiltration, commonly because of untreated rosacea.

Sternotomy Surgical procedure in which a vertical inline incision is made along the sternum, after which the sternum itself is divided. This procedure provides access to the heart and lungs for surgical procedures.
Vasectomy Minor surgical procedure wherein the vasa deferentia of a male are severed, and then tied or sealed in a manner such as to prevent sperm from entering the seminal stream.
Vasoepididymostomy Surgical creation of a passage between the vas deferens and the epididymis.
Vasovasostomy Procedure to reconnect the vas deferens tubes that were cut during a vasectomy.

Abbreviations

ACL	Anterior cruciate ligament
BMP-2	Bone morphogenetic protein-2
EGF	Epidermal growth factor
FGF	Fibroblast growth factor
GAG	Glycosaminoglycan
GDNF	Glial-derived neurotrophic factor
GFAP	Glial fibrillary acidic protein
IGF	Insulin-like growth factor
IGFBP	Insulin-like growth factor-binding protein
K1	Kringle1
KGF	Keratinocyte growth factor
MALP-2	Macrophage activator lipoprotein peptide-2
MCL	Medial collateral ligament
MSC	Mesenchymal stem cell
NGF	Nerve growth factor
NRK	Normal Rattusnorvegicus kidney
NT-3	Neurotrophin-3
PBS	Phosphate-buffered saline
PDGF	Platelet-derived growth factor
PEG	Polyethylene glycol
PEI	Polyethylenimine
PGA	Polyglycolic acid
PLGA	Polylactic-*co*-glycolic acid
PRP	Platelet-rich-plasma
PTFE	Polytetrafluoroethylene
PTH	Parathyroid hormone
PTN	Pleiotrophin
SDMSC	Skin-derived mesenchymal stem cell-like cells
β-TCP	β-Tricalcium phosphate
TGF-β	Transforming growth factor-β
VEGF	Vascular endothelial growth factor

2.217.1. Historical Perspective

The first scientific concepts of the blood coagulation process were developed only at the beginning of the nineteenth century,[1] and it is only in 1909 that the fibrin was first used for clinical applications by Bergel.[2] A few years later, and during the First World War, fibrin tampons and patches were used as parenchymal tissue dressings to control bleeding and for hemostasis in cerebral surgery.[3] In the 1940s, human fibrinogen and thrombin were produced in large quantities in a laboratory at Harvard led by Cohen, and in 1943, human plasminogen and thrombin were used by Tidrick and Warner as a biological adhesive for the fixation of skin grafts in humans.[4] These events constituted a significant step in the development of fibrin sealants. However, they were neglected for about three decades because of a rather poor clinical outcome of their early generation, mainly because of poor adhesive strength and poor durability, probably related to the absence of fractionation technologies to provide concentrated fibrinogen solutions and the lack of knowledge on fibrinolysis inhibitor.[4,5] It is only in the early 1970s that the use of fibrin sealants reappeared when Matras *et al.* successfully used a highly concentrated human plasma-derived fibrinogen solution in combination with factor XIII, thrombin, and calcium chloride to seal nerves in animal experiments.[6] The risk of viral transmission, which had also caused some issues in the 1940s, was reduced through careful donor selection, followed by a heat treatment.[7] The successes observed during the early 1970s led to the first commercial fibrin sealant in 1978 (Fibrinkleber Human Immuno®). Since then, improved versions of the product and other fibrin sealants have been introduced on the market. Newer developments have focused on the enhancement of viral safety profiles as well as improvement of handling properties and delivery methods without compromising the product properties. In addition to their initial intended use as a sealant for hemostasis, fibrin sealants have now become a growing platform for various other applications in the tissue engineering and regenerative medicine arenas.

2.217.2. Composition, Structure, and Properties

2.217.2.1. Composition and Polymerization

Fibrin is a natural biopolymer involved in the coagulation cascade and results from the conversion of fibrinogen to cross-linked fibrin by thrombin (Figure 1).

The fibrinogen molecule, a 340 000 Da hexamer, is a plasma protein, approximately 45 nm long. It consists of two outer D domains, each connected by a coiled-coil segment to the central E domain. The molecule is composed of two sets of three polypeptide chains termed Aα, Bβ, and γ, which are joined together in the N-terminal E domain by five symmetrical disulfide bridges[3,8–12] (Figure 2). The Aα, Bβ, and γ chains consist of 610, 461, and 411 residues, respectively.[13,14]

The conversion of fibrinogen to fibrin is catalyzed by the serine protease thrombin, which is generated by the blood coagulation cascade from the activation of prothrombin. Thrombin

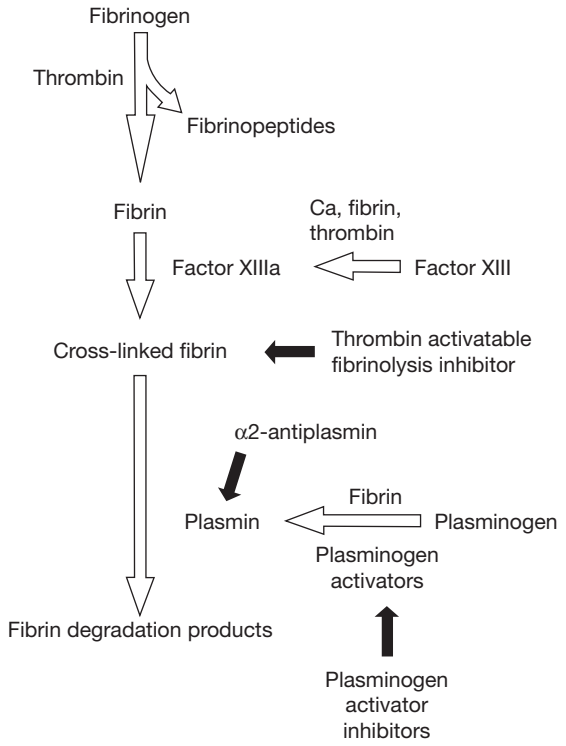

Figure 1 Basic scheme of fibrin polymerization and fibrinolysis. Black arrows represent inhibitory reactions. Images from Weisel, J. W. *Adv. Protein Chem.* **2005**, *70*, 247–299, reproduced with permission.

cleavage of two sets of small N-terminal fibrinopeptides (fibrinopeptide A (FpA) and fibrinopeptide B (FpB)) from the Aα and Bβ chains exposes binding sites E_A and E_B and initiates fibrin polymerization[12,15] (Figure 2). Each E_A-site combines with a constitutive complementary-binding pocket (Da) in the D domain of neighboring molecules.[16–18] The initial E_A:Da associations cause fibrin molecules (or fibrin monomers) to align in a staggered overlapping end-to-middle domain arrangement to form double-stranded twisting protofibrils with a periodicity of 22.5 nm (i.e., with a 22.5-nm repeat spacing of the individual fibrin monomers)[11,12] (Figure 3). These protofibrils further self-assemble laterally and into branched fiber bundles (Figure 3), resulting in the formation of a characteristic biopolymer gel material with an open three-dimensional (3D) porous network structure,[1] as depicted in Figure 4.

2.217.2.2. Structure and Mechanical Properties

Although the mechanical properties of *in vivo* fibrin clots are still largely unknown, there is no doubt that these properties are critical in clinical scenarios. For example, the viscoelastic properties of a thrombus in a blood vessel will determine whether the blood flow will rupture or embolize the clot. In the case of hemostasis, the structure must be strong enough to withstand the pressure of arterial blood flow.[19]

The properties of the fibrin clots vary greatly depending on the conditions of polymerization, which influence the clot structure. Negatively contrasted fibrin studies using transmission electron microscopy revealed the substructure of the fibers forming the fibrin clot and the presence of branch points[19] (Figure 5). During polymerization, two types of branching occur, and they both account for fibrin network.[12,20,21] Bilateral (or tetramolecular) branch junctions (i.e., lateral aggregation) occur when double-stranded protofibrils converge side to side, whereas equilateral (or trimolecular) branch points form by coalescence of three fibrin molecules that connect three double-stranded protofibrils of equal widths[12,20,21] (Figure 3). Hence, trimolecular branch points seem to be formed when protofibrils diverge instead of aggregating only laterally, and may therefore be formed early during the polymerization process while protofibrils are added to the network. Polymerization conditions that favor lateral aggregation would then tend to produce clots made of rather thick fibers with few branch points, whereas polymerization conditions that would inhibit lateral aggregation would tend to produce clots made of rather thin fibers with many branch points.[19,22] The rate of release of the fibrinopeptides FpA and FpB as well as other factors influencing the lateral association of the fibers during polymerization will regulate fiber thickness, degree of branching, and clot porosity, which, all together, influence the overall clot structure.

Some of the factors influencing the rate and extent of polymerization and the fiber formation include the fibrinogen and thrombin concentrations, the ionic strength, the presence of certain other plasma proteins (such as albumin), the pH, and the temperature. For example, when comparing the structure of fibrin clots prepared with different thrombin concentrations, Helgerson *et al.*[1] reported that the fiber structure formed was much finer with less porosity and many more branch points with a higher thrombin concentration compared to a structure with thicker and more laterally associated fibers with lower thrombin concentrations (Figure 6). The authors also reported that, similarly, increasing salt concentration produced thinner fibers with more branch points and lower porosity,[1] forming 'fine gels' as described earlier by Sierra,[3] in comparison to the 'coarse gels' presenting larger diameter fibers and higher porosity, observed with lower salt concentrations (Figure 7). Factor XIII, which, when activated, is responsible for cross-linking fibrin monomers that make up the fiber bundles and catalyses the formation of covalent bonds between fibrin chains, has been reported to have no effect on gel porosity[3] and fiber thickness.[23] Finally, the eventual presence of fibronectin also does not seem to influence the porosity, but it increases fiber diameter of the clots.[24]

The different constituents of the fibrin clot influencing its structure will also affect its mechanical properties. Fibrin is a viscoelastic polymer, and therefore, its properties may be characterized by stiffness (representing its elastic properties) and creep compliance (representing its inelastic properties).[25] As mentioned before, these properties will determine how the clot will respond to the stress to which it is subjected. A very stiff clot will not deform as much as a less stiff one under the same applied stress. As a consequence, under flowing blood pressure, for example, a clot with a greater elastic component will return to its original shape, whereas a clot with a greater inelastic component will incur more permanent deformation[19] and may be less subject to embolization.[19,22] In a review on mechanical characteristics of fibrin sealants, Sierra[3] reported that the compliance was dictated by the number of contacts and

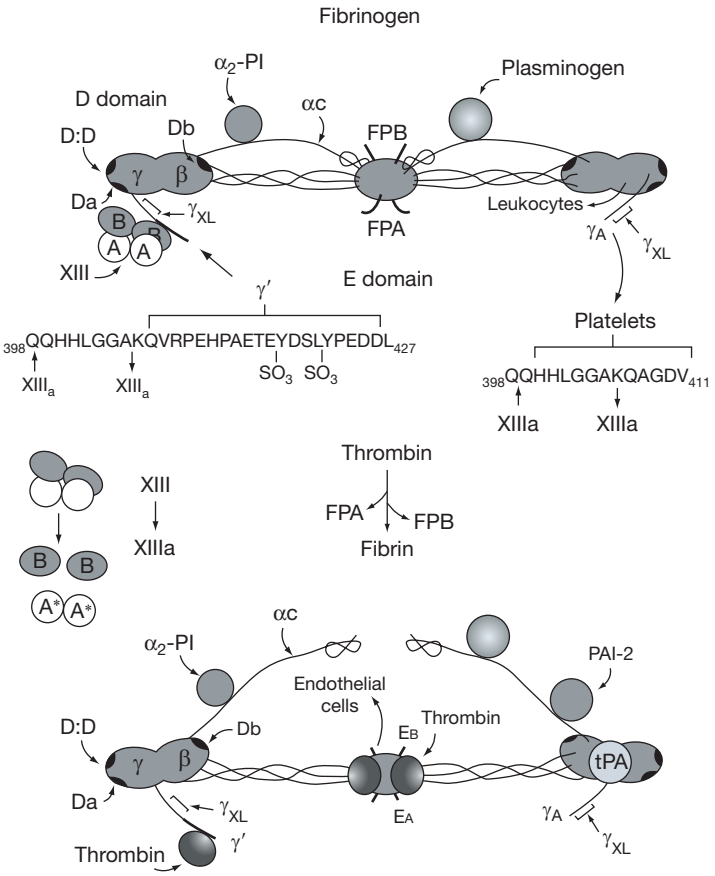

Figure 2 Schematic diagram of fibrinogen and fibrin showing the major structural domains, the association sites that participate in fibrin polymerization and cross-linking, and other molecular and cellular binding interactions. Bottom half of the figure: Thrombin cleavage of two sets of fibrinopeptides (fibrinopeptide A (FpA) and fibrinopeptide B (FpB)) from the Aα and Bβ chains of the fibrinogen molecules exposes sites E_A and E_B (initiation of the polymerization). Images from Mosesson, M. W.; Siebenlist, K. R.; Meh, D. A. *Ann. N. Y. Acad. Sci.* **2001**, *936*, 11–30, reproduced with permission.

interactions between the fibers. When comparing gels with or without fibronectin under shear loading, the author reported that coarse gels with added fibronectin (which has been reported to increase the diameter of the fibers) demonstrated a large increase in their modulus and a decrease in creep compliance, whereas fine gels exhibited a decrease in their modulus and a corresponding increase in creep compliance.

Other parameters commonly reported are the breaking strength and the adhesiveness. Some studies and reviews on fibrin mechanical properties reported an increase of the elastic modulus, tensile strength, and adhesive strength with increasing fibrinogen concentrations.[3,23,26,27] With regard to the effects of thrombin, a study from Rowe *et al.* reported that the elastic modulus and ultimate tensile strength of the clots increased with decreasing thrombin concentrations.[28] It is worth noting that in this latter study, fibrin gels were seeded with vascular smooth muscle cells. However, the authors attributed the changes in mechanical properties to the differences in thrombin concentration as they did not observe these changes in similar constructs made of collagen type I. A recent study by Akpalo and Larreta-Garde,[29] looking at the effects of varying concentrations of both thrombin and transglutaminase on the fibrin network and mechanical strength, reported that thrombin concentration influenced the kinetics of gelation (or polymerization), but not the evolution of the mechanical properties. The authors also showed an indirect relationship between the gel elasticity and thrombin concentration upon covalent binding. Finally, although factor XIII content does not seem to influence the clot structure, at least in terms of porosity[3] and fiber thickness,[23] some studies and reviews have reported that increasing the clot content of factor XIII increases the elastic modulus by enhancing clot rigidity and decreasing inelastic deformation.[22,30] This would be primarily explained by the stabilization of the interactions between preassembled protofibrils by cross-linking.[22] Such increase can be up to fivefold under physiological conditions.[30] The effects of cross-linking on the mechanical stability of clots are an important part of blood clotting that may be responsible for the serious bleeding problems of patients lacking factor XIII.[22]

2.217.2.3. Degradation Process: Fibrinolytic Properties

As described above, the viscoelastic properties of the fibrin clot are very important as the clot needs to fulfill a mechanical function and its stability will be greatly influenced by these properties. However, the clot stability will also be directly influenced by its fibrinolytic properties as in physiological

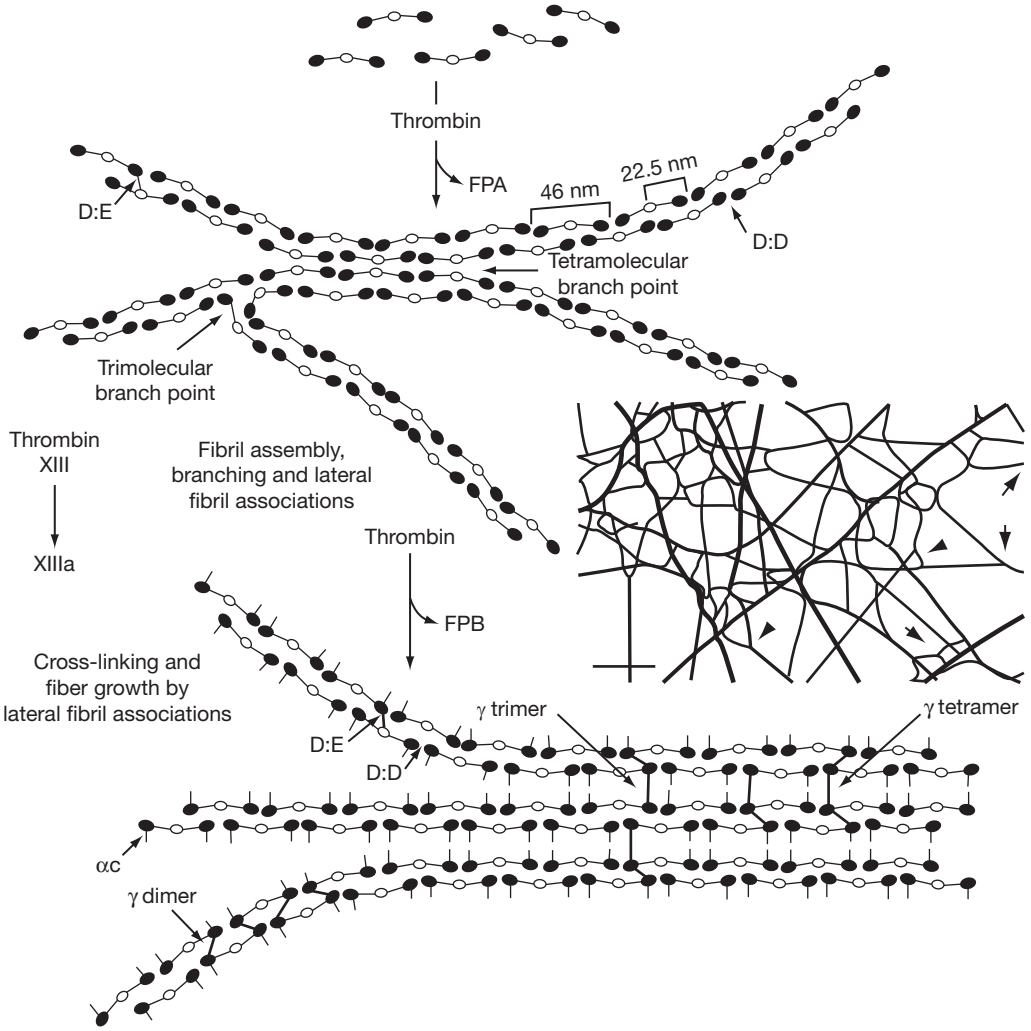

Figure 3 Schematic diagram of fibrin assembly and cross-linking. Thrombin cleavage of two sets of fibrinopeptides (fibrinopeptide A (FpA) (top half of the figure) and fibrinopeptide B (FpB) (bottom half of the figure)) from the Aα and Bβ chains of the fibrinogen molecules, respectively, exposes sites E_A and E_B and initiates fibrin polymerization. Each E_A site combines with a constitutive complementary-binding pocket (Da) (D:E on the diagram) in the D domain of neighboring molecules. These associations cause fibrin monomers to align in a staggered overlapping end-to-middle domain arrangement to form a double-stranded twisting protofibrils. The protofibrils further self-assemble laterally and into branched fiber bundles. Inset shows a critical point dried fiber matrix containing bilateral (arrowheads) and equilateral (arrows) branch junctions. Note: Bilateral (or tetramolecular) branch junction (i.e., lateral aggregation) occurs when double-stranded protofibrils converge side to side. Equilateral (or trimolecular) branch point (i.e., formation of branch point) forms by coalescence of three fibrin molecules that connect three double-stranded protofibrils of equal widths. Images from Mosesson, M. W.; Siebenlist, K. R.; Meh, D. A. *Ann. N. Y. Acad. Sci.* **2001**, *936*, 11–30, reproduced with permission.

conditions, the clot must be efficiently dissolved in a timely manner to avoid thrombosis.

Fibrinolysis under physiological conditions involves the binding of circulating plasminogen to fibrin, and the activation of plasminogen to the protease plasmin by tissue-type plasminogen activator (tPA), also bound to fibrin.[22,25] The activation of plasminogen is further stimulated by the initial cleavage of fibrin. Plasmin then cleaves fibrin at specific sites, creating new binding sites and leading to identifiable soluble, large, and complex fragments with portions of individual fibers and protofibrils.[22,25] A study by Veklich *et al.* using scanning electron microscopy imaging of clot surfaces being digested demonstrated that fibrinolysis proceeded by transverse cutting of fibrils and fibers, with the creation of gaps in the fiber continuity and free transected fiber segments that associate laterally within the matrix fiber structure to form thicker fiber bundles.[31] Similarly, a study by Collet *et al.*[32] using confocal electron microscopy to characterize the morphological changes at the fibrin network and fiber levels showed a progressive disaggregation of the fibrin fibers, also suggesting that fibrinolysis proceeded by transverse cutting rather than by progressive cleavage uniformly around the fibers. Finally, in a recent review, authors from the same group reported that fibrinolysis would involve the movement of plasmin laterally across fibers, binding to sites created by its own proteolytic activity.[33]

Numerous approaches have been used to measure the rate of fibrin degradation, including enzyme-linked immunosorbent assay to detect soluble cross-linked D dimers, measuring

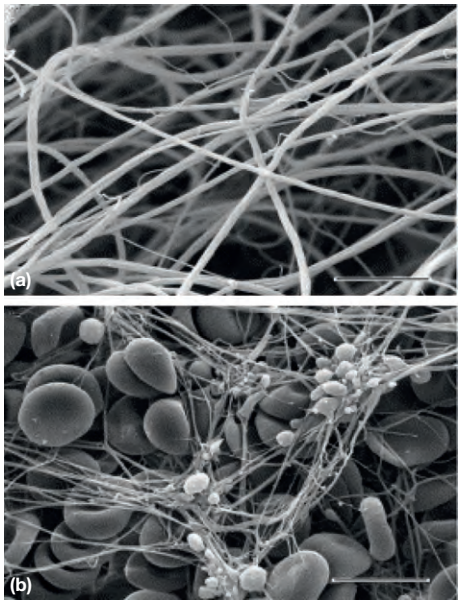

Figure 4 Scanning electron microscope images of fibrin clots. (a) Scanning electron micrograph of a clot formed by the addition of thrombin to purified fibrinogen. Magnification bar: 5 μm. Note the visible twisting of protofibrils making up the fibers on the surface of some fibers. (b) Electron micrograph of whole blood clot, made from freshly drawn blood with no addition. Magnification bar: 10 μm. Images from Weisel, J. W. *Adv. Protein Chem.* **2005**, *70*, 247–299, reproduced with permission.

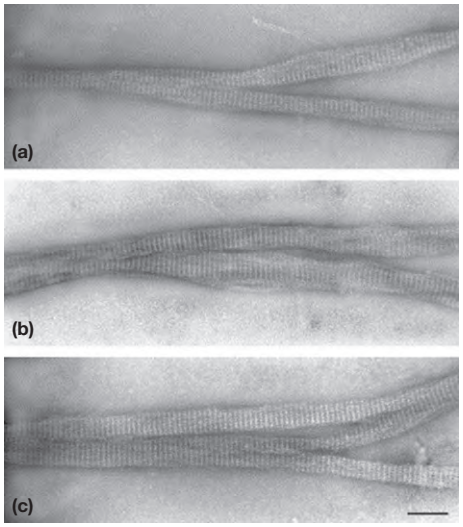

Figure 5 Transmission electron micrographs of negatively contrasted fibrin fibers showing the substructure of the fibers and the presence of branch points. Most branch points consist of three fiber segments that join at a small acute angle with band patterns aligned. The band pattern depicts the fiber repeat of 22.5 nm. Such pattern arises because areas with high protein density exclude stain and appear bright while areas with lower protein density allow more stain to penetrate and appear darker. Magnification bar = 200 nm. Images from Weisel, J. W. *Biophys. Chem.* **2004**, *112*, 267–276, reproduced with permission.

the absorbance of the clot supernate at 280 nm or the release of [^{125}I]-labeled fibrin degradation products to assess the release of soluble degradation products, analyzing changes in turbidity, or using thromboelastographic measurements of lysing clots.[34]

Overall, it appears that although the lysis rate is influenced by the structural properties of the clot, other physical and chemical properties of the clot also influence its dynamic changes and therefore its lysis. These properties and the fibrinolysis process of a natural clot need to be considered when using fibrin for clinical applications. In fact, in bleeding situations or in tissue regeneration applications where fibrin is used as a delivery system and/or as a free scaffold for tissue growth as detailed later in the chapter, a challenge is to keep the fibrin clot stable long enough to reach hemostasis or allow tissue regeneration. Fibrinolysis of the clots will highly depend not only on the surgery site but also on the fibrin composition. The presence of preseeded cells in the fibrin clots in some tissue engineering applications will also accelerate the clot lysis.

Strategies have been explored to prolong the life of fibrin matrices, including their reinforcement through the use of synthetic polymers such as polyethylene glycol (PEG) and the addition of protease inhibitors.[35] For example, the use of calcium chloride and/or a fibrinolysis inhibitor such as aprotinin in fibrin sealant mixtures will increase the retention of the clot and is essential for its efficacy. However, although aprotinin is an efficient inhibitor of fibrin degradation, it rapidly diffuses out of fibrin matrices. Methods have been developed to prevent this diffusion. For example, Smith *et al.* showed prolonged presence of fibrin in a chick chorioallantoic

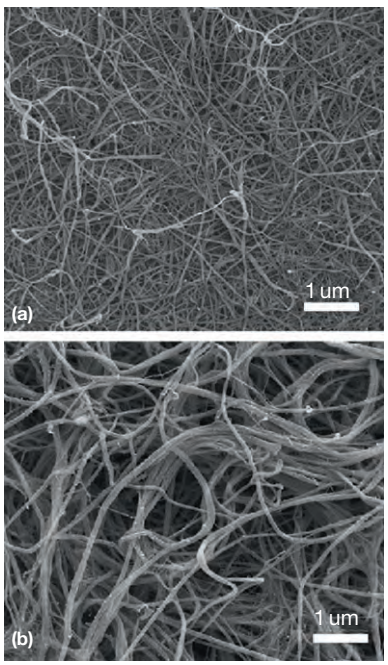

Figure 6 Effect of varying the thrombin concentration on fibrin clot structure. (a) 25 IU ml^{-1} of thrombin; (b) 0.25 IU ml^{-1} of thrombin (final concentrations). Fibrinogen complex concentration: 5 mg ml^{-1} (final concentration). Note the relatively thinner individual fibers and decreased overall porosity for the fibrin clot prepared with higher thrombin concentration (a). Images from Helgerson, S.; Seelich, T.; Diorio, J. P.; Tawil, B.; Bittner, K.; Spaethe, R. *Enc. Biomat. Biomed. Eng.* **2004**, *1*, 603–610, reproduced with permission.

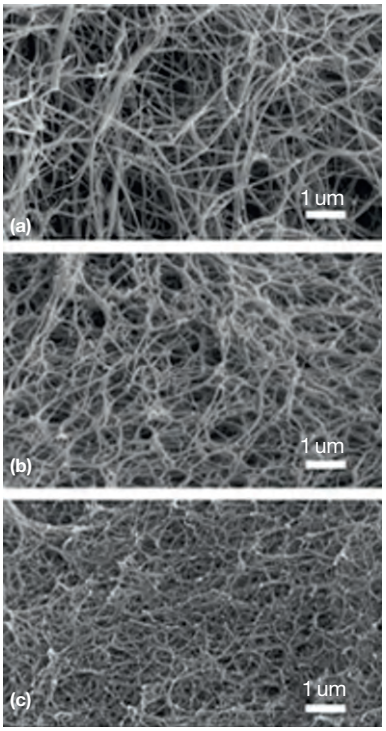

Figure 7 Effect of varying the salt concentration of the medium on fibrin clot structure. (a) 0.07 M; (b) 0.13 M; (c) 0.20 M. Fibrinogen complex concentration: 22.5 mg ml^{-1}; thrombin concentration: 75 IU ml^{-1} (final concentrations). Note the relatively thinner individual fibers and decreased overall porosity of the fibrin clot with increasing medium salt concentration. Images from Helgerson, S.; Seelich, T.; Diorio, J. P.; Tawil, B.; Bittner, K.; Spaethe, R. *Encyc. Biomat. Biomed. Eng.* **2004**, *1*, 603–610, reproduced with permission.

membrane invasion assay by chemically conjugating aprotinin to fibrinogen using a cysteine-based trifunctional cross-linker prior to gel formation.[36] Recently, Lorentz *et al.* reported an engineered aprotinin variant that could be immobilized within fibrin.[35] The authors showed that by recombinantly fusing aprotinin to a transglutaminase substrate domain from α2-plasmin inhibitor, the resulting variant (aprotinin-α2-plasmin inhibitor) could be covalently crosslinked into fibrin matrices during normal thrombin/factor XIIIa-mediated polymerization, leading to a 78% mass retention of the fibrin matrices submitted to physiological plasmin concentrations for 3 weeks *in vitro*. Fibrin matrices containing wild type aprotinin degraded completely within 1 week. These strategies constitute useful tools for possibly extending the applicability of fibrin-based biomaterials in tissue engineering as well as clinically.

2.217.2.4. Inherent Biological Properties

The first function of fibrin(ogen) in the blood coagulation process and wound healing is to rapidly control bleeding at the injury site. Once hemostasis is achieved, the fibrin clot serves as the basis of a complex matrix both to initiate and to support subsequent tissue repair[1,37] by providing a structural scaffold for the adhesion, proliferation, and migration of cells important in wound healing.

The exact mechanisms by which the different cell types interact with fibrin(ogen) are still not fully understood. However, some mechanisms have been proposed. Indeed, fibrin has peptide domains that facilitate cell adhesion to the clot, serving as binding sites for integrin receptors on cells involved in tissue repair.[1] The most established one is through the platelet integrin αIIbβ3 through the γ-chain C-terminal epitope containing Ala-Gly-Asp-Val (AGDV).[38] A number of cell attachment and adhesion epitopes have been proposed for fibrin(ogen). For example, RGD sequences found on the α-chains in human fibrinogen have been regarded as candidates for integrin-mediated cell binding to fibrinogen.[38,39] Another possible cell-interacting mechanism to fibrin may be based on the group of membrane proteins of the family of the cell marker CD44, which has been reported to be involved in cell proliferation, differentiation, migration, and signaling for cell survival.[38,40,41] In addition, the release of FpB from the β-chain of fibrinogen during fibrin polymerization results in the exposure of a new N-terminal peptide domain that will serve as a binding site for vascular endothelial cell surface receptor VE-cadherin, itself causing the vascular endothelial cells in injured blood vessels to migrate, proliferate, and differentiate to form new blood capillaries.[1] This angiogenesis process resulting in neovascularization is critical for the tissue regeneration, and will therefore also be critical for most tissue engineering applications.

The biological properties inherent to fibrin clots are not just limited to fibrin(ogen) but also include a complex mixture of other proteins that bind to fibrin matrix.[1,42] For example, factor XIIIa, which stabilizes the clot by covalently cross-linking fibrin monomers, also cross-links other plasma proteins to fibrin, such as plasma-derived proteins fibronectin, α2-antiplasmin, and plasmin activator inhibitor 2 (PAI-2), which help to control subsequent fibrinolysis of the clot. Residual fibronectin in fibrinogen, usually present in clots made of fibrin sealant preparations, as well as cross-linked plasma fibronectin might be responsible for cell-binding activity of the fibrin clot by providing specific receptor-binding sites for cells involved in wound healing, such as keratinocytes, fibroblasts, and vascular endothelial cells.[43]

Therefore, in addition to its favorable 3D structure as illustrated in previous paragraphs, fibrin also presents inherent biological properties that will be important for successful tissue regeneration. Moreover, these inherent biological properties can be enhanced by the addition of cells or bioactive molecules, for which fibrin can be used as a delivery system, as explained in the following section and summarized by Figure 8.

2.217.3. Fibrin Use as a Delivery System

2.217.3.1. Cell Delivery System

Fibrin sealants have been used for years to deliver autologous cells to various skin defects.[44] A study by Horch *et al.*[45] showed that the transplantation of actively proliferating and dividing human keratinocytes in a fibrin sealant matrix could be used in clinics for the treatment of chronic ulcers. A study by Kopp *et al.*[46] also showed the potential of a fibrin sealant matrix for delivering cultured human autologous keratinocytes and

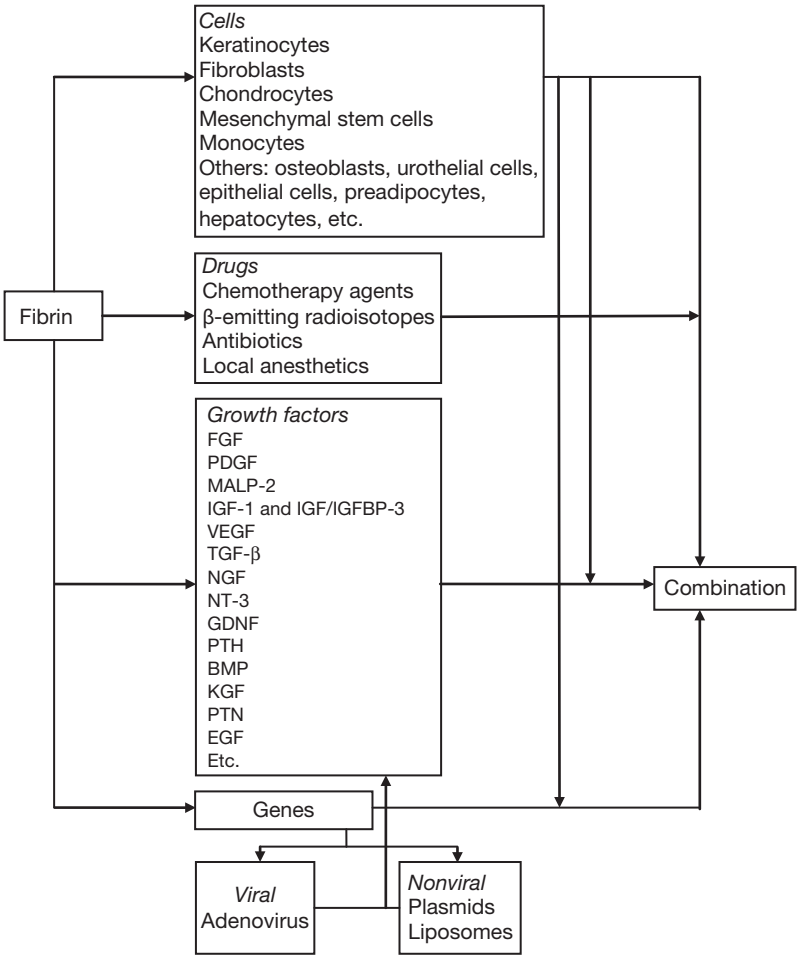

Figure 8 Schematic of the common cells and bioactive molecules delivered by fibrin scaffolds. Although the list is not exhaustive, all cells and bioactive molecules listed on this figure have been reported in the literature and illustrated in paragraph 3. Adapted from Breen, A.; O'Brien, T.; Pandit, A. *Tissue Eng. Part B* **2009**, *15*(2), 201–214.

leading to the reepithelialization of acute and chronic wounds. In an *in vitro* study, Tuan *et al.*[47] showed that fibroblasts seeded in fibrin gels synthesized collagen and remodeled the matrix into a collagen-rich granulation tissue-like matrix. When used as a delivery system for cultured keratinocytes and fibroblasts, fibrin sealants may actually provide similar advantages to those proven with conventional skin grafts,[48] and, at the same time, at least partially overcome some of the common disadvantages of standard sheet grafts such as uncertain attachment rate of cultured cells to the wound ground and difficulty in handling the grafts.[45]

Several groups have also reported on the use of fibrin as a delivery system for chondrocytes.[49–54] For example, a study by Homminga *et al.*[52] demonstrated that chondrocytes encapsulated in a fibrin sealant retained their morphology and synthesized matrix. Ameer *et al.*[49] showed a 2.6 times higher retention of synthesized glycosaminoglycans (GAG) when seeding pig chondrocytes in a biodegradable composite scaffold made of fibrin gel and polyglycolic acid (PGA) nonwoven mesh compared to a scaffold made of PGA only. Kirilak *et al.*[53] showed that fibrin sealant could promote the migration and proliferation of human articular chondrocytes, possibly via thrombin-induced protease-activated receptors-1 signaling. Dare *et al.*[51] showed that, when cultured in chondrogenic medium, fibrin-encapsulated C5.18 cells (a chondrogenic precursor cell line) elaborated an extracellular matrix containing type II collagen, as well as aggrecan, components of hyaline cartilage. A study by Pettersson *et al.*[54] showed that human autologous chondrocytes seeded in biodegradable macroporous gelatin microcarriers embedded in fibrin glue led to chondrocyte adhesion and expansion as well as extracellular matrix synthesis. However, this study also showed that the presence of the microcarriers was essential for the fibrin glue to support the structural takeover of extracellular matrix proteins produced by the embedded chondrocytes, as exclusion of the microcarriers resulted in unstable structures that dissolved before matrix formation could occur. In a study investigating whether a fibrin sealant could provide a suitable scaffold for *in vitro* generation of cartilage transplants using human mesenchymal stem cells (MSC), Baumgartner *et al.*[50] demonstrated that under chondrogenic differentiation conditions, especially under hypoxic conditions, stem cells seeded in the fibrin sealant differentiated into rounded chondrocyte-like cells with a chondrogenic phenotype.

Other studies investigated the use of fibrin for the delivery of other cell types such as osteoblasts,[55] urothelial cells,[56–58] tracheal epithelial cells,[57] preadipocytes,[57] and hepatocytes.[59] Those studies showed the potential of fibrin as a cell delivery vehicle for successful reimplantation of these different cells to reconstruct the tissue in which they are implanted.

Interestingly, some *in vitro* studies have shown that by simply varying the concentration of fibrinogen and thrombin, one could optimize the environment for delivering various cell types such as fibroblasts, keratinocytes, monocytes, and MSC.[60–64] For example, Cox *et al.*[61] reported that fibroblasts proliferated well within fibrin clots containing fibrinogen concentrations ranging from 5 to 17 mg ml^{-1} and thrombin concentrations from 1 to 167 IU ml^{-1}. In addition, the cells retained their morphology and growth characteristics after migrating out of the gels. When looking at the delivery of skin keratinocytes in fibrin, Harkin *et al.*[62] showed optimized keratinocyte cell growth in fibrin containing 1–3 mg ml^{-1} fibrinogen and 2–5 IU ml^{-1} thrombin. Mana *et al.*[64] reported that while all fibrin formulations analyzed supported monocyte proliferation, the highest cell proliferation was reached with a fibrinogen concentration between 26 and 50 mg ml^{-1} and a thrombin concentration of 250 IU ml^{-1} (final concentrations in the clots). The profiles of cell proliferation and cell adhesion were similar. Investigations of MSC proliferation within various fibrin formulations showed that lower fibrinogen concentrations favored a higher proliferation.[60,63,65] For example, Bensaid *et al.*[65] reported that a concentration of 18 mg ml^{-1} for the fibrinogen component and that of 100 IU ml^{-1} for thrombin were optimal for human MSC spreading and proliferation. The authors also showed that MSC were able to migrate out of the fibrin gels and invade a calcium carbonate-based ceramic scaffold (coral) implanted within the peritoneal cavity of nude mice, supporting the concept of using fibrin sealant as a delivery system for human MSC.[65] When looking at the osteogenic differentiation of the seeded MSC with no additional osteogenic agent in the culture medium, Catelas *et al.*[60] reported that increasing the concentration of fibrinogen component favored early osteogenic differentiation of the cells, as demonstrated by a higher expression of alkaline phosphatase activity. However, the rather small size of calcium phosphate nodules and low expression of specific osteogenic genes revealed that the cells were not fully differentiated. A study from Trombi *et al.*[66] also analyzed the capability of fibrin gels to support osteogenic differentiation of MSC. The authors reported an increase in alkaline phosphatase activity, calcium phosphate deposition, and osteopontin expression in samples cultured with osteogenic medium and concluded on the potential of fibrin gels to support osteogenic differentiation. A study from Zhang *et al.*[67] showed that PEGylation of fibrin patch made of 10 mg ml^{-1} fibrinogen and 100 IU ml^{-1} thrombin (final concentrations in the clots) could increase the viability and differentiation of MSC isolated from the sternum of healthy pigs. More recently, the same group also showed that modifying fibrinogen with various PEG derivatives, which resulted in different physical and mechanical characteristics of the fibrin matrix, affected the differentiation of MSC towards the endothelial phenotype.[68] Finally, a recent study by Huang *et al.*[69] demonstrated that fibrin could regulate MSC gene expression of phenotypic markers across multiple lineages. However, the effect of fibrin appeared to be limited as MSC did not differentiate into fully mature cells considering the absence of distinctive immunofluorescence expression of mature lineage-specific markers after 12 days.

Despite differences in the cell and/or fibrin sources that have been reported to affect the results,[70] all these studies support the capability of fibrin to be used as a cell delivery system and show the potential of fibrin as a biomaterial for various cell-based therapy or tissue engineering applications, which will be detailed later in this chapter.

2.217.3.2. Drug and Growth Factor Delivery System

2.217.3.2.1. Drug delivery system

Systemic administration of antibiotics is generally adequate but in some situations, such as severe trauma and large-area burns, local delivery of high levels of antibiotics may be desirable or necessary.[7] Fibrin has been used as a delivery system for chemotherapy agents and antibiotics for some years, but the challenge has always been to sustain the delivery of the drug for adequate periods of time.[7] Therefore, different forms of fibrin have been investigated, such as microparticles, fibrin-coated drug particulates, fibrin discs, drug-containing beads embedded within fibrin gels, or fibrin sheets with the entrapped drug.

In the oncology arena, fibrin gels have been used for the delivery of chemotherapy agents such as carboplatin to the retina,[71,72] or for delivery of beta-emitting radioisotopes in microspheres in the treatment of brain tumor.[73] A study by Yoshida *et al.*[74] also demonstrated the importance of the hydrophobicity of the anticancer drugs influencing their release from fibrin gels. The release rate of various drugs, such as mitomycin C, fluorouracil, and enocitabine, was evaluated. While the first two were quickly released from fibrin gels, whether or not they contained aprotinin, the last one was gradually released from fibrin-containing aprotinin. The authors concluded that the release rate of each drug from fibrin containing aprotinin correlated with the drug hydrophobicity and that lipophilic anticancer drugs should be used to favor a sustained release from fibrin.

With regard to the treatment of localized infections, various studies have been looking at the use of fibrin to deliver tetracycline, erythromycin, cefazolin, ciprofloxacin, aminoglycoside, cefotaxim, mezlocillin, or even vancomycin alginate beads. For example, Woolverton *et al.*[75] evaluated the use of fibrin discs to deliver tetracycline for the treatment of peritoneal infection initiated with *Staphylococcus aureus (S. aureus)* in rats and mice. Results showed that the mice prophylactically treated with fibrin sealant-tetracycline 2 days prior to an infection with *S. aureus* cleared the infection, resulting in 100% survival. In addition, the same treatment in rats showed no detectable serum tetracycline levels. A study by Kumar *et al.*[76] also evaluated the release of soluble tetracycline, but using a freeze-dried fibrin disc. The *in vitro* release kinetics of the drug in phosphate, buffered saline (PBS) solution and serum were compared. Results showed that the release rate of tetracycline from the fibrin disc into serum remained steady from day 1 to 12, whereas the delivery of the drug from the discs into PBS was found to be high for up to the third day, followed by a sharp decline. The authors concluded that fibrin disc may be a suitable candidate as a drug delivery implant for short-term use.

A study by Tredwell *et al.*[77] evaluated the encapsulation, stability, and controlled release of erythromycin and cefazolin from fibrin sealants. Results showed that erythromycin was released slowly from the fibrin clots over the first 2 h and then degraded rapidly. Cefazolin, however, appeared to be very stable over a period of 2 days, suggesting the potential use of cefazolin-loaded fibrin sealants as an antibiotic delivery system postoperatively. A recent study by Tsouvakas *et al.*[78] investigated the *in vitro* release of ciprofloxacin from acrylic bone cement and fibrin clot for the treatment of bone infections. Results revealed that the diffusion of ciprofloxacin from bone cement was rapid at first and decreased gradually over a period of 365 days. The release from fibrin clots was high up to 65 days, that is, enough time to treat a bone infection. It is, however, surprising that the authors were able to maintain the fibrin clots *in vitro* for such a long time. In a previous study, the same authors had reported that ciprofloxaxin–fibrin clot complexes usually disintegrated after 60 days,[79] which was already surprisingly long. Also in the context of bone infection treatment, Hou *et al.*[80] evaluated the *in vitro* use of fibrin for the simultaneous codelivery of vancomycin alginate beads to treat the infection and MSC to promote bone formation. Results showed that cell behavior was affected by the addition of the vancomycin beads. Interestingly, the addition of the beads seemed to increase the osteogenic differentiation of the MSC, as depicted by a higher ALP activity, and higher osteogenic gene expression. With regard to the antibiotic release kinetics, results revealed that vancomycin concentrations remained above the breakpoint sensitivity for 22 days.

Finally, Zhibo and Miaobo[81] recently reported on the use of fibrin to deliver lidocaine as a local anesthetic to reduce pain after subpectoral breast augmentation. The positive results of this study suggested the possibility of using fibrin for local anesthetic delivery. However, the study only included a limited number of patients, and therefore, results need to be confirmed through a larger randomized, double-blind study.

2.217.3.2.2. Growth factor delivery system

Although fibrin possesses inherent biological properties that make it particularly attractive as a cell delivery system for tissue regeneration, the incorporation of an exogenous growth factor can enhance and accelerate tissue repair through a synergistic effect. Many studies have been reported on the use of fibrin for the delivery of growth factors. A comprehensive review detailing some of these key studies has been provided by Breen *et al.*[15]

For example, a study by Pandit *et al.*[82] looking at the effects of the addition of fibroblast growth factor (FGF)-1 in fibrin for wound healing in a rabbit model showed that the combination of FGF-1 and fibrin improved the mechanical properties of the healed tissue compared to fibrin alone or growth factor alone. Mogford *et al.*[83] showed that the combination of fibroblasts and platelet-derived growth factor (PDGF)-BB delivered using fibrin sealant enhanced ear cutaneous wound healing in the rabbit. Ucuzian *et al.*[84] showed that the delivery of PDGF-BB and FGF-2 (also known as basic FGF (bFGF)) could promote smooth muscle cell invasion into fibrin gels *in vitro*. In a study on bone regeneration, Park *et al.*[85] showed that fibrin delivery of bFGF and osteoblasts resulted in two and nine times more bone formation and calcium content, respectively, than fibrin delivery of osteoblasts alone. A study by Cole *et al.*[86] showed that monocytes seeded on fibrin containing macrophage activator lipoprotein peptide-2 (MALP-2) secreted more cytokines such as interleukin-6 and tumor necrosis factor-α, as well as chemoattractants such as macrophage inflammatory protein-1α and monocyte chemoattractant protein-1, than monocytes seeded on fibrin with no added MALP-2. Finally, a study by Bhang *et al.*[87] using fibrin gel as a delivery vehicle to release bFGF and human bone marrow stromal cells in rat traumatic brain injury showed that the addition of bFGF enhanced neural tissue regeneration compared to the control group (fibrin with human bone marrow stromal cells alone).

Some of the growth factors used for tissue regeneration applications, including bFGF,[88] the insulin-like growth factor-1 (IGF-1)/IGF-binding protein-3 complex (IGFBP-3) (IGF-1/IGFBP-3),[89] and vascular endothelial growth factor (VEGF) isoform 165[90] specifically bind to fibrin(ogen). Therefore, fibrin acts as a natural reservoir for such growth factors.[1,91] The natural fibrin(ogen)-binding affinity of these growth factors allows for their controlled release and delivery from fibrin-based gels as demonstrated both *in vitro*[91,92] and *in vivo*.[93] In this case, the growth factors are released primarily upon cellular infiltration of the scaffold and subsequent scaffold degradation. For example, a study by Wong *et al.*[91] showed a slower release of bFGF and VEGF-165 (added prior to the formation of the fibrin sealant clots) compared to VEGF-121 that is not binding to fibrin(ogen), or at least not binding to the same extent, and that is readily released from the clots by free diffusion. The authors suggested that VEGF-165 binding to fibrin(ogen) and to fibronectin contained in fibrin may be associated with the 44-residue C-terminal domain that was previously shown to contain the heparin-binding site to VEGF-165. This study suggested a controlled release of bFGF and VEGF-165 from fibrin clots. Catelas *et al.*[92] also reported the possibility of controlling the release of transforming growth factor-β1 (TGF-β1) by varying the concentrations of fibrinogen component and thrombin. The authors showed that increasing the concentration of the fibrinogen component decreased TGF-β1 release. Indeed, the cumulative release reached 75% of the initially added amount after 10 days *in vitro* when using 5 mg ml^{-1} of fibrinogen component and 2 IU ml^{-1} of thrombin. On the other hand, it only reached approximately 50% when using a fibrin gel formulation containing 25 mg ml^{-1} of fibrinogen component and the same amount (2 IU ml^{-1}) of thrombin. These results suggested a binding affinity of TGF-β1 with fibrin(ogen), possibly related to factor XIII content. The released TGF-β1 remained biologically active as demonstrated by its chondrogenic effects on human MSC cultured in 2D with fibrin gel supernatants containing the released TGF-β1.

Several linkage approaches have been studied to enhance the retention of growth factors. As described by Bhang *et al.*,[94] a possible approach is to incorporate free heparin into the fibrin matrix to sequester and protect the growth factors, mimicking the natural extracellular matrix.[15] Indeed, the authors showed that the rate and duration of nerve growth factor (NGF) release were controlled by heparin and by the concentration of fibrinogen and thrombin in the gels.[94] The authors also showed that the release was lower when adding heparin or increasing fibrinogen and thrombin concentrations, with fibrinogen concentration having the largest effect.

Released NGF was biologically active as depicted by a higher viability and differentiation of pheochromocytoma (PC12) cells cultured with medium containing released NGF. Other strategies have been carried out to attach heparin-binding domains to the fibrin matrix through the use of factor XIIIa substrate as explained later in this section. Another linkage approach was recently reported by Zhao *et al.*[95] Aiming to improve therapeutic neovascularization and wound repair, the authors fused bFGF with the fibrin-peptide Kringle1 (K1), derived from human plasminogen. The resulting recombinant K1bFGF showed high fibrin and plasma-clot-binding affinity. It also induced neovascularization and improved wound healing when applied in wound sites. The authors then developed a fibrin-scaffold/K1bFGF system, which promoted localized neovascularization and tissue regeneration when implanted subcutaneously. The same authors recently reported similar results when using the Kringle4 domain (K4).[96] Finally, Drinnan *et al.*[97] reported on a multimodal release system of PDGF-BB and TGF-β1 using PEGylated fibrin gels to potentially stabilize neovascularization in the treatment of ischemic tissue. While PDGF-BB was entrapped during thrombin-mediated crosslinking leading to a diffusion-controlled release, TGF-β1 was conjugated through a homobifunctional amine reactive PEG linker as well as physical affinity with the fibrin matrix. The authors showed that by modulating the molar ratio of PEG to fibrinogen, the release rate of TGF-β1 could be controlled without affecting the release of PDGF-BB.

In the case of VEGF, the protein domain of the VEGF-165 isoform responsible for conferring the binding affinity to fibrin(ogen) has been identified by Helgerson and coworkers.[98] The VEGF gene consists of eight exons that give rise to different protein isoforms (VEGF-121, VEGF-145, VEGF-165, VEGF-183, VEGF-189, VEGF-206) as a result of alternative splicing of the pre-mRNA transcript.[99,100] The activity of these VEGF isoforms is associated with the N-terminal domain common to all the isoforms, that is, the VEGF-121 protein sequence. The alternate domain sequences contained in the other VEGF isoforms confer increasing binding affinity of the proteins for extracellular matrix proteins as evidenced for heparin and heparin sulfate *in vitro*.[101] The observation that VEGF-165 was released more slowly from fibrin-based clots compared to VEGF-121[91] led to the hypothesis that the C-terminal domain sequence of VEGF-165 coded by the VEGF gene Exon 7 was responsible for fibrin(ogen) binding. Subsequently, a recombinant fusion protein that added the C-terminal domain of VEGF-165 to leptin, a protein with no significant heparin or fibrin(ogen)-binding affinity, was designed and expressed.[98] This engineered protein was shown to have binding affinity for heparin, and also, to be released from fibrin-based clots with a controlled release kinetic.

Additional methods have been developed to modify the fibrin-based matrix with the intent to control the time and extent of delivery of growth factors that do not naturally bind to fibrin(ogen), or at least not strongly. In particular, covalent linkages between the growth factors and fibrin gels have been used extensively to control the growth factor release.[102] Some of these methods include the design of a bi-domain peptide with a factor XIIIa substrate in one domain and a bioactive peptide in another domain, both covalently incorporated into fibrin gels during coagulation through the action of the transglutaminase factor XIIIa as described by Schense and Hubbell.[103] In this study, the authors determined the cross-linking characteristics for two bi-domain peptides with factor XIIIa substrates based on fibrinogen, as well as one bi-domain peptide with a substrate sequence based on α2-plasmin inhibitor, and another one with a nonbiological oligolysine substrate. Results showed that each of these peptides was able to cross-link into the fibrin gels during coagulation, without changing the structural characteristics of the resulting gels. The bioactivity of the incorporated active factors was tested in a neuronal culture model using two bioactive sequences (RGD and DGEA) and one inactive control sequence (RDG). Results showed that each of the tested peptides influenced the extension of neurites from chicken dorsal root ganglia. Further use of this approach has been reported for covalent incorporation of other molecules such as lamin peptides, VEGF-121, and ephrin B2.[104–106]

Utilizing this method of covalently cross-linking bi-domain peptides to fibrin matrices using the transglutaminase activity of factor XIIIa, Sakiyama-Elbert and Hubbell[107] created an affinity-based delivery system sequesting growth factors inside the matrix through the use of a bi-domain heparin-binding peptide. One domain within this heparin-binding peptide consists of a transglutaminase substrate to facilitate peptide cross-linking into fibrin matrices, while the other domain consists of a heparin-binding domain that allows non-covalent immobilization of heparin to the peptide. The authors used bFGF as an example of a heparin-binding growth factor, and showed enhanced neurite extension relative to unmodified fibrin. The use of this system was further tested for other growth factors with heparin affinity, such as neurotrophin-3 (NT-3) in the context of spinal cord injury.[108] However, although such scaffolds allowed growth factor control delivery thereby enhancing the initial regenerative response by increasing neuronal fiber sprouting and cell migration into the lesion, they were not sufficient to produce functional motor recovery.[109] In a more recent study using a subacute rat model, Johnson *et al.*[110] showed promising results for functional recovery following spinal cord injury by demonstrating enhanced survival of embryonic stem-cell derived neural progenitor cells as well as differentiation of the cells into neurons when embedding them in fibrin scaffolds containing NT-3, PDGF and the heparin-binding delivery system. Sakiyama-Elbert and Hubbell[111] also reported on the controlled release of NGF from their fibrin-based heparin-binding delivery system. Surprisingly, in that study, the release rate of NGF reported by the authors showed a higher initial burst release and was not lower than that found by Bhang *et al.*[94] using free heparin. However, it is likely that the difference in the concentrations of fibrinogen and thrombin (3.5 vs. 94.3 mg ml^{-1} fibrinogen for Sakiyama-Elbert and Bhang *et al.*, respectively; and 2 vs. 33.3 IU ml^{-1} thrombin for Sakiyama-Elbert and Bhang *et al.*, respectively) accounted for the differences in the release kinetic profiles between the two studies. More recent studies from Sakiyama-Elbert's group showed that the delivery of NGF and glial-derived neurotrophic factor (GDNF) from fibrin matrices containing the bi-domain heparin-binding peptide could promote peripheral nerve regeneration[112,113] and selectively promote motor neuron regeneration as well as functional recovery in a rat sciatic nerve model.[114]

Finally, utilizing the multidomain peptide technology, Sakiyama-Elbert *et al.* designed a fusion protein system consisting of a factor XIIIa substrate and a β-NGF sequence, but with the addition of a plasmin substrate sequence linker.[115] The theory behind the incorporation of a plasmin substrate sequence linker was that such a linker would enable cleavage by endogenous plasmin, resulting in a release on cell demand of the bioactive molecules *in situ*.[115,116] Such modified fibrin system incorporating β-NGF enhanced neurite extension from embryonic chick dorsal root ganglia by 50% compared to the use of soluble native β-NGF alone. In the bone regeneration field, a fusion protein system was also used to deliver bone morphogenetic protein (BMP)-2 and parathyroid hormone (PTH)1–34.[116–118] In a study comparing the retention of the engineered human recombinant nonglycosylated BMP-2 fusion protein (referred as TG-pl-BMP-2 with TG denoting a transglutaminase-sensitive binding domain and pl the plasmin-sensitive linking domain) with the retention of glycosylated BMP-2 without using the fusion protein technology, Schmoekel *et al.*[118] reported that the retention of the TG-pl-BMP-2 was higher than that of the glycosylated BMP-2 alone (60% ± 5% vs. 27 ± 1% after 60 h and 50 wash volumes). The authors also showed a higher healing at 3 weeks in the rat calvaria model when using 1 μg of TG-pl-BMP-2 (81 ± 5%) compared to the healing observed when using 1 μg of glycosylated BMP-2 (46 ± 14%). Interestingly, however, in a previous separate study, the same authors had reported a retention rate of 83 ± 6% after 60 h and 50 wash volumes, and a bone healing of 74 ± 4% in the rat model at 3 weeks with nonglycosylated BMP-2 without the use of the fusion protein technology.[117] Therefore, the comparison of the two separate studies shows that the retention rate of nonglycosylated BMP-2 without using the fusion technology was higher than that using the fusion technology (83 ± 6% vs. 60 ± 5%, respectively), while the induced bone healing at 3 weeks in the rat model was comparable (74 ± 4% vs. 81 ± 5%, respectively). This would mean that using the fusion protein technology was, in the case of nonglycosylated BMP-2, not increasing the retention of the protein, nor significantly improving bone healing in rat calvaria. Results reported by the authors in a canine pancarpal arthrodesis were also similar, with 100% of the dogs demonstrating clinical bridging within 12 weeks when using the TG-pl-BMP-2,[118] versus 88% when not using the fusion protein technology.[117]

Other methods aiming to control the time and extent of growth factor delivery are looking into modifying the bioactive substance itself, be it therapeutic proteins, drugs, or DNA as explained in the following section.

2.217.3.3. Gene Delivery System

As described above, fibrin constitutes an attractive carrier system for recombinant growth factors that have been used successfully to promote and improve tissue healing in various clinical applications. However, growth factor applicability remains restricted by their limited commercial availability, high costs, as well as their limited half-lives *in vivo*, requiring high and repeated doses that are associated with undesired systemic side effects.[119] Some studies have been looking at the use of fibrin-encapsulated liposomes as a protein delivery system.[120,121] In general, such studies revealed that the protein-filled liposomes protect the protein during fibrin polymerization process and are retained in fibrin until its degradation by plasmin. Therefore, such technology helps in keeping the protein stable and prolonging its biological activity.

As gene therapy represents an alternative to protein-based therapies, an alternative method to deliver growth factors consists of transfecting or transducing their respective cDNAs under the control of suitable promoters in target cells *ex vivo* or *in vivo*.[119] Recent studies have been reported on fibrin scaffold efficacy for gene vector delivery, either viral or nonviral. A comprehensive review of some of those studies has been provided by Breen *et al.*[15]

2.217.3.3.1. Viral delivery

Of all the viruses developed for use in gene therapy, recombinant adenoviruses represent an appealing gene delivery method, when considering viral systems. However, some limitations of their use include an inflammatory response to the vector and the transient nature of transgene expression,[122] which can be overcome, at least to some extent, by the use of an appropriate scaffold. Fibrin has recently been evaluated for its use as such a scaffold. Applications that have been evaluated include bone, esophagus, vasculature, and dermal ulcer,[15] all showing promising results. For example, a study by Teraishi *et al.*[124] evaluated the endoscopic local delivery of recombinant adenoviruses in aerosolized fibrin glues through a multiluminal catheter. Results showed that such technique could be optimal for gene transfer into epithelial cells in the mucosal surface. A study by Schek *et al.*[123] showed that the bioactivity of an adenovirus expressing β-galactosidase and suspended in medium or collagen decreased to half-maximal activity after 15 h incubation, whereas the virus suspended in fibrin exhibited a threefold extension of bioactivity and did not reach half-maximal activity for 45 h. The study also reported bone formation after 4 weeks following intramuscular implantation of BMP-7 expressing adenovirus in collagen, fibrin, or liquid in nude mice. However, bone formation occurred in 80% of muscles with the adenovirus implanted with collagen or fibrin, compared to 50% of muscles with the adenovirus implanted with liquid. Fibrin also led to significantly larger ossicles. A study by Breen *et al.*[125] investigating the use of fibrin to enhance the delivery of adenovirus encoding endothelial nitric oxide (NO) synthase (eNOS), one of the enzymes responsible for NO production, showed more NO production and enhanced healing of diabetic wound sites, normally characterized by NO deficiency, when using fibrin containing the adenovirus encoding eNOS. Another study by the same authors analyzed whether fibrin could deliver a low single dose of a viral vector to a wound site, without compromising transfection efficiency.[126] Groups with fibrin containing adenovirus encoding β-galactosidase, fibrin alone, adenovirus alone, and no treatment were studied using the rabbit ear ulcer model. Results showed that fibrin helped in the delivery of a low-dose viral vector, thereby avoiding a chronic inflammation response and allowing superior transfection than the viral vector alone.

Another study of Breen *et al.*[122] showed that fibrinogen and thrombin concentrations could affect the release of the adenovirus. Different fibrin formulations were analyzed incorporating an adenoviral vector encoding β-galactosidase.

Results showed that the optimum concentrations of fibrinogen and thrombin were 60 mg ml^{-1} and 4 IU ml^{-1}, respectively, in order to sustain a release of the adenovirus up to 192 h.

Finally, in order to avoid direct exposure to viral vectors, some studies have been reported on the combined use of cell and gene therapy. In this case, cells are manipulated with the vector and are embedded within the fibrin scaffold. For example, in the attempt to promote skin wound healing, Escamez *et al.*[127] compared the efficacy of keratinocyte growth factor (KGF)-adenoviral gene-transferred human fibroblasts embedded in fibrin, with KGF gene transfer by adenoviral vector immobilized in fibrin with no cells, and with KGF gene transfer by intradermal adenoviral injection. Results showed that the use of genetically modified fibroblast-containing matrix as an *in situ* protein bioreactor was highly reproducible and was leading to a significant improvement of the overall healing process.

2.217.3.3.2. Nonviral delivery

In terms of nonviral delivery, various studies have been reported on plasmid delivery and liposome-based vector delivery from fibrin. Indeed, because of low transfection efficiency of naked plasmid injections, polymer matrix such as fibrin has been examined.[128] By encapsulating the plasmid in the fibrin matrix, the DNA would be released more slowly as the matrix degrades, thus increasing chances of plasmid–cell interaction and transfection efficiency.[129] Using such technology in a rabbit hind-limb ischemia model, Jozkowicz *et al.*[130] tested the angiogenic potency of plasmid encoding human VEGF-165 (pSG5-VEGF165) entrapped in fibrin sealant or dissolved in PBS. Results showed that injection of pSG5-VEGF165 into ischemic adductor muscle led to synthesis of human VEGF and increased the number of capillaries, but, surprisingly, the mode of delivery did not influence the results. A study by Michlits *et al.*[131] also reported on the topical fibrin-mediated administration of a VEGF-A plasmid to the wound bed of rat abdominal skin flaps to evaluate if such a method could protect the tissue from necrosis. Results showed that flaps treated with fibrin-mediated VEGF plasmids in the presence of uptake-enhancing Lipofectamine transfection reagent increased significantly the flap survival 7 days postoperatively, with markedly elevated tissue perfusion and enhanced tissue VEGF-A protein expression. Fibrin delivery of plasmid VEGF-A without Lipofectamine, however, was not beneficial. A study by Christman *et al.*[129] examined the use of pleiotrophin (PTN) plasmid in fibrin for the treatment of ischemic myocardium. The authors demonstrated that delivery of PTN plasmid in fibrin increased neovasculature formation compared to injection of the naked plasmid in saline solution.

Nonviral delivery studies have also been conducted using cells as the gene vector. For example, Andree *et al.*[132] inoculated a fibrin matrix with human epidermal growth factor (EGF) expression plasmid and human keratinocytes. Transfection rates were reported to be up to 100-fold higher compared to controls containing no EGF expression plasmid. Transplantation of such constructs to full-thickness wounds in athymic mice led to a 180-fold increase in EGF concentration compared to controls for up to 7 days. A study by Lee *et al.*[133] analyzed the feasibility of using fibrin as a scaffold for normal Rattusnorvegicus kidney (NRK) cells carrying BMP-2 for rabbit spinal fusion. Cells were first transfected with plasmid cytomegalovirus (pCMV)-BMP-2 vectors by FuGENE6, a multicomponent nonviral reagent that forms a complex with DNA and can then be used to transport the complex into mammalian cells. They were then encapsulated and evenly suspended in the fibrin scaffold before being implanted. Results showed prominent new bone formation in 67% animals and moderate new bone formation in the remaining 33%, compared to no new bone formation in the control group (gelatine sponge). The authors concluded that fibrin gel could encapsulate pCMV-BMP-2 transfected NRK cells and deliver them successfully in lumbar spine spaces in rabbits, with no sign of rejection. Hence, fibrin gel appeared to be a promising scaffold for future gene therapy applications.

In a study looking at generating a lyophilized gene-vector-doted fibrin glue, Schillinger *et al.*[119] examined clotting parameters, vector release, and structural characteristics after formulating a copolymer-protected polyethylenimine (PEI)–DNA vector, naked DNA, and PEI–DNA with the lyophilized fibrinogen component of a fibrin sealant. Reporter and growth factor gene delivery to primary keratinocytes and chondrocytes was examined *in vitro*. Results showed that the material containing copolymer-protected PEI–DNA vector was suitable to mediate growth factor gene delivery to primary keratinocytes and chondrocytes admixed before fibrin clotting. Copolymer-protected PEI–DNA vectors also remained tightly immobilized over extended periods of time (0.29% release per day) compared to naked DNA that was rapidly released from fibrin clots (>70% within the first 7 days). *In situ* BMP-2 gene transfection and subsequent expression in chondrocytes grown in fibrin clots containing BMP-2-copolymer-protected PEI–DNA vectors also resulted in alkaline phosphatase expression as well as in an increased extracellular matrix formation when the chondrocyte-colonized clots were cultured in medium supplemented with 50 μg ml^{-1} ascorbic acid *in vitro*. This study showed that fibrinogen could possibly be used in clinics as the gene vector carrier that could be lyophilized and mixed with thrombin to form a fibrin clot containing a gene vector.

Finally, using lipoplexes, NIH-3T3 cells, and plasmids encoding for luciferase, des Rieux *et al.*[134] analyzed the effects of two different *in vitro* models on cell transfection: encapsulating the cells in the fibrin gels versus seeding the cells onto the fibrin gels. Results showed that transfection was dependent on fibrinogen and DNA concentrations. In the case of encapsulated cells, all cells had intracellular plasmid and transgene expression persisting for at least 10 days, with greatest levels at day 1. When seeding cells onto the fibrin gels, the expression levels were less, but increased throughout the culture period.

2.217.4. Fibrin in Tissue Engineering Applications

An appropriate biomatrix is a key structural element for tissue regeneration since a provisional extracellular matrix is required to support the highly organized remodeling and repair processes involved in forming new tissue.[1] As explained earlier in this chapter, fibrin provides a biocompatible physical structure and many of the important

biological properties needed for successful tissue regeneration. It can, therefore, be used as a biocompatible matrix in addition to being used as a delivery system for cells or bioactive molecules. Fibrin matrix also allows a uniform distribution of the cells and nutrients throughout the scaffold, which remains a critical challenge in many tissue engineering applications that require cell seeding of the scaffolds. Finally, fibrin matrix is readily remodeled and resorbed through normal fibrinolytic processes as cells deposit the tissue-specific extracellular matrix components during the regeneration of functional tissues, making it an attractive platform for tissue engineering applications.

Some of the tissue engineering applications using fibrin as a starting matrix include vascular grafts and cardiovascular tissues, bone, cartilage, neurite regeneration, and others, as detailed below.

2.217.4.1. Vascular Tissue Engineering

Examples of studies using cell, growth factor, and/or gene delivery to induce angiogenesis and neovascularization have been presented when reviewing fibrin as a delivery system (Section 2.217.3). The present section illustrates some examples of the use of fibrin for vascular tissue engineering (i.e., vascular grafts and engineered tissues).

2.217.4.1.1. Vascular grafts

Small-caliber vessels constructed from synthetic materials for coronary bypass or peripheral vascular repair have been reported to have poor intermediate and long-term patency rates, probably because of thrombogenic occlusion of the lumen caused by the blood-contacting surface.[135] Autologous grafts remain the standard for small-caliber vessel replacement procedures, but they are not an option for some patients with severe pathological conditions. The development of tissue-engineered grafts is therefore promising. Aper *et al.*[136] reported on the use of fibrin and a polyglactin mesh seeded with endothelial cells and myofibroblasts for engineering a vascular graft. Results showed that a hierarchically organized vessel wall structure could be achieved with this combination. However, the layer thickness of the viable vascular structure was limited and remained to be investigated. Tschoeke *et al.*[135] recently developed a small-caliber vascular graft made of a bioabsorbable, macroporous poly(L/D) lactide 96/4 [P(L/D)LA 96/4] mesh combined with fibrin. The authors tested the graft seeded with arterial smooth muscle cells/fibroblasts and lined with endothelial cells in a bioreactor. After 21 days in culture, cells deposited extracellular matrix proteins into the graft wall, with a significant increase in both cell number and collagen content. A luminal endothelial cell lining was also evidenced by Von Willebrand factor staining. The same group then reported promising results in a sheep carotid artery model for up to 6 months using such vascular composite graft seeded with autologous arterial-derived cells and submitted to mechanical conditioning in a bioreactor prior to implantation.[137]

Some studies demonstrated the importance of mechanical stimulation when developing small-diameter vascular grafts. For example, a study by Cummings *et al.*[138] analyzed the mechanical properties of constructs made of collagen, fibrin, and 1:1 mixtures of collagen and fibrin in order to evaluate the use of fibrin as an alternative, or additional matrix for engineered blood vessels. The authors showed that the properties of engineered vessels could be modulated by the application of mechanical stimulation. Pure collagen had the highest linear modulus and pure fibrin had the lowest. The ultimate tensile stress was strongly dependent on the degree of gel compaction, which was increased by the application of cyclic mechanical strain. Collagen–fibrin mixtures at $2\,mg\,ml^{-1}$ total protein content showed the highest values. A study by Stekelenburg *et al.*[139] also showed that dynamic conditioning enhanced the mechanical properties of the grafts engineered using a fast-degrading PGA scaffold coated with poly-4-hydroxybutyrate combined with fibrin gel and seeded with myofibroblasts. Finally, using a pulsed flow-stretch bioreactor in which fibrin-based grafts seeded with fibroblasts were subjected to cyclic distension and transmural flow, Syedain *et al.*[140] showed extensive remodeling of the grafts into circumferentially-aligned tubes of collagen and other extracellular matrix, with a compliance comparable to native arteries.

2.217.4.1.2. Engineered cardiovascular tissues

Some *in vivo* animal studies have shown promising results when using fibrin as a carrier system for cell delivery and/or growth factors to restore injured heart muscles. For example, transplanted skeletal myoblasts or cardiomyocytes using fibrin sealant have been shown to survive in myocardial infarction area and improve heart function in rats with myocardial ischemia.[141,142] Using a porcine model of post-infarction left ventricular remodeling, Xiong *et al.*[143] recently showed that a fibrin patch-based transplantation of human embryonic stem cell-derived vascular cells (endothelial cells and smooth muscle cells) led to a significant cell engraftment, accompanied by a significant increase of neovascularization and left ventricular contractile functional improvement, which in turn resulted in a significant reduction of regional wall stress and infarct size.

Other studies have been exploring the use of fibrin to generate a tissue construct *in vitro*. For example, a recent study by Divya and Krishnan[144] showed that the combination of fibrin with GAG, hyaluronic acid, and heparin sulphate induced endothelial cell growth and extracellular matrix remodeling, with simultaneous degradation of the fibrin matrix and deposition of collagen IV and elastin. The authors concluded that this combination may be suitable for generating a cardiovascular tissue *in vitro*. A study by Montano *et al.*[145] also showed promising results for engineering prevascularized matrices. Using a 3D culture system consisting of human microvascular endothelial cells seeded into fibrin-based hydrogels, the authors were able to demonstrate capillary lumen formation, followed by the generation of intracellular vacuoles, successive fusion of these vacuoles, and finally the formation of a continuous lumen. The transplanted prevascularized matrices onto the back of immunoincompetent rats showed that mural cells recruited from the underlying recipient mesenchyme stabilized the newly formed vessels. However, to be used for reconstruction of tissue defects, engineered grafts need to be axially vascularized to enable transplantation without graft loss due to hypoxia.[146] Promising results in generating such a tissue have been reported using an

arteriovenous loop (AV-loop) embedded in an isolation chamber filled with fibrin matrix in the rat,[147] and more recently in larger animal models such as the sheep.[146]

2.217.4.2. Bone Tissue Engineering

Although some studies reported no direct osteoinductive property of fibrin sealant when implanted alone in dogs[148] or in rats,[149] other studies reported a stimulation of osseous repair in osteochondral fractures sealed with fibrin sealant in dogs[150] compared to fractures fixed with pins.

The suitability of fibrin as a cell delivery system as described earlier in this chapter represents a great potential for bone formation if fibrin is seeded with osteoprogenitor cells and induces their differentiation before their release. By injecting cultured periosteal cells with fibrin glue into the subcutaneous space on the dorsum of athymic nude mice, Isogai *et al.*[151] showed the feasibility of initiating site-directed formation of bone structures at heterotopic tissue sites. The fibrin carrier contained 64 mg ml^{-1} of fibrinogen and 50 IU ml^{-1} of thrombin (final concentrations in the gels). When injected alone, fibrin did not initiate any bone formation. By using a combination of fibrin with MSC and platelet-rich plasma (PRP) to fill bone defects after placing dental implants in dogs, Ito *et al.*[152] showed more bone–implant contact in the group containing cells, PRP and fibrin, compared to the group containing only cells and fibrin (no PRP) for up to 4 weeks. In a recent study, Kang *et al.*[153] reported on the *in vitro* and *in vivo* osteogenenesis of skin-derived mesenchymal stem cell-like cells (SDMSC) with a demineralized bone and fibrin glue scaffold. Scaffolds seeded with autologous SDMSC were grafted into the maxillary sinus of adult miniature pigs and compared with scaffolds alone. Results showed that trabecular bone formation and osteocalcin expression were more pronounced around the grafted material containing cells than around the scaffolds alone, with also new bone formation from the periphery to the center. The authors concluded that autologous SDMSC with a demineralized bone matrix and fibrin glue scaffold could serve as a predictable alternative to bone grafting in the maxillary sinus floor.

Because of its suitability for delivering exogenous growth factors, fibrin can also be used as a delivery system of BMP or angiogenic growth factors for bone tissue engineering applications. For example, when combining fibrin with BMP, Kawamura and Urist[154] reported a potential immunochemical function of fibrin clot, with the observation of more new bone formation than in the control group (BMP alone). Schmoeke *et al.*[117,118] also reported similar bone healing at 3 weeks in rat calvaria when using BMP-2 and fibrin compared to autograft. In addition, the authors reported bone bridging in a canine pancarpal arthrodesis within 12 weeks.

In addition to cells and growth factors, fibrin has also been combined with other biomaterials for bone regeneration applications. For example, despite some mixed results in the past, bioceramic-derived fibrin composites have been widely used,[155] possibly because of the improved surgical handling of such combination. While some studies showed negative effects of bioceramic–fibrin composites,[156,157] others showed osteogenic properties of these composites.[158,159] For example, Carmagnola *et al.*[156] showed a negative impact on bone colonization in alveolar bone defects in dogs when using a composite made of a bone graft (Bio-Oss®) and a fibrin sealant.[156] On the other hand, Le Guéhennec *et al.*[158] reported newly formed bone at a distance from the surface of Micro-macroporous Biphasic Calcium Phosphate (MBCP®) granules in rabbit femoral defects, suggesting an osteoinductive phenomenon, compared to the commonly described osteoconduction effect of calcium phosphate materials depicted by bone formation directly on the surface of the granules when not mixed with fibrin. To gain insight into the role of fibrin structural properties on bone wound healing *in vivo*, Karp *et al.*[160] conducted an experiment comparing bone healing in rat distal femur defects, filled with either poly(lactic-*co*-glycolic acid) (PLGA) scaffolds alone, PLGA scaffolds combined with a fibrin sealant (TISSEEL™) prepared with a low thrombin concentration (i.e., thick fibers and large pores), PLGA scaffolds combined with the fibrin sealant prepared with a high thrombin concentration (i.e., thin fibers and small pores), or nontreated (controls). Results showed that after 5 days, fibrin-filled PLGA scaffolds were infiltrated with less bone than empty scaffold, and after 11 days, they showed significantly delayed bony wound healing. The authors concluded that fibrin sealants in their present state were not ideal for enhancing bone-tissue invasion into PLGA scaffolds. However, they still observed a more rapid bone-tissue invasion during the first 5 days of healing within PLGA scaffolds filled with fibrin containing a low thrombin concentration compared to fibrin containing a high thrombin concentration. They also reported more disorganized thin collagen fibrils within scaffolds filled with fibrin containing a high thrombin concentration at early time points, and concluded that the structural properties of fibrin matrices may be an important design parameter for maximizing host-tissue invasion during wound healing. Indeed, large pores in fibrin containing a low thrombin concentration may have permitted deeper penetration of cell processes compared to smaller pores in fibrin containing a high thrombin concentration. Fibrin properties and retention on the surface of an endosseous implant are also expected to affect peri-implant bone healing. The influence of the microroughened surface of a titanium implant on the initial interactions of blood/cells has been investigated by Park and Davies.[161] The authors showed that these interactions influenced fibrin clot formation and thereby the migration and differentiation of osteogenic cells in the healing compartment,[161] which has been considered as the hallmark of osteoconduction.[162] Considering that osteogenic cells exert tractional forces while migrating through the fibrin covering the implant surface, the strength of fibrin adhesion (initially attached on the implant surface because of fibrin-adhesive properties) should be strong enough to withstand these tractional forces (http://www.ecf.utoronto.ca/~bonehead/). Davies defined the concept of effective fibrin retention versus inadequate fibrin retention by the implant surface and showed that an effective fibrin retention will allow the cells to migrate toward and stay on the implant surface where they will polarize and secrete bony matrix, thereby providing a good osteointegration. Davies also showed that fibrin retention on the implant surface is a function of the implant microtopography, which will therefore largely influence the implant fixation and its clinical outcome.

Studies described above have been looking at mixing fibrin with cells, growth factors, or biomaterials. Additional studies

investigated other types of combinations. For example, the mixture of fibrin glue with natural coral and TGF-β1 has proven effective in repairing rabbit skull defects.[163] In a recent study, Arkudas *et al.*[164] showed early improvement of vascularization by mixing VEGF-165 and bFGF with fibrin, used to fill a particulated porous hydroxyapatite and beta-tricalcium phosphate matrix in which an arteriovenous loop was created in the medial thigh of rats. The same group also showed successful axial vascularization in a large volume of the same construct but without the growth factors, when creating such arteriovenous loop in a large animal model (sheep).[165] Using a combination of fibrin, MSC and β-tricalcium phosphate (β-TCP), Yamada *et al.*[166] demonstrated that MSC/β-TCP fibrin glue admixtures (containing 40 mg ml^{-1} of fibrinogen and 125 IU ml^{-1} of thrombin – final concentrations in the gels) could result in successful bone formation, whereas β-TCP with fibrin glue only did not induce any bone formation in subcutaneous space on the dorsum of rats. Similarly, Bensaid *et al.*[65] reported that, when implanted in nude mice, MSC-fibrin scaffold-coral implants were invaded by numerous fibroblastic-like cells and a high number of blood vessels, in a larger extent than in the fibrin scaffold-coral implants (with no cells) and coral implant groups. Finally, a recent study by Kang *et al.*[153] showed osteogenic properties of a combination made of SDMSC, demineralized bone, and fibrin glue both *in vitro* and *in vivo*.

Overall, these studies show the potential synergistic effects between fibrin and other biomaterials as well as growth factors and seeded cells for bone tissue engineering applications.

2.217.4.3. Cartilage Tissue Engineering

Fibrin has been successfully used as a scaffold and adhesive to improve healing and regeneration of fibrocartilage, elastic cartilage, craniofacial cartilage, and articular cartilage.[167]

For example, the implantation of fibrin glue containing MSC into rat meniscal defects showed that the cells could survive and proliferate, as well as produce abundant extracellular matrix contributing to meniscal repair.[168] When implanting fibrin seeded with human pediatric auricular chondrocytes into nude mice, Ruszymah *et al.*[169] showed that the engineered cartilage resembled native elastic cartilage. While investigating the use of fibrin for craniofacial applications, Silverman *et al.*[170] showed that the implantation of fibrin (80 mg ml^{-1} of fibrinogen and 50 IU ml^{-1} thrombin) mixed with swine articular chondrocytes into a subcutaneous pocket on the back of nude mice led to the formation of a neocartilage layer between the two native cartilage discs after 6 weeks. The neocartilage also adhered to the normal cartilage matrix. With regard to articular cartilage, multiple studies reported on the use of fibrin with articular chondrocytes. For example, Hendrickson *et al.*[171] reported improved cartilage surface, a significantly greater aggrecan level, and a significantly higher proportion of type II collagen when using fibrin for articular chondrocyte transplantation in trochlea of horse distal femur compared to controls (empty defects). While implanting constructs made of fibrin with articulating chondrocytes into defects in swine knees, Peretti *et al.*[172] showed new cartilage formation and filling of the defects. Finally, while evaluating the use of a fibrin-based scaffold as a delivery vehicle for C5.18 cells for hyaline cartilage regeneration, Dare *et al.*[51] showed that when cultured in chondrogenic medium, fibrin-encapsulated C5.18 cells elaborated an extracellular matrix containing type II collagen as well as aggrecan, two components of hyaline cartilage. These results indicated a more articular-like chondrogenic differentiation of C5.18 cells encapsulated in fibrin, demonstrating that the C5.18 cell line could possibly be used as a tool to evaluate potential scaffolds for articular cartilage tissue engineering.

Biodegradable polymers have been one of the key components in cartilage tissue engineering, and synthetic and naturally derived biodegradable polymers have been widely used for the scaffolds. In order to incorporate the advantages of multiple biomaterials, fibrin has often been investigated in combination with other biodegradable polymers for cartilage tissue engineering applications. For example, Ameer *et al.*[49] evaluated the use of a biodegradable composite system made of pig chondrocytes entrapped in a fibrin gel phase and dispersed throughout the void volume of a PGA nonwoven mesh. After 28 days in culture, results showed an increase in GAG content up to 88% that of native pig cartilage. Total collagen content per cell represented 40% of the value determined for native cartilage. When implanting subcutaneously a fibrin–hyaluronan composite gel seeded with rabbit knee chondrocytes in the back of nude mice, Park *et al.*[173] detected the formation of cartilage-like tissue earlier than when using fibrin alone. Recently, the same group reported on the capacity of such composite to promote chondrogenic differentiation of rabbit MSC *in vitro*.[174] Sha'ban *et al.*[175] also used fibrin to immobilize rabbit articular chondrocytes and provide homogenous cell distribution in PLGA *in vitro*. Results showed that fibrin–PLGA constructs promoted early *in vitro* chondrogenesis and could therefore potentially be used for *in vitro* tissue-engineered articular cartilage. In a recent study, Jung *et al.*[176] showed that constructs made of poly(L-lactide-co-ε-caprolactone) scaffolds and fibrin gels promoted the secretion of cartilaginous extracellular matrix and the formation of mature cartilage tissue by seeded rabbit chondrocytes after implantation into the subcutaneous dorsum of mice.

Finally, other studies also investigated the combination of fibrin with cells, other biomaterials, and growth factors such as TGF-β1 to induce stem cell differentiation into the chondrogenic lineage in order to enhance repair strategies for damaged cartilage. For example, Jung *et al.*[177] showed that hybridization of fibrin and poly(lactide-*co*-caprolactone) scaffolds for 3D spatial organization of the cells as well as effective delivery of TGF-β1 using heparin-functionalized nanoparticles could induce the differentiation of human adipose tissue-derived stem cells. Dickhut *et al.*[178] analyzed whether the combination of collagen-type I/III carrier with fibrin glue into a biphasic construct could support *in vitro* chondrogenesis of MSC and allow for local release of bioactive TGF-β1. The authors reported that the biphasic carrier constructs showed a high biofunctionality with improved chondrogenesis and long-term local supply of bioactive TGF-β1. Very recently, Park *et al.*[179] showed increased chondrogenesis in human MSC seeded in fibrin hydrogels both *in vitro* and in nude mouse and rabbit defect models when the gels contained TGF-β3-loaded nanoparticles. Other studies have shown that, in addition to TGF-β, other factors could alternatively be used with fibrin for cartilage repair.[167] For example, using a model of extensive cartilage loss

in horses, Fortier *et al.*[180] showed that the addition of IGF-1 to composites made of chondrocytes and fibrin enhanced chondrogenesis in the defects as well as graft incorporation into the surrounding cartilage.

2.217.4.4. Nervous Tissue Engineering

Tissue-engineered neural structures may present an alternative strategy to treat serious clinical conditions of the nervous system, such as brain and spinal cord injuries as well as neurodegenerative diseases.[167]

As explained in **Section 2.217.3** of this chapter illustrating the use of fibrin matrices containing the heparin-based delivery system developed by Sakiyama-Elbert and Hubbell[107] for the delivery of growth factors, studies using such system and incorporating NGF showed an enhancement of neurite extension.[111,115] More recently, a study by Gao *et al.*[181] using a combination of fibrin and NGF without the heparin-based delivery system technology also showed more regenerated nerve fibers with the development of axons compared to fibrin alone or NGF alone. In addition, when combining NGF and GDNF with fibrin matrices containing the heparin-based delivery system, Wood *et al.* reported peripheral nerve regeneration[112,113] as well as motor neuron regeneration and functional recovery in a rat sciatic nerve model.[114]

Similarly, some studies illustrating the use of fibrin for the delivery of NT-3 showed an increase in neural fiber density in spinal cord lesions.[108,109] For example, as previously described in **Section 2.217.3**, a study by Taylor *et al.*[108] using the heparin-based delivery system to immobilize NT-3 within fibrin gels showed stimulated neural outgrowth from chick dorsal root ganglia by up to 54% *in vitro* and an increased neural density at 9 days in a rat accurate spinal cord injury model. Another study by the same authors using the accurate spinal cord injury model in rats showed an enhanced initial regenerative response when delivering NT-3 in a controlled manner using the same heparin-based delivery system in fibrin gels, as depicted by an increase in neuronal fiber sprouting and cell migration into spinal cord lesions.[109] Interesting, a more recent study from the same group showed that the controlled release of NT-3 could enhance neural fiber sprouting even when the treatment was delayed 2 weeks following injury.[182] Finally, when combining the controlled delivery of NT-3 and PDGF using, once again, the heparin-based delivery system in fibrin gels, the same authors showed promising results for enhancing functional recovery following spinal cord injury in a subacute rat model.[110]

In a recent study, Kalbermatten *et al.*[183] compared the use of fibrin versus poly-3-hydroxybutyrate as a conduit to guide nerve regeneration and bridge nerve defects using a rodent sciatic nerve injury model. Results showed a potential advantage of using fibrin as a conduit for the initial phase of peripheral nerve regeneration, demonstrated by a superior nerve regeneration distance after 1 month and an enhanced Schwann cell intrusion from the proximal and distal ends. A study by Isaacs *et al.*[184] investigating different commercially available fibrin sealants to suture nerve repairs and decrease the gapping at the repaired site, showed that fibrin sealants helped preventing the initial gapping in cadaveric nerve specimens. Johnson *et al.*[185] showed that the use of fibrin induced significantly higher levels of neural fibers in a rat spinal cord injury site at 2 and 4 weeks after treatment. In addition, the accumulation of glial fibrillary acidic protein (GFAP)-positive reactive astrocytes surrounding the lesion was delayed. Finally, Itosaka *et al.*[186] showed that the bone marrow stromal cell transplantation in rats using a fibrin construct led to a more pronounced recovery of neurologic function than fibrin alone or cells alone, concluding that fibrin matrix may be a promising scaffold candidate for spinal cord injury.

2.217.4.5. Other Tissue Engineering Applications

Fibrin has been evaluated for and used in many more tissue engineering applications, including those in skin, liver, muscles, tendons, and ligaments.

2.217.4.5.1. Skin

The use of fibrin for skin repair will be further discussed when reviewing fibrin use in plastic and reconstructive surgery in the next section of this review (**Section 2.217.5**). The present section will only summarize a few studies on the use of fibrin in *in vitro* models to induce wound reepithelialization and give some examples of the use of fibrin in skin substitutes in preclinical studies.

Geer *et al.*[187] developed a wound reepithelialization model based on engineered composite skin equivalents and human keratinocytes. Using this model, the authors evaluated fibrin as a substrate for keratinocyte growth and migration after incisional wounding, showing that the use of fibrin decreased the length of the lag phase of keratinocyte activation and increased the consistency of the healing response. Such models are also used to investigate regulatory mechanisms of cell growth and differentiation under conditions mimicking those *in vivo*. Using a combination of keratinocytes, fibrin suspension, and acellular dermis (AlloDerm®), Bannasch *et al.*[188] reported closure of full-thickness wounds in a porcine model, with reduced wound contraction. Finally, when using fibrin as a delivery vehicle for human umbilical cord perivascular cells, Zebardast *et al.*[189] showed accelerated early wound healing in full thickness skin defects created on the dorsum of Balb/c nude mice, with thicker and more organized dermal repair tissue compared to contralateral controls that had received fibrin only.

Because of the limited availability of autografts (especially in some patients with extended burns), the development of skin substitutes for wound coverage is very important for the care of burn wounds. Cultured skin substitutes, composed of keratinocytes and fibroblasts in fibrin matrix have been developed as an adjunctive burn wound therapy. For example, a study from Ronfard *et al.*[190] showed that human keratinocytes cultured on a fibrin matrix had the same growth capacity and transplantability as those cultured on plastic surfaces, but the presence of fibrin greatly facilitated the preparation, handling and surgical transplantation of the grafts. Recently, a study by Tanikawa *et al.*[191] evaluated the long-term growth and differentiation characteristics of keratinocytes cultured onto a fibrin gel under immerse and air-liquid interface culture conditions. Results showed that the resulting composite had promising ultrastructural, morphological and functional characteristics, suggesting that such composite may have some potential for clinical use. However, vascularization of such cultured skin substitutes is slower than that of split-thickness skin autografts,

and therefore grafted cells are exposed to ischemia and nutriment deprivation early on after implantation. In order to improve the vascularization of the substitutes, growth factors such as VEGF and bFGF have been added to these substitutes. Some studies showed increased angiogenesis when using such enhanced skin substitutes in athymic mice.[192,193]

2.217.4.5.2. Liver

Hepatocyte transplantation are under investigation as an alternative to liver transplantation (limited by donor organ shortage and immunosuppression), and therefore, 3D scaffolds have been investigated as carrier systems.[194] Fibrin matrices have been considered for such scaffolds. For example, a study by Bruns *et al.*[195] evaluated the use of fibrin as a carrier for hepatocytes in culture and developed an intrahepatic injection technique to transplant the fibrin gel-immobilized hepatocytes in rats. Culture of hepatocytes in the fibrin matrix allowed stable cell numbers and 3D neotissue formation, and *in vivo* results showed integration of hepatocytes and hepatic stellate cells into the host liver. A study by Gwak *et al.*[59] also showed that one week after transplantation of hepatocytes using fibrin matrix in an athymic mouse model, the cells retained their hepatocyte-specific functions whereas no transplanted cells were visible in the control groups (transplantation of hepatocytes suspended in culture medium).

2.217.4.5.3. Skeletal muscles

Tissue engineering of skeletal muscle tissue still remains a major challenge. Skeletal muscle tissue engineering aims to create autologous neomuscle, involving the differentiation of myoblasts to myofibers either *in vitro* or *in vivo* after implantation.[196] In a recent review of the current state of the art in tissue engineering of skeletal muscle, Koning *et al.*[197] reported that optimal scaffolding for structural support and regulation of proliferation and differentiation of muscle progenitor cells could comprise a fibrin gel and cultured monolayers of muscle satellite cells obtained through the cell sheet technique. A study by Beier *et al.*[198] showed that expanded primary rat myoblasts cultured for 1 week in a fibrin matrix were integrated into the host's skeletal muscle fibers after transplantation. Another study by the same authors also evaluated the possibility of filling the muscle defect with fibrin containing myoblasts using an injection system instead of implanting precultivated 3D myoblast cultures.[196] Results showed that injected myoblasts with fibrin increased integration into the host muscle fibers in a time-dependent manner, with a conservation of the transplanted cell phenotype. *In vitro*, Khodabukus and Baar[199] were able to rapidly (about 10 days) engineer a functional tissue using the C2C12 mouse myoblast cell line in fibrin supplemented with aprotinin and natural cross-linker genipin. Finally, Bian and Bursac[200] reported on combining cell-mediated fibrin gel compaction with precise microfabrication of polydimethylsiloxane molds to guide cell alignment along the microfabricated tissue pores and control the overall tissue porosity, size, and thickness. The interconnected muscle bundles within the porous tissue networks were composed of densely packed, aligned, and highly differentiated myofibers.

2.217.4.5.4. Tendons and ligaments

Injuries of tendons and ligaments are among the most common orthopedic injuries, and unfortunately, incomplete regeneration of the tissue often occurs during healing.[167] The properties of anterior cruciate ligament (ACL) and medial collateral ligament (MCL) fibroblasts were analyzed in a 3D fibrin matrix gel, with or without TGF-β1, to investigate the possible differences in ACL and MCL fibroblast ability to perform the key events of wound repair, including wound matrix contraction mimicked by fibrin matrix gel contraction.[201] Results showed that MCL fibroblasts synthesized a significantly higher amount of collagen per cell than ACL fibroblasts between days 2 and 6 of culture. The addition of 5 ng ml^{-1} of TGF-β1 caused a significantly faster rate of the 3D construct contraction than control (0.5% fetal bovine serum), without having to increase the initial cell number. By injecting a mixture of human bone marrow stem cells with fibrin glue into patellar tendon defects of immunodeficient rats, Hankemeier *et al.*[202] showed more mature tissue formation with more regular patterns of cell distribution compared to untreated defects or defects filled with fibrin glue only. Interestingly, using the same model, the authors more recently compared the effects of fibrin glue seeded with human bone marrow stem cells versus fibroblasts on the ultrastructural morphology, mRNA expression of essential extracellular matrix proteins, and material properties of the healing tissue.[203] Results showed that only the mean collagen fibril diameter was significantly higher compared to the defect group but the group with human bone marrow stem cells showed also more collagen I mRNA expression, collagen I/collagen III mRNA ratio, and an increase in the Young's modulus at 20 days postoperatively. Finally, Thomopoulos *et al.*[204] recently reported that the delivery of bFGF and PDGF-BB using the heparin-binding delivery system in fibrin gels initially developed by Sakiyama-Elbert and Hubbell[107] stimulated tendon fibroblast proliferation and promoted some changes in the expression of matrix genes related to tendon gliding, strength and remodeling *in vitro*. The authors concluded that the controlled delivery of these factors *in vivo* may allow for sustained biological stimulation in the early period after repair. However, such *in vivo* studies remain to be conducted to verify that the observed improvements *in vitro* translate to improvements *in vivo*. Previous studies from the same authors using PDGF-BB in a canine flexor tendon model had shown improved gliding but not improved strength.[205] Similarly, in a recent study, the authors showed that bFGF administration alone led to increased tendon cellularity and matrix synthesis but no improvement of the functional and mechanical properties of the repair.[206]

Mechanical properties still remain a challenge for the functionality of fibrin for tendon and ligament applications. Indeed, by injecting bone-marrow-derived MSC mixed with fibrin sealant in rabbit Achilles tendons, Chong *et al.*[207] showed improved modulus compared to control, but only at the early stages of healing. Similarly, a study by Thomopoulos *et al.*[208] analyzed both the functional and structural properties of the healing tissue in an intrasynovial flexor tendon repair model using fibrin/heparin-based delivery system of PDGF-BB. Results showed that cell activity was accelerated as a result of PDGF-BB at 14 days and tendon gliding properties were significantly higher for the PDGF-BB-treated tendons than for the repair-alone tendons at 42 days. However, there was no improvement in the tensile properties.

2.217.5. Fibrin in Clinical Practice

2.217.5.1. Commercially Available Fibrin Sealants

Commercial fibrin sealants are currently composed of plasma-derived complexes of purified, pathogen-inactivated human fibrinogen and thrombin.[209] Other components, such as factor XIII, tranexamic acid, or aprotinin (bovine origin or synthetic), are added in some fibrin sealants. Factor XIII, activated by thrombin in the presence of calcium ions, serves as the cross-linking reagent.[15] Either tranexamic acid or aprotinin, which acts as a fibrinolytic inhibitor (or plasmin inhibitor), is added in some fibrin sealants to prolong the life of the fibrin clot. For some formulations, however, a manufacturing step is added to remove the plasminogen from the fibrinogen component, so that no plasmin inhibitor is needed.

There are currently several commercially available fibrin sealant products, including ARTISS™ (Baxter Healthcare Corp., Westlake Village, CA), Beriplast® P Combi-Set (CSL Behring, King of Prussia, PA), Cryoseal® (Thermogenesis, Rancho Condova, CA), Evicel™ (replacement of Crosseal™/Quixil® (Omrix biopharmaceuticals Ltd. and Ethicon Inc. J&J, Somerville, NJ), and TISSEEL™/TISSUCOL™ (Baxter AG, Vienna, Austria; also available through Baxter Healthcare Corp., Westlake Village, CA). To ensure that clotting occurs quickly and effectively, commercial fibrin sealants need to be prepared with very high amounts of fibrinogen and thrombin, up to 60 mg ml^{-1} of fibrinogen and 300–500 IU ml^{-1} of thrombin after mixing.[209–211] The two component solutions are usually applied through a double-barreled syringe system, which allows simultaneous application of the fibrinogen and thrombin through a blunt-ended needle or spray tip.[5] The two components passively mix at the ends of the delivery needles or spray tip. The method of application can have a significant effect on the clinical outcome and should therefore be chosen carefully depending on the clinical need. Some concerns have indeed raised clinically with regard to the learning curve of the clinical staff for techniques of applications as well as for reconstitution of the fibrin sealants that can affect their usability.[212]

Production method generally includes several precipitation steps to enhance the purity of fibrinogen by decreasing the relative proportion of fibronectin, albumin, or immunoglobulins. Viral inactivation methods include two-step vapor heating, solvent–detergent step, and pasteurization. Therefore, in addition to the factor XIII and/or a plasmin inhibitor supplements in some fibrin sealants as explained above, the precipitation mode and purification, as well as the viral inactivation treatment influence the composition and behavior of the final product, including the stability after reconstitution or thawing, the speed of hemostasis, the preparation time, and the ease of use. The direct comparison between properties of different fibrin sealants remains difficult because of variable testing conditions between studies (such as differences in rheological devices, different animal models, etc.). However, because of the variations between formulations, outcomes for a particular clinical application can vary depending on the fibrin sealant used.[213–215] Choice of the sealant should therefore be carefully considered. **Tables 1 and 2** illustrate the differences in composition (**Table 1**) as well as handling and storage requirements (**Table 2**) of some commercially available fibrin sealants in Europe.

Although fibrin sealants have been approved by the FDA for hemostasis in various surgical applications, as adhesives (e.g., burn wound skin graft attachment) and sealants (e.g., colon sealing),[216] they have also been used off-label in many other applications. Some of the clinical applications in which they have been applied include cardiovascular and thoracic surgeries, plastic and reconstructive surgeries, gastrointestinal surgeries, neurosurgeries, ophtalmology, urology, and others (some examples of these uses are provided below). They have been also used clinically as an adjunct therapy to replace sutures or staples because of their enhancement of healing, minimizing scarring, and ease of application.[211]

2.217.5.2. Examples of Fibrin Uses in Clinical Practice

2.217.5.2.1. Cardiovascular and thoracic surgeries

Cardiovascular applications for fibrin sealants are numerous, including bypass surgery, vascular graft attachment, cardiovascular patches, heart valve implantation, and synthetic vascular grafts or preclotting of porous vascular grafts. This is probably the surgical area where fibrin sealants have been the most applied, with a primary use as an adjunct to hemostasis during vascular and cardiac procedures. Study examples of some of these clinical applications are given below.

2.217.5.2.1.1. Applications as a hemostatic agent in cardiac surgeries

A randomized clinical trial of fibrin sealant in 333 patients undergoing resternotomy or reoperative cardiac surgery was

Table 1 Comparison of the composition of some commercial fibrin sealants

Product	*Plasma protein fraction (mg ml^{-1})*	*Human fibrinogen (mg ml^{-1})*	*Human factor XIII (U ml^{-1})*	*Human thrombin (IU ml^{-1})*	*Fibrinolytic inhibitor*
Quixil	60–80	40–60	Not available	1000 (800–1200)	Tranexamic acid, 100 mg ml^{-1}
Tisseel/Tissucol Duo	75–115	70–110	~1 (USA, UK); 10–50 (mainland Europe)	500	Bovine aprotinin, 3000 KIU ml^{-1}
Tisseel/Tissucol Kit	75–115	70–110	~1 (USA, UK); 10–50 (mainland Europe)	4 or 500	Bovine aprotinin, 3000 KIU ml^{-1}
Beriplast P	90 (65–115)	90	60 (40–80)	500	Bovine aprotinin, 1000 KIU ml^{-1}

Adapted from Tredree, R.; Beierlein, W.; Debrix, I.; *et al*. *EJHPScience* **2006**, *12*, 3–9.

Table 2 Comparison of the handling and storage requirements of some commercial fibrin sealants

Product	*Presentation*	*Applicator*	*Storage*	*Preparation*	*Time of preparation*	*Shelf-life after thawing/reconstitution*
Quixil	Frozen components in vials	Triple lumen, drip and spray	Below −18 °C	Thaw, draw into applicator	5–7 min thawing in the hand; <1 min after thawing	30 days at 2–8 °C
Tisseel/ Tissucol Duo	Frozen components in syringes	Single lumen blunt needle (by default). Spray also available for purchase	Below −18 °C	Thaw, warm to 37 °C, attach tip to syringe	20–30 min if thawed at room temperature; warming to 37 °C recommended	36 h
Tisseel/ Tissucol kit	Lyophilized components for reconstitution	Single lumen blunt needle (by default). Spray also available for purchase	2–8 °C	Reconstitute, warm to 37 °C, assemble applicator	About 40 min warming/stirring	4 h
Beriplast P	Lyophilized components for reconstitution	Single lumen blunt needle (by default). Spray also available for purchase	2–8 °C	Reconstitute, warm to 37 °C, assemble applicator	10–15 min waiting time for components to mix	8–24 h

Table from Tredree, R.; Beierlein, W.; Debrix, I.; *et al*. *EJHPScience* **2006**, *12*, 3–9, reproduced with permission.

published by Rousou *et al.*[217] The study was conducted to test the efficacy and safety of fibrin sealant as a topical hemostatic agent. Results showed a 92.6% success rate for fibrin sealant in controlling bleeding within 5 min of application, compared to only a 12.4% success rate with conventional topical agents. By using fibrin sealant, 82.0% of those bleeding episodes not initially controlled by conventional agents were also more rapidly controlled, and postoperative blood loss was significantly less in the fibrin sealant group than in the matched controls. Additionally, resternotomy rates after re-operations were significantly lower in the fibrin sealant group (5.6%) than in the control group (10%). A more recent randomized, double-blind clinical study (phase 3) evaluated the topical hemostatic efficacy and safety of a fibrin sealant (TISSEEL VH S/D™) compared to a previous formulation (TISSEEL VH™) during cardiac surgery.[218] Results showed that 88.2% of the patients treated with TISSEEL VH S/D and 89.6% of the ones treated with TISSEEL VH achieved hemostasis within 5 min and maintained it until surgical closure. These results suggested that both fibrin sealants were safe and effective for use as an adjunct to hemostasis in patients undergoing cardiac surgery. In a recent prospective randomized controlled trial, Chalmers *et al.*[219] showed that the use of another fibrin sealant (EVICEL™) compared to manual compression in PTFE arterial anastomoses shortened the time to haemostasis and reduced the incidence of treatment failure.

2.217.5.2.1.2. Applications in synthetic vascular grafts

A prospective randomized multicenter trial evaluating the safety and efficacy of a fibrin sealant (Beriplast® P) in stopping bleeding from needle or suture holes in polytetrafluoroethylene (PTFE) grafts after anastomosis to the femoral artery of 201 patients was published by Taylor *et al.*[220] The fibrin sealant was compared to a thrombin-soaked gelatin sponge. The authors reported that time to hemostasis was shorter in the fibrin sealant group, blood loss was less, and time to wound closure was shorter. There was no difference in recurrent bleeding or any other adverse events. The authors concluded that the fibrin sealant was more effective than the thrombin-soaked gelatin sponge for achieving hemostasis after needle or suture hole bleeding in PTFE femoral artery grafts.

2.217.5.2.1.3. Applications in cardio patches

A prospective randomized trial including 20 patients investigated whether the application of Quixil® sealant to the suture line of an expended PTFE (ePTFE) patch could improve the time to achieve hemostasis and reduce local blood loss compared to standard topical hemostat Kaltostat® (a soft, white, sterile nonwoven dressing of calcium sodium alginate containing 80% calcium and 20% sodium).[221] Results showed that the blood loss and the time to achieve hemostasis after clamp release were significantly lower in the Quixil® group compared to controls. A study by Aigner *et al.*[222] reported on the use of a double pericardial patch with a layer of human fibrin glue in between (sandwich technique) to cover the defect caused by intraoperative coronary sinus rupture, a rare event but potentially mortal. The study included four patients. The authors reported that all patients could be treated successfully, with excellent bleeding control. Finally, in a case study report by Toda *et al.*,[223] a patient with penetrating cardiac injuries to both ventricles was treated by two different methods: buttressed sutures on one side, and a collagen mesh dressing covered by a fibrin glue (TachoComb® patch) on the other side. The study reported that the patient recovered without a ventricular pseudoaneurysm.

2.217.5.2.2. Plastic and reconstructive surgeries

Fibrin has been widely used as an adhesive in plastic and reconstructive surgeries, including burn surgeries, craniofacial surgeries, and microvascular surgeries,[224] mainly because of its graft adherence and hemostasis properties. As mentioned at the beginning of this chapter, fibrin has been used as an adhesive for skin grafts as early as in the 1940s. Grafting of skin has been successful regardless of the fibrin sealant production method in areas such as hands in burn patients, face lifts, and rhynophyma repair.[3]

2.217.5.2.2.1. Graft adherence

Fibrin has been shown to improve the percentage of skin graft take, especially in difficult grafting sites or sites with unavoidable movement.[48] By facilitating graft adherence, fibrin sealants can improve the graft survival and cosmetic results.[225] In 1983, Vibe and Pless[226] reported an improvement in skin graft area take from 83 to 92% with the use of a fibrin glue (TISSEEL™) in 20 patients. The authors reported that, in difficult areas such as over mobile muscle or close to skin folds, 88% of cases were successful when using fibrin to glue the tissue and only 44% without using fibrin. A study by Stuart *et al.*[227] a few years later also achieved 99% graft take in 16 patients when using a single-donor fibrin glue as an adjunct in early excision and grafting hand-burned patients.

A recent multicentered, prospective, randomized, and evaluator-blinded phase 3 clinical study evaluated ARTISS™ for skin graft adherence compared to staples in burn wounds.[228] The study reported that, by day 14, complete wound closure occurred in 48.8% when using the sealant compared to 42.6% when using staples. These numbers reached 70.3% versus 65.8%, respectively, at day 28. The sealant also scored better by the investigators in terms of graft adherence, preference for method of fixation, satisfaction with the graft fixation, and overall quality of healing. This study was carried out after a multicenter, randomized, and controlled phase 1/2 clinical study comparing the fibrin sealant and staples for the same purpose, that is, attaching split-thickness autologous sheet grafts in patients with deep, partial, or full-thickness burn wounds.[229] In the latter study, the authors had showed that the percentage of completely closed sites was generally greater with the sealant than with the staples, with the maximum difference at day 28 (79.5% vs. 59%, $p = 0.0215$).

2.217.5.2.2.2. Hemostasis

Several studies have been reported on the effects of fibrin sealants on wound hemostasis. A phase III multicenter, randomized, comparative clinical trial was performed by Nervi *et al.*[230] to evaluate the topical hemostatic efficacy of a fibrin sealant in burn patients undergoing skin graft procedures. The sealant evaluated in that study consisted of a human topical fibrinogen complex and a solution of human α-thrombin at 250–350 IU ml^{-1} once reconstituted. Each patient served as his or her own control. A contiguous donor skin harvest site was bisected into two equal halves, and one of them was treated with the fibrin sealant. The time of hemostasis in each of the donor site halves was identified by the operating surgeon. The study reported a significant difference in the mean time to hemostasis between the fibrin sealant-treated donor sites compared to the control sites. In a previous study in 95 burn patients and investigating the hemostatic effect of a human fibrin sealant (which appears to be similar to the one used later by Nervi *et al.*[230]), McGill *et al.*[231] (same group of researchers as Nervi *et al.*) had previously reported an estimated blood loss/graft ratio of 0.50 ± 0.30 ml cm^{-2} (median = 0.46) for the study group versus 0.98 ± 2.4 ml cm^{-2} (median = 0.56) for the control group. The difference was not statistically significant unless considering only patients more than 16 years old. Although the use of the fibrin sealant did not show a major improvement in the clinical outcome in terms of hemostasis, the authors had reported a reduced need for blood transfusion, as well as a reduced alloantigen exposure and a reduced blood-borne viral infection risk when using fibrin compared to controls. A former study by Achauer *et al.*[232] including ten patients with burns had also not reported any significant difference in the bleeding between the donor site sprayed with fibrinogen and thrombin (i.e., fibrin glue) compared to the site sprayed with thrombin and plasma placebo. Likewise, when evaluating the safety and potential efficacy of a solvent/detergent-treated commercial fibrin sealant (same as the one previously described by McGill *et al.*[231]) for topical hemostasis in skin grafting, Greenhalgh *et al.*[233] did not report any differences between the fibrin sealant-treated site and the control site (no treatment) with regard to acceleration of donor site healing, graft take, or scar maturation. A subjective observation by the investigators revealed that graft sites treated with the fibrin sealant may, however, progress through the maturation phase of healing more rapidly than other burn wounds that were not treated with the fibrin sealant, but such observation would need to be investigated further.

2.217.5.2.2.3. Face-lift surgeries and seroma prevention

Although some studies did not show clear advantages of fibrin for face-lift surgery, others have shown benefits. For example, a prospective, randomized, nonblinded controlled trial published by Marchac and Greensmith[234] showed only minimal differences when comparing scores among grades of haematomas, ecchymosis, and edema between sprayed fibrin sealant (TISSEEL™) and drainage versus drainage treatment only in 30 face-lift patients. On the other hand, another prospective, randomized, double-blind trial in 20 consecutive patients undergoing bilateral face lifts showed a significant difference in drainage between the two sides at 24 h.[235] The side treated with the fibrin sealant had a median drainage of 10 ml compared to 30 ml for the control side. In a recent review of ten different papers on the topic, Por *et al.*[236] concluded that there was no statistically significant benefit from the use of tissue sealants in face-lift surgery. The parameters analyzed were postoperative drainage at 24 h and ecchymosis, as well as postoperative edema measurement.

On the basis of the tissue-adhesive qualities of fibrin glue, seroma prevention is a natural avenue of exploration for clinical use.[224] Few studies have been published on the use of fibrin sealants to prevent seroma formation after breast cancer surgery, abdominoplasty, and body-contouring surgery.[237,238] However, these reports seem to be too few to draw conclusions on the use of fibrin for these applications, and more randomized clinical trials should be performed to determine the efficacy of fibrin for such applications.

2.217.5.2.3. Other clinical applications

2.217.5.2.3.1. Gastrointestinal

Bleeding in the upper gastrointestinal tract is often managed by local endoscopic injection of hemostatic agents.[5] The injection of a fibrin sealant provides an effective therapy that can be administered repeatedly as required. For example, fibrin sealant can help control the diffuse oozing associated with liver surgery.[239] In a large randomized multicenter study, 854 patients with ulcers or active gastroduodenal bleeding (spurting, oozing) received either a single application of polidocanol 1%, a single application of a fibrin sealant (Beriplast®P), or repeated applications of the fibrin sealant.[240] Results showed that patients treated with repeated applications of the fibrin sealant were significantly less likely to have recurrent bleeding compared to those treated with polidocanol. In a retrospective analysis of bleeding upper gastrointestinal ulcers, 452 patients with benign gastric or duodenal ulcers were examined.[241] Eighty-five patients exhibiting stigmata or fresh bleeding were treated endoscopically by injection of a fibrin sealant. Results showed that initial endoscopic hemostasis was achieved in all patients, and permanent hemostasis was reached in 85.9%. In another prospective and randomized study, 121 patients undergoing liver resection were treated either with Crosseal™ fibrin sealant (58 patients) or using standard commercially available topical hemostatic agents (44 patients).[242] Results showed that hemostasis was achieved within 10 min in 91.4% of the patients treated with the fibrin sealant versus 69.8% of the patients treated with standard topical hemostatic agents. In addition, the time to hemostasis was 282s with the fibrin sealant compared with 468s with the standard topical hemostatic agents. Finally, postoperative complication rate was also lower with the fibrin sealant.

Another potential organ for fibrin use in gastrointestinal applications is the pancreas. For example, Jang *et al.*[243] reported on the efficacy of a fibrin sealant (TISSEEL™) injected endoscopically for closure of pancreatocutaneous fistula and abdominal wall defects following transgastric endoscopic necrosectomy. A systematic literature search was actually recently performed by Fingerhut *et al.*[244] to determine the use of fibrin sealants in pancreatic surgery. The authors reported on 24 studies that included six controlled randomized trials. However, because of the heterogeneity and lack of high-level evidence, they concluded that, as of today, it is hard to say if fibrin sealants are of any real utility in pancreatic surgery. Further large-scale controlled trials may be necessary before concluding on the use of fibrin sealants in this surgery field.

2.217.5.2.3.2. Neurosurgery

Fibrin sealants have been used in various neurosurgery applications, including the prevention and treatment of cerebrospinal fluid leakage after neurosurgery,[245,246] as well as peripheral nerve repair.[247,248] Kamada *et al.*[245] reported a successful treatment of a spontaneous intracranial hypotension due to a cerebrospinal fluid leak at the C2 level by epidural fibrin glue patching (Beriplast® P). A prospective randomized study evaluating the efficacy of autologous and commercial (Beriplast®) fibrin sealants to decrease postoperative cerebrospinal fluid leak in spinal cord surgery reported that the volume of drainage fluid was significantly lower in the groups with fibrin sealants (both autologous and commercial) than in the group without fibrin sealant.[246] On the other hand, a study by Jankowitz *et al.*[249] did not report any difference in dural repair when using a fibrin glue (TISSEEL VH™) in patients who experienced a durotomy during lumbar spine surgery. However, Narakas[247] had previously reported earlier that using a fibrin glue in repair of peripheral nerves offered an advantage on suturing alone and allowed a considerable gain of operative time. A significant advantage of fibrin glue over microsuturing is based on the fact that the expected nerve appositioning can be fixed into place with no significant migration, making the procedure easier and faster, and reducing or avoiding the use of sutures.[3,4]

2.217.5.2.3.3. Ophthalmology

Fibrin-based matrices have been used extensively for the treatments of many corneal diseases, including total limbal cell deficiency and corneal perforation.[167] For example, in their attempt to restore corneal integrity in patients with total limbal stem cell deficiency, Rama *et al.*[250] evaluated the efficacy of the transplantation of fibrin-cultured limbal stem cell constructs (using TISSUCOL™) and showed successful results in 14 out of 18 patients, with reepithelialization within the first week. A study by Siatiri *et al.*[251] evaluated the use of a fibrin sealant (TISSEEL VH™) for the repair of corneal perforations up to 3 mm in diameter and showed successful healing in 15 out of 18 patients after 3 months.

Amniotic membrane has been commonly used as a substrate for limbal stem cell transplantation.[252] A study by Kim and Park[253] evaluated the use of a fibrin glue (Green Plast) to create a multilayered amniotic membrane (five to seven ply of amniotic membrane with fibrin applied to each sheet) for transplantation into large corneal perforations, which eliminates the requirement for sutures. The authors reported that 90% of the patients showed complete epithelialization over the amniotic membrane with a mean reepithelialization time of 14.9 ± 4.9 days.

2.217.5.2.3.4. Urology

Fibrin sealants have been used in a large number of applications in urology, including hemostasis during partial nephrectomy, renal reconstruction after trauma, bladder surgery, ureteral anastomosis, microsurgical vasal anastomosis (vasovasostomy and vasoepididymostomy), and fistula repair. For example, the use of a commercial fibrin sealant (TISSEEL™) was successful in obtaining strict hemostasis during laparoscopic partial nephrectomy in 15 patients following conventional hemostatic measures of electrocauterization and argon-beam coagulation.[254] There was also no evidence of urinary leak during or after surgery, a common complication after laparoscopic partial nephrectomy, suggesting that the fibrin sealant may have helped to prevent such complication by helping to seal or close small defects in the urinary collecting system. Similarly, percutaneous fibrin glue (TISSUCOL™) injection allowed controlling urine leakage in a 71-year-old man with a single kidney and renal cell carcinoma who subsequently underwent laparoscopic partial nephrectomy.[255]

Reviews have been reported on the use of fibrin sealants in urology.[256,257] For example, Shekarriz and Stoller[257] reported on a number of case series and case reports showing the

efficacy of fibrin sealant for ureteral anastomosis, microsurgical vasal anastomosis, fistula repair, and other reconstruction applications, and concluded that fibrin sealant was an effective and safe topical agent for controlling surface bleeding during elective and trauma-related urological procedures. Evans and Morey[256] detailed diverse urological applications of fibrin sealant in the management of genitourinary injuries, surgeries, and complications. The authors concluded that fibrin sealant offered an effective adjunct for hemostasis, tissue adhesion, and reinforcement of urinary tract sealing.

2.217.6. Conclusion

The literature on fibrin is extremely large and continues to expand. This chapter provided a summary of the main characteristics and properties of fibrin and presented a wide range of fibrin uses in tissue engineering approaches as well as in clinical practice. It was shown that fibrin can serve as a cell and/or bioactive substance delivery system and be used as a bioactive matrix on its own or combined with other biomaterials. This versatility, in addition to unique intrinsic biological properties, make fibrin a very attractive candidate for the development of the next generation of biomaterials designed to achieve site-directed stimulation of tissue regeneration processes. Because fibrin mechanical and fibrinolytic properties greatly vary depending on the fibrin components and their concentrations, it will be important to keep in mind the matrix parameters necessary for a specific application. For example, whereas a fast degradation and a more open matrix structure may be beneficial for applications requiring a rapid cell or bioactive substance delivery, a more stable matrix may be necessary for tissue growth applications where cells need time to differentiate and produce their own matrix. By varying fibrin composition, many different structures of fibrin gels with different overall properties can be developed, which will make fibrin suitable for multiple new applications in tissue engineering and clinical practice.

References

1. Helgerson, S.; Seelich, T.; Diorio, J. P.; Tawil, B.; Bittner, K.; Spaethe, R. *Encyc. Biomat. Biomed. Eng.* **2004**, *1*, 603–610. doi:10.1081/E-EBBE 1200007295.
2. Bergel, S. *Dtsch Med. Wochenschr.* **1909**, *35*, 663–665.
3. Sierra, D. H. *J. Biomater. Appl.* **1993**, *7*, 309–352.
4. Radosevich, M.; Goubran, H. I.; Burnouf, T. *Vox Sang.* **1997**, *72*, 133–143.
5. Jackson, M. R. *Am. J. Surg.* **2001**, *182*, 1S–7S.
6. Matras, H.; Dinges, H. P.; Lassmann, H.; Mamoli, B. *Wien. Med. Wochenschr.* **1972**, *122*, 517–523.
7. Jackson, M. R.; Macphee, M. J.; Drohan, W. N.; Alving, B. M. *Blood Coagul. Fibrinolysis* **1996**, *7*, 737–746.
8. Clark, R. A. *J. Invest. Dermatol.* **2003**, *121*, xxi–xxii.
9. Laurens, N.; Koolwijk, P.; De Maat, M. P. *J. Thromb. Haemost.* **2006**, *4*, 932–939.
10. Mosesson, M. W. *J. Thromb. Haemost.* **2003**, *1*, 231–238.
11. Mosesson, M. W. *J. Thromb. Haemost.* **2005**, *3*, 1894–1904.
12. Mosesson, M. W.; Siebenlist, K. R.; Meh, D. A. *Ann. N. Y. Acad. Sci.* **2001**, *936*, 11–30.
13. Henschen, A.; Lottspeich, F.; Kehl, M.; Southan, C. *Ann. N. Y. Acad. Sci.* **1983**, *408*, 28–43.
14. Standeven, K. F.; Ariens, R. A.; Grant, P. J. *Blood Rev.* **2005**, *19*, 275–288.
15. Breen, A.; O'Brien, T.; Pandit, A. *Tissue Eng. Part B* **2009**, *15*(2), 201–214.
16. Everse, S. J.; Spraggon, G.; Veerapandian, L.; Riley, M.; Doolittle, R. F. *Biochemistry* **1998**, *37*, 8637–8642.
17. Pratt, K. P.; Cote, H. C.; Chung, D. W.; Stenkamp, R. E.; Davie, E. W. *Proc. Natl. Acad. Sci. USA* **1997**, *94*, 7176–7181.
18. Shimizu, A.; Nagel, G. M.; Doolittle, R. F. *Proc. Natl. Acad. Sci. USA* **1992**, *89*, 2888–2892.
19. Weisel, J. W. *Biophys. Chem.* **2004**, *112*, 267–276.
20. Mosesson, M. W.; Diorio, J. P.; Siebenlist, K. R.; Wall, J. S.; Hainfeld, J. F. *Blood* **1993**, *82*, 1517–1521.
21. Mosesson, M. W.; Siebenlist, K. R.; Amrani, D. L.; Diorio, J. P. *Proc. Natl. Acad. Sci. USA* **1989**, *86*, 1113–1117.
22. Weisel, J. W. *J. Thromb. Haemost.* **2007**, *5*(Suppl. 1), 116–124.
23. Khare, A.; Woo, L.; Mclean, A.; *et al. Blood Coagul. Fibrinolysis* **1998**, *9*, 105.
24. Okada, M.; Blomback, B.; Chang, M. D.; Horowitz, B. *J. Biol. Chem.* **1985**, *260*, 1811–1820.
25. Weisel, J. W. *Adv. Protein Chem.* **2005**, *70*, 247–299.
26. Blomback, B. *Thromb. Res.* **1994**, *75*, 327–328.
27. Sierra, D. H.; Feldman, D. S.; Saltz, R.; Huang, S. *J. Appl. Biomater.* **1992**, *3*, 147–151.
28. Rowe, S. L.; Lee, S.; Stegemann, J. P. *Acta Biomater.* **2007**, *3*, 59–67.
29. Akpalo, E.; Larreta-Garde, V. *Acta Biomater.* **2010**, *6*(2), 396–402.
30. Roberts, W. W.; Lorand, L.; Mockros, L. F. *Biorheology* **1973**, *10*, 29–42.
31. Veklich, Y.; Francis, C. W.; White, J.; Weisel, J. W. *Blood* **1998**, *92*, 4721–4729.
32. Collet, J. P.; Park, D.; Lesty, C.; *et al. Arterioscler. Thromb. Vasc. Biol.* **2000**, *20*, 1354–1361.
33. Weisel, J. W.; Litvinov, R. I. *Cardiovasc. Hematol. Agents Med. Chem.* **2008**, *6*, 161–180.
34. Meh, D. A.; Mosesson, M. W.; Diorio, J. P.; *et al. Blood Coagul. Fibrinolysis* **2001**, *12*, 627–637.
35. Lorentz, K. M.; Kontos, S.; Frey, P.; Hubbell, J. A. *Biomaterials* **2011**, *32*, 430–438.
36. Smith, J. D.; Chen, A.; Ernst, L. A.; Waggoner, A. S.; Campbell, P. G. *Bioconjug. Chem.* **2007**, *18*, 695–701.
37. Martin, P. *Science* **1997**, *276*, 75–81.
38. Gorodetsky, R. *Expert Opin. Biol. Ther.* **2008**, *8*, 1831–1846.
39. Suehiro, K.; Mizuguchi, J.; Nishiyama, K.; Iwanaga, S.; Farrell, D. H.; Ohtaki, S. *J. Biochem.* **2000**, *128*, 705–710.
40. Bajorath, J. *Proteins* **2000**, *39*, 103–111.
41. Turley, E. A.; Noble, P. W.; Bourguignon, L. Y. *J. Biol. Chem.* **2002**, *277*, 4589–4592.
42. Clark, R. A. *Thromb. Haemost.* **2003**, *90*, 1003–1006.
43. Clark, R. A.; An, J. Q.; Greiling, D.; Khan, A.; Schwarzbauer, J. E. *J. Invest. Dermatol.* **2003**, *121*, 695–705.
44. Tawil, B. In *An Introduction to Biomaterials*; Guelcher, S. A., Hollinger, J. O., Eds.; CRC Press Taylor and Francis Group: Boca Raton, FL, 2006; pp 105–120.
45. Horch, R. E.; Bannasch, H.; Stark, G. B. *Transplant. Proc.* **2001**, *33*, 642–644.
46. Kopp, J.; Jeschke, M. G.; Bach, A. D.; Kneser, U.; Horch, R. E. *Cell Tissue Bank.* **2004**, *5*, 89–96.
47. Tuan, T. L.; Zhu, J. Y.; Sun, B.; Nichter, L. S.; Nimni, M. E.; Laug, W. E. *J. Invest. Dermatol.* **1996**, *106*, 1007–1011.
48. Currie, L. J.; Sharpe, J. R.; Martin, R. *Plast. Reconstr. Surg.* **2001**, *108*, 1713–1726.
49. Ameer, G. A.; Mahmood, T. A.; Langer, R. *J. Orthop. Res.* **2002**, *20*, 16–19.
50. Baumgartner, L.; Arnhold, S.; Brixius, K.; Addicks, K.; Bloch, W. *J. Biomed. Mater. Res. A* **2010**, *93*(3), 930–940.
51. Dare, E. V.; Vascotto, S. G.; Carlsson, D.; Hincke, M. T.; Griffith, M. *Int. J. Artif. Organs* **2007**, *30*, 619–627.
52. Homminga, G. N.; Buma, P.; Koot, H. W.; Van der Kraan, P. M.; Van den Berg, W. B. *Acta Orthop. Scand.* **1993**, *64*, 441–445.
53. Kirilak, Y.; Pavlos, N. J.; Willers, C. R.; *et al. Int. J. Mol. Med.* **2006**, *17*, 551–558.
54. Pettersson, S.; Wettero, J.; Tengvall, P.; Kratz, G. *J. Tissue Eng. Regen. Med.* **2009**, *3*, 450–460.
55. Kim, S. J.; Jang, J. D.; Lee, S. K. *Cytotechnology* **2007**, *54*, 115–120.
56. Bach, A. D.; Bannasch, H.; Galla, T. J.; Bittner, K. M.; Stark, G. B. *Tissue Eng.* **2001**, *7*, 45–53.
57. Wechselberger, G.; Russell, R. C.; Neumeister, M. W.; Schoeller, T.; Piza-Katzer, H.; Rainer, C. *Plast. Reconstr. Surg.* **2002**, *110*, 123–129.
58. Wechselberger, G.; Schoeller, T.; Stenzl, A.; Ninkovic, M.; Lille, S.; Russell, R. C. *J. Urol.* **1998**, *160*, 583–586.
59. Gwak, S. J.; Choi, D.; Paik, S. S.; Lee, E. Y.; Lees, K. S.; Kim, B. S. *Biotechnol. Lett.* **2004**, *26*, 505–508.
60. Catelas, I.; Sese, N.; Wu, B. M.; Dunn, J. C.; Helgerson, S.; Tawil, B. *Tissue Eng.* **2006**, *12*, 2385–2396.
61. Cox, S.; Cole, M.; Tawil, B. *Tissue Eng.* **2004**, *10*, 942–954.

62. Harkin, D. G.; Dawson, R. A.; Upton, Z. *Wound Repair Regen.* **2006**, *14*, 354–363.
63. Ho, W.; Tawil, B.; Dunn, J. C.; Wu, B. M. *Tissue Eng.* **2006**, *12*, 1587–1595.
64. Mana, M.; Cole, M.; Cox, S.; Tawil, B. *Wound Repair Regen.* **2006**, *14*, 72–80.
65. Bensaid, W.; Triffitt, J. T.; Blanchat, C.; Oudina, K.; Sedel, L.; Petite, H. *Biomaterials* **2003**, *24*, 2497–2502.
66. Trombi, L.; D'Alessandro, D.; Pacini, S.; *et al*. *Transfusion* **2008**, *48*, 2246–2251.
67. Zhang, G.; Wang, X.; Wang, Z.; Zhang, J.; Suggs, L. *Tissue Eng.* **2006**, *12*, 9–19.
68. Zhang, G.; Drinnan, C. T.; Geuss, L. R.; Suggs, L. J. *Acta Biomater.* **2010**, *6*, 3395–3403.
69. Huang, N. F.; Chu, J.; Lee, R. J.; Li, S. *Acta Biomater.* **2010**, *6*, 3947–3956.
70. Macasev, D.; Diorio, J. P.; Gugerell, A.; Goppelt, A.; Gulle, H.; Bittner, M. *J. Biomater. Appl.* **2010**.
71. Pardue, M. T.; Hejny, C.; Gilbert, J. A.; Phillips, M. J.; Geroski, D. H.; Edelhauser, H. F. *Retina* **2004**, *24*, 776–782.
72. Simpson, A. E.; Gilbert, J. A.; Rudnick, D. E.; Geroski, D. H.; Aaberg, T. M., Jr.; Edelhauser, H. F. *Arch. Ophthalmol.* **2002**, *120*, 1069–1074.
73. Hafeli, U. O.; Pauer, G. J.; Unnithan, J.; Prayson, R. A. *Eur. J. Pharm. Biopharm.* **2007**, *65*, 282–288.
74. Yoshida, H.; Yamaoka, Y.; Shinoyama, M.; Kamiya, A. *Biol. Pharm. Bull.* **2000**, *23*, 371–374.
75. Woolverton, C. J.; Fulton, J. A.; Salstrom, S. J.; *et al*. *J. Antimicrob. Chemother.* **2001**, *48*, 861–867.
76. Kumar, T. R.; Vasantha Bai, M.; Krishnan, L. K. *Biologicals* **2004**, *32*, 49–55.
77. Tredwell, S.; Jackson, J. K.; Hamilton, D.; Lee, V.; Burt, H. M. *Can. J. Surg.* **2006**, *49*, 347–352.
78. Tsourvakas, S.; Alexandropoulos, C.; Karatzios, C.; Egnatiadis, N.; Kampagiannis, N. *Acta Orthop. Belg.* **2009**, *75*, 537–542.
79. Tsourvakas, S.; Hatzigrigoris, P.; Tsibinos, A.; Kanellakopoulou, K.; Giamarellou, H.; Dounis, E. *Arch. Orthop. Trauma. Surg.* **1995**, *114*, 295–297.
80. Hou, T.; Xu, J.; Li, Q.; Feng, J.; Zen, L. *Tissue Eng. A* **2008**, *14*, 1173–1182.
81. Zhibo, X.; Miaobo, Z. *Aesthet. Surg. J.* **2009**, *29*, 32–34.
82. Pandit, A. S.; Wilson, D. J.; Feldman, D. S. *J. Biomater. Appl.* **2000**, *14*, 229–242.
83. Mogford, J. E.; Tawil, B.; Jia, S.; Mustoe, T. A. *Wound Repair Regen.* **2009**, *17*, 405–410.
84. Ucuzian, A. A.; Brewster, L. P.; East, A. T.; Pang, Y.; Gassman, A. A.; Greisler, H. P. *J. Biomed. Mater. Res. A* **2010**, *94*, 988–996.
85. Park, M. S.; Kim, S. S.; Cho, S. W.; Choi, C. Y.; Kim, B. S. *J. Biomed. Mater. Res. B Appl. Biomater.* **2006**, *79*, 353–359.
86. Cole, M.; Cox, S.; Inman, E.; *et al*. *Wound Repair Regen.* **2007**, *15*, 521–529.
87. Bhang, S. H.; Lee, Y. E.; Cho, S. W.; *et al*. *Biochem. Biophys. Res. Commun.* **2007**, *359*, 40–45.
88. Sahni, A.; Odrljin, T.; Francis, C. W. *J. Biol. Chem.* **1998**, *273*, 7554–7559.
89. Campbell, P. G.; Durham, S. K.; Hayes, J. D.; Suwanichkul, A.; Powell, D. R. *J. Biol. Chem.* **1999**, *274*, 30215–30221.
90. Sahni, A.; Francis, C. W. *Blood* **2000**, *96*, 3772–3778.
91. Wong, C.; Inman, E.; Spaethe, R.; Helgerson, S. *Thromb. Haemost.* **2003**, *89*, 573–582.
92. Catelas, I.; Dwyer, J. F.; Helgerson, S. *Tissue Eng. C Methods* **2008**, *14*, 119–128.
93. Mittermayr, R.; Morton, T.; Hofmann, M.; Helgerson, S.; Van Griensven, M.; Redl, H. *Wound Repair Regen.* **2008**, *16*, 542–550.
94. Bhang, S. H.; Jeon, O.; Choi, C. Y.; Kwon, Y. H.; Kim, B. S. *J. Biomed. Mater. Res. A* **2007**, *80*, 998–1002.
95. Zhao, W.; Han, Q.; Lin, H.; *et al*. *J. Mol. Med.* **2008**, *86*, 1127–1138.
96. Zhao, W.; Han, Q.; Lin, H.; *et al*. *Tissue Eng. A* **2009**, *15*, 991–998.
97. Drinnan, C. T.; Zhang, G.; Alexander, M. A.; Pulido, A. S.; Suggs, L. J. *J. Control Release* **2010**, *147*, 180–186.
98. Redl, H.; Fuerst, W.; Kneidlinger, R.; *et al*. Fibrin/Fibrinogen-Binding Conjugate. US Patent 6,713,453 B2, 2004.
99. Houck, K. A.; Ferrara, N.; Winer, J.; Cachianes, G.; Li, B.; Leung, D. W. *Mol. Endocrinol.* **1991**, *5*, 1806–1814.
100. Robinson, C. J.; Stringer, S. E. *J. Cell Sci.* **2001**, *114*, 853–865.
101. Houck, K. A.; Leung, D. W.; Rowland, A. M.; Winer, J.; Ferrara, N. *J. Biol. Chem.* **1992**, *267*, 26031–26037.
102. Spicer, P. P.; Mikos, A. G. *J. Control. Release* **2010**, *148*, 49–55.
103. Schense, J. C.; Hubbell, J. A. *Bioconjug. Chem.* **1999**, *10*, 75–81.
104. Ehrbar, M.; Djonov, V. G.; Schnell, C.; *et al*. *Circ. Res.* **2004**, *94*, 1124–1132.
105. Schense, J. C.; Bloch, J.; Aebischer, P.; Hubbell, J. A. *Nat. Biotechnol.* **2000**, *18*, 415–419.
106. Zisch, A. H.; Zeisberger, S. M.; Ehrbar, M.; *et al*. *Biomaterials* **2004**, *25*, 3245–3257.
107. Sakiyama-Elbert, S. E.; Hubbell, J. A. *J. Control Release* **2000**, *65*, 389–402.
108. Taylor, S. J.; McDonald, J. W., III; Sakiyama-Elbert, S. E. *J. Control. Release* **2004**, *98*, 281–294.
109. Taylor, S. J.; Rosenzweig, E. S.; McDonald, J. W., III; Sakiyama-Elbert, S. E. *J. Control. Release* **2006**, *113*, 226–235.
110. Johnson, P. J.; Tatara, A.; Shiu, A.; Sakiyama-Elbert, S. E. *Cell Transplant.* **2010**, *19*, 89–101.
111. Sakiyama-Elbert, S. E.; Hubbell, J. A. *J. Control. Release* **2000**, *69*, 149–158.
112. Wood, M. D.; Moore, A. M.; Hunter, D. A. *Acta Biomater.* **2009**, *5*, 959–968.
113. Wood, M. D.; Hunter, D.; Mackinnon, S. E.; Sakiyama-Elbert, S. E. *J. Biomater. Sci. Polym. Ed.* **2010**, *21*, 771–787.
114. Wood, M. D.; Macewan, M. R.; French, A. R.; *et al*. *Biotechnol. Bioeng.* **2010**, *106*, 970–979.
115. Sakiyama-Elbert, S. E.; Panitch, A.; Hubbell, J. A. *FASEB J.* **2001**, *15*, 1300–1302.
116. Arrighi, I.; Mark, S.; Alvisi, M.; Von Rechenberg, B.; Hubbell, J. A.; Schense, J. C. *Biomaterials* **2009**, *30*, 1763–1771.
117. Schmoekel, H.; Schense, J. C.; Weber, F. E.; *et al*. *J. Orthop. Res.* **2004**, *22*, 376–381.
118. Schmoekel, H. G.; Weber, F. E.; Schense, J. C.; Gratz, K. W.; Schawalder, P.; Hubbell, J. A. *Biotechnol. Bioeng.* **2005**, *89*, 253–262.
119. Schillinger, U.; Wexel, G.; Hacker, C.; *et al*. *Pharm. Res.* **2008**, *25*, 2946–2962.
120. Giannoni, P.; Hunziker, E. B. *Biotechnol. Bioeng.* **2003**, *83*, 121–123.
121. Meyenburg, S.; Lilie, H.; Panzner, S.; Rudolph, R. *J. Control. Release* **2000**, *69*, 159–168.
122. Breen, A.; Strappe, P.; Kumar, A.; O'Brien, T.; Pandit, A. *J. Biomed. Mater. Res. A* **2006**, *78*, 702–708.
123. Schek, R. M.; Hollister, S. J.; Krebsbach, P. H. *Mol. Ther.* **2004**, *9*, 130–138.
124. Teraishi, F.; Umeoka, T.; Saito, T.; Tsukagoshi, T.; Tanaka, N.; Fujiwara, T. *Surg. Endosc.* **2003**, *17*, 1845–1848.
125. Breen, A. M.; Dockery, P.; O'Brien, T.; Pandit, A. S. *Biomaterials* **2008**, *29*, 3143–3151.
126. Breen, A.; Dockery, P.; O'Brien, T.; Pandit, A. *J. Biomed. Mater. Res. A* **2009**, *89*, 876–884.
127. Escamez, M. J.; Carretero, M.; Garcia, M.; *et al*. *J. Invest. Dermatol.* **2008**, *128*, 1565–1575.
128. Bonadio, J. *J. Mol. Med.* **2000**, *78*, 303–311.
129. Christman, K. L.; Fang, Q.; Yee, M. S.; Johnson, K. R.; Sievers, R. E.; Lee, R. J. *Biomaterials* **2005**, *26*, 1139–1144.
130. Jozkowicz, A.; Fugl, A.; Nanobashvili, J.; *et al*. *Int. J. Artif. Organs* **2003**, *26*, 161–169.
131. Michlits, W.; Mittermayr, R.; Schafer, R.; Redl, H.; Aharinejad, S. *Wound Repair Regen.* **2007**, *15*, 360–367.
132. Andree, C.; Voigt, M.; Wenger, A.; *et al*. *Tissue Eng.* **2001**, *7*, 757–766.
133. Lee, T. C.; Ho, J. T.; Hung, K. S.; Chen, W. F.; Chung, Y. H.; Yang, Y. L. *Neurosurgery* **2006**, *58*, 373–380; discussion 373–380.
134. des Rieux, A.; Shikanov, A.; Shea, L. D. *J. Control. Release* **2009**, *136*, 148–154.
135. Tschoeke, B.; Flanagan, T. C.; Koch, S.; *et al*. *Tissue Eng. A* **2009**, *15*, 1909–1918.
136. Aper, T.; Teebken, O. E.; Steinhoff, G.; Haverich, A. *Eur. J. Vasc. Endovasc. Surg.* **2004**, *28*, 296–302.
137. Koch, S.; Flanagan, T. C.; Sachweh, J. S. *Biomaterials* **2010**, *31*, 4731–4739.
138. Cummings, C. L.; Gawlitta, D.; Nerem, R. M.; Stegemann, J. P. *Biomaterials* **2004**, *25*, 3699–3706.
139. Stekelenburg, M.; Rutten, M. C.; Snoeckx, L. H.; Baaijens, F. P. *Tissue Eng. A* **2009**, *15*, 1081–1089.
140. Syedain, Z. H.; Meier, L. A.; Bjork, J. W.; Lee, A.; Tranquillo, R. T. *Biomaterials* **2011**, *32*, 714–722.
141. Christman, K. L.; Vardanian, A. J.; Fang, Q.; Sievers, R. E.; Fok, H. H.; Lee, R. J. *J. Am. Coll. Cardiol.* **2004**, *44*, 654–660.
142. Li, Y. S.; Gao, B. R. *Chin. Med. J. (Engl.)* **2007**, *120*, 2022–2027.
143. Xiong, Q.; Hill, K. L.; Li, Q.; *et al*. *Stem Cell* **2011**, *29*(2), 367–375.
144. Divya, P.; Krishnan, L. K. *J. Tissue Eng. Regen. Med.* **2009**, *3*, 377–388.
145. Montano, I.; Schiestl, C.; Schneider, J.; *et al*. *Tissue Eng. A* **2009**, *16*, 269–282.
146. Beier, J. P.; Horch, R. E.; Arkudas, A.; *et al*. *Microsurgery* **2009**, *29*, 42–51.
147. Kneser, U.; Polykandriotis, E.; Ohnolz, J.; *et al*. *Tissue Eng.* **2006**, *12*, 1721–1731.
148. Zilch, H.; Wolff, R. *Z. Orthop. Ihre Grenzgeb.* **1987**, *125*, 214–218.
149. Schwarz, N.; Redl, H.; Zeng, L.; Schlag, G.; Dinges, H. P.; Eschberger, J. *Clin. Orthop. Relat. Res.* **1993**, *293*, 353–359.
150. Meyers, M. H.; Herron, M. *Clin. Orthop. Relat. Res.* **1984**, *182*, 258–263.

151. Isogai, N.; Landis, W. J.; Mori, R.; *et al*. *Plast. Reconstr. Surg.* **2000**, *105*, 953–963.
152. Ito, K.; Yamada, Y.; Naiki, T.; Ueda, M. *Clin. Oral Implants Res.* **2006**, *17*, 579–586.
153. Kang, E. J.; Byun, J. H.; Choi, Y. J.; *et al*. *Tissue Eng. A* **2010**, *16*(3), 815–827.
154. Kawamura, M.; Urist, M. R. *Clin. Orthop. Relat. Res.* **1988**, *235*, 302–310.
155. Le Guehennec, L.; Layrolle, P.; Daculsi, G. *Eur. Cell Mater.* **2004**, *8*, 1–10; discussion 10–11.
156. Carmagnola, D.; Berglundh, T.; Araujo, M.; Albrektsson, T.; Lindhe, J. *J. Clin. Periodontol.* **2000**, *27*, 799–805.
157. Cunin, G.; Boissonnet, H.; Petite, H.; Blanchat, C.; Guillemin, G. *Spine (Phila Pa 1976)* **2000**, *25*, 1070–1076.
158. Le Guehennec, L.; Goyenvalle, E.; Aguado, E.; *et al*. *J. Mater. Sci. Mater. Med.* **2005**, *16*, 29–35.
159. Re, S.; Corrente, G.; Abundo, R.; Cardaropoli, D. *Int. J. Periodontics Restorative Dent.* **2002**, *22*, 138–145.
160. Karp, J. M.; Sarraf, F.; Shoichet, M. S.; Davies, J. E. *J. Biomed. Mater. Res. A* **2004**, *71*, 162–171.
161. Park, J. Y.; Davies, J. E. *Clin. Oral Implants Res.* **2000**, *11*, 530–539.
162. Davies, J. E. *Int. J. Prosthodont.* **1998**, *11*, 391–401.
163. Arnaud, E. *Childs Nerv. Syst.* **2000**, *16*, 659–668.
164. Arkudas, A.; Beier, J. P.; Pryymachuk, G.; *et al*. *Tissue Eng. Part C Methods* **2010**, *16*, 1503–1514.
165. Beier, J. P.; Horch, R. E.; Hess, A.; *et al*. *J. Tissue Eng. Regen. Med.* **2010**, *4*, 216–223.
166. Yamada, Y.; Boo, J. S.; Ozawa, R.; *et al*. *J. Craniomaxillofac. Surg.* **2003**, *31*, 27–33.
167. Ahmed, T. A.; Dare, E. V.; Hincke, M. *Tissue Eng. B Rev.* **2008**, *14*, 199–215.
168. Izuta, Y.; Ochi, M.; Adachi, N.; Deie, M.; Yamasaki, T.; Shinomiya, R. *Knee* **2005**, *12*, 217–223.
169. Ruszymah, B. H.; Lokman, B. S.; Asma, A.; *et al*. *Int. J. Pediatr. Otorhinolaryngol.* **2007**, *71*, 1225–1234.
170. Silverman, R. P.; Bonasser, L.; Passaretti, D.; Randolph, M. A.; Yaremchuk, M. J. *Plast. Reconstr. Surg.* **2000**, *105*, 1393–1398.
171. Hendrickson, D. A.; Nixon, A. J.; Grande, D. A.; *et al*. *J. Orthop. Res.* **1994**, *12*, 485–497.
172. Peretti, G. M.; Xu, J. W.; Bonassar, L. J.; Kirchhoff, C. H.; Yaremchuk, M. J.; Randolph, M. A. *Tissue Eng.* **2006**, *12*, 1151–1168.
173. Park, S. H.; Park, S. R.; Chung, S. I.; Pai, K. S.; Min, B. H. *Artif. Organs* **2005**, *29*, 838–845.
174. Park, S. H.; Choi, B. H.; Park, S. R.; Min, B. H. *Tissue Eng. Part A* **2011**, *17*, 1277–1286.
175. Sha'Ban, M.; Kim, S. H.; Idrus, R. B.; Khang, G. *J. Orthop. Surg.* **2008**, *3*, 17.
176. Jung, Y.; Kim, S. H.; Kim, Y. H. *J. Biomater. Sci. Polym. Ed.* **2010**, *21*, 581–592.
177. Jung, Y.; Chung, Y. I.; Kim, S. H.; Tae, G.; Kim, Y. H.; Rhie, J. W. *Biomaterials* **2009**, *30*, 4657–4664.
178. Dickhut, A.; Dexheimer, V.; Martin, K.; Lauinger, R.; Heisel, C.; Richter, W. *Tissue Eng. A* **2010**, *16*, 453–464.
179. Park, J. S.; Yang, H. N.; Woo, D. G.; Jeon, S. Y.; Park, K. H. *Biomaterials* **2011**, *32*, 1495–1507.
180. Fortier, L. A.; Mohammed, H. O.; Lust, G.; Nixon, A. J. *J. Bone Joint Surg. Br.* **2002**, *84*, 276–288.
181. Gao, C.; Ma, S.; Ji, Y.; Wang, J. E.; Li, J. *Injury* **2008**, *39*, 1414–1420.
182. Johnson, P. J.; Parker, S. R.; Sakiyama-Elbert, S. E. *Biotechnol. Bioeng.* **2009**, *104*, 1207–1214.
183. Kalbermatten, D. F.; Pettersson, J.; Kingham, P. J.; Pierer, G.; Wiberg, M.; Terenghi, G. *J. Reconstr. Microsurg.* **2009**, *25*, 27–33.
184. Isaacs, J. E.; Mcdaniel, C. O.; Owen, J. R.; Wayne, J. S. *J. Hand Surg. Am.* **2008**, *33*, 893–899.
185. Johnson, P. J.; Parker, S. R.; Sakiyama-Elbert, S. E. *J. Biomed. Mater. Res. A* **2010**, *92A*(1), 152–163.
186. Itosaka, H.; Kuroda, S.; Shichinohe, H.; *et al*. *Neuropathology* **2009**, *29*, 248–257.
187. Geer, D. J.; Swartz, D. D.; Andreadis, S. T. *Tissue Eng.* **2002**, *8*, 787–798.
188. Bannasch, H.; Unterberg, T.; Fohn, M.; Weyand, B.; Horch, R. E.; Stark, G. B. *Burns* **2008**, *34*, 1015–1021.
189. Zebardast, N.; Lickorish, D.; Davies, J. E. *Organogenesis* **2010**, *6*, 197–203.
190. Ronfard, V.; Rives, J. M.; Neveux, Y.; Carsin, H.; Barrandon, Y. *Transplantation* **2010**, *70*, 1588–1598.
191. Tanikawa, D. Y.; Alonso, N.; Herson, M. R.; *et al*. *Acta Cir. Bras.* **2010**, *25*, 541–548.
192. Hojo, M.; Inokuchi, S.; Kidokoro, M.; *et al*. *Plast. Reconstr. Surg.* **2003**, *111*, 1638–1645.
193. Inoue, S.; Kijima, H.; Kidokoro, M.; *et al*. *J. Burn Care Res.* **2009**, *30*, 514–519.
194. Fiegel, H. C.; Kneser, U.; Kluth, D.; Metzger, R.; Till, H.; Rolle, U. *Pediatr. Surg. Int.* **2009**, *25*, 667–673.
195. Bruns, H.; Kneser, U.; Holzhuter, S.; *et al*. *Tissue Eng.* **2005**, *11*, 1718–1726.
196. Beier, J. P.; Stern-Straeter, J.; Foerster, V. T.; Kneser, U.; Stark, G. B.; Bach, A. D. *Plast. Reconstr. Surg.* **2006**, *118*, 1113–1121; discussion 1122–1124.
197. Koning, M.; Harmsen, M. C.; Van Luyn, M. J.; Werker, P. M. *J. Tissue Eng. Regen. Med.* **2009**, *3*, 407–415.
198. Beier, J. P.; Kneser, U.; Stern-Strater, J.; Stark, G. B.; Bach, A. D. *Cell Transplant.* **2004**, *13*, 45–53.
199. Khodabukus, A.; Baar, K. *Tissue Eng. C Methods* **2009**, *15*, 501–511.
200. Bian, W.; Bursac, N. *Biomaterials* **2009**, *30*, 1401–1412.
201. Chun, J.; Tuan, T. L.; Han, B.; Vangsness, C. T.; Nimni, M. E. *Connect. Tissue Res.* **2003**, *44*, 81–87.
202. Hankemeier, S.; Van Griensven, M.; Ezechieli, M.; *et al*. *Arch. Orthop. Trauma Surg.* **2007**, *127*, 815–821.
203. Hankemeier, S.; Hurschler, C.; Zeichen, J.; *et al*. *Tissue Eng. A* **2009**, *15*, 1019–1030.
204. Thomopoulos, S.; Das, R.; Sakiyama-Elbert, S.; Silva, M. J.; Charlton, N.; Gelberman, R. H. *Ann. Biomed. Eng.* **2010**, *38*, 225–234.
205. Thomopoulos, S.; Das, R.; Silva, M. J. *J. Orthop. Res.* **2009**, *27*, 1209–1215.
206. Thomopoulos, S.; Kim, H. M.; Das, R.; *et al*. *J. Bone Joint Surg. Am.* **2010**, *92*, 2285–2293.
207. Chong, A. K.; Ang, A. D.; Goh, J. C.; *et al*. *J. Bone Joint Surg. Am.* **2007**, *89*, 74–81.
208. Thomopoulos, S.; Das, R.; Silva, M. J.; *et al*. *J. Orthop. Res.* **2009**, *27*, 1209–1215.
209. Amrani, D. L.; Diorio, J. P.; Delmotte, Y. *Ann. N. Y. Acad. Sci.* **2001**, *936*, 566–579.
210. Buchta, C.; Hedrich, H. C.; Macher, M.; Hocker, P.; Redl, H. *Biomaterials* **2005**, *26*, 6233–6241.
211. Janmey, P. A.; Winer, J. P.; Weisel, J. W. *J. R. Soc. Interface* **2009**, *6*, 1–10.
212. Spotnitz, W. D.; Burks, S. *Clin. Appl. Thromb. Hemost.* **2010**, *16*, 497–514.
213. Clark, R. A. *Expert Opin. Investig. Drugs* **2000**, *9*, 2371–2392.
214. Dickneite, G.; Metzner, H.; Pfeifer, T.; Kroez, M.; Witzke, G. *Thromb. Res.* **2003**, *112*, 73–82.
215. Tredree, R.; Beierlein, W.; Debrix, I.; *et al*. *EJHPScience* **2006**, *12*, 3–9.
216. Spotnitz, W. D. *World J. Surg.* **2010**, *34*, 632–634.
217. Rousou, J.; Levitsky, S.; Gonzalez-Lavin, L.; *et al*. *J. Thorac. Cardiovasc. Surg.* **1989**, *97*, 194–203.
218. Lowe, J.; Luber, J.; Levitsky, S.; *et al*. *J. Cardiovasc. Surg. (Torino)* **2007**, *48*, 323–331.
219. Chalmers, R. T.; Darling, R. C., III; Wingard, J. T.; *et al*. *Br. J. Surg.* **2010**, *97*, 1784–1789.
220. Taylor, L. M., Jr.; Mueller-Velten, G.; Koslow, A.; Hunter, G.; Naslund, T.; Kline, R. *J. Vasc. Surg.* **2003**, *38*, 766–771.
221. Sintler, M. P.; Mahmood, A.; Smith, S. R.; Simms, M. H.; Vohra, R. K. *World J. Surg.* **2005**, *29*, 1259–1262.
222. Aigner, C.; Wolner, E.; Mohl, W. *Ann. Thorac. Surg.* **2006**, *81*, 1275–1278.
223. Toda, K.; Yoshitatsu, M.; Izutani, H.; Ihara, K. *Interact. Cardiovasc. Thorac. Surg.* **2007**, *6*, 577–578.
224. Mooney, E.; Loh, C.; Pu, L. L. *Plast. Reconstr. Surg.* **2009**, *124*, 989–992.
225. Foster, K. *Surgery* **2007**, *142*, S50–S54.
226. Vibe, P.; Pless, J. *Scand. J. Plast. Reconstr. Surg.* **1983**, *17*, 263–264.
227. Stuart, J. D.; Morgan, R. F.; Kenney, J. G. *Ann. Plast. Surg.* **1990**, *24*, 524–527.
228. Foster, K.; Greenhalgh, D.; Gamelli, R. L.; *et al*. *J. Burn Care Res.* **2008**, *29*, 293–303.
229. Gibran, N.; Luterman, A.; Herndon, D.; *et al*. *J. Burn Care Res.* **2007**, *28*, 401–408.
230. Nervi, C.; Gamelli, R. L.; Greenhalgh, D. G.; *et al*. *J. Burn Care Rehabil.* **2001**, *22*, 99–103.
231. Mcgill, V.; Kowal-Vern, A.; Lee, M.; *et al*. *J. Burn Care Rehabil.* **1997**, *18*, 429–434.
232. Achauer, B. M.; Miller, S. R.; Lee, T. E. *J. Burn Care Rehabil.* **1994**, *15*, 24–28.
233. Greenhalgh, D. G.; Gamelli, R. L.; Lee, M.; *et al*. *J. Trauma* **1999**, *46*, 433–440.
234. Marchac, D.; Greensmith, A. L. *Plast. Reconstr. Surg.* **2005**, *115*, 911–916; discussion 917–918.

235. Oliver, D. W.; Hamilton, S. A.; Figle, A. A.; Wood, S. H.; Lamberty, B. G. *Plast. Reconstr. Surg.* **2001**, *108*, 2101–2105; discussion 2106–2107.
236. Por, Y. C.; Shi, L.; Samuel, M.; Song, C.; Yeow, V. K. *Aesthetic Plast. Surg.* **2009**, *33*, 336–339.
237. Carless, P. A.; Henry, D. A. *Br. J. Surg.* **2006**, *93*, 810–819.
238. Toman, N.; Buschmann, A.; Muehlberger, T. *Chirurg* **2007**, *78*, 531–535.
239. Albala, D. M.; Lawson, J. H. *J. Am. Coll. Surg.* **2006**, *202*, 685–697.
240. Rutgeerts, P.; Rauws, E.; Wara, P.; *et al*. *Lancet* **1997**, *350*, 692–696.
241. Herold, G.; Preclik, G.; Stange, F. *Hepatogastroenterology* **1994**, *41*, 116–119.
242. Schwartz, M.; Madariaga, J.; Hirose, R.; *et al*. *Arch. Surg.* **2004**, *139*, 1148–1154.
243. Jang, J. W.; Park, D. H.; Moon, S. H.; *et al*. *World J. Gastroenterol.* **2008**, *14*, 6093–6095.
244. Fingerhut, A.; Veyrie, N.; Ata, T.; Alexakis, N.; Leandros, E. *Dig. Surg.* **2009**, *26*, 7–14.
245. Kamada, M.; Fujita, Y.; Ishii, R.; Endoh, S. *Headache* **2000**, *40*, 844–847.
246. Nakamura, H.; Matsuyama, Y.; Yoshihara, H.; *et al*. *Spine (Phila Pa 1976)* **2005**, *30*, E347–E351.
247. Narakas, A. *Orthop. Clin. North Am.* **1988**, *19*, 187–199.
248. Silver, F. H.; Wang, M. C.; Pins, G. D. *Biomaterials* **1995**, *16*, 891–903.
249. Jankowitz, B. T.; Atteberry, D. S.; Gerszten, P. C.; *et al*. *Eur. Spine J.* **2009**, *18*, 1169–1174.
250. Rama, P.; Bonini, S.; Lambiase, A.; *et al*. *Transplantation* **2001**, *72*, 1478–1485.
251. Siatiri, H.; Moghimi, S.; Malihi, M.; Khodabande, A. *Cornea* **2008**, *27*, 988–991.
252. Levis, H.; Daniels, J. T. *Curr. Opin. Biotectnol.* **2009**, *20*(5), 593–597.
253. Kim, H. K.; Park, H. S. *Cornea* **2009**, *28*, 170–176.
254. Pruthi, R. S.; Chun, J.; Richman, M. *BJU Int.* **2004**, *93*, 813–817.
255. Seo, I. Y.; Lee, Y. H.; Rim, J. S. *J. Endourol.* **2008**, *22*, 959–962.
256. Evans, L. A.; Morey, A. F. *Int. Braz. J. Urol.* **2006**, *32*, 131–141.
257. Shekarriz, B.; Stoller, M. L. *J. Urol.* **2002**, *167*, 1218–1225.

Relevant Websites

http://www.ecf.utoronto.ca/~bonehead/

2.218. Elastin Biopolymers

J Rnjak-Kovacina*, Tufts University, Massachusetts, USA
W F Daamen*, Radboud University Nijmegen Medical Centre, Nijmegen, The Netherlands
M Pierna and J C Rodríguez-Cabello, Universidad de Valladolid, Paseo de Belén, Valladolid, Spain
A S Weiss, University of Sydney, Sydney, NSW, Australia

© 2011 Elsevier Ltd. All rights reserved.

2.218.1. Recombinant Human Tropoelastin-Based Constructs 330
2.218.1.1. Introduction 330
2.218.1.2. Synthetic Human Elastin Hydrogels 330
2.218.1.2.1. Chemically cross-linked SHE hydrogels 330
2.218.1.2.2. Enzymatically cross-linked SHE hydrogels 331
2.218.1.2.3. SHE hydrogels formed under alkaline conditions in the absence of a cross-linker 331
2.218.1.3. Electrospun rhTE Fibers 331
2.218.1.3.1. Electrospun rhTE and vascular tissue engineering 332
2.218.1.3.2. Electrospun rhTE and skin tissue engineering 332
2.218.1.4. Functionalized Surfaces 332
2.218.2. The Elastin-Like Recombinamers 333
2.218.2.1. Introduction 333
2.218.2.2. The Extraordinary Properties of ELRs 333
2.218.2.3. Genetic Engineering of ELRs 334
2.218.2.4. The Stimuli-Responsive Behavior and Self-Assembly Properties of ELRs 335
2.218.2.5. Biomedical and Biotechnological Applications 335
2.218.2.5.1. Tissue engineering 335
2.218.2.5.2. Functionalized surfaces 338
2.218.2.5.3. Fibers 339
2.218.2.5.4. Drug delivery 339
2.218.2.5.5. ELR-fusion constructions 340
2.218.2.6. Outlook 340
2.218.3. Animal-Derived Solubilized Elastin 341
2.218.3.1. Introduction 341
2.218.3.2. Types of Solubilized Elastin 341
2.218.3.2.1. α- and β-elastin 341
2.218.3.2.2. κ-elastin 341
2.218.3.2.3. Enzymatically solubilized elastin 341
2.218.3.3. Biomaterials Containing Animal-Derived Solubilized Elastin 341
2.218.3.4. *In Vitro* Experiments 341
2.218.3.4.1. Blends with natural materials 342
2.218.3.4.2. Blends with polymers 342
2.218.3.5. *In Vivo* Experiments 342
2.218.3.6. Clinical Applications 343
2.218.3.7. Future Directions 344
References 344

Abbreviations

BS3	Bis-sulfosuccinimidyl suberate
DSP	4-hydroxyphenyldimethylsulfoniummethyl-sulfate
EBP	Elastin-binding protein
ECM	Extracellular matrix protein
EDC	1-ethyl-3-(3-dimethylaminopropyl) carbodiimide hydrochloride
EDC/NHS	Ethyl(dimethyllaminopropyl) carbodiimide/N-Hydroxysuccinimide
EGDE	Ethylene–diglycidyl ether
ELP	Elastin-like polypeptide
ePTFE	Expanded polytetrafluoroethylene
FGF	Fibroblast growth factor
GA	Glutaraldehyde
GAG	Glycosaminoglycan
GO	Gene ontology
HFP	Hexafluoropropanol
HMDI	Hexamethylene diisocyanate
HUVEC	Human umbilical vein endothelial cells

*Both the authors contributed equally.

LO	Lysyl oxidase
MMP12	Matrix metalloproteinase 12
PBS	Phosphate buffered saline
PCL	Polycaprolactone
PET	Polyethylene terephthalate
PIII	Plasma immersion ion implantation
rhTE	Recombinant human tropoelastin
SHE	Synthetic human elastin
TFE	Trifluoroethanol
TMC	Trimethylene carbonate
VEGF	Vascular endothelial growth factor

2.218.1. Recombinant Human Tropoelastin-Based Constructs

2.218.1.1. Introduction

Research into elastin-containing biomaterials has for many years been hampered by elastin's extreme insolubility and the short *in vivo* lifetime of its precursor tropoelastin, making the formulation of constructs from intact elastic fibers exceedingly difficult.[1] The increased availability of soluble animal-derived elastin, obtained through alkaline (κ-elastin), acid (α-elastin), and enzymatic hydrolysis, and of elastin-based peptides, and in particular the development of the recombinant full-length elastin precursor tropoelastin (rhTE) now allow for enhanced and improved use of this class of protein in the development of advanced biomaterials.

Tropoelastin is a 60–70 kDa protein (whose size is dependent on the splice variant) encoded by a single copy gene located in the 7q12.2 region in humans.[2,3] It is characterized by alternating hydrophobic and hydrophilic domains, encoded by separate exons.[4] The hydrophobic domains are implicated in the association of the monomer in solution and the elastic function of the polymer, while the lysine- and alanine-rich hydrophilic domains are involved in polymerization of the monomer through cross-linking.[5] The lysyl oxidase (LO)-mediated formation of lysine-derived cross-links is preceded by coacervation, the self-association of tropoelastin monomers at physiological temperature and salt concentration.[6,7]

rhTE was first expressed in a bacterial expression system following the construction of the vector containing the human cDNA sequence.[8] This expression and purification system was further optimized to reproducibly generate multigram quantities of the most common splice variant of human tropoelastin.[9] The extensive study of this 60 kDa protein has since contributed vastly to our understanding of the tropoelastin structure, assembly, and function. rhTE has also been developed into a range of promising biomaterials for vascular and skin tissue engineering purposes and has been used to functionalize a number of polymer and metallic surfaces for improved biocompatibility.

As a recombinant human protein, rhTE carries little risk of immunorejection and pathogen transfer. It is isolated from bacterial cells through a tightly controlled and highly reproducible process that gives rise to little batch-to-batch inconsistency often observed in preparations isolated from animal sources.

2.218.1.2. Synthetic Human Elastin Hydrogels

Hydrogels are highly hydrated hydrophilic polymer networks.[10] Because of their tissue-like water content, their ability to transport nutrients and waste, and the versatile range of materials that can be used in their construction, hydrogels have proved to be particularly effective tissue engineered scaffolds.[11] Hydrogels can be cast into a variety of different macromolecular structures and physical forms. Their tissue-engineering applications are wide ranging and include soft contact lenses,[12] pills and capsules,[13] implants and catheters,[14] and wound dressings.[15]

The potential of elastin-based hydrogels in soft tissue bioengineering has long been recognized. Elastin-based hydrogels have been engineered from α-elastin,[16–18] recombinant elastin-like polypeptides (ELPs),[19–21] and rhTE.[22–26] Polymerization of rhTE into synthetic human elastin (SHE) hydrogels has been achieved by (i) introducing chemical cross-linkers to coacervating rhTE,[22,25] (ii) enzymatic cross-linking of rhTE by yeast LO,[24] or (iii) exposure of rhTE solutions to alkaline conditions in the absence of a cross-linker.[23]

2.218.1.2.1. Chemically cross-linked SHE hydrogels

In the presence of sixfold molar excess of chemical cross-linker bis-sulfosuccinimidyl suberate (BS3), over 80% of rhTE monomers are incorporated into the elastic array to form SHE hydrogels. BS3 is an amine-reactive homobifunctional cross-linker that inserts an 11.4 Å spacer arm between closely placed lysine residues of rhTE.[22] SHE hydrogels self-assemble in distinct stages, involving the association of rhTE monomers in spheres that coalesce into open-linked networks, which finally consolidate to form the porous SHE scaffold (**Figure 1**).[27] These constructs are highly elastic, displaying a Young's modulus of 220–280 kPa, similar to that of native elastin, which has a Young's modulus of 300–600 kPa. SHE hydrogels display a purely elastic region to above 150% strain and elongation at break ranging from 200% to 370%.[22] They show stimuli-responsive characteristics to salt concentration, where they absorb 33 times their weight in water and only 3.8 times their weight in PBS at 37 °C.[22]

SHE hydrogels have been shown to possess favorable biological properties *in vitro* and *in vivo*. They support cellular interactions with a range of adherent epithelial cell lines and with dermal fibroblasts.[22] Dermal fibroblasts also interact favourably with SHE hydrogels[25] coblended with α-elastin,[18] heparin, and dermatan sulfate.[26] Interestingly, when rhTE is coblended with glycosaminoglycans (GAGs) such as heparin and dermatan sulfate, the resultant hydrogels displayed increased porosity, pore size, and therefore cell penetration into the scaffold.[26] Fibroblasts grown on SHE hydrogels express ECM proteins including fibronectin and type I collagen.[25] These scaffolds are well tolerated *in vivo*, generating at most a bland immunological response when implanted subcutaneously in guinea pigs. Unlike collagen which is largely dispersed by week 4 postimplantation, SHE hydrogels remain intact up to 13 weeks postimplantation, showing only minor breakdown of the material.[22]

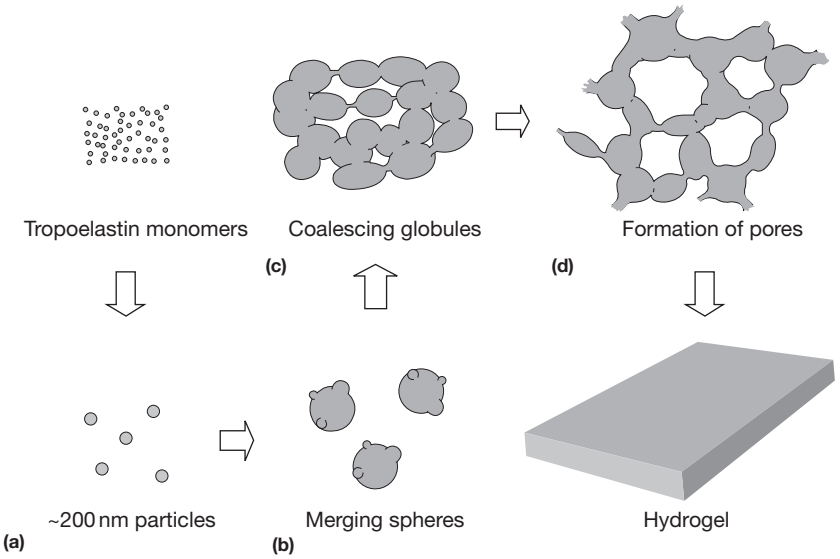

Figure 1 Stages of SHE hydrogel formation. Reproduced from Tu, Y.; Wise, S. G.; *et al*. *Micron* **2010**, *41*(3), 268–272.

2.218.1.2.2. Enzymatically cross-linked SHE hydrogels

rhTE can be cross-linked by LO isolated from a yeast strain *Pichia pastoris* in a process that mimics the cross-links formed in mammalian elastin.[24] Yeast LO oxidizes the lysine residues of rhTE *in vitro* to form cross-links found in natural elastin polymers, including lysinonorleucine, allysine aldol, and desmosine. However, the cross-linking efficiency in this system is reduced compared to that in natural elastin, resulting in 25-fold reduction in desmosine cross-links and ten times higher number of residual lysines compared to elastin isolated from horse *ligamentum nuchae*. A lower Young's modulus and greater swelling in water in these artificially cross-linked constructs also point to a lower number of cross-links formed. While resulting in less efficiently cross-linked materials compared to natural and chemically cross-linked elastin, these scaffolds are the first successful demonstration of LO cross-linking of rhTE *in vitro* and are therefore a valuable model in gaining a better understanding of the elastin cross-linking process, including mapping of regions involved in the intra- and intermolecular cross-links formed between tropoelastin molecules *in vivo*.[24]

2.218.1.2.3. SHE hydrogels formed under alkaline conditions in the absence of a cross-linker

Exposing rhTE to an alkaline environment at physiological temperature results in a sol–gel transition that enables the formation of stable, highly elastic hydrogels without the need for chemical or enzymatic cross-linking.[23] These materials consist of coacervated rhTE spherules that have self-assembled through association of the exposed hydrophobic rhTE side chains.[28] The resulting hydrogel is a stable, porous material that can be cast into a variety of shapes *in vitro* or injected *in vivo*. The material is highly flexible and elastic, with a Young's modulus of 1.69 ± 0.04 MPa. It displays favorable biological properties, supporting dermal fibroblast attachment and proliferation *in vitro* and persisting for up to 2 weeks subcutaneously *in vivo*, while eliciting only a mild foreign body response.[23] This material shows promise as a bulking agent or a biomaterial for the treatment of soft tissue injuries or defects, especially where the use of chemical cross-linkers raises biocompatibility concerns and impacts on the material approval process.

2.218.1.3. Electrospun rhTE Fibers

Electrospinning is a novel way of producing nano- to microscale fibers from a variety of natural and synthetic polymers.[29] It utilizes a strong electric field to process a polymer solution into a fibrous construct.[30] It has generated much interest in the tissue-engineering field in the past two decades as a simple, inexpensive means of mimicking native ECM fiber morphology.[30] Electrospinning results in thin, continuous fibers with a high surface area-to-volume ratio that promotes cellular adhesion.[29–32] The high porosity and pore interconnectivity of electrospun scaffolds allow for nutrient and metabolic waste transport necessary for cell survival and proliferation.[33,34] Compositional, structural, and functional properties of electrospun scaffolds can be easily controlled and adapted to a range of tissue-engineering applications.[32] Electrospun scaffolds are currently being investigated as a means of replacing and regenerating a range of tissues including skin, tendon, bone, cartilage, and blood vessels (for reviews see Liao *et al.*,[35] Kumbar *et al.*,[33] Ramachandran and Gouma,[36] Sell *et al.*[37]). They also present a potential for drug and gene delivery and coating of medical and dental implants.[33,38]

A number of elastin derivatives including solubilized bovine elastin,[39–48] elastin-mimetic peptide polymers,[49,50] cell culture-produced ECM sheets containing tropoelastin,[51] and rhTE[25,44,52,53] have been successfully electrospun. The majority of electrospun elastin-containing constructs have been generated by co-electrospinning α-elastin with other natural or synthetic polymers to mimic the components of the native tissue or increase the mechanical and structural stability of the electrospun construct.

Elastin-based scaffolds are generally electrospun from hexafluoropropanol (HFP),[41–48,51] but electrospinning from

trifluoroethanol (TFE)[49,50] and hydrochloric acid[40] has also been achieved. During the electrospinning process, α-elastin and rhTE adopt flat, ribbon-like fiber morphologies that are independent of the electrospinning parameters. Interestingly, when rhTE and α-elastin are electrospun alone, rhTE fibers are always two to three times wider than α-elastin fibers under identical electrospinning conditions. Electrospun rhTE fibers are also more elastic and possess higher tensile strength than electrospun α-elastin fibers.[44]

Elastin-based scaffolds require chemical cross-linking following electrospinning to retain the structural and mechanical integrity of the scaffold. Electrospun elastin scaffolds have been successfully cross-linked with glutaraldehyde (GA) vapors,[42,43,46,52,53] 1,6-diisocyanatohexane (HMDI),[44,52] and *N*-(3-dimethylaminopropyl)-*N*′-ethylcarbodiimide hydrochloride and *N*-hydroxysuccinimide (EDC/NHS).[40]

Solubilized bovine elastin[39–48] is the most commonly electrospun elastin derivative, but electrospun rhTE-based scaffolds are proving to be promising constructs in vascular and skin tissue engineering. rhTE was first electrospun in 2005[44] and its electrospinning and cross-linking parameters have since been optimized to generate a range of constructs with different physical and biological properties. rhTE can be electrospun into flat scaffolds of different shapes and sizes and into hollow tubular constructs. rhTE can be electrospun into randomly oriented or aligned fibers of different widths, and the scaffold pore size and porosity can be altered by changing the electrospinning parameters. Altered electrospinning parameters as well as introduction of other natural and synthetic polymers have also been shown to allow fine tuning of the mechanical and biological properties of electrospun rhTE-based scaffolds, including modulation of the scaffolds elasticity, tensile strength, and cellular interactions.

rhTE retains its functional activity following electrospinning. The electrospinning process does not negatively impact on the molecular weight, secondary structure, coacervation properties, or cell binding on rhTE.[52] Cross-linked electrospun rhTE scaffolds interact favorably with a number of cell types, including embryonic palatal mesenchymal cells,[44] human umbilical vein endothelial cells (HUVECs),[52,53] and primary dermal fibroblasts.[25]

2.218.1.3.1. Electrospun rhTE and vascular tissue engineering

Elastin is a promising candidate for vascular tissue engineering because of its prevalence in vessel walls, favorable cellular interactions, and blood compatibility. Elastin comprises up to 50% of the dry weight of major arteries, where it provides elastic recoil, resilience, and durability.[4] Additionally, it offers important cell signaling cues that promote attachment and proliferation of endothelial[54,55] but not smooth muscle cells[56] and results in reduced platelet adhesion and activation.[53,57,58] Its particular promise lies in the design of small diameter (<6 mm) vascular conduits where compliance mismatch between stiff commercially available conduits and native vessels results in graft failure.[59]

An rhTE-based small-diameter vascular conduit was constructed by electrospinning a multilayer construct comprising a GA cross-linked rhTE luminal layer and rhTE-polycaprolactone (PCL) hybrid outer layers. Cross-linked rhTE supported HUVEC attachment and proliferation *in vitro* allowing the establishment of a fully confluent cell layer on the scaffold surface by day 3 post seeding. Platelet attachment to these constructs was significantly lower than on commercially available ePTFE or on PCL-based constructs. Mechanical properties of the rhTE-based conduit were optimized to mimic the permeability, compliance, elastic modulus, and burst pressure of the human internal mammary artery. Importantly, these conduits were well tolerated and retained their superior mechanical properties for at least 1 month in a rabbit carotid interposition model.[53]

2.218.1.3.2. Electrospun rhTE and skin tissue engineering

Electrospun scaffolds hold immense potential as both dermal substitutes and wound dressings. The porous nature of electrospun scaffolds promotes the drainage of wound exudates, while retaining wound moisture and promoting the exchange of gases.[60] While much effort has been invested into the design of electrospun elastin-containing vascular grafts,[39,42,43,45–48,51] the addition of elastin to electrospun dermal substitutes has been largely overlooked. Dermal elastic network is a strong determinant of skin resilience, texture, and quality, but is not sufficiently regenerated following burn injury.[61–64] Elastin-based dermal substitutes have the potential to decrease wound contraction, improve scar appearance and functionality, and contribute to wound-healing outcomes through a combination of elastin's mechanical and cell signaling properties.[65]

A dermal substitute scaffold electrospun entirely from rhTE and cross-linked with GA vapors was found to support the attachment, spreading, and proliferation of primary dermal fibroblasts. This scaffold consists of flat, ribbon-like fibers that resemble the size and morphology of native elastin fibers, showing an average fiber width of $2.3 \pm 0.5\,\mu m$. Its elasticity is similar to that of native elastin, with a Young's modulus of $265 \pm 17\,kPa$. Altering the electrospinning conditions allows for easy modification of the scaffold properties to generate highly porous and open-weave scaffolds that promote fibroblast infiltration.[25] Dermal fibroblasts actively migrate into the scaffold and secrete ECM proteins, including type I collagen and fibronectin. These scaffolds are well tolerated *in vivo* in a rat full-thickness excision model, where they support fibroblast infiltration and collagen deposition.[65] Electrospinning also allows for addition of other ECM proteins, such as collagen to rhTE-based scaffolds, to further improve their handling and cell interactive properties without negatively impacting on the scaffold elasticity.[65]

2.218.1.4. Functionalized Surfaces

Synthetic polymers and metal alloys are vastly employed in the development of medical devices. Many commercially available vascular grafts, heart valves, bone and joint implants, and wound dressings are manufactured from synthetic polymers, while many cardiovascular devices such as heart valves, pacemaker components, and stents are composed of metal alloys, including stainless steel, titanium, and cobalt chromium. These materials are mostly biologically inert and therefore do not promote cellular interactions necessary for the long-term success of the device *in vivo*.[66] Many of the metallic surfaces are also not sufficiently blood compatible and therefore cause thrombosis and device failure.[67,68]

Coating of polymer and metal devices with rhTE has the potential to overcome these problems, as elastin modulates the behavior of a number of cell types and is known to be nonthrombogenic. Multiple peptides from the alternating hydrophobic domains of tropoelastin modify cell behavior. These include the hexapeptide VGVAPG and peptides containing a GXXPG motif, as well as the recently identified C-terminal GRKRK motif. Cells interact with elastin and its derivatives via several different cell surface receptors, including the elastin-binding protein (EBP), αvβ3 integrin and through GAGs on the cell surface (for review see Almine *et al.*[69] and references therein).

Covalent immobilization of rhTE onto a polymer surface was demonstrated on plasma immersion ion implantation (PIII) treated polystyrene. Covalent binding of proteins to polymer surfaces ensures presentation of proteins in a conformationally relevant state and reduces protein resorption following implantation. This treatment can be used to selectively guide fibroblast spreading on rhTE-coated surfaces, as was demonstrated by patterning the surface to achieve cell spreading on rhTE treated areas only.[70]

Covalent immobilization of rhTE onto stainless steel was achieved by creating a plasma deposited interface on the metal surface.[55] This new, rhTE-coated surface significantly enhances HUVEC attachment, spreading, and proliferation compared to untreated stainless steel and to plasma treated steel alone.[54,55] The plasma-treated surface in the presence and absence of rhTE reduced the thrombus weight by more than tenfold after 30 min under flow in a modified Chadler loop and delayed the time to thrombus formation by threefold.[54] The plasma-modified rhTE-coated surface therefore has the potential to enhance endothelialization and reduce thrombosis of endovascular stents. Importantly, this technique was not only demonstrated on flat pieces of stainless steel, but the coating technology was also translated to modification of coronary stents.[54]

The use of stem cells is of extreme importance in tissue engineering and the ability to propagate these cells while maintaining them in undifferentiated state is challenging. rhTE-coated surfaces have recently been demonstrated to enhance the propagation of human and murine hemopoietic stem and progenitor cells. This phenomenon is attributed to the elastic nature of rhTE rather than specific signaling roles of the protein, as truncated and cross-linked forms of rhTE do not display the same effect. Furthermore, inhibition of mechanotransduction abolishes the positive effects of rhTE.[71]

2.218.2. The Elastin-Like Recombinamers

2.218.2.1. Introduction

In the last few decades polymer science has developed rapidly and has had a profound impact on society showing that macromolecules can be excellent candidates to create highly functional materials. Within macromolecules, we can find proteins as indispensable part of biological structures and systems, especially as regards control of tissue formation, biological functions, or physical performance.[72]

Natural proteins are usually large and very complex linear polymers, which contain diverse specific functional groups that generate and promote self-assembly and function. Nature has designed proteins with specific practical functionality, such as ability to self-assemble, specific recognition, energy interconversion, or monodispersity, and enhances these attributes in protein-based biomaterials. All of this amazing functionality displayed by natural proteins seems to be based on a simple fact: a complex and completely defined primary structure. In living cells, protein biosynthesis is carried out with an absolute control of the amino acid sequence, from the first amino acid to the last with a complete absence of randomness.[73] For this reason, a basic understanding of amino acid-based peptides and proteins forms the foundation for the current development of peptide-based biomaterials. As such, peptides and high molecular weight polypeptides are emerging as a new class of biomaterials because of their unique chemical, physical, and biological properties.

This explosion of new peptide-based materials is founded on parallel developments in both our understanding of protein function and the maturation of recombinant DNA technologies to obtain recombinant protein-based polymers, also known as 'recombinamers.'[74] These macromolecules, with total lack of randomness in their sequence, permit the required functionalities to be designed in the final material in a highly precise manner with an exponential increase of complexity and low costs.

The genetic engineering of recombinamers enables the easy and highly effective design and synthesis of complex and highly functional molecules with selected and sophisticated properties, such as the incorporation of selected exogenous bioactivities in order to develop materials for cutting-edge applications in biomedicine and nano(bio)technology.[75] Furthermore, genetic engineering can recreate simple or complex properties that are present in natural proteins in these recombinamers. Additionally, as it is possible to construct any coding gene required, base by base, on the basis of original designs without being restricted to the gene fragments present in living organisms, materials and systems exhibiting functions of particular technological interest that are not displayed in living organisms can also be designed and produced.[76] As an example of these approaches (**Figure 2**), we show here how elastin-like recombinamers (ELRs), which combine sequential and architectural molecular complexity with diverse bioactivities, play an important role in the synthesis of advanced materials for biomedical and nano(bio)technological applications.

2.218.2.2. The Extraordinary Properties of ELRs

ELRs are a promising model of biocompatible protein-based polymers. The basic structure of ELRs involves a repeating sequence based on the recurring sequences found in the mammalian elastic protein elastin.[77] As far as their properties are concerned, some of their main characteristics are derived from those of the natural protein. Elastin is an extracellular matrix protein that is present in all vertebrate connective tissues. Its functions include the provision of elasticity and resilience to tissues, such as large elastic blood vessels (aorta), elastic ligaments, lung, and skin, which are subjected to repetitive and reversible deformation.[4,78]

The importance of ELRs resides in the fact that these polymers show a versatile and broad range of interesting properties

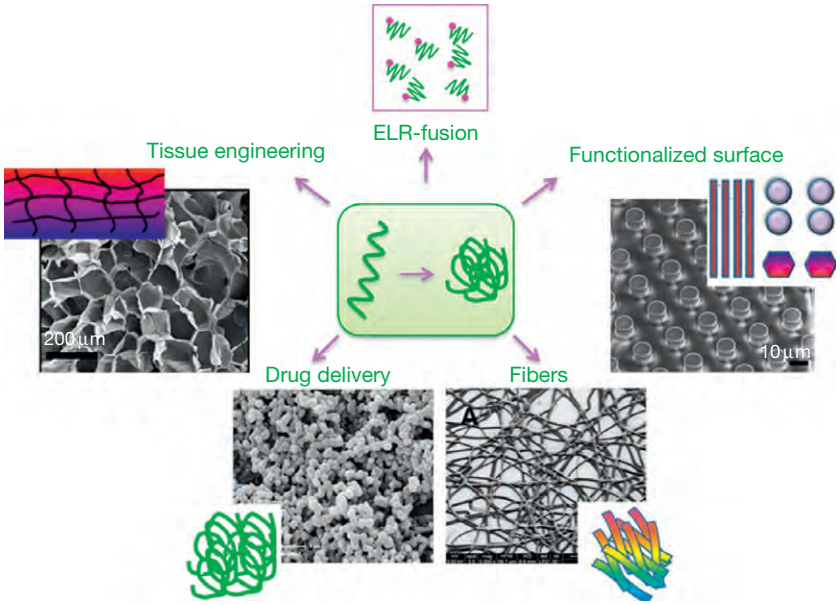

Figure 2 Different applications of elastin-like recombinamers, including tissue engineering, drug delivery, fibers, functionalized surface, and ELRs-fusion constructions.

above and beyond their simple mechanical performance that are not easily found together in other materials, including stimuli-responsive behavior or the ability to self-assemble. These properties arise because of a molecular transition of the polymer chain in the presence of water at temperatures above a certain level. This transition, known as the 'inverse temperature transition' (ITT),[79–81] has become the key issue in the development of peptide-based polymers for use as molecular machines and materials.

ELRs show an additional property – an outstanding high biocompatibility – which is highly relevant for the use of these polymers in advanced biomedical applications such as tissue engineering and controlled drug delivery. Indeed, the complete series of ASTM generic biological tests for materials and devices in contact with tissues and tissue fluids and blood demonstrate their unmatched biocompatibility.[82] Perhaps somewhat surprisingly, it appears that the immune system simply ignores these polymers as it cannot distinguish them from natural elastin because the β-spiral, the common structural feature of all ELRs, strongly contributes to preventing their identification.[83] In addition, their degradation products – natural amino acids – are nontoxic.[84–87]

The polymer poly(VPGVG) (V=L-valine; P=L-proline; G=glycine) is considered to be a model for all ELRs.[81] Indeed, most ELRs are based on the pentapeptide VPGVG (or its permutations), with amino acid side chains, other than glycine, comprising simple aliphatic and mainly hydrophobic chains, without further functionalization. A wide variety of ELRs based on the ELP model, with the general formula VPGXG, where X is any natural or modified amino acid other than L-proline, have been (bio)synthesized.

Initially, the monomers, oligomers, and higher polymers of this repeat, and modifications thereof, were chemically synthesized. More recently, however, with the increased development of molecular biology, these and more complex ELRs have been produced using genetic-engineering techniques.[88,89]

2.218.2.3. Genetic Engineering of ELRs

The use of genetic-engineering techniques to produce these polymers as recombinant proteins has several advantages over their synthetic counterparts. These techniques permit precise control over ELR sequence and chain length, as well as construction of new polymers with physical, mechanical, and/or biological features, such as variations of folding, chain interactions within protein structure, temperature or pH responsiveness, etc.[84,90]

The design of an appropriate strategy at the nucleotide level is critical for the efficient synthesis of the protein encoding sequence and to produce a uniform protein product with an optimal quality and yield. The biosynthesis of any artificial protein generally includes (1) the construction of a synthetic gene that encodes the protein of interest in a plasmid with close transcription control; (2) the cloning of a recombinant gene with the necessary transcriptional regulatory elements into competent cells; (3) the screening of plasmids containing the desired clones and verification of their DNA sequence; (4) transformation of the chosen plasmids into expression-competent host cells; (5) the growth of appropriate volumes of host cells and induction of protein expression; and (6) purification of the protein of interest from cell lysates.[91]

Molecular biology techniques are typically employed to self-ligate monomer DNA fragments in an oligomerization process that relies on restriction enzyme-based approaches when designing genes that encode repetitive recombinamers. In this case, the monomer fragments must be oligomerized in a 'head-to-tail' orientation and can either be seamless in sequence or can contain intervening linkers between the desired repeats. Approaches to oligomerization can be classified as (1) iterative, where a DNA segment is oligomerized in a series of single, uniform steps, each of which extends the oligomer by one unit length of the monomer gene; (2) random method or 'concatemerization,' where an uncontrolled

number of monomer DNA segments are oligomerized in a single step to create a population of oligomerized clones with different lengths; and finally, (3) recursive directional ligation (RDL), an alternative method in which DNA segments with two different restriction sites flanking the insert are joined in sequential steps, with the length of the ligated segments growing geometrically in each step. This approach is suitable for the synthesis of repetitive polypeptides with a specific and predetermined chain length as it seamlessly joins the two monomeric inserts and also eliminates the restriction sites placed at either end of the dimerized gene.[79,80,92]

2.218.2.4. The Stimuli-Responsive Behavior and Self-Assembly Properties of ELRs

The responsive behavior of ELRs has been defined as their ability to respond to external stimuli. This property is based on the molecular transition of the polymer chain in the presence of water at a temperature above a certain level, known as the ITT. Below a specific transition temperature (T_t), the free polymer chains remain as disordered, random coils that are fully hydrated in aqueous solution, mainly by hydrophobic hydration.[93] This hydration is characterized by ordered, clathrate-like water structures somewhat similar to those described for crystalline gas hydrates,[94,95] although somewhat more heterogeneous and of varying perfection and stability surrounding the apolar moieties of the polymer.[96] However, above T_t, the chains fold hydrophobically and assemble to form a phase-separated state containing 63% water and 37% polymer by weight.[97] In this folded state, the polymer chains adopt a dynamic, regular, nonrandom structure, known as a β-spiral, which contains type II β-turns as the main secondary feature and is stabilized by intraspiral, interturn, and interspiral hydrophobic contacts.[93] The ITT process is completely reversible, and the polymer returns to its initial state when the temperature drops below T_t.[98] During the initial stages of polymer dehydration, hydrophobic association of the β-spirals results in their taking on a fibrillar form. According to Urry's model, this process begins with the formation of filaments composed of three-stranded, dynamic polypeptide β-spirals that grow to lengths of several hundred nanometers before settling into a visible phase-separated state.[93,97]

The specific T_t can be measured by different techniques (see **Figure 3**), such as turbidity analysis or calorimetric methods. The T_t values obtained by these methods usually differ because of the influence of several factors.[99]

The magnitude of T_t also depends on several factors. For example, any intrinsic modification to the composition of the polymer chain as a result of changing the sequence or distribution of the different domains, or extrinsic factors such as salt additions, that modifies the tendency of water molecules to take part in hydrophilic versus hydrophobic hydration will alter the clathrate structure and modify the T_t. This effect is a result of both the mean polarity of the polymer chain and the molecular architecture and distribution of the different amino acid domains in the ELRs.[100] T_t can also be affected by the polymer concentration and by other factors, such as changes in pH or the oxidation state of a side chain or functional group, the addition of extrinsic factors such as salts and organic solutes, the presence of other ions and molecules, or pressure changes.[101–103]

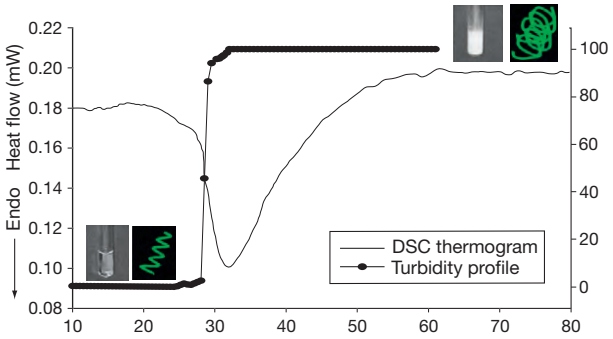

Figure 3 Turbidity profile as a function of temperature for poly(VPGVG) (5 mg l^{-1}) in water. The two photographs are below (5 °C) and above (40 °C) its T_t. Also, a DSC thermogram of a 50 mg l^{-1} aqueous solution of the same polymer is shown (heating rate 5 °C min^{-1}). Reproduced from Rodriguez-Cabello, J. C.; Prieto, S.; *et al. J. Biomater. Sci. Polym. Ed.* **2007**, *18*(3), 269–286, with permission from Brill.

As far as self-assembly is concerned, many synthetic strategies have been developed to obtain advanced devices in an attempt to mimic the efficiency of biology in nature. These techniques are usually developed on the basis of the concepts of self-organization and self-assembly, both of which are widely found in nature, to arrange hierarchically ordered systems in such a way that they can be exploited in synthetic devices. Proteins are useful building blocks for the formation of ordered nanostructures via self-assembly because of their well-understood folding, stability, and protein–protein interactions.[104] Natural elastin undergoes a self-aggregation process in its natural environment that leads to the formation of nanofibers.[83] However, genetic engineering and the tailored molecular design of ELRs allow this possibility to be extended to other topologies and nanostructures that involve the directed self-assembly of ELRs[105,106] such as nanopores.[107]

2.218.2.5. Biomedical and Biotechnological Applications

2.218.2.5.1. Tissue engineering

ELRs are useful for tissue engineering because they are soluble in aqueous solutions, have good *in vivo* biocompatibility, a controllable degradation rate *in vivo*, and break down into natural amino acids that can be metabolized by the body to produce nontoxic degradation products.[84] Besides this proven compatibility, their smart and self-assembling characteristics and their ability to be easily genetically functionalized to enhance their interactions with cells provide an optimal platform for cellular activities and tissue functions. Thus, they are excellent candidates for use in regenerative and reparative medicine.[108] They are also highly versatile as these properties can be tuned and extended in many different ways simply by changing their amino acid sequence, thereby opening up new possibilities for the formation of biomimetic advanced bio- and nanomaterials that can actively participate in the formation of functional tissue.

The first candidates for tissue-engineering applications were simple polymers of the type poly(VPGVG) and their

cross-linked matrices that promote unspecific cell adhesion because of lack of specific bioactivities. But, immediately these simple molecules were subsequently enriched with short peptides having specific bioactivities, such as cell-adhesion peptides RGD (R, L-arginine; D, L-aspartic acid) and REDV (E, L-glutamic acid). The complexity of these still relatively simple ELRs was subsequently increased by adding different functionalities such as cross-linking domains.[109–113] Numerous examples based on more complex designs, including various bioactivities[114,115] and other functionalities,[116–119] have since been synthesized in an effort to mimic the complex composition and function of the natural ECM. Thus, the addition of different functionalities such as cross-linking domains results in more uniform substrates, which are usually based on lysine residues, incorporated in the elastin-based repeat unit (VPGXG).[109,113,120]

ELRs are able to form stable viscoelastic hydrogels that mimic many of the characteristics of the ECM. These ELR hydrogels can be produced by photoinitiation,[121] irradiation,[122,123] amine reactivity,[124,125] or enzymatic cross-linking by tissue transglutaminase[114] to maintain their interesting properties as stimuli-responsive substrates. Furthermore, they are a new class of soft materials, which, in response to a small change in temperature, light, or other environmental stimulus, swell to several times their original volume or shrink to the same degree.[126,127] These materials have proved very useful in biomedical and pharmaceutical applications because of their high water content and rubbery nature, which are similar to that of natural tissue.

The physical properties of chemically cross-linked hydrogels can be modulated by varying the ELR's concentration, molecular mass, and lysine content. This ability to prepare 'tunable' hydrogels allows these ELRs to be used in a wide range of applications. Although there are many examples of ELRs hydrogels cross-linked in organic solvents, the application of *in situ* cross-linking in aqueous solution is limited by factors such as the toxicity of the reagents and by products, and slow gelation kinetics. Lim *et al.*[19] have reported that the chemical gelation of ELRs under physiological conditions results in a biocompatible and injectable biomaterial for support tissue regeneration. Similarly, Tirrell's group has developed this idea further and has demonstrated that chemically cross-linked hydrogels from ELRs-containing fibronectin cell-binding domains can successfully be used to support the growth and spreading of endothelial cells.[109,128] The tunable, elastin-like mechanical properties of ELR hydrogels and their ability to mediate cellular adhesion and proliferation make them suitable candidates for use in small diameter vascular grafts.[108] In addition, ELR hydrogels have also demonstrated the ability to induce the differentiation of adult human adipose stem cells into the chondrocytic phenotype and the accumulation of cartilage-specific extracellular matrix in the absence of exogenous chondrogenic supplements *in vitro*, thereby potentially simplifying and reducing the cost of the differentiation process.[129] Likewise, we have reported the production of 3D-ELR structured hydrogels with controlled microtopography and different size and depths by replica molding (see **Figure 4**).[130] These hydrogels may find a use in the study and control of cell behavior by controlling their topography and their smart nature enables changing the dimension of the microstructures during cell culture.[124,125]

One of the ELRs bioproduced by a group associated with some of the authors is an 877 amino acid complex polymer (REDV-ELR biopolymer) (see **Figure 5**) whose monomer unit contains four different functional domains in order

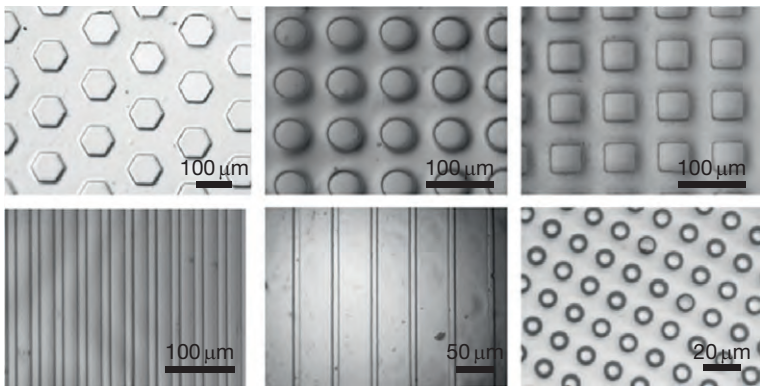

Figure 4 Micropatterned gels with different features obtained by replica molding. Optical micrographs of swollen gels in PBS by DIC microscopy. Reproduced from Martin, L.; Arias, F. J.; *et al. Soft Matter* **2010**, *6*(6), 1121–1124, with permission.



Figure 5 Schematic composition of monomer used in ELP design described in the text. The scheme shows the different functional domains of the monomer that can be identified with their corresponding peptide sequences. Reproduced from Rodriguez-Cabello, J. C.; Prieto, S.; *et al. J. Biomater. Sci. Polym. Ed.* **2007**, *18*(3), 269–286, with permission from Brill.

to achieve a suitable balance between mechanical and bioactive responses.[102,103] The polymer framework contains two elastomeric pentapeptides (VPGIG and VPGKG), which provide the desired mechanical properties, stimuli-responsive nature, biocompatibility, and cross-linking domains, namely, the CS5 domain from fibronectin, which contains the cell-selective adhesion REDV motif,[131] and the human elastin hexapeptide VGVAPG, which is targeted by the elastases that rearrange and renew the ECM. Three-dimensional matrices with controlled pore sizes formed from chemically cross-linked REDV-ELR have been obtained for use in cell culture, and salt-leaching and gas-foaming techniques have been used to improve the homogeneity of the pore size, the mechanical properties, and their interconnectivity. The 3D culture of HUVEC endothelial cells has shown the suitability of these scaffolds, with infiltration of these cells inside the porous network being essentially complete.[124,125] A study of the physical changes which occurred as a result of their temperature responsiveness showed that the collapse due to the phase transition above T_t decreased the mean pore size by about 30% (see **Figure 6**). This technique should provide a simple method for the fabrication of advanced scaffolds with tunable biological and physical applications.

This ELR-containing REDV cell-adhesion sequence has also been used to prepare hybrid scaffolds. Thus, the ELR was introduced as an elastic element in collagen-based scaffolds with a view to providing increased proteolytic sensitivity and increased functionality to the scaffolds by carrying a specific sequence for microbial transglutaminase cross-linking, endothelial cell adhesion, and drug delivery. These scaffolds showed that cross-linking ELR–collagen affects the physicochemical properties of the scaffolds such as their porosity, presence of cross-linking, thermal behavior, and mechanical strength. These enzymatic cross-linked ELR–collagen scaffolds were tested *in vitro* as substrates to study cell viability with different cell lines. An increasing ELR fraction in the scaffold was found to have an antifouling effect in fibroblasts, whereas endothelial cells displayed normal behavior and proliferation in the hybrid scaffolds. This differential colonization of the scaffolds with a specific cell type makes these scaffolds an attractive platform for biomedical applications, as varying the proportion of both materials should allow us to design the optimal requirements for future applications, such as vascular tissue or skin wound healing.[114] Other complex hybrid scaffolds containing ELR and collagen have been produced with the aim of creating an innovative acellular arterial substitute. For instance, Caves *et al.*[132] described the creation of artificial multilamellar vessel-like scaffolds consisting of several layers of an ELR matrix reinforced with synthetic collagen microfibers.

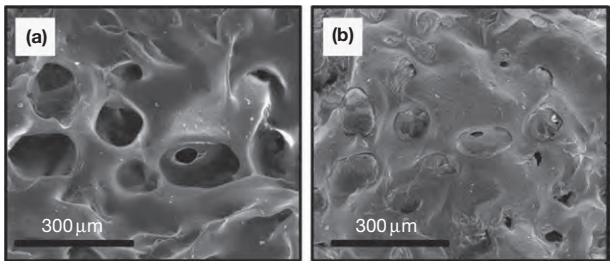

Figure 6 ESEM micrograph showing the change in pore size with temperature in swollen hydrogels: (a) 4 °C and (b) 37 °C. Reproduced from Martin, L.; Alonso, M.; *et al*. *Biomacromolecules* **2009**, *10*(11), 3015–3122, with permission from American Chemical Society.

Another type of hybrid scaffold has been synthesized for use as a provisional bone tissue. Thus, ELRs were amalgamated with chitosan to develop hydrogels with applications in bone tissue engineering, which requires temporary scaffolds to regenerate bone and improve its healing rate. These hydrogels can be injected into the body, as a liquid that gels *in situ*, thus allowing the material and cells to be implanted using a minimally invasive procedure. In this work, the ELR was incorporated into two different hydrogel formulations. First, physically cross-linked chitosan/β-glycerophosphate (Cht-β/GP) thermosensitive hydrogels were prepared where incorporation of the ELR into the (Cht-β/GP) formulation seemed to drastically improve the mechanical properties of this gel under physiological conditions. Second, chemically cross-linked chitosan hydrogels were prepared with the ELR acting as a coating. An ELR containing an osteoconductive sequence was found to improve the bioactive properties of chitosan-based systems and besides this, the mechanical properties of this gel under physiological conditions induced precipitation of calcium phosphate when the materials were soaked in simulated body fluids for 7 days.[117]

The REDV-containing polymer described above has also been used as a substrate to culture cells from the ocular surface. Epithelial cell adhesion and proliferation were investigated on this ELR, which mimics the functional characteristics of extracellular matrices. Corneal wound healing requires cell adhesion and proliferation, both of which are mediated by binding of epithelial membrane-bound integrins to substrate ligands such as fibronectin. A significant improvement in the adhesion and proliferation of the conjunctival epithelial cell line on the ELR-coated surface containing REDV peptides was observed. ELR-coated surfaces containing REDV peptides supported the normal phenotype and functions of epithelial cells *in vitro*, thus confirming that this recombinant polymer resembling the ocular surface extracellular matrix is a suitable substrate for sustaining epithelial cell attachment and growth. One of the potential applications we envision for this kind of protein-based polymer is the preparation of scaffolds to be used for ocular surface tissue engineering.[115]

Other examples of ELRs demonstrate the complexity attainable for this class of biomaterials. Thus, a sophisticated ELR has been biosynthesized to generate temporary scaffolds that support neural regeneration, thereby helping to repair injuries to the central nervous system (CNS). This engineered protein includes cell-adhesion sequences to enable neural attachment as well as sequences sensitive to cleavage by urokinase plasminogen activator (uPA), a protease secreted locally at the tips of growing neurites, to enable highly localized and tunable degradation. These ELRs were chemically cross-linked into highly swollen hydrogels with controllable mechanical properties. In addition, it was found that increasing the density of RGD peptides present in the protein substrates led to increased cell adhesion and more extensive neurite growth.[133]

It is also possible to make use of the thermosensitive behavior of ELRs to form hydrogels. Thus, raising the temperature of

a concentrated solution of an ELR above its T_t results in aggregation of the ELR's chains and the formation of an insoluble coacervate phase. Reverse thermosensitive polymers are very promising base materials for '*in situ* generated implants' because of their ability to form low viscosity physiological solutions at room temperature which gel at higher temperature. This property opens up numerous possibilities, although the two principal areas of research involve hydrophobic materials, which acquire desired mechanical properties, or water-based systems for the controlled release of hydrophilic macromolecules. The structural complexity of ELRs with specific mechanical, chemical, and biological properties allows us to design specific features that make it possible to acquire some or all of these properties. The self-assembly behavior of ELRs, for example, has been triggered by the addition of different main peptide blocks in the structure, with the hydrophilic block providing conformationally elastic properties[134] and the hydrophobic blocks forming physical cross-links through hydrophobic aggregation.[74]

In a recent example, ELR triblock copolymers with different hydrophobic architectures were found to form gels with a complex shear modulus, which can be varied by changing the hydrophobicity of the inner block.[49] Although the modification of ELRs allows some control of their mechanical properties, the physically cross-linked ELR hydrogels lack the strength required for some tissue-engineering applications. When greater mechanical integrity is desired, the elastic modulus can be enhanced by including additional chemical cross-linking sites between the ELR chains,[134,135] thus making them excellent candidates for biomedical applications. Sallach *et al.* have also developed a recombinant elastin-mimetic triblock copolymer in the absence of either chemical or ionic cross-linking that shows minimal inflammatory response and robust *in vivo* stability for periods exceeding 1 year. This example demonstrates the high and extraordinary biocompatibility of ELRs. These triblock copolymers could also be used as structural components of artificial organs and engineered living tissues, as carriers for controlled drug release, or as biocompatible surface coatings.[136]

2.218.2.5.2. Functionalized surfaces

One of the most active research areas in the field of materials science concerns the control and modification of surfaces and interfaces, also known as surface engineering.[102,103,137] The surface can be functionalized with fouling/antifouling properties, specific groups to promote cell material interactions, smart behavior (stimuli responsive or environmentally sensitive), or with micro- or nanopatterns.

Surfaces modified with stimuli-responsive biopolymers change their physical and chemical properties in response to changes in the environment or under external stimuli. This advantage has been exploited in some smart surfaces covered with a chemically synthesized polymer that exhibits a lower critical solution temperature, especially poly(*N*-isopropylacrylamide) (pNIPAM) and its derivatives. A change in the environment causes such a surface to undergo a significant change in its bioactive properties, for instance, protein adsorption/desorption or cell or bacterial attachment/detachment.[138–141] For instance, Ozturk *et al.* have demonstrated recently that RGD-ELR adsorbed on micropatterned pNIPAM films is crucial to maintain the cell attachment in dynamic cell culturing. Thus, cell behavior was studied upon application of mechanical stress generated by changing the temperature to shrink and stretch pNIPAM films under *in vitro* conditions. This is a promising strategy to obtain smart cell carriers for bone formation.[142] The major disadvantage of this system is the nondegradability of pNIPAM, although it should be possible to resolve this problem by replacing it with an ELR-containing biodegradable sequences, such as that described by Girotti *et al.*[102,103]

ELRs have some additional advantages that make them excellent candidates for the development of smart surfaces, especially the fact that they can be obtained by recombinant technologies, thus enabling a close control of their sequence, length, and stereochemistry. This allows, among others, a nanometer level of control of the position where functionality is located along the polypeptide chain and leads to a tremendous potential for the self-assembling and other advanced functionalities displayed by these systems.

Chilkoti's group has also created what they refer to as the 'thermodynamically reversible addressing of proteins' (TRAP),[137,143] where an ELR is covalently micropatterned onto a glass surface against an inert background. This TRAP technology enables the reversible, spatial–temporal modulation of protein binding at the solid–liquid interface and can be applied in different systems for bioanalytical applications, such as protein-based microsensors for detecting single biomolecules. The adhesion of other binding proteins coupled to designed polypeptides on solid surface has also been reported.[144] Along similar lines, a novel protein for controlling cellular functions has been constructed by combining the RGD sequence, epidermal growth factor (EGF), and a hydrophobic sequence into a single molecule. This protein was found to have both cell-adhesive and growth factor activity, while its hydrophobic sequence contributed to assembly of the RGD and retention of its activity on a solid-phase surface. This fusion protein could therefore prove to be of use for wound healing and tissue regeneration.[145]

A novel temperature-responsive culture surface, consisting of a cell sheet harvested from a culture dish, that exploits the stimuli-responsive characteristics of ELRs has been developed. This technique involves changing the temperature once the cells have become confluent in order to reverse the coaggregation. The cells are then detached from the culture dish as a single sheet and subsequently transferred to new surfaces, thereby suggesting the potential of this approach for the fabrication of multilayer cell sheets.[87] Na *et al.* have also taken advantage of the rapid response of a smart material surface created by adsorption of ELRs to external stimuli for use in cell-based biochips. The smart transition of ELR micropatterns between a hydrophobic and hydrophilic surface glass at T_t enabled these authors to control the reversible cell adhesion by way of the incubation temperature.[146]

Another simple technique commonly used in the field of ELRs is the layer-by-layer deposition of alternating ELR–polyelectrolytes, which is a simple technique for generating bioactive surfaces.[147] In this way, cells were cultured on multilayer substrates formed by depositing alternating layers of ELR and a polyelectrolyte to show that the thickness and the mechanical integrity of the multilayer substratum are important to regulating cell proliferation and formation of focal

adhesions.[147] Costa *et al.*[118] have also developed thermoresponsive thin coatings by electrostatic self-assembly (ESA), which involves simple deposition of an ELR containing the cell-attachment sequence RGD from an aqueous solution onto chitosan surfaces. The thermoresponsive behavior of these coatings can be exploited for tunable cell adhesion and controlled protein adsorption by nanoscale surface tailoring.[118]

The chemical functionalization of ELRs has also been used in biomimetic surface modification strategies to obtain metallic (commercial pure titanium, Cp Ti) dental implants with osteostimulative capabilities. A simple process using silane chemistry has been shown to be specific, rapid, and reliable for the covalent immobilization of biomolecules on the Cp Ti surface to obtain mechanically and thermochemically stable ELR-containing coatings.[148]

2.218.2.5.3. Fibers

The ability to generate micro/nanoscale fibers from synthetic and natural polymers has been improved by electrospinning.[149,150] This technique generates an electrically charged jet of the polymer solution, which dries to leave a polymer nanofiber network containing fibers with diameters ranging from a few micrometers to less than a hundred nanometers, depending on processing parameters such as polymer concentration and viscosity, flow rate, and applied voltage, among others.[151] The ability to vary the fiber size in the nanometer range opens up the possibility of mimicking the size scale of fibrous proteins found in the natural extracellular matrix. Thus, electrospinning techniques were employed to produce fibers with different morphologies (beaded fibers, thin filaments, and broad ribbon-like structures) in a form that mimics the diameter of native elastin utilizing a genetically engineered ELR,[152] and as in other ELR constructions, the inclusion of specific biofunctionalities may provide a wide range of possibilities.

Recently, and continuing with the theme of nanofiber architecture formation, core–shell nanostructures of CdSe nanoparticles with a shell of ELRs have been used as building blocks to fabricate functional 1D nanostructures. The ELR stabilizes the CdSe nanoparticles in an aqueous medium and controls their nucleation, growth, and spatial distribution, thus leading to the self-assembly of core–shell building blocks into fibril architectures. Moreover, in presence of ELR the material is potentially noncytotoxic; thus, these types of nanofibers could find future applications in fields such as medical nanotechnology and the diagnosis and treatment of various diseases.[153]

2.218.2.5.4. Drug delivery

When traditional oral or injectable drug formulations cannot be used, controlled drug delivery can be an important factor. A wide range of materials have been employed to control the release of drugs and other active agents, although polymeric systems are the most common because of their desirable physical properties.[154] Here, ELRs display several properties that can be useful for drug-delivery purposes, including precise control over size and sequence, smart behavior, self-assembly, biocompatibility, biodegradability, and monodisperse character, parameters that are critical to tune the pharmacokinetics of polymers. The genetic engineering of ELRs permits the incorporation of targeting peptides, such as cell-penetrating domains[155–157] or receptor ligands, and the introduction of reactive sites for chemical conjugation of drugs[158] or fluorescent probes[159] into the ELR sequences. ELRs can also be designed to self-assemble in response to an extrinsic temperature stimulus for applications such as soluble macromolecular carriers that can be used for the systemic delivery of antitumor agents or the local delivery of therapeutics directly to the tumor.[84]

The first ELR-based drug-delivery systems were reported by Urry. These systems were quite simple devices in which γ-radiated cross-linked poly(VPGVG) hydrogels were loaded with the model water-soluble drug (Biebrich Scarlet), which was then released by diffusion. Additionally, the introduction of various chemical functions along the polymer chain led to enhanced performance and release efficiency.[160]

In a different example, the ability of some ELRs, to form stable, drug-loaded, nano- and microparticles has facilitated the development of injectable systems for controlled release.[161] The drug is entrapped in these nano- and microparticles when the particles self-assemble as the temperature is raised above T_t and then it is released. Thus, the production of self-assembled nanoparticles for the combined release of bone morphogenetic protein-2 (BMP-2) and bone morphogenetic protein-14 (BMP-14) by exploiting the ITT of the poly(VPAVG) in a period of 14 days has been reported to show significant potential for future bone tissue-engineering applications.[162] More recent studies showed a hysteresis behavior in this polymer, with thermal absorption/release of components depending on the salt concentration of the polymer solution.[162]

The ability to control the ELR aggregation both *in vivo* and *in vitro* opens the way to a series of advanced medical applications, such as hyperthermia-induced localized extravascular drug accumulation, drug depot formation, and the design of novel materials suitable for tissue repair or engineering. For example, ELRs specially designed for targeted intracellular drug delivery have been produced by taking advantage of the soluble–insoluble transition of ELRs to target a solid tumor by local hyperthermia.[79,80,163] This mild hyperthermia-assisted approach to enhancing the accumulation of thermally responsive polymer carriers in tumors following systemic delivery has been demonstrated by Dreher *et al.*[159] Besides, this drug-delivery system could serve as an alternative to fusogenic peptides in gene-therapy formulations and to enhance the intracellular delivery of protein therapeutics that function in the cytoplasm.[79,80,135,164]

Continuing with this idea, but following a different strategy that involves enhancing the complexity of ELRs, a simple ELR-fusion form of the cell-penetrating Tat peptide (derived from the HIV-1 Tat protein) has been developed with an antimetastatic potential in an experimental ovarian cancer metastasis model *in vivo*.[165] By adding the L12 peptide (lactoferrin-derived peptide) to the previous construction, it was able to overcome several obstacles that commonly thwart drug development, including poor pharmacokinetics and systemic toxicity. These conjugates are therefore promising candidates for future *in vivo* studies because of their degree of selectivity in inducing cancer cell inhibition under hyperthermal conditions.[166] Other ELR fusions have been developed such as Bac-ELR1-p21, being promising macromolecular carriers for the delivery of cell cycle inhibitory peptides to solid tumors.[165]

Electrospraying, which is a versatile, efficient, and flexible technique, has also been used to generate nanoscale

bioresponsive peptide-based particles of defined morphology that can encapsulate drugs, such as in the preparation of ELR particles that contain the chemotherapy agent doxorubicin.[163,167]

Polymer vesicles and micelles have recently received an increasing amount of attention as potential carriers for hydrophobic drugs or genes. ELR-based block copolymers can be tailor-made to form smart, self-assembling, protein-like micellar systems with controlled structure and function. Chilkoti *et al.*, for instance, have focused on the potential therapeutic application of heat-triggered, reversible ELR-containing micelles.[168] Similarly, Dreher *et al.* have utilized ELRs in a linear diblock architecture with an N-terminal peptide ligand to form multivalent spherical micelles when heated slightly above body temperature. The critical micelle temperature is controlled by the length of the hydrophobic block, and the size of the micelle is controlled by both the total ELR length and hydrophilic-to-hydrophobic ratio. This study also identified a subset of elastin-like block co-recombinamers that could be useful for drug targeting by thermally triggered multivalency.[169] Recently, Kim *et al.*[170] have developed stabilized nanoparticles through the use of disulfide cross-linking between two amphiphilic diblock polypeptides modified with cysteine residues incorporated at the core–shell interface that could be stable under complex, physiological conditions. Most of these studies involve diblocks, although there are also some examples based on triblocks, including one where a reversible change in micelle compacticity is triggered by a helix-to-sheet protein folding transition upon raising the temperature above T_t.[171] Moreover, it has been shown that these triblocks, which can be produced in the absence of either chemical or ionic cross-linking, show minimal inflammatory response and robust *in vivo* stability for periods exceeding 1 year.[136]

As a further example, the 'one-pot' synthesis of pH- and temperature-sensitive gold clusters mediated by an ELR has been reported recently by some of the authors. This ELR promoted the formation of 2D linear arrangements of gold clusters with interparticle distances ranging from 10 to 40 nm. Furthermore, the gold–biopolymer hybrid displayed spectroscopic properties (UV–vis absorption) that could be modulated by varying the pH and temperature of the environment as a result of reversible aggregation and expansion of gold particles.[172]

In a subsequent step, Álvarez-Rodríguez *et al.*[173] have explored the use of cyclodextrins and the formation of alkanethiol mixed monolayers over the previously described hybrid ELR in order to decouple the photoisomerization of azobenzene from the bulk phase absorption. If they can be tuned to work under physiological conditions, these smart gold–ELR hybrids could be interesting for the development of multistimuli biosensors and drug-delivery applications.

2.218.2.5.5. ELR-fusion constructions

A great amount of ELR-fusion construction has been demonstrated during the writing of this manuscript in different applications. The emergence of the genetic engineering of ELRs has permitted the incorporation of targeting peptides, such as cell-penetrating domains,[155–157] growth factors,[145] proteases sequences[133] or receptor ligands, and the introduction of reactive sites for chemical conjugation of drugs[158] or fluorescent probes[159] into the ELR sequences.

However, in the last few years, the most acclaimed applications of the ELR-fusion constructions have resulted in an improvement in the recovery and purification efficiency of fusion proteins, an alternative to conventional chromatography methods approaching the thermal phase transitions of this type of polymer. Although chromatography-based protein purification methods yield proteins of high purity, they also have several drawbacks that limit their industrial scale-up, including their high cost, and specialized equipment.[108]

The temperature-dependent, reversible aggregation of ELRs provides a novel means to avoid this cost-intensive affinity chromatography by one of several strategies, including direct ELR tagging by simple ELR-based protein purification or ELR coaggregation and purification by ELR-mediated affinity capture. In the first case, cleavage of the ELR moiety from the fusion protein by treatment with specific proteases could raise cost issues for large-scale protein production and could also result in some of the problems inherent to protein recovery using conventional chromatographic procedures mentioned above. However, a combination of ELR and intein technology, which is designed to induce self-cleavage, eliminates the need for postpurification enzymatic or chemical cleavage of the ELRs. In the second case, namely, ELR-mediated affinity capture, the ELR can bind the fusion protein specifically and reversibly, thereby eliminating the need for postpurification enzymatic or chemical cleavage and possibly allowing reuse of the ELR-capture molecule.[174] In this regard, Araújo *et al.*[175] have reported the microbial production of a functionalized high molecular weight subtilisin for controlled enzymatic hydrolysis of wool surface whose activity was successfully restricted to the cuticle of wool, thereby allowing a significant reduction in pilling, weight loss, and loss of tensile strength of the wool fibers.

Another novel approach is a new platform known as ELR-mediated affinity capture, EMAC, which has been proposed to improve antibody purification. The main advantage of this new platform is its universality as it does not require the construction of a fusion protein for each individual antibody of interest, and involves the construction of a fusion protein in which the ELR is joined to an antibody-binding domain. Selective affinity interaction between the antibody and the antibody-binding domain allows recovery of the antibody after triggering the transition of the ELR.[176]

2.218.2.6. Outlook

The wide spectrum of biomedical and biotechnological applications in tissue engineering, surface engineering, drug delivery, and protein purification are some examples of the enormous potential of these versatile materials due to their numerous advantages, superior properties, and unconventional features with respect to any other polymer family. Here, we have attempted to highlight the enormous potential of genetic engineering for producing highly complex functional polymers characterized by extreme biocompatibility, smart and self-assembling characteristics, and programmed biodegradation providing them a huge potential for this wide range of applications in many different fields. Moreover,

these recombinamers have a monodisperse character and are obtained with a precise sequence and molecular weight, which makes them highly valuable as biomaterials.

However, these polymers are still far from reaching their full potential. It is therefore reasonable to expect that the near future will bring new recombinamers with widely diverse functionalities, which will establish a new standard in polymer function and, perhaps, a clear quantitative and qualitative leap that will contrast with the current slow but nevertheless continual development of polymer-based innovation, along with encouraging applications.

2.218.3. Animal-Derived Solubilized Elastin

2.218.3.1. Introduction

Solubilized elastin is equivalent to partly hydrolyzed elastin, and can also be referred to as elastin peptides, although the latter term is not confined to solubilized elastin alone. Peptide bonds of the insoluble elastin are hydrolyzed, thereby fragmenting the insoluble elastin and reducing its molecular weight.

Solubilized elastin can – as does tropoelastin – signal through the elastin–laminin receptor.[177] Elastin synthesis,[178] chemotaxis,[179] and proliferation of fibroblasts,[180] keratinocytes,[181] and smooth muscle cells[182] are examples of effects of (solubilized) elastin mediated by this receptor. These are important effects that may guide cells in a biomaterial construct in a certain direction. More elastin–laminin receptor-related effects can be found in other reviews.[183,184]

2.218.3.2. Types of Solubilized Elastin

2.218.3.2.1. α- and β-elastin

The most commonly used method to hydrolyze insoluble elastin is treatment with 0.25 M oxalic acid at 100 °C. The produced solubilized elastin preparation can be coacervated in 10 mM sodium acetate with 10 mM NaCl (set to pH 5.5 with acetic acid) at 37 °C. After centrifugation, two fractions will appear: α-elastin as the viscous coacervate with an average molecular weight of 60 kDa, and β-elastin in the supernatant with an average molecular weight of 3–10 kDa.[185,186]

2.218.3.2.2. κ-elastin

Another widely applied solubilized elastin is prepared by treatment with 1 M potassium hydroxide in 80% (w/v) ethanol at 37 °C. The elastin solubilized with KOH is called κ-elastin and is a heterogeneous mixture of elastin peptides with a mean molecular mass of approximately 70 kDa, soluble in aqueous solutions.[187]

2.218.3.2.3. Enzymatically solubilized elastin

Insoluble elastin can also be enzymatically digested with proteolytic enzymes that are able to degrade the elastin, mostly the elastases like serine-type elastases from neutrophils and pancreas and metalloelastases, for example, matrix metalloproteinase 12 (MMP12) of monocyte/macrophage origin.[183]

In one of these solubilization methods, human neutrophil elastase was used to digest elastin in PBS (pH 8.0) at 37 °C for 24 h, followed by centrifugation to remove remaining insoluble aortic elastin. The enzyme was subsequently removed by affinity chromatography for over 99%.[179] In another method, elastin was solubilized with porcine pancreatic elastase in 0.1% (w/v) ammonium bicarbonate, pH 7.8. After a 24 h incubation at 37 °C, over 90% of the elastase activity in the starting reaction mixture was removed by multiple affinity absorptions with coarse-mesh elastin and separation of the digested elastin from the insoluble elastin by centrifugation.[188] When using MMP12 on a larger scale, usually (the catalytic domain of) recombinant human MMP12 is used.[189]

2.218.3.3. Biomaterials Containing Animal-Derived Solubilized Elastin

Solubilized elastin has been employed in biomaterials as a component of porous scaffolds, as hydrogels, as (electrospun) tubes, and as coatings to materials. We will further introduce the various biomaterials by their stage of research, that is, *in vitro* experimentation including biomaterial preparation and cell culture experiments (see 2.218.3.4), *in vivo* experimentation using animal models (see 2.218.3.5), and clinical application (see 2.218.3.6).

2.218.3.4. *In Vitro* Experiments

Early biomaterials containing solubilized elastin were made by Rabaud and coworkers and included a matrix with collagen and κ-elastin,[190,191] a collagen matrix with κ-elastin and heparan sulfate or hyaluronic acid,[192] and a collagen matrix with κ-elastin and calcium phosphate.[193] Some of these biomaterials, including type I + III collagen containing κ-elastin, were tested in animal models, for example, for its use as a tympanic membrane.[194]

In 2005, solid disks from α-elastin were prepared by polymerizing coacervated elastin with a diepoxy cross-linker. By influencing the degree of cross-linking, the elastic modulus could be modified to some extent. Although vascular smooth muscle cells could adhere to the disks, proliferation capacity was decreased.[195] However, succeeding publications on these elastin disks are sparse.

Elastin hydrogels were prepared from α-elastin by mixing with GA, directly followed by pipetting the mixture into a Teflon mold (without and with high pressure CO_2) and leaving the material at 37 °C for 15 min to 24 h. Cross-linked hydrogels were washed with water and quenched with a Tris-based buffer. Increased pressure resulted in an increased swelling rate of the hydrogel and substantially increased pore interconnectivity together with a reduction in wall thickness and pore size.[16,17] In a preceding study, high pressure CO_2 was seen to impede the coacervation of an α-elastin solution.[196] Elastin-based hybrid gels were made using 50% tropoelastin and 50% α-elastin blends by the same procedure to introduce more lysine residues for cross-linking and to increase mechanical integrity. It indeed enhanced the mechanical properties, that is, compressive modulus 6-fold, elastic modulus 2.5-fold, and stress at break 2-fold, as compared to hydrogels without tropoelastin.[18] In a similar setup, but using another cross-linker (hexamethylene diisocyanate, HMDI), high pressure CO_2 also increased pore size and swelling ratio, which

stimulated the penetration and proliferation of fibroblasts through the hydrogels.[16,17]

2.218.3.4.1. Blends with natural materials

Next to biomaterials which are made solely out of elastin, blends with natural materials are often used to create an artificial extracellular matrix. A set of 48 fully characterized biomaterials based on collagen, insoluble elastin, α-elastin, and GAGs was screened by Lammers *et al.*[197] for stimulating proliferation of human primary keratinocytes. Scaffolds consisting of 80% collagen and 20% α-elastin induced proliferation, but further analysis revealed that proliferating cells were mainly of fibroblast morphology. Especially, scaffolds containing insoluble elastin fibers (80% collagen and 20% elastin fibers, and to less extent 50% collagen and 50% elastin fibers) increased keratinocyte proliferation, but not fibroblast proliferation.

Rat tail tendon collagen with κ-elastin (90–10%) was used to prepare biomaterial films. The κ-elastin component mainly functioned as an inductor of thermal cross-linking for collagen after treatment at 60 °C.[198]

Other elastic biomaterials were made from oxalic acid-solubilized elastin and combined with silk fibroin and/or hyaluronan with chemically introduced amine groups.[199] Starting from a 25% (w/v) solubilized elastin solution, 0–2.3% (w/v) hyaluronan, and 0–5.8% (w/v) silk fibroin were introduced followed by BS3 cross-linking. Using different contents, Young's moduli could be varied from 100 to 230 kPa and strain to failure from 15 to 40%, whereas ultimate tensile strengths were generally 30 kPa (higher for elastin only, 50 kPa). These materials sustained proliferation of human primary smooth muscle cells, but cell morphology differed on various materials, that is, isolated cells on elastin only, stretched cells that formed a network on elastin/hyaluronan, and cluster-forming cells on elastin/silk fibroin.

Miyamoto used specific fractions of oxalic acid-solubilized elastin for electrospinning in the presence of the new cross-linker 4-hydroxyphenyldimethylsulfoniummethylsulfate (DSP)-activated ester, and the oxalic acid-solubilized elastin isotype that formed fibers promoted by differentiation of vascular smooth muscle cells while suppressing the proliferative capacity.[200]

Matriderm is a clinically applied collagen scaffold containing 3% α-elastin (also see **Section 2.218.3.6**). In 2006, Matriderm was used as a scaffold for the cultivation of porcine primary chondrocytes, and cells not only maintained their proliferative capacity, but also showed improved differentiation as type II collagen synthesis was increased, even in the absence of a differentiation medium.[201] Specific follow-ups on this work are sparse in the literature.

Matriderm has also been used as a transport carrier system to transfer proliferating epidermal cells to human dermis *in vitro*,[202] for simultaneous culture of human keratinocytes and human preadipocytes,[203] and as a substrate to culture pancreatic stem cells *in vitro*.[204]

2.218.3.4.2. Blends with polymers

Electrospinning is often applied in combination with polymers, especially in the preparation of vascular tubes. Examples of these are described here. An electrospun bilayer scaffold composed of gelatine, elastin, PCL, and poliglecaprone (a copolymer of glycolide and ε-caprolactone) was used to construct a Ø 4-mm porous tubular graft,[205,206] which promoted human aortic endothelial cell proliferation and was functional as cells were able to form tight junctions and secrete prostacyclin.[205,206]

A no further specified soluble elastin from the Elastin Products Company was used to prepare polydioxanon–elastin Ø 6-mm tubes with different blending ratios in order to meet the mechanics of the native vessel.[45] Suture reinforced electrospun polydioxanon–elastin Ø 1.5-mm tubes were cross-linked with 1-ethyl-3-(3-dimethylaminopropyl) carbodiimide hydrochloride (EDC), GA vapor (at both 100 and 25 °C for 30 min and 1 h, respectively), or ethylene–diglycidyl ether (EGDE), but only EDC (45% cross-linking) and heated GA (17% cross-linking) tubes did not dissolve upon wetting.[207] The EDC-cross-linked tubes had burst pressures ten times higher than normal systolic pressures with a range of compliances, including those matching the native artery.

A three-layered PCL-soluble elastin-collagen electrospun matrix was made to further mimic the structure of the native artery, with an intimal layer (98-2-0 blend), medial layer (45-45-10; 55-35-10; 65-25-10 blends), and adventitial layer (70-0-30 blend).[208]

The copolymer of glycolide with trimethylene carbonate (TMC), known as Maxon, was used in combination with gelatin and elastin to prepare tubes for vascular grafts. A triple-layered tubular scaffold was prepared by sequential electrospinning of the blend.[47]

Combinations with polymers also include the coatings for vascular grafts. Dutoya *et al.*[209] also coated a layer of κ-elastin without (0.4–2 μm) and with (3 μm) insoluble elastin onto polyethylene terephthalate (PET).[209] The elastin–κ-elastin–PET biomaterial promoted endothelial cells growth while maintaining their phenotype. Such a biomaterial could eventually function as a small-caliber vascular prosthesis, but reports of an announced implantation at the abdominal femoral junction in a dog model were not found in the literature. In another study, coacervated α-elastin was coated onto Dacron vascular grafts, which resulted in an inhibition of smooth muscle cell migration without an effect on endothelial cell motility. Such a coating may therefore prevent intimal hyperplasia.[210]

2.218.3.5. *In Vivo* Experiments

Matriderm (collagen-solubilized elastin scaffold) was directly compared to Integra (collagen–chondroitin sulfate scaffold) in immune-incompetent rats.[211] A two-stage setup was used and the time between scaffold implantation and epidermal transplantation was either 1 or 2 weeks. No differences were found in epidermal graft take, vascularization, and neodermal regeneration. In order to make a good comparison, both scaffolds were used as 2-mm thick constructs, which means that the thickness of Matriderm was double that of those used in other studies, making it difficult to compare with other Matriderm studies.

Ring *et al.* used Matriderm to which a glow discharge technique was applied, a method more generally applied to

polymer surfaces. When applied to full-thickness grafts in balb/c mice, accelerated neovascularization was observed.[212]

Carbodiimide cross-linked scaffolds composed of 50% insoluble collagen and 50% oxalic acid-solubilized elastin induced angiogenesis and showed synthesis of small elastic fibers, as shown with antibodies against rat elastin and rat fibrillin-1. Rat fibrillin-2, however, mainly colocalized with elastin blood vessels.[213] Please note that the solubilized elastin was prepared by oxalic acid solubilization and was not coacervated but filtrated in centrifugal filter tubes. The resulting solubilized elastin had an isoelectric point of 6 and a mean molecular weight of 1100 kDa, much larger than the expected 60 kDa for α-elastin.[214] Nillesen *et al.*[215] used the same solubilized elastin preparation to create an acellular full-thickness skin graft. The dual-layered skin graft was composed of a dermal porous part composed of 80% collagen and 20% solubilized elastin, which was then chemically cross-linked by a carbodiimide in the presence of the GAGs dermatan sulfate and heparin (3:1) and the growth factors vascular endothelial growth factor (VEGF) and fibroblast growth factor 2 (FGF2); the epidermal layer was composed of a dense structure of collagen cross-linked with heparin and containing fibroblast growth factor 7 (FGF7 or keratinocyte growth factor). Both layers were attached to each other using a collagen suspension, frozen and lyophilized. The construct was both biochemically and structurally characterized and used as an acellular full-thickness skin graft in a rat wound model where it was compared to the commercially available Integra dermal regeneration template and untreated wounds. At early time points, the double-layered skin construct showed more cell influx, significantly less contraction, and increased blood vessel formation. At the latest time point (day 112), it showed more elastic fibers than both other groups. Strikingly, structures resembling hair follicles and sebaceous glands were found in the double-layered skin construct and the untreated wound, but these were scarce in the Integra-treated wound. Lammers *et al.*[216] used the explants from the double-layered skin construct and the untreated wounds to run high-density gene expression microarrays and studied the biological processes in an unbiased manner using gene ontology (GO) analysis with the freely available program DAVID. They showed that microarray analysis is a promising tool that can be used complementarily to other methods like histology. However, the method is still in its infancy as for this rat study not all genes were annotated, GO terms were not well defined, and not all genes that belonged to a certain biological process were incorporated. This may explain why not all processes that were observed by histology, for example, elastic fiber development, were picked up in the GO analysis.

2.218.3.6. Clinical Applications

To our knowledge, Matriderm is the only clinically applied biomaterial that contains solubilized elastin. Matriderm is a 1-mm thick matrix made of porous insoluble collagen scaffold obtained by washing bovine skin (containing type I, III, and IV collagen) which is then coated with 3% oxalic acid-solubilized elastin obtained by hydrolysis of bovine nuchal ligament. The scaffold is cryogenically cross-linked and sterilized by gamma irradiation.[217–219]

Matriderm has been used as a dermal graft in clinical trials, and can be used either in a one or two-stage grafting procedure. This means that an epidermal (split skin) graft can be applied at the same time as applying the collagen–elastin matrix (one-stage) or some time (usually 2–3 weeks) after introducing the collagen–elastin matrix (two-stage). One-stage grafting is of course favored when it does not negatively influence the outcome of grafting. For Integra, only two-stage grafting is indicated, and time is needed to let the collagen–chondroitin sulfate (nonelastin) matrix be vascularized to allow a good epidermal graft take.[220]

In an early clinical trial concerning an intraindividual comparison study, the number of regrafting procedures was similar when using Matriderm with split skin in a one-stage procedure compared to split skin alone. When followed up on the short term, skin elasticity was considerably improved by Matriderm as analyzed by cutometer measurements,[221] but after 1 year, this difference was no longer statistically significant.[222] In a 12-year follow-up of this study, an objective scar assessment was performed and patients treated with Matriderm generally showed more improved scar parameters than patients treated with the epidermal graft alone. Examples of this are that scars treated with Matriderm and a largely expanded meshed skin graft were significantly more elastic and that a specific surface roughness parameter was significantly improved in Matriderm-treated reconstructed scars. In addition, pliability, relief, and the general observer score were better in acute and reconstructive burn scars which were initially treated with the collagen–elastin matrix.[223]

Ryssel *et al.* also intraindividually compared Matriderm with a split-thickness skin graft (one-stage procedure) to split-thickness skin graft alone in burn patients. In one study, results from ten burn patients showed a similar take and number of regrafting procedures, with improved elasticity for the Matriderm group.[224] In another study from 18 patients with hand burns, after 6 months a significantly improved range of motion was observed as well as a significantly better skin quality.[225] Ryssel *et al.*[219] also used Matriderm with split-thickness skin graft in one step after high voltage injuries (nine patients) and necrotizing fasciitis defects (five patients),[226] complex cases that often need to cover exposed bone and tendon, and saw promising results. Clinical comparative studies for treatment in these cases still need to be performed.

Generally, most studies have not used (in-patient) comparative studies. In one clinical study, Matriderm was applied after severe burn injuries of the hand in a one-stage procedure in ten patients which resulted in good take of the split-thickness skin graft. After 3 months, excellent pliability and full range of motion were observed.[217] After 12 months, scars showed good pliability and height and a well-established hand and wrist motion function. Also critical care patients, for example, patients with burns that covered a large percentage of the total body surface area, showed good results.[227] Improved cosmetics, facial contour, texture, and expression were found 4 months after treatment of a patient with a full-thickness chemical burn to almost all of the face with Matriderm and a homogenous graft.[228] Other case studies include the use of Matriderm in a breast reconstruction,[229] in the covering of exposed Achilles tendon secondary to burn injury,[230] and the surgical treatment of diabetic ulcers,[231] all with satisfying results.

The use of the collagen–elastin matrix looks highly auspicious, but so far few studies have made a direct comparison between Matriderm treatment and current treatments. Only such direct comparisons can persuade clinicians to explicitly choose a dermal matrix in specific one-stage grafting procedures.

2.218.3.7. Future Directions

Biomaterials containing solubilized elastin have been mainly used in skin (dermal substitute) and cardiovascular applications (small diameter blood vessel or coating of stents). Because of the wide range of cells that are capable of responding to solubilized elastin, because they carry the elastin–laminin receptor, its biological function can be exploited much more in biomaterials. Examples of effects of solubilized elastin that may be utilized are its function as a protector from ischemia by binding to S-Gal,[232] its capacity as a cell-surviving factor antagonizing apoptosis,[233] and its role as an inhibitor of platelet aggregation.[234]

References

1. Daamen, W. F.; Hafmans, T.; *et al*. *Biomaterials* **2001**, *22*(14), 1997–2005.
2. Fazio, M. J.; Mattei, M. G.; *et al*. *Am. J. Hum. Genet*. **1991**, *48*(4), 696–703.
3. Mithieux, S. M.; Weiss, A. S. *Adv. Protein Chem*. **2005**, *70*, 437–461.
4. Rosenbloom, J.; Abrams, W. R.; *et al*. *FASEB J*. **1993**, *7*(13), 1208–1218.
5. Muiznieks, L. D.; Jensen, S. A.; *et al*. *Arch. Biochem. Biophys*. **2003**, *410*(2), 317–323.
6. Cox, B. A.; Starcher, B. C.; *et al*. *Biochim. Biophys. Acta* **1973**, *317*(1), 209–213.
7. Kagan, H. M.; Sullivan, K. A. *Methods Enzymol*. **1982**, *82*(Pt A), 637–650.
8. Indik, Z.; Abrams, W. R.; *et al*. *Arch. Biochem. Biophys*. **1990**, *280*(1), 80–86.
9. Martin, S. L.; Vrhovski, B.; *et al*. *Gene* **1995**, *154*(2), 159–166.
10. Drury, J. L.; Mooney, D. J. *Biomaterials* **2003**, *24*(24), 4337–4351.
11. Ahmed, T. A.; Dare, E. V.; *et al*. *Tissue Eng. B Rev*. **2008**, *14*(2), 199–215.
12. Nicolson, P. C.; Vogt, J. *Biomaterials* **2001**, *22*(24), 3273–3283.
13. Bikiaris, D.; Koutris, E.; *et al*. *Recent Pat. Drug Deliv. Formul*. **2007**, *1*(3), 201–213.
14. DiTizio, V.; Ferguson, G. W.; *et al*. *Biomaterials* **1998**, *19*(20), 1877–1884.
15. Boateng, J. S.; Matthews, K. H.; *et al*. *J. Pharm. Sci*. **2008**, *97*(8), 2892–2923.
16. Annabi, N.; Mithieux, S. M.; *et al*. *Biomaterials* **2009**, *30*(27), 4550–4557.
17. Annabi, N.; Mithieux, S. M.; *et al*. *Biomaterials* **2009**, *30*(1), 1–7.
18. Annabi, N.; Mithieux, S. M.; *et al*. *Biomaterials* **2010**, *31*(7), 1655–1665.
19. Lim, D. W.; Nettles, D. L.; *et al*. *Biomacromolecules* **2007**, *8*(5), 1463–1470.
20. Lim, D. W.; Nettles, D. L.; *et al*. *Biomacromolecules* **2008**, *9*(1), 222–230.
21. McHale, M. K.; Setton, L. A.; *et al*. *Tissue Eng*. **2005**, *11*(11–12), 1768–1779.
22. Mithieux, S. M.; Rasko, J. E. J.; *et al*. *Biomaterials* **2004**, *25*, 4921–4927.
23. Mithieux, S. M.; Tu, Y.; *et al*. *Biomaterials* **2009**, *30*(4), 431–435.
24. Mithieux, S. M.; Wise, S. G.; *et al*. *J. Struct. Biol*. **2005**, *149*(3), 282–289.
25. Rnjak, J.; Li, Z.; *et al*. *Biomaterials* **2009**, *30*(32), 6469–6477.
26. Tu, Y.; Mithieux, S. M.; *et al*. *J. Biomed. Mater. Res. A* **2010**, *95*(4), 1215–1222.
27. Tu, Y.; Wise, S. G.; *et al*. *Micron* **2010**, *41*(3), 268–272.
28. Naumann, C.; Mithieux, S. M.; *et al*. *Biopolymers* **2009**, *91*(5), 321–330.
29. Rutledge, G. C.; Fridrikh, S. V. *Adv. Drug Deliv. Rev*. **2007**, *59*(14), 1384–1391.
30. Ayres, C. E.; Jha, B. S.; *et al*. *Wiley Interdiscip. Rev. Nanomed. Nanobiotechnol*. **2010**, *2*(1), 20–34.
31. Boudriot, U.; Dersch, R.; *et al*. *Artif. Organs* **2006**, *30*(10), 785–792.
32. Kriegel, C.; Arrechi, A.; *et al*. *Crit. Rev. Food Sci. Nutr*. **2008**, *48*(8), 775–797.
33. Kumbar, S. G.; James, R.; *et al*. *Biomed. Mater*. **2008**, *3*(3), 034002.
34. Matthews, J. A.; Wnek, G. E.; *et al*. *Biomacromolecules* **2002**, *3*(2), 232–238.
35. Liao, S.; Li, B.; *et al*. *Biomed. Mater*. **2006**, *1*(3), R45–R53.
36. Ramachandran, K.; Gouma, P. I. *Recent Pat. Nanotechnol*. **2008**, *2*(1), 1–7.
37. Sell, S. A.; McClure, M. J.; *et al*. *Adv. Drug Deliv. Rev*. **2009**, *61*(12), 1007–1019.
38. Ashammakhi, N.; Wimpenny, I.; *et al*. *J. Biomed. Nanotechnol*. **2009**, *5*(1), 1–19.
39. Boland, E. D.; Matthews, J. A.; *et al*. *Front. Biosci*. **2004**, *9*, 1422–1432.
40. Buttafoco, L.; Kolkman, N. G.; *et al*. *Biomaterials* **2006**, *27*(5), 724–734.
41. El-Kurdi, M. S.; Hong, Y.; *et al*. *Biomaterials* **2008**, *29*(22), 3213–3220.
42. Heydarkhan-Hagvall, S.; Schenke-Layland, K.; *et al*. *Biomaterials* **2008**, *29*(19), 2907–2914.
43. Lee, S. J.; Yoo, J. J.; *et al*. *J. Biomed. Mater. Res. A* **2007**, *83*(4), 999–1008.
44. Li, M.; Mondrinos, M. J.; *et al*. *Biomaterials* **2005**, *26*, 5999–6008.
45. Sell, S. A.; McClure, M. J.; *et al*. *Biomed. Mater*. **2006**, *1*(2), 72–80.
46. Stitzel, J.; Liu, J.; *et al*. *Biomaterials* **2006**, *27*(7), 1088–1094.
47. Thomas, V.; Zhang, X.; *et al*. *Biomed. Mater*. **2007**, *2*(4), 224–232.
48. Thomas, V.; Zhang, X.; *et al*. *Biotechnol. Bioeng*. **2009**, *104*(5), 1025–1033.
49. Nagapudi, K.; Brinkman, W. T.; *et al*. *Biomaterials* **2005**, *26*(23), 4695–4706.
50. Sallach, R. E.; Leisen, J.; *et al*. *J. Biomater. Sci. Polym. Ed*. **2009**, *20*(11), 1629–1644.
51. Schenke-Layland, K.; Rofail, F.; *et al*. *Biomaterials* **2009**, *30*(27), 4665–4675.
52. Nivison-Smith, L.; Rnjak, J.; *et al*. *Acta Biomater*. **2010**, *6*(2), 354–359.
53. Wise, S. G.; Byrom, M. J.; *et al*. *Acta Biomater*. **2011**, *7*(1), 295–303.
54. Waterhouse, A.; Yin, Y.; *et al*. *Biomaterials* **2010**, *31*(32), 8332–8340.
55. Yin, Y.; Wise, S. G.; *et al*. *Biomaterials* **2009**, *30*(9), 1675–1681.
56. Brooke, B. S.; Bayes-Genis, A.; *et al*. *Trends Cardiovasc. Med*. **2003**, *13*(5), 176–181.
57. Jordan, S. W.; Haller, C. A.; *et al*. *Biomaterials* **2007**, *28*(6), 1191–1197.
58. Woodhouse, K. A.; Klement, P.; *et al*. *Biomaterials* **2004**, *25*(19), 4543–4553.
59. Conte, M. S. *FASEB J*. **1998**, *12*(1), 43–45.
60. Zahedi, P.; Rezaeian, I.; *et al*. *Polym. Adv. Technol*. **2010**, *21*, 77–95.
61. Amadeu, T. P.; Braune, A. S.; *et al*. *Wound Repair Regen*. **2004**, *12*(2), 169–174.
62. Chen, G.; Chen, J.; *et al*. *Br. J. Dermatol*. **2009**, *161*(1), 48–55.
63. Kielty, C. M. *Expert Rev. Mol. Med*. **2006**, *8*(19), 1–23.
64. Tsuji, T.; Sawabe, M. *J. Cutan. Pathol*. **1987**, *14*(2), 106–113.
65. Rnjak, J.; Wise, S. G.; Mithieux, S. M.; Weiss, A. S. *Tissue Eng. B Rev*. **2010**, *17*, 81–91.
66. Bacakova, L.; Filova, E.; *et al*. *Physiol. Res*. **2004**, *53*(Suppl. 1), S35–S45.
67. Hong, J.; Azens, A.; *et al*. *Biomaterials* **2005**, *26*(12), 1397–1403.
68. Singh, R.; Dahotre, N. B. *J. Mater. Sci. Mater. Med*. **2007**, *18*(5), 725–751.
69. Almine, J. F.; Bax, D. V.; *et al*. *Chem. Soc. Rev*. **2010**, *39*(9), 3371–3379.
70. Bax, D. V.; McKenzieal, D. R.; *et al*. *Acta Biomater*. **2009**, *5*(9), 3371–3381.
71. Holst, J.; Watson, S.; *et al*. *Nat. Biotechnol*. **2010**, *28*(10), 1123–1128.
72. Sarikaya, M.; Tamerler, C.; *et al*. *Nat. Mater*. **2003**, *2*(9), 577–585.
73. Rodriguez-Cabello, J. C.; Reguera, J.; *et al*. *Ordered Polymeric Nanostructures at Surfaces* **2006**, *200*, 119–167.
74. Rodríguez-Cabello, J. C.; Martín, L.; *et al*. *Polymer* **2009**, *50*(22), 5159–5169.
75. Arias, F. J.; Reboto, V.; *et al*. *Biotechnol. Lett*. **2006**, *28*(10), 687–695.
76. Rodríguez-Cabello, J. C.; Prieto, S.; *et al*. *Nanomedicine* **2006**, *1*(3), 267–280.
77. Miao, M.; Bellingham, C. M.; *et al*. *J. Biol. Chem*. **2003**, *278*(49), 48553–48562.
78. Keeley, F. W.; Bellingham, C. M.; *et al*. *Philos. Trans. R. Soc. Lond. B Biol. Sci*. **2002**, *357*(1418), 185–189.
79. Chilkoti, A.; Dreher, M. R.; *et al*. *Adv. Drug Deliv. Rev*. **2002**, *54*(8), 1093–1111.
80. Chilkoti, A.; Dreher, M. R.; *et al*. *Adv. Drug Deliv. Rev*. **2002**, *54*(5), 613–630.
81. Rodriguez-Cabello, J. C.; Prieto, S.; *et al*. *J. Biomater. Sci. Polym. Ed*. **2007**, *18*(3), 269–286.
82. Urry, D. W.; Parker, T. M.; *et al*. *J. Bioact. Compat. Polym*. **1991**, *6*(3), 263–282.
83. Urry, D. W. *What Sustains Life? Consilient Mechanisms for Protein-Based Machines and Materials*. Springer-Verlag: New York, 2006.
84. Macewan, S. R.; Chilkoti, A. *Biopolymers* **2010**, *94*(1), 60–77.
85. Urry, D. W. *Trends Biotechnol*. **1999**, *17*(6), 249–257.
86. Urry, D. W.; Pattanaik, A.; *et al*. *J. Biomater. Sci. Polym. Ed*. **1998**, *9*(10), 1015–1048.
87. Zhang, H.; Iwama, M.; *et al*. *Tissue Eng*. **2006**, *12*(2), 391–401.
88. Betre, H.; Setton, L. A.; *et al*. *Biomacromolecules* **2002**, *3*(5), 910–916.
89. McPherson, D. T.; Xu, J.; *et al*. *Protein Expr. Purif*. **1996**, *7*(1), 51–57.
90. Qiu, W.; Teng, W.; *et al*. *Biomacromolecules* **2009**, *10*(3), 602–608.
91. Mi, L. X. *Biomacromolecules* **2006**, *7*(7), 2099–2107.

92. Rodríguez-Cabello, J. C.; A. G.; Ribeiro, A.; Arias, F. J. *Meth. Mol. Biol.* **2010**.
93. San Biagio, P. L.; Madonia, F.; *et al. Chem. Phys. Lett.* **1988**, *145*(6), 571–574.
94. Pauling, L.; Marsh, R. E. *Proc. Natl. Acad. Sci. USA* **1952**, *38*(2), 112–118.
95. Tanford, C. *The Hydrophobic Effect: Formation of Micelles and Biological Membranes*. Wiley: New York, 1973; p 200.
96. Rodriguez-Cabello, J. C.; Alonso, M.; *et al. Biopolymers* **2000**, *54*(4), 282–288.
97. Manno, M.; Emanuele, A.; *et al. Biopolymers* **2001**, *59*(1), 51–64.
98. Urry, D. W. *Angew. Chem. Int. Ed.* **1993**, *32*(6), 819–841.
99. Rodriguez-Cabello, J. C.; Reguera, J.; *et al. Prog. Polym. Sci.* **2005**, *30*(11), 1119–1145.
100. Ribeiro, A.; Arias, F. J.; *et al. Biophys. J.* **2009**, *97*(1), 312–320.
101. Alonso, M.; Reboto, V.; *et al. Macromolecules* **2001**, *34*(23), 8072–8077.
102. Girotti, A.; Reguera, J.; *et al. Macromolecules* **2004**, *37*(9), 3396–3400.
103. Girotti, A.; Reguera, J.; *et al. J. Mater. Sci. Mater. Med.* **2004**, *15*(4), 479–484.
104. Rajagopal, K.; Schneider, J. P. *Curr. Opin. Struct. Biol.* **2004**, *14*(4), 480–486.
105. Flamia, R.; Zhdan, P. A.; *et al. Biomacromolecules* **2004**, *5*(4), 1511–1518.
106. Wright, E. R.; Conticello, V. P. *Adv. Drug Deliv. Rev.* **2002**, *54*(8), 1057–1073.
107. Reguera, J.; Fahmi, A.; *et al. J. Am. Chem. Soc.* **2004**, *126*(41), 13212–13213.
108. Chow, D.; Nunalee, M. L.; *et al. Mater. Sci. Eng. Rep.* **2008**, *62*(4), 125–155.
109. Di Zio, K.; Tirrell, D. A. *Macromolecules* **2003**, *36*(5), 1553–1558.
110. Heilshorn, S. C.; Liu, J. C.; *et al. Biomacromolecules* **2005**, *6*(1), 318–323.
111. Liu, J. C.; Heilshorn, S. C.; *et al. Biomacromolecules* **2004**, *5*(2), 497–504.
112. Richman, G. P.; Tirrell, D. A.; *et al. J. Control. Release* **2005**, *101*(1–3), 3–12.
113. Welsh, E. R.; Tirrell, D. A. *Biomacromolecules* **2000**, *1*(1), 23–30.
114. Garcia, Y.; Hemantkumar, N.; *et al. Tissue Eng. A* **2009**, *15*(4), 887–899.
115. Martinez-Osorio, H.; Juarez-Campo, M.; *et al. Curr. Eye Res.* **2009**, *34*(1), 48–56.
116. Barbosa, J. S.; Costa, R. R.; *et al. Nanoscale Res. Lett.* **2009**, *4*(10), 1247–1253.
117. Barbosa, J. S.; Ribeiro, A.; *et al. Adv. Eng. Mater.* **2010**, *12*(1–2), B37–B44.
118. Costa, R. R.; Custodio, C. A.; *et al. Adv. Funct. Mater.* **2009**, *19*(20), 3210–3218.
119. Senior, R. M.; Griffin, G. L.; *et al. J. Cell Biol.* **1984**, *99*(3), 870–874.
120. Nowatzki, P. J.; Tirrell, D. A. *Biomaterials* **2004**, *25*(7–8), 1261–1267.
121. Nagapudi, K.; Brinkman, W. T.; *et al. Macromolecules* **2002**, *35*(5), 1730–1737.
122. Lee, J.; Macosko, C. W.; *et al. Macromolecules* **2001**, *34*(17), 5968–5974.
123. Lee, J.; Macosko, C. W.; *et al. Macromolecules* **2001**, *34*(12), 4114–4123.
124. Martin, L.; Alonso, M.; *et al. Biomacromolecules* **2009**, *10*(11), 3015–3022.
125. Martin, L.; Alonso, M.; *et al. Soft Matter* **2009**, *5*(8), 1591–1593.
126. Furth, M. E.; Atala, A.; *et al. Biomaterials* **2007**, *28*(34), 5068–5073.
127. Kopecek, J. *Biomaterials* **2007**, *28*(34), 5185–5192.
128. Liu, J. C.; Tirrell, D. A. *Biomacromolecules* **2008**, *9*(11), 2984–2988.
129. Betre, H.; Ong, S. R.; *et al. Biomaterials* **2006**, *27*(1), 91–99.
130. Martin, L.; Arias, F. J.; *et al. Soft Matter* **2010**, *6*(6), 1121–1124.
131. Plouffe, B. D.; Njoka, D. N.; *et al. Langmuir* **2007**, *23*(9), 5050–5055.
132. Caves, J. M.; Kumar, V. A.; *et al. Biomaterials* **2010**, *31*(27), 7175–7182.
133. Straley, K.; Heilshorn, S. C. *Conf. Proc. IEEE Eng. Med. Biol. Soc.* **2009**, *2009*, 2101–2102.
134. Sallach, R. E.; Cui, W.; *et al. Biomaterials* **2009**, *30*(3), 409–422.
135. Wu, X. Y.; Sallach, R.; *et al. Biomacromolecules* **2005**, *6*(6), 3037–3044.
136. Sallach, R. E.; Cui, W.; *et al. Biomaterials* **2010**, *31*(4), 779–791.
137. Nath, N.; Hyun, J.; *et al. Surf. Sci.* **2004**, *570*(1–2), 98–110.
138. Akiyama, Y.; Kikuchi, A.; *et al. Langmuir* **2004**, *20*(13), 5506–5511.
139. Cho, E. C.; Kim, Y. D.; *et al. Polymer* **2004**, *45*(10), 3195–3204.
140. Jones, D. M.; Smith, J. R.; *et al. Adv. Mater.* **2002**, *14*(16), 1130–1134.
141. Kushida, A.; Yamato, M.; *et al. J. Biomed. Mater. Res.* **1999**, *45*(4), 355–362.
142. Ozturk, N.; Girotti, A.; *et al. Biomaterials* **2009**, *30*(29), 5417–5426.
143. Nath, N.; Chilkoti, A. *Adv. Mater.* **2002**, *14*(17), 1243–1247.
144. Wada, A.; Mie, M.; *et al. J. Am. Chem. Soc.* **2003**, *125*(52), 16228–16234.
145. Elloumi, I.; Kobayashi, R.; *et al. Biomaterials* **2006**, *27*(18), 3451–3458.
146. Na, K.; Jung, J.; *et al. Langmuir* **2008**, *24*(9), 4917–4923.
147. Swierczewska, M.; Hajicharalambous, C. S.; *et al. Acta Biomater.* **2008**, *4*(4), 827–837.
148. Aparicio, C.; Salvagni, E.; *et al. J. Med. Devices* **2009**, *3*(2), 027555.
149. Huang, Z.-M.; Zhang, Y. Z.; *et al. Compos. Sci. Technol.* **2003**, *63*(15), 2223–2253.
150. Li, D.; Xia, Y. N. *Adv. Mater.* **2004**, *16*(14), 1151–1170.
151. Sill, T. J.; von Recum, H. A. *Biomaterials* **2008**, *29*(13), 1989–2006.
152. Huang, L.; McMillan, R. A.; *et al. Macromolecules* **2000**, *33*(8), 2989–2997.
153. Fahmi, A.; Pietsch, T.; *et al. Adv. Funct. Mater.* **2010**, *20*, 1011–1018.
154. Kost, J.; Langer, R. *Adv. Drug Deliv. Rev.* **1991**, *6*(1), 19–50.
155. Bidwell, G. L.; Raucher, D. *Mol. Cancer Ther.* **2005**, *4*(7), 1076–1085.
156. Bidwell, G. L., III; Davis, A. N.; *et al. J. Control. Release* **2009**, *135*(1), 2–10.
157. Massodi, I.; Bidwell, G. L., III; *et al. J. Control. Release* **2005**, *108*(2–3), 396–408.
158. Furgeson, D. Y.; Dreher, M. R.; *et al. J. Control. Release* **2006**, *110*(2), 362–369.
159. Dreher, M. R.; Liu, W.; *et al. Cancer Res.* **2007**, *67*(9), 4418–4424.
160. Urry, D. W. *Abstr. Papers Am. Chem. Soc.* **1990**, *200*, 74.
161. Herrero-Vanrell, R.; Rincon, A. C.; *et al. J. Control. Release* **2005**, *102*(1), 113–122.
162. Bessa, P. C.; Machado, R.; *et al. J. Control. Release* **2010**, *142*(3), 312–318.
163. Dreher, M. R.; Raucher, D.; *et al. J. Control. Release* **2003**, *91*(1–2), 31–43.
164. Stayton, P. S.; Hoffman, A. S.; *et al. J. Control. Release* **2000**, *65*(1–2), 203–220.
165. Massodi, I.; Bidwell, G.; *et al. Clin. Exp. Metastasis* **2009**, *26*(3), 251–260.
166. Massodi, I.; Thomas, E.; *et al. Molecules* **2009**, *14*(6), 1999–2015.
167. Wu, Y.; MacKay, J. A.; *et al. Biomacromolecules* **2009**, *10*(1), 19–24.
168. MacKay, J. A.; Chen, M.; *et al. Nat. Mater.* **2009**, *8*(12), 993–999.
169. Dreher, M. R.; Simnick, A. J.; *et al. J. Am. Chem. Soc.* **2008**, *130*(2), 687–694.
170. Kim, W.; Thévenot, J.; *et al. Angew. Chem. Int. Ed.* **2010**, *49*(25), 4257–4260.
171. Sallach, R. E.; Wei, M.; *et al. J. Am. Chem. Soc.* **2006**, *128*(36), 12014–12019.
172. Alvarez-Rodriguez, R.; Alonso, M.; *et al. Eur. Polym. J.* **2010**, *46*(4), 643–650.
173. Alvarez-Rodríguez, R.; Arias, F. J.; *et al. Macromol. Rapid Commun.* **2010**, *31*(6), 568–573.
174. Floss, D. M.; Schallau, K.; *et al. Trends Biotechnol.* **2010**, *28*(1), 37–45.
175. Araujo, R.; Silva, C.; *et al. Biomacromolecules* **2009**, *10*(6), 1655–1661.
176. Kim, J. Y.; Mulchandani, A.; *et al. Biotechnol. Bioeng.* **2005**, *90*(3), 373–379.
177. Hinek, A.; Wrenn, D. S.; *et al. Science* **1988**, *239*(4847), 1539–1541.
178. Hinek, A.; Wang, Y. T.; *et al. J. Dermatol. Sci.* **2005**, *39*(3), 155–166.
179. Senior, R. M.; Griffin, G. L.; *et al. J. Clin. Invest.* **1980**, *66*(4), 859–862.
180. Kamoun, A.; Landeau, J. M.; *et al. Cell Adhes. Commun.* **1995**, *3*(4), 273–281.
181. Fujimoto, N.; Tajima, S.; *et al. J. Invest. Dermatol.* **2000**, *115*(4), 633–639.
182. Mochizuki, S.; Brassart, B.; *et al. J. Biol. Chem.* **2002**, *277*(47), 44854–44863.
183. Antonicelli, F.; Bellon, G.; *et al. Curr. Top. Dev. Biol.* **2007**, *79*, 99–155.
184. Fulop, T.; Jacob, M. P.; *et al. Pathol. Biol.* **1998**, *46*(7), 497–506.
185. Mecham, R. P.; Lange, G. *Biochemistry* **1982**, *21*(4), 669–673.
186. Partridge, S.; Davis, H.; *et al. J. Biol. Chem.* **1955**, *61*, 11–21.
187. Jacob, M. P.; Hornebeck, W. In *Methods of Connective Tissue Research*; Robert, L., Moczar, M., Moczar, E., Eds.; Karger: Basel, 1985; pp 92–129.
188. Senior, R. M.; Griffin, G. L.; *et al. J. Clin. Invest.* **1982**, *70*(3), 614–618.
189. Taddese, S.; Weiss, A. S.; *et al. Matrix Biol.* **2008**, *27*(5), 420–428.
190. Lefebvre, F.; Gorecki, S.; *et al. Biomaterials* **1992**, *13*(1), 28–33.
191. Rabaud, M.; Lefebvre, F.; *et al. Biomaterials* **1991**, *12*(3), 313–319.
192. Lefebvre, F.; Pilet, P.; *et al. Biomaterials* **1996**, *17*(18), 1813–1818.
193. Rovira, A.; Amedee, J.; *et al. Biomaterials* **1996**, *17*(15), 1535–1540.
194. Bonzon, N.; Carrat, X.; *et al. Biomaterials* **1995**, *16*(11), 881–885.
195. Leach, J. B.; Wolinsky, J. B.; *et al. Acta Biomater.* **2005**, *1*(2), 155–164.
196. Dehghani, F.; Annabi, N.; *et al. Biomacromolecules* **2008**, *9*(4), 1100–1105.
197. Lammers, G.; Tjabringa, G. S.; *et al. Biomaterials* **2009**, *30*(31), 6213–6220.
198. Sionkowska, A.; Skopinska-Wisniewska, J.; *et al. Int. J. Biol. Macromol.* **2010**, *47*(4), 570–577.
199. Serban, M. A.; Kluge, J. A.; *et al. Biomacromolecules* **2010**, *11*(9), 2230–2237.
200. Miyamoto, K.; Atarashi, M.; *et al. Int. J. Biol. Macromol.* **2009**, *45*(1), 33–41.
201. Stark, Y.; Suck, K.; *et al. Exp. Toxicol. Pathol.* **2006**, *57*(4), 305–311.
202. Waaijman, T.; Breetveld, M.; Ulrich, M.; Middelkoop, E.; Scheper, R. J.; Gibbs, S. *Cell Transplant.* **2010**, *19*(10), 1339–1348.
203. Keck, M.; Haluza, D.; Lumenta, D. B.; Burjak, S.; Eisenbock, B.; Kamolz, L. P.; Frey, M. *Burns.* **2011**, *37*(4), 626–630.
204. Salem, H.; Ciba, R.; *et al. Biomaterials* **2009**, *30*(5), 789–796.
205. Zhang, X.; Thomas, V.; *et al. J. Mater. Sci. Mater. Med.* **2010**, *21*(2), 541–549.
206. Zhang, X.; Thomas, V.; *et al. Biomaterials* **2010**, *31*(15), 4376–4381.
207. Smith, M. J.; McClure, M. J.; *et al. Acta Biomater.* **2008**, *4*(1), 58–66.
208. McClure, M. J.; Sell, S. A.; *et al. Acta Biomater.* **2010**, *6*(7), 2422–2433.
209. Dutoya, S.; Verna, A.; *et al. Biomaterials* **2000**, *21*(15), 1521–1529.
210. Ito, S.; Ishimaru, S.; *et al. ASAIO J.* **1998**, *44*(5), M501–M505.
211. Schneider, J.; Biedermann, T.; *et al. Burns* **2009**, *35*(1), 51–57.
212. Ring, A.; Langer, S.; *et al. Burns* **2010**, *36*, 1222–1227.
213. Daamen, W. F.; Nillesen, S. T.; *et al. Tissue Eng. A* **2008**, *14*(3), 349–360.
214. Daamen, W. F.; Geutjes, P. J.; *et al. Adv. Mater.* **2007**, *19*(5), 673–677.

215. Nillesen, S. T.; Lammers, G.; Wismans, R. G.; Ulrich, M. M.; Middelkoop, E.; Spauwen, P. H.; Faraj, K. A.; Schalkwijk, J.; Daamen, W. F.; van Kuppevelt, T. H. *Acta Biomater.* **2011**, *7*(3), 1063–1071.
216. Lammers, G.; Gilissen, C.; *et al*. *Biomaterials* **2010**, *31*(32), 8299–8312.
217. Haslik, W.; Kamolz, L. P.; *et al*. *Burns* **2007**, *33*(3), 364–368.
218. Lamme, E. N.; Van Leeuwen, R. T.; *et al*. *J. Pathol.* **2000**, *190*(5), 595–603.
219. Ryssel, H.; Radu, C. A.; *et al*. *Int. Wound J.* **2007**, *2010*(7), 385–392.
220. Ruszczak, Z. *Adv. Drug Deliv. Rev.* **2003**, *55*, 1595–1611.
221. van Zuijlen, P. P.; van Trier, A. J.; *et al*. *Plast. Reconstr. Surg.* **2000**, *106*(3), 615–623.
222. van Zuijlen, P. P.; Vloemans, J. F.; *et al*. *Plast. Reconstr. Surg.* **2001**, *108*(7), 1938–1946.
223. Bloemen, M. C.; van Leeuwen, M. C.; *et al*. *Plast. Reconstr. Surg.* **2010**, *125*(5), 1450–1459.
224. Ryssel, H.; Gazyakan, E.; *et al*. *Burns* **2008**, *34*(1), 93–97.
225. Radu, C. A.; Germann, G.; *et al*. *Burns* **2010**, *36*(8), 1248–1253.
226. Ryssel, H.; Germann, G.; *et al*. *Burns* **2010**, *36*(7), 1107–1111.
227. Haslik, W.; Kamolz, L. P.; *et al*. *J. Plast. Reconstr. Aesthet. Surg.* **2008**, *63*(2), 360–364.
228. Atherton, D. D.; Tang, R.; *et al*. *Plast. Reconstr. Surg.* **2010**, *125*, 60e–61e.
229. Murphy, K. D.; McGoldrick, C.; *et al*. *J. Plast. Reconstr. Aesthet. Surg.* **2009**, *62*(12), E658–E660.
230. Boyce, A.; Atherton, D. D.; *et al*. *J. Plast. Reconstr. Aesthet. Surg.* **2010**, *63*(2), E206–E207.
231. Cervelli, V.; Lucarini, L.; *et al*. *Int. Wound J.* **2010**, *7*, 291–296.
232. Robinet, A.; Millart, H.; *et al*. *FASEB J.* **2007**, *21*(9), 1968–1978.
233. Cantarelli, B.; Duca, L.; *et al*. *FEBS Lett.* **2009**, *583*(14), 2385–2391.
234. Shiratsuchi, E.; Ura, M.; *et al*. *J. Pept. Sci.* **2010**, *16*(11), 652–658.
235. Machado, R.; Ribeiro, A. J.; Padrão, J.; *et al*. *J. Nano Res.* **2009**, *6*, 133–145.

2.219. Biophysical Analysis of Amyloid Formation

I Segers-Nolten, M van Raaij, and V Subramaniam, University of Twente, Enschede, The Netherlands

© 2011 Elsevier Ltd. All rights reserved.

2.219.1.	**Introduction**	348
2.219.2.	**Monomer Folding**	349
2.219.2.1.	α-Synuclein Structural Heterogeneity	349
2.219.2.2.	Antiparallel Arrangement of α-Synuclein Helices	351
2.219.3.	**Aggregation Intermediates**	352
2.219.3.1.	Aggregation Kinetics	352
2.219.3.2.	Morphology of Aggregation Intermediates	352
2.219.3.3.	Secondary Structure of Aggregation Intermediates	353
2.219.3.4.	Protein Interactions	353
2.219.4.	**Mature Amyloid Fibrils**	354
2.219.4.1.	Structural Polymorphism of Amyloid Fibrils	354
2.219.4.2.	Mechanical Deformation of Fibrils	357
2.219.5.	**Conclusion**	358
References		358

Glossary

Amphipathic Containing polar and nonpolar regions.
Amyloidosis Disease resulting from abnormal deposition of amyloid.
CMC Critical micelle concentration, minimum phospholipid concentration that forms micelles in water.
Cross-β conformation β-sheet secondary protein structure with parallel β-strands oriented perpendicular to the assembly axis.
Curli Extracellular bacterial amyloid used for surface adhesion and colony formation.
Lewy body Amyloid-containing inclusions found in neurons in the brain of Parkinson's patients.
Melanosome Mammalian cellular organelle containing melanin residing in skin and eye cells.
Micelle Around 5-nm-diameter spherical aggregate, formed from phospholipids in water above a characteristic concentration, the critical micelle concentration.
Neurodegenerative disease Disease characterized by progressive loss of functional neurons in the brain, like Parkinson's and Alzheimer's disease.
Oligomer Assembly of a limited number of identical monomers.
Pme117 A transmembrane protein that mediates the early steps in the formation of melanosomes.
Polymorphism The variety of morphologies exhibited by assemblies of identical subunits.
Protofibril Intermediate amyloid aggregation state between protofilament and mature fibril.
Protofilament Intermediate amyloid aggregation state between monomer and protofibril.
Raman spectroscopy Vibrational spectroscopy that yields insight into the secondary structure and chemical composition of a sample by measuring the intensity and spectral distribution of light emitted by a sample after excitation with high-intensity laser light.

Abbreviations

Aβ	Amyloid-β
$Aβ_{1-42}$	Amyloid-β; N-terminal 1–42 residues
AFM	Atomic force microscopy
CD	Circular dichroism
CM-AFM	Contact mode AFM
CMC	Critical micelle concentration
DNA	Deoxyribonucleic acid
EPR	Electron paramagnetic resonance spectroscopy
FRET	Förster resonance energy transfer
FWHM	Full width half maximum
HAM	Hierarchical assembly model
LUV	Large unilamellar vesicle
MTSL	1-Oxy-2,2,5,5 tetramethylpyrroline-3-methyl-methanethiosulfonate
NMR	Nuclear magnetic resonance
PD	Parkinson disease
POPG	1-Palmitoyl-2-oleoyl-*sn*-glycero-3-(phosphorac-(1-glycerol))
S129	Serine residue 129
SDS	Sodium dodecyl sulfate
SEM	Scanning electron microscope

SM-FRET	Single-molecule Förster resonance energy transfer	**Triton X-100**	Detergent
STM	Scanning tunneling microscope	**Trp**	Tryptophan
SUV	Small unilamellar vesicle	**tTG**	Tissue transglutaminase
ThioT	Thioflavin T	**UV**	Ultraviolet
TM-AFM	Tapping mode AFM		

Symbols

E_{obs}	Observed FRET efficiency
Θ	Ellipticity

2.219.1. Introduction

Insoluble amyloid fibrils self-assemble from a wide variety of proteins that are soluble under physiological conditions. In general, fibrillar amyloid nanostructures have typical diameters of around 10 nm, can grow to several micrometers in length, are extremely stable, and consist mainly of β-sheet folded protein in a typical hydrogen-bonded cross-β conformation (**Chapter 2.204, Peptoids: Synthesis, Characterization, and Nanostructures**). Amyloid formation has long been associated with disease. Besides neurodegenerative disorders, such as Alzheimer's, Parkinson's, Huntington's, and Creutzfeld–Jacob disease, other diseases such as type II diabetes and cardiovascular amyloidosis are also accompanied by the development of amyloid fibrils.[1] Amyloids have also gained more positive recognition since several functional amyloid-containing materials have been identified in nature, from bacteria to humans.[2] Examples are spider silk, biofilms formed from bacterial curli, fibrillar chorion proteins in insect egg shells,[3] and Pme117 fibers in human melanosomes.[4] Amyloid formation also plays an important role in the food industry, where food processing induces fibrillar aggregation of globular proteins, for instance, during heating.[5] In particular, there is a specific interest in the use of amyloid structures for optimization of food texture.

The extreme stability of amyloid fibrils, with a reported mechanical strength similar to polystyrene and nylon, has instigated the interest for use in novel bionanotechnological applications.[6,7] The fibrillar character is particularly interesting for fabrication of nanostructured scaffolds. The spontaneous self-assembly of specific proteins enables the formation of biomaterials with extraordinary characteristics. The proteinaceous nature offers the possibility of using the toolbox of molecular biology to specifically functionalize the fibrils with a variety of chemical or biological conjugation partners resulting in a biomaterial with unique biophysical and physicochemical properties. Compared to chemically synthesized materials, amyloid-based materials have advantageous qualities with respect to biocompatibility and biodegradability. Their versatility offers great potential for creative applications in bionanotechnology. An obvious possibility is the fabrication of nanophotonic or nanoelectronic devices from amyloid-based nanowires.[8,9]

Although protein aggregation in general has been studied extensively for many years, the mechanism of amyloid fibril formation has not been resolved. Full understanding of the assembly mechanism is however essential, not only for development of therapeutic means to fight hitherto incurable diseases but also for optimal utilization of amyloid as nanobiomaterials. To achieve these aims, a range of available biophysical approaches can be deployed that provide molecular level information on the structure of amyloid fibrils.

This chapter gives an overview of biophysical methods that we have applied to the amyloid-forming Parkinson disease (PD) related *α-synuclein* protein,[10,11] but may be considered as relevant for amyloids in general. We describe the revealed information with a focus on those aspects of amyloid formation that are most relevant for a better understanding of the aggregation mechanism, concurrently enhancing insights into the material properties of amyloids. The molecular level assembly process (in this case of α-synuclein) is reflected in characteristics of the monomeric protein and oligomeric folding intermediates, kinetics of fibril formation, fibrillar ultrastructure, and mechanical fibril properties (**Figure 1**).

We describe recent progress in the application of advanced biophysical methods such as (single-molecule) fluorescence spectroscopy, electron paramagnetic resonance (EPR) spectroscopy, circular dichroism (CD) spectroscopy, and atomic force

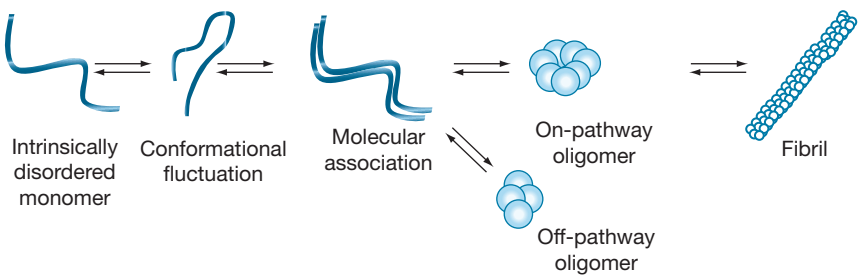

Figure 1 Schematic representation of the proposed amyloid formation mechanism for human α-synuclein.

microscopy (AFM) to study α-synuclein aggregation. This broad ensemble of approaches provides a deeper perspective into the fascinating research field of amyloids, both from a mechanistic and a materials perspective.

2.219.2. Monomer Folding

2.219.2.1. α-Synuclein Structural Heterogeneity

It has long been believed that protein stability and function are inevitably associated with proper folding into a characteristic three-dimensional conformation. In recent years, it has become apparent that there exist a large number of intrinsically disordered proteins, such as human α-synuclein, that are functional without having a structured conformation.[12] Both classes of proteins, structured and unstructured, are able to aggregate into amyloid fibrils, requiring partial unfolding of globular proteins or partial acquisition of structure by intrinsically disordered proteins, respectively.[13] The assembly of amyloid fibrils from protein monomers is believed to take place by a nucleation-dependent polymerization process. Partially folded/unfolded monomers may assemble to form oligomers of still unidentified size and conformation, possibly functioning as nuclei, followed by transformation into elongated protofibrillar structures and finally into mature fibrils.[1,14–16]

Human α-synuclein protein (**Figure 2**), a 140 residue intrinsically disordered protein, plays a central role in the etiology of PD,[10] and forms fibrillar aggregates that are found in Lewy bodies in the brain, structures which are the hallmark of the disease.[11,17,18] Three point mutations (A30P, A53T, and E46K) are associated with early onset PD.[19–21] Modifications such as phosphorylation of the serine residue at position 129, and truncations of the protein, are reported to play an important role in the toxicity of α-synuclein.[22–26]

The conformation of the intrinsically disordered protein α-synuclein is known to depend on the environment, binding to targets, and the aggregation state. Although its exact function remains obscure, α-synuclein has been associated with dopamine neurotransmission and regulation of the synaptic vesicular pool.[27] Furthermore, it has been suggested to act at the presynaptic membrane interface.[28] Free in solution, α-synuclein has random-coil-like conformations,[29] but on binding to negatively charged membranes α-helical structures dominate.[30,31] In the fibrillar state, a rigid cross-β structure is prominent,[32] likely lining up the fibril core. Obviously, the protein is structurally highly flexible, which may be fundamental to its putative biological function and implications for disease. The structural transition of the unstructured protein into β-sheet-rich fibrils may be initiated and driven by the occurrence of local structure in α-synuclein molecules. The transient nature, inherent heterogeneity, and low frequencies of occurrence of intramolecular fluctuations and intermolecular associations at physiological concentrations can be addressed only by advanced single-molecule spectroscopy approaches that can detect distributions of structures in ensembles.

Therefore, we and others have used *single-molecule confocal fluorescence microscopy* to study the flexibility and to map the 'structure' of individual α-synuclein monomers, both free in solution and upon binding to SDS (sodium dodecyl sulfate) molecules of monomeric or micellar nature.[33,34] The interaction with SDS is particularly interesting because of its resemblance to membrane components. Single-molecule techniques are specifically required to resolve the occurrence and characteristics of substructures within a population of protein monomers, information that is impossible to obtain from ensemble methods. We have used *single-molecule Förster resonance energy transfer* (SM-FRET) to investigate the structural architecture of α-synuclein.[34] FRET is a nonradiative transfer of the excitation energy from a donor to an acceptor chromophore that involves a distance-dependent interaction between the emission and the absorption transition dipole moments of the donor and acceptor, respectively.[35–37] The rate of energy transfer depends on the spectral overlap of the donor emission and acceptor absorbance, the donor fluorescence quantum yield, the relative orientation of their transition dipole moments, and the distance between donor and acceptor molecules. FRET efficiencies depend on the donor–acceptor separation distance with an inverse sixth power law. The Förster radius, the characteristic distance for a given donor–acceptor pair at which the energy transfer efficiency is 50%, is comparable to the size of biological macromolecules. Therefore, FRET is very useful for measuring distances between different sites on proteins.[38–40]

The N-terminal domain of the α-synuclein protein is known to be involved in membrane binding.[30] Using recombinant techniques, we have engineered a variant of α-synuclein with two cysteines in the putative membrane-binding domain (amino acids 9 and 69). These engineered cysteines act as molecular 'hooks,' and were specifically labeled with donor and acceptor dyes suitable for SM-FRET. FRET efficiency (E_{obs}) histograms of 100 pM Alexa Fluor 488 and Alexa Fluor 568 labeled α-synuclein-9C/69C at increasing concentrations of SDS are presented in **Figure 3**. Initially, without SDS, α-synuclein adopts conformations resulting in an E_{obs} centered at 0.54 (first panel, 0 mM, **Figure 3**).

At low SDS concentrations (up to ~0.5 mM), no apparent changes in the histograms were observed. However, upon

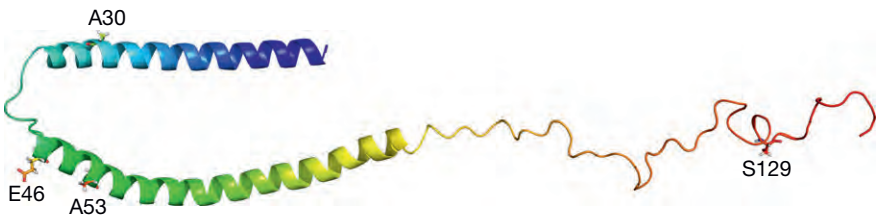

Figure 2 Representation of the α-synuclein protein indicating the Parkinson's disease-related mutation sites (A30P, E46K, and A53T) and the S129 phosphorylation site.

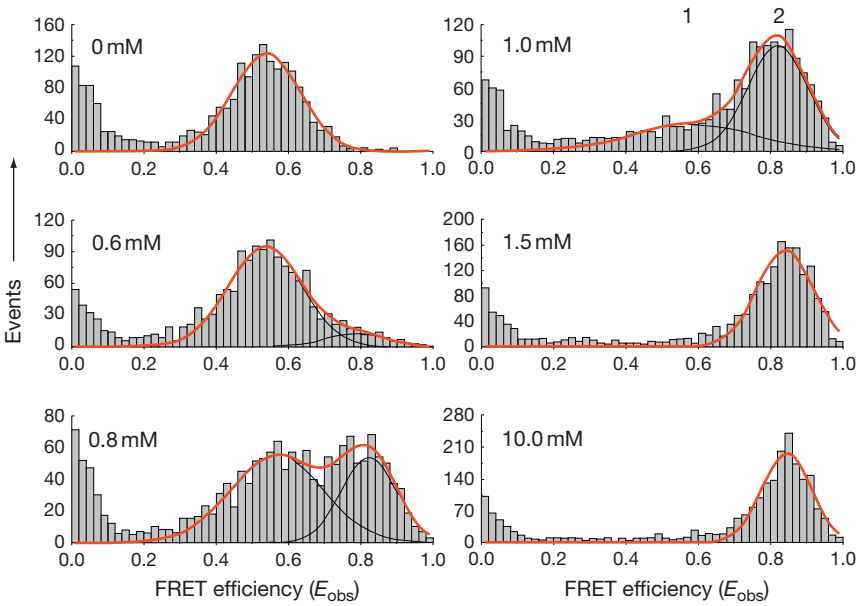

Figure 3 FRET efficiency histograms of α-synuclein-9C/69C as a function of SDS concentration. Solid lines indicate Gaussian fits to one or two populations (marked 1 and 2). Where applicable, individual Gaussians are shown.

increasing the SDS concentration from 0.5 to 1.0 mM, a clear second distribution centered at E_{obs} ~0.82 and of smaller width appeared (peak 2). The higher E_{obs}-value is indicative of a population of proteins where positions 9 and 69 are closer together, leading to increased FRET. The area of the first peak decreased concomitantly with the increase in area of the second peak, suggesting that SDS-induced structural changes in α-synuclein result in one or the other of the conformers, at least within the 1 ms time frame of the experiment. At even higher SDS concentrations (1.5–10.0 mM), the first distribution completely disappeared. Remarkably, above 1.5 mM SDS, although the mean value of the peak did not alter significantly, the width decreased further by ~15% (with an error in the full width half maximum (FWHM) below 5%). We attribute this narrowing of the distribution width to a further stabilization of the horseshoe structure as has been structurally resolved with NMR (nuclear magnetic resonance)[41] (see Figure 4).

We also used *CD spectroscopy* to assess the α-synuclein secondary structure content over the applied SDS concentration range. CD spectroscopy measures directly, without a need for additional labeling, the presence and abundance of specific secondary structures.[42] In CD spectroscopy, the differential absorbance of left- and right-circularly polarized light that is alternately radiated into a sample is detected. A CD spectrum is recorded by measuring this differential absorption as a function of wavelength. CD spectroscopy is mostly performed in the far-UV spectral region, where peptide bonds generate CD signals dependent on the environment. Thus, the CD signals are determined by the secondary structure of the protein and can even be used to semiquantitatively estimate the α-helix, β-sheet, and random-coil content.

CD measurements, with a five orders of magnitude higher protein concentration than that used in the SM-FRET experiments, revealed an increase in α-helix content that corresponded very well with the peak positions and relative areas

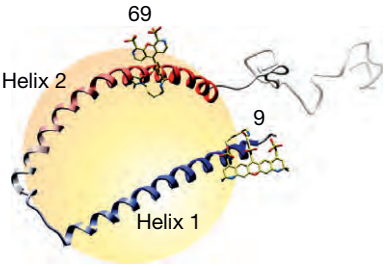

Figure 4 Representation of the horseshoe conformation of SDS micelle bound AF488 and AF568-labeled α-synuclein-9C/69C. Helix 1 and helix 2 indicate the two putative membrane-binding helices. The unstructured C-terminal tail is also shown.

determined from the FRET efficiency histograms (Figure 5). These data confirm previously reported SDS-induced structural alterations in wild-type α-synuclein.[43]

Taking into account the reported value of 62 Å for the Förster radius of the dye pair used and the mean E_{obs}-value at SDS concentrations >1.5 mM, the most frequently found distance between the two dyes in the SDS-bound state can be estimated at 45 Å. This value is higher than the 32 Å distance between amino acid positions 9 and 69 obtained from either NMR[41] or EPR.[44] One should keep in mind, however, that the labels have ~10 Å linkers between the maleimide and fluorophore moiety (Figure 4) and that the observed distance is the distance between the centers of the two fluorophores. As the exact orientation of the dyes with respect to α-synuclein bound to the SDS micelle is not known, it is in this case not possible to translate the observed distance to exact topological distance information within the α-synuclein molecule.

It has been shown that α-synuclein in solution does not behave as a fully random-coil protein; apparently it contains

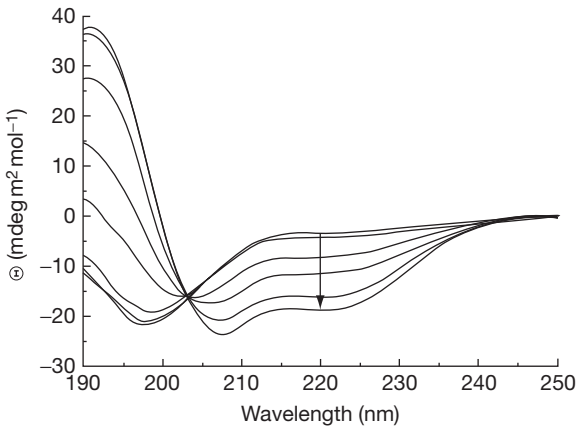

Figure 5 Structural changes in α-synuclein-9C/69C (unlabeled) induced by increasing concentrations of SDS measured with far-UV circular dichroism. The arrow indicates increasing concentrations of SDS and an increase of α-helix content.

some residual structure in the polypeptide chain.[30,45] The rather wide distributions of the histograms found for free α-synuclein in solution could point to the presence of residual structure within α-synuclein. However, care should be taken in interpreting the distribution widths as they are highly dependent on the timescale of chain motions relative to the observation time of each molecule.[46–50] The apparent broadening (an increase in the FWHM of 35%) of the low FRET peak in the histograms at SDS concentrations up to at least 0.8 mM could point to an increased heterogeneity and/or altered flexibility within this population caused by binding of SDS monomers to the polypeptide chain. However, the broadening could also arise from slower conformer interconversion or chain stiffening caused by SDS binding, especially as the average E_{obs}-value did not shift. Although techniques resolving faster timescales will be necessary to elucidate the detailed mechanism, the observed broadening does indicate dynamic structural alterations within α-synuclein, potentially induced by selective SDS binding.

The α-synuclein protein, with its amphipathic motif in the N-terminal region,[29] has been shown to adopt a horseshoe-like structure upon binding to SDS micelles[41] (see **Section 2.219.2.2**) and large unilamellar vesicles (LUVs).[44] Upon closer inspection of our data, we observe that the appearance of peak 2 in SM-FRET occurs just at the onset of α-helix formation measured with CD. This observation is a strong indication that peak 2 contains the conformers with high α-helical content, while peak 1 represents largely unstructured conformers. Furthermore, peak 2 very likely represents the horseshoe conformation,[41] as judged from the high mean E_{obs} and the width corresponding to the state bound to fully formed micelles at much higher SDS concentrations.

The existence of two peaks within the narrow SDS concentration regime (~0.5–1.0 mM) suggests that α-synuclein is able to adopt metastable structures via some sort of all-or-none mechanism for structural rearrangement (on the timescale of the experiment). Even more surprising is that these transitions occur below the CMC (critical micelle concentration) of SDS (6.5 mM at our experimental conditions), as has been reported before.[43] We hypothesize that α-synuclein may locally induce micelle formation at such low amounts that it is not detectable. Interestingly, tryptophan (Trp) residues engineered at positions 9 and 69, probing local polarity, also displayed a dependence on the SDS concentration. However, the blue shifts of the Trp fluorescence approached their maxima already at ~0.6 mM SDS, just at the onset of α-helix formation measured with CD and the appearance of peak 2 in SM-FRET. Thus, below the apparent CMC of SDS, Trps report apolar environments very likely arising from the apolar hydrocarbon tails of SDS, suggesting either micelle formation or at least some sort of SDS encapsulation or binding around the Trp. It is interesting to speculate whether this putative micelle formation is induced by α-synuclein. Once SDS monomers were bound (blue shift) and α-helical structure formation was induced (increase in ellipticity), the second distribution became prominent (SM-FRET). Although analysis of more double-cysteine and single-Trp mutants will be necessary to probe if these transitions occur along the whole peptide, it will also be interesting to resolve whether these apparent sharp transitions also occur *in vivo* and what their role may be.

In conclusion, the SM-FRET approach in combination with ensemble CD and Trp fluorescence spectroscopy has enabled us to discriminate two apparent conformational states of α-synuclein and to analyze these conformers in terms of distribution and heterogeneity, information that is otherwise impossible to extract from ensemble measurements.

2.219.2.2. Antiparallel Arrangement of α-Synuclein Helices

The mode of binding of α-synuclein to membranes has generated significant discussion in the literature. It was proposed that α-synuclein binds to membranes either as an extended, continuous helix (residues 1–100)[51–53] or in a horseshoe-like conformation, consisting of helix 1 (residues 3–37), a bend around residue 42, and helix 2 (residues 45–92),[41] with the two helices in an antiparallel arrangement but not touching (see **Figure 4**).[54,55] Supporting evidence for the latter proposal was given by the single-molecule fluorescence study described in the previous paragraph, revealing structural information from interaction of α-synuclein with monomeric and micellar SDS. Micelles have typical diameters[56] of 5 nm and may thus be too small to accommodate α-synuclein in the extended conformation (around 15 nm for an extended helix of 100 residues).[57] Therefore, micelles could enforce an antiparallel configuration of the helices even if that is not the preferred state of α-synuclein on a larger surface such as that of a biological membrane. In contrast, even small unilamellar vesicles (SUVs) have diameters on the order of 20–30 nm,[30] providing a surface area that is large compared to the dimensions of α-synuclein[57] and a larger radius of curvature than that of micelles. Therefore, SUVs are more suitable models for biological membranes than micelles.

In collaboration with the group of Martina Huber at the University of Leiden, we have investigated the structure of α-synuclein on SUVs using pulsed EPR techniques[44] that enable the acquisition of long-range information on the conformation of α-synuclein bound to the vesicle surface. In short, the distances between pairs of spin labels introduced by site-selective cysteine mutagenesis were measured for four double-cysteine mutants, α-synuclein-9/90, α-synuclein-18/90, α-synuclein-18/69, and α-synuclein-9/69, each containing one

label in the proposed helix 1, and a second label in helix 2 (see Figure 4). These cysteine residues were labeled with MTSL (1-oxy-2,2,5,5 tetramethylpyrroline-3-methyl-methanethiosulfonate). EPR measurements on labeled α-synuclein in the presence of SUVs of POPG [1-palmitoyl-2-oleoyl-*sn*-glycero-3-(phosphorac-(1-glycerol))] lipids yielded distance distributions that provided a redundant set of distances that proves that the arrangement of the two helices must be antiparallel, as shown in Figure 4. This result has implications for the conformation of α-synuclein *in vivo*, where α-synuclein interacts with synaptic vesicles with diameters of around 40 nm.

2.219.3. Aggregation Intermediates

2.219.3.1. Aggregation Kinetics

The development of cross-β conformation during amyloid formation is commonly detected by the interaction with specific *fluorescent dyes*, such as Congo red and thioflavin T. The most frequently used dye, thioflavin T, shows significantly enhanced fluorescence emission upon binding to cross-β conformations,[58–60] and is therefore a very useful dye to follow the kinetics of amyloid formation. In general, *in vitro* kinetics studies utilize purified, often recombinantly produced, proteins that spontaneously form amyloid fibrils when incubated at specific conditions of protein concentration, temperature, pH, ion concentration, and agitation.

The formation of amyloid fibrils usually involves a lag phase, during which a sufficient concentration of nucleating species is formed to initiate the subsequent rapid development of protofilaments, protofibrils, and mature fibrils. Elimination of the lag phase can be accomplished by seeding; the addition of a small amount of preassembled fibrils to monomers induces the start of amyloid formation almost instantaneously. Considering disease-related amyloid formation, it is important to note that during the lag phase, oligomers are formed that have been hypothesized to be the potentially toxic species.[61–63] Figure 6 illustrates the difference in aggregation kinetics for an unseeded and a seeded aggregation reaction of recombinantly produced α-synuclein performed with constant shaking. For the unseeded aggregation, the thioflavin T fluorescence intensity curve clearly displays a lag phase, followed by a phase of rapid growth and the saturated final stage. Upon seeding, the thioflavin T emission intensity increases right from the beginning.

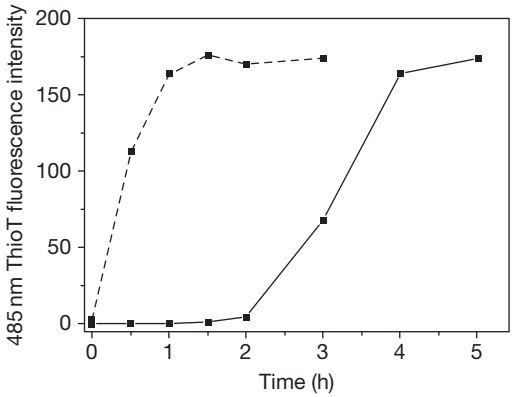

Figure 6 Aggregation of α-synuclein followed in time by thioflavin T fluorescence. Solid line: without seeding; dashed line: with seeding.

Thioflavin T is a popular and useful dye to follow the kinetics of amyloid fibril formation, although the binding is rather unspecific and the sensitivity quite poor. Especially in the lag phase, where processes from dimerization to oligomerization take place, thioflavin T is not sufficiently sensitive to resolve these important stages. Therefore, in search for better alternatives, novel dyes have been developed and synthesized that are promising specifically for detection of early stage aggregates.[64–68]

2.219.3.2. Morphology of Aggregation Intermediates

Aggregation intermediates of amyloidogenic proteins have characteristic dimensions in the nanometer range, which makes them ideally suited for study by *AFM*. AFM[69] is a scanning probe microscopy technique derived from scanning tunneling microscopy (STM) (**Chapter 3.302, Atomic Force Microscopy**). In AFM, a cantilever with a sharp (typically 10 nm) tip scans across a surface and records topography and material properties of the sample surface through the variation in tip–sample interaction forces experienced by the cantilever. Specifically for imaging of relatively soft biological samples such as DNA, proteins, and cells, and also for amyloid fibrils, the AFM technique has several advantages over scanning electron microscopy (SEM): no special sample treatment is required; measurements can be performed in ambient air and in physiologically relevant aqueous milieus without a need for a vacuum environment;[70,71] and measurement of true heights in the nanometer range is possible. The application of AFM to biological and supramolecular systems has been reviewed in recent publications.[70–74] In amyloid fibril research, AFM can be used as an imaging modality, mapping the topography and material properties of the protein aggregates, and also for force spectroscopy measurements, where the tip is used to push and pull individual protein molecules, dimers, or (proto-) fibrils in a controlled fashion.

The high-resolution AFM technique can be effectively employed to study the aggregation kinetics by imaging the intermediate structures formed after different incubation times[75] or by time-lapse imaging of *in situ* growing fibrils[76] on a surface. Figure 7 gives representative AFM images taken during the α-synuclein aggregation presented in Figure 6 by thioflavin T fluorescence. The early phase images from the unseeded aggregation are dominated by small dot-like aggregates that represent oligomeric structures.

The oligomeric species form a focal point of attention in the field of amyloid fibril formation, because of their proposed toxic function. In the course of the aggregation, the oligomeric species is replaced by an increasing number of fibrils. The AFM images demonstrate that thioflavin T is indeed not suitable as an early indicator of amyloid formation; after 90 min, the thioflavin T emission intensity of the unseeded aggregation reaction is still at background level, while the AFM images already show some fibrils.

Because of its exceptionally high spatial resolution, the AFM technique is applicable not only for kinetic studies but also for

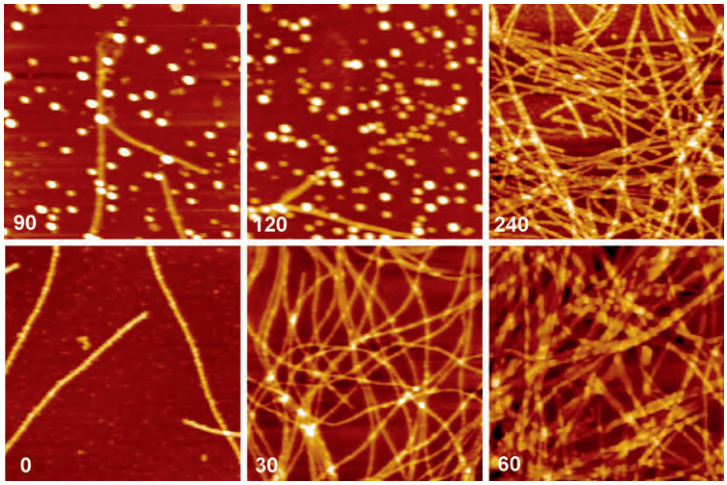

Figure 7 AFM images taken at different time points, indicated in hours, during aggregation of α-synuclein. Top row unseeded aggregation; bottom row seeded aggregation. Image size: 2.5 × 2.5 μm. Height scale: 10 nm.

quantitative morphological analysis of the fibrillar aggregation products formed (see Section 2.219.4.1).

2.219.3.3. Secondary Structure of Aggregation Intermediates

CD spectroscopy is an attractive method to monitor conformational changes and transitions in the course of the amyloid formation process[77] (see also Section 2.219.2.1). Figure 8 shows far-UV CD spectra measured from monomeric and oligomeric (lag phase) α-synuclein indicating random-coil and β-sheet structure, respectively. The CD spectrum of monomeric α-synuclein shows a minimum at 198 nm and close to zero CD signals in the 210–220 nm region, which is characteristic for an unfolded protein. The spectrum of the oligomers is completely different, and with a minimum at 220 nm typical for β-sheet structure. Specifically, in the early aggregation phase, where thioflavin T is not sufficiently sensitive, CD spectroscopy is able to demonstrate changes in protein conformation.

Alternatively, *Raman spectroscopy*[78–80] is another method that may be applied to obtain information on the secondary structure content of aggregation intermediates (Chapter 3.322, Infrared and Raman Microscopy and Imaging of Biomaterials).

2.219.3.4. Protein Interactions

In a natural *in vivo* environment, amyloid formation takes place in the presence of many other components. Interactions with various chemical and biological components such as metal ions, proteins, and enzymes, are therefore likely. In this context, we have studied the interaction of the enzyme tissue transglutaminase (tTG) with α-synuclein protein variants at physiologically relevant concentrations. The tTG enzyme catalyzes cross-link formation between protein-bound glutamine residues and primary amines and plays a role in various neurodegenerative diseases.[81] tTG enzyme activity has been shown to be upregulated in PD affected brain.[82] tTG-catalyzed cross-links have been found colocalized with Lewy bodies, the cytoplasmic inclusions composed of fibrillar α-synuclein that are characteristic of PD,[11] suggesting a role for tTG in the

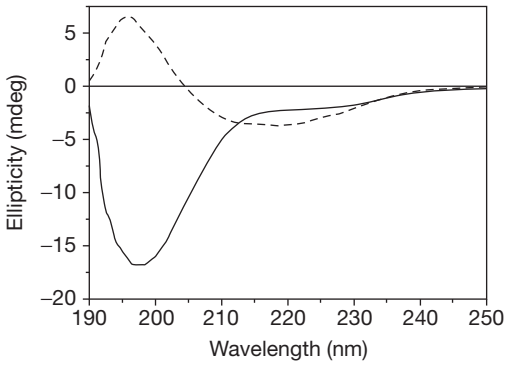

Figure 8 CD spectra of monomeric (solid line) and oligomeric (dashed line) α-synuclein.

pathophysiology of PD.[83] Cross-linked α-synuclein appeared to correlate with disease progression, indicating that tTG cross-linking may change the structure of monomeric α-synuclein resulting in altered functionality. Intramolecular cross-linking by tTG was hypothesized to be protective in PD, by inhibiting the assembly of monomeric α-synuclein into amyloid fibrils and its potentially toxic oligomeric precursors.[84]

To shed light on the pathological relevance of tTG cross-linking, we have systematically investigated tTG cross-linking of wild-type and disease-related mutant A30P, E46K, and A53T α-synuclein.[85] We evaluated the effect of physiologically relevant[86,87] nanomolar tTG concentrations on cross-linking kinetics, on affected α-synuclein fraction, and on inhibition of aggregation.

Figure 9(a) shows that nanomolar tTG concentrations are sufficient for complete inhibition of fibrillization by effective α-synuclein cross-linking, resulting predominantly in intramolecularly cross-linked monomers accompanied by an oligomeric fraction. AFM indicated the formation of very distinct, uniform, oligomeric species (Figure 9(b)). As oligomeric α-synuclein structures are most likely implicated in the pathophysiology of PD,[84] we determined the secondary structure, foldability, and vesicle permeabilization properties of

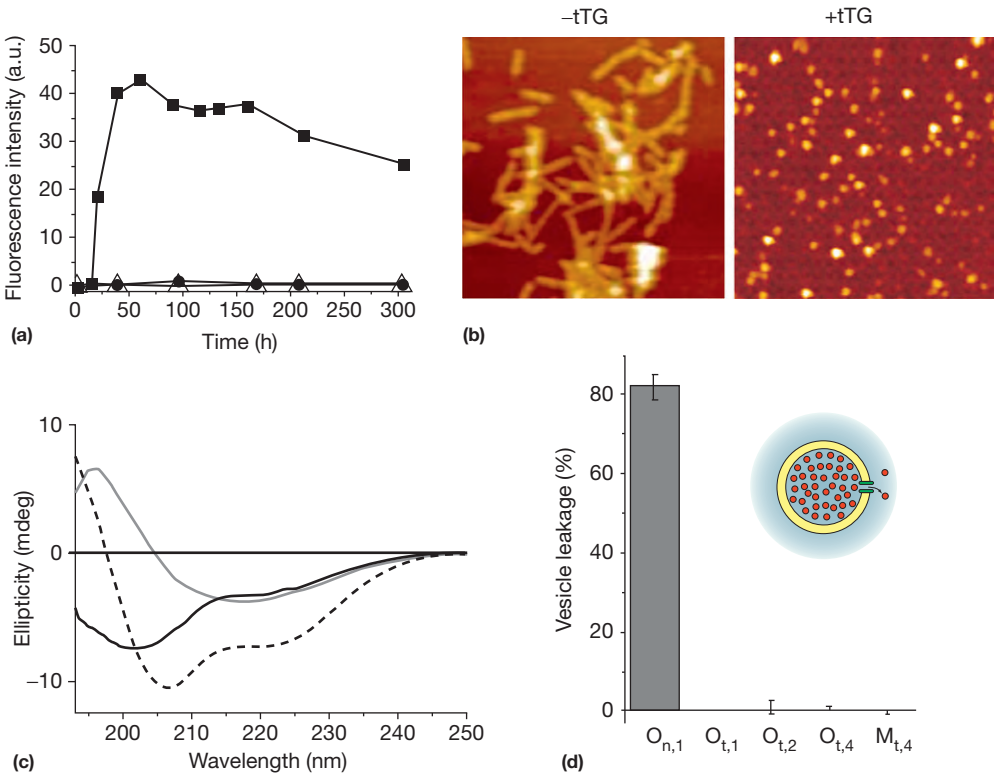

Figure 9 Aggregation of 100 μM E46K α-synuclein in the presence and absence of tTG. (a) Thioflavin T fluorescence assay: without (squares), and with 50 nM (circles) and 1.3 μM tTG (triangles). (b) AFM images: after 214 h without tTG (left) and after 310 h with 1.3 μM tTG. Images are $1.25 \times 1.25\ \mu m^2$. (c) CD spectra of tTG/α-synuclein oligomers and normal α-synuclein oligomers. Black spectra: oligomeric tTG/α-synuclein, before (solid line) and after (dashed line) addition of 0.1% (w/v) SDS. Gray spectrum: normal α-synuclein oligomers. (d) Vesicle permeabilization assay. $O_{n,1}$: normal α-synuclein oligomers used at 1 μM; $O_{t,1}$, $O_{t,2}$, and $O_{t,4}$: tTG/α-synuclein oligomers used at 1, 2, and 4 μM, respectively. $M_{t,4}$: tTG/α-synuclein monomers used at 4 μM.

purified tTG/α-synuclein oligomers compared to normal oligomers. Our results demonstrate that although tTG/α-synuclein oligomers contain no secondary structure (Figure 9(c)), they are nevertheless able to fold into α-helix conformation on binding SDS. To investigate the membrane permeabilization capability of the tTG/α-synuclein oligomers, we performed a dye efflux assay.[88] POPG LUVs were prepared by drying an aliquot of a solution in chloroform. After rehydration in a buffer solution containing the fluorescent dye calcein, the solution was extruded through a 100 nm pore size polycarbonate membrane filter. Free dye was removed by gel filtration and the phospholipid concentration of the calcein-filled LUVs was determined.[89] In the permeabilization assay, 40 μM phospholipid-containing vesicle solution was mixed 1:1 (v/v) with α-synuclein solution and incubated for 30 min at room temperature. Fluorescence (emission: 505–550 nm, excitation: 494 nm) was measured using a spectrofluorimeter. From the background-corrected fluorescence, the vesicle leakage was calculated relative to maximum vesicle disruption induced by 0.5% (w/v) Triton X-100. Figure 9(d) indicates that the tTG/α-synuclein oligomers, unlike normal oligomers, are not capable of permeabilizing phospholipid vesicles.

The comprehensive data that we have acquired suggest that tTG binds to all α-synuclein variants effectively and prevents formation of toxic oligomers and successive progression into fibrils by forming intramolecular cross-links, imposing structural constraints on α-synuclein. The formation of small, harmless, tTG cross-linked, α-synuclein assemblies suitable for removal by intracellular degradation systems may be a mechanism to prevent formation of pathogenic aggregates. We speculate that intramolecular cross-linking may be the predominant process early in PD, while at later stages, with higher tTG and α-synuclein concentrations[81,90] the probability of intermolecular cross-linking and formation of large, insoluble protein clusters may increase.

2.219.4. Mature Amyloid Fibrils

2.219.4.1. Structural Polymorphism of Amyloid Fibrils

The structural polymorphism of amyloid fibrils, resulting in a multitude of distinct morphologies, is a particularly important element in scientific understanding of amyloid fibrillogenesis[91] because polymorphism suggests that it is likely that there are multiple pathways of amyloid fibril formation and potential neurodamage. Particularly in this area, nanoscale imaging methods such as AFM can contribute to the understanding of amyloid fibril formation. From high-resolution AFM images, the multitude of aggregate morphologies that occur both *in vivo* and *in vitro* may be classified. In general, amyloid fibrils are unbranched, linear fibrils with a diameter of around 10 nm and lengths that run into the micrometer range.

The discovery by AFM imaging of several types of filaments differing in their diameter, and the observation of periodicity or even twist in the thicker fibrils, has led to the development of the hierarchical assembly model (HAM).[59] This model describes that mature fibrils consist of a twisted pair of protofibrils, each of which is composed of two thinner intertwined protofilaments. However, polymorphism observed by AFM and scanning transmission electron microscopy in amyloid-β (Aβ) fibrils suggests that other mechanisms, not involving protofilaments, may also play a role in the assembly of amyloid fibrils.[92] Possibly mature fibrils are also formed by assembly of discrete independent entities, morphologically resembling twisted fibrils.

Mature fibrils formed by various proteins differ in the number of constituent filaments. For example, β_2-microglobulin fibrils, involved in dialysis-related amyloidosis, form three types of mature fibrils: consisting of two or four intertwined filaments, or consisting of four filaments and forming a twisted-ribbon structure.[93] These authors also found fibrils exhibiting supercoiling: the superhelical twist period was twice the twist period, which gives the fibrils a zig-zag appearance. Whether the various species form sequentially or in parallel is as yet unclear.

Polymorphism is evident not only when comparing different fibrils. Fibrils formed by full-length prion protein display polymorphism even within individual fibrils, differing in number of constituent filaments and twisting at different points along their length.[22,23] One assembly mechanism that may contribute to this behavior is 'lateral seeding': monomers and oligomers from solution may attach to an existing fibril surface and initiate a new filament alongside an existing filament. This mechanism has been proposed for insulin,[94] when fibrils were formed at an unusual condition of high pressure. However, an argument against the generality of lateral seeding is that the mechanism implies that fibrils would grow in width indefinitely, whereas it has been shown on fibrils formed by many different proteins and peptides that only a small range of fibril diameters is formed.

We have used different contrast modes of high-resolution AFM to study in detail the morphology of α-synuclein fibrils prepared *in vitro* from recombinantly produced wild-type human α-synuclein and the familial disease-related A30P, E46K, and A53T mutant proteins.[95] Aggregation half-times measured using thioflavin T fluorescence spectroscopy at low salt reaction conditions indicated different aggregation kinetics for the variants: 150 h for wild-type and 75, 100, and 250 h for A53T, E46K, and A30P, respectively. These results are consistent with the literature.[96] AFM images in air (**Figure 10(a)–10(d)**) were recorded to verify if the different aggregation kinetics influence the fibril morphologies. Visual inspection of the images suggests that the morphology is not identical for all variants.

Quantitative analysis was performed of heights, modulation depths, and periodicities of a large number of fibrils for each variant (**Figure 10(e)** and **10(f)** and **Table 1**).[97] Wild-type fibrils exhibit the lowest height; A30P and E46K have intermediate values, while A53T fibrils are highest. The modulation depth is not significantly different among the mutant proteins, although wild-type protein has a smaller modulation depth commensurate with the lower measured fibril height. Together with the fibril height, the periodicity of the fibrils is the most characteristic parameter for each α-synuclein variant. The E46K mutant displays a very distinct average periodicity of about 60 nm, A53T an intermediate value of 110 nm, and wild-type and A30P display the largest periodicities of ~140 nm. The distribution of period lengths is narrowest for E46K (main mode at 40–50 nm), whereas A30P and A53T display wider distributions. Wild-type protein displays a main

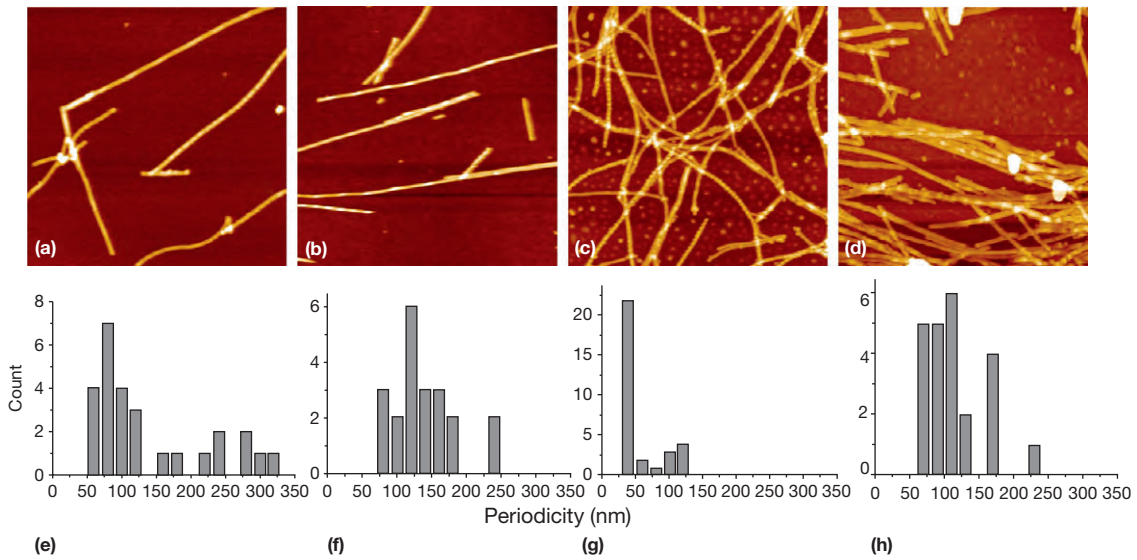

Figure 10 Representative tapping mode AFM images of wild-type (a), A30P (b), E46K (c), and A53T (d) variants of α-synuclein in air. The color scale represents 15.6 nm in height for wild-type, 20.2 nm for A30P, 22.4 nm for E46K, and 31.3 nm for A53T α-synuclein. Image size is 2500 × 2500 nm. Distributions of fibril periodicities are given for wild-type (e), A30P (f), E46K (g), and A53T (h) variants of α-synuclein. The number of fibrils analyzed is indicated in **Table 1**. Histogram bin size is 20 nm.

periodicity of around 80 nm, but larger periodicities were also observed. The fibril heights and modulation depths measured in air for A30P and E46K variants are consistent, within the accuracy of the data, with earlier AFM results in liquid.[97] The measured heights and modulation depths of wild-type protein are somewhat smaller in air than in liquid. Periodicities measured for A30P and E46K are similar in air and in liquid, and also for wild-type protein considering the main mode in the broad distribution.

Table 1 summarizes the quantitative data obtained and indicates that a single-point mutation in the α-synuclein protein has significant consequences for the ultrastructure of the fibrils formed.

High-resolution phase images were recorded to examine the nanoscale structure of individual α-synuclein fibrils in detail. Phase imaging is sensitive to differences in material properties like sample viscoelasticity or hydrophobicity, and is a complementary contrast mode yielding more details than can be observed in height images.[98] Fibrils shown in Figure 11(a) clearly display twisted fibril morphology, providing evidence for the presence of a skewed pitch. In contrast, Figure 11(b) shows a high-resolution image of a small area scan revealing assembly of fibril segments of 100–150 nm in length. Figure 11(c) and 11(d) demonstrate that both assembly modes can be found within one sample, an observation made for all α-synuclein variants.

Our results indicate that the aggregation of genetic variants of α-synuclein not only follows different kinetics but is also accompanied by the formation of morphologically different fibrils. Individual mutant forms of α-synuclein fibrils may be distinguished on the basis of their characteristic heights and periodicities. Specific point mutations appear to affect fibril assembly and may drive fibril formation into energetically more favorable structures with characteristic periodicity. The measured modulation depths in relation to the fibril heights are compatible with a twisted HAM within the accuracy of the data. For this model, we expect the modulation depth not to exceed 25% of the maximum height of the fibril, an expectation supported by the data shown in Table 1. However, we also observe morphologies that do not resemble the expected twisted structure, but appear like a series of associated segments. This type of morphology has also been observed for insulin fibrils.[94] We thus have evidence for both hierarchical and segmented α-synuclein fibril formation, potentially on the basis of a multipathway mechanism. We speculate that segmented assembly may precede the twist formation, because we mainly observe segmented morphologies in lower height fibrils (protofibrils). Higher resolution imaging and further analysis are required for definitive conclusions.

Tapping mode AFM (TM-AFM) *phase imaging* provides another unique source of information on the mechanical properties of amyloid fibrils.[99] The contrast mechanism in TM-AFM phase contrast imaging is the time lag between the oscillation of the cantilever and the driving oscillation. This lag is due to the interaction between the tip and the sample/substrate, which may depend on any number of material properties and the electrical charge of tip and sample. For good phase contrast imaging, the correct choice of tapping frequency, tapping amplitude, set-point ratio, humidity, the thickness of a potential thin water layer on the dry sample, and surface charges on the tip and/or the sample are important. We have recently obtained high-resolution AFM phase contrast images (Figure 12) that demonstrate that the ends of the α-synuclein fibrils and certain specific points in the bulk of the fibrils have a decidedly different phase lag than the rest of the fibril, possibly representing local differences in material properties. The resolution of these patches of alternate tip–sample interaction is higher than the resolution of the height image, presumably because only just the 'tip of the tip' participates in the interactions that cause the phase difference. Possibly for the same reason, tip–sample convolution does not reduce the phase resolution in the same way as it reduces the lateral resolution

Table 1 Quantitative characteristics of fibrils of α-synuclein variants

α-synuclein variant	*N fibrils*	*Fibril top height (nm)*	*Modulation depth (nm)*	*Periodicity (nm)*
Wild-type	33 (27)	7.5 ± 0.9	1.5 ± 0.4	141 ± 82
A30P	41 (21)	8.7 ± 1.4	2.3 ± 0.7	139 ± 46
E46K	37 (29)	9.8 ± 1.2	2.1 ± 0.6	59 ± 28
A53T	33 (20)	10.4 ± 1.3	2.2 ± 0.8	115 ± 41

N fibrils is the total number of fibrils analyzed per mutant; the number of periodic fibrils is in brackets. The fibrils classified as nonperiodic were irregular in height. Height values are averages over all *N* fibrils; the modulation depth and periodicity are calculated over only the periodic fibrils. The standard deviation is used as the measurement error.

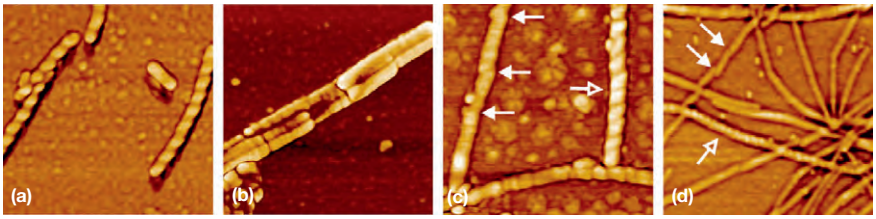

Figure 11 Tapping mode AFM phase images in air. (a) E46K fibrils displaying twisted morphology. (b) Wild-type fibril with appearance of associated segments. (c) and (d) Contain both twisted and segmented E46K fibrils. Image sizes are for (a), (b), and (c): 620×620 nm, for (d) 1250×1250 nm. Closed arrows point out segmented fibrils, open arrows twisted fibrils.

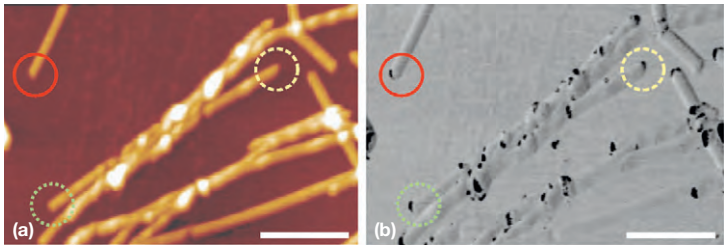

Figure 12 AFM phase contrast shows high-resolution fibril features TM-AFM height image of α-synuclein fibrils (a) with the corresponding simultaneously recorded AFM phase contrast image (b). The phase image (b) shows that fibril ends (*circles*) and certain specific parts of the fibril bulk have material properties different from those of the bulk fibril. Scale bar 500 nm, resolution 256 pixels/line.

of height images. The exact origin of the oscillation lag and thus of the phase contrast is unclear, but probably involves the higher harmonic mode of the cantilever oscillation as the tapping cantilever touches the sample surface.

The examples given here indicate that phase contrast imaging holds great promise as a method for characterization of material properties of amyloid fibrils. Phase imaging may play an important role in providing the necessary differential contrast and sensitivity that are lacking in height images to reveal differences in material properties at fibril segment interfaces.

2.219.4.2. Mechanical Deformation of Fibrils

The application of AFM imaging is not limited to characterization of fibril morphology properties under various conditions by imaging; also the mechanical properties of the fibrils may be deduced from the images. In contact mode AFM (CM-AFM), the tip is in constant contact with the surface. The tip is effectively 'dragged along' the sample while the feedback loop keeps the interaction force constant by maintaining the deflection at a set-point value. This mode allows for very high lateral resolution on periodic samples with low corrugation, but is typically too damaging for fibrillar protein aggregates, especially in liquid. The damaging nature of CM-AFM can be used as a tool to study the effect of controlled damage applied to fibrillar aggregates. **Figure 13(a)** depicts an image of A30P mutant fibrils obtained by scanning in tapping mode. Then the same area was rescanned in contact mode, followed by another larger scan in tapping mode. The combined images taken before and after contact mode scanning clearly show deformed fibrils in the area scanned in contact mode; outside this area the fibrils are not affected. The regular pattern of nanoscale deformations is the result of the force imposed on the fibrils during contact mode scanning (**Figure 13(b)**). A closer look at a single fibril reveals that the spacing between the deformations corresponds to the 140 nm periodicity of the original intact fibrils (**Figure 13(c)** and **13(d)**). **Figure 13** shows that α-synuclein fibrils have 'weak spots' at intervals corresponding to their periodicity.[95,97] This same effect was found for Aβ: N-terminal 1–42 residues ($A\beta_{1\text{-}42}$) fibrils.[100] Fibrils may be damaged by indentation forces ranging from 40 to 100 nN.[101,102]

Lateral forces in contact mode are much higher than in tapping mode because the tip is continuously in contact with the sample. The contact force is mainly dominated by the adhesion force between the Si_3N_4 tip and the sample. The periodicity of the deformations may arise from the

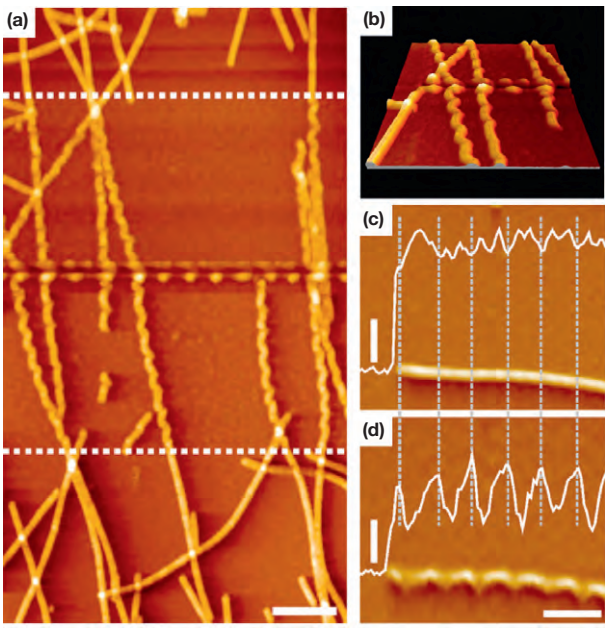

Figure 13 Contact mode AFM imaging reveals mechanical weak spots in α-synuclein fibrils. (a) Composite tapping mode AFM height image of A30P α-synuclein fibrils. The section between the *dotted lines* has been subjected to contact mode imaging before this image was made. The horizontal track in the middle results from repeated line scanning for optimization of imaging parameters. Scale bar 500 nm. (b) 3D rendering of affected area. Comparison of morphology of one fibril before (c) and after (d) contact mode imaging. The height profiles show that least damage was done on those sections that were lowest before scanning (*gray dashed lines*, scan direction was vertical). Horizontal scale bar 200 nm, vertical scale bars 2 nm.

characteristic fibril structure, assembled in such a way that it is locally more sensitive to deformation by lateral force. Another reason may be the intrinsic variation in adhesion force. Hydrophilic parts of the sample will display higher adhesion forces.[103] Possibly, these fibril parts are more prone to damage by high local lateral forces. The fibril deformation results may support both hierarchical and segmented α-synuclein fibril assembly. This AFM-based fibril deformation method may be applied more generally to study the mechanical properties of various fibrillar structures. The extent of the deformations may be even converted into quantitative mechanical data.

2.219.5. Conclusion

Amyloids experience a growing scientific interest, from both a fundamental biomedical and a materials science perspective. Initially amyloid formation was observed as a pathological hallmark of several neurodegenerative diseases. More recently functional amyloids have been discovered in many species, and these structures also play a role in industrial processes, such as in the optimization of food texture. Nevertheless, the process of amyloid formation is still not well understood. More knowledge about the mechanism and about factors that may affect fibril formation will improve our understanding of the molecular origin of amyloid diseases and about the role of functional amyloid. In the case of pathogenic amyloid, this information is indispensable in the search for effective medication, when targeting of a specific aggregation stage may be considered. Widespread application and exploitation of amyloid nanobiomaterials require further information about not only the details of the aggregation process, but also the final material properties.

This chapter describes the application of a variety of biophysical approaches to understand important aspects of amyloid fibril formation. Although we have mainly focused on a single model system, the human α-synuclein protein, the approaches are generally applicable to the broader genre of amyloid-forming proteins.

Acknowledgments

The authors thank Kees van der Werf for assistance and advice on atomic force microscopy; Kirsten van Leijenhorst-Groener, Yvonne Kraan, and Marloes ten Haaff-Kolkman are acknowledged for production and purification of α-synuclein protein. We acknowledge a fruitful collaboration with Martina Huber at Leiden University, and Malte Drescher at the University of Konstanz for the EPR work. The described work is part of the research program of the 'Stichting voor Fundamenteel Onderzoek der Materie (FOM),' which is financially supported by the 'Nederlandse Organisatie voor Wetenschappelijk Onderzoek (NWO).' Financial support is also provided by the Stichting Internationaal Parkinson Fonds, Hoofddorp, The Netherlands.

References

1. Dobson, C. M. *Nature* **2003**, *426*, 884–890.
2. Otzen, D.; Nielsen, P. H. *Cell. Mol. Life Sci.* **2008**, *65*, 910–927.
3. Fowler, D. M.; Koulov, A. V.; Balch, W. E.; Kelly, J. W. *Trends Biochem. Sci.* **2007**, *32*, 217–224.
4. Fowler, D. M.; Koulov, A. V.; Alory-Jost, C.; Marks, M. S.; Balch, W. E.; Kelly, J. W. *PLoS Biol.* **2006**, *4*, 100–107.
5. Pearce, F. G.; Mackintosh, S. H.; Gerrard, J. A. *J. Agric. Food Chem.* **2007**, *55*, 318–322.
6. Gras, S. L.; Squires, A. M.; Dobson, C. M.; MacPhee, C. E. Functionalised fibrils for bio-nanotechnology. In *Proceedings of the 2006 International Conference on Nanoscience and Nanotechnology*, ICONN, South Korea, 2006; Vols. 1 and 2 265–267.
7. Wang, C.; Hunag, L.; Wang, L.; Hong, Y.; Sha, Y. *Biopolymers* **2007**, *86*, 23–31.
8. Malisauskas, M.; Meskys, R.; Morozova-Roche, L. A. *Biotechnol. Prog.* **2008**, *24*, 1166–1170.
9. Rambaran, R. N.; Serpell, L. C. *Prion* **2008**, *2*, 112–117.
10. Goedert, M. *Nat. Rev. Neurosci.* **2001**, *2*, 492–501.
11. Spillantini, M. G.; Schmidt, M. L.; Lee, V. M.-Y.; Trojanowski, J. Q.; Jakes, R.; Goedert, M. *Nature* **1997**, *388*, 839–840.
12. Tompa, P. *Structure and Function of Intrinsically Disordered Proteins*; CRC Press: Boca Raton, FL, 2010.
13. Chiti, F.; Dobson, C. M. *Annu. Rev. Biochem.* **2006**, *75*, 333–366.
14. Buxbaum, J. N. *Trends Biochem. Sci.* **2003**, *28*, 585–592.
15. Selkoe, D. J. *Nature* **2003**, *426*, 900–904.
16. Soto, C. *Nat. Rev. Neurosci.* **2003**, *4*, 49–60.
17. Shults, C. W. *Proc. Natl Acad. Sci. USA* **2006**, *103*, 1661–1668.
18. Spillantini, M. G.; Crowther, R. A.; Jakes, R.; Hasegawa, M.; Goedert, M. *Proc. Natl Acad. Sci. USA* **1998**, *95*, 6469–6473.
19. Krüger, R.; Kuhn, W.; Müller, T.; *et al. Nat. Genet.* **1998**, *18*, 106–108.
20. Polymeropoulos, M. H.; Lavedan, C.; Leroy, E.; *et al. Science* **1997**, *276*, 2045–2047.
21. Zarranz, J. J.; Alegre, J.; Gómez-Esteban, J. C.; *et al. Ann. Neurol.* **2004**, *55*, 164–173.
22. Anderson, M.; Bocharova, O. V.; Makarava, N.; Breydo, L.; Salnikov, V. V.; Baskakov, I. V. *J. Mol. Biol.* **2006**, *358*, 580–596.
23. Anderson, J. P.; Walker, D. E.; Goldstein, J. M.; *et al. J. Biol. Chem.* **2006**, *281*, 29739–29752.
24. Chen, L.; Feany, M. B. *Nat. Neurosci.* **2005**, *8*, 657–663.
25. Fujiwara, H.; Hasegawa, M.; Dohmae, N.; *et al. Nat. Cell Biol.* **2002**, *4*, 160–164.
26. Okochi, M.; Walter, J.; Koyama, A.; *et al. J. Biol. Chem.* **2000**, *275*, 390–397.
27. Murphy, D. D.; Rueter, S. M.; Trojanowski, J. Q.; Lee, V. M.-Y. *J. Neurosci.* **2000**, *20*, 3214–3220.
28. Chandra, S.; Gallardo, G.; Fernández-Chacón, R.; Schlüter, O. M.; Südhof, T. C. *Cell* **2005**, *123*, 383–396.
29. Weinreb, P. H.; Zhen, W.; Poon, A. W.; Conway, K. A.; Lansbury, P. T., Jr. *Biochemistry* **1996**, *35*, 13709–13715.
30. Davidson, W. S.; Jonas, A.; Clayton, D. F.; George, J. M. *J. Biol. Chem.* **1998**, *273*, 9443–9449.
31. Eliezer, D.; Kutluay, E.; Bussel, R., Jr.; Browne, G. *J. Mol. Biol.* **2001**, *307*, 1061–1073.
32. Serpell, L. C.; Berriman, J.; Jakes, R.; Goedert, M.; Crowther, R. A. *Proc. Natl Acad. Sci. USA* **2000**, *97*, 4897–4902.
33. Gambin, Y.; Schug, A.; Lemke, E. A.; *et al. Proc. Natl Acad. Sci. USA* **2009**, *106*, 10153–10158.
34. Veldhuis, G.; Segers-Nolten, I.; Ferlemann, E.; Subramaniam, V. *Chembiochem* **2009**, *10*, 436–439.
35. Jares-Erijman, E. A.; Jovin, T. M. *Nat. Biotechnol.* **2003**, *21*, 1387–1395.
36. Lakowicz, J. R. *Principles of Fluorescence Spectroscopy*, 2nd ed.; Kluwer Academic/Plenum Publishers: New York, 2002.
37. Wu, P.; Brand, L. *Anal. Biochem.* **1994**, *218*, 1–13.
38. Periasamy, A. *J. Biomed. Opt.* **2001**, *6*, 287–291.
39. dos Remedios, C. G.; Moens, P. D. *J. Struct. Biol.* **1995**, *115*, 175–185.
40. Stryer, L. *Annu. Rev. Biochem.* **1978**, *47*, 819–846.
41. Ulmer, T. S.; Bax, A.; Cole, N. B.; Nussbaum, R. L. *J. Biol. Chem.* **2005**, *280*, 9595–9603.
42. Pelton, J. T.; McLean, L. R. *Anal. Biochem.* **2000**, *277*, 167–176.
43. Ferreon, A. C. M.; Deniz, A. A. *Biochemistry* **2007**, *46*, 4499–4509.
44. Drescher, M.; Veldhuis, G.; van Rooijen, B. D.; Milikisyants, S.; Subramaniam, V.; Huber, M. *J. Am. Chem. Soc.* **2008**, *130*, 7796–7797.
45. Bussell, A., Jr.; Eliezer, D. *J. Biol. Chem.* **2001**, *276*, 45996–46003.
46. Deniz, A. A.; Laurence, T. A.; Beligere, G. S.; *et al. Proc. Natl Acad. Sci. USA* **2000**, *97*, 5179–5184.
47. Merchant, K. A.; Best, R. B.; Louis, J. M.; Gopich, I. V.; Eaton, W. A. *Proc. Natl Acad. Sci. USA* **2007**, *104*, 1528–1533.
48. Mukhopadhyay, S.; Krishnan, R.; Lemke, E. A.; Lindquist, S.; Deniz, A. A. *Proc. Natl Acad. Sci. USA* **2007**, *104*, 2649–2654.
49. Schuler, B.; Eaton, W. A. *Curr. Opin. Struct. Biol.* **2008**, *18*, 16–26.
50. Schuler, B.; Lipman, E. A.; Eaton, W. A. *Nature* **2002**, *419*, 743–747.
51. Bisaglia, M.; Tessari, I.; Pinato, L.; *et al. Biochemistry* **2005**, *44*, 329–339.
52. Bussell, R., Jr.; Eliezer, D. *J. Mol. Biol.* **2003**, *329*, 763–778.
53. Jao, C. C.; Der-Sarkissian, A.; Chen, J.; Langen, R. *Proc. Natl Acad. Sci. USA* **2004**, *101*, 8331–8336.
54. Bussell, R., Jr.; Ramlall, T. F.; Eliezer, D. *Protein Sci.* **2005**, *14*, 862–872.
55. Chandra, S.; Chen, X.; Rizo, J.; Jahn, R.; Südhof, T. C. *J. Biol. Chem.* **2003**, *278*, 15313–15318.
56. Itri, R.; Amaral, L. Q. *J. Phys. Chem.* **1991**, *95*, 423–427.
57. Rhoades, E.; Ramlall, T. F.; Webb, W. W.; Eliezer, D. *Biophys. J.* **2006**, *90*, 4692–4700.

58. Ban, T.; Hamada, D.; Hasegawa, K.; Naiki, H.; Goto, Y. *J. Biol. Chem.* **2003**, *278*, 16462–16465.
59. Khurana, R.; Coleman, C.; Ionescu-Zanetti, C.; *et al. J. Struct. Biol.* **2005**, *151*, 229–238.
60. Krebs, M. R. H.; Bromley, E. H. C.; Donald, A. M. *J. Structur. Biol.* **2005**, *149*, 30–37.
61. Conway, K. A.; Lee, S.-J.; Rochet, J.-C.; Ding, T.; Williamson, R. E.; Lansbury, P. T., Jr. *Proc. Natl Acad. Sci. USA* **2000**, *97*, 571–576.
62. Danzer, K. M.; Haasen, D.; Karow, A. R.; *et al. J. Neurosci.* **2007**, *27*, 9220–9232.
63. Kayed, R.; Head, E.; Thompson, J.; *et al. Science* **2003**, *300*, 486–489.
64. Celej, M. S.; Caarls, W.; Demchenko, A. P.; Jovin, T. M. *Biochemistry* **2009**, *48*, 7465–7472.
65. Celej, M. S.; Jares-Erijman, E. A.; Jovin, T. M. *Biophys. J.* **2008**, *94*, 4867–4879.
66. Volkova, K. D.; Kovalska, V. B.; Balanda, A. O.; *et al. Bioorg. Med. Chem.* **2008**, *16*, 1452–1459.
67. Volkova, K. D.; Kovalska, V. B.; Balanda, A. O.; *et al. J. Biochem. Biophys. Meth.* **2007**, *70*, 727–733.
68. Volkova, K. D.; Kovalska, V. B.; Segers-Nolten, G. M.; Veldhuis, G.; Subramaniam, V.; Yarmoluk, S. M. *Biotech. Histochem.* **2009**, *84*, 55–61.
69. Binnig, G.; Quate, C. F.; Gerber, C. *Phys. Rev. Lett.* **1986**, *56*, 930–933.
70. Cohen, S. R.; Bitler, A. *Curr. Opin. Colloid Interface Sci.* **2008**, *13*, 316–325.
71. Müller, D. J.; Dufrêne, Y. F. *Nat. Nanotechnol.* **2008**, *3*, 261–269.
72. Gaczynska, M.; Osmulski, P. A. *Curr. Opin. Colloid Interface Sci.* **2008**, *13*, 351–367.
73. Gosal, W. S.; Myers, S. L.; Radford, S.; Thomson, N. H. *Protein Pept. Lett.* **2006**, *13*, 261–270.
74. Samori, P. *Chem. Soc. Rev.* **2005**, *34*, 551–561.
75. Dong, M.; Hovgaard, M.; Xu, S.; Otzen, D. E.; Besenbacher, F. *Nanotechnology* **2006**, *17*, 4003–4009.
76. Goldsbury, C.; Kistler, J.; Aebi, U.; Arvinte, T.; Cooper, G. J. S. *J. Mol. Biol.* **1999**, *285*, 33–39.
77. Uversky, V. N.; Li, J.; Fink, A. L. *J. Biol. Chem.* **2001**, *276*, 10737–10744.
78. Apetri, M. M.; Maiti, N. C.; Zagorski, M. G.; Carey, P. R.; Anderson, V. E. *J. Mol. Biol.* **2006**, *355*, 63–71.
79. Maiti, N.; Apetri, M.; Zagorski, M.; Carey, P.; Anderson, V. *J. Am. Chem. Soc.* **2004**, *126*, 2399–2408.
80. Thomas, G. J., Jr. *Annu. Rev. Biophys. Biomol. Struct.* **1999**, *28*, 1–27.
81. Muma, N. A. *J. Neuropathol. Exp. Neurol.* **2007**, *66*, 258–263.
82. Kim, S.-Y.; Grant, P.; Lee, J.-H.; Pant, H. C.; Steinert, P. M. *J. Biol. Chem.* **1999**, *274*, 30715–30721.
83. Junn, E.; Ronchetti, R. D.; Quezado, M. M.; Kim, S.-Y.; Mouradian, M. M. *Proc. Natl Acad. Sci. USA* **2003**, *100*, 2047–2052.
84. Lashuel, H. A.; Petre, B. M.; Wall, J.; *et al. J. Mol. Biol.* **2002**, *322*, 1089–1102.
85. Segers-Nolten, I. M. J.; Wilhelmus, M. M. M.; Veldhuis, G.; van Rooijen, B. D.; Drukarch, B.; Subramaniam, V. *Protein Sci.* **2008**, *17*, 1395–1402.
86. Konno, T.; Morii, T.; Shimizu, H.; Oiki, S.; Ikura, K. *J. Biol. Chem.* **2005**, *280*, 17520–17525.
87. Murtaugh, M. P.; Arend, W. P.; Davies, P. J. A. *J. Exp. Med.* **1984**, *159*, 114–125.
88. van Rooijen, B. D.; Claessens, M. M. A. E.; Subramaniam, V. *Biochim. Biophys. Acta* **2009**, *1788*, 1271–1278.
89. Chen, P. S.; Toribara, T. Y.; Warner, H. *Anal. Chem.* **1956**, *28*, 1756–1758.
90. Rockenstein, E.; Hansen, L. A.; Mallory, M.; Trojanowski, J. Q.; Galasko, D.; Masliah, E. *Brain Res.* **2001**, *914*, 48–56.
91. Kodali, R.; Wetzel, R. *Curr. Opin. Struct. Biol.* **2007**, *17*, 48–57.
92. Goldsbury, C.; Frey, P.; Olivieri, V.; Aebi, U.; Müller, S. A. *J. Mol. Biol.* **2005**, *352*, 282–298.
93. Kad, N. M.; Myers, S. L.; Smith, D. P.; Smith, D. A.; Radford, S. E.; Thomson, N. H. *J. Mol. Biol.* **2003**, *330*, 785–797.
94. Jansen, R.; Dzwolak, W.; Winter, R. *Biophys. J.* **2005**, *88*, 1344–1353.
95. Segers-Nolten, I.; van der Werf, K.; van Raaij, M.; Subramaniam, V. Quantitative characterization of protein nanostructures using atomic force microscopy. In *Conference Proceedings of the 2007 Annual International Conference of the IEEE Engineering in Medicine and Biology Society*, Lyon, France, 2007; Vols. 1–16, 6609–6612.
96. Hoyer, W.; Cherny, D.; Subramaniam, V.; Jovin, T. M. *Biochemistry* **2004**, *43*, 16233–16242.
97. van Raaij, M. E.; Segers-Nolten, I. M. J.; Subramaniam, V. *Biophys. J.* **2006**, *91*, L96–L98.
98. Argaman, M.; Golan, R.; Thomson, N. H.; Hansma, H. G. *Nucleic Acids Res.* **1997**, *25*, 4379–4384.
99. Moreno-Herrero, F.; Pérez, M.; Baró, A. M.; Avila, J. *Biophys. J.* **2004**, *86*, 517–525.
100. Arimon, M.; Díez-Pérez, I.; Kogan, M. J.; *et al. FASEB J.* **2005**, *19*, 1344–1346.
101. Fukuma, T.; Mostaert, A. S.; Jarvis, S. P. *Tribol. Lett.* **2006**, *22*, 233–237.
102. Mesquida, P.; Riener, C. K.; MacPhee, C. E.; McKendry, R. A. *J. Mater. Sci. Mater. Med.* **2007**, *18*, 1325–1331.
103. van Noort, S. J.; van der Werf, K. O.; de Grooth, B. G.; van Hulst, N. F.; Greve, J. *Ultramicroscopy* **1997**, *69*, 117–127.

2.220. Extracellular Matrix as Biomimetic Biomaterial: Biological Matrices for Tissue Regeneration

H Walles, Julius-Maximilians-University Hospital Würzburg, Würzburg, Germany
T Walles, Robert-Bosch-Hospital GmbH, Gerlingen, Germany

© 2011 Elsevier Ltd. All rights reserved.

2.220.1.	**Extracellular Matrix**	362
2.220.2.	**Materials Applied in TE**	363
2.220.2.1.	Synthetic Materials	363
2.220.2.2.	Biological Materials	363
2.220.2.2.1.	Synthetic biological materials	363
2.220.2.2.2.	Decellularized biological materials	363
2.220.3.	**Induction of Graft Vascularization**	364
2.220.3.1.	Indirect Revascularization	364
2.220.3.2.	Induction of Angiogenesis *In Vitro*	365
2.220.4.	**Biological Vascularized Scaffold**	365
2.220.4.1.	Generation	365
2.220.4.2.	Application as *In Vitro* Test System	365
2.220.4.3.	Application as Transplant	365
2.220.5.	**Summary and Future Directions**	366
References		366

Glossary

Biological vascularized scaffold (BioVaSc) XXX
Biomechanical stimuli XXX
Biomimicry XXX
Extracellular matrix XXX
Indirect revascularization XXX
Matrix XXX
Revascularization XXX
Scaffold XXX
Tissue differentiation XXX

Abbreviations

BioVaSc	Biological vascularized scaffold
ECM	Extracellular matrix
PERV	Porcine endogenous retrovirus
RGD	Arginine-glycine-aspartate sequence on integrins, which mediates adhesion between cells and the extracellular matrix
SFF	Solid free-form fabrication
SIS	Small intestinal submucosa
TE	Tissue engineering

Tissue engineering (TE) is an interdisciplinary field that applies the principles of engineering and the life sciences toward the development of biological substitutes that restore, maintain, or improve tissue function.[1] It offers the potential to fabricate new, physiologic, functioning tissues from biodegradable scaffolds and autologous cells[2] by

1. Guided tissue regeneration with engineered matrices,
2. Use of cells seeded on or within matrices (cell matrix construct), or
3. Injection of autologous or allogenic or xenogenic cells (cell therapy).

with the latter two approaches being the most common. This chapter, however, will not address cell therapies, but focus on the use of cell-free or seeded matrices as scaffolds to generate bioartificial tissues.

Scaffolds give bioartificial tissues their macroscopic three-dimensional shape and their matrix functions as carrier structure for cells, establishing a three-dimensional framework for cell seeding. Besides its role in providing mechanical support it participates in cellular communication pathways. Porosity, surface chemistry, topography, three-dimensional architecture, immunogenecity, and mechanic parameters are matrix properties.[3]

Without going into great detail it has to be acknowledged that cells and the extracellular components of the surrounding matrix (extracellular matrix (ECM)) interact with each other, resulting in a complex interplay composed of cell–cell and

cell–matrix interactions (Figure 1). Additionally, biomechanical stimuli and soluble factors within the physiological tissue environment influence tissue differentiation and growth (microenvironment). Unfortunately, this complex interplay is currently only beginning to be understood.

Therefore, one of the most difficult obstacles facing tissue engineers is defining the conditions that direct cell behavior, and recapitulating these conditions in a suitable *in vitro* growth environment.[4] Additionally, the arrangement of assorted cells into correct spatial organization is of fundamental importance.

Initial success has been achieved primarily in tissues of relatively simple architecture, including skin and cartilage. In comparison, engineering tissues with greater complexity has been rather unsuccessful. These tissues comprise multiple cell types within a highly structured and defined organization. Reproducing this organization in an engineered tissue constrains the juxtaposition of specific cells with various gradients of soluble factors, specific ECM scaffolds, physical forces, and other cell types, and therefore is likely to be required to recapitulate the signals that drive cell and tissue function.[4]

Depending on the intended application, matrices have to meet numerous requirements for tissue suitability (Table 1). Therefore, the composition of the tissue-specific ECM composition is analyzed to develop biomimetic materials.

2.220.1. Extracellular Matrix

In vivo, cells are embedded in a complex ECM and exposed to a wide range of stimuli. Depending on the tissue type, cells communicate by cell–cell contacts with neighboring cells or secrete soluble factors. Examples for the biomolecules released into the intercellular environment are hormones, growth factors, and neurotransmitters. One of the most important stimuli for cellular behavior is the cell's interaction with its surrounding ECM.[5] The ECM is generated from biological molecules synthesized by these cells and maintained in a dynamic milieu. It provides the substrate for anchorage-dependent cells to firmly adhere and organize.

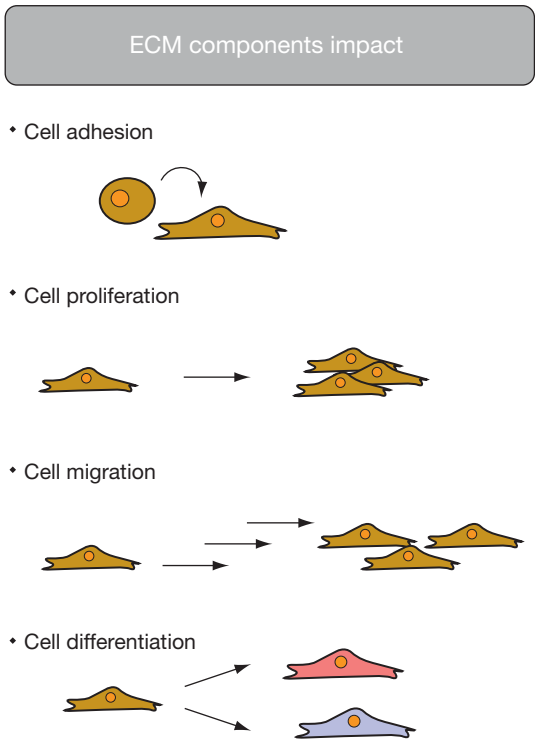

Figure 1 The matrix interacts with the fundamental cell functions.

The extracellular microenvironment, which surrounds cells and comprises the molecular signals, is a highly hydrated network hosting three main effectors: (1) insoluble hydrated macromolecules (fibrillar proteins such as collagens, noncollagenous glycoproteins such as elastin, laminin or fibronectin, and hydrophilic proteoglycans with large glycosaminoglycan side chains), (2) soluble macromolecules (growth factors, chemokines and cytokines), and (3) proteins on the surfaces of neighboring cells. Thus, the ultimate decision of a cell to differentiate, proliferate, migrate, apoptose, or perform other specific functions is a coordinated response to the molecular interactions with these ECM effectors. It is noteworthy that the flow of information between cells and their ECM is highly bidirectional, as, for example, observed in processes involving ECM degradation and remodeling.[6]

Considering the multitude of different tissues, a wide variety of ECM compositions becomes apparent: While bone ECM is characterized by its durability and porosity, brain ECM resembles a flexible hydrogel. According to this, the ECM-associated stimuli like topography of globular, porous, crystalline or febrile structures, stability, elasticity, roughness, wettability and water storage capacity, chemical composition, and ligands vary. These various material properties and compositions define the tissue-specific properties.[7]

Basically, the ECM is composed of febrile and globular proteins.[8] In higher vertebrates, collagen is the most abundant protein found. Twenty-nine types have been identified with type I being the most abundant. Over 90% of the collagen in the body, however, is of type I, II, III, and IV, as indicated by Table 2. Elastic fibers are composed of fibrillin and elastin.[9] Additionally, the ECM contains globular proteins (i.e., laminin or fibronectin), which frequently present specific amino acid sequences for the specific adhesion of cells – with the

Table 1 Ideal properties of matrices for tissue engineering

Biocompatibility
Bioabsorbability
Nonimmunogenicity
Support cell attachment and growth
Induction of angiogenesis
Three-dimensional structure
Affording sterilization

Table 2 Collagen distribution in human tissues

Collagen type	*Occurrence*
I	Skin, tendon, vasculature, ligaments, organs, bone
II	Cartilage
III	Reticular fibers
IV	Cell basement membrane
V	Cell surfaces

arginine-glycine-aspartate (RGD) sequence being the most common.[10,11] Glycosaminoglycans represent another large group of ECM macromolecules. They are long-chained polysaccharides that form proteoglycans by association with proteins. The diversity and interaction of proteins, glycosaminoglycans, and proteoglycans set the basis for the various ECM properties.[12]

To initiate signaling cascades that lead to changes in cell growth, proliferation, migration, differentiation, and survival soluble factors were applied in cell culture media and incorporated into TE scaffolds. For example, hepatocytes dedifferentiate *in vitro* in the absence of collagen I, dynamic culture maintain endothelial cells (EC) in a quiescent, whereas cells cultured in static conditions resemble cells in an inflammatory state. Simply combining cells with matrix proteins in culture is not sufficient to generate bioartificial tissues with specific and long-term function. A specified spatial arrangement, the application of physical factors, surrounding proteins, and neighboring cells control the degree to which cells are in contact with matrix versus neighboring cells. This balance is important to direct cell and tissue behavior *in vitro*[4] (**Figure 2**).

2.220.2. Materials Applied in TE

2.220.2.1. Synthetic Materials

Ample experience exists regarding the use and biocompatibility of synthetic materials as implants in reconstructive surgery. For decades they have been applied mainly in dentistry and orthopedic- and cardiovascular surgery. Synthetic materials currently used for biomedical applications include metals and alloys, polymers, and ceramics (see **Chapter 1.102, Metals for Use in Medicine**; **Chapter 1.104, Shape Memory Alloys for Use in Medicine**; and **Chapter 1.109, Bioactive Ceramics**, Inert ceramics, Polymers).

2.220.2.2. Biological Materials

Biological materials can be (1) composed artificially from single or few ECM components, such as collagen and fibronectin or (2) generated from three-dimensional biologic auto-, allo-, or xenogenic tissues.

2.220.2.2.1. Synthetic biological materials

Biological materials can be fabricated from single or multiple ECM proteins. The material properties can be tailored to the specific needs by adding various additives such as, growth factors or RGD-peptides to optimize cellular microenvironment and graft stability. However, these synthesized biological materials lack the physiological three-dimensional structure and various ECM components, changing the microenvironment for seeded and in growing cells (**Table 3**). Especially, the speed of material degradation has been shown to depend on the material's elastin content.[14]

Various fabrication techniques have been applied for material generation:

1. solid freeform fabrication (SSF),[15]
2. electrospinning,[16] and
3. bioprinting.[17]

As a result of these new technologies, tissue-engineered constructs that contain a controlled spatial distribution of cells and growth factors, as well as engineered gradients of scaffold materials with a predicted microstructure can be generated.[15]

2.220.2.2.2. Decellularized biological materials

In contrast to fabricated synthetic biological materials, biological tissues that are decellularized adequately provide a naive ECM composition, a biomimetic environment, and physiological three-dimensional scaffold composition that may serve as structural landmark for reseeding and tissue differentiation. Auto-, allo-, and xenogenic tissues may serve as starter materials to generate cell-free biological scaffolds for TE applications (**Table 4**).

The specific properties of every scaffold preparation, however, largely depend on the applied fabrication methods. Decellularized biological materials may be (1) implanted as

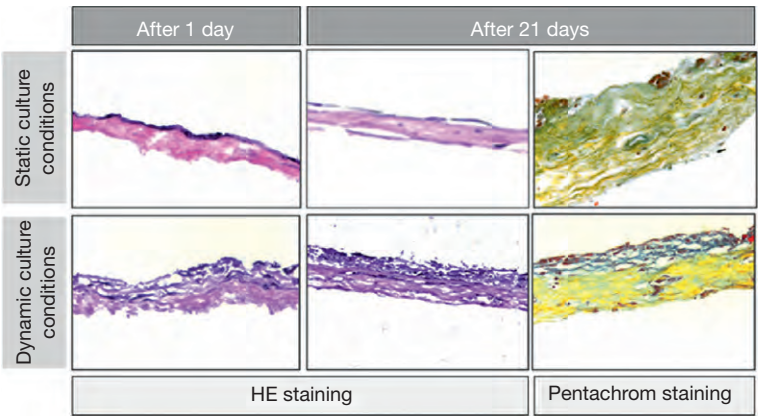

Figure 2 Biomechanical stimulation supporting tissue differentiation. Porcine jejunal segments were decellularized chemically, reseeded with allogenic fibroblasts and cultured for 3 weeks under static culture conditions (upper row) and dynamic culture conditions (lower row). In the static culture, cell proliferation and migration are detectable (HE staining), but only scarce collagen synthesis (PC staining). In the dynamic culture, there is evidence of additional matrix synthesis (HE staining). The entire extracellular matrix shows a higher degree of organization (PC staining). (HE staining: nuclei are stained blue, collagen is stained pink; PC staining: nuclei are stained brown, collagen is stained yellow, proteoglycans are stained green, elastic fibers are stained red, calcifications are stained black).

cell-free scaffolds (guided tissue regeneration), (2) lyophilized and injected as hydrogel or (3) recellularized *in vitro* and implanted as cell–matrix construct (TE). As a matter of fact, a good portion of the potential interdependencies, however, has not been understood so far and is currently the subject of ongoing research. For example, ECM isolated from heart tissue supports myocardial regeneration far better than the ECM of a different origin.[30]

Regarding the potential threats of decellularized porcine tissues, concerns regarding the possibility of porcine endogenous retrovirus (PERV) transmission[37] onto human recipients have been disproved by experimental and clinical findings.[38]

2.220.3. Induction of Graft Vascularization

The advances in cell and tissue culture techniques and the progress in materials research led to the development of uncounted bioartificial tissues for experimental and clinical applications, as was already indicated in Table 4.

Table 3 Important noncollagenous ECM components

Component	*Function*
Fibrin	Controls stiffness, resists tension, easily degraded, and remodeled
Elastin	Provides elastic recoil, hinders degradation processes
Proteoglycan	Resists compression, hinders water transport, hinders macromolecular transport, binds growth factors and chemokines

Source: Retrieved from Griffith and Swartz[13].

The multitudinous transplantation studies of the past displayed the elementary importance of tissue vascularization for graft function: When *in vitro* engineered cellular constructs are transplanted *in vivo* they have to rely on processes like interstitial fluid diffusion and blood perfusion. Here resides a core limitation for transfer of TE models from the *in vitro* to the *in vivo* environment.[4] With one exception, the (clinically) realized TE applications represent simple tissues that are supplied by diffusion, but not by vascularization. Therefore, one of the major obstacles in TE of thick, complex tissues is to keep the construct viable *in vitro* (during cultivation and formation of the tissue) as well as *in vivo* (on implantation).[39] *In vivo*, the construct must be vascularized immediately to allow for its survival and later integration as the host's vascularization is not sufficient to feed the implant.[40] The importance of this issue led to the development of various strategies and experimental approaches to vascularize bioengineered grafts directly or indirectly.[41]

2.220.3.1. Indirect Revascularization

Diffusion is the initial process involved following tissue transplantation, but it can only provide for cell support within a maximum range of 200 μm[42] into the matrix. Therefore, prompt formation of new blood vessels by budding or sprouting of preexisting vessels is necessary to sustain the newly formed tissue. Animal experiments investigating the capillary ingrowth in a rodent transplant model showed that avascular tissues with a diameter of less than 1 mm are supplied by diffusion over a time period of 2 weeks.[40] Tissue revascularization was detectable about 2 weeks following transplantation and continued up to the 8th postoperative week.[14]

Table 4 Various tissue types applied as biological scaffolds for tissue engineering applications[a]

Target tissue	*Decellularized donor tissue*	*Applied*			*Reference*
		In vitro	*Preclinically*	*Clinically*	
Bladder	Small intestine submucosa (SIS)	x	x	(x)	18
	Bladder	x			19
	Amniotic membrane	x			20
Blood vessels	Blood vessels	x	x	x	21
	SIS	x	x		22
Bone	Trabecular bone	x			23
Cornea	Cornea	x	x		24
Esophagus	Bladder	x	x		25
Heart valves	Aortic valves	x	x	x	26
	Pericardial valves	x	x		26
	SIS	x			27
Myocard	SIS		x		28
	Myocardium		x		29
	Ventricular ECM		x		30
	Pericardial ECM		x		30
Peripheral nerve tissue	Nerve graft	x	x		31
Skin	Amniotic membrane	x	x		32
	Skin	x	x		33
Trachea	Trachea			x	34
	Porcine jejunum	x	x	x	35
Uretera	SIS	x	x		36
	Bladder	x	x		36

Indirect revascularization, the concept of wrapping the TE graft with viable tissue (i.e., greater omentum, peritoneum, muscle, subcutaneous tissue) and stimulating ingrowth of microvessels, has been intensively investigated in the experimental literature.[43] In this approach, the new capillaries emerge from neighboring vessels induced by an inflammatory wound-healing response as a reaction to the surgical implantation.[44] This, combined with the hypoxia within the implant evokes local expression of angiogenic growth factors. Recently, it was shown clinically that this approach may result in vascularized tissue transplants.[45] However, this process took 4 months.

2.220.3.2. Induction of Angiogenesis *In Vitro*

The vascular network branches in a hierarchical fashion and is organized spatially to provide adequate nutrients to the cells of all organs and supporting structures by diffusion and convection. The maturation of nascent vasculature requires recruitment of mural cells, generation of an ECM and specialization of the vessel wall for structural support, and regulation of vessel function. In addition, the vascular network must be organized so that the parenchymal cells receive adequate nutrients. All of the processes are orchestrated by physical forces as well as by a constellation of ligands and receptors whose spatiotemporal patterns of expression and concentration are tightly regulated.[46]

Physicists, chemists, engineers, material scientists, biologists, and physicians try to mimic the only partially understood biological processes of vasculogenesis, angiogenesis, and vessel maturation. Three approaches have been used for vascularization of bioengineered tissues[41]:

1. incorporation of angiogenic factors in the bioengineered tissue,
2. seeding EC with other cell types, and
3. prevascularization of matrices prior to cell seeding.

Optimized surgical implantation techniques are one more essential step toward clinical application of engineered bioartificial tissues.[47]

2.220.4. Biological Vascularized Scaffold

As the angiogenic capabilities of most engineered tissues are not sufficient, complex bioartificial tissues that are viable and functional can currently be generated only by implementation of a fully developed capillary network. Recently, a biological vascularized matrix (BioVaSc) was introduced that supplies a capillary bed for the nutrition of complex man-made biological tissues[48] including clinical transplants[35,49] (Figure 3).

2.220.4.1. Generation

The BioVaSc represents an acellular collagenous network generated from a porcine jejunal segment by removal of all cellular components. Its histologic composition is similar to the small intestinal submucosa (SIS) matrix, which has been shown to

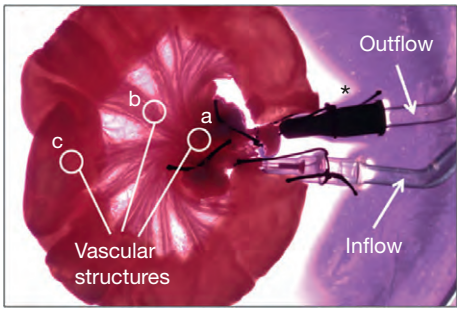

Figure 3 The biological vascularized scaffold represents an acellular biological matrix that is endued with a capillary network and feeding vascular structures. It is obtained from a porcine jejunal segment that is explanted with its feeding artery and draining vein and decellularized chemically by flushing the vascular structures. For reseeding, the acellular matrix is perfused in a bioreactor. The asterisk symbol indicates the canula in the draining vein, (a), (b), and (c) indicate different sections of the vascular network within the BioVaSc.

- represent a complete absorbable biocompatible framework,[50]
- enable cellular migration and differentiation,[51]
- show early capillary ingrowth and endothelialization,[51]
- provide high infection resistance,[52] and
- be nonimmunogenic.[50]

The SIS has been successfully applied as a biological matrix for numerous body tissues in animal studies and human clinical trials including

- musculoskeletal,[53]
- cardiovascular,[54]
- urogenital,[55] and
- laryngeal applications.[56]

Although the SIS shows excellent biomimetic and therefore favorable remodeling properties,[57] its applicability is limited by the lack of graft vascularization.[41] The BioVaSc may surmount this difficulty.

2.220.4.2. Application as *In Vitro* Test System

Given the documented favorable biomimetic properties of the SIS, complex bioengineered human tissues built on the BioVaSc represent sustainable alternatives to animal models for pharmaceutical, chemical, cosmetic, and nutritional investigations. Additionally, they can be applied as model systems for basic research to study cell–cell and cell–matrix interactions as well as angiogenesis processes[58] (Figure 4). Moreover, they afford antiangiogenesis studies and the *in vitro* growth of human tumor tissues.[59]

2.220.4.3. Application as Transplant

If nothing else, clinical applications have confirmed the assumable outstanding healing properties of the BioVaSc including its nonimmunogenicity (see Section 2.220.4.1).[35,49,57] Short-term implantations confirmed the functionality of the generated vascular structures affording transplant survival.[35] Applied for tracheal reconstruction, the BioVaSc showed a substantial tissue maturation process within the first 3 months following

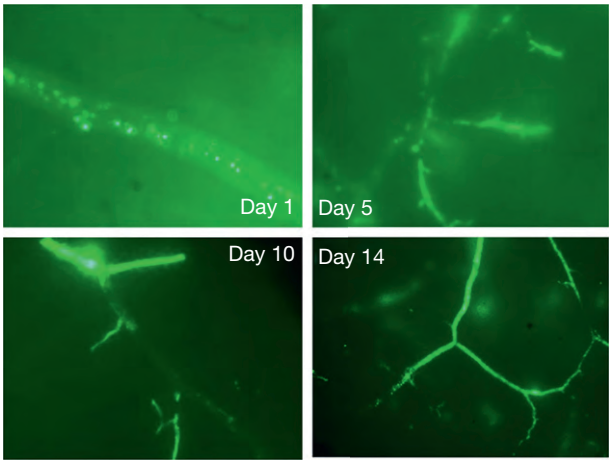

Figure 4 Angiogenetic *in vitro* studies afforded by the biological vascularized scaffold (BioVaSc). Human microvascular endothelial cells were cultivated on the BioVaSc for 2 weeks. Endothelial cells were labeled green with carboxyfluorescein diacetate succinimidyl ester.

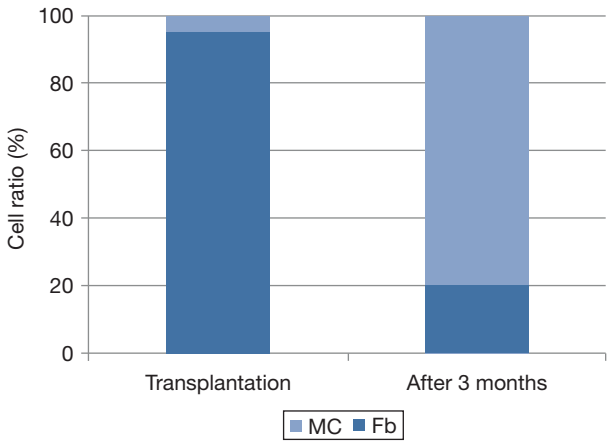

Figure 5 The bioartificial tissue undergoes a significant remodeling process within the first 3 months following transplantation (MC = muscle cells, Fb = fibroblasts).

transplantation, mirrored by shifted cell-populations, epithelial repopulation of the surfaces and vascularization[49] (Figure 5).

2.220.5. Summary and Future Directions

Many applications in the TE field currently depend on the identification of biological materials that support and stimulate the self-assembly and organization of cells, tissues and organs. Today, TE provides numerous promising medical applications and may expand the spectrum of methods in basic and applied research. In the light of a growing understanding of biomimetic signals, vasculogenesis, and angiogenesis, it is foreseeable that the complexity and applicability of the artificial tissues will increase.

Despite apparent successes using synthetic materials, at present the biological materials set the basis for studying the underlying mechanisms and interactions to develop easier available and manageable artificial materials for future applications. Looking into the future, a further diversification of the field is foreseeable. For example, the potential impact of nanomedicine will radically change the composition of materials applied for TE.

Besides the importance of material-specific interactions, clinical applications have taught the paramount importance of the physiological microenvironment for the artificial tissues. These have to be studied and understood to be calculable in future applications.

References

1. Langer, R.; Vacanti, J. P. *Science* **1993**, *260*, 920–926.
2. Fuchs, J. R.; *et al*. *Ann. Thorac. Surg.* **2001**, *72*, 577–591.
3. Vacanti, J. P.; Langer, R. *Lancet* **1999**, *354*, 132–134.
4. Liu, W. F.; Chen, C. S. *Adv. Drug Deliv. Rev.* **2007**, *59*, 1319–1328.
5. Liu, W. F.; Chen, C. S. *Mater. Today* **2005**, *8*, 28–35.
6. Lutolf, M. P.; Hubbell, J. A. *Nat. Biotechnol.* **2005**, *23*, 47–55.
7. Shin, H. *Biomaterials* **2007**, *28*, 126–133.
8. Alberts, B., *et al*. Eds.; In *Molecular Biology of the Cell*, 5 edn.; Garland Science: New York, 2008.
9. Ushiki, T. *Arch. Histol. Cytol.* **2002**, *65*, 109–126.
10. Aumailley, M.; Rousselle, P. *Matrix Biol.* **1999**, *18*, 19–28.
11. Hersel, U.; *et al*. *Biomaterials* **2003**, *24*, 4385–4415.
12. Timpl, R. *Experientia* **1993**, *49*, 417–428.
13. Griffith, L. G.; Swartz, M. A. *Nat. Rev. Mol. Cell Biol.* **2006**, *7*, 211–224.
14. Walles, T.; *et al*. *Int. J. Artif. Organs* **2003**, *26*, 225–234.
15. Hutmacher, D. W.; *et al*. *Trends Biotechnol.* **2004**, *22*, 354–362.
16. Matthews, J. A.; *et al*. *Biomacromolecules* **2002**, *3*, 232–238.
17. Skardal, A.; *et al*. *Biomaterials* **2010**, *31*, 6173–6181.
18. Cheng, E. Y.; Kropp, B. P. *World J. Urol.* **2000**, *18*, 26–30.
19. Liu, Y.; *et al*. *Biomaterials* **2009**, *30*, 3865–3873.
20. Sharifiaghdas, F.; *et al*. *Urol. J.* **2009**, *6*, 283–288.
21. Gui, L.; *et al*. *Tissue Eng. A* **2009**, *15*, 2665–2676.
22. Vinatier, C.; *et al*. *Trends Biotechnol.* **2009**, *27*, 307–314.
23. Grayson, W. L.; *et al*. *Proc. Natl. Acad. Sci. USA* **2010**, *23*, 3299–3304.
24. Zhang, C.; *et al*. *Cell Tissue Res.* **2007**, *329*, 249–257.
25. Badylaks, S. F.; *et al*. *J. Surg. Res.* **2005**, *128*, 87–97.
26. Schmidt, D. *Meth. Mol. Med.* **2007**, *140*, 319–330.
27. Johnston, D. E.; *et al*. *J. Biomed. Mater. Res. A* **2006**, *78*, 383–393.
28. Zhao, Z. Q.; *et al*. *J. Am. Coll. Cardiol.* **2010**, *23*, 1250–1261.
29. Singelyn, J. M.; *et al*. *Biomaterials* **2009**, *30*, 5409–5416.
30. Singelyn, J. M.; Christman, K. L. *J. Cardiovasc. Transl. Res.* **2010**, *3*, 478–486.
31. Hudson, T. W.; *et al*. *Tissue Eng.* **2004**, *10*, 1641–1651.
32. Wilshaw, S. P.; *et al*. *Tissue Eng. A* **2008**, *14*, 463–472.
33. Prasertsung, I.; *et al*. *J. Biomed. Mater. Res. B Appl. Biomater.* **2008**, *85*, 210–219.
34. Asnaghi, M. A.; *et al*. *Biomaterials* **2009**, *30*, 5260–5269.
35. Mertsching, H.; *et al*. *Transplantation* **2009**, *88*, 203–210.
36. Fu, Q.; *et al*. *BJU Int.* **2007**, *99*, 1162–1165.
37. Patience, C.; *et al*. *Nat. Med.* **1997**, *3*, 282–286.
38. Walles, T.; *et al*. *Eur. J. Cardiothorac. Surg.* **2003**, *24*, 358–563.
39. Levenberg, S.; Langer, R. *Curr. Top. Dev. Biol.* **2004**, *61*, 113–128.
40. Walles, T.; *et al*. *Biomaterials* **2003**, *24*, 1233–1239.
41. Walles, T.; Mertsching, H. In *Biomaterials Research Advances*; Kendall, J. B., Ed.; Nova Science: New York, 2007; pp 183–203.
42. Folkman, J.; Hochberg, M. *J. Exp. Med.* **1973**, *138*, 745–753.
43. Walles, T. *Expert Rev. Med. Devices* **2004**, *1*, 241–250.
44. Eiselt, P.; *et al*. *Biotechnol. Prog.* **1998**, *14*, 134–140.
45. Delaere, P.; *et al*. *N. Engl. J. Med.* **2010**, *362*, 138–145.
46. Jain, R. K. *Nat. Med.* **2003**, *9*, 685–693.
47. Kneser, U.; *et al*. *J. Cell. Mol. Med.* **2006**, *10*, 7–19.
48. Mertsching, H.; *et al*. *Biomaterials* **2005**, *26*, 6610–6617.
49. Walles, T.; *et al*. *Transplantation* **2005**, *80*, 284–285.
50. Hodde, J. *Tissue Eng.* **2002**, *8*, 295–308.
51. Badylak, S. F.; *et al*. *Biomaterials* **1999**, *20*, 2257–2263.
52. Lantz, G. C.; *et al*. *J. Invest. Surg.* **1993**, *6*, 297–310.
53. Nguyen, T. D.; *et al*. *Tissue Eng. A* **2009**, *15*, 957–963.

54. Badylak, S. F.; *et al*. *Heart Surg. Forum* **2003**, *6*, E20–E26.
55. Record, R. D.; *et al*. *Biomaterials* **2001**, *22*, 2653–2659.
56. Huber, J. E.; *et al*. *Ann. Otol. Rhinol. Laryngol*. **2003**, *112*, 428–433.
57. Macchiarini, P.; *et al*. *J. Thorac. Cardiovasc. Surg*. **2004**, *128*, 638–641.
58. Schanz, J.; *et al*. *J. Biotechnol*. **2010**, *148*, 56–63.
59. Walles, T.; *et al*. *Onkologie* **2007**, *30*, 388–394.
60. Fiegel, H. C.; *et al*. *J. Cell. Mol. Med*. **2008**, *12*, 56–66.
61. González-Andrades, M.; *et al*. *J. Tissue Eng. Regen. Med*. **2009**, *3*, 442–449.
62. Hood, B.; *et al*. *Neurosurg. Focus* **2009**, *26*, E4.
63. Ichihara, S.; *et al*. *Injury* **2008**, *39*(Suppl. 4), 29–39.
64. Kokemueller, H.; *et al*. *Int. J. Oral Maxillofac. Surg*. **2010**, *39*, 379–387.
65. Mirensky, T. L.; Breuer, C. K. *Pediatr. Res*. **2008**, *63*, 559–568.
66. Shevchenko, R. V.; *et al*. *J. R. Soc. Interface* **2010**, *7*, 229–258.
67. Villalona, G. A. *Tissue Eng. B* **2010**, *16*, 341–350.
68. Wood, D.; Southgate, J. *Curr. Opin. Urol*. **2008**, *18*, 564–569.
69. Yoshikawa, H.; *et al*. *J. R. Soc. Interface* **2009**, *6*(Suppl. 3), S341–S348.

2.221. Decellularized Scaffolds

E M Srokowski, University of Toronto, Toronto, ON, Canada
K A Woodhouse, University of Toronto, Toronto, ON, Canada; Queen's University, Kingston, ON, Canada

© 2011 Elsevier Ltd. All rights reserved.

2.221.1.	**Introduction**	370
2.221.1.1.	What is Decellularization	370
2.221.1.2.	Benefits and Challenges of Decellularization	370
2.221.2.	**Decellularization Methodology**	371
2.221.2.1.	Physical Methods	371
2.221.2.2.	Chemical Methods	373
2.221.2.2.1.	Solvent extraction	373
2.221.2.2.2.	Alkaline and acid treatments	373
2.221.2.2.3.	Detergent extraction	374
2.221.2.2.4.	Hypotonic and hypertonic treatment	375
2.221.2.2.5.	Enzymatic treatment	375
2.221.2.3.	Additional Reagents	376
2.221.2.4.	Additional Processing	376
2.221.2.5.	Important Considerations	376
2.221.2.5.1.	Characterization of decellularization	376
2.221.2.5.2.	Host response to decellularized scaffolds	377
2.221.3.	**Origin of Decellularized Scaffolds and their Applications**	379
2.221.3.1.	Small Intestine	379
2.221.3.2.	Dermis	380
2.221.3.3.	Urinary Bladder	381
2.221.3.4.	Vascular and Cardiac Tissue	382
2.221.3.5.	Embryoid Body Matrix	383
2.221.4.	**Concluding Remarks**	383
References		383

Abbreviations

α-Gal epitope	Galα1-3Galβ1-4GlcNAc-R
Ab	Antibody
ACL	Anterior cruciate ligament
ADM	Acellular dermal matrix
anti-α-Gal	Galactose-α-1,3-galactose antibody
BAM	Bladder acellular matrix
BAMG	Bladder acellular matrix graft
bFGF	Basic fibroblast growth factor
C-ECM	Cardiac extracellular matrix
CHAPS	3-[(3-Cholamidopropyl)dimethylammonio]-1-propanesulfonate
CS	Chondroitin sulfate
CS-A	Chondroitin sulfate A
CS-B	Chondroitin sulfate B
CTAB	Cetyltriethylammonium bromide
DNA	Deoxyribonucleic acid
DNase	Deoxyribonuclease
DSC	Differential scanning calorimetry
EBs	Embryoid bodies
ECM	Extracellular matrix
EDTA	Ethylenediaminetetraacetic acid
ESCs	Embryonic stem cells
ETO	Ethylene oxide
GAGs	Glycosaminoglycans
HA	Hyaluronan
H&E	Hematoxylin and Eosin
HS	Heparan sulfate
Ig	Immunoglobulins
LS	Lauroyl sarcosinate
MGP	Methyl green-pyronine
MHC	Major histocompatibility complex
PAA	Peracetic acid
PDM	Placental decellular matrix
PES	Ethanol peracetic acid solution
PMSF	Phenylmethylsulfonylfluoride
RGD	Amino acid residues arginine-glycine-asparagine (Arg-Gly-Asp)
RNA	Ribonucleic acid
RNase	Ribonuclease
SB-10	Sulfobetaine-10
SB-16	Sulfobetaine-16
SDS	Sodium dodecyl sulfate
SD	Sodium deoxycholate (deoxycholic acid)
SEM	Scanning electron microscopy
SIS	Small intestinal submucosa
TEM	Transmission electron microscopy

TGF-β1	Transforming growth factor beta 1	**UBM**	Urinary bladder matrix
TnBP	Tri(*n*-butyl)phosphate	**UBS**	Urinary bladder submucosa
Triton® X-100	Octyl phenol ethoxylate	**VEGF**	Vascular endothelial growth factor

2.221.1. Introduction

Organ demand is a major healthcare issue that is growing in magnitude, globally. Although organ donations are increasing, the number of patients waiting for a transplant is increasing more rapidly. In 2006, the world market for organ replacement therapy was estimated to be in excess of $350 billion and expected to surpass $500 billion within 20 years.[1] An area of study that holds great potential to combat this ever-increasing crisis is tissue engineering. Tissue engineering applies the principles of cell transplantation, material science, and engineering to develop biological substitutes that can restore and maintain normal function.[2] The pioneering work of Robert Langer, Joseph Vacanti, and colleagues introduced the concept of using a degradable three-dimensional (3D) scaffold as a temporary substitute for the extracellular matrix (ECM).[3–6] The ECM is, by definition, nature's ideal biologic scaffold material.[7] The composition and ultrastructure of the ECM consists of a complex combination of structural and functional proteins, glycosaminoglycans (GAGs), glycoproteins, and small molecules all arranged in a unique, tissue-specific 3D architecture.[8] In addition to providing structural support, the ECM modulates cellular behavior by regulating the activity of growth factors, cytokines, matrix-degrading enzymes, and their inhibitors. More importantly, the ECM is in a state of dynamic equilibrium with its surrounding microenvironment.[8] Consequently, the ECM facilitates the bidirectional flow of information between adjacent cells and the external environment, which is crucial in a number of biological processes such as embryonic development, wound repair, and hemostasis.

Briefly, native ECM is composed primarily of collagen (collagen type I being the predominant type), providing the necessary mechanical strength to the scaffold. Elastin is another dominant structural protein found in the ECM that provides elasticity and resilience to connective tissues. Fibronectin, a glycoprotein, is also found in abundance within the ECM, in particular in the basement membrane, submucosal structures, and in interstitial tissues. Fibronectin is important in mediating cell–matrix communication, due to its rich content of Arg-Gly-Asp (RGD) subunits that are important for cell adhesion.[8] Laminin, another adhesion protein found abundantly in the basement membrane of the ECM, plays an important role in early embryonic development as well as a critical role in the process of cell and tissue differentiation.[8] In addition, the ECM contains various mixtures of GAGs such as chondroitin sulfate A (CS-A) and B (CS-B), heparin, heparan sulfate (HS), and hyaluronan (HA). The GAGs bind various growth factors and cytokines in the ECM, as well as promote water retention and contribute to the gel properties of the ECM.[8,9] Moreover, although native ECM contains very small quantities of growth factors and cytokines, they are vital in modulating a variety of cellular activities (i.e., cell migration, proliferation, differentiation, and maturation).[8,9]

An important characteristic of native ECM that distinguishes it from the variety of other scaffolds used in tissue engineering applications is its diversity of structural and functional proteins. In general, the scaffold approach in tissue engineering falls under two categories: (1) the use of synthetic matrices; and (2) the use of natural matrices, which include decellularized matrices. The objective of this chapter is to provide an overview of the current knowledge surrounding decellularized matrices including the various methods used to decellularize tissues, the manufacturing effects of decellularization, and lastly the origin and applicability of decellularized matrices in a therapeutic tissue engineering context.

2.221.1.1. What is Decellularization

Decellularization is the process of removing the allogeneic or xenogeneic cellular antigens from a tissue that would initiate an immune response while leaving behind an intact ECM comprising a mixture of structural and functional molecules. Decellularization results in a decellularized matrix also referred to as acellular or devitalized matrix in the literature. The particular terminology used to denote a decellularized matrix in this chapter has been kept consistent as that referred to the referenced publication. Decellularization strategies vary depending on the tissue being processed. In general, the manufacturing process involves a series or combination of physical, chemical, and enzymatic treatments that ideally removes all cellular and nuclear materials without adversely affecting the composition, organization, biological activity, and mechanical integrity of the native ECM tissue. The efficiency of decellularization is a factor of both the processing methodology and the nature of the tissue.[10,11]

2.221.1.2. Benefits and Challenges of Decellularization

Decellularization of tissue has been widely shown to be an attractive method of obtaining scaffolds for tissue engineering. An alternative to decellularization is the use of synthetic scaffold materials. These materials are typically characterized by uniform and reproducible mechanical and material properties. However, synthetic materials can lack the bioinductive and constructive remodeling properties inherently characteristic of ECM-derived scaffolds.[10,12–14]

The use of decellularized scaffolds for a tissue engineering approach provides a number of benefits, as listed in **Table 1**. First, removal of allogeneic or xenogeneic cellular antigens not only minimizes the source of immunogenicity on implantation, but also preserves the ECM components, which are highly conserved among species allowing the use of xenogeneic materials.[15] Moreover, decellularized scaffolds can retain a

Table 1 Comparison of the benefits and challenges of decellularization

Benefits
Minimizes immunological response upon implantation
Allows for the use of xenogeneic materials
Ability to conserve the mechanical integrity of native tissue
Ability to retain the biochemical composition of native tissue
Ability to retain the three-dimensional microarchitecture of native tissue
Retains the bioinductive properties (cryptic peptides) to facilitate tissue remodeling
Widely applicable and economical
Long-term storage capability
Potential for an off-the-shelf product
Challenges
Requires optimization of decellularization process for each tissue source
Immunological response from incomplete cellular removal
Decellularization efficiency dependent on tissue source, thickness, and architecture
Bioactivity and structural integrity of tissue may be impaired during manufacturing process
Difficulty in characterizing efficiency of decellularization
Scaffold properties constrained by the tissue source characteristics
Reliance on host cell availability and infiltration
Rapid *in vivo* degradation before recellularization

more physiologically relevant composition and microenvironment to the native ECM tissue. For instance, the ultrastructure and 3D architecture of the tissue can be preserved throughout the decellularizing process, retaining defining structures such as laminin and collagen type IV of the basement membrane in urinary bladder matrix (UBM)[16] and placental decellular matrix (PDM),[17] which are crucial in modulating cellular behavior. Moreover, decellularization may preserve the alignment and organization of collagen fibers,[10,18] as well as elastic fibers,[14,19] that aid in retaining not only elasticity to the scaffold but also biological activity.[20,21] Consequently, the functionality and mechanical stability of decellularized scaffolds can provide the closest match to that of native tissues.[22] Decellularized scaffold may also function as resorbable, provisional matrices whose degradation products release cryptic peptides such as endostatin, angiostatin, and canstatin, which actively participate in long-term tissue remodeling.[7,23] Lastly, decellularized scaffolds present a widely applicable yet economical option with the potential for an off-the-shelf product with long-term storage capabilities for clinical applications.[8,24–29]

Despite the numerous benefits decellularized scaffolds provide, some challenges still exist. First, the decellularization process needs to be optimized for each tissue source, as the ECM harvested from the tissue contains a unique arrangement and composition of structural and functional components specific to that particular tissue or organ.[11] As a result, incomplete cellular removal may elicit immune reactions on implantation. In addition, tissue variability may exist in terms of tissue thickness or the age of the tissue, which further complicates the efficacy of decellularization.[7,11,12,15,30] Likewise, depending on the methods and/or reagents used in the manufacturing process, the bioactivity and structural integrity of the scaffold may be impaired. Therefore, a systematic and perhaps lengthy approach may be needed to fine tune the decellularization strategy. Challenges in characterizing the decellularized scaffold also exist in terms of accurately identifying and quantifying both the bioactive components and residual decellularizing agents in the matrix.[11,15] Moreover, the material properties of the decellularized scaffold are inherently constrained by the characteristics of the tissue source including shape, and mechanical behavior.[10] Thus, additional processing such as cross-linking may need to be introduced to improve the versatility of the scaffold. Decellularized scaffolds, by definition, also rely on cellular infiltration by host cells whose availability *in vivo* may be limited or whose infiltration may be inhomogeneous.[29,31] Lastly, decellularized scaffold can degrade quickly *in vivo*, however, before complete recellularization[23,25,32]

2.221.2. Decellularization Methodology

In 1975, Meezan *et al.* described the first decellularization strategy for extracting cells from the ECM through a multistep chemical and enzymatic process in preparation of basement membranes from several tissues.[33] In recent years, there have been a number of methods developed to manufacture biologic scaffolds derived from decellularized tissues and organs, as summarized in **Table 2**. The resulting decellularized ECM-derived scaffolds have been broadly applied to a multitude of applications including adipose,[17] bladder,[53,77,85–88] nerve,[83,89–92] and cardiovascular[27,57,69,73,93–100] tissues. The most robust and effective decellularization protocols include a combination of physical, chemical, and enzymatic treatments.[11] In general, a typical decellularization protocol contains the following series of steps: (1) lysis of cell membranes by physical treatments or ionic solutions, (2) separation of cellular component from the ECM using enzymatic treatments, (3) solubilization of cytoplasmic and nuclear cellular components by detergent treatment, and finally (4) rinsing and removal of cellular remnants from the ECM. Each of these steps may be coupled with mechanical agitation, and repeated a number of times to increase the effectiveness. The effectiveness of decellularization and preservation of the native ECM can be evaluated at each of the steps by a variety of methods, as will be discussed. Nonetheless, it is important to acknowledge that tissues depending on their origin, composition, structure, and thickness may respond variably to a decellularization process. Decellularization strategies must therefore be optimized for each tissue by controlling the concentration and duration of each treatment, and subsequently analyzing their effects on the composition, architecture, as well as function of the remaining decellularized ECM.[68,101]

2.221.2.1. Physical Methods

To facilitate the decellularization of tissue, physical methods such as lyophilization, repeated freeze-thawing, sonication, direct pressure, and agitation may be used. The premise for each method employed is to disrupt the cell's plasma membrane resulting in cell lysis and removal from the tissue. These methods provide a direct and rapid means of decellularization. However, these methods typically need to be used in conjugation with chemical extraction treatments to increase their effectiveness.[40]

Table 2 Common decellularization methods and reagents

Method	*Mode of action*	*Effects on ECM*	*Examples of tissue/organ*	*References*
Physical				
Snap freezing & lyophilization	Intracellular ice crystal formation resulting in permeabilization of cell membrane	ECM is disrupted or fractured during rapid freezing	Ligament; cardiac valves; pericardium; bone matrix; amniotic membrane; embryoid bodies; liver	34–41
Repeated freeze–thaw			Heart valves leaflets; meniscus; ligament; nerve; embryonic chick knee; dermis; embryoid bodies	40,42–48
Mechanical force (delamination and pressure)	Pressure can burst cells and tissue layer removal eliminates cells	Mechanical force can damage ECM components	SIS; UBM; UBS; aorta; tendon; meniscus	16,49–52
Mechanical flow (agitation and perfusion)	Facilitates chemical exposure and removal of cellular debris; may lyse cells	Aggressive conditions may harm ECM components	Heart valves; bladder; heart; placenta; umbilical veins	17,19,53–59
Chemical				
Solvent extraction (ethanol, xylene, butanol, acetone)	Facilitates membrane lipid removal, specifically triglycerides and cholesterol	Prolonged exposure may induce collagen structural changes in the ECM	Blood vessels; heart valves; umbilical veins	12,56,60,61
Tri(*n*-butyl)phosphate	Organic solvent that disrupts protein–protein interactions	Variable outcome with cell removal and disruption to ECM	Articular cartilage; tendon; ligament	62–65
Alkaline and acidic treatments	Solubilizes cytoplasmic components of cells; disrupts nucleic acids	Potential oxidative damage to GAGs such as HA, as well as microscopic structural changes to collagen	SIS; UBM; UBS; blood vessels; gallbladder; embryoid bodies	50,60,66–68
Detergent extraction				
Nonionic detergents (Triton® X-100, Tween® 20, Tween® 80)	Disrupts lipid–lipid and lipid–protein interactions but leaves protein–protein interactions intact	Variable outcome dependent on tissue type	Ligaments; tendons; cartilage; aortic valves; embryoid bodies	62,63,65,68–70
Ionic detergents (SDS, sodium deoxycholate, Triton® X-200, lauroyl sarcosinate)	Solubilizes cytoplasmic and nuclear cellular membranes; tends to denature proteins	Variable outcome dependent on tissue type, detergent concentration, and treatment duration; potential loss of GAG content, collagen structural change, and change to mechanical integrity	Cartilage; ligament; tendon; pericardium; meniscus; heart valves; blood vessels; bladder; skin; placenta	17,33,53,62,63,71–82
Cationic detergents (CTAB)	Disrupts cellular membrane and solubilizes cellular content	Structural damage to ECM proteins	Nerve	83
Zwitterionic detergents (CHAPS, Empigen BB, SB-10, SB-16)	Exhibits properties of both nonionic and ionic detergents	Sufficient cell removal and minimal ECM disruption	Umbilical arteries; nerve	27,83,84
Hypotonic and hypertonic solutions	Cell lysis by osmotic shock	Effective at cell lysis but requires additional processing for removal of cellular debris	Bladder; blood vessels; aortic valves; meniscus; ligament	22,53,58,74,77,79,81
Enzymatic				
Trypsin	Serine protease, cleaves proteins at the C-side of Arg and Lys residues; chelating agents (EDTA) typically used with trypsin	Longer incubations may disrupt ECM structure and composition	Heart valves; blood vessels; pericardium	12–14,19,70,76,82
Endonucleases	Cleaves the interior phosphodiester bond of ribonucleotide and deoxyribonucleotide chains	Difficult to remove from the tissue and could invoke an immune response	Heart valves; pericardium; bladder; placenta; embryoid bodies	17,53,58,68,69,73,74,77,80,82
Exonucleases	Cleaves the terminal phosphodiester bond of ribonucleotide and deoxyribonucleotide chains			

Adapted and reprinted with permission from Gilbert W.; Sellaro L.; Badylak F. *Biomaterials* **2006**, *27*, 3675–3683. © Elsevier.

Snap freezing followed by lyophilization has been utilized to decellularize a variety of tissues prior to therapeutic application, including ligaments,[36,37,41] cardiac valves,[34] pericardium,[38,102] bone matrix,[35] amniotic membrane,[103] and more recently embryoid bodies.[40] Rapid freezing of the tissue or matrices results in intracellular ice crystal formation, disrupting the cellular membrane and thereby cell lysis. Subsequent removal of water molecules by freeze-drying may also facilitate removal of cellular debris. Freeze–thaw cycling is another physical technique consisting of submerging the tissue in liquid nitrogen (snap freezing) followed by room temperature thawing in a buffered aqueous solution. Multiple tissues have been decellularized by freeze–thaw cycling including peripheral nerve grafts,[43,92] meniscal tissue,[46,47,79] embryonic chick knees,[48] and human dermis.[42] In both techniques, the rate of temperature change needs to be optimized for each tissue or matrix in order to prevent damage to ECM components.[11]

Application of direct pressure is another physical technique,[11,16,49,51,52,104] but this technique is only effective for tissues that are not characterized by densely organized ECM (e.g., liver, lung); otherwise, the treatment may leave cellular debris behind thereby inducing potential immunogenic reactions.[11,78] Recently, supercritical carbon dioxide containing a small amount of ethanol has been used as an extraction medium to decellularize porcine aortas.[52] Physical separation or delamination of tissue layers is a common technique reported by the Badylak group[16,50,105,106] in creation of the small intestinal submucosa (SIS)-ECM as well as the urinary bladder submucosa (UBS) and urinary bladder matrix (UBM)-ECM. Delamination has proven to be an effective physical technique in decellularization of the tissue without disruption to the native ECM structure and architecture.[11,16,50,107,108] Mechanical agitation using a magnetic stir plate or an orbital shaker and the introduction of sonication are among other common physical techniques used in decellularization procedures.[11]

In many decellularization protocols, physical techniques are employed in conjugation with chemical treatments to assist in decellularizing the tissue. The latter strategies are largely based on passive diffusion, which require extensive washing steps to not only remove the cellular debris from the ECM, but also remove any residual chemical compounds. In addition, the optimal speed, volume of reagent, and length of agitation all affect the efficiency of decellularization, which in turn is dependent on the composition, architecture, and thickness of the tissue.[11,56] More recently in the literature,[17,54,56,57,59] the application of convective flow or perfusion has been commonly reported as an effective decellularization strategy, especially in thick tissues. For instance, Flynn *et al.* used a perfusion system to aid decellularization of human placenta,[17] while Ott *et al.* decellularized whole rat hearts using a modified Langendorff apparatus.[57]

2.221.2.2. Chemical Methods

A variety of chemical treatments can be used independently or in a multistep extraction process to decellularize tissues. As summarized in **Table 2**, the reagents used to decellularize different tissues can be generally categorized into solvents for extraction, alkaline or acidic detergents, hypotonic and hypertonic solutions, and enzymes.[11] The choice of reagent(s) is largely dependent on the suitability to effectively treat the tissue source, in terms of conserving the native ECM's biochemical and structural properties and also simultaneously removing the undesirable cellular elements.[68] It is important to recognize, however, that the extraction process may result in cell damage and death, which can consequently produce divergent secondary signals on implantation. For instance, capase found on the cell surface of apoptotic cells can degrade elastin, where the resulting peptides can signal through the elastin–laminin receptor in the presence of transforming growth factor β 1 (TGF-β1) to ultimately produce bone.[109] Therefore, as with each decellularization treatment, care must be taken to optimize the extraction process best suited for the tissue of interest.

2.221.2.2.1. Solvent extraction

Solvent extraction through the use of reagents such as ethanol,[12,56,60,61] xylene, and butanol[12] as well as acetone[56] has been reported to facilitate decellularization of blood vessels,[12,60] heart valves,[110] and umbilical veins.[56] Predominantly used in combination with other chemical treatments, this pretreatment has been reported to extract membrane-bound lipids such as phospholipids, triglycerides, and cholesterol while minimizing tissue calcification.[12,61] In comparison to proteins, the chemistry of the phospholipid molecules, for example, allows for greater solubilization by organic solvents. However, disruptions to the ECM structural components and biomechanical behavior have been observed post solvent extraction treatment.[12,61]

Tri(*n*-butyl)phosphate (TnBP) is another commonly used organic solvent, reported to aid in the extraction of cells from blood derivatives as well as lipid-enveloped viruses,[111,112] articular cartilage,[63] tendon,[62] and anterior cruciate ligament (ACL).[64,65] Unlike other solvents, TnBP disrupts protein–protein interactions.[11] To date, mixed outcomes on the effectiveness of cellular removal and disruption to the ECM with TnBP treatment have been reported. Decellularization of rat tail tendon with 1% TnBP for 48 h yielded complete removal of nuclear remnants and preserved the natural structure and mechanical properties of the tissue.[62] On the other hand, treatment of articular cartilage with 2% TnBP had a minimal effect on tissue decellularization but exhibited a decrease in GAG content and change in mechanical integrity in comparison to native tissue.[63] Similarly, decellularization of an ACL graft with a Triton–TnBP treatment showed equivalent levels of cellular extraction to that with Triton–sodium dodecyl sulfate (SDS) in the midsubstance of the graft; however, incomplete decellularization was observed at the femoral insertion.[65] Moreover, ACL treatment with TnBP preserved both the ECM structure and mechanical behavior of the tissue better than other extraction techniques, although disruption to the GAG content and collagen structure was reported.[64,65]

2.221.2.2.2. Alkaline and acid treatments

Alkaline and acidic treatments have been used to decellularize tissues such as SIS, UBM, UBS,[50,66] blood vessels,[60] the cholecyst wall (gallbladder),[67] and, more recently, mineralized human primary osteoblast-derived matrices.[113] Alkaline extraction procedures use alkaline salts such as those of sodium or

potassium as well as alkaline earth metals such as calcium.[60] Acidic treatments may involve the use of acetic acid, peracetic acid (PAA), hydrochloric acid, and sulfuric acid.[11] These treatments not only disrupt the cellular membrane but can also solubilize major cytoplasmic components of the cells (i.e., organelles), which aids in the removal of nucleic acids from the matrices.[11] Goissis and colleagues[60] devitalized small and large blood vessels from beagle dogs using a multistep process centered on an alkaline extraction process, and showed that the efficiency of cell removal is dependent on the segment and the type of blood vessel. Moreover, despite the harsh alkaline conditions used, no denaturation of the collagen matrix was found and the collagen and elastic fibers were preserved. On the other hand, Badylak *et al.*[50,66] have decellularized a variety of porcine tissues including SIS, UBM, and UBS using PAA at concentrations of ~0.10–0.15% (w/v).[11] The PAA treatment has been reported to effectively decellularize thin intact ECM matrices[11] while simultaneously disinfecting the matrices by penetrating into microorganisms and oxidizing microbial enzymes.[114,115] Despite the oxidative nature of PAA, the treatment has been found to retain both structural and functional molecules of the native ECM such as collagen,[16] sulfated GAGs (HA, heparin, HS, CS-A, and dermatan sulfate),[9,116] and various growth factors (vascular endothelial growth factor (VEGF), basic fibroblast growth factor (bFGF), TGF-β1).[9,116–118] However, oxidative damage to HA in SIS after PAA treatment[117] and microscopic changes to the structural integrity of collagen fibers are issues that have been raised in the literature.[50,116,117]

2.221.2.2.3. Detergent extraction

Detergents are water-soluble molecules that have the ability to incorporate themselves into the lipid bilayer of the cellular membrane. Consequently, they solubilize the lipid membrane by disrupting the lipid–lipid and lipid–protein interactions and encapsulate proteins within detergent micelles at certain concentrations.[11,119] A variety of detergent extraction techniques have been utilized to decellularize tissues, which can range from the use of nonionic, ionic, cationic, or zwitterionic detergents.[11,119] Differences in the size, charge, denaturing ability, and critical micelle concentration may determine the tissue penetration, membrane disruption, and pattern of protein–detergent interaction, all of which may ultimately influence the effect on the ECM.[119] Regardless of the type of detergent used in the decellularization protocol, steps must be taken to efficiently remove residual detergent from the matrices to avoid pronounced immune responses.[75,120]

2.221.2.2.3.1. Nonionic detergents

Nonionic detergents, such as octyl phenol ethoxylate (Triton® X-100), Tween® 20, and Tween® 80, are mild or nondenaturants capable of breaking lipid–lipid and protein–lipid interactions but leaving protein–protein interactions intact.[11,119] Triton® X-100 is the most widely studied nonionic detergent used to decellularize a variety of tissues such as ligaments,[65] tendons,[62] cartilage,[63] bladder,[24,53] nerve,[83] liver,[39] aortic valves,[69,70] blood vessels[121] and embryoid bodies.[122] However, the effectiveness of Triton® X-100 in terms of complete cellular and nuclear removal as well as preservation of ECM components is variable, depending on the nature of the tissue. For instance, similar cellularity and nuclear content to controls were observed after 1% Triton® X-100 treatment of carotid arteries[121] and tendons[62] while complete removal of cellular remnants from aortic valve leaflets has been observed with the same treatment.[70,74] Mixed results on collagen density and structure, GAG content, and mechanical integrity of tissues after Triton® X-100 treatment have also been reported. For example, Triton® X-100 treatment of aortic valves showed a reduction in the collagen density,[69,70] as well as loss of GAG content (especially CS) and loss of adhesion molecules, laminin, and fibronectin.[70] Conversely, treatment of ACL with Triton® X-100 showed no effect on the collagen and GAG content, as well as on mechanical properties. As such, the effectiveness of using a mild, nonionic detergent to decellularize largely depends on both the type of tissue as well as the subsequent decellularization treatments used.

2.221.2.2.3.2. Ionic detergents

Ionic detergents such as sodium dodecyl sulfate (SDS), sodium deoxycholate (SD), Triton® X-200, and more recently lauroyl sarcosinate (LS) are commonly used in decellularization protocols as they are effective in solubilizing both cytoplasmic and nuclear cellular membranes.[11] In general, ionic detergents are denaturants. They disrupt the noncovalent bonds within proteins, causing them to lose their native conformation,[119] and in terms of the ECM, potentially disrupt the integrity of collagen.[56]

In a number of extraction protocols, sufficient levels of cell removal from tissues such as cartilage,[63] tendon,[62] ligament,[22] skin,[72] and heart valves[74,76] have been achieved through the use of the surfactant SDS. As an amphipathic molecule, SDS effectively binds to proteins via its hydrophobic domain, resulting in an increased negative charge that can lead to both swelling of the tissue and destabilization of the collagen triple helical domain.[73,76] In the literature, there have been concerns about the use of SDS in extraction protocols because of its effects on collagen stability, potential toxicity, and retention within the matrix.[62,64,76,123] However, recent reports suggest SDS to be an effective decellularization agent with minimal ECM disruption but favorable cellular repopulation that can, in part, be linked to detergent concentration, treatment duration, and the nature of the tissue.[22,63,78,79,120,124] Gratzer *et al.*[22] found that residual SDS in decellularized porcine ACL tissue did not influence the viability and repopulation of autologous ACL fibroblasts. However, treatment with 1% SDS for 48 h significantly reduced GAGs levels and caused structural changes to collagen while no significant change in mechanical behavior was noted in the decellularized ACL tissue. On the other hand, Lichtenberg *et al.*[124] re-endothelialized decellularized ovine pulmonary valves post 0.5% SDS treatment, and not only maintained a confluent layer of endothelial cells under physiological pulmonary flow conditions, but also found preservation of the ECM structure and mechanical integrity of the decellularized scaffold to be comparable to that of the native tissue. Lastly, Elder *et al.*[63] found that the duration of SDS treatment in decellularizing articular cartilage determined the level of biochemical and ultrastructural change in the tissue. For instance, treatment with 2% SDS for 1 or 2 h resulted in a 33% reduction in DNA content but maintained the biochemical (i.e., GAG and collagen content) and biomechanical

properties of the tissues. In contrast, 2% SDS treatment for 6 or 8 h resulted in a greater reduction in DNA content, and significantly decreased both the GAG content and compressive properties of the tissue.

SD is another ionic detergent that is very effective in removing cellular remnant, but tends to have even more significant impact on the ECM structure than SDS.[11] The specific effect of SD on decellularized ECM is unclear to date[11] as it is typically used in conjunction with other decellularizing agents.[76,82]

2.221.2.2.3.3. Cationic detergents

In general, for decellularization, the class of cationic detergents is typically deemed to be that of the most cytotoxic as well as too strong detergents that cause structural proteins in the native ECM to denature.[83] Cetyltriethylammonium bromide (CTAB) is a cationic detergent used as part of a detergent-based decellularization method for nerve tissue. Although CTAB was found to be effective at removing cellular components from the nerve tissue, it was unable to preserve the ECM structure.[83]

2.221.2.2.3.4. Zwitterionic detergents

A variety of zwitterionic or amphoteric detergents have also been incorporated in decellularization methodologies, such as 3-[(3-cholamidopropyl)dimethylammonio]-1-propanesulfonate (CHAPS), as well as sulfobetaine-10 (SB-10) and -16 (SB-16). Zwitterionic detergents exhibit properties of both nonionic and ionic detergents, but have a greater tendency to denature proteins than nonionic detergents.[11] In the literature, zwitterionic detergents are typically used in combination with an ionic detergent that allows for tighter packing of the detergent micelles.[83] More specifically, the use of both a zwitterionic and an ionic detergent allows the neutrally charged zwitterionic molecules to intersperse between the ionic molecules, lowering the repulsion between head groups and thus, increasing the packing density of the micelles. A tighter packing density is presumed to result in smaller, more robust micelles that are able to better penetrate into the tissue and mediate the removal of more hydrophobic materials (i.e., cell membranes).[83] Zwitterionic detergents have been used in decellularization strategies for nerves[83] and umbilical arteries.[27,84] In general, zwitterionic detergents are considered to be mild detergents as they yield sufficient cell removal and preserve the ECM to some extent.[11,83]

2.221.2.2.4. Hypotonic and hypertonic treatment

To enhance the action of detergents or as a measure on its own, osmotic shock may be incorporated into the decellularization strategy as a means to effectively lyse cells. Osmotic shock has been used in decellularization strategies for a number of tissues including bladder,[53,58,77] blood vessels,[81] placenta,[17] aortic valves,[74] meniscus,[79] and ligament.[22] Its introduction generally involves treatment with a hypotonic solution followed by treatment with a hypertonic solution. Osmotic lysis with a hypotonic solution causes the cells to swell and burst. Swelling of the cell, caused by the inward movement of water, may also enhance the uptake of detergents into the cellular membrane. The opposite effect occurs in a hypertonic solution where water moves outward from the cell causing cellular dehydration and shrinkage, which aids in cellular death and detachment from the matrix.[119] Although this strategy is highly effective at lysing cells, additional processing is required to remove the resultant cellular debris from the tissue, especially residual nucleic acids. Therefore, an additional nuclease enzyme digestion step typically follows the osmotic shock treatment.[11,119]

2.221.2.2.5. Enzymatic treatment

Enzymatic treatments, involving proteases and nucleases, are incorporated into the decellularization strategy to aid in the removal of cellular proteins and nucleic remnants. Trypsin is one of the most commonly used proteolytic enzymes in decellularization methodologies, and is typically used in combination with the calcium chelating agent, ethylenediaminetetraacetic acid (EDTA).[11,119] EDTA is used to inactivate intracellular proteases that are released by the trypsinized cells and are capable of degrading the ECM constituents. Trypsin is a serine protease that cleaves proteins at the carboxyl side of lysine and arginine residues except when followed by proline, as is the case with collagen. It is predominantly used in decellularization protocols to aid in the detachment of cells from the surrounding ECM proteins by disrupting protein interactions, resulting in a more open matrix that can facilitate the removal of cellular debris.[11,119] Trypsin has been part of enzymatic treatments for decellularization of a number of tissues including heart valves,[13,19,70,76] vascular grafts,[12,14] and pericardium.[82] Nonetheless, variable cell loss has been reported in the literature following trypsin treatment.[13,19,76] Schenke-Layland and colleagues reported insufficient cell removal from pulmonary valves but preservation of ECM components (GAG, collagen, and elastin) following shorter trypsin-EDTA incubation times (5 and 8 h). At a longer incubation period (24 h), complete cellular removal was reported. However, the ECM biochemical composition (especially in terms of *o*-sulfated GAGs as well as acid and salt soluble collagens) and ECM integrity were negatively impacted in a time-dependent manner.[19] On the other hand, complete cellular removal and well-conserved and arranged collagen and elastin fibers were found by Teebken *et al.* who used a multistep enzymatic extraction method with trypsin-EDTA, deoxyribonuclease (DNase), and ribonuclease (RNase) to decellularize thoracic aortas.[14] Therefore, the nature of the tissue as well as the duration of enzymatic digestion must be taken into consideration when incorporating trypsin-EDTA into a decellularization strategy.[11,12,76]

Nucleases such as endonucleases and exonucleases may also be incorporated in enzymatic treatments.[11] DNases and RNases have been commonly used in decellularization methodologies in combination with detergent extraction treatments to aid in the removal of nuclear debris. Many of the nucleases used in decellularization protocols are extracted from bovine tissues running the risk for prion disease transmission.[11] An alternative may be to use recombinant nucleases. As with protease treatment, the duration of nuclease treatment must also be optimized in order to effectively remove cellular antigens without harming the ECM composition and structure.[68,122] As such, decellularization protocols using either proteases or nucleases must incorporate effective steps for the removal of residual enzymes in the tissue prior to *in vivo* implantation.

2.221.2.3. Additional Reagents

Lysing of cellular membranes during decellularization may also release a number of cellular proteases into the environment, causing additional, yet unintentional damage to the ECM. Moreover, maintaining the tissue above 4 °C for any length of time after removal can result in tissue breakdown.[109] In order to account for these disruptions, a number of lengthy decellularization processes are run in cooler conditions and include protease inhibitors such as phenylmethylsulfonylfluoride (PMSF), aprotonin, and leupeptin.[11] In addition, decellularization may be conducted in buffered solutions of pH 7–8, as proteases function optimally in acidic conditions.

Lastly, many decellularization protocols include antibiotic solutions such as those of penicillin, streptomycin, or amphotericin to prevent bacterial contamination.[11] However, special attention must be taken to ensure that residual antibiotic does not remain in the decellular matrix prior to *in vivo* implantation; otherwise regulatory approval for clinical use will be difficult.[11]

2.221.2.4. Additional Processing

Following physical, chemical, and/or enzymatic treatments, decellularized ECM scaffolds are typically disinfected and/or terminally sterilized before being used or stored. Decellularized scaffolds are commonly disinfected using oxidizing agents such as hydrogen peroxide, sodium peroxide, PAA, or an ethanol–peracetic acid solution (PES).[25,50,114,116,125] However, long exposure periods of these disinfectants may cause oxidative damage to collagen fibers and GAGs, ultimately reducing the structural integrity of the matrix.[26,50,116] Prior to *in vivo* implantation, decellularized scaffolds are also subjected to terminal sterilization usually by ethylene oxide (ETO) treatment, gamma irradiation, or electron beam irradiation.[25,50,117,126] Several studies have shown that these sterilants can have detrimental effects on the mechanical behavior of the scaffolds. However, certain sterilants can cause more significant damage to the matrix than others. For instance, Freytes and colleagues found that in comparison to the ionizing radiation treatments, ETO treatment had the least detrimental effect on the mechanical properties of a lyophilized form of the UBM.[25] Moreover, they also suggested that the overall effect of sterilization depends on the relative amounts, density, and distribution of the ECM constituents, as well as dosage of the sterilant.[25]

Decellularized ECM scaffolds may also take on a variety of different forms upon additional processing steps to not only improve their shelf life but also expand their clinical applicability, as recently reviewed elsewhere.[10] For instance, decellularized scaffolds can be hydrated or dehydrated,[127] comminuted into a powdered ECM form,[128,129] or solubilized into a liquid or gel form.[130,131] **Table 3** summarizes some of the commercially available decellularized scaffolds that have been packaged and stored under various conditions, including hydrated (Pelvicol™, Bard), laminated and vacuum dried (Restore™, Depuy Orthopedics), and freeze-dried (Bard® Dermal Allografts, Bard).[7,10,127] Storage of processed ECM scaffolds in a hydrated state helps to maintain the native tissue architecture. However, continuous leaching and/or hydrolysis of structural (i.e., collagen) and nonstructural (i.e., growth factors) components may disrupt the functionality and shelf life of the scaffold.[10,127] Dehydration of processed ECM scaffolds, by lyophilization or by vacuum pressing, may minimize hydrolytic degradation during storage. However, dehydration may also result in scaffold ultrastructural changes that can consequently affect cellular attachment, infiltration, and remodeling.[10,127] Powdered or gelated forms of decellularized scaffolds can potentially conform to any 3D shape as well as have the capability of being delivered to a site of interest by minimally invasive techniques.[129,130] Regardless of the manufacturing process, the effect of storage duration and temperature on the scaffold's structural and functional properties must also be taken into consideration in order to have a therapeutically relevant material.[26]

2.221.2.5. Important Considerations

2.221.2.5.1. Characterization of decellularization

Decellularization strategies aim to remove all cellular debris while preserving the composition, mechanical integrity, and biological activity of the remaining ECM. Therefore, decellularization efficiency and reproducibility are characterized not only by the cellular constituents that are removed, but also by the desired components of the ECM that are retained. In this chapter, there is very little information comparing the effectiveness of different decellularization methods in treating a tissue of interest.[82] Nonetheless, it is important to recognize that the decellularization process needs to be optimized for each harvested tissue to account for tissue variability. A number of different techniques can be used to characterize a decellularized scaffold that in general fall under the following categories: (a) histological, immunohistochemical, and biochemical assessment; (b) scaffold architecture assessment; (c) biomechanical assessment; (d) biofunctionality assessment; and (e) microbiological assessment, as summarized in **Table 4**.

A simple yet effective initial test that is commonly performed to detect any residual nucleated cells or cell fragments throughout the decellularization process is the histological stain Hematoxylin and Eosin (H&E). A variety of other histological stains such as Masson's Trichrome, Movat's Pentachrome, and methyl green-pyronine (MGP) can be used to evaluate the intracellular components of the decellularized tissue, as depicted in **Figure 1** for a PDM.[17] Immunohistochemical assessment for collagen, laminin, actin, and fibronectin can be used to gain a qualitative understanding of the biological composition, while a combination of biochemical assays such as for DNA content, GAG content, and/or collagen content can be used to quantify the biological composition of the decellularized tissue in comparison to its native form. Assessment of both scaffold ultrastructure and biomechanical behavior provides insight into the structural integrity of the decellularized scaffold. Assessment of collagen denaturation temperature and tissue shrinkage temperature has also been routinely performed to determine the structural stability of collagen.[60,73,74,82] The biofunctionality of the decellularized scaffold can be evaluated through *in vivo* and/or *in vitro* biocompatibility markers such as cytotoxicity and cellular infiltration.[17,53,80,120,133] Lastly, prior to their use, decellularized scaffolds are commonly disinfected and/or terminally sterilized; therefore, the effectiveness of the sterilization procedure should be evaluated against microbial viability and growth.[77,120]

Table 3 Commercially available devices composed of naturally derived extracellular matrix

Product	*Company*	*Material*	*Chemical modification*	*Form*	*Use*
Acell Vet®	Acell, Inc.	Porcine urinary bladder	Natural	Powder	Treatment of canine arthritic hips
AlloDerm®/Cymetra®	LifeCell Corp.	Human dermis	Natural	Dry sheet/ gel	Hernia, abdominal wall repair and breast reconstruction, soft tissue defects
AlloPatch HD™	MTF Sports Medicine	Human fascia lata	Natural	Dry sheet	Tendon augmentation
Axis™ dermis	Mentor	Human dermis	Natural	Dry sheet	Pelvis organ prolapse
Bard® Dermal Allograft	Bard	Cadaveric human dermis	Natural	Dry sheet	Pelvic floor reconstruction
CardioGRAFT®	LifeNet Health	Human cardiac tissue	Natural		Cardiovascular repair
CuffPatch™	Arthrotek	Porcine SIS	Cross-linked	Hydrated	Soft tissue reinforcement
CryoValve® SG	CryoLife, Inc.	Human pulmonary valve	Natural	Hydrated	Cardiac valve repair
DurADAPT™	Synovis Life Technologies, Inc.	Equine pericardium	Cross-linked	Dry sheet	Repair dura matter
Dura-Guard®	Synovis Life Technologies, Inc.	Bovine pericardium	Cross-linked	Hydrated	Spinal and cranial repair
Durasis®	Cook SIS	Porcine SIS	Natural	Dry sheet	Repair dura matter
Durepair®	TEI Biosciences	Fetal bovine skin	Natural	Dry sheet	Repair of cranial or spinal dura
FasLata®	Bard	Cadaveric fascia lata	Natural	Dry sheet	Urological repair
FlexHD®	Ethicon 360, Inc.	Human dermis		Hydrated	Connective and soft tissue reinforcement
Graft Jacket®	Wright Medical Tech	Human dermis	Natural	Dry sheet	Foot ulcers
MatrixP/ MatrixP plus™	AutoTissue^{GmbH}	Porcine pulmonary valve	Natural		Pulmonary valve reconstruction
MatriStem®	ACell, Inc.	Urinary bladder matrix	Natural	Dry sheet or powder	Soft tissue reconstruction
Oasis®	Healthpoint	Porcine SIS	Natural	Dry sheet	Partial and full thickness wounds & superficial and second degree burns
OrthADAPT™	Synovis Life Technologies, Inc.	Equine pericardium	Cross-linked	Dry sheet	Rotator cuff and Achilles tendon repair
Pelvicol®	Bard	Porcine dermis	Cross-linked	Hydrated	Pelvic floor reconstruction
Peri-Guard®	Synovis Life Technologies, Inc.	Bovine pericardium	Cross-linked	Dry sheet	Pericardial and soft tissue repair
Permacol™	Tissue Science Laboratories	Porcine dermis	Cross-linked	Hydrated	Soft connective tissue repair
PriMatrix™	TEI Biosciences	Fetal bovine skin	Cross-linked	Hydrated	Wound management
Prima™	Edwards Lifesciences	Porcine heart valve	Cross-linked	Dry sheet	Valve reconstruction
ProPatch®	CryoLife, Inc.	Bovine pericardium	Natural	Hydrated	Soft tissue reconstruction
Restore® Orthobiologic	DePuy Ortho Tech	Porcine SIS	Natural	Dry sheet	Soft tissue treatment
Stratasis®	Cook SIS	Porcine SIS	Natural	Dry sheet	Urinary incontinence treatment
Strattice™ (formerly XenoDerm)	LifeCell Corp.	Porcine dermis	Natural	Dry sheet	Soft tissue reinforcement
SurgiMend™	TEI Biosciences	Fetal bovine skin	Natural	Dry sheet	Soft tissue membrane repair
Surgisis®	Cook SIS	Porcine SIS	Natural	Dry sheet	Soft tissue repair and reinforcement
Suspend™	Mentor	Human fascia lata	Natural	Dry sheet	Urethral sling
TissueMend®	TEI Biosciences	Fetal bovine skin	Natural	Dry sheet	Rotator cuff reconstruction
Vascu-Guard®	Synovis Life Technologies, Inc.	Bovine pericardium	Cross-linked	Dry sheet	Vascular reconstruction
Veritas®	Synovis Life Technologies, Inc.	Bovine pericardium	Cross-linked	Hydrated	Soft tissue repair
Xelma™	Molnlycke	Amelogenins in propylene glycol alginate and water		Gel	Venous leg ulcer repair
Xenform™	TEI Biosciences	Fetal bovine skin	Natural	Dry sheet	Soft tissue reenforcement
Zimmer Collagen Patch®	Tissue Science Laboratories	Porcine dermis	Cross-linked	Hydrated	Rotator cuff repair

Adapted and reprinted with permission from Badylak, S. F.; Freytes, D. O.; Gilbert, T. W. *Acta Biomater*. **2009**, *5*, 1–13. © Elsevier.

2.221.2.5.2. Host response to decellularized scaffolds

Decellularization aims to remove cellular antigens that are recognized as foreign by the host in response to the ECM-derived scaffold, which if unsuccessfully decellularized can ultimately result in an adverse inflammatory response or immune-mediated rejection on implantation.[7,10,136] With decellularized scaffolds, the host is presented with a different scenario from what is normally encountered with autogenous, allogenous, or xenogeneic whole organ grafts. In a typical tissue graft, immune recognition of cellular antigens occurs

Table 4 Summary of decellularization characterization techniques

A. Histological, Immunohistochemical, Biochemical Assessment	
Histological evaluation:	17,58,59,75,80,82
Hematoxylin and Eosin (H&E) – detects residual nucleated cells or cell fragments	
Masson's Trichrome – characterizes collagen structure	
Van Gieson – differentiates between collagen and elastin	
Miller's Elastin stain – detects elastin	
Picrosirius Red stain – detects collagen	
Hoechst – detects DNA	
Methyl Green-Pyronine (MGP) – detects DNA and RNA	
Movat's Pentachrome – detects collagen, elastin, nuclei, GAGs	
Alizarin stain – detects calcification	
Gomori Trichrome stain – detects connective tissue	
Herovici stain – discriminates between collagen type I and III	
Immunohistochemical evaluation:	17,58,65,70,79
Various markers – collagen type I, III, and IV; laminin; chondroitin sulfate; peripherin; van Willebrand factor; fibronectin; α-Gal; major histocompatibility complex (MHC) molecules	
Biochemical evaluation:	11,12,19,22,27,40,59,63,68,73–75,77,80,124
DNA quantification – Hoechst; DAPI; propidium iodide; PicoGreen	
Total protein content – Bradford method; Bicinchoninic acid	
Collagen content – Hydroxyproline assessment; Sircol Assay	
Denatured collagen content – Hydroxyproline assessement post digestion	
GAG content – Dimethylene blue; Blyscan Assay	
Elastin content – Fastin Elastin Assay, Hydroxyproline assessment post digestion	
Triglyceride content: Triglyceride SL Assay	
B. Scaffold Ultrastructure Assessment	
SEM, TEM, Near-infrared multiphoton laser scanning microscopy	60,73,82,132
DSC – collagen denaturation temperature, tissue shrinkage temperature	
C. Biomechanical Assessment	
Uniaxial tensile properties	25,50,59,73,77,80,130
Biaxial tensile properties	
Viscoelastic behavior	
D. Biofunctionality Assessment	
In vivo/in vitro biocompatibility – cytotoxicity, cellular infiltration	17,53,80,120,133–135
E. Microbiological Assessment	
Effectiveness of sterilization – detection of microorganism (bacterial/fungi) viability and growth	77,120

followed by the production of proinflammatory mediators and cytotoxicity, ultimately resulting in organ rejection.[8,137] However, in the case of the decellular scaffold, only the constituent proteins of the ECM and their degradation products are present, eliciting a different inflammatory and immunologic response. Unlike whole organ transplantation, the mechanisms of the host immune response to allogeneic or xenogeneic decellular scaffolds are neither well studied nor well understood.[137] In the literature, decellularized scaffolds have been noted to be immunologically tolerated as allografts for dural or dermis,[138] heart valve,[13,139] and nerve[28,91] replacement. However, concerns over the use of decellular xenogeneic grafts have been raised.[139–143] A comprehensive analysis of the immune response to biologic materials has been recently reviewed by Badylak and Gilbert; therefore, the reader is directed to this literature for a more thorough discussion.[136]

In brief, one of the major obstacles facing transplantation of living animal tissue to humans (i.e., xenotransplantation) is the interaction between the human natural galactose-α-1,3-galactose antibody (anti-α-Gal) and the α-Gal epitope (Galα1-3Galβ1-4GlcNAc-R), the latter being found in high density as a cell-surface molecule in nonprimate mammals and New World monkeys.[144,145] In humans, apes, and Old World monkeys, the α-Gal epitope is not expressed because of two frameshift mutations in the α1-3-galactosyltransferase gene. Instead, they produce large amounts of anti-Gal antibodies (Ab) constituting approximately 1% of circulating immunoglobulins (Ig) such as IgG, IgM, and IgA, which consequently mediate hyperacute or delayed rejection of xenotransplants.[140,145,146] A number of studies have attempted to identify and/or quantify the presence of the α-Gal epitope post decellularization including in porcine medial meniscus,[79] porcine heart valves,[143] porcine pericardium,[141] and porcine SIS.[147] In the decellularized scaffold of porcine pericardium, the decellularization process was able to completely remove the α-Gal epitope, some of which incorporated the use of α-galactosidase to aid in xenogeneic antigen removal.[141] In contrast, porcine SIS has been found to contain small amounts of the α-Gal epitope,[147] but its presence was unable to either activate the complement pathway in human plasma or influence its ability to serve as a bioscaffold for tissue remodeling following implantation.[148] More specifically, implantation of SIS was found to elicit an immune response but the response was restricted to the Th-2 pathway and not to the Th-1 pathway, which allowed acceptance and remodeling of the xenogeneic graft.[149]

Another area of concern with decellular xenogeneic grafts, in particular porcine grafts, is the presence of porcine DNA

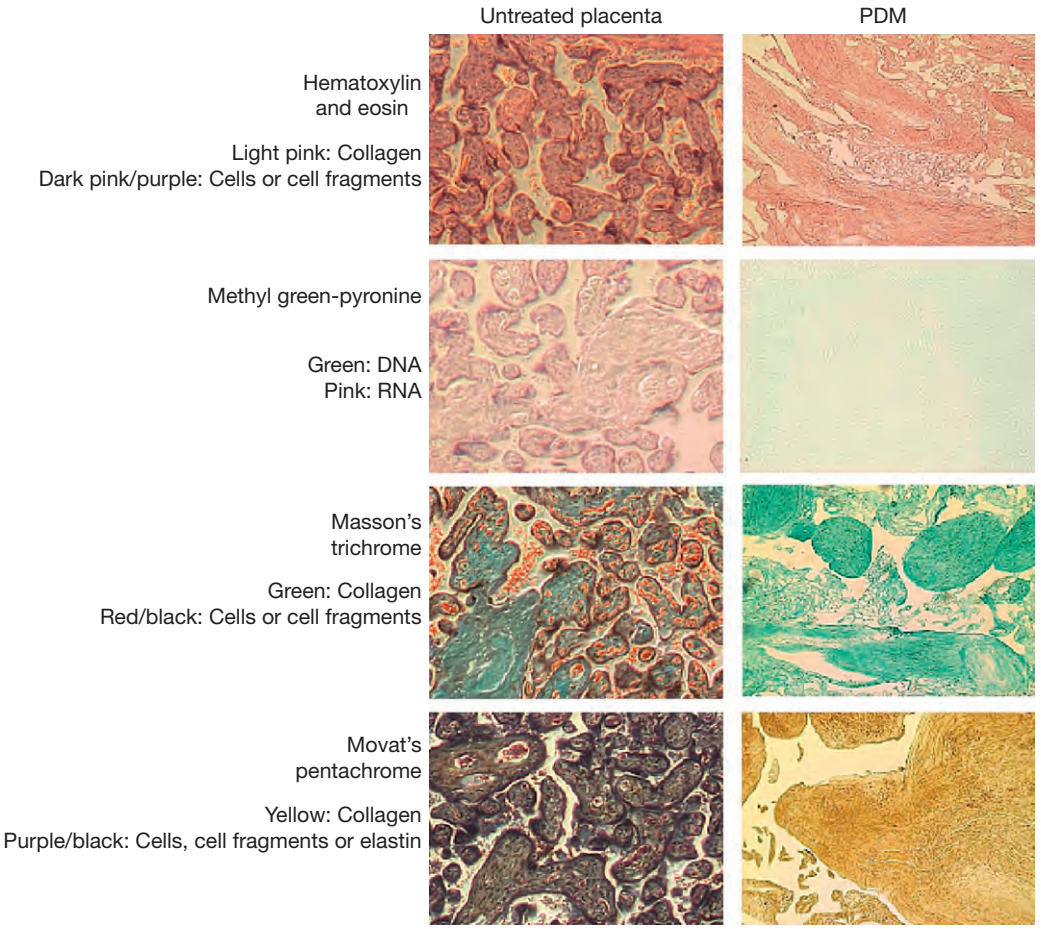

Figure 1 Histological assessment of placental decellular matrix (PDM) following the completion of decellularization, and untreated placenta. Hematoxylin and Eosin, Masson's trichrome, and Movat's pentachrome stainings indicate that there are no cells or cellular debris in the PDM following processing. The MGP staining shows that the PDM is free of residual RNA and DNA. Original magnification × 50. Adapted and reprinted with permission from Flynn, L.; Semple, J. L.; Woodhouse, K. A. *J. Biomed. Mater. Res. A* **2006**, *79*, 359–369. © Wiley InterScience.

remnants. It has been suggested that these remnants may be the cause of 'inflammatory reactions' following implantation in orthopedic applications.[150] However, a number of commercially available decellularized scaffolds such as Restore® (porcine SIS), GraftJacket™ (human dermis), and TissueMend™ (bovine dermis) contain trace amounts of DNA remnants.[150–152] In a recent study by Gilbert and colleagues, it was found that in all of the decellularized products investigated, small amounts of remnant DNA were present. However, the remaining DNA was present as small fragments (<300 bps) in most of the scaffolds with the exception of GraftJacket™ that contained full DNA strands.[152] Even with the most rigorous decellularization protocol, complete cellular removal is very unlikely.[152] Nonetheless, despite the presence of DNA remnants, the investigated commercially available decellularized scaffolds have been clinically effective for their intended applications.[136,152]

2.221.3. Origin of Decellularized Scaffolds and their Applications

Decellularization of tissues has yielded a variety of naturally derived decellular matrices, many of which are commercially available to treat an assortment of conditions such as rotator cuff repair, bladder repair, and spinal and cranial repair, as listed in Table 3. Decellularized scaffolds have a rich history and this section will highlight the origin of some tissues used to produce decellularized matrices and their applicability to tissue engineering.

2.221.3.1. Small Intestine

SIS is a resorbable xenogeneic bioscaffold derived from porcine small intestine, as shown in Figure 2.[105] SIS is prepared by mechanically removing the tunica mucosa, serosa, and tunica muscularis from the inner and outer surfaces of the intestine. The material is thoroughly rinsed in water, treated with peracetic acid, and then rinsed with buffered saline or water to yield a neutral pH. The resultant thin, translucent matrix (0.1 mm wall thickness) is composed primarily of 90% collagen (mostly collagen type I), fibronectin, laminin, proteoglycans (decorin), glycoproteins (biglycan and entactin), GAGs (HA, heparin, HS, CS-A, CS-C, dermatan sulfate), and growth factors (bFGF, VEGF, TGF-β).[10,105] This milieu of structural and functional molecules establishes a unique 3D scaffold that may assist in cell migration, cell-to-cell interactions, as well as cell

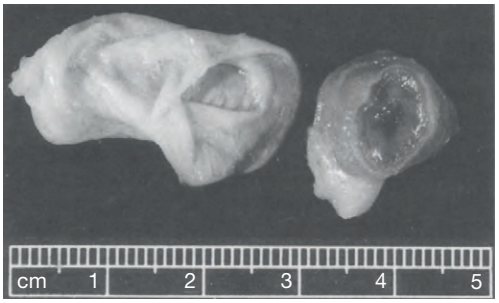

Figure 2 A cross section of intact small intestine with an attached piece of mesenteric adipose tissue (about 7 O'clock position) is shown on the right side of this figure. The tissue on the left is a longitudinal view of the SIS graft material after the superficial mucosa, the serosa and mesenteric connective tissue, and the muscularis externa have been removed. This material is very flexible and strong and is partially transparent when viewed against the light. Reprinted with permission from Badylak, S. F.; Lantz, G. C.; Coffey, A.; Geddes, L. A. *J. Surg. Res.* **1989**, *47*, 74–80. © Elsevier Ltd.

growth and differentiation during the regenerative process. The exact cellular mechanisms involved in remodeling following SIS implantation are not completely understood. However, the remodeling process has been strongly associated with angiogenesis, cell migration, and differentiation, and deposition of extensive ECM.[9] SIS grafts also have the ability to rapidly and completely degrade within a short term following implantation.[32,153,154]

The capacity of SIS to induce site-specific *in vivo* cellular repopulation and regeneration without *in vitro* cell seeding in a variety of applications has been well documented throughout the literature, as summarized in **Table 5**. Despite its xenogeneic nature, implanted SIS grafts are capable of surviving without signs of rejection in a number of animal systems including rat, mice, dog, and rabbit as well as in human patients.[7,136,140,147]

Early studies found SIS to function well as arterial and venous grafts with rapid replacement by native tissue.[105,156,157] Despite SIS's significant potential as vascular grafts, challenges of endothelialization and long-term vascular patency rates (>18 months) have been raised.[105,156,183] SIS has also been extensively used in the genitourinary system. Kropp *et al.*[108,171] found successful histological and functional regeneration of both rodent and canine bladders using SIS in a partial (40%) cystectomy model. For instance, at 15 months postoperative, histological analysis of the SIS augmented bladders showed significant regeneration of all three major layers of the bladder wall (urothelium, smooth muscle, and serosa) with no evidence of scar formation. *In vitro* contractility studies on SIS regenerated bladder strips demonstrated that the contractile activity of the augmented bladder tissue matched that of the native tissue. Similarly, *in vitro* tensile testing demonstrated no significant differences in the stress–strain properties of the graft tissue versus native bladder. The regenerated bladders also showed functional nerve regeneration and innervation comparable to native bladder.[171,172] Nonetheless, recent SIS studies have been inconsistent with regard to bladder regeneration.[184,185] For instance, significant morphological and histological differences between distal and proximal segments of SIS in bladder regeneration and calcification within the regeneration bladder have been observed.[184,185] Larger SIS grafts in a subtotal cystectomy (90%) model were unable to induce the same quality and quantity of bladder regeneration as previously observed with a partial (40%) cystectomy model.[186] Lastly, long-term bladder reconstitution with SIS augmented bladders has shown variable outcomes with regard to fibrosis, capacity, and compliance.[187–189]

Table 5 Applications of SIS in tissue engineering

Application	*Model*	*References*
Vascular	Canine, porcine	105,155–161
Cardiac	Canine, porcine	162–164
Dura mater	Rodent, canine	165,166
Abdominal wall	Canine, rodent	167,168
Bladder	Rabbit, canine, rodent	108,169–173
Bowel	Canine	174
Esophagus	Canine	175
Tendon	Canine, rabbit	107,176
Ligament	Canine	177
Cartilage (Meniscus)	Rabbit, canine	178–180
Dermal	Rodent	168
Bone	Rodent	181,182

Despite mixed results with certain applications of SIS grafts between various studies, a multitude of positive clinical outcomes have been reported. In addition, as of 2007, more than one million human patients have received an SIS graft to reconstruct a variety of tissues.[7] To date, the reasons for the disparate results are unknown but may be related to patient selection, surgical technique, and/or lack of our understanding regarding optimal use of an inductive scaffold for reconstruction of certain tissues.[7]

2.221.3.2. Dermis

Decellularized dermal tissue or acellular dermal matrix (ADM) can be derived from full or split-thickness skin from which the cellular components (keratinocytes, sweat glands, sebaceous glands, fibroblasts, vascular endothelium, and smooth muscle) are removed or extracted.[135] Studies with an ADM, AlloDerm® (LifeCell Corp.), processed from banked human cadaver skin have shown the material to be safe and efficacious in a variety of surgical procedures.[190] These procedures include treatment of full-thickness burns,[135,191] use as a substrate for oral resurfacing and periodontics,[192] a substrate for dural replacement,[190] a small-caliber vessel substitute,[193] as well as a soft tissue filler in plastic surgery.[194,195] A porcine equivalent of AlloDerm®, XenoDerm (LifeCell Corp.), has also shown efficacy as a viable dura substitute in a mini-pig model.[138] In both cases, porcine and human dermis are decellularized by first removing the epidermis by incubating the skin in 1 M sodium chloride (NaCl) at 37 °C for 8 h. Dermal fibroblast and epithelial cells are then removed by incubating the material in 2% SD containing 10 mM EDTA at room temperature overnight. The dermis is then cryoprotected with a combination of 35% maltodextrin and 10 mM disodium-EDTA and packaged as a freeze-dried sheet until it is rehydrated at the time of surgery.[138,190] This decellularization process has shown to reduce major histocompatability complex (MHC) Class I and Class II molecules, as well as preserve the normal architecture of the dermis.[138,190,196] Decellularized dermis has been noted to be

rich in collagen type I, type IV, and type VII as well as in elastin content, providing the graft with favorable elastic properties.[183] Grafted acellular dermal matrix has also been shown to support fibroblast infiltration, neovasculation, and epithelialization in the absence of an inflammatory response.[135]

A number of other methods have been attempted to decellularize dermal tissue using a combination of extraction (i.e., Triton® X-100, SDS) and enzymatic (i.e., trypsin, dispase, DNase/RNase) treatments resulting in varying degrees of decellularization efficiency.[72,197–200] For instance, Walter *et al.* prepared an ADM by two different methods using either dispase followed by Triton® X-100 treatment (dispase–Triton) or hypertonic NaCl solution followed by SDS (NaCl–SDS) treatment. Both methods completely removed the epidermis and most cellular components from the dermis while preserving the basic dermal architecture. However, the NaCl–SDS method retained a greater amount of cell-surface antigens as well as ECM components in comparison to the dispase–Triton method.[200] Moreover, despite the clinical effectiveness of allogeneic decellularized dermis, challenges such as limited availability of cadaver skin, high cost of commercially available human ADM, and the risk of disease transmission (i.e., Cruetzfeldt–Jakob disease) exist.[197,198] Lastly, variable outcomes have been reported in the literature regarding the histological and biocompatible differences between ADM xenografts and allografts,[197,198,201] warranting further investigation into the underlying mechanisms.

2.221.3.3. Urinary Bladder

The bladder is a soft tissue organ and despite its relative structural simplicity, it is one of the most distensible and strongest muscles in the body.[202] Early work by Badylak *et al.* showed promising results for esophageal repair using UBS produced by mechanical delamination, resulting in only the tunica submucosa.[175] More recently, decellularized bladder tissue, in the form of UBM, has been used for esophageal repair[203,204] as well as for treatment as a cardiac patch,[162,164,205,206] and thoracic wall repair,[207] displaying great potential for tissue restoration. UBM is prepared by first trimming the residual external connective tissue and soaking the urothelial layer in saline before the remaining bladder tissue is mechanically delaminated to remove the epithelium, serosa, muscularis externa, and the tunica submucosa. The remaining basement membrane of the tunica mucosa and the subjacent tunica propria, collectively termed UBM, is disinfected in a PES solution followed by a saline solution rinse.

Pioneering work by Tanagho[208–211] and Atala,[24,212,213] has driven the use of decellularized bladder tissue to a number of urological applications such as urethral, ureteral, bladder wall, and vaginal replacement, as shown in **Figure 3**.[214] Tanagho and colleagues[208,215–219] decellularized bladder tissue, termed bladder acellular matrix graft (BAMG), according to an adapted methodology described by Meezan *et al.*[33] The decellularization process consisted of a combination of hypotonic cell lysis, DNase digestion, and lipid membrane solubilization by an anionic detergent. This process has been applied to a variety of species' bladder tissue such as hamster, rabbit, dog, rat, pig, and human bladder tissue, and subsequently evaluated for bladder regeneration in homologous or heterogenous bladder augmentation. Early studies showed promising results of morphologic and functional rat bladder regeneration following homologous BAMG augmentation cystoplasty.[208,209,218] Findings by Sutherland *et al.* confirmed these results with a similar rat BAMG homologous *in vivo* model.[220] However, concerns of bladder stone formation and clinical relevancy were raised over the rat model. Subsequently, homologous BAMG augmentation in a canine model was performed and showed that the augmented bladders were functionally compliant and closely resembled native bladder with only minimal scar formation.[219]

Work in our own and collaborator's laboratory[53,55,58] decellularized porcine bladder tissue, termed bladder acellular matrix (BAM), using a multistep detergent-enzymatic extraction process originally established by Wilson *et al.*[99]

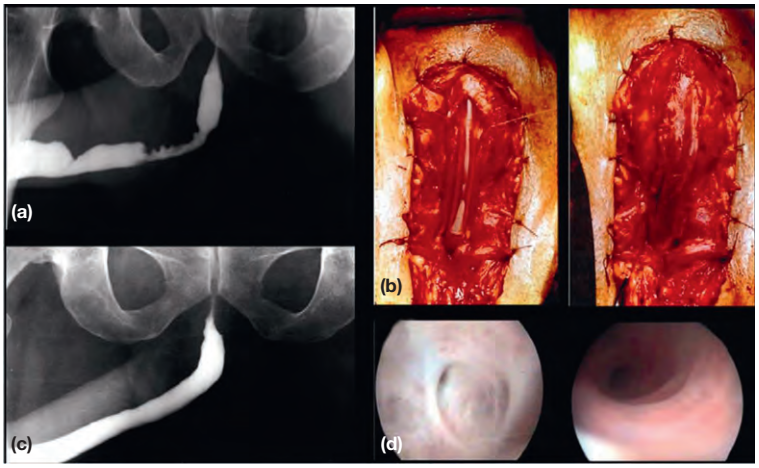

Figure 3 Tissue engineering of the urethra using an acellular collagen matrix obtained and processed from porcine bladder submucosa. (a) Representative case of a patient with a bulbar stricture. (b) During the urethral repair surgery, strictured tissue is excised, preserving the urethral plate on the left side, and matrix is anastamosed to the urethral plate in an onlay fashion on the right. (c) Urethrogram 6 months after repair. (d) Cystoscopic view of urethra before surgery on the left side, and 4 months after repair on the right side. Reprinted with permission from Atala, A. *Curr. Opin. Biotechnol.* **2009**, *20*, 575–592. © Elsevier Ltd.

to decellularize small-diameter blood vessels. Initial work demonstrated that BAM, used in an *in vivo* short-term (12 week) homologous model of bladder augmentation, promoted the ingrowth of urothelium, smooth muscle, and blood vessels. By 12 weeks postoperatively, the augmented bladders also exhibited capacity and compliance comparable to normal bladders.[58] However, in a follow-up study evaluating BAM at a longer time frame (22 weeks), histological results were less encouraging indicating a fibroproliferative response resulting in gross graft contracture and decrease in elasticity. As with many decellularized scaffolds, the mechanisms promoting regeneration with restoration of bladder tissue function have not been fully elucidated. A desire to understand the dynamic and reciprocal dialogue between the cells and their extracellular microenvironment has prompted studies to incorporate cell-based models and bioactive molecules as a means to potentially improve *in vivo* organ restoration following implantation.[133,221–223]

2.221.3.4. Vascular and Cardiac Tissue

Decellularization of vascular tissue is an encouraging approach for treatment of cardiovascular disease, including coronary artery and peripheral vascular disease. A number of vascular tissues have been decellularized including umbilical arteries,[27,56] carotid arteries,[12,14,224] pulmonary arteries,[75] and iliac arteries[60,71] for the intended application as either small or large caliber vascular grafts. Although decellularized vascular grafts provide the ease of procurement and availability, concerns of incomplete cellular repopulation[75] as well as susceptibility of the elastin-based scaffolds to vascular calcification[225–227] have been raised.

A number of studies report decellularization of cardiac valves including pulmonary valves[13,76,81,124,132,228] and aortic valves.[69,70,74,81,96,229–232] Cardiac valves from a wide variety of species have also been used, such as canine, porcine, ovine, and rodent, all for their intended organ-specific application. Challenges with these particular decellularized scaffolds include maintenance of hemodynamic function,[233] control of early calcification,[228] cellular repopulation, and matrix generation.[132,234] Moreover, the importance of ensuring complete decellularization has been exemplified with the Synergraft™ (CryoLife, Inc.) decellularized porcine aortic valves. Although *in vitro* and *in vivo* experimental results with Synergraft™ were encouraging, early clinical performance in young children was not successful. Macroscopically and histologically, the explanted grafts showed fibrous overgrowth and a strong inflammatory response, initially attributed to a foreign-body-type reaction.[235] In this follow-up study, not only was incomplete decellularization confirmed using the Synergraft™ method, but also detection of the α-Gal epitope suggested that it might have triggered hyperacute rejection.[235] However, to what extent and quantity the presence of α-Gal epitope in heart valve bioprostheses triggers a host inflammatory response needs to be further investigated.

Recently, as a means to meet the growing demand for a bioartificial heart for end-stage heart failure, Ott and colleagues decellularized whole rat hearts by retrograde coronary perfusion (Langendorff) using a SDS-Triton® X-100 extraction method to generate a biocompatible whole-heart scaffold with a perfusable vascular tree, patent valves, and a four-chamber geometry.[57] Subsequently, the whole-heart scaffolds were recellularized with cardiac and endothelial cells and allowed to mature under physiologically relevant conditions in a bioreactor. By 28 days in perfused organ culture, whole heart constructs showed electric and contractile response as well as pump function equivalent to 2% of adult or 25% of 16-week fetal heart function. On a larger scale, Badylak and colleagues have recently decellularized in a reproducible and time-effective manner (<10 h) porcine whole hearts by pulsatile retrograde aortic perfusion to generate cardiac-ECM (C-ECM).[59] The perfused decellularization process consists of an enzymatic (trypsin), nonionic detergent (Triton® X-100), ionic detergent (deoxycholic acid), and acid solution (PES) treatment with systematic hypotonic and hypertonic rinses to remove cellular debris, as depicted in Figure 4. The resultant C-ECM preserved the composition and complex 3D

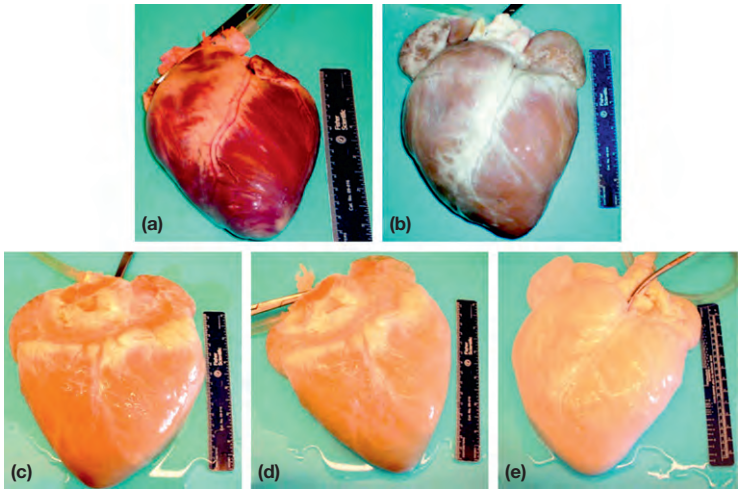

Figure 4 Representative images of the gross appearance of intact porcine hearts subjected to decellularization by retrograde perfusion. (a) Before decellularization, (b) after 0.02% trypsin, (c) after 3% Triton® X-100, (d) after 4% sodium deoxycholate, and (e) after 0.1% peracetic acid/4% ethanol. Reprinted with permission from Wainwright, J. M.; Czajka, C. A.; Patel, U. B.; *et al*. *Tissue Eng. C Methods* **2009**, *16*(3), 525–532. © Mary Ann Liebert, Inc.

architecture of the native heart. Moreover, C-ECM was found to be a suitable substrate for chicken embryonic cardiomyocyte attachment and maintenance of phenotype. Collectively, both investigations identify the significant potential this novel whole organ decellularization approach may bring to the field for tissue engineering. Not only is this technique potentially scalable to hearts of human size and complexity, but also adaptable to a wide range of other organs such as lung, liver, and kidney.

2.221.3.5. Embryoid Body Matrix

New to the area of decellularization, ECM has recently been isolated from differentiating mouse embryonic stem cells (ESCs), termed embryoid bodies (EBs), as a means to recapitulate the dynamic stem cell niche.[40,68,122] Recent evidence suggests that the spatiotemporal composition of biomolecular factors synthesized and released by ESCs *in vivo* plays an indispensible role of regulating stem cell behavior and thus, regenerative events.[236–240] Studies by the McDevitt group have decellularized EBs in a scalable manner at different time-points along their differentiation pathway by two different strategies: (1) chemical treatment consisting of Triton® X-100 in combination with DNase[68,122], and (2) physical disruption by either lyophilization or freeze–thaw cycling in combination with DNase treatment.[40] For both strategies, decellularization efficiency was assessed on the basis of cell viability, DNA removal, ultrastructure assessment, and protein retention. Not only were the EBs successfully decellularized, but retention and distribution of adhesive ECM proteins (i.e., collagen type IV, laminin, fibronectin) and the sulfated GAG hyaluronan were found to vary as a function of differentiation time in the acellular EB matrices in a similar fashion as native EBs. Moreover, the acellular EB matrices permitted exogenous repopulation and attachment of fibroblast *in vitro*.[40]

Many of the existing decellularized scaffolds originate from adult tissue sources that have limited regenerative capacity. The concept of using decellular matrices from stem cells actively undergoing morphogenic differentiation provides a unique and inherently flexible route to deliver morphogenic factors, in particular morphogens and mitogens, to an injured or diseased adult tissue that can potentially mimic early stages of embryogenesis and promote functional regeneration.

2.221.4. Concluding Remarks

The area of decellularization has contributed significantly to the progression of where tissue engineering is today and perhaps more importantly, toward its future direction. In comparison to other tissue engineering approaches that use synthetic matrices or single purified ECM matrices (e.g., collagen, elastin, or fibrin-based matrices), decellularized scaffolds offer the advantage of a more physiologically relevant composition of ECM components that is organ and tissue specific. With an optimized decellularization process, decellularized scaffolds can preserve the intricate complexities of the spatial and temporal ECM microenvironment that plays an integral role in modulating cellular behavior such as migration, proliferation, and differentiation. Moreover, decellularization offers the possibility of using xenogeneic tissues under the condition that all cellular antigens have been effectively removed to minimize an adverse immunologic response. Despite the significant advancements made in the area of decellularization to date, questions remain unanswered.[241] These include the following: Is there an optimal decellularization strategy for each tissue in the body? Is there an optimal method of storage/preservation so that an 'off-the-shelf' product is achievable? Is it necessary for recellularization of the bioscaffold prior to implantation? Although these questions exist, it is encouraging to realize from the results observed both experimentally and clinically from the vast number of different decellularized tissues and more recently embryonic stems cells and whole organs that our ultimate goal of functional tissue restoration is achievable.

References

1. Chan-Park, M. B.; Shen, J. Y.; Cao, Y.; *et al*. *J. Biomed. Mater. Res. A* **2009**, *88*, 1104–1121.
2. Atala, A. *J. Tissue Eng. Regen. Med*. **2007**, *1*, 83–96.
3. Cima, L. G.; Vacanti, J. P.; Vacanti, C.; Ingber, D.; Mooney, D.; Langer, R. *J. Biomech. Eng*. **1991**, *113*, 143–151.
4. Langer, R.; Cima, L. G.; Tamada, J. A.; Wintermantel, E. *Biomaterials* **1990**, *11*, 738–745.
5. Langer, R.; Vacanti, J. P. *Science* **1993**, *260*, 920–926.
6. Langer, R. S.; Vacanti, J. P. *Sci. Am*. **1999**, *280*, 86–89.
7. Badylak, S. F. *Biomaterials* **2007**, *28*, 3587–3593.
8. Badylak, S. F. *Transpl. Immunol*. **2004**, *12*, 367–377.
9. Hodde, J. P.; Badylak, S. F.; Brightman, A. O.; Voytik-Harbin, S. L. *Tissue Eng*. **1996**, *2*, 209–217.
10. Badylak, S. F.; Freytes, D. O.; Gilbert, T. W. *Acta Biomater*. **2009**, *5*, 1–13.
11. Gilbert, T. W.; Sellaro, T. L.; Badylak, S. F. *Biomaterials* **2006**, *27*, 3675–3683.
12. Mcfetridge, P. S.; Daniel, J. W.; Bodamyali, T.; Horrocks, M.; Chaudhuri, J. B. *J. Biomed. Mater. Res. A* **2004**, *70*, 224–234.
13. Steinhoff, G.; Stock, U.; Karim, N.; *et al*. *Circulation* **2000**, *102*, 50–55.
14. Teebken, O. E.; Bader, A.; Steinhoff, G.; Haverich, A. *Eur. J. Vasc. Endovasc. Surg*. **2000**, *19*, 381–386.
15. Furth, M. E.; Atala, A.; Van Dyke, M. E. *Biomaterials* **2007**, *28*, 5068–5073.
16. Brown, B.; Lindberg, K.; Reing, J.; Stolz, D. B.; Badylak, S. F. *Tissue Eng*. **2006**, *12*, 519–526.
17. Flynn, L.; Semple, J. L.; Woodhouse, K. A. *J. Biomed. Mater. Res. A* **2006**, *79*, 359–369.
18. Sacks, M. S.; Gloeckner, D. C. *J. Biomed. Mater. Res*. **1999**, *46*, 1–10.
19. Schenke-Layland, K.; Vasilevski, O.; Opitz, F.; *et al*. *J. Struct. Biol*. **2003**, *143*, 201–208.
20. Hinds, M. T.; Rowe, R. C.; Ren, Z.; *et al*. *J. Biomed. Mater. Res. A* **2006**, *77*, 458–469.
21. Karnik, S. K.; Brooke, B. S.; Bayes-Genis, A.; *et al*. *Development* **2003**, *130*, 411–423.
22. Gratzer, P. F.; Harrison, R. D.; Woods, T. *Tissue Eng*. **2006**, *12*, 2975–2983.
23. Gilbert, T. W.; Stewart-Akers, A. M.; Badylak, S. F. *Biomaterials* **2007**, *28*, 147–150.
24. Chen, F.; Yoo, J. J.; Atala, A. *Urology* **1999**, *54*, 407–410.
25. Freytes, D. O.; Stoner, R. M.; Badylak, S. F. *J. Biomed. Mater. Res. B Appl. Biomater*. **2008**, *84*, 408–414.
26. Freytes, D. O.; Tullius, R. S.; Badylak, S. F. *J. Biomed. Mater. Res. B Appl. Biomater*. **2006**, *78*, 327–333.
27. Gui, L. Q.; Muto, A.; Chan, S. A.; Breuer, C. K.; Niklason, L. E. *Tissue Eng. A* **2009**, *15*, 2665–2676.
28. Hudson, T. W.; Zawko, S.; Deister, C.; *et al*. *Tissue Eng*. **2004**, *10*, 1641–1651.
29. Ritter, A. B.; Reisman, S.; Michniak, B. B. *Biomedical Engineering Principles*. CRC Press: Boca Raton, FL, 2005.
30. Chan, G.; Mooney, D. J. *Trends Biotechnol*. **2008**, *26*, 382–392.
31. Chan, B. P.; Leong, K. W. In *First Japanese Meeting on Spine Research – The Intervertebral Disc*. Kyoto, Japan, 2008.

32. Gilbert, T. W.; Stewart-Akers, A. M.; Simmons-Byrd, A.; Badylak, S. F. *J. Bone Joint Surg. Am.* **2007**, *89A*, 621–630.
33. Meezan, E.; Hjelle, J. T.; Brendel, K. *Life Sci.* **1975**, *17*, 1721–1732.
34. Curtil, A.; Pegg, D. E.; Wilson, A. *Cryobiology* **1997**, *34*, 13–22.
35. El-Sabban, M. E.; El-Khoury, H.; Hamdan-Khalil, R.; Sindet-Pedersen, S.; Bazarbachi, A. *Regen. Med.* **2007**, *2*, 383–390.
36. Jackson, D. W.; Grood, E. S.; Arnoczky, S. P.; Butler, D. L.; Simon, T. M. *Am. J. Sports Med.* **1987**, *15*, 528–538.
37. Jackson, D. W.; Grood, E. S.; Arnoczky, S. P.; Butler, D. L.; Simon, T. M. *Am. J. Sports Med.* **1987**, *15*, 295–303.
38. Laun, A.; Tonn, J. C.; Jerusalem, C. *Acta Neurochir. (Wien)* **1990**, *107*, 16–21.
39. Lin, P.; Chan, W. C.; Badylak, S. F.; Bhatia, S. N. *Tissue Eng.* **2004**, *10*, 1046–1053.
40. Ngangan, A. V.; Mcdevitt, T. C. *Biomaterials* **2009**, *30*, 1143–1149.
41. Roberts, T. S.; Drez, D., Jr.; Mccarthy, W.; Paine, R. *Am. J. Sports Med.* **1991**, *19*, 35–41.
42. Bullard, K. M.; Banda, M. J.; Arbeit, J. M.; Bergsland, E.; Young, D. M. *Invasion Metastasis* **1997**, *17*, 42–52.
43. Ide, C. *Arch. Histol. Jpn* **1983**, *46*, 243–257.
44. Jackson, D. W.; Grood, E. S.; Cohn, B. T.; Arnoczky, S. P.; Simon, T. M.; Cummings, J. F. *J. Bone Joint Surg. Am.* **1991**, *73*, 201–213.
45. Kim, W. G.; Park, J. K.; Lee, W. Y. *Int. J. Artif. Organs* **2002**, *25*, 791–797.
46. Lewis, P. B.; Williams, J. M.; Hallab, N.; Virdi, A.; Yanke, A.; Cole, B. J. *J. Orthop. Res.* **2008**, *26*, 49–55.
47. Yamasaki, T.; Deie, M.; Shinomiya, R.; *et al. J. Biomed. Mater. Res. A* **2005**, *75*, 23–30.
48. Zaleske, D.; Peretti, G.; Allemann, F.; *et al. Tissue Eng.* **2003**, *9*, 949–956.
49. Diehl, P.; Steinhauser, E.; Gollwitzer, H.; *et al. J. Orthop. Sci.* **2006**, *11*, 380–385.
50. Freytes, D. O.; Badylak, S. F.; Webster, T. J.; Geddes, L. A.; Rundell, A. E. *Biomaterials* **2004**, *25*, 2353–2361.
51. Naal, F. D.; Schauwecker, J.; Steinhauser, E.; *et al. J. Biomed. Mater. Res. B Appl. Biomater.* **2008**, *87*, 19–25.
52. Sawada, K.; Terada, D.; Yamaoka, T.; Kitamura, S.; Fujisato, T. *J. Chem. Technol. Biotechnol.* **2008**, *83*, 943–949.
53. Brown, A. L.; Farhat, W.; Merguerian, P. A.; Wilson, G. J.; Khoury, A. E.; Woodhouse, K. A. *Biomaterials* **2002**, *23*, 2179–2190.
54. Karim, N.; Golz, K.; Bader, A. *Artif. Organs* **2006**, *30*, 809–814.
55. Merguerian, P. A.; Reddy, P. P.; Barrieras, D. J.; *et al. BJU Int.* **2000**, *85*, 894–898.
56. Montoya, C. V.; Mcfetridge, P. S. *Tissue Eng. C Meth.* **2009**, *15*, 191–200.
57. Ott, H. C.; Matthiesen, T. S.; Goh, S. K.; *et al. Nat. Med.* **2008**, *14*, 213–221.
58. Reddy, P. P.; Barrieras, D. J.; Wilson, G.; *et al. J. Urol.* **2000**, *164*, 936–941.
59. Wainwright, J. M.; Czajka, C. A.; Patel, U. B.; *et al. Tissue Eng. C Meth.* **2009**, *16*(3), 525–532.
60. Goissis, G.; Suzigan, S.; Parreira, D. R.; Maniglia, J. V.; Braile, D. M.; Raymundo, S. *Artif. Organs* **2000**, *24*, 217–223.
61. Vyavahare, N.; Hirsch, D.; Lerner, E.; *et al. Circulation* **1997**, *95*, 479–488.
62. Cartmell, J. S.; Dunn, M. G. *J. Biomed. Mater. Res.* **2000**, *49*, 134–140.
63. Elder, B. D.; Eleswarapu, S. V.; Athanasiou, K. A. *Biomaterials* **2009**, *30*, 3749–3756.
64. Harrison, R. D.; Gratzer, P. F. *J. Biomed. Mater. Res. A* **2005**, *75*, 841–854.
65. Woods, T.; Gratzer, P. F. *Biomaterials* **2005**, *26*, 7339–7349.
66. Badylak, S.; Liang, A.; Record, R.; Tullius, R.; Hodde, J. *Biomaterials* **1999**, *20*, 2257–2263.
67. Burugapalli, K.; Thapasimuttu, A.; Chan, J. C.; *et al. Biomacromolecules* **2007**, *8*, 928–936.
68. Nair, R.; Ngangan, A. V.; Mcdevitt, T. C. *J. Biomater. Sci. Polym. Ed.* **2008**, *19*, 801–819.
69. Bader, A.; Schilling, T.; Teebken, O. E.; *et al. Eur. J. Cardiothorac. Surg.* **1998**, *14*, 279–284.
70. Grauss, R. W.; Hazekamp, M. G.; Oppenhuizen, F.; Van Munsteren, C. J.; Gittenberger-De Groot, A. C.; Deruiter, M. C. *Eur. J. Cardiothorac. Surg.* **2005**, *27*, 566–571.
71. Borschel, G. H.; Huang, Y. C.; Calve, S.; *et al. Tissue Eng.* **2005**, *11*, 778–786.
72. Chen, R. N.; Ho, H. O.; Tsai, Y. T.; Sheu, M. T. *Biomaterials* **2004**, *25*, 2679–2686.
73. Courtman, D. W.; Pereira, C. A.; Kashef, V.; Mccomb, D.; Lee, J. M.; Wilson, G. J. *J. Biomed. Mater. Res.* **1994**, *28*, 655–666.
74. Courtman, D. W.; Pereira, C. A.; Omar, S.; Langdon, S. E.; Lee, J. M.; Wilson, G. J. *J. Biomed. Mater. Res.* **1995**, *29*, 1507–1516.
75. Ketchedjian, A.; Jones, A. L.; Krueger, P.; *et al. Ann. Thorac. Surg.* **2005**, *79*, 888–896; discussion 896.
76. Rieder, E.; Kasimir, M. T.; Silberhumer, G.; *et al. J. Thorac. Cardiovasc. Surg.* **2004**, *127*, 399–405.
77. Rosario, D. J.; Reilly, G. C.; Salah, E. A.; Glover, M.; Bullock, A. J.; Macneil, S. *Regen. Med.* **2008**, *3*, 145–156.
78. Sandmann, G. H.; Eichhorn, S.; Vogt, S.; *et al. J. Biomed. Mater. Res. A* **2009**, *91*, 567–574.
79. Stapleton, T. W.; Ingram, J.; Katta, J.; *et al. Tissue Eng. A* **2008**, *14*, 505–518.
80. Wilshaw, S. P.; Kearney, J. N.; Fisher, J.; Ingham, E. *Tissue Eng.* **2006**, *12*, 2117–2129.
81. Wilson, G. J.; Courtman, D. W.; Klement, P.; Lee, J. M.; Yeger, H. *Ann. Thorac. Surg.* **1995**, *60*, S353–S358.
82. Yang, M.; Chen, C. Z.; Wang, X. N.; Zhu, Y. B.; Gu, Y. J. *J. Biomed. Mater. Res. B Appl. Biomater.* **2009**, *91*, 354–361.
83. Hudson, T. W.; Liu, S. Y.; Schmidt, C. E. *Tissue Eng.* **2004**, *10*, 1346–1358.
84. Gui, L.; Chan, S.; Breuer, C.; Niklason, L. *Tissue Eng. C Meth.* **2009**, *16*(2), 173–184.
85. Bolland, F.; Korossis, S.; Wilshaw, S. P.; *et al. Biomaterials* **2007**, *28*, 1061–1070.
86. Chun, S. Y.; Lim, G. J.; Kwon, T. G.; *et al. Biomaterials* **2007**, *28*, 4251–4256.
87. Gilbert, T. W.; Wognum, S.; Joyce, E. M.; Freytes, D. O.; Sacks, M. S.; Badylak, S. F. *Biomaterials* **2008**, *29*, 4775–4782.
88. Liu, Y.; Bharadwaj, S.; Lee, S. J.; Atala, A.; Zhang, Y. Y. *Biomaterials* **2009**, *30*, 3865–3873.
89. Chalfoun, C. T.; Wirth, G. A.; Evans, G. R. D. *J. Cell. Mol. Med.* **2006**, *10*, 309–317.
90. Dumont, C. E.; Hentz, V. R. *Transplantation* **1997**, *63*, 1210–1215.
91. Fansa, H.; Schneider, W.; Wolf, G.; Keilhoff, G. *Transplantation* **2002**, *74*, 381–387.
92. Gulati, A. K. *J. Neurosurg.* **1988**, *68*, 117–123.
93. Erdbrugger, W.; Konertz, W.; Dohmen, P. M.; *et al. Tissue Eng.* **2006**, *12*, 2059–2068.
94. Kasimir, M. T.; Weigel, G.; Sharma, J.; *et al. Thromb. Haemost.* **2005**, *94*, 562–567.
95. Li, W.; Liu, W. Y.; Yi, D. H.; Yu, S. Q.; Jin, Z. X. *Asian Cardiovasc. Thorac. Ann.* **2007**, *15*, 91–96.
96. Meyer, S. R.; Nagendran, J.; Desai, L. S.; *et al. J. Thorac. Cardiovasc. Surg.* **2005**, *130*, 469–476.
97. Mirsadraee, S.; Wilcox, H. E.; Korossis, S. A.; *et al. Tissue Eng.* **2006**, *12*, 763–773.
98. Schmidt, C. E.; Baier, J. M. *Biomaterials* **2000**, *21*, 2215–2231.
99. Wilson, G. J.; Yeger, H.; Klement, P.; Lee, J. M.; Courtman, D. W. *ASAIO Trans.* **1990**, *36*, M340–M343.
100. Zhou, M.; Liu, Z.; Wei, Z. Q.; *et al. Artif. Organs* **2009**, *33*, 230–239.
101. Marquez, S. P.; Martinez, V. S.; Ambrose, W. M.; *et al. Acta Biomater.* **2009**, *5*, 1839–1847.
102. Aimoli, C. G.; Nogueira, G. M.; Nascimento, L. S.; *et al. Artif. Organs* **2007**, *31*, 278–283.
103. Ahn, J. I.; Lee, D. H.; Ryu, Y. H.; *et al. Artif. Organs* **2007**, *31*, 711–721.
104. Murakoshi, A.; Kimura, T.; Funamoto, S.; *et al.* In *TERMIS-EU*, London, UK, 2007 (Meeting Abstract 136).
105. Badylak, S. F.; Lantz, G. C.; Coffey, A.; Geddes, L. A. *J. Surg. Res.* **1989**, *47*, 74–80.
106. Badylak, S. F.; Record, R.; Lindberg, K.; Hodde, J.; Park, K. *J. Biomater. Sci. Polym. Ed.* **1998**, *9*, 863–878.
107. Badylak, S. F.; Tullius, R.; Kokini, K.; *et al. J. Biomed. Mater. Res.* **1995**, *29*, 977–985.
108. Kropp, B. P.; Eppley, B. L.; Prevel, C. D.; *et al. Urology* **1995**, *46*, 396–400.
109. Aitken, K. J.; Bagli, D. J. *Nat. Rev. Urol.* **2009**, *6*, 612–621.
110. Voytik-Harbin, S. L.; Brightman, A. O.; Kraine, M. R.; Waisner, B.; Badylak, S. F. *J. Cell. Biochem.* **1997**, *67*, 478–491.
111. Horowitz, B. *Curr. Stud. Hematol. Blood Transfus.* **1989**, (56), 83–96.
112. Horowitz, B.; Bonomo, R.; Prince, A. M.; Chin, S. N.; Brotman, B.; Shulman, R. W. *Blood* **1992**, *79*, 826–831.
113. Reichert, J. C.; Quent, V. M.; Burke, L. J.; Stansfield, S. H.; Clements, J. A.; Hutmacher, D. W. *Biomaterials* **2010**, *31*(31), 7928–7936.
114. Hodde, J.; Hiles, M. *Biotechnol. Bioeng.* **2002**, *79*, 211–216.
115. Pruss, A.; Kao, M.; Kiesewetter, H.; Von Versen, R.; Pauli, G. *Biologicals* **1999**, *27*, 195–201.
116. Hodde, J.; Janis, A.; Hiles, M. *J. Mater. Sci. Mater. Med.* **2007**, *18*, 545–550.
117. Hodde, J.; Janis, A.; Ernst, D.; Zopf, D.; Sherman, D.; Johnson, C. *J. Mater. Sci. Mater. Med.* **2007**, *18*, 537–543.
118. Hodde, J. P.; Record, R. D.; Liang, H. A.; Badylak, S. F. *Endothelium* **2001**, *8*, 11–24.
119. Knight, R. L.; Wilcox, H. E.; Korossis, S. A.; Fisher, J.; Ingham, E. *Proc. Inst. Mech. Eng. H* **2008**, *222*, 129–143.

120. Wilshaw, S. P.; Kearney, J.; Fisher, J.; Ingham, E. *Tissue Eng. A* **2008**, *14*, 463–472.
121. Dahl, S. L.; Koh, J.; Prabhakar, V.; Niklason, L. E. *Cell Transplant*. **2003**, *12*, 659–666.
122. Nair, R.; Shukla, S.; Mcdevitt, T. C. *J. Biomed. Mater. Res. A* **2008**, *87*, 1075–1085.
123. Bodnar, E.; Olsen, E. G.; Florio, R.; Dobrin, J. *Thorac. Cardiovasc. Surg.* **1986**, *34*, 82–85.
124. Lichtenberg, A.; Tudorache, I.; Cebotari, S.; *et al*. *Biomaterials* **2006**, *27*, 4221–4229.
125. Pruss, A.; Baumann, B.; Seibold, M.; *et al*. *Biologicals* **2001**, *29*, 59–66.
126. Gouk, S. S.; Lim, T. M.; Teoh, S. H.; Sun, W. Q. *J. Biomed. Mater. Res. B Appl. Biomater.* **2008**, *84*, 205–217.
127. Freytes, D. O.; Tullius, R. S.; Valentin, J. E.; Stewart-Akers, A. M.; Badylak, S. F. *J. Biomed. Mater. Res. A* **2008**, *87*, 862–872.
128. Brennan, E. P.; Reing, J.; Chew, D.; Myers-Irvin, J. M.; Young, E. J.; Badylak, S. F. *Tissue Eng.* **2006**, *12*, 2949–2955.
129. Gilbert, T. W.; Stolz, D. B.; Biancaniello, F.; Simmons-Byrd, A.; Badylak, S. F. *Biomaterials* **2005**, *26*, 1431–1435.
130. Freytes, D. O.; Martin, J.; Velankar, S. S.; Lee, A. S.; Badylak, S. F. *Biomaterials* **2008**, *29*, 1630–1637.
131. Singelyn, J. M.; Dequach, J. A.; Seif-Naraghi, S. B.; Littlefield, R. B.; Schup-Magoffin, P. J.; Christman, K. L. *Biomaterials* **2009**, *30*, 5409–5416.
132. Schenke-Layland, K.; Riemann, I.; Opitz, F.; Konig, K.; Halbhuber, K. J.; Stock, U. A. *Matrix Biol*. **2004**, *23*, 113–125.
133. Brown, A. L.; Brook-Allred, T. T.; Waddell, J. E.; *et al*. *Biomaterials* **2005**, *26*, 529–543.
134. Lindberg, K.; Badylak, S. F. *Burns* **2001**, *27*, 254–266.
135. Wainwright, D. J. *Burns* **1995**, *21*, 243–248.
136. Badylak, S. F.; Gilbert, T. W. *Semin. Immunol*. **2008**, *20*, 109–116.
137. Brown, B. N.; Valentin, J. E.; Stewart-Akers, A. M.; Mccabe, G. P.; Badylak, S. F. *Biomaterials* **2009**, *30*, 1482–1491.
138. Chaplin, J. M.; Costantino, P. D.; Wolpoe, M. E.; Bederson, J. B.; Griffey, E. S.; Zhang, W. X. *Neurosurgery* **1999**, *45*, 320–327.
139. Rieder, E.; Seebacher, G.; Kasimir, M. T.; *et al*. *Circulation* **2005**, *111*, 2792–2797.
140. Ansaloni, L.; Cambrini, P.; Catena, F.; *et al*. *J. Invest. Surg.* **2007**, *20*, 237–241.
141. Goncalves, A. C.; Griffiths, L. G.; Anthony, R. V.; Orton, E. C. *J. Heart Valve Dis.* **2005**, *14*, 212–217.
142. Griffiths, L. G.; Choe, L. H.; Reardon, K. F.; Dow, S. W.; Christopher Orton, E. *Biomaterials* **2008**, *29*, 3514–3520.
143. Kasimir, M. T.; Rieder, E.; Seebacher, G.; Wolner, E.; Weigel, G.; Simon, P. *Tissue Eng.* **2005**, *11*, 1274–1280.
144. Galili, U. *Biochimie* **2001**, *83*, 557–563.
145. Galili, U. *Immunol. Cell Biol*. **2005**, *83*, 674–686.
146. Badylak, S. E.; Gilbert, T. W. *Semin. Immunol*. **2008**, *20*, 109–116.
147. Mcpherson, T. B.; Liang, H.; Record, R. D.; Badylak, S. F. *Tissue Eng.* **2000**, *6*, 233–239.
148. Raeder, R. H.; Badylak, S. F.; Sheehan, C.; Kallakury, B.; Metzger, D. W. *Transpl. Immunol*. **2002**, *10*, 15–24.
149. Allman, A. J.; Mcpherson, T. B.; Badylak, S. F.; *et al*. *Transplantation* **2001**, *71*, 1631–1640.
150. Zheng, M. H.; Chen, J.; Kirilak, Y.; Willers, C.; Xu, J.; Wood, D. *J. Biomed. Mater. Res. B Appl. Biomater.* **2005**, *73*, 61–67.
151. Derwin, K. A.; Baker, A. R.; Spragg, R. K.; Leigh, D. R.; Iannotti, J. P. *J. Bone Joint Surg. Am.* **2006**, *88*, 2665–2672.
152. Gilbert, T. W.; Freund, J. M.; Badylak, S. F. *J. Invest. Surg.* **2009**, *152*, 135–139.
153. Badylak, S.; Kokini, K.; Tullius, B.; Whitson, B. *J. Surg. Res.* **2001**, *99*, 282–287.
154. Record, R. D.; Hillegonds, D.; Simmons, C.; *et al*. *Biomaterials* **2001**, *22*, 2653–2659.
155. Hiles, M. C.; Badylak, S. F.; Lantz, G. C.; Kokini, K.; Geddes, L. A.; Morff, R. J. *J. Biomed. Mater. Res.* **1995**, *29*, 883–891.
156. Lantz, G. C.; Badylak, S. F.; Coffey, A. C.; Geddes, L. A.; Blevins, W. E. *J. Invest. Surg.* **1990**, *3*, 217–227.
157. Lantz, G. C.; Badylak, S. F.; Coffey, A. C.; Geddes, L. A.; Sandusky, G. E. *J. Surg. Res.* **1992**, *53*, 175–181.
158. Lantz, G. C.; Badylak, S. F.; Hiles, M. C.; *et al*. *J. Invest. Surg.* **1993**, *6*, 297–310.
159. Robotin-Johnson, M. C.; Swanson, P. E.; Johnson, D. C.; Schuessler, R. B.; Cox, J. L. *J. Thorac. Cardiovasc. Surg.* **1998**, *116*, 805–811.
160. Sandusky, G. E., Jr.; Badylak, S. F.; Morff, R. J.; Johnson, W. D.; Lantz, G. *Am. J. Pathol*. **1992**, *140*, 317–324.
161. Sandusky, G. E.; Lantz, G. C.; Badylak, S. F. *J. Surg. Res.* **1995**, *58*, 415–420.
162. Badylak, S.; Obermiller, J.; Geddes, L.; Matheny, R. *Heart Surg. Forum* **2003**, *6*, E20–E26.
163. Matheny, R. G.; Hutchison, M. L.; Dryden, P. E.; Hiles, M. D.; Shaar, C. J. *J. Heart Valve Dis.* **2000**, *9*, 769–774; discussion 774–775.
164. Robinson, K. A.; Li, J.; Mathison, M.; *et al*. *Circulation* **2005**, *112*, I135–I143.
165. Cobb, M. A.; Badylak, S. F.; Janas, W.; Boop, F. A. *Surg. Neurol*. **1996**, *46*, 389–393; discussion 393–394.
166. Cobb, M. A.; Badylak, S. F.; Janas, W.; Simmons-Byrd, A.; Boop, F. A. *Surg. Neurol*. **1999**, *51*, 99–104.
167. Clarke, K. M.; Lantz, G. C.; Salisbury, S. K.; Badylak, S. F.; Hiles, M. C.; Voytik, S. L. *J. Surg. Res.* **1996**, *60*, 107–114.
168. Prevel, C. D.; Eppley, B. L.; Summerlin, D. J.; *et al*. *Ann. Plast. Surg.* **1995**, *35*, 381–388.
169. Knapp, P. M.; Lingeman, J. E.; Siegel, Y. I.; Badylak, S. F.; Demeter, R. J. *J. Endourol*. **1994**, *8*, 125–130.
170. Kropp, B. P.; Ludlow, J. K.; Spicer, D.; *et al*. *Urology* **1998**, *52*, 138–142.
171. Kropp, B. P.; Rippy, M. K.; Badylak, S. F.; *et al*. *J. Urol*. **1996**, *155*, 2098–2104.
172. Kropp, B. P.; Sawyer, B. D.; Shannon, H. E.; *et al*. *J. Urol*. **1996**, *156*, 599–607.
173. Vaught, J. D.; Kropp, B. P.; Sawyer, B. D.; *et al*. *J. Urol*. **1996**, *155*, 374–378.
174. Chen, M. K.; Badylak, S. F. *J. Surg. Res.* **2001**, *99*, 352–358.
175. Badylak, S.; Meurling, S.; Chen, M.; Spievack, A.; Simmons-Byrd, A. *J. Pediatr. Surg.* **2000**, *35*, 1097–1103.
176. Hodde, J. P.; Badylak, S. F.; Shelbourne, K. D. *Tissue Eng.* **1997**, *3*, 27–37.
177. Aiken, S. W.; Badylak, S. F.; Toombs, J. P.; *et al*. *Vet. Comp. Orthop. Traumatol*. **1994**, *7*, 124–128.
178. Cook, J. L.; Tomlinson, J. L.; Arnoczky, S. P.; Fox, D. B.; Reeves Cook, C.; Kreeger, J. M. *Tissue Eng.* **2001**, *7*, 321–334.
179. Fox, D. B.; Cook, J. L.; Arnoczky, S. P.; *et al*. *Tissue Eng.* **2004**, *10*, 129–137.
180. Peel, S. A. F.; Chen, H.; Renlund, R.; Badylak, S. F.; Kandel, R. A. *Tissue Eng.* **1998**, *4*, 143–155.
181. Moore, D. C.; Pedrozo, H. A.; Crisco, J. J., III; Ehrlich, M. G. *J. Biomed. Mater. Res. A* **2004**, *69*, 259–266.
182. Suckow, M. A.; Voytik-Harbin, S. L.; Terril, L. A.; Badylak, S. F. *J. Invest. Surg.* **1999**, *12*, 277–287.
183. Hodde, J. *Tissue Eng.* **2002**, *8*, 295–308.
184. Kropp, B. P.; Cheng, E. Y.; Lin, H. K.; Zhang, Y. *J. Urol*. **2004**, *172*, 1710–1713.
185. Raghavan, D.; Kropp, B. P.; Lin, H. K.; Zhang, Y.; Cowan, R.; Madihally, S. V. *J. Biomed. Mater. Res. A* **2005**, *73*, 90–96.
186. Zhang, Y.; Frimberger, D.; Cheng, E. Y.; Lin, H. K.; Kropp, B. P. *BJU Int*. **2006**, *98*, 1100–1105.
187. Chung, S. Y.; Krivorov, N. P.; Rausei, V.; *et al*. *J. Urol*. **2005**, *174*, 353–359.
188. Landman, J.; Olweny, E.; Sundaram, C. P.; *et al*. *J. Urol*. **2004**, *171*, 2450–2455.
189. Paterson, R. F.; Lifshitz, D. A.; Beck, S. D.; *et al*. *J. Urol*. **2002**, *168*, 2253–2257.
190. Costantino, P. D.; Wolpoe, M. E.; Govindaraj, S.; *et al*. *Head Neck* **2000**, *22*, 765–771.
191. Wainwright, D.; Madden, M.; Luterman, A.; *et al*. *J. Burn Care Rehabil*. **1996**, *17*, 124–136.
192. Silverstein, L. H.; Gornstein, R. A.; Callan, D. P. *Dent. Today* **1999**, *18*, 76–79.
193. Inoue, Y.; Anthony, J. P.; Lleon, P.; Young, D. M. *J. Reconstr. Microsurg.* **1996**, *12*, 307–311.
194. Sclafani, A. P.; Romo, T., III; Jacono, A. A.; Mccormick, S.; Cocker, R.; Parker, A. *Arch. Facial Plast. Surg.* **2000**, *2*, 130–136.
195. Sclafani, A. P.; Romo, T., III; Jacono, A. A.; Mccormick, S. A.; Cocker, R.; Parker, A. *Arch. Facial Plast. Surg.* **2001**, *3*, 101–103.
196. Livesey, S. A.; Herndon, D. N.; Hollyoak, M. A.; Atkinson, Y. H.; Nag, A. *Transplantation* **1995**, *60*, 1–9.
197. Armour, A. D.; Fish, J. S.; Woodhouse, K. A.; Semple, J. L. *Plast. Reconstr. Surg.* **2006**, *117*, 845–856.
198. Srivastava, A.; Desagun, E. Z.; Jennings, L. J.; *et al*. *Ann. Surg.* **2001**, *233*, 400–408.
199. Takami, Y.; Matsuda, T.; Yoshitake, M.; Hanumadass, M.; Walter, R. J. *Burns* **1996**, *22*, 182–190.
200. Walter, R. J.; Matsuda, T.; Reyes, H. M.; Walter, J. M.; Hanumadass, M. *Burns* **1998**, *24*, 104–113.
201. Ge, L.; Zheng, S.; Wei, H. *Burns* **2009**, *35*, 46–50.
202. Aitken, K. J.; Bagli, D. J. *Nat. Rev. Urol*. **2009**, *6*, 596–611.
203. Badylak, S. F.; Vorp, D. A.; Spievack, A. R.; *et al*. *J. Surg. Res.* **2005**, *128*, 87–97.
204. Nieponice, A.; Gilbert, T. W.; Badylak, S. F. *Ann. Thorac. Surg.* **2006**, *82*, 2050–2058.
205. Badylak, S. F.; Kochupura, P. V.; Cohen, I. S.; *et al*. *Cell Transplant*. **2006**, *15* (Suppl. 1), S29–S40.
206. Kelly, D. J.; Rosen, A. B.; Schuldt, A. J.; *et al*. *Tissue Eng. A* **2009**, *15*, 2189–2201.

207. Gilbert, T. W.; Nieponice, A.; Spievack, A. R.; Holcomb, J.; Gilbert, S.; Badylak, S. F. *J. Surg. Res.* **2008**, *147*, 61–67.
208. Piechota, H. J.; Dahms, S. E.; Nunes, L. S.; Dahiya, R.; Lue, T. F.; Tanagho, E. A. *J. Urol.* **1998**, *159*, 1717–1724.
209. Probst, M.; Dahiya, R.; Carrier, S.; Tanagho, E. A. *Br. J. Urol.* **1997**, *79*, 505–515.
210. Sievert, K. D.; Bakircioglu, M. E.; Nunes, L.; Tu, R.; Dahiya, R.; Tanagho, E. A. *J. Urol.* **2000**, *163*, 1958–1965.
211. Sievert, K. D.; Tanagho, E. A. *World J. Urol.* **2000**, *18*, 19–25.
212. Oberpenning, F.; Meng, J.; Yoo, J. J.; Atala, A. *Nat. Biotechnol.* **1999**, *17*, 149–155.
213. Yoo, J. J.; Meng, J.; Oberpenning, F.; Atala, A. *Urology* **1998**, *51*, 221–225.
214. Atala, A. *Curr. Opin. Biotechnol.* **2009**, *20*, 575–592.
215. Dahms, S. E.; Piechota, H. J.; Dahiya, R.; Lue, T. F.; Tanagho, E. A. *Br. J. Urol.* **1998**, *82*, 411–419.
216. Dahms, S. E.; Piechota, H. J.; Nunes, L.; Dahiya, R.; Lue, T. F.; Tanagho, E. A. *Urology* **1997**, *50*, 818–825.
217. Piechota, H. J.; Dahms, S. E.; Probst, M.; *et al. Br. J. Urol.* **1998**, *81*, 548–559.
218. Piechota, H. J.; Gleason, C. A.; Dahms, S. E.; *et al. Urol. Res.* **1999**, *27*, 206–213.
219. Probst, M.; Piechota, H. J.; Dahiya, R.; Tanagho, E. A. *BJU Int.* **2000**, *85*, 362–371.
220. Sutherland, R. S.; Baskin, L. S.; Hayward, S. W.; Cunha, G. R. *J. Urol.* **1996**, *156*, 571–577.
221. Atala, A.; Bauer, S. B.; Soker, S.; Yoo, J. J.; Retik, A. B. *Lancet* **2006**, *367*, 1241–1246.
222. Brown, A. L.; Ringuette, M. J.; Prestwich, G. D.; Bagli, D. J.; Woodhouse, K. A. *Biomaterials* **2006**, *27*, 3825–3835.
223. Youssif, M.; Shiina, H.; Urakami, S.; *et al. Urology* **2005**, *66*, 201–207.
224. Amiel, G. E.; Komura, M.; Shapira, O.; *et al. Tissue Eng.* **2006**, *12*, 2355–2365.
225. Hilbert, S. L.; Boerboom, L. E.; Livesey, S. A.; Ferrans, V. J. *J. Biomed. Mater. Res. A* **2004**, *69*, 197–204.
226. Hinds, M. T.; Courtman, D. W.; Goodell, T.; *et al. J. Biomed. Mater. Res. A* **2004**, *69*, 55–64.
227. Kurane, A.; Simionescu, D. T.; Vyavahare, N. R. *Biomaterials* **2007**, *28*, 2830–2838.
228. Leyh, R. G.; Wilhelmi, M.; Rebe, P.; *et al. Ann. Thorac. Surg.* **2003**, *75*, 1457–1463; discussion 1463.
229. Booth, C.; Korossis, S. A.; Wilcox, H. E.; *et al. J. Heart Valve Dis.* **2002**, *11*, 457–462.
230. Korossis, S. A.; Booth, C.; Wilcox, H. E.; *et al. J. Heart Valve Dis.* **2002**, *11*, 463–471.
231. Ota, T.; Taketani, S.; Iwai, S.; *et al. Ann. Thorac. Surg.* **2007**, *83*, 1501–1507.
232. Wilcox, H. E.; Korossis, S. A.; Booth, C.; *et al. J. Heart Valve Dis.* **2005**, *14*, 228–236; discussion 236–237.
233. Korossis, S. A.; Wilcox, H. E.; Watterson, K. G.; Kearney, J. N.; Ingham, E.; Fisher, J. *J. Heart Valve Dis.* **2005**, *14*, 408–421; discussion 422.
234. Schenke-Layland, K.; Opitz, F.; Gross, M.; *et al. Cardiovasc. Res.* **2003**, *60*, 497–509.
235. Simon, P.; Kasimir, M. T.; Seebacher, G.; *et al. Eur. J. Cardiothorac. Surg.* **2003**, *23*, 1002–1006; discussion 1006.
236. Fraidenraich, D.; Stillwell, E.; Romero, E.; *et al. Science* **2004**, *306*, 247–252.
237. Guo, Y.; Graham-Evans, B.; Broxmeyer, H. E. *Stem Cells* **2006**, *24*, 850–856.
238. Guttinger, M.; Fedele, D.; Koch, P.; *et al. Epilepsia* **2005**, *46*, 1162–1169.
239. Shenghui, H.; Nakada, D.; Morrison, S. J. *Annu. Rev. Cell Dev. Biol.* **2009**, *25*, 377–406.
240. Singla, D. K.; Singla, R. D.; Mcdonald, D. E. *Am. J. Physiol. Heart Circ. Physiol.* **2008**, *295*, H907–H913.
241. Badylak, S. F.; Gilbert, T. *Ann. Thorac. Surg.* **2009**, *87*, 868.

2.222. Xenogenic Tissues and Biomaterials for the Skeletal System

D I Zeugolis, M Keeney, E Collin, G Fontana, and A Pandit, National University of Ireland, Galway, Ireland

© 2011 Elsevier Ltd. All rights reserved.

2.222.1.	**Introduction**	387
2.222.2.	**ECM Composition**	388
2.222.2.1.	Collagen and Elastin	388
2.222.2.2.	Proteoglycans and Glycosaminoglycans	389
2.222.2.3.	Fibronectin and Laminin	389
2.222.2.4.	Growth Factors	390
2.222.3.	**Xenogenic Tissues, ECM Biopolymers, or Cells in Tissue Engineering**	390
2.222.3.1.	Bone Reconstruction	390
2.222.3.2.	Intervertebral Disc Reconstruction	393
2.222.3.3.	Tendon Reconstruction	395
2.222.4.	**Limitations**	396
2.222.5.	**Future Perspectives**	397
References		398

Glossary

Allograft A tissue graft that is harvested from one individual and transplanted in a genetically nonidentical individual of the same species.

Autograft A tissue graft that is harvested from and implanted in the same individual.

Extracellular matrix Cell-secreted molecules that form highly ordered insoluble aggregates around a given tissue or organ.

Xenograft A tissue graft that is harvested from one individual and implanted in another individual of different species.

Abbreviations

ADSCs	Adipose tissue-derived stem cells
BMP	Bone morphogenetic protein
bMSCs	Bone marrow-derived mesenchymal stem cells
DDD	Disc degeneration disease
ECM	Extracellular matrix
FGF	Fibroblast growth factor
GAGs	Glycosaminoglycans
HA	Hyaluronic acid
IVD	Intervertebral disk
NP	Nucleus pulposus
NSAIDs	Nonsteroidal anti-inflammatory drugs
PDGF	Platelet-derived growth factor
PGA	Polyglycolide
PLLA	Poly(L-lactide)
rhBMP	Human recombinant bone morphogenetic protein
SAARDs	Slow acting antirheumatic drugs
TGF-β	Transforming growth factor beta
VEGF	Vascular endothelial cell growth factor

2.222.1. Introduction

Autografts, allografts, and xenografts are currently being considered as the gold standard in many clinical applications, including those for bone, skin, tendon and ligament, nerve, and heart valves, because their structure is identical to the tissue being replaced. Properties such as rapid fixation, fast healing, imitation of native tissue architecture, and the ability to promote functional regeneration have led to several, commercially available, tissue grafts, which have demonstrated normal tissue ingrowth and have be shown to facilitate functional regeneration of injured or degenerated tissues, both in preclinical animal models and in human clinical studies.[1–14]

However, allografts are associated with the potential risk of transmitting infectious diseases and autografts have the disadvantage of creating a secondary morbid site during harvesting.[15–18] For this reason, tissue-engineering strategies that provide a valuable solution to shortfalls in the availability of tissue grafts have been developed. Tissue engineering started with the use of materials that were designed to interact with the body, encourage tissue regeneration, and restore its function.[19–21] The ideal tissue substitute should enable its easy processing to end-products of different textures that are similar in structural conformation and mechanical integrity to the tissue being replaced. To this end, advancements in micro- and nanofabrication technologies have enabled topographical and spatial control over cellular behavior and have facilitated the creation of more functional tissue facsimiles.[22–32] It is also important that the engineered device be composed of materials that will elicit neither an immunological response nor a

clinically detectable foreign body reaction. It is also desirable that the scaffold material offers opportunities for functionalization, such as facilitating delivery of bioactive or therapeutic molecules to the site of injury.[26,33–36] Currently, there are several types of material, such as (a) synthetic biodegradable and bioresorbable polymers (e.g., polyglycolide (PGA), racemic polylactides, polydioxanone, polyvinyl alcohol, polycaprolactone, polyethylene glycol); (b) nonabsorbable polymers (e.g., polyetherketone, polytetrafluoroethylene, polypropylene, silicone); and (c) responsive to stimuli 'smart' polymers (e.g., *N*-ethyl morpholine metacrylate, *N*-ethyl morpholine methacrylamide, *N*-ethyl pyrrolidine methacrylamide, *N*-isopropylacrylamide), that are commercially available. These have been shown to stimulate repair and regeneration of tissues *in vivo*.[26,37–40]

Nondegradable synthetic materials, however, may be harmful due to mechanical impingement or infection and may require a second operation for their removal,[41] while the degradation products of biodegradable synthetic materials could be deleterious to the surrounding cells and tissue.[42–44] Moreover, synthetic materials are associated with a foreign body reaction[45–48] because they lack cell-recognition signals and also because their hydrophobic property hinders cell adhesion.[49–51] For these reasons, biological scaffolds, composed of natural polymers (e.g., collagen, elastin, fibrin, hyaluronan), have been evaluated for biomedical applications.[38,52–56] Such materials possess several inherent advantages such as the ability to present receptor-binding ligands to cells, susceptibility to cell initiated proteolytic degradation, and enhancement of natural remodeling.[13,38,52,57,58] The following section will provide an overview of the most abundant extracellular matrix (ECM) components that are used in tissue-engineering applications.

2.222.2. ECM Composition

ECM can be defined as the cell-secreted molecules that form highly ordered insoluble aggregates, which combine to form various tissues and organs. The cell-ECM has been characterized as a 'dynamic equilibrium' between the cells and the matrix; the composition, conformation, and architecture of the matrix depend upon the phenotype of the resident cells and the biochemical/biomechanical milieu, while the matrix influences the behavior and phenotype of the surrounding cells.[11] The primary function of the matrix is to provide structural support. Collagen and elastin are typical examples of structural proteins. However, the ECM has manifold effects, apart from providing structural integrity.[59] For example, ECM proteins, including laminin and fibronectin, contain and bind to adhesion receptors (e.g., integrins) that mediate cell–matrix adhesion, cell migration, proliferation and apoptosis, transduce signals into cells, and are involved in developmental and inflammatory processes.[60–62] Growth factors constitute another functional unit of the matrix; the matrix is responsible for their distribution, activation, and presentation to cells.[63,64] Proteoglycans and their constituent glycosaminoglycans, despite their minor proportion in the ECM, influence many physiological processes, including collagen fibrillogenesis, cell–cell interactions, growth factor binding and cell regulation.[65–68] For these reasons, all the above molecules, either alone or combined, are used as constructive scaffolds that can induce functional regeneration.

2.222.2.1. Collagen and Elastin

The term collagen is often used to describe a family of protein molecules. Forty vertebrate collagen genes have been described to date, the products of which combine to form 29 distinct homo- and/or heterotrimeric molecules,[69–74] each having, as a common feature, at least one tripeptide helical sequence of repeated $(Gly–X–Y)_{100\text{-}400}$, where X is often proline and Y is sometimes hydroxyproline.[71,72,75–77] These distinct collagens differ by minor alterations in the properties of the collagen molecule such as changes in the length of the triple helix, the Mw, the charge profile along the helix, interruptions in the integrity of the triple helix, the size and shape of the terminal globular domains, the cleavage or retention of the latter in the supramolecular aggregate, and by variations in posttranslational modifications.[76,77] The most acceptable approach to categorizing these forms of collagens is based upon the structure of the aggregate. As such, four main groups have been identified, named fibrous, nonfibrous, filamentous, and fibril-associated collagens with interrupted triple helices.[69–72,76–84] Most of the research into the assembly and molecular organization of collagen is based on type I collagen, which is abundant in the skin, bone, cornea, dentin, ligament, and tendon.[85–90] Although type I collagen accounts for up to 70–90% of the collagen found in the body and is normally encountered in biomaterial applications, when it comes to evaluating the performance of biomaterials *in vivo*, however, the distribution and roles of the other less abundant collagen types is also important.[72,80] For example, type II collagen is important while evaluating the properties of a scaffold designed to replace cartilaginous tissues;[91–94] type III[95–102] and type V[100,103] collagens are important modulators of fiber diameter. The pathway of collagen synthesis, from gene transcription to secretion and assembly into functional fibrils in tissues, is a complex multistep process that requires the coordination of temporal and spatial biochemical events. Briefly, fibril-forming collagens are synthesized in their precursor form, termed procollagens, with N- and C-terminal propeptide extensions. Following or during secretion into the ECM, the propeptides are cleaved by specific procollagen proteinases[71,78,80,85,97,99,104–108] that leave short, non-triple-helical domains, termed telopeptides, at each end of the collagen molecule.[80,104,106,109–112] Individual collagen molecules then aggregate spontaneously in a quarter-staggered arrangement to form elongated fibers (termed fibrils). After fibril formation, the lysyl-oxidase pathway forms cross links in a head-to-tail fashion, which gives exceptional strength to collagen fibers.[76,77,79,105,113–120]

Collagen is extensively used in tissue-engineering applications due to its inherent properties, such as high tensile strength; being inexpensive and easy to prepare in large reproducible quantities; biodegradability; hemostatic properties; low antigenicity; high degree of resistance to proteolysis; biostability; low inflammatory and cytotoxic properties; and the ability to interact with cells and other ECM molecules, which promotes cellular attachment and growth, and consequently, tissue healing and regeneration.[71,72,121–139] Collagen type I is primarily extracted

from skin and tendons, while cartilaginous tissues are used for extracting type II collagen. Dilute acidic solutions are used to break intermolecular crosslinks of the aldimine type, while proteolytic enzymes, such as pepsin, are used to cleave the more stable crosslinks of the ketoimine type. Limited pepsin digestion will cleave only the non-triple-helical C- and N-telopeptides, leaving the triple-helical molecule intact,[98,132,140–142] unless it has been partially unfolded, molten or broken.[143] Extracted collagen, under appropriate conditions of temperature, pH, ionic strength, collagen concentration and composition, and in the presence of other connective tissue macromolecules, will spontaneously self-assemble to form microscopic fibrils, fibril bundles and macroscopic fibers with structural characteristics that are virtually indistinguishable from their native counterparts.[88,98,144–161] The lysyl-oxidase-mediated crosslinking does not occur *in vitro*, and consequently, reconstituted collagen constructs lack sufficient strength and may disintegrate upon handling or collapse under the pressure from surrounding tissue upon implantation. To this end, a number of crosslinking methods (chemical, physical, and biological) have been introduced that offer control over mechanical and thermal properties, biological stability, residence time in the body, and to some extent, the immunogenicity and antigenicity of the device.[127,132,134,162–171]

Elastin is an ECM protein that is responsible for the elasticity and resilience of tissues and organs such as skin, blood vessels, lung, and elastic ligaments.[172,173] The amount of elastin in a tissue depends on the tissue function; elastin comprises 1–2% of tendons, 2–4% of skin, 30% of lung, 50% of large arteries, and 70% of elastic ligaments by dry weight mass.[174–179] Under physiological conditions, smooth muscle cells, endothelial cells, fibroblasts, and chondrocytes synthesize elastin as a 72-kDa soluble precursor (termed tropoelastin).[180–187] Elastin has also been reported to be produced by neoplastic cells.[188] Tropoelastin undergoes a number of post-translational modifications before it is assembled into the elastic fibers. Each elastin molecule is composed of alternating hydrophobic and lysine-rich crosslinking domains that are critical for extracellular assembly and elastic function. Lysine side chain oxidation (by lysyl-oxidase) allows the formation of covalent crosslinks with neighboring molecules.[180,189–193] A transglutaminase crosslink between tropoelastin and fibrillin-1 has also been identified.[194] Crosslinking results in mature elastin, which is insoluble and extremely stable. Overextension of tissues is prevented by these crosslinks; these enable almost complete recovery of the wavy configuration of the collagen fibers after muscle contraction.[191,195–197] These elastic fibers are composed of an abundant amorphous core, of which elastin is the major constituent, and a highly ordered microfibrillar structure of about 10–12 nm in diameter, which is located around the amorphous core and is composed of fibrillin 1 and/or 2.[150,173,198–203] Fibrillins, together with the elastin microfibril interface located proteins (EMILINS), act as a template for the organization of the elastic tissue and are distributed in tissues where resilience and elastic recoil are prominent.[198,202–207] Elastin, its degradation products, and synthetic elastin-like peptides interact with the elastin–laminin receptor, and mediate elastin synthesis, chemotaxis, inhibit vascular calcification, proliferation, migration and differentiation of numerous cells, and other biological processes.[208–211] It is for these reasons that elastin-based biomaterials of different physical forms are used for skin regeneration and as vascular constructs.[33,212–218]

2.222.2.2. Proteoglycans and Glycosaminoglycans

Proteoglycans are a family of glycoproteins that consist of a protein core with a variable number of covalently attached carbohydrate moieties.[219] These ECM molecules form a gel-like structure in which collagen fibrils are embedded.[220] There are two major classes of proteoglycans present in connective tissues; the first is represented by large molecules (>1000 kDa), having the capacity to form aggregates with hyaluronan,[221–223] while the second class is characterized by low-molecular weight aggregates (<100 kDa) that are not capable of interacting with hyaluronate.[224] Although proteoglycans and their constituent glycosaminoglycans are found in very low quantities in connective tissues, they influence many physiological processes, including collagen fibrillogenesis, cell–cell interactions, growth factor binding, and cell regulation.[65–68] Small, leucine-rich proteoglycans (e.g., decorin, biglycan, fibromodulin, and lumican)[225–231] regulate collagen fibril assembly and growth by preventing aberrant, lateral fusion of collagen fibrils in connective tissues such as the tendon.[232–234] Chondroitin sulfate and hyaluronate are primarily encountered in fetal tendon tissue, while dermatan sulfate is the main glycosaminoglycan in the mature tendon,[235] and have been shown to facilitate structural integrity of collagen fibrils.[116,236] Due to the important biological functions of proteoglycans and glycosaminoglycans in native tissues, these molecules are frequently used to enhance the properties of implantable devices for several tissue-engineering applications,[237] including those for cartilage,[238] nucleus pulposus (NP),[239] tendon,[240] bone,[241] and skin[242,243] regeneration.

2.222.2.3. Fibronectin and Laminin

Fibronectin is the major product of diploid fibroblasts[244] organized in discrete ECM fibrils that also contain procollagen types I and III.[245,246] Fibronectin is a dimmer with a molecular weight of 250 kDa and is found in the ECM at an early stage of embryonic development. During this period, a dynamic relationship between fibronectin, laminin, and collagen type IV has been documented.[247] Fibronectin is an abundant component of the ECM of the submucosa, basement membranes, and the interstitial tissues.[248,249] It possesses ligand binding sites, such as Arg-Gly-Asp (RGD sequence), for adhesion and migration of many cell types. Specifically, fibronectin induces receptor clustering by binding to two integrins, which, subsequently, creates a relatively high local concentration of fibronectin. This promotes self-association and also facilitates attachment to the actin cytoskeleton through interactions with the cytoplasmic domain of the receptor.[250–252] Fibronectin has also been shown to modulate the deposition of several ECM molecules, including type I and type III collagens,[253–256] and is involved in wound healing.[257] For these reasons, fibronectin is extensively used to enhance the biological properties of biomaterials for bone,[258] tendon,[259] and other tissue-engineering applications.[260]

Laminins are extracellular, cross-shaped molecules with one long and two or three short arms, heterotrimeric

glycoproteins of molecular weight between 400 and 900 kDa. Laminins consist of noncovalently associated α, β, and γ chains that facilitate the assembly and structural integrity of basement membranes.[248,261–264] Laminin molecules bind to each other in the extracellular space and form laminin networks that are located close to the cell surface.[265,266] Extracellular assembly of a laminin network has been postulated to be important in epithelial morphogenesis.[267] Laminins are adhesion molecules that contain specific domains that are capable of interacting with cellular receptors or ECM ligands, thereby influencing cell proliferation, differentiation, adhesion, and migration under normal and pathological conditions.[262,268–271] Laminin is crucial in early embryonic development and tissue morphogenesis[272] and deletion of any of its subunits results in periimplantation lethality.[273,274] Laminin 2 and 4 are present in the basement membrane of skeletal muscle.[275,276] It has also been shown that laminin is essential for myo-differentiation, muscle cell survival *in vitro* and *in vivo*, and muscle integrity.[277] Absence of laminin leads to different types of muscular dystrophy and myopathies that are manifested by discontinuities in or breakdown of the myofiber basement membrane under constant stress of contractions.[278–283] Laminin has also been shown to influence nerve regeneration by facilitating the extension of neurites.[252,284–286] Laminin also plays an important role in wound healing, and keratinocytes activated at the leading edges of wounds have been shown to express high levels of laminin.[287–289] Mutations in the isoforms of laminin 5 are associated with epidermolysis bullosa, a group of inherited disorders of the dermoepidermal region in the skin, where blistering occurs as a result of even slight mechanical trauma.[290–292] Given the importance of laminins in physiological and pathophysiological conditions, therapeutic approaches based on laminin are under investigation. For example, gene therapy studies have been used to successfully treat epidermolysis bullosa,[293,294] while biomaterials coated with laminin have been used for nerve regeneration.[295–298]

2.222.2.4. Growth Factors

Growth factors are ECM molecules with specific biological activity. Although they are present in very small quantities, growth factors act as potent modulators of cell behavior, including differentiation, migration, adhesion, and gene expression.[299] Growth factors initially interact with receptors on the plasma membrane to deliver mitogenic signals that are required for cell proliferation.[300,301] The association of microtubules and microfilaments with proteins of the plasma membrane also plays a regulatory role in conveying the signals delivered by the growth factors to specific intracellular targets,[302–305] even when the cytoskeleton is not intact.[306] Several growth factors, including the vascular endothelial cell growth factor (VEGF), fibroblast growth factor (FGF), transforming growth factor beta (TGF-β), platelet-derived growth factor (PDGF), and the bone morphogenetic protein (BMP), are used to enhance the biological functions of biomaterials and modulate cell functions.[171,307–314] For example, incorporation of growth factors in scaffolds has been shown to be crucial at the early stages of the repair and it is likely to result in superior repair, and therefore, a functional tissue. VEGF, insulin-like growth factor, PDGF, basic FGF, and TGF-β have all been shown to increase the mechanical properties of the tissue, to enhance intrinsic reparative processes after tendon injury, to enhance tendon healing and, in general, to modulate cell proliferation and to stimulate matrix synthesis.[312,315–327] However, growth factors are typically labile; when intravenously administered, the biological half-lives of PDGF, basic FGF, and VEGF are 2, 3, and 50 min, respectively.[64] As a result, the use of polymeric drug-delivery vehicles, to encapsulate the active molecules and maintain a sustained localized delivery to the target site, has been adopted.[328–331] Gradients in the concentration of growth factors have also been investigated as a means to enable directional cell migration, create patterns of cellular differentiation and direct tissue organization into complex structures, such as the branching networks of vascular or nervous systems.[332–335]

2.222.3. Xenogenic Tissues, ECM Biopolymers, or Cells in Tissue Engineering

More than 33 million musculoskeletal injuries occur annually in the United States alone.[336–341] As the human population ages and life expectancy increases, injuries and degenerative conditions of the skeletal system will continue to rise, adding to the physical and financial strain of healthcare systems. It is therefore of paramount importance to develop strategies that enable functional regeneration of tissue. This section provides an overview of the current tissue-engineering solutions aimed at musculoskeletal regeneration.

2.222.3.1. Bone Reconstruction

Early attempts at xenogenic bone grafting used fresh, fresh frozen, or freeze-dried calf bone. Boplant® is an example of an early, commercialized xenograft. Unfortunately, these xenografts were poorly tolerated by the body and were ineffective at bone regeneration.[342] Currently, two types of xenografts are available: those in which the inorganic matrix has been removed and those in which the organic matrix has been removed. The former are known as demineralized bone matrix (DBM), while the latter are biologically produced hydroxyapatite. The most common sources of a xenograft are bovine bone or natural coral. Unlike autografts, xenografts must undergo substantial processing before they can be implanted into a human recipient. Such processing involves the removal of host cells, the organic or inorganic matrix, and sterilization. Freeze/thaw cycles are used to kill the host cells; alternatively, the xenograft is treated with gamma radiation, which simultaneously kills the cells and sterilizes the implant. The xenograft can also be immersed in alcohol, detergents, or in a glycosidase solution to remove fatty components and antigens, or soaked in demineralization solution to remove the inorganic structure, leaving a porous collagenous xenograft. It has been hypothesized that the removal of the inorganic phase allows greater access to proteins within the collagenous structure, which may aid in osteoinduction. For removal of the organic phase, the xenograft is either subjected to high temperature treatment or to deproteinization using chemicals such as hydrogen peroxidase. The reason for removing the organic phase is

to reduce the risk of cross-species reactivity and the transmission of any disease, for example, the Creutzfeldt–Jakob disease. A number of deproteinized bovine-derived bone substitutes are commercially available, such as Bio-Oss®, Cerabone®, Endobon®, and Osteograf®.[343,344] All of these products provide an osteoconductive surface for bone growth and a structure that mimicks the natural environment.

Bone xenografts are commonly mixed with bone marrow aspirate to enhance the regenerative process. The first clinical attempt to use bone xenografts combined with bone marrow was reported in 1978 by Salama *et al*. This study used partially deproteinized bovine bone (Kiel Bone) mixed with bone marrow from the iliac crest and implanted them in 28 patients. The results were promising and infection occurred only in one case.[345] Horowitz *et al*. used the same xenografts, mixed with bone marrow aspirate, to treat cystic defects in the jaws of 20 patients. On a 4-year follow up, the success rate was 80%; however, none of the failures were attributed to host rejection.[346] The Kiel bone has been used in almost every bone-grafting situation but with mixed results. Salama and Horowitz, as mentioned above, have found excellent success rates, while McMurray *et al*. have found it unsuitable in orthopedic practice.[347] The Kiel bone, when used by McMurray, was infiltrated with fibrous tissue by as early as 6 weeks, and was still present at 17 months after the operation. It was concluded from this study that the Kiel bone only provides a temporary structural support for the invasion of fibrous tissue and eventually leads to tissue necrosis due to the absence of a vascular network. As the popularity of the Kiel bone decreased, the market was gradually taken over by the fully deproteinized bone. Bio-Oss®, which is a biologically produced hydroxyapatite, is the current world leader in xenograft materials. There have been reports of varying and unpredictable degradation rates;[348] however, a review of 20 patients, who in 1999 received Bio-Oss® for maxillary sinus reconstruction, over a period of 6 months to 4 years showed that the material was surrounded by host bone *in vivo* and that osteoclasts were present, suggesting a slow degradation profile.[349] Bio-Oss® is now available in combination with porcine collagen, that is, Bio-Oss Collagen®, to improve the regenerative process.

Xenograft materials for bone tissue engineering can also be derived from marine animals as their ECM mainly comprises hydroxyapatite. Ewers performed a 15-year study in 118 patients who were implanted with marine-derived xenografts for maxillary sinus grafting.[350] The biomaterials used were AlgiPore®, C Graft™, and AlgOss™, and were implanted along with 10% autogenous bone mixed with either venous blood or platelet-rich plasma (PRP). The dental implants were placed six months after maxilla grafting. The survival rate of the resulting dental implants was 95.6%, indicating that sufficient bone regeneration had occurred in the 6-month interim period. Schopper *et al*. have examined biopsies from 26 patients who had received Algipore® implants in the maxilla.[351] They found that new bone had formed around the xenograft after 7 months. Multinucleated giant cells were observed within the implanted material and resorption was evident. Algipore® and C Graft™ have also been successfully used along with autologous bone in maxilla graft operations.[352]

Xenografts that have been processed for implantation purposes, however, are not without limitations. Despite xenografts being osteoconductive, they offer little toward osteoinduction. It is hypothesized that the absence of the protein component leads to the loss of osteoinduction properties. It is for this reason that xenografts are commonly combined with autologous bone, bone marrow, or growth factors. Despite the advances in processing techniques and sterilization, there still exists a fear of cross-species contamination, thus limiting their use as grafting material.

Before the introduction of biomaterials, the obvious high strength and structural stability of bone left surgeons with no choice but to replace irreversibly damaged bone tissue with more bone tissue, hence the use of xenografts. Gallie published a paper in 1914 entitled 'The history of a bone graft,'[353] which investigated the fate of autologous bone grafts, boiled bone grafts, and xenogenic bone grafts. This paper also highlighted the early, practical search for new materials to replace bone. The use of metal plates to stabilize long bone fractures has also been discussed by Lane in 1895;[354] however, the development of the first generation of modern biomaterials did not begin until the mid-twentieth century. The first biomaterials were permanent structures designed to support the bone and prevent fracture reoccurrence, however, the tissue engineering had one further goal, namely regeneration. If tissue regeneration was to be achieved then degradable biomaterials were a necessity. Such degradable biomaterials can be divided into two distinct groups: natural and synthetic.

Synthetic polymers are the most versatile of all materials used in tissue engineering. Mechanical and degradation properties can be tailored by blending a series of polymers with few limitations on the scaffold architecture. A discussion of the commonly used polymers has been provided by Hutmacher.[355] Polyester is a type of polymer defined by ester linkages in its main chain. Poly(L-lactide) (PLLA) and PGA are the types of polyesters that have been extensively used in tissue engineering. These polymers are a promising scaffolding material; however, the by-products created during *in vivo* degradation are a major disadvantage. A clinical trial in patients receiving PLLA bone plates or screws has been reported to result in swelling at the site of implantation.[356] Remnants of the implant were surrounded by a fibrous capsule, and on closer examination, highly crystalline particles were found both intra- and extracellularly at 5.7 years postimplantation. Bostman *et al*. have also frequently observed clinical foreign body reaction to PLLA and PGA materials.[357–360] It should also be noted that there have been many successful clinical outcomes using these materials,[361,362] however, given the frequent incidence of foreign body reaction, this is not an ideal implant material.

It is for this reason that xenogenic biopolymers (polymers derived from natural origins) are processed before use as biomaterials. The most commonly used natural material is collagen type I. Other examples include chitosan, glycosaminoglycan, hyaluronan, fibrin, and silk; however, collagen or composites of collagen are the only xenogenic biomaterials that are being widely used in bone tissue engineering today. As these materials are derived from natural materials, they have the advantages of biological recognition, availability of receptor-binding ligands, a natural hierarchical structure and susceptibility to cell- triggered proteolytic degradation.[363] Natural polymers such as collagen are composed of polypeptides which contain chains of amino

acids. Most natural polymers contain a higher level of complexity compared to synthetic polymers. There is a hierarchy in structure, for example, in collagen, amino acid chains form peptides, peptides combine to form polypeptides, polypeptides form helical chains which are referred to as tropocollagens, tropocollagen chains combine to form fibrils which eventually unite to make fibers of collagen.[132,364] Due to this structure, these materials also revert to their lower hierarchical forms upon degradation,which can be easily cleared by the body.[364] Many natural polymers are commercially available either individually or as composites, such as, Collagraft® (collagen plus biphasic calcium phosphate), Healos® (collagen plus hydroxyapatite), DuraGen™ (collagen), Veritas® (collagen), and Integra™ (collagen). Most scaffolds that are based on naturally occurring materials, however, are suitable only for nonload bearing applications or when in combination with a metallic implant, for example, collagen has been used as a carrier for rhBMP-2 in spinal interbody fusion when used in combination with a titanium cage.[365,366] Collagen is ideal for such applications as it is pliable, absorbent, and highly biocompatible. Collagen sponges loaded with rhBMP-2 have also been used for maxillary sinus reconstruction followed by successful dental implant placement[367] and also in the repair of open tibial fractures.[368] Although collagen has been used for bone tissue engineering, it is more suitable when combined with either ceramic or a polymer. Collagen and calcium phosphate have often been combined to form composites as their composition is similar to that of the bone, for example, Collagraft® and Healos®.

In a clinical trial in 213 patients, autologous bone grafts were compared with a collagen/biphasic calcium phosphate ceramic (Collagraft®) mixed with autologous marrow.[369] At 24-month postoperation, 98% of the autografts resulted in fracture healing, while 97% of the Collagraft® treated fractures had also healed. In a separate study by Cornell *et al.*, which monitored 267 patients over a 12-month period, Collagraft® appeared to function as well as an autograft.[370] Neen *et al.* have performed a study using Healos® along with bone marrow aspirate to treat posterolateral lumbar fusions and lumbar interbody fusions. They found that Healos® was effective in the posterolateral lumbar spine fusion model but was radiographically ineffective in lumbar interbody fusions.[371] Carter *et al.* have used Healos® for transforaminal lumbar interbody fusion in combination with interbody cages and posterior pedicle screws; however, patient numbers are low ($n = 20$) and no controls were applied.[372] Despite these inadequacies Healos® was shown to be effective in achieving a successful fusion. DePuy, manufactures of Healos®, have released an injectable version of this product, Healos® Fx., in 2009. An injectable product is always desirable as it can be used during minimally invasive surgery and has the added benefit of complete defect filling.

Despite these advances in tissue-engineering scaffolds, they have failed to become the primary choice of surgeons, which suggests inadequate healing. The majority of tissue-engineering scaffolds described above are empty templates, and depend on a compromised healing site to upregulate the genes necessary for osteogenesis. It is therefore not surprising that a scaffold alone is inadequate in regenerating the defective site. As collagen is a hydrophilic material and well tolerated in the body, it has received a lot of attention for use as a drug carrier. Some of the studies described above have used BMPs to aid the regenerative process. This combination of xenogenic biopolymers and growth factor delivery has been shown to be an effective for the treatment for critical-sized bone defects. Chung *et al.* have developed a nanoparticles–hydrogel complex consisting of fibrin, heparin functionalized nanoparticles, and BMP-2. **Figure 1** shows the regeneration of six critical-sized defects over a 4-week period.[373] Such technologies have resulted in the commercialization of the OP-1® putty available from Stryker® and the INFUSE® bone graft available from Medtronic; however, more recent developments have also used collagen as a carrier for plasmid DNA for bone regeneration.[374–376] The collagen scaffolding material acts as a reservoir for controlled release, and hence, prolonged delivery of the therapeutic agent can be achieved.[377] **Figure 2** shows an osteosarcoma cell transfected with plasmid DNA that was released from a collagen/calcium phosphate scaffold developed for bone tissue engineering.[378] The same material was then used to correct femoral defects in mice.[379] The collagen/calcium phosphate scaffold was loaded with plasmid DNA encoding $VEGF_{165}$. **Figure 3** shows remnants of the scaffold material and evidence of bone regeneration at the defect site. There was a statistically significant increase in bone formation when scaffolds loaded with the $VEGF_{165}$ plasmid were used compared to plain scaffolds. This study heralds an exciting, new age for xenogenic biopolymers.[379]

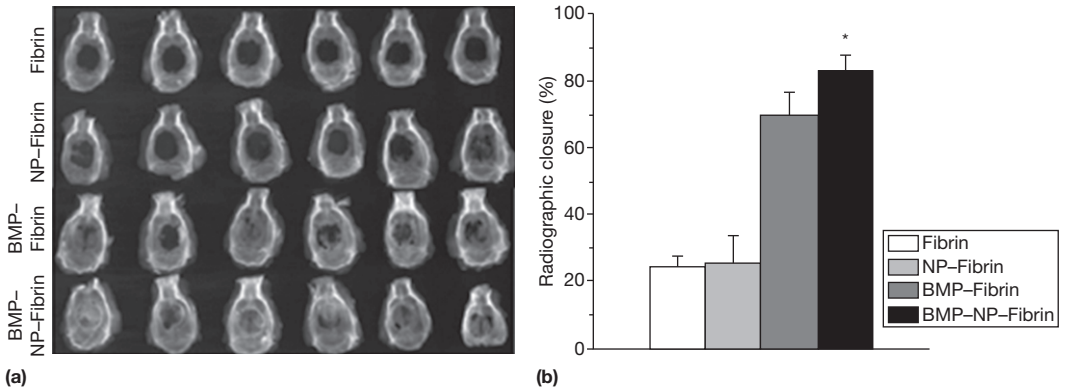

Figure 1 Regeneration of critical-sized defects over a 4-week period using functionalized with heparin and BMP-2 fibrin systems. Reproduced from Chung, Y. I.; Ahn, K. M.; Jeon, S. H.; Lee, S. Y.; Lee, J. H.; Tae, G. *J. Control. Release* **2007**, *121*, 91–99.

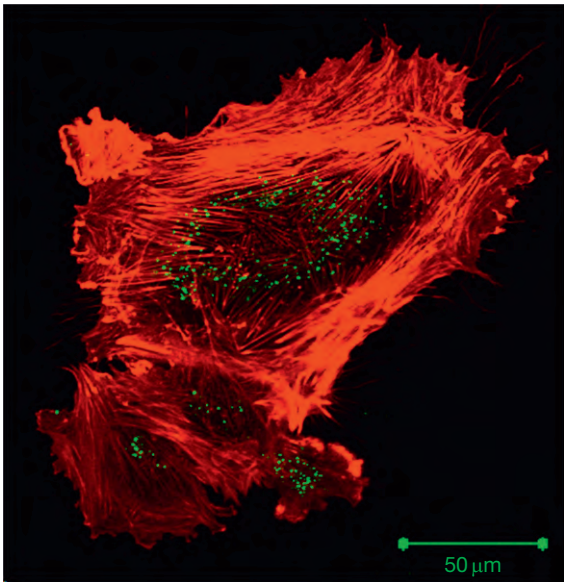

Figure 2 Uptake of plasmid DNA by a marrow stromal cell following delivery from a collagen/calcium phosphate scaffold. Plasmid DNA has been labeled with a cyanine 3 (green) marker, while the phalloidin filaments have been stained with rhodamine (red). Plasmid DNA was complexed with a commercially available transfection agent for efficient delivery.

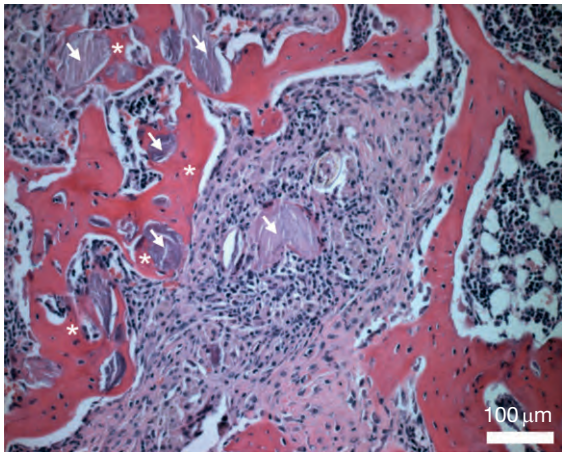

Figure 3 Resorption of a collagen/calcium phosphate scaffold and replacement with bone in a mouse femur after 4 weeks of implantation. The scaffold was loaded with plasmid DNA encoding vascular endothelial growth factor 165. Arrows indicate remenants of scaffold, while asterisks indicate bone formation with the defect site. Decalcified histological section stained with hematoxylin and eosin. Image captured at 200×.

2.222.3.2. Intervertebral Disc Reconstruction

Neck and low back pain are the two highest causes of job-related disability, with significant associated social and economic costs,[380] accounting for a total annual direct healthcare cost estimated between $50 and $90 billion each year in the United States alone.[381] These pathologies are strongly associated with degeneration of the intervertebral disc (IVD).[382] Disc degeneration disease (DDD) is defined as 'an aberrant cell mediated response to progressive failure.'[383] The onset of the degeneration process results in the IVD being inherently incapable of adequate self-repair.[382] Currently, the most prevalent treatment modalities associated with DDD involve conservative methods, including physical therapy, drugs, and interbody fusion surgery.[380,381] Tissue-engineering strategies offer many advantages in the treatment of DDD. This will potentially have a significant impact on medical practices and will facilitate a reduction in the social and economic costs associated with DDD.[384]

Current technologies for disc replacement are designed to preserve flexion, extension, and lateral bending motions, and ultimately, to restore disc space height.[385] The use of the poly(vinyl)alcohol hydrogels has been advocated, although a significant delay in the regeneration process has been observed after implantation into baboon and rabbits.[386,387] It is also worth pointing out that their long-term behavior is still unknown[388] and that ejection of the implant (out of the disc) due to mechanical movements and the absence of adherence of this material to the native tissue limit its use in clinical practice.[387] Furthermore, the inability of such materials to biointegrate, and subsequently, remodel the tissue, imposes the need for developing new strategies. To respond to these problems, other types of hydrogels are under investigation. A promising preclinical trial of an injectable hydrogel 'NuCore™' (Spine Wave, USA) has been carried out recently. This commercial hydrogel is composed of an *in situ* crosslinked copolymer of elastin and silk which mimics the biomechanical properties of the native nucleus. The disc maintained 93% of its original height at the central region and 92% at the posterior disc region after 24 weeks during this preclinical trial.[389] However, this material can only replace, but not regenerate, a damaged disc.

New tissue-engineering approaches are based on either the regeneration or replacement of the IVD using biomaterials that are enriched with cells and/or bioactive macromolecules. Cell implantation, generally associated with scaffolds, has received great attention in recent years. Cells-based tissue engineering can be envisaged in two ways: either injection of cells alone[390] or injection of cells with a carrier system (often a biodegradable scaffold).[391] These carriers provide physical support for cell placement into the disc. Furthermore, with these, a specific cellular environment can be created[392] to direct a desired cellular activity, such as cell proliferation or production of ECM. These scaffolds can be functionalized by gene or drug carriers, which can influence signaling pathways[393] and/or enable the production of new functional ECM[394] (**Figure 4**).

The major challenge in cell-based therapies is the identification and development of a material, which resembles native tissue, and is capable of promoting phenotype maintenance, proliferation and differentiation of NP cells, and/or stem cells. Cell carriers such as alginate,[395] bioactive composite scaffolds including chitosan–glycerophosphate,[396] type II collagen–aggrecan–hyaluronan,[384] fibrin–hyaluronan scaffolds,[397] and gene carriers such as nanoscaffolds including nanoshells, dendrimers, and polymers[398] have the following advantages when used as therapeutic solutions: (a) biodegradability; (b) injectability (less invasive than the use of surgical techniques); (c) preservation of the native tissue; and (d) nonpreclusion of future spinal surgery and multilevel disc

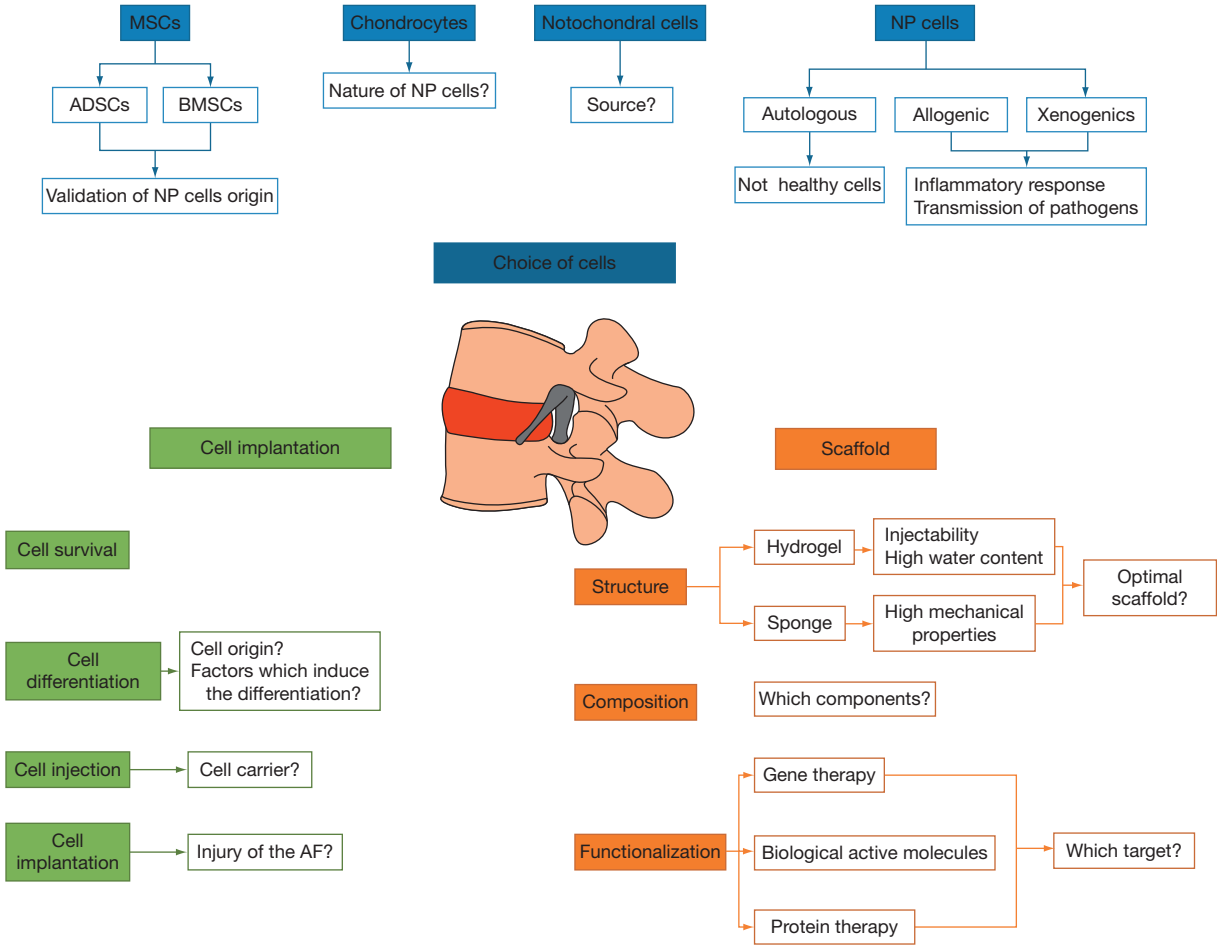

Figure 4 Potential strategies for the treatment of the intervertebral disc.

treatments.[399] Ideally, this three-dimensional matrix should closely mimic the environment of the native tissue at the site of interest.[400] An ideal scaffold should be biodegradable at a rate that matches ECM deposition without any toxic or inhibitory products. In addition to being highly biocompatible, the scaffold should have a chemical/structural make-up that permits the transport of nutrients, metabolites, and regulatory molecules to and from the cells[401] and should not affect cell phenotype and differentiation.[402]

The composition of the hydrogels used for cell delivery is important for NP regeneration. It has been shown that the low antigenic character of type II collagen, its mechanical properties and its dominance in the composition of the native tissue make it a candidate of choice for IVD tissue engineering.[54,403] Copolymers of type II collagen have been reported to be promising scaffolds for cartilage and disc regeneration,[239,404,405] inducing, notably, the regeneration of the disc after bone marrow-derived mesenchymal stem cell (bMSCs) implantation (**Figure 5**).[406] Type II collagen hydrogels have also been shown to enhance chondrogenesis of adipose tissue-derived stem cells (ADSCs) at a greater rate than hydrogels of collagen type I.[402] Furthermore, microenvironments of chondroitin sulfate and hyaluronic acid (HA) have been shown to promote cell aggregation and chondrogenic differentiation. These molecules also help maintain the NP cell phenotype.[397,407]

HA is an abundant glycosaminoglycan in NP tissue. Tissue-engineering strategies are based on molecules derived from HA. Studies have shown that acellular hydrogels (HYAFF-R 120) and cell-loaded hydrogels (HYADD-R 3) are capable of inducing repair of an IVD following nucleotomy. Although the biological effect of hyaluronan-derived materials has not been studied,[408] it has been reported that HA has a positive effect in stimulating ECM biosynthesis, cell proliferation, cell migration, and phenotype maintenance in chondrocytes and NP cells.[397,409–411] Furthermore, an anti-inflammatory effect of this molecule has also been shown that prevent arthritis formation in joints and discs.[412] Soluble HA, blended within collagen gels, can provide the biological benefits of HA without the associated mechanical limitations.[413]

Different cell sources have been envisaged for cell therapy of IVD, such as autologous and xenogenic cells from the NP and mesenchymal stem cells. The use of autologous and xenogenic cells is limited by the low number of cells available in the disc. For this reason, mesenchymal stem cells have been investigated extensively with regard to their availability, proliferation, and differentiation properties.[400] Two types of mesenchymal stem cells are used for IVD therapy: bMSCs and ADSCs.

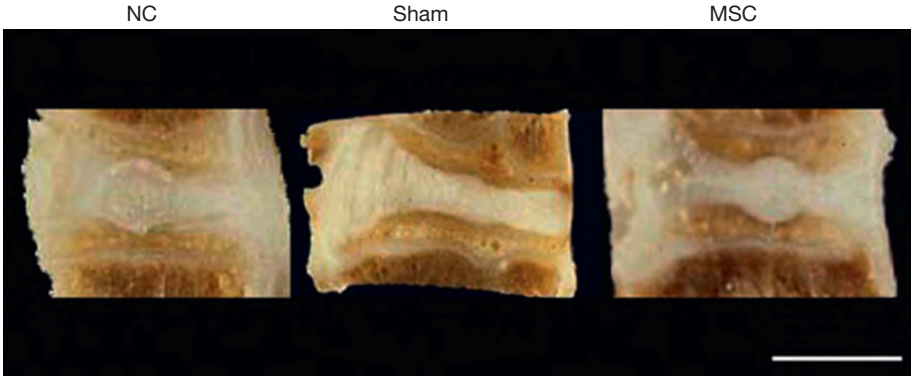

Figure 5 Macroscopic view of normal control (NC), sham-operated (Sham), and mesenchymal adult stem cell (MSC)-transplanted discs (MSC) after MSC transplantation using a type II collagen hydrogel as cell carrier. Reproduced from Sakai, D.; Mochida, J.; Iwashina, T.; *et al*. *Biomaterials* **2006**, *27*, 335–345.

In vitro, cocultures of bMSCs and ADSCs with NP cells have been shown to induce the production of type II collagen, GAGs, and a decrease in type I collagen production and markers of differentiation into a NP cell-like lineage.[414–416] The environment of culture of stem cells affects their properties and differentiation. Micro-mass cultures have shown a significant improvement in the production of type II collagen and aggrecans.[92] ADSCs have been the subjected to extensive research in orthopedic tissue engineering in recent years. They have been described in literature as having the same properties as bone marrow stem cells. However, ADSCs present distinct advantages compared to bone marrow stem cells, that is, widely available sources and larger numbers. ADSCs have shown properties of differentiation into IVD cell-like and chondrogenic lineages.[417] Mesenchymal stem cells could be a good alternative to cell therapy for IVD. However, the origin of NP cells is still unknown and the use of mesenchymal stem cells is under debate.[418,419]

A combination of the datasets suggests that the association of different types of ECM molecules would help guide the differentiation of stem cells into a NP cell-like phenotype. O'Halloran *et al.* have shown that a composite hydrogel of HA and type II collagen was most suitable for maintaining a NP cell phenotype.[384] Consequently, a cell carrier with a composition that closely mimics the native environment could be envisaged as ideal for IVD regeneration. Therapies that use direct injection of growth factors or cytokine inhibitors have been shown to be unsuccessful because of their short half-life *in vivo*.[382] Furthermore, a degenerated disc in a more advanced stage of degeneration may require prolonged exposure to growth factors to restore biochemical composition and disc function. It appears that the use of gene therapy can prolong the exposure period of IVD cells to these therapeutic molecules (e.g., growth factors,[393] transcription factors,[420] RNA interferent[394]). In order to keep the composition of the biodegradable carriers closer to the native tissue, carriers based on ECM proteins are currently being developed. The advantages of these carriers are their biocompatibility due to their similarity to the ECM and their biodegradability. Nagae *et al.* have shown that the delivery of PRP-impregnated gelatin microspheres slowes down the process of degeneration.[421] The biodegradability of the microsphere, controlled by the degree of crosslinking, induces a time-dependent release of the molecule of interest. However, repeated injections are essential for continuous inhibition of the degeneration factors.[420,421]

The treatment of the IVD seems to be a complex association of cells and biologically active molecules, all embedded within a biodegradable polymeric carrier. It is anticipated that an association of the macroscale (carrier of cells) and the microscale (carrier of gene or/and proteins) components will provide a solution that not only will slow down the process of IVD degeneration but also promote its regeneration (**Figure 4**).

2.222.3.3. Tendon Reconstruction

There are over 15 million tendon- and ligament-related injuries in the United States alone with approximately 95 000 new cases per year.[336–341] As the life expectancy increases, it is anticipated that tendon injuries will remain the most common cause of morbidity throughout the world. Therefore, it is essential to develop therapeutic strategies for functional tendon regeneration. Noninvasive pharmacological strategies for the prevention of ligament and tendon injuries, based on slow acting antirheumatic drugs (SAARDs) or nonsteroidal anti-inflammatory drugs (NSAIDs), have been introduced.[422–425] However, SAARDs and NSAIDs are effective only during the early stages of disease, are associated with severe side effects[426–428] and have an inhibitory effect on proteoglycan synthesis and cell proliferation.[429] For these reasons, their use has been limited.

The use of tissue grafts has been advocated repeatedly due to superior functional results in a clinical set up for anterior cruciate ligament and extensor tendon.[430–433] Palmaris longus and plantaris longus tendon autografts are commonly employed for tendon reconstruction in the digit, hand, and wrist, as they are similar in size and have been proven to be reliable.[433–435] Allografts have also been used extensively for tendon regeneration with variable results that range from limited success[436–439] to properties similar or even superior to autografts.[5,440–442] Xenogenic tissues have also been used for tendon and ligament repair. Xenogenic tissues have a structure that is identical to the host tissue and do not compromise patient's tissues. Early drawbacks[3,443–445] have now been addressed[446,447] and recent data demonstrate normal tissue ingrowth in several animal models.[2,448–450] Despite the very

promising results with the use of tissue grafts, allografts still face the risk of potential transmission of infectious diseases[15–18] and autografts have the disadvantage of creating a secondary morbid site during harvesting. Development of tissue-engineering strategies is therefore essential to address shortfalls of tissue grafts.

Synthetic and natural scaffolds have the potential to significantly improve the treatment of tendon and ligament injuries, especially those associated with degenerative and congenital conditions, where autografts or allografts may not be available in sufficient quantity.[433,435,451–454] Numerous synthetic materials have been evaluated for tendon regeneration including polylactic acid,[455] carbon–polylactic acid polymer composite,[456,457] polytetrafluoroethylene,[458,459] polyethylene terephthalate,[460,461] poly(glycolic acid) and Dacron® composite,[462–464] nylon,[323,465] polypropylene,[466,467] PGA/polyglyconate/polydioxanone,[457,468] and polyglactin.[469] Since synthetic materials are associated with foreign body reaction[45–48] and a lack of cell-recognition signals and also because their hydrophobic properties hinder smooth cell seeding,[49–51] biological molecules (collagen, gelatin, HA, growth factors, and RGD peptides sequences) have been used to modulate cell attachment, decrease adhesions, accelerate tendon healing and improve the quality of repair tissue.[259,323,470–485] Despite the early promising results, several drawbacks in the use of synthetic devices have been identified. For example, Dacron® does not allow the functional orientation of neotissue[486] and fails to protect the patellar tendon graft during neovascularization.[487] Polyglycolic acid fibers induced a thinner and significantly weaker neotissue compared to natural tendon.[488] Nylon-based repair approaches have failed to successfully produce a new functional substitute.[489] Polypropylene devices were characterized by a disordered fibrous capsule.[490] The use of carbon fibers has also been limited due to the association of carbon with skin diseases.[491–493] Potential toxic degradation products of synthetic materials have also been shown to be deleterious to the surrounding tissue and have suppressed cell growth.[43,494,495] For these reasons, no artificial materials have been able to meet the requirements of functional tissue remodeling.[496]

Given that natural polymers (e.g., fibrin, silk, chitosan, and collagen) possess several inherent advantages such as ability to present receptor-binding ligands to cells, susceptibility to cell initiated proteolytic degradation, and natural remodeling,[13,38,52,57,58] they are preferred for scaffold fabrication for tendon repair. Although it has been shown that fibrin glue demonstrates significantly better functional and cosmetic results compared to treatment with sutures[497,498] and that it also promotes a smooth gliding surface and restricts adhesion after repair of the flexor tendon,[499–501] the properties of the regenerated tissue did not match those of the original tissue.[502] Silk has been used extensively for tendon reconstruction due to its exceptional mechanical and biological properties.[503–506] Moreover, silk-based biomaterials support cell attachment, expansion and differentiation of adult human progenitor bone marrow stromal cells and promote the expression of collagen types I and III and tenascin-C, all of which are characteristics of ligament.[507] However, early unsuccessful results[489] and potential allergic reactions have restricted its use in tissue engineering.[508] Chitosan has also been used successfully for tendon and ligament regeneration; in fact neotissue formation following implantation of chitosan-based scaffolds was characterized by very good mechanical properties.[509–513] Collagen-based devices have also been used very successfully for tendon and ligament regeneration. Self-assembled collagen fibers (**Figure 6**) have been shown to closely imitate native ECM supramolecular assemblies with regard to structural and mechanical properties,[88,156,162,168,514–529] while their unique nanotexture topography has been shown to facilitate directional cell migration, which is essential for neotissue formation.[527] Cross-linking approaches (chemical, physical, and biological) that have been investigated over the years have offered control over mechanical and thermal properties, biological stability, residence time in the body and, to some extent, the immunogenicity and antigenicity of the device.[127,132,134,162–171] Moreover, using transglutaminase, an enzyme that catalyze several posttranslational modifications of proteins in the ECM in a Ca^{2+}-dependent manner,[530–534] we have been able to functionalize collagen scaffolds.[93,168,535–539] Collagen fibers also avoid the problems that are associated with long-term foreign body implantation or a granuloma that could interfere with the smooth gliding of tendon repairs.[240,514,515,518,522,529] Indeed, it has been shown in animal studies that an aligned neotissue, similar to the one obtained from an autograft and almost identical to a normal tendon, is formed.[516,540] For ligament repair, self assembled collagen fibers have been shown to remodel host tissue within 12 weeks,[529] and an organized and crimped neoligament tissue was observed at 20 weeks postimplantation.[521] A combination of mesenchymal adult stem cells (MSCs), biological cues, and scaffolds have also been investigated for tendon injuries.[541] The hypothesis in this case was that MSCs could replace the limited number of host cells that reside in the endotendon tissue between the collagen fascicles and adjacent to the vasculature, and therefore, can potentially regenerate or repair the tendon and ligaments.[542,543] To this end, it has been shown that MSCs have proliferation rates and function that are comparable to tenocytes, while adipose-derived MSCs have been shown to proliferate fast *in vitro* and have been used to successfully repopulate acellularized tendon *in vivo*.[544,545] Animal models and human clinical trials have demonstrated significantly improved mechanical, structural, biological, and biochemical properties in the repaired tendon.[341,546–554]

2.222.4. Limitations

Allogeneic and xenogenic biological scaffolds based on ECM are being customarily used for numerous tissue-engineering applications because of their superior inherent properties, although the effects of such scaffolds on the host immune response are yet to be fully investigated.[141,555,556] Despite the advancements in extraction and purification procedures and the minimal regulatory requirements already in place, ECM components could potentially be responsible for disease transmission.[557–562] For example, the transmission of Bovine Spongiform Encephalopathy across species barriers has proven to be a significant drawback in manufacturing bovine-derived biomaterials despite reports that state that the transmission of this disease to humans, if at all it occurs, requires an effective dose for a sufficiently prolonged period of time.[563]

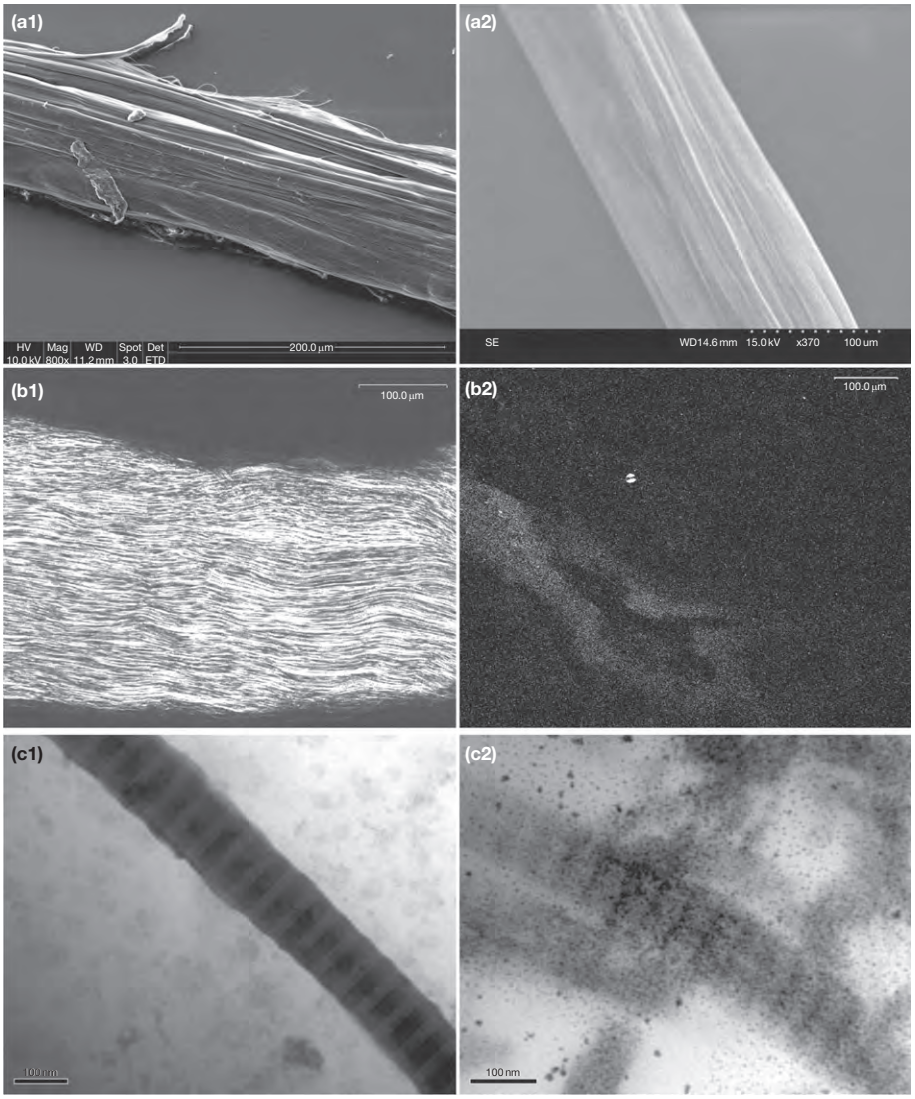

Figure 6 Extruded collagen fibers (a2) exhibit similar surface topography to native tendon (a1) as revealed by scanning electron microscopy. Second harmonic generation analysis demonstrates that extruded collagen fibers (b2) possess high level of crystallinity and structural alignment proportional to native tendons (b1). Transmission electron microscopy reveals that extruded collagen fibers (c2) are quarter-staggered arranged as native tendons (c1).

Recombinant and peptide synthesis technologies, have in the recent years, introduced a means of producing ECM-like components[564] such as collagen[565–569] and elastin.[570–573] Invaluable insights into physiological[574,575] and pathophysiological[576] collagen folding pathways, as well as information about triple-helix stability[577–579] and biological functions, including cell-adhesion and crosslinking sites,[580–583] have been obtained using collagen-like peptides. Similarly, several expression systems including transfected mammalian cells,[584,585] insect cells,[586,587] yeast,[588,589] bacteria,[590–592] transgenic mice,[593] transgenic plants such as tobacco[594,595] and corn,[596] and silkworms[597] have been successfully employed to produce human recombinant procollagens which avoids the problems related to variations between batches, interspecies transmission of disease and possible xenogenic immuno-responses induced by animal-extracted collagens.[598–600] However, the expression of fully functional molecules has been difficult due to the complex nature of procollagen synthesis.[601] Moreover, in all cases, the expression levels of procollagen have been very low and therefore have limited broad commercialization potential.[587,602,603] Moreover, recombinant collagens lack specific domains which are otherwise present in native fibrillar collagens,[564,604] which further compromises their biological function and reduces their use.

2.222.5. Future Perspectives

The use of xenogenic tissues and natural biomaterials in the skeletal system has been extensive. Future applications lie in how we can effectively overcome the current limitations in their manufacturing. A strategy to restore the instructive assembly of the natural scaffold is by the incorporation of signaling cues. This incorporation can be done by the use of functionalization strategies. Adding missing functionality to the

resultant manufactured biomaterial is an attractive option. This can be achieved by deciphering the linking strategies already existing in natural tissues. Natural enzymatic linkers can be synthesized using the advances made in peptide synthesis and click chemistry. However, much of the functionality can be achieved when basic fundamental transcriptomic signatures of various cell types, during their differentiation phases, are understood. Ultimately, the final EC matrix is a result of what the cells express. Hence, this critical piece of the puzzle needs to be deciphered to develop the ultimate biomaterial – the true EC matrix.

Acknowledgments

D. Z. would like to acknowledge the Engineering and Physical Sciences Research Council, UK; the Faculty Research Committee of the Faculty of Engineering, National University of Singapore; the Irish Research Council for Science Engineering and Technology (RCS740); Science Foundation Ireland (SFI_09-RFP-ENM2483); and the National University of Ireland Galway Millennium Research Fund (MF08-P11) for financial support. A. P. would like to acknowledge Science Foundation Ireland (SFI_07/RFP/ENMF482 and 07/SRC/B1163); the Irish Research Council for Science Engineering and Technology; The National Development Plan; the European Molecular Biology Organisation; the Enterprise Ireland Research Innovation Fund; the Health Research Board (RP/2008/188); and the European Commission (NMP3-LA-2008-213904) for financial support.

References

1. Pham, C.; Greenwood, J.; Cleland, H.; Woodruff, P.; Maddern, G. *Burns* **2007**, *33*, 946–957.
2. Stone, K.; Walgenbach, A.; Turek, T.; Somers, D.; Wicomb, W.; Galili, U. *Arthroscopy* **2007**, *23*, 411–419.
3. Milthorpe, B. K. *Biomaterials* **1994**, *15*, 745–752.
4. Scheffler, S. U.; Schmidt, T.; Gangéy, I.; Dustmann, M.; Unterhauser, F.; Weiler, A. *Arthroscopy* **2008**, *24*, 448–458.
5. Alcid, J. G.; Powell, S. E.; Tibone, J. E. *J. Shoulder Elbow Surg.* **2007**, *16*, 268–272.
6. Stock, U. A.; Schenke-Layland, K. *Biomaterials* **2006**, *27*, 1–2.
7. Tu, Q.; Zhang, Y.; Ge, D.; Wu, J.; Chen, H. *Appl. Surf. Sci.* **2008**, *255*, 282–285.
8. Lumpkins, S. B.; Pierre, N.; McFetridge, P. S. *Acta Biomater.* **2008**, *4*, 808–816.
9. Kim, S. W.; Seo, D. S.; Lee, J. K. *Appl. Surf. Sci.* **2008**, *255*, 388–390.
10. Xie, H.; Yang, F.; Deng, L.; *et al. Biomaterials* **2007**, *28*, 3314–3324.
11. Badylak, S. F. *Transpl. Immunol.* **2004**, *12*, 367–377.
12. Schenke-Layland, K.; Vasilevski, O.; Opitz, F.; *et al. J. Struct. Biol.* **2003**, *143*, 201–208.
13. Badylak, S. F.; Freytes, D. O.; Gilbert, T. W. *Acta Biomater.* **2009**, *5*, 1–13.
14. Goldblatt, J. P.; Fitzsimmons, S. E.; Balk, E.; Richmond, J. C. *Arthroscopy* **2005**, *21*, 791–803.
15. Evans, P.; Mackinnon, S.; Levi, A.; *et al. Muscle Nerve* **1998**, *21*, 1507–1522.
16. Conrad, E.; Gretch, D.; Obermeyer, K.; Moogk, M.; Sayers, M.; Wilson, J. *J. Bone Joint Surg. Am.* **1995**, *77A*, 214–224.
17. Asselmeier, M. A.; Caspari, R. B.; Bottenfield, S. *Am. J. Sports Med.* **1993**, *21*, 170–175.
18. Ireland, L.; Spelman, D. *Cell Tissue Bank.* **2005**, *6*, 181–189.
19. Bonassar, L. J.; Vacanti, C. A. *J. Cell. Biochem. Suppl.* **1998**, *30–31*, 297–303.
20. Butler, D. L.; Goldstein, S. A.; Guilak, F. *J. Biomech. Eng.* **2000**, *122*, 570–575.
21. Lanza, R. P., Langer, R., Vacanti, J., Eds.; In *Principles of Tissue Engineering*; Academic Press: London, 2000.
22. Chai, C.; Leong, K. W. *Mol. Ther.* **2007**, *15*, 467–480.
23. Stitzel, J.; Liu, J.; Lee, S. J.; *et al. Biomaterials* **2006**, *27*, 1088–1094.
24. Lee, L. J. *Ann. Biomed. Eng.* **2006**, *34*, 75–88.
25. Hollister, S. J. *Nat. Mater.* **2005**, *4*, 518–524.
26. Hutmacher, D. W. *J. Biomater. Sci. Polym. Ed.* **2001**, *12*, 107–124.
27. Desai, T. A. *Med. Eng. Phys.* **2000**, *22*, 595–606.
28. Zeltinger, J.; Sherwood, J. K.; Graham, D. A.; Mueller, R.; Griffith, L. G. *Tissue Eng.* **2001**, *7*, 557–572.
29. Carnell, L. S.; Siochi, E. J.; Holloway, N. M.; *et al. Macromolecules* **2008**.
30. Khademhosseini, A.; Langer, R.; Borenstein, J.; Vacanti, J. P. *Proc. Natl. Acad. Sci. USA* **2006**, *103*, 2480–2487.
31. Xia, Y. *Nat. Mater.* **2008**, *7*, 758–760.
32. Ladet, S.; David, L.; Domard, A. *Nature* **2008**, *452*, 76–80.
33. Heydarkhan-Hagvall, S.; Schenke-Layland, K.; Dhanasopon, A. P.; *et al. Biomaterials* **2008**, *29*, 2907–2914.
34. Ker, R. F. *Int. J. Fatigue* **2007**, *29*, 1001–1009.
35. Williams, D. F. *Biomaterials* **2008**, *29*, 2941–2953.
36. Laporte, L. D.; Shea, L. D. *Adv. Drug Deliv. Rev.* **2007**, *59*, 292–307.
37. Hutmacher, D. W.; Woodruff, M. A. In *Handbook of Engineering Biopolymers: Homopolymers, Blens and Composites*; Fakirov, S., Bhattacharyya, D., Eds.; Hanser: Munich, 2007; pp 773–794.
38. Nair, L. S.; Laurencin, C. T. *Prog. Polym. Sci.* **2007**, *32*, 762–798.
39. Liu, Y.; Ramanath, H. S.; Wang, D.-A. *Trends Biotechnol.* **2008**, *26*, 201–209.
40. Martina, M.; Hutmacher, D. *Polym. Int.* **2007**, *56*, 145–157.
41. Merle, M.; Dellon, A.; Campbell, J.; Chang, P. *Microsurgery* **1989**, *10*, 130–133.
42. Agrawal, C.; Athanasiou, K. *J. Biomed. Mater. Res.* **1997**, *38*, 105–114.
43. Agrawal, C.; McKinney, J.; Lanctot, D.; Athanasiou, K. *Biomaterials* **2000**, *21*, 2443–2452.
44. Suganuma, J.; Alexander, H. *J. Appl. Biomater.* **1993**, *4*, 13–27.
45. Mastrokalos, D. S.; Paessler, H. H. *Arthroscopy* **2008**, *24*, 732–733.
46. Heidemann, W.; Jeschkeit, S.; Ruffieux, K.; *et al. Biomaterials* **2001**, *22*, 2371–2381.
47. Jozsa, L.; Reffy, A.; Demel, S.; Balint, J. B. *J. Hand Surg. J. Br. Soc. Surg. Hand* **1989**, *14*, 84–85.
48. Burger, C.; Kabir, K.; Rangger, C.; Mueller, M.; Minor, T.; Tolba, R. *Arch. Orthop. Trauma Surg.* **2006**, *126*, 695–705.
49. Suh, J. K.; Matthew, H. W. *Biomaterials* **2000**, *21*, 2589–2598.
50. Chen, G.; Ushida, T.; Tateishi, T. *Mater. Sci. Eng. C* **2001**, *17*, 63–69.
51. Chen, G.; Ushida, T.; Tateishi, T. *J. Biomed. Mater. Res.* **2000**, *51*, 273–279.
52. Mano, J. F.; Silva, G. A.; Azevedo, H. S.; *et al. J. R. Soc. Interface* **2007**, *4*, 999–1030.
53. Coombes, A. G. A.; Verderio, E.; Shaw, B.; Li, X.; Griffin, M.; Downes, S. *Biomaterials* **2002**, *23*, 2113–2118.
54. Chevallay, B.; Herbage, D. *Med. Biol. Eng. Comput.* **2000**, *38*, 211–218.
55. Venkatesh, S.; Sizemore, S. P.; Byrne, M. E. *Biomaterials* **2007**, *28*, 717–724.
56. Wang, Y.; Kim, H.-J.; Vunjak-Novakovic, G.; Kaplan, D. L. *Biomaterials* **2006**, *27*, 6064–6082.
57. Knight, C. G.; Morton, L. F.; Peachey, A. R.; Tuckwell, D. S.; Farndale, R. W.; Barnes, M. J. *J. Biol. Chem.* **2000**, *275*, 35–40.
58. Vaidyanathan, J.; Vaidyanathan, T. K.; Yadav, P.; Linaras, C. E. *Biomaterials* **2001**, *22*, 2911–2920.
59. Hynes, R. O. *Science* **2009**, *326*, 1216–1219.
60. Lemons, M.; Condic, M. *Exp. Neurol.* **2008**, *209*, 343–352.
61. García, A. J. *Biomaterials* **2005**, *26*, 7525–7529.
62. White, D. J.; Puranen, S.; Johnson, M. S.; Heino, J. *Int. J. Biochem. Cell Biol.* **2004**, *36*, 1405–1410.
63. Schultz, G.; Wysocki, A. *Wound Repair Regen.* **2009**, *17*, 153–162.
64. Chen, R.; Mooney, D. *Pharm. Res.* **2003**, *20*, 1103–1112.
65. Riley, G. P.; Harrall, R. L.; Constant, C. R.; Chard, M. D.; Cawston, T. E.; Hazleman, B. L. *Ann. Rheum. Dis.* **1994**, *53*, 367–376.
66. Hardingham, T. E.; Fosang, A. J. *FASEB J.* **1992**, *6*, 861–870.
67. Scott, J. E. *Biochem. J.* **1988**, *252*, 313–323.
68. Ruoslahti, E. *J. Biol. Chem.* **1989**, *264*, 13369–13372.
69. Jenkins, E.; Moss, J. B.; Pace, J. M.; Bridgewater, L. C. *Matrix Biol.* **2005**, *24*, 177–184.
70. Pace, J. M.; Corrado, M.; Missero, C.; Byers, P. H. *Matrix Biol.* **2003**, *22*, 3–14.
71. van der Rest, M.; Garrone, R.; Herbage, D. In *Advances in Molecular and Cell Biology*; Kleinman, H. K., Ed.; JAI Press Inc: Greenwich, CT, 1993; vol. 6, pp 1–67.
72. Kielty, C. M.; Grant, M. E. In *Connective Tissue and Its Heritable Disorders: Molecular, Genetic and Medical Aspects*; Royce, P. M., Steinmann, B., Eds.; Wiley: New York, 2002; pp 159–221.
73. Veit, G.; Kobbe, B.; Keene, D. R.; Paulsson, M.; Koch, M.; Wagener, R. *J. Biol. Chem.* **2006**, *281*, 3494–3504.
74. Söderhäll, C.; Marenholz, I.; Kerscher, T.; *et al. PLoS Biol.* **2007**, *5*, e242.
75. van Der Rest, M.; Bruckner, P. *Curr. Opin. Struct. Biol.* **1993**, *3*, 430–436.

76. Bailey, A. J. *J. Soc. Leather Technol. Chem.* **1992**, *76*, 111–127.
77. Bailey, A. J.; Paul, R. G. *J. Soc. Leather Technol. Chem.* **1998**, *82*, 104–110.
78. Hulmes, D. J. S. *J. Struct. Biol.* **2002**, *137*, 2–10.
79. Bailey, A. J.; Paul, R. G.; Knott, L. *Mech. Ageing Dev.* **1998**, *106*, 1–56.
80. Ramshaw, J. A. M.; Werkmeister, J. A.; Glattauer, V. *Biotechnol. Genet. Eng. Rev.* **1995**, *13*, 335–382.
81. Hulmes, D. J. S. *Essays Biochem.* **1992**, *27*, 49–67.
82. Elamaa, H.; Snellman, A.; Rehn, M.; Autio-Harmainen, H.; Pihlajaniemi, T. *Matrix Biol.* **2003**, *22*, 427–442.
83. Rehn, M.; Pihlajaniemi, T. *Semin. Cell Dev. Biol.* **1996**, *7*, 673–679.
84. Rehn, M.; Hintikka, E.; Pihlajaniemi, T. *Genomics* **1996**, *32*, 436–446.
85. Birk, D. E.; Lande, M. A. *Biochim. Biophys. Acta Protein Struct.* **1981**, *670*, 362–369.
86. Meek, K. M.; Boote, C. *Exp. Eye Res.* **2004**, *78*, 503–512.
87. Bos, K. J.; Holmes, D. F.; Kadler, K. E.; McLeod, D.; Morris, N. P.; Bishop, P. N. *J. Mol. Biol.* **2001**, *306*, 1011–1022.
88. Pins, G. D.; Silver, F. H. *Mater. Sci. Eng. C* **1995**, *3*, 101–107.
89. Hofman, S.; Sidqui, M.; Abensur, D.; Valentini, P.; Missika, P. *Biomaterials* **1999**, *20*, 1155–1166.
90. Holmes, D. F.; Graham, H. K.; Kadler, K. E. *J. Mol. Biol.* **1998**, *283*, 1049–1058.
91. Lu, Z.; Doulabi, B.; Huang, C.; Bank, R. A.; Helder, M. N. *Tissue Eng. A* **2010**, *16*, 81–90.
92. Lu, Z.; Doulabi, B.; Wuisman, P. I.; Bank, R. A.; Helder, M. N. *J. Cell. Mol. Med.* **2008**, *12*, 2812–2822.
93. O Halloran, D. M.; Collighan, R. J.; Griffin, M.; Pandit, A. S. *Tissue Eng.* **2006**, *12*, 1467–1474.
94. Pieper, J. S.; van der Kraan, P. M.; Hafmans, T.; *et al. Biomaterials* **2002**, *23*, 3183–3192.
95. Cameron, G. J.; Alberts, I. L.; Laing, J. H.; Wess, T. J. *J. Struct. Biol.* **2002**, *137*, 15–22.
96. Keene, D. R.; Sakai, L. Y.; Bachinger, H. P. *J. Cell Biol.* **1987**, *105*, 2393–2402.
97. Birk, D. E.; Silver, F. H. *Arch. Biochem. Biophys.* **1984**, *235*, 178–185.
98. Zeugolis, D. I.; Paul, R. G.; Attenburrow, G. *J. Biomed. Mater. Res.* **2008**, *86A*, 892–904.
99. Lapiere, C.; Nusgens, B.; Pierard, G. *Connect. Tissue Res.* **1977**, *5*, 21–29.
100. Silver, F. H.; Birk, D. E. *Int. J. Biol. Macromol.* **1984**, *6*, 125–132.
101. Tajima, S. *J. Dermatol. Sci.* **1996**, *12*, 104–109.
102. Jarvinen, T.; Jarvinen, T.; Kannus, P.; Jozsa, L.; Jarvinen, M. *J. Orthop. Res.* **2004**, *22*, 1303–1309.
103. Birk, D. E.; Fitch, J. M.; Babiarz, J. P.; Doane, K. J.; Linsenmayer, T. F. *J. Cell Sci.* **1990**, *95*, 649–657.
104. Holmes, D. F.; Graham, H. K.; Trotter, J. A.; Kadler, K. E. *Micron* **2001**, *32*, 273–285.
105. Canty, E. G.; Kadler, K. E. *Comp. Biochem. Physiol. A Mol. Integr. Physiol.* **2002**, *133*, 979–985.
106. Gorham, S. D. In *Biomaterials. Novel Materials from Biological Sources*; Byrom, D., Ed.; Macmillan Publishers Ltd and ICI Biological Products Business: New York, 1991; pp 55–122.
107. Fleischmajer, R.; MacDonald, E. D.; Perlish, J. S.; Burgeson, R. E.; Fisher, L. W. *J. Struct. Biol.* **1990**, *105*, 162–169.
108. Ploetz, C.; Zycband, E. I.; Birk, D. E. *J. Struct. Biol.* **1991**, *106*, 73–81.
109. Grassmann, W. In *Biochemie et Physiologie du Tissu Conjonctif, Symposium International*; Compte, P., Ed.; Societe Ormeco et Imprimerie du Sud-Est: Lyon, France, 1965; pp 205–218.
110. Woodley, D. T.; Yamauchi, M.; Wynn, K. C.; Mechanic, G.; Briggaman, R. A. *J. Invest. Dermatol.* **1991**, *97*, 580–585.
111. Wess, T. J.; Hammersley, A. P.; Wess, L.; Miller, A. *J. Mol. Biol.* **1998**, *275*, 255–267.
112. Roveri, N.; Falini, G.; Sidoti, M. C.; *et al. Mater. Sci. Eng. C* **2003**, *23*, 441–446.
113. Bailey, A. J.; Peach, C. M. *Biochem. Biophys. Res. Commun.* **1968**, *33*, 812–819.
114. Heathcote, J. G.; Bailey, A. J.; Grant, M. E. *Cell Biol. Int. Rep.* **1980**, *4*, 780.
115. Knott, L.; Bailey, A. J. *Bone* **1998**, *22*, 181–187.
116. Danielsen, C. C. *Development* **1981**, *15*, 269–278.
117. Tanzer, M. L.; Mechanic, G. *Biochem. Biophys. Res. Commun.* **1970**, *39*, 183–189.
118. Mechanic, G. L.; Kuboki, Y.; Shimokawa, H.; Nakamoto, K.; Sasaki, S.; Kawanishi, Y. *Biochem. Biophys. Res. Commun.* **1974**, *60*, 756–763.
119. Mechanic, G. L. *Biochem. Biophys. Res. Commun.* **1974**, *56*, 923–927.
120. Yamauchi, M.; Woodley, D. T.; Mechanic, G. L. *Biochem. Biophys. Res. Commun.* **1988**, *152*, 898–903.
121. Scott, J. E. *Biochem. J.* **1980**, *187*, 887–891.
122. Danielsen, C. C. *Connect. Tissue Res.* **1982**, *9*, 219–225.
123. Pieper, J. S.; van Wachem, P. B.; van Luyn, M. J. A.; *et al. Biomaterials* **2000**, *21*, 1689–1699.
124. Yarat, A.; Ozcelik, F.; Emekli, N. *J. Marmara Univ. Dent. Facult.* **1996**, *2*, 527–529.
125. Hey, K. B.; Lachs, C. M.; Raxworthy, M. J.; Wood, E. J. *Biotechnol. Appl. Biochem.* **1990**, *12*, 85–93.
126. Charulatha, V.; Rajaram, A. *J. Biomed. Mater. Res.* **2001**, *54*, 122–128.
127. McKegney, M.; Taggart, I.; Grant, M. H. *J. Mater. Sci. Mater. Med.* **2001**, *12*, 833–844.
128. Wells, M. R.; Kraus, K.; Batter, D. K.; *et al. Exp. Neurol.* **1997**, *146*, 395–402.
129. Matsumoto, K.; Nakamura, T.; Shimizu, Y.; *et al. Am. Soc. Artif. Intern. Organs J.* **1999**, *45*, 288–292.
130. Rocha, L. B.; Goissis, G.; Rossi, M. A. *Biomaterials* **2002**, *23*, 449–456.
131. Liu, L. S.; Thompson, A. Y.; Heidaran, M. A.; Poser, J. W.; Spiro, R. C. *Biomaterials* **1999**, *20*, 1097–1108.
132. Friess, W. *Eur. J. Pharm. Biopharm.* **1998**, *45*, 113–136.
133. Fratzl, P.; Weinkamer, R. *Prog. Mater. Sci.* **2007**, *52*, 1263–1334.
134. Paul, R. G.; Bailey, A. J. *Sci. World J.* **2003**, *3*, 138–155.
135. Pandit, A.; Ashar, R.; Feldman, D.; Thompson, A. *Plast. Reconstr. Surg.* **1998**, *101*, 766–775.
136. Marks, M. G.; Doillon, C.; Silver, F. H. *J. Biomed. Mater. Res.* **1991**, *25*, 683–696.
137. Stompro, B. E. *Curr. Surg.* **1990**, *47*, 35–37.
138. Wissink, M. J. B.; Beernink, R.; Poot, A. A.; *et al. J. Control. Release* **2000**, *64*, 103–114.
139. Yao, C.; Prével, P.; Koch, S.; *et al. Cells Tissues Organs* **2004**, *178*, 189–196.
140. Light, N. D. In *Methods in Skin Research*; Skerrow, D., Skerrow, C. J., Eds.; John Wiley and Sons: New York, 1985; pp 559–586.
141. Lynn, A. K.; Yannas, I. V.; Bonfield, W. *J. Biomed. Mater. Res. B Appl. Biomater.* **2004**, *71B*, 343–354.
142. Gelman, R. A.; Poppke, D. C.; Piez, K. A. *J. Biol. Chem.* **1979**, *254*, 11741–11745.
143. Bruckner, P.; Prockop, D. J. *Anal. Biochem.* **1981**, *110*, 360–368.
144. Delorenzi, N. J.; Gatti, C. A. *Matrix (Stuttgart, Germany)* **1993**, *13*, 407–413.
145. Hsu, S.; Jamieson, A. M.; Blackwell, J. *Biorheology* **1994**, *31*, 21–36.
146. Silver, F. H.; Trelstad, R. L. *J. Biol. Chem.* **1980**, *255*, 9427–9433.
147. Li, G. Y.; Fukunaga, S.; Takenouchi, K.; Nakamura, F. *J. Soc. Leather Technol. Chem. Technol.* **2004**, *88*, 66–71.
148. Farber, S.; Garg, A. K.; Birk, D. E.; Silver, F. H. *Int. J. Biol. Macromol.* **1986**, *8*, 37–42.
149. Brokaw, J. L.; Doillon, C. J.; Hahn, R. A.; Birk, D. E.; Berg, R. A.; Silver, F. H. *Int. J. Biol. Macromol.* **1985**, *7*, 135–140.
150. Gross, J. *J. Exp. Med.* **1949**, *89*, 699–708.
151. Gross, J.; Highberger, J. H.; Schmitt, F. O. *Proc. Natl. Acad. Sci. USA* **1954**, *40*, 679–688.
152. Gross, J.; Highberger, J. H.; Schmitt, F. O. *Proc. Natl. Acad. Sci. USA* **1955**, *41*, 1–7.
153. Miller, A.; Wray, J. S. *Nature* **1971**, *230*, 437–439.
154. Ward, N. P.; Hulmes, D. J. S.; Chapman, J. A. *J. Mol. Biol.* **1986**, *190*, 107–112.
155. Chapman, J. A.; Tzaphlidou, M.; Meek, K. M.; Kadler, K. E. *Electron Microsc. Rev.* **1990**, *3*, 143–182.
156. Zeugolis, D. I.; Khew, S. T.; Yew, E. S. Y.; *et al. Biomaterials* **2008**, *29*, 2293–2305.
157. Brokaw, J. L.; Doillon, C. J.; Hahn, R. A.; Birk, D. E.; Berg, R. A. *Int. J. Biol. Macromol.* **1985**, *7*, 135–140.
158. Williams, B. R.; Gelman, R. A.; Poppke, D. C.; Piez, K. A. *J. Biol. Chem.* **1978**, *253*, 6578–6585.
159. Zeugolis, D. I.; Paul, R. G.; Attenburrow, G. *J. Biomater. Sci. Polym. Ed.* **2009**, *20*, 219–234.
160. Zeugolis, D. I.; Paul, R. G.; Attenburrow, G. *J. Biomed. Mater. Res. B Appl. Biomater.* **2008**, *85B*, 343–352.
161. Zeugolis, D. I.; Paul, R. G.; Attenburrow, G. *J. Appl. Polym. Sci.* **2008**, *108*, 2886–2894.
162. Koob, T. J.; Hernandez, D. J. *Biomaterials* **2002**, *23*, 203–212.
163. Cote, M. F.; Sirois, E.; Doillon, C. J. *J. Biomater. Sci. Polym. Ed.* **1992**, *3*, 301–313.
164. Rault, I.; Frei, V.; Herbage, D.; Abdul-Malak, N.; Huc, A. *J. Mater. Sci. Mater. Med.* **1996**, *7*, 215–221.
165. Chen, C. N.; Wu, C. C.; Tsai, C. C.; Sung, H. W.; Chang, Y. *J. Chin. Inst. Chem. Eng.* **1997**, *28*, 389–397.
166. Osborne, C. S.; Barbenel, J. C.; Smith, D.; Savakis, M.; Grant, M. H. *Med. Biol. Eng. Comput.* **1998**, *36*, 129–134.
167. Friess, W.; Lee, G. *Biomaterials* **1996**, *17*, 2289–2294.

168. Zeugolis, D. I.; Paul, G. R.; Attenburrow, G. *J. Biomed. Mater. Res. A* **2009**, *89*(4), 895–908.
169. Charulatha, V.; Rajaram, A. *Biomaterials* **2003**, *24*, 759–767.
170. Weadock, K.; Olson, R. M.; Silver, F. H. *Biomater. Med. Devices Artif. Organs* **1983–84**, *11*, 293–318.
171. Yao, C.; Markowicz, M.; Pallua, N.; Noah, E. M.; Steffens, G. *Biomaterials* **2008**, *29*, 66–74.
172. Pasquali-Ronchetti, I.; Baccarani-Contri, M. *Microsc. Res. Technol.* **1997**, *38*, 428–435.
173. Kielty, C.; Sherratt, M.; Shuttleworth, C. *J. Cell Sci.* **2002**, *115*, 2817–2828.
174. Gemmill, J. F. *J. Anat. Physiol.* **1906**, *40*, 396–399.
175. Kannus, P. *Scand. J. Med. Sci. Sports* **2000**, *10*, 312–320.
176. Chrzanowski, P.; Keller, S.; Cerreta, J.; Mandl, I.; Turino, G. *Am. J. Med.* **1980**, *69*, 351–359.
177. Rosenbloom, J.; Abrams, W.; Mecham, R. *FASEB J.* **1993**, *7*, 1208–1218.
178. Lowry, O.; Gilligan, D.; Katersky, E. *J. Biol. Chem.* **1941**, *139*, 795–804.
179. Weinstein, G.; Boucek, R. *J. Invest. Dermatol.* **1960**, *35*, 227–230.
180. Bailey, A. J. *J. Clin. Pathol. Suppl. R. Coll. Pathol.* **1978**, *12*, 49–58.
181. Jones, P.; Scott-Burden, T.; Gevers, W. *Proc. Natl. Acad. Sci. USA* **1979**, *76*, 353–357.
182. Madsen, K.; Moskalewski, S.; von der Mark, K.; Friberg, U. *Dev. Biol.* **1983**, *96*, 63–73.
183. Sephel, G.; Davidson, J. *J. Invest. Dermatol.* **1986**, *86*, 279–285.
184. Mecham, R.; Madaras, J.; Senior, R. *J. Cell Biol.* **1984**, *98*, 1804–1812.
185. Mandl, I.; Cantor, J.; Osman, M.; Turino, G. M. *Connect. Tissue Res.* **1986**, *15*, 9–12.
186. Mecham, R. P.; Madaras, J.; McDonald, J. A.; Ryan, U. *J. Cell. Physiol.* **1983**, *116*, 282–288.
187. Zhang, M.-C.; Giro, M.-G.; Quaglino, D. J.; Davidson, J. M. *J. Clin. Invest.* **1995**, *95*, 986–994.
188. Grosso, L. *J. Oral Pathol. Med.* **1996**, *25*, 5–9.
189. Kielty, C.; Stephan, S.; Sherratt, M.; Williamson, M.; Shuttleworth, C. *Philos. Trans. R. Soc. B* **2007**, *362*, 1293–1312.
190. Rucker, R.; Dubick, M. *Environ. Health Perspect.* **1984**, *55*, 179–191.
191. Bailey, A. J.; Etherington, D. J. *Comp. Biochem.* **1980**, *19B*, 299–460.
192. Brown-Augsburger, P.; Tisdale, C.; Broekelmann, T.; Sloan, C. *J. Biol. Chem.* **1995**, *270*, 17778–17783.
193. Umeda, H.; Takeuchi, M. *J. Biol. Chem.* **2001**, *276*, 12579–12587.
194. Rock, M.; Cain, S.; Freeman, L.; *et al. J. Biol. Chem.* **2004**, *279*, 23748–23758.
195. Bailey, A. J. *Amino Acids* **1991**, *1*, 293–306.
196. Butler, D.; Grood, E.; Noyes, F.; Zernicke, R. *Exerc. Sport Sci. Rev.* **1978**, *6*, 125–181.
197. Partridge, S. M.; Elsden, D. F.; Thomas, J. *Nature* **1963**, *197*, 1297–1298.
198. Doliana, R.; Bot, S.; Mungiguerra, G.; Canton, A.; Cilli, S.; Colombatti, A. *J. Biol. Chem.* **2001**, *276*, 12003–12011.
199. Strocchi, R.; Leonardi, L.; Guizzardi, S.; Marchini, M.; Ruggeri, A. *J. Anat.* **1985**, *140*, 57–67.
200. Chaplin, D. M.; Greenlee, T. K. J. *J. Anat.* **1975**, *120*, 253–274.
201. Haust, M. *Am. J. Pathol.* **1965**, *47*, 1113–1137.
202. Bailey, A. J. *Mech. Ageing Dev.* **2001**, *122*, 735–755.
203. Sakai, L. Y.; Keene, D. R.; Engvall, E. *J. Cell Biol.* **1986**, *103*, 2499–2509.
204. Bressan, G. M.; Castellani, I.; Colombatti, A.; Volpin, D. *J. Biol. Chem.* **1983**, *258*, 13262–13267.
205. Mongiat, M.; Ligresti, G.; Marastoni, S.; Lorenzon, E.; Doliana, R.; Colombatti, A. *Mol. Cell. Biol.* **2007**, *27*, 7176–7187.
206. Colombatti, A.; Doliana, R.; Bot, S.; *et al. Matrix Biol.* **2000**, *19*, 289–301.
207. Zanetti, M.; Braghetta, P.; Sabatelli, P.; *et al. Mol. Cell. Biol.* **2004**, *24*, 638–650.
208. Mochizuki, S.; Brassart, B.; Hinek, A. *J. Biol. Chem.* **2002**, *277*, 44854–44863.
209. Senior, R.; Griffin, G.; Mecham, R. *J. Clin. Invest.* **1980**, *66*, 859–862.
210. Jung, S.; Rutka, J.; Hinek, A. *J. Neuropathol. Exp. Neurol.* **1998**, *57*, 439–448.
211. Wachi, H.; Sugitani, H.; Murata, H.; Nakazawa, J.; Mecham, R.; Seyama, Y. *J. Atheroscler. Thromb.* **2004**, *11*, 159–166.
212. Daamen, W.; Veerkamp, J.; van Hest, J.; Van Kuppevelt, T. *Biomaterials* **2007**, *28*, 4378–4398.
213. Lu, Q.; Ganesan, K.; Simionescu, D. T.; Vyavahare, N. R. *Biomaterials* **2004**, *25*, 5227–5237.
214. Flanagan, T. C.; Wilkins, B.; Black, A.; Jockenhoevel, S.; Smith, T. J.; Pandit, A. S. *Biomaterials* **2006**, *27*, 2233–2246.
215. Garcia, Y.; Hemantkumar, N.; Collighan, R.; Griffin, M.; Rodriguez-Cabello, J.; Pandit, A. *Tissue Eng. A* **2009**, *15*, 887–899.
216. Li, M.; Mondrinos, M. J.; Gandhi, M. R.; Ko, F. K.; Weiss, A. S.; Lelkes, P. I. *Biomaterials* **2005**, *26*, 5999–6008.
217. Leach, J. B.; Wolinsky, J. B.; Stone, P. J.; Wong, J. Y. *Acta Biomater.* **2005**, *1*, 155–164.
218. Wu, Y.; MacKay, J.; McDaniel, J.; Chilkoti, A.; Clark, R. *Biomacromolecules* **2009**, *10*, 19–24.
219. Kjellen, L.; Lindahl, U. *Annu. Rev. Biochem.* **1991**, *60*, 443–475.
220. Elliott, D. *Biol. Rev.* **1965**, *40*, 392–421.
221. Heinegard, D.; Bjorne-Persson, A.; Coster, L.; *et al. Biochem. J.* **1985**, *230*, 181–194.
222. Morgelin, M.; Paulsson, M.; Malmstrom, A.; Heinegard, D. *J. Biol. Chem.* **1989**, *264*, 12080–12090.
223. Vogel, K.; Evanko, S. *J. Biol. Chem.* **1987**, *262*, 13607–13613.
224. Heinegard, D.; Paulsson, M.; Inerot, S.; Carlstrom, C. *Biochem. J.* **1981**, *197*, 355–366.
225. Hedbom, E.; Heinegard, D. *J. Biol. Chem.* **1993**, *268*, 27307–27312.
226. Vesentini, S.; Redaelli, A.; Montevecchi, F. M. *J. Biomech.* **2005**, *38*, 433–443.
227. Iozzo, R. V. *Annu. Rev. Biochem.* **1998**, *67*, 609–652.
228. Iozzo, R. V. *J. Biol. Chem. Mater.* **1999**, *274*, 18843–18846.
229. Weber, I. T.; Harrison, R. W.; Iozzo, R. V. *J. Biol. Chem.* **1996**, *271*, 31767–31770.
230. Svensson, L.; Närlid, I.; Oldberg, Å. *FEBS Lett.* **2000**, *470*, 178–182.
231. Brown, D. C.; Vogel, K. G. *Matrix (Stuttgart, Germany)* **1989**, *9*, 468–478.
232. Birk, D. E.; Nurminskaya, M. V.; Zycband, E. I. *Dev. Dyn.* **1995**, *202*, 229–243.
233. Orgel, J. P. R. O.; Irving, T. C.; Miller, A.; Wess, T. J. *Proc. Natl. Acad. Sci. USA* **2006**, *103*, 9001–9005.
234. Ezura, Y.; Chakravarti, S.; Oldberg, A.; Chervoneva, I.; Birk, D. E. *J. Cell Biol.* **2000**, *151*, 779–788.
235. Scott, J. E.; Orford, C. R.; Hughes, E. W. *Biochem. J.* **1981**, *195*, 573–581.
236. Lam, R.; Claffey, W. J.; Ceil, P. H. *Biophys. J.* **1978**, *24*, 613–628.
237. Harley, B. A. C.; Gibson, L. J. *Chem. Eng. J.* **2008**, *137*, 102–121.
238. Venkatesan, N.; Barre, L.; Benani, A.; *et al. Proc. Natl. Acad. Sci.* **2004**, *101*, 18087–18092.
239. O Halloran, D. M.; Grad, S.; Stoddart, M.; Dockery, P.; Alini, M.; Pandit, A. S. *Biomaterials* **2008**, *29*, 438–447.
240. Pins, G. D.; Christiansen, D. L.; Patel, R.; Silver, F. H. *Biophys. J.* **1997**, *73*, 2164–2172.
241. Douglas, T.; Hempel, U.; Mietrach, C.; *et al. J. Biomed. Mater. Res.* **2008**, *84A*, 805–816.
242. Damour, O.; Gueugniaud, P. Y. *Clin. Mater.* **1994**, *15*, 273–276.
243. Yannas, I. V.; Burke, J. F.; Gordon, P. L.; Huang, C.; Rubenstein, R. H. *J. Biomed. Mater. Res.* **1980**, *14*, 107–132.
244. Baum, B.; McDonald, J. A.; Crystal, R. G. *Biochem. Biophys. Res. Commun.* **1977**, *79*, 8–15.
245. McDonald, J. A.; Kelley, D. G.; Broekelmann, T. J. *J. Cell Biol.* **1982**, *92*, 485–492.
246. Schwarzbauer, J. E.; Sechler, J. L. *Curr. Opin. Cell Biol.* **1999**, *11*, 622–627.
247. Saylam, C.; Özdemir, N.; Itil, I. M.; Sendag, F.; Terek, M. C. *Arch. Gynecol. Obstet.* **2002**, *266*, 83–85.
248. Schwarzbauer, J. *Curr. Biol.* **1999**, *9*, R242–R244.
249. Schwarzbauer, J. *Curr. Opin. Cell Biol.* **1991**, *3*, 786–791.
250. Rhoads, D. S.; Guan, J.-L. *Exp. Cell Res.* **2007**, *313*, 3859–3867.
251. Comut, A. A.; Shortkroff, S.; Zhang, X.; Spector, M. *Biomaterials* **2000**, *21*, 1887–1896.
252. Hari, A.; Djohar, B.; Skutella, T.; Montazeri, S. *Int. J. Dev. Neurosci.* **2004**, *22*, 113–117.
253. Sottile, J.; Hocking, D. *Mol. Biol. Cell* **2002**, *13*, 3546–3559.
254. Velling, T.; Risteli, J.; Wennerberg, K.; Mosher, D.; Johansson, S. *J. Biol. Chem.* **2002**, *277*, 37377–37381.
255. Sottile, J.; Shi, F.; Rublyevska, I.; Chiang, H.-Y.; Lust, J.; Chandler, J. *Am. J. Physiol. Cell Physiol.* **2007**, *293*, 1934–1946.
256. Santoro, S.; Cunningham, L. *Proc. Natl. Acad. Sci.* **1979**, *76*, 2644–2648.
257. Grinnell, F.; Billingham, R. E.; Burgess, L. *J. Invest. Dermatol.* **1981**, *76*, 181–189.
258. Ball, M. D.; O'Connor, D.; Pandit, A. *J. Mater. Sci. Mater. Med.* **2009**, *20*, 113–122.
259. Yao, J.; Korotkova, T.; Riboh, J.; Chong, A.; Chang, J.; Smith, R. L. *J. Hand Surg.* **2008**, *33*, 1558–1564.
260. Brown, R. A.; Phillips, J. B.; Kwang, W. J. In *International Review of Cytology*, Academic Press: San Diego, CA, 2007; pp 75–150.
261. Ackley, B. D.; Kang, S. H.; Crew, J. R.; Suh, C.; Jin, Y.; Kramer, J. M. *J. Neurosci.* **2003**, *23*, 3577–3587.
262. Tzu, J.; Marinkovich, M. *Int. J. Biochem. Cell Biol.* **2008**, *40*, 199–214.
263. Hamill, K. J.; Langbein, L.; Jones, J. C. R.; McLean, W. H. I. *J. Biol. Chem.* **2009**, *284*, 35588–35596.

264. Schéele, S.; Nyström, A.; Durbeej, M.; Talts, J. F.; Ekblom, M.; Ekblom, P. *J. Mol. Med.* **2007**, *85*, 825–836.
265. Yurchenco, P.; O'Rear, J. J. *Curr. Opin. Cell Biol.* **1994**, *6*, 674–681.
266. Timpl, R.; Brown, J. *Bioessays* **1996**, *18*, 123–132.
267. Ekblom, M.; Falk, M.; Salmivirta, K.; Durbeej, M.; Ekblom, P. *Ann. N. Y. Acad. Sci.* **1998**, *857*, 194–211.
268. Allamand, V.; Sunada, Y.; Salih, M.; *et al. Hum. Mol. Genet.* **1997**, *6*, 747–752.
269. Colognato, H.; Yurchenco, P. *Dev. Dyn.* **2000**, *218*, 213–234.
270. Belkin, A.; Stepp, M. *Microsc. Res. Tech.* **2000**, *51*, 280–301.
271. Hallmann, R.; Horn, N.; Selg, M.; Wendler, O.; Pausch, F.; Sorokin, L. M. *Physiol. Rev.* **2005**, *85*, 979–1000.
272. Miner, J.; Yurchenco, P. *Annu. Rev. Cell Dev. Biol.* **2004**, *20*, 255–284.
273. Yurchenco, P.; Wadsworth, W. *Curr. Opin. Cell Biol.* **2004**, *16*, 572–579.
274. Bader, B.; Smyth, N.; Nedbal, S.; *et al. Mol. Cell. Biol.* **2005**, *25*, 6846–6856.
275. Patton, B. *Microsc. Res. Technol.* **2000**, *51*, 247–261.
276. Sasaki, T.; Mann, K.; Miner, J.; Miosge, N.; Timpl, R. *Eur. J. Biochem.* **2002**, *269*, 431–442.
277. Vachon, P.; Loechel, F.; Xu, H.; Wewer, U.; Engvall, E. *J. Cell Biol.* **1996**, *134*, 1483–1497.
278. Pedrosa-Domellöf, F.; Tiger, C. F.; Virtanen, I.; Thornell, L. E.; Gullberg, D. *J. Histochem. Cytochem.* **2000**, *48*, 201–209.
279. Hillaire, D.; Leclerc, A.; Faure, S.; *et al. Hum. Mol. Genet.* **1994**, *3*, 1657–1661.
280. Xu, H.; Christmas, P.; Wu, X.; Wewer, U.; Engvall, E. *Proc. Natl. Acad. Sci. USA* **1994**, *91*, 5572–5576.
281. Helbling-Leclerc, A.; Zhang, X.; Topaloglu, H.; *et al. Nat. Genet.* **1995**, *11*, 216–218.
282. Mayer, U.; Saher, G.; Fassler, R.; *et al. Nat. Genet.* **1997**, *17*, 318–323.
283. Miner, J. *Microsc. Res. Tech.* **2008**, *71*, 349–356.
284. Baron-Van Evercooren, A.; Kleinman, H.; Ohno, S.; Marangos, P.; Schwartz, J.; Dubois-Dalcq, M. *J. Neurosci. Res.* **1982**, *8*, 179–193.
285. Palm, S.; Furcht, L. *J. Cell Biol.* **1983**, *96*, 1218–1226.
286. Bignami, A.; Chi, N.; Dahl, D. *Exp. Neurol.* **1984**, *85*, 426–436.
287. Frank, D.; Carter, W. *J. Cell Sci.* **2004**, *117*, 1351–1363.
288. Goldfinger, L.; Hopkinson, S. *J. Cell Sci.* **1999**, *112*, 2615–2629.
289. Nguyen, B.; Ren, X.; Schwartz, M.; Carter, W. *J. Biol. Chem.* **2001**, *276*, 43860–43870.
290. Pulkkinen, L.; Christiano, A. M.; Gerecke, D.; Tryggavason, K.; Burgeson, R. E.; Uitto, J. *Matrix Biol.* **1994**, *14*, 393–394.
291. Uitto, J.; Richard, G. *Am. J. Med. Genet.* **2004**, *131C*, 61–74.
292. Mitsuhashi, Y.; Hashimoto, I. *Arch. Dermatol. Res.* **2003**, *295*, S29–S33.
293. Mavilio, F.; Pellegrini, G.; Ferrari, S.; *et al. Nat. Med.* **2006**, *12*, 1397–1402.
294. Nunzio, F. D.; Maruggi, G.; Ferrari, S.; *et al. Mol. Ther.* **2008**, *16*, 1977–1985.
295. Yao, L.; Damodaran, G.; Nikolskaya, N.; Gorman, A.; Windebank, A.; Pandit, A. *J. Biomed. Mater. Res. A* **2010**, *92*(2), 484–492.
296. Rosner, B. I.; Hang, T.; Tranquillo, R. T. *Exp. Neurol.* **2005**, *195*, 81–91.
297. Hobson, M. I. *Ann. R. Coll. Surg. Engl.* **2002**, *84*, 47–53.
298. Madison, R.; da Silva, C.; Dikkes, P.; Chiu, T.; Sidman, R. *Exp. Neurol.* **1985**, *88*, 767–772.
299. Rudland, P. S. *Biochim. Biophys. Acta* **1979**, *560*, 91–133.
300. Schlessinger, J.; Schechter, Y.; Willingham, M. C.; Pastan, I. H. *Proc. Natl. Acad. Sci. USA* **1978**, *75*, 2659–2663.
301. Schlessinger, J.; Shechter, Y.; Cuatrecasas, P.; Willingham, M. C.; Pastan, I. *Proc. Natl. Acad. Sci. USA* **1978**, *75*, 5353–5357.
302. Edelman, G. M.; Yahara, I. *Proc. Natl. Acad. Sci. USA* **1976**, *73*, 2047–2051.
303. McClain, D. A.; D'Eustachio, P.; Edelman, G. H. *Proc. Natl. Acad. Sci. USA* **1977**, *74*, 666–670.
304. Friedkin, M.; Legg, A.; Rozengurt, E. *Proc. Natl. Acad. Sci. USA* **1979**, *76*, 3909–3912.
305. De Mey, J.; Joniau, M.; De Brabander, M.; Moens, W.; Geuens, G. *Proc. Natl. Acad. Sci. USA* **1978**, *75*, 1339–1343.
306. Otto, A.; Zumbe, A.; Gibson, L.; Kubler, A.; Jimenez De Asua, L. *Proc. Natl. Acad. Sci. USA* **1979**, *76*, 6435–6438.
307. Sakiyama-Elbert, S. E.; Hubbell, J. A. *J. Control. Release* **2000**, *65*, 389–402.
308. Shen, Y. H.; Shoichet, M. S.; Radisic, M. *Acta Biomater.* **2008**, *4*, 477–489.
309. Roberts, R.; Gallagher, J.; Spooncer, E.; Allen, T.; Bloomfield, F.; Dexter, T. *Nature* **1988**, *332*, 376–378.
310. Bonewald, L. *Crit. Rev. Eukaryot. Gene Expr.* **1999**, *9*, 33–44.
311. Friess, W.; Uludag, H.; Foskett, S.; Biron, R. *Pharm. Dev. Technol.* **1999**, *4*, 387–396.
312. Sakiyama-Elbert, S. E.; Das, R.; Gelberman, R. H.; Harwood, F.; Amiel, D.; Thomopoulos, S. *J. Hand Surg.* **2008**, *33*, 1548–1557.
313. Fontana, A.; Spolaore, B.; Mero, A.; Veronese, F. M. *Adv. Drug Deliv. Rev.* **2008**, *60*, 13–28.
314. Liman, S. T.; Kara, C. O.; Bir, F.; Yildirim, B.; Topcu, S.; Sahin, B. *Int. J. Pediatr. Otorhinolaryngol.* **2005**, *69*, 1327–1331.
315. Hsu, C.; Chang, J. *J. Hand Surg.* **2004**, *29*, 551–563.
316. Petersen, W.; Varoga, D.; Zantop, T.; Hassenpflug, J.; Mentlein, R.; Pufe, T. *J. Orthop. Res.* **2004**, *22*, 847–853.
317. Thomopoulos, S.; Harwood, F. L.; Silva, M. J.; Amiel, D.; Gelberman, R. H. *J. Hand Surg.* **2005**, *30*, 441–447.
318. Wang, X. T.; Liu, P. Y.; Tang, J. B. *J. Hand Surg.* **2005**, *30*, 222–229.
319. Würgler-Hauri, C. C.; Dourte, L. M.; Baradet, T. C.; Williams, G. R.; Soslowsky, L. J. *J. Shoulder Elbow Surg.* **2007**, *16*, S198–S203.
320. Wang, X. T.; Liu, P. Y.; Xin, K.-Q.; Tang, J. B. *J. Hand Surg.* **2005**, *30*, 1255–1261.
321. Kobayashi, M.; Itoi, E.; Minagawa, H.; *et al. J. Shoulder Elbow Surg.* **2006**, *15*, 371–377.
322. Gelberman, R. H.; Thomopoulos, S.; Sakiyama-Elbert, S. E.; Das, R.; Silva, M. J. *J. Hand Surg.* **2007**, *32*, 373–379.
323. Hamada, Y.; Katoh, S.; Hibino, N.; Kosaka, H.; Hamada, D.; Yasui, N. *J. Hand Surg.* **2006**, *31*, 530–540.
324. James, R.; Kesturu, G.; Balian, G.; Chhabra, A. B. *J. Hand Surg.* **2008**, *33*, 102–112.
325. Murphy, K. D.; Mushkudiani, I. A.; Kao, D.; Levesque, A. Y.; Hawkins, H. K.; Gould, L. J. *J. Hand Surg.* **2008**, *33*, 1168–1178.
326. Mehta, V.; Mass, D. *J. Hand Ther.* **2005**, *18*, 87–92.
327. Yamazaki, S.; Yasuda, K.; Tomita, F.; Tohyama, H.; Minami, A. *Arthroscopy* **2005**, *21*, 1034–1041.
328. Barras, F.; Pasche, P.; Bouche, N.; Aebischer, P.; Zurn, A. *J. Neurosci. Res.* **2002**, *70*, 746–755.
329. Tornqvist, N.; Bjorklund, L.; Almqvist, P.; Wahlberg, L.; Stromberg, I. *Exp. Neurol.* **2000**, *164*, 130–138.
330. Bensadoun, J.; Pereira de Almeida, L.; Fine, E.; Tseng, J.; Deglon, N.; Aebischer, P. *J. Control. Release* **2003**, *87*, 107–115.
331. Silva, A.; Richard, C.; Bessodes, M.; Scherman, D.; Merten, O. *Biomacromolecules* **2009**, *10*, 9–18.
332. Cheng, X.; Gurkan, U. A.; Dehen, C. J.; *et al. Biomaterials* **2008**, *29*, 3278–3288.
333. Elliott, J. T.; Woodward, J. T.; Umarji, A.; Mei, Y.; Tona, A. *Biomaterials* **2007**, *28*, 576–585.
334. Kim, J. A.; Cho, K.; Shin, Y. S.; Jung, N.; Chung, C.; Chang, J. K. *Biosens. Bioelectron.* **2007**, *22*, 3273–3277.
335. Harley, B. A.; Hastings, A. Z.; Yannas, I. V.; Sannino, A. *Biomaterials* **2006**, *27*, 866–874.
336. Laurencin, C.; Gelberman, R. In *Musculoskeletal Soft-Tissue Aging: Impact on Mobility*; Buckwalter, J., Goldberg, V., Woo, S., Eds.; American Academy Orthopaedic Surgeons Publishers: Rosemont, IL, 1992.
337. Lippiello, L. *eCAM* **2007**, *4*, 219–224.
338. Frank, C.; Jackson, D. *J. Bone Joint Surg. Am.* **1997**, *79*, 1556–1576.
339. Calve, S.; Dennis, R. G.; Kosnik, P. E.; Baar, K.; Grosh, K.; Arruda, E. M. *Tissue Eng.* **2004**, *10*, 755–761.
340. Butler, D. L.; Awad, H. A. *Clin. Orthop. Relat. Res.* **1999**, S324–S332.
341. Bullough, R.; Finnigan, T.; Kay, A.; Maffulli, N.; Forsyth, N. *Disabil. Rehabil.* **2008**, *30*, 1746–1751.
342. Heiple, K. G.; Kendrick, R. E.; Herndon, C. H.; Chase, S. W. *J. Bone Joint Surg. Am.* **1967**, *49*, 1119–1127.
343. Gisep, A. *Injury* **2002**, *33*, 88–92.
344. Tadic, D.; Epple, M. *Biomaterials* **2004**, *25*, 987–994.
345. Salama, R.; Weissman, S. L. *J. Bone Joint Surg. Br.* **1978**, *60*, 111–115.
346. Horowitz, I.; Bodner, L. *Head Neck* **1989**, *11*, 516–523.
347. McMurray, G. N. *J. Bone Joint Surg. Br.* **1982**, *64*, 101–104.
348. Schlegel, A. K.; Donath, K. *J. Long Term Eff. Med. Implants* **1998**, *8*, 201–209.
349. Piattelli, M.; Favero, G. A.; Scarano, A.; Orsini, G.; Piattelli, A. *Int. J. Oral Maxillofac. Implants* **1999**, *14*, 835–840.
350. Ewers, R. *J. Oral Maxillofac. Surg.* **2005**, *63*, 1712–1723.
351. Schopper, C.; Moser, D.; Sabbas, A.; *et al. Clin. Oral Implants Res.* **2003**, *14*, 743–749.
352. Yerit, K. C.; Posch, M.; Hainich, S.; *et al. Clin. Oral Implants Res.* **2004**, *15*, 693–699.
353. Gallie, W. E. *J. Bone Joint Surg. Am.* **1914**, 201–212.
354. Lane, W. A. *Br. Med. J.* **1895**, 861–863.
355. Hutmacher, D. W. *Biomaterials* **2000**, *21*, 2529–2543.
356. Bergsma, J. E.; Debruijn, W. C.; Rozema, F. R.; Bos, R. R. M.; Boering, G. *Biomaterials* **1995**, *16*, 25–31.

357. Bostman, O.; Partio, E.; Hirvensalo, E.; Rokkanen, P. *Acta Orthop. Scand.* **1992**, *63*, 173–176.
358. Bostman, O. M. *J. Bone Joint Surg. Br.* **1991**, *73*, 679–682.
359. Bostman, O. M. *Clin. Orthop. Relat. Res.* **1992**, *278*, 193–199.
360. Bostman, O. M.; Pihlajamaki, H. K. *J. Bone Joint Surg. Am.* **1998**, *80A*, 1791–1794.
361. Bostman, O.; Makela, E. A.; Sodergard, J.; Hirvensalo, E.; Tormala, P.; Rokkanen, P. *J. Pediatr. Orthop.* **1993**, *13*, 242–245.
362. Bucholz, R. W.; Henry, S.; Henley, M. B. *J. Bone Joint Surg. Am.* **1994**, *76A*, 319–324.
363. Lutolf, M. P.; Hubbell, J. A. *Nat. Biotechnol.* **2005**, *23*, 47–55.
364. Stenzel, K. H.; Miyata, T.; Rubin, A. L. *Annu. Rev. Biophys. Bioeng.* **1974**, *3*, 231–253.
365. Geiger, M.; Li, R. H.; Friess, W. *Adv. Drug Deliv. Rev.* **2003**, *55*, 1613–1629.
366. Boden, S. D.; Martin, G. J., Jr.; Horton, W. C.; Truss, T. L.; Sandhu, H. S. *J. Spinal Disord.* **1998**, *11*, 95–101.
367. Boyne, P. J.; Marx, R. E.; Nevins, M.; *et al*. *Int. J. Periodontics Restorative Dent.* **1997**, *17*, 10–25.
368. Govender, S.; Csimma, C.; Genant, H. K.; *et al*. *J. Bone Joint Surg. Am.* **2002**, *84A*, 2123–2134.
369. Chapman, M. W.; Bucholz, R.; Cornell, C. *J. Bone Joint Surg. Am.* **1997**, *79A*, 495–502.
370. Cornell, C. N.; Lane, J. M.; Chapman, M.; *et al*. *J. Orthop. Trauma* **1991**, *5*, 1–8.
371. Neen, D.; Noyes, D.; Shaw, M.; Gwilym, S.; Fairlie, N.; Birch, N. *Spine* **2006**, *31*, E636–E640.
372. Carter, J. D.; Swearingen, A. B.; Chaput, C. D.; Rahm, M. D. *Spine J.* **2009**, *9*, 434–438.
373. Chung, Y. I.; Ahn, K. M.; Jeon, S. H.; Lee, S. Y.; Lee, J. H.; Tae, G. *J. Control. Release* **2007**, *121*, 91–99.
374. Bonadio, J.; Smiley, E.; Patil, P.; Goldstein, S. *Nat. Med.* **1999**, *5*, 753–759.
375. Endo, M.; Kuroda, S.; Kondo, H.; Maruoka, Y.; Ohya, K.; Kasugai, S. *Tissue Eng.* **2006**, *12*, 489–497.
376. Fang, J.; Zhu, Y. Y.; Smiley, E.; *et al*. *Proc. Natl. Acad. Sci. USA* **1996**, *93*, 5753–5758.
377. Holladay, C.; Keeney, M.; Greiser, U.; Murphy, M.; O'Brien, T.; Pandit, A. *J. Control. Release* **2009**, *136*, 220–225.
378. Keeney, M.; Collin, E.; Pandit, A. *Tissue Eng. C Meth.* **2009**, *15*, 265–273.
379. Keeney, M.; van den Beucken, J.; van der Kraan, P.; Jansen, J.; Pandit, A. *Biomaterials* **2010**, *31*(10), 2893–2902.
380. Strine, T. W.; Hootman, J. M. *Arthritis Rheum.* **2007**, *57*, 656–665.
381. Fritz, J. M.; Cleland, J. A.; Speckman, M.; Brennan, G. P.; Hunter, S. J. *Spine* **2008**, *33*, 1800–1805.
382. Urban, J. P.; Roberts, S. *Arthritis Res. Ther.* **2003**, *5*, 120–130.
383. Adams, M. A.; Roughley, P. J. *Spine* **2006**, *31*, 2151–2161.
384. Halloran, D. O.; Grad, S.; Stoddart, M.; Dockery, P.; Alini, M.; Pandit, A. S. *Biomaterials* **2008**, *29*, 438–447.
385. Nesti, L. J.; Li, W. J.; Shanti, R. M.; *et al*. *Tissue Eng. A* **2008**, *14*, 1527–1537.
386. So, K.; Takemoto, M.; Fujibayashi, S.; *et al*. *Spine (Phila Pa 1976)* **2007**, *32*, 1586–1591.
387. Allen, M. J.; Schoonmaker, J. E.; Bauer, T. W.; Williams, P. F.; Higham, P. A.; Yuan, H. A. *Spine (Phila Pa 1976)* **2004**, *29*, 515–523.
388. Kobayashi, M.; Toguchida, J.; Oka, M. *Biomaterials* **2003**, *24*, 639–647.
389. Berlemann, U.; Schwarzenbach, O. *Eur. Spine J.* **2009**, *18*, 1706–1712.
390. Sakai, D. *Eur. Spine J.* **2008**, *17*(Suppl. 4), 452–458.
391. Gruber, H. E.; Hanley, E. N., Jr. *Expert Opin. Biol. Ther.* **2003**, *3*, 1209–1214.
392. Gruber, H. E.; Leslie, K.; Ingram, J.; Norton, H. J.; Hanley, E. N. *Spine J.* **2004**, *4*, 44–55.
393. Masuda, K.; An, H. S. *Spine J.* **2004**, *4*, 330S–340S.
394. Kakutani, K.; Nishida, K.; Uno, K.; *et al*. *J. Orthop. Res.* **2006**, *24*, 1271–1278.
395. Baer, A. E.; Wang, J. Y.; Kraus, V. B.; Setton, L. A. *J. Orthop. Res.* **2001**, *19*, 2–10.
396. Wan, Y.; Feng, G.; Shen, F. H.; Laurencin, C. T.; Li, X. *Biomaterials* **2008**, *29*, 643–652.
397. Stern, S.; Lindenhayn, K.; Schultz, O.; Perka, C. *Acta Orthop. Scand.* **2000**, *71*, 496–502.
398. Storrie, H.; Mooney, D. J. *Adv. Drug Deliv. Rev.* **2006**, *58*, 500–514.
399. O'Halloran, D.; Pandit, A. *Tissue Eng.* **2007**, *13*, 1927–1954.
400. Anderson, D. G.; Risbud, M. V.; Shapiro, I. M.; Vaccaro, A. R.; Albert, T. J. *Spine J.* **2005**, *5*, 297S–303S.
401. Vunjak-Novakovic, G. *Novartis Found Symp.* **2003**, *249*, 34–46; discussion 46–51, 170–174, 239–141.
402. Lu, Z.; Zandieh-Doulabi, B.; Huang, C.; Bank, R. A.; Helder, M. *Tissue Eng. A* **2010**, *16*(1), 81–90.
403. Riesle, J.; Hollander, A. P.; Langer, R.; Freed, L. E.; Vunjak-Novakovic, G. *J. Cell. Biochem.* **1998**, *71*, 313–327.
404. Barnes, C. P.; Pemble, C. W.; Brand, D. D.; Simpson, D. G.; Bowlin, G. L. *Tissue Eng.* **2007**, *13*, 1593–1605.
405. Veilleux, N.; Spector, M. *Osteoarthr. Cartilage* **2005**, *13*, 278–286.
406. Sakai, D.; Mochida, J.; Iwashina, T.; *et al*. *Biomaterials* **2006**, *27*, 335–345.
407. Wu, C. H.; Ko, C. S.; Huang, J. W.; Huang, H. J.; Chu, I. M. *J. Mater. Sci. Mater. Med.* **2009**.
408. Revell, P. A.; Damien, E.; Di Silvio, L.; Gurav, N.; Longinotti, C.; Ambrosio, L. *J. Mater. Sci. Mater. Med.* **2007**, *18*, 303–308.
409. Kawasaki, K.; Ochi, M.; Uchio, Y.; Adachi, N.; Matsusaki, M. *J. Cell. Physiol.* **1999**, *179*, 142–148.
410. Tang, S.; Spector, M. *Biomed. Mater.* **2007**, *2*, S135–S141.
411. Pek, Y. S.; Kurisawa, M.; Gao, S.; Chung, J. E.; Ying, J. Y. *Biomaterials* **2009**, *30*, 822–828.
412. Strauss, E. J.; Hart, J. A.; Miller, M. D.; Altman, R. D.; Rosen, J. E. *Am. J. Sports Med.* **2009**, *37*(8), 1636–1644.
413. Kuo, S. M.; Wang, Y. J.; Niu, G. C.; Lu, H. E.; Chang, S. J. *J. Mater. Sci. Mater. Med.* **2008**, *19*, 1235–1241.
414. Steck, E.; Bertram, H.; Abel, R.; Chen, B.; Winter, A.; Richter, W. *Stem Cells* **2005**, *23*, 403–411.
415. Sobajima, S.; Vadala, G.; Shimer, A.; Kim, J. S.; Gilbertson, L. G.; Kang, J. D. *Spine J.* **2007**.
416. Kim, D.; Kim, S.; Heo, S.; *et al*. *J. Biosci. Bioeng.* **2009**, *108*, 63–67.
417. Hoogendoorn, R. J.; Lu, Z. F.; Kroeze, R. J.; Bank, R. A.; Wuisman, P. I.; Helder, M. N. *J. Cell. Mol. Med.* **2008**, *12*(6A), 2205–2216.
418. Kandel, R.; Roberts, S.; Urban, J. P. *Eur. Spine J.* **2008**, *17*(Suppl. 4), 480–491.
419. Hunter, C. J.; Matyas, J. R.; Duncan, N. A. *Tissue Eng.* **2003**, *9*, 667–677.
420. Yoon, S. T. *Spine J.* **2005**, *5*, 280S–286S.
421. Nagae, M.; Ikeda, T.; Mikami, Y.; *et al*. *Tissue Eng.* **2007**, *13*, 147–158.
422. Vogel, H. *Connect. Tissue Res.* **1975**, *3*, 237–244.
423. Vogel, H. *Connect. Tissue Res.* **1974**, *2*, 177–182.
424. Vogel, H. *Connect. Tissue Res.* **1977**, *5*, 91–95.
425. Ferry, S. T.; Dahners, L. E.; Afshari, H. M.; Weinhold, P. S. *Am. J. Sports Med.* **2007**, *35*, 1326–1333.
426. Dawes, P. T.; Symmons, D. P. M. *Baillières Clin. Rheumatol.* **1992**, *6*, 117–140.
427. Andrews, J. R. *Arthroscopy* **2005**, *21*, 333–347.
428. Andres, B. M.; Murrell, G. A. C. *Clin. Orthop. Relat. Res.* **2008**, *466*, 1539–1554.
429. Riley, G.; Cox, M.; Harrall, R.; Clements, S.; Hazleman, B. *J. Hand Surg.* **2001**, *26*, 224–228.
430. Chan, Y.-S.; Yang, S.-C.; Chang, C.-H.; *et al*. *Arthroscopy* **2006**, *22*, 762–770.
431. Wu, C.-H.; Chen, A. C.-Y.; Yuan, L.-J.; *et al*. *Arthroscopy* **2007**, *23,* 420. e422–427.e422.
432. Antonogiannakis, E.; Yiannakopoulos, C. K.; Hiotis, I.; Karabalis, C.; Babalis, G. *Arthroscopy* **2005**, *21*, 894.e891–894.e895.
433. Chu, P. J.; Lee, H. M.; Hou, Y. T.; Hung, S. T.; Chen, J. K.; Shih, J. T. *J. Orthop. Surg.* **2008**, *3*, 16.
434. Hunter, J. M.; Salisbury, R. E. *J. Bone Joint Surg. Am.* **1971**, *53*, 829–858.
435. Bora, F. W., Jr.; Osterman, A. L.; Thomas, V. J.; Maitin, E. C.; Polineni, S. *J. Hand Surg. Am.* **1987**, *12*, 1038–1040.
436. Crossett, L. S.; Sinha, R. K.; Sechriest, V. F.; Rubash, H. E. *J. Bone Joint Surg. Am.* **2002**, *84A*, 1354–1361.
437. Sanchez-Sotelo, J.; Morrey, B. F.; Adams, R. A.; O'Driscoll, S. W. *J. Bone Joint Surg. Am.* **2002**, *84A*, 999–1005.
438. Zanotti, R. M.; Freiberg, A. A.; Matthews, L. S. *J. Arthroplasty* **1995**, *10*, 271–274.
439. Arnoczky, S.; Warren, R.; Ashlock, M. *J. Bone Joint Surg. Am.* **1986**, *68*, 376–385.
440. Ahn, J. H.; Yoo, J. C.; Wang, J. H. *Arthroscopy* **2005**, *21*, 965–969.
441. Poehling, G. G.; Curl, W. W.; Lee, C. A.; *et al*. *Arthroscopy* **2005**, *21,* 774. e715–774.e771.
442. Cole, D. W.; Ginn, T. A.; Chen, G. J.; *et al*. *Arthroscopy* **2005**, *21*, 786–790.
443. Roe, S. C.; Milthorpe, B. K.; True, K.; Rogers, G. J.; Schindhelm, K. *Clin. Mater.* **1992**, *9*, 149–154.
444. Madden, K. N.; Johnson, K. A.; Howlett, C. R.; *et al*. *Biomaterials* **1997**, *18*, 225–234.
445. van Steensel, C.; Schreuder, O.; van den Bosch, B.; *et al*. *J. Bone Joint Surg. Am.* **1987**, *69*, 860–864.
446. Badylak, S. F.; Tullius, R.; Kokini, K.; *et al*. *J. Biomed. Mater. Res.* **1995**, *29*, 977–985.

447. Johnson, K. A.; Rogers, G. J.; Roe, S. C.; *et al*. *Biomaterials* **1999**, *20*, 1003–1015.
448. Whitlock, P. W.; Smith, T. L.; Poehling, G. G.; Shilt, J. S.; Van Dyke, M. *Biomaterials* **2007**, *28*, 4321–4329.
449. Metcalf, M.; Savoie, F.; Kellum, B. *Oper. Tech. Orthop.* **2002**, *12*, 204–208.
450. Gilbert, T. W.; Stewart-Akers, A. M.; Simmons-Byrd, A.; Badylak, S. F. *J. Bone Joint Surg. Am.* **2007**, *89*, 621–630.
451. Nakamura, S.; Katsuki, M. *J. Hand Surg. Br.* **2002**, *27*, 326–328.
452. Mountney, J.; Blundell, C. M.; McArthur, P.; Stanley, D. *J. Hand Surg. Br.* **1998**, *23*, 662–665.
453. Oka, Y. *Tokai J. Exp. Clin. Med*. **2000**, *25*, 23–26.
454. Wajid, M. A.; Rangan, A. *J. R. Coll. Surg. Edinb*. **2001**, *46*, 57–58.
455. Freeman, J. W.; Woods, M. D.; Laurencin, C. T. *J. Biomech*. **2007**, *40*, 2029–2036.
456. Aragona, J.; Parsons, J. R.; Alexander, H.; Weiss, A. B. *Clin. Orthop. Relat. Res.* **1981**, 268–278.
457. Makela, P.; Pohjonen, T.; Tormala, P.; Waris, T.; Ashammakhi, N. *Biomaterials* **2002**, *23*, 2587–2592.
458. Brown, T. D.; Fu, F. H.; Hanley, E. N., Jr. *J. Trauma* **1981**, *21*, 951–957.
459. Li, Y.; Ma, T.; Yang, S. T.; Kniss, D. A. *Biomaterials* **2001**, *22*, 609–618.
460. Lieberman, J. R.; Lozman, J.; Czajka, J.; Dougherty, J. *Clin. Orthop. Relat. Res.* **1988**, 204–208.
461. Amstutz, H. C.; Coulson, W. F.; David, E. *J. Biomed. Mater. Res.* **1976**, *10*, 47–59.
462. Rodkey, W. G.; Cabaud, H. E.; Feagin, J. A.; Perlik, P. C. *Am. J. Sports Med*. **1985**, *13*, 242–247.
463. Phaneuf, M. D.; Dempsey, D. J.; Bide, M. J.; Quist, W. C.; LoGerfo, F. W. *Biomaterials* **2001**, *22*, 463–469.
464. Chandy, T.; Das, G. S.; Wilson, R. F.; Rao, G. H. *Biomaterials* **2000**, *21*, 699–712.
465. Vizesi, F.; Jones, C.; Lotz, N.; Gianoutsos, M.; Walsh, W. R. *J. Hand Surg.* **2008**, *33*, 241–246.
466. Ozaki, J.; Fujiki, J.; Sugimoto, K.; Tamai, S.; Masuhara, K. *Clin. Orthop. Relat. Res*. **1989**, 204–208.
467. Huber, C.; Eckstein, F. S.; Halbeisen, M.; Carrel, T. P. *Ann. Thorac. Surg.* **2003**, *75*, 1318–1321.
468. Wada, A.; Kubota, H.; Taketa, M.; Miura, H.; Iwamoto, Y. *J. Hand Surg. J. Br. Soc. Surg. Hand* **2002**, *27*, 329–332.
469. Roberts, J. M.; Goldstrohm, G. L.; Brown, T. D.; Mears, D. C. *Clin. Orthop. Relat. Res*. **1983**, 244–249.
470. Noga, D. E.; Petrie, T. A.; Kumar, A.; Weck, M.; García, A. J.; Collard, D. M. *Biomacromolecules* **2008**, *9*, 2056–2062.
471. Sawyer, A. A.; Hennessy, K. M.; Bellis, S. L. *Biomaterials* **2007**, *28*, 383–392.
472. Hwang, D. S.; Sim, S. B.; Cha, H. J. *Biomaterials* **2007**, *28*, 4039–4046.
473. Dankers, P.; Harmsen, M.; Brouwer, L.; Luyn, M. V.; Meijer, E. *Nat. Mater.* **2005**, *4*, 568–574.
474. Ma, K.; Chan, C. K.; Liao, S.; Hwang, W. Y. K.; Feng, Q.; Ramakrishna, S. *Biomaterials* **2008**, *29*, 2096–2103.
475. Wu, W.; Feng, X.; Mao, T.; *et al*. *Br. J. Oral Maxillofac. Surg.* **2007**, *45*, 272–278.
476. Martin, T.; William, M.; Carroll, W.; Selezneva, I.; Gorelov, A.; Rochev, Y. *J. Biomed. Mater. Res. A* **2007**, *81*, 870–876.
477. Dines, J. S.; Weber, L.; Razzano, P.; *et al*. *J. Shoulder Elbow Surg.* **2007**, *16*, S215–S221.
478. He, W.; Yong, T.; Ma, Z. W.; Inai, R.; Teo, W. E.; Ramakrishna, S. *Tissue Eng.* **2006**, *12*, 2457–2466.
479. Li, M.; Guo, Y.; Wei, Y.; MacDiarmid, A. G.; Lelkes, P. I. *Biomaterials* **2006**, *27*, 2705–2715.
480. He, W.; Ma, Z.; Yong, T.; Teo, W. E.; Ramakrishna, S. *Biomaterials* **2005**, *26*, 7606–7615.
481. Venugopal, J.; Ma, L. L.; Yong, T.; Ramakrishna, S. *Cell Biol. Int.* **2005**, *29*, 861–867.
482. Prager, M.; Polterauer, P.; Bohmig, H.-J.; *et al*. *Surgery* **2001**, *130*, 408–414.
483. Sahoo, S.; Cho-Hong, J.; Siew-Lok, T. *Biomed. Mater.* **2007**, *2*, 169–173.
484. Dines, J. S.; Grande, D. A.; Dines, D. M. *J. Shoulder Elbow Surg.* **2007**, *16*, S204–S207.
485. Tanaka, T.; Zhao, C.; Sun, Y.-L.; Zobitz, M. E.; An, K.-N.; Amadio, P. C. *J. Hand Surg.* **2007**, *32*, 876–881.
486. Arnoczky, S.; Warren, R.; Minei, J. *Am. J. Sports Med*. **1986**, *14*, 1–6.
487. Andrish, J.; Woods, L. *Clin. Orthop. Relat. Res* **1984**, *183*, 298–302.
488. Cao, D.; Liu, W.; Wei, X.; Xu, F.; Cui, L.; Cao, Y. *Tissue Eng.* **2006**, *12*, 1369–1377.
489. Foster, I.; Ralis, Z.; McKibbin, B.; Jenkins, D. *Clin. Orthop. Relat. Res*. **1978**, *131*, 299–307.
490. McPherson, G.; Mendenhall, H.; Gibbons, D.; *et al*. *Clin. Orthop. Relat. Res.* **1985**, *196*, 186–195.
491. Singh, S.; Nalwa, H. *J. Nanosci. Nanotechnol*. **2007**, *7*, 3048–3070.
492. Shvedova, A.; Castranova, V.; Kisin, E.; *et al*. *J. Toxicol. Environ. Health A* **2003**, *66*, 1909–1926.
493. Lam, C.; James, J.; McCluskey, R.; Hunter, R. *Toxicol. Sci*. **2004**, *77*, 3–5.
494. Hiraoka, Y.; Kimura, Y.; Ueda, H.; Tabata, Y. *Tissue Eng.* **2003**, *9*, 1101–1112.
495. Hemmrich, K.; Salber, J.; Meersch, M.; *et al*. *J. Mater. Sci. Mater. Med*. **2008**, *19*, 257–267.
496. Bagnaninchi, P. O.; Yang, Y.; Haj, A. J. E.; Maffulli, N. *Br. J. Sports Med*. **2007**, *41*, 1–5.
497. Redaelli, C.; Niederhäuser, U.; Carrel, T.; Meier, U.; Trentz, O. *Chirurg* **1992**, *63*, 572–576.
498. Hohendorff, B.; Siepen, W.; Spiering, L.; Staub, L.; Schmuck, T.; Boss, A. *J. Foot Ankle Surg.* **2008**, *47*, 392–399.
499. Lusardi, D.; Cain, J. *J. Foot Ankle Surg.* **1994**, *33*, 443–447.
500. Thermann, H.; Frerichs, O.; Biewener, A.; Krettek, C. *Foot Ankle Int.* **2001**, *22*, 478–483.
501. Frykman, E.; Jacobsson, S.; Widenfalk, B. *J. Hand Surg.* **1993**, *18*, 68–75.
502. Thomopoulos, S.; Soslowsky, L.; Flanagan, C.; *et al*. *J. Shoulder Elbow Surg.* **2002**, *11*, 239–247.
503. Key, J. A. *Am. J. Surg.* **1939**, *44*, 166–177.
504. Hooker, D. H.; Lam, C. R. *Am. J. Surg.* **1941**, *54*, 412–416.
505. Buehler, M. J.; Keten, S.; Ackbarow, T. *Prog. Mater. Sci*. **2008**, *53*, 1101–1241.
506. Vepari, C.; Kaplan, D. L. *Prog. Polym. Sci*. **2007**, *32*, 991–1007.
507. Altman, G. H.; Horan, R. L.; Lu, H. H.; *et al*. *Biomaterials* **2002**, *23*, 4131–4141.
508. Altman, G. H.; Diaz, F.; Jakuba, C.; *et al*. *Biomaterials* **2003**, *24*, 401–416.
509. Majima, T.; Irie, T.; Sawaguchi, N.; *et al*. *Proc. Inst. Mech. Eng.* **2007**, *221*, 537–546.
510. Funakoshi, T.; Majima, T.; Iwasaki, N.; *et al*. *Am. J. Sports Med*. **2005**, *33*, 1193–1201.
511. Funakoshi, T.; Majima, T.; Iwasaki, N.; *et al*. *J. Biomed. Mater. Res. A* **2005**, *74*, 338–346.
512. Majima, T.; Funakosi, T.; Iwasaki, N.; *et al*. *J. Orthop. Sci*. **2005**, *10*, 302–307.
513. Bagnaninchi, P. O.; Yang, Y.; Zghoul, N.; Maffulli, N.; Wang, R. K.; Haj, A. J. E. *Tissue Eng.* **2007**, *13*.
514. Goldstein, J. D.; Tria, A. J.; Zawadsky, J. P.; Kato, K. Y.; Christiansen, D.; Silver, F. H. *J. Bone Joint Surg.* **1989**, *71A*, 1183–1191.
515. Kato, Y. P.; Christiansen, D. L.; Hahn, R. A.; Shieh, S.-J.; Goldstein, J. D.; Silver, F. H. *Biomaterials* **1989**, *10*, 38–42.
516. Wasserman, A. J.; Kato, Y. P.; Christiansen, D.; Dunn, M. G.; Silver, F. H. *Scanning Microsc.* **1989**, *3*, 1183–1197; discussion 1197–1200.
517. Rizvi, A. H.; Pins, G. D.; Silver, F. H. *Clin. Mater.* **1994**, *16*, 73–80.
518. Kato, Y. P.; Silver, F. H. *Biomaterials* **1990**, *11*, 169–175.
519. Zeugolis, D. I.; Paul, G. R.; Attenburrow, G. *Acta Biomater.* **2008**, *4*, 1646–1656.
520. Dunn, M. G.; Avasarala, P. N.; Zawadsky, J. P. *J. Biomed. Mater. Res.* **1993**, *27*, 1545–1552.
521. Dunn, M. G.; Tria, A. J.; Kato, Y. P.; *et al*. *Am. J. Sports Med*. **1992**, *20*, 507–515.
522. Wang, M. C.; Pins, G. D.; Silver, F. H. *Biomaterials* **1994**, *15*, 507–512.
523. Koob, T. J.; Willis, T. A.; Hernandez, D. J. *J. Biomed. Mater. Res.* **2001**, *56*, 31–39.
524. Koob, T. J.; Willis, T. A.; Qiu, Y. S.; Hernandez, D. J. *J. Biomed. Mater. Res.* **2001**, *56*, 40–48.
525. Koob, T. J. *Comp. Biochem. Physiol. A Mol. Integr. Physiol*. **2002**, *133*, 1171–1192.
526. Gentleman, E.; Lay, A. N.; Dickerson, D. A.; Nauman, E. A.; Livesay, G. A.; Dee, K. C. *Biomaterials* **2003**, *24*, 3805–3813.
527. Cornwell, K. G.; Downing, B.; Pins, G. D. *J. Biomed. Mater. Res.* **2004**, *71A*, 55–62.
528. Cornwell, K. G.; Lei, P.; Andreadis, S. T.; Pins, G. D. *J. Biomed. Mater. Res.* **2007**, *80A*, 362–371.
529. Cavallaro, J. F.; Kemp, P. D.; Kraus, K. H. *Biotechnol. Bioeng.* **1994**, *43*, 781–791.
530. Bersten, A. M.; Ahkong, Q. F.; Hallinan, T.; Nelson, S. J.; Lucy, J. A. *Biochim. Biophys. Acta Mol. Cell Res.* **1983**, *762*, 429–436.
531. Hevessy, Z.; Patthy, A.; Karpati, L.; Muszbek, L. *Thromb. Res.* **2000**, *99*, 399–406.
532. Case, A.; Ni, J.; Yeh, L.-A.; Stein, R. L. *Anal. Biochem.* **2005**, *338*, 237–244.
533. Lorand, L. *Neurochem. Int.* **2002**, *40*, 7–12.
534. Hucho, F.; Bandini, G. *FEBS Lett*. **1986**, *200*, 279–282.
535. Garcia, Y.; Wilkins, B.; Collighan, R. J.; Griffin, M.; Pandit, A. *Biomaterials* **2008**, *29*, 857–868.

536. Orban, J. M.; Wilson, L. B.; Kofroth, J. A.; El-Kurdi, M. S.; Maul, T. M.; Vorp, D. A. *J. Biomed. Mater. Res.* **2004**, *68A*, 756–762.
537. Chau, D. Y. S.; Collighan, R. J.; Verderio, E. A. M.; Addy, V. L.; Griffin, M. *Biomaterials* **2005**, *26*, 6518–6529.
538. Chen, R.-N.; Ho, H.-O.; Sheu, M.-T. *Biomaterials* **2005**, *26*, 4229–4235.
539. Zeugolis, D. I.; Pradeep-Paul, P.; Yew, E. S. Y.; Sheppard, C.; Phan, T. T.; Raghunath, M. *J. Biomed. Mater. Res. A* **2010**, *92*(4), 1310–1320.
540. Kato, Y. P.; Dunn, M. G.; Zawadsky, J. P.; Tria, A. J.; Silver, F. H. *J. Bone Joint Surg. Am.* **1991**, *73*, 561–574.
541. Huang, D.; Balian, G.; Chhabra, A. B. *J. Hand Surg.* **2006**, *31*, 693–704.
542. Richardson, L. E.; Dudhia, J.; Clegg, P. D.; Smith, R. *Trends Biotechnol.* **2007**, *25*, 409–416.
543. Sutter, W. W. *Clin. Tech. Equine Pract.* **2007**, *6*, 198–208.
544. Kryger, G. S.; Chong, A. K. S.; Costa, M.; Pham, H.; Bates, S. J.; Chang, J. *J. Hand Surg.* **2007**, *32*, 597–605.
545. Kryger, G. S.; Pham, H.; Wu, C.; Bates, S.; Chang, J. *J. Am. Coll. Surg.* **2005**, *201*, S45–S46.
546. Harris, M. T.; Butler, D. L.; Boivin, G. P.; Florer, J. B.; Schantz, E. J.; Wenstrup, R. J. *J. Orthop. Res.* **2004**, *22*, 998–1003.
547. Awad, H. A.; Butler, D. L.; Boivin, G. P.; *et al. Tissue Eng.* **1999**, *5*, 267–277.
548. Ringe, J.; Kaps, C.; Burmester, G.-R.; Sittinger, M. *Naturwissenschaften* **2002**, *89*, 338–351.
549. Young, R. G.; Butler, D. L.; Weber, W.; Caplan, A. I.; Gordon, S. L.; Fink, D. J. *J. Orthop. Res.* **1998**, *16*, 406–413.
550. Moioli, E. K.; Clark, P. A.; Sumner, D. R.; Mao, J. J. *Bone* **2008**, *42*, 332–340.
551. Qiao, C.; Xu, W.; Zhu, W.; *et al. Cell Biol. Int.* **2008**, *32*, 8–15.
552. Juncosa-Melvin, N.; Boivin, G. P.; Gooch, C.; *et al. Tissue Eng.* **2006**, *12*, 369–379.
553. Caplan, A. I.; Fink, D. J.; Bruder, S. P.; *et al. The Regeneration of Skeletal Tissues with Mesenchymal Stem Cells. Frontiers in Tissue Engineering*; Pergamon: Oxford, 1998; pp 471–480.
554. Wang, Q. W.; Chen, Z. L.; Piao, Y. J. *J. Biosci. Bioeng.* **2005**, *100*, 418–422.
555. Remes, A.; Williams, D. F. In *The Biomaterials: Silver Jubilee Compendium*; Williams, D. F., Ed.; Elsevier Science: Oxford, 2006; pp 79–91.
556. Badylak, S. F.; Gilbert, T. W. *Semin. Immunol.* **2008**, *20*, 109–116.
557. Trentham, D. E.; Townes, A. S.; Kang, A. H. *J. Exp. Med.* **1977**, *146*, 857–868.
558. Rutala, W.; Weber, D. *Clin. Infect. Dis.* **2001**, *32*, 1348–1356.
559. Tiwari, A.; Patnayak, D.; Chander, Y.; Minakshi, P.; Goyal, S. *Avian Dis.* **2006**, *50*, 284–287.
560. Joly, J.; Nguyen, V.; Bourrat, F. *Prod. Anim.* **2001**, *14*, 91–96.
561. Louz, D.; Bergmans, H.; Loos, B.; Hoeben, R. *J. Gene Med.* **2005**, *7*, 1263–1274.
562. Louz, D.; Bergmans, H.; Loos, B.; Hoeben, R. *Rev. Med. Virol.* **2008**, *18*, 53–65.
563. Narotam, P. K.; Van Dellen, J. R.; Bhoola, K.; Raidoo, D. *Br. J. Neurosurg.* **1993**, *7*, 635–641.
564. Ruggiero, F.; Koch, M. *Methods* **2008**, *45*, 75–85.
565. Koide, T. *Philos. Trans. R. Soc. B* **2007**, *362*, 1281–1291.
566. Koide, T. *Connect. Tissue Res.* **2005**, *46*, 131–141.
567. Ito, H.; Steplewski, A.; Alabyeva, T.; Fertala, A. *J. Biomed. Mater. Res.* **2006**, *76A*, 551–560.
568. Nokelainen, M. *Recombinant Human Collagens. Medical Biochemistry*; University of Oulu: Oulu, 2000.
569. Olsen, D.; Yang, C.; Bodo, M.; *et al. Adv. Drug Deliv. Rev.* **2003**, *55*, 1547–1567.
570. McHale, M. K.; Setton, L. A.; Chilkoti, A. *Tissue Eng.* **2005**, *11*, 1768–1779.
571. Shamji, M. F.; Betre, H.; Kraus, V. B.; *et al. Arthritis Rheum.* **2007**, *56*, 3650–3661.
572. Bellingham, C. M.; Lillie, M. A.; Gosline, J. M.; *et al. Biopolymers* **2003**, *70*, 445–455.
573. Huang, L.; McMillan, R. A.; Apkarian, R. P.; Pourdeyhimi, B.; Conticello, V. P.; Chaikof, E. L. *Macromolecules* **2000**, *33*, 2989–2997.
574. Stultz, C. *Protein Sci.* **2006**, *15*, 2166–2177.
575. Long, C.; Braswell, E.; Zhu, D.; Apigo, J.; Baum, J.; Brodsky, B. *Biochemistry* **1993**, *32*, 11688–11695.
576. Gauba, V.; Hartgerink, J. D. *J. Am. Chem. Soc.* **2008**, *130*, 7509–7515.
577. Miles, C. A.; Bailey, A. J. *J. Mol. Biol.* **2004**, *337*, 917–931.
578. Venugopal, M.; Ramshaw, J.; Braswell, E.; Zhu, D.; Brodsky, B. *Biochemistry* **1994**, *33*, 7948–7956.
579. Krishna, O.; Kiick, K. *Biomacromolecules* **2009**, *10*, 2626–2631.
580. Yao, J.; Yanagisawa, S.; Asakura, T. *J. Biochem.* **2004**, *136*, 643–649.
581. Khew, S. T.; Yang, Q. J.; Tong, Y. W. *Biomaterials* **2008**, *29*, 3034–3045.
582. Pêcher, J.; Pires, V.; Djaafri, I.; *et al. Eur. J. Med. Chem.* **2009**, *44*, 2643–2650.
583. Cejas, M.; Kinney, W.; Chen, C.; *et al. Proc. Natl. Acad. Sci. USA* **2008**, *105*, 8513–8518.
584. Geddis, A. E.; Prockop, D. J. *Matrix Biol.* **1993**, *13*, 399–405.
585. Fertala, A.; Sieron, A. L.; Ganguly, A.; *et al. Biochem. J.* **1994**, *298*, 31–37.
586. Lamberg, A.; Helaakoski, T.; Myllyharju, J.; *et al. J. Biol. Chem.* **1996**, *271*, 11988–11995.
587. Myllyharju, J.; Lamberg, A.; Notbohm, H.; Fietzek, P.; Pihlajaniemi, T.; Kivirikko, K. *J. Biol. Chem.* **1997**, *272*, 21824–21830.
588. Toman, P. D.; Chisholm, G.; McMullin, H.; *et al. J. Biol. Chem.* **2000**, *275*, 23303–23309.
589. Olsen, D. R.; Leigh, S. D.; Chang, R.; *et al. J. Biol. Chem.* **2001**, *276*, 24038–24043.
590. Buechter, D. D.; Paolella, D. N.; Lelie, B. S.; Brown, M. S.; Mehos, K. A.; Gruskin, E. A. *J. Biol. Chem.* **2003**, *278*, 645–650.
591. Xue, W.; Fan, D.; Shang, L.; Zhu, C.; Ma, X.; Yu, Y. *Biotechnol. Lett.* **2009**, *31*, 221–226.
592. Xu, C.; Yu, Z.; Inouye, M.; Brodsky, B.; Mirochnitchenko, O. *Biomacromolecules* **2010**, *11*(2), 348–356.
593. Toman, P. D.; Pieper, F.; Sakai, N.; Karatzas, C.; Platenburg, E. *Transgenic Res.* **1999**, *8*, 415–427.
594. Ruggiero, F.; Exposito, J. Y.; Bournat, P.; *et al. FEBS Lett.* **2000**, *469*, 132–136.
595. Stein, H.; Wilensky, M.; Tsafrir, Y.; *et al. Biomacromolecules* **2009**, *10*, 2640–2645.
596. Zhang, C.; Baez, J.; Pappu, K.; Glatz, C. *Biotechnol. Prog.* **2009**, *25*, 1660–1668.
597. Tomita, M.; Munetsuna, H.; Sato, T.; *et al. Nat. Biotechnol.* **2003**, *21*, 52–56.
598. Yang, C.; Hillas, P.; Báez, J.; *et al. BioDrugs* **2004**, *18*, 103–119.
599. Báez, J.; Olsen, D.; Polarek, J. *Appl. Microbiol. Biotechnol.* **2005**, *69*, 245–252.
600. Liu, W.; Merrett, K.; Griffith, M.; *et al. Biomaterials* **2008**, *29*, 1147–1158.
601. Bulleid, N.; John, D.; Kadler, K. *Biochem. Soc. Trans.* **2000**, *28*, 350–353.
602. Fichard, A.; Tillet, E.; Delacoux, F.; Garrone, R.; Ruggiero, F. *J. Biol. Chem.* **1997**, *272*, 30083–30087.
603. Vuorela, A.; Myllyharju, J.; Nissi, R.; Pihlajaniemi, T.; Kivirikko, K. *EMBO J.* **1997**, *16*, 6702–6712.
604. Majsterek, I.; McAdams, E.; Adachi, E.; Dhuma, S. T.; Fertala, A. *Protein Sci.* **2003**, *12*, 2063–2072.

2.223. Bacterial Cellulose as Biomaterial

A Bodin, Biopolymer Technology, Göteborg, Sweden
H Bäckdahl, SP Technical Research Institute of Sweden, Borås, Sweden
N Petersen, University of Virginia, Charlottesville, VA, USA
P Gatenholm, Biopolymer Technology, Göteborg, Sweden; Wake Forest Institute for Regenerative Medicine, Winston-Salem, NC, USA

© 2011 Elsevier Ltd. All rights reserved.

2.223.1. Introduction 405
2.223.2. Bacterial Cellulose: Growth 405
2.223.3. Modification of Nanostructure 406
2.223.4. Engineering of Morphology 407
2.223.5. Shaping in 3D Structure 407
2.223.6. Biocompatibility 408
2.223.7. Biomechanics 408
2.223.8. Cell Interactions and Migration 408
2.223.9. Biomedical Applications 409
2.223.10. Future Outlook 409
References 410

Abbreviations

BC	Bacterial cellulose
CHO	Chinese hamster ovary
CMC	Carboxy methyl cellulose
GPa	Gigapascal
SMC	Smooth muscle cells
UDP	Uridine diphosphate
UDPG	UDP-glucose

2.223.1. Introduction

The development of biomaterials coincides with the beginning of surgery. The Indian surgeon Sushruta as early as 2800 years ago conducted advanced surgeries and used sutures made of cellulose from hemp and cotton. Cellulose was first isolated in 1838 from the cell walls of plants.[1] Since then, its structural importance and presence in other organisms has been further elucidated. In plants, cellulose provides structural integrity where it is found in conjunction with hemicelluloses, lignin, and other materials. The bacteria *Acetobacter xylinum* has been particularly noted for its production of cellulose in which it plays a protective role rather than being a load-bearing material. *A. xylinum* is a nonpathogenic obligate aerobic Gram-negative rod. It is a common contaminant of wine and beer and is found naturally on the surface of fruits and flowers where it produces a cellulose film.[2] This biofilm helps to retain moisture, protects the bacteria from UV radiation, and, in liquids, helps the bacteria stay near the oxygen-rich surface, thanks to its natural buoyancy.[2–4] On fruit, it has been shown that the biofilm promotes *A. xylinum* colonization while inhibiting colonization of competing organisms.[3] The cellulose produced by bacteria is pure, without contaminant molecules. This remarkable purity is combined with high water-holding capacity. Bacterial cellulose (BC) contains 99 wt% water and is essentially a hydrogel.[5] The architecture of the entangled nanoscale fiber network makes it mechanically strong (see Section 2.223.7). Taken together, all these unique properties of the BC network make it a very interesting candidate to be used for various biomedical applications (Figure 1).

2.223.2. Bacterial Cellulose: Growth

BC, like all cellulose, is a natural polymer synthesized from UDP-glucose (UDPG) monomers. Cellulose synthase is the enzyme that catalyzes the covalent attachment of these glucose subunits into a linear chain. In the process, UDP is cleaved off and the remaining D-glucose subunits are attached via β-1,4 linkages, forming β-1,4 glucan chains. In addition to the β-1,4 covalent bond between adjacent D-glucose monomers, each D-glucose subunit also hydrogen bonds with adjacent D-glucose monomers within its chain. As chains are brought into close proximity, interchain hydrogen bonding also occurs between the exposed hydroxyl groups of aligned chains (Figure 2).

A. xylinum is not limited to six-carbon sugars as substrates for cellulose synthesis. It can utilize a variety of molecules as carbon sources including hexoses, hexanoates, pyruvate, glycerol, dihydroxyacetone, and dicarboxylic acids.[3] The benefit of this diversity of usable substrates is that there is potential for growing BC in a variety of media, including biomass waste material. A wide range of alternative growth media has been investigated. Waste broth from beer culture, pineapple juice, coconut milk, konjac powder, and sugarcane molasses are some of the sources investigated in the past several years.[6–10]

Individual chain polymerization and subsequent association of multiple chains into larger microfibrils occurs in series. Cellulose synthase is thought to be located on the cytoplasmic membrane. Multiple chain synthesis sites are located in close proximity so that newly polymerized polyglucan chains associate in parallel, forming intermolecular hydrogen bonds. The method of extrusion from the cell differs in bacteria and plants. In plants, cellulose aggregates are extruded from rosette structures whereas in bacteria, they are extruded from a linear array of 50–80 extrusion pores running longitudinally along the side of each bacterium. In cellulose-producing bacteria, initial aggregates of 10–15 polyglucan chains form first.[3] These premicrofibril aggregates then assemble to form larger microfibrils. Microfibrils associate to form larger microfibril bundles, and bundles ultimately associate loosely to form the cellulose ribbon extending from each cellulose-producing bacterium. Bacteria replicate and continue 'spinning' cellulose until a dense intertwined mesh is created, thus enclosing and protecting the bacteria. The result of a colony of such bacteria-producing cellulose ribbons is a highly pure, nanofibrillar mesh composed of 99% water (Figure 3).[5]

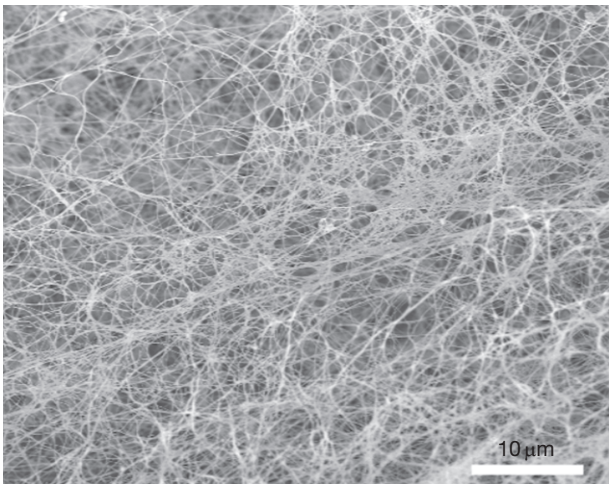

Figure 1 Bacterial cellulose: nanostructure.

2.223.3. Modification of Nanostructure

The polymerization of individual polyglucan chains and the ultimate crystallization of these large cellulose ribbons are coupled processes, occurring simultaneously and in linear physical connection.[3] However, the crystallization process can be disrupted by the addition of interfering molecules to

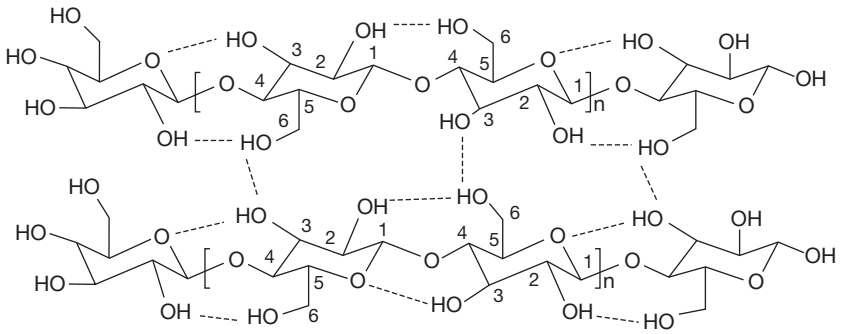

Figure 2 Cellulose, showing the hydrogen bonding network and the numbering of the atoms. Each glucose residue forms two intramolecular hydrogen bonds ($O_6 \cdots H–O_2$) and ($O_3–H \cdots O$ ring) and one intermolecular bond ($O_6–H \cdots O_3$).

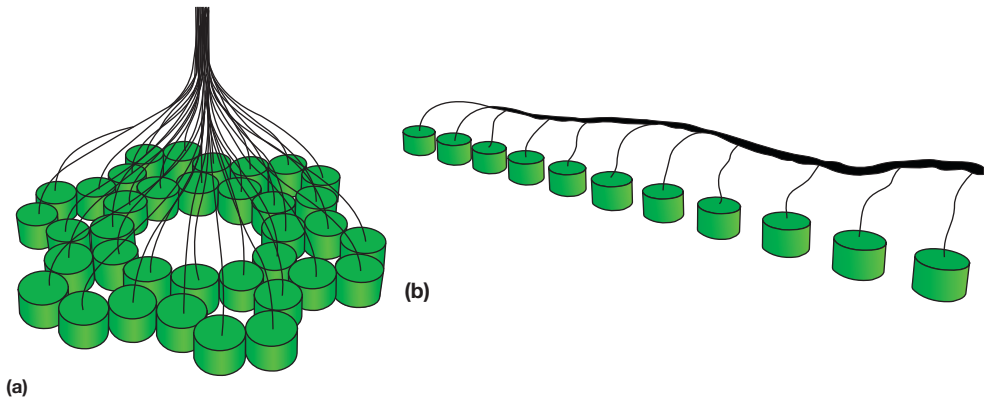

Figure 3 (a) Rosette-type terminal complex as found in algae and vascular plants. (b) Linear arrangement of cellulose extrusion pores, as found in cellulose-producing bacteria, forming a cellulose premicrofibril aggregate strand.

the culture medium (e.g., Congo red dye, calcofluor, carboxymethyl cellulose).[3,11,12]

There have been many efforts to modify the nanostructure of BC. One example is to supply different oxygen tensions. Watanabe *et al.* reported that a denser BC network formed in a static culture with a higher oxygen ratio (50%) than in air. BC nanofibrils branched in association with cell division, and those branches produced a ramified network. The length of the segments between branches varied from 700 µm at 10% oxygen to 200 µm at 50% oxygen tension.[13] It has been recently discovered that the synthesis of the nanofibril by bacteria can be involved in generating movement of the cell. By adding carboxymethylcellulose sodium salt (CMC) to the culture medium, bacteria moved faster in the culture medium, resulting in changes to the nanofiber compared to a normal cellulose nanofiber.[14]

2.223.4. Engineering of Morphology

One of the greatest advantages of BC is its ability to be molded into almost any size and shape during its synthesis without causing any significant alteration of its physical properties.

When cultured statically, BC accumulates at the surface of the culture medium as a pellicle.

The BC pellicle that is formed has a great number of almost parallel thin cellulose layers.[15] These layers propagate downward during culture. New layers always form at the upper film surface, resulting in a steady increase in the pellicle's thickness with time.[16] The pellicle can be used in its native state for several biomedical applications (see **Section 2.223.9**). It is also possible to reform the pellicle into desired shapes. For example, if the culture surface has a 'meniscus-like' shape, the resulting pellicle will be similar in appearance to a meniscus (**Figure 4**).[17]

Several patents and articles cover the production of BC tubes by utilizing different fermentation methods.[18–21] Many techniques use a surface that acts as a template for BC deposition and as a membrane for oxygen delivery. In some, the culture is encapsulated, which makes the BC network fill out the area between, for example, two glass cylinders, resulting in a tube-shaped BC network. Since the production techniques vary, the properties of the resulting tubes are not the same, even though they are all composed of a BC network.

2.223.5. Shaping in 3D Structure

A scaffold seeded with cells is generally considered the paradigm of tissue engineering. It has been found that when the scaffold has a nanoscale morphology, cell attachment, proliferation, and expression of matrix components are increased.[22] Compared with macroscale scaffolds, nanoscale scaffolds possess larger surface areas for the adsorption of proteins and present many more binding sites to cell membrane receptors.[23] BC fibrils are in the nanometer scale and are microscopically similar to collagen fibers.[24] This makes them interesting for use as a building block in scaffolds. The BC pellicle has too high a nanofibril density to be able to house cells other than in the outermost regions when acting as a scaffold for smooth muscle cells (SMCs).[24] The porosity can be altered with a

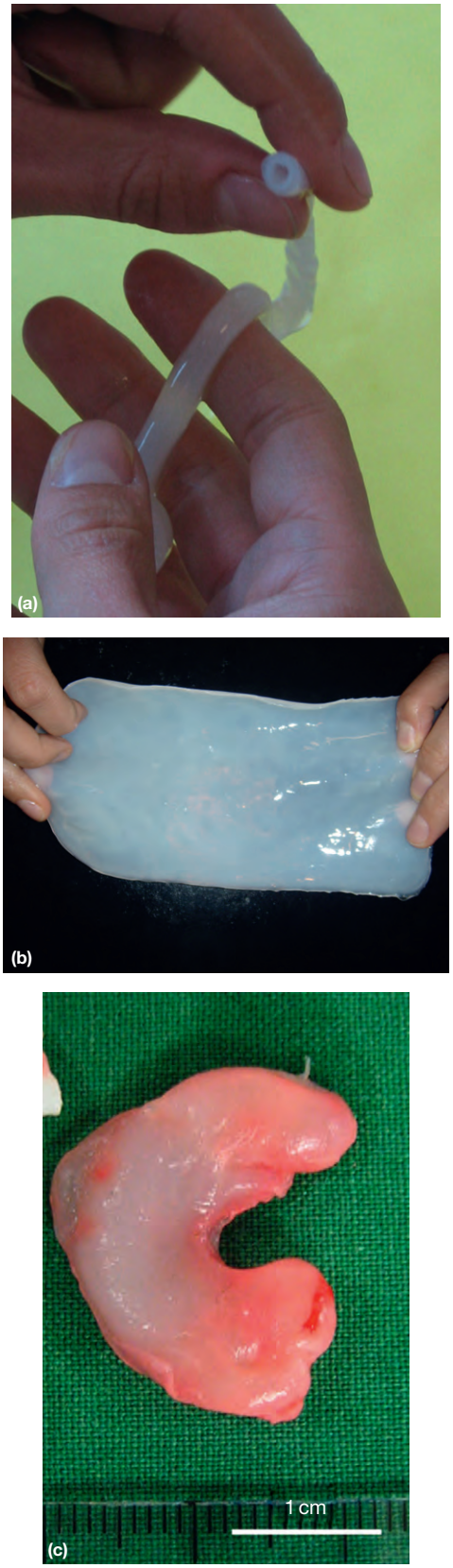

Figure 4 Bacterial cellulose in various shapes, tube to be used as vascular graft (a), membrane to be used as burn dressing (b), meniscus implant (c).

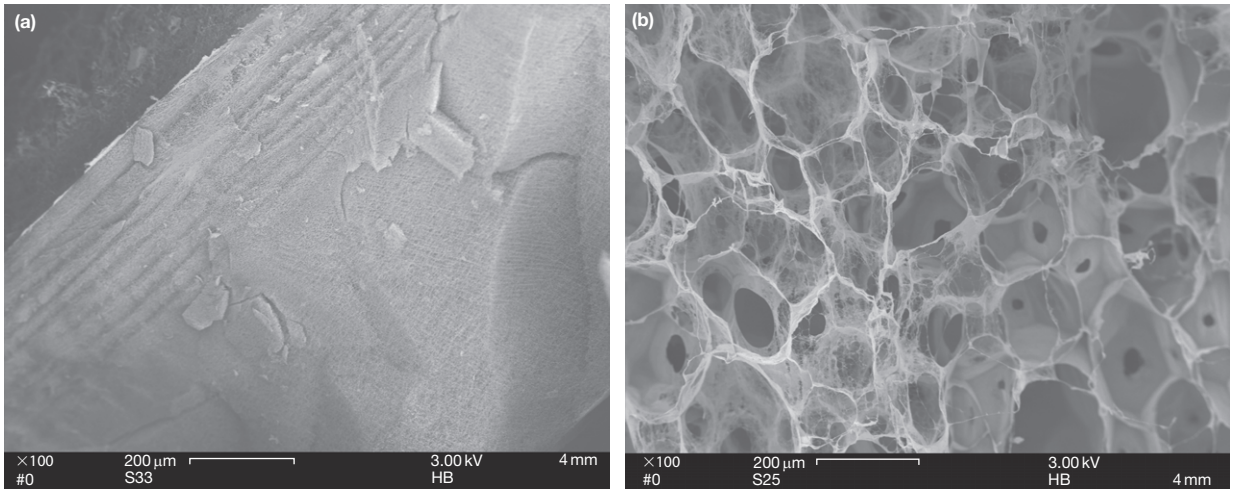

Figure 5 Scanning electron microscopic image of a pellicle and a porous bacterial cellulose (BC) network made with paraffin particles. The cross section of a BC pellicle is seen in (a) while (b) shows a scaffold made with paraffin particles in the size range of 300–500 µm. The porosity has greatly been altered with the help of the particle-leaching technique.

particle-leaching technique where paraffin wax particles are introduced into the culture, and removed when the culture is finished. This results in a microporous BC scaffold that can house SMCs (Figure 5).[24]

2.223.6. Biocompatibility

BC's high water content, around 99%, suggests that it can be seen as a hydrogel, although not by definition as it is not a network of polymer chains that are water soluble. Hydrogels are known for their favorable biocompatibility properties, largely due to little protein adsorption.

A biocompatibility evaluation of a BC pellicle has been made in Wistar rats by subcutaneous implantation and evaluation. At 1, 4, and 12 weeks, Helenius *et al.* reported that there were no macroscopic signs of inflammation, that is, redness, edema, or exudates, around the implanted BC pieces or in the incision at any time point.[25] No histological signs of inflammation in the specimens were found. Fibrosis, capsule formations, or giant cells were not detected around the implants. Instead, the rat connective tissue integrated very nicely with the BC structure at all the studied time points. Newly formed blood vessels were present around and in the implant at all studied time points. The formation of new blood vessels around and in a biomaterial is very important for the healing process and long-term success of a scaffold.[25] BC was further evaluated *in vivo* and *in vitro* by Mendes *et al.*[26] They found that BC induced a mild inflammatory response *in vivo*.

Genotoxicity evaluation has been conducted on BC nanofibers by Moreira *et al.* They reported that BC was not genotoxic under the conditions tested.[27]

Yamanaka *et al.* and Klemm *et al.* have reported data on BC blood compatibility.[19,20] BC was found to be blood compatible, although no systematic study has been carried out to elucidate BC properties toward blood. Klemm *et al.* further claimed to get endothelial cells to cover the lumen when they implanted microbial cellulose vessels, BASYC®, into a rat. As yet, there have been no studies on retention of endothelial cells on BC tubes or on endothelialization of BC tubes in large animal models.

Degradability of regenerated cellulose implants has been shown to be limited. The degradation is induced by chemical modifications that alter its ordered and rigid structure.[28,29] The degradability of BC has not been fully evaluated either *in vivo* or *in vitro*. Mendes *et al.* reported that subcutaneous implanted BC membranes remained intact for at least 90 days.[26] That is similar to what Helenius *et al.* have reported.[25]

2.223.7. Biomechanics

The bonding pattern between cellulose chains gives cellulose remarkable strength. Young's modulus in the plane of a thin BC sheet in the dry state has been reported to be >15 GPa, exceeding any previously tested polymeric film by more than 5 GPa, with tensile strength comparable to that of steel.[3,30]

The high Young's modulus has been ascribed to the unique supermolecular structure in which the microfibrils are tightly bound by hydrogen bonds (see Section 2.223.2). It is important to note that these studies have been conducted on dry films of BC. The reported tensile strength of BC in its wet state has been expressed in Newtons, which makes it difficult to compare results with other values for Young's modulus.[20,31] The Young's modulus in tensile load of wet BC gel has been reported to be 1 MPa, and the elasticity varies depending on sample preparation and probably also on fermentation method.[24,32] Another favorable property of BC is that it can be easily sterilized by autoclaving.

2.223.8. Cell Interactions and Migration

The high water content of BC makes the material a poor substrate for cell adhesion. The low irritation to the skin caused by BC, reported in the patents for wound-care products, is

probably due to some extent to the high water content, which might prevent adhesion to the healing skin and dressing.[33] Its less advantageous properties for cell adhesion have been addressed by Watanabe *et al.* when growing mammalian cells onto BC.[34] Adhesion was somewhat improved if the membranes were preincubated with proteins such as laminin, collagen, or fibronectin. The best results were obtained when the material was chemically modified and negative groups were introduced onto the surface. Watanabe *et al.* claim to have achieved an improvement of protein adsorption and thereby cell adhesion.[34] This is somewhat contradictory to common surface modifications, made to improve biocompatibility, where negatively charged groups are introduced precisely because they effectively decrease protein adsorption.[35] *In vivo* results of BC have, however, revealed good cell adhesion and migration into the material *in vitro*, using growth factors as an attractant.[24,25] Inducing porosity to the BC improves adhesion and migration of SMCs into the cellulose network.[36]

Other cell types have also been cultured on BC. Mendes *et al.* concluded that the material may prove useful as a scaffold for mesenchymal stem cells.[26] A cell proliferation evaluation has been conducted on BC nanofibers by Moreira *et al*. They used a proliferation assay to evaluate fibroblast and Chinese hamster ovary (CHO) cell proliferation on the nanofibers. A slight reduction in cell proliferation was revealed, although no modification in the cell morphology was observed.[27]

2.223.9. Biomedical Applications

Interest in BC as a biomaterial is not new; several products have been registered since the late 1980s (Biofill®, Gengiflex®). The use of microbial-derived cellulose in the medical industry has, however, been limited to liquid-loaded pads, wound dressings, and other external applications. There are several clinical studies by the BioFill company (BioFill Produtos Biotechnologicos, Curitiba, Pr Brazil) on BC in applications for regeneration of bone. In one case in which Gengiflex® was grafted with hydroxyapatite, a complete restoration of an osseous defect could be seen.[37] In 1996, Xylos negotiated exclusive licensing agreements with Johnson & Johnson to use their patents on cellulose-based wound-care products. Since that time, the company has been able to successfully obtain FDA approval for its product, XCell®.[38] XCell® is for external application (so far), Biofill® is partially dried BC, and Gengiflex® is partly modified BC.[15,33,39,40] However, BC has interesting properties in its wet, unmodified state. The versatility of BC allows it to be manufactured in various sizes and shapes depending on the product requirements. BC in different shapes has already been applied to treat several types of injuries. Sheets (or pellicles) of BC have been used as a barrier in the regeneration of periodontal tissue, to repair abdominal defects (peritoneum) and as a dura mater substitute.[37,41,42] Furthermore, chronic wounds and burns have been treated with BC sheets.[15,38] Attempts have been made toward regeneration of cartilage, bone graft material, and meniscus replacements.[4,17,20,37,40,42–47] Tubular-shaped BC has been suggested for use as a blood vessel replacement and for nerve surgery.[19,20] The utilization of BC vascular grafts has recently been reported.[48]

BC has also been used as a coating to reduce the coagulation effect on polyester vascular grafts and stents.[46,49]

There are several variables that influence the overall production process and performance of the final BC biomaterial, for example, choice of fermentation method, bacterial strain, media, and purification method. The commercialization of BC as a biomaterial will of course depend upon successful technical and economic solutions and market requirements.[43,50]

2.223.10. Future Outlook

This brief presentation of the unique properties of microbial cellulose probably raises the question of why microbial cellulose has not been used by industry. In fact, it has; however, certain hurdles have prevented its widespread use. These have included the need for better understanding of the biosynthetic process itself, optimizing the fermentation process, and enhancing cell proliferation and BC biosynthesis for more efficient, lower-cost production.[51]

In 1983 the Weyerhaeuser Co., in collaboration with Cetus, started process development, manufacturing, and marketing of microbial cellulose as a dough-like solid and a viscous liquid suspension called Cellulon®. The unique properties of BC mentioned earlier make it applicable in different fields, such as in the paper and textile industry as a binding and coating material and in the food industry to act as a thickener, stabilizer, texturizer, and/or calorie reducer. Despite the interesting properties of BC, Cellulon® never obtained commercial success, probably because cost reductions to make the product competitive with other biopolymers were never realized. The business was later sold to Kelco and has recently been purchased by Monsanto. Opportunities for expansion of microbial cellulose now exist; however, significant gains will be necessary in upgrading fermentation techniques.[43,51,52]

BC resembles human tissue in the sense that it is soft and is composed of highly hydrated nanofibrils with high mechanical strength. The material is versatile and can be manufactured in various sizes and shapes, depending on the product requirements. This makes it interesting to explore BC for use in several biomedical applications. Beyond controlling the size and shape of the BC, the microscopic morphology and even chemistry of the network can be altered in many ways.

A deeper understanding of network formation and various possibilities to control the direction of the extruded nanocellulose is important if we wish to tailor-make advanced 3D biomedical materials. Moreover, it is essential to screen the different strains of *A. xylinum*, to measure the specific dimensions of the nanocellulose fibers produced by each, and then to correlate this with the mechanical properties and porosities of the networks formed.

It is also important to elucidate the mechanism of the observed high biocompatibility of BC. How is the water bound in the network? How are fluids adsorbed and transported in the material? Also, knowledge of the durability and possible degradation of BC *in vivo* will be important for long-term implants. Can *in vivo* BC degradation rates be controlled? To conclude, there are several things to be learned about BC as

an implant, and collaboration between various disciplines will be necessary for successful implementation of BC as a medical material in the clinical setting.

References

1. Wisniak, J. *Educ. Quim.* **2005**, *16*, 568–580.
2. Klemm, D.; Heublein, B.; Fink, H.-P.; Bohn, A. *Angew. Chem. Int. Ed.* **2005**, *44*, 3358–3393.
3. Ross, P.; Mayer, R.; Benziman, M. *Microbiol. Rev.* **1991**, *55*, 35–58.
4. Hutchens, S. A.; Benson, R. S.; Evans, B. R.; O'Neill, H. M.; Rawn, C. J. *Biomaterials* **2006**, *27*, 4661–4670.
5. Gelin, K.; Bodin, A.; Gatenholm, P.; Mihranyan, A.; Edwards, K.; Stromme, M. *Polymer* **2007**, *48*, 7623.
6. Ha, J. H.; Shehzad, O.; Khan, S.; *et al. Korean J. Chem. Eng.* **2008**, *25*(4), 812–815.
7. Kongruang, S. *Appl. Biochem. Biotechnol.* **2008**, *148*, 245–256.
8. Radiman, C.; Yulianil, G. *Polym. Int.* **2008**, *57*, 502–508.
9. Hong, L.; Qiu, K. Y. *Carbohydr. Polym.* **2008**, *72*(3), 545–549.
10. Premjet, S.; Premjet, D.; Ohtani, Y. *Seni Gakkaishi* **2007**, *63*(8), 193–199.
11. Colvin, J. R.; Witter, D. E. *Protoplasma* **1983**, *116*, 34–40.
12. Haigler, C. H.; Brown, R. M., Jr.; Benziman, M. *Science* **1980**, *210*, 903–906.
13. Watanabe, K.; Yamanaka, S. *Biosci. Biotechnol. Biochem.* **1995**, *59*, 65–68.
14. Tomitaa, Y.; Kondo, T. *Carbohydr. Polym.* **2009**, *77*, 754–759.
15. Fontana, J. D.; *et al. Appl. Biochem. Biotechnol.* **1990**, *24–25*, 253–264.
16. Borzani, W.; de Souza, S. J. *Biotechnol. Lett.* **1995**, *17*, 1271–1272.
17. Bodin, A.; Concaro, S.; Brittberg, M.; Gatenholm, P. *J. Tissue Eng. Regen. Med.* **2007**, *1*, 406–408.
18. Roberts, E. M.; Hardison, L. K.; Brown, R. M. Microbial Cellulose, University of Texas System: USA, Eur. Pat. Appl., 1986; p 22.
19. Yamanaka, S.; Ono, E.; Watanabe, K.; Kusakabe, M.; Suzuki, Y. Production of Hollow Cellulose Produced by Microorganisms for Artificial Blood Vessels, Ajinomoto Co., Inc: Japan, Sony Corp., Eur. Pat. Appl., 1990; p 7.
20. Klemm, D.; Schumann, D.; Udhardt, U.; Marsch, S. *Prog. Polym. Sci.* **2001**, *26*, 1561–1603.
21. Bodin, A.; Backdahl, H.; Fink, H.; Gustafsson, L.; Risberg, B.; Gatenholm, P. *Biotechnol. Bioeng.* **2007**, *97*(2), 425–434.
22. Pattison, M.; Hardison, L. K.; Brown, R. M. *Biomaterials* **2005**, *26*, 2491–2500.
23. Stevens, M. M.; George, J. M. *Science* **2005**, *310*, 1135–1138.
24. Backdahl, H.; Helenius, G.; Bodin, A.; *et al. Biomaterials* **2006**, *27*, 2141–2149.
25. Helenius, G.; Backdahl, H.; Bodin, A.; Nannmark, U.; Gatenholm, P.; Risberg, B. *J. Biomed. Mater. Res. A* **2006**, *76*, 431–438.
26. Mendes, P. N.; Rahal, S. C.; Pereira, O. C. M., Jr.; *et al. Acta Vet. Scand.* **2009**, *51*, 12.
27. Moreiraa, S.; Silvab, N. B.; Almeida-Limab, J.; *et al. Toxicol. Lett.* **2009**, *18*, 235–241.
28. Miyamoto, T.; Takahashi, S.; Ito, H.; Inagaki, H.; Noishiki, Y. *J. Biomed. Mater. Res.* **1989**, *23*, 125–133.
29. Hayashi, T. *Prog. Polym. Sci.* **1994**, *19*, 663–700.
30. Yamanaka, S.; Ishihara, M.; Sugiyama, J. *Cellulose* **2000**, *7*, 213–225.
31. Oster, G. A.; Lentz, K.; Koehler, K.; Hoon, R.; Serafica, G.; Mormino, R. Solvent Dehydrated Microbially-Derived Cellulose for In Vivo Implantationed, US Pat. Appl., 2002; p 27.
32. Bodin, A.; Backdahl, H.; Gustafsson, L.; Gatenholm, P. In *Modern Multidisciplinary Applied Microbiology: Exploiting Microbes and Their Interactions*; Mendez-Vilas, A., Ed.; Wiley-VCH: Weinheim, 2006; Vol. XVI, pp 619–622.
33. dos Anjos, B.; Novaes, A. B., Jr.; Meffert, R.; Barboza, E. P. *J. Periodontol.* **1998**, *69*, 454–459.
34. Watanabe, K.; Eto, Y.; Takano, S.; Nakamori, S.; Shibai, H.; Yamanaka, S. *Cytotechnology* **1993**, *13*, 107–114.
35. Sun, S.; Yue, Y.; Huang, X.; Meng, D. *J. Membr. Sci.* **2003**, *222*, 3–18.
36. Bäckdahl, H.; Esguerra, M.; Delbro, D.; Risberg, B.; Gatenholm, P. *J. Tissue Eng. Regen. Med.* **2008**, *2*, 320–330.
37. Novaes, A. B., Jr.; Novaes, A. B. *Clin. Oral Implants Res.* **1993**, *4*(2), 106–110.
38. Czaja, W.; Krystynowicz, A.; Bielecki, S.; Brown, R. M., Jr. *Biomaterials* **2006**, *27*, 145–151.
39. Novaes, A. B., Jr.; Novaes, A. B. *Int. J. Oral Maxillofac. Implants* **1992**, *7*(4), 536–540.
40. Novaes, A. B., Jr.; Novaes, A. B. *Int. J. Oral Maxillofac. Implants* **1997**, *12*(1), 84–87.
41. Falcão, S. C.; Neto, E. J.; Coelho, A. R. B. *Acta Cir. Bras.* **2008**, *23*, 78–83.
42. Mello, L. R.; Feltrin, L. T.; Fontes Neto, P. T.; Ferraz, F. A. *J. Neurosurg.* **1997**, *86*, 143–150.
43. White, D. G.; Brown, R. M., Jr. In *Cellulose and Wood – Chemistry and Technology*; Schuerch, C., Ed.; Wiley: New York, 1989; pp 573–590.
44. Bodin, A.; Gustafsson, L.; Gatenholm, P. *J. Biomater. Sci. Polym. Ed.* **2006**, *17*, 435–447.
45. Hutchens, S. A.; Woodward, J.; Evans, B. R.; O'Neill, H. M. Composite Biocompatible Hydrogel Material Including Calcium Phosphate and Bacterial Cellulose, US Pat. Appl., 2004; p 12.
46. Charpentier, P. A.; Maguire, A.; Wan, W.-K. *Appl. Surf. Sci.* **2006**, *252*, 6360–6367.
47. Svensson, A.; Nicklasson, E.; Harrah, T.; *et al. Biomaterials* **2005**, *26*, 419–431.
48. Wippermann, J.; Schumann, D.; Klemm, D.; Kosmehl, H.; Salehi-Gelani, S.; Wahlers, T. *Eur. J. Vasc. Endovasc. Surg.* **2009**, *37*, 592–596.
49. Bueno, R. R. L.; Tanguay, J.-F.; Brito, F. S.; *et al. J. Invasive Cardiol.* **2009**, *21*, 392–396.
50. Bielecki, S.; Krystynowicz, A.; Turkiewicz, M.; Kalinowska, H. *Biopolymers* **2002**, *5*, 37–90.
51. Vandamme, E. J.; De Baets, S.; Vanbaelen, A.; Joris, K.; De Wulf, P. *Polym. Degrad. Stab.* **1998**, *59*, 93–99.
52. Jonas, R.; Farah, L. F. *Polym. Degrad. Stab.* **1998**, *59*, 101–106.

Relevant Websites

www.arterion.se – Arterion AB.
http://www.botany.utexas.edu/mbrown/ – Prof. Malcolm Brown.
http://www.xyloscorp.com/ – Xyloscorp.
http://www.dermafill.com/ – Dermafill.
http://www.jenpolymers.de/ – Jenpolymers.

3.301. Surface Analysis and Biointerfaces: Vacuum and Ambient *In Situ* Techniques

D W Grainger, University of Utah, Salt Lake City, UT, USA
D G Castner, University of Washington, Seattle, WA, USA

© 2011 Elsevier Ltd. All rights reserved.

3.301.1.	**Introduction**	2
3.301.1.1.	Needs Assessment for Surface Analysis	3
3.301.1.2.	Defining the Surface of Interest	4
3.301.1.3.	Sample Preparation and Handling for Surface Analysis	4
3.301.1.4.	Sample Analysis Strategy	6
3.301.1.5.	Surface Analysis Methods	6
3.301.2.	**Ambient Analytical Methods**	6
3.301.2.1.	Contact Angle and Surface Energy Measurements	6
3.301.2.2.	Ambient Surface Spectroscopy and Optical Waveguide Methods	8
3.301.2.3.	Surface-Sensitive Infrared Spectroscopy	9
3.301.2.4.	Ellipsometry	10
3.301.2.5.	Surface Plasmon Resonance and Other Total Internal Reflection Optical Sensing Tools	11
3.301.2.6.	Scanning Probe Surface Imaging Techniques	12
3.301.2.7.	Surface Analytical Detection Using Shear-Mode and Surface Acoustic Wave Oscillator Devices	12
3.301.2.7.1.	TSM oscillator	13
3.301.2.7.2.	QCM with dissipation monitoring	14
3.301.3.	**Ultrahigh Vacuum Surface Analytical Techniques**	14
3.301.3.1.	Electron Spectroscopy for Chemical Analysis	14
3.301.3.2.	Secondary Ion Mass Spectrometry	16
3.301.3.3.	Auger Electron Spectroscopy	17
3.301.4.	**Next Challenges: Nanomaterial Surfaces**	17
3.301.5.	**Conclusions**	19
References		20

Glossary

AFM Atomic force microscopy, one of several surface scanning probe tools used to image and assess the outer atomic levels of a surface with a cantilever.

Contamination Unwanted species adsorbed onto the surface of materials, originating from air (e.g., ubiquitous siliceous, hydrocarbon, and volatile surface-reactive species) or from the sample environment (aqueous adsorbates), or from the analytical methodology (vacuum oils, salts, fingerprints).

Evanescent field A surface-bound electromagnetic field decaying exponentially orthogonal to a surface and external to a medium, created from total internal reflection of coherent energy within that same medium.

Inelastic mean free path The average distance that an emitted photoelectron moves before experiencing inelastic collisions with another electron or nucleus of a material's constituent atoms, dissipating its energy within the material.

Sampling depth The surface penetration depth of analytical reporting for a specific surface analysis method.

SIMS Secondary ion mass spectrometry, a family of related methods that analyzes under UHV conditions secondary ion fragments sputtered from the surface of a sample by an incident primary ion beam.

SPM Scanning probe microscopy, the general family of scanning probe methods comprising many diverse modes of monitoring interactions of a cantilever tip with the outermost atoms on a surface.

SPR Surface plasmon resonance, one of several optical methods used to measure kinetics and amounts of adsorbing or desorbing species to a surface using surface-localized perturbations and attenuations in evanescent electromagnetic energy.

Surface zone The portion of a medium's surface region that is sampled by the chosen analytical method. This zone is highly variable, depending on the technique used, from outermost atomic levels (e.g., AFM) to a few atomic layers (static SIMS) to thousands of atomic layers (FTIR).

UHV Ultrahigh vacuum conditions used for surface analysis in which nearly all atmospheric components (gases, water vapor) are removed by pumping, leaving the sample to be analyzed in a desiccated state at or below 10^{-9} Torr.

XPS X-ray photoelectron spectroscopy, a UHV-based surface analytical method using incident X-ray interrogation of a surface to produce surface-emitted photoelectrons that are characteristic of surface elemental composition and chemical bonding species.

Abbreviations

AES	Auger electron spectroscopy
AFM	Atomic force microscopy
ATR-FTIR	Attenuated total reflection Fourier transform infrared spectroscopy
BAW	Bulk acoustic wave
BE	Binding energy
D	Dissipation factor
EELS	Electron energy loss spectroscopy
ESCA	Electron spectroscopy for chemical analysis
FPW	Flexural plate wave
FTIR	Fourier transform infrared spectroscopy
KE	Kinetic energy
LFM	Lateral force microscopy
NEXAFS	Near edge X-ray absorption fine structure
OWLS	Optical waveguide lightmode spectroscopy
QCM	Quartz crystal microbalance
QCM-D	Quartz crystal microbalance with dissipation monitoring
QSR	Quality system regulations
RMS	Root-mean squared
SAM	Scanning Auger microscopy
SAW	Surface acoustic wave
SECM	Scanning electrochemical microscopy
SEM	Scanning electron microscopy
SIMS	Secondary ion mass spectrometry
SH-APM	Shear-horizontal acoustic plate mode
SH-SAW	Shear-horizontal surface acoustic wave
SPR	Surface plasmon resonance
SSBW	Surface-skimming bulk wave
STM	Scanning tunneling microscopy
STW	Surface transverse wave
TIR	Total internal reflection
ToF-SIMS	Time-of-flight secondary ion mass spectrometry
TSM	Thickness shear mode
UHV	Ultra-high vacuum
XPS	X-ray photoelectron spectroscopy

3.301.1. Introduction

Widespread recognition that the surface of a biomaterial, employed either in a medical device or in an assay, is a critical determinant of the biological response to the material has led to the use of an array of surface analytical methods aimed at biomaterials surface characterization. In addition, surface characterization can be an important component of the fabrication protocol, design process, and performance evaluation of materials and devices used in any industry that involves macromolecular or cellular contact with synthetic materials. Elucidation of specific surface properties of a material is important for a number of reasons. First, materials surfaces interact with macromolecules (e.g., proteins, lipids, oligosaccharides) and cells in ways that influence subsequent biological responses (see **Chapter 4.403, The Innate Response to Biomaterials**; **Chapter 4.404, Adaptive Immune Responses to Biomaterials**; **Chapter 4.405, Leukocyte–Biomaterial Interaction *In Vitro***; **Chapter 4.406, Protein Interactions with Biomaterials**; and **Chapter 4.407, Bacterial Adhesion and Biomaterial Surfaces**). Second, because of interfacial thermodynamics, surface chemistry is distinct from that of the bulk material. Surfaces have intrinsic energy associated with the discontinuity of the interface, its asymmetry, and associated chemical properties from this unique environment. Surfaces actively minimize their free energy through continual processes of adsorption, restructuring, and chemical reactions, leading to a dynamic surface evolution through diverse physical and chemical responses. Surfaces are a challenge to understand fully because they change continuously with their environment and are readily contaminated: defining both kinetics and equilibrium in surface states is intrinsically problematic. Finally, the issue of analytical sensitivity is important: surfaces comprise a small fraction of a given material, limiting the amount of material interrogated by any surface analytical method. If a 'typical' single crystal surface density is 10^{15} atoms cm^{-2} ($\sim$0.2 nmol cm^{-2}), then surface analytical methods must be able to resolve this relatively minute amount of material in this specific zone from signals emanating from the bulk material. Performance requires both chemical selectivity and sensitivity – two common analytical figures of merit – to distinguish sufficient signals from a background and, importantly, in a specific, desired surface sampling depth.

This chapter presents a concise introduction to numerous common approaches to the comprehensive analysis of a biomaterial's surface. It is beyond the scope of this chapter to provide specific details of the various methods used in biointerface and surface analysis: entire books, monologues, and reviews are available to guide one further.[1–11] A wide range of surface-sensitive techniques are available to study the performance of materials and to aid in solving problems associated with devices fabricated from these materials in a biomedical context. For example, polymeric, ceramic, and metallic components of devices can be characterized both in terms of their surface chemistry and elemental composition with X-ray photoelectron spectroscopy (XPS or ESCA), Auger electron spectroscopy (AES), static and dynamic secondary ion mass spectrometry (SIMS), and attenuated total reflection Fourier transform infrared spectroscopy (ATR-FTIR). Rapidly evolving, diverse probe microscopy techniques such as scanning probe methods (i.e., atomic force microscopy, AFM) in various forms are used to characterize the outermost three-dimensional (3D) topography of a surface and much more that is associated with the atomic features of surfaces. Optical methods such as ellipsometry, optical interferometry and evanescent field methods, and surface plasmon spectroscopy and imaging methods[12–14] provide accurate information regarding the thickness of overlayers, adsorbed layers, or coatings on optically compatible or reflective materials such as metals and metal oxides. **Figure 1** shows a flowchart outlining the various surface analytical methods currently available to the biomaterials researcher. While all the techniques are not commonly

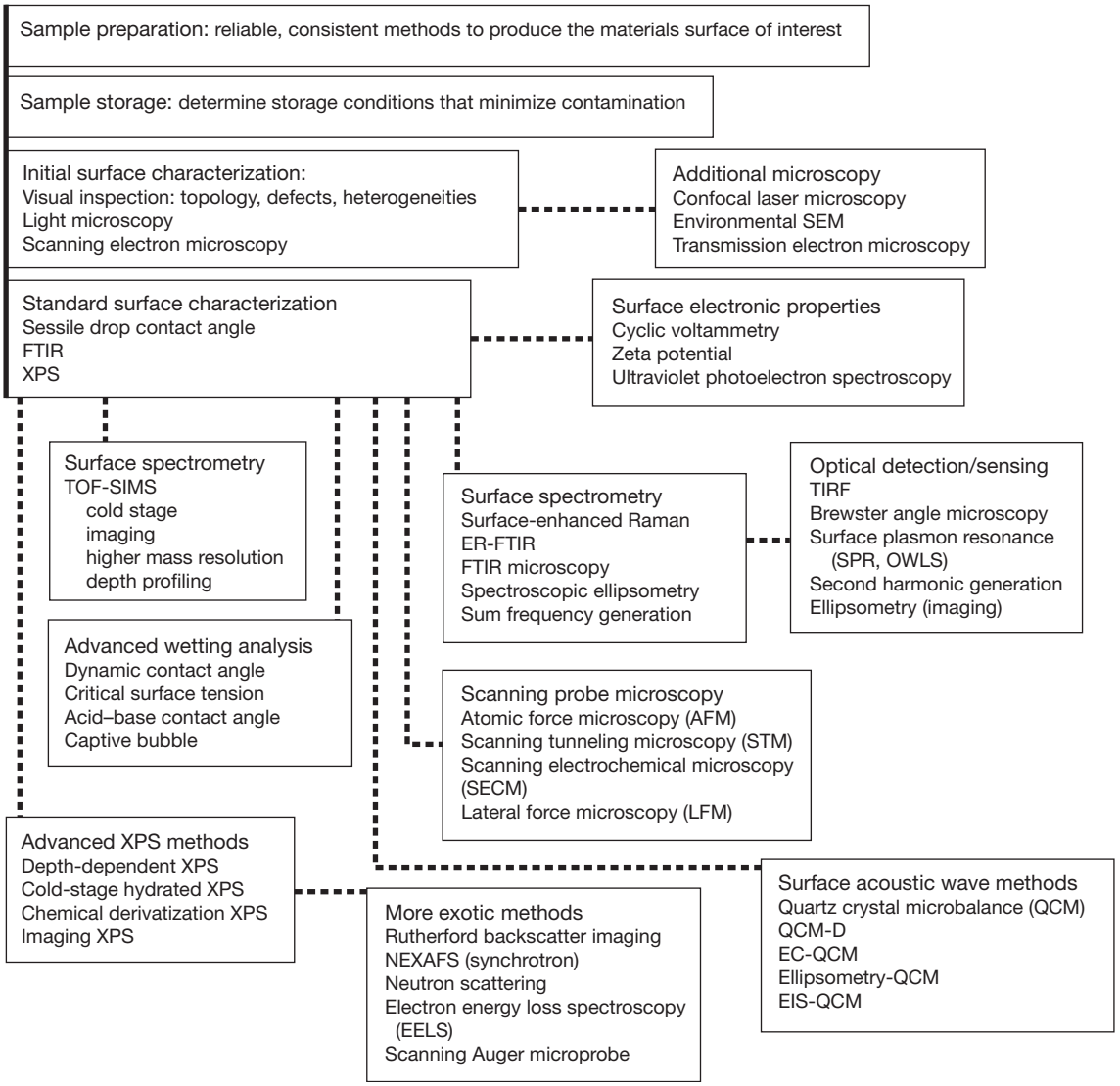

Figure 1 Methods flowchart for navigating various surface analytical approaches and instruments available for characterizing biomaterials. Adapted from Grainger, D. W.; Healy, K. In *Handbook of Biomaterials Evaluation*, 2nd ed.; von Recum, A. F., ed., MacMillan: New York, 1998; pp 115–141.

available at a single location, specialized surface analytical centers exist at industrial sites, many academic institutions, government research institutes (e.g., National Physical Laboratory, UK; NIST, ALS, PNNL, Sandia and Brookhaven, USA; CSIRO, Australia), and for-profit commercial analytical companies (e.g., Charles Evans, USA) that collectively utilize many of the methods detailed in Figure 1. The flowchart begins with relatively common and inexpensive surface analytical methods and moves to more exotic, specialized, and expensive techniques that are not often readily available. To understand the method of selection of certain techniques and the order of progression from one technique to the next requires an appreciation of the surface physical chemistry of the material, knowledge of a specific question that could be addressed by surface analysis, and some idea of the level of resolution required for the surface examination. For example, characterization of surface modifications to improve device performance, and identification of either contaminants or adsorbates requires the use of surface analytical equipment capable of detecting changes in surface chemistry and elemental composition at the outer nanometer level (i.e., 10 Å), while a general, comparative approximation between materials might require only a few inexpensive routine analyses of lower surface resolution and information content. It is critical to realize that because a surface is dynamic and many methods provide only partial information content at differing sampling depths with different resolutions, sensitivities, and selectivities, if one uses only one technique, one obtains only partial, incomplete information about the surface. A full understanding of the surface requires careful comparison and coordination of many complementary techniques that provide different information about the same sample.

3.301.1.1. Needs Assessment for Surface Analysis

A preliminary analytical approach is useful for all potential biomaterials surface characterization. A significant amount

of effort (and money) can be spared by making a few careful choices at the beginning of any analysis. The decision of when to employ these techniques depends on the type of information desired and the depth of the material surface from which the information should be collected. As it is rare for a single technique to provide sufficient information for complete surface characterization of a material, knowledge of how data from multiple techniques can be combined to generate a complete picture of the surface chemistry and structure is important.

3.301.1.2. Defining the Surface of Interest

Table 1 shows that each surface analytical method probes the 'surface zone' differently. This is shown schematically in Figure 2. Specifically, the depth of analytical interrogation (i.e., the sampling depth) and the type of analytical information returned must be considered when selecting methods. The surface-sensitive region for an ATR-FTIR experiment (up to ~2300 Å) is obviously not the surface zone analyzed by the atomic force microscope (top 10 Å) or a static SIMS experiment (top 10 Å). In addition, the type of information returned by each analysis is distinctly different. Regardless of surface depth resolution, the type of information required may dictate the sampling requirements (e.g., spectroscopic vs. surface energy vs. topology). Hence, one must decide the appropriate information to be gained from the surface analysis, and the method to obtain it. Appropriate questions to ask in this regard include

- How deep is the relevant surface of my biomaterial of interest?
- What methods probe this surface zone?
- What type of surface information is required? (e.g., compositional, energetic, dynamic, topological)
- What analytical environment is appropriate? (e.g., vacuum, ambient, or aqueous conditions)

In addition, quasistable surfaces (typically polymers) can exhibit lateral structural and chemical heterogeneities, as well as depth compositional gradients, confounded by the structural dynamics of intrinsic surface reorganization of these surface components either laterally or within the material's bulk. In these cases, methods that probe specifically at different zone depths or with different lateral spatial resolution would be better suited to the interrogation of these surface properties, which might not be accurately assessed by a general method. Protocols for the analysis of a specific surface may be developed by formulating specific objectives for performing surface characterization and by matching goals with techniques, cost, and access. Relevant goals for a typical surface analysis are provided in Table 2.

3.301.1.3. Sample Preparation and Handling for Surface Analysis

In vitro and *in vivo* biomedical devices are designed and tested to ensure reliability, consistency, and predictable performance. Quality control of surface composition and structure for all components in a biomedical device should be built into the quality analysis routine under a Quality System Regulations (QSR) mandate. Surface analysis should be performed on

Table 1 Surface analytical techniques commonly used for biomaterials characterization

Technique	*Physical principle*	*Measured quantity*	*Depth of analysis*	*Analytical sensitivity*
XPS (ESCA)	Photoelectron effect: incident X-rays induce photoelectron emission	Kinetic energy (eV) (or electron binding energy) of emitted photoelectrons	10–100 Å	0.1 at.%
AES	Incident electrons or X-rays cause emission of Auger electrons	Kinetic energy of Auger electrons (eV)	5–50 Å	0.1 at.%
SIMS	Incident primary ions emit secondary ions of different mass	Mass:charge (m/z) ratio of emitted ions	10 Å–1 μm	ppm
ATR-FTIR	Incident IR radiation is absorbed by surface molecules producing vibrations of interatomic bonds	Optical energy absorbance as function of wave number (or energy) characteristic of specific molecular vibrations	1–5 μm	1 mol%
AFM	Surface topography-induced deflection of a proximal cantilever is detected by reflected laser light and a photodiode	Quantitative three-dimensional images and surface physical properties in contact or noncontact modes of many types	Depth or lateral resolution: 1 Å	Atoms and molecules
SPR/OWLS	Backside incident laser radiation produces evanescent field at metal surface	Changes in maximum light reflectivity, intensity, or angle of reflected light associated with surface binding events; used to detect amounts or image adsorbates	Exponentially decaying optical field extending a few hundred nm away from metal surface	0.5–1 ng cm^{-2} adsorbate sensitivity
Ellipsometry	Detects changes in reflected coherent polarized laser light at an interface	Measures Δ and ψ that are then used to calculate film thickness and refractive index, and can be used to image surfaces	nm to μm	0.2 nm film thickness differentiation
QCM-D	Applied transverse propagating acoustic wave sensitive to adsorbing surface species and resulting viscoelastic properties of adlayer	Resonant frequency shift and impedance ratio (dissipation factor, D), proportional to mass loading	Few hundred nanometers	~ng cm^{-2} adsorbate sensitivity

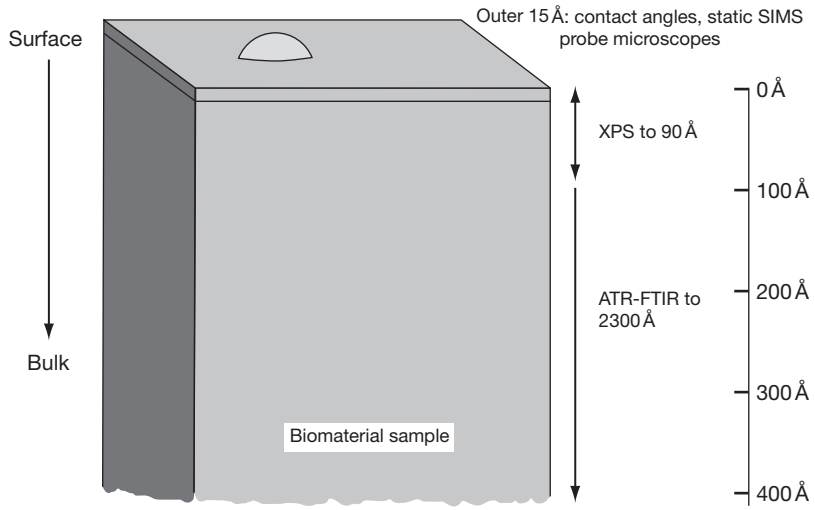

Figure 2 Schematic of an ideal biomaterial cross-section showing different surface analytical zones sampled by different analytical techniques. The surface analysis technique essentially defines the 'surface of interest' by the depth of its information retrieval and analytical reporting figures of merit. Adapted from Grainger, D. W.; Healy, K. In *Handbook of Biomaterials Evaluation*, 2nd ed.; von Recum, A. F., ed., MacMillan: New York, 1998; pp 115–141.

Table 2 Relevant goals for biomaterial surface characterization strategies

- Development of surface quality control criteria to monitor surface contamination and provide a means to establish the true identity of a biomaterial surface in context
- Monitoring surface-active leachables contained within a sample bulk that collect on biomaterial surfaces. Examples: plasticizers, polymer fillers, oligomeric or unreacted chemical species, catalysts, extrusion aids, mold-release agents, polishing compounds, and surfactant processing agents
- Assess the impact of sterilization protocols on surface chemistry and shelf-life
- Evaluate surface oxidation, degradation, corrosions, or chemical reactions over time in given environments
- Compare the effects of different biomaterial fabrication methods on surface properties. Molding and casting surfaces of different chemistries (e.g., metal, glass-ceramic, glass, ambient air) are well known to produce distinctly different surface properties in a given polymer film, metallic, or ceramic sample
- Correlate surface chemistry with biological responses, including activation of clotting factors, protein deposition, inactivation of immobilized enzymes and antibodies, cell and bacterial growth and phenotypes, macrophages activation, and fibrosis

samples in a state as close as possible to the state in which they exist in the actual device, subject to final packaging, and to the environment in which they are intended to be used. Once samples have been chosen, care should be taken to preserve the sample surface in its 'original' state. As most biomaterials are fabricated and manipulated under controlled but atmospheric conditions, certain levels of ubiquitous air- and water-borne contamination (hydrocarbons, water vapor, ambient siliceous species) should be expected – even clean rooms and hoods do *not eliminate* these adsorbates. If rigorous sample preparation and handling protocols are consistently followed, then ambient contamination should remain at relatively low and consistent levels. Common inadvertent, avoidable contaminants include human fingerprints (deposits of hydrocarbons and salts, typically sodium chloride), packaging or sealing materials (adhesive tape, parafilm, paper, or plastic wraps), and poor quality/contaminated solvents used for surface rinsing/cleaning. For example, many envelopes and copy papers have surface finishes (metal salts, clays) that abrade away and deposit onto a sample surface when they are placed in contact with the sample surface. Plastic bags frequently contain highly surface-active silicone oils and plasticizers (e.g., dioctyl phthalate is often detectable in any lab environment) that are readily transferred to a biomaterials surface. Therefore, sample storage or shipping protocols could substantially contaminate the surfaces being prepared and shipped for analysis.

An important 'first-step,' therefore, is to determine the cleanliness and reliability of all sample preparation, and handling and storage procedures/materials. The potential for contamination transfer to the biomaterials surface must be ascertained, typically by a time-dependent study of sample surface changes during storage and/or shipment. Commonly used clean storage containers include Fluoroware® twist-top single silicon wafer boats, acid-etched glass (borosilicate) dishes, cell-culture plastic ware (polystyrene), and zip-lock-type electron microscopy polyethylene bags. However, quality control and suppliers for these items are not guaranteed and checks should be run periodically to analyze for any variability in the surface composition of these materials. In addition, samples rinsed with alcohols or distilled water from common plastic laboratory squirt-bottles will often be contaminated by surface-active leachables introduced during the manufacturing of the squirt-bottles and thus these leachables will also be present in the rinsing media.

3.301.1.4. Sample Analysis Strategy

A common rule for best analytical results is that all conclusions regarding materials surface properties should be drawn from as many different analytical methods as financially and technically feasible. Therefore, conclusions drawn from any single surface data set are sure to be incomplete and possibly misleading. Several principles govern the selection of a surface analytical protocol. First, various biological environments intended for biomaterial applications are extremely heterogeneous and complex. Many surface analysis methods do not operate in conditions even close to biological complexity, or even simple hydration (e.g., ultrahigh vacuum (UHV) techniques including AES, XPS, and SIMS). Nevertheless, surface information provided by UHV techniques is often extremely valuable and useful, and can be correlated to biological performance even though the data are not collected under biological (i.e., aqueous) conditions.

The second guiding principle is that surface analysis data from many characterization techniques provide a logical, coherent, and integrated picture of the biomaterials surface. Contradictory data between several methods should be suspect and reconciled to avoid misleading or erroneous conclusions. An integrated approach allows a system of checks. Poorly reproducible data should be carefully scrutinized and checked by at least two alternative methods.

A third guiding principle is that all fabricated biomaterials surfaces are impure and imperfect. No chemical derivatization technique is perfect, no surface is without defects and heterogeneities at some scale, and all surfaces are contaminated to some degree. To date, no synthetic and fabrication expertise used in biomaterials development has resulted in ideal interfacial performance in any biomedical context. So, the more relevant, practical questions for surface analysis should focus on finding and relating the effects of ubiquitous, controlled levels of surface contamination and possible different defects present on all biomaterials to their observed biological reactions. Biological fluids, tissues, and cells respond to surface microenvironments (defects and heterogeneities). Identifying the types of surface properties, the chemistry, and structures, and how these influence biomedical device performance and consistency in a given application over time should be the goal.

A fourth important principle is that surface analytical methods have the potential to change a surface during the process of interrogation. That is, surface analytical techniques can damage or alter the surfaces being analyzed. Common examples are the sorption of probe liquid drops from wetting analysis into the material surface, loss of fluorine from fluorinated polymer samples exposed to nonmonochromatized X-rays under XPS analysis, and electron beam-induced reduction of metal oxides during AES analyses. Even state-of-the-art XPS X-ray sources can remove fluorine from certain polymers in some environments and induce oxidation of sulfur-containing compounds. Again, careful controls must assess the potential for generating misleading data from fragile/labile surfaces.

3.301.1.5. Surface Analysis Methods

The following sections survey some of the recommended methods and approaches to permit a thorough assessment of surface properties and compositions, and judgment of suitable criteria for either acceptance or rejection for a particular use. As every device or materials performance is context dependent, specific biomaterials surface properties that might promote or prevent certain biological responses are not described – only methods for surface analysis. Indeed, such understandings of surface design for specific biological performance remain premature and speculative, or at least empirical. General design rules for controlling surface-biological behaviors are often scientifically unfounded and their implications are dangerous to extrapolate. Nonetheless, early bio-surface adsorption events occurring spontaneously and rapidly upon exposure of a biomaterial to biological fluids determine subsequent biological responses, sometimes reflecting the relative 'biocompatibility' of this specific scenario (see **Chapter 4.401, The Concept of Biocompatibility** and **Chapter 4.402, Biocompatibility and the Relationship to Standards: Meaning and Scope of Biomaterials Testing**). These early interfacial events (occurring as fast as diffusional limitations dictate approximately microseconds) include adsorption of small solutes, salts, and organic molecules, then small proteins, and ultimately large proteins and cells to a biomaterial's surface (see **Chapter 4.406, Protein Interactions with Biomaterials** and **Chapter 3.311, Molecular Simulation Methods to Investigate Protein Adsorption Behavior at the Atomic Level**). Certainly, material surface parameters including surface composition, display of polar and apolar chemistries (surface energy), surface formal charge, hydrogen bonding, and topology are relevant to these critical events as reported by many past surface analysis studies.[1,2,4,5,8–11]

3.301.2. Ambient Analytical Methods

3.301.2.1. Contact Angle and Surface Energy Measurements

While many surface analytical methods require sophisticated equipment and expert operators, information on the outer few atomic layers of a material surface can be obtained with a relatively simple, inexpensive method called contact angle analysis. The three-phase intersection between a pure probe liquid of known surface tension, the biomaterial surface of interest, and ambient air (or gas bubbles) defines an angle in equilibrium: the contact angle. If the three-phase line is in motion, then the hysteresis between the reversible advancing and retreating angles of the line provides data on surface roughness, heterogeneity, and surface chemical mobility. Once defined, this angle can be related to solid materials interfacial free energies. Surface energy, in turn, is a reflection of the surface chemical and physical constitution – functional groups, polar or apolar species, and even acidic or basic chemistry, or topological features – in the material's outer 2–10 Å. Because hydrophilicity and hydrophobicity remain two important surface classifications correlating biological interfacial behavior, wetting analyses even in their crudest approximations are valuable surface interrogation methods. Interpretation of contact angle data depends on the suitability of certain assumptions regarding the three-phase scenario: misleading data will be obtained from misuse or ignorance of these assumptions.

Wetting analysis is perhaps the most used and also the most misused surface analytical method. Classic sources of information on wetting, capillarity, and surface tension are

recommended reading to understand the dynamics and thermodynamics of the three-phase line.[1,7,11,15,16] Because the three-phase line is sensitive generally to the outer atomic layers, this simple analysis, if done correctly, can provide surface energy information. Such contact angle analysis is also known as 'wetting analysis' due to the convention of using liquids to probe solid surfaces in air. In combination with other surface techniques mentioned in this chapter, contact angles provide a readily accessible, valuable first-line-of-analysis proven to be useful in virtually all areas of surface chemistry and engineering. As simple as this method appears, it is one of only few *in situ* techniques to characterize the aqueous–biomaterial interface.

The basis for contact angle or wetting analysis lies most often in the interaction of a liquid with a solid surface in the presence of a vapor. A liquid drop placed on a solid surface (a sessile drop) often will not wet the surface (i.e., spread spontaneously) but, instead, will remain as a drop having a definite angle of contact on the surface. The idealized interface is one between an ideal nondeformable smooth, clean solid, an infinitely deformable pure liquid, and a pure vapor. For this ideal scenario, the classic energy balance for the sessile drop in equilibrium on the surface is provided by Young's equation:

$$\gamma_{SV} = \gamma_{LV} \cos\theta + \gamma_{SL} \quad [1]$$

where θ is the three-phase contact angle, and the various interfacial free energies are given by γ_{SV} for the solid–vapor, γ_{SL} for the solid–liquid, and γ_{LV} for the liquid–vapor.

Contact angles can be interpreted in terms of Young's equation directly if the following assumptions are valid[1]:

- The solid surface is rigid and nondeformable (surface modulus of elasticity should exceed 3.5×10^5 dynes cm^{-2}). Gels and soft materials (e.g., biomembranes, surfactants, soft elastomers) often do *not* satisfy this assumption.
- The solid surface is immobile and cannot reorient in response to the liquid probe. Many polymer surfaces cannot fulfill this assumption.
- The solid surface is smooth (~0.1 μm root mean squared (RMS) surface roughness regime): optically or visibly featureless is generally acceptable. Most solid surfaces do not satisfy this assumption.
- The solid surface is homogeneous and uniform, lacking heterogeneous surface domains, patches, leachables, or contaminants. Unclean surfaces (i.e., all real surfaces and those tested ambiently) most frequently violate this assumption.
- The liquid phase surface tension is known and remains constant. Importantly, transfer of surface contamination and leachables to the liquid surface from either the solid or vapor phases will change the liquid surface tension. Temperature variations affect surface tension.
- The solid and liquid phases do not interact beyond the three-phase equilibrium (i.e., no surface swelling by the liquid, no extraction of the solid). Surface swelling violates this assumption.
- The spreading pressure for the liquid on the solid is zero, meaning that the liquid vapor does not adsorb onto the solid surface and change the solid surface free energy.

Contact angle hysteresis, inaccurate wetting, and invalid surface energy determinations result from scenarios where these assumptions are unfulfilled. Importantly, because most assumptions for ideal contact angle measurements are violated by actual measurement conditions, all contact angles measured must consider in their reporting and analysis the impact of these nonideal issues. True (reproducible, reversibly invariant) contact angle hysteresis in dynamic, mobile assays (i.e., Wilhelmy plate hysteresis-style) can be a useful diagnostic tool, but must be distinguished from hysteresis related to sample nonadherence to the assumptions listed above.

Several different methods have been developed for contact angle measurements[1,7,15]:

- Direct, microscopic measurements of the three-phase line for liquid drops in air, or vapor bubbles in bulk liquids, against solid surfaces.
- Dimensional determinations for drops on surfaces, allowing contact angle determination from well-known trigonometric relationships.
- Capillary rise of a liquid with a known surface tension within a small tube or capillary coated with the material of interest.
- DuNouy ring methods.
- Wilhelmy plate methods.

Many of these techniques are commercially available as turn-key, automated instruments. The Wilhelmy plate method can be adapted to nonplanar geometries, including cylindrical shapes relevant to catheters and tubing, fibers, and discs.[1,17]

Important differences between so-called static and dynamic contact angle measurements should be considered. If the solid–liquid interface is in motion, the measurement is dynamic and may not be at equilibrium. Wilhelmy plate hysteresis determinations are generally dynamic, although slow three-phase interfacial velocities can approximate static measurements. Immersion of the solid surface into the probe liquid produces an *advancing* contact angle, θ_A while emersion of the solid from the liquid produces a *receding* contact angle, θ_R. The difference between advancing and receding angles, $\Delta\theta$, is termed the contact angle hysteresis. A solid–liquid pair fulfilling all the assumptions listed above should exhibit only one contact angle and, therefore, no hysteresis. However, because most real systems cannot fulfill these assumptions, hysteresis is commonly observed and this information can be exploited. A critical assessment must always be directed at the source of hysteresis as two general types of hysteresis have been identified:

1. Thermodynamically stable hysteresis reproducible over many emersion–immersion cycles.
2. Kinetic hysteresis that changes with sample placement, time, and cycling frequency.

Interpretations of hysteresis must consider violations of the above-mentioned assumptions, including effects of surface heterogeneity (adsorbed contamination, domains), reactivity (i.e., polar, apolar interactions between probe liquid and surface), metastable surface structures and chemistries (reorganization, reorientation), surface roughness (texture, particle adhesion, pinholes, pitting), solid surface swelling and liquid penetration, adsorption of contaminants onto the liquid interface, and surface deformation (mobility). Only careful assessment of these interfacial factors in tandem with surface-sensitive knowledge from other analytical methods makes contact angle analysis a valuable surface characterization tool.

A popular extension of contact angle analysis is the determination of solid surface critical surface tension, γ_c, as originally described by Zisman's group.[18] This approach leads to an empirical determination of a solid surface energy related to the extrapolated solid surface free energy. Experimentally, a series of pure probe liquids of varying surface tension are applied as drops to the sample solid surface. Contact angles are assessed for sessile drops for test liquids that span a highly nonwetting (contact angle $\theta > 90°$, $\cos\theta \sim 0°$) to a highly wetting (contact angle $\theta \sim 0°$, $\cos\theta \sim 1.0$ for complete wetting) regime. When these data are plotted against the known liquid surface tensions, the critical surface tension is defined by the x-intercept at $\cos\theta = 1$ (complete wetting) from the liquid series. The method has proven useful for empirical correlations of solid surface energies with interfacial performance in various applications, including interesting relationships between materials bulk elastic modulus and γ_c. Values of γ_c for various polymers are tabulated in the *Polymer Handbook*.[19]

3.301.2.2. Ambient Surface Spectroscopy and Optical Waveguide Methods

Nondestructive, real-time label-free surface detection methods are attractive for monitoring interfacial reactions and adsorption events, mapping surface spatial reactivity and chemical patterning, and monitoring film thickness, even in aqueous and biological milieu. Figures 3 and 4 show several optical spectroscopic configurations. Several optical waveguide methods have shown nanomolar concentration (pg mm^{-2} mass) sensitivity for detecting adsorbates including proteins and cells, as well as applicability to a wide variety of biomaterials.[12–14] Label-free optical sensing is preferred, given the benefits of not introducing an extrinsic label to the adsorbate to detect it. However, optical compatibility between the analytical optical energy coupling and the material is required for detection, and intrinsic optically active signals from many molecules of interest are not strong, limiting utility in some cases. Regardless, these waveguide and evanescent methods are increasing in popularity and versatility, and have been commercialized in many different forms.

Most such analytical spectroscopy systems exploit evanescent electromagnetic fields directly external to a tailored waveguide to sense interactions with the waveguide surface (and often associated thin film). Optical sensing energy must be coupled into the waveguide, transmitted internally within the waveguide, and propagated such that internal reflection rules are satisfied to establish and maintain evanescent external fields.[20] In many cases, this must be accomplished within the biomedical test system of interest, that is, in the presence of a biomaterial coating on the waveguide and within a liquid flow cell or static aqueous milieu containing complex biological species in contact with the biomaterial-coated waveguide. The energy intensity and depth of sensitivity of the surface-bound evanescent field emanating from the waveguide into the external milieu depend upon many factors, including the input optical energy, the refractive indices of the waveguide and external media, and the refractive index of the adsorbing species.[14] In addition, the evanescent field intensity decays exponentially with distance from the waveguide surface, with

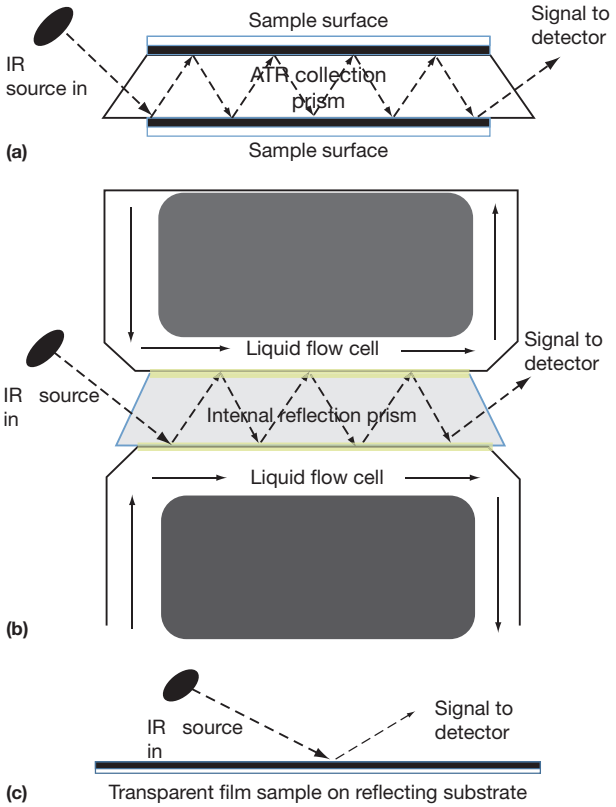

Figure 3 Modes of surface-sensitive measurement for infrared spectroscopic interrogation of biomaterials surfaces: (a) an attenuated total reflection (ATR) prism sandwiched by sample surfaces pressed against each prism surface, (b) ATR in a liquid flow cell with internal immersed collection prism, (c) grazing IR incidence external reflection off a surface in single-reflection mode.

a decay length of approximately $\lambda/2\pi$, where λ is the wavelength of the in-coupled optical energy. For an optical excitation wavelength of $\lambda = 500–800$ nm, which is characteristic of many common laser inputs, the evanescent field extends ~100–150 nm into the external milieu above the waveguide surface. This short evanescent field sensing distance provides the innate advantage that the waveguide-bound sensing field interacts with adsorbing material only in direct proximity to the waveguide surface, largely uninfluenced by species suspended in bulk solution. This improves the signal:noise ratio for adsorbate detection. This also presents the limitation that modifications to the waveguide surface (i.e., use of biomedical coatings or deposits) must be very thin and uniform on the waveguide for the evanescent field to penetrate with sufficient energy to produce a surface signal at the surface of the coating. The farther from the waveguide surface the target detection is desired, the (exponentially) weaker the bound evanescent signal is due to decay. Different designs for optical biosensors manipulate evanescent field properties to extend either well beyond or confined tightly to the waveguide surface. Improved detection sensitivity can be achieved by matching locations of largest biochemical binding to those waveguide zones of highest evanescent field intensity.[21]

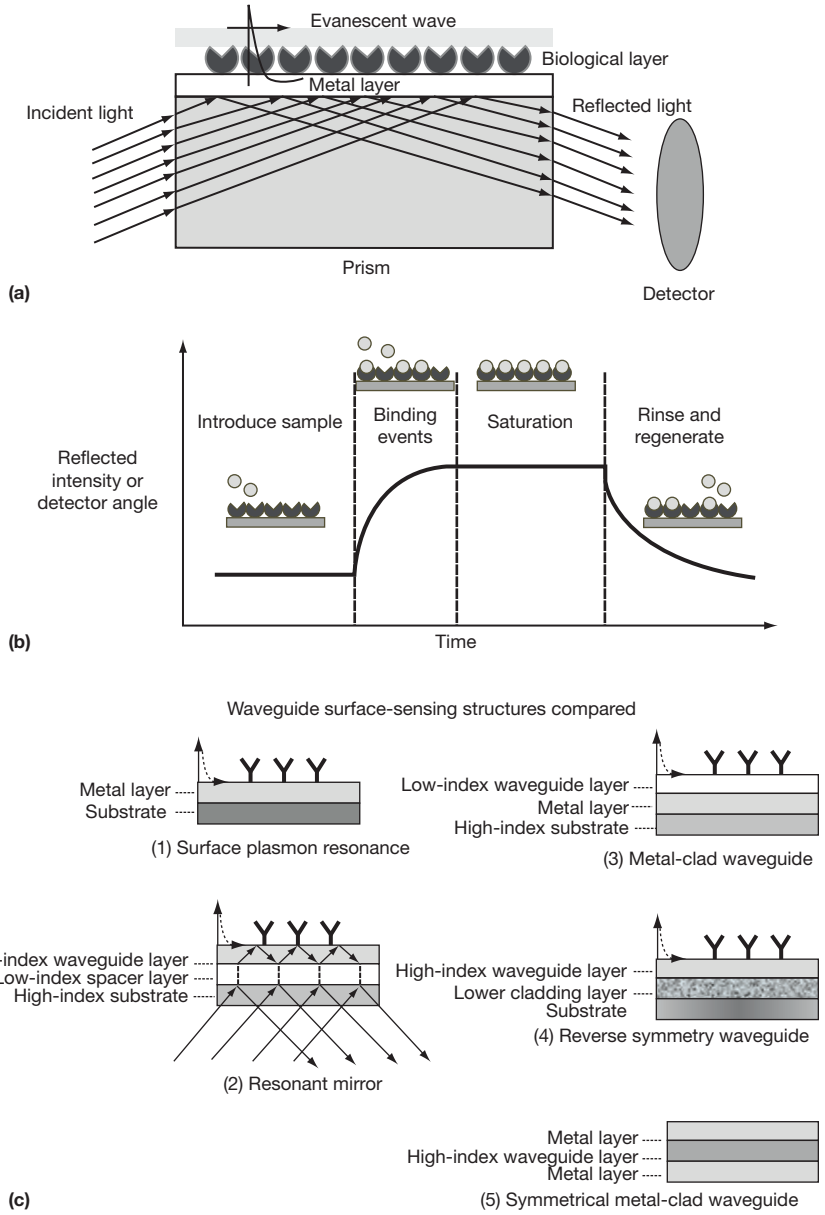

Figure 4 Optical waveguide sensing configurations for surface binding and interfacial interaction analysis. (a) Surface plasmon resonance (SPR) backside illumination of a plasmon-active metal substrate, creating a front-side evanescent field capable of detecting surface-adsorbing species, (b) schematic description of SPR optical signal intensity as a kinetic function of the surface-adsorbate experiment, and (c) several common optical waveguide configurations for interfacial sensing using surface-localized evanescent field interactions and total internal reflection optical conditions.

3.301.2.3. Surface-Sensitive Infrared Spectroscopy

Infrared (IR) absorption spectroscopy is a classical bulk characterization method providing chemical information about the molecular structure of a material based on identifying characteristic vibrational bands of bonded units. IR interrogation of surfaces has been greatly enhanced by applying Fourier methods to enhance signal:noise ratios and resolution for generally weak IR vibrational signals associated with biomedically relevant species. Nevertheless, in many cases, FTIR of surfaces remains signal-limited, and certainly not very specific, as many characteristic IR absorption bands are shared among many species of interest. In addition, when a sufficient surface signal is obtained, the problem of distinguishing and resolving the specific surface analytical zone from bulk-derived IR signals is difficult due to the large IR sampling depth (up to a micron). Many actual FTIR 'surface analytical' configurations return information from thousands of molecular layers beneath the actual interface unless they are configured to remove this bulk signal.

Several different FTIR surface-sensitive modes of analysis have been developed for obtaining representative surface IR spectra.[22–25] Different commercially available sampling

'rigs' allow convenient access to spectroscopic analysis of material surfaces, adsorbate reactions, and kinetic events in aqueous media (Figure 3). Transparent films coated onto reflecting metal mirrors are successfully analyzed by grazing incidence external reflection geometries (Figure 3(c)), with acceptable signal:noise ratios even for monolayers of material.[26–28] Films can be dip-coated or cast onto metal substrates (e.g., gold mirrors) to produce these samples. Nonreflecting surfaces and powders can be analyzed in the diffuse reflectance mode.[24] Attenuated total reflection (ATR-FTIR) methods (Figure 3(a)–3(c)) have often been applied to biomaterials surfaces because hydrated and flow-cell samples in simplified aqueous solution can be analyzed using commercial components in an IR-active evanescent sensing mode extending several microns into the external medium. An IR-transparent prism (typically germanium, ZnSe, or silicon, Figure 3(a)) is used as a waveguide to propagate the analytical IR signal through the FTIR prism. IR internal reflection generates a localized evanescent electromagnetic field outside the prism. External samples or media placed adjacent to the prism surface are sampled by this evanescent field, producing IR absorption/IR spectra for all IR-active species within the evanescent field (Figure 3(a) and 3(b)). Acceptable signal:noise ratios often require high adsorbate surface coverages and intimate physical compression (close contact) of the sample against the prism surface, a problem for rough or rigid irregular samples or parts. An ATR-FTIR circle cell (flow cell, Figure 3(b)) has been used in the ATR mode to study protein interactions in real time with thin biomaterial films coated onto prisms.[29–31]

3.301.2.4. Ellipsometry

Ellipsometry in its diverse surface measurement formats represents a valuable optical technique for determining the thickness and surface density of overlayers on reflective materials (e.g., SiO_2, titanium, gold, aluminum, platinum, etc.). Organic films and polymers can also be studied with ellipsometry as model biomaterials if they are presented as a thin film on an optically reflective surface. The strength of ellipsometry lies in the technique's ability to report thickness and optical properties of either metal oxides, grafted organic molecules, or adsorbed proteins with good accuracy in a nondestructive manner.[32] Spectroscopic ellipsometry has found widespread use in the materials science community to determine the optical properties of unknown films, overlayers and materials, assess dissolution and swelling of thin polymer films, and analyze oxidation and corrosion of metals and *in situ* kinetics of macromolecular adsorption to materials in aqueous environments.[33–35] Spectroscopic ellipsometry has been employed in the biomaterials community using Cauchy optical models to interpret data to better reflect the physical interfacial situation, including film thickness and refractive index.[36]

Ellipsometry exploits changes in the reflected polarization of elliptically polarized light from an interface of interrogation. The ellipsometer actually measures the quantities 'del' (Δ) and psi (ψ), which are then used to calculate the index of refraction and the thickness of the layer interacting with the light. The quantity Δ is the change in phase difference between the parallel component and perpendicular component of light (with respect to the reflected plane) occurring upon reflection from either a surface or interface. By definition, ψ is the angle whose tangent is the ratio of the magnitudes of the total reflection coefficients, r_p and r_s.[37] Both Δ and ψ are functions of wavelength (λ) or energy and are used in the fundamental equation governing ellipsometry [2]:

$$\tan(\psi)e^{(i\Delta)} = r_p/r_s \qquad [2]$$

to calculate the total reflection coefficients, r_p and r_s. The total reflection coefficients are then used in conjunction with appropriate physical and mathematical models to calculate the parameter of interest, for example, adsorbed (protein) layer thickness and surface density. The accuracy of the physical parameters calculated depends on the model used to make the estimate. Thus, materials properties and other physical parameters determined by ellipsometry are inherently dependent on the physical model assumed by the user, its basis in reality, and the mathematical treatment of that model. A more complete review of the practical issues of ellipsometry is published,[33] and its theoretical aspects are treated extensively in textbooks.[37,38]

Use of ellipsometry in biomaterials science has been somewhat limited to protein adsorption kinetics and isotherm measurements of proteins from media containing only single proteins.[34,35] Recently, the scope of research employing ellipsometry has been broadened to include interactions of proteins with organic surfaces,[39,40] and the identification of the composition of proteins adsorbed to metals from human plasma,[41] or organic surface modifications.[42,43] Composition of proteins adsorbed to a surface was identified using an indirect immuno-ellipsometry technique to measure the increase in thickness associated with antibody binding directed toward specific proteins bound to the surface. A common problem associated with the measurement of overlayer thicknesses by ellipsometry is that the indexes of refraction ($N = n + ik$) of the layer and substrate need to be known *a priori* or determined simultaneously.[44] Accurate values of the index of refraction for proteins, thin polymer films, and organic layers are not usually available, so the researcher is left to estimate N. This problem is minimized by using a spectroscopic ellipsometer (commercially available), where plots of Δ and ψ as a function of wavelength (or energy) are used to accurately determine the optical properties of the layer, and calculate the parameter of interest from multiple wavelengths simultaneously. The accuracy of layer thicknesses and surface density in multilayer structures is also improved by making measurements with a spectroscopic ellipsometer.[45]

Imaging ellipsometry (IE), a powerful widely available tool for measuring thin films of many different materials adsorbed/deposited onto a substrate, combines the spatial resolution of optical microscopy with ellipsometry's thin film assessment capabilities. Interest in IE is surging, and it is now used for applications in biomedical surface imaging. Traditional IE is a qualitative technique; ellipsometry imaging shows surface topology variation mapped by optical changes. As a quasi-quantitative tool, changes in optical ellipsometry surface images can help elucidate lateral changes in film thicknesses or densities. IE overcomes spatial resolution limitations in normal ellipsometry that averages information over the fully irradiated spot size (typically 50–100 μm to >1 mm spots). Optics used in IE in combination with a CCD camera provide

spatial resolution to 1–2 μm, <0.1 nm thickness resolution (e.g., SiO_2 on Si) and real-time sample observation, providing unprecedented measurement control and analysis of sample homogeneity. In addition to taking measurements on multiple fields on a surface, IE can provide *n*, *k*, and thickness maps over the full field-of-view. IE also enables use of liquid flow cells for measurements in fluids using a standard reflective setup.[46,47]

3.301.2.5. Surface Plasmon Resonance and Other Total Internal Reflection Optical Sensing Tools

A distinct total internal reflection (TIR) optical (or evanescent field) sensing tool now very popular for *in situ* surface analysis of biomaterials utilizes surface plasmon resonance (SPR, **Figure 4(a)**).[48–57] Using backside optical excitation of surface plasmons in certain metallic thin films (particularly gold), incoming light guided to the metallic surface at the appropriate resonant angle and matched wavelength conditions excites a standing evanescent field propagating along both the metal and bound dielectric (i.e., biological) adlayer on the *opposite* metal surface. Adlayer optical changes from any adsorption or desorption events at this metal surface cause the optical resonance conditions to change, and this change can be used to follow the adsorption or desorption process (both kinetics and amounts) in real time under static or flow conditions. Two common methods are used to detect changes in the assay resonance conditions. One uses a fixed wavelength incident light source (i.e., a laser) and detects the intensity of the reflected light as a function of angle of light at the surface maintaining TIR. The other uses a multiple wavelength incident light source (i.e., white light) and detects the intensity of the reflected light as a function of wavelength. Since the resonance angle or wavelength is proportional to the optical properties of the adsorbed film, changes in those quantities can be used to determine amounts and kinetics of species adsorbing and desorbing from the metallic surface.

SPR sensing relies on the principle that any changes on the dielectric sensing surface will cause a shift in the angle or wavelength of the TIR light, followed in real time by a detector, to satisfy the plasmon excitation resonance conditions at the surface. Many SPR detection configurations and analytical instrumentation systems are commercialized[58–60] and perform versatile experimental tasks for mass sensing of biomolecules in liquid milieu adsorbed to or very near a biomaterial's interface.

As shown in **Figure 4(b)**, SPR reports kinetic changes in the mass of material adsorbed or desorbed from the metal surface within the evanescent field, but has no intrinsic chemical or biological specificity. Adsorption and desorption events can be monitored in flow cells, with addition of components, different milieu, and rinsing. Interfacial mass is indirectly reported as an optical SPR-instrument-specific unit and actual SPR mass must be converted using algorithms correlating the optical sensitivity of the instrument to the changes in the local refractive index and adsorbate-specific properties. The chemical and biological specificity must be introduced by modification of the metal surface (e.g., attachment of antibodies binding only specific species, labeling with resonance-enhancing probes or optically excitable dyes, or use of affinity ligands immobilized in a nonfouling surface background). Significantly, while SPR-derived rate constants are routinely reported for kinetic data, apparent surface binding or adsorption kinetics must be carefully interpreted in terms of mass transfer limitations imposed by the immobilized surface layer or matrix where surface interactions occur. Also, experimental conditions such as temperature changes that also change the resonance conditions must be controlled so that they do not confound measured changes in the SPR resonance angle or wavelength.

In other TIR sensor modes (**Figure 4(c)**), a resonant mirror (RM) configuration is used to create an evanescent field external to the sensing element (shown in **Figure 4(c)**). Again, optical resonance conditions are established in the waveguide that become changed by the adsorption of molecules on the external surface of the sensing surface. The RM TIR design is a 'leaky' waveguide strategy similar to SPR's Kretschmann prism configuration (e.g., **Figure 4(a)**), but differs in that the coupling of incident light through a prism is interfaced with a high-index dielectric layer, rather than a metal surface. The SPR design is married with the enhanced sensitivity of new waveguide structures to produce sharper resonance peaks than SPR, thereby increasing the sensitivity of the technique. Measurements made in real time using a flow cell configuration and adsorption or ligand–receptor interactions can be observed conveniently and rapidly in any number of environments. In addition, sensing surfaces can be chemically and physically modified with a number of known conjugation chemistries to yield interfaces with relevant chemical features for the biomaterials investigator.

Dual polarization interferometry (DPI) represents another evanescent sensing technique, first commercialized a decade ago (Farfield Group, Ltd., UK), that is now seeing increased application. DPI utilizes waveguide structures comprising stacked dielectric layers, with reference and sensing layers separated by a cladding layer (**Figure 4(c)**).[61] A top dielectric layer is etched to reveal the sensing layer so that two separate channels can be present on a single sensor chip. Laser light passed through the sandwiched waveguide structure produces an interference pattern detected by a CCD camera. Any changes in refractive index that occur at the surface as a result of adsorption alter the phase position of the fringes relative to the reference layer, are detected in real time, and deconvoluted to the amounts of adsorbed species. As opposed to reporting only relative changes in refractive index upon adsorption using one polarization, DPI's use of two optical waveguide polarization modes to determine both effective refractive index and adlayer thickness values provides distinct advantages over SPR, RM, and other optical sensor methods.

Optical waveguide lightmode spectroscopy (OWLS) also monitors changes in both transverse electric and magnetic polarization modes of optical excitation energy by adsorbing molecules. The optical thickness and the refractive index of thin and homogeneous adsorbed layers can be determined from the mode phase shifts and the absolute amount of adsorbed molecules is calculated based on the difference in refractive indices of adsorbed molecules versus external medium (solvent molecules do not contribute to detected mass). OWLS is sensitive ($\sim$1 ng cm^{-2}) and facilitates direct real-time monitoring of macromolecular adsorption to surfaces.[62]

Applications for these optical surface sensors are now being fully explored.[52,63,64] Sensing surfaces can be dip-coated, spin-coated, plasma modified, chemically derivatized, and serially exchanged. Quantification of adsorbed amounts, and binding and desorption kinetics are possible from both gas and liquid phases in flow/rinsing configurations. Tandem or synergistic surface-localized binding events can also be monitored. Fiber optic sensing waveguides for *in vitro* and *in vivo* analysis are widely reported for different applications and analytical capabilities.[65,66]

High-contrast SPR microscopy or imaging[67] has been proposed to increase the throughput of standard SPR sensors.[68–70] Imaging SPR once exhibited reduced sensitivity compared to conventional SPR but is currently capable of mapping surface topology using comparable mass/optical detection.[71] Twenty-micron lateral resolution for surface features several angstrom thick can be obtained. More recent work has demonstrated SPR imaging of DNA and protein monolayers on surfaces with applications to sandwich sensors, microarrays, and other protein-electrode-based devices.[72,73] Innovations to improve signal-based images using phase shift discrimination and angle scanning, and spatial arraying multiplex imaging techniques are now incorporated into commercial devices.[74] In addition, SPR and waveguide evanescent field fluorescence-based interfacial sensing and imaging applications are also reported to increase sensitivity and resolution.[75–77]

3.301.2.6. Scanning Probe Surface Imaging Techniques

As the tool of choice for nanometer imaging of surfaces, membranes, and molecules, the AFM now represents a diversified family of related scanning force microscopies (SFMs) with various unprecedented surface analytical capabilities.[78,79] SFMs are relatively new surface techniques (invented in 1986[80]), falling under the broader selection of 'scanning probe microscopies.' These surface profiling methods provide nondestructive quantitative topographical images of a surface with atomic-level resolution (well below the optical diffraction limit) on rigid, semisoft and soft materials, using several different force-feedback modes to produce surface images. These methods can also provide molecular-level resolution of 'shapes' or morphologies of biomolecules and some soft-modulus materials (e.g., membranes, polymer coatings, gels) attached to ultra-flat surfaces (see **Chapter 3.302, Atomic Force Microscopy** for further details).

AFM surface interrogation is performed by mechanical feedback from a stylus-like, microfabricated (commercial) cantilever probe held in contact with or very proximal to the surface while scanning in-plane in x and y directions. Laser tracking of the stylus interactions and cantilever surface trajectory scanning across the surface 'maps' the surface topology. Two AFM measurement modes are used: static and dynamic. In the static (or contact) mode, the AFM tip is placed in contact with the surface and 'dragged or pushed' in a scan to measure surface features directly by cantilever deflections. Constant force between the tip and the surface is maintained, using continuous rapid feedback from the laser tracking system.[71] Two piezoelectric translators adjust the z-axis of the sample while the sample is scanned laterally under constant probe force, termed optical lever detection,[80] used in most commercial instruments. In the dynamic mode (i.e., both noncontact and tapping measurement modes), the cantilever is oscillated at a desired frequency close to its resonance frequency, using external oscillator controls. Cantilever interactions with the surface change this oscillating frequency, both the amplitude and phase, producing the information base that yields the surface image.[81]

Significantly, scanning probe techniques can often be used in aqueous environments, an enormous advantage for biomaterials research where few methods provide this utility. Operating the AFM in a physiologically relevant medium such as water or buffered salt solutions turns out to be an advantage because in air capillary forces tend to distort the precision of the applied force.[80] AFM in particular is valued because it provides 3D topological information incomparable to other methods in these conditions. In addition, other cantilever surface feedback modes, including electrical potential, current, capacitance, frictional and affinity interactions, can map different surface properties. AFM has become the technique of choice for imaging synthetic biomaterials (commercial polymers, thin polymer films, ceramics, metal oxides, etc.), native biological materials (red blood cells, platelets, cell membranes, bacteria, bone, dentin, etc.), and patterned surfaces of all kinds. With these advantages, it also has disadvantages including its speed of surface scanning (several minutes per scan, leading to thermal drift problems), and image scan size: the AFM can image only a maximum height of $\sim$10–20 μm, and has a maximum scanning area of $\sim 150 \times 150$ μm. Image artifacts from AFM tip defects or contamination, along with the inability to measure sidewalls, overhangs, or narrow features where the tip geometry precludes surface size sampling, are also limitations of AFM. Even so, AFM images of microporous materials are possible.[82]

AFM has been used in numerous applications including structural characterization of organic thin films,[83] analysis of thin polymer films,[84] nanoscale tribology of polymer films,[85] protein adsorption onto mica surfaces,[81,86,87] measurement of the elastic properties of biological materials such as bone,[88] and monitoring of the demineralizing effect of conditioning agents on the structure of dentin.[89] AFM analyses on clinically available biomaterials include assessment of bone response to titanium implants with different morphology,[90] and analysis of a solvent extraction process on biomedical polyurethane morphology.[91–93]

3.301.2.7. Surface Analytical Detection Using Shear-Mode and Surface Acoustic Wave Oscillator Devices

Shear-mode and acoustic wave sensors exploit a sensing detection mechanism from an induced traveling mechanical (i.e., acoustic) wave in the sensor.[94,95] Acoustic wave propagation properties (e.g., wave velocity and/or amplitude) through or on the surface of a material responds to changes in the wave propagation pathway. Changes in wave velocity are monitored by measuring the sensor's wave frequency or phase change characteristics. These changes can be quantitatively correlated to corresponding events monitored by the sensor (i.e., surface adsorption). Acoustic wave and shear-mode devices as sensors use piezoelectric materials interfaces with an electrical pulse generator to generate their acoustic

wave. Piezoelectricity is characteristic of select materials that spontaneously and reversibly produce an electrical charge or field by an applied mechanical stress, or the reciprocal effect of applying an electrical field to a piezoelectric material to yield a mechanical stress. This piezoelectric property leads to their being named 'shear mode' oscillators: applying an oscillating electric field to the material creates a transverse mechanical wave that propagates through the substrate and then can be converted back to an electric field for measurement. Piezoelectric substrate materials possible for use as acoustic wave sensors and devices include quartz (SiO_2), lithium tantalate ($LiTaO_3$), and, in principle, lithium niobate ($LiNbO_3$), although rarely used. Each material exhibits specific advantages and disadvantages, involving crystal cost, their frequency-temperature dependence, and wave attenuation and propagation velocities. Quartz is versatile in that its temperature dependence can be selected by its substrate cut angle and the wave propagation direction such that ideally, temperature effects on wave propagation are minimized. Alternatively, a quartz acoustic wave temperature sensor may be designed by maximizing this effect. By contrast, lithium niobate or lithium tantalite, both exhibiting linear temperature dependences for all material cuts and propagation directions, cannot be exploited this way. Other piezo-active substrate materials include gallium arsenide (GaAs), silicon carbide (SiC), langasite (LGS), zinc oxide (ZnO), aluminum nitride (AlN), lead zirconium titanate (PZT), and polyvinylidene fluoride (PVDF).

Acoustic wave devices can be characterized by the mode of wave propagation through or on top of a piezoelectric substrate, distinguished by wave velocities and displacement directions. Two bulk acoustic wave (BAW) devices, all with transverse waves propagating through the substrate, are most commonly thickness shear mode (TSM) oscillators, and shear-horizontal acoustic plate mode (SH-APM) sensors. Alternatively, waves propagating on the surface of the substrate are known as surface waves. Surface acoustic wave (SAW) and shear-horizontal surface acoustic wave (SH-SAW) sensors, known also as surface transverse wave (STW) sensors, are the most widely used surface wave devices.

All acoustic wave devices can report their intrinsic sensitivity to wave perturbations from many different physical parameters. Any alterations in the propagating path characteristics over which the acoustic wave moves on or in the substrate produce a change in the output. While all such designs function in gaseous or vacuum environments, significantly, only a few devices operate efficiently in liquids. The TSM, SH-APM, and SH-SAW all generate waves propagating principally with shear horizontal motion and this does not dissipate appreciable energy into liquids. This facilitates their use in liquids without excessive wave damping. In contrast, the SAW sensor produces a substantial surface-normal displacement that radiates compression waves into the liquid above the surface, yielding excessive damping. Importantly, however, devices producing waves propagating at a velocity below the sound velocity in the liquid do not suffer appreciably from this damping. Other acoustic waves with attractive applications as sensors include the flexural plate wave (FPW), Love wave, surface-skimming bulk wave (SSBW), and Lamb wave.

3.301.2.7.1. TSM oscillator

The TSM is now better known as the quartz crystal microbalance (QCM) – the oldest and simplest SAW device, deployed for vapor sensing over 50 years ago and commercialized in many forms. The QCM typically consists of a thin disk of AT-cut (i.e., cut from quartz mineral piece at a 35.25° orientation to its optical axis) quartz with parallel circular electrodes, generally of evaporated conductive metal, patterned on both sides. Application of a voltage across these electrodes yields a shear deformation of the crystal due to the piezoelectric effect. This device is known as a resonator because the crystal resonates as electromechanical standing waves are created. Maximum displacement is at the AT-cut crystal faces, resulting in a device intrinsically sensitive to surface interactions. The QCM shear acoustic wave velocity depends highly on the quartz crystal properties, especially the stiffness (i.e., Young's modulus) and density, allowing these resonators to determine material-specific parameters not readily accessible using other sensors with direct transduction, such as SPR. Relationships between QCM crystal mass and its density allow prediction of the QCM resonant frequency variation associated with small mass increases at the QCM surface. This is based on the so-called Sauerbrey equation establishing a linear relationship between crystal resonant frequency and small mass increments, based importantly on the assumption that the mass deposited at the QCM surface is tightly or rigidly coupled to the crystal surface. Hence, the loaded crystal should simply behave as if it were a thicker crystal. Under these conditions, the effective crystal wavelength is increased, and consequently its resonant frequency decreases under such mass loading. As no energy dissipation occurs, this assumption will only be valid for thin, rigid, and uniform adsorbed surface films with similar acoustic properties to the bulk crystal material. QCM was originally used to measure metal thin-film deposition rates in vacuum systems, deployed in an oscillator circuit. The crystal oscillation frequency tracks the crystal resonance and directly reflects mass accumulation on the device surface in systems like these where the adsorbing layer is rigid and coupled to the QCM surface. This piezoelectric signal transduction in principle enables label-free detection of surface binding, adsorption and immobilization events in a variety of different applications, such as monitoring and characterization of protein adsorption, (bio)film deposition, detection of specific antigens, biomolecule binding kinetics, cell adhesion, and DNA detection.[94,95]

Importantly, certain adsorbing and assay conditions violate the Sauerbrey assumptions. Specifically, when the QCM is immersed in a fluid, as is often desired in biosensing applications, or when the surface-adsorbed layer or film has radically different viscoelastic, mechanical, or acoustic properties from the crystal sensor, mechanical wave energy is lost to the fluid phase through viscous coupling. In this case, the shear acoustic waves propagate from the crystal into the fluid, decreasing the sensor resonant frequency from (1) liquid damping proportional to the viscosity and density of the fluid and (2) exponentially decaying transverse shear wave energy dissipation into the bulk fluid, normal to the crystal surface, with a decay characteristic length depending on the crystal oscillating frequency. For example, a penetration depth (decay length) of 250 nm exists for a shear acoustic wave

propagating in water at a 5-MHz crystal frequency. Exploiting this same dependence of wave decay length on the crystal resonance frequency enables probing at different distances from the crystal surface and allows analysis of different 'layers' external to the crystal surface by measuring at the crystal frequency overtones. Importantly, crystal resonant frequency variations are also affected by changes in the roughness of the crystal surface, adsorbate heterogeneity, including nonuniform layers, solution permittivity and conductivity, and charged species near the surface. Many of these are serious limitations to QCM use in biological systems and must be treated differently.[94]

3.301.2.7.2. QCM with dissipation monitoring

The classic analytical treatment of surface adsorption using the Sauerbrey equation treats the sensor resonance frequency and its variation from adsorption as the sole experimental parameter. However, as the crystal resonance frequency is influenced by several factors that must be accounted for to accurately quantify analytes or kinetic adsorption data, and the 'rigid coupling' assumption does not often apply to adsorbed 'soft materials' such as many proteins, cells, lipids, and bacteria, alternatives to the Sauerbrey QCM treatment have been developed.[84] Significantly, impedance analysis enables a full description of the acoustic loading of the crystal surface and thus allows identification and elimination of interfering signals. Physically, impedance is the ratio of the applied voltage across the crystal and current flowing through the crystal between electrodes. In impedance analysis, the incident voltage versus the reflected sinusoidal voltage from the quartz crystal is measured within the resonant frequency, and the impedance magnitude and phase angle are calculated. The magnitude of the impedance provides a measure of signal attenuation, whereas the phase measures the lag between the applied field and the resulting displacement. Different SAW/QCM devices depend on the propagation of acoustic waves in a multilayer structure (i.e., crystal plus adsorbate layers). The acoustic load impedance reflects these changes, independently of whether these wave frequency changes result from actual surface mass accumulation, changes in the adsorbed material properties (e.g., swelling, softening, melting, or rigidity), or chemical (e.g., cross-linking) and physical (e.g., phase transition) changes. Dissipation monitoring in QCM, known as QCM-D and embedded in several commercial SAW instruments, employs on-board impedance analysis of QCM signals. Under conditions of low acoustic load, the impedance of the loaded QCM crystal surface can be expressed as an additional element in series with the equivalent circuit. That is, the impedance of the crystal mass loading under multiple layers is described as linear combinations of the impedance of each layer. Thus, when liquid is added or mass is deposited onto the crystal surface, new elements can be added to the model to describe the new overall impedance. This makes it possible to identify the effect of each of the layers simply by measuring the impedance in a stepwise manner as each component of the measuring sample (e.g., buffer, or target molecules) is added. The Q factor, defined as the ratio between the height of the QCM resonance peak and its width at half maximum in a given media, can also be obtained from impedance spectra. In physical terms, the Q factor represents the fractional energy stored and the energy lost in a single QCM oscillation. This is a quantitative measure for energy dissipation. However, the most commonly determined parameter to account for QCM dissipation is the dissipation factor, D, defined as the reciprocal of the Q factor.[94]

QCM-D improves on the traditional QCM capabilities with dissipation analysis, and enables real-time, label-free measurements of molecular adsorption and/or interactions on various surfaces in liquid media. In addition to sensing adsorbed mass with ng cm^{-2} sensitivity, measured as changes in quartz crystal frequency, the dissipation parameter (D) provides novel insights regarding the structural (viscoelastic) properties of adsorbed layers and their solvated states or of evolving soft matter properties. QCM-D has recently been coupled with real-time dual surface measurements using QCM-ellipsometry and QCM-electrochemistry and electrical impedance spectroscopy, and QCM-Raman spectroscopy. These tandem techniques enrich the information content available from each QCM assay.

3.301.3. Ultrahigh Vacuum Surface Analytical Techniques

3.301.3.1. Electron Spectroscopy for Chemical Analysis

Also known by the synonym XPS, electron spectroscopy for chemical analysis (ESCA) is the method of choice to provide high-resolution compositional information about biomaterials surfaces.[1,96,97] ESCA surface sensitivity results from the production of photoelectrons within a material, and the surface selectivity of their emission and characteristic analysis. X-ray excitation of a material produces classic photoelectron emission processes, resulting in the ejection of core-level electrons from atoms in a relatively deep surface zone (~μm), depending on X-ray energy. However, these ejected photoelectrons have kinetic energies ranging from 30 to 2500 eV, so their inelastic mean free path of travel within a material is about 0.5–3 nm for most materials. The inelastic mean free path is the average distance that an electron can move before experiencing inelastic collisions with another electron or nucleus of any atom in the material that results in loss of energy. As a result, very few photoelectrons created by X-ray-induced emission at depths >2–3 times the mean free path will leave the bulk material with their initial photo-emitted kinetic energy (KE). Photoelectrons produced at depths deeper than this undergo many collisions with atoms and electrons in the bulk and if they reach the ESCA energy analyzer, they will just contribute to the background signal. Owing to their strong interactions with matter, the intensity of photoelectrons decreases exponentially with the depth from the surface where they are created, meaning that XPS is most sensitive to the outer atomic level photoemission processes. This produces the ESCA sampling depth of ~10 nm for many materials. As each photoelectron KE is characteristic of the atom from which the electron was originally derived, all photoelectrons reaching the KE analyzer in ESCA are 'counted' and attributed to the abundance of their source atoms in the surface zone. All elements with an atomic number (Z) of 3 or greater create sufficient photoelectrons to be detected. Using ESCA, most elements can be detected to 0.1 at.% (atomic percent)

sensitivity, and relative atomic amounts are calculated for surface composition. ESCA methods allow access to a rich variety of data, as summarized in Table 3.

ESCA is based on photoemission of core- and valence-level electrons in an atom. Incident X-rays with energy ($h\nu$), usually monochromatic on modern systems, liberate core- and valence-level electrons with sufficient KE to escape from the material and pass through the vacuum chamber to the energy spectrum analyzer to determine their binding energies (BEs). The general form of the energy balance ($BE = h\nu - KE$) was proposed by Einstein in 1905. Additional terms (e.g., spectrometer work function) need to be included in the energy balance to account for the experimental conditions.[97] Figure 5 schematically shows the photoemission process along with a survey spectrum and high-resolution spectra acquired from poly(methyl methacrylate) (PMMA). Data are typically collected as survey spectra spanning the BE range of 0–1000 eV. Then high-resolution spectra may be collected in a region of interest to examine the fine structure of specific core-level peaks (e.g., carbon 1s, oxygen 1s, titanium 2p, etc.). The BE of the photoelectrons emitted depends on the atomic orbital from which they originated, the parent atom, and the chemical environment of the atom. A survey spectrum covering 0–1000 eV will contain photoemission peaks from all elements (excluding H and He) present in the surface of a material (up to 100 Å depth). Shifts in these ESCA peaks can be used to identify chemical state information of the atoms of this surface region.

Innovations in ESCA sampling methods include angle-dependent capabilities for depth compositional mapping,[98–100]

Table 3 Information obtainable from XPS analysis of the biomaterials interface

- Identification of all elements except H and He present in the outer 10 nm of a surface at concentrations exceeding 0.1 at.%
- Quantitative determination of approximate surface composition (±10%)
- Bonding information and molecular environments (oxidation states, bonding partners) in the surface zone
- Identification of unsaturated and aromatic species from satellite ($\pi \rightarrow \pi^*$) transitions
- Further information on surface-exposed organic functional groups using chemical derivatization methods
- Elemental depth profiles to 10 nm deep using angle-dependent XPS analysis or photoelectrons with different depths and depth profiling models
- Sputter depth profiling using various ion sources
- Lateral resolution of surface domains/heterogeneities using models applied to angular-resolved data, or using small spot imaging methods (~10 μm) and data handling models
- Identification of materials using valence bond spectra and bonding orbital information

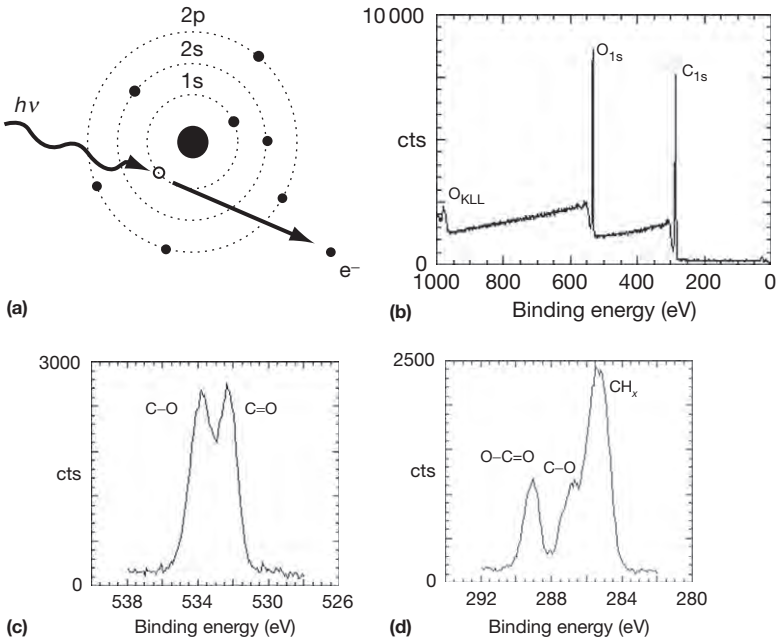

Figure 5 (a) Schematic of the photoemission process. An incident X-ray with energy ($h\nu$) liberates a photoelectron from an atom in the sample with sufficient kinetic energy to be measured by the analyzer. The binding energy (BE) of a photoelectron emitted from conducting sample in electrical contact with the spectrometer is described by the equation: $BE = h\nu - KE - \phi$, where ϕ is the spectrometer work function. Changes in binding energy (ΔBE) for a particular photoelectron (i.e., 2s) occur when the chemical environment changes. (b) A survey spectrum obtained from a poly(methyl methacrylate) (PMMA) sample using monochromatized Al K_α X-rays. Both photoelectrons (C 1s and O 1s) and Auger electrons (O KLL) are detected in the survey spectrum. High-resolution spectra of the O 1s and C 1s regions are shown in (c) and (d). Peaks due to the different oxygen and carbon species present in PMMA can be observed in the high-resolution spectra.

cryogenic freezing of volatile or hydrated specimens for UHV analysis,[101,102] surface spatial mapping of chemistry,[103–106] and surface derivatization reactions to identify functional groups[107–110] and new X-ray sources.[111] While standard sampled areas in a conventional ESCA instrument are millimeter in size or larger, the latest commercial instruments can analyze areas <10 μm in size. Both microprobe (focused X-ray source) and microscope (imaging detector) style ESCA instruments are available.[112–116] In addition, some microprobe style instruments can raster the X-ray beam across selected spots. The primary benefit of these new instruments is the capability of selecting smaller sample areas and 'mapping' surface chemistry in these areas. Disadvantages include a greater risk of sample damage due to a higher flux of focused X-rays (microprobe mode), X-ray exposure of the sample outside the analyzed area (microscope mode), a lower signal-to-noise ratio as smaller irradiated areas produce less photoelectrons (both modes), and significant charge neutralization problems on nonconducting samples. Submicron spatial resolution for biological samples is now possible with ESCA using synchrotron radiation soft X-rays (e.g., at the Berkeley Advanced Light Source).

Together, these ESCA methods offer numerous advantages for biomedical materials surface analysis. Parts or pieces of biomedical devices can be analyzed readily as retrieved, fabricated, or modified. In addition, ESCA provides the capability to evaluate hydrated specimens, to yield rich information on chemistries within a surface zone up to 100 Å deep, and to achieve relatively small sample destruction when using monochromatized X-ray sources. It has established precedents for numerous data interpretation modes, allows rapid sampling, and requires little sample preparation. Disadvantages include (1) the requirement for eliminating sample out-gassing in the UHV environment, (2) the need for access to specialized ESCA resources and expert operators with associated analytical costs, and (3) the potential for sample damage if extended analysis times are required. The first disadvantage can be greatly reduced using the cryogenic sampling methods mentioned above. The second disadvantage diminishes each year with the increased availability of these resources around the world.

Applications of ESCA to biomedical materials surface characterization and biocompatibility studies have been extensive. Studies of polymer surface dynamics,[1,117] protein adsorption to surfaces,[118] and analysis of commercially available materials and medical devices have been performed.[117–119] Inorganic materials have also been studied using ESCA. Orthopedic and dental applications include characterization of commonly prepared titanium implants,[10,120–122] contamination of dental implants from sterilization,[123] failure analysis of ceramic-to-metal bonding,[124] corrosion and oxidation of implants materials,[125–128] and characterization of dental amalgams.[129]

3.301.3.2. Secondary Ion Mass Spectrometry

SIMS is another UHV method that can supplement and augment surface analytical data available from ESCA.[130–138] This method produces a surface mass spectrum of surface species, analogous to long-standing bulk mass-spectrum techniques, using a primary ion beam impacting the surface to generate secondary molecular and ion fragments from the chemistry residing in the top few namometers of the surface of interest. A wide range of primary ion sources is commercially available. Initial SIMS experiments used rare gas ions such as Ar^+ and Xe^+ as primary ion sources. Then liquid metal ion sources using Ga^+ were developed for their improved imaging capabilities. Cs^+ ion sources have also been extensively used. Recent developments in cluster ion sources have significantly expanded the information that can be obtained from SIMS analysis.[139–141] Some of the commercially available cluster ion beams include C_{60}, Bi_3, and Au_3. Typical energies of the incident ion beam range from 200 eV to 30 keV. When the incident primary ion beam strikes the sample surface, ion energy and momentum transfer eject multitudes of different molecular, fragment, and atomic species from the surface zone. A small percentage (typically <1%) of these ejected species are positive or negative ions, which are collected and detected in an interfaced mass analyzer typical of mass spectrometers (i.e., measuring mass/charge ratio, m/z). With monoatomic primary ions, the flux of bombarding primary ions must be kept low (typical ion doses $<10^{13}$ ions per cm^2) to minimize surface etching and damage of surface chemistry. These conditions are termed static SIMS.[130,131] However, with the advent of cluster ion beams, such as C_{60}, that produce little residual surface damage (i.e., most of the material in the impact zone is sputtered away), the static SIMS requirements of low primary ion doses are no longer necessary. This has resulted in the new SIMS capabilities and analytical performance in surface molecular depth profiling and 3D imaging of organic and biological materials.[140,142–145]

The development of time-of-flight SIMS (ToF-SIMS) represented a major improvement in the method and now commercially available SIMS instruments capable of high mass resolution and imaging of surface species are widely available.[26,27,146] The ToF detection mass spectrometry configuration enables enhanced mass-measurement sensitivity and surface mapping of selected species into images. The advantages of SIMS plus enhanced mass-measurement capabilities mean that synthetic polymer surfaces and high mass adsorbates (proteins, contaminants, genetic material) can be analyzed on surfaces at high precision. Complex fragmentation patterns presented by macromolecule mass spectroscopy data are often difficult to interpret unless simpler model studies are performed as a basis for understanding fragmentation. However, newer multivariate statistical methods[147–151] improve enhanced analytical capabilities for both spectroscopic and imaging SIMS studies of organic and biological materials.

Information provided by SIMS analysis is shown in **Table 4**. This information is complementary in many respects to ESCA analysis and provides new, corroborative data from a different surface zone (see **Figure 2**). An example of ToF-SIMS analysis of PMMA, used frequently in bone cements and other biomedical applications, is shown in **Figure 6**. The negative (**Figure 6(a)**) and positive (**Figure 6(b)**) ToF-SIMS survey spectra along with high-resolution spectra (**Figure 6(c)**) demonstrate the ability to determine chemical species present at the surface with extremely high mass resolution. Since a focused primary ion beam is used to generate the secondary ions, it can be rastered across the surface to generate ion-specific images. **Figure 7** shows ToF-SIMS images from secondary ions that show the spatial distributions of chemical species on a surface.[145,152] In addition to chemical information associated with the

Table 4 Surface information obtained from SIMS experiments

- Surface sampling zone restricted to top 1–3 nm of material in the static mode
- Identification of hydrogen
- Molecular structure inferred from fragmentation patterns per mass spectrometry analysis
- Detection of higher molecular weight fragments (polymers, biopolymers)
- Useful for polymer, metal, and ceramic samples
- Applicable to devices and samples with complex geometries (e.g., powders, fibers, films, sponges, etc.)
- Spatial resolution of composition in imaging mode (<1 μm)
- High sensitivity to low surface concentrations (ppm to ppb for many atomic secondary ions)
- Molecular depth profiling and 3D imaging with cluster ion beam sputtering sources

outermost materials surface chemistry, recent work has demonstrated that SIMS is useful in identifying proteins adsorbed to interfaces.[152–154]

3.301.3.3. Auger Electron Spectroscopy

In AES, as in ESCA (XPS), energy deliberately directed to a surface (e.g., an electron beam or X-ray usually 2–20 keV in energy) ejects a core- or valence-level electron in an atom in the typical photoemission process. Subsequently, another electron from a higher energy level within this atom 'falls' into the vacated electron level. Two energy relaxation processes in this atom are then possible: an X-ray can be emitted from this electron relaxation, or a third electron can be ejected from the atom. The emitted electron in this latter process, shown in **Figure 8**, is an Auger electron, and is distinct from the ESCA photoelectrons. AES and scanning Auger microscopy (SAM) both use electrons as both the incident excitation source and the detected analytical signature. The process of Auger electron emission leaves an atom in a doubly ionized final state. A thorough discussion of the nomenclature used to describe Auger emission, instrumentation, and spectral interpretation can be found in the literature.[155,156]

AES and SAM are versatile techniques capable of characterizing the top few molecular layers (0.5–5 nm) with detection limits on the order of 0.1–0.5 at.%. In AES (and SAM), the KE of Auger electrons emitted from a parent atom is measured. All elements above He can be detected with either method. The strength of SAM is the excellent lateral resolution (<20 nm) obtainable with modern field emission electron sources. Owing to this excellent spatial resolution, SAM is routinely coupled with scanning electron microscopy and has found wide acceptance in the fields of biomaterials, microelectronics, catalysis, corrosion science, tribology, metallurgy, adhesion science, and oxidation of metals. Depth profiling measurements are made by monitoring the Auger signal intensities while eroding the sample by ion sputtering. The combination of surface sensitivity, excellent lateral resolution, and depth profiling capabilities allows SAM/AES to be used to investigate numerous phenomena associated with biomaterials fabrication, characterization, and performance testing. AES and SAM data are influenced by electron beam (incident electrons) interactions with the sample; so, considerable care must be taken to minimize electron beam-induced reduction or stimulated desorption of a sample, and in the case of depth profiling prevent ion dependent changes in peak shape and preferential sputtering of specific elements. The major drawback of these techniques is that they are limited in practice to the examination of inorganic materials, thin organic/inorganic coatings on base inorganic substrates, or inorganic coatings on organic materials. Comprehensive reviews of AES and SAM can be found elsewhere.[2,155] As a newer modification, Auger photoelectron coincidence spectroscopy (APECS) is now being developed as a surface analytical tool.

Standard AES analysis provides data describing the elemental composition of the near surface region, and possibly the chemical state of a particular atom. Data are typically collected as a survey spectrum spanning the KE range of 0–1000 eV; subsequently, high-resolution spectra may be collected in a region of interest to examine the fine structure of the Auger peaks. SAM studies provide the spatial distribution of the elemental composition, or the elemental composition at specific positions on a sample surface. AES and SAM have also been used extensively to analyze the surface of orthopedic and dental implants as a function of preparation,[120,157,158] surface modifications or bioactive coatings,[159,160] oxidation and corrosion of biomaterials,[127,128,161] implant failure,[162] and bone response to the implant.[90,163]

AES depth profiling measurements are useful in analyzing the thickness and composition of metal oxides on implant materials,[120,127,157,163] surface modifications such as ion implantation or bioactive coatings on metal surfaces,[160,161] and composition gradients at either a surface or interface. Quantitative depth profiling requires the use of a well-calibrated ion sputtering source to determine instrument parameters that minimize the interfacial depth resolution.[164] Furthermore, standards that model the actual sample are necessary to calibrate the ion sputtering rate. For example, an anodically oxidized titanium standard of known oxide thickness has been used to calibrate the sputter etch rate so that the oxide thickness of a titanium film exposed to a model biological environment could be measured.[127,128] Thorough discussions addressing quantitative depth profiling are given in the literature.[165,166]

3.301.4. Next Challenges: Nanomaterial Surfaces

Nanomaterials are the latest generation of new biomaterials, with novel properties and enormous potential for both *in vitro* and *in vivo* applications. Current increasing interests and use of engineered nanoparticles in both research and product development in biomedical areas has created substantial challenges for the surface analytical community to provide adequate tools for these materials. In a 2-nm diameter particle, over 60% of the atoms in particles of this size reside at their surface; specific surface areas for many of these nanomaterials are unprecedented (200–800 $m^2 g^{-1}$). Surface issues with these materials are indeed acute. As with all biomaterials, biomedical uses for nanomaterials also require full understanding of their properties and behaviors as they are synthesized, fabricated, applied, and as they age in a particular environment, process, or application. Accompanying this from the producer side is an increasing awareness of the need to understand the health,

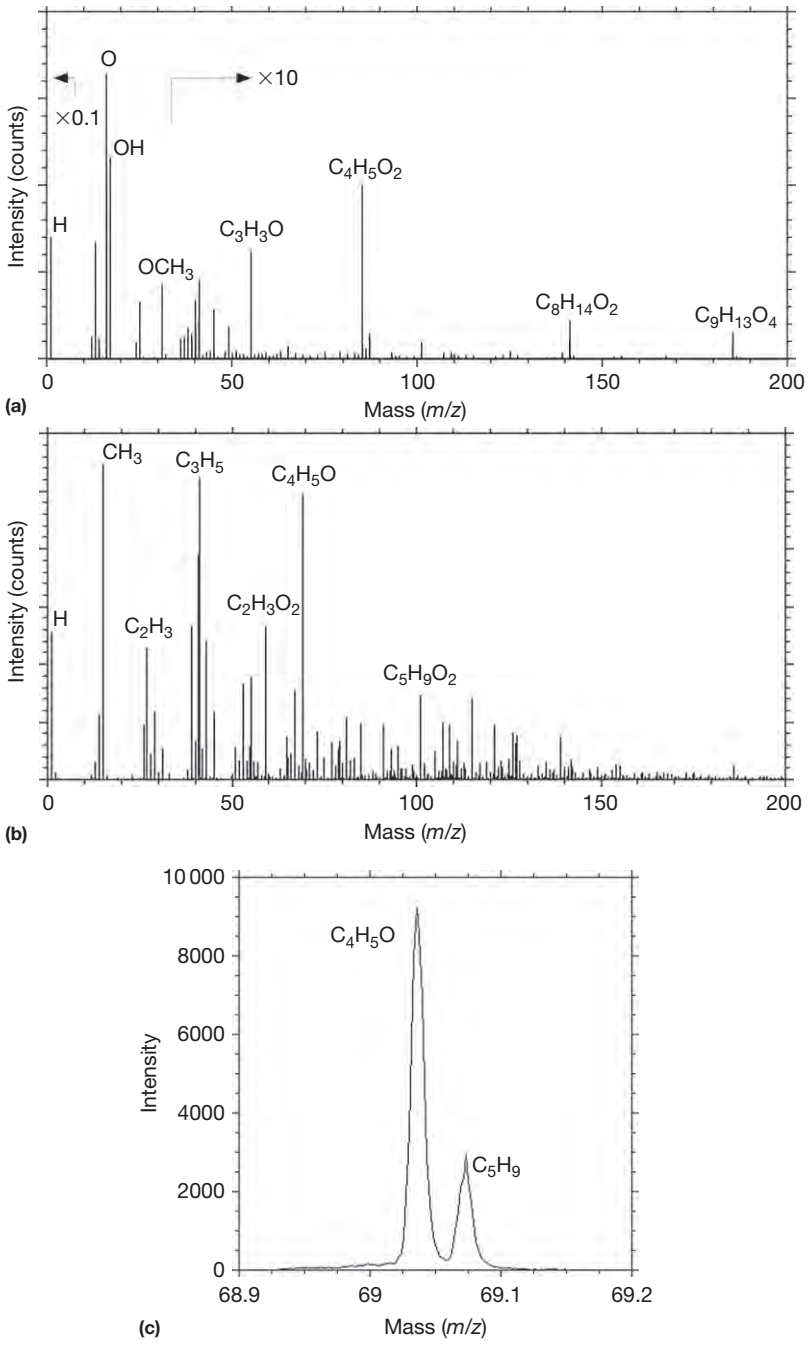

Figure 6 (a) Negative and (b) positive time-of-flight secondary ion mass spectrometry survey spectra of a poly(methyl methacrylate) (PMMA) sample for $m/z = 0$–200. Selected fragments related to the PMMA structure have been labeled. Examples in the negative ion spectrum include the methoxy peak at $m/z = 31$, the M – CH_3 peak at $m/z = 85$, and the 2 M – CH_3 peak at $m/z = 185$ (M = the PMMA monomer). Examples in the positive ion spectrum include the M – OCH_3 peak at $m/z = 69$ and M + H peak at $m/z = 101$. In some cases, multiple species are present at the same nominal mass. In (c), the high mass resolution spectrum for the positive $m/z = 69$ region shows both C_4H_5O ($m/z = 69.03$) and C_5H_9 ($m/z = 69.07$) are present.

safety, and environmental impacts of nanoparticles in all forms of possible interaction, both from consumers and regulatory agencies. Nevertheless, important physical properties required to understand the unique physical and chemical behaviors of many nanomaterials are unreported in research reports and apparently often go unmeasured, especially in biomedical conditions (*in vitro* or *in vivo*). Under these conditions, nanoparticles are often deliberately treated with surface-active stabilizing agents, and then exposed to many biological agents with surfactant or contaminants properties. The dynamics of interfacial structure–property relationships in these cases is unknown. None of these situations have methods sensitive enough to enable their direct analysis even in a dilute biological milieu. As a result, nanomaterials in their

operational conditions are often poorly characterized and, many times, their surface chemistry is not even adequately described. Increasingly, it is recognized that reports on the properties of nanoparticles and other nanomaterials are based on inadequate characterization, certainly not to the standards that historically have governed conventional biomaterials. Consequently, the validity of some conclusions correlating surface properties with performance, efficacy, function, and safety may be questionable. Development of surface analytical techniques to sufficiently characterize nanomaterials in biological contexts represents the next challenge.[167,168]

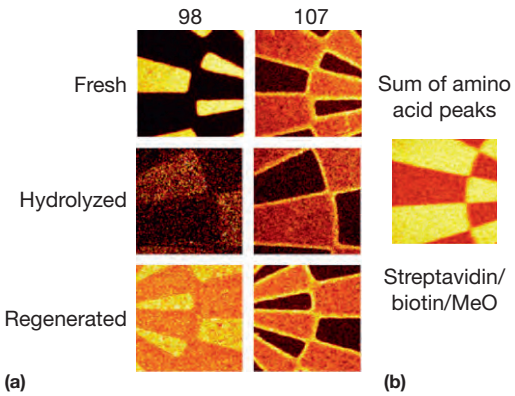

Figure 7 Time-of-flight secondary ion mass spectrometry (ToF-SIMS) images of hydrogel-coated glass slides with methoxy (MeO) and *n*-hydroxysuccinimde (NHS) pinwheel patterned surface chemistries. (a) Negative ToF-SIMS images of fragments from NHS ($m/z = 98$) and processing photoresist ($m/z = 107$) as the sample goes from fresh to hydrolyzed to regenerated. Note that the intensity of the photoresist residue (an organic contaminant on an organic surface) does not change significantly during this treatment sequence while the intensity of the NHS fragment does. (b) The NHS region of the NHS/MeO surface has been treated with an amine-terminated biotin molecule and then exposed to streptavidin. The positive ToF-SIMS image is a the sum of intensities from the amino acid fragments and shows the streptavidin only attaches to the biotin regions of the patterned surface. Adapted from Dubey, M.; Brison, J.; Grainger, D. W.; Castner, D. G. *Surf. Interface Anal.* **2010**, *42*, DOI: 10.1002/sia.3537; Dubey, M.; Emoto, K.; Takahashi, H.; Castner, D.G.; Grainger, D. W. *Adv. Funct. Mater.* **2009**, *19*, 3046–3055.

3.301.5. Conclusions

Surface characterization of biomaterials has enjoyed a renaissance of development and technological improvement with the recognition that the material interface plays a key role in mediating biological response and reactivity. New methods are continually evolving, improving the capabilities to probe materials surfaces and their interfaces with biology in many new and valuable ways. While a variety of surface analytical methods are now available to the biomaterial scientist, each case of surface characterization must be carefully evaluated to match desired analytical information with the method(s) and their respective capabilities. Few techniques actually are able to provide surface data of direct relevance to the biological implant environment: few methods operate under water or in the presence of complex milieu such as serum. Instead, some of the more valuable methods (e.g., ESCA) often operate in high vacuum – far from the aqueous environment of biomaterial applications. At best, only simulated environments approximating biological sites (for example, the evanescent wave biosensors, environmental SEM or hydrated ESCA or SIMS) are currently available to address this gap between analysis and application environments. Much of a biomaterial's surface description, therefore, must be inferred and extrapolated from the environment of the surface in the analytical scenario (e.g., UHV) to the material site of application (aqueous). Because surfaces of many biomaterials are synthetic polymers or proteins capable of metastable states of surface relaxation and restructuring, analytical methods must account for possible 'chameleon-like' changes in surfaces (e.g., topology, chemistry)

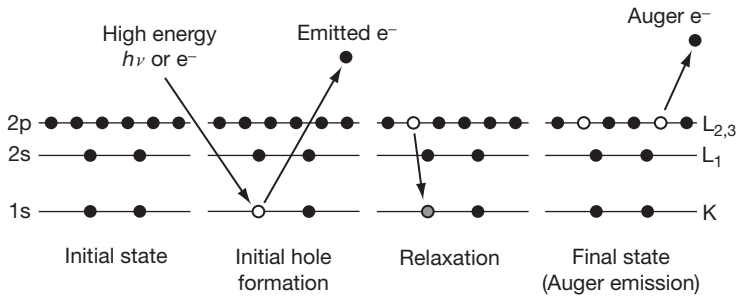

Figure 8 Schematic diagram of Auger electron emission process. The atom starts out with its full complement of electrons (far left). Then either a high-energy X-ray or electron beam is used to ionize a core or valence electron (ionization of a 1s or K electron shown, second from left). An outer shell electron then relaxes and fills the initial hole (relaxation of an 2p or $L_{2,3}$ electron is shown, second from right). The excess energy from the relaxation process is then either emitted as X-ray (not shown) or transferred to another electron which is then emitted (shown, far right). This is the Auger electron (shown as emission of an $L_{2,3}$ electron). The kinetic energy (KE) of the emitted Auger electron depends on the specific Auger transition that occurs (i.e., $KL_{2,3}\,L_{2,3}$ shown in this figure) and the chemical environment of the atom. It does not depend on the energy of the primary X-ray or electron beam used to create the initial hole as long as the beam has sufficient energy to ionize that electron. After emission of an Auger electron the atom has a charge of +2 due to loss of two electrons (the initial ionized electron plus the Auger electron). The energy balance for a $KL_{2,3}\,L_{2,3}$ Auger electron is $KE_{KL2,3L2,3} = BE_K - BE_{L2,3} - BE_{L2,3}$, where the first BE term represents the binding energy of the initial core hole, the second BE term represents the binding energy of the electron that fills the initial core hole, and the third BE term represents the binding energy of the electron that is emitted as an Auger electron.

between vacuum, air, and water environments. The more complete the knowledge of the material and its possible surface composition and physical chemistry, the more confident the investigator may be regarding the surface's reactivity in a biological setting. The fullest impact of surface analysis in the biomaterials field will be realized by coupling surface characterization to a broader set of disciplines common to biomaterials development. This sets the stage then for the biomaterials specialist to become adept with a number of scientific concepts regarding surfaces and their behavior. Comprehensive understanding of the influence of materials interfacial chemistry in biological systems will be derived from an ability to direct diverse principles of surface physics, surface analysis, materials science and engineering, surface electrochemistry, synthetic chemistry, and cellular and molecular biology to the application of biomaterials in specific sites.

Acknowledgments

D.W.G. gratefully acknowledges NIH grant EB-001473 and D.G.C. gratefully acknowledges NIH grant EB-002027 for support during the preparation of this manuscript as well as for some the experiments described in it.

References

1. Andrade, J. D. In *Surface and Interfacial Aspects of Biomedical Polymers*; Plenum Press: New York, 1985; Vols. 1 and 2.
2. Briggs, D., Seah, M. P., Eds.; In *Practical Surface Analysis*, 2nd ed.; Wiley: New York, 1990; Vols. 1 and 2.
3. Ratner, B. D. In *Concise Encyclopedia of Medical and Dental Materials*; Williams, D. F., Ed.; Pergamon: Oxford, 1990; pp 337–346.
4. Castner, D. G.; Ratner, B. D. *Surf. Sci.* **2002**, *500*, 28–60.
5. Konradi, R.; Textor, M.; Reimhult, E. In *Surface Analysis and Techniques in Biology*; Smentkowski, V. S., Ed.; Springer Verlag: Berlin, (in press).
6. Somorjai, G. A. *Chemistry in Two Dimensions: Surfaces*. Cornell University Press: Ithaca, NY, 1981.
7. Adamson, A. W. *Physical Chemistry of Surfaces*, 4th ed.; Wiley-Interscience: New York, 1990.
8. Horbett, T. A., Brash, J. D., Eds.; *Proteins at Interfaces*; ACS: Washington, DC, 1987; Vols. 1 and 2; 1995.
9. Ratner, B. D., Ed.; *Progress in Biomedical Engineering: Surface Characterization of Biomaterials*; Elsevier: Amsterdam, 1988; Vol. 6.
10. Kasemo, B.; Lausmaa, J. In *CRC Critical Reviews in Biocompatibility*; CRC Press: Boca Raton, FL, 1986; Vol. 4, pp 335–380.
11. Aveyard, R.; Haydon, D. A. *Introduction to Principles of Surface Chemistry*. Cambridge Press: London, 1973.
12. Bally, M.; Halter, M.; Vörös, J.; Grandin, H. M. *Surf. Interface Anal.* **2006**, *38*, 1442–1458.
13. Velasco-Garcia, M. N. *Semin. Cell Dev. Biol.* **2009**, *20*, 27–33.
14. Fan, X. *Anal. Chim. Acta* **2008**, *620*, 8–26.
15. Neumann, A. W. In *Wetting, Spreading and Adhesion*; Padday, J. F., Ed.; Academic Press: New York, 1978; pp 3–35.
16. Mittal, K. L., Ed.; In *Contact Angle, Wettability and Adhesion*; VCP: Weinheim, 1993.
17. Pitt, W. L.; Young, B. R.; Cooper, S. L. *Colloids Surf.* **1987**, *27*, 345–355.
18. Zisman, W. In *Contact Angle, Wettability and Adhesion*; Fowkes, F. M., Ed.; Adv. Chem. Ser.; ACS: Washington, DC, 1964; Vol. 43, pp 1–51.
19. Brandup, I. J., Immergut, E. H., Eds.; In *Polymer Handbook*, 3rd ed.; Wiley: New York, 1990.
20. Daghestani, H. N.; Day, B. W. *Sensors* **2010**, *10*, 9630–9646.
21. Cooper, M. A., Ed.; In *Label-Free Biosensors: Techniques and Applications*; Cambridge University Press: Cambridge, 2009.
22. Reichert, W. M. *Crit. Rev. Biocompat.* **1989**, *5*, 173–205.
23. Mirabella, F. M. *Appl. Spectrosc. Rev.* **1985**, *21*, 145–178.
24. Urban, M. *Vibrational Spectroscopy of Molecules and Macromolecules on Surfaces*. Wiley-Interscience: New York, 1993.
25. Knutson, K.; Lyman, D. J. In *Surface and Interfacial Aspects of Biomedical Polymers*; Andrade, J. D., Ed.; Plenum: New York, 1985; Vol. 1, pp 197–247.
26. Wang, W.; Castner, D. G.; Grainger, D. W. *Supramol. Sci.* **1997**, *4*, 83–99.
27. Sun, F.; Castner, D. G.; Mao, G.; Wang, W.; McKeown, P.; Grainger, D. W. *J. Am. Chem. Soc.* **1996**, *118*, 1856–1866.
28. Porter, M. D. *Anal. Chem.* **1988**, *60*, 1143A–1154A.
29. Magnani, A.; Busi, E.; Barbucci, R. *J. Mater. Sci. Mater. Med.* **1994**, *5*, 839–847.
30. Lenk, T. J.; Ratner, B. D.; Gendreau, R. M. *J. Biomed. Mater. Res.* **1989**, *23*, 549–557.
31. Cheng, S.-S.; Chittur, K. K.; Sukenik, C. N.; Culp, L. A.; Lewondowska, K. *J. Colloid Interface Sci.* **1994**, *162*, 135–147.
32. Keddie, J. L. *Curr. Opin. Colloid Interface Sci.* **2001**, *6*, 102–110.
33. Tompkins, H. G. *A User's Guide to Ellipsometry*. Academic Press: San Diego, CA, 1993.
34. Cuypers, P. A.; Corsel, J. W.; Janssen, M. P.; Kop, J. M. M.; Hermens, W. T.; Hemker, H. C. *J. Biol. Chem.* **1983**, *258*, 2426–2431.
35. Ivarsson, B.; Lundström, I. In *CRC Critical Reviews in Biocompatibility*; CRC Press: Boca Raton, FL, 1986; Vol. 2, pp 1–95.
36. Byrne, T. *Surf. Sci.* **2008**, *602*, 2927–2935.
37. Azzam, R. M. A.; Bashara, N. M. *Ellipsometry and Polarized Light*. North-Holland: Amsterdam, 1977.
38. Born, M.; Wolf, E. *Principles of Optics: Electromagnetic Theory of Propagation Interference and Diffraction of Light*, 4th ed.; Pergamon: New York, 1969.
39. Prime, K. L.; Whitesides, G. M. *Science* **1991**, *252*, 1164–1167.
40. Wahlgren, M. C.; Paulsson, M. A.; Arnebrant, T. *Colloids Surf. A* **1993**, *70*, 139–149.
41. Wälivaara, B.; Askendal, A.; Elwing, H.; Lundström, I.; Tengvall, P. *J. Biomed. Mater. Res.* **1992**, *26*, 1205–1216.
42. Tengvall, P.; Lestelius, M.; Liedberg, B.; Lundström, I. *Langmuir* **1992**, *8*, 1236–1238.
43. Lestelius, M.; Liedberg, B.; Lundström, I.; Tengvall, P. *J. Biomed. Mater. Res.* **1994**, *28*, 871–880.
44. Arwin, H. *Appl. Spectrosc.* **1986**, *40*, 313–318.
45. Arwin, H.; Mårtensson, J.; Lundström, I. *Appl. Phys. Commun.* **1992**, *11*, 41–48.
46. Asinovski, L.; Beaglehole, D.; Clarkson, M. T. *Phys. Status Solidi* **2008**, *205*, 764–771.
47. Jin, G.; Jansson, R.; Arwin, H. *Rev. Sci. Instrum.* **1996**, *67*, 2930–2936.
48. Kooyman, R. P. H.; Kolkman, H.; Van Gent, J.; Greve, J. *Anal. Chim. Acta* **1988**, *213*, 35–45.
49. Kooyman, R. P. H.; De Bruin, H. E.; Eenik, R. G.; Greve, J. *J. Mol. Struct.* **1990**, *218*, 345–350.
50. Jönsson, U.; Fägerstam, L.; Ivarsson, B.; *et al. Biotechniques* **1991**, *11*, 620–627.
51. Fägerstam, L.; Frostell-Karlsson, A.; Karlsson, R.; Persson, B.; Rönnberg, I. *J. Chromatogr.* **1992**, *597*, 397–410.
52. Davies, J. *Nanobiology* **1994**, *3*, 5–16.
53. Cush, R.; Cronin, J. M.; Stewart, W. J.; Maule, C. H.; Molloy, J.; Goddard, N. J. *Biosens. Bioelectron.* **1993**, *8*, 347–364.
54. Buckle, P. E.; Davies, R. D.; Kinning, T.; *et al. Biosens. Bioelectron.* **1993**, *8*, 365–370.
55. Davies, R. D.; Edwards, P. R.; Watts, H. J.; *et al. Tech. Protein Chem.* **1994**, *5*, 285–292.
56. Homola, J.; Yee, S. S.; Myszka, D. In *Optical Biosensors: Today and Tomorrow*, 2nd ed.; Ligler, F. S., Taitt, C. R., Eds.; Elsevier: Amsterdam, 2008; Chapter 4, pp 185–242.
57. Zhang, H.; Orosz, K. S.; Takahashi, H.; Saavedra, S. S. *Appl. Spectrosc.* **2009**, *63*, 1062–1067.
58. Davies, R. J.; Pollard-Knight, D. *Am. Biotechnol. Lab.* **1993**, *11*(8), 52–54.
59. Malmqvist, M. *Nature* **1993**, *361*, 186–187.
60. Mukhopadhyay, R. *Anal. Chem.* **2005**, *77*, 313A–317A.
61. Cross, G. H.; Reeves, A.; Brand, S. *J. Phys. D Appl. Phys.* **2004**, *37*, 74–80.
62. Vörös, J. *Biophys. J.* **2004**, *87*, 553–561.
63. Malmqvist, M. In *Nanofabrication and Biosystems: Integrating Material Science, Engineering, and Biology*; Hoch, H., Jelinski, L., Craighead, H., Eds.; Cambridge University Press: New York, 1996; pp 103–122.
64. O'Shannessy, D. J. *Curr. Opin. Biotechnol.* **1994**, *5*, 65–71.
65. Narayanaswamy, R., Wolfbeis, O. S., Eds.; In *Optical Sensors: Industrial, Environmental and Diagnostic Applications*; Springer Series on Chemical Sensors and Biosensors; Springer: Berlin, Heidelberg, 2004; Vol. 1.
66. Wolfbeis, O. S. *Anal. Chem.* **2006**, *78*, 3859–3873.
67. Rothenhausler, B.; Knoll, W. *Nature* **1988**, *332*, 615–617.

68. Jordan, C. E.; Frutos, A. G.; Thiel, A. J.; Corn, R. M. *Anal. Chem.* **1997**, *69*, 4939–4947.
69. Bassil, N.; Maillart, E.; Canva, M.; *et al. Sens. Actuators B* **2003**, *94*, 313–323.
70. Shumaker-Parry, J. S.; Aebersold, R.; Campbell, C. T. *Anal. Chem.* **2004**, *76*, 2071–2082.
71. Yeatman, E. M.; Ash, E. A. *SPIE* **1988**, *897*, 100–107.
72. Schmidt, A.; Spinke, J.; Bayeri, T.; Sackmann, E.; Knoll, W. *Biophys. J.* **1992**, *63*, 1385–1392.
73. Zourob, M., Lakhtakia, A., Eds.; In *Optical Guided-Wave Chemical and Biosensors II*; Springer Series on Chemical Sensors and Biosensors; Springer-Verlag: Berlin, 2010; Vol. 8.
74. Steiner, G. *Anal. Bioanal. Chem.* **2005**, *379*, 328–331.
75. Grandin, H. M.; Bonderer, L.; Städler, B.; Textor, M.; Vörös, J. *Biosens. Bioelectron.* **2006**, *21*, 1476–1482.
76. Fang, Y. In *Optical Guided-Wave Chemical and Biosensors II*; Zourob, M., Lakhtakia, A., Eds.; Springer Series on Chemical Sensors and Biosensors; Springer-Verlag: Berlin, 2010; Vol. 8, pp 27–42.
77. Campbell, C. T.; Kim, G. *Biomaterials* **2007**, *28*, 2380–2392.
78. Giessibl, F. J. *Rev. Mod. Phys.* **2003**, *75*, 949–983.
79. Jalili, N.; Laxminarayana, K. *Mechatronics* **2004**, *14*, 907–945.
80. Binnig, G.; Quate, C. F.; Gerber, C. H. *Phys. Rev. Lett.* **1986**, *56*, 930.
81. Marchant, R. E.; Leas, S. A.; Andrade, J. D.; Bockenstedt, P. J. *J. Colloid Interface Sci.* **1992**, *148*, 261–272.
82. Paredes, J. I.; Martínez-Alonso, A.; Tascón, J. M. D. *Stud. Surf. Sci. Catal.* **2002**, *144*, 1–10.
83. Zasadzinski, J. A.; Viswanathan, R.; Schwartz, D. K.; *et al. Colloids Surf. A Physicochem. Eng. Asp.* **1994**, *93*, 305–333.
84. Berquier, J.-M.; Creuzet, F.; Grimal, J.-M. *Langmuir* **1996**, *12*, 597–598.
85. Smithson, R. L. W.; Evans, D. F.; Monfils, J. D.; Guire, P. E. *Colliods Surf. B Biointerfaces* **1993**, *1*, 349–355.
86. Fritz, M.; Radmacher, M.; Cleveland, J. P.; *et al. Langmuir* **1995**, *11*, 3529–3535.
87. Taborelli, M.; Eng, L.; Descouts, P.; Ranieri, J. P.; Bellamkonda, R.; Aebischer, P. *J. Biomed. Mater. Res.* **1995**, *29*, 707–714.
88. Tao, N. J.; Lindsay, S. M.; Lees, S. *Biophys. J.* **1992**, *63*, 1165–1168.
89. Marshall, G. W.; Balooch, M.; Kinney, J. H.; Marshall, S. J. *J. Biomed. Mater. Res.* **1995**, *29*, 1381–1387.
90. Larsson, C.; Thomsen, P.; Lausmaa, J.; Rodahl, M.; Kasemo, B.; Ericson, L. E. *Biomaterials* **1994**, *15*, 1062–1074.
91. Nurdin, N.; Descourts, P. *J. Biomater. Sci. Polym. Ed.* **1995**, *7*, 425–438.
92. Dvorak, J. A. *Methods* **2003**, *29*, 86–96.
93. Haupt, B. J.; Pelling, A. E.; Horton, M. A. *Sci. World J.* **2006**, *15*, 1609–1618.
94. Ferreira, G. N. M. *Trends Biotechnol.* **2009**, *27*(12), 689–697.
95. Marx, K. A. *Biomacromolecules* **2003**, *4*(5), 1099–1120.
96. Dilks, A. In *Electron Spectroscopy: Theory, Techniques and Applications*; Baker, A. O., Brudle, C. R., Eds.; Academic Press: London, 1981; pp 277–359.
97. Ratner, B. D.; Castner, D. G. In *Surface Analysis-Principle Techniques*, 2nd ed.; Vickerman, J. C., Gilmore, I., Eds.; Wiley: Chichester, 2009; pp 47–112.
98. Fadley, C. S. *Prog. Solid State Chem.* **1976**, *11*, 265–343.
99. Tyler, B. J.; Castner, D. G.; Ratner, B. D. *Surf. Interface Anal.* **1989**, *14*, 443–450.
100. Ratner, B. D.; Paynter, R. W. In *Polyurethanes in Biomedical Engineering, Progress in Biomedical Engineering*; Planck, H., Engbers, G., Syre, I., Eds.; Elsevier: Amsterdam, 1984; Vol. 1, pp 41–68.
101. Ratner, B. D.; Weathersby, P. K.; Hoffman, A. S.; Kelly, M. A.; Scharpen, L. H. *J. Appl. Polym. Sci.* **1978**, *22*, 643–664.
102. Lewis, K. B.; Ratner, B. D.; Klumb, L. A.; Ertel, S. I. *Trans. Soc. Biomater.* **1991**, *14*, 176.
103. Seah, M. P.; Smith, G. C. *Surf. Interface Anal.* **1988**, *11*, 69–79.
104. Hoffmann, D. P.; Proctor, A.; Hercules, D. M. *Appl. Spectrosc.* **1989**, *43*, 899–908.
105. Ebel, H.; Ebel, M. F.; Mantler, M.; Barnegg-Golwig, G.; Svagera, R.; Gurker, N. *Surf. Sci.* **1990**, *231*, 233–239.
106. Briggs, D. *Polymer* **1985**, *25*, 1379–1391.
107. Chilkoti, A.; Ratner, B. D.; Briggs, D. *Chem. Mater.* **1991**, *3*, 51–61.
108. Chilkoti, A.; Ratner, B. D. *Surf. Interface Anal.* **1991**, *17*, 567–574.
109. Batich, C. D. *Appl. Surf. Sci.* **1988**, *32*, 57–73.
110. Chilkoti, A.; Ratner, B. D. In *Surface Characterization of Advanced Polymers*; Sabbatini, L., Zambonin, P. G., Eds.; VCH Verlag: Weinheim, Germany, 1993; pp 221–256.
111. Paynter, R. W. In *Techniques of Biocompatibility Testing*; Williams, D. F., Ed.; CRC Press: Boca Raton, FL, 1986; Vol. 2, pp 49–80.
112. Baer, D. R.; Engelhard, M. H. *Surf. Interface Anal.* **2000**, *29*(11), 766–772.
113. Coxon, P.; Krizek, J.; Humpherson, M.; Wardell, I. R. M. *J. Electron Spectros. Relat. Phenomena* **1990**, *52*, 821–836.
114. Drummond, I. W.; Street, F. J.; Ogden, L. P.; Surman, D. J. *Scanning* **1991**, *13*(2), 149–163.
115. Vohrer, U.; Blomfield, C.; Page, S.; Roberts, A. *Appl. Surf. Sci.* **2005**, *252*(1), 61–65.
116. Walton, J.; Fairley, N. *Surf. Interface Anal.* **2006**, *38*(8), 1230–1235.
117. Mori, H.; Hirao, A.; Nakahama, S.; Senshu, K. *Macromolecules* **1994**, *27*, 4093–4100.
118. Paynter, R. W.; Rantner, B. D. In *Surface and Interfacial Aspects of Biomedical Polymers*; Andrade, J. D., Ed.; Plenum: New York, 1985; Vol. 2, pp 189–216.
119. Castner, D. G.; Ratner, B. D.; Hoffman, A. S. *J. Biomater. Sci. Polym. Ed.* **1990**, *1*, 191–206.
120. Lausmaa, J.; Kasemo, B.; Mattsson, H. *Appl. Surf. Sci.* **1990**, *44*, 133–146.
121. Klauber, C.; Lenz, L. J.; Henry, P. J. *Int. J. Oral Maxillofac. Implants* **1990**, *5*, 264–271.
122. Healy, K. E.; Ducheyne, P. *Biomaterials* **1992**, *13*, 553–561.
123. Lausmaa, J.; Kasemo, B.; Hansson, S. *Biomaterials* **1985**, *6*, 23–27.
124. Anusavice, K. J.; Ringle, R. D.; Fairhurst, C. W. *J. Prosthet. Dent.* **1979**, *42*, 417–421.
125. Hofmann, J.; Michel, R.; Holm, R.; Zilkens, J. *Surf. Interface Anal.* **1981**, *3*, 110–117.
126. Ohnsorge, J.; Holm, R. *Med. Prog. Technol.* **1978**, *5*, 171–177.
127. Healy, K. E.; Ducheyne, P. *J. Colloid Interface Sci.* **1992**, *150*, 404–417.
128. Healy, K. E.; Ducheyne, P. *J. Biomed. Mater. Res.* **1992**, *26*, 319–338.
129. Hanawa, T.; Takahashi, H.; Ota, M.; Pinizzotto, R. F.; Ferracane, J. L.; Okabe, T. *J. Dent. Res.* **1987**, *66*, 1470–1478.
130. Castner, D. G.; Ratner, B. D. In *Surface Characterization of Biomaterials. Progress in Biomedical Engineering*; Ratner, B. D., Ed.; Elsevier: Amsterdam, 1988; Vol. 6, pp 65–81.
131. Vickerman, J. C.; Brown, A.; Reed, N. M. *Secondary Ion Mass Spectrometry, Principles and Applications*. Clarendon: Oxford, 1989.
132. Pignataro, S.; Licciadello, A. *Gazz. Chim. Ital.* **1990**, *120*, 351–363.
133. Katz, W.; Newman, J. G. *MRS Bull.* **1987**, *7*, 40–46.
134. Niehuis, E. In *Proceedings of the Sixth International Conference on Secondary Ion Mass Spectrometry (SIMS VI)*; Benninghoven, A., Huber, A. M., Werner, H. W., Eds.; Wiley: Chichester, 1988; Vol. 1, pp 591–598.
135. Davies, M. C.; Lynn, R. A. P. *CRC Crit. Rev. Biocompat.* **1990**, *5*, 297–341.
136. Belu, A.; Graham, D. J.; Castner, D. G. *Biomaterials* **2003**, *24*, 3635–3653.
137. Vickerman, J. C. *Surf. Sci.* **2009**, *603*, 1926–1936.
138. Vickerman, J. C., Briggs, D., Eds.; In *ToF-SIMS: Surface Analysis by Mass Spectrometry*; IM Publications: Chichester, 2003.
139. Weibel, D.; Wong, S.; Lockyer, N.; Blenkinsopp, P.; Hill, R.; Vickerman, J. C. *Anal. Chem.* **2003**, *75*, 1754–1764.
140. Winograd, N. *Anal. Chem.* **2005**, *77*, 142A–149A.
141. Kollmer, F. *Appl. Surf. Sci.* **2004**, *231–232*, 153–158.
142. Fletcher, J. S. *Mass Spectrom. Rev.* **2011**, *30*, 142–174.
143. Mahoney, C. *Mass Spectrom. Rev.* **2010**, *29*, 247–293.
144. Brison, J.; Muramoto, S.; Castner, D. G. *J. Phys. Chem. C* **2010**, *114*, 5565–5573.
145. Dubey, M.; Brison, J.; Grainger, D. W.; Castner, D. G. *Surf. Interface Anal.* **2011**, *43*, 261–264.
146. Price, D. *Trends Anal. Chem.* **1990**, *9*, 21–25.
147. Chilkoti, A.; Ratner, B. D.; Briggs, D. In *SIMS VIII*; Benninghoven, A., Janssen, K. T. F., Tumpner, J., Werner, H. W., Eds.; Wiley: Chichester, 1992; pp 815–818.
148. Chilkoti, A.; Ratner, B. D.; Briggs, D. *Anal. Chem.* **1993**, *65*, 1736–1745.
149. Wagner, M. S.; Graham, D. J.; Ratner, B. D.; Castner, D. G. *Surf. Sci.* **2004**, *570*, 78–97.
150. Tyler, B. J.; Rayal, G.; Castner, D. G. *Biomaterials* **2007**, *28*, 2412–2423.
151. Graham, D. J.; Wagner, M. S.; Castner, D. G. *Appl. Surf. Sci.* **2006**, *252*, 6860–6868.
152. Dubey, M.; Emoto, K.; Takahashi, H.; Castner, D. G.; Grainger, D. W. *Adv. Funct. Mater.* **2009**, *19*, 3046–3055.
153. Mantus, D. S.; Ratner, B. D.; Carlson, B. A.; Moulder, J. F. *Anal. Chem.* **1993**, *65*, 1431–1437.
154. Wagner, M. S.; Castner, D. G. *Langmuir* **2001**, *17*, 4649–4660.
155. Hofmann, S. *Mikrochim. Acta (Wein)* **1987**, *1*, 321–345.
156. Briggs, D.; Rivière, J. C. In *Auger and X-ray Photoelectron Spectroscopy*, 2nd ed.; Briggs, D., Seah, M. P., Eds.; Practical Surface Analysis; Wiley: New York, 1990; Vol. 1, pp 85–141.
157. Binon, P. P.; Weir, D. J.; Marshall, S. J. *Int. J. Oral Maxillofac. Implants* **1992**, *7*, 168–175.

158. Lausmaa, J.; Kasemo, B.; Rolander, U.; *et al*. In *Progress in Biomedical Engineering: Surface Characterization of Biomaterials*; Ratner, B. D., Ed.; Elsevier: Amsterdam, 1988; Vol. 6, pp 161–174.
159. Van Raemdonck, W.; Ducheyne, P.; De Meester, P. *J. Am. Ceram. Soc.* **1984**, *67*, 381–384.
160. Kim, C. S.; Ducheyne, P. *Biomaterials* **1991**, *12*, 461–469.
161. Ducheyne, P.; Healy, K. E. *J. Biomed. Mater. Res.* **1988**, *22*, 1137–1163.
162. Aparicio, C.; Olivé, J. *Int. J. Oral Maxillofac. Implants* **1992**, *7*, 94–103.
163. Sundgren, J.-E.; Bodö, P.; Lundström, I. *J. Colloid Interface Sci.* **1992**, *110*, 9–20.
164. Hunt, C. P.; Seah, M. P. *Surf. Interface Anal.* **1984**, *6*, 82–93.
165. Mathieu, H. J.; Datta, M.; Landolt, D. *J. Vasc. Sci. Technol. A* **1985**, *3*, 331–335.
166. Hofmann, S. In *Auger and X-ray Photoelectron Spectroscopy*, 2nd ed.; Briggs, D., Seah, M. P., Eds.; Practical Surface Analysis; Wiley: New York, 1990; Vol. 1, pp 143–199.
167. Grainger, D. W.; Castner, D. G. *Adv. Mater.* **2008**, *20*, 867–877.
168. Baer, D. R.; Gaspar, D. J.; Nachimuthu, P.; Techane, S. D.; Castner, D. G. *Anal. Bioanal. Chem.* **2010**, *396*, 983–1002.
169. Grainger, D. W.; Healy, K. In *Handbook of Biomaterials Evaluation*, 2nd ed.; von Recum, A. F., Ed.; MacMillan: New York, 1998; pp 115–141.

3.302. Atomic Force Microscopy

L-C Xu and C A Siedlecki, The Pennsylvania State University, College of Medicine, Hershey, PA, USA

© 2011 Elsevier Ltd. All rights reserved.

3.302.1.	**Introduction**	24
3.302.2.	**Fundamentals of the AFM**	24
3.302.2.1.	Principles of AFM	24
3.302.2.2.	Contact Mode Imaging	25
3.302.2.3.	Dynamic Imaging Modes	26
3.302.2.3.1.	Intermittent-contact imaging	26
3.302.2.3.2.	Force modulation and phase imaging	26
3.302.2.3.3.	Noncontact imaging modes	28
3.302.3.	**Force–Distance Measurement and Force Mapping**	28
3.302.3.1.	Force–Distance Curve	28
3.302.3.2.	Force Mapping	29
3.302.4.	**Nanoindentation and Measurement of Near-Surface Nanomechanical Properties of Polymeric Biomaterials**	29
3.302.5.	**Probing Molecular Interaction and Recognition Sites on Biosurfaces**	31
3.302.5.1.	Modification of AFM Probes	31
3.302.5.2.	Measuring Adhesion Forces of Protein to Biomaterial Surfaces	32
3.302.5.3.	Molecular Recognition of Proteins in Dual Component Protein Film	32
3.302.5.4.	Measuring the Functional Activity of Adsorbed Proteins	33
3.302.6.	**Limitations and Perspectives**	33
References		34

Abbreviations

2D	2-dimensional
AFM	Atomic force microscope
BSA	Bovine serum albumin
EFM	Electric force microscopy
JKR	Johnson–Kendall–Roberts
LFM	Lateral force microscopy
mAb	Monoclonal antibody
MFM	Magnetic force microscopy
NHS	*N*-hydroxysuccinimide
pAb	Polyclonal antibody
PDMS	Polydimethylsiloxane
PE	Polyethylene
PU	Polyurethane
RMS	Root mean square
SAM	Self-assembled monolayer
SEM	Scanning electron microscope
SPM	Scanning probe microscope
STM	Scanning tunneling microscope
TEM	Transmission electron microscope

Symbols

A	Set point amplitude
A_0	Free amplitude of oscillation
d	The deflection of cantilever (nm)
E	Young's modulus (GPa)
E_s	Separation energy
F	Force (nN)
F_{adh}	Adhesion force (nN or pN)
h	Indentation depth (nm)
k	The cantilever spring constant (N/m)
r_{sp}	Ratio of set point amplitude and free amplitude of oscillation (A/A_0)
R	Tip radius (nm)
Z_{defl}	cantilever deflection (nm)
Z_{pos}	z-piezo movement (nm)
α	Half of the pyramidal angle of the indentor
β	= 2 for elastic deformation of a sphere and $(\pi/2)^2$ for pyramidal and conic shapes
Δ	Cantilever deflection at the point where the probe loses contact with the surface
ν	Poisson's ratio

3.302.1. Introduction

The atomic force microscope (AFM) is a member of a broad family of scanning near-field tools generally known as the scanning probe microscopes (SPMs). The primary distinguishing feature of SPMs is that the measurements are performed by bringing a small probe to close proximity with a surface, and the surface is then scanned, generating a contrast map. The first microscope in the SPM class was the scanning tunneling microscope (STM), invented by Binnig and Rohrer in 1981,[1] and the STM quickly demonstrated the imaging of surface structure with true atomic resolution.[1,2] Binnig and Rohrer were awarded the Nobel Prize in 1986 for the development of the STM. The STM uses the tunneling current between probe and sample to make maps of the surface structure, including the ability to resolve single atoms as noted. One central limitation of the STM is that the surface of the sample must be conductive. This limitation contributed to the development of the AFM in 1986.[3] The AFM uses a very sharp probe to measure and map the morphology of nearly any surface, without the limitation of conducting surfaces. This development quickly attracted the attention of the biophysical community and led to the development of a variety of high-resolution imaging techniques applicable to biological systems.[4–7] Although the initial emphasis of the AFM was primarily on improved imaging resolution in physiologic environments, it was soon recognized that the AFM had the capacity to be much more than just a high-resolution microscope. The possibilities for localized spectroscopic analysis, direct and selective surface modification, and molecular manipulation gave rise to a variety of technological breakthroughs across the realm of AFM use.[8,9]

One of the most important advantages of the AFM for biomaterials and biological applications is that measurement of samples can be performed under physiologically relevant conditions without complex sample preparations. This is significantly different from techniques such as the scanning electron microscopy (SEM) and the transmission electron microscopy (TEM), which generally operate under high vacuum, and must necessarily operate under high vacuum for very high-resolution imaging. Within the biomedical field, innumerable biological samples have been investigated, ranging from smallest biomolecules such as DNA,[10,11] proteins,[12,13] lipids,[14,15] and polysaccharides[16,17] all the way up to living cells[18–21] and tissues,[22,23] to name just a few. The focus of these studies is not just high-resolution imaging of structural properties, but also measurements of the mechanical, chemical, and functional properties[24] of these biological materials. Moreover, biological events can be observed in near real time by AFM, offering unparalleled opportunities for investigating dynamic, biochemical, and physiological processes while simultaneously acquiring structural and functional information on the materials,[25] for example, receptor–ligand interactions[26,27] and biological adhesion phenomena at material surfaces.[28]

The development of these AFM techniques has made a considerable impact across the many disciplines of biomaterials research.[25] Surface properties are known to play a major role in determining the host response to a biomaterial,[29,30] whether it be orthopedic, neural, vascular, or other soft tissues, as the molecular interactions occurring at the interface between material and host (protein adsorption, surface-induced thrombosis, cell–surface interactions, and tissue integration among others), are important determinants of the ultimate biologic response to a biomaterial.[31–33] The AFM provides unique opportunities for visualizing these and other surface-dependent cellular and molecular interactions in three dimensions, on a nanometer scale, and under physiological conditions. This chapter introduces the principles of the AFM techniques and their application to biomaterials research. Examples of selected studies of the structural properties of biomaterials as well as the dynamic biological properties and responses of biomaterials will illustrate the utility of the technique. Common concerns in optimizing AFM experiments as well as the future potential of the AFM in biomaterials research are also discussed.

3.302.2. Fundamentals of the AFM

3.302.2.1. Principles of AFM

Fundamental details of the AFM as related to instrumental aspects can be found throughout the literature.[34–36] This section briefly describes the most standard operating principles of the AFM and summarizes some of the common operating modes with examples of research that are likely to be of interest to the biomaterials scientific community.

The most common basic configuration of an AFM is shown schematically in Figure 1. The primary components of a typical system include a probe mounted at the end of a microcantilever that scans over the surface and detects a physical property that provides a contrast mechanism; a piezoscanner that controls the probe–surface separation and provides motion across the x, y, z directions, generally with angstrom-level accuracy; and a feedback electronic system that monitors and controls the probe near the surface. For topographic imaging, this control mechanism usually involves holding the probe at a preset vertical separation distance between the tip and surface. As the probe scans over the surface and interacts with the sample, the microcantilever deflects in response to some desired contrast

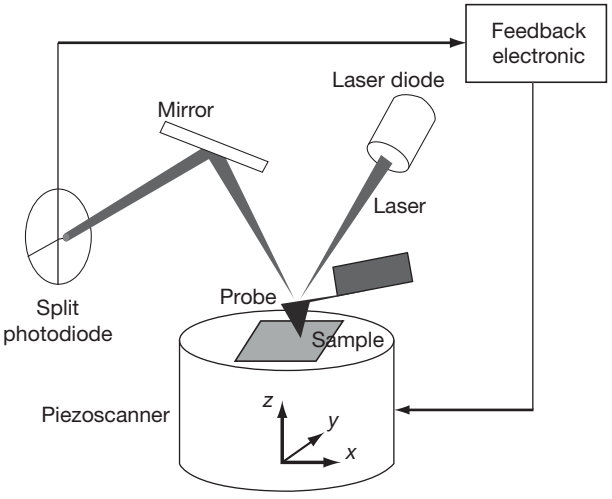

Figure 1 Schematic of the basic atomic force microscope configuration.

mechanism. The tip–sample interaction is commonly monitored by a laser beam targeted to the back of the cantilever. The beam is reflected toward a multisegment photodetector, configuring an optical lever which amplifies the sub-nanometer-level cantilever deflections. This interaction between the probe and sample is measured at each scanning point of a two-dimensional (2D) (X,Y) matrix, and when coupled with the recorded interaction forms a 3D reconstruction of the sample. In many designs, an optical microscope is coupled with the AFM to locate the position of the cantilever and to simultaneously acquire an optical image of the sample. Of course, some variations to this basic setup exist. For example, in some cases, the piezoscanner may directly raster the probe so that an optical system can be included in the setup. There are a multitude of variations and combinations of these systems, and the reader is encouraged to consult the literature for specific designs of interest.

The scanning probe is in large part the central component of the AFM, and serves as the method by which the various contrast mechanisms are achieved. The standard topographic imaging AFM probe consists of a sharp tip attached at the end of a flexible cantilever. The shape and sharpness of the tip are important in the ultimate resolution of the image obtained. The most common cantilevers are fabricated by photolithographic processes, using standard semiconductor materials such as Si, SiO_2, or Si_3N_4. The use of carbon nanotubes as ultrafine AFM probes represents a breakthrough in terms of resolution and accuracy.[37,38] Carbon nanotube probes, possessing a high aspect ratio and ultrasharpness, reduce the artifacts associated with imaging surface features.[39] Both standard semiconductor-based probes and carbon nanotube probes can be chemically functionalized, and nanotubes are sometimes regarded as important probes for biological applications of the AFM, particularly for the study of structural biology. However, a limitation of the ultrasharp tip is that the high pressures produced may damage delicate biological samples. Colloidal probes have been used for force and mechanical property measurements after attaching a sphere of known size to the end of the cantilever.[40] These spherical particles have a well-defined radius, can be glass, polymer, or other materials, and are often easy to modify with chemical functional groups or biomolecules. As a result, colloidal probes are often used to directly measure surface–surface interaction forces, colloidal interactions on the single particle–particle level, cellular mechanics, and adhesion forces under a variety of conditions.[40–43] AFM probes can be conductive, magnetic, or wear resistant, depending on the operation mode and the specific properties that one wishes to measure.

The appropriate choice of cantilever and probe is dependent on the imaging mode and the characteristics of surface features of interest. The stiffness of the cantilever should be as low as possible when the AFM is operated in contact mode to avoid damage to the sample, whereas in dynamic imaging modes, the higher spring constant values of the cantilevers may help reduce noise and instabilities. Commercially available silicon nitride and silicon probes may be satisfactory for many applications using contact and dynamic imaging modes, respectively. Another important criterion for choosing a probe is minimization or avoidance of the most common artifacts in imaging generated from the tip geometry, as illustrated in Figure 2.[44–47]

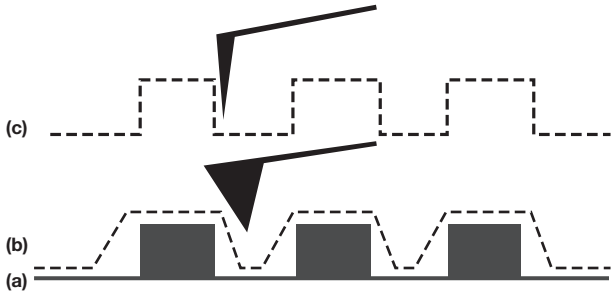

Figure 2 Artifacts can arise from atomic force microscope imaging as a result of the tip geometry. (a) The actual topography, (b) the image produced by a typical pyramidal probe showing an enlargement artifact, and (c) the surface as measured by an ultrasharp, high aspect ratio probe showing less enlargement.

The spring constant of the cantilever represents yet another important parameter of the AFM probe that should be considered, particularly for making measurements of interaction forces. Typical spring constants for commercial AFM cantilevers range from 0.001 to 100 $N\,m^{-1}$, enabling force sensitivity down to the piconewton level. Although manufacturers provide the nominal spring constants, actual spring constants are known to vary over wide ranges, even from the same batch of probes, with cantilevers fabricated from the same wafer varying by 10%. Fortunately, this issue was recognized early and techniques have been developed to directly measure the individual cantilever spring constants. These techniques can be grouped into three general categories: (1) dimensional models where theoretical models or semiempirical formulas are used to calculate the cantilever spring constants on the basis of their dimensions, geometry, and material properties[48,49]; (2) static deflection measurements where the spring constant is determined by loading the cantilever with a known force[50,51]; and (3) dynamic deflection measurements where the resonance behavior of the cantilever is related back to its spring constant.[52–55] Other methods may sometimes be used in specific situations; for example, the hydrodynamic drag force can be used to determine the spring constant of the colloidal probe cantilever.[56]

3.302.2.2. Contact Mode Imaging

As mentioned, a wide range of AFM operating modes can be used to examine different structure–property relationships under ambient or aqueous conditions. The most common (and original) mode of AFM imaging is termed contact mode. In this mode, the probe is brought into gentle contact with the sample surface so that the force between the probe and sample is repulsive. As the scanner gently traces the tip across the sample, the contact force causes the cantilever to deflect. Often, a Z-feedback loop is used to maintain a constant cantilever deflection, although for some high-resolution, small-area imaging applications, one might turn off this feedback loop. Images are created by recording the piezovertical position required to keep the force constant against the laser probe position if the feedback loop is on, or simply monitoring the cantilever deflection if the loop is off. Contact mode can be operated under aqueous environments, which remove the capillary forces seen in

ambient environments as a result of thin water films on probe and sample, thereby reducing the interaction forces and potentially minimizing tip-induced damage.[57]

Contact mode imaging is generally suitable for samples that are flat and rather rigid, for example, fixed cells, hard inorganic surfaces, metals, and common polymeric biomaterials such as polyethylene, PTFE, silicone, and polyurethane elastomers.[58] However, the shear forces applied to the sample during contact mode imaging can be sufficient to disrupt a delicate sample or sweep an adsorbed molecule to the periphery of the imaging area.[59,60] As a result, contact mode is often deemed unsuitable for reliable imaging of isolated proteins, live cell surfaces, or low modulus biomaterials under aqueous conditions.

When the probe scans the surface in contact mode, a torsion or twist of the cantilever arises from the lateral forces applied by the sample onto the probe, resulting in a deviation in the signal striking the two lateral segments of the photodiode. This operation mode is usually referred to as lateral force mode or lateral force microscopy (LFM),[61,62] and the torsion of the cantilever scanning across the surface yields information arising primarily from changes in surface friction (chemistry) and changes in surface slope (topography). To separate these effects, LFM and AFM images are often collected simultaneously. LFM allows identification of heterogeneities in materials, thin films, or monolayers at high spatial resolution, and illustrates the frictional properties of polymers,[63–65] although quantification of friction forces can be difficult. The use of a chemically modified probe to measure the difference between areas of a surface having distinct chemical properties is also referred to as chemical force microscopy.[66] This technique has been shown to be useful to map the chemical properties and even the different compositions of the surfaces of block copolymers.[67–69]

3.302.2.3. Dynamic Imaging Modes

3.302.2.3.1. Intermittent-contact imaging

As mentioned previously, contact mode imaging can result in the development of lateral forces associated with the raster scanning of the probe against the sample. To overcome this problem, a number of dynamic imaging modes have been developed.[70] One of the most commonly used of these is the intermittent-contact mode. A second piezoelement is used to oscillate the cantilever near its resonance frequency while the oscillation amplitude is monitored. The deviation of the magnitude of oscillation is measured as the cantilever approaches and contacts the surface. The cantilever's oscillation amplitude changes with sample surface topography, and a topography image is obtained by recording the feedback signal necessary to keep the amplitude of oscillation at a constant value. This intermittent-contact imaging is the most common dynamic mode, available on nearly all commercial instruments, and maps topography by lightly touching the surface with an oscillating probe tip. In this mode, the tip experiences both attractive and repulsive forces with the sample during oscillation,[71,72] and as the tip is only intermittently in contact with the sample, the lateral forces are greatly reduced.

Intermittent-contact mode can be performed in either ambient or aqueous conditions and has proved to be the most successful mode for high-resolution imaging of soft or delicate samples such as proteins and cell surfaces under aqueous conditions.[73–76] A representative example of proteins studied by intermittent-contact mode AFM on a surface is fibrinogen adsorption.[77] Fibrinogen is the third most abundant protein plasma in blood and plays a prominent role in platelet adhesion and development of surface-induced thrombosis. **Figure 3** shows images of fibrinogen on a hydrophobic graphite surface and hydrophilic mica surface, with both images obtained under phosphate buffer. The 3D trinodular structure of fibrinogen is clearly visible and the dimensions of adsorbed molecules can be measured.[73] The conformational structure of protein adsorbed on the material surface is known to be influenced by substrate surface property but also changed with adsorption time.[78,79] In the case of fibrinogen shown here, the operation of intermittent-contact mode in an aqueous environment provided the possibility to directly visualize the time-dependent conformational changes of this protein by measuring changes in the heights of the individual domains of the molecule.[73]

3.302.2.3.2. Force modulation and phase imaging

3.302.2.3.2.1. Force modulation

Force modulation and phase imaging comprise the second type of dynamic force microscopy. Force modulation imaging is a variation of the contact mode AFM technique, which can be used to identify and map differences in surface stiffness or elasticity.[80] The probe in force modulation mode scans in

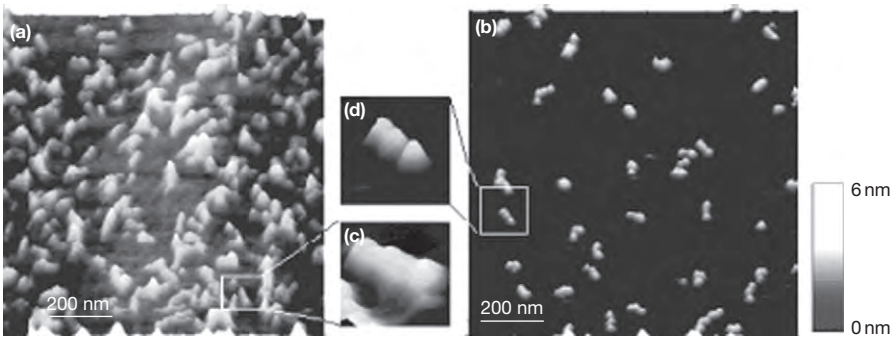

Figure 3 Molecular-scale atomic force microscope images of fibrinogen on (a) hydrophobic HOPG and (b) hydrophilic mica surfaces. (c, d) Higher magnification images of individual fibrinogen molecules illustrating the trinodular structure. The *z*-scale for (a) and (b) is 6 nm and 3 nm for (c) and (d). Reproduced from Agnihotri, A.; Siedlecki, C. A. *Langmuir* **2004**, *20*(20), 8846–8852.

contact with the surface, but has a superimposed secondary vertical sinusoidal oscillation (modulation) that is significantly faster than raster scan. The force applied on the sample or cantilever is modulated so that the force is equal to that in contact mode. The variation (RMS) in cantilever deflection amplitude at the frequency of modulation can be used to obtain information on the mechanical properties of the sample. Topographical information is collected simultaneously with force modulation data. Force modulation has been used to characterize mixed composite and polymer blends as well as phase-separated block copolymers.[81,82]

3.302.2.3.2.2. Phase imaging

Phase imaging is a secondary imaging mode derived from the intermittent-contact mode that goes beyond the topographical data to characterize variations in composition, adhesion, friction, viscoelasticity, and other properties for a multitude of sample types.[70] Phase imaging monitors the phase lag between the periodic signal that drives the cantilever near resonance and the resulting oscillation of the cantilever. Changes in this phase lag are indicative of changes in the properties of the sample surface. Phase imaging has been a powerful tool in surface characterization of biomaterials, as the phase image is able to detect subtle chemical and mechanical variations in materials and can reveal more detailed surface properties than topography alone.[83,84]

An important application of phase imaging in biomaterials science is differentiating between the component phases of composite materials, including biomaterial stalwarts such as polyurethane (PU) copolymers.[85] PU materials are segmented block copolymers constructed from a mixture of 'soft' and 'hard' segments. These materials are frequently used in a variety of blood-contacting medical devices because of their desirable mechanical properties, fatigue resistance, and acceptable hemocompatibility for many applications, including circulatory support devices, vascular grafts, and heart valves.[86] **Figure 4** illustrates topographic and phase images of a PU material in an ambient environment.[87] The PU film surface appears relatively smooth across the $500 \times 500\text{-nm}^2$ scan area, with only a few occasional topographic features observed, whereas the distribution of the microphase structures can be clearly visualized from the phase image. In this image, high phase angle (light colors) represents the 'harder' regions, and these hard microphases appear as spherical or cylindrical features that are dispersed within a soft segment matrix. The lateral dimensions of the hard domains are 15–50 nm, similar in dimension to many plasma proteins such as fibrinogen.

Because phase imaging can be operated in physiological conditions, the technique provides an excellent opportunity for detection of dynamic reorientation in polymers during hydration. By collecting a series of sequential *in situ* phase images of a PU film following hydration in phosphate-buffered saline, hard domains were observed undergoing reorientation and enrichment at the surface.[88] It should be noted that the phase detection is affected by the force applied by the scanning probe to the polymer surface, which is presented by the ratio of set point amplitude and free amplitude of oscillation ($r_{sp} = A/A_0$).[89,90] **Figure 5** shows phase images of a PU material under increasing tapping forces.[87] At a very light tapping force (**Figure 5(a)** and **5(b)**; $r_{sp} = 0.95$ and 0.90, respectively), few phases are observed, suggesting the presence of a soft segment overlayer on the surface. As the imaging force increases (**Figure 5(c)** and **5(d)**; $r_{sp} = 0.85$ and 0.75, respectively), randomly oriented cylindrical and spherical structures are observed, indicating that hard domains are being detected in the subsurface region. This increasing tapping force can be used to sequentially probe deeper into a sample and to examine vertical sections.

AFM topographic imaging of adsorbed proteins is generally limited to smooth model substrates such as mica, graphite, silicon, and gold and polished metals. The inherent roughness of traditional biomaterial surfaces such as polymers has largely prevented observation of adsorbed proteins in topographic images. Phase imaging provides information on differences

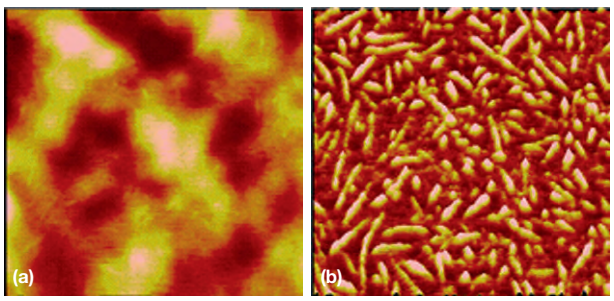

Figure 4 Atomic force microscope (a) topographic and (b) phase images of polyurethane in air. Scan size: $500 \times 500\,\text{nm}^2$; scale: height 50 nm, phase 25°. Reprinted from Xu, L. C.; Soman, P.; *et al. Atomic Force Microscopy Methods for Characterizing Protein Interactions with Microphase-Separated Polyurethane Biomaterials*. Springer: Heidelberg, 2009.

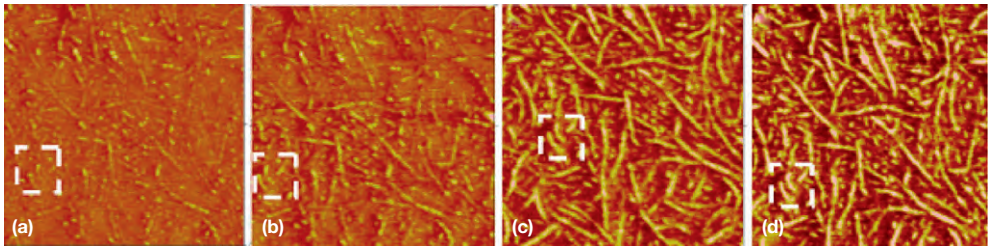

Figure 5 Atomic force microscope phase images of polyurethane under increasing tapping forces. Scan size: $500 \times 500\,\text{nm}^2$; scale: 25°. The box indicates a reference feature common in all images: (a) $r_{sp} = 0.95$; (b) $r_{sp} = 0.90$; (c) $r_{sp} = 0.85$; (d) $r_{sp} = 0.75$. Reprinted from Xu, L. C.; Soman, P.; *et al. Atomic Force Microscopy Methods for Characterizing Protein Interactions with Microphase-Separated Polyurethane Biomaterials*. Springer: Heidelberg, 2009.

in material properties of the surface, and offers the possibility to distinguish the adsorbed protein molecules from the underlying polymer surface. Holland and Marchant[91] reported imaging of fibrinogen molecules adsorbed on National Heart Lung and Blood Institute reference materials polydimethylsiloxane (PDMS) and low-density polyethylene (PE) *in situ* using phase imaging AFM. However, it was shown to be difficult to observe the individual proteins adsorbed on the microphase-separated polyurethane biomaterials because of the strong phase signal from hard and soft domains, and the comparable dimensions of fibrinogen and hard domains.

An alternative approach to detect protein adsorption on rough materials is to add a label to the proteins that can be detected by the AFM probe. For example, nanogold particles with well-defined dimensions are suitable for labeling proteins and are easily detected by AFM phase imaging. Figure 6 illustrates the topography and phase images of a PU film following adsorption of bovine serum albumin (BSA) conjugated with 6-nm nanogold particles. The protein-conjugated nanogold particles are detected in the phase image, allowing quantitative measurements of the labeled proteins to the different phases. The data showed that more proteins were adsorbed to soft regions of polymer, suggesting that the macrophase separation properties of polymer appear to be linked to local surface chemical properties (hard and soft domains) and proteins preferentially adsorb to soft segments. Similar gold label techniques were used by Eppell to monitor ligand binding to platelets using multiple microscopy techniques.[92]

3.302.2.3.3. Noncontact imaging modes

The final mode of dynamic microscopy to be discussed is noncontact AFM. Similar to the intermittent-contact imaging discussed previously, in noncontact imaging, the cantilever is oscillated near its resonance frequency, but in noncontact mode, the probe does not contact the sample.[93] As the probe tip approaches the sample, force gradients arising from van der Waals, electrostatic, or magnetic forces lead to shifts in the cantilever resonance frequency, which can be measured using either frequency or amplitude detection techniques.[94,95] The applications of noncontact AFM include electric force microscopy (EFM) and magnetic force microscopy (MFM). EFM provides the possibility for investigating the surface electrical characteristics, including localized charge distribution on surfaces and biomolecules,[96] surface potential, and doping profiles. MFM measures the gradient of the magnetic field of the material surface, and is mainly applied in magnetic data storage or micro-/nanomagnetic materials.

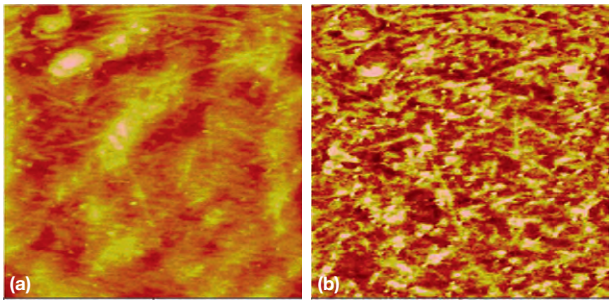

Figure 6 Atomic force microscope images of bovine serum albumin conjugated with 6-nm nanogold labels, adsorbed on polyurethane and imaged under PBS buffer. Gold beads are seen in both height (a) and (b) phase images. Quantification reveals a more than twofold increase in number of labeled proteins per unit area on the soft segment regions compared to the hard segment. Scan size: $500 \times 500\ nm^2$; scale: height 25 nm, phase, 10°. Reprinted from Xu, L. C.; Siedlecki, C. A. *J. Biomed. Mater. Res. A* **2010**, *92*(1): 126–136.

3.302.3. Force–Distance Measurement and Force Mapping

3.302.3.1. Force–Distance Curve

The interests of the biophysical and biomaterial communities in the potential of the AFM did not arise solely from the high-resolution imaging capabilities of this technique, but also because AFM offers the unique possibility of obtaining quantitative information on intra- and intermolecular forces at the single molecule scale.[8] This mode of operation is generally termed a force–distance measurement, and detailed interpretation and application can be found in the literature.[97,98] Briefly, the force curve produced by these measures shows the cantilever deflection measured as a function of the relative probe motion as it approaches and then retracts, or separates, from the surface. An example of a typical force–distance curve is shown in Figure 7. Starting from the right (position A), the probe is far from the sample and no interaction is detected. As the probe approaches the surface (moving toward the left side of the plot), long-range forces such as electrostatic and hydrophobic forces can be detected. When the probe reaches position B, the attractive force increases because of van der Waals forces, until the force gradient becomes greater than the spring constant of the cantilever and the probe jumps to contact with the sample (position C) with the cantilever bending downward (negative, or attractive force). After contact, the probe begins to compress the sample, and as the probe moves farther, an upward deflection of the cantilever (positive, or repulsive force) is measured. This contact region of the force curve can be used to measure the elastic properties of the sample. Eventually, the sample and probe begin separating. The cantilever deflection will move largely down the same path, although some hysteresis in the piezoposition might be expected.

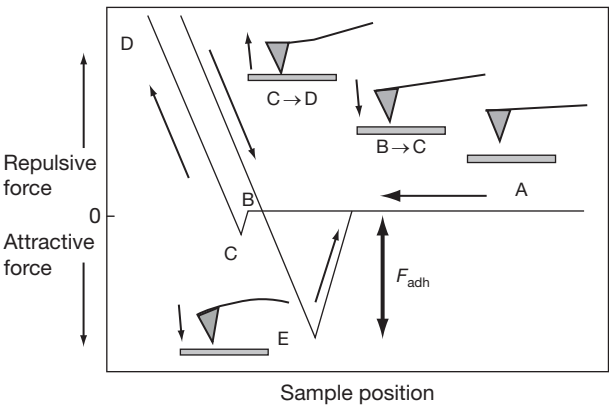

Figure 7 Schematic of a typical force–distance curve. The images illustrate typical cantilever deflections in each region of the curve.

Adhesion between the probe and the sample leads to an additional deflection of the cantilever downward until the adhesion force is overcome by the cantilever restoration force, and the probe separates from the surface. This additional downward deflection of the cantilever is the value that is most often measured as the adhesion force or debonding force. The AFM typically measures the cantilever deflection as a function of the z-piezodisplacement, which differs from the actual tip–sample distance. However, by subtracting the cantilever deflection from the z-piezomovement, the actual tip–sample displacement can be calculated (Figure 8).

A deflection–position force can be converted to a force–distance curve force via Hooke's law: $F = -kd$, where k is the cantilever spring constant and d is the deflection of the cantilever during imaging; thus, quantitative information on the interaction between an AFM probe and a surface can be extracted from force curves. Further, the AFM probe can be modified with specific functionalities, including chemical groups, ligands, proteins, and other biomolecules. This capacity enables the measurement of fundamental interactions between biological molecules such as proteins and a biomaterial surface,[99,100] and assesses ligand and receptor intermolecular bond strengths for cells on materials, for example.[101] Generally, long-range and short-range forces and the elasticity of the sample can be obtained from the approach portion of the curve, and intermolecular interactions such as adhesion force or debonding force measured from the retracting portion.

A variety of parameters can be obtained from the retracting portion of the force curve (Figure 8). The adhesion force (F_{adh}) is usually defined as the force at maximum cantilever deflection during separation from the surface. A pull-off or rupture length is the distance that the tip moves from the zero interaction force during separation to the position where the probe has separated and returned to zero deflection. The separation energy, E_s, is obtained by integration of the force holding the probe to the surface and the distance moved by the cantilever during probe separation from the surface. Each force at each point, $F_{s,i}$, is calculated for a scan split into n intervals, whereas the distance moved by the cantilever in each interval is $l = L/n$, where L is the total scanning distance between the start of approach and subsequent reversal. The total separation energy is thus calculated as the total area in the attraction-force region (shadow area in Figure 8) in a retracting curve as

$$E_s = \sum_{i=1}^{a} lF_{s,i} = -\sum_{i=1}^{a} lkd_{d,i}$$

3.302.3.2. Force Mapping

Maps of the distribution of intra- and intermolecular forces can be collected over the sample scanning area. Individual force curves are obtained at unique x–y positions on the sample, so that interaction forces can be measured at each location. This array of force curves forms a 3D force map, illustrating the distribution of any particular interaction of interest. For example, most simply, an array of adhesion forces extracted from force–distance curves would produce an adhesion map of the sample. Through selective modification of the AFM probe, this adhesion map can be tailored to isolate a particular interaction, thereby showing the distribution of an otherwise unknown entity. Figure 9 illustrates a schematic representation of adhesion mapping of proteins in a multicomponent protein layer on a material surface. In this case, the probe is modified with an antibody of interest, and interactions between the antibody-modified probe and the substrate demonstrate the presence of the desired antigen.

3.302.4. Nanoindentation and Measurement of Near-Surface Nanomechanical Properties of Polymeric Biomaterials

Information on the elasticity and other mechanical properties of a biomaterial surface or biological sample can be obtained from the approach, or compression, region of the force curve. Once the probe comes into contact with the surface, continued compression will lead to sample indentation. The indentation depth (h) can be calculated from the z-piezomovement (Z_{pos}) and the cantilever deflection (Z_{defl}) as

$$h = Z_{pos} - Z_{defl}$$

By measuring the amount of indentation at a given force, the local elasticity of the sample in terms of the Young's modulus

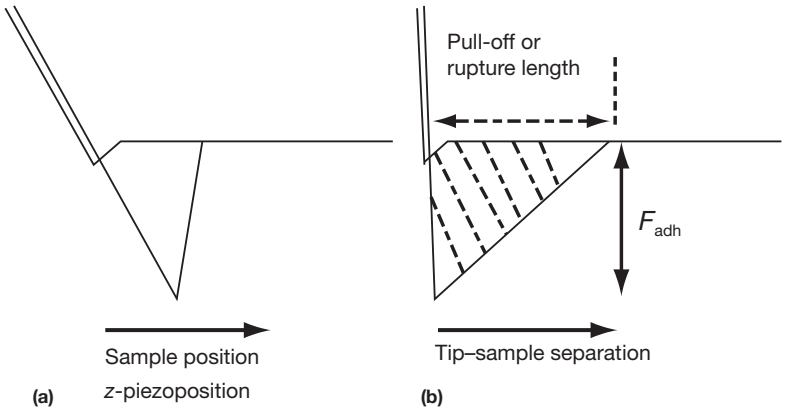

Figure 8 Conversion of a force curve (a) as a function of z-piezomovement and (b) as a function of probe–sample separation. The shaded area is used for calculation of separation energy.

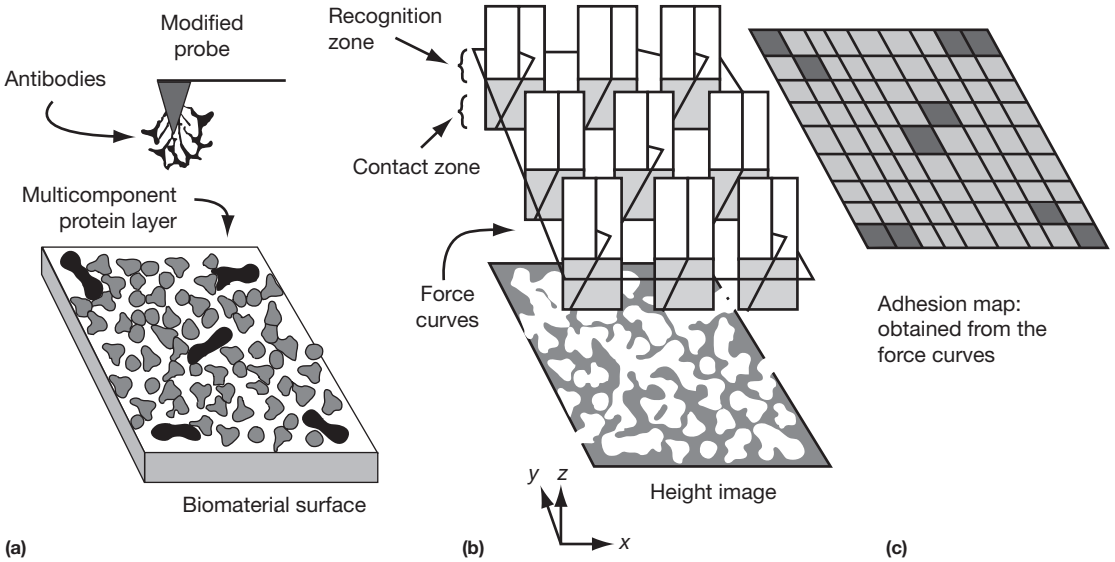

Figure 9 Schematic representation of adhesion imaging. (a) A functionalized probe scanning a multicomponent surface, (b) a topography image and array of force curves are obtained across the surface, and (c) an adhesion map is generated by calculating the strength of adhesion from individual force curves.

can be obtained from various classic models, including the Hertzian, Johnson, Kendall, Roberts, and Sneddon's.[102,103] Derivation of Young's modulus from the Hertzian model gives

$$E = \frac{3}{4}(1-\upsilon^2)\frac{k}{R^{1/2}}\frac{Z_{\text{defl}}}{h^{3/2}}$$

where v is Poisson's ratio, k is the spring constant of cantilever, and R is the tip radius, and the JKR model gives:

$$E = \frac{9}{4}(1-\upsilon^2)Rk\Delta\left[\frac{P_1}{3Rh}\right]^{3/2}$$

where $P_1 = (3P_2 - 1)[1/9(P_2+1)]^{1/3}$, $P_2 = (Z_{\text{defl}}/\Delta + 1)^{1/2}$, and Δ is the cantilever deflection at the point where the probe loses contact with the surface.

Sneddon's model accounts for the particular geometry of the indenter:

$$E = \frac{\sqrt{\pi}}{2\sqrt{2}\beta\tan\alpha}(1-\upsilon^2)k\frac{\Delta Z_{\text{defl},i,i-1}}{h\Delta h_{i,i-1}}\ (\text{pyramidal indenter shape})$$

$$E = \frac{1}{2\sqrt{R}\beta}(1-\upsilon^2)k\frac{\Delta Z_{\text{defl},i,i-1}}{\sqrt{h}\Delta h_{i,i-1}}\ (\text{parabolic indenter shape})$$

where $\beta = A_{\text{cros}}/A$, A_{cros} is the cross-sectional area of the indenter at the indentation depth h from the apex, β is equal to 2 for elastic deformation of a sphere and $(\pi/2)^2$ for pyramidal and conic shapes, α is half of the pyramidal angle of the indentor, and i, $i-1$ refers to the adjacent indentor displacements. Chizhik *et al.*[102] tested the elasticity of polyisoprene rubber, polyurethane, polystyrene, and polyvinylchloride by these models, and found that Sneddon's and Hertzian elastic models gave consistent results at indentation depths up to 200 nm, and were close to the JKR solution. The Hertzian model is relatively simple and does not require additional assumptions or measurements of interfacial energies as needed for the JKR theory. This model is often selected for calculation of elasticity of polymeric material[104] and cell surfaces.[105]

Figure 10 illustrates representative indentation and modulus curves for one region of a PDMS homopolymer surface as well as a segmented polyurethane material. In this example, the modulus is being measured at various indentation depths by looking at the local deformations of the cantilever as the probe compresses the surface. The PDMS is a uniform, single component polymer and used as a reference sample here. The data shows a uniform modulus down to approximately 50 nm indentation depth, and that the indentation curve increases with applied force in an approximately linear manner. The polyurethane material exhibits marked differences in the indentation depth and modulus profiles compared to the PDMS (Figure 10(b)). As the polyurethane copolymer contains both soft and hard phases, a nonuniform indentation depth curve is expected, and measurements of the indentation depth and modulus curves confirm a soft segment overlayer on the material surface, with the thickness of the soft overlayer being about 5–10 nm in this case. Once the soft segment overlayer is penetrated, hard segments with a high modulus are encountered in the sample.

As discussed previously, the AFM can be used to acquire an array of force–distance curves across the surface during scanning. Each force curve can be extracted and analyzed to produce a modulus profile as a function of indentation depth, as shown in Figure 10. By combining this depth sampling with an array of force curves across a small area, a modulus map for different subsurface depths was created, as shown in Figure 11. This figure illustrates the material modulus across a hydrated (1 h) polyurethane material at indentation depths of 3, 5, 7, 9, and 11 nm. The warmer colors in the maps represent higher modulus ('hard' segment regions) while the cooler colors represent lower modulus ('soft' regions). These modulus maps demonstrate the presence of an outer soft segment-rich layer for the 1-h hydrated sample, and as the sampling depth increases, more hard regions (higher modulus) are detected. Through measurements of polyurethane materials with

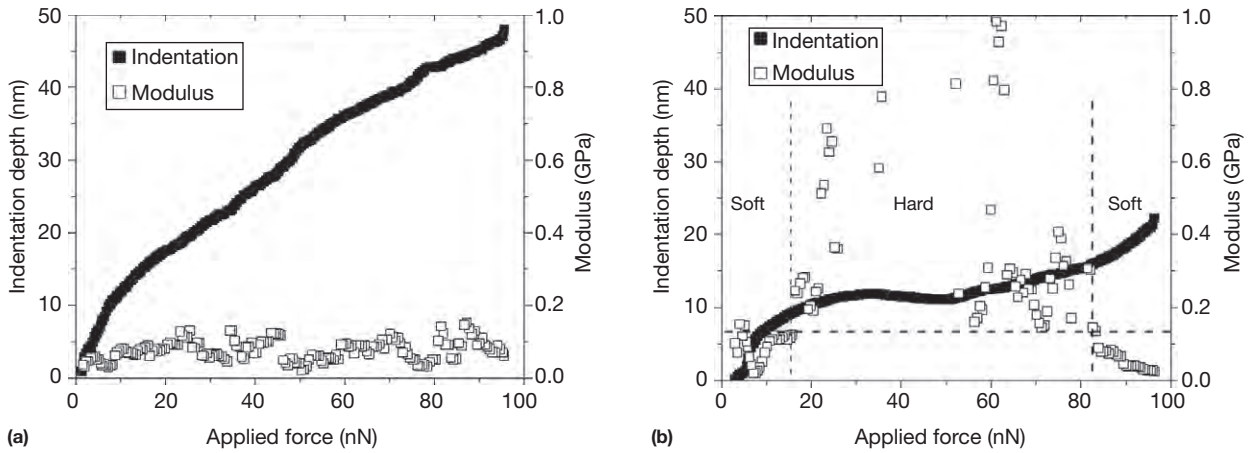

Figure 10 Representative indentation and modulus curves for (a) polydimethylsiloxane and (b) a polyurethane material, as functions of applied force. Reprinted from Xu, L. C.; Runt, J.; *et al*. *Acta Biomater*. **2010**, *6*(6), 1938–1947.

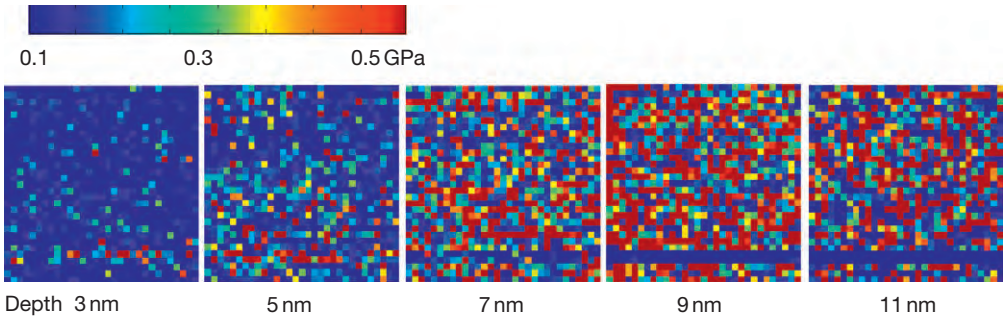

Figure 11 Depth-dependent modulus maps for a polyurethane material at 3, 5, 7, 9, and 11 nm following hydration in PBS for 1 h. Reprinted from Xu, L. C.; Runt, J.; *et al*. *Acta Biomater*. **2010**, *6*(6), 1938–1947.

different hydration times, dynamic phase restructuring can be observed as changes in hard domain distribution.

3.302.5. Probing Molecular Interaction and Recognition Sites on Biosurfaces

The retraction, or separation, portion of force–distance curves allows measurement of a wide variety of interactions between a probe and a surface at or near the single molecule level. This ability enables measurements of the interactions of proteins and surfaces if the probe is appropriately modified with proteins of interest. Using this tool, one can explore the adhesion (adsorption) properties of proteins on material surfaces, or by using a probe modified with a specific functionality such as an antibody or a ligand, AFM allows detection or recognition of proteins and binding sites on biosurfaces (e.g., biomaterials, microbial cells). These techniques can be useful for studying the conformation, orientation, and activity of adsorbed proteins on surfaces.

3.302.5.1. Modification of AFM Probes

As AFM probes are generally fabricated from silicon-based semiconductor materials, there are a number of standard approaches available for probe–surface modification.[106,107] Chemically functionalized tips can be obtained by modifying their surface self-assembled monolayers (SAMs) terminated by specific functional groups. The SAMs can be formed on standard silicon and silicon nitride probes directly through surface modification with silane-based monolayers, or alternatively probes can be coated with a thin layer of gold so that alkanethiol-based systems can be used. These modified probes may be used to directly map surface chemical/physical properties, such as mapping the hydrophobicity of a surface,[108] or used as the substrates for subsequent biological modification.

Functionalizing of probes with proteins or other relevant biomolecules is an essential step for molecular interaction measurements.[109] The first functionalized biological AFM probe was used to measure the interactions between biotin and avidin.[110] The silicon nitride probe was incubated with biotinylated BSA solution overnight, and then the adsorbed biotinylated BSA was subsequently exposed to avidin. A second approach to preparing biological probes involves the use of the chemically modified probes. Proteins or macromolecules having thiol groups can be directly immobilized on gold surfaces, or biomolecules can be attached through standard coupling chemistries using, for example, carbodiimides and *N*-hydroxysuccinimide (NHS).[111] Amine functionalization[112] of probes allows for simple coupling approaches such as glutaraldehyde coupling, which has been

shown to allow proteins sufficient mobility and flexibility to rotate and orient themselves for binding and identification.[113]

Cells can be directly placed onto AFM probes for measuring interactions with surfaces. Bacterial cells have been immobilized using glutaraldehyde treatment to create covalent cross-links between the cells and the probe,[114] by attaching single cells using a small amount of glue,[115] or by physically adsorbing onto poly-L-lysine-coated tips.[116] Using any of these methods, the cells can be used to make measurements of interaction forces with surfaces, other cells, or immobilized proteins.

3.302.5.2. Measuring Adhesion Forces of Protein to Biomaterial Surfaces

Protein-modified AFM probes can be used to directly measure one of the most fundamental interactions in biomaterials science, the interaction forces between proteins and surfaces. Maps of these interactions can be used to determine the distribution of protein adsorption properties across a heterogeneous biomaterial surface, or to identify the location of protein adsorption/activity using biorecognition techniques. By combining the various techniques discussed so far in this chapter, it becomes possible to actually make direct measurements of the structure–function relationships in biomaterials. As an example, the compression region of the force curve provides information on material deformability or modulus, and at the same time, the separation region of the curve contains information on the adhesion of the probe with the surface at the same location. By combining techniques, the relationship between material microstructures (e.g., microphase structure in PU in this case) and protein interactions (the adhesion force) is obtained. Figure 12 displays the adhesion force map for an albumin-modified AFM probe, and the corresponding modulus map obtained simultaneously, for a hydrated PU film. In this figure, warm colors represent larger adhesion forces while cool colors indicate the smaller adhesion forces. The modulus map was generated from the compression region of the same force curves, and shows a distribution of hard and soft domains in the material. Strong correlations between the hard segment domains and low adhesion forces were clearly observed, as denoted by the white lines showing the overlay of the hard domain regions with the low adhesion force areas. The results provide direct evidence of decreased protein adhesion forces to the hard segment regions in PU, as one would expect on the basis of known material properties.

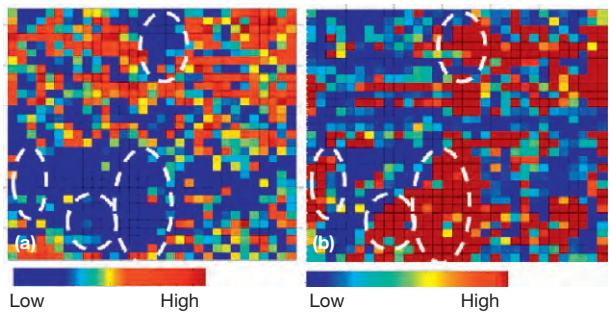

Figure 12 (a) Adhesion map and (b) modulus map of a polyurethane surface as measured by a bovine serum albumin-modified probe. Size: $500 \times 500\ nm^2$. Reprinted from Xu, L. C.; Siedlecki, C. A. *J. Biomed. Mater. Res. A* **2010**, *92*(1): 126–136.

3.302.5.3. Molecular Recognition of Proteins in Dual Component Protein Film

A critical step in using AFM to study protein adsorption at the molecular scale is the ability to detect specific proteins when numerous proteins simultaneously adsorb to the same material surface. Although molecular recognition of a specific protein might be feasible through topography alone on an ideally smooth surface, clinically used biomaterials have much rougher topographies, and it is difficult to detect proteins on these surfaces through standard imaging techniques, let alone identify different proteins.

Following the pioneering work on the biotin–avidin interaction, a variety of ligand–receptor forces have been measured at the single molecule level, including the forces between antibody and antigen for recognition purposes.[117] The group of Hinterdorfer and colleagues has led the way on this type of work, although their main emphasis has not been in the field of biomaterials. Antibodies are attached to probes using any of the methods described earlier, generating an AFM-based immunoassay with high spatial resolution, allowing for examination of multicomponent protein films on biomaterial surfaces without the tedious sample preparation necessary for

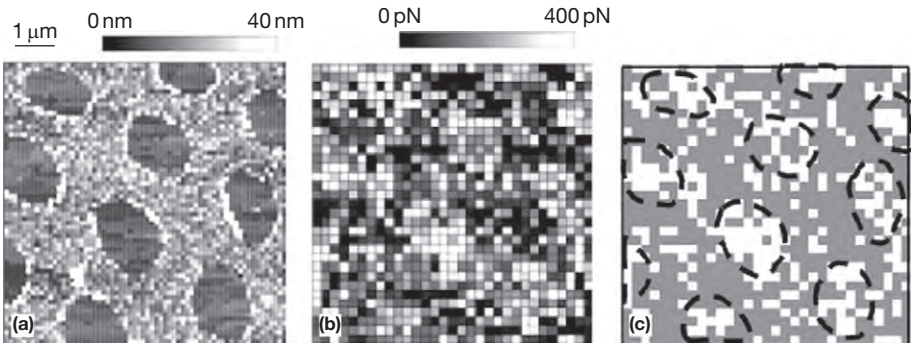

Figure 13 Images of microcontact printing patterned bovine serum albumin on mica after backfilling with fibrinogen. (a) Topographic image of the pattern, (b) adhesion map showing the interaction strength, and (c) binary recognition map showing fibrinogen recognition as white pixels and nonspecific interactions with bovine serum albumin as black pixels. Reprinted from Agnihotri, A.; Siedlecki, C. A. *Ultramicroscopy* **2005**, *102*(4), 257–268.

other techniques such as electron microscopy. Figure 13 illustrates an example of this work using proteins patterned into a known distribution. Albumin was patterned by microcontact printing on a mica surface, and fibrinogen was then allowed to adsorb into the nonpatterned areas (seen here as holes). An AFM probe coupled with a polyclonal antibody (pAb) against human fibrinogen was used to simultaneously measure both topography and interaction forces across the substrate surface. The adhesive force measured at each point is used to generate an adhesion map (Figure 13(b)) where the lighter regions showing higher adhesive forces correspond well with the holes in the height image, indicating the presence of fibrinogen in these regions. Control measurements were used to differentiate the nonspecific interaction of BSA and the antibody-modified probes from the specific fibrinogen–probe interactions, with that data being used to generate a binary recognition image showing the distribution of specific proteins (Figure 13(c)). This technique has subsequently been used to measure the distribution of fibrinogen on a series of PU biomaterials having different soft chemistry and hard segment contents.[87]

3.302.5.4. Measuring the Functional Activity of Adsorbed Proteins

The conformational structures and bioactivity of plasma proteins on biomaterial surfaces are important measurements for understanding the mechanism of biologic response to implants. While more traditional analytical techniques have been used to study the conformation, structure, and activity of proteins, these are generally not capable of providing the detailed level of information on proteins on surfaces under aqueous conditions, which the AFM can. Alternative approaches have used monoclonal antibodies (mAb) to detect the availability of specific functional regions in proteins.[78,118,119]

An example of the utility of combining probe microscopy with monoclonal identification techniques can be found in the study of fibrinogen. Fibrinogen is a central molecule in blood coagulation and thrombosis. It possesses three pairs of potential platelet-binding peptide sequences: two RGD sequences that are found in each of the Aα chains and a dodecapeptide sequence in each of the γ chains. There is ample evidence that the γ chain dodecapeptide sequence is the primary ligand for platelet binding to adsorbed fibrinogen. A commercially available mAb that recognizes the last 20 amino acids of the γ chain of fibrinogen (γ392–411) was coupled to an AFM probe, and interactions between this antibody-modified probe and fibrinogen were measured for a variety of substrates. Figure 14(a) illustrates the probability of the mAb against fibrinogen γ392–411 encountering the antigen in the platelet-binding region during any individual force measurement plotted as a function of fibrinogen residence time following exposure to a hydrophilic muscovite mica surface. The maximum likelihood of recognition occurred near 45 min, and decreased with increasing adsorption times. Time-dependent macroscale platelet adhesion measurements on the same muscovite mica substrates were carried out under similar experimental conditions.[120] Results illustrated in Figure 14(b) show that platelet adhesion similarly reaches a peak at ~45 min of fibrinogen residence time, correlating well with the molecular-scale AFM results and demonstrating the use of probe microscopy to measure protein function in single molecules.

3.302.6. Limitations and Perspectives

Despite the great potential of AFM in biomaterial research, there is still much to be improved for the AFM to be routinely used in applications beyond that of a characterization tool for surface topography. The outcome of AFM studies is dependent on several key factors, including the nature and quality of sample, the quality of probe used and methods for modifying/characterizing probe modifications, careful control of experimental conditions, the accuracy of data collection and robust methods for data interpretation, and attention to potential

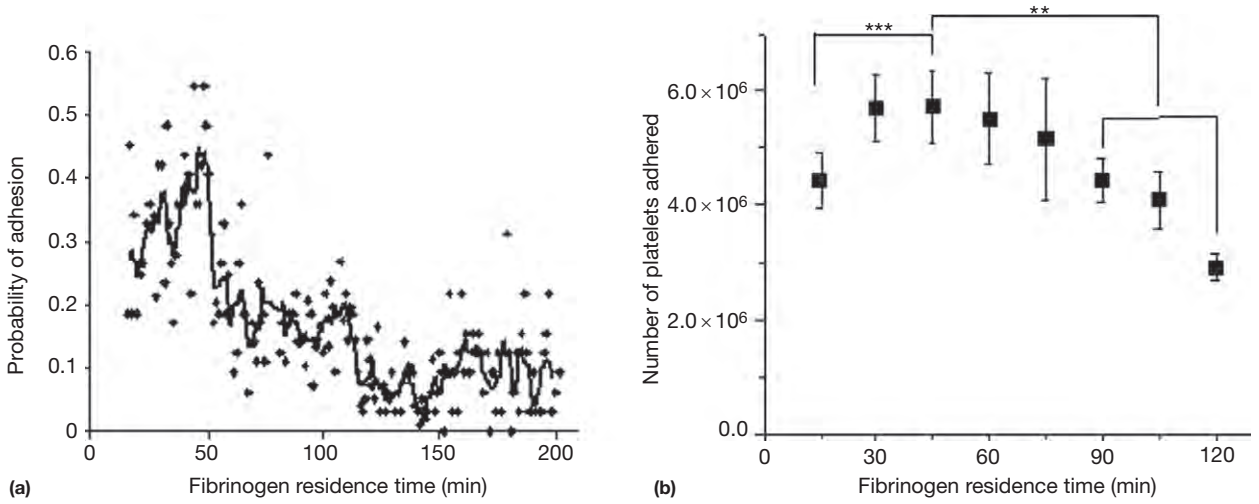

Figure 14 (a) Probability of interaction between a mAb against γ chain 392–411 and its antigen on fibrinogen measured by atomic force microscope. The solid line, the average of five points, is included for visualization purposes. (b) Platelet adhesion data from multiple experiments ($n \geq 6$ for each time point) showing changes in platelet adhesion as a function of fibrinogen residence time on mica substrates. Reprinted from Soman, P.; Rice, Z.; *et al*. *Langmuir* **2008**, *24*(16), 8801–8806.

artifact. Samples generally must be immobilized for scanning whether the sample is in an air or an aqueous environment. As a result, materials that are designed to minimize adsorption of proteins might not be suitable for AFM studies, a dichotomy in that these are the types of surfaces that are becoming increasingly important in biomaterials. While many studies of biomaterials are intended to understand how they influence biology, the immobilization of molecules either on the sample or on the probe may change the properties of these molecules in ways different from that in the biological environment. In force spectroscopy measurements, a modified probe may encounter the sample hundreds and even thousands of times, a situation vastly different from that found *in vivo* where it is usually an initial interaction that provides the impetus to biological response. Simple experimental factors such as probe loading force, loading rates, scanning rates, and contact time are all important parameters that affect the interaction forces and therefore may skew outcomes.[43,121] Experience is often necessary to understand how these factors affect the data obtained.

Although there are clearly important considerations to be kept in mind for all AFM work, the field has seen, and will continue to see, an increased use of novel, high-resolution AFM techniques for biomaterials science. Combinations of AFM with imaging and spectroscopic techniques[122,123] have greatly expanded the amount and types of data one can obtain simultaneously. AFM has become a routine surface characterization technique in many laboratories and research centers, and there has been a rapidly increasing use of AFM for characterization of the biologic responses to materials including cell–cell and cell–material interactions. With the development of micromachining and nanofabrication technologies, ultrasharp, ultrasensitive probes are being used more routinely, allowing more access to data that formerly required devoted facilities. As new developments in instrumentation and accessories continue to appear, it is also likely that the versatility of the AFM as a standard tool in biomaterials science will continue to progress.

References

1. Binnig, G.; Rohrer, H. *Helv. Phys. Acta* **1982**, *55*(6), 726–735.
2. Binnig, G.; Quate, C. F.; Gerber, C. *Phys. Rev. Lett.* **1986**, *56*(9), 930–933.
3. Engel, A. *Annu. Rev. Biophys. Biophys. Chem.* **1991**, *20*, 79–108.
4. Marti, O.; *et al*. *J. Microsc. Oxford* **1988**, *152*, 803–809.
5. Radmacher, M.; Tillmann, R. W.; Fritz, M.; Gaub, H. E. *Science* **1992**, *257*(5078), 1900–1905.
6. Shao, Z. F.; Yang, J.; Somlyo, A. P. *Annu. Rev. Cell Dev. Biol.* **1995**, *11*, 241–265.
7. Alessandrini, A.; Facci, P. *Meas. Sci. Technol.* **2005**, *16*(6), R65–R92.
8. Cohen, S. R.; Bitler, A. *Curr. Opin. Colloid. Interf. Sci.* **2008**, *13*(5), 316–325.
9. Lyubchenko, Y. L.; Shlyakhtenko, L. S. *Proc. Natl. Acad. Sci. USA* **1997**, *94*(2), 496–501.
10. Tanigawa, M.; Okada, T. *Anal. Chim. Acta* **1998**, *365*(1–3), 19–25.
11. Arakawa, H.; Umemura, K.; Ikai, A. *Nature* **1992**, *358*(6382), 171.
12. Wadu-Mesthrige, K.; Amro, N. A.; Liu, G. Y. *Scanning* **2000**, *22*(6), 380–388.
13. Hui, S. W.; Viswanathan, R.; Zasadzinski, J. A.; Israelachvili, J. N. *Biophys. J.* **1995**, *68*(1), 171–178.
14. Muscatello, U.; Valdre, G.; Valdre, U. *J. Microsc. Oxford* **1996**, *182*, 200–207.
15. Gunning, A. P.; Kirby, A. R.; Morris, V. J.; Wells, B.; Brooker, B. E. *Polym. Bull.* **1995**, *34*(5–6), 615–619.
16. Sun, R. G.; Zhang, J. *Acta Chim. Sin.* **2006**, *64*(24), 2467–2472.
17. Henderson, E. *Prog. Surf. Sci.* **1994**, *46*(1), 39–60.
18. Nagao, E.; Dvorak, J. A. *J. Microsc. Oxford* **1998**, *191*, 8–19.
19. Nagao, E.; Dvorak, J. A. *Biophys. J.* **1999**, *76*(6), 3289–3297.
20. Kang, I.; Panneerselvam, D.; Panoskaltsis, V. P.; Eppell, S. J.; Marchant, R. E.; Doerschuk, C. M. *Biophys. J.* **2008**, *94*(8), 3273–3285.
21. Ge, G. L.; *et al*. *Ultramicroscopy* **2007**, *107*(4–5), 299–307.
22. Weischer, C. H. *Eur. J. Cell Biol.* **1997**, *74*, 70.
23. Scheuring, S.; Dufrene, Y. F. *Mol. Microbiol.* **2010**, *75*(6), 1327–1336.
24. Vansteenkiste, S. O.; Davies, M. C.; Roberts, C. J.; Tendler, S. J. B. *Prog. Surf. Sci.* **1998**, *57*(2), 95–136.
25. Florin, E. L.; Moy, V. T.; Gaub, H. E. *Science* **1994**, *264*(5157), 415–417.
26. Merkel, R.; Nassoy, P.; Leung, A.; Ritchie, K.; Evans, E. *Nature* **1999**, *397*(6714), 50–53.
27. Zhu, C. *J. Biomech.* **2000**, *33*(1), 23–33.
28. Montdargent, B.; Letourneur, D. *Infect. Control Hosp. Epidemiol.* **2000**, *21*(6), 404–410.
29. Thevenot, P.; Hu, W. J.; Tang, L. P. *Curr. Top. Med. Chem.* **2008**, *8*(4), 270–280.
30. Horbett, T. A. *Cardiovasc. Pathol.* **1993**, *2*(3), S137–S148.
31. Castner, D. G.; Ratner, B. D. *Surf. Sci.* **2002**, *500*(1–3), 28–60.
32. Gorbet, M. B.; Sefton, M. V. M. V. *Biomaterials* **2004**, *25*(26), 5681–5703.
33. Sarid, D. *Scanning Force Microscopy: With Application to Electric, Magnetic and Atomic Forces*, Revised ed.; Oxford University Press: New York, 1994.
34. Wiesendanger, R. *Scanning Probe Microscopy and Spectroscopy: Methods and Applications*. Cambridge University Press: Cambridge, 1994.
35. Giessibl, F. J. *Rev. Mod. Phys.* **2003**, *75*, 949–983.
36. Hafner, J. H.; Cheung, C. L.; Lieber, C. M. *Nature* **1999**, *398*(6730), 761–762.
37. Stevens, R. M. *Mater. Today* **2009**, *12*(10), 42–45.
38. Kuwahara, M.; Abe, H.; Tokumoto, H.; Shima, T.; Tominaga, J.; Fukuda, H. *Mater. Charact.* **2004**, *52*(1), 43–48.
39. Ducker, W. A.; Senden, T. J.; Pashley, R. M. *Nature* **1991**, *353*(6341), 239–241.
40. Kappl, M.; Butt, H. J. *Part. Part. Syst. Character.* **2002**, *19*(3), 129–143.
41. Xu, L. C.; Logan, B. E. *Environ. Sci. Technol.* **2005**, *39*(10), 3592–3600.
42. Xu, L. C.; Logan, B. E. *Langmuir* **2006**, *22*(10), 4720–4727.
43. Xu, L. C.; Vadillo-Rodriguez, V.; Logan, B. E. *Langmuir* **2005**, *21*(16), 7491–7500.
44. Westra, K. L.; Mitchell, A. W.; Thomson, D. J. *J. Appl. Phys.* **1993**, *74*(5), 3608–3610.
45. Velegol, S. B.; Pardi, S.; Li, X.; Velegol, D.; Logan, B. E. *Langmuir* **2003**, *19*(3), 851–857.
46. Wilson, D. L.; Kump, K. S.; Eppell, S. J.; Marchant, R. E. *Langmuir* **1995**, *11*, 265–272.
47. Wilson, D. L.; Dalal, P.; Kump, K. S.; Benard, W.; Xue, P.; Marchant, R. E.; Eppell, S. J. *J. Vacuum Sci. Technol. B* **1996**, *14*(4), 2407–2416.
48. Sader, J. E.; White, L. *J. Appl. Phys.* **1993**, *74*(1), 1–9.
49. Sader, J. E. *Rev. Sci. Instrum.* **1995**, *66*(9), 4583–4587.
50. Senden, T. J.; Ducker, W. A. *Langmuir* **1994**, *10*(4), 1003–1004.
51. Cumpson, P. J.; Clifford, C. A.; Hedley, J. *Meas. Sci. Technol.* **2004**, *15*(7), 1337–1346.
52. Cleveland, J. P.; Manne, S.; Bocek, D.; Hansma, P. K. *Review of Scientific Instruments* **1993**, *64*(2), 403–405.
53. Sader, J. E.; Chon, J. W. M.; Mulvaney, P. *Review of Scientific Instruments* **1999**, *70*(10), 3967–3969.
54. Hutter, J. L.; Bechhoefer, J. *Review of Scientific Instruments* **1993**, *64*(7), 1868–1873.
55. Levy, R.; Maaloum, M. *Nanotechnology* **2002**, *13*(1), 33–37.
56. Craig, V. S. J.; Neto, C. *Langmuir* **2001**, *17*(19), 6018–6022.
57. Grigg, D. A.; Russell, P. E.; Griffith, J. E. *J. Vacuum Sci. Technol. A* **1992**, *10*(4), 680–683.
58. Siedlecki, C. A.; Marchant, R. E. *Biomaterials* **1998**, *19*(4–5), 441–454.
59. Oshea, S. J.; Welland, M. E.; Wong, T. M. H. *Ultramicroscopy* **1993**, *52*(1), 55–64.
60. Warmack, R. J.; Zheng, X. Y.; Thundat, T.; Allison, D. P. *Review of Scientific Instruments* **1994**, *65*(2), 394–399.
61. Quintanilla, M. A. S.; Goddard, D. T. *Review of Scientific Instruments* **2008**, *79* (2), 11.
62. Munz, M. *J. Phys. D Appl. Phys.* **2010**, *43*(6).
63. Vancso, G. J.; Forster, S.; Leist, H. *Macromolecules* **1996**, *29*(6), 2158–2162.
64. Raczkowska, J.; *et al*. *Langmuir* **2007**, *23*(13), 7235–7240.
65. Ho, S. P.; Nakabayashi, N.; Iwasaki, Y.; Boland, T.; LaBerge, M. *Biomaterials* **2003**, *24*(28), 5121–5129.
66. Frisbie, C. D.; Rozsnyai, L. F.; Noy, A.; Wrighton, M. S.; Lieber, C. M. *Science* **1994**, *265*(5181), 2071–2074.
67. Werts, M. P. L.; van der Vegte, E. W.; Grayer, V.; Esselink, E.; Tsitsilianis, C.; Hadziioannou, G. *Adv. Mater.* **1998**, *10*(6), 452.
68. Ibrahim, S.; Ito, T. *Langmuir* **2010**, *26*(3), 2119–2123.

69. Schonherr, H.; Feng, C. L.; Tomczak, N.; Vancso, G. J. *Macromol. Symp.* **2005**, *230*, 149–157.
70. Garcia, R.; Perez, R. *Surf. Sci. Rep.* **2002**, *47*(6–8), 197–301.
71. Garcia, R.; San Paulo, A. *Phys. Rev. B* **1999**, *60*(7), 4961–4967.
72. San Paulo, A.; Garcia, R. *Phys. Rev. B* **2001**, *64*(19) art. no. 193411.
73. Moller, C.; Allen, M.; Elings, V.; Engel, A.; Muller, D. J. *Biophys. J.* **1999**, *77*(2), 1150–1158.
74. San Paulo, A.; Garcia, R. *Biophys. J.* **2000**, *78*(3), 1599–1605.
75. Hussain, M. A.; Agnihotri, A.; Siedlecki, C. A. *Langmuir* **2005**, *21*(15), 6979–6986.
76. Agnihotri, A.; Siedlecki, C. A. *Langmuir* **2004**, *20*(20), 8846–8852.
77. Averett, L. E.; Schoenfisch, M. H. *Analyst* **2010**, *135*(6), 1201–1209.
78. Balasubramanian, V.; Grusin, N. K.; Bucher, R. W.; Turitto, V. T.; Slack, S. M. *J. Biomed. Mater. Res.* **1999**, *44*(3), 253–260.
79. Wertz, C. F.; Santore, M. M. *Langmuir* **2002**, *18*(3), 706–715.
80. Maivald, P.; Butt, H. J.; Gould, S. A. C.; Prater, C. B.; Drake, B.; Burley, J. A.; Elings, V. B.; Hansma, P. K. *Nanotechnology* **1991**, *2*, 103–106.
81. Chen, J. T.; Thomas, E. L. *J. Mater. Sci.* **1996**, *31*(10), 2531–2538.
82. Lin, H. N.; Hung, T. T.; Chang, E. C.; Chen, S. A. *Appl. Phys. Lett.* **1999**, *74*(19), 2785–2787.
83. Downing, T. D.; Kumar, R.; Cross, W. M.; Kjerengtroen, L.; Kellar, J. J. *J. Adhes. Sci. Technol.* **2000**, *14*(14), 1801–1812.
84. Ye, Z.; Zhao, X. *J. Microsc. Oxford* **2010**, *238*(1), 27–35.
85. Garrett, J. T.; Runt, J.; Lin, J. S. *Macromolecules* **2000**, *33*(17), 6353–6359.
86. Lamba, N. M. K.; Woodhouse, K. A.; Cooper, S. L. *Polyurethanes in Biomedical Applications*. CRC Press: Boca Raton, FL, 1998.
87. Xu, L. C.; Soman, P.; Agnihotri, A.; Siedlecki, C. A. In *Biological Interactions on Materials Surfaces*; Puleo, D. A., Bizios, R., Eds.; Springer: Dordrecht, 2009; pp 44–69.
88. Xu, L. C.; Siedlecki, C. A. *J. Biomed. Mater. Res. A* **2010**, *92A*(1), 126–136.
89. Garrett, J. T.; Siedlecki, C. A.; Runt, J. *Macromolecules* **2001**, *34*(20), 7066–7070.
90. Thormann, E.; Pettersson, T.; Kettle, J.; Claesson, P. M. *Ultramicroscopy* **2010**, *110*(4), 313–319.
91. Holland, N. B.; Marchant, R. E. *J. Biomed. Mater. Res.* **2000**, *51*(3), 307–315.
92. Eppell, S. J.; Simmons, S. R.; Albrecht, R. M.; Marchant, R. E. *Biophys. J.* **1995**, *68*(2), 671–680.
93. Miyahara, Y.; Deschler, M.; Fujii, T.; Watanabe, S.; Bleuler, H. *Appl. Surf. Sci.* **2002**, *188*(3–4), 450–455.
94. Florin, E. L.; Radmacher, M.; Fleck, B.; Gaub, H. E. *Review of Scientific Instruments* **1994**, *65*(3), 639–643.
95. Kitamura, S.; Suzuki, K.; Iwatsuki, M. *Appl. Surf. Sci.* **1999**, *140*(3–4), 265–270.
96. Todd, B. A.; Eppell, S. J. *Langmuir* **2004**, *20*(12), 4892–4897.
97. Cappella, B.; Dietler, G. *Surf. Sci. Rep.* **1999**, *34*(1–3), 1.
98. Butt, H. J.; Cappella, B.; Kappl, M. *Surf. Sci. Rep.* **2005**, *59*(1–6), 1–152.
99. Wang, M. S.; Palmer, L. B.; Schwartz, J. D.; Razatos, A. *Langmuir* **2004**, *20*(18), 7753–7759.
100. Kidoaki, S.; Matsuda, T. *Colloids Surf. B Biointerfaces* **2002**, *23*(2–3), 153–163.
101. Marshall, B. T.; Sarangapani, K. K.; Lou, J. H.; McEver, R. P.; Zhu, C. *Biophys. J.* **2005**, *88*(2), 1458–1466.
102. Chizhik, S. A.; Huang, Z.; Gorbunov, V. V.; Myshkin, N. K.; Tsukruk, V. V. *Langmuir* **1998**, *14*(10), 2606–2609.
103. Tsukruk, V. V.; Huang, Z.; Chizhik, S. A.; Gorbunov, V. V. *J. Mater. Sci.* **1998**, *33* (20), 4905–4909.
104. Tsukruk, V. V.; Gorbunov, V. V.; Huang, Z.; Chizhik, S. A. *Polym. Int.* **2000**, *49* (5), 441–444.
105. Hansen, J. C.; Lim, J. Y.; Xu, L. C.; Siedlecki, C. A.; Mauger, D. T.; Donahue, H. J. *J. Biomech.* **2007**, *40*, 2865–2871.
106. Dupres, V.; Verbelen, C.; Dufrene, Y. F. *Biomaterials* **2007**, *28*(15), 2393–2402.
107. Barattin, R.; Voyer, N. *Chem. Commun.* **2008**, *13*, 1513–1532.
108. Dufrene, Y. F. *Biophys. J.* **2000**, *78*(6), 3286–3291.
109. Hinterdorfer, P.; Dufrene, Y. F. *Nat. Methods* **2006**, *3*(5), 347–355.
110. Lee, G. U.; Kidwell, D. A.; Colton, R. J. *Langmuir* **1994**, *10*(2), 354–357.
111. Dammer, U.; Popescu, O.; Wagner, P.; Anselmetti, D.; Guntherodt, H. J.; Misevic, G. N. *Science* **1995**, *267*(5201), 1173–1175.
112. Hinterdorfer, P.; Baumgartner, W.; Gruber, H. J.; Schilcher, K.; Schindler, H. *Proceedings of the National Academy of Sciences of the United States of America* **1996**, *93*(8), 3477–3481.
113. Chowdhury, P. B.; Luckham, P. F. *Colloids Surf. A Physicochem. Eng. Aspects* **1998**, *143*(1), 53–57.
114. Razatos, A.; Ong, Y. L.; Sharma, M. M.; Georgiou, G. *Proceedings of the National Academy of Sciences of the United States of America* **1998**, *95*(19), 11059–11064.
115. Bowen, W. R.; Hilal, N.; Lovitt, R. W.; Wright, C. J. *Colloids Surf. A Physicochem. Eng. Aspects* **1998**, *136*(1–2), 231–234.
116. Liu, Y.; Strauss, J.; Camesano, T. A. *Biomaterials* **2008**, *29*(33), 4374–4382.
117. Willemsen, O. H.; *et al*. *Biophys. J.* **1998**, *75*(5), 2220–2228.
118. Hemmersam, A. G.; Foss, M.; Chevallier, J.; Besenbacher, F. *Colloids Surf. B Biointerfaces* **2005**, *43*(3–4), 208–215.
119. Shiba, E.; *et al*. *Am. J. Physiol.* **1991**, *260*(5), C965–C974.
120. Tamada, Y.; Kulik, E. A.; Ikada, Y. *Biomaterials* **1995**, *16*(3), 259–261.
121. Dufrene, Y. F. *Nat. Protoc.* **2008**, *3*(7), 1132–1138.
122. Kassies, R.; *et al*. *J. Microsc. Oxford* **2005**, *217*, 109–116.
123. Schmidt, U.; Hild, S.; Ibach, W.; Hollricher, O. *Macromol. Symp.* **2005**, *230*, 133–143.

3.303. Proteomic and Advanced Biochemical Techniques to Study Protein Adsorption

D L Elbert, Washington University in St. Louis, St. Louis, MO, USA

© 2011 Elsevier Ltd. All rights reserved.

3.303.1.	Introduction	37
3.303.2.	Unbiased Analysis of Adsorbed Proteins by Polyacrylamide Gel Electrophoresis	37
3.303.3.	Analysis of Adsorbed Proteins by 2DPAGE	39
3.303.3.1.	Identification of Proteins by Mass Spectrometry	41
3.303.4.	Quantification of Protein Amounts by Mass Spectrometry	43
3.303.5.	Proteomics to Study Protein Denaturation on Surfaces	43
3.303.6.	Challenges of the Proteomics Approach	44
3.303.7.	Conclusions	44
References		44

Abbreviations

ECMO	Extracorporeal membrane oxygenators
HA	Hydroxyapatite
HMWK	High molecular weight kininogen
LTIC	Low temperature isotropic carbon
MALDI-TOF	Matrix-assisted light desorption/ionization-time of flight (mass spectrometry)
PEG	Poly(ethylene glycol)
SDS-PAGE	Sodium dodecylsulfate polyacrylamide gel electrophoresis
TOF-SIMS	Time-of-flight secondary ion mass spectrometry

3.303.1. Introduction

Researchers in the field of proteomics seek to apply unbiased methods to obtain a comprehensive understanding of complex mixtures of proteins. Traditional biochemical methods used to study proteins are well suited to address specific hypotheses but are biased by the use of specific antibodies or the labeling of single proteins. With traditional methods, high-quality information is gained about one protein at the expense of information about the multitude of other proteins in the sample. Unbiased methods instead seek to identify and quantify proteins that are exceptional under some set of experimental conditions, for example, proteins that adsorb well to a particular biomaterial. Identification of the observed proteins is an important goal of proteomics, which distinguishes the proteomics approach from the many methods that measure averaged properties of mixtures of adsorbed proteins, for example, ellipsometry, surface plasmon resonance, OWLS, quartz crystal microbalance, circular dichroism, attenuated total reflectance Fourier transform infrared spectroscopy (ATR-FTIR), etc. Proteomics typically combines electrophoresis, often two-dimensional (2D) electrophoresis, with mass spectrometry (see **Figure 1**). However, current technical limitations mean that proteomics approaches are far from comprehensive, and absolute quantification continues to be a major challenge. Methods continue to evolve, and it is likely that unbiased methods will eventually become the methods of choice to study proteins adsorbed to biomaterials.

3.303.2. Unbiased Analysis of Adsorbed Proteins by Polyacrylamide Gel Electrophoresis

In the field of biomaterials, several unbiased approaches were developed to study protein adsorption long before the field of proteomics emerged. In 1974, Lyman *et al*. eluted blood proteins from polyurethane, silastic, and Teflon FEP tubes exposed to blood in an *ex vivo* shunt model. Proteins were removed from the surfaces by incubation with 1% Triton X-100 for 2 days.[1] The proteins were concentrated and analyzed by alkaline polyacrylamide gel electrophoresis (PAGE). This type of PAGE leads to the identification of albumin, two α-globulin bands, two β-globulin, bands, and a γ-globulin band. The different surfaces had different amounts of albumin relative to the globulin bands. Surfaces with more intense albumin bands also showed decreased platelet adhesion, suggesting that surfaces that attract albumin have higher blood compatibility than those that attract the globulin proteins.

Limber and Mason subsequently examined proteins eluted from Cuprophane dialysis membranes that were coated with albumin or heparin and exposed to platelet poor plasma.[2] Proteins were eluted into flowing buffer, but continual desorption of adsorbed proteins was observed regardless of the length of the buffer wash. This may have been a result of the relative hydrophilicity of the substrates. A protocol was developed to elute proteins with a 250 ml buffer wash, then an elution with a 1% Triton X-100 solution to remove more tightly bound proteins, followed by another 1000 ml buffer wash and a

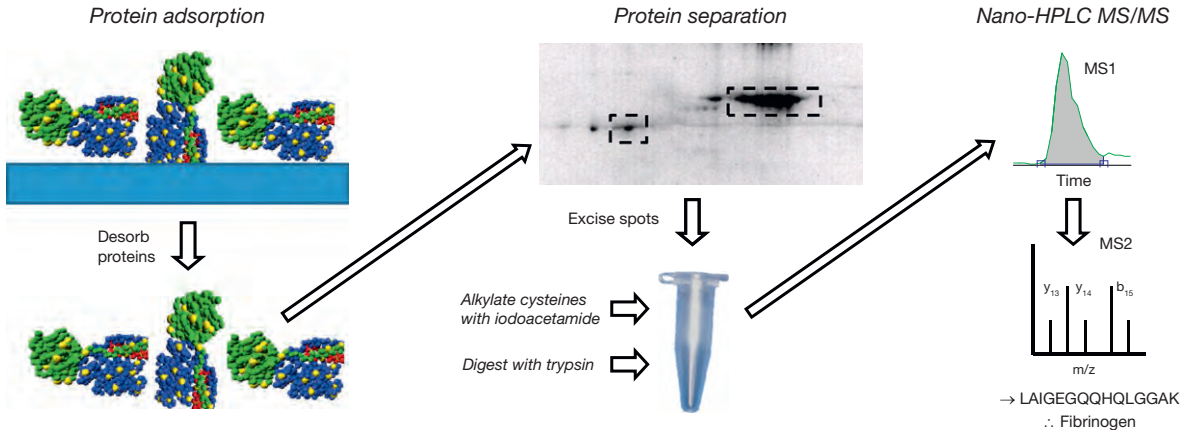

Figure 1 Workflow of a typical proteomics experiment to study protein adsorption. Many alternative protocols have also been developed, as described in the text.

second elution with Triton X-100. Up to seven protein bands could be observed by PAGE. However, only albumin and IgG could be definitively identified by immunoelectrophoresis, most likely due to the small amounts of protein present. The limited amounts of protein adsorbed to surfaces, typically about 200 ng cm^{-2} of surface area, and the difficulty in removing adsorbed proteins, still present challenges today.

Weathersby and coworkers enhanced these early techniques by radiolabeling proteins that had already adsorbed to surfaces.[3,4] Proteins were labeled with radioactive iodine and then eluted from the surfaces with 1% sodium dodecylsulfate (SDS) and sonication. The advantage of this method was the high sensitivity afforded by radiolabeling and the ability to detect noneluted protein. Proteins eluted from the surface were separated by SDS-PAGE. Identification of eluted proteins was based on molecular weights alone, as protein amounts were too low for Edman microsequencing. By comparing native and reduced gels, fibrinogen, IgG, and hemoglobin were identified based on the differences in peak locations following the disruption of disulfide bonds. However, six other major peaks could not be identified definitively. The relative change in the amount of each protein was measured on surfaces of different hydrophilicity (various copolymers of hydroxyethylmethacrylate (HEMA) and ethylmethacrylate (EMA). Some proteins were found to be more difficult to radioiodinate than others, complicating quantification of relative protein amounts. Further, a subsequent survey of a wide panel of surfactants revealed that a substantial fraction of adsorbed protein was not eluted.[5] Many of the proteomic methods in current use also rely on elution of adsorbed proteins prior to analysis, complicating interpretation of the results.

Unbiased methods may be used to demonstrate activation of the intrinsic coagulation cascade and the Vroman effect. Fibrinogen initially adsorbs to glass surfaces from plasma, but within a few minutes, can no longer be detected.[6] This process is known as the Vroman effect. Glass surfaces also promote the adsorption of Factor XII, which becomes more susceptible to enzymatic cleavage and activation upon adsorption.[7] Following enzymatic activation, Factor XIIa activates prekallikrein to form kallikrein. Kallikrein then may activate high molecular weight kininogen (HMWK). Activated HMWK binds to glass with high affinity and efficiently displaces fibrinogen.[8] To better understand this process, Brash and colleagues examined adsorbed human plasma proteins eluted from glass beads with 1 M Tris followed by 2% SDS and analysis by SDS-PAGE.[9] Most of the eluted proteins could not be definitively identified based on molecular weight alone. Immunoelectrophoresis demonstrated the presence of albumin, IgG, fibrinogen, and plasminogen, but the presence of other plasma proteins could not be confirmed. Bands consistent with intact fibrinogen were found in the 2% SDS wash, while bands consistent with plasmin-degraded fibrinogen were found in the 1 M Tris wash. In contrast, Factor XII-deficient plasma or plasminogen-deficient plasma had intact fibrinogen bands in the 1 M Tris wash. To better identify the proteins eluted from glass, Western blots were performed for 16 major plasma proteins. All 16 proteins were detected in the eluates by Western blot. Although degraded fibrinogen could be detected in normal plasma by Western blot, the proportion of degraded fibrinogen was highest in the 1 M Tris eluate. Compared to native plasma, Factor XII and HMWK eluted from the glass were found in their cleaved forms, indicating that they had been activated after contact with glass. Although Western blots allowed identification of the proteins eluted from materials, quantification of amounts of proteins relative to each other was not attempted. Due to the high sensitivity of the technique, bands on a Western blot may be undetectable on SDS-PAGE gels, while prominent bands on SDS-PAGE gels might not correspond to proteins examined by Western blot.

The large-scale Western blot approach was also applied to proteins eluted from hemodialyzers after clinical use.[10] The membranes consisted of poly(methyl methacrylate) (PMMA), cellulose acetate, saponified cellulose ester, or Cuprophane. Proteins were eluted with 2% SDS. Extensive degradation of many of the 16 proteins was observed, much more so than with human plasma *in vitro*, suggesting the presence of cell-derived proteases not present in platelet poor plasma. Little fibrinogen was present on PMMA membranes, while fibrinogen degradation products were mainly found on the other materials.

Large amounts of degraded complement protein C3 were found on all membranes. This was consistent with the activation of the complement cascade on the hemodialyzer units.[11]

3.303.3. Analysis of Adsorbed Proteins by 2DPAGE

The limitations of SDS-PAGE led to the use of 2DPAGE to better resolve plasma proteins (see **Figure 2**). 2D gel electrophoresis subjects proteins to isoelectric focusing prior to separation by SDS-PAGE.[12] In this way, hundreds of plasma proteins may be identified on a single gel based only on molecular weight and isoelectric point (pI).[13–15] Owen *et al.* used 2D electrophoresis in 1985 to examine proteins bound to extracorporeal membrane oxygenators (ECMO). On an ECMO that failed due to massive coagulation, hemoglobin and IgG were the most prominent proteins. A successfully used ECMO in the same patient revealed a large albumin spot in addition to hemoglobin and IgG.[16] Subsequently, Andrade and colleagues utilized 2D electrophoresis to detect heparin-binding proteins present in plasma.[17] Rather than eluting the proteins bound to heparin–agarose particles, depletion of proteins from plasma was measured. The adsorption kinetics of antithrombin-III, complement protein C3, Apolipoprotein (Apo) A-I, and Apo A-IV were quantified by observing the disappearance of spots corresponding to these proteins on 2D gels.

One of the drawbacks of unbiased proteomics techniques is the large amount of protein required for analysis. Assuming 200 ng cm^{-2} of adsorbed protein, 50 cm^2 of surface area would be required to obtain 10 μg of protein that is typically loaded in each lane of an SDS-PAGE gel. Even more protein is required for 2D gel electrophoresis. Thus, proteomic methods are more amenable to the analysis of high surface area materials, such as packed beds of microspheres. Not only is more surface area available, but the entire surface area may be exposed to a low volume of eluent, potentially eliminating the need to concentrate the eluted proteins prior to analysis. Thus, proteomic analyses of protein adsorption have largely focused on materials in the form of powders, fibers, microspheres, and nanoparticles.

2D electrophoresis has been used extensively to better understand the opsonization of microspheres and nanoparticles. Müller and colleagues used 2D electrophoresis to determine the effects of surface chemistry on protein adsorption and subsequent uptake by macrophages. Different polyethylene glycol (PEG)-based copolymer surfactants were adsorbed to polystyrene beads, and the more hydrophilic copolymers adsorbed, the less total protein.[18] Similar to previous studies, most of the proteins found in plasma were also found adsorbed to the nanoparticle surfaces. However, some proteins, such as albumin and haptoglobin were less abundant on the nanoparticle surfaces compared to plasma, while transferrin and Apo C-III were enriched. For most proteins, the adsorbed

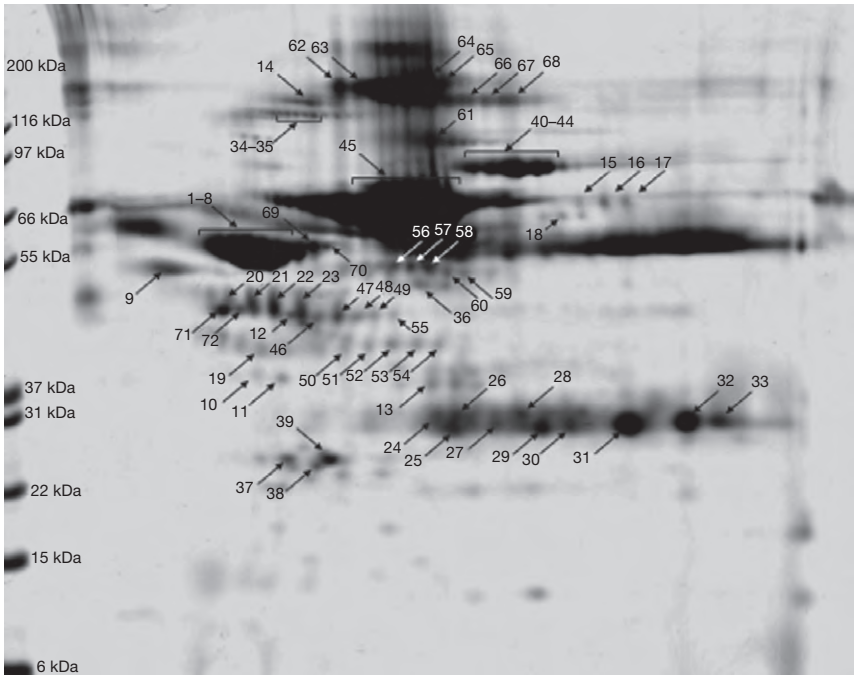

Figure 2 Two-dimensional gel electrophoresis of proteins eluted from an extracorporeal liver support device. Lower isoelectric point proteins are on the left side of the gel. Spots were cut from the gel and proteins in the spots were digested with trypsin. The peptide mixture was analyzed by matrix-assisted light desorption/ionization-time of flight/time of flight, with fragmentation of ions to allow identifications as in **Figure 3**. The largest spot (45) is serum albumin. Sixteen unique proteins were identified. The proteins that adsorbed to the device largely reflected the composition of proteins found in blood plasma. While the technique may, in principle, be used to determine the kinetics of protein adsorption, in practice, the throughput and cost of the method are still limiting factors. Reprinted in part with permission from Mares, J.; Thongboonkerd, V.; Tuma, Z.; Moravec, J.; Karvunidis, T.; Matejovic, M. *J. Proteome Res.* **2009**, *8*, 1756–1764. Copyright 2009 American Chemical Society.

amount was correlated with the hydrophobicity of the copolymer coating, but Apo A-IV and Apo E showed the lowest adsorption on the surfaces of intermediate hydrophilicity. PEG-based copolymer surfactants greatly lowered opsonization of polystyrene nanoparticles and increased circulation half-life.[19] However, proteomics analysis showed that protein adsorption still occurred on the so-called 'stealth' particles and that some proteins may actually be enriched on these surfaces. An extensive study of different PEG coatings on polystyrene microspheres revealed that the PEG coatings that were best able to reduce protein adsorption adsorbed slightly more albumin and Apo A-I, proteins that are not opsonins.[20] This suggested that hydrophilic coatings not only reduce protein adsorption but also recruit proteins that are not recognized by macrophages. Müller's group has published over 30 manuscripts characterizing protein adsorption to various particles, for example, emulsions,[21,22] iron oxide particles,[23] degradable PEG-containing microspheres, and nanoparticles,[24,25] polycyanoacrylate nanoparticles,[26] lipid–drug conjugates,[27] and transfection reagents.[28] Using similar methods, protein adsorption to liposomes was also studied by another group.[29]

LeRoux and colleagues used 2D electrophoresis to determine the mechanism by which PEG reduced uptake of polylactic acid nanoparticles by monocytes in plasma. Reduction of monocyte uptake due to the PEG coating was confirmed, yet the only differences in proteins adsorbed to the surfaces seemed to be Apo A-IV and Apo E.[30] In a later study by the same group, albumin adsorption to poly(D,L-lactide) nanoparticles decreased over the course of 60 min, while complement protein C3 adsorption increased dramatically.[31] This suggested that complement activation was initiated by the nanoparticles, consistent with previous work showing that complement promotes opsonization of these nanoparticles.[32] From the studies of Müller and LeRoux, it may be concluded that the protein composition in an adsorbed layer strongly resembles the protein composition of plasma, but PEG coatings reduce the total amount of adsorbed protein. However, the studies also suggest that the small differences observed between the adsorbed protein layer and the proteins in bulk plasma may be of tremendous importance in the biocompatibility of 'stealth' materials.

Müller and colleagues further used 2D gel electrophoresis to discover the mechanism by which some polysorbate-coated nanoparticles pass through the blood–brain barrier. The protein Apo E was found adsorbed to the nanoparticles in large amounts, which suggested a novel hypothesis for passage of these nanoparticles into the brain. The hypothesis was then experimentally validated, resulting in a novel discovery that may have not emerged using traditional methods.[33] Subsequently, another group found that PEG-polyhexadecylcyanoacrylate nanoparticles also crossed the blood–brain barrier. Using 2D electrophoresis and Western blotting, these nanoparticles were shown to also exhibit enhanced adsorption of Apo E.[34] Thus, unbiased approaches, when ideally practiced, may lead to the development of new hypotheses that may then be verified using more traditional methods.

In 1995, Feng and Andrade used 2D electrophoresis to analyze proteins adsorbed to powders of low temperature isotropic carbon (LTIC). The potential issue of nonelutable proteins was addressed by examining proteins that remained in plasma in the presence of the LTIC or silica powders. 2D electrophoresis allowed the identification and quantification of adsorption of 25 plasma proteins, inferred by the decrease in the intensity of spots on the gel due to adsorption to the powders. Twenty-one of the proteins had >50% depletion on silica at 12 h (with 1.5 m^2 surface area per 1.7 ml of plasma). All the proteins were >50% depleted on LTIC under similar conditions. Both materials adsorbed similar amounts of protein, about 200 ng cm^{-2} of total protein. The proteins with the highest surface activity could be discerned by using lower amounts of LTIC. The proteins that were >80% depleted under these conditions were Apo C, Apo E, complement protein C4, fibrinogen, α_2-HS-glycoprotein, α_2-macroglobulin, and plasminogen. On silica, the most readily depleted proteins were Apo C, Apo E, fibrinogen, and α_2-macroglobulin. After 5 min of adsorption on LTIC, the most depleted protein was fibrinogen. However, no Vroman effect was observed on either surface, as fibrinogen was still depleted at longer time points. This was inconsistent with many prior studies, as the silica surface would be expected to activate the intrinsic coagulation cascade leading to displacement of fibrinogen by activated HMWK. However, activation of the intrinsic coagulation cascade also results in the activation of plasminogen.[35] Activated plasminogen may have lead to fibrinogen degradation on the surface and in solution, reducing the intensity of the fibrinogen band on the 2D gel. This was consistent with the fibrinogen degradation products previously detected by Brash and colleagues.[9] Using similar methods, Rosengran *et al*. later analyzed the proteins depleted from plasma after exposure to ceramic particles (hydroxyapatite (HA), alumina, zirconia, and two bioactive glasses) along with proteins desorbed from the surfaces. Most of the major plasma proteins were found to adsorb to the surfaces, but Apo J (clusterin) was substantially depleted on all surfaces.[36,37]

Also in 1995, Stanislawski *et al*. used SDS-PAGE and 2D electrophoresis to examine protein adsorption to fibers used in ligament repair.[38] The fibers were made of polyarylamide, polyester (Dacron), polypropylene, or polylactic acid. After incubation with human plasma, the fibers were washed ten times with buffer and proteins were eluted from the materials with 3% SDS and 0.75% β-mercaptoethanol. Polyarylamide, the most hydrophilic material tested, exhibited a distinct pattern of adsorbed proteins compared with the more hydrophobic materials. In particular, a band at 115 kDa was present that was likely to be HMWK. The band was not present if HMWK-deficient plasma was incubated with the polyarylamide, although immunoblots failed to detect HMWK. Western blots demonstrated adsorption of fibrinogen, albumin, IgG, α_1-antitrypsin, transferrin, α_2-macroglobulin, prothrombin, Apo A-I, and Apo E. Some tightly packed bands on the SDS-PAGE gel were then resolved by 2D electrophoresis. Western blotting of the 2D gels allowed identification of the three fibrinogen chains, albumin, and the heavy chain of IgG. Nine other proteins were identified based on molecular weight and isoelectric point. Although HMWK may have been present on polyarylamide, no Vroman effect was observed. In fact, fibrinogen adsorption to polyarylamide was much higher than to the other surfaces, while Apo A-I adsorption was much lower. This agreed with previous reports that Apo A-I and fibrinogen adsorption are inversely correlated.[39]

Adsorption to hydrophilic surfaces has also been studied by proteomic methods. Magnani *et al.* used a two-step elution protocol to remove serum proteins adsorbed to glass, aminophase glass, and hyaluronic acid-modified glass. Proteins were eluted with 0.1% SDS followed by the sample buffer used for isoelectric focusing, containing 8 M urea, 4% CHAPS, and dithioerythritol. Using this protocol, over 1000 protein spots could be resolved on 2D gels. However, most of the spots on a 2D gel represent isoforms of the serum proteins with different amounts of glycosylation. The total number of unique plasma proteins has been estimated to be about 700.[40] Using manual processing, 30 unique proteins were identified by matching the spots on the 2D gels with those on a plasma protein 2D gel found in the Swiss-2DPAGE database (http://www.expasy.org). The most abundant proteins that adsorbed to glass and hyaluronic acid were albumin, α_1-antitrypsin, IgG, transferrin, fetuin, complement protein C3, and Apo A-I. Using similar methods, Berna *et al.* characterized adsorption of proteins to agarose-based chromatography resins in the presence of salts and sugars that promote protein phase separation.[41,42]

Materials commonly used in orthopedic implants are also amenable to proteomic analysis. In 2003, Sun *et al.* used 2D gels followed by Edman microsequencing to identify proteins adsorbed to titanium alloy, cobalt chromium molybdenum alloy, PMMA, and polyethylene particles, relevant to the failure of orthopedic implants.[43] Microsequencing resulted in the identification of only three proteins, albumin, α_1-antitrypsin, and Apo A-I. Albumin and α_1-antitrypsin were present as major peaks on all surfaces, while Apo A-I was only present on the polymeric surfaces. Using similar methods, Xie *et al.* found, in the course of studying proteins expressed by osteoblasts on hydroxyapatite (HA), that fetuin strongly adsorbed to the HA surface. This led to the development of a specific and novel hypothesis that adsorbed fetuin mediates osteoblast responses to HA. The researchers did not find that adsorbed fetuin affected osteoblast gene expression, but instead found that osteoblasts adhere normally to HA even in the absence of serum proteins.[44] However, this demonstrates how unbiased methods may lead to unexpected insights into complex biological responses.

3.303.3.1. Identification of Proteins by Mass Spectrometry

Mass spectrometry can greatly aid in protein identification. In 1999, Kingshott *et al.* studied proteins adsorbed to contact lenses using matrix-assisted light desorption/ionization-time of flight (MALDI-TOF) mass spectrometry. With this method, 2D gels were not necessary as the intact proteins were removed from the materials within the mass spectrometer. The proteins were adsorbed to the materials, washed, overlaid with light-absorbing molecules (matrix), and placed in the high vacuum of the MALDI-TOF. Whole proteins were removed from the surface upon exposure to laser light. Lysozyme was detected adsorbed to the contact lens after only 10 min in the eye.[45] In 2000, Oleschuk *et al.* used this method to analyze blood plasma proteins adsorbed to polyurethanes. The proteins were identified based on molecular weights observed in the mass spectra. Proteins as small as Apo C-I (6630 Da) and as large as IgG (150 000 Da) could be identified in a single spectrum. The limitation of the technique is the inability to measure absolute concentrations of the proteins. However, peak intensities are qualitatively related to adsorbed protein concentrations,[46,47] and albumin was found to be the most prominent peak, as expected.[48] Time-of-flight secondary ion mass spectrometry (TOF-SIMS) may also be performed on intact adsorbed proteins. By bombarding the adsorbed proteins with a beam of heavy ions, small fragments of the protein can be removed. On the basis of the differences in the ratio of the 20 amino acids in different proteins, the fragments can reveal the identities of proteins adsorbed to the surface (a detailed description is included in **Chapter 3.301, Surface Analysis and Biointerfaces: Vacuum and Ambient *In Situ* Techniques**).[49–52]

The major enabling technology that launched the field of proteomics was the use of mass spectrometry to identify protein spots on 2D gels following digestion of the proteins with proteases. Although quantification of protein amounts is still usually based on the intensity of the spot on the 2D gel, mass spectrometry allows identification of minor spots that previously would have only been the subject of speculation. In a typical protocol, spots on the 2D gel are cut out, washed to remove the protein stain, and then incubated with an enzyme such as trypsin. Trypsin cleaves proteins with high fidelity after lysines and arginines that are not followed by proline. By MALDI-TOF, a series of peaks are observed at different mass-to-charge (m/z) ratios, each corresponding to different peptides generated from the enzymatic digestion of the protein (a 'peptide mass fingerprint'). The sequence of the entire known proteome is available for download from the National Center for Biotechnology Information (NCBI). Prediction of the peptides that will be generated by proteolytic degradation of a particular protein is straightforward and performed automatically by a number of different software packages. The molecular weights of the predicted peptides may then be compared to peaks found in a MALDI-TOF peptide mass fingerprint.

In 2001, Derhami *et al.* used the sample buffer for isoelectric focusing, which contained dithiothreitol (DTT) and the surfactant CHAPS, to remove adsorbed serum proteins from titanium and tissue culture polystyrene. After 2D electrophoresis, spots were excised from the gel and digested with trypsin. The digest from each spot was analyzed by MALDI-TOF mass spectrometry. The peptide mass fingerprints were compared to predicted peptides of proteins found in a database with similar isoelectric points and molecular weights. Several proteins adsorbed to the materials were identified by MALDI-TOF, including α_2-HS-glycoprotein (fetuin), thrombospondin-1, α-fetoprotein, plasminogen, albumin, transferrin, and complement protein C3.[53]

If more than one protein is present within a spot, identification of the proteins by peptide mass fingerprints is more tenuous, but this may be overcome by further fragmenting each peptide ion in the mass spectrometer ('tandem mass spectrometry,' see **Figure 3**). In tandem mass spectrometry, a peptide mass fingerprint is obtained (a 'precursor ion scan'). Then a quadropole or ion trap is used to isolate ions at a particular m/z ratio, usually focusing on one of the more intense peaks in the precursor ion scan. The isolated ions are then fragmented, generally by collision with helium gas ('MS/MS scan'). Fragmentation by these collisions tends to occur at the peptide bond. Often, only one bond in the peptide backbone is broken, generating an N-terminal fragment and a C-terminal fragment referred to as *b* and *y* ions, respectively. The *b* and *y*

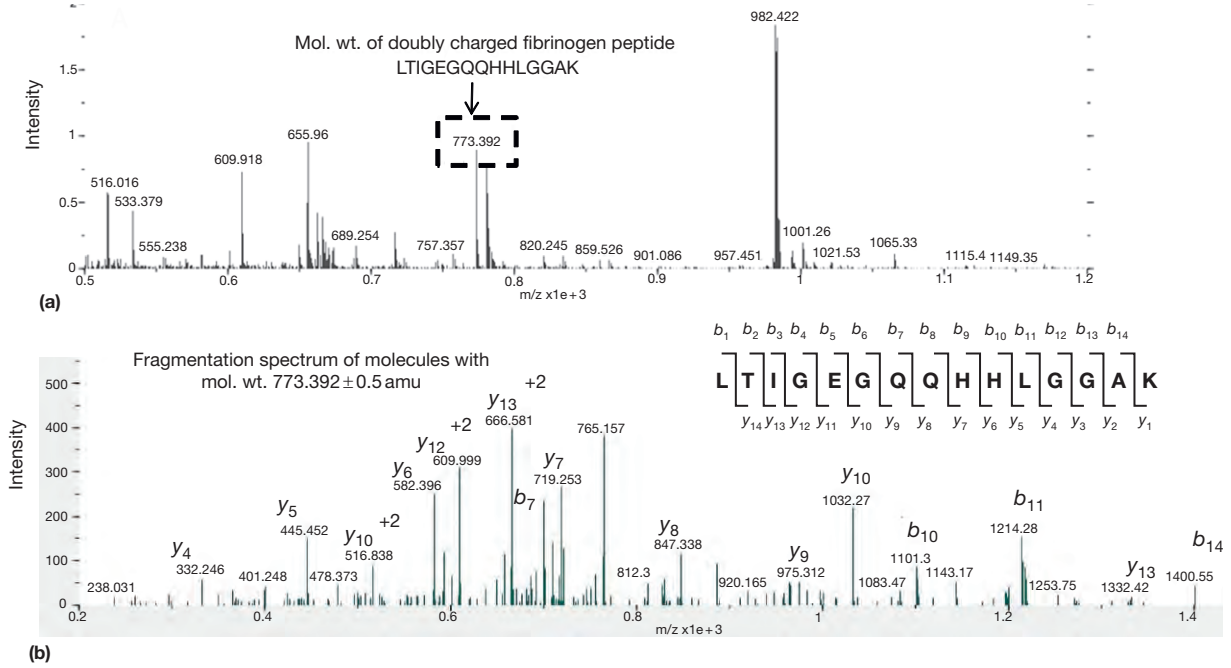

Figure 3 Protein identification by tandem mass spectrometry. A protein sample, often a band or spot following gel electrophoresis, is digested with the enzyme trypsin. The peptide mixture may be purified by high performance liquid chromatography run at extremely low flow rates. The eluent in some cases is directly electrosprayed into the mass spectrometer. (a) The peptides that enter the mass spectrometer may be detected in a 'precursor ion scan' (MS1 scan). The most intense peaks in the precursor ion scan are selected for fragmentation. In this example, a doubly charged ion (m/z 773.392) was selected and fragmented by collision with helium gas. (b) The fragmentation spectrum generated from the precursor ion peak shows peaks consistent with cleavage at different peptide bonds of the peptide with the shown sequence. While only some of the fragments are present, the assignment to this peptide can be made with high confidence. The *b* ions are fragments containing the N-terminus of the peptide, and *y* ions are the fragments containing the C-terminus of the peptide. The limitation of mass spectrometry is that while identification is robust, quantification is still challenging.

ions generated by fragmentation of a peptide yield a great deal of sequence information. In the ideal case, the full sequence of the peptide may be easily determined due to the presence of all possible *b* and *y* ions in the fragmentation spectrum. In real spectra, only some of the possible *b* and *y* ions are present. However, by matching the m/z of observed ions in the MS/MS scan with the masses of *b* and *y* ion predicted from peptides found in a protein database, assignments to a particular peptide may be made with extremely high confidence. Tandem mass spectrometry is not greatly affected by the presence of multiple proteins, since identifications are made of individual peptides at a narrow range of m/z, while peptides generated by trypsin have a wide range of m/z ratios. Nonetheless, high abundance proteins (e.g., albumin in plasma samples, actin, and histones in cellular samples) will generate intense peaks in the precursor ion scan and will dominate the scans selected for fragmentation. To increase the dynamic range of the measurement when multiple proteins may be present, peptides obtained from spots on the 2D gel may be separated by nanoliter-per-minute high performance liquid chromatography (nanoHPLC). Peptides separated by nanoHPLC enter the mass spectrometer over a range of times, increasing the ability to detect lower abundance proteins.

Kim *et al*. used tandem mass spectrometry to study plasma and serum proteins eluted from polypropylene, tissue culture polystyrene, poly(ethylene terephthalate) (PET), and polydimethylsiloxane.[54] The eluted proteins were first separated by 2D or SDS-PAGE gels. Bands or spots were sliced from the gels and treated with trypsin. The tryptic peptides were separated by nanoHPLC (run at 300 nl min) followed immediately by electrospray ionization and tandem mass spectrometry. Many of the same proteins found in previous studies were observed to be adsorbed to the different surfaces. However, one protein, serum amyloid P, was found to be one of the major proteins that adsorbed from serum onto the materials. The amount of adsorbed serum amyloid P increased over the course of hours to days of incubation with serum. On an SDS-page gel, serum amyloid P was identified along with Apo A-I and IgG light chain in the 20–30 kDa range after 7 days of incubation with serum. After 1 h, only IgG light chain was detected, while after 7 days in plasma, only Apo A-I was identified. Serum amyloid P had previously been demonstrated to bind to Fcγ receptors on leukocytes and opsonize particles for phagocytosis[55] It was hypothesized that adsorbed serum amyloid P promotes the attachment of leukocytes to biomaterials. Adsorbed serum amyloid P did in fact promote attachment and spreading of both monocytes and granulocytes onto the materials.[54] Similar methods were subsequently used to analyze proteins adsorbed to clinical low density lipoprotein (LDL) apheresis units. Seventy proteins were identified, including serum amyloid P.[56]

In recent years, characterization of protein adsorption to clinical devices by proteomics has become more common. Mares *et al*. used 2D electrophoresis and MALDI-TOF/TOF to study blood proteins adsorbed to liver support devices[57]

and polysulfone hemodialyzers[58] that had been used in human patients. MALDI-TOF/TOF is a type of tandem mass spectrometry and therefore yields high-confidence protein identifications. Some proteins were enriched by adsorption to the liver support devices: transthyretin, prothrombin, hyaluronan-binding protein, and plasma retinol-binding protein. Hyaluronan-binding protein is known to be upregulated by liver injury and is linked to protease activation. It was hypothesized that removal of this protein from the blood potentially could help to limit liver damage, but this was not experimentally verified. On the polysulfone hemodialyzers, ficolin-2, clusterin, and complement C3 were preferentially adsorbed. Ficolin-2 is an activator of the lectin pathway of the complement cascade. Along with the presence of complement C3 and clusterin (a C5b-9 inhibitor), a mechanism for complement activation on these membranes was suggested. The high abundance proteins from plasma such as albumin, transferrin, and α_1-antitrypsin were also present on the dialyzer units, consistent with an earlier proteomics study of cellulose diacetate and ethylenevinyl acetate hemodialyzers.[59]

3.303.4. Quantification of Protein Amounts by Mass Spectrometry

Tandem mass spectrometry is exceptionally adept at identifying proteins, but quantification of protein amounts by mass spectrometry continues to be a major challenge.[60] Generally, the intensity of ion peaks in the precursor ion mass spectrum is correlated with the concentration of the ion. However, in complex mixtures of proteins, unrelated peptides may elute from the nanoHPLC system at the same time, complicating the use of peak intensities from the precursor ion scan for quantification. Further, ionization is greatly affected by the presence of multiple peptides with different side chain chemistries,[61] making comparisons of amounts between different peptides quite difficult. The use of isotope-labeled internal standard peptides may help to account for differences in ionization efficiency.[62,63] However, this is limited by the availability of isotope-labeled peptides and proteins. In the absence of isotope-labeled standards, it has been found that simply counting the number of scans in which peptides from a particular protein are identified is a surprisingly accurate measure of protein concentration.[64] Further, the intensities of the *b* and *y* ions in the MS/MS scan are well correlated with protein concentrations and less sensitive to simultaneous elution of multiple proteins.[65] Strategies that combine these approaches are emerging which may improve the accuracy, precision, and dynamic range of mass spec-based quantification.[66] However, the current lack of quantification limits the usefulness of proteomics for the study of protein adsorption. Until then, radiolabeling remains the gold standard for quantification of protein adsorption.

3.303.5. Proteomics to Study Protein Denaturation on Surfaces

Adsorbed fibrinogen undergoes dramatic changes in conformation upon adsorption. The increase in surface area covered by each fibrinogen molecule is directly observable by atomic force microscopy (AFM) over the course of about an hour.[67] It has been proposed that resting platelets recognize two motifs on adsorbed fibrinogen, the α-chain 572–575 RGDS sequence and the γ-chain dodecapeptide.[68,69] The latter peptide is responsible for the aggregation of activated platelets in solution.[70] Binding of monoclonal antibodies suggests that the domains containing these peptides may undergo conformational changes following adsorption to surfaces.[71,72] A high-throughput proteomics method to detect exposure of protein domains upon adsorption may allow more detailed study of these processes.

The accessibility of side chain amino acids to reaction with chemical labels is commonly used to map protein structures.[73] Combined with mass spectrometry, the locations of the modified amino acids may be identified. Side-chain labeling methods may potentially reveal changes in conformation following adsorption to surfaces. Using a side-chain labeling approach, lysine groups on fibrinogen were reacted with NHS-activated biotin, following adsorption to PET microparticles.[74] Fibrinogen was eluted from the polymer and digested with trypsin. Using MALDI-TOF mass spectrometry, the presence of peaks corresponding to biotin-labeled peptides was used to estimate the extent of labeling, consistent with the exposure of these sites due to conformational changes that are more likely due to the slower kinetics of adsorption from low concentration solutions. Proteins adsorbed from less concentrated solutions had increased numbers of biotin-labeled peptides, and the two adhesion sites were only observed at lower solution protein concentrations.

Latour and colleagues utilized a tryptophan modification chemistry to probe conformational changes of adsorbed enzymes. Lysozyme or glucose oxidase was adsorbed to alkanethiol monolayers on gold. With lysozyme, tryptophan modification was lower on $-CH_3$ and –COOH surfaces compared to –OH and $-NH_2$ surfaces, and all surfaces had less labeling than the enzyme in solution. With glucose oxidase, tryptophan labeling was more extensive following adsorption. Circular dichroism could be applied to the protein-adsorbed self-assembled monolayers, and a decrease in helicity was correlated with tryptophan modification in glucose oxidase but not lysozyme. Activity of the enzymes adsorbed on the surfaces was also measured. A decrease in enzymatic activity was well correlated with a lack of tryptophan labeling of lysozyme, but tryptophan labeling was not correlated with the activity of glucose oxidase. The activity of glucose oxidase adsorbed on the $-CH_3$ and –COOH surfaces was actually higher than in solution. It was hypothesized that the tryptophans present near the active site of lysozyme are in a hydrophobic pocket that may orient toward the $-CH_3$ surface, decreasing activity. Tandem mass spectrometry was used to identify the tryptophan residues modified in lysozyme. On the $-CH_3$ surface, only one tryptophan was found to be labeled, which is far away from the active cleft of the enzyme. In solution, this tryptophan was unlabeled, but tryptophans near the active cleft were labeled.[75] Mass spectrometry thus could aid in deciphering the predominant orientations of adsorbed proteins. When proteins adsorb in preferred orientations, the side-chain labeling strategy may be useful to determine how conformational changes affect biological activity.

Future improvements in quantitative mass spectrometry may also allow characterization of preferred adsorbed orientations in complex mixtures of proteins.

3.303.6. Challenges of the Proteomics Approach

Despite the promise of proteomics for the study of protein adsorption, several limitations must be overcome. Ideally, proteomics should result not just in a large body of information, but to the emergence of novel, testable hypotheses. Unbiased approaches are difficult to reconcile with the cornerstone of the scientific method – the testing of specific hypotheses. Biased approaches are currently far superior to address specific hypotheses. Due to the wide range of concentrations of proteins in biological samples, proteomic methods are currently far from comprehensive. The most abundant proteins in biological samples, for example, albumin, actin, and histones, are often of little interest, yet dominate the signal from proteomic methods. Contamination of the sample with dust, skin, or hair may also result in a large signal from keratin. Proteins of great interest, such as growth factors, may be at concentrations that are far too low to detect without extensive purification, for example, by immunoprecipitation. However, the approach would then no longer be unbiased. Although proteomic methods are considered to be high throughput, the actual throughput may be relatively low. A typical sample run on nanoHPLC and a tandem mass spectrometer may require about 1 h of mass spectrometer time. To extensively characterize a single 2D gel could require days of mass spectrometer time, yielding typically only protein identification with no information on protein amount. Improvements in the throughput of mass spectrometers should greatly enhance the usefulness of these methods. Enhancement of the quantitative nature of mass spectrometry may also allow the methods to become competitive with radiolabeling. Compared to radiolabeling, proteomic methods are also challenged by the presence of adsorbed proteins that are difficult to elute. Elution of proteins from surfaces, particularly hydrophobic surfaces, will likely be incomplete.[76,77] On hydrophobic surfaces, the most highly denatured proteins that are most difficult to elute may also have the most biological activity due to more extensive conformational changes.

3.303.7. Conclusions

The use of unbiased methods has changed our understanding of the process of protein adsorption. It is clear that the proteins that adsorb to a surface largely reflect the proteins found in solution. Proteins such as Apo A-I, transferrin, and α_2-macroglobulin that are typically not studied by radiolabeling may be present in large amounts on surfaces. The impact of such proteins on biocompatibility, either directly or indirectly by affecting adsorption of active proteins, is unclear. However, the presence of a wide range of proteins should be taken into account to fully understand the role of adsorbed proteins in biological responses to materials. High-throughput, unbiased methods may lead to a comprehensive understanding of protein adsorption, although substantial method development will be required to surpass the quality of data obtained using traditional biochemical techniques.

References

1. Lyman, D. J.; Metcalf, L. C.; Albo, D., Jr.; Richards, K. F.; Lamb, J. *Trans. Am. Soc. Artif. Intern. Organs* **1974**, *20B*, 474–478.
2. Limber, G. K.; Mason, R. G. *Thromb. Res.* **1975**, *6*, 421–430.
3. Horbett, T. A.; Weathersby, P. K. *J. Biomed. Mater. Res.* **1981**, *15*, 403–423.
4. Weathersby, P. K.; Horbett, T. A.; Hoffman, A. S. *Trans. Am. Soc. Artif. Intern. Organs* **1976**, *22*, 242–252.
5. Rapoza, R. J.; Horbett, T. A. *J. Colloid Interface Sci.* **1990**, *136*, 480–493.
6. Vroman, L.; Adams, A. L.; Fischer, G. C.; Munoz, P. C. *Blood* **1980**, *55*, 156–159.
7. Griffin, J. H. *Proc. Natl. Acad. Sci. USA* **1978**, *75*, 1998–2002.
8. Scott, C. F. *J. Biomater. Sci. Polym. Ed.* **1991**, *2*, 173–181.
9. Brash, J. L.; Thibodeau, J. A. *J. Biomed. Mater. Res.* **1986**, *20*, 1263–1275.
10. Mulzer, S. R.; Brash, J. L. *J. Biomed. Mater. Res.* **1989**, *23*, 1483–1504.
11. Craddock, P. R.; Fehr, J.; Dalmasso, A. P.; Brighan, K. L.; Jacob, H. S. *J. Clin. Invest.* **1977**, *59*, 879–888.
12. O'Farrell, P. H. *J. Biol. Chem.* **1975**, *250*, 4007–4021.
13. Anderson, L.; Anderson, N. G. *Proc. Natl. Acad. Sci. USA* **1977**, *74*, 5421–5425.
14. Anderson, N. L.; Anderson, N. G. *Electrophoresis* **1991**, *12*, 883–906.
15. Anderson, N. L.; Polanski, M.; Pieper, R.; *et al. Mol. Cell. Proteomics* **2004**, *3*, 311–326.
16. Owen, D. R.; Chen, C. M.; Oschner, J. A.; Zone, R. M. *Trans. Am. Soc. Artif. Intern. Organs* **1985**, *31*, 240–243.
17. Ho, C. H.; Hlady, V.; Nyquist, G.; Andrade, J. D.; Caldwell, K. D. *J. Biomed. Mater. Res.* **1991**, *25*, 423–441.
18. Blunk, T.; Hochstrasser, D. F.; Sanchez, J. C.; Muller, B. W.; Muller, R. H. *Electrophoresis* **1993**, *14*, 1382–1387.
19. Moghimi, S. M.; Muir, I. S.; Illum, L.; Davis, S. S.; Kolb-Bachofen, V. *Biochim. Biophys. Acta* **1993**, *1179*, 157–165.
20. Meng, F.; Engbers, G. H.; Gessner, A.; Muller, R. H.; Feijen, J. *J. Biomed. Mater. Res.* **2004**, *70A*, 97–106.
21. Harnisch, S.; Muller, R. H. *Electrophoresis* **1998**, *19*, 349–354.
22. Hedeman, H.; Luck, M.; Blunk, T.; Frokjaer, S.; Muller, R. H. *Clin. Nutr.* **1996**, *15*, 175–178.
23. Thode, K.; Luck, M.; Schroder, W.; *et al. J. Drug Target.* **1997**, *5*, 35–43.
24. Gref, R.; Luck, M.; Quellec, P.; *et al. Coll. Surf. B Biointer.* **2000**, *18*, 301–313.
25. Luck, M.; Pistel, K. F.; Li, Y. X.; Blunk, T.; Muller, R. H.; Kissel, T. *J. Control Release* **1998**, *55*, 107–120.
26. Peracchia, M. T.; Harnisch, S.; Pinto-Alphandary, H.; *et al. Biomaterials* **1999**, *20*, 1269–1275.
27. Gessner, A.; Olbrich, C.; Schroder, W.; Kayser, O.; Muller, R. H. *Int. J. Pharm.* **2001**, *214*, 87–91.
28. Olbrich, C.; Bakowsky, U.; Lehr, C. M.; Muller, R. H.; Kneuer, C. *J. Control. Release* **2001**, *77*, 345–355.
29. Diederichs, J. E. *Electrophoresis* **1996**, *17*, 607–611.
30. Leroux, J. C.; Gravel, P.; Balant, L.; *et al. J. Biomed. Mater. Res.* **1994**, *28*, 471–481.
31. Allemann, E.; Gravel, P.; Leroux, J. C.; Balant, L.; Gurny, R. *J. Biomed. Mater. Res.* **1997**, *37*, 229–234.
32. Leroux, J. C.; De Jaeghere, F.; Anner, B.; Doelker, E.; Gurny, R. *Life Sci.* **1995**, *57*, 695–703.
33. Kreuter, J.; Shamenkov, D.; Petrov, V.; *et al. J. Drug Target.* **2002**, *10*, 317–325.
34. Kim, H. R.; Andrieux, K.; Delomenie, C.; *et al. Electrophoresis* **2007**, *28*, 2252–2261.
35. Brash, J. L.; Scott, C. F.; Ten Hove, P.; Wojciechowski, P.; Colman, R. W. *Blood* **1988**, *71*, 932–939.
36. Rosengren, A.; Oscarsson, S.; Mazzocchi, M.; Krajewski, A.; Ravaglioli, A. *Biomaterials* **2003**, *24*, 147–155.
37. Rosengren, A.; Pavlovic, E.; Oscarsson, S.; Krajewski, A.; Ravaglioli, A.; Piancastelli, A. *Biomaterials* **2002**, *23*, 1237–1247.
38. Stanislawski, L.; De Nechaud, B.; Christel, P. *J. Biomed. Mater. Res.* **1995**, *29*, 315–323.
39. Poot, A.; Beugeling, T.; Van Aken, W. G.; Bantjes, A. *J. Biomed. Mater. Res.* **1990**, *24*, 1021–1036.
40. Schenk, S.; Schoenhals, G. J.; De Souza, G.; Mann, M. *BMC Med. Genomics* **2008**, *1*, 41.
41. Berna, N.; Berna, P.; Oscarsson, S. *Arch. Biochem. Biophys.* **1996**, *330*, 188–192.

42. Berna, N.; Berna, P.; Oscarsson, S. *J. Chromatogr. A* **1997**, *764*, 193–200.
43. Sun, D. H.; Trindade, M. C.; Nakashima, Y.; *et al*. *J. Biomed. Mater. Res.* **2003**, *65A*, 290–298.
44. Xie, J.; Baumann, M. J.; McCabe, L. R. *J. Biomed. Mater. Res. A* **2005**, *73*, 39–47.
45. Kingshott, P.; St John, H. A. W.; Griesser, H. J. *Anal. Biochem.* **1999**, *273*, 156–162.
46. Leize, E. M.; Leize, E. J.; Leize, M. C.; Voegel, J. C.; Van Dorsselaer, A. *Anal. Biochem.* **1999**, *272*, 19–25.
47. Walker, A. K.; Qiu, H.; Wu, Y.; Timmons, R. B.; Kinsel, G. R. *Anal. Biochem.* **1999**, *271*, 123–130.
48. Oleschuk, R. D.; Mccomb, M. E.; Chow, A.; *et al*. *Biomaterials* **2000**, *21*, 1701–1710.
49. Lhoest, J. B.; Wagner, M. S.; Tidwell, C. D.; Castner, D. G. *J. Biomed. Mater. Res.* **2001**, *57*, 432–440.
50. Wagner, M. S.; Horbett, T. A.; Castner, D. G. *Biomaterials* **2003**, *24*, 1897–1908.
51. Wagner, M. S.; McArthur, S. L.; Shen, M.; Horbett, T. A.; Castner, D. G. *J. Biomater. Sci. Polym. Ed.* **2002**, *13*, 407–428.
52. Wagner, M. S.; Tyler, B. J.; Castner, D. G. *Anal. Chem.* **2002**, *74*, 1824–1835.
53. Derhami, K.; Zheng, J.; Li, L.; Wolfaardt, J. F.; Scott, P. G. *J. Biomed. Mater. Res.* **2001**, *56*, 234–244.
54. Kim, J. K.; Scott, E. A.; Elbert, D. L. *J. Biomed. Mater. Res. A* **2005**, *75*, 199–209.
55. Bharadwaj, D.; Mold, C.; Markham, E.; Du Clos, T. W. *J. Immunol.* **2001**, *166*, 6735–6741.
56. Dihazi, H.; Koziolek, M. J.; Sollner, T.; *et al*. *Nephrol. Dial. Transplant.* **2008**, *23*, 2925–2935.
57. Mares, J.; Thongboonkerd, V.; Tuma, Z.; Moravec, J.; Karvunidis, T.; Matejovic, M. *J. Proteome Res.* **2009**, *8*, 1756–1764.
58. Mares, J.; Thongboonkerd, V.; Tuma, Z.; Moravec, J.; Matejovic, M. *Kidney Int.* **2009**, *76*, 404–413.
59. Bonomini, M.; Pavone, B.; Sirolli, V.; *et al*. *J. Proteome Res.* **2006**, *5*, 2666–2674.
60. Turck, C. W.; Falick, A. M.; Kowalak, J. A.; *et al*. *Mol. Cell. Proteomics* **2007**, *6*, 1291–1298.
61. Pan, P.; Mcluckey, S. A. *Anal. Chem.* **2003**, *75*, 5468–5474.
62. Gygi, S. P.; Rist, B.; Gerber, S. A.; Turecek, F.; Gelb, M. H.; Aebersold, R. *Nat. Biotechnol.* **1999**, *17*, 994–999.
63. Ong, S. E.; Blagoev, B.; Kratchmarova, I.; *et al*. *Mol. Cell. Proteomics* **2002**, *1*, 376–386.
64. Liu, H.; Sadygov, R. G.; Yates, J. R., III *Anal. Chem.* **2004**, *76*, 4193–4201.
65. Bateman, R. J.; Munsell, L. Y.; Chen, X.; Holtzman, D. M.; Yarasheski, K. E. *J. Am. Soc. Mass Spectrom.* **2007**, *18*, 997–1006.
66. Griffin, N. M.; Yu, J.; Long, F.; *et al*. *Nat. Biotech.* **2010**, *28*, 83–89.
67. Sit, P. S.; Marchant, R. E. *Thromb. Haemost.* **1999**, *82*, 1053–1060.
68. Kieffer, N.; Fitzgerald, L. A.; Wolf, D.; Cheresh, D. A.; Phillips, D. R. *J. Cell Biol.* **1991**, *113*, 451–461.
69. Savage, B.; Ruggeri, Z. M. *J. Biol. Chem.* **1991**, *266*, 11227–11233.
70. Farrell, D. H.; Thiagarajan, P.; Chung, D. W.; Davie, E. W. *Proc. Natl. Acad. Sci. USA* **1992**, *89*, 10729–10732.
71. Grunkemeier, J.; Wan, C.; Horbett, T. *J. Biomater. Sci. Polym. Ed.* **1996**, *8*, 189–209.
72. Horbett, T. A.; Lew, K. R. *J. Biomater. Sci. Polym. Ed.* **1994**, *6*, 15–33.
73. Bennett, K. L.; Matthiesen, T.; Roepstorff, P. *Meth. Mol. Biol.* **2000**, *146*, 113–131.
74. Scott, E. A.; Elbert, D. L. *Biomaterials* **2007**, *28*, 3904–3917.
75. Fears, K. P.; Sivaraman, B.; Powell, G. L.; Wu, Y.; Latour, R. A. *Langmuir* **2009**, *25*, 9319–9327.
76. Magnani, A.; Barbucci, R.; Lamponi, S.; *et al*. *Electrophoresis* **2004**, *25*, 2413–2424.
77. Ombelli, M.; Composto, R. J.; Meng, Q. C.; Eckmann, D. M. *J. Chromatogr. B Analyt. Technol. Biomed. Life Sci.* **2005**, *826*, 198–205.

3.304. Developments in High-Resolution CT: Studying Bioregeneration by Hard X-ray Synchrotron-Based Microtomography

A Rack, European Synchrotron Radiation Facility, Grenoble, France
M Stiller, O Dalügge, and T Rack, Charité Medical University, Berlin, Germany
H Riesemeier, BAM – Federal Institute for Materials Research and Testing, Berlin, Germany
C Knabe, Philipps University Marburg, Marburg, Germany

© 2011 Elsevier Ltd. All rights reserved.

3.304.1.	**Hard X-ray Microimaging**	48
3.304.1.1.	Laboratory Approach	48
3.304.1.2.	Synchrotron Light Sources	49
3.304.1.3.	Quantitative Volume Image Analysis	51
3.304.1.4.	Microtomography: Life Sciences, Biomaterials and Bone Research	51
3.304.2.	**Comparative Animal Study of Bioceramic-Supported Bone Regeneration**	53
3.304.2.1.	Surgery and Specimen Retrieval	53
3.304.2.2.	Microtomography and Volume Image Processing	55
3.304.2.3.	Results	55
3.304.3.	**Bone Regeneration After Sinus Floor Augmentation in Humans**	57
3.304.3.1.	Surgery and Biopsy	57
3.304.3.2.	Microtomography and Volume Image Analysis	58
3.304.3.3.	Results	58
3.304.4.	**Summary**	59
References		61

Glossary

Boolean image Also binary image, a digital image with only two possible values for each pixel (commonly, '1' and '0').

Insertion device Array of spatially periodic magnets inserted into the straight section of the storage ring of a synchrotron source, different types are known: wavelength shifters, undulators, and wigglers; they all cause acceleration of the electrons in the storage ring which results in the emission of synchrotron light.

Multilayer monochromator Multilayer films for X-rays can be described as an extension of optical coatings to shorter wavelengths or of natural crystals to larger lattice spacings; a multilayer monochromator for X-rays selects a wavelength out of a polychromatic spectrum, commonly with an energy spread of a few percentage.

(Partial) Spatial coherence A property of a wavefront which allows for interference, that is, X-ray phase contrast within the content of this chapter.

Pixel Acronym for picture element which represents a value within an image interpreted as two-dimensional matrix (per definition, a pixel is shapeless).

Scintillation A subcategory of luminescence: ionizing radiation of high energy is converted into a flash of visible light photons.

Sinogram Also Radon transform, a visualization of the acquired raw tomographic data along the rotation angle which corresponds to one slice after the reconstruction.

Spatial resolution/point spread function Imaging detectors record an ideal point-shaped signal with a specific broadening, described with the point spread function (PSF); frequently, the width of the PSF is used as measurement for the spatial resolution of the detector (while the detector's pixel size needs to be adapted to the PSF according to Shannon's theorem).

Synchrotron light source The synchrotron itself is a cyclic particle accelerator based on synchronized magnetic and electric fields; frequently, electrons are accelerated close to the speed of light and then inserted into a storage ring where the light to be used is created when the electrons pass through magnetic fields (see as well insertion device).

Voxel Acronym for volume(tric) picture element which represents a value within, for example, a tomographic image interpreted as three-dimensional matrix (per definition, a voxel is shapeless).

X-ray phase contrast Also inline phase contrast, objects with negligible X-ray attenuation contrast can be visualized in terms of their edges when a source with a certain coherence is used for the illumination: the refraction of the X-rays at interfaces leads to an intensity modulation within the images.

Abbreviations

352i	Calcium alkali orthophosphate with the main crystalline phase $Ca_{10}KNa(PO_4)_2$
CCD	Charge-coupled device
CMOS	Complementary metal oxide semiconductor
CT	Computed tomography
ESRF	European Synchrotron Radiation Facility
GB9	Material with the main crystalline phase $Ca_2KNa(PO_4)_2$ and small amorphous phase containing silica phosphates
HZB	Helmholtz Zentrum Berlin für Materialien und Energie
MAVI	Modular Algorithms for Volume Images
PSF	Point spread function
PyHST	Python-based high speed tomographic reconstruction
SPIE	International Society for Optics and Photonics
SμCT	Synchrotron-based microtomography
TCP	Beta-tricalcium phosphate with 35% porosity
TCP-P	Beta-tricalcium phosphate with 60% porosity
WLS	Wavelength shifter
μCT	Microtomography

3.304.1. Hard X-ray Microimaging

Since the discovery of X-rays by W. C. Röntgen more than a 100 years ago ('Über eine neue Art von Strahlen,' in: Secretary of the Physical-Medical Society, Würzburg, 1895), radiographic imaging has been established as one of the fundamental techniques for medical diagnosis. In addition, various other applications, for example, for nondestructive evaluation emphasize the high value of imaging the interior of an object without the need of damaging it.[1]

During in the 1970s, X-ray imaging was extended into the third dimension by combining radiographic images of an object taken from different angles: computed (axial scanning) tomography (CT).[2,3] Like radiography, CT established itself as a fundamental technique in medicine, and is presently extended by sophisticated contrast modes such as positron-emission tomography using different types of radiation, respectively.[4]

In the early 1980s, first successful approaches were reported in which CT was applied outside medical fields, for example, to study cracks in concrete.[5] In this case, the instrumentation development pushed the reachable spatial resolutions to the micrometer range: microtomography (μCT).[6,7] In the same decade, first publications were introducing μCT as performed using synchrotron light (SμCT).[8–13] During the 1990s, with the first so-called third generation synchrotron light sources starting operations, SμCT was established as a standard technique with spatial resolutions available up to the (sub-)micrometer range[14] and specific contrast modes.[15] This development has been well documented in the SPIE conference series *Developments in X-ray Tomography I–VII* and the corresponding proceedings. A detailed review on tomographic techniques for materials research and engineering using different contrast modes as well as radiation sources is given in Banhart,[16] specifically for synchrotron light sources in Graeff and Engelke.[13]

The content of this chapter is dedicated to *ex vivo* investigations performed using SμCT in the so-called absorption contrast mode. The specimens under investigation are human and sheep bone, taken several months after the implantation of bioceramic particles.[17] The following sections are dedicated to the introduction of the methods in a brief manner while results are presented in the following paragraphs.

3.304.1.1. Laboratory Approach

The basic principle of CT relies on the fact the interior mass distribution inside an object can be reconstructed from its radiographic projection images taken from different projection angles. Presently, various robust algorithms performing this task have been established as a standard solution, providing virtual slices of the analyzed object which arranged as a stack represent the volume image. One approach, known as algebraic reconstruction, formulates the problem as a set of independent equations to be solved via matrix operations. Other methods such as the filtered-backprojection algorithm or the direct Fourier inversion reconstruct a virtual slice by summation of the measured integral attenuation profiles in real or Fourier space.[18] An excellent description of the different basic principles of tomographic reconstruction was published by Kalender.[19]

The common scanning geometry known from medical CT keeps the patient fixed while the X-ray source and the detector are rotated around him to perform the CT scan.[4] For μCT, with the specimen commonly being small and of static nature, the X-ray source and the detector are fixed while the sample is rotated (see **Figure 1**). Consequently, demands on the mechanics are less extensive, especially for achieving a spatial precision in the (deep sub-)micrometer range.

With respect to the following section about synchrotron-based microtomography, two different beam geometries for full-field imaging have to be considered (see **Figure 1**): X-ray tubes emit the light in a broad cone or fan. The advantage of this cone beam geometry is that the imaging magnification and hence, the spatial resolution can be chosen by the distance between the sample and the X-ray source. But, this limits the maximum distance between the sample as well as the source in a practical manner: with the increasing distance the photon flux density decreases. Thus, the finite source size can deteriorate the achievable resolution by means of penumbral blurring. Furthermore, artifacts are introduced due to the incomplete projection data acquired when using a cone beam. Synchrotron light sources frequently deliver a nearly parallel beam. Here, the sample-to-detector distance can be extended up to several 100 m but the spatial resolution to be achieved requires a corresponding high resolving power of the X-ray detection scheme used.[4,14,16,18,20]

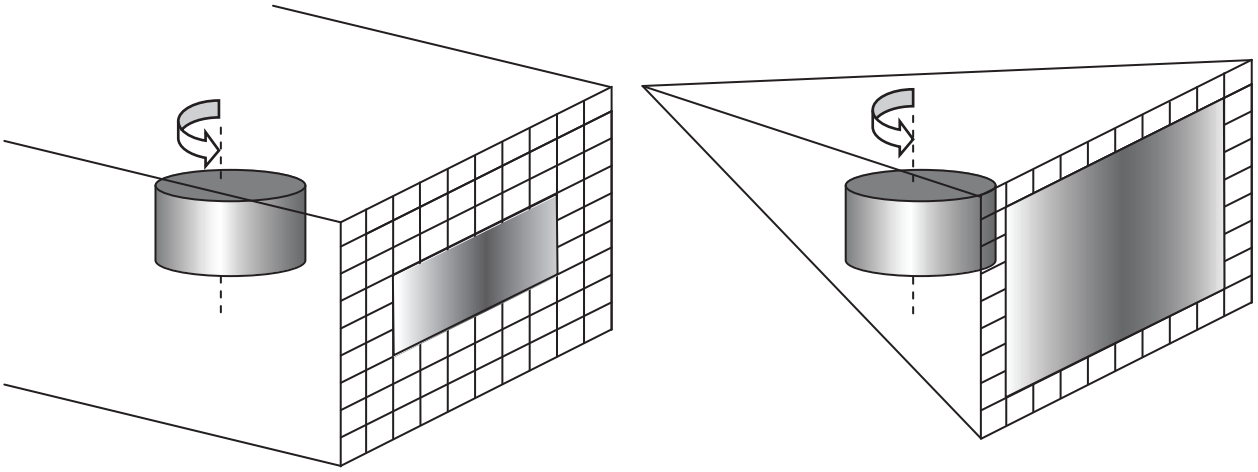

Figure 1 The two relevant beam geometries in full-field microtomography and radiography: parallel beam (left) allowing for large source-to-experiment distances but with high demands on the resolving power of the X-ray detector; the cone beam geometry (right) allows one to tune the imaging magnification via the sample-to-detector distance but is practically more sensitive to the finite source size extension.

The contrast in a standard laboratory μCT scan is given by the local X-ray attenuation behavior of the sample. This is in a first approximation related to the local density, the chemical components and the X-ray photon energy employed. The density-related material contrast is directly connected to the photon flux density available for imaging in a strongly nonlinear manner, for example, to double the detectable contrast an increase of the photons involved by a factor of four is required.[21,22] Additionally, for example, the X-ray photon energy used needs to be adapted for the individual sample as specific transmission values are optimal for the tomographic reconstruction.[13,23,24]

Full-field microtomography using laboratory X-ray sources is an excellent tool applied within a broad range of scientific and industrial fields. Successful approaches of μCT employed, for example, in bone research were already reported during the 1980s.[25–27] In the same decade, the demand for using the powerful synchrotron light sources with orders of magnitude higher than photon flux density for X-ray microimaging was formulated, since it would allow for pushing the limits of the achievable resolution in space and time.[7,14,28–31]

3.304.1.2. Synchrotron Light Sources

While laboratory X-ray tubes generate the light via accelerated electrons hitting a target, synchrotron light sources use electrons passing with relativistic speeds (close to the speed of light) through magnetic fields. Due to the magnetic field, the trajectory of the electrons is bent and as known from a classical dipole (antenna), accelerated electrons emit electromagnetic waves. The relativistic speed of the electrons deforms the dipole emission characteristic so that the light is emitted as a bundle in one direction tangential to the flight direction only. The speed of the electrons and their density as well as the magnetic field and the numbers of magnets roughly determine the emission spectra and photon flux density as well as the brilliance of the source.[32]

For imaging applications, the major advantages of synchrotron light sources in comparison with other sources are: the orders of magnitude higher than photon flux density, the almost parallel beam propagation and the coherence properties of the beam at the position of the experiment. As an example, see **Figure 2** in which the available monochromatic photon flux density of the imaging station located at the BAM*line* (BESSY-II light source of the Helmholtz Zentrum Berlin für Materialien und Energie GmbH, Germany) is compared with standard laboratory sources.[33,34] Other imaging stations at synchrotron light sources such as the European Synchrotron Radiation Facility (Grenoble, France) and the Advanced Photon Source (Chicago, United States) or SPring-8 (Hyogo, Japan) provide even much higher photon flux densities. The large amount of photons allows for using monochromators: monochromatic radiation employed for X-ray imaging increases generally the contrast while reducing artifacts.[35] A high photon flux density specifically allows for increasing the detectable density-related material contrast.[21,22] As mentioned in the previous section, due to the parallel beam the distance between source and experiment can be extended up to several hundred meters which suppresses the influence of the finite source size on the achievable spatial resolution. Another effect of this long distance is a certain coherence of the X-ray wave fronts at the position of the experiment, hence, interference effects can give access to more sophisticated contrast modes like the inline X-ray phase contrast or holotomography.[15,36–38] Other contrast modes such as the local chemical species distribution or the local crystal phase information are accessible when employing a scanning approach instead of the full-field imaging technique.[39] A detailed discussion about the advantages of using synchrotron light for μCT is given in Bonse and Busch[20] while the more general overview of the different contrast modes in combination with different radiation types is available, for example, by Banhart.[16]

The common design of a microimaging experimental station at a synchrotron light source is depicted in **Figure 3**, again using the BAM*line* as an example.[33,34] From the polychromatic radiation generated by the source inside the storage ring, a certain wavelength is selected via an X-ray monochromator. The light travels through a long vacuum pipe toward the

experimental hutch. Here, the sample is placed on a manipulator allowing for rotation, tilt alignments and translation. Behind the sample, a digital X-ray pixel detector is placed which records the light as transmitted by the specimen.

In Figure 3 an additional schematic is shown which displays the common indirect detection scheme applied for high resolution imaging with a parallel beam, based on the concepts of Hartmann *et al.*[41] and Bonse and Busch[20]: the luminescence image of a scintillator screen (powder or single-crystal) is projected via diffraction-limited visible light optics onto a camera (CCD or CMOS). Here, the maximum achievable spatial resolution is determined by the wavelength of emission of the scintillator as well as the numerical aperture of the objective used (Abbe's theorem). By introducing transparent thin single-crystal film scintillators, resolutions up to the (sub-)micrometer range can be reached as standard application.[14] The high resolution is only accessible at the expense of the field of view of the detector and its efficiency. In order to reach for a spatial resolution around 1 µm, pixel sizes below 0.5 µm have to be used, with the common 2048 × 2048 pixel CCD camera the remaining field of view is less than 1 mm^2. The required numerical aperture for this type of resolution reduces the depth of focus to a few micrometer in which the active layer of the scintillator screen has to fit. For example, at an X-ray photon energy of 15 keV a $Lu_3Al_5O_{12}$ (LAG) screen with the required thickness of 5 µm transmits 75% of the flux which therefore cannot be used for imaging.[40] Further increase of the resolution in the nanometer range can be achieved by employing X-ray optics.[42–44] This facilitated even studying structures as small as single cells.[45,46]

Commonly, access to experimental stations at synchrotron light sources is free of charge for scientific users. Experiments have to be approved after submitting proposals which are evaluated by independent committees. The beamtime is then allocated according to the availability and the ranking of the rated proposals.[47] A compilation of synchrotron light sources worldwide which operate microimaging facilities is listed in

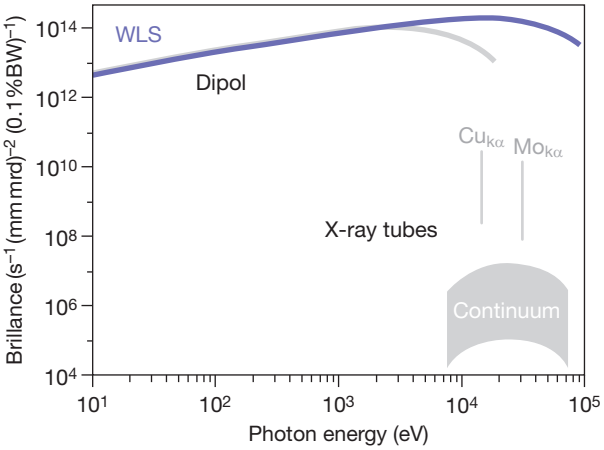

Figure 2 The available monochromatic photon flux at the BAM*line* imaging station of the BESSY-II light source (Berlin, Germany) in comparison with standard laboratory sources. See as well Görner, W.; Hentschel, M. P.; Müller, B. R.; *et al. Nucl. Instrum. Meth. Phys. Res. A* **2001**, *467*, 703–706; Rack, A.; Zabler, S.; Müller, B.; *et al. Nucl. Instrum. Meth. Phys. Res. A* **2008**, *586*, 327–344.

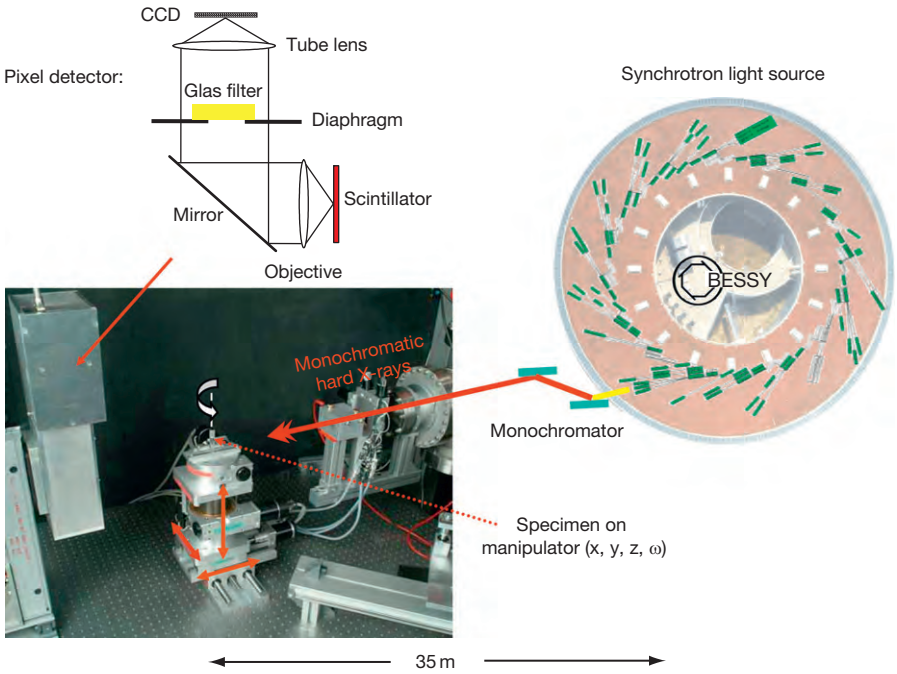

Figure 3 The imaging station of the BAM*line* as example for a common full-field microtomography design at a synchrotron light source: from the polychromatic radiation of the source, a wavelength is selected by a monochromator. The light reaches through a long vacuum pipe the experimental station. The sample is placed on a manipulator allowing for rotation, tilt alignment and translation. The X-rays as transmitted by the sample are collected by a high resolution X-ray pixel detector. The sketch shows the common indirect detection scheme used, see Graafsma and Martin[40] and Rack *et al.*[34]

Table 1 Overview of synchrotron light sources worldwide operating hard X-ray microimaging facilities

Name, country	*Website*	*Beamline(s)*
Advanced Light Source, USA	http://www.als.lbl.gov	Beamline 8.3.2
Advanced Photon Source, USA	http://www.aps.anl.gov	2-BM, 5-BM, 13-BM, 26-ID, 32-ID
ANKA, Germany	http://ankaweb.fzk.de	TopoTomo
Australian Synchrotron, Australia	http://www.synchrotron.org.au	Imaging and Medical Beamline (under construction)
BESSY-II, Germany	http://www.bessy.de, http://www.bam.de	BAM*line*
CAMD, USA	http://www.camd.lsu.edu	Tomography
Canadian Light Source, Canada	http://www.lightsource.ca	Medical beamline BMIT-ID
DESY, Germany	http://www.desy.de	IBL, HEMS (Petra3, under construction), HARWII, BW2 (Doris)
Diamond Light Source, UK	http://www.diamond.ac.uk	JEEP, I13 (under construction)
ELETTRA, Italy	http://www.elettra.trieste.it	SYRMEP
European Synchrotron Radiation Facility, France	http://www.esrf.eu	BM05, ID15a, ID17, ID19, ID22
National Synchrotron Light Source, USA	http://www.nsls.bnl.gov	X2B, X15a
Pohang Light Source, Korea	http://pal.postech.ac.kr	1B2/microprobe
Shanghai Synchrotron Radiation Facility, China	http://ssrf.sinap.ac.cn/english	BL10W1 (under construction)
Singapore Synchrotron Light Source, Singapore	http://ssls.nus.edu.sg	PCI
Soleil, France	http://www.synchrotron-soleil.fr	PSICHÉ, PUMA (both under construction)
Stanford Synchrotron Radiation Lightsource, USA	http://www-ssrl.slac.stanford.edu	BL6-2
SPring-8, Japan	http://www.spring8.or.jp	BL19B2, BL20XU, BL20B2
Swiss Light Source, Switzerland	http://sls.web.psi.ch	TOMCAT

Table 1. A detailed list of all synchrotron light sources and further information can be accessed via the URL http://www.lightsources.org.

3.304.1.3. Quantitative Volume Image Analysis

Tomographic data sets are volume images in the sense of a three-dimensional matrix filled with values which, for example, can be considered as gray-scales for visualization purposes. Depending on the acquisition mode, these values represent, for example, the linear X-ray attenuation coefficient (μCT), density of metabolized isotopes (positron emission tomography), hydrogen concentration (magnetic resonance imaging), or the electron density (holotomography).

The first step in the analysis of a multiconstituent volume image is commonly the separation of morphological components (e.g., pores, bone, or bioceramic particles) into independent Boolean images. In such an image, pixels (picture elements, frequently called voxels for volume images) belonging to one phase are marked with a Boolean '1' while the remaining part of the image contains only '0.' In Figure 4, these steps are depicted via an example of cross-sections of a tomographic data set acquired *ex vivo* using synchrotron light showing a sheep bone specimen sampled 3 months after sinus floor augmentation with bioceramic bone grafting particles. Creating a Boolean image of the bioceramic is straight forward due to the excellent contrast and well-defined morphological structure. This Boolean image is used to remove the ceramic information from the original image which allows for separating the bone information from the remaining noise in a second step.[48] The crucial task of creating Boolean images, frequently called binarization, is one of the main challenges for the image analysis and subsequently, a broad range of techniques were developed, ranging from simple thresholds to sophisticated algorithms such as the watershed transformation or region growing in combination with a threshold hysteresis.[49,50]

Once a set of Boolean images is created, further data processing can derive quantitative results like spatial cross-correlations between different constituents in the image[51] or the Boolean images are used to determine properties of a structure based on numerical simulations.[52,53] In our case, the separated images are also the basis for high quality volume renderings as shown in Figure 4. Further details regarding the analysis and rendering of volume images are outlined in Schladitz and Ohser[54] and Ohser and Schladitz,[55] for example. Common software packages employed for the analysis and visualization of volume images, are MAVI by the Fraunhofer ITWM, Department of Image Processing[56] or, for example, VGStudioMax, see Reinhart *et al.*,[57] both are commercially available.

For bone histomorphometry, the standardization of nomenclature, symbols and units has already been performed.[58] These standards can then be applied when analyzing tomographic data sets of bone,[27,104] thus, it becomes possible to progress to bone histovolumetry when combining μCT with quantitative volume image analysis.[59]

3.304.1.4. Microtomography: Life Sciences, Biomaterials and Bone Research

While μCT for medical and clinical applications as well as life sciences in general is presently aiming for *in vivo* scanning of animals and humans,[60–62] the use of SμCT is more challenging in this context. This is due to dose issues,[63] but in addition because of the limited availability and high costs of beamtime at synchrotron light sources. The outstanding contrast accessible with SμCT as demonstrated for, for example, investigating breast tissue,[64] tumor tissue,[65] or cartilage,[66] however, emphasized the high value of these techniques as tool for medical diagnosis. For a review of selected biomedical imaging techniques using synchrotron light, the reader is referred to Baruchel *et al.*[67]

Successful imaging investigations based on utilizing synchrotron light have already been reported in various fields

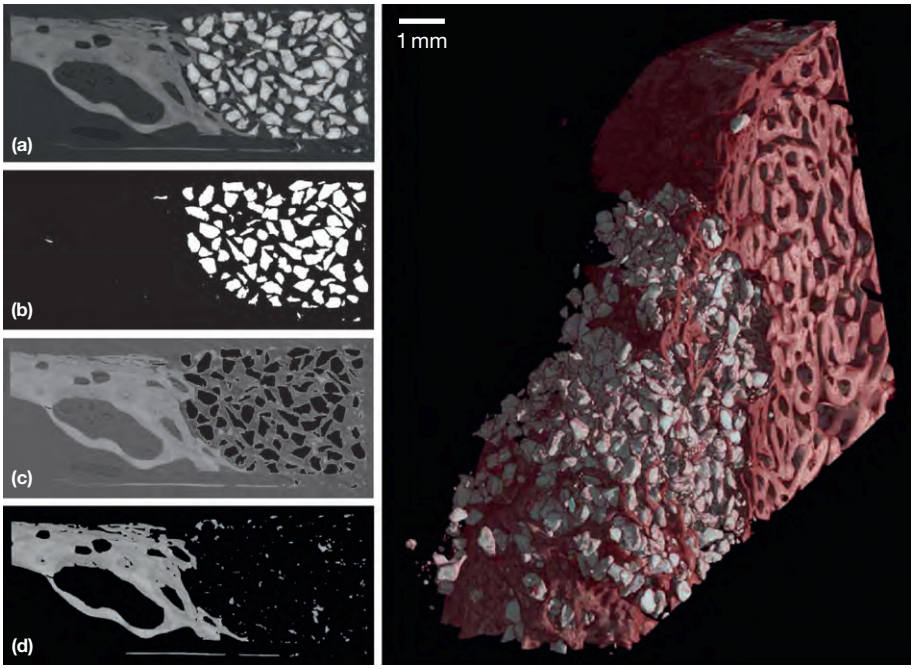

Figure 4 Left: from the gray-scaled image showing bioceramic particles after implantation for bone regeneration in sheep (a), through Boolean images of the individual material phases (e.g., ceramic particles, b) one can separate the gray-scale information of the different morphological components into independent images (c, d) which are the basis for high quality volume renderings as shown on the right. Adapted from Rack, A. Ph.D. Thesis, Technical University, Berlin, 2006 [in German]; See as well Schladitz, K.; Ohser, J. In *Advanced Tomographic Methods in Materials Research and Engineering*; Banhart. J., Ed.; Oxford University Press: Oxford, 2008; pp 37–106; Ohser, J.; Schladitz, K; *3D Images of Materials Structures: Processing and Analysis*. Wiley-VCH: Weinheim, 2009.

of the life sciences, such as biomineralization,[68] for studying endo- and exoskeletons[69] and biology, for imaging structure, function, and physiology of (living) organisms.[70,71] Due to the excellent contrast available, biomaterials have been studied with synchrotron-based microimaging for many years.[72–76] A few selected examples underscoring the high potential of synchrotron-based X-ray imaging with high resolution and in three dimensions are shown in **Figure 5**: the head of Forficula auricularia (Dermaptera),[71] a rat heart imaged with phase sensitive contrast[78] and newly formed bone onto the inner surface of a hydroxyapatite scaffold.[77] An example of a thorough comparative study of synchrotron radiation and laboratory X-ray sources for biomedical imaging (mammography) was published by Moeckli *et al.*[79]

Following the demonstration of the high potential of μCT for bone research,[26,27] SμCT was pioneered in this field already during the 1990s.[80] By virtue of the high density-sensitivity of the technique, it is excellently suited for the analysis of (trabecular) bone[81] or quantifying its degree of mineralization (see **Chapter 3.325, Imaging Mineralized Tissues in Vertebrates** and **Chapter 3.323, Magnetic Resonance of Bone Microstructure and Chemistry**).[82,83] The latter has also been applied for analyzing mineral concentrations in sound and carious enamel.[84] Other possibilities only available at synchrotron light sources include *in situ* investigations of bone under load to visualize crack formation[85] or *in vitro* studies of microgap formation between dental implants and their abutments.[86]

Recent developments, which also should be mentioned, are tomographic techniques using synchrotron radiation with very specific contrast modes for analyzing the local crystal structure[87] or chemical species distribution[88] of bone. Spatial nano-resolution in combination high density contrast has been achieved by ptychographic X-ray CT.[89] An outlook regarding synchrotron imaging contrast modes with micro- to nano-resolution to specifically study bone was published elsewhere.[90]

The widely nondestructive nature of μCT as performed by using laboratory or synchrotron sources also allows for an analysis of errors which arise when only classical (two-dimensional) techniques like histomorphometry of hard-tissue sections are applied for analyzing the amounts of newly formed bone rather than three-dimensional volumetric approaches (see **Chapter 3.313, Histological Analysis**). Already by comparing histological two-dimensional images with corresponding tomographic slices the strong effect of the sectioning of the specimens on the derived results can be demonstrated.[80] A first approach to quantify this effect using μCT with moderate resolution and contrast found discrepancies in the range of ±10%.[91–93] Recent studies with SμCT employing higher spatial resolution confirmed these observations, relating this effect both to the loss of substance which occurs during the sectioning as well to general limitations of histology originating from its two-dimensional nature.[59]

Exciting results are achieved when SμCT is used to study bone and biomaterials in a combined manner,[94] that is, the regeneration of tissue in a bony defect either around implants[95,96] or supported by ceramic bone substitute materials.[73] These studies are commonly performed *ex vivo* with animals, where biomaterials are implanted in artificial defects,

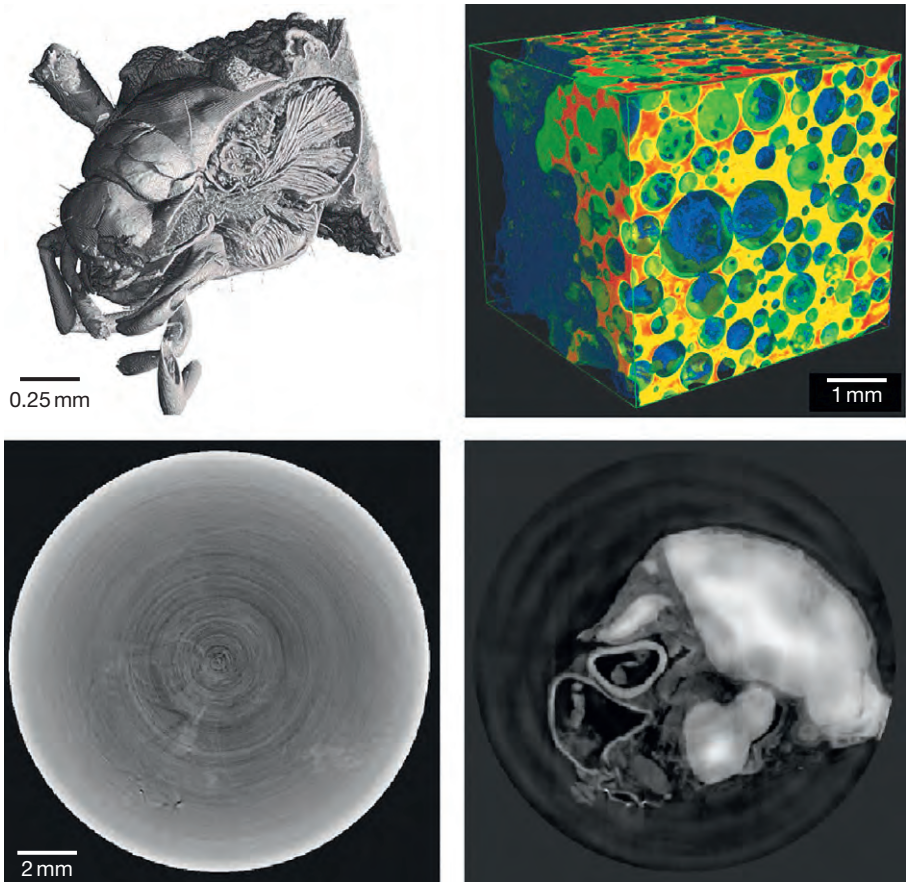

Figure 5 Top, left: volume rendering showing a CT-dataset of the head of Forficula auricularia (Dermaptera) as acquired by the means of synchrotron X-ray microtomography. See as well Betz, O.; Wegst, U.; Weide, D.; *et al. J. Microsc.* **2007**, *227*, 51–71. Right: hydroxyapatite scaffold (Engipore) loaded with sheep BMSC and implanted in an immunodeficient mouse, showing newly formed bone (green) onto the inner surface of the scaffold (yellow and red); the organic phase is blue. Reproduced from Cancedda, R.; Cedola, A.; Giuliani, A.; *et al. Biomaterials* **2007**, *28*, 2505–2524. Bottom, left: tomographic slice through the upper part of a rat heart, absorption contrast; right: the same slice when working with phase sensitive contrast, here achieved by an interferometric approach. Adapted from Weitkamp, T.; David, C.; Bunk, O.; Bruder, J.; Cloetens, P.; Pfeiffer, F. *Eur. J. Radiol.* **2008**, *68*, S13–S17.

specimens taken after sacrificing and then analyzed using SμCT and additional techniques, as reported by Weiss *et al.*[73] An example for an *in vivo* clinical study using laboratory CT studying bone cement in the rat spine has been published by Wang *et al.*[97] Often these type of studies are referred to as *in vivo* studies, due to the fact that the performance of the biomaterials was evaluated using an *in vivo* animal model while *ex vivo* modes of analysis are employed subsequent to specimen retrieval.[98] The following two paragraphs focus on results achieved *ex vivo* as part of two studies with humans and with animals, where the response of bone to different bioceramic materials was imaged using synchrotron-based microtomography.

3.304.2. Comparative Animal Study of Bioceramic-Supported Bone Regeneration

3.304.2.1. Surgery and Specimen Retrieval

An animal study (DFG-grant: KN 377/3-1) was performed in order to investigate the osteogenic potential and biodegradability of various resorbable calcium phosphate bone grafting materials. The biomaterials studies included two rapidly resorbable calcium alkali orthophosphate ceramics, first a glassy crystalline material with the main crystalline phase $Ca_2KNa(PO_4)_2$ and small amorphous phase containing silica phosphates (material denominated GB9) and second a calcium alkali orthophosphate with the novel main crystalline phase $Ca_{10}KNa(PO_4)_2$ (material denominated 352i).

These bioceramics were designed for higher biodegradability compared to tricalcium phosphate, which was used as a clinically established reference material in the current study. All biomaterials included in this study had a mean particle size of 300–355 μm. The various test materials were implanted bilaterally in the sheep mandible and maxilla for 1, 4, 12, and 24 weeks and examined with respect to their potential to regenerate critical-size bone defects and their biodegradability.

In the maxilla, these materials were used for sinus floor augmentation which entailed close contact of a significant amount of the bone grafting material with the Schneiderian membrane, while close contact with the local bony tissue of the sinus floor was only present at the bottom of the defect (Figures 4 and 7). In order to prevent the migration

of fibroblasts into the implantation sites, which may potentially disrupt bone regeneration, the lateral access window to the sinus was covered with a titanium membrane. In this sheep study, an extraoral approach was chosen in order to access to the maxillary sinus. To this end, a lateral window was created.

In the sheep mandible chronicle critical-size membrane-protected defects as described by von Arx *et al.*[99] were applied. To this end, two premolars and molars were extracted and two rectangular defects 1.5 cm in width were created bilaterally. These were allowed to heal for 8 weeks, which was followed by removal of the granulation tissue and augmentation of the defects with the various bone grafting materials (**Figure 6**). The volume of the biomaterial granules inserted into the critical-size defects was about 1 cm^3. The defects were then covered with titanium membranes, thus applying the principle of guided bone regeneration.

After completion of the various implantation periods, the animals were sacrificed and the implantation sites with the surrounding bone tissue were retrieved for histological and synchrotron microtomographical analysis. The tissue blocks were fixed in an alcohol-based fixative Neofix^R (Merck KgaA, Darmstadt, Germany), then embedded in a resin, which contained methylmethacrylat and buthylmethacrylat. Prior to histological sectioning the embedded tissue blocks were examined with synchronton microtomography. This was followed by cutting 50-µm-thick sections using a sawing microtome and subsequent grinding and polishing of the sections, which were then used for histological, histomorphometric, and immunhistochemical analysis as described previously.[100]

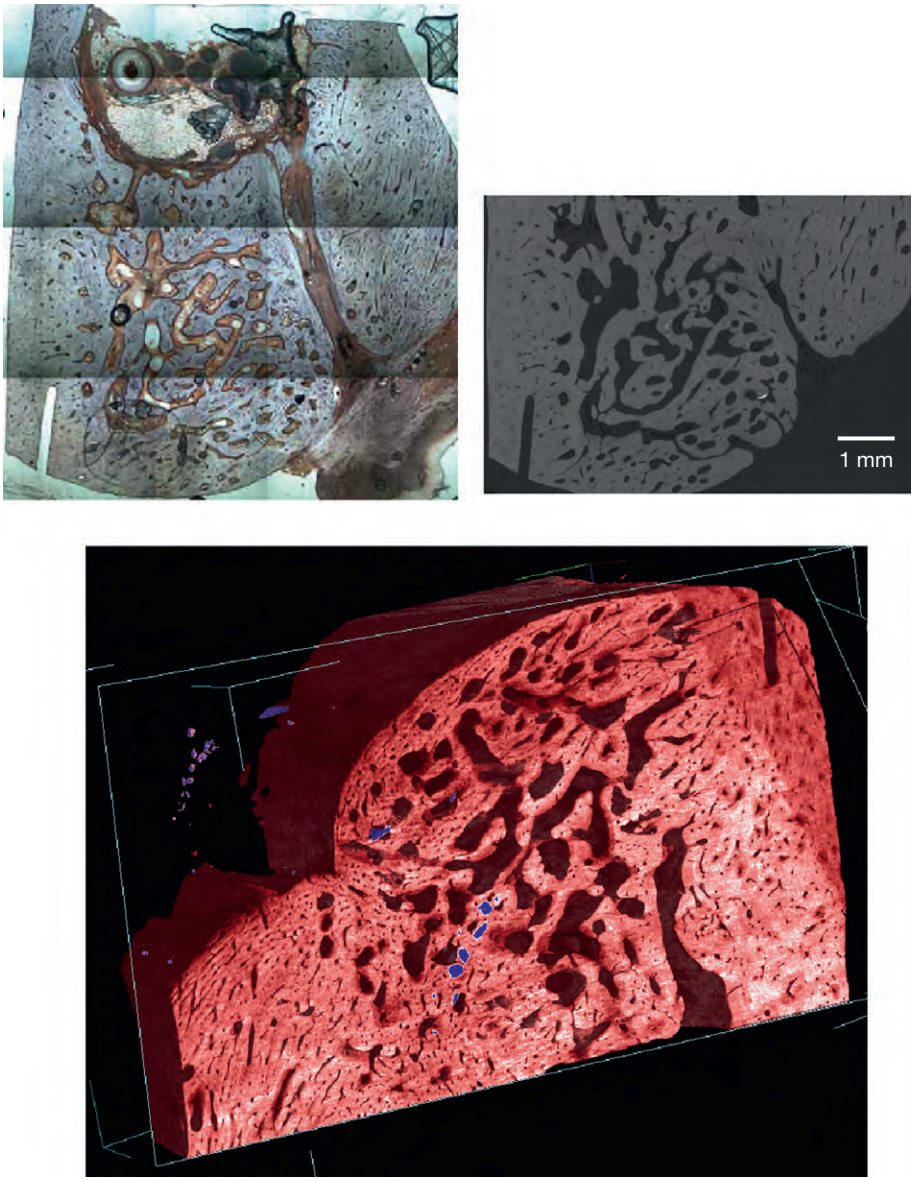

Figure 6 Specimen sampled 24 weeks after implantation of GB9 particles in the sheep mandible – top, left: histological section (bone in gray-blue, marrow spaces and areas staining positive for type I collagen appear in a brownish-red color), top, right: corresponding tomographic slice, bottom: volume rendering of the segmented tomographic data set (frontal cropped), residual bioceramic particles are distinguishable (deep blue).

3.304.2.2. Microtomography and Volume Image Processing

The microtomography experiments were performed at the BAM*line*, one of the hard X-ray beamlines of the BESSY-II light source (Berlin Electron Storage Ring Company for Synchrotron Radiation) at the Helmholtz Zentrum Berlin für Materialien und Energie (HZB), Germany.[33,34] The BAM*line*'s SμCT facility is operated by the Bundesanstalt fur Materialforschung und -prüfung (Federal Institute for Materials Research and Testing, Berlin, Germany) in cooperation with the HZB (Institute of Applied Materials). A detailed description of the experimental setup for microtomography can be found in Rack *et al.*,[34] a photo and a sketch of the imaging station is shown in Figure 3. The optimal X-ray energy for the tomographic scans was determined experimentally to be ~28 keV (monochromatic): assuming that the best contrast is given when the condition $\mu D = 2$ (μ: linear X-ray attenuation coefficient, D: sample diameter) is fulfilled, which equals to an overall X-ray transmission T by the sample of $T = 13.5\%$.[24]

For the experiments, the high resolution indirect detector was equipped with a nominal 10-μm-thick Gadox (Gd_2O_2S) scintillator powder screen because of its high stopping power and excellent photon yield. For the microscope objective, a Rodenstock 'XR-Heliflex' (focal length $f = 100$ mm, maximum $NA = 0.4$) was chosen in combination with a Nikon 'Nikkor 180/2.8 ED' ($f = 180$ mm) objective, resulting in a magnification factor of 1.8×. In the parallel section of the optical path, a diaphragm is placed to adjust the ratio of absorbed X-ray photons (Gadox) versus detected luminescence photons (CCD) and to compensate for defect focus. The optics project the luminescence image onto the back-illuminated CCD chip of a Princeton Instruments VersArray: 2048B (11 000:1 dynamic range with 1 MHz readout speed, 2048 × 2048 pixels, each 13.5 μm in size). The resulting effective pixel size is 7 μm which leads to a $14 \times 14\ mm^2$ field of view, large enough to investigate the usually $25 \times 12 \times 5\ mm^3$ sized specimen. In the radiographic projection the resolution was estimated to about 20 μm with the help of a copper edge (10% of the modulation transfer function). For the reconstruction of the tomographic images the filtered-backprojection algorithm is used via the ESRF software package PyHST.[101]

The absorption contrast in this microtomographic scans is determined by the local X-ray attenuation coefficient which mainly depends on the local density of the material as well as the atomic number of its elements. Here, the dependence on the X-ray energy can be omitted since a monochromatic beam is used. After the tomographic reconstruction, the resulting pixel values are translated into gray-scales and the whole volume data set can then be rendered in three dimensions. For the rendering, a commercial software package by Volume Graphics GmbH (Heidelberg, Germany) was used – VGStudioMAX.[57] In order to derive images which can be considered as an extension of histology into three dimensions, first the spatial information of the different material phases (bone and ceramic particles, *cf.*, e.g., Figure 4) was separated into Boolean images which contain only the morphological information of one phase. The algorithm applied is using a threshold hysteresis in combination with a region growing approach: an initial range of gray values, manually selected, is used to define, for example, what certainly is bone information within the image. In a second step, a broader range of gray values is selected, defining what might be the bone information. The algorithm extends in successive stages already identified bone phase with image pixels which are (i) direct neighbors of already identified bone and (ii) contain gray values within the above-mentioned second range. The algorithm terminates when no more pixels remain which fulfill these two conditions.[49] A further manual optimization of the input parameters is required, frequently performed by visual inspection of selected slides in gray-scales and Boolean. The results are volume images in which the very pixels associated with the bone information are marked as '1' and the remaining background is set to '0.' Once separated, the Boolean images can be individually cleaned from noise, for example, by using morphological transformations as well as being colored. A combined rendering of these individual volume images is shown in Figure 4, right side.

3.304.2.3. Results

Of the calcium alkali phosphate bioceramic GB9: two specimens were imaged, one sampled after 12 and one sampled at 24 weeks of implantation in the sheep mandible. The corresponding volume rendering of the 24-week sample is displayed in Figure 6 (bottom). Parts of the bony tissue are set transparent in order to give insight into the bony volume. At 24 weeks, only very few residual particles, which show excellent bone-bonding behavior, can be detected in the tomographic volume image (also after 12 weeks, only minor amounts of residual particles were distinguishable, data not shown here). Consequently, the GB9 ceramic supported bone formation and regeneration of the bony defect and then biodegraded rapidly, while new bone is formed, with hardly any residual particles remaining.

In order to validate our results, histological sections of the 24 weeks specimen were cut and prepared for immunohistochemical analysis. The corresponding section was identified (see below) and visualized using a light microscope in combination with a digital camera (Colourview III) and SIS Analysis software (Olympus, Germany) (see Figure 6 (top, left)). Here, the bone can be recognized by the gray-bluish color. Marrow spaces and areas staining positive for type I collagen appear in a brownish-red color. The volume data set of the 24-week sample was compared manually slice by slice with the histological image until the corresponding section was found (see Figure 6 (top, right)). No major differences between the detected bone structure in the tomographic image and the histological image are visible. Due to the density-related absorption contrast within the SμCT image it can be concluded that for this sample the bone is fully developed, that is, mineralized as all bony tissue detected in the chemical contrasted histological image is also visible in the tomographic slice.

The bone substitute material 352i, however, displayed a rather different behavior. A sample examined 12 weeks after sinus floor augmentation is depicted in Figure 7. In contrast to GB9 (see Figure 6) the majority of the ceramic particles are still present while only a small amount of newly formed bone becomes visible between the 352i particles. In addition, these particles show very limited bone-particle contact, that is, very poor bone-bonding behavior. Here, it is noteworthy that

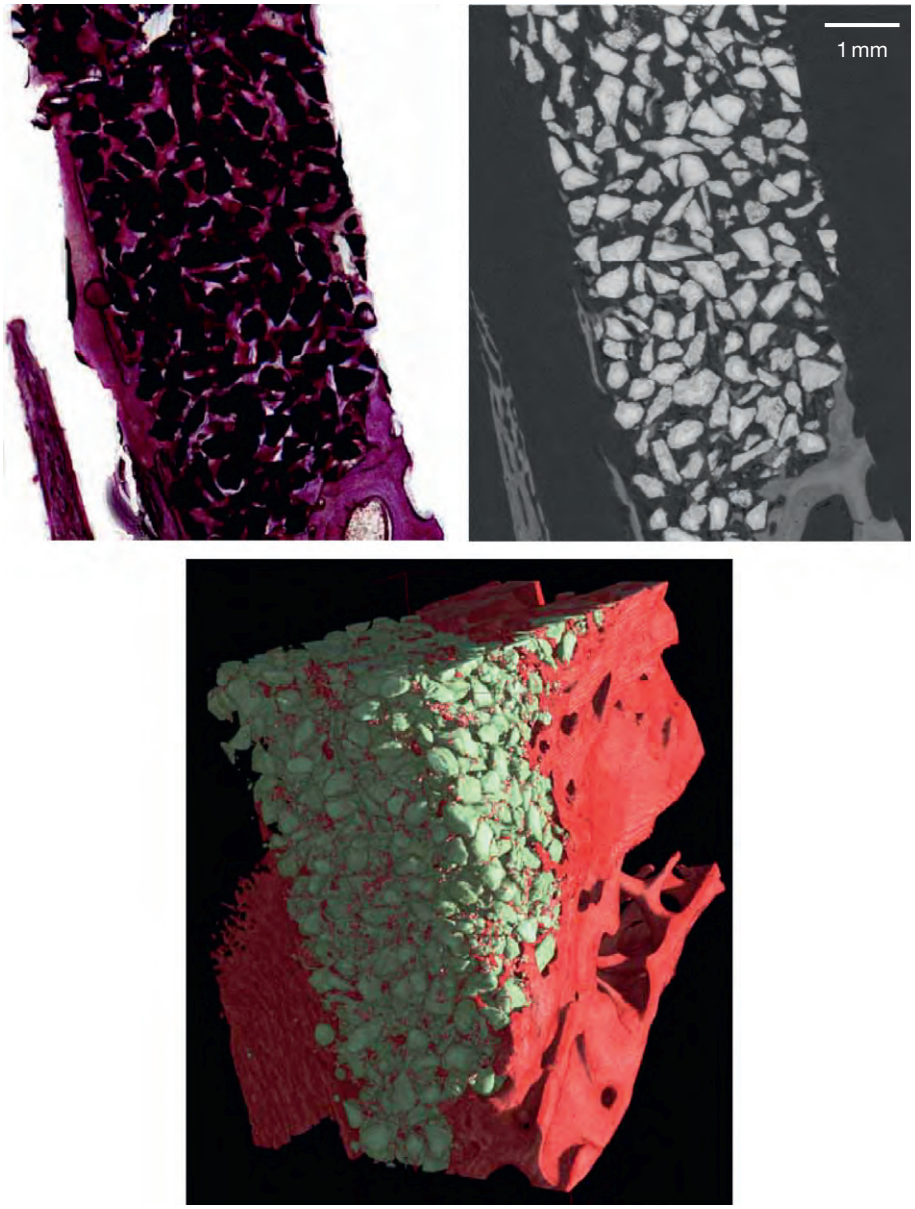

Figure 7 Specimen harvested 12 weeks after sinus floor augmentation with 352i – top, left: histologically prepared section (bone in cyan, ceramic particles black, soft tissue: scarlet red and light pink), top, right: corresponding tomographic slice, bottom: volume rendering of the segmented tomographic data set, bioceramic particles (white) are dominantly present in the augmented site (red). Adapted from Rack, A.; Zabler, S.; Müller, B. R.; *et al*. *Nucl. Instrum. Meth. Phys. Res. A* **2008**, *586*, 327–344.

these particles display a very limited biodegradability. At the same time, they only support limited bone formation at their surface, thereby resulting in a high soft-tissue particle contact and poor bone-bonding behavior. Again, to validate and also to extend the results derived from SμCT, histological sections were prepared (see Figure 7 (top)).

For comparison, the SμCT volume image showing bone and ceramic particles was sectioned and orientated so that the slice corresponding to the histological image becomes visible (*cf*. Figure 7). The amount of detected bone differs between the two images. When taking a closer look it becomes evident that the amount of bone visible in the lower right of the images is identical for both the tomographical as well as the histological image. This is bone tissue adjacent to the implantation site which was already present prior to implantation. However, in between the 352i particles a slightly greater amount of bone appears to be visible in the histological image when compared to the tomographical image. This appears to be newly forming bone tissue which is not fully mineralized. In the early stages of the bone formation, the tissue exhibits a lower degree of mineralization, thereby being less dense than a mature bone.[102] As a result it cannot be detected in the absorption contrast microtomography image due to its low density contrast whereas it is visible in the histological images. However, in the histological image, the considerable amount of soft tissue in contact with the bone substitute particles also becomes evident.

The use of microtomographic and histological images for characterizing the bone-regenerative capacity and biodegradability of GB9 and 352i facilitates analyzing the significant differences in how fast these materials degrade. With respect to the rapidly resorbable material, GB9 formation of mature and fully mineralized bone could be demonstrated after 12 and 24 weeks of implantation, whereas for the material 352i, limited bone formation and bone tissue with a low degree of mineralization was detected at 12 weeks.

By performing a qualitative comparison between a microtomographic slice and the corresponding histological section, the matching (or nonmatching) of the information collected by the two differing imaging techniques for a selected sample can be evaluated (see **Figure 6** vs. **Figure 7**). In case of a high level of congruence, the tomographic data set extends the capacity of hard-tissue histologic images into three dimensions. Hence, the bioregeneration of bone can be studied in a true spatial as well as nondestructive manner. The next section will underscore the value of the tomographic approach using hard X-ray synchrotron radiation to not only qualitatively but also to quantitatively determine the amount of bone regeneration in a given defect.

3.304.3. Bone Regeneration After Sinus Floor Augmentation in Humans

3.304.3.1. Surgery and Biopsy

In order to study bone regeneration in the human case, the effect of two particulate tricalcium phosphate materials (porosity 35% and 60%, respectively) on osteogenic marker expression and bone formation was evaluated in biopsies sampled 6 months after augmentation of the sinus floor.[103] This was in addition to examining the biodegradability. Two of these patients were selected for SμCT-analysis. Sinus floor augmentation was performed using β-tricalcium phosphate (TCP) particles with either 35% porosity (TCP, grain size 1000–2000 μm, product label: Cerasorb, Curasan AG, Kleinostheim, Germany) or 60% porosity (TCP-P, grain size 1000–2000 μm, product label: Ceros, Mathys AG, Bettlach, Switzerland).

Sinus floor augmentation elevation was carried out under local anesthesia. A staged surgical approach was used in which dental implant placement is performed 6 months after sinus floor augmentation. This was due to the fact that the height of the residual alveolar process was only 1 mm in the posterior maxillary region. Then the newly created space between the maxillary alveolar process and the elevated Schneiderian membrane was filled using a mixture (4:1 ratio) of β-TCP particles and autogenous bone chips. X-ray images were taken postoperative which allowed to examine the volume of the augmented sinus floor directly after sinus floor elevation as well as to determine volume alterations after the healing period of 6 month, that is, prior to implant placement.[59]

The dental implant placement as well as biopsy sampling were also performed in local anesthesia. One biopsy from each patient was harvested utilizing a trephine burr (2.75 mm inner diameter and 3.50 mm outer diameter), at one of the dental implant sites, in which the height of the original residual alveolar crest prior to augmentation was ~1 mm and the depth of the implant bed prepared after augmentation was roughly 12 mm (after augmentation). The biopsies were 2.5 mm in diameter and roughly 8 mm in length. Specimens underwent histological, histomorphometric, and SμCT examination. They contained the grafted area as well as the native alveolar crest of the sinus floor, which was ~1 mm in height. We would like to note that the residual native crest was not included in any analysis.

For the histological as well histomorphometric analysis, a novel technique which facilitated performing immunohistochemical analysis on undecalcified hard-tissue sections as described previously was used.[100,103] In brief, samples were fixed immediately in an ethanol-based fixative Neofix^R (Merck KGaA, Darmstadt, Germany) commonly for 3 days at room temperature. This was followed by infiltration and dehydration. Then the specimens were embedded in a resin, which was composed of metylmetacrylate and *n*-butyl-metracrylate to which benzoyl peroxide (BPO catalyst, Merck KGaA, Darmstadt, Germany) and polyethylene glycol 400 (Merck KGaA, Darmstadt, Germany) and 1.5 ml *N*,*N*-dimethyl-*p*-toluidine (Merck KGaA, Darmstadt, Germany) were added. Samples were polymerized in polyethylene vials. This resin was selected because it maintained the antigenicity of the tissue and at the same time also provided adequate material properties for cutting the 50-μm-thick sections with a sawing microtome. After polymerization, the blocks were removed from the vials and excess resin was trimmed away. Both tissue blocks, which contained the entire biopsy cylinders, underwent SμCT scans prior to histological sectioning and histomorphometrical evaluation. Further details on the SμCT scans are given in the next section.

Following the tomographic data acquisition at the synchrotron light source the resin blocks which contained the biopsies were glued to acrylic slides (Plexiglas GS 209, Rohm GmbH & Co. KG, Darmstadt, Germany) by applying an epoxy resin based two-component adhesive (UHU GmbH & Co. KG, Buhl, Germany). Fifty microns sections were then cut with a Leitz 1600 sawing microtome (Leitz, Wetzlar, Germany). These sections were then grounded and polished. Prior to the immuno-histochemical staining, deacrylation of sections was done by immersion in toluene, xylene and acetone. Subsequently the sections were rinsed in distilled water and placed in *Tris*-buffer (pH 7.4). Immunohistochemical staining was then performed as described previously,[103] Mayer's haematoxylin was used as a counterstain.

Histomorphometric analysis was performed on pairs of 20–30-μm-sections which were ~150 μm apart. Both sections were measured semiautomatically using a light microscope (Olympus, Hamburg, Germany) in combination with a digital camera (Colourview III) and the SIS Analysis™ software (Olympus, Hamburg, Germany). Additionally, a square area of 6.25 mm^2 was defined within the longitudinal plane of each specimen. For both biopsies, the surface area that consisted of bone and the area that consisted of graft material were measured in square millimeters. Additionally, the area fraction of bone, as well as the area fraction of grafted material, was analyzed as a percentage of the total area and were averaged. Because there were no histomorphometric discrepancies between both sections of each biopsy specimen, one section was chosen as a representative for the later SμCT comparison in the following sections.

3.304.3.2. Microtomography and Volume Image Analysis

Like in the previous section, the microtomography experiments were performed at the BAM*line* of the BESSY-II light source (Helmholtz Zentrum Berlin für Materialien und Energie (HZB), Germany), see as well Görner *et al.*[33] and Rack *et al.*[34] A photograph and a schematic of the imaging station are shown in Figure 3. The optimal X-ray energy for the tomographic scans was determined experimentally to be ~20 keV (monochromatic): assuming that the best contrast is given when the condition $\mu D = 2$ (μ: linear X-ray attenuation coefficient, D: sample diameter) is fulfilled, which equals to an overall X-ray transmission T by the sample of $T = 13.5\%$.[24]

For the indirect detector, a 50-μm-thick cadmium tungstate ($CdWO_4$) single-crystal scintillator glued on top of a 0.5-mm-thick yttrium–aluminum garnet substrate ($Y_3Al_5O_{12}$) was chosen. Its luminescence image is projected onto the CCD chip of a Princeton Instruments camera VersArray:2048B with an effective 9× magnification (leading to an effective pixel size of 1.5 μm and a real spatial resolution of ~4 μm) using a Rodenstock 'TV-Heligon' (front objective, $f = 21$ mm, maximum $NA = 0.5$) in combination with the Nikon 'Nikkor 180/2.8 ED' ($f = 180$ mm). The choice of the pixel size was determined by the dimensions of the sample (2.5 mm in diameter) as well as the finite size of the CCD sensor (leading to a $3.2 \times 3.2\,mm^2$ field of view). In order to achieve a good reconstruction quality, 1500 projection images were recorded for each SμCT scan of one of the specimens. For the reconstruction, the filtered back projection algorithm[18] was applied utilizing a software package which was developed by the SciSoft group of the European Synchrotron Radiation Facility (ESRF) – PyHST.[101]

Due to correspondingly short detector-to-sample distance chosen, the contrast in the acquired SμCT images is dominated by the absorption, common phase contrast edge enhancements are only slightly present. This is as well due to the spatial resolution of the employed indirect detector setup as well as the coherence properties of the BAM*line* (~165 μm horizontal source size). Similar to the previous section, the contrast of the fully developed mature, that is, mineralized bone was used to create Boolean images of the bone phase by applying a region growing algorithm in combination with a threshold hysteresis (*cf.* example images in Figure 4). While in the sheep study, the focus was on the volume renderings, in case of the human specimens, we consider a quantitative approach in order to compare the two-dimensional histological results with the volumetric analysis performed via SμCT. Therefore, for the specimens investigated, a histologic section as well as a SμCT image was acquired. Manual scanning of the tomographic data set in meridional and sagittal orientation allowed us to find the slice in the volume image which corresponds to the histologic section (see, e.g., Figure 8). Plain voxel counting in the Boolean slice which shows the same information as the histologic section gives access to the two-dimensional bone density. The same procedure when applied to the whole volume image determines the true three-dimensional bone density. Thus, it opens to the possibility of comparing histologic results with a truly three-dimensional approach in a quantitative manner.

3.304.3.3. Results

A scan of the central portion of a human specimen which shows regenerated bone after augmentation with Cerasorb particles (β-TCP with 35% porosity) is depicted in Figure 8. In the top portion the histological image as compared to the SμCT slice containing the same information is shown. Below the volume rendering of the complete data set, sectioned along the same slice which corresponds to the histologic section. The three-dimensional visualization shows the new bone which formed in conjunction with degradation of the TCP particles. The newly formed bone was predominantly a lamellar bone with different degrees of mineralization – higher degrees in the central areas (light red colored) and lower degrees in the marginal areas of the regenerated bone (dark red colored).

As described in the previous sections, two-dimensional histomorphometric image analysis was performed on the histological image in a manual manner. Histomorphometrically the bone area fraction was determined to be 53.3%. From the Boolean image of the corresponding tomographic slice a value of 54.9% was calculated. The absolute difference of only 1.6% between the two results underscores the good correspondence of the information gathered by microtomography and histomorphometry in terms of contrast. Consequently, this facilitates using tomographic data to measure the real bone volume fraction in a three-dimensional manner. The volume image analysis after processing the SμCT data set showed 48.8% of the entire volume of the central portion of the biopsy to consist of newly formed bone 6 months after sinus floor augmentation. So, the measurements of the bone volume determined by calculating it via the three-dimensional SμCT data differed from the values of the bone area fraction (histomorphometry) by 8.5%.

Concerning the second specimen, a scan of a human biopsy after augmentation with Ceros particles (β-TCP with 60% porosity) is shown in Figure 9. Again, in the top portion the histological image is shown as compared to the corresponding SμCT slice. In the bottom portion of the image, a volume rendering of the complete data set is depicted, sectioned along the slice which is shown in the top portion of the figure. Here, 6 months after sinus floor augmentation the volume image shows different degrees of mineralization of the newly formed bone, clearly visible in terms of different shades of red. Residual β-TCP particles are clearly visible (blue color). When taking a comparative look on the three-dimensional images shown in Figures 8 and 9 it becomes evident that the TCP-P (Ceros) bone biopsy specimen exhibits a tightly-meshed bone pattern with increased density. This is associated with a decreasing volume of bone marrow spaces and the yet unmineralized fibrous matrix. Furthermore, residual particles of the degrading ceramic material display good bone formation at their surface, that is, good bone-bonding behavior.

Identical to the Cerasorb specimen, two-dimensional image analysis was done manually on the histological section. In this case, the bone area fraction measured histomorphometrically was 38.8%. Here the two-dimensional image analysis of the tomographic data as transformed into a Boolean image revealed a bone area fraction of 39.0%. Like in the previous case, both methods of two-dimensional analysis delivered similar results. Hence, it was possible to progress

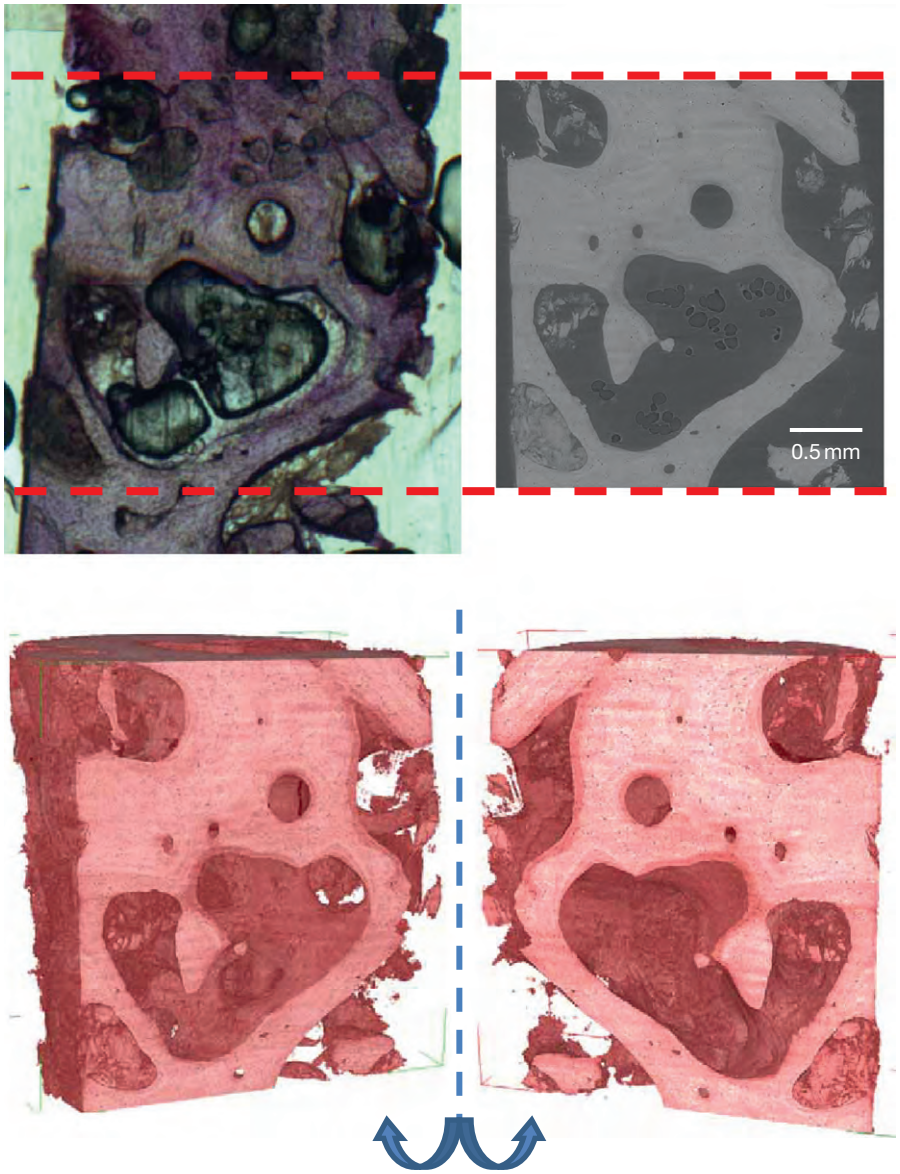

Figure 8 Human bone biopsy sampled 6 months after sinus floor augmentation with Cerasorb particles (35% porosity) – top: histologically prepared section (left, bone in violet-blue, bone marrow spaces and soft tissue in brownish-gray) and corresponding tomographic slice (right). Bottom: volume rendering of the complete tomographic image, sectioned along the slice representing as well the histological information. Adapted from Stiller, M.; Rack, A.; Zabler, S.; *et al*. *Bone* **2009**, *44*, 619–628.

then to measure the real three-dimensional bone volume fraction based on the Boolean image of the SμCT data set. In this case, the data processing resulted in a value of 36.3% for the bone volume fraction of the examined portion of the biopsy. The difference between the bone area fraction measured using conventional histomorphometry versus the bone volume as determined by SμCT is 6.5% and therefore less compared to the case in which the less porous β-TCP was used and in which a more cancellous pattern of bone regeneration pattern was observed.

But, in both cases it became evident that the application of only classical two-dimensional methods for analysis like histomorphometry is associated with significant errors in the results. By applying synchrotron-based microtomography with its widely nondestructive manner, three-dimensional nature, as well as high contrast, it is possible to progress to histovolumetry which allows for a more precise analysis of, for example, bone regeneration.

3.304.4. Summary

Synchrotron-based microtomography is an established technique available at various synchrotron light sources worldwide (see Table 1). The combination of high resolution with high signal-to-noise ratio and different contrast modalities renders SμCT as an excellently suited analytical tool for studies in biomedical fields such as bone research and hard-tissue research.

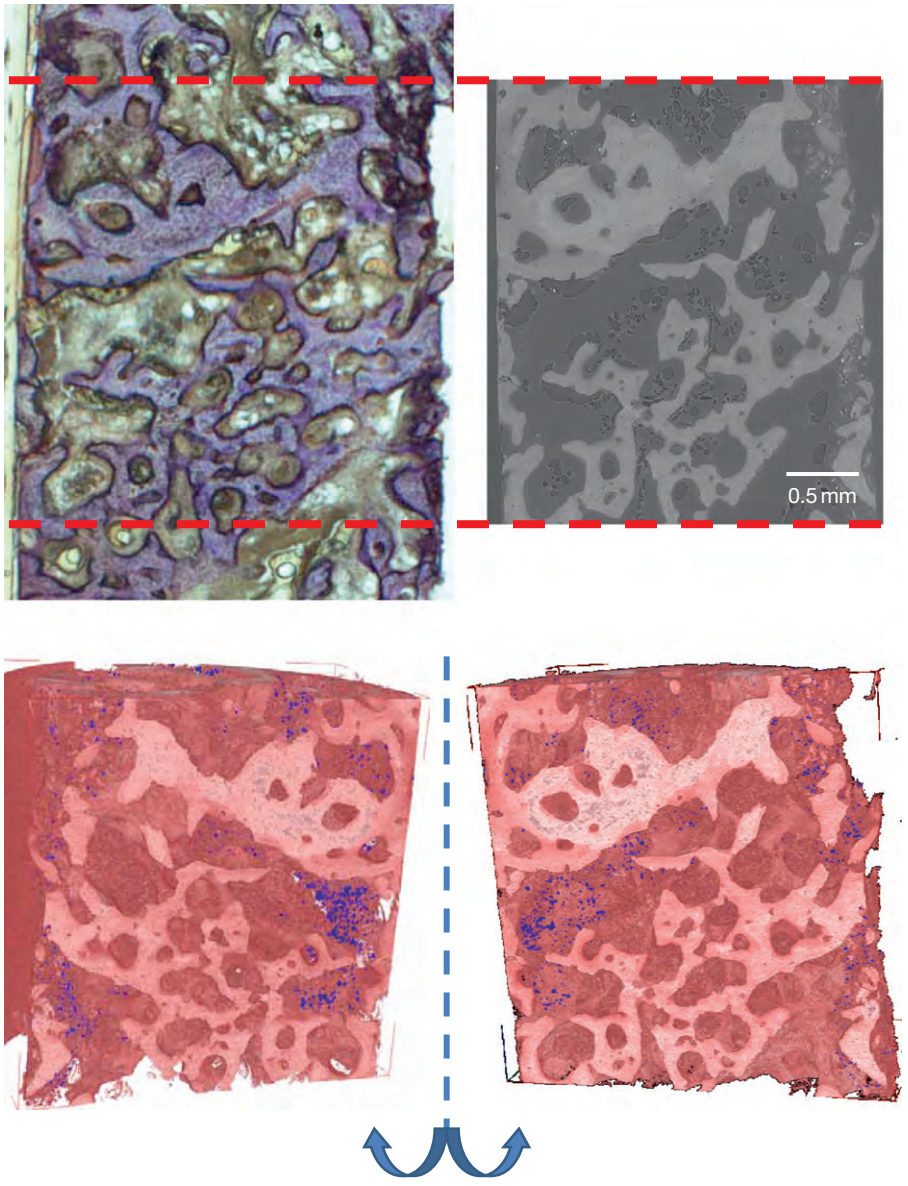

Figure 9 Human bone biopsy sampled 6 months after sinus floor augmentation with Ceros particles (60% porosity) – top: histologically prepared section (left, bone in blue, bone marrow spaces and soft tissue in gray, residual particles black) and corresponding tomographic slice (right). Bottom: volume rendering of the complete tomographic image, sectioned along the slice representing the histological information. Residual bioceramic particles are detectable (deep blue color). Adapted from Stiller, M.; Rack, A.; Zabler, S.; *et al*. *Bone* **2009**, *44*, 619–628.

Countless successful applications have been published in recent years, a selection of which has been outlined in the first section of this chapter.

The analysis of bone regeneration supported by different bioceramic materials using SμCT has been described as one of the many potential applications in the field of biomaterials research. Here, comparing bioceramic compositions with different resorbability in the context of an animal study showed that based on the qualitative agreement between histological sections and corresponding tomographic slices, SμCT can be considered as an extension of the classical histology into three dimensions. In addition to the three-dimensional approach, SμCT compared to the sectioning of specimens provides information in a widely nondestructive manner. The increased reliability of the achieved results was demonstrated in a second study, in which quantitative analysis was employed to compare the amount of regenerated bone as analyzed using histomorphometry to the results yielded by SμCT in combination with volume image analysis. A significant difference with respect to the amount of bone determined was demonstrated. Consequently, so-called histovolumetry needs to be considered for future studies in order to verify, qualify or falsify the results based on classical two-dimensional techniques.

Besides the high potential of synchrotron-based imaging techniques, a drawback will remain which is the limited beamtime available and the high costs of synchrotron light. Therefore, this analytical tool, will be dedicated to the analysis of selected specimens and cases. A fact, which is not going to be

changed within the near future, despite the many light sources which have recently started operations.

For the future, two main developments are supposed to open new possibilities for biomedical and biomaterials research using synchrotron light. One is based on the extended resolution capabilities when X-ray optics are employed. Hierarchical imaging showing, for example, the structure of a specimen on the macroscopic, microscopic, and nanoscopic scale combined with different contrast modalities (multimodal imaging) will be a goal only to be reached when synchrotron light sources are employed. Furthermore, a second development is the increased data acquisition speed which will push further for *in situ* examination of specimens in combination with time-resolution.

Acknowledgments

We like to acknowledge the support of J. Goebbels, B. R. Müller, T. Wolk, and G. Weidemann (BAM) during the data acquisition at the BAM*line*, G. Berger, R. Gildenhaar (BAM) for developing and fabricating the calcium alkali orthophosphate bone substitute materials, Ch. Koch, H. Seeligmann, I. Borchert, A. Besnarek, and A. Kopp (Charité) for the histologic sections, T. Weitkamp (ESRF) for the tomographic slices of the rat heart, O. Betz (Universität Tübingen) for the tomographic image of the head of Forficula auricularia (Dermaptera) and F. Peyrin (ESRF) for the volume rendering of the hydroxyapatite scaffold with newly formed mouse bone. Parts of this work were founded by the German Research Foundation (DFG-grant no. KN 377/3-1).

References

1. Johns, H. E.; Cunningham, J. R. *The Physics of Radiology*; Charles C Thomas: Springfield, IL, 1983; 4th edn.
2. Cormack, A. C. *J. Appl. Phys.* **1963**, *34*, 2722–2727.
3. Hounsfield, G. N. *Br. J. Radiol.* **1973**, *46*, 1016–1022.
4. Hsieh, J. *Computed Tomography: Principles, Design, Artifacts and Recent Advances*; SPIE: Bellingham, WA, 2009, 2nd edn.
5. Reimers, P.; Goebbels, J. *Mater. Eval.* **1983**, *41*, 732–737.
6. Elliott, J. C.; Dover, S. D. *J. Microsc.* **1982**, *126*, 211–213.
7. Flannery, B. P.; Deckmann, H. W.; Roberge, W. G.; D'Amico, K. L. *Science* **1987**, *237*, 1439–1444.
8. Thompson, A. C.; Llacer, J.; Campbell Finman, L.; *et al. Nucl. Instrum. Meth.* **1984**, *222*, 319–323.
9. Bowen, D. K.; Elliott, J. C.; Stock, S. R.; Dover, S. D. In *X-Ray Imaging II*, *Proceedings of SPIE*; Bowen, D. K., Knight, L. V., Eds.; SPIE: Bellingham, WA, 1986; Vol. 691, pp 94–98.
10. Spanne, P.; Rivers, M. L. *Nucl. Instrum. Meth. Phys. Res. B* **1987**, *24–25*, 1063–1067.
11. Kinney, J. H.; Johnson, Q. C.; Nichols, M. C.; *et al. Rev. Sci. Instrum.* **1989**, *60*, 2471–2474.
12. Bonse, U.; Nusshardt, R.; Busch, F.; *et al. Rev. Sci. Instrum.* **1989**, *60*, 2478–2481.
13. Graeff, W.; Engelke, K. In *Handbook on Synchrotron Radiation*; Ebashi, S., Koch, M., Rubenstein, E., Eds.; North-Holland: Amsterdam, 1991; Vol. 4, pp 361–406.
14. Koch, A.; Raven, C.; Spanne, P.; Snigirev, A. *J. Opt. Soc. Am.* **1998**, *15*, 1940–1951.
15. Cloetens, P.; Ludwig, W.; Baruchel, J.; *et al. Appl. Phys. Lett.* **1999**, *75*, 2912–2914.
16. Banhart, J., Ed.; In *Advanced Tomographic Methods in Materials Research and Engineering*; Oxford University Press: Oxford, 2008.
17. Knabe, C.; Ducheyne, P. In *Bio-ceramics and Their Clinical Applications*; Kokubo, T., Ed.; Wood-head: Cambridge, 2008; pp 133–164.
18. Kak, A. C.; Slaney, M. *Principles of Computerized Tomographic Imaging*. IEEE: New York, 1988.
19. Kalender, W. A. *Computed Tomography*. Publicis MCD Verlag: Munich, 2000.
20. Bonse, U.; Busch, F. *Prog. Biophys. Mol. Biol.* **1996**, *65*, 133–169.
21. Brooks, R. A.; Di Chiro, G. *Med. Phys.* **1976**, *3*, 237–240.
22. Flannery, B.; Roberge, W. *J. Appl. Phys.* **1987**, *62*, 4668–4674.
23. Grodzins, L. *Nucl. Instrum. Meth. Phys. Res.* **1983**, *206*, 547–552.
24. Grodzins, L. *Nucl. Instrum. Meth. Phys. Res.* **1983**, *206*, 541–545.
25. Elliott, J. C.; Dover, S. D. *Metab. Bone Dis. Relat. Res.* **1984**, *5*, 219–221.
26. Elliott, J. C.; Dover, S. D. *J. Microsc.* **1985**, *138*, 329–331.
27. Feldkamp, L.; Goldstein, S.; Parfitt, A.; Jesion, G.; Kleerekope, M. *J. Bone Miner. Res.* **1989**, *4*, 3–11.
28. Spiller, E. *Nucl. Instrum. Meth.* **1980**, *177*, 187–192.
29. Hughes, E. B.; Zeman, H. D.; Campbell, L. E.; *et al. Nucl. Instrum. Meth.* **1983**, *208*, 665–675.
30. Rack, A.; García-Moreno, F.; Baumbach, T.; Banhart, J. *J. Synchrotron Radiat.* **2009**, *16*, 432–434.
31. Wang, Y.; Liu, X.; Im, K.-S.; *et al. Nat. Phys.* **2008**, *4*, 305–309.
32. Wiedemann, H. *Synchrotron Radiation*. Springer: Berlin, 2002.
33. Görner, W.; Hentschel, M. P.; Müller, B. R.; *et al. Nucl. Instrum. Meth. Phys. Res. A* **2001**, *467*, 703–706.
34. Rack, A.; Zabler, S.; Müller, B. R.; *et al. Nucl. Instrum. Meth. Phys. Res. A* **2008**, *586*, 327–344.
35. Brooks, R. A.; Di Chiro, G. *Phys. Med. Biol.* **1976**, *21*, 390–398.
36. Snigirev, A.; Snigireva, I.; Kohn, V.; Kuznetsov, S. *Rev. Sci. Instrum.* **1995**, *66*, 5486–5492.
37. Cloetens, P.; Barrett, R.; Baruchel, J.; Guigay, J.-P.; Schlenker, M. *J. Phys. D Appl. Phys.* **1996**, *29*, 133–146.
38. Nugent, K. A.; Gureyev, T. E.; Cookson, D. F.; Paganin, D.; Barnea, Z. *Phys. Rev. Lett.* **1996**, *77*, 2961–2964.
39. Bleuet, P.; Welcomme, E.; Doorhyée, E.; Susini, J.; Hodeau, J.-L.; Walter, P. *Nat. Mater.* **2008**, *7*, 468–472.
40. Graafsma, H.; Martin, T. In *Advanced Tomographic Methods in Materials Research and Engineering*; Banhart, J., Ed.; Oxford University Press: Oxford, 2008; pp 277–302.
41. Hartmann, W.; Markewitz, G.; Rettenmaier, U.; Queisser, H. J. *Appl. Phys. Lett.* **1975**, *27*, 308–309.
42. Schroer, C. G.; Meyer, J.; Kuhlmann, M.; *et al. Appl. Phys. Lett.* **2002**, *81*, 1527–1529.
43. Feser, M.; Gelb, J.; Chang, H.; *et al. Meas. Sci. Technol.* **2008**, *19*, 094001.
44. Withers, P. J. *Mater. Today* **2007**, *10*, 26–34.
45. Schneider, G.; Guttmann, P.; Heim, S.; Rehbein, S.; *et al. Nat. Meth.* **2010**, *7*, 985–987.
46. Ortega, R.; Cloetens, P.; Devès, G.; Carmona, A.; Bohic, S. *PLoS One* **2007**, *2*, e925.
47. Sinha, S. K.; Glyde, H.; Briber, R.; Takata, M. *Synchroton Radiat. News* **2010**, *23*, 33–38.
48. Rack, A. Ph.D. Thesis, Technical University, Berlin, 2006. [in German]
49. Pal, N. R.; Pal, S. K. *Pattern Recognit.* **1993**, *26*, 1277–1294.
50. Pal, N. R.; Bhandari, D. *Signal Process.* **1993**, *33*, 139–158.
51. Rack, A.; Helfen, L.; Baumbach, T.; *et al. J. Microsc.* **2008**, *232*, 282–292.
52. Knackstedt, M. A.; Arns, C. H.; Senden, T. J.; Gross, K. *Biomaterials* **2006**, *27*, 2776–2786.
53. Janssen, D.; Mann, K. A.; Verdonschot, N. *J. Biomech.* **2008**, *41*, 3158–3163.
54. Schladitz, K.; Ohser, J. In *Advanced Tomographic Methods in Materials Research and Engineering*; Banhart, J., Ed.; Oxford University Press: Oxford, 2008; pp 37–106.
55. Ohser, J.; Schladitz, K. *3D Images of Materials Structures: Processing and Analysis*. Wiley-VCH: Weinheim, 2009.
56. Fraunhofer ITWM, Department of Image Processing 2009. MAVI – Modular Algorithms for Volume Images. http://www.itwm.fhg.de/mab/projects/MAVI/.
57. Reinhart, C.; Poliwoda, C.; Günther, T.; Roemer, W.; Maass, S.; Gosch, C. In *Proceedings of 16th World Conference on Nondestructive Testing (WCNDT2004)*, Montreal, Canada, 2004.
58. Parfitt, A. M.; Drezner, M. K.; Glorieux, F. H.; *et al. J. Bone Miner. Res.* **1987**, *2*, 595–610.
59. Stiller, M.; Rack, A.; Zabler, S.; *et al. Bone* **2009**, *44*, 619–628.
60. Paulus, M. J.; Gleason, S. S.; Kennel, S. J.; Hunsicker, P. R.; Johnson, D. K. *Neoplasia* **2000**, *2*, 62–70.
61. Ritman, E. L. *Annu. Rev. Biomed. Eng.* **2004**, *6*, 185–208.
62. Aghaloo, T.; Cowan, C. M.; Zhang, X.; *et al. J. Oral Maxillofac. Surg.* **2010**, *68*, 300–308.
63. Spanne, P. *Phys. Med. Biol.* **1989**, *34*, 679–690.

64. Keyrilainen, J.; Fernandez, M.; Karjalainen-Lindsberg, M.-L.; *et al*. *Radiology* **2008**, *249*, 321–327.
65. Balvay, D.; Troprès, I.; Billet, R.; *et al*. *Radiology* **2009**, *250*, 692–702.
66. Issever, A. S.; Diederichs, G.; Majumdar, S.; *et al*. *J. Synchrotron Radiat.* **2008**, *15*, 525–527.
67. Baruchel, J.; Bleuet, P.; Bohic, S.; *et al*. *Synchroton Radiat. News* **2008**, *21*, 30–41.
68. Fratzl, P.; Weinkamer, R. *Prog. Mater. Sci*. **2007**, *52*, 1263–1334.
69. Neues, F.; Epple, M. *Chem. Rev.* **2008**, *108*, 4734–4741.
70. Westneat, M. W.; Socha, J. J.; Lee, W.-K. *Annu. Rev. Physiol*. **2008**, *70*, 119–142.
71. Betz, O.; Wegst, U.; Weide, D.; *et al*. *J. Microsc.* **2007**, *227*, 51–71.
72. Baruchel, J.; Lodini, A.; Romanzetti, S.; Rustichelli, F.; Scrivani, A. *Biomaterials* **2001**, *22*, 1515–1520.
73. Weiss, P.; Obadia, L.; Magne, D.; *et al*. *Biomaterials* **2003**, *24*, 4591–4601.
74. Ho, S. T.; Hutmacher, D. W. *Biomaterials* **2006**, *27*, 1362–1376.
75. Tanaka, T.; Uesugi, K.; Takeuchi, A.; Suzuki, Y.; Iwata, T. *Polymer* **2007**, *48*, 6145–6151.
76. Mastrogiacomo, M.; Papadimitropoulos, A.; Cedola, A.; *et al*. *Biomaterials* **2007**, *28*, 1376–1384.
77. Cancedda, R.; Cedola, A.; Giuliani, A.; *et al*. *Biomaterials* **2007**, *28*, 2505–2524.
78. Weitkamp, T.; David, C.; Bunk, O.; Bruder, J.; Cloetens, P.; Pfeiffer, F. *Eur. J. Radiol*. **2008**, *68*, S13–S17; Proceedings of the 5th Medical Application of Synchrotron Radiation 2007.
79. Moeckli, R.; Verdun, F. R.; Fiedler, S.; Pachoud, M.; Schnyder, P.; Valley, J.-F. *Phys. Med. Biol*. **2000**, *45*, 3509–3523.
80. Bonse, U.; Busch, F.; Günnewig, O.; *et al*. *Bone Miner*. **1994**, *25*, 25–38.
81. Salomé, M.; Peyrin, F.; Cloetens, P.; *et al*. *Med. Phys*. **1999**, *26*, 2194–2204.
82. Nuzzo, S.; Peyrin, F.; Cloetens, P.; Baruchel, J.; Boivin, G. *Med. Phys*. **2002**, *29*, 2672–2681.
83. Griffith, J. F.; Genant, H. K. *Best Pract. Res. Clin. Endocrinol. Metab*. **2008**, *22*, 737–764.
84. Dowker, S. E. P.; Elliott, J. C.; Davis, G. R.; Wilson, R. M.; Cloetens, P. *Caries Res*. **2004**, *38*, 514–522.
85. Bleuet, P.; Roux, J.-P.; Dabin, Y.; Boivin, G. In *Developments in X-Ray Tomography IV*, *Proceedings of SPIE*; Bonse, U., Ed.; SPIE: Bellingham, WA, 2004; Vol. 5535, pp 129–136.
86. Rack, A.; Rack, T.; Stiller, M.; Riesemeier, H.; Zabler, S.; Nelson, K. *J. Synchrotron Radiat*. **2010**, *17*, 289–294.
87. Stock, S. R.; De Carlo, F.; Almer, J. D. *J. Struct. Biol*. **2008**, *161*, 144–150.
88. Zoeger, N.; Streli, C.; Wobrauscheck, P.; *et al*. *X-Ray Spectrom*. **2008**, *37*, 3–11.
89. Dierolf, M.; Menzel, A.; Thibault, P.; *et al*. *Nature* **2010**, *467*, 436–440.
90. Peyrin, F. *Osteoporos. Int*. **2009**, *20*, 1057–1063.
91. Müller, R.; Van Campenhout, H.; Van Damme, B.; *et al*. *Bone* **1998**, *23*, 59–66.
92. Gielkens, P. F. M.; Schortinghuis, J.; de Jong, J. R.; *et al*. *Arch. Oral Biol*. **2008**, *53*, 558–566.
93. Park, E.-A.; Hong, S. H.; Kim, K. G.; Choi, J.-Y.; Shin, C. S.; Kang, H. S. *Acad. Radiol*. **2009**, *16*, 332–340.
94. Guldberg, R. E.; Duvall, C. L.; Peister, A.; *et al*. *Biomaterials* **2008**, *29*, 3757–3761.
95. Bernhardt, R.; van den Dolder, J.; Bierbaum, S.; *et al*. *Biomaterials* **2005**, *26*, 3009–3019.
96. Wagner, A.; Sachse, A.; Keller, M.; *et al*. *Phys. Med. Biol*. **2006**, *51*, 1313–1324.
97. Wang, M. L.; Massie, J.; Allen, R. T.; Lee, Y.-P.; Kim, C. W. *Spine J*. **2008**, *8*, 340–350.
98. Monjo, M.; Rubert, M.; Wohlfahrt, J. C.; Rønold, H. J.; Ellingsen, J. E.; Lyngstadaas, S. P. *Acta Biomater*. **2010**, *6*, 1405–1412.
99. von Arx, T.; Cochran, D. L.; Schenk, R. K.; Buser, D. *Int. J. Oral Maxillofac. Surg*. **2002**, *31*, 190–199.
100. Knabe, C.; Kraska, B.; Koch, C.; Gross, U.; Zreiquat, H.; Stiller, M. *Biotech. Histochem*. **2006**, *81*, 31–39.
101. Mirone, A.; Wilcke, R.; Hammersley, A.; Ferrero, C. last visit 2010. PyHST – High Speed Tomographic Reconstruction. http://www.esrf.eu/UsersAndScience/Experiments/TBS/SciSoft/.
102. Sodek, J.; Cheifetz, S. In *Bone Engineering*; Davies, J. E., Ed.; Em Squared: Canada, 2002; pp 31–43.
103. Knabe, C.; Koch, C.; Rack, A.; Stiller, M. *Biomaterials* **2008**, *29*, 2249–2258.
104. Kallai, I.; Mizrahi, O.; Tawackoli, W.; Gazit, Z.; Pelled, G.; Gazit, D. *Nat. Prot*. **2011**, *6*, 105–110.

3.305. Biomedical Thin Films: Mechanical Properties

B Ben-Nissan, University of Technology, Sydney, NSW, Australia
B A Latella, Commonwealth Scientific and Industrial Research Organisation, Perth, WA, Australia
A Bendavid, Commonwealth Scientific and Industrial Research Organisation, Lindfield, NSW, Australia

© 2011 Elsevier Ltd. All rights reserved.

3.305.1. Introduction 63
3.305.1.1. Why Surface Engineering? 64
3.305.2. Coating Techniques 64
3.305.2.1. Plasma Coating of Calcium Phosphates 64
3.305.2.2. Nanocrystalline Coatings 65
3.305.2.2.1. Physical vapor deposition 65
3.305.2.2.2. Chemical vapor deposition 66
3.305.2.2.3. Sol–gel nanocoating method 66
3.305.2.3. Diamond-like Carbon 66
3.305.3. Thin Film Mechanical Testing: Methods 66
3.305.3.1. Instrumented Nanoindentation 67
3.305.3.2. Adhesion and Wear Test Methods 68
3.305.3.2.1. Pull-off testing 68
3.305.3.2.2. Scratch testing 68
3.305.3.2.3. Pin on disk 69
3.305.3.3. Microtensile Testing 69
3.305.3.4. Bending Tests 70
3.305.3.5. Bulge and Blister Testing 70
3.305.3.6. Stress Measurements 71
3.305.4. Concluding Remarks 71
References 72

Abbreviations

CVD	Chemical vapor deposition
DLC	Diamond-like carbon
HR	Hip resurfacing
HVOF	High velocity oxyfuel
M–M	All metal
M–PE	Metal–polyethylene
OA	Osteoarthritis
PACVD	Plasma-assisted chemical vapor deposition
PVD	Physical vapor deposition
THR	Total hip replacement
UHMWPE	Ultra-high molecular weight polyethylene

3.305.1. Introduction

Degenerative joint disease is recognized as an increasing problem for society as a direct result of an ageing population. More than 700 000 primary total hip and knee replacements are performed each year in the United States, and demand for the surgery is expected to double in the next 10 years. When a person has joint pain and joint immobility, the main concern is the relief of that pain and the return to a healthy and functional lifestyle. The degeneration of joints often makes surgical repair or replacement necessary. Most of the implants used in orthopedics usually utilize a surface modification method such as protective, hard, or bioactive coatings to improve reliability and long-term performance.

Osteoarthritis is the degeneration of the articular surface of the joint. The word arthritis literally means joint inflammation. There are two basic and separate causes of arthritis, inflammation, and mechanical damage. Mechanical damage is related to osteoarthritis where either a limb fracture or prolonged mechanical overload initiates degradation of the articular cartilage. Osteoarthritis is the most common form, and the hip is one of the common joints affected by this. It is a degenerative process, which directly results in the wearing out of the articulating cartilage on the joint's surface. Over time, the joint surfaces slowly deteriorate until the underlying bone is exposed. Exposed bone results in a painful joint when it moves and bears weight. As a result, hip pain and stiffness increase and the bones articulate without the load-distributing effect of the cartilage.[1] Other hip problems that produce similar symptoms include rheumatoid arthritis and avascular necrosis (injury and loss of blood supply to the bones).

Osteoarthritis (OA), also known as degenerative joint disease, is a painful and debilitating condition that affects many people, including the relatively young. It is said to be the most common musculoskeletal disorder affecting the western world. Overall OA affects 13.9% of adults aged 25 and older

and 33.6% (12.4 million) of those older than 65; an estimated 26.9 million US adults in 2005. In OA of the hip, the most common surgical treatment is some form of hip replacement (or arthroplasty). In Australia, in the period from September 1999 to the end of 2007, there were just over 125 000 primary total hip replacement (THR) surgeries, almost 90% of them for OA.[2] THR has been described as an orthopedic success story, enabling hundreds of thousands of people to live fuller, more active lives. Despite the success of THR it has been observed that it is not so suitable for younger patients who wish to return to a more active lifestyle.[3]

The probability of survival of THRs in younger patients is around 80% after 10 years and drops to 50% after 20 years. Therefore, patients under 50 years old would be likely to outlive their implants.

Hip resurfacing (HR) is proposed as a bone-conserving alternative for younger, heavier, and more active patients for whom a total hip replacement is less suitable. Despite its popularity, and increasing acceptance and use by orthopedic surgeons, there still remains controversy and disagreement over whether it should be used or not.[4,5] One of the main concerns is the incidence of early, postoperative, hip fracture.[6,7] The other main cause of failure of HR is loosening of the femoral implant.

In Australia, in the period from September 1999 to December 2007, there were almost 11 000 HR with 150 revised because of femoral fracture and 89 because of loosening.[2] There are several anatomical and surgical parameters that affect the incidence and likelihood of hip fracture and loosening.

As early as the 1960s and 1970s in Europe, Charnley, Scales, McKee, Ring, and Muller developed either metal–polyethylene (M–PE) bearings for total hip replacements (THR) or all metal (M–M) cobalt–chromium–molybdenum (CoCr) heads and cups.[8]

Currently, bearing surfaces for hip joints fall into two broad categories. Firstly, the so-called *hard-on-soft* combinations in which hard materials such as metal or ceramic implants articulate against polyethylene. Secondly, the so-called *hard-on-hard* bearing surfaces in which the same hard components articulate against themselves. New bearing surfaces are being sought, which give significant reductions in both the volume of wear debris generated and its effect on the body.[9]

3.305.1.1. Why Surface Engineering?

The release of particulate matter derived from THRs is important in determining the long-term survival of the prosthesis. Polyethylene debris derived from a M–PE coupling appears to cause the most pronounced tissue reaction. Phagocytosis of wear debris induces an inflammatory reaction associated with the release of cytokines and other inflammatory mediators. Once osteolysis has occurred, it tends to progress and may ultimately lead to failure of the implant. Consequently, it is appropriate to consider the use of bearing surfaces with a greater resistance to the production of osteolytic wear debris, such as metal-on-metal and ceramic-on-ceramic systems.[10]

Wear in metal-on-metal components is known to consist of two distinct phases. A relatively high-wear running-in phase followed by a steady-state phase when the wear rate is relatively constant and much lower. Metal-on-metal components have given good clinical results but there are still concerns over long-term exposure to elevated levels of metal ions.[9]

Surface engineering of the metallic bearing surface offers an alternative approach to reduce metallic wear debris in metal-on-metal bearing couples for hip prostheses. Fully surface-engineered bearing systems are used to reduce the wear rates for metal-on-metal prostheses and to minimize the generation of wear debris and the release of metal ions. After 2 million cycles in a physiological anatomical hip joint simulator test, it has been shown that the wear rates of full surface-engineered (surface-coated) prostheses were at least 23-fold lower for the heads and 6-fold lower for the inserts than the traditional clinical metal-on-metal prostheses, which leads to at least an 18-fold reduction in the overall wear rates.[11]

3.305.2. Coating Techniques

Coatings offer the possibility of modifying the surface properties of surgical-grade materials to achieve improvements in performance, reliability, and biocompatibility. Techniques such as physical vapor deposition (PVD), chemical vapor deposition (CVD), metal–organic chemical vapor deposition (MOCVD), electrochemical vapor deposition, thermal or diffusion conversion, and sol–gel processing have been used to produce both micro- and nanocoatings.

3.305.2.1. Plasma Coating of Calcium Phosphates

Hydroxyapatite, $Ca_{10}(PO_4)_6(OH)_2$, is widely accepted as a biocompatible material, which resembles the mineral component of bone and teeth.[12,13]

Since the early 1980s calcium phosphates have been used as porous coating materials on a range of metallic implants for orthopedic and maxillofacial applications.[14,15]

This was initiated to compensate for the poor mechanical properties of porous bulk calcium phosphate materials and utilize the excellent mechanical properties of the metallic substrates.

Over the years, a large number of coating methods have been investigated, ranging from thermal processes to sophisticated ion implantation methods, to produce calcium phosphate coatings, but plasma spraying has been the only commercial method widely applied to metallic implants.

A mixture of amorphous and crystalline phases results from the spraying process leading to variable solubility, dictated by the amount of the amorphous phase. While some manufacturers prefer a more crystalline coating, others prefer faster dissolving amorphous or calcium oxide containing coatings.

The advantage lies in the supply of calcium and phosphate ions that stimulate bone tissue growth toward the surface. However, a good balance must be reached between the solubility and the bone growth rate to allow good mechanical bonding and properties at the implant–tissue interface. Pure hydroxyapatite coatings are now being substituted by chitosan/hydroxyapatite composites[16] to improve bone adhesion or by fluorohydroxyapatite coatings to improve bone integration.[17]

The ideal environment for bone growth is established whereby metal ion release is reduced, good mechanical interlocking is established, and a bioactive surface is available.[18]

Thermal spraying is a well-established technology for forming hard coatings on selected component substrates. The coating material is heated in a gaseous medium and projected at high velocity as molten droplets onto a substrate surface. Upon impact, the droplets become flattened, heat is transferred to the cold substrate and the droplets solidify rapidly to form the 'splat.' Powders, rod, and wires can be used as feedstock materials.[19,20]

Thermal processing of hydroxyapatite has been controversial. The complexity of plasma processing requires a high degree of skill to ensure that the desired product is deposited. Every particle travels through the heat source and is subjected to a unique processing environment dictated by the thermokinetic history of the particle. Several approaches are being used to provide a reproducible environment. Axial powder delivery, unlike transverse delivery, provides injection directly into the heat source.

Several thermal processing routes can be employed depending on the materials and desired coating. These include plasma spraying, high velocity oxyfuel (HVOF) spraying, detonation flame spraying, and flame spraying. Plasma spraying can be carried out in an ambient atmosphere (atmospheric plasma spraying, APS), under vacuum (vacuum plasma spraying, VPS), or under controlled atmospheres, such as nitrogen. Plasma spraying uses a direct current arc to produce gas plasma, although other sources, such as radiofrequency-generated plasmas can be used. Each is capable of producing coatings of thickness ranging from a few microns to a few millimeters. The high-temperature decomposition during plasma spraying impedes the deposition of hydroxyapatite coatings.[18]

A narrow particle size distribution provides each particle with a comparable heat history. Atmospheric plasma spraying causes turbulence that introduces cold pockets into the spray stream. Turbulence can be reduced by plasma spraying in a vacuum or with a flame.

The control of particle melting leads the way to predictable solidified droplet microstructures. Electron microscopy has long been a useful technique to visually identify the appearance of the deposit. Micro-Raman provides the ability to assess the chemical bonding within each flattened droplet. Micro-X-ray diffraction, available at synchrotron light sources, provides an analysis of the crystal structure. Nanoindentation testing, also known as depth-sensing indentation, is ideally suited for measuring hardness and elastic modulus of droplets or thin films/coatings and will be discussed later in this chapter.

3.305.2.2. Nanocrystalline Coatings

Nanocrystalline coatings with grain sizes in the nanometer range are known to exhibit superior hardness and strength. The search for nanostructured coatings is driven by the improvement in nanocoating techniques and the availability of various kinds of precursor materials and sources.

Coating is a technique for the surface modification of the base material in order to enhance the physical and/or mechanical performances of tools and structural components. Existing PVD and CVD processes for preparing microcrystalline coatings can be used to produce nanostructured coatings by modifying the processing parameters or by using feedstock powders having nanograined structures. In addition, conventional plasma spraying and high velocity oxygen fuel thermal spraying are viable high-rate deposition techniques to produce nanocrystalline coatings using nanosized feedstock powders.

Hard ceramic coatings have attracted increasing attention due to their potential applications in cutting and forming tools, bearings, engine parts, and seals. Hard coatings improve the durability of substrate materials in hostile environments against abrasive wear, to prolong the component life. The ever-growing need for superior materials to withstand severe operating conditions has driven the search for superhard coatings with hardness values above 40 GPa.[21–23] Until recently, hardness enhancement in a single layer could only be achieved by introducing mechanical stresses into the coatings. The limitations of conventional coatings due to inferior hardness, elastic modulus, and poor oxidation stability are overcome by nanocomposite hard coatings such as nc-TiN/α-SiN_x, which consist of nanocrystalline TiN and a noncrystalline tissue phase of SiN_x, which are mutually immiscible. The improved mechanical properties of these nanocomposites can be explained by their nanostructure. Nanocomposite thin films exhibit hardness values significantly exceeding the microhardness that is given by the rule of mixture. Several research groups have reported on various superhard coatings with hardness exceeding 40 GPa. However, there is a distinguishable difference between superhard films where the high hardness values originate from the high compressive stress induced during the deposition by energetic ion bombardment and a second 'family' of coatings for which the hardness is due to the nanostructure arrangement.[22] Superhard nanocomposite thin films are at the early stage of development and appear to have a wide range of applications.

Although many different coating techniques and their modified versions exist, we will briefly explain only three basic methods. There are a number of review papers that cover each in more detail.[24,25]

3.305.2.2.1. Physical vapor deposition

Deposition of thin films by PVD techniques has found widespread use in many industrial sectors. State-of-the-art magnetron sputtering processes allow the deposition of metals, alloys, ceramic, and polymer thin films onto a wide range of substrate materials. Therefore, it is used in many coating applications, for example, metal-working industry, biomedical applications, and optical or electrical components. There is an increasing demand for coatings with tailored and enhanced properties such as high hardness, wear and corrosion resistance, low friction, and specific optical or electrical properties as well as decorative colors, and often, complex combinations of those properties are required.

PVD is a versatile synthesis method and is capable of preparing thin film materials with structural control at the atomic or nanometer scale by careful monitoring of the processing conditions. PVD involves the generation of vapor phase species either via evaporation, sputtering, laser ablation, or ion beam. In most PVD-based processing approaches, it is not possible to uniformly coat nonplanar substrates without sophisticated substrate translation/rotation or the use of multiple, spatially distributed sources. This arises because the vapor atoms are created in high vacuum that results in nearly collisionless vapor transport to the substrate. As a result, only regions in the line-of-sight of the vapor source are coated.[26]

3.305.2.2.2. Chemical vapor deposition

CVD of films and coatings involves the chemical reactions of gaseous reactants on or near the vicinity of a heated substrate surface. This atomistic deposition method can provide highly pure materials with structural control at atomic or nanometer-scale levels. Moreover, it can produce single layer, multilayer, composite, nanostructured, and functionally graded coating materials with well-controlled dimension and unique structure at low processing temperatures.

Furthermore, the unique feature of CVD over other deposition techniques such as the non-line-of-sight-deposition capability has allowed the coating of complex-shaped engineering components and the fabrication of nanodevices and composites. The versatility of CVD has led to rapid growth in the use of functional devices and it has become one of the main processing methods for the deposition of thin films and coatings for a wide range of applications, including refractory ceramic materials used for hard coatings and metallic films for protective coatings.[27]

3.305.2.2.3. Sol–gel nanocoating method

Sol–gel-derived nanocoatings are one of the preferred thin film production methods due to the relative ease of production and the inexpensive equipment utilized. The advantages of the process are based on its ability to form a physically and chemically pure and uniform coating over complex geometric shapes and the potential to deliver exceptional mechanical properties.

By definition, a sol is a suspension of colloidal particles in a liquid. A sol differs from a solution in that a solution is a single-phase system, whereas a sol is a two-phase, solid–liquid system. Colloidal particles can be in the approximate size range of 1–1000 nm; hence gravitational forces on these particles are negligible and interactions are dominated by short-range forces and surface charges.

Reducing their surface charge can modify the stability of the sol particles. If the surface charge is reduced sufficiently, 'gelation' is induced and the resultant product is able to maintain its shape without the assistance of a mould. Gels are regarded as composites, since they consist of a solid skeleton or network that encloses a liquid phase or excess of solvent. Depending on their chemistry, they can be soft and have a low elastic modulus, usually obtained through controlled polymerization of the hydrolyzed starting compound. In this case, a three-dimensional network forms, resulting ultimately in a high molecular weight polymeric gel. The gel can be thought of as a macroscopic molecule that extends throughout the solution. The gelation point is the time taken for the last bond in this network to form. This gelation can be used to produce nanostructured monoliths, powders, platelets, or nanosized coatings, depending on the process applied. Shrinkage problems are the main concerns in monolithic structures.

Sol–gel processing is unique in that it can be used to produce different forms, such as powders, platelets, coatings, fibers, and monoliths of the same composition, merely by varying the chemistry, viscosity, and other factors of a given solution. Furthermore, the range of different compositions that can be produced includes single oxides, mixed oxides, and nonoxides such as nitrides, borides, and chlorides.[28]

The advantages of the sol–gel techniques are numerous; it is nanoscale; it results in a stoichiometric, homogeneous, and pure product owing to mixing on the molecular scale; high purity can be maintained as grinding can be avoided; it allows reduced firing temperatures due to its small particle sizes with high surface areas; it has the ability to produce uniform fine-grained structures; it allows the use of different chemical routes; and it is easily applied to complex shapes with a range of coating techniques, including dip, spin, and spray deposition.[29–31]

Furthermore, sol–gel coatings have the added advantages that the costs of precursor materials are relatively unimportant, owing to small amounts of material requirements. Shrinkage for a number of coatings, depending on the chemistry, is fairly uniform perpendicular to the substrate and the coating can dry rapidly without cracking. A single layer coating is ~70–100 nm. Several layers can be applied, but cracking is typically an issue when more than four layers are applied, even with alternating sol gel deposition and sintering.[31–34]

Sol–gel film deposition also offers the advantage over other film depositions techniques in that thickness, pore volume, size, and surface area can be relatively easily controlled by synthesis methods or chemistry. Significant research has been conducted on the design of hard coatings with excellent strength, hardness, and toughness characteristics. One of the design concepts is based on the formation of multilayered gradient structures or superlattices having a difference in the elastic modulus between the layers. The thickness of each layer is in the nanometer range and a number of methods are used to produce multilayered films with desired nanohardness values. Another design approach utilizes the formation of single-layer nanocomposite coatings with microstructures comprising nanocrystallites embedded in an amorphous matrix.[35]

3.305.2.3. Diamond-like Carbon

Diamond-like carbon (DLC) has been the focus of extensive research in recent years due to its potential application in many technological areas. The combination of low friction, wear resistance, high hardness, biocompatibility, hemocompatibility, and chemical inertness makes it suitable for a number of applications ranging from the coatings of stents, heart valves, orthopedic components, and prostheses in the biomedical industry.[36,37] DLC and doped DLC have been investigated extensively for possible biomedical applications. It has been demonstrated that doping with elements such as Si, N, F, Ca, and P improves the properties of DLC such as biocompatibility, infection resistance, and mechanical properties.[38–41] DLC films have been used to coat the surfaces of blood-interfacing prostheses. A number of different deposition technologies have been described for synthesizing DLC films.[42] The most common deposition technique used is RF-based (13.56 MHz) plasma-assisted chemical vapor deposition (PACVD). This technique allows high-quality DLC coatings to be deposited onto complex-shaped items at low temperature (**Table 1**).

3.305.3. Thin Film Mechanical Testing: Methods

With the ever increasing demands imposed by the use of bioimplants and devices, novel techniques are required to assess their mechanical reliability. Methods for ascertaining mechanical properties and adhesion have been stimulated by developments

Table 1 Thin film mechanical properties of some common thin films showing according to their deposition techniques, nanoindentation hardness, and Young's modulus values

Thin film material	*Hardness (GPa)*	*Elastic modulus (GPa)*	*Deposition process*	*References*
Hydroxyapatite	1.5–5.0	60–100	Microplasma spraying	84
Hydroxyapatite	2.5–3.0	65–140	PLD	19
Hydroxyapatite	4.5–5.2	100–120	RF magnetron	20
DLC	20–47	180–415	PLD	85
DLC	10–16	70–120	RF magnetron	86
DLC	16	150	PACVD	36
DLC-Si	12–16	110–150	PACVD	36
DLC-F	6–16	80–150	PACVD	39
DLC-SiO_x	11–16	100–150	PACVD	40
DLC-TiO_x	10–16	160–130	PACVD	38
TiN	15	250	CVD	87
TiN	25–27	250–280	FAD	21
TiO_2	17–18	200–210	FAD	88
TiO_2	4–7	–	PACVD	89
ta-C	34–42	295–345	FAD	90
ZrO_2	14–18	180–225	FAD	91
ZrO_2	6–12	120	Sol–gel	34,71
nc-TiN/α-SiN_x	40	300	FAD	21
SiO_2	2.5 $\pm$ 0.27	13.6 $\pm$ 0.4	Sol–gel	92
$ZrO_2/Al_2O_3/ZrO_2$	10.4$\pm$ 0.8	240 $\pm$ 22	Sol–gel	30

This table is designed to give some examples of the work carried out in the field. In most if not in all studies different thicknesses on and a number of different substrates were used. FAD, Filtered arc deposition; PACVD, Plasma assisted chemical vapor deposition; PLD, Pulsed laser deposition; RF magnetron, radio frequency magnetron; CVD, Chemical vapor deposition; SOL, Sol–gel deposition.

of bio-inspired coatings (i.e., hydroxyapatite) on metallic substrates, as discussed in the previous section. Methods to quantitatively determine the mechanical properties of these thin coatings on substrates or free-standing films are required. There have been constant improvements and developments in equipment capable of extracting the properties of the structure or film and also the adhesion of the coating to an underlying substrate.[43]

In general, we typically think of thin films in terms of their electronic, magnetic, or optical properties but many such devices are limited by their mechanical properties. Furthermore, for medical devices that are mainly used in very harsh physiological environments, it is extremely important to understand mechanical properties. A common definition of thin films is based on the substrate thickness and geometry, which influence the mechanical, and in general, physical properties.[44]

In biomedical applications, implants are usually much thicker than the thin film coatings applied to them. Some of the new generation coatings can be from a few nanometers in thickness up to a few millimeters thick. The question arises, can a 30–50 μm plasma-sprayed coating be classified as a thin film coating?

In the context of biomedical applications, coatings greater than 1000 μm should be considered 'thick' or 'macrocoatings', 1–1000 μm as 'thin film coatings' or 'microcoatings' and below 1 μm should be considered 'nanocoatings.'

An overview of some of the most widely used test methods for measuring mechanical properties and adhesion performance of micro- and nanocoatings on substrates pertinent to biomedical materials development is given. These methods can broadly be divided into the measurement of (i) coating properties and (ii) adhesion properties, although there may be some overlap with some techniques. For an excellent and comprehensive compilation of methods for studying film adhesion, the reader is referred to Lacombe.[45]

3.305.3.1. Instrumented Nanoindentation

The starting point and method of choice by many practitioners in the biomedical field for measuring the mechanical properties of coatings and implants is nanoindentation. The methodology and instrumentation have developed in leaps and bounds over the years and it is now considered a simple and effective means of obtaining meaningful measures of hardness, *H*, and Young's modulus, *E*, of coatings. The main requirements for obtaining the best possible results with such testing are in sample preparation, calibration of equipment and corrections for thermal drift, initial penetration, frame compliance, and indenter tip shape.[46–53]

In macro/microindentation, a load is applied and then removed and the area of the residual impression is measured.[54] By contrast, in nanoindentation, a set load (in the mN range) is applied to the indenter in contact with the specimen. As the load is applied, the penetration depth is measured (nm range). At maximum load, the area of contact is determined by the depth of the impression and the known angle or radius of the indenter. The result is a load–displacement curve as shown in **Figure 1** for pure hydroxyapatite, which yields contact pressure or hardness and Young's modulus from the shape of the unloading curve using software based on the model and indenter type (pointed, i.e., Berkovich, Vickers, Knoop, or spherical).[47] Likewise, different types of loading and unloading methods can be used to extract desired properties as a function of depth of penetration.[32,33,48,55] The application

of nanoindentation can also be directed toward the measurement of residual stress and film adhesion from direct indentation or transverse scratching as described by Fischer-Cripps.[48]

3.305.3.2. Adhesion and Wear Test Methods

Adhesion testing is necessary to ensure the coating will adhere properly to the substrate to which it is applied. Many techniques have been employed for adhesion measurement of films and coatings as demonstrated by Mittal.[56] The most popular test methods for measuring the adhesive bonding to substrates include pull-off, cross-cut, indentation scratching (increasing load), and pin-on-disk.

3.305.3.2.1. Pull-off testing

This is perhaps the most common method to determine the strength of a bond between a thin film and a thick substrate. Many types of configurations have been proposed[57] using universal testing machines or dedicated tensile testers. The main requirements are that the alignment of grips and sample fixture is precise to ensure uniform loading and that the adhesive used to bond the sample to the fixture is sufficiently strong (stronger than the bond strength of the film–substrate) and does not penetrate the interface of interest. The bond strength is determined from the critical load required to separate the film–substrate contact area. The main advantage of this technique is its versatility and applicability to a wide range of coating–substrate systems. It can be used for both soft flexible coating as well as hard brittle ones. The weakness in typical pull testing is the wide variation in data. One must perform multiple tests on a given sample and statistical analysis to obtain reliable quantitative data. In biomaterials, pull out is a more common mode of failure of a bone implant than bone fracture. Pull out may not necessarily occur at the interface between bone and coating, but instead between the metal and the hydroxyapatite coating.

3.305.3.2.2. Scratch testing

Scratch testers such as that shown in Figure 2 use a small diamond stylus or hard metal (WC; normally 200 μm radius), which is drawn across the coated surface at a constant velocity at increasing load. The load on the diamond causes stresses to be increased at the interface between the coating and the substrate, which can result in delamination or chipping of the coating. The load at which the coating first delaminates is called the critical load and is a measure of coating adhesion. Coating failure can be determined from load and the distance at which delamination begins using microscopy, or from the change in friction or using an acoustic emission sensor. In addition to the critical load, the applied normal force, the tangential (friction) force, and the penetration depth are obtained.

Figure 3 shows the typical cracking and delamination that occurs on scratching a hard titania coating on a polycarbonate substrate.

Analyzing scratch test results is difficult due to the complex stress states involved and the broad array of damage processes that can occur depending on film thickness and the mechanical properties of the film and substrate. The test is sensitive to loading rate, stylus shape, environment (humidity), and scratch speed. Thus, it is difficult to relate the critical load to film adhesion.

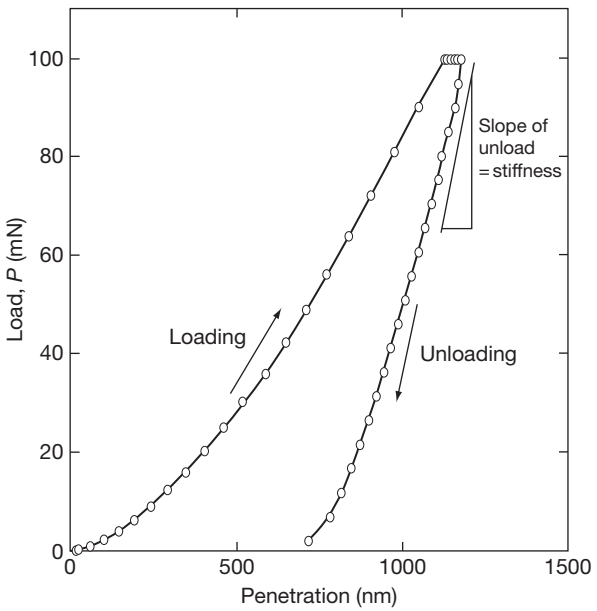

Figure 1 Indentation load–displacement curve for a pure hydroxyapatite using a Berkovich indenter ($H = 9.9$ GPa, $E = 110$ GPa).

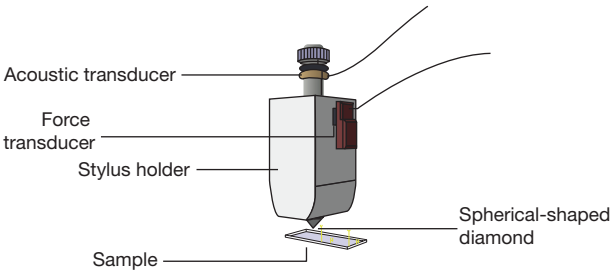

Figure 2 Typical scratch testing device (based on the Quad Group Inc. Romulus III universal test equipment).

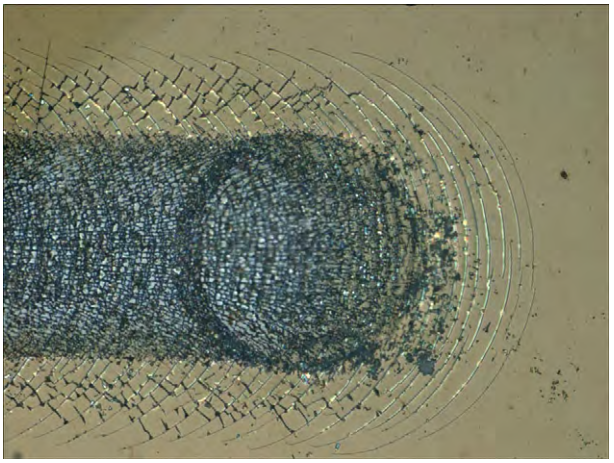

Figure 3 Scratch damage in a titanium oxide coating on a polycarbonate substrate. Horizontal field of view is 400 μm.

3.305.3.2.3. Pin on disk

Pin-on-disk tribometers are used to determine the friction coefficient and wear resistance of surfaces. The tester consists of a pin (normally a ruby, WC, or metal sphere) under a static load in contact with a rotating sample. The test can be run for an extended period of time either in air or a simulated body environment to provide information on the degradation of the coating with time (sliding distance). Similar devices that are used in biomaterials research are pin-on-plate type wear testing machines, such as the Ortho-Pod instrument (Advanced Mechanical Testing, Inc., Watertown, MA). This has six stations for the pins with independent servo-controlled variables that correspond to rotary motion of both the plate and the pins and the normal load applied to each of the six pins. The pin rotation feature gives this machine the ability to generate pin–plate sliding motions that are typically not available on standard pin-on-disk machines. The Ortho-Pod is an excellent tool for testing implant materials whose wear characteristics depend upon various sliding directions (crossings) as well as load, in either dry or a fully lubricated environment (serum or other fluids).

3.305.3.3. Microtensile Testing

In microtensile testing, the coating is deposited on a tensile coupon, which can then be pulled in a universal testing machine or specialized device that can be placed under an optical microscope or in a scanning electron microscope (**Figure 4**). The damage evolution in the coating can be viewed *in situ* or *ex situ* after application of specific strains. The method is suitable to determine properties of thin or thick coatings on a variety of ductile substrates.[58–62]

This type of test is advantageous in that the stress field is uniform and small specimens can be used. Likewise, using optical or scanning electron microscopy to view the damage *in situ* during loading offers useful insights into material failure mechanisms.[63,64] The drawback with such tests is that for analysis of the coating behavior, the residual stress and Young's modulus of the coating are required by other means, such as from curvature measurements (see later) and nanoindentation, respectively.

Thin brittle coatings on ductile substrates when uniaxially stressed produce parallel cracks in the coating layer perpendicular to the tensile axis and normal to the interface. These cracks generally extend along the width of the sample and increase in number with additional elongation, leading to a decrease in the crack spacing. For some systems, cracks may also be accompanied by localized delamination of the coating from the substrate. Ultimately, the delamination of the coating signals the end of the lifetime of the coated system. For softer and more compliant films, cracking can be irregular and film debonding reduced substantially. The drawback with these semibrittle films is that quantitative analysis cannot be performed.

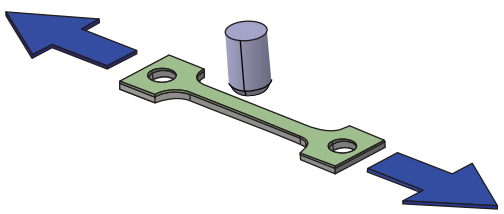

Figure 4 Schematic of the *in situ* tensile test specimen pulled while viewing with optical microscope.

In situ tensile tests provide insights into fracture and delamination processes and for ranking the practical adhesion performance of different coatings. The film debonding behavior is key to the reliability of film–substrate systems, particularly where mechanical loading and chemical interactions are encountered. For films that crack and debond in a controlled fashion, one can use linear elastic fracture mechanics relations to extract intrinsic film properties (strength and fracture toughness) and interfacial adhesion characteristics.[65–67]

Zirconia films (both nano and macro) have been produced by a number of different methods and are of great interest for variety of orthopedic applications. The phase transformation in bulk zirconia has been found to be a clinical concern in femoral heads of THA due to the unexpected failures observed in early 2000.[8,68] However, zirconia nanocoatings of 70–100 nm thickness are not affected by the dilation due to phase transformations and behave differently from their bulk forms.[34] As a result, a wide range of different deposition techniques for zirconia have been proposed. Characterization techniques also proved that adhesion of these coatings to a number of metallic biocompatible substrates and new generation femoral components has been extremely good.[69]

As an example, microtensile testing was used to determine the mechanical properties and adhesion characteristics of surface-modified pure titanium metal substrates coated with a sol–gel-derived alkoxide-based zirconia to improve its wear properties and corrosion resistance is briefly described. In addition to microtensile testing, tribological pin-on-plate wear tests were also carried out for assessment of wear properties.

The morphology, adhesion, and tribological properties of the zirconia sol–gel coating on as-polished and 25 V anodized titanium surfaces were compared.[70] The anodization of titanium involves the formation of a thin, compact, oxide layer, which improves the wettability for further coating. These samples were spin coated with zirconia, yielding 100 nm thick films. The nanocoatings were prepared by alkoxide sol–gel chemistry, using techniques and protocols developed in an earlier work, and were examined with X-ray diffraction and scanning electron microscopy.[34,71]

Interfacial adhesion properties were measured using the tensile test as described above. The tribological properties were investigated using an Ortho-Pod machine, with commercial grade ultra-high molecular weight polyethylene (UHMWPE) pins (3/8 in. diameter) that can articulate in number of different combinations against opposing coated and control specimens. The UHMWPE pins were used in a bovine serum environment. The amount of wear was measured gravimetrically and wear features were observed using SEM. Preliminary Ortho-Pod results indicate a lower wear rate on the anodized titanium substrate in comparison to the as-polished substrate. The calculated H statistic of 38.563 indicated that indeed there are statistically different wear rates among the groups ($p < 0.001$). No *post-hoc* analysis is available to test for differences between individual groups – the Kruskal–Wallis approach simply provides a ranking of best to worst. In this light, the four best performing surfaces were, from best to worst, surfaces Cp Ti

once coated with ZrO_2, uncoated anodized Cp Ti, uncoated Ti6Al4V samples, and uncoated Ti6Al4V anodized samples.

Table 2 shows the film properties and interfacial adhesion energies for the as-polished and anodized titanium substrate. The film properties are essentially equivalent but the anodized layer has improved the interfacial adhesion of the zirconia film to the substrate by a factor of about 7.

The fracture toughness of the films depends on the integrity of the film, the bonding to the substrate, interphases between coating and substrate, and the nature of the substrate itself. The production of a homogeneous solution is necessary to ensure good mechanical properties for the film as well as protection of the substrate. No cracking of the coatings were observed for any of the preparation conditions. Bonding to the substrate was also found to be good for all films, as evidenced by the lack of any severe spalling in all samples (Figure 5). The pattern of fracture lines on the sample in Figure 5 are through thickness cracks initiated mainly by slip bands from the substrate deformation. The tortuous crack paths shown demonstrate good fracture toughness and adhesion of the nanocoatings.

3.305.3.4. Bending Tests

Three- and four-point bending methods have been used to characterize the interfacial fracture between dissimilar materials and films on substrates, and to quantitatively evaluate the interfacial fracture energy. The thicknesses of these substrates are usually much smaller than their lateral dimensions, so that simple beam bending mechanics can be applied to describe their elastic response.[72]

A fracture-mechanics-based method for four-point bending developed by Charalambides and coworkers[73] for interfaces between dissimilar materials has been applied in many areas including biomaterials research successfully[74–78] to measure interface fracture energy. The method requires a bend bar of the coated substrate with a notch machined in the coated layer as shown in Figure 6. As the bending moment increases a crack initiates from the notch and propagates to the interface. For a sufficiently weak interface bond, the crack deflects and propagates along the interface. The interfacial fracture energy is given in eqn [1]:

$$\gamma = \frac{21P_c^2 l^2\left(1-\nu_s^2\right)}{16E_s b^2 h^3} \qquad [1]$$

where b is the specimen or beam width, h is the total thickness, l is the moment arm (distance between inner and outer loading lines), P_c is the critical load for stable crack propagation, and ν_s and E_s are Poisson's ratio and Young's modulus of the substrate, respectively. This method has the advantage that the interface fracture energy is independent of the crack length as long as the crack tip is not too close to the precrack or the loading points.

Table 2 Zirconia film properties and interfacial fracture energies for as-polished and anodized titanium substrates

	As-polished pure Ti	*Anodized pure Ti*
Zirconia film strength (MPa)	480 ± 50	530 ± 50
Zirconia film fracture toughness (MPa $m^{1/2}$)	0.34 ± 0.02	0.37 ± 0.05
Interfacial fracture energy (J m^{-2})	4 ± 0.8	30 ± 0.8

3.305.3.5. Bulge and Blister Testing

In bulge and blister testing, the film–substrate system is pressurized with gas or a fluid through a hole in the substrate. The height of the resulting hemispherical bulge in the film is then measured by optical microscopy or an interferometer. The pressure and deflection height can be used to provide information on elastic, plastic, and time-dependent deformation. In blister testing the pressure is increased until the film starts to debond from the substrate. The interfacial energy can be determined from the critical pressure for debonding as shown in eqn [2][79]:

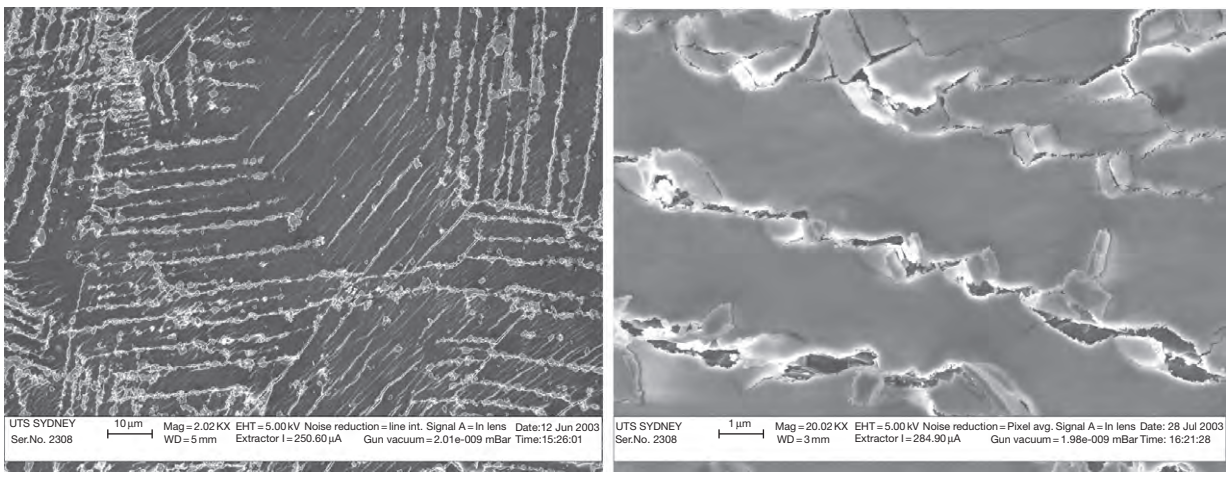

Figure 5 Scanning electron microscopy images of the sol–gel-derived zirconia-coated titanium alloy substrate after tensile testing showing the parallel micro-cracks in the coating which are dictated by the shear bands in the substrate (left, scale 10 µm) and at higher magnification the torturous path of the crack propagation within the film that is still well adhered to the substrate (right, scale 1 µm). Sample strained to about 10%.

$$\gamma = \frac{p^2(3 - v_f^2)r^4}{16E_f t_f^3} \quad [2]$$

where p is the applied pressure, r is the radius of the hole, E_f is the Young's modulus of the film, v_f is the Poisson's ratio of the film, and t_f is the film thickness.

3.305.3.6. Stress Measurements

The evaluation of the stress in a coating due to deposition and or temperature can be crucial in regards to mechanical stability. The stress in a film is made up of the following components (eqn [3]): intrinsic (deposition, mode of growth, structure), thermal expansion mismatch between film and substrate, and externally applied stresses[80]:

$$\sigma_f = \sigma(\text{intrinsic}) + \sigma(\text{thermal}) + \sigma(\text{external}) \quad [3]$$

Substrate curvature is a simple method requiring a stylus profilometer capable of long scans, generally no less than 10 mm length, or by using a phase shifting interferometer. The advantages of using an optical method such as interferometry are high accuracy of about 6 nm, substrates with curvature of up to 3 μm are acceptable, and rapid and straightforward to use. Furthermore, the substrate needs to be sufficiently thin for adequate measurement of the curvature. The stylus profilometry method requires careful and precise placement of the sample, so that a cross scan in the x- and y-directions is made on the surface (preferably both sides) before and after coating. A second method of measuring the curvature of substrate is by using a phase shifting interferometer (Figure 7).

The stress in the coating (intrinsic+thermal) can be determined using the Stoney formula without prior knowledge of the coating properties. The information that is required is coating thickness, substrate thickness, and Young's modulus. Stoney's equation[81] shows the relationship between the change in the radius of a coated and uncoated substrate and the corresponding stress in the layer (eqn [4]):

$$\sigma = \frac{1}{6}\left[\frac{1}{R_f} - \frac{1}{R_i}\right]\frac{E_s}{(1 - v_s)}\frac{t_s^2}{t_f} \quad [4]$$

where R_i is the radius of curvature before coating, R_f after coating, E_s and v_s the modulus and Poisson's ratio of the substrate, t_s the substrate thickness, and t_f the film thickness. Assuming that the scan length L of the substrate is much greater than the final bow B of the substrate, the radius R can be calculated using eqn [5].

$$R = \frac{L^2}{8B} \quad [5]$$

Compressive stress in the film leads to a convex deflection, whereas tensile stress results in concave deflection (as shown in Figure 8). The reader is referred to the text by Freund and Suresh,[82] which provides a comprehensive resource on stresses in films.

Measurements can be made *in situ* during deposition or thermal treatment with optical means by interferometry or deflection method (cantilever beam) using a low power laser. Likewise, elastic strain in films can be measured by X-ray diffraction from the change in crystal lattice d-spacing, from which the stress can be determined, given knowledge of the Young's modulus and strain-free lattice spacing (which may be unknown in many cases).[83]

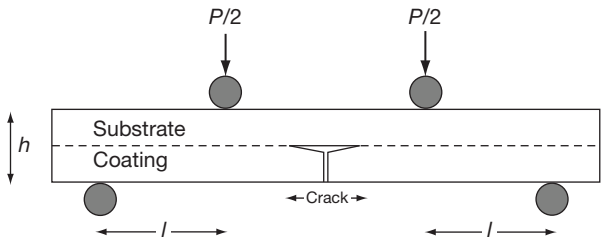

Figure 6 Schematic of the four-point bend delamination method.

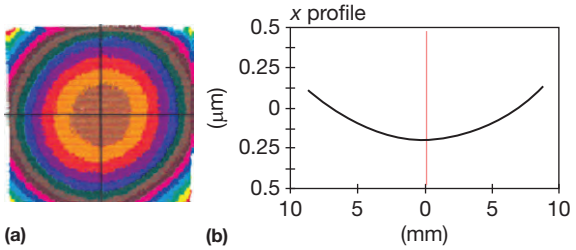

Figure 7 (a) A typical interference pattern (obtained by using a phase shifting interferometer) of the curvature of Si substrate coated with a film with tensile stress and (b) showing the curvature profile in the x-axis.

3.305.4. Concluding Remarks

In the biomedical field, the surface modification of metallic materials aims to inhibit wear, reduce corrosion and ion release, and promote biocompatibility. Surface coatings offer the possibility of modifying the properties of a component, and hence, improve both performance and reliability.

To date, many deposition methods have been used to produce wear-resistant, bioactive, and/or protective corrosion-resistant coatings on various substrates.

Many of the common barrier and corrosion-resistant coatings use plasma or thermal spraying, while several more recent techniques that have been used include PVD, plasma MOCVD, electrochemical vapor deposition, and sol–gel processing.

Microcoatings (30–50 μm) applied by plasma methods have produced in specific instances a range of problems. However, thin nanoscale coatings avoid problems associated with thermal expansion mismatch with metallic or ceramic substrates.

The term sol–gel is currently used to describe any chemical procedure or process capable of producing ceramic oxides, nonoxides, and mixed oxides from solutions.

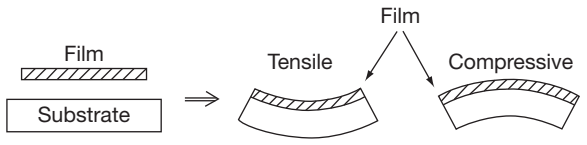

Figure 8 Film strained in tension results in tensile stress or strained in compression results in compressive stress.

Sol–gel-derived ceramic nanoscale coatings (40–200 nm) show promise due to their relative ease of production, ability to form a physically and chemically uniform coating over complex geometric shapes, consolidated at relatively low temperatures, and their potential to deliver exceptional mechanical properties and wear resistance due to their nanocrystalline structure.

The mechanical properties of biomaterial coatings and the substrate (implant) are strongly dependent on the film microstructure and deposition process as well as on the influence of interfacial constraint. These properties can differ from the bulk, and accurate measurement techniques are essential for determination of the properties of the coatings. In particular, better techniques are required for quantitative measurements of hardness, friction, adhesion strength or particularly the coating–substrate interfacial fracture toughness. Nanoindentation and microscratch measurements are essential tools for characterizing submicron coating properties, and further understanding of mechanical processes involved in these and other tests will help in obtaining valuable information, as well as in identifying their limitations. Likewise, the advent of microfabrication/machining technology and lithography has allowed micron-sized samples and free-standing films to be produced and tested *in situ* using SEM and/or TEM. In addition, theoretical modeling approaches are essential for progress in understanding thin film–substrate interfacial behavior which may lead to better choice and design of thin film–substrate materials selection.

The relationship between materials surface properties and biological responses is one of the major issues in biomedical materials research. Surface modification by thin film deposition has become a valuable tool for research aimed at understanding how structural and chemical surface properties influence material–biosystem interactions. As better understanding is achieved, one can expect that surface modifications for the purpose of controlling tissue response will open up avenues for developing new and superior implants and medical devices in a more systematic manner and at a faster rate than at present. This is possibly where the greatest potential of surface engineering lies in this field.

Bone–implant interactions, in addition to biological factors, are influenced by functionally applied multiaxial forces and biomechanics. The ultimate understanding of biological systems can only be achieved with appropriate nanoscale mechanical properties of biogenic structures and the influence of the nanostructures and nanoloading on these biological systems.

Our push to measure and determine thin film mechanical properties at the nanoscale will inevitably open new avenues in understanding the influence of stresses and micro/nanodeformations in the growth and repair mechanisms of biologic systems to allow us to use new materials, systems, and tools in tissue regeneration.

Acknowledgments

The authors thank Dr. Richard Roest for his contribution on nanocoated zirconia films and Drs. Tony Murphy and Phil Martin for their critical proofreading of this chapter.

References

1. Bierbaum, B. E.; Sweet, R. *Orthop. Clin. N. Am.* **1982**, *13*, 761–775.
2. Australian Orthopaedic Association National Joint Replacement Registry Annual Report. Adelaide: AOA, 2008.
3. Beckenbaugh, R. D.; Ilstrup, D. M. *J. Bone Joint Surg. Am.* **1978**, *60*, 306–313.
4. McKellop, H.; Park, S.; Chisa, R. *Clin. Orthop.* **1989**, *249*, 129–140.
5. Schmalzried, T. P.; Fowble, V. A.; Ure, K. J.; Amstutz, H. C. *Clin. Orthop. Relat. R* **1996**, *329*(Suppl.), 106–114.
6. Howie, D. W.; Cornish, B. L.; Vernon-Roberts, B. *Classification of loosening the role of prosthesis wear particles. Clin. Orthop. Relat. R.* **1990**, *225*, 144–159.
7. Wagner, M.; Wagner, H. *Clin. Orthop. Relat. R.* **1996**, *329*, 78–88.
8. Clarke, I. C.; Green, D. D.; Pezzotti, G.; Sakakura, S.; Ben-Nissan, B. In *Bioceramics: Materials Applications IV: Ceramic Transactions;* Sundar, V. V., Rusin, R. P., Rutiser, C. A., Eds.; American Ceramic Society: Nashville, Tennessee, 2004; Vol. 147, pp 155–166.
9. Isaac, G. H.; Thompson, J.; Williams, S.; Fisher, J. *Proc. IMechE* **2006**, *220H*, 119–133.
10. Savarino, L.; Greco, M.; Cenni, E.; Cavasinni, L.; Rotini, R.; Baldini, N.; Giunti, A. *J. Bone Joint Surg. Br.* **2006**, *88B*, 472–476.
11. Fisher, J.; Hu, X. Q.; Stewart, T. D.; Williams, S.; Tipper, J. L.; Ingham, E.; Stone, M. H.; Davies, C.; Hatto, P.; Bolton, J.; Riley, M.; Hardaker, C.; Isaac, G. H.; Berry, G. *J. Mater. Sci.: Mater. Med.* **2004**, *15*, 225–235.
12. De Groot, K. R.; Geesink, R.; Klein, C. P. A. T.; Serekian, P. *J. Biomed. Mater. Res.* **1987**, *21*(12), 1375–1381.
13. Hench, L. L. *J. Am. Cerm. Soc.* **1991**, *74*, 1487–1510.
14. Ducheyne, P.; Hench, L. L.; Kagan, A.; Martens, M.; Bursens, A.; Mulier, C. *J. Biomed. Mater. Res.* **1980**, *14*, 225–237.
15. Jarcho, M. *Clin. Orthop.* **1981**, *157*, 259–279.
16. Redepenning, J.; Venkataram, G.; Chen, J.; Stafford, N. *J. Biomed. Mater. Res.* **2003**, *66A*(2), 411–416.
17. Savarino, L.; Fini, M.; *et al. J. Biomed. Mater. Res.* **2003**, *66A*(3), 652–661.
18. Berndt, C. C.; *et al. Mater. Forum* **1990**, *14*, 161–173.
19. Nelea, V.; Morosanu, C.; Iliescu, M. *Appl. Surf. Sci.* **2004**, *228*, 346–356.
20. Nelea, V.; Pelletier, H.; Mille, P.; Muller, D. *Thin Solid Films* **2004**, *453*, 208–214.
21. Bendavid, A.; Martin, P. J.; Preston, E.; Cairney, J.; Xie, Z.-H.; Hoffman, M. *Surf. Coat. Technol.* **2006**, *201*, 4139–4144.
22. Vepřek, S. *J. Vac. Sci. Technol. A* **1999**, *17*(5), 2401–2420.
23. Vepřek, S. Reiprich, *Thin Solid Films* **1995**, *268*, 64–71.
24. Doerner, M. F.; Gardner, D. S.; Nix, W. D. *Mater. Res.* **1986**, *1*, 845–852.
25. Pelletier, H.; Nelea, V.; Mille, P.; Muller, D. *Nucl. Instrum. Meth. Phys. Res. B* **2004**, *216*, 269–274.
26. Hass, D. D.; Marciano, Y.; Wadley, H. N. G. *Surf. Coat. Technol.* **2004**, *185*, 283–291.
27. Choy, K. L. *Prog. Mater. Sci.* **2003**, *48*, 57–170.
28. Ben-Nissan, B.; Choi, A. H. *Nanomedicine* **2006**, *1*(3), 311–319.
29. Brinker, C. J.; Scherer, G. W. *Sol–Gel Science: The Physics and Chemistry of Sol–Gel Processing*. Academic Press: New York, 1990.
30. Miao, X.; Ben-Nissan, B. *J. Mater. Sci.* **2000**, *35*(2), 497–502.
31. Strawbridge, I.; James, P. F. *J. Non-Cryst. Solids* **1986**, *99*, 381–393.
32. Gan, L.; Ben-Nissan, B. *Comput. Mater. Sci.* **1997**, *8*, 273–281.
33. Gan, L. B.; Ben-Nissan, B. *J. Aust. Ceram. Soc.* **1997**, *32*(1–2), 51–55.
34. Paterson, M. J.; Paterson, P. J. K.; Ben-Nissan, B. *J. Mater. Res.* **1998**, *13*(2), 388–395.
35. Tjong, T.; Chen, H. *Mater. Sci. Eng. R* **2004**, *45*, 1–88.
36. Bendavid, A.; Martin, P. J.; Comte, C.; *et al. Diam. Relat. Mater.* **2007**, *16*, 1616–1622.
37. Dearnaley, G.; Arps, J. H. *Surf. Coat. Technol.* **2005**, *200*, 2518–2524.
38. Amin, M. S.; Randenyia, L. K.; Bendavid, A.; Martin, P. J.; Preston, E. W. *Diam. Relat. Mater.* **2009**, *18*, 1139–1144.
39. Bendavid, A.; Martin, P. J.; Randeniya, L. K.; Amin, M. S. *Diam. Relat. Mater.* **2009**, *18*, 66–71.
40. Randeniya, L. K.; Bendavid, A.; Martin, P. J.; Amin Md, S.; Preston, E. W.; Ismail Magdon, F. S.; Coe, S. *Acta Biomater.* **2009**, *5*, 1791–1797.
41. Uzumaki, E. T.; Lambert, C. S.; Belangero, W. D.; Freire, C. M. A.; Zavaglia, C. A. C. *Diam. Relat. Mater.* **2006**, *15*, 982–988.
42. Robertson, J. *Mater. Sci. Eng. R* **2002**, *37*, 129–281.
43. Ben-Nissan, B.; Pezzotti, G. *J. Ceram. Soc. Jpn.* **2002**, *110*(7), 601–608.
44. Ben-Nissan, B.; Pezzotti, G.; Muller, W. In *Mechanical Tribology: Materials Characterisation Applications*; Totten, G. E., Liang, H., Dekker, M., Eds.; Marcel Dekker: New York, 2004; pp 135–184.

45. Lacombe, R. *Adhesion Measurement Methods: Theory and Practice*. Taylor & Francis: Boca Raton, 2006.
46. Field, J. S.; Swain, M. V. *J. Mater. Res.* **1993**, *8*, 297–306.
47. Field, J. S.; Swain, M. V. *J. Mater. Res.* **1995**, *10*, 101–112.
48. Fischer-Cripps, A. C. *Introduction to Nanoindentation*. Springer: New York, 2002.
49. Gan, L. B.; Ben-Nissan, B.; Ben-David, A. *Thin Solid Films* **1996**, *290–291*, 362–366.
50. Mencik, J.; Munz, D.; Qut, E.; Weppelmann, E. R.; Swain, M. V. *J. Mater. Res.* **1997**, *12*, 2475–2484.
51. Mencik, J.; Swain, M. V. *J. Mater. Res.* **1995**, *10*, 1491–1501.
52. Oliver, W. C.; Pharr, G. M. *J. Mater. Res.* **1982**, *7*, 1564–1583.
53. Swain, M. V.; Menčík, J. *Thin Solid Films* **1994**, *253*, 204–211.
54. Kealley, C.; Latella, B. A.; Van Riessen, A.; Elcombe, M.; Ben-Nissan, B. *J. Nanosci. Technol.* **2008**, *8*, 3936–3941.
55. Fischer-Cripps, A. C. *Surf. Coat. Technol.* **2006**, *200*, 4153–4165.
56. Mittal, K. L. In *Adhesion Measurements of Films Coatings*; Mittal, K. L., Ed.; VSP: Utrecht, 1995.
57. Vallin, O.; Jonsson, K.; Lindberg, U. *Mater. Sci. Eng. Rep.* **2005**, *50*, 109–165.
58. Filiaggi, M. J.; Pilliar, R. M.; Abdulla, D. *J. Biomed. Mater. Res.* **1996**, *33*, 239–256.
59. Latella, B. A.; Gan, B.; Li, H. *Surf. Coat. Technol.* **2007**, *201*, 6325–6331.
60. Latella, B. A.; Triagni, G.; Evans, P. *Scr. Mater.* **2007**, *56*, 493–496.
61. Roest, R.; Eberhardt, A. W.; Latella, B. A.; Wuhrer, R.; Ben-Nissan, B. *Key Eng. Mater.* **2004**, *254–256*, 455–458.
62. Wang, J. S.; Sugimura, Y.; Evans, A. G.; Tredway, W. K. *Thin Solid Films* **1998**, *325*, 163–174.
63. Ignat, M.; Marieb, T.; Fukimoto, H.; Flinn, P. A. *Thin Solid Films.* **1999**, *353*, 201–207.
64. Latella, B. A.; Ignat, M.; Barbé, C. J.; Cassidy, D. J.; Li, H. *J. Sol Gel Sci. Technol.* **2004**, *31*, 143–149.
65. Harry, E.; Rouzaud, A.; Ignat, M.; Juliet, P. *Thin Solid Films* **1998**, *332*, 195–201.
66. Ignat, M. *Key Eng. Mater.* **1996**, *116–117*, 279–290.
67. Scafidi, P.; Ignat, M. *J. Adhes. Sci. Technol.* **1998**, *12*, 1219–1242.
68. Clarke, I. C.; Manaka, M.; Green, D. D.; *et al. J. Bone Joint Surg. Am.* **2003**, *85A*(Suppl. 4), 73–84.
69. Cordingley, R.; Kohan, L.; Ben-Nissan, B.; Pezzotti, G. *J. Aust. Ceram. Soc.* **2003**, *39*(1), 20–35.
70. Roest, R.; Atanacio, A. J.; Latella, B. A.; Wuhrer, R.; Ben-Nissan, B. *Mater. Forum* **2007**, *31*, 160–163.
71. Anast, M.; Bell, J.; Bell, T.; Ben-Nissan, B. *J. Mater. Sci. Lett.* **1992**, *11*, 1483–1485.
72. Saha, R.; Nix, W. D. *Acta Mater.* **2002**, *50*(1), 23–38.
73. Charalambides, P. G.; Lund, J.; Evans, A. G.; McMeeking, R. M. *J. Appl. Mech.* **1989**, *56*, 77–82.
74. Angelelis, C.; Ducarroir, M.; Felder, E.; Ignat, M.; Scordo, S. *Ann. Chimie Sci. Materiaux* **1998**, *23*, 891–898.
75. Dauskardt, R. H.; Lane, M.; Ma, Q. *Eng. Fract. Mech.* **1998**, *61*, 141–162.
76. Hofinger, I.; Oechsner, M.; Bahr, H. A.; Swain, M. V. *Int. J. Fract.* **1998**, *92*, 213–220.
77. Kuper, A.; Clissold, R.; Martin, P. J.; Swain, M. V. *Thin Solid Films* **1997**, *308–309*, 329–333.
78. Suansuwan, N.; Swain, M. V. *J. Dent.* **2003**, *31*, 509–518.
79. Bennet, S. J.; Devries, K. L.; Williams, M. L. *Int. J. Fract.* **1974**, *10*, 33–43.
80. Lepienski, C. M.; *et al. Thin Solid Films* **2004**, *447–448*, 251–257.
81. Stoney, G. G. *Proc. R. Soc. Lond. A* **1909**, *82*, 172–173.
82. Freund, L. B.; Suresh, S. *Thin Film Materials: Stress, Defect Formation and Surface Evolution*. Cambridge University Press: Cambridge, 2003.
83. Tsui, Y. C.; Doyle, C.; Clyne, T. W. *Biomaterials* **1998**, *19*(22), 2015–2029.
84. Dey, A.; Mukhopadhyay, A. K.; Gangadharan, S.; Sinha, M. K.; Basu, D.; Bandyopadhyay, N. R. *Ceram. Int.* **2009**, *35*, 2295–2304.
85. Tabbal, M.; Merel, P.; Chaker, M.; *et al. Surf. Coat. Technol.* **1999**, *116–119*, 452–455.
86. Anita, V.; Saito, N.; Takai, O. *Thin Solid Films* **2006**, *506–507*, 63–67.
87. Ramanujan, N.; Levy, R. A.; *et al. Mater. Lett.* **2001**, *57*(2), 261–269.
88. Bendavid, A.; Martin, P. J.; Preston, E. W. *Thin Solid Films* **2008**, *517*, 494–499.
89. Mathur, S.; Kuhn, P. *Surf. Coat. Technol.* **2006**, *201*, 807–814.
90. Xu, S.; Tay, B. K.; Tan, H. S.; *et al. J. Appl. Phys.* **1996**, *79*, 7234–7240.
91. Yu, G. O.; Tay, B. K. *Appl. Phys. A Mater. Sci. Process.* **2005**, *81*, 405–411.
92. Chan, C. M.; Cao, G. Z.; Fong, H.; Sarikaya, M.; Robinson, T.; Nelson, L. *MRS Bull.* **2000**, *15*, 148–154.

3.306. Microindentation

L-H He, University of Otago, Dunedin, New Zealand
M V Swain, University of Otago, Dunedin, New Zealand; The University of Sydney, Sydney, NSW, Australia

© 2011 Elsevier Ltd. All rights reserved.

3.306.1.	**Introduction**	75
3.306.2.	**Overview of Nanoindentation Technique**	76
3.306.2.1.	Measurement of Elastic Modulus and Hardness	76
3.306.2.2.	Instrument Calibration	78
3.306.2.2.1.	Basic calibration of force and depth measurement systems	78
3.306.2.2.2.	The determination of the load frame compliance, C_f	78
3.306.2.2.3.	Indenter tip shape calibration	78
3.306.2.3.	Indentation Stress–Strain Relationship	79
3.306.2.4.	Measurement of Fracture Toughness and Residual Stress	80
3.306.2.4.1.	Fracture toughness	80
3.306.2.4.2.	Residual stresses	82
3.306.2.5.	Indentation Creep	82
3.306.2.6.	Other Factors that Influence the Accuracy of the Results	83
3.306.3.	**Application of Nanoindentation to Biomaterials**	85
3.306.3.1.	Elastic Modulus and Hardness of Enamel	85
3.306.3.2.	Stress–strain Relationship of Enamel	86
3.306.3.3.	Creep Behavior of Enamel	87
3.306.3.4.	Nanoindentation of Caries Lesions	88
3.306.4.	**Summary**	89
References		89

Abbreviations

μm	micro-meter
μN	micro-Newton
mN	milli-Newton
nm	nano-meter
GPa	giga-pascal
N	Newton
s	second

3.306.1. Introduction

The mechanical characterization of biological tissues and biomaterials is of utmost importance in clinical medicine. However, there is a paucity of information regarding the role of mechanics of biomaterials associated with clinical treatments. Biological tissues and biomaterials used *in vivo* oftentimes have small dimensions or are composed of hierarchical structures with important features at the nanometer to the millimeter scale. A technique that can probe mechanical properties at these scales has the potential to address numerous questions that are relevant to the biomedical community. Nanoindentation, also known as instrumented or depth-sensing indentation, involves the application of a controlled load to the surface to induce local surface deformation. With a typical working force range of 1 μN to 500 mN and a displacement range of 1 nm to 20 μm,[1] this technique, originally developed for the metallurgical thin films community, has become a commonplace tool for the measurement of nano- and microscale mechanical properties of tissues and synthetic biomaterials. Because of its small probe size, nanoindentation can be used to measure local material properties in small, thin, and heterogeneous samples. This allows testing of specimens that are unsuitable for traditional mechanical testing techniques, such as biopsy specimens or tissue samples from small animals. Nanoindentation is also useful for measuring mechanical properties of microstructural features within bulk samples of biomaterials/tissues, characterizing the properties of individual constituents within composite or heterogeneous samples, or mapping mechanical properties across a sample surface. As a result, nanoindentation is emerging as a valuable mechanical testing technique for biomaterials.

A simplified schematic illustration representative of many instrumented indentation systems is shown in **Figure 1**.[2,3] Commercially available systems include MTS (Oak Ridge, TN), Hysitron (Minneapolis, MN), Micro Materials (UK), UMIS (CSIRO, Australia), and CSM Instruments (Switzerland). Force is often applied using either electromagnetic or electrostatic actuation, and a capacitive or inductive sensor is typically used to measure displacement. Regardless of the operational differences, the raw force and raw displacement data for these systems are generally coupled due to the leaf springs, and in fact, a plot of the raw force as a function of the raw displacement with the tip out of contact is characteristic of the spring stiffness.[4]

3.306.2. Overview of Nanoindentation Technique

3.306.2.1. Measurement of Elastic Modulus and Hardness

The most common application of nanoindentation is to measure the basic mechanical properties such as elastic modulus and hardness of small volume samples.

The analysis of force–displacement curves produced by instrumented indentation systems is often based on the work by Oliver and Pharr.[3] Their analyses were in turn based upon Sneddon's theoretical work[5] for the penetration of a flat elastic half space by different probes with particular axisymmetric shapes (e.g., a flat-ended cylindrical punch, a paraboloid of revolution, and a cone). Consider the case of the elastic contact for a cone and a flat specimen. The force and the indenter displacement are given by Sneddon's equation:

$$P = \frac{2}{\pi} E^* \tan\alpha h^2 \qquad [1]$$

in which P is the maximum force, E^* is the reduced modulus, α is the indenter cone half-angle (Figure 2), and h is the displacement of the specimen-free surface beneath the indenter.

The reduced modulus is determined by the elastic modulus and Poisson's ratio (which is the ratio of transverse contraction strain to longitudinal extension strain in the direction of the stretching force) of sample and indenter based upon the following relationship

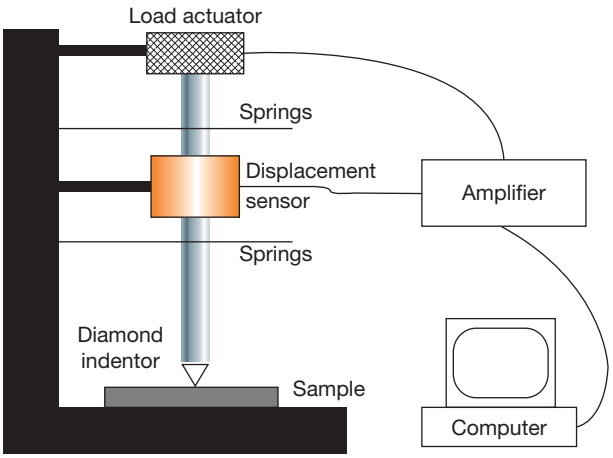

Figure 1 Schematic illustration of an instrumented indentation system.

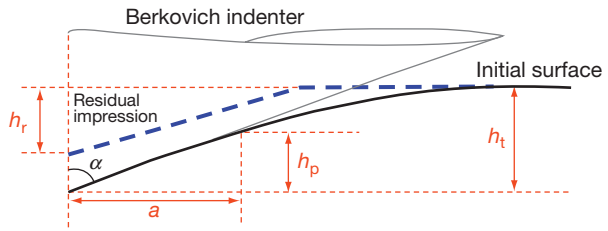

Figure 2 Schematic illustration of an equivalent axisymmetric contact between a Berkovich indenter and a flat specimen. h_t is total penetration depth, h_p is contact depth, h_r is final unloading depth (residual depth), α is the indenter equivalent cone half-angle, and a is the equivalent contact radius of the indenter at maximum load.

$$\frac{1}{E^*} = \frac{(1-\nu^2)}{E} + \frac{(1-\nu_i^2)}{E_i} \qquad [2]$$

where E, E_i and ν, ν_i are elastic modulus and Poisson's ratio of the sample and indenter, respectively.

Taking the derivative of P with respect to h in eqn. [1], it now becomes

$$\frac{dP}{dh} = 2\left[\frac{2}{\pi} E^* \tan\alpha\right] h \qquad [3]$$

where dP/dh is defined as the contact stiffness, S, which is a very important quantity in the analysis of nanoindentation test data.

The displacement of the indenter and the radius of the circle of contact are related by

$$h = \frac{\pi}{2} a \cot\alpha \qquad [4]$$

and since $A = \pi a^2$, it is straightforward to obtain

$$E^* = \frac{1}{2}\frac{dP}{dh}\frac{\sqrt{\pi}}{\sqrt{A}} \qquad [5]$$

The last equation applies to the elastic contact of any axisymmetric indenter (such as a sphere, cone, and cylindrical punch) and allows the combined elastic modulus of the indenter and the specimen to be calculated from the contact stiffness and the contact radius. The contact stiffness can be measured experimentally. The contact radius can be found from the contact depth, h_p, and the geometry of the indenter as $A = \pi a^2 = \pi(\tan\alpha h_p)^2$. The contact depth, h_p, is related to the deformation behavior of the material and the shape of the indenter, which can be obtained from[3]

$$h_p = h_t - \frac{\varepsilon P}{S} \qquad [6]$$

where S is the contact stiffness and ε is a function of the particular tip geometry. (For example, the flat-ended cylindrical punch has the value of 1, paraboloid of revolution has the value of 0.75, while cone-shaped tip has the value of $2(\pi-2)/\pi$).

These elasticity-based analyses are normally applied to the unloading data of an indentation measurement, assuming the unloading behavior of the material is characterized by elastic recovery only. In general, the relationships between penetration depth, h, and force, P, during unloading can be represented in the form

$$P = \alpha(h - h_r)^m \qquad [7]$$

The parameter α contains geometric constants, the sample elastic modulus E, the sample Poisson's ratio ν, the indenter elastic modulus E_i, and the indenter Poisson's ratio ν_i; the parameter h_r is the final unloading depth (Figure 2); and m is a power-law exponent (typically with a value between 1 and 2) that is related to the geometry of the indenter. Once an appropriate fit of the unloading indentation force–displacement curve (see Figure 3) is obtained, the derivative, dP/dh, determined at the maximum loading point (h_{max}, P_{max}) is used to determine the contact stiffness S. With the knowledge of elastic modulus and Poisson's ratio of diamond, which are ~1000 GPa and 0.007, the elastic modulus of the sample can be calculated from eqns. [2] and [5].

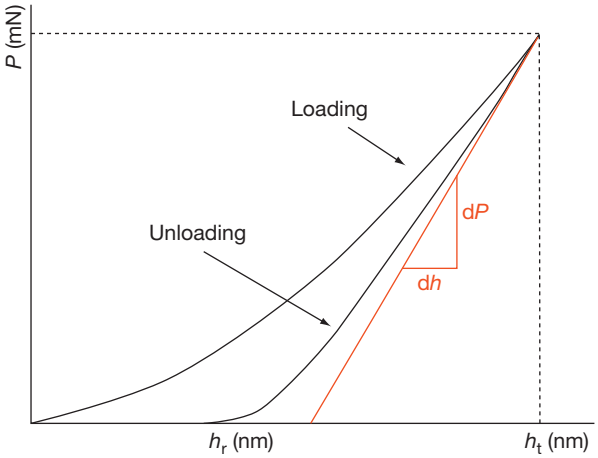

Figure 3 Schematic diagram of indentation force–displacement curve with the unloading stiffness S at the maximum force illustrated.

The hardness H of a solid is defined as its resistance to local plastic/permanent deformation. The simplest method to determine H, or the contact pressure, is to press a hard indenter of known geometry and to divide the applied load P by the contact area A produced by the indentation, $H = P/A$. The indentation hardness parameter originated with dead weight loading and optical measurement of the indentation residual impression.[6] Good examples include most microhardness tests (e.g., Vickers hardness test), in which the elastic recovery of the material coupled with difficulty in determining the edge of the impression may influence the measured size of the residual impression. In nanoindentation testing, the residual indent impression is frequently too small to be measured optically, and is not measured, but the area is inferred from the assumption that the residual area is the same as the contacted area at maximum load, A_c, which is in turn calculated from the indentation depth h_t (eqn. [2]). The contact hardness (H_c) can then be defined as the hardness at peak load[3]:

$$H_c = \frac{P_{max}}{A_c} = \frac{P_{max}}{\pi(\tan\alpha h_t)^2} \quad [8]$$

where α is the indenter cone half-angle and h_t is the total penetration depth (**Figure 2**). For a Berkovich indenter, α is 70.3°.

Obviously, both elastic and plastic deformations contribute to the total contact at peak load.[7] The aforementioned analysis was originally derived for metals[6] in which the elastic deformation was negligible compared with the plastic component. However, for most biomaterials, elasticity or viscoelasticity is significant and important for their performance. The classic contact hardness is not an accurate basis to describe the resistance to local plastic/permanent deformation of these materials. Based on a contact hardness model assuming 'springs in series' for elastic and plastic deformation,[8] Oyen developed a parameter to express the plastic deformation component of a material using indentation hardness testing.[9]

In her analysis, Oyen pointed out that both elastic (h_{El}) and plastic (h_{Pl}) deformations contribute to the total contact displacement (h_t) as mechanical elements in series such that the displacements sum

$$h_c = h_{El} + h_{Pl} \quad [9]$$

The known form of the elastic load–displacement relation is[5]

$$P_E = \alpha_2 E' h_{El}^2 \quad [10]$$

and α_2 is a constant dependent upon indenter geometry and is 4.4 for a Berkovich indenter,[10] E' is the plain strain modulus ($E' = E/(1-\nu^2)$), where ν is Poisson's ratio) and P_E is the elastic load component. Similarly, the plastic load–displacement relation is

$$P_P = \alpha_1 H h_{Pl}^2 \quad [11]$$

where α_2 is again dependent upon indenter geometry and is 24.5 for a Berkovich indenter, P_P is the plastic load component, and H is a term quantifying resistance to permanent deformation.

Knowing that for elastic and plastic elements in series the loads are equal ($P_E = P_P$), the contact hardness can be written by combining eqns. [8]–[11][8] as

$$H_C = \frac{1}{\alpha_1((\alpha_2 E')^{-1/2} + (\alpha_1 H)^{-1/2})^2} \quad [12]$$

by which the resistance to plastic deformation, H, can be extracted from the indentation hardness. Also, the proportion of elastic and plastic deformation can be calculated. A simple analysis for bone and teeth reveals that plastic deformation resistance H of mineralized tissues is three to six times higher than the apparent indentation hardness and plastic deformation of these biomaterials only occupies ~50% of the total indentation deformation.[9]

The effort associated with the plastic deformation resistance during the generation of nanoindentation data may also be considered from the energy point of view.

Mechanical work done or energy consumed is defined as the product of force and displacement. Therefore, the area below the loading curve in the load–displacement (P–h) diagram (**Figure 3**) corresponds to the total energy spent pressing an indenter into the material, U_T. The area below the unloading curve corresponds to the elastic energy recovered from the system during unloading, U_E. Their difference, $U_P = U_T - U_E$, (the area between loading and unloading curve), expresses the unrecoverable energy, consisting of the work spent in plastic deformation or other irreversible processes (e.g., cracking), and stored elastic energy associated with the residual stresses caused by the resultant impression. All these energies can be easily calculated from P–h curves. However, since all these values correspond to a particular test with special values of load and depth, it is more informative to normalize them. This is typically done by determining the ratio of the unrecoverable energy to the total energy

$$U(\%) = U_P/U_T \times 100 \quad [13]$$

and is used to normalize the energy expenditure of each test. This value may also be denoted as the 'plasticity index' to characterize the plasticity or nonlinear response of the material. This U_P/U_T ratio ranges from 0 for an ideally elastic material (all energy is returned on unloading) to 1 for an ideally plastic material (no energy is returned). In addition, the

concept of 'work of indentation'[1,11] is considered as the basis for analysis. The energy to create a unit volume of indentation is called the 'work of indentation' and is given by

$$W = \frac{U}{V} \quad [14]$$

in which U is the energy used to create the indentation volume, V, on the surface of the sample. During loading procedure, the energy used to create the volume, V_T, at maximum load should be U_T. After unloading, the residual impression with the volume V_R is a reflection of unrecoverable energy, U_P. The volume of indent produced by a spherical indenter is a segment of a sphere which can be calculated with the following equation:

$$V = \frac{\pi}{3}h^2(3R - h) \quad [15]$$

As there is a geometrical relationship between contact radius, a, contact depth, h, and tip radius, R, namely

$$R = \frac{h^2 + a^2}{2h} \quad [16]$$

eqn. [15] can be rewritten as

$$V = \frac{\pi}{6}h(h^2 + 3a^2) \quad [17]$$

in which h is generated from the analysis software and contact radius, a, is calculated using a tip calibration function, $a = f(h_P)$, established with fused silica.

For a Berkovich indenter, the volume of an equivalent conical shape was determined by using the nominal indenter face angle of 70.3°. Therefore, the volume can be calculated from

$$V = \frac{1}{3}\pi a^2 h \quad [18]$$

in which contact radius, a, is calculated by

$$a = \eta \tan \alpha h_p \quad [19]$$

with η being the area function ratio between a perfect indenter ($\eta = 1$) and the actual indenter.[12]

For the residual impression V_R after unloading, h in the aforementioned equations is the residual depth, h_r, of the indentation (see **Figure 2**). The calculation of the residual volume V_R is based on Stilwell and Tabor's observation,[13] who assumed the elastic recovery in the horizontal direction is small enough so that the radius of residual impression is the same as the maximum contact radius of the indentation, a, in eqns. [16] and [17]. With U_P and V_R values, the plastic work of indentation ('true hardness' defined by Sakai), W_P, values can be calculated with eqn. [14].

The method has been applied on the investigation of dental enamel.[14]

3.306.2.2. Instrument Calibration

As a delicate measuring system working at small displacement and using very light forces, calibration is essential for nanoindentation to acquire repeatable and reliable results. Although most manufacturers provide details of calibration procedure of the system in the software of the user's menu, little discussion of calibration related to nanoindentation can be found in the literature. Basically, for a nanoindentation system, calibration should be done from the following different aspects before the machine becomes suitable for any real testing.

3.306.2.2.1. Basic calibration of force and depth measurement systems

For the purpose of accuracy of the data, it is important that both the force and displacement sensors are properly calibrated against traceable reference standards. Calibration of the instrument is normally done at the time of manufacturing and not by the end user.

3.306.2.2.2. The determination of the load frame compliance, C_f

Consideration of the load frame compliance (defined as $C = h/P$) effects is critical for accurate interpretation of force–displacement response. Apart from the load frame, the compliance is influenced by the specific indenter tip used. The displacement output readings and the effect are equivalent to a spring in series with the load train and depend linearly upon the load applied. Prior to calibration (i.e., C_f is unknown), the measured displacement, h_{total}, is a combination of displacement of the load frame, h_f, and displacement of the sample, h_s. Treating the system as two springs (the load frame and the sample) in series under a given force, P, $h_{total} = h_f + h_s$. Dividing both sides by P,

$$C_{total} = C_f + C_s = C_f + \frac{\sqrt{\pi}}{2E^*}\frac{1}{\sqrt{A}} \quad [20]$$

Usually, the load frame compliance, C_f, can be calibrated by using reference samples with known elastic modulus and Poisson's ratio. With the concept of compliance and known geometrical details of the indenter, eqn. [20] can be rewritten as

$$\frac{dh}{dP} = \frac{1}{2\tan\alpha E^*}\frac{1}{h_p} + C_f \quad [21]$$

Typically, a series of indentation measurements are made on a single reference sample, and a plot of dh/dP against $1/h_p$ is linear with an intercept given by C_f. The choice of the reference sample should be made with an objective of maximizing contact stiffness (minimizing C_s) so that C_{total} is dominated by C_f. Thus, relatively large indentation forces and depths are normally applied to a reference material that either has a high modulus or exhibits significant plastic deformation, that is, a sample that has a high ratio of E/H.

3.306.2.2.3. Indenter tip shape calibration

The analysis equations for nanoindentation testing rely on the dimensions of the indenter being ideal, since the projected area of the impression is calculated from the depth and the geometry of the indenter. However, for sharp indenters, the tip of the indenter is usually rounded. For spherical indenters, the actual radius can be either larger or smaller depending on the quality of manufacture. To account for these variations in indenter geometry, a 'tip' correction, or area function, is needed to apply to the results. The objective of tip shape calibration is to estimate the cross-section area of the indenter tip as a function of distance from the apex. Usually, a series of indentation measurements are made on a single reference sample to

cover a large range of force and penetration depth data. At any given force, P, the contact area, A, is the cross-section area of the indenter tip at a distance, h_p, from the tip apex. For each indentation, from load–displacement curve, A and h_p can be calculated by eqns. [5] and [6], respectively. With sufficient number of measurements over a range of h_p values, a tip shape function, $A(h_p)$, can be determined by fitting the A versus h_p data, typically using a multiterm polynomial fit of the form

$$A(h_p) = B_o h_p^2 + B_1 h_p + B_2 h_p^{1/2} + \ldots \quad [22]$$

in which B_0, B_1, . . ., B_n are constant coefficients determined by the curve fitting. Ideally, B_0 should be equal to $\pi \tan^2 \alpha$ (for a conical indenter) representing the perfect tip, while additional terms attempt to account for deviations from ideal geometry, such as blunting of the tip.

An alternative approach in the software of some instruments uses a simple ratio between the actual contact area (A_h) versus the theoretical contact area for a perfect sharp indenter tip ($A_t = 3\sqrt{3} \tan \omega h_p^2$) where ω is the indenter apical angle. That is

$$\eta(h) = A_h / A_t \quad [23]$$

The value of $\eta \sim 1$ for large depths of penetration, whereas for shallow depths, the magnitude of η increases as $h \to 0$, especially for blunter tips with larger equivalent indenter tip radii.[12] The latter authors also point out the influence of pile-up and sink-in about the edges of the impression on the determination of the contact area.

3.306.2.3. Indentation Stress–Strain Relationship

As mentioned earlier, the instrumented indentation technique has become a popular method to measure the mechanical properties of different biomaterials. However, most investigators use a sharp tip such as a Berkovich indenter from which the hardness and elastic modulus may be determined. Relatively few investigators choose a spherical tipped indenter. Theoretically, a sharp tipped indenter does not allow the transition from elastic to plastic behavior of a material to be deduced because these indenters produce a nominally constant plastic strain impression. A spherical tip, in contrast, with increasing depth of penetration, develops increasing contact stress with load, the mechanics of which will now be considered, so that the elastic to plastic transition response and the determination of the contact stress–strain property of a material may be investigated.[15,16]

The use of spherical tipped indenters has a long history for characterizing metallic materials.[17] Tabor[6] found a simple empirical relationship between contact pressure or hardness and contact strain (contact radius/indenter radius, a/R). This approach and the relationships between hardness and true stress as well as contact strain and true strain have been an area of further study such as that by Matthews[18] and have been analytically confirmed by Hill *et al.*[19] Recently, Lawn and colleagues[20–23] have investigated the behavior of dental ceramics with a spherical indenter. The latter research has mainly concentrated on the macroscale damage mode of brittle material and multilayer structures.

Besides the Oliver and Pharr[3] method discussed earlier for the determination of the hardness and elastic modulus mechanical properties of materials, Field and Swain[24] developed an alternate method to analyze force–displacement data using a spherical tipped indenter. Later, Oliver and Pharr[25] and Suganuma and Swain[12] verified the equivalence of the two approaches.

The models chosen to interpret the indentation data were that of Hertz,[17] Oliver and Pharr,[3] and Tabor.[6] Unfortunately, on a microscale level, it is impossible to produce a perfect polished diamond spherical indenter with a constant radius. In the case of a spherical tipped indenter, Hertz's analysis provides an elastic contact relationship between indenter and samples (see **Figure 4**).

The radius of contact circle, a, can be calculated as[17]

$$a^3 = \frac{3}{4}\frac{PR}{E^*} \quad [24]$$

in which $\frac{1}{E^*} = \frac{1-\nu^2}{E} + \frac{1-\nu'^2}{E'}$, E, E' and ν, ν' are Young's modulus and Poisson's ratio of specimen and indenter (usually diamond), P is the contact load, and a is the contact radius.

The total depth of penetration, h_t, is given by

$$h_t^3 = \left(\frac{3}{4E^*}\right)^2 \frac{P^2}{R} \quad [25]$$

Contact pressure, P_m, can be calculated by the definition of the pressure,

$$P_m = \frac{P}{\pi a^2} \quad [26]$$

Hertz also established the simple relationship between the elastic total displacement into the sample, h_t, and the contact depth, h_p,

$$h_t = 2h_p \quad [27]$$

Combining eqns. [24] and [26], the relationship between the contact pressure, P_m, and the contact radius, a, is

$$P_m = \left(\frac{4E^*}{3\pi}\right)\frac{a}{R} \quad [28]$$

where E^* is the reduced modulus and R is the nominal radius of the indenter tip. This expression establishes the linear relationship between contact pressure and contact strain, a/R, during the elastic loading of a material.

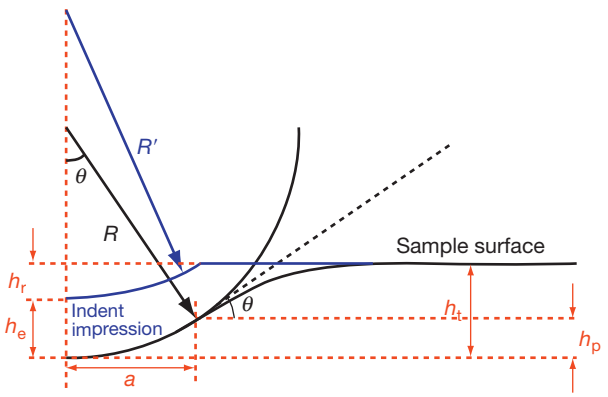

Figure 4 Schematic illustration of contact between a spherical indenter and a flat specimen.

In the case of a conical tipped indenter, Tabor[6] showed that

$$\varepsilon_r \approx 0.2 \tan\theta \quad [29]$$

$$\sigma \approx P_m/3 \quad [30]$$

are appropriate expressions for representative strain, εr, and stress, σ, where θ is the angle between the indenter flank and the original surface. Matthews,[18] on the other hand, suggested that the divisor in eqn. [30] should be 2.8 rather than 3.

For spherical indentation, strain increases continuously with indentation impression depth, and an appropriate equivalent expression is

$$\varepsilon_r \approx 0.2a/R \quad [31]$$

where for small θ, $\tan\theta \approx \sin\theta \approx a/R$.

The approach of Tabor, namely the H–a/R curve generated for a material, is generally regarded as the contact stress–strain curve.

In the case of elastic–plastic response of materials to pointed indenters, Oliver and Pharr[3] recommended a simple method to fit the nanoindentation P–h unloading curve (see eqn. [7]). This method applies to all axisymmetric indenters, including spheres. With this equation, the elastic contact stiffness, dP/dh, can be calculated from the upper portion of the unloading data.

There is a constant relationship between the elastic contact stiffness, dP/dh, the projected area of contact, A, and the reduced or indentation modulus, E^*,

$$\frac{dP}{dh} = \beta \frac{2}{\sqrt{\pi}} E^* \sqrt{A} \quad [32]$$

in which $A = \pi a^2$ and β is a constant dependent upon indenter shape. For a spherical indenter, $\beta = 1$.

In this context, by assuming that the elastic modulus, E, of a material is known, the radius of contact area, a, at a certain loading force, can be calculated from eqn. [32], namely

$$a = \frac{dP/dh}{2E^*} \quad [33]$$

At the same time, a relationship between the indenter radius, R, contact radius, a, and contact depth h_p, can be derived from Figure 4,

$$a = \sqrt{2h_pR - h_p^2} \quad [34]$$

By combining eqns. [33] and [34], it is not difficult to show[28]

$$\frac{a}{R} = \frac{\frac{dP/dh}{E^*} h_p}{\left(\frac{dP/dh}{2E^*}\right)^2 + h_p^2} \quad [35]$$

Based on the definition of hardness, H,

$$H = \frac{P_{max}}{A} \quad [36]$$

the nanoindentation system can record the P–h response of a material from which P_{max}, h_p, and dP/dh may be automatically calculated. Thus, a relationship between H–a/R curve of the sample may be determined.

Because of the inevitable deviation of the tip shape from that of a sphere, the real radius of the tip at different contact depths may not be as constant as the nominal value reported by the manufacturer. Therefore, a better method is required to avoid using the parameter of tip radius, R, in the calculation.

From Figure 4, it is not difficult to show that the contact area of a spherical indenter with a specimen can be described by the h_p–a curve. The tangent angle of this curve, θ, may also be easily calculated from the derivative of the function $h_p(a)$. Moreover, to facilitate calculation, the equation of the curve can be expressed as $a = f(h_p)$ and its derivative (da/dh) as $a' = \tan\beta = f'(h_p)$, in which β is the tangent angle of the curve. In this way, the stress–strain curve of any material can be acquired by collecting P and h_p data alone. For $\theta + \beta = 90°$, $\tan\theta$ can be calculated as

$$\tan\theta = 1/\tan\beta = 1/f'(h_p) \quad [37]$$

Contact pressure, H, can be calculated as

$$H = \frac{P_t}{A} \quad [38]$$

in which $A = \pi a^2$ and $a = f(h_p)$. With eqns. [37] and [38], the stress–strain curve (H–$\tan\theta$ curve) may be calculated. Another geometrical relationship evident from Figure 4 is

$$a/R = \sin\theta = 1/\sqrt{(\tan^{-2}\theta + 1)} \quad [39]$$

By a combination of eqns. [37] and [39], an effective indenter radius, R, may be determined. The elastic modulus of the sample may be calculated from eqn. [33] as

$$E^* = \frac{dP/dh}{2a} \quad [40]$$

With the help of the known tip shape function $a = f(h_p)$, the elastic modulus of any sample can be measured with nominally spherical tips by using only h_p and dP/dh data.

Although the indentation stress–strain is an empirical relationship as the actual stress and strain about an indentation impression has severe gradients, it is not surprising that some investigations have shown that the nominal stress–strain curve from this approach did not superimpose with standard uniaxial stress–strain curves.[26] Therefore, it might be wiser to retain the values of H and $\tan\theta$ in the results to avoid misunderstanding that the plots are standard stress–strain curves. However, using the same method, the H–$\tan\theta$ curves enable comparison between different materials and are indicative of stress–strain behavior. The method has been applied to the measurement of stress–strain relationship of human enamel and dental materials.[27,28]

3.306.2.4. Measurement of Fracture Toughness and Residual Stress

3.306.2.4.1. Fracture toughness

Indentation methods have been used for many years to determine the fracture toughness of brittle materials. The most popular method uses a Vickers indenter and micro- to macro-indentation-based loads (1–500 N). For brittle materials, radial/median crack patterns form around the indenter, and from the size of the radial cracks or the remaining strength of the indented object, the fracture toughness may be estimated. This approach was initially proposed by Palmqvist[29] to determine the fracture toughness of hard metals (WC–Co alloys).

Follow-up studies by a number of authors led to the development of a basic understanding of the median radial fracture response about pointed indenters.[30–32] The most widely used approach to determine fracture toughness is that by Anstis *et al.*[33] There have also been many other expressions for the determination of the critical stress intensity factor (K_{1c}) based upon Vickers indentation tests. A critical review of the various expressions and their validity for the determination of toughness for brittle ceramics and glasses is given by Ponton and Rawlings.[34] More recently, Quinn and Bradt[35] have drawn attention to the fact that Vickers indentation-derived values for fracture toughness may be at variance with standardized values from classic methods. However for many situations, such as localized phases and small samples, traditional methods are not appropriate for the determination of fracture toughness.

Lawn *et al.*[31] described the evolution of a half-penny median/radial crack system in the far field of a sharp indenter. Based upon this analysis, it is possible to derive a simple relation between the measured radial crack length, c, the hardness, H, the elastic modulus, E, and the fracture toughness of a material, namely

$$K_{1c} = \kappa \left(\frac{E}{H}\right)^{1/2} \left(\frac{P}{c^{3/2}}\right) \qquad [41]$$

where κ is given by

$$\kappa = \Psi(\cot \phi)^{2/3} \qquad [42]$$

ψ is an empirical constant and ϕ is the equivalent conical angle of the indenter geometry; for a standard Vickers indenter, κ is 0.016. This approach was shown to be suitable for a wide range of brittle materials.[33] Recently, Leonardi *et al.*[36] have developed a fracture-mechanics-based analysis to determine κ and ψ for both wedge and point force approaches to the crack extension about triangular pyramid indenters.

Nanoindentation typically uses a Berkovich indenter tip that only generates three radial cracks rather than four as for the Vickers indenter. Dukino and Swain[37] compared the fracture toughness of a number of brittle materials when measured with a Vickers and Berkovich indenter. In all instances, the size of the radial cracks with the three-sided Berkovich indenter was ~ 10% larger than for the Vickers indenter at the same load. These authors also developed a specific expression to account for the difference in the number of cracks and also because the radial cracks were shallow surface cracks rather than median/radial cracks as is the case for a Vickers indenter at moderate loads.

More recently, researchers have used sharper corner cube indenters to evaluate the fracture toughness of brittle materials at loads commensurate with nanoindenter systems.[38,39] Scholz *et al.*,[39] using an atomic force microscopy (AFM)-based nanoindenter system, were able to derive the fracture toughness of materials from submicron-sized radial cracks. A typical set of data generated by these authors is shown in **Figure 5**. The value of the constant κ was found to be slightly dependent upon the ratio of the crack size to the residual hardness impression size and varied from 0.022 to 0.028. The extension of this approach, although not with nanoindenter loads, has been undertaken on bone[40] and dentine.[41]

Another approach to estimate the fracture toughness of brittle materials has used the force–displacement response

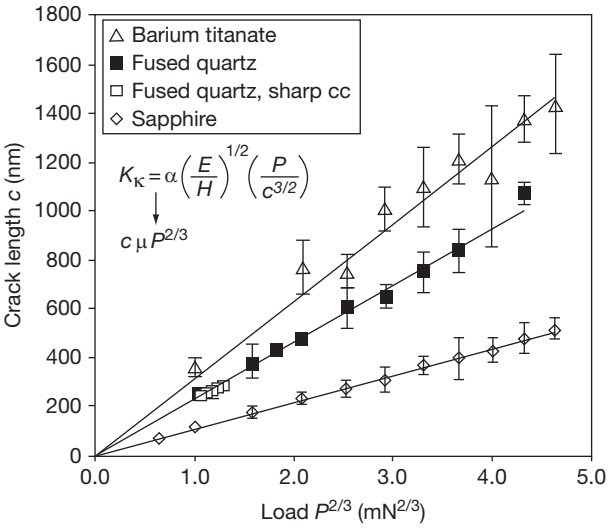

Figure 5 Measured crack lengths for a number of materials using a cube corner indenter and AFM-based nanoindenter system. Derived from Scholz, T.; Schneider, G. A.; Munoz-Saldana, J.; Swain, M. V. *Appl. Phys. Lett.* **2004**, *84*, 3055–3057.

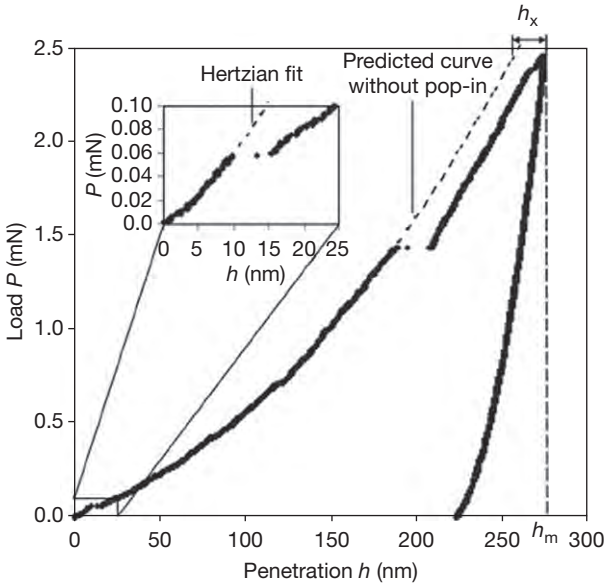

Figure 6 Force–displacement curve for a sharp (tip radius ~ 70 nm) corner cube indenter being loaded into barium titanate. The first pop-in event at low load (see insert) is associated with the transition from elastic to elastic–plastic behavior and the second pop-in is associated with crack formation about the indenter. The additional penetration associated with radial crack formation is h_x.

of a corner cube indenter to determine the fracture toughness. Specifically, often pop-in events are observed during indentation of brittle materials with a sharp indenter. Field *et al.*[42] developed an approach that used the additional pop-in displacement associated with radial crack formation to quantify the K_{1c}. This was further extended by Scholz *et al.*[39] who identified there were two pop-in events during indentation, as shown in **Figure 6**. The response prior to the first pop-in was associated with the Hertzian elastic response of the slightly

rounded cube corner indenter tip (radius ~70 nm). At a critical contact pressure, the material around the indenter tip yields and the first pop-in occurs. With increased loading, the material behaves in an elastic–plastic manner, which is predictable based on the hardness and elastic modulus of the material.[43] At a critical load, radial cracks are formed about the indenter and the second pop-in event occurs. This additional displacement with the second pop-in is associated with the crack opening displacement that is related to the size of the cracks, the elastic modulus, and fracture toughness of the material.[42]

3.306.2.4.2. Residual stresses

The presence of residual stresses in a material may have an influence on the hardness, and on the extent of radial crack extension around the impression in the case of a brittle materials indented with a sharp indenter. There have been a number of studies that have explored the influence of residual or applied stress on the hardness of metallic materials.[44] These studies generally have considered the presence of biaxial tensile or compressive stresses; the situation becomes more complex in the case where uniaxial stresses are present. The latter creates a nonaxially symmetric deformation problem. In addition, residual stresses in materials, except for low yield stress metallic materials, are generally small compared with the magnitude of the hardness, and as such, the perturbation of yield stress or hardness by their presence will be minor. A critical analysis and experimental procedure to quantify the residual or applied stresses on the hardness or to determine the residual stress from change of hardness is given by Suresh and Giannakopoulos.[45]

The presence of residual stresses is more apparent on the extent of radial crack extension around the residual impression. Marshall and Lawn[46] developed a simple analysis of this problem. The presence of residual or applied tensile or compressive stress on the surface of the material being indented introduces an additional term in the expression for the stress intensity factor, as given by eqn. [41]. A complete 2D fracture mechanics analysis of this problem was also developed by Lawn and Marshall[47] for a number of cases which included linear and parabolic stress distributions. For the situation where the indentation crack size is small compared with the gradient of stress, the expression for the stress intensity factor is composed of two terms:

$$K_{1c} = K_{Ind} + K_{App/Res} \quad [43]$$

where K_{Ind} is the indentation stress intensity factor given by eqn. [41] and $K_{App/Res}$ is the stress intensity factor for a crack in the residual or applied stress field and is given by

$$K_{App/Res} = Y\sigma_{App/Res}\sqrt{c} \quad [44]$$

where Y is the shape factor for a half-penny surface crack and $\sigma_{App/Res}$ is the applied or residual stress present. Combining eqns. [41], [43], and [44] we have

$$K_{1c} = \kappa\left(\frac{E}{H}\right)^{1/2}\frac{P}{c^{3/2}} \pm Y\sigma_{App/Res}\sqrt{c} \quad [45]$$

The second term in eqn. [45] may be positive or negative depending upon whether the stresses on the surface are either tensile or compressive, respectively. The aforementioned approach has been used to determine the tempering residual stresses developed in veneering porcelains as a consequence of rapid cooling.[48,49] Kase and Rowcliffe[50] used this approach with a corner cube nanoindenter to plot the stress field about indentation impressions in soda lime glass.

3.306.2.5. Indentation Creep

Viscous response of natural biomaterials plays an important role in their function to bear and distribute force, especially for bone, and has attracted considerable attention.[51–56] Jäger[52] summarized the characteristics of typical viscous deformation of biological tissues as (1) the force necessary for deformation depends on the deformation rate; (2) force–displacement hysteresis occurs during loading and unloading; (3) application of a (constant) force leads to transient and/or permanent creep; (4) after removing the deformation force, there is stress–relaxation/recovery.

Restricted by measurement methods, the limited viscosity, and temperature range over which natural biomaterials operate, the viscous responses, especially creep behavior, are difficult to quantify. For metallic and polymeric materials, traditional tensile and/or compressive tests are used to investigate the creep response of a specimen. Two main problems limit the usage of these methods for biological materials such as enamel or dentine. Firstly, these tests need multiple identical specimens and are time consuming to conduct. Secondly, the accuracy of these methods depends on the creep response of the material. For small samples with limited creep, such as enamel, it is not very reliable. Torsion[55,56] and three-point bending tests[51] were used to measure the relaxation and the elastic modulus and shear modulus of bovine bone. Furthermore, because of the anisotropic property of natural biomaterials, the loading direction must be controlled. This limitation, along with the size of teeth, severely restricts the usage of bulk methods for the evaluation of dental tissue. In the field of biomaterials, only limited indentation creep tests have been done on biological hard tissues.

Indentation creep tests are a powerful technique for studying the rheological properties and relaxation dynamics of different materials such as metals,[57] polymers,[10,58,59] and other materials.[60,61] Lucas and Oliver[57] reviewed the depth-sensing creep tests and recognized four types: (1) indentation load (at fixed displacement) relaxation tests, (2) constant rate of loading tests, (3) constant-load indentation creep tests, and (4) impression creep tests. The most common method is the constant-load indentation creep test, which records the change of the depth with time.

In some nonlinear solids, especially power-law creep materials, the mechanical response depends upon the strain rate, $\dot{\varepsilon}$, namely[1]

$$\sigma = K\dot{\varepsilon}^m \quad [46]$$

where K and m are material constants and m is the creep rate sensitivity. This equation is derived from Norton's finding that $d\varepsilon/dt = (\sigma/\sigma_c)^n$, where ε, σ, t are strain, stress, and time, respectively and σ_c, n are material parameters.[62]

The complex stress state beneath an indenter tip requires a somewhat different approach to evaluate the creep response generated. Because of geometrical similarity for conical and pyramidal indenter tips, the Berkovich tip has a constant effective strain value; from Tabor's empirical relationship, the effective contact strains

are $\varepsilon_r \approx 0.2 \tan \theta$.[6] Therefore, the strain rate of an indentation test can be extracted from the h–t curve as the indenter displacement velocity divided by the plastic depth of penetration[63]:

$$\dot{\varepsilon} = \dot{h}/h \qquad [47]$$

where the indentation rate $\dot{h} = \mathrm{d}h/\mathrm{d}t$. Strictly speaking, h should be the contact depth of indenter, h_p. However, to facilitate the measurement and calculation, total displacement, h_t, is generally used in this equation. By assuming a constant ratio of h_p/h_t, which is what is commonly observed for most materials including enamel, the use of ht instead of h_p will not significantly influence the final results.[64]

Another independent analysis derived from the definition of hardness also supports the concept of strain rate dependence in eqn. [47].[57] As has been mentioned in eqn. [8], the definition of contact hardness, H, can be written as

$$H = \frac{P}{A} = \frac{P}{ch^2} \qquad [48]$$

where H is hardness, P is the load, h is the contact depth (and total depth, h_t, is often chosen), and c is a geometrical constant of the indenter (24.5 for perfect Berkovich tip). Equation [48] can be differentiated and reorganized into

$$\frac{\dot{h}}{h} = \frac{1}{2}\left(\frac{\dot{P}}{P} - \frac{\dot{H}}{H}\right) = \dot{\varepsilon} \qquad [49]$$

in which $\dot{\varepsilon}$ is the strain rate defined in eqn. [47]. This equation suggests that, during the holding period of a creep test, because the force is kept constant ($\dot{P} = 0$), strain rate $\dot{\varepsilon}$ is expressed by $\dot{h}/h$. This conclusion is the same as eqn. [47].

Based on the aforementioned analysis, the creep behavior and the creep rate sensitivity, m, of material can be calculated from the depth–time (h–t) curve of the creep test at maximum load. By fitting and determining the differential equation of the h_e depth–time (h–t) curve, the indentation rate $\dot{h} = \mathrm{d}h/\mathrm{d}t$ needed by eqn. [47] can be calculated. From eqn. [48], the contact pressure (hardness, H) can be acquired. Therefore, creep rate sensitivity value of the sample can be read from the logarithmic plot of $H - \dot{\varepsilon}$ curve. The method has been applied to human enamel research.[64]

An alternative approach for the time-dependent properties may be described in a more classical way, such as universal rheological models, consisting of springs and dashpots (Figure 7). The parameters in these models can be obtained by fitting the time course of indenter penetration by a creep function, depending on the material, indenter shape, and loading history (see, e.g., Mencik *et al.*[65]).

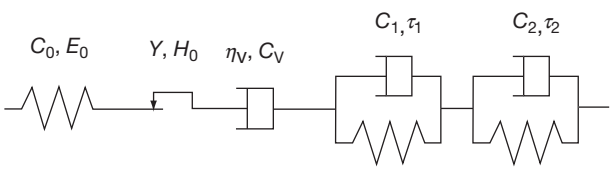

Figure 7 Viscoelastic–plastic model 'spring + plastic element + dashpot + 2 Kelvin-Voigt bodies'. C_0, C_1, and C_2: compliances; E_0 and H_0: instantaneous elastic modulus and hardness; c_v: viscous compliance; τ_1, τ_2: retardation times.

The relationship between indenter load and the depth of penetration into elastic or viscoelastic material under monotonic loading can be expressed generally as

$$f[h(T)] = K\psi(P, J, t) \qquad [50]$$

where f is some function of the indenter shape and penetration depth, K is a constant characterizing the indenter geometry, and Ψ (P, J, t) is a function depending on the load magnitude and history, on material parameters, and on time.

3.306.2.6. Other Factors that Influence the Accuracy of the Results

1. Environmental conditions may have significant effect on nanoindentation test results. Thermal drift and mechanical stability are two main issues to consider. Because the nanoindentation displacement sensor is sensitive to sub-nanometer displacements, any thermal expansion of the indenter, indenter shaft, and specimen as a result of temperature changes during a test can be incorporated into the test results. The thermal expansion need only be very small to make a significant effect. For example, an indentation test lasting 1 minute to a penetration depth of 100 nm can easily be in error by more than 10% if the change in displacement sensor output due to thermal expansion is 10 nm over that minute. For this reason, the temperature of the system and the sample must be very well controlled and maintained throughout the test. It is always good to allow the indenter and newly installed sample some time to reach thermal balance before starting the test. Also, any environmental vibration that is transferred to the system may influence the displacement accuracy of the test. Therefore, sufficient vibrational damping is important to ensure the mechanical stability of the whole system.
2. The viscous properties of the sample have significant influence on the results as well. This is because the compliance method, on the analysis of force–displacement data, (as described in **Sections 3.306.2.1–3.306.2.3**) is based on the assumption of elastic–plastic, isotropic sample materials.[3,25] Polymeric biomaterials and tissues often exhibit viscoelastic or time-dependent behavior. These characteristics can lead to errors in modulus determination using the compliance method. The most readily observed effect of viscoelasticity on indentation is creep, or a sinking of the tip into the sample under a constant load. In cases where creep behavior dominates the elastic response of the material, a 'nose' is observed on the indentation unloading curve, as illustrated in **Figure 8**.[66] In short, it was found that when loading is followed by unloading without a hold at peak load, displacement increases slightly in the initial portion of the unloading phase, because the creep rate of the material is initially higher than the imposed unloading rate. This phenomenon results in a negative slope in the initial unloading region (**Figure 8(a)**), making it impossible to use the compliance method to measure modulus as well as overestimating the hardness. To eliminate this creep-induced nose effect, Briscoe and colleagues[66] incorporated a 10 s hold period at peak load into their applied load–unload functions in order to allow the material to approach equilibrium prior to unloading. The effect of this hold period on

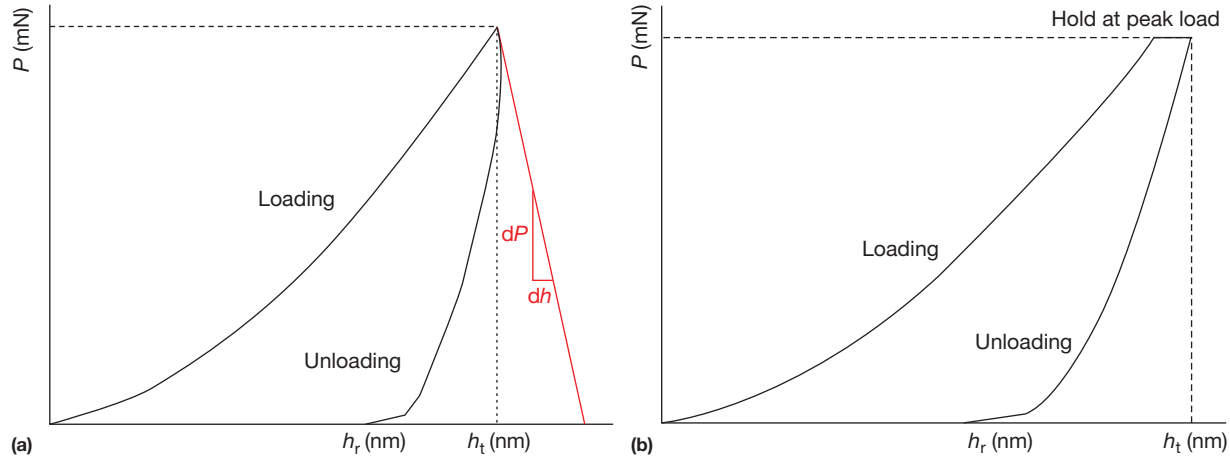

Figure 8 (a) Illustration of the nose effect resulting from indenting a viscous material. (b) Illustrates the elimination of the nose effect by adding a hold period at peak load.

load–displacement data is illustrated in **Figure 8(b)**. This same approach has been used in many indentation studies of biomaterials, with different hold periods to allow the creep rate to dissipate prior to unloading.[67,68] An appropriate hold time should be selected based on the creep and unloading rates used in the experiment. More details about indentation creep have been discussed in the previous sections.

More recently, Guidoni *et al.*[69] also investigated the possible role of indentation recovery during unloading on the unloading slope compliance during testing of bovine enamel. Using the compliance method, these authors found that a threefold change in E modulus occurred depending upon whether tests were conducted wet or dry using a cube corner indenter. However, when the same samples were tested using blunter indenter tips, differences of <20% were observed. The major differences in the case of the cube corner indenter between wet and dry were considered to be associated with significant pile-up about the indenter for the dry specimen.

3. As with most biomaterials function under conditions of complete hydration, the history of sample storage will influence the mechanical behavior of the biomaterials. It has long been recognized that, for biological samples, E and H of the specimen is significantly affected by the hydration status. In bovine femur cortical bone, dehydration increased E in osteonal tissue and interstitial lamellae by 15.4% and 9.7% (when using a Bekovich indenter), respectively, which was attributed to the fact that drying contracts the individual fibrils in the tissue.[70] Another study of bone specimens reports increases in indentation moduli of 11–28% after dehydration, with further increases after embedding in resin.[71] An investigation of human enamel under different environmental conditions also showed substantial changes in elastic modulus, hardness, and creep response after ethanol dehydration, water rehydration, and dry.[72] These studies demonstrate the importance not only of testing fully hydrated specimens but also of avoiding prolonged dehydration during sample preparation and testing. Other studies illustrate the importance of selecting an appropriate storage medium and time. It was demonstrated that storage of dentin and enamel specimens in Hank's balanced salt solution (HBSS) maintained the low load corner cube-derived mechanical properties, while storage in deionized water or $CaCl_2$ solution resulted in a decrease in modulus and hardness that was attributed to demineralization of the surface.[73] Observation on dog trabecular bone reveals that long-term storage in epoxy (3–6 months) increased the E of the specimen significantly (26%), which was attributed to the increase of modulus of embedding resin, desiccation of the bone tissue, and hardening of the porous space in the tissue.[74]
4. The method of surface preparation can also affect mechanical properties, as surface roughness can have a significant impact on the measurement of modulus using nanoindentation.[75] For mineralized hard tissue, the most common sample preparation methods are microtome sectioning and mechanical polishing. A comparison of these two preparation methods prior to testing lamellar bone specimens illustrated that, depending on the thickness of the specimen required, the surface preparation methods can significantly influence the roughness and resultant mechanical properties of the specimens.[76] Usually, to minimize errors arising from surface roughness, biomaterials are polished (usually down to a 1 μm or even finer particle size) prior to indentation.[77,78] It has been suggested that indent penetration depths then be chosen such that the surface roughness (Ra) is <10% of the total penetration depth.[79]
5. A feature evident with many materials evaluated using nano- and microindentation is the presence of the so-called indentation size effects (ISE). This effect is generally seen using pointed indenters, but does occur with spherical indenters, where the hardness decreases with increasing load. On the other hand, for metallic and ceramic materials, the elastic modulus of a material is usually considered invariant with contact size, and this is one aspect that should be confirmed initially when size-dependent effects are observed. There have been a number of explanations rationalizing ISE developed over the past 5 decades for metallic and ceramic materials, which have been critically reviewed.[80]

6. For the measurement of thin film, the thickness of the film and the properties of the substrate material have influence on the nanoindentation results. Details have been discussed in **Chapter 3.305, Biomedical Thin Films: Mechanical Properties** by Ben-Nissan *et al.*

3.306.3. Application of Nanoindentation to Biomaterials

Nature endows different natural hard materials unique structures, which offer potential for the development of biomimetic materials. The nanoindentation technique provides the ability to explore the mechanical properties, including anisotropy of these naturally designed biomaterials, in respect to their multiple hierarchical microstructures. The use of nanoindentation for characterizing the properties of biological materials has been well reviewed elsewhere.[81–83] It is impossible to cover the whole literature database within a few pages in this chapter. Therefore, here we illustrate the application of nanoindentation research on human enamel.

As the hardest organ of our body, teeth must retain their shape as well as resist fracture and wear during load-bearing function for the life of an individual. Teeth experience a range of loading situations[84]: firstly, they contact directly other objects and/or opposing teeth; secondly, they encounter normal and sliding contact loading resulting in wear, and thirdly, unlike bone, damage of teeth is not repairable. To meet all of these functional requirements, teeth have evolved with a unique hierarchical microstructure. What is the relationship between the hierarchial microstructure and the excellent mechanical behavior of the natural biomaterials? Nanoindentation becomes a basic tool to explore this area. Numerous nanoindentation investigations have been conducted on human teeth, as they do not readily lend themselves to more conventional property evaluation procedures.

3.306.3.1. Elastic Modulus and Hardness of Enamel

The mechanical tests to determine the elastic modulus and hardness of enamel have experienced several stages of development from the macroscale to the micro- and nanoscale over the last few decades. Due to the size limit of human enamel samples, it has been difficult to perform macroscale tests. Therefore, most recent investigations on the mechanical properties of human enamel have been done using nanoindentation.[27,73,79,85–94] These micro- and nanoscale investigations revealed some very interesting features of this natural ceramic-like biocomposite.

Firstly, the high mineral level (about 96 wt%) as well as the unique microstructure of enamel contribute to its high mechanical properties.[79,86,95] The stiffness of a composite material like enamel is a combination of the stiffness of its multiphase components and associated microstructures; the inorganic-hydroxyapatite (HAP) crystals and organic tissues which may be considered as a fibrous composite model.[96]

Secondly, the hardness and elastic modulus of enamel were found to be a function of enamel rod alignments.[27,79,92] The measured elastic modulus varies with the direction of load application relative to the apatite crystals of enamel. Higher elastic modulus values were generated when the force is applied parallel to enamel rods, as the deflection will be resisted primarily by the aligned crystals in that direction within the rods. In the perpendicular directions, the displacement will be influenced more by the less stiff organic tissue surrounding the crystals, thereby resulting in lower elastic moduli. The rod orientation dependence is also seen in a numerical uniaxial loading 3D finite element analysis simulation of enamel.[96] This also explains the discrepancy in the elasticity data of the localized values of enamel rod and interrod regions. The interrod region was reported to have hardness and elastic modulus of about only 25 and 50%, respectively of the values of the core region of the rod.[88]

Thirdly, the mechanical properties of the enamel are intra-tooth site dependent. The inner enamel near the dentino-enamel junction (DEJ) has on average a reduced hardness and elastic modulus values by typically 26% compared to the outer enamel.[86,89] The size of enamel rods decreases with distance toward the DEJ; consequently, the volume fraction of softer protein-rich interrods has a twofold increase, which undoubtedly contributes to a decrease in composite hardness and stiffness.[92]

Lastly, recent systemic nanoindentation investigation on sound enamel of permanent teeth with different tips and various loads reveals that the elastic modulus of enamel does not have a constant value but a noticeable size effect dependent on the indentation contact areas.[27] This behavior is shown in **Figure 9**, which illustrates a consistent decrease in elastic modulus with an effective contact diameter for all indenters. This shows that the elastic modulus, in the case of enamel, is a function of the contact area and the effective volume of the contact stress field from which the elastic modulus is determined, irrespective of what type of indenter tip is used. This can be rationalized by the unique rod–interrod microstructure of the biocomposite, in which the nanohardness and elastic modulus of the interrod region were respectively 73.6% and 52.7% lower than those of the rod.[88] Upon consideration of the rod structure of enamel, with increasing peak load during nanoindentation, more and more prism-sheath units are involved in the indentation stress field and contribute to the measured nanoindentation elastic modulus (**Figure 10**). Due to the reduced modulus of the protein-rich sheath region,

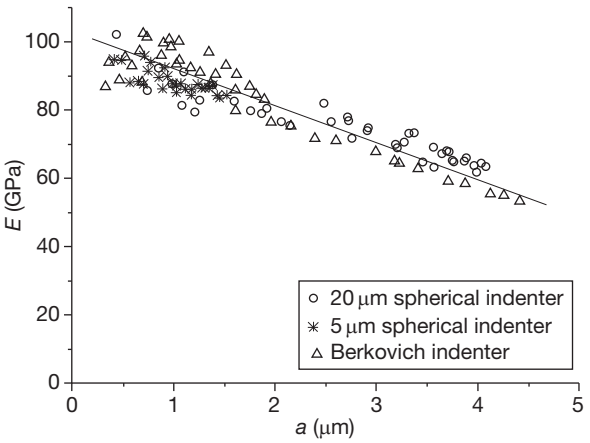

Figure 9 Elastic modulus, E, of human enamel parallel to the rod axis plotted against contact radius, a, for the three different indenters.

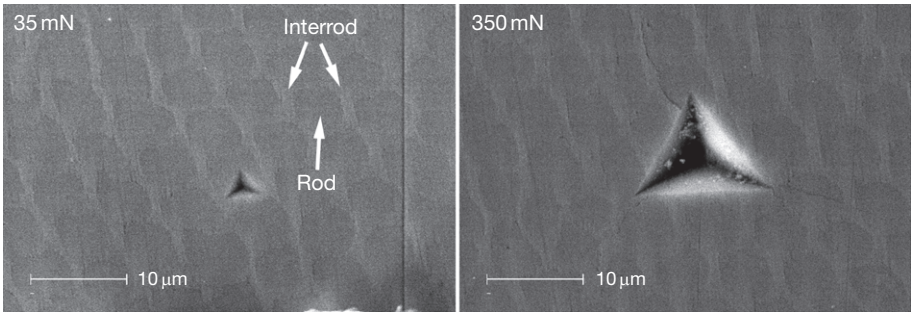

Figure 10 Indenter impressions from different peak loads are compared and also with the rod-like features within the enamel. (a) Shows that under a load of 35 mN, the Berkovich impression was located within one prism unit. In contrast, (b) illustrated that a 350 mN load generated a much bigger impression with the same indenter now covering more than three prism units.

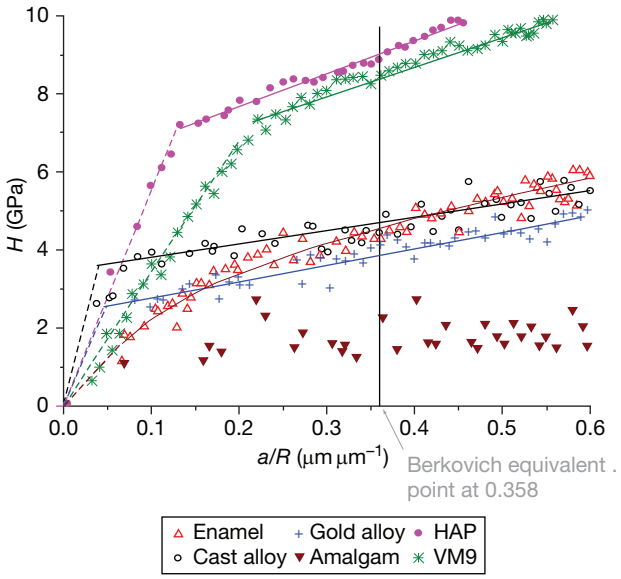

Figure 11 Indentation-derived stress–strain (H–tan θ) relationships of different dental restorative materials and enamel. Solid lines represent plastic part and short dotted lines represent the elastic part of materials, which were calculated from the Hertz equation [25].

the more the sheath area becomes involved in the deformation field, the lower the stiffness of the measured area. This may also partially assist in explaining the wide range of elastic modulus reported in other investigations and wider standard deviations from AFM-based nanoindentation tests.

3.306.3.2. Stress–strain Relationship of Enamel

With the method described in Section 3.306.2.3, nanoindentation stress–strain relationships for enamel have been evaluated,[27] and some interesting results were found.

As shown in Figure 11, enamel exhibited smooth stress–strain curves without a prominent elastic–plastic transition point. This is mainly caused by the unique composite rod structure of enamel and its organic-rich interrod region, which enables it to be more deformable and less damage prone than pure HAP. In the case where the indentation force was parallel to the prism (rod) direction, the yield behavior was primarily determined by shear deformation of the very thin protein 'glue' between the individual apatite crystallites. In the case of the load perpendicular to the axis of the enamel rods, the loaded rods deflect under the force because the contact load is supported not only by the rod structure but also by the more deformable and thicker interrod structure surrounding the rods.

A comparison of indentation-based stress–strain curves generated with small spherical tipped indenters for a range of dental materials is shown in Figure 11. Enamel was found to behave more like a metallic material than a ceramic. A comparison with dense HAP, which is the main component of the enamel, indicated that enamel had much lower stress–strain response. This suggests that the minor organic components in enamel influence the mechanical behavior of this highly mineralized biocomposite significantly. From this point of view and the aforementioned results, traditional criteria of dental material selection based on elastic modulus and hardness may not be appropriate for choice of restorative materials which can protect opposing teeth from excessive attrition. The nanoindentation stress–strain evaluation should also be involved in future dental restorative material selection and development studies.

As proposed in Section 3.306.2.1, the plastic deformation resistance can be extracted from nanoindentation data by either a hardness approach[9] or an energy approach.[14] For enamel, plastic energy expenditure ratio, U%, from eqn. [13] begins at 30% and has a monotonic increase with the contact strain, tan θ, with no obvious elastic part (Figure 12). In contrast, HAP showed a linear U%–strain part for strain values <0.5 and the curve started from 0%. Although the major component of the two materials in Figure 12 was very similar, enamel had a slightly higher energy dissipation ability (~10%) than HAP at the same strain level.

A question arising from Figure 12 is, where has the extra energy in enamel dissipated? If we initially consider the apatite crystals, their very small size would have near theoretical strength, ~10% of the shear modulus of ~10 GPa. The mean contact stresses for enamel do not approach this value and only in the vicinity of the tip in the case of the Berkovich indenter may such stresses be achieved. Hence, it is not considered that energy loss by conventional dislocation-based plastic deformation of the inorganic phase is important for enamel. Therefore, the focus of the discussion is centered on the role of the organic protein components between and surrounding HAP crystallite rods.[28]

Spears in a finite element numerical model of the elastic response of enamel cited the elastic modulus of HAP crystals and organic tissues as 114 and 4.3 GPa, respectively.[96] Moreover, AFM nanoindentation[88] also reinforced the argument that the protein-rich sheath between the rods has a lower elastic modulus and hardness than the apatite containing cores of rods: the nanohardness and elastic modulus of the sheaths as reported earlier were 73.6% and 52.7% lower than those of the rods, respectively. The nanoindentation curves shown by Ge *et al.*[88] showed that sheaths exhibited more energy absorption than rods. White *et al.*[97] also established that mineral apatite crystals had a microhardness ~1.8 times greater than human enamel. These studies indicate that the minor components of enamel, namely protein and water, have a profound softening/plasticizing effect. Other possible mechanisms responsible for the greater energy loss include fracture of the apatite crystallites, deformation of the very thin protein layers between the crystallites within the prisms, or deformation of the protein and movement of fluid in the nanoscale porous structure.

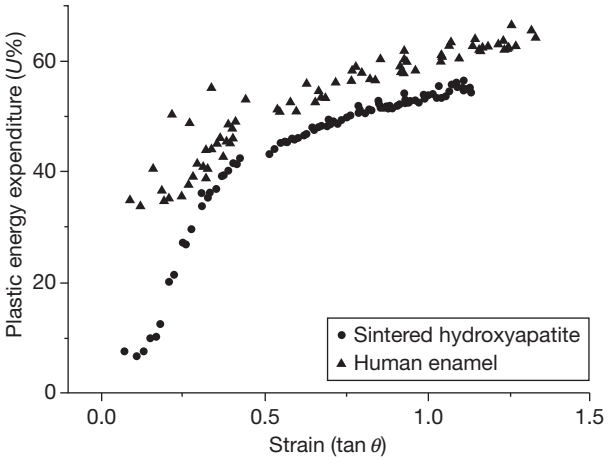

Figure 12 Comparison of plastic energy absorption ability between enamel and dense hydroxyapatite based on indentation data generated with a nominally 10 μm spherical indenter.

It was argued by He and Swain[14] that higher energy expenditure behavior of the enamel was primarily related to the minor organic components. Three different mechanisms were considered to potentially contribute to the measured energy absorption, namely fluid flow within the sheath structure as proposed by Fox,[98] protein 'sacrificial bond' extension as proposed by Smith *et al.*[99] for nacre and Fantner *et al.*[100] for bone, or nanoscale friction within sheaths associated with the degustation of enamel rods as considered by Macho *et al.*[101] Further work is required to more quantitatively assign the energy loss observations to these or other mechanisms.

3.306.3.3. Creep Behavior of Enamel

In recent investigations,[64,102] the creep behavior of enamel was described and compared with dental materials by a one-step nanoindentation loading–unloading method with a Berkovich indenter. Samples were indented at the maximum force of 250 mN with a one-step loading method. Holding time at maximum load was 900 s for all tests. During one-step unloading, another holding at 5 mN was activated. This unload-holding time was 900 s as well.

In Figure 13, the relative penetration depth, h'_t, was calculated by subtracting the initial depth at the beginning of the holding time from the increasing depths with time during the holding period at maximum and minimum loads. Creep data, while holding at maximum load, exhibited increasing penetration depth with time for most of the investigated materials (Figure 13(a)). Pure titanium showed the greatest extent of creep followed by enamel. In contrast, the indentation creep depths of dense HAP were very limited (<0.025 μm during the 900 s holding period). Such limited creep response, ~0.03 nm s^{-1}, is within the system thermal drift stability range and implies that the viscous properties of HAP materials are negligible compared with their elastic–plastic properties.

At the minimum-load holding period (named *backcreep* period), the recovery was prominent only for enamel but remained within the instrument's stability range (<0.03 nm s^{-1}) for other samples (Figure 13(b)). The displacement rate and limited backcreep of HAP (~0.03 nm s^{-1}) and

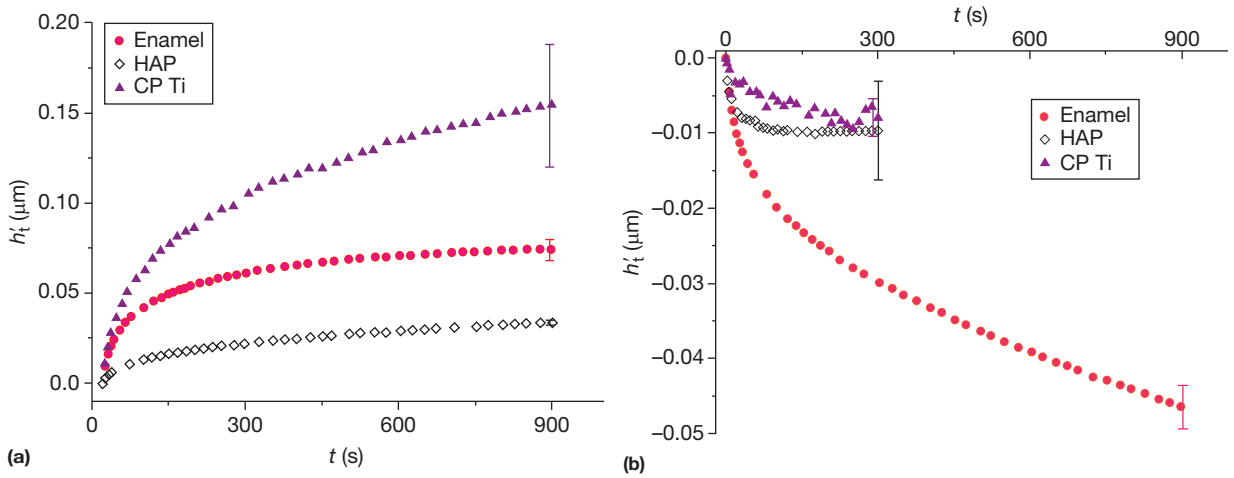

Figure 13 Indentation depth against time, $h'_t - t$ curves generated with a Berkovich indenter of (a) creep at 250 mN and (b) backcreep at 5 mN of different materials.

titanium ($\sim$0.02 nm s^{-1}) were all within the limit of system thermal drift. Therefore, only enamel exhibited significant backcreep response.

This phenomenological result implies that enamel and some dental metallic materials all exhibit creep behavior but with different characteristics. This indicates that different mechanisms are responsible for such behavior. The viscoelastic behavior of enamel may be considered as follows: first, the proteins and other organic (and water) components within enamel may be regarded as a biopolymer. Viscoplastic properties of these biopolymers stem from the configurational rearrangements, disposition, and interaction among the macromolecules in both their short- and long-range network interactions.[103] Under indentation load, high stresses around the indenter tip cause a rapid redistribution response of the structure, while in the lower stressed regions more remote from the tip, long-range interaction response is slow due to the time-dependent macromolecular rearrangement. Upon unloading, because of the memory effects associated with the cross-linked network, the molecules have a tendency to return to their initial form and positions.[103] In the case of indentation, the surrounding elastically deformed hinterland about the residual impression provides an additional driving force for such backcreep deformation. These factors result in the recovery of the indentation impression being also time-dependent. Second, proteins within enamel may behave similar to the recovery domain bond within many proteins, called a 'sacrificial bond.'[104] Rief *et al.*[104] also noted that the longer the delay before the next application of force, the more reformation or recovery of the bond occurred during relaxation; refolding of protein domains was also observed during this process. Similarly, proteins within the organic-rich sheath and between the apatite crystallites of enamel may have a similar function and response as those in bone.

In short, this reversible viscoelastic property of enamel may help teeth redistribute the localized high contact/impact stresses resulting from chewing forces, especially the high localized contacts from asperities/small hard particles trapped between teeth. Also, sliding wear between teeth and food particles may introduce high local tensile, compressive, and shear forces around the sliding contact area. This reversible inelastic property may be vital to limit damage accumulation and prevent excessive wear in enamel.

3.306.3.4. Nanoindentation of Caries Lesions

Nanoindentation has also been employed by researchers of structures that have experienced human diseases. Dental caries may be defined as a bacterial disease of calcified tissues of teeth and is characterized by demineralization of the inorganic and destruction of the organic substance of the tooth.[105] Due to its long history and wide prevalence, dental caries has attracted considerable attention of both clinical practitioners and researchers.

From a materials science point of view, caries and precaries or precavitated lesions (e.g., white spot lesions (WSLs) in clinic) would be anticipated to have markedly inferior mechanical properties than their healthy counterparts. By considering the aforementioned hierarchical microstructures of both enamel and dentin, and the natural procedure of acid invasion and mineral dissolution, the changes of mechanical properties may have certain characteristics, which may be able to help us understand the formation and development of the lesion so that remineralization treatments may be developed. In this field, nanoindentation is obviously a powerful tool.

Recently, a nanoindentation characterization of artificially generated WSLs has been reported.[106] After a certain period of time soaking in a mild acidic solution, sound teeth samples showed certain degrees of subsurface demineralization. The partially demineralized lesion areas had lower elastic modulus and hardness than sound areas, due to the loss of mineral crystals. On the surface of these natural lesions (WSLs), a harder, less demineralized surface layer up to 50-μm thickness was found (unpublished data).

Another recent nanoindentation on WSLs (unpublished data) exhibited a number of specific mechanical property features: (1) there is a rapid gradient and reduction in mechanical properties from sound enamel to the WSL body; (2) the body of the lesion appears inhomogeneous with some islands that show higher or lower elastic modulus and hardness; (3) the surface layer of the lesion showed higher elastic modulus and hardness than the lesion body. Moreover, the reduction of elastic modulus and hardness of natural WSLs was considered as a consequence of mineral loss. Therefore, a correlation analysis of elastic modulus and mineral density was performed on the natural WSL samples. Mineral density were measured and calculated from the gray value of calibrated micro-CT images.[107] By taking the mineral density of sound enamel ρ_{sound} as 3.0 g cm^{-3}, the porosity of every indented lesion point can be calculated with the equation: Porosity $= \rho_{lesion}/\rho_{sound}$ and correlated with the elastic modulus of that point (**Figure 14**). An exponential relationship was found to fit the data very well and the result can be related to Rice's minimum solid area model for porous materials.[108] In addition, recent high resolution electron microscopy observation provided direct evidence on the dissolution and pore formation of enamel HAP crystals as a consequence of caries degradation.[109]

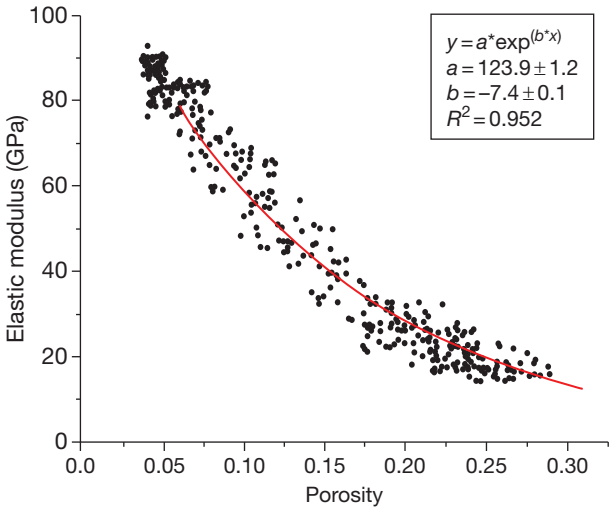

Figure 14 Nanoindentation-derived values of elastic modulus plotted against the mineral porosity of white spot lesion sample determined from quantitative micro-CT.

Developmental defects of dental hard tissues, mainly including amelogenesis imperfecta (defects of enamel) and dentinogenesis imperfacta (defects of dentine), are others conditions where nanoindentation has application. The etiology of these developmental defects is complex, including genetic, environmental, and systemic factors. Amelogenesis imperfecta has two subtypes: hypoplastic type (defective matrix production) and hypomineralized type (defective maturation/mineralization).[105] In general, most of these defective enamel and dentine tissues have less mineral and higher organic contents. Theoretically, from Spears' finite element model,[96] the change of the mineral/organic ratio of the composite will decrease the mechanical properties of the nature biocomposite significantly. In recent nanoindentation investigation, the hardness and elastic modulus of the hypomineralized enamel were reported as 0.53 ± 0.31 and 14.49 ± 7.56 GPa, respectively, which are much lower than the sound counterpart.[110] Similarly, another nanoindentation mapping showed that the hardness and elastic modulus of the hypomineralized region ranged from 0.07–1.7 to 3.2–40.9 GPa, respectively, which are less than a quarter of that of the normal enamel.[111] It was also suggested that this reduction is not only due to variations in mineralization, but more likely from differences in the apatite crystalline and crystal orientations of the hypoplastic enamel. Moreover, a newly published report showed that hypomineralized enamel also exhibited a profound elastic modulus size effect upon nanoindentation, as described in **Section 3.306.3.1**, but the decreasing trend was more significant than sound enamel.[112] The accompanying transmission electron microscopy (TEM) observations illustrated thicker interrod structures, with higher levels of organic content surrounding the HAP crystals within both rod and interrod regions.[112] By employing Spears' finite element model, the inferior mechanical properties can be reasonably explained in respect of the microstructure of the hypomineralized enamel.

3.306.4. Summary

In conclusion, nanoindentation provides a powerful way to explore the mechanical properties of biological materials in respect to their hierarchical microstructures. The nanoindentation investigations on natural biomaterials have contributed significantly to biomimetics and the development of new composite materials. However, as a newly developed technique, some aspects regarding the special properties of biomaterials need further development and investigations. These include:

1. Nanoindentation investigation of viscoelastic–plastic properties of biomaterials. As stated previously, viscous behavior of the material may generate a 'nose' effect on the force–displacement curve upon unloading and affect the accuracy of the result. How to resolve the problem needs more theoretical and experimental research.
2. Nanoindentation of fluid-filled porous structures.
3. Investigation and characterization of creep properties of biomaterials by nanoindentation. Unlike the uniaxial tests, nanoindentation generates a complex stress field on the sample. Procedures to adequately quantify the creep ability of materials by nanoindentation need further consideration.
4. Indentation size effects (ISE). Usually, this is a term related to metallic and ceramic materials related to hardness. However, as illustrated in this chapter, biomaterials may present similar size effect on the elastic properties due to the hierarchical microstructures. How to interpret and apply the results containing size effects becomes a question for further research on biomaterials.

References

1. Fischer-Cripps, A. C. *Nanoindentation*; Springer: New York, 2002.
2. Doerner, M. F.; Nix, W. D. *J. Mater. Res.* **1986**, *1*, 601–609.
3. Oliver, W. C.; Pharr, G. M. *J. Mater. Res.* **1992**, *7*, 1564–1583.
4. Vanlandingham, M. R. *J. Res. Natl. Inst. Stand. Technol.* **2003**, *108*, 249–265.
5. Sneddon, I. N. *Int. J. Eng. Sci.* **1965**, *3*, 47–57.
6. Tabor, D. *Hardness of Metals*; Clarendon Press: Oxford, 1951.
7. Cook, R. F.; Pharr, G. M. *J. Hard Mater.* **1994**, *5*, 179–190.
8. Sakai, M. *J. Mater. Res.* **1999**, *14*, 3630–3639.
9. Oyen, M. L. *J. Biomech.* **2006**, *39*, 2699–2702.
10. Oyen, M.; Cook, R. *J. Mater. Res.* **2003**, *18*, 139–149.
11. Sakai, M. *Acta Metall. Mater.* **1993**, *41*, 1751–1758.
12. Suganuma, M.; Swain, M. V. *J. Mater. Res.* **2004**, *19*, 3490–3502.
13. Stilwell, N. A.; Tabor, D. *Proc. Phys. Soc.* **1961**, *78*, 169–179.
14. He, L. H.; Swain, M. V. *J. Biomed. Mater. Res.* **2007**, *81A*, 484–492.
15. Fujisawa, N.; Li, W.; Swain, M. V. *J. Mater. Res.* **2004**, *19*, 3474–3483.
16. Swain, M. V. *Mater. Sci. Eng. A* **1998**, *253*, 160–166.
17. Hertz, H. *Miscellaneous Papers*; Macmillan: London, 1863 (translated by D. E. Jones and G. A. Schott).
18. Matthews, J. R. *Acta Metall.* **1980**, *28*, 311–318.
19. Hill, R.; Storakers, B.; Zdunek, A. B. *Proc. R. Soc. Lond.* **1989**, *A423*, 301–330.
20. Lawn, B. R.; Deng, Y.; Lioyd, I. K.; Janal, M. N.; Rekow, E. D.; Thompson, V. P. *J. Dent. Res.* **2002**, *81*, 433–438.
21. Lawn, B. R.; Deng, Y.; Thompson, V. P. *J. Prosthet. Dent.* **2001**, *86*, 495–501.
22. Lawn, B. R.; Pajares, A.; Zhang, Y.; *et al. Biomaterials* **2004**, *25*, 2885–2892.
23. Peterson, I. M.; Pajares, A.; Lawn, B. R.; Thompson, V. P.; Rekow, E. D. *J. Dent. Res.* **1998**, *77*, 589–602.
24. Field, J. S.; Swain, M. V. *J. Mater. Res.* **1993**, *8*, 297–305.
25. Oliver, W. C.; Pharr, G. M. *J. Mater. Res.* **2004**, *19*, 3–20.
26. Herbert, E. G.; Pharr, G. M.; Oliver, W. C.; Lucas, B. N.; Hay, J. L. *Thin Solid Films* **2001**, *398–399*, 331–335.
27. He, L. H.; Fujisawa, N.; Swain, M. V. *Biomaterials* **2006**, *27*, 4388–4398.
28. He, L. H.; Swain, M. V. *Dent. Mater.* **2007**, *23*, 814–821.
29. Palmqvist, S. *Arch. Eisenhuettenwesen* **1962**, *33*, 333–629.
30. Lawn, B. R.; Fuller, E. R. *J. Mater. Sci.* **1975**, *10*, 2016–2024.
31. Lawn, B. R.; Marshall, D. B.; Chantikul, P.; Anstis, G. R. *J. Aust. Ceram. Soc.* **1980**, *16*, 4–9.
32. Lawn, B. R.; Swain, M. V.; Phillips, K. *J. Mater. Sci.* **1975**, *10*, 1236–1239.
33. Anstis, G. R.; Chantikul, P.; Lawn, B. R.; Marshall, D. B. *J. Am. Ceram. Soc.* **1981**, *64*, 533–538.
34. Ponton, C. B.; Rawlings, R. D. *Mater. Sci. Technol.* **1989**, *5*, 865–872.
35. Quinn, G. D.; Bradt, R. C. *J. Am. Ceram. Soc.* **2007**, *90*, 673–680.
36. Leonardi, A.; Furgiuele, F.; Syngellakis, S.; Wood, R. J. K. *J. Am. Ceram. Soc.* **2009**, *92*, 1093–1097.
37. Dukino, R. D.; Swain, M. V. *J. Am. Ceram. Soc.* **1992**, *75*, 3299–3304.
38. Morris, D. J.; Myers, S. B.; Cook, R. F. *J. Mater. Res.* **2004**, *19*, 165–175.
39. Scholz, T.; Schneider, G. A.; Munoz-Saldana, J.; Swain, M. V. *Appl. Phys. Lett.* **2004**, *84*, 3055–3057.
40. Mullins, L. P.; Bruzzi, M. S.; Mchugh, P. E. *J. Biomech.* **2007**, *40*, 3285–3288.
41. Imbeni, V.; Kruzic, J. J.; Marshall, G. W.; Marshall, S. J.; Ritchie, R. O. *Nat. Mater.* **2005**, *4*, 229–232.
42. Field, J. S.; Swain, M. V.; Dukino, R. D. *J. Mater. Res.* **2003**, *18*, 1412–1419.
43. Bradby, J. E.; Williams, J. S.; Swain, M. V. *J. Mater. Res.* **2004**, *19*, 380–386.
44. Tsui, T. Y.; Oliver, W. C.; Pharr, G. M. *J. Mater. Res.* **1996**, *11*, 752–759.
45. Suresh, S.; Giannakopoulos, A. E. *Acta Mater.* **1998**, *46*, 5755–5767.
46. Marshall, D. B.; Lawn, B. R. *J. Am. Ceram. Soc.* **1977**, *60*, 86–87.
47. Lawn, B. R.; Marshall, D. B. *Phys. Chem. Glasses* **1977**, *18*, 7–18.
48. Anusavice, K. J.; Dehoff, P. H.; Hojjatie, B.; Gray, A. *J. Dent. Res.* **1989**, *68*, 1182–1187.
49. Asaoka, K.; Kuwayama, N.; Tesk, J. A. *J. Dent. Res.* **1992**, *71*, 1623–1627.
50. Kese, K.; Rowcliffe, D. J. *J. Am. Ceram. Soc.* **2003**, *86*, 811–816.

51. Goto, T.; Sasaki, N.; Hikichi, K. *J. Biomech.* **1999**, *32*, 93–97.
52. Jäger, I. L. *J. Biomech.* **2005**, *38*, 1451–1458.
53. Jäger, I. L.; Fratzl, P. *Biophys. J.* **2000**, *79*, 1737–1746.
54. Mcelhaney, J. H. *J. Appl. Phys.* **1966**, *21*, 1231–1236.
55. Sasaki, N.; Enyo, A. *J. Biomech.* **1995**, *28*, 809–815.
56. Sasaki, N.; Yoshikawa, M.; Enyo, A. *J. Biomech.* **1993**, *26*, 1369–1376.
57. Lucas, B. N.; Oliver, W. C. *Metal. Mater. Trans.* **1999**, *30A*, 601–610.
58. Tweedie, C. A.; Van-Vliet, K. J. *J. Mater. Res.* **2006**, *21*, 1576–1589.
59. Yang, S.; Zhang, Y. W.; Zeng, K. A. *J. Appl. Phys.* **2004**, *95*, 3655–3666.
60. Bembey, A. K.; Oyen, M. L.; Bushby, A. J.; Boyde, A. *Phil. Mag.* **2006**, *86*, 5691–5703.
61. Wei, B. C.; Zhang, T. H.; Li, W. H.; Xing, D. M.; Zhang, L. C.; Wang, Y. R. *Mater. Trans.* **2005**, *46*, 2959–2962.
62. Norton, F. H. *Creep of Steel at High Temperatures*; McGraw-Hill: New York, 1929.
63. Mayo, M. J.; Nix, W. D. *Acta Metall.* **1988**, *36*, 2183–2192.
64. He, L. H.; Swain, M. V. *J. Biomed. Mater. Res.* **2009**, *91A*, 352–359.
65. Mencik, J.; He, L. H.; Swain, M. V. *J. Mech. Behav. Biomed. Mater.* **2009**, *2*, 318–325.
66. Briscoe, B. J.; Fiori, L.; Pelillo, E. *J. Phys. D Appl. Phys.* **1998**, *31*, 2395–2405.
67. Angker, L.; Swain, M. V.; Kilpatrick, N. *J. Biomech.* **2005**, *38*, 1535–1542.
68. Shibata, Y.; He, L. H.; Kataoka, Y.; Miyazaki, T.; Swain, M. V. *J. Dent. Res.* **2008**, *87*, 233–237.
69. Guidoni, G. M.; He, L. H.; Schoberl, T.; Jager, I.; Dehm, G.; Swain, M. V. *J. Mater. Res.* **2009**, *24*, 616–625.
70. Rho, J. Y.; Pharr, G. M. *J. Mater. Sci. Mater. Med.* **1999**, *10*, 485–488.
71. Bushby, A. J.; Ferguson, V. L.; Boyde, A. *J. Mater. Res.* **2004**, *19*, 249–259.
72. He, L. H.; Swain, M. V. *Biomaterials* **2007**, *28*, 4512–4520.
73. Habelitz, S.; Marshall, G. W.; Baloochb, M.; Marshalla, S. J. *J. Biomech.* **2002**, *35*, 995–998.
74. Mittra, E.; Akella, S.; Qin, Y. X. *J. Biomed. Mater. Res.* **2006**, *79A*, 86–93.
75. Donnelly, E.; Baker, S. P.; Boskey, A. L.; Van Der Meulen, M. C. H. *J. Biomed. Mater. Res.* **2006**, *77A*, 426–435.
76. Xu, J.; Rho, J. Y.; Mishra, S. R.; Fan, Z. *J. Biomed. Mater. Res.* **2003**, *67A*, 719–726.
77. He, L. H.; Standard, O. C.; Huang, T. T. Y.; Latella, B. A.; Swain, M. V. *Acta Biomater.* **2008**, *4*, 577–586.
78. Ho, S. P.; Goodis, H.; Balooch, M.; Nonomura, G.; Marshall, S. J.; Marshall, G. *Biomaterials* **2004**, *25*, 4847–4857.
79. Habelitz, S.; Marshall, S. J.; Marshall, G. W.; Balooch, M. *Arch. Oral Biol.* **2001**, *46*, 173–183.
80. Sangwal, K. *Cryst. Res. Technol.* **2009**, *44*, 1019–1037.
81. Angker, L.; Swain, M. V. *J. Mater. Res.* **2006**, *21*, 1893–1905.
82. Ebenstein, D. M.; Pruitt, L. A. *Nano Today* **2006**, *1*, 26–33.
83. Lewis, G.; Nyman, J. S. *J. Biomed. Mater. Res. B Appl. Biomater.* **2008**, *87B*, 286–301.
84. Rensberger, J. M. *Mechanical Adaptation in Enamel*; Balkema: Rotterdam, 1997.
85. Barbour, M. E.; Parker, D. M.; Jandt, K. D. *J. Colloid Interface Sci.* **2003**, *265*, 9–14.
86. Cuy, J. L.; Manna, A. B.; Livi, K. J.; Teaford, M. F.; Weihs, T. P. *Arch. Oral Biol.* **2002**, *47*, 281–291.
87. Fong, H.; Sarikaya, M.; White, S. N.; Snead, M. L. *Mater. Sci. Eng. C* **2000**, *7*, 119–128.
88. Ge, J.; Cui, F. Z.; Wang, X. M.; Feng, H. L. *Biomaterials* **2005**, *26*, 3333–3339.
89. He, L. H.; Swain, M. V. *J. Dent.* **2009**, *37*, 596–603.
90. Mahoney, E.; Holt, A.; Swain, M.; Kilpatrick, N. *J. Dent.* **2000**, *28*, 589–594.
91. Marshall, G. W.; Balooch, M.; Gallagher, R. R.; Gansky, S. A.; Marshal, S. J. *J. Biomed. Mater. Res.* **2000**, *54*, 87–95.
92. Poolthong, S. Ph.D. Thesis, University of Sydney, New South Wales, 1998.
93. Willems, G.; Celis, J. P.; Lambrechts, P.; Braem, M.; Vanherle, G. *J. Biomed. Mater. Res.* **1993**, *27*, 747–755.
94. Zhou, J.; Hsiung, L. L. *J. Biomed. Mater. Res.* **2007**, *81A*, 66–74.
95. Anderson, P.; Elliott, J. C. *Caries Res.* **2000**, *34*, 33–40.
96. Spears, I. R. *J. Dent. Res.* **1997**, *76*, 1690–1697.
97. White, S. N.; Luo, W.; Paine, M. L.; Fong, H.; Sarikaya, M.; Snead, M. L. *J. Dent. Res.* **2001**, *80*, 321–327.
98. Fox, P. G. *J. Mater. Sci.* **1980**, *15*, 3113–3121.
99. Smith, B.; Schaffer, T.; Viani, M.; *et al. Nature* **1999**, *399*, 761–763.
100. Fantner, G. E.; Hassenkam, T.; Kindt, J. H.; *et al. Nat. Mater.* **2005**, *4*, 612–616.
101. Macho, G. A.; Jiang, Y.; Spears, I. R. *J. Hum. Evol.* **2003**, *45*, 81–90.
102. He, L. H.; Swain, M. V. *J. Dent.* **2007**, *35*, 431–437.
103. Ji, B.; Gao, H. *J. Mech. Phys. Solids* **2004**, *52*, 1963–1990.
104. Rief, M.; Gautel, M.; Oesterhelt, F.; Fernandez, J.; Gaub, H. *Science* **1997**, *276*, 1109–1112.
105. Soames, J. V.; Southam, J. C. *Oral Pathology*; Oxford University Press: New York, 2005.
106. Dickinson, M. E.; Wolf, K. V.; Mann, A. B. *Arch. Oral Biol.* **2007**, *52*, 753–760.
107. Huang, T.; Jones, A. S.; He, L. H.; Darendeliler, M. A.; Swain, M. V. *J. Dent.* **2007**, *35*, 737–743.
108. Rice, R. W. *J. Mater. Sci.* **1996**, *31*, 102–118.
109. Yanagisawa, T.; Miake, Y. *J. Electron Microsc.* **2003**, *52*, 605–613.
110. Mahoney, E. K.; Rohanizadeh, R.; Ismail, F. S. M.; Kilpatrick, N. M.; Swain, M. V. *Biomaterials* **2004**, *25*, 5091–5100.
111. Mahoney, E.; Ismail, F. S.; Kilpatrick, N.; Swain, M. *Eur. J. Oral Sci.* **2004**, *112*, 497–502.
112. Xie, Z. H.; Mahoney, E. K.; Kilpatrick, N. M.; Swain, M. V.; Hoffman, M. *Acta Biomater.* **2007**, *3*, 865–872.

3.307. Finite Element Analysis in Bone Research: A Computational Method Relating Structure to Mechanical Function

D Ruffoni, Institute for Biomechanics, ETH Zurich, Zurich, Switzerland
G H van Lenthe, Institute for Biomechanics, ETH Zurich, Zurich, Switzerland; K.U.Leuven, Leuven, Belgium

© 2011 Elsevier Ltd. All rights reserved.

3.307.1.	**Introduction**	92
3.307.1.1.	The Finite Element Analysis	93
3.307.2.	**Macroscale: Whole Bone**	94
3.307.2.1.	Continuum-Level FE	95
3.307.2.2.	Microstructural FE	95
3.307.2.3.	Femur	96
3.307.2.3.1.	Continuum FE models	96
3.307.2.3.2.	μFE models	96
3.307.2.4.	Radius	97
3.307.2.4.1.	μFE models	97
3.307.2.5.	Vertebra	99
3.307.2.5.1.	Continuum FE models	99
3.307.2.5.2.	μFE models	100
3.307.3.	**Mesoscale: Trabecular Bone**	100
3.307.3.1.	Conceptual Cellular Solids Modeling	100
3.307.3.1.1.	Role of architectural disorder and defects	100
3.307.3.1.2.	Trabecular thinning versus trabecular loss	102
3.307.3.1.3.	Towards patient-specific stiffness and strength predictions	102
3.307.3.2.	μFE Modeling	102
3.307.3.2.1.	Homogeneous versus heterogeneous tissue at the trabecular level	102
3.307.3.2.2.	Failure properties	104
3.307.3.2.3.	Structural and mechanical anisotropy	104
3.307.3.2.4.	The role of structural indices	105
3.307.3.2.5.	Mechanical behavior of single rods and plates	105
3.307.4.	**Microscale: Ultrastructural Features**	106
3.307.4.1.	Osteocyte Lacunae	106
3.307.4.2.	Canal Network	107
3.307.5.	**Nanoscale: Mineral and Collagen**	108
3.307.5.1.	Mechanics of the Mineral–Collagen Nanocomposite	108
3.307.6.	**Conclusions and Future Directions**	108
References		110

Glossary

Alendronate (also alendronic acid) Is a bisphosphonates drug used for osteoporosis.

Anabolic agent Substance which stimulates the formation of new bone. One of the most common anabolic agents is the parathyroid hormone (PTH) which regulates the levels of calcium in the serum. The use of anabolic agents is common in therapies against osteoporosis.

Antiresorptive therapy A type of medical treatment used against osteoporosis which inhibits bone resorption. Antiresorptive therapies are often based on bisphosphonates.

Bone quality Various skeletal factors which contribute to bone strength in addition to bone mass. For example, bone quality includes bone microarchitecture, bone material properties, bone remodeling.

Colles' fractures (also Colles fracture) Distal fracture of the radius in the forearm with dorsal posterior displacement of the wrist.

Compact bone (also cortical bone) A common type of bone which forms the outer shell of most bones. Compact bone is much denser and has different mechanical properties than trabecular bone.

Osteocyte A type of bone cell found inside the mineralized bone matrix. It is located within a small hole called osteocyte lacuna. Osteocytes can communicate with each other through cell processes which run inside small channels called canaliculi. Osteocytes are believed to act as sensors which transform mechanical inputs into biological signals.

Osteoporosis One of the most prevalent bone diseases which increases bone fragility and, consequently, fracture risk. Osteoporosis is accompanied by a decrease in bone mass and by a deterioration of bone microarchitecture

leading to a general decrease in bone quality. Osteoporosis is most common in women after menopause (so-called postmenopausal osteoporosis), but also develops in men.
Teriparatide A form of parathyroid hormone (PTH) used in the treatment of osteoporosis.

Trabecular bone (also cancellous bone and spongy bone) A common type of bone which is found, for instance, inside the vertebral body and at the end of long bones. Trabecular bone is highly porous and it is composed of small struts called trabeculae.

Abbreviations

BEI	Back-scattered electron imaging
BMD	Bone mineral density
BV/TV	Bone volume fraction
CT	Computed tomography
DXA	Dual-energy X-ray absorptiometry
FE	Finite element
FEA	Finite element analysis
FEM	Finite element method
HR-pQCT	High-resolution peripheral quantitative computed tomography
MIL	Mean intercept length
MR	Magnetic resonance
MRI	Magnetic resonance imaging
OVX	Ovariectomized
pQCT	Peripheral quantitative computed tomography
QCT	Quantitative computed tomography
SED	Strain energy density
SR nCT	Synchrotron radiation nanocomputed tomography
SR μCT	Synchrotron radiation microcomputed tomography
Tb.N	Trabecular number
Tb.Sp	Trabecular spacing
Tb.Th	Trabecular thickness
WHO	World Health Organization
μCT	Microcomputed tomography
μFE	Microstructural finite element
μMRI	Micromagnetic resonance imaging

3.307.1. Introduction

Bone is the most frequently investigated biological material and finite element analysis (FEA) is currently the computational tool most commonly used for the analysis of bone biomechanical function. FEA has been used in bone research for more than 30 years and has had a substantial impact on our understanding of the complex behavior of bone.[1] Bone is structured in a hierarchical way over many length scales[2] and this chapter reflects this hierarchical organization. In particular, we focus on the applications of FEA for understanding the relationship between bone structure and its mechanical function at specific hierarchical levels. A better understanding of the relationship between structure and mechanical function is supposed to be important for the current trend of (bio)materials design, where the structure of biological materials is considered as a possible source of inspiration.[3] Furthermore, an improved understanding could lead to more successful approaches in the prevention and treatment of age- and disease-related fractures.

FEA has been extensively used in bone research for a variety of purposes. This chapter does not attempt to give an in-depth review of all the FE studies in the bone field. Neither do we consider traditional aspects directly related to the design and analysis of orthopedic implants; for this topic, the reviews of Prendergast[4] and Wirth *et al.*[5] can be consulted. In addition, we limit our review by only considering bone from a 'static' point of view; hence, time-dependent processes such as bone adaption and healing are not included. FE simulations in the field of bone remodeling and adaption have been recently reviewed by Gerhard and colleagues,[6] whereas FE studies on bone healing have been collected by Doblaré *et al.*[7]

In this chapter, the basic concepts of FEA are briefly discussed in Section 3.307.1.1. The reader looking for a more exhaustive description of the principles and numerical implementations of FEA is referred to classical textbooks.[8] Afterward, we focus on some specific levels of bone hierarchical structure, ranging from the macroscale to the nanoscale. At each level, the most common FE modeling strategies are introduced. Depending on the hierarchical level, different research questions have been investigated with FE simulations: from more clinically oriented issues connected with bone quality (e.g., predicting bone strength at the radius) to more fundamental problems (e.g., basic mechanisms of damage accumulation in mineralized collagen fibrils).

At the macroscopic or organ level (Figure 1(a)), bones have quite different shapes that relate to their specific functions and loading conditions. Bones are loaded through direct contact within joints and through the action of muscles and tendons; hence, the resulting loading scenarios can be very complex. Nevertheless, a proper and accurate description of the boundary conditions is fundamental for meaningful calculations of physiological tissue loading, and this can be done only when whole bones are represented. Furthermore, the effects of bone diseases such as osteoporosis become specifically apparent at the organ level where they can cause spontaneous fractures. In Section 3.307.2, FE studies on whole bones are reviewed focusing on the specific locations that are most prone to osteoporotic fractures, which are the femur, radius, and vertebra.

At the mesoscale, the next hierarchical level with typical dimensions of hundreds of micrometer, trabecular bone can be distinguished from compact bone (Figure 1(b)). Trabecular bone is found at the ends of long bones (e.g., in the femoral head or in the distal radius) and inside the vertebral bodies; it has a porous nature and it is composed of small rod-like and plate-like struts. The mechanical behavior of trabecular bone,

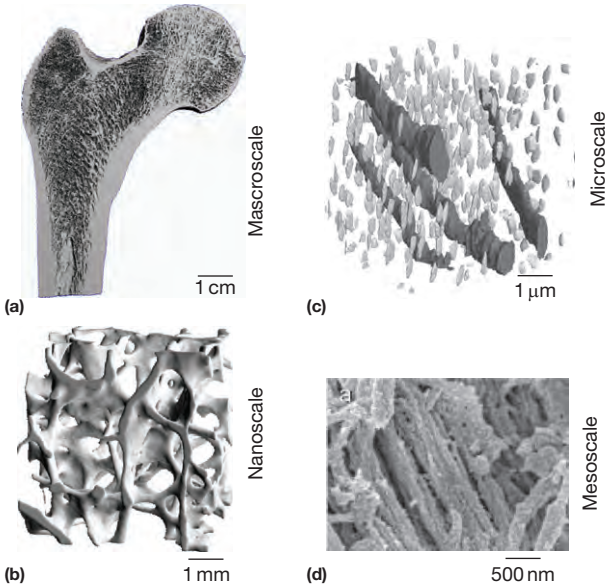

Figure 1 Schematic overview of the hierarchical levels of bone considered in this chapter. (a) At the macroscale, a microcomputed tomography (μCT) image of a section across the femur shows the trabecular core as well as the compact cortical shell around it (image courtesy of Thomas Mueller, ETH Zurich, Zurich, Switzerland). (b) At the mesoscale, close-up on the three-dimensional microarchitecture of a trabecular bone sample coming from the femoral head and imaged with μCT. (c) At the microscale, the main ultrastructural features of cortical bone (canal network and osteocyte lacunae) are visible with synchrotron radiation nanocomputed tomography. Adapted from Schneider, P.; Stauber, M.; Voide, R.; Stampanoni, M.; Donahue, L. R.; Müller, R. *J. Bone Miner. Res.* **2007**, with permission. (d) At the nanoscale, scanning electron micrographs of mineralized collagen fibrils coming out from a fracture surface in a human bone specimen (image courtesy of Paul Hansma, UCSB, Santa Barbara, USA).

explored with FE strategies, is reported in Section 3.307.3. The extent of this section reflects the considerable amount of literature focusing on trabecular bone. In fact, trabecular bone has been extensively characterized for mainly two reasons. First, bone loss and architectural deterioration occurring in osteoporotic patients primarily weaken the trabecular network. Second, trabecular bone is a natural material that efficiently combines low weight with high mechanical performance: hence, the study of the relationship between architectural and mechanical properties (e.g., stiffness, strength, and failure modes) could be inspiring for biomaterial applications.

Compact or cortical bone appears dense at a level of hundreds of micrometer, but considering a higher magnification (3–5 μm), several ultrastructural features such as the osteocyte lacunae and the canal network can be distinguished (Figure 1(c)). The influence of such features on the mechanics of bone tissue at the microscale as assessed by FE is explored in Section 3.307.4.

At the material level, the basic building blocks of bone are a soft but tough protein matrix and stiff but brittle mineral crystals (Figure 1(d)). The relative geometrical arrangement of the two components influences the stress transfer between mineral and collagen as well as the propagation of cracks in this composite material. FE applications at the nanoscale are reviewed in Section 3.307.5.

3.307.1.1. The Finite Element Analysis

Due to the application of external loads, internal forces (stresses), and deformations (strains) are generated inside a structure. The magnitude and direction of stress and strain are influenced by various aspects including magnitude and direction of the loading conditions, shape and internal architecture of the structure, and local material properties. The transmission of forces from the boundary of an object to the inside of that structure is well described with a set of partial differential equations that constitute the so-called boundary-value problem. From a mathematical point of view, the elastic problem can be formulated by considering a three-dimensional body of volume V, delimited by a surface S into a coordinate system x_i ($i = 1, 2, 3$). The body is subjected to some prescribed displacement on its boundary and to external forces which can be point loads f_P, surface loads f_S, or volume loads f_V. A coordinate system is also attached to the body. Due to loads and boundary constrains, the body will deform and the strain tensor $\boldsymbol{\varepsilon}$ can be computed by differentiating the displacement vector $\boldsymbol{u}(\boldsymbol{x})$ (small strain assumption):

$$\varepsilon_{ij} = \frac{1}{2}\left[\frac{\partial u_i}{\partial x_j} + \frac{\partial u_j}{\partial x_i}\right] \qquad [1]$$

The diagonal components of the strain tensor ($i = j$) represent the relative length variation along the directions of the coordinate system whereas the nondiagonal components ($i \neq j$) express the relative angle variations between two faces initially parallel to the directions of the coordinate system. Considering a linear elastic constitutive behavior, the relationship between the stress tensor $\boldsymbol{\sigma}$ and strain tensor $\boldsymbol{\varepsilon}$ is given by:

$$\sigma_{ij} = C_{ijkl}\varepsilon_{lk} \qquad [2]$$

The diagonal components of the stress tensor ($i = j$) represent the area-normalized force acting along the directions of the coordinate system and perpendicular to a considered infinitesimal area, whereas the nondiagonal components ($i \neq j$) describe the area-normalized force acting along the directions of the coordinate system but parallel to an infinitesimal area. If the material is isotropic, only two independent material properties are needed to describe the material mechanical behavior and the stiffness matrix $\boldsymbol{C}$ becomes:

$$\boldsymbol{C} = \frac{E}{(1+\nu)(1-2\nu)}\begin{bmatrix} 1-\nu & \nu & \nu & 0 & 0 & 0 \\ \nu & 1-\nu & \nu & 0 & 0 & 0 \\ \nu & \nu & 1-\nu & 0 & 0 & 0 \\ 0 & 0 & 0 & 1/2-\nu & 0 & 0 \\ 0 & 0 & 0 & 0 & 1/2-\nu & 0 \\ 0 & 0 & 0 & 0 & 0 & 1/2-\nu \end{bmatrix} \qquad [3]$$

where E is the Young's modulus and ν the Poisson's ratio.

The constitutive equation (eqn [2]) has to be solved under two constraints. First, the equilibrium condition on the stress tensor states that (assuming $f_v = 0$):

$$\frac{\partial \sigma_{ij}}{\partial x_j} = 0 \quad \text{in } V \qquad [4]$$

Second, the strain field must satisfy the compatibility relations to assure the existence of a displacement field:

$$\frac{\partial^2 \varepsilon_{ij}}{\partial x_k \partial x_l} + \frac{\partial^2 \varepsilon_{kl}}{\partial x_i \partial x_j} - \frac{\partial^2 \varepsilon_{ik}}{\partial x_j \partial x_l} - \frac{\partial^2 \varepsilon_{jl}}{\partial x_i \partial x_k} = 0, \quad i,j,k,l = 1,2,3 \qquad [5]$$

Equations [2], [4], and [5] can be combined into a single equation for the displacement:

$$(\lambda+\mu)\frac{\partial}{\partial x_i}\left(\frac{\partial u_k}{\partial x_k}\right)+\mu\frac{\partial^2 u_i}{\partial x_j^2}=0 \qquad [6]$$

λ and μ are the Lamè coefficients defined as:

$$\lambda=\frac{E\,v}{(1+v)(1-2v)},\quad \mu=\frac{E}{2(1+v)} \qquad [7]$$

Equation [6] is a second-order partial differential equation that describes the displacement field inside a three-dimensional object. Only in very simple cases it can be solved analytically; in most of the situations encountered in bone research, geometries, loading conditions, and material properties are complex, and numerical solutions of the elastic problem are needed.

The FEA is the most adopted numerical procedure for solving boundary-value problems. The finite element method (FEM) does not directly attempt to discretize eqn [6]; instead, it is based on alternative formulations of the elastic problem such as, for instance, the potential energy method or the principle of virtual works. Such formulations are preferred since they can be solved directly using simple linear matrix operations and indirectly when used in combination with powerful minimization methods. Considering the potential energy principle, it states that a mechanical system is at equilibrium when its total potential energy reaches its minimum value. The total potential energy Π is obtained by summing up the total strain energy inside the system and the work done by the external forces W:

$$\Pi=\frac{1}{2}\int_V \boldsymbol{\sigma}\boldsymbol{\varepsilon}\,\mathrm{d}V-\int_V \boldsymbol{u}\boldsymbol{f}_\mathrm{V}\,\mathrm{d}V-\int_S \boldsymbol{u}\boldsymbol{f}_\mathrm{S}\,\mathrm{d}S-\sum_P \boldsymbol{u}\boldsymbol{f}_\mathrm{P} \qquad [8]$$

The formulation of the total potential energy given in eqn [8] is valid for a continuum system whereas for FEA a discrete implementation is required. The basic idea of the FEM is to discretize a complex structure into small elements with simple shapes. The size of the elements must be chosen according to the length scale of interest. The elements are interconnected through nodes situated at specific locations within the elements and at the elements boundaries. The displacement field inside each element is assumed to be a function of the displacement of the nodes; the displacement functions, also called shape functions, are generally linear, quadratic, or cubic. The first step in the discretization procedure is to substitute the continuum displacement vector $\boldsymbol{u}$ with the nodal displacement $\boldsymbol{U}_\mathrm{N}$. The displacements of the nodes are the main unknowns of the FEM. The displacement and the strain within each element ($\boldsymbol{U}_\mathrm{M}$ and $\boldsymbol{\varepsilon}_\mathrm{M}$, respectively) can be calculated as a function of the nodal displacement by introducing the shape-function matrix $\boldsymbol{S}_\mathrm{M}$ and the strain-displacement matrix $\boldsymbol{B}_\mathrm{M}$:

$$\boldsymbol{U}_\mathrm{M}=\boldsymbol{S}_\mathrm{M}\boldsymbol{U}_\mathrm{N} \qquad [9]$$

$$\boldsymbol{\varepsilon}_\mathrm{M}=\boldsymbol{B}_\mathrm{M}\boldsymbol{U}_\mathrm{N} \qquad [10]$$

The stress inside each element $\boldsymbol{\sigma}_\mathrm{M}$ is defined based on the element strain $\boldsymbol{\varepsilon}_\mathrm{M}$ and on the element constitutive properties reported in the constitutive matrix $\boldsymbol{D}_\mathrm{M}$:

$$\boldsymbol{\sigma}_\mathrm{M}=\boldsymbol{D}_\mathrm{M}\boldsymbol{\varepsilon}_\mathrm{M} \qquad [11]$$

Similar to the displacement, all the forces acting within each element can also be transformed into equivalent forces acting at the nodal points, which must be in equilibrium with the boundary stresses and with all the loads acting on the element ($\boldsymbol{f}_\mathrm{P}$, $\boldsymbol{f}_\mathrm{S}$, and $\boldsymbol{f}_\mathrm{V}$). Inserting eqns [9]–[11] into eqn [8] and putting together all the force terms into a global force vector $\boldsymbol{F}$ and all the displacement terms into a global displacement vector $\boldsymbol{U}$, eqn [8] becomes:

$$\Pi=\frac{1}{2}\boldsymbol{U}^\mathrm{T}\boldsymbol{K}\boldsymbol{U}-\boldsymbol{U}^\mathrm{T}\boldsymbol{F} \qquad [12]$$

where $\boldsymbol{K}$ is the so-called global stiffness matrix. The minimum value of the total potential strain energy of the finite system is computed by imposing:

$$\frac{\partial\Pi}{\partial\boldsymbol{U}_i}=\begin{bmatrix}\dfrac{\partial\Pi}{\partial\boldsymbol{U}_1}\\ \vdots\\ \dfrac{\partial\Pi}{\partial\boldsymbol{U}_N}\end{bmatrix}=0,\quad i=1,\ldots,N \qquad [13]$$

which leads to the following system of N algebraic equations (in three dimensions N is equal to three times the number of nodes in the system):

$$\boldsymbol{K}\boldsymbol{U}=\boldsymbol{F} \qquad [14]$$

With the FEM, the problem of solving a second-order partial differential equation [6] is reduced to the easier task of solving a set of algebraic equations.

In FEA, two typical drawbacks resulting from the element discretization should be mentioned. First, the displacement functions can very well represent the displacement field within each element but may give rise to discontinuity in the displacement between adjacent elements, therefore violating the compatibility criterion. Second, equilibrium is computed and ensured only at nodes where equivalent forces are considered; inside the elements, equilibrium requirements are often violated. Therefore, the solution obtained with FEA is approximate and concepts such as accuracy and validity should be considered. The accuracy of a FE model quantifies how close the model output is to the real solution of the boundary-value problem. Since the real solution is not known, the accuracy can be estimated with a so-called convergence test: the size of the element is decreased and a new solution is obtained and compared with the old one. From a mathematical point of view, if the element size approaches zero, the numerical solution will converge to the correct solution. The model validity, a fundamental issue unfortunately often disregarded, tells to which extent the results of the model can represent or can predict the behavior of the investigated mechanical system. The validation of a model is often performed by comparing model predictions with experimental results. Where the accuracy of a FEA can be quite easily assessed, it can be challenging (and sometimes even not possible) to verify the validity of a FE model.

3.307.2. Macroscale: Whole Bone

The natural ability of the skeleton to withstand loads can be greatly compromised in case of bone diseases such as

osteoporosis. A fundamental task of bone research is to provide tools for improving the prediction of bone strength, ideally *in vivo* and at the organ level. Nowadays, the main diagnostic method to assess fracture risk connected with skeletal disorders such as osteoporosis is to measure *in vivo* the amount of bone. This is often performed with a technique called dual-energy X-ray absorptiometry (DXA), which estimates from the quantity of the adsorbed radiation how much bone is present.[9] The result of DXA measurements, corrected by body size, is the bone mineral density (BMD) characterizing with a single scalar value the bone under investigation. According to the instruction of the World Health Organization (WHO), a reference value of BMD for healthy people as a function of age is established and variations of 2.5 standard deviations or more below this value define an osteoporotic individual.[10,11] When thinking at the intricate structure of bone (**Figure 1**), it is obvious that there are several limitations in estimating bone mechanics, and in particular, bone strength using BMD only. Estimating the probability of fracture with BMD does not identify all the people at risk and does not tell who will and who will not have a nontraumatic fracture.[10] The poor predictive power of BMD is also evident from the effects of antiresorptive therapies where the significant reduction observed in fracture risk has almost no correlation with the small increase in BMD.[12–14]

Two computational approaches have been employed for estimating the mechanical behavior of bone (primarily bone strength) at the organ level: continuum-level FE (or continuum FE) and microstructural-level FE (or continuum FE) (μFE). Those methods are based on three-dimensional virtual reconstructions of the skeletal system which can be obtained nondestructively with computed tomography (CT) or magnetic resonance (MR) imaging.[15,16] The development of FE simulations in bone research has run parallel to the improvement in the resolution of imaging systems based on X-rays and MR. *In vivo* scanners for the whole body based on quantitative CT (QCT) have a resolution of about 1 mm. QCT measures the specific external shape of bones and gives estimations of BMD but it does not include microstructural details (i.e., at the level of individual trabeculae) which are only visible in the submillimeter range. For the extremities of the musculoskeletal system, scanners with higher resolution have been developed. Peripheral QCT (pQCT) initially had a resolution of about 170 μm and nowadays high-resolution pQCT (HR-pQCT) can resolve bone microstructure with a voxel size of 80 μm.[17] The widely spread desktop micro-CT (μCT) system, used in bone research starting from the 1990s,[18] is now capable of resolving bone structure even at the submicrometer range but requires small bone samples. In animals, the feasibility of performing *in vivo* μCT was first demonstrated in the rat proximal tibia using synchrotron radiation,[19] and was used to depict bone loss after OVX.[20] The recent introduction of desktop μCT systems for *in vivo* scanning of small animals[21,22] with resolution better than 10 μm has opened the way to more practical and better accessible systems.[23]

3.307.2.1. Continuum-Level FE

Continuum FE models are commonly based on QCT imaging. In continuum FE different degrees of material complexity such as inhomogeneity, anisotropy, and nonlinearity can be introduced within manageable computational time. Elastic moduli for continuum-level FE elements are commonly derived from BMD values through empirical conversions,[24] which however, are still quite controversial.[25] It has been demonstrated that continuum FE, based on QCT images, can give better predictions of bone strength than BMD.[26,27] For the skeletal locations where only QCT imaging is clinically feasible, such as femur and vertebra, continuum FE could be considered the actual state of the art computational method to predict bone strength *in vivo*. The method has a great potential to become a valuable tool in cross-sectional studies, where bones of different healthy and osteoporotic individuals are scanned and compared; conversely, it might not be precise enough to track more subtle changes in bone stiffness and strength in follow-up studies, where the very same skeletal regions of the same patient is followed over time.[16] It has been suggested that a possible cause for the nonperfect ability to predict bone strength from QCT-based FE models is the lack of information on bone microstructure. By definition, continuum FE models do not represent the internal microarchitecture of bones; hence, features such as the orientation of individual trabeculae or the thin cortical shell surrounding the trabecular core cannot be resolved. However, these structural aspects could be fundamental for a better understanding of the mechanisms of deformation and failure of bones. The use of more refined FE models, which accurately represent bone microarchitecture, might be a way to overcome this problem and therefore to better predict bone failure.[16] Increasing the complexity of the material behavior is considered another possible strategy to compensate for the lack of microstructural information.[28]

3.307.2.2. Microstructural FE

During the last two decades, a novel approach to investigate the mechanical properties of bone, which takes into account bone microarchitecture has been developed. The approach combines three-dimensional imaging with FE and is referred to as microstructural FE (μFE) analysis or voxel FEA. The strategy normally adopted to exploit high-resolution images for FE simulations is to directly convert each image voxel into (typically) a brick-shaped element.[28–30] Alternatively, image processing algorithms (e.g., marching cube) are adopted to generate smoother meshes of tetrahedral elements.[31] Obviously, as a result of the voxel-to-element conversion approach, the resulting μFE models are made up of a very large number of elements: an entire human vertebra can possess up to 60 million elements and 200 million degrees of freedom.[32,33] Special solving strategies have been developed for such large systems. The element-by-element method,[30] for instance, exploits the fact that all elements are identically shaped bricks for making very efficient use of the memory. More advanced numerical methods based on the concept of preconditioners have been recently introduced for large parallel computer architectures.[28,34] Currently, the maximum number of degrees of freedom that can be analyzed in μFE is about 1 billion and, when using supercomputers, the solution time required can range from minutes to a few hours depending on the number of CPUs and the complexity of the model.

The tissue properties normally adopted in μFE are quite simple: it has been shown by comparison with biomechanical

testing that isotropic and linear elastic material models give very accurate predictions (for small deformations) of the apparent mechanical behavior of bone samples and of whole bones.[16,35,36] Even if the tissue modulus is assumed isotropic, the directional dependence of bone mechanical properties emerges automatically due to the directional nature of the trabecular network. The role of tissue properties as well as of nonlinearity in the material behavior will be discussed in more details when specifically considering trabecular bone (Section 3.307.3.2). Another advantage of μFE is the possibility to calculate stress and strain locally, in the individual trabeculae; this knowledge can be fundamental to understand bone adaption in healthy and osteoporotic conditions.[33,37]

In the following three sections, some examples of continuum FE and μFE studies focusing on whole bones will be presented. Three locations of the musculoskeletal system which are often subjected to osteoporotic fractures[38,39] will be considered: the femur (Section 3.307.2.3), the radius (Section 3.307.2.4), and the vertebra (Section 3.307.2.5). For each of these regions we will not attempt to give an exhaustive review of the literature, instead, some significant applications of FE simulations will be discussed. Our aim is to give the reader an idea of the current state of the art applications of FE in bone research, including advantages and potential pitfalls.

3.307.2.3. Femur

One of the musculoskeletal sites where osteoporotic fractures are most frequent is the femur and in particular the femoral neck.[39] The femur is also one of the most studied bones of the skeleton. It was by looking at the trabecular arrangement inside a human femur that, more than a century ago, the first thoughts on bone remodeling and adaption were made.[40] Hence, it may not be surprising that the first FEA of a whole bone reported in literature was performed on a femur.[41] Since the original work of Brekelmans,[41] FE studies have been extensively used to assess the mechanical properties of human femurs, with a special interest in predicting failure characteristics as well as stresses and strains at the tissue level in healthy and osteoporotic conditions.

3.307.2.3.1. Continuum FE models

Continuum FE models take in consideration the specific shape of the femur but do not model the internal architecture. This method has been often employed to study femoral fractures: it has been shown that continuum FE performs better than BMD in quantifying bone strength, with R^2 values typically ranging from 0.75 to 0.83.[42,43] Keyak and colleagues[43] used linear continuum FE, with geometry and material properties automatically generated from QCT scans, to investigate the prediction of fracture locations. Several human femurs ($N = 18$) were tested under two different loading conditions: single-limb stance and fall to the side. The model could predict different fracture locations for the different loading scenarios; however, the agreement with experimentally determined failure locations was limited to 72% and 67% for stance and fall loading case, respectively. In a subsequent study, the model was refined by including nonlinear material behavior (an elastic region, a perfectly plastic region, and a strain-softening phase were considered).[44] The nonlinear properties improved the strength prediction ($R^2 = 0.92$) but also resulted in a huge overestimation of stiffness. Considering failure properties, one obvious question is which type of failure criterion for bone tissue can better identify the risk of fracture? Schileo and colleagues[45] combined subject-specific continuum FE models and experimental mechanical testing to compare the performance of a failure model based on maximum principal strain versus stress-based criteria in predicting the failure patterns of human femurs. The authors considered only three femurs and a single loading condition; nevertheless, the results clearly indicated that a principal strain criterion better identified the level of failure risk and the location of fracture. The use of a failure mode based on strain is supported by experimental data showing that the failure strains of bone tissue appear to be fairly constant.[46]

Currently, QCT-based continuum FE models appear to be the best technology to determine femoral bone strength *in vivo*. However, no technological standard exists for quantifying bone fracture from FEA. More experimental data on bone failure characteristics is needed to justify or adapt currently incorporated bone fracture mechanics models in the FE analyses. With that in place continuum FE seems to be a promising approach towards a clinical implementation of patient-specific strength prediction in the femur.

3.307.2.3.2. μFE models

The femur has been analyzed with μFE simulations also with different aims than strength prediction. In particular, this methodology has been used to explore the link between microstructural changes occurring with osteoporosis and their impact on the load distribution at the tissue level. This aspect is quite important in view of the ability of bone to adapt to its mechanical demands. It is not clear to which extent bones are adapted to normal or habitual loads of daily life and, therefore, how dangerous are nonhabitual or error loads, for instance originating from accidents or during sport activities.[37] In addition, the adaption mechanism might differ in healthy and osteoporotic conditions. Researchers have tried to answer those issues by focusing on the analysis of local stress/strain distributions in healthy and osteoporotic bone under different loading scenarios.[33,37,47] One study of van Rietbergen[37] analyzed the stress and strain distributions inside an healthy and an osteoporotic human femur with high level of details. μCT images of a region of about 100 mm in length (including the femoral head and neck) at a resolution of 80 μm were converted into μFE models which had approximately 96 millions of elements (Figure 2(a) and 2(b)). Cortical and trabecular bone were modeled with different tissue moduli (22.5 and 15 GPa, respectively) and proper boundary conditions were applied to simulate the maximum load occurring during the stance phase of walking. The simulations showed that the mean tissue strain was almost 1.7 times higher in the osteoporotic femur compared to the healthy one (520 and 304 mean microstrains, respectively) (Figure 2(c) and 2(d)). Additionally, the tissue of the osteoporotic specimen was less uniformly strained, as shown by its broader strain distribution. Interestingly, osteoporotic bone presented a higher percentage of tissue both high-loaded and low-loaded than healthy bone. Finally, the authors observed that by reducing the external load by approximately 41%, the mean strains in the two femurs

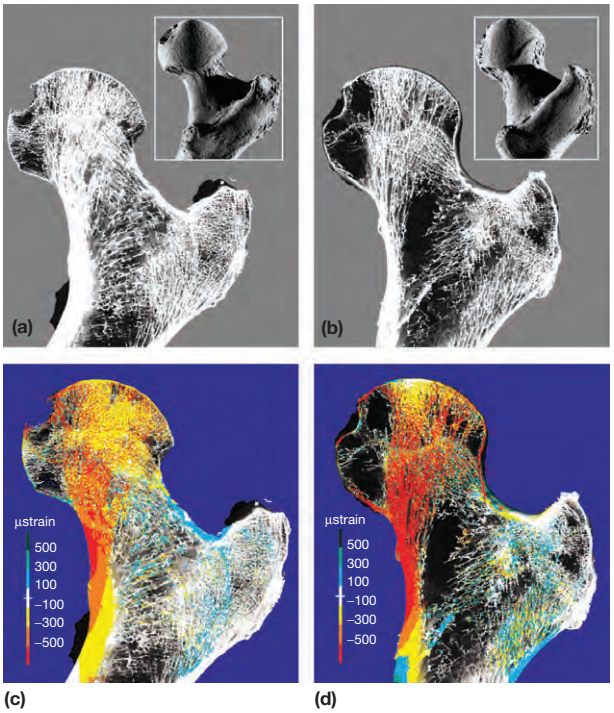

Figure 2 Three-dimensional reconstructions of a healthy (a) and osteoporotic (b) proximal femur. Sections across the femurs as well as the entire models are shown. A large hole can be seen in the (b) osteoporotic femur, devoid of any trabeculae; contour plots for the principal strains at the tissue level inside the healthy (c) and osteoporotic (d) human femur. The strains were computed with micro-finite element analysis (element size 80 μm). For loading conditions the stance-phase of walking was assumed. In the color map, negative values (from yellow to red) correspond to compressive strains and positive values (from blue to green) to tensile strains. The loading patterns in the two femurs are similar; however, higher strains both in tension and compression are present in the osteoporotic femur. Adapted from Van Rietbergen, B.; Huiskes, R.; Eckstein, F.; Ruegsegger, P. *J. Bone Miner. Res.* **2003**, *18*, 1781–1788, with permission.

were quite similar, hence suggesting that osteoporotic bone might be adapted to lower load levels. A similar approach based on μFE was followed by Verhulp *et al.*[47] to characterize the tissue stresses and strains for nonhabitual loads. More specifically, the authors simulated and analyzed a fall to the side onto the greater trochanter for the same healthy and osteoporotic femurs used by van Rietbergen *et al.*[37] In this study the relative contribution of cortical and trabecular bone in taking up the load was also calculated. This estimation was done by measuring the ratio of the elastic energies stored in the two bone compartments was alos calculated. The μFE calculations indicated that both for healthy and osteoporotic femur, the anatomical location subjected to the highest strain was always the cortex of the femoral neck. Also for the case of a fall to the side, broader distributions of the strain energy density (SED) were found for the osteoporotic femur. However, the relative amounts of strain energy stored by the inner trabecular bone in the two models were comparable (67.8% and 70.3% for the healthy and osteoporotic femur, respectively). Similar strain distributions in the two femurs were obtained if the loading force acting on the osteoporotic femur was reduced by 39%. Surprisingly, this values is very similar to the one reported by van Rietbergen for physiological loading configurations.[37] This fact may indicate that the relative weakness of the osteoporotic femurs compared to the healthy one does not depend on habitual or nonhabitual loading conditions. A limitation of these two studies was that only one healthy and one osteoporotic sample were considered. It would be interesting to test to what extent the findings are valid when analyzing femurs from a more heterogeneous population with different degrees of osteoporosis.

3.307.2.4. Radius

Fractures at the distal radius are very spread among osteoporotic individuals. They have less severe consequences than femoral fractures but cause great pain and often require surgical interventions. In addition, those fractures are also considered good indicators of an increased probability of having other fractures in the future at different skeletal locations.[48] Similar to other bones, the prediction of fracture risk at the radius has been based on the measurement of BMD. However, this approach presents several limitations, as discussed at the beginning of Section 3.307.2. Not only from a clinical, but also from a technological point of view, the radius is an interesting anatomical site because it can be imaged *in vivo* with high-resolution techniques such as pQCT and HR-pQCT; having such *in vivo* detailed measures makes image-based μFE the preferred computational method for assessing and predicting the stiffness and, more important, the strength of this skeletal region. For this reason, in this section we will only consider studies were μFE has been used in combination with pQCT or HR-pQCT to investigate the mechanical behavior of the radius.

3.307.2.4.1. μFE models

One of the first aims of μFE studies based on pQCT of human radii has been to determine whether a correlation exists between common regions of fractures observed in clinical practice and locations of high mechanical stresses or strains computed with μFE. A study of Ulrich and colleagues[48] focused on a distal radius of a healthy volunteer, which was imaged along with the two adjacent carpal bones, at a resolution of 165 μm. Bone tissue was assumed to be linear elastic with an isotropic tissue modulus of 10 GPa and the model had about 1.6 millions of elements. The inclusion of the carpal bones and of a cartilage layer between these bones and the radius was done in an effort to improve the boundary conditions for modeling high impact forces resulting from a fall. In fact, the loading scenario at the distal radius is quite complex, and the relative fraction of load coming from the carpal bones (scaphoid and lunate) depends on the specific position of the hand and it is still not too well characterized. Ulrich *et al.*[48] considered different loading scenarios, corresponding to the same applied maximum force of 1000 N and showed that the ratio of the forces acting on the carpal bones had a strong influence on the stresses and strains inside the radius. A quite interesting result was that for all load cases, the location of highest SED absorption was always in a region adjacent to the articular surface. This region well corresponds with locations where radius fractures are observed in clinics.[49] The study of Ulrich *et al.*[48] was probably the first attempt to

estimate tissue-level stress and strain in a living human subject. Subsequently, Pistoia and coworkers[50] investigated the influence of image resolution on the predicted mechanical behavior of bone with μFE. The study showed an excellent correlation between elastic moduli calculated from the pQCT-based models (165 μm) and those calculated from high-resolution μCT (28 μm) based models ($R^2 > 0.95$). They also investigated failure properties and, in particular, strength prediction.[36] For that purpose they combined linear elastic μFE based on pQCT scans with experimental mechanical testing. In the study, 54 human arms from cadavers were scanned with pQCT (voxel size 165 μm) and then tested until failure in a simplified experimental configuration adopted to reproduce the Colles' fractures. The ultimate (or failure) load was defined as the maximum force measured in the experimental tests. Failure loads were also estimated with linear elastic μFE by computing the force required to have a certain percentage of bone tissue loaded beyond the tissue yield strain, which was assumed at 7000 microstrains.[51] The best correlation ($R^2 = 0.75$) between experimentally and computationally determined failure forces was obtained when 2% of the tissue resulted loaded beyond the yield point. The predicted ultimate force, however, was always overestimated by approximately 30%. From a technical point of view, the resolution of the FE analysis could be a first source of inaccuracy. In fact, the voxel size of the first generation *in vivo* systems, like the one used in the study of Pistoia,[36] is 165 μm. This could lead to overestimating trabecular thickness (Tb.Th).[52] Such models would overestimate bone failure loads because, for the same applied load, a network with thicker trabeculae will experience less strain. Clearly, strength prediction is hampered here by the adopted methodology of deriving failure, which is a highly nonlinear phenomenon, from linear elastic analyses. An improvement in failure prediction is foreseen with increasing the resolution and with the inclusion of nonlinear properties in μFE.

Assessing bone strength and fracture risk with HR-pQCT is obviously more promising than with normal pQCT and BMD because of the higher degree of details obtained at the microstructural level. *In vivo* HR-pQCT images of the whole radius are not accessible since in clinical practice only a section of the radius is scanned. If the entire geometry of the radius is not available, one potential concern is whether μFE studies based on only subregions are able to predict bone strength. Additionally, it is not clear which type of boundary conditions should be applied to such subregions since the load transmission from the joint is not taken into account. In two recent works, Mueller *et al.*[53] and Varga *et al.*[54] have explored those issues. The study of Varga *et al.*, for instance, was based on 21 radii which were scanned at 82 μm isotropic voxel size using HR-pQCT. Two different subregions of 9 mm were virtually cut and analyzed with μFE. The first subregion was located in the standard position adopted for clinical scanning at a distance of 9.5 mm from the endplate. The second location was more distal and in contact with the endplate (**Figure 3(a)**). Isotropic and homogeneous tissue properties were used (Young's modulus of 15 GPa and Poisson's ratio of 0.3) and boundary conditions were imposed to simulate compression tests. Concomitantly, experimental mechanical test-to-failure were performed with a setup adopted to reproduce Colles' fractures (**Figure 3(b)**).[55] The strength estimation with FE was done with the threshold method, introduced by Pistoia[36] and previously explained. The authors reported high correlations between experimental and computed strength for both regions ($R^2 = 0.96$ and $R^2 = 0.92$, for the most distal and for the standard location, respectively). From these results, it can be inferred that FE analysis based on single subregions seems very promising for predicting bone strength and, surprisingly, the role of the boundary conditions might be only of second order.

If μFE based on high-resolution images of the radius has to become the standard clinical tool for assessing bone strength and fracture risk, two important issues need further discussion. First, appropriate mechanical procedures to directly estimate bone strength needs to be identified and standardized. Second, the reproducibility of such procedures has to be quantified. The first aspect has been explored by MacNeil and Boyd.[56]

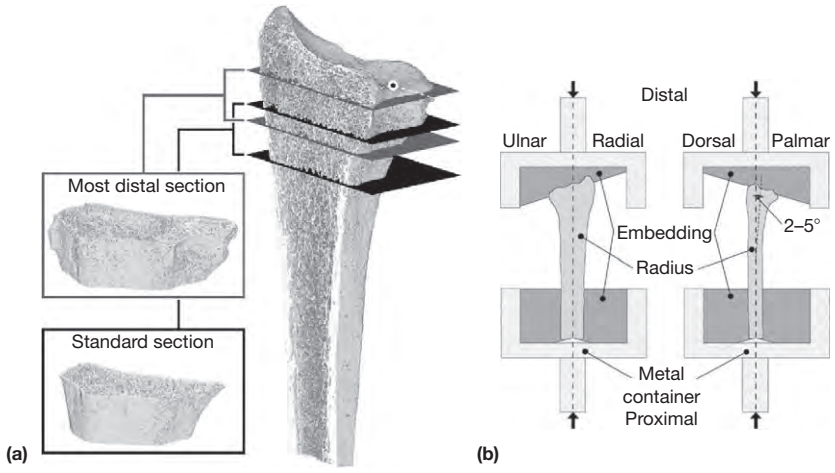

Figure 3 (a) Location of the two regions selected on HR-pQCT of the distal radius. The standard region is measured 9.5 mm away from the endplate whereas a new location is selected more distal and in contact with the endplate. (b) Schematic representation of a setup for mechanical testing of human radii. The specific testing configuration is chosen to reproduce Colles' fractures. Adapted from Varga, P.; Pahr, D. H.; Baumbach, S.; Zysset, P. K. *Bone* **2010**, with permission.

The authors considered the role of various μFE modeling assumptions (e.g., homogenous vs. heterogeneous tissue modulus, linear and nonlinear material behavior) on the simulated strength. μFE models with a homogeneous tissue modulus were compared versus models where the modulus varied locally according to the attenuation values of the CT. Additionally, both linear and nonlinear simulations (using an asymmetric, bilinear yield strain criterion) were run. Direct mechanical compression testing was also performed to have a gold standard value for failure strength. The experimental dataset was not the entire radius but several specimens of approximately 9 mm in thickness cut from several locations in human cadaver radii. The samples were scanned with HR-pQCT (82 μm voxel size) and then tested in uniaxial compression. A typical μFE mesh had approximately 7 millions of elements and was solved in an average of 2.6 h. Also in this study, the apparent elastic properties estimated with linear μFE correlated highly with failure strength, and the correlation was only slightly higher when local tissue moduli were assigned based on CT-attenuation values than when an homogeneous modulus (6.8 GPa) was used ($R^2 = 0.98$ and $R^2 = 0.97$, respectively). The nonlinear analysis was as well in excellent agreement with the experimental strength ($R^2 = 0.95$) and, additionally, it could capture the behavior of the tissue beyond the yield point. Reproducibility of the μFE-based mechanical assessment is the second important aspect which has been investigated by several authors.[57–60] A useful parameter to define the reproducibility is a measurement of the precision error, previously introduced for bone densitometry measurements.[61] Stiffness and strength computed with μFE based on HR-pQCT seems to be highly reproducible, with reported precision error in the range 0.48–2.93%.[59]

In conclusion, considering the recent developments in high-resolution imaging, where the microarchitecture of the distal radius can be easily quantified *in vivo* with a resolution of approximately 80 μm, it is foreseen that μFE based on HR-pQCT imaging might, in the future, be used as a tool for the analysis of bone quality and fracture risk in patient populations.

3.307.2.5. Vertebra

Several FE models of the vertebra have been developed over the last 15–20 years.[62] In analogy with radius and femur, *in silico* research on human vertebrae has been driven by the need for having accurate predictors of strength and risk of fracture which could replace the use of BMD.[63] It is well known that fractures connected with osteoporosis occur frequently in the vertebral body and that increased bone fragility could even lead to a spontaneous collapse of the vertebrae.

3.307.2.5.1. Continuum FE models

In terms of *in vivo* strength assessment and prediction, the current computational state of the art employs continuum FE in conjunction with QCT. This methodology can provide better estimates of vertebral compressive strength than QCT alone. Crawford and colleagues,[26] for example, compared the FE-based bone strength and the QCT-based bone strength against gold standard strength values assessed with experimental tests. In their study the authors considered 13 human vertebral bodies which were scanned with QCT (0.674 mm pixel size). The QCT voxel values were converted into elastic moduli (along the vertical direction) using a simple linear correlation between elastic modulus and mineral density.[64] The material behavior was assumed transversely isotropic and the remaining elastic constants were derived accordingly. The resulting FE models were heterogeneous at the material level: microstructural details were not directly considered but the models were able to detect lower Young's modulus in the core of the vertebra, which reflects the presence of the porous cancellous bone (Figure 4). The vertebral strength was positively correlated with the FE measures of strength ($R^2 = 0.86$) and only poorly correlated with BMD values ($R^2 = 0.53$). Although the study has several limitations, it is one of the first works that has demonstrated the better performance of FE models with respect to correlation-based QCT methods in predicting vertebral compressive strength. Improvement in the prediction of the mechanical behavior (also considering off-axis loading) can be obtained by employing more complex material laws. Chevalier *et al.*[65] used a calibration method to derive local bone volume fraction (BV/TV) from BMD values and a fabric-based model[66] was adapted to convert local voxel volume fractions into elastic values. With this novel procedure, each element of the FE model carries information on local elasticity as well as on the anisotropy of the trabecular network. The prediction of the ultimate force from the FE models was again linearly related to the experimental values ($R^2 = 0.77$) but this time the slopes and intercepts of the linear regression equation

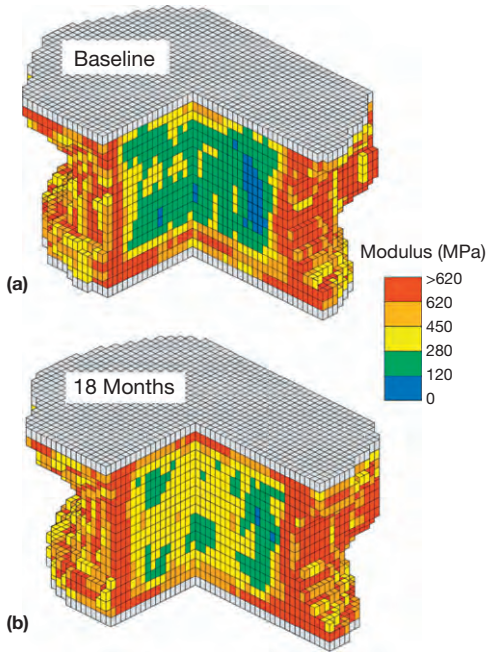

Figure 4 Continuum-level finite element models of a lumbar vertebra scanned *in vivo* with quantitative computed tomography (QCT) (a) at the base line and (b) after 18 months of anabolic treatment. Each element in the FE model is assigned a different Young's modulus based on the gray values of the QCT. The osteoporotic treatment alters the distribution of density within the vertebra, as seen by comparing (a) and (b).
Adapted from Keaveny, T. M.; Donley, D. W.; Hoffmann, P. F.; Mitlak, B. H.; Glass, E. V.; San Martin, J. A. *J. Bone Miner. Res.* **2007**, *22*, 149–157, with permission.

were not significantly different from 1 and 0, respectively. This is an important result which means that FE can predict bone strength in an absolute sense, without any need of additional correction factors. In the same study, the authors also extended the use of continuum FE for investigating the location and accumulation of damage during different applied loads. For this purpose, a newly developed constitutive law for elasticity, plasticity, and damage was employed.[67] It could be shown that, independent from the loading modes, damage accumulation always occurred in the vertebral core, where trabecular bone is located.

Recently, the FE framework based on QCT has been used to evaluate the effectiveness of various osteoporotic therapies.[68–70] In all the investigated scenarios the FE approach provided more information on the effects of osteoporotic treatments than only BMD. For instance, Keaveny and coworkers[70] compared the effect of an anabolic agent (teriparatide) versus an antiresorptive therapy (with alendronate) in a study on human patients. A total of 53 subjects were considered and QCT scans were taken before starting the treatment and after 18 months of treatment. For all the subjects the compressive strength of the L3 vertebra was assessed with continuum-level FE modeling (Figure 4). The two treatments changed BMD and strength in a quite different way: the median percentage increase for the anabolic agent was significantly greater than for the antiresorptive one (13.0% and 4.9%, respectively). In addition, the anabolic agent increased the vertebral strength not only by increasing BMD but also by altering the distribution of density within the vertebra. In conclusion, FE studies have been able to overcome the limitations of BMD in discriminating vertebral fracture and can more precisely evaluate the effects of treatments.

3.307.2.5.2. μFE models

μFE methods require high-resolution images, which are currently not available *in vivo* for the vertebra. However, this technique has been fundamental to understand the micromechanical behavior of vertebral bone and also bone adaption in healthy and diseased situations.[32,33,71–73] Two novel studies[32,71] explored the relative contribution of the cortical shell and of the vertebral core in the mechanical properties of the vertebra. For these studies, 13 human vertebrae were scanned with μCT (voxel size 60 μm) and the corresponding specimen-specific FE models (with more than 13 million elements) were generated. An automated image processing procedure was developed to identify and digitally separate the cortical shell; compression tests were simulated with and without the cortical shell. Despite its thin nature (average thickness of 0.38 ± 0.06 mm), the shell had a predominant role in the load transfer mechanism: at the narrowest section of the vertebrae, the shell carried between 38 and 54% of the load.[32] Such improved understanding of the biomechanics of the vertebra may be beneficial for identifying changes occurring with aging, diseases, and after clinical treatments.

3.307.3. Mesoscale: Trabecular Bone

As described in Section 3.307.1, a distinction is made between cortical and trabecular bone. Trabecular bone, also called cancellous bone, is found at the end of long bones as well as in the spine. It has a complex internal network of small rod-like and plate-like struts called trabeculae. Depending on the specific location, trabecular bone can have quite different microarchitectures, even within one subject (Figure 5(a)). In addition, even at the same location cancellous bone can have a variety of densities and morphologies among different individuals depending on age, genetics, and disease-related aspects (Figure 5(b)). The mechanical properties of trabecular bone, which also vary a lot with anatomical location, age and disease, depend on three main factors: apparent density, internal microarchitecture, and local tissue properties. For the same apparent density, a large variability in stiffness and strength has been reported which might be due to the specific role of microarchitecture and of material properties. A better understanding of the interplay among these three factors is of high importance, especially for the clinical assessment of bone fragility and fracture risk as well as for the design of new scaffolds and implants for osteoporotic bone. In fact, bone fractures associated with osteoporosis, occur frequently in anatomical locations dominated by trabecular bone, like the femoral head, the vertebral body, and the radius (Section 3.307.2). The complex mechanical behavior of trabecular bone has been extensively investigated with computational models based on FEA for the last 20 years. In particular, two different types of modeling approaches have been considered.[46] The first approach, more conceptual and based on cellular solids theories, will be reviewed in Section 3.307.3.1; the second one, more recent, adopts μFE combined with high-resolution images and it will be introduced in Section 3.307.3.2.

3.307.3.1. Conceptual Cellular Solids Modeling

The main philosophy of the cellular solids approach is to reduce the complexity of the trabecular network while still being able to describe its most relevant micromechanical aspects. The reduction in complexity is carried out by mapping only certain aspects of the trabecular network into simplified two- or three-dimensional lattice models. The microstructure of a cellular solids model is often composed of a collection of elements (or beams) which have in general the same shape but different length and thickness. The elements can be regularly arranged in space (e.g., periodic honeycombs) or can have a more random distribution (e.g., Voronoi honeycombs). From a computational point of view, such models can be efficiently solved with coarse-grained FEA based on beam elements. In short, compared to continuum-level FE and μFE models, each beam inside a cellular solid structure is modeled with special purpose elements called beam elements which allow only for specific deformation modes (typically bending, stretching, and shear deformations) and therefore can greatly reduce the number of degrees of freedom of the models. In addition, with such idealized representations of the trabecular architecture, it is feasible to introduce controlled variations in given architectural parameters and to assess their impact on the mechanical performance. In this section, we will focus on the main questions related to bone research which have been addressed with cellular solids modeling.

3.307.3.1.1. Role of architectural disorder and defects

The architecture of trabecular bone is neither completely regular nor random[2] and cellular solid models have been used to

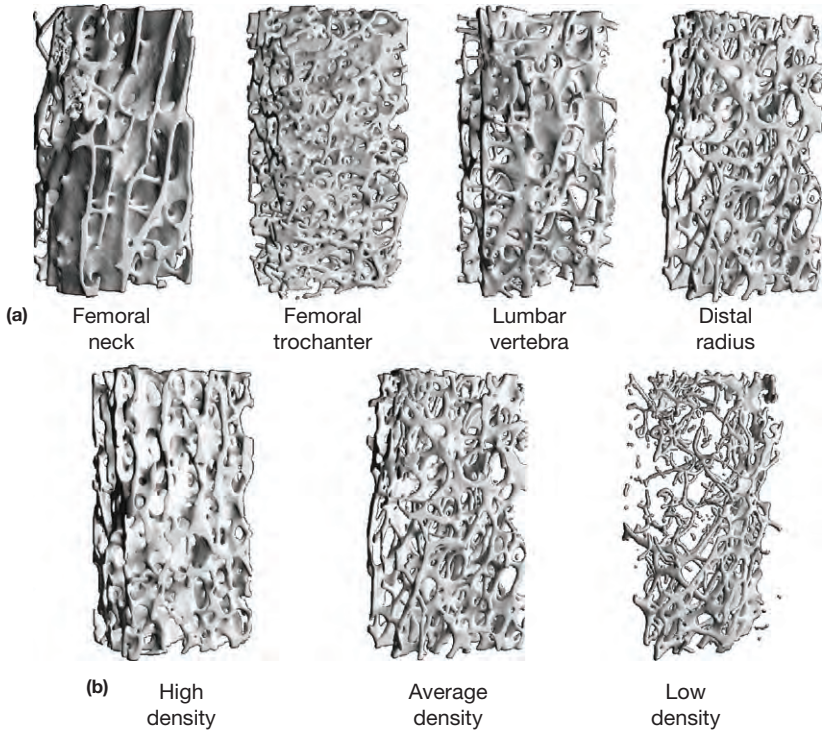

Figure 5 Three-dimensional microcomputed tomography reconstructions of trabecular specimens from various skeletal locations (a) within the same individual and (b) at the same location (distal radius) among different individuals. Within the same subject, trabecular bone can have quite different relative densities and microarchitectures: from very dense plate-like structure (e.g., femoral neck) to a combination of rod-like and plate-like network (e.g., distal radius). At the same skeletal location, the microarchitecture of trabecular bone is subject-specific and it is influenced by factors like age and health status. Dense trabecular specimens are often seen in young and healthy people, whereas with aging or osteoporosis the trabecular network becomes coarser and the plates transform into rods. Data courtesy of Felix Eckstein, Ludwig-Maximilians-University Munich, Germany.

investigate the effect of different degrees of randomness (or disorder) on apparent stiffness and strength of various types of architectures including honeycomb, Voronoi, and cubic lattices.[74–77] In two-dimensional Voronoi honeycombs, introducing structural disorder (in terms of nonperiodic microstructure) weakened the structure at the apparent level and the Voronoi honeycombs resulted approximately 30% less strong than periodic, hexagonal honeycombs of the same density.[76] At the local level of single beams, the nonperiodic microstructure affected the strain distribution: higher strains were seen in a relatively small number of struts compared to periodic, hexagonal honeycombs.[76] In addition, in Voronoi honeycombs, the axial strains in the cell walls have been found to be approximately normally distributed.[78] In general, the redistribution of forces inside a cellular structure depends critically on the degree of randomness of the structure, with increasing randomness resulting in a broader distribution.[79] The effect of randomness is different in three-dimensional regular cubic lattices. In fact, these regular structures are highly ordered and, consequently, extremely sensitive to both strain localization and orientation effects.[80] Luxner and colleagues[75] showed that introducing some disorder had a positive mechanical outcome since it reduced the tendency of deformation localization (**Figure 6**) and it decreased the strong anisotropy of the cubic lattice. Interpreting these results for trabecular bone structures, one could assume that some disorder in the arrangement of trabeculae might be beneficial to prevent or retard catastrophic failure.[75] In addition to disorder, the role of defects on the local and the apparent mechanical properties of cellular solids has also been intensively analyzed with FE. In particular, different types of morphological imperfections such as struts waviness, struts misalignment, and missing struts, have been considered. Chen and coworkers[81,82] and performed systematic studies to investigate the role of different types of defects and imperfections on the apparent properties of two-dimensional cellular solids. The authors unraveled a link between the reduction in the mechanical properties and the switching in the main deformation mechanisms from stretching to bending induced by the defects. The largest reduction in the apparent yield of the models was caused by fractured struts whereas variation in the thickness of the beam had only second-order effects. Other authors have considered the load distribution around defects.[83,84] Ruffoni and coworkers,[84] for example, studied the relationship between the geometry of a point defect and the spatial distribution of the SED in an otherwise regular two-dimensional honeycomb. For hydrostatic loading, the SED was concentrated in the defect; conversely, uniaxial loading resulted in intricate distribution of the SED, with its highest values not in the defect but in its nearer environment. Sites of concentrated loading might be potential locations for failure initiation and thus, to understand the weakening of a structure they need to be investigated.

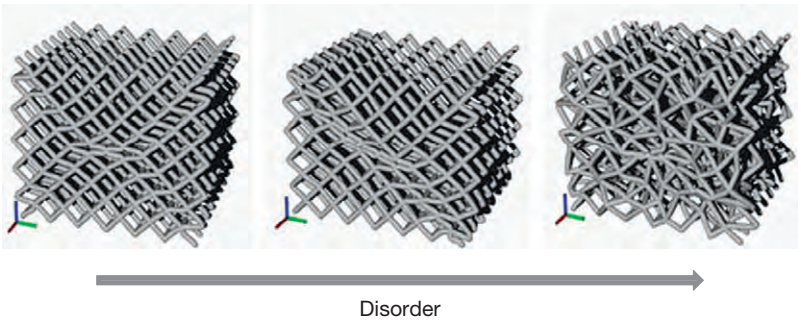

Figure 6 FE simulations of cubic lattices with increasing disorder (from left to right). The disorder is introduced by adding a random displacement to the original position of the vertices of the regular cubic lattice. Failure bands which represent highly localized deformations can be seen in the first structure; increasing the amount of disorder strengthens the structures by preventing the formation of localized failure regions. Adapted from Luxner, M. H.; Woesz, A.; Stampfl, J.; Fratzl, P.; Pettermann, H. E. *Acta Biomater.* **2009**, *5*, 381–390, with permission.

3.307.3.1.2. Trabecular thinning versus trabecular loss

Trabecular architecture changes with age and bone is lost due to a reduction in the number of trabeculae as well as to thinning of trabeculae.[85] An important clinical issue connected with these changes is which of the two mechanisms (thinning vs. loss) causes the strongest reduction in bone strength for a similar amount of bone loss. Various computational studies on two- and three-dimensional cellular solids models have predicted trabecular loss as the worst scenario for the mechanical properties.[76,86] Guo and Kim[87] considered both rod-like and plate-like cellular architectures and, assuming an elasto-plastic material law, they were able to predict the behavior of both stiffness and strength following bone loss. Independently of the model microstructure (plate-like or rod-like), stiffness and strength were much more reduced when the reduction in BV/TV occurred through loss of trabeculae than through trabeculae thinning. In addition, the authors considered whether increasing the thickness of the remaining trabeculae after bone loss could recover the initial stiffness and strength of the system; that was not the case. Hence, to improve the clinical outcome of osteoporotic treatments it might be fundamental to start osteoporotic therapies at early stages, in order to preserve trabecular number (Tb.N) and connectivity.

3.307.3.1.3. Towards patient-specific stiffness and strength predictions

A recent study of van Lenthe *et al.*[88] has demonstrated the feasibility to apply cellular solids models to predict the mechanical behavior of trabecular bone specimens in a fast and accurate way. In order to generate a cellular solids model starting from high-resolution μCT images of trabecular bone, the first step is to decompose the trabecular network into its basic rod and plate elements. Slightly different procedures to obtain this decomposition have been presented.[89–91] In short, decomposition starts with a shape preserving skeletonization algorithm with a topological optimization procedure which is applied on a digital image of trabecular bone (**Figure 7(a)**). As a result, the bone architecture is reduced to a one-voxel thick skeleton. Subsequently a point classification algorithm which is able to say, for each point in the skeleton, whether it belonged to a rod or to a plate, is employed (**Figure 7(b)**). Eventually, according to this new classification, a final algorithm is utilized to expand the elements of the skeleton to their original size. This operation results in a spatially decomposed bone structure where rods and plates are labeled with a different color (**Figure 7(c)**). The structure can then be used to generate beam FE models. van Lenthe *et al.*[88] modeled each rod with one beam (circular cross-section) with length and thickness corresponding to the average morphometric values of the single element to be represented; for plates several crossing beams forming a shell-like structure were used (**Figure 7(d)**). In the study, the same μCT images were also directly converted into μFE and both models were solved with the same boundary conditions simulating uniaxial compression tests. Experimental compression tests were also performed to have gold standard measures for the apparent stiffness and strength of the specimens. The main advantage of the idealized approach is the reduction of the computational complexity of the models: the beam FE presented, with respect to high-resolution μFE, a reduction by two orders of magnitude of the number of nodes, which corresponded to 1000-fold reductions in CPUs time.[88] Despite the strong reduction in the complexity of the trabecular network, the 'coarse-grained' beam FE models introduced in that study were in excellent agreement with the results of both experimental and voxel-based FE models ($R^2 = 0.85$ and $R^2 = 0.97$, respectively; **Figure 7(e)**). Hence, the beam representation seems to be detailed enough to accurately estimate the overall mechanical properties and the deformation mechanisms of the samples.

3.307.3.2. μFE Modeling

As extensively explained throughout **Section 3.307.2**, μFE are based on high-resolution images obtained for instance with μCT or μMRI. Considering trabecular bone specimens, those images are three-dimensional virtual reconstructions with a resolution up to 10 μm. μFE have been widely used to investigate the mechanical properties of trabecular bone, with a special focus in linking mechanical behavior to microstructural characteristics. In this section, we will review the main modeling assumptions and the main findings of μFE modeling of trabecular bone.

3.307.3.2.1. Homogeneous versus heterogeneous tissue at the trabecular level

In most of the μFE studies on trabecular bone (likewise on whole bone, **Section 3.307.2**), trabecular tissue is normally considered homogeneous and isotropic and each element is

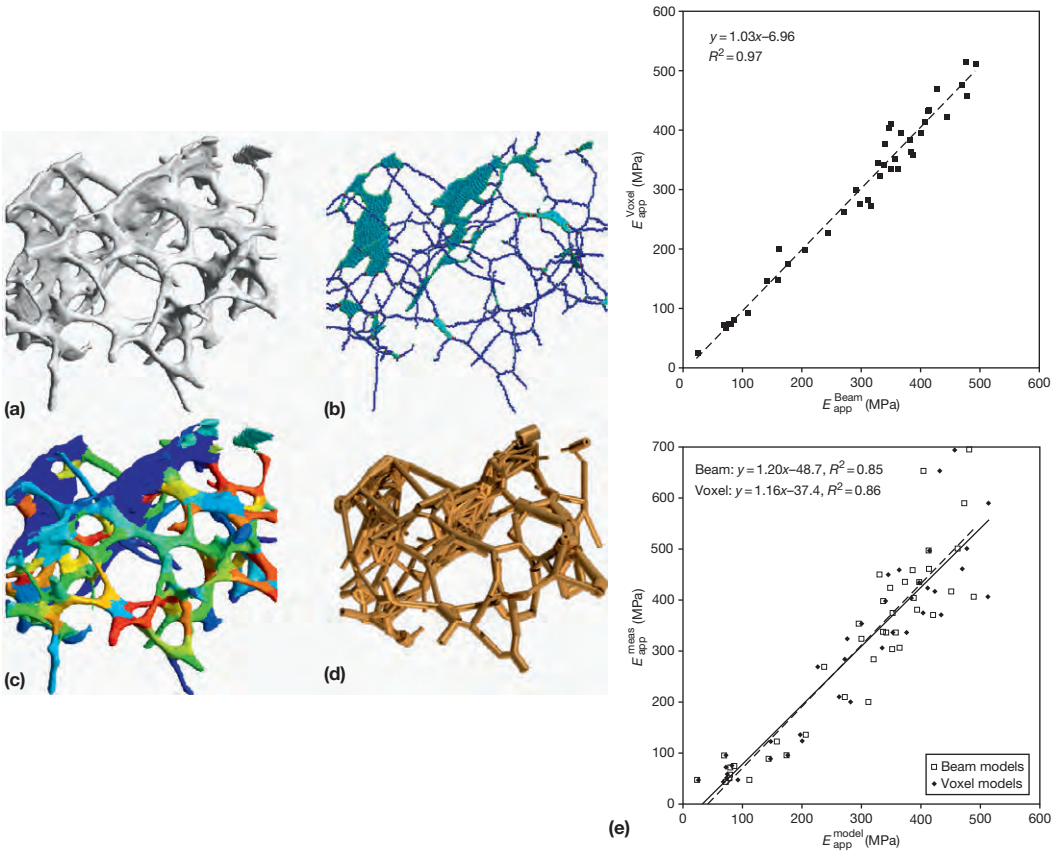

Figure 7 The procedure to generate a specimen-specific beam finite element model comprises various steps: (a) starting from a microcomputed tomography image of a trabecular bone specimen, (b) skeletonization and point classification are applied. Subsequently (c) an algorithm for multicolor dilation is used and (d) local values for thickness and volume of each decomposed trabecular element are then assigned to the beam model. Finally (e) the performance of the beam finite element model (in terms of stiffness) can be compared against predictions of high-resolution micro-finite element ($R^2 = 0.97$) and experimental results ($R^2 = 0.85$). Adapted from Van Lenthe, G. H.; Stauber, M.; Müller, R. *Bone* **2006**, *39*, 1182–1189, with permission.

given the same Young's modulus. This assumption is accurate enough for predicting the apparent elastic properties of trabecular bone specimen, as reported by several authors.[30,35,92,93] By comparing experimental versus μFE models is even possible to derive an apparent or effective modulus for the trabecular tissue. With such procedure different values for Young's modulus have been reported in the range 5–18 GPa. Most probably this wide range reflects natural biological variability (e.g., anatomical site, age) as well as differences in the experimental techniques, specimen size and element size.[16,46] Whereas for quantifying the elastic properties at the apparent level an effective tissue modulus works well, when considering the mechanical behavior of individual trabeculae this assumption might not be too accurate. In fact, trabecular tissue is quite heterogeneous and anisotropic; as a result of bone remodeling and mineralization, the trabeculae appear like a patchwork of different bone packets which have different mineral contents (**Figure 8**)[94,95] and different elastic moduli, as indicated by nanoindentation.[96] In addition, the distribution of the mineral content changes in osteoporotic patients (which have less mineral content and a strong heterogeneous distribution of the mineral) and after clinical antiresorptive therapies.[97] The effect of material inhomogeneity could be taken into account with μFE by assigning at each bone element a different tissue modulus; nevertheless, this procedure, especially at the trabecular level, is still quite controversial because of the following two issues. First, it is not clear how to correctly convert the gray levels of a μCT image into proper mineral contents. One adopted solution has been to consider gray values proportional to the local mineral content after a proper calibration with phantoms containing different known concentrations of hydroxyapatite.[98,99] Even if calibration procedures are implemented, the voxel values of μCT images are still somewhat influenced by image artifacts like beam hardening and they can only give qualitative information on mineral content.[100,101] In spite of these difficulties, the assessment of bone mineral content with μCT is a fascinating possibility and a lot of research is currently ongoing. The second uncertainty is the relationship between local mineral content and local elastic properties. Previous μFE studies have demonstrated that the nonuniform mineral distribution as well as the specific law used to correlate mineral content with Young's modulus can have a significant effect on the mechanical behavior computed with μFE.[102,103] Van der Linden *et al.*[103] considered trabecular specimens coming from human vertebrae and employed different relationships between mineral content

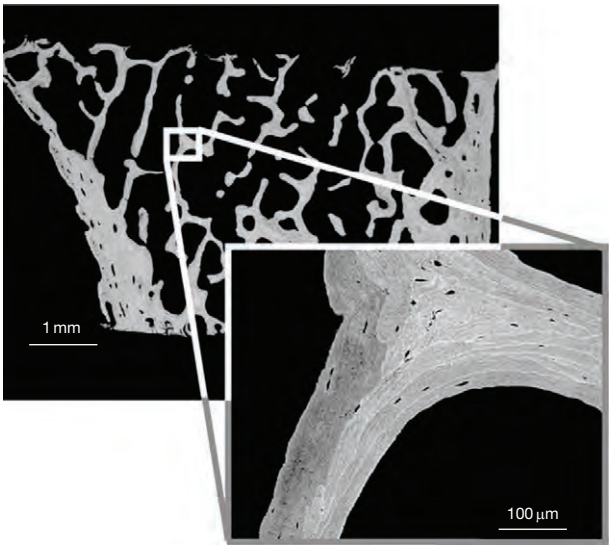

Figure 8 Section of a transiliac bone biopsy visualized with back-scattered electron imaging (BEI). The gray-level values are directly proportional to local mineral content. By increasing the resolution, the individual bone packets inside a trabecula can be seen. Each bone packet has different mineral content due to the processes of bone remodeling and mineralization. Dark gray represents young low mineralized bone and light gray means old high mineralized bone. Adapted from Ruffoni, D.; Fratzl, P.; Roschger, P.; Klaushofer, K.; Weinkamer, R. *Bone* **2007**, *40*, 1308–1319, with permission.

and Young's modulus. For a linear relationship, the apparent stiffness of the specimens varied only slightly (up to 8%) compared to the uniform tissue model. Instead, with an exponential law, the apparent stiffness varied up to 20%. Results along the same line have been obtained considering trabecular samples coming from human mandibles: the incorporation of different mineralization values decreased the apparent elastic moduli to a maximum of 21% in comparison to the homogeneous models.[102] More insights into the correlation between mineral content and tissue stiffness has been obtained experimentally by combining nanoindentation[96] with accurate measures of local mineral content by means of back-scattered electron imaging (BEI).[104] In conclusion, µFE modeling provides excellent estimates of trabecular bone mechanical properties when considered at a scale where it behaves as a continuum. Whether it currently provides the same accuracy at the level of single trabeculae still remains to be established. For that purpose, more studies which combine µFE with accurate experimental measures of local mineral content and local tissue moduli are needed; it appears that the heterogeneous material distributions as seen in trabeculae could have a strong effect on the mechanism of deformation and failure especially for those trabeculae subjected to large deformations.

3.307.3.2.2. Failure properties

Although some work on bone failure characteristics with µFE has been performed on whole bone (or at least on large parts of entire bones, Section 3.307.2.4), the trabecular level – for obvious computational aspects – is still considered the preferred one for such types of investigations. Even at the trabecular level, only a few studies have incorporated nonlinear material properties in FE analysis in an attempt to better describe and understand bone failure.[16] No consensus has been reached as to what would be the best implementation of bone failure in µFE. This is not surprising because the precise failure mechanism and associated material properties (especially after yielding) of trabecular bone are still not well understood. One of the first attempts to add nonlinear material behavior to µFE analysis was done by Niebur and coworkers.[51] They proposed a bilinear constitutive model with asymmetric tissue yield strains in tension and compression, including a reduction of the tissue modulus by 95% after yield strains. The values of the yield strains could be obtained by a direct comparison with experimental testing and were 0.60% in tension and 1.01% in compression. The authors demonstrated that the proposed model, along with the assumption that yield properties were the same for all the considered specimens (trabecular samples coming from bovine tibias) was able to accurately describe the apparent yield in compression, tension, and shear. In addition to material nonlinearity, Stölken and Kinney[105] performed a computational study on a single trabecula and showed that local deformations could be very large. Therefore, also geometrical nonlinearity should be accounted for. Recently, more complex postyield behavior has also started to be characterized. Verhulp and colleagues,[106] for instance, introduced an iterative fitting procedure in order to determine the set of parameters to be used in µFE simulations to have the best agreement with experimental linear and failure results. In the study they considered both material and geometrical nonlinear behavior combined with µFE. It was found that accurate descriptions of the experimental compression tests were obtained by including a negative postyield modulus (compression softening) at the tissue level. Furthermore, variations in the postyield properties were less important than variations in the elastic and yield properties for the simulated apparent mechanical behavior.

3.307.3.2.3. Structural and mechanical anisotropy

µFE is a valuable tool to investigate the directional dependence of the mechanical properties of trabecular bone. It has been demonstrated that trabecular bone has an anisotropic behavior which is mainly governed by the orientation of the trabeculae[16]; hence, bone anisotropy has been mainly investigated at the trabecular level. The main advantage of µFE over more traditional experimental testing is that virtual mechanical tests can be run always on the same specimen in order to measure the apparent elastic properties along different directions. Using µFE it has been found that trabecular bone can be well described as an orthotropic material with nine independent parameters.[107] The orthotropic parameters can be determined by running only six FE simulations. Here, FE expands experimental techniques, because, accurate measurements of the orthotropic elastic constants of a given trabecular specimen with experimental mechanical testing are extremely difficult if not impossible. Mechanical anisotropy of trabecular bone is a manifestation of its structural anisotropy. Structural anisotropy has been characterized with the fabric tensor which is defined as a symmetric second-order tensor.[66] Various methods have been proposed to measure structural anisotropy and one of the most common is with the mean intercept length (MIL).[108]

The idea of the MIL method is to superimpose a linear grid with different orientations on a bone section; for each orientation, the mean length of the intersections between the grid and the bone–marrow interface is computed. A plot of the MIL as a function of the grid orientation can, in two dimensions, be fitted well by an ellipse and in three dimensions by an ellipsoid. The eigenvalues of the fabric tensor correspond to the principal axis of the ellipsoid and are used to describe bone structural anisotropy. μFE simulations has been employed to establish the relationships between the stiffness tensor and the fabric tensor in human cancellous bone samples.[66,109]

3.307.3.2.4. The role of structural indices

A main application of μFE modeling based on realistic trabecular geometries is the investigation of the relationship between mechanical properties and architectural features like BV/TV, anisotropy (fabric tensor), Tb.Th, Tb.N, trabecular separation (Tb.Sp), and connectivity. This topic is closely related to clinical research, in particular to the task of predicting in a robust manner bone fragility by looking at microarchitectural measures. One way to asses to which extent the use of architectural descriptors, in addition to BMD, improves the prediction of bone mechanical properties is to correlate the results of μFE calculations with geometrical measures based, for instance, on μCT images. Ulrich and coworkers[110] investigated more than 200 different cancellous bone samples taken from the iliac crest, lumbar spine, femoral head, and calcaneus and computed different geometrical parameters (BV/TV, Tb.Th, Tb.Sp, Tb.N, fabric tensor) as well as the mechanical competence of those samples (Young's moduli, shear moduli, and Poisson's ratios). The main finding of the study was that the prediction of mechanical properties increased from a value of 53% when considering only BV/TV (which is related to BMD) to 82% just by adding the anisotropy of the structure described by the fabric tensor. A maximum correlation of 92% was obtained with three parameters: BV/TV, Tb.Sp, and fabric tensor. Despite the promising evidence that including various architectural parameters (in addition to BMD) resulted in strong correlation with bone mechanical properties (stiffness), these results should be interpreted only in a statistical sense. They do not explain the real physical contribution of the microarchitecture to the mechanical behavior of bone. In fact, to understand how differences in bone microarchitecture influence bone stiffness and strength, insight into load transfer through the bone architecture is needed.[59] Additionally, it is not possible to find a general mathematical formulation that links structural indices and mechanics since the combinations of the structural parameters are strongly depended on anatomical sites.[111]

Considering connectivity, its role is still quite debated. Theoretical considerations based on cellular solids predict that connectivity strongly influences the main deformation modes. If a three-dimensional network has connectivity less than 12, its architecture is bending dominated and therefore quite soft. Conversely, if the connectivity is bigger than 12, the deformation mode becomes stretching dominated and hence the stiffness of the structure increases substantially.[2,112] In simple cellular solids the connectivity coincides with the coordination number, that is, the number of struts which meet at a node, whereas for more complex networks like trabecular bone, the definition of connectivity is more complicated. Intuitively connectivity describes the number of redundant trabeculae in the network, that is, the number of trabeculae that may be cut without increasing the numbers of separate parts in the bone structure.[113] Connectivity is a general topological property of a network and can be calculated through the Euler number. In a voxel-based image, the Euler number is computed by looking at the voxel filled with bone and combining the number of voxel corners, voxel edges, voxel faces, and voxel volumes inside a given volume of interest.[113] In addition, a correction for the artificially unconnected trabeculae that are generated when analyzing only a subregion of the entire trabecular network needs to be performed.[113] Interestingly, studies using μFE on human trabecular samples from various anatomical regions have reported no relationship between stiffness and connectivity.[114,115] One possible reason for this lack of correlation could be associated to the presence of both rod-like and plate-like structures inside the trabecular network. If during bone remodeling a plate is perforated, most probably the stiffness of the structure will decrease whereas the connectivity will increase as the fenestrated plate will be considered as a combination of new rods.[115] In addition, the high connectivity values of artificial structures are never present in trabecular bone. For example, in vertebral trabecular bone, the trabeculae are mainly oriented along the horizontal and the vertical direction which results in quite low connectivity values. Trabeculae that run diagonally though the vertebrae and hence that would substantially increase the connectivity are not observed.[2]

3.307.3.2.5. Mechanical behavior of single rods and plates

The relative amount of rods and plates in the trabecular network is another important determinant of the mechanical behavior of cancellous bone.[116,117] It is known that trabecular bone morphology is more plate-like for high volume fraction and more rod-like for low-volume fraction.[118] Additionally, with aging bone plates get perforated and therefore plate-like architectures tend to become more rod-like.[118] As reported in **Section 3.307.3.1**, various algorithms have been recently proposed to decompose the trabecular structure into basic rod and plate elements.[90,91] Such procedures, combined with newly developed local morphological descriptors for rods and plates, have been applied by Stauber and coworkers[117] to a cohort of 42 human vertebral trabecular bone samples to assess the role of local morphometry (i.e., the shape and form of each single bone element) in the measurement of bone architecture and its relative contribution to the mechanics of human vertebral bone. Specifically, the apparent Young's modulus of the trabecular specimens has been computed both with direct experimental compression testing and with μFE; the two methods correlated quite well ($R^2 = 0.85$). Furthermore, the authors proposed a multiple linear regression model based on local morphology which included mean trabecular spacing, mean slenderness of the rods, and the relative rod volume fraction and which was able to predict up to 90% of the variance of the computed apparent Young's moduli.[117] Liu and colleagues[89] have applied volumetric decomposition to better understand the influence of rods and plates on the anisotropic elastic properties of trabecular bone. The authors included bone specimens from femoral neck, tibia, and vertebral body. They reported significant differences in the relative arrangements of rods and plates: the majority of trabecular

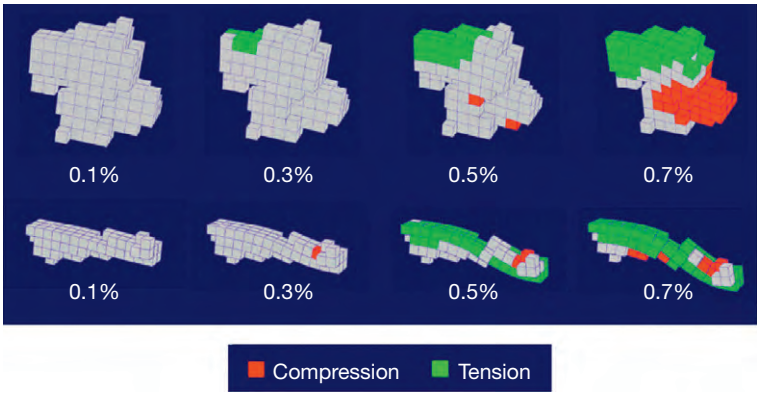

Figure 9 Qualitative visualization of failure in a plate (top) and a rod (bottom) during a simulated uniaxial compression test with microstructural finite element on a trabecular bone specimen. The plate and the rod had different orientations with respect to the main loading direction: the plate was oriented longitudinally whereas the rod was oriented transversally. The elements which failed in tension (colored greed) and compression (colored red) can be visualized for different values of the applied apparent strain. Adapted from Liu, X. S.; Bevill, G.; Keaveny, T. M.; Sajda, P.; Guo, X. E. *J. Biomech*. **2009**, *42*, 249–256, with permission.

plates were orientated along the principal direction of loading, whereas most of trabecular rods serve as transverse connections between longitudinal plates.[89] In a subsequent study, Liu and collaborators,[116] analyzed the micromechanical behavior of trabecular bone in terms of failure initiation and progression considering individual rod and plate elements. The novelty of the study resides in the combination of local trabecular decomposition with nonlinear μFE. The authors performed virtual compression tests on 15 human vertebral trabecular bone samples up to 1% apparent strain. The amount of failed trabecular plates and rods were recorded during loading and data were classified according to the trabecular orientation (Figure 9). Results indicated that trabecular rods tended to fail at the initiation of the compression (i.e., 0.1–0.2% apparent strain) whereas plates failed around the apparent yield point (i.e., 0.7% apparent strain). Interestingly, there was a strong correlation between the volume fraction of plates and the apparent yield strength whereas the volume fraction of rods was only poorly related with the yielding. Considering orientations, the weakest elements where most of the tissue failure was observed were longitudinal trabecular plates and transverse rods.

In conclusion, studies combining local decomposition in rods and plates with μFE seem quite promising to get a better picture of the role of architecture on deformations and failure in trabecular bone.

3.307.4. Microscale: Ultrastructural Features

At a length scale of about 1–3 μm bone ultrastructure becomes visible. In cortical bone the main ultrastructural features are the canal network and the osteocyte lacunae (Figure 10(a) and 10 (b)). Osteocyte lacunae are small holes inside the mineralized bone matrix containing a type of bone cell called osteocyte. Osteocytes are connected to each other and to the canal network through long processes located in small channels called canaliculi. These canaliculi have a diameter of about hundred nanometers. Bone canals are much bigger than osteocyte lacunae and they enclose blood vessels and nerves. The porosity of human cortical bone can vary quite a lot and values in the range from 5 to 38% have been measured using synchrotron radiation-based μCT (SR μCT).[119] The canal network gives the main contribution to cortical porosity and morphological descriptors of this intricate system, such as canal volume, canal diameter, canal length, and canal orientation, have been introduced.[120] In addition to canal network, the osteocyte lacunae have also been visualized and analyzed with respect to number and shape.[120,121] Those ultrastructural characteristics have been shown to influence the mechanical behavior of whole bones[122] as well as the initiation and propagations of cracks in the bone matrix.[123,124] In addition, osteocytes are believed to act as sensors which transform mechanical inputs into biological signals.[125] Hence, both for structural and biological aspects, it is of primary interest to characterize the mechanical environment around osteocyte lacunae as well as their microstructural response under loading.[126,127]

3.307.4.1. Osteocyte Lacunae

FE modeling can be employed to compute the stresses and strains around osteocyte lacunae. Recently, Bonivtch and colleagues[128] performed a parametric FE study of an idealized osteocyte lacuna modeled as an ellipsoid (Figure 10(c)). In addition to the lacuna geometry, the authors considered the role of canalicular diameters, perilacunar tissue modulus, and perilacunar tissue thickness. The main aim of the study was to compute the strain amplification factor (i.e., the ratio between the maximum strain around the lacuna and the applied strain) in the tissue due to the presence of the lacuna. Linear elastic FE analysis were performed and a deformation of 2000 microstrains was imposed; it is believed that this value might be close to the maximum physiological strain experienced in human long bones.[129] The maximum strain amplification factor predicted with the model was around 3. The presence of the canaliculi substantially contributed to increase the computed strains around the lacuna. Decreasing the perilacunar tissue modulus increased the

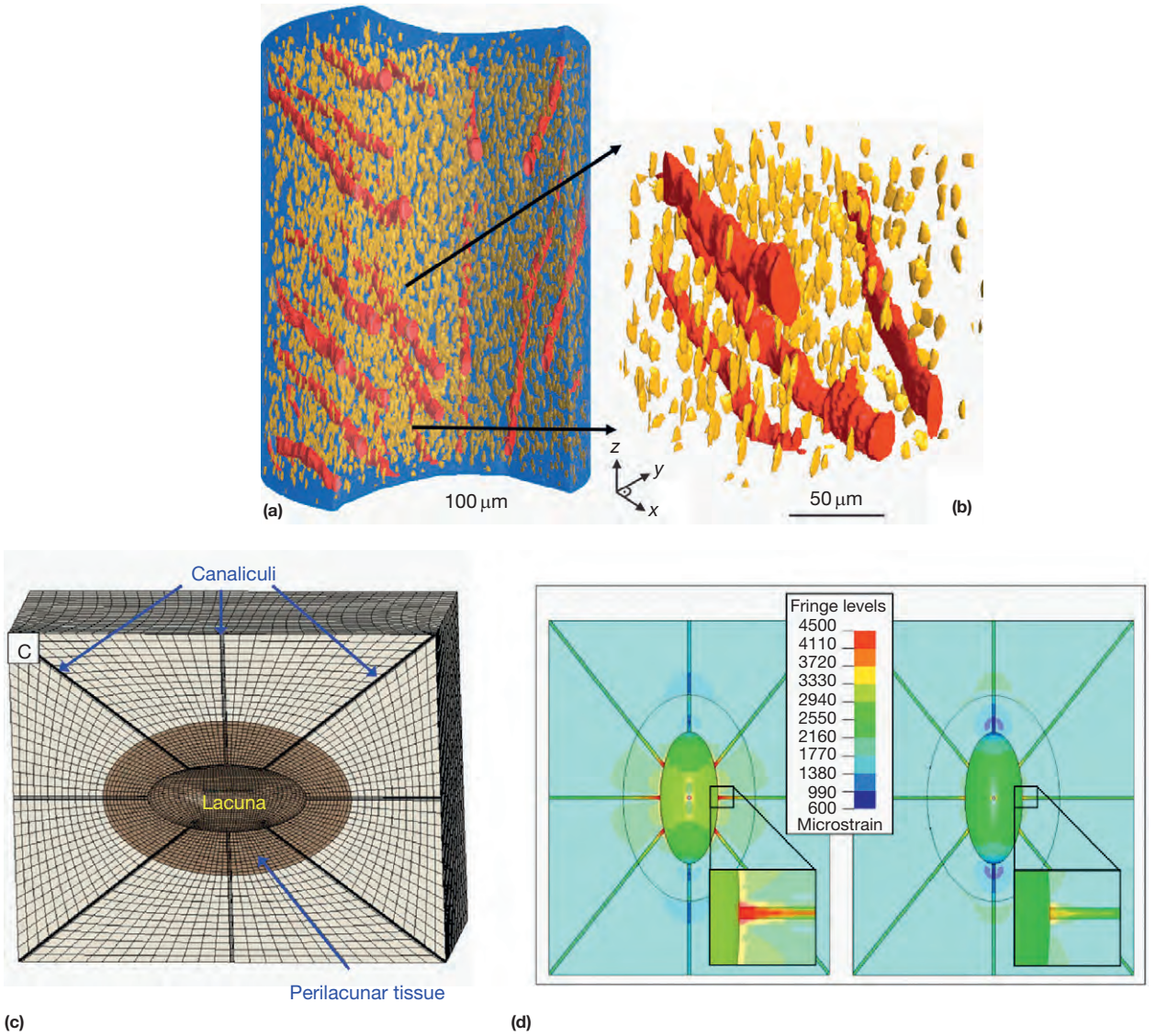

Figure 10 The ultrastractural features of cortical bone at a resolution of 700 nm measured with synchrotron radiation nanocomputed tomography. (a) Three-dimensional visualization of a cortical subregion in a mouse femur with the canal network (red) and osteocyte lacunae (yellow). (b) Close-up on the three-dimensional arrangement of lacunae and canals obtained by inverting the background voxel with the image voxel (negative imaging). (c) Finite element mesh for a region around an osteocyte lacuna including the lacuna, the perilacunar tissue, and the canaliculi. The tissue in close proximity to the lacuna (dark gray) is modeled with different material properties than the tissue further away from the lacuna (light gray). (d) Contour plots of the microstrains computed with FE simulations in the perilacunar region. Strain concentration is observed at the junction between lacuna and canaliculi. In addition, a low perilacunar modulus (left) causes higher strains than a high modulus (right). Adapted from Schneider, P.; Stauber, M.; Voide, R.; Stampanoni, M.; Donahue, L. R.; Müller, R. *J. Bone Miner. Res.* **2007**, *22*, 1557–1570; Bonivtch, A. R.; Bonewald, L. F.; Nicolella, D. P. *J. Biomech.* **2007**, *40*, 2199–2206, with permission.

maximum strain whereas the thickness of the perilacunar region had only a minor role (Figure 10(d)). Although the study contains quite strong assumptions like the idealized lacunar shape and the isotropic material properties (which, at this length scale, are obviously strongly anisotropic), the results clearly suggest that the application of macroscopic strains with magnitudes close to the *in vivo* values can produce quite high strain concentration around the osteocyte lacunae.[128] Hence, the hypothesized role of strain risers of these small holes inside bone tissue[130] can be quantified with FE simulations.

3.307.4.2. Canal Network

The role of cortical canals and of the lacunar canalicular network has been investigated mainly in connection with fluid flow and bone poroelasticity. It is assumed that the process of transducing external mechanical loads into internal stimuli at the level of osteocytes is mediated via fluid flow inside the canal and canalicular networks.[125] The main focus of the computational modeling in this area has been to compute flow-related parameters like pressure and velocity as a function of the applied external load. The canal network has been

in most of the cases modeled with idealized geometries. Reviewing those studies is outside the scope of this chapter. The reader interested in flow dynamic simulations in connection with bone ultrastructural features could consult the works of several investigators.[131–137] One possible way to include ultrastructure when assessing bone mechanical competence is with the so-called multilevel FE modeling.[138] Although the idea of a multiscale approach seems very promising,[28] the main limitation of such models is currently the strong idealization of the hierarchical levels, especially of bone ultrastructure. In fact, accurate three-dimensional reconstructions of bone ultrastructure require technologies which are not widely available, like synchrotron radiation-based nano-CT (SR nCT). In addition, the possible interactions between each hierarchical level are currently difficult to be assessed and modeled.

3.307.5. Nanoscale: Mineral and Collagen

In bone, at the material level, stiff mineral nanoparticles are embedded in a tough polymeric matrix. The matrix is mainly composed of type I collagen molecules, which self-assemble in a staggered fashion to form collagen fibrils.[2] The collagen matrix is stabilized by covalent cross-links between the collagen molecules; the amount of cross-linking changes during aging and metabolic bone diseases such as osteoporosis and it influences bone mechanical performance.[139,140] In addition to the organic matrix, bone contains nanocrystals of calcium phosphate which are periodically located along the collagen fibrils.[141] Also the physicochemical properties of mineral crystals are age-dependent and their changes can be correlated with impaired mechanical function of bone.[142] Hydroxyapatite is very stiff but brittle whereas collagen is two orders of magnitude softer but approximately three orders of magnitude tougher. Bone tissue at the nanoscale has a fibrillar nature: mineral and collagen are combined in the so-called mineralized collagen fibril. A simple mechanical model able to explain how to combine stiffness of the mineral and toughness of the matrix in bone at the nanoscale has been introduced by Jäger and Fratzl.[143] The model considers the mineralized collagen fibril and it is based on pure geometrical arguments. The main assumption is the staggered arrangement of stiff (mineral) elements embedded in a soft (protein) matrix. With this geometry, under applied tensile load, the mineral platelets carry tensile stresses while the main task of the protein layer is to transfer the load between adjacent mineral crystals by shear.[2,143,144]

3.307.5.1. Mechanics of the Mineral–Collagen Nanocomposite

The model introduced by Jäger and Fratzl for the mineralized collagen fibril[143] has been the starting point for subsequent investigations using FE simulations to assess bone properties at the nanoscale.[140,144–146] Siegmund and colleagues[140] investigated the specific role of the collagen matrix. In particular, different types of collagen cross-links were assumed and the deformation and failure of mineralized collagen fibrils were simulated. A composite material model for bone and mineral was developed and computer simulations were run for three different scenarios: without collagen cross-links, with only enzymatic cross-links, and with only nonenzymatic cross-links. The enzymatic cross-links were described by connecting the end terminal position of each collagen domain whereas the nonenzymatic cross-links, which have a more stochastic nature, were modeled by a random placement of cross-links at the interface between two collagen molecules. The study reported that the cross-links with the strongest influence on the mechanical behavior of the model were the nonenzymatic ones. From a mechanical point of view, at the nanolevel, these cross-links inhibited the sliding of the collagen and, therefore, increased the amount of load which was transferred to the mineral. This finding provides a micromechanical explanation on the negative influence of nonenzymatic collagen cross-links on bone toughness.[140] In a subsequent study, Dong and coworkers[145] implemented a two-dimensional probabilistic FE model based on mineralized collagen fibrils, to explore the propagation of microdamage at the tissue level. The model was composed of alternating layers of mineral and collagen and an initial defect was introduced in the form of a small hole in the mineral layer (**Figure 11(a)**). For the interface between mineral and collagen two situations were considered: a perfectly bonded interface and some degree of debonding in the vicinity of the defect. Material properties for mineral and collagen as well as geometrical dimensions were described in a statistical sense, that is, with random variables having a Gaussian distribution. A total of 200 different model realizations were simulated. The role of the mineral–collagen interface was pivotal for the failure propagation. For a perfectly bonded interface the most likely failure location was close to the defect (**Figure 11(b)**) whereas with some degree of interfacial debonding the failure location moved far away from the defect (**Figure 11(c)**), thus suggesting the formation of diffuse damage. Possible future refinements of the presented models might be the extension in the third dimension and the inclusion of more realistic material and geometrical properties for mineral and collagen.

3.307.6. Conclusions and Future Directions

The mechanical properties of bone depend on its hierarchical structure. In this chapter, we have discussed various FE applications that have increased our understanding of the relationship between bone structure and its mechanical function. Here, we have mainly focused on human bones. At the organ level we showed that the combination of microarchitectural bone imaging with FE is a powerful tool to improve strength assessment and individual fracture risk prediction. Whether the sophisticated engineering approaches presented in this chapter will find their way from research to the clinic is yet to be determined, but the high level of automation, the continuing increase in computational power and above all the improved predictive capacity over predictions based on bone mass, make clear that there is great potential in the clinical arena for *in vivo* FE simulations.[16] At the trabecular level, FEA has elucidated several mechanical aspects such as the role of trabeculae in defining the anisotropic mechanical behavior of bone and the relationship between structural indices and trabecular bone mechanical

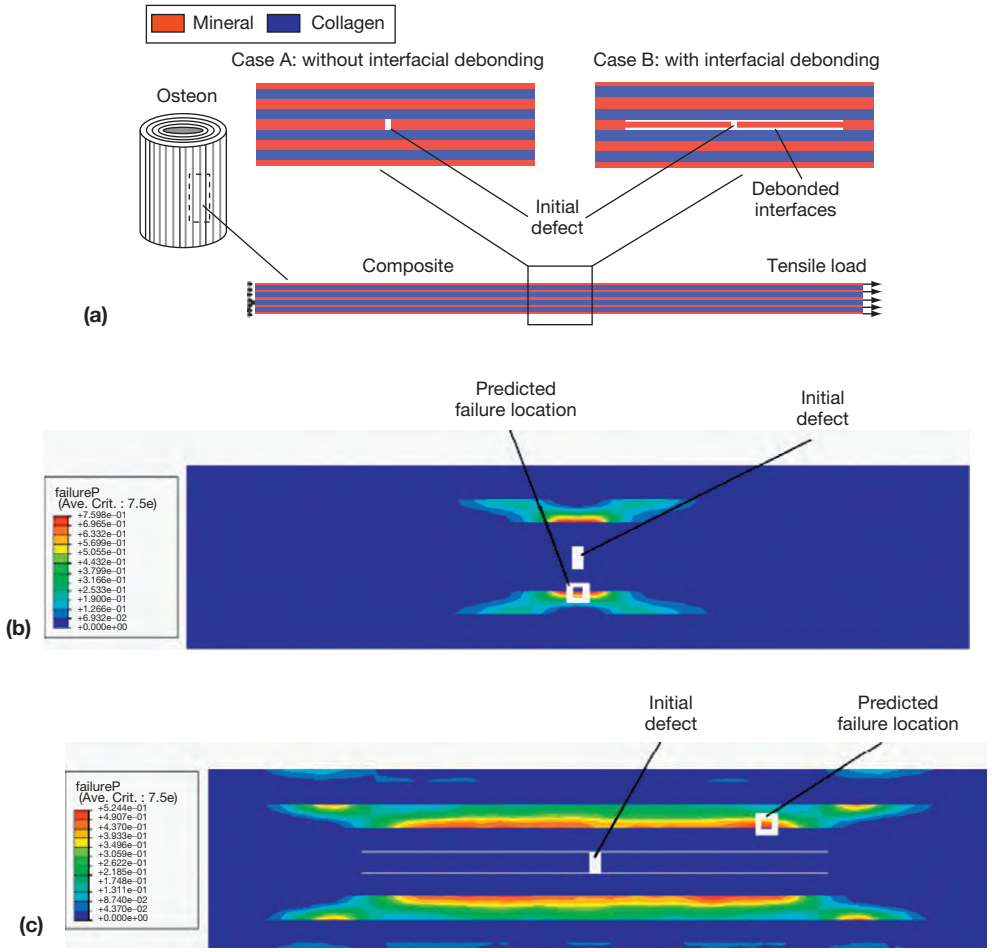

Figure 11 (a) Sketch of an idealized mineralized collagen fibril composed of alternating layers of mineral (red) and collagen (blue). An initial defect (white) is present in the mineral layer and two situations are condidered: (right) with and (left) withouth interfacial debonding at the collagen mineral interface. Contour plots of the failure distributions computed with FE analysis for (b) pefect bonding between mineral and collagen and (c) with some degree of debonding at the interface. In the first scenario, the most probable failure locations are very close to the defect; conversely, with interfacial debonding the failure is observed away from the defect. Adapted from Dong, X. N.; Guda, T.; Millwater, H. R.; Wang, X. *J. Biomech*. **2009**, *42*, 202–209, with permission.

properties. Future FE studies should aim to improve the failure prediction by considering, for example, the precise locations where failure will initiate and the modes of failure propagation. For that purpose, more accurate material models and constitutive laws for bone tissue have to be developed. Furthermore, a quantification of the contribution of individual architectural elements (in healthy and osteoporotic trabecular bone) to the strength of the trabecular structure would be beneficial, because it would provide further insights into which are the key elements to target in anti-osteoporosis therapy.

Experimental data at the microscale of bone has demonstrated that bone ultrastructure changes with age, with bone diseases or after drugs administration. Hence, ultrastructural features are nowadays considered important targets for the assessment of bone mechanical properties and pharmacological treatments.[121] Consequently, it can be expected that more FE studies which consider bone ultrastructure will be performed in the near future. One novel approach might be to perform FE simulations based on experimental measures of bone ultrastructure at the micrometer and submicrometer scale. One fascinating possibility might be to model the role of ultrastructural features on the formation and propagation of cracks inside bone tissue. However, for such models to work, information on the material behavior at the micro- and nanoscale would be needed. This knowledge might be provided by nanoscale FE where it might soon become feasible to investigate damage propagation in three dimensions at the level of the mineral–collagen nanocomposite.

In conclusion, FE analysis has been an indispensable computational tool in elucidating the relationship between bone structure and its mechanical function. It is expected to stay important considering the subject-specific analysis of bone strength based on subject-specific structural measures; an improved understanding of bone strength, fracture initiation, and progression could lead to more successful approaches in the prevention and treatment of age- and disease-related fractures. We expect that FE will become even more important in materials research considering the current trends in (bio)materials design, where the structure of biological materials is considered as a possible source of inspiration.

References

1. Huiskes, R.; Chao, E. Y. *J. Biomech.* **1983**, *16*, 385–409.
2. Fratzl, P.; Weinkamer, R. *Prog. Mater. Sci.* **2007**, *52*, 1263–1334.
3. Sarikaya, M. *Proc. Natl. Acad. Sci. USA* **1999**, *96*, 14183–14185.
4. Prendergast, P. J. *Clin. Biomech. (Bristol, Avon)* **1997**, *12*, 343–366.
5. Wirth, A. J.; Mueller, T. L.; Vereecken, W.; *et al. Arch. Appl. Mech.* **2010**, *80*, 513–525.
6. Gerhard, F. A.; Webster, D. J.; Van Lenthe, G. H.; Müller, R. *Philos. Transact. A Math. Phys. Eng. Sci.* **2009**, *367*, 2011–2030.
7. Doblaré, M.; Garcia, J. M.; Gomez, M. J. *Eng. Fract. Mech.* **2004**, *71*, 1809–1840.
8. Zienkiewicz, O. C.; Taylor, R. L. *The Finite Element Method*; Butterworth-Heinemann: Oxford; Boston, 2000.
9. Kanis, J. A. *Curr. Rheumatol. Rep.* **2000**, *2*, 62–66.
10. Kanis, J. A.; Borgstrom, F.; De Laet, C.; *et al. Osteoporos. Int.* **2005**, *16*, 581–589.
11. Koller, D. L.; Econs, M. J.; Rodriguez, L. A.; *et al. J. Bone Miner. Res.* **1999**, *14*, S141.
12. Delmas, P. D.; Seeman, E. *Bone* **2004**, *34*, 599–604.
13. Fratzl, P.; Roschger, P.; Fratzl-Zelman, N.; Paschalis, E. P.; Phipps, R.; Klaushofer, K. *Calcif. Tissue Int.* **2007**, *81*, 73–80.
14. Watts, N. B.; Cooper, C.; Lindsay, R.; *et al. J. Clin. Densitom.* **2004**, *7*, 255–261.
15. Majumdar, S.; Genant, H. K.; Grampp, S.; *et al. J. Bone Miner. Res.* **1997**, *12*, 111–118.
16. Van Lenthe, G. H.; Müller, R. *Drug Discov. Today Technol.* **2006**, *3*, 221–229.
17. Boutroy, S.; Sornay-Rendu, E.; Munoz, F.; Delmas, P. D. *Osteoporos. Int.* **2006**, *17*, S135.
18. Ruegsegger, P.; Koller, B.; Müller, R. *Calcif. Tissue Int.* **1996**, *58*, 24–29.
19. Kinney, J. H.; Lane, N. E.; Haupt, D. L. *J. Bone Miner. Res.* **1995**, *10*, 264–270.
20. Lane, N. E.; Thompson, J. M.; Haupt, D.; Kimmel, D. B.; Modin, G.; Kinney, J. H. *J. Bone Miner. Res.* **1998**, *13*, 229–236.
21. David, V.; Laroche, N.; Boudignon, B.; *et al. J. Bone Miner. Res.* **2003**, *18*, 1622–1631.
22. Waarsing, J. H.; Day, J. S.; Van Der Linden, J. C.; *et al. Bone* **2004**, *34*, 163–169.
23. Van Lenthe, G. H.; Müller, R. *IBMS BoneKEy* **2008**, *5*, 410–425.
24. Taddei, F.; Schileo, E.; Helgason, B.; Cristofolini, L.; Viceconti, M. *Med. Eng. Phys.* **2007**, *29*, 973–979.
25. Helgason, B.; Perilli, E.; Schileo, E.; Taddei, F.; Brynjolfsson, S.; Viceconti, M. *Clin. Biomech. (Bristol, Avon)* **2008**, *23*, 135–146.
26. Crawford, R. P.; Cann, C. E.; Keaveny, T. M. *Bone* **2003**, *33*, 744–750.
27. Homminga, J.; Huiskes, R.; Van Rietbergen, B.; Ruegsegger, P.; Weinans, H. *J. Biomech.* **2001**, *34*, 513–517.
28. Christen, D.; Webster, D. J.; Müller, R. *Philos. Transact. A Math. Phys. Eng. Sci.* **2010**, *368*, 2653–2668.
29. Müller, R.; Ruegsegger, P. *Med. Eng. Phys.* **1995**, *17*, 126–133.
30. Van Rietbergen, B.; Weinans, H.; Huiskes, R.; Odgaard, A. *J. Biomech.* **1995**, *28*, 69.
31. Hollister, S. J.; Riemer, B. A. *Math. Meth. Med. Imaging II* **1993**, *2035*, 95–106.
32. Eswaran, S. K.; Gupta, A.; Adams, M. F.; Keaveny, T. M. *J. Bone Miner. Res.* **2006**, *21*, 307–314.
33. Homminga, J.; Van-Rietbergen, B.; Lochmuller, E. M.; Weinans, H.; Eckstein, F.; Huiskes, R. *Bone* **2004**, *34*, 510–516.
34. Arbenz, P.; Van Lenthe, G. H.; Mennel, U.; Müller, R.; Sala, M. *Int. J. Numer. Methods Eng.* **2008**, *73*, 927–947.
35. Kabel, J.; Vanrietbergen, B.; Dalstra, M.; Odgaard, A.; Huiskes, R. *J. Biomech.* **1999**, *32*, 673–680.
36. Pistoia, W.; Van Rietbergen, B.; Lochmuller, E. M.; Lill, C. A.; Eckstein, F.; Ruegsegger, P. *Bone* **2002**, *30*, 842–848.
37. Van Rietbergen, B.; Huiskes, R.; Eckstein, F.; Ruegsegger, P. *J. Bone Miner. Res.* **2003**, *18*, 1781–1788.
38. Burge, R.; Dawson-Hughes, B.; Solomon, D. H.; Wong, J. B.; King, A.; Tosteson, A. *J. Bone Miner. Res.* **2007**, *22*, 465–475.
39. Cummings, S. R.; Black, D. M.; Rubin, S. M. *Arch. Intern. Med.* **1989**, *149*, 2445–2448.
40. Wolff, J. *Clin. Orthop. Relat. Res.* **2010**, *468*, 1056–1065.
41. Brekelmans, W. A.; Poort, H. W.; Slooff, T. J. *Acta Orthop. Scand.* **1972**, *43*, 301–317.
42. Cody, D. D.; Gross, G. J.; Hou, F. J.; Spencer, H. J.; Goldstein, S. A.; Fyhrie, D. P. *J. Biomech.* **1999**, *32*, 1013–1020.
43. Keyak, J. H.; Rossi, S. A.; Jones, K. A.; Les, C. M.; Skinner, H. B. *Med. Eng. Phys.* **2001**, *23*, 657–664.
44. Keyak, J. H. *Med. Eng. Phys.* **2001**, *23*, 165–173.
45. Schileo, E.; Taddei, F.; Cristofolini, L.; Viceconti, M. *J. Biomech.* **2008**, *41*, 356–367.
46. Keaveny, T. M.; Morgan, E. F.; Niebur, G. L.; Yeh, O. C. *Annu. Rev. Biomed. Eng.* **2001**, *3*, 307–333.
47. Verhulp, E.; Van Rietbergen, B.; Huiskes, R. *Bone* **2008**, *42*, 30–35.
48. Ulrich, D.; Van Rietbergen, B.; Laib, A.; Ruegsegger, P. *J. Biomech.* **1999**, *32*, 821–828.
49. Tajima, T.; Saito, H. *Handchir. Mikrochir. Plast. Chir.* **1991**, *23*, 227–235.
50. Pistoia, W.; Van Rietbergen, B.; Laib, A.; Ruegsegger, P. *J. Biomech. Eng.* **2001**, *123*, 176–183.
51. Niebur, G. L.; Feldstein, M. J.; Yuen, J. C.; Chen, T. J.; Keaveny, T. M. *J. Biomech.* **2000**, *33*, 1575–1583.
52. Laib, A.; Ruegsegger, P. *Bone* **1999**, *24*, 35–39.
53. Mueller, T. L.; Wirth, A. J.; Müller, R.; Van Lenthe, G. H. *J. Biomech.* **2008**, *41*(Suppl. 1), S154.
54. Varga, P.; Pahr, D. H.; Baumbach, S.; Zysset, P. *K. Bone* **2010**, *47*, 982–988.
55. Varga, P.; Baumbach, S.; Pahr, D.; Zysset, P. K. *J. Biomech.* **2009**, *42*, 1726–1731.
56. Macneil, J. A.; Boyd, S. K. *Bone* **2008**, *42*, 1203–1213.
57. Boutroy, S.; Bouxsein, M. L.; Munoz, F.; Delmas, P. D. *J. Clin. Endocrinol. Metab.* **2005**, *90*, 6508–6515.
58. Macneil, J. A.; Boyd, S. K. *Med. Eng. Phys.* **2008**, *30*, 792–799.
59. Mueller, T. L.; Stauber, M.; Kohler, T.; Eckstein, F.; Müller, R.; Van Lenthe, G. H. *Bone* **2009**, *44*, 364–371.
60. Müller, R.; Hildebrand, T.; Hauselmann, H. J.; Ruegsegger, P. *J. Bone Miner. Res.* **1996**, *11*, 1745–1750.
61. Gluer, C. C.; Blake, G.; Lu, Y.; Blunt, B. A.; Jergas, M.; Genant, H. K. *Osteoporos. Int.* **1995**, *5*, 262–270.
62. Jones, A. C.; Wilcox, R. K. *Med. Eng. Phys.* **2008**, *30*, 1287–1304.
63. Buckley, J. M.; Loo, K.; Motherway, J. *Bone* **2007**, *40*, 767–774.
64. Kopperdahl, D. L.; Morgan, E. F.; Keaveny, T. M. *J. Orthop. Res.* **2002**, *20*, 801–805.
65. Chevalier, Y.; Charlebois, M.; Pahra, D.; *et al. Comput. Meth. Biomech. Biomed. Eng.* **2008**, *11*, 477–487.
66. Zysset, P. K. *J. Biomech.* **2003**, *36*, 1469–1485.
67. Garcia, D.; Zysset, P. K.; Charlebois, M.; Curnier, A. *Arch. Appl. Mech.* **2010**, *80*, 543–555.
68. Chevalier, Y.; Quek, E.; Borah, B.; *et al. Bone* **2010**, *46*, 41–48.
69. Imai, K.; Ohnishi, I.; Matsumoto, T.; Yamamoto, S.; Nakamura, K. *Osteoporos. Int.* **2009**, *20*, 801–810.
70. Keaveny, T. M.; Donley, D. W.; Hoffmann, P. F.; Mitlak, B. H.; Glass, E. V.; San Martin, J. A. *J. Bone Miner. Res.* **2007**, *22*, 149–157.
71. Eswaran, S. K.; Bayraktar, H. H.; Adams, M. F.; *et al. Comput. Meth. Appl. Mech. Eng.* **2007**, *196*, 3025–3032.
72. Eswaran, S. K.; Gupta, A.; Keaveny, T. M. *Bone* **2007**, *41*, 733–739.
73. Fields, A. J.; Eswaran, S. K.; Jekir, M. G.; Keaveny, T. M. *J. Bone Miner. Res.* **2009**, *24*, 1523–1530.
74. Jensen, K. S.; Mosekilde, L.; Mosekilde, L. *Bone* **1990**, *11*, 417–423.
75. Luxner, M. H.; Woesz, A.; Stampfl, J.; Fratzl, P.; Pettermann, H. E. *Acta Biomater.* **2009**, *5*, 381–390.
76. Silva, M. J.; Gibson, L. J. *Int. J. Mech. Sci.* **1997**, *39*, 549–563.
77. Silva, M. J.; Hayes, W. C.; Gibson, L. J. *Int. J. Mech. Sci.* **1995**, *37*, 1161–1177.
78. Zhu, H. X.; Hobdell, J. R.; Windle, A. H. *Acta Mater.* **2000**, *48*, 4893–4900.
79. Ngan, A. H. W. *Proc. R Soc. Lond. A Math. Phys. Eng. Sci.* **2005**, *461*, 433–458.
80. Luxner, M. H.; Stampfl, J.; Pettermann, H. E. *Int. J. Solids Struct.* **2007**, *44*, 2990–3003.
81. Chen, C.; Lu, T. J.; Fleck, N. A. *J. Mech. Phys. Solids* **1999**, *47*, 2235–2272.
82. Chen, C.; Lu, T. J.; Fleck, N. A. *Int. J. Mech. Sci.* **2001**, *43*, 487–504.
83. Chen, D. H.; Ozaki, S. *Compos. Struct.* **2009**, *89*, 52–59.
84. Ruffoni, D.; Dunlop, J. W. C.; Fratzl, P.; Weinkamer, R. *Philos. Mag.* **2010**, *90*, 1807–1818.
85. Mosekilde, L. *Bone* **1988**, *9*, 247–250.
86. Vajjhala, S.; Kraynik, A. M.; Gibson, L. J. *J. Biomech. Eng. Trans. ASME* **2000**, *122*, 511–515.
87. Guo, X. E.; Kim, C. H. *Bone* **2002**, *30*, 404–411.
88. Van Lenthe, G. H.; Stauber, M.; Müller, R. *Bone* **2006**, *39*, 1182–1189.
89. Liu, X. S.; Sajda, P.; Saha, P. K.; *et al. J. Bone Miner. Res.* **2008**, *23*, 223–235.
90. Liu, X. W. S.; Sajda, P.; Saha, P. K.; Wehrli, F. W.; Guo, X. E. *J. Bone Miner. Res.* **2006**, *21*, 1608–1617.

91. Stauber, M.; Müller, R. *Bone* **2006**, *38*, 475–484.
92. Ladd, A. J. C.; Kinney, J. H.; Haupt, D. L.; Goldstein, S. A. *J. Orthop. Res.* **1998**, *16*, 622–628.
93. Verhulp, E.; Van Rietbergen, B.; Müller, R.; Huiskes, R. *J. Biomech.* **2008**, *41*, 1479–1485.
94. Roschger, P.; Paschalis, E. P.; Fratzl, P.; Klaushofer, K. *Bone* **2008**, *42*, 456–466.
95. Ruffoni, D.; Fratzl, P.; Roschger, P.; Klaushofer, K.; Weinkamer, R. *Bone* **2007**, *40*, 1308–1319.
96. Gupta, H. S.; Schratter, S.; Tesch, W.; *et al. J. Struct. Biol.* **2005**, *149*, 138–148.
97. Ruffoni, D.; Fratzl, P.; Roschger, P.; Phipps, R.; Klaushofer, K.; Weinkamer, R. *J. Bone Miner. Res.* **2008**, *23*, 1905–1914.
98. Meganck, J. A.; Kozloff, K. M.; Thornton, M. M.; Broski, S. M.; Goldstein, S. A. *Bone* **2009**, *45*, 1104–1116.
99. Nazarian, A.; Snyder, B. D.; Zurakowski, D.; Müller, R. *Bone* **2008**, *43*, 302–311.
100. Fajardo, R. J.; Cory, E.; Patel, N. D.; *et al. Bone* **2009**, *44*, 176–184.
101. Nuzzo, S.; Peyrin, F.; Cloetens, P.; Baruchel, J. *Med. Phys.* **2002**, *29*, 2672–2681.
102. Renders, G. A. P.; Mulder, L.; Langenbach, G. E. J.; Van Ruijven, L. J.; Van Eijden, T. M. G. J. *J. Biomech.* **2008**, *41*, 2793–2798.
103. Van Der Linden, J. C.; Birkenhager-Frenkel, D. H.; Verhaar, J. A. N.; Weinans, H. *J. Biomech.* **2001**, *34*, 1573–1580.
104. Roschger, P.; Fratzl, P.; Eschberger, J.; Klaushofer, K. *Bone* **1998**, *23*, 319–326.
105. Stolken, J. S.; Kinney, J. H. *Bone* **2003**, *33*, 494–504.
106. Verhulp, E.; Van Rietbergen, B.; Müller, R.; Huiskes, R. *J. Biomech.* **2008**, *41*, 1479–1485.
107. Yang, G. Y.; Kabel, J.; Van Rietbergen, B.; Odgaard, A.; Huiskes, R.; Cowin, S. C. *J. Elast.* **1998**, *53*, 125–146.
108. Whitehouse, W. J. *J. Microsc.* **1974**, *101*, 153–168.
109. Kabel, J.; Van Rietbergen, B.; Odgaard, A.; Huiskes, R. *Bone* **1999**, *25*, 481–486.
110. Ulrich, D.; Van Rietbergen, B.; Laib, A.; Ruegsegger, P. *Bone* **1999**, *25*, 55–60.
111. Morgan, E. F.; Bayraktar, H. H.; Keaveny, T. M. *J. Biomech.* **2003**, *36*, 897–904.
112. Deshpande, V. S.; Ashby, M. F.; Fleck, N. A. *Acta Mater.* **2001**, *49*, 1035–1040.
113. Odgaard, A.; Gundersen, H. J. G. *Bone* **1993**, *14*, 173–182.
114. Kabel, J.; Odgaard, A.; Van Rietbergen, B.; Huiskes, R. *Bone* **1999**, *24*, 115–120.
115. Kinney, J. H.; Ladd, A. J. C. *J. Bone Miner. Res.* **1998**, *13*, 839–845.
116. Liu, X. S.; Bevill, G.; Keaveny, T. M.; Sajda, P.; Guo, X. E. *J. Biomech.* **2009**, *42*, 249–256.
117. Stauber, M.; Rapillard, L.; Van Lenthe, G. H.; Zysset, P.; Müller, R. *J. Bone Miner. Res.* **2006**, *21*, 586–595.
118. Stauber, M.; Müller, R. *Osteoporos. Int.* **2006**, *17*, 616–626.
119. Bousson, V.; Peyrin, F.; Berot, C.; Hausard, M.; Sautet, A.; Laredo, J. D. *J. Bone Miner. Res.* **2004**, *19*, 794–801.
120. Schneider, P.; Stauber, M.; Voide, R.; Stampanoni, M.; Donahue, L. R.; Müller, R. *J. Bone Miner. Res.* **2007**, *22*, 1557–1570.
121. Müller, R. *Nat. Rev. Rheumatol.* **2009**, *5*, 373–381.
122. Voide, R.; Van Lenthe, G. H.; Müller, R. *J. Bone Miner. Res.* **2008**, *23*, 1194–1203.
123. Koester, K. J.; Ager, J. W.; Ritchie, R. O. *Nat. Mater.* **2008**, *7*, 672–677.
124. Voide, R.; Schneider, P.; Stauber, M.; *et al. Bone* **2009**, *45*, 164–173.
125. Robling, A. G.; Castillo, A. B.; Turner, C. H. *Annu. Rev. Biomed. Eng.* **2006**, *8*, 455–498.
126. Ascenzi, M. G.; Gill, J.; Lomovtsev, A. *J. Biomech.* **2008**, *41*, 3426–3435.
127. Prendergast, P. J.; Huiskes, R. *J. Biomech. Eng. Trans. ASME* **1996**, *118*, 240–246.
128. Bonivtch, A. R.; Bonewald, L. F.; Nicolella, D. P. *J. Biomech.* **2007**, *40*, 2199–2206.
129. Burr, D. B.; Milgrom, C.; Fyhrie, D.; *et al. Bone* **1996**, *18*, 405–410.
130. Currey, J. D. *J. Biomech.* **2003**, *36*, 1487–1495.
131. Cowin, S. C.; Gailani, G.; Benalla, M. *Philos. Transact. A Math. Phys. Eng. Sci.* **2009**, *367*, 3401–3444.
132. Goulet, G. C.; Cooper, D. M.; Coombe, D.; Zernicke, R. F. *Comput. Meth. Biomech. Biomed. Eng.* **2008**, *11*, 379–387.
133. Goulet, G. C.; Hamilton, N.; Cooper, D.; *et al. J. Biomech.* **2008**, *41*, 2169–2175.
134. Malachanne, E.; Dureisseix, D.; Canadas, P.; Jourdan, F. *J. Biomech.* **2008**, *41*, 721–725.
135. Nguyen, V. H.; Lemaire, T.; Naili, S. *Med. Eng. Phys.* **2010**, *32*, 384–390.
136. Remond, A.; Naili, S.; Lemaire, T. *Biomech. Model. Mechanobiol.* **2008**, *7*, 487–495.
137. Steck, R.; Niederer, P.; Tate, M. L. K. *J. Theor. Biol.* **2003**, *220*, 249–259.
138. Deligianni, D. D.; Apostolopoulos, C. A. *Biomech. Model. Mechanobiol.* **2008**, *7*, 151–159.
139. Banse, X.; Sims, T. J.; Bailey, A. J. *J. Bone Miner. Res.* **2002**, *17*, 1621–1628.
140. Siegmund, T.; Allen, M. R.; Burr, D. B. *J. Biomech.* **2008**, *41*, 1427–1435.
141. Fratzl, P.; Fratzl-Zelman, N.; Klaushofer, K.; Vogl, G.; Koller, K. *Calcif. Tissue Int.* **1991**, *48*, 407–413.
142. Akkus, O.; Adar, F.; Schaffler, M. B. *Bone* **2004**, *34*, 443–453.
143. Jäger, I.; Fratzl, P. *Biophys. J.* **2000**, *79*, 1737–1746.
144. Gao, H.; Ji, B.; Jager, I. L.; Arzt, E.; Fratzl, P. *Proc. Natl. Acad. Sci. USA* **2003**, *100*, 5597–5600.
145. Dong, X. N.; Guda, T.; Millwater, H. R.; Wang, X. *J. Biomech.* **2009**, *42*, 202–209.
146. Gao, H. J. *Int. J. Fract.* **2006**, *138*, 101–137.

Relevant Websites

www.top500.org – High performance computing.
www.en.wikipedia.org/wiki/Finite_element_analysis – Introduction to finite element analysis.
www.en.wikipedia.org/wiki/Microtomography – Introduction to microtomographic imaging.
http://en.wikipedia.org/wiki/Osteoporosis – Introduction to osteoporosis.

3.308. The Mechanics of Native and Engineered Cardiac Soft Tissues

M S Sacks, University of Pittsburgh, Pittsburgh, PA, USA
S Wognum, Academic Medical Center, Amsterdam, The Netherlands
J Stella, University of Pittsburgh, Pittsburgh, PA, USA
E Joyce, University of Pittsburgh, Pittsburgh, PA, USA
A D'Amore, University of Pittsburgh, Pittsburgh, PA, USA; Fondazione RiMED, Italy

© 2011 Elsevier Ltd. All rights reserved.

3.308.1. Introduction 114
3.308.1.1. Background 114
3.308.1.2. Structure–Function Relationships in Cardiovascular Tissues 114
3.308.1.3. Nonlinearity of Soft Tissues 116
3.308.2. Heart Valve Tissues 116
3.308.2.1. Heart Valve Tissue Biomechanics 116
3.308.2.2. Planar Biaxial Tensile Biomechanical Behavior of the Aortic Valve Leaflet 117
3.308.2.3. Flexural Response of Native Valvular Tissues 118
3.308.2.4. Micromechanics of Heart Valve Cells 119
3.308.3. Myocardium 120
3.308.4. Constitutive Models of Soft Tissues 122
3.308.4.1. Introduction 122
3.308.4.2. Stress and Strain Definitions 122
3.308.4.3. Phenomenological Hyperelastic Constitutive Models 122
3.308.4.4. Fung and Coworkers 123
3.308.4.5. Structural Constitutive Models for Multiphase Soft Tissues 124
3.308.5. Emulating Native Tissue Mechanical Behavior in Engineered Tissues 127
3.308.5.1. Introduction 127
3.308.5.2. Electrospun Scaffolds 127
3.308.5.3. Modeling Scaffold Structure–Function Relationships 128
References 131

Glossary

Electrospinning A technique to stretch an electrically charged liquid into the form of a yarn.
Extracellular matrix The extracellular part of tissue that usually provides structural support to the cells in addition to performing various other important functions.
Glycosaminoglycans Long unbranched polysaccharides that maintain the function of collagen and elastin.
Micromechanics The analysis of composite or heterogeneous materials on the level of the individual constituents that constitute these materials.
Scaffold A temporary structure supporting materials and tissues in their synthesis.
Soft tissues Tissues that connect, support, or surround other structures and organs of the body, not being bone.

Abbreviations

AV	Aortic Valve
AVIC	Aortic valve interstitial cell
EC	Endothelial cell
ECM	Extracellular matrix
GAG	Glycosaminoglycans
HV	Heart valve
LV	Left ventricle
MTM	Maximum tangent modulus
MVAL	Mitral valve anterior leaflet
NAR	Nuclear aspect ratio
PEUU	Poly(ester urethane)urea
RVE	Representative volume element
RVFW	Right ventricular free wall
VEC	Valvular endothelial cells
VIC	Valve interstitial cell

3.308.1. Introduction

3.308.1.1. Background

Particular challenges are encountered in constitutive modeling for cardiac/cardiovascular tissues due to their complex mechanical behavior. For example, because of their oriented fibrous structures, they often exhibit pronounced mechanical anisotropy. In addition, they exhibit highly nonlinear stress–strain relationships, large deformations, viscoelasticity, and strong axial coupling. Taken as a whole, cardiac soft biological tissues defy simple material models. Mechanical investigations have usually been confined to uniaxial studies because of the difficulties in controlling two or even three-dimensional (3D) boundary conditions. However, due to anisotropy, uniaxial data cannot be used to extrapolate to the fully generalized 3D constitutive equations, even if multidimensional strain data from the uniaxial experiment is available. There have also been investigations using inflation of circular membranes, which under assumption of isotropy can provide the necessary experimental data. All tissues are anisotropic, however, and hence this method cannot be applied. Further, when attempting to determine material constants for complex material models, multiaxial testing methods that include complex testing protocols, which allow large variations in stress and strain states for full characterization, are required.[1] As with all soft biological tissues, multiaxial tests on cardiovascular structures are generally difficult to perform. Just a few of the experimental problems include small specimen sizes, structural and compositional heterogeneity, difficulty in gripping (without doing damage), dramatic effects of different gripping techniques (St. Venant-like effects), difficulty in precisely identifying material axes, difficulty in assuring constant forces along specimen edges, large specimen-to-specimen variability, and time-dependent changes due to biological degradation. In addition, the question of homogeneity of deformation within the specimen is paramount. These issues can often frustrate the application of even the most straightforward of attempts to develop a constitutive model. In addition to the above experimental issues, relating the observed mechanical response to tissue structure is perhaps more paramount than in other more traditional material applications, where the continuum scale is usually at most of the size of large polymer molecules. In contrast, cardiac tissues are comprised of a dense network of primarily myocytes, and collagen and elastin various fibers, which indicates a continuum scale at the fiber-scale (typically $\sim$1 μm). In addition, the fibers can undergo large rotations and exhibit nonlinear stress–strain behavior that can induce complex behaviors at the macrospecimen scale not easily accounted for in classic material models. Accounting for these behaviors in both experimental evaluation and formulation of appropriate constitutive models continues to be a challenge. The focus of this chapter is to review these problems and present solutions and future trends.

3.308.1.2. Structure–Function Relationships in Cardiovascular Tissues

The strength of any material, natural or synthetic, depends on the substances of which it is composed. Yet, despite a wide range of physiological function and variation in specific behavior, all soft connective tissues share the same principal constituents: collagen, elastin, muscle fibers, and glycosaminoglycans (GAGs). The unique properties of each tissue are a result of its distinctive structure, which is determined by the constituents present and their arrangement. Type I and Type III collagen form undulated fibers that provide support under tension whereas elastin, an aggregate fiber from microfibrils, provides elastic properties and the ability to undergo large extensions. In contrast to these fibrous components, GAGs are composed of long unbranched polysaccharides usually attached to a protein core to form proteoglycans, whose high negative charge makes GAGs hydrophilic. It is well known that collagen fibers can withstand high tensile forces, but have low torsional and flexural stiffness. Thus, the directions in which the fibers are oriented can be identified with the directions in which the tissue is able to withstand the greatest tensile stresses.[2]

Cardiovascular soft tissues, like all connective tissues, are complex composite materials comprised of insoluble fibers, microfibrils and a wide range of soluble proteins and glycoproteins. In particular, their extracellular matrix (ECM) provides specific mechanical and physiochemical properties, in addition to providing scaffolding for cell attachment and migration.[3] The most abundant proteins in the body and the predominant components of the ECM are members of the collagen family of proteins, which form the major structural elements of connective tissues.[3,4] Collagens are the major structural elements of most load-bearing connective tissues, where they contribute to mechanical stability as well as maintain their structural integrity. Many reviews exist that provide a detailed description of their structure,[5] and the interested reader is referred to these publications. Thus, the ability of collagen to transmit load and maintain the structural integrity of tissue is a consequence of the aggregation of collagen fibrils, which have a well-defined tensile function, into collagen fibers. It has been experimentally demonstrated that fibrils can have a wide range of diameters. The ultimate tensile strength of fibers is largely dictated by their diameter size. As a result, when tissue undergoes high tensile loading, the collagen fibers will have a larger cross-sectional area due to the large fibril diameters, allowing the tissue to maintain its integrity in the harsh loading environment.[6]

To provide an excellent example of a connective tissue that elucidates many of the key features of cardiovascular tissues, we present a brief background to tendon structure, formed primarily from dense networks of collagen fibers. When the tendon is placed between crossed polarizers and then viewed under a light microscope, an alternating dark and light banding appears.[7] This banding pattern is referred to as crimp, and can be found in all fibrillar collagens (i.e., collagen types I–III) of most mammalian tissues, with the exception of bone and articular cartilage.[8] Although collagen crimp is observed at the fiber level, Diamant and coworkers[7,8] determined that fiber crimp is a property of individual collagen fibrils. In spite of the ubiquitous nature of collagen crimp, the cause of crimping has yet to be determined. An early explanation for collagen crimp was that contraction of elastin fibers within the collagen structure induced crimp.[9] This theory was dispelled because rat tail tendon, which does not contain elastin, clearly demonstrates collagen crimp.[9] Some speculate that contraction of the mucopolysaccharide matrix, in which the fibrils are embedded, causes the fibrils to buckle.[9] Determination of the crimp

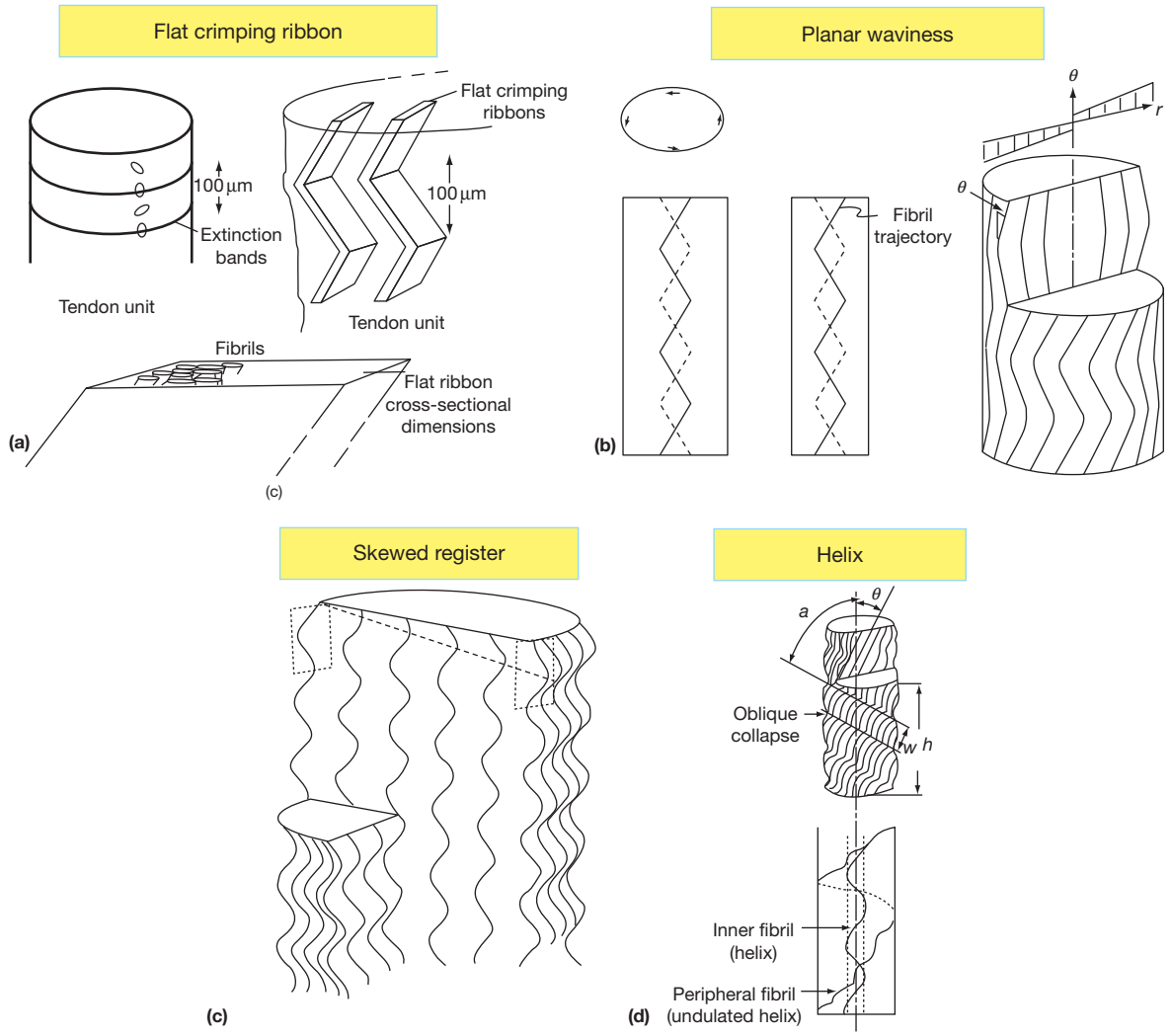

Figure 1 Proposed models for collagen crimp patterns. (a) Baer *et al.* proposed a flat crimping ribbon model. In this model, it is assumed that the fibrils have a ribbon-like cross-section that results in the flattened cylinder cross-section of the tendon unit, that is, fibers that give rise to the horizontally elongated tendon cross-section. (b) Kastelic *et al.* proposed that fibrils follow a wavy or zig-zag crimped course and are packed cylindrically. (c) Rowe *et al.* suggested the skewed register crimp model and stated that their findings did not support the cylindrical symmetry model of fibril packing. (d) Yahia *et al.* proposed that fibrils are helically organized around the fiber axis.

pattern, a result of fibril aggregation, is also not trivial and has led to various theories (Figure 1).[8]

Various models have been proposed for the crimp pattern found in tendons and ligaments. The models proposed are as follows: (1) a flat crimping ribbon model (Figure 1(a)),[10] (2) a planar waviness model (Figure 1(b)),[7,11–13] (3) a skewed register model (Figure 1(c)),[14] and (4) a helix model (Figure 1(d)).[15] The flat crimping ribbon model assumes that fibrils aggregate laterally to form a tendon unit, and the tendon units are bundled together with elastic fibers and fibroblasts, resulting in the macroscopic tendon. This model assumes that the fibrils have a ribbon-like cross-section that results in the flattened cylinder cross-section of the tendon unit, which gives rise to a horizontally elongated tendon cross-section. Polarizing microscopy has demonstrated that the crimped ribbons are all in phase, with their ribbon planes parallel throughout the tendon. It is to be noted that the flat crimped ribbons are thought to be responsible for the extinction bands that are evident under polarizing light. In the planar waviness model, fibrils are not straight and follow a wavy or zig-zag crimped course, and are packed cylindrically to form a collagen fiber.[11–13] Diamant *et al.*[7] claim that the fibril cross-sectional appears cylindrical and not like a flat ribbon, as was claimed by Baer *et al.*[16] Diamant *et al.* employed polarizing microscopy and demonstrated that collagen fibers of native tendons display a planar zig-zag morphology. Under polarizing light, collagen fibers gave rise to a periodic pattern of light and dark bands, which appeared and disappeared systematically as the crossed polarizers were rotated, or as the specimen was rotated about its longitudinal axis.[12] Small angle X-ray data presented by Gathercole and Keller supported this zig-zag morphology. Rowe *et al.* presented the skewed register crimp model and concluded that their findings did not support the cylindrical symmetry model of fibril packing. Instead, collagen

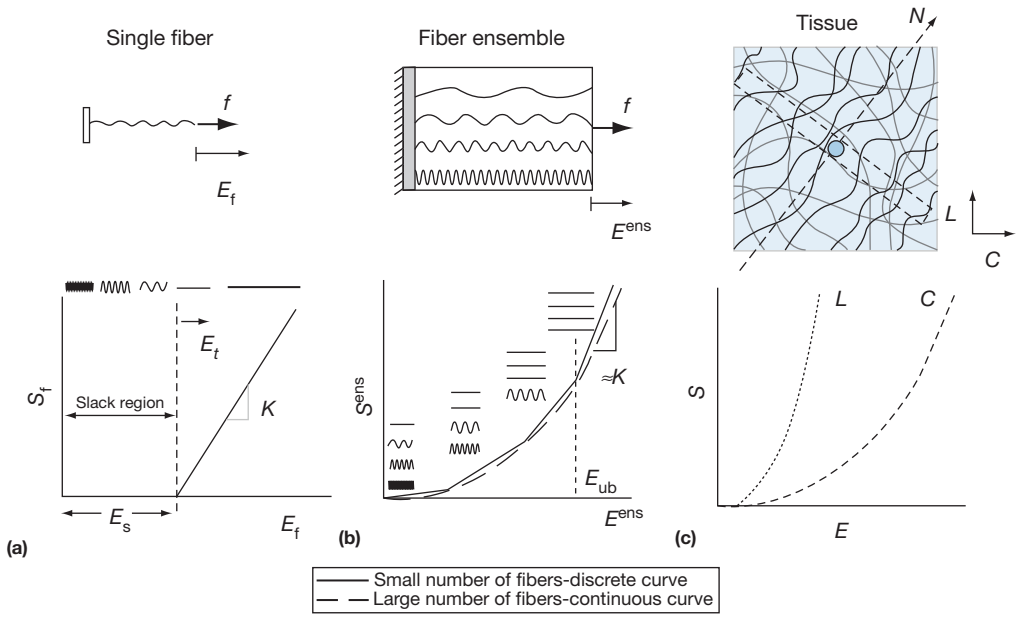

Figure 2 A general framework for collagenous soft tissue mechanical behavior, built from a single fiber. (a) The uniaxial loading of a crimped fiber, with the corresponding stress–strain curve, where *K* is the fiber modulus. (b) Uniaxial loading of an ensemble of fibers with the corresponding stress–strain curve, indicating how the recruitment of individual fibers results in a nonlinear stress–strain curve. (c) Scaling up to the tissue level produces an anisotropic mechanical behavior resulting from the specific distribution of fiber ensembles (see **Section 3.308.4** for term definitions).

fibrils appeared to aggregate side by side with flexibility in any direction in the register of wave patterns across the thickness of the fiber.[14] This configuration demonstrates that the peripheral fibrils are undulated helices while the central ones are normal helices.[15]

Not surprisingly, there is a strong correlation between fiber orientation and the functional requirements of tissues. Thus, collagen fiber orientation significantly affects the mechanical properties of a tissue. For example, when a tissue is loaded in only one direction *in vivo*, the collagen fibers of that tissue will orient in the direction of load, and the resulting mechanical properties will be anisotropic. However, if a tissue is loaded in all directions, the collagen fibers of that tissue will be oriented in all directions, and the tissue will possess an isotropic mechanical behavior. Thus, fiber direction is indicative of the dominant tensile stresses that a tissue undergoes, because fiber reorientation is the most efficient and selective way to optimize strength without increasing weight and metabolic cost, or "The least material is used in the most strategic locations to carry the greatest loads with the least strain."[6]

3.308.1.3. Nonlinearity of Soft Tissues

Mechanically, soft tissues exhibit a characteristic nonlinear stress–strain behavior. Following our focus on collagen, we note that this nonlinearity is a result of the particular structure of collagen fibers. Specifically, collagen fibers are crimped and transmit load only if stretched beyond the point where all the crimp has disappeared (**Figure 2(a)**). Once straightened, fibers are assumed to follow a linear elastic material model. Next, we extend this simple concept to a unidirectional ensemble of fibers, composed of fibers each of which has a separate degree of undulation (**Figure 2(b)**). Collagen fibers are recruited (straightened) with different amounts of strain due to the difference in their original degrees of crimping (**Figure 2(b)**), resulting in a nonlinear response. However, once all the collagen fibers are straightened, the stress–strain curve becomes linear. This linear elastic region is generally considered to be the threshold of reversibility. Next, to extend this to a complete tissue, we consider the tissue as a collection of fiber ensembles with varying orientation (**Figure 2(c)**). Tissues are composed of a large number of such ensembles with varying orientations. The angular distribution of these ensembles results in a unique and complex nonlinear bulk tissue response.

3.308.2. Heart Valve Tissues

3.308.2.1. Heart Valve Tissue Biomechanics

As our first example for cardiac tissues, we explore the valves of the heart, which are a remarkable example of highly developed structure and function.[17] For example, when open, the aortic valve (AV) allows for unobstructed outflow of blood from the ventricle during systole; with flow deceleration, it closes via Bernoulli effects, and the leaflet provides a complete closure to prevent valve regurgitation. All this is achieved through the unique and complex structure of the AV tissue, which consists of three layers (the fibrosa, spongiosa, and ventricularis), constructed principally of collagen, elastin, and GAGs.[18–23] The ventricularis layer faces the left ventricle and is composed primarily of collagen and elastin.[18–24] On the opposite face of the valve is the fibrosa layer. This layer faces the outflow and is composed predominantly of a dense network of type I collagen fibers, which exhibit macroscopic crimp and are aligned primarily in the circumferential direction.[19,23] The hydrophobic GAGs largely make up the central spongiosa,

resulting in a highly hydrated layer.[25–27] As its name implies, the ventricularis layer faces the left ventricular chamber and is composed of a dense network of collagen and elastin fibers. The spongiosa layer contains a high concentration of proteoglycans. The fibrosa layer is composed predominantly of a dense network of collagen fibers, and is thought to be the major stress-bearing layer. Interstitial cells (myofibroblasts) permeate the entire tissue structure, although they are generally more numerous in the spongiosa.

Further evidence of an adaptive structure is the unique structure of the commissure region, which approximately corresponds to the coaptation region. The coaptation region is not under any transvalvular pressure; it is loaded instead in a uniaxial-like manner due to the tethering forces generated at the attachment of the commissures to the aortic root. Unlike the biaxially loaded belly region, the uniaxial loading of the commissures would tend to make their structure more highly aligned, that is, more like a tendon. Like tendons, a highly aligned fiber network would have a very short transition region from low to high stiffness, as evidenced by rapid fiber uncrimping with stress. The highly aligned nature of the commissure region in the unloaded state and the more rapid realignment with transvalvular pressure in these regions are consistent with the pretransition strain level behavior of tendon-like materials. The results presented in **Section 3.308.1** suggest a complex structure-mechanical behavior and interactions in heart valve leaflets. It is useful to divide the study of the tissue-level biomechanics of heart valve (HV) leaflets into in-plane stretch and flexural deformation modes. These occur cyclically as the valve opens (flexure) and experiences surface shear stress from the local blood flow, followed by closure (flexure), then coaptation and full loading (tension). A detailed description of the three individual loading modes is presented in the following section.

3.308.2.2. Planar Biaxial Tensile Biomechanical Behavior of the Aortic Valve Leaflet

The mechanics of valvular tissues are complex: they exhibit a highly nonlinear stress–strain relationship; undergo large deformations; and express complex time-dependent behaviors that defy simple experiments and material models. Much of this behavior is a direct result of changes in their internal structure with strain, which involves both the straightening of highly crimped collagen fibers and rotation of these fibers toward the stretch axis. For valvular tissues, much of the previous work on the mechanical properties of the native and chemically treated aortic valve has relied on uniaxial mechanical testing.[23,28,29] These studies demonstrate that chemical fixation of intact valves, especially under pressure, alters the mechanical properties of the leaflets. Marked decreases in the extensibility are generally attributed to the 'locking' of the collagen fibers in the uncrimped state.[18,30] Tests on thin tissue strips, however, cannot mimic the heterogeneous multiaxial deformation fields, combined loading sequences, and native fiber kinematics found in the physiological environment. Mayne *et al.*[31] and Christie and Barratt-Boyes[32] have performed equibiaxial testing (i.e., equal levels of tension applied to each test axis), which overcomes many of the above limitations of uniaxial loading. However, derivation of a constitutive relationship solely from equibiaxial test data is limited due to multiple colinearities, which confound the ability to obtain reliable, unique model parameter values.[33]

The mechanical behavior and material parameters of tissues are determined through mechanical testing. Whole organ testing is more physiological, but the complex stress and strain boundary conditions on most organs, due to external loading by the surrounding organs or an irregular geometry, prevent an accurate investigation of isolated tissue response. For planar membrane or thin tissue sections, planar biaxial tests can be successfully used to investigate the mechanical behavior of various planar soft tissues[34–40] (**Figure 3**). Billiar and Sacks[34] generated the first complete biaxial mechanical data necessary for constitutive modeling of the aortic valve leaflet. Due to the small size and heterogeneous structure of the aortic valve leaflet, testing methods were developed and validated. Leaflet specimens were subjected to biaxial tests utilizing seven loading protocols to provide a range of loading states that encompass the physiological loading state (**Figure 4**). The leaflets demonstrated a complex, highly anisotropic mechanical behavior, including pronounced mechanical coupling between the circumferential and radial directions. Mechanical coupling between the axes produced negative strains along the circumferential direction and/or nonmonotonic stress–strain

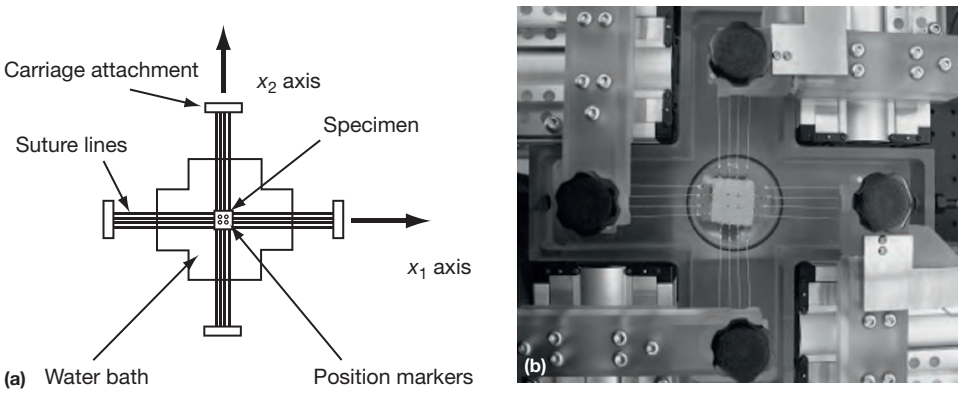

Figure 3 Schematic of a biaxial test (a) and photo of actual device (b). Note the use of four self-equilibrating suture lines to facilitate uniform loading along each of the specimen edges.

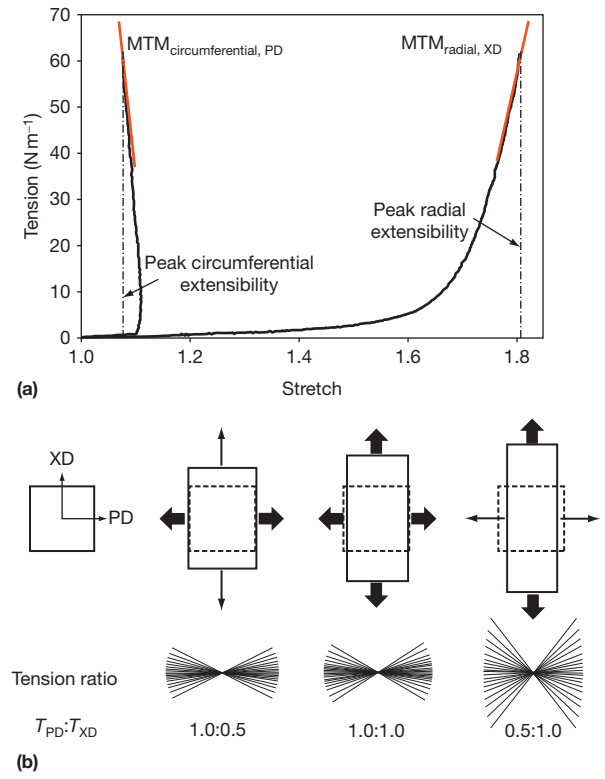

Figure 4 Application of traditional engineering metrics of material behavior is often inadequate as a descriptor of the complex behaviors observed in biological materials. (a) Load-bearing matrix-rich biological materials, such as native aortic valve leaflets, typically exhibit highly nonlinear and highly anisotropic tensile behaviors. (b) The extreme anisotropy and sharp transition from low to high stiffness is attributed to a coupled fiber recruitment process capable of exhibiting lateral contraction at high stress levels (circumferential shortening). As a consequence, the determination of traditional engineering indices of material behavior, such as tensile modulus, has little meaning (i.e., negative modulus). Adequate characterization of biological materials can necessitate more sophisticated methods to characterize their true mechanical behaviors.

behavior when subjected to equibiaxial tension, a behavior noted by Mayne *et al.*[31] but not explained. Moreover, Adamczyk and Vesely[41] measured AV leaflet strains *in situ* and found that negative strains can occur in the noncoronary leaflet.

In our laboratory and others,[31,42,43] biomechanical tissue analyses were conducted at quasistatic (strain rates of 4% per second to 12% per second) experimental conditions. However, we have shown that the deformations of heart valve leaflets can reach strain rates in excess of 300% per second. These findings have raised an important question: Are the quasistatic leaflet mechanical properties truly representative of their physiological behavior? The strain rate dependence of the mechanical properties of soft tissues has been extensively studied. Yet the literature indicates a wide range of findings, which are very much a function of the specific tissue composition and structure, as well as the specific testing methods utilized. Thus, the strain rate dependence of any one tissue needs to be properly investigated under realistic physiological loading states to model physiological functions. We explored, for the first time, the effects of strain rate (from quasistatic to physiologic) on the planar biaxial mechanical properties of the mitral valve anterior leaflet (MVAL).[44,45] A novel high-speed biaxial testing device capable of achieving strain rates was developed. Porcine MVAL specimens were loaded to physiological load levels with cycle periods of 15, 1, 0.5, 0.1, and 0.05 s. The resulting loading stress–strain responses were found to be remarkably independent of strain rate. The hysteresis, defined as the fraction of the membrane strain energy between the loading and unloading tension-areal stretch curves, was low (~12%) and did not vary with strain rate.

The underlying structural basis for this unique mechanical behavior is presently unknown. As collagen is the major structural component of the MVAL, we investigated the relation between collagen fibril kinematics (rotation and stretch) and tissue-level mechanical properties in the MVAL under biaxial loading using small angle X-ray scattering (SAXS).[46] A novel device was developed and utilized to perform simultaneous measurements of tissue-level forces and strain under a planar biaxial loading state. Collagen fibril D-period strain (ε_D) and the fibrillar angular distribution were measured under equibiaxial tension, creep, and stress relaxation to a peak tension of 90 N m^{-1}. The results indicated that, under equibiaxial tension, collagen fibril straining did not initiate until the end of the nonlinear region of the tissue-level stress– strain curve. At higher tissue tension levels, ε_D increased linearly with increasing tension. In creep tests, both tissue strain and ε_D remained constant, with no observable changes over the test length. These results suggest that valve leaflets can be modeled as 'functionally elastic' biological materials. In a follow-up study, we expanded these results to provide a more complete picture of the time-dependent mechanical properties of the MVAL. To accomplish this, biaxial stress relaxation and creep studies were performed on porcine MVAL specimens. Our primary finding was that while the MVAL leaflet exhibited significant stress relaxation, it exhibited negligible creep over the 3 h test. These results strengthened our assertion that the MVAL functionally behaves not as a linear or nonlinear viscoelastic material, but rather as an *anisotropic functionally elastic material*. These results appear to be largely unique in the soft tissue literature, suggesting as they do that valvular tissues are unique in their ability to withstand significant loading without time-dependent material effects.

3.308.2.3. Flexural Response of Native Valvular Tissues

During valve opening and closing, the leaflet is primarily deformed through flexure. While opening, the leaflet bends to straighten, and then curvature reverses as the leaflet conforms to the blood flow profile before reaching the full open position; during valve closing, the leaflet bends with the curve toward the ventricle as it approaches its morphologic closed state.[47] As GAGs largely make up the central spongiosa layer, it has been speculated that this layer serves to reduce the shear stresses resulting from the differential movement of the fibrosa and ventricularis during leaflet bending.[19,24,25,48–50] Further, it has been shown that larger strains in AVs compared to pulmonary valves are associated with the increase in collagen fiber rotation as well as crimp area.[51] Moreover, it has

been shown that the biaxial tensile biomechanical response of the AV is primarily from the collagenous fibrosa and ventricularis layers, with the response dominated by the fibrosa layer.[52] From these studies, it is hypothesized that under the quasistatic tensile loading, GAGs do not play a substantial role in the load-bearing mechanics as the biomechanical behavior is dominated by collagen and elastin. However, the role of GAGs in the time-dependent biomechanical behavior remains unclear.

We recently completed a study to determine GAGs' primary contribution to AV leaflet biomechanics utilizing enzymatic removal under planar tension and flexure: the two primary deformation modes experienced by the AV. Specimens were removed from the belly region of porcine AVs and subsequently treated with either an enzyme solution to remove the GAGs or a control (buffer with no enzyme) solution. Planar biaxial loading was conducted both on-axis and at 45° off-axis to induce maximum shear, with a separate group subjected to flexural testing. The results indicated that the removal of GAGs (1) did not affect extensional mechanical properties (either on- or 45° off-axis), including peak stretch, hysteresis, or creep, and (2) neither was the flexural effective modulus affected (**Figure 5(a)**); yet, the flexural hysteresis was markedly reduced from $35.96\% \pm 2.65\%$ to $25.00\% \pm 1.64\%$ ($p < 0.001$) in the control group as a result of GAG removal (**Figure 5(b)**). Collectively, these novel results suggest that GAGs do not play a role in the tensile properties of the valvular tissues, but rather may be important in providing a damping mechanism to reduce leaflet flutter. The results of this study support our hypothesis that GAGs do not play a measurable role in the tensile biomechanics of aortic valve tissues. Under extensional deformation and shear, collagen fibers rotate and straighten. GAGs interacting with the collagen fibers to contribute to the biomechanics under this loading state would induce viscous effects via fiber–matrix interactions, yet none were observed. In flexure, however, the biomechanical behavior is likely dominated by the crimped collagen fibers (not straightened ones) interacting with the GAGs. While it was noted that there were no bending direction effects in stiffness, it was observed that GAGs do play a significant role in the flexural hysteresis. These results suggest a damping role of GAGs in the aortic valve leaflet, reducing flutter during full systolic flow. This information can be utilized in the design and evaluation of novel engineered heart valves; minimizing valve flutter via enforcing hysteretic properties in flexure could assist in improving the long-term durability of these valve replacement options.

3.308.2.4. Micromechanics of Heart Valve Cells

The leaflets of all four HVs are sheathed by a single layer of valvular endothelial cells (VECs) that have been shown to be morphologically different from aortic endothelial cells (ECs).[53,54] Additionally, VECs are aligned with the collagen architecture of the valve, which is circumferentially oriented.[55] The VECs are believed to regulate vascular tone, inflammation, thrombosis, and remodeling, and their dysfunction has been linked with multiple disorders.[56] Within the proximal third of the leaflets, where they are innervated, there is believed to be a feedback mechanism between the VECs and the valve interstitial cells (VICs) wherein the nerves transmit information regarding released substances from the VECs.[57] Primarily, the release of cytokines has been shown to cause changes in interstitial cell structure and function.[58,59] VICs serve to maintain tissue structural integrity via protein synthesis and enzymatic degradation. Aortic valve interstitial cells (AVICs) are typically characterized as myofibroblasts; they exhibit phenotypic plasticity and may play an important role in valve pathophysiology. It has also been speculated that there exists some physical communication between the VECs and the VICs. However, to date no direct junctions have been observed between the two cell populations.[60]

While it is known that AVICs can respond to mechanical stimuli *in vitro*, the level of *in vivo* AVIC deformation and its relation to local collagen fiber reorientation during the cardiac cycle remain unknown. We have investigated the deformation of AVICs using porcine AV glutaraldehyde fixed under 0–90 mmHg transvalvular pressures. The resulting

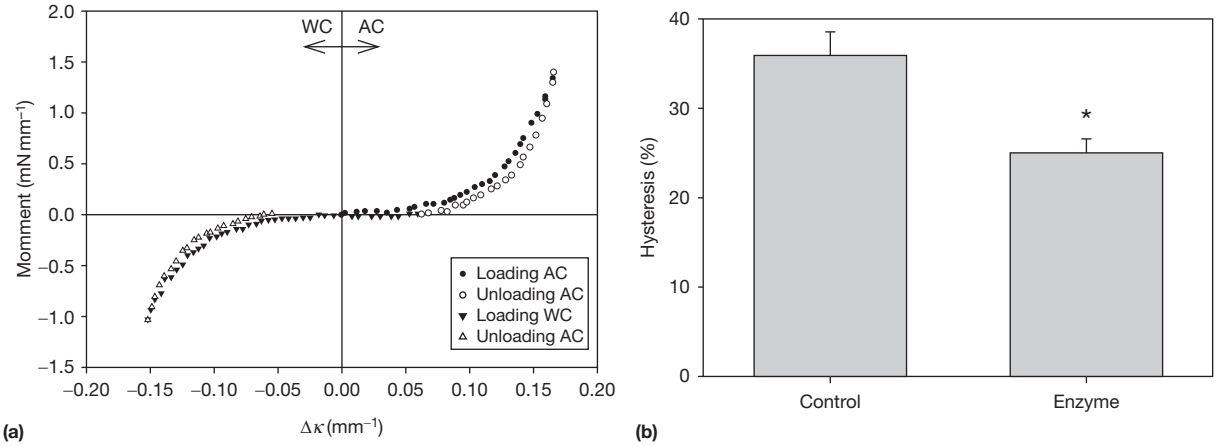

Figure 5 (a) Representative M versus $\Delta\kappa$ loading and unloading curve in both the WC and AC directions; the nonlinear sigmoidal response was present in the native, control, and enzyme treated groups. (b) Combined hysteresis in both directions exhibited a significant decrease from the control to the enzyme treated group ($p < 0.001$).

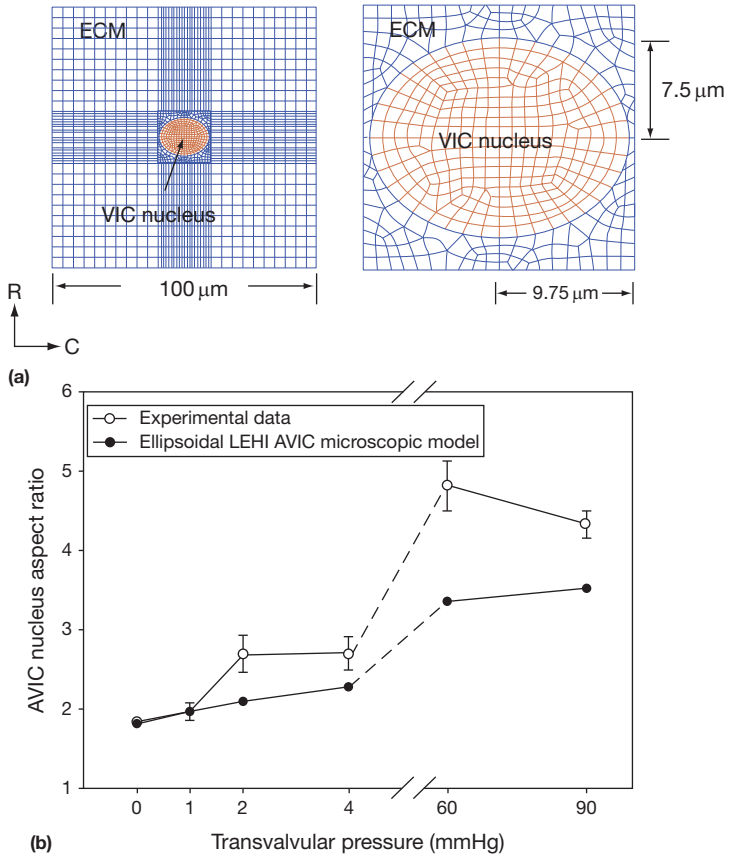

Figure 6 (a) The finite element mesh consisting of an AVIC nucleus within leaflet extracellular matrix, with the contributions of the cell membrane and cytoplasm being considered negligible. (b) A comparison of experimentally measured AVIC nuclear aspect ratio values with values predicted by the representative volume element (RVE) model plotted against the experimentally applied levels of transvalvular pressure (TVP). While the RVE model captured the overall trend, discrepancies with the experimental data increased at greater TVPs. This result indicated that significant compression of the AVICs was induced by local fiber compaction.

change in nuclear aspect ratio (NAR) was used as an index of overall cellular strain, and dependencies on spatial location and pressure loading levels quantified. A tissue-level finite element (FE) model of an AVIC embedded in the AV ECM was also used to explore the relation between AV tissue- and cellular-level deformations (Figure 6(a)). The results indicated large, consistent increases in AVIC NAR with transvalvular pressure (e.g., from a mean of 1.8 at 0 mmHg to a mean of 4.8 at 90 mmHg), as well as pronounced layer-specific dependencies. Associated changes in collagen fiber alignment indicated that little AVIC deformation occurs with the large amount of fiber straightening for pressures below ~1 mmHg, followed by substantial increases in AVIC NAR from 4 to 90 mmHg (Figure 6(a)). While the tissue-level FE model was able to capture the qualitative response, it also underpredicted the extent of AVIC deformation. This result suggested that additional micromechanical and fiber-compaction effects occur at high pressure levels. The results of this study form the basis for the understanding of transvalvular pressure-mediated mechanotransduction within the native AV and first-time quantitative data correlating AVIC nuclei deformation with AV tissue microstructure and deformation.

3.308.3. Myocardium

Myocardium, the muscle of the heart, has had a long history of biomechanical investigations, and wall stress is a major factor in heart function and physiology.[61] As for the previous mentioned tissues, essential to the understanding of the myocardial mechanical behavior is constitutive (stress–strain) relationship. Biaxial mechanical tests have been used to quantify the passive mechanical properties of left ventricle (LV) midwall myocardium, which have revealed its regionally dependent, anisotropic, and viscoelastic behavior.[62–68] In contrast, there is comparatively little data yet available on the mechanical properties of the right ventricle (RV) myocardium.

Our group has reported the passive biaxial mechanical properties of the right ventricle free wall (RVFW) myocardium as follows.[69,70] Hearts from five mongrel dogs (~20 kg), used in unrelated studies, were harvested using a chilled high-potassium cardioplegic solution. The sinus or conus region was first dissected from the RVFW. Any visible coronary vessels in the remaining RVFW myocardium were plugged with adhesive to minimize leakage of the cardioplegic solution from the excision boundaries during reinjection, which allowed for adequate perfusion of the remaining myocardium.

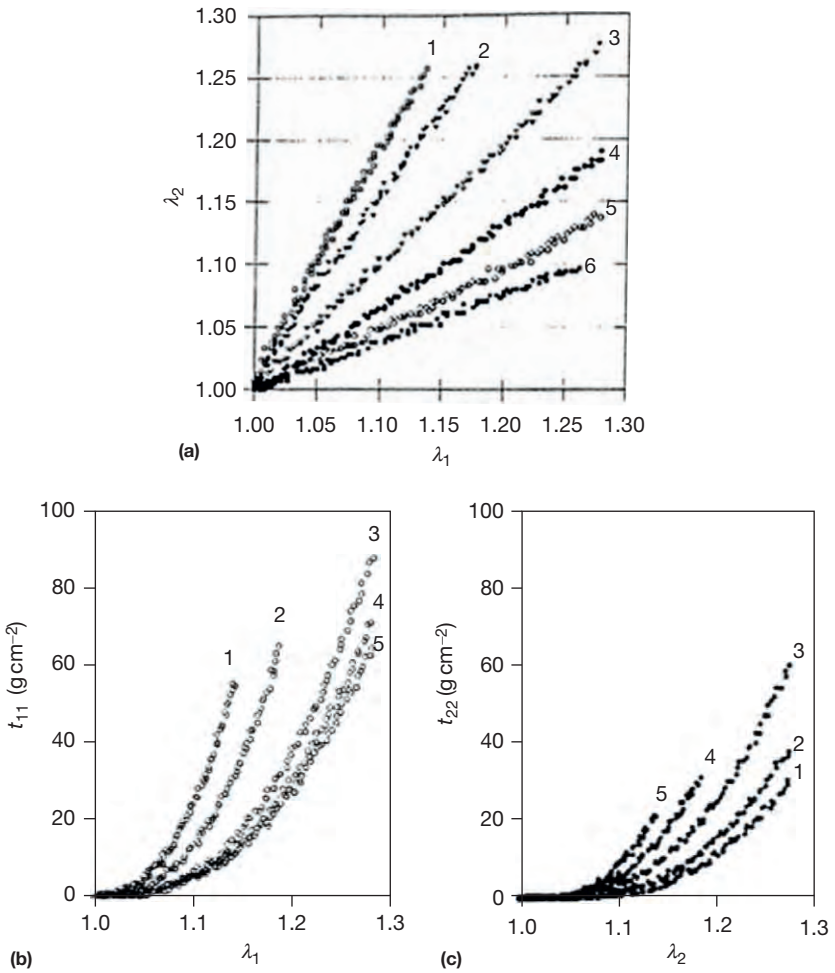

Figure 7 (a) Illustration of the six loading protocols used to characterize the passive RVFW myocardium mechanical properties. In each protocol, the ratio of the percentage elongation along each stretch axes was kept constant. The ratios used were 1:2, 1:1.5, 1:1, 1.5:1, 2:1, and 2.5:1, labeled as 1–6 on curves, respectively. (b, c) Typical stress–strain responses for the five loading protocols, with the labels on curves referring to the protocol numbers.

The remaining heart was placed in a chilled cardioplegic bath and reinjected with fresh chilled cardioplegic solution at 10–15 min intervals. A 2–3 mm sheet of fairly uniform thickness was prepared from the excised sections ~1 mm from the epicardial surface. After test completion, another specimen from the remaining RVFW region was similarly prepared and tested. All testing was performed in an oxygenated cardioplegic solution at room temperature within 3 h from the time of sacrifice. Specimens were preconditioned by performing ten cycles of equibiaxial stretch, with the load at either axes never exceeding 200 g. Immediately afterward, the unstressed specimen's optical target dimensions were recorded. This sequence was repeated until the optical target dimensions did not change by more than 3% from the prior measurement. Once stable optical target dimensions were obtained, the outer specimen dimensions were measured with a digital caliper. These dimensions were used as the references in all subsequent testing and analysis. The test protocol consisted of six tests in which the ratio of the percentage elongation along each stretch axes was kept constant (Figure 7(a)).

Both RVFW regions showed a greater stiffness in the fiber than the cross-fiber direction (Figure 7(b) and 7(c)). Both RVFW regions show a larger stiffness in the fiber than the cross-fiber direction. In general, we found that:

1. The overall qualitative response of the RVFW myocardium was similar to that of the LV myocardium. In both cases, the fiber direction was the direction of greater stiffness.
2. A greater degree of anisotropy was found for the RVFW myocardium compared to the LV midwall myocardium.
3. The conus region of the RVFW showed a greater degree of anisotropy compared to the sinus region.

Although qualitatively similar to the LV myocardium, the RVFW myocardium showed a consistently greater degree of anisotropy. Further, the RVFW showed clear regional differences in passive mechanical properties. The reasons for these differences are at present unknown, but they may be due to microstructural variations in the myocardium in different regions of the heart. Comparisons to other data for the LV is complicated by the different test protocols used. In earlier studies by Yin *et al.* cited above, similar degrees of varying anisotropy were

seen on the LV midwall myocardium. One may ask what mechanical advantages to the RVFW an increased level of anisotropy would bring. Like other biological structures, the heart is a paradigm of efficiency, and it is reasonable to expect that the observed differences satisfy the functional needs of their respective regions. A possible explanation is the close relation between the direction of maximum systolic deformation and mean fiber direction found in the RVFW.[71] It is possible that during systole the predominate stress component for each layer of the RVFW myocardium is in this same direction. A greater stiffness along this direction would tend to better support larger stresses. In the LV, no such similarity between the fiber direction and maximum deformation was found;[72] therefore, a less anisotropic property may be more mechanically advantageous in the LV. However, more studies of the stress distribution in the heart are required for a better understanding of the underlying causes of the differences in regional RV myocardial mechanical properties.

3.308.4. Constitutive Models of Soft Tissues

3.308.4.1. Introduction

Fung is considered the pioneer of phenomenological constitutive models for soft tissues, and many researchers have used variations of the so-called 'Fung-type' models for many different soft tissue applications.[37,73–76] Fung models are widely used because they are capable of capturing highly nonlinear mechanical behavior over a wide strain range. However, while Fung models and phenomenological models in general capture the general stress–strain behavior, they lack the ability to capture the underlying mechanisms contributing to tissue behavior, and the model parameters are not based on physiological phenomena. Structural models, on the other hand, are based on microstructural tissue features that are experimentally measurable and have the ability to relate tissue-level mechanical response to individual fibrillar constituent properties. Most soft tissues behave in a viscoelastic or related time-dependent manner. However, the mechanical behavior can be simplified by assuming a pseudoelastic behavior wherein the tissue is preconditioned and the stress–strain relation repeatable. The loading and unloading branches continue to be represented by a unique constitutive equation, but with differing parameter sets. We adopt this approach in the following section.

3.308.4.2. Stress and Strain Definitions

In the case of finite deformations, several different definitions of stress and strain are used. Let the vector $\mathbf{X}$ represent the position of a point P in the reference configuration, and $\mathbf{x}$ the position of that same material point in a deformed configuration. Then, the deformation gradient tensor $\mathbf{F}$ describes the transformation of the line segment $d\mathbf{X}$ to $d\mathbf{x}$ as $\mathbf{F} = \partial\mathbf{x}/\partial\mathbf{X}$. A change in an infinitesimal volume element (dV) from the reference to the deformed configuration is defined as $J = dV/dV_0 = \det\ \mathbf{F}$, which is equivalent to $J = \rho/\rho_0 = \det\ \mathbf{F}$ due to conservation of mass. Here, ρ is the tissue density in the current configuration and $\det\ \mathbf{F}$ is the determinant of $\mathbf{F}$. Because $\mathbf{F}$ contains rigid body motions, alternative measures of strains are defined that purely represent deformations giving rise to strain energy. The Right Cauchy-Green tensor $\mathbf{C}$, the Left Cauchy-Green tensor $\mathbf{B}$, and the Green–Lagrange or Green's strain tensor $\mathbf{E}$ are defined as

$$\begin{aligned}\mathbf{C} &= \mathbf{F}^T\mathbf{F}\\ \mathbf{B} &= \mathbf{F}\mathbf{F}^T\\ \mathbf{E} &= \frac{1}{2}(\mathbf{C}-\mathbf{I})\end{aligned} \quad [1]$$

where $\mathbf{I}$ is the identity tensor. Moving on to the most commonly used definitions of stress, the most natural definition is in the Cauchy sense, wherein the Cauchy stress tensor $\mathbf{t}$ is derived from the traction vectors acting on a body's surfaces and is defined in the deformed configuration. The first Piola–Kirchhoff stress tensor $\mathbf{P}$ is defined in the referential configuration. The second Piola–Kirchhoff stress tensor $\mathbf{S}$, while not having a simple physical meaning, represents a very useful stress measure. The following equations represent an overview of the relations between these stress tensors

$$\begin{aligned}\mathbf{P} &= J\mathbf{F}^{-1}\mathbf{t} = J\mathbf{t}\mathbf{F}^{-T}\\ \mathbf{S} &= J\mathbf{F}^{-1}\mathbf{t}\mathbf{F}^{-T}\\ \mathbf{P} &= \mathbf{F}\mathbf{S} = \mathbf{S}\mathbf{F}^T\\ \mathbf{S} &= \mathbf{F}^{-1}\mathbf{P} = \mathbf{P}\mathbf{F}^{-T}\end{aligned} \quad [2]$$

In the case of isothermal conditions (which is considered to be the case for biological tissues) and under the assumption of elastic behavior, we can define a scalar strain energy density function Ψ per unit undeformed volume. During an isothermal deformation, the strain energy is associated with the free energy per unit undeformed (reference) volume, and the strain energy is zero in the reference state. Under the assumption of hyperelasticity, we can then define

$$\mathbf{S} = \frac{\partial\Psi}{\partial\mathbf{E}} \quad [3]$$

so that $\mathbf{S}$ can be derived from Ψ. The goal for all constitutive modeling is thus to obtain the form and the parameter values for the scalar strain energy density function. A material with a constitutive relation of the form described by eqn [3] is called a hyperelastic material. In other words, the mechanical properties of a hyperelastic material are characterized completely by a scalar strain energy density function.

3.308.4.3. Phenomenological Hyperelastic Constitutive Models

Materials that keep the volume constant throughout a deformation are characterized by the incompressibility constraint $J = \det\ \mathbf{F} = 1$. For this class of materials, eqn [3] is expressed as

$$\mathbf{S} = 2\frac{\partial\Psi}{\partial\mathbf{C}} - p\mathbf{C}^{-1} = \frac{\partial\Psi}{\partial\mathbf{E}} - p\mathbf{C}^{-1} \quad [4]$$

where p is a Lagrange multiplier that is determined from the equations of motion and boundary conditions (kinematic constraints) and is usually associated with the hydrostatic pressure in a tissue. Note particularly that p does not generally have a direct physical interpretation, but under volume-changing deformations can only be interpreted as the hydrostatic pressure required to enforce incompressibility.[77] Under the assumption of pseudoelasticity, the strain energy function should technically be referred to as a pseudostrain-energy

function. Under the condition of plane stress (with $S_{13} = S_{23} = S_{33} = 0$) for planar biaxial deformation, the strain energy is dependent on the strain components E_{11}, E_{22}, E_{12}, E_{33}. Because of the incompressibility constraint, a reduced strain energy function can be defined as

$$\hat{\Psi}(E_{11}, E_{22}, E_{12}) = \Psi(E_{11}, E_{22}, E_{12}, E_{33}) \quad [5]$$

where the stress tensor components are

$$S_{11} = \frac{\partial \hat{\Psi}}{\partial E_{11}}$$
$$S_{22} = \frac{\partial \hat{\Psi}}{\partial E_{22}}$$
$$S_{12} = \frac{\partial \hat{\Psi}}{\partial E_{12}} - C_{12}C_{33}^2 \frac{\partial \Psi}{\partial E_{33}} \quad [6]$$

3.308.4.4. Fung and Coworkers

The first investigators to develop and utilize planar biaxial testing for soft biological tissues were Lanir and Fung, who, in 1974,[37,78] investigated the mechanical properties of rabbit skin. Briefly, a 3–6-cm square skin specimen was mounted in a trampoline-like fashion with up to 68 individual attachments distributed equally over the four specimen sides (17/side). As in the experiments by Rivlin and Saunders,[79] the tension on each line could be individually adjusted to ensure that a reasonably uniform stress was applied on each specimen side. Actuator motion was controlled utilizing a function generator. To avoid the effects of local stress concentrations of the suture attachments, bidirectional tissue strain was measured in a central region by monitoring the distance between pairs of lines separated by 5 mm along each axis using a video dimensional analyzers (VDAs).[80] Experimental results demonstrated that skin exhibited a nonlinear, orthotropic stress–strain response whose material axis depended on the specimen's anatomic orientation. While differences were observed between the loading and unloading curves due to hysteresis, the loading and unloading stress–strain responses were essentially independent of strain rate. It is important to note that these results *underscore the major phenomenon found in all subsequent biaxial mechanical investigations of soft tissues*.

Based on these experimental observations and data, Tong and Fung[81] used the above biaxial data to develop a constitutive model. Because of their insensitivity to strain rate, separate pseudostrain-energy functions could be developed for the loading and unloading phases of the stress–strain curve.[35] Thus, for the loading and unloading phases, the in-plane second Piola–Kirchhoff stresses are derived from a 2D strain energy function W

$$S_{ij} = \frac{\partial W}{\partial E_{ij}} \quad [7]$$

For this form of W (using their original notation), Tong and Fung observed from the experimental data that the stress–strain curves had a very shallow slope followed by an abrupt transition to a very high stiffness. For all practical purposes, the 'Fung' type model was developed

$$\rho_0 W = \frac{c}{2}(e^Q - 1) \quad [8]$$

where $Q = c_{ijkl}E_{ij}E_{kl}$. This is perhaps the most broadly used constitutive model to date for the biaxial response of soft biological tissues (as well as other loading states), including skin,[81] pericardium,[82] epicardium,[83] visceral pleura,[84] and myocardium. However, one of the difficulties in applying eqn [8] to biological tissue is the high amount of interspecimen variability, which in turn translates into wide variability in material parameter values. The sources of variability have been attributed to experimental noise or numerical instability of the fitting algorithms resulting from the nonlinearity. These problems can confound the ability to obtain a unique set of material constants either for a given specimen or for a class of biomaterials. Further, the residuals in nonlinear regression may not be normally distributed, disallowing conventional statistical analysis.

In their study of canine pericardium, Yin *et al.*[66] developed a statistical approach to assess the sources of the variability in material constants in describing biaxial stress–strain data and to account for them. Using experimental data for canine pericardium,[82] they determined a strain energy function (including exploration of the use of noninteger powers of the Green strain). They performed a residual analysis to determine if standard statistical methods could be used to assess the variability, and, if they were not, they used nonparameteric methods (boot strapping). The use of a five parameter exponential strain energy function found pericardial tissue to be strain-history dependent and anisotropic, which could not be attributed to either experimental noise or instability in the numerical algorithms.

Another form of the phenomenological constitutive equation is expressed in terms of a set of independent strain invariants of $\mathbf{C}$ or $\mathbf{B}$.[85] The first three (principal) invariants are defined in terms of principal stretches as

$$I_1 = tr\mathbf{C} = tr\mathbf{B} = \lambda_1^2 + \lambda_2^2 + \lambda_1^2$$
$$I_2 = \frac{1}{2}\left[(tr\mathbf{B})^2 - tr\mathbf{B}^2\right] = \lambda_1^2\lambda_2^2 + \lambda_1^2\lambda_3^2 + \lambda_2^2\lambda_3^2$$
$$I_3 = \det\mathbf{C} = \det\mathbf{B} = J^2 = \lambda_1^2\lambda_2^2\lambda_1^2 \quad [9]$$

Most biological tissues are characterized as anisotropic and can be viewed as being composed of an isotropic matrix material (i.e., ground substance) and one or more families of fibers responsible for the anisotropy, with the derivation of the constitutive relation based on the principle of *material symmetry*. This approach was initially proposed by Spencer[85,86] for elastomeric materials and is now being increasingly used.[87] The simplest representation of this is transverse isotropy, consisting of one family of fibers. The fiber direction in the reference configuration is defined by a unit vector $\mathbf{a}$, and its structural tensor is defined as $\mathbf{a}\otimes\mathbf{a}$. The pseudoinvariants of $\mathbf{C}$ and $\mathbf{a}$ are

$$I_4 = \mathbf{a}^T\mathbf{C}\mathbf{a} = \lambda_A^2$$
$$I_5 = \mathbf{a}^T\mathbf{C}^2\mathbf{a} \quad [10]$$

where λ_A is the fiber stretch in the direction of $\mathbf{a}$. Thus, for transversely isotropic materials, the strain energy is written as $\Psi = \Psi(I_1, I_2, I_3, I_4, I_5)$.

Humphrey *et al.* developed the following functional form for myocardium biaxial mechanical properties. In this approach, a subclass of transversely isotropic materials that are a function of two strain invariants were used[88]

$$W = W(I_1, I_4) \quad [11]$$

where W is the strain energy function, and I_1 and I_4 are the first and fourth strain invariants, respectively, with $I_4 = \alpha^2$ where α is the stretch ratio along the muscle fiber direction. This form allows the determination of the dependence of W_1 and W_α on I_1 and α directly from the experimentally obtained stress and deformation data[88]

$$2W_1 = \frac{\xi_4 \mathbf{t}_{11} - \xi_2 \mathbf{t}_{22}}{\xi_1 \xi_4 - \xi_2 \xi_3} \quad W_\alpha = \alpha \frac{\xi_1 \mathbf{t}_{22} - \xi_3 \mathbf{t}_{11}}{\xi_1 \xi_4 - \xi_2 \xi_3} \qquad [12]$$

where $W_1 = \partial W/\partial I_1$ and $W_\alpha = \partial W/\partial \alpha$, t_{ij} are the physical components of the Cauchy stress tensor, and

$$\begin{aligned}
\xi_1 &= \lambda_1^2 + \kappa_1^2 - \lambda_3^2 \\
\xi_2 &= \lambda_1^2 \cos^2(\theta) + 2\lambda_1\kappa_1 \cos(\theta)\sin(\theta) + \kappa_1^2 \sin^2(\theta) \\
\xi_3 &= \lambda_2^2 + \kappa_2^2 - \lambda_3^2 \\
\xi_4 &= \kappa_2^2 \cos^2(\theta) + 2\lambda_2\kappa_2 \cos(\theta)\sin(\theta) + \lambda_2^2 \sin^2(\theta) \\
\xi_5 &= \kappa_1\lambda_2 + \kappa_2\lambda_1 \\
\xi_6 &= \lambda_1\kappa_2 \cos^2(\theta) + (\lambda_1\lambda_2 + \kappa_1\kappa_2)\cos(\theta)\sin(\theta) + \kappa_1\lambda_2 \sin^2(\theta)
\end{aligned} \qquad [13]$$

where λ_i and κ_i are components of the deformation gradient tensor, and θ is the fiber angle with respect to the x_1 axis. Next, based on experimental plots of W_1 and W_α versus I_1 and α, they assumed the following functional form for $W(I_1, \alpha)$

$$W(I_1, \alpha) = \sum_{i=0}^{n} \sum_{j=0}^{m} c_{ij} (I_1 - 3)^i (\alpha - 1)^j \qquad [14]$$

where c_{ij} are material parameters. The interested reader is referred to[88] for details of the derivation. Based on the resulting response functions, as well as the theoretical restrictions on the values of c_{ij} (e.g., at zero strain $W(3, 1) = 0$, requiring $c_{00} = 0$), the following form for passive myocardium was derived

$$\begin{aligned}
W(I_1, \alpha) = {} & c_1(\alpha - 1) + c_2(\alpha - 1)^3 + c_3(I_1 - 3) \\
& + c_4(I_1 - 3)(\alpha - 1) + c_5(I_1 - 3)^2
\end{aligned} \qquad [15]$$

where c_i are the material constants. In obtaining the material constants, additional empirical inequalities were applied to set bounds on the values for c_i. The constant invariant tests used to derive eqn [15] require that the tissue specimen be subjected to simultaneous loading and unloading, which strictly violates pseudoelasticity.[35] Thus, data from only the loading portion of the equibiaxial strain and constant α tests were used to determine values for c_i. The data from constant I_1 tests were used to find only the functional form, and were hence excluded as the tissue experiences simultaneous loading and unloading during these tests. The resulting model was found to fit the biaxial data quite well, and was also found not to be overparameterized.[89] The results also emphasized the need for good data, including accurate measurement of the applied forces, original dimensions, and experimental deformations. Later, Sacks and Chuong[70] successfully applied eqn [15] to right ventricular myocardium, where the effects of a fiber splay were incorporated within the specimen. May-Newman and Yin[90] also applied a similar approach to the biaxial mechanical properties of the mitral valve. It is also interesting to note that the overall approach of using theoretically guided experiments is not restricted to the form of eqn [20], but it has also been successfully applied to the epicardium (a thin connective tissue layer surrounding the heart)[83] using the Fung model (eqn [8]) and constant E_{11} and E_{22} tests.

Clearly, the strength of the above approach is that it allows the derivation of the functional form of W to be based on direct evaluation of the experimental data. This avoids the limitations of the trial-and-error approach of earlier work, and is an elegant example of how theory and experiment can be successfully integrated. In principal, the approach can be applied to specimens where there is a nonzero distribution of fiber orientations. However, the author has found the model to be weakly dependent with respect to trans-mural layer orientations, potentially because of the transverse isotropy assumption (Sacks, unpublished data). More detailed, realistic interlayer models may need to be developed. Further, in order to determine the form of W, strict pseudoelasticity must be violated (i.e., the tissue must be subjected to simultaneous loading and unloading protocols). While the loading and unloading curves are qualitatively similar, differences do exist and may influence the sensitivity and final choice of the form. Moreover, one can extend this approach to two families of fibers, where the second fiber family is defined by the unit vector $\mathbf{b}$; additional strain invariants are defined as associated with this additional fiber family and the interaction between the two families. The invariants I_6–I_8 are defined as

$$\begin{aligned}
I_6 &= \mathbf{b}^T \mathbf{C} \mathbf{b} = \lambda_B^2 \\
I_7 &= \mathbf{b}^T \mathbf{C}^2 \mathbf{b} \\
I_8 &= \mathbf{a}^T \mathbf{C} \mathbf{b}
\end{aligned} \qquad [16]$$

Strain energy functions are often divided into an isotropic and an anisotropic part representing the isotropic matrix and the fibers, respectively, resulting in

$$\Psi = \Psi_{\text{iso}}(I_1, I_2) + \Psi_{\text{aniso}}(I_4, I_5, \ldots) \qquad [17]$$

when assuming incompressibility ($I_3 = 1$), which can be simplified to[87]

$$\Psi = \Psi_{\text{iso}}(I_1) + \Psi_{\text{aniso}}(I_4, I_6, \ldots) \qquad [18]$$

Different specific functional forms of Ψ_{iso} and Ψ_{aniso} have been proposed in the literature, where a neo-Hookean formulation is often used for Ψ_{iso}

$$\Psi_{\text{iso}} = \frac{C}{2}(I_1 - 3) \qquad [19]$$

For Ψ_{aniso}, many different phenomenological expressions have been proposed (e.g., Holzapfel *et al.*,[74] Holzapfel and Gasser,[87] Humphrey *et al.*,[88] Holzapfel,[91] Humphrey and Yin,[65] Natali *et al.*,[92] Yang *et al.*[93]). An interesting generalization of the invariant-based method has been presented by Ehret and coworkers.[94] They present a constitutive model for fiber-reinforced materials consisting of an arbitrary number of fibers, where each fiber is represented by its individual structural tensor and a weight factor.

3.308.4.5. Structural Constitutive Models for Multiphase Soft Tissues

The structural approach as introduced where each model parameter has physiological significance, allows for separate investigation of the contribution of each individual tissue component to the tissue's mechanical behavior, and will eventually provide the ability to elucidate changes as a result of

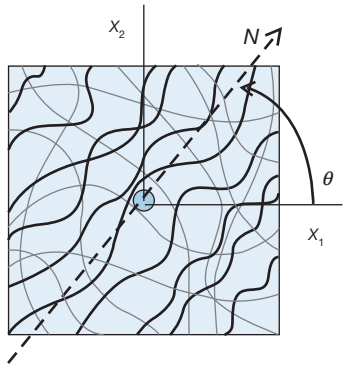

Figure 8 Schematic of the representative volume element. Fiber ensembles are an idealized group of fibers of varying undulation, aligned along the same angle θ, represented by the unit vector N.

pathological processes. The structural constitutive model described herein builds upon the theoretical work formally introduced by Lanir and coworkers[95–98] and extended by Sacks and coworkers,[1,99,100] in which the tissue-level response is related to the collective contribution of individual fiber ensembles. The term fiber ensemble refers to a collection of fibers sharing a common orientation. This modeling technique treats the fibrillar ECM component by homogenizing the fiber ensemble response. It is assumed that a representative volume element (RVE) can be identified that is large enough to represent the processes associated with the microstructure of the material in an average sense, yet sufficiently small compared to the characteristic length scale of the microstructure (Figure 8). The RVE is treated as a 3D continuum, and within the RVE, the following assumptions are made (see also Sacks[100]):

1. The tissue can be idealized as a network of fibers of varying types and structures, all embedded within a compliant ground matrix. The two fiber families considered in the current study are collagen and muscle.
2. Fiber–fiber and fiber–matrix interactions are ignored so that the net tissue response is the sum of the individual fiber responses.
3. Hydrostatic forces generated by the matrix are considered negligible compared to the fiber forces, and are handled by assuming that these components collectively induce an incompressible behavior at tissue level.
4. Contributions from nonload-bearing constituents are combined with the ground matrix.
5. Collagen fibers are intrinsically undulated (also called crimped) and gradually straighten with increased stretch. The load required to straighten the collagen fiber is considered negligible compared to the load transmitted by the stretched fiber. Once a fiber has been stretched to a straightened state, it will transmit load and be considered linear elastic.

The tissue-level strain energy density Ψ of the RVE is assumed to result from the contribution of muscle (M) and ECM, weighted by their respective volume fractions ϕ and is defined as

$$\Psi(\mathbf{E}) = \sum_i \phi_i \Psi(\mathbf{E}) = \phi_{\mathrm{ECM}} \Psi_{\mathrm{ECM}}(\mathbf{E}) + \phi_{\mathrm{M}} \Psi_{\mathrm{M}}(\mathbf{E}) \qquad [20]$$

If the tissue is considered to consist mostly of water (tissue density $= \sim 1\,\mathrm{g\,ml^{-1}}$), and if individual constituent densities are assumed to be equal, volume fractions can be approximated by mass fractions. Assuming a pseudoelastic, hyperelastic material response, the tissue-level second Piola–Kirchhoff stress $\mathbf{S}$ is derived from the strain energy as

$$\begin{aligned}\mathbf{S}(\mathbf{E}) &= \frac{\partial \Psi(\mathbf{E})}{\partial \mathbf{E}} - p\mathbf{C}^{-1} \\ &= \phi_{\mathrm{ECM}} \frac{\alpha \Psi_{\mathrm{ECM}}(\mathbf{E})}{\partial \mathbf{E}} + \phi_{\mathrm{M}} \frac{\partial \Psi_{\mathrm{M}}(\mathbf{E})}{\partial \mathbf{E}} - p\mathbf{C}^{-1}\end{aligned} \qquad [21]$$

where the Lagrange multiplier p accounts for the incompressible nature of the tissue.

A structurally based modeling approach for planar collagenous tissues is employed for the ECM strain energy function, where the contribution of individual fiber ensembles acting at independent orientations is summed over all orientations, using a statistical fiber orientation distribution function. Thus, it assumes the form

$$\begin{aligned}\Psi_{\mathrm{ecm}}(\mathbf{E}) &= \int_\theta R(\theta) \Psi_{\mathrm{col}}^{\mathrm{ens}}(\theta, \mathbf{E}) \mathrm{d}\theta \\ &= \int_\theta R(\theta) \Psi_{\mathrm{col}}^{\mathrm{ens}}(E^{\mathrm{ens}}(\theta)) \mathrm{d}\theta\end{aligned} \qquad [22]$$

where col stands for collagen, $R(\theta)$ is the fiber angular density function, $\Psi_{\mathrm{col}}^{\mathrm{ens}}$ is the strain energy associated with an individual collagen fiber ensemble (ens), and $E^{\mathrm{ens}} = \mathbf{N}^T \mathbf{E} \mathbf{N}$ is the uniaxial Green–Lagrange strain acting in the ensemble direction, defined by a unit vector parallel to the fiber axis in the reference configuration $\mathbf{N}$. The effective ensemble response has been modeled with a phenomenological expression[34,99,100] as well as with a formulation accounting for the recruitment process.[100]

The structural formulation for collagen fibers assumes that the fibers are crimped and transmit load only if stretched beyond the point where all the crimp has disappeared, that is, the slack stretch or strain. In the straightened condition, fibers are assumed to follow a linear elastic material model. In the case of straight fibers without slack, this implies $S_{\mathrm{f}} = \eta E_{\mathrm{t}}$ or $\Psi_{\mathrm{f}} = \frac{\eta}{2} E_{\mathrm{t}}^2$, where η is the fiber modulus and E_{t} is the true fiber strain. In the case of undulated fibers, E_{t} is related to the ensemble or fiber strain by $E_{\mathrm{t}} = \frac{E^{\mathrm{ens}} - E_{\mathrm{s}}}{1 + 2E_{\mathrm{s}}}$, where E_{s} is the fiber slack strain. In terms of E_{t}, the fiber stress–strain relation for an undulated fiber is

$$S_{\mathrm{f}} = \frac{\partial \Psi_{\mathrm{f}}}{\partial E_{\mathrm{f}}} = \frac{\partial E_{\mathrm{f}}}{\partial E_{\mathrm{t}}} \frac{\partial E_{\mathrm{t}}}{\partial E_{\mathrm{f}}} = \eta \frac{E_{\mathrm{f}} - E_{\mathrm{s}}}{1 + 2E_{\mathrm{s}}} \frac{1}{1 + 2E_{\mathrm{s}}} = \eta \frac{E_{\mathrm{f}} - E_{\mathrm{s}}}{(1 + 2E_{\mathrm{s}})^2} \qquad [23]$$

The ensuing fiber ensemble strain energy and stress–strain relation are then described as the sum of the individual fiber strain energies of the ensemble (Figure 8), weighted by the distribution of slack strains D, as

$$\begin{aligned}\Psi_{\mathrm{col}}^{\mathrm{ens}}(E^{\mathrm{ens}}) &= \int_0^{E^{\mathrm{ens}}} D(x) \Psi_{\mathrm{f}}(x) \mathrm{d}x = \frac{\eta}{2} \phi_{\mathrm{f}} \int_0^{E^{\mathrm{ens}}} D(x) \left[\frac{E^{\mathrm{ens}} - x}{1 + 2x} \right]^2 \mathrm{d}x \\ S_{\mathrm{col}}^{\mathrm{ens}}(E^{\mathrm{ens}}) &= \int_0^{E^{\mathrm{ens}}} D(x) S_{\mathrm{f}}(x) \mathrm{d}x = \eta \phi_{\mathrm{f}} \int_0^{E^{\mathrm{ens}}} D(x) \frac{E^{\mathrm{ens}} - x}{[1 + 2x]^2} \mathrm{d}x\end{aligned} \qquad [24]$$

Here, η is the collagen fiber modulus, ϕ_f the collagen fiber fraction, and $D(x)$ a recruitment function. For convenience, ϕ_f is often absorbed in the effective fiber modulus K

$$K = \phi_f \eta \quad [25]$$

Here, $D(x)$ describes the fraction of fibers realizing a fully straightened state at a given strain magnitude, which is effectively the distribution of slack strains $D(E_s)$. D is defined over $E_s \in [E_{lb}, E_{ub}]$, where E_{ub} is the upper bound strain defining an ensemble strain state where all fibers are straight, and E_{lb} the ensemble strain where recruitment begins (E_{lb} can be assumed to equal zero in many cases). Under equibiaxial strain conditions, E_{11} equals E_{22}, and zero shear is assumed ($E_{12} = 0$). Because of the fact that $D(x)$ is not directionally dependent, the fiber ensemble stress–strain relationship can be obtained directly from the experimental data using $S^{ens} = S_{11} + S_{22}$, and $E^{ens} = E_{11} = E_{22}$.[98,100] Hence, the parameters of the fiber ensemble model could be experimentally determined directly from an equibiaxial stretch protocol. Combining the above leads to a complete formulation for stress in the ECM component

$$\mathbf{S}(\mathbf{E}) = \eta\phi_f \int_{-\frac{\pi}{2}}^{\frac{\pi}{2}} R(\theta) \left\{ \int_0^{E^{ens}(\theta)} D(x) \frac{E^{ens}(\theta) - x}{[1+2x]^2} dx \right\} \mathbf{N} \otimes \mathbf{N} \, d\theta \quad [26]$$

The fiber distribution function R is represented by a β-distribution function with mean μ_R and standard deviation σ_R.

Forms and functions describing fiber recruitment, a process in which fibers in an individual ensemble engage into load transmission as they become fully straightened, have been presented in the literature.[100] The recruitment function $D(E_s)$ can be represented by different functions. The simplest relation is exponential in form:

$$D(E_s) = \frac{\left[\exp\left(a \frac{E_s}{E_{ub}}\right) - 1 + b \frac{E_s}{E_{ub}} \right]}{E_{ub}\left[\frac{b}{2} + \frac{(\exp(a) - 1)}{a} - 1\right]} \quad [27]$$

where the denominator is introduced to ensure $\int_0^{E_{ub}} D(x)dx = 1$. As an initial step, the recruitment function $D(E_s)$ is represented by means of a unimodal modified β-distribution with mean μ and standard deviation σ.[101] The β-distribution $B(\gamma)$ is defined on the interval $\gamma \in [0, 1]$, which is modified to be defined on the interval $[0, E_{ub}]$, with $\gamma = E_s/E_{ub}$, so that

$$D(E_s, \mu, \sigma) = \begin{cases} \dfrac{B(\gamma, s_1, s_2)}{E_{ub}} & 0 \le E_s \le E_{ub} \\ 0 & \text{otherwise} \end{cases} \quad [28]$$

where s_1 and s_2 are shape parameters computed from μ and σ using

$$s_1 = \frac{\mu^2 - \mu^3 - \mu\sigma^2}{\sigma^2}, \quad s_2 = s_1 \frac{1-\mu}{\mu} \quad [29]$$

the β-function is restricted to a unimodal shape with a lower bound of zero, and $s_1, s_2 > 1$ is enforced to prevent the upper bound going to infinity. Note, that for an unbound function $\mu, \sigma \in [0, 1]$.

Next, this model is extended by adopting a structurally guided form for the fiber ensemble strain energy. To take into account both levels of fiber uncoiling present in the bladder collagen fiber network, $D(E_s)$ is modified to the following bimodal distribution (with $j = 1$, 2, and γ a scaling factor):

$$D(E_s, \mu_j, \sigma_j, \gamma) = \gamma D_1 + (1-\gamma) D_2 \quad [30]$$

The parameters are bound in a similar manner, that is, the shape parameters are larger than 1 to enforce two distinguishable peaks, $\mu_1 < \mu_2$.

To estimate the fiber effective modulus, we note that if the tissue consisted of all straight fibers, the maximum tangent modulus (MTM) would equal K. At strain values $E^{ens} > E_{ub}$, all fibers are recruited, and MTM is determined using

$$\text{MTM} = \frac{\partial S^{ens}(E^{ens})}{\partial E^{ens}} \Big|_{E^{ens} \ge E_{ub}} = K \int_0^{E_{ub}} \frac{D(x)}{(1+2x)^2} dx \quad [31]$$

The greater the degree of slacked fibers in the tissue (either a longer slack length per fiber, or more slacked fibers), the lower is the MTM as compared to K. Hence, MTM provides a lower bound value for K, the integral on the right hand side of eqn [31] being lower than 1 because of the presence of fiber slack.

Experimentally, the E_{ub} is determined by finding the onset of constant stiffness from the S_{ens}-E_{ens} response curve, best determined from strain value, where the tangent modulus plateaus (**Figure 9(a)** and **9(b)**). To determine the ensemble model parameters K, μ, and σ, eqn [31] was fitted to the to S'–E' data using the Marquardt–Levenberg nonlinear least squares algorithm.[102] The posttransition tangent modulus value (equivalent to the MTM) was used as an initial estimate for the collagen fiber elastic modulus K. When applied to the native MVAL, mitral valve posterior leaflet (MVPL), and AV, the recruitment model was found to fit the data quite well, with an $r_2 \cong 0.99$. Aortic valve leaflet (AVL) was found to have the $E_{ub} = 0.3013 \pm 0.0323$, in comparison with MVAL (0.2692 ± 0.0487) and MVPL (0.2473 ± 0.01181). Moreover, the model predicted the very similar average K values for each valve leaflet type (mean ± s.e.m., $n = 6$ each): MVAL 123.443 ± 3.324 MPa, MVPL $= 124.114 \pm 7.830$ MPa, and AV $= 101.220 \pm 6.030$ MPa. It is interesting to note that these values are very similar to the 95.5 MPa measured using SAXS for the MVAL.[46] In addition to having greater structural realism, the recruitment model can perform better in stress overload situations. For example, both the exponential model and the recruitment model were fitted to the same equibiaxial strain data (**Figure 9(c)** and **9(d)**). We then simulated the trend beyond the used data range and examined the predicted trend with the ten real datum points. As anticipated, the exponential model predicted a continuous increase in tensile modulus with increased strain, whereas the fiber recruitment model provided accurately predicted the linear stress–strain relationship beyond the data range (**Figure 9(b)**). This result indicates the need for realistic constitutive models capable of prediction outside the range used to define the model, especially in situations where stress overloads need to be accurately predicted.

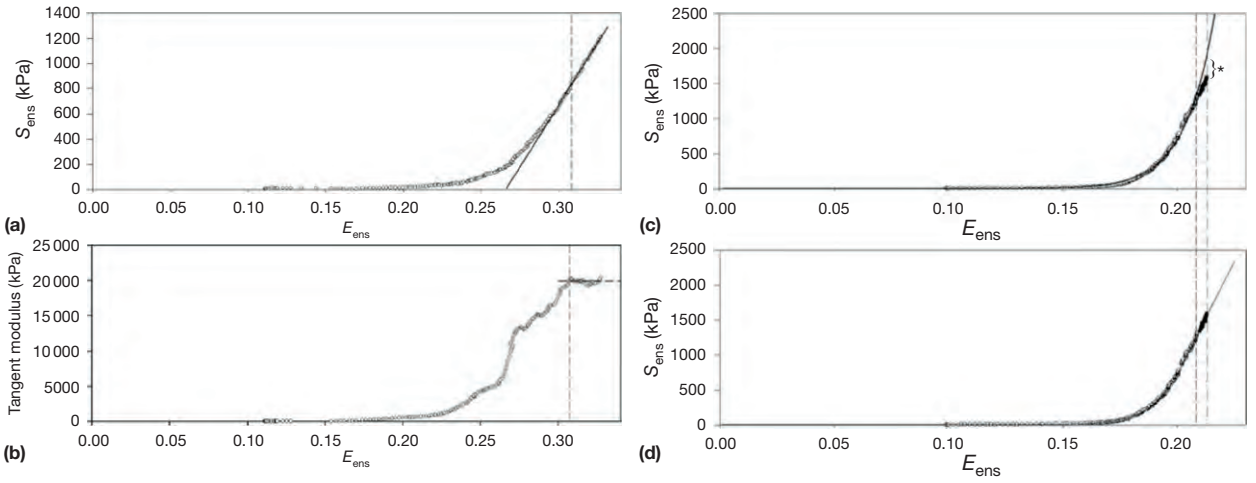

Figure 9 (a) A representative example of the effective fiber stress–strain curve of heart valve leaflets (MVAL), showing the characteristic long toe region, transitional region, and subsequent linear region. (b) Corresponding tangent modulus of the fiber stress–strain curve. Note the sharp rise of tangent modulus in the middle of the transitional region and the following plateau that shows a constant tensile modulus in the linear region. (c) The standard exponential model fitted to the data predicts a continuous increase of stiffness beyond the used data range, whereas the fiber recruitment model correctly predicts a linear stress–strain relationship beyond the used data range.

3.308.5. Emulating Native Tissue Mechanical Behavior in Engineered Tissues

3.308.5.1. Introduction

Surgical replacement of cardiac tissues using engineered tissue/regenerative medicine approaches has become a major research focus in the field of biomaterials and biomechanics. For example, in pediatric applications, growth of the replacement valve is essential to eliminate the need for reoperations as the patient grows. The ultimate heart valve replacement characterized as a nonobstructive, nonthrombogenic living tissue valve substitute that lasts the lifetime of the patient, provides ongoing remodeling and repair of cumulative injury, and potentially grows with the recipient is an important goal.[103] Such a valve would be particularly useful in the treatment of the ~20 000 children with congenital heart disease born in the United States each year and especially those with valvular disease. In this population, the anticoagulation required with mechanical valves is particularly dangerous and tissue valve substitutes undergo accelerated calcification. Thus, a fundamental problem inherent in the use of existing mechanical and biological prostheses in the pediatric population is their failure to grow, repair, and remodel. Engineered tissue approaches have the potential to address these and related tissues.[103]

However, engineered tissue approaches in cardiac tissue engineering ultimately have to function mechanically at the tissue and organ levels. As shown earlier in the text, collagenous soft tissues exhibit a wide array of unique mechanical behaviors, which can be probed by a variety of testing modes (tension, shear, bending, torsion, etc.). Practically speaking, the application of traditional engineering metrics of material behavior to soft biological materials can be not only difficult but also potentially unsuitable. When characterizing material performance, it is important to consider the functional relevance of a chosen method of mechanical testing and its interpretation relating to tissue function. For instance, valvular tissue stiffness with the highly anisotropic and nonlinear behavior of the tissues as discussed in the preceding sections cannot be adequately described by singular indices of material behavior. This is apparent in the circumferential response of valvular tissues under biaxial loading, where specimen contraction is observed at high stress states rendering the calculation of a MTM erroneous (Figure 4). The basis for this coupled, anisotropic response between material directions is the result of a reorganization of the fiber constituents (i.e., structural anisotropy). While helpful in providing potentially comparable metrics of tissue behavior, tabulated values, which appear in contemporary literature, can be misleading and belie the complex mechanical responses characteristically observed in soft load-bearing tissues. While the matching of metrics related to tensile strength (i.e., ultimate tensile stress and ultimate percent elongation) or tensile modulus has merit when applied appropriately, this approach gives little indication of the full material response during loading. Again, in the case of valvular tissues, if one was to simply match peak stress–strain values without considering the native material loading response, it would likely lead to inadequate coaptation or closing of the heart valve and result in poor function. Native cardiac tissues often exhibit highly specific, complex mechanical behaviors necessitating more sophisticated and thorough methods of characterization. This is also true for scaffolds and engineered constructs, as discussed in the following sections.

3.308.5.2. Electrospun Scaffolds

Elastomeric scaffolds fabricated by electrospinning natural polymers, synthetic polymers, or polymer blends have received widespread attention, largely due to their ability to produce biocompatible polymer constructs that exhibit many soft tissue-like mechanical behaviors.[104–106] Electrospinning is a highly versatile process capable of creating a wide array of material behaviors through the alteration of production

parameters or polymer choice. As such, it is necessary to assess these mechanical behaviors in a systematic manner. For practical reasons, uniaxial tensile testing is often employed to obtain basic material properties such as the elastic modulus, strain at the onset of yielding, and ultimate tensile strength.[107–113] From the systematic mechanical evaluation conducted by Courtney *et al.*, several scaffolds were manufactured with varying degrees of structural anisotropy or fiber alignment, which was controlled by altering the rotational velocity of the collection mandrel. Increase in rotational velocity results in an increase in fiber alignment,[105,114–116] and this was experimentally measured from scanning electron microscopy (SEM) micrographs via an image analysis algorithm.

The controlled structural anisotropy produced during manufacturing directly led to more nonlinear, anisotropic material responses. These structural properties form a complex 3D scaffold with tunable tissue-level mechanical behavior that can be remarkably similar to the gross biaxial mechanical response of the native pulmonary valve leaflet.[104] It has also been shown that the tensile response of some musculoskeletal tissues, namely, knee meniscus and annulus fibrosis tissues, can be emulated well by electrospun scaffolds.[105,117] Much of the work found in the recent literature has focused on the structural and mechanical characterization of electrospun materials with limited effort made in the development of modeling frameworks to further assess our understanding of electrospun material behavior. Nerurkar *et al.* have adapted a homogenization modeling approach originally presented by Yin and Elliot to compare predicted mechanical behaviors of electrospun poly-ε-caprolatone and the inner and outer lamella of native annulus fibrosus tissue. Structure-based modeling attempts originally developed for dense collagenous planar tissues have proven quite successful in capturing the mechanical behavior of electrospun scaffolds under biaxial modes of deformation.[104] It was noted that the model predicted a higher degree of fiber orientation than measured experimentally. This is attributed to structural characteristics of the polymer fibers measured in the image analysis algorithm but not accounted for in the model formulation.

In order to improve upon these initial modeling efforts and gain a better appreciation of how these materials function across multiple length scales, work was recently undertaken by Stella *et al.* to quantify additional structural characteristics. The electrospun scaffolds investigated in this study exhibited complex, hierarchical architectures spanning multiple length scales.[118] As a result, understanding the mechanisms by which these materials deform and behave under various loading conditions was not a simple task. Fiber tortuosity, diameter, and fiber orientation distributions were all quantified as the electrospun specimen underwent planar biaxial modes of deformation. In addition, the deformation behavior of the scaffold was investigated across multiple scales by defining three characteristic lengths (micro (1–2 μm), meso (40–50 μm), and macro (1–3 mm)). Fiber tortuosity, a measure of how much a fiber deviated from being straight in the unloaded scaffold, was observed to be dependent on mandrel velocity during both production and orientation. As the scaffold underwent planar biaxial modes of deformation, fiber tortuosity was eliminated and substantial fiber rotational kinematics was observed, contributing to an intricate fiber recruitment process.[119] Electrospun constructs were observed to follow gross affine fiber transformations and can be described in a manner similar to collagenous scaffolds.[120] Interestingly, some fibers were observed to rotate or change their direction of orientation during deformation, while as a population, no net change was measured. This is likely an additional manifestation of the local heterogeneity that exists at the microscale. With increased specimen deformation, a monotonic decrease in poly(ester urethane)urea (PEUU) fiber diameter was measured for all specimens. Furthermore, it was observed that the neighboring fibers were well attached where they overlapped or intersected, impeding translation of fibers with respect to one another; but this did not appear to inhibit rotational fiber kinematics about these points of intersection. Johnson *et al.*[121] presented a similar hypothesis for reduced fiber mobility in electrospun polymers exhibiting 'point bonding.' In short, polymer sintering was utilized on electrospun poly (ε-caprolatone) scaffolds to invoke definite point bonds between fibers. Scale-dependent variations in deformation were observed and these were attributed to the complex, spatially variant structure that results from the electrospinning process. These heterogeneous variations occur at the microscale that a cell might experience. The overall strain behavior tends to become increasingly more homogenous as the scale of interest approaches the tissue level.

The unique coupled matrix–cell deformation response of electrospun scaffolds integrated with cells was also recently investigated (**Figure 10**).[119] The scaffolds exhibited microfiber morphologies and kinematics that were shown to directly influence local cellular deformations. For instance, in the unstrained configuration, the electrospun fibers exhibited a tortuous architecture that transitioned to a web-like network of straight, interconnected fibers at high levels of strain. The deformations of the microintegrated cells were found to be primarily mediated primarily by this phenomenon. The cell-integrated constructs underwent fully recoverable large deformations akin to many native tissues. Initially, the integrated cells exhibited a rapid increase in NAR as the fibers straightened and tortuosity was reduced. Once the PEUU fibers became straightened and the architecture transitioned to an interconnected web-like structure, changes in NAR were observed to remain constant. Microintegrated cell deformation was mediated by the local reduction of tortuosity or straightening of the PEUU fibers. Thus, cell–scaffold interactions can be subtle and can bring about unique deformation behaviors. These results indicate that it may be possible to successfully emulate gross native tissue behavior without exactly replicating their highly complex microarchitectures. Attempts to delineate the individual contributions of structural fiber characteristics such as tortuosity and fiber kinematics to the construct's mechanical behavior would be quite cumbersome and might better lend itself to the development of a numerical framework to explore this unique, interrelated phenomenon.

3.308.5.3. Modeling Scaffold Structure–Function Relationships

Elucidation of the mechanical behavior of native biological materials is further confounded by tissue-specific, highly specialized multiscale constituent arrangements, which dictate their unique mechanical functions. While the

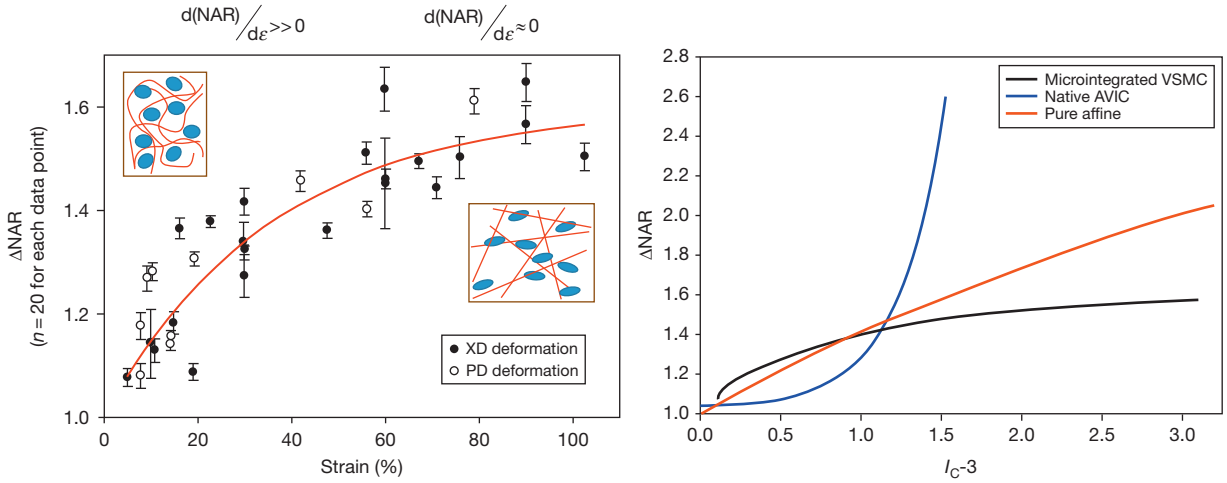

Figure 10 Strain-induced changes in electrospun polyester microarchitecture and resulting nuclei deformation. A composite of all nuclear aspect ratio measurements (mean ± s.e.m.) demonstrated a rapid increase to 60% strain, after which a plateau was observed with further strain increases, indicating that nuclei deformations are dominated by local fiber straightening. A composite cell–scaffold deformation response (bottom) is provided for native porcine aortic valve leaflet, cell-integrated electrospun poly(ester urethane)urea, and a theoretical purely affine cell deformation response to macroscopic strain.

development of new materials continues to be the focus of ongoing research, achievement of material behavior that is functionally comparable to native tissue is currently limited. Despite advancements made in recent years, there continue to be a multitude of unanswered fundamental questions, which inhibit the production of truly functional tissue surrogates. While more thorough methods for the characterization of native and engineered biological tissues are necessary, the answers to many fundamental biological or structural questions cannot be ascertained through experimental testing alone. By combining well-posed theoretical frameworks with experimentally derived observations, it is possible to elucidate the complex interrelated mechanisms presented by nature. Modeling approaches can serve as valuable tools not only to simplify and test our understanding of complex biological systems but also to guide future hypothesis-based investigations. Correspondingly, methods to restore, maintain, or improve tissue or whole organ function must incorporate a thorough understanding of the intricate multiscale hierarchical arrangements typically found in nature. Engineering sustainable solutions concerned only with tissue or organ-level function disregards the multifaceted, coordinated function of these tissue structures and their constituents, which are in turn a result of cellular or subcellular processes that reach down to the molecular scale of protein interactions and gene transcription. Surely, one model cannot incorporate this large range in scales with our current understanding of biological processes. Rather, a hierarchy of models and approaches is necessary to connect the established continuum-level relationships (i.e., phenomenological,[91,122–125] structural[64,87,97,98,100,126–128]) with underpinning cell and subcellular events. From a modeling point of view, a vital aspect of these models consists of the difficult task of seamlessly coupling various length scales.

For materials with regular, repeating structures, unit cell-based modeling approaches can successfully relate microstructural responses to global material behavior. Stylianopoulos and coworkers[129–131] have developed such a model for the mechanical behavior of collagen fiber networks. Briefly, the unit cell, the representative unit of the continuum that encompasses the periodicity of the microstructural parameters, contains an idealized fiber mesh generated in-silico. A group of unit cells are then perturbed in a defined manner (i.e., uniaxial tension) and a force balance within each unit cell results in a volume-averaged macroscopic response. In related work, Zahalak *et al.*[132] and Marquez *et al.*[133,134] have developed constitutive relations to relate individual cellular contributions to macroscopic material response in an effort to elucidate active and passive cell deformation responses and material properties. The fundamental unit of this model comprised cells, idealized as contractile rods, within a compliant matrix. Both constituents were parametrically assigned linear elastic, isotropic material properties. Because of these assumptions, the predictive capabilities are limited as biologic materials typically exhibit nonlinear viscoelastic behaviors. However, they did show that the strain experience by the cell can be related to macroscopic strain via a scalar valued strain factor and that reasonable approximations of cell stiffness can be determined from measured tissue properties. One shortcoming of the unit cell approach is that it neglects the structural heterogeneity seen in biological tissues and the incorporation of increased structural complexity is penalized by significant computational demands. Moreover, native dense collagenous tissues are long fiber composites with fiber lengths up to the millimeter scale while the characteristic length scale of this model is much shorter as defined by unit cell dimensions.

Additionally, efforts spent on assessing appropriate material specific RVE size have been insufficient. Morphology descriptors produced through image analysis such as material porosity, fiber density, fiber alignment distribution, fiber connectivity distribution, and fiber diameter strongly depend on the material architecture at micromeso level. This can be

demonstrated by studying the evolution of these parameters over regions of interest of increasing sizes and/or repeating the image analysis over analogous regions differing in location. Morphology feature fluctuations and location dependency gradually cease as the analyzed region of interest approaches an appropriate RVE size. A direct implication is that an image analysis technique remains incomplete if it does not identify an appropriate RVE for the variable of interest. RVE size in random composites can be derived by statistically, numerically, or empirically studying the stabilization of the analyzed variable over RVEs of increasing sizes.[135,136] Thus, the importance of identifying the appropriate RVE size is twofold. First, in terms of material characterization, it contributes to the development of reliable tools to assess scaffold manufacturing process repeatability and second, in terms of mechanical modeling, the analysis performed at the RVE can provide physically meaningful data. In particular, structural deterministic models depend greatly on rigorously defined material structural descriptions. This need, where the model capability relies prevalently on the accuracy of the network topology, has been extensively highlighted in the recent literature.[129–131,137,138]

Furthermore, microarchitectural data extraction accuracy is not only crucial but also fundamental in stochastic representations of engineered scaffolds for the minimization of the gap between the real and the simulated structure. The potential of a structural deterministic approach in elucidating the inherently multiscale nature of native and engineered soft tissue response seems to justify its apparent complexity.[129–131,138] An alternative path for deterministic modeling is the reproduction of the entire scaffold area or volume without duplicating the RVE. The main benefits of this alternative solution are that the implicit error introduced by the multiscale approach is removed and the information at the meso level is preserved. For instance, tortuosity measurements of a collagen fiber can be performed in a heart valve leaflet under loaded and unloaded configurations, which would otherwise be neglected in the multiscale approach where the fibers cannot cross element boundaries. However, these expected benefits are counterbalanced by a significant increase in computational cost.

The modeling strategies outlined above also have potential use for the rational design of future scaffold morphologies at the macro (tissue-engineered construct size, shape, etc.) and microlevel (fiber connectivity, fiber density, fiber alignment, etc.). This has the potential to profoundly impact the fields of tissue engineering and mechanobiology, whereby empirically driven experimentation can be augmented or replaced with more rational design approaches. Relating macroscopic kinematic events to the cell environment and understanding the cellular responses to these cues are critical to the production of engineered tissue surrogates. It has been shown that mechanical cues modulate many cellular processes and the ability to understand and predict the events leading to healthy tissue accretion or adaptive repair/growth can guide mechanical training regimes to produce robust tissue formation. Efficacious repair or replacement of abnormal or lost tissue relies on our ability to reproducibly control cellular responses to exogenous cues.

Clearly, a better understanding of the effects of cardiac-engineered tissue scaffold architecture on cell morphology, metabolism, phenotypic expression, and prediction of material mechanical behavior have recently begun to receive increased attention. A novel image-based analysis approach has been

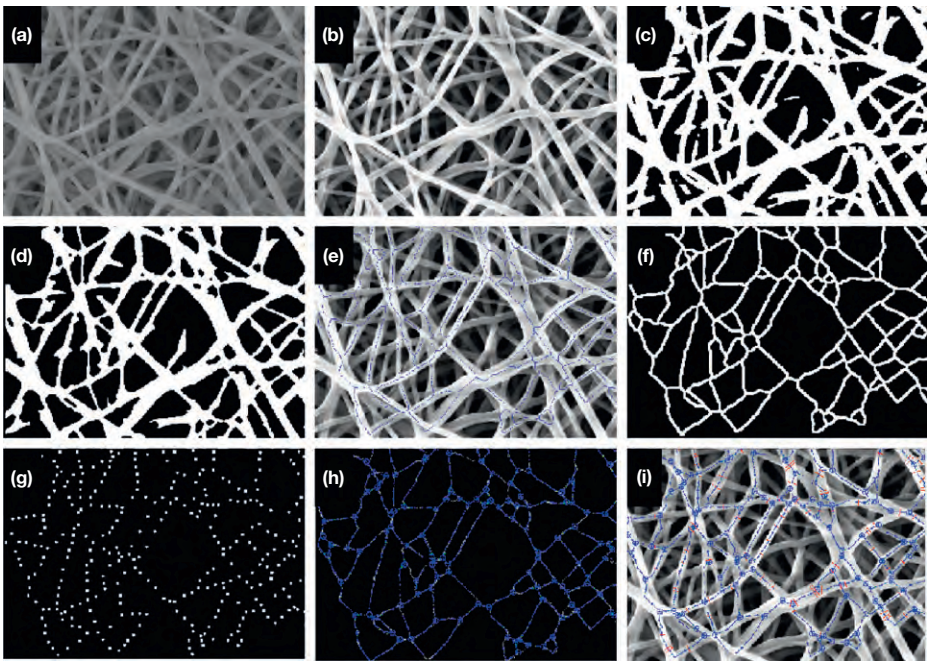

Figure 11 (a) Starting scanning electron microscopy image. (b) Image histogram equalization followed by 3 by 3 median filtering. (c) Local thresholding through Otsu method. (d) Thinning, smoothing, and removal of isolated pixel areas through a cascade of different morphological operators. (e) Skeletonization. (f, g) Binary filters for Delaunay network refinement. (h) Modified Delaunay network associated to the real fiber network. (i) Final network and fiber diameters as detected.

recently developed to automatically characterize engineered tissue fiber network topology.[139] Microarchitectural features that fully defined fiber network topology, including fiber orientation, connectivity, intersection spatial density, and diameter (Figure 11), were detected and quantified. Algorithm performance was tested using SEM images of electrospun PEUU (ES-PEUU) scaffolds. SEM images of rabbit mesenchymal stem cell (MSC) seeded collagen gel scaffolds and decellularized rat carotid arteries were also analyzed to further evaluate the ability of the algorithm to capture fiber network morphology regardless of the scaffold type and the evaluated size scale. The image analysis procedure was validated qualitatively and quantitatively, comparing fiber network topology manually detected by human operators ($n = 5$) with that automatically detected by the algorithm. Correlation values between manually detected and algorithm-detected results for the fiber angle distribution and for the fiber connectivity distribution were 0.86 and 0.93, respectively. Algorithm-detected fiber intersections and fiber diameter values were comparable (within the mean $\pm$ standard deviation) with those detected by human operators. This automated approach identifies and quantifies fiber network morphology as demonstrated for three relevant scaffold types and provides a means to (1) guarantee objectivity, (2) significantly reduce analysis time, and (3) potentiate broader analysis of scaffold architecture effects on cell behavior and tissue development both *in vitro* and *in vivo*.

Acknowledgment

This work was supported by the National Institute of Health grants R01 HL08975 and HL68816.

References

1. Sacks, M. S.; Sun, W. *Annu. Rev. Biomed. Eng.* **2003**, *5*, 251–284.
2. Sacks, M. S.; Smith, D. B.; Hiester, E. D. *Ann. Biomed. Eng.* **1997**, *25*, 678–689.
3. Batemen, J. F.; Lamande, S. R.; Ramshaw, J. A. M. In *Extracellular Matrix, Molecular Components and Interactions*; Comper, W. D., Ed.; Harwood Academic: Amsterdam, Netherlands, 1996; Vol. 2.
4. Koide, T. *Connect. Tissue Res.* **2005**, *46*, 131–141.
5. Gelse, K.; Poschl, E.; Aigner, T. *Adv. Drug Deliv. Rev.* **2003**, *55*, 1531–1546.
6. Ottani, V.; Raspanti, M.; Ruggeri, A. *Micron* **2001**, *32*, 251–260.
7. Diamant, J.; *et al. Proc. R. Soc. Lond. B* **1972**, *180*, 293–315.
8. Hukins, D. W. L. In *Connective Tissue Matrix*; Hukins, D. W. L., Ed.; Verlag Chemie: Weinheim, 1984.
9. Betsch, D. F.; Baer, E. *Biorheology* **1980**, *17*, 83–94.
10. Baer, E.; Cassidy, J. J.; Hiltner, A. In *Collagen*; Nimni, M. E., Ed.; CRC: Boca Raton, FL, 1988.
11. Kastelic, J.; Baer, E. In *The Mechanical Properties of Biological Materials*; Vincient, J. F., Currey, J. D., Eds.; Society for Experimental Biology: Great Britain, 1980.
12. Kastelic, J.; Galeski, A.; Baer, E. *Connect. Tissue Res.* **1978**, *6*, 11–23.
13. Kastelic, J.; Palley, I.; Baer, E. *J. Biomech.* **1980**, *13*, 887–893.
14. Rowe, R. W. *Connect. Tissue Res.* **1985**, *14*, 21–30.
15. Yahia, L. H.; Drouin, G. *J. Orthop. Res.* **1989**, *7*, 243–251.
16. Baer, E.; Hiltner, A.; Friedman, B. *Mech. Compos. Mater.* **1976**, *12*, 619–629.
17. Sacks, M. S.; Merryman, D. W.; Schmidt, D. E. *J. Biomech.* **2009**, *42*, 1804–1824.
18. Christie, G. W. *Eur. J. Cardiothorac. Surg.* **1992**, *6*, S25–S33.
19. Schoen, F.; Levy, R. *J. Biomed. Mater. Res.* **1999**, *47*, 439–465.
20. Scott, M.; Vesely, I. *Ann. Thorac. Surg.* **1995**, *60*, S391–S394.
21. Scott, M. J.; Vesely, I. *J. Heart Valve Dis.* **1996**, *5*, 464–471.
22. Vesely, I.; Boughner, D. *J. Biomech.* **1989**, *22*, 655–671.
23. Vesely, I.; Noseworthy, R. *J. Biomech.* **1992**, *25*, 101–113.
24. Vyavahare, N.; Ogle, M.; Schoen, F. J.; *et al. J. Biomed. Mater. Res.* **1999**, *46*, 44–50.
25. Simionescu, D. T.; Lovekamp, J. J.; Vyavahare, N. R. *J. Heart Valve Dis.* **2003**, *12*, 226–234.
26. Talman, E. A.; Boughner, D. R. *J. Heart Valve Dis.* **1996**, *5*, 152–159.
27. Talman, E. A.; Boughner, D. R. *Ann. Thorac. Surg.* **1995**, *60*, S369–S373.
28. Lee, J. M.; Courtman, D. W.; Boughner, D. R. *J. Biomed. Mater. Res.* **1984**, *18*, 61–77.
29. Lee, J. M.; Boughner, D. R.; Courtman, D. W. *J. Biomed. Mater. Res.* **1984**, *18*, 79–98.
30. Broom, N.; Christie, G. W. In *Cardiac Bioprosthesis*; Cohn, L. H., Gallucci, V., Eds.; Yorke Medical Books: New York, 1982.
31. Mayne, A. S.; Christie, G. W.; Smaill, B. H.; Hunter, P. J.; Barratt-Boyes, B. G. *J. Thorac. Cardiovasc. Surg.* **1989**, *98*, 170–180.
32. Christie, G. W.; Barratt-Boyes, B. G. *Ann. Thorac. Surg.* **1995**, *60*, S156–S159.
33. Brossollet, L. J.; Vito, R. P. *J. Biomech.* **1995**, *28*, 679–687.
34. Billiar, K. L.; Sacks, M. S. *J. Biomech. Eng.* **2000**, *122*, 327–335.
35. Fung, Y. C. *Biomechanics: Mechanical Properties of Living Tissues*. Springer Verlag: New York, 1993.
36. Gloeckner, D. C.; Sacks, M. S.; Fraser, M. O.; Somogyi, G. T.; De Groat, W. C.; Chancellor, M. B. *J. Urol.* **2002**, *167*, 2247–2252.
37. Lanir, Y.; Fung, Y. C. *J. Biomech.* **1974**, *7*, 171–182.
38. Lin, D. H.; Yin, F. C. *J. Biomech. Eng.* **1998**, *120*, 504–517.
39. Strumpf, R. K.; Humphrey, J. D.; Yin, F. C. *Am. J. Physiol.* **1993**, *265*, H469–H475.
40. Wells, P. B.; Harris, J. L.; Humphrey, J. D. *J. Biomech. Eng.* **2004**, *126*, 492–497.
41. Adamczyk, M. M.; Vesely, I. *J. Heart Valve Dis.* **2002**, *11*, 75–83.
42. Christie, G. W.; Barratt-Boyes, B. G. *Ann. Thorac. Surg.* **1995**, *60*, S160–S164.
43. May-Newman, K.; Yin, F. C. *Am. J. Physiol.* **1995**, *269*, H1319–H1327.
44. Grashow, J. S.; Sacks, M. S.; Liao, J.; Yoganathan, A. P. *Ann. Biomed. Eng.* **2006**, *34*, 1509–1518.
45. Grashow, J. S.; Yoganathan, A. P.; Sacks, M. S. *Ann. Biomed. Eng.* **2006**, *34*, 315–325.
46. Liao, J.; Yang, L.; Grashow, J.; Sacks, M. S. *J. Biomech. Eng.* **2007**, *129*, 78–87.
47. Thubrikar, M. J.; Heckman, J. L.; Nolan, S. P. *J. Heart Valve Dis.* **1993**, *2*, 653–661.
48. Schoen, F. J. *J. Heart Valve Dis.* **1999**, *8*, 350–358.
49. Thubrikar, M.; Eppink, R. T. *J. Biomech.* **1982**, *15*, 529–535.
50. Thubrikar, M. J.; Skinner, J. R.; Eppink, R. T.; Nolan, S. P. *J. Biomed. Mater. Res.* **1982**, *16*, 811–826.
51. Joyce, E. M.; Liao, J.; Schoen, F. J.; Mayer, J. E., JR.; Sacks, M. S. *Ann. Thorac. Surg.* **2009**, *87*, 1240–1249.
52. Stella, J. A.; Sacks, M. S. *J. Biomech. Eng.* **2007**, *129*, 757–766.
53. Butcher, J. T.; Nerem, R. M. *J. Heart Valve Dis.* **2004**, *13*, 478–485; discussion 485–486.
54. Butcher, J. T.; Penrod, A. M.; Garcia, A. J.; Nerem, R. M. *Arterioscler. Thromb. Vasc. Biol.* **2004**, *24*, 1429–1434.
55. Deck, J. D. *Cardiovasc. Res.* **1986**, *20*, 760–767.
56. Leask, R. L.; Jain, N.; Butany, J. *Microsc. Res. Tech.* **2003**, *60*, 129–137.
57. Marron, K.; Yacoub, M. H.; Polak, J. M.; *et al. Circulation* **1996**, *94*, 368–375.
58. Davies, P. F. *Atherosclerosis* **1997**, (Suppl. 131), S15–S17.
59. Davies, P. F.; Tripathi, S. C. *Circ. Res.* **1993**, *72*, 239–245.
60. Filip, D. A.; Radu, A.; Simionescu, M. *Circ. Res.* **1986**, *59*, 310–320.
61. Yin, F. C. *Circ. Res.* **1981**, *49*, 829–842.
62. Demer, L.; Strumpf, R.; Yin, F. *Biophys. J.* **1983**, *41*, 245.
63. Demer, L. L.; Yin, F. C. *J. Physiol. Lond.* **1983**, *339*, 615–630.
64. Humphrey, J. D.; Yin, F. C. *Biophys. J.* **1987**, *52*, 563–570.
65. Humphrey, J. D.; Yin, F. C. *J. Biomech. Eng.* **1987**, *109*, 298–304.
66. Yin, F. C.; Chew, P. H.; Zeger, S. L. *J. Biomech.* **1986**, *19*, 27–37.
67. Yin, F. C.; Strumpf, R. K.; Chew, P. H.; Zeger, S. L. *J. Biomech.* **1987**, *20*, 577–589.
68. Yin, F. C. P.; Spurgeon, H. A.; Weisfeldt, M. L.; Lakatta, E. G. *Circ. Res.* **1980**, *46*, 292–300.
69. Sacks, M. S.; Chuong, C. J. *J. Biomech. Eng.* **1993**, *115*, 202–205.
70. Sacks, M. S.; Chuong, C. J. *J. Biomech.* **1993**, *26*, 1341–1345.
71. Chuong, C. J.; Sacks, M. S.; Templeton, G.; Schwiep, F.; Johnson, R. L. *Am. J. Physiol.* **1991**, *260*, H1224–H1235.
72. Waldman, L. K.; Nosan, D.; Villarreal, F.; Covell, J. W. *Circ. Res.* **1988**, *63*, 550–562.
73. Fung, Y. C. *Biomechanics: Mechanical Properties of Living Tissues*. Springer-Verlag: New York, 1981.

74. Holzapfel, G. A.; Gasser, T. C.; Ogden, R. W. *J. Biomech. Eng.* **2004**, *126*, 264–275.
75. Lanir, Y. *J. Biomech. Eng.* **1983**, *105*, 374–380.
76. Sun, W.; Sacks, M. S.; Sellaro, T. L.; Slaughter, W. S.; Scott, M. J. *J. Biomech. Eng.* **2003**, *125*, 372–380.
77. Taber, L. A. *Nonlinear Theory of Elasticity. Applications in Biomechanics*; World Scientific Publishing: Singapore, 2004.
78. Lanir, Y.; Fung, Y. C. *J. Biomech.* **1974**, *7*, 29–34.
79. Rivlin, R. S.; Saunders, D. W. *Philos. Trans. R. Soc.* **1951**, *A243*, 251–288.
80. Yin, F. C.; Tompkins, W. R.; Peterson, K. L.; Intaglietta, M. *IEEE Trans. Biomed. Eng.* **1972**, *19*, 376–381.
81. Tong, P.; Fung, Y. C. *J. Biomech.* **1976**, *9*, 649–657.
82. Chew, P. H.; Yin, F. C.; Zeger, S. L. *J. Mol. Cell. Cardiol.* **1986**, *18*, 567–578.
83. Humphrey, J. D.; Strumpf, R. K.; Yin, F. C. P. *J. Biomech. Eng.* **1992**, *114*, 461–466.
84. Humphrey, J. D.; Vawter, D. L.; Vito, R. P. *Ann. Biomed. Eng.* **1986**, *14*, 451–466.
85. Spencer, A. J. M. *Continuum Mechanics*; Longman Scientific & Technical: New York, 1980.
86. Spencer, A. *Deformations of Fibre-Reinforced Materials*; Oxford university press: Glasgow, 1972.
87. Holzapfel, G. A.; Gasser, T. C. *J. Elast.* **2000**, *61*, 1–48.
88. Humphrey, J. D.; Strumpf, R. K.; Yin, F. C. *J. Biomech. Eng.* **1990a**, *112*, 333–339.
89. Humphrey, J. D.; Strumpf, R. K.; Yin, F. C. *J. Biomech. Eng.* **1990b**, *112*, 340–346.
90. May-Newman, K.; Yin, F. C. *J. Biomech. Eng.* **1998**, *120*, 38–47.
91. Holzapfel, G. A. *J. Theor. Biol.* **2006**, *238*, 290–302.
92. Natali, A. N.; Carniel, E. L.; Gregersen, H. *Med. Eng. Phys.* **2009**, *31*, 1056–1062.
93. Yang, W.; Fung, T. C.; Chian, K. S.; Chong, C. K. *J. Biomech. Eng.* **2006**, *128*, 409–418.
94. Itskov, M.; Ehret, A. E.; Mavrilas, D. *Biomech. Model. Mechanobiol.* **2006**, *5*, 17–26.
95. Horowitz, A.; Lanir, Y.; Yin, F. C.; Perl, M.; Sheinman, I.; Strumpf, R. K. *J. Biomech. Eng.* **1988**, *110*, 200–207.
96. Lanir, Y. *J. Biomech.* **1979**, *12*, 423–436.
97. Lanir, Y. *J. Biomech.* **1983**, *16*, 1–12.
98. Lanir, Y.; Lichtenstein, O.; Imanuel, O. *J. Biomech. Eng.* **1996**, *118*, 41–47.
99. Billiar, K. L.; Sacks, M. S. *J. Biomech. Eng.* **2000**, *122*, 23–30.
100. Sacks, M. S. *J. Biomech. Eng.* **2003**, *125*, 280–287.
101. Mendenhall, W.; Sincich, T. *Statistics for the Engineering and Computer Sciences*; Dellen: San Francisco, CA, 1988.
102. Press, W. H.; Flannery, B. P.; Teukolsky, S. A.; Vetterling, W. T. *Numerical Receipes in C*. Cambridge University Press: Cambridge, 1988.
103. Sacks, M. S.; Schoen, F. J.; Mayer, J. E., Jr. *Annu. Rev. Biomed. Eng.* **2009**, *11*, 289–313.
104. Courtney, T.; Sacks, M. S.; Stankus, J.; Guan, J.; Wagner, W. R. *Biomaterials* **2006**, *27*, 3631–3638.
105. Nerurkar, N. L.; Elliott, D. M.; Mauck, R. L. *J. Orthop. Res.* **2007**, *25*, 1018–1028.
106. Yoshimoto, H.; Shin, Y. M.; Teral, H.; Vacanti, J. P. *Biomaterials* **2003**, *24*, 2077–2082.
107. Bibekananda, S.; Subramanian, V.; Natarajan, T. S.; Rong-Zheng, X.; Chia-Cheng, C.; Wun-Shain, F. *Appl. Phys. Lett.* **2004**, *84*, 1222–1224.
108. Li, W. J.; Cooper, J. A., Jr.; Mauck, R. L.; Tuan, R. S. *Acta Biomater.* **2006**, *2*, 377–385.
109. Li, W. J.; Laurencin, C. T.; Caterson, E. J.; Tuan, R. S.; Ko, F. K. *J. Biomed. Mater. Res.* **2002**, *60*, 613–621.
110. Matthews, J. A.; Wnek, G. E.; Simpson, D. G.; Bowlin, G. L. *Biomacromolecules* **2002**, *3*, 232–238.
111. Pedicini, A.; Farris, R. J. *Polymer* **2003**, *44*, 6857–6862.
112. Stankus, J. J.; Guan, J.; Wagner, W. R. *J. Biomed. Mater. Res.* **2004**, *70A*, 603–614.
113. Yarin, A. L.; Zussman, E. *Polymer* **2004**, *45*, 2977–2980.
114. Li, W. J.; Mauck, R. L.; Cooper, J. A.; Yuan, X.; Tuan, R. S. *J. Biomech.* **2007**, *40*, 1686–1693.
115. Pham, Q. P.; Sharma, U.; Mikos, A. G. *Tissue Eng.* **2006**, *12*, 1197–1211.
116. Teo, W. E.; He, W.; Ramakrishna, S. *Biotechnol. J.* **2006**, *1*, 918–929.
117. Mauck, R. L.; Baker, B. M.; Nerurkar, N. L.; *et al. Tissue Eng. B Rev.* **2009**, *15*, 171–193.
118. Stella, J. A.; D'Amore, A.; Wagner, W. R.; Sacks, M. S. *Acta Biomater.* **2010**, *6*(7), 2365–2381. Epub 2010 Jan 7. Review. PMID: 20060509.
119. Stella, J. A.; Liao, J.; Hong, Y.; David Merryman, W.; Wagner, W. R.; Sacks, M. S. *Biomaterials* **2008**, *29*, 3228–3236.
120. Gilbert, T. W.; Sacks, M. S.; Grashow, J. S.; Woo, S. L.; Badylak, S. F.; Chancellor, M. B. *J. Biomech. Eng.* **2006**, *128*, 890–898.
121. Johnson, J.; Ghosh, A.; Lannutti, J. *J. Appl. Polym. Sci.* **2007**, *104*, 2919–2927.
122. Choi, H. S.; Vito, R. P. *J. Biomech. Eng.* **1990**, *112*, 153–159.
123. Fung, Y. C. *J. Appl. Physiol.* **1988**, *64*, 2132–2141.
124. Fung, Y. C.; Fronek, K.; Patitucci, P. *Am. J. Physiol.* **1979**, *237*, H620–H631.
125. Humphrey, J. D.; Vawter, D. L.; Vito, R. P. *J. Biomech. Eng.* **1987**, *109*, 115–120.
126. David, G.; Pedrigi, R. M.; Heistand, M. R.; Humphrey, J. D. *J. Biomech. Eng.* **2007**, *129*, 97–104.
127. Lanir, Y. *J. Appl. Mech. Trans. ASME* **1994**, *61*, 695–702.
128. Sacks, M. S. *Comput. Mech.* **2000**, *26*, 243–249.
129. Agoram, B.; Barocas, V. H. *J. Biomech. Eng.* **2001**, *123*, 362–369.
130. Preethi, L. C.; Victor, H. B. *J. Biomech. Eng.* **2007**, *129*, 137–147.
131. Stylianopoulos, T.; Barocas, V. H. *Comput. Meth. Appl. Mech. Eng.* **2007**, *196*, 2981–2990.
132. Zahalak, G. I.; Wagenseil, J. E.; Wakatsuki, T.; Elson, E. L. *Biophys. J.* **2000**, *79*, 2369–2381.
133. Marquez, J. P.; Genin, G. M.; Zahalak, G. I.; Elson, E. L. *Biophys. J.* **2005a**, *88*, 778–789.
134. Marquez, J. P.; Genin, G. M.; Zahalak, G. I.; Elson, E. L. *Biophys. J.* **2005b**, *88*, 765–777.
135. Kanit, T.; Forest, S.; Galliet, I. *Int. J. Solids Struct.* **2003**, *40*, 3647–3679.
136. Khisaeva, Z. F.; Ostoja-Starzewski, A. M. *J. Elast.* **2006**, *85*, 153–173.
137. Burd, H. J. *Biomech. Model. Mechanobiol.* **2009**, *8*(3), 217–231.
138. Stylianopoulos, A.; Bashur, C. A.; Goldstein, A. S.; Guelcher, S. A.; Barocas, V. H. *J. Mech. Behav. Biomed. Mater.* **2008**, *1*, 326–335.
139. D'Amore, A.; Stella, J. A.; Wagner, W. R.; Sacks, M. S. *Biomaterials* **2010**, *31*, 5345–5354.

3.309. Fluid Mechanics: Transport and Diffusion Analyses as Applied in Biomaterials Studies

K Mukundakrishnan, University of Pennsylvania, Philadelphia, PA, USA
P S Ayyaswamy, University of Pennsylvania, Philadelphia, PA, USA

© 2011 Elsevier Ltd. All rights reserved.

3.309.1.	**Introduction**	134
3.309.2.	**Transport Phenomena: Diffusive, Convective, and Reactive Transport Mechanisms**	136
3.309.3.	**Analysis of Transport Models in Porous Media**	137
3.309.3.1.	Flow Field Evaluation	137
3.309.3.1.1.	Direct numerical simulations: mathematical formulation	137
3.309.3.1.2.	Numerical methods	138
3.309.3.1.3.	Pore-scale geometry description	140
3.309.3.1.4.	Macroscopic averaged equations	141
3.309.3.1.5.	Volume averaging technique: mathematical formulation	141
3.309.3.1.6.	Correlations for estimating porous scaffold permeability	146
3.309.3.1.7.	Direct methods for the estimation of permeabilities	147
3.309.3.1.8.	Comparison of direct estimations with correlations	148
3.309.3.2.	Mass Transfer Equations	148
3.309.3.2.1.	Direct numerical simulations	149
3.309.3.2.2.	Macroscopic averaged equations	150
3.309.3.2.3.	Cell growth kinetics	151
3.309.3.2.4.	Cell growth and modification of flow field equations	151
3.309.3.2.5.	Evaluation of effective diffusivities	151
3.309.4.	**Conclusion**	152
References		152

Abbreviations

CFD	Computational fluid dynamics
CFL	Courant–Friedrichs–Lewy
CT	Computed tomography
CV	Control volume
DNS	Direct numerical simulation
DVI	Digital volumetric imaging
ECM	Extracellular matrix
FCC	Face-centered cubic
FEM	Finite element method
LB	Lattice-Boltzmann
MRI	Magnetic resonance imaging
MRM	Magnetic resonance microscopy
PBT	Polybutylene terephthalate
PDLLA	Poly D,L-lactic acid
PEG	Polyethylene glycol
PEGT	Polyethylene glycol terephthalate
PEOT	Polyethylene oxide terephthalate
PGA	Polyglycolic acid
PLA	Polylactic acid
PLAGA	Polylactic-*co*-glycolic acid
REV	Representative elementary volume
RHS	Right-hand side

Symbols

a	Average radius of the fiber (m)
a_p	Specific area of the particle (m^2)
$\mathbf{A}$	Discretized convective operator
$A_{\beta e}$	Area of entrances and exits of the averaging volume
$A_{\beta\sigma}$	Area between the fluid and solid phases
$\mathbf{b}$	Closure vector for pressure deviation
$\mathbf{B}_G$	Discretized gradient operator
$\mathbf{B}$	Second-order closure tensor for velocity deviation
c	Artificial compressibility factor
C_F	Forchheimer coefficient
c_g	Intrinsic average concentrations of glucose ($mol\,m^{-3}$)
C_i	Concentration of species i ($mol\,m^{-3}$)
C_l	Intrinsic average concentrations of lactate ($mol\,m^{-3}$)
C_o	Intrinsic average concentrations of oxygen ($mol\,m^{-3}$)
d_p	Average diameter of the fibers (m)
d_{pore}	Pore diameter (m)

$\mathbf{d}$	Alternate closure vector for pressure deviation
$\mathbf{D}$	Alternate second-order closure tensor for velocity deviation
$\mathbf{D}_{\mathrm{eff}}$	Effective diffusivity tensor of each species ($m^2\,s^{-1}$)
$\mathbf{D}_i$	Diffusion coefficient of species i ($m^2\,s^{-1}$)
$\mathcal{D}_{i\beta}$	Diffusivity of species i in the culture medium ($m^2\,s^{-1}$)
E_0	Surface concentration of the transporter proteins ($mol\,m^{-2}$)
$\mathbf{F}$	Forchheimer correction tensor
$\mathbf{F}_b$, $\mathbf{f}$	Body force vector (N)
$\mathbf{g}$	Velocity imposed at the boundaries of the averaging volume ($m\,s^{-1}$)
G	Hydraulic conductivity
$\mathbf{I}$	Identity tensor
$\mathbf{J}_{\mathrm{conv}}$	Convective flux of species ($mol\,m^{-2}\,s^{-1}$)
$\mathbf{J}_{\mathrm{diff}}$	Diffusive flux of species ($mol\,m^{-2}\,s^{-1}$)
$\mathbf{J}_{\mathrm{total}}$	Total flux of species ($mol\,m^{-2}\,s^{-1}$)
k_d	Death coefficient due to apoptosis
k_g	Homogenous cell growth rate coefficient
k_k	Carman–Kozeny constant
K	Isotropic permeability value ($m^2\,s^{-1}$)
K_0 and K_1	Modified Bessel functions of the second kind of orders 0 and 1
$K_{\parallel}$	Permeability parallel to the flow direction ($m^2\,s^{-1}$)
$K_{\perp}$	Permeability perpendicular to the flow direction ($m^2\,s^{-1}$)
K_c	Modified Contois saturation constant
K_{eq}	Equilibrium constant
K_m	Michaelis–Menten constant ($mol\,m^{-3}$)
K_{pr}	Product susceptibility constant
$\mathbf{K}$	Permeability tensor ($m^2\,s^{-1}$)
$\mathbf{K}_{\mathrm{visc}}$	Discretized viscous operator
$\mathbf{l}$	Computational lattice vector
L	Length scale (m)
L_f	Average length of the fibers (m)
l_β	Characteristic length scale of the liquid phase (average pore size) (m)
l_σ	Characteristic length scale of the solid phase (scaffold matrix and cells) (m)
m_s	Maintenance coefficient
$\mathbf{M}$	Discretized mass matrix
$\mathbf{n}$	Outward pointing unit normal vector
$\mathbf{n}_{\beta\sigma}$	Normal vector at the scaffold matrix–fluid interface
p	Fluid pressure ($N\,m^{-2}$)
$\hat{p}$	Variation of pressure
$\tilde{p}$	Pressure deviation about the intrinsic averaged pressure
r	Radius of the averaging volume (m)
$\dot{R}$	Production/consumption rate of species ($mol\,m^{-3}\,s^{-1}$)
Re	Reynolds number
S	Surface area (m^2)
t	Time (s)
$\mathbf{T}$	Traction vector
$\mathbf{u}$	Fluid velocity vector ($m\,s^{-1}$)
$\tilde{\mathbf{u}}$	Velocity deviation about the intrinsic averaged velocity ($m\,s^{-1}$)
$\hat{\mathbf{u}}$	Variation of velocity vector
V	Volume (m^3)
V_{max}	Half-maximal rate of species consumption ($mol\,m^{-3}\,s^{-1}$)
Y_{XS}	Yield of cells per unit oxygen
α_2, α_3, α_4, α_5	Transport kinetic parameters
γ, γ_1	Adjustable parameters
ε_s	Volume fraction of the scaffold matrix
ε_β	Volume fraction of the fluid or porosity
ε_σ	Volume fraction of the cells
θ	Weight for the time-stepping scheme
κ_i	Relative measure of the importance of intercellular diffusivity
λ	Tortuosity of the porous medium
μ	Newtonian viscosity ($N\,s\,m^{-2}$)
μ_{max}	Maximal cell specific growth rate (s^{-1})
ρ	Fluid density ($kg\,m^{-3}$)
ρ_{cd}	Cell density within scaffold
ρ_{cell}	Specific cell density (m^{-3})
ϕ	Volume fraction of the scaffold
ψ	Generic variable
Ψ_{fibers}	Mass flow rates at the porous fibers
Ψ_{inlet}	Mass flow rates at the inlet pipe (s^{-1})
Ψ_{outet}	Mass flow rates at the outlet pipe

3.309.1. Introduction

This chapter reviews the mathematical and computational models used to predict the transport processes involving biomaterials. Transport processes involve both fluid momentum transfer and mass transfer of species. This review will be restricted to isothermal processes and consequently heat transport will not be discussed. The intention here is to provide bioengineers with references to important state-of-the-art models that can be employed to accurately predict transport processes in biotechnological applications of recent interest. While the models described are general in nature, specific focus is given to the area of tissue engineering involving porous scaffolds exposed to dynamic flow conditions such as those that prevail in many modern-day bioreactors.

Tissue engineering is the application of principles and methods of engineering and life sciences toward the development of biological substitutes to restore, maintain, or improve physiological functions. Engineered tissues are very useful in basic biological studies, pharmacological and toxicological screens, and as replacement tissues for clinical applications. Most cells require cues from a three-dimensional (3D) environment to form relevant physiological tissue structures in vitro. Traditionally developed 2D surfaces have been shown to be insufficient to reproduce the true morphology and functionalities of cells compared to 3D cultures and

associated 3D tissue-like structures. The 3D matrix affects the mass transfer of solutes, growth factors, and enzymes thereby establishing proper tissue-scale solute concentration gradients, as well as local pericellular gradients. Also, morphogenetic and remodeling events that occur over larger-length scales may be modeled only using the 3D cell culture environments.[1,2] For 3D cell culture employed in tissue engineering, porous 3D scaffolds are extensively used to manipulate cell function and guide new tissue formation.[3] The formation of cohesive, organized, and functional 3D tissues in a 3D matrix (scaffold) is an exceedingly complex event.[4] An important requirement for such scaffolds is that they should balance mechanical function and mass transport to aid biological delivery and tissue regeneration.[5]

A suitable environment for the proliferation and differentiation of cells seeded within a porous scaffold is afforded by a dynamic bioreactor. Many such bioreactors that aim at reproducing the physiological environment (including biochemical and mechanical functions) specific to the tissue to be regenerated have been developed over the past several years. Some of the common types of bioreactors widely employed in tissue engineering include spinner flasks,[6] rotating wall vessels,[7–15] perfusion culture bioreactors,[16] and more recently, the wavy-walled reactors.[17] A review of several types of bioreactors is reported in Freed *et al.*[18] In general, improved cell viability, proliferation, and extracellular matrix production have been demonstrated in such bioreactors relative to static controls. While the chemical and mechanical properties of many of the scaffold materials employed in these bioreactors are well characterized, the prevailing fluid dynamics and mass transport of species inside the complex microenvironment of the scaffolds are not so well understood.[19] It is well known that an important factor for the growth of cells is the mass transfer of species such as oxygen, and nutrients such as glucose. Supplying the cells seeded within the support scaffold with sufficient nutrients and oxygen requires a knowledge of transport phenomena of these species.[20] Cells relying only upon the diffusion of nutrients inside the porous scaffold such as that would occur in static cultures produce thinner tissues.[21] Also, diffusion-limited growth of cells is often confined to the outer parts of the porous scaffolds while the central core becomes necrotic due to the nonavailability of nutrients.[22]

Transport of oxygen and nutrients can be improved by using dynamic bioreactors that enhance mass transfer of species through convection. The transport processes in such bioreactors usually occur on multiple scales, namely, the microscopic scales of the individual cell and the scaffold to the macroscopic scale of the bioreactors.[23] Therefore, to correctly characterize and evaluate the mass transfer processes, an understanding of these processes occurring at both the micro and macro levels is required. A large number of experimental and computational methods have been developed for biotechnological studies involving cell culture in bioreactors. Many of these studies have focused mainly on the characterization of macroscale flows and some involving solid and porous microcarriers.[11–15,24] However, detailed models of the complex transport processes occurring at the pore scale (microscopic scale) within a porous 3D scaffold are few in number largely due to the complexity presented by the scaffold architecture. Optimization of such scaffold architectures requires a detailed evaluation of design parameters such as the distribution of local shear stress, local concentration of the solutes, and material–cell interactions within these scaffolds in order to obtain the most appropriate conditions of growth for various cell types.[25] Experimental quantification of the dynamics of flow and mass transfer within the microscale environment of the 3D scaffold is usually very difficult and time-consuming. However, these aspects may be understood and evaluated employing mathematical models and numerical methods such as computational fluid dynamics (CFD). In this chapter, we present some of the important and useful mathematical models for characterizing the transport of species through 3D porous scaffolds through which there is flow of a cell culture medium (in contrast to pure static cultures). In particular, a perfusion culture system is picked as the representative bioreactor. The perfusion culture system represents an important class of bioreactors that enable efficient and uniform seeding of scaffolds of various compositions, architectures, and porosities through direct perfusion of a cell suspension through the pores of a 3D scaffold.[26] A schematic of a perfusion culture system is shown in **Figure 1**. A known flow rate or fluid velocity is prescribed at the inlet. Fluid flows through the porous scaffold and exits through the outlet. The objectives are to characterize the flow dynamics and transport of species within such a scaffold.

To accomplish the various objectives of this chapter, it is organized as follows. First, the basic concepts involved in transport phenomena such as the integral and differential forms of species conservation equations are explained. This is followed by detailed models of flow and species transport in porous media. Both direct simulation models that contain no approximation to the governing equations and averaged equations based on various upscaling theorems are included. For the latter, although the averaging procedure is presented here in a succinct manner, the reader is referred to Whitaker,[27] Wood *et al.*,[28] and Lasseux *et al.*[29] for details. This is followed by a discussion on mass transfer models in the context of direct numerical simulations. Finally, detailed mass transfer equations for important species such as oxygen, glucose, and lactate coupled with models for cell growth kinetics are presented.

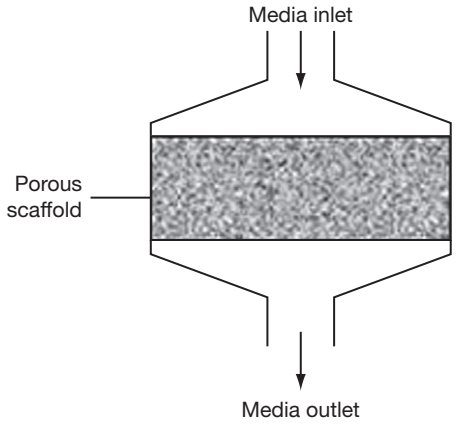

Figure 1 Schematic of a perfusion culture system.

3.309.2. Transport Phenomena: Diffusive, Convective, and Reactive Transport Mechanisms

Some of the important concepts of transport phenomena are first reviewed. In this section, for brevity purposes, we consider only the mass transport mechanisms of a representative species such as oxygen, glucose, or lactate. For full details on the derivation of fluid mass and momentum conservation equations (also referred to as the Navier–Stokes equations), readers are referred to Deen[30] and Batchelor.[31] The discussions that follow in this paper assume that the fluid is of constant density which is generally valid for cell culture media.

The fundamental transport mechanisms governing the mass transport of a representative species both in the bulk medium and within the scaffolds are convection, diffusion, and reaction. In general, the pore-scale fluid flow within the 3D scaffolds may be assumed to be laminar. Assuming an idealized cylindrical pore structure, the laminar flow is characterized by a low to moderate Reynolds number (typically less than 2300), where the Reynolds number Re is defined as

$$Re = \frac{\rho |\mathbf{u}| d_{\text{pore}}}{\mu} \qquad [1]$$

Here, ρ is the density of the fluid (culture medium) permeating the pores in the scaffold, $|\mathbf{u}|$ is a characteristic speed of the fluid inside the scaffold which is usually obtained from the macroscopic bulk motion prevailing outside the scaffold or the specified boundary condition, and d_{pore} is a characteristic pore diameter.

Diffusion of species occurs due to the migration of molecules from regions of higher concentration to regions of lower concentration resulting in a nonzero flux. The diffusive flux, $\mathbf{J}_{\text{diff}}$, depends on the local gradient of the concentration of a given species (e.g., oxygen or nutrients) and is mathematically represented by Fick's law of diffusion.

$$\mathbf{J}_{\text{diff}} = -\mathbf{D}_i \cdot \nabla C_i \qquad [2]$$

where C_i refers to the local concentration of the species, and $\mathbf{D}_i$ is the diffusivity tensor. A negative sign indicates that the flux is positive when there is movement of molecules down the gradient (negative sign cancels the negative gradient along the direction of positive flux). For isotropic scaffolds (i.e., the arrangement of pores are statistically the same across all directions), the diffusivity tensor can be replaced by a single scalar, namely, the diffusion coefficient D_i.

Convection occurs due to bulk motion of the fluid within the porous channels of a scaffold. The convective or advective flux, $\mathbf{J}_{\text{conv}}$, depends on the local concentration, C_i, and the mass-averaged velocity, $\mathbf{u}$. It may be noted that in modeling most transport processes, the preferred mixture velocity is the mass-averaged velocity which is also the fluid velocity $\mathbf{u}$.

$$\mathbf{J}_{\text{conv}} = \mathbf{u} C_i \qquad [3]$$

The details of evaluating this local fluid velocity $\mathbf{u}$ within the porous scaffold are deferred to **Section 3.309.3**. The total flux is given by the sum of eqns [2] and [3] as follows:

$$\mathbf{J}_{\text{total}} = \mathbf{J}_{\text{diff}} + \mathbf{J}_{\text{conv}} = -\mathbf{D}_i \cdot \nabla C_i + \mathbf{u} C_i \qquad [4]$$

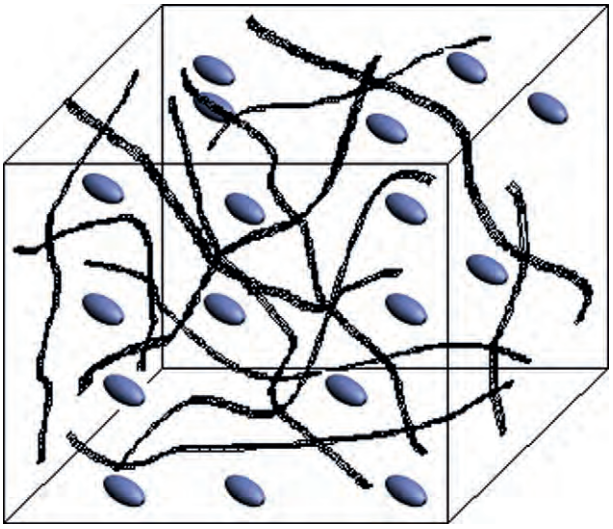

Figure 2 A schematic of a control volume (CV) for a porous fibrous scaffold seeded with cells (represented as ellipsoids). Transport into and out of this CV occurs due to diffusive and convective fluxes while the cells contribute to species production or consumption within the CV.

The conservation equation for C_i can then be written in terms of eqn [4] as given below.

Now consider a fixed control volume (CV) for a porous scaffold seeded with cells as shown in **Figure 2**.

Applying the standard integral form of conservation equation[30] for species C_i within this CV yields

$$\frac{\mathrm{d}}{\mathrm{d}t}\int_V C_i \,\mathrm{d}V = -\int_S \mathbf{J}_{\text{total}} \cdot \mathbf{n} \,\mathrm{d}S + \int_V \rho_{\text{cd}} \dot{R} \,\mathrm{d}V \qquad [5]$$

This equation states that the rate of change of the concentration of species i within the CV is equal to the net balance of the convective and diffusive fluxes occurring across the surface of the CV and the rate of consumption or production of the species by the cells that reside within the CV. In the above, V is the CV, S is the CV surface, $\mathbf{n}$ is the unit normal vector on the surface of the CV (pointed outward), and $\dot{R}$ is the reactive flux which is the rate of consumption (reaction) or production of species C_i within the CV per unit cell density and ρ_{cd} is the cell density within the scaffold. For species that are consumed such as oxygen and nutrients, $\dot{R}$ is negative, while for the metabolic waste products that are produced, $\dot{R}$ is positive. For a fixed CV applying Leibniz's theorem for eqn [5] and using eqn [4] for $\mathbf{J}_{\text{total}}$, yields the following:

$$\int_V \frac{\partial C_i}{\partial t} \,\mathrm{d}V = -\int_S [-\mathbf{D}_i \cdot \nabla C_i + \mathbf{u} C_i] \cdot \mathbf{n} \,\mathrm{d}S + \int_V \rho_{\text{cd}} \dot{R} \,\mathrm{d}V \qquad [6]$$

If the concentration field is smooth and if the size of the CV is chosen to be very small compared to the linear dimensions of the scaffold, Gauss' divergence theorem can be applied to eqn [6]. This yields the differential form of the above integral conservation law for the species C_i given by the following equation.

$$\frac{\partial C_i}{\partial t} + \mathbf{u} \cdot \nabla C_i = \nabla \cdot (\mathbf{D}_i \cdot \nabla C_i) + \rho_{\text{cd}} \dot{R} \qquad [7]$$

For constant isotropic diffusivities, the above equation simplifies to

$$\frac{\partial C_i}{\partial t} + \mathbf{u} \cdot \nabla C_i = D_i \nabla^2 C_i + \rho_{cd} \dot{R} \quad [8]$$

Equations [7] and [8] are the fundamental forms of differential equations that are usually employed in most of the transport studies of oxygen and nutrients within biomaterials. The consumption rate of species such as oxygen or nutrients by the cells usually follows a Michaelis–Menten type kinetics[32–34] and is described by

$$\dot{R} = -\frac{V_{max} C_i}{K_m + C_i} \quad [9]$$

where V_{max} is the half-maximal rate of species consumption and K_m is the Michaelis–Menten constant. Other kinetics such as Monod kinetics can also be used to describe the consumption rates of species such as oxygen.[35] Following Croll *et al.*,[35] the Monod kinetics for oxygen consumption by cells is given by

$$\dot{R} = -\left(\frac{\mu_{max}}{Y_{XS}} + m_s\right) \frac{C_i}{K_m + C_i} \quad [10]$$

where μ_{max} is the maximal cell specific growth rate, Y_{XS} is the yield of cells per unit oxygen, and m_s is the maintenance coefficient, the minimum oxygen consumption required to keep the cells alive. Still other kinetics such as zeroth-order kinetics have also been described for species consumption.[36]

In the following sections, the details of computing the flow field within a porous scaffold and subsequently evaluating the mass transport equations described in this section are presented.

3.309.3. Analysis of Transport Models in Porous Media

In many of the biotechnological applications involving bioreactors and porous scaffolds, the flow field usually does not directly depend on the concentration fields of the species. However, this may not be the case if the presence of the cells and consideration of cell growth within the scaffold are taken into account. In the latter case, the fluid velocity depends on the cell volume fraction which in turn depends on the concentration of species. The discussion of this situation is deferred until Section 3.309.3.2. In any case, first the fluid velocity field is obtained for a given geometry which is subsequently used to solve for the transport of species. Therefore, we first consider the problem of evaluating the flow field within a porous scaffold in Section 3.309.3.1. This is followed by Section 3.309.3.2 where the mass transfer models for important species such as glucose, oxygen, and lactate are reviewed in greater detail.

3.309.3.1. Flow Field Evaluation

A number of earlier studies have presented analytical solutions of the flow field in porous media for idealized configurations where the elements in the media are arranged in a very regular and defined way. In this regard, some of the salient works and their references are provided in the review by Jackson and James[37] on fibrous porous media. While these analytical results are limited in their applicability, they are nevertheless useful for obtaining an estimate of the flow field under limit conditions. Due to the necessity for finding accurate solutions to more complex scaffold configurations and for a wide range of Reynolds numbers where obtaining analytical solutions are difficult or impossible, numerical and computational tools are employed.

The different computational approaches used for solving the flow problem within a porous scaffold can be broadly classified into the following two modeling categories depending on the level of approximations involved in obtaining the solution: (i) direct numerical simulations and (ii) macroscopic averaged equations. A review of these two approaches is presented below.

3.309.3.1.1. Direct numerical simulations: mathematical formulation

Direct numerical simulation aims at resolving the fluid flow structure in its entirety without any underlying approximations of the governing equations. Any locally discontinuous and inhomogeneous flow fields due to the presence of fibers and other pore-scale structures may be predicted accurately without any averaging assumptions on the microstructure of the porous matrix.

The flow of an incompressible Newtonian fluid is governed by the equations of continuity and momentum (Navier–Stokes) which are expressed as follows:

$$\nabla \cdot \mathbf{u} = 0 \quad [11]$$

$$\rho\left(\frac{\partial \mathbf{u}}{\partial t} + \mathbf{u} \cdot \nabla \mathbf{u}\right) = -\nabla p + \nabla \cdot \mu\left[\frac{\nabla \mathbf{u} + (\nabla \mathbf{u})^T}{2}\right] + \mathbf{F}_b \quad [12]$$

Here, ρ is the density and μ is the Newtonian viscosity of the culture medium which are assumed constants, $\mathbf{u}$ is the local velocity vector of the fluid, p is the fluid pressure, and $\mathbf{F}_b$ is the body force vector. The first term on the left hand side of eqn [12] denotes the local fluid acceleration, and the second term represents fluid inertia. On the right hand side, the first term represents the pressure gradient force, the second term represents the viscous forces, and the last term represents the body forces. Usually, body force due to gravity is absorbed into the pressure as a hydrostatic head contribution giving rise to a modified pressure. With the pressure so modified, in the absence of any other body forces, $\mathbf{F}_b$ is set to zero. If the Reynolds number of the medium is such that *Re* given by eqn [1] is $\ll 1$, the inertia of the fluid can be neglected and eqn [12] simplifies to an unsteady Stokes equation:

$$\rho \frac{\partial \mathbf{u}}{\partial t} = -\nabla p + \mu \nabla \cdot \left[\frac{\nabla \mathbf{u} + (\nabla \mathbf{u})^T}{2}\right] \quad [13]$$

Furthermore, if the flow is steady, eqn [13] takes the form of the steady Stokes flow equation commonly employed in many fluid flow analysis through a porous scaffold used in biological applications:

$$\mu \nabla \cdot \left[\frac{\nabla \mathbf{u} + (\nabla \mathbf{u})^T}{2}\right] - \nabla p = 0 \quad [14]$$

The assumption of low Reynolds number is justified only for very small pore diameters (of the order of few microns) and low flow perfusion rates. For medium and large pore

diameters, and for nominal to high flow rates, eqn [12] or its steady state version needs to be employed in order to get accurate solutions.

3.309.3.1.1.1. Initial and boundary conditions

Two commonly employed boundary conditions consists of (i) periodic boundary conditions for velocities and pressure at all the boundaries and (ii) a prescribed inlet flow rate (velocity) boundary condition specified at one of the boundaries. With the latter, a traction free boundary condition is usually prescribed at the outlet of the computational domain. The flow rate prescribed at the inlet is often determined from the experiments and is a prescribed quantity. At all other boundaries, a periodic boundary condition is imposed. For unsteady problems, a zero flow initial condition is specified in the interior of the computational domain.

3.309.3.1.2. Numerical methods

The main computational methods for solving the equations of the continuum models can be broadly classified in four types, namely: (i) finite difference method, (ii) finite element, (iii) finite volume methods, and (iv) Lattice Boltzmann method. A brief discussion on each of these methods is provided below.

3.309.3.1.2.1. Finite difference method

The basis of the finite difference method is the construction of a discrete grid, the replacement of continuous derivatives in the governing equation (eqn [12]) by equivalent finite difference expressions using Taylor series expansion techniques, and solving the resultant algebraic equations. Consider a discrete point in the grid uniquely specified by the spatial indices (i, j, k) such that the coordinates are given by $(i\,\Delta x, j\,\Delta y, k\,\Delta z)$, where Δx, Δy, and Δz are the mesh discretization sizes. Let the time level be denoted by n such that $t^n = n\,\Delta t$, where Δt is the discrete time step size. For a generic variable ψ which can denote either the velocity components or pressure, the Taylor series expansions in space along ith direction and time are given by

$$\text{Space}: \psi_{i+1}^n = \sum_{m=0}^{\infty} \frac{\Delta x^m}{m!} \left[\frac{\partial^m \psi_i}{\partial x^m}\right]^n$$

$$\text{Space}: \psi_i^{n+1} = \sum_{m=0}^{\infty} \frac{\Delta t^m}{m!} \left[\frac{\partial^m \psi_i}{\partial t^m}\right]^n \qquad [15]$$

Based on eqn [15], some of the most often used difference expressions are given below:

$$\text{Central difference}:$$

$$\frac{\partial \psi_i}{\partial x} = \frac{\psi_{i+1} - \psi_{i-1}}{2\Delta x} + O(\Delta x^2)$$

$$\frac{\partial^2 \psi_i}{\partial x^2} = \frac{\psi_{i+1} - 2\psi_i + \psi_{i-1}}{\Delta x^2} + O(\Delta x^2) \qquad [16]$$

$$\text{Forward difference}: \frac{\partial \psi_i}{\partial x} = \frac{\psi_{i+1} - \psi_i}{\Delta x} + O(\Delta x) \qquad [17]$$

$$\text{Backward difference}: \frac{\partial \psi_i}{\partial x} = \frac{\psi_i - \psi_{i-1}}{\Delta x} + O(\Delta x) \qquad [18]$$

It can be noted that the central difference formulae given by eqn [16] are second-order accurate while the forward and backward difference formulae given by eqns [17] and [18] are first-order accurate. Application of a second-order spatial discretization to eqn [12] (neglecting the body forces) yields the following time-dependent linear system of equations:

$$\mathbf{M}\dot{\mathbf{u}} = -\mathbf{A}(\mathbf{u})\mathbf{u} - \mathbf{B}_G p + \mathbf{K}_{visc}\mathbf{u} \qquad [19]$$

where $\mathbf{M}$ is the discretized mass matrix (first term of LHS in eqn [12]), $\mathbf{A}(\mathbf{u})$ is the discretized convective operator (second term of LHS in eqn [12]), $\mathbf{B}$ is the discretized gradient operator (first term of RHS in eqn [12]), and $\mathbf{K}_{visc}$ is the discretized viscous operator (second term of RHS in eqn [12]). It should be noted the term $\mathbf{A}(\mathbf{u})\mathbf{u}$ is nonlinear and the degree of nonlinearity scales with Re. The time derivative $\dot{\mathbf{u}}$ can be discretized using a Taylor series expansion such as the one given for spatial terms in eqn [15]. Depending on the time level at which the spatial operators (RHS of eqn [19]) are evaluated, the finite difference method can be classified as explicit or implicit. If the current time level n is used, the scheme is implicit and if the previous level $(n-1)$ is used, the scheme is explicit. Following Peyret and Taylor,[38] a θ method may be employed to discretize eqn [19] and this results in the following linear algebraic system:

$$\frac{\mathbf{M}\mathbf{u}^n - \mathbf{M}\mathbf{u}^{n-1}}{\Delta t} = \theta\left[-\mathbf{A}(\mathbf{u})\mathbf{u} + \mathbf{B}_G p + \mathbf{K}_{visc}\mathbf{u}\right]^n + (1-\theta)\left[-\mathbf{A}(\mathbf{u})\mathbf{u} + \mathbf{B}_G p + \mathbf{K}_{visc}\mathbf{u}\right]^{n-1} \qquad [20]$$

It should be noted that $\theta = 1$ results in a fully implicit scheme and $\theta = 0$ results in a fully explicit scheme. Both the implicit and explicit schemes are only first-order accurate in time. A value of $\theta = \frac{1}{2}$ results in a Crank–Nicolson type discretization which is second-order accurate both in space and time. A fully explicit scheme has both viscous and convective (also called the CFL) time step restrictions because of numerical stability issues (see, Peyret and Taylor[38]). A fully implicit scheme has no time step restrictions but requires highly sophisticated iterative techniques to solve the above linear algebraic system. Such solution techniques used in implicit schemes are the most time-consuming part of any DNS simulations. The discrete form of the continuity eqn [11] is given as

$$\mathbf{B}_G^T u = 0 \qquad [21]$$

where $\mathbf{B}^T$ is the divergence operator and is equal to the transpose of the gradient operator given in eqn [19]. In general, eqns [20] and [21] need to be solved instantaneously to advance both the velocity and pressure fields in time. Several other methods of discretization can be employed to treat the individual terms in eqn [19] depending on the nature of the problem. In many numerical schemes and commercial codes, it is usual to treat the convective terms explicitly and viscous terms implicitly. This is mainly done to avoid severe nonlinearities introduced in the linear algebraic systems associated with high Re and implicit treatment of convective terms. However, such a treatment of convective terms especially for high Re flows needs to be done with care. For example, an explicit treatment of convective terms with a second-order spatial differencing of the velocity derivatives results in numerical instabilities. Usually, upwinding techniques in which the spatial derivatives of velocities are biased

along the flow direction are used to alleviate such problems.[38] A detailed discussion of many upwinding schemes, treatment of various boundary conditions, and other sophisticated forms of finite difference discretizations, such as projection methods, fractional step methods, and compact finite difference schemes, can be found in the works of Peyret and Taylor,[38] Ferziger *et al.*,[39] Brown *et al.*,[40] Mahesh,[41] and the references mentioned therein. In any case, the discretization of eqns [11] and [12] always results in a linear algebraic system similar to the one given by eqn [19] whose solution yields the velocity and pressure field.

The matrices that arise in eqn [20] are generally sparse (few nonzero elements) due to the compact nature of the finite difference stencil used in the discretization procedure. The solution of such sparse linear systems is a computational bottleneck for many large-scale numerical simulations involving millions of elements. Direct solution methods for solving such linear systems based on Gaussian elimination are usually not practical due to excessive memory requirements and intensive use of computational (CPU) resources. In such cases, iterative methods are the most preferred solution techniques because of their lesser memory requirements even for fully 3D problems and also due to the ease of implementation for parallel computations. A review of many sparse linear iterative methods including the popular Krylov-family of solvers such as GMRES methods and advanced multigrid solution acceleration techniques are provided by Saad.[42]

3.309.3.1.2.2. Finite element method

The finite element method (FEM) is another popular numerical technique that employs an integral or variational formulation for solving the governing equations. The most commonly used integral approach is the method of weighted residuals. This technique forms an integral equation by multiplying the governing eqns [11] and [12] by weighting or test functions $\hat{\mathbf{u}}$ and $\hat{p}$, followed by integrating them over the domain of interest (computational domain). Assuming $\mathbf{F}_b = 0$, the weighted integral formulations are given by

$$\int_V \hat{\mathbf{u}}\cdot\left[\rho\left(\frac{\partial \mathbf{u}}{\partial t}+\mathbf{u}\cdot\nabla\mathbf{u}\right)\right]\mathrm{d}V = \int_V \hat{\mathbf{u}}\cdot\left[-\nabla p+\nabla\cdot u\left(\frac{\nabla\mathbf{u}+\nabla\mathbf{u}^{\mathrm{T}}}{2}\right)\right]\mathrm{d}V \quad [22]$$

$$\int_V \hat{p}\nabla\cdot\mathbf{u}\,\mathrm{d}V = 0. \quad [23]$$

The test functions $\hat{\mathbf{u}}$ and $\hat{p}$ essentially denote the variations of velocity and pressure. The domain of interest is then discretized using nonoverlapping elements such as triangles or quadrilaterals in 2D and hexahedrons and tetrahedrons in 3D. Both the variations and the independent variables are then expanded using known complete function spaces such as polynomials, Legendre functions, Chebyshev functions etc., with unknown coefficients which are then substituted into the integral equations. If the variations $\hat{\mathbf{u}}$, $\hat{p}$, and the independent variables $\mathbf{u}$ and p are expanded using the same function space, then the methods is known Galerkin FEM which is one of the most popular method used in many commercial CFD softwares. The next step involves the weak formulation of which is obtained by integrating the first two terms in the RHS of eqn [22] by parts and is given by

$$\int_V \hat{\mathbf{u}}\cdot\left[\rho\left(\frac{\partial \mathbf{u}}{\partial t}+\mathbf{u}\cdot\nabla\mathbf{u}\right)\right] = \int_S \hat{\mathbf{u}}\cdot\left[-p\mathbf{I}+\mu\left(\frac{\nabla\mathbf{u}+\nabla\mathbf{u}^{\mathrm{T}}}{2}\right)\right]\cdot\mathbf{n}\,\mathrm{d}S - \int_V \nabla\hat{\mathbf{u}}:\left[-p\mathbf{I}+\mu\left(\frac{\nabla\mathbf{u}+\nabla\mathbf{u}^{\mathrm{T}}}{2}\right)\right]\mathrm{d}V \quad [24]$$

where $\mathbf{I}$ is the identity tensor and $\mathbf{n}$ is the unit normal vector on the domain boundary (pointed outward). Equation [23] remains unaltered and is usually not integrated into its weak form. The first term in the RHS of this equation is a boundary integral term where S denotes the boundaries of the computational domain. For those boundaries where an inlet velocity or mass flux is specified, the variation $\tilde{\mathbf{u}}$ vanishes and for those boundaries where a traction $\mathbf{T}$ is specified, the term $\left[-p\mathbf{I}+\mu\left(\frac{\nabla\mathbf{u}+\nabla\mathbf{u}^{\mathrm{T}}}{2}\right)\right]\cdot\mathbf{n}$ is substituted with $\mathbf{T}$.

Details of the matrix formulation for the Galerkin FEM, the stabilized treatment of convective terms for high *Re* flows, and other forms of FEMs such as penalty FEM, least-squares FEM can be found in Reddy and Gartling[43] and are not discussed here for brevity. The discretization procedure in all these cases once again leads to a sparse linear system of equations similar to the one given by eqn [19]. The time marching procedure and the solution methodologies are similar to the ones discussed earlier and hence will not be repeated.

3.309.3.1.2.3. Finite volume method

The basis of finite volume method is that, an integral form of the conservation equation [12] is used to derive the discretized approximations. The integral form of the fluid momentum equation (neglecting $\mathbf{F}_b$) is obtained as follows

$$\int_V\cdot\left[\rho\left(\frac{\partial \mathbf{u}}{\partial t}+\mathbf{u}\cdot\nabla\mathbf{u}\right)\right]\mathrm{d}V = \int_V\left[-\nabla_p+\nabla\cdot\mu\left(\frac{\nabla\mathbf{u}+\nabla\mathbf{u}^{\mathrm{T}}}{2}\right)\right]\mathrm{d}V \quad [25]$$

Applying Gauss' divergence theorem yields the integral conservation law for fluid momentum

$$\int_V \rho\frac{\partial \mathbf{u}}{\partial t}\,\mathrm{d}V+\rho\int_S \mathbf{u}(\mathbf{u}\cdot\mathbf{n})\mathrm{d}S = \int_S\left[-p\mathbf{I}+\mu\left(\frac{\nabla\mathbf{u}+\nabla\mathbf{u}^{\mathrm{T}}}{2}\right)\right]\cdot\mathbf{n}\,\mathrm{d}S \quad [26]$$

The first step in the finite volume method is to divide the physical domain into a number of nonoverlapping CVs such that there is one CV surrounding each grid point. In the second step, the governing equation [26] for the unknown velocity is integrated over each CV. Finally, the integrals are evaluated by assuming a piecewise profile for the variation of each velocity component and this results in a linear system of algebraic equations for the grid point and its neighbors under consideration. The linear system is once again similar to eqn [19] and the solution procedure for this system follows the same procedure as explained earlier. The important aspect of the finite volume formulation is that the resulting solution satisfies an integral conservation property on the whole domain. The details of the discretization procedure, differences between cell-centered versus vertex-centered CV procedures, and the evaluation of the advective and diffusive fluxes given in eqn [26] are provided in Ferziger *et al.*[39]

3.309.3.1.2.4. Lattice-Boltzmann method

Another efficient direct numerical method to solve for the flow field inside realistic scaffold geometries is the Lattice-Boltzmann (LB) method.[44,45] LB method breaks physical space into discrete nodes, and each node is associated with a particle distribution function. In each timestep, these distributions translate between neighboring nodes and these translations are governed by an LB equation. Such translations results in collisions whose dynamics is governed by the Boltzmann theory that conserves physical properties such as mass and momentum. Application of the Chapman–Enskog multiscale expansion on the LB equation approximates the Navier–Stokes equations to the second order.[44] Thus, LB methods are used to simulate flow physics governed by the continuity and Navier–Stokes equations.

The methods described in this section constitute the DNS techniques used for obtaining the velocity and pressure fields. The only approximations involved are those introduced by the discretization procedures. In order to avoid under resolution of the flow structures, the discretization procedure in a DNS method usually involves a large number of elements in order to accurately represent the complex microarchitecture of the porous scaffold. Direct numerical simulations of the flow through a full porous scaffold are prohibitive in terms of computational costs because of the demand on accuracy to resolve widely disparate length scales. While the pore diameter is usually of the order of few microns, the typical dimension of the scaffold may be of the order of millimeters or even centimeters. However, a reasonable yet meaningful description of the flow field can be achieved by using simplified geometries or by reducing the size of the computational domains or both. A review of the computational models that have employed both detailed pore-scale resolutions of biomaterial scaffolds and simplifications of the size of the computational domains is provided in the following.

3.309.3.1.3. Pore-scale geometry description

The most common simplification is to consider a representative unit cell (a smaller portion of the complete scaffold) consisting of a regular lattice made of cylinders or spheres, or a random arrangement of rigid cylindrical fibers. For example, Vossenberg *et al.*[46] have considered a regular cylindrical lattice of cylinders arranged both parallel and perpendicular to the flow direction and solved for the velocity field using the commercial software COMSOL Multiphysics 3.3 which is based on FEM. Singh *et al.*[47] have calculated the flow field within the entire scaffold structure (5 mm × 5 mm × 5 mm) consisting of cylindrical fibers arranged to form a 90° (parallel and perpendicular) lay-down pattern using the commercial finite volume solver Fluent (ANSYS).[48] Cantini *et al.*,[36] Boschetti *et al.*,[49] and Raimondi *et al.*[50] have considered a periodic lattice of spheres for describing their porous scaffold. The latter study has also considered the presence of the biological cell clusters (approximated as spheres) embedded within the porous scaffold structure. Olivares *et al.*[51] have employed regular scaffold structures such as gyroid and hexagonal scaffolds in their computational study to determine the mechanical stimuli at the cellular level where the cells are cultured in a perfusion bioreactor. Such regular geometry of the scaffold structures provides for a greater control of the transport mechanisms.[5]

Many scaffolds used in tissue engineering do not possess a regular geometrical structure and simplifications using standard lattice structures may provide incorrect estimates of the local shear stress and fluid velocities. Recently, many state-of-the-art imaging techniques together with computer aided design tools have emerged that attempt to closely approximate the real structure of scaffolds in three dimensions (3D). With the advent of powerful computers and the development of efficient computational codes, calculation of 3D flow fields inside such complex and realistic scaffold microarchitectures with or without cells seeded in them has become more feasible. One of the most widely used imaging technique for generating an accurate 3D description of a porous scaffold is the microcomputed tomography (microCT or μCT).[52] μCT is a nondestructive imaging technique to quantify the internal structure of an object in three dimensions. It provides hierarchical biological imaging capabilities with isotropic resolutions ranging from the millimeter down to nanometer length scales.[53] The **Figure 3** shows a typical image obtained from a μCT scan of a porous β-tricalcium phosphate scaffold.[53]

These images can then be converted to computational meshes which can then be used to evaluate the fluid flow and shear stresses by solving eqns [11], [12], and [14] with appropriate boundary and initial conditions. Some of the very recent studies that have utilized the μCT images for computing the fluid flow include the contribution by Anderson *et al.*,[54] Raimondi *et al.*,[55] Cioffi *et al.*,[56] Maes *et al.*,[57] Jungreuthmayer *et al.*,[58] and Sandino *et al.*[59] Jungreuthmayer *et al.*[58] have additionally considered a linear elastostatics model to calculate the deformation of the cells within the scaffold. Their model employs numerically seeded cells of two common morphologies where cells are either attached flatly on the scaffold wall or bridging two struts of the scaffold. In Sandino *et al.*,[59] finite element models have been used to analyze the behavior of the mechanical stimuli within some calcium phosphate-based porous scaffolds in terms of stress and strain distributions in the solid material phase and fluid velocity, pressure and fluid shear stress distributions in the pores. For modeling purposes, two porous materials, namely, calcium phosphate-based cement and biodegradable glass have been used. The microstructural details have been obtained by means of micro-computed tomography. Steady state version of the Navier–Stokes equation [12] has been used to simulate the-flow with an inlet velocity of 10 $\mu m\,s^{-1}$. The fluid pressure p is set to zero at the oulet and all other boundaries are considered as no-slip walls. In **Figure 4**, a representative plot of the fluid velocity, pressure, and shear stress distributions within a porous scaffold has been shown.[53]

Porter *et al.*[60] have used the LB method to simulate the 3D flow field inside a porous scaffold whose geometry was obtained from μCT images.

Other state-of-the-art imaging techniques such as X-ray tomography,[61] magnetic resonance microscopy (MRM) to generate tomographic mappings of a porous medium at micron-scale resolution,[62] high-resolution magnetic resonance imaging (MRI) images,[63] and 3D digital volumetric imaging (DVI)[64] have also been used to characterize the porous scaffold architecture. In Jaganathan *et al.*,[64] the DVI technique has been used to generate the geometry of the porous scaffold

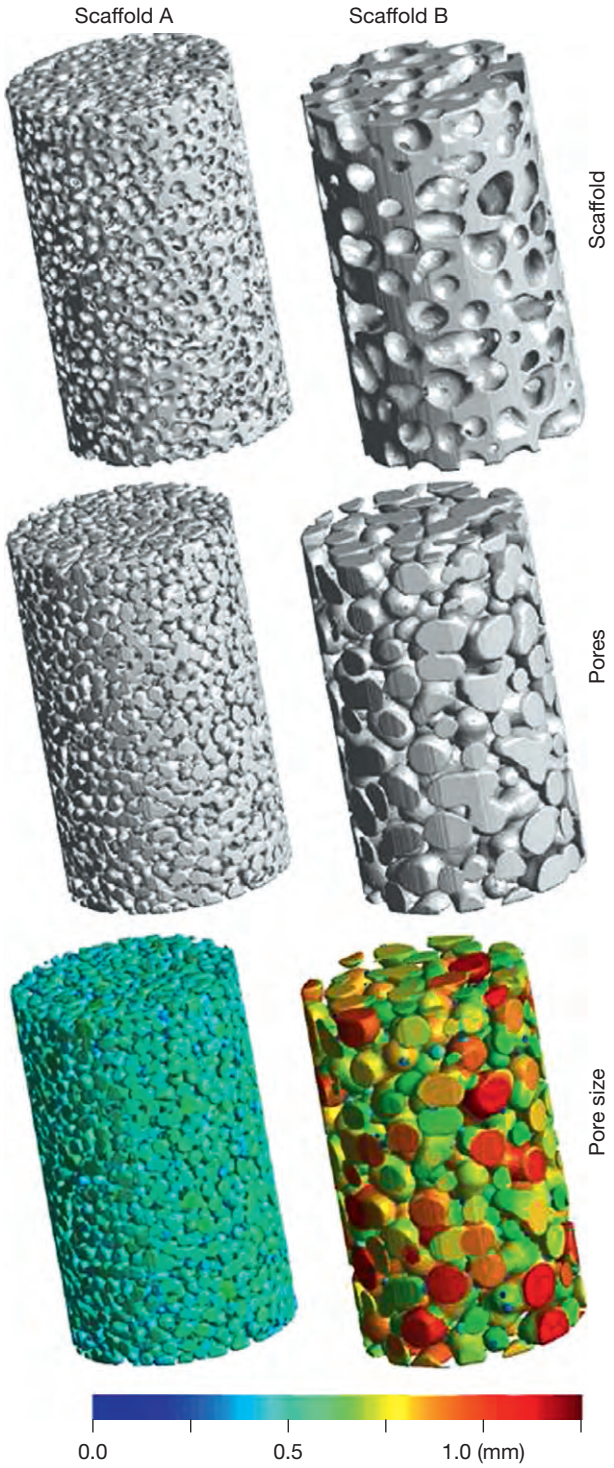

Figure 3 μCT scan of porous β-tricalcium phosphate scaffolds imaged using μCT scanning, showing the scaffold, the pores, and a color-coded visualization of pore size. Reproduced with permission from van Lenthe, G. H.; Hagenmuller, H.; Bohner, M.; Hollister, S. J.; Meinel, L.; Muller, R. *Biomaterials* **2007**, *28*(15), 2479–2490.

which is then used for their finite volume computations (see Section 3.309.3.1.1) of the flow field. The computational domain representing a unit cell of the porous fibrous scaffold and the imposed boundary conditions on this computational cell are shown in Figure 5. The governing equations employed by them include eqns [11] and [12] with $\mathbf{F}_b = 0$.

The results for the flow field is displayed in Figure 6 which show the details of the complex flow structures prevailing around individual fibers of such a fibrous scaffold.

These state-of-the-art techniques in conjunction with the DNS methods often enable sufficiently accurate estimations of the flow field even for complex geometries. The flow fields so obtained may then be used to estimate the shear stress distributions within the porous scaffolds. The knowledge of the flow and shear stress fields can then be used to accurately evaluate the concentration fields of important species. Such a knowledge of mass transfer that takes into account the microscopic structure is a critical issue that needs to be considered in the design of scaffolds for optimizing tissue-engineering treatments.[5]

The second method for predicting the fluid flow, namely the macroscopic averaged equations is described next.

3.309.3.1.4. Macroscopic averaged equations

While the DNS simulations can provide detailed solutions on the pore scale for a given system they are still computationally expensive, and as described above, require detailed knowledge of the pore-scale microstructure. Also, the possibility of considering the differentiation and expansion of biological cells, which result in a change of the geometry, poses significant challenges for DNS. For many engineering purposes, it is sufficient to know the flow field in an average sense, the average performed over the pores, cells, and scaffold matrix phases. The volume averaging method is one such technique used to analyze flow and transport in porous media on a macroscopic scale.[27] The Navier–Stokes equations representing the transport of momentum together with the mass transport equation for every species in particular phases of the multiphase systems (the scaffold material, cells, and the liquid media constitute the different phases) can be spatially smoothed to obtain continuum equations that are valid everywhere. These equations are called volume averaged equations. The techniques of the volume averaging procedure are described in the following section for the case of Stokes flow.

3.309.3.1.5. Volume averaging technique: mathematical formulation

This method mainly consists of averaging the microscale equations over a representative elementary volume (REV), which is chosen such that it is sufficiently larger than the characteristic length scales present in the porous scaffold (the pore size and the individual biological cell size) while much smaller than the total system volume.

3.309.3.1.5.1. Mathematical formulation

Consider the REV shown in Figure 7.

Let L be the macroscopic length scale, V be the averaging volume with radius r, and l_σ, l_β be the characteristic length scales of the solid phase (scaffold matrix and cells) and the liquid phase (average pore size), respectively. In Figures 7 and 8, let $A_{\beta\sigma}$ refers to the area between the fluid and solid phases, and $A_{\beta e}$ is the area of entrances and exits for the volume V. Assuming a homogenous porous media, the size

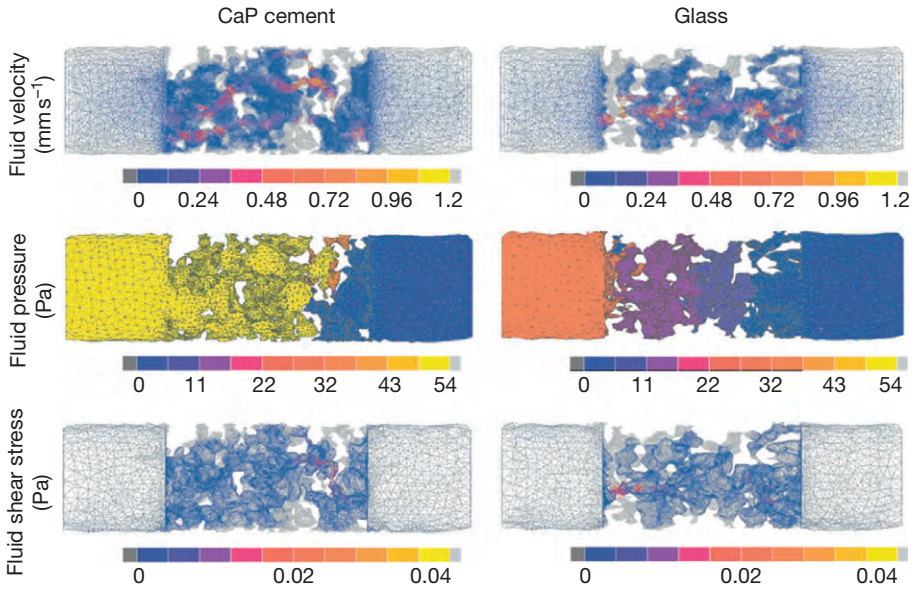

Figure 4 The flow field (velocity and pressure) and derived quantities (shear stress) obtained using a finite element DNS solution within a porous scaffold. Reproduced with permission from Sandino, C.; Planell, J. A.; Lacroix, D. *J. Biomech.* **2008**, *41*(5), 1005–1014.

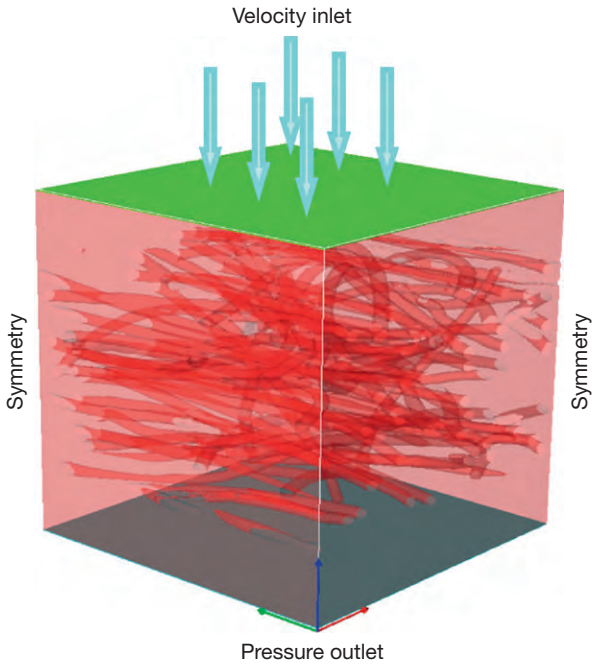

Figure 5 Computational domain and boundary conditions used in the DNS study of Jaganathan *et al.*[64] Reproduced with permission from Jaganathan, S.; Vahedi Tafreshi, H.; Pourdeyhimi, B. *Chem. Eng. Sci.* **2008**, *63*(1), 244–252.

of the REV is chosen such that the following length scale constraint holds true:

$$l_\sigma, l_\beta \ll r \ll L \qquad [27]$$

The following volume averages for any generic quantity ψ within the REV are defined as follows:

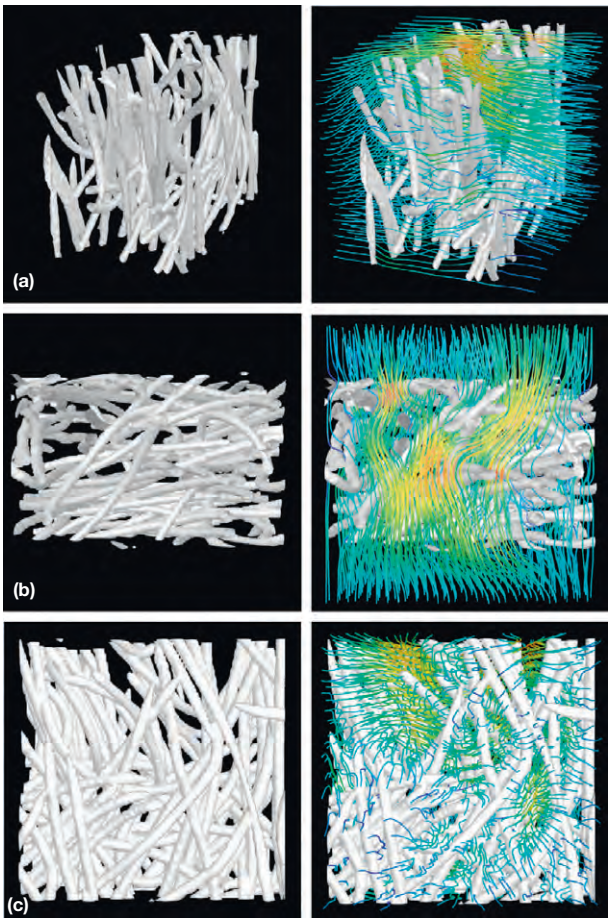

Figure 6 Flow path lines through a fibrous media rendered using results obtained from DNS: (a) isometric view, (b) side view, and (c) bottom view. Reproduced with permission from Jaganathan, S.; Vahedi Tafreshi, H.; Pourdeyhimi, B. *Chem. Eng. Sci.* **2008**, *63*(1), 244–252.

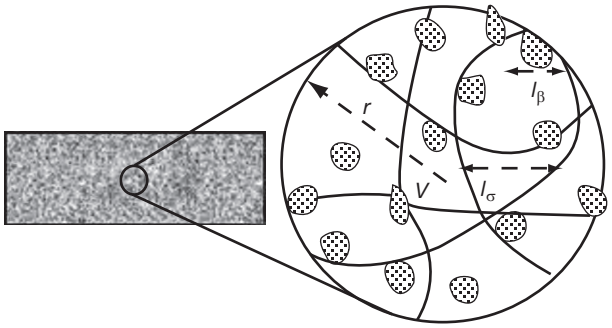

Figure 7 Schematic of a fibrous porous scaffold along with a representative element volume (REV). V is the averaging volume with radius r, and l_σ, l_β are the characteristic length scales of the scaffold matrix and the liquid phase (average pore size), respectively.

$$\langle\psi\rangle = \frac{1}{V}\int_{V_\beta}\psi\,dV \qquad [28]$$

is the superficial phase average or the average over the total volume V, and

$$\langle\psi\rangle^\beta = \frac{1}{V_\beta}\int_{V_\beta}\psi\,dV \qquad [29]$$

is the intrinsic phase average or average over the fluid phase. Here, V_β is the volume of the β-phase (fluid) contained within the representative or averaging volume V. These two averages are related by:

$$\langle\psi\rangle = \varepsilon_\beta\langle\psi\rangle^\beta \qquad [30]$$

where $\varepsilon_\beta = \frac{V_\beta}{V}$ is the porosity.

The governing equations for fluid flow for $Re < 1$ are the continuity and Stokes equations given by

$$-\nabla p + \mathbf{f} + \mu\nabla^2\mathbf{u} = \mathbf{0} \qquad [31]$$

and,

$$\nabla\cdot\mathbf{u} = 0 \qquad [32]$$

where $\mathbf{f}$ is a constant body force vector such as gravity. The associated boundary conditions are:

$$\begin{aligned}&\text{At } A_{\beta\sigma}: \mathbf{u} = 0\\ &\text{At } A_{\beta e}: \mathbf{u} = \mathbf{g}(\mathbf{r}, t)\end{aligned} \qquad [33]$$

where $\mathbf{g}(\mathbf{r}, t)$ is the velocity imposed at the boundaries of the REV.

The volume averaging method consists in applying the average procedure using eqn [28] to the governing eqns [31] and [32] in order to obtain the volume-averaged version of the continuity and Stokes equation. Along with this averaging, it is necessary to use Gray's decomposition, which is expressed as:

$$\begin{aligned}p &= \langle p\rangle^\beta + \tilde{p}\\ \mathbf{u} &= \langle\mathbf{u}\rangle^\beta + \tilde{\mathbf{u}}\end{aligned} \qquad [34]$$

where $\tilde{p}$ and $\tilde{\mathbf{u}}$ are the deviations or fluctuations about the intrinsic averaged pressure and velocity, respectively. Using eqn [34] in eqns [31] and [32] results in a set of equations containing both the averaged quantities and the deviations. In order to solve the system of equations, closure relations

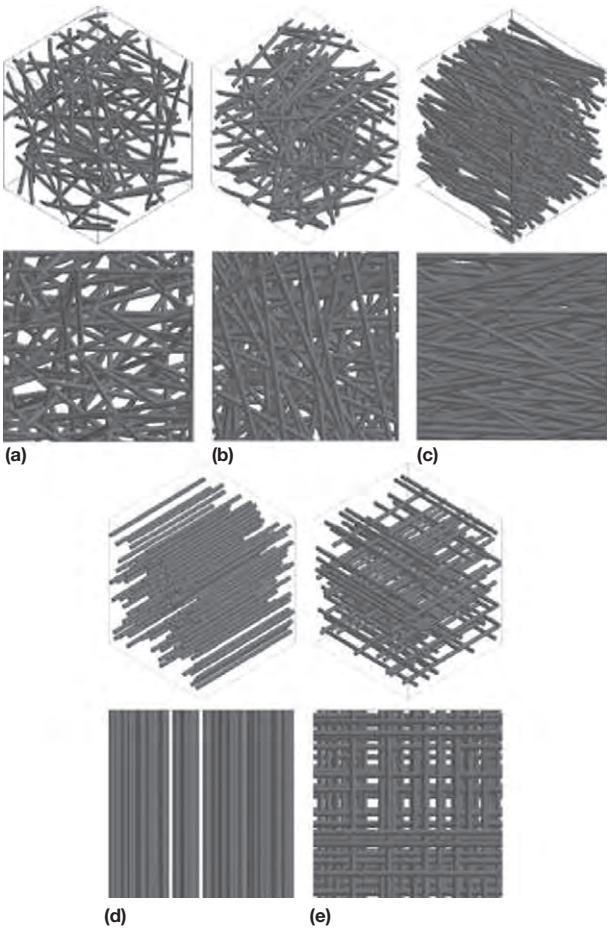

Figure 8 Different fiber orientations in isometric and side views: (a) 3D isotropic, (b) layered with random in-plane fiber orientation, (c) highly oriented layered, d) disordered unidirectional, and (e) disordered orthogonal media. Reproduced with permission from Tahir, M. A.; Tafreshi, H. V. *Phys. Fluids* **2009**, *21*, 083604.

expressing the deviations in terms of the averaged quantities are required. Following Whitaker,[65] one such closure problem is obtained by first expressing $\tilde{p}$ and $\tilde{\mathbf{u}}_\beta$ as follows.

$$\begin{aligned}\tilde{p} &= \mu\mathbf{b}\cdot\langle\mathbf{u}\rangle^\beta\\ \tilde{\mathbf{u}} &= \mathbf{B}\cdot\langle\mathbf{u}\rangle^\beta\end{aligned} \qquad [35]$$

where $\mathbf{b}$ and $\mathbf{B}$ are the unknown vector and second-order tensor used to represent the pressure and velocity deviations in terms of the averaged quantities. Both $\mathbf{b}$ and $\mathbf{B}$ are determined from the following integro-differential boundary value problems (see Whitaker[65] for more details):

$$\begin{aligned}&\nabla\cdot\mathbf{B} = 0\\ &-\nabla\mathbf{b} + \nabla^2\mathbf{B} = \frac{1}{V_\beta}\int_{V_\beta}\left[-\nabla\mathbf{b} + \nabla^2\mathbf{B}\right]dV\end{aligned} \qquad [36]$$

These equations are subjected to the following boundary conditions. At the fluid–scaffold matrix boundary ($A_{\beta\sigma}$),

$$\mathbf{B} = -\mathbf{I} \qquad [37]$$

where $\mathbf{I}$ is the identity tensor. At the entrance and exit of the scaffold ($A_{\beta e}$)

$$\mathbf{B}(\mathbf{r}+\mathbf{1}) = \mathbf{B}(\mathbf{r})$$
$$\mathbf{b}(\mathbf{r}+\mathbf{1}) = \mathbf{b}(\mathbf{r}), \quad i = 1, 2, 3 \qquad [38]$$

where $\mathbf{l}$ is the computational lattice vector. $\mathbf{B}$ and $\mathbf{b}$ are also subjected to the following conditions as well that reflect the assumption that the intrinsic averages of $\tilde{p}$ and $\tilde{\mathbf{u}}$ vanish:

$$\langle \mathbf{b} \rangle^{\beta} = \langle \mathbf{B} \rangle^{\beta} = 0 \qquad [39]$$

It is worth noting that the boundary condition related to the velocity at $A_{\beta e}$ as given by eqn [33] has been simplified and changed to a spatially periodic condition in the closure model given by eqn [38] in order to solve the closure problem.[65] However, such a change will not limit the validity of the equations to periodic structures alone and can be applied even for nonperiodic heterogeneous media as long as the scale constraints (given by eqn [27]) are satisfied.[65,66]

Based on the averaging procedure and the closure problem described so far, Darcy's law and the associated fluid mass conservation equations can be derived in the classical form and expressed as:

$$\langle \mathbf{u} \rangle = -\frac{\mathbf{K}}{\mu} \cdot \left[\nabla \langle p \rangle^{\beta} - \mathbf{f} \right] \qquad [40]$$

$$\nabla \cdot \langle \mathbf{u} \rangle = 0 \qquad [41]$$

where the permeability tensor $\mathbf{K}$ is defined as follows:

$$\mathbf{K} = \varepsilon_{\beta} \mathbf{C}^{-1} \qquad [42]$$

$$\mathbf{C} = \frac{1}{V_{\beta}} \int_{A_{\beta\sigma}} \mathbf{n}_{\beta\sigma} \cdot (\nabla \mathbf{B} - \mathbf{I}\mathbf{b}) \mathrm{d}A \qquad [43]$$

Here, $\mathbf{n}_{\beta\sigma}$ is the normal vector at the scaffold matrix–fluid interface.

An alternate and simpler form of closure equations (given by eqn [36]) can be derived based on the following transformations[27]:

$$\mathbf{D} = -\varepsilon_{\beta}^{-1} (\mathbf{B} + \mathbf{I}) \cdot \mathbf{K}$$
$$\mathbf{d} = -\varepsilon_{\beta}^{-1} \mathbf{B} \cdot \mathbf{K} \qquad [44]$$

Substituting eqn [44] into eqn [36] leads to the following Stokes-like set of equations.

$$\nabla \cdot \mathbf{D} = 0 \qquad [45]$$

$$-\nabla \mathbf{d} + \nabla^2 \mathbf{D} = \mathbf{I} \qquad [46]$$

These equations are subjected to the following boundary conditions

$$\text{At } A_{\beta\sigma} : \mathbf{D} = \mathbf{0} \qquad [47]$$

and at $A_{\beta e}$:

$$\mathbf{D}(\mathbf{r}+\mathbf{1}) = \mathbf{D}(\mathbf{r})$$
$$\mathbf{d}(\mathbf{r}+\mathbf{1}) = \mathbf{d}(\mathbf{r}), \quad i = 1, 2, 3 \qquad [48]$$

Also,

$$\langle \mathbf{d} \rangle^{\beta} = 0 \qquad [49]$$

$$\langle \mathbf{D} \rangle^{\beta} = -\varepsilon_{\beta}^{-1} \mathbf{K} \qquad [50]$$

The solution to eqns [45] and [46] subjected to boundary conditions given by eqns [47] and [48] helps in determining the permeability tensor $\mathbf{K}$ from eqn [50]. It is through the solution procedure of the above set of equations and through the averaging procedure in eqn [50] that the microscopic details of the scaffold structure enters the permeability calculations. Hence, an accurate estimation of the permeability tensor $\mathbf{K}$ depends on how well the microstructure of the porous scaffold is represented.

3.309.3.1.5.2. Numerical solution procedure

Equations [45] and [46] can be considered as a generalized Stokes problem for the components of $\mathbf{d}$ and $\mathbf{D}$. Anguy *et al.*[67] and Bernard *et al.*[68] have used an artificial compressibility method to obtain the solution for eqns [45] and [46]. Following Anguy *et al.*,[67] the equations governing the artificial compressibility method is given as follows:

$$\frac{\partial \mathbf{d}}{\partial t} + c^2 \nabla \cdot \mathbf{D} = 0 \qquad [51]$$

$$\frac{\partial \mathbf{D}}{\partial t} + \nabla \mathbf{d} - \nabla^2 \mathbf{D} = -\mathbf{I} \qquad [52]$$

where c is the artificial compressibility factor and t is pseudo-time. Equations [51] and [52] are subjected to the boundary conditions given by eqns [47] and [48] and initial conditions given as follows

$$\mathbf{d} = \mathbf{d}_0$$
$$\mathbf{D} = \mathbf{D}_0 \qquad [53]$$

where $\mathbf{d}_0$ and $\mathbf{D}_0$ are the specified initial conditions. The steady-state solution for eqns [51] and [52] yields the solution for $\mathbf{d}$ and $\mathbf{D}$, and this has been obtained using a standard finite volume solver and an explicit scheme (with $\theta = 0$ scheme described in **Section 3.309.3.1.2**). Expressions for the stable time step Δt and the artificial compressibility c have been provided in Anguy *et al.*[67] Following Anguy *et al.*,[67] for a 2D problem with a given stable Δt and grid spacings δx and δy, the expression for c is given by

$$c^2 = \min\left(\frac{1}{4\Delta t^2} (\delta x^2 - 8\Delta t), \frac{1}{4\Delta t^2} (\delta y^2 - 8\Delta t) \right) \qquad [54]$$

With the permeability tensor $\mathbf{K}$ of the medium so obtained, it may be used in the macroscopic averaged equations such as the Darcy's model given by eqn [40]. Some of the important macroscopic models including Darcy's model that are typically used in porous media calculations are listed below.

3.309.3.1.5.2.1. Darcy's law model As described earlier, Darcy's law given by eqn [40] results from the volume-averaging of the Stokes equation governing fluid flow in the porous medium. It relates the superficial average of the velocity, $\langle \mathbf{u} \rangle$ to the intrinsic average of the pressure $\langle p \rangle^{\beta}$. The superficial average velocity is chosen in the derivation because of its solenoidal characteristic represented by eqn [41]. The superficial average velocity is also directly related to the experimentally determined mass flow rate in the perfusion reactor. However, an intrinsic average of pressure is preferred because it more closely resembles the pressure that one could measure or the pressure that one could impose as a boundary condition see, Ochoa-Tapia and Whitaker.[69] The main drawback of Darcy's law is that it cannot satisfy a no-slip boundary condition at a solid surface bounding the porous material since there are no second derivatives of velocities.

3.309.3.1.5.2.2. Darcy–Brinkman model The Brinkmann model[70] was proposed to account for the presence of solid boundaries by introducing a term involving the second derivative of velocity in the Darcy's model. The semiempirical Darcy–Brinkman equation is a combination of Stokes equation [14] and Darcy's law. Following Khaled and Vafai,[71] the Darcy–Brinkman equation takes the following form:

$$\frac{\mu}{\varepsilon_\beta}\lambda\Delta^2\langle\mathbf{u}\rangle - \mu\mathbf{K}^{-1}\langle\mathbf{u}\rangle = -\nabla\langle p\rangle^\beta \qquad [55]$$

where ε_β is the porosity of the scaffold and λ is the tortuosity of the porous medium. For a highly porous medium, which is usually the case with many porous biomaterials, λ is usually taken to be equal to 1.

3.309.3.1.5.2.3. Darcy–Brinkman–Forchheimer model Both Darcy and Brinkman models do not account for the inertial effects of the fluid within the porous medium. For cases in which inertial effects ($Re > 1$) in the flow are significant, the Darcy–Brinkman equation is extended to the so-called Darcy–Forchheimer–Brinkman formulation.[72] Following Nithiarasu *et al.*,[73,74] the Darcy–Forchheimer–Brinkman model for an anisotropic porous medium characterized by the porosity ε_β and permeability tensor $\mathbf{K}$ is given as follows.

$$\frac{\rho}{\varepsilon_\beta}\left[\frac{\partial\langle\mathbf{u}\rangle}{\partial t} + \nabla\cdot\left(\frac{\langle\mathbf{u}\rangle\langle\mathbf{u}\rangle}{\varepsilon_\beta}\right)\right] = -\frac{1}{\varepsilon_\beta}\nabla(\varepsilon_\beta\langle p\rangle^\beta) + \frac{\mu}{\varepsilon_\beta}\nabla^2\langle\mathbf{u}\rangle - \mu\mathbf{K}^{-1}\langle\mathbf{u}\rangle - \rho C_F\mathbf{K}^{-\frac{1}{2}}\left|\langle\mathbf{u}\rangle\right|\langle\mathbf{u}\rangle \qquad [56]$$

where $|\langle\mathbf{u}\rangle|$ denotes the magnitude of the velocity vector at any given location. Also, C_F is the Forchheimer coefficient and is expressed as,

$$C_F = \frac{1.75}{\sqrt{150\varepsilon_\beta^3}} \qquad [57]$$

A more general form of the Darcy–Forchheimer–Brinkman model has been proposed by Bousquet-Melou *et al.*[66] that takes into account porosity variations within a porous scaffold along with a generalized form of continuity equation that are given as follows:

$$\frac{\partial}{\partial t}(\varepsilon_\beta\rho + \varepsilon_\sigma\rho_\sigma) + \nabla\cdot(\rho\langle\mathbf{u}\rangle) = 0 \qquad [58]$$

$$\varepsilon_\beta{}^{-1}\frac{\partial}{\partial t}(\rho\langle\mathbf{u}\rangle) + \varepsilon_\beta{}^{-1}\nabla\cdot\left(\varepsilon_\beta{}^{-1}\rho\langle\mathbf{u}\rangle\langle\mathbf{u}\rangle\right) = -\nabla\langle p\rangle^\beta + \mathbf{f} + \mu\varepsilon_\beta{}^{-1}\nabla^2\langle\mathbf{u}\rangle - \mu\varepsilon_\beta{}^{-1}\nabla\varepsilon_\beta\cdot\nabla(\varepsilon_\beta{}^{-1}\langle\mathbf{u}\rangle) - \mu\mathbf{K}^{-1}\cdot\langle\mathbf{u}\rangle - \mu\mathbf{K}^{-1}\cdot\mathbf{F}\cdot\langle\mathbf{u}\rangle \qquad [59]$$

where $\mathbf{F}$ is the Forchheimer correction tensor. The solution procedure for $\mathbf{F}$, which involves a closure problem similar to the one described in **Section 3.309.3.1.5**, is still an open research problem.[75] Usually, the last term of the RHS of eqn [59] is approximated by the last term of the RHS given in eqn [56]. The fourth term of the RHS in eqn [59] denotes the second Brinkman correction term that explicitly involves porosity gradients. Hence, this form of equation may be useful for modeling tissue growth in porous scaffolds. It may be noted that eqns [40], [55], and [56] are special cases of eqn [59].

All of the model equations have been employed in various recent studies to evaluate the flow within porous scaffolds. Botchwey *et al.*[76] used Darcy's law to estimate shear stresses inside 3D microcarrier scaffolds during rotation in a high aspect ratio vessel. Whittaker *et al.*[77] developed a mathematical model based on Darcy's law for forced flow of culture medium through a porous scaffold to predict the nutrient and shear-stress distributions. In this study, the authors have investigated the role of fluid flow within a porous scaffold that included both an externally driven flow using inlet and outlet pipes, and additional perfusion using porous fibers within the scaffold. The scaffold has been modeled as a uniform isotropic porous medium with distributed mass sources representing both the external flows and perfusion from porous fibers. Mathematically, this can be described using the following modified continuity equation:

$$\nabla\cdot\langle\mathbf{u}\rangle = \Psi_{\text{inlet}} - \Psi_{\text{outlet}} + \Psi_{\text{fibers}} \qquad [60]$$

where Ψ_{inlet}, Ψ_{outlet}, and Ψ_{fibers} denote the mass flow rates from the inlet pipe, the outlet pipe, and the porous fibers. The fiber core is assumed to be a slender cylinder and flow within the core is modeled using Navier–Stokes equations with inertia and radial pressure gradients neglected. The walls of the fibers are modeled as an axisymmetric and axially uniform porous medium governed by Darcy's law (eqn [40]). Chung *et al.*[78] have used the Darcy–Brinkman equation to characterize the fluid dynamics within a porous construct placed in a perfusion reactor. Using a finite volume method, Yu *et al.*[79] have numerically investigated the effect of cell density on the fluid dynamics and mass transfer of oxygen inside a porous isotropic tissue engineering scaffold placed within a rotating bioreactor. The external flow to the porous scaffold has also been considered. The microbioreactor consisted of an open cylinder chamber filled with culture medium. For the external flow, the fluid velocities and oxygen concentration fields are solved numerically using eqns [11] and [12]. The flow inside the scaffold has been modeled using the Darcy–Brinkman–Forchheimer model given by eqn [56] along with eqn [57] (also, see Yu *et al.*[80]). The external and internal flows are coupled through boundary conditions at the scaffold surface. Following Chen *et al.*,[81] the boundary conditions needed to couple the macroscopic flow described by DNS at the bioreactor macroscopic scale and the microscopic flow inside the porous scaffold governed by the Darcy–Brinkman–Forchheimer model are given as follows:

Continuity of velocity and normal stress :

$$\langle\mathbf{u}\rangle\big|_{\text{Fluid}} = \langle\mathbf{u}\rangle\big|_{\text{Porous}} = \langle\mathbf{u}\rangle\big|_{\text{Interface}} \qquad [61]$$

$$\frac{\mu}{\varepsilon}\frac{\partial\langle u\rangle_t}{\partial n}\bigg|_{\text{Porous}} - \mu\frac{\partial\langle u\rangle_t}{\partial n}\bigg|_{\text{Fluid}} = 0 \qquad [62]$$

Tangential stress jump condition :

$$\frac{\mu}{\varepsilon}\frac{\partial\langle u\rangle_t}{\partial n}\bigg|_{\text{Porous}} - \mu\frac{\partial\langle u\rangle_t}{\partial n}\bigg|_{\text{Porous}} = \gamma\frac{\mu}{\sqrt{K}}\bigg|_{\text{Interface}} + \gamma_1\rho\langle u\rangle_t{}^2 \qquad [63]$$

where $\langle u\rangle_n$ and $\langle u\rangle_t$ are the normal and tangential components of the velocity vector $\langle\mathbf{u}\rangle$ and γ, γ_1 are adjustable parameters which account for the stress jump at the interface and are usually determined from experiments (see, Ochoa-Tapia and Whitaker[82]). The parameter γ usually varies in the range -1 to 0.7[83] and γ_1 is assumed to vary in the range -0.7 to 0.7.[81]

The application of the above models for computing interstitial fluid flow within biological tissues can be found in the reviews of Khaled and Vafai[71] and Swartz and Fleury.[84]

3.309.3.1.6. Correlations for estimating porous scaffold permeability

An estimation of the macroscopic permeability tensor of the porous scaffold **K** is critical to solving the averaged equations for fluid flow described earlier. As shown in **Section 3.309.3.1.5**, the permeability tensor **K** arises as a result of the volume averaging procedure and is obtained by solving a closure problem (eqns [45]–[50]) on a reasonably well approximated porous microstructure. For the case of realistic fibrous scaffold architecture obtaining solutions for such a closure problem requires a lot of computational resource and is therefore noted to be a difficult problem (see, Serrat[85]).

Simpler models/correlations that provide a good estimate of the permeability values are often sought. Such models need to consider the dependence of the permeability on the geometry of the porous medium, the orientation of the pores/fibers with respect to the flow, and the porosity ε_β or the solid volume fraction, $\phi = 1 - \varepsilon_\beta$, of the scaffold. The dependence of the permeability on ε_β (or ϕ) is critical for tissue engineering purposes because the porosity of the microstructure changes with time as the cells proliferate and grow.

Early models that studied flow in fibrous media were confined to 2D geometries, used Stokes flow equations, and utilized a unit cell model consisting of a single fiber or a periodic array of fibers. By solving the creeping flow equations for parallel or transverse orientation of fiber axis, expressions for the hydraulic permeability were derived. A review of such models is given by Jackson and James.[37] For realistic 3D fibrous media used in biotechnology applications, the second-order permeability tensor **K** is usually diagonally dominant and the off-diagonal components are usually two or three orders of magnitude smaller Ashari *et al.*[86] The scaffold materials are approximated as orthotropic materials, and if the diagonal components are nearly the same, they are treated as isotropic materials. Based on these approximations, analytical expressions/correlations of permeabilities have been derived using simplified geometries of the porous microstructure and these serve as good estimates for modeling the flow using the averaged equations. Some of the important and more widely used correlations for the permeability of porous media involving relatively low solid volume fraction (typically, $\phi < 0.3$) are listed below.

1. Carman–Kozeny equation:

   Carman–Kozeny expression predicts a single (isotropic) scalar value for the permeability of the fibrous porous medium in terms of the porosity of the medium. The permeability expression is[87]:

$$K = \frac{\varepsilon_\beta^3}{k_k(1-\varepsilon_\beta)^2 a_p^2} \qquad [64]$$

   where, k_k is the Carman–Kozeny constant which accounts for the tortuosity and nonuniformity of the pores, a_p is the specific area of the particle, and ε_β is the porosity of the scaffold. Here, a_p is given by:

$$a_p = \frac{2(2\lambda+1)}{\lambda d_p} \qquad [65]$$

   where, d_p is the average diameter of the fibers, $\lambda = L_f/d_p$ is the aspect ratio of the fiber, where L_f is the average length of the fibers. It may be noted that for large values of λ, $a_p \approx 4/d_p$, the eqn [64] reduces to:

$$K = \frac{\varepsilon_\beta^3 d_p^2}{16 k_k (1-\varepsilon_\beta)^2}, \lambda \gg 1. \qquad [66]$$

   Values of k_k as a function of ε_β and r_p for randomly stacked fibers are given in Rahli *et al.*[87] Studies that have employed Carman–Kozeny equations include those by Botchwey *et al.*,[76] Chung *et al.*,[78,88] and Whittaker *et al.*[77]

2. Spielman–Goren model:

   Using Brinkman equation for the fluid flow, Spielman and Goren[89] have derived a set of implicit equations for the permeability of different fibrous microstructures. Their expressions for layered (eqn [67]) and 3-D random microstructures (eqn [68]) in terms of the solid volume fraction ($\phi = 1 - \varepsilon_\beta$)are given as follows (see, Jackson and James[37]):

$$\text{Layered}: \frac{1}{2} + \frac{\sqrt{K}}{a}\frac{K_1\left(\frac{a}{\sqrt{K}}\right)}{K_0\left(\frac{a}{\sqrt{K}}\right)} = \frac{1}{4\phi} \qquad [67]$$

$$\text{3D Random}: \frac{1}{3} + \frac{5}{6}\frac{\sqrt{K}}{a}\frac{K_1\left(\frac{a}{\sqrt{K}}\right)}{K_0\left(\frac{a}{\sqrt{K}}\right)} = \frac{1}{4\phi} \qquad [68]$$

   where a is the average radius of the fiber, K_0 and K_1 are modified Bessel functions of the second kind of orders 0 and 1, respectively.

3. Jackson and James model:

   Jackson and James[37] have proposed the following correlation for the permeability of 3D random arrays of cylinders based on a simple weighted averaging of the streamwise and transverse permeability values.

$$\frac{K}{a^2} = \frac{3}{20\phi}(-\ln\phi - 0.931) \qquad [69]$$

   The authors have also provided a large compilation of the values of permeabilities for various fibrous materials as a function of porosity.

4. Parallel and transverse flows through fibers:

   Drummond and Tahir[90] and Sangani and Acrivos[91] have obtained permeability expressions for parallel and transverse flows through periodic arrays of fibers aligned parallel to each other.

$$\frac{K_{||}}{a^2} = \frac{1}{4\phi}\left(-\ln(\phi) - 1.476 + 2\phi - \frac{\phi^2}{2} + O(\phi^4)\right) \qquad [70]$$

$$\frac{K_\perp}{a^2} = \frac{1}{8\phi}(-\ln(\phi) - 1.476 + 2\phi - 1.774\phi^2 + 4.076\phi^3 + O(\phi^4)) \qquad [71]$$

   where $K_{||;}$ and $K_\perp$ are the permeabilities parallel and perpendicular to the flow direction. Based on these expressions, the

permeability of the scaffold with randomly oriented fibers in three dimensions is given as follows[84,92,93]:

$$\frac{1}{K} = \frac{1}{(\phi/3)K_{||}} + \frac{1}{(2\phi/3)K_{\perp}} \quad [72]$$

5. Experimental correlation of Davies:

Davies[94] has obtained an experimental correlation for the permeability of planar fibrous sheets as described by:

$$K = \frac{a^2}{16\phi^{3/2}(1+56\phi^3)} \quad [73]$$

The values of the isotropic permeability K for some of the commonly used porous scaffolds are listed in **Table 1**. For the cases where both porosity and permeability change due to cell growth, the values provided in the table represent the initial conditions.

3.309.3.1.7. Direct methods for the estimation of permeabilities

One direct method for the estimation of the permeability tensor is through the solution of the closure equations (eqns [45]–[50]) using the microarchitecture of porous medium. The permeabilities of the porous microstructure have also been determined using the following approach based on DNS methods. First, a steady state Stokes flow field prevailing within the microstructure is solved using DNS as described in **Section 3.309.3.1**. The small Re approximation used in Stokes flow is usually justified for porous biomaterials because of the smallness of the pore size. Once the flow field is calculated, the scalar value of permeability K, along a given direction is usually obtained using eqn [40]. Specifically,

$$K = \mu\langle u\rangle\left(\frac{\Delta p}{\Delta L}\right)^{-1} \quad [74]$$

where $\Delta p/\Delta L$ is the numerically estimated magnitude of the pressure drop along the particular direction for which K is to be determined. Clague and Phillips[92] calculated hydraulic permeabilities for monomodal and bimodal, periodic and random fibrous media using the following equation:

$$K = \frac{V}{|\mathbf{F}|} \quad [75]$$

where V is the total volume of a unit cell normalized by a^3, where a is the radius of the fibers (assumed as cylindrical rods), and $|\mathbf{F}|$ is the total force acting on the cylinders in the cell normalized by the product of the imposed fluid velocity, the fluid viscosity, and the cylinder (fiber) radius. In the numerical technique employed by Clague and Phillips,[92] each fiber was represented as a line distribution of point forces, and the no-slip condition was enforced in an integral form. Although they have reported results mainly for dilute volume fractions, the method can be used for more concentrated suspensions with the addition of quadropole terms and by using additional point singularities on the rigid fiber surfaces.

In this manner, the accurate results from DNS can be used to compare the results obtained from correlations in order to check the regime under which the correlations may be used as valid simplifications. Some of the results obtained using detailed DNS simulations have been compared with the results of correlations described earlier and are presented in the following section.

Apart from DNS, other modeling techniques such as network modeling have also been employed to calculate the permeabilities of fibrous media and the methodology has been described for low and high fiber volume fractions in Thompson.[97] Here, the pore space is discretized into an interconnected set of pores and pore throats using Voronoi networks. By assigning hydraulic conductivities to pore throats based on an effective radius approach and Hagen–Poiseuille law, the flow problem is cast as a pipe network (or resistor network) problem. Mass conservation equation applied to each pore in the network produces a set of linear equations as given below that is solved for individual pore pressures.

$$\sum_{j=1}^{n} \frac{G_{ij}}{\mu}(P_j - P_i) = 0 \quad [76]$$

where G_{ij} is the hydraulic conductivity for the ijth and n is the total number of neighbors to a pore i. The solution of the system of equations also gives the total flow rate through the network (if boundary pressures are specified), or the pressure drop across the network (if the flow rate is imposed). These quantities can then be used in the Darcy's law to calculate the permeability of the fibrous medium along a given direction. If the material is anisotropic, the permeability tensor may be defined by repeating the flow calculation in the other coordi-

Table 1 Isotropic permeability values for some commonly used scaffold materials

Scaffold	*Porosity (ε_β)*	*Permeability (m^2)*	*References*
PEOT, PBT, and PEG copolymer	0.8	2.28×10^{-10}	Vossenberg *et al.*[46]
PLA and PGA copolymer	0.8–0.92	2.1×10^{-12}–1.6×10^{-11}	Agrawal *et al.*[95]
Generic polymeric scaffold	0.97	5.1×10^{-11}	Coletti *et al.*[96]
Microsphere scaffold	0.6	5×10^{-10}	Yu *et al.*[79]
Amorphous polylactic acid (PDLLA)	0.77	3.34×10^{-12}	Boschetti *et al.*[49]
Poly(lactic-*co*-glycolic acid) (PLAGA)	0.31	1.25×10^{-8}–1.13×10^{-7}	Botchwey *et al.*[76]
Coralline hydroxyapatite	0.642	2.66×10^{-10}	Swider *et al.*[63]
Hydroentangled nonwoven fabric	0.83–0.94	4.5×10^{-11}–2.4×10^{-10}	Jaganathan *et al.*[64]
Gyroid and hexagonal scaffolds	0.55–0.7	0.52×10^{-11}–3.95×10^{-10}	Olivares *et al.*[51]
Synthetic microporous scaffolds	0.85	5.41×10^{-10}	Cantini *et al.*[36]

A dynamic viscosity of $\mu = 1\times10^{-3}\,\mathrm{N\,s\,m^{-2}}$ has been assumed for the calculation of permeabilities of some of the scaffold materials whose units are reported in $\mathrm{m^4\,(N\,s)^{-1}}$.

nate directions. In this method, the distinction between pores and pore throats has been neglected and a simplified relationship between discrete nodal pressures and flow has been assumed. However, it has been noted that the simplicity of the method in obtaining the solutions and the reasonable accuracy of the calculated permeabilities at low volume fractions of the fibrous network ($\phi < 0.3$) overweigh such limitations.

3.309.3.1.8. Comparison of direct estimations with correlations

Higdon and Ford[98] have calculated the permeability K for ordered fibrous media based on simple cubic, body-centered cubic and face-centered cubic (FCC) lattices. In this study, accurate numerical results based on spectral boundary element DNS methods for the full range of volume fractions have been presented. Their results compare reasonably well with the correlation of Jackson and James (eqn [69]) for $\phi < 0.3$. Clague *et al.*[99] have calculated hydraulic permeabilities from eqn [74] for ordered and disordered media using the flow fields obtained from LB simulations. Good agreement with the semi-analytical results of Sangani and Acrivos[91] (see eqn [71]) has been demonstrated for the ordered media simulations. The simulation results for the disordered media are in good agreement with the results of Jackson and James (eqn [69]) and the permeability calculations of Higdon and Ford's FCC lattices.[98] Jaganathan *et al.*[64] have calculated the permeabilities of 3D hydroentangled fibrous scaffolds using eqn [74]. The flow fields have been obtained using a DVI technique in conjunction with a finite volume-based flow solver. At low values of ϕ, their results for permeabilities are in close agreement with those of eqns [67] and [73]. Tahir and Tafreshi[100] have studied the influence of fiber orientation on the permeability of a fibrous medium. The different orientations of the fibers used in this study are shown in **Figure 8**. A commercial finite volume flow solver (ANSYS) was used to solve for the flow fields, and eqn [74] was subsequently employed to obtain the permeabilities for various fiber orientations. Good agreement of the predicted results with those of eqns [67], [68], and [73] are noted. In Stylianopoulos *et al.*,[101] permeability calculations are then performed for isotropic and oriented fiber networks within the fiber volume fraction range of 0.3–15% using FEM-based DNS. Good agreement is noted between their results and the results predicted with eqn [69] and also with the numerical results of Clague and Phillips,[92] and Higdon and Ford.[98]

Many of the correlations for permeabilities compare quite well with the results of direct simulations for low values of solid volume fraction that are characteristic of applications involving porous biomaterials. With the values of permeabilities so obtained, the flow velocity field within the porous scaffolds may be calculated using averaged equations. The main disadvantage of the averaging procedure is that it smoothes many of the flow structures occurring at the length scales of the pores. In some cases, averaged equations may under predict shear stress variations at the cellular scale inside the scaffolds.[102] This is shown in **Figure 9** where the shear stress results of a fibrous porous medium obtained with DNS simulations using eqns [11] and [12] using the finite volume solver Fluent (ANSYS) is compared with those obtained using the Darcy–Brinkman's model (eqn [55]). A value of $K = 2.23 \times 10^{-12}\,\mathrm{m}^2$ has been used for the Brinkman model. The values of shear stresses predicted by the DNS model are approximately twice as high as the Brinkman model predictions. Therefore, with averaged equations, there always results a trade-off between the level of accuracy obtained and the ease of calculations.

The velocity field obtained using the DNS methods or using the averaged equations may now be used to calculate the mass transport of species as described in the following sections.

3.309.3.2. Mass Transfer Equations

An understanding of the nutrient transport process within a porous scaffold represents one of the key processes in determining the success of a tissue engineering protocol. A review on the need for nutrient transport modeling within a porous scaffold is provided by Sengers *et al.*[103] If the cells are uniformly distributed within a porous scaffold saturated with culture medium, then eqn [7] governs the transport of species such as nutrients, oxygen, and waste products. Assuming a Michaelis–Menten kinetics for the consumption rate $\dot{R}$, the individual species mass transfer equations may then be expressed as

$$\frac{\partial C_i}{\partial t} + \mathbf{u} \cdot \nabla C_i = \nabla \cdot (\mathbf{D}_i \cdot \nabla C_i) - \frac{V_{\max} C_i}{K_m + C_i} \qquad [77]$$

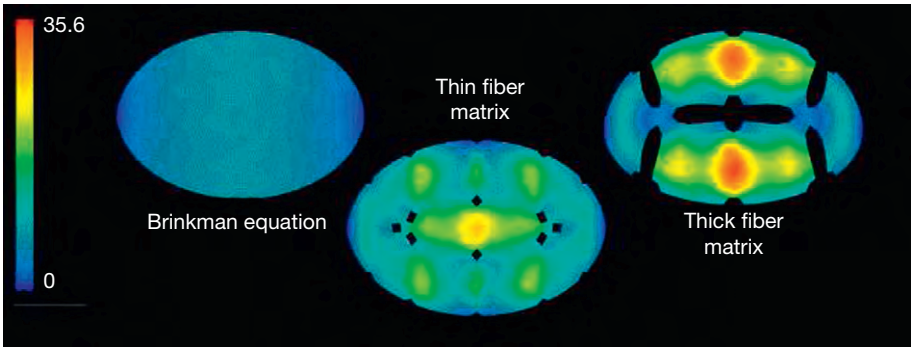

Figure 9 Comparison of shear stress results obtained for a fibrous porous media using Darcy–Brinkan model (left panel) with those obtained using DNS methods for two different fiber thickness but with same permeability, $K = 2.23 \times 10^{-12}\,\mathrm{m}^2$ (the two right panels). Reproduced with permission from Pedersen, J. A.; Boschetti, F.; Swartz, M. A. *J. Biomech.* **2007**, *40*(7), 1484–1492.

As with the flow field estimation, the mass transfer may be evaluated using DNS methods or by employing macroscopic averaged equations that are described in the following sections.

3.309.3.2.1. Direct numerical simulations

The evolution of species concentration within a porous scaffold may be accurately estimated using direct numerical simulations for a known geometry of the porous medium and the associated flow field. As mentioned under **Section 3.309.3.1** for the pore-scale geometry description, the studies of Anderson *et al.*,[54] Raimondi *et al.*,[55] Cioffi *et al.*,[56] Maes *et al.*,[57] and Jungreuthmayer *et al.*[58] have provided detailed microscale pore-level flow field evaluations using the exact geometry obtained from μCT methods. However, none of these studies have evaluated nutrient transport within the scaffolds. Cantini *et al.*[36] have used DNS methods both for the flow and mass transfer to optimize the microenvironment inside porous scaffolds placed in a perfusion bioreactor used for hematopoietic stem cell culture. For computational purposes, the porous scaffold was represented by a periodic unit cell consisting of interconnected spheres representing the pores. The steady-state Navier–Stokes equations (steady-state version of eqn [12] coupled with eqn [11]) were solved with periodic boundary conditions for pressure and velocity using the commercial finite volume code Fluent (ANSYS). For oxygen transport analysis, a nonperiodic model was used that consisted of superimposed periodic units. Oxygen transport was modeled using the steady-state version of eqn [8], with a diffusivity value set equal to $3.29 \times 10^{9}\,\mathrm{m^2\,s^{-1}}$ and partial pressure at the inlet set equal to 152 mmHg (20%). The volumetric oxygen consumption rate $\dot{R}$ representing cellular uptake was modeled using a zeroth-order kinetics and was set equal to a value 1.25×10^{-17} $\mathrm{mol\,s^{-1}}$ per cell. The cell density value ρ_{cd} in eqn [8] was set equal to 10^{12} cells per cubic meter for hematopoietic stem cells and 9×10^{12} cells per cubic meter for stromal cells.

Cioffi *et al.*[104] have quantified in detail the transport of species within a complex 3D porous scaffold using DNS techniques. In this study, a combined macroscale/microscale computational approach was used to quantify oxygen transport and flow-mediated shear stress to human chondrocytes cultured in 3D poly(ethylene glycol terephthalate)/poly(butylene terephthalate) (PEGT/PBT) scaffolds placed in a perfusion bioreactor system. Cells were assumed to form a single layer on the walls of the pores during the initial culture period and hence the wall shear stress on the scaffold surface was assumed to approximate the shear stress on cell surfaces. The boundary conditions for the DNS microscale simulations of the flow field inside the scaffold were obtained by solving an averaged macroscale model based on the Darcy–Brinkman model given by eqn [55]. For the macroscale model, the scaffold was considered isotropic and the permeability K was set to a value of $4 \times 10^{-11}\,\mathrm{m^2}$ and the viscosity value μ was set to 8.1×10^{-4} Pa s. A constant flat velocity profile computed from a specified flow rate is set as the boundary condition at the inlet. For the pore-scale DNS model, the geometry description was obtained using a μCT reconstruction of a foam scaffold. The schematic of the μCT model, the mesh, and the boundary conditions used are given in **Figure 10**.

The steady-state oxygen (O_2) mass transfer distribution was obtained by solving eqn [77] using a finite volume solver Fluent (ANSYS). The volumetric oxygen consumption rate was assumed to follow a Michaelis–Menten type kinetics (eqn [9]). The value for D_i was set equal to $3.23 \times 10^{-12}\,\mathrm{m^2\,s^{-1}}$. **Figure 11** shows the contours of oxygen distribution obtained using the DNS method inside the porous scaffold as given in Cioffi *et al.*[104]

In the DNS methods, although the presence of cells may be directly taken into account as demonstrated by Jungreuthmayer *et al.*[58] and Olivares *et al.*,[51] the modeling of transient development of an engineered tissue within the scaffold still remains an open challenge. The techniques for addressing some of the relevant issues such as tissue growth and the associated changes

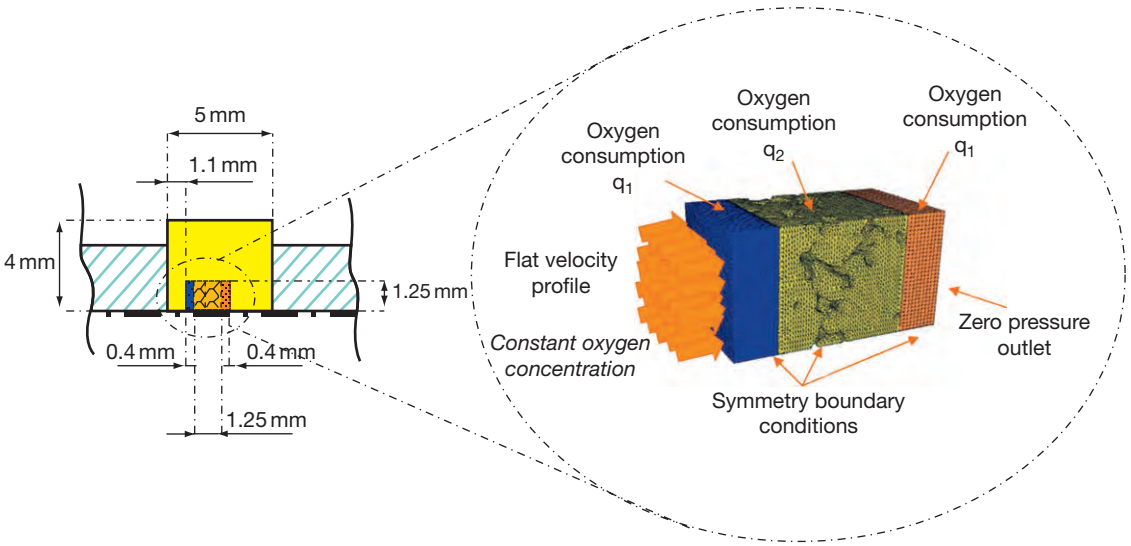

Figure 10 The schematic of μCT model of a porous scaffold used in the study of Cioffi *et al.*[104] The mesh and the boundary conditions used in the DNS simulations of the pore-scale flow and mass transfer are also shown. Reproduced with permission from Cioffi, M.; Kuffer, J.; Strobel, S.; Dubini, G.; Martin, I.; Wendt, D. *J. Biomech.* **2008**, *41*(14), 2918–2925.

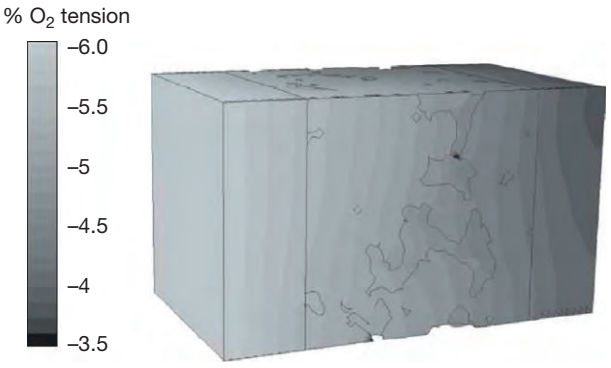

Figure 11 Contours of oxygen distribution in a porous scaffold obtained using DNS simulations. Reproduced with permission from Cioffi, M.; Kuffer, J.; Strobel, S.; Dubini, G.; Martin, I.; Wendt, D. *J. Biomech.* **2008**, *41*(14), 2918–2925.

in porosity and permeability that are difficult to model with DNS are next addressed in the context of volume averaged equations of the mass transport process.

3.309.3.2.2. Macroscopic averaged equations

Averaged equations provide a useful and an efficient way to obtain meaningful solutions both for the flow and the mass transport within a porous scaffold. While providing a reasonable estimate of the fluid flow within a porous construct, the macroscopic averaged flow equations (see **Section 3.309.3.1**) can also account for cell density variations occurring due to proliferation. The changes in the microstructure of the porous medium due to cell growth may be accounted through the changes in porosity values ε_β. This change in ε_β (or ϕ) directly affects the permeability in the macroscopic averaged equations (refer to eqns [64]–[73]). Following Wood *et al.*,[28] a model for species transport inside a porous tissue engineering scaffold taking into account the variations in cell density and corresponding variations in permeability and porosity is presented below. Specifically, the quantification of the consumption/production rates of basic metabolites, such as glucose, oxygen, and lactate are highlighted. The following major assumptions are invoked in the development of the mass transfer models:

1. The cells are assumed to be uniformly attached to the scaffold and hence no cells are suspended in the culture medium (β-phase).
2. The cellular phase (σ-phase) comprises both the cells and the extracellular matrix (ECM).
3. Diffusion mechanism alone is considered to take place in the cellular σ-phase and the diffusion coefficients are the same both inside the cell and in the ECM.
4. The intrinsic average concentration of species in the fluid (c_i^β) and cell (c_i^σ) phases are in local thermodynamic equilibrium. Mathematically, this condition may be expressed for a species i as

$$c_i^\beta = K_{eq} c_i^\sigma \qquad [78]$$

where K_{eq} is the equilibrium constant. The physical constraints for local mass equilibrium assumptions are explained in greater detail in Golfier *et al.*[62] Usually, such conditions apply for transport in biomaterials.

Under these conditions, a single macroscale transport equation can be used to describe the species transport within the porous scaffold.[28] Let ε_β and ε_σ denote the volume fractions of the culture medium and cells, respectively. Also, let ε_s denote the constant volume fraction of the scaffold matrix (fibers). Then, from the definition of volume fractions, we have

$$\varepsilon_\beta + \varepsilon_\sigma + \varepsilon_s = 1 \qquad [79]$$

The solid volume fraction, ϕ, is given by

$$\phi = \varepsilon_\sigma + \varepsilon_s \qquad [80]$$

For highly porous scaffolds, ε_s can be assumed to be negligible. Let c_g^β, c_l^β, and c_o^β represent the intrinsic average concentrations of glucose (subscript g), lactate (subscript l), and oxygen (subscript o), respectively. Following Wood *et al.*,[28] the macroscale balance equations for each of the species may be written as

$$\frac{\partial}{\partial t}\left[\left(\varepsilon_\beta + \varepsilon_\sigma K_{eq_i}\right)c_i^\beta\right] + \nabla\cdot\left(\langle\mathbf{u}\rangle c_i^\beta\right) = \nabla\cdot\left(\mathbf{D}_{eff_i}\nabla c_i^\beta\right) + \varepsilon_\sigma \dot{R}_i \qquad [81]$$

The effective diffusivity tensor of each species is denoted by $\mathbf{D}_{eff_i}$ while K_{eq_i} is given by eqn [78]. Details on the evaluation of $\mathbf{D}_{eff_i}$ is provided in a subsequent section. Here, $\langle\mathbf{u}\rangle$ is the known fluid velocity vector obtained as described in **Section 3.309.3.1**. Glucose and oxygen are consumed by the cells in the σ-phase and their consumption rates are assumed to follow a Michaelis–Menten kinetics.

$$\dot{R}_{(g,\,o)} = -\frac{V_{max(g,\,o)}c_i^\beta}{K_{m(g,\,o)} + c_i^\beta} \qquad [82]$$

In eqn [82], $V_{max(g,o)}$ are the half-maximal rates of consumption and $K_{m(g,o)}$ are the Michaelis–Menten constants for glucose and oxygen, respectively. The lactate production rate of the cells $\dot{R}_l$, in general, depends on $\dot{R}_g$ and $\dot{R}_o$ through the metabolic mass balance equation involving both aerobic and anaerobic processes.[105,106] Generalizing the relation provided in Sengers *et al.*,[105] the following equation may be deduced:

$$\dot{R}_l = \alpha\dot{R}_g + \gamma\dot{R}_o \qquad [83]$$

where α and γ are constants and $\dot{R}_g$ and $\dot{R}_o$ are given by eqn [82]. Sengers *et al.*[105,106] have chosen the values of α and γ to be -2 and $\frac{1}{3}$, respectively. In their studies, it has been assumed that all oxygen uptake is fully used to break down glucose aerobically and none is used for matrix synthesis. In the work of Chung *et al.*,[88] a lower value of $\alpha = 1.6$ has been assumed and γ is set to 0 (the aerobic metabolic pathway is neglected). The values of the various mass transfer parameters for the kinetics appearing in eqns [81] and [82] for glucose, lactate, and oxygen are given in Sengers *et al.*[106] and Chung *et al.*[78] along with the diffusivities of each of the above species both in the culture medium and within the cell (these diffusivities are not the same as $\mathbf{D}_{eff_i}$).

Thus, the concentration of the given species c_i^β is determined by solving the coupled set of equations given by

eqns [79], [81], [82], and [83]. A finite element solution procedure using a commercial solver (Multiphysics 3.2 (COMSOL)) is described in the studies of Chung *et al.*[78,88] It should be noted that in these studies, the definition of K_{eq} is the inverse of one defined in eqn [78].

3.309.3.2.3. Cell growth kinetics

In the most general case, the cell volume fraction ε_σ is not a constant but evolves with time due to cell proliferation and cell death (apoptosis). Using a cell mass balance equation and under the assumption that the cells are immobilized (no bulk motion of cells within the scaffold), the evolution of ε_σ may be modeled using the mechanisms of cell diffusion within the scaffolds and cell growth kinetics. Here, cell diffusion occurs due to random motion of the cells within the scaffold, and in a macroscopic sense, it can be characterized by a diffusion coefficient, D_{cell}[107] and may be assumed as a constant.[78] As described by Galban and Locke,[108] the cell growth kinetics may be modeled using a modified Contois kinetics. The modified Contois growth kinetics incorporates the effect of glucose and lactate in determining the cell population. Following Galban and Locke,[108] the following equation for cell growth rate in terms of the cell volume fraction ε_σ applies:

$$\frac{\partial \varepsilon_\sigma}{\partial t} = D_{cell}\nabla^2\varepsilon_\sigma + \left[\frac{k_g c_g^\beta}{K_c \rho_{cell}\varepsilon_\sigma\left(K_{eq}^{-1} + K_{pr}^{-1}c_l^\beta\right)} - k_d\right]\varepsilon_\sigma \quad [84]$$

Here, k_g is the homogenous cell growth rate coefficient, k_d is the death coefficient (due to apoptosis), K_c is the modified Contois saturation constant, ρ_{cell} is the specific cell density, and K_{pr} is the product susceptibility constant (lactate, in this case). The values of the above parameters typically used in tissue engineering are provided in Galban and Locke,[108] and Chung *et al.*[78,88] It should be noted that other growth kinetics have also been used to study cell growth. For example, in Galban and Locke,[109] Moser and *n*th-order heterogenous kinetics for cell growth have been employed. Lewis *et al.*[110] have used a linear model for cell growth kinetics to investigate the interactions between oxygen concentration field and cell distributions within a seeded 3D scaffold structure.

3.309.3.2.4. Cell growth and modification of flow field equations

Since the volume fraction of the pores change with time, the continuity equation [41] for the fluid needs to be changed to reflect this effect. The general form of continuity equation is given by eqn [58]. If the porosity of a constant density scaffold is such that $\varepsilon_\beta \gg (\varepsilon_\sigma + \varepsilon_s)$, eqn [58] can be simplified to the following equation:

$$\frac{\partial \varepsilon_\beta}{\partial t} + \nabla \cdot \langle \mathbf{u} \rangle = 0 \quad [85]$$

This form of the continuity equation has been used in the studies of Chung *et al.*[78,88] The evaluation of $\mathbf{D}_{eff}$ required to solve eqn [81] is provided below.

3.309.3.2.5. Evaluation of effective diffusivities

Similar to the permeability tensor $\mathbf{K}$, the diffusivity tensor $\mathbf{D}_{eff_i}$ of a given species arises in the volume-averaging procedure of the microscopic mass transfer equations. The evaluation of $\mathbf{D}_{eff_i}$ requires a direct numerical solution to a closure problem very similar to the ones provided for velocity in **Section 3.309.3.1.5**. As noted in that section, the solution procedure for such a closure equation is complicated for realistically structured porous scaffolds. The direct simulation while providing accurate results also requires detailed information about the pore microstructure. One such numerical method for solving the closure problem for the effective diffusivity tensor and the associated boundary conditions has been provided in great detail in the study by Wood *et al.*[28] for the cases of biofilms and tissues. A similar procedure has also been employed and numerically solved by Lux *et al.*[61] using a flux continuous and locally conservative finite volume approach to determine the effective thermal conductivity tensor of real fibrous materials featuring local anisotropic thermal properties. While it is possible to obtain a detailed pore scale structure using methods described in **Section 3.309.3.1**, in many biotechnological applications, such a detailed solution may not be critical.[111] Many of the fibrous scaffolds used in tissue engineering are generally isotropic in the microstructure. For such isotropic systems, $\mathbf{D}_{eff_i}$ may not be very sensitive to the geometry of the microstructure.[28,111] Therefore, just as with the case of permeabilities, simplified geometries may be used to describe the microscale pore structure and analytical solutions may be derived to get reasonable estimates for the effective diffusivities. In this regard, the most popular models/correlations for evaluating the isotropic diffusivities are given below.

1. Chang's unit cell model

   Following the unit cell model given in Chang,[112] Wood and Whitaker[111] have solved the closure problem and obtained the following relation for the isotropic effective diffusivity:

$$\frac{\mathbf{D}_{eff_i}}{\mathcal{D}_{i\beta}} = \frac{3\kappa_i - 2\varepsilon_\beta(\kappa_i - 1) + 2\varepsilon_\beta\varepsilon_\sigma^{-1/3}(4\pi/3)^{\frac{1}{3}}(\gamma_i/l)}{3 + \varepsilon_\beta(\kappa_i - 1) + (3 - \varepsilon_\beta)\varepsilon_\sigma^{-1/3}(4\pi/3)^{\frac{1}{3}}(\gamma_i/l)} \quad [86]$$

Here, $\mathcal{D}_{i\beta}$ is the diffusivity of species i in the culture medium (β-phase), $\kappa_i = \frac{\mathcal{D}_{i\sigma}}{K_{eq}\mathcal{D}_{i\beta}}$ is a relative measure of the importance of intercellular diffusivity $\mathcal{D}_{i\sigma}$ to the diffusivity in the medium $\mathcal{D}_{i\beta}$, and γ_i is a parameter that measures of relative importance of extracellular transport in the β-phase to that of the intercellular reaction and is given by:

$$\gamma_i = \mathcal{D}_{i\sigma}\left(\alpha_2 + \alpha_3 c_i^\beta + \alpha_4 c_i^\sigma + \alpha_5 c_i^\beta c_i^\sigma\right)/(K_{eq}E_0) \quad [87]$$

where α_2–α_5 represent the transport kinetic parameters for facilitated membrane transport mechanism of species i, E_0 represents surface concentration of the transporter proteins, and K_{eq_i} is given by eqn [78]. The details of the facilitated membrane transport mechanisms are given in Wood and Whitaker.[113] The values of κ_i and γ_i are usually determined from experiments. Based on the available experimental data, Wood and Whitaker[111] have suggested γ_i to be in the range 0 to 10, and κ_i in the range 0 to 1. The length scale l appearing in eqn [86] is related to the diameter of a spherical cell (d_p) through the following expression[28]:

$$l = \left(\frac{1}{2}\left[\frac{4\pi}{3\varepsilon_\sigma}\right]^{1/3}\right)d_p \quad [88]$$

Table 2 Representative values for isotropic diffusivities for different species in the fluid (culture medium, β-phase) and in the cellular phase (σ-phase)

Species	$\mathcal{D}_{i\beta}$ ($m^2\,s^{-1}$)	*References*	$\mathcal{D}_{i\sigma}$ ($m^2\,s^{-1}$)	*References*
Glucose	9.17×10^{-10}	34	7.5×10^{-10}	78
Lactate	1.39×10^{-9}	34	1.15×10^{-10}	88
Oxygen	3.29×10^{-9}	33	1.59×10^{-10}	33

2. Maxwell's model

When the rate of transmembrane transport is instantaneous ($\gamma_i \to 0$), eqn [86] may be simplified to yield

$$\frac{\mathbf{D}_{\mathrm{eff}_i}}{\mathcal{D}_{i\beta}} = \frac{3\kappa_i - 2\varepsilon_\beta(\kappa_i - 1)}{3 + \varepsilon_\beta(\kappa_i - 1)} \qquad [89]$$

Equation [89] is referred to as the Maxwell's equation for effective diffusivity.

In Table 2, the representative values of $\mathcal{D}_{i\beta}$ and $\mathcal{D}_{i\sigma}$ of the important species, namely, glucose, lactate, and oxygen are provided.

In recent studies by Chung *et al.*,[78,88] eqn [89] has been used to estimate the diffusivities of glucose and lactate for predicting the mass transfer of nutrients in porous scaffolds. Other correlations for calculating the effective diffusivities as a function of $\mathcal{D}_{i\sigma}$, $\mathcal{D}_{i\beta}$, and ε_σ can be found in the review of Riley *et al.*[114,115] Coletti *et al.*[96] have coupled the macroscale and microscale mass transfer models for a porous scaffold placed in a perfusion bioreactor. They have solved for the transient mass transfer of oxygen within a 3D polymeric scaffold placed inside a perfusion bioreactor combined with cell growth kinetics described by Contois kinetics. The flow external to the scaffold has been described through the Navier–Stokes equations for incompressible fluids while the flow through the scaffold is modeled using Darcy–Brinkman model. Continuity of pressure between the external flow and the inlet of the scaffold and a continuity of velocity at the outlet of the scaffold and external fluid have been assumed. The oxygen uptake rate in the mass transfer model has been described by Michaelis–Menten kinetics. The values of the various parameters used have been provided in their study.

3.309.4. Conclusion

This chapter consists of a review of some of the most recent mathematical models used for solving transport problems involving porous biomaterial scaffolds. While the majority of discussions have been related to perfusion reactors, the model equations have been presented in their most general form and can thus be applied to other bioreactor studies as well. Both direct numerical simulation (DNS) methods and macroscopic averaged equations for porous media have been reviewed in sufficient detail. DNS methods provide the most accurate details of the flow, shear stress, and species concentration fields. The state-of-the-art imaging techniques coupled with DNS serve to be very helpful in pore-scale optimization studies of the scaffold geometry.[36,104] However, the dynamic changes in the geometry of the scaffold architecture due to cell growth and proliferation pose significant research challenges for DNS methods. Even with the advent of powerful computers, DNS calculations are still computationally intensive for large scale optimization studies. On the other hand, macroscopic averaged equations are simpler to solve and by the very nature of their construction may be scaled up for the system level (up to the length scale of bioreactors) optimization. The disadvantage of the averaging procedure is that it smoothes the flow structure at the pore scales and, in some cases, may under predict shear stress variations at the cellular scale inside the scaffolds.[102] However, in most situations, they do produce reasonable engineering estimates of the flow and concentrations fields. While each of the described methods has its own advantages and disadvantages, the choice of any particular method depends on the desired level of accuracy sought for a given application. Both DNS and averaged methods will continue to serve as powerful tools for performing quantitative engineering studies of transport involving bioreactors and biomaterials. Combining the best features of both the methods may enable multiscale optimization studies involving both the bioreactor scale (macroscale) and the pore scale (microscale).[96,104]

References

1. Griffith, L. G.; Swartz, M. A. *Nat. Rev. Mol. Cell Biol.* **2006**, *7*, 211–224.
2. Lee, J.; Cuddihy, M. J.; Kotov, N. A. *Tissue Eng. B Rev.* **2008**, *14*, 61–86.
3. Chen, G. P.; Ushida, T.; Tateishi, T. *Macromol. Biosci.* **2002**, *2*(2), 67–77.
4. Hutmacher, D. W.; Singh, H. *Trends Biotechnol.* **2008**, *26*(4), 166–172.
5. Hollister, S. J. *Nat. Mater.* **2005**, *4*(7), 518–524.
6. Sikavitsas, V. I.; Bancroft, G. N.; Mikos, A. G. *J. Biomed. Mater. Res.* **2002**, *62*(1), 136–148.
7. Bucaro, M. A.; Zahm, A. M.; Risbud, M. V.; *et al. J. Bone Miner. Res.* **2004**, *19*(Suppl. 1), S392.
8. Cummings, L. J.; Waters, S. L. *Math. Med. Biol.* **2007**, *24*(2), 169–208.
9. Cummings, L. J.; Sawyer, N. B. E.; Morgan, S. P.; Rose, F.; Waters, S. L. *Biotechnol. Bioeng.* **2009**, *104*(6), 1224–1234.
10. Hammond, T. G.; Hammond, J. M. *Am. J. Physiol. Ren. Physiol.* **2001**, *281*(1), 12.
11. Lynch, S. V.; Mukundakrishnan, K.; Benoit, M. R.; Ayyaswamy, P. S.; Matin, A. *Appl. Environ. Microbiol.* **2006**, *72*(12), 7701.
12. Qiu, Q. Q.; Ducheyne, P.; Gao, H.; Ayyaswamy, P. S. *Tissue Eng.* **1998**, *4*(1), 19–34.
13. Qiu, Q. Q.; Ducheyne, P.; Ayyaswamy, P. S. *Biomaterials* **1999**, *20*(11), 989–1001.
14. Qiu, Q. Q.; Ducheyne, P.; Ayyaswamy, P. S. *J. Biomed. Mater. Res.* **2000**, *52*(1), 66–76.
15. Qiu, Q. Q.; Ducheyne, P.; Ayyaswamy, P. S. *In Vitro Cell. Dev. Biol. Anim.* **2001**, *37*(3), 157–165.
16. Bancroft, G. N.; Sikavitsas, V. I.; Mikos, A. G. *Tissue Eng.* **2003**, *9*(3), 549–554.
17. Bilgen, B.; Uygun, K.; Bueno, E. M.; Sucosky, P.; Barabino, G. A. *Tissue Eng. A* **2008**, *15*(4), 761–771.
18. Freed, L. E.; Guilak, F.; Guo, X. E.; *et al. Tissue Eng.* **2006**, *12*(12), 3285–3305.
19. Choi, N. W.; Cabodi, M.; Held, B.; Gleghorn, J. P.; Bonassar, L. J.; Stroock, A. D. *Nat. Mater.* **2007**, *6*, 908–915.
20. Fisher, R. J.; Peattie, R. A. *Adv. Biochem. Eng. Biotechnol.* **2007**, *103*, 1–73.
21. Vunjak-Novakovic, G.; Freed, L. E. *Adv. Drug Deliv. Rev.* **1998**, *33*, 15–30.
22. Rose, F. R.; Cyster, L. A.; Grant, D. M.; Scotchford, C. A.; Howdle, S. M.; Shakesheff, K. M. *Biomaterials* **2004**, *25*, 5507–5514.
23. Das, D. B. *Chem. Eng. Sci.* **2007**, *62*(13), 3627–3639.
24. Ayyaswamy, P. S.; Mukundakrishnan, K. *Acta Astronaut.* **2007**, *60*(4–7), 397–405.
25. Khademhosseini, A.; Langer, R.; Borenstein, J.; Vacanti, J. P. *Proc. Natl. Acad. Sci. USA* **2006**, *103*, 2480–2487.
26. Wendt, D.; Riboldi, S. A.; Cioffi, M.; Martin, I. *Adv. Mater.* **2009**, *21*(32–33, Spl. Iss.), 3352–3367.
27. Whitaker, S. *Theory and Applications of Transport in Porous Media: The Method of Volume Averaging*; Kluwer Academic: London, 1999.

28. Wood, B. D.; Quintard, M.; Whitaker, S. *Biotechnol. Bioeng.* **2002**, *77*(5), 495–516.
29. Lasseux, D.; Ahmadi, A.; Cleis, X.; Garnier, J. *Chem. Eng. Sci.* **2004**, *59*(10), 1949–1964.
30. Deen, W. M. *Analysis of Transport Phenomena*; Oxford University Press: New York, 1998.
31. Batchelor, G. K. *An Introduction to Fluid Dynamics*; Cambridge University Press: Oxford, 2000.
32. Mukundakrishnan, K.; Ayyaswamy, P. S.; Risbud, M.; Hu, H. H.; Shapiro, I. M.; Shapiro, I. M. *Ann. N. Y. Acad. Sci.* **2004**, *1027*, 85–98.
33. Pathi, P.; Ma, T.; Locke, B. R. *Biotechnol. Bioeng.* **2005**, *89*(7), 743–758.
34. Zhou, S.; Cui, Z.; Urban, J. P. *Biotechnol. Bioeng.* **2008**, *101*, 408–421.
35. Croll, T. I.; Gentz, S.; Mueller, K.; *et al. Chem. Eng. Sci.* **2005**, *60*(17), 4924–4934.
36. Cantini, M.; Fiore, G. B.; Redaelli, A.; Soncini, M. *Tissue Eng. A* **2008**, *15*(3), 615–623.
37. Jackson, G. W.; James, D. F. *Can. J. Chem. Eng.* **1986**, *64*(3), 364–374.
38. Peyret, R.; Taylor, T. D. *Computational Methods for Fluid Flow*; Springer: Berlin, 1983.
39. Ferziger, J. H.; Peric, M.; Morton, K. W. *Computational Methods for Fluid Dynamics*; Springer: Berlin, 1999.
40. Brown, D. L.; Cortez, R.; Minion, M. L. *J. Comput. Phys.* **2001**, *168*(2), 464–499.
41. Mahesh, K. *J. Comput. Phys.* **1998**, *145*(1), 332–358.
42. Saad, Y. *Iterative Methods for Sparse Linear Systems*; Society for Industrial Mathematics: Philadelphia, PA, 2003.
43. Reddy, J. N.; Gartling, D. K. *The Finite Element Method in Heat Transfer and Fluid Dynamics*; CRC Press: Boca Raton, FL, 2000.
44. Chen, S.; Doolen, G. D. *Annu. Rev. Fluid Mech.* **1998**, *30*(1), 329–364.
45. Martys, N. S.; Chen, H. *Phys. Rev. E* **1996**, *53*(1), 743–750.
46. Vossenberg, P.; Higuera, G. A.; van Straten, G.; van Blitterswijk, C. A.; van Boxtel, A. J. B. *Biomech. Model. Mechanobiol.* **2009**, *8*, 1–9.
47. Singh, H.; Teoh, S. H.; Low, H. T.; Hutmacher, D. W. *J. Biotechnol.* **2005**, *119*(2), 181–196.
48. ANSYS. Fluent 6.3 Users Guide. Southpointe: ANSYS Inc.
49. Boschetti, F.; Raimondi, M. T.; Migliavacca, F.; Dubini, G. *J. Biomech.* **2006**, *39*(3), 418–425.
50. Raimondi, M. T.; Boschetti, F.; Falcone, L.; Migliavacca, F.; Remuzzi, A.; Dubini, G. *Biorheology* **2004**, *41*(3–4), 401.
51. Olivares, A. L.; Marsal, È.; Planell, J. A.; Lacroix, D. *Biomaterials* **2009**, *30*(30), 6142–6149.
52. Tuan, H. S.; Hutmacher, D. W. *Comput. Aided Des.* **2005**, *37*(11), 1151–1161.
53. van Lenthe, G. H.; Hagenmuller, H.; Bohner, M.; Hollister, S. J.; Meinel, L.; Muller, R. *Biomaterials* **2007**, *28*(15), 2479–2490.
54. Anderson, E. J.; Savrin, J.; Cooke, M.; Dean, D.; Knothe Tate, M. L. In *ASME Summer Bioengineering Conference*, Vail, CO, 2005.
55. Raimondi, M. T.; Moretti, M.; Cioffi, M.; *et al. Biorheology* **2006**, *43*(3), 215–222.
56. Cioffi, M.; Boschetti, F.; Raimondi, M. T.; Dubini, G. *Biotechnol. Bioeng.* **2006**, *93*(3), 500–510.
57. Maes, F.; Van Ransbeeck, P.; Van Oosterwyck, H.; Verdonck, P. *J. Biomech.* **2008**, *41*(1), 306.
58. Jungreuthmayer, C.; Jaasma, M. J.; Al-Munajjed, A. A.; Zanghellini, J.; Kelly, D. J.; OBrien, F. J. *Med. Eng. Phys.* **2009**, *31*(4), 420–427.
59. Sandino, C.; Planell, J. A.; Lacroix, D. *J. Biomech.* **2008**, *41*(5), 1005–1014.
60. Porter, B.; Zauel, R.; Stockman, H.; Guldberg, R.; Fyhrie, D. *J. Biomech.* **2005**, *38*(3), 543–549.
61. Lux, J.; Ahmadi, A.; Gobbé, C.; Delisée, C. *Int. J. Heat Mass Transfer* **2006**, *49*(11–12), 1958–1973.
62. Golfier, F.; Wood, B. D.; Orgogozo, L.; Quintard, M.; Buès, M. *Adv. Water Resour.* **2009**, *32*(3), 463–485.
63. Swider, P.; Conroy, M.; Pedrono, A.; *et al. J. Biomech.* **2007**, *40*(9), 2112–2118.
64. Jaganathan, S.; Vahedi Tafreshi, H.; Pourdeyhimi, B. *Chem. Eng. Sci.* **2008**, *63*(1), 244–252.
65. Whitaker, S. *Transp. Porous Media* **1986**, *1*(1), 3–25.
66. Bousquet-Melou, P.; Goyeau, B.; Quintard, M.; Fichot, F.; Gobin, D. *Int. J. Heat Mass Transfer* **2002**, *45*(17), 3651–3665.
67. Anguy, Y.; Bernard, D.; Ehrlich, R. *Adv. Water Resources* **1994**, *17*(6), 337–351.
68. Bernard, D.; Nielsen, Ø.; Salvo, L.; Cloetens, P. *Mater. Sci. Eng. A* **2005**, *392*(1–2), 112–120.
69. Ochoa-Tapia, J. A.; Whitaker, S. *Int. J. Heat Mass Transfer* **1995**, *38*(14), 2635–2646.
70. Brinkman, H. C. *Appl. Sci. Res.* **1949**, *1*(1), 27–34.
71. Khaled, A. R. A.; Vafai, K. *Int. J. Heat Mass Transfer* **2003**, *46*(26), 4989–5003.
72. Vafai, K.; Kim, S. J. *Int. J. Heat Fluid Flow* **1995**, *16*(1), 11–15.
73. Nithiarasu, P.; Sujatha, K. S.; Ravindran, K.; Sundararajan, T.; Seetharamu, K. N. *Comput. Meth. Appl. Mech. Eng.* **2000**, *188*(1–3), 413–430.
74. Nithiarasu, P.; Seetharamu, K. N.; Sundararajan, T. *Arch. Comput. Meth. Eng.* **2002**, *9*(1), 3–42.
75. Goyeau, B.; Bousquet-Melou, P.; Gobin, D.; Quintard, M.; Fichot, F. *Comput. Appl. Math.* **2004**, *23*, 381–400.
76. Botchwey, E. A.; Pollack, S. R.; El-Amin, S.; Levine, E. M.; Tuan, R. S.; Laurencin, C. T. *Biorheology* **2003**, *40*(1–3), 299.
77. Whittaker, R. J.; Booth, R.; Dyson, R.; *et al. J. Theor. Biol.* **2009**, *256*(4), 533–546.
78. Chung, C. A.; Chen, C. W.; Chen, C. P.; Tseng, C. S. *Biotechnol. Bioeng.* **2007**, *97*(6), 1603–1616.
79. Yu, P.; Zeng, Y.; Lee, T. S.; Low, H. T. *Int. Commun. Heat Mass Transfer* **2009**, *36*, 569–573.
80. Yu, P.; Zeng, Y.; Lee, T. S.; Bai, H. X.; Low, H. T. *Int. J. Heat Fluid Flow* **2010**, *9*, 99.
81. Chen, X.; Yu, P.; Winoto, S. H.; Low, H. T. *Int. J. Numer. Methods Heat Fluid Flow* **2008**, *18*(5–6), 635–655.
82. Ochoa-Tapia, J. A.; Whitaker, S. *J. Porous Media* **1998**, *1*, 201–218.
83. Ochoa-Tapia, J. A.; Whitaker, S. *Int. J. Heat Mass Transfer* **1995**, *38*(14), 2647–2655.
84. Swartz, M. A.; Fleury, M. E. *Annu. Rev. Biomed. Eng.* **2007**, *9*, 229–256.
85. Serrat, P. J. L. Master's Thesis, Georgia Institute of Technology, USA, 2001.
86. Ashari, A.; Bucher, T. M.; Tafreshi, H. V.; Tahir, M. A.; Rahman, M. S. A. *Int. J. Heat Mass Transfer* **2010**, *53*, 1750–1758.
87. Rahli, O.; Tadrist, L.; Miscevic, M.; Santini, R. *J. Fluids Eng.* **1997**, *119*, 188.
88. Chung, C. A.; Chen, C. P.; Lin, T. H.; Tseng, C. S. *Biotechnol. Bioeng.* **2008**, *99*(6), 1535–1541.
89. Spielman, L.; Goren, S. L. *Environ. Sci. Technol.* **1968**, *2*(4), 279–287.
90. Drummond, J. E.; Tahir, M. I. *Int. J. Multiph. Flow* **1984**, *10*(5), 515–540.
91. Sangani, A. S.; Acrivos, A. *Int. J. Multiph. Flow* **1982**, *8*(3), 193–206.
92. Clague, D. S.; Phillips, R. J. *Phys. Fluids* **1997**, *9*, 1562.
93. Levick, J. R. *Q. J. Exp. Physiol.* **1987**, *72*(4), 409–437.
94. Davies, C. N. *Air Filtration*; Academic Press: London, 1973.
95. Agrawal, C. M.; McKinney, J. S.; Lanctot, D.; Athanasiou, K. A. *Biomaterials* **2000**, *21*(23), 2443–2452.
96. Coletti, F.; Macchietto, S.; Elvassore, N. *Ind. Eng. Chem. Res.* **2006**, *45*(24), 8158–8169.
97. Thompson, K. E. *AIChE J.* **2002**, *48*(7), 1369–1389.
98. Higdon, J. J. L.; Ford, G. D. *J. Fluid Mech.* **1996**, *308*, 341–361.
99. Clague, D. S.; Kandhai, B. D.; Zhang, R.; Sloot, P. M. A. *Phys. Rev. E* **2000**, *61*(1), 616–625.
100. Tahir, M. A.; Tafreshi, H. V. *Phys. Fluids* **2009**, *21*, 083604.
101. Stylianopoulos, T.; Yeckel, A.; Derby, J. J.; *et al. Phys. Fluids* **2008**, *20*, 123601.
102. Pedersen, J. A.; Boschetti, F.; Swartz, M. A. *J. Biomech.* **2007**, *40*(7), 1484–1492.
103. Sengers, B. G.; Taylor, M.; Please, C. P.; Oreffo, R. O. C. *Biomaterials* **2007**, *28*(10), 1926–1940.
104. Cioffi, M.; Kuffer, J.; Strobel, S.; Dubini, G.; Martin, I.; Wendt, D. *J. Biomech.* **2008**, *41*(14), 2918–2925.
105. Sengers, B. G.; Heywood, H. K.; Lee, D. A.; Oomens, C. W. J.; Bader, D. L. *J. Biomech. Eng.* **2005**, *127*, 758.
106. Sengers, B. G.; Van Donkelaar, C. C.; Oomens, C. W. J.; Baaijens, F. P. T. *Biotechnol. Prog.* **2005**, *21*(4), 1252–1261.
107. Berg, H. C. *Random Walks in Biology*; Princeton University Press: Princeton, NJ, 1993.
108. Galban, C. J.; Locke, B. R. *Biotechnol. Bioeng.* **1999**, *64*(6), 633–643.
109. Galban, C. J.; Locke, B. R. *Biotechnol. Bioeng.* **1999**, *65*(2), 121–132.
110. Lewis, M. C.; MacArthur, B. D.; Malda, J.; Pettet, G.; Please, C. P. *Biotechnol. Bioeng.* **2005**, *91*(5), 607–615.
111. Wood, B. D.; Whitaker, S. *Chem. Eng. Sci.* **2000**, *55*(17), 3397–3418.
112. Chang, H. C. *AIChE J.* **1983**, *29*(5), 846–853.
113. Wood, B. D.; Whitaker, S. *Chem. Eng. Sci.* **1998**, *53*(3), 397–425.
114. Riley, M. R.; Muzzio, F. J.; Buettner, H. M.; Reyes, S. C. *Biotechnol. Bioeng.* **1996**, *49*(2), 223–227.
115. Riley, M. R.; Muzzio, F. J.; Reyes, S. C. *Appl. Biochem. Biotechnol.* **1999**, *80*(2), 151–188.

3.310. Computational Methods Related to Reaction Chemistry

A J Shih*, S E Telesco* and Y Liu, University of Pennsylvania, Philadelphia, PA, USA
R Venkatramani, Duke University, Durham, NC, USA
R Radhakrishnan#, University of Pennsylvania, Philadelphia, PA, USA

© 2011 Elsevier Ltd. All rights reserved.

3.310.1.	**Introduction**	155
3.310.2.	**Computational Methods**	156
3.310.2.1.	Molecular Dynamics	156
3.310.2.2.	Homology Modeling	157
3.310.2.3.	Free Energy	158
3.310.2.3.1.	Free-energy perturbation	158
3.310.2.3.2.	Umbrella sampling	159
3.310.2.4.	Electronic Structure Methods	159
3.310.2.4.1.	Electronic structure methods in force-field development	159
3.310.2.4.2.	QM/MM simulations	160
3.310.2.5.	Methods for Determining Reaction Paths	161
3.310.2.5.1.	Transition path sampling[142,143]	161
3.310.2.5.2.	BOLAS sampling for calculating free energies	162
3.310.2.6.	Effect of Force on Biomolecules	162
3.310.2.7.	Limitations and Caveats	164
3.310.3.	**Applications**	164
3.310.3.1.	*Ab Initio* Simulations of Material Properties	164
3.310.3.2.	Surfaces with Tailored Functionality Through Self-Assembly Techniques	165
3.310.3.3.	Slow Dynamical Modes in Adhesion, Catalysis, and Force	165
3.310.3.3.1.	Computational modeling of the attachment function of fibronectin	165
3.310.3.4.	Future Directions	167
References		167

Abbreviations

CHELPG	CHarges from ELectrostatic Potentials using a Grid based method
DFT	Density functional theory
ECM	Extracellular matrix
FEP	Free energy perturbation
FRET	Fluorescence resonance energy transfer
GA	Genetic algorithm
HF	Hartree-Fock
LSCF	Local self-consistent field
MD	Molecular dynamics
MMPBSA	Molecular mechanics Poisson-Boltzmann/surface area
NMR	Nuclear magnetic resonance
PC	Principal component
PCA	Principal component analysis
PDB	Protein Data Bank (www.pdb.org)
QM/MM	Quantum mechanics molecular mechanics
REM	Replica exchange molecular dynamics
SAM	Self-assembling monolayer
SMD	Steered molecular dynamics
TPS	Transition path sampling
WHAM	Weighted histogram analysis method

3.310.1. Introduction

Biomaterials have been an important consideration for medicine, specifically medical implants, for a long time. Recent advances in biomaterials have even helped expand their uses beyond compatibility, from smart delivery of drugs to directing cell fates.[1] Many synthetic biomaterials, including metals, ceramics, and polymers, are used for bone and joint replacements. Although clinical outcomes with these existing biomaterials are excellent using current surgical techniques, a fundamental understanding of biocompatibility, and possibly, the bioactivity of these biomaterials is still not complete. Evidence is accumulating that the best biomaterials elicit the normal tissue at their surface, and thereby, engender continuous transition to the tissues in which they are inserted. For example, such behavior has been described for titanium, titanium alloys, bioactive glasses, and tyrosine-derived

*These authors contributed equally.
#Corresponding author.

polycarbonates, among others, with underlying mechanisms ranging from hydroxylation to formation of calcium phosphate layers.[2,3] Such processes are initiated and sustained through rich reaction chemistry including leaching of network modifying ions and formation of Si–OH bonds; dissolution and repolymerization resulting in a SiO_2 gel layer; formation of an amorphous calcium phosphate layer, etc. Current challenges lie in unraveling the molecular mechanisms that underlie this rich chemistry surrounding the interaction of material surface with tissue, which govern bone biocompatibility.[4] Understanding these challenges involves synthesis/characterization (discussed in other chapters) as well as computational simulations (topic of this chapter) of inorganic materials and biomaterials. Rational design of such materials involves development of highly controlled surface chemistry using experimental as well as computational approaches. Experimentally, for example, model surfaces are created using self-assembling monolayer (SAM) chemistry in order to create hydroxylated surfaces, and then proceed to a controlled functionalization (e.g., calcification) of these SAM layers. Computationally, molecular-based simulation tools predict likely recognition sequences and the corresponding conformations at the interface between the material surface and the extracellular matrix (ECM) as well as the cell membrane. Focusing on the molecular mechanisms and how molecular interactions feedback into the signaling environment will lead to new insight into the bioactivity of existing biomaterials. It will be possible to utilize this fundamental knowledge to create new and improved bioengineered constructs for use in bone tissue repair therapies.

3.310.2. Computational Methods

The acceptance of multiscale simulation techniques has helped bridge the gap between theory and experiment.[5] Electronic structure (quantum level or *ab initio*) simulations can reveal how specific molecules assume stable geometrical configurations and charge distributions when subject to specific chemical environment. By examining the charge distributions and structure, it is possible to quantify and predict structural properties as well as chemical reactivity pertaining to the molecule, which are particularly pertinent when investigating novel materials. Although quantum simulations provide a wealth of information regarding structure and reactivity, it is currently not possible to model much more than a few hundred atoms at the most. Molecular dynamics (MD) simulations based on classical (empirical) force fields can model hundreds of thousands of atoms for tens of nanoseconds, and for some systems, up to microseconds. Since MD simulations can be set up at atomic resolution, they are uniquely suited to examine thermodynamic and statistical properties of (bio)materials: such properties include (but are not limited to) Young's modulus, surface hydration energies, and protein adsorption to different surfaces.[6] Coarse-grained or mesoscale simulations are used to bridge the gap between the atomistic scale of MD simulations and continuum approaches such as elasticity theory or hydrodynamics at the macroscale (i.e., milliseconds, millimeters, and beyond).[5]

3.310.2.1. Molecular Dynamics

MD simulation techniques are one of the most commonly used model systems of biomolecules and biomaterials because they can track individual atoms, and therefore, answer questions pertaining to specific material properties.[7,8] To perform MD simulations, the starting point is to define the initial coordinates and initial velocities of the atoms characterizing the model system, for example, the desired biomolecule plus the biologically relevant environment, that is, water molecules or other solvent and/or membranes. The coordinates of the desired biomolecule can usually be found as structural data (X-ray or nuclear magnetic resonance (NMR)) deposited into the protein data bank (PDB)[9] (www.pdb.org); otherwise it is possible to derive initial geometry and coordinate data from model building techniques, including homology methods (see **Section 3.310.2.2**). This step also typically includes the placement and positioning of the environment of the molecules (solvation, ionic strength, etc.). The initial velocities are typically derived from the Maxwell–Boltzmann distributions at the desired temperature of the simulation. The potential of interactions of each of the atoms are calculated using a force field, which parameterizes the nonbonded and bonded interaction terms of each atom depending on its constituent atom connectivity: bond terms, angle terms, dihedral terms, improper dihedral terms, nonbonded Lennard-Jones terms, and electrostatic terms. The potential interactions are summed across all the atoms contained in the system, to compute an overall potential energy function for the system[10–14]:

$$U(R) = \sum_{\text{bonds}} K_b(b - b_0)^2 + \sum_{\text{angles}} K_\theta(\theta - \theta_0)^2 + \sum_{\text{dihedrals}} K_\chi(1 + \cos(\eta\chi - \delta)) + \sum_{\text{impropers}} K_\phi(\phi - \phi_0)^2 + \sum_{\text{nonbonded}} \left(\varepsilon_{ij}\left[\left(\frac{R_{\min_{ij}}}{r_{ij}}\right)\right]\right)$$

Taking the derivative of the potential energy function yields the force, and from Newton's second law, this is equal to mass times acceleration. Although the process seems simple, the derivative function results in a set of $3N$ coupled second-order ordinary differential equations that must be solved numerically. The solution consists of a numerical recipe to advance the positions and the velocities by one time step. This process is repeated over and over again to generate MD trajectories of constant energy. Constant-temperature dynamics are derived by coupling the system to a thermostat using well-established formulations such as the Langevin dynamics or the Nose–Hoover methodologies.[15] Application of MD simulations to biomolecules is facilitated by several popular choices of force fields such as CHARMM[16] (www.charmm.org), AMBER[17] (www.ambermd.org), and GROMOS[18] (www.gromacs.org), as well as dynamic simulations packages and visualization/analysis tools such as NAMD[19] (www.ks.uiuc.edu/Research/namd/) and VMD[20] (www.ks.uiuc.edu/Research/vmd/).

With analysis of MD trajectories, it is possible to calculate statistical properties under a variety of initial and other external conditions[5] such as hydrogen-bond analyses for hydrophilic interactions and solvent-accessible surface area for hydrophobic interactions. For example, by analyzing the relative positions of the hydrogen-bond donors to the hydrogen-bond

acceptors with a preset cutoff angle and a bond length, the hydrogen bonds present in the majority of a given trajectory can be identified to record permanent stabilizing interactions and differentiate them from transient interactions.[21] Similarly, statistical data based on solvent accessible surface area analysis, which maps a surface area by rolling a probe sphere (typically 1.4A) on the protein surface, provides a quantitative metric of hydrophobic stabilization of the solvated protein.

A popular statistical approach to analyze biomolecular dynamics is principal component analysis (PCA).[22,23] PCA solves the eigenvalue equation: $[\sigma - \mathbf{\lambda I}]\xi = 0$ to project out principal components (PCs) or independent modes of atomic motion captured in an MD trajectory and sort them by their variance (in decreasing order). Here, σ is a two-dimensional variance–covariance matrix of atomic fluctuations about the trajectory average, with elements $\sigma_{ij} = \langle (x_i - \langle x_i \rangle)(x_j - \langle x_j \rangle) \rangle$ $(i,j = 1, \ldots, 3N$, N being the total number of atoms with position given by the Cartesian coordinates $x)$; $\xi = (\xi_1, \xi_2, \ldots, \xi_{3N})$ are the $3N$ independent (uncorrelated) eigenvectors (PCs) with eigenvalues $\lambda = (\lambda_1, \lambda_2, \ldots, \lambda_{3N})$ sorted in descending order that is, $\lambda_1 > \lambda_2, \ldots, \lambda_{3N-7} > \lambda_{3N-6}$. All global translations/rotations about the center of mass are removed prior to evaluating σ, and the six eigenvalues corresponding to these degrees of freedom are close to zero. The resulting eigenvectors represent the uncoupled PCs (modes orthogonal to each other), and the eigenvalues reflect their magnitude (strength) in the trajectory. Generally, the top ten PCs contain most of the atomic fluctuations in the MD trajectory ($>$ 40–90%); moreover, pairwise correlations between motions of atoms in an extended region of interest, such as the active site of an enzyme, can provide valuable information in relating structure to function through dynamics (or fluctuations) captured in the MD trajectory.[22]

The utility of MD simulations generally depends on the accuracy of the underlying force field. Since force fields are created using empirical energy functions, they are parameterized and tuned to a specific class of molecules; this introduces a constraint on their transferability to model non-native systems or environments and results must often be compared to experimental data, not only to verify their accuracy, but also to identify where methodological improvements can be made. Thus, there is continued development of the basic force field as well as the simulation methodology.

Another important consideration is the ability to perform sufficient sampling of the combinatorially large number of conformations available to even the simplest of biomolecules.[24,25] In this respect, a potential disadvantage of MD calculations is that there is an inherent limitation upon the maximum time step used for the simulation ($\leq$ 2 fs). Solvated systems of protein monomers typically consist of 40 000 atoms, and those of higher order complexes such as dimers or membrane-bound proteins can be as large as 200 000–500 000 atoms. For such system sizes, with current hardware and software, simulation times extending into the microsecond regime and beyond is an exceedingly difficult and labor-intensive endeavor, which requires a combination of algorithmic enhancements as well as the utilization of high-performance computing hardware infrastructure. For example, cutoff distances reduce the number of interactions to be computed without loss of accuracy for short-range interactions but not for long-range (electrostatic) interactions; to help maintain accuracy, long-range corrections such as the particle mesh Ewald algorithm[26] along with periodic boundary conditions are typically implemented. Parallelization techniques enable the execution of the simulations on supercomputing resources of thousands of processors on of a networked Linux cluster. Although a cluster of this size is a big investment, its accessibility is feasible through the US National Science Foundation's TeraGrid Initiative (founded in 2001) for academic researchers. TeraGrid resources (www.teragrid.org) currently include more than a petaflop of computing capability and more than 30 petabytes of online and archival data storage, with rapid access and retrieval over high-performance networks. Capitalizing on advances in hardware architecture, another approach is the creation of custom hardware for MD simulations, and offers one to two orders of magnitude enhancement in performance; examples include MDGRAPE-3[27,28] and ANTON.[29,30] Recently, graphical processing unit (GPU) accelerated computation has come into the forefront to enable massive speed enhancements for easily parallelizable tasks, with early data indicating that GPU accelerated computing may allow for the power of a supercomputing cluster in a desktop, see examples Friedrichs *et al.*[31] and Stone *et al.*[32]

3.310.2.2. Homology Modeling

Protein structure prediction is a fast-growing research field with applications to biotechnology.[33–35] Current experimental techniques for resolving protein structure through X-ray crystallography or NMR spectroscopy are laborious, and thus can solve only a small fraction of proteins sequenced by large-scale genome-sequencing endeavors. At present, at least 6 800 000 protein sequences have been deposited in the nonredundant protein sequence database (NR; accessible through the National Center for Biotechnology Information: ftp://ftp.ncbi.nlm.nih.gov/blast/db/), yet the PDB (http://www.rcsb.org/pdb/) contains fewer than 50 000 protein structures.[36] Given this discrepancy, computational modeling of protein structure has proven to be an invaluable tool for bridging the gap between protein sequence and structure. In particular, homology modeling, or prediction of an unknown structure by using a related protein with a known structure as a template, has been one of the most successful computational techniques for protein structure prediction[37–40]; see also several computer programs and web servers: Swiss-Model server (http://www.expasy.ch/swissmod/), CPH models (http://www.cbs.dtu.dk/services/CPHmodels/), MODELLER[41] (http://salilab.org/modeller/). Homology modeling typically consists of the following steps: search for homologous protein structures, selection of an appropriate template, target-template alignment, model construction, and model quality assessment.

The search for homologous or highly related protein structures to be used as the template for model building typically involves querying the PDB with the target sequence: the target sequence is compared with the sequence of every structure in the database, and potential templates are identified. In order to select the best template for comparative modeling, several factors must be considered. First, the higher the degree of sequence identity between the target and template, the better the quality of the template. Secondly, the similarity between

the environment (i.e., the type of solvent, pH, presence of ligands) of the template and the environment of the target should be considered.[41] In addition, the quality of the template structure, which has been experimentally derived, must be taken into account. For example, resolution of a crystallographic structure is an indicator of the structure quality. Once a template structure has been selected, a target-template alignment must be performed, which can be done by using standard sequence alignment methods.[42–44] However, if the degree of sequence identity between the target and template is below 40%, user intervention is required to correct any gaps or misaligned residues generated in the alignment. More accurate alignments can be generated by incorporating structural information from the template, and some modeling programs, including MODELLER, utilize a combination of sequence and structure information in the alignment algorithm.

Once a target-template alignment is created, several algorithms may be used to build a 3D model of the target protein.[33,35] One commonly employed method is to use distance geometry to satisfy spatial restraints determined from the target-template alignment.[45–47] MODELLER, for instance, imposes spatial restraints that are derived from two sources: homology-derived restraints on the bond distances and angles in the target structure that are based on its alignment with the template structure, and stereochemical restraints on bond distance and dihedral angle preferences that are obtained from a representative set of all known protein structures. The model is then constructed using MD methods to minimize violations of the spatial restraints.

A reliable homology modeling program should allow for modeling of insertions (i.e., loops) during model building. The *ab initio* loop modeling method involves exploring multiple conformations for the specified loop region, and each is then scored by an energy function to identify the most likely loop conformation.[48] Alternatively, a database approach may be employed, which involves identification of a main chain segment that fits the two stem regions of a loop by searching a database of many known protein structures. A limitation of the database approach is the availability of only a small number of known protein structures,[49] whereas the *ab initio* approach is more widely applicable to loop regions bound to ligands or other molecules. Currently, loop regions of up to 12 residues can be modeled accurately using these techniques, provided that the loop environment is well-defined.[41]

The final step in homology modeling is model quality assessment. Over the past couple of decades, several techniques have been developed to assess the quality and correctness of protein structural models. These methods analyze the stereochemical quality of the model, including bonds, bond angles, dihedral angles, and nonbonded atom–atom distances. Several programs, including PROCHECK (www.ebi.ac.uk/thornton-srv/software/PROCHECK[50]) and (WhatCheck swift.cmbi.ru.nl/gv/whatcheck[51]), perform this type of analysis. When there is less than approximately 30% sequence identity between the target and template, external assessment methods must be applied to determine whether a correct template was used.[52] Thus, several different alignments for the same template may be tested, in addition to alternative templates. The model can be further analyzed by computing a residue-by-residue energy profile, where peaks in the profile represent model errors. However, a potential pitfall of this method is that a segment of residues may appear to be erroneous, when in fact it is only interacting with an erroneously modeled region. Therefore, the use of energy profiles should not be the only means of model assessment.

Despite the predictive power and utility of homology modeling, several challenges persist. First, the level of target-template structural conservation and the accuracy of the alignment are key determinants of the quality of the resulting model. If the target-template sequence identity is <20%, approximately half of the residues in the model may be misaligned.[53] This issue can be addressed by modeling based on more than one template, to integrate the most relevant features from each template. Another challenge is that homology modeling programs must evolve new techniques to keep pace with the increasing number of known protein structures. Precomputing structural relationships within the PDB may be helpful in addressing this issue, as many irrelevant structures may be excluded without the need to align them explicitly.[53] An additional challenge in comparative modeling is determination of side-chain conformation. Many side-chain programs are based on rotamer libraries,[54] which contain values for side-chain torsional angles for preferred conformations of specific side chains. However, as the number of rotamers increases, the issue of sampling all potential conformations becomes a combinatorial problem. Xiang *et al.*[55] have recently shown that the use of a rotamer library based on Cartesian coordinates of known structures, rather than optimal bond lengths and angles, can successfully predict side-chain conformation. Thus, local minima for side-chain prediction may be nearly as reliable as the global minimum, and renders the combinatorial problem less of an issue. Despite these present challenges, homology modeling remains a powerful tool for reliable prediction of protein structure. As the accuracy of the technique increases over the next several years, comparative modeling will further close the gap between the number of known sequences and the number of available structures, as well as deepen our understanding of the relationship between protein structure and function.

3.310.2.3. Free Energy

The second law of thermodynamics states that natural systems seek a state of minimum free energy at equilibrium. Thus computation of free energy of a system is important in comparing the results of simulation and experiment. Several different methods have been implemented for calculation of the free energy of various biological systems, and here we will discuss two of the more commonly employed techniques, namely, the free-energy perturbation (FEP) method[56] and umbrella sampling.[57]

3.310.2.3.1. Free-energy perturbation

In molecular systems, the free-energy problem is typically presented in terms of computing a free-energy difference, ΔF, between two defined thermodynamic states, for example, a ligand-bound versus unbound molecule. The free-energy difference between the two states is expressed as[58]:

$$\Delta F = -\frac{1}{\beta} \ln \langle \exp[-\beta \Delta v(x)] \rangle_0; \ \beta = \frac{1}{k_B T}$$

where the subscript zero indicates configurational averaging over the ensemble of configurations representative of the initial state of the system, k_B is the Boltzmann constant, T is the temperature, and $v(x)$ is the potential energy function that depends on the Cartesian coordinates of the system, $[x]$. ΔF can also be computed by the reverse integration:

$$\Delta F = -\frac{1}{\beta} \ln \langle \exp[-\beta \Delta v(x)] \rangle_1$$

where the subscript '1' indicates averaging over the ensemble of configurations representative of the final state of the system. The most straightforward implementation of the FEP method involves defining the potential energy function for each state and performing an MD simulation for the initial state of the system, thus calculating the ensemble average in eqn [1]. Both forward and backward integrations may be run to obtain an estimate of the statistical uncertainty in ΔF. This uncertainty arises from configurations sampled in the ensemble representative of the initial state but not the final state and vice versa, and is typically small when the initial and final states of the system are very similar (i.e., the free-energy difference between the initial and final states is in the order of $2k_BT$, or 1.5 kcal mol^{-1}).[59] However, for systems in which the free-energy difference is significantly larger, a series of intermediate states must be defined and must differ by no more than $2k_BT$. The total ΔF can then be computed by summing the ΔF's between the intermediate states:

$$\Delta F = -\frac{1}{\beta} \sum_{i=1}^{M+1} \ln \langle \exp[-\beta[v(x;\lambda_{i+1}) - v(x;\lambda_i)]] \rangle_{\lambda_i}$$

where M indicates the number of intermediate states and λ is the coupling parameter, which is a continuous parameter that marks the extent of the transition from the initial to the final state. As λ is varied from 0 (initial state) to 1 (final state), the potential energy function $v(x;\lambda)$ passes from v_0 to v_1.

A limitation of this method is that the end points of the transformation, which correspond to the creation or elimination of a group of atoms, are subject to van der Waals (VDW) clashes that result in end-point catastrophes.[60,61] To obtain an accurate estimate of the free energy at the diverging end points, the number of windows at the beginning and end of the FEP simulations can be increased to collect data at several points with λ values close to 0 or 1. Another challenge is particularly relevant to biological systems, as there are often multiple ways that a ligand can bind to a receptor.[58] Indeed, some of these possibilities will result in comparable free-energy estimates. However, the current FEP methodology must improve upon ways to distinguish among the alternative possibilities and thoroughly sample the possible conformations at a binding site. Despite these limitations, the FEP method is capable of providing an accurate theoretical estimate of the free energy of numerous biomolecular systems.[62–65]

3.310.2.3.2. Umbrella sampling

This procedure enables the calculation of the potential of mean force (free-energy density) along an *a priori* chosen set of reaction coordinates or order parameters, from which free-energy changes can be calculated by numerical integration (see for example Chandler[66]). For the free-energy calculation, the probability distribution $P(\chi_i)$ is calculated by dividing the range of order parameter χ_i into several windows. The histograms for each window are collected by harvesting and binning trajectories in that window, from which the potential of mean force $\Lambda(\chi_i)$ is calculated; the potential of mean force $\Lambda_i(\chi_i)$ is given by[67,68]

$$\Lambda_i(\chi_i) = -k_BT \ln(P(\chi_i)) + \text{Constant; then, } \exp(-\beta \Delta F) = \int \exp(-\beta \Lambda_i(\chi_i)) d\chi_i$$

The functions $\Lambda_i(\chi_i)$ in different windows are pieced together by matching the constants such that the Λ_i function is continuous at the boundaries of the windows. Thus, the arbitrary constant associated with each window is adjusted to make the Λ function continuous. The standard deviation in each window of the potential of mean force calculations is estimated by dividing the set of trajectories in two blocks and collecting separate histograms. The calculation of the multidimensional potential of mean force (multiple reaction coordinates) using the weighted histogram analysis method (WHAM) has been reviewed by Roux,[69] which enables an easy and accurate recipe for unbiasing and combining the results of umbrella sampling calculations and simplifies considerably the task of recombining the various windows of sampling in complex systems and of computing ΔF.[68–72]

3.310.2.4. Electronic Structure Methods

Molecular simulations using the empirical force-field approach are rooted in the validity of classical mechanics. Electronic structure methods[73–75] that relieve this fundamental assumption are often necessary in force-field development as well as in understanding chemical reaction pathways and catalytic mechanisms. While electronic structure methods are computationally rather demanding, recent advances in mixed quantum mechanics molecular mechanics (QM/MM) methods also enable us to combine high-level electronic structure methods with MM.[76–87] This multiscale description of force fields provides a route to extend the electronic structure methods to the nanometer scale to enable the study of biomolecular systems. Compared to their classical counterparts,[11,88–112] the quantum approaches (such as the empirical valence bond[76,77]) and mixed QM/MM approaches are more challenging to apply in the biochemical context, though several successful demonstrations are available.[62,84,113–116] Here, we describe the utility of electronic structure methods in force-field development as well as in the study of catalytic reaction mechanisms.

3.310.2.4.1. Electronic structure methods in force-field development

In order to obtain an accurate description of molecular parameters (force field), we require specification of geometric parameters such as bond, angle, dihedral angles, etc., energetic terms such as partial charges, bond/angle/dihedral stiffness, and contributions of solvation–desolvation. Consistent with existing biomolecular force fields, it is thus essential to parameterize any new compound/molecule/chemical modification in the model and extend the force field for accurate representation of the model system. This procedure usually involves a series of steps[10,12] described below.

The geometry of new compounds is optimized using an electronic structure method such as Hartree–Fock (HF)[73] and by using a set of basis functions to represent the electronic wave function. Such calculations are facilitated by the aid of quantum chemistry software such as GAUSSIAN (www.gaussian.com[73]). Geometry optimization yields the spatial electron density 0 K, from which the partial (Mulliken) charges on each atom are inferred. Moreover, the frequency spectrum of the molecule to characterize its vibration spectrum in the ground state is also computed using the analysis of normal modes (**Figure 1(a)**). In order to represent delocalized (low-frequency) motions such as torsional oscillations, a torsional energy scan is also performed (**Figure 1(b)**).

In determining empirical force-field parameters for new compounds, consistency and compatibility with the parent force field is an important criterion. For example, the CHARMM27 force field is commonly used as an all-atom empirical force field for biomolecules; it is therefore necessary to develop force-field parameters for new compounds consistent with the rest of the CHARMM27 force field.

To obtain these parameters,[117] partial atomic charges are calculated using CHarges from ELectrostatic Potentials using a Grid based method (CHELPG)[118] in GAUSSIAN and further adjusted to reproduce interaction energy of H-bond donor/acceptor atoms in the compounds with water molecules. The intramolecular parameters such as molecule geometry and force constants are determined by using structural and vibrational data derived from electronic structure calculations (**Figure 1(a)**). Intramolecular force constants are initially assigned on the basis of existing parameters of compounds with similar structure and further refined following an automatic procedure using a genetic algorithm (GA) to optimize a merit function,[106] which matches both eigenvalues and eigenvectors estimated using the electronic structure calculations (i.e., using GAUSSIAN) to those resulting from a normal mode analysis calculated from classical molecular mechanics calculations, that is, using CHARMM[119] (see **Figure 2**).

3.310.2.4.2. QM/MM simulations

In the QM/MM simulations, the system is subdivided into two subregions, the quantum mechanical subregion (QM region) where the reactive events take place, and the molecular mechanical subregion (which provides the complete environment around the reactive chemistry).[77,79] Since electronic structure methods are limited by the number of atoms they can handle (typically 50–500), the QM subregion is restricted to a small number of atoms of the total system. For example, in an enzymatic system, the quantum region can consist of catalytic ions, water molecules within 3Å of the catalytic ions, parts of the substrate molecules, and the catalytic amino acid residues (such as aspartic acids). The remaining protein and solvent molecules are treated classically using the regular classical force field (such as CHARMM27).

In QM/MM simulations, wave function optimizations are typically performed in the quantum (or QM) subregion of the system using an electronic structure method such as density functional theory (DFT).[74] In this step, the electrostatic coupling between the QM and the MM subregions is accounted for: that is, the charges in the MM subregion are allowed to polarize the electronic wave functions in the QM subregion. The forces in the quantum subregion are calculated using DFT on the fly, assuming that the system moves on the Born–Oppenheimer surface.[79,120] That is, we assume a clear

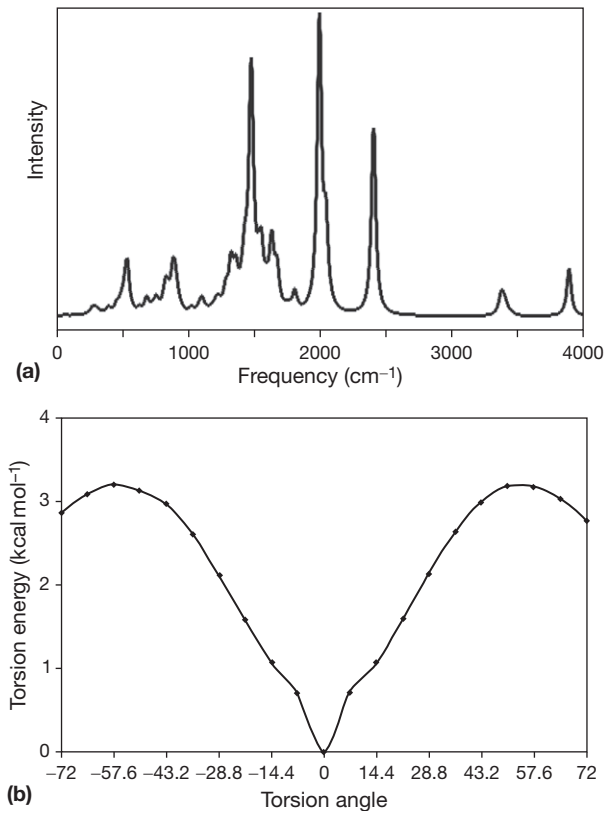

Figure 1 (a) Calculated infrared spectrum of model compound at 300 K and (b) calculated torsional energy scan of the compound.

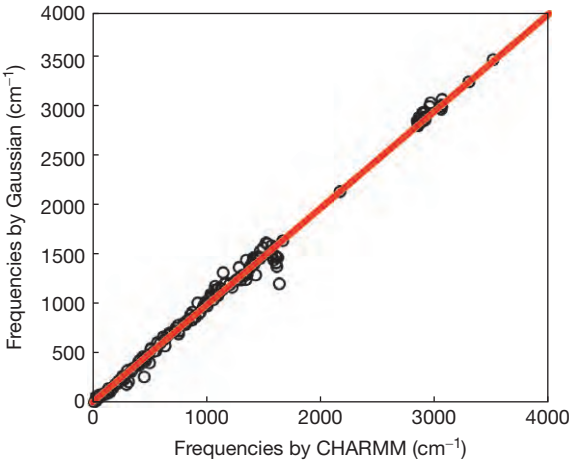

Figure 2 Frequency-matching for electronic structure and molecular mechanics calculations.

timescale of separation between the electronic and nuclear degrees of freedom, and the electronic degrees of freedom are in their ground state around the instantaneous configurations of the nuclei. The forces on the classical region are calculated using a classical force field. In addition, a mixed Hamiltonian (energy function) accounts for the interaction of the classical and the quantum subregions. Since the QM/MM boundary often cuts across covalent bonds, one can use a link atom procedure[82] to satisfy the valences of broken bonds in the QM subregion. Also, bonded terms and electrostatic terms between the atoms of the QM region and those of the classical region are typically included.[80]

From a practitioner's standpoint, QM/MM methods are implemented on the basis of existing interfaces between the electronic structure and the MD programs, one implementation is between GAMESS-UK (www.cfs.dl.ac.uk[121]) (an *ab initio* electronic structure prediction package) and CHARMM.[16] The model system can then be subjected to the usual energy minimization and constant-temperature equilibration runs at the desired temperature using the regular integration procedures in operation for pure MM systems; it is customary to carry out QM/MM dynamics runs (typically limited to 10–100 ps because of the computationally intensive electronic structure calculations) using a standard 1 fs time step of integration. The main advantage of the QM/MM simulations is that one can follow reactive events and dissect reaction mechanisms in the active site while considering the explicit coupling to the extended region. In practice, sufficient experience and care is needed in the choices of the QM subregion and the many alternative choices of system sizes, as well as the link atom schemes need to be compared to ensure convergence and accuracy of results.[80] The shorter length of the dynamics runs in the QM/MM simulations (ps) relative to the MM MD simulations (ns) implies that sufficiently high-resolution structures are usually necessary for setting up such runs as the simulations only explore a limited conformational space available to the system. Another challenge is an accurate and reliable representation of the mixed QM/MM interaction terms.[83] These challenges are currently being overcome by the suitable design of next-generation methods for electronic structure and molecular mechanics simulations.[122,123]

3.310.2.5. Methods for Determining Reaction Paths

Brute-force MD simulations of realistic models are restricted to the nano- to microsecond regimes. The development of long-time dynamics and sampling algorithms is a well-appreciated central objective of single-molecule biophysics, as the prediction of biologically relevant properties that occur in the timescale upward of a microsecond has remained a problem. Sampling the complex configurational space of biomolecules is a challenge, but can be partially overcome via smart sampling techniques,[124–127] umbrella sampling,[63,69]steered and targeted dynamics,[98,128] meta-dynamics,[129,130] Tsallis statistics,[131,132] adaptive sampling,[133] and density-of-states Monte Carlo.[134,135] Path-based methodologies seek to describe transition pathways connecting two well-defined states[93,136,137]; practical applications of this ideology are available through methods such as stochastic path approach,[138] nudged elastic band,[139–141] finite temperature string,[133] and transition path sampling (TPS),[142–144] each of which exploits the separation in timescales in activated processes, namely, the existence of a shorter timescale of relaxation at the kinetic bottleneck or the transition state (τ_{relax}), in comparison to a much longer timescale of activation at the transition state itself (τ_{TS}). Below, we review the path-based method of TPS and the related method of Bolas sampling.

3.310.2.5.1. Transition path sampling[142,143]

TPS aims to capture rare events (excursions or jumps between metastable basins in the free-energy landscape) in molecular processes by essentially performing Monte Carlo sampling of dynamics trajectories; the acceptance or rejection criteria are determined by selected statistical objectives that characterize the ensemble of trajectories. In TPS, time reversible MD trajectories in each transition state region are harvested using the shooting algorithm[144] to connect two metastable states via a Monte Carlo protocol in trajectory space. Essentially, for a given dynamics trajectory, the state of the system (i.e., basin A or B) is characterized by defining a set of order parameters $\chi = [\chi_1, \chi_2, \ldots]$. Each trajectory is expressed as a time series of length τ. To formally identify a basin, the population operator $h_A = 1$ if and only if a particular molecular configuration associated with a time t of a trajectory belongs to basin A; otherwise $h_A = 0$. The trajectory operator $H_B = 1$ if and only if the trajectory visits basin B in duration τ, that is, there is at least one time slice for which $h_B = 1$; otherwise $H_B = 0$. The idea in TPS is to generate many trajectories that connect A to B from one such existing pathway. This is accomplished by a Metropolis algorithm that generates an ensemble of trajectories $[\chi^\tau]$ according to a path action $S[\chi^\tau]$ given by: $S[\chi^\tau] = \rho(0)h_A(\chi_0)H_B[\chi^\tau]$, where $\rho(0)$ is the probability of observing the configuration at $t = 0$ ($\rho(0) \propto \exp(-E(0)/k_BT)$, in the canonical ensemble. Trajectories are harvested using the shooting algorithm[144]: a new trajectory $\chi^{*\tau}$ is generated from an existing one χ^τ by perturbing the momenta of atoms at a randomly chosen time t in a symmetric manner,[144] that is, by conserving detailed balance. The perturbation scheme is symmetric, that is, the probability of generating a new set of momenta from the old set is the same as the reverse probability. Moreover, the scheme conserves the equilibrium distribution of momenta and the total linear momentum (and, if desired, the total angular momentum). The acceptance probability implied by the above procedure is given by $P_{acc} = \min(1, S[\chi^{*\tau}]/S[\chi^\tau])$. With sufficient sampling in trajectory space, the protocol converges to yield physically meaningful trajectories passing through the true transition state (saddle) region.

The convergence of each sampling run is monitored by calculating the autocorrelation function of the order parameter. The characteristic relaxation time τ_{mol} associated with the crossing of each transition state region is given by the time taken for the gradual transition of the autocorrelation function $\langle\chi_i(0)\chi_i(t)\rangle$, where $\langle\cdot\rangle$ denotes the average over the ensemble of generated trajectories. Order parameter autocorrelation functions transition from an initial value $\langle\chi_i(0)\chi_i(\tau)\rangle \approx \langle\chi_A^2\rangle$ to a final value $\langle\chi_i(0)\chi_i(\tau)\rangle \approx \langle\chi_A\rangle^*\langle\chi_B\rangle$, to indicate crossing of the barrier region between two metastable regions A and B over

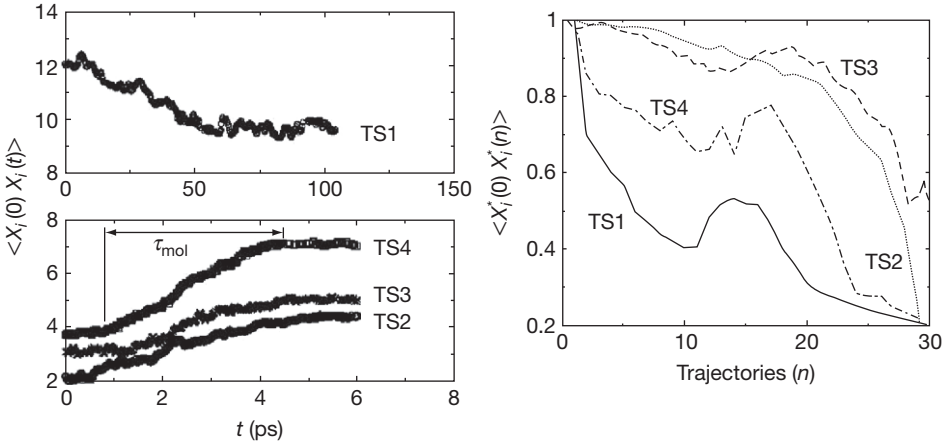

Figure 3 Convergence analysis in TPS simulations. Left: order parameter correlation functions transitioning between $\sim \chi_A^2$ and $\sim \chi_A\chi_B$ in a timescale of τ_{mol}. Right: decorrelation of transition paths.

time τ. The timescale of barrier relaxation τ_{mol} is inferred from these correlation functions graphically. Shown in Figure 3 are these functions for four different sampling runs. The top left panel captures a large subdomain motion, while the bottom left panel captures three residue flips during the closing conformational change.[145] The gradual change in the order parameters indicates the decorrelation in each TPS run. In addition to the autocorrelation functions associated with order parameters, an assessment of the quality of our sampling by checking for the decorrelation of order parameters in path (Monte Carlo) space is necessary. This is achieved by calculating the function $\langle \chi_i^*(0)\chi_i^*(n)\rangle$, where n represents the harvested trajectory number, and χ_i^* is the value of the order parameter evaluated at a particular time slice at the bottleneck of the transition. In calculating this correlation function, no shifting with respect to the first trajectory is done. This removes the trivial decorrelation because of the shifting moves. Figure 3 shows such correlation functions; it is evident from Figure 3 that, on average, every 10th to 20th trajectory is statistically decorrelated; therefore the 200–300 trajectories that are generated for each TS ensure sufficiently good sampling, see examples Radhakrishnan and Schlick[145] and Bolhuis.[146]

3.310.2.5.2. BOLAS sampling for calculating free energies

BOLAS is motivated by the method of TPS. BOLAS generates an ensemble of MD trajectories using a Monte Carlo protocol with an appropriate action S based on shooting perturbations. Below, we define the BOLAS action S and show that using BOLAS, the free energy as a function of a reaction coordinate or order parameter chosen *a priori* can be computed. The BOLAS path action (different from the TPS path action) is $S[\chi^\tau] = \rho(0)$. The need to use a modified path action for BOLAS stems from our requirement to compute the unbiased probability distribution of a given order parameter at equilibrium. In principle, configurations contained within the trajectories harvested by TPS are also obtained from the shooting algorithm. However, the bias imposed at the boundaries due to the $h_A(\chi_0)$ and $H_B[\chi^\tau]$ in the TPS action prevents the correct estimation of the equilibrium probability distribution $P(\chi)$. This is because the contribution to $P(\chi)$ comes from six classes of trajectories: trajectories that start in A and visit B in time interval τ; trajectories that start in B and visit A; trajectories that neither originate in A nor B, but visit both the states in the time interval τ; trajectories that visit A and not B; trajectories that visit B and not A; and trajectories that neither visit A nor B. The TPS action includes only the first class of trajectories; an action defined by $S[\chi^\tau] = \rho(0)H_A[\chi^\tau]$ $H_B[\chi^\tau]$ includes the first three classes of trajectories; the BOLAS action includes all six classes of trajectories.

Since detailed balance is preserved for the momentum perturbation move of the shooting algorithm and the individual MD trajectories conserve a stationary (equilibrium) distribution ρ, the configurations contained within the ensemble of the generated trajectories are also distributed according to the equilibrium distribution ρ (see derivation in Radhakrishnan, and Schlick[70]). Thus, from the ensemble of trajectories generated using the BOLAS action, the equilibrium probability distribution of the order parameter can be calculated by binning the data from accepted trajectories into histograms of the order parameters. In our implementation, the desired range of χ is divided up in terms of smaller windows and the BOLAS protocol is used to independently sample the configurations in each of these windows. This is equivalent to performing an umbrella sampling. The functions in different windows are then pieced together by using the WHAM algorithm.[69] The validity and application of BOLAS have been illustrated in several applications of protein–nucleic acid interactions.[70,145,147]

3.310.2.6. Effect of Force on Biomolecules

In single-molecule experiments, a force applied can linearly couple to a reaction coordinate and alter the free-energy landscape. If A and B denote the ground and transition states for a given transition (associated with catalysis or a ligand-binding event), then according to transition state theory the equilibrium constant for the system to switch from state A to B in the absence of any external force is $K_{eq}(0) \propto \exp(-\Delta G/k_B T)$, where ΔG is the free-energy difference between A and B.[148] Within the linear response limit, the applied force will shift the

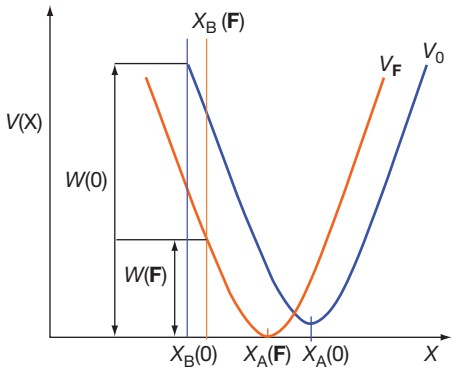

Figure 4 Schematic of the effect of the force on the free-energy landscape.

ground state equilibrium position $X_A(\mathbf{F})$ and the position of the transition state $X_B(\mathbf{F})$.[148] Thus, the change in the total (free) energy cost to transition from state A to state B, that is, $\Delta W = W(0) - W(\mathbf{F})$, under an applied force $\mathbf{F}$ acting along X is $\Delta W(\mathbf{F}) = W(0) - 0.5k_x[X_B(\mathbf{F}) - X_A(\mathbf{F})]^2$, which will alter the equilibrium constant (see Figure 4)[148]:

$$K_{eq}(\mathbf{F}) \propto \exp\left(-[\Delta G - \Delta W(\mathbf{F})]/k_B T\right)$$

Such a linear response, which assumes a perfect alignment of the applied force and the reaction coordinate, is assumed in the Bell model for receptor–ligand interactions, as well as in models of two-state transitions used to interpret single-molecule experiments.[148,149] However, the force will change X only if a coupling exists between X and the applied force. We can explore this coupling by carrying out a PCA (see Section 3.310.2.1).[23] The coupling between the applied force and a coordinate X occurs through the alignment of the force and the PCs and how the PCs impact the coordinate X. While the former can be quantified by projecting the force component along the eigenvectors, the latter can be quantified linearly combining the PCs to describe the motion along X, as we illustrate below.[150]

An external force applied to a molecule will displace atoms in a given active site. Let $\Delta\mathbf{x} = (\Delta x_1, \Delta y_1, \Delta z_1, \Delta x_2, \Delta y_2, \Delta z_2, \ldots, \Delta x_{3N}, \Delta y_{3N}, \Delta z_{3N})$ be the $3N$-dimensional displacement vector that represents the displacement of the N atoms in the active site due to the applied force $\mathbf{F}$. We can express this displacement vector in terms of the $3N$ normalized PC modes ξ_m which forms a complete basis as, $\Delta\mathbf{x} = \sum_m a_m \xi_m$, with expansion coefficients a_m. Under the quasiharmonic approximation and linear response, the Hamiltonian (energy function) for the system is given by:

$$H = \frac{1}{2}\sum_{m=1}^{3N} k_m (a_m \xi_m)^2 - \sum_{m=1}^{3N} \mathbf{F}\cdot(a_m \xi_m)$$

That is, in the quasiharmonic approximation, for each eigenvector ξ_m the spring constant corresponds to $k_m = k_B T/\lambda_m$.[23] At equilibrium, we have $\partial H/\partial a_m = 0$ for each a_m which gives:

$$a_m = \frac{\mathbf{F}\cdot\xi_m}{k_m} = \frac{|\mathbf{F}|\cos\theta_m}{k_m}$$

Here, $\mathbf{F}$ is a $3N$-dimensional vector representing the force on the active site fragment and θ_m is a generalized angle between $\mathbf{F}$ and ξ_m (PCs are normalized):

$$\cos\theta_m = \frac{\mathbf{F}\cdot\xi_m}{|\mathbf{F}|} = \frac{\sum_{i=1,\ldots,N}^{j=x,y,z} F_i^j \xi_{mi}^j}{\sqrt{\sum_{i=1,\ldots,N}^{j=x,y,z} (F_i^j)^2}}$$

where F_i^j denotes the component of applied force acting on the ith atom of the active site fragment in the direction j. In the experiments, the force is applied by tethering polymer chains (e.g., DNA) to the ends of the molecule, based on which we can define the applied force to be

$$F_i^j = F_0(i) n_j \quad \forall i \in [x_T]$$

$$F_i^j = 0 \quad \forall i \notin$$

Here $F_0(i)$ is the magnitude of force acting on the ith atom $\left(|\mathbf{F}| = \sqrt{\sum_{i=1}^{N_T} (F_0(i))^2}\right)$ and $[x_T]$ is a subset of N_T atoms subject to the force. The components n_j $(j = x, y, z)$ belong to a unit vector along the applied force direction. We generally assume that $[x_T]$ includes only the heavy atoms and that the region subject to the force is small enough so that the same force $F_0(i) = |\mathbf{F}|/\sqrt{N_T}$ acts on all the atoms. Calculations are performed by varying $|\mathbf{F}|$ to get the resultant change in the active site geometry due to the applied force $\mathbf{F}$: $\mathbf{R}(\mathbf{F}) - \mathbf{R}(0) = \sum_m a_m \xi_m$, where, $\mathbf{R} = (x_1, x_2, \ldots, x_{3N})$ is the vector representing the geometry of the active site. Here, $\mathbf{R}(0)$ is the ground state active site geometry at zero force for which $X = X_A(0)$, and $\mathbf{R}(\mathbf{F})$ is the new active state geometry due to $\mathbf{F}$ for which $X = X_A(\mathbf{F})$. The force along X which causes a displacement, $\Delta X_A(\mathbf{F}) = X_A(\mathbf{F}) - X_A(0)$ is $F_x(\mathrm{F}) = -k_x \Delta X_A(\mathrm{F})$. The spring constants k_x can simply be obtained from the distribution (histogram) of X values P_x in MD trajectories by fitting a harmonic function to the energy of the distribution $E(X) = (1/2)k_x X^2 = -k_B T \ln(P_x)$. Since the free-energy surface projected along the reaction coordinate has a maximum at the transition state, the negative curvature is approximated as $k_{ts} = -\mu(\omega_{ts})^2$, where μ is the reduced mass of the coordinate at the transition state and ω_{ts} is the passage time in transition state theory: $\omega_{ts} = -k_B T/\hbar$. Assuming that the same force acts on X throughout the system's passage from the ground to the transition state (the dynamic coupling is unaltered), the displacement of the transition state value of X, $\Delta X_B(\mathbf{F}) = X_B(\mathbf{F}) - X_B(0)$, is given as:

$$\Delta X_B(\mathbf{F}) = \frac{F_x(\mathbf{F})}{k_{ts}} = -\frac{k_x}{k_{ts}} \Delta X_A(\mathbf{F})$$

Note that the displacements $\Delta X_A(\mathbf{F})$ and $\Delta X_B(\mathbf{F})$ have opposite signs due to positive/negative curvatures of the free energy for ground/transition states. We employ the full

set of $3N-6$ PC modes to calculate the displacements $\Delta X_A(\mathbf{F})$ and $\Delta X_B(\mathbf{F})$ and obtain the ratio $K_{eq}(\mathbf{F})/K_{eq}(0) = \exp(\Delta W(\mathbf{F})/k_BT)$.[150]

3.310.2.7. Limitations and Caveats

MD simulations suffer from inherent modeling limitations (force-field uncertainties, solvent approximations, limited sampling, finite size effects, etc.). Some of these issues (e.g., finite size effects) are difficult to overcome because of constraints posed by computational resources, while others can be addressed to some degree. It is prudent to test the effect of force fields on active site geometry by comparing, for example, different force fields such as CHARMM and AMBER. While solvent effects are taken into account by explicitly treating water molecules, there is, in general, the problem of determining the protonation states. This can be dealt with at the mean field level by using Debye–Huckel calculations for titratable side-chain residues and by Poisson–Boltzmann (MMPBSA)[151] evaluation of the relative free energies for residues participating in the catalytic reaction. QM/MM calculations can be used to further assess the relative stabilities of the different protonation states. The QM/MM methodologies make some approximations as well. Perhaps the most significant is the choice of the QM/MM boundary. Since the boundary between the MM and QM regions cuts through covalent bonds, the single link atom procedure satisfies valences of broken bonds. In particular, the electrostatic terms involving the MM host atoms that connect to the QM region need to be excluded from the Hamiltonian. The test cases[80] have shown that the double link atom method yields better numerical accuracy to the other popular approaches using the local self-consistent field (LSCF) formalism and single link atom approach.[82] The study also notes that single link with partially visible MM atoms yields comparable results with the double link procedure. Other benchmark recipes for link atoms such as the pseudobond method[83] are also available. In order to handle complex chemistry, there is generally a need employ a high-level electronic structure method such as DFT, with a reliable energy functional and a high-level set of basis functions often allowing for polarization.

The issue of limited timescales explored in MD simulations can be overcome to an extent by smart sampling algorithms as discussed in **Section 3.310.2.5**. Of course, these long-time algorithms have shortcomings of their own: these include issues of multiple pathways and choice of order parameters. In general, there is a need to devise several assessment tools to monitor the quality of sampling and to control the statistical error. The limitations of PCA in extracting dominant modes of protein dynamics arise because of the finite simulation time of the MD trajectory.[152,153] While PCA is not reliable for describing the slow modes of the system beyond what is captured in the dynamics trajectory it is based on, it does provide an approximate description of the slow modes faster than the timescale of the trajectory (t). The error in the eigenvalue propagates as $(tv_i)^{-1/2}$, where v_i is the frequency of the ith mode. Despite the methodological approximations and limitations, we vouch for the notion that the predictions from such simulations can be made to have sufficient accuracy to make meaningful contact with experimental literature.

3.310.3. Applications

3.310.3.1. *Ab Initio* Simulations of Material Properties

The advantages of employing titanium (Ti) alloys in biomedical implant applications, such as hip and knee prostheses, include high fatigue resistance, good ductility and wear resistance, low cytotoxicity, and low elastic modulus[154–156] (see also **Chapter 1.102, Metals for Use in Medicine**). Ti and Ti-based alloys typically occur in either one or a mixture of two crystalline structures: the α-phase, which assumes the hexagonal structure, and the β-phase, which assumes the body-centered cubic (bcc) structure. Several recent studies have demonstrated that many of the biomedical constraints for implant applications can be met by designing Ti alloys that use the most biocompatible elements, such as Ta, Mo, and Nb, as alloy components for preferentially stabilizing the bcc β-phase over the α- or α–β-phases.[157–159] In particular, β-Ti alloys have an elastic modulus that is lower than that of most commonly used α- or α–β-Ti alloys. This is important because bone-replacing implants must have a low elastic stiffness that simulates that of the surrounding bone tissue.[155,156] Thus, key criteria for optimizing the design of Ti alloys include the stabilization of the bcc β-phase at room temperature and the reduction of the elastic stiffness relative to currently employed Ti-based alloys.

Raabe *et al.* (http://adsabs.harvard.edu/abs/2008arXiv0811.0157R) addressed these biomedical constraints by applying both quantum mechanical simulations and experiments to the design of biocompatible β-titanium (β-Ti) alloys with a small elastic modulus. Specifically, they restrained their search to binary alloys composed of Ti–Mo and Ti–Nb, and obey the following constraints: composed of nontoxic elements, stable in the β-phase, and low Young's modulus. The binary alloys were computationally represented as supercells composed of $20\times 2\times 2$ cubic or hexagonal unit cells with a total of 16 atoms. In this way, many different alloy compositions could be investigated by systematically substituting Nb or Mo atoms for Ti atoms. The group then calculated the alloy formation energy for each composition, which is the fundamental quantity representing the thermodynamic stability of an alloy in its ground state. For an alloy to be thermodynamically stable, its formation energy must be negative. Raabe *et al.* found that Mo is an intrinsic stabilizer of the β-phase (i.e., exhibited negative formation energy) even at concentrations as low as 25%, in the absence of any entropy-driven temperature effects. In contrast, stabilization of the β-phase (i.e., negative formation energy) by Nb was temperature-dependent. Thus, Nb acts as an entropy-driven β stabilizer. To experimentally validate their findings, the group determined the volume fractions of the α- and β-phases using X-ray wide angle diffraction experiments for the binary Ti–Nb and Ti–Mo alloys.

To determine the mechanical properties of the various alloys, the group first computationally predicted the Young's modulus by simulating a uniaxial tensile test along the crystallographic [001] direction of the β-phase, and then comparing it with experimental measurements of the Young's modulus using ultrasonic resonance frequency to assess the natural period of the transient vibration and results from a mechanical disturbance of the object tested. The best alloy identified, Ti–30% Nb, had a Young's modulus of 72.1 GPa, which, compared to the reference modulus of a polycrystalline Ti

sample, equates to a drop in stiffness of 37%. Thus the computational simulations allowed for a faster and more efficient method of alloy design and characterization of the alloys' mechanical properties. This shows that it is possible to screen the elastic properties of new alloys before actually preparing and casting them, resulting in a more streamlined alloy design process. Theory-guided design of biocompatible Ti alloys will help to reduce the amount of time required by conventional metallurgical alloy screening.

In a different study, Malavasi *et al.* modeled the bioactive glass 45S5, a reactive glass with low SiO_2 content and with potent effect on bone tissue formation[160] (see also **Chapter 1.110, Bioactive Glass-Ceramics**). The simulations showed that the Muliken charges were close to the ionic charges, implying that the bioglass is an ionic material. The authors also computed the bandgap of the material to be of 6.5 eV, indicating that the material is an insulator.

3.310.3.2. Surfaces with Tailored Functionality Through Self-Assembly Techniques

When a medical device is implanted, the surrounding proteins quickly adsorb onto the surface of the device. The biocompatibility is determined by the specific biochemical signaling potential of these proteins[161,162] (see also **Chapter 4.406, Protein Interactions with Biomaterials**). Therefore, the control of how proteins adsorb onto a surface can be important for the design of compatible biomaterials (see also **Chapter 3.311, Molecular Simulation Methods to Investigate Protein Adsorption Behavior at the Atomic Level**). Hydroxylated surfaces can be made in a highly controlled manner using ultrathin organic films. These films are typically prepared by Langmuir–Blodgett and SAM techniques (see also **Chapter 2.205, Self-Assembling Biomaterials**). SAMs are used as model biomaterial surfaces because they present well-defined chemistries. The substrate surface can be negatively or positively charged as well as hydrophilic or hydrophobic by selecting carboxyl-terminated, amine-terminated, hydroxyl-terminated, or methyl-terminated SAMs.

Using MD simulations and experiments, Rout *et al.* and Verneker *et al.* studied the specific contributions of variable residues to adsorption free energy between a G_4–X–G_4 peptide (G is glycine, X is variable residue) and functionalized Au–alkanethiol SAMs.[163,164] An initial challenge was that the SAMs were not parameterized in the GROMOS force field; so, using a protocol similar to that described in **Section 3.310.2.4**, the SAM model geometry and charges were assigned. Following the system simulation, the adsorption free energy was calculated by using the probability ratio method,[72] where tracking the surface separation distance (the distance between the C_α of the peptide and the plane of the SAMs) versus time is transformed into an adsorption free energy. In performing the simulations, the investigators combined an adaptive implementation of the umbrella sampling methodology described in **Section 3.310.2.3** with an enhanced sampling method known as replica exchange MD (REMD)[165–167] to help gain accuracy in the calculation of the adsorption free energy. In particular, using an adaptive implementation of the umbrella sampling in conjunction with REMD overcomes the high energy barrier inherent in solvent–solute–surface system and provides adequate sampling. The simulations and experiments were in agreement in that the G_4–G–G_4 and G_4–K–G_4 peptides showed minimal-to-no adsorption to the OH-SAM surfaces whereas the G_4–K–G_4 showed strong adsorption to the COOH-SAM surface. The simulations also predicted a relatively strong adsorption of the G_4–G–G_4 peptide to the COOH-SAM surface and both peptides were predicted to adsorb to the oligo(ethylene glycol) (OEG) surface.[163]

3.310.3.3. Slow Dynamical Modes in Adhesion, Catalysis, and Force

Theoretical and experimental studies have argued that thermal motions in proteins and their substrates with a diverse range of timescales (long-range or global as well as short-range or local motions) tend to couple to bring together the essential elements required for activity.[168–172] This implies that distal mutations can affect function by disrupting equilibrium distributions of the protein conformations to favor optimal organization of the active site and by providing a favorable electrostatic environment for the reaction.[168,173–176] Similar trends are reported for other proteins,[168,177] and show that the slow structural rearrangements of the enzyme–substrate complex play an important role in lowering the barrier for catalysis. For example, identifying the slow structural motions of the enzyme–substrate complex, which couple to the fast local coordinates at the catalytic site to lower the barrier for catalysis, may prove to be important in the delineation of reaction pathways.[71] Using novel tools for single-molecule experimentation,[178–181] pioneering studies of polymerases replicating DNA stretched under differing tensions[182,183] show that the replication rate is highly sensitive to forces exerted on the template strand (replication rate increases with forces <4–7 pN and decreases for higher values of the force); this implies that the applied force affects the rate-limiting step. Theoretical models parameterized by experimental data[182,183] and atomistic simulations[184] suggest that the rate-limiting step in this case involves the rearrangement of more than one base pair. Such models are instructive regarding the force-mediated coupling between the complex cooperative motion of polymerase and DNA degrees of freedom at the catalytic site.[150,185,186] More generally, the models help to delineate the effect of force on the recognition of receptor–ligand bonds and how the adhesion is mediated between cells and substrates.[187–191] Such interactions are also generally applicable in the context of biomaterials embedded in a tissue environment, as the interaction with the ECM will introduce forces and stresses at the biomaterial–matrix interface, which can trigger many signaling responses governed by the mechanobiology as described in an application summarized below.

3.310.3.3.1. Computational modeling of the attachment function of fibronectin

It is well known that cell adhesion to ECM proteins is primarily mediated by integrins, a widely expressed family of heterodimeric transmembrane adhesion receptors consisting of noncovalently associated α and β subunits (see also **Chapter 4.408, Integrin-Activated Reactions to Metallic Implant Surfaces** and **Chapter 2.207, Extracellular Matrix: Inspired Biomaterials**). Integrins bind to specific amino acid sequences on ECM

proteins, such as the well-known arginine–glycine–aspartic acid (RGD) motifs. Fibronectin is composed of three repeating structural motifs, one of which is the FN-III module (see also **Chapter 2.217, Fibrin**). The 10th type III module of fibronectin, FN-III$_{10}$, possesses the RGD motif. Since the attachment function of fibronectin is the result of its RGD binding domain, it is important to control the conformation and orientation of fibronectin on the surface of biomaterials, especially the accessibility of this RGD sequence. Recent experimental and computational efforts have demonstrated that external forces generated by cells regulate the conformation of fibronectin, thus altering its functional state and the accessibility of the RGD loop.[192–194] These studies have shown that integrin binding to fibronectin RGD loops on FN-III$_{10}$, resulting in the formation of a cytoskeletal apparatus that mechanically couples actin contractility to ECM fibronectin fibers. In addition, these studies have revealed that supramolecular assembly of fibronectin modules into fibrillar matrix confers functions not present in individual proteins and controls the exposure of the RGD binding site. As part of a larger supramolecular complex, fibronectin is mechanically coupled to other proteins so that the force applied to fibronectin is propagated to these molecules, thus affecting their function.

To determine how the organization of fibronectin into fibrillar matrix allows cells to control its structure, Baneyx *et al.*[195] employed intramolecular fluorescence resonance energy transfer (FRET) as an indicator of fibronectin conformation within the fibrillar matrix of NIH 3T3 fibroblasts. The FRET results revealed that in many fibrils, fibronectin was stretched by cells so that one or more FN-III modules were unfolded, yet this effect could be reversed by addition of cytoskeletal inhibitors such as cytochalasin D, which promotes refolding. The group concluded that the force generated by cells is necessary to maintain fibronectin in partially unfolded conformations, supporting a model in which fibronectin in cell fibrils is hyperextended relative to fibronectin bound to the cell membrane. The observation that fibronectin in fibroblast fibrils is stretched into partially unfolded conformations has functional implications. Hyperextension of FN-III modules may expose buried binding sites, termed 'cryptic sites,' that are inaccessible in the native state, in addition to altering the distance between binding sites or straightening the hydrophilic loops that contain binding sites.[196] Indeed, FN-III$_1$, FN-III$_{7–8}$, and FN-III$_{10}$ all possess cryptic binding sites that must be exposed to allow fibronectin matrix assembly.[197–199]

These experimental studies on FN-III modules suggest that the force-induced unfolding of FN-III$_{10}$ is capable of significantly altering the biochemical events occurring in the surrounding cells. To delineate the unfolding pathway of FN-III modules, other experimental techniques, including atomic force microscopy (AFM), have been employed[200–202] (see also **Chapter 3.302, Atomic Force Microscopy**). However, AFM studies alone cannot provide atomic-level detail of the unfolding process. As a result, computational modeling and simulation of the fibronectin unfolding pathway have been invaluable tools for dissecting the unfolding process at atomic-level resolution. Steered MD (SMD) simulations have demonstrated that, prior to complete unfolding of FN-III modules (see **Figure 5**, left), cryptic binding sites may become exposed in an intermediate state of the force-induced

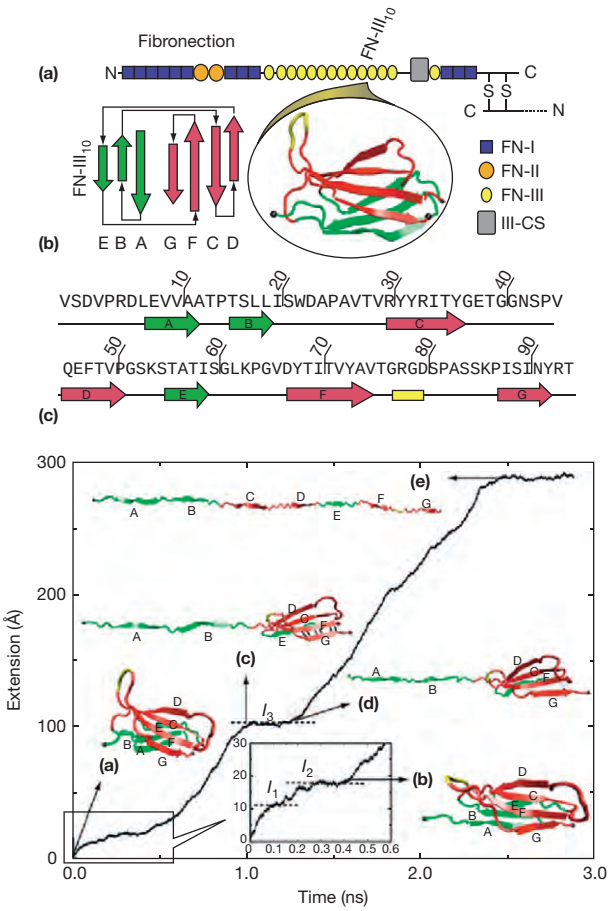

Figure 5 Unfolding intermediates of FN-III$_{10}$ by steered molecular dynamics. Left panel: schematic representation of the fibronectin monomer. (a) The modular structure. FN-III modules are shown as yellow ovals. (b) FN-III$_{10}$ is illustrated through two representations highlighting its secondary (left) and tertiary (right) structure. The RGD loop is shown in yellow. (c) Primary sequence of FN-III$_{10}$ and corresponding β-strands. Right panel: Extension–time profile from a steered molecular dynamics simulation and representative snapshots (a)–(e) illustrated during unfolding. Here (a) is the native structure and (e) is the fully unfolded structure. A total of three metastable intermediates were observed in the extension–time plot generated by SMD stretching of FN-III$_{10}$ (see right). The first and second intermediates represented alignment of the β sheets along the direction of the external force prior to unfolding of FN-III$_{10}$ β-strands. The third intermediate, which was extended by 100 Å, corresponded to unraveling of individual β-strands. Reproduced with permission from Gao, M.; Craig, D.; Vogel, V.; Schulten, K. *J. Mol. Biol.* **2002**, *323*, 939–950.

unfolding pathway.[203–205] SMD simulations also predicted that extension of the FN-III$_{10}$ module into this intermediate state decreases binding to $\alpha_5\beta_1$ integrins by increasing the separation distance between the RGD loop and its synergy site, which is required for $\alpha_5\beta_1$ (but not other integrins) binding to fibronectin.[206] The functional implication of this is that $\alpha_5\beta_1$-mediated signaling may predominate in cells bound to unstretched fibronectin, whereas other integrin-mediated pathways may begin to predominate as fibronectin is extended and the synergy site is separated from the RGD loop. If the FN-III modules become completely unraveled, the RGD loop may

straighten, decreasing integrin affinity.[204] This is one example of how regulation of the extent of fibronectin unfolding within fibrils may control the biochemical activity of the surrounding cells. The majority of these computational studies explored the early stages of fibronectin unfolding. Gao *et al.*[207] constructed an extended computational model in which FN-III_{10} was solvated in a box of water large enough to allow stretching of FN-III_{10} into its fully unfolded conformation (see **Figure 5**, right).

Based on **Figure 5**, the authors suggested that there is a consensus unfolding pathway prior to unraveling of β-strands, at which point the unfolding trajectory diverges into three alternate pathways for separation of β-strands from the main module: A-strand separating first, G-strand separating first, or both A- and G-strands separating simultaneously. The identification of multiple unfolding pathways for FN-III_{10} has several functional implications. First, the authors suggest that binding of fibronectin to specific integrins or to other fibronectin proteins may change the unfolding pathway. For example, Gao *et al.*[207] predict that binding of an integrin to the RGD loop between the F- and G-strands of FN-III_{10} may promote the interaction between these β-strands, thereby biasing the unfolding pathway toward separation of the A-strand first. The authors also suggest that the existence of unfolding intermediates lends support to a currently proposed mechanism of fibrillogenesis, which predicts that the process occurs via β-strand swapping among fibronectin modules.[208] Indeed, one of the partially unfolded intermediates identified in the SMD simulations is able to swap its β-strands with other fibronectin molecules, as the unraveled A- and B-strands can assemble with other FN-III modules. Thus, one model for fibrillogenesis is that integrin-generated force would unravel the A- and B-strands from FN-III_{10}, allowing other FN-III modules, such as FN-III_1, to assemble with FN-III_{10}. Indeed, experimental studies have found that FN-III_{10} contains a cryptic site that binds to FN-III_1 modules.[209] SMD simulations thus provide an atomic-level of detail to the complex process of fibronectin unfolding and suggest new mechanisms of fibrillogenesis that can be tested experimentally. In the future, it will be important to apply these simulation results to better control the conformation of fibronectin adsorbed to the surface of novel biomaterials.

3.310.3.4. Future Directions

As multiscale modeling techniques are becoming more sophisticated, their applications to increasingly complex biological systems are being explored. Therefore, a renewed focus on direct connection with experiments to enable proper validation is critical. One strategic approach is to compare the results of the models and experiments as well as require consistency at multiple length- and timescales, which can be realized by comparing to a hierarchy of experiments. For example, structural features can be investigated by means of a combination of experimental approaches such as Fourier transform infrared (FTIR), NMR, electron paramagnetic resonance (EPR) spectroscopy, AFM, scanning electron microscopy (SEM), transmission electron microscopy (TEM), X-ray diffraction, etc. One can simultaneously employ thermal (differential scanning colorimetry (DSC) and thermogravimetry (TG)), mechanical (hardness and elastic modulus), and biological properties for validation and require the modeling to predict a range of properties. In the future, the utility of well-validated models and simulation is in directing the rational design and modifications of novel materials. This includes creation of well-controlled surfaces that mimic multiple recognition sites for compatibility with the ECM and quantifying the effect of chemical heterogeneity (OH^- and PO_4^{3-} groups distributed randomly as dangling bonds or the presence of divalent metal ions) in inducing conformational shifts in biomolecules (such as fibronectin) as well as the effect of applied force mediated through protein–ligand interactions in orchestrating and triggering signaling events in the constituent cells.

Acknowledgments

We thank Dr. Paul Ducheyne for helpful suggestions. We acknowledge funding from National Science Foundation CBET-0853539 and CBET-0853389, National Institutes of Health NIBIB-1R01EB006818 and NHLBI-1R01HL087036, and computational support from National Partnerships for Advanced Computational Infrastructure NPACI-MCB060006. S.E.T. acknowledges funding through a GAANN fellowship and a NSF graduate fellowship.

References

1. Huebsch, N.; Mooney, D. J. *Nature* **2009**, *462*, 426–432.
2. Ducheyne, P.; Qiu, Q. Q. *Biomaterials* **1999**, *20*, 2287–2303.
3. Ducheyne, P.; Kokubo, T.; VanBlitterswijk, D., Eds. In *Bone Bonding Biomaterials*; Reed-Elsevier: Amsterdam, 1993.
4. Place, E. S.; Evans, N. D.; Stevens, M. M. *Nat. Mater.* **2009**, *8*, 457–470.
5. Redondo, A.; LeSar, R. *Annu. Rev. Mater. Res.* **2004**, *34*, 279–314.
6. Giuseppina, R.; Fabio, G. *Macromol. Biosci.* **2007**, *7*, 552–566.
7. Karplus, M.; Kuriyan, J. *Proc. Natl. Acad. Sci. USA* **2005**, *102*, 6679–6685.
8. Karplus, M.; Brunger, A. T.; Elber, R.; Kuriyan, J. *Cold Spring Harb. Symp. Quant. Biol.* **1987**, *52*, 381–390.
9. Berman, H. M.; Westbrook, J.; Feng, Z.; *et al. Nucleic Acids Res.* **2000**, *28*, 235–242.
10. MacKerell, A. D.; Bashford, D.; Bellott, M.; *et al. J. Phys. Chem. B* **1998**, *102*, 3586–3616.
11. Ferrara, P.; Apostolakis, J.; Caflisch, A. *Proteins* **2000**, *39*, 252–260.
12. MacKerell, A. D., Jr.; Banavali, N. K. *J. Comp. Chem.* **2000**, *21*, 105–120.
13. Cheatham, T. E., 3rd; Cieplak, P.; Kollman, P. A. *J. Biomol. Struct. Dyn.* **1999**, *16*, 845–862.
14. Wang, W.; Donini, O.; Reyes, C. M.; Kollman, P. A. *Annu. Rev. Biophys. Biomol. Struct.* **2001**, *30*, 211–243.
15. Glenn, J. M.; Douglas, J. T.; Michael, L. K. *J. Chem. Phys.* **1994**, *101*, 4177–4189.
16. Brooks, B. R.; Bruccoleri, R. E.; Olafson, B. D.; States, D. J.; Swaminathan, S.; Karplus, M. *J. Comput. Chem.* **1983**, *4*, 187–217.
17. Weiner, P. W.; Kollman, P. A. *J. Comput. Chem.* **1981**, *2*, 287–303.
18. Scott, W. R. P. *J. Phys. Chem. A* **1999**, *103*, 3596–3607.
19. Phillips, J. C.; Braun, R.; Wang, W.; *et al. J. Comput. Chem.* **2005**, *26*, 1781–1802.
20. Humphrey, W.; Dalke, A.; Schulten, K. *J. Mol. Graph.* **1996**, *14*, 33–38.
21. Shih, A. J.; Purvis, J.; Radhakrishnan, R. *Mol. Biosyst.* **2008**, DOI:10.1039/B803806F.
22. Amadei, A.; Linssen, A. B. M.; Berendsen, H. J. C. *Proteins: Struct. Funct. Genet.* **1993**, *17*, 412–425.
23. Amadei, A.; Linssen, A. B. M.; deGroot, B. L.; van Aalten, D. M. F.; Berendsen, H. J. C. *J. Biomol. Struct. Dynam.* **1996**, *13*, 615–625.
24. McCammon, J. A.; Harvey, S. C. *Dynamics of Proteins and Nucleic Acids*; Cambridge University Press: Cambridge, MA, 1987.
25. McCammon, J. A.; Gelin, B. R.; Karplus, M. *Nature* **1977**, *267*, 585–590.

26. Essmann, U. *J. Chem. Phys.* **1995**, *103*, 8577–8593.
27. Gota, K.; Rossen, A.; Narutoshi, K.; *et al*. *J. Comput. Chem.* **2009**, *30*, 110–118.
28. Suenaga, A.; Hatakeyama, M.; Kiyatkin, A. B.; Radhakrishnan, R.; Taiji, M.; Kholodenko, B. N. *Biophys. J.* **2009**, *96*, 2278–2288.
29. Shaw, D. E.; Deneroff, M. M.; Dror, R. O.; *et al*. *Commun. ACM* **2008**, *51*, 91–97.
30. Shan, Y.; Seeliger, M. A.; Eastwood, M. P.; *et al*. *Proc. Natl. Acad. Sci. USA* **2009**, *106*, 139–144.
31. Friedrichs, M. S.; Eastman, P.; Vaidyanathan, V.; *et al*. *J. Comput. Chem.* **2009**, *30*, 864–872.
32. Stone, J. E.; Phillips, J. C.; Freddolino, P. L.; Hardy, D. J.; Trabuco, L. G.; Schulten, K. *J. Comput. Chem.* **2007**, *28*, 2618–2640.
33. Bajorath, J.; Stenkamp, R.; Aruffo, A. *Protein Sci.* **1993**, *2*, 1798–1810.
34. Baker, D. *Nature* **2000**, *405*, 39–42.
35. Marti-Renom, M. A.; Stuart, A. C.; Fiser, A.; Sanchez, R.; Melo, F.; Sali, A. *Annu. Rev. Biophys. Biomol. Struct.* **2000**, *29*, 291–325.
36. Kryshtafovych, A.; Fidelis, K. *Drug Discov. Today* **2009**, *14*, 386–393.
37. Dunbrack, R. L., Jr. *Curr. Opin. Struct. Biol.* **2006**, *16*, 374–384.
38. Ginalski, K. *Curr. Opin. Struct. Biol.* **2006**, *16*, 172–177.
39. Moult, J. *Structure* **2008**, *16*, 14–16.
40. Schueler-Furman, O.; Wang, C.; Bradley, P.; Misura, K.; Baker, D. *Science* **2005**, *310*, 638–642.
41. Fiser, A.; Sali, A. *Meth. Enzymol.* **2003**, *374*, 461–491.
42. Blake, J. D.; Cohen, F. E. *J. Mol. Biol.* **2001**, *307*, 721–735.
43. Dewey, T. G. *J. Comput. Biol.* **2001**, *8*, 177–190.
44. Sanchez, R.; Sali, A. *Proc. Natl. Acad. Sci. USA* **1998**, *95*, 13597–13602.
45. Aszodi, A.; Taylor, W. R. *Fold Des.* **1996**, *1*, 325–334.
46. Havel, T. F.; Snow, M. E. *J. Mol. Biol.* **1991**, *217*, 1–7.
47. Srinivasan, S.; March, C. J.; Sudarsanam, S. *Protein Sci.* **1993**, *2*, 277–289.
48. Fiser, A.; Do, R. K.; Sali, A. *Protein Sci.* **2000**, *9*, 1753–1773.
49. Fidelis, K.; Stern, P. S.; Bacon, D.; Moult, J. *Protein Eng.* **1994**, *7*, 953–960.
50. Laskowski, R. A.; MacArthur, M. W.; Moss, D. S.; Thornton, J. M. *J. Appl. Cryst.* **1993**, *26*, 283–291.
51. Hooft, R. W.; Vriend, G.; Sander, C.; Abola, E. E. *Nature* **1996**, *381*, 272.
52. Luthy, R.; Bowie, J. U.; Eisenberg, D. *Nature* **1992**, *356*, 83–85.
53. Xiang, Z. *Curr. Protein Pept. Sci.* **2006**, *7*, 217–227.
54. Ponder, J. W.; Richard, F. M. *J. Mol. Biol.* **1987**, *193*, 775–791.
55. Xiang, Z. W. *J. Mol. Biol.* **2001**, *311*, 421–430.
56. Zwanzig, R. W. *J. Chem. Phys.* **1954**, *22*, 1420–1426.
57. Frenkel, D.; Smit, B. *Understanding Molecular Simulations from Algorithms to Applications*; Academic Press: San Diego, CA, 1996.
58. Beveridge, D. L.; DiCapua, F. M. *Annu. Rev. Biophys. Biophys. Chem.* **1989**, *18*, 431–492.
59. Straatsma, T. P.; Berendsen, H. J. C.; Postma, J. P. M. *J. Chem. Phys.* **1986**, *85*, 6720–6727.
60. Beutler, T. C.; Mark, A. E.; van Schaik, R. C.; Gerber, P. R.; van Gunsteren, W. F. *Chem. Phys. Lett.* **1994**, *222*, 529–539.
61. Pitera, J. W.; van Gunsteren, W. F. *Mol. Simul.* **2002**, *28*, 45–65.
62. Florian, J.; Goodman, M. F.; Warshel, A. *J. Am. Chem. Soc.* **2003**, *125*, 8163–8177.
63. Radmer, R. J.; Kollman, P. A. *J. Comput. Chem.* **1997**, *18*, 902–919.
64. Wang, J. Y.; Deng, Y. Q.; Roux, B. *Biophys. J.* **2006**, *91*, 2798–2814.
65. Zhou, R.; Das, P.; Royyuru, A. K. *J. Phys. Chem. B* **2008**, PMID 18975892.
66. Chandler, D. *Introduction to Modern Statistical Mechanics*; Oxford University Press: New York, NY, 1987.
67. Chandler, D. *J. Chem. Phys.* **1978**, *68*, 2959–2970.
68. Bartels, C.; Karplus, M. *J. Phys. Chem. B* **1998**, *102*, 865–880.
69. Roux, B. *Comput. Phys. Commun.* **1995**, *91*, 275–282.
70. Radhakrishnan, R.; Schlick, T. *J. Chem. Phys.* **2004**, *121*, 2436–2444.
71. Radhakrishnan, R. *Biophys. J.* **2007**, *93*, 2391–2399.
72. Mezei, M. *Mol. Simul.* **1989**, *3*, 301–313.
73. Szabo, A.; Ostlund, N. S. *Modern Quantum Chemistry*; Dover: Mineola, NY, 1996.
74. Parr, R. G.; Yang, W. *Density-Functional Theory of Atoms and Molecules*; Oxford University Press: Oxford, 1989.
75. Jensen, F. *Introduction to Computational Chemistry*; Wiley: Chichester, 2007.
76. Warshel, A.; Parson, W. W. *Quart. Rev. Biophys.* **2001**, *34*, 563–679.
77. Warshel, A. *Computer Modeling of Chemical Reactions in Enzymes and Solution*; Wiley: New York, 1989.
78. Shurki, A.; Warshel, A. *Protein Simul.* **2003**, *66*, 249–313.
79. Senn, H. M.; Thiel, W. In *Atomistic Approaches in Modern Biology: From Quantum Chemistry to Molecular Simulations*; Springer-Verlag: Berlin, 2007; pp 173–290.
80. Das, D.; Eurenius, K. P.; Billings, E. M.; *et al*. *J. Chem. Phys.* **2002**, *117*, 10534–10547.
81. Reuter, N.; Dejaegere, A.; Maigret, B.; Karplus, M. *J. Phys. Chem. A* **2000**, *104*, 1720–1735.
82. Field, M. J.; Bash, P. A.; Karplus, M. *J. Comput. Chem.* **2002**, *11*, 700–733.
83. Zhang, Y.; Yang, W. *J. Chem. Phys.* **1999**, *110*, 46–54.
84. Garcia-Viloca, M.; Gao, J. *Theor. Chem. Acc.* **2004**, *111*, 280–286.
85. Pu, J.; Truhlar, D. G.; Gao, J. *J. Phys. Chem. A* **2004**, *108*, 632–650.
86. Friesner, R. A.; Baik, M. H.; Guallar, V.; *et al*. *Coord. Chem. Rev.* **2003**, *238–239*, 267–290.
87. Rega, N.; Iyengar, S. S.; Voth, G. A.; Schlegel, H. B.; Vreven, T.; Frisch, M. J. *J. Phys. Chem. B* **2004**, *108*, 4210–4220.
88. Zhou, R.; Berne, B. J.; Germain, R. *Proc. Natl. Acad. Sci. USA* **2001**, *98*, 14931–14936.
89. Snow, C. D.; Nguyen, H.; Pande, V. S.; Gruebele, M. *Nature* **2002**, *420*, 102–106.
90. Zagrovic, B.; Sorin, E. J.; Pande, V. *J. Mol. Biol.* **2001**, *313*, 151–169.
91. Duan, Y.; Kollman, P. A. *Science* **1998**, *282*, 740–744.
92. Daggett, V. *Curr. Opin. Struct. Biol.* **2000**, *10*, 160–164.
93. Elber, R.; Meller, J.; Olender, R. *J. Phys. Chem. B* **1999**, *103*, 899–911.
94. Zaloj, V.; Elber, R. *Comput. Phys. Commun.* **2000**, *128*, 118–127.
95. Daura, X.; Jaun, B.; Seebach, D.; Gunsteren, W. F. V.; Mark, A. *J. Mol. Biol.* **1998**, *280*, 925–932.
96. Schlick, T. *Biophys. J.* **2003**, *85*, 1–4.
97. Israelewitz, B.; Baudry, J.; Gullingsrud, J.; Kosztin, D.; Schulten, K. *J. Mol. Graph. Model.* **2001**, *19*, 13–25.
98. Isralewitz, B.; Gao, M.; Schulten, K. *Curr. Opin. Struct. Biol.* **2001**, *11*, 224–230.
99. Izrailev, S.; Crofts, A. R.; Berry, E. A.; Schulten, K. *Biophys. J.* **1999**, *77*, 1753–1768.
100. Grayson, P.; Tajkhorshid, E.; Schulten, K. *Biophys. J.* **2003**, *119*, 36–48.
101. Yang, L.; Beard, W. A.; Wilson, S. H.; Broyde, S.; Schlick, T. *J. Mol. Biol.* **2002**, *317*, 651–671.
102. Young, M. A.; Gonfloni, S.; Superti-Furga, G.; Roux, B.; Kuriyan, J. *Cell* **2001**, *105*, 115–126.
103. Ferrara, P.; Apostolakis, J.; Caflisch, A. *J. Phys. Chem. B.* **2000**, *104*, 4511–4518.
104. Yang, J. *J. Comput. Chem.* **2004**, *25*, 843–857.
105. Kirkpatrick, S.; Gelatt, C.; Vecchi, M. *Science* **1983**, *220*, 671–680.
106. Morris, G. M.; Goodsell, D. S.; Halliday, R. S.; *et al*. *J. Comput. Chem.* **1998**, *19*, 1639–1662.
107. Lee, K.; Czaplewski, C.; Kim, S. Y.; Lee, J. *J. Comput. Chem.* **2005**, *26*, 78–87.
108. Camacho, J. C.; Gatchell, D. W.; Kimura, S. R.; Vajda, S. *Proteins* **2000**, *40*, 525–537.
109. Bindewald, E.; Skolnick, J. *J. Comput. Chem.* **2005**, *26*, 374–383.
110. Bursulaya, B. D.; Totrov, M.; Abagyan, R. C. L. B.3rd. *J. Comput. Aided Mol. Des.* **2003**, *17*, 755–763.
111. Pearlman, D. A. *J. Med. Chem.* **1999**, *42*, 4313–4324.
112. Pearlman, D. A.; Charifson, P. S. *J. Med. Chem.* **2001**, *44*, 3417–3423.
113. Banerjee, A.; Yang, W.; Karplus, M.; Verdine, G. L. *Nature* **2005**, *434*, 612–618.
114. Zhang, Y.; Kua, J.; McCammon, J. A. *J. Am. Chem. Soc.* **2002**, *124*, 10572–10577.
115. Guo, H.; Cui, Q.; Lipscomb, W. N.; Karplus, M. *Proc. Natl. Acad. Sci. USA* **2001**, *98*, 9032–9037.
116. Cui, Q.; Karplus, M. *J. Am. Chem. Soc.* **2001**, *123*, 2284–2290.
117. Floppe, N.; MacKerell, J. A. D. *Biophys. J.* **1999**, *76*, 3206–3218.
118. Breneman, C. M.; Wiberg, K. B. *J. Comput. Chem.* **1990**, *11*, 361–373.
119. Vaiana, A. C.; Cournia, Z.; Costescu, I. B.; Smith, J. C. *Comput. Phys. Commun.* **2005**, *167*, 34–42.
120. Mulholland, A. J. *Drug Discov. Today* **2005**, *10*, 1393–1402.
121. Schmidt, M. W.; Baldridge, K. K.; Boatz, J. A.; *et al*. *J. Comput. Chem.* **1993**, *14*, 1347–1363.
122. Shimojo, F.; Kalia, R. K.; Nakano, A.; Vashishta, P. *Comput. Phys. Commun.* **2005**, *167*, 151–164.
123. Zhou, R.; Berne, B. J. *J. Chem. Phys.* **1995**, *103*, 9444–9459.
124. Berne, B. J.; Straub, J. E. *Curr. Opin. Struct. Biol.* **1997**, *7*, 181–189.
125. Berneche, S.; Roux, B. *Nature* **2001**, *414*, 73–77.
126. Simonson, T.; Archontis, G.; Karplus, M. *Acc. Chem. Res.* **2002**, *35*, 430–437.
127. Boczko, E. M.; Brooks, C. L. *Science* **1995**, *269*, 393–396.
128. Schlitter, J.; Engels, M.; Kruger, P. *J. Mol. Graph.* **1994**, *12*, 84–89.
129. Laio, A.; Parrinello, M. *Proc. Natl. Acad. Sci. USA* **2002**, *99*, 12562–12566.
130. Ensing, B.; Klein, M. *Proc. Natl. Acad. Sci. USA* **2005**, *102*, 6755–6759.
131. Barth, E. J.; Laird, B. B.; Leimkuhler, B. J. *J. Chem. Phys.* **2003**, *118*, 5759–5768.

132. Tsallis, C. *J. Stat. Phys.* **1988**, *542*, 479–487.
133. Weinan, E.; Ren, W.; Vanden-Eijnden, E. *J. Phys. Chem. B* **2005**, *109*, 6688–6693.
134. Wang, F.; Landau, D. P. *Phys. Rev. Lett.* **2001**, *86*, 2050–2053.
135. Yan, Q.; de Pablo, J. J. *Phys. Rev. Lett.* **2003**, *90*, 035701.
136. Weinan, E.; Ren, W. Q.; Vanden-Eijnden, E. *Chem. Phys. Lett.* **2005**, *413*, 242–247.
137. Elber, R.; Ghosh, A.; Cardenas, A. *Acc. Chem. Res.* **2002**, *35*, 396–403.
138. Elber, R.; Cárdenas, A.; Ghosh, A.; Stern, H. *Adv. Chem. Phys.* **2003**, *126*, 93–129.
139. Henkelman, G.; Jonsson, H. *J. Chem. Phys.* **2000**, *113*, 9978.
140. Henkelman, G.; Uberuaga, B. P.; Jonsson, H. *J. Chem. Phys.* **2000**, *113*, 9901.
141. Jonsson, H.; Mills, G.; Jacobsen, K. W. In *Classical and Quantum Dynamics in Condensed Phase Simulations*; Berne, B. J.; Ciccotti, G.; Coker, D. F.; Eds. World Scientific, 1998.
142. Bolhuis, P. G.; Chandler, D.; Dellago, C.; Geissler, P. L. *Annu. Rev. Phys. Chem.* **2002**, *53*, 291–318.
143. Dellago, C.; Bolhuis, P. G.; Geissler, P. L. *Adv. Chem. Phys.* **2002**, *123*, 1–81.
144. Bolhuis, P. G.; Dellago, C.; Chandler, D. *Faraday Discuss.* **1998**, *110*, 421–436.
145. Radhakrishnan, R.; Schlick, T. *Proc. Natl. Acad. Sci. USA* **2004**, *101*, 5970–5975.
146. Bolhuis, P. G. *Proc. Natl. Acad. Sci. USA* **2003**, *100*, 12129–12134.
147. Radhakrishnan, R.; Schlick, T. *J. Am. Chem. Soc.* **2005**, *127*, 13245–13253.
148. Bustamante, C.; Chemla, Y. R.; Forde, N. R.; Izhaky, D. *Annu. Rev. Biochem.* **2004**, *73*, 705–748.
149. Bustamante, C. *FEBS J.* **2005**, *272*, 337–337.
150. Venkatramani, R.; Radhakrishnan, R. *Phys. Rev. Lett.* **2008**, *100*, 088102.
151. Kollman, P. A.; Massova, I.; Reyes, C.; *et al. Accounts. Chem. Res.* **2000**, *33*, 889–897.
152. Balsera, M. A.; Wriggers, W.; Oono, Y.; Schulten, K. Principal component analysis and long time protein dynamics. *J. Phys. Chem.* **1996**, *100*, 2567–2572.
153. Arora, K.; Schlick, T. *Biophys. J.* **2004**, *87*, 3088–3099.
154. Burstone, C. J.; Goldberg, A. J. *Am. J. Orthod.* **1980**, *77*, 121–132.
155. Goldberg, J.; Burstone, C. J. *J. Dent. Res.* **1979**, *58*, 593–599.
156. Long, M.; Rack, H. J. *Biomaterials* **1998**, *19*, 1621–1639.
157. Banerjee, R.; Nag, S.; Samuel, S.; Fraser, H. L. *J. Biomed. Mater. Res. A* **2006**, *78*, 298–305.
158. Banerjee, R.; Nag, S.; Stechschulte, J.; Fraser, H. L. *Biomaterials* **2004**, *25*, 3413–3419.
159. Nag, S.; Banerjee, R.; Stechschulte, J.; Fraser, H. L. *J. Mater. Sci. Mater. Med.* **2005**, *16*, 679–685.
160. Malavasi, G.; Menziani, M.; Pedone, A.; Civalleri, B.; Corno, M.; Ugliengo, P. *Theor. Chem. Accounts Theor. Comput. Model. (Theor. Chim. Acta)* **2007**, *117*, 933–942.
161. Anderson, J. M.; Bonfield, T. L.; Ziats, N. P. *Int. J. Artif. Organs* **1990**, *13*, 375–382.
162. Ratner, B. D.; Hoffmann, A. S.; Schoen, F. J.; Lemons, J. E. *Biomaterials Science: An Introduction to Materials in Medicine*; Academic Press: San Diego, 1996.
163. Raut, V. P.; Agashe, M. A.; Stuart, S. J.; Latour, R. A. *Langmuir* **2005**, *21*, 1629–1639.
164. Vernekar, V. N.; Latour, R. A. *Mater. Res. Innovat.* **2005**, *9*, 53–55.
165. Sugita, Y.; Okamoto, Y. *Chem. Phys. Lett.* **2000**, *329*, 261–270.
166. Metropolis, N.; Rosenbluth, A. W.; Rosenbluth, M. N.; Teller, A. H.; Teller, E. *J. Chem. Phys.* **1953**, *21*, 1087–1092.
167. Feng, W.; Steven, J. S.; Robert, A. L. *Biointerphases* **2008**, *3*, 9–18.
168. Hammes-Schiffer, S.; Benkovic, S. J. *Annu. Rev. Biochem.* **2006**, *75*, 519–541.
169. Vendruscolo, M.; Dobson, C. M. *Science* **2006**, *313*, 1586–1587.
170. Agarwal, P. K.; Billeter, S. R.; Rajagopalan, P. T.; Benkovic, S. J.; Hammes-Schiffer, S. *Proc. Natl. Acad. Sci. USA* **2002**, *99*, 2794–2799.
171. Huang, Z.; Wagner, C. R.; Benkovic, S. J. *Biochemistry* **1994**, *33*, 11576–11585.
172. Radkiewicz, J. L.; Brook, I. C. L. *J. Am. Chem. Soc.* **2000**, *122*, 225–231.
173. Stephens, P.; Hunter, C.; Bignell, G.; *et al. Nature* **2004**, *431*, 525–526.
174. Benkovic, S. J.; Hammes-Schiffer, S. *Science* **2006**, *312*, 208–209.
175. Wong, K. F.; Selzer, T.; Benkovic, S. J.; Hammes-Schiffer, S. *Proc. Natl. Acad. Sci. USA* **2005**, *102*, 6807–6812.
176. Benkovic, S. J.; Hammes-Schiffer, S. *Science* **2003**, *301*, 1196–1202.
177. Eisenmesser, E. Z.; Millet, O.; Labeikovsky, W.; *et al. Nature* **2005**, *438*, 117–121.
178. Bustamante, C.; Bryant, Z.; Smith, S. B. *Nature* **2003**, *421*, 423–427.
179. Lavery, R.; Lebrun, A.; Allemand, J. F.; Bensimon, D.; Croquette, V. *J. Phys. Condens. Matter* **2002**, *14*, R383–R414.
180. Schnitzer, M. J.; Visscher, K.; Block, S. M. *Nat. Cell Biol.* **2000**, *2*, 718–723.
181. Guo, Q.; Sousa, R. *J. Mol. Biol.* **2006**, *358*, 241–254.
182. Wuite, G. J. L.; Smith, S. B.; Young, M.; Keller, D.; Bustamante, C. *Nature* **2000**, *404*, 103–106.
183. Maier, B.; Bensimon, D.; Croquette, V. *Proc. Natl. Acad. Sci. USA* **2000**, *97*, 12002–12007.
184. Andricioaei, I.; Goel, A.; Herschbach, D.; Karplus, M. *Biophys. J.* **2004**, *87*, 1478–1497.
185. Venkatramani, R.; Radhakrishnan, R. *Protein. Struct. Funct. Bioinform.* **2008**, *71*, 1360–1372.
186. Venkatramani, R.; Radhakrishnan, R. *Proteins Sci.* **2010**, *19*, 815–825.
187. Bell, G.; Dembo, M.; Bongrand, P. *Biophys. J.* **1984**, *45*, 1051.
188. Bell, G. I. *Science* **1978**, *200*, 618.
189. Alon, R. R.; Hammer, D. A.; Springer, T. A. *Nature* **1995**, *374*, 539.
190. Chang, K. C.; Tees, D. F.; Hammer, D. A. *Proc. Natl. Acad. Sci. USA* **2000**, *97*, 11262.
191. Hanley, W.; McCarty, O.; Jadhav, S.; Tseng, Y.; Wirtz, D.; Konstantopoulos, K. *J. Biol. Chem.* **2003**, *278*, 10556–10561.
192. Darribere, T.; Schwarzbauer, J. E. *Mech. Dev.* **2000**, *92*, 239–250.
193. Zamir, E.; Katz, B. Z.; Aota, S.; Yamada, K. M.; Geiger, B.; Kam, Z. *J. Cell Sci.* **1999**, *112*(Pt 11), 1655–1669.
194. Zamir, E.; Katz, M.; Posen, Y.; *et al. Nat. Cell Biol.* **2000**, *2*, 191–196.
195. Baneyx, G.; Baugh, L.; Vogel, V. *Proc. Natl. Acad. Sci. USA* **2002**, *99*, 5139–5143.
196. Vogel, V.; Thomas, W. E.; Craig, D. W.; Krammer, A.; Baneyx, G. *Trends Biotechnol.* **2001**, *19*, 416–423.
197. Hocking, D. C.; Sottile, J.; McKeown-Longo, P. J. *J. Biol. Chem.* **1994**, *269*, 19183–19187.
198. Ingham, K. C.; Brew, S. A.; Huff, S.; Litvinovich, S. V. *J. Biol. Chem.* **1997**, *272*, 1718–1724.
199. Langenbach, K. J.; Sottile, J. *J. Biol. Chem.* **1999**, *274*, 7032–7038.
200. Oberhauser, A. F.; Badilla-Fernandez, C.; Carrion-Vazquez, M.; Fernandez, J. M. *J. Mol. Biol.* **2002**, *319*, 433–447.
201. Oberhauser, A. F.; Marszalek, P. E.; Erickson, H. P.; Fernandez, J. M. *Nature* **1998**, *393*, 181–185.
202. Rief, M.; Gautel, M.; Gaub, H. E. *Adv. Exp. Med. Biol.* **2000**, *481*, 129–136; discussion 137–141.
203. Craig, D.; Krammer, A.; Schulten, K.; Vogel, V. *Proc. Natl. Acad. Sci. USA* **2001**, *98*, 5590–5595.
204. Krammer, A.; Lu, H.; Isralewitz, B.; Schulten, K.; Vogel, V. *Proc. Natl. Acad. Sci. USA* **1999**, *96*, 1351–1356.
205. Paci, E.; Karplus, M. *J. Mol. Biol.* **1999**, *288*, 441–459.
206. Krammer, A.; Craig, D.; Thomas, W. E.; Schulten, K.; Vogel, V. *Matrix Biol.* **2002**, *21*, 139–147.
207. Gao, M.; Craig, D.; Vogel, V.; Schulten, K. *J. Mol. Biol.* **2002**, *323*, 939–950.
208. Litvinovich, S. V.; Brew, S. A.; Aota, S.; Akiyama, S. K.; Haudenschild, C.; Ingham, K. C. *J. Mol. Biol.* **1998**, *280*, 245–258.
209. Hocking, D. C.; Smith, R. K.; McKeown-Longo, P. J. *J. Cell Biol.* **1996**, *133*, 431–444.

Relevant Websites

www.ambermd.org – AMBER forcefield.
www.charmm.org – CHARMM forcefield.
www.cbs.dtu.dk/services/CPHmodels – CPH Models.
www.cfs.dl.ac.uk – GAMESS-UK.
www.gaussian.com – Gaussian.
www.gromacs.org – GROMOS forcefield.
salilab.org/modeler – Modeller.
www.ks.uiuc.edu/Research/namd – NAMD.
ftp://ftp.ncbi.nlm.nih.gov/blast/db – Non-redundant Sequence Database.
www.ebi.ac.uk/thornton-srv/software/PROCHECK – PROCHECK.
www.rcsb.org/pdb – Protein Data Bank.
www.seas.upenn.edu/∼biophys – Radhakrishnan Lab Site.
www.expasy.ch/swissmod – Swiss-Model server.
www.teragrid.org – Teragrid Supercomputing.
www.ks.uiuc.edu/Research/vmd – VMD.
swift.cmbi.ru.nl/gv/whatcheck – WhatCHECK.

3.311. Molecular Simulation Methods to Investigate Protein Adsorption Behavior at the Atomic Level

R A Latour, Clemson University, Clemson, SC, USA

© 2011 Elsevier Ltd. All rights reserved.

3.311.1.	**Introduction**	172
3.311.2.	**Fundamental Aspects of Protein Adsorption Behavior**	173
3.311.3.	**Molecular Simulation Methods and Their Relevance to Protein Adsorption**	175
3.311.3.1.	Overview	175
3.311.3.2.	QM Methods	175
3.311.3.3.	Classical Mechanics Methods	176
3.311.3.3.1.	Overview	176
3.311.3.3.2.	Empirical force field equations	176
3.311.3.3.3.	Representation of solvation effects	178
3.311.3.3.4.	Set up, control, and calculation of properties in a CM simulation	179
3.311.3.3.5.	MC and MD methods	180
3.311.3.3.6.	Accelerated sampling methods	182
3.311.4.	**Application of All-Atom Modeling Methods to Simulate Protein–Surface Interactions**	184
3.311.4.1.	Early Efforts Beginning in the Late 1980s	184
3.311.4.1.1.	Simulations with limited conformational sampling and treatment of solvation effects due to computational limitations	184
3.311.4.1.2.	Early MD simulations of protein–surface interactions with increased conformational sampling and explicit solvation	185
3.311.4.1.3.	Early matched experimental and simulation efforts to support force field parameterization for protein–surface interactions	185
3.311.4.1.4.	Early MD simulations of protein–surface interactions with minimal constraints	186
3.311.4.2.	Advancements in Protein–Surface Simulations in the First Decade of the Twenty-First Century	186
3.311.4.2.1.	Protein interactions with surfaces presenting organic functional groups	186
3.311.4.2.2.	Protein interactions focused on surfaces presenting inorganic functional groups	188
3.311.5.	**Current Limitations and Directions for Further Development**	189
3.311.5.1.	Force Field Transferability for Protein–Surface Interactions	189
3.311.5.2.	Representation of Solvation Effects for Protein–Surface Interactions	189
3.311.5.3.	Phase-Space Sampling for Protein–Surface Interactions	190
3.311.5.4.	Coarse-Grained Molecular Modeling Methods	190
3.311.6.	**Concluding Remarks**	190
References		191

Abbreviations

CM	Classical mechanics
DDD	Distance dependent dielectric function
GB	Generalized-Born
KE	Kinetic energy
L-J	Lennard-Jones
MC	Monte Carlo
MD	Molecular dynamics
MM	Molecular mechanics
P–B	Poisson–Boltzmann
PBC	Period boundary condition
QM	Quantum mechanics

Symbols

$a(t)$	Acceleration of an atom at time t
b	Bond length parameter
b_o	Minimum-energy bond length
B_{ij}	Biased energy function acting between states x_j and x_i
B_u	Biasing energy umbrella function
E_i	Potential energy of molecular system when in conformational state x_i
$E(x_i)$	Potential energy of molecular system when in conformational state x_i
F_{ij}	Force vector acting on atom i from atom j
k_B	Boltzmann constant
k_b	Stiffness coefficient for bond stretching
k_θ	Stiffness coefficient for bond bending
k_ϕ	Stiffness coefficient for bond torsional rotation
k_u	Stiffness constant for umbrella function
k_χ	Stiffness coefficient for improper bond torsion

m_i	Mass of atom i	v_i	Velocity i
M	Number of total conformational states sampled during a simulation	$v(t)$	Velocity of an atom at time t
		V	Volume
N	Number of atoms	x_i	Molecular system in ith conformational state
N_c	Number of constraints limiting the degrees of freedom	$<X>$	Average value of parameter X
		ΔG	Change in free energy
P	Pressure	ΔH	Change in enthalpy
$P(x_i)$	Probability of system being in conformational state x_i	ΔS	Change in entropy
		β	Parameter representing $(k_BT)^{-1}$
P_{ij}	Relative probability to be in state x_j compared to state x_i	χ	Improper bond torsional angle
		χ_o	Minimum-energy improper bond torsional angle
$\overline{P}_{ij}$	Biased Relative probability to be in state x_j compared to state x_i	δ	Offset torsional rotation angle
		ε_o	Permittivity of free space
q_i	Partial charge of atom i.	ε_r	Relative dielectric constant
Q	Partition function	ε_{ij}	Minimum energy for Lennard-Jones nonbonded interaction
r_{ij}	Distance between centers of atoms i and j, or position vector from atom j to i		
		ϕ	Torsional rotation angle
$r(t)$	Position of an atom at time t	λ	Designated parameter for umbrella function
Rnd (0_1)	Random number between 0 and 1	λ_u	Value of designated parameter that umbrella function is applied around
t	time	κ	Inverse Debye length
T	Temperature (absolute scale)	θ	Bond angle
U	Average potential energy of a molecular system	θ_o	Minimum-energy bond angle
		σ_{ij}	Atomic collision diameter between atoms i and j

3.311.1. Introduction

In order to understand the importance of protein adsorption to biomaterial surfaces and its relationship to the biocompatibility of medical devices, it is first necessary to recognize that cells in the body generally do not have receptors that are able to specifically interact with a synthetic material. For this reason, cells have no means of responding to chemically stable nonbiologically-based materials that are placed inside the body. Of course, cells in the body do respond to these types of materials, which raises the question: How does this occur? The answer to this question is simply that cells do not directly respond to synthetic biomaterials placed inside the body; rather they respond to the layer of adsorbed proteins that rapidly adsorb to and coat a biomaterial surface within seconds following its contact with biological fluids, such as blood and interstitial fluid.[1] Based on this understanding, it must be understood that cellular response is largely directed by the bioactive sites that are present in this layer of adsorbed proteins, with the presence of these bioactive sites being dependent on the types of proteins adsorbed and their orientation, conformation, packing arrangement, and dynamic behavior on a biomaterial's surface.[2–4] The realization that protein adsorption is fundamental to the biocompatibility of biomaterials has caused this to be one of the major topics of investigation in the biomaterials field over the past several decades. While much has been learned from these studies, we still have a very incomplete and largely qualitative understanding of protein adsorption behavior, with little knowledge at this time of how to design biomaterial surfaces to control protein adsorption and subsequent cellular responses to biomaterials. Because of this situation, biomaterials design can still largely be only approached through trial-and-error methods.

One of the primary reasons for this lack of quantitative understanding is the lack of methods that enable protein adsorption processes to be investigated at the molecular level. This underscores the need for the development of new technologies that will provide this capability. Molecular simulation methods provide the potential to meet this need. These methods have come to represent essential technologies in areas such as biophysics for understanding protein folding behavior,[5–7] and in pharmaceutical science, for drug design.[8–10] Similar potential exists for molecular simulations to complement experimental studies in the biomaterials field to help us finally understand and control protein adsorption behavior, and to then apply this understanding to guide biomaterial surface design. However, as will be highlighted in this chapter, these methods cannot simply be borrowed from other disciplines, but rather they must be specifically developed and adapted to meet the needs that are unique to the biomaterials field.

Before we can properly understand what factors need to be addressed in order to develop molecular simulation methods for applications of biomaterials, it is first necessary to have a general understanding of the fundamental principles that govern the kinetics and the thermodynamics of protein–surface interactions. An overview of these principles is provided in Section 3.311.2. Following this, the basic principles of molecular simulation are addressed in Section 3.311.3, with a focus on all-atom classical mechanics (CM) simulation methods and their application to model protein–surface interactions. Section 3.311.4 then highlights some of the key studies that have been conducted over the past two decades toward the development and application of CM

methods to simulate protein adsorption behavior. This is followed by Section 3.311.5, which addresses some of the current limitations and future trends for further development, with final concluding remarks provided in Section 3.311.6.

3.311.2. Fundamental Aspects of Protein Adsorption Behavior

To begin to understand protein adsorption behavior, it is first necessary to understand the basic structural makeup of proteins and how a protein's structure is generally influenced when it interacts with a surface. Proteins are essentially very complex organic copolymers of amino acids.[11,12] There are 20 different types of naturally occurring amino acids, each of which have the basic chemical formula of (NH_2–CHR–COOH), with R representing the amino acid's side chain. The chemical makeup of the side chain of an amino acid determines its nature, or functionality, which is generally characterized as being nonpolar, polar, or charged. The enormous versatility provided by this type of molecular system (i.e., a copolymer with 20 different mer units) can be appreciated by the realization that even a simple oligopeptide chain that is only 15 amino acids long will thus have $20^{15} \approx 10^{20}$ different possible sequence combinations, each with a slightly different chemical and physical characteristic. To appreciate the size of this number, this is 500 times larger than the age of the known universe as expressed in seconds, which is about 4×10^{17} s (i.e., about 14 billion years).[13] Many proteins have polypeptide chains that are thousands of amino acids long.

Proteins are composed of four levels of organization, which are termed primary, secondary, tertiary, and quaternary structure.[11,12] The primary structure represents the specific sequence of amino acids along a polypeptide chain, with each amino acid referred to as an amino acid residue. The amino acids are covalently linked together by condensation reactions to form covalent bonds between the main-chain carboxyl and amine groups of adjacent amino acids along the polypeptide chain, with the first and last amino acids of the chain referred to as the N-terminus and the C-terminus, respectively, and the direction of the chain designated as running from the N- to the C-terminus. The secondary structure of a protein represents the way that the polypeptide chain of the protein is organized into helical, planar, and random loop elements, with the helical and planar secondary structures stabilized by hydrogen bonds between the amine and carboxyl functional groups of the polypeptide main chain. There are three basic types of helical structures (typically right-handed helices), which are designated as α-helices, 3_{10}-helices, and π-helices, with 3.7, 3, and 5 amino acid residues per full rotation of the polypeptide chain, respectively, each of which organizes in such a way that their side chains radiate outward from the helix. The planar secondary structures are formed by relatively straight β-strands. These elements are organized into two basic chain configurations, which are designated as parallel and antiparallel β-sheets, depending on whether adjacent strands are running in the same or opposite direction, respectively, with their amino acid side chains extending above and below the sheet in each case. Helical and β-strand elements are covalently connected by random loop segments, which, as the name implies, do not have any specifically defined structure. The tertiary structure of a protein is determined by the manner in which the secondary structures organize together, with van der Waals interactions between the side chains extending outward from each of the secondary structural elements stabilizing the tertiary structure. In addition, covalent cross-links can also exist between adjacent secondary structures by the formation of disulfide bonds between adjacent cysteine residues, which have (R: CH_2–SH) as their side-chain structures. Finally, if a protein is composed of more than one polypeptide chain, with each chain having its own N- and C-termini, it is then referred to as having a quaternary structure, with the interactions between the chains being mediated by the same types of bonds that hold tertiary structures together (i.e., van der Waals interactions and disulfide covalent bonds between the amino acid side chains making up secondary structural elements). The end result of the final folded state of a protein is the formation of bioactive sites, which are created from the functional groups presented by the specific amino acids forming the particular region of the protein combined with their spatial arrangement. These sites provide a protein with its biological activity to perform its designated function, whether that be as an enzyme, a factor in a biological process, an extracellular matrix protein, or a membrane-bound cell receptor.

Each protein has a defined native-state folded structure that is formed by the unique combination of its primary through tertiary or quaternary levels of organization. It is generally believed that this structure is determined by thermodynamics, with the native-state folded structure representing the global minimum free energy state of the protein.[12] This folding behavior has been illustrated by what is referred to as the protein folding funnel,[14,15] which conceptually represents all possible conformational states that a given polypeptide chain can exist in along the x-axis and the relative free energy state of the protein in aqueous solution along the γ-axis, as schematically depicted in Figure 1. This folding process is largely driven by the thermodynamic tendency of a protein to fold in a manner so as to reduce the solvent-accessible surface area of its nonpolar amino acid residues. Accordingly, proteins tend to fold in such a way that they bury their nonpolar residues within their structure so as to minimize their exposure to the surrounding aqueous solution while maintaining their hydrophilic amino acid residues (i.e., polar and charged amino acids) on the outer surface of the protein, thus providing aqueous solubility.

Based on this understanding of the principles that govern a protein's native-state structure and thermodynamics, we can begin to understand how interactions between a protein with a synthetic surface will take place. We start with the general thermodynamic principle that any spontaneously occurring process must result in a reduction in free energy of the system, with the change in free energy at constant temperature (T) expressed as $\Delta G = \Delta H - T\Delta S$, where ΔG, ΔH, and ΔS represent the change in free energy, enthalpy, and entropy, respectively. Accordingly, when exposed to a hydrophobic surface, there is a thermodynamic driving force to reduce the overall solvent-accessible surface area of the nonpolar groups of the system, which is generally driven by the fact that water molecules next to a nonpolar surface at room or body temperature are generally in a higher free energy state than water molecules in the

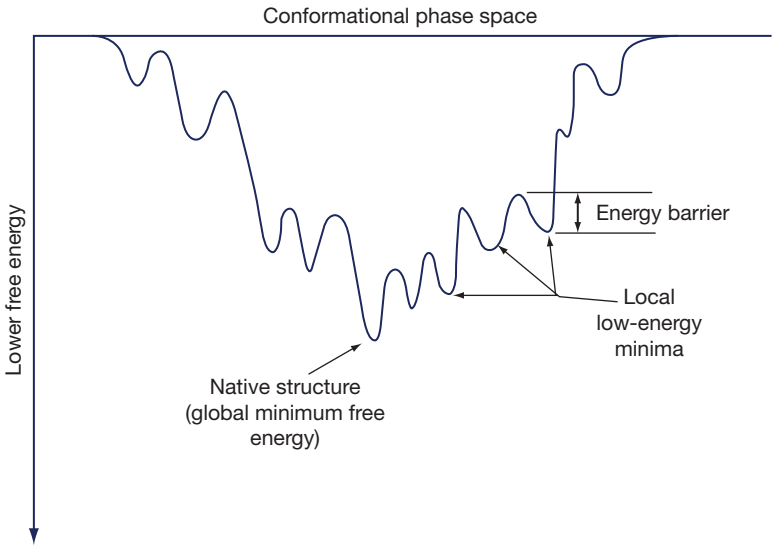

Figure 1 Illustration of the protein folding funnel for the folding of a protein in aqueous solution. Horizontal axis represents the set of all possible conformational states of the protein and the vertical axis represents the free energy state for each conformation. A protein will fold in a manner to attain its global minimum free energy conformation, which represents the protein's native-state structure.

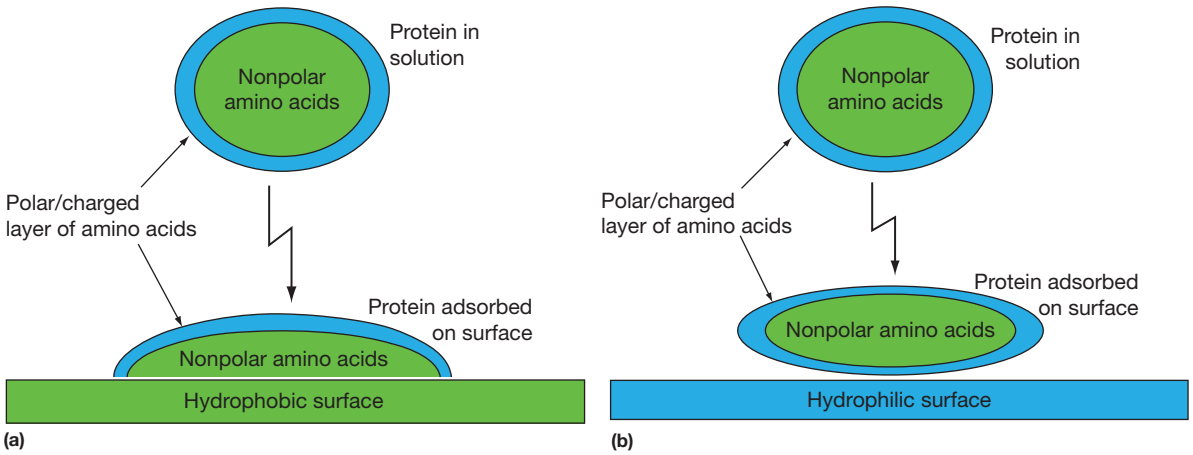

Figure 2 (a) Protein adsorption on a hydrophobic surface. An adsorbed protein tends to unfold/refold to cover the nonpolar functional groups of the surface with its nonpolar amino acid residues while maintaining a layer of polar/charged amino acid residues over its own solvent-exposed surface. (b) Protein adsorption on a hydrophilic surface. A protein tends to adsorb in a manner such that it maintains its nonpolar amino acids buried within its core to avoid their exposure to either the hydrophilic groups of the adsorbent surface or the solution.

bulk aqueous solution. This generally causes a protein to unfold and spread out over a hydrophobic surface to displace the water and cover the hydrophobic groups of the surface with its own nonpolar amino acids (i.e., hydrophobic interactions) while maintaining a layer of hydrophilic amino acids over its own solvent-accessible surface.[4,16] In contrast to this, exposure of a protein to a hydrophilic surface (i.e., a surface with polar and/or charged groups) will tend to cause a protein to adsorb and spread out over a surface in a manner where it maintains its nonpolar amino acid residues buried within itself and shielded from both the solvent and the surface, with the protein's own polar and charged residues interacting with the surface functional groups via hydrogen bonding and salt-bridge associations, possibly with a bridging, hydrogen-bonded layer of water.[4,16] The bonds formed between the functional groups of the protein and the surface can thus be considered to replace similar types of bonds that were previously formed with water and/or salt ions of the solution, resulting in relatively little change in the enthalpic state of the system. In this case, the reduction in free energy that occurs to induce protein adsorption can be understood to be largely driven by the release of bound water and ions from the surface and protein to bulk solution, which represents an increase in the entropy of the system that more than compensates for the reduction of entropy that occurs from the binding of the protein. These concepts are illustrated in **Figure 2**.

The processes involved in protein adsorption to a surface can also be illustrated by representing how interactions with a surface will perturb the shape of the protein's folding funnel.[17] As depicted in **Figure 3**, when a protein is exposed to a

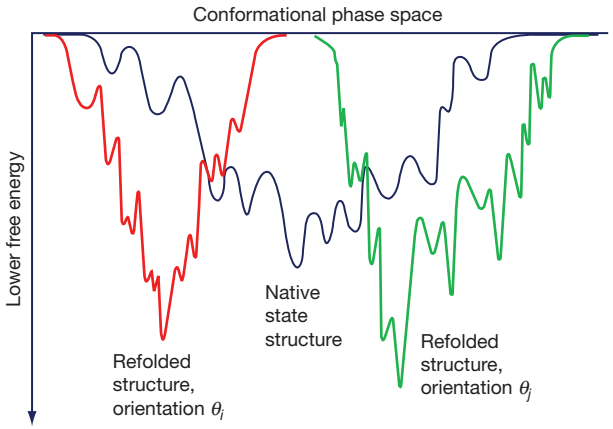

Figure 3 Illustration of the effect of the presence of a surface on the shape of the protein folding funnel. Each orientation of a protein on a surface will result in different forces being applied to the protein, which will perturb the aqueous-solution folding funnel in a different manner. One orientation will provide the overall global minimum free energy for the adsorbed protein. Large free energy barriers between local low-energy conformations and the global minimum energy conformation may cause adsorbed proteins to be trapped in many different metastable states on a surface.

synthetic surface in a given orientation, the functional groups of the adsorbing surface will exert forces on the adjacent surface of the protein that are not present when the protein is in bulk solution. These forces will tend to perturb the thermodynamics of the system, causing the protein's native conformation to no longer represent the global minimum free energy state of the system. This may result in a shifting of the protein's folding funnel in a manner to cause the protein to restructure or refold into a new low free energy conformation. Because it can be expected that each orientation of a protein will result in a different set of forces acting on the protein, each initial orientation of a protein on a surface can be expected to result in a different shape in the protein's folding funnel, with one specific orientation out of this total set of perturbed systems resulting in the global minimum free energy of the system. However, because of the ruggedness of the protein folding funnel (i.e., relatively large free energy barriers separating the various local free energy minima), a protein may be trapped in a metastable local low free energy state. This type of behavior can be expected to result in proteins existing over a wide range of orientations and metastable configurational states following adsorption from a solution onto a surface, which may then continue to change over a long period of time.

Based on the earlier description of some of the fundamentals of protein adsorption behavior, it is no wonder that it has been so difficult to obtain a quantitative atomistic level of understanding of protein adsorption behavior through the use of experimental methods alone. Complementary methods are needed that enable the interactions between the functional groups presented by a protein, a surface, and an aqueous solution to be depicted on an atomistic level. This represents a situation that is extremely well suited for the application of molecular simulation methods. However, as emphasized in the following sections, these methods cannot simply be borrowed from methods that were previously developed for other applications, but rather they must be specifically developed to meet the unique set of conditions that are needed for the accurate representation of protein–surface interactions.

3.311.3. Molecular Simulation Methods and Their Relevance to Protein Adsorption

3.311.3.1. Overview

Molecular simulation methods can basically be separated into quantum mechanics (QM) methods, which treat electrons as the fundamental interactive particles of the system, and CM methods, which treat individual atoms or groups of atoms as the fundamental interactive particles of the system. Because of the size of the molecular systems involved in the simulation of protein adsorption behavior, CM methods are most widely used, with QM methods providing a very important supporting role. In this section, a brief summary of QM methods will be first provided followed by a relatively in-depth coverage of CM methods with a focus on some of the key areas that are particularly important for the simulation of protein–surface interactions; namely, the empirical force field and its parameterization, the handling of solvation effects, and the sampling of the phase space of the molecular system.

3.311.3.2. QM Methods

QM methods can be divided up into *ab initio*, semiempirical, and density functional theory (DFT) methods.[18,19] *Ab initio* methods, as the name implies, require no empirical information about the molecular system being considered but rather apply various approximations to solve Schrödinger's equation through the use of wave functions to describe atomic orbitals for the calculation of molecular properties. Semiempirical QM (SEQM) methods use similar calculational methods, but only for valence electrons, thus substantially reducing the computational cost of the calculations. DFT methods, on the other hand, determine properties from calculations based on the electron density of the molecular system. Because QM calculations are extremely rigorous, the size of the molecular systems to which they can be applied is fairly limited. For example, high-level QM methods (e.g., Møller–Plesset (MP) methods such as MP2) are even able to account for electron-correlation effects between nonbonded atoms, thus enabling them to represent London dispersion interactions. These methods are so computationally intensive that they may only be able to be applied to systems composed of a dozen or so atoms at a time. Other less rigorous QM methods such as DFT methods can be used for systems involving hundreds of atoms. However, DFT methods have the drawback of generally not being able to account for electron-correlation effects, which may be substantially important depending on the molecular system being considered.

The current limitations in the size of the molecular system that can be handled with QM methods make them largely unsuitable for direct application to simulate protein–surface interactions. On the other hand, because these types of methods can represent both intra and intermolecular interactions very accurately without requiring any

empirical information, they are extremely valuable and widely used to establish parameter values for empirical force fields for CM simulations.[20]

3.311.3.3. Classical Mechanics Methods

3.311.3.3.1. Overview

In contrast to QM methods, CM methods are much less computationally expensive and can easily be used to conduct simulations containing tens of thousands of atoms, or even much larger systems if united-atom methods are used, thus making them well suited for the simulation of protein–surface interactions. This reduction in computational complexity, however, comes at a cost of the simulations being largely dependent on the accuracy of the empirical equation form and parameter sets that are used to determine how the atoms or groups of atoms in the modeled system interact with one another during the simulation.

CM simulation methods are subdivided into three basic types: molecular mechanics (MM), Monte Carlo (MC), and molecular dynamics (MD) methods.[18,21,22] Each of these methods use an analytical function along with an empirically derived set of constants that dictate how the atoms or particles in the system interact with one another as a function of their state of bonding and their coordinate positions; these are referred to as the force field equation and force field parameter set. MM methods are used to calculate the potential energy of a molecular structure based on the molecular configuration of the system and are most commonly used to calculate the geometry of a molecular system that will minimize its overall potential energy, which is referred to as energy minimization or geometry optimization. It should be recognized, however, that this represents the condition of the molecular structure under absolute zero temperature conditions. In addition to being useful for predicting minimum energy geometries for a given molecule or molecular system, MM methods are commonly used prior to beginning an MC or MD simulation in order to relax improperly stretched, bent, or twisted covalent bonds in a system and to avoid energetically unfavorable overlaps between atoms. This step is especially useful when representing a condensed-phase system, with the molecules of the solvent being explicitly represented.

MC and MD methods are similar to MM methods in that they use an empirical force field for the calculation of the potential energy of the system as a function of the coordinate positions and the bonded state of the atoms. These methods, however, implement additional statistical mechanics-based algorithms to incorporate temperature in the simulation, which provides the capability of evaluating the thermodynamic behavior of the system at a designated temperature (e.g., adsorption free energy at 298 K) when using MC, and evaluating both the thermodynamic and the kinetic behavior of a system at a given temperature when using MD.

3.311.3.3.2. Empirical force field equations

The empirical force field is the equation that is used in MM, MC, and MD simulations to calculate the potential energy (E) of the system as a summation of the individual energetic contributions from each atom in the system.[18] This is called a 'force field' equation because when differentiated with respect to the coordinate positions of the atoms (x_i), it yields an expression that provides the force acting on each atom (i.e., $F_i = -\mathrm{d}E/\mathrm{d}x_i$). These forces are then used in an MD simulation to determine how the atoms will move over the next time-step of the simulation (further addressed below in Section 3.311.3.3.5). Two basic types of force field equations have been primarily developed over the past several decades, which are referred to as Class I and Class II force fields.

Class I force fields, which are relatively simple in form, have mainly been developed for use with biological molecules. The general form of a Class I force field equation that is most widely used for biomolecular simulations (e.g., proteins, carbohydrates, phospholipids, RNA, and DNA) is shown in eqn [1]:

$$\begin{aligned} E = &\sum_{\text{bonds}} k_b(b-b_0)^2 + \sum_{\text{angles}} k_\theta(\theta-\theta_0)^2 \\ &+ \sum_{\text{dihedrals}} k_\phi[1+\cos(n\phi-\delta)] \sum_{\text{improp}} k_\chi(\chi-\chi_0)^2 \\ &+ \sum_{\text{L–J}} 4\varepsilon_{ij}\left[\left(\frac{\sigma_{ij}}{r_{ij}}\right)^{12} - \left(\frac{\sigma_{ij}}{r_{ij}}\right)^{6}\right] + \sum_{\text{Coulomb}} \frac{q_i q_j}{4\pi\varepsilon_0\varepsilon_r r_{ij}} \end{aligned} \quad [1]$$

The first three terms on the right-hand side of eqn [1] represent the potential energy of the covalently bonded atoms in the system due to covalent bond stretching, bending, and rotation. For these terms, the parameters b, θ, ϕ, and χ represent the bond length, bond angle, dihedral angle (torsion), and out-of-plane bending (also called improper torsion), respectively, of the bonded state, relative to a reference position (designated by force field parameters b_0, θ_0, ϕ_0, δ, and χ_0). The k parameters in eqn [1] represent additional empirical force field parameters that reflect the stiffness of each of the bond types in the system. The last two terms of the force field equation represent the contributions of the nonbonded interactions to the potential energy of the system. The first of these two terms represents Lennard-Jones (L–J) 12–6 interactions, which are considered as being pairwise interactions for all nonbonded atoms (i.e., atoms separated by more than two covalent bonds along a covalently bonded chain or between two atoms in different molecules in the system). In this term, ε_{ij} and σ_{ij} represent the L-J well depth and the collision diameter between the designated pairs of atoms, respectively, for atoms i and j. The second nonbonded term represents the energy contributions from the electrostatic interactions between pairs of atoms, which are represented by Coulomb's law, where q_i and q_j represent the partial charges centered on atoms i and j, ε_0 is the permittivity of free space, and ε_r is the relative dielectric constant. ε_r is typically set to 1.0 or about 79 depending on whether an explicit or implicit solvation method is being used, respectively (this aspect is further addressed in Section 3.311.3.3.3). Some of the most popular Class I force fields in use today are AMBER,[23,24] CHARMM,[25,26] GROMOS,[27] and OPLS-AA.[28]

Class II force fields capture the same general types of energetic contributions as do Class I force fields, but include expanded sets of terms for the bonded parameters (i.e., bond stretching, bond bending, dihedral rotation) as well as cross-terms between bonded terms (e.g., a bond stretch–bend term).[29] These terms enable the behavior of molecules to be represented more accurately than Class I force fields, especially for molecular behavior under relatively highly strained

conditions; however, this comes at a cost of additional complexity and computational expense. An example of the form of a Class II force field is shown in eqn [2]:

$$\begin{aligned}E = &\sum_{\text{bonds}}\left[k_{b2}(b-b_0)^2 + k_{b3}(b-b_0)^3 + k_{b4}(b-b_0)^4\right]\\ &+\sum_{\text{angles}}\left[k_{\theta2}(\theta-\theta_0)^2 + k_{\theta3}(\theta-\theta_0)^3 + k_{\theta4}(\theta-\theta_0)^4\right]\\ &+\sum_{\text{dihedrals}} k_{\phi1}[1-\cos\phi] + k_{\phi2}[1-\cos 2\phi] + k_{\phi3}[1-\cos 3\phi]\\ &+\sum_{\chi} k_{\chi}\chi^2\\ &+\sum_{b,b'} k_{b,b'}(b-b_0)(b'-b_0') + \sum_{b,\theta} k_{b,\theta}(b-b_0)(\theta-\theta_0)\\ &+\sum_{b,\phi}(b-b_0)[k_{b,\phi1}\cos\phi + k_{b,\phi2}\cos 2\phi + k_{b,\phi3}\cos 3\phi]\\ &+\sum_{\theta,\phi}(\theta-\theta_0)[k_{\theta,\phi1}\cos\phi + k_{\theta,\phi2}\cos 2\phi + k_{\theta,\phi3}\cos 3\phi]\\ &+\sum_{\theta,\theta'} k_{\theta,\theta'}(\theta-\theta_0)(\theta'-\theta_0')\\ &+\sum_{\theta,\theta',\phi} k_{\theta,\theta',\phi}(\theta-\theta_0)(\theta'-\theta_0')\cos\phi\\ &+\sum_{\text{L-J}}\varepsilon_{ij}\left[2\left(\frac{\sigma_{ij}}{r_{ij}}\right)^9 - 3\left(\frac{\sigma_{ij}}{r_{ij}}\right)^6\right] + \sum_{\text{Coulomb}}\frac{q_iq_j}{4\pi\varepsilon_0\varepsilon_r r_{ij}}\end{aligned} \quad [2]$$

where the same variable descriptions apply as for the Class I force field shown in eqn [1], with the addition of additional constants to represent the contributions from higher order terms for bond stretching, bending, dihedral rotation, and out-of-plane bending, and cross-terms for bond stretch–stretch (b, b' combined terms), stretch–bend (b, θ combined terms), stretch–torsion (b, ϕ combined terms), bend–torsion (θ, ϕ combined terms), bend–bend (θ, θ' combined terms), and bend–bend–torsion (θ, θ, ϕ combined terms). In addition, Class II force fields typically use a 9-6 L-J potential form while using the same Coulomb's law expression for electrostatic interactions. While Class II force fields can be used to represent biological molecules, the additional complexity and subsequent computational cost is generally not considered to be necessary for these types of molecules near room temperature. Class II force fields are commonly used in the materials science field to represent the behavior of synthetic polymer, metal, and ceramic solid-phase materials and whenever the additional computational cost is needed to achieve a more accurate prediction of potential energies, structures, and vibrational frequencies of a molecule or molecular system. Examples of Class II force fields include CFF,[29] PCFF (polymer CFF),[30] the MM# series,[31] and COMPASS.[32]

A force field for a given molecular simulation is thus described by both the form of the force field equation (e.g., eqn [1] or [2]) and the values of the empirical force field parameters that are assigned for each designated set of atom and bond type in the system. For example, a C–C covalent bond in a Class I force field will have one set of defined k_b and b_0 values, while a C–O bond will have another. The L-J parameters (i.e., ε_{ij} and σ_{ij}) are handled slightly differently, with each individual atom type 'i' given its own ε_i and σ_i parameter value. These values are then combined for a given 'ij' atom–atom pair interaction using Lorentz–Berthelot combination rules,[18] in which ε_{ij} and σ_{ij} are derived for any given pair of atoms using either the geometric or arithmetic mean of the two individual atom's values (depending on the rules of the type of force field used). The values of these empirical parameters for both the bonded and nonbonded terms are generally determined from either QM calculations of small molecules containing similar functional groups with empirical parameters then adjusted to optimally match the QM-predicted behavior, or by adjusting the empirical parameters to match experimentally determined properties, such as density, heat of vaporization, or vibrational frequencies. If parameterized properly, an empirical force field can provide a very accurate representation for a given molecular system. However, if not, the predicted behavior of the system can be very far from reality.

One of the difficulties involved in force field parameterization is that an appropriate set of force field parameters for one set of atoms in one type of molecular environment may not be appropriate for the same set of atoms in a different type of molecular environment; this situation is referred to as the issue of 'force field transferability.' Force field transferability is particularly a problem for the fixed partial charges assigned to each atom type in a fixed-charge empirical force field (i.e., q_i), because, in reality, the effective partial charge state of an atom in a molecule will substantially shift depending on its polarizability and the distribution of partial charges in the atoms in its immediate surroundings. As an excellent example of this problem, van Gunsteren and coworkers[33] showed that two different sets of partial charge parameters were needed to accurately represent the behavior of the same set of molecules depending on whether they were represented in their pure condensed liquid state compared to when they were represented as individual molecules in aqueous solution. It is therefore important to use a validated set of parameters for a given molecular environment.

The question of force field transferability raises a particularly important issue for the use of empirical force field-based methods for the simulation of protein–surface interactions. Generally, a force field is validated for a given molecular system by using the force field to conduct simulations for the calculation of experimentally measurable properties of the system (e.g., density, structure, vibrational frequencies, heat of evaporation, and free energy of solvation). By comparing calculated values to experimentally measured data, the validity of the force field to accurately represent the behavior of the given molecular system can then be assessed. If substantial errors are found in the calculated values, the experimental data can subsequently serve as a benchmark set to which the force field can be tuned and validated. The difficulty that this approach presents for the simulation of protein–surface interactions is that presently there are relatively little experimental data available that can be used to determine whether the results from a molecular simulation of protein adsorption behavior are correct or not. Without such data, it is very difficult to determine whether or not a simulation realistically portrays the molecular behavior of the system. As one approach to address this deficiency, the Latour group has been conducting carefully matched experimental and simulation studies to measure and calculate the free energy of adsorption for a broad series of peptide–surface systems using a custom-designed host–guest peptide model and a series of alkanethiol self-assembled monolayer (SAM) surfaces with surface functionality set to represent common functional groups present in

polymeric biomaterials.[34–38] This approach provides a means of assessing the validity of a given force field for the simulation of protein–surface interactions. Similar efforts are also needed to develop experimental methods that can be used to quantitatively measure the orientation, conformation, and bioactive state of adsorbed proteins,[39,40] from which the accuracy of simulations of protein adsorption behavior, using a given force field, can be further assessed.

Another problem for the implementation of current sets of force field parameterization for the simulation of protein–surface interactions is the fact that the protein modeling community has primarily developed force field parameterization for the simulation of protein behavior in solution using a Class I force field equation format, while the materials science community has primarily developed force field parameterization for polymers, metals, and ceramic materials using the Class II force field equation format. Current commercially available molecular simulation programs, however, require that only one type of force field (i.e., either Class I or Class II) be used in a simulation. This then creates a dilemma for the simulation of protein–surface interactions where it is desired to represent both a protein solution phase and a solid materials phase in the same simulation. In this case, it is necessary to reparameterize one phase or the other to be able to run the simulation with a single type of force field, which would be an extremely time-consuming endeavor. To make this situation even more complicated, because the interface between two phases of such a molecular system represents a substantially different molecular environment than either phase by itself, it can be expected that separate parameterization will need to be developed to accurately represent molecular interactions at this interface. One possible approach to solving this problem, which the Latour group has been exploring, is the development of a hybrid force field molecular simulation program that is specifically designed for the simulation of multiphase systems to enable either a Class I or a Class II force field to be used to separately control the behavior of the atoms in each phase of the system, with a third set of independent parameters used to control the interactions at the interface between the two phases of the system. By this approach, a program will be able to make combined use of the decades of efforts that have already been spent on the development and validation of force field parameters from both the materials science and the biophysical science communities, while enabling the parameterization of interfacial interactions to be separately optimized to accurately represent protein–surface interactions at the solid–liquid interface.

3.311.3.3.3. Representation of solvation effects

Because most applications where protein–surface interactions are of interest in the biomaterials field take place in aqueous solution, the accurate representation of solvation effects is extremely important in a simulation of protein adsorption behavior. The most direct way of representing solvation effects in an MC or MD simulation of protein–surface interactions is to include water molecules and salt ions as explicitly represented atoms in the simulation. Many different water models, and their associated force field parameters, have been developed that generally provide excellent representations of solvation effects at around 298 K. Some of the most popular water models are SPC,[41] SPC/E,[42] TIP3P,[43] TIP4P,[44,45] TIP4P/Ew,[44] and TIP5P.[46] Decisions regarding which water model should be used for a given simulation of protein–surface interactions should primarily be made based on selecting the water model that is recommended by the force field developers to go with the force field that is being used to represent the protein. For example, the CHARMM force field was parameterized with CHARMMs version of TIP3P water.[25] The explicit representation of solvation, however, comes at a very high computational cost because it greatly increases the number of atoms that must be represented in a molecular simulation, which directly translates into the need for much greater computing capacity and/or much longer wall-clock time to perform a given simulation.

To circumvent this problem, several methods have been developed to represent solvation effects using mean-field continuum approximations, which are referred to as 'implicit solvation' methods. The simplest of these methods involves merely changing the relative dielectric constant (ε_r) in the Coulomb's term of the force field (see eqn [1] or [2]) from a value of 1.0, which is used in explicit solvation simulations, to a value of about 79, which is the relative dielectric constant of bulk water at about 298 K.[18] A related technique involves setting $\varepsilon_r = r_{ij}$, or a function of r_{ij} (i.e., the distance between atoms i and j), which provides a situation where electrostatic interactions are very strong when atoms are close to one another, but rapidly dampen out as the separation distance increases to represent the influence of intervening water molecules that effectively shield electrostatic interactions between atoms. This procedure is known as the 'distant-dependent dielectric' (DDD) method.[18] This method was developed as a very crude approach to represent the dampening of electrostatic effects for protein folding simulations. While arguably better than not representing solvation effects at all, the use of this method alone is strongly recommended against because of the substantial artifacts in simulated behavior that it tends to cause.[18,47,48] The use of dielectric constant-based methods alone for the representation of solvation effects is even more problematic for the treatment of solute adsorption behavior in aqueous solution (e.g., protein adsorption), because these types of interactions are completely dominated by nonbonded interactions without the mediating effects of covalent bonds. In this case, this procedure will completely neglect the competitive interaction of water for the atoms of the solute and the material surface through both electrostatic and L-J interactions, thus tending to substantially overestimate the strength of adsorption, particularly for polar and charged functional groups. For example, Sun and Latour[49] have shown that the use of a DDD method alone will cause polar hydrophilic groups of the amino acid residues of a protein to be attracted to polar groups on a material surface nearly as strongly as they would in vacuum. Experimental studies have shown the exact opposite behavior, with these types of interactions being extremely weak due to the competitive adsorption behavior of water for polar functional groups of both the protein and a surface.[38]

A much more sophisticated and accurate form of implicitly representing solvation effects due to electrostatic interactions is provided through the use of the Poisson–Boltzmann (P–B) equation to calculate the free energy of molecular salvation.[50,51] However, this method is generally considered to be

too computationally rigorous (i.e., slow) to be used in MC and MD simulations, and thus, its use is primarily limited to MM simulations for the calculation of the electrostatic solvation free energy contribution of molecules in a given conformation. A much less computationally expensive approximation of the P–B equation, known as the generalized Born (GB) equation, has been developed and widely applied as an implicit solvation method for MD simulations of peptide and protein folding with a reasonable degree of accuracy.[52,53] P–B and GB methods, however, only address the electrostatic component of solvation effects but do not address molecular interactions that are driven by hydrophobic effects. To address this omission, an additional term is required in the force field equation. This term is generally expressed in the form of a surface tension per unit area parameter that is then multiplied by the surface area of the molecule in solution, thus providing a thermodynamic driving force for minimizing the exposure of nonpolar surface areas of a molecule to a surrounding aqueous solution.

As with all situations with molecular modeling, any implicit solvation method that is used for a given type of simulation should be checked and validated before it can be considered to be reliable for use. This is particularly important for protein–surface interactions where solvation effects play such a dominant role in the behavior of the system, and where relatively small imbalances in the representation of solvation effects can be expected to have large effects on predicted adsorption behavior.

3.311.3.3.4. Set up, control, and calculation of properties in a CM simulation

To prepare to conduct an MC or MD simulation of a given molecular system, the first step is to establish the coordinate positions and the bonded state of the atoms in the system.[18] For simulations involving proteins, coordinate positions are typically obtained by downloading structural information of the desired protein from the protein data bank (PDB). Coordinate positions for solid-phase materials are typically obtained from experimentally determined structures using nuclear magnetic resonance (NMR) spectroscopy or X-ray crystallography. The system to be modeled is then represented in a designated spatial volume defined by boundaries. If it is desired to represent conditions where the molecules of interest are contained in aqueous solution with the use of explicitly represented solvation, the free space in the bounded system is filled with solvent molecules (e.g., water molecules and salt ions) at the desired density (i.e., 1.0 g cm^{-3}). This is then generally followed by an energy minimization step using MM methods, which serve to adjust the positions of the atoms in the system to eliminate atom–atom overlap. In order to represent a continuous system, boundaries are typically represented using what are called periodic boundary conditions (PBCs), in which case, the molecular system contained within the boundaries is treated as a unit cell, which is replicated as periodic images in all directions surrounding the central, or primary, unit cell. With this type of system representation, when an atom or molecule moves across the boundary from the primary cell to an adjacent image of the periodic system, another atom or molecule of the same type and structure enters the system through the opposite boundary, thus providing a mechanism to maintain a constant number of atoms in the system throughout the simulation (see Figure 4). Because this then effectively represents an infinitely sized system, the use of PBCs creates a problem for the calculation of the nonbonded interaction terms of the force field, since atoms in the primary cell of the system will be influenced by the atoms in the infinite array of surrounding images of the unit cell of the system. To address this problem, nonbonded L-J interactions are only considered between atoms that are separated by less than a designated cutoff distance (typically around 8–12 Å), with this cutoff applied in a manner to smoothly truncate these interactions. This type of truncation can be done with minimal artifacts for L-J interactions because of their relatively short-range behavior (i.e., L-J interactions diminish as a function of r_{ij}^{-6}). In order to minimize artifacts due to atoms contained within the primary cell of the periodic system from interacting with images of themselves that are represented in the adjacent unit cell representations of the system, which can result in nonphysical correlations in atomic motion, the dimensions of the primary unit cell of the system should be at least twice the length of the cutoffs used for the the L-J interactions between atoms in the system. The use of cutoffs is generally not advised for handling nonbonded electrostatic interactions between atoms, which diminish on the order of only r_{ij}^{-1}. Electrostatic effects are therefore generally recommended to be handled through the use of Ewald summation methods,[54,55] which effectively account for the long-range nature of these types of interactions.[56]

Once the model of the molecular system is established, MC or MD simulations can be performed to simulate the molecular behavior of the system under defined sets of conditions (or ensembles), such as constant number of atoms (N), primary cell volume (V), temperature (T) (canonical ensemble) or constant N, pressure (P), and T (isobaric–isothermal ensemble). With respect to these parameters, N and V are obviously defined by the number of atoms modeled in the simulation and the size of the primary simulation cell, while T and P are determined from statistical thermodynamic relationships. For example, for MD simulations, T and P are determined by Leach[18]

$$T = \frac{2}{(3N - N_c)k_B}\langle \mathrm{KE}\rangle = \frac{\langle m_i v_i^2\rangle}{(3N - N_c)k_B};$$
$$P = \frac{1}{V}\left[Nk_BT - \frac{1}{3k_BT}\sum_{i=1}^{N}\sum_{j=i+1}^{N} r_{ij}\cdot F_{ij}\right] \quad [3]$$

where N_c is the number of constraints in the system (i.e., reduction in degrees of freedom), the brackets ($\langle\ \rangle$) represent the average value of the property contained within the brackets, KE is the kinetic energy of the system, m_i and v_i are the mass and velocity of atom 'i,' k_B is Boltzmann's constant, and r_{ij} and F_{ij} are the position vector and the force vector between atoms 'i' and 'j,' with the summation run over all atom pairs in the system. Ideally, a simulation is first run until the system equilibrates under the designated conditions (equilibration phase of the simulation), following which the simulation is then continued with the molecular coordinates and properties periodically saved and subsequently used to calculate the average properties of the system (production phase of the simulation) by averaging the values for the entire set of sampled states. For example,

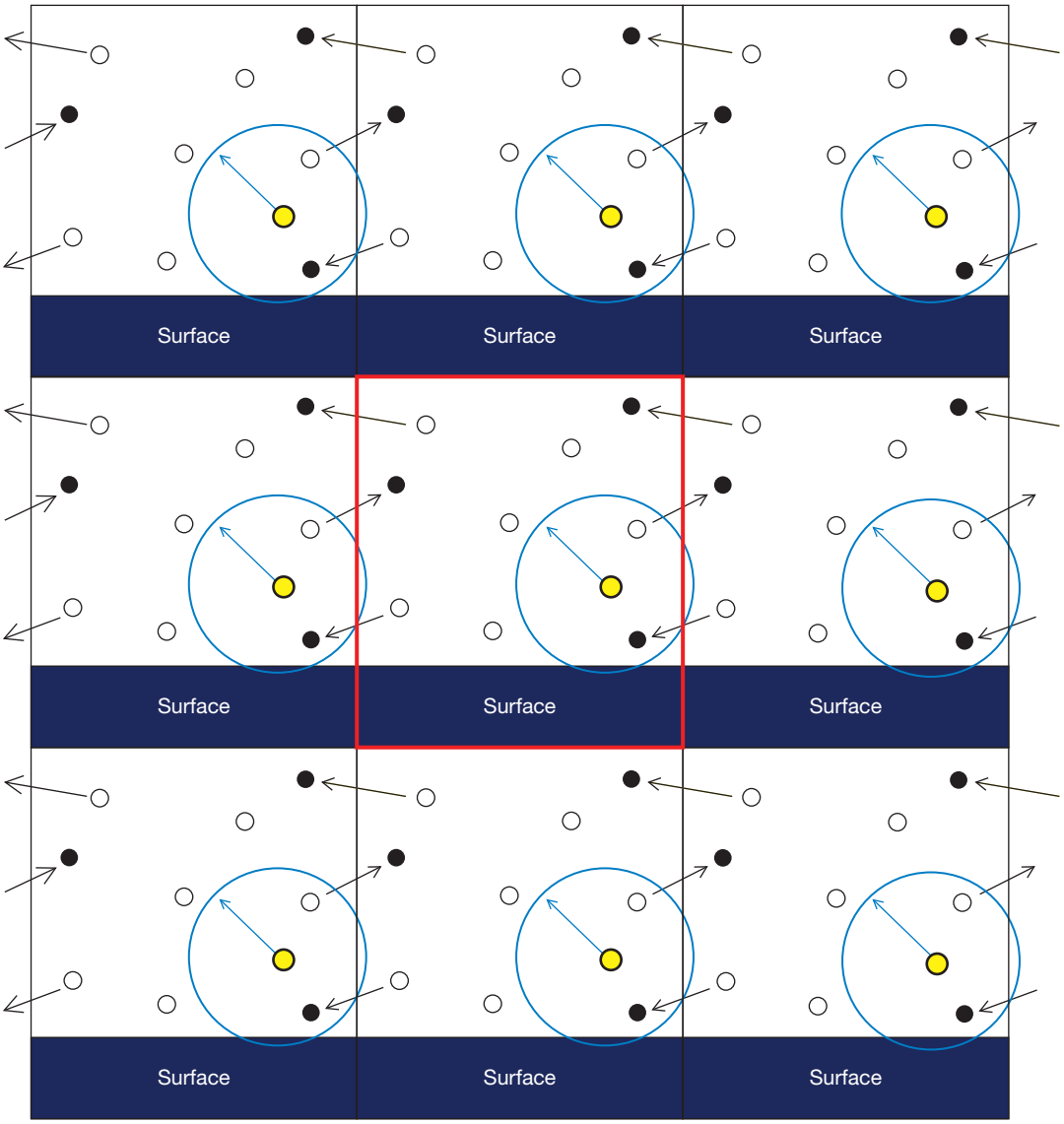

Figure 4 Illustration of periodic boundary conditions with the primary unit cell highlighted in red and surrounded by periodic images of itself. Molecules leaving the side of the primary cell enter back into the cell from the opposite side from another image, thus maintaining a constant number of atoms in the primary unit cell. The light blue circle surrounding the yellow atom indicates the cutoff radius for the calculation of L-J interactions for surrounding atoms acting on the yellow atom.

$$U = \langle E \rangle = \frac{1}{M}\sum_{i=1}^{M} E_i \qquad [4]$$

calculates the average potential energy (U) of the system, where M represents the number of individual states of the system that were sampled during the production phase of the simulation. These general methods are applicable for both MC and MD simulations. A summary of how each of these types of simulations is typically conducted is presented in the following section.

3.311.3.3.5. MC and MD methods

MC methods, which are most typically conducted in the canonical ensemble (i.e., NVT conditions), are used to efficiently search the conformational phase space of a molecular system.[18] The conformational phase space represents the potential energy surface of the system as a function of all of the coordinate degrees of freedom in the system. An MC simulation is conducted by applying various algorithms to move the positions of the atoms following a defined move set (e.g., random atom translation or dihedral rotation around a covalent bond) to efficiently explore the conformational phase space of the system. MC simulations typically employ what is referred to as 'importance sampling,' which was developed by Metropolis in the 1950s, and involves a random move to a new configurational state (x_i) combined with a decision algorithm that determines whether or not the newly sampled state should be accepted into the overall Boltzmann-weighted ensemble of

states that is being collected to represent the thermodynamic behavior of the system. The decision algorithm that provides this capability can be expressed thus:

$$\begin{aligned} &\text{If } E(x_j) \le E(x_i), \text{then accept new sampled state into} \\ &\quad \text{the ensemble of accepted sampled states} \\ &\text{If } E(x_j) > E(x_i), \text{then accept new state into ensemble} \\ &\quad \text{if } \mathrm{Rnd}(0-1) < exp[-(E(x_j) - E(x_i))/k_B T]. \end{aligned} \quad [5]$$

where $E(x_j)$ and $E(x_i)$ represent the potential energies of the newly sampled conformational state (x_j) and the previously accepted state (x_i), respectively, with these energies being calculated by the force field equation, and Rnd(0−1) represents a random number generated between 0 and 1. By design, this algorithm results in the probability of a sampled state, with energy $E(x_j)$ being accepted into the ensemble of previously accepted states with a Boltzmann-weighted probability ($P(x_j)$) equal to

$$P(x_i) = \{exp(-E(x_i)/k_B T)\}/Q; \quad \text{with } Q = \sum_i exp(-E(x_i)/k_B T) \quad [6]$$

where Q is the partition function of the system, thus generating a Boltzmann-weighted ensemble of sampled states. The implementation of this sampling process enables representative thermodynamic properties of a system to be directly determined simply by averaging the values of the accepted sampled set of states obtained from the simulation.

Because the move algorithms applied in an MC simulation are not time-dependent, MC simulations have the drawback of not providing direct information regarding the rate (or the kinetics) of a molecular process, but rather primarily only provide a means to determine the values of thermodynamic properties of a system. On the other hand, because the move set used to sample the phase space of a molecular system is not related to the kinetics of molecular motion, an MC simulation may provide an extremely fast and efficient method to sample the phase space of the system.

In contrast to an MC simulation, MD simulations use Newton's equations of motion to predict the behavior of the molecules in the system over time, typically under either NVT or NPT conditions, in a manner that reflects both the thermodynamic and the kinetic behavior of the system. In addition to needing the starting coordinates for each atom in a molecular system, an MD simulation also requires initial atomic velocities, which are typically obtained from a Maxwell–Boltzmann distribution of velocities for the designated temperature of the system,[18] with the additional requirement that the average velocity of the entire system is zero. Once the initial positions and velocities are set, the forces acting on each atom in the system are then calculated by the force field equation as a function of the atomic coordinate positions. Newton's second law (i.e., $F_i = ma_i$) is then applied to calculate the subsequent acceleration of each atom under the applied net force vector acting upon it. The acceleration is then numerically integrated over a short time-step to calculate each atom's new velocity and position, with the new coordinate positions of all of the atoms then used to calculate new force vectors for the next MD cycle. As an example, one of the commonly applied numerical integration algorithms that is used to determine the movement of atoms in an MD simulation is called the velocity Verlet algorithm, with the equations of motion expressed as[18]

$$\begin{aligned} r(t + \Delta t) &= r(t) + \Delta t\, v(t) + 0.5\Delta t^2\, a(t) \\ v(t + \Delta t) &= v(t) + 0.5\Delta t[a(t) + a(t + \Delta t) \end{aligned} \quad [7]$$

where r, v, and a are the position, velocity, and acceleration of a given atom, and t and Δt are the previous time point and the increment in time over which the system moves over each cycle of the simulation. The time-step used in an all-atom MD simulation must be small enough to enable the fastest motions of the system (i.e., covalent bond stretching vibrations) to be smoothly followed during the simulation: A time-step of 1.0 fs is often used in all-atom MD simulations, or if covalent bonds with hydrogen atoms are held fixed (by the application of algorithms such as SHAKE[57] or RATTLE[58]), a 2.0 fs time-step can be applied. This then reduces the amount of wall-clock time needed to cover a designated period of simulated time by a factor of 2 (i.e., a 2-month-long simulation can be completed in only 1 month).

As with the Metropolis MC method, the set of sampled states obtained from an MD simulation can be used to calculate the average values of thermodynamic properties of a molecular system. In this case, the probability of sampling a given state does not have to be established through the use of a Metropolis criterion, but rather the Newtonian dynamics process itself provides a Boltzmann-weighted sampling of states, ideally similar to that which occurs for the real system. The ability of both MC and MD simulations to serve as equivalent methods to determine the average properties of a molecular system is supported by the ergotic hypothesis, which states that the average value of a property determined from an ensemble average of sampled states (e.g., from an MC simulation) is equal to the time-averaged property of the same molecular system (e.g., from an MD simulation).[18,22] A critical requirement for either of these approaches, however, is that the phase space of the system must be sampled ergotically, meaning that all of the relevant conformational states of the system must be thoroughly sampled in the simulation. One of the key problems in this requirement is that it is often very difficult to know when either an MC or MD simulation has run sufficiently long (or sampled the system sufficiently well) to represent a properly equilibrated, ergotically sampled system. In fact, in systems with complex free energy landscapes, such as the case of protein folding (see **Figure 1**) or protein adsorption (see **Figure 3**), it is generally impossible with today's computational resources to run a conventional MC or MD simulation long enough to ergotically sample the system. Instead, simulations generally tend to be trapped in local low-energy regions without adequately exploring the full conformational phase space of the system, with averaged values obtained from the simulation then providing poor estimates of the desired properties. To overcome this limitation, several types of advanced, accelerated sampling methods have been developed that enable energy barriers to be more rapidly crossed that tend to trap a molecular system in a particular region of phase space, thus enabling systems to be equilibrated in a much shorter

computational time frame than can be achieved with conventional MC or MD methods. A few of these accelerated sampling methods are addressed in Section 3.311.3.3.6.

The decision of whether an MC or an MD method would be the best choice for the simulation of protein–surface interactions will depend on the system being reproduced and the properties that are desired. For example, if it is desired to conduct a simulation to address which face of a protein will be most strongly attracted to a given surface, thus addressing the issue of the initial adsorbed protein orientation, and if the solvent is being represented using a validated mean-field implicit solvation algorithm, an MC method would probably be the most efficient. In this case, the protein could be represented as a rigid molecule that is rotated and translated over a designated set of incremental moves to rapidly generate a converged set of states that depict how the potential energy of the system changes as a function of the protein's initial orientation on the surface. An MD simulation in this case would not be nearly as efficient because of the relatively slow kinetics involved for a protein rotating over a material surface. In comparison, if protein adsorption behavior were to be investigated in a simulation using explicitly represented solvation, MC moves are limited to very small increments because any large change in the position of the atoms of the protein would cause it to overlap with the neighboring atoms of the solvent, leading to unacceptably high values of potential energy due to the repulsive component of the L-J term in the force field. In this case, MC and MD methods would both be expected to provide about the same general degree of efficiency for sampling the various states of the system, with an MD simulation providing additional data regarding the predicted time course of the simulation.

3.311.3.3.6. Accelerated sampling methods

Accelerated sampling methods that are used in MC and MD simulations involve the application of specifically designed algorithms that enable energy barriers separating the various microstates in a molecular system to be rapidly crossed, thus facilitating the ability to ergotically sample a molecular system with a rugged potential energy landscape much more efficiently than in a conventional simulation. The basic principles behind most advanced sampling algorithms can be understood based on the statistical mechanics relationships that describe the probability (P_i) of a given state for a molecular system and the probability of sampling a different state, P_j, relative to P_i (i.e., P_j/P_i). These relationships can be described by the following set of equations[59]:

$$P_i = \frac{e^{-E(x_i)/k_B T}}{Q}, \quad \text{with } Q = \sum_i e^{-E(x_i)/k_B T} \text{ and } P_{ij} \equiv \frac{P_j}{P_i} = e^{-\Delta E_{ij}/k_B T} \qquad [8]$$

The first two of these equations are equivalent to those shown in eqn [6], and the third equation represents the relative probability of sampling the system in conformal state x_j verses x_i where ΔE_{ij} is the difference in potential energy between states x_j and x_i. Given these relationships, the probability of the system being in a given energy state can be adjusted by altering the value of the group of parameters in the exponential part of the probability expression (i.e., $E(x_i)/k_B T$), either by introducing a biasing energy function into the force field equation to influence the energy state of the system (E_i) or by adjusting the temperature of the system (T).

The introduction of a biasing energy function (B_{ij}) can be done by adding a user-defined term directly into the force field equation that controls how the atoms interact with one another during the simulation in a manner that lowers the energy barriers separating the various states of the system that one wishes to sample during the simulation.[60] The introduction of a biasing function can be expressed mathematically by eqn [9][36]:

$$\overline{P}_{ij} \equiv \frac{P_j}{P_i} e^{-B_{ij}/k_B T} = e^{-(\Delta E_{ij} + B_{ij})/k_B T} \qquad [9]$$

where $\overline{P}_{ij}$ represents the biased probability distribution that results from the addition of the biased-energy function. As is clear from the relationship expressed on the far right-hand side of eqn [9], if B_{ij} is set to exactly cancel the potential energy difference between two states of the system (i.e., $B_{ij} = -\Delta E_{ij}$), then the net energy difference separating them will be zero, creating a situation where there is equal probability of being in either state, thus eliminating the sampling problem. After the simulation is completed, the biased probability ratio that is obtained from the trajectory of the simulation is then corrected to remove the applied bias to obtain the unbiased probability distribution by inverting eqn [9] to obtain eqn [10]:

$$P_{ij} \equiv \frac{P_j}{P_j} = \overline{P}_{ij} e^{B_{ij}/k_B T} \qquad [10]$$

This method is highly effective if the coordinate position and the depth of a given local low-energy well are known such that a biasing energy function can be appropriately determined and applied in the simulation. If these parameters are not known *a priori*, they can be determined by running preliminary simulations to assess where the system tends to become trapped, and then adaptively adding in a biasing function until the sampling problem is removed.[61,62]

The use of a biased-energy function is most widely used to force sampling over a single designated system coordinate, such as either the dihedral rotation about a bond in a peptide chain[60,63] or the separation distance between a solute and a material surface.[36] For these types of applications, an umbrella sampling technique[60,64] is typically used in the form of

$$B_u = k_u (\lambda - \lambda_u)^2, \qquad [11]$$

which is also referred to as a 'restraining potential,' where k_u is the stiffness constant, λ_u is the coordinate parameter of interest (which is set at a designated coordinate value), and λ is the sampled value of the coordinate at a given point in the simulation. In this form, the biasing energy function (B_u) penalizes the system in a quadratically increasing manner as it deviates from the designated position, λ_u. A series of independent parallel simulations, referred to as 'windows,' can then be carried out with the value of λ_u incrementally varied over the full range of interest, with the increments set such that the neighboring sampled populations overlap one another. The resulting overlapping sampled distributions from all of these simulations can then be combined using the weighted histogram analysis

method (WHAM),[65,66] which serves to remove the applied bias from the combined set of sampled distributions and generate an unbiased probability distribution of states over the full range of the parameter of interest (i.e., over the full range of λ).

More recently, a biased-energy method has been developed, which is called metadynamics,[67,68] that adds relatively small Gaussian-shaped biasing energy functions to the system in an incremental manner to effectively 'fill up' a given low low-energy well that the simulation may be trapped in, causing the simulation to then move on to explore other areas of phase space. This process is continued in an automated manner until the energy landscape is effectively smoothed out such that all relevant energy barriers are removed, with the simulation then progressing with essentially equal probability to sample all areas of phase space. The resulting summation of the applied biasing functions then effectively represents a 'mold' of the full potential energy surface from which the thermodynamic properties of the system can be properly determined.

As an alternative to biasing the energy function in a simulation, temperature can also be used to accelerate sampling in a molecular system. In this case, sampling is accelerated not by lowering the free energy barriers, but by providing increased thermal energy to enable the barriers to be much more rapidly crossed. The use of temperature is particularly effective because it simultaneously acts on all degrees of freedom in the system. One of the most widely used methods that uses temperature to accelerate sampling is known as parallel tempering (PT),[69] which was developed for implementation in MC simulations, with a very similar type of algorithm called replica-exchange MD (REMD) being developed for MD simulations.[70,71] In each of these methods, independent simulations are run in parallel for a series of replicas of the molecular system, with each replica being simulated at an increasingly higher temperature level above the baseline temperature of interest, for example, 298 K. After a given period of simulation (e.g., 250 steps of MC or cycles of MD), a Metropolis-like statistical mechanics-based exchange algorithm is applied in the following form:

$$\text{If } E(x_j)_n \leq E(x_i)_m, \quad \text{then exchange temperatures between replicas} \tag{12}$$

$$\begin{aligned} &\text{If } E(x_j)_n > E(x_i)_m, \quad \text{then exchange temperatures} \\ &\quad \text{if } \mathrm{Rnd}(0-1) < \exp[-(\Delta\beta_{imn}\Delta E_{ij})], \quad \text{with } \Delta E_{ij} \\ &= E(x_j)_n - E(x_i)_m \text{ and } \Delta\beta_{mn} = \left(\frac{1}{k_B T_m} - \frac{1}{k_B T_n}\right) \end{aligned}$$

where $E(x_j)_n$ and $E(x_i)_m$ represent the potential energy of the system sampled at temperature T_n and T_m, respectively, with T_n being the next higher temperature interval above T_m along the 'temperature ladder' in the overall system. If an exchange is accepted, then the temperatures between the pair of replicas are swapped. If it is not, the replicas remain at their prior temperature levels for another cycle of sampling, following which the swapping decision process is repeated again. A diagram depicting this process is shown in Figure 5. By this method, a replica that is trapped in a local low-energy well that actually represents a relative high-energy state of the system tends to be exchanged upward in temperature, which provides additional thermal energy to help the replica

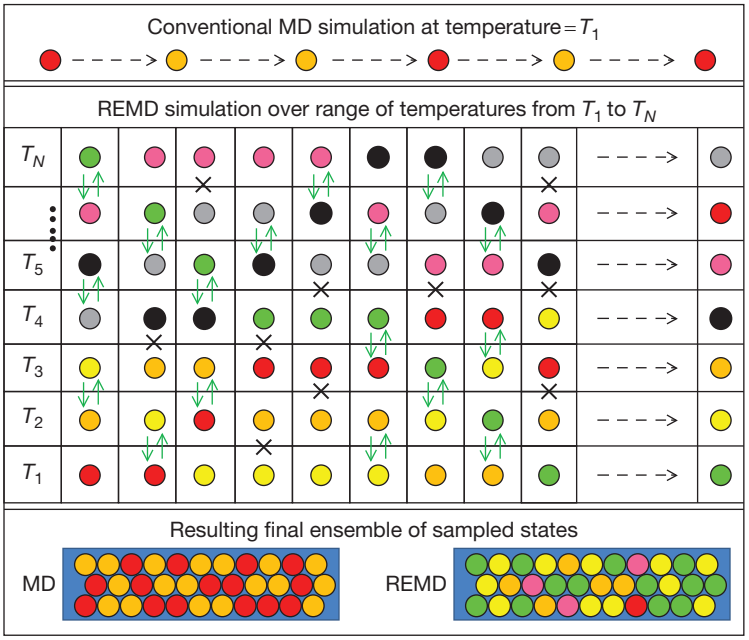

Figure 5 Illustration of a replica-exchange molecular dynamic (REMD) simulation in contrast with a conventional MD simulation. Each colored circle represents a different region of the phase space that is sampled in the simulation. The MD simulation (top of figure) tends to be trapped by the energy barriers in the system, thus greatly limiting the regions of phase space that are sampled. In the REMD simulation, the elevated temperature levels provide additional thermal energy to speed up the crossing of energy barriers. The Metropolis-like exchange process is represented by a set of green arrows (exchange accepted) and black 'Xs' (exchange not accepted). The exchange process enables the replicas to change temperature levels, which provides much better sampling over the phase space and results in a Boltzmann-weighted distribution of states being sampled at each temperature level.

escape from that local energy well to explore other regions of the phase space of the system. Similarly, replicas that move into relatively low-energy states tend to be exchanged downward in temperature, thus increasing their probability of being sampled at the baseline temperature. This somewhat complicated process greatly enhances the sampling of the conformational phase space of a given molecular system and generates a Boltzmann-weighted ensemble of states at each temperature level from which ensemble-averaged thermodynamic properties of the system can be calculated.

While PT and REMD are extremely useful computational techniques, because the number of replicas that are needed to perform a simulation is proportional to the square root of the number of atoms in the system, they can rapidly become very computationally expensive for a large molecular system. Furthermore, the time taken for a replica to move from the high-to-low temperature levels in the simulation is proportional to the square of the number of replicas used in simulation, thus substantially increasing the amount of wall-clock time required to equilibrate a system with a large number of replicas.[72] The combination of these two factors can make a conventional PT or REMD simulation too computationally expensive for practical use for the simulation of a large molecular system. To address these limitations, many different versions of these methods have been (and are being) developed to improve computational efficiency.[73,74] Along these lines, the Latour group has recently developed a new advanced sampling method, which is called 'temperature intervals with global exchange of replicas' (TIGER),[75] and a revised method called TIGER2.[72] These methods were specifically designed to uncouple the number of replicas that must be used to span a given temperature range from the size of the simulation, thus enabling REMD-like simulations to be conducted with a much smaller number of replicas than must be used for a conventional REMD simulation.

3.311.4. Application of All-Atom Modeling Methods to Simulate Protein–Surface Interactions

Atomic-level molecular simulations of protein–surface and peptide–surface interactions have been conducted over about the past two decades. In this section, an overview of several of these efforts is presented with a focus on selected studies that have addressed key issues in this field, with specific emphasis applied to the types of force fields used, the methods used to represent solvation effects, and the issues related to system sampling. As shown, the sophistication of these efforts has continued to dramatically increase over the years as computational power has continued to grow at an exponential pace, and investigators have developed a better understanding of the issues that must be addressed to accurately simulate this type of molecular system.

3.311.4.1. Early Efforts Beginning in the Late 1980s

3.311.4.1.1. Simulations with limited conformational sampling and treatment of solvation effects due to computational limitations

Some of the first studies to use empirical force field-based molecular modeling to investigate protein–surface interactions were published by Park and coworkers from 1989 to 1994.[76–78] In their first paper, simulations were conducted to calculate the initial potential energies of interaction between a set of four proteins (lysozyme, trypsin, an immunoglobulin fragment, and hemoglobin) on five polymer surfaces (polystyrene, polyethylene, polypropylene, poly(hydroxyethyl methacrylate), and poly(vinyl alcohol)), with the proteins treated as rigid elements that were rotated over a broad range of orientations over each polymer surface. The force field used to calculate interactions included terms for electrostatic, dipole (e.g., hydrogen bonding), dispersion, and overlap repulsion. At this early stage of development, a force field term for solvation effects was not included. The results from these studies predicted interaction energies ranging from about -200 to $+150\,\mathrm{kcal\,mol^{-1}}$. The results of these simulations predicted that the strongest interactions occurred for protein adsorption on the strongly hydrophilic poly(vinyl alcohol) surface rather than on the hydrophobic polymers. These results can be understood by realizing that without including solvation effects, these simulations actually represented the adsorption behavior of the proteins under vacuum conditions instead of aqueous solution, with the expected result that the polymer with the most polar functional groups (i.e., poly(vinyl alcohol)) would yield the strongest adsorption behavior. While this would be expected under vacuum conditions, the presence of the competitive interactions by water would be expected to actually make protein adsorption to this very hydrophilic polymer relatively weak compared to a hydrophobic surface such as polyethylene, where hydrophobic effects are known to cause very strong adsorption.[79] Despite these initial limitations, this work represented quite an ambitious start to model the complexities of protein adsorption behavior.

Park and coworkers followed up their initial paper with a subsequent study published in 1991[77] for this same set of proteins and polymers where the interaction energies due to solvation effects were included in their calculations. In this new set of simulations, solvation effects were based on experimental data regarding the partitioning of amino acids between water and various organic solvents. These new data predicted adsorption energies to be between about -62 and $-20\,\mathrm{kcal\,mol^{-1}}$ on the hydrophobic polymers, with positive adsorption energies for the hydrophilic polymers. These results are thus much more in agreement with the experimentally observed behavior that proteins adsorb more strongly on hydrophobic than hydrophilic polymers and nicely demonstrated the importance of including solvation effects in these types of calculations. Lee and Park then published a follow-up study in 1994[76] in which they used their methods to calculate how adsorption energy changed as a function of separation distance between proteins and polymer surfaces. In these studies, the L-J parameters were borrowed from the CHARMM force field, partial charges for atoms were borrowed from the AMBER force field, and solvation effects were treated implicitly based on experimental solvation free energies for amino acids and the changes in solvent-accessible surface area of the amino acid residues as a function of a protein's position over a surface. Due to limitations of computational power at that time, it was necessary to keep the protein and polymer molecules rigid, with interaction energies then calculated for two different orientations of each protein over each surface as the proteins were translated in 1.0 Å increments away from the surface. From these simulations, the authors predicted that adsorption

energies reduced to zero once the proteins were 20–30 Å away from the surface. They also made a specific note that while this method of implicitly accounting for solvation effects was much more reliable than using a simple dielectric constant method, there was a distinct need for increased computational power so that the solvent could be explicitly represented in the simulations. In addition, increased computing power was needed to allow mobility for both the protein and polymer functional groups, thus providing much better sampling of the system.

Another relatively early paper addressing protein–surface interactions was published by Noinville *et al.*[80] In this study, the interactions between an acidic protein (α-lactalbumin) and a basic protein (hen egg-white lysozyme) were simulated over a positively charged poly(vinyl imidazole) polymer surface, which is used in anion-exchange chromatography. In these simulations, the structure and partial charge distribution for the polymer model was predicted from SEQM simulations, and the polymer surface was constructed to provide a net surface change density of 0.10 C m^{-2} to match experimentally determined properties of this ion-exchange polymer on a silica substrate. The protein structures were obtained from the PDB and they were rigidly fixed for the simulations. The simulations were then performed by rotating the proteins in 5° increments and translating them between 1 and 100 Å over the surface for a total of 2592 different configurations over the surface. The interaction energies between the proteins and the surface were calculated for each configuration using the AMBER force field. Solvation effects were represented using a DDD function in the denominator of the Coulomb's law expression, with an additional exponential term added in the numerator of the function in the form of $\exp(-\kappa r_{ij})$ to account for the dampening of electrostatic effects due to the concentration of salts in solution, where r_{ij} represented the distance between an atom of the protein and an atom of the surface, and κ was the inverse Debye length calculated for a 150 mM Na_2SO_4 salt solution. The simulation results were subsequently used to calculate the average values of the interaction energy, predict preferred orientations of each protein over the polymer surface, and which amino acid residues of the proteins were most strongly attracted to the surface. While the results from these simulations were judged to be in general agreement with experimental results for similar systems, the authors recognized the limitations of the simulations due to the need to use an implicit solvation method to account for solvation effects and the lack of conformational freedom of the protein, with these approximations again being necessary given the limitations of computing power at that time.

3.311.4.1.2. Early MD simulations of protein–surface interactions with increased conformational sampling and explicit solvation

One of the first set of studies using MD simulation to investigate protein–surface interactions that included explicitly represented solvation effects was reported by Pitt and coworkers in 1997 and 1998.[81,82] In these studies, a small pentapeptide protein called leucine-enkephalin was modeled over a crystalline polyethylene surface. This peptide was predicted to fold into a conformation that resulted in a hydrophobic surface on one side and a hydrophilic surface on the other. In their simulations, the protein was modeled with either all atoms fixed in position or with only the α-carbons of each amino acid residue fixed, and the explicitly represented water molecules were allowed to be fully mobile. The MD simulation was performed with PBCs using the consistent valence force field (CVFF) using the InsightII/Discover software programs with a cutoff of 8 Å used for all nonbonded interactions. The protein was placed in different orientations over the surface and translated in increments of 0.4 Å from 1.5 to 9.5 Å over the surface for each orientation while MD simulations were performed to allow the solvent molecules to adapt and interact with the solute–surface system. The MD simulations were run using a 1.5 fs time-step with 300 steps of energy minimization applied, followed by 1000 steps (i.e., about 1.5 ps) for initial system equilibration to 298 K, followed by 12 000 steps (i.e., 18 ps) of production-run simulation, with the average net force acting on the protein calculated from the production-run phase of the simulation. The results from these simulations showed a significant influence of protein orientation over the surface, with an attractive adsorption force occurring when the protein was orientated with its hydrophobic side facing the surface and with a repulsive adsorption force occurring when the hydrophilic side of the protein was oriented toward the surface. The dipole orientation of the water over the polymer surface was also analyzed and found to be much more highly ordered than in the bulk water. Significant differences in the adsorption force were found to occur between simulations when the protein was held fully rigid as opposed to only fixing the five α-carbons and leaving the rest of the atoms of the protein free to move. In their discussion in their 1997 paper, Pitt and Weaver did an excellent job in assessing the limitations of their simulation methods. While their simulations yielded reasonable results, they commented on the fact that they had little basis to judge the accuracy of the L-J interactions between the protein, polymer surface, and water because these interactions were calculated using force field parameterization that was neither developed nor validated for this type of application. They also reflected on the short duration of their simulations and the influence that fixing the atoms of both the protein and the polymer surface may have had on the accuracy of the average properties determined from this very limited degree of sampling. This relatively early paper thus highlighted three key issues that are extremely important for the accurate simulation of protein–surface interactions: (i) the importance of accurately representing solvation effects through the use of explicitly represented water in their simulation, (ii) the question of the accuracy of their force field parameters to represent interfacial interactions, and (iii) the importance of adequately sampling the phase space of the molecular system.

3.311.4.1.3. Early matched experimental and simulation efforts to support force field parameterization for protein–surface interactions

Recognizing the lack of experimental studies that provide quantitative data on the thermodynamics of the interactions between individual amino acids within a polypeptide chain and surface functional groups, Latour and colleagues planned a combined set of experimental and computational studies to investigate the energetics related to the adsorption of individual lysine amino acid residues of a polylysine chain and a silica glass surface.[83–86] The experimental studies involved the generation of isotherms from the adsorption of polylysine chains

varying from about 1000 to 25 000 Da in molecular weight onto silica glass beads over a range of concentration and temperature. Simulations were conducted using SEQM methods with AM1 parameterization to calculate the enthalpy of interactions between the amine group of a lysine side chain and the hydroxyl group of individual silica rings of a silica glass surface. MM methods using MM2 parameterization were then also conducted to predict the conformational behavior of a polylysine chain to estimate the likely number of amino acid side chains that would be able to interact with a silica glass surface when a polylysine chain adsorbed. The results from the experimental studies yielded an average value of about −0.23 kcal per mol per residue for the enthalpy of interaction between a polylysine chain and silica glass. The SEQM AM1 results predicted that an individual hydrogen between a lysine side chain and a hydroxyl group of a silica ring to be $-3.7\ \text{kcal mol}^{-1}$, which was about an order of magnitude lower than the experimental value. However, the MM calculations suggested that the polypeptide chain should exist in a helical conformation with about one turn per eight amino acid residues, thus suggesting that only about one out of eight of the lysines of the polypeptide chain may actually be able to form a hydrogen bond to the silica when adsorbed. This effect combined with the composition of the silica glass, resulted in an estimated value of −0.34 kcal per mol per residue of a polylyine chain, which provides very reasonable agreement with the experimental results. The developed methods, however, also had several recognized limitations. The experimental methods had the inherent problem of limited applicability to other types of surfaces, and adsorption results were considered to be very susceptible to the conformational behavior of the relatively long polypeptide chains. Recognized limitations in the simulation methods included the fact that SEQM models were limited to only small sets of atoms, thus only being able to address the interactions between individual amino acid residues and units of silica structure as opposed to a larger polypeptide chain or protein interacting with a silica surface, and the lack of the explicit inclusion of solvation effects in the SEQM models. In addition, the calculations only represented the enthalpic contributions of amino acid–surface interactions but not the free energy of these types of interactions, which would require the inclusion of entropic effects as well. Despite these limitations, these studies provided some of the earliest attempts to combine experimental and molecular simulation studies to understand the molecular-level interactions between individual amino acid residues of a polypeptide chain and functional groups presented by a biomaterials surface, and to provide the types of experimental data that are necessary to support the evaluation, modification, and validation of force field parameters that will accurately represent protein–surface interactions.

3.311.4.1.4. Early MD simulations of protein–surface interactions with minimal constraints

One of the first MD simulations performed with a relatively large unconstrained protein was presented by Klein and coworkers in 1996,[87] in which simulations were conducted using the CHARMM19 force field to investigate the interactions between cytochrome c (an electron transfer protein) and alkanethiol SAM surfaces functionalized by either methyl (hydrophobic) or thiol (hydrophilic) functional groups. This system was of particular interest to help understand protein–surface interactions that were related to electron transfer processes in cell membranes and for the possible development of biomimetic devices. Because the intended devices were used in air, solvation effects were not included, with vacuum conditions thus being represented surrounding the protein and SAM surface. The MD simulations were conducted with the protein and SAM surface atoms fully free to move with the exception of a layer of locked sulfur atoms at the base of the SAM surface to represent a foundational support. The temperature was maintained at 300 K using a Nosé-Hoover thermostat to control temperature, with PBCs applied. The L-J interactions were truncated at 10 Å and long-range electrostatic effects were represented using Ewald summation. The simulations were conducted for about 1.1 ns using a 1.5 fs time-step. The results from these simulations showed that the protein actually interacted much more strongly with the hydrophilic than the hydrophobic surface, which is to be expected in vacuum given the fact that under such conditions, the hydrophilic groups of a surface will attract the protein through both weak dispersion and relatively stronger electrostatic interactions, while the nonpolar surface will only attract the protein by relatively weak dispersion forces. While this work represented a substantial advancement in the simulation of protein–surface interactions by treating the protein and surface in a largely unconstrained manner, the representation of vacuum conditions in the simulations was certainly less than ideal compared to experimental conditions where this protein was adsorbed to these types of surfaces under an air environment with a designated degree of humidity.

3.311.4.2. Advancements in Protein–Surface Simulations in the First Decade of the Twenty-First Century

3.311.4.2.1. Protein interactions with surfaces presenting organic functional groups

One of the first papers involving protein–surface interactions that was published in the first decade of the twenty-first century was a follow-up study reported by Klein and coworkers to investigate the influence of condensed water vapor on the adsorption behavior of cytochrome c on SAM surfaces functionalized with hydroxyl and methyl surface groups.[88] In these simulations, 100–500 TIP3P water molecules were added to the system to represent different degrees of condensation, and the hydrophilic thiol functional groups from the first study were replaced by hydroxyl groups. Not surprisingly, the results from these studies showed that the water molecules primarily clustered around the protein but not the surface for the hydrophobic SAM, while wetting both the protein and the surface for the hydrophilic SAM. As with the previous study under vacuum conditions, the 2002 study also indicated stronger interactions of the protein with the hydrophilic SAM surface, which demonstrates that simply adding a relatively small number of water molecules to a protein–surface system surrounded by vacuum to represent condensed water vapor (as purposely intended by the authors) represents conditions far different from protein–surface interactions in bulk aqueous solution. The results from these simulations showed that the angle between the plane of the heme group of cytochrome c with respect to the surface favorably compared with optical linear dichroism measurements of similar systems. While these simulations represented

some of the most ambitious and well-carried out studies to date, it must be realized that 1.5 ns still represents very limited sampling for this type of complex molecular system, with orders of magnitude longer simulation times most likely being needed for proper system equilibration.

Beginning in 2002, Raffaini and Ganazzoli[89–93] began publishing their efforts to conduct MD simulations to study protein interactions with surfaces, such as graphite and polyvinyl alcohol, using a set of methods that they have put forth as a standard approach for conducting these types of simulations. Their simulations were conducted using the InsightII/Discover software program with the CVFF force field. By their standardized approach, a protein is first placed over a surface and energy minimized with solvation effects represented using a DDD method alone. MD simulations are then run for about 1 ns at 300 K with the same implicit solvation function. The resulting structures are then once again energy minimized, following which several thousand explicitly represented water molecules are added to the simulation with an additional 10 ps of MD simulation run to provide time for a water structure to develop around the functional groups of the protein–surface system. While this group has been extremely prolific in publishing results, this procedure being applied to a broad range of protein–surface systems, it is important to realize that there are, unfortunately, several serious problems with this approach. First of all, as has been well documented by others and addressed in **Section 3.311.3.3.3**, the representation of solvation effects solely using a DDD function causes severe artifacts in a simulation, with the resulting molecular behavior being far different than that which would occur under aqueous solution conditions.[18,47,48] This type of implicit solvation method only serves to weaken electrostatic effects and does not represent the competitive binding behavior of water for polar and charged functional groups in the system. The use of this approach thus effectively represents a vacuum environment with dampened long-range electrostatic effects as opposed to an aqueous solution environment, and explains why most of the simulations conducted using these methods have predicted the complete unfolding of a protein over a surface, with the protein ending up adsorbed as a randomly coiled single-layer thickness of amino acid residues. While the subsequent addition of explicit water to the system followed by 10 ps of MD simulation is sufficient to enable a water structure to form around the functional groups of the protein and surface, this period of time is many orders of magnitude off of what would be needed to actually reequilibrate this complex type of molecular system. Therefore, while this group has made a serious attempt to develop a very computationally efficient method of simulating protein–-surface interactions, the use of a DDD function alone to represent solvation effects creates conditions very far from reality and simply should never be used alone to represent the simulation of protein adsorption behavior under aqueous solution conditions.

In another relatively early effort to provide a more realistic implicit solvation model for the simulation of protein interactions with organic functional groups, and to extend their previous modeling efforts, the Latour group conducted a series of SEQM simulations to calculate adsorption free energy versus surface separation distance (SSD) profiles for amino acid interactions with various types of functionalized surfaces.[94–97] In these SEQM simulations, solvation effects were represented using a conductor-like screening model algorithm (COSMO)[98] to represent electrostatic interactions combined with a surface energy versus solvent-accessible surface area term to represent entropic effects related to functional group desolvation. The developed free energy versus SSD profiles were then used to adjust force field parameters using the InsightII software program with InsightII's version of the CHARMM force field, with this modified force field then applied to characterize the adsorption behavior of a fibronectin fragment over various alkanethiol SAM surfaces. The protein fragment was first rotated around its long axis in 15° increments for a full 360° of rotation, with energy minimization performed at each step. The lowest energy orientation of the protein fragment over each surface was then used to perform a short 50 ps MD simulation to evaluate the initial phase of adsorption of the protein fragment on each surface. The results of these simulations were used to predict the relative adsorption strength of this protein fragment on each type of functionalized surface and the accessibility of the integrin binding sites in the protein fragment following adsorption. Despite the extremely short duration and limited degree of sampling provided by these simulations, the results were qualitatively found to be in close agreement with experimentally determined adsorption behavior of this protein fragment on similar SAM surfaces.

The Jiang group has also served as one of the pioneering groups working toward the development and application of methods to simulate protein interactions with surface functionalized with organic functional groups.[99–103] They have developed a combined MC/MD approach using the CHARMM force field. As recognized by the Jiang group, before conducting an MD simulation to investigate protein adsorption behavior on a surface, it is necessary to first select a given orientation of the protein on the surface, which poses a very complex problem in its own right. This group's approach to address this problem was to first conduct an MC simulation with the protein held in a fixed conformation while rotating and translating it over the surface to thoroughly sample the phase space for this type of defined system (e.g., 10^6 different sampled states) while calculating the potential energy of the system for each configuration. Because this type of MC simulation cannot be efficiently conducted using explicitly represented solvation, an implicit solvation method must be used. The method selected by the Jiang group for their MC simulations was once again the DDD function. While the same criticism applies for the use of this type of implicit solvation method as previously discussed, the method of using an MC simulation with implicit solvation to identify initial low-energy orientations of a protein over a surface provides a much more sophisticated approach for selecting starting orientations for MD simulations than simply randomly selecting orientations for subsequent MD simulations. Using this method, predicted low-energy orientations of the protein over the surface were identified and subsequently used as the starting structures to perform 1.0 ns long simulations in explicitly represented solvent using TIP3P water with Na^+ and Cl^- ions added to maintain charge neutrality, with both L-J and electrostatic interactions truncated at 11 Å. The Jiang group has applied these methods to study a broad range of protein–surface interactions, primarily for surfaces with organic functional groups, and have particularly contributed to understanding the molecular basis of surfaces that provide high levels of protein adsorption resistance.

3.311.4.2.2. Protein interactions focused on surfaces presenting inorganic functional groups

While the majority of molecular simulations of protein adsorption behavior conducted in the 1990s and early 2000s involved interactions with organic surfaces, more recently, several groups have been developing and applying molecular simulation methods to study the interactions of proteins on inorganic surfaces, including metals, metal oxides, and minerals. In addition, as computational power and algorithm development have continued to expand, many of these efforts have employed relatively new, more sophisticated techniques with the potential to improve the accuracy of protein adsorption simulations. In particular, increased attention has been paid to force field parameterization to accurately represent interactions at the peptide–surface interface.

As an excellent example of some of these more recent developments, the Walsh group has conducted combined MC and MD simulations to investigate the atomic-level interactions between various peptides and inorganic surfaces, including TiO_2,[104,105] quartz,[106] and carbon nanotubes.[107] In preparations for simulations to study the adsorption behavior of peptides and TiO_2 surfaces, DFT simulations were first conducted between water and TiO_2 (110) surfaces for comparison with MD simulations using a TIP3P water model in the TINKER molecular simulation program. Force field parameters for the TiO_2 surface were obtained from previous studies.[105] Comparisons between the water structure over the surface (e.g., density profile and dipole orientation distribution) predicted by both methods confirmed that the TIP3P water model was able to provide a very reasonable representation of solvation effects over a TiO_2 surface. A subsequent paper then reported on combined MC/MD simulations that were conducted to predict the adsorption behavior of specifically sequenced hexapeptides on TiO_2 surfaces.[104] These simulations were conducted using the DL-Poly simulation program, with the parameters for TiO_2 and TIP3P water obtained from their previous study and the parameters for the peptide obtained from the CHARMM force field. Similar to the approach used by the Jiang group, initial orientations of the peptide over the surface were determined by an MC simulation using implicit solvation. In this case, however, a more sophisticated implicit solvation method was used instead of the simple DDD method. The Walsh group instead represented solvation effects using the atomic solvation parameter (ASP) method, which is based on experimentally measured solvation free energies of amino acids coupled with the calculation of solvent-accessible surface areas during the simulation. In addition, recognizing that the accuracy of this solvation method still has not been validated for this type of application, a large number of alternative conformations of the peptide over the TiO_2 surface were also considered. Low-energy orientations were subsequently selected, the system was solvated with TIP3P water and counter ions, and 2.0 ns MD simulations were conducted, with PBCs and Ewald summation being used for representing long-range electrostatic interactions. The results of the simulations were then analyzed to assess the conformation and structure of both the peptide and water over the TiO_2 surface, and to determine which amino acid residues of the peptide were predicted to strongly mediate the association of the peptide with the TiO_2 surface.

The Walsh group has also recently published one of the first sets of studies of peptide–surface interactions with the use of a polarizable force field.[107,108] As mentioned in Section 3.311.3.3.2, one of the limitations with fixed-charge force fields is that atoms in the system are not able to change their assigned partial charges to adjust to changes in their local surroundings. The ability to adapt in this manner can be particularly important for accurately capturing the adsorption behavior between peptides containing aromatic amino acids (e.g., tryptophan) and surfaces containing aromatic ring structures, such as graphite and carbon nanotubes where π-stacking interactions can substantially influence adsorption behavior. Recognizing these issues, Walsh and coworkers conducted simulations of the interactions of peptides with both single-walled carbon nanotubes (SWNT) and graphite surfaces with various degrees of curvature using the AMOEBA polarizable force field in the TINKER simulation package.[109,110] The AMOEBA force field incorporates methods to address electrostatic interactions in a much more sophisticated manner than fixed-charged force fields by using distributed multipole approximations[111,112] and atom-based polarizabilities, thus enabling atoms in a CM simulation to adapt their partial charge state to their surrounding molecular environment in a manner somewhat analogous to a QM simulation. Because the AMOEBA force field was specifically developed for peptides and proteins, the Walsh group had to generate their own multipole parameters for their graphite and SWNT surfaces. These were generated by performing calculations using the Gaussian software program with functional groups represented at the Hartree–Fock (HF)/6–31G* level of theory. L-J and polarizability parameters for the aromatic ring carbons were then borrowed from the existing AMOEBA parameterization library for aromatic carbons. One of the limitations of polarizable force fields is that they are much more computationally expensive than fixed-charged force fields. For this reason, the 1.0 ns MD simulations that were performed to investigate peptide interactions with the graphite and SWNT surfaces had to be conducted with solvation effects represented implicitly, which was implemented using the ASP method. The developed methods were applied to simulate the adsorption behavior of a set of phage-display designed peptides that had been experimentally determined to exhibit a wide range of binding affinities for these types of surfaces. Analysis of the simulation results predicted trends in binding affinity that were similar to what has been observed experimentally, thus qualitatively supporting the developed simulation methods.

The simulation of peptide adsorption behavior on metallic surfaces represents another unique challenge for molecular simulation where simple fixed-charged force fields are inherently problematic. This occurs because the mobility of the valence electrons around the atoms making up a metallic surface results in a situation where the partial charge state of the metal atoms, which will be neutral when unperturbed, will shift in response to an electric field; such as the field generated by an approaching atom with ionic charge. This shift in the partial charge of the atoms in a metallic surface is referred to as the image-charge effect, and these types of dynamic responses cannot be captured when representing the atoms making up a metal surface using a simple fixed-charge force field. To address this problem for applications such as biosensor development, Corni and coworkers[113,114] have developed a force field with

atomic polarization capabilities to represent image-charge effects for a gold (111) surface for the simulation of protein adsorption behavior. Force field parameters to represent the interactions between a gold surface and surrounding water and amino acid residues of a protein were then generated based on extensive QM calculations using both MP2 and DFT levels of theory. In order to be compatible with most widely used protein force fields, parameters fitting the 12-6 L-J nonbonded term of a Class I force field were then fit to the QM results to represent the interactions between amino acid functional groups and the gold surface. OPLS-AA parameters were used for amino acid functional groups and the SPC model used for water. The validity of the developed force field parameterization was then established by comparing interaction energies from simulation results for small molecules representing amino acid-like functional groups adsorbed on gold with available experimental data sets.

While the majority of the methods that have been applied to simulate protein–surface interactions have been based on MD simulations, with MC methods occasionally used to predict initial conformations, the Gray group has developed an all-atom, fully unconstrained Metropolis MC method combined with energy minimization to predict protein adsorption behavior.[115,116] This method is based on an extension of the Rosetta protein folding program and is called RosettaSurface. Similar to Rosetta,[117] RosettaSurface uses rapid structure prediction techniques to widely sample conformational space using discrete protein fragment and side-chain rotamer libraries from high-resolution protein structures coupled with force field terms for van der Waals interactions, hydrogen bonding, and solvation energy. As previously noted, the ability to rapidly move around conformational phase space with large MC moves requires the use of an implicit method to represent solvation effects. The RosettaSurface program uses an implicit solvation method developed by Lazaridis and Karplus,[118] which is called the effective energy function (EEF1) method. EFF1 is based on the sum of functional group-based solvation energy contributions that were developed for validating protein folding applications. Prediction of statherin adsorption to hydroxyapatite surfaces using this method has been found to be consistent with solid-state NMR results, thus supporting the validity of this approach.

3.311.5. Current Limitations and Directions for Further Development

As noted in Section 3.311.4, three recurrent critical issues arise when molecular simulation methods are applied for the simulation of protein–surface interactions[119]: (i) the issue of force field transferability for protein–surface interactions, (ii) the adequate representation of solvation effects (including implicit solvation), and (iii) phase-space sampling to adequately represent equilibrated properties of a protein–surface system for comparison with experimentally observed values.

3.311.5.1. Force Field Transferability for Protein–Surface Interactions

Because protein–surface interactions are primarily governed by nonbonded interactions, the accurate representation of protein–surface interactions involves the parameterization of the L-J terms and the partial charge terms of the force field. Protein–surface interactions are particularly sensitive to these parameters because adsorption behavior is dependent on relatively small differences between protein–surface versus protein–water and water–surface interactions. Unfortunately, at this time, there is little basis to assess the transferability of existing force fields that have been developed for protein folding or materials science applications to accurately represent protein–surface interactions at the interface between a solid-phase material and a protein-containing solution phase. As presented in Section 3.311.4.2, several groups have addressed this issue by conducting QM simulations of representative amino acid functional groups and water with representative functional groups of a surface. While this should theoretically enable force field parameters to be obtained that provide a proper balance between amino acids, water, and surfaces, accurate experimental data is still needed for representative properties (e.g., adsorption free energy) that can be directly used to quantitatively evaluate the accuracy of force field parameters for the simulation of protein adsorption behavior. For this purpose, Wei and Latour[38] have generated a large experimental data set to characterize the free energy of adsorption of peptides on surfaces presenting the types of organic functional groups that are used in many different types of polymers. The results from these studies provide an experimental data set that can be used to evaluate, modify, and validate any given force field for protein adsorption behavior on surfaces presenting similar types of functional groups. Latour and coworkers[120] have used this data set to evaluate the CHARMM22 force field by conducting simulations to calculate the adsorption free energy for 38 of the same peptide–SAM surface systems that were experimentally evaluated by Wei and Latour. Comparison between the simulation results has revealed that the CHARMM22 force field substantially underestimates the strength of adsorption of amino acid residues on hydrophobic surfaces and positively charged amine surfaces, while slightly overestimating the strength of interactions between amino acid residues and neutral hydrophilic and negatively charged carboxylate surfaces. Latour and coworkers are currently working on the development of a modified version of the CHARMM program, called dual-force-field CHARMM, which will provide the capabilities to design an interfacial force field to control protein–surface interactions while using conventional CHARMM force field parameters to control the behavior of a protein in solution. This program should thus provide the capabilities to tune an interfacial force field to accurately represent amino acid residue interactions with surfaces presenting organic functional groups, thus providing a validated interfacial force field for the accurate simulation of protein adsorption behavior to these types of surfaces. Similar data sets are needed for inorganic surfaces, including metals, metal oxides, and ceramic materials, in order to obtain validated force field parameters for the accurate simulation of protein adsorption behavior to these types of surfaces as well.

3.311.5.2. Representation of Solvation Effects for Protein–Surface Interactions

The second critical issue that needs to be addressed is the development of appropriate methods to represent solvation

effects for protein–surface interactions. Presently, explicit solvation represents the gold standard for use in peptide and protein adsorption simulations; however, the appropriateness of existing water models such as TIP3P and SPC for this type of application still remains to be verified. A more difficult issue involves the development and validation of implicit solvation models for protein–surface interactions. As an initial assessment of this issue, Sun *et al.* have conducted simulations comparing several of the currently available implicit solvation models (including DDD, ASP, and EEF1) that have primarily been developed by the protein folding community.[49,121] The results from these simulations have shown widely differing predicted adsorption energies for each method, with little basis at this time to assess which method provides the most accurate results. The substantial savings in computational time that is provided by the ability to implicitly represent solvation effects create a large incentive for the development and validation of implicit solvation methods for the simulation of protein–surface interactions. There is no theoretical reason why accurate implicit solvation methods cannot be developed for this application, and this remains a promising area for continued research.

3.311.5.3. Phase-Space Sampling for Protein–Surface Interactions

The third critical issue for the development of simulation methods to accurately represent protein adsorption behavior is the need for advanced sampling methods that can be applied to accelerate the exploration of phase space for large molecular systems. As presented in Section 3.311.4, most MD simulations that have been conducted to investigate protein–surface interactions have involved the application of conventional MD sampling over time periods extending no longer than a few nanoseconds. While these simulations can represent extremely large expenditures of computational time, it must be recognized that surface-induced refolding/unfolding processes that occur when proteins interact with a surface can be expected to require many orders of magnitude and longer periods of time. As a clear example of this, a study by Agashe *et al.*[122] involved the simulation of the adsorption behavior of a relatively modest-sized 30 kDa fragment of the blood-clotting protein fibrinogen over various functionalized surfaces, including a hydrophobic CH_3-functionalized SAM surface. These simulations, which included explicitly represented SPC water, were simulated for 5.0 ns. Experimental studies of the adsorption behavior of fibrinogen on a CH_3-SAM surface have been shown to induce a substantial degree of unfolding,[16,123] which was the type of behavior expected to be observed in the simulation. However, the 5.0 ns simulation only resulted in the rotation of the protein fragment over about a 45° angle over the surface, with the nonpolar amino acid residues near the protein's outer surface strongly adsorbing to the surface and the polar and charged amino acids remaining hydrated and away from the surface. Thus, while the general initial type of interactions were observed in this simulation (i.e., the adsorption of protein to the surface via its nonpolar residues), it was clearly apparent that a much longer simulated time frame was necessary to be able to capture the anticipated unfolding behavior of the protein on the surface. As addressed in Section 3.311.3.3.6, several accelerated sampling methods have already been developed that are readily applicable to accelerate phase-space sampling for protein–surface interactions, and this also represents a very important area of continued research for the development of methods that are specifically applicable for the simulation of protein–surface interactions.

3.311.5.4. Coarse-Grained Molecular Modeling Methods

Although this chapter has primarily focused on the development and application of all-atom molecular simulation methods, coarse-grained (CG) CM methods, where individual particles in the system represent groups of atoms, also represent an important area for development for the simulation of protein–surface interactions.[102] These methods have the distinct advantage of substantially reducing the number of degrees of freedom in the molecular system, thus greatly accelerating the ability to simulate a molecular process. However, the derivation and validation of force field parameters that are needed for the development of these types of methods, which includes the implicit representation of solvation effects, represent even bigger challenges than those faced in the development of force field parameters for all-atom simulations. Indeed, the force field parameterization of most currently available CG methods were produced and validated by comparison with all-atom simulations, analogous to the way that all-atom force field parameters are often derived from QM simulations. Thus, while CG methods may provide the opportunity to extend simulations over much greater time and length scales than can be currently achieved by all-atom simulations, accurate all-atom simulation methods must first be developed before they will be able to be extended for the development of accurate CG and higher order multiscale methods.

3.311.6. Concluding Remarks

In this chapter, a general overview of the topic of molecular simulation was presented with a focus on the use of all-atom MC and MD methods for the simulation of protein–surface interactions. Emphasis was placed on addressing some of the key issues and limitations that must be considered when conducting simulations of peptide and protein adsorption behavior; namely, the validity of force field parameterization for the system being considered, the accurate representation of solvation effects, and statistical sampling to obtain converged results that are representative of an equilibrated system.

Molecular simulation methods have the potential to provide the biomaterials field with an extremely valuable tool for the design of surfaces at the atomic level that will enable the adsorption behavior and subsequent bioactivity of adsorbed proteins to be manipulated and controlled in a desired manner. This capability should directly translate into the development of biomaterial systems with improved performance for a broad range of applications in biomedical engineering and biotechnology. This situation, however, will only be realized if the biomaterials field will recognize this potential and work to further the development of these types of methods specifically for application to study protein–surface interactions. Although many challenges and limitations currently exist that prevent this potential

from being fully realized at this time, the rapidly expanding pace of the development of algorithms with improved efficiency combined with the continued exponential growth in computational system capabilities suggest that this area of research and development and the potential benefits that it can provide will only continue to grow and expand well into the foreseeable future.

Acknowledgments

I would like to acknowledge the contributions made by the graduate students, postdoctoral fellows, and research associates with whom I have worked over the past 15 years for the development of both computational and experimental methods to study protein–surface interactions. I would also like to specifically acknowledge my colleague Prof. Steven Stuart of the Department of Chemistry at Clemson University for numerous insightful discussions over the years regarding molecular simulation and statistical thermodynamics. Finally, I sincerely thank the NIH and NSF for providing funding support for my research program on the development of molecular simulation methods to simulate protein–surface interactions: NIH R01 EB006163, R01 GM074511, the NJ Center for Biomaterials (RESBIO) at Rutgers University (funded by NIH, P41 EB001046), and the Center for Advanced Engineering Fibers and Films at Clemson University (CAEFF, previously funded by NSF-ERC, EPS-0296165).

References

1. Dee, K. C.; Puleo, D. A.; Bizios, R. *Protein–Surface Interactions*; Wiley: Hoboken, NJ, 2002; Chapter 3.
2. Castner, D. G.; Ratner, B. D. *Surf. Sci.* **2002**, *500*, 28–60.
3. Hlady, V.; Buijs, J. *Curr. Opin. Biotechnol.* **1996**, *7*, 72–77.
4. Latour, R. A. In *The Encyclopedia of Biomaterials and Bioengineering*, 2nd ed.; Wnek, G. E.; Bowlin, G. L., Eds.; Informa Healthcare: New York, NY, 2008; Vol. 1, pp 270–284.
5. Beck, D. A. C.; Daggett, V. *Methods* **2004**, *34*, 112–120.
6. Brooks, C. L., III. *Curr. Opin. Struct. Biol.* **1998**, *8*, 222–226.
7. Gnanakaran, S.; Nymeyer, H.; Portman, J.; Sanbonmatsu, K. Y.; Garcia, A. E. *Curr. Opin. Struct. Biol.* **2003**, *13*, 168–174.
8. Bernard, D.; Coop, A.; Mackerell, A. D. *J. Med. Chem.* **2005**, *48*, 7773–7780.
9. Chen, H. F. *Chem. Biol. Drug Des.* **2008**, *71*, 434–446.
10. Muegge, I. *Med. Res. Rev.* **2003**, *23*, 302–321.
11. Brandon, C.; Tooze, J. *Introduction to Protein Structure*, 2nd ed.; Garland: New York, NY, 1999.
12. Voet, D.; Voet, J. G.; Pratt, C. W. *Fundamentals of Biochemistry*; Wiley: New York, NY, 2002.
13. Mishra, S. *Int. J. Theor. Phys.* **2008**, *47*, 2655–2662.
14. Bryngelson, J. D.; Onuchic, J. N.; Socci, N. D.; Wolynes, P. G. *Proteins* **1995**, *21*, 167–195.
15. Onuchic, J. N.; Wolynes, P. G.; Lutheyschulten, Z.; Socci, N. D. *Proc. Natl. Acad. Sci. USA* **1995**, *92*, 3626–3630.
16. Wertz, C. F.; Santore, M. M. *Langmuir* **2001**, *17*, 3006–3016.
17. Latour, R. A. In *Biological Interactions on Materials Surfaces: Understanding and Controlling Protein, Cell, and Tissue Responses*; Bizios, R., Puleo, D. A., Eds.; Springer: New York, NY, 2009; pp 69–95.
18. Leach, A. R. *Molecular Modelling: Principles and Applications*; Pearson: Harlow, UK, 1996.
19. Levine, I. N. *Quantum Chemistry*; Prentice-Hall: Upper Saddle River, NJ, 2000.
20. Becker, O. M.; MacKerrel, A. D.; Roux, B.; Watanabe, M., Eds. *Computational Biochemistry and Biophysics*; Marcel Dekker: New York, NY, 2001.
21. Allen, M. P.; Tildesley, D. J. *Computer Simulation of Liquids*; Oxford University Press: New York, NY, 1987.
22. Frenkel, D.; Smit, B. *Understanding Molecular Simulation*; Academic Press: New York, NY, 1996.
23. Cornell, W. D.; Cieplak, P.; Bayly, C. I.; *et al. J. Am. Chem. Soc.* **1995**, *117*, 5179–5197.
24. Weiner, S. J.; Kollman, P. A.; Case, D. A.; *et al. J. Am. Chem. Soc.* **1984**, *106*, 765–784.
25. MacKerell, A. D.; Bashford, D.; Bellott, M.; *et al. J. Phys. Chem. B* **1998**, *102*, 3586–3616.
26. MacKerell, A. D.; Brooks, B.; Brooks, C. L. I.; *et al*. In *Encyclopedia of Computational Chemistry*; Wiley: New York, NY, 1998; Vol. 1 (A–D), pp 271–277.
27. van Gunsteren, W. F.; Daura, X.; Mark, A. E. In *Encyclopedia of Compuational Chemistry;* Schleyer, P. v. R., Ed.; Wiley: New York, NY, 1998; Vol. 2 (E–L), pp 1211–1216.
28. Kaminski, G. A.; Friesner, R. A.; Tirado-Rives, J.; Jorgensen, W. L. *J. Phys. Chem. B.* **2001**, *105*, 6474–6487.
29. Hwang, M. J.; Stockfisch, T. P.; Hagler, A. T. *J. Am. Chem. Soc.* **1994**, *116*, 2515–2525.
30. Soldera, A. *Polymer* **2002**, *43*, 4269–4275.
31. Allinger, N. L.; Chen, K.; Lii, L. H. *J. Comp. Chem.* **1996**, *17*, 642–668.
32. Sun, H. *J. Phys. Chem. B* **1998**, *102*, 7338–7364.
33. Oostenbrink, C.; Villa, A.; Mark, A. E.; van Gunsteren, W. F. *J. Comput. Chem.* **2004**, *25*, 1656–1676.
34. Raut, V. P.; Agashe, M. A.; Stuart, S. J.; Latour, R. A. *Langmuir* **2006**, *22*, 2402–2402.
35. Vernekar, V. N.; Latour, R. A. *Mater. Res. Innovations* **2005**, *9*, 337–353.
36. Wang, F.; Stuart, S. J.; Latour, R. A. *Biointerphases* **2008**, *3*, 9–18.
37. Wei, Y.; Latour, R. A. *Langmuir* **2008**, *24*, 6721–6729.
38. Wei, Y.; Latour, R. A. *Langmuir* **2009**, *25*, 5637–5646.
39. Fears, K. P.; Sivaraman, B.; Powell, G. L.; Wu, Y.; Latour, R. A. *Langmuir* **2009**, *25*, 9319–9327.
40. Sivaraman, B.; Fears, K. P.; Latour, R. A. *Langmuir* **2009**, *25*, 3050–5056.
41. Glattli, A.; Daura, X.; van Gunsteren, W. F. *J. Chem. Phys.* **2002**, *116*, 9811–9828.
42. Mark, P.; Nilsson, L. *J. Phys. Chem. A* **2001**, *105*, 9954–9960.
43. Jorgensen, W. L.; Chandrasekhar, J.; Madura, J. D.; Impey, R. W.; Klein, M. L. *J. Chem. Phys.* **1983**, *79*, 926–935.
44. Horn, H. W.; Swope, W. C.; Pitera, J. W.; *et al. J. Chem. Phys.* **2004**, *120*, 9665–9678.
45. Jorgensen, W. L.; Madura, J. D. *Mol. Phys.* **1985**, *56*, 1381–1392.
46. Mahoney, M. W.; Jorgensen, W. L. *J. Chem. Phys.* **2001**, *114*, 363–366.
47. Schaefer, M.; Bartels, C.; Karplus, M. *Theor. Chem. Accounts* **1999**, *101*, 194–204.
48. Yeh, I. C.; Lee, M. S.; Olson, M. A. *J. Phys. Chem. B* **2008**, *112*, 15064–15073.
49. Sun, Y.; Latour, R. A. *J. Comput. Chem.* **2006**, *27*, 1908–1922.
50. Bertonati, C.; Honig, B.; Alexov, E. *Biophys. J.* **2007**, *92*, 1891–1899.
51. Sharp, K. A.; Honig, B. *J. Phys. Chem.* **1990**, *94*, 7684–7692.
52. Feig, M.; Onufriev, A.; Lee, M. S.; Im, W.; Case, D. A.; Brooks, C. L. *J. Comput. Chem.* **2004**, *25*, 265–284.
53. Still, W. C.; Tempczyk, A.; Hawley, R. C.; Hendrickson, T. *J. Am. Chem. Soc.* **1990**, *112*, 6127–6129.
54. Darden, T.; York, D.; Pedersen, L. *J. Chem. Phys.* **1993**, *98*, 10089–10092.
55. Essmann, U.; Perera, L.; Berkowitz, M. L.; Darden, T.; Lee, H.; Pedersen, L. G. *J. Chem. Phys.* **1995**, *103*, 8577–8593.
56. Collier, G.; Vellore, N. A.; Stuart, S. J.; Latour, R. A. *Biointerphases* **2009**, *4*, 57–64.
57. Ryckaert, J. P.; Ciccotti, G.; Berendsen, H. J. C. *J. Comput. Phys.* **1977**, *23*, 327–341.
58. Andersen, H. C. *J. Comput. Phys.* **1983**, *52*, 24–34.
59. McQuarrie, D. A. In *Statistical Thermodynamics*; Harper & Row: New York, NY, 1976; pp 35–47.
60. Beutler, T. C.; Van Gunsteren, W. F. *J. Chem. Phys.* **1994**, *100*, 1492–1497.
61. Bartels, C.; Karplus, M. *J. Phys. Chem. B* **1998**, *102*, 865–880.
62. Bartels, C.; Schaefer, M.; Karplus, M. *Theor. Chem. Accounts* **1999**, *101*, 62–66.
63. Souaille, M.; Roux, B. *Comput. Phys. Commun.* **2001**, *135*, 40–57.
64. Harvey, S. C.; Prabhakaran, M. *J. Phys. Chem.* **1987**, *91*, 4799–4801.
65. Kumar, S.; Bouzida, D.; Swendsen, R. H.; Kollman, P. A.; Rosenberg, J. M. *J. Comput. Chem.* **1992**, *13*, 1011–1021.
66. Kumar, S.; Rosenberg, J. M.; Bouzida, D.; Swendsen, R. H.; Kollman, P. A. *J. Comput. Chem.* **1995**, *16*, 1339–1350.
67. Laio, A.; Gervasio, F. L. *Rep. Prog. Phys.* **2008**, *71*(126601), 1–22.
68. Laio, A.; Parrinello, M. *Proc. Natl. Acad. Sci. USA* **2002**, *99*, 12562–12566.
69. Hansmann, U. H. E. *Chem. Phys. Lett.* **1997**, *281*, 140–150.
70. Gallicchio, E.; Andrec, M.; Felts, A. K.; Levy, R. M. *J. Phys. Chem. B.* **2005**, *109*, 6722–6731.
71. Sugita, Y.; Okamoto, Y. *Chem. Phys. Lett.* **1999**, *314*, 141–151.

72. Li, X.; Stuart, S. J.; Latour, R. A. *J. Chem. Phys.* **2009**, *130*(174106), 1–9.
73. Okamoto, Y. *J. Mol. Graph. Model.* **2004**, *22*, 425–439.
74. Okur, A.; Wickstrom, L.; Layten, M.; *et al. J. Chem. Theory Comput.* **2006**, *2*, 420–433.
75. Li, X.; O´Brien, C. P.; Collier, G.; *et al. J. Chem. Phys.* **2007**, *127*(164116), 1–10.
76. Lee, S. J.; Park, K. *J. Vac. Sci. Technol. A* **1994**, *12*, 2949–2955.
77. Lu, D. R.; Lee, S. J.; Park, K. *J. Biomater. Sci. Polym. Ed.* **1991**, *3*, 127–147.
78. Lu, D. R.; Park, K. *J. Biomater. Sci. Polym. Ed.* **1989**, *1*, 243–260.
79. Wertz, C. F.; Santore, M. M. *Langmuir* **2002**, *18*, 706–715.
80. Noinville, V.; Vidal-Madjar, C.; Sebille, B. *J. Phys. Chem.* **1995**, *99*, 1516–1522.
81. Bujnowski, A. M.; Pitt, W. G. *J. Colloid Interface Sci.* **1998**, *203*, 47–58.
82. Pitt, W. G.; Weaver, D. R. *J. Colloid Interface Sci.* **1997**, *185*, 258–264.
83. Latour, R. A. *Curr. Opin. Solid State Mater* **1999**, *4*, 413–417.
84. Latour, R. A.; Trembley, S. D.; Tian, Y.; Lickfield, G. C.; Wheeler, A. P. *J. Biomed. Mater. Res.* **2000**, *49*, 58–65.
85. Latour, R. A.; West, J. K.; Hench, L. L.; *et al.* In *Bioceramics*; Sedel, L., Rey, C., Eds.; Elsevier: New York, NY, 1997; Vol. 10, pp 541–544.
86. West, J. K.; Latour, R. A.; Hench, L. L. *J. Biomed. Mater. Res.* **1997**, *37*, 585–591.
87. Tobias, D. J.; Mar, W.; Blasie, J. K.; Klein, M. L. *Biophys. J.* **1996**, *71*, 2933–2941.
88. Nordgren, C. E.; Tobias, D. J.; Klein, M. L.; Blasie, J. K. *Biophys. J.* **2002**, *83*, 2906–2917.
89. Mantero, S.; Piuri, D.; Montevecchi, F. M.; Vesentini, S.; Ganazzoli, F.; Raffaini, G. *J. Biomed. Mater. Sci.* **2002**, *59*, 329–339.
90. Raffaini, G.; Ganazzoli, F. *Langmuir* **2003**, *19*, 3403–3412.
91. Raffaini, G.; Ganazzoli, F. *Langmuir* **2004**, *20*, 3371–3378.
92. Raffaini, G.; Ganazzoli, F. *Phys. Chem. Chem. Phys.* **2006**, *8*, 2765–2772.
93. Raffaini, G.; Ganazzoli, F. *J. Mater. Sci. Mater. Med.* **2007**, *18*, 309–316.
94. Basalyga, D. M.; Latour, R. A. *J. Biomed. Mater. Res.* **2003**, *64A*, 120–130.
95. Latour, R. A.; Hench, L. L. *Biomaterials* **2002**, *23*, 4633–4648.
96. Latour, R. A.; Rini, C. J. *J. Biomed. Mater. Res.* **2002**, *60*, 564–577.
97. Wilson, K.; Stuart, S. J.; Garcia, A.; Latour, R. A. *J. Biomed. Mater. Res.* **2004**, *69A*, 686–698.
98. Klamt, A.; Schuurmann, G. *J. Chem. Soc. Perkin Trans.* **1993**, *2*, 799–805.
99. He, Y.; Hower, J.; Chen, S. F.; Bernards, M. T.; Chang, Y.; Jiang, S. Y. *Langmuir* **2008**, *24*, 10358–10364.
100. Hower, J. C.; Bernards, M. T.; Chen, S. F.; Tsao, H. K.; Sheng, Y. J.; Jiang, S. Y. *J. Phys. Chem. B* **2009**, *113*, 197–201.
101. Hower, J. C.; He, Y.; Bernards, M. T.; Jiang, S. Y. *J. Chem. Phys.* **2006**, *125*, Article 214704.
102. Zhou, J.; Chen, S.; Jiang, S. *Langmuir* **2003**, *19*, 3472–3478.
103. Zhou, J.; Zheng, J.; Jiang, S. Y. *J. Phys. Chem. B* **2004**, *108*, 17418–17424.
104. Skelton, A. A.; Liang, T. N.; Walsh, T. R. *Interfaces* **2009**, *1*, 1482–1491.
105. Skelton, A. A.; Walsh, T. R. *Mol. Simulat.* **2007**, *33*, 379–389.
106. Notman, R.; Walsh, T. R. *Langmuir* **2009**, *25*, 1638–1644.
107. Tomasio, S. D.; Walsh, T. R. *Mol. Phys.* **2007**, *105*, 221–229.
108. Tomasio, S. M.; Walsh, T. R. *J. Phys. Chem. C* **2009**, *113*, 8778–8785.
109. Grossfield, A.; Ren, P. Y.; Ponder, J. W. *J. Am. Chem. Soc.* **2003**, *125*, 15671–15682.
110. Schnieders, M. J.; Baker, N. A.; Ren, P. Y.; Ponder, J. W. *J. Chem. Phys.* **2007**, *126*, Article 124114.
111. Stone, A. J. *Chem. Phys. Lett.* **1981**, *83*, 233–239.
112. Stone, A. J.; Alderton, M. *Mol. Phys.* **1985**, *56*, 1047–1064.
113. Iori, F.; Corni, S. *J. Comput. Chem.* **2008**, *29*, 1656–1666.
114. Iori, F.; Di Felice, R.; Molinari, E.; Corni, S. *J. Comput. Chem.* **2009**, *30*, 1465–1476.
115. Makrodimitris, K.; Masica, D. L.; Kim, E. T.; Gray, J. J. *J. Am. Chem. Soc.* **2007**, *129*, 13713–13722.
116. Masica, D. L.; Gray, J. J. *Biophys. J.* **2009**, *96*, 3082–3091.
117. Bradley, P.; Misura, K. M. S.; Baker, D. *Science* **2005**, *309*, 1868–1871.
118. Lazaridis, T.; Karplus, M. *Proteins* **1999**, *35*, 133–152.
119. Latour, R. A. *Biointerphases* **2008**, *3*, FC2–FC12.
120. Vellore, N. A.; Yancey, J.; Collier, G.; Stuart, S. J.; Latour, R. A. *Langmuir* **2010**, , *26*, 7396–7404, DOI: 10.1021/la904415d.
121. Sun, Y.; Dominy, B. N.; Latour, R. A. *J. Comput. Chem.* **2007**, *28*, 1883–1892.
122. Agashe, M.; Raut, V.; Stuart, S. J.; Latour, R. A. *Langmuir* **2005**, *21*, 1103–1117.
123. Sivaraman, B.; Latour, R. A. *Biomaterials* **2010**, *31*, 832–839.

Relevant Websites

http://www.rcsb.org/pdb/home/home.do – Protein data bank for protein structures.
Molecular simulation programs:
http://ambermd.org/ – AMBER.
http://www.charmm.org/ – CHARMM.
http://www.gaussian.com/ – Gaussian.
http://www.gromacs.org/ – GROMACS.
http://accelrys.com/products/materials-studio/ – Materials Studio.
http://www.ks.uiuc.edu/Research/namd/ – NAMD.
http://www.schrodinger.com/ – Schrodinger.

3.312. Cell Culture Systems for Studying Biomaterial Interactions with Biological Barriers

R E Unger, C Pohl, I Hermanns, C Freese, and C J Kirkpatrick, Johannes Gutenberg University, Mainz, Germany

© 2011 Elsevier Ltd. All rights reserved.

3.312.1.	**Introduction**	194
3.312.1.1.	Major Epithelial and Endothelial Barriers in Drug Transport	194
3.312.1.1.1.	Epithelial barriers of the gastrointestinal tract	194
3.312.1.1.2.	Inhalation barriers: airway epithelium	195
3.312.1.2.	Skin	195
3.312.1.3.	Blood–Brain Barrier	195
3.312.1.4.	Other Routes for Drug Delivery	195
3.312.1.5.	Tissue Targeting	195
3.312.2.	**The Upper Respiratory Tract: Barrier Functions of the Bronchial Epithelium**	195
3.312.2.1.	Introduction	195
3.312.2.2.	Mucociliary Clearance	196
3.312.2.3.	Integrity of the Bronchial Epithelium	196
3.312.2.4.	Cell Culture Models of Bronchial Epithelial Cells	196
3.312.2.5.	Human Primary Cell Bronchial Coculture Models	196
3.312.2.6.	Specific Applications	197
3.312.2.6.1.	Transport through barriers	197
3.312.2.6.2.	Ciliary beat frequency	199
3.312.2.7.	Potential and Limitations of the Bronchial Models	199
3.312.3.	**The Lower Respiratory Tract: Cell Culture Models Mimicking the Biological Barriers of the Distal Lung**	200
3.312.3.1.	The Biological Barriers of the Distal Lung	200
3.312.3.1.1.	Cell culture models of alveolar epithelial cells	201
3.312.3.1.2.	Characterization of alveolar epithelial cells	201
3.312.3.2.	Primary Isolated Human Alveolar Type II Epithelial Cells	201
3.312.3.3.	Human Cell Lines with Alveolar Epithelial Cell Characteristics	202
3.312.3.4.	Cell Culture Models of the Alveolar–Capillary Barrier	203
3.312.3.5.	Characterization of Human Pulmonary Capillary Endothelial Cells	203
3.312.3.6.	Primary Alveolar Epithelial Cells and Microvascular Endothelial Cells in Coculture	204
3.312.3.7.	Coculture of NCI H441 with ISO-HAS-1	204
3.312.3.8.	Specific Applications	205
3.312.3.8.1.	Transport studies	205
3.312.3.8.2.	Uptake of micro- and nanoparticles	205
3.312.3.8.3.	Influence of cytokines on barrier properties	206
3.312.3.9.	Potential and Limitations of Available Cell Culture Models	207
3.312.4.	***In Vitro* Studies with Endothelial Cells from the BBB**	207
3.312.4.1.	Introduction	207
3.312.4.2.	Characteristics of the BBB	208
3.312.4.3.	Characterization of Brain Endothelial Cells	208
3.312.4.4.	Primary Isolated Human Brain Endothelial Cells	209
3.312.4.5.	Primary Porcine Brain Endothelial Cells and Pericytes	209
3.312.4.5.1.	Isolation	209
3.312.4.5.2.	Characterization	209
3.312.4.5.3.	*In vitro* coculture model with PBECs and pericytes	210
3.312.4.6.	Analysis of Novel Biomaterials with Cells from the BBB	210
3.312.5.	**Conclusion and Future Perspectives**	212
References		212

Abbreviations

AJ	Adherens junctions	**ATP**	Adenosine triphosphate
AJC	Apical junctional complex	**BBB**	Blood–brain barrier
AQP-5	Aquaporin-5	**CBF**	Ciliary beat frequency
		CD31	Cluster of differentiation

CLSM	Confocal laser scanning microscopy
CNS	Central nervous system
DPPC	Dipalmitoylphosphatidyl-choline
EC	Endothelial cells
FACS	Fluorescence-activated cell sorting
FITC	Fluorescein isothiocyanate
GI	Gastrointestinal tract
hATII	Human alveolar type II cells
hATI-like	Human alveolar type I-like cells
hCMEC/D3	Human cerebral microvascular endothelial cell line
HPMEC	Human pulmonary microvascular endothelial cells
IFN-γ	Interferon gamma
LDH	Lactate dehydrogenase
MTS	(3-(4,5-dimethylthiazol-2-yl)-5-(3-carboxymethoxyphenyl)-2-(4-sulfophenyl)-2H-tetrazolium
MTT	(3-(4,5-Dimethylthiazol-2-yl)-2,5-diphenyltetrazolium bromide
NG-2	Neuron-glial 2
Papp	Apparent permeability coefficient
PBECs	Porcine brain endothelial cells
PDGFR-β	Platelet-derived growth factor receptor-beta
PECAM-1	Platelet endothelial cell adhesion molecule-1
PEI-OG	Oregon green-coupled polyethyleneimine
PLGA	Poly(D,L)-lactic-*co*-glycolic acid
RAGE	Receptor for advanced glycation end products
RT-PCR	Reverse-transcription polymerase chain reaction
SEM	Scanning electron microscopy
SMA	(α) Smooth muscle actin
SP-A (B, C, D)	Surfactant protein A (B, C, D)
TEER	Transepithelial electrical resistance
TEM	Transmission electron microscopy
TER	Transbilayer electrical resistance
TJ	Tight junctions
TNF-α	Tumor necrosis factor alpha
TT1	Transformed type I cells
TTF-1	Thyroid transcription factor-1
VE-cadherin	Vascular endothelial cadherin (cadherin-5)
vWF	von Willebrand factor
ZO-1	Zonula occludens protein 1

3.312.1. Introduction

Heterotypic cell interactions, that is, the interactions between cells of different types, are essential for establishing functional tissues and models mimicking organs from the body. The study of cell–cell interactions in models of higher complexity is very relevant for studies in tissue regeneration and possible application to drug and gene delivery.[1] In the past few years, nanomedicine has become a major topic along with the development of nano-scale therapeutic systems.[2] Although there is considerable knowledge about the physicochemical properties of nanostructures, much less is known about nanobiology, including the mechanisms of uptake of nanoparticles and how the human body reacts to nanostructures of different size and surface chemistry.

Nanoparticles can enter the body by passing through biological barriers, which include the skin, the cornea of the eyes, and the membranes lining the respiratory, digestive, urinary, and reproductive tracts. Epithelial and endothelial barriers separate the body from the external environment and the compartments of the body from each other. The plasma membrane of polarized cells is divided into an apical compartment which is exposed to foreign compounds and a basolateral region which communicates with the underlying structures.[3]

Tight junctions (TJs) are generated between adjacent cells and are necessary to form a functional barrier by the epithelial and endothelial cell types.[4] TJs located at the apical borders of the cells are responsible for the transport of ions and neutral molecules through the paracellular space.[5] However, this paracellular movement restricts the uptake especially of macromolecules. Desmosomes and intermediate junctions are located at the lateral borders, and the basal side is generally characterized by a basal lamina.[6] Membranes in both the apical and basolateral compartments are composed of a lipid bilayer in which proteins are integrated. These are complex systems which nano- and macromolecules have to enter or to leave via a specific transport system across the barrier.[2] The mucus layer protecting epithelial surfaces is an additional extracellular barrier, which also plays a major role in drug and gene delivery in the lung and the gastrointestinal tract (GI).[7] The mucus is formed by lipids, mucins, and glycoproteins and exists as a bilayer. An outer viscous gel-like fraction is layered upon a more firm epithelial-cell adherent fraction.[8] It is evident that all of these major components need to be considered in any assay system designed to simulate barriers in order to study biomaterial uptake.

3.312.1.1. Major Epithelial and Endothelial Barriers in Drug Transport

3.312.1.1.1. Epithelial barriers of the gastrointestinal tract

Oral administration of drugs is the most used method of drug therapy. Absorption of these drugs is given by the membrane permeability. The transepithelial electrical resistance is one of the methods used to measure the integrity and tightness of the barrier and is the lowest in the small intestine.[9] The barrier is formed by a columnar epithelial cell layer covered with a mucus membrane that protects and physically separates the epithelial cells from the gut contents. Because of the leaky paracellular TJs as compared to the other parts of the GI, jejunum, and ileum are considered as the weakest barrier and therefore the major target of drug absorption in the body.[9] Differences in anatomical structure, distinct lipid alignment of the membranes, and different expression patterns of the TJ family lead to the distinction in paracellular permeability between the regions of the GI tract.[10]

3.312.1.1.2. Inhalation barriers: airway epithelium

The respiratory tract is a main portal for inhaled particles and toxic substances. During inhalation, particles and organisms present in the inhaled air are immobilized in the mucus lining fluid and mostly filtered out by the coordinated beating of cilia. The bronchial region is an integral part of the pulmonary system and consists of the trachea, the main bronchi, and the bronchioles.[11] The trachea branches into two main bronchi that continue to branch and eventually give rise to the bronchioles which lead to the alveoli. Although the human alveolar barrier has a much larger surface area of about 120 m^2 compared to the upper airways that have a surface area of about 0.24 m^2, the upper respiratory system with the mucociliary clearance is the first line of defence against foreign substances.[12–14]

Drug delivery across the ciliated and nonciliated epithelial cells, the type I and II pneumocytes on the apical side of the alveoli, and the pulmonary endothelial cells on the basolateral side is regarded as a realistic possibility for systemic therapy.[15]

3.312.1.2. Skin

Because of its anatomical structure with a keratinized layer, the skin is the least permeable to both small molecules and macromolecules. The skin is composed of two major layers, an upper multilayer of cells (epidermis) consisting primarily of keratinocytes of varying stages of differentiation attached to one another by desmosomes and an underlying connective tissue layer (dermis) separated by a basal membrane. The upper layer of the epidermis is known as the stratum corneum and consists of various keratinocyte cells surrounded by cross-linked proteins and a covalently bound lipid membrane which is responsible for the extremely low permeability to water and solutes. Transdermal drug delivery is the most used nonoral technology for therapeutic application offering drug delivery over a large surface area.[16]

3.312.1.3. Blood–Brain Barrier

The blood–brain barrier (BBB) is the major portal of entry for drug delivery to the central nervous system (CNS) and has an essential function in protecting the brain tissue. The integrity of the BBB is guaranteed by cell–cell interactions between three major cell types, namely, the brain capillary endothelial cells (ECs) and closely apposed pericytes and astrocytes. The endothelial cells of the brain in contrast to endothelial cells from other sites of the body are attached to each other by TJs. These structures are similar to those seen in epithelial barriers and represent the morphological basis of the integrity of the BBB. The endothelial TJs of the BBB contain occludin, junctional adhesion molecule, and claudin and are linked to the cytoskeleton of the endothelial cells via zonula occludins. Furthermore, the endothelial cells of the BBB contain numerous systems that tightly regulate the transcellular transport of ions and molecules into and out of the brain. These include efflux transporters to passively transport lipophilic molecules from the blood to the brain and back again and brain endothelial-specific transporters that deliver specific nutrients such as glucose, amino acids, and vitamins from the blood to the brain. A difference between the BBB endothelial cells and the epithelial barriers in the body is that the barrier formed by the endothelial cells in the brain vasculature is entirely regulated by the interactions and cell–cell communication that take place with the endothelial cells and their close contact to the pericytes, the astrocytes, and the neural cells of the brain.

3.312.1.4. Other Routes for Drug Delivery

Besides the barriers mentioned above, other barriers are built, for example, from the olfactory system, which consists of epithelial and endothelial cells.[17] Other barriers are the cornea of the eyes and the uroepithelial barrier.[18,19] Another important one is the vascular system, made up of vessels that carry blood and lymph through the body. Micro- and nanoparticles delivery directly to the circulation will reach practically all tissues of the body, so that this portal of entry demands an effective, targeting system. The latter represents a major challenge for the life sciences with respect to defining specific molecules which characterize the various target organs.

3.312.1.5. Tissue Targeting

Drug and gene delivery is often limited by inefficient transport through the heterotypic cell interactions and complex biological environments. The route a particle takes through the epithelium is not yet known. The particle can cross the barrier for instance through the cell or can pass the barrier between the cells or can pass it via the TJs. Developments of new targeted delivery of therapeutic agents to specific tissues are often limited by the available *in vitro* models. Thus, for example, a model for the GI tract or the lungs must be able to built mucus and TJs to study the biological mechanism and to mimic more realistic conditions. Therefore, it is essential to develop biological systems for understanding the complexity of cell–biomaterial or cell–nanoparticle interactions.[1,20,21]

To avoid loss of promising compounds and biomaterials in clinical studies, the design of the study and the limitations or settings of the different models, cultures, and cells must be clarified. Several models and systems using different stages of complexity have been established and extend from whole animal studies through cell culture systems and 3D models[22–24] to the point of isolated liposomes.[25] The choice of the test system is often a compromise between high throughput or higher complexity and significance. However, not all screenings can be done in animal testing which has the transferability of the results to humans, so that *in vitro* cell culture models offer an alternative to preselect and test drug and gene delivery.[7]

In the sections below, potentials and limitations of different models of the blood–air barrier and the BBB are described with regard to their barrier properties, the uptake, intracellular transport, and localization of the compounds within the cell, and the effects on cell–cell interactions. Importantly, how these model systems can be applied to the study of novel biomaterials is described.

3.312.2. The Upper Respiratory Tract: Barrier Functions of the Bronchial Epithelium

3.312.2.1. Introduction

The respiratory tract is a main portal for inhaled particles and toxic substances. The bronchial region is part of the pulmonary

system and consists of the trachea, the main bronchi, and the bronchioles.[11] The epithelium of the bronchi consists of cuboidal cells which include several cell types, with the most prominent being basal, ciliated, and secretory cells.[26,27]

Ciliated cells amount to about 50% of the tracheal epithelium, while basal calls, Clara cells (bronchioles), and secretory cells form the rest. The secretory cells exhibit a higher number in the distal airways and are present in lower numbers in the large airways.[28] Ciliated cells are 20–60 μm tall and exhibit about 250 cilia on the apical surface of each cell and these cells play a very important role in mucociliary clearance.[29,30] Secretory cells build a viscoelastic layer about 5–10 μm in height, which covers the pulmonary system on top of the cilia.[31–33] Basal cells are flattened cells which remain on the basolateral side between the other cells but do not contribute to the apical region of the pulmonary layer.[34] These may be progenitor cells differentiating to the ciliated form as well as secretory cells.[29,35–37]

3.312.2.2. Mucociliary Clearance

Inhaled bacteria, viruses, or particles are cleared from the airways by mucociliary clearance. Mucus transport is controlled by a coordinated ciliary beating and airflow. The mucus layer forms two or three layers and lies superficial to the cilia. Oligomerized glycoproteins ensure that the mucus layer is both elastic and viscous.[38,39] It is evident that the presence of this mucus layer is highly relevant for biomaterial particle interactions with the barrier.

Mucociliary clearance is driven by two major mechanisms: primarily the ciliary action and secondarily by coughing when ciliary beating fails or is overloaded. Mucus is synthesized by serous cells, goblet cells, Clara cells, and type II alveolar cells.[40,41] The amount of mucus in a section is dependent on the number of mucus-producing cells in this particular region, so that the degree of mucociliary clearance is higher in the peripheral than in the central airways and therefore, ciliated cells per section decrease from the peripheral to the central airways.[42] Cilia beat at a rate of 700–1000 beats min^{-1}.[43] The coordinated metachronal waves generated by cilia flow is in opposite direction to the mucus flow. Mucociliary clearance which extends to the terminal bronchioles is normally complete within hours or extends up to one day.[44]

3.312.2.3. Integrity of the Bronchial Epithelium

In addition to mucociliary activity, the formation of diffusion barriers is a fundamental requirement for the physiological functioning of the respiratory epithelium.[45] To form a functional barrier, TJs[4] and adherens junctions (AJ) have to be generated between adjacent cells. Proximal lung epithelial barrier function is regulated by an apical junctional complex (AJC) consisting of proteins of TJs and AJs. TJs, located at the apical borders of the cells, are responsible for the transport of ions and neutral molecules through the paracellular space and several lung diseases are due to a disruption to these proteins.[46]

The transepithelial electrical resistance (TEER), the transbilayer electrical resistance (TER), and the paracellular movement are methods used to measure the integrity and tightness of the barrier.

3.312.2.4. Cell Culture Models of Bronchial Epithelial Cells

Although primary bronchial cells are available, cell lines are widely used for toxicological studies of the respiratory tract. Among these cell lines Calu-3, BEAS-2B, and 16HBE14o− are well established.

The immortalized bronchial cell line (16HBE14o−) was generated from a 1-year-old heart–lung patient and transformed with the SV40 large antigen. This cell line retains different epithelial functions such as the presence of both TJs and AJs.[47] 16HBE14o− cells in coculture with fibroblasts under air–liquid interface conditions induced a multilayered growth, but no bronchial tissue-like differentiation was seen.[7,48] Additionally, 16HBE14o− cells do not form an organized epithelial layer. Although 16HBE14o− cells were immortalized from primary isolated bronchial epithelial cells they did not have the capacity to differentiate to the three main bronchial phenotypes as is the case for primary isolated HBECs (human bronchial epithelial cells) cells from explant-outgrowth cultures. An additional cocultivation with the fibroblast cell line Wi-38 used in certain sudies also failed to trigger 16HBE14o− cell differentiation. Although the cellular organization of 16HBE14o− was less distinctive, 16HBE14o− in coculture with Wi-38 showed higher maximum TER and lower P_{app} values (apparent permeability coefficients) than HBEC in coculture. This effect is most likely because of the physical barrier generated by the 16HBE14o− cells, multilayered growth properties and not because of a tighter barrier formed by 16HBE14o− cells at cell–cell junctions (see **Section 3.312.2.6**).[49]

Calu-3 cells are a submucosal gland cell line, which was generated from a bronchial adenocarcinoma. Under air–liquid interface conditions Calu-3 cells grow in monolayers, producing mucus and cilia-like microvilli. Because of the presence of TJs, Calu-3 cells are often used for transport studies.[50,51]

BEAS-2B is also a human epithelial cell line which is commercially available and is an adenovirus-12 SV40 hybrid virus-transformed and nontumorigenic cell line. This cell line is often used for toxicity studies and to study airway epithelial structures, but does not form TJs.[34,52–54] In addition, there is no mucus secretion (**Table 1**).[58]

The cell lines are useful for certain studies, although they are not feasible for studies of mucociliary clearance.

3.312.2.5. Human Primary Cell Bronchial Coculture Models

A number of human bronchial models based on epithelial–fibroblast cocultures have been described[59–61] as well as a variety of animal models regarding the bronchial tract.[62] In the section below, a coculture model of the bronchial tract established by our group is described.[49,63,64]

Table 1 Expression of different mucins in the cell lines and primary cells; mucins in the coculture were measured with immunofluorescence and RT-PCR

	MUC 2	*MUC 4*	*MUC 5AC*	*MUC 5B*	*MUC 8*
16HBE14o−	−[55]	+/−[55]		+/−[55]	
Calu-3	−[55]	+/−[55]		+/−[55]	
Native lung	+[56]	+[57]	+[56]	+[56]	+/−[56]
Coculture		+	+	+	+/−

Human bronchial epithelial explant-outgrowth cells (HBECs) were isolated according to a method of Lechner[65] and modified as previously described.[49,64] Small bronchi (diameter <5 mm) were first dissected from the remaining peripheral lung tissue and cut into defined pieces of 1–2 cm^2 size. The small explants were cultivated in tissue culture flasks coated with rat-tail collagen type 1. HBECs migrated out of the explants after 1 week. The bronchial models were established as a bilayer coculture of the isolated HBEC with the lung fibroblast cell line Wi-38. For cocultures, the upper surface of Transwells was coated with a solution of collagen type 1 in 0.1 M acetic acid and air-dried at room temperature. Fibroblasts ($1 \times 10^4\ cm^{-2}$) were placed on the lower surface of inverted 24-well HTS-Transwell filter membranes and incubated for 2 h at 37 °C and 5% CO_2. The filter plates were then inverted and placed in 24 well plates filled with 1 ml medium per well. The bronchial cells ($5 \times 10^4\ cm^{-2}$) were subsequently seeded on the top surface of the HTS 24-Transwell filter membranes and grown to confluence simultaneously with the Wi-38 cells on the lower surface. After 3 days of coculture, bronchial models were placed at an air–liquid interface and only fed basolaterally with media. Media were replaced twice weekly.

After the explant outgrowth from the small bronchial tissue fragments, the HBEC showed cuboidal morphology and stained positively for the basal cell markers, cytokeratin 14 (CK14), and aquaporin 3 (AQP-3). Immunofluorescent staining for different types of mucins (MUC 2, MUC 5AC, MUC 5B) as well as for β-tubulin, a structural protein of cilia, was negative (Figure 1).

The HBEC differentiated to a ciliated pseudostratified airway epithelium in the cocultures in the 24 Transwells. During the first two weeks of cocultivation, the morphological phenotype of the HBEC changed from a more squamous to a pseudostratified epithelium. Within 21 days of coculture, all three major cell types of the bronchi (basal, ciliated, secretory) could be observed.

In coculture with the fibroblast cell line Wi-38, the HBEC showed ciliated cells after 21 days in culture (Figure 2(c) and 2(d)). At this time point, the HBEC in monoculture merely formed apical extensions similar to the cell lines 16HBE14o− and the Calu-3 (Figure 2(a) and 2(b)), but no mature cilia with the typical 9-plus-2 pattern of microtubules were detected, this being in marked contrast to that observed in the coculture (Figure 3(b)). After 21 days in coculture, a bronchial layer showing the tight junctional protein ZO-1 at the cell–cell contact areas and β-tubulin within the cilia was observed by immunofluorescence (Figure 3(c)).

During the cocultivation period, the proportion of ciliated cells slightly increased but the principal finding was that the cilia gained in length. Furthermore, the cilia generated were actively beating (frequency between 14 and 19 Hz depending on the donor). After 4 weeks of coculture, a distinct film of acid mucosubstances (Figure 3(d)) was observed on top of the epithelial layer which persisted for up to 12 weeks in culture. From 4 to 12 weeks in coculture, the thickness of the epithelial layer stayed constant but the proportion of ciliated cells and the length of the cilia increased significantly.[49]

3.312.2.6. Specific Applications

3.312.2.6.1. Transport through barriers

TEER is a measure of the tightness of intercellular TJs. The electrical resistance across the cultures is usually measured using an EVOM voltohmmeter (World Precision Instruments,

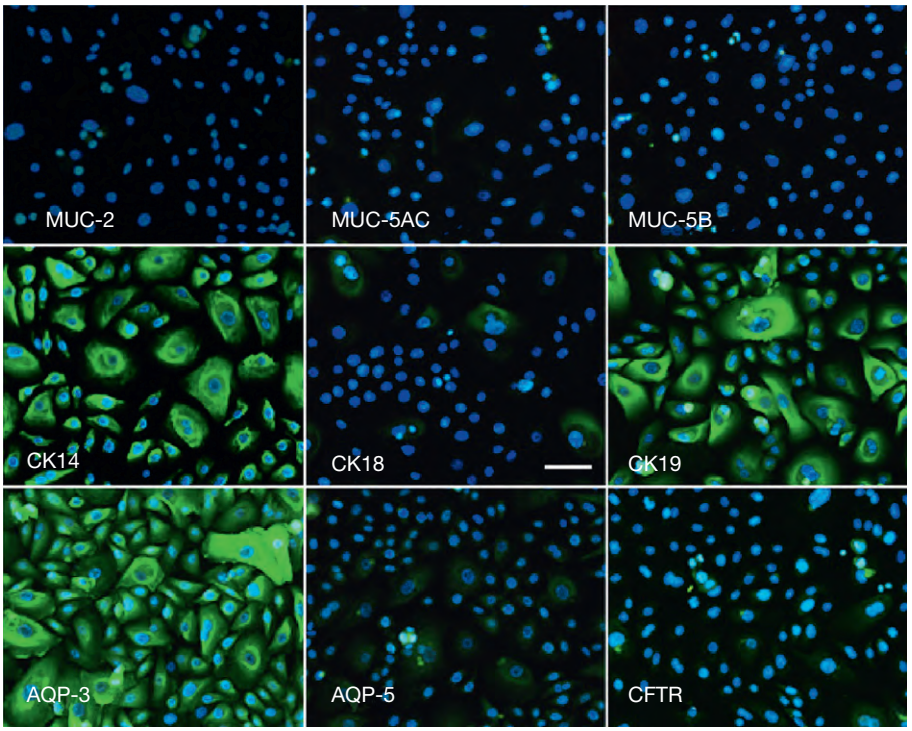

Figure 1 Immunofluorescent staining of outgrowth cells (scale bar = 20 μm; all images were taken at the same magnification).

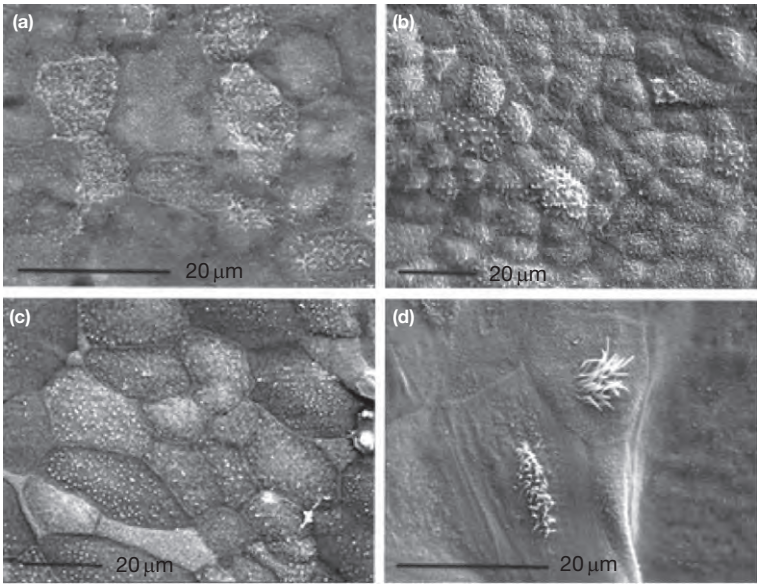

Figure 2 Scanning electron microscopic images of 16HBE14o− (a), Calu-3 (b), and HBEC (c and d) on Transwell filter membranes after 28 days in coculture with Wi-38. 16HBE14o− and Calu-3 formed apical extensions, but only cocultures with the primary HBEC formed functioning cilia.

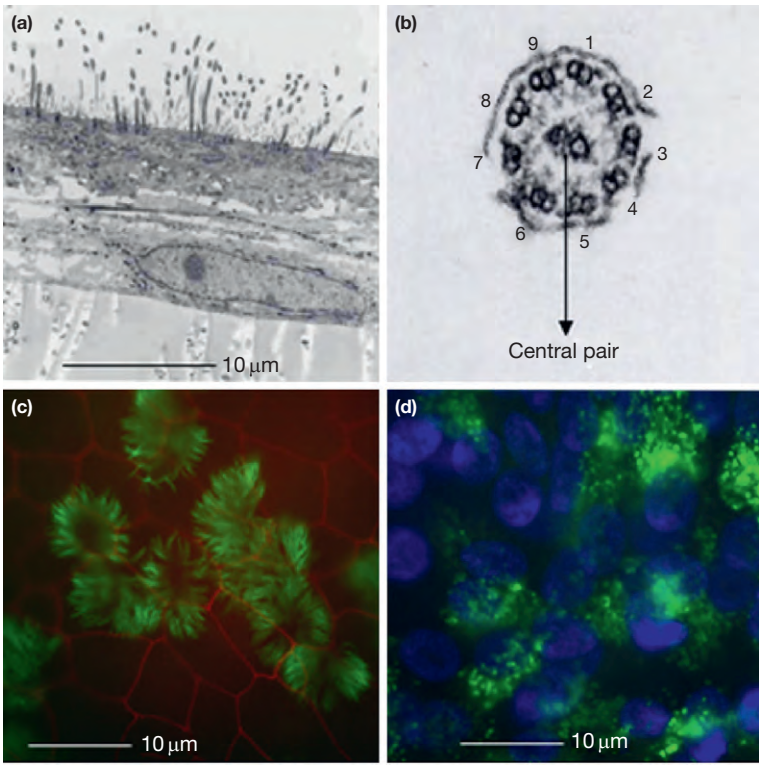

Figure 3 Image (a) shows a transmission electron micrograph of the differentiated primary cell culture model performed after 28 days in coculture, demonstrating basal, ciliated, and secretory cells. Cilia present their normal structure of nine outer doublet microtubules surrounding the central pair of single microtubules, similar to that found *in vivo* (b). Immunofluorescent staining of bronchial cells in coculture with Wi-38 on Transwell filter membranes with β-tubulin (green fluorescence) and ZO-1 (red fluorescence) is shown in (c). The apical intercellular TJ complex is present between adjacent ciliated and nonciliated cells. The mucus layer generated by the cells is shown by immunofluorescence of Muc5Ac (d).

Berlin, Germany) with chopstick electrodes. The electrical resistance is obtained by multiplying the meter readings by the effective surface area of the filter membrane. The resistance is inversely proportional to the surface area. Thus, the larger the membrane, the lower the resistance is

$$\text{Resistance of a unit area} = \text{Resistance } (\Omega) \times \text{Effective membrane area } (\text{cm}^2)$$

After 10 days in coculture, the HBEC showed a detectable transepithelial resistance. TER increased during the cultivation time to a maximum of 600–800 $\Omega\,\text{cm}^2$ (depending on the donor) at day 14–17 and remained relatively constant during long term cultivation, that is, over 3 months.[49,63,64]

The electrical resistance of the cell line 16HBE14o− is heavily dependent on the culture conditions. 16HBE14o− show TEER values of about 600–700 $\Omega\,\text{cm}^2$ after 10 days in monoculture grown under submerged conditions and about 100 $\Omega\,\text{cm}^2$ grown under air–liquid interface conditions. In coculture with Wi-38, TER values reached a maximum of 1000–1200 $\Omega\,\text{cm}^2$ during the cultivation time of 10 days and stayed constant for 4 days before TER decreased.[7,48,49,66–68]

Calu-3 reached a maximum TEER at day 10–11 of about 400–700 $\Omega\,\text{cm}^2$ under air–liquid interface culture conditions. Under submerged conditions, Calu-3 cells were able to build tighter junctions with TEER values up to 1000 $\Omega\,\text{cm}^2$ (Table 2).

Another assessment of the tightness of the barrier in the epithelial layer is to measure the paracellular movement. Substances often used for transport are the anionic hydrophilic marker sodium-fluorescein and FITC-labeled dextrans with different molecular weights. The apparent permeability coefficients (P_{app}) were calculated using the following equation:

$$P_{app} = \frac{V_{res}}{A \times c_{t0,\,don}} \times \frac{dc_{res}}{dt}\,(\text{cm s}^{-1})$$

with V_{res} value in the receiver compartment; dc_{res}/dt solute flux; A surface area of the filter; $c_{t0,\,don}$ the initial drug concentration (Table 3).

Table 2 Transepithelial and transbilayer electrical resistance ($\Omega\,\text{cm}^2$)

	Submerged	*Air–liquid interface*	*Coculture with Wi-38 at air–liquid interface*
16HBE14o−	600–700[7,68]	100[7,66]	1000–1200[49]
Calu-3	1000[7,69]	400–700[70,71]	900–1000 (unpublished results)
HBEC	100[49]	100–200[49]	600–700[49,63,64]

Table 3 P_{app} values for the transport of sodium fluorescein (a) FITC-dextran 20 kDa (b) across the different cell layers P_{app} ($10^{-6}\,\text{cm s}^{-1}$)

	Submerged	*Air–liquid interface*	*Coculture with Wi-38 at air–liquid interface*
16HBE14o−	(a) 0.85[72]	(a) 4.9[72]	(a) 1.1[49] (b) 0.0043[49]
Calu-3	(a) 0.11[7] (b) 0.001[73]	(a) 0.23[71]	
HBEC			(a) 0.9[49] (b) 0.0015[49]

3.312.2.6.2. Ciliary beat frequency

In host defence and in the removal of foreign material, mucociliary transport plays a very important role. A dysfunction of ciliary beating may lead to a variety of respiratory problems. This sensitive system can be influenced by several factors such as hormones as well as parasympathetic or sympathetic neurotransmitters.[74] Most studies addressing the regulation of ciliary function used biopsies or freshly isolated nasal and tracheal epithelial cells where a ciliary beat frequency (CBF) comparable to the *in vivo* situation was retained for no longer than 1 week.[75] In response to a variety of substances such as ATP, NO, or β-agonists, the CBF has been shown to increase.[76,77] On the other hand, a decrease in CBF was shown when interferon-γ (IFN-γ) was added to the culture medium (Table 4).[82,83]

The ciliary beat frequency was measured using a method established by the group of König and Kummer *et al.*[38,42] using rat trachea cells. The coculture model described above with human cells was cultivated over a period of 3 months to obtain a well-differentiated ciliated epithelium. Filters were dissected and mounted on dishes filled with Sylgard gel and then studied by video-optical microscopy. Cells from the coculture were found to beat at a frequency of 14–19 Hz.[49]

In order to be useful as a model system to investigate how nanoparticles or other modulating influences interact with the barrier, the latter must be shown to be responsive to microenvironmental change. Thus, in experiments with cytokines, such as TNF-α and IFN-γ in concentrations found in the mucosa of patients with cystic fibrosis,[84] the following results were obtained: IFN-γ (100 ng ml^{-1}) elicited after 5 min a statistically significant decrease of 11–13 Hz in CBF, but cells then recovered and after 10 min the CBF value did not differ from that at the start of the experiment. The cells were still able to respond to ATP after 70 min. After adding TNF-α and IFN-γ, the cytokines induced a reduction (9–10 Hz) of CBF which was still statistically significant after 30 min. However, the 60 min value did not differ markedly from the value determined at the beginning of the measurement (Figure 4). After 70 min, cilia were again able to respond to ATP. The combination of the cytokines appeared to potentiate the effects on CBF. Such cytokine influences underline the fact the coculture assay is responsive and can undergo recovery.

3.312.2.7. Potential and Limitations of the Bronchial Models

Bronchial epithelial cells represent not only the first line of defence against various toxic and pollutant substances, but also one of the first barriers encountered by inhaled particles designed for drug and gene delivery. One of the early consequences of injury to bronchial epithelium is a change in

Table 4 Ciliary beat frequency in different tissues

Tissue	*Frequency (Hz)*	*References*
Bronchial biopsies	9–14	78,79
Nasal ciliated epithelium	11–16	80
Rat trachea	8–10	81
Coculture model	14–19	49

mucociliary function. The epithelium of the proximal airways include several cell types, among which basal, ciliated, and secretory cells are the most abundant.[26,27] To study human airway epithelial cells *in vitro*, numerous cell culture models using cell lines have been described, but most of these cultures only partially mimic the *in vivo* situation. Immortalized bronchial epithelial cell lines, such as Calu-3, BEAS-2B, or 16HBE14o−, are widely used for toxicology studies of the respiratory tract. Compared to *in vivo* studies, such cell lines have the benefit of flexibility and specific phenotypic traits.[85,86] However, they lack the ability to mimic the different cell types of bronchial epithelium *in vivo*. An alternative to the use of cell lines are primary isolated bronchial cells which contain all phenotypes of the bronchial epithelium. Unfortunately, most primary isolated bronchial epithelial cells rapidly lose their differentiated phenotype *in vitro*, possibly caused by the absence of extracellular matrix, growth factors, and essential hormones.[87]

For nasal, tracheal, and bronchial cultures, primary cells from different species that also demonstrate the formation of cilia and mucus production have been described.[62,88] A human primary coculture which utilizes epithelial–fibroblast interactions to induce a redifferentiation of explant-outgrowth bronchial cells to the main bronchial phenotypes with beating cilia is described by Pohl *et al.*[49] Such epithelial–fibroblast cocultures have also been described by other groups.[59–61]

In host defence and in the removal of foreign material, mucociliary transport plays a very important role. A dysfunction of ciliary beating may lead to a variety of respiratory problems. This sensitive system can be influenced by several factors such as hormones as well as parasympathetic or sympathetic neurotransmitters.[74] Most studies addressing the regulation of ciliary function used biopsies or freshly isolated nasal and tracheal epithelial cells where a CBF comparable to the *in vivo* situation was retained for no longer than 1 week.[75]

Ciliary beat activity of human bronchial epithelial cells *in vitro* is so far only described for human tissue-culture preparations[89] or lung slices[82] and could not be sustained for longer than 25 days. In the already described coculture tissue culture preparations or lung slices, cilia showed a synchronized beating pattern. In the coculture model, we could observe a synchronization between all cilia from one cluster and the beating activity could be maintained for a period of at least 3 months. The primary bronchial model still has to be modified in order to study mucociliary clearance, but could be very useful to investigate not only the long-term effects of toxic or pharmaceutical substances on the ciliary beat frequency, but also the possible interaction and uptake of engineered nanoparticles.

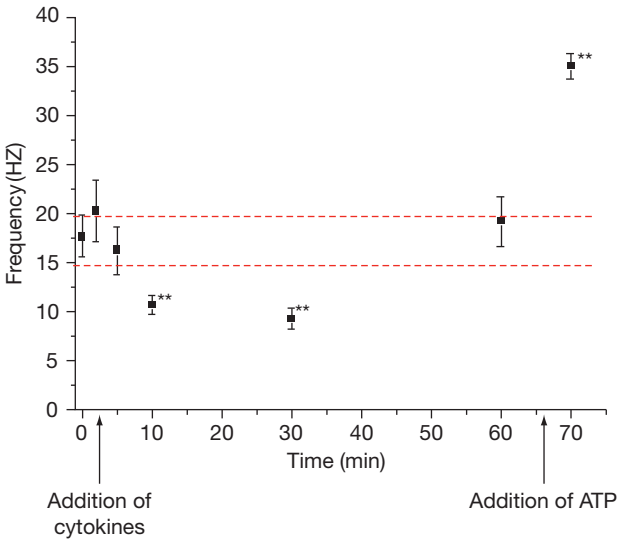

Figure 4 Ciliary beat frequency over a time period of 70 min after treatment with a combination of the cytokines TNF-α and IFN-γ. For every time point at which CBF was measured, 1000 video frames were taken and evaluated with a Fourier transformation. ATP was used as a positive control to determine whether the cilia were still able to respond after cytokine treatment. Data are depicted as means ± SD from $n = 9$ filters from three different donors. Significantly different ($^{*}p < 0.05$ or $^{**}p < 0.01$) from the vehicle-treated control.

3.312.3. The Lower Respiratory Tract: Cell Culture Models Mimicking the Biological Barriers of the Distal Lung

3.312.3.1. The Biological Barriers of the Distal Lung

In the healthy lung, the distal lung barrier is formed by several layers of defence (**Figure 5**). The surface of the alveoli is covered by a thin layer of surfactant with phospholipids and surfactant apolipoproteins acting as a surface active substance lowering the air–liquid surface tension and also functioning as a component of local defence mechanisms in the lung.[90] Alveolar macrophages occur on all epithelial lung surfaces with prevalence in the distal regions. Their number shows great variability, depending on biological parameters such as gender and behavioural parameters such as smoking.[90] With their phagocytic activity, alveolar macrophages function as a first line of cellular defence and patrol the extensive surface area of the alveolar epithelium. The alveolar epithelium itself forms a tight cellular barrier that continuously lines the distal air space, covering more than 99% of the internal surface area of the lungs.[13] It is composed of a monolayer of two morphologically distinct types of cells, namely, type I and type II alveolar

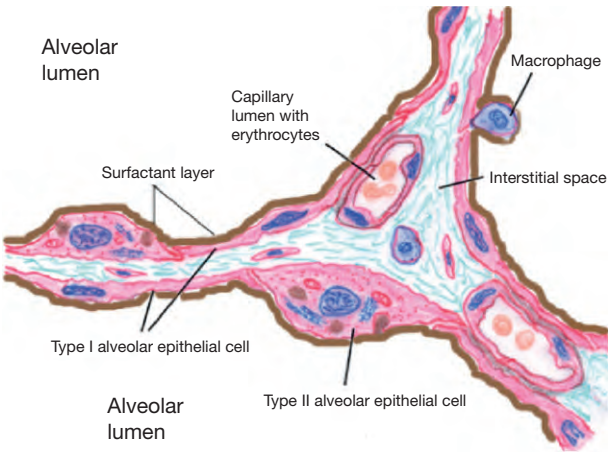

Figure 5 Composition of the distal lung tissue (lower respiratoy tract).

epithelial cells.[91] Both epithelial cell types are involved in gas exchange and fluid homeostasis (reviewed by Matthay *et al.*[92]). Type I cells are characterized by their flattened morphology and cover >95% of the alveolar surface.[93] Alveolar type II (ATII) cells are surfactant-producing cuboidal cells showing many additional metabolic and immunological functions.[4,94–96] Their apical surface is covered with microvilli and their cytoplasm is notable for numerous lamellated inclusions. While the type II cells only cover 7% of the alveolar surface area, they constitute 67% of the epithelial cell number within the alveoli[93] pointing to their biochemical importance. Together with the surfactant proteins, ATII cells play an important role in the clearance of macromolecules by means of the alveolar lining fluid. Type II cells also serve as progenitors for alveolar type I cells during normal lung development[97] or in case of type I cell injury,[98–100] as the latter cells are unable to regenerate themselves. During these repair process, type II alveolar epithelial cells undergo mitosis and a subset of daughter cells initiates the expression of type I cell-associated markers and acquires characteristic type I morphology.[98–101] This process, often termed as transdifferentiation, has also been described *in vitro*. However, the parallels between *in vitro* and *in vivo* ATII transdifferentiation remain to be fully defined, and the term ATI-like cell to represent the *in vitro*-derived ATI phenotype is often adopted. Another cell type also contributing to the distal lung barrier is capillary endothelial cells, which amount up to 30% of all lung cells. The capillary endothelium of the lung does not merely function as a barrier, but also critically regulates systemic and pulmonary vascular function, involving numerous physiological, immunological, and metabolic tasks.[102–105] Moreover, a number of different interstitial cells, mainly fibroblasts and myofibroblasts, exist in the interstitial space, comprising 37% of the total lung cells.

Both alveolar epithelial cell types are interconnected by TJs.[4] The formation of these TJs is accompanied by AJs and these two distinct junctions show not only an intimate spatial but also a functional relationship.[106–108] In contrast to the epithelium, endothelium does not show a clear morphologic differentiation into AJ and apical TJ, with both junctional structures present along the complete lateral aspect of the endothelial contacting zones.[109,110] Because of the large surface area offered by the alveolo-capillary (or air–blood) barrier, there is great interest in using this as a portal of entry for the delivery of drugs or genes in micro- or nanoparticulate form. However, because of its complexity, a rational approach to using this barrier requires a functional model *in vitro* with which to study mechanisms of surface interaction, cellular uptake, and transcellular transport. This is described in the following sections.

3.312.3.1.1. Cell culture models of alveolar epithelial cells

Primary alveolar epithelial cells isolated from rat lungs are one of the best-established and mostly used *in vitro* models for alveolar epithelium. They have been well characterized, and are accompanied by a high reproducibility, convenient availability, and economics of pathogen-free animals.[91] For several decades, these rat-based monolayers have been considered the gold standard in analysis of alveolar epithelial cell physiology and biology. Therefore, it seemed obvious that the same well-established primary rat alveolar epithelial model could be employed for drug delivery studies.[111–113] However, recently models have been developed that are based on animal species which more closely resemble human physiology, for example, porcine lung alveolar epithelial cells.[58] Moreover, a number of laboratories started establishing primary cultures of human alveolar epithelial cells.[96,114–119]

For the human alveolar epithelium, several cell culture models of interest exist, namely, primary culture of alveolar epithelial cells isolated from distal lung tissue, and in terms of cell lines, the TT1, A549, and H441 cells, which will be described in more detail in the following sections. In order to use *in vitro* results as a predictive tool to estimate *in vivo* interactions, the utility and validity of such models must be proven and optimized.[120]

3.312.3.1.2. Characterization of alveolar epithelial cells

Human alveolar type II synthesize and secrete lung phospholipids, a characteristic of pulmonary surface-active material, the surfactant proteins A, B, C, and D (SP-A, SP-B, SP-C, and SP-D),[121] and are responsible for local immunomodulation. In addition, they are the alveolar epithelial repair system after lung injury and during normal cellular turnover.[100] An exclusive marker for type II cells is surfactant protein C (SP-C) or pro-SP-C. All other surfactant proteins are also expressed in cells of the bronchial epithelium or even other epithelial cells of the body. Further markers for the ATII phenotype are the storage organelles of lung surfactant, the lamellar bodies, alkaline phosphatase activity, and the expression of thyroid transcription factor-1 (TTF-1), a transcription regulator of the surfactant proteins A, B, and C.[122,123] With respect to markers for ATI cells, there is still some discordance.[124,125] Varieties of glycocalyx appear to be expressed in ATI versus ATII cells, which can be distinguished by the binding of specific lectins.[126,127] The expression of caveolin-1, the main structural protein of caveolae, has also been used to distinguish ATI from ATII cells, as ATI (but not ATII) cells contain numerous caveolae.[128] Caveolin-1, however, is also highly expressed in lung capillary endothelial cells.[129] Furthermore, aquaporin-5 (AQP-5), a protein localized specifically in the apical plasma membrane of ATI cells[130,131] has received some attention as an ATI cell marker. Different reports from *in situ* studies have shown that transmembrane receptor for advanced glycation end products (RAGE) is localized to the basolateral plasma membrane of ATI cells.[132–134]

3.312.3.2. Primary Isolated Human Alveolar Type II Epithelial Cells

An approach close to the *in vivo* situation uses primary isolated human alveolar type II epithelial cells (hATII) derived from peripheral lung tissue after surgery.[117,118,135,136] Cultivation on permeable filter supports leads to the establishment of a confluent monolayer with hATII cells partly transdifferentiated to alveolar type I-like (hATI-like) cells within 8–10 days of culture. This model appears to be a valuable *in vitro* model for pulmonary drug delivery and transport studies, as TEER values of more than $1000\,\Omega\,cm^2$ can be detected within 8–10 days of culture.[117,118] In addition, cells exhibit TJs as well as desmosomes and show cell-specific lectin binding.[117] In terms of morphological differentiation, they demonstrate a characteristic flattening of cells and transition from a cuboidal

(type II) morphology in early culture stages to a type I-like morphology with flattened extensions.[118] Additionally, a shift in the synthesis of important marker proteins toward the type I phenotype can be shown. Thus, the protein biosynthesis switches with time in culture from low caveolin-1 and high SP-C to high caveolin-1 and low SP-C levels.[118] Moreover, the expression of AQP-5[130] and RAGE[119,130] was shown to increase during the shift of type II to type I phenotype. Nevertheless, in cultures at the age of 7–10 days, cuboidal cells are still occasionally found interspersed in the monolayer and they also contain the typical multilamellar bodies of hATII cells.[119] Figure 6 shows the characteristic transdifferentiation of the hATII cells (with numerous lamellar bodies at day 3) toward the flattened type I phenotype on Transwell filters over time.

3.312.3.3. Human Cell Lines with Alveolar Epithelial Cell Characteristics

In contrast to primary cells, cell lines are often preferred, because of their availability, purity, and reproducibility due to the lack of donor dependency. Although it is possible to isolate primary rodent ATI cells,[125] to our knowledge, there are no methods to isolate hATI cells. Recently, an immortalized alveolar type I-like cell (transformed type I; TT1) was generated by transduction of hATII cells with the catalytic subunit of telomerase and simian virus 40 large-tumour antigen.[39,137] The ATI-like cell phenotype was characterized by immunochemical and morphological methods.[137] Unlike primary hATII cells, the immortalized cells no longer expressed alkaline phosphatase, pro-SP-C, and TTF-1, but expressed increased levels of caveolin-1 and RAGE. Live cell imaging using scanning ion conductance microscopy showed that the TT1 cells were ~40 μm in size, resembling hATI cells *in situ*. Transmission electron microscopy highlighted the attenuated morphology and showed endosomal vesicles in some TT1 cells. Unfortunately, confluent TT1 cell monolayer formation with electrically tight characteristics could not yet be demonstrated.[39] However, the fact that there are characteristic endosomal vesicles in TT1 cells, similar to those found *in situ*, holds much promise as a model to investigate the uptake and transport mechanisms of micro- and nanosized carriers in hATI-like cells, without the need for primary cultures.

The cell line A549 belongs to the group of well-characterized and widely used *in vitro* models for the alveolar type II phenotype. This human lung carcinoma cell line was initiated through explant culture of lung carcinomatous tissue from a 58-year-old Caucasian man[138,139] and is available from the ATCC (American Type Culture Collection). A549 cells exhibit features of alveolar type II cells,[29,34,140] but on account of the production of mucins they also show characteristics of bronchial cells.[141] Although the cell monolayer phenotype of A549 is commonly accepted to be primarily type II in nature, A549 differ from isolated or cultured primary alveolar type II cells in several aspects. In terms of lipid content, phosphatidylglycerol, one of the characteristic phospholipids of pulmonary surface-active material in primary isolated human type II cells (8.9%), is nearly absent in A549 cells (0.1–0.2%).[142] Further distinctive indications are that A549 cells do not express detectable levels of surfactant protein A (SP-A) nor of its mRNA,[143,144] and that they lack the formation of domes (indicating active transepithelial ion transport), whereas human type II cells do.[121] Finally, A549 monolayers show TEER values close to zero even after several days of culture to confluence.[145] This absence of any significant electrical resistance in monolayers of immortalized cell lines is most likely caused by a lack of functional TJs.[146,147] The difference from the 1000 Ω cm^2 TEER values for primary cells may be explained by different intercellular junctions between type II-like cells alone (= A549), type I-like cells alone, or type I and II cells (= primary culture).[148] Differences in the expression of TJs between A549 and primary cells are confirmed by a comparative immunostaining for the TJ protein ZO-1 in primary human cells hATII/hATI-like cells and the A549 cell line. As demonstrated in Figure 7 the protein itself is present in both models. In the case of the hATII/hATI-like cells, it is located at the cell–cell contact zones showing the

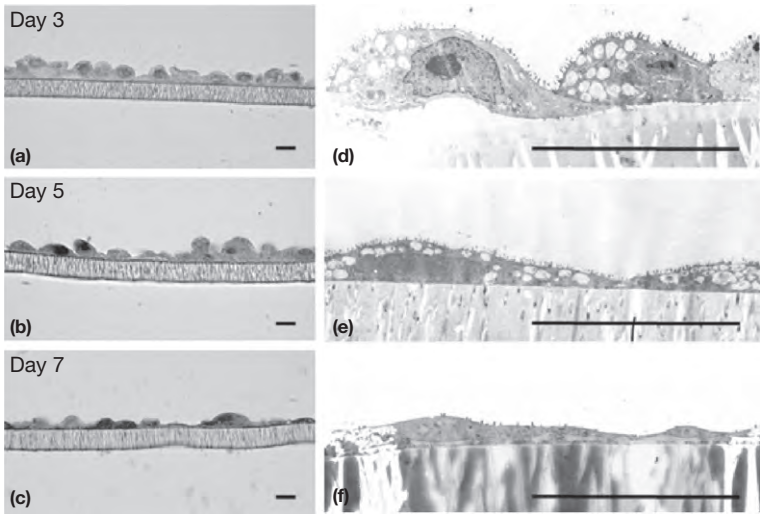

Figure 6 Cross-sections through cultured human alveolar epithelial cells (hATII /hATI-like) in monoculture at different times of culture (a–c), visualized by light microscopy or TEM (d–f). Scale bar = 10 μm.

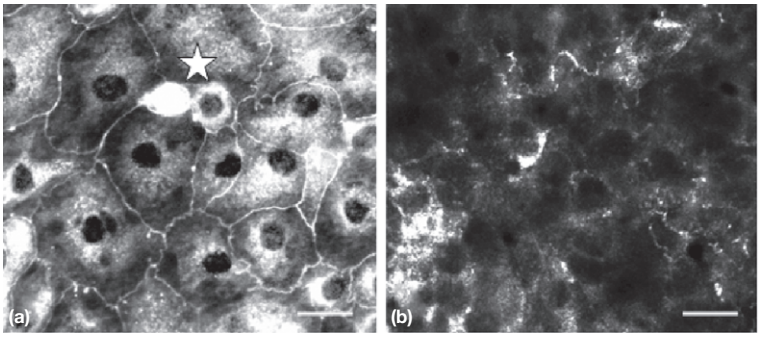

Figure 7 Different morphology of tight junctions compared between primary alveolar epithelial cells and the cell line A549 *in vitro*. (a) Primary human alveolar epithelial cells on day 10 in culture, hATI-like cells with intermediate hATII cells (star). (b) Filter-grown monolayer of A549, 10 days after plating. Both are immunostained for ZO-1 protein (nuclei appear dark). Scale bar = 10 μm. Observation by confocal laser scanning microscopy.

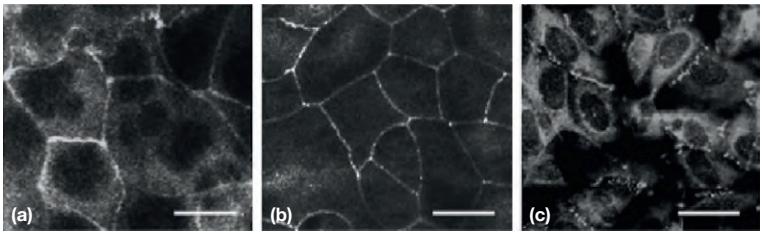

Figure 8 Expression of tight junctions compared between the cell lines NCI H441 and A549 without and with dexamethasone treatment. (a) Filter-grown monolayer of NCI H441 cells 10 days after plating. (b) Filter-grown monolayer of NCI H441 cells and (c) A549 on day 10 in culture with 1 μM dexamethasone. Immunostaining for ZO-1 protein (nuclei appear dark). Scale bar = 10 μm. Observation by confocal laser scanning microscopy.

characteristic circumferential staining pattern, whereas the cell line A549 reveals a fragmented staining pattern of ZO-1.

The cell line NCI H441, also available from ATCC, was derived from the pericardial fluid of a patient with papillary adenocarcinoma of the lung and shows morphological characteristics of both hATII and Clara cells.[138] Clara cells and hATII cells share several markers, such as the production of surfactant proteins SP-A, SP-D, and SP-B and the associated expression of the nuclear factor TTF-1. Besides these attributes, recent studies have shown that NCI H441 exhibited responses to mitogenic growth factors similar to primary isolated hATII cells.[149] NCI H441 shows several type II characteristics, such as the formation of lamellar bodies, storage organelles for SP-B and SP-C, and associated phospholipids, such as dipalmitoylphosphatidyl-choline (DPPC),[136] and, under dexamethasone treatment, a positive immunocytochemical staining for the ATII-marker SP-C.[145] Several *in vitro* models have shown that glucocorticoids also tighten cellular contacts in mammary epithelium, retinal endothelium, and brain microvascular epithelium.[150–153] Treatment with dexamethasone caused reproducible TER values of $273 \pm 11\,\Omega\,cm^2$ for NCI H441 cells after 10–12 days of filter culture and regular distribution of ZO-1 at the cell–cell contact zones. As was shown in previous studies, A549 failed to develop substantial TER[68,146] and showed TJ of a beaded appearance in freeze–fracture studies.[154] For A549, dexamethasone treatment led to a slightly increased ZO-1 localization between adjacent cells (see **Figure 8(c)**) but no increase in TER.[145]

3.312.3.4. Cell Culture Models of the Alveolar–Capillary Barrier

When an extra-pulmonary transport as well as systemic delivery of the drug load is the goal, carriers also have to pass the adjacent endothelium before entering the pulmonary and then the systemic circulation. Therefore, to study drug and gene delivery across the distal lung barrier, a coculture of alveolar epithelial and endothelial cells is required, and this is on the basis of the close proximity of both cell types *in vivo*. A barrier-forming bilayer model permits communication and interaction of alveolar type II epithelial cells and microvascular endothelial cells cultured on opposite sides of Transwell® filter growth supports (**Figure 9**).

3.312.3.5. Characterization of Human Pulmonary Capillary Endothelial Cells

Human primary isolated pulmonary microvascular endothelial cells (HPMECs) can be isolated from peripheral lung tissue using PECAM-1 (platelet endothelial cell adhesion molecule-1) microbeads, a characteristic marker for endothelial cells.[155] Exclusive markers for a microvascular phenotype are a positive immunofluorescent staining for CD36 (thrombospondin receptor)[156] and CD105 (Endoglin).[157] Additionally, CD143 (angiotensin converting enzyme, ACE) is expressed at high level in lung capillary endothelial cells *in situ*.[158] All of these markers were shown to be present in HPMEC isolated by our group.[119] Furthermore, these cells expressed GM-CSF[103] and were able to react to proinflammatory cytokines with the

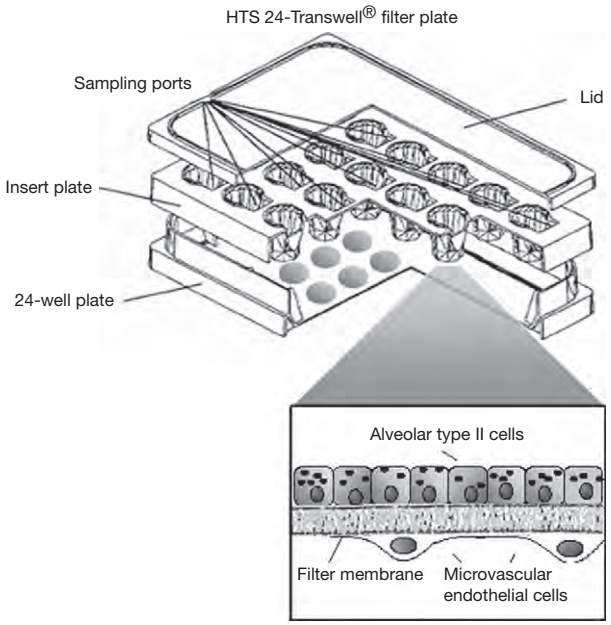

Figure 9 Schematic of the 24-Transwell® filter setup of the alveolar–capillary model *in vitro*.

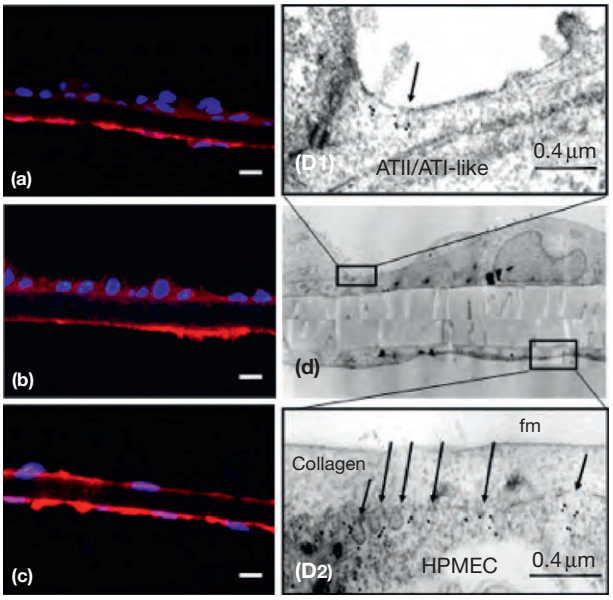

Figure 10 Cross-sections through human alveolar epithelial cells (hATII/hATI-like) cultured with HPMEC at day 3 (a), day 5 (b), and day 7 (c) of coculture, visualized by confocal laser scanning microscopy with staining of caveolin-1 or TEM with immunogold labeling of caveolin-1 at day 10 (d) in hATI-like cells (D1) or HPMEC (D2). fm = filter membrane. Scale bar = 10 µm.

induction of adhesion molecules (ICAM-1 and VCAM-1) and selectins (P-selectin, E-selectin).[159] *In vitro*, they also released several secondary cytokines, for example, IL-6, IL-8, and MCP-1 on stimulation.[119]

3.312.3.6. Primary Alveolar Epithelial Cells and Microvascular Endothelial Cells in Coculture

In this section, we describe a barrier-forming bilayer model of hATII/hATI-like alveolar epithelial cells and primary isolated pulmonary microvascular endothelial cells (HPMECs) cultured on opposite sides of Transwell® filter growth supports developed by our group.[119] Similar to monocultures, hATII cells in coculture with HPMEC established a confluent monolayer with hATII cells that partly transdifferentiated to hATI-like cells within 7–11 days.[119] The hATII cells showed nearly no caveolin-1 expression on day 3 of coculture (**Figure 10**). With ongoing culture, the HATII cells partially transdifferentiated to flattened HATI-like cells. Up to day 5, in coculture the epithelial cells on the upper surface of the filter membrane showed a slightly increased fluorescence for caveolin-1 (**Figure 10(b)**). On day 7, the intensity of the caveolin-1 signal for HATII/HATI-like cells was as strong as for the HPMEC, which showed a constant fluorescent labeling for caveolin-1 with ongoing culture (**Figure 10(c)**). Caveolar structures with immunogold labeling for caveolin-1 were visualized by TEM on day 10 of coculture (**Figure 10(d)**).

Two functional barriers were established in bilayer coculture with a maximum TER (transbilayer electrical resistance) of approximately $1730 \pm 460\,\Omega\,cm^2$.[119] Additionally, immunolabeling revealed the formation of confluent monolayers on both sides of the filter membrane with TJ and AJ for epithelial and endothelial cells. The two barriers formed, that is, the heterocellular alveolar epithelium and the microvascular endothelial cell monolayer, create a system with two distinct compartments. This compartmentalization reflects the physiological and morphological properties of the human alveolar–capillary barrier *in vivo*. Therefore, the primary coculture model appears to be a highly valuable *in vitro* model for pulmonary drug delivery studies across the main cellular barriers at the distal lung.

3.312.3.7. Coculture of NCI H441 with ISO-HAS-1

Because of a high donor variability and a limited source of human tissue specimens, there is still a need to develop an alveolar–capillary model based on cell lines. A precondition for drug delivery and transport studies is barrier formation *in vitro*. Hence, a bilayer model of the barrier-forming cell line NCI H441, exhibiting features of alveolar type II cells, with a microvascular endothelial cell line (ISO-HAS-1) was recently developed by our group.[135] The microvascular endothelial cell line ISO-HAS-1, derived from a dermal angiosarcoma, showed features most akin to microvascular endothelial cells. Reproducible maximum TER values of $480 \pm 100\,\Omega\,cm^2$ after 10–12 days of cocultivation were achieved.[135] The treatment with dexamethasone (1 µM), as well as the coculture with ISO-HAS-1, reduced proliferation of NCI H441 cells (less Ki67 positive cells compared to nontreated cells, **Figure 11(a)**, and compared to green nuclear staining, **Figure 11(d)**). Additionally, a tight polarized monolayer of NCI H441 cells was developed (regular apical ZO-1 distribution, see **Figure 11(d)**). Without dexamethasone, ISO-HAS-1 on the opposite side of the filter membrane adopted a more proangiogenic phenotype and formed vessel-like structures (**Figure 11(c)**), whereas with dexamethasone they developed a confluent monolayer

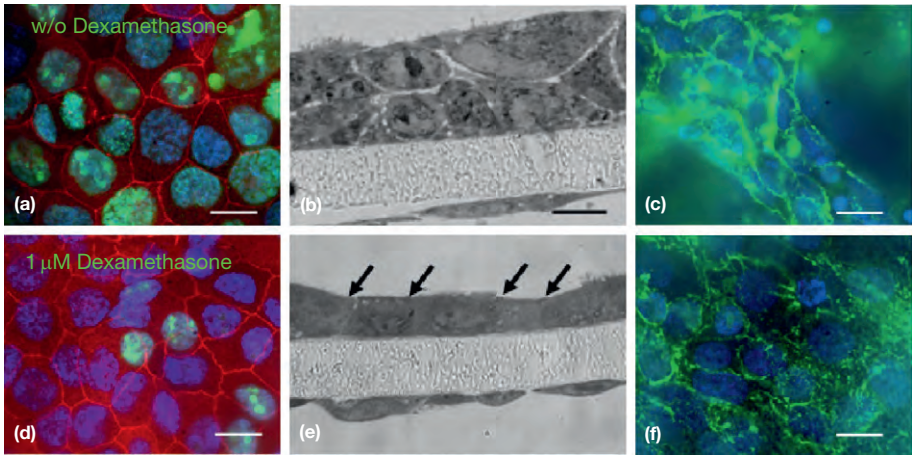

Figure 11 Cross-sections of NCI H441 or ISO-HAS-1 cell layers at day 10 of coculture without (w/o, a–c) and with dexamethasone (1 μM, d–f), visualized by confocal laser scanning microscopy with staining of ZO-1 (red) and Ki67 (green) for NCI H441 (a, d), and of VE-cadherin (green) for ISO-HAS-1 (c, f) or TEM (b, e). Scale bar = 5 μm.

Table 5 P_{app} values for the transport of sodium fluorescein (a) FITC-dextran 20 kDa (b) across the different cell layers P_{app} (10^{-6} cm s^{-1})

	Submerged	*Coculture with HPMEC*	*Coculture with ISO-HAS-1*
A549	(a) 0.28–0.35[160] (b) 1.2 ± 0.1[148]	ND	ND
NCI H441 (1μM Dex)	(a) 1.11 ± 0.23[145]	(a) 0.181 ± 0.021[145]	(a) 0.146 ± 0.032[135]
ATII/ATI-like	(a) 0.104–0.85 porcine[58] (b) 0.08 ± 0.004 human[117]	(a) 0.184 ± 0.027 human (unpublished)	ND

ND = not done

with VE-cadherin located at the cell–cell contact zones, showing a characteristic circumferential staining pattern (**Figure 11(f)**) as in a quiescent microcirculation.

3.312.3.8. Specific Applications

3.312.3.8.1. Transport studies

The paracellular movement of the anionic hydrophilic marker sodium-fluorescein or FITC-labeled dextrans with different molecular weights is often used to quantify the tightness of epithelial layers *in vitro*. Apparent permeability coefficients (P_{app}) are calculated using an equation already described in the subsection 'Cell culture models of the bronchial epithelium.' Transport studies with hydrophilic macromolecular FITC-dextrans across heterocelllular (hATII/ATI-like) epithelial cell monolayers revealed an inverse relation between permeability and molecular size.[117] **Table 5** specifies the P_{app} values for the transport of sodium fluorescein (a) or FITC-dextran 20 kDa (b) across different cell layers.

The apparent permeability coefficients of FITC dextrans (4400–150 000 Da) of A549 turned out to be more than 100-fold higher than that found in primary cultured alveolar epithelial cells.[117,148]

3.312.3.8.2. Uptake of micro- and nanoparticles

With the already described coculture systems for the upper and lower respiratory tracts, it is now possible to study systematically how micro- and nanoparticle biomaterials interact with these important barriers. The function of such carriers as drug or gene delivery systems is not merely restricted to surface adhesion. Particles that can adhere to the epithelial surface and that can be taken up in intact form could serve as carriers for labile substances that need to be delivered to the underlying tissue or the systemic circulation. However, the real situation *in vivo* is much more complex than can be modeled by taking a well-known cancer cell line, such as HeLa cells, and studying how the micro-/nanocarriers of interest enter the cell cytoplasm. In both the upper and lower respiratory tract, there are interactions with a protein–mucus layer (proximal) and a protein–surfactant layer (distal) before a micro- or nanoparticle 'sees' any plasma membrane. The presented coculture systems offer the possibility to study these sequential interactions in a manner which simulates the *in vivo* situation in a more realistic way than any monoculture model.

Inhaled micro-/nanocarriers may interact with the apical plasma membrane of the polarized alveolar epithelial cells and enter or pass them by a number of different processes, including passive (diffusive) and active mechanisms. Particles that express human proteins on their surface may be able to penetrate epithelial cells via receptor-mediated endocytosis[161] that involves caveolae-[162] or clathrin-mediated[163] lipid raft pathways and/or other yet unknown pathways of uptake. For each biomedical application, detailed mechanisms of how physical properties affect biological barrier properties, as well as the interplay between various physicochemical properties, may have to be elucidated case by case. Active transport

mechanisms by which some compounds traverse the distal lung barrier are more likely to provide new insights and improved strategies for pulmonary delivery of drugs into the systemic circulation and/or targeting drugs to lung parenchymal cells. These considerations are far from trivial. Thus, if a biomaterial carrier system is being primarily developed to treat lung diseases, the biomaterial must enter the lung and not be transported to the lumen of the pulmonary microcirculation. On the other hand, using the lung merely as a portal of entry for targeted delivery to another organ system will require active transport across all barrier components without intracellular accumulation of the carrier in the lung cells. The latter requirement is a major challenge, as our own work has shown that microcirculatory endothelial cells have an enormous capacity for uptake and intracellular sequestration of nanoparticles.[164]

To detect an uptake of micro-/nanocarriers, several methods should be combined to gain reliable results. Methods of choice are electron microscopic techniques, such as scanning or transmission electron microscopy (TEM), and, in the case of a fluorescent label, confocal laser scanning microscopy (CLSM). Trafficking of fluorescent carriers should be followed by colocalization with markers of the cellular uptake and intracellular transport machinery, for example, caveolin-1, clathrin, early/late endosomal markers, and lysosomal markers. Figure 12 illustrates the importance of the use of different methods to detect mechanisms of micro-/nanocarrier interaction with cells. Barrier-forming NCI H441 and ISO-HAS-1 cells show a clearly differing interaction with biodegradable poly(D,L)-lactic-*co*-glycolic acid (PLGA) microspheres. For polarized NCI H441 cells, the PLGA-spheres seem to adhere preferably to the apical contact zones of adjacent cells as shown by CLSM. Whereas a selective adhesion was shown, an uptake of spheres could not clearly be confirmed by SEM and TEM (Figure 12(a)). For microvascular endothelial cells in coculture, PLGA-microspheres were taken up and partly transported through the cells (Figure 12(b) asterisk). Here all applied methods of detection, CLSM, SEM, and TEM, demonstrated a perinuclear localization of PLGA-microspheres in ISO-HAS-1 cells.

3.312.3.8.3. Influence of cytokines on barrier properties

Alveolar epithelial cells are localized at the critical interface with the external environment and are the first to be exposed to inhaled irritants, allergens, and noxious stimuli. As well as maintaining their barrier function, alveolar epithelial cells also serve as a part of the local immune system. Their function in host defense has been reviewed recently. Moreover, this review covers alterations of the epithelium associated with airway diseases and potential therapeutic implications for the treatment of respiratory diseases.[165] Damage to the alveolar–capillary barrier is the major critical element occurring during many pathological processes in the lung, for example, acute inflammatory responses, as reviewed in *Lucas et al.*[166] As treatment with drugs is often necessary under such pathophysiological conditions, *in vitro* models that mimic an impaired barrier could be useful, and indeed necessary, to predict drug effects on an alveolar epithelium with altered barrier function. TJs are highly dynamic structures capable of rapid alterations in disease and in response to functional stress.[154] A basolateral exposure of the coculture (NCI H441 and ISO-HAS-1) to TNF-α and IFN-γ, for example, caused a local disruption of the TJ with the loss of ZO-1 labeling in NCI H441 cells, accompanied by a decrease of TER.[135] At these areas of local TJ disruption, an increased adhesion/uptake of Oregon green-coupled 25 kDa polyethyleneimine nanoparticles was detected. In contrast, polarized NCI H441 with intact TJ showed no adhesion/uptake of Oregon green-coupled 25 kDa polyethyleneimine nanoparticles (Figure 13).

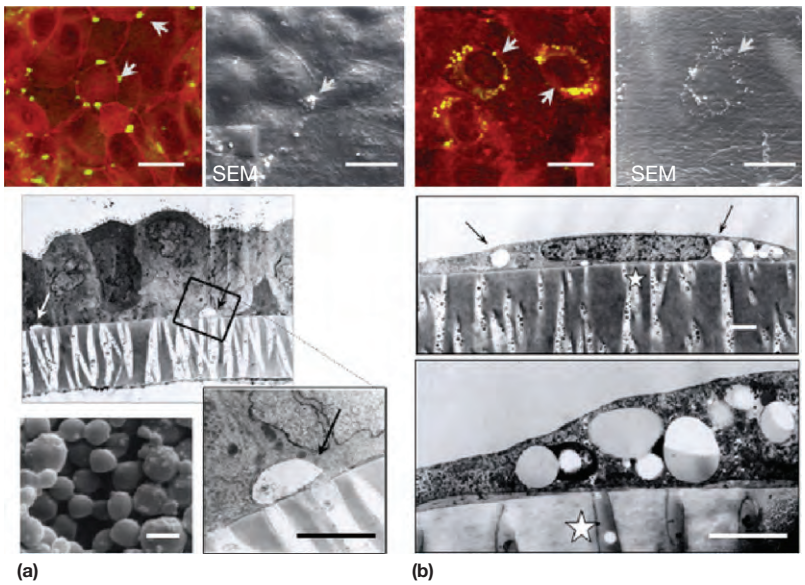

Figure 12 Selective interaction of PLGA microparticles with NCI H441 or ISO-HAS-1 cell layers at day 10 of coculture. Distribution of PLGA-Cumarin 6 (green) in NCI H441 (a) and in ISO-HAS-1 (b), visualized by confocal laser scanning microscopy with staining of the actin cytoskeleton (red), SEM or TEM. Scale bar = 1 μm.

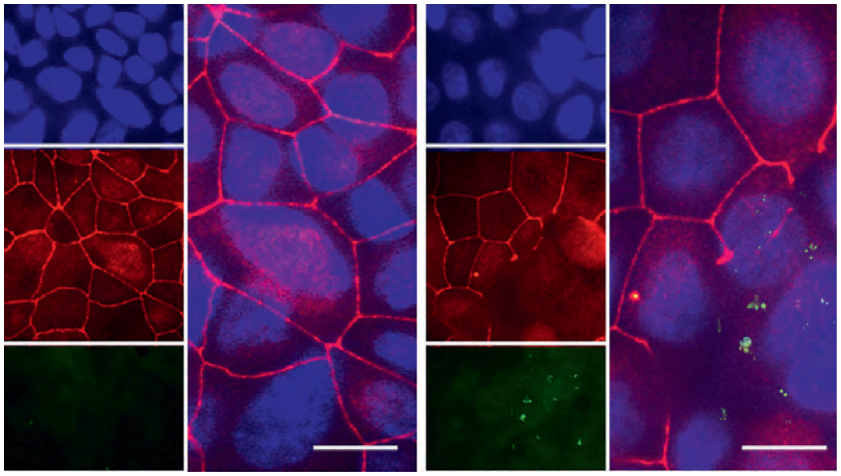

Figure 13 Selective interaction of Oregon green-coupled 25 kDa polyethyleneimine nanoparticles (PEI-OG) with NCI H441 cell layers at day 10 of coculture. Distribution of PEI-OG (green) in polarized NCI H441 (a) and in NCI H441 with disrupted tight junctions (b), cells were treated with tumor necrosis factor-α and interferon-γ for 12 h before incubation with PEI-OG), visualized by confocal laser scanning microscopy with staining of the nuclei (blue) and ZO-1 (red). Scale bar = 5 μm.

3.312.3.9. Potential and Limitations of Available Cell Culture Models

The *in vitro* model of the alveolar–capillary barrier that most closely mimics the *in vivo* situation is a primary coculture of heterocellular alveolar epithelial cells with HPMEC.[119] Because of ethical considerations, a commercial use of normal primary human cells will hardly be accepted. Moreover, the human material is mainly derived from lung surgery, that is, from tumor patients, who are often elderly people. Another drawback to be faced is the risk of biological variability, for example, smokers versus nonsmokers, as well as the incidence of lung or hereditary diseases. Finally, in addition to a quite complex isolation procedure, the sources for tissue material are limited, thus confining the availability of this model and not recommending it for first stage high throughput screening. The recently generated type I-like cell line TT1 could serve as an efficient tool to investigate the human alveolar type I phenotype. As confluent TT1 cell monolayer formation with electrically tight characteristics has not yet been shown,[39] its usefulness as a drug absorption model appears questionable, unless specific data can be generated.

Type II cell lines, such as A549, were used in human coculture models for leukocyte transmigration or microbial infection in the lower airways,[167,168] but the formation of a functional barrier was not adequately characterized. Overall, the low values for transepithelial resistance for A549 make it difficult to interpret transport data (including drug trafficking) obtained from such a cell line.[147] Nevertheless, A549 cells have in fact been used to study alveolar drug absorption,[148] metabolism,[146] and gene delivery[169] and are widely accepted as a valuable model for studies in pulmonary toxicity with widespread use even in recent years.[170–172] The great majority of studies within this scope of metabolism (e.g., of certain classes of xenobiotics) used the A549 cell line as *in vitro* model. For the cell line NCI H441, there is still a need to further characterize its metabolic properties as an acceptable substitute for alveolar epithelium. As NCI H441 cells possess functional barrier properties, they may be a suitable tool to predict micro-/nanocarrier interaction in the lower respiratory tract. The addition of the endothelium as the second barrier component raises the potential of the coculture (NCI H441 with ISO-HAS-1) as a model for the assessment of drug efficacy, toxicity, and rapid evaluation of drug permeability in the deep lung. It further allows assessment of the contributions of microvascular endothelium (systemic drug delivery) and epithelium (inhaled drug delivery) to pulmonary adsorption of new drug carrier systems, delivering drugs to peripheral lung epithelial cells and across an alveolar–capillary barrier. With ongoing refinement of such coculture systems, additional cell types (e.g., macrophages, lymphocytes, dendritic cells, and/or polymorphonuclear leukocytes) can be added to the culture to study various cell biology-related questions. Notwithstanding the difficulties and challenges in various aspects of the *in vitro* distal lung models, mechanistic studies of pulmonary drug delivery using the alveolar–capillary barrier as the main portal of entry into the systemic circulation from the lung airspaces are expected to provide us a wealth of information in coming years. These models will enable us to study more efficient ways of treating lung-specific diseases using targeting approaches as well as improved bioavailability of those therapeutics that yield very poor absorption via other routes.

3.312.4. *In Vitro* Studies with Endothelial Cells from the BBB

3.312.4.1. Introduction

The brain is not exposed to the outside environment such as the skin, the eyes, or the membranes lining the respiratory, digestive, urinary, and reproductive tracts. The brain is enclosed in the body and is protected by a barrier that prevents most foreign compounds from entering the brain. This barrier

is formed by microcapillaries that are part of the vessels that transport blood throughout the body. However, the capillaries in the BBB differ from those of other tissues. These microcapillaries are made up of brain-specific capillary endothelial cells that exhibit unique morphological characteristics, such as the presence of TJs between individual endothelial cells, the absence of fenestrations, and the near absence of pinocytotic activity. These characteristics are due to the interaction and direct contact of the microvascular endothelial cells with pericytes, astrocytes, and microglia cells found within the brain. These brain-specific endothelial characteristics also limit the types of substances that can pass into the brain. The exchange of nutrients and oxygen between blood and tissues readily takes place at the capillary walls in other parts of the body. However, many nutrients needed by the brain do not pass directly into the brain but are transported by specific systems in endothelial cells that move the substances the brain needs across the BBB. The presence of the TJs limits or excludes many useful therapeutic compounds such as antibiotics, chemotherapeutic compounds, peptides, and proteins from moving into the brain from the blood.

3.312.4.2. Characteristics of the BBB

The primary characteristic that differentiates the BBB microvasculature from the vasculature from other parts of the body is the presence of AJs and TJs which limit the permeation of solutes in the blood by diffusion between endothelial cells into the brain extracellular spaces. The TJs are formed by endothelial cells at the interface between blood and brain and are associated with astrocytes from the brain. The TJs are formed primarily by transmembrane adherens proteins such as claudins, occludins, and junctional adhesion molecules, which are in turn anchored to the endothelial cells by cytoplasmic scaffolding and the regulatory proteins ZO-1, ZO-2, ZO-3, and cingulin. Any disruption to these proteins decreases TJ resistance and results in leaky BBB. The way these proteins are organized and interact plays an important role in the degree of barrier integrity. The integrity of the BBB and the presence of TJs are demonstrated by an inhibition of ion movement via paracellular diffusion between endothelial cells and can be demonstrated by a high *in vivo* trans-electrical resistance of the BBB. The association of microglia, astrocytes, nerve terminals, and pericytes are necessary for the formation of TJs by the brain endothelial cells. These cells release vasoactive agents and cytokines that can modify TJ assembly and barrier permeability, and influence the polarized expression of specific transporters within the brain endothelial cells at the luminal and abluminal membranes. The importance of these cell–cell interactions and the formation, stabilization, and increase of TJs has been demonstrated in many *in vitro* studies by increases of the TER or trans-electrical resistance across monolayers of endothelial cells compared to cocultures.[3,20,173]

Many different and unique mechanisms have been identified for the transport of nutrients across the BBB and into and out of the endothelial cells. These include the ATP-binding cassette or ABC transporter (lipid soluble, nonpolar compounds), solute carriers (glucose, amino acids, nucleosides, small peptides), and receptor-mediated (transferrin, lipoproteins, immunoglobulins, cytokines) and adsorptive-mediated transcytosis (histones, cell-penetrating peptides). Many other mechanisms are used to specifically transport unique compounds across the microvascular endothelial cell of the BBB.

3.312.4.3. Characterization of Brain Endothelial Cells

As mentioned above, the inner layer of all microcapillary vessels in the BBB is formed by endothelial cells. Although these endothelial cells can differ in their barrier properties, they share some characteristics with endothelial cells in all parts of the body. These special endothelial cell markers allow a distinction between endothelial and nonendothelial cells. One of the major endothelial cell markers is von Willebrand factor (vWF, also called factor VIII). This blood glycoprotein is expressed by endothelial cells and after release into the blood it is important for blood clotting (*haemostasis*). The second endothelial cell marker is PECAM-1. PECAM-1 (platelet endothelial cell adhesion molecule), also called CD31 (cluster of differentiation), is expressed at the cell surface of endothelial cells. It is involved in cell–cell adhesion and interacts with other CD-31 molecules or proteins of the integrin family. Also VE-cadherin (cadherin-5), a cell adhesion protein, is specifically expressed on endothelial cells. The cytoplasmic domain of this interendothelial protein is connected to the actin cytoskeleton via α-, β-, and γ-catenins. VE-cadherin is important for the organization of new blood vessels and is involved in several regulatory processes of endothelial cells. These markers can be stained by specific antibodies and visualized by fluorescence microscopy as shown in Figure 14.

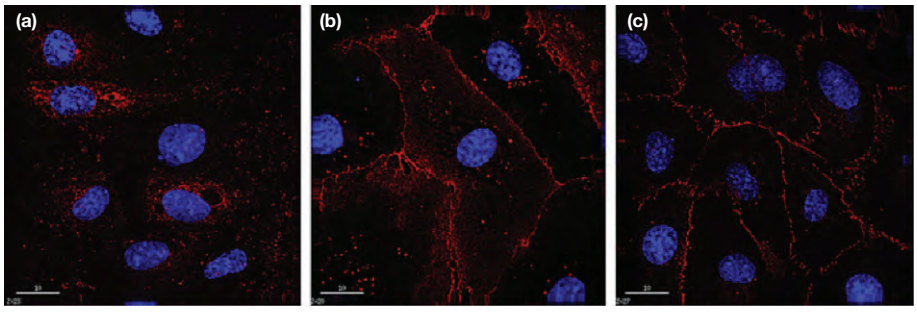

Figure 14 Specific endothelial cell markers. Typical endothelial cell markers are stained with antibodies against vWF (a), CD31 (b), and VE-cadherin (c) (all in red) in a human brain endothelial cell line. The nuclei are stained with Hoechst (blue). Fluorescence microscopy (60×).

3.312.4.4. Primary Isolated Human Brain Endothelial Cells

Different coculture models from various parts of the body such as the air–blood barrier (lung) or BBB have been developed and have been shown to exhibit structures and functions similar to those in the *in vivo* situation.[174,175] The use of freshly isolated primary cells for generating an *in vitro* model has the advantage that the isolated cells generally express most of the important cell properties and functions and under the proper conditions can generate the characteristics of a tight barrier. Major disadvantages are the difficulty in obtaining fresh human brain tissue and the purity of the cells after isolation, and the variability of cell isolation success and functions dependent on the donor. A number of brain-endothelial cell lines are available that exhibit most of the characteristics and properties, although the barrier properties of primary cells such as TER are generally higher and closer to the *in vivo* situation. Thus, most *in vitro* models utilize primary cells of different animals. A few well-established primary cell-based rat, porcine, and especially bovine BBB models are routinely used.[3,20,173] The isolated brain endothelial cells are often cocultivated with astrocytes or pericytes as this has been shown to increase the TER and TJ properties and to induce and stabilize the expression of barrier-specific proteins. In the section below various methods will be described using porcine brain endothelial cells (PBECs) with or without pericytes to examine novel biomaterials and their interaction with and uptake and transport in brain-derived endothelial cells.

3.312.4.5. Primary Porcine Brain Endothelial Cells and Pericytes

3.312.4.5.1. Isolation

We have previously developed a method to isolate human brain microcapillary endothelial cells from brain tissue.[175] This method has been adapted and found to function for the isolation of endothelial cells from porcine brain tissue. Brains from freshly slaughtered pigs were used for the isolation of primary PBECs and porcine pericytes. After carefully removing the meninges and larger blood vessels, the gray matter was separated from the white matter and used in the following isolation steps. The brain tissue was digested with collagenase type IV and afterwards the small capillaries were separated from myelin debris by a percoll gradient (GE Healthcare, Sweden). A second digestion with a mixture of collagenase/dispase and an additional percoll gradient and washing step were carried out. This step has been found to ensure high purification of the microvessels with few additional contaminating cells. The microvessels were resuspended in basic endothelial growth medium with supplement mix (PromoCell, Germany), 1% penicillin/streptomycin, and 3 $\mu g\,ml^{-1}$ puromycin (Calbiochem, USA). The medium was changed daily and addition of 3 $\mu g\,ml^{-1}$ puromycin was contined for two additional days. On day 3, cells were switched to a medium without the addition of puromycin and cultured until confluent. Puromycin is a nucleoside-antibiotic that is toxic for fibroblasts and other contaminating cells but can be transported by efflux transporters out of the brain endothelial cells without exhibition of a toxic effect. This method resulted in a significant enhancement in the purity of the porcine brain capillary-cell isolated.

To isolate brain pericytes, the microvessels were resuspended in the above medium with puromycin for 24 h, and then switched to a medium without puromycin. Pericytes exhibit a significantly higher replication rate than endothelial cells and rapidly outgrow these cells. Generally, after one to two passages, no endothelial cells remained (as detected by immunohistochemical staining; see below).

3.312.4.5.2. Characterization

The purity of the isolated cells and their proper characterization is essential for further experimentation. The characterization of cells can be done by immunostaining with endothelial cell-specific markers (see **Section 3.312.4.3**) or by using these same markers for FACS (fluorescence activated cell sorting) analysis. Also, a characterization by reverse-transcription polymerase chain reaction (RT-PCR) with primers to specific cell marker genes is possible.[175] The outgrowing PBECs after isolation of microcapillaries are shown in **Figure 15(a)**. The expression of a typical endothelial cell marker for endothelial cells (CD31) was used to stain porcine brain capillary endothelial cells (PBCECs) (**Figure 15(b)**). In comparison to the endothelial cells, the morphology and the staining of smooth muscle actin of pericytes are demonstrated in **Figure 15(c)** and **15(d)**, respectively.

A precise characterization of pericytes is difficult.[176] One criterion is the morphological structure of the cells, namely, long, thin, and stretched structure. These cells are also positive on staining the cells for smooth muscle actin (**Figure 15(d)**), desmin (class III muscle-specific intermediate filament), NG-2

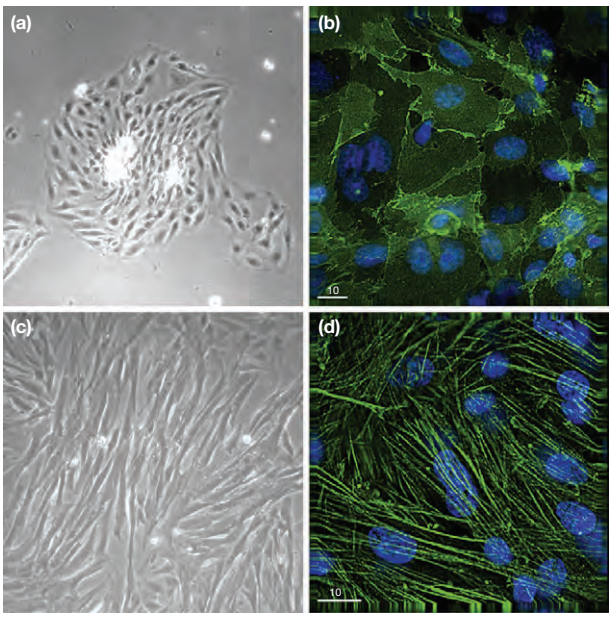

Figure 15 Morphology and staining of specific cell markers of PBECs and pericytes. Phase contrast microscope images showing the different morphologies of PBECs (a) and pericytes (c). The staining of CD31 in PBECs (b) and SMA (d) in pericytes (all in green) represents specific markers of each cell type. The nuclei are stained with Höchst (blue). Fluorescence microscopy (60×); light microscopy (20×).

(Neuron-glial 2), platelet-derived growth factor receptor (PDGFR)-β, and aminopeptidase A and N. However, none of these markers is absolutely specific for pericytes and none of the markers recognizes all pericytes because their expression is dynamic, differs depending on the location of cell source, and is dependent on the cell development stage. The identification of pericytes is generally based on a combination of staining methods, structural morphology, and a high resolution confocal imaging. Another useful pericyte marker, 3G5, has been identified and has been used for enriching these cells, but is unfortunately not commercially available.[177]

3.312.4.5.3. In vitro *coculture model with PBECs and pericytes*

A coculture of primary porcine brain endothelial cells and pericytes can be used to generate an *in vitro* model for the brain mimicking the *in vivo* situation.[178] To generate this barrier, PBECs are seeded on the top of a Transwell filter (Transwell, see section lung–air barrier) and pericytes on the other side of the filter. With time, the expression of TJ and AJ barrier proteins, such as zonula occludens (ZO-1), β-catenin, and VE-cadherin, can be seen (Figure 16). This indicates that barrier proteins are generated and correlates with higher TER values.

3.312.4.6. Analysis of Novel Biomaterials with Cells from the BBB

The investigation of new biomaterials for brain delivery is focused primarily on methods to target the BBB or to act as a carrier across the barrier. Most research strategies are focused on the use of specifically designed peptides or nanoparticles targeted to unique characteristics of the BBB in order to be transported across the barrier. Thus, *in vitro* studies of these compounds with models of the BBB are necessary to understand interactions between the new materials and living cells and to validate the possibility of transport. Carrying out studies with each new compound *in vivo* would not be possible. Therefore, to mimic the *in vivo* situation, a well-characterized *in vitro* single or coculture model is needed. On the one hand, it provides the opportunity to prevent unnecessary animal experiments and on the other hand, it allows detailed analysis of individual mechanistic characteristics in a particular cell type in the absence of other interfering cells that are operative *in vivo*. However, prior to studies with complex coculture models, or single cell cultures of primary brain capillary endothelial cells, other investigations are necessary to determine the biocompatibility and toxicological effects of the novel biomaterials. Toxicity and biocompatibility studies are best examined in monoculture cell culture systems of either brain endothelial cells or microvascular endothelial cells.

To determine whether a novel compound or nanoparticle is biocompatible and exhibits no toxic effects, a number of different tests are generally used. The MTT or MTS is the most widely used test to examine the effects of compounds on cell viability. In this test, cells are incubated in the presence or absence of the novel compound and then MTS/MTT is added. The level of the reduction of the MTS/MTT substrate by dehydrogenases located in the mitochondrial membranes of cells to formazan is directly correlated with the viability of the cells. Thus, the more the MTT enzymatically converted to formazan, the higher the cell viability is. In addtion to cell viability, cell toxicity must also be evaluated. The LDH-test is the most commonly used test for examining cell toxicity of a compound. LDH (lactate dehydrogenase) is a cytoplasmic enzyme and if a biomaterial/nanoparticle causes cell toxicity the cell membrane of the affected cell becomes leaky. After exposure of cells to a test compound, the supernatant is collected and the LDH content of the supernatant is determined and compared to controls. The more toxic a compound, the more LDH is present in the supernatant and the more substrate is converted. In certain cases, it has been found that particular novel compounds may have an inhibitory effect in one or the other test systems. Therefore, it is important to use more than one test to exclude an impairment of a test system by new biomaterials/nanoparticles.

Initial studies of the interaction of novel compounds with the BBB are conducted with single-cell systems. In addition to the toxicity studies described above, which are not directly dependent on whether the compounds are present extracellulary or intracellulary, the next step is to examine how the compounds interact with the cells. Nanoparticles are often internalized. The internalization itself can cause decreased cell viability and/or increased cell toxicity. The level of impairment of cells by nanoparticles can be associated with different properties such as the concentration, shape, size, and chemical composition of the nanomaterials or combinations thereof. In addition to the toxicological effects on the cells, if a compound is taken up, then the fate after internalization of the nanoparticles within the cell is generally the question that

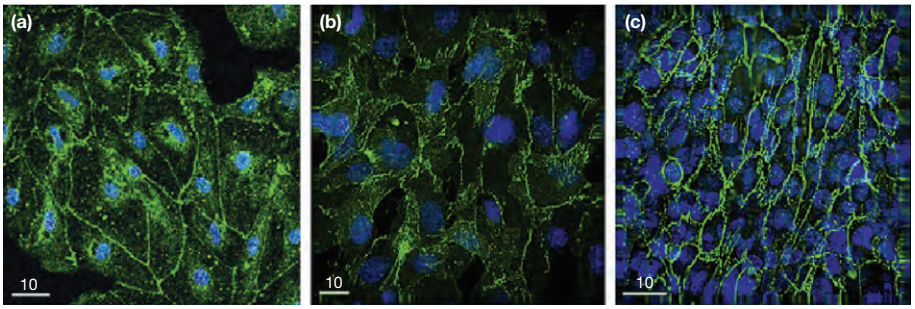

Figure 16 Staining of tight and adherens junctions in porcine brain endothelial cells. Staining pattern of different tight and adherens junction proteins on endothelial cells. (a) ZO-1 staining, (b) β-catenin, and (c) VE-cadherin; all in green. The nuclei are stained with Höchst (blue). Fluorescence microscopy (60×).

needs to be answered, especially if the nanoparticles are to be used to transport compounds across the barrier. To investigate uptake mechanisms such as pinocytosis or receptor-mediated endocytosis, specific inhibitors of these systems can be used. In addition, specific antibodies are available to stain individual intracellular structures and organelles and these can be used to follow or localize nanoparticles within cells. One criterion for studying nanoparticles or other peptides/proteins is that they contain a suitable method of detection, the optimal being a fluorescent label or visibility by light microscopy. One of drawbacks in the study of nanoparticles in cells is that the detection of the nanoparticle is limited by the numerical aperture and the wavelength of visible light attainable by microscopy. Because of the small size of single nanoparticles, these lie below the maximum resolution that is obtainable by microscopy. Generally it is only possible to detect agglomerations of nanoparticles within the cells. An example of nanoparticles in cells can be seen in Figure 17(a). Transferrin, which is taken up by clathrin-mediated endocytosis, is often used as a model to show the colocalization of transferrin and endocytotic vesicles (Figure 17(b)).

To detect single nanoparticles at the cell surface or even within the cells, it is necessary to use electron microscopes with a higher resolution maximum. Although the resolution of transmission electron microscope or scanning electron microscopes is higher compared to optical microscopes, not all nanoparticles or compounds can be detected. Only nanoparticles with a high atomic number or density such as gold or silver can be detected by these techniques. Other nanomaterials or compounds with a lower atomic number can be coated with a thin gold layer to make them suitable for electron microscopy. An example of the uptake of gold nanoparticles in brain endothelial cells is shown in Figure18.

The internalized nanoparticles are often in vesicles in the perinuclear region (Figure 18). Similar agglomerations of gold nanoparticles can also be detected by optical microscopy. In Figure 19, the difference in the amount of uptake of two nanoparticles which differ only in the surface modification is shown. Figure 19(a) shows the uptake of a gold nanoparticle with a neutral net charge while in Figure 19(b) the uptake of nanoparticles with a negative net charge is shown. Prior to the use of more complex coculture systems,

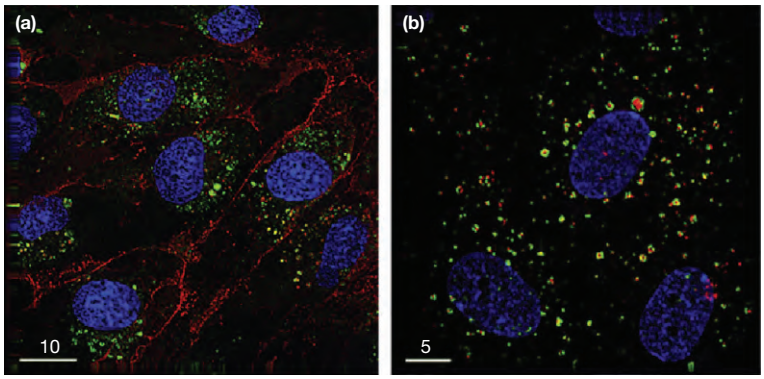

Figure 17 Uptake of 100 nm liposome nanoparticles (a) and transferrin (b) in brain endothelial cells. The uptake of fluorescent nanoparticles (liposomes, 100 nm) in human cerebral microcapillary endothelial cells is shown after a treatment for 4 h (a). The internalization of transferrin Texas Red (Molecular Probes) after 30 min of treatment and the colocalization with EEA (early endosomal marker, green) in brain endothelial cells is shown. The nuclei are stained with Höchst (blue). Fluorescence microscopy (a) 60× and (b) 100×.

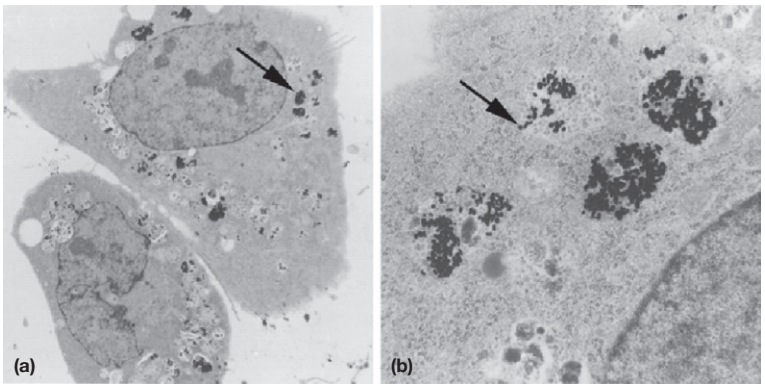

Figure 18 Transmission electron micrographs of the uptake of gold nanoparticles in human cerebral microcapillary endothelial cells (hCMEC) after 4 h. After 4 h of treatment with 100 μg ml^{-1} gold nanoparticles hCMEC were fixed and prepared for TEM analysis. (a) shows an overview of two cells with gold nanoparticles, while (b) demonstrates the uptake of gold particles and storage in vesicle-like structures in the perinuclear region. The arrows indicate the localization of gold agglomerates (a) and single gold nanoparticles (b). Magnification (a) 860×; (b) 8900×.

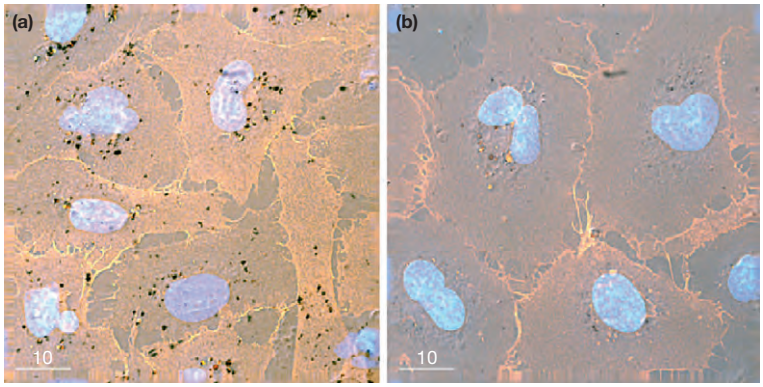

Figure 19 Uptake of gold nanoparticles (35 nm) with different surface modifications in brain capillary endothelial cells. After 4 h of treatment with 100 μg ml^{-1} gold nanoparticles (35 nm), human cerebral microcapillary endothelial cells were fixed and stained with CD31 (red) to highlight the cytoplasmic membrane. In (a), the uptake of gold nanoparticles with a hydroxpropylamine (neutral net charge) is shown. Less uptake can be detected after the treatment with gold nanoparticles coated with taurine (negative net charge; b). Fluorescence microscopy (60×).

single-cell culture systems can be used to evaluate how the size, shape, charge, surface modification, and chemical composition of a compound affect the ability of uptake and localization within a cell.

3.312.5. Conclusion and Future Perspectives

The advent of sophisticated nanocarrier-based systems for drug and gene delivery has faced the life sciences with the challenge of providing suitable model systems with which to investigate the mechanisms of cell–biomaterial interactions. Complex systems which possess an *in vivo* similarity are essential not only to adequately exclude toxic side-effects, but also to provide structure–function correlations. Thus, in design and application of nanocarriers the determination of biological response by physicochemical characteristics takes on fundamental importance. *In vivo*-like systems are best established *in vitro* using those primary human cells to be found in the various natural barriers encountered during nanocarrier delivery. This chapter has concentrated on those in the respiratory tract and the BBB. In some cases, it is possible to replace the primary cells with a phenotypically stable permanent cell line. Among the major challenges for future research are understanding the mechanisms of protein and surfactant molecule interaction with nanoparticles and the identification of specific targeting molecules which are genuine molecular addresses of the tissue and cells to be targeted. This is particularly important in any form of systemic application of nanocarriers.

Acknowledgments

The authors would like to thank S. Barth, L. Meyer, M. Moisch, K. Molter, K. Müller, A. Sartoris, and E. Stahr for their excellent technical assistance and C. Brochhausen and J. Kasper for many useful discussions. This work was supported by the German Defence Ministry, BMVg (M/SAB1/7A011) and the Integrated Project NanoBioPharmaceutics (026723-1) from the European Union.

References

1. James Kirkpatrick, C.; Fuchs, S.; Iris Hermanns, M.; Peters, K.; Unger, R. E. *Biomaterials* **2007**, *28*, 5193–5198.
2. Mrsny, R. J. *Adv. Drug Deliv. Rev.* **2009**, *61*, 172–192.
3. Kido, Y.; Tamai, I.; Nakanishi, T.; *et al*. *Drug Metab. Pharmacokinet*. **2002**, *17*, 34–41.
4. Paine, R.; Rolfe, M.; Standiford, T.; Burdick, M.; Rollins, B.; Strieter, R. *J. Immunol*. **1993**, *150*, 4561–4570.
5. Utech, M.; Bruwer, M.; Nusrat, A. *Meth. Mol. Biol*. **2006**, *341*, 185–195.
6. Simons, K.; Fuller, S. D. *Annu. Rev. Cell Biol*. **1985**, *1*, 243–288.
7. Ehrhardt, C.; Fiegel, J.; Fuchs, S.; *et al*. *J. Aerosol Med*. **2002**, *15*, 131–139.
8. Suh, J.; Dawson, M.; Hanes, J. *Adv. Drug Deliv. Rev*. **2005**, *57*, 63–78.
9. Ward, P. D.; Tippin, T. K.; Thakker, D. R. *Pharm. Sci. Technol. Today* **2000**, *3*, 346–358.
10. Masaoka, Y.; Tanaka, Y.; Kataoka, M.; Sakuma, S.; Yamashita, S. *Eur. J. Pharm. Sci*. **2006**, *29*, 240–250.
11. Patton, J. S. *Adv. Drug Deliv. Rev*. **1996**, *19*, 3–36.
12. Dahl, A. R. *Toxicol. Appl. Pharmacol*. **1990**, *103*, 185–197.
13. Mercer, R. R.; Russell, M. L.; Crapo, J. D. *J. Appl. Physiol*. **1994**, *77*, 1060–1066.
14. Mercer, R. R.; Russell, M. L.; Roggli, V. L.; Crapo, J. D. *Am. J. Respir. Cell Mol. Biol*. **1994**, *10*, 613–624.
15. Scheuch, G.; Kohlhaeufl, M. J.; Brand, P.; Siekmeier, R. *Adv. Drug Deliv. Rev*. **2006**, *58*, 996–1008.
16. Naik, A.; Kalia, Y. N.; Guy, R. H. *Pharm. Sci. Technol. Today* **2000**, *3*, 318–326.
17. Wolburg, H.; Wolburg-Buchholz, K.; Sam, H.; Horvat, S.; Deli, M. A.; Mack, A. F. *Histochem. Cell Biol*. **2008**, *130*, 127–140.
18. Jost, S. P.; Gosling, J. A.; Dixon, J. S. *J. Anat*. **1989**, *167*, 103–115.
19. Khandelwal, P.; Abraham, S. N.; Apodaca, G. *Am. J. Physiol. Ren. Physiol*. **2009**, *297*, F1477–F1501.
20. Gaillard, P. J.; Voorwinden, L. H.; Nielsen, J. L.; *et al*. *Eur. J. Pharm. Sci*. **2001**, *12*, 215–222.
21. Gruenert, D. C.; Finkbeiner, W. E.; Widdicombe, J. H. *Am. J. Physiol*. **1995**, *268*, L347–L360.
22. Leonard, F.; Collnot, E. M.; Lehr, C. M. *Mol. Pharm*. **2010**, *7*(6), 2103–2119.
23. Rothen-Rutishauser, B. M.; Kiama, S. G.; Gehr, P. *Am. J. Respir. Cell Mol. Biol*. **2005**, *32*, 281–289.
24. Wottrich, R.; Diabate, S.; Krug, H. F. *Int. J. Hyg. Environ. Health* **2004**, *207*, 353–361.
25. Braun, A.; Hammerle, S.; Suda, K.; *et al*. *Eur. J. Pharm. Sci*. **2000**, *11*(Suppl. 2), S51–S60.
26. Knowles, M. R.; Boucher, R. C. *J. Clin. Invest*. **2002**, *109*, 571–577.
27. Travis, S. M.; Singh, P. K.; Welsh, M. J. *Curr. Opin. Immunol*. **2001**, *13*, 89–95.
28. Plopper, C. G.; Mariassy, A. T.; Wilson, D. W.; Alley, J. L.; Nishio, S. J.; Nettesheim, P. *Exp. Lung Res*. **1983**, *5*, 281–294.
29. Mathias, N. R.; Yamashita, F.; Lee, V. H. L. *Adv. Drug Deliv. Rev*. **1996**, *22*, 215–249.
30. Sleigh, M. A.; Blake, J. R.; Liron, N. *Am. Rev. Respir. Dis*. **1988**, *137*, 726–741.
31. Breeze, R. G.; Wheeldon, E. B. *Am. Rev. Respir. Dis*. **1977**, *116*, 705–777.
32. King, M. *Eur. Respir. J*. **1998**, *11*, 222–228.

33. Patton, J. S.; Byron, P. R. *Nat. Rev. Drug Discov.* **2007**, *6*, 67–74.
34. Forbes, I. I. *Pharm. Sci. Technol. Today* **2000**, *3*, 18–27.
35. Evans, M. J.; Shami, S. G.; Cabral-Anderson, L. J.; Dekker, N. P. *Am. J. Pathol.* **1986**, *123*, 126–133.
36. Hong, K. U.; Reynolds, S. D.; Watkins, S.; Fuchs, E.; Stripp, B. R. *Am. J. Pathol.* **2004**, *164*, 577–588.
37. Inayama, Y.; Hook, G. E.; Brody, A. R.; *et al. Lab. Invest.* **1988**, *58*, 706–717.
38. Klein, M. K.; Haberberger, R. V.; Hartmann, P.; *et al. Eur. Respir. J.* **2009**, *33*, 1113–1121.
39. Van Den Bogaard, E. H.; Dailey, L. A.; Thorley, A. J.; Tetley, T. D.; Forbes, B. *Pharm. Res.* **2009**, *26*, 1172–1180.
40. Lopez-Vidriero, M. T. *Chest* **1981**, *80*, 799–804.
41. McWilliams AS, H. P.; Gehr, P. In *Particle–Lung Interaction*; Gehr, P., Heyder, J., Eds.; Marcel Decker: Basel, New York, 2000; pp 473–489.
42. Van Der Schans, C. P. *Respir. Care* **2007**, *52*, 1150–1156; discussion 1156–8.
43. Clarke, S. W.; Pavia, D. *Br. J. Clin. Pharmacol.* **1980**, *9*, 537–546.
44. Camner, P.; Philipson, K. *Arch. Environ. Health* **1978**, *33*, 181–185.
45. Balda, M. S.; Matter, K. *J. Cell Sci.* **1998**, *111*(Pt 5), 541–547.
46. Schmitz, H.; Barmeyer, C.; Fromm, M.; *et al. Gastroenterology* **1999**, *116*, 301–309.
47. Cozens, A. L.; Yezzi, M. J.; Kunzelmann, K.; *et al. Am. J. Respir. Cell Mol. Biol.* **1994**, *10*, 38–47.
48. Forbes, B.; Ehrhardt, C. *Eur. J. Pharm. Biopharm.* **2005**, *60*, 193–205.
49. Pohl, C.; Hermanns, M. I.; Uboldi, C.; *et al. Eur. J. Pharm. Biopharm.* **2009**, *72*, 339–349.
50. Shen, B. Q.; Finkbeiner, W. E.; Wine, J. J.; Mrsny, R. J.; Widdicombe, J. H. *Am. J. Physiol.* **1994**, *266*, L493–L501.
51. Wan, H.; Winton, H. L.; Soeller, C.; *et al. Eur. Respir. J.* **2000**, *15*, 1058–1068.
52. Herzog, E.; Casey, A.; Lyng, F. M.; Chambers, G.; Byrne, H. J.; Davoren, M. *Toxicol. Lett.* **2007**, *174*, 49–60.
53. Penn, A.; Murphy, G.; Barker, S.; Henk, W.; Penn, L. *Environ. Health Perspect.* **2005**, *113*, 956–963.
54. Veranth, J. M.; Kaser, E. G.; Veranth, M. M.; Koch, M.; Yost, G. S. *Part. Fibre Toxicol.* **2007**, *4*, 2.
55. Berger, J. T.; Voynow, J. A.; Peters, K. W.; Rose, M. C. *Am. J. Respir. Cell Mol. Biol.* **1999**, *20*, 500–510.
56. Yoon, J. H.; Moon, H. J.; Seong, J. K.; *et al. Differentiation* **2002**, *70*, 77–83.
57. Bernacki, S. H.; Nelson, A. L.; Abdullah, L.; *et al. Am. J. Respir. Cell Mol. Biol.* **1999**, *20*, 595–604.
58. Steimer, A.; Haltner, E.; Lehr, C. M. *J. Aerosol Med.* **2005**, *18*, 137–182.
59. Araya, J.; Cambier, S.; Morris, A.; Finkbeiner, W.; Nishimura, S. L. *Am. J. Pathol.* **2006**, *169*, 405–415.
60. Choe, M. M.; Sporn, P. H.; Swartz, M. A. *Am. J. Physiol. Lung Cell. Mol. Physiol.* **2003**, *285*, L427–L433.
61. Shoji, S.; Rickard, K. A.; Takizawa, H.; Ertl, R. F.; Linder, J.; Rennard, S. I. *Am. Rev. Respir. Dis.* **1990**, *141*, 433–439.
62. Antunes, M. B.; Woodworth, B. A.; Bhargave, G.; *et al. Biotechniques* **2007**, *43*, 195–196; 198, 200 passim.
63. Pohl, C.; Hofmann, H.; Moisch, M.; *et al. J. Biotechnol.* **2009**.
64. Pohl, C.; Papritz, M.; Moisch, M.; *et al. Toxicol. Sci.* **2009**.
65. Lechner, J. F.; Haugen, A.; Autrup, H.; Mcclendon, I. A.; Trump, B. F.; Harris, C. C. *Cancer Res.* **1981**, *41*, 2294–2304.
66. Forbes, B.; Shah, A.; Martin, G. P.; Lansley, A. B. *Int. J. Pharm.* **2003**, *257*, 161–167.
67. Steimer, A.; Laue, M.; Franke, H.; Haltner-Ukomado, E.; Lehr, C. M. *Pharm. Res.* **2006**, *23*, 2078–2093.
68. Winton, H.; Wan, H.; Cannell, M.; *et al. Clin. Exp. Allergy* **1998**, *28*, 1273–1285.
69. Patel, J.; Pal, D.; Vangal, V.; Gandhi, M.; Mitra, A. L. *Pharm. Res.* **2002**, *19*, 1696–1703.
70. Borchard, G.; Cassara, M. L.; Roemele, P. E.; Florea, B. I.; Junginger, H. E. *J. Pharm. Sci.* **2002**, *91*, 1561–1567.
71. Fiegel, J.; Ehrhardt, C.; Schaefer, U. F.; Lehr, C. M.; Hanes, J. *Pharm. Res.* **2003**, *20*, 788–796.
72. Ehrhardt, C.; Kneuer, C.; Fiegel, J.; *et al. Cell Tissue Res.* **2002**, *308*, 391–400.
73. Mathia, N. R.; Timoszyk, J.; Stetsko, P. I.; Megill, J. R.; Smith, R. L.; Wall, D. A. *J. Drug Target.* **2002**, *10*, 31–40.
74. Wanner, A.; Salathe, M.; O'riordan, T. G. *Am. J. Respir. Crit. Care Med.* **1996**, *154*, 1868–1902.
75. Rautiainen, M.; Matsune, S.; Yoshitsugu, M.; Ohyama, M. *Eur. Arch. Otorhinolaryngol.* **1993**, *250*, 97–100.
76. Uzlaner, N.; Priel, Z. *J. Physiol.* **1999**, *516*(Pt 1), 179–190.
77. Zhang, L.; Han, D.; Sanderson, M. J. *Ann. Otol. Rhinol. Laryngol.* **2005**, *114*, 399–403.
78. Laoukili, J.; Perret, E.; Willems, T.; *et al. J. Clin. Invest.* **2001**, *108*, 1817–1824.
79. Wohlsen, A.; Martin, C.; Vollmer, E.; *et al. Eur. Respir. J.* **2003**, *21*, 1024–1032.
80. Ahmad, I.; Drake-Lee, A. *Rhinology* **2003**, *41*, 69–71.
81. Iida, H.; Matsuura, S.; Shirakami, G.; Tanimoto, K.; Fukuda, K. *Can. J. Anaesth.* **2006**, *53*, 242–249.
82. Delmotte, P.; Sanderson, M. J. *Am. J. Respir. Cell Mol. Biol.* **2006**, *35*, 110–117.
83. Rhee, C. S.; Hong, S. K.; Min, Y. G.; *et al. Am. J. Rhinol.* **1999**, *13*, 27–30.
84. Oshima, T.; Laroux, F. S.; Coe, L. L.; *et al. Microvasc. Res.* **2001**, *61*, 130–143.
85. Halldorsson, S.; Asgrimsson, V.; Axelsson, I.; *et al. In Vitro Cell. Dev. Biol. Anim.* **2007**, *43*, 283–289.
86. Karp, P. H.; Moninger, T. O.; Weber, S. P.; *et al. Meth. Mol. Biol.* **2002**, *188*, 115–137.
87. Zabner, J.; Smith, J. J.; Karp, P. H.; Widdicombe, J. H.; Welsh, M. J. *Mol. Cell* **1998**, *2*, 397–403.
88. Wiszniewski, L.; Jornot, L.; Dudez, T.; *et al. Am. J. Respir. Cell Mol. Biol.* **2006**, *34*, 39–48.
89. Deslee, G.; Dury, S.; Perotin, J. M.; *et al. Respir. Res.* **2007**, *8*, 86.
90. Crouch, E.; Wright, J. R. *Annu. Rev. Physiol.* **2001**, *63*, 521–554.
91. Dobbs, L. G. *Am. J. Physiol.* **1990**, *258*, L134–L147.
92. Matthay, M. A.; Folkesson, H. G.; Clerici, C. *Physiol. Rev.* **2002**, *82*, 569–600.
93. Crapo, J.; Barry, B.; Gehr, P.; Bachofen, M.; Weibel, E. *Am. Rev. Respir. Dis.* **1982**, *126*, 332–337.
94. Strunk, R.; Eidlen, D.; Mason, R. *J. Clin. Invest.* **1988**, *81*, 1419–1426.
95. Vanderbilt, J. N.; Mager, E. M.; Allen, L.; *et al. Am. J. Respir. Cell Mol. Biol.* **2003**, *29*, 661–668.
96. Witherden, I. R.; Vanden Bon, E. J.; Goldstraw, P.; Ratcliffe, C.; Pastorino, U.; Tetley, T. D. *Am. J. Respir. Cell Mol. Biol.* **2004**, *30*, 500–509.
97. Adamson, I.; Bowden, D. *Lab. Invest.* **1975**, *32*, 736–745.
98. Adamson, I.; Bowden, D. *Lab. Invest.* **1974**, *30*, 35–42.
99. Evans, M. J.; Cabral, L. J.; Stephens, R. J.; Freeman, G. *Exp. Mol. Pathol.* **1975**, *22*, 142–150.
100. Uhal, B. D. *Am. J. Physiol.* **1997**, *272*, L1031–L1045.
101. Clegg, G. R.; Tyrrell, C.; Mckechnie, S. R.; Beers, M. F.; Harrison, D.; Mcelroy, M. C. *Am. J. Physiol. Lung Cell. Mol. Physiol.* **2005**, *289*, L382–L390.
102. Beck, G.; Yard, B.; Breedijk, A.; Van Ackern, K.; Van Der Woude, F. *Clin. Exp. Immunol.* **1999**, *118*, 298–303.
103. Burg, J.; Krump-Konvalinkova, V.; Bittinger, F.; Kirkpatrick, C. J. *Am. J. Physiol. Lung Cell. Mol. Physiol.* **2002**, *283*, L460–L467.
104. Moore, T. M.; Chetham, P. M.; Kelly, J. J.; Stevens, T. *Am. J. Physiol. Lung Cell Mol. Physiol.* **1998**, *275*, L203–L222.
105. Ryan, U. S. *Annu. Rev. Physiol.* **1986**, *48*, 263–277.
106. Ando-Akatsuka, Y.; Yonemura, S.; Itoh, M.; Furuse, M.; Tsukita, S. *J. Cell. Physiol.* **1999**, *179*, 115–125.
107. Suzuki, A.; Ishiyama, C.; Hashiba, K.; Shimizu, M.; Ebnet, K.; Ohno, S. *J. Cell Sci.* **2002**, *115*, 3565–3573.
108. Yonemura, S.; Itoh, M.; Nagafuchi, A.; Tsukita, S. *J. Cell Sci.* **1995**, *108*, 127–142.
109. Schnittler, H. *Basic Res. Cardiol.* **1998**, *93*, 30–39.
110. Vestweber, D. *J. Pathol.* **2000**, *190*, 281–291.
111. Forbes, B.; Wilson, C. G.; Gumbleton, M. *Int. J. Pharm.* **1999**, *180*, 225–234.
112. Patel, L. N.; Uchiyama, T.; Kim, K. J.; *et al. J. Pharm. Sci.* **2008**, *97*, 2340–2349.
113. Widera, A.; Kim, K. J.; Crandall, E. D.; Shen, W. C. *Pharm. Res.* **2003**, *20*, 1231–1238.
114. Armstrong, L.; Medford, A. R.; Uppington, K. M.; *et al. Am. J. Respir. Cell Mol. Biol.* **2004**, *31*, 241–245.
115. Cunningham, A. C.; Milne, D. S.; Wilkes, J.; Dark, J. H.; Tetley, T. D.; Kirby, J. A. *J. Cell Sci.* **1994**, *107*(Pt 2), 443–449.
116. Eghtesad, M.; Jackson, H. E.; Cunningham, A. C. *Immunology* **2001**, *102*, 157–164.
117. Elbert, K. J.; Schafer, U. F.; Schafers, H. J.; Kim, K. J.; Lee, V. H.; Lehr, C. M. *Pharm. Res.* **1999**, *16*, 601–608.
118. Fuchs, S.; Hollins, A. J.; Laue, M.; *et al. Cell Tissue Res.* **2003**, *311*, 31–45.
119. Hermanns, M. I.; Fuchs, S.; Bock, M.; *et al. Cell Tissue Res.* **2009**, *336*, 91–105.
120. Mathias, N. R.; Kim, K. J.; Robison, T. W.; Lee, V. H. *Pharm. Res.* **1995**, *12*, 1499–1505.
121. Robinson, P. C.; Voelker, D. R.; Mason, R. J. *Am. Rev. Respir. Dis.* **1984**, *130*, 1156–1160.
122. Ikeda, K.; Clark, J. C.; Shaw-White, J. R.; Stahlman, M. T.; Boutell, C. J.; Whitsett, J. A. *J. Biol. Chem.* **1995**, *270*, 8108–8114.
123. Wert, S. E.; Glasser, S. W.; Korfhagen, T. R.; Whitsett, J. A. *Dev. Biol.* **2002**, *242*, 75–87.

124. Dahlin, K.; Mager, E. M.; Allen, L.; *et al*. *Am. J. Respir. Cell Mol. Biol*. **2004**, *31*, 309–316.
125. Williams, M. C. *Annu. Rev. Physiol*. **2003**, *65*, 669–695.
126. Bankston, P. W.; Porter, G. A.; Milici, A. J.; Palade, G. E. *Eur. J. Cell Biol*. **1991**, *54*, 187–195.
127. Barkhordari, A.; Stoddart, R. W.; Mcclure, S. F.; Mcclure, J. *J. Mol. Histol*. **2004**, *35*, 147–156.
128. Campbell, L.; Hollins, A. J.; Al-Eid, A.; Newman, G. R.; Von Ruhland, C.; Gumbleton, M. *Biochem. Biophys. Res. Commun*. **1999**, *262*, 744–751.
129. Kasper, M.; Reimann, T.; Hempel, U.; *et al*. *Histochem. Cell Biol*. **1998**, *109*, 41–48.
130. Demling, N.; Ehrhardt, C.; Kasper, M.; Laue, M.; Knels, L.; Rieber, E. P. *Cell Tissue Res*. **2006**, *323*, 475–488.
131. Kreda, S. M.; Gynn, M. C.; Fenstermacher, D. A.; Boucher, R. C.; Gabriel, S. E. *Am. J. Respir. Cell Mol. Biol*. **2001**, *24*, 224–234.
132. Fehrenbach, H.; Kasper, M.; Tschernig, T.; Shearman, M. S.; Schuh, D.; Muller, M. *Cell Mol. Biol*. **1998**, *44*, 1147–1157.
133. Shirasawa, M.; Fujiwara, N.; Hirabayashi, S.; *et al*. *Genes Cells* **2004**, *9*, 165–174.
134. Uchida, T.; Shirasawa, M.; Ware, L. B.; *et al*. *Am. J. Respir. Crit. Care Med*. **2006**, *173*, 1008–1015.
135. Hermanns, M. I.; Kasper, J.; Dubruel, P.; *et al*. *J. R. Soc. Interface* **2009**, *7*(Suppl. 1), S41–S54.
136. Weaver, T. E.; Na, C. L.; Stahlman, M. *Semin. Cell Dev. Biol*. **2002**, *13*, 263–270.
137. Kemp, S. J.; Thorley, A. J.; Gorelik, J.; *et al*. *Am. J. Respir. Cell Mol. Biol*. **2008**, *39*, 591–597.
138. Gazdar, A.; Linnoila, R.; Kurita, Y.; *et al*. *Cancer Res.* **1990**, *50*, 5481–5487.
139. Lieber, M.; Smith, B.; Szakal, A.; Nelson-Rees, W.; Todaro, G. *Int. J. Cancer* **1976**, *17*, 62–70.
140. Shapiro, D. L.; Nardone, L. L.; Rooney, S. A.; Motoyama, E. K.; Munoz, J. L. *Biochim. Biophys. Acta* **1978**, *530*, 197–207.
141. Carterson, A. J.; Honer Zu Bentrup, K.; Ott, C. M.; *et al*. *Infect. Immun*. **2005**, *73*, 1129–1140.
142. Mason, R.; Williams, M. *Biochim. Biophys. Acta* **1980**, *617*, 36–50.
143. Alcorn, J. L.; Gao, E.; Chen, Q.; Smith, M. E.; Gerard, R. D.; Mendelson, C. R. *Mol. Endocrinol*. **1993**, *7*, 1072–1085.
144. Korst, R. J.; Bewig, B.; Crystal, R. G. *Hum. Gene Ther*. **1995**, *6*, 277–287.
145. Hermanns, M. I.; Unger, R. E.; Kehe, K.; Peters, K.; Kirkpatrick, C. J. *Lab. Invest*. **2004**, *84*, 736–752.
146. Foster, K. A.; Oster, C. G.; Mayer, M. M.; Avery, M. L.; Audus, K. L. *Exp. Cell Res*. **1998**, *243*, 359–366.
147. Kim, K. J.; Borok, Z.; Crandall, E. D. *Pharm. Res*. **2001**, *18*, 253–255.
148. Kobayashi, S.; Kondo, S.; Juni, K. *Pharm. Res*. **1995**, *12*, 1115–1119.
149. Chess, P.; Ryan, R.; Finkelstein, J. *Exp. Lung Res*. **1998**, *24*, 27–39.
150. Antonetti, D.; Wolpert, E.; Demaio, L.; Harhaj, N.; Scaduto, R. J. *J. Neurochem*. **2002**, *80*, 667–677.
151. Buse, P.; Woo, P. L.; Alexander, D. B.; Reza, A.; Firestone, G. L. *J. Biol. Chem*. **1995**, *270*, 28223–28227.
152. Hoheisel, D.; Nitz, T.; Franke, H.; *et al*. *Biochem. Biophys. Res. Commun*. **1998**, *247*, 312–315.
153. Zettl, K.; Sjaastad, M.; Riskin, P.; Parry, G.; Machen, T.; Firestone, G. *Proc. Natl. Acad. Sci. USA* **1992**, *89*, 9069–9073.
154. Godfrey, R. *Microsc. Res. Tech*. **1997**, *38*, 488–499.
155. Hewett, P. W.; Murray, J. C. *Microvasc. Res*. **1993**, *46*, 89–102.
156. Ge, Y.; Elghetany, M. T. *Lab. Hematol*. **2005**, *11*, 31–37.
157. Wong, S. H.; Hamel, L.; Chevalier, S.; Philip, A. *Eur. J. Biochem*. **2000**, *267*, 5550–5560.
158. Muller, A. M.; Gruhn, K.; Lange, S.; Franke, F. E.; Muller, K. M. *Pathologe* **2004**, *25*, 141–146.
159. Muller, A.; Hermanns, M.; Cronen, C.; Kirkpatrick, C. *Exp. Mol. Pathol*. **2002**, *73*, 171–180.
160. Nalayanda, D. D.; Puleo, C.; Fulton, W. B.; Sharpe, L. M.; Wang, T. H.; Abdullah, F. *Biomed. Microdevices* **2009**, *11*, 1081–1089.
161. Mo, Y.; Barnett, M. E.; Takemoto, D.; Davidson, H.; Kompella, U. B. *Mol. Vis*. **2007**, *13*, 746–757.
162. Lajoie, P.; Nabi, I. R. *J. Cell. Mol. Med*. **2007**, *11*, 644–653.
163. Young, A. *Semin. Cell Dev. Biol*. **2007**, *18*, 448–458.
164. Peters, K.; Unger, R. E.; Kirkpatrick, C. J.; Gatti, A. M.; Monari, E. *J. Mater. Sci. Mater. Med*. **2004**, *15*, 321–325.
165. Thompson, A. B.; Robbins, R. A.; Romberger, D. J.; *et al*. *Eur. Respir. J*. **1995**, *8*, 127–149.
166. Lucas, R.; Verin, A. D.; Black, S. M.; Catravas, J. D. *Biochem. Pharmacol*. **2009**, *77*, 1763–1772.
167. Birkness, K. A.; Deslauriers, M.; Bartlett, J. H.; White, E. H.; King, C. H.; Quinn, F. D. *Infect. Immun*. **1999**, *67*, 653–658.
168. Carolan, E. J.; Mower, D. A.; Casale, T. B. *Am. J. Respir. Cell Mol. Biol*. **1997**, *17*, 727–732.
169. Yanagihara, K.; Cheng, P. W. *Biochim. Biophys. Acta* **1999**, *1472*, 25–33.
170. Kauffman, H. F.; Tomee, J. F.; Van De Riet, M. A.; Timmerman, A. J.; Borger, P. *J. Allergy Clin. Immunol*. **2000**, *105*, 1185–1193.
171. Tomee, J. F.; Van Weissenbruch, R.; De Monchy, J. G.; Kauffman, H. F. *J. Allergy Clin. Immunol*. **1998**, *102*, 75–85.
172. Tomee, J. F.; Wierenga, A. T.; Hiemstra, P. S.; Kauffman, H. K. *J. Infect. Dis*. **1997**, *176*, 300–303.
173. Garcia-Garcia, E.; Gil, S.; Andrieux, K.; *et al*. *Cell. Mol. Life Sci*. **2005**, *62*, 1400–1408.
174. Jeliazkova-Mecheva, V. V.; Bobilya, D. J. *Brain Res. Brain Res. Protoc*. **2003**, *12*, 91–98.
175. Unger, R. E.; Oltrogge, J. B.; Von Briesen, H.; *et al*. *In Vitro Cell. Dev. Biol. Anim*. **2002**, *38*, 273–281.
176. Armulik, A.; Abramsson, A.; Betsholtz, C. *Circ. Res*. **2005**, *97*, 512–523.
177. Nayak, R. C.; Attawia, M. A.; Cahill, C. J.; King, G. L.; Ohashi, H.; Moromisato, R. *Kidney Int*. **1992**, *41*, 1638–1645.
178. Gerhardt, H.; Semb, H. *J. Mol. Med*. **2008**, *86*, 135–144.

3.313. Histological Analysis

C B Johansson, University of Gothenburg, Göteborg, Sweden
R Jimbo, Malmö University, Malmö; Göteborg University, Göteborg, Sweden
K Roeser, University Medical Center Hamburg-Eppendorf, Hamburg, Germany

© 2011 Elsevier Ltd. All rights reserved.

3.313.1. Introduction 216
3.313.2. Preservation of Tissue 217
3.313.2.1. Resolution Level 217
3.313.2.2. Storage 217
3.313.2.3. Fixation 217
3.313.2.4. Perfusion Fixation 218
3.313.2.5. Preserving the Immunoreactivity 218
3.313.2.6. Fixation for Bone Biopsy Samples (1 × 5 mm) up to Bone Slices (8–10 mm thickness) with Implants *In Situ* 218
3.313.2.7. Dehydration 219
3.313.2.8. Infiltration 219
3.313.2.9. Embedding of Bone Biopsies in Technovit® 9100 NEW Resin 220
3.313.2.10. Cutting the Small Bone Biopsies (see additional information below) 220
3.313.2.11. Artifacts 220
3.313.3. Undecalcified Versus Decalcified 220
3.313.3.1. Clarifications of the Intended Purpose 220
3.313.3.2. Solutions/Chemicals for Decalcification of Bone Tissue 220
3.313.3.3. Advantages and Disadvantages 221
3.313.3.4. Artifacts 221
3.313.4. Embedding Techniques 221
3.313.4.1. Undecalcified Versus Decalcified 222
3.313.4.2. Embedding Materials 222
3.313.4.2.1. Resin 222
3.313.4.2.2. Paraffin 222
3.313.4.3. Tissue Tech, OCT Compounds (Optimal Cutting Temperature) 222
3.313.4.4. Artifacts 222
3.313.4.4.1. Artifacts related to paraffin 223
3.313.4.4.2. Artifacts related to frozen sectioning 223
3.313.5. Sectioning Techniques 223
3.313.5.1. Ground Sections: Cutting and Grinding Technique Add Modum Donath 223
3.313.5.2. Artifacts 223
3.313.5.3. Microdissection 225
3.313.6. Staining Methods 225
3.313.6.1. Staining for Histological Observations 225
3.313.6.2. Immunohistochemistry 225
3.313.6.3. *In Situ* Hybridization 226
3.313.7. Quantification Methods 226
3.313.7.1. Level of Quantification 227
3.313.7.2. What and How to Quantify? 227
3.313.7.3. Methods and Equipment/Software 228
3.313.7.4. Reference Sections and Reference Quantifier: In-house Standard Rules 229
3.313.7.5. X-rays 229
3.313.7.6. Microcomputed Tomography and Synchrotron Radiation-Based μCT 229
3.313.7.7. Histological Versus Biomechanical Quantification 229
3.313.7.8. Combination of Techniques for Quantification of Bone Remodeling 231
3.313.7.8.1. Confocal laser scanning microscope 231
3.313.7.8.2. Gene expression 231
3.313.8. Summary and Future Directions 231
References 232

Abbreviations

AB	Antibody
ACP	Acidic phosphatase
ALP	Alkaline phosphatase
BA	Bone area
BIC	Bone implant contact
CLSM	Confocal laser scanning microscope
DAB	Diamino benzidine
DNA	Deoxyribonucleic acid
EDTA	Ethylenediamine tetraacetic acid
EDX	Energy-dispersive X-ray spectroscopy
FLC	Fluorescent
GMA	Glycol methacrylate
HE	Hematoxylin and eosin
HRP	Horseradish peroxidase
IHC	Immunohistochemistry
ISH	*In situ* hybridization
MEA	Methoxyethylacetate
MI	Mirror image
MMA	Methyl methacrylate
mRNA	Messenger ribonucleic acid
NaN_3	Sodium azide
NBF	Neutral buffered formaldehyde
PBS	Phosphate buffered saline
PCNA	Proliferating cell nuclear antigen
PMMA	Poly methyl methacrylate
PVC	Polyvinyl chloride
PVP	Polyvinylpyrrolidone
RFA	Resonance frequency analyses
RNA	Ribonucleic acid
RT	Room temperature
RTQ	Removal torque
SRμCT	Synchrotron radiation-based microcomputed tomography
SSC	Standard saline citrat
TEA	Tris base, acetic acid
THR	Total hip replacements
TRIS	Tris(hydroxymethyl)-aminomethan
μCT	Microcomputed tomography
X-ray	Radiography

3.313.1. Introduction

Histological evaluation of the tissue reactions to the biomaterial placed in the living body is of utmost importance and is an essential step in understanding its nature. By observing and evaluating histological sections, the aim is to determine whether or not the material is biocompatible. Histology has evolved so much and there are numerous techniques available that we can observe not only the shape of the cells, but further observe its gene expression or related protein localization. Hence, it can be said that with the tools we have today, a more precise evaluation of the tissue reactions to the biomaterial is possible. However, having multiple options for such evaluations may sometimes be a double-edged blade, since there are specific preparations for each type of sectioning, staining, or technique that one wrong step may lead to a failure, in other words, without proper preparations, we may not be able to observe the target. Therefore, before proceeding to the concrete contents, the importance of project planning and adequate project outlines should be addressed in this introduction part of the chapter.

During the course of project planning, certain issues or questions must be discussed or answered such as 'What do we want to observe?' or 'What type of evaluation, or what kind of staining?' or 'Decalcified or calcified sections?' or 'Paraffin sections or resin sections or frozen sections?' or 'How many samples are to be prepared?' or 'What is the expected size of the samples?' or 'What is the composition of the samples?' By answering to these questions, we will have a clear idea of the protocols we must follow. It is most important to obtain advice from the persons involved in the laboratory procedures at early stages of planning. The project planning must include consideration of the safety problems for the persons involved in the procedures because many steps involve using hazardous reagents.

Although the application of biomaterials has a wide range from soft tissues to hard tissues, this chapter mainly focuses on bone tissue reactions in relation to biomaterials.

The history of *artificial* materials placed in bone goes back as far as the age of the Roman empire,[1] where a wrought iron material was placed in the maxilla after tooth loss. Whether or not the material was in function will remain as a missing piece of the puzzle, this is a clear indication that we always had an idea that materials could replace once lost organs.

Around 1961, Brånemark and colleagues discovered the osseointegration phenomenon using commercially pure titanium,[2,3] and to this day, efforts to improve osseointegration have lead to a variety of innovations. And it is necessary to emphasize that the laboratory evaluation of osseointegration has always been dependent on histology. The original definition of osseointegration was based on the light microscopical level.[4] The method for preparing undecalcified sections in the 'early days' in the laboratories followed the guidelines of Hallén and Röckert.[5] These authors had modified the cutting and grinding methods that were presented by Pattern and Chase.[6] Nowadays, the specific histological sample preparation follows the cut and grinding technique described by Donath and Breuner,[7] and for a proper evaluation, the importance of sample thickness has been reported indicating its technique sensitivity.[8] Sample thickness is important for achieving proper/reliable histomorphometrical results; however, there are quite recent publications where sections of 50 μm and more are evaluated and to our knowledge, the thicker the section the greater the integration will appear.[9–11]

This chapter briefly describes some selected histological and histomorphometrical methods starting from sample preparation techniques to specific quantification methods in particular for bone tissue. Along with the basic histological staining techniques, standard immunohistochemistry, immunofluorescent stainings, enzyme histochemistry, and DNA/RNA

labeling technique using *in situ* hybridization will be presented. Furthermore, toward the end of this chapter, some state-of-the-art and novel techniques will be presented that will provide more knowledge and enhance our understanding related to histological analysis.

There are several excellent books available within this interesting field, and at the end of this chapter, we refer to some selected handbooks.

3.313.2. Preservation of Tissue

This section describes the preparation of the samples for adequate quality sections and/or stainings, focusing on fixation of the tissue. This is an utmost important task for adequate histological analyses, since the quality of the sections may easily be disturbed due to inappropriate procedures during the fixation step. Some critical aspects related to the fixation protocol are temperature, sample size and volume of fixative, pH, and time of fixation. Almost all fixatives contain toxic substances and safety aspects must be followed. For such issues, we refer to the paper by Titford.[12]

3.313.2.1. Resolution Level

Different resolution levels involved in analyses require the usage of specific fixative solutions in order to achieve the best results of tissue preservation for the intended investigation. The resolution level to be investigated must be known beforehand. This is crucial since not only sample size matters for achieving good results. Both overfixed and underfixed tissue will render 'preservation artifacts' irrespective of morphological, cytological, or histochemical level.

3.313.2.2. Storage

After adequate fixation has been performed, the samples should not be stored in the fixative since this will overfix the material. The fixation itself is a very critical part and later histological staining results will be hampered. Storage of fully fixed samples in 70% ethanol kept in a cool place is recommended. With proper handling of samples, they can be stored for a very long time and the material can be used for later analyses.

3.313.2.3. Fixation

Fixation is the first step in the preparation of the histological sections. It should preserve the tissue as it is so that we will be able to observe or evaluate the intended time point. Proper tissue fixation is important.

In general, for immunohistochemical detection of proteins in the tissue, a fixation time of 24 h at room temperature using 4% paraformaldehyde solution is adequate. If and when using 1.4% paraformaldehyde solution at 4 °C, the fixation time is prolonged and over fixation will not be a problem. However, the solution has to be changed very often because the concentration of paraformaldyde decreases with time. This low concentrated fixative can only be used on small tissue samples otherwise the fixation is too slow to protect the tissue from autolysis. Achieving excellent fixation of tissue surrounding implants is a challenge. Problems associated with histological analysis, especially in the interface region, refer to the penetration time of the fixative, that is influenced by the various different density properties involved in the sample (bone, soft tissue, biomaterial). There is the compact bone tissue on one side and the cell membranes with their semipermeable properties on the other side. Immuno- and enzyme histochemistry require a protein protective fixation. The fixative must stabilize cell membranes, render no shrinking, and thus reveal no osmotic differences. Nucleic acids need strong fixation such as 10% paraformaldehyde; however, over fixation by time renders negative results/consequences.

Preserving the tissue is intended to prevent autolysis and to immobilize the cells and/or tissues. Glutaraldehyde has a strong fixation effect due to the dual –CHO radicals, and it is mainly used for electron microscopic observations, for example, observing implant tissue interface or cells cultured on biomaterials as seen in **Figure 1**.[13] The advantage of this fixative is that it preserves the cell or the tissue morphology to be favorable for these types of observations. In normal procedures, 2–5% concentration in phosphate-buffered saline (PBS)

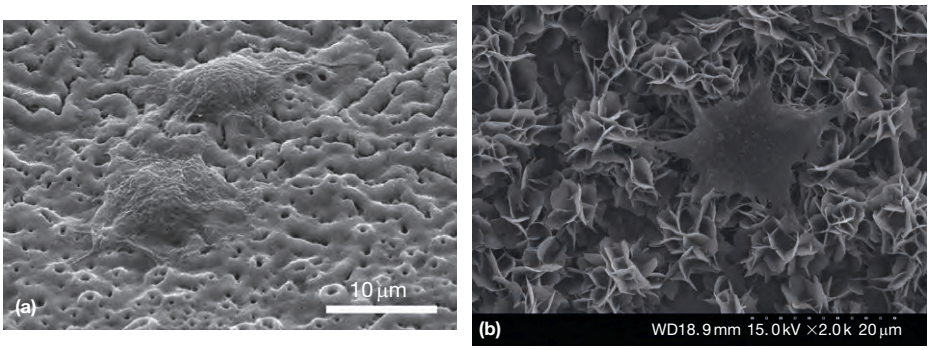

Figure 1 Scanning electron microscopic images of osteoblasts (MC3T3-E1) cultured on (a) laminin-incorporated hydroxyapatite surface (b) anodic-oxidized surface. Although observed at different time-points, the cells are well spread indicating the biocompatibility of the surface. Cells were fixed with glutaraldehyde fixatives, followed by series of dehydration. Note that the cell morphologies are well preserved after treatments. (a) Reproduced from Jimbo, R.; Sawase, T.; Baba, K.; *et al. Clin. Impl. Dent. Relat. Res.* **2008**, *10*, 55–61, with permission from Wiley.

is most commonly used. However, the time to fix takes longer compared with formaldehydes, hence most of the studies which involves electron microscopic observations use a mixture of formaldehyde and glutaraldehyde of around 2–3% each.[14] Due to their strong fixability, tissues fixed with glutaraldehydes tend to reduce their enzyme chemical reactions.[15] On the other hand, 4% formaldehyde solution in PBS is one of the most commonly used fixatives for diagnostic and research histological sample preparations. Moreover, by adding sucrose to the 4% formaldehyde solution in PBS, this will protect the cross-linking of the proteins, and this fixative is known to be effective for standard histological sections, immunohistochemistry, and enzyme histochemistry.[16]

The pH of the fixatives should be between 7.2 and 7.4 in order to prevent shrinkage or swelling of the cells. Needless to say, this adjustment will enhance the quality of the final sections, and in fact, it is crucial for obtaining good quality material/sections. The used fixative and the time for fixation cause the majority of problems in tissue preservation and later analyses. We must keep in mind that there is no standard time setting for the length of fixation, since this will differ depending on tissue type and size of the sample. In diagnostics, a sample size of $10 \times 10 \times 3$ mm is preferred and many methods and protocols are in fact designed for such sample size. As a rule of thumb, samples of this size are fixed within 6–24 h in neutral-buffered formaldehyde (NBF). For example, in our laboratories, we have a wide variety of fixation time from 24 h to more than 7 days depending on the tissue type and size as well as subsequent stainings and analysis to be performed.

3.313.2.4. Perfusion Fixation

Perfusion fixation is a research method, which will fixate the tissue by perfusing the fixative solution through the vascular system. It is known that this procedure will better fixate the samples to its smallest vessels compared to the immersion procedure. Perfusion fixation is normally operated by placing a catheter through the heart or large arteries such as the femoral or the inguinal artery. At first, blood and other residues will be removed by a reflux of saline or PBS, if necessary, anticoagulants such as heparin should be used. Thereafter, the fixatives prewarmed to body temperature should be perfused into the vessels at constant speed, preferably using a mechanically controlled pump.

3.313.2.5. Preserving the Immunoreactivity

As mentioned above, fixatives including aldehydes have a strong fixing effect. Even the formaldehyde may be too strong that the section may lose its immunoreactivity. When an antibody does not work, some blame on the quality of the antibody and never think about the fixatives and sample preparation. This section and further below may provide some ideas on what we can do to improve the immunoreactivity of the samples. High or low osmotic pressure between the tissue and the fixative will either make the tissues enlarged or contracted and may have some negative influence on the immunoreactivity and cell morphology. As mentioned before, by adding sucrose to the 4% formaldehyde solution in PBS, this will hinder the cross-binding of the proteins and thus both enzyme and immunohistochemistry can be successfully investigated.[16]

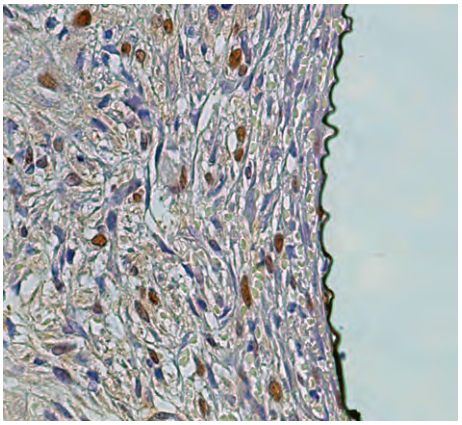

Figure 2 Immunohistochemical staining using antiproliferating cell nuclear antigen (PCNA) antibody. The objective of the staining was to observe cell proliferative activities around the implant. Magnification: ×40.

In some cases, reactivation of enzymes is possible. Samples being immersed in 4% NBF for no longer than 24 h can be 'reactivated' rendering positive enzyme histochemical detection of ALP (alkaline phosphatase) and ACP (acidic phosphatase). However, the best quality of the enzyme activity is of course obtained when using the most adequate fixative to start with.[17]

Addition of zinc ions to the formalin (4% zinc-formaldehyde, Mallinckrodt Baker B.V., Holland) has also proven to be an effective way to preserve the immunoreactivity (Figure 2). The role of the zinc ions is to prevent the cross-linkage between proteins and tissue that may disturb the immunoreactions.[18]

3.313.2.6. Fixation for Bone Biopsy Samples (1×5 mm) up to Bone Slices (8–10 mm thickness) with Implants *In Situ*

The time for fixation of smaller biopsies is usually between 12 and 24 h and takes place in different solutions depending not only upon the composition of the specimen but also on the antigen or enzyme to be labeled. The larger bone samples may need a fixation time of 1 week. To enhance the preservation of the tissue, we recommend that the fixation be performed with the aid of agitation and vacuum treatment.

In general, both for diagnostics and for research purposes, the 4% NBF is accepted and regarded as a state-of-the-art fixative. However, for specific demands, one has to go beyond the routine. Below is some useful information regarding tissue treatment for such demands of 'higher magnification investigation.'

The following methods of fixation have been used for detecting antigens or enzymes.

(a) 4% neutral-buffered formalin (0.02 mol l^{-1} phosphate buffer) – 4–8 °C for 24–48 h, suitable for all histological staining methods (tissue and cell structures), immunohistochemistry (proteins and antigens), *in situ* hybridization techniques (nucleic acids). A fixation at RT for 24–48 h is also possible if omitting the sucrose.

(b) 1.4% paraformaldehyde solution at 4–8 °C for 24–48 h and longer because overfixation will not be a problem by using this low concentration (suitable for sensitive detection of enzymes such as alkaline and acidic phosphatases and for antigens sensitive to denaturation/structural changes).

Fixative solutions

1. Paraformaldehyde stock solution (8%)
   40 g paraformaldehyde
   make up to 500 ml with distilled water
2. 1 M phosphate buffer (pH 7.0–7.4)
   112.5 g disodium hydrogen phosphate
   30.0 g potassium dihydrogen phosphate
   make up to1000 ml with distilled water
   adjust the pH to 7.0 with HCl
3. 0.4 M phosphate buffer with 10% sucrose
   40 ml 1 M phosphate buffer
   100 g sucrose
   10 ml 10% NaN_3
   make up to 500 ml with distilled water
4. Adjust the pH to 7.0 with HCl–paraformaldehyde solution (4%) = *Ready Enzyme Fixative Solution*
   100 ml paraformaldehyde stock solution (see above)
   100 ml 0.04 mol l^{-1} phosphate buffer with 10% sucrose, pH 7.4
5. Paraformaldehyde solution (1.4%) = *Ready Enzyme Fixative Solution*
   35 ml paraformaldehyde stock solution (see above)
   65 ml distilled water
   100 ml 0.04 mol l^{-1} phosphate buffer with 10% sucrose, pH 7.4

There are several variations of this fixative and the original is from Romeis.[19] In 1989, it was upgraded by Böck.[20] One variation of the fixative, with the addition of ethylenediaminetetraacetic acid (EDTA), demonstrated excellent results in standard histological staining, immunohistochemistry, and DNA isolation.[21]

The *Enzyme Fixative Solution* as mentioned above has successfully been used both for small bone biopsies as well as larger samples with implants *in situ* (Figure 3). The following steps have been followed for bone tissue with implants *in situ*.[22]

All solutions should be fresh and newly prepared as well as pH adjusted. Solutions can be stored in the refrigerator overnight before mixing. It is important to follow a strict protocol during fixation and the following is recommended for small bone biopsies:

1. Place the samples in cold (+4 °C) fixative for 6 h (keep cold)
2. Change the fixative to new solution (+4 °C) and continue 24 h (keep cold)
3. Change the fixative to new solution (+4 °C) and continue 24 h (keep cold)
4. Place samples in 70% ethanol
5. Dehydration: see Section 3.313.2.7.

3.313.2.7. Dehydration

Dehydration is routinely performed in increasing concentrations of ethanol and can be performed both manually and automatically in a suitable device at ambient temperature.

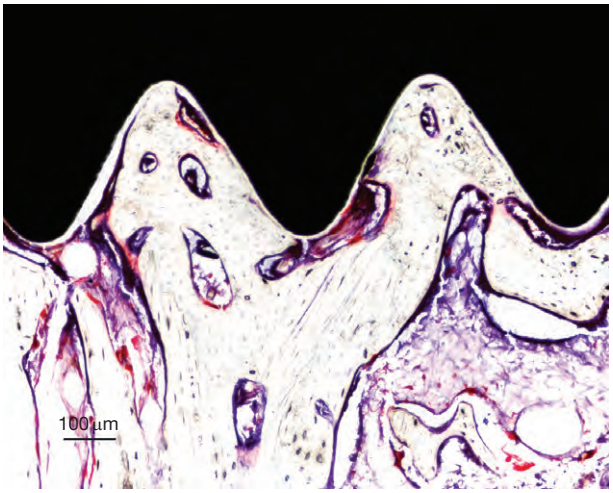

Figure 3 Cut and ground section of a sample retrieved from rabbit bone. Alkaline phosphatase (ALP) and acidic phosphatase (ACP) can be seen both in the interface region and in the bone remodeling cavities. Magnification: the distance between the thread peaks is 0.6 mm.

Two batches of xylene are then used as an intermediate solution before infiltration in resin. The time in each step varies depending on sample size, but for small biopsies 1 h per step is required. For larger samples, with implants *in situ*, agitation and vacuum will aid in all steps.

3.313.2.8. Infiltration

Our experience, with infiltration of samples to be resin embedded with the Technovit® 9100 NEW resin (Heraeus, Kulzer, Germany) suitable for enzyme and immunohistochemical investigations, is described here. Samples are immersed in three preinfiltration steps followed by infiltration in two batches of pure resin. Preinfiltration steps 1 and 2 can be performed both manually and automatically in a suitable dehydration device, whereas the two last steps should be carried out in a refrigerator. One hour per preinfiltration step is required for small spongy and cortical bone samples and pelvic biopsies. For large tissue samples (8–10 mm thickness), the times and volumes should be increased proportionally. Readers interested in additional information related to the following are referred to Wolf *et al.*[16] and Röser *et al.*[23]

The following steps are followed before embedding in Technovit® 9100 NEW:

Dehydration in ethanol (1 h per step)

1. 70%
2. 80%
3. 96% × 2
4. Absolute ethanol × 3
   Intermediate (1 h per step)
5. Xylene × 2
   Preinfiltration (1 h per step)
6. Xylene: Technovit 9100 NEW. Basic (Stabilized), 1:1
7. Technovit 9100 NEW, Basic (Stabilized) + Hardener-1
8. Technovit 9100 NEW, Basic (Destabilized) + Hardener-1
   Infiltration (1 h to 2–3 days per step for small biopsies and prolonged for larger samples)

9. Technovit 9100 NEW, Basic (Destabilized) + Hardener-1+ PMMA-powder.

The table below shows the preparation of preinfiltration and infiltration as well as stock solutions from the five components that are included in the Technovit 9100® New Kit.

Component	1. Basic solution	2. PMMA powder	3. Hardener 1	4. Hardener 2	5. Regulator	Storage
Preinfiltration	200 ml		1 g			Room temp
Infiltration	add 250 ml	20 g	1 g/2 g[a]			4 °C
Stock-sol A	add 500 ml	80 g	3 g/4 g[a]			4 °C
Stock-sol B	add 50 ml			4 ml	2 ml	4 °C

[a]The usage of stabilized Technovit 9100®NEW requires the larger amount of Hardener 1.

Preparation of embedding solution (polymerization mixture): The cooled stock solutions A and B are mixed before usage in a glass beaker during stirring in proportions; 9 parts A plus 1 part B.

3.313.2.9. Embedding of Bone Biopsies in Technovit® 9100 NEW Resin

Embedding molds vary depending on sample size, from gelatin capsule to PVC cups.

The precooled embedding solutions should be poured over the sample and a complete covering is necessary. Samples are placed in a cooled desiccator under vacuum at 4 °C for about 10 min.

The resin is hardened in an oxygen free chamber (sealed container) placed in −8 to −20 °C. The polymerization setting time is dependent on the amount of resin but in general 24–48 h. Following this, the samples are placed in a refrigerator for a few hours (overnight) before reaching room temperature.

3.313.2.10. Cutting the Small Bone Biopsies (see additional information below)

Bone biopsies can be successfully cut using a knife with a D-shaped cutting edge in a stabile rotation microtome. Use 30% ethanol as a stretching media when cutting the sections. Place sections on super frost plus slides and mount with 50% ethanol followed by covering the sections with PVC foil. Remove the excess fluid with filter paper. Place the sections in a press in an oven over night.

The following steps are recommended for deacrylation of sections before staining

1. Xylene 2–3 × 20 min
2. 2-Methoxyethylacetate (2-MEA) 1 × 20 min
3. Pure acetone 2 × 5 min
4. Distilled water 2 × 2 min
5. Alternatively 2-MEA 3 × 20 min
   Constant stirring during the steps and room temperature is recommended.

3.313.2.11. Artifacts

Biopsies with a 'foggy appearance' containing 'white spots' ('Lunker-Stellen') of polymer in the bone tissue are due to inappropriate dehydration and/or infiltration. Such artifacts negatively influence the cutting of the block as well as the quality of the sections. According to our experience, such biopsies can be divided and reinfiltrated in resin under stirring and then repolymerized. However, caution must be taken since dividing the biopsies also result in the loss of material. This treatment renders acceptable sections.

3.313.3. Undecalcified Versus Decalcified

This section refers to our in-house routine methods and thus will not cover all aspects relate to un-decalcification versus decalcification. For more information related to other decalcifying methods, the readers are referred to Sheehan and Hrapchak[24] and the review by Callis and Sterchi.[25]

3.313.3.1. Clarifications of the Intended Purpose

Bone tissue and teeth/dentin are the hardest components of the body, due to the incorporation of great amounts of calcium salts. While un-decalcified bone involves a long time for tissue processing until histological sectioning is possible, the decalcified samples can be rather quickly processed. The latter preparation is more often conducted in diagnostic/routine pathological laboratories, while the former of un-decalcifications are commonly used in research laboratories. Moreover, when biomaterials are involved in the bone tissue, most often the tissue is not decalcified since the interface between the bone tissue and the biomaterial is of great importance. Processing of un-decalcified cut and ground sections with biomaterials *in situ* are thus most often associated with research laboratories. However, there are times when the research project has a specific purpose for preparation of decalcified samples. If no biomaterial is present in the tissue and if it is urgent, it has been shown that decalcification can be successfully carried out using microwaves also for *in situ* hybridization studies.[26] The need to clarify the intended purpose of the sampling process is important and this should be kept in mind when designing the study.

3.313.3.2. Solutions/Chemicals for Decalcification of Bone Tissue

The fixed bone sample must be thoroughly rinsed in water before decalcification can start.

While various acids such as modified formic acid and acetic acid are effective, cheap, and rapid for decalcification purposes, the usage of milder solutions such as EDTA takes a longer time since calcium is removed by chelation and involves a higher

cost. However, the use of EDTA renders better quality of the histological features compared to other decalcifying solutions. In a study by Alers *et al.*[27] using EDTA, the antigenic sites, DNA, and mRNA were preserved compared to tissue dehydrated in an acidic decalcifying solution (RDO, Apex Engineering Products; Plainfield, IL, USA). Our own experience over the years, and recently on decalcified and paraffin sectioned rat bone, is that it works well for immunohistochemical analyses.[28]

Decalcifying solution EDTA with PVP applicable for enzyme- and immunohistochemical analyses

Chemicals

1. Ethylenediaminetetraacetic acid disodium salt dihydrate, EDTA
   $C_{10}H_{14}N_2Na_2O_8 \cdot 2H_2O$, MW 372.24
2. Tris(hydroxymethyl)aminomethane
   $C_4H_{11}NO_3$ M, MW 121.14
3. Potassium hydroxide, ≥85% KOH basis, pellets, MW 56.11
4. Polyvinylpyrrolidone, PVP, MW 24 000 g mol^{-1}

Method

1. Dissolve 12.11 g Tris in 800 ml distilled H_2O
2. Add 100 g EDTA
3. Adjust pH to 6.95 with KOH pellets
4. Add 75 g PVP

When completely dissolved, fill up to 1000 ml with distilled H_2O. The solution should be light-yellow.

Storage: Dark bottle in refrigerator. Durability: about 2 months. Decalcification time: several days to weeks. Posttreatment: H_2O.

3.313.3.3. Advantages and Disadvantages

Decalcification using acidic solutions destroys the structure of proteins to various degrees. Epitopes can be affected which are necessary for the immunohistological detection of certain proteins. However, the EDTA decalcifying solution can be used due to its preservation effect on the epitopes/proteins, although it is time-consuming (ref. compact vs. spongeous bone). In our laboratories, we use EDTA with addition of PVP (polyvinylpyrolidone). The PVP is added since it resists protein precipitation. However, the time to decalcify, for example, a slice of rat tibia bone (about 3 mm thick) takes around 3 weeks. This is the main disadvantage of using EDTA. The process is performed in the refrigerator, changing the solution every third day and using agitation. Paraffin sectioning of such samples and immunohistochemical detection of positively stained megakaryocytes in bone marrow, using Factor VIII (Biocare Medical, USA), were successfully demonstrated by Nyberg *et al.*[28] (**Figure 4**). The reasons for these results are probably due to a combination of a good fixative and a mild decalcifying solution. The retrieved material was immersed in 4% zinc-formaldehyde (Mallinckrodt Baker B.V., Holland). This fixative was used because of its ability to preserve enzyme activity. The disadvantages using acids are that the process must be interrupted immediately after the decalcification is ready in order not to damage the ability of a proper histological staining. The acids are prone to negatively affect the staining of nuclei and thus a poorer morphology can be expected compared to tissue decalcified in EDTA. The endpoint of fixation cannot be exactly determined beforehand. However, there are ways to investigate if a proper

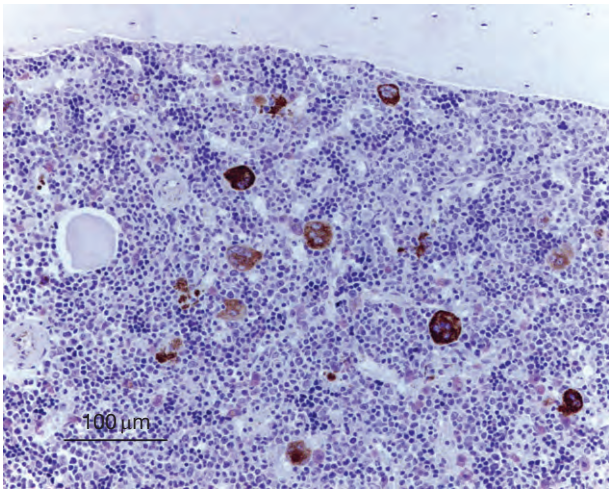

Figure 4 Paraffin section of a rat bone, initially fixed with Zn-formaldehyde solution and decalcified with EDTA (including PVP). Note the positively stained megakaryocytes in the bone marrow. Bar = 100 µm.

decalcification has been achieved, and one commonly used method is to perform X-ray tests. The existing calcium content will show up as brighter regions compared to decalcified areas being darker. In former days, the X-ray tests were a time-consuming method. Nowadays, with the state-of-the-art techniques available (ref. dental equipment), the time to perform such tests is rapid. Moreover, since the X-ray images can be stored in the computer at once, one would think that a standard recipe, guiding when the end-point should be expected, will be available. Another test, albeit rough and with persistent artifacts, is to apply the smallest needle available and pinch a part of the bone that is out of interest for later analyses. Yet another way is to include a 'test sample' with similar properties as the 'real sample' into the same decalcifying batch. This test sample can be manually tested by piercing, bending, and cutting and thus leave the real sample without man-made manual artifacts.

Most acidic decalcification protocols recommend direct posttreatment in ethanol, while EDTA samples can be rinsed in water prior to the commencement of the dehydration process.

3.313.3.4. Artifacts

Artifacts that appear due to the decalcification solutions used relate to poor morphology and destruction of intracellular components as well as impaired staining ability. With this in mind, one should balance between the fixative of choice, the speed, and the time of the decalcification in order to reduce the negative effects that appear in the morphology.

3.313.4. Embedding Techniques

Embedding tissue means that the materials will be surrounded by a supporting material that prevents the tissue from being destroyed when further processed to histological sections. The preferred embedding technique depends on the question of what is going to be observed. For light microscopic

observations, there is a greater variety of what materials and techniques one can use, while for electron microscopical purposes the choice is less and mostly resins (epoxy or acrylic) are used for the latter.

The most commonly used embedding material for diagnostic purposes on fixed, decalcified bone, dehydrated and infiltrated tissue samples without hard unsectionable biomaterials *in situ* is paraffin. However, for rapid diagnostic purposes, the tissue can be frozen and sections prepared using a cryostat, which is a cryosectioning equipment. Yet another technique, when undecalcified bone and biomaterials are involved, is to use various resins as a supporting material (see below).

3.313.4.1. Undecalcified Versus Decalcified

Bone tissue with biomaterials *in situ* requires preparation of undecalcified cut and ground sections. The state-of-the-art technique of undecalcified sectioning is referred to as the 'Donath technique.'[7,29] The advantage of this technique is that one can prepare sections from sample sizes of a few millimeter (e.g., cochlea wall implants) to THR (total hip replacements) from research animals and humans using the same equipment. The major drawback is that it is time-consuming and expensive. Moreover, a skillful technician is a must in order to obtain excellent results.

For diagnostic purposes, when the time for sample processing is urgent and when biomaterials interactions with bone tissue are not the major focus, decalcification of the bone tissue with subsequent processing to paraffin sections is the method of choice. The decalcification process itself can be speeded up with, for example, various decalcifying solutions and microwave processing.

3.313.4.2. Embedding Materials

3.313.4.2.1. Resin

A great variety of resin embedding materials exists. Commonly used ones are methyl methacrylate (MMA) and glycol methacrylate (GMA). The MMA is mostly used for undecalcified bone samples. The latter GMA can be mixed in water and thus the sample need not be fully dehydrated. However, once polymerized, it is not water soluble. Irrespective of resin used, all methacrylates must be regarded as hazardous to health.

The choice of resin is dependent on the aim of the study, and thus tissue processing and time vary substantially. For example, when processing bone with biomaterials *in situ* for subsequent processing to undecalcified sections add modum Donath, we recommend a 'hard' light-curing resin such as Technovit 7200 VLC (Heraeus Kulzer GmbH, Germany). This is due to the fact that softer resins cover the diamond/bore nitride/ layers on the sawing bands and by such clotting there will be a prolonged cutting time. The fact that the band itself is very expensive also motivates the laboratories to use harder resins for preparing cut and ground sections. Harder resins also render better quality sections, that is, more even sections without pronounced artifacts (see below).

In earlier times, we routinely used the hard grade LR White resin (polyhydroxy aromatic resin, London Resin Co. Ltd., Hampshire, England) for cut and ground-sectioning, but to our experience, this resin is 'softer' (even if using the 'hardest' one of the available ones). If the aim is to prepare various resolution levels, that is, light and electron microscopical investigations of the very same sample, both Technovit 7200 VLC and LR White are too 'hard' compared to 'ordinary SEM resins.' Technovit is more brittle compared to LR White and more problematic to section even by a very experienced electron microscopist.

For many years, there was no resin available for the purpose of preparing adequate enzyme and immunohistochemical investigations on undecalcified bone tissue (with biomaterials *in situ*). Research laboratory tests with 'in-house-made' resin on bone biopsies and bone with biomaterials *in situ* rendered excellent results of both enzyme- and immunohistochemical detection of proteins in bone tissue.[16,22,23] By trial and error, we learnt that the first and most important step in reaching such results were the fixative used (Johansson and Röser, unpublished data). Nowadays, this MMA resin, that hardens at low temperature in an oxygen free chamber and can be dissolved, is commercially available and referred to as Technovit 9100® NEW (Heraeus Kulzer GmbH, Germany). The Embedding Kit contains two components, which can be mixed in different portions, which enables the user to determine the hardness of the resin; meaning the same kit can be used for sectioning as well as cutting and grinding.

3.313.4.2.2. Paraffin

Sections for routine diagnostics purposes demand a quick processing time. For this purpose, one may need to divide the undecalcified bone into various samples where some must be treated with decalcification solutions and subsequent paraffin sectioning. If using appropriate fixatives, paraffin-sectioned decalcified bone can be investigated in terms of proteins present in the tissue.[28,30]

3.313.4.3. Tissue Tech, OCT Compounds (Optimal Cutting Temperature)

The frozen- or cryosectioning technique is never the method of choice if one need good or excellent histology. However, this technique is required for specific purposes, such as rapid diagnostics. In order to glue the prefixed thin biopsy and have it secure to the embedding-supporting plate, the Tissue-Tech compound is used. The media freezes and thaws rapidly. The tissue can be snap frozen in, for example, *iso*-pentane that is precooled in liquid nitrogen, followed by 'embedding' in Tissue Tech. For more information, we refer the readers interested in this method to the handbooks recommended in the last part of this chapter.

3.313.4.4. Artifacts

In general, all steps in tissue handling, from fixation, dehydration, infiltration as well as sectioning followed by staining and finally cover slipping are equally important irrespective of what embedding and sectioning techniques are used. Each and every step can cause artifacts. As mentioned earlier, related to fixation, both over-fixed and under-fixed tissue will render 'preservation artifacts' irrespective of morphological, cytological, and histochemical levels. Unexpected, uncommon, and unwanted artifacts arise even if the materials and

methods are routinely performed according to internal guidelines. We have experienced such artifacts appearing as severe thin crack-propagations even with brand new batches of Technovit 7200 VLC. These cracks were observed on the final sections only and not during processing. All ten bottles were tested but cracks appeared and thus the entire batch was discarded. These types of artifacts have not been noted since then. Other artifacts can occur such as large cracks and bubble formation irrespective of resin used. When such artifacts are present, the polymerization process may have been too rapidly performed or the tissue is not perfectly processed, that is, not fully dehydrated and or infiltrated.

Another type of unexpected artifact, that is, unwanted self-polymerization, occurred resulting in a large clump with several samples internalized, when using the LR White resin. Unfortunately, the reasons for these problems cannot be explained. However, such problems have so far not been noted when using the Technovit resins.

3.313.4.4.1. Artifacts related to paraffin

Inappropriate dehydration of the tissue (as well as clearing and/or infiltration of the paraffin) will result in difficulties to sectioning the paraffin block. There will be regions of 'air' in the paraffin block. Such artifacts can be minimized by slowly returning the sample to some previous steps carried out. However, if the sample is poorly handled during the primary tissue processing, no proper results will be achieved. Moreover, the melting temperature of paraffin is critical for keeping the protein structure intact.

3.313.4.4.2. Artifacts related to frozen sectioning

In general, the morphological details and the resolution of frozen sections are of less good quality compared to tissue which has been paraffin sectioned. In order to avoid freezing artifacts the sample must be frozen rapidly. Severe cracks in the tissue may be due to the fact that a too large sample is used. Moreover, the sample structure, with various components from soft and fat tissue to hard, challenges even the technician with the greatest stamina. The cryostat itself may also be a cause for artifacts of, for example, variations in section thickness.

3.313.5. Sectioning Techniques

The next step in sample processing after embedding is to prepare adequate sections for later staining procedures. In Section 3.313.4, some methods were mentioned that use various types of so called microtomes for sectioning decalcified samples. For routine diagnostic purposes, more technically advanced microtomes both for paraffin and resin embedded samples are available nowadays. The cryomicrotomes have not gone through major technical modifications, and thus such microtomes are still placed in a cooling box operated from outside. Sections from 5 to 10 μm thickness are most often prepared irrespective of microtome used.

If sectioning smaller undecalcified bone biopsy samples, our experience is that one needs a heavy-duty rotation microtome and an adequate knife (so called D-knife). The collection of sections in the latter case requires more attention, for example, related to stretching the section on the precoated supporting objective glass. Moreover, the section should be dried under pressure (preventing it from later loosening). The procedure is time-consuming but renders good quality sections that can be stained for diagnostic histology as well as enzyme and immunohistochemistry.

3.313.5.1. Ground Sections: Cutting and Grinding Technique Add Modum Donath

In order to study bone implant integration, that is, osseointegration, the biomaterial must not be removed from the tissue before sectioning since this will cause an interruption of the interfacial zone. The state-of-the-art technique for processing undecalcified samples to cut and ground sections with the implant *in situ* is referred to as the 'Donath technique.'[29] Among various cutting and grinding equipments on the market, we use the so called Exakt equipment which has been on the market for about 30 years (Exakt Apparatebau, Norderstedt, Germany). The entire machine-park consists of several units where the most used ones are: the sample polymerization unit (polymerization of the resin takes place in white- and UV light), modified band-saw with either diamond- or bore nitride-coated cutting bands, polymerization unit for sections and grinding machines where Si-coated wet grinding papers of various roughness can be mounted (with the possibility to predecide the material to be grinded off).

The cutting and grinding technique is rough and does not allow for serial sectioning and may be considered a drawback compared to other techniques. However, to the best of our knowledge, having 25 years of experience, there are no other techniques available related to cutting and grinding that can create thin (10 μm and less) sections of undecalcified bone with implants *in situ* in a reproducible manner. In brief, the technique involves all steps from retrieval of sample, preservation of the tissue with adequate fixation solution to the final section of an adequate thickness (depending on the biomaterial *in situ* this can be from some μm and up several micrometers) and histologically stained. The steps involved in our in-house routine methods and techniques related to undecalcified cut and ground sections with biomaterials *in situ* are illustrated in Figure 5.

3.313.5.2. Artifacts

According to our experience, the most common artifact that arises when preparing undecalcified sections relates to resin curing. To speed up the curing time may unfortunately result in several cracks in the resin and the greater the sample the more pronounced are the cracks if the curing time is too short. Yet another artifact arising is related to inappropriate infiltration. This is not always observed until the sample is divided, but in general, it helps out to go back and reinfiltrate the sample in resin during vacuum and stirring followed by reembedding.

By using harder resins and less weight when grinding, artifacts referred to as the water planning effect can be minimized. This will result in a more even section thickness compared to if a softer resin is being used. When the cut and ground section of an implant in bone reveals that the metal part is thicker

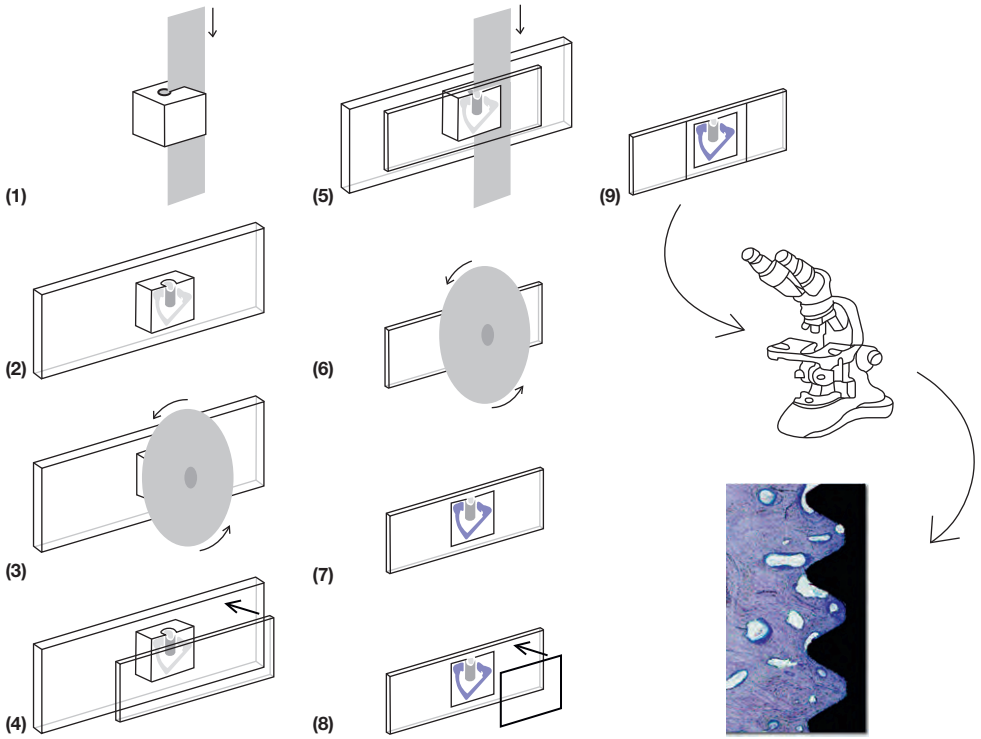

Figure 5 Schematic illustration of the cutting and grinding steps involved in preparing undecalcified cut and ground sections with implants *in situ*. The embedded sample is following the route below. (1) Divide the resin embedded sample in a band saw – resulting in two half's of the implant with surrounding tissue. (2) Attach/cement the backside of the sample(s) on a supporting plexis glass. (3) Grind the sample surface in a water-cooled grinding machine. (4) Clean the surface, measure the thickness of 'the block' (i.e., the sample including the supporting glass) and glue an object glass (of known thickness), onto the sample surface. Calculate the glue thickness since this varies depending on sample size and glue; measure the entire thickness of the 'sandwich' (= calculate the thickness of the glue: since you know the thickness of the object glass and the entire block before gluing, the glue can be calculated. This is important to know during the final grinding procedure). (5) Cut a section (~150–200 μm thick) in the band saw. (6) Grind the section in the water-cooled grinding machine to a desired thickness (start with rough and go to finer grinding papers, be careful and do not use too much weight during grinding; during grinding, control the thickness both by measurements and in the light microscope) a section thickness of 10–15 μm is routinely performed. (7) Clean the surface and stain the section followed by rinsing the section and let it dry. (8) Coverslip the sections (using mounting media of choice). (9) Qualitative inspection in the light microscope followed by histomorphometry, that is, quantification of, for example, BIC, BA, and MI around the implant. © Lotta Persson.

than the bone, this may also be due to the water planning effect. If the biomaterial is harder than, for example, commercially pure titanium, we advise to start the grinding procedure using a rough paper or even start on the diamond plate. Worn out and soft grinding papers negatively affect the preparation of plan parallel section and result in water planning effect especially if a too high weight is applied during grinding. It is a compromise between plan parallel section and scratches in such cases. The latter will most likely diminish when the stained section is coverslipped and thus later analyses will not be affected.

The very first grinding step, that is, to prepare the surface for the first section, is crucial as well. If too much grinding and too heavy weight is applied, with too smooth papers, already here the water planning effect will be introduced and later result in more problems of unevenly thick sections. These artifacts will be depicted as 'shadow effects' in the interface region when observed in the microscope.

As with all machinery in a laboratory, careful maintenance of the machine park should be a daily routine. The most commonly observed cutting artifacts on sections that relates to the band-saw is an uneven section (thick at one end and thinner at the other). There are various reasons for this and to mention but a few:

1. the cutting band is not adjusted parallel to the vacuum plate holding the sample in place,
2. the supporting vacuum-plate is not properly adjusted, that is, nonparallel to the cutting band,
3. the cutting band is clotted,
4. the ball bearings are worn out resulting in movement of the band,
5. the rubber bands on the wheels, holding the cutting band in place, are dirty and thus the bands are not hold in place during cutting,
6. too much force is applied, that is, too much weight is used during the cutting process. This can also create 'burning artifacts' and such artifacts are devastating for the tissue if the cooling water is not functioning.

Of course, there are other reasons and artifacts involved in the cutting and grinding procedure, but in general, proper maintenance of the machine-park is the first step in achieving successful results.

3.313.5.3. Microdissection

This technique involves a laser that is used for cutting out regions of interest as well as cells in a section during light microscopic observations. Applying the microdissection technique is ongoing technique especially in the tumor research field, and genetic screening of tissue from the tumor invasion front with laser microdissection was successfully performed using DNA sequencing.[31] The use of the technique as a potential and future tool for routine diagnostic purposes is not fully known but most likely it will become a state-of-the-art technique in pathology laboratories. The laser microdissection technique may be a promising tool in our research field of interest, that is, bone–biomaterials, since it is possible to collect samples from cut and ground sections in close vicinity to metal implants. Trials are ongoing and extrapolating artifacts, that is, the influence of the chemical fixatives and the used resins is a challenge.

The readers interested in the technique are referred to www.zeiss.de/microdissection

3.313.6. Staining Methods

Both qualitative and quantitative tissue reactions around biomaterials, irrespective of whether it is for diagnostic or for research purposes, rely on the primary observation of histologically stained tissue.

The basic approach in histological diagnostic is an automatic staining processing of tissue sections mounted on glass slides. However, routine-staining procedures in research laboratories is still dependent on the technician's often man-made staining by following a recipe and subsequent hand-made staining of the sections.

3.313.6.1. Staining for Histological Observations

Routine staining methods, especially for bone tissue, involve various connective tissue staining protocols. It is out of the scope to include staining recipe here since almost all handbooks mentioned in part 8 contain excellent recipes. Our experience with staining bone tissue on undecalcified cut and ground sections is that one needs routine staining methods that differentiate between various bone quality components and preferably render no overstained cellular components. The in-house routine staining that we use frequently is toluidine blue mixed with pyronin G. The bone tissue is stained in various degrees of purple (old bone pale purple compared to young bone dark purple). The toluidine blue itself stains most tissue blue, but it also demonstrates certain components such as mast cell granules being purple. This phenomenon is referred to as metachromasia. Moreover, the cellular details are well distinguished.

Irrespective of the staining used, the results should precisely demonstrate specific components. These components can sometimes be enhanced by adding a counter stain. Counterstaining the tissue means applying a contrasting color. For example, when using the bulk staining method that stains the microcracks in bone red[32] or the enzyme-histochemical method to capture ALP (blue) and ACP (red), it is common to use light green as a counter stain since this staining renders qualitative (and quantitative) discrimination between the specific parts of interest.

Counterstaining must be of a contrasting color, and it should not be too intense so that it masks the specific staining.

Special stains are important tools and the usage of such specific stains is of key importance in detecting various pathogens. From observations on the light microscopy level, one can continue with immunohistochemical protein stains as well as other technical methods not possible just a few years ago.

Molecular techniques are becoming diagnostic tools and applying such techniques enables us to identify specific genes involved in various diseases. Moreover, since the biomaterials research field focuses intensely on the implant surface morphology and the nanolevel, we foresee a combination of methods that depict the tissue reaction to medical devices in magnifications which is not possible until now.

3.313.6.2. Immunohistochemistry

Immunohistochemistry (IHC) is used to detect target antigens in the histological sections using specific antibodies. Since the following chapter is about IHC, discussing the methodology and further details will be beyond the scope of this chapter. Hence, in this section, we focus more on 'what can be done' and 'what has been done' with IHC on bone tissue samples.

It is uncommon to use IHC on cut and ground sections since IHC is rather difficult to perform on such sections. The reason for this may be the type of fixatives, type of resin used for embedding, the thickness of the sections, or it could be that the antibody we want to use is just not suited for resin cut and ground sections. However, in our laboratories, we have ongoing research to improve the immunoreactivity in the cut and ground sections.[17] The improvement will definitely provide additional information that will be useful for the evaluation of biomaterials in bone tissue. The IHC technique will clarify the localization or the intensity of the antigens. However, it is extremely important to understand the limits. IHC is not intended to determine or quantify gene expression. For readers interested in this field, we recommend *in situ* hybridization, which will be described in the next section or polymerase chain reaction using total RNA extracted from paraffin sections, the protocol of which can be easily found elsewhere.

The ability to remove the resin is an essential step in applying immunohistochemical methods on bone tissue successfully. Therefore, it is only possible on paraffin sections after decalcification of the bone with all the disadvantages mentioned above or on methylmethacrylate (Technovit 9100 New) thin or ground sections.

After removing the resin, all routine immunohistochemical methods can be carried out. All commercially available antibodies recommended to be suitable for paraffin-embedded and formalin-fixed tissue samples can be used.[16] Here, we describe a modified method taking into account that new products are on the marked with advantages regarding sensitivity and time.

Nonbiotin-HRP/DAB immunohistochemistry

1. after removing the resin, the sections were rehydrated in a descending series of ethanol till distilled water
2. rinse slides in washing buffer
3. antigen-demasking by using citrate buffer (pH 6.0) or EDTA buffer (pH 9.0) (AB dependent)

4. incubate sections for 30 min at 98 ± 2 °C
5. after cooling down rinse slides in washing buffer
6. blocking of endogenous peroxidase by incubating sides for 20 min in 1% H_2O_2
7. rinse slides in washing buffer (two times)
8. inhibition of unspecific binding by using a Powerblock-Solution (BioGenex HK085-5K): incubate for 10 min
9. Primary-AB: incubate for 30 min at RT in humidified atmosphere
10. rinse slides in washing buffer (three times)
11. Enhancer*: incubate for 20 min at RT
12. rinse slides in washing buffer (three times)
13. Polymer*: incubate for 30 min at RT
14. rinse slides in washing buffer (three times)
15. Chromogen (DAB)*: cover for max. 5 min (visual check)
16. Counter staining: hematoxylin solution for about 10 s
17. dehydration and mounting of sections

*BioGenex SuperSensitive NonBiotin-HRP/DAB; QD430-XAK.

3.313.6.3. *In Situ* Hybridization

The *in situ* hybridization (ISH) technique enables us to investigate the distribution or expression of specific DNA or RNA sequences.[33] For example, during the course of osteogenesis, the involved cells, for example, mesenchymal stem cells, pre-osteoblasts, osteoblasts, or osteocytes produce bone related proteins at appropriate time points. Figure 6 shows a paraffin section of a sectionable test implant placed in the mouse femur, *in situ* hybridized with an osteocalcin cRNA probe. It shows the distribution of responsible fibroblastic cells in the vicinity of the implant surface. With ISH, we can detect which cell is responsible for specific protein production. This is the major difference compared to IHC because IHC only allows us to detect the localization of proteins and we do not know for sure which cells are responsible for its production. For interested readers, the above reference is recommended.

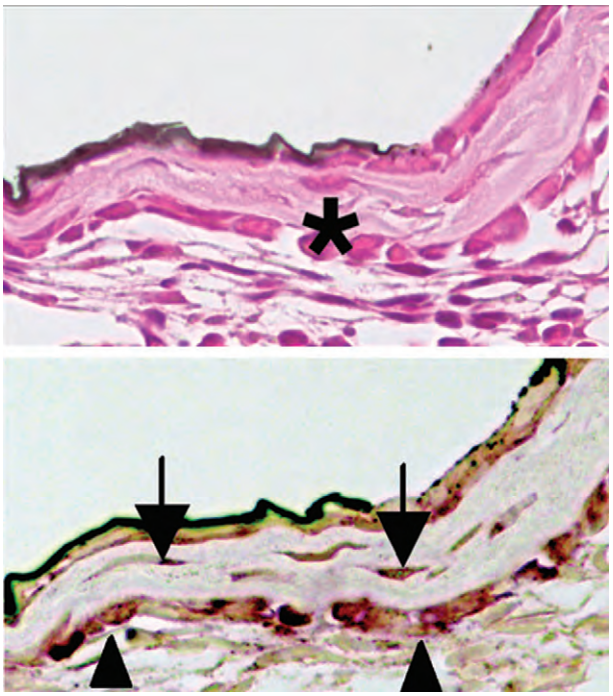

Figure 6 *In situ* hybridization using osteocalcin probe. Asterisk in the HE section indicates fibroblastic cells. Corresponding hybridized section shows that the fibroblastic cells are expressing osteocalcin mRNA. Magnification: ×40. Reproduced from Jimbo, R.; Sawase, T.; Shibata, Y.; *et al*. *Biomaterials* **2007**, *28*, 3469–3477, with permission from Elsevier.

Unfortunately, for cut and ground sections, this technique is inapplicable, due to resin embedding and contamination from cut and grinding procedures. However, we introduce this technique to the readers because when applicable to samples regarding bone and biomaterials, this technique is extremely useful and will provide us more information.

After removing the resin, all kinds of ISH techniques can be conducted on bone tissue. We used RNA ISH using Dig-labeled probes to collagen type I, II, and III as described by Plenz *et al.*[34]

Nonradioactive RNA ISH

1. Air-dried deparaffinized or deacrylated sections
2. Pretreatment with proteinase K
3. Postfixation in an ice-cold 4% paraformaldehyde solution
4. Washing in PBS
5. Acetylation: 0.1M TEA buffer (pH 8.0) + 0.25% acetic anhydride
6. Prehybridization
7. Hybridization: hybridization mix containing the dig-labeled RNA-probe; incubate over night at 42 °C in an humidified atmosphere
8. Posthybridization by washing sections in a descending series of SSC (2× SSC, 1× SSC, 0.1× SSC)
9. Detection by using antibodies targeted to dig
10. Counterstaining
11. Mounting.

3.313.7. Quantification Methods

Both quantitative and qualitative evaluation of tissue reactions around implants are of utmost importance in bone biomaterials research. Each laboratory has its own in-house standard related to histomorphometrical analysis and no 'out-house' consensus exists regarding what or how to perform such biomaterial-related analyses. The methods of sample preparation rendering high quality nondecalcified cut and ground sections with biomaterials *in situ* also vary between different laboratories although it is referred to the 'Donath technique.' Sample preparation is time-consuming and expensive and requires specially trained and experienced technicians for achieving high-quality sections. While some laboratories work with thick sections (100 µm and more), our laboratory routine is to prepare cut and ground sections of a thickness of 10–15 µm (and even thinner if the aim is related to enzyme- and immunohistochemical analyses). Such appropriately stained sections render good quality and visualization of specific cells and tissue components and thus reliable histomorphometrical interfacial analyses of, for example, bone implant contact (BIC) can be performed. We have shown that the thicker the section the greater is the overestimation of the

BIC, that is, the osseointegration. Sections of 10 and 30 μm compared to 100 μm resulted in 30% overestimations compared to sections of 10 and 30 μm only (no overestimations in the latter case). Two independent persons performed the histomorphometrical analyses, and there were no significant differences between the investigators.[8] Another study has shown the importance of sectioning directions and from those results it is obvious that all samples in a research study must be sectioned in the same anatomical manner in order not to compare 'apples to pears.'[35]

3.313.7.1. Level of Quantification

The level of quantification needs to be determined beforehand and the very same magnification must be used for the entire material involved in a study. As a rule of thumb and in order to 'get to know' your material, we always perform high magnification qualitative inspections in the light microscope before the commencement of the measurements. Moreover, the same person should perform the histomorphometrical analyses. If the person is a trainee, it is mandatory that a skilled person perform measurements on the very same material as well and that the results are discussed in order to set the baseline. For students, working on their diploma, it is mandatory that our in-house routine histomorphometry and image analyses tests are performed under the guidance of skilled persons. Naturally, questions arise and if there is lack of clarity related to the material, a consensus is called on.

3.313.7.2. What and How to Quantify?

Histomorphometrical analysis involves various bone quality aspects that can be quantified. Irrespective of what or how to quantify, it is time-consuming. Bone remodeling around implants involves both contact measurements as well as area measurements. The former is related to BIC and the latter is related to bone area (BA) both inside and outside (mirror image, MI) the inner threads. The latter quantification method may, for example, depict bone remodeling differences if ratios between inner and outer regions (threads) are compared.[36] Figure 7 illustrates the in-house routine quantitative measurement performed in the light microscope. Routine animal research experiments often involve one follow-up time, and to distinguish between the parameters to be measured, good quality histological staining reactions are of the utmost importance. Heavily stained sections are sometimes needed for illustration purposes but often these sections are overstained and thus cellular reactions cannot be depicted due to such artifacts and this results in difficulties to perform accurate interpretation of the tissue components. Accurate histomorphometry requires not only high-quality sections but also trained personnel with histological knowledge. The latter is important since artifacts arising from sample preparation must be interpreted correctly and thus does not result in false qualitative or quantitative data.

Investigations of bone remodeling around implants retrieved from patients for various reasons are ongoing in

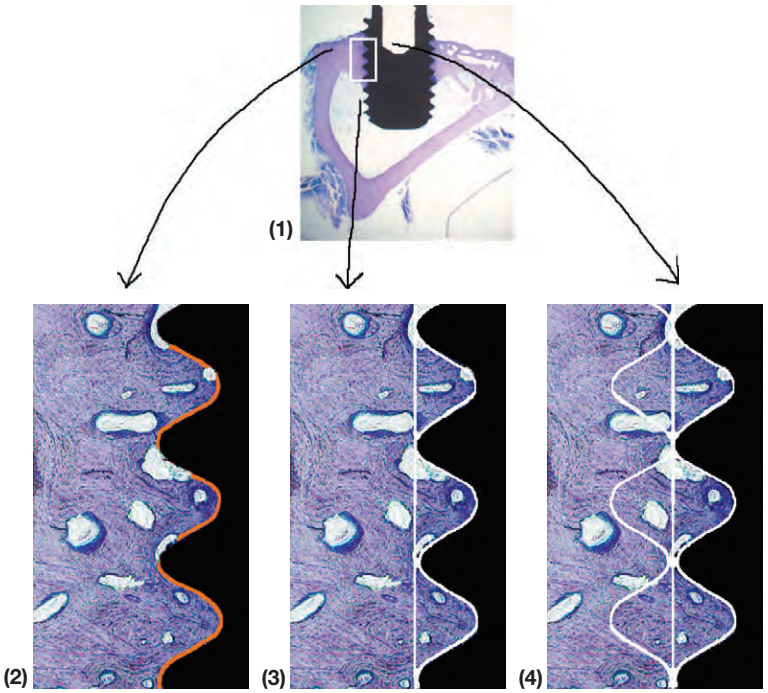

Figure 7 This is an illustration of the in-house routine quantitative measurement performed in the light microscope. The top survey picture (1) is an undecalcified cut and ground sample with an implant *in situ* stained in toluidien blue mixed with pyronin G. The enlarged sample in (2) illustrates the BIC (bone implant contact) measurement in the three best consecutive threads. (3) demonstrates the BA (bone area) measurement in the inner threads while the outlined areas in (4) demonstrate the MI (mirror image area) measurements, that is, the inner area region is mirrored out. The BA and MI measurements involve comparisons of the relationship between inner:outer area. All true measurements are performed with one thread enlarged.
© Lotta Persson.

several studies in-house. To mention one such study where implants of the very same design were retrieved after being (i) nonloaded and compared to (ii) various times loading (from 1 year to more than 5 years), some interesting and different remodeling activities were observed along the threads.[37] The unloaded implants had the greatest BIC below the thread peak and this percentage increased with time of loading. The bone contact in the thread peak region (often referred to as the stress shielding area) showed the greatest BIC when loaded between 2.5 and 5 years and thereafter decreased, that is, the bone resorption was most pronounced in this region up to a period of 5 years of loading. The bottom region of the thread demonstrated the lowest BIC to start with (unloaded implants) but increased with time of loading. Similar observation was made on the flat surface above the thread peak, and this region showed the highest BIC percentage after a loading time of more than 5 years (Figure 8).

Another paper related to bone remodeling activity around implants placed in the tibia of rabbits, and evaluations performed on cut and ground sections with the implants *in situ* were performed by Sul *et al.*[38] The quantitative BIC and new formed BA were greater around porous anodized implants compared to nonporous controls. The enzyme-histochemical observations focused on the activity of ALP and ACP in the interface region (both enzymes being present) as well as in the new formed bone (mostly ALP) periosteally and endosteally on the sections. Based on the overall observations, the remodeling activity was greater in the endosteal region compared to the periosteal and in general there was a greater ALP activity compared to the ACP.

3.313.7.3. Methods and Equipment/Software

Histomorphometry of bone tissue around biomaterials shows great variations both related to the methods and the equipment/software used. While some softwares are more 'general,' that is, the user must program the application needed (often a time-consuming and complex task), others are more 'application-specific,' where no programming is needed but the usability is limited.

Within the same laboratory, various equipments are used. The usage and preference of equipments depends on the question: what and how to quantify? It is our opinion, after several years of histomorphometrical analyses as well as tests and trials of various equipments, that there is no fully automatic equipment that can be used. Artifacts will render higher

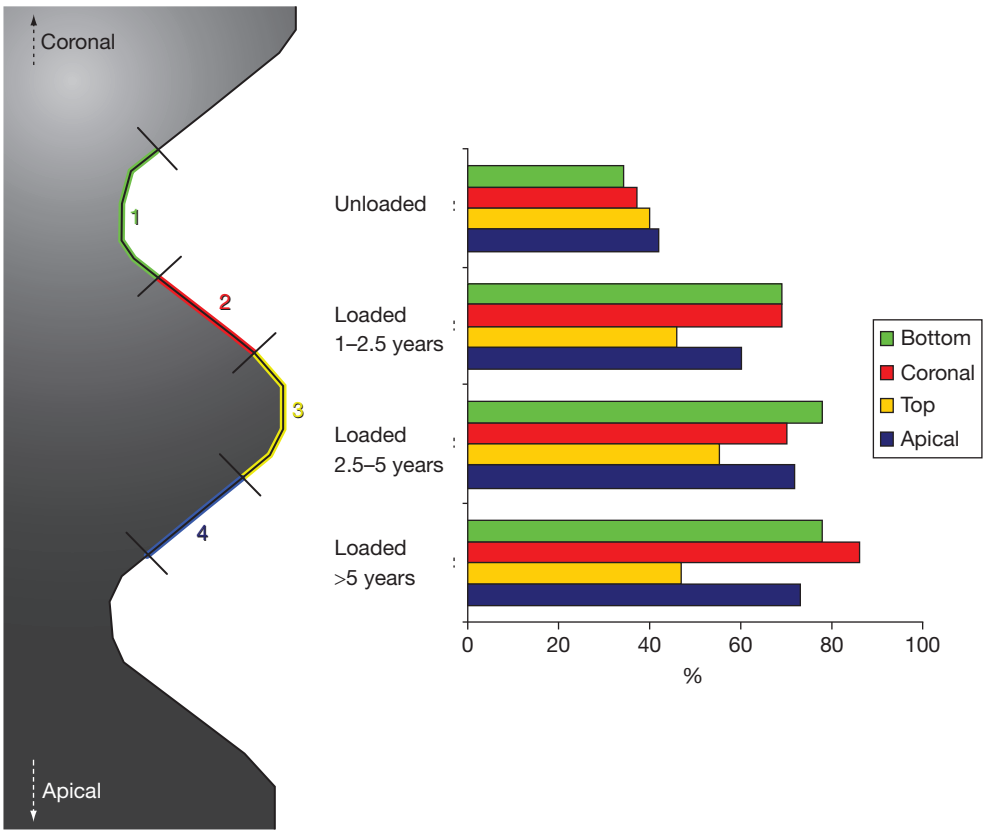

Figure 8 This is an illustration of bone remodeling data. The results obtained from cut and ground sections of retrieved human oral implants ($n = 40$) being unloaded and loaded between 1 and 2.5 years, 2.5 and 5 years and loaded more than 5 years. Histomorphometrical calculations involved of bone implant contact (BIC) in various regions along the implant thread surface. The region facing the coronal portion (1), the flat surface below (2), the thread peak (3) often referred to as the stress shielding area, and (4) is the flat portion below the thread peak. The nonloaded implants had greatest BIC in region 4. After more than 5 years of loading, the greatest BIC values were observed in region 2. Irrespective of unloaded or various loading times, the stress shielding region (3) always demonstrated the lowest BIC value.

or lower estimations automatically compared to the naked eye of experienced investigators that can differentiate between the tissue structures and components in a way that no computer as of now can. This topic of comparisons between manual and automatic methods of bone tissue remodeling around implants is ongoing within our network. Comparable and similar data of BA (bone area) and MI (mirror image area) were obtained irrespective of manual or automatic method.[39,40] However, the BIC values showed significant differences and the automatic programs rendered higher BIC percentages compared to the manual measurements performed directly in the eyepiece of the microscope oculars using the Microvid Image Analysis program (Leitz, Germany). This latter state-of-the-art quantifying method is very time-consuming, and thus within our network, we are presently working on a more user friendly and semiautomatic image analysis application. It allows the user to easily correct falsely estimated results of the analysis. Such research tools will not only speed up the histomorphometrical process but also render more time for the more complex tasks, that is, the qualitative biological responses related to osseointegration of biomaterials.

3.313.7.4. Reference Sections and Reference Quantifier: In-house Standard Rules

To the best of our knowledge, no commercially available reference section exists for histomorphometrical tests related to bone–biomaterial research. However, in the laboratories, we have utilized a variety of sections for internal comparisons both interindividual and intraindividual throughout the years. Needless to say but having good quality sections and being aware of how to interpret, for example, artifacts arising from shrinkage the histomorphometry are easy albeit time-consuming. A recently performed in-house study, comparing data obtained by three persons (with different experience in histomorphometry), from sections of various quality (i.e., artifactual staining errors as well as sections being 'perfect'), rendered similar and nonsignificant differences between the evaluators.[41]

There may be 'extreme cases' when the evaluator has difficulties to interpret the tissue reaction to the material. Such problems have occurred when evaluating bone tissue around hydroxyapatite-coated implants.[42] In such cases, we refer to 'unidentified areas' and in the latter case about 10% of such areas were presented. These regions were analyzed with a higher magnification tool (EDX) showing Ca, S, and P ions in the unidentified region, but if it was 'bone to be' or 'not to be' remained unclear.

To the best of our knowledge, artifacts or problems related to quantifications are neglected. It is an issue that is not discussed and elaborated on. Theoretically, it can be that such unidentified areas are of great importance both for the tissue tolerance to the material and for the material itself. This issue needs greater attention.

3.313.7.5. X-rays

In our laboratories ordinary X-ray images are seldom used for quantification purposes due to the poor resolution level but X-ray images are perfect for localization of buried implants. Microradiography, on the other hand, of rather thick (80 μm) cut and ground sections with implants *in situ* may sometimes be of interest and, for example, if various gray levels need to be quantified, these glass plates can be sufficient. If good quality microradiographs are prepared, it is also possible to perform automatic image analysis of bone tissue areas.[43,44] Irrespective of ordinary X-ray or microradiography and compared to histological sections, they all render 2D images.

3.313.7.6. Microcomputed Tomography and Synchrotron Radiation-Based μCT

High-resolution volume imaging techniques, that is, the 3D techniques available in bone biomaterials research are related to microcomputed tomography (μCT) and synchrotron radiation-based microcomputed tomography (SRμCT).[45,46] While the former technique is one that several laboratories have implemented as an in-house technique, the latter is not. The former 'standard' μCT device often renders physics-based artifacts such as a bright aura surrounding the implant in bone which prevents a reliable discrimination of the interface region.[47] The latter technique requires access to synchrotron facilities that exists in various countries worldwide. Beam line time is limited and the scans are time-consuming so that routine experiments cannot be performed using such facilities. We have recently performed SRμCT experiments using the facilities at the Institute for Materials Research, GKSS Research Centre Geesthacht, Germany (www.desy.de). Our studies so far reveal that the SRμCT technique provides satisfactory results of the interface region. The resolution is improved compared to the μCT device due to the parallel beam and the small beam size (**Figure 9**). The aura still exists but is limited and can be removed by image analysis methods.[48] Furthermore, the higher resolutions enable a more extensive quantitative 3D analysis which is an ongoing challenge.

3.313.7.7. Histological Versus Biomechanical Quantification

In vivo bone biomaterial integration can be performed with various biomechanical tests. The nondestructive resonance frequency analyses (RFA) test is performed clinically and relates to the 'implant stability as a function of the stiffness.' The test is referred to as 'a bending test of the implant bone complex where a transducer applies an extremely small bending force'.[49]

However, RFA tests performed in research animals is not a simple task and the readers interested in more details related to this are referred to the papers by Sennerby *et al.*[50] and Sul *et al.*[51] In the latter study, RFA measurements were performed on six groups of implants, with various topographies and surface chemical properties, at the time of installation in rabbit bone and 6 weeks later. Significant differences were observed for measurements performed both in the longitudinal and perpendicular manner of the bone comparing baseline to 6 weeks.

Destructive biomechanical tests of implant integration in research animals is performed with a variety of equipment, ranging from manual hand-hold Tonichi devices[36] to commercially available and larger apparatus such as the Instron equipment.[52–54] For the readers interested in more

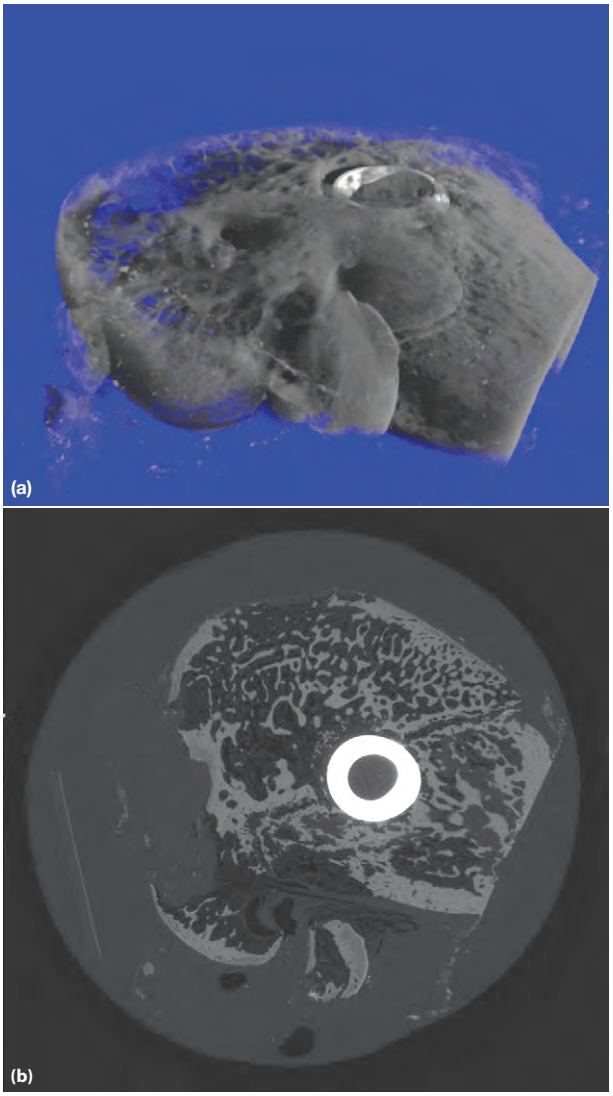

Figure 9 (a) Rendering of an SRμCT image volume demonstrating an irradiated bone sample with an implant inserted in the femur region of a rat. (b) Transverse cut from the same sample showing the destroyed femur condyle region in 2D. Implant diameter 2.2 mm.

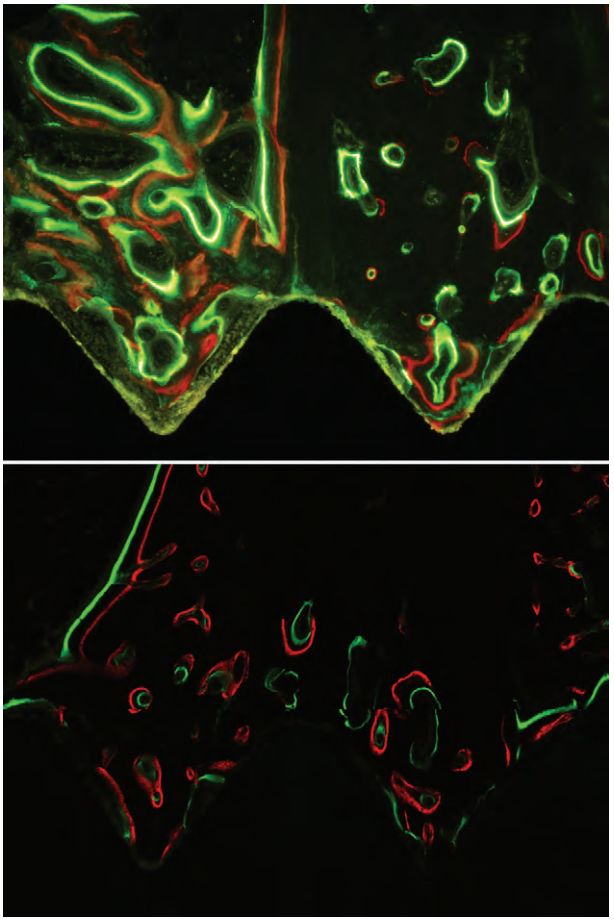

Figure 10 Fluorescent microscopic images prepared with a conventional microscope (top) and confocal laser scanning microscope (bottom), of implant interfaces with two different fluorochromes (green: calcein green; red: alizarin complexon). Note the blurry and saturated image obtained by the conventional microscope and sharp images obtained by confocal laser scanning microscope. The *in vivo* labeling regime and the preparation of samples were the same; however, there are qualitative differences. Both sections are about 50 μm thick.

information related to biomechanical tests of implant integration, we refer to **Chapter 3.316, Immunohistochemistry**.

Bone implant contact data are most often achieved from one central section only. Our in-house comparisons of 2D BIC data to 3D biomechanical data often points to the same direction, that is, if the former is high so is the latter.[55] However, both types of results are important for determining the osseointegration of a biomaterial. The ideal situation would be to combine such data. For research animal purposes, we conduct destructive biomechanical tests of screw-shaped implant integration by removal torque tests (RTQ) using an electronic device which is our in-house standard technique since several years (Detektor AB, Göteborg, Sweden). The results of such 3D measurements are given in N cm and in order to convert the data to shear strength values (N mm^{-2}) we prepare cut and ground sections of the loosened implant which is left *in situ* in the bone bed.[56] This method of conversion of the 3D removal torque data to shear strength values by measuring bone lengths on the 2D cut and ground sections was first presented and elaborated on in the paper by DeRezende and Johansson.[57] Moreover, when testing implants of various morphologies and materials *in vivo* several studies have shown an agreement between removal torque and shear strength values, although the former is a 3D measurement compared to the 2D length measurements involved in the conversion to shear strengths.[58–61] Recently, we have demonstrated a good reproducibility also when it comes to tests of new biomechanical devices on implants molded in materials with different hardness.[62] Moreover, if biomaterials with different diameters are tested, it is of the utmost importance not only to show the RTQ values in N cm but also to supply information of the N mm^{-2} data.[63] As mentioned earlier, it is a challenge to combine various quantitative and qualitative analysis techniques and to do so a titanium device was developed

by Sul *et al.*[67] that can be used for *in vivo* measurements of biomechanical and histomorphometrical tests as well as qualitative histological analysis. This device combines pull away tests measuring the bone bonding force between a disk shaped implant and bone tissue on one hand and removal torque/shear strength measurements on the other hand on the screws that are attached in bone and holds the device in place. Such a device is of great value for the investigation of biochemical bonds involved in osseointegration.

3.313.7.8. Combination of Techniques for Quantification of Bone Remodeling

3.313.7.8.1. Confocal laser scanning microscope

The confocal laser scanning microscope (CLSM) is a microscope which focuses only on a single focal plane, and the unfocused plane will not be visualized. In the past, the traditional laser microscope excited the whole thickness of the sample, resulting in saturated, blurry images and sometimes visualizing false colocalization images. Since the CLSM excites a single focal plane, this technique is suitable for quantification and visualizing 'true' images. **Figure 10** is an image of fluorochrome-labeled bone tissue around the implant obtained from a conventional fluorescent microscope[64] and from CLSM. The section thickness is similar, although it is obvious that the CLSM image is less blurry and less saturated. Another interesting feature of this microscope is that it can reconstruct 3D images by building up multiple single focal planes. The obtained data can be analyzed simultaneously using appropriate software and most of the times can be exported as an Excel file. **Figure 11** demonstrates data from trials of combining the biomechanical data with the fluorescence data, which is ongoing and such combinations seem promising. One factor to keep in mind is that the CLSM can change the intensity of the image. The advantage of this feature is that the microscope can pick up the weakest signals expressed in the sections. However, on the other hand, misuse of this feature may lead to the collection of false data. It is extremely important to set a standard for the intensity level before starting the measurements.

3.313.7.8.2. Gene expression

Gene expression analyses are approaching the biomaterial research field. Initial reports revealed the possibility to study functional attachment and the biological mechanisms related to the biomechanics data by combining information gathered from gene expression results of proteins related to bone remodeling in retrieved tissue.[65] Other gene expression studies where both the implant and the tissue surrounding the implant have been investigated reveal interesting data that will add important knowledge to the field of osseointegration not possible before.[66] Yet another recently performed study involved removal of torque data coupled to the amount of various bone formation and bone resorption as well as inflammatory genes both on the retrieved implant and in the surrounding tissue.[41] In a study comparing machined (control) and sand blasted (test) implants placed in mice femur, we found remarkable differences in bone formation histologically, and the corresponding results from northern blot analysis showed significantly higher expression of osteocalcin mRNA for the test group (**Figure 12**) (unpublished data). This field of research is now attracting more attention and is expected to advance further. Yet again, to be able to conduct as many tests as possible on the very same sample, a careful study design needs to be outlined before the commencement of the study.

3.313.8. Summary and Future Directions

Tissue preservation methods and subsequent techniques used leading to histological sections have not changed dramatically over the last decade. In fact, some techniques described in this

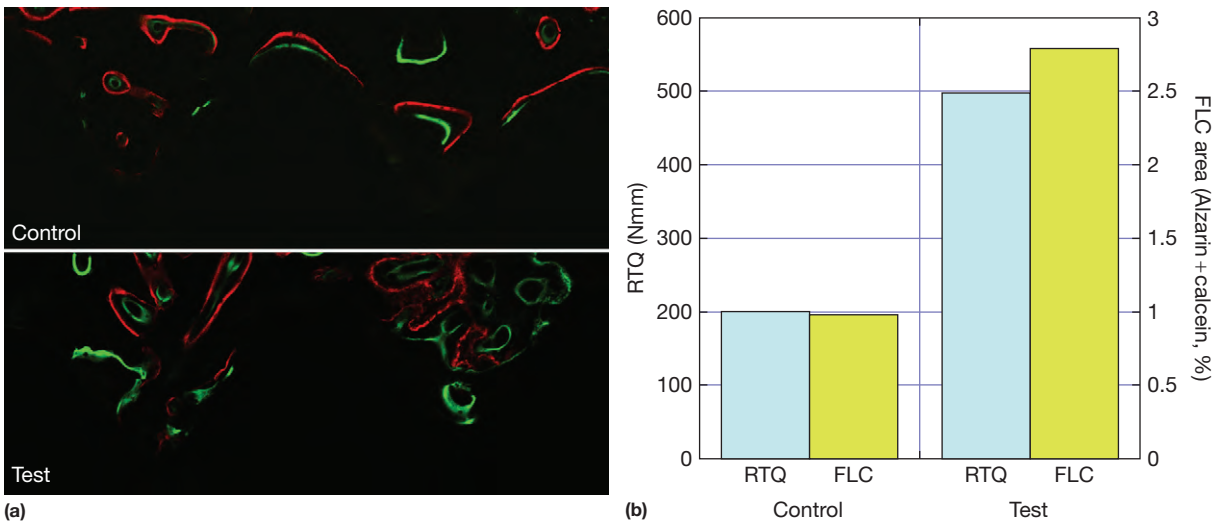

Figure 11 (a) Ongoing study comparing biomechanics (removal torque values) to the fluorochrome positive areas (images prepared with confocal laser scanning microscope). (b) Graph shows a correlation between the two parameters and clear differences between test and control group were seen for both parameters. The corresponding image shows more fluorochrome labeling for the test group compared to the control group.

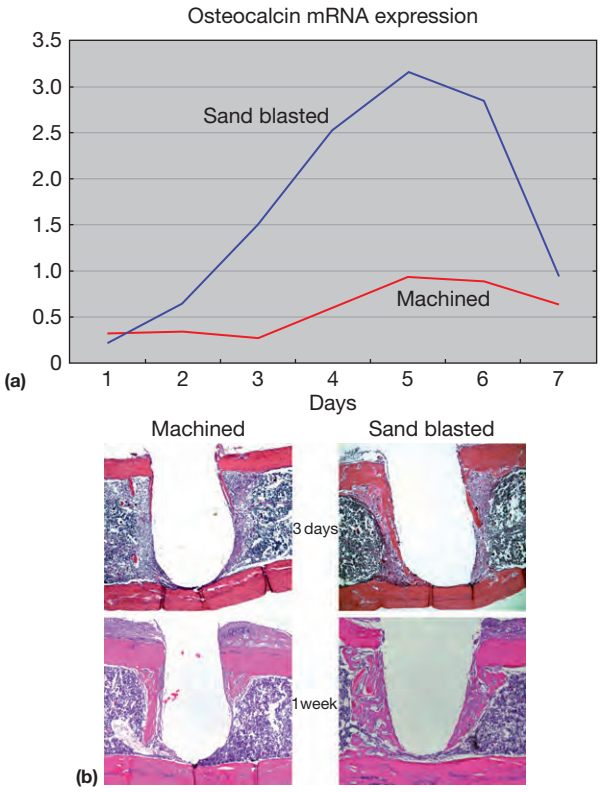

Figure 12 (a) Northern blot analysis of machined and sand-blasted implants placed in the mouse femur. The osteocalcin mRNA expression was followed from day 1 to day 7. (b) Corresponding HE (hematoxylin–eosin)-stained paraffin section at day 3 and 1 week (day 7) for both groups. The implant diameter is in millimeters.

chapter are still considered state of the art. Unfortunately, much research material is wasted not only due to inadequate knowledge and handling of the material outside the histological laboratories but also because of a poor study design. The biomaterials research field involves various, equally important, disciplines. Sophisticated manipulation of medical devices and especially nowadays focusing on the implant morphology (all surface-related aspects) may not always be observed in the subsequent and most important step, that is, tissue reactions to the materials. The reasons for this are complex but in general the first and most important step must be decided: What level is of importance for the study and what is to be used to target this level? If several levels are of equal importance one must prepare a detailed plan. The questions as to how to perform these analyses require various individual competences. The steps from ordinary light microscopical analyses to gene and chromosome levels challenge all disciplines in the biomaterials field. We foresee that a combination of several novel analysis tools should be included in the very same study to be conducted. By the end of the day, when it comes to the very important task, the histological analysis of tissue reactions to the medical devices, that is, the qualitative and quantitative analyses – these methods needs to be upgraded.

Histomorphometrical analyses are important but one should not underestimate the qualitative observations. The latter needs greater attention and demands more focus, especially nowadays when mimicking the medical devices tends to focus on the nanolevel. Here, we foresee involvement of even more various disciplines in every study. Nothing is impossible – as long as you have a good formulated question – methods can be modified accordingly.

References

1. Crubézy, E.; Murai, L. P.; Girard, L.; Bernadou, J. P. *Nature* **1998**, *391*.
2. Albrektsson, T.; Johansson, C. B. *Eur. Spine J.* **2001**, *10*, 96–101.
3. Brånemark, P.-I.; Breiner, U.; Lindström, J.; Adell, R.; Hansson, B. O.; Ohlsson, P. *Cand. J. Plastic Reconstr. Surg.* **1969**, *3*, 81.
4. Albrektsson, T.; Brånemark, P. I.; Hansson, H. A.; Lindström, J. *Acta Orthop. Scand.* **1981**, *52*, 155–179.
5. Hallén, O.; Röckert, H. *Särtryck Odontologisk Tidskrift* **1960**, *68*(3), 1960; Abstract in English.
6. Pattern, B. M.; Chase, S. W. *Anat. Rec.* **1925**, *30*, 123.
7. Donath, K.; Breuner, G. *J. Oral Pathol.* **1982**, *11*, 318–326.
8. Johansson, C. B.; Morberg, P. *Biomaterials* **1995**, *16*(2), 91–95.
9. Becker, J.; Kirsch, A.; Schwarz, F.; *et al. Clin. Oral Invest.* **2006**, *10*, 217–224.
10. Iwaniec, U. T.; Wronski, T. J.; Turner, R. T. In *Alcohol: Methods and Protocols*; Nagy, L. E., Ed.; Methods in Molecular Biology; Humana Press: New York, 2008; Vol. 447, p 325.
11. Ohashi, H.; Kobayashi, A.; Kadoya, Y.; Yamano, Y.; Oonishi, H.; Iwaki, H. *J. Mater. Sci. Mater. Med.* **2000**, *11*, 255–259.
12. Titford, M. *J. Histotechnol.* **2001**, *24*, 165–171.
13. Jimbo, R.; Sawase, T.; Baba, K.; Kurogi, T.; Shibata, Y.; Atsuta, M. *Clin. Implant Dent. Relat. Res.* **2008**, *10*, 55–61.
14. Sennerby, L.; Ericsson, L. E.; Thomsen, P.; Lekholm, U.; Astrand, P. *Clin. Oral Implants Res.* **1991**, *2*, 103–111.
15. Hopwood, D. *J. Anatomy* **1967**, *101*, 83–92.
16. Wolf, E.; Röser, K.; Hahn, M.; Werkerling, H.; Delling, G. *Virchows Arch. A* **1992**, *420*, 17–24.
17. Johansson, P.; Röser, K.; Johansson, C. B. Enzyme preservation in bone tissue through the usage of appropriate fixative. In *European Society for Biomaterials (ESB) Conference 26th ESB Anniversary Conference*, Barcelona, Spain, Sept 2002; Abstract.
18. Dapson, R. W. *Biotechnic Histochem.* **1993**, *68*, 75–82.
19. Romeis, B. *Microskopische Technik*, 16th ed.; R. Oldenbourg: Munchen, Wien, 1968.
20. Böck, P. *Romeis Mikroskopische Technik*. 17te neubearbeitete Auflage Urban and Schwarzenberg: Munchen/Wien/Baltimore, 1989.
21. Krenacs, T.; Bagdi, E.; Stelkovics, E.; Bereczki, L.; Krenacs, L. *J. Clin. Pathol.* **2005**, *58*, 897–903.
22. Johansson, C. B.; Röser, K.; Bolind, P.; Donath, K.; Albrektsson, T. *Clin. Implant Dent. Relat. Res.* **1999**, *1*(1), 33–40.
23. Röser, K.; Johansson, C. B.; Donath, K.; Albrektsson, T. *J. Biomed. Mater. Res.* **2000**, *51*(2), 280–291.
24. Sheehan, D. C., Hrapchak, B. B., Eds. *Theory and Practice of Histotechnology*, 2nd ed.; Battelle Press, 1987; ISBN 0-935470-39-5.
25. Callis, G. M.; Sterchi, D. L. *J. Histotechnol.* **1998**, *21*(1), 49–58.
26. Kaneko, M.; Tomita, T.; Nakase, T.; *et al. Biotechnic Histochem.* **1999**, *74*(1), 49–54.
27. Alers, J. C.; Krijtenburg, P. J.; Vissers, K. J.; van Dekken, H. *J. Histochem. Cytochem.* **1999**, *47*(5), 703–709.
28. Nyberg, J.; Hertzman, S.; Svensson, B.; Johansson, P.; Granström, G.; Johansson, C. B. *J. Osseointegration* **2010**, *2*(2), 93–101.
29. Donath, K. *Pathol. Res. Pract.* **1985**, *179*, 631–633.
30. Jimbo, R.; Sawase, T.; Shibata, Y.; *et al. Biomaterials* **2007**, *28*, 3469–3477.
31. Hahn Strömberg, V. H.; Edvardsson, E.; Bodin, L.; Franzén, L. *Acta Pathol. Microbiol. Immunol. Scand.* **2008**, *116*(4), 253–256.
32. Burr, D. B.; Hooser, M. *Bone* **1995**, *17*(4), 431–433.
33. Koji, T. *Molecular Histochemical Techiniques: Springer Lab Manual*. 2000.
34. Plenz, G.; Gan, Y.; Raabe, H. M.; Müller, P. K. *Cell Tissue Res.* **1993**, *273*(2), 381–389.
35. Johansson, C. B.; Morberg, P. *Biomaterials* **1995**, *16*(13), 1037–1039.
36. Johansson, C. B. PhD. Thesis, Department of Handicap Research, Biomaterials, University of Gothenburg, Gothenburg, Sweden, 1991.
37. Bolind, P.; Johansson, C. B.; Balshi, T.; Langer, B.; Albrektsson, T. *Int. J. Periodontics Restorative Dent.* **2005**, *25*(5), 425–437.
38. Sul, Y. T.; Johansson, C. B.; Röser, K.; Albrektsson, T. *Biomaterials* **2002**, *23*(8), 1809–1817.

39. Ballerini, L.; Franke-Stenport, V.; Borgefors, G.; Johansson, C. B. *J. Mater. Sci. Mater. Med.* **2007**.
40. Sarve, H.; Lindblad, J.; Johansson, C. B.; Borgefors, G.; Franke-Stenport, V. In CAIP 2007. *Lecture Notes in Computer Science*; Kropatsch, W. G., Kampel, M., Hanbury, A., Eds.; 2007; Vol. 4673, pp 253–260.
41. Johansson, C. B.; Lennerås, M.; Nyberg, J.; Nannmark, U. Gene expression analyses in tissue and on retrieved implants after removal torque tests. in preparation.
42. Gottlander, M.; Johansson, C.; Albrektsson, T. *Clin. Oral Implants Res.* **1997**, *8*, 345–351.
43. Klinge, B.; Johansson, C.; Albrektsson, T.; Hallström, H.; Engdahl, T. *Clin. Oral Implants Res.* **1995**, *6*, 91–95.
44. Mashiba, T.; Mori, S.; Burr, D. B.; *et al. J. Bone and Miner. Res.* 23(Suppl.) 2005, pp 36–42.
45. Bernhardt, R.; Scharnweber, D.; Muller, B.; *et al. Proc. SPIE* **2006**, *6318*.
46. Irsen, S. H.; Leukers, B.; Tille, C.; *et al. Adv. Med. Eng.* **2007**, *114*.
47. Barrett, J. F.; Keat, N. *RadioGraphics* **2004**, *24*, 1679–1691.
48. Sarve, H.; Lindblad, J.; Johansson, C. B. In *Lecture Notes in Computer Science*; 2009; Vol. 5575, pp 770–779.
49. Sennerby, L.; Meredith, N. *Periodontology 2000* **2008**, *47*, 51–65.
50. Sennerby, L.; Persson, L. G.; Berglundh, T.; Wennerberg, A.; Lindhe, J. *Clin. Implant Dent. Relat. Res.* **2005**, *7*, 136–140.
51. Sul, Y. T.; Jönsson, J.; Yoon, G. S.; Johansson, C. B. *Clin. Oral Implants Res.* **2009**, *20*(10), 1146–1155.
52. Brånemark, R. Ph.D. Thesis, University of Göteborg, Göteborg, Sweden, 1996; ISBN 91-628-2267-5.
53. Brånemark, R.; Ohrnell, L. O.; Skalak, R.; Carlsson, L.; Brånemark, P. I. *J. Orthop. Res.* **1998**, *16*(1), 61–69.
54. Brånemark, R.; Skalak, R. *Med. Eng. Phys.* **1998**, *20*(3), 216–219.
55. Sul, Y. T. Ph.D. Thesis, Department of Biomaterials/Handicap Research, Göteborg University, Gothenburg, Sweden, 2002, pp 1–189.
56. Franke-Stenport, V. F.; Johansson, C. B. *Clin. Implant Dent. Relat. Res.* **2008**, *10*(3), 191–199.
57. DeRezende Rubo, M. L.; Johansson, C. B. *J. Mater. Sci. Mater. Med.* **1993**, *4*, 233–239.
58. Ellingsen, J. E.; Johansson, C. B.; Wennerberg, A.; Holmen, A. *Int. J. Oral Maxillofac. Implants* **2004**, *19*(5), 659–666.
59. Han, C. H.; Johansson, C. B.; Wennerberg, A.; Albrektsson, T. *Clin. Oral Implants Res.* **1998**, *9*(1), 1–10.
60. Johansson, C. B.; Han, C. H.; Wennerberg, A.; Albrektsson, T. *Int. J. Oral Maxillofac. Implants* **1998**, *13*(3), 315–321.
61. Reigstad, O.; Johansson, C. B.; Franke-Stenport, V.; Wennerberg, A.; Rökkum, M.; Reigstad, A. *J. Biomed. Mater. Res. B* **2007**.
62. Johansson, C. B.; Jimbo, R.; Stefenson, P. *Clin. Implant Dent. Relat. Res.* **2010**.
63. Ivanoff, C. J.; Sennerby, L.; Johansson, C.; Rangert, B.; Lekholm, U. *Int. J. Oral Maxillofac. Surg.* **1997**, *26*, 141–148.
64. Carlsson, C.; Holmgren-Peterson, K.; Jönsson, J.; *et al. Online TITANIUM Int. Sci. J. Dental Implants Biomater.* **2009**, *1*(1), 61–70.
65. Monjo, M.; Lamolle, S. F.; Lyngstadaas, S. P.; Rönold, H. J.; Ellingsen, J. E. *Biomaterials* **2008**, *29*, 3771–3780; Epub 2008 Jun 27.
66. Omar, O.; Suska, F.; Lennerås, M.; *et al. Clin. Implant Dent. Relat. Res.* **2009**.
67. Sul, Y. T.; Johansson, C. B.; Albrektsson, T. *J. R. Soc. Interf.* **2010**, *7*(42), 81–90.

Recommended Handbooks

1. Sheehan, D. C., Hrapchak, B. B., Eds. *Theory and Practice of Histotechnology*, 2nd ed.; Battelle Press: Columbus, OH, 1987; ISBN 0-935470-39-5.
2. An, Y. H., Martin, K. L., Eds. *Handbook of Histology Methods for Bone and Cartilage*, 1st ed.; Humana Press: Totowa, NY, 2003; ISBN-10 0896039609.
3. Carson, F. L. *Histotechnology: A Self-Assessment Workbook*, 2nd ed.; American Society Clinical Pathology: Chicago, 1997; ISBN-10 0891894128.
4. Carson, F. L.; Hladik, C. *Histotechnology: A Self-Instructional Text*, 3rd ed.; American Society for Clinical Pathology: Chicago, 2009; ISBN-10 0891895817.
5. Bancroft, J. D.; Gamble, M. *Theory and Practice of Histological Techniques*, 6th ed.; Churchill Livingstone: Edinburg, 2007; ISBN-10 0443102791.
6. Kiernan, J. A. *Histological and Histochemical Methods: Theory and Practice*, 4th ed.; Cold Spring Harbor Laboratory Press, Scion: Bloxham, 2008; ISBN-10 1904842429.
7. Cook, D. J. *Cellular Pathology: An Introduction to Techniques and Applications*, 2nd ed.; Scion: Bloxham, Oxfordshire, 2006; ISBN-10 1904842305.

3.314. Materials to Control and Measure Cell Function

K Anselme, A Ponche, and L Ploux, Institut de Science des Matériaux de Mulhouse (IS2M), Université de Haute Alsace, Mulhouse, France

© 2011 Elsevier Ltd. All rights reserved.

3.314.1.	**Introduction**	235
3.314.2.	**Influence of Surface Features on Cell Function**	237
3.314.2.1.	Cell Adhesion	237
3.314.2.2.	Cell Migration/Contact Guidance	238
3.314.2.3.	Cell Proliferation and Differentiation	239
3.314.3.	**Influence of Surface Features on Bacteria Function**	240
3.314.3.1.	Initial Adhesion	240
3.314.3.2.	Biofilm Formation	241
3.314.4.	**Applications in BioMEMs/Microsystems Fields**	241
3.314.4.1.	Cell Culture	241
3.314.4.1.1.	Control of adhesion, migration, proliferation, and differentiation	241
3.314.4.1.2.	Cocultures	242
3.314.4.1.3.	3D cultures	244
3.314.4.2.	Cell Docking	245
3.314.4.3.	Cell Separation and Enrichment	247
3.314.4.4.	Cell Transfection	248
3.314.4.5.	Contact Guidance/Cell Migration	248
3.314.4.6.	Cell Mechanobiology	250
3.314.4.7.	Use of Cell Properties	251
3.314.5.	**Conclusions**	252
References		252

Abbreviations

ADSCs	Adipose-derived stem cells
AFM	Atomic force microscope
BioMEMs	Biological microelectromechanical systems
BSA	Bovine serum albumin
DEP	Dielectrophoretic forces
DSQ50	Surfaces presenting 120-nm diameter pits placed with the displaced square ±50 nm from the center
ECM	Extracellular matrix
EDTA	Ethylenediaminetetraacetic acid
EG4SH	Tetraethyleneglycol-terminated alkanethiols
ELISA	Enzyme-linked immunosorbent assays
ES	Embryonic cells
FBS	Fetal bovine serum
FISH	Fluorescent *in situ* hybridization
HA	Hyaluronic acid
hESCs	Human embryonic stem cells
hMSCs	Human mesenchymal stem cells
LINC	Link between nucleoskeleton and cytoskeleton
μCCA	Microcell culture analog
MBAs	Microbioreactor arrays
mES	Murine embryonic cells
ModSLA	Modified SLA surfaces
MSCs	Mesenchymal stem cells
NVOC	Nonvolatile organic compounds
PC	Polycaprolactone
PCR	Polymerase chain reaction
PDMS	Polydimethylsiloxane
PEG	Polyethylene glycol
PLLA	Poly-L-lactic acid
PMMA	Polymethymethacrylate
PNIPAAm	Poly(*N*-isopropylacrylamide)
PS	Polystyrene
RBCs	Red blood cells
REDV	Arginine–glutamine–aspartic acid–valine
RGD	Arginine–glycine–aspartic acid
RGDS	Arginine–glycine–aspartic acid–serine
RT-PCR	Reverse transcription polymerase chain reaction
SAM	Self-assembled monolayer
SERS	Surface-enhanced Raman scattering
SLA	Titanium implant surfaces modified by sandblasting and acid-etching
VAPG	Valine–alanine–proline–glycine

3.314.1. Introduction

Surface modifications of materials have been used to control and measure cell function for several decades. An example is the possibility to control the tissue integration of medical prostheses by changing their material composition, surface chemistry, surface energy, or surface topography. Similarly, the control of material surface is also a key determinant in the efficiency of diagnostic tools, cell culture disposables, biosensors, or drug delivery systems. Cells and bacteria have been

shown to posses the ability to discriminate and react specifically to surface chemistry and surface topography at the micro and nanoscales.[1–7]

In recent years, the biological and biomedical applications of micro and nanotechnology have become increasingly prevalent because these techniques allow the production of surfaces with precise features and high aspect ratios.[8] With the advent of these techniques, it is now possible to develop devices with features on a scale relevant to cells and bacteria. These devices can be made reproducibly in large quantities. They can have a small size, and they facilitate incorporation of integrated circuit technology for biological micro-electromechanical systems (BioMEMs).[9] Moreover, the use of microfluidic perfusion in these microsystem technologies allows controlled delivery and removal of soluble molecules in the extracellular environment, the use of small culture volume, and the application of mechanical forces on cells via fluid flow.[10] The BioMEMs and other Lab-on-Chip microsystems present several advantages compared to conventional *in vitro* cell culture systems that utilize culture dishes or microwells plates. In fact, these conventional approaches are labor-intensive and time consuming, and require technical expertise and specific facilities to handle cell harvesting, media exchange, and cell subculturing procedures, which are not necessary anymore with most of the microsystems.

After a general description of how cellular and bacterial functions can be controlled by materials, this chapter focuses on how materials are used and modified in microsystems with the same goal, namely controlling cellular and bacterial function. Specifically, only studies dealing with surface modification of materials to control cell function are reviewed. The use of microfluidics or electrical and optical stimulations in BioMEMs is not the subject of this chapter, except if they are associated with a modification of materials. For further details on BioMEMs please refer to **Chapter 3.315, Biological Microelectromechanical Systems (BioMEMS) Devices**. Lab-on-Chip microsystems achieving the step of cell manipulation uniquely (culture, docking, separation, guidance, and transfection) with subsequent detection of the signal by techniques, such as fluorescence microscopy or colorimetric assays, are also considered. In the following, the term 'microsystem' is mainly used for referring to all these different systems, while 'BioMEMs' is used only for electromechanical integrated systems.

Concerning the last point, microsystems have historically been fabricated with materials related to microelectronics such as glass or silicon. On such substrates, manufacturing techniques such as lithography or etching are well established. Polymer substrates have appeared in the field more recently due to their increased biocompatibility, optical properties, and simple fabrication methods.[8] Usually, the substrate is chosen for its bulk properties and the control of its surface topography is done by photolithography and hard or soft machining.[11,12] Further, chemical modifications are applied to the material surface to confer on the microsystem its specificity for cells. Techniques such as plasma treatments, plasma polymerization, physical vapor deposition, or self-assembled monolayers are used to control the chemistry, energy, and biomolecule immobilization on the surface of materials. They are also used to develop electrodes for electrical stimulation and detection, or to control the velocity in microchannels (**Table 1**).

Concerning the control of cell function, modifications of the material surface or specific materials are used to develop innovative cell culture systems and to control cell adhesion, migration, proliferation, and differentiation as well as to achieve cocultures or three-dimensional (3D) cultures. The interest in microfabrication is due to the fact that it offers the possibility of capturing or separating cells for single-cell analysis. This is

Table 1 Chemical/physical treatments applied on materials used in bioMEMs and microsystems

Chemical/physical treatment	*Bulk material*	*Chemical functionality*	*Applications*	*References*
Plasma polymerization	Silicon, silicon nitride	Polyethylene glycol (tetraglyme, Crown ether)	Biofouling	11,13
	Platinum, gold electrodes	Acetonitrile	Control of surface wettability, biomolecule immobilization	14
	Glass	Hexamethyldisiloxane	Biomolecule immobilization	14–16
	Glass/silicon	Acrylic acid	Velocity control in microchannels	17
Plasma treatments	Polydimethylsiloxane (PDMS)	Air plasma treatment	Bonding on glass substrate, control of surface wettability	18,19
	Glass	Oxygen plasma	Microfluidic channel	20,21
Physical vapor deposition	Silicon	Titanium	Biocompatibility	22
	Silicon	Gold	Electrodes	23
	Polymethylmethacrylate, poly (ethylene terephtalate), polycarbonate, polyimide	Gold	Electrodes	24,25
Self assembled monolayers (SAMs)	Silicon oxide	Methoxypoly(ethylene glycol) silane	Biofouling	26–28
	Silicon oxide	Polynucleic acid–polyethylene glycol functionalized phosphonate	Biomolecule immobilization	29
	Gold	COOH terminated alkanethiol	Biomolecule immobilization	26,28
Electrostatic interactions	Glass	Poly(lysine)-*g*-poly(ethylene glycol)	Biofouling	30

particularly important in cell biology, immunology, stem cell research, and cancer research. Some experiments of cell transfection in microsystems have been developed by combining electroporation and micromachining of the substrates. The possibility to control cell migration and contact guidance by modifying surface topography and surface chemistry inside BioMEMs and other microsystems has also been largely exploited.

The use of materials with different stiffnesses has allowed probing cell mechanics and also evaluation of the forces generated by cells or their capacity to respond to mechanical stimuli. Finally, the microfabrication approach is also very useful to develop artificial machines using materials and cells. These systems use cell properties, such as the autonomous beating capacity of cardiac cells, to develop pumps, microactuators, or microrobots.

Similarly, microsystems are largely developed for studying bacteria. However, as the bacteria's capacity to live in suspension is high in comparison to mammalian cells, and even though it is now accepted that biofilms constitute the most frequent bacterial mode of life, most examples of BioMEMs and other microsystems in microbiology concern suspensions of bacteria individually or in colonies. In this review, we focus on the microsystems involving bacteria–material interactions or material modifications for achieving, improving, or studying microbial culture, docking, separation, or migration. For more details on bacterial adhesion and biomaterials surfaces please refer to **Chapter 4.407, Bacterial Adhesion and Biomaterial Surfaces**.

3.314.2. Influence of Surface Features on Cell Function

Cells are filled with cytoplasm, which is a liquid that contains organelles such as the nucleus, the Golgi apparatus, and the mitochondria. They are surrounded by a membrane made of a phospholipid bilayer containing receptors such as integrins, cadherins, etc., allowing their interactions, respectively, with extracellular matrices (ECMs) or other cells. Their architecture is maintained by a cytoskeleton made of three types of filaments: actin microfilaments, tubulin microtubules, and intermediate filaments made of vimentin, keratin, desmin, or lamin. The cytoskeleton is physically 'hard-wired' both to the plasma membrane at focal adhesions by proteins such as vinculin, paxillin, talin, etc., and to the nuclear membrane by proteins forming the LINC complex (link between nucleoskeleton and cytoskeleton). Cytoskeleton is then involved in the mechanotransduction system, which is the basis of the cell's response to surface topography. Besides this direct signaling pathway, a biochemical signaling pathway exists between the cell membrane and the nucleus, which involves integrin receptors, kinases, and transcription factors that will translocate across the cytoplasm and nuclear membrane inside the nucleus and transmit information coming from integrins connected to proteins adsorbed on the surface of the cell substrate.

The majority of cells (except blood cells) need to adhere to survive and further proliferate and differentiate. For more information on cell adhesion onto materials, the reader must refer to other reviews.[1–5]

In this section, we describe the current knowledge on the influence of surface features on cell function in general. In particular, we detail the influence of surface topography, chemistry, energy, and stiffness.

3.314.2.1. Cell Adhesion

The influence of surface roughness on cell adhesion can be separated into the influence of roughness amplitude (height), roughness organization, lateral distance between features, or shape of features at both the microscale and the nanoscale. Many experiments have demonstrated that cells react differently to surfaces with different topographies.[1–5,31–33] For details on influence of surface roughness on cells please refer to **Chapter 6.622, The Effect of Substrate Microtopography on Osseointegration of Titanium Implants** in this comprehensive. However, the difficulty in this field is the comparison of results from studies performed using different cell types or on surfaces defined by their manufacturing processes rather than by a sufficient number of roughness parameters.[34] Most authors are satisfied with some amplitude roughness parameters, while frequency, hybridization, or fractal parameters are not measured. Now, it has been shown that surface topography must be characterized for all these parameters to be correctly and totally defined.[2–5,35]

The influence of the topography on cells cannot be generalized. Different cell types can respond in different ways depending on their origin. For example, bone-derived cells are known to 'prefer' rough surfaces, whereas fibroblasts 'prefer' smooth surfaces.

An interesting approach to appreciate the influence of roughness on cell response is to use surfaces presenting a gradient of increasing roughness amplitudes obtained by the same process. We have previously shown that the topography must be considered as a function of the cell scale in order to better interpret biological results.[2–5,36–39] Human osteoblasts adhered better on rough electroeroded metallic surfaces than on smooth ones. Above the cell scale, the surfaces produced by electroerosion were considered as rough with melted relief with smooth edges, whereas below the cell scale, they were relatively smooth and presented a large number of smooth and flat areas permitting the adhesion of cells.[39]

The organization of topography has also been shown to be a major influencing factor on cell adhesion. Cells are able to differentiate isotropic and anisotropic surfaces. Notably, human primary bone cells adhered better to isotropic, rough metallic surfaces obtained by electroerosion or sandblasting compared to anisotropic or polished surfaces.[39]

Anisotropic structures have allowed us to highlight recently a fascinating phenomenon of nuclear deformation of human cancer-derived cells.[40,41] Cells were cultured on poly-L-lactic acid (PLLA) substrates presenting square micropillars with 7 μm width and 4 μm height with 7 μm spacing. The most surprising aspect of this deformation is that the cell's capacity to survive, proliferate, and differentiate was not significantly impaired. More recently, this deformation was also observed on immortalized bone cells[40,41] and keratinocytes as well as on cancer cells derived from colon (unpublished data), although normal cells did not deform their nuclei on the same substrates (**Figure 1**). The modification of the spacing between pillars or of their dimensions did not change these observations. Normal cells did not deform their nuclei whatever the

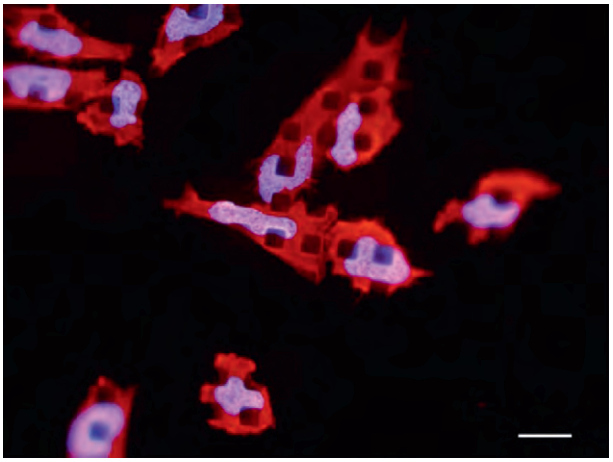

Figure 1 SaOs-2 osteosarcoma-derived cells cultured on PLLA micropillars measuring 7 × 6 μm and showing a nuclear deformation never seen before (nucleus: pink, actin cytoskeleton: red). Scale bar is 20 μm.

dimensions of the pillars, whereas this nuclear deformation was systematically observed in cancerous cells.[40,41] These observations confirm that tumor-derived cells have a lower rigidity than normal cells[42,43] which can be related to their capacity for deformation during invasion in metastasis. Moreover, these results highlight clearly that cell experiments using tumor-derived cells to study the influence of surface topography are now open to criticism because of these cells' evident abnormal response to the topography. Primary cells derived from healthy tissues must be clearly preferred.

Cell adhesion is also largely influenced by nanotopography. Using polymer-demixed nanotopography, Dalby *et al.* have shown that fibroblasts are able to identify the presence of 10-nm high nanotopographic surfaces.[44–47] Their initial adhesion was increased on islands less that 35 nm high, while long-term adhesion was increased only on 13-nm islands.[44–47] On 13-nm islands, cells displayed a spread morphology with a well-defined cytoskeleton, while on taller islands the cell cytoskeleton appeared disorganized.[44–47] Some recent studies have focused on diameter-controlled TiO_2 nanotube surfaces. Cells adhered and spread well on smaller nanotubes (30 and 50 nm), whereas on larger nanotubes they exhibited considerable elongation. Indeed, increasing the size of nanotubes did result in a smaller surface area for attachment with larger spacing, which might have disrupted the formation of focal adhesions.[48,49] For details on nanostructured surfaces and cell behavior, please refer to **Chapter 4.409, Surfaces and Cell Behavior**.

The shape of the features was shown also to influence cell adhesion at the nanoscale. Aligned nanopatterns of varying heights and tip shapes (needle- or blade-like tips) induced smaller fibroblastic cell sizes on needle-like posts and enhanced elongation on blade-like nanogrates. Fibroblasts exhibited punctuated adhesion complexes on the top of needle-like posts and dash-like adhesion complexes on nanogrates.[50]

The distance between nanofeatures is also visible for cell adhesions. Spatz *et al.* demonstrated in an elegant study, using gold nanoparticles bearing an RGD (arginine–glycine–aspartic acid) peptide and separated by polyethylene glycol (PEG) to prevent cell adhesion, that the minimal spacing to allow the formation of focal contacts by cells was in the range of 58–73 nm.[51]

In a study where nano and microtopography were voluntarily associated, it was demonstrated that nano- and microtopography exerted a synergistic influence on human osteosarcoma cell adhesion.[52]

The surface chemistry also influences cell adhesion. Some of the different ways to modify the surface chemistry are described in **Table 1**. However, the processes used to induce roughness can also sometimes have a strong influence on surface chemistry and consequently on cell adhesion.[2–5] Apparently, the chemical composition of the material can be identified by the cells. Titanium alloy modified by ion beam implantation influenced differently the spreading capacity of primary bone cells. These differences were associated with different activations of the signaling molecules.[53] Recent interesting works have focused on the influence of hydrophilicity on cell adhesion, using linear gradients with increasing surface energy. Platelet adhesion was improved by a positive charge character,[54] whereas adhesion of endothelial cells[55] or neural cells[56] was increased more on positions with moderate hydrophilicity than on the more hydrophilic or hydrophobic positions. On gradients with self-assembled monolayers (SAMs) treated by UV light, the adhesion and spreading of murine osteoblastic cells were not modified.[57] On the contrary, fibroblasts adhered better on the hydrophilic part of gradients formed by association of a hydrophobic hexane polymer and a hydrophilic allylamine polymer.[58]

In order to control the surface chemistry, some authors have coated the surfaces with another material or made replicas of the surfaces. For example, gold coatings on titanium or stainless steel substrates treated to induce various surface topography and morphology have allowed us to demonstrate that the short-term cell adhesion is mainly modulated by the surface chemistry, while the long-term cell adhesion is mainly related to the surface topography.[36–39,59] Ti-coated replicas were used to investigate the effects on cells of surfaces with varying roughness and constant chemical composition.[60,61] Another approach to control the surface chemistry is to covalently graft active molecules on the material surface. The most studied one involves the grafting of peptides or oligopeptides derived from bioadhesive molecules like proteins of the ECM, such as fibronectin or collagen. The best known peptide is RGD, which was shown to increase *in vitro* cell adhesion.[62,63] However, the use of RGD grafting for increasing *in vivo* tissue integration of implants is still controversial.[64] For more details, please refer to **Chapter 4.411, Peptide- and Protein-Modified Surfaces** in this comprehensive.

3.314.2.2. Cell Migration/Contact Guidance

After the cells have adhered and spread on the surface, their cytoskeleton will be prestressed as a result of the equilibrium between the tension applied by actin microfilaments and the compression maintained by microtubules.[65,66] Then the cells will be able to move on the surface and eventually react to or follow the surface features. When they migrate, the cells will first polarize, extend the membrane in the direction of movement, and form an attachment between the leading membrane

and the substrate. Further, the cell body will move forward and the attachment at the rear will be released. The migration and contact guidance capacity of cells are thus based on the mechanotransduction process.[65–67] The capacity of cells to follow surface features and, for example, align following the underlying grooves has been defined as 'contact guidance.' This phenomenon was first described at the beginning of the twentieth century,[68,69] and is almost universal among cell phenotypes or scales since it exists as well on nanotopography[2–5] as on microtopography.[33,70–75] Contact guidance can be explained by the inhibition of cell spreading by a physical step on the surface. The cells will follow the edge step and finally elongate following the groove direction. A recent work on living cells on nanogrooves has shown that cells emit filopodia that probe their environment. When they come across a favorable site, they form focal adhesions before forming cell protrusions. Depending on the quality of the focal adhesions formed on the grooves, the adhesion of cells is either improved or decreased. The best adhesion is obtained when focal adhesions can be formed parallel to the ridge.[76]

The first demonstration of the contact guidance capacity of cells was shown on fibroblasts.[70] Rat dermal fibroblasts oriented systematically on grooves measuring 1, 2, 5, and 10 μm wide on polystyrene (PS), whereas they oriented only on 1- and 2-μm wide grooves on titanium.[77] The orientation increased with the depth of the microgrooves[74,75] or nanogrooves.[78] Recently, interesting results have been obtained using topography gradients.[79–81] By maintaining the ridge width and depth constant (1 μm and 400 nm, respectively) but varying the groove width between 1 and 91 μm, it was shown that fibroblasts aligned more strongly along denser patterns compared to sparser patterns.[79–81] On the contrary, cells did migrate more rapidly at an intermediate ridge density. Similarly, interesting results were obtained on surfaces displaying a variable local density of square pits.[79–81] Fibroblasts migrated following the direction of patterns of higher anisotropy from spacer to denser areas. This allows us to envision more sophisticated design of biomedical devices to better control their colonization by cells. Also, the contact guidance capacity of cells has been exploited for muskuloskeletal myogenesis and for developing artificial muscular structures on grooves or fibers[82,83] mostly for the regeneration of injury gaps in neurites.[72,84–86] Interesting observations were made recently on surfaces presenting concave and convex circular structures measuring 100 μm in diameter and 50 μm in depth demonstrating the migration of fibroblasts and human mesenchymal stem cells (MSCs) toward convex structures and thus the capacity of cells to sense the curvature of surfaces.[87,88]

The surface chemistry is also a means to control cell contact guidance. Using photolithography and cold plasma discharge in oxygen, lines presenting adhesive properties have been developed on PS. Oxidized PS lines adsorbed more proteins (fibronectin or collagen) than unoxidized ones and permitted cell adhesion unlike untreated PS lines.[89,90] Adhesive guidance was developed on quartz by making aminosilane/methylsilane tracks of 5–100 μm period either parallel or perpendicular to topographic gratings of the same period and 0.1–6.0 μm in depth. This combination, on the same substrate, of adhesive and topographic guidance revealed that the adhesive response was consistently dominant.[91]

Mechanical stiffness of the substrates has also been shown to be a means to control cell migration. 3T3 fibroblastic cells were cultured on flexible polyacrylamide sheets coated with type I collagen, presenting a transition in rigidity in the central region. Cells approaching the transition region from the soft side could easily migrate across the boundary, with a concurrent increase in spreading area and traction forces. In contrast, cells migrating from the stiff side turned around or retracted as they reached the boundary. This apparent preference for a stiff substrate was called 'durotaxis'.[92] It was shown that this cellular sensitivity to substrate flexibility involves myosin-generated forces and protein tyrosine phosphorylation with highly dynamic and irregularly shaped focal adhesions on flexible substrates.[93]

3.314.2.3. Cell Proliferation and Differentiation

In the field of bone implants, the influence of surface microtopography on cell proliferation and differentiation was largely studied. It was notably shown that the proliferation and differentiation potential of osteosarcoma-derived cells on titanium was positively influenced by the roughness.[94–96] Cells were more differentiated on rough surfaces and their responses to systemic or regulation factors were also stimulated by the roughness. Their sensitivity to roughness was shown to depend on their maturity state, immature cells being more sensitive to roughness.[97] The role of integrins in the response of cells to roughness was also recently demonstrated. On roughness gradients, it was shown that rat calvaria osteoblasts showed a linear increase of proliferation with roughness, whereas human gingival fibroblasts showed the opposite, demonstrating again the influence of the cell phenotype on the response to surface features.[98]

Nanotopography also influences the cell's proliferation and differentiation capacity.[2–5]On nanotubes produced by anodization, human MSCs (hMSCs) differentiation was shown to depend on the tube diameter. Smaller tubes promoted less cellular differentiation than larger ones. This observation was related to a more dramatic cell elongation on larger nanotubes, which was supposed to stimulate their differentiation.[49] However, the same experiment with rat MSCs gave opposite results.[99–101] This was explained by the authors as due to a different nature of the nanotubes, which were anodized and amorphous in the case of Park *et al.*[99–101] versus heat-treated and crystallized in the anatase phase in Oh *et al.*,[49] illustrating the capacity of the cells to respond also to slight differences in surface chemistry.

Other fascinating results were obtained by modifying the nanotopography organization. Dalby *et al.* showed that hMSCs cultured on polymer surfaces presenting 120-nm diameter pits placed with the hexagonal, square, or displaced square (±50 nm from the center = DSQ50) organization differentiated differently. Cells cultured on DSQ50 surfaces differentiated more compared to those on other surfaces and, more surprisingly, they differentiated as if stimulated with the osteogenic medium that is generally used to induce their differentiation *in vitro*.[44–47]

As previously shown in the case of cell migration, substrate stiffness can also control the differentiation of hMSCs. Engler *et al.* have observed that soft matrices that mimicked brain were

neurogenic, that stiffer matrices that mimicked muscle were myogenic, and that rigid matrices that mimicked collagenous bone were osteogenic.[102] For more details, please refer to **Chapter 5.504, Effect of Substrate Modulus on Cell Function and Differentiation** in this comprehensive.

Concerning surface chemistry, it was shown, using model surfaces covered with SAMs, that the differentiation of osteoblasts was higher on hydrophilic substrates than on hydrophobic ones.[103] *In vivo* studies with SAM-coated implants confirmed these results.[104] Using gradients of polymers, the influence of surface energy on osteoblasts was elucidated.[56] Cells proliferated more on the hydrophilic positions in the gradient. This was also confirmed on gradients produced by plasma polymers.[58] These studies developed on model surfaces were also carried out on titanium implant surfaces modified by sandblasting and acid etching (SLA).[105–107] These SLA surfaces have induced high proliferation and differentiation of bone cells *in vitro*[94–96] and osseointegration *in vivo*.[108–110] However, in order to improve their performance further, a modification was proposed in which the samples were rinsed and immersed in NaCl under N_2 protection during the preparation process and storage until the implantation. These modified SLA surfaces (ModSLA) increased the differentiation of osteoblasts *in vitro*[111,112] as well as the osseointegration of implants *in vivo*.[109,113] This modification by improving the wetting of surfaces by biological fluids and the adsorption of proteins on them is a demonstration of the possibility to control cell response *in vitro* and *in vivo* not only by mechanical input on cells using surface topography or surface stiffness but also by controlling surface energy. In this case, the mediators are the proteins adsorbed on the surface.

3.314.3. Influence of Surface Features on Bacteria Function

Bacteria can live as planktonic cells but prefer to attach to a surface in community known as biofilms.[114] This assembly of microbial cells and extracellular biopolymers is the result of the initial adhesion of planktonic bacteria that have proliferated and synthesized species-dependent polysaccharides and other metabolites (proteins, lipids) once attached to the surface. The crucial step of adhesion is affected by bacterial characteristics as well as features such as the physicochemical properties of the cell wall and protein- or carbohydrate-based filament-like appendages named flagella, pili, curli, and other fimbriae, or lipopolysacharrides.[115,116] Bacterial adhesion is also highly influenced by the properties of the material on which the biofilm is developing, in particular by its chemical and topographical characteristics.[6,7] Material surface properties seem to play a relatively small role in further biofilm development, but some evidence already exists that surface properties can also affect the biofilm characteristics.

3.314.3.1. Initial Adhesion

Topographic features at the microscale are commonly considered as favorable material characteristics for bacterial adhesion. Indeed, bacteria are preferentially observed in crevices and holes of their own size, which may be attributed to the protection that these features may offer to bacteria. Various works have confirmed this phenomenon in general.[117–119] However, it is not clear whether this is the result of cell entrapment or of a real adhesion phenomenon. Moreover, analyses are usually performed by quantifying adherent bacteria without the determination of bacterial localization, which prevents us from drawing conclusions as to the potential influence not only of the topographical features but also of their organization, as already shown in the case of mammalian cell adhesion.[2–5] Concerning the chemical features, typical dimensions of bacteria of around a few micrometers lead to the conclusion that chemical patterns at the microscale, that is, larger than bacterial dimensions, play for bacteria similar roles as separate surfaces with different chemical properties. As an example, preferential adhesion can occur on surface areas functionalized with favorable chemical functionalities, such as mannose for *Escherichia coli*.[120] It has also been demonstrated that bacteria can detach differently according to surface chemistry.[121] Bacteria may be able to migrate from one favorable pattern to another. Specific material characteristics such as surface wettability or surface roughness may also affect bacterial migration, although this topic has only rarely been treated so far.

Due to their small size compared to mammalian cells, bacteria may be expected to react also to chemical and topographical surface features at the nanoscale. However, the bacterial membrane is not as deformable as the mammalian one. In particular, the bacterial membrane does not have the ability to form filopod-like appendices or to orientate cytoskeleton with grooves or other geometrical topographic surface features. Only weak modifications of the cell shape occur throughout the bacterial life. Therefore, while topographic features at the microscale should be expected to influence the adhesion of bacteria onto surfaces, the effect of nanometric features on bacterial adhesion and further biofilm formation is not obvious. The lack of deformation capability may affect also the capability of bacteria to access potentially favorable chemical patterns of nanometric size on surfaces, and therefore their capability to react to nanometric chemical surface features.

However, as pointed out above, bacteria can possess protein- or carbohydrate-based macromolecules anchored in their membranes, creating filament-like appendages of various sizes (from a few hundred nanometers to a few micrometers) according to the species and strains. These structures (flagella, pili, curli, and other fimbriae, but also lipopolysacharrides) may participate in the sensing of the surface by bacteria, allowing them to detect surface features at the nanoscale.[122,123] This hypothesis has not yet been directly proved. Nevertheless, some of the previously evoked membrane structures have been implicated in the adhesion capability of bacteria[124–127] as well as their mobility on material surfaces.[128,129] In addition, some evidence already exists that surface properties at the nanoscale are able to influence the adhesion of bacteria, although studies on this topic are rare. Several authors have concluded on the general increase in bacterial adhesion when the surface roughness increases. However, the response of bacteria to topography is a complex phenomenon, as demonstrated by frequent contradictory results published in the literature. For example, Campoccia *et al.*[130] observed similar bacterial adhesion on surfaces with various roughnesses, while the study of Mitik-Dineva *et al.*[131] showed a decrease in the number of adherent bacteria when material surface roughness increased. In addition, the organization and size of the topographic features

may play an important role as suggested by a few works,[132,133] although the relationship between feature organization and size on one hand, and bacterial localization and amount on the other, has not been addressed so far. As well, the effect of surface chemical features at the nanoscale on bacterial adhesion and retention has rarely been studied. Nevertheless, knowing that bacteria interact with chemically complex surroundings (other bacteria or tissues, for example), their capability to recognize the chemical heterogeneities at the molecular scale should be expected. A few studies have been conducted with SAM model surfaces chemically mixed at the molecular scale, demonstrating that bacteria are sensitive to variation of chemical function densities.[134–136] However, bacterial capability to distinguish between nanoscale patterns of similar chemistry but different numbers of molecules is still unknown.

3.314.3.2. Biofilm Formation

The influence of topographic and chemical surface properties on the development and the characteristics of biofilms is largely unknown. It is even commonly considered that biofilm evolution is independent of the surface. However, a few studies have already provided evidence that the surface chemistry can affect bacterial colonization at further stages than the initial adhesion. Thus, it has been demonstrated that surface colonization after 12 h (*Staphylococcus epidermidis*)[137] and the colonization kinetics (*E. coli*)[6,7] can be influenced by surface wettability, whereas initial adhesions do not differ between surfaces. Also, effect of surface charge on bacterial colonization has been shown to vary with the incubation time.[138] Nevertheless, much work has still to be done to understand biofilm development and behavior in response to specific chemical and topographic surface characteristics.

Finally, important questions about the influence of surface properties on bacterial adhesion and biofilm formation and behavior remain unclear. Thanks to the scale and precision reached by microsystem technologies, essential improvements can be expected from their use in studies addressing these questions. On the other hand, bacterial behavior in response to surface features can be exploited for improving microsystem performances. For example, bacterial response to topography should allow docking of bacteria on microsystem surfaces, resulting in easier quantification, identification, or characterization of the microbial cells. Both these aspects are addressed in the following section.

3.314.4. Applications in BioMEMs/Microsystems Fields

3.314.4.1. Cell Culture

The previous concepts have been found out essentially using classical culture techniques, that is, in 2D cultures in Petri dishes or multiwell plates. However, it is well known that these techniques present several disadvantages. The major disadvantage is that cells are cultured under conditions that are very different from their natural life conditions where they live in three dimensions and make connections with each other. Attempts have been made for several years to develop 3D cultures in bioreactors to overcome these disadvantages. However, these techniques are applicable only when large amounts of cells are available or when the objective is to produce several centimeter cubes or grams of cells, with or without ECM, for example for tissue engineering applications. Coculture systems have also been developed and used to understand the relationships between two – or maximum three – different cell types.[139–141] However, the need exists for culture techniques that allow culturing together more than two cell types under the same conditions or in their real environment, that is, in three dimensions inside an ECM and in connection with other cell types. Moreover, the maintenance of cells in three dimensions imposes the use of dynamic circulation of body fluids to oxygenate and to permit mass transport to the cells. The control of the circulation of fluids inside a bioreactor of several milliliters or more is relatively complex and does not allow the test in parallel of several fluid circulation conditions or different medium compositions.[142]

Microfluidics and BioMEMs give now the possibility to overcome most of the limitations of current culture methods. Microfluidics allow perfect control of the circulation of fluids inside the circuits, circulation of several fluids in parallel that can be mixed at will, and development of gradients of concentrations of the active products, and in a very small volume, thus allowing one to work on rare and precious products. In parallel, research in microsystems focus on the development of systems that allow 3D cultures in different materials based on natural and synthetic hydrogels fed by microfluidics. By modifying the construction of the microfluidic circuits, it is possible to coculture different cell types and to control their interactions. The approaches based on microfluidics not only allow the feeding of cocultures but also permit following dynamically the response of cells in living cultures with time. The capability of microsystems to reduce the volume of the culture and the volume of reaction allows us to consider testing in the same system several products or drugs on several cell types or associations of different cell types. Aside from improvements in sample treatment throughput for routine assays, the reduction of culture volume allows us to decrease the number of cells, which, in the case of pathogenic microorganisms, should reduce also the infection-associated risks to the environment. Finally, contrary to the classical culture techniques, in which the cell detachment necessary to isolate cells for gene expression or protein synthesis analysis is mainly carried out by enzymatic methods, the microsystems approach has allowed the diversification of the techniques for harvesting cells or for carrying out these analyses.

3.314.4.1.1. Control of adhesion, migration, proliferation, and differentiation

As described previously, the first phase of adhesion is essential for the mammalian cell survival and further cell migration, proliferation, and differentiation. The control of adhesion by the modification of surface topography and surface chemistry has been at the center of an intense research activity for several decades.[31,32,143] The quality of adhesion of the cells is mainly assessed by quantifying the energy needed to detach them.[1] In general, to evaluate directly the adhesion strength, physical constraints are applied by techniques such as fluid flow, centrifugation, micropipette aspiration, jet impingement, etc. Thermoresponsive polymers have also been shown to be particularly efficient for controlling cell detachment.[144–146] This

concept has been applied in microsystems by synthesizing the thermoresponsive polymer poly(*N*-isopropylacrylamide)–poly (ethylene glycol)-thiol (PNIPAAm–PEG-thiol), which was used for the formation of SAMs on gold substrates. The polymer chains passed from an extended and highly hydrated state above 37 °C to a collapsed coil state below 37 °C. At 37 °C, the cultivated fibroblasts adhered and spread normally on these surfaces, whereas they detached on reducing the temperature to 25 °C. Thus, the use of these SAMs in a microfluidic device allowed the quantification of the forces needed to detach cells using laminar flow.[147] The control of culture conditions in microsystems can also be done through the control of the architecture and the chemistry of the microfluidic perfusion system. Cell-adhesive surface microdomains alternating with cell-repellent coatings have been used to mimic *in vivo* spatial cues for muscle assembly. This system allowed the confinement of the fusion of myoblasts into aligned and isolated multinucleated myotubes. Moreover, the microfluidic system provided accurate control of the perfusion rates and biochemical composition of the environment surrounding the cells.[20] A microcell chip based on five layers of poly (dimethylsiloxane) (PDMS) alternating with borosilicate substrates presenting holes of various diameters was designed. It allowed the development of a microcell stimulator based on a pneumatic actuator with a flexible diaphragm, which consisted of an air chamber and several cell chambers. This system was designed to apply compressive pressure to hMSCs for inducing osteogenesis. A cyclic compressive stimulus of 5 kPa twice a day for 10 min during 7 days showed to be the best condition for stimulating cell proliferation and cell differentiation.[148] A microfluidic device was filled with a pregelled alginate solution where calcium was chelated by DM-nitrophen™. The UV exposure of the caged calcium provoked its release from DM-nitrophen causing alginate cross-linking. This elegant approach allowed the 3D coculture of endothelial cells and osteoblastic cells in a microchannel.[149] The same principle of photocaging was applied to RGDS peptides caged inside a hyaluronic acid (HA) hydrogel. Line patterns were made with this modified hydrogel material, which allowed the control of the adhesion and proliferation of fibroblasts.[150]

So far, contrary to the case with mammalian cells, the intensity of adhesion of individual bacteria to surfaces has not been measured in microsystems. Nevertheless, bacterial growth has been studied by using microdevices, mainly in suspensions. The main studies have concerned the response of microorganisms to specific environmental conditions. Extreme and unusual environments have been mimicked by adjusting, for example, fluid velocity, pH, and ammonium concentration for methanogen cultivation.[151] Even the screening at microscale of unusual growth conditions has allowed the successful cultivation of previously uncultivated bacteria.[152,153] Microtube- and microcapsule-associated microdevices have been also realized for studying the behavior of microorganisms in confined growth conditions. The microtubes proposed by Huang *et al.*[154] are transparent for cell observation and display variable diameters, which should allow the investigation of the influence of the confinement diameter on the shape and arrangement of microbial cells. Semipermeable microcapsules composed of an alginate–poly-L-lysine membrane and entrapped in microfluidic system were created by Morimoto *et al.* for encapsulating cells and microorganisms. Their permeability should allow the transport of nutrient and waste through the membrane, allowing the growth of cells encapsulated inside. This was already demonstrated for *Chlamydomonas* unicellular alga and opens the door of the easy observation of several microorganism subpopulations growing under different specific conditions.[155] Finally, microfluidic devices have been also exploited for studying the growth and detachment of bacterial biofilms (*S. epidermidis*) in response to the hydrodynamics of the local environment as well as to a hydrolyzing enzyme or antibiotic treatments. In particular, by comparing biofilm morphology according to the location in the device, and to the hydrodynamic microenvironments, this study confirmed that biofilms tend to be elongated along the flow direction when grown under high shear, whereas they tend to form filamentous streamers when grown under low shear.[156,157] Micropatterned devices have also been used for the investigation of cell–cell communication in *E. coli* communities, a prelude to quorum sensing, which is another crucial aspect of the biofilm-associated bacterial mode of life.[158]

3.314.4.1.2. Cocultures

The development of cocultures started less than 5 years ago in the BioMEMs and microsystems field. One challenge in the field is to be able to control spatially and also temporally the cocultures and the cell–cell interactions. The difficulty is (1) to reversibly control the interactions between different cell populations that are in patterns on molecularly defined surfaces and (2) to serially manipulate the surface to control the duration of the cell–cell interactions.[159] Diverse approaches have been followed. Mainly microfabrication techniques were used to develop complementary cell substrates that could be displaced or changed to control cell–cell interactions. Lee *et al.*[159] developed an original method combining a photoelectroactive surface chemistry strategy with a microcontact printing patterning method. They first used microcontact printing to pattern hexadecanethiols onto a gold surface backfilled with a mixed solution of tetraethyleneglycol-terminated alkanethiols (EG4SH) to render the unpatterned region inert to cell attachment. Nonvolatile organic compounds (NVOC)-protected hydroquinone-terminated alkanethiols were added to the unpatterned region and further deprotected, electrochemically oxidized to quinone, and grafted with oxyamine–RGD. This approach allowed the addition of a second cell type besides the first one adhering on the microcontact-printed regions, which then allowed the spatial control of their interactions. For achieving temporal control, the second cell type could be released from the pattern by the application of a mild reductive electrochemical potential to break the oxime linkage, leading to the release the RGD ligand. The possibility of developing gradient surfaces with RGD–oxyamine peptide was also demonstrated.[159] By using a micromachined silicon substrate with moving parts, Hui and Bhatia[160] studied in an elegant manner the need for cell–cell interactions in hepatocytes/stromal cells cocultures for maintenance of the hepatocellular phenotype. They developed silicon plates with comb fingers that could be placed in contact or slightly separated (**Figure 2**). After coating the silicon plates by irradiated PS, cells were cultured on the top surfaces. Sliding the two silicon plates by 1.6 mm changed the gap between fingers by

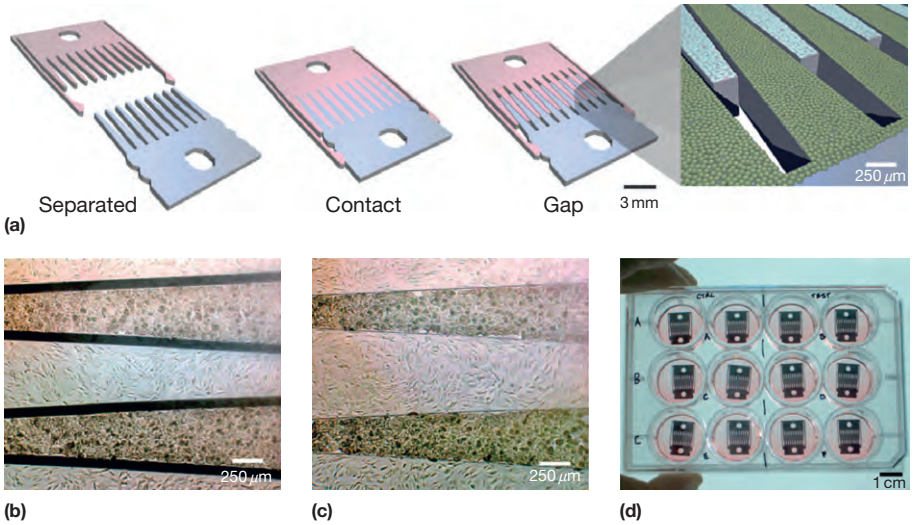

Figure 2 Micromechanical substrates enabling cell positioning with micrometer resolution. (a) Microfabricated silicon parts can be fully separated (left), locked together with comb fingers in contact (center), or slightly separated (right). Cells are cultured on the top surfaces; manual scraping can be used to restrict cells to the comb fingers only (inset). The slope of the tapered comb fingers results in a 20:1 mechanical transmission ratio; that is, sliding the parts by 1.6 mm changes the gap between the fingers by only 80 μm. Together with the integrated snap-lock mechanism, it is thereby possible to control the separation with repeatable micrometer-scale precision by using unassisted manual actuation. (b, c) Bright-field images of hepatocytes (darker cells) and of 3T3 fibroblasts cultured on the comb fingers. The silicon is first functionalized by spin-coating with polystyrene (PS) followed by plasma treatment, resulting in a surface comparable to tissue-culture plastic. Devices can be reused multiple times (>20). (d) Devices in a standard 12-well plate. Cell culture and functional assays were performed with standard methods. Actuation is also performed directly on the plate with sterile tweezers. Reproduced from Hui, E. E; Bhatia, S. N. *Proc. Natl. Acad. Sci. USA* **2007**, *104*, 5722–5726, copyright (2007), National Academy of Sciences, USA.

80 μm. Therefore, it was possible to control the separation between the two cell layers very easily.[160] The combination of two PS and PDMS complementary cell substrates covered by confluent layers of two different cell types was used to develop a tumor/endothelium model. Using this model, the migration of tumor cells toward the endothelial cells and the simultaneous retreat of these last ones were observed. The possibility of separating the two types of cells by a gap-type barrier allowed to demonstrate that when direct contact between the two cell types was prevented, the endothelial cells initially migrated toward the tumor cells before retreating.[161] Another method based on cell crushing by a controlled force applied on the top of culture chamber presenting 100-μm thick microstamps was developed. The possibility to perform cocultures after cell crushing and rinsing was demonstrated on mouse fibroblasts and liver hepatocarcinoma. The main advantage of this technique is that the same microchip can be used several times for micropatterning and microfluidic cocultures.[162] Other coculture systems were developed using Parylene-C to fabricate patterned stencils presenting round holes. After activation by plasma, the stencils were coated with HA and deposited on a fibronectin-coated substrate. Murine embryonic cells (mES) deposited at the surface adhered mainly inside the holes on the fibronectin-coated substrate. Upon removal of the Parylene-C stencil, a cell micropattern was formed. The subsequent seeding of AML-12 hepatocytes allowed the formation of cocultures that were qualified as static cultures. The possibility of controlling temporally the cocultures qualified as dynamic cultures was also demonstrated. A first coculture of mES and fibroblasts was carried out with the fibroblasts cultured on the collagen-coated Parylene-C and maintained in contact with the mES inside holes. The Parylene-C with fibroblasts was further removed and AML-12 hepatocytes were seeded around mES patches.[163] All these approaches are a means to engineer more complex cell–cell interactions in a spatially and temporally regulated manner. The development of cocultures was also applied to 3D cultures in a microfluidic device. 3D hydrogel cell cocultures have been developed notably to test the cytotoxicity of anticancer drugs while reproducing multiorgan interactions.[164] A chamber with liver cells was connected to another with colon tumor cells cultured both in matrigel, while a third chamber was filled with marrow cells in alginate gel (**Figure 3**). Two different anticancer drugs were inoculated in this microcell culture analog (μCCA), one being metabolized by enzymes in the liver to be active (Tegafur) and the other one not (5-FU). The μCCA allowed the observation of a cytotoxic effect on colon cancer cells with Tegafur in a time-dependent manner compared to control cultures in a 96-well microtiter plate. When liver cells were absent in the circuit, Tegafur showed a considerably weaker cytotoxic effect than when the liver cells were present. This indicates that Tegafur was converted in 5-FU by liver cells and that 5-FU recirculated into the tumor chamber and exerted its toxic effect on tumor cells. These results demonstrate that μCCA, which provides a more physiologically realistic environment than conventional static multiwell plate systems, can be very useful tools to test the pharmackinetic profiles of drugs.[164] The cocultures in 3D hydrogel-based cultures were also applied on liver cell cultures. Upregulation of hepatic functions was observed by cocultures with nonparenchymal liver cells.[165] Bilayered cultures of epithelium and a supporting cell layer were achieved

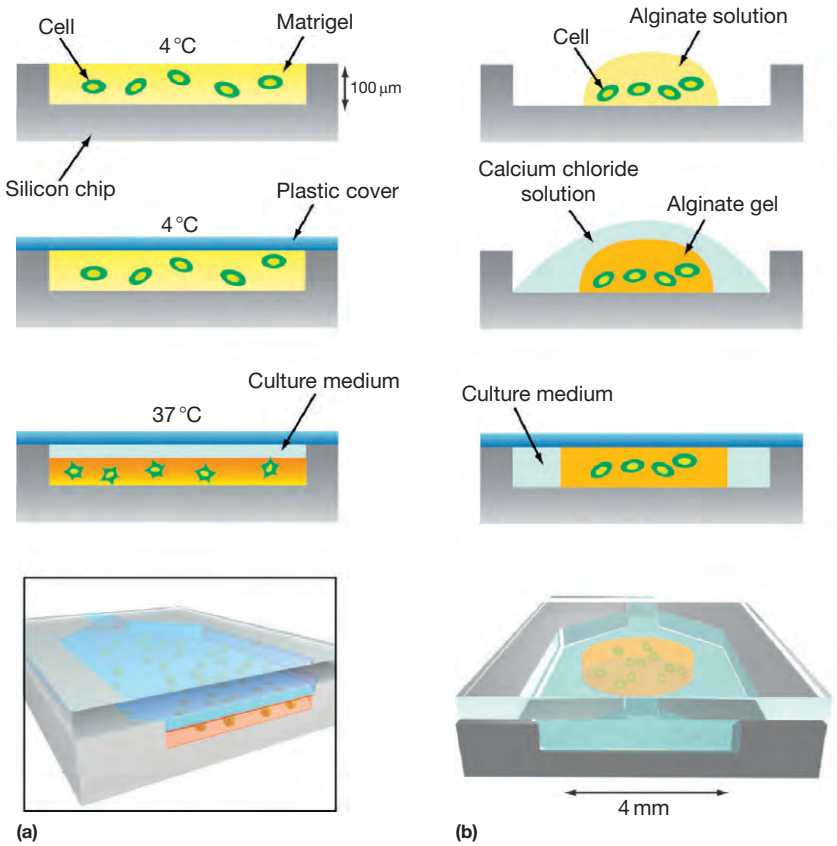

Figure 3 (a) Schematic diagrams describing the incorporation of matrigel hydrogel into a μCCA. Cell-embedded matrigel is inserted into a chamber in a liquid state and the device is sealed with a plastic top cover and a bottom housing piece. After the sealing, the gel is formed by raising the temperature. The bottom housing piece is omitted in the figure for simplicity. (b) Incorporation of alginate hydrogel into a μCCA. A drop of cell suspension in alginate solution is placed inside a chamber and the gel is formed by addition of calcium chloride solution. By sealing with the top cover, a disk-shaped hydrogel is formed inside the chamber. Reprinted with permission from Sung, J. H.; Shuler, M. L. *Lab Chip* **2009**, *9*, 1385–1394.

on the apical and basal side, respectively, of a collagen vitrigel in a microfluidic device with the objective to develop corneal microtissue patches.[166]

Lee *et al*. demonstrated recently the high potential of microfluidic coculture approaches to develop physiologically and clinically relevant models of implant-associated bacterial infection. A microfluidic system was used for imaging MC3T3-E1 murine calvarial preosteoblast proliferation in response to *S. epidermidis* environment contamination. A surface of polished TiAl6V4 alloy was integrated into a PDMS microfluidic system, and various amounts of bacteria were considered. With a small number of bacteria (10^2–10^5 colony forming units), osteoblast adhesion, spreading, and proliferation were not significantly affected during the early stages of the culture. But, interestingly, the results suggested that, when the number of bacteria was small, they did not compete with osteoblasts for the Ti alloy surface. However, when bacterial proliferation occurred, it changed the microenvironment, making it unfavorable for cell viability.[156,157]

3.314.4.1.3. 3D cultures

One challenge in the field is to develop 3D cultures that will better mimic the *in vivo* environment of cells. The microsystems associated with microfluidics are particularly convenient tools to achieve 3D cultures notably because they can be carried out in a small volume with a small quantity of the culture medium. 3D cultures in hydrogels associated with microfluidics have been used to assess the effects of pharmacological and/or microenvironmental influences on tumor cell invasion.[167–169] A microfluidic platform was built for real-time imaging of the interactions between multiple cell types exposed to autocrine and paracrine signaling molecules. Collagen and matrigel hydrogels were polymerized in alternating gel channels containing fluorescently labeled breast cancer cells and macrophage cells. A two-photon fluorescence microscope was used to visualize the migration and the capacity of collagen remodeling of cancer cells.[170] Similarly, the invasive capacity of BALB3T3/v-src cells was studied on three cell culture arrays with collagen gel-coated surfaces in presence or absence of a collagenase inhibitor.[169] Collagen gel microstructure was also used as a matrix for bacterial immobilization in on-chip incubation systems dedicated to high-throughput screening in antibacterial drug research and to pathogenic bacterial identification. Combined with electrochemical detection of the microbial respiration activity, this system allowed the cultivation of small amounts of bacteria while maintaining bacterial viability.[171]

Hydrogel-based microfluidic devices are also useful for studying cell migration. Using a system capable of generating

steady and long-term linear chemical concentration gradients, the chemotactic response of wild-type *E. coli* and differentiated human neutrophils versus attractant products was analyzed.[172] Porous polymeric materials were used instead of hydrogels to study cancer migration in a microsystem.[173] Microbioreactor arrays (MBAs) combining 12 microbioreactors have been developed in which cells were either attached to the substrates or encapsulated in HA hydrogels.[174] They were notably used to study the vascular differentiation of human embryonic stem cells (hESCs). The effects of cell density and flow regimes on hESC differentiation were tested. The hESCs cultured with a higher level of shear exhibited a higher level of differentiation, whereas the cell density had a negative effect on cell differentiation. The interest of MBAs is that each of their wells is independent, that is, without interactions with other wells, and that the medium at the outlet of each well is sent to waste instead of being recirculated back to the cells. By this way, there is no interaction between the wells and no confusion with paracrine signals. 3D pillared microstructures in PDMS were also used to induce the formation of three-dimensionally organized hepatocyte aggregates inside microsystems.[175]

3D cultures were also developed using microwell arrays. With such systems, it becomes possible to cultivate either single cells[176] or cell aggregates.[99–101,177] The modification of the geometry of the microwells displaying the same volume as one cell showed that the actin cytoskeleton of cells whose 3D shapes were fully confined by microwells was remarkably 3D and that prominent actin fibers were often aligned along the long axis of the microwells (**Figure 4**).[176] Change of the material composing the microwells was used to favor cell adhesion or, on the contrary, to inhibit their adhesion and favor the formation of aggregates.[177–181] Notably, the formation of embryoid bodies has been favored by using PEG microwells. By this way, it was possible to control the sizes and shapes of ES cell aggregates.[177]

Nanofiber polymer networks were also incorporated into cell chips to mimic the cellular microenvironment. Proliferation of hMSCs on electrospun nanofiber matrices inside cell chip was comparable to their proliferation in classical cell culture environment.[178,179] Microwells structurally bonded to a sheet of electrospun fibers were constructed from several polymers, which showed their ability to control the cell cluster environment and cocultures.[182] Pure chitosan microfibers were synthesized directly in a microfluidic circuit and used as a cell support in a bioartificial liver chip.[178,179]

In conclusion, the fabrication of biomimetic environments is one of the important issues in the current BioMEM and microsystem research fields. They must be developed and used as cell culture tools, providing miniaturized versions of conventional laboratory techniques. In addition, they will bring new insights into investigations on cell–cell or cell–ECM interactions and simulate *in vivo* situations.

3.314.4.2. Cell Docking

The capture of single cells in microfluidic devices is essential for the development of integrated microsystems for single-cell analysis. Various techniques have been used with this objective. Some are based on material surface chemistry

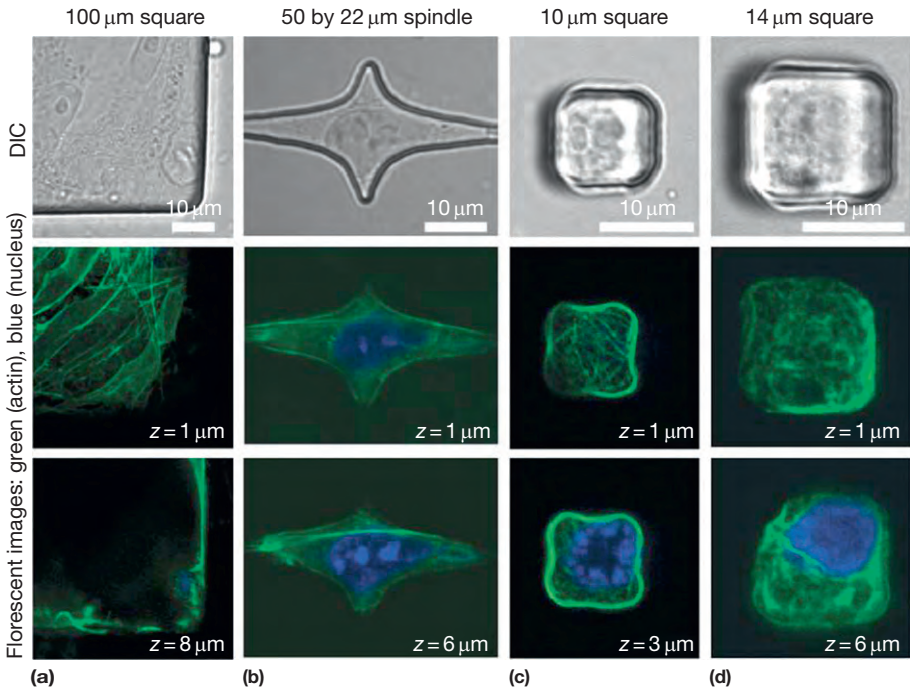

Figure 4 Differential interference contrast (DIC) and fluorescent confocal images are shown of cell nuclei (ethidium homodimer; blue) and actin cytoskeletal networks (Alexa 488-phalloidin; green). Human vascular endothelial cells (HUVECs) cultured for 24 h are shown in a large microwell (a), a spindle-shaped microwell that was slightly bigger than the confined cell (b), and 10 (c) and 14 mm square (d) microwells that adequately controlled the 3D shape of cells. Confocal slices are shown at different height positions in the microwells, where $z = 0$ indicates the microwell bottom. Reprinted with permission from Ochsner, M.; Dusseiller, M. R.; Grandin, H. M.; *et al*. *Lab Chip* **2007**, *7*, 1074–1077.

modification by microcontact printing or by grafting of biological molecules such as DNA, antibodies, or RGD peptides with the capacity to link to cell membrane by biological recognition. However, in the most part, the techniques used for docking mammalian cells are based on physical approaches such as the application of electromagnetic and acoustic wave fields, laser trapping, dielectrophoretic trapping, or micromolding to make microstructures capable of capturing cells. On the contrary, such physical techniques are only rarely proposed for docking bacterial cells. These techniques are not in the focus of this review.

However, some applications of cell docking approaches concern the concept of cell retainers for nonadherent cells such as blood-derived cells (**Figure 5**).[183–186] These cell retainers are generally produced by photolithography-based approaches. These devices have been used, for example, to investigate the effect of drugs on individual cells, which were further analyzed for their reactive oxygen species generation, intracellular enzymatic activity, calcium flux, etc., through fluorescence-based imaging and automatic analysis.[185] Another important application of cell docking approaches is the possibility to isolate embryoid bodies.[187] By controlling the size and the concentration of the cell suspension, it is possible to control the initial size of aggregates, thereby influencing the lineage commitment of embryoid bodies. Moreover, the control of the bottom of wells and notably the possibility to make them round using a laser-jet-printer-based method and replica molding have allowed the maintenance of the spherical morphology of embryoid bodies and controlling their growth and differentiation.[187]

Other ways for docking cells are based on hydrogels. Some authors have used PEG hydrogel microwells to protect cells from medium flow in channels of microfluidic systems and to dock cells within predefined locations.[188] The interest in entrapping cells inside hydrogels comes from the fact that, in the case of an alginate hydrogel, a reversible immobilization of cells can be achieved, which offers the potential of long-term cell culture.[189] Using a patterned agarose hydrogel forming a cell layer, a microelectrode array was developed to culture and study the spontaneous electrical activities of primary hippocampal neurons. This system allowed the monitoring of their response to drugs. Moreover, the development of spontaneous network activity was observed.[190] Dielectrophoretic forces (DEPs) were also used to pull cells on patterned electrodes and to accurately position single cells on a substrate. Negative[191] or positive DEP[192] has been used with this objective. Magnetic-based methods are also sometimes used for aligning cells on geometrical arrays.[193–195] By labeling cells with immunomagnetic labels and by generating magnetic flux density peaks at predefined locations, Liu *et al.*[193,194] were able to randomly array up to 136 single cells per square millimeter. Optical tweezers have also been used alternatively.[196]

Finally, many studies have utilized the functionalization of surfaces micropatterned by microcontactprinting with biomolecules such as fibronectin or RGD peptides derived from fibronectin on a background that otherwise prevents cell adhesion.[30,197] This approach has allowed the production of adhesive patches of different sizes and morphologies and the study of the adhesion of single cells on each patch. The influence of the size and shape of the patches on the formation of focal adhesions, stress fibers, and lamellipodia by the adherent cells has been studied in depth.[198–200]

The possibility to use RGD peptides to functionalize alginate gels in microfluidic channels was also demonstrated.[201,202] Peptide-functionalized alginate was adsorbed on the surface of a device and converted into a thin hydrogel layer by rinsing

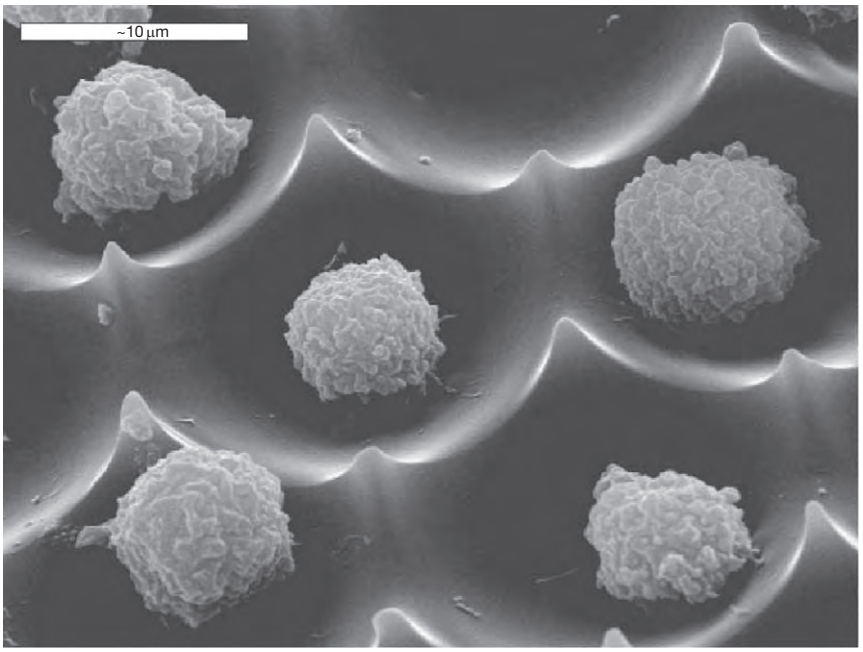

Figure 5 Scanning electron micrograph of U937 promonocyte cells in PDMS array made as described in Deutsch *et al.*[183] Reprinted with permission from Deutsch, A.; Zurgil, N.; Hurevich, I.; *et al*. *Biomed. Microdevices* **2006**, *8*, 361–374.

with a Ca^{2+} ionic solution. Primary rat cardiac fibroblasts were injected into the device, which were captured by the peptide-functionalized gel. Following capture, the hydrogel was dissolved using ethylenediaminetetraacetic acid (EDTA), thereby releasing the captured cells. This very simple method could be adapted to all microsystems operating in a low shear stress regime.[201,202] DNA was also used to capture cells directly in microfluidic devices. The interest of this approach lies in the fact that, in contrast to adhesion proteins such as fibronectin, it is independent of specific receptors possessed by individual cells. Consequently, both naturally adherent and nonadherent cells are compatible with this method. The addition of artificial DNA to the cell surface is a versatile coding strategy allowing the generation of complex cellular arrays with many cell types. Moreover, the patterning of DNA on the capture surfaces can be accomplished with standard methods used to prepare DNA microarrays.[203,204] This approach was used to develop a microdevice on an array of pH-sensitive microelectrodes for metabolic analysis.[203,204] The sensor area of the microelectrodes was functionalized with the DNA complementary strand of the cell membrane-bound single-stranded DNA. With this system, it was possible to demonstrate a higher extracellular acidification rate for Jurkat T lymphoma cells compared to normal primary T cells.[203,204]

In the field of microorganisms, cells are mainly docked for further detection and identification. Especially, this approach is of high interest for controlling water quality as well as for detecting the presence of pathogens in biological fluids. In most of these applications, the bacterial capture is provided in microsystems by immunorecognition. Antibodies specific to the bacterial species of interest are chemically immobilized on chips. Using an interesting approach, Yang *et al*. enhanced the efficiency of bacterial (*Listeria monocytogenes*) capture by coupling immunocapture to dielectrophoresis for concentrating cells prior to docking. This strategy allowed achievement of immunocapture efficiencies between 55 and 65% for *Salmonella* cells with 15–30 min DEP, while efficiencies were between 10 and 20% for similar detections time without DEP.[205] In such approaches, the targeted bacteria are usually further detected and/or identified using enzyme-linked immunosorbent assay (ELISA) methods,[205,206] immunoassays coupled to laser-induced fluorescence,[207] impedance measurements[208] or microscale polymerase chain reaction (PCR).[209]

Capture of microorganisms is also useful for selecting single bacteria or subpopulations of bacteria, in order to study their behavior under specific growth conditions. In this field, docking has been achieved by entrapment in grooves for selecting persistent individual cells in subpopulations,[210] and by encapsulation in microdroplets for screening optimum growth media in order to cultivate previously uncultivated bacteria. Encapsulation in microcapsules[155] and confinement in microtubes[154,170] are also potential new ways for capturing single cells or cell subpopulation for further cultivation or analysis.

3.314.4.3. Cell Separation and Enrichment

The isolation and characterization of single cells from a heterogeneous population are important processes in cell biology, immunology, stem cell research, and cancer research. In the development of novel cell-based therapies, there is considerable need of targeting specific cell types to allow further analysis and amplification *ex vivo*. Microfluidics was largely developed to reach this objective. This can be achieved by adapting the channel architecture and sorting cells using DEP, fluorescence or magnetic-based methods[211–214] but here we only describe examples where material surface modifications were used.

Optical tweezers were used to separate single yeast cells, which were further immobilized in a thermosensible hydrogel using a transparent microheater placed under the channels. The major interest of this approach is that single cells can be further collected and analyzed by switching off the microheater.[215]

The affinity of different cell types (endothelial cells, fibroblasts, smooth muscle cells) for different adhesion peptides was used to develop an adhesion-based negative selection method.[201,202,211] REDV (Arg-Glu-Asp-Val), VAPG (Val-Ala-Pro-Gly), and RGDS peptides were coated inside spiral-shaped microfluidic channels designed for a three-stage separation process. This process was based on the connection in series of three spiral-shaped channels of different widths. The width of channels for each stage was calculated on the basis of the optimal shear stress for separating the different cell types. Further, a heterogeneous suspension of endothelial cells, fibroblasts, and smooth muscle cells spiked with a small number of adipose-derived stem cells (ADSCs) were injected into the device and the number of each cell type in the suspension emerging from each stage was measured. Finally, by this method it was possible to recover a small number of ADSCs from the heterogeneous cell suspension. The functionalization of PDMS surfaces with aptamers was used in microfluidics to develop devices for enrichment, sorting, and detection of cancer cells.[216,217] The possibility of using an antibody-coated microfluidic chamber to negatively deplete undesired cell types, thereby obtaining an enriched cell subpopulation at the outlet, was demonstrated.[218] Association of antibodies for immunospecific cell capture as well as fibronectin for cell adhesion and growth was used for selective breast cancer cell capture and culture on self-assembled magnetic bead patterns in a microfluidic chip.[219] The immobilization of antibodies on columns was used for the separation of CD34+ and CD34– cells. The parameters such as graft copolymerization, column tilt angle, and medium flow rate were modified to control cell separation. Using this cell sorting system, it was found that populations containing a high density of CD34 could be eluted in the delayed fractions.[220]

Picoliter droplets produced by a gentle acoustic field in agarose hydrogels were used to encapsulate single to a few cells of different phenotypes at rates of 1–10 000 droplets per second.[221] This technique may be applied to extract data from single cells or to generate large cell population from single cells by direct tissue printing.

Finally, an elegant approach of label-free microfluidic method has been developed for the separation and enrichment of human breast cancer cells. The principle of this method is based on the difference in adhesion between normal epithelial and cancer cells on nanostructured polymer surfaces presenting pillars or lines. These surfaces were constructed at the bottom of PDMS microfluidic channels. The detachment of

cells on these nanostructured surfaces with increasing flow rates after some hours of culture was different between normal and cancer cells, the latter showing the lowest adhesion.[222] The differential response of normal and cancer cells to 3D microstructures was recently confirmed by us[40,41] and others.[223] In another approach, multiple arrays of crescent-shaped isolation wells were created in a microchannel to isolate cancer cells from peripheral blood (Figure 6). The gaps of 5 μm in each of the traps ensured the exit of blood constituents because of the highly deformable nature of erythrocytes and because large white blood cells are of comparable dimensions to but more deformable than cancer cells. Clogging prevention was ensured by a pitch of 500 μm between each trap. This microsystem showed a potential of isolation from 40 to 80% of cancer cells depending to the pressure differentials used.[224]

Many microfluidic systems have been developed for sorting bacteria before detecting or identifying them using fluorescent *in situ* hybridization (FISH) or PCR, for example. Given the possibility of cultivating bacteria in suspension in contrast to mammalian cells, these systems are mainly based on liquid-phase separation. Typically, bacteria are individually confined in aqueous microdroplets before sorting.[193,194,225] Separation microfluidic systems exploiting surface properties are rare. As previously mentioned (see Section 3.314.4.2), isolation of persistent microbial cells in a subpopulation has been also realized after physical docking. Using confinement in microscale grooves, the authors isolated individual bacterial cells. Replacement of the initial culture medium by a medium supplemented with appropriate antibiotics killed nonpersistent cells while allowing persistent cells to grow.[210] Bacteria have been also isolated using micro-Petri dishes based on porous aluminum oxide membranes that allow nutrients to pass through, associated to sidewalls obtained by reactive ion etching of acrylic polymer[226] or UV polymerization of PEG.[208] In these microwells, single bacteria or small colonies can be micromanipulated for specific detection or identification using immunorecognition, for example, and for further selection.[226] An elegant approach, which nevertheless does not allow separation of bacterial cells but permits their identification, allowing further selection, was reported by Grow *et al*. This approach is based on surface-enhanced Raman scattering (SERS) microscopy for label-free detection of bacteria and their toxins. After biomolecule or/and cell capture by the usual selective ligand–receptor affinity, pathogens and toxins could be individually identified by their SERS fingerprints. Moreover, the SERS fingerprint reflects the physiological state of a bacterial cell. For example, changes in pathogen virulence or viability in response to specific growth conditions can be then identified by this method.[227]

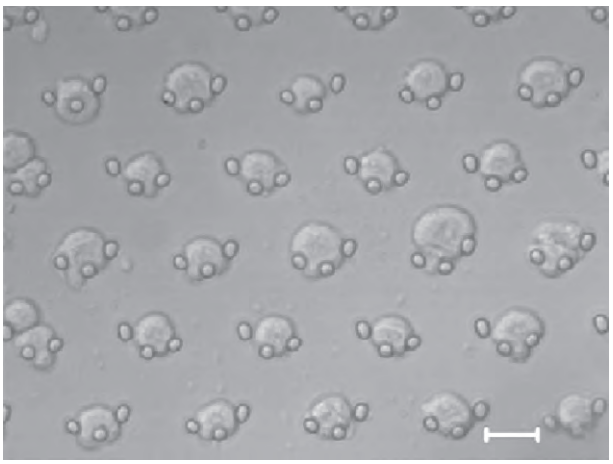

Figure 6 Cancer cell isolation and microsystem efficiency characterization. (a) Overview of the cell isolation region showing mostly single cells trapped in each crescent-shaped structure. (Scale bar represents 20 μm.) Reprinted with permission from Tan, S. J.; Yobas, L.; Lee, G. Y. H.; Ong, C. N.; Lim, C. T. *Biomed. Microdevices* **2009**, *11*, 883–892.

3.314.4.4. Cell Transfection

Besides the possibility of analyzing gene expression on single cells and even on single-cell processes such as filopod, there exists a need for gene transfection in single cells. Several methods have been developed to introduce nucleic acids into adherent cells, such as chemical-based transfection, particulate-based methods, electrotransfer, sonoporation, and electroporation. The possibility of transferring gene using microspiked electrodes has been demonstrated.[228] The combination of a novel microfluidic device and lipoplex-based transfection method allowed improving the transfection efficiency of primary rat cortical neurons.[229] However, most transfection studies on microfluidic or BioMEMS platforms were based on electroporation,[230] some of them exploiting ionic conductivity. Moreover, one difficulty is to adapt these transfection methods to microwell arrays. A nozzle array was micromachined in silicon or plastic to develop an electrosonic ejector microarray for gene delivery. The device comprises piezoelectric transducers for ultrasound wave generation, a reservoir for storing the sample mixture, and a set of acoustic horn structures that form the nozzle array. When the device is driven at a particular resonant frequency of the acoustic horn structures, the sample containing the mixture of cells and transfection agents is ejected from orifices located at the nozzle tips enabling gene transfection.[231] Jain *et al.* have recently described proof-of-principle experiments on 484-microwell arrays with electroporation-ready transparent substrate. They showed that it was possible to achieve highly efficient parallel introduction of exogenous molecules into human cell lines and mouse primary macrophages.[232]

3.314.4.5. Contact Guidance/Cell Migration

Nano and microstructured substrates have been developed to control and analyze the contact guidance and cell migration of diverse cell types. All adherent cell phenotypes are susceptible to orientate themselves and to migrate on anisotropically structured substrates. Notably, the contact guidance capacity has applications for directing axon outgrowth and migration of neurons and permitting nervous regeneration of injured tissues.[71,84–86] The study of this textural guidance has been carried out also using BioMEMS and microfluidic systems.[214,233] Mammalian neurons showed two different growth regimes as a function of textural features (Figure 7). On surfaces presenting posts of 100 μm diameter separated by 200 μm spacing,

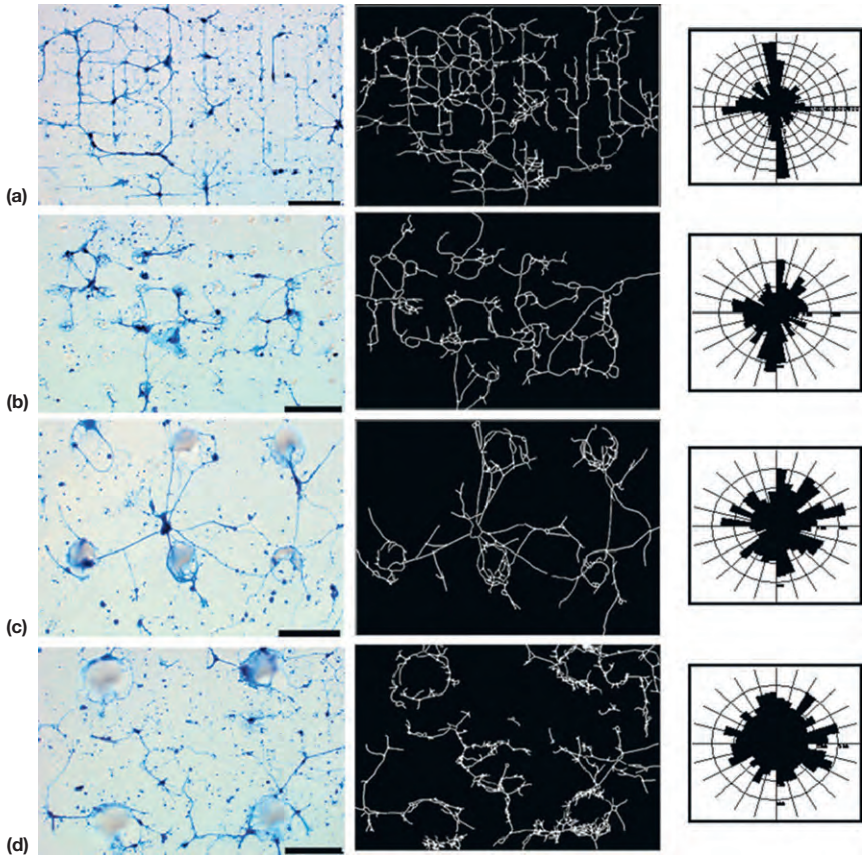

Figure 7 Optical micrographs, under the same magnification and light settings, of hippocampal neurons plated on glass substrates patterned with conical posts of PDMS (first column), the corresponding trace of neuronal networks on patterned substrates (Neurolucida) (middle column), and subsequent polar histograms (third column) representing branching angle characteristics of the neuronal network (Neurolucida Explorer) created from each trace. Polar histograms visually represent the amount of process length (scaled to total process length for each examined cell network) at a given branching angle range. (a) 10 mm diameter, 10 mm spacing; (b) 20 mm diameter, 40 mm spacing; (c) 50 mm diameter, 100 mm spacing; and (d) 100 mm diameter, 200 mm spacing. Scale bar is 90 mm. Reprinted with permission from Hanson, J. N.; Motala, M. J.; Heien, M. L.; Gillette, M.; Sweedler, J.; Nuzzo, R. G. *Lab Chip* **2009**, *9*, 122–131.

neuronal outgrowth showed a process of wrapping and looping around posts but with a low alignment of the process. On the contrary, the smaller the feature size (until $10 \times 10\,\mu m$), the more the process appeared to migrate directly to the posts as they follow the pattern.[233] This capacity was used to isolate axons and to allow their direct analysis after separation from the rest of cells by 1D or 2D electrophoresis, western blot, and RT-PCR.[214]

Cell migration is really important, notably in wound healing of soft tissues such as the skin. The influence of surface features on cell migration has been described in **Section 3.314.2**. A recent work has described the development of a microchannel-based device for the study of cell migration on defined surfaces.[234] PDMS microchannels were coated with ECM molecules before inoculating with human SaOs-2 osteosarcoma cells or mouse 3T3 fibroblasts. The significant advantage of this microfluidic-based technique was its ability to maintain a virgin surface prior to the commencement of the cell migration assay. Cells were first inoculated and cultured in a main chamber connected on each side to five migration channels. The medium did not enter the migration channels because surface tension prevented spontaneous flow down the channel opening. Thus after some hours of adhesion inside the main chamber, the migration channels were backfilled with the culture medium and photographs were taken at T_0 and after 18, 24, and 36 h to quantify cell migration. The analysis of cell migration showed that 3T3 and SaOs-2 cells migrated at different rates on various surfaces. The highest migration rate was $11\,\mu m\,h^{-1}$ for fibroblasts on untreated glass, collagen I, fetal bovine serum (FBS), and FBS blocked with bovine serum albumin (BSA), whereas the highest rate was $5.5\,\mu m\,h^{-1}$ for SaOs-2 cells on collagen I, collagen IV, collagen IV blocked with BSA, FBS, and FBS blocked by BSA.[234] A microfluidic PDMS imaging chamber was developed for the direct observation of chemotactic transmigration.[235] The chamber consisted of two channels separated by a vertical barrier with multiple bays of pores with widths varying from 6 to 16 μm and lengths varying from 25 to 50 μm. The cells were plated in the channel on one side of the barrier, while the chemoattractant was flowed through the channel on the other side of the barrier. The chemotactic transmigration of breast-cancer cells was studied in presence or absence of blebbistatin, which is an inhibitor of myosin II. Two different rates of cell migration through narrow pores were identified.

Either the cell body rapidly contracted to fit within the pore, or the cell continued to extend through the pores until the cell body was slowly pulled behind it. This microfluidic system is particularly interesting since it can improve dramatically the imaging potential relative to other *in vitro* transmigration systems such as Boyden chambers.[235] The same approach of barrier with pores was used to study the migration of cancer cells after coating the microgaps with matrigel.[236] 3D chemotaxis studies were developed using an agarose-based microfluidic platform. A gradient was preestablished in an agarose layer above the cell compartment before adding the 3D cell-containing matrix based on collagen and matrigel.[237]

Differences in cell migration velocity and flow direction under electrophoretic forces have been exploited for sorting cells. Although sorting is performed in suspension and is highly dependent on the buffer ionic strength, the chemical properties of the material surface is also of high importance for an efficient sorting since electro-osmotic flow is dependent on the surface charge of the material. In this study, polymethylmethacrylate (PMMA) and polycaprolactone (PC) were used. Their surfaces were chemically modified by the introduction of ionizable groups on the surface in order to reach appropriate electroosmotic flow. With this system, selective introduction of *E. coli* and red blood cells (RBCs) into the device's microchannel was achieved.[238]

Microfluidic devices provide an indispensable and elegant way for studying bacterial chemotaxis. In a basic research work, Takeuchi *et al*. were able to control the shape of filamentous *E. coli* (phenotype resulting from cephalexin antibiotic supplementation). Bacteria were cultivated in agarose or PDMS microchambers with diverse topographic shapes and organizations creating various shapes of confinement, and they adopted the shapes of the structures (zigzags, sinusoids, spirals) and retained them even after releasing.[239] Cheng *et al*. proposed a three-channel system created by patterning on a thin piece of agarose gel. One extreme channel was filled with buffer and the other one with attractant chemical (α-methyl-DL-aspartate), while bacterial cells were injected in the central channel. Diffusion of the attractant molecule through the hydrogel led to a concentration gradient in the central channel, which resulted in higher concentration of bacteria at the wall closer to the source channel of the attractant molecule.[172] The influence of the confined environment on the development and the migration of bacterial colonies has also been studied in a microfluidic chemostat displaying chambers of various shapes but identical depth of 1 μm, which was close to the diameter of the bacteria. Surprisingly, the orientation of cells was shown to be anisotropic at high densities, and was dictated by the chamber walls and the locations of chamber exits. This self-organization, which probably increases the access of nutrients into and the evacuation of waste out of the colonies, may be crucial for the early stage development of biofilms in small, confined growth niches.[240] Park *et al*. investigated also chemotaxis of bacterial colonies in confined environments. Using microstructured PDMS devices creating a maze, starved bacteria were shown to form colonies in the smallest confining structures. This organization was demonstrated to be the cell's response to a gradient of chemoattractant that bacteria excrete in an environment depleted in exogeneous nutrients. Bacteria actively moved and collapsed into the small cavity to form colonies, rather than waiting until the bulk density of bacteria reached the necessary threshold. Such behavior may be critical for bacterial survival during periods of stress.[158]

3.314.4.6. Cell Mechanobiology

Materials have been used to demonstrate the cell mechanics, the capacity of cells to apply mechanical strength to their environment, and the influence of the mechanical characteristics of their environment on the cells themselves.[241] Microsystems are an excellent means to deliver physical cues that affect cell mechanics, such as fluid flow, substrate topography, and stiffness, to create *in vitro* models for probing the mechanics or measuring the intrinsic mechanical properties of cells.[242] There are a wide variety of techniques available to quantify mechanical force on single cells *in vitro*.[241,243] BioMEMs have been also developed with this objective.[244] Among them, atomic force microscopy (AFM) allows characterization of the viscoelastic properties of different cell types.[245,246] A uniaxial microsystem was developed recently for imaging cell response in real time during quantitative force–displacement measurements. The viscoelastic response of fibroblasts measured using this device fitted well with the previously published values.[247] Cell deformability is an important biomarker that can be used to distinguish between healthy and cancer cells. A microfluidic channel design was used to study the biorheological behavior of benign breast epithelial cells and nonmetastatic tumor breast cells.[248] The time taken for the cell to squeeze into the microchannel as well as the speed of the cell flowing through the microchannel was measured, which demonstrated the difference in stiffness between benign and cancerous breast cells, the latter being more deformable.[248]

Culture of cells on flexible substrates was also used to demonstrate the capacity of cells to apply mechanical forces on their environment. The first demonstration of that was done by Harris *et al*.,[249] who observed that fibroblasts were able to wrinkle the silicone substrates upon which they were crawling. Alternatively, flexible posts were made in PDMS.[250–252] Platelets play an important role in hemostasis by forming a thrombotic plug that seals the vessels. A recent paper describes a means to measure the contractile force generated by platelets using a flexible post force-sensor array. By measuring the volume of the clot formed between posts from the images, the force applied per platelet was calculated to be 2.1 ± 0.1 nN after 60 min.[251] The forces of heart muscle cells suspended between elastic micropillars was evaluated to be 140 nN in the relaxed state and 400 nN in the contracted state (**Figure 8**).[250] The use of cytoskeleton inhibitors impedes the flexion of elastomeric microneedle-like posts by cells. By this approach, it was shown that cell morphology regulates the magnitude of the traction force generated by cells.[252] This approach was used recently to measure and manipulate forces from microtissues consisting of cells encapsulated within 3D micropatterned matrices and anchored to the tips of microcantilevers. Microcantilevers were used to simultaneously constrain the remodeling of the collagen gel and to report forces generated during this process. This system allowed highlighting the complex and dynamic relationship between cellular forces, ECM remodeling, and cellular phenotype, giving essential input for future engineering of 3D tissues.[253]

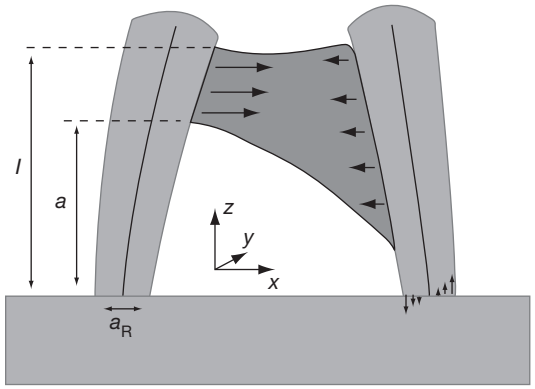

Figure 8 Basic features of the micropillar system developed by Kajzar *et al.*[250] Two micropillars (light shaded) connected by a cell (dark shaded). Cells apply transversal tensions (solid arrows) to both beams (neutral axes are depicted). The torque acting on each beam is balanced by normal tensions within the beam, depicted for the right beam. Further shown are the coordinate system and the geometrical parameters of the beams. Reprinted with permission from Kajzar, A.; Cesa, C. M.; Kirchgessner, N.; Hoffmann, B.; Merkel, R. *Biophys. J.* **2008**, *94*, 1854–1866.

The influence of substrate rigidity on cell migration and differentiation was previously described in Section 3.314.2. However, several microsystems have been developed recently for studying the influence of mechanical stimuli to cells. Individually programmable cell-stretching microwell arrays have been developed. They display flexible bottom chambers made of PDMS that can be deformed by pins moving upwards to apply strain to the cells and actuated by a refreshable Braille display.[254] Similarly, Moraes *et al.* developed a novel microarray capable of simultaneously applying cyclic equibiaxial strains ranging from 2 to 15% to small populations of adherent cells. The array consisted of 9×12 loading posts suspended over an actuation cavity within a 6.5 cm^2 area. Positive pressure applied to this cavity distended the loading post upwards, deforming a flexible cell culture substrate.[255,256] This approach was adapted for 3D cultures. As a first demonstration of this technology, nuclear and cellular deformation in response to applied compression was assessed in C3H10T1/2 mouse mesenchymal stem cells encapsulated within PEG hydrogels.[255,256] For more information on these aspects, the reader is referred to recent reviews.[79–81,241]

Compared to mammalian cells, the behavior of bacteria under mechanical stress has been rarely studied, and the main studies have been conducted using AFM. To our knowledge, BioMEMs and microfluidic devices have not been applied to this topic. However, microsystems display several advantages to address this question since hydrodynamic flow and physical confinement can be simply used to provide the necessary mechanical stress to be applied. The study published by Takeuchi *et al.*[239] on individual filamentous cells that adopted the shape corresponding to the organization and shape of the microstructures present in the microfluidic chamber can be considered as a preliminary study on this topic. Moreover, some microsystems already exist that could be used for such applications, such as the microtubes developed by Huang *et al.*[154,170]

3.314.4.7. Use of Cell Properties

Synthesis of the smallest machines capable of producing work is a challenge of today's interdisciplinary research. Biomimetic artificial machines built with hybrid components combining synthetic and biological materials offer the opportunity to develop pumps, microactuators, or microrobots using cardiomyocytes,[87,88,257–260] vascular smooth muscle cells,[258–260] or insect dorsal vessel tissue, the latter presenting the advantage to work at room temperature.[261] A pioneering work in this field was published in 2005. One hybrid machine powered by a muscle bundle was fabricated through an elegant assembly procedure. The originality of this work was that the muscle bundles were formed directly on the silicon cantilevers starting from single muscle cells. A photolithography approach was used to produce a free-standing silicon microcantilever coupled to a solid support at one end and a post a few micrometers away from the end of the cantilever, which were further filled with PNIPAAm polymer and bridged with a thin gold strip. Since the muscle cells were not able to adhere to the polymer, they aligned along the gold strip and formed mature muscle bundles. By lowering the temperature below 32 °C, the PNIPAAm polymer dissolved and released the microcantilever coupled to the post by the gold bridge covered with muscle bundle. This approach allowed the realization of the first microsystem that moves as a consequence of collective contraction of muscle bundles.[262]

Another microactuator was developed based on a cardiomyocyte-polymer hybrid.[87,88] An Au/Cr–PDMS composite membrane in the shape of a dome shape was fabricated on a bulk-etched cavity of a silicon wafer. After coating the gold surface by SAMs, it was covered with fibronectin and gelatin for permitting rat cardiomyocyte adhesion. The beating of cells started at 2 days after seeding and continued over 5–6 days. During this time, the beating of cells actuated the membrane in a vertical movement of about 8 µm, forming a net flow rate in the chamber of approximately 0.226 nl min^{-1}.[87,88] By culturing cardiomyocytes around a hollow PDMS sphere connected to Teflon capillaries, it was possible to generate a flow by each chamber contraction (Figure 9).[258–260] A microrobot was developed by designing a backbone in PDMS consisting of three strips of 'legs' connected across a 'body.' The backbone surface was grooved and coated with fibronectin in order to favor the adhesion of cardiomyocytes. This approach enabled the microrobot to 'walk' continuously for over 10 days.[257]

Several bacterial properties have been proposed to be used in BioMEMs or microsystems. Bacteria are able to produce diverse biominerals and magnetic particles, as well as a large range of bioactive molecules including therapeutic agents, surfactants, and lubricants. These components can be synthesized and used directly in a microsystem (example of biosurfactants and biolubricants) or used as template (example of extracellular polysaccharides) or scaffolds (example of functionalized flagella).[263] Microorganisms can be also used as motors, as precisely described by Spetzler *et al.*[264] in their review. In order to avoid eventual microorganism contaminations, 'ghost' mycoplasma cells obtained by membrane permeabilization were even used by Uenoyama *et al.* They demonstrated that mycoplasma cells were still capable of gliding movement

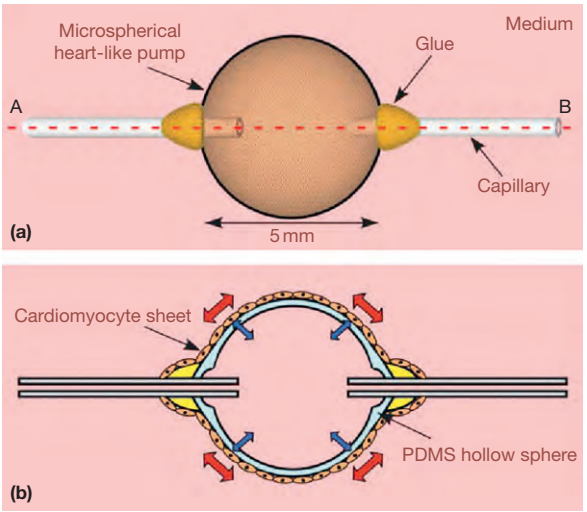

Figure 9 Design of a microspherical heart-like pump. (a) Schematic view. (b) Cross-sectional view along line A–B. A cultured cardiomyocyte sheet of contiguous pulsating cells is rolled onto a hollow sphere of poly(dimethylsiloxane) (PDMS) elastomer and allowed to adhere. The sphere is strained by the collective contractile motions of the attached cardiomyocyte sheet, and the fluid volume inside the hollow sphere chamber is reduced, producing flow into the attached Teflon2 capillary. To detect the flow generated by each chamber contraction, motion of PS microspheres is followed in the capillaries using *in situ* microscopy. The chamber diameter is of the order of millimeters. Reprinted with permission from Tanaka, Y.; Sato, K.; Shimizu, T.; Yamato, M.; Okano, T.; Kitamori, T. *Lab Chip* **2007**, *7*, 207–212.

and proposed therefore the replacement of living cells in microbial motors.[265] More frequently, bacteria have been used as a sensitive detection tool for toxicants and other pollutants. Several biosensors have been developed for water toxicity analysis, based on the use of particular bacterial strains engineered for being able to generate signals in the presence of specific pollutants.[266–268] Typically, a cascade of biological reactions is induced in the genetically engineered bacteria by the presence of toxicants, producing a directly detectable green fluorescent protein[265] or an enzyme able to convert a substrate to an electroactive species which can be further detected by an appropriate system.[266,267]

3.314.5. Conclusions

In recent years, biological and biomedical applications of micro and nanotechnology have become increasingly prevalent because it is now easy to develop devices with feature scales relevant to cells and bacteria and offering ease of *en masse* fabrication, small device size, and facile incorporation of integrated circuit technology. Moreover, the use of microfluidic perfusion in these microsystems allows controlled delivery and removal of soluble molecules in the extracellular environment and the use of small culture volumes. Finally, microsystems present several advantages since cell harvesting, media exchange, and cell subculturing procedures are easier to handle than in conventional *in vitro* cell culture systems. Here, we have highlighted how microsystems allow developing new culture devices and present a very high potential for cocultures or 3D cultures that are both difficult to achieve with classical culture methods. We have shown that working on materials and surface modifications of these materials is one of the major ways besides microfluidics to improve the growth capacity of cells inside microsystems. Moreover, BioMEMS or microsystems are the ideal tools for separating, docking, and analyzing isolated cells from a heterogeneous population. Aside from physical approaches, material modifications such as surface functionalization or microstructuration are promising routes for improving cell sorting and cell docking. Nano- and microstructuration of cell substrates are also a means to control and measure cell migration and contact guidance. Similarly, materials with different stiffnesses are particularly convenient for measuring cell mechanics, the capacity of cells to apply mechanical strength to their environment, or the influence of the mechanical characteristics of their environment on the cells themselves. By combining synthetic materials with biological ones, such as muscle cells, it is now possible to develop artificial machines with autonomous activity, such as microactuators or microrobots. The potential of BioMEMs and microsystems for controlling and measuring bacterial functions is also very important. Actually, the research in this field is highly dynamic and perhaps more developed than on mammalian cells, but the control of bacterial cells by using the material properties is less developed probably because bacteria are less adherent than mammalian cells. Finally, the materials currently used for microsystems are relatively restricted in term of diversity, and the field should profit from the research already developed in materials science. This has already started with the use of hydrogels or functionalization of silicon and glass substrates and the field should benefit more and more from the discoveries of new materials and new functionalization methods. This should further increase significantly the potential of materials in the field of BioMEMs and microsystems for applications in biology and medicine in the near future.

References

1. Anselme, K. *Biomaterials* **2000**, *21*, 667–681.
2. Anselme, K.; Davidson, P.; Popa, A. M.; Giazzon, M.; Liley, M.; Ploux, L. *Acta Biomater.* **2010**, *6*, 3824–3846.
3. Anselme, K.; Linez, P.; Bigerelle, M.; *et al. Biomaterials* **2000**, *21*, 1567–1577.
4. Anselme, K.; Ploux, L.; Ponche, A. *J. Adhes. Sci. Technol.* **2010**, *24*, 831–852.
5. Anselme, K.; Ponche, A.; Bigerelle, M. *Proc. IMechE, H: J. Eng. Med.* **2010**, *224*(12), 1487–1507.
6. Ploux, L.; Beckendorff, S.; Nardin, M.; Neunlist, S. *Colloids Surf. B Biointerfaces* **2007**, *57*, 174–181.
7. Ploux, L.; Ponche, A.; Anselme, K. *J. Adhes. Sci. Technol.* **2010**, *24*, 2165–2201.
8. Bashir, R. *Adv. Drug Deliv. Rev.* **2004**, *56*, 1565–1586.
9. Ainslie, K. M.; Desai, T. A. *Lab Chip* **2008**, *8*, 1864–1878.
10. Kim, L.; Toh, Y. C.; Voldman, J.; Yu, H. *Lab Chip* **2007**, *7*, 681–694.
11. Hanein, Y.; Pan, Y. V.; Ratner, B. D.; Denton, D. D.; Bohringer, K. F. *Sens. Actuators B Chem.* **2001**, *81*, 49–54.
12. Ziaie, B.; Baldi, A.; Lei, M.; Gu, Y. D.; Siegel, R. A. *Adv. Drug Deliv. Rev.* **2004**, *56*, 145–172.
13. Bouaidat, S.; Berendsen, C.; Thomsen, P.; Petersen, S. G.; Wolff, A.; Jonsmann, J. *Lab Chip* **2004**, *4*, 632–637.
14. Hiratsuka, A.; Muguruma, H.; Lee, K. H.; Karube, I. *Biosens. Bioelectron.* **2004**, *19*, 1667–1672.
15. Kojima, K.; Hiratsuka, A.; Suzuki, H.; Yano, K.; Ikebukuro, K.; Karube, I. *Anal. Chem.* **2003**, *75*, 1116–1122.
16. Miyachi, H.; Hiratsuka, A.; Ikebukuro, K.; Yano, K.; Muguruma, H.; Karube, I. *Biotechnol. Bioeng.* **2000**, *69*, 323–329.

17. Dhayal, M.; Choi, J. S.; So, C. H. *Vacuum* **2006**, *80*, 876–879.
18. Chau, L.; Doran, M.; Cooper-White, J. *Lab Chip* **2009**, *9*, 1897–1902.
19. Kim, C.; Lee, K. S.; Kim, Y. E.; *et al*. *Lab Chip* **2009**, *9*, 1294–1297.
20. Tourovskaia, A.; Figueroa-Masot, X.; Folch, A. *Lab Chip* **2005**, *5*, 14–19.
21. Weston, D. F.; Smekal, T.; Rhine, D. B.; Blackwell, J. *J. Vac. Sci. Technol. B* **2001**, *19*, 2846–2851.
22. Kotzar, G.; Freas, M.; Abel, P.; *et al*. *Biomaterials* **2002**, *23*, 2737–2750.
23. Rowe, L.; Almasri, M.; Lee, K.; *et al*. *Lab Chip* **2007**, *7*, 475–482.
24. Cheng, J.; Jandik, P.; Avdalovic, N. *Anal. Chem.* **2003**, *75*, 572–579.
25. Lin, Y. C.; Jen, C. M.; Huang, M. Y.; Wu, C. Y.; Lin, X. Z. *Sens. Actuators B Chem.* **2001**, *79*, 137–143.
26. Lan, S.; Veiseh, M.; Zhang, M. Q. *Biosens. Bioelectron.* **2005**, *20*, 1697–1708.
27. Li, N.; Ho, C. M. *JALA* **2008**, *13*, 237–242.
28. Veiseh, M.; Zareie, M. H.; Zhang, M. Q. *Langmuir* **2002**, *18*, 6671–6678.
29. Cattani-Scholz, A.; Pedone, D.; Blobner, F.; *et al*. *Biomacromolecules* **2009**, *10*, 489–496.
30. Fink, J.; Thery, M.; Azioune, A.; *et al*. *Lab Chip* **2007**, *7*, 672–680.
31. Boyan, B. D.; Hummert, T. W.; Dean, D. D.; Schwartz, Z. *Biomaterials* **1996**, *17*, 137–146.
32. Boyan, B. D.; Lohmann, C. H.; Dean, D. D.; Cochran, D. L.; Schwartz, Z. *Annu. Rev. Mater. Res.* **2001**, *31*, 357–371.
33. Brunette, D. M.; Chehroudi, B. *J. Biomech. Eng.* **1999**, *121*, 49–57.
34. Meyer, U.; Büchter, A.; Wiesmann, H. P.; Joos, U.; Jones, D. B. *Eur. Cells Mater.* **2005**, *9*, 39–49.
35. Ponche, A.; Bigerelle, M.; Anselme, K. *Proc. IMechE, H: J. Eng. Med.* **2010**, *224*(12), 1471–1486.
36. Anselme, K.; Bigerelle, M. *Surf. Coat. Technol.* **2006**, *200*, 6325–6330.
37. Anselme, K.; Bigerelle, M. *Biomaterials* **2006**, *27*, 1187–1199.
38. Anselme, K.; Bigerelle, M. *J. Mater. Sci. Mater. Med.* **2006**, *17*, 471–479.
39. Bigerelle, M.; Anselme, K.; Noël, B.; Ruderman, I.; Hardouin, P.; Iost, A. *Biomaterials* **2002**, *23*, 1563–1577.
40. Davidson, P.; Fromigue, O.; Marie, P.; Hasirci, V.; Reiter, G.; Anselme, K. *J. Mater. Sci. Mater. Med.* **2010**, *31*, 939–946.
41. Davidson, P.; Özçelik, H.; Hasirci, V.; Reiter, G.; Anselme, K. *Adv. Mater.* **2009**, *21*, 3586–3590.
42. Guck, J.; Schinkinger, S.; Lincoln, B.; *et al*. *Biophys. J.* **2005**, *88*, 3689–3698.
43. Ochalek, T.; Nordt, F. J.; Tullberg, K.; Burger, M. M. *Cancer Res.* **1988**, *48*, 5124–5128.
44. Dalby, M. J.; Gadegaard, N.; Tare, R. S.; *et al*. *Nat. Mater.* **2007**, *6*, 997–1003.
45. Dalby, M. J.; Giannaras, D.; Riehle, M. O.; Gadegaard, N.; Affrossman, S.; Curtis, A. S. *Biomaterials* **2004**, *25*, 77–83.
46. Dalby, M. J.; Riehle, M. O.; Johnstone, H.; Affrossman, S.; Curtis, A. S. *Biomaterials* **2002**, *23*, 2945–2954.
47. Dalby, M. J.; Riehle, M. O.; Johnstone, H.; Affrossman, S.; Curtis, A. S. *Cell Biol. Int.* **2004**, *28*, 229–236.
48. Brammer, K. S.; Oh, S.; Cobb, C. J.; Bjursten, L. M.; van der Heyde, H.; Jin, S. *Acta Biomater.* **2009**, *5*, 3215–3223.
49. Oh, S.; Brammer, K. S.; Li, Y. S. J.; *et al*. *Proc. Natl. Acad. Sci. USA* **2009**, *106*, 2130–2135.
50. Choi, C. H.; Hagvall, S. H.; Wu, B. M.; Dunn, J. C. Y.; Beygui, R. E.; Kim, C. J. *Biomaterials* **2007**, *28*, 1672–1679.
51. Arnold, M.; Cavalcanti-Adam, E. A.; Glass, R.; *et al*. *Chemphyschem* **2004**, *5*, 383–388.
52. Zinger, O.; Anselme, K.; Denzer, A.; *et al*. *Biomaterials* **2004**, *25*, 2695–2711.
53. Zreiqat, H.; Valenzuela, S. M.; Nissan, B. B.; *et al*. *Biomaterials* **2005**, *26*, 7579–7586.
54. Lee, J. H.; Khang, G.; Lee, J. W.; Lee, H. B. *J. Biomed. Mater. Res.* **1998**, *40*, 180–186.
55. Lee, J. H.; Lee, S. J.; Khang, G.; Lee, H. B. *J. Colloid Interface Sci.* **2000**, *230*, 84–90.
56. Lim, J. Y.; Liu, X.; Vogler, E. A.; Donahue, H. J. *J. Biomed. Mater. Res. A* **2004**, *68*, 504–512.
57. Kennedy, S. B.; Washburn, N. R.; Simon, C. G.; Amis, E. J. *Biomaterials* **2006**, *27*, 3817–3824.
58. Zelzer, M.; Majani, R.; Bradley, J. W.; Rose, F. R.; Davies, M. C.; Alexander, M. R. *Biomaterials* **2008**, *29*, 172–184.
59. Bigerelle, M.; Anselme, K. *J. Biomed. Mater. Res. A* **2005**, *72*, 36–46.
60. Kunzler, T. P.; Drobek, T.; Sprecher, C. M.; Schuler, M.; Spencer, N. D. *Appl. Surf. Sci.* **2006**, *253*, 2148–2153.
61. Schuler, M.; Kunzler, T. P.; de Wild, M.; *et al*. *J. Biomed. Mater. Res. A* **2009**, *88*, 12–22.
62. D'Souza, S. E.; Ginsberg, M. H.; Plow, E. F. *Trends Biochem. Sci.* **1991**, *16*, 246–250.
63. Durrieu, M. C. *ITBM RBM* **2005**, *26*, 229–237.
64. Petrie, T. A.; Raynor, J. E.; Reyes, C. D.; Burns, K. L.; Collard, D. M.; Garcia, A. J. *Biomaterials* **2008**, *29*, 2849–2857.
65. Ingber, D. E. *Annu. Rev. Physiol.* **1997**, *59*, 575–599.
66. Ingber, D. E. *FASEB J.* **2006**, *20*, 811–827.
67. Alenghat, F. J.; Ingber, D. E. *Sci. STKE* **2002**, *2002*, E6.
68. Weiss, P. *J. Exp. Zool.* **1934**, *68*, 393–448.
69. Weiss, P. *J. Exp. Zool.* **1945**, *100*, 353–386.
70. Dunn, G. A.; Heath, J. P. *Exp. Cell Res.* **1976**, *101*, 1–14.
71. Rajnicek, A. M.; Britland, S.; McCaig, C. D. *J. Cell Sci.* **1997**, *110*, 2905–2913.
72. Sorensen, A.; Alekseeva, T.; Katechia, K.; Robertson, M.; Riehle, M. O.; Barnett, S. C. *Biomaterials* **2007**, *28*, 5498–5508.
73. Teixeira, A. I.; Abrams, G. A.; Bertics, P. J.; Murphy, C. J.; Nealey, P. F. *J. Cell Sci.* **2003**, *116*, 1881–1892.
74. Walboomers, X. F.; Croes, H. J. E.; Ginsel, L. A.; Jansen, J. A. *J. Biomed. Mater. Res.* **1999**, *47*, 204–212.
75. Walboomers, X. F.; Ginsel, L. A.; Jansen, J. A. *J. Biomed. Mater. Res.* **2000**, *51*, 529–534.
76. Fujita, S.; Ohshima, M.; Iwata, H. *J. R. Soc. Interface* **2009**, *6*, S269–S277.
77. Den Braber, E. T.; Jansen, H. V.; de Boer, M. J.; *et al*. *J. Biomed. Mater. Res.* **1998**, *40*, 425–433.
78. Lipski, A. M.; Pino, C. J.; Haselton, F. R.; Chen, I. W.; Shastri, V. P. *Biomaterials* **2008**, *29*, 3836–3846.
79. Kim, D. H.; Han, K.; Gupta, K.; Kwon, K. W.; Suh, K. Y.; Levchenko, A. *Biomaterials* **2009**, *30*, 5433–5444.
80. Kim, D. H.; Seo, C. H.; Han, K.; Kwon, K. W.; Levchenko, A.; Suh, K. Y. *Adv. Funct. Mater.* **2009**, *19*, 1579–1586.
81. Kim, D. H.; Wong, P. K.; Park, J.; Levchenko, A.; Sun, Y. *Annu. Rev. Biomed. Eng.* **2009**, *11*, 203–233.
82. Motlagh, D.; Hartman, T. J.; Desai, T. A.; Russell, B. *J. Biomed. Mater. Res. A* **2003**, *67A*, 148–157.
83. Williamson, M. R.; Adams, E. F.; Coombes, A. G. A. *Biomaterials* **2006**, *27*, 1019–1026.
84. Johansson, F.; Carlberg, P.; Danielsen, N.; Montelius, L.; Kanje, M. *Biomaterials* **2006**, *27*, 1251–1258.
85. Wang, X.; Ohlin, C. A.; Lu, Q.; Hu, J. *Biomaterials* **2008**, *29*, 2049–2059.
86. Zhu, B.; Zhang, Q.; Lu, Q.; *et al*. *Biomaterials* **2004**, *25*, 4215–4223.
87. Park, J. Y.; Kim, I. C.; Baek, J. G.; *et al*. *Lab Chip* **2007**, *7*, 1367–1370.
88. Park, J. Y.; Lee, D. H.; Lee, E. J.; Lee, S. H. *Lab Chip* **2009**, *9*, 2043–2049.
89. Dupont-Gillain, C. C.; Alaerts, J. A.; Dewez, J. L.; Rouxhet, P. G. *Biomed. Mater. Eng.* **2004**, *14*, 281–291.
90. Lhoest, J. B.; Detrait, E.; Dewez, J. L.; deAguilar, P. V.; Bertrand, P. *J. Biomater. Sci. Polym. Ed.* **1996**, *7*, 1039–1054.
91. Britland, S.; Morgan, H.; WojiakStodart, B.; Riehle, M.; Curtis, A.; Wilkinson, C. *Exp. Cell Res.* **1996**, *228*, 313–325.
92. Lo, C. M.; Wang, H. B.; Dembo, M.; Wang, Y. L. *Biophys. J.* **2000**, *79*, 144–152.
93. Pelham, R. J.; Wang, Y. L. *Proc. Natl. Acad. Sci. USA* **1997**, *94*, 13661–13665.
94. Kieswetter, K.; Schwartz, Z.; Hummert, T. W.; *et al*. *J. Biomed. Mater. Res.* **1996**, *32*, 55–63.
95. Links, J.; Boyan, B. D.; Blanchard, C. R.; *et al*. *Biomaterials* **1998**, *19*, 2219–2232.
96. Martin, J. Y.; Schwartz, Z.; Hummert, T. W.; *et al*. *J. Biomed. Mater. Res.* **1995**, *29*, 389–401.
97. Lohmann, C. H.; Tandy, E. M.; Sylvia, V. L.; *et al*. *J. Biomed. Mater. Res.* **2002**, *62*, 204–213.
98. Wang, L.; Zhao, G.; Olivares-Navarrete, R.; *et al*. *Biomaterials* **2006**, *27*, 3716–3725.
99. Park, J.; Bauer, S.; Schlegel, K. A.; Neukam, F. W.; von der Mark, K.; Schmuki, P. *Small* **2009**, *5*, 666–671.
100. Park, J.; Bauer, S.; von der Mark, K.; Schmuki, P. *Nano Lett.* **2007**, *7*, 1686–1691.
101. Park, J.; Cho, C. H.; Parashurama, N.; *et al*. *Lab Chip* **2007**, *7*, 1018–1028.
102. Engler, A. J.; Sen, S.; Sweeney, H. L.; Discher, D. E. *Cell* **2006**, *126*, 677–689.
103. Keselowsky, B. G.; Collard, D. M.; Garcia, A. J. *Proc. Natl. Acad. Sci. USA* **2005**, *102*, 5953–5957.
104. Barbosa, J. N.; Madureira, P.; Barbosa, M. A.; Aguas, A. P. *J. Biomed. Mater. Res. A* **2006**, *76*, 737–743.
105. Braceras, I.; De Maeztu, M. A.; Alava, J. I.; Gay-Escoda, C. *Int. J. Oral Maxillofac. Surg.* **2009**, *38*, 274–278.
106. Ferguson, S. J.; Broggini, N.; Wieland, M.; *et al*. *J. Biomed. Mater. Res. A* **2006**, *78*, 291–297.

107. Kim, H.; Choi, S. H.; Ryu, J. J.; Koh, S. Y.; Park, J. H.; Lee, I. S. *Biomed. Mater. Eng.* **2008**, *3*, 1–6.
108. Bornstein, M. M.; Schmid, B.; Belser, U. C.; Lussi, A.; Buser, D. *Clin. Oral Implants Res.* **2005**, *16*, 631–638.
109. Buser, D.; Broggini, N.; Wieland, M.; *et al. J. Dent. Res.* **2004**, *83*, 529–533.
110. Cochran, D. L.; Buser, D.; ten Bruggenkate, C. M.; *et al. Clin. Oral Implants Res.* **2002**, *13*, 144–153.
111. Zhao, G.; Raines, A. L.; Wieland, M.; Schwartz, Z.; Boyan, B. D. *Biomaterials* **2007**, *28*, 2821–2829.
112. Zhao, G.; Schwartz, Z.; Wieland, M.; *et al. J. Biomed. Mater. Res. A* **2005**, *74*, 49–58.
113. Schatzle, M.; Mannchen, R.; Balbach, U.; Hammerle, C. H.; Toutenburg, H.; Jung, R. E. *Clin. Oral Implants Res.* **2009**, *20*, 489–495.
114. Costerton, J. W.; Stewart, P. S.; Greenberg, E. P. *Science* **1999**, *284*, 1318–1322.
115. Proft, T.; Baker, E. N. *Cell. Mol. Life Sci.* **2009**, *66*, 613–635.
116. Srivastava, S.; Srivastava, P. S. *Understanding Bacteria*. Kluwer: Dordrecht, 2003.
117. Edwards, K. J.; Rutenberg, A. D. *Chem. Geol.* **2001**, *180*, 19–32.
118. Flint, S. H.; Brooks, J. D.; Bremer, P. J. *J. Food Eng.* **2000**, *43*, 235–242.
119. Whitehead, K. A.; Verran, J. *Food Bioprod. Process.* **2006**, *84*, 253–259.
120. Coullerez, G.; Seeberger, P. H.; Textor, M. *Macromol. Biosci.* **2006**, *6*, 634–647.
121. Bos, R.; Van der Mei, H. C.; Gold, J.; Busscher, H. J. *FEMS Microbiol. Lett.* **2000**, *189*, 311–315.
122. Otto, J.; Norbeck, J.; Larsson, T.; Karlsson, K. A.; Hermansson, M. *J. Bacteriol.* **2001**, *183*, 2445–2453.
123. Prigent-Combaret, C.; Vidal, O.; Dorel, C.; Lejeune, P. *J. Bacteriol.* **1999**, *181*, 5993–6002.
124. Bakker, D. P.; Busscher, H. J.; van Zanten, J.; de Vries, J.; Klijnstra, J. W.; Van der Mei, H. C. *Microbiology* **2004**, *150*, 1779–1784.
125. Houry, A.; Briandet, R.; Aymerich, S.; Gohar, M. *Microbiology* **2010**, *156*, 1009–1018.
126. Medilanski, E.; Kaufmann, K.; Wick, L. Y.; Wanner, O.; Harms, H. *Biofouling* **2002**, *18*, 193–203.
127. Scheuerman, T. R.; Camper, A. K.; Hamilton, M. A. *J. Colloid Interface Sci.* **1998**, *208*, 23–33.
128. Harshey, R. M. *Annu. Rev. Microbiol.* **2003**, *57*, 249–273.
129. Merz, A. J.; So, M.; Sheetz, M. P. *Nature* **2000**, *407*, 98–102.
130. Campoccia, D.; Montanaro, L.; Agheli, H.; *et al. Int. J. Artif. Organs* **2006**, *29*, 622–629.
131. Mitik-Dineva, N.; Wang, J.; Truong, V. K.; *et al. Biofouling* **2009**, *25*, 621–631.
132. Puckett, S. D.; Taylor, E.; Raimondo, T.; Webster, T. J. *Biomaterials* **2010**, *31*, 706–713.
133. Whitehead, K. A.; Colligon, J.; Verran, J. *Colloids Surf. B* **2005**, *41*, 129–138.
134. Barth, K. A.; Coullerez, G.; Nilsson, L. M.; *et al. Adv. Funct. Mater.* **2008**, *18*, 1459–1469.
135. Burton, E. A.; Sirnon, K. A.; Hou, S. Y.; Ren, D. C.; Luk, Y. Y. *Langmuir* **2009**, *25*, 1547–1553.
136. Wiencek, K. M.; Fletcher, M. *J. Bacteriol.* **1995**, *177*, 1959–1966.
137. Patel, J. D.; Ebert, M.; Ward, R.; Anderson, J. M. *J. Biomed. Mater. Res. A* **2007**, *80A*, 742–751.
138. Gottenbos, B.; Van der Mei, H. C.; Busscher, H. J. *J. Biomed. Mater. Res.* **2000**, *50*, 208–214.
139. Bhatia, S. N.; Yarmush, M. L.; Toner, M. *J. Biomed. Mater. Res.* **1997**, *34*, 189–199.
140. Fuchs, S.; Hofmann, A.; Kirkpatrick, C. J. *Tissue Eng.* **2007**, *13*, 2577–2588.
141. Villars, F.; Guillotin, B.; Amedee, T.; *et al. Am. J. Physiol. Cell Physiol.* **2002**, *282*, C775–C785.
142. Martin, I.; Wendt, D.; Heberer, M. *Trends Biotechnol.* **2004**, *22*, 80–86.
143. Curtis, A. S. G.; Wilkinson, C. *Biomaterials* **1997**, *18*, 1573–1583.
144. Nagase, K.; Kobayashi, J.; Okano, T. *J. R. Soc. Interface* **2009**, *6*, S293–S309.
145. Tsuda, Y.; Kikuchi, A.; Yamato, M.; Sakurai, Y.; Umezu, M.; Okano, T. *J. Biomed. Mater. Res.* **2004**, *69A*, 70–78.
146. Yamato, M.; Konno, C.; Kushida, A.; *et al. Biomaterials* **2000**, *21*, 981–986.
147. Ernst, O.; Lieske, A.; Jager, M.; Lankenau, A.; Duschl, C. *Lab Chip* **2007**, *7*, 1322–1329.
148. Sim, W. Y.; Park, S. W.; Park, S. H.; Min, B. H.; Park, S. R.; Yang, S. S. *Lab Chip* **2007**, *7*, 1775–1782.
149. Chueh, B. H.; Zheng, Y.; Torisawa, Y. S.; *et al. Biomed. Microdevices* **2010**, *12*, 145–151.
150. Goubko, C. A.; Majumdar, S.; Basak, A.; Cao, X. D. *Biomed. Microdevices* **2010**, *12*, 555–568.
151. Steinhaus, B.; Garcia, M. L.; Shen, A. Q.; Angenent, L. T. *Appl. Environ. Microbiol.* **2007**, *73*, 1653–1658.
152. Kaeberlein, T.; Lewis, K.; Epstein, S. S. *Science* **2002**, *296*, 1127–1129.
153. Zengler, K.; Toledo, G.; Rappé, M.; *et al. Proc. Natl. Acad. Sci. USA* **2002**, *99*, 15681–15686.
154. Huang, G.; Mei, Y.; Thurmer, D. J.; Coric, E.; Schmidt, O. G. *Lab Chip* **2009**, *9*, 263–268.
155. Morimoto, Y.; Tan, W.; Tsuda, Y.; Takeuchi, S. *Lab Chip* **2009**, *9*, 2217–2223.
156. Lee, J.-H.; Kaplan, J.; Lee, W. *Biomed. Microdevices* **2008**, *10*, 489–498.
157. Lee, J.-H.; Wang, H.; Kaplan, J. B.; Lee, W. Y. *Acta Biomater.* **2010**, *6*, 4422–4429.
158. Park, S.; Wolanin, P. M.; Yuzbashyan, E. A.; *et al. Proc. Natl. Acad. Sci. USA* **2003**, *100*, 13910–13915.
159. Lee, E. J.; Chan, E. W. L.; Yousaf, M. N. *Chembiochem* **2009**, *10*, 1648–1653.
160. Hui, E. E.; Bhatia, S. N. *Proc. Natl. Acad. Sci. USA* **2007**, *104*, 5722–5726.
161. Kaji, H.; Yokoi, T.; Kawashima, T.; Nishizawa, M. *Lab Chip* **2009**, *9*, 427–432.
162. Leclerc, E.; El Kirat, K.; Griscom, L. *Biomed. Microdevices* **2008**, *10*, 169–177.
163. Wright, D.; Rajalingam, B.; Selvarasah, S.; Dokmeci, M. R.; Khademhosseini, A. *Lab Chip* **2007**, *7*, 1272–1279.
164. Sung, J. H.; Shuler, M. L. *Lab Chip* **2009**, *9*, 1385–1394.
165. Kojima, R.; Yoshimoto, K.; Takahashi, E.; Ichino, M.; Miyoshi, H.; Nagasaki, Y. *Lab Chip* **2009**, *9*, 1991–1993.
166. Puleo, C. M.; Ambrose, W. M.; Takezawa, T.; Elisseeff, J.; Wang, T. H. *Lab Chip* **2009**, *9*, 3221–3227.
167. Chen, M. C. W.; Gupta, M.; Cheung, K. C. *Biomed. Microdevices* **2010**, *12*, 647–654.
168. Kim, M. S.; Yeon, J. H.; Park, J. K. *Biomed. Microdevices* **2007**, *9*, 25–34.
169. Okochi, M.; Takano, S.; Isaji, Y.; Senga, T.; Hamaguchi, M.; Honda, H. *Lab Chip* **2009**, *9*, 3378–3384.
170. Huang, C. P.; Lu, J.; Seon, H.; *et al. Lab Chip* **2009**, *9*, 1740–1748.
171. Kaya, T.; Nagamine, K.; Oyamatsu, D.; Shiku, H.; Nishizawa, M.; Matsue, T. *Lab Chip* **2003**, *3*, 313–317.
172. Cheng, S. Y.; Heilman, S.; Wasserman, M.; Archer, S.; Shuler, M. L.; Wu, M. M. *Lab Chip* **2007**, *7*, 763–769.
173. Ma, L.; Zhou, C.; Lin, B.; Li, W. *Biomed. Microdevices* **2010**, *12*, 753–760.
174. Figallo, E.; Cannizzaro, C.; Gerecht, S.; *et al. Lab Chip* **2007**, *7*, 710–719.
175. Evenou, F.; Fujii, T.; Sakai, Y. *Biomed. Microdevices* **2010**, *12*, 465–475.
176. Ochsner, M.; Dusseiller, M. R.; Grandin, H. M.; *et al. Lab Chip* **2007**, *7*, 1074–1077.
177. Karp, J. M.; Yeh, J.; Eng, G.; *et al. Lab Chip* **2007**, *7*, 786–794.
178. Lee, K. H.; Kwon, G. H.; Shin, S. J.; *et al. J. Biomed. Mater. Res* **2009**, *90A*, 619–628.
179. Lee, K. H.; Shin, S. J.; Kim, C. B.; *et al. Lab Chip* **2010**, *10*, 1328–1334.
180. Ling, Y.; Rubin, J.; Deng, Y.; *et al. Lab Chip* **2007**, *7*, 756–762.
181. Paguirigan, A.; Beebe, D. J. *Lab Chip* **2006**, *6*, 407–413.
182. Gallego-Perez, D.; Higuita-Castro, N.; Sharma, S.; *et al. Lab Chip* **2010**, *10*, 775–782.
183. Deutsch, A.; Zurgil, N.; Hurevich, I.; *et al. Biomed. Microdevices* **2006**, *8*, 361–374.
184. Deutsch, M.; Deutsch, A.; Shirihai, O.; *et al. Lab Chip* **2006**, *6*, 995–1000.
185. Schiffenbauer, Y. S.; Kalma, Y.; Trubniykov, E.; *et al. Lab Chip* **2009**, *9*, 2965–2972.
186. Zhang, B. Y.; Kim, M. C.; Thorsen, T.; Wang, Z. H. *Biomed. Microdevices* **2009**, *11*, 1233–1237.
187. Nguyen, D.; Sa, S.; Pegan, J. D.; *et al. Lab Chip* **2009**, *9*, 3338–3344.
188. Khademhosseini, A.; Yeh, J.; Jon, S.; *et al. Lab Chip* **2004**, *4*, 425–430.
189. Braschler, T.; Johann, R.; Heule, M.; Metref, L.; Renaud, P. *Lab Chip* **2005**, *5*, 553–559.
190. Kang, G.; Lee, J. H.; Lee, C. S.; Nam, Y. *Lab Chip* **2009**, *9*, 3236–3242.
191. Mittal, N.; Rosenthal, A.; Voldman, J. *Lab Chip* **2007**, *7*, 1146–1153.
192. Zou, H.; Mellon, S.; Syms, R. R. A.; Tanner, K. E. *Biomed. Microdevices* **2006**, *8*, 353–359.
193. Liu, W.; Dechev, N.; Foulds, I. G.; Burke, R.; Parameswaran, A.; Park, E. J. *Lab Chip* **2009**, *9*, 2381–2390.
194. Liu, W.; Kim, H. J.; Lucchetta, E. M.; Du, W.; Ismagilov, R. F. *Lab Chip* **2009**, *9*, 2153–2162.
195. Tanase, M.; Felton, E. J.; Gray, D. S.; Hultgren, A.; Chen, C. S.; Reich, D. H. *Lab Chip* **2005**, *5*, 598–605.
196. Eriksson, E.; Sott, K.; Lundqvist, F.; *et al. Lab Chip* **2010**, *10*, 617–625.
197. Azioune, A.; Storch, M.; Bornens, M.; Thery, M.; Piel, M. *Lab Chip* **2009**, *9*, 1640–1642.
198. Chen, C. S.; Alonso, J. L.; Ostuni, E.; Whitesides, G. M.; Ingber, D. E. *Biochem. Biophys. Res. Commun.* **2003**, *307*, 355–361.
199. James, J.; Goluch, E. D.; Hu, H.; Liu, C.; Mrksich, M. *Cell Motil. Cytoskeleton* **2008**, *65*, 841–852.

200. Thery, M.; Pepin, A.; Dressaire, E.; Chen, Y.; Bornens, M. *Cell Motil Cytoskeleton* **2006**, *63*, 341–355.
201. Plouffe, B. D.; Brown, M. A.; Iyer, R. K.; Radisic, M.; Murthy, S. K. *Lab Chip* **2009**, *9*, 1507–1510.
202. Plouffe, B. D.; Radisic, M.; Murthy, S. K. *Lab Chip* **2008**, *8*, 462–472.
203. Douglas, E. S.; Chandra, R. A.; Bertozzi, C. R.; Mathies, R. A.; Francis, M. B. *Lab Chip* **2007**, *7*, 1442–1448.
204. Douglas, E. S.; Hsiao, S. C.; Onoe, H.; Bertozzi, C. R.; Francis, M. B.; Mathies, R. A. *Lab Chip* **2009**, *9*, 2010–2015.
205. Yang, L. *Talanta* **2009**, *80*, 551–558.
206. Song, J. M.; Culha, M.; Kasili, P. M.; Griffin, G. D.; Vo-Dinh, T. *Biosens. Bioelectron.* **2005**, *20*, 2203–2209.
207. Song, J. M.; Vo-Dinh, T. *Anal. Chim. Acta* **2004**, *507*, 115–121.
208. Yu, J.; Liu, Z.; Liu, Q.; *et al*. *Sens. Actuators A Phys.* **2009**, *154*, 288–294.
209. Hwang, K.-Y.; Jeong, S.-Y.; Kim, Y.-R.; *et al*. *Sens. Actuators B Chem.* **2011**. http://dx.doi.org/10.1016/j.snb.2009.11.005.
210. Balaban, N. Q.; Merrin, J.; Chait, R.; Kowalik, L.; Leibler, S. *Science* **2004**, *305*, 1622–1625.
211. Green, J. V.; Murthy, S. K. *Lab Chip* **2009**, *9*, 2245–2248.
212. Kobel, S.; Valero, A.; Latt, J.; Renaud, P.; Lutolf, M. *Lab Chip* **2010**, *10*, 857–863.
213. Shevkoplyas, S. S.; Yoshida, T.; Munn, L. L.; Bitensky, M. W. *Anal. Chem.* **2005**, *77*, 933–937.
214. Wu, H. I.; Cheng, G. H.; Wong, Y. Y.; *et al*. *Lab Chip* **2010**, *10*, 647–653.
215. Arai, F.; Ng, C.; Maruyama, H.; Ichikawa, A.; El-Shimy, H.; Fukuda, T. *Lab Chip* **2005**, *5*, 1399–1403.
216. Phillips, J. A.; Xu, Y.; Xia, Z.; Fan, Z. H.; Tan, W. H. *Anal. Chem.* **2009**, *81*, 1033–1039.
217. Xu, Y.; Phillips, J. A.; Yan, J. L.; Li, Q. G.; Fan, Z. H.; Tan, W. H. *Anal. Chem.* **2009**, *81*, 7436–7442.
218. Sin, A.; Murthy, S. K.; Revzin, A.; Tompkins, R. G.; Toner, M. *Biotechnol. Bioeng.* **2005**, *91*, 816–826.
219. Sivagnanam, V.; Song, B.; Vandevyver, C.; Bunzli, J. C. G.; Gijs, M. A. M. *Langmuir* **2010**, *26*, 6091–6096.
220. Mahara, A.; Yamaoka, T. *Biotechnol. Prog.* **2010**, *26*, 441–447.
221. Demirci, U.; Montesano, G. *Lab Chip* **2007**, *7*, 1139–1145.
222. Kwon, K. W.; Choi, S. S.; Lee, S. H.; *et al*. *Lab Chip* **2007**, *7*, 1461–1468.
223. Nikkhah, M.; Strobl, J.; Agah, M. *Biomed. Microdevices* **2009**, *11*, 429–441.
224. Tan, S. J.; Yobas, L.; Lee, G. Y. H.; Ong, C. N.; Lim, C. T. *Biomed. Microdevices* **2009**, *11*, 883–892.
225. Baret, J.-C.; Miller, O. J.; Taly, V.; *et al*. *Lab Chip* **2009**, *9*, 1850–1858.
226. Ingham, C. J.; Sprenkels, A.; Bomer, J.; *et al*. *Proc. Natl. Acad. Sci. USA* **2007**, *104*, 18217–18222.
227. Grow, A. E.; Wood, L. L.; Claycomb, J. L.; Thompson, P. A. *J. Microbiol. Meth.* **2003**, *53*, 221–233.
228. Miyano, N.; Inoue, Y.; Teramura, Y.; *et al*. *Lab Chip* **2008**, *8*, 1104–1109.
229. Shin, H. S.; Kim, H. J.; Sim, S. J.; Jeon, N. L. *J. Nanosci. Nanotechnol.* **2009**, *9*, 7330–7335.
230. Fox, M. B.; Esveld, D. C.; Valero, A.; *et al*. *Anal. Bioanal. Chem.* **2006**, *385*, 474–485.
231. Zarnitsyn, V. G.; Meacham, J. M.; Varady, M. J.; Hao, C. H.; Degertekin, F. L.; Fedorov, A. G. *Biomed. Microdevices* **2008**, *10*, 299–308.
232. Jain, T.; McBride, R.; Head, S.; Saez, E. *Lab Chip* **2009**, *9*, 3557–3566.
233. Hanson, J. N.; Motala, M. J.; Heien, M. L.; Gillette, M.; Sweedler, J.; Nuzzo, R. G. *Lab Chip* **2009**, *9*, 122–131.
234. Doran, M. R.; Mills, R. J.; Parker, A. J.; Landman, K. A.; Cooper-White, J. J. *Lab Chip* **2009**, *9*, 2364–2369.
235. Breckenridge, M. T.; Egelhoff, T. T.; Baskaran, H. *Biomed. Microdevices* **2010**, *12*, 543–553.
236. Chaw, K. C.; Manimaran, M.; Tay, F. E. H.; Swaminathan, S. *Biomed. Microdevices* **2007**, *9*, 597–602.
237. Haessler, U.; Kalinin, Y.; Swartz, M. A.; Wu, M. W. *Biomed. Microdevices* **2009**, *11*, 827–835.
238. Witek, M. A.; Wei, S.; Vaidya, B.; *et al*. *Lab Chip* **2004**, *4*, 464–472.
239. Takeuchi, S.; DiLuzio, W. R.; Weibel, D. B.; Whitesides, G. M. *Nano Lett.* **2005**, *5*, 1819–1823.
240. Cho, H.; Jönsson, H.; Campbell, K.; *et al*. *PLoS Biol*. **2007**, *5*, e302.
241. Addae-Mensah, K. A.; Wikswo, J. P. *Exp. Biol. Med.* **2008**, *233*, 792–809.
242. Vanapalli, S. A.; Duits, M. H. G.; Mugele, F. *Biomicrofluidics* **2009**, *3*, 012006.
243. Kasza, K. E.; Rowat, A. C.; Liu, J. Y.; *et al*. *Curr. Opin. Cell Biol.* **2007**, *19*, 101–107.
244. Loh, O.; Vaziri, A.; Espinosa, H. D. S. M. *Exp. Mech.* **2009**, *49*, 105–124.
245. Darling, E. M.; Topel, M.; Zauscher, S.; Vail, T. P.; Guilak, F. *J. Biomech.* **2008**, *41*, 454–464.
246. Docheva, D.; Padula, D.; Popov, C.; Mutschler, W.; Clausen-Schaumann, H.; Schieker, M. *J. Cell. Mol. Med.* **2008**, *12*, 537–552.
247. Serrell, D. B.; Law, J.; Slifka, A. J.; Mahajan, R. L.; Finch, D. S. *Biomed. Microdevices* **2008**, *10*, 883–889.
248. Hou, H. W.; Li, Q. S.; Lee, G. Y. H.; Kumar, A. P.; Ong, C. N.; Lim, C. T. *Biomed. Microdevices* **2009**, *11*, 557–564.
249. Harris, A. K.; Wild, P.; Stopak, D. *Science* **1980**, *208*, 177–179.
250. Kajzar, A.; Cesa, C. M.; Kirchgessner, N.; Hoffmann, B.; Merkel, R. *Biophys. J.* **2008**, *94*, 1854–1866.
251. Liang, X. M.; Han, S. J.; Reems, J. A.; Gao, D. Y.; Sniadecki, N. J. *Lab Chip* **2010**, *10*, 991–998.
252. Tan, J. L.; Tien, J.; Pirone, D. M.; Gray, D. S.; Bhadriraju, K.; Chen, C. S. *Proc. Natl. Acad. Sci. USA* **2003**, *100*, 1484–1489.
253. Legant, W. R.; Pathak, A.; Yang, M. T.; Deshpande, V. S.; McMeeking, R. M.; Chen, C. S. *Proc. Natl. Acad. Sci. USA* **2009**, *106*, 10097–10102.
254. Kamotani, Y.; Bersano-Begey, T.; Kato, N.; *et al*. *Biomaterials* **2008**, *29*, 2646–2655.
255. Moraes, C.; Chen, J. H.; Sun, Y.; Simmons, C. A. *Lab Chip* **2010**, *10*, 227–234.
256. Moraes, C.; Wang, G. H.; Sun, Y.; Simmons, C. A. *Biomaterials* **2010**, *31*, 577–584.
257. Kim, J.; Park, J.; Yang, S.; *et al*. *Lab Chip* **2007**, *7*, 1504–1508.
258. Tanaka, Y.; Morishima, K.; Shimizu, T.; *et al*. *Lab Chip* **2006**, *6*, 362–368.
259. Tanaka, Y.; Sato, K.; Shimizu, T.; Yamato, M.; Okano, T.; Kitamori, T. *Lab Chip* **2007**, *7*, 207–212.
260. Tanaka, Y.; Sato, K.; Shimizu, T.; *et al*. *Lab Chip* **2008**, *8*, 58–61.
261. Akiyama, Y.; Iwabuchi, K.; Furukawa, Y.; Morishima, K. *Lab Chip* **2009**, *9*, 140–144.
262. Xi, J. Z.; Schmidt, J. J.; Montemagno, C. D. *Nat. Mater.* **2005**, *4*, 180–184.
263. Ingham, C. J.; van Hylckama Vlieg, J. E. T. *Lab Chip* **2008**, *8*, 1604–1616.
264. Spetzler, D.; York, J.; Dobbin, C.; *et al*. *Lab Chip* **2007**, *7*, 1633–1643.
265. Uenoyama, A.; Miyata, M. *Proc. Natl. Acad. Sci. USA* **2005**, *102*, 12754–12758.
266. Ben-Yoav, H.; Biran, A.; Pedahzur, R.; *et al*. *Electrochim. Acta* **2009**, *54*, 6113–6118.
267. Popovtzer, R.; Neufeld, T.; Ron, E. Z.; Rishpon, J.; Shacham-Diamand, Y. *Sens. Actuators B Chem.* **2006**, *119*, 664–672.
268. Theytaz, J.; Braschler, T.; van Lintel, H.; *et al*. *Procedia Chem.* **2009**, *1*, 1003–1006.

3.315. Biological Microelectromechanical Systems (BioMEMS) Devices

L H Ting and N J Sniadecki, University of Washington, Seattle, WA, USA

© 2011 Elsevier Ltd. All rights reserved.

3.315.1.	**Introduction**	258
3.315.2.	**Cell Adhesions to the Microenvironment**	258
3.315.3.	**BioMEMS Devices to Measure Traction Forces**	260
3.315.3.1.	Membrane Wrinkling	260
3.315.3.2.	Traction Force Microscopy	261
3.315.3.3.	MEMS Adapted Tools	261
3.315.3.4.	Microposts	262
3.315.4.	**BioMEMS Devices to Apply Forces to Cells**	265
3.315.4.1.	Micromanipulation	265
3.315.4.2.	Magnetic Bead Forces	265
3.315.4.3.	Optical Traps/Tweezers	267
3.315.4.4.	Magnetic Microposts	267
3.315.4.5.	Cytoskeletal Force Response	268
3.315.4.6.	Nanoscissors	269
3.315.5.	**Microfluidic Systems**	269
3.315.5.1.	Fluid Shear Stress	269
3.315.5.2.	BioMEMS Reactors	270
3.315.5.3.	Bioreactor Pumping	270
3.315.5.4.	Bioreactor Configuration	270
3.315.5.5.	Interstitial Shear	271
3.315.5.6.	Single Cell Analysis	272
3.315.5.7.	Cell Sorting	272
3.315.5.8.	Organ on Chip Microfluidic Devices	273
3.315.5.9.	Analysis of Mechanotransduction or Morphogenesis Biomarkers	274
3.315.6.	**Future Directions**	274
References		275

Glossary

Actin A protein present in all eukaryotic cells that compromises the cytoskeleton of a cell. Actin monomers polymerize together to form a double helical strand known as a microfilament or thin filament. The pointed end of actin has slower rate of adding new actin monomers to the strand than the barbed end.

Adherens junction Cadherin and catenin protein complexes at the cell membrane that serve as intracellular attachments linking neighboring cell cytoskeletons together. Traction forces can be transmitted from one cell actin structure through an adherens junction to a cell in contact.

Extracellular matrix Network of complex macromolecules that form a scaffold that cells adhere to. Common structural extracellular matrix proteins are collagen and elastin and common adhesive proteins are fibronectin and laminin.

Focal adhesion Large protein assemblies at the cell membrane that anchor a cell to the extracellular matrix through integrin receptors. Focal adhesion formation is a GTPase-dependent process and serves to transmit forces between the extracellular matrix and the cell's cytoskeleton.

Focal adhesion kinase (FAK) A tyrosine kinase present at focal adhesions that promotes turnover of cell contacts with the extracellular matrix.

Microcontact printing Protein transfer technique akin to a stamp and ink procedure that is used to control available binding sites for biomolecules or cells. A soft elastomer stamp has a protein absorbed to it and is put in contact with the target surface transferring the protein pattern over.

Myosin Motor proteins that interact with actin filaments for motile processes within a cell. Many isoforms exist, with myosin I and myosin II being the most frequently referred to. Myosin I has a single head binding domain and an ATP independent actin-binding site. Myosin II comprises two heavy chain ATPase domain heads and four light chain tails. With ATP present, heavy chains alternate attachment to an actin filament and walk along the filament to generate force.

Rho A GTPase protein encoded by the Rho genes that regulates actin dynamics. Downstream protein signal regulators include Dia1 and the ROCK subfamily. Their broad range of action affects cell adhesion, gene expression, motility, and proliferation.

Soft lithography Replication of a surface or topography by applying a liquid elastomer onto a surface, curing it, and then peeling the surfaces apart to form a negative mold. Repeating this procedure with the negative mold reproduces the original features.

Traction force The force exerted by a cell through its actin–myosin contractile apparatus that allows it to migrate. Traction forces are transmitted through the focal adhesions of a cell.

Abbreviations

AFM	Atomic force microscopy
BioMEMS	Biological microelectromechanical systems
DEP	Dielectrophoresis
ECM	Extracellular matrix
ELISA	Enzyme-linked immunosorbent assay
F-actin	Filamental actin
FAK	Focal adhesion kinase
G-actin	Globular actin
GAG	Glycosaminoglycan
GFP	Green fluorescent protein
GTPase	Guanosine triphosphatase
MEMS	Microelectromechanical systems
MTC	Magnetic twisting cytometry
PDMS	Polydimethylsiloxane
ROCK	Rho kinase
UV	Ultraviolet

3.315.1. Introduction

Cells respond to biochemical and biomechanical stimuli through changes in their proliferation, apoptosis, differentiation, secretion, contraction, motility, and adhesion. To better understand these changes in cellular behavior, researchers have developed biological microelectromechanical systems (BioMEMS) that provide a high degree of control over the stimuli that cells receive from their surroundings. Cells are cultured commonly on dishes, which are not only stiffer and flatter than a cell's native tissue, but they also lack the appropriate chemical and mechanical signals that cells experience *in vivo*. The techniques and processes from BioMEMS can provide a means to control a wide variety of microenvironmental cues in order to better understand the nature of the cellular response.[1,2] Findings that have come from the use of BioMEMS have influenced the design of biomaterials and tissue-engineered constructs because engineers and scientists can begin to incorporate the appropriate interactions for cells.

Cells in living tissue have different levels of cues than their counterparts in culture. The vascular and lymphatic systems provide cells with the appropriate nutrients and hormones for their survival and function. Likewise, the levels of oxygen and growth factors in culture can be excessive for cells and overdrive their response. These chemical interactions influence cell behavior by engaging surface receptors that activate specific signal pathways. Gradients in signal molecules can also serve to attract cells to locations or activate particular responses. In addition to these soluble factors, the insoluble cues that a cell encounters from its extracellular matrix (ECM) are different than those in tissue. Tissue culture dishes are coated usually with one kind of ECM protein such as collagen or fibronectin or reconstituted extracts such as Matrigel, whose contents are poorly defined. These insoluble factors are not well-matched to the different variety of adhesive ligands that a cell type may require. Moreover, cells experience a variety of extracellular forces from their surroundings that act on the mechanosensory structures in a cell that influence its behavior.[3,4] These forces come from the range of physiological phenomena such as pressure forces from muscle contraction, shear forces from vascular hemodynamics, traction forces from surrounding cells, or stretching forces from musculoskeletal locomotion. Emerging evidence shows that biomechanical factors such as substrate stiffness and cell geometry can influence cell functions such as migration,[5] cytokinesis,[6] differentiation,[7,8] and growth.[9,10] These findings are important because they implicate that cells in one kind of environment respond differently than those in another. Since the influence of different factors must be careful examined, robust means to explore these factors are required.

BioMEMS has provided important insights in improving the development of biomaterials or tissue-constructs to better represent the cellular microenvironment, either by closely matching the native one or specifically activating a cellular response. Many of these tools are derived from microelectromechanical systems (MEMS) such as actuators or posts but have been adapted by researchers interested in probing cells at the nanoscale. BioMEMS devices can be used to measure traction forces that cells produce against a surface, which is important to maintain stable adhesion against a substrate. These tools can also be incorporated with techniques to impart forces onto the surface of a cell to examine the mechanotransduction response. Cell culture and microfluidics can be combined to create chemical gradients or shearing forces that cells experience *in vivo*. In all these cases, BioMEMS provides a powerful way to manipulate physical forces and chemical factors that interact with a cell to better understand the role of a cell's microenvironment.

3.315.2. Cell Adhesions to the Microenvironment

Cells in living organisms bind and adhere to a network of ECM proteins. This meshwork of protein provides the structural scaffold necessary for cells to form stable adhesions (**Figure 1**). ECM proteins include collagen, elastin, laminin,

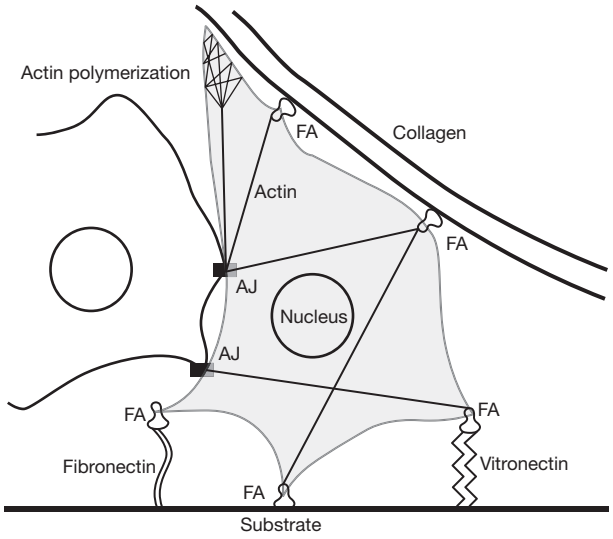

Figure 1 Cells adhere to the extracellular matrix through focal adhesion (FA) sites that connect intracellularly to the actin cytoskeleton. Neighboring cells connect their cytoskeletons at adherens junctions (AJ). A cell changes its shape in order to spread or migrate by polymerizing its actin filaments so that they can push against the cell membrane.

fibronectin, vitronectin, and many other proteins to varying degrees of concentration and spatial organization. The main function of the ECM is to provide cells with ligands for the binding of their integrin receptors, which are not only essential for cell adhesion but also activate signaling pathways that affect cell function.[11] Integrins also coordinate activities within a cell's cytoskeleton, such as actin filament polymerization and focal adhesion assembly, which are important in stabilizing the adhesion of a cell against a substrate.[12,13]

When an integrin receptor contacts a ligand site on an ECM protein, signal pathways associated with RhoGTPases Rho and Rac are activated. In eukaryotic cells, there is an abundant quantity of the monomeric, globular actin (G-actin) within the cell. Rho and Rac can activate actin-binding proteins that cause G-actins to bind to each other to create filamental actin (F-actin).[14] F-actin elongation occurs as more G-actins become recruited to the growing filament, but with the pointed end growing faster than the barbed end. F-actin growth can be prevented by capping proteins that inhibit the addition of G-actin at the free ends, severing proteins that cleave the filament at points along its length, or depolymerizing proteins that promote the dissociation of G-actin from the ends.[15] This dynamic remodeling of actin allows the filaments to push the cellular membrane forward during spreading, a critical component of cell survival[9] and migration. It also provides the freedom for the cell to adapt its structure to response to its surroundings.

When myosin and α-actinin bind to F-actin, the structure is called a stress fiber and has the ability to shorten its length to create tension inside the cell. Myosin acts to slide two or more F-actin filaments past one another so that the cell can contract.[16] A cell then produces traction forces by transmitting its cytoskeletal tension from actin and myosin to its focal adhesions where integrins are clustered together and firmly bound to ligands in the ECM. The major signaling pathway for stress fiber regulation is Rho and its downstream effectors Rho kinase (ROCK or ROK) and mDia1.[14] The dual action of ROCK directly phosphorylates myosin light chain and inhibits myosin light chain phosphatase. The Rho effector mDia1 serves as a nucleating agent at the cell membrane for new actin polymerization.[17]

Focal adhesions are not static structures, but respond to ligand binding and applied forces. They are large, multiprotein complexes that structurally connect the actin cytoskeleton to the ECM and can activate signaling networks that are essential for morphogenesis, migration, proliferation, differentiation, and survival.[18] Focal adhesions form at the cytoplasmic side of the cell membrane after integrins bind to the ECM. Focal adhesion proteins such as talin, vinculin, and paxillin colocalize with integrins and help to improve the bond strength of the adhesion site by gathering many integrins within a close proximity and also by mechanically coupling the integrins to the actin.[13] Interestingly, cytoskeletal tension from actin and myosin is needed to promote the growth of focal adhesions, indicating that these structures have a mechanotransduction response to force. Focal adhesions also serve as docking sites for signaling proteins such as focal adhesion kinase (FAK) and Src that regulate tyrosine phosphorylation pathways and guanine–nucleotide exchange factors (GEFs) and GTPase-activating proteins (GAPs) that regulate Rho GTPases.[18] Specifically, an important balance exists between pathways associated with Rho and FAK, which serve to encourage adhesion reinforcement or disassembly. Rho activity increases focal adhesion formation,[19] but FAK can act to suppress Rho and therefore promote detachment of focal adhesions during cell motility.[20]

The compliance in ECM proteins gives some insight into how cells interact with their microenvironment. At the molecular level, ECM proteins are surprisingly stiff materials. Collagen, for example, has an elastic modulus of around 5 GPa,[21] but as a reconstituted gel, it is significantly softer. Comparatively, bone is between 10 and 20 GPa and soft tissue is between 10 and 100 kPa,[22,23] so there is a significant range of stiffness that cells can experience in their native environment. Common engineered materials used in biological applications such as titanium alloy and stainless steel are 114 and 190 GPa, respectively[24] and many plastics, including polystyrene which is used in tissue culture dishes, have an elastic modulus between 2 and 4 GPa. Thus, it is important to be aware that in designing biomaterials and tissue-constructs that their material properties need to be matched to the native tissue so as to illicit the appropriate mechanotransduction effect on the cells.

The compliance of the ECM has been shown to play a role in the dynamic binding of a cell's integrins. Certain ECM proteins such as fibronectin can be unraveled under tension to reveal new ligand sites on which a cell can bind.[25] These 'cryptic' sites become available under force and are therefore hypothesized to be regulated by traction forces of a cell or external forces from physiological motion.[26] Cells have also been observed to bind differently to synthetic matrices that are highly compliant. On polyacrylamide gels, cells show changes in their spreading and motility that depended on the environmental stiffness (**Figure 2**).[27] Focal adhesion structures are also noticeably reduced on softer gels and have lower kinase activity as compared to cells on stiffer gels or plastic tissue culture dishes. This suggests that ECM stiffness increases focal adhesion formation in addition to cytoskeletal tension. In fact,

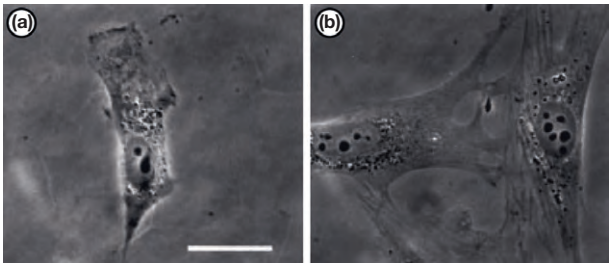

Figure 2 (a) Cell on a soft substrate spreads less than (b) cells on a stiff substrate. Scale bar is 10 μm. Reproduced from Pelham, R. J., Jr.; Wang, Y. *Proc. Natl. Acad. Sci. USA* **1997**, *94*, 13661–13665 with permission, Copyright 1997 National Academy of Sciences, USA.

gradients in stiffness can also affect the direction of cell migration as cells have been observed to move toward stiff regions and away from softer regions.[5]

Much of the native interaction that cells have with their microenvironment is lost with traditional cell culture. Common procedures seed cells onto polystyrene dishes or flasks and grow the cells in an incubator to maintain correct temperatures and pH levels. Polystyrene dishes are convenient, cost-effective, and well-established surfaces on which to culture and observe cells. Manufacturing standards have made it possible for dishes from different suppliers to elicit the same cell attachments and behaviors while remaining inert to cells and chemicals. Polystyrene is certainly the most widely used surface to culture and experiment with cells, offering high optical clarity and visibility, and complete compatible with phase light, fluorescent, and confocal microscopy techniques, but it is also a more rigid environment than cells experience *in vivo*.

By departing from traditional culture approaches, it has been possible to observe how cells regulate their function in response to the stiffness of their environment. Cardiomyocytes improve their contractile performance when plated onto gels that match the stiffness of the native myocardium.[28] Stem cells are able to commit to a neurogenic lineage on soft gels and osteogenic lineages on stiff gels based on their ability to generate cytoskeletal tension.[7] A three-dimensional matrix environment also affects cells for they show reduced levels of cytoskeletal and focal adhesion activities as compared with cells on ECM-coated substrates.[29] Thus, there needs to be a better understanding on the biochemical and biomechanical factors that drives these changes in cell adhesions and BioMEMS can provide important insights for the design of biomaterials and tissue-constructs. For additional information, see **Chapter 4.403, The Innate Response to Biomaterials**.

3.315.3. BioMEMS Devices to Measure Traction Forces

Cell force measurement tools arose in response to observations that cells in culture were motile and so it was likely that they were imparting forces to move. It was suspected that they produced traction forces against the surface of the culture dish, but techniques were limited in measuring these nanoscale forces. The advent of MEMS fabrication techniques provided a means to create tools and sensors that matched the size of the cell. Researchers adopted these techniques to create new tools that followed a common macroscale approach to measure force: direct contact with a flexible, calibrated structure and observation of its deflection under a load. Sensor structures such as these can be fabricated and designed to measure a wide range of physiological cell forces, such as single cell contraction and multicellular interactions.

3.315.3.1. Membrane Wrinkling

A pioneering development that laid the groundwork for future BioMEMS devices was Albert Harris' work in 1980. He and his colleagues observed that cells exerted traction forces by culturing cells on a deformable, silicone membrane substrate.[30] To make the surface, a layer of silicone fluid, polydimethylsiloxane (PDMS), was spread out on a glass coverslip. Flame was then used to cross-link the top layer of the silicone to create a thin, elastic film on top of the remaining liquid silicone film, which acted as a support and lubricant for deflection. Cells placed on this film distorted the top surface and caused wrinkles that were due to the tangential forces they exerted from actin and myosin contraction (**Figure 3(a)**).[31,32] By correlating the membrane wrinkle length with a magnitude of force, the technique was later able to provide a closer measure of the traction forces, but the approach was still semiquantitative.[33] An important finding from Harris' pioneering work was that fibroblast forces were far larger than what is needed for locomotion, in fact two or three magnitudes more. This led to the theory that these strong forces are necessary for the physical remodeling of the ECM.[34] When fibroblasts were seeded onto collagen gels, they observed that the traction forces of the cells pulled the gel into a dense capsule of collagen fibers similar to the formation of wrinkles in the silicone films. They theorized that the traction fields created by the cells can form the aligned collagen fiber structures seen in tissues such as tendons or ligament, rather than relying on an existing matrix to induce the alignment.

A limitation of PDMS wrinkling films is that there is low resolution in measuring traction forces because there exists a mechanical coupling between a wrinkle in a substrate and the traction forces nearby. A traction force is applied at a single focal adhesion of a cell, but the surface strains in the film leads to wrinkling over a wider area. The overlap in strains from nearby traction forces makes it difficult to determine how much each one contributes to a visible wrinkle in the film. The elasticity of the silicone film also means that the traction forces of a cell can cause a strain in the film over a widespread area, which can subject neighboring cells to an external stretch or wrinkled surface topology. Quantifying wrinkles is also a vague approach because it is difficult to interpret what is and what is not a wrinkle due to debris or surface defects in the silicone film.

Refinements were made to the silicone wrinkling technique by using surface markers that enabled a higher resolution and a better understanding of the deformations caused by traction forces. Marker beads were placed on top of the PDMS film to track displacement of the film over a high number of spatial points. To create this substrate, one micrometer diameter latex beads were deposited onto the PDMS fluid and its top surface was cross-linked in a glow discharge chamber.[35] An improved mathematical and statistical model for the deformation of the film used the tracking of the beads, rather than wrinkles.[36] Additionally, the

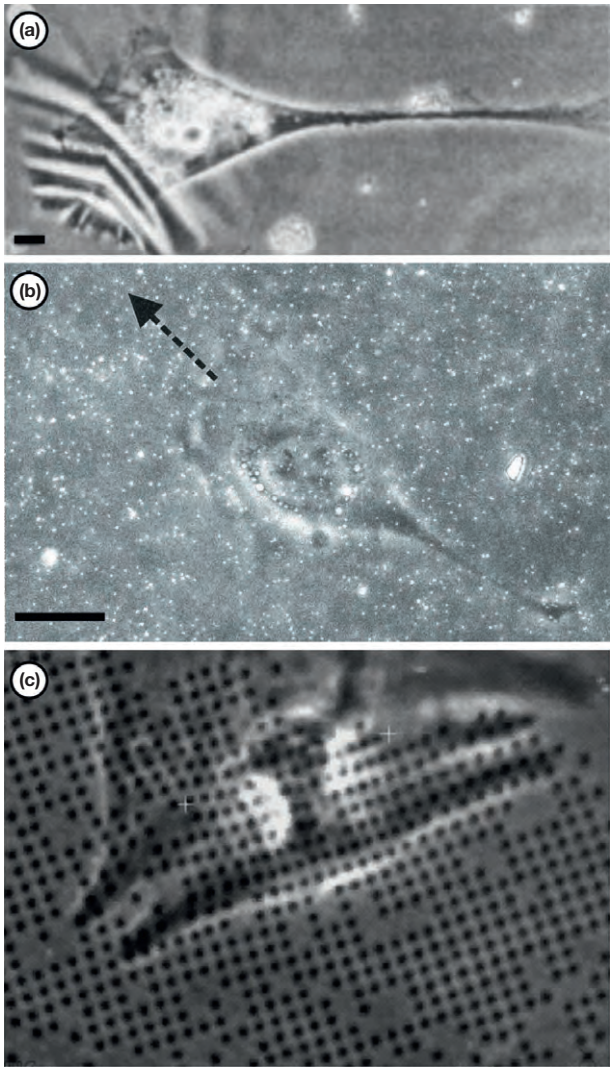

Figure 3 (a) Cell wrinkling of a silicone membrane floating on silicone fluid. Force is orthogonal to the long axis of each wrinkle and the stretch of the traction force correlates with the length of the wrinkles. Scale bar is 10 μm. (b) Traction force microscopy technique with cell on polyacrylamide gel containing embedded fluorescent beads, which act as fiduciary markers of strain at the surface of the substrate. Scale bar is 20 μm. (c) BioMEMS traction force microscopy where marker dots are patterned into a 2-μm grid pitch. Some dots are missing from the fabrication process, but surface strains are evident by the displacements of the markers from their original positions as evenly spaced rows and columns. Adapted from Harris, A. K.; Stopak, D.; Wild, P. *Nature* **1981**, *290*, 249–251; Munevar, S.; Wang, Y.; Dembo, M. *Biophys. J.* **2001**, *80*, 1744–1757; Balaban, N. Q.; Schwarz, U. S.; Riveline, D.; *et al. Nat. Cell Biol.* **2001**, *3*, 466–472.

approach allowed for an order of magnitude improvement in detectable forces compared to wrinkling membranes.

3.315.3.2. Traction Force Microscopy

A popular method to measure subcellular level forces is traction force microscopy which measures traction forces by the distortion of cells on polyacrylamide gels instead of on PDMS films.[37] The gel is mixed with fluorescent beads that are a few micrometers or smaller in diameter and spread out as a thin film on a glass coverslip on which cells can be cultured (Figure 3(b)). To engage integrins to bind and promote cell adhesion, an ECM protein such as collagen or fibronectin can be coated onto the surface of the gel. The completed fabrication process results in a deformable gel on which cells can be cultured and whose embedded fluorescent particles can be tracked to measure cellular traction forces. Cells seeded into this environment adhere to the ECM protein, form focal adhesions and actin stress fibers, and exert cytoskeletal traction forces onto the substrate. The deformation of the gel pulls with it the fluorescent particles. Their positions can be recorded under fluorescence microscopy and compared to the original, undeflected positions of the particles to obtain the deflection field. Calculation of a traction force field from a measured deflection field in an elastic material is known as a Boussinesq problem in the field of mechanics and can be readily solved. Traction force microscopy has been used to show that the forces of a cell increase with stiffness of a substrate, adhesive ligand density, and contact area.[5,38,39] Normal and transformed cells also exhibit distinct patterns of traction forces across the leading and tail edges when migrating with normal cells having organized zones of forces and transformed cells displaying weak disorganized mechanical domains.[40]

Patterns of traceable markers can be generated for traction force microscopy by using a microfabricated stamp from a silicon wafer that has arrays of dot-like features (Figure 3(c)).[41] The stamp can be used to deposit fluorescent material onto the surface of a PDMS substrate to create a uniform array of marker dots. Cells deform the surface, and traction forces can be measured with more accuracy due to the regularity of the pattern as opposed to the random placement of beads in polyacrylamide gels. One disadvantage of traction force microscopy is that it shares the same problem as silicon wrinkling films in that the gels or PDMS is a continuous material and so the solution for the traction forces is difficult to obtain without a degree of uncertainty.

3.315.3.3. MEMS Adapted Tools

MEMS techniques and devices have played a key role in developing an understanding of traction forces. Atomic force microscopy (AFM) was one of the first tools used to reveal cellular properties. Extreme sensitivity and miniscule local sampling area on the order of 0.01 μm^2 means that researchers can use it to sample very localized responses.[42] AFM takes measurements by lowering a nanometer scale tip onto the surface of interest. A piezoelectric sensor detects cantilever deflection and can also impart simple or cyclic deflections to the tip giving a way to impart force as well. The AFM technique opened the field to direct force measurements of properties of whole cells,[43] cell cytoskeletons,[44] subcellular organelles, and biomolecules.[45]

A novel approach is the fabrication of a set of horizontal cantilevers that have micrometer-scale dimensions (Figure 4).[46] Micromachining is used to create the cantilever, which is a manufacturing process where thin layers of polysilicon, silicon dioxide, and metals are deposited onto a wafer and then each layer is selective etched to create a final structure. The horizontal cantilever is built underneath the surface of the device but

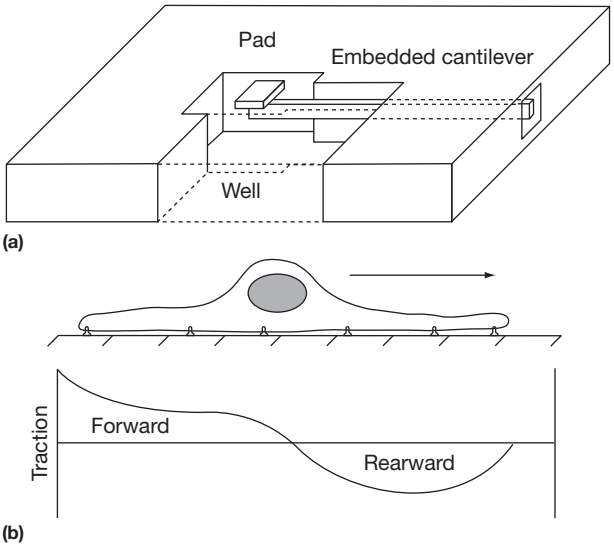

Figure 4 (a) BioMEMS traction force device with embedded, horizontal cantilever inside a well. A migrating cell can attach to the pad at the opening of the well and deflect the cantilever under its traction force. (b) Traction forces of a migrating cell measured with the device show pulling forces at the leading edge and pushing forces at the tail. Reproduced from Galbraith, C. G.; Sheetz, M. P. *Proc. Natl. Acad. Sci. USA* **1997**, *94*, 9114–9118 with permission. Copyright 1997 National Academy of Sciences, USA.

surrounded by a well that was etched to allow the cantilever to freely deflect. A pad is attached at the free end of a cantilever to allow the cell to bind and is used to mark the displacement of the cantilever tip. Cells placed onto this device can adhere and spread on the top surface. As a cell migrates, it comes in contact with a cantilever's pad and forms a focal adhesion. The traction force produced by actin and myosin causes the cantilever to bend. The deflection of the cantilever is readily visible under optical microscopy, which then allows the calculation of traction forces during migration. The use of BioMEMS cantilevers showed that the magnitude of traction forces differs across regions of the cell during migration. As the cell proceeds in one direction, the leading edge creates contractile forces toward the nucleus, increasing this traction force in the region behind the lamellipodia. These traction forces reverse in the rear of the cell, indicating the cell is pushing against the substrate to propel itself. Fibroblast cells move by continuous generation of focal adhesions at the front and release of adhesions at the rear, again through the influence of actin and myosin. The measurement of traction forces by a single cantilever, however, prevents simultaneous force measurement across all regions of the cell as seen with traction force microscopy. The force that is measured can only be determined on an axis perpendicular to the length of the cantilever, so the true strength and direction of the force are not directly resolved.

3.315.3.4. Microposts

Soft lithography can be used to create arrays of vertically aligned PDMS cantilevers, which are referred to as microposts.[47] To form the master, a thick film of photoresist is patterned on a silicon wafer using photolithography to create arrays of microposts that are up to tens of micrometers in height and a few micrometers in diameter (**Figure 5(a)**). Fluorosilane is applied during this process to act as a nonadhesive release layer. Uncured PDMS is poured on top of the microposts features of the master and subsequently cured by heat to create a negative mold with 'microholes.' The negative mold then can be used to replicate the micropost features of the master. PDMS is poured on top of the mold, cured, and then peeled off to create the arrays of PDMS microposts used for cell culture. The elastic stiffness of the posts can be controlled by the physical dimensions of diameter and height of the microposts giving the sensors multicellular capabilities with different cell types.

PDMS is a useful material for BioMEMS researchers due to its high biocompatibility, surface chemistry, and ease of use and fabrication. Favorable mechanical properties include predictable elastomeric properties, thermal stability, gas permeability for cell culture purposes, and optical transparency in imaging and observation.[48] PDMS can be sterilized through several means: immersion in 70% ethanol, UV exposure, or autoclaving.[49] It also has a hydrophobic surface that can be useful in certain applications, but it can also be modified with plasma oxidation to render it temporarily hydrophilic.[50] In microcontact printing, changing the hydrophobicity of PDMS is useful in order to allow proteins to transfer from a hydrophobic PDMS stamp onto a hydrophilic PDMS substrate.[51] In microfluidics, a temporarily hydrophilic surface is desirable to enhance the wetting of the fluid into small channels. Plasma oxidation of PDMS also allows it to covalently bond to other polymers and glass. Ozone treatment can produce a similar result as plasma oxidation, but is significantly slower and does not weaken the PDMS structure.[48] Silane is a common surface treatment for PDMS because it reacts with available hydroxyl groups on the surface to form covalently bonded Si–O–Si molecules on the surface. A wide variety of silanes are available that can be used to create new functional groups on the PDMS surface.[48,52] In replica molding of the PDMS micropost array, the negative molds are treated with fluorosilane in order to ensure easy peeling of the arrays from the mold.

Biofunctionalization of the micropost array is achieved by patterning ECM proteins onto the top surface of the micropost tips. A PDMS stamp with the appropriate pattern is molded from an SU-8 or a silicon structure (**Figure 5(b)**). ECM proteins in solution are deposited onto the surface of the PDMS stamp and then the stamp is used to print a pattern of ECM onto the tips of the micropost array (**Figure 5(c)**). Subsequent treatment with Pluronics can be used to prevent cell adhesion at any surface of the microposts that has not been stamped with ECM protein. Pluronics is a nonionic copolymer consisting of ethylene oxide and propylene oxide, whose amphiphilic nature makes it a powerful surfactant. It adheres to the unstamped regions of PDMS to form a single-molecule thick coating that prevents other molecules from adsorbing to the surface. Thus, cells are confined to form focal adhesions to only the stamped tips of the posts (**Figure 6(a)**).

In order to measure strength of the traction forces on the posts, it is important to accurately track the displacement of the tips.[53,54] Originally, the displacements were identified by immunofluorescently staining the ECM at the tips of the posts.[47] A common treatment now is to submerge the micropost arrays in DiI solution, which is a hydrophobic dye which

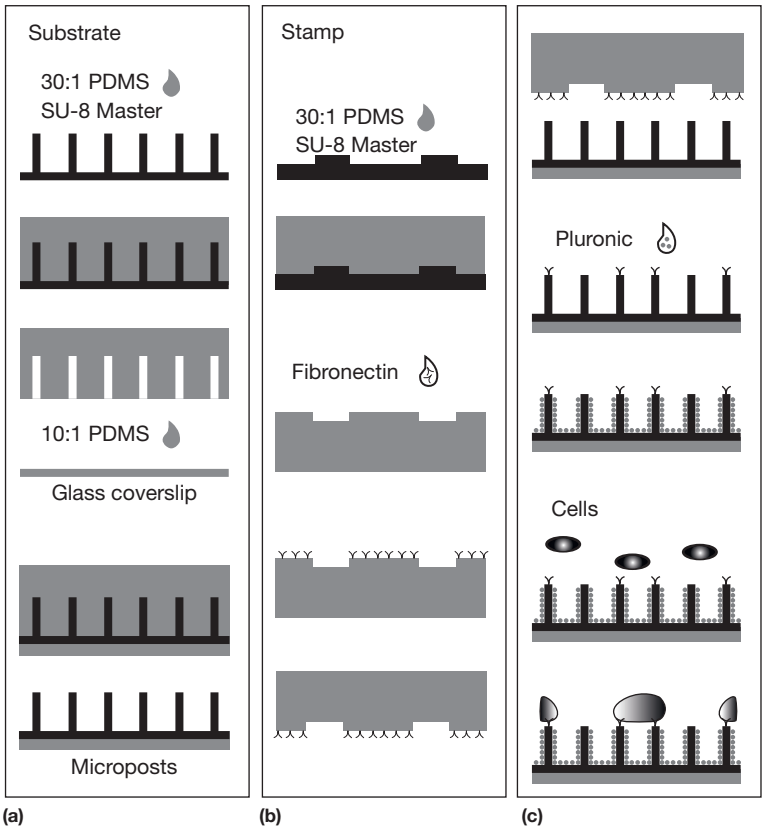

Figure 5 Micropost fabrication technique. (a) A master is created using photolithography of SU-8 or silicon (not shown) and then double-cast in PDMS to produce arrays of micropost. (b) For microcontact printing, stamps are created to pattern ECM proteins on the surface of the posts. (c) After stamping, Pluronic is used to block the adsorption of proteins onto unstamped surfaces in order to control cell adhesion.

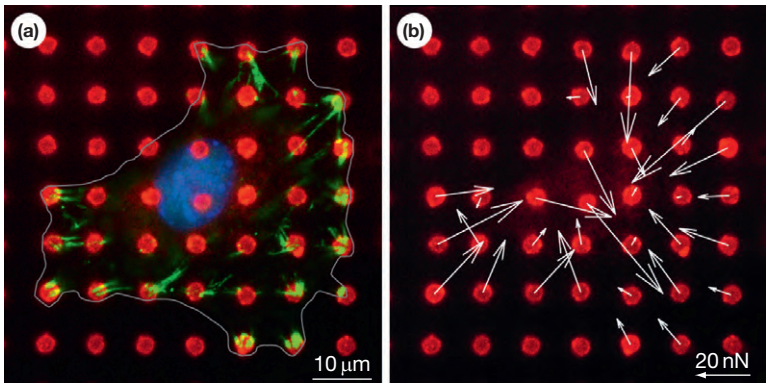

Figure 6 (a) A cell spreads across the tips of multiple microposts and forms focal adhesions. (b) Fluorescent labeling of the posts allows for traction force measurements as force vectors. Scale bar is 10 μm and scale arrow is 20 nN. Adapted from Sniadecki, N. J.; Anguelouch, A.; Yang, M. T.; *et al. Proc. Natl. Acad. Sci. USA* **2007**, *104*, 14553–14558.

labels the PDMS in the infrared spectrum. Microposts can also be marked by depositing quantum dots in the tips of the posts[55] or by phase contrast microscopy.[56,57] A local traction force is determined from the post's deflection δ and is given by $F = 3\pi ED^4\delta/64L^3$, where E is the elastic modulus of PDMS, D is the diameter, and L is the length of the post. Microposts have been made with diameters between 2 and 5 μm and lengths between 5 and 15 μm. From these measurements, it is possible to determine the traction force field that cells exert on the microposts (Figure 6(b)). By adjusting the dimensions of the microposts, it is possible to tailor the stiffness of the array to look at how cells adjust their traction forces in response to matrix compliance[58] or anisotropic material properties.[59]

Microposts are a useful tool for examining individual cells, but the idea can be extended to larger and smaller scales as well. Micropost flexibility can be adjusted by increasing the dimensions to measure the high forces generated by cardiac myocytes (Figure 7(a)).[60] Large microposts ('megaposts') have been

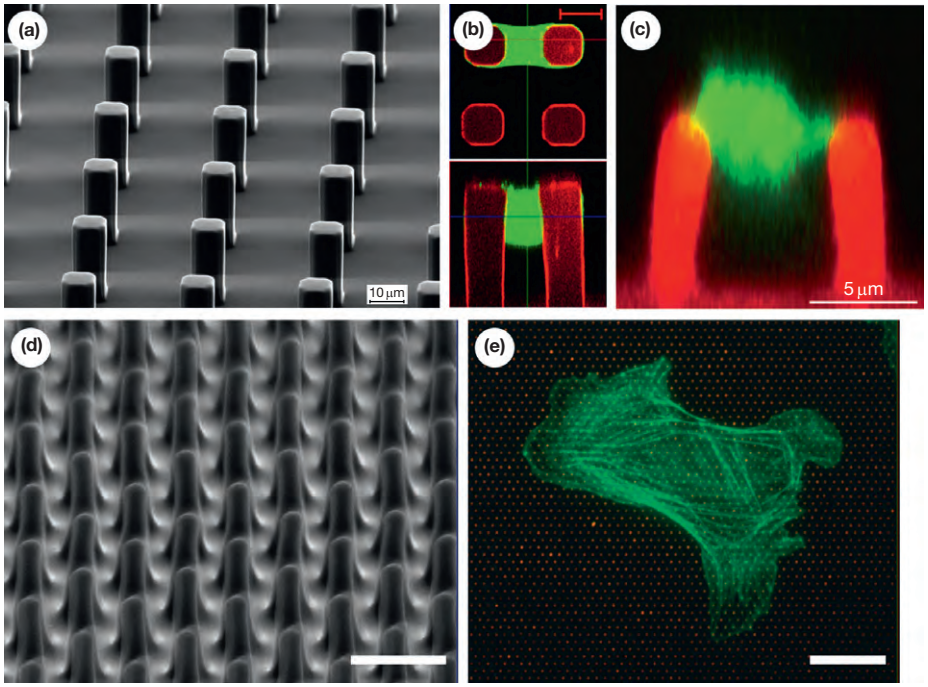

Figure 7 (a) Scanning electron microscope (SEM) image of megaposts. (b) Actin-labeled cardiac myocyte suspended between two megaposts. Scale bar is 10 μm. (c) Platelet microclot suspended between a pair of microposts. (d) SEM image of nanoposts. Scale bar is 10 μm. (e) Cell spread on nanoposts and have more defined cytoskeletal structures. Scale bar is 10 μm. Adapted from Kajzar, A.; Cesa, C. M.; Kirchgessner, N.; Hoffmann, B.; Merkel, R. *Biophys. J.* **2008**, *94*, 1854–1866; Liang, X. M.; Han, S. J.; Reems, J. A.; Gao, D.; Sniadecki, N. J. *Lab Chip* **2010**, *10*, 991–998; Yang, M. T.; Sniadecki, N. J.; Chen, C. S. *Adv. Mater.* **2007**, *19*, 3119.

used to test single cardiac myocytes that have been isolated to adhere to pairs of large posts (Figure 7(b)). Observation shows periodic myocyte contraction rates and large force ranges of 140–400 nN, which is beyond the measurable range with other techniques. The megapost approach has also been used to measure tissue-construct forces that arise from the combination of cells and ECM into a microtissue.[61] The samples are made by seeding cells and collagen into molds that were hundreds of microns long and containing two megaposts at either end. As the cells gather with collagen, they pull on the megaposts revealing bulk dynamics. In an approach similar to megaposts, pairs of microposts were used to measure the contractile forces that platelets generate when they aggregate together to form a clot and then retract (Figure 7(c)).[62] Recent developments have reduced the dimensions of the microposts to create nanoposts (Figure 7(d)).[63] These smaller dimensions allow for a significantly higher packing density of posts underneath a cell that creates a quasismooth surface on which a cell can spread (Figure 7(e)). The cytoskeletons in cells on the nanoposts closely resemble those observed for cells on flat surfaces. The reduced spacing also allows cells or cellular structures to be analyzed that are too small to fit between individual microposts. As the technology to fabricate BioMEMS improves, it is likely that the adhesive and physical interactions between smaller cells and subcellular structures will be more deeply explored.

Unlike the deformation of continuous films or gels, individual microposts are independent sensors because the deflection at one post does not affect the measurement of force at another post. Thus, these arrays lend themselves to measuring a large field of forces from multiple cells and different configurations of patterning can be done to test a wide gamut of multicellular interactions. Cells in a monolayer form adherens junctions with neighboring cells, and microposts have been used to examine the mechanical interactions in sheets of cells.[56,64] Bowtie patterns can also be used so that the tugging force between pairs of cells can be measured in isolation (Figure 8(a)).[65] Fibronectin was patterned onto the microposts to confine the contact between two cells. Since the pair of cells is connected through their adherens junctions, the vector sum of traction forces of one of the cells is not zero, but is in fact the tugging force from the neighbor cell. It was found cells that had a greater length of adherens junction with each other were able to support a higher tugging force. It was found that Rho mediated the tugging force and the Rac regulated the increased adherens junction assembly length. This mechanical interplay between cells shows that with groups of cells on the microposts, maximum forces are at the edge of the monolayer and exceed those of a single cell, indicating that collective mechanical signaling may be occurring.[56] This signaling can lead to a mechanotransduction response because cells at the edges or corners of a monolayer had higher traction stresses against the ECM due to the tugging forces of their neighbors, and this stress caused increased proliferation of cells at the edge (Figure 8(b)).[64] Heterogeneous cell–cell interactions can also promote higher traction forces because individual endothelial cells within a monolayer exerted higher forces on the microposts when they were in contact with a transmigrating monocyte (Figure 8(c)).[66]

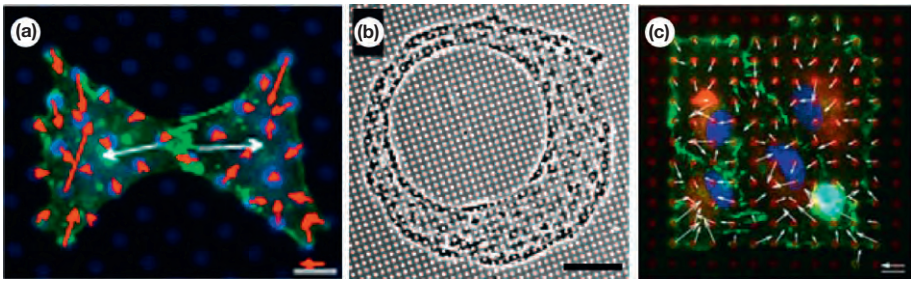

Figure 8 (a) Cells patterned to bowties on microposts can be used to measure the tugging force at adherens junctions. Scale bar is 10 μm, scale arrow is 10 nN. (b) Endothelial cells patterned into an eccentric circle shape on the microposts. Scale bar is 100 μm. (c) Monocyte transmigration through endothelial cells can be measured on microposts. Scale bar is 10 μm, scale arrow is 32 nN. Adapted from Liu, Z.; Tan, J. L.; Cohen, D. M.; *et al*. *Proc. Natl. Acad. Sci. USA* **2010**, *107*, 9944–9949; Nelson, C. M.; Jean, R. P.; Tan, J. L.; *et al*. *Proc. Natl. Acad. Sci. USA* **2005**, *102*, 11594–11599; Liu, Z. J.; Sniadecki, N. J.; Chen, C. S. *Cell. Mol. Bioeng.* **2010**, *3*, 50–59.

3.315.4. BioMEMS Devices to Apply Forces to Cells

Cells sense forces and modulate their cytoskeleton and regulatory proteins accordingly.[67] The three main cytoskeletal filaments actin, intermediate filaments, and microtubules transmit forces within a cell, and can become linked to neighboring cells cytoskeleton through transmembrane junction proteins such as at adherens junctions. Cells therefore relay forces to cells around them, as well as experience forces acting on them from their microenvironment. The importance of these transmitted forces in tissue is important in the development of the cardiovascular, musculoskeletal, and nervous systems, all of which have been shown to be influenced by mechanical forces.[68]

Arterial remodeling provides an interesting example of cellular mechanotransduction. Arteries are mechanically compliant, and when blood is driven through them, they expand elastically with each pressure wave from the cardiac cycle. The distensible nature of the arterial tissue acts as a stretchable substrate on which endothelial cells adhere. Strains up to 10% are normal for arterial tissue, and these strains can be recreated *in vitro* by culturing cells on flexible PDMS membranes that are stretched uniaxially. Cells have been observed to change their shape and realign their actin cytoskeletons in a direction perpendicular to the applied strain. However, when Rho activity is inhibited, these cells align in a direction parallel to the stretching, suggesting that external force is sufficient to induce actin remodeling.[69]

Mechanotransduction has been hypothesized to occur at a variety of cellular structures, but the cytoskeleton has been strongly implicated to have a central role since it connects to the focal adhesions and adherens junctions. When cells on a PDMS membrane were treated with a detergent to keep the cytoskeletons intact but strip away the lipid membranes and cytoplasmic proteins, it was found that cytoskeletons that were stretched had significantly higher amounts of focal adhesion proteins.[70] This response is similar to the growth response at the focal adhesion due to traction forces.[41] Additionally, the protein response at the focal adhesion suggests that mechanotransduction occurs from conformation changes.[71] Force may cause unfolding of focal adhesion proteins to reveal new domains for the binding of adaptor or signaling proteins or it may also expose enzymatic domains that then activate signaling activity associated with mechanotransduction. For additional information, see **Chapter 5.527, Cardiovascular Tissue Engineering**.

3.315.4.1. Micromanipulation

Tests with large strains and stresses are useful for simulating tissue level dynamics but single cell systems are of equal interest. Cellular responses to a localized force can be useful in examining a mechanosensor in a cell. The most direct approach is to use micromanipulation techniques with a glass pipette.[72] To form this tool, a pipette is heated until its melting temperatures and then pulled into a long, sharp tip before being allowed to cool. Because the tip diameter can be as small as 1 μm, its deflection can be used to measure the amount of force applied to the cells. These tool tips can be biofunctionalized by coating with an ECM protein such as fibronectin to ensure that integrins adhere to the tip and form focal adhesions. It has been observed that applied force can create growth at focal adhesions near the tip. It has also been shown that the externally applied mechanical stress can bypass the need for ROCK-mediated cytoskeletal tension in order to cause the growth of focal adhesions.

AFM has been used to impart forces to biological materials,[73] but larger forces and more degrees of freedom in positioning the manipulator may be of interest. MEMs micromachining can produce probing tools for applying localized cell forces with wider force ranges than AFM and with greater accuracy than glass micropipette techniques. A micromachined device consisting of suspended, flexible beams has been created from silicon wafers (**Figure 9(a)**).[74] A probe tip on a translatable backbone beam is connected to pairs of flexible beams that are fixed to the base silicon structure. As the probe tip is pushed against a cell, the change in lateral distance between the tip and a fixed reference point can be used to indicate the force (**Figure 9(b)**). Applying pulling force to axons has shown that tension causes vesicles that contain neurotransmitters to accumulate at the presynaptic terminal, indicating that neuromuscular synapses use tensile forces in regulating synaptic function (**Figure 9(c)**).[75]

3.315.4.2. Magnetic Bead Forces

A technique for applying forces is magnetic twisting cytometry (MTC).[76] Here, a ferromagnetic microbead is coated with an Arg-Gly-Asp (RGD) peptide sequence, which is a ligand for integrins. These beads can then be bound to the surface of a cell and mechanical stress applied by rotating the beads through a magnetic field (**Figure 10**). Probing individual

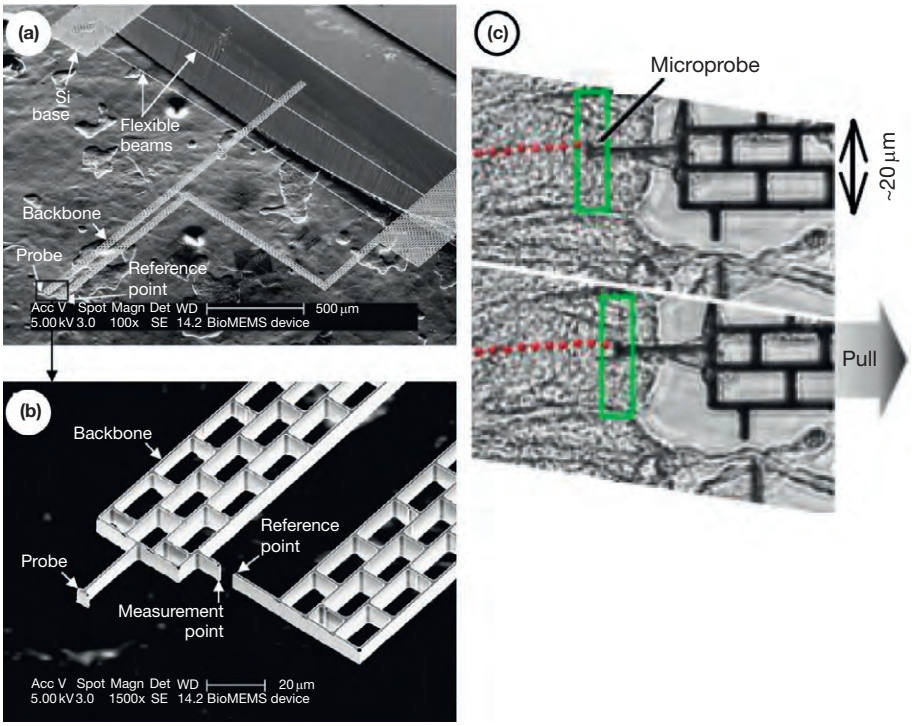

Figure 9 (a) Suspended BioMEMS manipulator structure made from silicon. (b) Force measurement is conducted by monitoring the distance between the probe and reference point on a fixed beam. (c) Force from the manipulator can be used to examine mechanotransduction in nervous tissue. Adapted from Yang, S.; Saif, T. *Rev. Sci. Instrum.* **2005**, *76*; Siechen, S.; Yang, S. Y.; Chiba, A.; Saif, T. *Proc. Natl. Acad. Sci. USA* **2009**, *106*, 12611–12616.

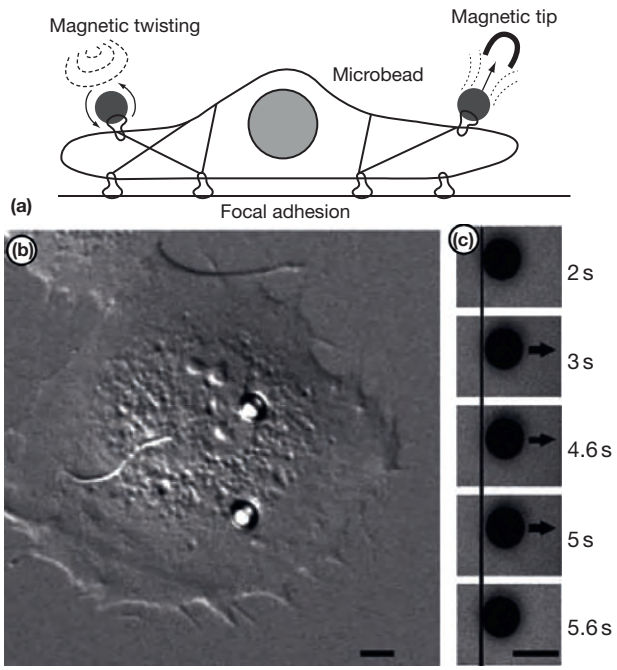

Figure 10 (a) Magnetic microbeads bound to integrins on a cell are rotated by a uniform magnetic field or pulled into the gradient of a magnetic field emanating from magnetic tip. (b) Two microbeads attached on a cell's surface are pulled on and (c) the response shows a displacement starting at time of 3 s and ending after 5 s. Scale bars are 5 μm. Adapted from Matthews, B. D.; Overby, D. R.; Alenghat, F. J.; *et al. Biochem. Biophys. Res. Commun.* **2004**, *313*, 758–764, with permission from Elsevier.

focal adhesions through MTC demonstrated that a cell stiffens its mechanical attachment to the bead to prevent it from twisting. A similar response was observed with magnetic tweezers, where an integrin-bound magnetic bead is pulled into the gradient of a magnetic field.[77] Early reinforcement depends on the structural integrity of the cytoskeleton, but the active strengthening of the adhesion site to a sustained force from the bead requires Rho, ROCK, Src, and stretch-activated ion channels.[78] Combining MTC with fluorescence resonance energy transfer gives a way to visually observe the activation of proteins under applied loads.[79] In particular, Src has been observed to become activated at both the local focal adhesion where force is applied and at remote sites. The rate of activation at the remote sites is 50 times faster than what is possible through soluble factor-induced signaling and can be inhibited by pharmacologically disrupting microtubule and actin filaments to prevent the transmission of force along the cytoskeleton.[79,80] Thus, mechanical forces acting through the cytoskeleton might be a rapid and efficient signaling cue to inform cells about their microenvironment as opposed to diffusive, soluble signals. It has been revealed by using MTC that mechanotransduction signals can also propagate across adjacent cells through their adherens junctions.[81] Interestingly, vinculin, which is a protein that is associated with both the focal adhesion and with the adherens junctions, has been observed to accumulate at the E-cadherin adhesion complex under applied force.[82] Since cell–cell adhesions appear to have a similar mechanotransduction response as cell–ECM adhesions, the cytoskeleton likely plays an integral role in directing these mechanical forces to the appropriate mechanosensory structures.[83]

3.315.4.3. Optical Traps/Tweezers

Optical traps are another method that can measure and induce forces at the subcellular level. The technique uses a focused laser to produce a force on a dielectric microbead, which can be embedded at the surface or in the cytoplasm of a cell. Beads can be used to apply forces to focal adhesions, but non-ECM proteins can be coated onto the beads to probe a variety of biophysical interactions within a cell. As long as the bead's dielectric material has a higher refractive index than the surrounding medium, when the bead is in focal point of the beam, it experiences an optical force toward the center of the beam. This restoring force is due to change in momentum of the photons from refraction as the laser light passes through the bead. If the center of the beam is moved, the bead will experience a stronger restoring force that moves it toward the position of the laser's focal point. The distance of the bead from the center of the focal point is a close approximation to the strength of the restoring force and is usually measured using a photodiode.

Optical tweezers have been used to show that focal adhesion strengthening occurs with applied force.[84] Vinculin is observed to accumulate at the site of applied force using beads coated with only the cell-binding domains of fibronectin.[85] The accumulation of the focal adhesion proteins likely involves the early binding of talin to the fibronectin-integrin complex that provide initial strength to the adhesion site.[86] The applied force also activates Src, which regulates the growth of the integrin–cytoskeleton connection.[87] The stiffness at the cellular membrane can also be examined with optical tweezers, where an isoform of myosin, myosin-1a, has been found to be essential in linking the membrane to the underlying cortical cytoskeleton.[88]

Larger field effects for applying forces to cells can also be created. An optical method, known as optical stretching, uses two lasers that face one another (**Figure 11(a)**).[89] A cell trapped between the two lasers is trapped at the focal point, but also experiences a gradient of forces from the refracted beams that cause a stretch to its entire volume (**Figure 12(b)–12(d)**). This technique functions as long the refractive index of the cell is higher than the surrounding fluid environment. The stretching force that can be generated by the gradients is significantly larger than for two beads pulling with optical tweezers. Also the use of divergent beams produces less risk of radiation damage to the biomolecule or cell. An important consideration for optical stretching is that it is limited to the study of nonadhesive cells as many cells will undergo apoptosis without adequate integrin engagement.

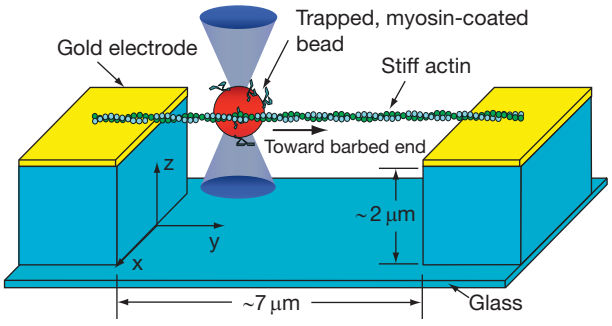

Figure 11 Myosin coated bead placed with optical tweezers migrating on an actin filament, which is held in tension between two gold adhesion pads. Adapted from Arsenault, M. E.; Sun, Y.; Bau, H. H.; Goldman, Y. E. *Phys. Chem. Chem. Phys.* **2009**, *11*, 4834–4839, with permission from Royal Society of Chemistry.

Optical techniques provide high sensitivity at the nanoscale and can be used to measure single biomolecule mechanics.[90] To do so, a bead is attached to one end of a molecule with the other end anchored to a nonmoving surface. It is possible to examine the stretch response in a molecule under an applied load by moving the optical trap away from the anchored molecule and observing the bead's change in distance from the trap's focal point. Sensitivity is so high that in fact optical traps are limited only by environmental noise from the substrate, since it is theoretically possible to resolve angstrom scale length changes. To address the noise, a second optical trap and microbead can replace the anchored point on a biomolecule, enabling even finer forces to be measured.[91] Not only does it provide a way to study how force can change the structure of a protein or biomolecule such as DNA, it also provides a measure of strain recovery times, spring constants, and internal molecular coefficients of friction, thus providing a richer mechanical analysis of single molecules.[90]

In particular, the mechanical interactions between actin and myosin can be examined to better understand how this fundamental process underlies the mechanics of cells. Optical tweezers have been used to determine that myosin bound to a nonmoving surface can produce 3 pN of force on average with each power stroke against a single actin filament that is held in an optical trap.[92] Improvements to this approach have demonstrated that actin filaments can be aligned across a gap between two gold electrode by using an AC field (**Figure 12**).[93] Tension in the filament is controlled by the electric field which allows a straight actin filament to be formed between the gold electrodes. A bead coated with myosin V or myosin X is brought in contact with the actin filament and released from the optical tweezer. Interestingly, the path that the bead took under myosin's motor action was helical as it traversed toward the barbed end of the filament. A similar helical path has been seen for myosin II,[94] suggesting that the motor action of myosin involves a degree of torque as it progresses along the length of actin.

3.315.4.4. Magnetic Microposts

A recent development in BioMEMS has been the use of PDMS micropost arrays with embedded magnetic nanowires. Magnetic cobalt nanowires are manufactured through electrochemical deposition into a sacrificial alumina template with 300 nm diameter pores. Once released from the template, the nanowires are suspended in ethanol and then aliquoted onto the PDMS negative mold under a magnetic field, which pulls the nanowires down into the wells that form the microposts. Once the ethanol is evaporated away, PDMS is then poured into the negative mold to form the micropost arrays. The PDMS encapsulates the nanowires that are deposited into the wells, and once the PDMS array is peeled from the mold, the nanowires are found to be embedded inside individual posts, which are referred to as magnetic posts (**Figure 13(a)**).[95] Biofunctionalization of the microposts is performed using the

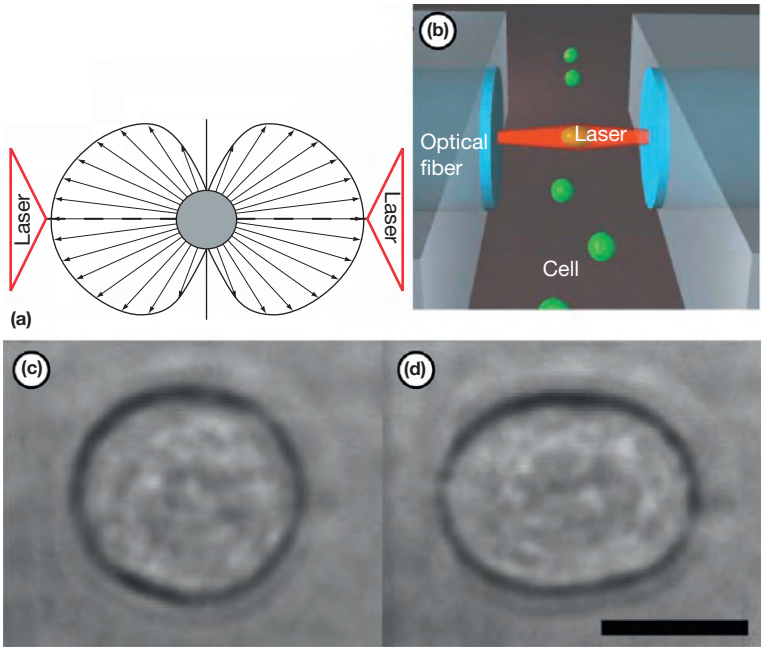

Figure 12 (a) Divergent focusing of two optical tweezers results in whole-cell stretching forces. (b) Combining the optical stretcher within a microfluidic channel allows for high-throughput trapping and stretching of a cell. (c) Phase light images of a trapped cell without stretch and (d) under optical stretch. Scale bar is 10 μm. Adapted from Guck, J.; Schinkinger, S.; Lincoln, B.; *et al. Biophys. J.* **2005**, *88*, 3689–3698, with permission from Elsevier.

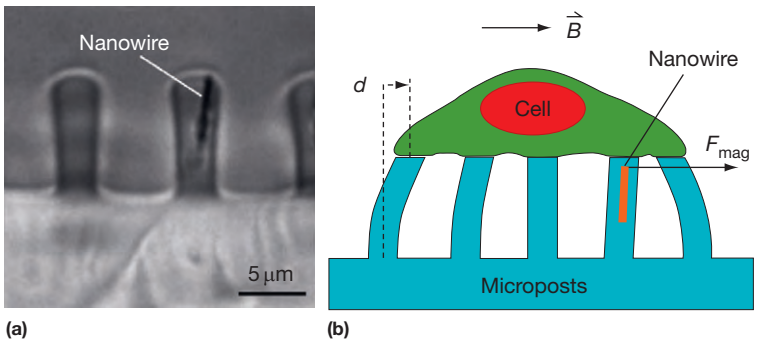

Figure 13 (a) Phase image of micropost cross section with embedded cobalt nanowire. (b) External force can be imparted to a cell at the magnetic post by applying a magnetic field, while traction forces can be measured at the nearby nonmagnetic posts. Adapted from Sniadecki, N. J.; Anguelouch, A.; Yang, M. T.; *et al. Proc. Natl. Acad. Sci. USA* **2007**, *104*, 14553–14558.

same techniques as with nonmagnetic micropost arrays. When a cell is seeded onto the surface of the microposts, they adhere at the tips and form focal adhesions and stress fibers just as if they were on flat substrates. PDMS posts that have the magnetic nanowires are able to be actuated when a horizontally applied uniform magnetic field is presented (**Figure 13(b)**). Deflection of a magnetic post introduces a controlled stress to the basal contact surface of the cell that induces growth at the local focal adhesion. Since a cell spreads onto multiple posts, its traction forces can be measured through the surrounding nonmagnetic posts. The posts are mechanically isolated from each other, so force actuation at a magnetic post does not impact the measuring ability at its neighbors. This has the advantage of being able to exert clearly measurable directionality and magnitude of force without worrying about force contributions from neighboring regions. The use of magnetic microposts has revealed that a cell responsds to an applied force at one or more of its focal adhesions with a rapid loss in cytoskeletal tension that slowly recovers after the stimulation.[54] This suggests that a cell can adjust its cytoskeletal structure in response to mechanical cues in its microenvironment.

3.315.4.5. Cytoskeletal Force Response

Under stretch from a silicone membrane, a cell's cytoskeleton tends to quickly fluidize before recovering and solidifying over time.[96] Under the solid-like state, biochemical interactions within a cell are highly specific, where the stable structures of the cytoskeleton are formed from distinct ligand-binding site interactions. Upon stretching a cell, it experiences a

structural transition into a chaotic, glassy-like phase where nonspecific interactions from proteins released from the disrupted cytoskeleton cause a crowded, molecular environment. Specifically, the stretching stimulus acts as a kind of 'enzymatic trigger' that causes the actin cytoskeleton to rapidly depolymerize. As a cell's structure turns over into a glassy-like state, there is a transitional drop in its stiffness. Newly freed G-actin monomers then polymerize into F-actin to resolidify the cell and cause its stiffness to return to prestretch levels. Treating cells with F-actin stabilizer jasplakinolide and applying stretch shows that the cell has a larger decrease in stiffness, but also recovers quickly to its pretreatment stiffness. Recent research has also examined fluidization and recovery in response to stretch using traction microscopy tools. Cells placed on polyacrylamide gels with isotropic or anisotropic stretches have traction forces that rapidly decrease after stretch which then recovers over time. These responses are seen in other diverse cells such as smooth muscle, endothelial, and osteocytes.[97]

3.315.4.6. Nanoscissors

The structural recovery of actin can be observed directly by snipping actin stress fibers inside a cell using a highly focused, femtosecond laser. Actin filaments in cells expressing GFP-actin can be targeted for ablation without causing large spread heating effects to the cell.[98,99] Cutting actin with a laser causes the filaments to instantaneously pull apart and continue to retract over many seconds. This is interpreted as the release of elastic tension in the strand, as well as gives insight to the viscoelasticity of the filaments and the fluid resistance of the cytoplasm.[98] Combining nanoscissor with traction force microscopy gives researchers the ability to measure the force contributions of single stress fibers. Severing a single fiber revealed a progressive loss in cytoskeletal tension for a cell. For cells on stiff substrates, cutting a fiber with the laser resulted in very minor cell elongation. On soft substrates, however, the severed stress fiber caused significantly higher cell elongation. Traction force mapping showed that the focal adhesion linked to the severed stress fiber displaced outward from the cell, furthering the evidence that cytoskeletal tensions are responsible for cell morphology and adhesion stability. The viscoelastic relaxation seen for cutting a single fiber is distinct from the rapid relaxation for cells stretched on silicone membranes or pulled on with magnetic posts. It is likely that local severing of actin causes a slow response because the remaining cytoskeletal structure is intact while the other techniques stimulate focal adhesion signals that cause massive disruption to the cytoskeleton's structural integrity.

3.315.5. Microfluidic Systems

BioMEMS provides tools that give better control over the microenvironment of the cell and, in particular, can be employed to present a myriad of mechanical and chemical factors to the cells. Constant or varied fluidic shear can be applied across single or multiple cells. Other factors that cells would see in their native environment such as stretch or pressure responses may be added. The microscale approach lends itself to the analysis of single cells in a high-throughput manner, which can be useful in filtering out heterogeneous responses within a subpopulation of the cells.[100] Moreover, more than one cell type may be cocultured together in a microfluidic system to gauge responses to released soluble factors and transmembrane signaling at their cell–cell contacts.

An added benefit of microfluidics is the high degree of control over waste product removal and nutrient addition. Typical protocols require that one changes a culture's nutrient media every 48 h.[101] Common growth factors such as serum become depleted in these intermittent times, while proliferating cells produce increasing amounts of undesirable waste products. Compared to static cell cultures, microfluidic systems and bioreactors typically have large volumes of media which translates to a volumetric buffer that minimizes chemical profile changes over time. The motion of the media also continuously refreshes the local media at the cell level, maintaining a steady amount of available biomolecules. Compared to static culture, cells in microfluidics can be confined to far narrower bands of available growth factor or signaler molecule concentrations.

3.315.5.1. Fluid Shear Stress

In many biological systems, mechanical shear stress from fluid flow plays a vital role in regulating cell morphology and function. These effects can be seen in flow systems as diverse as cardiovascular blood flow and interstitial cell flow. It has been well documented that the structure and physiology of the vasculature is heavily influenced by shear rate and flow type.[4,102] Vascular cells are exposed to a wide variety of flow conditions ranging from highly turbulent flows in the heart and major arteries to extremely laminar flows in arterioles and venules.

Mechanotransduction response by endothelial cells is of particular interest because of its close relation to atherosclerosis development. In normal function, the endothelium acts as a nonadhesive and nonclotting layer that protects arterial tissue from developing fatty lipids and invasive leukocytes in the intima. When the endothelium is damaged by shear, its barrier function deteriorates and lipids and macrophages are found to be in abundance in the artery wall. Once there, cytokines released from the affected area recruit additional leukocytes to the site where they accumulate lipids and swell the artery wall. Vascular smooth muscle cells proliferate within the damaged region and contribute to wall thickening by further releasing growth factors, chemoattractants, and vascular cell adhesion molecule.[103]

Initial damage can be caused by direct injury or endothelial cell remodeling in response to below average shear or disturbed shear regimes with high shear gradients. Endothelial cells express an atheroprone gene profile when exposed to these flow conditions.[104] However, laminar shear stresses cause a conformal remodeling of individual cells to reinforce their barrier function by promoting cell–cell junctions.[105] As mentioned previously, cells can align in response to applied stretch. However, different cells have different mechanotransduction responses. Mouse 3T3 fibroblasts align parallel to the applied strain, while endothelials align perpendicular.[69] Specific response also exists in shear stress as endothelial cells align parallel, but vascular smooth muscle cells align perpendicularly.[106] Endothelial cell realignment under fluidic shear has

also been confirmed with AFM examination of the surface topology.[107] Results show that shear-aligned cells display distinct surface ridges comprised of cytoskeletal actin. Non-sheared cells have smooth surfaces devoid of these features.

Platelets are another blood cell type that respond to mechanical shear. Decelerating hemodynamic shear microgradient profiles can activate platelets and cause thrombus formation.[108] Microfluidic experimentation has been a way to reveal this behavior. Other studies have shown that a critical rate of shear and exposure exists that, once passed, initiates activation regardless of shear conditions afterward. This can present problems downstream in the vasculature.[109] Platelet formation from megakaryocytes can be examined using BioMEMS apparatuses as well. Megakaryocytes are grown in a layered chamber separated by a porous membrane. Shear forces are applied to the system by gentle agitation. The megakaryocytes are seen to extend proplatelet-like protrusions through the membrane with an observation that agitated cells break off fragments of themselves.[110]

In examining the cellular response to shear, it is critical to know the flow conditions that a cell experiences *in vivo*, as well as the flows that are produced within a bioreactor or microfluidic device. Computer simulation of actual arteries utilizes magnetic resonance imaging or ultrasound scanning to generate a contoured interior surface of vessels for fluid flow simulations.[111] Direct methods exist for characterizing the flow inside a microchannel or flow chamber. Microscale particle image velocimetry is a technique that can be used to visualize and measure patterns in the flow field.[112] Here, microbeads or other tracer particles are added to a fluid and as they are carried along with the fluid, they report the local direction and velocity of the flow. These techniques are helpful in calibrating the flow conditions applied to cells.

3.315.5.2. BioMEMS Reactors

BioMEMS microfluidic devices are frequently used to apply moving fluid to cells. To do so, a channel is formed with biocompatible materials and functionalized. Channel shape, dimensions, and flow rates are all parameters that can be adjusted to control the flow dynamics. A proven and well documented method of channel fabrication is through PDMS replication molding of channels on a silicon wafer created through surface micromachining or photolithography techniques.[50] Complex geometries can be fabricated with this method, and valves and multiple flow conditions can be incorporated into one device. The material used to fabricate the device is flexible in many cases. For most applications, glass is the desired material due to its optical clarity, robustness, nonporous nature, and resistance to all sterilization techniques. However, machining glass and maintaining optical clarity and surface smoothness is a difficult task. Other common biocompatible replacement materials are acrylic, polystyrene, and polycarbonate. These offer similar optical transparency, can still be sterilized, and are easy to reconfigure in a laboratory setting. Plasma treatment of glass or a polymer creates a highly adhesive surface that forms a watertight seal with PDMS and is employed in many bioreactor designs.[48] For live-cell observation, a glass coverslip makes an ideal bottom surface of a bioreactor due to its thinness, a requirement for high magnification microscope objectives.

Cells are introduced to microfluidic systems by suspending them in media and injecting media through the microchannel. The cells settle and adhere to the surface and washing steps remove unattached cells. Since the vascular wall is comprised of more than endothelial cells, researchers have examined the effects of coculture on alignment and adhesion.[113] First, a layer of smooth muscle cells is seeded onto a substrate and grown to quiescent confluence. Next, endothelial cells can be directly seeded on top of the first layer and allowed to proliferate to confluence. The result is a bilayer of cells that closely resembles the endothelium in structure. The two cell types are able to form transmembrane gap junctions for chemical signaling, as well as respond to mechanical stresses through adherens junctions.

3.315.5.3. Bioreactor Pumping

To create fluid flow, different pumping schemes are used to achieve the desired flow in the microchannels. In the most basic flow device, pressure produced either through a raised fluid reservoir or gas source can drive fluid through a microfluidic system while a pump cycles the fluid back into the reservoir source. However, the lack of feedback-control means that researchers require more precise means. Syringe pumps provide excellent control if low flow rates are needed, but with limited volumes. Configuring multiple syringes and valves together can create a unidirectional flow that can recirculate to maintain the supply volume. Large flow rates use a peristaltic pump, also known as a roller pump, to have precise control of the flow. Peristaltic pumps produce a nonsteady pressure to the flow, which can be desirable if researchers want pulsatile flow. In most cases, a steady flow rate is desired, so air dampeners are placed in the fluid path to remove the effect of the pulses.[114] For additional information on other types of fluid flow devices, see **Chapter 5.511, Rotating-Wall Vessels for Cell Culture**.

3.315.5.4. Bioreactor Configuration

In BioMEMS microfluidic applications, ducts are the most common channel shape because shear is well defined and can be controlled precisely by dimensional considerations (**Figure 14(a, 1–8)**). Certain assumptions about the length-to-width aspect ratio mean that the wall shear stresses in the microchannels can be approximated to shear stress in parallel-plate flow. Shear forces at the wall can be calculated using: $\tau = 6\,\mu Q/WH^2$, where τ is shear stress, μ is viscosity, Q is fluid volumetric flow rate, W is the width, and H is the height of the channel. With steady pumping schemes, a constant level of shear stress gradient is produced at the wall surface. Adding a weir or obstruction in the channel initiates a disturbance in the flow that causes recirculation or vorticity at a region downstream. Between the weir and the vorticity reattachment point, a range of shear stresses and shear stress gradient exists.

Research has been done to determine the role of shear on endothelial cell morphogenesis. Endothelial cells placed into a duct with weir configuration display alignment characteristics that depend on their location in the channel. In steady, positive-direction laminar shear or steady, negative-direction laminar shear, the cells align parallel to the direction of flow.

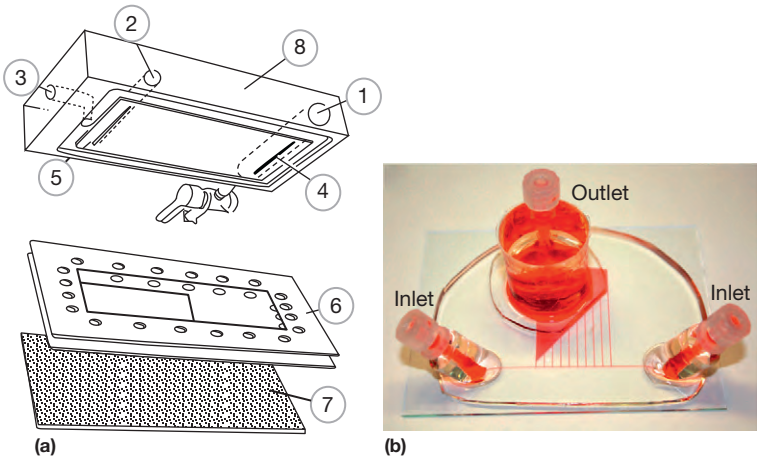

Figure 14 (a) Fluidic shear chamber utilizing parallel-plate channels. Fluid enters at (1), runs into the channel at slit (4), out of the channel (5), and leaves the device at (2). A gasket (6) seals a glass cover slide (7) with the polycarbonate top plate (8). Vacuum pressure through the (3) perimeter channel forms a seal for the device. (b) BioMEMS can be used to create multiple fluidic shears that are applied simultaneously to a common culture of cells by using differing channel lengths. The device is fabricated from replica molding of PDMS and treated with plasma to bond it to an underlying glass slide. Adapted from Chiu, J. J.; Wang, D. L.; Chien, S.; Skalak, R.; Usami, S. *J. Biomech. Eng.* **1998**, *120*, 2–8; Chau, L.; Doran, M.; Cooper-White, J. *Lab Chip* **2009**, *9*, 1897–1902.

Cells in regions with vorticity and below average shear stress have visible gaps between the cells, indicating a breakdown in their protective barrier function. Immunofluorescent imaging for F-actin filaments and microtubules additionally shows cytoskeletal fibers align in the direction of steady laminar flow and with no distinct alignment for low shear.[115]

A BioMEMS device fabricated with multiple channels of different lengths produces shear stress over a range of different magnitudes to the same culture of cells (**Figure 14(b)**).[116] The advantage here is that a single passage of cells can be used in the experiment and scarce samples can be tested efficiently. Mechanosensing of endothelial cells activates Weibel–Palade bodies to secrete von Willebrand factor, a glycoprotein that mediates the adhesion of platelets. Endothelial cells tested in this device display shear regulation of von Willebrand factor, supporting the idea that mechanosensing is a necessary component of hemostasis and wound healing.

Fluidic shear stresses not only influences morphogenesis, but also migration behavior. Endothelial cell mechanotaxis under hemodynamic flow is an important function for wound healing and vascular repair. Cells at the edge of a wound increase their motility toward regions that are damaged, extending the leading edge and possibly modifying the ECM to allow other cells to proliferate and move in that direction. Microfluidic devices are used to investigate this behavior by applying a shear across monolayers of cells. Wounding assays are commonly done by dragging a sterile glass pipette or razor blade across a confluent layer of endothelial cells creating a fissure in the monolayer. By taking time-lapse images of the cells at the fissure, it is seen that cell migration is the dominant response in wound healing versus cell proliferation. Regardless of the wound direction, whether it is parallel or perpendicular to the fluid flow, shear stress increases wound closure rates. Migration rates through mechanotaxis have an impact on angiogenesis in developing organisms and vascular health and so the use of a bioreactor device aids in research understanding.[117] Other methods for creating wound simulation is to seed cells onto a surface with a thin film PDMS layer containing cut out areas. Cells grow to confluence and the film is removed exposing a patterned monolayer of cells.[118] The wound model demonstrates that cells at the leading edge of the wounded area sense the void and exhibit 'leader-cell' behavior, becoming highly mobile and acting to drag the cell layer into the missing region.

Microfluidics can be combined with other systems to better replicate *in vivo* conditions. Most commonly, factors or chemicals are added to media which is washed over cells. Combinations or gradients of factors can be created within devices to perform many experiments simultaneously.[119] Cell seeding density determines the number of cells in microchannels and can be changed to isolate single cells or create confluent monolayers. Force during the transmigration of leukocytes can be studied by combining fluid shear and endothelial cells on microposts. As cells such as neutrophils adhere during shear and pass through the endothelium, they impart forces to push the endothelial cells apart, which in experiments is detected by underlying micropost sensors.[120] Coculture of cells through the use of integrated three-dimensional ECM scaffolds in microfluidic devices can examine capillary growth, endothelial cell migration, and gradient growth factor effects.[121] For additional information, see **Chapter 5.512, *In Vivo* Bioreactors**.

3.315.5.5. Interstitial Shear

Mechanical shear is experienced by cells outside the vascular system as well. Interstitial flow is the slow movement of lymphatic fluid or blood plasma between ECM structures and cells. The fluid driving force is thought to be from difference in hydrostatic and osmotic pressures between the lymphatic system and vascular capillaries. The slow nature of the fluid flow is also explained by the presence of the proteoglycans fiber network that impedes the flow. Proteoglycans in the ECM are formed out of protein filaments with many glycosaminoglycan (GAG) side chain connections. These GAGs are able to bind to signal molecules or cytokines in the fluid by being negatively

charged. The physical geometry of the GAG side chains means that they present a densely packed but porous structure of overlapping strands. The combination of the hydrostatic or osmotic pressure differences and the flow resistance presented by the cell–ECM architecture work together to control the interchange rates of lymphatic fluid.

Interstitial flow is of interest due to its role in molecular transport within tissue and cells. In particular, tumors have been shown to have more permeable vasculature but a limited lymphatic path outward, causing them to tend to retain biomolecules. Specific micro- or nanoparticles can be designed to become concentrated in tumors and deliver therapeutic drugs.[122] Cell–ECM constructs or size controlled membranes are one route to simulate and examine interstitial flow on cultured cells while molecular fluorescent-labeling allows observation of the particles exchange rates. Integrated microfluidic systems that incorporate three-dimensional scaffolds and cell encapsulation can create interstitial flow effects by creating pressure differentials across different surfaces of the cell, maintaining a more native-like environment for examining phenomenon such as angiogenesis.[123]

3.315.5.6. Single Cell Analysis

In some cases, cell responses from a large population of cells can be misleading. One may observe that the expression levels of a particular protein is not centered on a point, but may have two distinct peak levels due to a bimodal behavior. Bulk measurements through immunoassays or gel electrophoresis techniques would suggest that the expression level is the average of the two peaks; however, this is flawed because it fails to resolve the two individual peaks. Probing individual cells is important to capture these phenomena.[124] BioMEMS cytometry tools exist such as fluorescent flow and laser scanning cytometry.[125] In fluorescent flow cytometry, cells in suspension have their specific biomolecules labeled with a fluorescent probe and are flowed past an illumination source and sensor. Concentration of the biomolecule on the surface of the cell is gathered through signal intensity and large numbers of cells can be screened this way. Laser scanning cytometry also uses fluorescent labeling, but individual cells in culture are positioned under the sensor for measurement. Advantages of this include being able to take time-lapse images of many cells in one experiment, and the cell does not need to be adherent. However, the process is slower than with flow cytometry.

BioMEMS techniques for physical trapping also exist, such as creating substrates with arrays of wells with room for cells. Cells are seeded into the wells, and nonadherent cells are washed away. This approach has been used to monitor the differentiation of mesenchymal stem cells that were exposed to different mixtures of adipogenic or osteogenic media conditions.[126] Confined growth channels have been applied to create micropatterns of muscle cells for long-term differentiation studies and fluorescent labeling.[127] Fluidic forces can be utilized like in hydrodynamic trap devices, which use small cross-flow channels to position cells within larger microchannels. Configurations have been used to examine cell–cell interactions by placing hydrodynamic traps across a channel to capture single cells and bring them in contact.[128] Microfluidic systems can also physically separate individual cells for analysis.[124] Examples include a novel design of microchannels that divert cells into cup-shaped wells. The hydrodynamics of a well with an occupied cell site prevents further cell occupation and allows for arrays of single cells to be analyzed (**Figure 16**). By creating channel systems with integrated valves, flow paths can be systemically changed to isolate out single cells for extraction of biomolecules such as messenger RNA[129] or by combining it with on-device electrophoresis, amino acid contents of single cells can be examined as well.[130]

3.315.5.7. Cell Sorting

Microfluidic sorting is possible with other BioMEMS tools. Antibody capture is one method that can select out target cells from a population because of cell surface chemistry changes upon differentiation. An antigen or antibody is applied to microstructures with high surface areas such as arrays of microposts or serpentine channels, and suspended cells are flowed across. Cell surface affinity for the antibody draws the cells to the structure while nontarget cells continue to pass (**Figure 15**). This is a robust technique that has been used to sort circulating prostate tumor cells from cell groups.[131]

As mentioned previously, optical traps have been used to stretch cells, but this technique can also be used to detect phenotypic difference between normal and cancerous cells and then sort the cells into different groups.[132] Cancerous cells have different cytoskeletal elastic and viscoelastic properties than normal cells. Research using normal 3T3 mouse fibroblast and malignant SV-T2 mouse fibroblasts under stretch has shown that optically induced deformations are statistically higher in the cancerous cells. Refractive index between the two cells is generally indistinguishable so similar optical stretch forces are exerted on both types. Cellular deformation then directly reflects the cytoskeletal deformation and compliance. Breast epithelial cells can also be distinguished despite a relatively low sampling count. Normal MCF10 breast epithelial cells have the least compliance, or are the stiffest. Cancerous MCF7 cells have more compliance and metastatic modMCF7 cells are the most compliant. This technique has a high throughput compared to previous techniques and a statistical conclusion can be reached rapidly. Phenotype sorting can be performed without potentially damaging physical or biochemical alteration to the cell populations such as with genomic techniques.

Optical sorting of dielectric particles and whole cells can be achieved by splitting a laser beam and focusing it to create interferometric patterns. These can be arranged into optical lattices of any dimension. Microchannel flow through these lattices generates a directional gradient that exerts different forces to alter the trajectory of the particle through a microchannel for sorting.[133] Optimization of the lattice focusing can give high sorting accuracy comparable with fluorescence sorting or flow cytometry techniques.

Integrating electrical fields on microfluidic systems can be done to use dielectrophoresis (DEP) for sorting and cell micromanipulation. A cell's membrane can act as a dielectric material and when an electrical field is applied, the field exerts a force on the cell in the direction of the strongest gradient. These forces can be used to trap cells in suspension for analysis using arrays of electrodes to generate standing electrical gradients.[134]

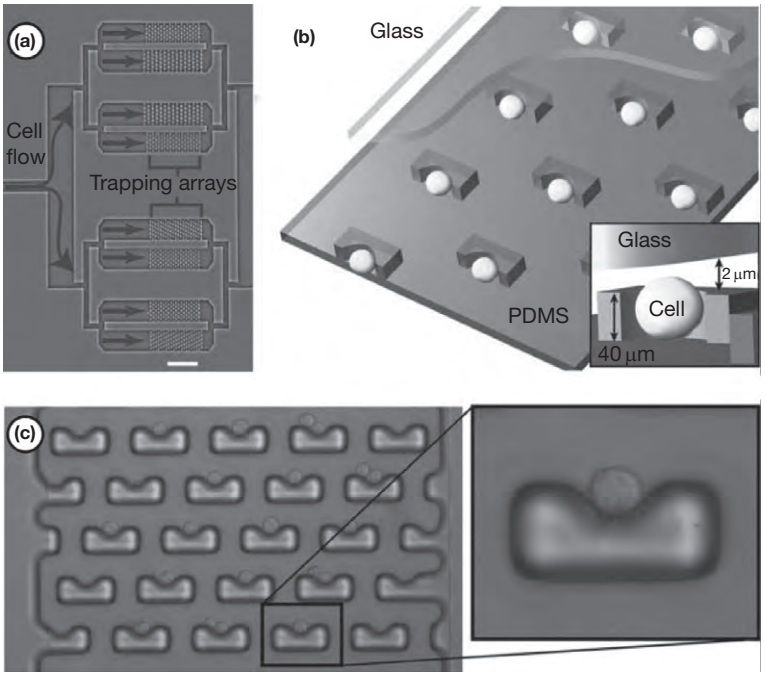

Figure 15 (a) Cell separation using (b) dimensioned heights and wells to (c) isolate single cells. Adapted from Di Carlo, D.D.; Wu, L.Y.; Lee, L.P.; *Lab Chip*, **2006**, *6*, 1445–1449, with permission from Royal Society of Chemistry.

The electrical properties of a cell's membrane can change depending on the proteins, biomolecules, or ions present in a cell during different differentiation states or cellular activities.[135] When a population of cells is exposed to electrical fields, DEP forces are exerted to differing degrees on the cells and allows for sorting them in a microfluidic system.[136]

3.315.5.8. Organ on Chip Microfluidic Devices

Research into the engineering of complete organ systems has benefited from microfluidic device studies as well. It has been possible to culture microtissue consisting of the heptatocytes in a fluidic bioreactor that supports cell viability and metabolic functionality of the liver.[137,138] Recently, a significant microfluidic system has been achieved that recreates the coculture cues and mechanical stimuli for cells of the pulmonary system.[139] The lung comprises individual alveolus which exchanges gas and chemicals with the blood. Similar to the endothelium, the alveolus are comprised of a single layer of alveolar epithelial cells with a meshwork of capillaries covering them. Gas and molecular exchange occurs through a thin ECM layer separating the epithelial cells and the endothelial cells of the capillaries as blood is pumped through the alveolus. There is also a strain effect induced as the alveolus fills with air during each respiratory cycle, with the elastic ECM aiding to expel the waste gas afterward. This is a complex system that is difficult to recreate with macroscale devices but has been achieved with a microfluidic system. First, a set of three parallel microchannels were constructed and bonded between a porous membrane (Figure 16(a)). The membrane is etched away in the left and right channels, but in the middle channel, it is partially etched so that a thin membrane separates the upper and lower

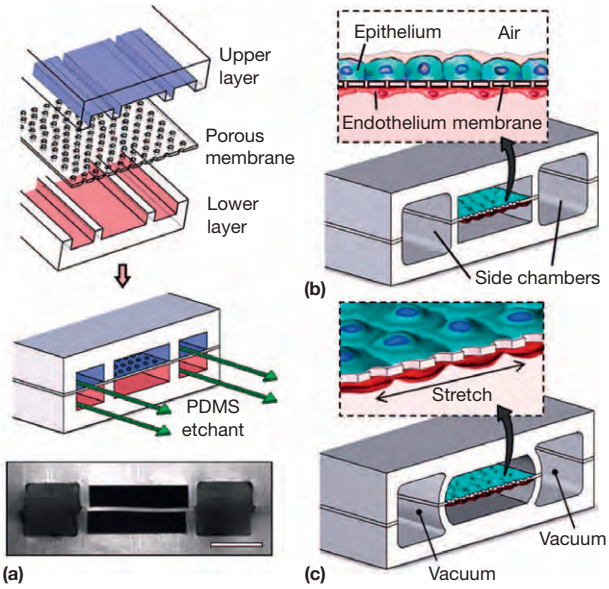

Figure 16 Lung-on-a-chip microdevice fabricated by (a) bonding two parallel PDMS microchannels around a PDMS membrane containing arrays of holes and etching steps. (b) Endothelial and epithelial cells can be grown on opposing sides of the membrane and exposed to shear and (c) stretch from applied vacuum. Adapted from Huh, D.; Matthews, B. D.; Mammoto, A.; Montoya-Zavala, M.; Hsin, H. Y.; Ingber, D. E. *Science* **2010**, *328*, 1662–1668.

channels. Alveolar epithelial cells can then be grown in the upper, center channel and pulmonary microvascular endothelial cells in the lower, center channel (Figure 16(b)). The left and right channels can be used to simulate strain from

respiratory cycling (Figure 16(c)). Researchers have used such devices to study coculture interactions between pulmonary cells and found that the barrier function of the alveolar epithelial cells and endothelial cells improved. Mechanical stretch used to mimic the motion of breathing accentuated the proinflammatory response to nanoparticles. These types of devices greatly improve the environmental cues seen by cells and can possibly replace animal testing by recreating whole-tissue physiology. For additional information, see **Chapter 3.309, Fluid Mechanics: Transport and Diffusion Analyses as Applied in Biomaterials Studies**.

3.315.5.9. Analysis of Mechanotransduction or Morphogenesis Biomarkers

In many BioMEMS applications and experiments, the presence or concentration of a protein is of interest to better understand the biochemical and biomechanical response of cells. To measure these, cell lysis is necessary to release intercellular contents of interest and can be performed through different BioMEMS techniques. Purely mechanical methods exist, such as forcing cells against micromachined barbs.[140] Another tool has been the development of micro system incorporated electroporation to disrupt the cell membrane without damaging organelle membranes.[141]

Immunofluoresence labeling is popular with researchers due to its target specificity. By using protein antibodies, single or multiple proteins to be examined together in one experimental sample to look at colocalization or compare expression levels. It is possible to perform the steps of immunostaining to cells inside a microfluidic device. To do so, the cells are washed with a fixative such as formalin or paraformaldehyde, whose aldehyde groups form methylene bridges between the nitrogen atoms of neighboring proteins. This treatment effectively cross-links the structure of the cell in place. The cell membrane is made permeable by adding a surfactant such as Triton X-100. Immunofluorescent staining utilizes a primary IgG antibody with affinity for specific antigens in a target protein of a cell. Blocking of nonspecific ligands in the cell can be accomplished by exposing samples to serum, which washes out unbound antibodies and serves to occupy nontargeted sites. A secondary antibody consisting of a fluorescent molecule conjugated to an IgG antibody to the primary antibody is then washed over the cell. The secondary antibody excites under a specific wavelength and emits photons at a higher wavelength. Single or multiple proteins can be placed on different excitation wavelengths to avoid signal interference. Because only targeted proteins or ligands are fluorescent, comparison between images for experimental and control samples gives researchers a method to cross-examine protein expression levels through signal intensity and an accurate way to identify protein colocalization sites. ELISA assays work under similar principles of antibody/antigen reactivity to detect presence or concentration in a sample. ELISA plates are scanned by a plate reader, and the intensity of the fluorescent signal indicates the amount of protein present in the sample. Microfluidic systems that perform ELISA on-chip have been used for disease detection and have an advantage over traditional assays by only requiring small amounts of biomarkers and reagents.[87]

In genomic techniques, microfluidics is a growing technology because of scaling advantages in biomolecular analysis.[142] In laboratory settings, amplification of DNA is traditionally done through polymerase chain reaction (PCR) techniques, but these generally require a sizeable sample from a population of at least 5000 cells, for which rare cells such as stem cells or circulating tumor cells may be difficult to obtain in large quantities. PCR and other amplification methodologies using BioMEMS can require as little as 150 cells, or only 300 pg. This technology and the level of sensitivity and detection have been demonstrated through human genome-wide transcriptome analysis.[143] Since external fluid handling is kept to a minimum, there is an improved sample accuracy in sensitive analyses such as PCR and electrophoresis.[144] In addition to mammalian cells, systems exist for the analysis of bacterial pathogens and viruses such as influenza.[145]

An interesting set of tools and assays are lab-on-disc or lab-on-CD technologies. These devices use microfluidic channels, gates, and switches imprinted into a spinning disc to perform many parallel evaluations of experimental samples. The microchannels are formed on a disc by photolithography and PDMS molding or injection molding plastics such as PMMA.[146] Force generated by spinning the device powers centrifugal pumping of fluid through the microchannels.[147] Different spin speeds cause the fluid to travel through channels that are gated by hydrophobic zones that act as burst valves. A fluid is able to move past a burst valve when the centrifugal force is large enough to overcome the surface tension of the fluid at the hydrophobic zone. Laser diode switchable gates can also be used to dynamically control the flow through the channels as the heat locally melts a barrier to the flow.[148] The design of the devices allows for processes such as mixing, metering, washing, reacting, and observation to occur in serial, entirely on disc, and is controlled by the spin speed profile.[149] Cell culture capabilities include growth and handling processes such as cell lysis.[150] ELISA assays have been converted to operate on discs and require less reagents and time than the standard large-scale assay.[151] Lab-on-disc is not limited to just fluids in the system but can also incorporate reagents bound on microbeads to increase surface area available for reactions. Immunoassays of whole blood in lab-on-disc have been performed to screen for diseases such as hepatitis and incorporate such protocols.[146] These microfluidic systems create a new opportunity to more completely investigate the spatial and temporal aspects of cell behavior by controlling the biochemical and biomechanical factors that a cell experiences and subsequently analyzing the response with integrated detection assays.

3.315.6. Future Directions

Many researchers are working toward better prosthetic integration with natural tissue. Currently, prosthetics are still largely perceived as foreign objects by the body. Few human-made materials can be accepted by living tissue on a cellular level and become incorporated with the native tissue. Through an understanding of migration, proliferation, differentiation, and adhesion that is aided by BioMEMS tools, future designs can better enhance biomaterial acceptance. This progress can be achieved by tailoring the material properties or soluble biochemistry to encourage migration through mechanotaxis or chemotaxis. BioMEMS tools also allow researchers to better control a cell's

microenvironment in order to elicit desirable behaviors from a cell. The development of new tools can offer better control of the biochemical and biomechanical environment properties or provide more powerful measurements. BioMEMS will continue to adapt from traditional MEMS application in order to improve. One such novel implementation has been the use of microfabricated nozzles for inkjet printers, which have been modified to deliver plasmids to targeted cells for gene transfection.[152] Microfluidics is particularly useful for engineering improvements for the cardiovascular system. For example, endothelial cell permeability from hemodynamic shear could be exploited for increased targeting of drugs to atherosclerotic lesions. Bioreactors could be used to culture megakaryocytes in order to generate large numbers of platelets to aid in blood transfusion. Surgical materials for stents can be biofunctionalized to prevent reocclusion of vessel walls after angioplasty, or can be constructed entirely of native ECM that can become fully incorporated into the tissue by encouraging cell motility and wound healing. Tools to impart microenvironment control for stem cells can enable better tissue engineering techniques in the future. These and many more examples demonstrate the potential for BioMEMS techniques and microenvironmental theories, which have merit for closer investigation.

Acknowledgments

The authors are grateful for support in part from grants from the National Institutes of Health (HL097284) and the National Science Foundation's CAREER Award.

References

1. Norman, J. J.; Mukundan, V.; Bernstein, D.; Pruitt, B. L. *Pediatr. Res.* **2008**, *63*, 576–583.
2. Sniadecki, N. J.; Desai, R. A.; Ruiz, S. A.; Chen, C. S. *Ann. Biomed. Eng.* **2006**, *34*, 59–74.
3. Geiger, B.; Spatz, J. P.; Bershadsky, A. D. *Nat. Rev. Mol. Cell Biol.* **2009**, *10*, 21–33.
4. Hahn, C.; Schwartz, M. A. *Nat. Rev. Mol. Cell Biol.* **2009**, *10*, 53–62.
5. Lo, C. M.; Wang, H. B.; Dembo, M.; Wang, Y. L. *Biophys. J.* **2000**, *79*, 144–152.
6. Thery, M.; Racine, V.; Pepin, A.; *et al. Nat. Cell Biol.* **2005**, *7*, 947–953.
7. Engler, A. J.; Sen, S.; Sweeney, H. L.; Discher, D. E. *Cell* **2006**, *126*, 677–689.
8. Mcbeath, R.; Pirone, D. M.; Nelson, C. M.; Bhadriraju, K.; Chen, C. S. *Dev. Cell* **2004**, *6*, 483–495.
9. Chen, C. S.; Mrksich, M.; Huang, S.; Whitesides, G. M.; Ingber, D. E. *Science* **1997**, *276*, 1425–1428.
10. Klein, E. A.; Yin, L.; Kothapalli, D.; *et al. Curr. Biol.* **2009**, *19*, 1511–1518.
11. Giancotti, F. G.; Ruoslahti, E. *Science* **1999**, *285*, 1028–1032.
12. Garcia, A. J.; Huber, F.; Boettiger, D. *J. Biol. Chem.* **1998**, *273*, 10988–10993.
13. Geiger, B.; Bershadsky, A.; Pankov, R.; Yamada, K. M. *Nat. Rev. Mol. Cell Biol.* **2001**, *2*, 793–805.
14. Burridge, K.; Wennerberg, K. *Cell* **2004**, *116*, 167–179.
15. Winder, S. J.; Ayscough, K. R. *J. Cell Sci.* **2005**, *118*, 651–654.
16. Bray, D. *Cell Movements: From Molecules to Motility*. Garland: New York, 2001.
17. Pellegrin, S.; Mellor, H. *J. Cell Sci.* **2007**, *120*, 3491–3499.
18. Zaidel-Bar, R.; Geiger, B. *J. Cell Sci.* **2010**, *123*, 1385–1388.
19. Ridley, A. J.; Hall, A. *Cell* **1992**, *70*, 389–399.
20. Ren, X. D.; Kiosses, W. B.; Sieg, D. J.; Otey, C. A.; Schlaepfer, D. D.; Schwartz, M. A. *J. Cell Sci.* **2000**, *113*(Pt 20), 3673–3678.
21. Lorenzo, A. C.; Caffarena, E. R. *J. Biomech.* **2005**, *38*, 1527–1533.
22. Ethier, C. R.; Simmons, C. A. *Introductory Biomechanics from Cells to Organisms*. Cambridge University Press: Cambridge, New York, 2007.
23. Suki, B.; Ito, S.; Stamenovic, D.; Lutchen, K. R.; Ingenito, E. P. *J. Appl. Physiol.* **2005**, *98*, 1892–1899.
24. Budynas, R. G.; Keith Nisbett, J. *Shigley's Mechanical Engineering Design*. McGraw-Hill: New York, 2008.
25. Vogel, V. *Annu. Rev. Biophys. Biomol. Struct.* **2006**, *35*, 459–488.
26. Vogel, V.; Sheetz, M. P. *Curr. Opin. Cell Biol.* **2009**, *21*, 38–46.
27. Pelham, R. J., Jr.; Wang, Y. *Proc. Natl. Acad. Sci. USA* **1997**, *94*, 13661–13665.
28. Jacot, J. G.; Mcculloch, A. D.; Omens, J. H. *Biophys. J.* **2008**, *95*, 3479–3487.
29. Cukierman, E.; Pankov, R.; Stevens, D. R.; Yamada, K. M. *Science* **2001**, *294*, 1708–1712.
30. Harris, A. K.; Wild, P.; Stopak, D. *Science* **1980**, *208*, 177–179.
31. Chrzanowska-Wodnicka, M.; Burridge, K. *J. Cell Biol.* **1996**, *133*, 1403–1415.
32. Helfman, D. M.; Levy, E. T.; Berthier, C.; *et al. Mol. Biol. Cell* **1999**, *10*, 3097–3112.
33. Burton, K.; Taylor, D. L. *Nature* **1997**, *385*, 450–454.
34. Harris, A. K.; Stopak, D.; Wild, P. *Nature* **1981**, *290*, 249–251.
35. Lee, J.; Leonard, M.; Oliver, T.; Ishihara, A.; Jacobson, K. *J. Cell Biol.* **1994**, *127*, 1957–1964.
36. Dembo, M.; Oliver, T.; Ishihara, A.; Jacobson, K. *Biophys. J.* **1996**, *70*, 2008–2022.
37. Dembo, M.; Wang, Y. L. *Biophys. J.* **1999**, *76*, 2307–2316.
38. Rajagopalan, P.; Marganski, W. A.; Brown, X. Q.; Wong, J. Y. *Biophys. J.* **2004**, *87*, 2818–2827.
39. Reinhart-King, C. A.; Dembo, M.; Hammer, D. A. *Mol. Biol. Cell* **2004**, *15*, 174a.
40. Munevar, S.; Wang, Y.; Dembo, M. *Biophys. J.* **2001**, *80*, 1744–1757.
41. Balaban, N. Q.; Schwarz, U. S.; Riveline, D.; *et al. Nat. Cell Biol.* **2001**, *3*, 466–472.
42. Shroff, S. G.; Saner, D. R.; Lal, R. *Am. J. Physiol. Cell Physiol.* **1995**, *38*, C286–C292.
43. Yuan, Y.; Verma, R. *Colloids Surf. B Biointerfaces* **2006**, *48*, 6–12.
44. Lal, R.; Drake, B.; Blumberg, D.; Saner, D. R.; Hansma, P. K.; Feinstein, S. C. *Am. J. Physiol. Cell Physiol.* **1995**, *38*, C275–C285.
45. Lal, R.; John, S. A. *Am. J. Physiol.* **1994**, *266*, C1.
46. Galbraith, C. G.; Sheetz, M. P. *Proc. Natl. Acad. Sci. USA* **1997**, *94*, 9114–9118.
47. Tan, J. L.; Tien, J.; Pirone, D. M.; Gray, D. S.; Bhadriraju, K.; Chen, C. S. *Proc. Natl. Acad. Sci. USA* **2003**, *100*, 1484–1489.
48. Zhou, J.; Ellis, A. V.; Voelcker, N. H. *Electrophoresis* **2010**, *31*, 2–16.
49. Mata, A.; Fleischman, A. J.; Roy, S. *Biomed. Microdevices* **2005**, *7*, 281–293.
50. Duffy, D. C.; McDonald, J. C.; Schueller, O. J. A.; Whitesides, G. M. *Anal. Chem.* **1998**, *70*, 4974–4984.
51. Tan, A.; Rodgers, K.; Murrihy, J.; O'Mathuna, C.; Glennon, J. D. *Lab Chip* **2001**, *1*, 7–9.
52. Slentz, B. E.; Penner, N. A.; Lugowska, E.; Regnier, F. *Electrophoresis* **2001**, *22*, 3736–3743.
53. Lemmon, C. A.; Sniadecki, N. J.; Ruiz, S. A.; Tan, J. L.; Romer, L. H.; Chen, C. S. *Mech. Chem. Biosyst.* **2005**, *2*, 1–16.
54. Sniadecki, N. J.; Lamb, C. M.; Liu, Y.; Chen, C. S.; Reich, D. H. *Rev. Sci. Instrum.* **2008**, *79*, 044302.
55. Addae-Mensah, K. A.; Kassebaum, N. J.; Bowers, M. J.; *et al. Sens. Actuators A Phys.* **2007**, *136*, 385–397.
56. Du Roure, O.; Saez, A.; Buguin, A.; *et al. Proc. Natl. Acad. Sci. USA* **2005**, *102*, 2390–2395.
57. Li, B.; Xie, L.; Starr, Z. C.; Yang, Z.; Lin, J. S.; Wang, J. H. *Cell Motil. Cytoskeleton* **2007**, *64*, 509–518.
58. Saez, A.; Buguin, A.; Silberzan, P.; Ladoux, B. *Biophys. J.* **2005**, *89*, L52–L54.
59. Saez, A.; Ghibaudo, M.; Buguin, A.; Silberzan, P.; Ladoux, B. *Proc. Natl. Acad. Sci. USA* **2007**, *104*, 8281–8286.
60. Kajzar, A.; Cesa, C. M.; Kirchgessner, N.; Hoffmann, B.; Merkel, R. *Biophys. J.* **2008**, *94*, 1854–1866.
61. Legant, W. R.; Pathak, A.; Yang, M. T.; Deshpande, V. S.; Mcmeeking, R. M.; Chen, C. S. *Proc. Natl. Acad. Sci. USA* **2009**, *106*, 10097–10102.
62. Liang, X. M.; Han, S. J.; Reems, J. A.; Gao, D.; Sniadecki, N. J. *Lab Chip* **2010**, *10*, 991–998.
63. Yang, M. T.; Sniadecki, N. J.; Chen, C. S. *Adv. Mater.* **2007**, *19*, 3119.
64. Nelson, C. M.; Jean, R. P.; Tan, J. L.; *et al. Proc. Natl. Acad. Sci. USA* **2005**, *102*, 11594–11599.
65. Liu, Z.; Tan, J. L.; Cohen, D. M.; *et al. Proc. Natl. Acad. Sci. USA* **2010**, *107*, 9944–9949.
66. Liu, Z. J.; Sniadecki, N. J.; Chen, C. S. *Cell. Mol. Bioeng.* **2010**, *3*, 50–59.
67. Fletcher, D. A.; Mullins, R. D. *Nature* **2010**, *463*, 485–492.
68. Mammoto, T.; Ingber, D. E. *Development* **2010**, *137*, 1407–1420.
69. Kaunas, R.; Nguyen, P.; Usami, S.; Chien, S. *Proc. Natl. Acad. Sci. USA* **2005**, *102*, 15895–15900.

70. Sawada, Y.; Sheetz, M. P. *J. Cell Biol.* **2002**, *156*, 609–615.
71. Giannone, G.; Sheetz, M. P. *Trends Cell Biol.* **2006**, *16*, 213–223.
72. Riveline, D.; Zamir, E.; Balaban, N. Q.; *et al. J. Cell Biol.* **2001**, *153*, 1175–1186.
73. Radmacher, M.; Tillmann, R. W.; Gaub, H. E. *Biophys. J.* **1993**, *64*, 735–742.
74. Yang, S.; Saif, T. *Rev. Sci. Instrum.* **2005**, *76*, 044301–044301-8.
75. Siechen, S.; Yang, S. Y.; Chiba, A.; Saif, T. *Proc. Natl. Acad. Sci. USA* **2009**, *106*, 12611–12616.
76. Wang, N.; Butler, J. P.; Ingber, D. E. *Science* **1993**, *260*, 1124–1127.
77. Matthews, B. D.; Overby, D. R.; Alenghat, F. J.; *et al. Biochem. Biophys. Res. Commun.* **2004**, *313*, 758–764.
78. Matthews, B. D.; Overby, D. R.; Mannix, R.; Ingber, D. E. *J. Cell Sci.* **2006**, *119*, 508–518.
79. Na, S.; Wang, N. *Sci. Signal.* **2008**, *1*, l1.
80. Hu, S.; Chen, J.; Fabry, B.; *et al. Am. J. Physiol. Cell Physiol.* **2003**, *285*, C1082–C1090.
81. Potard, U. S.; Butler, J. P.; Wang, N. *Am. J. Physiol.* **1997**, *272*, C1654–C1663.
82. Le Duc, Q.; Shi, Q.; Blonk, I.; *et al. J. Cell Biol.* **2010**, *189*, 1107–1115.
83. Chen, C. S.; Tan, J.; Tien, J. *Annu. Rev. Biomed. Eng.* **2004**, *6*, 275–302.
84. Choquet, D.; Felsenfeld, D. P.; Sheetz, M. P. *Cell* **1997**, *88*, 39–48.
85. Galbraith, C. G.; Yamada, K. M.; Sheetz, M. P. *J. Cell Biol.* **2002**, *159*, 695–705.
86. Jiang, G.; Giannone, G.; Critchley, D. R.; Fukumoto, E.; Sheetz, M. P. *Nature* **2003**, *424*, 334–337.
87. Wang, Y.; Botvinick, E. L.; Zhao, Y.; *et al. Nature* **2005**, *434*, 1040–1045.
88. Nambiar, R.; McConnell, R. E.; Tyska, M. J. *Proc. Natl. Acad. Sci. USA* **2009**, *106*, 11972–11977.
89. Guck, J.; Ananthakrishnan, R.; Moon, T. J.; Cunningham, C. C.; Kas, J. *Phys. Rev. Lett.* **2000**, *84*, 5451–5454.
90. Meiners, J. C.; Quake, S. R. *Phys. Rev. Lett.* **2000**, *84*, 5014–5017.
91. Moffitt, J. R.; Chemla, Y. R.; Izhaky, D.; Bustamante, C. *Proc. Natl. Acad. Sci. USA* **2006**, *103*, 9006–9011.
92. Finer, J. T.; Simmons, R. M.; Spudich, J. A. *Nature* **1994**, *368*, 113–119.
93. Arsenault, M. E.; Sun, Y.; Bau, H. H.; Goldman, Y. E. *Phys. Chem. Chem. Phys.* **2009**, *11*, 4834–4839.
94. Beausang, J. F.; Schroeder, H. W., III; Nelson, P. C.; Goldman, Y. E. *Biophys. J.* **2008**, *95*, 5820–5831.
95. Sniadecki, N. J.; Anguelouch, A.; Yang, M. T.; *et al. Proc. Natl. Acad. Sci. USA* **2007**, *104*, 14553–14558.
96. Trepat, X.; Deng, L.; An, S. S.; *et al. Nature* **2007**, *447*, 592–595.
97. Krishnan, R.; Park, C. Y.; Lin, Y. C.; *et al. PLoS One* **2009**, *4*, e5486.
98. Colombelli, J.; Besser, A.; Kress, H.; *et al. J. Cell Sci.* **2009**, *122*, 1665–1679.
99. Kumar, S.; Maxwell, I. Z.; Heisterkamp, A.; *et al. Biophys. J.* **2006**, *90*, 3762–3773.
100. El-Ali, J.; Sorger, P. K.; Jensen, K. F. *Nature* **2006**, *442*, 403–411.
101. Masters, J. R.; Stacey, G. N. *Nat. Protoc.* **2007**, *2*, 2276–2284.
102. Malek, A. M.; Alper, S. L.; Izumo, S. *J. Am. Med. Assoc.* **1999**, *282*, 2035–2042.
103. Cunningham, K. S.; Gotlieb, A. I. *Lab. Invest.* **2005**, *85*, 9–23.
104. Garcia-Cardena, G.; Comander, J.; Anderson, K. R.; Blackman, B. R.; Gimbrone, M. A., Jr. *Proc. Natl. Acad. Sci. USA* **2001**, *98*, 4478–4485.
105. Dai, G.; Kaazempur-Mofrad, M. R.; Natarajan, S.; *et al. Proc. Natl. Acad. Sci. USA* **2004**, *101*, 14871–14876.
106. Steward, R. L., Jr.; Cheng, C. M.; Wang, D. L.; Leduc, P. R. *Cell Biochem. Biophys.* **2010**, *56*, 115–124.
107. Barbee, K. A.; Davies, P. F.; Lal, R. *Circ. Res.* **1994**, *74*, 163–171.
108. Nesbitt, W. S.; Westein, E.; Tovar-Lopez, F. J.; *et al. Nat. Med.* **2009**, *15*, 665–673.
109. Rubenstein, D. A.; Yin, W. *J. Thromb. Thrombolysis* **2010**, *30*, 36–45.
110. Junt, T.; Schulze, H.; Chen, Z.; *et al. Science* **2007**, *317*, 1767–1770.
111. Reneman, R. S.; Arts, T.; Hoeks, A. P. *J. Vasc. Res.* **2006**, *43*, 251–269.
112. Santiago, J. G.; Wereley, S. T.; Meinhart, C. D.; Beebe, D. J.; Adrian, R. J. *Exp. Fluids* **1998**, *25*, 316–319.
113. Wallace, C. S.; Champion, J. C.; Truskey, G. A. *Ann. Biomed. Eng.* **2007**, *35*, 375–386.
114. Frangos, J. A.; Eskin, S. G.; Mcintire, L. V.; Ives, C. L. *Science* **1985**, *227*, 1477–1479.
115. Chiu, J. J.; Wang, D. L.; Chien, S.; Skalak, R.; Usami, S. *J. Biomech. Eng.* **1998**, *120*, 2–8.
116. Chau, L.; Doran, M.; Cooper-White, J. *Lab Chip* **2009**, *9*, 1897–1902.
117. Li, S.; Huang, N. F.; Hsu, S. *J. Cell Biochem.* **2005**, *96*, 1110–1126.
118. Poujade, M.; Grasland-Mongrain, E.; Hertzog, A.; *et al. Proc. Natl. Acad. Sci. USA* **2007**, *104*, 15988–15993.
119. Neils, C.; Tyree, Z.; Finlayson, B.; Folch, A. *Lab Chip* **2004**, *4*, 342–350.
120. Rabodzey, A.; Alcaide, P.; Luscinskas, F. W.; Ladoux, B. *Biophys. J.* **2008**, *95*, 1428–1438.
121. Chung, S.; Sudo, R.; Mack, P. J.; Wan, C. R.; Vickerman, V.; Kamm, R. D. *Lab Chip* **2009**, *9*, 269–275.
122. Swartz, M. A.; Fleury, M. E. *Annu. Rev. Biomed. Eng.* **2007**, *9*, 229–256.
123. Vickerman, V.; Blundo, J.; Chung, S.; Kamm, R. *Lab Chip* **2008**, *8*, 1468–1477.
124. Di Carlo, D.; Lee, L. P. *Anal. Chem.* **2006**, *78*, 7918–7925.
125. Mach, W. J.; Thimmesch, A. R.; Orr, J. A.; Slusser, J. G.; Pierce, J. D. *J. Clin. Monit. Comput.* **2010**, *24*(4), 251–259.
126. Gomez-Sjoberg, R.; Leyrat, A. A.; Pirone, D. M.; Chen, C. S.; Quake, S. R. *Anal. Chem.* **2007**, *79*, 8557–8563.
127. Tourovskaia, A.; Figueroa-Masot, X.; Folch, A. *Lab Chip* **2005**, *5*, 14–19.
128. Lee, P. J.; Hung, P. J.; Shaw, R.; Jan, L.; Lee, L. P. *Appl. Phys. Lett.* **2005**, *86*, 223902–223902-3.
129. Hong, J. W.; Studer, V.; Hang, G.; Anderson, W. F.; Quake, S. R. *Nat. Biotechnol.* **2004**, *22*, 435–439.
130. Wu, H.; Wheeler, A.; Zare, R. N. *Proc. Natl. Acad. Sci. USA* **2004**, *101*, 12809–12813.
131. Stott, S. L.; Lee, R. J.; Nagrath, S.; *et al. Sci. Transl. Med.* **2010**, *2*, 25ra23.
132. Guck, J.; Schinkinger, S.; Lincoln, B.; *et al. Biophys. J.* **2005**, *88*, 3689–3698.
133. MacDonald, M. P.; Spalding, G. C.; Dholakia, K. *Nature* **2003**, *426*, 421–424.
134. Voldman, J.; Gray, M. L.; Toner, M.; Schmidt, M. A. *Anal. Chem.* **2002**, *74*, 3984–3990.
135. Hu, X.; Arnold, W. M.; Zimmermann, U. *Biochim. Biophys. Acta* **1990**, *1021*, 191–200.
136. Gascoyne, P. R.; Vykoukal, J. V. *Proc. IEEE Inst. Electr. Electron. Eng.* **2004**, *92*, 22–42.
137. Powers, M. J.; Domansky, K.; Kaazempur-Mofrad, M. R.; *et al. Biotechnol. Bioeng.* **2002**, *78*, 257–269.
138. Powers, M. J.; Janigian, D. M.; Wack, K. E.; Baker, C. S.; Beer Stolz, D.; Griffith, L. G. *Tissue Eng.* **2002**, *8*, 499–513.
139. Huh, D.; Matthews, B. D.; Mammoto, A.; Montoya-Zavala, M.; Hsin, H. Y.; Ingber, D. E. *Science* **2010**, *328*, 1662–1668.
140. Di Carlo, D.; Jeong, K. H.; Lee, L. P. *Lab Chip* **2003**, *3*, 287–291.
141. Lu, H.; Schmidt, M. A.; Jensen, K. F. *Lab Chip* **2005**, *5*, 23–29.
142. Zhang, C.; Xu, J.; Ma, W.; Zheng, W. *Biotechnol. Adv.* **2006**, *24*, 243–284.
143. Irimia, D.; Mindrinos, M.; Russom, A.; *et al. Integr. Biol. (Camb.)* **2009**, *1*, 99–107.
144. Lagally, E. T.; Medintz, I.; Mathies, R. A. *Anal. Chem.* **2001**, *73*, 565–570.
145. Pal, R.; Yang, M.; Lin, R.; *et al. Lab Chip* **2005**, *5*, 1024–1032.
146. Lee, B. S.; Lee, J. N.; Park, J. M.; *et al. Lab Chip* **2009**, *9*, 1548–1555.
147. Madou, M.; Zoval, J.; Jia, G. Y.; Kido, H.; Kim, J.; Kim, N. *Annu. Rev. Biomed. Eng.* **2006**, *8*, 601–628.
148. Park, J. M.; Cho, Y. K.; Lee, B. S.; Lee, J. G.; Ko, C. *Lab Chip* **2007**, *7*, 557–564.
149. Duffy, D. C.; Gillis, H. L.; Lin, J.; Sheppard, N. F.; Kellogg, G. J. *Anal. Chem.* **1999**, *71*, 4669–4678.
150. Kim, J.; Hee Jang, S.; Jia, G.; Zoval, J. V.; da Silva, N. A.; Madou, M. J. *Lab Chip* **2004**, *4*, 516–522.
151. Lai, S.; Wang, S.; Luo, J.; Lee, L. J.; Yang, S. T.; Madou, M. J. *Anal. Chem.* **2004**, *76*, 1832–1837.
152. Xu, T.; Rohozinski, J.; Zhao, W.; Moorefield, E. C.; Atala, A.; Yoo, J. J. *Tissue Eng. A* **2009**, *15*, 95–101.

3.316. Immunohistochemistry

E Aikawa, Harvard Medical School, Boston, MA, USA

© 2011 Elsevier Ltd. All rights reserved.

3.316.1.	**Introduction to Immunohistochemistry**	278
3.316.2.	**Factors Contributing to Antibody–Antigen Interaction**	278
3.316.2.1.	Affinity	278
3.316.2.2.	Avidity	278
3.316.2.3.	Specificity	279
3.316.2.4.	Stability	279
3.316.3.	**Visualization of Antibody by Enzymatic or Fluorescent Labeling and The Advantages and Disadvantages**	279
3.316.3.1.	Enzymatic Labeling and Common Chromogens	279
3.316.3.2.	Fluorescence Labeling and Fluorophores	280
3.316.4.	**Basic Immunohistochemistry Protocols and Their Advantages and Disadvantages for Biomaterial Science**	280
3.316.4.1.	Tissue Preparation	280
3.316.4.1.1.	Paraffin-embedded tissues	281
3.316.4.1.2.	Frozen tissues	282
3.316.4.2.	Immunohistochemical Staining Protocols	282
3.316.4.3.	Counterstaining and Mounting	284
3.316.4.3.1.	Counterstaining following immunohistochemical staining	284
3.316.4.3.2.	Mounting following immunohistochemical staining	284
3.316.4.4.	Data Interpretation	284
3.316.5.	**Detection of Pathobiological Processes and Associated Cellular Events in an Implanted Site**	284
3.316.5.1.	Wound-Healing Response	285
3.316.5.1.1.	Inflammatory phase	285
3.316.5.1.2.	Proliferative phase	285
3.316.5.1.3.	Maturation/remodeling phase	287
3.316.5.1.4.	Cytokines	287
3.316.5.2.	Angiogenesis	287
3.316.5.3.	Immune Response	288
3.316.5.4.	Encapsulation	288
3.316.5.5.	Calcification	288
3.316.6.	**Implant Evaluation Using Immunohistochemical Methods**	289
3.316.6.1.	Heart Valve Prostheses	289
3.316.6.2.	Polymer-Based Engineered Tissues	289
3.316.6.3.	Vascular Grafts	289
3.316.6.4.	Intravascular Stents	290
3.316.6.5.	Cardiac Assist Devices and Artificial Hearts	290
References		290

Abbreviations

AEC	3-Amino-9-ethylcarbasole
AM-3K	Anti macrophage antibody, clone AM-3K
bFGF	Basic fibroblast growth factor
BMP	Bone matrix protein
Cbfa 1	Core binding factor alpha 1
DAB	3,3 Diaminobenzidine
DAPI	4′6-Diamidino-2-phenylindole
DDR2	Discoidin domain receptor 2
ECM	Extracellular matrix
ED-1	Ectodermal dysplasia 1
EGF	Epidermal growth factor
FBGC	Foreign-body giant cells
FGF	Fibroblast growth factor
FITC	Fluorescein isothiocyanate
GBP-1	Guanylate-binding protein 1
GMA	Glycolmethacrylate
HAM-56	Human alveolar macrophage 56
HLA	Human leukocyte antigen
ICAM-1	Intracellular adhesion molecule 1
IFNγ	Interferon gamma
IgG	Immunoglobulin G
IL-1	Interleukin 1
LRP5	Low-density lipoprotein 5
LYVE-1	Lymphatic vessel endothelial 1
MCH	Myosin heavy chain
MMA	Methyl methacrylate
MMP	Matrix metalloproteinase
OCT	Optimal cutting temperature
OPG	Osteoprotegerin

PBS	Phosphate buffered saline
PCNA	Proliferating cell nuclear antigen
PDGF	Platelet-derived growth factor
PECAM 1	Platelet endothelial cell adhesion molecule 1
PFA	Paraformaldehyde
RUNX 2	Runt-related transcription factor 2
TGF-β1	Transforming growth factor beta 1
TM	Thrombomodulin
TNF-α	Tumor necrosis factor alpha
vWF	von Willebrand factor
VCAM-1	Vascular adhesion molecule 1
VE-Cadherin	Vascular endothelial cadherin
VEGF	Vascular endothelial growth factor
VEGFR-1	Vascular endothelial growth factor receptor 1
α-SMA	Alpha smooth muscle actin

3.316.1. Introduction to Immunohistochemistry

Antibodies are an essential component of the immune response. Their function is to identify and then specifically bind foreign molecules, which results in the generation of immune responses such as complement activation and phagocytosis. In order to maintain a proper defense, an antibody must have exquisite specificity for the foreign molecule. This ability of antibodies to specifically recognize numerous distinctive molecules makes them indispensable research tools. In addition, their ability to identify biological molecules in cells and tissues serves as a foundation for an immunohistochemical approach.

Karl Landsteiner first demonstrated a specific binding of antibody to antigen in the 1930s. An antigen-binding site, also known as an epitope, consists of amino acid sequences and confers antigen recognition. A simplified antibody structure depicting an antigen-binding site is shown in Figure 1. Typically, the epitopes for antibodies raised against native proteins develop clusters of three-dimensional protein conformation (tertiary structure). Therefore, the conformation of the protein is a key determinant of antibody recognition when the antibody is raised against a native or recombinant protein. Many traditional immunohistochemistry methods employ fixation, tissue processing, and antigen retrieval, which may significantly alter the target protein's tertiary structure. These changes in the protein structure can be due to chemical modification, such as oxidation, reduction of disulfide bonds, and modification of primary amines by cross-linking fixatives such as formaldehyde. In addition, gross changes in protein structure can be caused by denaturation, fixation, proteolytic cleavage, changes in pH, and dehydration. Moreover, antibodies raised against peptide immunogens that mimic continuous epitopes on the target protein may detect both folded and denaturated protein.

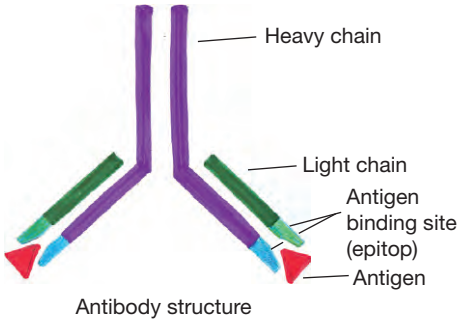

Figure 1 Schematic antigen structure depicting heavy chain, light chain, and antigen-binding site (epitope).

Therefore, testing various fixatives and antigen retrieval solutions and optimization of the tissue preparation and staining techniques are needed to understand whether the antibody will recognize the antigen after tissue processing. Thus each new antibody has to be evaluated individually for each experimental condition and immunohistochemical application.

3.316.2. Factors Contributing to Antibody–Antigen Interaction

3.316.2.1. Affinity

Antibody affinity is defined as strength of the binding interaction between antigen and antibody. It depends on the closeness of the stereochemical fit between antibody sites and antigen determinants, the size of the area of contact between them, and the distribution of charged and hydrophobic groups. In stable condition, where the associated form of the antigen and antibody is favored, the antibody is referred to as being of higher affinity. Normally the binding of an antibody to an antigen occurs within 1 h at room temperature, when the antibody–antigen system achieves equilibrium. Antigen–antibody interaction is slower at a lower temperature (usually at 4 °C) and will require more time for antibody incubation (usually overnight). While the affinity of monoclonal antibodies can be characterized, the affinity of polyclonal antibodies cannot be determined, because polyclonal serum contains a combination of antibodies with different affinities.

3.316.2.2. Avidity

Antibody avidity also considerably contributes to the success of immunohistochemical staining and refers to the strength of antigen–antibody binding. Avidity is a measure of the contribution of multivalent interactions to the stability of the antigen–antibody complex – which is different from affinity – that describes the strength of a single bond. Multivalent interactions can take place when there is a high local concentration of the protein of interest, or when an antigen contains multiple copies of an epitope. Thus, the intrinsic flexibility of antibody structure allows the recognition of various antigens in an array of conformations. Antigens displaying multiple epitopes can be cross-linked by antibodies to form stable complexes, resulting in signal amplification and further enhancement of the experimental results. An excess of either the antibody or the antigen, however, may limit the formation of stable complexes and lead to signal loss. This phenomenon is observed occasionally during immunohistochemical staining experiments.

Therefore, optimizing each of the parameters – particularly titration of the primary antibody – is critical to successful immunostaining, and higher concentration of an antibody may not always be better for immunological applications. Additional common problems in immunohistochemical techniques include background staining, which is influenced by primary antibody concentration, tissue preparation, and endogenous enzyme activity, and unwanted cross-reactivity with proteins other than the target protein.

3.316.2.3. Specificity

The specificity of an antibody is its ability to distinguish between different epitopes. The specificity of some antibodies can be so precise that they are able to discriminate between enantiomers (one of a pair of optical isomers) of the same molecule, but this term is more commonly used in reference to the variety of species that an antibody is raised against or to refer to a target protein. In immunohistochemistry, specificity is harder to determine, as compared to Western blotting or immunoprecipitation, as subcellular staining is limited to nuclear or cytoplasmic localization. Inclusion of suitable controls (e.g., negative control antibodies, control tissues, control cell preparations) is required to confirm observations. The most appropriate control samples are knockout tissues or cell preparations, but data interpretation may be complicated by compensatory expression of related proteins that show cross-reactivity with the primary antibody.

3.316.2.4. Stability

Antibodies are stable proteins, and usually, with careful handling, the shelf life of a purified antibody can be as long as 10 years. The stability of antibodies depends on their purification method. For example, exposure to acidic conditions can cause aggregation and affect antibody stability. This, in turn, may influence the results obtained from immunohistochemical experiments by increasing nonspecific background staining. In addition, conjugation to fluorophores, enzymes, and small molecules can also have an effect on antibody stability, shelf life, and background staining, and should be considered when troubleshooting unexpected patterns.

Antibodies are susceptible to freeze–thaw cycles and should be properly aliquotted and stored. In the long term, most antibodies are best preserved at −80 °C in a freezer that does not go through repeated freeze–thaw cycles. If glycerol is present as a cryoprotectant, antibodies can be stored at −20 °C, because at this temperature, the antibody solution does not freeze. Short-term storage at 2–8 °C is also possible to facilitate handling, but care must be taken to prevent bacterial or fungal growth. Antibody contaminated with bacterial or fungal matter should not be used, as it will result in unspecific background staining.

3.316.3. Visualization of Antibody by Enzymatic or Fluorescent Labeling and The Advantages and Disadvantages

A reporter label is used to visualize an antibody–protein reaction in a tissue section. An enzymatic or fluorescent label could bind directly to the primary antibody, which is raised against the target protein to a secondary antibody, which in turn recognizes the primary antibody or a compound of an amplification system. The enzymatic labeling technique is broadly used in research and clinical laboratories. The recent advances in the fluorochrome-conjugated antibody approach have made possible the creation of brightly colored images and multilabeled stains because a fluorochrome absorbs and emits light in a specific spectrum viewed under a particular filter. Several fluorochromes can be used simultaneously, enabling the study of immunobiological processes in depth and in combination with other fluorescence approaches (e.g., near-infrared fluorescence molecular imaging).

The selection of the proper reporter label detection system is not trivial as both enzymatic and fluorescent labels have their advantages and disadvantages. Hence, the appropriate and careful choice of histological methods and microscopy techniques enables the successful localization of the target (Figure 2). In general, it is preferable to begin immunohistochemical studies using enzymatic labeling, which requires no more than bright-field microscopy. Light microscopy allows researchers to identify cell-specific protein expression in association with overall morphological changes in the tissue. Follow-up fluorescence microscopy studies, and particularly double or triple labeling, could be done afterward to address more specific questions regarding protein–protein colocalization.

3.316.3.1. Enzymatic Labeling and Common Chromogens

Several labeling enzymes are used in immunohistochemistry in combination with various chromogens. The chromogen determines the color of the reaction precipitate product. The chromogen choice is largely dependent on personal preference and overall research design. Peroxidase and phosphatase enzymes are commonly used as enzymatic labels in both research and clinical laboratories. Particularly, peroxidase-chromogen combinations such as 3-amino-9-ethylcarbasole (AEC) and

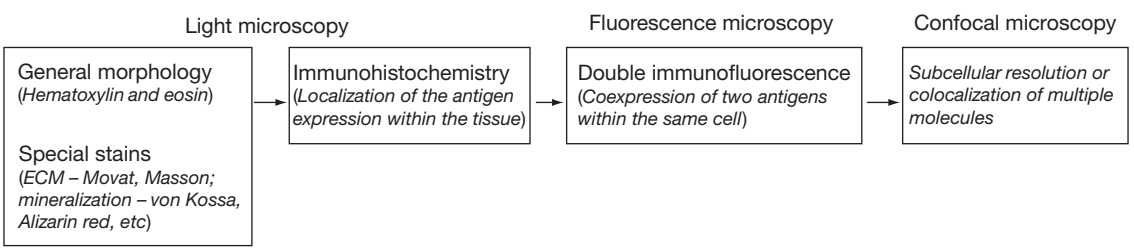

Figure 2 Sequence of histological techniques and microscopy methods for successful target identification.

3,3-diaminobenzidine (DAB) are the most frequent choices because they provide optimal contrast with counterstains (e.g., hematoxylin) and because they are simple to use, reducing the workload involved in time consuming and labor-intensive experiments. AEC produces a bright red product, which is soluble in alcohol, and therefore, requires an aqueous mounting medium. The disadvantage of AEC is that the intensity of the staining decreases over time, especially with exposure to light; hence, AEC-developed slides should be stored in the dark. DAB generates a brown or black polymerized precipitate that is insoluble in alcohol. DAB-developed slides require dehydration in increasing concentrations of alcohol, followed by mounting in organic medium. The advantage of DAB is that it produces permanent preservation of the immunohistochemical signal, with a favorable signal-to-background ratio. But DAB is a carcinogenic chemical, and care must be taken to handle it properly.

The intensity of an enzyme–chromogen reaction signal depends on the amount of target protein, the concentration of primary and secondary antibodies, and the development time. A tissue containing a large amount of target protein or stained using a highly concentrated antibody is expected to produce a strong signal in <3–5 min. A tissue containing a small amount of target protein requires incubation for up to 30 min. As reaction time fluctuates, it is strongly recommended to examine the sections regularly using a light microscope during the development stage until the desired result is achieved.

3.316.3.2. Fluorescence Labeling and Fluorophores

Immunofluorescence technique employs fluorescent labels to visualize the subcellular distribution of the molecule of interest. Usually tissue sections are incubated with fluorochrome-conjugated secondary antibody or avidin–biotin complexes. In some cases, primary antibody conjugated with fluorescent labels is applied directly to tissue sections. This direct labeling decreases the number of steps in the staining protocol, and more importantly, often prevents cross-reactivity and high background staining. Following immunofluorescence staining, the tissue sections are viewed using a fluorescence microscope equipped with a set of filters for imaging fluorochromes according to their emission and excitation characteristics. In immunohistochemistry, the most commonly used fluorescent dyes are fluorescein (e.g., fluorescein isothiocyanate (FITC), green, excitation 494 nm, emission 521 nm) and rhodamine (e.g., Texas Red, red, excitation 595 nm, emission 615 nm) derivates. Other derivatives of rhodamine include fluorophores such as Alexa Fluor dyes. The excitation and emission spectra of the Alexa Fluor series cover the visible spectrum and extend into the infrared (e.g., Alexa Fluor 350, blue; Alexa Fluor 488, green; Alexa Fluor 680, red). This new group of fluorescent dyes has been recently developed for various applications where higher photostability, increased brightness, different spectra characteristics, or different attachment groups are needed (e.g., molecular imaging).

As with most fluorescence techniques, a significant problem with immunofluorescence is rapid photobleaching. Reducing exposure to light, increasing the concentration of the flourophore, or employing more robust fluorophores such as Alexa Fluors can control the loss of signal intensity caused by photobleaching. Notably, image acquisition and quantification should be done within days after the staining procedure. Interestingly, in some cases, tissue-inherent autoimmunofluorescence properties can be used as a landmark to help with the orientation of the tissue section. For example, elastin autofluorescence serves as an excellent marker of arterial media (Figure 3). Overall, excellent color contrast, high resolution, and the capacity to produce simultaneous multicolor imaging of proteins in the same cell make immunofluorescence imaging a convenient and reliable tool for studying pathobiological processes.

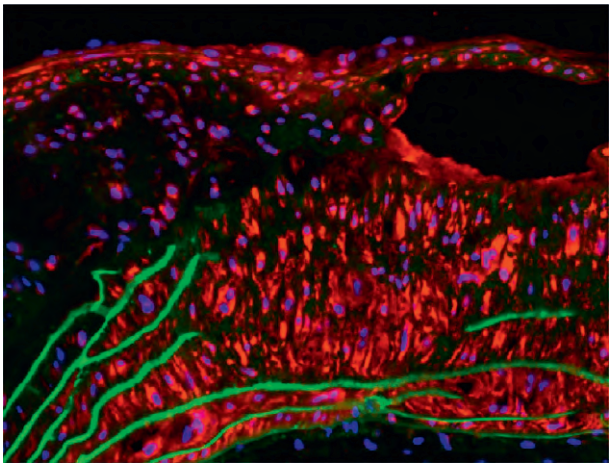

Figure 3 Immunofluorescence staining with anticathepsin S antibody (Texas Red). Autofluorescence of elastin in the media of mouse aorta (green). Original magnification ×200. Modified from Aikawa, E.; *et al*. *Circulation* **2009**, *119*, 1785–1794.

3.316.4. Basic Immunohistochemistry Protocols and Their Advantages and Disadvantages for Biomaterial Science

3.316.4.1. Tissue Preparation

Tissue preparation is a critical step in obtaining reliable and reproducible results in immunohistochemistry. There are two major types of specimen preparation commonly used in immunohistochemistry staining experiments: paraffin-embedded and fresh-frozen tissue samples. These two conventional tissue preparation techniques are remarkably successful in small soft tissues; however, there are many sample types for which these techniques do not work well, including large samples, complex samples containing soft and hard tissue parts, and hard tissues. In particular, the biggest obstacle to the application of cryosectioning and paraffin sectioning to large samples is that the tissue structure is extensively damaged during cutting. Therefore, occasionally a polymer embedding is preferable, and methyl methacrylate (MMA) can be a good alternative to glycolmethacrylate (GMA) embedding as it preserves both enzymatic activity and tissue antigenicity. Although this chapter is primarily focused on the most commonly used immunohistochemistry protocols, the various

issues concerning tissue preparation – including the processing, fixation, orientation, and embedding of specimens in relation to biomaterials and tissue engineering – will be discussed in greater detail.

3.316.4.1.1. Paraffin-embedded tissues

Paraffin-embedded tissues are a common type of specimen used for immunohistochemistry. Prior to paraffin embedding, tissues undergo fixation and processing.

3.316.4.1.1.1. Fixation

The choice of a fixative should be made with several considerations in mind, including the preservation of antibody–antigen interaction properties and short-term and long-term storage. Fixation preserves tissues by preventing autolytic changes, and thus allows tissues to remain unchanged during subsequent treatment. It is crucial that tissue is collected and fixed immediately after harvesting, as delay will promote hypoxia, proteolytic enzyme activation, autolysis, and drying – factors deleterious to antigen preservation. On the other hand, fixation causes changes in the protein structure, rendering it biologically inactive. In addition, cross-linking fixatives create marked differences in the chemical and antigenic properties of the proteins compared to their native forms.

For special studies, a wide variety of fixatives are available. The investigator should be aware of the advantages and disadvantages of each fixative and the artifacts associated with them. The most popular fixatives used for immunohistochemical staining techniques are aldehyde fixatives (e.g., paraformaldehyde (PFA), formalin, glutaraldehyde), protein-denaturing agents (e.g., methanol, ethanol), and acetone.

3.316.4.1.1.1.1. Formalin Ten-percent buffered neutral formalin is considered the best general fixative for pathological specimens because it preserves the broad range of biological structures, requires a relatively short fixation time, penetrates rapidly, and can be used for long-term storage. Tissue samples can remain in 10% buffered formalin for many months without undesirable effects or unwanted precipitates. Formalin does not precipitate protein or harden albumin. Cellular components such as nucleic acids, carbohydrates, and lipids are not fixed directly, but rather trapped in the network of insoluble cross-links. Of note, formalin reacts with DNA and RNA only at 65 and 45 °C, respectively, due to uncoiling of DNA and RNA at these temperatures. Such temperatures can be reached only in the tissue processor when wax impregnation takes place; by that time, however, the majority of the fixative has been washed out. Although formalin fixation provides excellent preservation of tissue morphology and architecture, it often results in antigen masking due to aggressive and excessive cross-linking of proteins. In addition, fixation with formalin increases tissue hydrophobicity, leading to an increased incidence of general background staining.

3.316.4.1.1.1.2. Paraformaldehyde Based on the experience of our laboratory, low concentrations of PFA (2–4%) are most favorable for immunohistochemical applications. While providing excellent ultrastructural preservation, PFA fixation keeps antigen masking to a minimum. A disadvantage of 4% PFA fixation is that tissue penetration is slow, and as a result, incubation requires more time and a small sample size is preferred.

3.316.4.1.1.1.3. Ethanol, methanol, and acetone Ethanol, methanol, and acetone penetrate tissue poorly and are generally used on tissue sections only before staining rather than on pieces of tissue. Absolute alcohol preserves glycogen but causes distortion of nuclear detail and shrinks cytoplasm. Fixation with acetone creates undesirable morphological changes, such as the loss of cell membranes and chromatolysis. In addition, extended fixation with acetone makes tissue brittle.

3.316.4.1.1.2. Antigen retrieval

The antigen-masking effects of fixation are reversible to varying degrees by a process known as antigen retrieval. It involves exposing the tissue sections to heat or proteolytic enzyme digestion before performing immunohistochemical staining. The success of retrieval depends on the fixative, the duration of fixation, and the antigen of interest. The mechanism of antigen retrieval is disruption of the methylene bridge cross-links formed between proteins during fixation, which allows antibody access to the epitope. The harsh conditions of heat and proteolytic enzyme digestion methods often cause tissue sections to lift off the slides. Therefore, tissue–adhesive-coated slides should be used.

3.316.4.1.1.3. Tissue processing

Basic tissue processing consists of three stages: dehydration, clearing, and infiltration. These steps are intended to remove the fixative and water and replace them with a medium that solidifies tissue. Use of graded alcohols from a lower to a higher concentration is a standard procedure for tissue dehydration. The dehydration step is followed by the replacement of alcohol with xylene, a clearing solution. Recently, many immunohistological laboratories have used automatic tissue processors, which promote tissue infiltration using heat, vacuum, pressure, and agitation. But such tissue processors are costly and space consuming. In addition, the heat used in the tissue processors melts paraffin wax at 50–60 °C, which can be harmful to antigen staining. Paraffin-embedded tissue sections are also exposed to high temperatures during oven slide drying in order to increase tissue adherence to the slide. The duration and intensity of heating tissues during embedding or slide drying should be kept to a minimum.

In biomaterials research, the tissue samples collected for patho-immunohistological analyses are considerably larger than clinical samples (e.g., biopsies) and often contain biopolymers and other hard materials. The tissue processing therefore may require more time. Taking shortcuts in processing may result in poorly and incompletely dehydrated, cleared, and infiltrated specimens, which will cause further problems with sectioning, staining, and examining the tissues. A protocol for paraffin embedding of relatively large ($\sim 2.5 \times 2.5$ cm) tissue samples is given below.

Protocol for paraffin embedding

1. 80% alcohol, 1 h
2. 95% alcohol, three changes, 1 h each
3. Absolute alcohol, three changes, 1 h each
4. Xylene, three changes, 1 h each
5. Paraffin, three changes, 1 h each
6. Embedding

3.316.4.1.1.4. Specimen orientation

The quality of a tissue section depends on every step of processing. Even with adequate fixation, processing, and sectioning, a tissue section can be destroyed by improper orientation. Every tissue fragment, especially tissue containing heterogeneous material (e.g., graft, tissue-engineered scaffold, and stent), should be analyzed in order to decide how to position the tissue in the block. A broad knowledge of gross tissue structure and anatomy and explicit communication with the pathologist are critical for proper tissue placement. Tissue sections should be embedded entirely flat to assure that a complete section will be obtained. Care must be taken to prevent causing artifacts by rough handling of the specimen. Large or dense specimens should be oriented at a slight angle to the knife-edge in order to minimize the risk of pulling the tissue out of the block and diminishing knife vibration. Importantly, tubular structures such as arteries should be placed as vertically as possible, so that the knife cuts perpendicular to the long axis of the tube and across the lumen.

3.316.4.1.1.5. Embedding

Paraffin is the most popular and widely used embedding medium. Care should be taken, however, to prevent the paraffin wax from overheating (as described earlier in the section on tissue processing). The paraffin-embedding technique used in immunohistochemistry is similar to that used in general histological methods, and therefore will not be described in this chapter.

3.316.4.1.2. Frozen tissues

Fresh-frozen, unfixed tissue is the most suitable preparation for immunohistochemistry, but improperly frozen tissue introduces ice crystal artifacts that can make morphological interpretation difficult. If frozen slowly, large ice crystals are allowed to form in the tissue, creating cracks, enlarging intracellular and extracellular spaces, and rupturing cell membranes. Alternatively, 'snap freezing' employs liquid nitrogen (−190 °C) for rapid freezing. While quick freezing is achieved, liquid nitrogen still has its disadvantages, as tissue often cracks due to the rapid expansion of ice, thus producing problems with sectioning. The vapor phase of liquid nitrogen can act as an insulator, resulting in uneven tissue freezing and contributing further to ice crystal formation. The artifacts due to slow and rapid freezing techniques can be overcome by freezing the tissue in chilled/dry ice isopentane (2-methylbutane) where the tissue freezes without expansion and the resultant tissue damage. Therefore, this freezing method is preferable for histological and immunologistochemical applications. Handling the tissue after freezing should be kept to a minimum to prevent thawing.

Protocol for dry ice/isopentane freezing

1. Place the container with isopentane onto dry ice 15–20 min before embedding so that the isopentane becomes cold.
2. Dissect the tissue (~1 × 1 cm).
3. Incubate the tissue in optimal cutting temperature (OCT) compound at room temperature (two to three changes, 1 min each).
4. Add OCT into plastic cryomold.
5. Place tissue in cryomold with OCT (make sure that tissue is completely covered by OCT).
6. Using long forceps, place the cryomold into cold isopentane until OCT stops bubbling (~1–3 min).
7. Place frozen mold onto dry ice until isopentane fumes evaporate before going to −80 °C freezer.

Following cryotomy, frozen sections are transferred to slides and then left to air dry at room temperature up to 30 min. The contrast in heat melts OCT compound on the slide, thus providing better tissue adhesion. The sections are then stored at −20 or −80 °C until needed. This brief freeze–thaw cycle usually does not have any harmful effects on immunohistochemical staining.

Occasionally, it is required to freeze tissue samples that have previously been fixed. The advantage of prefixed tissues is that fixation prevents the diffusion of enzymes and antigens during freezing. The increased water content of the tissue may contribute to severe ice crystal formation and tissue artifacts, but this can be avoided by immersing the tissue samples into sucrose solution. As it has a lower freezing temperature than water, sucrose solution acts as a cryoprotectant and prevents ice crystal formation.

3.316.4.2. Immunohistochemical Staining Protocols

Immunohistochemical staining protocols can vary from one-step procedures, where the label is conjugated directly to the primary antibody, to multiple-step procedures, where the label is conjugated to a secondary antibody or avidin–biotin complex (Figure 4). These protocols can easily be adapted for use with fresh-frozen and formalin-fixed paraffin-embedded tissue sections or enzymatic and fluorescent labels. To achieve the highest intensity of positive specific staining with the

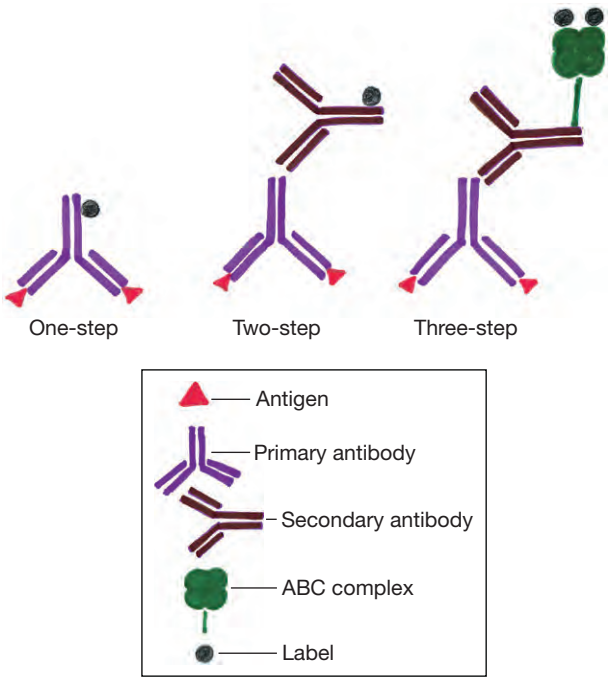

Figure 4 Single (one-step) and multiple (two-step and three-step) indirect immunohistochemistry. ABC, avidin–biotin complex.

lowest amount of background staining, an optimization of antibody dilutions should be performed using a known positive-control tissue. This section provides the most common immunohistochemistry staining protocols that are being successfully used in our laboratory.

Immunohistochemical (indirect, three-step) staining protocol for formalin-fixed, paraffin-embedded sections

1. Place slides in oven 60 °C for 1 h.
2. Let slides cool for 30 min at room temperature.
3. Place slides in xylene for 5 min, two changes. In a similar fashion, place slides for 5 min each in: 100% ethanol, two changes; 95% ethanol, two changes; 70% ethanol, two changes. Rinse slides for 5 min in dH_2O.
4. Place slides in 0.3% H_2O_2 solution for 3 min to inhibit endogenous peroxidase activity. Wash well in dH_2O. Wash in phosphate buffered saline (PBS) for 5 min.
5. Prepare the moisture chamber with water-soaked paper towels. Remove excess moisture around the section using a Kimwipe. Do not let the sections dry out.
6. Perform any necessary antigen-retrieval techniques. Wash in PBS for 5 min.
7. Cover each section with blocking serum (4% normal serum, depending on primary antibody source) for 30 min in moisture chamber.
8. Tap off blocking serum and wipe excess solution off the slide with a Kimwipe. Cover each section with primary antibody solution (make the appropriate dilution of antibody in the blocking solution). Incubate in the moisture chamber for 60–90 min.
9. Tap off the primary antibody solution and wash twice, 5 min each time in PBS.
10. Cover each section with the appropriate secondary antibody solution (1:100) and incubate for 30 min in moisture chamber. Prepare ABC solution (see Step 11).
11. Tap off the secondary antibody solution as above and wash the slides in PBS (twice, 5 min each).
12. Cover each slide with ABC (horseradish peroxidase) kit, prepared in Step 9 (solution must stand for 30 min at room temperature after being prepared).
13. Wash the slides in PBS (twice, 5 min each).
14. Prepare the chromogen solution. Check the reaction under the microscope.
15. Rinse in H_2O twice, 5 min each.
16. Counterstain with Harris's hematoxylin solution for 3–5 min.
17. If DAB is used, dehydrate slides. Place slides for 3 min each in: 70% ethanol, 95% ethanol, 100% ethanol, xylene, twice in each solution. Place one drop of Permount on section and coverslip.

Immunohistochemical staining protocol for frozen sections

1. Dry sections for 30 min at room temperature.
2. Wash the slides in PBS (twice, 5 min each).
3. Fix sections in 4% PFA (5 min).
4. Wash the slides in H_2O and PBS (twice, 5 min each).
5. Place slides in 0.3% H_2O_2 solution to inhibit endogenous peroxidase activity for 1 min. Wash well in dH_2O. Wash in PBS for 5 min.
6. Do not let the sections dry out. Draw a circle around each section with a wax pencil.
7. Cover each section with blocking serum (4% normal serum, depending on primary antibody source) for 30 min in moisture chamber.
8. Tap off blocking serum and cover each section with primary antibody solution (make the appropriate dilution of antibody in the blocking solution). Incubate in the moisture chamber for 60 min.
9. Tap off the primary antibody solution and wash twice, 3 min each time in PBS.
10. Cover each section with the appropriate secondary antibody solution and incubate for 30 min in moisture chamber. Prepare ABC solution (see Step 11).
11. Tap off the secondary antibody solution as above and wash the slides in PBS (twice, 3 min each).
12. Cover each slide with ABC (horseradish peroxidase) kit prepared in Step 9 (solution must stand for 30 min at room temperature after being prepared).
13. Wash the slides in PBS (twice, 3 min each).
14. Prepare the chromogen solution. Check the reaction under the microscope.
15. Rinse in H_2O for 3 min twice.
16. Counterstain with Gill's hematoxylin solution for 1 min.
17. If AEC is used, rinse with tap water for 5–10 min and coverslip with aqueous mounting medium.

Immunofluorescence protocol for frozen sections (single and double labeling)

1. Fix cryostat sections (6–7 mm) in 4% PFA for 5 min and wash the slides in H_2O followed by PBS (twice, 5 min each).
2. Block nonspecific binding of primary antibody with 4% species-appropriate normal serum by incubation for 30 min. Do not rinse sections after blocking.
3. Apply primary antibody diluted in PBS supplemented with 4% of the species-appropriate normal serum and incubate for 90 min. Wash in PBS (3 times each).
4. Apply biotinylated secondary antibody diluted in PBS supplemented with 4% of the species-appropriate normal serum and incubate for 45 min. Wash in PBS (3 times each).
5. Incubate with Streptavidin-conjugated Texas Red for 20 min. Wash in PBS (3 times each).
   For single labeling, continue to Step 8.
   For double labeling, continue to Step 6.
6. In the case of double immunolabeling, the sections after the first part of staining undergo two blocking procedures:
   a. Treatment with an avidin–biotin blocking kit (Vector): solution A (15 min) followed by 15 min washing; and solution B (15 min) followed by 15 min washing.
   b. Blocking with 4% appropriate normal serum (20 min).
7. For the second antigen, apply primary antibody (overnight at +4 °C), followed by biotinylated secondary antibody (45 min) and streptavidin-coupled FITC (20 min). Wash in PBS (3 times each).
8. Counterstain nuclei with 4'6-diamidino-2-phenylindole (DAPI) for 2 min.
9. Coverslip and place in the box at +4 °C.

3.316.4.3. Counterstaining and Mounting

3.316.4.3.1. Counterstaining following immunohistochemical staining

Many investigators underestimate the importance of nuclear counterstaining after completion of immunohistochemical staining. It is necessary, however, for the evaluation of overall tissue morphology and the nuclear-cytoplasmic structural relationship. In general, counterstains are designed to provide a contrast of nucleus with cytoplasmic immunostaining and surrounding tissue. It is important to use a color that is different from that of the enzymatic label in order to avoid confusion. The most common colors are blue (e.g., hematoxylin, toluiding blue, methylene blue), red (e.g., fast red), and green (e.g., light green). Hematoxylin is the most popular nuclear counterstain and provides the perfect contrast when used with AEC or DAB chromogens, which produce red and brown reaction products, respectively. Hematoxylins can be used in progressive (Mayer's or Gill's) or regressive (Harris's) staining protocols. During regressive staining, tissue sections are incubated with hematoxylin for a long time to achieve overstaining, and then differentiated to remove extra stain by immersion in an acid solution. Initially, hematoxylin stains nuclei red, until the pH changes to alkaline and the color changes to blue. This is an important step to reach visible contrast between nuclei and cytoplasm, and the reaction is commonly accomplished by washing the slides in tap water (in most locations, running tap water provides enough alkalinity) or in a solution of ammonia. When using AEC chromogen that is soluble in alcohol, the use of nonalcohol-containing hematoxylins (e.g., Mayer's or Gill's) is preferable. If Harris's hematoxylin is used, the staining duration should be kept to the minimum because it contains alcohol. Harris's hematoxylin is a good choice, however, for DAB.

Staining intensity depends on several factors, including the concentration of the hematoxylin solution, the duration of staining, the duration of differentiation time, and tissue preparation (paraffin-embedded vs. fresh-frozen). It is important to maintain a balance between obtaining a good nuclear morphology and not overstaining the other tissue components.

3.316.4.3.2. Mounting following immunohistochemical staining

Mounting medium is used to protect stained tissue sections from physical damage and to improve the clarity and contrast of the image during microscopy. The choice of mounting medium depends largely on the label and the chromogen used. Mounting media can be categorized into two groups: organic and aqueous. Organic mounting medium is designed for the permanent preservation of insoluble chromagen substrates such as DAB; it is not suitable for fluorescent labels. Aqueous mounting medium is suitable for all enzymatic label/chromogen combinations, as well as fluorescent labels. Tissue sections mounted in such medium do not need dehydration or clearing steps; however, the clarity and contrast tend to be of poor quality compared to organic mounting medium.

3.316.4.4. Data Interpretation

The interpretation of staining results relies heavily on the skill and experience of the reader, and is often the most difficult aspect of immunohistochemistry. The reader, usually a pathologist, should identify the antigen while taking into consideration all possible artifacts due to fixation, tissue processing, sectioning, and staining. In addition, the interpreter must know what the staining should look like both in normal tissue and in a pathological specimen. Assessment of the pattern of staining is a critical step. Specific staining could associate with cytoplasm, nuclei, or cell membrane. Staining could be focal or diffuse. Focal staining localizes with smaller, distinct areas of cells, while diffuse staining associates with larger areas and is often nonspecific. Nonspecific or background staining usually associates with connective tissue, adipocytes, and collagen, and is often present when polyclonal antibodies are employed. Problems with staining interpretation frequently occur due to poor blocking of endogenous enzyme activity or lack of fixation. Poorly fixed tissue may have a preserved antigen, but morphology is often sacrificed. While longer fixation will preserve tissue morphology, antigens may be altered, masked, depleted, or destroyed. Cells that have undergone necrosis, autolysis, or have been damaged will likely show nonspecific staining. The most challenging staining to interpret is immunofluorescence because in addition to nonspecific staining, various tissues and cells have inherent autofluorescence (e.g., collagen, elastin, macrophages/foam cells). Tissue fixed in formalin provides additional problems in interpretation due to autofluorescence. Therefore, interpretation of immunofluorescence staining should always be done in conjunction with bright-field microscopy.

3.316.5. Detection of Pathobiological Processes and Associated Cellular Events in an Implanted Site

Implantation of an artificial prosthesis in the body interferes with the function of the tissue site of implantation, initiating the processes of 'host integration' and inducing a wound-healing response. Wound-healing response is determined by the degree of surgical trauma, the mechanical stresses applied to the tissue by an implant, and biocompatibility of the biomaterial. Normal healing is a complex cascade of cellular events characterized by three phases: inflammation, proliferation, and maturation/remodeling. In addition, newly formed blood vessels connect the construct to the circulation to provide the constructs with oxygen, which is critical for maintaining viability of the implanted cells. Finally, the immune response to the implanted construct plays a key role in the long-term outcome by defending the body from foreign matter. These three biological responses – wound-healing, angiogenesis, and immune response – are multicellular processes that are highly regulated as a series of interacting events. Each process can be characterized by cell-specific phenotype, growth factors, and cytokine expression, and therefore can be detected using specific antigen–antibody reaction. In addition to a normal wound-healing reaction, tissue interaction with an implant involves biomaterial-specific responses (e.g., foreign body reaction, encapsulation). Understanding of biomaterial–tissue interactions requires consideration of local and systemic effects of material on host tissues (e.g., inflammation, pannus formation, encapsulation) as well as biological effects of host environment on material (e.g., calcification). In this section, immunohistochemistry is presented in the context of

biomaterial implantation and tissue engineering. We focus on current understanding of the mechanisms of healing and rejection of biomaterials and provide a brief summary of wound-healing-associated cellular events that can be characterized using immunohistochemistry.

3.316.5.1. Wound-Healing Response

Wound-healing is a coordinated tissue process characterized by an inflammatory phase (hours), a proliferation phase (days), and a maturation/remodeling phase (weeks).

3.316.5.1.1. Inflammatory phase

The cellular aspect of the inflammatory phase occurs within hours of injury.

3.316.5.1.1.1. Neutrophils

Neutrophils are the predominant cell type during the first 48 h after implantation but they do not appear essential to the wound-healing process. Phagocytic neutrophils clean bacteria and necrotic material from the wound and release proinflammatory mediators. In some cases, the neutrophil number is low, but their absence does not prevent healing. This inflammatory phase can be detected by immunohistochemistry, using antineutrophil cytoplasmic antibodies, a group of IgG antibodies against antigens of neutrophil granulocytes that show a diffusely granular cytoplasmic staining pattern.

3.316.5.1.1.2. Macrophages

Once at the site of injury, monocytes differentiate into macrophages. Macrophages are essential to healing and are the most important cell type in the early phase of wound-healing. Phagocytic macrophages eliminate necrotic debris and bacteria. Recent studies identified two distinct phases of monocyte/macrophage participation in wound-healing, and showed the divergent properties of these cells in this process. Ly-6C^{hi} monocytes dominate early (phase I) and exhibit phagocytic, proteolytic, and inflammatory functions. Ly-6C^{lo} monocytes dominate later (phase II), have attenuated inflammatory properties, and express vascular endothelial growth factor (VEGF). Consequently, Ly-6C^{hi} monocytes digest damaged tissue, whereas Ly-6C^{lo} monocytes promote healing via myofibroblast accumulation, angiogenesis, and deposition of collagen.

Macrophages also secrete collagenases (matrix metalloproteinases MMP-1 and MMP-13), gelatinases (MMP-2 and MMP-9), and elastolytic cathepsins (cathepsin K, cathepsin S) that break down injured tissue. In addition, macrophages release platelet-derived growth factor (PDGF), a cytokine that stimulates the chemotaxis and proliferation of fibroblasts and smooth-muscle cells. In particular, it plays a significant role in angiogenesis. Macrophages also secrete several substances such as chemotactic factors, coagulation factors, and complement components that are important for healing. Thus, immunohistochemical assessment of macrophage subsets – their function, activation, and expression of cytokines and growth factors – may reveal delayed or defective wound repair.

The following macrophage markers could be assessed using immunohistochemistry:

- AM-3K: immunohistochemical staining of routinely processed specimens demonstrated that this antibody recognized a specialized subpopulation of antiinflammatory macrophages that are distinct from inflammatory or classically activated macrophages;
- CD 68: a classical macrophage marker expressed by human monocytes and tissue macrophages;
- F4/80: the best macrophage marker to date;
- HAM-56: a pan-macrophage marker; can be expressed by endothelial cells;
- MAC-1/MAC-3: monoclonal antibodies against the human mannose receptor, a specific marker for macrophages;
- CD 163: a specific marker of macrophages in paraffin-embedded tissue samples; is not restricted to 'mature' macrophages;
- 25F9: a late-stage inflammation marker;
- Ly6C: an early-stage inflammation marker;
- RM3/1: an intermediate- and late-phase inflammation marker;
- 27E10: a distinct marker of macrophage activation and differentiation, an early-stage inflammation marker;
- ED-1: used as a marker for rat macrophages;
- ED-2: a resident macrophage marker;
- Carboxypeptidase M (CPM): a marker of macrophage maturation *in vivo* and *in vitro*;
- Chitotriosidase: a marker of macrophage stimulation;
- Cathepsin K: a marker of macrophage differentiation; also expressed in osteoclasts.

3.316.5.1.1.3. Lymphocytes

T lymphocytes migrate into the wound during the inflammatory phase, ~72 h after injury. These cells are attracted to the wound by the cellular release of interleukin 1 (IL-1). Lymphocytes secrete lymphokines, such as heparin-binding epidermal growth factor (EGF) and basic fibroblast growth factor (bFGF), which have been shown to play a role in wound-healing and angiogenesis. Lymphocytes also play a role in cellular immunity and antibody production. Lymphocytes, their subsets, and lymphocyte-derived factors can be detected using commercially available antibodies (see **Section 3.316.5.3**).

3.316.5.1.2. Proliferative phase

Formation of granulation tissue or foreign body reaction is a central event during the proliferative phase. Inflammatory cells (mostly macrophages and foreign-body giant cells (FBGC)), fibroblasts, and newly formed vessels immersed in extracellular matrix (ECM) (fibronectin, collage, and proteoglycans) comprise the granulation tissue. FBGC are multinucleated cells thought to form through fusion of macrophages. These cells retain the functional capability of macrophages, and in that capacity, they contribute to the healing process. Granulation tissue formation occurs 3–5 days after injury and overlaps with the preceding inflammatory phase. This phase and the extent of involvement of each component are highly variable, depending on the form, type, and topography of the biomaterial surface.

3.316.5.1.2.1. Epithelialization

Epithelialization is the formation of epithelium over a wound incision, which involves the migration of cells at the wound edges over a distance of <1 mm. In humans, incisional wounds

are normally epithelialized within 24–48 h. Epidermal cells undergo structural changes and secrete collagenases that break down collagen and plasminogen activator, which stimulates the production of plasmin to promote clot dissolution. This epithelial layer provides a seal between the wound and the external environment.

3.316.5.1.2.2. Fibroblasts

Fibroblasts are critical components of granulation tissue. Fibroblast accumulation begins 3–5 days after injury and may last up to 14 days. Following biomaterial implantation, fibroblasts undergo a response known as 'activation,' characterized by a transition of quiescent cells into myofibroblast-like phenotype. Stimuli that initiate fibroblast activation mostly derive from macrophages. Responses of fibroblasts to activation include proliferation, fibrinogenesis, and release of cytokine and proteolytic enzymes. The number of fibroblasts increases in the healing wound while the number of inflammatory cells decreases. Increased numbers of fibroblasts around the implant occur primarily due to local proliferation in response to fibronectin, PDGF, and fibroblast growth factor (FGF). Detection of fibroblasts through immunohistochemistry is difficult, and only a couple of antifibroblast antibodies are available – including mouse antihuman fibroblast monoclonal antibody (clone 5B5), vimentin, and polyclonal anti-DDR2 (Discoidin Domain Receptor 2), which regulates fibroblast proliferation and migration. (Personal communication with Dr. Thomas K. Borg, Medical University of South Carolina.)

3.316.5.1.2.3. Myofibroblasts

A myofibroblast is an activated form of fibroblast that is capable of contraction due to the presence of cytoskeletal proteins that are normally found in smooth-muscle cells – in particular, α-smooth muscle actin. These cells participate in wound repair by contracting the edges of the wound.

The detection of myofibroblasts is complex, and thus a combination of different antibodies should be used (see below). The following myofibroblast markers could be assessed by immunohistochemistry:

- α-actin (α-SMA): a commonly used myofibroblast marker, also expressed in smooth-muscle cells; a marker of fibroblast-to-myofibroblast phenotypic modulation;
- Desmin: should be used in combination with α-smooth muscle actin;
- Vimentin: an intermediate filament;
- Palladin 4lg: a novel marker of myofibroblast conversion *in vivo* and *in vitro*;
- TGF-β1 (transforming growth factor β1): a marker of myofibroblast proliferation, differentiation, and survival.

3.316.5.1.2.4. Smooth muscle cells

Smooth muscle cells are a phenotypically heterogeneous cell population. Studies of these cells, therefore, have long been hampered by the lack of suitable markers. For example, both smooth muscle cells and myofibroblasts are characterized by the expression of α-smooth muscle actin. To distinguish smooth muscle cells from myofibroblast-like cells, a combination of specific markers of smooth muscle cells should be employed.

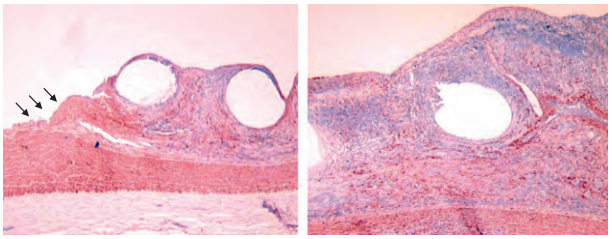

Figure 5 Left: 'good' healing with minimal inflammatory reaction around stent studs. Note, pannus formation/tissue overgrowth (arrows) detected using anti-α-smooth muscle actin antibody. Right: poor healing with abundant inflammation and substantial granulation tissue formation around stent studs. Original magnification ×100.

The following markers of differentiated smooth muscle cells can be assessed by immunohistochemistry:

- α-actin (α-SMA): expressed in differentiated and undifferentiated smooth-muscle cells and myofibroblasts; important component of pannus formation due to tissue overgrowth on the site of anastomosis or implantation (Figure 5);
- Calponin: most highly expressed in terminally differentiated and nonreplicating smooth muscle cells;
- Caldesmon: a specific marker of fully differentiated and nonproliferating smooth muscle cells;
- Smoothelin: a structural protein of differentiated, contractile smooth muscle cells;
- Transgelin (SM22): a marker of differentiating smooth muscle cells;
- SM2: a smooth muscle myosin heavy chain (MHC) isoform; an excellent marker for differentiated phenotype of smooth muscle cells;
- SM1: a MHC isoform; an excellent marker of mature smooth muscle cells;
- SMemb: a nonmuscle myosin that is expressed in embryonic smooth muscle cells or activated mesenchymal cells;
- Desmin: an intermediate filament protein of both smooth and striated muscles.

3.316.5.1.2.5. Differentiation of fibroblast, myofibroblasts, and smooth muscle cells using immunohistochemistry

We identified fibroblasts, myofibroblasts, and smooth muscle cells using a panel of antibodies that work on formalin-fixed paraffin-embedded human samples. We demonstrated the following expression patterns of cell-type markers:

Fibroblasts: α-SMA−, vimentin+, desmin−, SMemb−, SM1−, SM2−

Myofibroblasts: α-SMA+, vimentin+, desmin±, SMemb+, SM1−, SM2−

Smooth muscle cells: α-SMA+, vimentin±, desmin−, SMemb−, SM1+, SM2+

The challenge to detect 'dedifferentiated' cells remains, as they may lose their cell-type-specific markers.

3.316.5.1.3. Maturation/remodeling phase

3.316.5.1.3.1. Collagen

Remodeling begins ~21 days after injury, and may continue indefinitely. The synthesis and deposition of collagen is a critical event in wound-healing. Collagen is secreted to the extracellular space in the form of procollagen. Cleaved procollagen is converted into tropocollagen, which then aggregates to form collagen filaments. Filament, fibril, and collagen fiber formation occur within a matrix gel of glycosaminoglycans, hyaluronic acid, chondroitin sulfate, and heparin sulfate produced by fibroblasts. Collagen remodeling is controlled by the presence of collagenases, so that a balance exists between the formation of new collagen and old collagen. Approximately 80% of the collagen in healthy tissue (e.g., heart valve, artery, skin) is type I collagen, while type III collagen is the primary component of early granulation tissue and is abundant in embryonic tissue. During remodeling, collagen becomes increasingly organized. Fibronectin gradually disappears, and hyaluronic acid and glycosaminoglycans are replaced by proteoglycans. Water is resorbed from the scar, which allows collagen fibrils to get closer together, ultimately decreasing scar thickness. During scar maturation, the collagen subtype synthesis may shift, and type III collagen is replaced by type I collagen. Therefore, immunohistochemical characterization of collagen subtypes, followed by digital image analysis, can be used to quantify collagen organization and tissue maturity.

3.316.5.1.3.2. Proteolytic enzymes

The MMPs or proteolytic enzymes are able to initiate ECM degradation during tissue remodeling. Both macrophage- and fibroblast-derived MMPs contribute to this process. There are at least three mammalian collagenases capable of initiating the degradation of interstitial collagen – collagenase-1 (MMP-1), collagenase-2 (MMP-8), and collagenase-3 (MMP-13). Although increases in total proteolytic activity have been reported in tissue response for a long time after implantation of biomaterials, it is likely that early local expression and activity of these enzymes are necessary for the initial activation of resident fibroblasts. The other proteolytic enzymes that play important roles in tissue remodeling and cell activation include gelatinases (MMP-2 and MMP-9) and elastases (cathepsin S and cathepsin L). The antibodies for identification of these enzymes and other proteolytic enzymes are readily available from various sources.

3.316.5.1.4. Cytokines

Cytokines are important mediators of wound-healing that are released from various cell sources, including neutrophils, macrophages, and myofibroblasts. The following are key mediators that participate in wound-healing responses:

- FGF is a mitogen for endothelial cells, myofibroblasts, and fibroblasts. FGF is also an important activator of angiogenesis. This factor stimulates production of collagen, fibronectin, and proteoglycans, thereby contributing to wound-healing and remodeling.
- PDGF is released from the α-granules of platelets and is responsible for the stimulation of neutrophils and macrophages and the production of TGF-β. PDGF is a mitogen and chemotactic agent for fibroblasts and smooth-muscle cells. This factor stimulates angiogenesis, collagen production, and collagenase expression.
- VEGF is mitogenic for endothelial cells and plays an important role in angiogenesis.
- TGF-β is an important stimulant for fibroblast proliferation, activation, and phenotypic differentiation into myofibroblasts. This factor promotes the production of collagen, proteoglycans, and fibrin, as well as the accumulation of the ECM and fibrosis.
- Tumor necrosis factor α (TNF-α) is produced by macrophages and stimulates angiogenesis, collagen synthesis, and collagenase expression.

3.316.5.2. Angiogenesis

In order for the cell-based construct to function appropriately and integrate into host tissue, blood vessels should form to connect the construct to the circulation, for access to nutrients and oxygen and to remove waste. New blood vessel formation is a complex process that begins with the release of angiogenic factors such as VEGF, angiogenin, angiotropin, and fibronectin from macrophages, platelets, or ECM. The newly formed vessels extend by release of MMPs, which degrade surrounding ECM and facilitate endothelial cell migration and proliferation. Finally, these newly formed vessels are stabilized by recruitment of surrounding mesenchymal cells. New vessels that become unnecessary disappear by apoptosis.

The following endothelial cell markers could be assessed by immunohistochemistry:

- CD 31 (PECAM 1): a cell adhesion and signaling molecule that is enriched at the endothelial cell junctions;
- VE-Cadherin (7B4 antigen): an endothelial-specific marker that plays a role in the organization of lateral endothelial junctions and in the control of permeability properties of vascular endothelium;
- vWF (von Willebrand factor): routinely used to identify vessels in tissue sections;
- VCAM-1 (vascular adhesion molecule-1): a marker of endothelial cell activation, expressed during development and pathological conditions such as inflammation, transplantation, and rejection; mediator of cell migration from blood into tissue;
- CD 34: human progenitor cell antigen, localized on endothelial cells;
- CD 54 (intracellular adhesion molecule-1, ICAM-1): participates in endothelial cell migration;
- ICAM-2 (intracellular adhesion molecule-2): mediates angiogenesis, expressed at the endothelial junctions of vascular endothelial cells;
- CD 62P (P Selectin): a platelet activation marker;
- E Selectin: a marker of endothelial cell activation;
- CD 105 (Endoglin): a highly specific endothelial cell marker expressed on proliferating endothelial cells;
- CD 146 (P1H12): a novel cell adhesion molecule localized at the endothelial cell junction;
- Eotaxin-3: expressed in IL-4-stimulated vascular endothelial cells;
- CD 141 (Thrombomodulin, TM): a marker for microvasculature, but not macrovasculature, endothelial damage;

- VEGF: a key regulator of angiogenesis;
- VEGFR-1 (Flt-1): a high-affinity tyrosine kinase receptor for VEGF, expressed almost exclusively on vascular endothelial cells;
- GBP-1 (guanylate-binding protein-1): a novel endothelial cell marker expressed in a broad range of human tissues; characterizes the activated phenotype;
- MECA-32: a monoclonal antibody that shows high specificity for mouse endothelium in both embryonic and mature tissues;
- MECA-79 antibody: stains HEV (high endothelial venule)-like vessels at various sites of inflammation;
- BNH9/BNF13: reacts with endothelial cells in routinely fixed and embedded tissues;
- Nucleolin: a specific marker of angiogenic endothelial cells within the vasculature;
- D2-40: a recently available antibody that has been used as a lymphatic endothelial cell marker;
- LYVE-1: expressed by endothelial cells of normal lymphatic vessels, but not blood vessels.

3.316.5.3. Immune Response

The immune response to the implanted construct plays a key role in defending the body from foreign matter. It is composed of two complementary pathways known as innate and adaptive immunity. The innate immune system is the dominant system of host defense that responds to pathogens in a generic way. There are two arms of the innate system: biochemical and cellular. The biochemical cascade involves at least 20 proteins of the complement system, which attacks the surfaces of foreign bodies. The cellular components are innate leukocytes that include both phagocytic cells (e.g., macrophages and neutrophils) and natural killer cells. These cells destroy foreign particles by conveying them to intracellular lysosomes. Adaptive immunity allows for a stronger immune response and immunological memory. It also has two arms of defense: humoral and cell-mediated. B and T lymphocytes are two major cell types involved in adaptive immunity. B cells are involved in the humoral immune response, and T cells are involved in cell-mediated immune response. As with B cells, each type of T cell recognizes a different antigen that can be determined using immunohistochemistry:

- CD 4 and CD 8: functionally analogous molecules expressed on mature T cells; the cells have either CD 4 or CD 8 but not both;
- CD 11a/CD 18 (lymphocyte functional antigen-1, LFA-1): a member of the β-integrin family, present on most leukocytes;
- Intracellular adhesion molecule-3 (ICAM-3): an adhesion molecule present on many leukocytes following lymphocyte activation;
- CD 2 (LFA-2) and CD 58 (LFA-3): a pair of molecules involved in T-cell activation;
- CD 2: expressed on all T cells;
- CD 3: expressed on mature T lymphocytes;
- CD 28 and CD 152: present on mature T cells and critically involved in T cell activation;
- CD 80 and CD 86: induced on activated B cells;
- CD 40: a surface protein present on B cells, macrophages, and endothelial cells;
- CD 40L (CD 154): the ligand for CD 40, induced transiently on activated T cells;
- CD 45 (leucocyte common antigen): a phosphatase present on all leukocytes.

3.316.5.4. Encapsulation

Complete tissue regeneration and restoration of function is rare. Fibrous encapsulation is the more typical course of isolation of the implanted biomaterial. Granulation tissue that began to form earlier in the healing process builds to form a capsule that surrounds the implant, isolating it from the local tissue environment. At this point, it is possible for normal local processes to resume and function to be restored if the degree of injury permits. This stage is characterized by collagen accumulation and organization (scar formation) and reduction of the number of inflammatory cells. Overall tissue morphology at the stage of implant encapsulation can typically be demonstrated by hematoxylin and eosin staining and special stains showing collagen (e.g., Masson's, Movat's, picrosirius red), as reagent cost and technician effort are greater when immunohistochemistry is used.

3.316.5.5. Calcification

Calcification often occurs as a consequence of medical device implantation owing to reaction to tissue damage and inflammation. It was recently proposed that arterial and aortic valve calcification, particularly in prevailing dysmetabolic populations, is an inflammatory disease. Advanced calcification such as hydroxyapatite, the crystalline form of calcium phosphate, can be determined by routine histological methods such as von Kossa or alizarin red. However, earlier stages of host tissue mineralization (osteogenic activity and phenotypic changes of smooth muscle cells and myofibroblasts to osteoblast-like cells) could be revealed only using special immunohistochemical staining.

The following osteogenic and chondrogenic markers could be assessed by immunohistochemistry:

- Osteocalcin: a marker of differentiated osteoblasts;
- Osteopontin: a noncollagenous protein; inhibitor of calcification;
- Osteonectin: an inhibitor of hydroxyapatite formation;
- Cbfa1 (Runx2): a master osteoblast transcription factor;
- Osterix: a transcription factor downstream of Cbfa1;
- BMP (2, 4, 7): regulate mesenchymal progenitor cells differentiated along smooth muscle cells, chondrocyte, osteoblast, or adipocytic lineages;
- Osteoactivin: osteoblast-related glycoprotein that plays a role in osteoblast differentiation and function (downstream mediator of BMP-2);
- SOX9: master chondroblast transcription factor;
- Smad6: antagonist for BMP2/4 signaling;
- Osteoprotegerin (OPG): inhibitor of vascular calcification/osteoblastic phenotype;
- LRP5: plays an important role in osteoblastogenesis via β-catenin signaling pathway;
- Msx-2: promotes calcification.

3.316.6. Implant Evaluation Using Immunohistochemical Methods

Teamwork among surgeons, biomaterials engineers, and pathologists is extremely important for success in implant evaluation. Evaluation of the implant without understanding the specific pathological processes in the surrounding tissues will be incomplete. As described above, the key pathological tissue changes at the site of biomaterial implantation involve the wound-healing and host responses. In addition, the evaluation of cell viability, proliferation/apoptosis ratio, and phenotypic changes will be needed to assess devices that modify healing or improve tissue regeneration. Therefore, immunohistological techniques offer an important tool for the assessment of various cellular pathobiological events in implanted tissues.

3.316.6.1. Heart Valve Prostheses

Currently, cardiac valve replacement is the only treatment for calcific aortic valve disease. Approximately 172 000 valves are implanted worldwide each year. The majority of implanted valves are carbon bileaflet tilting disk valves (St. Jude Medical), and flexible-stent-mounted porcine aortic valve bioprostheses (Carpentier-Edwards and Hancock models) fabricated from a gluteraldehyde-fixed pig aortic valve. Patients with mechanical valves have a high risk of thromboembolic complications, while patients with bioprosthetic valve leaflets are susceptible to tissue deterioration, including calcification. Most implant retrieval involves examination of failed valves that are surgically removed or obtained at autopsy. Explanted valves should be inspected for evidence of thrombosis, infection, paravalvular leaks, and calcification. Combined histological and immunohistochemical approaches can be used to assess tissue ingrowth into cloth-covered studs, inflammation, and dystrophic calcification. Immunohistochemical analyses may include evaluation of pannus formation using α-smooth muscle actin antibody; macrophage (e.g., CD 68) and T-cell (e.g., CD 3) infiltration; and noncollagenous proteins (e.g., osteopontin, osteocalcin, osteonectin).

3.316.6.2. Polymer-Based Engineered Tissues

In 1986, Weinberg and Bell reconstructed blood vessels in test tubes using endothelial cells, vascular smooth-muscle cells, adventitial fibroblasts, and collagen. Since then, the field of cardiovascular tissue engineering has advanced significantly and considerable research has been conducted using seeded synthetic scaffold vascular grafts implanted in large and small animal models. One of the major problems related to these polymer scaffolds, however, is their long-term presence at the site of implantation as foreign bodies. As a result, in addition to normal wound-healing, the tissue-engineered vascular grafts would generate biomaterial-specific responses, such as foreign body reaction and encapsulation/scar formation. Notably, the leaflets of implanted tissue-engineered cardiac valves would undergo more severe destructive changes compared to the vascular wall, due to higher hemodynamical stresses. That would likely result in systemic responses to blood-circulated polymer particles.

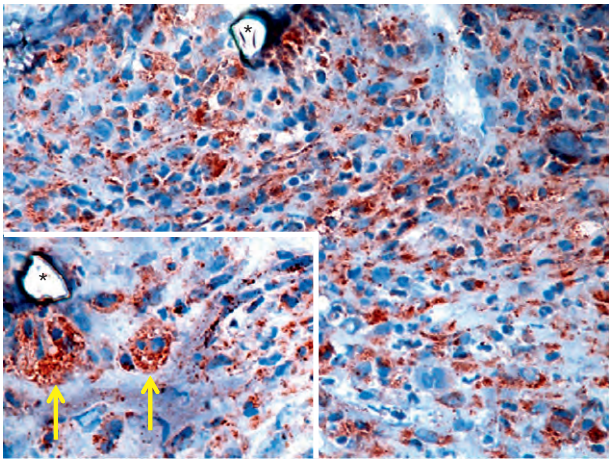

Figure 6 Macrophages detected using anti-mac 3 antibody (red reaction product) in vascular tissue engineered graft implanted into mouse carotid artery. Original magnification ×400. Inset: Giant cells (arrows) adjacent to polymer residue (asterisk). Magnification ×600.

We recently demonstrated the remodeling potential of tissue-engineered small-diameter vascular grafts implanted in mouse carotid artery, using comprehensive immunohistochemistry and molecular imaging analyses. We showed that remodeling is initiated by macrophage invasion, and that by 35 days after implantation, the majority of the initially seeded human mesenchymal cells were replaced by host murine cells, as detected by immunohistochemistry to mouse-specific antibodies (Figure 6). Over time, the remodeling enzyme expression (e.g., MMP-2, MMP-9, cathepsin B) and activity decreased, and grafts displayed layered collagenous structure. Multispectral intravital molecular imaging corroborated our histological findings. This imaging approach offered the advantage of data collection in real time without animal sacrifice and thus could be an additional diagnostic tool for evaluation of small-diameter tissue-engineered vascular grafts implanted in mice.

3.316.6.3. Vascular Grafts

Transplantation medicine has provided insights into the mechanisms of organ rejection that could be applied to tissue-engineered vascular grafts and xenografts. Xenografts are typically rejected by complement-mediated hyperacute mechanisms, but delayed forms of rejection also have been described. Therefore, analyses of immune responses, as well as of inflammation induced by xenogenic matrices or tissue-engineered scaffolds, are required for successful evaluation. Assessment by immunohistochemistry includes but is not limited to analysis of immune cell subpopulations (e.g., CD 3, CD 4, CD 8), expression of activation markers (e.g., CD 25, HLA-DR), cytokines (e.g., TNF-α, IFN-γ), and markers of cell proliferation (e.g., Ki 67). Specifically, examination should record the extent of endothelialization, perigraft tissue reaction, and anastomotic tissue structure (e.g., cell morphology and phenotypes, thickness, and tissue ingrowth).

3.316.6.4. Intravascular Stents

The purpose of stents is to decrease thrombus formation and reduce intimal thickness due to angioplasty. As most stent types use metal struts, the method used for tissue sampling and sectioning must either initially remove the metal inclusions or use specialized techniques for tissue processing and embedding. In such circumstances, a resin MMA-embedding method could be useful, as it preserves both enzymatic activity and tissue antigenicity. Prior to immunohistochemistry, the sections should be deplasticized and permeabilized in 1% Tween 20-PBS. Most cellular reactions to stents occur immediately around the struts, and include cell proliferation (e.g., PCNA), inflammation (e.g., CD 68, HAM 56), endothelialization (e.g., vWF), and tissue overgrowth and pannus formation (e.g., α-SMA, vimentin). These antibodies have been shown to work on resin-embedded tissue sections.

3.316.6.5. Cardiac Assist Devices and Artificial Hearts

Immunohistochemical assessment of explanted cardiac assist devices or artificial hearts may include examination of pseudointimal thickness along the pumping bladder surface for inflammatory cellular components such as leukocytes (neutrophils and macrophages). Endothelialization of the device surface is possible, and can be assessed using endothelial cell markers (e.g., CD 31, vWF). Fibroblasts and noncellular ECM components such as fibrin could be evaluated using an appropriate antibody. Pump bladder calcification in experimental devices has been reported, but the underlying mechanisms are unknown. Therefore it would be of interest to perform analysis of osteogenic regulating proteins and transcriptional factors, including osteocalcin, osteonectin, osteopontin, BMP (2, 4, 7), Cbfa 1, and Osterix.

References

1. Scion, S. R. S. *Immunohistochemistry: Methods Express Series*. 2005.
2. Ratner, B. D.; Schoen, F. J.; Lemons, J. E. *Biomaterial Science. An Introduction to Materials in Medicine*. Academic Press: New York, 1996.
3. Barbucci, R. *Integrated Biomaterial Science*. Kluwer Academic/Plenum: New York, 2001.
4. Von Recum, A.; Von Recum, A. F. *Handbook of Biomaterials Evaluation. Scientific, Technical and Clinical Testing of Implanted Materials*, 2nd ed.; CRC Press: Boca Raton, FL, 1998.
5. Palsson, B. O.; Bhatia, S. N. *Tissue Engineering*. Prentice Hall: Englewood Cliffs, NJ, 2003.
6. Aikawa, M.; Rabkin, E.; Okada, Y.; *et al*. *Circulation* **1998**, *97*, 2433–2444.
7. Nahrendorf, M.; Swirski, F.; Aikawa, E.; *et al*. *J. Exp. Med*. **2007**, *204*, 3037–3047.
8. Rabkin, E.; Hoerstrup, S. P.; Aikawa, M.; Mayer, J. E.; Schoen, F. J. *J. Heart Valve Dis*. **2002**, *11*, 308–314.
9. Aikawa, E.; Whittaker, P.; Farber, M.; Mendelson, K.; Padera, R. F.; Schoen, F. J. *Circulation* **2006**, *113*, 1344–1352.
10. Aikawa, E.; Nahrendorf, M.; Figueiredo, J. L.; *et al*. *Circulation* **2007**, *116*, 2841–2850.
11. Aikawa, M.; Rabkin, E.; Voglic, S. J.; *et al*. *Circ. Res*. **1998**, *83*, 1015–1026.
12. Manji, R. A.; Zhu, L.; Nijjar, N. K.; *et al*. *Circulation* **2006**, *114*, 318–327.
13. Hjortnaes, J.; Gotlieb, D.; Figueiredo, J. L.; *et al*. *Tissue Eng*. **2010**, *16*, 597–607.

Relevant Websites

http://www.ihcworld.com – This site offers information on basic histology and many aspects of immunohistochemistry, including antigen retrieval, positive controls, antibodies and immunohistochemistry protocols.

http://www.immunoportal.com – This site provides a database of staining protocols, and references articles relating to immunohistochemistry.

http://www.antibodyresource.com – This site helps to find companies that sell monoclonal and polyclonal antibodies.

http://www.linscottsdirectory.com/# – Linscott's Directory of Immunological and Biological Reagents is available free of charge. It contains more than 110 000 commercial and governmental supplier listings including suppliers of antibodies, immunoassays, and custom services.

http://www.histosearch.com – This site provides comprehensive information when troubleshooting immunohistochemistry protocols.

http://tumor.informatics.jax.org/mtbwi/immunohistochemistry.jsp – The Jackson Laboratory Mouse Tumor biology Database resource of 206 different antibodies for use in mice.

3.317. Fluorescence Imaging of Cell–Biomaterial Interactions

E Liu, S Vega and M D Treiser, Rutgers University, Piscataway, NJ, USA
H-J Sung, Vanderbilt University, Nashville, TN, USA
P V Moghe, Rutgers University, Piscataway, NJ, USA

© 2011 Elsevier Ltd. All rights reserved.

3.317.1.	**Introduction**	291
3.317.2.	**Principles, Instrumentation, and Methodology for Cell Imaging**	292
3.317.2.1.	Epifluorescence Microscopy and Deconvolution Microscopy	292
3.317.2.2.	Confocal Microscopy	292
3.317.2.3.	Multiphoton Microscopy	294
3.317.2.4.	Other Advanced Fluorescence Imaging Techniques	295
3.317.3.	**Probing Cell–Biomaterial Interactions**	296
3.317.3.1.	Introduction to Fluorescence-Based Probes	296
3.317.3.1.1.	Fluorophore-tagged antibodies	296
3.317.3.1.2.	Quantum dot-based probes	296
3.317.3.1.3.	GFP and variants	297
3.317.3.2.	Case Studies of Imaging Cell–Biomaterial Interactions	297
3.317.3.2.1.	Case study 1: Fluororeporter imaging of cell cytoskeletal remodeling and apoptosis on biomaterials	297
3.317.3.2.2.	Case study 2: Multiphoton fluorescence imaging of 3D polymer scaffolds and cellular organization	299
3.317.3.2.3.	Case study 3: Confocal microscopy of cell-based fluororeporters for high-content imaging of cell–biomaterial interactions	299
3.317.3.2.4.	Case study 4: Combination of high-content and high-throughput fluorescence imaging for cell–biomaterial interactions on biomaterials with spatially graded properties	300
3.317.4.	**Looking to the Future**	301
References		302

Abbreviations

CCD camera	Charged-coupled device camera
CLSM	Confocal laser scanning microscopy
FISH	Fluorescence *in situ* hybridization
FITC	Fluorescein isothiocyanate
FRET	Fluorescence resonance energy transfer
GFP	Green fluorescent protein
MDS	Multidimensional scaling
Micro-CT	Microtomography
MPM	Multiphoton microscopy
mRNA	Messenger ribonucleic acid
NA	Numerical aperture
PEG	Poly(ethylene glycol)
PMT	Photomultiplier tube
ROS	Reactive oxygen species
STED microscopy	Stimulated emission depletion microscopy
TIRFM	Total internal reflectance fluorescence microscopy
TPE	Two-photon excitation
WFM	Wide-field fluorescence microscopy

3.317.1. Introduction

Numerous studies document the potential role of biomaterials in tissue engineering and regenerative medicine.[1–4] Biomaterials can modulate a wide range of cellular phenomena, including cell attachment, spreading, migration, survival, growth, differentiation, and immune response.[5–10] The characterization of chemical and mechanical properties of biomaterials is a well-established field of study. However, the biological characterization of cellular responses to biomaterials is typified by a large number of divergent readouts that are challenged by the lack of standardized conditions and objective standards. Methods based on optical imaging, in general, and fluorescence microscopy, in particular, have witnessed rapid growth and gained widespread acceptance in real-time, high-resolution studies of cell cultures as well as high-throughput cell screening assays. Not surprisingly, these advances have inspired the application of a new generation of techniques to the field of cell–biomaterial interactions. Some of these leading methods are reviewed in this chapter.

Advances in fluorescence microscopy have heralded the development of single-cell and intracellular imaging methods and fluorophores. As epifluorescence microscopy became an entrenched tool in cell biology laboratories, multilabeled indirect immunofluorescence techniques enabled biologists to examine the associations of different antigens within the same subcellular compartments.[11] Thereafter, advances in fluorescence *in situ* hybridization (FISH) permitted the localization

of individual genes on chromosomes and specific mRNAs.[12–15] The more recent introduction of high-resolution confocal and multiphoton microscope systems has made it possible to capture three-dimensional (3D) images resolving the organization of structures within cells, with speeds in the order of milliseconds.[16–19]

Fixed cellular images acquired from high-resolution immunofluorescence techniques have revealed the remarkable complexity of cellular architecture and provided important insights into major cellular structures, including different cytoskeletal proteins, the nucleus and its various compartments, and membranous organelles.[20–22] However, images of fixed and stained cells are static, providing only a brief snapshot of the organization and properties of these structures. This drawback has inspired biologists and microscopists alike to develop fluorescence-based methods with high sensitivity for studying specific types of molecules and multicomponent complexes in living cells.

Some of the first proteins that were tracked via fluorescence imaging were cytoskeletal proteins such as actin, paxillin, or vinculin directly conjugated with a fluorophore such as X-FITC or X-Texas Red. These fluorophore-conjugated proteins were microinjected into cells, resulting in the FITC or Texas Red incorporation into targeted endogenous structures.[23–25] More recently, fluorescent imaging technology heralded the development of genetically encoded fluorescent proteins that could be expressed in cells and organisms through the use of green fluorescent protein (GFP), a protein that revolutionized the use of fluororeporters in cell biology.[26] The use of GFP-tagged proteins has many advantages as described later in this chapter, but primary among these is the ability to capture more time-resolved images, which enables the tracking of the dynamic properties of tagged molecules for extended periods of time.

This chapter is divided into two major sections. In Section 3.317.2, the technical aspects of cell imaging are presented. In Section 3.317.3, specific cell–biomaterial case studies are presented.

3.317.2. Principles, Instrumentation, and Methodology for Cell Imaging

3.317.2.1. Epifluorescence Microscopy and Deconvolution Microscopy

Epifluorescence microscopy, also referred to as wide-field fluorescence microscopy (WFM), is the most commonly used fluorescence microscopy method in life sciences. Fluorescence microscopy allows visualization of cell morphology, cellular/subcellular compartments as well as cellular markers of disease (e.g., cancer vs. normal cells) or phenotype (e.g., stem cell lineage). The optics of an epifluorescence microscope are illustrated in Figure 1(a). Briefly, light of a specific wavelength (usually in the ultraviolet or blue, green regions of the visible spectrum) is generated by passing multispectral light from an arc-discharge lamp or other source through a wavelength-selective bandpass filter (excitation filter). Selected wavelengths passed by the excitation filter are then reflected from a dichromatic mirror or beamsplitter through the microscope object to expose the specimen with intense light. If the specimen fluoresces, the emission light gathered by the object passes back through the dichromatic mirror and is subsequently filtered by another bandpass filter (emission filter), which blocks the unwanted excitation wavelengths. Emitted light is then collected by a detector such as a CCD camera.

The application of an array of fluorophores has made it possible to identify cells and subcellular components with a high degree of specificity amidst nonfluorescing material. Through the use of multiple-fluorophore labeling, different probes can simultaneously identify several target molecules. Conventional epifluorescence microscopy can also be used to visualize 3D samples from a series of 2D images taken at different focal planes. The drawback of this method is that light emitted from planes above and below the in-focus regions are also captured in each optical section. This is because the entire specimen is illuminated by excitation light source, which causes the whole sample specimen to emit fluorescence in the form of radiated light that is collected by the CCD camera (detector). This results in a reduction of both lateral resolution and depth discrimination.

In order to remove unwanted out-of-focus information from each 2D image in the series, deconvolution, based on the underlying physics of image information, can be used to improve the quality of images. Deconvolution methods determine how much out-of-focus light is expected for the optics in use and then seeks to redistribute this light to its points of origin in the specimen. In order to restore the original 'clean' image from the convolved 'blurred' 3D image, mathematical algorithms are utilized to segregate the original distribution of point sources that gave rise to the specimen image. Widely used methods include: nearest neighbors, wiener filters, linear least squares, nonlinear least squares, maximum likelihood, blind deconvolution, and Lucy–Richardson deconvolution.[27–31] In general, there is no 'universally optimal' deconvolution algorithm. Methods that require more computing power yield better image restoration results. However, the advent of confocal and more recently two-photon imaging has limited the use of deconvolution-based methods.

3.317.2.2. Confocal Microscopy

Confocal microscopy on the other hand addresses this problem physically by introducing pinholes to reject out-of-focus light.[17,32] In contrast, deconvolution seeks to solve the 'image restoration problem' in a mathematical/computational way. The principles and schematics of confocal microscopy are illustrated in Figure 1(b) and are described below.

The name 'confocal' originates from the configuration based on the use of point illumination and a pinhole in an optically conjugate plane in front of a detector to eliminate out-of-focus information. Excitation light that is focused on the specimen by the object is initially passed through a small aperture, often a slit or a pinhole. Fluorescence emissions that originate from above or below the plane of focus are then blocked by a second aperture or slit in front of the detector. The smaller the second aperture, the higher the rejection rate of out-of-focus light and the thinner the resulting optical sections. Thin optical sections have greatly improved contrast and axial resolution, but they are obtained at the expense of overall specimen brightness or signal strength.

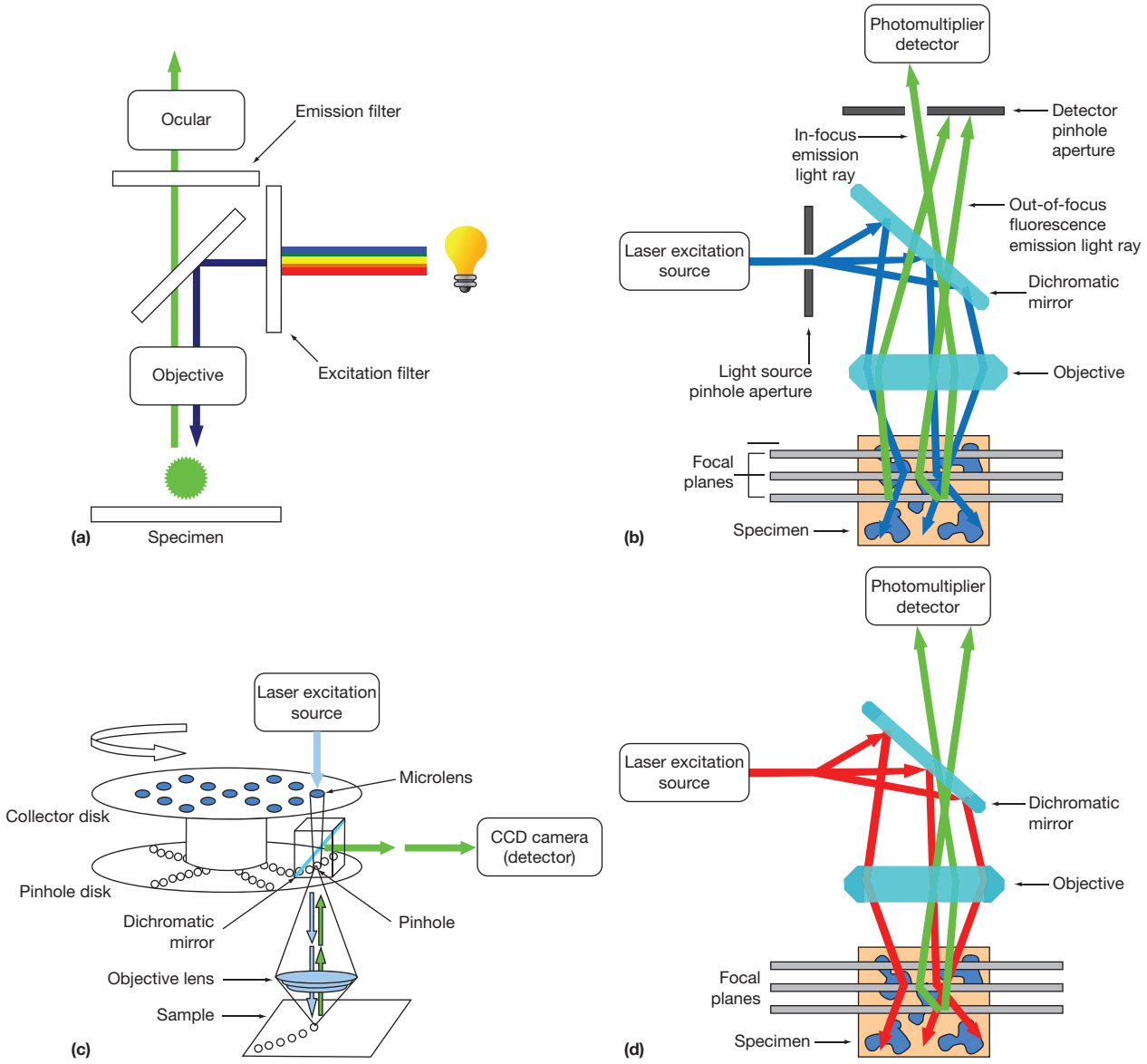

Figure 1 Schematic of various fluorescence microscope systems. (a) Epifluorescence microscope system, (b) laser scanning confocal microscope system, (c) spinning disk confocal microscope system, and (d) multiphoton (two photon).

There are two major approaches to achieve confocal microscopy using commercial instruments: point scanning confocal laser scanning microscopy (CLSM) and spinning disk confocal microscopy. CLSM is the most widely used confocal microscopy in life sciences; the basic principle is illustrated in Figure 1(b). An excitation laser source is scanned across the specimen in a point-by-point raster pattern. The emitted light is then collected by the object, passed through a small pinhole, and detected by a photomultiplier tube (PMT). The output from the PMT is assembled into an image and displayed by the computer.

CLSM has many advantages. It allows for extremely thin optical sectioning of specimens, permitting the imaging of structures and intracellular features in greater detail than conventional epifluorescence microscopy. The drawbacks of CLSM are that these systems compromise detectable fluorescence in order to deliver their high degree of confocality. Because of the small apertures of the pinhole, a large amount of light gets rejected, thus detectable emissions from the specimen must be bright enough to be captured through the use of high numerical aperture (NA) objectives. The use of intense lasers addresses the low-light emission problem; however, it also has its own shortcomings. The intensity of the laser light causes photobleaching in fluorescent probes and phototoxicity in the specimen itself. Additionally, CLSM's point-by-point acquisition technique is time consuming, making this system less capable of recording short-time biological events. For example, acquiring a 1024 by 1024 high-resolution single optical section image from most laser scanning confocal microscopes requires approximately 0.5–1 s. This is not rapid enough to capture

certain dynamic cellular phenomena, in particular, intracellular dynamics such as the visualization of calcium ion transients that occur in 1/10th to 1/5th of a second.[33–35]

The speed limitations imposed by CLSM can be overcome by using the second approach used to achieve confocal microscopy: a spinning disk confocal system. An array of beams can be used in parallel, which make it potentially useful for higher speed image acquisition in comparison to CLSM. The inherent parallelism of a spinning disk confocal system avoids fluorophore saturation, enabling higher levels of excitation to be used.[36–39] The spinning disk confocal is also called the Nipkow spinning disk confocal system, named after Paul Nipkow, who first proposed the principle of generating images using an array of pinholes in 1883.[39]

Figure 1(c) shows a diagram of the Nipkow spinning disk system. A conventional light source (mercury or xenon arc lamp) or laser passes through an excitation filter before being directed onto a spinning Nipkow disk in which 20 000–200 000 pinholes are arranged in spirals of constant pitch.[38] As light falls on one side of the disk, a subregion corresponding to about a thousand pinholes is illuminated and imaged. A partial rotation of a Nipsow disk (ranging from 1800 to 5000 rpm) scans the sample; the induced fluorescence (reflected light) produced by the specimen is collected by the objective lens and reflected off a beam splitter to highly reflective mirrors which amplify the collected light to the conjugate apertures on the other side of the spinning disk. Thin in-focus fluorescence from the specimen passes through the conjugate apertures and a barrier filter before being detected. In contrast, out-of-focus light from the specimen does not have a conjugate aperture to pass through, and is blocked by the disk. The time taken to traverse the field of view is so short that images can be seen in real time by an eyepiece or acquired using a camera that is synchronized with the rotation of the disk.[36–39]

Many of the biological applications using microscopy entail imaging living specimens or deep tissues. The complex nature of cellular materials means that the passage of light is affected in ways that cannot be accurately modeled, resulting in image quality falling well below theoretical resolution limits. Different imaging systems are not equally affected by this decrease in spatial accuracy as the focal plane moves further from the sample. CLSM is generally more tolerant to increasing working distance than wide-field microscopy systems, where out-of-focus light poses a major challenge. Absorption and scattering of light also contribute to the reduction in image quality, particularly, in thicker 3D specimens, although these factors become less pronounced with increasing excitation wavelength. The typical spatial limit of penetration of confocal microscopy for highly scattered cells/tissue samples is about 200 nm,[16,32,40] which may limit imaging of living specimens or deep tissues. This is one of the main reasons multiphoton microscopy (MPM) is the technique of choice for 3D tissue imaging.

3.317.2.3. Multiphoton Microscopy

Multiphoton microscopy (MPM) presents a major advantage over confocal microscopy because of deeper tissue penetration (on the order of millimeters), more efficient light detection, reduced photobleaching/phototoxicity, and enhanced spectral accessibility and flexibility.[16–19,41,42] The term MPM is a generic term for the following techniques: two-photon excitation (TPE) microscopy, three-photon excitation microscopy, second-harmonic generation MPM, and third-harmonic generation MPM.[19] All of these techniques use nonlinear excitation to generate fluorescence limited to a thin raster-scanned plane. With the advent of ultrafast (in the order of femtoseconds) pulsating lasers, such as Ti:Sapphire and Nd:YLF lasers, MPM, particularly TPE microscopy has become a viable tool to monitor complex biological samples.

The phenomenon of TPE arises from simultaneous absorption of two photons in a single quantized event.[19] Since the energy of a photon is inversely proportional to its wavelength, the two absorbed photons must have a wavelength of about twice that required for one-photon excitation. For example, a fluorophore that normally absorbs blue light (~488 nm wavelength) can also be excited by two photons of infrared light (~960 nm wavelength). Since TPE depends on simultaneous absorption, the resulting fluorescence emission varies with the square of the excitation intensity. In order to produce a significant number of two-photon absorption events, photon density must be ~1 million times that required to generate the same number of one-photon excitations.

In a MPM microscope, TPE is generated by focusing a single pulsed laser through the microscope optics. As the laser beam is focused, the photon density increases as it approaches the focal plane and the probability of two photons interacting simultaneously with a single fluorophore increases. The laser focal point is the location with highest probability along the optical path where the photons are crowded enough to generate significant occurrence of TPE. **Figure 1(d)** illustrates the generation of TPE in a fluorophore-containing specimen at the microscope focal point and peripheral areas. Above the focal point, the photon density is not sufficient for two photons to pass within the absorption cross-section of a single fluorophore at the same instant. However, at the focal point, the photons are so closely spaced that it is possible to find two of them within the absorption cross-section of a single fluorophore simultaneously.

The narrow localization of TPE to the illumination focal point is the basis for the technique's most significant advantages over confocal microscopy. In a conventional confocal microscope, although fluorescence is excited throughout the specimen's entire illuminated volume, only signals originating from the focal plane pass through the confocal pinhole, allowing background-free images to be collected. By contrast, TPE only generates fluorescence at the focal plane, and since no background fluorescence is produced, a pinhole is not necessary.

This dramatic difference between the excitation regions of confocal and TPE microscopy results in divergent photo bleaching patterns in each method. The laser of a confocal system excites fluorophores above and below the focal plane, contributing to the bleaching observed in these extensive areas. In contrast, TPE only occurs at the focal plane; therefore, bleaching is confined to this area.

The most powerful advantage of TPE is the ability to provide superior optical sectioning at greater depths in thick specimens than conventional CLSM or WFM due to the effect of three factors[16,18,19,40,43]: (i) absence of out-of-focus absorption allows for more of the excitation light photons to reach the

Table 1 Comparison of wide-field, confocal microscopy, and multiphoton microscopy

Imaging techniques	*Wide field*	*Confocal*		*Multiphoton excitation*
		Laser scanning	*Spinning disk*	
Light source	Wide band lamp	Narrow band laser (UV-far red)	Wide band lamp or narrow band laser	Tunable infrared laser
Lateral resolution	Poor	~250 nm	~250 nm	Slightly worse than 250 nm
Axial resolution	Poor	500–800 nm	500–800 nm	~500 nm
Detection approach	Volume detection	Limit detection to single plane		Limit excitation to single focal plane
Aperture requirement	No	Yes	Yes	No
Image penetration depth	–	<200 μm	<200 μm	Up to 1 mm
3D sectioning capability	No	Yes	Yes	Yes
Multiobjectives	No	No	Yes	No
Comments	Good for regular uses	High resolution but relatively low sensitivity and low speed. High intensity excitation can cause photodamage and limits use for some live cell imaging	Equipped with thousands of microlenses. Imaging of entire field. Fast imaging speed, less photodamage. Not as flexible as CLSM. Good for time-lapse imaging	Longer wavelength excitation renders deeper penetration. Less photodamage

desired specimen region, and (ii) red and infrared light scatters less than light at shorter wavelengths, (iii) the effects of light scattering are less detrimental in TPE than in conventional CLSM systems. Further comparisons between multiphoton and confocal microscopy can be found in **Table 1**.

It should be noted that the image resolution obtained with TPE is not better than that achieved in a well-aligned confocal microscope in spite of the advantages of TPE mentioned earlier. The utilization of longer excitation wavelengths actually results in a larger resolution spot. If a biological structure cannot be resolved in an ideal confocal microscope, it will similarly not be resolved in a TPE laser scanning microscope. It is also important to note that imaging thin specimens using TPE microscopy does not necessarily benefit significantly over conventional CLSM. The reason is that slightly increased photobleaching may occur in the focal plane when using TPE over CLSM in thin specimens, although total photobleaching in a thick specimen is greatly reduced in TPE when compared to CLSM.

Despite the advantages of MPM in 3D tissue imaging, the depth of penetration and image quality are limited by the ability to effectively label thick samples such as tissues. Introducing fluorescence labels into tissues becomes increasingly difficult at greater depths. One way to overcome this difficulty is by expressing GFP within transgenic animals and imaging with TPE mode *in vivo*, where conventional immunolabeling deep into tissue organs is barely accessible.[42]

3.317.2.4. Other Advanced Fluorescence Imaging Techniques

We briefly review two other high-resolution imaging approaches that have been adapted to the study of cell–biomaterial interactions, but with limited success. These methods are fluorescence resonance energy transfer (FRET) imaging and total internal reflectance fluorescence microscopy (TIRFM).

FRET, a widespread technique in molecular biology and biophysics, has been typically used to screen molecular conformation, molecular proximity, protein–protein interactions, and biosensing in cell biology.[44–46] More recently, FRET has been adapted to quantitatively analyze parameters of cell adhesion-related phenomena, such as molecular changes in matrix proteins, bonds between integrins and ligands, and changes in the cross-linking density of hydrogel-based extracellular matrix analogs.[47]

FRET is an interaction between the electronic excited states of two dye molecules. Excitation is transferred from a donor molecule to an acceptor molecule without the emission of a photon. The emission spectrum of the donor must overlap the excitation spectrum of the acceptor; the extent of this overlap determines the FRET efficiency. Furthermore, donor–acceptor transition dipole orientations must be approximately parallel.[44–46,48] FRET's intermolecular separation depends on the inverse sixth power of the distance, so it falls off rapidly with distance, usually in the order of 10 nm which is comparable to dimensions of biological macromolecules. When FRET occurs, the fluorescence of the donor molecule is quenched, the emission of the acceptor fluorophore is sensitized, and the donor lifetime is reduced. Therefore, FRET has a direct effect on rates of donor photobleaching and acceptor fluorescence depolarization. There are several ways that FRET can be measured depending on which of the consequences is being monitored. These methods are based on: quenching of donor fluorescence, sensitized emission of acceptor fluorescence, reduction in donor lifetime, and depolarization of acceptor fluorescence.

Because energy transfer is limited to distances of <10 nm, the detection of FRET provides valuable information about the

spatial relationships of fusion proteins on a subresolution scale. Moreover, it gives us a powerful tool for measuring the proximity of molecular species at a level beyond the resolution of any optical microscope.

Another high-resolution imaging approach that has been recently adapted to study cell–biomaterial interactions is TIRFM. TIRFM has gained popularity in the study of cellular processes and single biological molecules. Briefly, it utilizes an evanescent field generated in the lower refractive index medium during total internal reflection. Light from the fluorescent molecules can then be collected by an objective lens and recorded using a detector such as a CCD camera.[49] The chief advantage of this method is the thinness and exponential decay of the illumination.

Currently, TIRFM can be broken down into two categories: prism-type TIRFM and objective-type TIRFM. Prism-type TIRFM makes use of a prism made of higher refractive material than the biological sample. Light at an acute angle travels through the prism, a refractive index-matched immersion fluid, and the sample's coverslip until finally reaching the interface between the sample and the coverslip, where it undergoes total internal reflection. Since the prism is on the coverslip, prism-type TIRFM usually requires illumination and the light collection to come from opposite sides of the microscope. In contrast, objective-type TIRFM uses a high-NA objective lens instead of a prism to introduce light at a supercritical angle, which is implemented either through the use of an opaque disk in the conjugate back focal plane of the microscope (to block all subcritical angles of light), or by focusing a laser beam off-axis toward the back focal plane of the objective lens. Light focused at the back focal plane by either method is then redirected toward the sample with angles dependent upon the position of the focused beam with angles of excitation increasing with distance from the center of the back focal plane.

TIRFM has a wide range of applications in cell and molecular biology, particularly, for viewing single molecules anchored to planar surfaces and to study the position and dynamics of molecules and organelles in living culture cells near the contact regions with glass substrates.[50] In the biomaterials community, TIRFM has been applied to study cell adhesion-related responses on biomaterials, such as changes in the contact area and adhesion strength on biomaterial surfaces, analysis of bond strength, and real-time measurement of cell/substrate separation distances following exposure to flow.[51,52]

Despite the simplicity of TIRFM, it provides remarkably good optical sectioning equal to or better than any other technique. However, its utility is limited to the study of fluorescent molecules within 100 nm of the sample's coverslip. Thus, it cannot be applied to the necessary resolution of cell–biomaterial interactions in 3D scaffolds or thick tissue sections.

3.317.3. Probing Cell–Biomaterial Interactions

3.317.3.1. Introduction to Fluorescence-Based Probes

The high-resolution imaging methods presented in this chapter would not be possible without the use of fluorophores. Fluorophore-tagged markers are capable of identifying specific molecular targets and have been used for numerous applications, including the observation and analysis of various cell–biomaterial interactions. In this section, an overview of three different fluorophore markers is discussed: fluorophore-tagged antibodies, quantum dot-based probes, and fluorescent proteins.

3.317.3.1.1. Fluorophore-tagged antibodies

Immunostaining is a general term in biochemistry that applies to any use of an antibody-based method to detect a specific protein in a sample. Tagging of a fluorophore to an antibody improves the visualization of the antigens or antigen epitopes where the antibody binds. Antibodies can come in different varieties known as isotypes or classes. There are five antibody isotypes: IgA, IgD, IgE, IgG, and IgM.[53] They are each named with an 'Ig' prefix that stands for immunoglobulin, another name for antibody, and differ in their biological properties, functional locations, and ability to deal with different antigens. Due to their high specificity, IgGs are the most common antibody isotype for immunostaining applications. The Ig monomer is a 'Y'-shaped molecule that consists of two identical heavy chains and two identical light chains. Each chain is composed of structural domains called Ig domains. While the arms of Y-shape antibodies have antigen-recognition sites, the root of the antibodies where the heavy chains reside provide a site to tag a fluorophore.

There are two ways to detect target protein molecules. A directly labeled fluorophore-conjugated primary antibody can be used to detect a target protein; this immunostaining technique is known as the direct method. Alternatively, a broader species-specific fluorophore-labeled secondary antibody is used to detect and attach to a primary antibody bound to a target protein; this is known as the indirect method.[20,54–57] Both methods have their respective advantages and disadvantages. The direct method is simpler, more convenient, and less prone to artifacts than the indirect method. Although the indirect method is more cumbersome, it offers better signal amplification. This is achieved by several fluorophore-conjugated secondary antibodies binding to a single primary antibody. Moreover, secondary antibodies with fluorophores at various excitation/emission spectra are readily available from commercial sources, which make it easier to select probes for multicolor imaging applications.

3.317.3.1.2. Quantum dot-based probes

Quantum dots, also known as fluorescent semiconductor nanocrystal probes or qdots, are increasingly being used for biological applications. They are a new class of inorganic fluorophores that have gained extensive recognition as a result of their exceptional photophysical properties.

Quantum dots are nanoscale semiconductors and defined as particles with physical dimensions smaller than the exciton Bohr radius.[58] Metal and semiconductor nanoparticles, usually composed of groups II–VI or II–V elements, with 2–6 nm in diameter have been used extensively due to their similarity in physical size to biological components such as nucleic acids and proteins.[59] Quantum dots have been used in the following applications: FRET analysis, gene technology via qdot-conjugated oligonucleotide probes, fluorescent labeling of cellular proteins, tracking of cellular movement, pathogen and toxin detection, *in vivo* imaging, and tumor biology research.[45,58,60–68] Despite the growing impact of qdots, there

are several barriers that need to be overcome, such as cytotoxicity and alteration of cell functions that accompanies the cellular uptake of qdots.

3.317.3.1.3. GFP and variants

GFP was originally derived from the jellyfish Aequorea Victoria.[69] It has 238 amino acid residues and a green fluorophore which is comprised of only three amino acids: Ser65–Tyr66–Gly67. The stable protein structure is formed by beta sheets, which have a conformation that makes up an 11-stranded drum-like structure.[26] The stability of GFP allows it to withstand pH levels ranging from mildly acidic (pH = 5.5) to extremely basic (pH = 12) and can also resist temperatures of up to 65 °C. GFP has major and minor excitation peaks at wavelengths of 395 and 475 nm, respectively. Several modifications have been made from the original GFP, most notably the reduction of the dual excitation peaks of 395 and 475 nm down to one excitation peak of 488 nm, which is in the visible blue-light range. The emission peak of original and modified GFP is detected at 509 nm, which is in the visible green region of the electromagnetic spectrum.[26,69] XFP variants with spectra that range from blue to red (shown in Table 2) can be used for live cell–biomaterial interaction imaging.

In order for biomaterial scientists to utilize GFP fusion proteins to capture cellular and subcellular responses to biomaterials, the construction and expression of GFP can be easily accomplished via standard molecular biology techniques. While a complete discussion is beyond the scope of this chapter, the readers are referred to molecular biology protocols, and in particular, to the book by David L. Spector, Robert D. Goldman, and Rusty Lansford.[70] By introducing GFP into host cells, one can visualize GFP-tagged whole cells, subcellular organisms, and cytoskeletal structure/organization. This form of targeting allows the microscopist and the biomaterial scientist alike to study cellular behavior by observing GFP-tagged proteins and capture information at a level that was previously inaccessible, both spatially and temporally.[71] Apart from aforementioned GFP-based markers, phytochromes, light-sensitive photoreceptor, along with other proteins in the phytochrome signaling network, have been utilized to reversibly control the translocation of proteins to the cell membrane.[72]

Table 2 List of common fluorescence proteins

Species/ source	*Fluorescence proteins*	*Excitation (nm)*	*Emission (nm)*
Green	EGFP	489	508
Cyan	ECFP	434/453	477/501
Yellow	EYFP	514	527
Red	DsRed	558	583

3.317.3.2. Case Studies of Imaging Cell–Biomaterial Interactions

In this section, we highlight four different case studies that utilize these labeling methods and advanced fluorescence imaging modalities to capture cellular interactions with polymeric biomaterials. All case studies use members of a tyrosine-derived polycarbonate library with generic composition poly (desaminotyrosyl-tyrosine alkyl ester carbonates) (Figure 2).[73]

In the first study, WFM was used to track cells tagged with GFP-actin, and confocal microscopy was utilized to characterize the nuclear translocation of GFP-GAPDH when cells were cultured in a library of polycarbonate-derived substrates.[74] In the second study, we review the application of MPM to visualize cells in 3D synthetic biomaterial scaffolds.[43] The third case study illustrates the concept of using high-content imaging to identify cell adhesion, spreading, membrane modifications, and cytoskeletal organization on biomaterials.[75] In the final study, an advanced method combining high-throughput and high-content imaging platforms is highlighted in terms of its ability to screen cellular responses to gradient properties of biomaterials. This case study represents one of the future directions in biomaterial design and optimization.[76]

3.317.3.2.1. Case study 1: Fluororeporter imaging of cell cytoskeletal remodeling and apoptosis on biomaterials

This case study shows the role of reactive oxygen species (ROS) in cell apoptosis on biomaterials. Polymers derived from the amino acid L-tyrosine were used as synthetic matrix substrates.[74] Tyrosine-derived polycarbonates were synthesized by copolymerizing hydrophobic L-tyrosine derivatives with uncharged hydrophilic poly(ethylene glycol) (PEG, MW = 1000 Da), and negatively charged desaminotyrosyl-tyrosine (DT). These substrates were characterized in terms of their intrinsic ability to generate ROS, as well as their ability to regulate intracellular ROS production, actin remodeling, and apoptosis in Saos-2 cells (Figure 3(a)).

PEG-containing substrates induced both exogenous and intracellular ROS production, whereas the DT-containing anionic polymeric substrates reduced the production of both types, indicating a coupling of exogenous ROS generation and intracellular ROS production. The effects of ROS activity on the cytoskeletal actin reorganization was probed using a GFP-fluororeporter for actin (Figure 3(b)). In order to visualize dynamic changes in actin, live time-lapse imaging

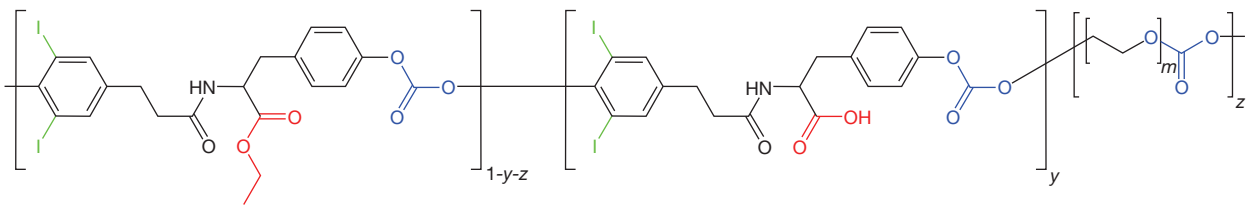

Figure 2 Chemical structure of a library of tyrosine-derived polycarbonates.

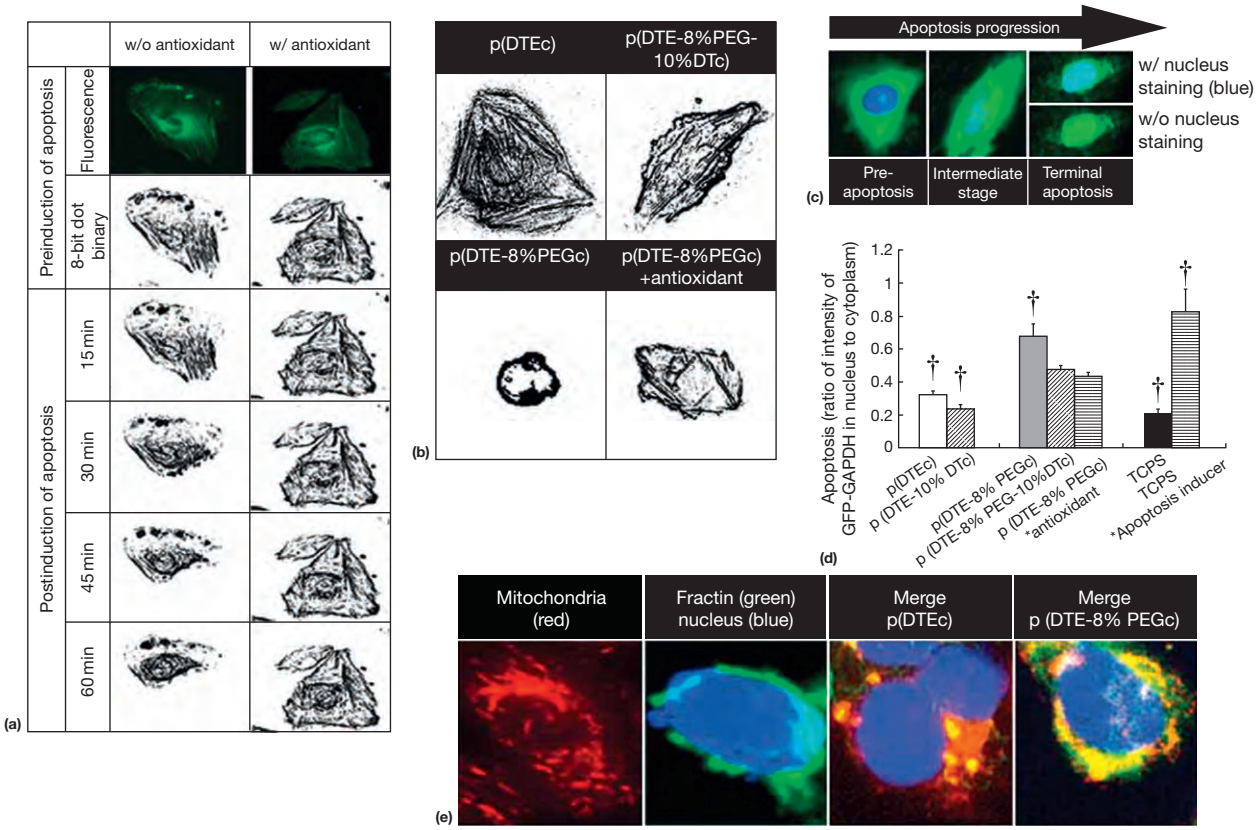

Figure 3 Imaging of cytoskeleton (GFP-actin) and functional reporters (GFP-GAPDH) during the process of apoptosis in the context of biomaterials. (a) Time lapse of GFP-actin Saos-2 cells during apoptosis with apoptosis promoter treatment. Morphologic changes over time were observed with and without the presence of an antioxidant. (b) Visualization of actin organization (GFP-actin Saos2 cells) on various biomaterial substrates with and without the presence of antioxidant. Images were converted to 8-bit binary images to improve the identification of the actin cytoskeleton. (c) Demonstration of nuclear translocation of GFP-GAPDH (green) to the nucleus (blue) during apoptosis. (d) Ratio of GFP-GAPDH signal within the nucleus to the cytoplasm was utilized to assess oxidative stress resulting from substrate chemistry. (e) Visualization of fractin formation via staining with a polyclonal antifractin antibody. Fractins (green) localized to the mitochondria (red). Colocalization (yellow) was more evident in PEG-containing samples. † indicates statistical differences.

of GFP-actin Saos-2 cells were performed on a heated chamber (Harvard Apparatus, Holliston, MA) perfused with carbon dioxide (CO_2). Images were taken every 3 min for 1 h with a Zeiss fluorescence microscope fitted with a 60X objective lens (Carl Zeiss MicroImaging, Inc., Thornwood, NY). Six single cells from three independent experiments were imaged in each condition ($n=6$, where n is the total number of cells imaged). Image contrast and brightness were adjusted to equalize fluorescence intensity using Microsoft PhotoDraw v2 (Microsoft). Contrast-adjusted images were then filtered utilizing a series of flattened filters in Image Pro Plus Version 5.1 (Media Cybernetics, Bethesda, MD). Fluorescence pixels were then converted to 8-bit dots with a constant thresholding process to allow the individual actin proteins to be segmented using ImageJ software (NIH). The 8-bit dot images provided a higher resolution of actin organization. To measure actin area fraction, 12 single cells were live-imaged at 72 h postseeding on four replicates of each substrate type ($n=12$, where n is the total number of cells imaged). From the 8-bit dot image, a summated dot area, which represents the total actin area, was obtained through particle analysis using ImageJ. A ratio of the actin area to the whole cell area was presented as an actin area fraction.

This study showed that the dynamic processes of actin remodeling were regulated by biomaterials induced with ROS and played causative roles in cellular apoptosis. Briefly, PEG-mediated ROS induction caused nuclear translocation of glyceraldehyde-3-phosphate dehydrogenase and an increase in caspase-3 activity, confirming a link with apoptosis. PEG-rich prooxidant substrates caused cytoskeletal actin remodeling through β-actin cleavage by caspase-3 into fractins. The fractins colocalized to the mitochondria and reduced the mitochondrial membrane potential. The remnant cytosolic beta-actin was polymerized and condensed, events consistent with apoptotic cell shrinkage (**Figure 3(c)–3(e)**). The cytoskeletal remodeling was integral to the further augmentation of intracellular ROS production. Conversely, the antioxidant DT-containing charged substrates suppressed the entire cascade of apoptotic progression. It was demonstrated that ROS activity serves as an important role in 'outside-in' signaling for cells grown on substrates. The ROS activity couples exogenous stress, driven by substrate composition to changes in

intracellular signaling. This signaling causes cell apoptosis, which is mediated by actin remodeling.

3.317.3.2.2. Case study 2: Multiphoton fluorescence imaging of 3D polymer scaffolds and cellular organization

Because confocal imaging of 3D substrates is limited by light scattering, MPM was used as an alternative approach to image and quantitatively characterize the microstructure and cell–substrate interactions within microporous scaffold substrates fabricated from synthetic biodegradable polymers. Poly(desaminotyrosyl-tyrosine ethyl carbonate) (pDTEc) and poly(desaminotyrosyl-tyrosine octyl carbonate) (pDTOc) were blended, and a fluorescent dye was mixed with the blend to visualize the scaffold architecture. The porosity of pDTEc/pDTOc blend scaffolds was varied to achieve the distribution of microporous and macroporous regions in the porous scaffolds. The GFP-engineered fibroblasts were seeded onto the scaffolds, which allowed the imaging of both cell morphological patterns and the porous scaffolds (Figure 4(a)). The porosity, pore size and distribution, strut size, pore interconnectivity, and orientation of both macroscale and microscale pores in the 3D scaffolds were effectively quantified and validated using complementary imaging techniques. MPM was used to obtain images of scaffold thicknesses $>100\,\mu m$, with a high signal-to-noise ratio that resulted in reduced bulk photobleaching and eliminated the need for deconvolution (Figure 4(b)). In this study, the morphology and cytoskeletal organization in cells located inside the scaffolds could be tracked with high resolution within the limits of penetration of the excitation beam. Thus, this study showed that MPM offers a promising integrated platform for imaging cell–material interactions within polymeric biomaterial scaffolds.

3.317.3.2.3. Case study 3: Confocal microscopy of cell-based fluororeporters for high-content imaging of cell–biomaterial interactions

Traditionally, the mainstream high-throughput cell assays were primarily fluorescent intensity-based detection systems such as plate readers and flow cytometers. Such cellular assays only focused on bulk changes in intensity of fluorescent probes of whole cell or cell lysates. Such cell assays can provide quick readouts but provide much less information than can be captured by analyzing cells at the microscopic level. Methods such as flow cytometry can render pseudo high-content readouts by detecting multiple fluorescent probes associated with individual cells.

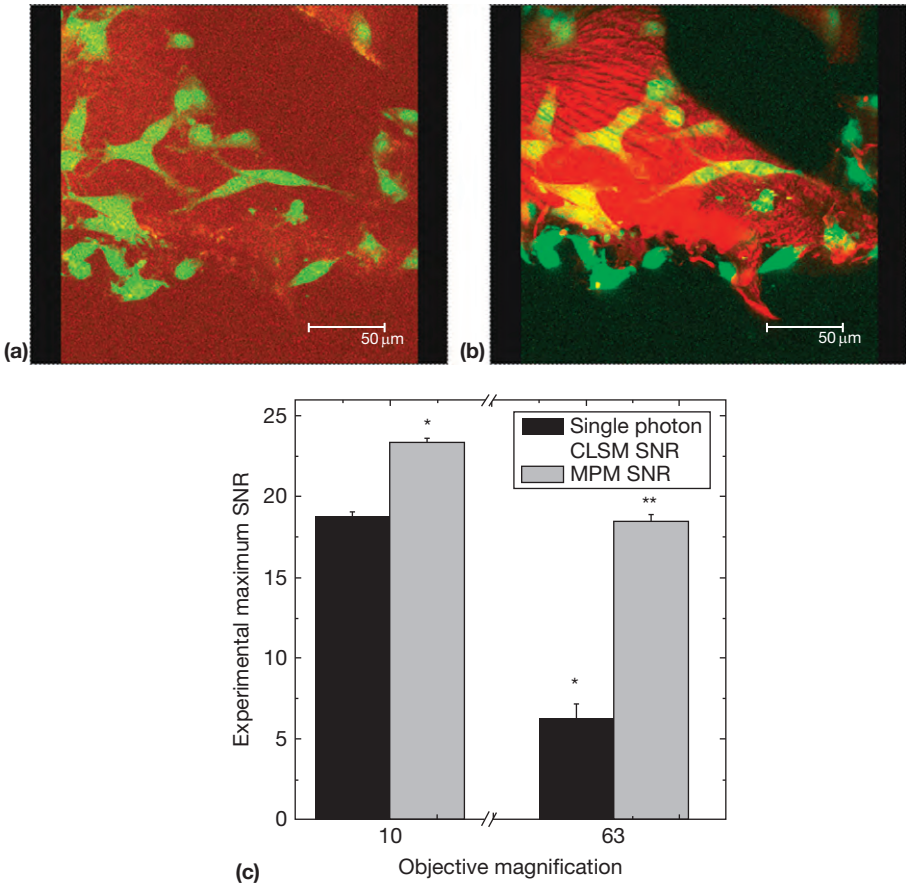

Figure 4 Comparison of multiphoton microscopy (MPM) and confocal laser scanning microscopy (CLSM) images of green fluorescent protein (GFP)-fibroblast cells in Texas Red dyed pDTEc/pDTOc scaffolds. (a and b) CLSM and MPM images of GFP-fibroblast cells on 50/50 pDTEc/pDTOc blend scaffold. (c) Comparison of experimental maximum signal-to-noise ratio of CLSM and MPM images of Texas Red doped pDTEc/pDTOc blends scaffold with macro and micro pores. A single asterix (*) represents a statistically significant difference, $p<0.05$, compared with 10X single-photon CLSM images. A double asterix (**) represents a statistically significant difference, $p<0.05$, compared with 63X single-photon CLSM images.

A recent study utilized a high-content imaging approach to correlate cytoskeletal organizational responses of cells to systematically varied chemical changes in biomaterial substrate chemistry.[75] Cell–biomaterial interactions were captured utilizing high-resolution images obtained with confocal microscopy. Mammalian cell lines (CHO and Saos-2) were transfected with GFP fusion proteins to highlight functional and morphological responses of the cells. The fusion proteins used in this study were GFP-actin, GFP-actinin, and GFP-paxillin. Actin, actinin, and paxillin represent cytoskeletal proteins involved in both the structural determination of cell shape as well as integrated members of a number of biochemical pathways that mediate the 'outside-in' signaling of cells. High-resolution images of the GFP-transfected cells in the context of a subset of a library of polycarbonates were captured using confocal microscopy. Single-cell morphometric features (cell descriptors) were then extracted from the images through the use of commercially available software Image Pro Plus 5.1 (Media Cybernetics Inc., MD). The general feature extraction steps include contrast enhancement, background subtraction, segmentation of whole cells and individual cytoskeletal proteins (actin), and parametric measurement. The extracted cell descriptors contain three categories of subcellular features including: (i) cellular morphologic parameters such as area, perimeter, mean radius, mean diameter, roundness, protrusions, and protrusion length; (ii) reporter localization and texture parameters such as heterogeneity of actin stress fibers, clumpiness, average fiber length/width, focal adhesions per cell, strength of focal adhesion region, and total area of paxillin-rich structures per cell; and (iii) reporter expression parameters such as integrated optical density per cell, and mean fluorescence (**Figure 5(a)**).

As an example, the morphological changes of reporter cells in response to changes of substrate properties are summarized in the 'heat map' shown in **Figure 5(b)**. A strong statistical difference in descriptor value (Student's *t*-test, p value $\rightarrow 0$) is represented by blue, a moderate difference by turquoise, a minor difference by orange, and no statistical difference (p value $\rightarrow 1$) by red. This study shows how descriptors can be used to discern combinatorial variations in substrate composition, and how living GFP reporters are uniquely suited to generate such descriptors unlike fixed tissue preparations.[75]

A more recent study shows how high-content imaging can be used to discern early morphological changes in stem cells cultured on synthetic biomaterials.[77] Actin-based morphology, texture, and intensity descriptors were obtained by single-cell imaging of human mesenchymal stem cells. The descriptors were reduced in dimensionality using multidimensional scaling (MDS), which combines the large number of descriptors into three groupings. The use of such groupings allowed the classification of heterogeneous subpopulations of stem cells within the first 24 h of stem cell culture on biomaterials. The use of high-content imaging allowed this classification early on, much before biochemical and molecular assays established the lineage classification of stem cells toward osteogenic (bone) versus adipogenic (fat) lineages. Thus, the quantitative approach of fluororeporter cell imaging provides information-rich high-content datasets that may be valuable for elucidating and benchmarking cell–biomaterial interactions.

3.317.3.2.4. Case study 4: Combination of high-content and high-throughput fluorescence imaging for cell–biomaterial interactions on biomaterials with spatially graded properties

Advances in polymeric biomaterial synthesis have allowed for the transition from synthesizing a small number of materials to the design and execution of large libraries of bipolymer blends derived from systematic combinations of biomaterials.[78–80] In a recent report, a combination of high-content imaging and higher throughput screening was proposed in the context of cell–biomaterial interactions. The substrate processing platform was based on different combinations of polymer blends exhibiting a continuous range of chemical and

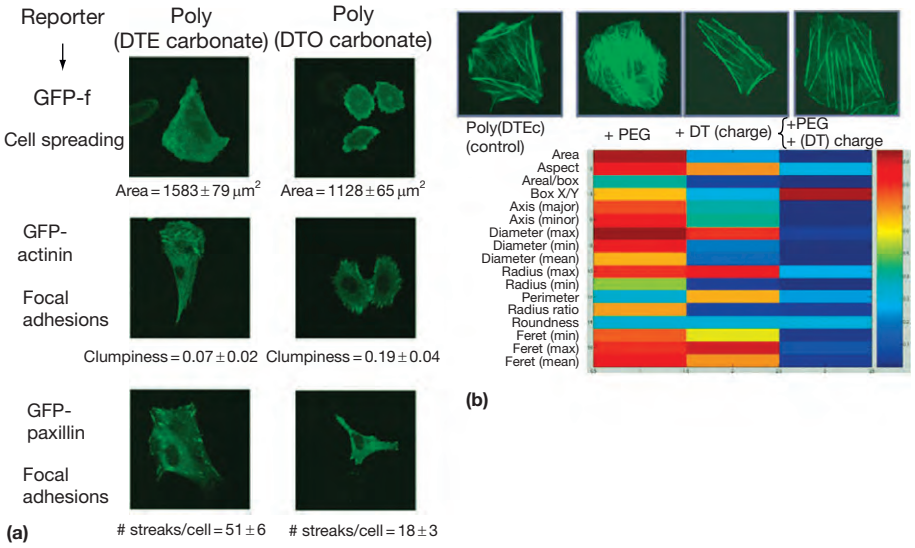

Figure 5 Various green fluorescent protein (GFP)-tagged subcellular reporters on a subset of tyrosine-derived polycarbonates. (a) Confocal micrographs of GFP-engineered Saos-2 cells on two polymeric substrates with different backbone compositions leading to differing hydrophobicities. (b) Cell responses to a combinatorial variation in substrate properties can be discerned using high-content imaging of GFP reporters and a heat map representation of variations in morphometric descriptors.

topographical properties on a single 42 mm round cover glass. As an example, the tyrosine-derived polycarbonates, pDTEc (E: ethyl) and pDTOc (O; octyl) homopolymers and their blends (70/30, 50/50, 30/70 ratio pDTEc/pDTOc, by mass), were flow coated on round glass cover slips. The fabricated pDTEc/pDTOc blends exhibited well-characterized surface gradients in hydrophobicity and surface roughness. Human Saos-2 cells transfected with GFP-tagged farnesylation (GFP-f) gene were examined for their responsiveness to the surface texture gradients of pDTEc and pDTOc blends. The morphology and organization of Saos-2 cells were examined in real time using a temperature-controlled chamber on the motorized stage of a confocal laser scanning microscope (CLSM).

The adhesion of Saos-2 cells was rapidly screened via tile scanning and was found to be maximized at intermediate regions, characterized by intermediate levels of roughness and the steepest roughness gradient (Figure 6(a)–6(c)). Through high-content imaging, we identified different morphometric parameters of the organization and intensity of GFP-f that correlate with the most adhesive substrate compositions (chemistry) or with the degree of surface roughness (Figure 7(a)–7(d)). The correlation between defined polymer blend parameters and cellular function was obtained. In conclusion, this study showed that by quantifying descriptors of GFP-f Saos-2 cells, the cellular adhesive responses to texture and compositional variations of polymer blends could be dissected via CLSM.

3.317.4. Looking to the Future

The field of imaging cell–biomaterial interactions has matured significantly over the past two decades. Earlier studies were largely focused on qualitative approaches related to epifluorescence and transmitted light microscopy. More recent methods have integrated advances in high-resolution imaging platforms such as confocal and TPE microscopy, new generation fluorophores and fluororeporters, and real-time intracellular imaging. These methods now enable a substantial paradigm shift in design criteria for screening and evaluating synthetic biomaterials, fully integrating principles from cell and molecular biology. Although considerable progress has been made already, ongoing challenges remain in capturing the dynamics of multiple cellular functional readouts and signals in physiological and complex biological milieu. A major challenge lies ahead regarding imaging of cellular phenomena within 3D microscale scaffolds. With newer imaging modalities, one of the limitations may be the maximum attainable resolution as photons become scarce within

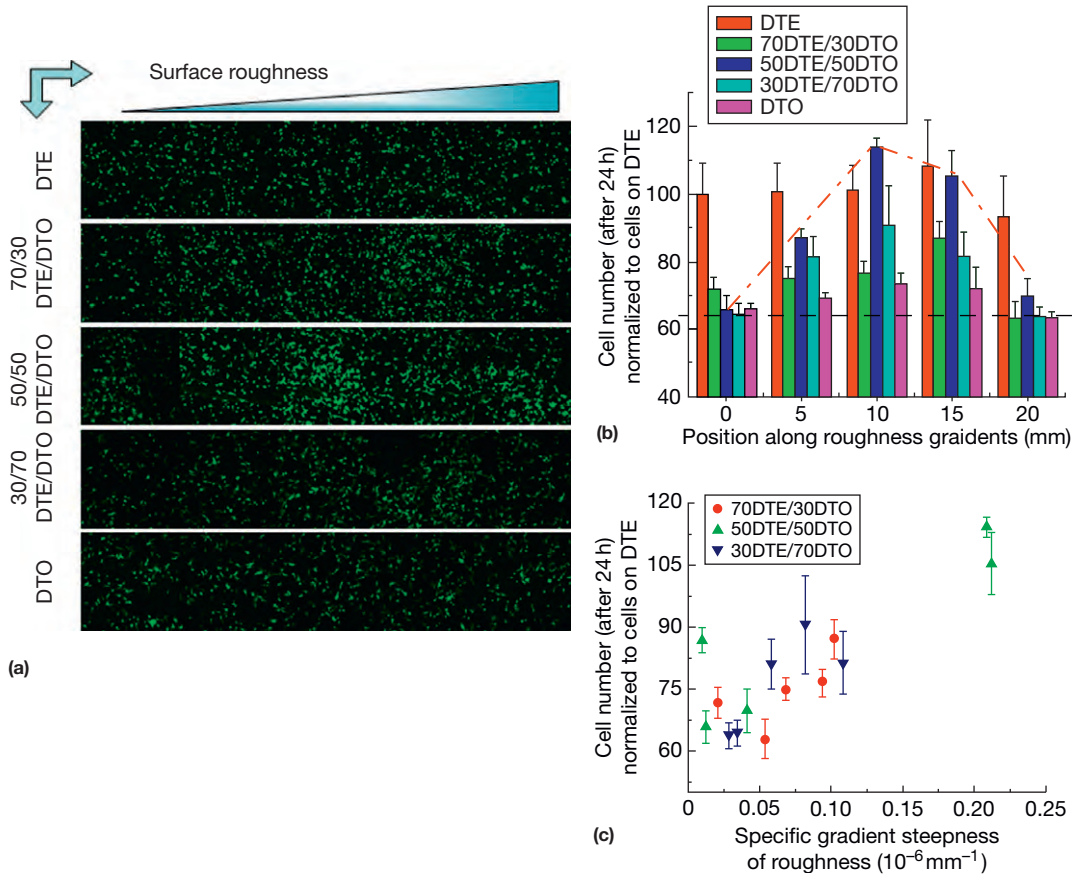

Figure 6 Screening cell attachment/adhesion on roughness gradient chip. (a) Green fluorescent protein-farnesylation (GFP-f) Saos-2 cells on a roughness gradient chip at low magnifications. (b and c) Quantification of cell attachment on the roughness gradient chip. Saos-2 GFP-f cell attachment was plotted against the roughness (b) or the local steepness of the roughness gradient (c).

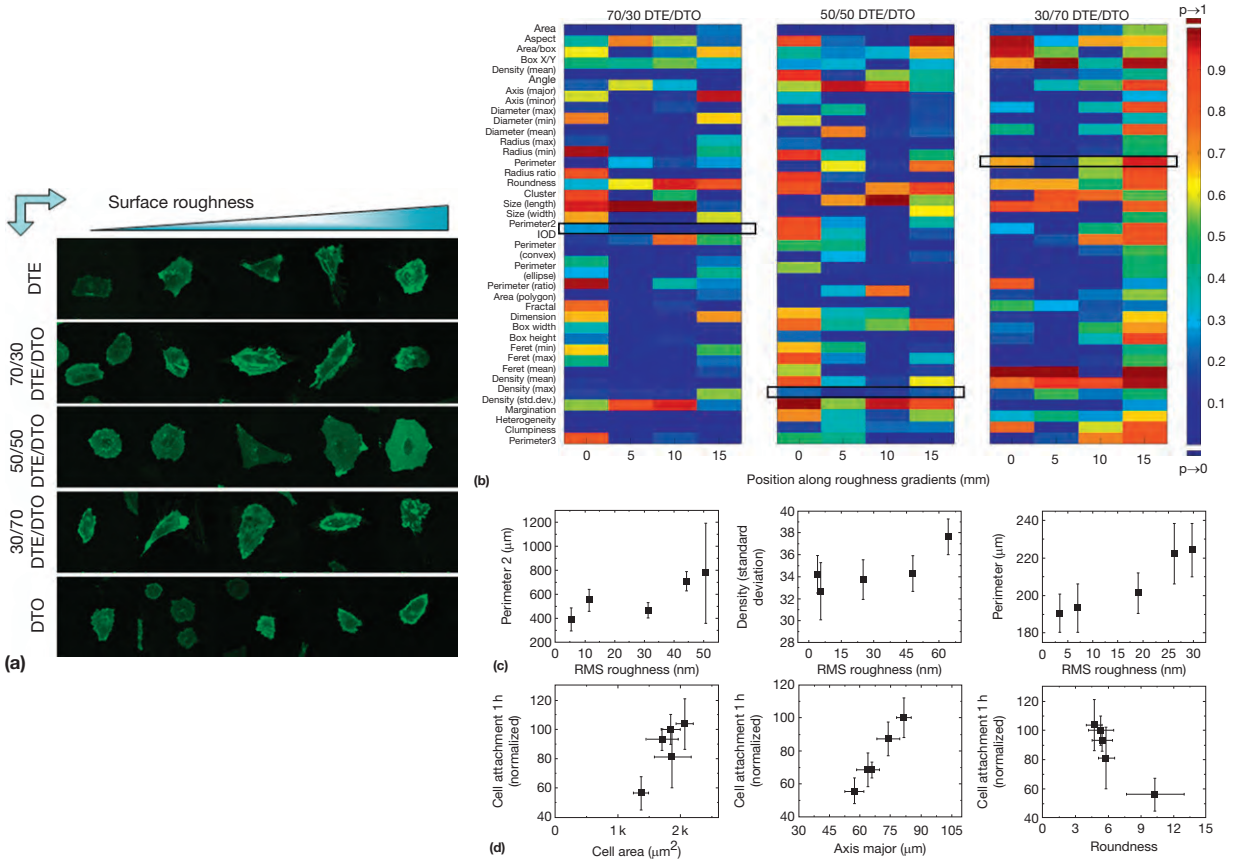

Figure 7 High-content imaging of green fluorescent protein-farnesylation (GFP-f) Saos-2 cells on roughness gradient. (a) High-resolution single-cell imaging of GFP-farnesylation Saos-2 cells on a roughness gradient chip. (b) Heatmap representation of a pool of cell descriptors along roughness gradients. (c) Correlation study of cell descriptors with substrate surface roughness. (d) Correlation study of cell descriptors with cell function (adhesion).

small imaging volumes. New powerful imaging techniques such as 4Pi confocal microscopy and stimulated emission depletion (STED) microscopy are currently being commercialized. The commercialization of STED and other emerging imaging techniques such as three-photon excitation imaging and second-harmonic imaging should further complement the current high-resolution platforms. The convergence of better transgenic animal models, radio-opaque or fluorescent biomaterials, and improved imaging hardware platforms should improve our ability to resolve tissue remodeling and track the long-term fates of implanted biomaterials *in vivo*. Another challenge is that of *in vivo* high-content imaging to allow for better *in silico* predictions of the *in vivo* fates of biomaterials. For example, microscale computer tomography-based molecular imaging methods may be particularly promising.[6,81,82] Combination of confocal and micro-CT approaches is also being proposed[83] to bring a full complement of the size scales over which these two methods enable imaging.

Acknowledgments

We gratefully acknowledge primary support under the auspices of NIH Grant P41 EB001046 for the biomedical technology resource RESBIO. Er Liu was supported by the RESBIO program. Sebastian Vega was also supported by a NSF DGE 0801620 IGERT fellowship on stem cells. Additional support was received from the Equipment Lease Fund, the Strategic Resource Opportunity Award, the Academic Excellence Fund at Rutgers University, and the New Jersey Center for Biomaterials.

References

1. Abraham, S.; Eroshenko, N.; Rao, R. R. *Regen. Med.* **2009**, *4*, 561–578.
2. Nolan, K.; Millet, Y.; Ricordi, C.; Stabler, C. L. *Cell Transplant.* **2008**, *17*, 241–243.
3. Stosich, M. S.; *et al. Methods* **2009**, *47*, 116–121.
4. Sundelacruz, S.; Kaplan, D. L. *Semin. Cell Dev. Biol.* **2009**, *20*, 646–655.
5. Causa, F.; Netti, P. A.; Ambrosio, L. *Biomaterials* **2007**, *28*, 5093–5099.
6. Choy, G.; Choyke, P.; Libutti, S. K. *Mol. Imaging* **2003**, *2*, 303–312.
7. Pasquinelli, G.; *et al. J. Anat.* **2008**, *213*, 520–530.
8. Reed, C. R.; *et al. Ann. Plast Surg.* **2009**, *62*, 505–512.
9. Shea, L. D.; Wang, D.; Franceschi, R. T.; Mooney, D. J. *Tissue Eng.* **2000**, *6*, 605–617.
10. Sun, T.; *et al. Biotechnol. Bioeng.* **2007**, *97*, 1318–1328.
11. Sundqvist, T.; Jakobson, M.; Magnusson, K. E. *Int. J. Biomed. Comput.* **1985**, *17*, 107–114.
12. Chaumeil, J.; Augui, S.; Chow, J. C.; Heard, E. *Methods Mol. Biol.* **2008**, *463*, 297–308.
13. Griffin, D. K.; Handyside, A. H.; Penketh, R. J.; Winston, R. M.; Delhanty, J. D. *Hum. Reprod.* **1991**, *6*, 101–105.
14. Han, K.; *et al. Leukemia* **1994**, *8*, 81–86.
15. Kraker, W. J.; *et al. Mayo Clin. Proc.* **1992**, *67*, 658–662.

16. Konig, K. *J. Microsc.* **2000**, *200*, 83–104.
17. Masters, B. R.; So, P. T.; Kim, K. H.; Buehler, C.; Gratton, E. *Meth. Enzymol.* **1999**, *307*, 513–536.
18. Xu, C.; Zipfel, W.; Shear, J. B.; Williams, R. M.; Webb, W. W. *Proc. Natl. Acad. Sci. USA* **1996**, *93*, 10763–10768.
19. Zipfel, W. R.; Williams, R. M.; Webb, W. W. *Nat. Biotechnol.* **2003**, *21*, 1369–1377.
20. Nadakavukaren, K. K.; Griffith, O. H. *Ultramicroscopy* **1985**, *17*, 31–42.
21. Pereira, M. C.; Costa, M.; Chagas Filho, C.; de Meirelles, M. N. *J. Submicrosc. Cytol. Pathol.* **1993**, *25*, 559–569.
22. Pietrasanta, L. I.; Schaper, A.; Jovin, T. M. *J. Cell Sci.* **1994**, *107*(Pt 9), 2427–2437.
23. Becker, B. E.; Romney, S. J.; Gard, D. L. *Dev. Biol.* **2003**, *261*, 488–505.
24. Dammermann, A.; Merdes, A. *J. Cell Biol.* **2002**, *159*, 255–266.
25. Elson, E. L.; Qian, H. *Meth. Cell Biol.* **1989**, *30*, 307–332.
26. Chalfie, M. *Photochem. Photobiol.* **1995**, *62*, 651–656.
27. Conchello, J. A.; Dresser, M. E. *J. Biomed. Optic.* **2007**, *12*, 064026-1:7.
28. Pankajakshan, P.; Zhang, B.; Blanc-Feraud, L.; Kam, Z.; Olivo-Marin, J.-C.; Zerubia, J. *Conference on Proceedings of the IEEE Engineering in Medicine and Biology Society*; INRIA/CNRS/UNSA, Sophia Antipolis, 2007; pp 6532–6535.
29. Sibarita, J. B. *Adv. Biochem. Eng. Biotechnol.* **2005**, *95*, 201–243.
30. Swedlow, J. R. *Meth. Cell Biol.* **2003**, *72*, 349–367.
31. Vicidomini, G.; Boccacci, P.; Diaspro, A.; Bertero, M. *J. Microsc.* **2009**, *234*, 47–61.
32. Periasamy, A.; Skoglund, P.; Noakes, C.; Keller, R. *Microsc. Res. Tech.* **1999**, *47*, 172–181.
33. Aigner, J.; Wilmes, E.; Naumann, A.; Bujia, J. *Laryngorhinootologie* **1997**, *76*, 248–251.
34. Coley, H. M.; Amos, W. B.; Twentyman, P. R.; Workman, P. *Br. J. Cancer* **1993**, *67*, 1316–1323.
35. Lopez, C.; Pons, M. N.; Morgenroth, E. *Water Res.* **2005**, *39*, 456–468.
36. Adams, M. C.; *et al. Methods* **2003**, *29*, 29–41.
37. Maddox, P. S.; Moree, B.; Canman, J. C.; Salmon, E. D. *Meth. Enzymol.* **2003**, *360*, 597–617.
38. McAllister, R. G.; Sisan, D. R.; Urbach, J. S. *J. Biomed. Optic.* **2008**, *13*, 054058-1:7.
39. Nakano, A. *Cell Struct. Funct.* **2002**, *27*, 349–355.
40. Rubart, M. *Circ. Res.* **2004**, *95*, 1154–1166.
41. Goksor, M.; Enger, J.; Hanstorp, D. *Appl. Opt.* **2004**, *43*, 4831–4837.
42. Sahai, E.; *et al. BMC Biotechnol.* **2005**, *5*, 14.
43. Liu, E.; *et al. J. Biomed. Mater. Res. B Appl. Biomater.* **2007**, *82*, 284–297.
44. Gertler, A.; Biener, E.; Ramanujan, K. V.; Djiane, J.; Herman, B. *J. Dairy Res.* **2005**, *72* (Spec No. 14–19).
45. Jares-Erijman, E. A.; Jovin, T. M. *Curr. Opin. Chem. Biol.* **2006**, *10*, 409–416.
46. Xu, X.; Brzostowski, J. A.; Jin, T. *Meth. Mol. Biol.* **2006**, *346*, 281–296.
47. Huebsch, N. D.; Mooney, D. J. *Biomaterials* **2007**, *28*, 2424–2437.
48. Periasamy, A.; Day, R. N. *Meth. Cell Biol.* **1999**, *58*, 293–314.
49. Nishikawa, S. *Nippon Rinsho* **2007**, *65*, 263–269.
50. Axelrod, D. *Meth. Cell Biol.* **2008**, *89*, 169–221.
51. Burmeister, J. S.; Olivier, L. A.; Reichert, W. M.; Truskey, G. A. *Biomaterials* **1998**, *19*, 307–325.
52. Curtis, A. S. *Eur. Cell Mater.* **2001**, *1*, 59–65.
53. Cox, G. *Optical Imaging Techniques in Cell Biology*; CRC Press: Boca Raton, FL, 2007.
54. Faulk, W. P.; Hijmans, W. *Prog. Allergy* **1972**, *16*, 9–39.
55. Harris, P. J. *Meth. Cell Biol.* **1986**, *27*, 243–262.
56. Javois, L. C.; Mullins, J. M. *Meth. Mol. Biol.* **1994**, *34*, 331–334.
57. Matthews, J. B. *J. Oral Pathol.* **1987**, *16*, 189–195.
58. Jamieson, T.; *et al. Biomaterials* **2007**, *28*, 4717–4732.
59. Chan, W. C.; *et al. Curr. Opin. Biotechnol.* **2002**, *13*, 40–46.
60. Jaiswal, J. K.; Goldman, E. R.; Mattoussi, H.; Simon, S. M. *Nat. Meth.* **2004**, *1*, 73–78.
61. Misra, R. D. *Nanomedicine* **2008**, *3*, 271–274.
62. Pinaud, F.; *et al. Biomaterials* **2006**, *27*, 679–1687.
63. Smith, A. M.; Duan, H.; Mohs, A. M.; Nie, S. *Adv. Drug Deliv. Rev.* **2008**, *60*, 1226–1240.
64. Sunbul, M.; Yen, M.; Zou, Y.; Yin, J. *Chem Commun (Camb.)* **2008**, 5927–5929.
65. Tian, J.; Liu, R.; Zhao, Y.; Xu, Q.; Zhao, S. *J. Colloid Interface Sci.* **2009**, *336*, 504–509.
66. Walling, M. A.; Novak, J. A.; Shepard, J. R. *Int. J. Mol. Sci.* **2009**, *10*, 441–491.
67. Weng, J.; *et al. Talanta* **2006**, *70*, 397–402.
68. Yang, D. Z.; Xu, S. K.; Chen, Q. F. *Guang Pu Xue Yu Guang Pu Fen Xi* **2007**, *27*, 1807–1810.
69. Prendergast, F. G.; Mann, K. G. *Biochemistry* **1978**, *17*, 3448–3453.
70. Goldman, R. D.; Spector, D. L. *Live Cell Imaging: A Laboratory Manual*; Cold Spring Harbor Laboratory Press: New York, NY, 2005.
71. March, J. C.; Rao, G.; Bentley, W. E. *Appl. Microbiol. Biotechnol.* **2003**, *62*, 303–315.
72. Levskaya, A.; Weiner, O.; Lim, W.; Voigt, C. *Nature* **2009**, *461*(7266), 997–1001.
73. Bourke, S. L.; Kohn, J. *Adv. Drug Deliv. Rev.* **2003**, *55*, 447–466.
74. Sung, H.-J.; *et al. J. Cell Physiol.* **2009**, *218*, 549–557.
75. Treiser, M. D.; *et al. Biotechniques* **2007**, *43*, 361–366, 368.
76. Liu, E.; *et al. Comb. Chem. High Throughput Screen.* **2009**, *12*, 646–655.
77. Treiser, M.; *et al. Proc. Natl. Acad. Sci. USA* **2009**, *107*(2), 610–615.
78. Amis, E. J. *Nat. Mater.* **2004**, *3*, 83–85.
79. Becker, M. L.; *et al. Am. Chem. Soc.* (Abstracts) **2005**, *230*, U3786.
80. Meredith, J. C.; Smith, A. P.; Karim, A.; Amis, E. J. *Macromolecules* **2000**, *33*, 9747–9756.
81. Blankenberg, F. G.; Mari, C.; Strauss, H. W. *Am. J. Cardiovasc. Drugs* **2002**, *2*, 357–365.
82. Wyss, C.; *et al. Eur. Radiol.* **2009**, *19*, 2487–2494.
83. Bradu, A.; Ma, L.; Bloor, J. W.; Podoleanu, A. *J. Biophotonics* **2009**, *2*, 380–388.

Relevant Websites

http://www.leica-microsystems.com/ – Leica Microsystems.
http://www.microscopyu.com/ – Nikon MicroscopyU.
http://www.olympusfluoview.com/ – Olympus FV1000 Confocal Microscope.
http://www.confocal.rutgers.edu/ – Rutgers Facility for Confocal Microscopy.
http://probes.invitrogen.com/ – Invitrogen Molecular Probes.
http://www.promega.com/ – Promega.
http://www.clontech.com/ – Clontech.
http://www.highcontentanalysis.com/ – High-Content Imaging / Analysis Conference.
http://www.moleculardevices.com/ – Molecular Devices.
http://www.biacore.com/ – Biacore.
http://www.nist.gov/ – National Institute of Standards and Technology (NIST).
http://www.njbiomaterials.org/ – New Jersey Center for Biomaterials (NJCBM).

3.318. Molecular Imaging

S H Crayton, A K Chen, Z Cheng and A Tsourkas, University of Pennsylvania, Philadelphia, PA, USA

© 2011 Elsevier Ltd. All rights reserved.

3.318.1.	**Introduction**	306
3.318.2.	**Nanomaterials**	307
3.318.2.1.	Quantum Dots	307
3.318.2.1.1.	Structure and properties	307
3.318.2.1.2.	Synthesis	308
3.318.2.1.3.	Biological interaction	309
3.318.2.1.4.	Applications	310
3.318.2.1.5.	Perspectives and challenges	311
3.318.2.2.	Gold Nanomaterials	311
3.318.2.2.1.	Structure and properties	311
3.318.2.2.2.	Synthesis	312
3.318.2.2.3.	Biological interactions	313
3.318.2.2.4.	Applications	313
3.318.2.3.	Superparamagnetic Nanoparticles	313
3.318.2.3.1.	Structure and properties	313
3.318.2.3.2.	Synthesis	315
3.318.2.3.3.	Biological interactions	316
3.318.2.3.4.	Applications	316
3.318.2.3.5.	Perspective and challenges	318
3.318.3.	**Nanovesicles**	318
3.318.3.1.	Liposomes	318
3.318.3.1.1.	Structure and properties	318
3.318.3.1.2.	Synthesis	319
3.318.3.1.3.	Applications	319
3.318.3.1.4.	Perspective and challenges	321
3.318.3.2.	Polymersomes	321
3.318.3.2.1.	Structure and properties	321
3.318.3.2.2.	Synthesis	322
3.318.3.2.3.	Biological interactions	322
3.318.3.2.4.	Applications	322
3.318.4.	**Polymeric Assemblies**	323
3.318.4.1.	Dendrimers	323
3.318.4.1.1.	Structure and properties	323
3.318.4.1.2.	Synthesis	323
3.318.4.1.3.	Biological interactions	324
3.318.4.1.4.	Applications	324
3.318.5.	**Future Outlook**	325
References		325

Glossary

Blood half-life The time it takes for the blood plasma concentrations of a contrast agent (or other substance) to be reduced to half its initial concentration.

Dendrimer nanoclusters A nanoparticle formed by chemically cross-linking dendrimers.

Dendrimers Spheroid polymeric nanostructures that repeatedly branch outward from an inner multimeric core.

Molecular imaging (Society of Nuclear Medicine Definition) The visualization, characterization, and measurement of biological processes at the molecular and cellular levels in living subjects.

Photoacoustic imaging A form of imaging where nonionizing laser pulses are delivered into biological tissues and ultrasonic emission is returned and detected. The delivered photons are absorbed and converted into heat, leading to thermoelastic expansion and creating the ultrasonic emission.

Polymersomes A class of self-assembled nanovesicles that are composed of amphiphilic synthetic block copolymers.

Quantum dots (QDs) Luminescent semiconductor nanocrystals with a typical diameter of 2–100 nm containing roughly 200–10 000 atoms of periodic group II–VI (e.g., CdSe, CdTe, CdS, and ZnSe) and III–V (e.g., InP and InAs).

Reticuloendothelial system Part of the immune system that consists of phagocytic cells, primarily macrophages, macrophage precursors, and specialized endothelial cells lining the sinusoids of the liver, spleen, and bone marrow.
Sentinel lymph node The first lymph node to be reached by metastasizing cancer cells from a primary tumor.
Superparamagnetic nanoparticles Nanoparticles that are strongly magnetic in an applied magnetic field but nonmagnetic when the field is removed. In the absence of a magnetic field, Brownian motions are sufficient to randomly orient the nanoparticles.
Surface-enhanced Raman spectroscopy (SERS) Raman spectroscopy is based on the inelastic scattering of photons by molecules, thus the energies of the incident and scattered photons are different. The energy difference is related to the vibrational energies of the molecule. SERS is a technique that results in the enhancement of the Raman signal by molecules absorbed on rough metal surfaces.
TAT peptide A polycationic peptide derived from the HIV-Tat protein. The TAT peptide is often used to transport contrast agents into cells. The process of internalization is thought to involve the nonspecific association between the positively charged peptide and the negatively charged cell membrane followed by macropinocytosis.

Abbreviations

ASG	Asialoglycoprotein
AuNP	Gold nanoparticles
BRET	Bioluminescence resonance energy transfer
CAM	Cell adhesion molecule
CCK	Cholecystokinin
CL	Caprolactone
CLIO	Crosslinked iron oxide
CNS	Central nervous system
CT	Computed tomography
DC	Dendritic cell
DMAA-IPA	3-N-[(N0, N0-dimethylaminoacetyl)amino]-α-ethyl-2,4,6-triiodobenzenepropanoic acid
DNA	Deoxyribonucleic acid
DNC	Dendrimer nanoclusters
DTPA	Diethylenetriaminepentaacetic acid
EGF	Epidermal growth factor
EGFR	Epidermal growth factor receptor
EPR	Enhanced permeability and retention
Fab	Antigen-binding fragment
FISH	Fluorescence *in situ* hybridization
FITC	Fluorescein isothiocyanate
Gd-DTPA	Gadolinium-diethylenetriaminepentaacetic acid
HUVEC	Human umbilical vein endothelial cells
IF	Interdigitation-fusion
ITO	Indium tin oxide
LBL	Layer-by-layer
LMV	Large multilamellar vesicle
LUV	Large unilamellar vesicle
MION	Monocrystalline iron oxide nanoparticle
MR	Magnetic resonance
MRI	Magnetic resonance imaging
NIR	Near infrared
NIRF	Near infrared fluorophore
NMR	Nuclear magnetic resonance
PAMAM	Polyamidoamine
PBD-PEO	Polybutadiene-polyethylene oxide
PEG	Polyethylene glycol
PEI	Polyethylene imine
PEO	Polyethylene oxide
PEOCL	Polyethylene oxide-b-polycaprolactone
POPC	1-Palmitoyl-2-oleoyl-sn-glycero-3-phosphocholine
PSMA	Prostate-specific membrane antigen
QD	Quantum dot
QY	Quantum yield
R1	Longitudinal relaxivity
R2	Transverse relaxivity
RES	Reticuloendothelial system
RGD	Arginine–glycine–aspartate
RNA	Ribonucleic acid
RSD	Relative size distribution
scFv	Single-chain variable fragment
SERS	Surface-enhanced Raman spectroscopy
siRNA	Small interfering RNA
SPIO	Superparamagnetic iron oxide
SPR	Surface plasmon resonance
SSPIO	Standard superparamagnetic iron oxide
SUV	Small unilamellar vesicle
T1	Longitudinal relaxation time
T2	Transverse relaxation time
TOPO	Trioctylphosphine oxide
USPIO	Ultrasmall superparamagnetic iron oxide
UV	Ultraviolet
VCAM-1	Vascular cell adhesion molecule-1

3.318.1. Introduction

Molecular imaging is a relatively new, rapidly developing, and multidisciplinary field that seeks to improve upon conventional anatomic imaging by providing information on the molecular profiles of tissue. Owing to the large number of clinical and academic areas involved, there are many working definitions of molecular imaging. However, the official definition from the Society of Nuclear Medicine,[1] which states "molecular imaging is the visualization, characterization, and measurement of biological processes at the molecular and cellular levels in humans and other living systems," is

appropriately concise and comprehensive. It should be clear to the reader that molecular imaging spans a range of techniques, imaging modalities, and pathologies. As such, the field of molecular imaging can be organized and discussed from a number of different perspectives. The objective of this chapter is to provide an introduction to molecular imaging from the standpoint of materials science. After a brief general discussion of molecular imaging, a number of materials commonly used in molecular imaging applications are highlighted with a discussion on their properties, current use, and future challenges.

Medical imaging traditionally has been a diagnostic tool based on anatomy, allowing physicians to visualize the presence, location, and extent of disease. Many molecular imaging agents have these same objectives. For example, the nuclear medicine 'octreotide scan' allows the radiologist to diagnose and pinpoint the location of carcinoid tumors.[2] These rare tumors can be very difficult to detect with conventional anatomic imaging since they are frequently small and can reside in a wide variety of locations. However, one of the defining characteristics of these neuroendocrine tumors is their avidity for somatostatin. Therefore, radiolabeled octreotide (a pharmacological analog of somatostatin) localizes to carcinoid tumors with a high degree of specificity, not only identifying the source of the tumor but also allowing the surgeon to detect metastatic lesions and assess whether curative resection is possible. This serves as a simple and illustrative example of diagnostic molecular imaging since specific molecular information is obtained and subsequently influences the clinical management of the disease (see **Chapter 3.326, Imaging and Diagnosis of Biological Markers**).

Another important role for molecular imaging is the validation and monitoring of biomarkers that can allow physicians to assess a patient's response to treatment even before detectable anatomic changes are manifested. For example, the most common way to assess tumor response to chemotherapy and radiation regimens is to measure tumor shrinkage with conventional anatomic imaging modalities. It is commonly accepted, however, that changes at the molecular level (metabolism, apoptosis, and cellular proliferation) precede gross anatomic changes. Molecular imaging, therefore, could allow physicians to confirm treatment response much earlier and, perhaps more importantly, predict treatment failure and modify regimens without losing valuable time.

Additionally, the ability to characterize pathology at the molecular level can allow for treatments to be better tailored to the patient on an individual basis. For example, breast cancer patients are often treated with therapeutic agents that target the Her2 receptor (Herceptin, a monoclonal antibody) and the estrogen receptor (selective estrogen receptor modulators, e.g., tamoxifen). However, these treatments have little benefit for patients whose tumors do not express these receptors, and so knowing the receptor status of the tumor is critical for selecting the best treatment. Often, this information can be obtained through tissue biopsy, but a noninvasive imaging approach may be preferable, especially if the tumor is in an organ that is difficult or more risky to sample (e.g., brain, liver) or the patient cannot readily tolerate biopsy. This information is also very valuable to pharmaceutical companies as they develop treatments and assess them in clinical trials. Molecular imaging can help confirm *in vivo* if an agent designed to interfere with a particular pathway indeed does so. Also, tremendous amounts of time and money can be saved by using molecular imaging to select the best subset of patients most likely to respond to the treatment (i.e., only enroll patients with Her2-positive tumors in a clinical trial for Herceptin), and by terminating a trial early if molecular imaging studies suggest that no response to the treatment is occurring.

Current research in molecular imaging has not only been applied to clinical applications, but has also played an important role in basic biomedical research. For example, molecular imaging strategies have been used to visualize and characterize molecular mechanisms of disease in cell cultures and animal models, providing insight into cell function and fate. The use of minimally invasive molecular imaging agents hand-in-hand with other staples of the biomedical research toolkit (e.g., reporter systems, gene disruption, animal models of disease, etc.) offers insight into the pathogenesis of disease, and the two/they have even been used to identify targets for diagnosis and treatment.

Now that a preliminary description and the potential value of molecular imaging have been provided, the remainder of the chapter will highlight some of the materials that have been commonly incorporated into molecular imaging agents. In particular, quantum dots (QDs), gold nanomaterials, superparamagnetic iron oxide (SPIO), liposomes, polymersomes, and dendrimers will be discussed.

3.318.2. Nanomaterials

3.318.2.1. Quantum Dots

3.318.2.1.1. Structure and properties

Semiconductor nanocrystals, also known as quantum dots (QDs), are luminescent nanostructured particles with a typical diameter of 2–100 nm containing roughly 200–10 000 atoms from periodic groups II–VI (e.g., cadmium selenide (CdSe), cadmium telluride (CdTe), cadmium sulfide (CdS), and ZnSe) and III–V (e.g., InP and InAs). Compared to organic fluorophores and fluorescent proteins, QDs exhibit unique optical properties, including size-tunable spectra, superior photostability, and exceptional brightness. Since their invention in 1982,[3,4] QDs have extended their applications from microelectronics and optoelectronics to molecular imaging within single cells and animals. Key advances that have enabled the use of QDs in biological applications include the synthesis of highly luminescent and water-soluble QDs, and novel surface modifications that allow for the facile bioconjugation of targeting ligands (see **Chapter 5.523, Carbon Nanotubes: Applications for *In Situ* Implant Sensors** and **Chapter 3.324, Fluorescent Nanoparticles for Biological Imaging**).

The fluorescence properties of semiconductor materials are dictated by the minimum energy required to excite an electron from the ground state (i.e., valence band) to a higher energy level (i.e., conduction band) via absorption of a photon of energy greater than this bandgap. This transition results in a positively charged hole in the valence band. The promoted electron and the positively charged hole are collectively termed an exciton or Coulomb correlated electron–hole pair. The exciton can be thought of as analogous to the excited state of traditional fluorophores; however, excitons typically have much longer lifetimes (up to approximately microseconds). Relaxation of the excited electron from the conduction band

to the valence band results in a fluorescence emission of a photon. In bulk (macrostructured) semiconductors, energy levels within each energy state (band) are very close together so that they resemble a continuum. As a result, bulk semiconductor materials elicit fluorescence emission that is characterized by the fixed energy of the bandgap, which is solely determined by the composition of the materials. For QDs, however, the size of the semiconductor crystal becomes so small that it approaches the size of the material's Exciton Bohr Radius (i.e., the average physical separation between the electron and hole). Consequently, the electron energy levels within each band can no longer be considered continuous and must be treated as quantized. In this manner, the addition or subtraction of just a few atoms to the QD can alter the size of the bandgap, resulting in different emission properties. Generally, the smaller the size of the crystal, the greater the difference in energy between the valence band and the conduction band. Therefore, more energy is needed to excite the dot, and concurrently, more energy is released when the crystal returns to its resting state. This effect has been exploited in the synthesis of QDs. As larger crystal sizes are produced, lower frequency emission is obtained, resulting in a color shift from blue to red emission (**Figure 1**). Recent advances in the synthesis of QDs allow for precise size (and, therefore, emission) tunability.[5–10]

Since their first biological application, QDs have become an important class of optical probes and an attractive alternative to both organic fluorophores and fluorescent proteins for molecular imaging in living subjects. Due to their large absorption cross-section, QDs have large molar extinction coefficients, typically on the order of $0.5–5 \times 10^6\,M^{-1}\,cm^{-1}$.[11,12] Excitation wavelengths span a spectrum of UV to visible, with the extinction coefficient generally increasing at shorter excitation wavelengths. In comparison to organic dyes and fluorescent proteins, QDs are 10–100 times brighter, owing to their high photon absorbability. In addition, QDs are 100–1000 times more photostable than organic dyes and hence possess the potential for long-term intracellular and *in vivo* tracking experiments. Furthermore, a single excitation wavelength can be used to excite QDs with different emission wavelengths, permitting simultaneous imaging of multiple molecular targets. Finally, recall that the emission of QD can be tuned by controlling the size and the composition of QD. For example, CdSe QDs may be size-tuned to emit in the 450–650 nm range, whereas CdTe QDs can emit in the 500–750 nm range. In marked contrast to organic fluorophores, QDs have broad adsorption spectra and very narrow emission spectra (i.e., ~13 nm of full-width at half maximum at room temperature) thereby permitting imaging of multiple targets simultaneously, each indicated by a different color.[12]

3.318.2.1.2. Synthesis

Since the first synthesis of QDs in 1982 by Efros and Efros[3] and Ekimov and Onushchenko,[4] various methods have been developed for preparing them in different media, including aqueous solution, high boiling point organic solvents, solid substrates,[13–15] and amphibious baths.[16] Traditionally, QDs were prepared in an aqueous solution under thermodynamically favorable conditions for crystal growth in the presence of stabilizing agents (i.e., thioglycerol or polyphosphate), which function to kinetically control crystal growth and limit their size within the quantum-confinement size regime. However, this procedure yielded QDs with poor luminescent properties and large size variations. These qualities of QDs were improved significantly in 1993 when Bawendi and coworkers created highly luminescent and monodisperse QDs from CdS, CdSe, or CdTe in organic solvents using a high-temperature organometallic procedure.[17] In brief, the synthesis began with the rapid injection of organometallic reagents into a hot coordinating solvent to produce a temporarily discrete homogenous nucleation. Slow growth and annealing in the coordinating solvent resulted in uniform surface derivatization and regularity in core structure. The size of QDs can be controlled by varying the duration, temperature, and ligand molecules used in the synthesis. Once the QDs have reached the desired size and emission wavelength (i.e., the emission of QD has been size-tuned), the reaction mixture may be cooled to room temperature to arrest growth. Size-selective precipitation provides powders of nearly monodisperse nanocrystals that are soluble in organic solvents. For instance, CdSe QDs exhibited nearly perfect crystal structures and much improved size distribution (RSD $<5\%$) compared to traditional methods. Since then, QD synthesis has been predominantly carried out in polar organic solvents.

Although QDs synthesized via the high-temperature organometallic procedure exhibited much improved monodispersity, they generally exhibit a low fluorescence quantum yield



Figure 1 Ten distinguishable emission colors of ZnS-capped CdSe quantum dots excited with a near-UV lamp. From left to right (blue to red), the emission maxima are located at 443, 473, 481, 500, 518, 543, 565, 587, 610, and 655 nm. Adapted from Han, M.; Gao, X.; Su, J. Z.; Nie, S. *Nat. Biotechnol.* **2001**, *19*, 631–635, with permission from Nature Publishing Group.

(the ratio of emitted to absorbed photons) of ~10%. The low quantum yield is likely due to the large surface area to volume ratios of QDs, whereby a large fraction of the constituent atoms are exposed to the surface, resulting in atomic and/or molecular orbitals that are incompletely bonded. These dangling orbitals serve as defect sites to quench QD fluorescence. One common strategy to address this issue is to grow a shell of another semiconductor with a wider bandgap onto the surface of the core, providing electronic insulation. In particular, ZnS and CdS are the two commonly known shells that are used for capping CdSe QDs.[18–20] The resulting CdSe/ZnS core/shell QDs exhibit much improved photoluminescence efficiency (QY of 40–50%). In addition to the high quantum yields, surface capping also helps reduce the sensitivity of QD luminescence to the local environment. Specifically, it has been shown that ZnS/CdSe core/shell QDs exhibit enhanced chemical stability and photostability against oxidation, afforded by the capped ZnS shell being much more resistant to oxidation than CdSe.[21] The addition of the shell may also improve the colloidal stability of QDs in organic solvents.[22] This is because Zn^{2+} atoms bind more strongly than Cd^{2+} atoms to most basic ligands such as alkyl phosphines and alklyamines (hydrophobic molecules that are required to improve the solubility of QDs in organic solvents).

Because synthesis of core/shell QDs takes place in organic solvents, they are highly hydrophobic. Solubility in aqueous solution, a necessity for biological applications, can be achieved by modifying the surface structure of the QDs. In one method known as ligand exchange, a suspension of trioctylphosphine oxide (TOPO)-coated QDs is mixed with a solution containing excess of a heterobifunctional ligand, which has one functional group that binds to the QD surface and another functional group that is hydrophilic. In this manner, hydrophobic TOPO ligands are displaced from the QDs through mass action while the new bifunctional ligand absorbs to the QD, generating water solubility. Using this method, (CdSe)ZnS QDs have been coated with mercaptoacetic acid and (3-mercaptopropyl) trimethoxysilane. Both of these consist of basic thiol groups that bind to the QD surface atoms, and either carboxylic acids or silane monomers, respectively, that are presented to the solvent.[12,23] However, ligand exchange can decrease fluorescence efficiency and does not fully resolve the problem of QD instability in aqueous buffers. Similarly, QD solubilization has also been achieved by ligand exchange with dendrons,[23] oligomeric phosphines,[24] and peptides.[25]

In an alternative approach, hydrophobic QDs may be encapsulated into an amphiphilic polymer shell.[26,27] The hydrophobic block of the polymer provides additional stability on the surface of QD through hydrophobic interactions. Other water-soluble shells, such as in phospholipids micelles,[28] silica shells,[29] or polymer beads,[30] have also been used. Regardless of the type of the shell employed, in general, the size of QDs increases significantly when encapsulated into a water-soluble shell, compared to those coated with a monolayer of ligand.

It should be noted that synthesis of QD in organic solvents and the subsequent solubilization in aqueous solvents by either ligand exchange and/or encapsulation methods typically can be lengthy and cumbersome. Over the past decade, scientists have gone back to the synthesis of QDs in purely aqueous solvents.[28,31,32] For instance, Schumacher *et al.*[32] prepared CdSe/ZnS-based QDs in a one-pot synthesis in an aqueous solution using microwave irradiation to provide superior control of nucleation and growth of the QD colloids. These particles can be engulfed more readily by macrophages than QDs solubilized by traditional schemes. However, it has generally been observed that QDs prepared in aqueous solvents rarely achieve the level of monodispersity, stability, and fluorescent efficiency as the QDs produced in organic solvents.

To extend their utility for biological applications, the surface of the water-soluble QDs can be further coated with bioinert polymers such as polyethylene glycol or bovine serum albumin,[28] improving biocompatibility and preventing nonspecific binding. Furthermore, the surface of the QDs may also be functionalized to have reactive species, such as amines, thiols, and carboxyl groups, allowing the subsequent conjugation of QDs to biomolecules such as proteins,[31] antibodies,[33] oligonucleotides,[34] or receptor-specific ligands.[27]

3.318.2.1.3. Biological interaction

For most *in vivo* imaging applications, QDs have been introduced into the bloodstream via systemic intravenous delivery. Once in circulation, the two parameters that seem to influence the biodistribution, circulation time, and mechanism of QD clearance the most are size and susceptibility to opsonization by serum proteins. For instance, renal clearance of QDs is highly related to the hydrodynamic diameter of the QDs, with the renal filtration threshold being 5–6 nm.[35] QDs below this size threshold are quickly removed from circulation by the kidneys, for example, QDs that were 4.36 nm in diameter exhibited a blood half-life of only 48 min and were found intact in the urine. As the QDs are increased in size, their circulation time is also increased, and they are generally removed from circulation by the reticuloendothelial system (RES), which includes the liver, spleen, and the lymphatic system.[36–38] For example, QDs with a diameter of 8.65 nm exhibited a blood half-life of 20 h and high uptake by the liver. When calculating the size of QDs *in vivo*, the influence of surface-adsorbed proteins on the overall size should be taken into consideration. The shape and surface chemistry of QDs will, of course, also affect the rate of RES uptake. It should be noted that although it is generally observed that increased circulation time increases the chance of directing targeted QDs to specific tissues, thus resulting in higher tissue contrast, rapid renal clearance may be preferred since long residence times may lead to the biodegradation of QDs into toxic components.

Before clinical applications of QDs can be undertaken, concerns about their safety must be addressed thoroughly. It has already been established that cadmium and selenium, two metals commonly used in QD cores, can cause acute and chronic toxicities in vertebrates, likely through the generation of reactive oxygen species and oxidative stress. However, it is still not clear whether these toxic ions, when incorporated into a nanocrystalline core, surrounded by biologically inert molecules (i.e., ZnS) and encapsulated within polymers, would still be toxic to living subjects. Some studies report that intense UV excitation may degrade QDs and thereby release Cd^{2+} from the core.[39] However, contradictory observations supporting

the robustness of the shell (i.e., ZnS) in preventing leakage of the encapsulated materials have also been reported.[39–41] It has been suggested that the surface coating (i.e., polyethylene glycol (PEG) or polymers) may further inhibit degradation of QDs. But again, a recent study questions the protective effect of surface coating, as hypochlorous acid and hydrogen peroxide, both produced by phagocytic cells, may readily diffuse across polymeric secondary coatings and cause QD lattice defects and solubilization of the core.[42] Furthermore, some studies suggest that the size of QDs may be an inherent source of toxicity, regardless of the presence or absence of secondary coating. It has been observed that increased toxicity may be correlated with a decrease in QD size,[43,44] although once the renal filtration threshold is reached, rapid and efficient urinary excretion is expected to result in reduced biotoxicity.

Clearly, the disagreement in literature regarding the potential hazards of QDs may stem from the fact that not all QDs are the same, each exhibiting distinct physicochemical properties, core/shell chemistry, water solubility, and surface modifications, all of which influence the overall potential for toxicity. The confusion is further exacerbated by the limited number of toxicological studies and the variety of QD dosages and exposure concentrations tested in the literature. To propel QDs into human clinical use, a standardized and systematic toxicology methodology capable of addressing particle distribution, excretion, metabolism, pharmacokinetics, and pharmacodynamics *in vivo* must be established. Until then, the scientific community is unlikely to reach a consensus concerning QD safety.

3.318.2.1.4. Applications

The ability to functionalize the surface of water-soluble QDs with proteins, ligands, or antibodies that are specific for biomarkers of interest has allowed their use in many biomedical applications. In contrast to organic fluorophores, which typically have broad emission spectra, the narrow emission spectra of QDs can facilitate the studying of multiple targets simultaneously by eliminating the need for spectral unmixing. In fact, wavelength-and-intensity multiplexing with QDs in biological assays can distinguish vast numbers of unique nucleic acid or protein sequences.[45] QDs also have bright fluorescence emissions and do not suffer from photobleaching, making them ideal for imaging targets that are expressed in low copy numbers. Sensitivity can be further improved by photobleaching the autofluorescent signal present in cell samples. Specifically, while autofluorescence undergoes photobleaching with UV illumination,[46] QDs are highly photostable. Therefore, the specific QD signal can be easily distinguished from autofluorescence by preirradiating the specimens.

3.318.2.1.4.1. Cellular imaging

To date, QDs have been predominantly used in fixed specimens – for immunolabeling of fixed cells and tissues,[47] and fluorescence *in situ* hybridization of chromosomes[48] and DNA.[49] Applications of QDs for live-cell imaging have also emerged over the past few years, particularly for the imaging and tracking of cell membrane receptors. For instance, QDs have been conjugated to epidermal growth factor (EGF) for the targeting of erbB/HER membrane receptors on human cancer cells[50] and also to an antibody fragment specific for the targeting of glycine receptors on the membranes of living neurons.[51] The diffusion of various plasma membrane proteins (including tyrosine kinases,[52] integrins,[53] G-protein coupled receptors,[54] and membrane lipids associated with apoptosis[55]) has also been characterized using QDs.

3.318.2.1.4.2. In vivo imaging

In vivo applications of QDs for molecular imaging have thus far, generally been limited to animal models and have primarily focused on vascular and lymphatic imaging, tumor imaging, and cell tracking. In particular, QDs have been used for the nontargeted imaging of various vascular systems, ranging from illumination of the capillaries of adipose tissue and skin of a living mouse,[56] to imaging the blood vessels of chicken embryos,[57] to mapping the coronary vasculature of a rat heart.[58] Additionally, active targeting in the vasculature has been accomplished using QDs conjugated to antibodies recognizing different cell adhesion molecules (CAMs).[59] For example, following intravenous injection of the QD-conjugates into a diabetic rat, fluorescence angiography revealed CAM-specific increases in fluorescence within the retinal vasculature. In this manner, the floating, endothelial rolling and leukostasis of individual leukocytes were all successfully monitored.

When QDs are used to image the lymphatic system, the extent of the lymphatic network that can be imaged is primarily dictated by the size of the QD. For example, it has been observed that following intradermal administration of QDs of large hydrodynamic diameter (>16 nm), they are translocated to sentinel nodes and can be observed fluorescently up to 1 cm beneath the skin surface.[60] On the other hand, QDs of smaller size (~9 nm) can migrate further along the draining lymphatic system. In this manner, it may be possible to tailor QDs for specific applications (e.g., allowing the identification of lymph nodes downstream from the lungs,[38] esophagus,[61] or subcutaneous tumors,[62] or even mapping lymphatic drainage networks[63]) by manipulating the overall hydrodynamic size of the QDs.

QDs are excellent candidates for cell-tracking experiments, which allow the researcher to identify the origins and progeny of various cell populations within an organism. This is typically achieved by preloading cells with QDs (i.e., by nonspecific uptake, receptor-mediated endocytosis, or peptide-mediated macropinocytosis – Qtracker) and subsequently administering them into a living subject. For instance, following subcutaneous administration of cancer cells loaded with QDs into mice, the cells divided to form a solid tumor, and the portion of cells within the tumor mass that retained the QDs could be visualized fluorescently through the skin.[26] QDs have also been proposed as a means to monitor the efficacy of stem-cell therapy. For instance, QD-loaded stem cells have been seeded into an extracellular matrix that was implanted to help rescue canine hearts from surgically induced defects.[64] The locomotion and fate of the stem cells were then followed and used to assess therapeutic efficacy.

The potential of QDs as optical contrast agents for *in vivo* imaging of tumors has also been realized for many years. QDs can be directed to tumor sites via 'passive' or 'active' targeting. For passive tumor targeting, extravasation of QDs from the leaky tumor vessels at the tumor site, combined with poor lymphatic drainage, results in the accumulation of QDs in

the tumor microenvironment (i.e., the enhanced permeability and retention (EPR) effect).[65] To facilitate the uptake of QDs by tumor tissues and improve specificity, QDs have also been conjugated with targeting molecules such as antibodies or affinity peptides that recognize protein targets overexpressed on the surface of tumor cells (i.e., active targeting). Some targets that have already been examined include, but are not limited to, epidermal growth factor receptor,[66] the transferrin receptor,[67] the folate receptor,[68] integrin,[69] and prostate-specific membrane antigen (PSMA).[26]

3.318.2.1.5. Perspectives and challenges

Although molecular imaging applications using QDs as optical biosensors have proven tremendously useful in biological and medical research, several hurdles remain before their utility can be fully exploited in clinical applications. As discussed earlier, concerns about their safety *in vivo* have persisted for many years and a consensus has yet to be reached. Also, the ability to use QDs to track intracellular biomolecules is still limited by the lack of an appropriate intracellular delivery method. Furthermore, when viewed individually, QDs exhibit blinking behavior that may prevent their use for live-cell tracking of individual molecules that correlate with pathology. The latter two of these issues are elaborated subsequently.

In contrast to the widespread application of QDs for targeting and labeling cell surface biomarkers, the ability to use QDs to image and track intracellular biomolecules is very limited. The addition of biocompatible coatings (i.e., PEG) significantly increases the size of QDs, which severely impedes their ability to penetrate the cell membrane and gain access to targets in the cytoplasm of living cells. Studies have shown that QDs delivered to cells via commonly utilized methods, such as passive uptake,[70] receptor-mediated internalization,[33] macropinocytosis via cell-penetrating peptides (e.g., TAT peptide),[71] chemical transfection (i.e., lipofectamine),[72] or electroporation,[39] tend to aggregate inside cells and are often trapped in endocytotic vesicles. Although it has been shown that QDs can potentially be released from endosomes by coating them with multivalent and endosome-disrupting surface coatings such as polyethylenimine (PEI)[71] or via osmotic lysis,[73] none of the aforementioned procedures is capable of achieving uniform distribution of QDs within the cytosol. To date, microinjection is the most promising method to accomplish cytosolic delivery, but the technique is known to be tedious, time-consuming, and not feasible for the analysis of large numbers of cells. Regardless of the method of choice, however, it has often been speculated that the large size of QDs may result in slow diffusion within the cytoplasm, which is a complex environment containing solutes, RNA, and an assortment of cytoskeletal proteins organized in a lattice-like mesh. Such cytoplasmic scaffolding allows small solutes to 'sieve' freely through the cell but likely would restrict the movement of QDs. Consequently, the synthetic methods that reduce the size of QDs, while maintaining their brightness and photostability, are essential for intracellular studies to progress. Recently, researchers have turned from the standard PEG coating to multifunctional multidentate polymer ligands and synthesized biocompatible QDs with hydrodynamic sizes <10 nm.[74]

Potentially, an additional concern over using QDs to image cytosolic targets is that they tend to be 'sticky,' binding nonspecifically to intracellular biomolecules. In particular, QDs with highly charged surface groups, such as carboxylic acids and amines, have already been shown to bind nonspecifically to a variety of cells and tissues.[75] This nonspecific binding can cause a high level of background fluorescence (as nonspecifically bound QDs cannot be distinguished from QDs that have engaged their target), significantly reducing the signal-to-noise ratio, specificity, and detection sensitivity. While nonspecifically bound QDs can generally be washed away in fluroescence *in situ* hybridization (FISH) or immunohistological studies, this is clearly not possible for *in vivo*. It is likely that an 'activatable' QD probe (such as QD-BRET[76]), which can differentiate target-bound from unbound QDs, is needed for intracellular analysis of specific biomolecules.

Even though QDs could be successfully used to target intracellular (or extracellular) targets in living cells, the use of QDs to continuously track the fate of a single biomolecules is severely limited by the fact that they 'blink.'[77,78] That is, under continuous excitation and individual observation by fluorescence microscopy, QDs turn on and off intermittently. Over the past decade, significant effort has been devoted to investigating the mechanisms underlying the blinking behavior of single QDs. Although still not fully understood, it is generally proposed that blinking is caused by extra charges in the nanocrystal that greatly enhance nonradiative decay rates.[77,78] These charges arise from the separation of photoexcited electron–hole pairs and are long-lived, since one charge carrier of the pair probably resides at the QD surface, in a deep-trap energy state. Consequently, a charged nanocrystal could have its photoluminescence temporarily quenched because of the high efficiency of nonradiative (e.g., Auger) recombination processes between the extra charge and a subsequently excited electron–hole pair. Photoluminescence could resume only after the nanocrystal's charge becomes neutralized again. One route to suppress blinking would be to eliminate trap sites. Over decades of research, studies have found that it is possible to attenuate the blinking events by coating the QD core with a thick crystalline shell to electronically insulate it and prevent ionization,[79,80] or by adding surface-bound ligands.[81,82] While blinking is significantly reduced (i.e., QDs remain 'on' for 97% of the time), it has yet to be eliminated, since the fundamental processes responsible for blinking still persist.

Recently, significant progress in the field has been made by Wang *et al.*[83] who successfully synthesized alloyed core nanocrystals of CdZnSe capped with a semiconductor shell of ZnSe (CdZnSe/ZnSe). At the single-crystal level, these QDs exhibit complete suppression of blinking for hours, despite the presence of extra charges. It has been speculated that the gradient alloyed structure of these QDs allows them not to blink, because light is continuously emitted even when the QD is ionized. It is expected that continued refinement of the CdZnSe/ZnSe QD synthesis with regard to biocompatibility via surface modification (as has been done for traditional QDs) will lead to their widespread application in biology and medicine.

3.318.2.2. Gold Nanomaterials

3.318.2.2.1. Structure and properties

Gold nanoparticles (AuNPs), which are typically sized between 0.5 and 250 nm, have been used as contrast agents on multiple

imaging platforms and possess size and shape-tunable properties. AuNPs have been prepared in a wide variety of shapes, including spherical (nanospheres) and rod shapes (nanorods), with no partitioning of material contents (Figure 2). AuNPs have also been synthesized with a thin gold shell surrounding a dielectric and insulating core (e.g., silica), that is, nanoshells. Gold 'nanodogbones' have even been reported.[84] The use of AuNPs in biological applications began in 1971 when Faulk and Taylor[85] invented the immunogold staining procedure for electron microscopy. The straightforward synthesis, excellent stability, and ability to easily attach targeting ligands have permitted the application of AuNPs to both live-cell and *in vivo* imaging.

AuNPs are an attractive contrast agent since they can be visualized with a variety of modalities. In general, a number of properties can be controlled by varying the absolute size (for nanospheres), the aspect ratio (for nanorods), or the relative dimensions of the core and shell layers (for nanoshells). For example, AuNPs strongly absorb and scatter visible light, and their propensity to scatter versus absorb incident light can be modulated by changing the nanoparticle size. Furthermore, when electromagnetic radiation of a wavelength much smaller than the diameter of the AuNP interacts with the particle, it induces coherent and resonant oscillations of the metal electrons across the nanoparticle. These oscillations are known as the surface plasmon resonance (SPR) effect. The fluorescent emission of AuNPs is also tunable based on size and shape, permitting the labeling of cellular structures with different colors. Moreover, AuNPs >20 nm can be visualized with optical microscopy in phase contrast or differential interference contrast mode. When AuNPs aggregate, they can exhibit a phenomenon called plasmon–plasmon interaction, by which a colloidal solution of dispersed spherical AuNPs changes color from red to blue. This photo-switching effect based on AuNP aggregation has been useful in designing colorimetric assays for detecting biomolecules such as cell membrane receptors. Further, light absorbed by AuNPs leads to the generation of heat, making AuNPs useful contrast agents for photoacoustic and photothermal imaging.[86,87] Lastly, the ability of AuNPs to attenuate electron waves and X-rays has allowed them to be used for transmission electron microscopy and X-ray imaging applications.[88]

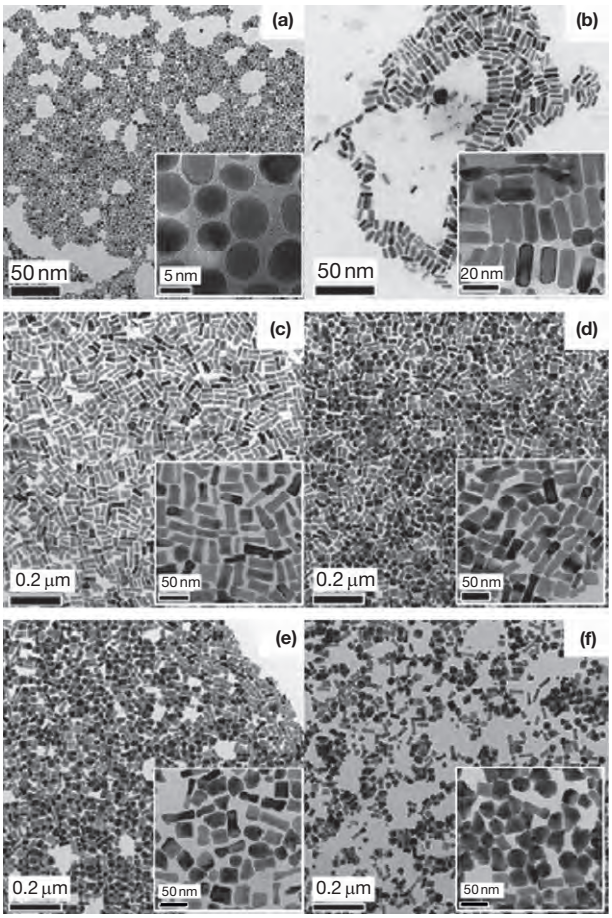

Figure 2 Transmission electron microscopy images of various gold nanomaterials. (a) Gold seed particles with spherical shape. (b) Gold nanorods. (c–f) Synthetic variations of gold 'nanodogbones.' Adapted from Huang, C.; Chiu, P.; Wang, Y.; Meen, T.; Yang, C. *Nanotechnology* **2007**, *18*, 395602, with permission from IOP Publishing Ltd.

3.318.2.2.2. Synthesis

Synthesis of gold nanospheres can take place in both aqueous solution and organic solvents via nucleated growth of gold salts.[89,90] In typical syntheses, gold salts such as $AuCl_3$ are reduced by the addition of a reducing agent, leading to nucleation of Au ions and the subsequent growth of the nanoparticles. In addition, a stabilizing agent is also required, which is either adsorbed or chemically bound to the surface of the Au nanoparticles. The stabilizing agent is typically charged, so that the like-charged nanoparticles repel each other and aggregation is prevented. For the synthesis in aqueous solution, citric acid can serve as both the reducing agent that triggers nucleation and as the stabilizing agent because of its negative charges. However, for a typical synthesis in organic solvent, the reducing agent is often different from the stabilizing agent, and colloidal stability of the AuNPs in organic solvents is typically imparted by the addition of surfactants, with hydrophobic alkane chains bound to the particle surface. Synthesis of nanorods can be achieved via seed-mediated growth in the presence of rod-shaped templates. Templates can include porous alumina,[91] polycarbonate membranes,[92] carbon nanotubes,[93] and micelles[94,95] whose shape can be modulated by varying the chemical and physical conditions. Small-size spherical AuNPs are first prepared to serve as seeds, and then the nanorods are grown under template-mediated shape control in the presence of a surfactant. The aspect ratios can also be partly controlled by varying the ratio of gold seed to gold salt. Lastly, the synthesis of gold nanoshells typically involves growing a layer of gold on the surface of a dielectric core, serving as a scaffold.[96] The relative thickness of the core and the shell can thus easily be modulated to influence the optical properties of the nanoshells.

After the synthesis of gold particles, the stabilizer molecules can be replaced by other stabilizer molecules in a ligand exchange reaction. Ligand exchange allows the transfer of AuNPs from an organic to aqueous phase (and vice versa) by exchanging hydrophobic surfactants and hydrophilic surfactants.[97] Like QDs, the utility of AuNPs for biological applications can be facilitated by coating the surface of the particles

with bioinert polymers such as polyethylene glycol or bovine serum albumin, which improve biocompatibility and prevent nonspecific binding.[98] Biomolecules such as proteins, antibodies, oligonucleotides, or receptor-specific ligands can be tethered to AuNPs directly or attached to reactive species such as amines, thiols, and carboxyl groups that have been introduced onto the AuNP surface.[89,90,99]

3.318.2.2.3. Biological interactions

It is generally perceived that AuNPs are safer than QDs, since gold is much less toxic than the primary materials composing QDs (cadmium and selenium). In fact, gold (as a bulk material) has been used clinically in the form of the antiinflammatory agents, Auranofin® and Tauredon®, for the treatment of rheumatoid arthritis.[100] However, some groups do question the safety of AuNPs and argue that as the size decreases to nanoscale dimensions, gold may behave very differently than in bulk.[101,102] Specifically, some research has found gold nanostructures to be toxic in the body, where elemental gold can become soluble by undergoing oxidation or cyanidation.[103,104] Studies have shown that gold is heavily concentrated by the kidneys (causing nephrotoxicity) and can also initiate eryptosis (erythrocyte suicidal death).[105,106] As with QDs, some of the disagreement concerning the safety of AuNPs is likely due to differences in size, surface charge, and shape exhibited in the extensive literature (see **Chapter 3.319, Characterization of Nanoparticles in Biological Environments**).

3.318.2.2.4. Applications

Although gold nanorods are not a molecular imaging application, they are being investigated as photothermal agents for *in vivo* use. In general, for the nanorods of smaller axial diameter (~10 nm), absorption dominates, whereas scattering is the primary effect for larger axial diameter nanorods (>35 nm).[107] Consequently, for *in vivo* applications of tumor ablation, small diameter gold nanorods are being used as photothermal converters of near infrared (NIR) light, due to their high absorption cross-sections. Short laser pulses can be directed onto AuNPs present in the tumor, and the laser energy converted into heat energy that destroys the tumor cells, which are typically more heat-sensitive than that of normal cells.[108]

3.318.2.2.4.1. Cellular imaging

The ability to functionalize AuNPs with various biomolecules allows for the targeting of intracellular contents in fixed cells. For instance, immunostaining is one of the traditional uses of AuNPs in biology. The labeled cellular structures can be visualized in bulk via fluorescence microscopy or at the single molecule level via electron microscopy. Immunostaining can also be performed on live cells with AuNPs. For example, AuNPs have been used to monitor the movement of cell surface receptors such as EGFR. Here, binding of multiple AuNPs on a single epidermal growth factor receptor (EGFR) resulted in a detectable red-shifted fluorescent signal.[109] However, as with QDs, live-cell imaging is generally restricted to imaging membrane receptors due to problems with intracellular delivery of the nanoparticle.

Importantly, the ability to detect cell surface receptors with AuNPs is not limited to conventional microscopy techniques but can also be accomplished by photoacoustic imaging. In this case, the local aggregation of the nanoparticles provides an enhanced photoacoustic signal that is not generated when the particles are dispersed in solution.[110]

3.318.2.2.4.2. In vivo imaging

In contrast to QDs, the literature is more coherent in its indication that AuNPs should be safe to use as contrast agents within living subjects. Consequently, over the past few years, there has been a push to use AuNPs as platforms for *in vivo* molecular imaging. For instance, AuNPs have been used to target tumors *in vivo* and have been detected using surface enhanced Raman spectroscopy (SERS).[111] The nanoparticles were encapsulated within a thiol-modified PEG coat that afforded biocompatibility and improved circulation time. These AuNPs were also surrounded by Raman reporters that led to light emission over 200 times brighter than QDs. Finally, the pegylated AuNPs were conjugated with an antibody (or an antibody fragment such as scFv) against EGFR to specifically target tumor cells. Using these AuNPs and SERS, the location of tumors was clearly delineated.

Recently, AuNPs have also been used as X-ray contrast agents. The small AuNPs (1.9 nm in diameter) were injected intravenously into tumor-bearing mice, and images were acquired over time with a standard mammography unit.[112] Tumors and other organs such as the kidneys were visualized with high spatial resolution. Furthermore, imaging of the microvasculature was possible, and increased vascularization and angiogenesis could be detected. Perhaps most interestingly, the large attenuation of AuNPs was found to provide superior contrast enhancement compared with iodine-based agents.

AuNPs have also been readily detected by photoacoustic tomography.[87] When AuNPs, ~50 nm in diameter, were injected intravenously into tumor-bearing mice, the tumors could be easily distinguished due to EPR of the AuNPs.

3.318.2.3. Superparamagnetic Nanoparticles

3.318.2.3.1. Structure and properties

Another nanomaterial at the forefront of current research in molecular imaging is the SPIO nanoparticle. The versatility, functionality, and magnetic properties of these nanoparticles make them attractive agents for a number of passive and active targeting applications in magnetic resonance imaging (MRI). Although over 45 years have passed since iron oxide particles were first used as magnetic contrast agents,[113] there has been increasing interest in their use over the past decade, primarily due to refinements in synthetic methods that have led to improved magnetic susceptibility and the introduction of new/modified surface coatings that have imparted diverse functionality. Importantly, both oral and intravenous forms of SPIO nanoparticles are currently approved for clinical use.

The basic structure of most SPIO nanoparticles currently under investigation consists of an iron oxide core and a hydrophilic surface coating. The iron oxide core is composed of magnetite (Fe_3O_4) and/or maghemite (γFe_2O_3) nanocrystals, and endows the particles with an MR detectable signal. Depending on the type of SPIO nanoparticle, the iron oxide core may be composed of a single individual nanocrystal or multiple crystals. Both magnetite and maghemite crystals have

similar lattice dimensions of 0.8396 and 0.8346 nm, respectively.[114] The two types of crystals also have similar magnetic properties, although maghemite does have a slightly lower saturation magnetization.[115,116] Further, magnetite has an inverse spinel crystal lattice structure, while maghemite has a cubic geometry and vacancies in the cationic sublattice. Post-synthetic oxidation of the iron core by exposure to oxygen and heat or oxidizing agents converts magnetite into maghemite and also leads to a visible change in color from a dark black-brown to a lighter red-brown.

The nanoscale size of the iron oxide core gives rise to the characteristic superparamagnetism of SPIO nanoparticles. Larger size crystals of magnetite and maghemite are ferromagnetic as a result of aligned unpaired electron spins, and consequently, magnetization is evident in these materials even in the absence of an external magnetic field. When a ferromagnetic material is not magnetized, magnetic domains (called Weiss domains) are aligned at short range, but antialigned at long range. Therefore, the bulk material consists of randomly oriented magnetic domains that exhibit no net magnetization. The transition between magnetic domains is termed the Bloch wall. At the nanoscale (~14 nm and below), the formation of such Bloch walls becomes thermodynamically unfavorable, resulting in the formation of single-domain crystals.[117,118] These single-domain crystals are classified as superparamagnetic, since they have significantly larger magnetic susceptibility than typically observed in paramagnetic materials, essentially because the entire nanocrystal aligns itself with the applied field as a single unit. The distinguishing features of paramagnetic materials are their ability to lose their magnetic remanence in the absence of a magnetic field. In other words, superparamagnetic materials align their magnetic dipoles with externally applied magnetic fields, creating a small positive magnetic susceptibility (i.e., the ability to strengthen the field into which they are placed), but once the magnetic field is removed, they become randomly oriented due to Brownian fluctuations, and the net magnetization of the solution is lost. Brownian forces are also capable of preventing the aggregation of SPIO nanoparticles that might otherwise be observed because of their magnetic attraction in solution.[119]

This ability of SPIO to generate local disturbances in the magnetic field results in the rapid dephasing of surrounding hydrogen nuclei and, therefore, produces a detectable change in their MR signal (**Figure 3**). Therefore, the imaging capability of SPIO nanoparticles arises through their influence on the longitudinal and transverse relaxation of surrounding protons, rather than inherently from the nanoparticles themselves. SPIO nanoparticles possess both high longitudinal relaxivity (R1) and transverse relaxivity (R2).[120,121] Accordingly, it has been demonstrated that they can generate levels of T1 and T2 contrast sufficient for biomedical applications. Nevertheless, the majority of molecular imaging applications have exploited SPIO as T2 contrast agents.[122–124]

A particularly important attribute of SPIO nanoparticles that are used for biological applications is the hydrophilic surface coating, which not only imparts improved colloidal stability and biocompatibility, but also allows for a variety of surface functionalizations and chemical conjugations.

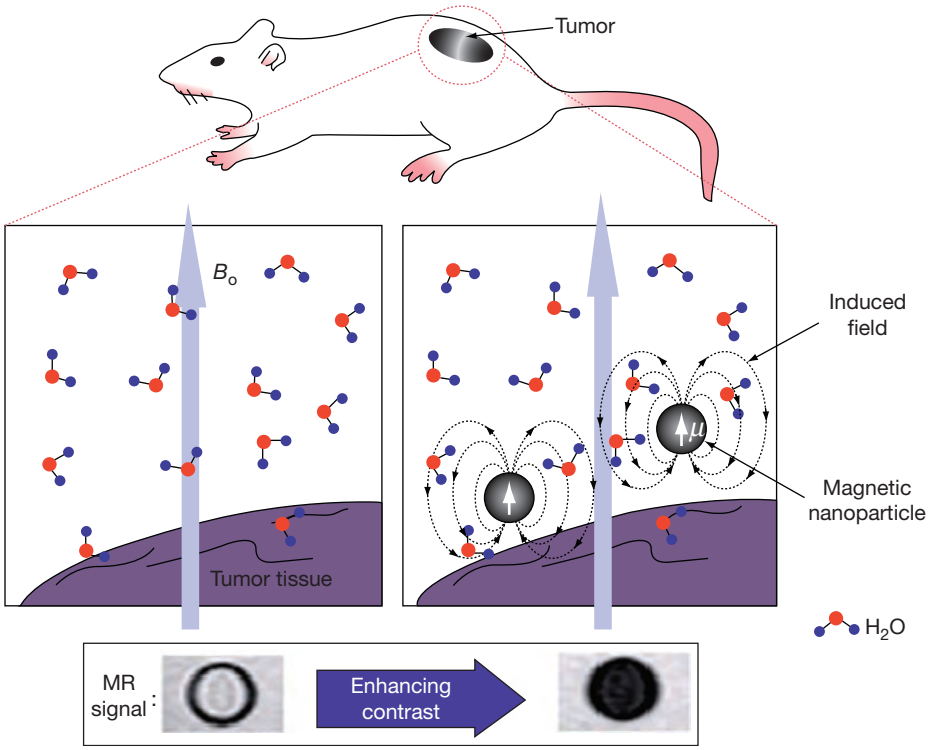

Figure 3 The presence of superparamagnetic iron oxide nanoparticles generates disruptions in the local magnetic field, leading to the rapid dephasing of nearby protons. Fast T2 relaxation results produces darker voxels on T2 weighted images. Adapted from Jun, Y. W.; Lee, J. H.; Cheon, J. *Angew. Chem. Int. Ed. Engl.* **2008**, *47*, 5122–5135. Copyright Wiley-VCH Verlag GmbH & Co.

These surface materials can also increase the circulation lifetime of SPIO[125] *in vivo*, as the coating prevents the rapid opsonization suffered by bare iron oxide.[126] To date, a wide variety of surface coatings have been used, but typical coatings are polysaccharides or synthetic polymers. An assortment of chemical modifications can also be applied to the surface-coating material to impart further improved stability, including stability at elevated temperatures. For example, the coating polymer may be crosslinked wih agents such as epichlorohydrin[128,129] or dextran may be substituted with carboxylmethyl reduced dextran[127] modifications. Depending on the synthetic method used, the coating material can either be adsorbed onto preformed bare iron oxide nanocrystals or incorporated onto the nanocrystals *in situ* as they are formed.

The size of SPIO nanoparticles can range over several orders of magnitude. For example, bare SPIO nanocrystals formed by citrate-inhibited growth are 2–3 nm,[130] polymer-coated polycrystalline SPIO nanoparticles are generally tens of nanometer in size, and ones formulated as orally ingestible contrast agents reach the micrometer scale. Although larger diameter particles have been synthesized and have utility for applications of cell tracking,[131,132] cell separation,[133] cell rheology,[134] membrane deformation,[135] and gastrointestinal contrast,[136] particles of this size have a limited role in molecular imaging since they cannot access neo- and microvasculature.

The classification and nomenclature for SPIO nanoparticles are based primarily on their overall hydrodynamic diameter, which includes the hydrated surface coating.[137] Particles >300 nm, ranging up to 3.5 μm, are termed oral-SPIO; standard SPIO (SSPIO) are ~60–150 nm; ultrasmall SPIO (USPIO) ~10–40 nm[138]; and monocrystalline iron oxide nanoparticles (MION – a subset of USPIO[139]) are ~10–30 nm.[140] MION nanoparticles are so named to denote that they have only a single SPIO nanocrystal in their iron oxide core, whereas the core of nanoparticles >50 nm typically comprises multiple iron oxide nanocrystals. Another commonly encountered classification is cross-linked iron oxide (CLIO), which denotes an SPIO nanoparticle with a cross-linked dextran surface coating. Generally, all SPIO agents with a hydrodynamic diameter <50 nm are used for similar molecular imaging applications *in vivo*, and therefore for the purposes of this review, all agents of this size will simply be referred to as SPIO.

3.318.2.3.2. Synthesis

Several synthetic methods that have been employed in the production of magnetic iron oxide nanoparticles will be briefly described below. The choice of the method used depends largely on the researcher's preferences for ease of synthesis and nanoparticle uniformity. The most commonly used procedure for SPIO nanoparticle synthesis involves the dropwise addition of concentrated base to effect the coprecipitation of ferrous and ferric salts.[141–143] This method is very popular for biomedical applications (along with microemulsion) since it is relatively simple to use, even if it produces a more polydisperse population of nanoparticles than other methods. When carried out in the absence of surface-complexing materials, it yields bare SPIO magnetite nanocrystals that typically have a mean diameter of ~10 nm and are roughly spherical in shape[144] (although these properties are highly dependent on the synthetic conditions). The original precipitate is collected by centrifugation or magnetic decantation, treated with nitric or perchloric acid, and then colloidally dispersed in water to produce an acidic magnetic sol. Alternatively, alkaline magnetic sols can be generated by substituting tetramethylammonium for the nitric or perchloric acid. A surface coating can then be subsequently applied to the nanoparticles through nonspecific adsorption.[145] Often however, the coating material is directly included in the original coprecipitation reaction mixture.[146] When nanoparticles are formed this way in the presence of dextran, the mean hydrodynamic radius of the polydisperse polymer-coated SPIO varies from 20 to >100 nm and can be controlled by adjusting several synthetic parameters such as the iron/dextran ratio. In general, the iron oxide core of these nanoparticles ranges from 2 to 15 nm.[147]

In an effort to reduce the polydispersity inherent in coprecipitation methods, synthetic techniques involving microemulsion (both oil-in-water and water-in-oil) are being pursued, since the size of microcavities formed can be tightly controlled between 2 and 12 nm.[148] Although some microemulsion approaches initially produce hydrophobic SPIO,[149] such nanoparticles can subsequently be given a water soluble surface coating.[150] Nanoparticles can be synthesized in the oil-in-water approach by suspending a ferrous salt-surfactant precipitate in an aqueous solution, and then adding a base, such as methylamine, to form the magnetic precipitate.[151] Alternatively, surfactant (oleic acid)-coated nanoparticles can be added to a solution composed of both a melted lipophilic suspension and an aqueous phase. Dispersing the warm transparent phase in cold water accomplishes lipid coating of the colloidal magnetite.[152] For biomedical applications, however, water-in-oil microemulsion is the more common approach. Typically, nanodroplets of aqueous iron are enclosed in a surfactant coat that separates them from the surrounding organic phase, forming reverse micelles.[153–155] Alkaline nanodroplets are then added to the solution, and SPIO is subsequently precipitated and oxidized inside the nanoscale micelle. Varying the temperature of reaction, as well as metal and base concentrations, yields nanoparticles of 3–12 nm diameter.[156] A major drawback of all microemulsion techniques is the relative inability to produce larger SPIO nanoparticles due to problems with disordered crystallinity at these sizes.[157]

Several other methods of SPIO nanoparticle synthesis have been explored, but they will be discussed only briefly here since they are still less commonly used. Ultrasound irradiation (sonochemical synthesis) uses the rapid collapse of sonically generated microcavities to produce nanosecond lifetime hot spots of ~5000 K in which ferrous salts are instantly driven to form SPIO. Following stabilization with oleic acid, a monodisperse colloid of 8 nm nanoparticles is formed.[158] SPIO nanoparticles have been produced via layer-by-layer (LBL) self-assembly, based on the repeated submersion of a substrate or colloidal template in solutions of oppositely charged polyelectrolytes.[159] In the method of spray pyrolysis, a solution is sprayed into a series of reactors where the solute condenses as the solvent evaporates. Ferric ions are reduced to a mixture of ferric and ferrous ions in an organic solvent, generating SPIO.[160] In laser pyrolysis, a laser heats a mixture of iron pentacarbonyl in air, producing nuclei that form small nanoparticles.[161]

This method requires less reaction volume than spray pyrolysis and allows uniform and well-crystallized nanoparticles to form in a single step.[162] Although these procedures offer high production rates, they require expensive equipment and meticulous control over the synthetic conditions.

One particularly promising approach for the ultra-large-scale synthesis of monodisperse iron oxide colloids relies on the thermal decomposition of various iron oxide precursors, at 250–300 °C in octylamine and trioctylamine.[163] This approach has generated a great deal of excitement because the synthetic process is inexpensive and utilizes nontoxic iron salts as reactants.

3.318.2.3.3. Biological interactions

For biological and medical research, the biodegradability and lack of toxicity of SPIO has made them a valuable tool for both imaging and therapeutic applications. In fact, the use of dextran–iron complexes *in vivo* stretches back over half a century, initially as a substitute for the ferritin complex as a treatment for anemia.[164,165] These complexes allowed the intravenous administration with much lower toxicity than soluble iron salts.[166]

The diameter and surface characteristics of SPIO significantly impact their clearance, cellular interactions, and toxicity. In general, nanoparticles above ~10 nm in diameter are sequestered in the liver and spleen as a consequence of uptake by phagocytic cells. On the other hand, particles under 10 nm are rapidly cleared through extravasation and renal excretion.[167] With regard to surface characteristics, amphiphilic coatings are preferred for generating prolonged plasma half-life; they can extend the circulation time from minutes to hours,[168] and thereby increase the targeting capabilities of SPIO contrast agents.

Polymer-coated SPIO nanoparticles have been shown, to date, to have minimal impact on cell viability and function. For instance, PEG-coated nanoparticles did not affect the cell adhesion behavior or morphology of cultured fibroblasts.[169] Similarly, dextran-coated SPIO labeled with TAT peptide demonstrated no significant effect on the cell viability, clonogenic efficiency, immunophenotype, or biodistribution of human hematopoietic cells.[170] However, studies have indicated that nanoparticle surface properties can influence nanoparticle uptake by phagocytic cells. Specifically, compared to dextran-coated SPIO, carboxydextran SPIO appear to be internalized more readily by macrophages.[171] Nevertheless, nanoparticle uptake is not associated with cell activation since no release of interleukin-1 is observed.[172] Following cellular internalization, SPIO generally accumulate in lysosomes where low pH exposure degrades the iron oxide core into iron ions, which are funneled into the hemoglobin pool.[173] Additionally, for dextran-coated SPIO nanoparticles, intracellular dextranase further assists with the degradation process.

As noted earlier, SPIO nanoparticles have already been used as contrast agents in living subjects. Adverse events associated with intravenously administered dextran-coated SPIO have been observed but are noted to be mild in severity and short in duration.[174] The most common reactions are headache, back pain, vasodilatation, and urticaria.

3.318.2.3.4. Applications

SPIO nanoparticles have been used as contrast agents in a wide range of applications involving the passive and active targeting of both anatomical sites and cell surface markers. They have also been used to track cell migration and trafficking,[175–178] and as highly sensitive biosensors (commonly referred to as magnetic relaxation switches[179–182]) to detect targeted cells, viruses, or biomolecules in aqueous samples. Magnetic relaxation switches and cell-tracking applications lie beyond the scope of this chapter and will not be discussed. Most applications for molecular imaging fall into the category of active targeting, and so these will be the primary focus of this section, following a brief introduction to passive targeting of SPIO (see **Chapter 3.327, Intracellular Probes**; **Chapter 3.328, Biosensors Based on Sol–Gel-Derived Materials**; **Chapter 3.329, Hydrogels in Biosensing Applications**; and **Chapter 3.330, Carbon Nanotube-Based Sensors: Overview**).

Nanoparticle probes lacking explicit molecular specificity are well known in the literature for the imaging of biological systems via naturally directed physiological processes. These include EPR in tumors, nontargeted cellular uptake, macrophage phagocytosis, and accumulation in the RES (liver, spleen, and lymph nodes). In these approaches, T2-weighted images reveal the presence of SPIO through the T2 relaxation shortening effect resulting from the accumulation of nanoparticles.[183–185] Perhaps the most important factors for passive targeting are the hydrodynamic radius and surface charge of the SPIO – properties that are dictated by the surface coating of the SPIO. These parameters control the circulation time of the nanoparticles as well as their accessibility to tissues, opsonization, and rate of cellular uptake.

For example, it has been demonstrated that larger nanoparticles (~150 nm hydrodynamic radius) such as dextran-coated SSPIO AMI-25 are nonspecifically engulfed by Kupffer cells in healthy liver tissue. The absence of Kupffer cells in liver lesions is then exploited as a means of discerning between healthy and malignant tissue through SPIO-enhanced contrast.[186–188] In contrast, smaller SPIO nanoparticles (~30 nm hydrodynamic radius) are found to extravasate into the interstitial space and are carried via lymph vessels to lymph nodes where they accumulate.[189,190] The presence of metastases in lymph nodes leads to disturbances in the flow of lymph and thus interferes with the ability of the SPIO nanoparticles to reach the node. This differential accumulation has allowed for significant increases in the positive predictive values and diagnostic accuracy of node metastases.[191] Finally, the observation that SPIO are efficiently internalized by macrophages and other phagocytic cells has led to their evaluation as contrast agents for the detection of inflammatory and degenerative disorders associated with the activity of those cells. For example, SPIO nanoparticles have been used to examine sites of transplant rejection,[192] atherosclerotic plaque,[193] ischemic strokes,[194] multiple sclerosis foci,[195] and CNS tumors.[196]

Active targeting is preferred to passive targeting, since it not only provides physiologic information but also offers insight into specific molecular mechanisms. Such information could allow for the early detection of disease and more accurate and specific grading. In order to achieve active targeting of SPIO nanoparticles against specific biomolecules, it is first necessary to conjugate targeting agents or ligands onto the SPIO surface – either directly or onto its hydrophilic coating. As mentioned earlier, one of the primary benefits of a polymer coating is its ability to be modified to possess a variety of reactive functional

groups (e.g., amines, sulfhydryls, carboxyls, etc.), which subsequently allow for more control over chemical conjugation to targeting ligands.

It should be noted that one of the primary weaknesses of MR as an imaging modality is its relatively low sensitivity. Therefore, perhaps the greatest hurdle for active targeting of SPIO is localizing adequate levels of nanoparticles at the disease site to generate sufficient contrast. Numerous approaches have been evaluated to improve the site-specific accumulation of SPIO, and thus enhance MR sensitivity. The most widely accepted technique is intracellular trapping,[197] whereby receptor-mediated uptake of SPIO nanoparticles leads to elevated levels of the contrast agent within the targeted tissue. An alternative strategy to improve MR contrast is two-step amplification.[198] Specifically, a biotinylated pretargeting antibody or antibody fragment is introduced intravenously and allowed to localize at the pathology of interest. Streptavidin-labeled SPIO nanoparticles are then administered to label each pretargeted antibody with multiple contrast agents. Although further development of this targeting method is still necessary, the extremely high binding affinity of the avidin–biotin system and the potential to extend this method to a wide range of targets just by using unique pretargeting antibodies make this approach quite promising.

Numerous studies have already demonstrated the ability of SPIO nanoparticles to actively target a wide variety of biomolecules implicated in a broad spectrum of disease states. By way of introduction to this fascinating and rapidly developing field, the following sections will highlight applications involving the detection of cancer, apoptosis, and cardiovascular disease.

3.318.2.3.4.1. Cancer imaging

In the field of cancer imaging with ligand-directed SPIO nanoparticles, the achievement of satisfactory image contrast generally requires that the target not only be overexpressed specifically on the tumor cells, but also undergo receptor-mediated endocytosis, allowing SPIO to accumulate intracellularly. One example of such a target is the transferrin receptor, which is overexpressed on a variety of malignant cell types – most notably, breast cancer.[199] Numerous studies have demonstrated that SPIO conjugated with transferrin can be used to monitor the expression and regulation of the transferrin receptor both *in vitro* and *in vivo*.[200–203]

Similarly, SPIO nanoparticles conjugated with folate experience rapid and efficient uptake by tumor cells that overexpress the folate receptor. *In vivo* MR postcontrast images of folate-receptor positive tumors revealed an average T2 intensity decrease of 38% from precontrast images.[204–206] In another study, the underglycosylated MUC-1 tumor antigen (uMUC-1) has been targeted with SPIO nanoparticles conjugated with the affinity peptide EPPT1.[207] This antigen is commonly found on a variety of epithelial cell adenocarcinomas, including breast, pancreatic, colorectal, lung, prostate, and gastric. Matrix metalloproteinase-2[208,209] (a membrane-bound endopeptidase found upregulated on gliomas) and Her2/neu tyrosine kinase receptor[210,211] (also called c-erb B-2, overexpressed on 25% of metastatic breast cancer) have also been imaged. These initial studies have set the groundwork for SPIO-enhanced imaging of tumors, and the number of cancer biomarkers being targeted *in vivo* continues to expand.

A parallel strategy for identifying tumors involves targeting receptors that are specifically expressed on normal cells of a particular type but not on cells that have undergone malignant transformation. Such an approach has been pursued for pancreatic tumors by targeting the cholecystokininA (CCKA) receptor present on normal pancreatic acinar cells. Upon administration of SPIO-CCK in rats, a significant decrease in T2 relaxation time was noted in areas of normal pancreatic tissue, but was not observed in the cancerous tissue.[212] Another organ to which this strategy has been applied is the liver, a common site for metastases from a variety of primary tumors, including breast, lung, and colorectal. Since detection of liver metastases is very important for cancer staging, and metastatic infiltration is not always clearly distinguishable from healthy liver, much effort has been expended in the research of liver-specific MR-contrast agents. One promising target is the asialoglycoprotein (ASG) receptor, which is expressed on normal hepatocytes but is missing from both primary and metastatic tumors in the liver.[213] Initial studies have shown that SPIO nanoparticles conjugated with the ASG receptor ligand arabinogalactan have allowed for enhanced tumor contrast in rats.

3.318.2.3.4.2. Apoptosis imaging

One specific cellular pathway that is critical to the pathogenesis of cancer and is being explored as a possible target for SPIO nanoparticles is apoptosis. Additionally, apoptosis plays a role in neurodegeneration, myocardial infarction, and chronic inflammation. Therefore, SPIO targeting of apoptotic cells could offer improved imaging of these disease processes and also allow for real-time monitoring of drug efficacy and treatment response. Recently, *in vivo* MR detection of apoptotic cells has been accomplished using the first C2 domain of synaptotagmin I as the targeting moiety.[214] SPIO nanoparticles conjugated with this element were able to generate significant increases in image contrast in regions of tumor with high apoptotic index. Another method of detecting apoptosis uses Annexin V-conjugated nanoparticles to target phosphatidylserine.[215] Apoptotic cells were detected with this method both *in vitro* and *in vivo*. In one study, distinct MR signal distributions were observed following ischemic and oxidative injury to heart tissue, suggesting that this approach may help identify 'at risk' cardiac cell populations.

3.318.2.3.4.3. Cardiovascular imaging

In addition to cancer and apoptosis, molecular imaging with SPIO nanoparticles has also made great strides to improve the contrast and early detection of various cardiovascular diseases, including atherosclerosis, thrombosis, and myocardial infarction. For example, detection of early atherosclerotic signatures was recently performed with SPIO conjugated to an anti-VCAM-1 (vascular adhesion molecule-1) antibody[216] or VCAM-1 affinity peptide.[197] Since VCAM-1 has been identified as an early marker of endothelial inflammation, it is envisioned that these nanoparticles could lead to earlier diagnosis and treatment. In the case of the affinity ligand, phage display was used to identify a VCAM-1 specific internalizing peptide. Through the increased uptake and subsequent compartmental accumulation of SPIO, sites of atherosclerosis were identified in an apolipoprotein-deficient mouse model through the resultant decrease in T2 signal. Reportedly, this targeting

peptide resulted in a 12-fold higher target-to-background signal ratio compared to SPIO targeted with the anti-VCAM-1 antibody. In addition to VCAM-1, E-selectin, a proinflammatory endothelial marker of atherosclerosis, angiogenesis, and tumor vasculature proliferation,[217–219] has also been validated as a potential target for SPIO. Using SPIO nanoparticles conjugated with antihuman E-selectin F(ab), the marker was detected in human endothelial cell culture with significant contrast enhancement over control cells.[220]

The molecular imaging of thrombi has recently been accomplished by the specific detection of αIIb-β3 integrin (expressed on activated platelets) and activated factor XIII[221] (a tissue transglutaminase in the coagulation cascade). For αIIb-β3, the targeting moiety used was RGD, a cyclic arginine-glycine-aspartate peptide well established to specifically bind the integrin.[222] SPIO-RGD resulted in better *ex vivo* thrombus visualization than nontargeted SPIO, and using its MR-contrast enhancement, clot visualization *in vivo* was achieved with an in-plane resolution of <0.2 mm by 0.2 mm.[223] Finally, for imaging of myocardial infarction, antimyosin Fab (R11D10), which is immunospecific for necrotic myocytes, was conjugated with SPIO. MR Imaging demonstrated significant signal decrease in the infarct relative to surrounding healthy myocardium.[140]

3.318.2.3.5. Perspective and challenges

Many of the advantages and disadvantages of SPIO nanoparticles as molecular imaging agents are inherent to the imaging modality in which they are used – magnetic resonance. One of the most powerful features of MR as a platform for *in vivo* molecular imaging is that molecular information can be gathered simultaneously with high-resolution anatomic information, regardless of tissue depth or the presence of overlying structures. In contrast, nuclear, optical, and ultrasound are limited by comparatively poor anatomic resolution and/or issues of signal penetration.

To date, the major shortcoming of MR (besides cost and availability) has been its relatively low sensitivity of detection. When compared to nuclear approaches that can detect probes down to the picomolar level,[224] the sensitivity of MR is several orders of magnitude worse. While it is possible to counter the inherently low signal-to-noise ratio of MR with longer scan times, this is difficult to achieve in the clinical setting, since the patient must remain very still throughout the image acquisition. Sensitivity can also be improved with the advent of higher magnetic field strengths. While MR instruments used for *in vivo* imaging in animal models have increased to 9.4 T or stronger, the majority of clinical instruments operate at 1.5 T. Nevertheless, it should be noted that imaging of individual cells can still be accomplished on a clinical scanner when some modifications are made.[225] Ultimately, the best approach to achieve higher signal and contrast-to-noise ratios in SPIO molecular imaging applications will be the various amplification strategies that were discussed (intracellular accumulation of targeted SPIO or pretargeting with a molecule possessing multiple binding sites for subsequent contrast agent). Another notable disadvantage of SPIO imaging (and MR in general) is the inability to simultaneously image multiple biomarkers, as is very commonly done with optical imaging.

Also, many SPIO-inherent challenges remain in the pursuit of ideal nanoparticle probes for molecular imaging. Chemical conjugation methods could be simplified and streamlined, synthetic approaches could be made to produce larger quantities of less polydisperse nanoparticles, and costs could be reduced. Also, there are some safety concerns over the CLIO particles that are commonly used in molecular imaging studies regarding the ability to completely remove the cross-linker. Nevertheless, given the versatility of SPIO, the large ongoing efforts in their research, and their established use in clinical medicine, these nanoparticle agents will continue to be a significantly important material in the future of molecular imaging.

3.318.3. Nanovesicles

3.318.3.1. Liposomes

3.318.3.1.1. Structure and properties

Liposomes are small artificial bilayer vesicles composed of either naturally occurring lipids or a number of commercially available synthetic products (**Figure 4(a)**). The natural or synthetic phospholipids have a hydrophobic lipid 'tail' and a polar 'head' constructed from various glycerylphosphate derivatives. Due to their amphiphilic nature, when phospholipid molecules are dispersed in aqueous media, they can self-assemble into spherical, closed structures consisting of an aqueous core surrounded by a highly ordered phospholipid bilayer.

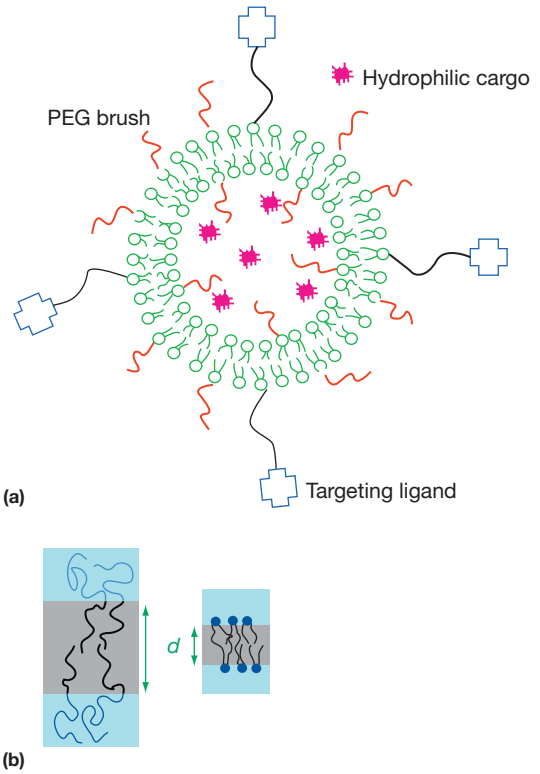

Figure 4 (a) Schematic representation of a multifunctional liposome. (b) Comparison of the liposome (right) and polymersome (left) bilayer membranes. The increased bilayer thickness of polymersomes (~8 nm) gives them improved mechanical stability. Adapted from Nallamothu, R.; Wood, G. C.; Pattillo, C. B.; *et al. AAPS PharmSciTech* **2006**, *7*, E32, with permission from Springer. Discher, B. M.; Won, Y. Y.; Ege, D. S.; *et al. Science* **1999**, *284*, 1143–1146, with permission from The American Association for the Advancement of Science.

Consequently, liposomes can encapsulate hydrophilic compounds in their aqueous cores and intercalate hydrophobic compounds in their lipid bilayers.

Liposomes vary widely in size, number of lamellae, surface charge, permeability, and bilayer rigidity, depending on the preparative technique, synthetic conditions, and types of lipids used. Liposome sizes range over three orders of magnitude, from tens of nanometers to tens of micrometers, and they can contain one, several, or many discrete bilayer membranes. These structural parameters affect the behavior of liposomes both *in vitro* and *in vivo*. Therefore, it is critical to carefully select the liposome constituents and preparative technique for the intended application. For example, conventional liposomes are rapidly cleared from the circulation by the phagocytic cells of the RES. Therefore, for *in vivo* applications, steps such as pegylation or steric stabilization must be taken to prolong circulation time.

Besides their application as contrast agents for molecular imaging, which will be highlighted in this section, liposomes have a wide variety of other uses. Since the lipid bilayer is the basic structural component of cell membranes, liposomes have been used extensively as a model system in basic research for studying the structure, properties, and functions of cell membranes. In addition, liposomes have been widely investigated for use in drug and gene delivery, cellular targeting, catalysis, food chemistry, cosmetics, energy conversion, and chemical separations. Liposome technology is a rapidly evolving field spanning both basic and applied science.

3.318.3.1.2. Synthesis

The most commonly used method to generate liposomes involves the hydration of dry lipid films. In general, this procedure consists of three steps: preparation of the lipid for hydration, hydration of the lipid with mechanical agitation, and liposome sizing to generate a homogeneous distribution of vesicles. First, the lipids must be dissolved in an organic solvent (typically chloroform or a chloroform–methanol mixture) to assure a homogeneous lipid mixture. Next, a thin lipid film is produced by evaporating the solvent with a stream of dry nitrogen or argon, or by rotary evaporation. Any residual organic solvent is removed by placing the film overnight in a vacuum pump evacuated chamber.

Second, hydration of the dry lipid film is accomplished by incubating an aqueous solution over the film and agitating the container. If the encapsulation of hydrophilic compounds in the liposomal core is desired, these compounds are simply included in the aqueous hydrating solution. During incubation, the temperature of the hydrating medium should be above the gel–liquid crystal transition temperature of the lipid. The products of hydration are large, multilamellar vesicles (LMV).

Finally, once a stable, hydrated LMV suspension has been produced, the liposomes can be reduced in size by a variety of techniques, including sonication or extrusion. Disruption of LMV suspensions using sonication typically produces small, unilamellar vesicles (SUV) with diameters in the range of 15–50 nm. Extrusion through filters of defined pore size typically yields large, unilamellar vesicles (LUV). The extrusion method yields liposomes with the most homogeneous size distribution, especially for larger (100–400 nm) diameters.

Several other synthetic approaches have also been employed in the construction of liposomes. In a similar procedure called the hydration/rehydration method, a lipid film is generated, dried under vacuum, and hydrated as before, to form a liposomal dispersion. This solution is then partially dehydrated a second time until the suspension becomes viscous. Then, an appropriate volume of water is reintroduced and the liposomes are allowed to equilibrate at a temperature above the phase transition point of the lipids.

Another synthetic variation using lipid films is the electroformation procedure. Again, the lipids are dissolved in a chloroform–methanol solvent and the resulting solution is spread onto glass coated with a conducting indium tin oxide (ITO) film. The film is dried under a vacuum for 1 h and then rehydrated while an AC electric field is applied and progressively increased, typically from 0 to 1.1 V, throughout the incubation.[226]

In the reverse-phase evaporation procedure, appropriate amounts of the lipid are dissolved in a chloroform–methanol mixture. Subsequently, isotonic buffer and additional methanol are added to yield a clear solution after brief sonication. The organic solvents and a small amount of water are then removed under nitrogen at a temperature above the phase transition temperature. Solvent removal proceeds until all foaming in the solution ceases.

Finally, liposomes can be prepared by simply injecting a lipid and ethanol solution directly into an aqueous solution. This ethanol injection method is a suitable technique to obtain the spontaneous formation of liposomes with small average diameter. Several parameters, including buffer composition and ionic strength, must be optimized in order to obtain the desired final formulation.

Once liposomes are formed, a variety of techniques, such as dynamic light scattering, electron microscopy, force microscopy, ultracentrifugation, viscometry, nuclear magnetic resonance (NMR) spectroscopy, and gel chromatography, are used for their characterization. These techniques report a number of different liposomal parameters such as size, shape, polydispersity, surface area, encapsulated volume, and stability. Analysis of these parameters is important in evaluating liposomes for subsequent use *in vivo*.

3.318.3.1.3. Applications

One of the most attractive attributes of liposomes is the functionality imparted by their amphiphilic structure. For example, one of the most promising applications of liposomes is drug delivery. Hydrophilic drugs can be loaded in the aqueous core and the hydrophobic domain serves as a natural carrier environment for hydrophobic drugs. The ideal liposomes for *in vivo* applications will encapsulate molecules with high efficiency, protect these molecules from degradation in plasma, and have a narrow size distribution, with dimensions allowing them to access the extravascular compartment. Furthermore, the ability to incorporate a wide range of lipids allows for enhanced liposome stability in circulation and a variety of surface modifications. The literature has many examples of liposomes with these features.

For instance, cationic lipids enhance the efficiency of gene delivery to cultured cells *in vitro*, in part because compared to the fate of free DNA, liposome-entrapped DNA is protected

to a varying extent from degradation or immediate dilution. Secondly, in order to prepare liposomes with prolonged circulation lifetimes *in vivo*, other specialized lipids (such as monosialoganglioside G_{M1} or PEG-modified phosphatidylethanolamine) have been investigated.[227] It has been proposed that these PEG-lipid conjugates provide 'steric stabilization' of the surface by virtue of the hydrophilic brush coat provided by the PEG polymer. The coat has been shown to inhibit serum protein binding to the liposomal surface, thereby stabilizing the liposomal membrane, limiting complement activation, and reducing reticuloendothelial system (RES) sequestration[228] (see **Chapter 4.424, Nanoparticles for Nucleic Acid Delivery**).

In addition to improved stability, the active targeting of liposome-encapsulated drugs or contrast agents to specific organs or pathologies further enhances the utility of liposomes for therapy and diagnosis. Targeted delivery of liposomes *in vivo* has been achieved by covalent and noncovalent coupling of site-directing ligands (such as monoclonal antibodies, proteins, vitamins, peptides, and glycolipids) to the surface of liposomes.[229] For example, PEG-shielded liposomes functionalized with cyclic RGD were used to target the antivascular agent combretastatin A4 to tumor vasculature.[230]

The significant majority of molecular imaging applications for liposomes involve the incorporation of contrast agents into the vesicles. When liposomes are used as carriers for imaging agents, they help overcome the rapid clearance, nonspecific cellular interaction, and toxicity of free contrast, all of which result in images of diminished contrast and resolution.[231] The following sections emphasize the development of novel liposome-based imaging contrast agents, organized by modality: MRI, optical imaging, computed tomography (CT), and ultrasound.

3.318.3.1.3.1. Optical contrast agents

As previously mentioned, liposomes have become a useful tool as drug delivery vehicles for the treatment of various diseases, including cancers. It is very important to track these nanocarriers at the cellular and subcellular level and to monitor drug distribution and concentration. Due to this need and the high sensitivity and good spatial resolution of optical methods, liposome-based optical contrast agents are being developed rapidly. Organic fluorophores are most commonly used in these preparations, since a large number of them are commercially available and possess interesting photophysical features. For *in vivo* optical imaging, NIR dyes are often chosen, since they offer deeper tissue penetration than dyes emitting in the visible region of the spectrum. For example, Mikhaylova *et al.* developed a nanocarrier based on liposome-mediated delivery of small interfering RNA (siRNA) to downregulate specific pathways in cancer growth and progression. To optically image the localization of these siRNA-containing liposomes *in vivo*, a DY647 moiety was covalently linked to the siRNA. Fluorescence was detected in tumor sections as early as 30 min following intravenous injection. Intracellular localization of DY647-labeled siRNA was observed in the tumor tissue even 24 h postinjection.[232]

Although organic fluorophores are versatile and easy to use, they present several limitations such as photodegradation and a high sensitivity to environmental factors. Consequently, there is growing interest in the development of new kinds of vesicle-based optical contrast agents by combining liposomes with QDs. As discussed previously, QDs are characterized by high photostability and their insensitivity to environmental factors. For example, Weng *et al.* developed multifunctional QD-conjugated immunoliposomes for imaging tumor cells *in vitro* and *in vivo*. Carboxyl-functionalized CdSe/ZnS core/shell QDs were chemically linked to amine-functionalized phospholipids present in the liposome bilayer. QD605 (λ_{max} ~605 nm) was used for *in vitro* analysis and pharmacokinetic studies, while QD800 (λ_{max} ~800 nm) was used for *in vivo* imaging experiments where deep tissue penetration is required. These studies indicated that QD-conjugated liposomes were able to provide (in a single nanoscale construct) tumor cell-targeting, imaging, and drug delivery functions.[233]

3.318.3.1.3.2. MR-contrast agents

Most MR agents in current clinical use are small, nontargeted, gadolinium (Gd)-based molecules that passively distribute into the intravascular and interstitial spaces to help generate clear anatomical images of the brain, spine, heart, and soft tissue. Recently, liposome-based MR-contrast agents have generated a particularly high degree of interest because of their ability to carry a large payload of these small Gd contrast agents, which can either be encapsulated within the liposome core or immobilized on the membrane surface. Such paramagnetic liposomes have been tested in many *in vivo* MRI studies in animal models.

The most common preparation involves encapsulating gadolinium-diethylenetriaminepentaacetate (Gd-DTPA) in different liposomal formulations.[234,235] For example, Freedman *et al.* developed a nanosized immunoliposome loaded with Gd-DTPA for detection of small metastases in lung cancer. Although current imaging methods can identify lung cancers, there are limits to the size of detectable nodules. Evidence also suggests that these current methods have difficultly in correctly distinguishing malignant nodules <7 mm from similarly appearing benign lesions. Thus, in an effort to improve specificity, Freedman *et al.* conjugated an antitransferrin receptor single-chain antibody fragment onto the surface of the liposomes loaded with Gd-DTPA. These paramagnetic liposomes can successfully enhance very small lung nodules (2–4 pixels, or even a single pixel in size).[234]

It should be noted that the ability of Gd-DTPA to provide effective T1 contrast relies on its ability to access and relax water protons. Thus, the relaxivity of liposome-encapsulated Gd-DTPA can decrease (or be 'quenched') by the low water permeability of the liposome membrane. This apparent disadvantage has been only partially overcome by the development of liposome MR probes with modified bilayers to improve water permeability, allowing bulk water molecules to exchange with water in the aqueous core and interact with the Gd-DTPA.[236] Therefore, the immobilization of chelated Gd on the surface of the bilayer membrane has become the preferred embodiment for liposome-based MR agents, since surface Gd has much better water access than that of core-encapsulated Gd. These liposomes can be made simply by doping the lipid bilayer with Gd-chelated phospholipids during preparation. For example, Mulder *et al.* incorporated Gd-DTPA-bis(sterylamide) into the bilayer of liposomes to generate paramagnetic MR agents. These liposomes do not leak upon incubation in

serum and also have a PEG coat and an anti-E-selectin antibody coupled to the distal end of the PEG-chains. MR studies revealed the specific association of the liposomal agent with stimulated human umbilical vein endothelial (HUVEC) cells. These data provide initial evidence that liposome-based MR-contrast agents can serve as useful diagnostic tools to investigate pathological processes *in vivo*.[237]

3.318.3.1.3.3. CT contrast agents

Recent reports have also explored the possibility of using liposomes as CT contrast agents. Heavily iodinated organic compounds are included primarily in the inner water compartment of liposomes or incorporated into the liposome membrane. These constructs have been shown to be effective CT contrast agents for enhancement of the liver in a number of different species, including rats, rabbits, pigs, and dogs. For example, Fouillet *et al.* developed vesicular agents using iomeprol-containing liposomes to detect small liver tumors in rats. After injection of these iomeprol-containing liposomes at a dose of 70 mg of (liposome-entrapped) iodine per kilogram of body weight, the normal liver parenchyma showed a contrast enhancement of more than 60% over precontrast intensity. As discussed earlier, liver tumors contain few or no Kupffer cells, and so are not enhanced, appearing as dark areas within the normal parenchyma. Both tumors and precancerous lesions as small as 3 mm in diameter could be distinguished using this noninvasive method.[238]

Seltzer *et al.* used interdigitation-fusion (IF) liposomes to carry the CT contrast agent iotrolan in their aqueous core. A high initial uptake (63–96% of the injected dose) was found in the liver and spleen. At 250 mg iodine per kilogram body weight, liver elimination proceeded with a half-life of 12.9 days. Thus, liposome-based CT contrast agents show promising attributes, including favorable biodistribution, clearance, and imaging properties.[239]

3.318.3.1.3.4. Ultrasound contrast agents

Ultrasound is a very attractive clinical imaging modality, since it is widely available, inexpensive, and easy to perform. Therefore, ultrasound contrast agents that exhibit an affinity for specific tissues or pathologies would have considerable clinical value. Since liposomes can be prepared by conjugating various targeting antibodies to the surface of the lipid bilayer, it thus becomes feasible to develop liposome-based ultrasound contrast agents. These vesicles can be used not only to identify and delineate diseased areas, but also release and activate a therapeutic agent *in situ*.

Ultrasound-activated liposomes are synthesized by incorporating air and the pharmaceutical of interest into liposomes of submicrometer size. These encapsulated air pockets are approximately tens to hundreds of nanometers in diameter, and thus can be considered nanobubbles. Exposure of these liposomes to suitable ultrasonic pulses disturbs the physical structure of the liposome bilayer and results in drug release. Because liposome activation by ultrasound can be controlled both spatially and temporally, these liposomes are potentially powerful tools for tissue or organ-specific drug delivery. Furthermore, the encapsulated air in the nanobubbles inherently produces ultrasound contrast, enabling the process of drug release and activation to be imaged in real time.

Recently, Tartis *et al.*[240] examined the cellular effects of ultrasound-mediated delivery of paclitaxel (a lipophilic chemotherapeutic agent) using acoustically activated lipospheres *in vitro*. In addition, Chen *et al.*[241] showed that acoustically activated liposomes can deliver DNA into cardiac muscle and pancreatic islet cells *in vivo*. Lastly, Kopechek *et al.*[242] compared ultrasound-mediated release of both hydrophilic and lipophilic agents from echogenic liposomes and found that water-soluble drugs were better candidates for the design and development of liposome-based ultrasound-controlled drug delivery systems (see **Chapter 4.422, pH-Responsive Polymers for the Intracellular Delivery of Biomolecular Drugs**).

3.318.3.1.4. Perspective and challenges

Liposomes demonstrate a lot of promise for advanced molecular imaging applications. However, to successfully bring these agents to fruition in the clinical environment, several challenges remain to be addressed. First, although effective on a small-scale basis, current synthetic methods lack the ability to produce commercial quantities of liposomal preparations with high entrapment efficiency of contrast agents. Also, even with the development of PEG-phospholipid-doped liposomes (sometimes referred to as stealth liposomes), further improvements are necessary to obtain the optimal chemical and physical stability that is important for biological application within the membrane-rich cellular environment.

3.318.3.2. Polymersomes

3.318.3.2.1. Structure and properties

Polymersomes represent a class of self-assembled nanovesicles that are composed of amphiphilic synthetic block copolymers. Compared to liposomes, polymersomes are far more robust, have lower membrane permeability, greater stability, and can be finely tuned through polymer selection to yield vesicles with diverse functionalities (**Figure 4(b)**). The improved stability largely stems from the higher molecular weight of the diblock copolymers and the presence of a thick hydrophobic domain, typically ~8–10 nm. This is significantly larger than the hydrophobic domain of most liposomes, which are typically ~3 nm in thickness.[243] Of course, with increasing membrane thickness, polymersome membrane fluidity and deformability generally decreases, bringing them closer to viral capsids than liposomes, in terms of mechanical properties (see **Chapter 1.129, Engineering the Biophysical Properties of Basement Membranes into Biomaterials: Fabrication and Effects on Cell Behavior**).

The vast majority of polymersomes are formed from diblock copolymers, with polyethylene oxide (PEO) as the hydrophilic block. This creates a relatively inert, brush-like outer shell, which imparts 'stealth-like' characteristics to the polymersomes and allows them to effectively avoid the RES.[244] Combined with their high stability, polymersomes have been found to exhibit long circulation times and low toxicity, qualities that are valued in molecular imaging applications.[244]

The amphiphoilic polymersomes are easily transformed into contrast agents through the encapsulation of hydrophilic contrast agents (e.g., Gd-DTPA, fluorescent dyes, etc.) within the aqueous core and/or hydrophobic fluorescent dyes within the hydrophobic domain. The exterior surface can also be readily functionalized with biologically active ligands for

targeted imaging applications.[245] Hence, polymersomes hold enormous potential as nanostructured biomaterials for future *in vivo* diagnostic imaging applications.

3.318.3.2.2. Synthesis

Polymersomes are synthesized using techniques similar to those used to form liposomes. Most often, the thin film hydration method is adopted, whereby diblock copolymers are first suspended in a volatile organic solvent and dried onto a glass or Teflon surface.[246] The film is then hydrated in an aqueous solution, sonicated, and extruded to the desired size. For imaging applications, most polymersomes are reduced to <150 nm in diameter to encourage long circulation times[247,248]; however, because of the high membrane stability, polymersomes that are tens of microns in diameter can also be synthesized.[246] It should be noted that polymersomes typically cannot be synthesized with diameters below 100 nm due to energetic constraints imparted by the thick hydrophobic domain.[247]

As an alternative to thin film hydration, polymersomes can also be formed by electroformation.[243] In this method, the diblock copolymer is dried on platinum wire electrodes and an alternating electric current is applied to form the vesicles. This method is generally preferred when large vesicles are desirable, since most of the polymersomes have diameters >10 μm. More recently, microfluidic techniques have also been used to produce polymersomes.[249] By varying the flow rates of several independently controlled fluid flows, the size, number of bilayers, and loading of the polymersomes can be controlled.

3.318.3.2.3. Biological interactions

The improved structural stability of the polymersome bilayer architecture has made them an attractive alternative to liposomes, which are often limited in clinical applications by their rapid dissolution in the circulation. Moreover, the high PEG (100%) content on the outer membrane of polymersomes has been shown to confer resistance to plasma protein deposition, resulting in longer circulation times.[245] Recent reports have indicated that polymersomes, ~125 nm in diameter, have a blood half-life of >15 h.[250] These findings provide evidence that the polymersomes can effectively evade the RES, which is generally desirable for targeted imaging studies.

It is generally agreed upon that the brush-like PEG layer on the outer shell also makes polymersomes highly biocompatible. To date, no obvious effects on cell proliferation have been noted, nor have any acute or chronic toxicities in vertebrates been reported. Of course, long-term toxicity data are lacking, as is information on the residence time and metabolism of the polymersome degradation products in living subjects. It is likely that any toxic side effects identified will depend largely on the composition of the diblock copolymers.

In anticipation of clinical translation, many studies have recently focused on the synthesis and evaluation of biodegradable polymersome formulations. Although PEG continues to be widely used as the hydrophilic block, a number of biodegradable polymer chains have been used within the hydrophobic block, including polylactic acid,[251] polycaprolactone,[252] poly(trimethylene carbonate),[253] and poly(2-vinylpyridine).[254] Alternatively, biodegradable linkages (e.g., disulfides[255] and poly(propylene sulfur)[256]) have also been inserted between the hydrophilic and hydrophobic blocks to promote the ultimate metabolism and clearance of polymersomes.

3.318.3.2.4. Applications

To date, polymersomes have been predominantly used as vehicles for drug delivery; however, several studies have demonstrated that they can also be transformed into very effective contrast agents. In the following sections, we will discuss how the unique properties of polymersomes have been exploited to create very promising optical and MR-contrast agents.

3.318.3.2.4.1. Optical contrast agents

Polymersomes have been transformed into optical contrast agents by simply introducing hydrophilic dyes into the aqueous core and by inserting hydrophobic dyes into the membrane. Membrane dyes have generated a particularly high degree of interest because the thick lamellar membrane allows for the insertion of dyes that would normally cause the dissolution of liposomes. For example, Ghoroghchian *et al.*[257] have successfully loaded multimeric porphyrin-based near infrared fluorophores (NIRFs), which are large in size and possess a rigid hydrophobic nature, into the hydrophobic bilayer of polybutadiene-polyethylene oxide (PBD-PEO) polymersomes. The porphyrin-based NIRFs exhibited photophysical properties within the polymersomal matrix that were akin to those observed when the dyes were in organic solvents. As a result, the total fluorescent signal emanating from the polymersomes was of sufficient intensity to penetrate through 1 cm of solid tumor.[257] Further, when these NIR-emissive polymersomes were injected into the tail-vein of mice, the biodistribution of the nanoparticles could be tracked noninvasively.

NIR-emissive polymersomes have also shown promise as contrast agents for cellular tracking. Christian *et al.*[258] have demonstrated the ability to label dendritic cells (DCs) *ex vivo* with polymersomes encapsulating porphyrin-based NIRFs; the TAT peptide was conjugated to these NIR-emissive polymersomes to facilitate efficient uptake of the polymer vesicles by DCs. It was found that DC surface-associated polymersomes shed over the first 24–48 h; but polymer vesicles that were fully internalized by the DCs remained stably incorporated for over 3 days.

3.318.3.2.4.2. MR-contrast agents

Recently, polymersomes have also been transformed into MR-contrast agents through the encapsulation of Gd-DTPA within the aqueous core. Although the entrapment of Gd within the lumen of polymersomes would normally result in a dramatic reduction in Gd relaxivity, this shortcoming was at least partly overcome through the introduction of pores within the bilayer. Two different approaches have thus far been taken to create porous polymersomes. In the first approach, polymersomes were produced from the aqueous assembly of diblock copolymers, PEO(1300)-b-PBD(2500) (PBdEO), and phospholipids, 1-palmitoyl-2-oleoyl-*sn*-glycero-3-phosphocholine (POPC) at an 85:15 molar ratio.[248] The PBdEO was cross-linked using a chemical initiator and the POPC was extracted with surfactant, generating a highly porous outer

membrane. The encapsulated Gd chelates were attached to dendrimers to prevent their leakage through the pores. It was estimated that, on average, nearly 44 000 Gd were encapsulated within each polymersome. As a result of the slower rotational correlation time of Gd-labeled dendrimers and the porous outer membrane, the paramagnetic porous polymersomes exhibited an R1 relaxivity of 7.2 mM^{-1} s^{-1} per Gd and 315 637 mM^{-1} s^{-1} per vesicle. This corresponds to a relaxivity that is amplified by a factor of $\sim 10^5$ compared with Gd-DTPA.

In the second approach, paramagnetic porous polymersomes were prepared using a synthetic method that did not require polymer cross-linking, thus reducing the number of required synthesis and purification steps and also likely improving biodegradability.[247] Specifically, the porous polymersomes were produced through the aqueous assembly of the polymers, polyethylene oxide-b-polybutadiene (PBdEO), and polyethylene oxide-b-polycaprolactone (PEOCL). Subsequent hydrolysis of the caprolactone (CL) block resulted in a highly permeable outer membrane. Again, to prevent the leakage of small Gd-chelate through the pores, Gd was conjugated to polyamidoamine (PAMAM) dendrimer via diethylenetriaminepentaacetic acid dianhydride (DTPA dianhydride) prior to encapsulation. These functional nanoparticles were found to exhibit a relaxivity similar to the cross-linked porous polymersomes described above. These polymersomes were also found to exhibit unique pharmacokinetics with a circulation half-life of >3.5 h and predominantly renal clearance, suggesting slow dissolution in circulation. This could provide an important advantage in regard to reducing toxicity compared with other long-circulating MR-contrast agents, which generally require metabolism of the contrast agent in the liver and exhibit prolonged retention in the body.

3.318.4. Polymeric Assemblies

3.318.4.1. Dendrimers

3.318.4.1.1. Structure and properties

Dendrimers are spheroid polymeric nanostructures that repeatedly branch outward from an inner multimeric core (Figure 5). Dendrimers are highly uniform with extremely low polydispersity and, in many cases, are monodisperse. Dendrimers are usually produced in an iterative sequence of reaction steps, in which every additional iteration leads to a higher generation material. Such a configuration results in an exponential increase in molecular weight for a geometric increase in volume.[259]

Lower generation dendrimers have highly asymmetric shapes and possess more open structures. As the chains are grown from the core, the dendrimers become densely packed, globular structures. When a critical branched state is reached, dendrimers cannot grow uniformly because of steric constraints.[260] For imaging applications, the most commonly used dendrimers are PAMAM dendrimers. These dendrimers are based on either an ethylenediamine core or ammonia core and possess amino groups on the surface, which provide attachment points for the conjugation of contrast agents.[261–264] Typical PAMAM dendrimers range in size from just over 1 nm to just over 10 nm, and the number of surface groups increases geometrically. For example, a generation 2 (G2) dendrimer has a diameter of 2.9 nm and 16 amine groups, while a G10 dendrimer has a diameter of about 13.5 nm and 4096 amine groups (Dendritech, Inc.).

Because of their molecular architecture, dendrimers show several significantly improved physical and chemical properties when compared to traditional linear polymers. For instance, dendrimer solutions have significantly lower viscosity than linear polymers. The presence of many chain-ends is responsible for high solubility and miscibility, and for high reactivity. Dendrimer solubility is strongly influenced by the nature of surface groups. Due to their globular shape and the presence of internal cavities, dendrimers can also encapsulate guest molecules in the macromolecule interior, a feature that has been exploited for a number of drug delivery applications.[265]

3.318.4.1.2. Synthesis

Dendrimers are generally synthesized using either divergent or convergent methods.[266,267] In the divergent methods, dendrimer branches are grown outward from a multimeric core through repetitive growth and activation steps. Specifically, each arm of the core molecule is reacted with a monomer that possesses one group capable of reacting with the core polymer and two groups that are blocked. Following the reaction between the core and the monomer, excess monomer can

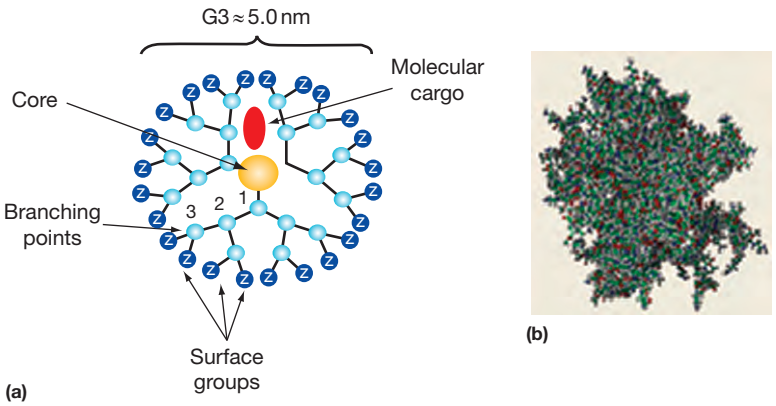

Figure 5 (a) Schematic 2D presentation of a G3 dendrimer containing three generations (branching points), as indicated by the numbers. (b) 3D presentation of G3 dendrimer as a space-filling structure. Copyright 2008 by Drug Delivery Solutions LLC.

be removed and the blocked groups can be activated. As a result, each functional group on the core is replaced by two new functional groups. This process can be repeated to build the dendrimer one generation at a time, until the desired size and/or number of functional groups is reached. PAMAM dendrimers are commonly synthesized using the divergent method, albeit with some slight modifications. Specifically, the ethylene diamine or ammonia core is first alkylated with methyl acrylate through Michael addition. Each amino group reacts with two methyl acrylate monomers. This step is followed by amidation of the resultant ester terminal group with excess ethylene diamine, creating a new dendrimer generation with twice the number of amines. Recently, the divergent synthetic method has been simplified by using two different monomers alternately during the growth process. This approach eliminates the need for an activation step and thus fewer synthetic and purification steps are required.[268] Of course, various dendrimer structures may be obtained by altering the initiator core, repeat units, and the surface groups; however, our discussion of dendrimers will be primarily limited to PAMAM dendrimers, since they have almost exclusively been used for molecular imaging applications.

In convergent methods, dendrimers are built from the outside in, that is, starting with the end groups and progressing inwards. Once dendron arms of sufficient size have been prepared, they are attached to the multimeric core molecule. Convergent methods are sometimes preferred because the number of simultaneous reactions is reduced, that is, fewer branching reactions are carried out in any given step. This results in more highly monodisperse samples and fewer side reactions.

3.318.4.1.3. Biological interactions

The cytotoxicity of dendrimers is largely governed by the size of the dendrimers and of the surface groups. Higher-generation dendrimers are generally found to promote more destructive interactions with the cell membrane, resulting in high cytotoxicity. This can perhaps be attributed to the higher charge density found on larger particles. For example, when cationic PAMAM dendrimers were incubated with V79 Chinese hamster lung fibroblasts (24 h), there was a size-dependent decrease in cell viability. The concentration producing 90% cell death was 1 mM for generation 3, 10 μM for generation 5, and 100 nM for generation 7.[269]

As would be expected, cytotoxicity has also been found to be dependent on the nature of the dendrimer surface.[270] For example, the cytotoxicity of the cationic dendrimers selected from a melamine-based dendrimer library including amine, guanidine, carboxylate, sulfonate, phosphonate, or PEGylated surfaces, showed that cationic dendrimers were much more cytotoxic than anionic or PEGylated dendrimers.[271] Similarly, quaternised PAMAM–OH derivatives showed a lower level of cytotoxicity than PAMAM–NH_2 because of shielding of the internal cationic charges by surface hydroxyl groups.[272] Therefore, despite the broad applicability of PAMAM dendrimers, it is generally necessary to modify the surface amino groups with neutral or anionic moieties to avoid cellular toxicity.

The biodistribution of intravenously administered dendrimers has been widely studied, particularly in relation to their development as imaging and therapeutic agents. In general, smaller generation dendrimers are subjected to rapid renal elimination, with blood half-lives of only a few minutes.[273] Those with charged (cationic or anionic) or hydrophobic surfaces are also rapidly cleared from the circulation, but tend to accumulate in the liver.[270] Therefore, it is generally desirable to neutralize the surface charge on PAMAM dendrimers to avoid accumulation in the liver. Dendrimers with a hydrophilic surface (e.g., –OH termini or pegylated dendrimers) exhibit much longer circulation times with blood half-lives that can reach many hours.[270]

To improve biocompatibility, some dendrimers have been designed to be biodegradable. Common approaches include using a cystamine core or the incorporation of monomer units that are chemical intermediates or products of metabolic pathways. Examples include peptide-based dendrimers formed from polylysine, dendrimers with PEO backbones, and polyester dendrimers incorporating monomers such as glycerol and lactic acid.[263,273,274]

3.318.4.1.4. Applications

The flexibility that dendrimers offer in terms of their size, shape, branching, length, and surface functionality have made them an attractive platform for drug delivery[275] and contrast agents. In the following section, we describe how dendrimers have been utilized as optical and MR-contrast agents in molecular imaging applications.

3.318.4.1.4.1. Optical contrast agents

Dendrimers are readily transformed into optical imaging agents through the attachment of NIR dyes to the terminal amino groups. Since the dendrimer itself simply provides a platform for attaching any organic (or inorganic) fluorophore, multiplexing experiments only require that each dendrimer be labeled with an optically distinct fluorophore. In one study, five-color optical lymphatic imaging was conducted using a multiple-excitation spectrally resolved fluorescence imaging technique.[276] Of course, fluorescently labeled dendrimers can also be targeted to cell surface biomarkers. Patri *et al.* functionalized generation 5 PAMAM dendrimers using fluorescein isothiocyanate (FITC) and J591 antibody, which is specific for the PSMA. This agent was used to monitor targeted prostate cancer therapy via confocal microscopy. Confocal microscopy studies also confirmed the binding and internalization of the antibody – dendrimer conjugate, while the dendrimer alone did not show significant binding or uptake into the cells.[277] It should be noted that while dendrimers can be used as fluorescent imaging agents, they do suffer from several inherent shortcomings. Most notably, only a small fraction of surface amines can be labeled with organic fluorophores before self-quenching becomes evident. Further, even though larger dendrimers can have thousands of amines, increasing dendrimer size does not generally allow for a corresponding increase in the number of fluorophores that can be conjugated before self-quenching is observed.

3.318.4.1.4.2. MR-contrast agents

The defined structure and large number of available surface amino groups of dendrimers has led to their use as platforms for the conjugation of large numbers of chelating agents for creating macromolecular MR-contrast agents. The earliest

dendrimer-based MRI contrast agents consisted of PAMAM dendrimers covalently labeled with Gd-DTPA.[261,278] Because self-quenching effects are not relevant for an MR-contrast agent, the number of Gd-DTPA that can be attached to a single dendrimer is only limited by steric effects. Gd-DTPA dendrimers have been used to enhance conventional MR images and 3D time of flight MR angiograms. It has been found that Gd-DTPA dendrimers with molecular weights of 8508 and 139 000 g mol^{-1} have enhancement half-lives of 40 and 200 min, respectively, much longer than the 24 min measured for Gd-DTPA alone.[279]

Langereis *et al.*[280] investigated different generations of Gd(III)DTPA-terminated poly(propylene imine) dendrimers (G0–G5) in terms of (1) longitudinal and transverse relaxivities in mouse blood plasma, (2) concentration detection limits *in vitro*, and (3) contrast-enhanced MR imaging in mice. They found that G0, G1, G3, and G5 dendrimers were all well suited for nontissue-specific MRI of submillimeter-sized blood vessels and evaluating tumor microcirculatory characteristics in mice. However, relaxivity, and thus sensitivity, did increase nonlinearly with molecular weight. Consequently, higher molecular weight dendrimers ($\geq$G5) are typically preferred for targeted molecular imaging applications.[280]

Recently, it was found that a significant improvement in MR sensitivity could be achieved through the formation of Gd-labeled dendrimer nanoclusters (DNCs).[281] DNCs are composed of individual Gd-DTPA-labeled PAMAM dendrimers that have been cross-linked to form larger nanoparticulate carriers. The improved MR sensitivity stems from the extremely high Gd payload per particle that was achieved. It was estimated that each DNC particle (~150 nm in diameter) was conjugated with ~300 000 Gd-DTPA and exhibited an R1 relaxivity of 3.6×10^6 mM^{-1} s^{-1} per particle. Further, it was shown that the Gd-labeled DNCs could readily be functionalized with targeting ligands (e.g., folic acid) and used for *in vivo* molecular imaging. Although this technology was validated on a tumor model, presumably by conjugating appropriate targeting ligands, the ultrasensitive MR detection of various diseases may be possible.

Before any new Gd-based contrast can be extended to the clinic, their toxicological profile must be carefully evaluated, especially with the increasing concerns over Gd-mediated toxicity (i.e., nephrogenic systemic fibrosis).[282] This is particularly relevant for Gd-labeled nanoparticles that are too large to be cleared via renal filtration, since they generally exhibit longer circulation and residence times.

3.318.4.1.4.3. CT contrast agents

Although, dendrimers have predominantly been used as nanoplatforms for MR and optical contrast agents, there have also been a few reports in the literature where dendrimers were used to support CT contrast agents. For example, Schumann and coworkers[283] synthesized water-soluble tin-based metallodendrimers as CT contrast agents and evaluated their toxicity in mice. Recently, another water-soluble iodinated dendritic nanoparticle, G-4-(DMAA-IPA)37, was developed by Yordanov and coworkers[284] and used as CT contrast agents. These particles consisted of a generation 4 Starburst PAMAM dendrimer core and 3-*N*-[(*N*′,*N*′-dimethylaminoacetyl)amino]-α-ethyl-2,4,6-triiodobenzenepropanoic acid (DMAA-IPA) molecules covalently attached to the surface. They possessed high iodine content (33.06%) while retaining their overall charge and water solubility. More recently, Fu *et al.* reported another type of dendritic iodinated contrast agent that has a PEG core with two dendritic polylysine dendrons and triiodobenzene derivatives at both PEG termini.[285] These dendrimers demonstrated several favorable characteristics, including prolonged intravascular enhancement in an animal model, adjustable and large apparent molecular weights, near monodispersity in size, high X-ray attenuation, high water solubility and hydrophilicity, low osmolality, and good chemical stability. It is expected that this new class of iodinated dendrimers will be applied in angiography and, more importantly, in the quantitative microvascular characterization of a wide variety of diseases and abnormalities including cancer, ischemic injury, inflammation, and altered states of angiogenesis.

3.318.5. Future Outlook

Molecular imaging gives scientists the ability to detect, visualize, and quantify cellular and molecular events *in situ*, opening up a myriad of possibilities to advance our understanding of biological systems. Consequently, molecular imaging, despite its relatively short history, has already made significant contributions to basic scientific research as well as academic and clinical medicine. As interest in the field continues to increase and more investigators from diverse disciplines join the effort, there is little doubt that molecular imaging will continue to progress exponentially and shape the future of biomedicine. Furthermore, since molecular imaging applications rely on the construction of specialized molecular probes, it should be evident that materials science plays a particularly invaluable role in the development and progress of molecular imaging. Materials scientists should, therefore, be conscious of this added impact of their work and consider molecular imaging applications when formulating potential research projects.

References

1. Mankoff, D. A. *J. Nucl. Med.* **2007**, *48*, 18N–21N.
2. Froidevaux, S.; Eberle, A. N. *Biopolymers* **2002**, *66*, 161–183.
3. Efros, A. L.; Efros, A. L. *Sov. Phys. Semiconduct.* **1982**, *16*, 772–775.
4. Ekimov, A. I.; Onushchenko, A. A. *Sov. Phys. Semiconduct.* **1982**, *16*, 775–778.
5. Bailey, R. E.; Nie, S. M. *J. Am. Chem. Soc.* **2003**, *125*, 7100–7106.
6. Hines, M. A.; Scholes, G. D. *Adv. Mater.* **2003**, *15*, 1844–1849.
7. Kim, S.; Fisher, B.; Eisler, H. J.; Bawendi, M. *J. Am. Chem. Soc.* **2003**, *125*, 11466–11467.
8. Pietryga, J. M.; Schaller, R. D.; Werder, D.; Stewart, M. H.; Klimov, V. I.; Hollingsworth, J. A. *J. Am. Chem. Soc.* **2004**, *126*, 11752–11753.
9. Qu, L. H.; Peng, X. G. *J. Am. Chem. Soc.* **2002**, *124*, 2049–2055.
10. Zhong, X. H.; Feng, Y. Y.; Knoll, W.; Han, M. Y. *J. Am. Chem. Soc.* **2003**, *125*, 13559–13563.
11. Alivisatos, A. P. *J. Phys. Chem.* **1996**, *100*, 13226–13239.
12. Chan, W. C. W.; Nie, S. M. *Science* **1998**, *281*, 2016–2018.
13. Alivisatos, A. P. *Science* **1996**, *271*, 933–937.
14. Bhattacharya, P.; Ghosh, S.; Stiff-Roberts, A. D. *Annu. Rev. Mater. Res.* **2004**, *34*, 1–40.
15. Crouch, D.; Norager, S.; O'brien, P.; Park, J. H.; Pickett, N. *Philos. Trans. R. Soc. Lond. A Math. Phys. Eng. Sci.* **2003**, *361*, 297–310.
16. Smith, A. M.; Nie, S. M. *Angew. Chem. Int. Ed.* **2008**, *47*, 9916–9921.
17. Murray, C. B.; Norris, D. J.; Bawendi, M. G. *J. Am. Chem. Soc.* **1993**, *115*, 8706–8715.

18. Dabbousi, B. O.; Rodriguezviejo, J.; Mikulec, F. V.; *et al*. *J. Phys. Chem. B* **1997**, *101*, 9463–9475.
19. Hines, M. A.; Guyot-Sionnest, P. *J. Phys. Chem.* **1996**, *100*, 468–471.
20. Peng, X. G.; Schlamp, M. C.; Kadavanich, A. V.; Alivisatos, A. P. *J. Am. Chem. Soc.* **1997**, *119*, 7019–7029.
21. Talapin, D. V.; Mekis, I.; Gotzinger, S.; Kornowski, A.; Benson, O.; Weller, H. *J. Phys. Chem. B* **2004**, *108*, 18826–18831.
22. Xie, R. G.; Kolb, U.; Li, J. X.; Basche, T.; Mews, A. *J. Am. Chem. Soc.* **2005**, *127*, 7480–7488.
23. Guo, W. H.; Li, J. J.; Wang, Y. A.; Peng, X. G. *J. Am. Chem. Soc.* **2003**, *125*, 3901–3909.
24. Kim, S.; Bawendi, M. G. *J. Am. Chem. Soc.* **2003**, *125*, 14652–14653.
25. Pinaud, F.; King, D.; Moore, H. P.; Weiss, S. *J. Am. Chem. Soc.* **2004**, *126*, 6115–6123.
26. Gao, X. H.; Cui, Y. Y.; Levenson, R. M.; Chung, L. W. K.; Nie, S. M. *Nat. Biotechnol.* **2004**, *22*, 969–976.
27. Wu, X. Y.; Liu, H. J.; Liu, J. Q.; *et al*. *Nat. Biotechnol.* **2003**, *21*, 452.
28. Hauck, T. S.; Anderson, R. E.; Fischer, H. C.; Newbigging, S.; Chan, W. C. *Small* **2010**, *6*, 138–144.
29. Bruchez, M.; Moronne, M.; Gin, P.; Weiss, S.; Alivisatos, A. P. *Science* **1998**, *281*, 2013–2016.
30. Gao, X. H.; Chan, W. C. W.; Nie, S. M. *J. Biomed. Opt.* **2002**, *7*, 532–537.
31. Howarth, M.; Takao, K.; Hayashi, Y.; Ting, A. Y. *Proc. Natl. Acad. Sci. USA* **2005**, *102*, 7583–7588.
32. Schumacher, W.; Nagy, A.; Waldman, W. J.; Dutta, P. K. *J. Phys. Chem. C* **2009**, *113*, 12132–12139.
33. Jaiswal, J. K.; Mattoussi, H.; Mauro, J. M.; Simon, S. M. *Nat. Biotechnol.* **2003**, *21*, 47–51.
34. Dubertret, B.; Skourides, P.; Norris, D. J.; Noireaux, V.; Brivanlou, A. H.; Libchaber, A. *Science* **2002**, *298*, 1759–1762.
35. Choi, H. S.; Liu, W.; Misra, P.; *et al*. *Nat. Biotechnol.* **2007**, *25*, 1165–1170.
36. Ballou, B.; Lagerholm, B. C.; Ernst, L. A.; Bruchez, M. P.; Waggoner, A. S. *Bioconjug. Chem.* **2004**, *15*, 79–86.
37. Fischer, H. C.; Liu, L. C.; Pang, K. S.; Chan, W. C. W. *Adv. Funct. Mater.* **2006**, *16*, 1299–1305.
38. Soltesz, E. G.; Kim, S.; Laurence, R. G.; *et al*. *Ann. Thorac. Surg.* **2005**, *79*, 269–277.
39. Derfus, A. M.; Chan, W. C. W.; Bhatia, S. N. *Nano Lett.* **2004**, *4*, 11–18.
40. Kirchner, C.; Liedl, T.; Kudera, S.; *et al*. *Nano Lett.* **2005**, *5*, 331–338.
41. Maysinger, D.; Behrendt, M.; Lalancette-Herbert, M.; Kriz, J. *Nano Lett.* **2007**, *7*, 2513–2520.
42. Mancini, M. C.; Kairdolf, B. A.; Smith, A. M.; Nie, S. M. *J. Am. Chem. Soc.* **2008**, *130*, 10836–10837.
43. Shiohara, A.; Hoshino, A.; Hanaki, K.; Suzuki, K.; Yamamoto, K. *Microbiol. Immunol.* **2004**, *48*, 669–675.
44. Zhang, Y. B.; Chen, W.; Zhang, J.; Liu, J.; Chen, G. P.; Pope, C. *J. Nanosci. Nanotechnol.* **2007**, *7*, 497–503.
45. Han, M.; Gao, X.; Su, J. Z.; Nie, S. *Nat. Biotechnol.* **2001**, *19*, 631–635.
46. Orcutt, K. M.; Ren, S. S.; Gundersen, K. *Sensors* **2009**, *9*, 7540–7549.
47. Alivisatos, P. *Nat. Biotechnol.* **2004**, *22*, 47–52.
48. Pathak, S.; Thompson, M. E.; Arnheim, N.; Choi, S. K. *Abstr. Pap. Am. Chem. Soc.* **2001**, *221*, U332.
49. Michalet, X.; Pinaud, F.; Lacoste, T. D.; *et al*. *Single Mol.* **2001**, *2*, 261–276.
50. Lidke, D. S.; Nagy, P.; Heintzmann, R.; *et al*. *Nat. Biotechnol.* **2004**, *22*, 198–203.
51. Dahan, M.; Levi, S.; Luccardini, C.; *et al*. *Science* **2003**, *302*, 442–445.
52. Echarte, M. M.; Bruno, L.; Arndt-Jovin, D. J.; Jovin, T. M.; Pietrasanta, L. I. *FEBS Lett.* **2007**, *581*, 2905–2913.
53. Chen, H. F.; Titushkin, I.; Stroscio, M.; Cho, M. *Biophys. J.* **2007**, *92*, 1399–1408.
54. Young, S. H.; Rozengurt, E. *Am. J. Physiol. Cell Physiol.* **2006**, *290*, C728–C732.
55. Le Gac, S.; Vermes, I.; Van Den Berg, A. *Nano Lett.* **2006**, *6*, 1863–1869.
56. Larson, D. R.; Zipfel, W. R.; Williams, R. M.; *et al*. *Science* **2003**, *300*, 1434–1436.
57. Smith, J. D.; Fisher, G. W.; Waggoner, A. S.; Campbell, P. G. *Microvasc. Res.* **2007**, *73*, 75–83.
58. Lim, Y. T.; Kim, S.; Nakayama, A.; Stott, N. E.; Bawendi, M. G.; Frangioni, J. V. *Mol. Imaging* **2003**, *2*, 50–64.
59. Jayagopal, A.; Russ, P. K.; Haselton, F. R. *Bioconjug. Chem.* **2007**, *18*, 1424–1433.
60. Kim, S.; Lim, Y. T.; Soltesz, E. G.; *et al*. *Nat. Biotechnol.* **2004**, *22*, 93–97.
61. Parungo, C. P.; Ohnishi, S.; Kim, S. W.; *et al*. *J. Thorac. Cardiovasc. Surg.* **2005**, *129*, 844–850.
62. Ballou, B.; Ernst, L. A.; Andreko, S.; *et al*. *Bioconjug. Chem.* **2007**, *18*, 389–396.
63. Kobayashi, H.; Hama, Y.; Koyama, Y.; *et al*. *Nano Lett.* **2007**, *7*, 1711–1716.
64. Rosen, A. B.; Kelly, D. J.; Schuldt, A. J. T.; *et al*. *Stem Cells* **2007**, *25*, 2128–2138.
65. Maeda, H.; Wu, J.; Sawa, T.; Matsumura, Y.; Hori, K. *J. Control. Release* **2000**, *65*, 271–284.
66. Tada, H.; Higuchi, H.; Wanatabe, T. M.; Ohuchi, N. *Cancer Res.* **2007**, *67*, 1138–1144.
67. Qian, J.; Yong, K. T.; Roy, I.; *et al*. *J. Phys. Chem. B* **2007**, *111*, 6969–6972.
68. Bharali, D. J.; Lucey, D. W.; Jayakumar, H.; Pudavar, H. E.; Prasad, P. N. *J. Am. Chem. Soc.* **2005**, *127*, 11364–11371.
69. Cai, W. B.; Shin, D. W.; Chen, K.; *et al*. *Nano Lett.* **2006**, *6*, 669–676.
70. Hanaki, K.; Momo, A.; Oku, T.; *et al*. *Biochem. Biophys. Res. Commun.* **2003**, *302*, 496–501.
71. Duan, H. W.; Nie, S. M. *J. Am. Chem. Soc.* **2007**, *129*, 3333–3338.
72. Voura, E. B.; Jaiswal, J. K.; Mattoussi, H.; Simon, S. M. *Nat. Med.* **2004**, *10*, 993–998.
73. Courty, S.; Luccardini, C.; Bellaiche, Y.; Cappello, G.; Dahan, M. *Nano Lett.* **2006**, *6*, 1491–1495.
74. Smith, A. M.; Nie, S. *J. Am. Chem. Soc.* **2008**, *130*, 11278–11279.
75. Kairdolf, B. A.; Mancini, M. C.; Smith, A. M.; Nie, S. M. *Anal. Chem.* **2008**, *80*, 3029–3034.
76. Xia, Z. Y.; Rao, J. H. *Curr. Opin. Biotechnol.* **2009**, *20*, 37–44.
77. Efros, A. L.; Rosen, M. *Phys. Rev. Lett.* **1997**, *78*, 1110–1113.
78. Frantsuzov, P.; Kuno, M.; Janko, B.; Marcus, R. A. *Nat. Phys.* **2008**, *4*, 519–522.
79. Chen, Y.; Vela, J.; Htoon, H.; *et al*. *J. Am. Chem. Soc.* **2008**, *130*, 5026–5027.
80. Mahler, B.; Spinicelli, P.; Buil, S.; Quelin, X.; Hermier, J. P.; Dubertret, B. *Nat. Mater.* **2008**, *7*, 659–664.
81. Fomenko, V.; Nesbitt, D. J. *Nano Lett.* **2008**, *8*, 287–293.
82. Hohng, S.; Ha, T. *J. Am. Chem. Soc.* **2004**, *126*, 1324–1325.
83. Wang, X. Y.; Ren, X. F.; Kahen, K.; *et al*. *Nature* **2009**, *459*, 686–689.
84. Huang, C.; Chiu, P.; Wang, Y.; Meen, T.; Yang, C. *Nanotechnology* **2007**, *18*, 395602.
85. Faulk, W. P.; Taylor, G. M. *Immunochemistry* **1971**, *8*, 1081–1083.
86. Boyer, D.; Tamarat, P.; Maali, A.; Lounis, B.; Orrit, M. *Science* **2002**, *297*, 1160–1163.
87. Zhang, Q.; Iwakuma, N.; Sharma, P.; *et al*. *Nanotechnology* **2009**, *20*, 395102.
88. Xu, C. J.; Tung, G. A.; Sun, S. H. *Chem. Mater.* **2008**, *20*, 4167–4169.
89. Sperling, R. A.; Pellegrino, T.; Li, J. K.; Chang, W. H.; Parak, W. J. *Adv. Funct. Mater.* **2006**, *16*, 943–948.
90. Zanchet, D.; Micheel, C. M.; Parak, W. J.; Gerion, D.; Alivisatos, A. P. *Nano Lett.* **2001**, *1*, 32–35.
91. Martin, B. R.; Dermody, D. J.; Reiss, B. D.; *et al*. *Adv. Mater.* **1999**, *11*, 1021–1025.
92. Schonenberger, C.; Vanderzande, B. M. I.; Fokkink, L. G. J.; *et al*. *J. Phys. Chem. B* **1997**, *101*, 5497–5505.
93. Govindaraj, A.; Satishkumar, B. C.; Nath, M.; Rao, C. N. R. *Chem. Mater.* **2000**, *12*, 202–205.
94. Pileni, M. P.; Gulik-Krzywicki, T.; Tanori, J.; Filankembo, A.; Dedieu, J. C. *Langmuir* **1998**, *14*, 7359–7363.
95. Pileni, M. P.; Ninham, B. W.; Gulik-Krzywicki, T.; Tanori, J.; Lisiecki, I.; Filankembo, A. *Adv. Mater.* **1999**, *11*, 1358–1362.
96. Kalele, S.; Gosavi, S. W.; Urban, J.; Kulkarni, S. K. *Curr. Sci.* **2006**, *91*, 1038–1052.
97. Pellegrino, T.; Kudera, S.; Liedl, T.; Javier, A. M.; Manna, L.; Parak, W. J. *Small* **2005**, *1*, 48–63.
98. Liu, L.; Zheng, H. Z.; Zhang, Z. J.; Huang, Y. M.; Chen, S. M.; Hu, Y. F. *Spectrochim. Acta A Mol. Biomol. Spectrosc.* **2008**, *69*, 701–705.
99. Levy, R.; Wang, Z. X.; Duchesne, L.; *et al*. *Chembiochem* **2006**, *7*, 592–594.
100. Murphy, C. J.; Gole, A. M.; Stone, J. W.; *et al*. *Acc. Chem. Res.* **2008**, *41*, 1721–1730.
101. De Jong, W. H.; Hagens, W. I.; Krystek, P.; Burger, M. C.; Sips, A. J. A. M.; Geertsma, R. E. *Biomaterials* **2008**, *29*, 1912–1919.
102. Sonavane, G.; Tomoda, K.; Makino, K. *Colloids Surf. B Biointerfaces* **2008**, *66*, 274–280.
103. Graham, G. G.; Whitehouse, M. W.; Bushell, G. R. *Inflammopharmacology* **2008**, *16*, 126–132.
104. Williams, M. L. *Inflammopharmacology* **2008**, *16*, 110–111.
105. Sereemaspun, A.; Rojanathanes, R.; Wiwanitkit, V. *Ren. Fail.* **2008**, *30*, 323–325.
106. Sopjani, M.; Foller, M.; Lang, F. *Toxicology* **2008**, *244*, 271–279.
107. Didychuk, C. L.; Ephrat, P.; Chamson-Reig, A.; Jacques, S. L.; Carson, J. J. L. *Nanotechnology* **2009**, *20*, 195102.
108. Huang, X.; Qian, W.; El-Sayed, I. H.; El-Sayed, M. A. *Lasers Surg. Med.* **2007**, *39*, 747–753.

109. Huang, X. H.; El-Sayed, I. H.; Qian, W.; El-Sayed, M. A. *J. Am. Chem. Soc.* **2006**, *128*, 2115–2120.
110. Wang, B.; Yantsen, E.; Larson, T.; *et al*. *Nano Lett.* **2009**, *9*, 2212–2217.
111. Qian, X. M.; Peng, X. H.; Ansari, D. O.; *et al*. *Nat. Biotechnol.* **2008**, *26*, 83–90.
112. Hainfeld, J. F.; Slatkin, D. N.; Focella, T. M.; Smilowitz, H. M. *Br. J. Radiol.* **2006**, *79*, 248–253.
113. Gilchrist, R. K.; Medal, R.; Shorey, W. D.; Hanselman, R. C.; Parrott, J. C.; Taylor, C. B. *Ann. Surg.* **1957**, *146*, 596–606.
114. Belin, T.; Guigue-Millot, N.; Caillot, T.; Aymes, D.; Niepce, J. C. *J. Solid State Chem.* **2002**, *163*, 459–465.
115. Cornell, R. M.; Schertmann, U. *The Iron Oxides: Structure, Properties, Reactions, Occurrence and Uses*; Weinheim: VCH, 1996.
116. Tebble, R. S.; Craik, D. J. *Magnetic Materials*; Wiley-Interscience: London, 1969.
117. Elliot, S. R. *The Physics and Chemistry of Solids*; Wiley: New York, 1998.
118. Sorensen, C. M. *Nanoscale Materials in Chemistry*; Wiley: New York, 2001.
119. Rosensweig, R. E. *Ferrohydrodynamics*; Cambridge University Press: Cambridge, 1985.
120. Reimer, P.; Landwehr, P. *Eur. Radiol.* **1998**, *8*, 858–872.
121. Saleh, A.; Schroeter, M.; Jonkmanns, C.; Hartung, H. P.; Modder, U.; Jander, S. *Brain* **2004**, *127*, 1670–1677.
122. Josephson, L.; Tung, C. H.; Moore, A.; Weissleder, R. *Bioconjug. Chem.* **1999**, *10*, 186–191.
123. Jun, Y. W.; Lee, J. H.; Cheon, J. *Angew. Chem. Int. Ed. Engl.* **2008**, *47*, 5122–5135.
124. Morawski, A. M.; Winter, P. M.; Crowder, K. C.; *et al*. *Magn. Reson. Med.* **2004**, *51*, 480–486.
125. Moore, A.; Marecos, E.; Bogdanov, A., Jr.; Weissleder, R. *Radiology* **2000**, *214*, 568–574.
126. Mornet, S.; Vasseur, S.; Grasset, F.; Duguet, E. *J. Mater. Chem.* **2004**, *14*, 2161–2175.
127. Groman, E. V.; Paul, G.; Frigo, T. B.; Bengele, H. H.; Lewis, J. M. Heat Stable Colloidal Iron Oxides Coated with Reduced Carbohydrates and Carbohydrate Derivatives. U.S. Patent 6599498, 2003.
128. Hogemann, D.; Josephson, L.; Weissleder, R.; Basilion, J. P. *Bioconjug. Chem.* **2000**, *11*, 941–946.
129. Palmacci, S.; Josephson, L. Synthesis of Polysaccharide Covered Superparamagnetic Oxide Colloids. U.S. Patent 5262176, 1993.
130. Massart, R.; Dubois, E.; Cabuil, V.; Hasmonay, E. *J. Magn. Magn. Mater.* **1995**, *149*, 1–5.
131. Hinds, K. A.; Hill, J. M.; Shapiro, E. M.; *et al*. *Blood* **2003**, *102*, 867–872.
132. Shapiro, E. M.; Skrtic, S.; Sharer, K.; Hill, J. M.; Dunbar, C. E.; Koretsky, A. P. *Proc. Natl. Acad. Sci. USA* **2004**, *101*, 10901–10906.
133. Kemshead, J. T.; Ugelstad, J. *Mol. Cell. Biochem.* **1985**, *67*, 11–18.
134. Fabry, B.; Maksym, G. N.; Butler, J. P.; Glogauer, M.; Navajas, D.; Fredberg, J. J. *Phys. Rev. Lett.* **2001**, *87*, 148102.
135. Wang, N.; Butler, J. P.; Ingber, D. E. *Science* **1993**, *260*, 1124–1127.
136. Hahn, P. F.; Stark, D. D.; Lewis, J. M.; *et al*. *Radiology* **1990**, *175*, 695–700.
137. Wang, Y. X. J.; Hussain, S. M.; Krestin, G. P. *Eur. Radiol.* **2001**, *11*, 2319–2331.
138. Weissleder, R.; Elizondo, G.; Wittenberg, J.; Rabito, C. A.; Bengele, H. H.; Josephson, L. *Radiology* **1990**, *175*, 489–493.
139. Edelman, R. R. *Radiology* **2004**, *232*, 653–668.
140. Weissleder, R.; Lee, A. S.; Khaw, B. A.; Shen, T.; Brady, T. J. *Radiology* **1992**, *182*, 381–385.
141. Massart, R. *IEEE Trans. Magn.* **1981**, *17*, 1247–1248.
142. Massart, R. Magnetic Fluids and Process for Obtaining Them. U.S. Patent 4329241, 1982.
143. Molday, R. S. Magnetic Iron–Dextran Microspheres. U.S. Patent 4452773, 1984.
144. Bee, A.; Massart, R.; Neveu, S. *J. Magn. Magn. Mater.* **1995**, *149*, 6–9.
145. Petri-Fink, A.; Chastellain, M.; Juillerat-Jeanneret, L.; Ferrari, A.; Hofmann, H. *Biomaterials* **2005**, *26*, 2685–2694.
146. Molday, R. S.; Mackenzie, D. *J. Immunol. Methods* **1982**, *52*, 353–367.
147. Shen, T.; Weissleder, R.; Papisov, M.; Bogdanov, A., Jr.; Brady, T. J. *Magn. Reson. Med.* **1993**, *29*, 599–604.
148. Pileni, M. P. *J. Phys. Chem.* **1993**, *97*, 6961–6973.
149. Laconte, L. E.; Nitin, N.; Bao, G. *Mater. Today* **2005**, *8*, 32–38.
150. Nitin, N.; Laconte, L. E.; Zurkiya, O.; Hu, X.; Bao, G. *J. Biol. Inorg. Chem.* **2004**, *9*, 706–712.
151. Hochepied, J. F.; Pileni, M. P. *J. Appl. Phys.* **2000**, *87*, 2472–2478.
152. Igartua, M.; Saulnier, P.; Heurtault, B.; *et al*. *Int. J. Pharm.* **2002**, *233*, 149–157.
153. Deng, Y.; Wang, L.; Yang, W.; Fu, S.; Elaissari, A. *J. Magn. Magn. Mater.* **2003**, *257*, 69–78.
154. Pillai, V.; Kumar, P.; Hou, M. J.; Ayyub, P.; Shah, D. O. *Adv. Colloid Interface Sci.* **1995**, *55*, 241–269.
155. Seip, C. T.; Carpenter, E. E.; O'connor, C. J.; John, V. T.; Li, S. C. *IEEE Trans. Magn.* **1998**, *34*, 1111–1113.
156. Pileni, M. P. *Nat. Mater.* **2003**, *2*, 145–150.
157. Ayyub, P.; Multani, M.; Barma, M.; Palkar, V. R.; Vijayaraghavan, R. *J. Phys. C Solid State Phys.* **1988**, *21*, 2229–2245.
158. Suslick, K. S.; Fang, M. M.; Hyeon, T. *J. Am. Chem. Soc.* **1996**, *118*, 11960–11961.
159. Decher, G. *Science* **1997**, *277*, 1232–1237.
160. Carreno, T. G.; Mifsud, A.; Serna, C. J.; Palacios, J. M. *Mater. Chem. Phys.* **1991**, *27*, 287–296.
161. Veintemillas-Verdaguer, S.; Morales, M. P.; Serna, C. J. *Appl. Organomet. Chem.* **2001**, *15*, 365–372.
162. Morales, M. P.; Veintemillas-Verdaguer, S.; Montero, M. I.; Serna, C. J. *Chem. Mater.* **1999**, *11*, 3058.
163. Rockenberger, J.; Scher, E. C.; Alivisatos, A. P. *J. Am. Chem. Soc.* **1999**, *121*, 11595–11596.
164. Fletcher, F.; London, E. *Br. Med. J.* **1954**, *1*, 984.
165. London, E. *J. Pharm. Sci.* **2004**, *93*, 1838–1846.
166. Gupta, A. *Nephrol. Dial. Transplant.* **2000**, *15*, 1482–1484.
167. Gupta, A. K.; Wells, S. *IEEE Trans. Nanobioscience* **2004**, *3*, 66–73.
168. Passirani, C.; Barratt, G.; Devissaguet, J. P.; Labarre, D. *Pharm. Res.* **1998**, *15*, 1046–1050.
169. Gupta, A. K.; Curtis, A. S. *J. Mater. Sci. Mater. Med.* **2004**, *15*, 493–496.
170. Lewin, M.; Carlesso, N.; Tung, C. H.; *et al*. *Nat. Biotechnol.* **2000**, *18*, 410–414.
171. Matuszewski, L.; Persigehl, T.; Wall, A.; *et al*. *Radiology* **2005**, *235*, 155–161.
172. Raynal, I.; Prigent, P.; Peyramaure, S.; Najid, A.; Rebuzzi, C.; Corot, C. *Invest. Radiol.* **2004**, *39*, 56–63.
173. Weissleder, R.; Bogdanov, A.; Neuwelt, E. A.; Papisov, M. *Adv. Drug Deliv. Rev.* **1995**, *16*, 321–334.
174. Anzai, Y.; Piccoli, C. W.; Outwater, E. K.; *et al*. *Radiology* **2003**, *228*, 777–788.
175. Bos, C.; Delmas, Y.; Desmouliere, A.; *et al*. *Radiology* **2004**, *233*, 781–789.
176. Bulte, J. W.; Zhang, S.; Van Gelderen, P.; *et al*. *Proc. Natl. Acad. Sci. USA* **1999**, *96*, 15256–15261.
177. Dodd, S. J.; Williams, M.; Suhan, J. P.; Williams, D. S.; Koretsky, A. P.; Ho, C. *Biophys. J.* **1999**, *76*, 103–109.
178. Frank, J. A.; Miller, B. R.; Arbab, A. S.; *et al*. *Radiology* **2003**, *228*, 480–487.
179. Perez, J. M.; Josephson, L.; O'loughlin, T.; Hogemann, D.; Weissleder, R. *Nat. Biotechnol.* **2002**, *20*, 816–820.
180. Perez, J. M.; Simeone, F.; Tsourkas, A.; Josephson, L.; Weissleder, R. *Nano Lett.* **2004**, *4*, 119–122.
181. Tsourkas, A.; Hofstetter, O.; Hofstetter, H.; Weissleder, R.; Josephson, L. *Angew. Chem. Int. Ed. Engl.* **2004**, *43*, 2395–2399.
182. Zhao, M.; Josephson, L.; Tang, Y.; Weissleder, R. *Angew. Chem. Int. Ed. Engl.* **2003**, *42*, 1375–1378.
183. Brooks, R. A. *Magn. Reson. Med.* **2002**, *47*, 388–391.
184. Gillis, P.; Moiny, F.; Brooks, R. A. *Magn. Reson. Med.* **2002**, *47*, 257–263.
185. Tanimoto, A.; Oshio, K.; Suematsu, M.; Pouliquen, D.; Stark, D. D. *J. Magn. Reson. Imaging* **2001**, *14*, 72–77.
186. Reimer, P.; Jahnke, N.; Fiebich, M.; *et al*. *Radiology* **2000**, *217*, 152–158.
187. Shamsi, K.; Balzer, T.; Saini, S.; *et al*. *Radiology* **1998**, *206*, 365–371.
188. Vogl, T. J.; Hammerstingl, R.; Schwarz, W.; *et al*. *Radiology* **1996**, *198*, 881–887.
189. Lind, K.; Kresse, M.; Debus, N. P.; Muller, R. H. *J. Drug Target.* **2002**, *10*, 221–230.
190. Mack, M. G.; Balzer, J. O.; Straub, R.; Eichler, K.; Vogl, T. J. *Radiology* **2002**, *222*, 239–244.
191. Harisinghani, M. G.; Barentsz, J.; Hahn, P. F.; *et al*. *N. Engl. J. Med.* **2003**, *348*, 2491–2499.
192. Kanno, S.; Wu, Y. J.; Lee, P. C.; *et al*. *Circulation* **2001**, *104*, 934–938.
193. Kooi, M. E.; Cappendijk, V. C.; Cleutjens, K. B.; *et al*. *Circulation* **2003**, *107*, 2453–2458.
194. Saleh, A.; Schroeter, M.; Jonkmanns, C.; Hartung, H. P.; Modder, U.; Jander, S. *Brain* **2004**, *127*, 1670–1677.
195. Dousset, V.; Delalande, C.; Ballarino, L.; *et al*. *Magn. Reson. Med.* **1999**, *41*, 329–333.
196. Enochs, W. S.; Harsh, G.; Hochberg, F.; Weissleder, R. *J. Magn. Reson. Imaging* **1999**, *9*, 228–232.
197. Kelly, K. A.; Allport, J. R.; Tsourkas, A.; Shinde-Patil, V. R.; Josephson, L.; Weissleder, R. *Circ. Res.* **2005**, *96*, 327–336.
198. Artemov, D.; Mori, N.; Okollie, B.; Bhujwalla, Z. M. *Magn. Reson. Med.* **2003**, *49*, 403–408.
199. Thorstensen, K.; Romslo, I. *Scand. J. Clin. Lab. Invest. Suppl.* **1993**, *215*, 113–120.
200. Ichikawa, T.; Hogemann, D.; Saeki, Y.; *et al*. *Neoplasia* **2002**, *4*, 523–530.

201. Kresse, M.; Wagner, S.; Pfefferer, D.; Lawaczeck, R.; Elste, V.; Semmler, W. *Magn. Reson. Med.* **1998**, *40*, 236–242.
202. Moore, A.; Basilion, J. P.; Chiocca, E. A.; Weissleder, R. *Biochim. Biophys. Acta* **1998**, *1402*, 239–249.
203. Qian, Z. M.; Li, H.; Sun, H.; Ho, K. *Pharmacol. Rev.* **2002**, *54*, 561–587.
204. Antony, A. C. *Annu. Rev. Nutr.* **1996**, *16*, 501–521.
205. Choi, H.; Choi, S. R.; Zhou, R.; Kung, H. F.; Chen, I. W. *Acad. Radiol.* **2004**, *11*, 996–1004.
206. Sudimack, J.; Lee, R. J. *Adv. Drug Deliv. Rev.* **2000**, *41*, 147–162.
207. Moore, A.; Medarova, Z.; Potthast, A.; Dai, G. *Cancer Res.* **2004**, *64*, 1821–1827.
208. Kachra, Z.; Beaulieu, E.; Delbecchi, L.; *et al. Clin. Exp. Metastasis* **1999**, *17*, 555–566.
209. Veiseh, O.; Sun, C.; Gunn, J.; *et al. Nano Lett.* **2005**, *5*, 1003–1008.
210. Artemov, D.; Mori, N.; Ravi, R.; Bhujwalla, Z. M. *Cancer Res.* **2003**, *63*, 2723–2727.
211. Funovics, M. A.; Kapeller, B.; Hoeller, C.; *et al. Magn. Reson. Imaging* **2004**, *22*, 843–850.
212. Reimer, P.; Weissleder, R.; Shen, T.; Knoefel, W. T.; Brady, T. J. *Radiology* **1994**, *193*, 527–531.
213. Reimer, P.; Weissleder, R.; Lee, A. S.; Wittenberg, J.; Brady, T. J. *Radiology* **1990**, *177*, 729–734.
214. Zhao, M.; Beauregard, D. A.; Loizou, L.; Davletov, B.; Brindle, K. M. *Nat. Med.* **2001**, *7*, 1241–1244.
215. Emoto, K.; Toyama-Sorimachi, N.; Karasuyama, H.; Inoue, K.; Umeda, M. *Exp. Cell Res.* **1997**, *232*, 430–434.
216. Tsourkas, A.; Shinde-Patil, V. R.; Kelly, K. A.; *et al. Bioconjug. Chem.* **2005**, *16*, 576–581.
217. Bischoff, J.; Brasel, C.; Kraling, B.; Vranovska, K. *Microcirculation* **1997**, *4*, 279–287.
218. Chapman, P. T.; Jamar, F.; Keelan, E. T.; Peters, A. M.; Haskard, D. O. *Arthritis Rheum.* **1996**, *39*, 1371–1375.
219. Kraling, B. M.; Razon, M. J.; Boon, L. M.; *et al. Am. J. Pathol.* **1996**, *148*, 1181–1191.
220. Kang, H. W.; Josephson, L.; Petrovsky, A.; Weissleder, R.; Bogdanov, A., Jr. *Bioconjug. Chem.* **2002**, *13*, 122–127.
221. Jaffer, F. A.; Weissleder, R. *Circ. Res.* **2004**, *94*, 433–445.
222. Ruoslahti, E. *Annu. Rev. Cell Dev. Biol.* **1996**, *12*, 697–715.
223. Johansson, L. O.; Bjornerud, A.; Ahlstrom, H. K.; Ladd, D. L.; Fujii, D. K. *J. Magn. Reson. Imaging* **2001**, *13*, 615–618.
224. Phelps, M. E. *Neurochem. Res.* **1991**, *16*, 929–940.
225. Foster-Gareau, P.; Heyn, C.; Alejski, A.; Rutt, B. K. *Magn. Reson. Med.* **2003**, *49*, 968–971.
226. Rodriguez, N.; Pincet, F.; Cribier, S. *Colloids Surf. B Biointerfaces* **2005**, *42*, 125–130.
227. Awasthi, V. D.; Garcia, D.; Goins, B. A.; Phillips, W. T. *Int. J. Pharm.* **2003**, *253*, 121–132.
228. Chonn, A.; Cullis, P. R. *Adv. Drug Deliv. Rev.* **1998**, *30*, 73–83.
229. Harasym, T. O.; Bally, M. B.; Tardi, P. *Adv. Drug Deliv. Rev.* **1998**, *32*, 99–118.
230. Nallamothu, R.; Wood, G. C.; Pattillo, C. B.; *et al. AAPS PharmSciTech* **2006**, *7*, E32.
231. Mody, V. V.; Nounou, M. I.; Bikram, M. *Adv. Drug Deliv. Rev.* **2009**, *61*, 795–807.
232. Mikhaylova, M.; Stasinopoulos, I.; Kato, Y.; Artemov, D.; Bhujwalla, Z. M. *Cancer Gene Ther.* **2009**, *16*, 217–226.
233. Weng, K. C.; Noble, C. O.; Papahadjopoulos-Sternberg, B.; *et al. Nano Lett.* **2008**, *8*, 2851–2857.
234. Freedman, M.; Chang, E. H.; Zhou, Q.; Pirollo, K. F. *Acad. Radiol.* **2009**, *16*, 627–637.
235. Zhang, D.; Feng, X. Y.; Henning, T. D.; *et al. Eur. J. Radiol.* **2009**, *70*, 180–189.
236. Aime, S.; Castelli, D. D.; Crich, S. G.; Gianolio, E.; Terreno, E. *Acc. Chem. Res.* **2009**, *42*, 822–831.
237. Mulder, W. J. M.; Strijkers, G. J.; Griffioen, A. W.; *et al. Bioconjug. Chem.* **2004**, *15*, 799–806.
238. Fouillet, X.; Tournier, H.; Khan, H.; *et al. Acad. Radiol.* **1995**, *2*, 576–583.
239. Seltzer, S. E.; Blau, M.; Herman, L. W.; *et al. Radiology* **1995**, *194*, 775–781.
240. Tartis, M. S.; Mccallan, J.; Lum, A. F. H.; *et al. Ultrasound Med. Biol.* **2006**, *32*, 1771–1780.
241. Chen, S. Y.; Ding, J. H.; Bekeredjian, R.; *et al. Proc. Natl. Acad. Sci. USA* **2006**, *103*, 8469–8474.
242. Kopechek, J. A.; Abruzzo, T. M.; Wang, B.; *et al. J. Ultrasound Med.* **2008**, *27*, 1597–1606.
243. Discher, B. M.; Won, Y. Y.; Ege, D. S.; *et al. Science* **1999**, *284*, 1143–1146.
244. Levine, D. H.; Ghoroghchian, P. P.; Freudenberg, J.; *et al. Methods* **2008**, *46*, 25–32.
245. Discher, D. E.; Ahmed, F. *Annu. Rev. Biomed. Eng.* **2006**, *8*, 323–341.
246. Robbins, G. P.; Jimbo, M.; Swift, J.; Therien, M. J.; Hammer, D. A.; Dmochowski, I. J. *J. Am. Chem. Soc.* **2009**, *131*, 3872–3874.
247. Cheng, Z. L.; Thorek, D. L. J.; Tsourkas, A. *Adv. Funct. Mater.* **2009**, *19*, 3753–3759.
248. Cheng, Z. L.; Tsourkas, A. *Langmuir* **2008**, *24*, 8169–8173.
249. Shum, H. C.; Kim, J. W.; Weitz, D. A. *J. Am. Chem. Soc.* **2008**, *130*, 9543–9549.
250. Photos, P. J.; Bacakova, L.; Discher, B.; Bates, F. S.; Discher, D. E. *J. Control. Release* **2003**, *90*, 323–334.
251. Rameez, S.; Alosta, H.; Palmer, A. F. *Bioconjug. Chem.* **2008**, *19*, 1025–1032.
252. Pang, Z. Q.; Lu, W.; Gao, H. L.; *et al. J. Control. Release* **2008**, *128*, 120–127.
253. Zhou, W.; Feijen, J. *J. Control. Release* **2008**, *132*, e35–e36.
254. Borchert, U.; Lipprandt, U.; Bilang, M.; *et al. Langmuir* **2006**, *22*, 5843–5847.
255. Cerritelli, S.; Velluto, D.; Hubbell, J. A. *Biomacromolecules* **2007**, *8*, 1966–1972.
256. Napoli, A.; Valentini, M.; Tirelli, N.; Muller, M.; Hubbell, J. A. *Nat. Mater.* **2004**, *3*, 183–189.
257. Ghoroghchian, P. P.; Frail, P. R.; Susumu, K.; *et al. Proc. Natl. Acad. Sci. USA* **2005**, *102*, 2922–2927.
258. Christian, N. A.; Milone, M. C.; Ranka, S. S.; *et al. Bioconjug. Chem.* **2007**, *18*, 31–40.
259. Gorman, C. B.; Smith, J. C. *Acc. Chem. Res.* **2001**, *34*, 60–71.
260. Brocorens, P.; Lazzaroni, R.; Bredas, J. L. *J. Phys. Chem. B* **2007**, *111*, 9218–9227.
261. Boswell, C. A.; Eck, P. K.; Regino, C. A. S.; *et al. Mol. Pharm.* **2008**, *5*, 527–539.
262. Xu, H.; Regino, C. A. S.; Koyama, Y.; *et al. Bioconjug. Chem.* **2007**, *18*, 1474–1482.
263. Xu, R. Z.; Wang, Y. L.; Wang, X. L.; Jeong, E. K.; Parker, D. L.; Lu, Z. R. *Exp. Biol. Med.* **2007**, *232*, 1081–1089.
264. Zhu, W. L.; Mollie, B.; Bhujwalla, Z. M.; Artemov, D. *Magn. Reson. Med.* **2008**, *59*, 679–685.
265. Cheng, Y. Y.; Qu, H.; Ma, M. L.; *et al. Eur. J. Med. Chem.* **2007**, *42*, 1032–1038.
266. Takanashi, K.; Yamamoto, K. *Org. Lett.* **2007**, *9*, 5151–5154.
267. Zhang, W.; Simanek, E. E. *Org. Lett.* **2000**, *2*, 843–845.
268. Antoni, P.; Nystrom, D.; Hawker, C. J.; Hult, A.; Malkoch, M. *Chem. Commun. (Camb.)* **2007**, 2249–2251.
269. Roberts, J. C.; Bhalgat, M. K.; Zera, R. T. *J. Biomed. Mater. Res.* **1996**, *30*, 53–65.
270. Duncan, R.; Izzo, L. *Adv. Drug Deliv. Rev.* **2005**, *57*, 2215–2237.
271. Chen, H. T.; Neerman, M. F.; Parrish, A. R.; Simanek, E. E. *J. Am. Chem. Soc.* **2004**, *126*, 10044–10048.
272. Lee, J. H.; Lim, Y. B.; Choi, J. S.; *et al. Bioconjug. Chem.* **2003**, *14*, 1214–1221.
273. Boyd, B. J.; Kaminskas, L. M.; Karellas, P.; Krippner, G.; Lessene, R.; Porter, C. J. H. *Mol. Pharm.* **2006**, *3*, 614–627.
274. Gillies, E. R.; Frechet, J. M. J. *Drug Discov. Today* **2005**, *10*, 35–43.
275. Svenson, S. *Eur. J. Pharm. Biopharm.* **2009**, *71*, 445–462.
276. Kobayashi, H.; Koyama, Y.; Barrett, T.; *et al. ACS Nano* **2007**, *1*, 258–264.
277. Patri, A. K.; Myc, A.; Beals, J.; Thomas, T. P.; Bander, N. H.; Baker, J. R. *Bioconjug. Chem.* **2004**, *15*, 1174–1181.
278. Kobayashi, H.; Brechbiel, M. W. *Adv. Drug Deliv. Rev.* **2005**, *57*, 2271–2286.
279. Wiener, E. C.; Brechbiel, M. W.; Brothers, H.; *et al. Magn. Reson. Med.* **1994**, *31*, 1–8.
280. Langereis, S.; De Lussanet, Q. G.; Van Genderen, M. H. P.; *et al. NMR Biomed.* **2006**, *19*, 133–141.
281. Cheng, Z. L.; Thorek, D. L. J.; Tsourkas, A. *Angew. Chem. Int. Ed.* **2010**, *49*, 346–350.
282. Boin, F.; Hummers, L. K. *Rheum. Dis. Clin. North Am.* **2008**, *34*, 199–220.
283. Schumann, H.; Wassermann, B. C.; Schutte, S.; *et al. Organometallics* **2003**, *22*, 2034–2041.
284. Yordanov, A. T.; Lodder, A. L.; Woller, E. K.; *et al. Nano Lett.* **2002**, *2*, 595–599.
285. Fu, Y. J.; Nitecki, D. E.; Maltby, D.; *et al. Bioconjug. Chem.* **2006**, *17*, 1043–1056.

Relevant Websites

http://www.ami-imaging.org/ – Academy of Molecular Imaging.
http://www.wmicmeeting.org/dev/ – World Molecular Imaging Congress.
http://www.molecularimaging.org/ – The Society for Molecular Imaging.
http://www.molecularimagingcenter.org/index.cfm?PageID=7165 – Molecular Imaging Center of Excellence.

3.319. Characterization of Nanoparticles in Biological Environments

M Maskos, BAM Bundesanstalt für Materialforschung und – prüfung, Berlin, Germany
R H Stauber, University Medical Center Mainz, Mainz, Germany

© 2011 Elsevier Ltd. All rights reserved.

3.319.1.	**Introduction**	329
3.319.1.1.	Definition of Nanoparticles	329
3.319.2.	**Interactions of Nanoparticles**	330
3.319.3.	**Characterization of Nanoparticles in or from Solution**	331
3.319.3.1.	Scattering Methods	331
3.319.3.2.	Microscopy-Based Methods	333
3.319.3.3.	Field-Flow Fractionation	333
3.319.4.	**Examples of Nanoparticles in Biological Environments**	334
3.319.4.1.	The Fate of Nanoparticles in Living, Biological Environments	335
3.319.4.2.	Influence of the Nano–Bio Interface on Nanomaterial-Mediated Biological Effects	337
3.319.5.	**Conclusions and Outlook**	338
References		338

Abbreviations

AFM	Atomic force microcopy
AmSil	Amorphous silica
ATII	Alveolar epithelial type II
DLS	Dynamic light scattering
DLVO	Derjaguin-Landau-Verwey-Overbeek
ENP	Engineered nanoparticle
FCS	Fetal calf serum
FFF	Field-flow fractionation
NP	Nanoparticle
SANS	Small angle neutron scattering
SAXS	Small angle X-ray scattering
SLS	Static light scattering
TEM	Transmission electron microscopy
VDW	van der Waals

3.319.1. Introduction

The investigation and the general discussion of the impact of nanoparticles on biological environments are accompanied by a steadily growing interest both within the scientific community and outside. This impact is being treated with increasing weariness, and therefore, the challenging tasks of understanding the structure–property relations and mechanisms of interactions on different levels have become increasingly important.

This chapter deals with the characterization of nanoparticles in biological environments and their interactions, mainly in aqueous-based solutions. After a short definition, the basic interactions between nanoparticles and their stabilization are summarized, followed by a short overview of some important methods of nanoparticles characterization. The last part then describes some aspects of interactions between nanoparticles and biomaterials in order to illustrate the current challenges.

3.319.1.1. Definition of Nanoparticles

It has been commonly accepted until now that nanoparticles possess dimensions between 1 and 100 nm. Additional important parameters are the size polydispersity, shape, and stabilization against aggregation.

Single particle properties differ from those of agglomerates and aggregates. Typically, agglomerates are a group of particles that are held together by relatively weak forces, including van der Waals (VDW) forces, electrostatic forces, and surface tension, whereas aggregates are heterogeneous particles in which the various components cannot be easily taken apart.

One of the prominent features of nanoparticles is the increase in their surface-to-volume ratio with decrease in size. Specific surface areas of up to a couple of thousand square meters per gram are theoretically possible. The characterization of nanoparticles is extremely challenging due to (i) their small size, which is typically below the wavelength limit of direct optical detection via light microscopy and (ii) their tendency to agglomerate or aggregate upon change in surrounding medium.

The interaction between material and biology is typically summarized by the term 'biocompatibility,' which refers to "the ability of a biomaterial to perform its desired function with respect to a medical therapy, without eliciting any undesirable local or systemic effects in the recipient or beneficiary of that therapy, but generating the most appropriate beneficial cellular or tissue response in that specific situation, and optimizing the clinically relevant performance of that therapy."[1] Proper and context-sensitive characterization is necessary to understand the impact of nanoparticles on biological environments.

3.319.2. Interactions of Nanoparticles

A recent review by Nel *et al.* very nicely summarizes the main features and properties that have to be dealt with when nanoparticles are under investigation. In a medium under investigation, important nanoparticle characteristics which determine the properties are the particle's chemical composition, surface functionalization, shape, and typically, also its polydispersity.[2–4] Other quantifiable properties, such as effective surface charge (ζ-potential), particle aggregation, state of dispersion, and stability are influenced by the characteristics of the suspending media,[2] including its ionic strength, pH, temperature, and the presence of large organic molecules (e.g., proteins) or surfactants.[5] Particle characteristics actively contribute to the interactions with the medium by promoting the adsorption of ions, proteins, natural organic materials, and detergents or by double layer formation.[6,7] Many of these particle properties determine the forces that operate at the particle–medium interface, and they have characteristic decay lengths[7] (Figure 1). These forces include those arising from attractive VDW and (typically) repulsive electrostatic interactions, plus short-range forces arising from steric and solvent interactions[7,8] (Table 1). Media interactions (e.g., protein interactions) could also induce large-scale changes, such as agglomeration, nanoparticle dissolution, or ion leaching.

At first glance, the interactions between nanoparticles and, for example, cells seem to embody some of the same principles as those between colloidal particles. VDW, electrostatic, salvation, and steric forces still apply, but due to their small size, many atoms are located at the surface of the nanoparticles.[7,9,10] Therefore, the accompanying VDW forces depend on the position of the atoms and their standard bulk permittivity functions (Table 1 and Figure 1).[10] This complexity further increases in biological media.

Typical interactions between silica particles in water involve VDW, electrostatic, and solvation forces (Figure 1).

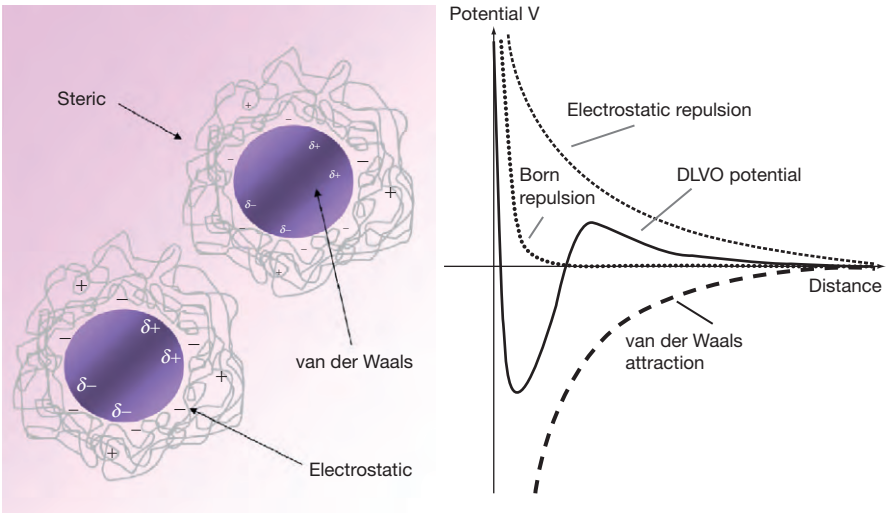

Figure 1 Interactions between nanoparticles. Traditional forces for colloidal stabilization (e.g., electrostatic, van der Waals, steric) that occur when particles are dispersed in aqueous media (left). van der Waals forces are attractive whereas the electrostatic forces are repulsive over a typical length scale (right). The Derjaguin–Landau–Verwey–Overbeek theory in colloid science considers the sum of these forces.

Table 1 Forces and their consequences on nanoparticle characteristics

Force	*Description*	*Range (nm)*	*Consequences*
Electrostatic interactions	Charged surfaces attract counter-ions and repel co-ions by Coulomb forces (double layer formation)	1–100	Typically repulsive, because most of the material carries negative charges in aqueous media; attractive for opposite charges
Electrodynamic interactions	van der Waals interactions through all interacting materials	1–100	Attractive in aqueous solution
Hydrodynamic interactions	At the nanoscale, classical Brownian diffusion and hydrodynamic forces are often hindered or enhanced	Typically $\gg$100 nm	Increase of frequency of collision of nanoparticles
Solubility	Interactions with solvent molecules	1–10	Influence on the thermodynamic stability of dispersed nanoparticles
Steric interactions	Polymers bound to the nanoparticles surface give rise to repulsive interactions	1–100 (depending on the length of the polymer)	Typically increase stability of individual particles

VDW forces result from the dynamic interaction of dipoles. At any moment, dipoles fluctuate and eventually induce a dipole moment in the atoms of the silica particle, thereby causing an attractive force. The electrostatic force in the system results from surface charges that are present on the silica particles. Silanol (Si–OH) groups dissociate in aqueous solution at pH greater than ~2 to yield negative surface charges, which then generate repulsive electrostatic forces between particles. For silica particles, the sum of the attractive VDW and repulsive electrostatic forces yields the well-established Derjaguin–Landau–Verwey–Overbeek (DLVO) potential[7,8,11] (Figure 1).

In biological fluids, the ionic strength is often about 150 mM, leading to the restriction of the electrostatic forces to a few nanometers from the surface. The high ionic strength also influences the zero frequency contribution of the VDW forces, whereas the higher frequency dispersion interactions still remain. Moreover, solvation is another issue that is important for nanoparticles, especially in aqueous solvents (Figure 1). The water molecules form a protective surface layer which decreases the tendency to adhere to other nanoparticles, leading to increased stability. In contrast, rapid dehydration and aggregation will occur if the relative affinity of two interacting surfaces for water molecules is much lower than that between the water molecules themselves ('hydrophobic effect'). All of these forces are described by theories.[10] Corresponding experimental measurements also tend to be reasonably consistent.

3.319.3. Characterization of Nanoparticles in or from Solution

The above-mentioned properties are a challenging task when nanoparticles are being characterized. This holds true for bare nanoparticles and becomes even more important when nanoparticles are analyzed in biological environments. The following part describes some of the main methods that are generally employed nowadays, especially for the characterization of nanoparticles in or from solution. This includes (i) scattering methods such as static and dynamic light scattering (SLS, DLS), small angle X-ray and neutron scattering (SAXS, SANS), and electrophoretic light scattering; (ii) microscopy-based methods, namely transmission electron microscopy (TEM) and atomic force microscopy (AFM); and (iii) field-flow fractionation (FFF).

3.319.3.1. Scattering Methods

Light, with wavelength in the visible range, is commonly used for static and dynamic light scattering (SLS, DLS), and the light scattered by dilute solutions is detected and subsequently analyzed.[12] Dust, which in solution is typically present in the size range of micrometers, needs to be removed, because the scattering intensity increases with the particle radius R as $I \sim R^6$. The time-averaged scattering intensity is detected in SLS and is used to determine the average molecular weight (M_w), the second virial coefficient (A_2), and the radius of gyration (R_g) of the particles in solution. The latter can only be determined if the size of the particles exceeds ~1/20 of the wavelength used. The scattering due to a known standard is used to calibrate the scattering intensity. The scattering itself is based on both concentration and density fluctuations (and of course, the difference in refractive index compared to the solvent; if this is zero, the particles become invisible); therefore the scattering due to the solvent is subtracted from that of the solution. Care should to be taken so that no additional effects, such as absorption or fluorescence, influence the measured intensity. The resulting inverse, reduced scattering intensity, the so-called Rayleigh ratio, is proportional to the scattering angle which is expressed in terms of the scattering vector q, and the sample concentration c. For particles with radii between ~10 and 50 nm, the application of the Zimm equation should yield a linear dependence of the inverse Rayleigh ratio and q^2 and c.

$$\frac{Kc}{R(\theta)} = \frac{1}{M_w}\left(1 + \frac{1}{3}q^2\left\langle R_g^2\right\rangle_z\right) + 2A_2c$$

where K is the optical constant (depends on the refractive index increment, the refractive index n of solvent, and the employed wavelength in vacuum l_0); c, the concentration; $R(\theta)$, measured Rayleigh ratio (defined as $R(\theta) = \frac{I_{solution} - I_{solv.}}{I_{std.}} R_{std.}$, scattering intensity of the solution, the solvent and a standard (typically toluene), and the independently determined Rayleigh ratio of the standard); θ, the scattering angle; M_w, the weight average molar mass; q, absolute value of the scattering vector ($q = |\vec{q}| = \frac{4\pi n}{\lambda_0}\sin(\theta/2)$), $\left\langle R_g^2\right\rangle_z$, z-average of the squared radius of gyration; and A_2 is the second osmotic virial coefficient.

Deviations from the linearity are observed if the particle size – and unfortunately also if the polydispersity – increases. In addition, this is also an important consideration in the case of charged particles in extremely low salt-containing solutions (such as deionized water), due to their potentially large interaction ranges.

In DLS, the time-dependent scattering intensity is detected, from which an autocorrelation function $g_1(t)$ can be derived. DLS yields particle hydrodynamic size (hydrodynamic radius R_h) in solution by the determination of the translational diffusion coefficient D. A recent review by Jones and Grainger points to the potential pitfalls that accompany DLS experiments:

> However, such nano-sizing analyses by DLS require a high degree of skill to perform, careful instrument calibration, positive and negative controls, attention to reagent purities, and some knowledge of optical data modeling algorithms to predict a sizing outcome consistent with many assumptions about the optical scattering physics in the solution. Many particle sizing studies, spanning metals, metal oxides, and polymers, treat the technique blindly as an automated method with default scattering models and curve-fitting assumptions that are neither described, justified nor validated for various sample types.[13]

The autocorrelation function $g_1(t)$ depends on D and the scattering angle (via θ), which, in the case of SLS, means that additional effects may need to be taken into account, especially with respect to the particle size and the polydispersity. In addition to the above, in the case of DLS, the anisotropy of the particles also needs to be taken into account, as it influences their diffusion properties.[12] For monodispers, spherical particles, $g_1(t)$ is defined by:

$$g_1(t) = \exp\left(-q^2\langle\Delta R^2(t)\rangle_\tau/6\right) = \exp\left(-Dq^2t\right) = \exp\left(-\frac{t}{t_D}\right)$$

$\langle\Delta R^2(t)\rangle_\tau$ is the average mean square displacement and t_D is the relaxation time.

For small spherical particles with moderate size distribution, DLS yields the inverse z-average of the hydrodynamic radius. The Stokes–Einstein relation combines the diffusion coefficient and the corresponding hydrodynamic radius. Typically, an extrapolation of $q \to 0$ and $c \to 0$ is needed to obtain $\langle D\rangle_z$. Otherwise, only apparent values are obtained.

$$\langle D\rangle_z \propto \langle R_h^{-1}\rangle_z, \quad R_h = \frac{k_B T}{6\pi\eta D}$$

where k_B is the Boltzmann constant; T, the absolute temperature; and η is the viscosity of the solvent.

Many nanoparticle systems in aqueous-based solutions are stabilized by electrostatic forces, as already discussed above. Therefore, contact with biological media such as cell culture medium often leads to destabilization due to the decrease in Debye length, and subsequently, to the formation of aggregates. This makes it challenging to distinguish between the impact of single dispersed nanoparticles and their aggregates in, subsequently performed cell experiments (Figure 15). One example of silica nanoparticles, analyzed by DLS in a low ionic strength aqueous solution and in a cell medium, is shown in Figure 2.[14,15]

Basically, small angle X-ray and neutron scattering (SAXS, SANS) are comparable to SLS. Major differences are the wavelength employed (typically in the order of 0.1–10 nm), and the scattering contrast, which in case of SAXS is the difference in electron density, and in case of neutrons, is the scattering length. Depending on the size of the particles, the determined angular-dependent scattering intensity of dilute solutions can yield the radius of gyration R_g and additional information about the shape and the internal structure of the particles, and is commonly expressed by a theoretically derived particle form factor $P(q)$ (Figure 3). Increasing polydispersity also leads to an increase in the ambiguity in the results.[16–18]

Specifically, during the characterization of nanoparticles, interesting particle properties can be derived from SAXS and SANS, including their internal structure (often called the fractal structure) and the ratio of surface to volume of the particles (in the so-called Porod regime).

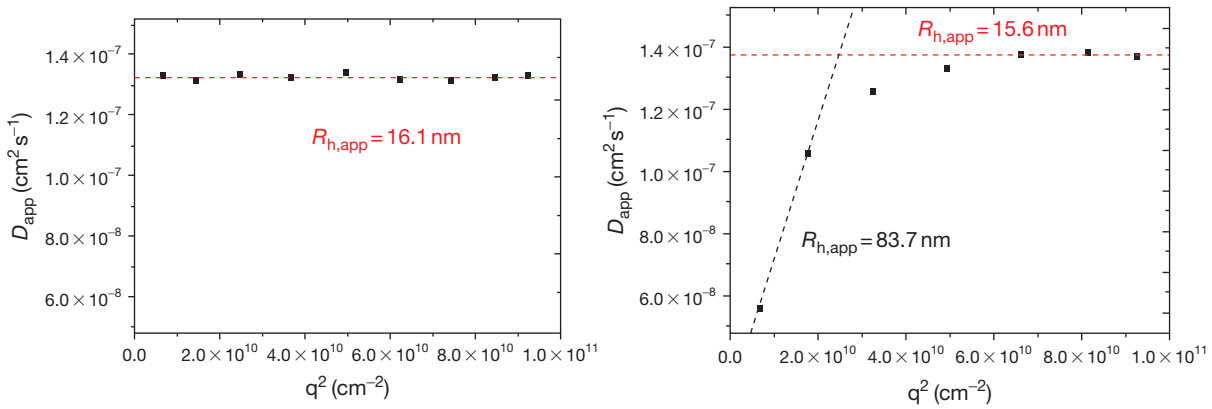

Figure 2 Apparent diffusion coefficient determined by dynamic light scattering for commercial silica nanoparticles (dispersions) in aqueous solution (concentration $c = 0.3\,g\,l^{-1}$, 24 h after sample preparation); left: in 0.01 M NaBr; right: in cell culture medium RPMI1640. Also shown are the corresponding extrapolation-based hydrodynamic radii; in case of medium, the extrapolations for high and for low q-values are shown.

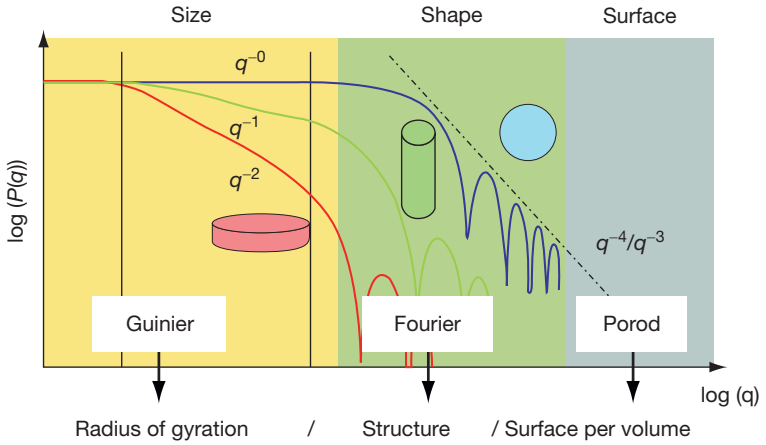

Figure 3 Evolution of the particle form factor $P(q)$ for different particle shapes.

Finally, electrophoretic light scattering is used to determine the effective charge in terms of the ζ-potential of the nanoparticles in solution.[11] In a very simple approach, the electrophoretic mobility μ of the particles can be linked to the ζ-potential according to:

$$\zeta = \mu \frac{4\pi\eta}{\varepsilon\varepsilon_0}$$

where h is the solvent viscosity; e_0, the permittivity; and e is the dielectric constant of the solvent.

Basically, the same parameters, as already discussed above for DLS, have to be considered here. In addition, the simple approach shown here becomes increasingly invalid in case of physiological conditions, mainly due to the high ionic strength of the solution.

3.319.3.2. Microscopy-Based Methods

Electron microscopy, especially transmission electron microscopy (TEM) is used to visualize nanoparticles and determine their size, polydispersity, and shape.[19] Typically, dried samples are analyzed on carbon-coated copper grids, which can potentially lead to additional effects such as induced aggregation. To minimize this effect, especially for aqueous-based solutions, a cryogenic sample preparation method can be employed (cryo-TEM, Figure 4).

The particle solution is again deposited on a carbon-coated copper grid, but now, typically, a Holey carbon film is used. After deposition, the sample is shock frozen in liquid propane, transferred into liquid nitrogen, and analyzed under external cooling. This preparation results in a thin, amorphously solidified water film that contains the nanoparticles.[20] As in light scattering, a high degree of the skill is needed, and in addition, the number of particles detected needs to be large enough to reduce the influence of potential artifacts due to insufficient statistical power. A comparison between ordinary sample preparation, including drying, and a cryogenic preparation of commercial silica nanoparticle dispersions, both analyzed by TEM, is shown in Figure 5.

The dry sample preparation shows aggregation of the particles upon drying. No reliable information on the existence of aggregates in solution is possible. On the other hand, the cryogenic sample preparation clearly shows individual particles.

A second modern technique to visualize nanoparticles on solid substrates, such as mica or graphite, is atomic force microscopy (AFM).[21] A small tip (typical radius of ~10 nm) is located on a cantilever and brought into contact with a surface to be analyzed (Figure 6).

Different modes of operation can be used, and mostly depend on sample characteristics and the forces involved. A topological picture of the surface is generated by incremental scanning of the surface. This can be used to obtain a topological picture of the surface or to measure force–distance curves. Modern instruments allow the characterization of the surface after drying or, especially for water-based solutions, in solution (after adsorption of the nanoparticles from solution). An example of polyorganosiloxane nanoparticles analyzed by AFM is given in Figure 7.[14]

3.319.3.3. Field-Flow Fractionation

FFF is a family of techniques, where a physical field acts perpendicular to a commonly ribbon-like channel, through which a solvent is pumped.[22,23] If the solvent viscosity is low enough, a laminar flow is generated. One method of exerting a force perpendicular to the channel is by inserting a semipermeable membrane as a physical barrier (Figure 8). The resulting

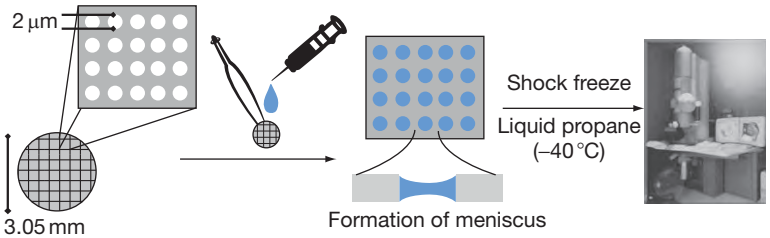

Figure 4 Sample preparation on cryo-TEM: Holey carbon-coated cupper grid (left), deposition of a solution droplet, pore spanning liquid film (middle), shock freezing in, for example, liquid propane and transfer into the TEM (right).

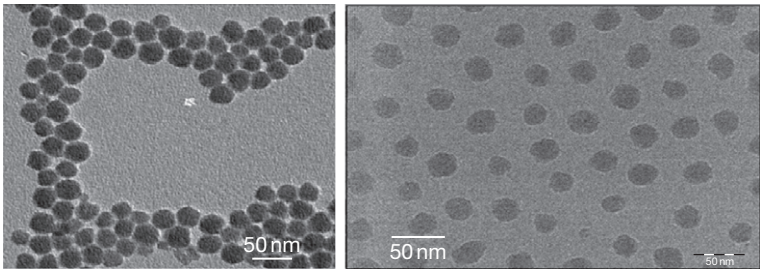

Figure 5 Transmission electron microscopy pictures of the same aqueous silica dispersion: after deposition on a carbon-coated cupper grid and subsequent drying (left) and after cryogenic sample preparation on Holey carbon-coated cupper grids (right).

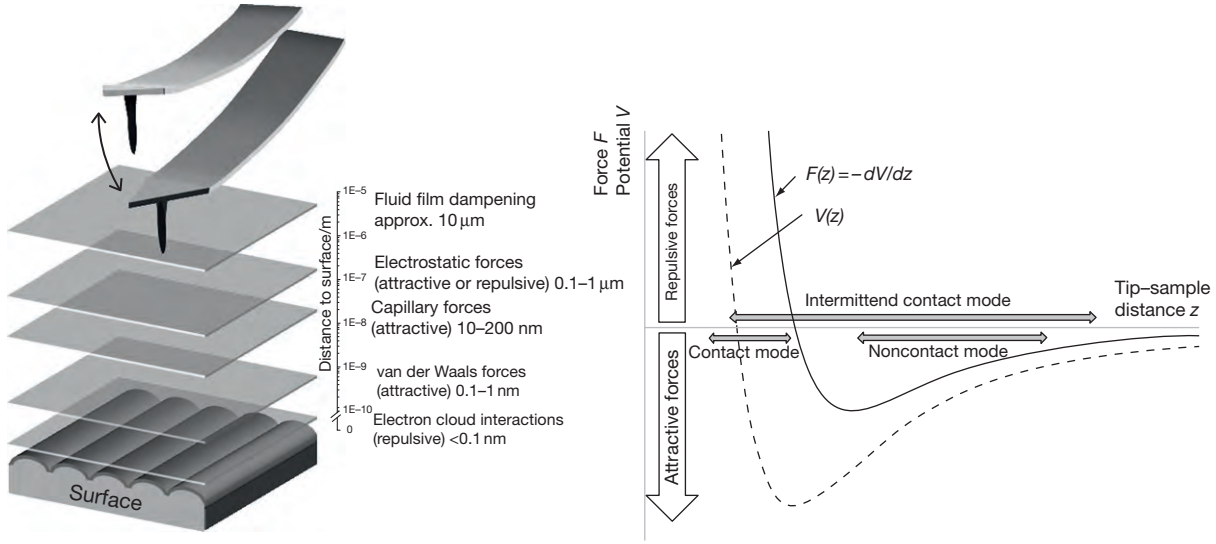

Figure 6 Schematic representation of the different modes used in AFM and the corresponding forces involved. (Adapted from Elings, V., Digital Instruments Nanoscope Command Reference Manual, Santa Barbara/CA (1995), now Bruker Nano Surfaces Division).

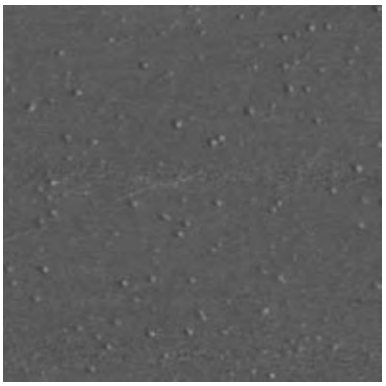

Figure 7 Atomic force microscopy picture (noncontact mode) obtained from an aqueous polyorganosiloxane–nanoparticle dispersion (average size 30 nm), spin cast from solution onto mica and subsequently dried; picture size 1 × 1 µm^2.

technique is commonly called asymmetrical flow FFF (AF-FFF) and works quite nicely, especially for aqueous-based solutions.[24] In this case, membranes typically used for ultrafiltration can be employed.

After the introduction and focusing of particles, a concentration profile is established from the membrane, depending on the diffusion coefficient. In a simple picture, and depending on the cross-flow, the smaller particles diffuse further into the channel compared to the larger ones. Subsequent turn-on of the laminar flow through the channel, while maintaining the cross-flow, leads to particle separation and subsequent detection (Figure 9).

This simple description breaks down when gravity needs to be included, or in other words, when the particle size increases to, for example, beyond micrometers in size, and is also dependent on the density of the particles. For smaller particles, the theoretical description yields a linear relation between the retention time t_R of the nanoparticles and their hydrodynamic radius R_h.

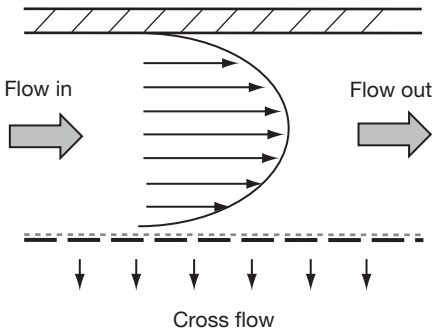

Figure 8 Schematic cut through an asymmetrical flow field-flow fractionation channel.

$$t_R = \frac{\pi\eta\dot{V}_c w^2}{\dot{V}k_B T}R_h$$

Where η is the solvent viscosity, $\dot{V}_c$, the cross-flow rate; w, the channel height; $\dot{V}$, channel flow rate; k_B, Boltzmann constant; and T is the absolute temperature.

An example of the AF-FFF characterization of polyorganosiloxane nanoparticles is shown in Figure 10.[25,26] In this case, a linearly decreasing cross-flow has been used to shorten the measuring time.

Due to technical constraints, such as compressible membranes or programmed flow conditions, AF-FFF is typically calibrated with particle standards of known sizes.[27]

3.319.4. Examples of Nanoparticles in Biological Environments

The expanding use of engineered nanoparticles (ENPs) has spurred an interest in defining their effects in biological environments.[2,28–30] The size-related properties of ENPs raise concerns about their potential adverse effects on biological and ecological systems, as a variety of studies have indicated

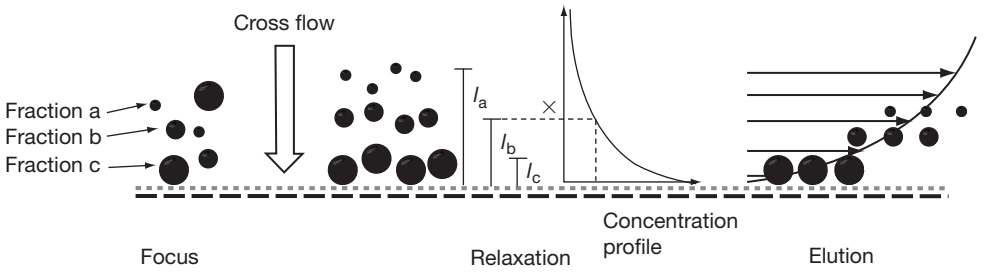

Figure 9 Scheme of the separation process in asymmetrical flow field-flow fractionation. Sample injection (left), evolution of the corresponding concentration profiles (middle), and separation after turn-on of the laminar flow (right).

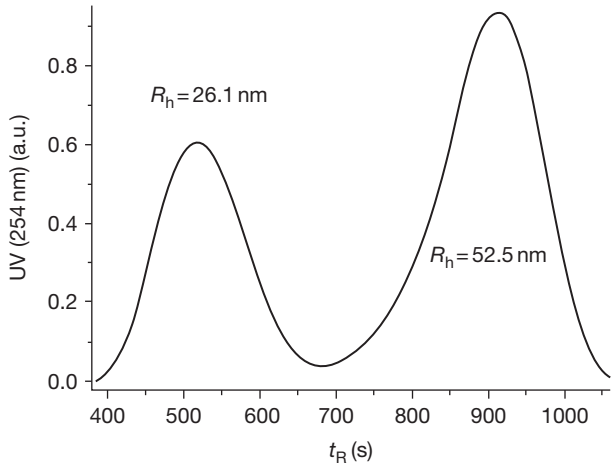

Figure 10 Separation of a bimodal nanoparticle mixture of polyorganosiloxanes in aqueous solution (10 mM NaCl, 100 mg l^{-1} TWEEN 20) by asymmetrical flow field-flow fractionation using a linearly decreasing cross-flow: UV signal at 254 nm versus retention time.

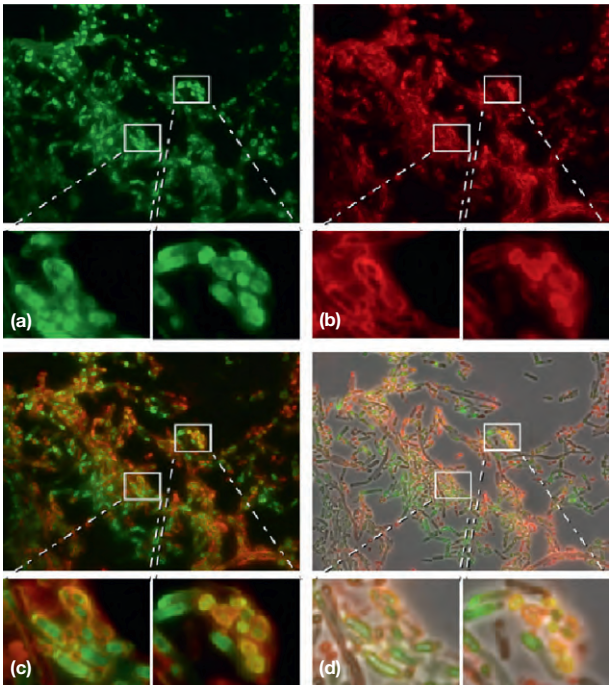

Figure 11 Binding of silica-engineered nanoparticles (SiNPs) to bacteria. *Escherichia coli* XL-2-bacteria expressing the green fluorescent protein (GFP) were incubated with red fluorescent silica NPs (10^{12} SiNP per milliliter) in PBS for 30 min, washed with PBS, and examined by fluorescence microscopy (for methods see Rücker *et al.*[37]). (a) GFP-expression marks bacterial cells. (b) Red fluorescent SiNPs bound to the outside of bacteria were detectable upon excitation with 509 nm. (c, d) Merge (yellow), combined with phase image.

that ENPs could exert toxic effects and pose hazards to the biological environment.[31–34] Traditionally, the *in vivo* biological and toxic effects of ENPs have been characterized by animal studies. However, the biological environment not only includes humans and higher animals, but also plants and simple microorganisms such as yeast, bacteria, phyto- and zooplankton[2,30,35,36] (Figure 11).

To even add a further level of complexity, certain ENPs may also enter the intracellular organelles, including the nucleus, which is a critical storage compartment of the genetic information.[2,29,38] Hence, the nano–bio interface, comprising the dynamic physicochemical interactions, kinetics, and thermodynamic exchanges between nanomaterial surfaces and (bio) molecules or ions present in the various biological environments, still awaits comprehensive characterization.[29,39] Such interactions lead to the formation of NP (protein) coronas which affect (intracellular) uptake and biocatalytic processes and may ultimately have biocompatible or bioadverse outcomes. Consequently, probing these various interfaces using the sophisticated methodologies described in the previous chapters is mandatory for the development of predictive relationships that describe the processes that occur at the nano–bio interface; these will be crucial for the safe use of nanomaterials.[1,40]

3.319.4.1. The Fate of Nanoparticles in Living, Biological Environments

The field of nano-eco(toxico)logy is highly relevant but complex.[35,41] Hence, we wish to focus on mammalian systems, and, predominantly on humans. Nanoparticles for medical applications are frequently delivered directly via parenteral administration. Among the most discussed entry sites for environmental ENPs are the skin and the respiratory and gastrointestinal tracts; the respiratory tract is considered as one of the main accidental entry routes for ENPs and can potentially lead to local or even systemic adverse effects[30,32,42,43] (Figure 12).

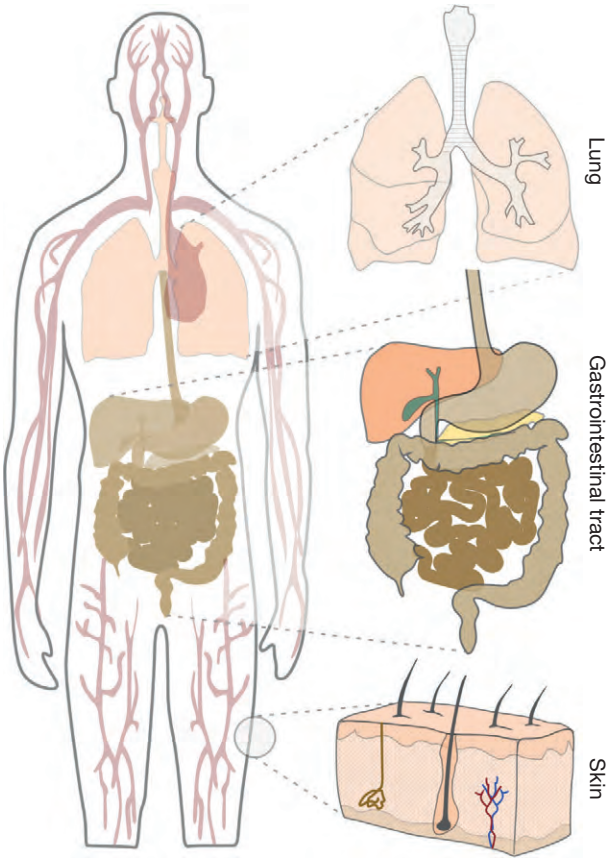

Figure 12 Schematic overview of the most relevant entry routes for nanoparticles into the human body.

The nasal mucosa, which is known to react to environmental toxins with irritation, infection, and allergies, is the first relevant biological interface that comes into contact with ENPs. The nasal mucosa has even been suggested to allow access of ENPs to the central nervous system.[44–46] Second, because of its large surface area (~120 m^2), and the less effective recognition of ENPs by alveolar macrophages which constitutes the first line of defense against particulates that have escaped the mucociliary escalator, the bronchial-/alveolo–capillary barrier is considered to be the key target of inhaled ENPs.[43,47] Moreover, only a thin barrier, composed of alveolar epithelial type I/type II and pulmonary capillary endothelial cells, separates the airspace from capillary blood (**Figure 13**), thus raising concerns about the potential systemic entry of ENPs.

After deep lung inhalation, ENPs may trigger (patho) biological effects not only by direct cell damage but also indirectly by inducing chronic inflammation, similar to that reported for carbon nanotubes.[48] Such inflammatory responses include alveolar macrophages and also alveolar epithelial type II (ATII) cells that can respond to noxious stimuli by producing proinflammatory cytokines.[38,49,50]

Irrespective of the entry route, the intrinsic characteristics of the ENPs are modified upon contact with the various biological matrices. Particularly, ENPs that target the respiratory and gastrointestinal tract first encounter mucus, a complex mixture containing glycoproteins (mucins), enzymes, immunoglobulins, and inorganic salts. Thus, ENPs in the deep lung do not directly interact with cellular membranes, but first meet the lung surfactant present over the epithelial cell layer (**Figure 13**).[51] The pulmonary surfactant is a lipid–protein composite that covers the air–water interface in vertebrate lungs. In this interface, the lipid monolayer regions most likely

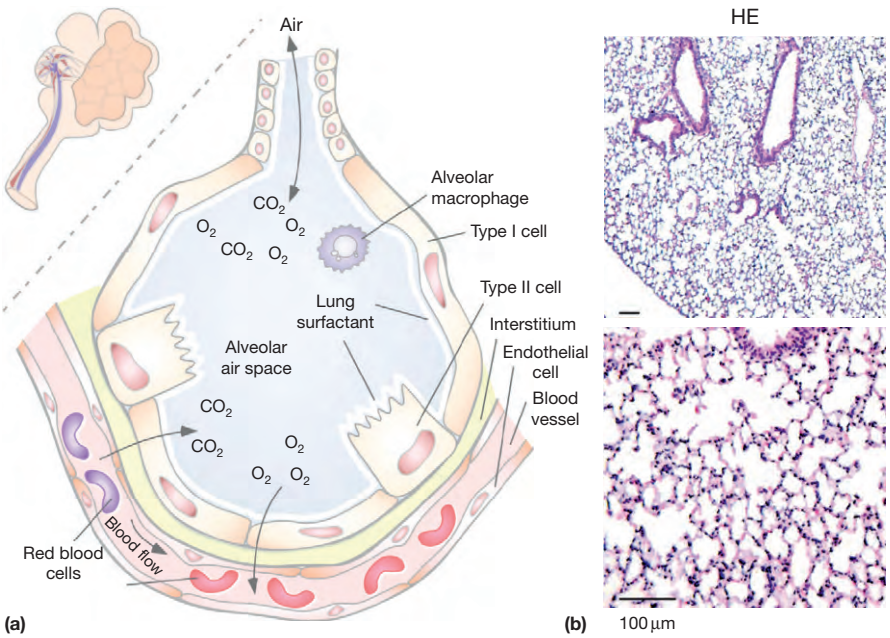

Figure 13 (a) Schematic illustration of alveolo–capillary barrier components. (b) Histologic specimen of murine lung tissue counterstained with hematoxylin and eosin. Bars: 100 μm.

coexist with surfactant protein containing multilayer structures, which may be disturbed by incoming ENPs. The essential function of the surfactant during the breathing process is to reduce the surface tension in order to prevent the collapse of the alveolar system during expiration, and to reduce the work of breathing.[52,53] Malfunction or lack of this crucial material might lead to diseases like the *Neonatal Respiratory Distress Syndrome*.[52] As ATII cells synthesize, secrete, and recycle the pulmonary surfactant, any interference in these processes by ENPs may affect the homeostasis and function of the pulmonary surfactant, and thereby contribute to ENP-induced (patho)biological consequences. Although animal studies have significantly aided in the discovery of such toxic effects,[48,54] the complexity of the alveolar microenvironment hampers studies on ENP-mediated effects at the molecular and mechanistic level. Therefore *in vitro* models mimicking the different biological layers of the alveolo-capillary barrier are used and are accepted as reliable experimental tools to investigate and predict the (patho)biological effects of ENPs.[49,55]

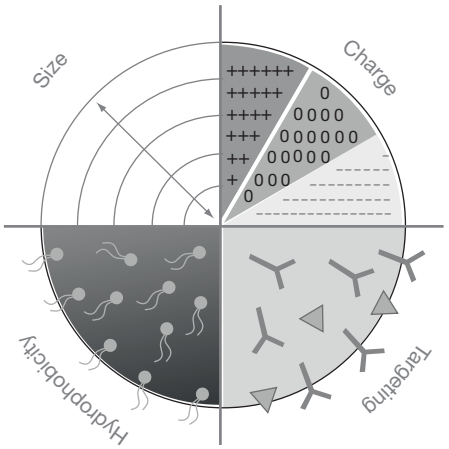

Figure 14 Schematic illustration of engineered nanoparticle characteristics affecting the nano–bio interface.

3.319.4.2. Influence of the Nano–Bio Interface on Nanomaterial-Mediated Biological Effects

The response of ENPs to the various biological environments is complex and results from the interplay of critical biophysicochemical forces that are active at the interface between nanomaterials and biological systems.[29,56] Nevertheless, such associations of proteins/biomolecules with nanoparticles are almost always the first step when nanoparticles enter a biological fluid.

Although clearly dependent on the entry route, for example, intravenous injection of ENPs for medical applications versus accidental inhalation, most ENPs, upon contact with biological matrices, are swiftly coated by proteins, leading to the formation of a so-called protein corona.

Such nano-biofilms largely define the biological identity of the particle, its interactions with biological surfaces, and hence, the induced (patho)biological responses. Several studies indicate that these responses tend to correlate with surface area rather than mass.[57,58] Nanoscale materials have far greater surface-to-volume ratios compared to larger particles, implying that more biomolecules/proteins will bind to a nanoparticle relative to its mass, compared to a particle of larger size.[57] Additionally, particle composition as well as its surface characteristics (e.g., size, radius of curvature, charge, hydrophobicity, etc.) will determine which types of biomolecules will interact with that particle and with what affinity[29,56,57] (**Figure 14**).

Thus, it is critical to characterize and understand the various chemicophysical binding forces that are involved in building the (dynamic) nano-biomolecule corona in order to be able predict the nature of the decorated particles that biological systems can face, and hence, their evoked biological responses (**Figure 15**).

Several proteins are already known to form (transient) complexes with nanoparticles. For example, upon intravenous ENP injection, human serum albumin and fibrinogen appear to dominate the particle surface, but it is not yet understood whether they also influence the biological effects induced by such particles. Likewise, albumin, immunoglobulins,

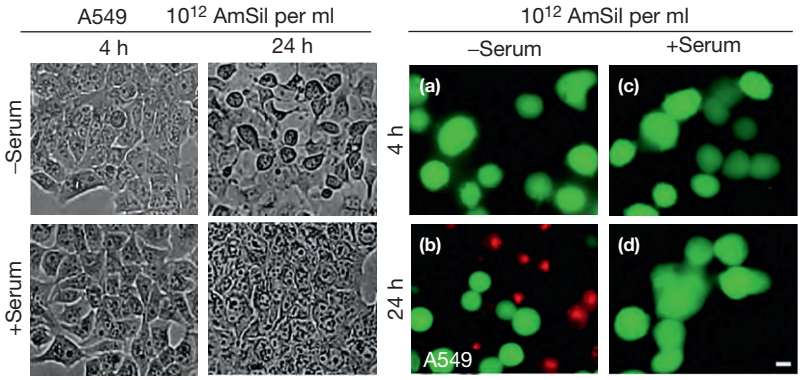

Figure 15 Serum proteins ameliorate the cytotoxicity of silica nanoparticles (NPs). The epithelial lung carcinoma cell line A549 was incubated with the indicated amounts of amorphous silica NPs (AmSil) suspended in cell culture medium (RPMI1640) in the absence or presence of 10% fetal calf serum (FCS). Four hours later, the medium was replaced by RPMI1640/10%FCS, and the cells were further cultivated for 24 h. At the indicated time points, cell morphology and vitality were analyzed by light microscopy (left, phase contrast images) or by using the *LIVE/DEAD® Viability/Cytotoxicity Kit* (Molecular Probes) (right, green fluorescence indicates vital cells, red fluorescent nuclei mark dead cells. Bar: 10 μm). AmSil-induced cell death was significantly reduced when exposure was performed in the presence of serum.

complement, fibrinogen, and apolipoproteins have been reported to bind most strongly to carbon nanotubes, iron oxide, and polymeric nanoparticles.[28,51] However, whether such nano-biofilms exist and are biologically relevant even upon inhalation or ingestion of these materials remains to be resolved. Again, depending on the respective biological microenvironment, the protein coating appears to determine the fate of the particular NP. Complement and immunoglobulin binding may trigger particle opsonization, thus leading to phagocytic ingestion; whereas particle-bound ligands may activate extracellular receptor-signaling and/or receptor-mediated endocytic uptake.[59,60] Reported cell-signaling pathways activated by NPs include receptor-tyrosine kinases, stress-activated protein kinases, pattern recognition receptors, as well as mitogen-activated protein kinases.[29,61] Also, direct NP penetration of the plasma membrane, without the need to involve endocytic compartments, has also been suggested, and this may contribute to nanomaterial toxicity.[60]

In addition to the complications described above, nanoparticles have a tendency to agglomerate, or form multiple single particle clusters when in a biological environment. Consequently, the observed differences in (patho)biological responses elicited by nanomaterials in the absence or presence of proteins (**Figure 15**) may also be due to protein-mediated NP aggregation, which reduces the effective cellular exposure dose[28,62] (**Figure 2**).

3.319.5. Conclusions and Outlook

Analyzing and predicting the impact of nanomaterials on biological systems is particularly complex. It combines numerous methodological challenges ranging from particle characterization in the absence and presence of biological fluids, their interactions with biological nanoscale or nanostructured surfaces as well as the dissection of NP-induced (patho) biological effects.

As outlined above, there are currently numerous highly sophisticated techniques available that allow the physicochemical characterization of nanomaterials in their respective (biological) environments. Also, various disciplines in the areas of life science hold an immense knowledge of how cells, organs, and whole organisms react to environmental nanoscale stimuli, such as viruses, proteins, and metabolites.

Despite this knowledge, we still lack an in-depth, mechanistic, molecular understanding of whether and how NP-induced biological responses are triggered; whether predominantly by extra- and/or intracellular NPs, and to what extent the physicochemical properties of these particles, as well as a (specific) protein/biomolecule-corona, is critical for these effects. This hurdle can only be overcome by an interdisciplinary joint endeavor. The identification and understanding of the large number of forces that determine these processes, such as the formation of the protein corona, cellular contact and signaling, particle entry as well as intracellular biocatalysis, demand systematic experimental approaches and improved technologies. The obtained insights will help us to comprehend the orchestration of the nano–bio interface and thus permit prediction of whether the nanomaterial is biocompatible or bioadverse for a given application.

Acknowledgments

Grant support: DFG Priority Programme SPP1313-BIONEERS, Medical University Mainz Priority Program (BIOMATICS), BMBF NanoKon, Novartis-Foundation for Therapeutic Research, Stiftung Rheinland-Pfalz für Innovationen.

References

1. Williams, D. F. *Biomaterials* **2008**, *29*, 2941–2953.
2. Nel, A.; Xia, T.; Madler, L.; Li, N. *Science* **2006**, *311*, 622–627.
3. Oberdorster, G.; Maynard, A.; Donaldson, K.; *et al*. *Part. Fibre Toxicol*. **2005**, *2*, 8.
4. Vertegel, A. A.; Siegel, R. W.; Dordick, J. S. *Langmuir* **2004**, *20*, 6800–6807.
5. Sigmund, W.; Pyrdiotakis, G.; Daga, A. *Chemical Processing of Ceramics*. CRC Press: Boca Raton, FL, 2005.
6. Gilbert, B.; Huang, F.; Zhang, H. Z.; Waychunas, G. A.; Banfield, J. F. *Science* **2004**, *305*, 651–654.
7. Min, Y. J.; Akbulut, M.; Kristiansen, K.; Golan, Y.; Israelachvili, J. *Nat. Mater*. **2008**, *7*, 527–538.
8. Velegol, D. *J. Nanophotonics* **2007**, *1*, 1–25.
9. Dagastine, R. R.; Manica, R.; Carnie, S. L.; Chan, D. Y. C.; Stevens, G. W.; Grieser, F. *Science* **2006**, *313*, 210–213.
10. Kim, H. Y.; Sofo, J. O.; Velegol, D.; Cole, M. W.; Lucas, A. A. *Langmuir* **2007**, *23*, 1735–1740.
11. Delgado, A. V.; Gonzalez-Caballero, F.; Hunter, R. J.; Koopal, L. K.; Lyklema, J. *J. Colloid Interface Sci*. **2007**, *309*, 194–224.
12. Schärtl, W. *Light Scattering from Polymer Solutions and Nanoparticle Dispersions*. Springer: New York, 2007.
13. Jones, C. F.; Grainger, D. W. *Adv. Drug Deliv. Rev*. **2009**, *61*, 438–456.
14. Diehl, C.; Fluegel, S.; Fischer, K.; Maskos, M. *Prog. Colloid Polym. Sci*. **2008**, *134*, 128.
15. Orts-Gil, G.; Natte, K.; Drescher, D.; *et al*. *J. Nanopart. Res*. **2010**, 1–12.
16. Glatter, O.; Kratky, O. *Small-Angle X-ray Scattering*. Academic Press: New York, 1982.
17. Glatter, O.; May, R. *International Tables for Crystallography C*. Kluwer Academic: Boston, MA, 1999.
18. Guinier, A.; Fournet, G. *Small-Angle Scattering of X-rays*. Wiley: New York, 1955.
19. Harris, J. R.; Roos, C.; Djalali, R.; Rheingans, O.; Maskos, M.; Schmidt, M. *Micron* **1999**, *30*, 289–298.
20. Müller, W.; Koynov, K.; Fischer, K.; *et al*. *Macromolecules* **2009**, *42*, 357–361.
21. Binnig, G.; Quate, C. F.; Gerber, C. *Phys. Rev. Lett*. **1986**, *56*, 930–933.
22. Cölfen, H., Antonietti, M., Eds.; In *Field-Flow Fractionation Techniques for Polymer and Colloid Analysis*; Springer: New York, 2000.
23. Schimpf, M.; Cadwell, K.; Giddings, J. C. *Field-Flow Fractionation Handbook*. Wiley-Interscience: New York, 2000.
24. Wahlhund, K. G.; Giddings, J. C. *Anal. Chem*. **1987**, *59*, 1332–1339.
25. Jungmann, N.; Schmidt, M.; Maskos, M. *Macromolecules* **2001**, *34*, 8347–8353.
26. Scherer, C.; Noskov, S.; Utech, S.; *et al*. *J. Nanosci. Nanotechnol*. **2010**, *10*, 6834–6839.
27. Tadjiki, S.; Assemi, S.; Deering, C. E.; Veranth, J. M.; Miller, J. D. *J. Nanopart. Res*. **2009**, *11*, 981–988.
28. Borm, P.; Klaessig, F. C.; Landry, T. D.; *et al*. *Toxicol. Sci*. **2006**, *90*, 23–32.
29. Nel, A. E.; Madler, L.; Velegol, D.; *et al*. *Nat. Mater*. **2009**, *8*, 543–557.
30. Stern, S. T.; McNeil, S. E. *Toxicol. Sci*. **2008**, *101*, 4–21.
31. Adiseshaiah, P. P.; Hall, J. B.; McNeil, S. E. *Wiley Interdiscip. Rev. Nanomed. Nanobiotechnol*. **2010**, *2*, 99–112.
32. Borm, P. J.; Robbins, D.; Haubold, S.; *et al*. *Part. Fibre Toxicol*. **2006**, *3*, 11.
33. Satterfield, T.; Kandlikar, M.; Beaudrie, C. E.; Conti, J.; Herr Harthorn, B. *Nat. Nanotechnol*. **2009**, *4*, 752–758.
34. Xia, X. R.; Monteiro-Riviere, N. A.; Riviere, J. E. *Nat. Nanotechnol*. **2010**, *5*, 671–675.
35. Nowack, B. *Environ. Pollut*. **2009**, *157*, 1063–1064.
36. Scown, T. M.; van Aerle, R.; Tyler, C. R. *Crit. Rev. Toxicol*. **2010**, *40*, 653–670.
37. Rücker, E.; Schneider, G.; Steinhäuser, K.; Löwer, R.; Hauber, J.; Stauber, R. H. *Protein Expr. Purif*. **2001**, *21*, 220–223.
38. Lehmann, A. D.; Parak, W. J.; Zhang, F.; *et al*. *Small* **2010**, *6*, 753–762.
39. Linse, S.; Cabaleiro-Lago, C.; Xue, W. F.; *et al*. *Proc. Natl. Acad. Sci. USA* **2007**, *104*, 8691–8696.
40. Leszczynski, J. *Nat. Nanotechnol*. **2010**, *5*, 633–634.

41. Barrena, R.; Casals, E.; Colon, J.; Font, X.; Sanchez, A.; Puntes, V. *Chemosphere* **2009**, *75*, 850–857.
42. Muhlfeld, C.; Rothen-Rutishauser, B.; Blank, F.; Vanhecke, D.; Ochs, M.; Gehr, P. *Am. J. Physiol. Lung Cell Mol. Physiol.* **2008**, *294*(5), L817–L829.
43. Tetley, T. D. *Biochem. Soc. Trans.* **2007**, *35*, 527–531.
44. Gao, X.; Chen, J.; Tao, W.; *et al. Int. J. Pharm.* **2007**, *340*, 207–215.
45. Oberdorster, G.; Elder, A.; Rinderknecht, A. *J. Nanosci. Nanotechnol.* **2009**, *9*, 4996–5007.
46. Wang, B.; Feng, W. Y.; Wang, M.; *et al. Biol. Trace Elem. Res.* **2007**, *118*, 233–243.
47. Adler, K. B.; Shapiro, S. D.; Gallup, M.; *et al. Am. J. Respir. Cell Mol. Biol.* **2006**, *34*, 523–526.
48. Poland, C. A.; Duffin, R.; Kinloch, I.; *et al. Nat. Nanotechnol.* **2008**, *3*, 423–428.
49. Hermanns, M. I.; Kasper, J.; Dubruel, P.; *et al. J. R. Soc. Interface* **2010**, *7*(Suppl. 1), S41–S54.
50. Lehmann, A. D.; Parak, W. J.; Zhang, F.; *et al. Small* **2010**, *6*.
51. Roy, I.; Vij, N. *Nanomedicine* **2010**, *6*, 237–244.
52. Harishchandra, R. K.; Saleem, M.; Galla, H. J. *J. R. Soc. Interface* **2010**, *7*(Suppl. 1), S15–S26.
53. Saleem, M.; Galla, H. J. *Biochim. Biophys. Acta* **2010**, *1798*, 730–740.
54. Puzyn, T.; Leszczynska, D.; Leszczynski, J. *Small* **2009**, *5*, 2494–2509.
55. Rothen-Rutishauser, B.; Blank, F.; Muhlfeld, C.; Gehr, P. *Expert Opin. Drug Metab. Toxicol.* **2008**, *4*, 1075–1089.
56. Rocker, C.; Potzl, M.; Zhang, F.; Parak, W. J.; Nienhaus, G. U. *Nat. Nanotechnol.* **2009**, *4*, 577–580.
57. Ferrari, M. *Nat. Nanotechnol.* **2008**, *3*, 131–132.
58. Verma, A.; Stellacci, F. *Small* **2010**, *6*, 12–21.
59. Decuzzi, P.; Ferrari, M. *Biomaterials* **2007**, *28*, 2915–2922.
60. Verma, A.; Uzun, O.; Hu, Y.; *et al. Nat. Mater.* **2008**, *7*, 588–595.
61. Ding, L.; Stilwell, J.; Zhang, T.; *et al. Nano Lett.* **2005**, *5*, 2448–2464.
62. Pettibone, J. M.; Cwiertny, D. M.; Scherer, M.; Grassian, V. H. *Langmuir* **2008**, *24*, 6659–6667.

3.320. Nanostructured Polymeric Films for Cell Biology

A D Presley and N Dube, University of California, Berkeley, CA, USA
T Xu, University of California, Berkeley, CA, USA; Lawrence Berkeley National Laboratory, Berkeley, CA, USA

© 2011 Elsevier Ltd. All rights reserved.

3.320.1.	**Introduction**	341
3.320.2.	**Controlled Protein Adsorption on BCP and Polymer Blend Surfaces**	342
3.320.2.1.	Protein Adsorption on Homopolymer Blend Surfaces	342
3.320.2.2.	Protein Adsorption on BCP Thin Film Templates	343
3.320.3.	**Protein and Cell Binding via Affinity Interactions Templated by Polymer Surfaces**	345
3.320.3.1.	Protein Immobilization and Patterning on Polymer Affinity Templates	345
3.320.3.2.	BCP Nanolithography and Its Application in Cell Biology	346
3.320.3.3.	Other BCP Platforms for Cell Culture Studies	348
3.320.4.	**Coassembly of BCPS with Peptides and Proteins in Thin Films**	348
3.320.5.	**BCP Surfaces for Biocompatibility and Antifouling Applications**	350
3.320.5.1.	Biocompatibility of Poly(2-hydroxyethyl methacrylate)-Based Copolymers	350
3.320.5.2.	Structural Implications for PU Biocompatibility	351
3.320.5.3.	BCP Surfaces for Marine Antifouling Applications	351
3.320.6.	**BCP Micelle Surfaces for Controlled Release Applications**	352
3.320.7.	**Conclusion**	353
References		353

Abbreviations

AFM	Atomic force microscopy
BCM	Block-copolymer micelle
BCP	Block copolymer
EBL	Electron beam lithography
QCM	Quartz crystal microbalance
SPM	Scanned-probed microscopy
SPR	Surface plasmon resonance
TEM	Transmission electron microscopy
TOF-SIMS	Time-of-flight secondary ion mass spectrometry
XPS	X-ray photoelectron spectroscopy

3.320.1. Introduction

Immobilized proteins have long found use in various applications including biosensing,[1] diagnostics,[2] and fine chemicals synthesis.[3] More recently, much effort has focused on immobilization of proteins in defined patterns resulting in arrays that allow for high-throughput, parallel assessment of proteins in proteomics studies[4] as biomarkers for cancer and other diseases,[5] and in drug discovery.[6] Present technologies rely in large part on patterns exhibiting micron- to millimeter-scale features. However, protein patterning on the nanoscale becomes ever more desirable as the scope of biochemical screening and demand for high-density platforms increase. As pattern density continues to increase, so will the scope and throughput for profiling of disease markers and other targets. Other potential benefits of nanoscale array platforms include lower sample volume requirements[7] and enhanced sensitivity for detection of low-abundance analytes.[8,9]

Furthermore, nanoscale patterning strategies enable the study of biophysical processes on length scales that are commensurate with the key protein effectors themselves. Cells and tissues exhibit hierarchically ordered structure including regular nanoscale morphologies such as collagen fibers in the extracellular matrix and hydroxyapatite crystals in bone tissue. Nonbiological substrates with defined nanotopography have been designed to mimic these biological structures as well as to elicit new responses from cells and tissues. Indeed, these designed substrates have been used to study and modulate processes including cellular adhesion, surface antigen presentation, and intracellular signaling pathways.[10] These processes are influenced not only by the physical topography of cellular nanostructures, but also by the arrangement of cell surface ligands and other chemical cues. As described below, nanoscale biochemical platforms have been developed to study spatial determinants of processes such as cell motility and apoptosis.[11,12] Further development of protein nanoarrays with defined topography may therefore create new fundamental biological knowledge.

Recent reviews have highlighted patterning of proteins and other biomolecules on the nanoscale by a variety of processes including photolithography and electron beam lithography (EBL), 'soft' lithographic techniques including microcontact printing, and scanned-probed microscopy (SPM)-based techniques such as dip-pen nanolithography.[13–15] Stamping processes allow for simple and rapid patterning of large areas, albeit with lower resolution than serial processes such as SPM- and EBL-based techniques. These serial processes can be more complicated and are relatively slow, although various

strategies have been developed to overcome throughput limitations. In total, these techniques have resulted in high-resolution protein patterns covering large areas.

Self-assembly of block copolymers (BCPs) is an attractive strategy for fabrication of materials systems with nanoscale control of biomolecules. This is because BCPs are characterized by well-defined nanometer-scale features due to the microphase separation of chemically incompatible polymers that are covalently linked together.[16,17] The size of the morphologies depends on the molecular weight ratio of the various blocks. Long-range order can be achieved with a variety of techniques, including annealing with selective solvents[18–20] or elevated temperatures;[21,22] application of external electric fields[23,24] and shear forces;[25] and use of topographically defined substrates.[26,27] This ready processability holds great promise for straightforward control of protein organization over large areas. BCP thin films and bulk preparations have been extensively utilized in various materials applications as templates for the synthesis of inorganic and magnetic materials,[28,29] masks for photolithography and other patterning techniques,[30] scaffolds for nanodevices,[30] and functional membrane materials.[22,31,32] The structure and functionality of conventional BCP thin films can be augmented through the incorporation of small molecules, homopolymers, and inorganic nanoparticles.

Several recent studies have demonstrated that biological molecules such as proteins can be incorporated in BCP assemblies, as reviewed in the following pages. In certain cases, systems have been developed for defined nanoscale patterning of proteins for biochemical assays as well as biological ligands for study of surface-mediated cellular processes. In other cases, polymer nanostructure has been used to modulate materials interactions with biological media, such as blood, in the context of biomedical devices. This review is limited to studies of protein interactions with surfaces of BCPs (as well as some polymer blends) in condensed phases – namely, BCP thin films. BCP self-assembly in solution has led to several examples of hydrogel and micelle materials that are particularly interesting as delivery vehicles for therapeutics and other cargo. While those solution-based systems are outside of the scope of this review, films and surface coatings containing BCP micelles for delivery applications are described. The reader is also directed to additional chapters in these volumes – including **Chapter 4.401, The Concept of Biocompatibility**; **Chapter 4.409, Surfaces and Cell Behavior**; **Chapter 1.129, Engineering the Biophysical Properties of Basement Membranes into Biomaterials: Fabrication and Effects on Cell Behavior**; **Chapter 4.411, Peptide- and Protein-Modified Surfaces**; and **Chapter 4.413, Patterned Biointerfaces** for in-depth review of nanostructured materials and their interactions with proteins, cells, and tissues.

3.320.2. Controlled Protein Adsorption on BCP and Polymer Blend Surfaces

3.320.2.1. Protein Adsorption on Homopolymer Blend Surfaces

Blending of immiscible polymers can result in composite materials with unique and useful physical and chemical properties. The thermodynamics of polymer–polymer phase behavior has been investigated experimentally and theoretically, and macrophase separation of immiscible polymers typically results in domains that are on the order of microns in size.[33] Polymer blend surface coatings, micropheres, and nanofibers have been studied with respect to cell culture, drug delivery, and tissue engineering in various biological systems.[34–36] Understanding of protein adsorption phenomena on polymer biomaterials is critically important because protein adsorption is usually the first event upon introduction to biological milieu, as in the case of *in vivo* implantation of biomedical devices. Adsorbed proteins, in turn, direct interactions with cells and tissues and control downstream biological processes.[37] For further insight on polymers and related protein adsorption phenomena, refer to **Chapter 4.406, Protein Interactions with Biomaterials**; **Chapter 1.122, Structural Biomedical Polymers (Nondegradable)**; and **Chapter 1.124, Polymer Films Using LbL Self-Assembly** in this series.

Libera and colleagues have studied the adsorption of ferritin, a protein nanocontainer with an iron core, on binary blends of hydrophobic poly(desaminotyrosyl-tyrosine dodecyl ester carbonate) (PDTD) with poly(ε-caprolactone) (PCL).[38,39] Adsorption was conveniently characterized by transmission electron microscopy (TEM) because of ferritin's electron-dense core, and pH-dependent behavior was discussed in terms of both hydrophilic and electrostatic interactions with the polymer surface. Near physiological pH, selective adsorption occurred on PDTD domains, which was attributed to repulsion of negatively charged ferritin by carboxylate groups of hydrolyzed PCL (**Figure 1(a)**). Selective adsorption did not occur under acidic conditions, when polymer surface charges are effectively neutralized.[39] When acidic ferritin residues were alkylated with dodecylamine, the resulting positively charged protein nanoparticles demonstrated strong preferential adsorption on negatively charged PCL phases (**Figure 1(b)**).[38] Direct incorporation of modified ferritin in PDTD/PEO blends was also investigated.[40] Alkylation of acidic amino acid residues with dodecylamine or amine-terminated poly (ethylene oxide) (PEO) imparted solubility in organic solvent to the ferritin nanoparticles. When blended with PDTD/PEO mixtures and cast in films, ferritin behavior depended on the surface functionalization. The ferritin–PEO conjugate was found to localize within PEO domains, while the ferritin–dodecylamine conjugate was localized within PDTD domains.

A number of analytical techniques have been employed for the study of protein adsorption on polymer surfaces and other materials. TEM and atomic force microscopy (AFM) provide direct visualization of protein adsorption with high resolution, while techniques such as X-ray photoelectron spectroscopy (XPS), time-of-flight secondary ion mass spectrometry (TOF-SIMS), and surface plasmon resonance (SPR) can be used to probe the proteins' chemical and biophysical properties.[41] For review of these and other analytical techniques (see **Chapter 3.302, Atomic Force Microscopy** and **Chapter 2.219, Biophysical Analysis of Amyloid Formation**). Recently, protein adsorption on polymer blend surfaces has also been used as a model biological system in the development of soft X-ray spectromicroscopy techniques.[42,43] These techniques have the potential to quantitatively probe chemical complexity with a resolution of 50 nm or better, on the basis of the distinct X-ray absorption fine structure

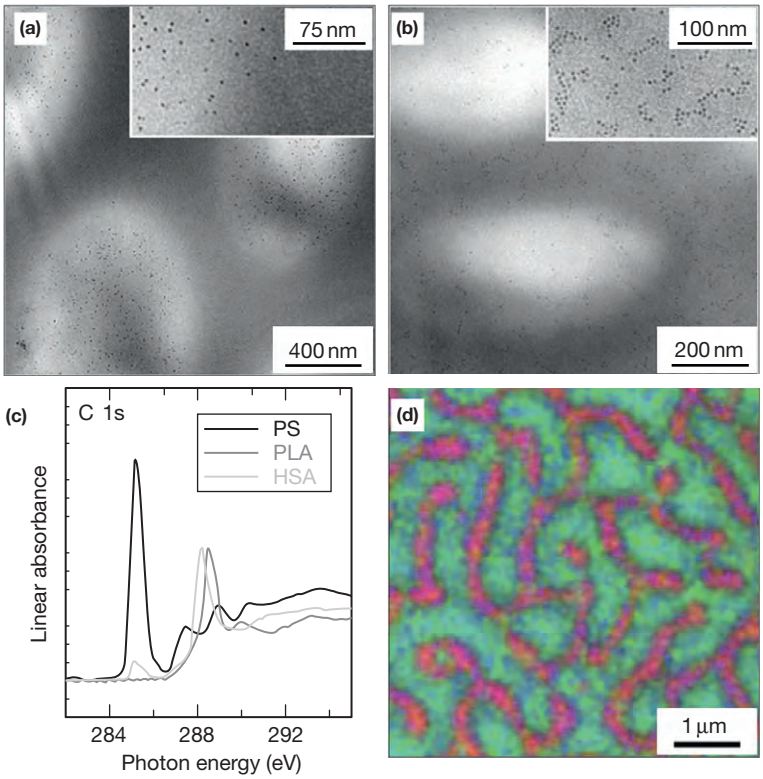

Figure 1 (a) and (b) Selective electrostatic adsorption of ferritin nanoparticles on homopolymer blend surfaces consisting of poly(desaminotyrosyl-tyrosine dodecyl ester carbonate) (PDTD) and poly(ε-caprolactone) (PCL). (a) At pH 5.8, unmodified wild-type ferritin adsorbs to PDTD domains (dark regions in TEM micrographs), which is attributed to repulsion of negatively charged proteins by negatively charged PCL domains. (b) Positively charged alkylated ferritin particles adsorb to negatively charged PCL domains (light regions in TEM micrographs) at pH 5.8. (a, b) Reprinted from Sengonul, M.; Sousa, A.; Libera, M. *Colloids Surf. B Biointerfaces* **2009**, *73*, 152–155, with permission from Elsevier. (c) and (d) X-ray photoemission electron microscopy (X-PEEM) analysis of human serum albumin (HSA) adsorption on homopolymer blend surfaces consisting of PS and polylactide (PLA). (c) C 1s X-ray absorption spectra of PS (black), PLA (dark gray), and HSA (light gray). Sample components can be identified and mapped in X-PEEM on the basis of their unique spectroscopic signatures. (d) Color composite map based on C 1s spectral data obtained by X-PEEM imaging (red, PS; green, PLA; blue, HSA). Preferential adsorption of HSA was observed at polymer domain interfaces. (c, d) Reprinted from Leung, B. O.; Hitchcock, A. P.; Cornelius, R.; Brash, J. L.; Scholl, A.; Doran, A. *Biomacromolecules* **2009**, *10*, 1838–1845, with permission from American Chemical Society.

of individual protein or polymer constituents (Figure 1(c)). Scanning transmission X-ray microscopy (STXM) measures wavelength-dependent optical density through a column of bulk material, and the technique can be applied to samples under vacuum, in air, or in a liquid cell. X-ray photoelectron emission microscopy (XPEEM) records the wavelength-dependent distribution of electrons ejected from a surface after X-ray absorption. XPEEM may therefore provide superior sensitivity for investigation of surface phenomena, as sampling depths are in the order of 5–10 nm, although the technique requires high-vacuum environments that may not be compatible with certain biological samples.

Protein adsorption behavior as characterized by XPEEM and STXM is consistent with phenomena as discussed above, although this behavior was observed to vary depending on the hydration state and sample treatment. Human serum albumin (HSA) was found to preferentially adsorb to the polystyrene (PS) domains in films consisting of a blend of PS and poly (methyl methacrylate) (PMMA), as characterized by XPEEM (Figure 1(d)). This was attributed to the hydrophobicity differential, as PS is more hydrophobic than PMMA. Highest adsorption levels, however, were observed at PS/PMMA interfaces.[43] Differential localization with varying pH was attributed to known conformational changes of HSA that modulate protein surface hydrophobicity.[42] When the same system was investigated under hydrated conditions using STXM, adsorption of HSA at PS/PMMA interfaces was observed along with adsorption of loosely bound HSA on PMMA.[44] This loosely bound protein could be removed with washing, and the resulting samples more closely resembled those characterized by XPEEM and other *ex situ* techniques. Other systems investigated by these X-ray techniques include adsorption of fibrinogen[45,46] and HSA[45,47] on polyurethane (PU) composite surfaces[45] and PS/polylactide (PLA) blends.[47]

3.320.2.2. Protein Adsorption on BCP Thin Film Templates

When immiscible polymers are tethered covalently as BCPs, self-assembled morphologies are reduced to length scales in the order of tens of nanometers.[16] As discussed above, BCP systems in this size regime may provide access to experimental platforms for basic research and new biotechnology. Hahm and coworkers demonstrated patterning of proteins via adsorption on self-assembled diblock-copolymer thin films.[48–51]

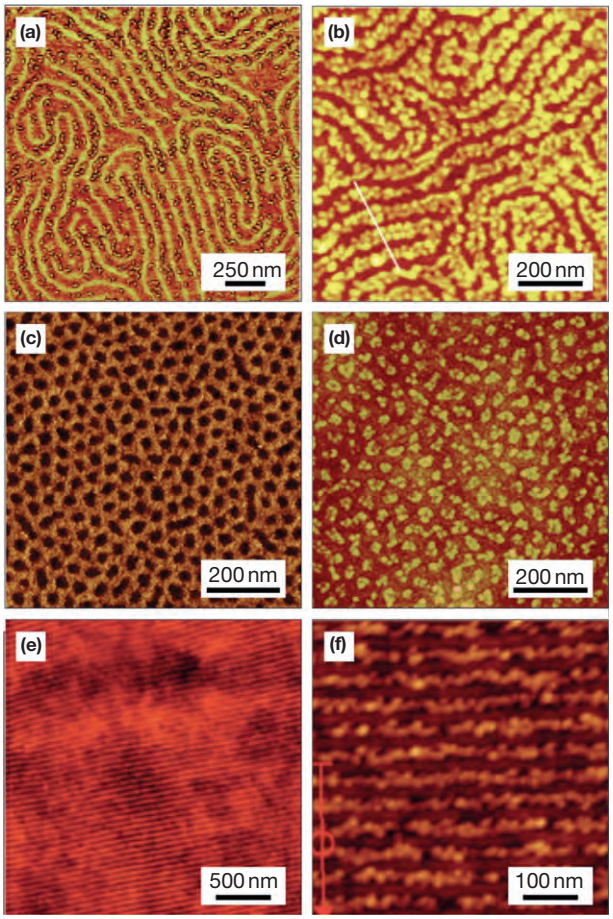

Figure 2 Patterning of proteins on thin film templates via preferential protein binding to hydrophobic microdomains. (a) and (b) IgG adsorbed on PS-*b*-PMMA thin films exhibiting lamellar morphology. IgG selectively adsorbs on PS microdomains, and density of adsorbed protein depends on solution concentration. (a, b) Reprinted from Kumar, N.; Hahm, J. I. *Langmuir* **2005**, *21*, 6652–6655, with permission from American Chemical Society. (c) PS-*b*-PMMA thin films exhibiting cylindrical morphology, (d) IgG adsorbed on PS-*b*-PMMA thin films exhibiting cylindrical morphology, (e) and (f) y-globulin adsorbed on ordered PS-*b*-PMMA thin films. Ordering of lamellar microdomains was accomplished via modulation of film thickness. (c, d) Reprinted from Li, Q.; Lau, K. H. A.; Sinner, E. K.; Kim, D. H.; Knoll, W. *Langmuir* **2009**, *25*, 12144–12150, with permission from American Chemical Society. (e, f) Reprinted from Matsusaki, M.; Omichi, M.; Kadowaki, K.; *et al*. *Chem. Commun*. **2010**, *46*, 1911–1913, with permission from The Royal Society of Chemistry.

Thermally annealed PS-*b*-PMMA thin films were prepared on silicon substrates, leading to phase-separated lamellar nanostructured films. Preferential adsorption of immunoglobulins (IgGs) and protein G, an IgG binder, on PS domains was demonstrated, as observed by AFM (Figure 2(a) and 2(b)).[48] Patterns were found to conform to the underlying film morphology, and hexagonal protein arrays were generated using copolymers with a minor PS fraction. Subsequent investigation demonstrated preferential adsorption at PS/PMMA interfaces, where films composed of diblock copolymers and homopolymer blends led to higher levels of protein adsorption than homogenous films composed of homopolymers alone.[50] Furthermore, a distance dependence was observed for homopolymer blend films where the number of adsorbed proteins decreased as distance from the interface increased. This suggests that film topography plays an important role in segregation behavior, and that BCP films – which are characterized by well-defined polymer interfaces at regular intervals – are uniquely suited to creation of high-density protein arrays.

Enzymatic activity of immobilized enzymes horseradish peroxidase (HRP) and mushroom tyrosinase was demonstrated, as judged by oxidation of small-molecule substrates such as tetramethylbenzidine and pyrocatechol in colorometric assays.[49] HRP, in particular, retained approximately 85% activity as compared to free enzyme in solution, indicating that the structure of the adsorbed proteins was maintained during patterning on BCP films.[51] Notably, maintenance of enzymatic activity over several months was demonstrated. Preservation of protein structure was also supported by confocal fluorescence microscopy experiments, which demonstrated the retention of structure-dependent fluorescence of enhanced green fluorescent protein (eGFP) and binding of fluorescently labeled IgGs by adsorbed protein G.

Patterning strategies have been developed for various iterations of other amphiphilic BCP systems. Preferential segregation of HRP and IgG was observed on PS phases of films consisting of polystyrene-*b*-poly(4-vinylpyridine) (PS-*b*-P4VP) micelles. Micelle morphology was controlled by exposure to selective solvent vapors, which in turn dictated the protein pattern morphology.[52] Derivatization of poly(acrylic acid) (PAA) blocks in PS-*b*-PAA thin films with amine-functionalized silanes resulted in positively charged domains that were used for patterning of negatively charged actin filaments via electrostatic interactions.[53]

Lau and coworkers employed PS-*b*-PMMA thin films as an antibody-array platform for immunoassays and DNA detection.[54–56] Gold-coated substrates were modified with a neutral brush layer consisting of poly(styrene-*r*-benzocyclobutene-*r*-methyl methacrylate)[57] prior to casting and thermal annealing of PS-*b*-PMMA films. The resulting templates exhibited hexagonally packed PS cylinders surrounded by a PMMA matrix (Figure 2(c) and 2(d)). After preferential adsorption of IgGs to PS domains in a manner similar to that described above, nonspecific binding of proteins during downstream operations was prevented by blocking with bovine serum albumin (BSA). Capture of rabbit-α-mouse antigens (RxM-IgGs) from solution by the patterned goat-α-rabbit antibodies (GxR-IgGs) was probed using SPR as shown in Figure 3.[55] Greater sensitivity was observed when the patterned GxR-IgGs were tested as antigens for mouse-α-goat antibodies (MxG-IgGs) in solution. This was interpreted as a result of randomly oriented immobilized IgGs leading to partial restriction of antigen binding. Fluorescence-based DNA detection was also demonstrated in a sandwich assay utilizing immobilized streptavidin and biotinylated peptide–nucleic acid probes. Interestingly, the protein patterns could be stabilized for use over extended periods by covalently cross-linking the adsorbed proteins.

The SPR techniques used in these experiments allowed for a quantitative study of binding preference on different BCP phases. As observed in other studies, IgGs exhibit preferential adsorption at PS/PMMA interfaces.[54] The amount

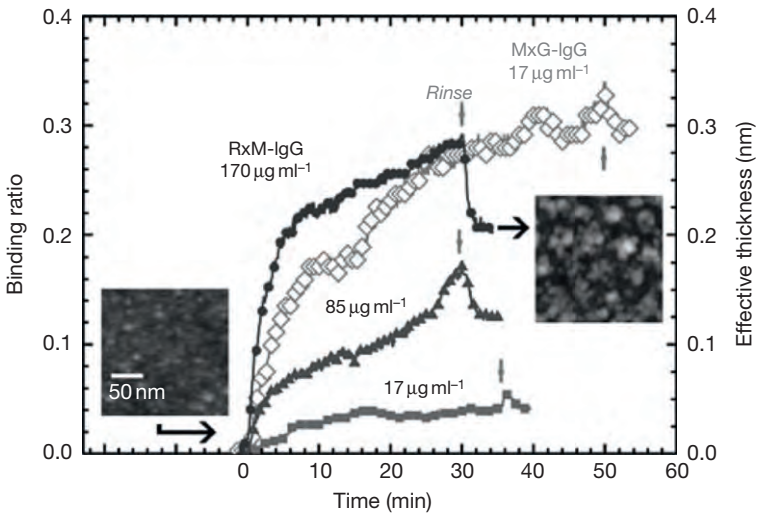

Figure 3 SPR analysis of antigen binding to GxR-IgG patterned on PS-*b*-PMMA templates. Binding of MxG-IgG to the immobilized antibodies is more efficient than capture of RxM-IgG by the immobilized antibodies. Film thickness (indicated on right axis) increases because of antigen binding, and bound antigens can be removed when rinsed with buffer (indicated by gray arrows above SPR traces). Antibody patterns are filled with BSA to block nonspecific antigen binding, resulting in smooth surfaces (as indicated by AFM topography image in left inset). Binding of antigens to immobilized antibodies results in reappearance of the nanoarray pattern (right inset). Reprinted from Lau, K. H. A.; Bang, J.; Kim, D. H.; Knoll, W. *Adv. Funct. Mater.* **2008**, *18*, 3148–3157, with permission from Wiley.

of 'excess' adsorbed protein on a given substrate (i.e., the amount exceeding levels expected based solely on the surface fractions of PS and PMMA) was found to depend on the length density of domain interfaces. Indeed, no direct relationship between excess adsorption and domain morphology or the surface fraction of either phase was discerned. Adsorption at domain interfaces was estimated to be approximately three times higher than on PS domains and approximately seven times higher than on PMMA domains.

Long-range ordering of BCP thin films can be achieved by a variety of means as described above. Recently, a controlled film thickness gradient was used to create PS-*b*-PMMA templates exhibiting highly aligned lamellae over large areas (**Figure 2(e)** and **2(f)**).[58] These thin film templates were then used for adsorption of serum proteins as well as cell adhesion proteins such as fibronectin (FN) and collagen. Again, protein adsorption was largely confined to hydrophobic PS domains as observed by AFM. Flexible fibrinogen fibers were observed to align along the length of the PS lamellae, whereas more rigid collagen fibers spanned both PS and PMMA lamellae in a grid-type morphology. The authors concluded that protein physical characteristics such as rigidity may play a significant role in determining the morphologies of resulting protein patterns.

Protein nanopatterning has not been limited to amphiphilic copolymers such as PS-*b*-PMMA. Protein nanopatterning using a diblock copolymer with two hydrophobic blocks, polystyrene-*block*-polyisoprene (PS-*b*-PI), was recently demonstrated.[59] Protein distributions were characterized by AFM and SIMS. BSA segregation on 'hard' (glassy) PS domains was observed, while 'soft' (rubbery) PI domains remained free of protein. Interestingly, pattern fidelity on this hydrophobic template was observed after BSA adsorption at higher concentrations ($\sim$1 mg ml^{-1}) and longer incubation times (>1 h) than for amphiphilic templates such as PS-*b*-PMMA, which could broaden the applicability of the technique for various patterning uses. Control of protein adsorption on nanostructured surfaces using fully hydrophilic BCPs requires polymer attachment to the underlying substrate in order to prevent film degradation in aqueous environments. Recently, surface-initiated atom transfer radical polymerization was employed for covalent modification of silicon substrates with poly(oligo (ethylene glycol) methacrylate)-*block*-poly(2-methacryloyloxy) ethyl trimethylammonium chloride (POEGMA-*b*-PMETAC).[60] Resulting surfaces contained a protein-resistant POEGMA matrix and protein-binding PMETAC domains. Phase separation of the two hydrophilic domains was induced by addition of sodium chloride, shielding positive charges in the polyelectrolyte PMETAC block, and various copolymer morphologies were achieved by adjusting the volume fraction of PMETAC in the copolymer. Quantification of ^{125}I-labeled protein adsorption was carried out by scintillation counting, and selective fibrinogen binding on PMETAC domains was observed by AFM. This preferential adsorption was attributed to electrostatic interactions between the protein and polyelectrolyte. Patterning employing fully hydrophilic polymers may prove useful for proteins that are particularly sensitive to denaturation caused by nonspecific hydrophobic surface interactions.

3.320.3. Protein and Cell Binding via Affinity Interactions Templated by Polymer Surfaces

3.320.3.1. Protein Immobilization and Patterning on Polymer Affinity Templates

Thus far, the systems outlined here rely primarily on nonspecific hydrophobic or electrostatic adsorption of proteins to polymer surfaces. This approach is operationally simple and widely employed to fabricate high-density biomolecular arrays, although significant drawbacks include restricted functionality due to randomly oriented proteins as well as reduced

activity due to varying degrees of denaturation. On the other hand, immobilization of target proteins via specific interactions with biological ligands can ensure proper protein orientation and limit denaturation. Furthermore, complex targets such as whole cells could be recruited to surfaces for the study of specific biological processes. Several studies have capitalized on such affinity interactions for specific protein binding on polymer surfaces.

Cresce and coworkers demonstrated chelation of nickel ions by poly(norbornenedicarboxylic acid) in a norbornene–norbornendicarboxylic acid BCP.[61] The nickel-BCP chelate was cast in thin films and used in the template binding of recombinant histidine-tagged GFP, which was observed by fluorescence spectroscopy. Selective GFP localization on the Ni-containing block was inferred from control experiments that indicated a lack of protein binding on thin films consisting of BCP in the absence of added nickel. Recently, histidine-tagged GFP was immobilized on PB-*b*-PEO surfaces bearing Ni^{2+}–nitrilotriacetic acid (NTA) groups at PEO chain ends.[62] In this case, a PB-*b*-PEO monolayer was formed at the air–water interface and transferred to a graphite substrate such that the surface layer was composed entirely of the PEO block. GFP binding to PB-*b*-PEO micelles in aqueous solution was also characterized. In another example, flexible patterned polymer substrates were fabricated by compressing alternating layers of polyethylene and an ethylene-*co*-(acrylic acid) (EAA) copolymer.[63] The resulting material was sectioned with a microtome to expose patterns containing 7-micron stripes, and the EAA layers were subsequently derivatized with amine-functionalized biotin via amide bond formation. Binding of dye-labeled streptavidin to the biotinylated EAA layers was observed by fluorescence microscopy, while the ethylene layers remained free of protein. Because streptavidin contains multiple biotin-binding sites, the streptavidin patterns could be used to recruit other biotinylated molecules of interest to the patterned surfaces.

3.320.3.2. BCP Nanolithography and Its Application in Cell Biology

Spatz and coworkers have developed an elegant and versatile technique, termed block-copolymer micelle (BCM) nanolithography, and used it to create nanopatterned surfaces with biological ligands placed at defined intervals (**Figure 4**).[64] In this technique, gold salts are complexed with the poly(vinylpyridine) block of PS-*b*-P2VP micelles. Films are formed by immersing a substrate in a micelle solution and withdrawing it at a controlled rate. Following exposure to gas plasma that removes the polymer and reduces the gold salts, hexagonal arrays of spherical gold nanoparticles are observed on the substrate surface. Biological ligands are introduced on the nanoparticle surfaces via formation of stable gold-thiol bonds, and bare regions of the substrate are passivated with coatings such as PEO. Much work has been done using cyclic RGD-containing peptides as ligands, which are bound by integrins on cell surfaces.[65–67] Substrates fabricated via BCP micelle nanolithography resulted in patterns of RGD with precise spacings of 30–90 nm, depending on the volume ratio of the PS-*b*-P2VP employed. The RGD patches in the arrays were ~8 nm in diameter, providing a binding site for one 8–12 nm integrin. MC3T3 osteoblasts were shown to adhere to patterns with RDG spacings ≤58 (**Figure 5(a)** and **5(b)**), but this behavior was drastically reduced with spacings ≥73 nm (**Figure 5(b)**). Furthermore, smaller RGD spacings led to greater spreading of cells, and recruitment of several key adhesion molecules (including integrin, vinculin, focal adhesion kinase, and actin) to focal adhesion points was visualized by immunohistochemical staining (**Figure 5(c)** and **5(d)**). Refer to **Chapter 3.316, Immunohistochemistry**; **Chapter 3.317, Fluorescence Imaging of CellBiomaterial Interactions**; and **Chapter 3.318, Molecular Imaging** for discussion of analytical techniques used in these and other cell-based experiments.

To determine whether this was due to an increase in ligand density rather than a decrease in ligand spacing, patterns were fabricated with small nanoparticle spacings and low nanoparticle densities through a combination of BCM nanolithography and EBL. Significantly lower numbers of RGD ligands promoted cell adhesion and spreading when ligand spacing was sufficiently low (58 nm), demonstrating that this effect arises primarily from ligand arrangement rather than ligand quantity. Such behavior was observed for a number of cell lines, including B16 melanocytes, REF52 fibroblasts, and 3T3 fibroblasts, suggesting a universal requirement that must be met for optimal integrin-mediated adhesion.[65,66]

The flexibility of the BCM nanolithography technique allows for patterning of other ligands for the study of other cell types. Neuron activity on nanopatterned surfaces was investigated by

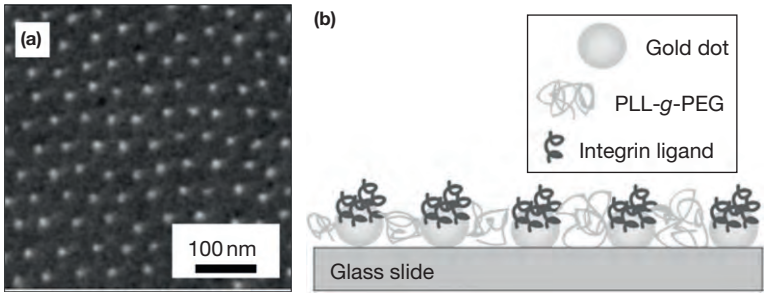

Figure 4 (a) SEM micrograph of gold nanodot array on a glass substrate, fabricated by BCP nanolithography. Dot spacing (55 ± 12 nm shown here) is dictated by the molecular weight and weight fraction of the PS-*b*-P2VP employed in the nanolithography process. (b) Schematic representation of a cell adhesion template based on the nanodot array. Glass surfaces are passivated with a cell-repellant PLL-*g*-PEG copolymer, and thiol-bearing integrin ligands (such as cyclic RGD-containing peptides) are covalently bound to the gold nanodots. Reprinted from Selhuber-Unkel, C.; Lûpez-Garcìa, M.; Kessler, H.; Spatz, J. P. *Biophys. J.* **2008**, *95*, 5424–5431, with permission from Elsevier.

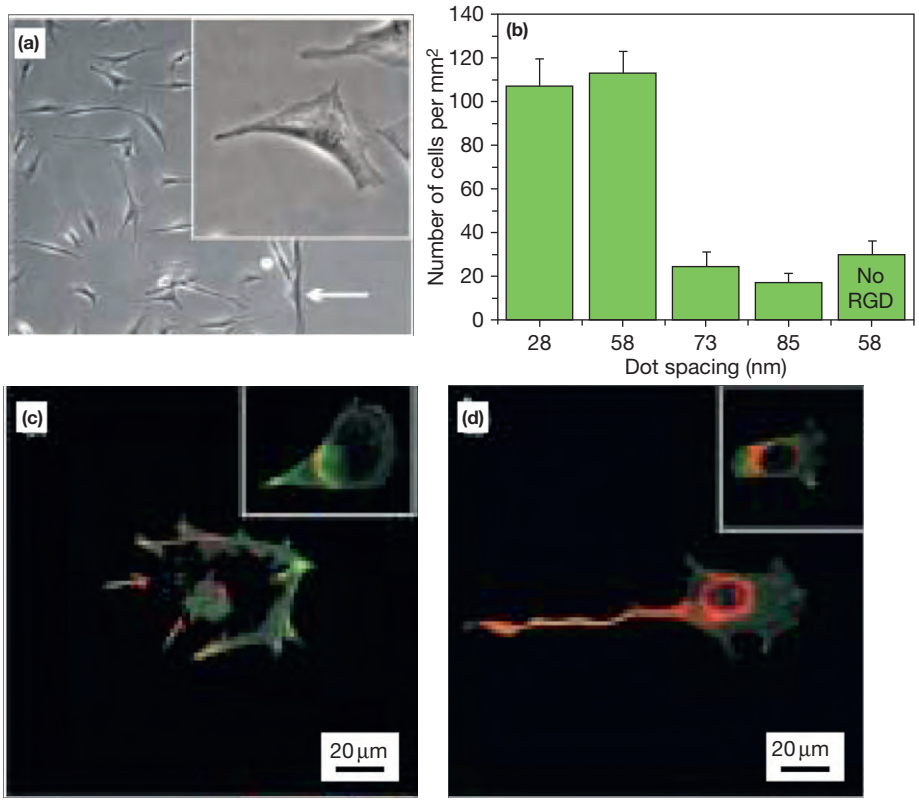

Figure 5 MC3T3-osteoblast adhesion on RGD-patterned surfaces prepared by BCP nanolithography. (a) Light micrograph of osteoblasts bound to RGD patterns with 58-nm spacing. White arrow indicates boundary between patterned (left) and PEG-passivated (right) surfaces. (b) Number of cells bound to patterned surfaces as a function of ligand spacing. (c) and (d) Characterization of adhesion molecules in B16 melanocytes bound to patterned surfaces by immunohistochemical staining and confocal microscopy. Cells expressing a GFP-integrin β3 (green) were stained for focal adhesion kinase (red) on surfaces with RGD spacings of 58 nm (c) and 73 nm (d). Inset: images of cells on patterned surfaces without RGD ligands. Recruitment of adhesion molecules to focal adhesion points is more pronounced for smaller RGD spacings. Reprinted from Arnold, M.; Cavalcanti-Adam, E. A.; Glass, R.; *et al*. *Chemphyschem* **2004**, *5*, 383–388, with permission from Joachim Spatz.

patterning the extracellular domain of DM-GRASP, an integral membrane protein and cell adhesion molecule from the immunoglobulin superfamily.[68] The patterns were fabricated by binding a recombinant, histidine-tagged DM-GRASP construct to gold nanoparticles modified with Ni^{2+}–NTA complexes. Resulting patterns were found to support adhesion of neuroblastoma cells via homophilic trans-interactions with DM-GRASP expressed on cell surfaces. Greater adhesion was observed for DM-GRASP patterns with smaller spacings, that is, 58 nm versus 78 nm, although neither pattern supported neurite growth.

Primary neuron behavior was investigated using dorsal root ganglion (DRG) cell culture containing neurons as well as mesenchymal stem cells. DM-GRASP patterns with small and large spacings were found to support adhesion, and 58-nm spacings were found to support neurite growth from neuron clusters. Neurites growing from single neurons were not observed on the nanopatterned surfaces, and furthermore neuron clusters were always in contact with mesenchymal cells. These results indicate that the patterned substrates are able to support but not initiate neurite formation. The authors note that the smaller DM-GRASP spacing, 58 nm, is commensurate with the dimensions of other molecules that are recruited to the focal adhesion sites and mediate adhesion and signaling. Other adhesion molecules including agrin[69] and cadherin[70] have also been arrayed via histidine/Ni^{2+}–NTA affinity patterning and studied with respect to neuronal cell culture. Tumor necrosis factor (TNF) was patterned to examine spacing effects on binding by TNF receptors on cultured cells and downstream apoptotic processes.[12]

BCM nanolithography can be engineered to fabricate patterns with varying degrees of complexity and to accommodate a range of substrate materials. As discussed above, the technique can be combined with photolithography or EBL to create hierarchically structured materials with micron-scale and nanoscale features.[65,71] Nanoparticle spacing can be varied along a controlled gradient by altering the draw velocity of substrates from BCP micelle solutions, and this spacing gradient has been shown to induce cell polarization and migration.[11,72] Initially fabricated on substrates such as glass, the nanoparticle patterns can be transferred to soft materials by coating nanoparticles with linker ligands that either physically attach or chemically bond to overlaid polymeric substrates. These soft substrates lend themselves to curved and rounded three-dimensional architectures that mimic tissue surfaces such as blood vessels and are difficult to realize on rigid materials.[73]

3.320.3.3. Other BCP Platforms for Cell Culture Studies

Cooper-White and colleagues have also developed a system for patterning of cell adhesion molecules employing covalent modification of BCP thin films. Initial investigation by AFM, quartz crystal microbalance (QCM), and fluorescence microscopy established that PEO microdomains in PS-*b*-PEO resist protein binding and prevent fibroblast adhesion and culture.[74] PS-*b*-PEO was then covalently modified at PEO chain ends with maleimide functionality. Subsequently, thin films were prepared and cysteine-bearing RGD peptides were covalently bound to the PEO microdomains via reaction with the maleimide groups. Histidine-tagged FN fragments were also bound to a Zn^{2+}-peptide chelate that was covalently immobilized on the PS-*b*-PEO template.

NIH-3T3 fibroblast adhesion on the templates was studied by fluorescence microscopy and found to occur only in the presence of both polymer maleimide functionality and immobilized RGD or FN peptides.[75] This result is consistent with cell adhesion due to binding of RGD and FN by integrins on fibroblast surfaces. This effect occurred in serum-free media, while adsorption of adhesion proteins to BCP surfaces from culture in serum led to nonspecific cell binding. This activity could be blocked with application of BSA or Pluronics to BCP films before cell experiments. PEO domain spacing was controlled via addition of PS homopolymer in the blends. As observed in experiments with BCM nanolithography-based templates, cell spreading was found to increase as spacing between PEO domains (and associated cell adhesion molecules) decreased. This property of the system might therefore be exploited to direct differentiation of mesenchymal stem cells, a process that is sensitive to mechanical stimuli such as cell spreading. This work was extended to three-dimensional cell culture scaffolds with hierarchical structure.[76] Temperature-induced macrophase separation of homopolymer PS and PS-*b*-PEO in solution followed by solvent removal resulted in porous bulk materials that exhibited microphase-separated nanostructure associated with the BCP (**Figure 6**). Following attachment of RGD adhesion peptides as described above, effects on adhesion and cell spreading were characterized as for the two-dimensional films. Use of PS-*b*-PAA in this system was also explored.

Other diblock-copolymer systems have been used to modulate cell adhesion and proliferation on tissue culture substrates. Khor examined the response of cultured fibroblasts and mesenchymal progenitor cells to BCP thin film morphology.[77] Ultrathin films composed of PS-*b*-P4VP and PS-*b*-P2VP were prepared on mica substrates resulting in patterns exhibiting dots and lamellae, respectively, following thermal annealing. The films were stable to sterilization and cell culture procedures, and cell growth was monitored using phase contrast and confocal laser microscopy. BCP nanopatterns, particularly the lamellar pattern, elicited earlier cell adhesion and greater proliferation than bare mica substrates. Microtubule and actin filament distribution varied as the substrate pattern changed, as did the morphology of the lamellipodia that propel the adhered cells across the substrates. Extracellular matrix proteins deposited by the cells on the substrates appeared to conform to the underlying nanostructure. Other recent studies have examined BCP thin films containing poly(2-methacryloyloxyethyl phosphorylcholine) (PMPC) blocks that resist protein adsorption and hydrophobic poly(dimethylsiloxane) (PDMS) that binds proteins.[78] Copolymers that contained higher weight fractions of PDMS were shown to adsorb higher levels of antibodies and FN, and these materials in turn led to more fibroblast adhesion. The materials supported adhesion only in the presence of serum, indicating that protein binding is necessary prior to cell adhesion.

3.320.4. Coassembly of BCPS with Peptides and Proteins in Thin Films

The examples discussed above primarily employ multistep processes in which proteins are adsorbed to or bound by preformed polymer templates. Relatively few studies have explored the simultaneous coassembly of polymers with peptides and proteins. Coassembly strategies are attractive because they may allow for integral incorporation of hierarchical structural complexity and functionality within the resulting materials. Ideal composite materials would also exhibit the superior processability of the polymeric matrices, enabling the incorporation of sensitive proteins in surface coatings, particles, and fibers. Practically speaking, coassembly requires cosolubilization of the BCPs and proteins. This constitutes a primary obstacle due to the chemical incompatibility of the two classes of materials. Peptides and proteins naturally exist in aqueous solution at or near physiological pH and usually have poor solubility in organic solvents.[79] BCPs, however, are frequently processed using volatile hydrocarbon solvents that can denature peptides and proteins. Many protein functionalities require noncovalent binding of small-molecule cofactors, so conditions must be also be chosen so as to preserve these cofactor complexes or to promote their reconstitution.[80,81] Meanwhile, conditions must allow for ready formation of BCP nanostructures in thin films. Solvents should be sufficiently volatile to allow for film casting, as well as for subsequent annealing if ordered structures are desired.

Russell and colleagues demonstrated patterning of ferritin-based nanoparticles in thin films via coassembly with poly(2-vinylpyridine)-*block*-poly(ethylene oxide) (P2VP-*b*-PEO).[82] Notably, covalent binding of PEO to ferritin, a protein-nanocage with an iron core, imparted solubility in organic solvents to the protein and allowed for direct incorporation in P2VP-*b*-PEO blends. Several developments in polymer–protein conjugation may be used in this manner to enhance protein stability and compatibility in polymeric systems.[83–85] The appended polymers may furthermore direct assembly of proteins within desired BCP microdomains, in the manner of homopolymer addition to BCP thin films.[19]

Recently, we reported the coassembly of PS-*b*-PEO with model heme proteins and enzymes.[86] A coiled-coil α-helix bundle was studied as a model protein because it is one of the simplest tertiary peptide motifs that retains a specific function, namely, small-molecule cofactor binding. The design of the peptide bundle employed in this case, termed H10H24, was based on the diheme cytochrome b subunit of cytochrome bc1.[87,88] In comparison to their natural counterparts, designed

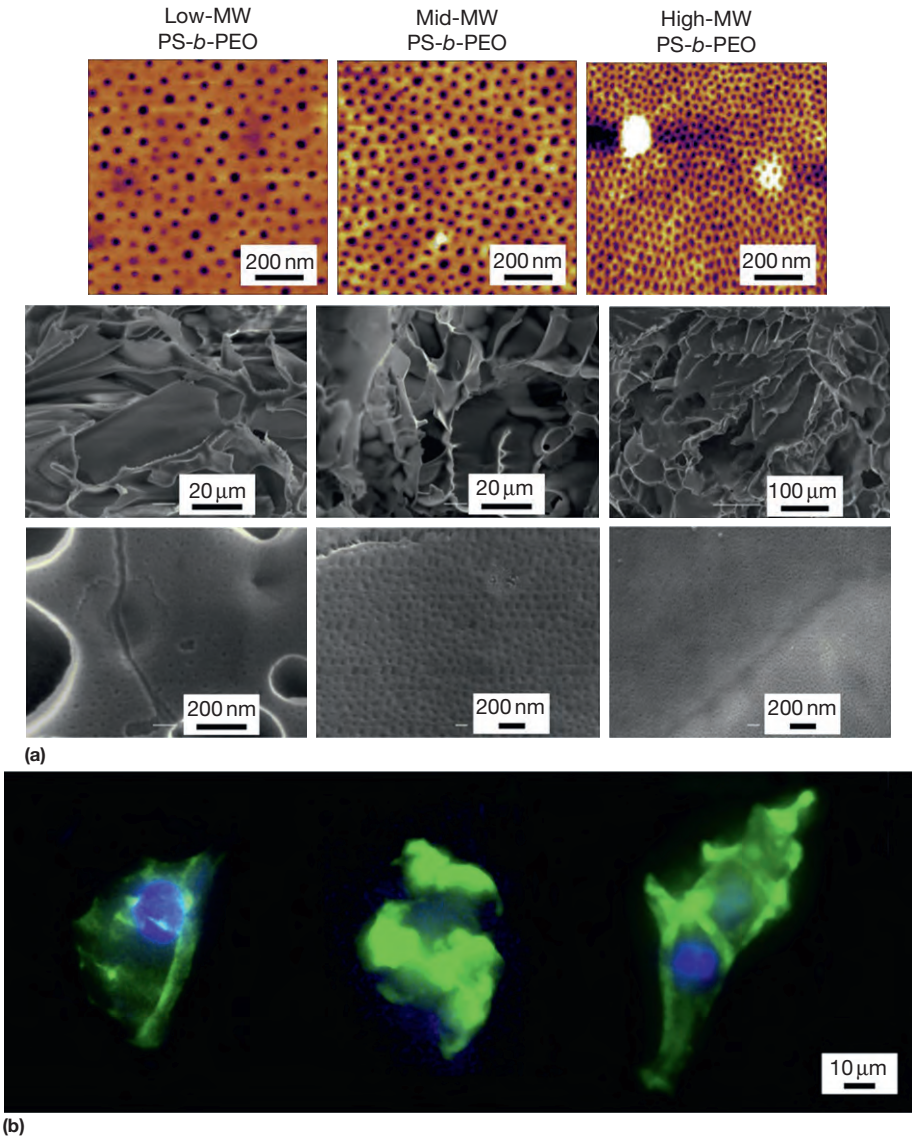

Figure 6 Fabrication of hierarchically ordered BCP scaffolds for 3D tissue culture. (a) AFM images (top row) depict dependence of PEO domain spacing on the molecular weight of the PS-*b*-PEO employed, with smaller spacings occurring for lower molecular weights. SEM images (middle and bottom row) depict polymer scaffold structure resulting from temperature-induced phase separation of PS-*b*-PEO and homopolymer PS, containing micron-scale porosity as well as nanoscale BCP morphologies. (b) Fluorescence microscopy images of NIH-3T3 fibroblasts cultured inside BCP scaffolds with stained actin (green) and nuclei (blue). Reprinted from George, P. A.; Quinn, K.; Cooper-White, J. J. *Biomaterials* **2010**, *31*, 641–647, with permission from Elsevier.

peptides have simple and robust secondary and tertiary structures and present an ideal starting point to explore the principles governing the coassembly of natural proteins with synthetic BCPs. Initially, the inherent chemical incompatibility between protein and polymer components prevented solution processing of the composite materials into thin films. As demonstrated previously in the case of ferritin, however, conjugation of PEO to helix bundles and larger heme proteins improved solubility in organic solution and compatibility with PS-*b*-PEO. In addition, polar cosolvents were used to solubilize the protein–PEO conjugates with the hydrophobic PS-*b*-PEO. Ordering of PS-*b*-PEO was induced by solvent annealing with a benzene–water vapor mixture.

Helical secondary structure of H10H24-PEO conjugate (H10H24-P2K) was maintained during thin film assembly and processing, as assessed by CD (Figure 7(b)). Binding of heme cofactors via bis-histidyl ligation as observed by UV-visible absorption spectroscopy was consistent with maintenance of the helix bundle tertiary structure (Figure 7(c)). The system was extended to include more complex, naturally occurring heme proteins. A myoglobin–PEO conjugate was compatible with thin film processing, and retention of enzymatic activity was consistent with preservation of protein structure within the composite materials. Conjugation of synthetic polymers to protein surfaces is expected to direct localization of protein–polymer conjugates within specific BCP microdomains,

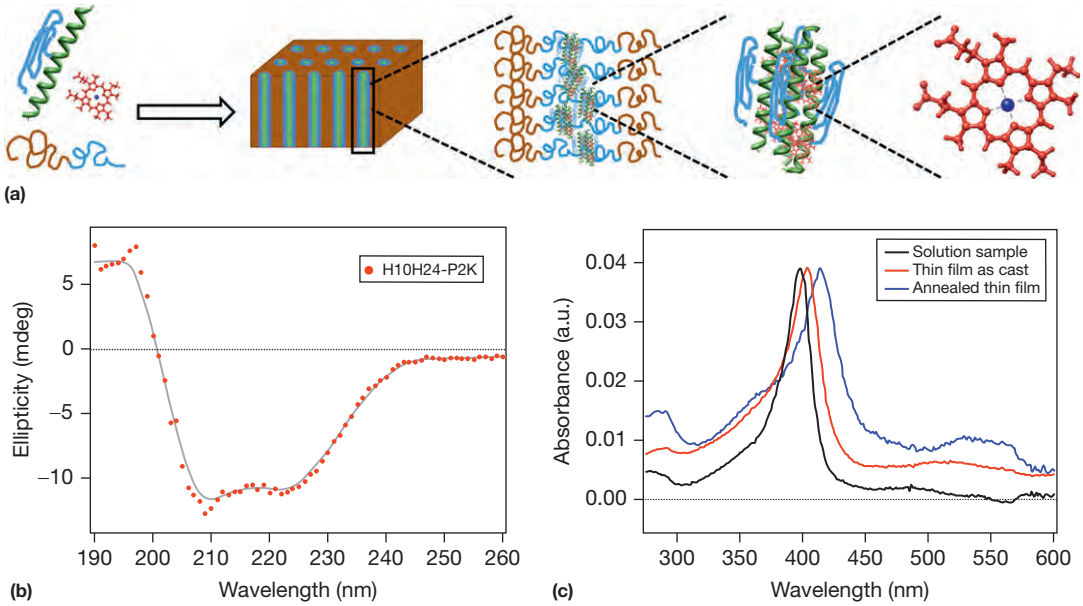

Figure 7 Coassembly of BCPs and heme proteins. (a) Schematic depiction of PS-*b*-PEO coassembly with a helix bundle peptide-PEO conjugate (H10H24-P2K) and heme cofactors. (b) Helical secondary structure of H10H24-P2K is retained, as indicated by circular dichroism. (c) Red-shifting and resolution of heme spectral features upon thin film casting and annealing, as observed by UV-vis absorption spectroscopy, are consistent with heme binding by H10H24-P2K and assembly of coiled-coil helix bundle tertiary structures. Reprinted from Presley, A. D.; Chang, J. J.; Xu, T. *Soft Matter*. **2011**, *7*, 172–179, with permission from The Royal Society of Chemistry.

as depicted schematically in Figure 7(a). Soft X-ray scattering techniques are currently being developed to unambiguously determine the location of the protein conjugates in the thin films.

3.320.5. BCP Surfaces for Biocompatibility and Antifouling Applications

3.320.5.1. Biocompatibility of Poly(2-hydroxyethyl methacrylate)-Based Copolymers

In contrast to the protein patterning strategies described above, much effort has been directed toward the prevention of protein and cell binding on polymer surfaces. Unwanted adsorption (termed biofouling) can prevent proper function of biomaterials and medical devices, causing problems such as thrombus formation in patients. The earliest systematic investigations of protein adsorption and cell adhesion on BCP surfaces in the context of biofouling prevention employed model polymer surfaces composed of triblock A–B–A copolymers containing poly(2-hydroxyethyl methyacrylate) (PHEMA) and PS.[89,90] TEM micrographs indicated that different serum proteins adsorb preferentially on different polymer phases, with albumins preferring hydrophilic PHEMA domains and γ-globulins preferring hydrophobic PS domains.[89] This is a particularly significant result because albumin is known to passivate surfaces against platelet adhesion, while the globulins and FN promote adhesion and thrombus formation. Surface antifouling properties might therefore be tuned by adjusting the copolymer composition and resulting protein distribution. When PHEMA polymer surfaces were exposed to whole blood, reduced platelet adhesion and deformation were observed on the BCP surfaces as compared to homopolymer or random copolymer surfaces (Figure 8(b)) similarly exposed.[90] Similar results were found for BCPs containing PEO, poly(propylene oxide) (PPO), and PDMS blocks in place of PS.[91,92] When used as a coating for various polyurethane (PU)-based arterial shunts *in vivo*, the HEMA copolymers were found to prevent thrombosis for significantly longer periods than uncoated or homopolymer-coated shunt tubing.[93]

Platelet adhesion to copolymer-coated surfaces was not abolished, suggesting that the BCP antithrombogenicity may be due to the prevention of platelet activation/deformation rather than the elimination of all surface binding. Indeed, decreased platelet activation was reflected in lower intracellular calcium levels detected with Ca^{2+}-specific probes as well as decreased release of serotonin, a known hemostatic agent, assessed by radiochemical techniques.[93,94] Platelet movement on different polymer surfaces has been characterized using computer-assisted analysis of microscopy images. Platelet movement on PHEMA copolymer-coated surfaces was qualitatively different from that on PEG-grafted surfaces. Rolling, spinning, and vibrating was observed to occur in an ATP-dependent fashion, and addition of sodium azide reduced cell metabolism and platelet mobility. Meanwhile, passive 'nonbiological' Brownian motion was observed on PEG-grafted surfaces. These results highlight the fact that contact with PHEMA copolymer surfaces alters biochemical processes that modulate cell adhesion, while the nonfouling character of PEG surfaces arises primarily from physical phenomena such as water structuring and excluded volume effects.[95,96] The authors of this study note that the dimensions of the phase-separated copolymer morphologies (on the order of 50 nm) are commensurate with biological structures, such as lipid rafts and integrin clusters in cell membranes, that play important roles in surface interactions and downstream processes.

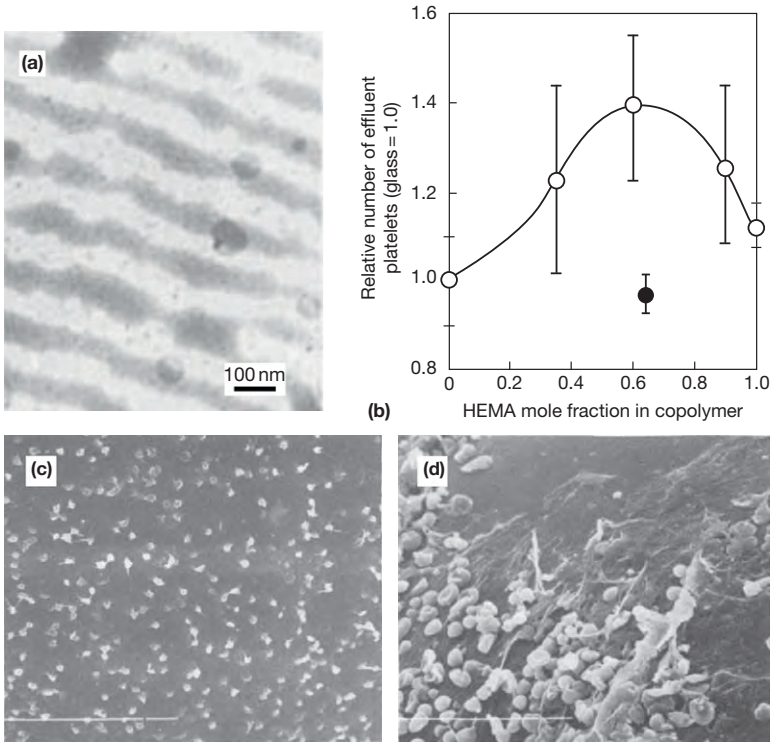

Figure 8 (a) TEM image of PS-PHEMA ABA triblock copolymer film containing a PHEMA weight fraction of 0.608, stained with osmium tetroxide. (b) Quantification of platelet binding to copolymer surfaces, assessed by platelet counting in canine blood effluents from columns packed with BCP-coated glass microspheres. Open circles correspond to block copolymers and the closed circle corresponds to a random copolymer. Platelet adhesion is lowest for copolymers with intermediate volume fraction of either block. (c) and (d) SEM images (2000× magnification) of platelets adhered to glass microspheres coated with triblock copolymer with a PHEMA weight fraction of 0.608 (c) and a random copolymer with a PHEMA weight fraction of 0.640 (d). Reprinted from Okano, T.; Nishiyama, S.; Shinohara, I.; *et al. J. Biomed. Mater. Res.* **1981**, *15*, 393–402, with permission from Wiley.

3.320.5.2. Structural Implications for PU Biocompatibility

PUs are the copolymers that are perhaps most relevant in the context of biocompatibility or antithrombogenicity, as they are widely employed in medical devices including catheters, cardiac devices, blood tubing, and wound dressings. For review of this important family, refer to **Chapter 1.125, Polyurethanes and Silicone Polyurethane Copolymers**. PUs possess several advantages including good mechanical properties, fatigue resistance, and low biofouling, and are marketed under several brand names with various compositions. So-called 'segmented' PUs are in fact multiblock copolymers consisting of hard segments (PU blocks derived from diisocyanates such as methylene bis(4-phenylisocyanate) and chain extenders such as butane diol or ethylene diamine) and soft segments (consisting of polyesters, polyethers, polycarbonates, or polyolefins). Various aspects of the biomedical applications of PUs have been reviewed elsewhere.[97,98]

Segmented PUs have exhibited better blood compatibility than their component homopolymers, as assessed by platelet adhesion and deformation, and compatibility was associated with the degree of surface microphase separation.[99] Blood compatibility is influenced by the weight fraction and chemistry of the soft segments,[100,101] as well as the diol or diamine chain extender contained in the hard segments.[102] A range of modifications has been made to PU surfaces to tune surface charge or hydrophobicity, improving blood compatibility to varying degrees.[103–106] However, few studies have directly examined protein adsorption on the length scale of the surface microdomains. Reorganization of PU microphases is known to occur upon hydration in biological samples, and polar hard segments typically orient toward the surface. Nevertheless, direct observation of PU surfaces by TEM[107] and AFM[108] has demonstrated that microphase-separated nanostructures remain present on hydrated surfaces. Protein adsorption has been shown to occur preferentially on soft segments consisting of hydrophobic polymers such as poly(tetramethylene oxide) and polybutadiene.[107,108] These and other studies have indicated that biocompatibility of PU and PUU materials is influenced by nanoscale microphase-separated morphology, although opinion on this matter appears to vary widely.[101]

3.320.5.3. BCP Surfaces for Marine Antifouling Applications

Several BCP systems have been studied as marine antifouling agents, preventing adhesion of organisms such as bacteria, algae, barnacles, and diatoms to surfaces in aquatic environments.[109] Most systems have consisted of di- and triblock copolymers of PS and various blocks including P2VP;[110] PMMA;[110] PAA and poly(4-vinylbenzoic acid) esterified with Zonyl FSO-100, a fluoroalkylalcohol-modified PEO;[111,112]

poly(ethylene-*ran*-butylene);[113,114] and amphiphilic blocks derived from epoxidized poly(isoprene), PEO, and fluoroalkanes.[113,114] Poly[poly(ethylene glycol)methyl ether methacrylate]-*block*-poly(2,3,4,5,6-pentafluorostyrene) has also been studied as an antifouling coating in marine environments.[115] Many of these systems have been specifically designed to incorporate extremes of wettability, and biofouling resistance has been attributed to both the low interfacial energy of PEO-like blocks in water and the low adhesiveness of fluorinated blocks.[114] Certain systems have high resistance to protein adsorption in general, which almost certainly contributes to prevention of marine organism adhesion in particular.[116] Another desirable characteristic of antifouling coatings is the ability to release adhered organisms from submerged surfaces, a property associated with pliant materials possessing low elastic moduli.[117] The elasticity of coating materials can be tuned by incorporating base layers of pliant polymers, such as PDMS and styrene-based elastomers, beneath BCP surface layers.[113,114] Surface topography has been indicated as an important variable affecting adhesion and release of fouling agents,[118] and the well-defined morphologies of phase-separated BCPs may make them particularly useful as antifouling coatings.

3.320.6. BCP Micelle Surfaces for Controlled Release Applications

BCMs have been studied extensively for their applications in drug delivery.[119,120] Amphiphilic BCPs assemble in aqueous solution to form core–shell BCMs, and highly versatile systems can result from chemical and physical tailoring of both the core and shell blocks. Small-molecule drugs can be sequestered in the BCM core, for example, while bioactive ligands can be conjugated to the BCM surface to target the therapeutics to specific cells or tissues *in vivo*. The discussion below focuses on solid-state films and surface coatings that incorporate BCMs for drug-delivery applications. Such materials may allow for fabrication of new implants or other biomedical devices with special therapeutic properties.

Special emphasis is placed on the fabrication of films and coatings by layer-by-layer (LbL) deposition of polymers that interact via electrostatics, hydrogen bonding, or covalent reaction.[121,122] The LbL technique has been employed to create a number of surface coatings incorporating small-molecule drugs, peptides and proteins, and nucleic acids for gene delivery.[123] These processes are largely conducted in aqueous solution, so the use of BCMs is particularly advantageous for incorporation of hydrophobic drugs without the functionality required for successful incorporation in LbL films. The multilayer nature of the films imparts a diffusion barrier and is expected to lead to a more controlled release of the incorporated cargoes. The incorporation of stimuli-responsive BCMs in LbL films will allow for drug loading and release that can be controlled through external parameters such as pH, temperature, and ionic strength.[124] Because various properties of micelles – such as size, morphology, and loading/release profiles – can be controlled with precision, novel nanomaterials may result from the combination of two or more BCMs in LbL films. Progress in this direction is expected to lead to the development of a general, versatile, and robust route to bringing multiple functional agents into layered and ordered thin films in a highly controlled manner.

Assembly of BCMs at surfaces has been investigated in organic and aqueous solvents, resulting in micelle assemblies that are physically adsorbed or covalently bonded to underlying substrates.[125–127] Surface assembly of BCMs has given rise to applications including BCP nanolithography as discussed above. Emoto and colleagues reported one of the earliest systems employing BCMs for release of small-molecule cargoes from surface coatings.[128,129] BCMs contained a methacryloyl-terminated PLA core and an acetal-terminated PEO corona. Cross-linking of the PLA core prevented micelle disruption upon contact with surfaces, and acetal hydrolysis resulted in aldehyde groups for BCM immobilization on amine-modified surfaces and multilayer formation with polyallylamine via reductive amination. Release of pyrene cargo from the PLA core was investigated, and loading capacity and release rate were found to depend on the number of layers in the LbL films. Pyrene release occurred on a timescale of minutes to hours.

Nguyen *et al.*[130] reported the LbL assembly of thin films formed by electrostatic interactions between anionic PAA and BCMs containing a cationic corona. The BCM corona consisted of dendritic poly(amidoamine) (PAMAM) and the hydrophobic core consisted of linear PPO. The BCMs were loaded with triclosan, a hydrophobic bactericide, and incorporated in the thin LBL films, which exhibited sustained drug release over a period of at least 2 weeks in a diffusion-controlled manner. The use of the linear-dendritic copolymer for BCM formation is this study led to significantly slower release of hydrophobic molecules than in earlier studies of LbL films containing BCMs consisting of linear–linear amphiphilic BCPs, including PS-*b*-PAA and (PAA-*b*-P4VP).[131,132] In another strategy employed for the delivery of multiple therapeutic agents using BCM films, cationic P2VEP-PCL micelles were loaded with hydrophobic drugs and assembled with polyanionic therapeutics heparin or dextran sulfate (**Figure 9**).[133] Controlled degradation was achieved through the incorporation of a degradable poly(β-amino ester) in the LbL films, and the release profiles were also found to depend on the identity of the anionic layering agents. Films containing both paclitaxel and heparin were found to be most effective against a human smooth muscle cell line.

LbL films based on hydrogen-bonding interactions between constituents are of interest because they are potentially responsive materials that are sensitive to changes in pH of their environment. Hammond and coworkers reported the incorporation of BCMs within polymer thin films by exploiting hydrogen bonding interactions.[134] Thin films were formed through hydrogen bonding between biologically compatible PAA, an H-bond donor, and BCMs consisting of poly(ethylene oxide)-*b*-poly(ε-caprolactone) (PEO-*b*-PCL), an H-bond acceptor. The biodegradable PCL micelle core was loaded with triclosan, and the LbL films were found to release the loaded micelles into the surrounding medium because of PAA deprotonation under physiological conditions and resulting disruption of H-bonding. In order to increase film stability and extend triclosan release over longer periods, PAA sidechains were thermally cross-linked to yield anhydride-stabilized LbL films. Drug-loaded BCM films were found to release significant amounts of triclosan to inhibit the growth of bacteria.

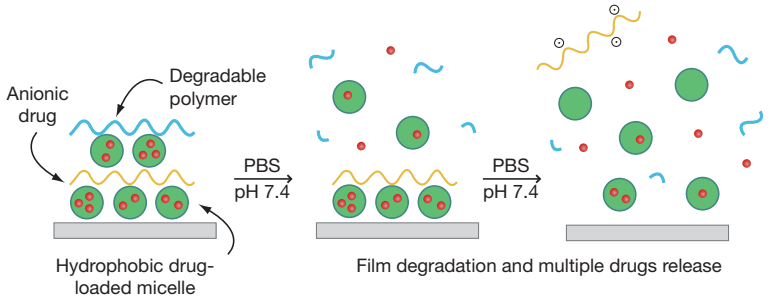

Figure 9 Assembly and evaluation of LbL films for multiagent drug delivery. A degradable polymer helps to stabilize interactions between polyanionic therapeutics and drug-containing micelles with a cationic corona. Upon hydrolysis of the degradable polymer under physiological conditions, polyanionic and hydrophobic therapeutics are released. Films with both small molecules and polyanions are most effective against cultured cell lines. Reprinted from Kim, B. S.; Smith, R. C.; Poon, Z.; Hammond, P. T. *Langmuir* **2009**, *25*, 14086–14092, with permission from American Chemical Society.

Hydrogen-bonded films assembled with a polymeric acid such as PAA as an H-bond donor are only stable in acidic media and spontaneously deconstruct at pH levels above the pK_a of the polyacid. In order to exploit hydrogen-bonding interactions for construction of stable BCM multilayer films at physiological pH, use of tannic acid, a water-soluble polyphenol (pK_a ~8.5), as the H-bond donator has been reported.[135] LbL films were formed through H-bonding between tannic acid H-bond donors and PEO H-bond acceptors in PEO-*b*-PHEMA BCMs. HEMA side chains were conjugated to chemotherapeutic doxorubicin (Dox) via a pH-sensitive carbamate linkage. Controlled release of Dox from the multilayers was found to elicit cytotoxic effects in human cervical cancer HeLa cell line. Furthermore, tannic acid is an attractive molecule for inclusion within surface films because of its known biofunctional properties, such as antitumor, antienzymatic, antibacterial, antimutagenic, and antioxidant activities.

The development of drug delivery systems where the drug release could be modulated by temperature changes is highly desirable. In one of the very few examples in the literature regarding the incorporation of BCMs in thin films for the design of temperature-responsive materials, Zhu and Sukhishvili[136] reported temperature triggered reversible swelling transitions in poly(*N*-vinylpyrrolidone)-*block*-poly(*N*-isopropylacrylamide) (PVPON-*b*-PNIPAM) BCMs assembled in LbL films with PMAA. PVPON-*b*-PNIPAM BCMs reversibly swelled within the films in response to decrease in temperature from 37 to 20 °C, reflecting collapse and dissolution of the micelle PNIPAM cores. The release of pyrene encapsulated in micelles was found to depend on the swelling rate of the film with slower release at higher temperature. Reversible swelling behavior and temperature-dependent release characteristics indicate promise for future controlled delivery applications.

3.320.7. Conclusion

As described here, several polymer platforms have allowed for the directed assembly of proteins on micron and nanometer length scales, as well as for the control of interactions of biomaterial surfaces with cells and tissues. BCPs in particular could potentially allow for rapid assembly of hierarchically ordered composite materials. In order to fully realize this potential, however, these systems will require further investigation and engineering. The BCPs used for solid-state nanostructure generation, in particular, usually consist of hydrophobic blocks that are virtually incompatible with proteins. 'Biofriendly' polymers, such as Pluronics and a few other amphiphilic BCPs, have been used effectively for immobilization of proteins in biosensor devices.[137,138] Much work remains, however, in order to direct the nanoscale assembly of these polymers and control long-range ordering. Certain amphiphilic polymersomes in solution have been employed for successful protein incorporation, and these studies may inform the development of biofriendly polymers for assembly of BCP/protein hybrid materials.[139] Such polymers may also be applied to delivery of proteins and peptides from BCM films and coatings designed for controlled-release applications. Multiplexing patterns and nanostructures to include more than one protein constitutes another significant challenge that has yet to be addressed. Use of multiblock copolymers, BCP blends, and BCP-based supramolecules can enrich the structural and functional complexity of polymer assemblies, which may provide multiple domains for protein attachment or sequestration.[140–142] Combination of BCP assembly with top-down patterning techniques such as EBL or soft lithography may also result in multielement protein arrays.[143,144] These functional hybrid materials, in turn, will facilitate fundamental research and enable new biotechnology.

References

1. Newman, J. D.; Setford, S. J. *Mol. Biotechnol.* **2006**, *32*, 249–268.
2. Clark, M. F.; Lister, R. M.; Barjoseph, M. *Meth. Enzymol.* **1986**, *118*, 742–766.
3. Brask, J. *Immobilized Enzymes in Organic Synthesis*. Wiley-VCH: Weinheim, Germany, 2009.
4. Templin, M. F.; Stoll, D.; Schwenk, J. M.; Potz, O.; Kramer, S.; Joos, T. O. *Proteomics* **2003**, *3*, 2155–2166.
5. Pollard, H. B.; Srivastava, M.; Eidelman, O.; *et al. Proteomics Clin. Appl.* **2007**, *1*, 934–952.
6. Weinrich, D.; Jonkheijm, P.; Niemeyer, C. M.; Waldmann, H. *Angew. Chem. Int. Ed.* **2009**, *48*, 7744–7751.
7. Lynch, M.; Mosher, C.; Huff, J.; Nettikadan, S.; Johnson, J.; Henderson, E. *Proteomics* **2004**, *4*, 1695–1702.
8. Lee, K. B.; Kim, E. Y.; Mirkin, C. A.; Wolinsky, S. M. *Nano Lett.* **2004**, *4*, 1869–1872.
9. Silzel, J. W.; Cercek, B.; Dodson, C.; Tsay, T.; Obremski, R. J. *Clin. Chem.* **1998**, *44*, 2036–2043.
10. Stevens, M. M.; George, J. H. *Science* **2005**, *310*, 1135–1138.
11. Arnold, M.; Hirschfeld-Warneken, V. C.; Lohmuller, T.; *et al. Nano Lett.* **2008**, *8*, 2063–2069.
12. Ranzinger, J.; Krippner-Heidenreich, A.; Haraszti, T.; *et al. Nano Lett.* **2009**, *9*, 4240–4245.

13. Christman, K. L.; Enriquez-Rios, V. D.; Maynard, H. D. *Soft Matter* **2006**, *2*, 928–939.
14. Mendes, P. M.; Yeung, C. L.; Preece, J. A. *Nanoscale Res. Lett.* **2007**, *2*, 373–384.
15. Schmidt, R. C.; Healy, K. E. *J. Biomed. Mater. Res.* **2009**, *90A*, 1252–1261.
16. Fasolka, M. J.; Mayes, A. M. *Annu. Rev. Mater. Res.* **2001**, *31*, 323–355.
17. Kim, J. K.; Lee, J. I.; Lee, D. H. *Macromol. Res.* **2008**, *16*, 267–292.
18. Di, Z. Y.; Posselt, D.; Smilgies, D. M.; Papadakis, C. M. *Macromolecules* **2010**, *43*, 418–427.
19. Kim, S. H.; Misner, M. J.; Russell, T. P. *Adv. Mater.* **2004**, *16*, 2119–2123.
20. Kim, S. H.; Misner, M. J.; Xu, T.; Kimura, M.; Russell, T. P. *Adv. Mater.* **2004**, *16*, 226–231.
21. Guarini, K. W.; Black, C. T.; Yeuing, S. H. I. *Adv. Mater.* **2002**, *14*, 1290–1294.
22. Thurn-Albrecht, T.; Steiner, R.; Derouchey, J.; *et al*. *Adv. Mater.* **2000**, *12*, 787–791.
23. Xu, T.; Goldbach, J. T.; Russell, T. P. *Macromolecules* **2003**, *36*, 7296–7300.
24. Xu, T.; Hawker, C. J.; Russell, T. P. *Macromolecules* **2003**, *36*, 6178–6182.
25. Angelescu, D. E.; Waller, J. H.; Adamson, D. H.; *et al*. *Adv. Mater.* **2004**, *16*, 1736–1740.
26. Cheng, J. Y.; Mayes, A. M.; Ross, C. A. *Nat. Mater.* **2004**, *3*, 823–828.
27. Park, S.; Lee, D. H.; Xu, J.; *et al*. *Science* **2009**, *323*, 1030–1033.
28. Hamley, I. W. *Nanotechnology* **2003**, *14*, R39–R54.
29. Lazzari, M.; Lopez-Quintela, M. A. *Adv. Mater.* **2003**, *15*, 1583–1594.
30. Segalman, R. A. *Mater. Sci. Eng. R Rep.* **2005**, *48*, 191–226.
31. Olson, D. A.; Chen, L.; Hillmyer, M. A. *Chem. Mater.* **2008**, *20*, 869–890.
32. Yang, S. Y.; Ryu, I.; Kim, H. Y.; Kim, J. K.; Jang, S. K.; Russell, T. P. *Adv. Mater.* **2006**, *18*, 709–712.
33. Bates, F. S. *Science* **1991**, *251*, 898–905.
34. Edlund, U.; Albertsson, A. C. *Degradable Aliphatic Polyesters*, Springer: Berlin, 2002.
35. Gunn, J.; Zhang, M. Q. *Trends Biotechnol.* **2010**, *28*, 189–197.
36. Meredith, J. C.; Sormana, J. L.; Keselowsky, B. G.; *et al*. *J. Biomed. Mater. Res. A* **2003**, *66*, 483–490.
37. Wilson, C. J.; Clegg, R. E.; Leavesley, D. I.; Pearcy, M. J. *Tissue Eng.* **2005**, *11*, 1–18.
38. Sengonul, M.; Sousa, A.; Libera, M. *Colloids Surf. B Biointerfaces* **2009**, *73*, 152–155.
39. Sousa, A.; Sengonul, M.; Latour, R.; Kohn, J.; Libera, M. *Langmuir* **2006**, *22*, 6286–6292.
40. Sengonul, M.; Ruzicka, J.; Attygalle, A. B.; Libera, M. *Polymer* **2007**, *48*, 3632–3640.
41. Merrett, K.; Cornelius, R. M.; Mcclung, W. G.; Unsworth, L. D.; Sheardown, H. *J. Biomater. Sci. Polym. Ed.* **2002**, *13*, 593–621.
42. Li, L.; Hitchcock, A. P.; Cornelius, R.; Brash, J. L.; Scholl, A.; Doran, A. *J. Phys. Chem. B* **2008**, *112*, 2150–2158.
43. Li, L.; Hitchcock, A. P.; Robar, N.; *et al*. *J. Phys. Chem. B* **2006**, *110*, 16763–16773.
44. Leung, B. O.; Wang, J.; Brash, J. L.; Hitchcock, A. P. *Langmuir* **2009**, *25*, 13332–13335.
45. Hitchcock, A. P.; Morin, C.; Heng, Y. M.; Cornelius, R. M.; Brash, J. L. *J. Biomater. Sci. Polym. Ed.* **2002**, *13*, 919–937.
46. Morin, C.; Hitchcock, A. R.; Cornelius, R. M.; *et al*. *J. Electron. Spectrosc. Relat. Phenom.* **2004**, *137*, 785–794.
47. Leung, B. O.; Hitchcock, A. P.; Cornelius, R.; Brash, J. L.; Scholl, A.; Doran, A. *Biomacromolecules* **2009**, *10*, 1838–1845.
48. Kumar, N.; Hahm, J. I. *Langmuir* **2005**, *21*, 6652–6655.
49. Kumar, N.; Parajuli, O.; Dorfman, A.; Kipp, D.; Hahm, J. I. *Langmuir* **2007**, *23*, 7416–7422.
50. Kumar, N.; Parajuli, O.; Gupta, A.; Hahm, J. I. *Langmuir* **2008**, *24*, 2688–2694.
51. Parajuli, O.; Gupta, A.; Kumar, N.; Hahm, J. I. *J. Phys. Chem. B* **2007**, *111*, 14022–14027.
52. Kumar, N.; Parajuli, O.; Hahm, J. I. *J. Phys. Chem. B* **2007**, *111*, 4581–4587.
53. Park, J. H.; Sun, Y.; Goldman, Y. E.; Composto, R. J. *Macromolecules* **2009**, *42*, 1017–1023.
54. Lau, K. H. A.; Bang, J.; Hawker, C. J.; Kim, D. H.; Knoll, W. *Biomacromolecules* **2009**, *10*, 1061–1066.
55. Lau, K. H. A.; Bang, J.; Kim, D. H.; Knoll, W. *Adv. Funct. Mater.* **2008**, *18*, 3148–3157.
56. Li, Q.; Lau, K. H. A.; Sinner, E. K.; Kim, D. H.; Knoll, W. *Langmuir* **2009**, *25*, 12144–12150.
57. Ryu, D. Y.; Shin, K.; Drockenmuller, E.; Hawker, C. J.; Russell, T. P. *Science* **2005**, *308*, 236–239.
58. Matsusaki, M.; Omichi, M.; Kadowaki, K.; *et al*. *Chem. Commun.* **2010**, *46*, 1911–1913.
59. Liu, D.; Wang, T.; Keddie, J. L. *Langmuir* **2009**, *25*, 4526–4534.
60. Gao, X.; Zhu, S. P.; Sheardown, H.; Brash, J. L. *Polymer* **2010**, *51*, 1771–1778.
61. Cresce, A. V.; Silverstein, J. S.; Bentley, W. E.; Kofinas, P. *Macromolecules* **2006**, *39*, 5826–5829.
62. Nehring, R.; Palivan, C. G.; Moreno-Flores, S.; *et al*. *Soft Matter* **2010**, *6*, 2815–2824.
63. Zhang, C.; Husson, S. M.; Hirt, D. E. *Macromol. Rapid Commun.* **2006**, *27*, 1173–1179.
64. Glass, R.; Moller, M.; Spatz, J. P. *Nanotechnology* **2003**, *14*, 1153–1160.
65. Arnold, M.; Cavalcanti-Adam, E. A.; Glass, R.; *et al*. *Chemphyschem* **2004**, *5*, 383–388.
66. Cavalcanti-Adam, E. A.; Micoulet, A.; Blummel, J.; Auernheimer, J.; Kessler, H.; Spatz, J. P. *Eur. J. Cell Biol.* **2006**, *85*, 219–224.
67. Huang, J. H.; Ding, J. D. *Soft Matter* **2010**, *6*, 3395–3401.
68. Thelen, K.; Wolfram, T.; Maier, B.; *et al*. *Soft Matter* **2007**, *3*, 1486–1491.
69. Wolfram, T.; Spatz, J. P.; Burgess, R. W. *BMC Cell Biol.* **2008**, *9*, 12.
70. Wolfram, T.; Belz, F.; Schoen, T.; Spatz, J. P. *Biointerphases* **2007**, *2*, 44–48.
71. Aydin, D.; Schwieder, M.; Louban, I.; *et al*. *Small* **2009**, *5*, 1014–1018.
72. Hirschfeld-Warneken, V. C.; Arnold, M.; Cavalcanti-Adam, A.; Lopez-Garcia, M.; Kessler, H.; Spatz, J. P. *Eur. J. Cell Biol.* **2008**, *87*, 743–750.
73. Graeter, S. V.; Huang, J. H.; Perschmann, N.; *et al*. *Nano Lett.* **2007**, *7*, 1413–1418.
74. George, P. A.; Donose, B. C.; Cooper-White, J. J. *Biomaterials* **2009**, *30*, 2449–2456.
75. George, P. A.; Doran, M. R.; Croll, T. I.; Munro, T. P.; Cooper-White, J. J. *Biomaterials* **2009**, *30*, 4732–4737.
76. George, P. A.; Quinn, K.; Cooper-White, J. J. *Biomaterials* **2010**, *31*, 641–647.
77. Khor, H. L.; Kuan, Y.; Kukula, H.; *et al*. *Biomacromolecules* **2007**, *8*, 1530–1540.
78. Seo, J. H.; Matsuno, R.; Takai, M.; Ishihara, K. *Biomaterials* **2009**, *30*, 5330–5340.
79. Chin, J. T.; Wheeler, S. L.; Klibanov, A. M. *Biotechnol. Bioeng.* **1994**, *44*, 140–145.
80. Hecht, M. H.; Das, A.; Go, A.; Bradley, L. H.; Wei, Y. N. *Protein Sci.* **2004**, *13*, 1711–1723.
81. Koder, R. L.; Dutton, P. L. *Dalton Trans.* **2006**, *25*, 3045–3051.
82. Lin, Y.; Boker, A.; He, J. B.; *et al*. *Nature* **2005**, *434*, 55–59.
83. Heredia, K. L.; Maynard, H. D. *Org. Biomol. Chem.* **2007**, *5*, 45–53.
84. Krishna, O. D.; Kiick, K. L. *Biopolymers* **2010**, *94*, 32–48.
85. Vandermeulen, G. W. M.; Klok, H. A. *Macromol. Biosci.* **2004**, *4*, 383–398.
86. Presley, A. D.; Chang, J. J.; Xu, T. *Soft Matter* **2011**, *7*, 172–179.
87. Huang, S. S.; Koder, R. L.; Lewis, M.; Wand, A. J.; Dutton, P. L. *Proc. Natl. Acad. Sci. USA* **2004**, *101*, 5536–5541.
88. Robertson, D. E.; Farid, R. S.; Moser, C. C.; *et al*. *Nature* **1994**, *368*, 425–431.
89. Okano, T.; Nishiyama, S.; Shinohara, I.; Akaike, T.; Sakurai, Y. *Polym. J.* **1978**, *10*, 223–228.
90. Okano, T.; Nishiyama, S.; Shinohara, I.; *et al*. *J. Biomed. Mater. Res.* **1981**, *15*, 393–402.
91. Okano, T.; Uruno, M.; Sugiyama, N.; *et al*. *J. Biomed. Mater. Res.* **1986**, *20*, 1035–1047.
92. Shimada, M.; Miyahara, M.; Tahara, H.; *et al*. *Polym. J.* **1983**, *15*, 649–656.
93. Nojiri, C.; Okano, T.; Grainger, D.; *et al*. *ASAIO J.* **1987**, *33*, 596–601.
94. Okano, T.; Suzuki, K.; Yui, N.; Sakurai, Y.; Nakahama, S. *J. Biomed. Mater. Res.* **1993**, *27*, 1519–1525.
95. Ito, E.; Suzuki, K.; Yamato, M.; Yokoyama, M.; Sakurai, Y.; Okano, T. *J. Biomed. Mater. Res.* **1998**, *42*, 148–155.
96. Uchida, K.; Yamato, M.; Ito, E.; *et al*. *J. Biomed. Mater. Res.* **2000**, *50*, 585–590.
97. Lamba, N. M. K.; Woodhouse, K. A.; Cooper, S. L.; Lelah, M. D. *Polyurethanes in Biomedical Applications*. CRC Press: Boca Raton, FL, 1998.
98. Zdrahala, R. J.; Zdrahala, I. J. *J. Biomater. Appl.* **1999**, *14*, 67–90.
99. Takahara, A.; Tashita, J.; Kajiyama, T.; Takayanagi, M.; Macknight, W. J. *Polymer* **1985**, *26*, 987–996.
100. Grasel, T. G.; Cooper, S. L. *Biomaterials* **1986**, *7*, 315–328.
101. Ma, C. F.; Hou, Y.; Liu, S.; Zhang, G. Z. *Langmuir* **2009**, *25*, 9467–9472.
102. Takahara, A.; Tashita, J.; Kajiyama, T.; Takayanagi, M.; Macknight, W. J. *Polymer* **1985**, *26*, 978–986.
103. Grasel, T. G.; Pierce, J. A.; Cooper, S. L. *J. Biomed. Mater. Res.* **1987**, *21*, 815–842.
104. Han, D. K.; Park, K. D.; Ryu, G. H.; Kim, U. Y.; Min, B. G.; Kim, Y. H. *J. Biomed. Mater. Res.* **1996**, *30*, 23–30.
105. Ito, Y.; Sisido, M.; Imanishi, Y. *J. Biomed. Mater. Res.* **1990**, *24*, 227–242.
106. Ryu, C.; Han, D.; Kim, Y.; Mini, B. *ASAIO J.* **1992**, *38*, M644–M648.

107. Goodman, S. L.; Simmons, S. R.; Cooper, S. L.; Albrecht, R. M. *J. Colloid Interface Sci*. **1990**, *139*, 561–570.
108. Xu, L. C.; Siedlecki, C. A. *J. Biomed. Mater. Res. A* **2010**, *92A*, 126–136.
109. Grozea, C. M.; Walker, G. C. *Soft Matter* **2009**, *5*, 4088–4100.
110. Grozea, C. M.; Gunari, N.; Finlay, J. A.; *et al*. *Biomacromolecules* **2009**, *10*, 1004–1012.
111. Krishnan, S.; Ayothi, R.; Hexemer, A.; *et al*. *Langmuir* **2006**, *22*, 5075–5086.
112. Martinelli, E.; Agostini, S.; Galli, G.; *et al*. *Langmuir* **2008**, *24*, 13138–13147.
113. Park, D.; Weinman, C. J.; Finlay, J. A.; *et al*. *Langmuir* **2010**, *26*, 9772–9781.
114. Weinman, C. J.; Finlay, J. A.; Park, D.; *et al*. *Langmuir* **2009**, *25*, 12266–12274.
115. Tan, B. H.; Hussain, H.; Chaw, K. C.; *et al*. *Polym. Chem.* **2010**, *1*, 276–279.
116. Weinman, C. J.; Gunari, N.; Krishnan, S.; *et al*. *Soft Matter* **2010**, *6*, 3237–3243.
117. Berglin, M.; Lonn, N.; Gatenholm, P. *Biofouling* **2003**, *19*, 63–69.
118. Schumacher, J. F.; Aldred, N.; Callow, M. E.; *et al*. *Biofouling* **2007**, *23*, 307–317.
119. Gaucher, G.; Dufresne, M. H.; Sant, V. P.; Kang, N.; Maysinger, D.; Leroux, J. C. *J. Control. Release* **2005**, *109*, 169–188.
120. Kataoka, K.; Harada, A.; Nagasaki, Y. *Adv. Drug Deliv. Rev.* **2001**, *47*, 113–131.
121. Boudou, T.; Crouzier, T.; Ren, K.; Blin, G.; Picart, C. *Adv. Mater.* **2010**, *22*, 441–467.
122. Quinn, J. F.; Johnston, A. P. R.; Such, G. K.; Zelikin, A. N.; Caruso, F. *Chem. Soc. Rev.* **2007**, *36*, 707–718.
123. Zelikin, A. N. *ACS Nano* **2010**, *4*, 2494–2509.
124. Rodriguez-Hernandez, J.; Checot, F.; Gnanou, Y.; Lecommandoux, S. *Prog. Polym. Sci*. **2005**, *30*, 691–724.
125. Karymov, M. A.; Procházka, K.; Mendenhall, J. M.; Martin, T. J.; Munk, P.; Webber, S. E. *Langmuir* **1996**, *12*, 4748–4753.
126. Meiners, J. C.; Quintel-Ritzi, A.; Mlynek, J.; Elbs, H.; Krausch, G. *Macromolecules* **1997**, *30*, 4945–4951.
127. Webber, S. E. *J. Phys. Chem. B* **1998**, *102*, 2618–2626.
128. Emoto, K.; Iijima, M.; Nagasaki, Y.; Kataoka, K. *J. Am. Chem. Soc.* **2000**, *122*, 2653–2654.
129. Emoto, K.; Nagasaki, Y.; Kataoka, K. *Langmuir* **2000**, *16*, 5738–5742.
130. Nguyen, P. M.; Zacharia, N. S.; Verploegen, E.; Hammond, P. T. *Chem. Mater.* **2007**, *19*, 5524–5530.
131. Ma, N.; Zhang, H. Y.; Song, B.; Wang, Z. Q.; Zhang, X. *Chem. Mater.* **2005**, *17*, 5065–5069.
132. Qi, B.; Tong, X.; Zhao, Y. *Macromolecules* **2006**, *39*, 5714–5719.
133. Kim, B. S.; Smith, R. C.; Poon, Z.; Hammond, P. T. *Langmuir* **2009**, *25*, 14086–14092.
134. Kim, B. S.; Park, S. W.; Hammond, P. T. *ACS Nano* **2008**, *2*, 386–392.
135. Kim, B. S.; Lee, H.; Min, Y. H.; Poon, Z.; Hammond, P. T. *Chem. Commun.* **2009**, *28*, 4194–4196.
136. Zhu, Z. C.; Sukhishvili, S. A. *ACS Nano* **2009**, *3*, 3595–3605.
137. Jia, S. S.; Fei, J. J.; Deng, J. J.; Cai, Y. L.; Li, J. A. *Sens. Actuators B Chem.* **2009**, *138*, 244–250.
138. Shan, W. J.; He, P. L.; Hu, N. F. *Electrochim. Acta* **2005**, *51*, 432–440.
139. Mecke, A.; Dittrich, C.; Meier, W. *Soft Matter* **2006**, *2*, 751–759.
140. Ikkala, O.; Ten Brinke, G. *Chem. Commun.* **2004**, *19*, 2131–2137.
141. Mao, H.; Arrechea, P. L.; Bailey, T. S.; Johnson, B. J. S.; Hillmyer, M. A. *Faraday Discuss.* **2005**, *128*, 149–162.
142. Tang, C.; Lennon, E. M.; Fredrickson, G. H.; Kramer, E. J.; Hawker, C. J. *Science* **2008**, *322*, 429–432.
143. Christman, K. L.; Schopf, E.; Broyer, R. M.; Li, R. C.; Chen, Y.; Maynard, H. D. *J. Am. Chem. Soc.* **2008**, *131*, 521–527.
144. Coyer, S.; García, A.; Delamarche, E. *Angew. Chem. Int. Ed.* **2007**, *46*, 6837–6840.

3.321. Microarrays in Biomaterials Research

Y Yamada, Nagoya University School of Medicine, Nagoya, Japan

© 2011 Elsevier Ltd. All rights reserved.

3.321.1.	**Introduction**	357
3.321.2.	**Principle of Microarray**	357
3.321.2.1.	Microarray Technology Method	357
3.321.2.1.1.	Biological question	357
3.321.2.1.2.	Sample preparation and microarray reaction	358
3.321.2.1.3.	Microarray detection, data analysis and modeling	358
3.321.3.	**Application of Microarray**	358
3.321.3.1.	Various Approaches to Biomaterial Research	358
3.321.3.2.	Functional Application of Microarray	360
3.321.3.2.1.	Essential stem cells study for biomaterial research	360
3.321.3.2.2.	Pathway dissection analysis	361
3.321.3.2.3.	Clustering analysis	362
3.321.4.	**Future Prospects of Microarray**	363
References		363

Abbreviations

3D	Three dimensional
AFM	Atomic force microscope
DPSCs	Dental pulp stem cells
GO	Gene-ontology
LCM	Laser capture microdissection
MSCs	Mesenchymal stem cells
SHED	Exfoliated deciduous teeth

3.321.1. Introduction

With the introduction of DNA microarrays in the 1990s, different types of arrays have gained increasing popularity in biosciences. The microarrays, which can comprise tens of thousands of spots on a single glass slide at addressable locations, have been extensively used in genomics with DNA- or protein-based probe molecules.[1–3] Moreover, the microarray format provides an ideal platform for the rapid assessment of material–cell interactions as it uses many materials in a manner that is amenable to cell culture. Cell propagation and cell encapsulation require some type of interaction between the cells and the supporting material to enable growth, function, and/or delivery,[4,5] and the cells are usually cultured in the presence of biomaterials. The response of cells to biomaterials is often initiated by cell contact and their adhesion to the biomaterial surface, and cell adhesion is regulated by proteins that are either part of the matrix or have adsorbed on the surface of the biomaterials.[6] Therefore, biomaterials can be used to provide the cells with specific, desirable matrices that mimic the native environment of the cells. Greater knowledge of the characteristics of the cells is also important for biomaterials research, and microarrays may be suitable for screening and testing a large number of combinations of biomaterials and microenvironments for cell adhesion, proliferation, and differentiation.[7]

On the other hand, biomaterials have been used for a variety of biomedical applications or as scaffolds in tissue engineering for many years.[4,8] In biomaterials research, many materials have been selected as being useful based on trial and error, availability, and macroscopic properties. Since the late 1800s, synthetic polymers are being increasingly used for biomedical purposes, and they are desirable as their chemical, biological, and mechanical properties can be easily engineered. Furthermore, biomaterials such as hydrogels provide a three-dimensional (3D) environment within which cells can be encapsulated. In addition, biomaterials provide sites for cell adhesion and initiation of matrix-generated signal transduction pathways, and also regulate stem cell differentiation through matrix elasticity and biomechanical cues.[9]

In this chapter, the potential of microarray methodology in biomaterials research and cell-based studies will be discussed.

3.321.2. Principle of Microarray

3.321.2.1. Microarray Technology Method

Microarray technology is emerging as a powerful platform for biological exploration as it allows entire genomes to be examined on glass chips. The microarray assay has five main steps: biological question, sample preparation, microarray reaction, microarray detection, and data analysis and modeling.[10] Therefore, every microarray experiment should begin with a biological question or query and proceed stepwise.

3.321.2.1.1. Biological question

Microarray analysis not only preserves the practice of query-based biology but has also made biological questioning

more important than ever; a recent proposal places 'the biological question' as the first step in a microarray experiment. Given the enormous power of microarray assays as data-generating devices, a single set of microarray experiments can generate a large amount of data and may require several months to analyze. Microarray analysis is fundamentally different from the traditional assays that employ gels and nylon membranes. In traditional assays, the ratio of analysis time to experimental time is small but in the microarray, this ratio is enormous. It is therefore suggested that a biological or technical question precede the other four basic steps of every microarray experiment.[10]

3.321.2.1.2. Sample preparation and microarray reaction

Microarray assays generate a large data flow, thus placing a premium on high-quality nucleic acid samples (RNA or DNA samples). Laser capture microdissection (LCM) can also be used in concert with microarray analysis to analyze gene expression. The LCM is used to capture specific cells from a section of cells, and the isolated RNA is converted to double-stranded complementary DNA (cDNA) using primers that contain T7 promoter sequences. The double-stranded cDNA is transcribed *in vitro* using the T7 polymerase to yield a large amount (~100-fold amplication per round) of amplified RNA (aRNA). The aRNA is then labeled with fluorescent nucleotides using reverse transcriptase to yield a fluorescent cDNA mixture that is hybridized to a DNA microarray. The location and extent of fluorescence provides a quantitative measure of gene expression in the sample. The use of multicolor schemes allows sensitive analysis of differential expression in multiple biological samples.[10]

3.321.2.1.3. Microarray detection, data analysis and modeling

Detection is the fourth step in a microarray experiment, and this critical step is currently being influenced by an explosion in fluorescence detection technology. DNA microarrays contain sequences of the known, predicted, or unknown genes and are probed with cDNA that has been labeled with different fluorophores (e.g., Cy3, green; Cy5, red). The relative abundance of each RNA message is measured by directly comparing the signals from the competitive hybridizations resulting in a red/green expression ratio for each gene. These microarray experiments generate an enormous amount of data, thus placing bioinformatics at the core of the microarray system. Attention has to be paid to output and data modeling, and once values are quantified from the microarray, the data are displayed in a variety of ways. One common method of depiction is the scatter plot, in which all the data points are plotted as a function of ratio and signal intensity; data points having a ratio >1.0 are plotted above the diagonal and those with ratios <1.0 plotted below the diagonal. The scatter plot provides a means of viewing, at a glance, very large datasets such as those involving expression profiles of thousands of genes (**Figure 1(a)** and **(b)**). Once the data are quantified and genes of interest are identified, a common method of data mining allows genes to be grouped or 'clustered' according to their expression profiles. The biological basis for clustering derives from the fact that gene expression correlates well with biological function. The clustering tools help in the identification of functionally related genes, such as those in common signaling pathways and those that share common biological activity.[11]

3.321.3. Application of Microarray

DNA microarrays also consists of a molecular technology that enable the process of gene interaction analysis. The data are analyzed by means of dedicated bioinformatics software which allows the detection of genes whose differential expression is signficant. This technology has been applied to a variety of studies, including those on cell differentiation, infection, inflammation, and cancer research.[12] A recent study has demonstrated that microarrays can be used to analyze pathways of genes involved in the differences in cellular proliferation between stem cells.[13] It can also be used to better understand the effects of different biomaterials on gene expression.[14]

3.321.3.1. Various Approaches to Biomaterial Research

The need for more informative biological assays and models has been essential in the development of predictive preclinical methods for drug discovery and clinical application processes. It has been stated that the study of cell–biomaterial interactions can be useful in a number of applications, such as tissue engineering,[15] drug discovery,[16] and so on. It is also important to control and understand the cellular microenvironment as it can affect gene expression and its regulation.[17]

Until now, differentiation of the cells had been studied using immunohistochemistry[18] and by atomic force microscopic (AFM) evaluation of cell morphology[19] and sizes.[20] They provide basic information about the response of the cell in the biomaterial environment. A more thorough characterization and analysis of these cell responses would require the study of gene expression either by PCR, DNA arrays, or proteomics. In general, these methods such as DNA array and proteomics have a limitation in that the analysis of the cellular responses is not easy, as these methods require large samples. It is often difficult to extract cellular material for analytical methods such as PCR or flow cytometry from cells that are embedded in biomaterials.[21] However, these methods, which can obtain greater information, play an important role in the analysis of selected biomaterials after the culture has been scaled to a larger size. Another dimension in cell assays is cellular manipulation by the use of transfections.[22] Transfections result in gene upregulation (with DNA or RNA) or knock down (with miRNA, siRNA, or antisense). This allows a systematic biological approach to the studies on cell responses. Reverse transfection is a commonly used procedure in cell array research and is related to the study of biological mechanisms. Such arrays allow studies on the mechanisms of the disease and a search for new drug targets. This is a powerful approach because it allows a systematic mapping of the cellular machinery by knocking down individual genes with siRNA and then noninvasively measuring the cellular response using fluorescent assays.[23] This functional assay must be selected case-by-case, and it depends on the cell type, end points, and goals of the study.

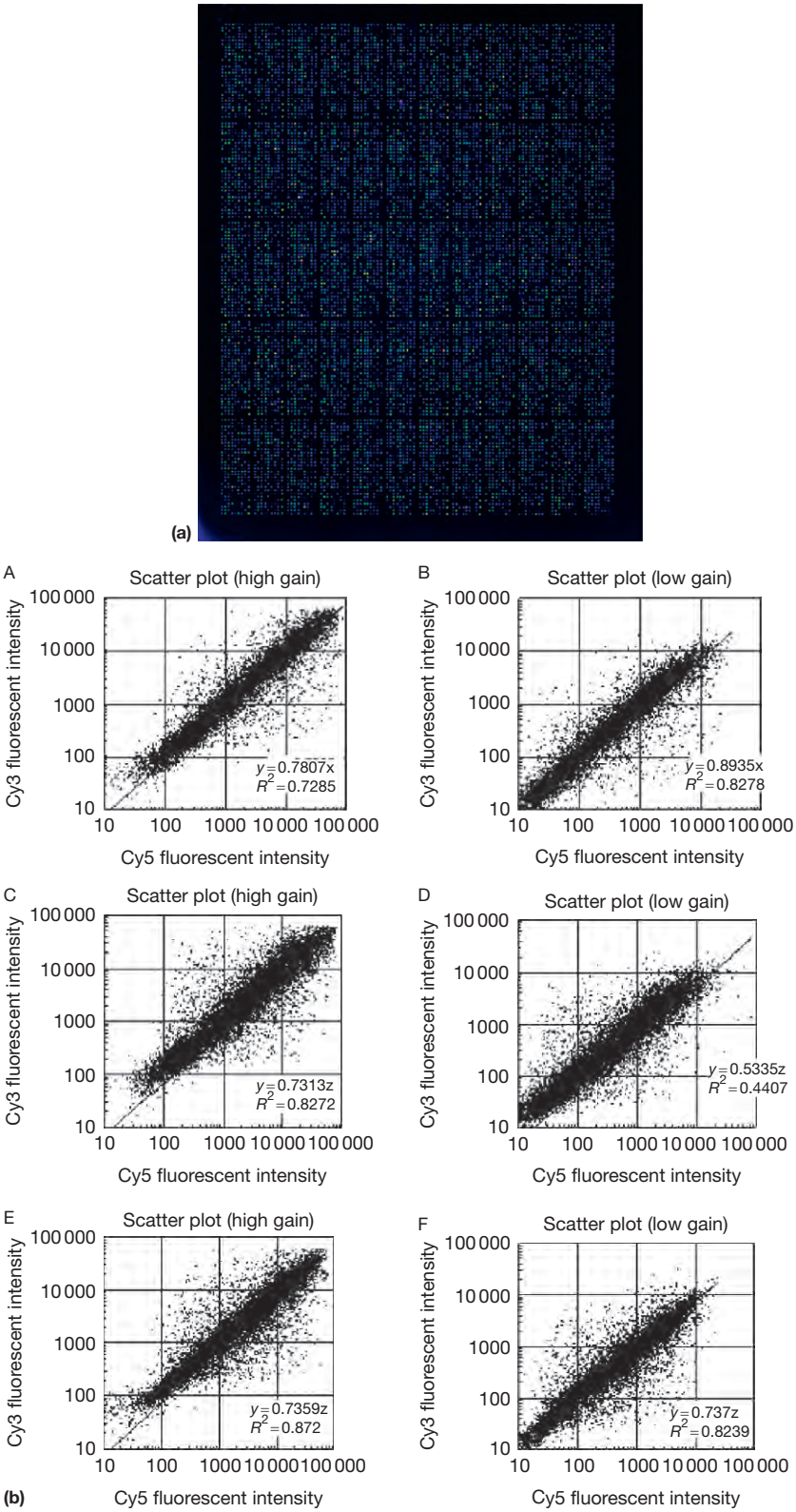

Figure 1 (a) Microarray scanned image. (b) Global comparison of the levels of gene expression in high (A, C, and E) and low (B, D, and F) gain human dental pulp stem cells (hDPSCs) or human mesenchymal stem cells (hMSCs). Each dot corresponds to the Cy3 and Cy5 fluorescent intensity of one single element on the microarray. The dot plot shows a (A): high or (B): low gain between hMSCs and hMSCs (osteoinduction), a (C): high or (D): low gain between hMSCs and hDPSCs, a (E): high or (F): low gain between hMSCs and hDPSCs (osteoinduction). Reproduced from Yamada, Y.; Fujimoto, A.; Ito, A.; Yoshimi, R.; Ueda, M. *Biomaterials* **2006**, *27*, 3766–3781, with permission from Elsevier.

3.321.3.2. Functional Application of Microarray

DNA microarrays are a useful means of quantifying tens of thousands of discrete sequences in a single assay. The most widespread use of microarrays, expression profiling,[24] has many applications, including in the discovery of gene functions,[25] pathway dissection,[26] and in the classification of clinical samples.[27] The development of microarray methods has enabled rapid and quantitative studies on the interaction between cells, such as stem cells and their microenvironment.

3.321.3.2.1. Essential stem cells study for biomaterial research

One emerging trend in biomaterials research is the design of biofunctional materials that can modulate cellular responses via the incorporation of necessary, instructive signals into the biomaterials. While much progress has been made in biomaterial design and application, the rational design of biomaterial cues to control stem cell behavior and differentiation has remained challenging due to the complexity of

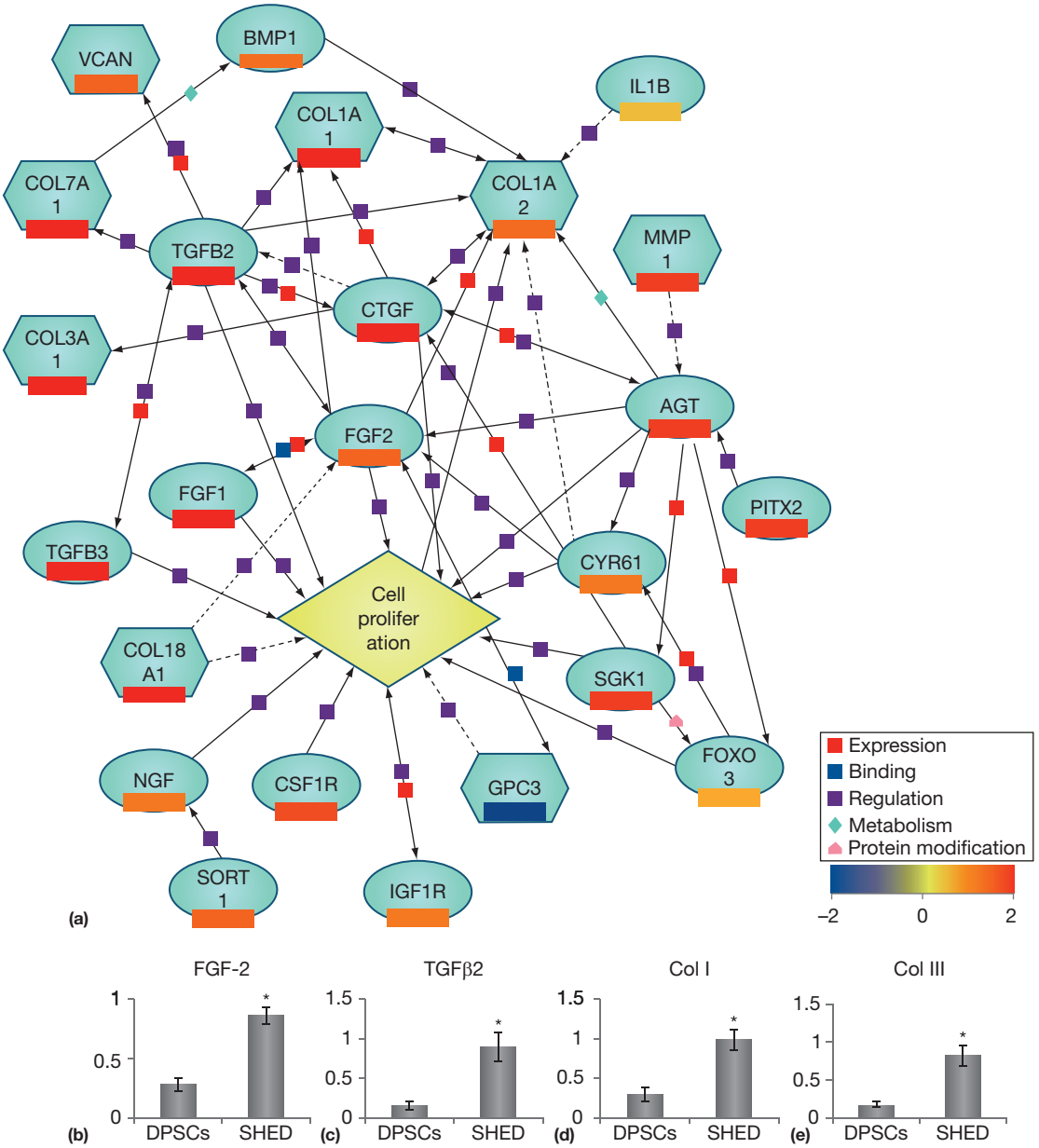

Figure 2 (a) Pathway analysis of gene categories that were prominent in stem cells from human exfoliated deciduous teeth (SHED) compared to dental pulp stem cells (DPSCs). The cell proliferation pathway was accelerated in SHED. The network is displayed as nodes (genes) and lines (biological relationships between nodes). Genes colored red showed increases, while genes colored blue showed decreases. Dotted lines denote downregulation. (b)–(e) Real-time PCR analysis was performed to validate the expression level of the genes involved in the cell proliferation pathway. FGF-2, TGF-β2, Col I, and Col III showed a significantly higher expression in SHED compared to DPSCs ($p < 0.05$). Reproduced from Nakamura, S.; Yamada, Y.; Katagiri, W.; Sugito, T.; Ito, K.; Ueda, M. *J. Endod*. **2009**, *35*, 1536–1542, with permission from Elsevier.

cell–biomaterial interactions.[28] On the other hand, stem cells are an essential element in the concept of tissue engineering for tissue regeneration. Tissue engineering is a relatively new field, in which new tissue is created for repair or replacement. According to this concept, it is possible to regenerate various tissues using three elements – living stem cells, appropriate scaffolds, and growth factors.[4] In recent tissue engineering studies, somatic stem cells, such as mesenchymal cells (bone marrow-derived mesenchymal stem cells (MSCs), dental pulp stem cells (DPSCs), stem cells from human exfoliated deciduous teeth (SHED), etc.), have been applied to regenerate tissues, as these stem cells readily self-replicate and are capable of replenishing the supply of tissue-forming cells. MSCs would also play an important role in tissue regeneration. DPSCs are able to differentiate into cells of the odontoblastic and osteoblastic lineage and have been reported to have the potential for use in cell-based therapy for systemic disease, such as neurological and cardiac diseases, and to ameliorate ischemic disease.[29,30] It must be stressed that tissue-engineered constructs, *ex vivo* cell propagation, and cell encapsulation–all require some type of interaction between cells and the supporting material for growth, function, and/or delivery, and stem cells are usually cultured such that they are in contact with biomaterials (as scaffolds or matrices). Therefore, information on the characteristics of cells is also important for design of biomaterials to be used as scaffolds. Microarray analysis or functional evaluation of the cellular gene expression profile has important implications for understanding stem cell characteristics, especially the mechanisms of cell capacities.

3.321.3.2.2. Pathway dissection analysis

There are two ways to carry the data analysis, beyond gene-ontology (GO) classification, deeper into biology: by going to the molecular level, which is promoter and regulatory network analysis, or by employing the vast knowledge that has already accumulated in the literature. The pathways focus on physical and functional interactions between genes rather than taking the gene-centered view of GO-based analyses.[31] Therefore, it is intriguing to map the list of significantly regulated genes onto the commonly precompiled pathways in order to elucidate the entire chain of events observed in a microarray experiment.

For example, it pays attention to the somatic stem cells of important role in clinical application. However, stem cells, such as SHED, DPSCs, and BMMSCs, which include a large proportion of the high growth- and differentiation-potential skeletal stem cells, have similar characteristics. On the

Table 1 Functional gene classification in clustering analysis

Major category	*Subcategory*	*a*	*b*	*c*	*d*	*e*	*f*	*g*	*h*	*i*
Cell division	DNA synthesis/replication	1		1						
	Apoptosis	2	1	9		6		1		
	Cell cycle	11		4		3		1		
	Chromosome	2				2				
	Subtotal	16	1	14	0	11	0	2	0	0
Cell signaling or cell communication	Cell adhesion	3	3	4	1	13		1		
	Channels/transport protein	2	1	4	2	6			1	
	Growth factors/cytokines	4		8		6		3		
	Metabolism	4		5		2				
	Protein modification	3		6		3				
	Receptors	9	4	10	1	16	2	9		
	Subtotal	25	8	37	4	46	2	13	1	0
Cell structure/motility	Cytoskeletal	1	1	1		1		1		
	Extracellular matrix	1	2			4	3	4		
	Microtubule-associated protein									
	Subtotal	2	3	1	0	5	3	5	0	0
Cell/organism defense	Homeostasis (stress response)	14	1	7		8	1	12		
	Immunology (immune response)	9	1	7		13	1	11		1
	Subtotal	23	2	14	0	21	2	23	0	1
Gene/protein expression	RNA synthesis (transcription factor)	6	2	8		12		4		
	Protein synthesis (protein binding)	1	1	1		1		1		
	Subtotal	7	3	9	0	13	0	5	0	0
Metabolism	Amino acid	1		4		1				1
	Energy/TCA cycle									
	Lipid	6		4		5		1		3
	Nucleotide	3				3				
	Protein modification	2		12		3		1		
	Transport	10	1	14	2	15		3		
	Subtotal	22	1	34	2	27	0	5	0	4
	Total	95	18	109	6	123	7	53	1	5
		166	53	145	23	233	9	58	6	11

Reproduced from Yamada, Y.; Fujimoto, A.; Ito, A.; Yoshimi, R.; Ueda, M. *Biomaterials* **2006**, *27*, 3766–3781.

other hand, because of their high proliferation ability, SHED and DPSCs, instead of BMMSCs, could be useful cell sources for cell-based therapy. Thus, there is an increasing focus on SHED and DPSCs and further analyses have been performed. cDNA microarray technology and pathway analysis have been used to compare multiple gene expression profiles that are representative of SHED and DPSCs. A fold-change cutoff of 2 for both upregulation and downregulation of genes and a *p*-value cutoff of 0.05 were set to identify the differentially expressed genes. One of the most significantly altered pathways was cell proliferation. The network of genes involved in cell proliferation is shown in **Figure 2(a)**. Extracellular matrix genes, including collagen (Col I, III, VII, and XIII) and proteoglycan (glypican and versican), were altered in the cell proliferation pathway. In addition, several cytokines were related to this pathway, and the results also showed that SHED expressed several growth factors such as FGF, TGF-β, CTGF, NGF, and BMP at higher levels (**Figure 2**).[13] A functional evaluation of the gene expression profile has important implications for understanding the stem cell characteristics, especially the mechanisms of cell potency. As it is quite important to have high proliferative capacity in order to be able to use MSCs in various medical applications, the high proliferation ability of SHEDs could be a great advantage. The pathways and individual genes that have been identified in this study might support SHED as an alternative useful cell source for future clinical applications that involve a novel therapy for systemic diseases.

3.321.3.2.3. Clustering analysis

A method for cluster analysis of genome-wide expression data from microarray hybridization that uses standard statistical algorithms to arrange genes according to the similarity in patterns of gene expression has been described. It combines clustering methods with a graphical representation of the primary data by representing each data point in color which quantitatively and qualitatively reflects the original experimental observations. Relationships among genes are represented by a dendrogram whose branch lengths reflect the degree of their similarity, as assessed by a pair-wise similarity function. Genes are displayed in the following colors: those with a log ratio of 0 (ratio of 1.0: genes unchanged) in yellow; those with increasingly positive log ratios in red of increasing intensity; and those with increasingly negative log ratios in blue of increasing intensity. The results suggest that the clustering algorithm successfully identifies cooperatively regulated genes according to their expression profiles. It thus enables a further clustering analysis of expression profiles of functionally categorized genes in order to investigate the relevance of the expression profiles and their functions. For example, gene expression patterns and functional classifications were investigated in human dental pulp stem cells (hDPSCs) and human mesenchymal stem cells (hMSCs) (**Figure 3**). The analyses of gene expression patterns indicated that several of the genes encoded extracellular matrix components, cell adhesion molecules, growth factors, and transcription regulators. Functional and clustering analyses of the differences in gene expression levels revealed genes involved in cell signaling, cell communication, or cell metabolism (**Table 1**).[32] In general, the classification scheme, such as functional and clustering analysis, consisted of six

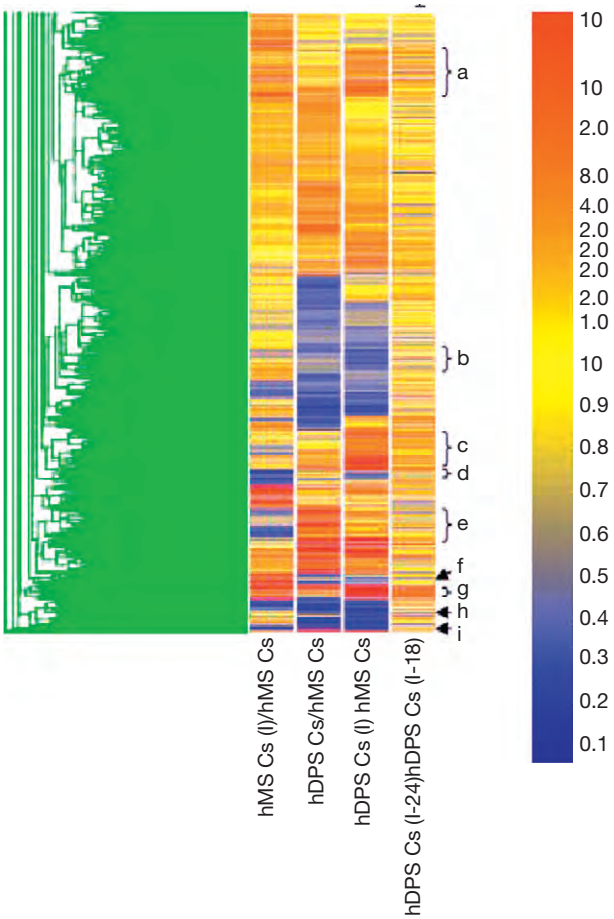

Figure 3 Representative global view of expression level changes by hierarchical clustering analysis. Significantly upregulated or downregulated genes were analyzed according to the clustering method. The cluster in yellow denotes no significant difference between samples; the clusters in red and blue denote transcripts which are more and less abundant in each cell, respectively. The intensity of the color is proportional to an *n*-fold increase or decrease, with the maximal intensity corresponding to a 15-fold increase or decrease as represented in the color scale (bottom). Annotations for the clusters given by the microarray data analysis software are shown on the right (magnified): the annotations in the clusters are a, b, c, d, e, f, g, h, and i. Reproduced from Yamada, Y.; Fujimoto, A.; Ito, A.; Yoshimi, R.; Ueda, M. *Biomaterials* **2006**, *27*, 3766–3781, with permission from Elsevier.

major functional categories (cell division, cell signaling/cell communication, cell structure/motility, cell/organism defense, gene/protein expression, and metabolism) with several minor functional categories within the major categories. The clustering analyses provided novel insights into cellular functions and enabled comprehension of the transcriptional regulatory mechanisms of several genes in each sample. Such information on the gene expression patterns of hDPSCs and hMSCs might be useful in determining the detailed functional roles of the relevant genes and may also be applicable in stem cell therapies. Moreover, these cells could also be used as sources of multipotent cells for gene technology and tissue engineering technology.

3.321.4. Future Prospects of Microarray

Microarray analysis is very appropriate for biomaterial research, especially for studying the interactions between cells, cellular behavior, and the microenvironment around biomaterials. Although the gene expression profiles should be further confirmed with other molecular biological methods such as quantitative real-time PCR, the method is valuable in its own right. In other words, gene microarray systems for profiling and analysis of gene expression offer abundant and useful information. They enable a functional classification of genes based on their protein-encoding functions. However, the assay should be selected case-by-case, depending on the cell type, end point, and goals of the study. In addition to gene expression profiles, technologies for pathway and clustering analysis using microarrays can provide new knowledge on how biomaterials interact with cells; this will enable progress in biomaterials research.

References

1. Heller, M. J. *Annu. Rev. Biomed. Eng.* **2002**, *4*, 129–153.
2. Lee, B. H.; Nagamune, T. *Biotechnol. Bioproc. Eng.* **2004**, *9*, 69–75.
3. Venkatasubbarao, S. *Trends Biotechnol.* **2004**, *22*, 630–637.
4. Langer, R.; Vacanti, J. P. *Science* **1993**, *260*, 920–926.
5. Lanza, R. P.; Langer, R. S.; Vacanti, J. *Principles of Tissue Engineering*, 2nd ed.; Academic Press: San Diego, 2000.
6. Fittakau, M. H.; Zilla, P.; Bezuidenhout, D.; *et al*. *Biomaterials* **2005**, *26*, 167–174.
7. Khademhosseini, A.; Langer, R.; Borenstein, J.; Vacanti, J. P. *Proc. Natl. Acad. Sci. USA* **2006**, *103*, 2480–2487.
8. Hubbell, J. A. *Nat. Biotech.* **2004**, *22*, 828–829.
9. Engler, A. J.; Sen, S.; Sweeney, H. L.; Discher, D. E. *Cell* **2006**, *126*, 677–689.
10. Mark, S. *Microarray Biochip Technology*; Eaton: Westborough, MA, 2000.
11. Eisen, M. B.; Spellman, P. T.; Brown, P. O.; Botstein, D. *Proc. Natl. Acad. Sci. USA* **1998**, *95*, 14863–14868.
12. Bednar, M. *Med. Sci. Mon.* **2000**, *6*, 796–800.
13. Nakamura, S.; Yamada, Y.; Katagiri, W.; Sugito, T.; Ito, K.; Ueda, M. *J. Endod.* **2009**, *35*, 1536–1542.
14. Bombonato-Prado, K. F.; Bellesini, L. S.; Junta, C. M.; Marques, M. M.; Passos, G. A.; Rosa, A. L. *J. Biomed. Mater. Res.* **2008**, *88*, 401–408.
15. Tan, W. J.; Teo, G. P.; Liao, K.; Leong, K. W.; Mao, H. Q.; Chan V. *Biomaterials* **2005**, *26*, 891–898.
16. Yang, X.; Parker, D.; Whitehead, L.; *et al*. *Comb. Chem. High Throughput Screen.* **2006**, *9*, 123–130.
17. Anderson, D. G.; Peng, W.; Akinc, A.; *et al*. *Proc. Natl. Acad. Sci. USA* **2004**, *101*, 16028–16033.
18. Flaim, C. J.; Chien, S.; Bhatia, S. N. *Nat. Meth.* **2005**, *2*, 119–125.
19. Simon, C. G.; Eidelman, N.; Kennedy, S. B.; Sehgai, A.; Khatri, C. A.; Washburn, N. R. *Biomaterials* **2005**, *26*, 6906–6915.
20. Karp, J. M.; Yeh, J.; Eng, G.; *et al*. *Lab Chip* **2007**, *7*, 786–794.
21. Goodman, S. L.; Sims, P. A.; Albrecht, R. M. *Biomaterials* **1996**, *17*, 2087–2095.
22. Brummelkamp, T. R.; Fabius, A. W.; Mullenders, J.; *et al*. *Nat. Chem. Biol.* **2006**, *2*, 202–206.
23. Yliperttula, M.; Chung, B. G.; Navaladi, A.; Manbachi, A.; Urtti, A. *Eur. J. Pharm. Sci.* **2008**, *35*, 151–160.
24. Schena, M.; Schalon, D.; Davis, R. W.; Brown, P. O. *Science* **1995**, *270*, 467–470.
25. Hughes, T. R.; Marton, M. J.; Jones, A. R.; *et al*. *Cell* **2000**, *102*, 109–126.
26. Roberts, C. J.; Nelson, B.; Marton, M. J.; *et al*. *Science* **2000**, *287*, 873–880.
27. Golob, T. R.; Slonim, D. K.; Tamayo, P.; *et al*. *Science* **1999**, *286*, 531–537.
28. Mei, Y.; Goldberg, M.; Anderson, D. *Curr. Opin. Chem. Biol.* **2007**, *11*, 388–393.
29. Iohara, K.; Zheng, L.; Wake, H.; *et al*. *Stem Cells* **2008**, *26*, 2408–2418.
30. Arthur, A.; Rychkov, G.; Shi, S.; Koblar, S. A.; Gronthos, S. *Stem Cells* **2008**, *26*, 1787–1795.
31. Thomas, P. D.; Mi, H.; Lewis, S. *Curr. Opin. Chem. Biol.* **2007**, *11*, 4–11.
32. Yamada, Y.; Fujimoto, A.; Ito, A.; Yoshimi, R.; Ueda, M. *Biomaterials* **2006**, *27*, 3766–3781.

3.323. Magnetic Resonance of Bone Microstructure and Chemistry

F W Wehrli, University of Pennsylvania, Philadelphia, PA, USA

© 2011 Elsevier Ltd. All rights reserved.

3.323.1.	**Introduction**	380
3.323.2.	**Fundamentals of Magnetic Resonance**	380
3.323.3.	**Quantitative MRI of Trabecular and Cortical Bone Microstructure**	381
3.323.3.1.	Role of Architecture: Structural Studies in Specimens	382
3.323.3.2.	*In Vivo* Spatial Resolution Regime	383
3.323.3.3.	Characterization of Trabecular Bone Architecture in Terms of Scale, Topology, and Orientation	384
3.323.3.3.1.	Trabecular bone volume fraction and thickness	384
3.323.3.3.2.	Topology of trabecular networks	384
3.323.3.3.3.	Structural orientation	385
3.323.4.	**Bone Water and Porosity**	385
3.323.5.	**NMR Spectroscopy and MRI of Bone Matrix and Mineral**	387
3.323.6.	**Summary and Conclusions**	389
References		389

Glossary

Apparent diffusion coefficient (ADC) Diffusion coefficient measured in the presence of barriers to diffusion. The ADC is smaller than the true diffusion coefficient of the diffusing molecules in the absence of structural hindering.

Cartesian imaging techniques Most common MRI method in which data are collected on a Cartesian grid, thereby allowing image reconstruction by 2D or 3D Fourier transformation.

Cross-polarization NMR method designed to transfer polarization from one nucleus (e.g., protons) to another (e.g., phosphorus).

Fabric tensor Symmetric second-rank tensor that characterizes the structural anisotropy of porous material microstructure such as trabecular bone networks.

Free induction decay (FID) Magnetic resonance signal induced in a receive coil by the precessing magnetic moments.

Larmor frequency Resonance or precession frequency of spins in a static magnetic field. The Larmor frequency is proportional to the magnetic field strength with a proportionality constant equal to the gyromagnetic ratio.

Mean intercept length Number of intersections between bone and surrounding narrow space along test lines of predetermined direction.

Pulse sequence Set of instructions to a MRI imaging device to turn magnetic field gradients and radio frequency fields on and off for the purpose of exciting spins and detecting their response.

Relaxation rate Reciprocal of relaxation time.

Relaxation times Time constants for the recovery of the nuclear magnetic moment or magnetization to its equilibrium state following a perturbation, with T_1 governing the return of the longitudinal magnetization and T_2 governing the return of the transverse magnetization.

Relaxivity Relaxation rate per unit concentration of the relaxant.

Solid-state MRI MRI technique designed to capture signals and image nuclei with extremely short transverse relaxation times as they occur in solids.

Spatial autocorrelation function Describes correlation among data as a method to probe the regularity of trabecular bone lattices.

Topology Study of spatial properties that are preserved under continuous deformation of the object, including stretching, an approach used for the characterization of trabecular bone networks.

Abbreviations

2D	Two-dimensional
3D	Three-dimensional
ACF	Autocorrelation function
BVF	Bone volume fraction
CBVF	Cortical bone volume fraction
CPMG	Carr–Purcell–Meiboom–Gill
CT	Computed tomography
DTA	Digital topological analysis
DXA	Dual-energy X-ray absorptiometry
FID	Free induction decay
HRpQCT	High-resolution peripheral quantitative computed tomography
MIL	Mean intercept length
MRI	Magnetic resonance imaging
NMR	Nuclear magnetic resonance
PSF	Point spread function
RF	Radiofrequency

S/C	Surface-to-curve	**μCT**	Micro-CT
SMI	Structure-model index	**YM**	Young's modulus
SNR	Signal-to-noise ratio		

3.323.1. Introduction

Bone is a composite, living biomaterial that dynamically adapts to the direction and intensity of the stresses to which it is subjected through a process called 'remodeling.' The same process enables the material to repair damage such as microcracks that form after the bone has undergone myriads of loading cycles during daily living through an elaborate interplay of cells (the osteoblasts or bone-forming cells and the osteoclasts or the bone-resorbing cells), mediated by osteocytes acting as pressure transducers and modulated by hormones and signaling molecules.

Remodeling-induced changes in bone material density can have significant implications on the bone's ability to withstand stresses. For example, decreased loading due to lack of exercise or prolonged exposure to microgravity leads to bone loss and thus increased fracture susceptibility. Similarly, depletion of estrogen levels following menopause in women causes a negative remodeling balance.

Bone derives its salient mechanical properties, in particular its high tensile and compressive strength, from its unique material composition and nanostructural organization.[1,2] Bone material is organized hierarchically starting at the molecular level, with basic building blocks being tropocollagen as the organic component and crystals of nonstoichiometric calcium hydroxyapatite interspersed in gaps in the collagen triple helix. An assembly of these basic building blocks forms fibrils, which, in turn, are organized into fibers. Arrays of parallel fibers make up sheets (lamellae) winding around Haversian canals, which, in cortical bone, make up the osteon, the basic building block at the microstructural level.

Bone's intrinsic material modulus ranges from about 15 to 25 GPa and is anisotropic, being stiffer in the direction of the osteonal axis than perpendicular to it. Bone is also unique in its toughness: that is, its capacity to absorb energy, critical to fracture resistance. In distinction to the mechanical properties (e.g., stiffness or ultimate strength) that are intrinsic to the material itself are their structural counterparts. Clearly, a given material density incompletely characterizes the bone's mechanical behavior, which is determined by the spatial distribution and the loading mode. The structural and mechanical properties of bone are well understood and have been described in detail in terms of continuum mechanics engineering math (see, e.g., Cowin[3]).

Imaging at virtually all length scales of resolution ranges from X-ray diffraction to scanning electron and confocal microscopy as tools to evaluate bone material nanostructure and microstructure, while the macrostructure is evaluated with X-ray radiography and computed tomography (CT). More recently, infrared and Raman spectroscopy and their spectroscopic imaging counterparts have provided new insights into the chemical makeup of the bone matrix and the mineral phases. However, other than CT, these imaging modalities are confined to the study of bone tissue *ex vivo* in cadaver specimens or bone biopsies.

This chapter briefly reviews the current state of the art and potential of magnetic resonance imaging (MRI) and nuclear magnetic resonance (NMR) spectroscopy for evaluating the structural and material properties of trabecular and cortical bone, both *ex vivo* and *in vivo* in live human subjects.

3.323.2. Fundamentals of Magnetic Resonance

MRI is currently the preeminent diagnostic imaging modality for most organ systems, including the musculoskeletal system. However, its salient strength lies in visualizing soft tissues and their abnormalities in tendons and ligaments, cartilage, muscle, intervertebral disk, bone marrow, etc.

While this is not the place to introduce the physics underlying the method, MRI's potential cannot be appreciated by the reader without some grasp of its fundamentals. MRI, or its parent, NMR, is based on detecting an electrical signal elicited by the nuclear magnetic moments (most typically protons in hydrogen, such as tissue water or lipids) after having been subjected to an intense, static, and homogeneous magnetic field B_0 of several tesla intensity ($1\,\mathrm{T} = 10\,000\,\mathrm{G}$). In this manner, the nuclear magnetic moments become polarized, or aligned with the field, thereby creating a macroscopic magnetic moment, also called *magnetization*. When then a second circularly polarized (radiofrequency, rf) magnetic field of amplitude B_1 is applied perpendicular to the static field for a short period of time, the magnetization is deflected into a plane transverse to the static field. The action of the rf pulse applied at the spins' resonance frequency ω_0 causes the magnetization to precess around the axis of the static field, thereby inducing a voltage in a suitably positioned receiver coil (Faraday's law of induction). The maximum signal that can be obtained with a given experimental arrangement is obtained by turning the field on for a period sufficient to rotate the magnetization by 90° into the transverse plane, that is, the plane perpendicular to the direction of the static field. The frequency $\omega_0 = \gamma B_0$ is called *Larmor* frequency, where γ is a nuclear constant. At a typical field strength of 3 T of a magnetic resonance imager, the resonance frequency is 128 MHz.

The signal obtained in this manner, also called *free induction decay* (FID), is a damped sinusoid with the damping time constant T_2, the *transverse relaxation time*. The finite lifetime of the signal results from mutual interference of the spins due small local variations in the magnetic field caused by external perturbations or mutual interactions among the nuclear magnetic moments. T_2 for protons in soft tissues ranges from a few milliseconds to about 100 ms. We will see later that the magnitude of T_2 critically affects our ability to detect the signal and, in general, that increased viscosity shortens T_2, resulting in extremely short values in the solid state. Examples are protons that are part of bone's collagen matrix or the phosphorus spins in calcium phosphate of the bone's mineral constituent.

Another time constant that affects the MRI signal is the longitudinal relaxation time T_1, so called because it characterizes the dynamics of the longitudinal component of the magnetization. Following a 90° rf pulse, for example, the longitudinal magnetization returns to its equilibrium value with a time constant T_1. Both T_1 and T_2 of the water protons in mammalian tissues are dependent on the strength of the static field, with T_1 increasing and T_2 decreasing. T_2 is 1–3 orders shorter than T_1, ranging from about 0.5 to 4 s.

In 1973, Lauterbur[4] showed that the NMR method lends itself to obtain cross-sectional images by spatially encoding the nuclear magnetic moments. Whereas in a uniform magnetic field all nuclei resonate at the same frequency, as pointed out above, this is no longer the case when a small, spatially variant field (a gradient magnetic field) is superimposed on the main field B_0. The effective field strength the spins experience then becomes a function of spatial position and, according to the Larmor relationship, also of their resonance frequency. By Fourier analysis of such a signal, which is a complex superposition of multiple sinusoids, a projection representation of the object is obtained, analogous to CT. By rotating the gradient field in small angular increments, a series of projections are collected, from which an image can be reconstructed using filtered backprojection.

While the above is not the most commonly used method for MRI, all current methods are based on spatial encoding with gradient magnetic fields. In the most commonly used Cartesian imaging techniques, two orthogonal gradient fields are applied, one immediately after excitation by a short pulse of the B_1 field, and a second one subsequently during signal collection. During each excitation signal-readout cycle, the pre-encoding gradient (also called phase-encoding gradient) assumes a different value. In this manner, a matrix of, for example 256×256, signal samples of the imaging object is obtained, each characterized by an amplitude and phase. The cycle of excitation and detection, followed by a recovery period, is called a *pulse sequence*. The recovery period inserted before the next following excitation is necessary to allow the magnetic moments to relax by exchanging their excess energy to their surroundings, also called 'lattice,' a process typically occurring with an exponential time constant T_1. An image is then obtained by subjecting the data to a two-dimensional (2D) Fourier transformation, upon which a 256×256 digital representation of the object is obtained wherein the amplitude of each picture element (pixel) is proportional to the proton concentration at a particular spatial location.

The smallest signal-producing element is the voxel (acronym for volume element), which is equal to the product of pixel area and slice thickness. Therefore, the relative signal strength is proportional to voxel volume. However, the quantity of relevance is the *signal-to-noise ratio* (SNR). The noise has a complicated dependence on various parameters, which include the field strength, size and design of the rf receive coil, and the volume of tissue 'seen' by the coil. Because of its stochastic nature, the noise amplitude increases only as the square root, whereas the signal increases linearly with the number of signal averages. Hence, it is possible to increase the SNR by repeatedly summing the signal from successive data collections.

Resolution in digital imaging modalities is often defined in terms of the length of the imaging voxel, Δr_i $(i = x, y, z)$, typically termed 'voxel size.' Equal voxel size along the three orthogonal directions ($\Delta x = \Delta y = \Delta z$) yields what is referred to as *isotropic* resolution. (The term is a misnomer since the resolution in non-orthogonal directions is less.) While a useful figure of merit for quantifying resolution, actual resolution is almost always less than suggested by voxel size in that true resolution is determined by the point spread function (PSF) of the imaging device. In Cartesian MR imaging, the PSF is at least 20% greater than voxel size. Nevertheless, for simplicity I shall here equate resolution with voxel size. This is not inappropriate as long as we compare different resolution regimes for essentially a given imaging method.

Figure 1 shows a cross-sectional high-resolution image of the distal tibia obtained *in vivo*, along with a volume-rendered 'virtual core' providing detailed insight into the architecture of the trabecular network.

3.323.3. Quantitative MRI of Trabecular and Cortical Bone Microstructure

Under typical imaging conditions, bone has near background intensity (unlike in X-ray imaging where the grayscale is determined by the attenuation coefficients, with hard tissues appearing with highest intensity). The contrast achieved, for example, between bone trabeculae and marrow, is caused by the large signal strength from the protons in fatty and hematopoietic marrow. The lack of a detectable signal from bone arises from the relatively low proton density and extremely short transverse relaxation times, in particular, not only of the protons in collagen of the osteoid (10–20 μs)[5] but also of the water in the Haversian and lacunocanalicular system as well as the significant fraction bound to collagen via hydrogen bonding, which possesses a T_2 on the order of 400–800 μs.[6] We will see in a later section in this chapter that bone water can be detected by appropriate imaging pulse sequences designed to capture the FID.

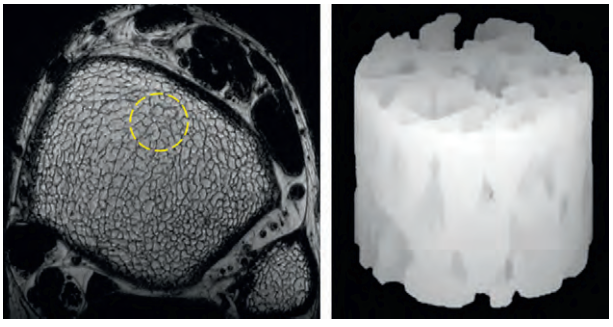

(a) (b)

Figure 1 (a) Magnetic resonance image at the location of the distal tibial metaphysis in a 37-year-old male, clearly showing trabecular and cortical bone at background intensity contrasting against the intense signal from fatty marrow in the endosteal cavity and other soft-tissue structures periosteally. The image obtained at 7 T field strength is one of 32 contiguous slices of 410 μm thickness and 137×137 μm^2 pixel size. (b) Volume-rendered 'virtual core' at the site indicated in panel a (circle), clearly showing the tubular, highly anisotropic, plate-like architecture with preferential orientation of the trabeculae along the bone's major loading direction.

In this section, we shall be concerned with imaging the marrow and reconstruct images of the 3D trabecular and cortical bone architecture by virtue of the contrast between the signal-less bone and the surrounding soft tissue. For details on imaging technology, including pulse sequences, image reconstruction, and processing, the reader is referred to some of the pertinent reviews on the subjects.[7–10]

The primary motivation for characterizing the 3D architecture of bone on the basis of structural images is to evaluate the relationship between mechanical competence and structure. Two fundamentally different approaches are being practiced. The first is to exploit structural information as a surrogate for measures of bone mechanical competence by quantitatively characterizing structure in terms of parameters of scale (typically bone volume fraction (BVF), mean trabecular separation, trabecular or cortical thickness[11]), topology (Euler numbers,[12] structure-model index (SMI),[13] digital and volume topological analysis),[14,15] and orientation.[16,17] The second approach seeks to directly estimate measures of the bone's mechanical behavior, such as compressive and shear moduli, failure strength, etc., via finite-element analysis after converting the binarized images into a mesh of finite elements directly from the voxel array.[18]

3.323.3.1. Role of Architecture: Structural Studies in Specimens

One needs to make a clear distinction between structure analysis performed at high spatial resolution – here defined as imaging at a voxel size less than the structural elements to be discerned, for example, the thickness of individual trabeculae – and the *in vivo* imaging regime where the voxel size is on the order of or exceeds trabecular thickness. Such a resolution is achievable on high-field microimaging systems designed to image specimens or small rodents *in vivo*. In this 'high-resolution' regime, bone and marrow phases can relatively easily be separated by simple threshold-based segmentation, which makes the data amenable to processing and analysis.[19]

A number of studies have been reported on extracting structural parameters from specimen MR images of human or animal trabecular bone.[19–25] The approach chosen involves marrow removal and immersion of the bone in water or saline doped with a relaxation reagent serving as a substitute for bone marrow to avoid artifacts from air inclusions due to fluid leaking out of the marrow matrix.[19] In recent years, specimen MRI of trabecular and cortical bone has largely been supplanted by micro-CT (μCT) (see, e.g., Stauber and Muller[26]), which provides superior SNR and thus resolution. We shall see that this situation is quite different for *in vivo* structural imaging application where radiation dose is a significant hurdle in CT imaging.

The role of 3D imaging of bone architecture is illustrated compellingly in a study by Hwang *et al.*[23] designed to predict the elastic modulus in trabecular bone on the basis of structural measures derived from high-resolution MR images. The work comprised 23 cylindrical trabecular bone specimens cored from the distal radius of 16 donors imaged at isotropic voxel size of 78 μm at 9.4 T on a microimaging system. The data suggested a moderate association between Young's modulus (YM) for compressive loading and Bone Volume Fraction (BVF) ($R^2 = 0.57$, $P < 0.0001$), confirming earlier studies relating YM to density.[27–29] From the 3D rendered images in **Figure 2(a)**, we see that the trabeculae are highly oriented along the radial axis, albeit to a variable extent. To quantify this effect, the authors conceived a method based on spatial autocorrelation analysis by

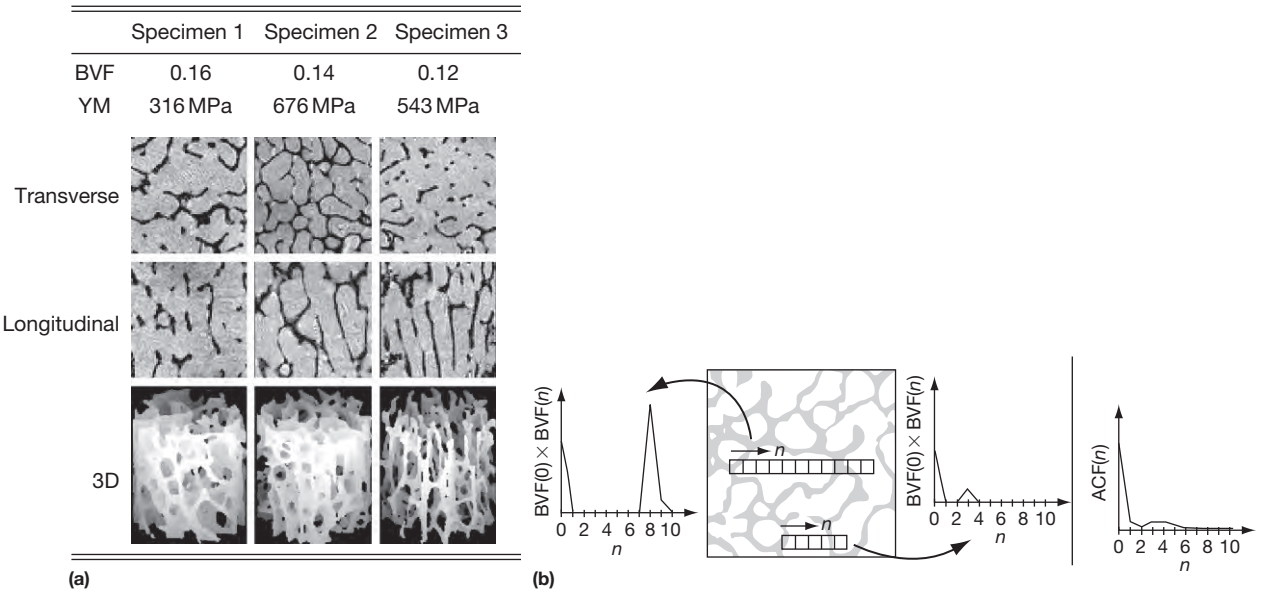

Figure 2 (a) The structural variability of trabecular bone in transverse, longitudinal, and 3D volume-rendered magnetic resonance images of specimens from a 76-year-old man (specimen 1), an 80-year-old man (specimen 2), and a 53-year-old woman (specimen 3). Note that in spite of highest BVF, the bone from specimen 1 has the lowest modulus. (b) Plots schematically showing the two-point probabilities for the two rows of voxels superimposed on the trabecular bone structure. The ACF is the average of the two-point probabilities of all pairs of voxels with a given offset with the distance between the peaks corresponding to the distance between trabeculae. Reproduced from Hwang, S. N.; Wehrli, F. W.; Williams, J. L. *Med. Phys.* **1997**, *24*, 1255, with permission from American Association of Physicists in Medicine.

treating the trabecular network as a quasiregular lattice. The principle of the method is illustrated in Figure 2(b). Whereas BVF of a voxel may be regarded as the probability $P(x, y, z)$ that a single randomly chosen point in voxel (x, y, z) is in bone, this concept was extended by considering the probability that two randomly chosen points are both in bone (Figure 2(b)). Here, we see that the distance to the second peak is equal to the distance between the trabeculae. Averaging of the two-point probabilities for all pairs of voxels with a given offset results in the autocorrelation function (ACF), which has previously been used to characterize porous materials (see, e.g., Barrall *et al.*[30]):

$$\mathrm{ACF}(n_x, n_y, n_z) = \langle P_1(x,y,z) P_1(x+n_x, y+n_y, z+n_z) \rangle_{x,y,z} \quad [1]$$

In eqn [1], $n_{x,y,z}$ are the voxel offsets in 3D space and the brackets indicate a spatial average over all possible voxel locations (x, y, z). Thus,

$$\mathrm{ACF}_{\mathrm{longitudinal}}(n_z) = \mathrm{ACF}(0, 0, n_z) = \langle P_1(x,y,z) P_1(x,y,z+n_z) \rangle_{x,y,z} \quad [2]$$

is the longitudinal spacing expressed as the distance to the second peak in the autocorrelation in axial (z) direction. We see from Figure 2(a) that the mean spacing between successive trabeculae is much larger in longitudinal than in transverse direction since the main loading direction is along the radial axis. On the other hand, there are significant interindividual differences in the degree of structural anisotropy. Hwang *et al.* developed a multiparameter model showing that a function of BVF and longitudinal spacing could predict over 90% of the variation in YM in this set of specimens, providing evidence that parameters other than density relating to the spatial distribution of the bone are important. Specifically, the data highlight the mechanical significance of structural orientation, first formulated theoretically by Cowin, who showed that the elastic properties of structured orthotropic materials can be described quantitatively in terms of 'fabric' and density.[31] We shall return to this topic in a later section of this chapter and review methods for quantification of structural orientation from 3D digital images.

It is also possible to obtain information on structural and possibly material properties by MRI without the need to resolve the trabeculae by making use of the induced inhomogeneous field caused by the difference in magnetic susceptibility between bone and marrow (or, for studies *ex vivo*, bone and water in the marrow spaces). Bone has been shown to be more diamagnetic than water – and, similarly, than hematopoietic or fatty marrow – by 2.5–3 ppm (Système International, S.I.)).[32,33] The induced inhomogeneous field in the vicinity of the bone trabeculae causes phase scrambling of the spin isochromats manifesting in a net loss of signal, particularly in gradient-echo imaging sequences in which dephasing effects are not reversed by a phase-reversal rf pulse. This effect has been studied extensively, both theoretically[34–37] and experimentally, in models of trabecular bone.[38,39]

3.323.3.2. *In Vivo* Spatial Resolution Regime

The holy grail of biomaterial science is to extract quantitative structural and mechanical information noninvasively by imaging, ultimately taking the place of bone-biopsy-based histology. A significant advantage of this approach is that it allows for time-series studies in which each subject or animal serves their own control, thereby significantly enhancing power. The author's laboratory has, during the past 15 years, striven toward this goal by developing image-based methods, leading to what has been referred to as 'virtual bone biopsy',[8–10] in analogy to a physical bone biopsy.

During the past decade, high-resolution MRI has proven its potential as a method to provide 3D images of trabecular and cortical bone at peripheral skeletal locations, including the distal and proximal tibia, calcaneus,[40–42] and distal radius.[43–46] Attempts have also been made to image the proximal femur.[47,48] MRI is of particular interest not just because of the absence of ionizing radiation but also because of the very wide availability of the technology. The latter is in contrast to MRI's closest competitor, high-resolution peripheral quantitative CT (HRpQCT), designed specifically for generating images at a resolution adequate to visualize and quantify essential features of the trabecular network at acceptable radiation dose (see, e.g., Khosla *et al.*[49]). Two areas of particular medical significance and interest involve the association between fracture susceptibility and structure and the evaluation of the structural implications of aging, disease progression, and regression in response to intervention.[43,50–53]

The resolution achievable *in vivo* is considerably below that possible in small specimens. As pointed out previously, resolution is largely determined by available SNR, which, in turn, is given by voxel volume. For image-analysis algorithms to operate reliably, SNR (typically expressed as mean marrow signal amplitude divided by the standard deviation of the background) should not fall below about 6–8,[54,55] even though SNR levels of >10 would be desirable. While signal averaging improves SNR, the gain scales as $\sqrt{T_s}$ with T_s being the total scan time. The practical upper limit of scan time is 10–15 min, which is largely governed by patient tolerance. At the current state of the art, adequate SNR and volume coverage are achievable at 3 T field strength to acquire images of the distal extremities with a voxel volume V_v of $4\times10^{-3}\,\mathrm{mm}^3$ in 11 min scan time.[56] This voxel volume yields an *apparent* linear resolution R_L, in all three orthogonal directions, of 160 µm ($R_L = \sqrt[3]{V_v}$).

Images such as those shown in Figure 1 are suited for deriving structural parameters that express various properties, which can broadly be categorized into *measures of scale* (BVF and thickness, either trabecular or cortical, and porosity), *orientation* (governed by the directional intensity of stresses, Wolff's law), and, lastly, *topology*. While topology has strict mathematical definition, it suffices to remember that topology is preserved under rubber-sheet deformation. Hence, stretching or twisting an object – in our case a hypothetical trabecular network – would not alter its topology. In contrast, breaking a connection between trabeculae or causing a perforation of a trabecular plate – both are common phenomena during aging and osteoporotic bone loss – would alter the structure's topology. It is readily recognized that the latter processes can have mechanical consequences that are disproportionately large relative to the amount of bone loss.

In the following, advanced methods designed to evaluate parameters falling into each of the three categories are briefly discussed and illustrated with data derived from *in vivo* images.

3.323.3.3. Characterization of Trabecular Bone Architecture in Terms of Scale, Topology, and Orientation

3.323.3.3.1. Trabecular bone volume fraction and thickness

As long as the voxel size is substantially less than trabecular thickness, the intensity histogram is bimodal (assuming the image contains only bone and marrow structures) and the image can easily be binarized by setting a threshold at the midpoint between the marrow and bone peaks. The resulting image has two discrete phases, that is, bone and marrow. Under these conditions, BVF can be obtained by summing all voxels within a 3D region pertaining to the phase assigned to bone. This approach is no longer possible once resolution becomes comparable to trabecular thickness since the histogram becomes monomodal and the choice of threshold becomes rather arbitrary. Contributing to the loss of bimodality is noise, since *in vivo* images typically have far lower SNR than their *ex vivo* counterparts. The loss of bimodality is caused by a process denoted 'partial volume averaging'; that is, the majority of voxels contain both bone and marrow even though the pure phases have unique intensity. While this appears to be an intractable problem, it actually is not and it has been shown that both BVF and trabecular thickness can be accurately retrieved in this regime.[54,55,57] An elegant algorithm conceived by Saha is based on the fuzzy distance transform, which allows computation of trabecular thickness under conditions of *in vivo* resolution and in the presence of noise.[55]

3.323.3.3.2. Topology of trabecular networks

Feldkamp *et al.*[12] were first to describe algorithms for extraction of topological quantities from digital images of trabecular bone obtained by 3D μCT. Connectivity, a quantity that characterizes the integrity of the trabecular network, can be derived from the 3D Euler number $N^{(3)}$. For an open network structure, the Euler number can be calculated from the number of nodes n and number of branches b, as $N^{(3)} = n - b$. For a network where at least one path exists between two nodes, the quantity $1 - N^{(3)}$ is a measure of connectivity in that it expresses the number of branches that can be broken before the structure becomes broken into disconnected elements. This approach requires the image to be skeletonized into a 3D line graph, which is a rather extreme form of data reduction since there is no longer a distinction between plates and rods. Nevertheless, the use of this metric has been practiced in the context of MRI of trabecular bone with some success.[24,58]

It is well known that at virtually all skeletal locations trabecular bone is a network of interconnected plates and rods, but that during aging, and particularly osteoporosis, heterogeneous erosion causes perforation of plates[59] leading to a more rod-like structure. Hildebrand and Rüegsegger[60] conceived an elegant algorithm for quantifying the bone's relative 'platelikeness' expressed by a quantity denoted structure-model index (SMI). The method is based on computing the relative change in surface area upon radial expansion of the structure. It is readily seen that for a rod-like element represented by a cylinder, the change in volume is far greater than for a plate. Using a normalization scheme, the SMI is calculated so as to yield values of 0 and 3 for perfect plates and rods, respectively. One difficulty with the SMI is that it is not easily applicable to *in vivo* MR or CT images since it requires triangulation of the surface and thus a binary image.

An alternative approach that has been widely applied to *in vivo* trabecular bone MR images is based on Saha and Chaudhuri's method termed digital topological analysis (DTA),[61] which was subsequently shown to yield detailed information on the topology of trabecular structures.[14] In DTA, a BVF image set is first derived from the raw images as a noiseless representation of the object, whereby each voxel represents the fractional occupancy of bone at each location in digital 3D space. To improve apparent resolution, the BVF maps are upsampled using interpolation (typically performed in k-space).[62] Another strategy is what has been referred to as 'subvoxel processing,' a method that mimics image acquisition at higher resolution.[63] The idea is to partition each voxel into subvoxels and redistribute the bone in such a way that each subvoxel receives additional material based on its proximity to bone under retention of total BVF. Thereafter, the images are binarized and skeletonized, converting trabecular plates to surfaces and rods to curves. Inspection of the $3 \times 3 \times 3$ neighborhood of each voxel then allows determination of its topological entity as to whether it is part of a surface or curve, or junctions between these basic structures, essentially using lookup tables.[64] A convenient measure for characterizing the bone's platelikeness is in terms of the topological surface-to-curve (S/C) ratio, which is essentially the sum of all surface-type voxels divided by the sum of all curve-type voxels. The substantial structural differences between subjects are illustrated with the color-coded 3D skeleton maps derived from high-resolution MR images of the distal tibia in **Figure 3**.

There is significant evidence that greater S/C is associated with lower prevalence of fractures of the vertebrae (quantified in terms of vertebral deformity index), even though the structural measurements were performed at a peripheral anatomic site, in this case the distal radius.[65,66] The method was also shown to be able to detect structural changes longitudinally, such as degradation of the trabecular architecture immediately following menopause and, conversely, maintenance of structural integrity with estrogen supplementation.[51] Another study showed large positive changes, exceeding those in BVF, in men with hypogonads after receiving testosterone.[50]

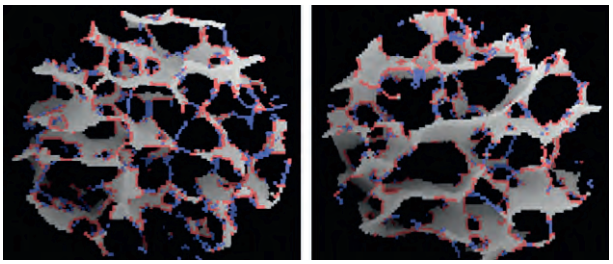

(a) (b)

Figure 3 Skeleton maps obtained showing surface interior voxels in gray, surface edges in red, and curves in blue in two subjects with substantially different topological makeup of the bone as expressed by their surface-to-curve ratio. Images are skeletonized from 7 mm diameter virtual core from the anterior distal tibial metaphysis: (a) woman, age 40 years, surface-to-curve ratio 5.61; (b) man, age 32 years, surface-to-curve ratio 9.11.

More recently, several other approaches have been described to characterize trabecular structure in terms of topology from MR or CT images at resolution and SNR levels achievable *in vivo*. Vasilic *et al.* describe a method that produces a continuous classification of voxels as belonging to plate-like or rod-like structures that determines their orientation and estimates their thickness. The method, denoted local inertial anisotropy (LIA), treats the *BVF* image as a distribution of mass density while the orientation of the trabeculae is determined from a locally calculated tensor of inertia at each voxel location.[67]

3.323.3.3.3. Structural orientation

We have seen above that structural orientation plays a pivotal role and that, even at a given anatomic site such as the distal radius, significant interindividual differences exist. It was Whitehouse who first showed that, when tracing the mean intercept length (MIL) through marrow as a function of orientation in polar diagram, the data trace an ellipse.[17] Harrigan and Mann showed that the degree of orientation in orthotropic materials can be described in terms of a second-rank tensor.[16] However, it was not before the advent of 3D digital imaging that this tensor could be mapped in a straightforward manner. Chung *et al.*, on the basis of 3D MR images of specimens, showed that the approach furnishes the MIL and fabric tensor that is characterized by three eigenvectors and three eigenvalues.[21] They developed an algorithm for determining MIL as a function of direction from 3D volume images through parallel test lines across the imaging volume. The MIL was then measured as the mean distance between adjacent trabeculae. The procedure is somewhat akin to that described by Dalstra *et al.*,[68] except that in that work 3D data were reconstructed from serial sections rather than volumetric imaging data. The orientation of the test lines, controlled by the polar and azimuthal angles, was chosen so as to uniformly sample the measurement volume. The MIL data obtained from all orientations were then transformed to a Cartesian coordinate system and fitted to the equation of an ellipsoid

$$ax^2 + bxy + cxz + dy^2 + eyz + fz^2 = 1 \qquad [3]$$

via least square error analysis, yielding the six coefficients from which a 3×3 matrix representing the fabric tensor in the measurement coordinate system is constructed[16]:

$$M = \begin{pmatrix} a & b/2 & c/2 \\ b/2 & d & e/2 \\ c/2 & e/2 & f \end{pmatrix} \qquad [4]$$

The eigenvectors of $\boldsymbol{M}$ correspond to the three orthogonal principal directions of the MIL ellipsoid. The lengths of the principal axes then are obtained as the reciprocal of the square root of the three eigenvalues of $\boldsymbol{M}$.

Figure 4 shows the MIL ellipsoid, which quantitatively measures the structural anisotropy, obtained from fitting the data measured directly from the 3D image set, along with volume-rendered projections for seven angles.

More recently, MIL in its 3D implementation has also been applied to *in vivo* MR images of trabecular bone of the distal tibia.[56,69]

Since bone models and remodels in response to the stresses to which it is subjected (Wolff's law), it is not surprising that structural anisotropy parallels mechanical anisotropy, shown experimentally by Odgaard *et al.*[70] Cowin had previously formulated a mathematical frame work relating the fabric tensor to the elasticity tensor for linearly elastic porous materials with intrinsically isotropic material properties.[71]

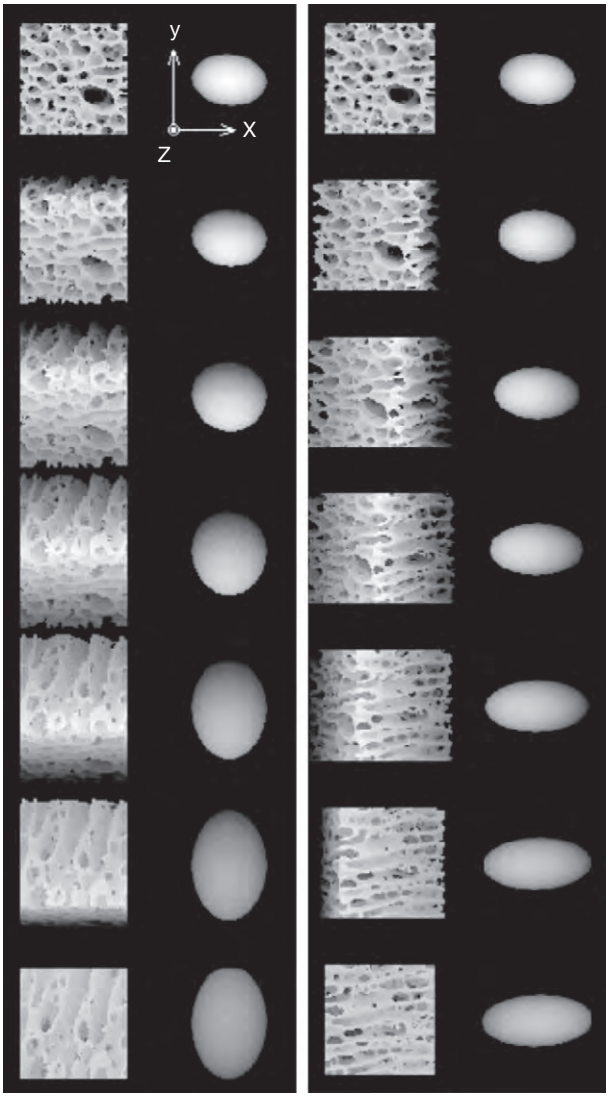

Figure 4 Volume-rendered projection magnetic resonance images of a bovine tibia specimen, along with anisotropy ellipsoid (magnified thrice). The $7 \times 7 \times 7$ mm^3 volume of interest is shown rotated in equal angular increments around (a) *x*-axis and (b) *y*-axis. The *z*-axis approximately corresponds to the anatomic long axis of the tibia. Adapted from Chung, H. W.; Wehrli, F. W.; Williams, J. L.; Wehrli, S. L. *J. Bone Miner. Res.* **1995**, *10*, 1452, with permission from Wiley.

3.323.4. Bone Water and Porosity

MRI and NMR spectroscopy have also provided detailed insight into the nature of water in the various compartments of osteonal bone.[72] Water plays a key role in bone by serving as a medium for transport of nutrients and waste products to and from osteocytes. Much of this transport is diffusion-driven

beyond the vascular conduit of the Haversian system. Moreover, water at its various locations in the matrix confers to bone its viscoelastic properties and its presence thus has important mechanical implications. Between 40 and 70% of the bone water, according to recent measurement in the author's laboratory, is bound to collagen of the osteoid, with most of the balance residing in the Haversian and Volkmann canals and a small portion occupying the osteocyte lacunae and canaliculi that interconnect osteocytes.[73] Haversian canals are 70–100 μm in diameter and thus are only resolvable *ex vivo* with μCT in small specimens.[74]

Quantification of porosity P, in particular if this were possible *in vivo* in patients, would of interest because it is inversely correlated with elastic modulus and ultimate strength. Currey found a roughly cubic relationship between YM and cortical bone volume fraction (CBVF): that is, $\mathrm{CBVF} = 1 - P$.[75] In a cadaver study, McCalden *et al.*[76] found that ultimate stress, strain, and energy absorption decreased by 5, 9, and 12% per decade, respectively, with porosity accounting for 76% of the reduction in strength. Cortical porosity increases with age,[77] particularly in women,[78] and the impaired mechanical competence is a major cause of hip fractures. The femoral neck, unlike other anatomic locations prone to fracture, has a significant portion of cortical bone. The etiology of age- and disease-related expansion of the Haversian canal system is believed to be the formation of composite osteons.[79]

We have seen in **Figure 1** that cortical and trabecular bone in MR images generally appear with background intensity. This is a consequence of the short T_2 relaxation time of bone water protons (<1 ms[6]) and the relatively low water proton density (~20%).[80] Key to capturing these signals is an imaging strategy that relies on radial sampling of the FID in conjunction with pulsed excitation[81,82] or excitation schemes that rely on frequency sweep approaches.[83]

Robson *et al.* reported images of the human midshaft tibia in which bone appears with high signal intensity, while suppressing signal from soft-tissue protons.[81] Again, we shall not be concerned with the details of the image acquisition process, for which the reader is referred to pertinent reviews of the subject.[84] The visibility of the proton bone, generally ascribed to bone water, can be further enhanced by selectively suppressing the signal from protons in soft tissue, including bone marrow and muscle, for which several strategies have been described.[81,85,86]

The large majority of the proton MRI signal detected with these techniques in cortical bone is due to water (rather than, e.g., protons in collagen or other organic matrix constituents. Evidence for this assignment stems from experiments involving heavy water (D_2O) exchange in cortical bone specimens, leading to almost complete loss of the signal[5]). More recently, Techawiboonwong *et al.* have developed a method for quantification of cortical bone water based on coimaging a sample of similar proton density and relaxation characteristics.[87,88] They ascribed the much greater bone water concentration measured at the midshaft tibia in a small group of postmenopausal women, relative to their premenopausal peers, to increased porosity in these subjects.[87]

There exist other MR-based indirect measurements of pore volume fraction, some of which allow estimation of the volume fractions of water on the basis of inverting the signal decay of either the FID (which yields T_2^*, the effective transverse relaxation time) or a Carr–Purcell–Meiboom–Gill (CPMG) spin-echo train (yielding T_2).[89,90] In the absence of exchange of water between the compartments, the signal consists of a weighted sum of exponentials

$$S(t) = \sum_i A_i \exp(-t/T_{ci}) \qquad [5]$$

where A_i and T_{ci} are the amplitude and time constant (T_2 or T_2^*) of the ith component from which a T_2 or T_2^* spectrum can be obtained via inverse Laplace transformation. Ni *et al.* recorded the CPMG decay signal at 2 MHz on a custom-built NMR system in cadaver specimens from the human femur and generated T_2 spectra.[89] They assigned the two peaks in the T_2 spectrum to water in Haversian canals and osteocytes, respectively, with the relative fractions in good agreement with data from porosimetry. For signal assignment, the authors resorted to Brownstein and Tarr's model[91] in which the T_2 relaxation rate is expressed as

$$1/T_2 = \rho(S/V) \qquad [6]$$

where ρ is the surface relaxivity and S/V the surface-to-volume ratio, based on the notion that smaller pores have larger S/V and thus the pore water greater relaxation rate. The approach described, while providing important insight into the nature of pore water, is only applicable *ex vivo*. In lieu of measuring T_2, the same methodology has more recently been practiced in order to obtain T_2^* spectra[90] by collecting the proton FID at 27 MHz and decomposing the signal, using the same inversion procedure. **Figure 5** shows the FID and relaxation spectrum from data of two donors, with three peaks centered at around 0.015, 0.15, and 200–200 ms, attributed to 'solid hydrogen,' bound water, and mobile water, respectively. The very short T_2^* protons are likely to arise from collagen backbone protons, which would be in agreement with observations in the authors' laboratory[5] the two remaining peaks have been ascribed to matrix water, presumably collagen-bound and pore water.

Fernandez *et al.* studied transport rates of water in cortical bone by analyzing the exchange of the native water in specimens of rabbit cortical bone immersed in D_2O and monitoring the temporal increase of the H_2O signal in the D_2O bath.[80] The area of the water signal is thus proportional to the amount of water diffused from bone into the D_2O bath. Since the cortical bone samples were shaped as thin plates, the H_2O–D_2O exchange is dominated by diffusion perpendicular to the sample's largest surface. If one assumes the bone to be homogeneous and the apparent diffusion coefficient to be constant, there exists an analytical solution for the relative signal amplitude[92]:

$$I(t) = I(\infty)\left[1 - \frac{8}{\pi^2}\sum_{n=0}^{\infty}\frac{1}{(2n+1)^2}\exp\left(-\frac{D_a(2n+1)^2\pi^2 t}{d^2}\right)\right] \qquad [7]$$

In eqn [7], $I(t)$ and $I(\infty)$ are the integrated signal intensities at time t and at equilibrium, D_a is the apparent diffusion coefficient of water through the bone matrix, d is the specimen thickness, and t is the exchange time. For small values of t, eqn [7] can be shown to be approximated by

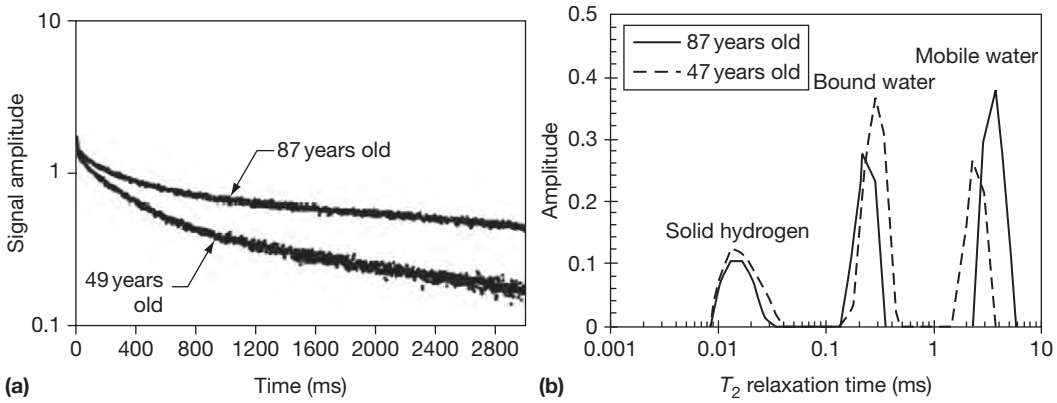

Figure 5 (a) FID signals from two specimens. (b) T_2^* relaxation spectrum in which the normalized signal intensity separated into three components. Reproduced from Nyman, J. S.; Ni, Q.; Nicolella, D. P.; Wang, X. *Bone* **2008**, *42*, 193–199, with permission, from Elsevier.

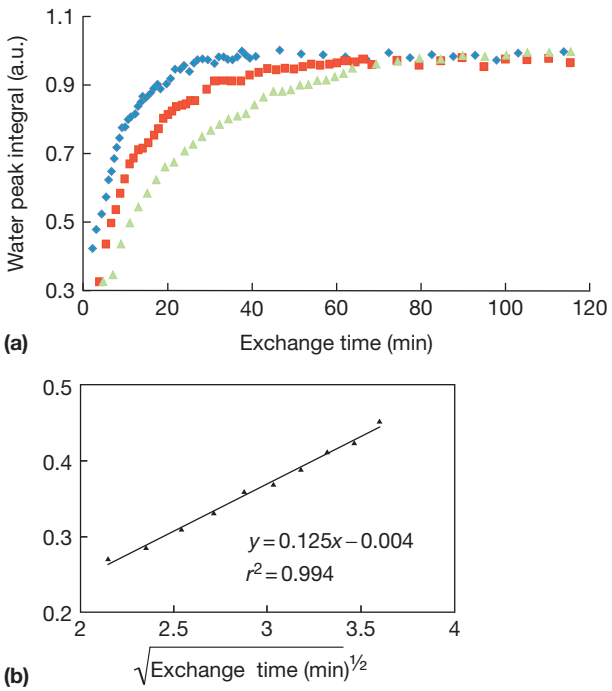

Figure 6 (a) Experimental exchange curves obtained at 25 °C (▲), 40 °C (○), and 55 °C (×) showing the temperature dependence of the diffusion rate. (b) Linear regression line obtained by fitting the 10 initial experimental data points for the data at 25 °C. The slope was used to compute D_a from eqn [8].

$$I(t) = I(\infty)\frac{4}{\pi^{1/2}}\left(\frac{D_a t}{d^2}\right)^{1/2} \quad [8]$$

The temporal evolution of the proton signal in the immersion fluid is shown in Figure 6(a). In Figure 6(b), the initial data is plotted along with a fit to the square root of the exchange time for one of the temperatures. From the apparent diffusion coefficient ($D_a = (7.8 \pm 1.5) \times 10^{-7}\,\text{cm}^2\,\text{s}^{-1}$) measured at 40 °C (i.e., near physiological temperature), the authors concluded that diffusive transport of small molecules from the bone vascular system to the osteocytes occurs within minutes, values that are in good agreement with those obtained by Tate *et al.*[93] by means of fluorescent tracers in rat bone. Finally, activation energy for water diffusion, derived from D_a measured at four different temperatures, indicated significant energy barriers to diffusion to be overcome for interactions between water molecules and matrix pores.

3.323.5. NMR Spectroscopy and MRI of Bone Matrix and Mineral

The study of bone mineral chemistry has a long history, and NMR spectroscopy has provided unique insight into this complex problem. Wet chemistry is problematic for this purpose since dissolution of the mineral into its ionic constituents provides limited information on the crystal structure of the calcium phosphates present in bone, typically regarded a non-stoichiometric calcium hydroxyapatite.

The advent of solid-state NMR with magic angle spinning, cross-polarization, and high-power proton decoupling in the 1970s[94] provided new tools to study bone mineral and synthetic phosphates by ^{31}P NMR (see, e.g., Rothwell *et al.*[95] and Wu *et al.*[96]). Rothwell *et al.* measured isotropic chemical shifts and principal components of the ^{31}P chemical shift tensors in various synthetic calcium phosphates as a means to detect these compounds in bone or enamel.[95] They found the isotropic shielding to increase upon protonation of the phosphate. Further, the chemical-shift anisotropy was found to be small for PO_4^{3-} groups, but significantly larger for HPO_4^{2-} and H_2PO^- constituents.

Even though it is known that synthetic calcium hydroxyapatite differs from bone mineral, only relatively recently spectroscopic techniques, notably infrared[97] and Raman microspectroscopy,[98] have provided detailed insight into the chemistry of bone mineral *in situ*. These techniques can provide compositional information such as the phosphate-to-amide or carbonate-to-phosphate ratio, based on the characteristic resonance bands, thereby providing information on mineralization and the nature of the anions balancing the positive charges of Ca^{2+}. But the techniques are unable to distinguish, for example, between different protonation states of the

phosphate, for instance. During the past two decades, ^{31}P and proton solid-state NMR have provided new insight into bone mineral chemistry during growth and remodeling as well as in osteoporosis.[96,99] Using a differential cross-polarization and magic angle spinning solid-state NMR spectroscopy technique, Wu *et al.* succeeded in selectively detecting minor phosphate constituents not present in synthetic Ca hydroxyapatite while suppressing the dominant orthophosphate (PO_4^{3-}) signal.[96] The ^{31}P isotropic chemical shift of this phosphate group was consistent with that of HPO_4^{2-} in octacalcium phosphate [$Ca_8(HPO_4)_2(PO_4)_4{\cdot}5H_2O$)], rather than brushite [$CaHPO_4{\cdot}2(H_2O)$]. In contrast, the bone acid phosphate anisotropic chemical shift parameters were found to be close to those of brushite, differing substantially from those in octacalcium phosphate. The authors concluded that the intimate structure of the hydrogen phosphate group in bone mineral is unique and does not match the nuclear shielding characteristics of the known synthetic calcium phosphates. Using 2D solid-state ^{1}H–^{31}P heterocorrelation NMR spectroscopy, researchers from the same laboratory determined the hydroxyl ion content in bone, variably reported previously as virtually absent, in spite of its presumed role as a constituent of the hydroxyapatite lattice.[100] In a series of elegant experiments in which the authors examined mixtures of brushite and hydroxyapatite and also of bone from various species, they identified a resonance at 0.2 ppm chemical shift, which could be unambiguously assigned to the hydroxyl moiety since in this experiment the corresponding phosphorus signal results from cross-polarization via contact with the hydroxyl proton. Figure 7 shows 2D solid-state ^{1}H–^{31}P heterocorrelation NMR spectra of synthetic apatite, showing characteristic cross-peaks assigned to the hydroxyl proton and phosphate resonances.

Matrix and mineral constituents are also amenable to imaging by proton and ^{31}P solid-state MRI techniques. One of the first reports showing the capability to obtain 3D images of bone mineral is by Wu *et al.*[101] The authors used a 3D radial projection imaging method in conjunction with nonselective rf pulses and achieved quantification of phosphorus density by relating the image intensities to those in reference samples after adjusting for relaxation times. Comparison of the results with dual-energy X-ray absorptiometry (DXA), gravimetric analysis, and chemical analysis of calcium and phosphorus demonstrated the method to be quantitatively accurate.

Among the motivations for solid-state MRI as opposed to X-ray-based densitometric techniques are absence of ionizing radiation, beam hardening, and other CT-specific artifacts. Further, the approach provides for direct measurement of a specific constituent of the mineral, thereby obviating reliance on assumptions about tissue composition. The latter is of particular importance for evaluating the two most common disorders of bone mineral homeostasis – osteoporosis and osteomalacia – which cannot be distinguished by densitometric techniques since both lead to loss of mineral, albeit via different mechanism. Osteomalacia is characterized by demineralization under volume retention, whereas in osteoporosis bone volume is lost while the bone is generally normally mineralized. However, in order to quantify true mineralization, the tissue volume needs to be known. Cao *et al.* developed and validated a solid-state ^{1}H MRI-based method in which protons from soft tissues are effectively suppressed, showing good agreement with independent measurements based on amino acid analysis and reference samples of known composition mimicking the properties of bone matrix protons.[102] Anumula *et al.* demonstrated the potential of high-field ^{31}P solid-state MRI and proton MRI in specimens of cortical bone from rabbits that had been subjected to a hypophosphatemic diet as a model for osteomalacia.[103] A second group of animals was, after induction of osteomalacia in the above manner, returned to a normophosphatemic diet for some period to evaluate whether the loss in mineralization was reversible. As expected, osteomalacia lowered phosphorus density, commensurate with a reduction in CT density and ultimate strength. However, these adverse effects on the bone's material and mechanical properties were largely reversible (Figure 8).

It is interesting that bone water (quantified in three different ways by proton–deuteron exchange NMR as described previously,[5] proton solid-state MRI, and drying) showed the

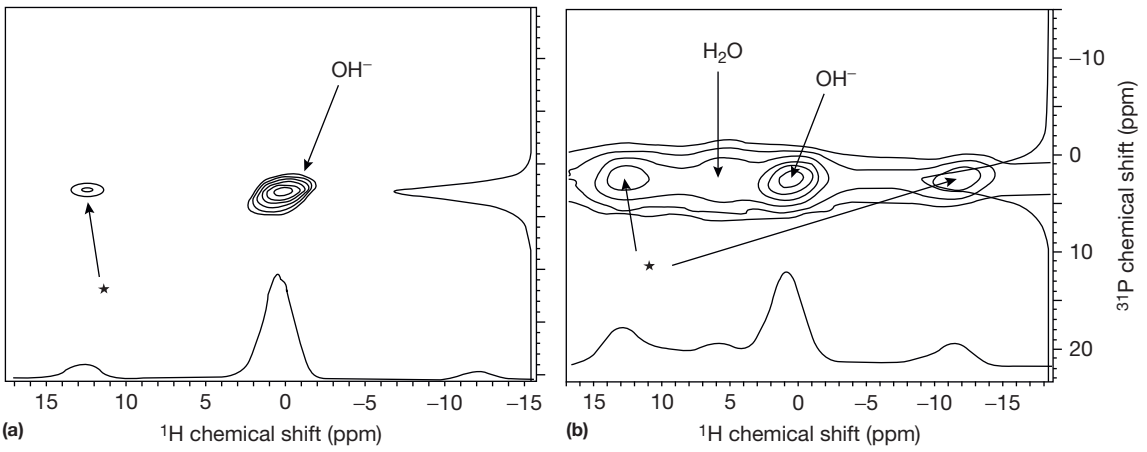

Figure 7 (a) 2D ^{1}H–^{31}P heterocorrelation NMR spectra of 95% hydroxyapatite/5% brushite at contact time = 0.3 ms. (b) Bovine cortical bone at contact time = 0.2 ms. In both spectra, a prominent hydroxyl proton cross-peak is present. A weak water peak is also observed in the bone spectrum. Peaks labeled with an asterisk are spinning sidebands. Reproduced from Cho, G.; Wu, Y.; Ackerman, J. L. *Science* **2003**, *300*, 1123, with permission.

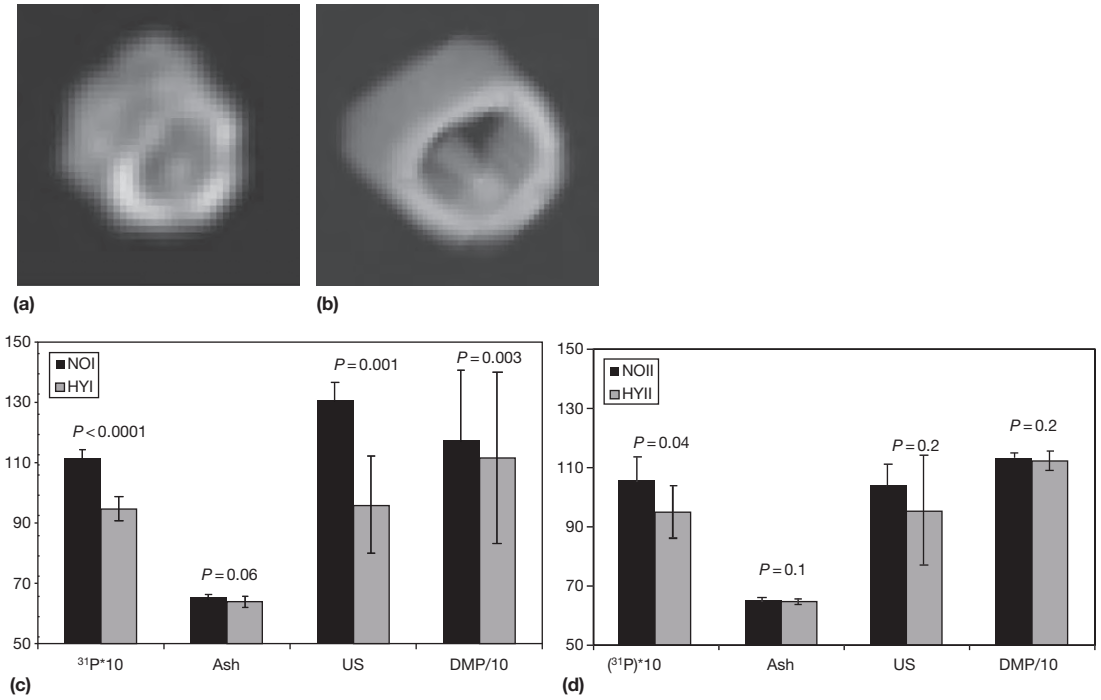

Figure 8 Volume-rendered solid-state ^{31}P (a) and ^{1}H (b) magnetic resonance images of sections of rabbit tibia at 9.4 T with reference capillary in the marrow cavity used for quantification of bone phosphorus and water content. (c) Group differences showing lower measures of bone phosphorus quantified by solid-state ^{31}P magnetic resonance imaging (wt%), ash (wt%), ultimate strength (US) in N mm^{-2}, and degree of mineralization of bone (DMB) in mg cm^{-3} in the hypophosphatemic group, measured by quantitative microcomputed tomography: HYI, hypophosphatemic animals; NOI: control group. Bars indicate means ± SD and *P* represents the statistical significance. (d) Same relationships shown for a second group of hypophosphatemic animals (HYII) after having been placed on normophosphatemic diet, again compared with age-matched controls (NOII). Modified from Anumula, S.; Magland, J.; Wehrli, S. L.; Ong, H.; Song, H. K.; Wehrli, F. W. *Bone* **2008**, *42*, 405–413, with permission from Elsevier.

reverse behavior, that is, increased water content in osteomalacic animals, commensurate with the notion that mineral and water densities are inversely related to each other.[104]

There have been several reports providing evidence that rapid bone turnover, as in ovariectomized rats or postmenopausal estrogen loss, leads to decreased mineralization density, as quantified, for example, by microradiography[105] or synchrotron micro-CT[106] and that, conversely, antiresorptive treatment increases mineral density.[105,107] In recent work from the author's laboratory, ^{31}P solid-state MRI performed in cortical bone from ovariectomized rats showed a reduction in phosphorus density by 8% relative to sham-operated animals.[72] Treatment with 25 μg kg^{-1} day^{-1} of alendronate for 50 days immediately after ovariectomy increased phosphorus density by 14% to values above those observed in sham-operated animals. Commensurate with these changes was increased bone water concentration in the ovariectomized animals and loss after alendronate treatment.

3.323.6. Summary and Conclusions

Magnetic resonance techniques, both NMR spectroscopy and MRI, are powerful tools for the study of bone architecture at multiple resolution levels, both *ex vivo* and increasingly *in vivo* in patients with degenerative and metabolic bone disorders. Recent work has shown that knowledge of trabecular structure, in terms of scale, topology, and orientation of the network, has important implications on the bone's mechanical competence independent of material density. MRI thus can provide new insight not previously amenable, and do so without exposing the subject to ionizing radiation. The technology has also proven its potential as an investigational tool to provide detailed information on mineral and matrix chemistry not amenable by other means. While much of the latter type of research has been conducted in specimens of bone, translation to human subject studies is in progress.

References

1. Rho, J. Y.; Kuhn-Spearing, L.; Zioupos, P. *Med. Eng. Phys.* **1998**, *20*, 92–102.
2. Ritchie, R.; Buehler, M.; Hansma, P. *Phys. Today* **2009**, *62*, 41–47.
3. Cowin, S. C., Ed.; In *Bone Mechanics*; CRC Press Inc.: Boca Raton, FL, 1989.
4. Lauterbur, P. C. *Nature* **1973**, *242*, 190.
5. Fernandez-Seara, M.; Wehrli, S. L.; Takahashi, M.; Wehrli, F. W. *J. Bone Miner. Res.* **2004**, *19*, 289–296.
6. Reichert, I. L.; Robson, M. D.; Gatehouse, P. D.; *et al. Magn. Reson. Imaging* **2005**, *23*, 611–618.
7. Majumdar, S. *Top. Magn. Reson. Imaging* **2002**, *13*, 323–334.
8. Wehrli, F. W. *J. Magn. Reson. Imaging* **2007**, *25*, 390–409.
9. Wehrli, F. W.; Saha, P. K.; Gomberg, B. R.; Song, H. K. *Proc. IEEE* **2003**, *91*, 1520–1542.
10. Wehrli, F. W.; Song, H. K.; Saha, P. K.; Wright, A. C. *NMR Biomed.* **2006**, *19*, 731–764.

11. Gomberg, B. R.; Saha, P. K.; Wehrli, F. W. *Acad. Radiol.* **2005**, *12*, 1320–1332.
12. Feldkamp, L. A.; Goldstein, S. A.; Parfitt, A. M.; Jesion, G.; Kleerekoper, M. *J. Bone Miner. Res.* **1989**, *4*, 3–11.
13. Hildebrand, T.; Laib, A.; Muller, R.; Dequeker, J.; Ruegsegger, P. *J. Bone Miner. Res.* **1999**, *14*, 1167–1174.
14. Gomberg, B. G.; Saha, P. K.; Song, H. K.; Hwang, S. N.; Wehrli, F. W. *IEEE Trans. Med. Imaging* **2000**, *19*, 166–174.
15. Saha, P.; Xu, Y.; Duan, H.; Heiner, A.; Liang, G. *IEEE Trans. Med. Imaging* **2010**, *29*(11), 1821–1838.
16. Harrigan, T. P.; Mann, R. W. *J. Mater. Sci.* **1984**, *19*, 761–767.
17. Whitehouse, W. J. *J. Microsc.* **1974**, *101*, 153–168.
18. Van Rietbergen, B.; Weinans, H.; Huiskes, R.; Odgaard, A. *J. Biomech.* **1995**, *28*, 69–81.
19. Chung, H. W.; Wehrli, F. W.; Williams, J. L.; Kugelmass, S. D.; Wehrli, S. L. *J. Bone Miner. Res.* **1995**, *10*, 803–811.
20. Chung, H.; Wehrli, F. W.; Williams, J. L.; Kugelmass, S. D. *Proc. Natl. Acad. Sci.* **1993**, *90*, 10250–10254.
21. Chung, H. W.; Wehrli, F. W.; Williams, J. L.; Wehrli, S. L. *J. Bone Miner. Res.* **1995**, *10*, 1452–1461.
22. Hipp, J. A.; Jansujwicz, A.; Simmons, C. A.; Snyder, B. D. *J. Bone Miner. Res.* **1996**, *11*, 286–297.
23. Hwang, S. N.; Wehrli, F. W.; Williams, J. L. *Med. Phys.* **1997**, *24*, 1255–1261.
24. Majumdar, S.; Kothari, M.; Augat, P.; *et al. Bone* **1998**, *22*, 445–454.
25. Wehrli, F. W.; Ford, J. C.; Chung, H. W.; *et al. Calcif. Tissue Int.* **1993**, *53*(Suppl. 1), S162–S169.
26. Stauber, M.; Muller, R. *Meth. Mol. Biol.* **2008**, *455*, 273–292.
27. Ciarelli, M. J.; Goldstein, S. A.; Kuhn, J. L.; Cody, D. D.; Brown, M. B. *J. Orthop. Res.* **1991**, *9*, 674–682.
28. Goldstein, S. A.; Goulet, R.; Mccubbrey, D. *Calcif. Tissue Int.* **1993**, *53*, S127–S133.
29. Hayes, W. C.; Piazza, S. J.; Zysset, P. K. *Radiol. Clin. North Am.* **1991**, *29*, 1–18.
30. Barrall, G.; Frydman, L.; Chingas, G. *Science* **1992**, *255*, 714–717.
31. Cowin, S. C. *J. Biomech. Eng.* **1986**, *108*, 83–88.
32. Hopkins, J. A.; Wehrli, F. W. *Magn. Reson. Med.* **1997**, *37*, 494–500.
33. Hwang, S. N.; Wehrli, F. W. *J. Magn. Reson.* **1999**, *139*, 35–45.
34. Ford, J. C.; Wehrli, F. W.; Chung, H. *Magn. Reson. Med.* **1993**, *30*, 373–379.
35. Hwang, S.; Wehrli, F. *J. Magn. Reson. B* **1995**, *109*, 126–145.
36. Majumdar, S. *Magn. Reson. Med.* **1991**, *22*, 101–110.
37. Yablonskiy, D. A.; Haacke, E. M. *Magn. Reson. Med.* **1994**, *32*, 749–763.
38. Yablonskiy, D. A. *Magn. Reson. Med.* **1998**, *39*, 417–428.
39. Yablonskiy, D. A.; Reinus, W. R.; Haacke, E. M.; Stark, H. *Magn. Reson. Med.* **1996**, *37*, 214–221.
40. Boutry, N.; Cortet, B.; Chappard, D.; *et al. Osteoporos. Int.* **2004**, *15*, 827–833.
41. Boutry, N.; Cortet, B.; Dubois, P.; Marchandise, X.; Cotten, A. *Radiology* **2003**, *227*, 708–717.
42. Majumdar, S.; Genant, H. K.; Gies, A. A.; Guglielmi, C. T. *J. Bone Miner. Res.* **1993**, *8*(Suppl.), 351.
43. Chesnut, C. H., 3rd; Majumdar, S.; Newitt, D. C.; *et al. J. Bone Miner. Res.* **2005**, *20*, 1548–1561.
44. Link, T. M.; Vieth, V.; Matheis, J.; *et al. Eur. Radiol.* **2002**, *12*, 401–408.
45. Majumdar, S.; Genant, H. K.; Grampp, S.; *et al. J. Bone Miner. Res.* **1997**, *12*, 111–118.
46. Wehrli, F. W.; Hwang, S. N.; Ma, J.; Song, H. K.; Ford, J. C.; Haddad, J. G. *Radiology* **1998**, *206*, 347–357.
47. Banerjee, S.; Han, E. T.; Krug, R.; Newitt, D. C.; Majumdar, S. *J. Magn. Reson. Imaging* **2005**, *21*, 818–825.
48. Krug, R.; Banerjee, S.; Han, E. T.; Newitt, D. C.; Link, T. M.; Majumdar, S. *Osteoporos. Int.* **2005**, *16*, 1307–1314.
49. Khosla, S.; Riggs, B. L.; Atkinson, E. J.; *et al. J. Bone Miner. Res.* **2006**, *21*, 124–131.
50. Benito, M.; Vasilic, B.; Wehrli, F. W.; *et al. J. Bone Miner. Res.* **2005**, *20*, 1785–1791.
51. Wehrli, F. W.; Ladinsky, G. A.; Jones, C.; *et al. J. Bone Miner. Res.* **2008**, *23*, 730–740.
52. Wehrli, F. W.; Rajapakse, C. S.; Magland, J. F.; Snyder, P. J. *J. Bone Miner. Res.* **2010**, *25*, 1406–1414.
53. Zhang, X. H.; Liu, X. S.; Vasilic, B.; *et al. J. Bone Miner. Res.* **2008**, *23*, 1426–1434.
54. Hwang, S. N.; Wehrli, F. W. *Int. J. Imaging Syst. Technol.* **1999**, *10*, 186–198.
55. Saha, P.; Wehrli, F. *IEEE Trans. Med. Imaging* **2004**, *23*, 53–62.
56. Wald, M. J.; Magland, J. F.; Rajapakse, C. S.; Wehrli, F. W. *J. Magn. Reson. Imaging* **2010**, *31*, 1157–1168.
57. Vasilic, B.; Wehrli, F. W. *IEEE Trans. Med. Imaging* **2005**, *24*, 1574–1585.
58. Majumdar, S.; Newitt, D.; Jergas, M.; *et al. Bone* **1995**, *17*, 417–430.
59. Parfitt, A. M.; Mathews, C. H. E.; Villanueva, A. R.; Kleerekoper, M.; Frame, B.; Rao, D. S. *J. Clin. Invest.* **1983**, *72*, 1396–1409.
60. Hildebrand, T.; Rüegsegger, P. *Comput. Meth. Biomech. Biomed. Eng.* **1997**, *1*, 15–23.
61. Saha, P. K.; Chaudhuri, B. B. *Comput. Vis. Image Underst.* **1996**, *63*, 418–429.
62. Magland, J. F.; Wehrli, F. W. *Acad. Radiol.* **2008**, *15*, 1482–1493.
63. Hwang, S. N.; Wehrli, F. W. *Magn. Reson. Med.* **2002**, *47*, 948–957.
64. Saha, P. K.; Gomberg, B. R.; Wehrli, F. W. *Int. J. Imaging Syst. Technol.* **2000**, *11*, 81–90.
65. Ladinsky, G. A.; Vasilic, B.; Popescu, A. M.; *et al. J. Bone Miner. Res.* **2008**, *23*, 64–74.
66. Wehrli, F. W.; Gomberg, B. R.; Saha, P. K.; Song, H. K.; Hwang, S. N.; Snyder, P. J. *J. Bone Miner. Res.* **2001**, *16*, 1520–1531.
67. Vasilic, B.; Rajapakse, C. S.; Wehrli, F. W. *Med. Phys.* **2009**, *36*, 3280–3291.
68. Dalstra, M.; Huiskes, R.; Odgaard, A.; Van Erning, L. *J. Biomech.* **1993**, *26*, 523–535.
69. Wald, M. J.; Vasilic, B.; Saha, P. K.; Wehrli, F. W. *Med. Phys.* **2007**, *34*, 1110–1120.
70. Odgaard, A.; Kabel, J.; Van Rietbergen, B.; Dalstra, M.; Huiskes, R. *J. Biomech.* **1997**, *30*, 487–495.
71. Cowin, S. C. *Mech. Mater.* **1985**, *4*, 137–147.
72. Anumula, S.; Wehrli, S. L.; Magland, J.; Wright, A. C.; Wehrli, F. W. *Bone* **2010**, *46*, 1391–1399.
73. Ong, H. H.; Wright, A. C.; Wehrli, F. W. In *Proceedings of the 18th Annual ISMRM Scientific Meeting*; ISMRM: Stockholm, Sweden, 2010.
74. Bousson, V.; Peyrin, F.; Bergot, C.; Hausard, M.; Sautet, A.; Laredo, J. D. *J. Bone Miner. Res.* **2004**, *19*, 794–801.
75. Currey, J. D. *J. Biomech.* **1988**, *21*, 131–139.
76. McCalden, R. W.; McGeough, J. A.; Barker, M. B.; Court-Brown, C. M. *J. Bone Joint Surg. Am.* **1993**, *75*, 1193–1205.
77. Laval-Jeantet, A. M.; Bergot, C.; Carroll, R.; Garcia-Schaefer, F. *Calcif. Tissue Int.* **1983**, *35*, 268–272.
78. Bousson, V.; Meunier, A.; Bergot, C.; *et al. J. Bone Miner. Res.* **2001**, *16*, 1308–1317.
79. Bell, K. L.; Loveridge, N.; Jordan, G. R.; Power, J.; Constant, C. R.; Reeve, J. *Bone* **2000**, *27*, 297–304.
80. Fernandez-Seara, M.; Wehrli, S. L.; Wehrli, F. W. *Biophys. J.* **2002**, *82*, 522–529.
81. Robson, M. D.; Gatehouse, P. D.; Bydder, M.; Bydder, G. M. *J. Comput. Assist. Tomogr.* **2003**, *27*, 825–846.
82. Wu, Y.; Chesler, D. A.; Glimcher, M. J.; *et al. Proc. Natl. Acad. Sci. USA* **1999**, *96*, 1574–1578.
83. Idiyatullin, D.; Corum, C.; Park, J. Y.; Garwood, M. *J. Magn. Reson.* **2006**, *181*, 342–349.
84. Robson, M. D.; Bydder, G. M. *NMR Biomed.* **2006**, *19*, 765–780.
85. Du, J.; Takahashi, A. M.; Bae, W. C.; Chung, C. B.; Bydder, G. M. *Magn. Reson. Med.* **2010**, *63*, 447–455.
86. Wu, Y.; Ackerman, J. L.; Chesler, D. A.; Graham, L.; Wang, Y.; Glimcher, M. J. *Magn. Reson. Med.* **2003**, *50*, 59–68.
87. Techawiboonwong, A.; Song, H. K.; Leonard, M. B.; Wehrli, F. W. *Radiology* **2008**, *248*, 824–833.
88. Techawiboonwong, A.; Song, H. K.; Wehrli, F. W. *NMR Biomed.* **2007**, *21*, 59–70.
89. Ni, Q.; King, J.; Wang, X. *Meas. Sci. Technol.* **2004**, *15*, 58–66.
90. Nyman, J. S.; Ni, Q.; Nicolella, D. P.; Wang, X. *Bone* **2008**, *42*, 193–199.
91. Fantazzini, P.; Brown, R. J.; Borgia, G. C. *Magn. Reson. Imaging* **2003**, *21*, 227–234.
92. Crank, J. *The Mathematics of Diffusion*; Oxford University Press: London, 1957.
93. Tate, M. L.; Niederer, P.; Knothe, U. *Bone* **1998**, *22*, 107–117.
94. Pines, A.; Gibby, M. G.; Waugh, J. S. *J. Chem. Phys.* **1973**, *59*, 569–590.
95. Rothwell, W. P.; Waugh, J. S.; Yesinowski, J. P. *J. Am. Chem. Soc.* **1980**, *102*, 2637–2643.
96. Wu, Y.; Glimcher, M. J.; Rey, C.; Ackerman, J. L. *J. Mol. Biol.* **1994**, *244*, 423–435.
97. Paschalis, E. P.; DiCarlo, E.; Betts, F.; Sherman, P.; Mendelsohn, R.; Boskey, A. L. *Calcif. Tissue Int.* **1996**, *59*, 480–487.
98. McCreadie, B. R.; Morris, M. D.; Chen, T. C.; *et al. Bone* **2006**, *39*, 1190–1195.
99. Wu, Y.; Ackerman, J. L.; Kim, H. M.; Rey, C.; Barroug, A.; Glimcher, M. J. *J. Bone Miner. Res.* **2002**, *17*, 472–480.

100. Cho, G.; Wu, Y.; Ackerman, J. L. *Science* **2003**, *300*, 1123–1127.
101. Wu, Y.; Ackerman, J. L.; Chesler, D. A.; *et al*. *Calcif. Tissue Int.* **1998**, *62*, 512–518.
102. Cao, H.; Ackerman, J. L.; Hrovat, M. I.; Graham, L.; Glimcher, M. J.; Wu, Y. *Magn. Reson. Med*. **2008**, *60*, 1433–1443.
103. Anumula, S.; Magland, J.; Wehrli, S. L.; Ong, H.; Song, H. K.; Wehrli, F. W. *Bone* **2008**, *42*, 405–413.
104. Robinson, R. A.; Elliot, S. R. *J. Bone Joint Surg.* **1957**, *39A*, 167–188.
105. Boivin, G. Y.; Chavassieux, P. M.; Santora, A. C.; Yates, J.; Meunier, P. J. *Bone* **2000**, *27*, 687–694.
106. Nuzzo, S.; Peyrin, F.; Cloetens, P.; Baruchel, J.; Boivin, G. *Med. Phys.* **2002**, *29*, 2672–2681.
107. Roschger, P.; Rinnerthaler, S.; Yates, J.; Rodan, G. A.; Fratzl, P.; Klaushofer, K. *Bone* **2001**, *29*, 185–191.

3.324. Fluorescent Nanoparticles for Biological Imaging

W Wu, Z Tian and A D Q Li, Washington State University, Pullman, WA, USA

© 2011 Elsevier Ltd. All rights reserved.

3.324.1.	**Introduction**	393
3.324.2.	**Fluorescent Nanoparticles: Synthesis and Surface Modification**	394
3.324.2.1.	Quantum Dots	394
3.324.2.2.	Fluorescent Silica Nanoparticles	395
3.324.2.3.	Metallic Fluorescent Nanoparticles	395
3.324.2.4.	Polymer Fluorescent Nanoparticles	396
3.324.3.	**Fluorescent Nanoparticles: *In Vitro* Applications**	397
3.324.3.1.	Replacing Fluorescent Dye in Cell Labeling and Imaging	397
3.324.3.2.	Imaging and Tracking Endocytosis	398
3.324.3.3.	Analyzing Biomolecular Interactions	398
3.324.3.4.	Fluorescent Nanoparticles as a Biosensor	400
3.324.4.	**Fluorescent Nanoparticles: *In Vivo* Applications**	401
3.324.4.1.	*In Vivo* Tumor Imaging	401
3.324.4.2.	*In Vivo* Tracking of Cell Migration in Living Animal	401
3.324.4.3.	*In Vivo* Imaging of Cardiovascular and Lymphatic Systems	402
3.324.5.	**Future Perspective**	402
References		403

Abbreviations

APPP	Atmospheric pressure plasma polymerization
CAMs	Cell adhesion molecules
DCs	Dendritic cells
EGF	Epidermal growth factor
EGFR	Epidermal growth factor receptor
ES	Embryonic stem
FITC	Fluorescein isothiocyanate
FRET	Forster resonance energy transfer
GFP	Green fluorescent protein
HMGA	High mobility group proteins A
IgG	Immunoglobulin G
IL-6	Interleukin-6
MEF	Metal-nanostructures enhancing fluorescence
MRI	Magnetic resonance imaging
NGF	Nerve growth factor
NIR	Near-infrared
NSPCs	Neural stem and progenitor cells
PET	Emission tomography
PFNPs	Polymer fluorescent nanoparticles
PMMA	Polymethyl methacrylate
PSMA	Prostate-specific membrane antigen
QDs	Quantum dots
RGD	Arginine–glycine–aspartic acid
RITC	Rhodamine 6G isothiocyanate
RRE	Rev responsive element
SLN	Sentinel lymph nodes
SPR	Surface plasmon resonance

3.324.1. Introduction

The invention of the fluorescence microscope has provided us with a powerful tool for direct viewing of dynamic protein interactions, intracellular networks, and materials transport in living cells. By labeling proteins, DNA, and other biomolecules with fluorescent tags, researchers can now track and study the behaviors of these biomolecules both *in vitro* and *in vivo*.[1] The widely used, traditional, fluorescent tags are organic dyes or genetically encoded fluorescent proteins.[2] However, their low photobleaching thresholds make them more vulnerable to light excitation.[3] To overcome these problems, fluorescent nanoparticles were introduced into the bioimaging arena and this opened a new vista in the research of biomolecular interaction and intracellular mechanics. Nanometer-sized fluorescent particles have unique functional and structural properties which distinguishes such particles from either discrete molecules or bulk materials.[4–8] For an individual fluorescent nanoparticle, the overall fluorescence signal output is proportional to the product of its fluorescence efficiency and loading density of the encapsulated dyes. As, typically, a large number of fluorophores are encapsulated inside a single nanoparticle, the nanoparticle produces a strong emission signal when properly excited. Thus, adaption of fluorescent nanoparticles is expected to overcome the weak fluorescence signal limit of the single-molecule fluorophore and therefore contribute to further developments in fluorescence imaging.

Among lots of fluorescent nanoparticles, semiconductor quantum dots (QDs), fluorescent dye-doped silica nanoparticles, metal fluorescent nanoparticles, and polymer fluorescent nanoparticles have garnered most of the research interest, from both the fundamental and technological viewpoints. The QDs

have the properties of size-tunable light emission, superior signal brightness, resistance to photobleaching, and broad absorption spectra for simultaneous excitation of multiple fluorescence colors. The fluorescent dye-doped silica nanoparticles are highly luminescent, exhibit minimal dye leaching and have excellent photostability.[9,10] The metal/metal oxide fluorescent nanoparticles combine magnetic and fluorescent properties into a single nanocrystal which enables simultaneous evaluations using magnetic resonance and fluorescence imaging techniques and thus provides more accurate diagnoses in biomedical applications.[11,12] The polymer fluorescent nanoparticles, made by polymerizing thousands of chromophores into a single nanoparticle, typically maintain their fluorescent properties, thus providing more optical features in bioimaging research.[13–19]

When conjugated with biomolecular ligands such as antibodies, peptides, DNA, and protein, these fluorescent nanoparticles can be used to trace intracellular transportation, to target tumors, monitor virus infection, and investigate biomolecular interaction. Recent advances have led to the development of many new types fluorescent nanoparticles, such as dual color fluorescent nanoparticles, photoswitchable fluorescent nanoparticles,[20,21] and magnetic fluorescent nanoparticles.[13,15,16,22] Exhibiting novel optical or magnetic properties, fluorescent nanoparticles have potential use in various applications such as high resolution imaging, bioseparation, and biosensing.[14,23,24] In this article, we will discuss recent developments in the synthesis and modification of myriad fluorescent nanocrystals, as well as their *in vitro* and *in vivo* applications in the bioimaging fields. Finally, we suggest some possible improvements to the design and construction of the fluorescent nanoparticles for future applications.

3.324.2. Fluorescent Nanoparticles: Synthesis and Surface Modification

3.324.2.1. Quantum Dots

QDs are semiconductor nanocrystals with all the three dimensions smaller than the Bohr exciton radius, within 1–10 nm, in most cases.[25–27] Typical QDs are constructed either from the elements combining from groups II and VI or groups III and V of the periodic table. In a typical semiconductor, an electron jumps from the filled valence band to the largely empty conduction band upon excitation, resulting in a positive vacancy 'hole' in the valence band. The photoluminescence of QDs originates from the radiative recombination of an excited electron–hole pair. The spatial separation (Bohr radius) of such an electron–hole pair, namely, the exciton, is typically in the range of 1–10 nm. The quantum confinement occurs when one of the dimensions of the semiconductor nanocrystals falls into the same range as that of the Bohr exciton radius, and therefore, leads to a finite band gap and discrete energy levels. QDs have many desired photophysical and electronic properties including good photostability, high quantum yield, and size-tunable photoluminescence ranging from visible to near-infrared (NIR) with narrow Gaussian emission profiles. Specifically, the past two decades have witnessed a great advancement in using QDs for biological applications ranging from immunoassays to cell and tissue imaging,[28–42] ever since Nie[43] and Alivisatos[44] reported their pioneering research in using QDs as fluorescence probes for biological imaging.

After the pioneering work of QD synthesis in the early 1980s,[45,46] great efforts have been invested in the synthesis of high quality fluorescent QDs.[47–61] In the earlier stages, QDs were mainly synthesized in an aqueous environment using stabilizing agents. For instance, a reverse micelle (w/o microemulsion)-based strategy was employed for the synthesis of the QDs.[62–65] QDs prepared using such a strategy usually displayed broad size distributions and poor fluorescence quantum yields. By introducing a high-temperature (~300 °C) organmetallic procedure, Bawendi and coworkers made a revolutionary breakthrough in 1993. In this procedure, high-quality QDs were synthesized by rapidly injecting the organometallic precursors into a hot coordinating organic solvent, which caused organmetallic reagents to undergo pyrolysis.[47] The presence of semiconductor-binding agents or surfactants enabled kinetic control of crystal growth, and consequently, helped maintain their size within the nanoscale.

For biological applications, QD synthesis typically involves four sequential steps. In the first step a QD core like CdSe is synthesized. In a typical protocol, an organometallic precursor containing cadmium is rapidly injected into a hot and vigorously stirred organic solution containing the other selenium precursor and ligands that bind to the QD surfaces. After the formation of nanocrystal nuclei at a high temperature (~300 °C), a large amount of solution is injected into the reaction to cool the reaction system and to stop nucleation. Next, an Ostwald ripening process takes place and the remaining precursors grow on the existing nuclei at a lower temperature. Once the QDs have reached the desired diameter, cooling the reaction system to ambient temperature stops the growth process. Second, the shell of another semiconductor is grown on the QD core to passivate the surface defects of the core by providing electronic insulation, and consequently, enhancing the photoluminescence efficiency.[46,47] An epitaxial growth strategy is usually involved in core–shell structures. Specifically, it is possible to make QDs with the same size but with different emission wavelengths by tuning their core sizes and shell thickness. The QDs formed using aliphatic coordinating ligands are soluble only in nonpolar organic solvents because they have hydrophobic alkyl monolayer caps their surfaces. Thus, the challenge has been to make these hydrophobic QDs water-dispersible for biological applications. Third, phase transfer of QDs from the organic solvent to an aqueous environment, using either ligand exchange or amphiphilic polymeric encapsulation, was required. The ligand exchange strategy replaced hydrophobic capping with an amphiphilic ligand, QDs thus having one functional group anchored at the shell and another hydrophilic group enabling water dispersibility.[43,44] The disadvantage of such a strategy is that the transformed QDs commonly display a decrease in luminescence quantum yield and are more vulnerable to aggregation and precipitation in biological buffers. As an alternative, encapsulation circumvented the aforementioned problems by retaining the native structure of the QDs while simultaneously adding amphiphilic polymers like polyethylene glycols (PEG), silica, or hydrophilic groups, thiol (–SH), carboxyl (–COOH), and amine (–NH_2) groups.[66–73] **Figure 1** depicts a surface modification and a bioconjugation, respectively.

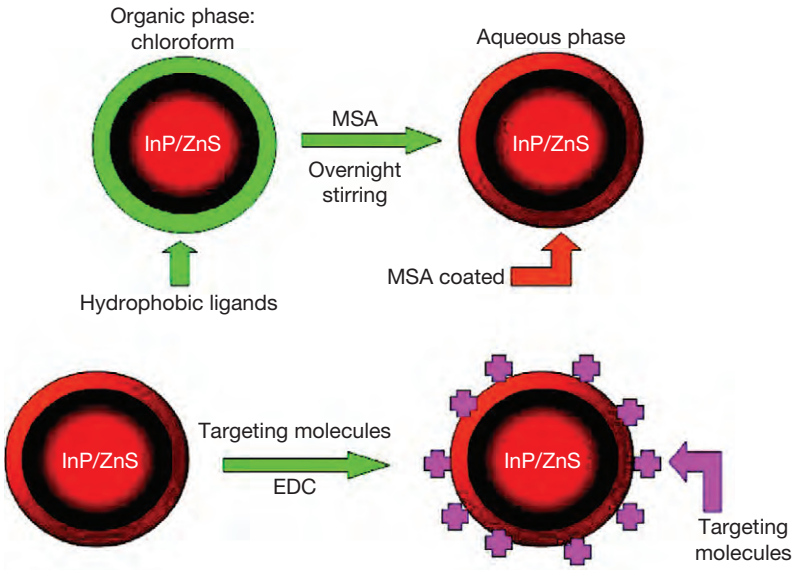

Figure 1 Schematic illustration shows the surface modification and bioconjugation of InP/ZnS quantum dots. MSA mercaptosuccinic acid, EDC 1-ethyl-3-(3-dimethylaminopropyl) carbodiimide hydrochloride. Reprinted with permission from Yong, K.; Ding, H.; Roy, I.; *et al*. *ACS Nano* **2009**, *3*, 502–510. Copyright 2009, American Chemical Society.

3.324.2.2. Fluorescent Silica Nanoparticles

Organic fluorescent dyes that are employed in biological labeling, suffer from rapid photobleaching and poor photostability. A strategy to overcome these problems is to incorporate multiple organic fluorophores into metal oxide-based scaffolds or hybrid siloxane-oxide networks which effectively protect the fluorophore dyes from environmental oxygen, and thereby, provide enhanced photostability. Among the various host matrices, silica is advantageous because it is biocompatible,[74] optically transparent,[75] and can be easily doped with functional organic moieties.[76] Additionally, dye-containing fluorescent silica nanoparticles contain a large number of dye molecules inside the silica matrix and therefore have greatly enhanced luminosity when compared to single-molecule fluorophores.[77] Also, encapsulation of fluorophores within silica matrices allows surface modification of the shell to enhance their hydrophilic character and cell uptake.[78–81] Therefore, silica is widely used to design hybrid organic–inorganic materials for various biological and medical applications.[82,83]

Traditionally, fluorescent dyes are incorporated into silica nanoparticles either by simple doping or by covalent attachment. In the doping strategy,[78,79,84–88] the fluorescent dyes are first solubilized within the core of the microemulsion and then trapped in the silica matrix during polymerization. In the absence of any covalent attachment, the dye molecules may leach out of the nanoparticles over time, consequently increasing the background signal and leading to cytotoxicity in some biological applications. In the covalent incorporation strategy, however, the fluorescent components are chemically bonded to the silica network.[89–92] This method effectively avoids any dye leaking during subsequent biological labeling. Subsequently, the silica nanoparticle surfaces can be modified using either amine ($-NH_2$) or carboxyl (–COOH) moieties. In most cases, such surface modification is done using a functional silane reagent, such as 3-(aminopropyl) triethoxysilane, during the condensation process, as shown in Figure 2.

3.324.2.3. Metallic Fluorescent Nanoparticles

Nanoparticles made from conventional noble metals such as gold and silver, usually do not fluoresce. These nanoparticles, however, are used in biological imaging as colorimetric contrast agents, induced by surface plasmon resonance (SPR) or as metal-nanostructures enhancing fluorescence (MEF). SPR contributes to bioimaging and biosensing by providing frequency dependent light absorption, which collectively originates from the electric field-induced oscillation of the conduction electrons at the surface of nanoparticles.[93,94] MEF, however, enhances the fluorescence of the fluorophores between the metallic nanoparticles.[95–98]

Nanoparticles containing rare-earth metals have been increasingly involved in biological applications for their unique optical properties, like for instance, upconversion luminescence and lower toxicity compared to QDs.[99–109] Many strategies were developed to construct rare-earth-metal-containing nanoparticles. The solvothermal approach was generally employed to synthesize such nanoparticles.[100–107] For instance, Xu and coworkers synthesized $NaYF_4$:Yb, Er nanoparticles using this method and subsequently constructed core–shell nanoparticles by coating $NaYF_4$:Yb, Er nanoparticles with a silica shell using the Stöber method.[103] In these composite nanoparticles, Yb^{3+} ions act as sensitizers that absorb NIR excitation light and Er^{3+} ions act as activators that emit upconversion luminescence with atomic-transition characteristics. Nanoparticles with similar structures and properties have also been synthesized by Zhang and coworkers.[105,106] Highly luminescent Eu^{3+} chelate nanoparticles with an alkyl alkoxysilane coating were synthesized by McNeill's group using the

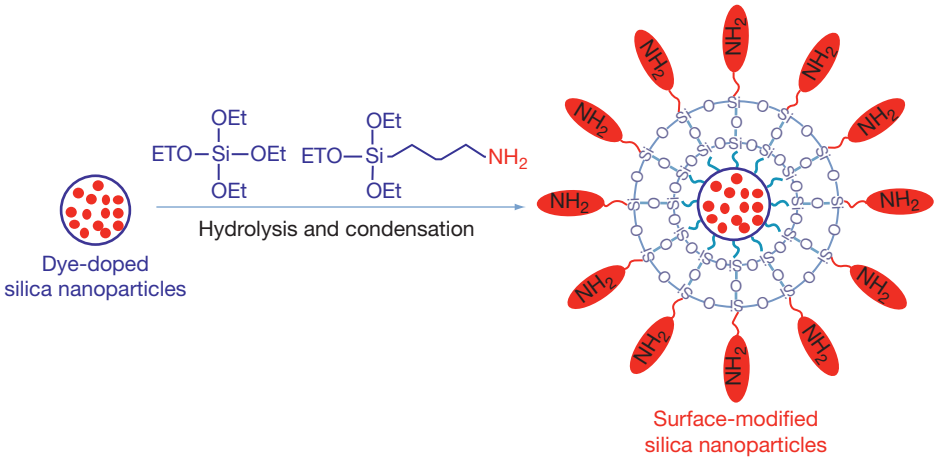

Figure 2 Schematic illustration shows the surface modification of dye-doped silica nanoparticles to result in dye-doped silica nanoparticles with shell containing primary amine groups for bioconjugation.

reprecipitation-encapsulation method.[108] In addition, rare-earth-metal-containing nanoparticles with different host materials were also synthesized by other groups. For example, a strategy based on the continuous supercritical water hydrothermal synthesis was applied by Lester's group[109] and Eu^{3+} doped ZrO_2 fluorescent nanoparticles were synthesized; and lanthanide-doped $NaYF_4^-$ PMMA (poly(methyl methacrylate)) composite nanoparticles were synthesized in Veggel's group via a situ polymerization approach.[110] Many strategies have been developed for the surface modification of these rare-earth nanoparticles, as shown in **Figure 3**.

3.324.2.4. Polymer Fluorescent Nanoparticles

Polymer fluorescent nanoparticles have also attracted considerable interest in diverse biological applications such as bioimaging and biosensing. For instance, fluorescent polystyrene nanoparticles were employed as probes to monitor the oxygen level in the brain and thus study the correlation between oxygen concentration and blood–brain barrier permeability to extravasated nanoparticles.[111]

Various strategies have been developed to synthesize polymer fluorescent nanoparticles. The commonly used strategy involves loading fluorescent components, for example, in most cases, organic fluorescent dyes, into an optically inactive polymer matrix, either by simple entrapment or by covalent linkage. Specifically, the microemulsion polymerization technique was used. Microemulsions are thermodynamically stable, transparent, or translucent equilibrium phases that contain immiscible liquids such as oil and water stabilized by a surfactant. Ranging from 10 to 100 nm in size, single-microemulsion droplets act as the microreactors for polymerization and polymer nanoparticles with sizes in the same range are synthesized.[112] For instance, Kopelman and coworkers[113,114] developed a strategy to fabricate spherical optical nanosensors by entrapping fluorescent indicators within the poly (acrylamide) nanoparticle matrix during microemulsion polymerization. By entrapping different fluorescent dyes, the resultant nanoparticles could be used as indicators to analyze pH, oxygen, and calcium concentration in living cells. Applying a similar strategy, Wu and coworkers[115] synthesized copolymer fluorescent nanoparticles with noncovalently embedded fluorescein dyes.

Nanoparticles with noncovalently encapsulated dyes carry the risk of the dye leaching out in biological applications. Thus, strategies that employed covalent linkage were preferred. Using a slightly modified microemulsion copolymerization method, Li and coworkers[13–16,116] synthesized core–shell fluorescent nanoparticles with fluorescent components that were covalently bonded to the core of the polymer nanoparticles, which significantly circumvented the problem of dye leaching and demonstrated excellent photostability. Additionally, these nanoparticles displayed greatly enhanced fluorescence brightness as compared to the molecularly dispersed solution sample because of their unique hydrophobic–hydrophilic core–shell structure. Another noteworthy advantage of such copolymerization over the other strategies is that the copolymer composition and sequence can be easily tuned. As a result, the surface properties of the final nanoparticles, for example, the nonspecific interactions with biological targets, could be largely controlled.[13] With a similar strategy, fluorescent polymer nanoparticles were also synthesized by other groups.[117–121] Besides the microemulsion polymerization approach, an atmospheric pressure plasma polymerization (APPP) technique was also developed to synthesize fluorescent polypyrrole nanoparticles by Yang and coworkers.[122] Many π-conjugated polymers are known to possess high extinction coefficients and high fluorescence quantum yields, making them feasible candidates for fluorescent nanoparticles. Such fluorescent nanoparticles primarily containing pi-conjugated polymers were synthesized in Masuhara's and McNeill's groups via a modified reprecipitation strategy.[123,124] Specifically, these fluorescent nanoparticles displayed high brightness in biological imaging applications. Surface –COOH groups on the polymer nanoparticles enabled convenient bioconjugation. For instance, Li and coworkers[13,14] synthesized photoswitchable fluorescent polymer nanoparticles and decorated their surfaces with the HMGA1 (high mobility group A1) protein and subsequently performed live cell fluorescence imaging.

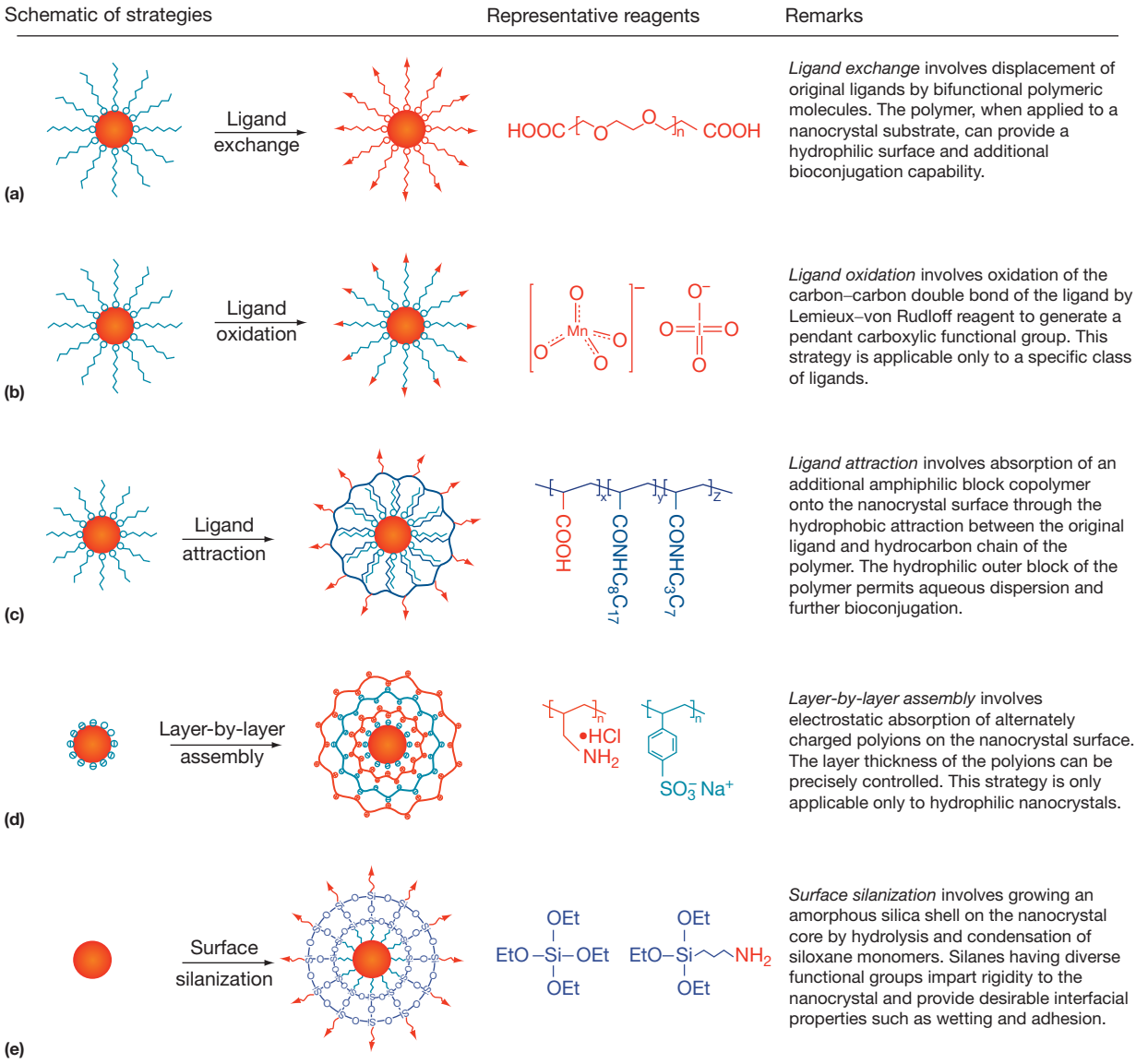

Figure 3 A summary of surface functionalization process of rare-earth-metal-contained nanoparticles for bioconjugation. Reprinted with permission from Wang, F.; Liu, X. *Chem. Soc. Rev.* **2009**, *38*, 976–989. Copyright 2009. The Royal Society of Chemistry.

3.324.3. Fluorescent Nanoparticles: *In Vitro* Applications

3.324.3.1. Replacing Fluorescent Dye in Cell Labeling and Imaging

Many superior properties make fluorescent nanoparticles good candidates for use in cellular labeling and imaging. For example, QDs have many advantages. The dye-doped nanoparticles also have high quantum yields and high molar extinction coefficients along with good resistance to both chemical and photodegradation. At the same time, the dimensions of the fluorescent nanoparticles are approximately three orders of magnitude smaller than that of the cell, and are thus small enough to stain the cells evenly.

Wu *et al.* used QDs linked to immunoglobulin G (IgG) and streptavidin to label the breast cancer marker Her2 on the surface of fixed and live cancer cells, to stain actin and microtubule fibers in the cytoplasm, and to detect nuclear antigens inside the nucleus.[125] They found that all labeling signals were specific for the intended targets and that the signals were brighter and considerably more photostable than comparable organic dyes. Lin *et al.*[126] evaluated the performance of different QDs in labeling mouse embryonic stem (ES) cells. They found that ES cell viability, proliferation, and differentiation were not adversely affected by QDs, and QD 800 offered the greatest fluorescent intensity compared to the other QDs tested.

Furthermore, the QDs were effective for simultaneously visualizing multiple proteins and nucleic acids in fixed tissues or cells. Compared to organic dyes, QDs have an attractive property – broad absorption spectra that gradually extend from the visible region to the ultraviolet region,

and the spectral positions of absorption and emission are tunable by particle size. Thus a light of single wavelength can excite different QDs, producing multiplex imaging. Sweeney *et al.*[127] used different QDs conjugated to biotinylated primary antibodies, thus enabling simultaneous multiplex staining of three proteins, CD34, Cytokeratin 18, and cleaved Caspase 3, in tonsillar tissue. This method enabled rapid measurement of multiple colocalized biomarkers on a single paraffin tissue section and was very useful in clinical trial studies. Smith *et al.*[128] used QD conjugates and molecular beacons to simultaneously detect the levels of expression of multiple biomarkers in tumor cells and tissue. Their multiplex imaging strategies provided important information that correlated the level of mRNA expression and the subsequent level of protein production for a given biomarker in the same sample.

The dye-doped nanoparticles have also been used for cell staining. He *et al.*[129] reported a method for staining HepG liver cancer cells using dye-doped fluorescent silica nanoparticles covalently linked to anti-human liver cancer monoclonal antibody HAb18. They observed that the bioassay, based on the dye-doped nanoparticles, could identify the target cells selectively and efficiently and that fluorescent nanoparticle labeling exhibited much higher photostability compared to traditional fluorescent dyes. In another paper, Santra *et al.*[130] applied dye-doped fluorescent silica nanoparticles successfully to stain human leukemia cells. The advantage of using dye-doped nanoparticles in the above papers was that many dye molecules were incorporated into one nanoparticle, hence the nanoparticle was much brighter and more photostable than a single dye. As the dye molecules were doped inside the protective silica network, the surrounding environment could not affect their emission properties. Thus dye-doped nanoparticles have very good optical properties compared to individual dyes.

3.324.3.2. Imaging and Tracking Endocytosis

Endocytosis is one of the most important functions of cells by which cells absorb molecules from the surrounding environment. Endocytosis intimately regulates many processes, including nutrient uptake, receptor signaling, pathogen entry, neurotransmission, cell growth and differentiation, and drug delivery. Research on endocytosis has been a hot topic since the invention of the fluorescence microscope.

QDs are the most frequently used fluorescent nanoparticles during endocytosis imaging. Functionalized by biomolecules, QDs can be endocytosed by many types of cells. Cambi *et al.*[131] exploited ligand-conjugated QDs to monitor antigen binding, its entry and trafficking in living dendritic cells (DCs). They demonstrated that DCs internalized virus-sized, ligand-conjugated QDs via clathrin-dependent endocytosis and the that internalized QDs could be detected inside living cells even after prolonged (up to 48 h) incubations. In this case, the biomolecule was covalently bound to the QDs.

Similarly, Lidke *et al.*[132] used biotinylated epidermal growth factor (EGF), complexed to commercial streptavidin QDs, to bind and activate the EGF receptor on CHO and A431 cells. They found that EGF-QDs were rapidly internalized into endosomes that exhibited active trafficking and extensive fusion. Through continuous monitoring of the moving EGF-QDs by confocal microscopy, they documented a previously unreported retrograde transport of the EGF-QDs from the filopodia to the cell body. Their results also demonstrated that noncovalently bound biomolecules on QDs still maintained their biological function; thus the QD-ligands should find widespread use in basic research and biotechnological applications.

The retrograde transport of nerve growth factor (NGF) was also observed in differentiated neurite-like PC12 cells using streptavidin-QDs coupled to monobiotin-NGF.[133] Due to the photostability and brightness of QDs, Echarte *et al.* were able to perform real-time analysis of the trafficking of individual QD–bNGF–receptor complexes within neurites. Their quantitative single particle tracking revealed a bidirectional step-like motion along the microtubules during endocytotic precession.

In addition to imaging endocytosis, QDs have also been used in the search to identify and localize proteins needed for endocytosis. Ogunkoya *et al.*[134] used quantum immune-electron microscopy to localize clathrin, the key protein in clathrin-mediated endocytosis, in a human adrenal cortical cell line SW-13. Their results demonstrated that the images obtained with QDs were much better than those obtained using traditional immunocytochemical light microscopic techniques, thus allowing accurate and specific localization of clathrin and the clathrin adaptor protein, AP-2, within cellular organelles.

The dye-doped fluorescent nanoparticles have also been used to monitor the endocytosis pathway. Xing *et al.*[135] have investigated the uptake of rhodamine 6G isothiocyanate (RITC)-doped silica-coated nanoparticles by HeLa cells. Their results indicated that the uptake of silica-coated nanoparticles by HeLa cells was a concentration-, time-, and energy-dependent, endocytic process. The silica-coated nanoparticles could be transported into HeLa cells partially through adsorptive endocytosis and partially through fluid-phase endocytosis.

Most recently, Li's group have applied the polymer fluorescent nanoparticles in endocytosis research.[13,136] Functionalized by high mobility group proteins A (HMGA protein), dual color or photoswitchable fluorescent nanoparticles were used to acquire images of cell endocytosis. Using confocal live-cell microscopy, they monitored the entire endocytic process in which the internalized HMGA1a-decorated nanoparticles were transported by motor proteins on microtubules and eventually arrived at the late endosomes/lysosomes (**Figure 4**).

3.324.3.3. Analyzing Biomolecular Interactions

Recent advances in single-molecule detection and nanotechnology hold exciting promises for *in vitro* biomolecular interaction analyses. The typical use of fluorescence nanoparticles in such studies is based on a technology named Forster resonance energy transfer (FRET), which is an interchromophore relaxation process that transmits the electronic excitation from an initially excited donor to a ground-state, acceptor fluorophore. FRET can be used to detect the proximity between two fluorophores separated by distances of 1–10 nm, thus allowing a study of the interactions of two or more fluorescent-nanoparticle-labeled biomolecules *in vitro*, even at the single-molecule level.

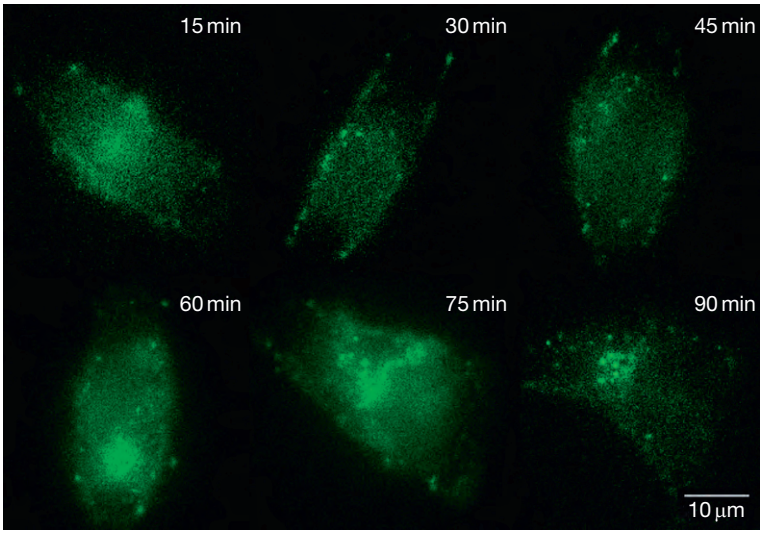

Figure 4 High mobility group AT-hook 1a (HMGA1a)-dual color fluorescent nanoparticles endocytic time trajectories. HMGA-functionalized nanoparticles and Hela cells were incubated together in DMEM medium. The cells were continuously cultured up to 90 min and every 15 min, a plate of cells was fixed and imaged using a 488-nm laser and representative images revealed HMGA-dual color nanoparticles inside the cell endosomes (green spots). Reprinted from Wu, W.; Wan, W.; Li, A. D. *J. Cell Biochem.* **2009**, *108*, 791–201, with permission from John Wiley and Sons.

One example of using fluorescent nanoparticles to investigate biomolecular interactions is the research on H(+)-ATPsynthases. The H(+)-ATPsynthase consists of a hydrophilic F1 part with subunits a3b3cde and a hydrophobic membrane integrated F0 part with subunits ab2c10. The whole H(+)-ATPsynthase couples transmembrane proton transport through the F0 subunit with ATP synthesis and hydrolysis within the F1 subunit. The coupling is occurs by the rotation of the rotor (subunits cec10) relative to the stator subunits a3b3dab2. When ATP molecules are produced, the relative positions of these subunits change. Galvez *et al.*[137] used QDs to label the subunits of the H(+)-ATPsynthases and studied the interactions of different subunits in real time. Using single-molecule spectroscopy and single-pair FRET analyses, they demonstrated the presence of three different conformations of the enzyme. Their results showed that the high photostability and brightness of the QDs allowed longer observation times of the same molecule compared to traditional dye labeling. Importantly, they showed that long observation time is the key to monitoring enzyme dynamics.

Zhang *et al.*[138] used QDs as the labeling tags to study protein–RNA interactions at the single-molecule level. Rev protein is an important HIV regulatory protein, which binds to the RRE (Rev responsive element) sequence in the RNA genome of the virus and is critical for HIV-1 replication. The sequence-specific binding between RRE RNA–Rev provides a useful *in vitro* system for evaluating the inhibitory effect of drugs on the RRE–Rev interactions in real time. In their experiments, the biotinylated RRE IIB RNA was linked to commercial streptavidin-coated QDs, the dye-labeled Rev peptide was added to the system and peptide–RNA interactions were monitored at the single-molecule level using FRET analyses. The authors demonstrated that the stoichiometry of Rev peptide binding to RRE could be accurately determined using the single-QD-based system. This system could sensitively quantify the inhibitory efficacy of proflavin (an anti-HIV drug) on Rev peptide–RRE binding, even in the presence of substantial levels of fluorescence interference from high concentrations of proflavin.

Hybridization is one of the most frequently used techniques to study biomolecular interactions. Both genome and proteome researchers use hybridization as a tool, and both protein–protein and DNA–DNA interaction assays have now been developed to the high throughput level. Many microarray products based on hybridization technology are available to study gene variation or protein expression levels *in vitro*. The signal read-out from the microarrays often suffers from photobleaching, low brightness, and background fluorescence. Fluorescent nanoparticles may prove to be an alternative to organic dyes that are used in microarray experiments.

Wu *et al.* have reported a microarray technology, based on RuDS dye-encapsulated silica nanoparticle labeling, to sensitively immuno-detect interleukin-6 (IL-6) protein *in vitro*.[139] The protein-modified nanoparticles with high fluorescence intensity, photostability, and biocompatibility were highly specific for IL-6, even in the presence of a range of cytokines or proteins, thus showing interesting promise for clinical diagnosis.

QDs have also been used in the microarray experiments. Ghazani *et al.*[140] used QDs to immuno-stain the membrane epidermal growth factor receptor (EGFR), pan cytokeratin, and E-cadherin on the tissue microarray. They found the quantitative analysis of tissue microarray using the QD-based immunoprofiling of proteins enabled accurate measurements of the tumor-derived antigen and delineated expression profiles of archival cancer tissue specimen. Goldman *et al.*[141] utilized streptavidin-coated QDs to visualize the protein toxins, which were immobilized in a galactoside polyacrylate hydrogel in a microarray format. And myriad examples have demonstrated that QDs are excellent candidates to increase the sensitivity of microarrays.[142–146]

3.324.3.4. Fluorescent Nanoparticles as a Biosensor

In the field of biosensing, fluorescence-based detection is one of the most common methods used because of its high sensitivity, simplicity, and diversity. Very recently, fluorescent nanoparticles have begun to replace traditional organic dyes as the sensing component in biosensor design. Fluorescent nanoparticles offer superior optical properties, such as brighter fluorescence, wider selections of excitation and emission wavelengths, higher photostability, and size- or shape-controlled optical characteristics.

Most fluorescent nanoparticle biosensors are based on FRET and the fluorescent nanoparticles usually serve as either the donor or acceptor, or both. In a typical sensor, the fluorescent nanoparticle is linked to biomolecules (protein, peptide, DNA, or RNA) and is quenched by another dye or particle. When the sensor meets its target, the target will interact with the biomolecules, break the link between the fluorescent nanoparticle and its quencher, thus releasing the fluorescent nanoparticle, which recovers its strong fluorescent signal.

Shi *et al.*[147] have developed a QD-based FRET probe which could be used to quantitatively sense trypsin and enable screening of trypsin inhibitors. This FRET-based probe used QDs as a donor and rhodamine as an acceptor; the rhodamine dye was immobilized onto the QD surface through peptide linkers. When trypsin was present in the solution, the probe would light up due to the enzymatic cleavage of the peptides and release of the rhodamine dye molecules from the surface of the QDs. Zhang *et al.*[148] have developed another single-QD-based aptameric sensor that was capable of detecting the presence of cocaine using both signal-off and signal-on modes. They functionalized the surface of QDs with aptamers, which could recognize cocaine. The FRET between 605QD and Cy5 and Iowa Black RQ sensed the binding of the cocaine to the aptamer and enabled detection of cocaine.

QDs of different colors can be simultaneously excited by one wavelength. This property allows multiple QD-mounted biosensors to be used to simultaneously and independently sense different targets in the same sample. Suzuki *et al.* have described a FRET-based QD bioprobe which was able to detect the actions of a protease, a deoxyribonuclease, a DNA polymerase, or changes in pH. Such QD bioprobes allow multiplex detection of the action of trypsin in the presence of a deoxyribonuclease[149] (**Figure 5**).

Ramadurai *et al.*[150] have also developed a nanosensor based on FRET between fluorescent QDs and organic quencher molecules, which could be used for the multiplex detection of biological antigens in solution. This multiplex detection could be accomplished by using several different sizes of QDs, with each QD of a given size labeled with an antibody for a different antigen. Their results demonstrated that QD-based nanosensors could detect several antigens simultaneously with high specificity and sensitivity almost in real time.

The dye-doped silica nanoparticles are also good candidate biosensors for bioanalyses. Tapec *et al.*[151] have made different kinds of biosensors using dye-doped silica nanoparticles. For example, avidin-coated nanoparticles were used to determine biotinylated bovine serum albumin, and glutamate dehydrogenase-coated nanoparticles were used as biosensors to measure glutamate.

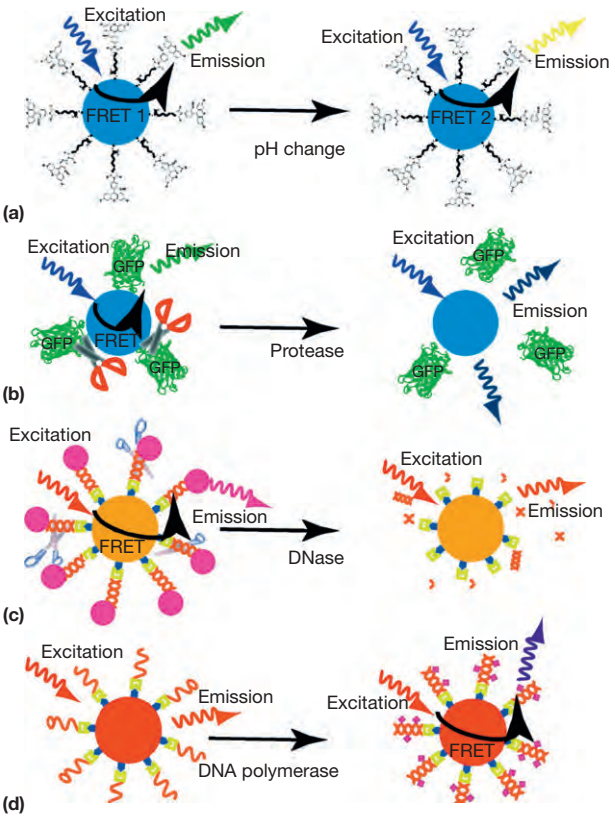

Figure 5 Forster resonance energy transfer (FRET)-based quantum dot (QD) bioprobes designed to give FRET changes upon (from top to bottom): (a) pH change via pH-sensing dyes attached to a QD; (b) cleavage of a green fluorescent protein (GFP) variant with an inserted sequence recognized by a protease (e.g., trypsin) to release GFP from the QD surface; (c) digestion of dsDNA by DNase (labeled with fluorescent dUTP) bound to a QD; (d) incorporation of fluorescently labeled dUTPs into ssDNA on a QD by extension with DNA polymerase. Reprinted from Suzuki, M.; Husimi, Y.; Komatsu, H.; Suzuki, K.; Douglas, K. T. *J. Am. Chem. Soc.* **2008**, *130*, 5720–5725, with permission from American Chemical Society.

Peng *et al.*[152] have made a pH sensor based on two-fluorophore-doped nanoparticles for noninvasive monitoring of intracellular pH changes induced by drug stimulation. This pH sensor contains a pH-sensitive indicator (fluorescein isothiocyanate, FITC) and a reference dye (tris(2,2′-bipyridyl) dichlororuthenium(II) hexahydrate, RuBPY). This sensor was used to monitor pH changes in living HeLa cells upon drug stimulation and was found to have excellent quantification, with high stability and excellent reversibility in the intracellular pH measurements. Doussineau *et al.*[153] have also used two-dye-doped silica nanoparticles for ratiometric pH measurements in the biologically relevant pH range. However, their sensors used a rhodamine derivative embedded in a silica core as the reference dye and a pH-sensitive naphthalimide dye immobilized on the amino-functionalized core as the sensing element.

Hong *et al.*[154] have developed some sensors for cardiac markers using nano-metallic fluorescent particles. In selected biocompatible solvents, the sensitivity of the nano-metallic fluorescent particles was improved because of enhancement

effects. Using those fluorescence enhancing nano-metallic particle reagents, they simultaneously quantified four cardiac markers in plasma with a very high signal-to-noise ratio.

3.324.4. Fluorescent Nanoparticles: *In Vivo* Applications

3.324.4.1. *In Vivo* Tumor Imaging

Tumor imaging is one of the hottest areas in bioimaging. Tumor cells have a lot of surface antigens, which are different from the normal cells and these serve as the targets in tumor imaging. Imaging tumor cells *in vivo* requires labeling the sensing agents such as dyes and nanoparticles with biomolecules that can specifically bind the tumor targets, thus detecting the tumor site effectively. Many different methods can be used to image live tumor cells such as X-ray imaging, positron emission tomography (PET), magnetic resonance imaging (MRI), and fluorescence imaging. With the development of highly fluorescent nanoparticles, *in vivo* fluorescent imaging of tumor cells has become easy, and some multifunctional fluorescent nanoparticles can even be used in multimodal imaging. For example, the metal fluorescent nanoparticles can be used for both MRI and fluorescent imaging.[155]

Due to their excellent optical and electronic properties, QDs are the most popular probes used in tumor imaging. Gao *et al.*[68] designed an ABC triblock copolymer-coated QD for *in vivo* imaging of growing human prostate cancer cells in nude mice. They conjugated the QDs with monoclonal antibody against the prostate-specific membrane antigen (PSMA). By injecting these QD-tagged cancer cells or antibody-QD probes into a live animal, they have achieved sensitive and multicolor fluorescent imaging of cancer cells *in vivo*.

Smith *et al.* have reported the use of peptide-conjugated QDs for noninvasive imaging of tumor vasculature markers in small animal models. The arginine–glycine–aspartic acid (RGD) peptides, which specifically bind to the newly formed/forming blood vessels in tumor tissues, were used as the target group to functionalize QDs in their experiments. Using intravital microscopy, they obtained a subcellular-resolution image of the tumor blood vessels in living subjects.[156] Cai *et al.*[157] have also used the RGD peptide-labeled QDs to image tumor blood vessels *in vivo*. The QDs used were QD705-RGD, a near-infraredQD. Their experiments showed that QD705-RGD had great potential as a universal NIR probe for detecting tumor vasculature in most cancer types *in vivo*. In another paper, they described the detailed procedure for the preparation of such peptide-conjugated QDs using commercially available PEG-coated QDs and RGD peptides.[158]

The use of polymer fluorescent nanoparticles is another newly developed area in tumor imaging. Hun *et al.*[159] have reported the use of polymer fluorescent nanoparticles (PFNPs), which were synthesized by precipitation polymerization using methacrylic acid (MAA) as the monomer, trimethylolpropane trimethacrylate (Trim) as the cross-linker, azobisisobutyronitrile (AIBN) as the radical initiator, and butyl rhodamine B (BTRB) as the fluorescent dye. These PFNPs were functionalized with anti-Her-2 monoclonal antibody and were used to detect ovarian cancer cells by fluorescence microscopy imaging *in vivo*. Their results demonstrated that the anti-Her-2 monoclonal antibody-conjugated PFNPs could effectively recognize ovarian cancer cells and that they exhibit good sensitivity and exceptional photostability.

Dye-doped silica nanoparticles can also be used in tumor imaging. Qian *et al.*[160] have synthesized a Nile Red-doped silica nanoparticle and conjugated it to apo-transferrin to target live HeLa cells. They further coconjugated the nanoparticles with PEG, which would improve the long *in vivo* circulation of these nanoparticles.

3.324.4.2. *In Vivo* Tracking of Cell Migration in Living Animal

In live animals, some cells will not stick to one place; instead they move around to execute their biological functions. Imaging such cells requires a strong and highly stable signaling tag. The recently developed fluorescent nanoparticles which are usually more stable and photobleach-resistant than organic dyes, are the latest tools used to track cell movements *in vivo*.

Noh *et al.*[161] have reported the use of near-infrared QDs for noninvasive, *in vivo*, tracking of DC migration into lymph nodes. DCs are phagocytic cells which play a key role in initiating the adaptive immune response. When DCs meet the antigen in circulation, they are activated and migrate to the lymph nodes where they present the antigen to the T cells. The ability to track their movements *in vivo* enables an exploration of their function and a better understanding of the immune system. Noh *et al.* found that labeling of the DCs with QDs had no effect on DC phenotype and migratory capacity, thus enabling the tracking of the QD-labeled DC movements, *in vivo*, using NIR fluorescence. Sen *et al.* have also used QDs to image DC behavior *in vitro* and *in vivo*. They found that when antigen-conjugated QDs were used, T cells formed stable clusters when in contact with DCs. Following subcutaneous injection of QDs in an adjuvant depot, DCs that had endocytosed QDs were visualized up to a depth of 400 μm within the draining lymph nodes.[162] Their results established the QDs as a versatile platform for immunoimaging of DCs and as an efficient nanoparticle-based antigen delivery system for priming an immune response.

During embryonic development, many cells migrate to new places to form different organs. The tracking and imaging of these cells are hot topics in development biology. Slotkin *et al.* have labeled the neural stem and progenitor cells (NSPCs) with QDs, and then monitored their behavior in early mammalian embryonic development.[163] Their results showed that the labeled NSPCs continued to develop in an apparently normal manner, implying that QDs could be effectively used to label mammalian NSPCs and to image their migration and differentiation during mammalian development *in vivo*.

Imaging the tumor cell migration may assist in the development of effective anti-cancer therapies. Labeling the tumor cells with fluorescent nanoparticles enables the observer to follow cells at high resolution in live animals. Voura *et al.*[164] have labeled tumor cells with QDs, intravenously injected the QDs into mice, and acquired images of QD migration into lung tissue. Their results showed that the behavior of QD-labeled tumor cells, *in vivo*, was indistinguishable from that of unlabeled cells, and that the QD fluorescent imaging allowed simultaneous identification of five different populations of cells using multiphoton laser excitation.

3.324.4.3. *In Vivo* Imaging of Cardiovascular and Lymphatic Systems

The cardiovascular and lymphatic systems are major components of the circulatory system in the human body. The cardiovascular system distributes blood while the lymphatic system distributes lymph. Both are hot topics in bioimaging research because they are very dynamic and are difficult to monitor *in vivo*. Many human diseases are related to cardiovascular and lymphatic systems. Cardiovascular disease is one of the leading causes of death in the world, and early accurate diagnosis of cardiovascular disease is crucial in saving lives. There are many cardiac muscle-specific biomarkers in the blood that can be targeted by functionalized fluorescent nanoparticles. The optical imaging of those markers *in vivo* may help in making a more accurate diagnosis of cardiovascular disease.

Ravnic *et al.*[165] used fluorescent nanoparticles as intravascular tracers to image the intravascular flow field in blood circulation *in vivo*. They modified the surface of the fluorescent nanoparticles to maximize plasma half-life as well as to minimize interactions with other blood components. Subsequent intravital imaging of the microcirculation demonstrated that the fluorescence nanoparticles could provide an accurate description of the localized intravascular flow field over time and space.

Jayagopal *et al.*[166] used QD-antibody bioconjugates (QD-mAb), which targeted to the cell adhesion molecules (CAMs) PECAM-1, ICAM-1, and VCAM-1 on the retinal endothelium, to image a rat model of diabetes *in vivo*. They incorporated PEG cross-linkers and Fc-shielding mAb fragments on to the surface of QDs to increase *in vivo* circulation times and targeting efficiency. They also imaged the circulating and adherent leukocyte subsets in live rats using QD-mAb targeted to RP-1 and CD45. After *in vivo* imaging, they examined the retinal whole mounts of the rat and confirmed the fluorescence patterns observed *in vivo*. Their results demonstrated that QDs are promising fluorescent tags that can specifically label vascular cells and be used to perform *in vivo* cardiovascular imaging.

The lymphatic system transports immune cells to and from the lymph nodes. In addition, the presence of lymph node metastases is an important prognostic marker in many types of tumors. Hence imaging lymphatic system *in vivo* can help in understanding the mechanisms of metastases and developing early diagnostic methods for cancer detection.

Soltesz *et al.*[167] used NIR fluorescent QDs as optimal lymphotrophic optical probes to image draining lymphatic channels and nodes in large animals, *in vivo*. They injected NIR QDs into the lobar parenchyma of 12 Yorkshire pigs (mean weight 35 kg) to get accurate maps of lymphatic drainage and sentinel lymph nodes (SLN). Their results showed that all SLNs were strongly fluorescent and could be easily visualized within 5 minutes of injection. Histological analyses confirmed that the fluorescent QDs and nodal tissue coexist, demonstrating that QDs were good noninvasive imaging tools, which provided real-time visual feedback for image-guided localization and resection.

Kobayashi *et al.*[168] used five QDs with similar physical sizes but different emission spectra to perform multicolor imaging of lymphatic system via direct interstitial injection. They simultaneously injected different QDs intracutaneously into five different sites in a mouse and monitored lymphatic drainages in the neck and in the upper trunk, *in vivo*. Their results showed that all major drainage trunks of the lymphatics in the upper body of the mouse could be depicted separately on five color images, indicating that such simultaneous visualization using nanoparticle-based technology could be very useful in predicting the route of cancer metastasis into the lymph nodes (**Figure 6**).

More recently, some multifunction polymer fluorescent nanoparticles, based on the dendrimer platform, were also used to image the lymphatic system *in vivo*. Mounzer *et al.* have developed a bimodal (fluorescence and MR) nanoparticulate composed of a polyamidoamine dendrimer core conjugated to paramagnetic contrast agents and fluorescent probes. They used this new bimodal nanoparticle to image the lymphatic vessels and lymph nodes by both fluorescence imaging and MRI.[169] The new bimodal nanoparticles provided much higher resolution and a clearer delineation of both lymph nodes and lymphatic vessels compared to traditional visualization methods. In another paper, Kobayashi *et al.* have also synthesized multimodal and multicolor nanoparticles based on the polyamidoamine dendrimer platform which are linked to both radionuclides and optical probes.[170] They used these nanoparticles to image the lymphatic system and obtained a dual-modality scintigraphic and spectrally resolved five-color NIR optical image via multiple excitation.

3.324.5. Future Perspective

Fluorescent nanoparticles are becoming the probes of choice for both *in vitro* and *in vivo* bioimaging. As fluorescent nanoparticles have strong signal strength, are resistant to photobleaching, and can be conjugated to biomolecules, they are being used more and more frequently to replace the traditional organic dyes. However, many issues still have to be addressed before these particles can be used to their full potential in practical biomedical and clinical diagnosis applications. In our opinion, further efforts should be focused on several key issues in the future. First of all, nanoprobes with smaller size are more suitable for labeling and detection of subcellular components or intracellular measurements, and for tagging a particular protein or studies on a group of proteins in an assembly. Thus, developing methods for constructing fluorescent nanoparticles with smaller sizes deserves special attention. Secondly, design and development of biocompatible fluorescent nanoparticles to overcome nonspecific binding and to facilitate their subsequent attachment to biological targets is highly desirable. Therefore, further efforts are needed to develop nanoprobes with 'smart' surfaces highly specific to target tissue that can interact minimally with the surrounding tissue. In addition, optimizing the size, shape, and surface chemistry of fluorescent nanoparticles is needed so that future nanoparticles can avoid nonspecific organ uptake or scavenging in the reticuloendothelial system in live animals. Thirdly, fluorescent nanoparticles with multiple signaling features are also desirable for highly accurate detection of complicated targets. Combinations of multiple modalities can yield complementary information and offer synergistic advantages over a single modality nanoparticles. For example, a single

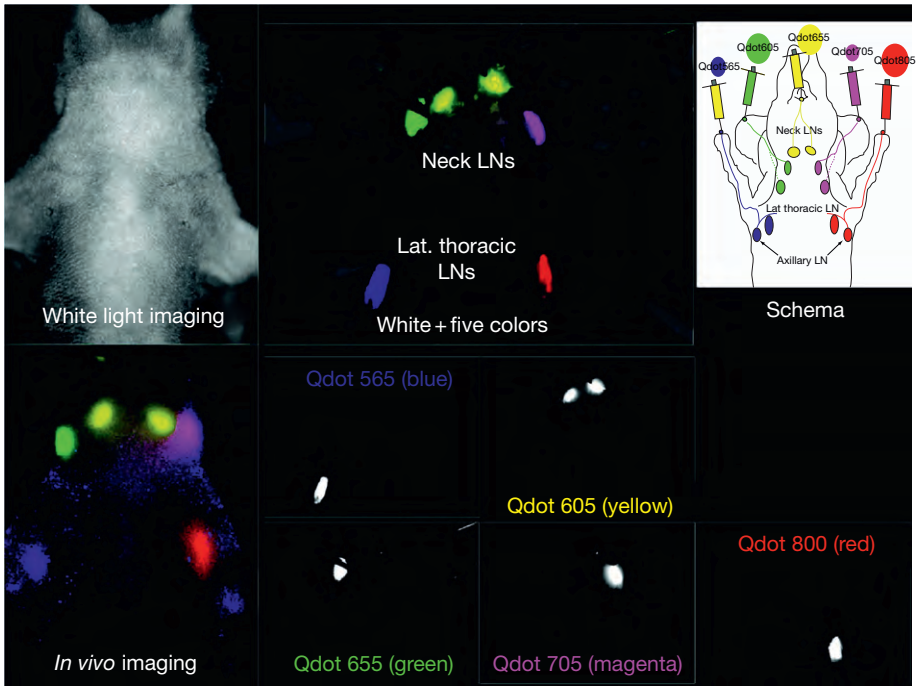

Figure 6 *In vivo* and intrasurgical spectral fluorescence imaging of a mouse injected with five carboxyl quantum dots (565, blue; 605, green; 655, yellow; 705, magenta; 800, red) intracutaneously into the middle digits of the bilateral upper extremities, the bilateral ears, and at the median chin. Five primary draining lymph nodes were simultaneously visualized with different colors through the skin in the *in vivo* image. Reprinted from Kobayashi, H.; Hama, Y.; Koyama, Y.; *et al. Nano Lett.* **2007**, *7*, 1711–1716, with permission from American Chemical Society.

nanoprobe possessing both fluorescence and magnetic properties will be a more powerful practical application because these two signal modes will complement each other, even though individually, each has its own strengths and weaknesses.[171] In summary, nanoparticles appear to have a bright future in imaging applications in both laboratory and clinical use.

Acknowledgments

The authors acknowledge the support of National Institute of General Medicine Sciences (GM065306) and National Science Foundation (CHE-0805547).

References

1. Ntziachristos, V. *Annu. Rev. Biomed. Eng.* **2006**, *8*, 1–33.
2. Lippincott-Schwartz, J.; Patterson, G. H. *Science* **2003**, *300*, 87–91.
3. Michalet, X.; Pinaud, F. F.; Bentolila, L. A.; *et al. Science* **2005**, *307*, 538–544.
4. Resch-Genger, U.; Grabolle, M.; Cavaliere-Jaricot, S.; Nitschke, R.; Nann, T. *Nat. Meth.* **2008**, *5*, 763–775.
5. Sun, C.; Lee, J. S.; Zhang, M. *Adv. Drug Deliv. Rev.* **2008**, *60*, 1252–1265.
6. Biju, V.; Itoh, T.; Anas, A.; Sujith, A.; Ishikawa, M. *Anal. Bioanal. Chem.* **2008**, *391*, 2469–2495.
7. Laurent, S.; Forge, D.; Port, M.; *et al. Chem. Rev.* **2008**, *108*, 2064–2110.
8. Chen, W. *J. Nanosci. Nanotechnol.* **2008**, *8*, 1019–1051.
9. He, X.; Duan, J.; Wang, K.; Tan, W.; Lin, X.; He, C. *J. Nanosci. Nanotechnol.* **2004**, *4*, 585–589.
10. Yao, G.; Wang, L.; Wu, Y.; *et al. Anal. Bioanal. Chem.* **2006**, *385*, 518–524.
11. Hwang, D. W.; Ko, H. Y.; Kim, S. K.; Kim, D.; Lee, D. S.; Kim, S. *Chemistry* **2009**, *15*(37), 9387–9393.
12. Frey, N. A.; Peng, S.; Cheng, K.; Sun, S. *Chem. Soc. Rev.* **2009**, *38*, 2532–2542.
13. Tian, Z.; Wu, W.; Wan, W.; Li, A. D. *J. Am. Chem. Soc.* **2009**, *131*, 4245–4252.
14. Hu, D.; Tian, Z.; Wu, W.; Wan, W.; Li, A. D. *J. Am. Chem. Soc.* **2008**, *130*, 15279–15281.
15. Zhu, L.; Wu, W.; Zhu, M. Q.; Han, J. J.; Hurst, J. K.; Li, A. D. *J. Am. Chem. Soc.* **2007**, *129*, 3524–3526.
16. Zhu, M. Q.; Zhu, L.; Han, J. J.; Wu, W.; Hurst, J. K.; Li, A. D. *J. Am. Chem. Soc.* **2006**, *128*, 4303–4309.
17. Chen, J.; Zeng, F.; Wu, S.; Su, J.; Tong, Z. *Small* **2009**, *5*, 970–978.
18. Kim, K.; Lee, M.; Park, H.; *et al. J. Am. Chem. Soc.* **2006**, *128*, 3490–3491.
19. Yang, Z.; Leon, J.; Martin, M.; *et al. Nanotechnology* **2009**, *20*, 165101.
20. Tian, Z.; Wu, W.; Li, A. D. *Chemphyschem* **2009**, *10*(15), 2577–2591.
21. Wu, W.; Li, A. D. *Nanomedicine* **2007**, *2*, 523–531.
22. Bertorelle, F.; Wilhelm, C.; Roger, J.; Gazeau, F.; Menager, C.; Cabuil, V. *Langmuir* **2006**, *22*, 5385–5391.
23. Di, C. R.; Piacenza, P.; Musaro, M.; *et al. Macromol. Biosci.* **2009**, *9*, 952–958.
24. Corr, S. A.; O'Byrne, A.; Gun'ko, Y. K.; *et al. Chem. Commun. (Camb.)* **2006**, 4474–4476.
25. Henglein, A. *Chem. Rev.* **2002**, *89*, 1861–1873.
26. Schmid, G. *Chem. Rev.* **1992**, *92*, 1709–1727.
27. Nirmal, M.; Brus, L. E. *Accounts Chem. Res.* **1998**, *32*, 407–414.
28. Niemeyer, C. M. *Angew. Chem. Int. Ed.* **2001**, *40*, 4128–4158.
29. Chan, W. C. W.; Maxwell, D. J.; Gao, X. H.; Bailey, R. E.; Han, M.; Nie, S. *Curr. Opin. Biotechnol.* **2002**, *13*, 40–46.
30. Jaiswal, J. K.; Simon, S. M. *Trends Cell Biol.* **2004**, *14*, 497–503.
31. Alivisatos, A. P.; Gu, W.; Larabell, C. *Annu. Rev. Bimed. Eng.* **2005**, *7*, 55–76.
32. Gao, X.; Yang, L.; Petros, J. A.; Marshall, F. F.; Simons, J. W.; Nie, S. *Curr. Opin. Biotech.* **2005**, *16*, 63–72.
33. Rhyner, M. N.; Smith, A. M.; Gao, X.; Mao, H.; Yang, L.; Nie, S. *Nanomedicine (Lond.)* **2006**, *1*, 209–217.
34. Smith, A. M.; Ruan, G.; Rhyner, M. N.; Nie, S. *Ann. Biomed. Eng.* **2006**, *31*, 3–14.
35. Warnement, M. R.; Tomlinson, I. D.; Rosenthal, S. J. *Curr. Nanosci.* **2007**, *3*, 273–284.
36. Zhang, Y.; Kaji, N.; Tokeshi, M.; Baba, Y. *Expert. Rev. Proteomics.* **2007**, *4*, 565–572.
37. Jamieson, T.; Bakhshi, R.; Petrova, D.; Pocock, R.; Imani, M.; Seifalian, A. M. *Biomaterials* **2007**, *28*, 4717–4732.
38. Courty, S.; Dahan, M. In *Single-Molecule Techniques: A Laboratory Manual*; Selvin, P. R. and Ha, T., Eds.; 2008; Chapter 9, pp 193–208.

39. Hild, W. A.; Breunig, M.; Goepferich, A. *Eur. J. Pharm. Biopharm.* **2008**, *68*, 153–168.
40. Hezinger, A. F. E.; Temar, J.; Gopferich, A. *Eur. J. Pharm. Biopharm.* **2008**, *68*, 138–152.
41. Smith, A. M.; Duan, H.; Mohs, A. M.; Nie, S. *Adv. Drug Deliv. Rev.* **2008**, *60*, 1226–1240.
42. Drbohlavova, J.; Adam, V.; Kizek, R.; Hubalek, J. *Int. J. Mol. Sci.* **2009**, *10*, 656–673.
43. Chan, W. C. W.; Nie, S. *Science* **1998**, *281*, 2016–2018.
44. Bruchez, M, Jr.; Moronne, M.; Gin, P.; Weiss, S.; Alivisatos, A. P. *Science* **1998**, *281*, 2013–2015.
45. Efros, A. I. L.; Efros, A. L. *Sov. Phys. Semiconduct.* **1982**, *16*, 772–775.
46. Ekimov, A. I.; Onushchenko, A. A. *Sov. Phys. Semiconduct.* **1982**, *16*, 775–778.
47. Murray, C. B.; Norris, D. J.; Bawendi, M. G. *J. Am. Chem. Soc.* **1993**, *115*, 8706–8715.
48. Alivisatos, A. P. *Science* **1996**, *271*, 933–937.
49. Peng, X. G.; Schlamp, M. C.; Kadavanich, A. V.; Alivisatos, A. P. *J. Am. Chem. Soc.* **1997**, *119*, 7019–7029.
50. Talapin, D. V.; Rogach, A. L.; Kornowski, A.; Haase, M.; Weller, H. *Nano Lett.* **2001**, *1*, 207–211.
51. Gaponik, N.; Talapin, D. V.; Rogach, A. L.; *et al. J. Phys. Chem. B* **2002**, *106*, 7177–7185.
52. Bailey, R. E.; Nie, S. *J. Am. Chem. Soc.* **2003**, *125*, 7100–7106.
53. Zhong, X.; Han, M.; Dong, Z.; White, T. J.; Knoll, W. *J. Am. Chem. Soc.* **2003**, *125*, 8589–8594.
54. Li, J. J.; Wang, Y. A.; Guo, W.; *et al. J. Am. Chem. Soc.* **2003**, *125*, 12567–12575.
55. Talapin, D. V.; Mekis, I.; Goötzinger, S.; Kornowski, A.; Benson, O.; Weller, H. *J. Phys. Chem. B* **2004**, *108*, 18826–18831.
56. Bao, H.; Gong, Y.; Li, Z.; Gao, M. Y. *Chem. Mater.* **2004**, *16*, 3853–3859.
57. Qian, H. F.; Dong, C. Q.; Weng, J. F.; Ren, J. C. *Small* **2006**, *2*, 747–751.
58. Xie, R. G.; Battaglia, D.; Peng, X. G. *J. Am. Chem. Soc.* **2007**, *129*, 15432–15433.
59. Zhu, C. Q.; Wang, P.; Wang, X.; Li, Y. *Nanoscale Res. Lett.* **2008**, *3*, 213–220.
60. Oluwafemi, S. O.; Revaprasadu, N.; Ramirez, A. J. *J. Cryst. Growth* **2008**, *310*, 3230–3234.
61. Gu, Z. Y.; Zou, L.; Fang, Z.; Zhu, W. H.; Zhong, X. H. *Nanotechnology* **2008**, *19*, 7.
62. Qi, L. M.; Ma, J. M.; Cheng, H. M.; Zhao, Z. G. *Colloid. Surface. A* **1996**, *111*, 195–202.
63. Quinlan, F. T.; Kuther, J.; Tremel, W.; Knoll, W.; Risbud, S.; Stroeve, P. *Langmuir* **2000**, *16*, 4049–4051.
64. Hirai, T.; Watanabe, T.; Komasawa, I. *J. Phys. Chem. B* **2000**, *104*, 8962–8966.
65. Pang, Q.; Guo, B. C.; Yang, C. L.; *et al. J. Cryst. Growth* **2004**, *269*, 213–217.
66. Dubertret, B.; Skourides, P.; Norris, D. J.; Noireaux, V.; Brivanlou, A. H.; Libchaber, A. *Science* **2002**, *298*, 1759–1762.
67. Wu, X. Y.; Liu, H. J.; Liu, J. Q.; *et al. Nat. Biotechnol.* **2003**, *21*, 41–46.
68. Gao, X. H.; Cui, Y. Y.; Levenson, R. M.; Chung, L. W. K.; Nie, S. M. *Nat. Biotechnol.* **2004**, *22*, 969–976.
69. Pellegrino, T.; Manna, L.; Kudera, S.; *et al. Nano Lett.* **2004**, *4*, 703–707.
70. Mattoussi, H.; Mauro, J. M.; Goldman, E. R.; *et al. J. Am. Chem. Soc.* **2000**, *122*, 12142–12150.
71. Gerion, D.; Pinaud, F.; Williams, S. C.; *et al. J. Phys. Chem. B* **2001**, *105*, 8861–8871.
72. Medintz, I. L.; Clapp, A. R.; Mattoussi, H.; Goldman, E. R.; Fisher, B.; Mauro, J. M. *Nat. Mater.* **2003**, *2*, 630–638.
73. Yong, K.; Ding, H.; Roy, I.; *et al. ACS Nano* **2009**, *3*, 502–510.
74. Smith, P. W. *J. Cell Biochem.* **2002**, *39*(Suppl), 54–59.
75. Velikov, K. P.; van Blaaderen, A. *Langmuir* **2001**, *17*, 4779–4786.
76. Vanblaaderen, A.; Vrij, A. *Langmuir* **1992**, *8*, 2921–2931.
77. Liang, S.; Pierce, D. T.; Amiot, C.; Zhao, X. J. *Synth. React. Inorg. Met.* **2005**, *35*, 661–668.
78. Santra, S.; Zhang, P.; Wang, K. M.; Tapec, R.; Tan, W. H. *Anal. Chem.* **2001**, *73*, 4988–4993.
79. Santra, S.; Wang, K. M.; Tapec, R.; Tan, W. H. *J. Biomed. Optic.* **2001**, *6*, 160–166.
80. Qhobosheane, M.; Santra, S.; Zhang, P.; Tan, W. H. *Analyst* **2001**, *126*, 1274–1278.
81. Qhobosheane, M.; Zhang, P.; Tan, W. H. *J. Nanosci. Nanotechnol.* **2004**, *4*, 635–640.
82. Sanchez, C.; Julián, B.; Belleville, P.; Popall, M. *J. Mater. Chem.* **2005**, *15*, 3559–3592.
83. Burns, A.; Ow, H.; Wiesner, U. *Chem. Soc. Rev.* **2006**, *35*, 1028–1042.
84. Zhao, X. J.; Bagwe, R. P.; Tan, W. H. *Adv. Mater.* **2004**, *16*, 173–176.
85. Lian, W.; Litherland, S. A.; Badrane, H.; *et al. Anal. Biochem.* **2004**, *334*, 135–144.
86. Rossi, L. M.; Shi, L.; Quina, F. H.; Rosenzweig, Z. *Langmuir* **2005**, *21*, 4277–4280.
87. Santra, S.; Bagwe, R.; Dutta, D.; *et al. Adv. Mater.* **2005**, *17*, 2165–2169.
88. Wang, L.; Tan, W. H. *Nano Lett.* **2006**, *6*, 84–88.
89. Verhaegh, N. A. M.; van Blaaderen, A. *Langmuir* **1994**, *10*, 1427–1438.
90. Imhof, A.; Megens, M.; Engelberts, J. J.; de Lang, D. T. N.; Sprik, R.; Vos, W. L. *J. Phys. Chem. B.* **1999**, *103*, 1408–1415.
91. Fölling, J.; Polyakova, S.; Belov, V.; Blaaderen, A.; Bossi, M.; Hell, S. *Small* **2008**, *4*, 134–142.
92. Langhals, H.; Esterbauer, A. J. *Chem. Eur. J.* **2009**, *15*, 4793–4796.
93. Nath, N.; Chilkoti, A. A. *Anal. Chem.* **2002**, *74*, 504–509.
94. Mafarland, A. D.; Van Duyne, R. P. *Nano. Lett.* **2003**, *3*, 1057–1062.
95. Malicka, J.; Gryczynski, I.; Kusba, J.; Lakowicz, J. R. *Biopolymers* **2003**, *70*, 595–603.
96. Aslan, K.; Leonenko, Z.; Lakowicz, J. R.; Geddes, C. D. *J. Fluoresc.* **2005**, *15*, 643–654.
97. Aslan, K.; Gryczynski, I.; Malicka, J.; Matveeva, E.; Lakowicz, J. R.; Geddes, C. D. *Curr. Opin. Biotechnol.* **2005**, *16*, 55–62.
98. Aslan, K.; Wu, M.; Lakowicz, J. R.; Geddes, C. D. *J. Am. Chem. Soc.* **2007**, *129*, 1524–1525.
99. Wang, F.; Liu, X. *Chem. Soc. Rev.* **2009**, *38*, 976–989.
100. Vetrone, F.; Capobianco, J. A. *Int. J. Nanotechnol.* **2008**, *5*, 1306–1339.
101. Heer, S.; Kompe, K.; Gudel, H. U.; Haase, M. *Adv. Mater.* **2004**, *16*, 2102–2105.
102. Mai, H.; Zhang, Y.; Sun, L.; Yan, C. *J. Phys. Chem. C* **2007**, *111*, 13721–13729.
103. Wang, M.; Mi, C.; Wang, W.; *et al. ACS Nano* **2009**, *3*, 1580–1586.
104. Wu, S.; Han, G.; Milliron, D. J.; *et al. Proc. Natl. Acad. Sci. USA* **2009**, *106*, 10917–10921.
105. Jalil, R. A.; Zhang, Y. *Biomaterials* **2008**, *29*, 4122–4128.
106. Idris, N.; Li, Z.; Ye, L.; *et al. Biomaterials* **2009**, *30*, 5104–5113.
107. Kim, W.; Nyk, M.; Prasad, P. *Nanotechnology* **2009**, *20*, 185301.
108. Peng, H.; Wu, C.; Jiang, Y.; Huang, S.; McNeill, J. *Langmuir* **2006**, *23*, 1591–1595.
109. Hobbs, H.; Briddon, S.; Lester, E. *Green Chem.* **2009**, *11*, 484–491.
110. Boyer, J. C.; Johnson, N. J. J.; van Veggel, F. C. J. M. *Chem. Mater.* **2009**, *21*, 2010–2012.
111. Yang, C.; Chang, C.; Tsai, P.; Chen, W.; Tseng, F.; Lo, L. *Anal. Chem.* **2004**, *76*, 4465–4471.
112. Candau, F. In *Handbook of Microemulsion Science and Technology*; Kumar, P., Mittal, K. L., Eds.; Marcel Dekker: New York, 1999; pp Chapter 22, pp 679–712.
113. Clark, H.; Hoyer, M.; Philbert, M.; Kopelman, R. *Langmuir* **1999**, *71*, 4831–4836.
114. Clark, H.; Kopelman, R.; Tjalkens, R.; Philbert, M. *Langmuir* **1999**, *71*, 4837–4943.
115. Lu, M.; Wu, D.; Guo, N. *J. Mater. Sci. Mater. Med.* **2009**, *20*, 563–572.
116. Tian, Z. Y.; Shaller, A. D.; Li, A. D. Q. *Chem. Comm* **2009**, 180–182.
117. Su, J.; Chen, J.; Zeng, F.; Chen, Q.; Wu, S.; Tong, Z. *Polymer Bull.* **2008**, *61*, 425–434.
118. Chen, J.; Zeng, F.; Wu, S.; Chen, Q.; Tong, Z. *Chem. Eur. J.* **2008**, *14*, 4851–4860.
119. Furukawa, H.; Misu, M.; Ando, K.; Kawaguchi, H. *Rapid Commun.* **2008**, *29*, 547–551.
120. Hu, Z.; Zhang, Q.; Xue, M.; Sheng, Q.; Liu, Y. *Opt. Mater.* **2008**, *30*, 851–856.
121. Hu, Z.; Zhang, Q.; Xue, M.; Sheng, Q.; Liu, Y. *J. Phys. Chem. Solids* **2008**, *69*, 206–210.
122. Yang, Y.; Zhang, J.; Guo, Y. *Appl. Surf. Sci.* **2009**, *255*, 6924–6929.
123. Kurokawa, N.; Yoshikawa, H.; Hirota, N.; Hyodo, K.; Masuhara, H. *Chem. Phys. Chem.* **2004**, *5*, 1609–1615.
124. Wu, C.; Bull, B.; Szymanski, C.; Christensen, K.; McNeill, J. *ACS Nano* **2008**, *2*, 2415–2423.
125. Wu, X.; Liu, H.; Liu, J.; *et al. Nat. Biotechnol.* **2003**, *21*, 41–46.
126. Lin, S.; Xie, X.; Patel, M. R.; *et al. BMC Biotechnol.* **2007**, *7*, 67.
127. Sweeney, E.; Ward, T. H.; Gray, N.; *et al. Biochem. Biophys. Res. Commun.* **2008**, *374*, 181–186.
128. Smith, M. Q.; Staley, C. A.; Kooby, D. A.; Styblo, T.; Wood, W. C.; Yang, L. *Curr. Mol. Med.* **2009**, *9*, 1017–1023.
129. He, X.; Duan, J.; Wang, K.; Tan, W.; Lin, X.; He, C. *J. Nanosci. Nanotechnol.* **2004**, *4*, 585–589.
130. Santra, S.; Wang, K.; Tapec, R.; Tan, W. *J. Biomed. Optic.* **2001**, *6*, 160–166.
131. Cambi, A.; Lidke, D. S.; Arndt-Jovin, D. J.; Figdor, C. G.; Jovin, T. M. *Nano. Lett.* **2007**, *7*, 970–977.
132. Lidke, D. S.; Nagy, P.; Heintzmann, R.; *et al. Nat. Biotechnol.* **2004**, *22*, 198–203.

133. Echarte, M. M.; Bruno, L.; Arndt-Jovin, D. J.; Jovin, T. M.; Pietrasanta, L. I. *FEBS Lett.* **2007**, *581*, 2905–2913.
134. Ogunkoya, Y.; Nickel, B. M.; Gay, V. L.; Murray, S. A. *Biotech. Histochem.* **2009**, *84*, 109–115.
135. Xing, X.; He, X.; Peng, J.; Wang, K.; Tan, W. J. *Nanosci. Nanotechnol.* **2005**, *5*, 1688–1693.
136. Wu, W.; Wan, W.; Li, A. D. *J. Cell Biochem.* **2009**, *108*, 791–801.
137. Galvez, E. M.; Zimmermann, B.; Rombach-Riegraf, V.; Bienert, R.; Graber, P. *Eur. Biophys. J.* **2008**, *37*, 1367–1371.
138. Zhang, C. Y.; Johnson, L. W. *Anal. Chem.* **2007**, *79*, 7775–7781.
139. Wu, H.; Huo, Q.; Varnum, S.; *et al. Analyst* **2008**, *133*, 1550–1555.
140. Ghazani, A. A.; Lee, J. A.; Klostranec, J.; *et al. Nano. Lett.* **2006**, *6*, 2881–2886.
141. Goldman, E. R.; O'Shaughnessy, T. J.; Soto, C. M.; *et al. Anal. Bioanal. Chem.* **2004**, *380*, 880–886.
142. Sarder, P.; Nehorai, A. *IEEE Trans. Nanobiosci.* **2008**, *7*, 284–297.
143. Karlin-Neumann, G.; Sedova, M.; Falkowski, M.; Wang, Z.; Lin, S.; Jain, M. *Meth. Mol. Biol.* **2007**, *374*, 239–251.
144. Pedroso, S.; Guillen, I. A. *Comb. Chem. High Throughput Screen.* **2006**, *9*, 389–397.
145. Eastman, P. S.; Ruan, W.; Doctolero, M.; *et al. Nano Lett.* **2006**, *6*, 1059–1064.
146. Geho, D.; Lahar, N.; Gurnani, P.; *et al. Bioconjugate Chem.* **2005**, *16*, 559–566.
147. Shi, L.; Rosenzweig, N.; Rosenzweig, Z. *Anal. Chem.* **2007**, *79*, 208–214.
148. Zhang, C. Y.; Johnson, L. W. *Anal. Chem.* **2009**, *81*, 3051–3055.
149. Suzuki, M.; Husimi, Y.; Komatsu, H.; Suzuki, K.; Douglas, K. T. *J. Am. Chem. Soc.* **2008**, *130*, 5720–5725.
150. Ramadurai, D.; Norton, E.; Hale, J.; *et al. IET Nanobiotechnol.* **2008**, *2*, 47.
151. Tapec, R.; Zhao, X. J.; Tan, W. *J. Nanosci. Nanotechnol.* **2002**, *2*, 405–409.
152. Peng, J.; He, X.; Wang, K.; Tan, W.; Wang, Y.; Liu, Y. *Anal. Bioanal. Chem.* **2007**, *388*, 645–654.
153. Doussineau, T.; Trupp, S.; Mohr, G. J. *J. Colloid Interface Sci.* **2009**, *339*, 266–270.
154. Hong, B.; Tang, L.; Ren, Y.; Kang, K. A. *Adv. Exp. Med. Biol.* **2007**, *599*, 23–29.
155. Li, L.; Li, H.; Chen, D.; *et al. J. Nanosci. Nanotechnol.* **2009**, *9*, 2540–2545.
156. Smith, B. R.; Cheng, Z.; De, A.; Koh, A. L.; Sinclair, R.; Gambhir, S. S. *Nano Lett.* **2008**, *8*, 2599–2606.
157. Cai, W.; Shin, D. W.; Chen, K.; *et al. Nano Lett.* **2006**, *6*, 669–676.
158. Cai, W.; Chen, X. *Nat. Protocol.* **2008**, *3*, 89–96.
159. Hun, X.; Zhang, Z.; Tiao, L. *Anal. Chim. Acta* **2008**, *625*, 201–206.
160. Qian, J.; Li, X.; Wei, M.; Gao, X.; Xu, Z.; He, S. *Optic. Express* **2008**, *16*, 19568–19578.
161. Noh, Y. W.; Lim, Y. T.; Chung, B. H. *Faseb J.* **2008**, *22*, 3908–3918.
162. Sen, D.; Deerinck, T. J.; Ellisman, M. H.; Parker, I.; Cahalan, M. D. *PLoS One* **2008**, *3*, e3290.
163. Slotkin, J. R.; Chakrabarti, L.; Dai, H. N.; *et al. Dev. Dynam.* **2007**, *236*, 3393–3401.
164. Voura, E. B.; Jaiswal, J. K.; Mattoussi, H.; Simon, S. M. *Nat. Med.* **2004**, *10*, 993–998.
165. Ravnic, D. J.; Zhang, Y. Z.; Turhan, A.; *et al. Microsc. Res. Tech.* **2007**, *70*, 776–781.
166. Jayagopal, A.; Russ, P. K.; Haselton, F. R. *Bioconjugate Chem.* **2007**, *18*, 1424–1433.
167. Soltesz, E. G.; Kim, S.; Laurence, R. G.; *et al. Ann. Thorac. Surg.* **2005**, *79*, 269–277.
168. Kobayashi, H.; Hama, Y.; Koyama, Y.; *et al. Nano Lett.* **2007**, *7*, 1711–1716.
169. Mounzer, R.; Shkarin, P.; Papademetris, X.; Constable, T.; Ruddle, N. H.; Fahmy, T. M. *Lymphat. Res. Biol.* **2007**, *5*, 151–158.
170. Kobayashi, H.; Koyama, Y.; Barrett, T.; *et al. ACS Nano* **2007**, *1*, 258–264.
171. Sun, P.; Zhang, H.; Liu, C.; *et al. Langmuir* **2010**, *26*, 1278–1284.

3.326. Imaging and Diagnosis of Biological Markers

K J Ooms and K Genuis, The King's University College, Edmonton, AB, Canada
K W Feindel, NRC Institute for Biodiagnostics (Atlantic), Halifax, NS, Canada

© 2011 Elsevier Ltd. All rights reserved.

3.326.1.	**Introduction**	429
3.326.2.	**Principles of MR and the Implications for Imaging and Diagnosis**	429
3.326.2.1.	The MR Interactions	429
3.326.2.1.1.	The Zeeman interaction	429
3.326.2.1.2.	Quadrupole interaction	430
3.326.2.1.3.	Interaction with an applied RF field	430
3.326.2.1.4.	Direct dipole–dipole interaction	430
3.326.2.1.5.	Magnetic shielding interaction	430
3.326.2.1.6.	Indirect spin–spin coupling	431
3.326.2.2.	Basics of MR Pulse Sequences	431
3.326.2.2.1.	Creating and detecting the MR response	431
3.326.2.3.	Relaxation in MR	431
3.326.2.3.1.	Longitudinal and transverse relaxation	431
3.326.2.3.2.	Rotating frame relaxation	432
3.326.2.4.	Diffusion in MR	432
3.326.2.5.	Magnetic Resonance Imaging	432
3.326.2.5.1.	Magnetic field gradients	432
3.326.2.5.2.	NMR signal and k-space	433
3.326.2.5.3.	Image contrast	433
3.326.2.5.4.	Example of MRI sequence	433
3.326.2.6.	Application to Imaging and Diagnosis of Biological Markers	434
3.326.2.7.	Summary	434
3.326.3.	**Viable Molecules, Nuclei, and Experiments for MR Studies**	434
3.326.3.1.	^{1}H Magnetic Resonance	435
3.326.3.1.1.	Water	435
3.326.3.1.2.	Fats	435
3.326.3.1.3.	Direct detection of small molecule metabolites	435
3.326.3.2.	^{31}P MR	435
3.326.3.3.	^{23}Na Magnetic Resonance	436
3.326.3.3.1.	Na^{+} concentration for diagnosis	436
3.326.3.3.2.	^{23}Na NMR parameters as biological markers for diagnosis	437
3.326.3.4.	^{13}C Magnetic Resonance	437
3.326.3.5.	Other Nuclei	437
3.326.3.6.	Summary	438
3.326.4.	**Case Study: Biological Markers for the Diagnosis of DDD**	438
3.326.4.1.	Molecular Changes During DDD	438
3.326.4.2.	^{2}H Double Quantum Filtered NMR Studies	439
3.326.4.3.	^{1}H $T_{1\rho}$ Studies of Water to Assess DDD	439
3.326.4.4.	Na^{+} Concentration Studies to Assess DDD	439
3.326.4.5.	^{23}Na Multiple Quantum Filtered NMR Studies	439
3.326.4.6.	Conclusions	440
3.326.5.	**Case Study: MR for Diagnosing Bone Disease and Treatment**	440
3.326.5.1.	Bone Structure and Markers of Disease	440
3.326.5.2.	Diagnosis of Bone Disease Using MR Techniques	441
3.326.5.2.1.	Collagen imaging	441
3.326.5.2.2.	Studies of HAp	441
3.326.5.2.3.	MRS of marrow fat	442
3.326.5.2.4.	Diffusion imaging of water in marrow	442

3.326.5.3. Developing and Assessing Biomaterial Treatments 442
3.326.5.3.1. Bioinert and resorbable bone materials 443
3.326.5.3.2. Bioactive bone implants 443
3.326.5.3.3. Hybrid bone biomaterials 443
3.326.5.4. Conclusions 444
3.326.6. Summary and Future of Imaging and Diagnosis of Biological Markers 444
References 444

Glossary

Annulus fibrosus The outer segment of the spinal disc.
Compact bone The inner segment of the spinal disc.
Nucleus pulposus The inner segment of the spinal disc.
Trabecular bone The porous inner region of the bone.

Abbreviations

BMD	Bone mineral density
CSI	Chemical shift imaging
CT	X-ray computed tomography
DCE	Dynamic contrast-enhanced
DDD	Degenerative disc disease
DQF, MQF, TQF	Double, multiple, triple quantum filtered
DWI	Diffusion-weighted imaging
EFG	Electric field gradient
HAp	Hydroxyapatite
MR	Magnetic resonance
MRI	Magnetic resonance imaging
MRS	Magnetic resonance spectroscopy
NMR	Nuclear magnetic resonance
SE	Spin echo
SNR	Signal-to-noise ratio
SQ, DQ, TQ	Single, double, triple quantum
SSNMR	Solid-state nuclear magnetic resonance
TWI	Tensor-weighted imaging

Symbols

B_0	External magnetic field
B_1	Applied magnetic field
d	Dipolar coupling constant
D	Diffusion constant
e	Electronic charge
G_x, G_y, G_z	Magnetic field gradients along the x, y, and z axes
h	Planck constant
$\hbar$	Planck constant divided by 2π
$\hat{H}_\sigma$	Magnetic shielding Hamiltonian
$\hat{H}_{DD}$	Direct dipole Hamiltonian
$\hat{H}_J$	Indirect spin–spin Hamiltonian
$\hat{H}_Q$	Quadrupolar Hamiltonian
$\hat{H}_{RF}$	Applied RF Hamiltonian
$\hat{H}_Z$	Zeeman Hamiltonian
I	Nuclear spin quantum number
I, S	Nuclear spin operator
I_Z	Azimuthal spin-angular momentum operator
J_{IS}	Isotropic spin–spin coupling constant
k	Reciprocal space vector
M_0	Initial magnetization
m_I	Magnetic quantum number
M_{xy}	Magnetization in the xy-plane of the laboratory frame
M_z	Magnetization along the z-axis of the laboratory frame
Q	Nuclear quadrupole moment
r_{IS}	Distance between spin I and S
t	Time
T_1	Longitudinal relaxation time
$T_{1\rho}$	Longitudinal relaxation time in the rotating frame
T_2	Transverse relaxation time
$T_{2\rho}$	Transverse relaxation time in the rotating frame
T_E	Echo time
T_R	Repetition time
V	Electric field gradient tensor
x, y, z	Cartesian coordinates
Δ	Time between two gradient pulses in a diffusion experiment
Θ	Angles that relate the direction of B_0 with respect to the principal axis system of the shielding tensor
γ	Magnetogyric ratio
δ_{iso}	Isotropic chemical shift
δ	Duration of the gradient pulses in a diffusion experiment
μ_0	Permeability of vacuum
ν_L	Larmor frequency
$\rho(r)$	Spin density as a function of position
σ_{iso}	Isotropic magnetic shielding
σ_{zz}	zz component of the shielding tensor
τ	Mixing time
τ_{max}	Time at which signal intensity in the DQF experiment is maximum

3.326.1. Introduction

Modern materials are changing the world of medicine. Metal, ceramic, polymer, hydrogel, and nanocomposite materials are all finding new applications to treat injuries and diseases. As these materials are developed and used, it is important to employ characterization techniques that probe the chemical changes that occur because of disease and the use of biomaterials in treatment. Magnetic resonance (MR) techniques, both nuclear magnetic resonance (NMR) spectroscopy and magnetic resonance imaging (MRI), are powerful methods for studying molecular level properties and therefore have the potential to be useful probes of the biochemical interactions between the body and biomaterials. Many MR phenomena have already found utility in clinical medicine. In particular, ^{1}H MRI techniques can provide contrast related to spin density, relaxation parameters (e.g., T_1- and T_2-weighted images), susceptibility changes (e.g., blood-oxygen-level-dependent contrast in functional MRI), flow, and diffusion. However, to fully exploit the potential of MR in novel and more specific ways, it is vital that researchers developing new techniques have a familiarity with the selection of biological markers that can be used for diagnosis, treatment, and monitoring a patient's response to treatment.[1]

The first important task when applying existing or developing new MR methods is to select the biological molecules that best characterize the changes caused by disease or treatment. Important criteria for selecting appropriate biological molecules are the presence of an element with an isotope that is amenable to MR studies and a molecule that is in high enough concentration that it can be detected with MR techniques. In conventional medical MRI, water is studied due to the ideal NMR properties of ^{1}H in water; however, other nuclei such as ^{23}Na or ^{31}P can be used as they also have favorable NMR properties. Finally, MR provides researchers a plethora of experimental methodologies that can be employed to measure a range of magnetic and chemical properties. In conventional ^{1}H MRI experiments that rely on water to provide the MR signal, proton density, and T_1 and T_2 relaxation properties are commonly probed. When developing new methods, other relaxation mechanisms (e.g., in the rotating frame), or nuclear spin interactions such as magnetic shielding (i.e., chemical shifts) or quadrupolar couplings, may provide more meaningful information, even for water.

The goal of this chapter is to illustrate how a deeper understanding of the fundamentals of MR, biochemistry, and biomaterial science can open up new methods for elucidating the biochemical implications of disease and biomaterial treatments. In this chapter, we define a biological marker as the molecule, the nuclear isotope used in the MR experiment, and the NMR property being probed, which in combination can be correlated to a disease, injury, or treatment response. By broadening the definition to include experimental techniques in addition to the molecules, the same molecule can be used as a biological marker to probe different biochemistries. The focus is on markers present in the body and not on those introduced specifically for imaging purposes such as contrast agents or MR tags. This chapter initially describes the basic concepts of MR and the properties that can be measured using NMR spectroscopy and imaging. Different biological markers will then be highlighted to illustrate how the choice of molecule, nucleus, and experiment is an important aspect of selecting the marker. Finally, we focus on two disease case studies where biomaterials are playing increasingly important roles and demonstrate how different biological markers are being used in imaging and diagnosis.

3.326.2. Principles of MR and the Implications for Imaging and Diagnosis

This section introduces basic concepts in MR, including fundamental theory, measurable interactions, pulse sequences, and experimental methodologies based on MR. Applications of these concepts to imaging and diagnosis of biomarkers are outlined.

3.326.2.1. The MR Interactions

NMR is a very sensitive probe of local molecular and electronic environment. In addition to the fundamental Zeeman interaction, the resonance frequencies, the shape of the resonance, and the relaxation times of an MR signal are related to the interaction of nuclear spins with each other, local and applied magnetic fields, electric field gradients (EFGs), and coupling to the surroundings. The energies of interaction for a spin system determine the resonance frequencies, and the total energy can be described by a Hamiltonian, $\hat{H}$:

$$\hat{H} = \hat{H}_Z + \hat{H}_Q + \hat{H}_{RF} + \hat{H}_{DD} + \hat{H}_\sigma + \hat{H}_J \qquad [1]$$

where the Zeeman interaction $\hat{H}_Z$ is the largest (MHz), followed by the quadrupole interaction $\hat{H}_Q$ (kHz to MHz), $\hat{H}_{RF}$ (kHz) which describes the coupling of the spins to the external applied radiofrequency (RF) field, the direct dipole–dipole coupling $\hat{H}_{DD}$ (kHz), the magnetic shielding $\hat{H}_\sigma$ (Hz to kHz), and the indirect dipole–dipole coupling $\hat{H}_J$ (Hz). Exploiting these interactions, NMR spectroscopy has long been recognized as a powerful tool for identification of molecular species and elucidation of molecular structure.[2] Herein, we describe briefly key information that can be obtained via characterization of each interaction, and the reader is referred to the literature for a complete description of the interaction Hamiltonians.[3–6]

3.326.2.1.1. The Zeeman interaction

The MR response relies on the fundamental interaction of a magnetic field with the magnetic dipole moment associated with the orbital angular momentum of a nucleus.[7] Many atomic nuclei possess half-integer or integer spin-angular momentum, $\mathbf{I}\hbar$, colinear with a magnetic dipole moment, $\mu = \gamma\mathbf{I}\hbar$, where γ is the magnetogyric ratio and $\hbar$ is the Planck constant h divided by 2π. As shown in eqn [2], the Zeeman Hamiltonian describes the energy of interaction of $\mathbf{I}\hbar$, with an external magnetic field, $\mathbf{B}_0$,

$$\hat{H}_Z = -\gamma\mathbf{I}\hbar\mathbf{B}_0 \qquad [2]$$

Typically, only the largest component of the $\mathbf{B}_0$ column vector (B_x, B_y, B_z) is considered, which defines the z-axis of the laboratory frame of reference, $\mathbf{B}_0 = (0, 0, B_0)$.

A proton (^{1}H) possesses a magnetic dipole moment and has a half-integer nuclear spin, $I = 1/2$. In the presence of an external magnetic field, the magnetic dipole moment aligns either parallel or antiparallel to the direction of B_0. As shown in Figure 1(a), different energies are obtained for the two possible projections with respect to the applied magnetic field, and correspond to the nondegenerate nuclear spin eigenstates: $m_I = 1/2$ (parallel) and $m_I = -1/2$ (antiparallel). The diagrams in Figure 1(b) and 1(c) illustrate the Zeeman splitting that results for a species with $I = 1$ (e.g., ^{2}H) and with $I = 3/2$ (e.g., ^{23}Na), respectively. Tables of nuclear spin properties are available.[8] The frequency corresponding to the difference in energy between adjacent states, ΔE, is defined by the Larmor equation:

$$\nu_L = \frac{|\gamma|B_0}{2\pi} = \frac{\Delta E}{h} \qquad [3]$$

where ν_L is referred to as the Larmor frequency. Transitions between energy levels with a change in magnetic quantum number equal to one (i.e., $m_I = 1/2 \rightarrow m_I = -1/2$) are called single-quantum (SQ) coherences, and are directly observable. Also, as shown in Figure 1(b) and 1(c), for nuclei with $I > 1/2$, coherences exist at multiples of the resonance frequency and are labeled on the basis of the order of the coherence, for example, double quantum (DQ), triple quantum (TQ), and so on. Both eqns [2] and [3] show the magnetic-field-dependent nature of the NMR frequency. The Larmor frequencies of nuclei in commercial superconducting MR magnets are on the order of 10^8 Hz, or in the RF range.

3.326.2.1.2. Quadrupole interaction

An NMR active nucleus with $I > 1/2$ possesses an asymmetric charge distribution, which gives rise to a quadrupole moment, Q. The quadrupole moment couples to the surrounding EFG, and therefore, the resultant interaction can provide valuable insight regarding electronic structure in the region around the nucleus. Rapid isotropic motion (e.g., solutes in solution, or liquids) leads to an averaging of the quadrupole coupling tensor to a value of 0; the EFG is properly described by a traceless second-rank tensor. When the Zeeman interaction dominates the total interaction Hamiltonian, the quadrupolar Hamiltonian can be written as shown in eqn [4]:

$$\hat{H}_Q = \frac{eQ}{6I(2I-1)\hbar}\mathbf{IVI} \qquad [4]$$

where e is the elementary charge and $\mathbf{V}$ is the traceless EFG tensor. The most common quadrupolar nuclei used for biological applications are ^{2}H ($I = 1$) and ^{23}Na ($I = 3/2$) (see Section 3.326.3).

3.326.2.1.3. Interaction with an applied RF field

Pulsed RF fields are used to apply an oscillating magnetic field, B_1, at the Larmor frequency and perpendicular to B_0. The net magnetization vector, M, of a sample is subject to a torque due to B_1, which causes M to rotate about the axis along which B_1 is applied. The angle of rotation of M is determined by the amplitude and duration of B_1. The amplitude of B_1 (on the order of kHz) typically dominates other interactions except for the Zeeman and quadrupole interactions. RF fields can be used to access information regarding slower NMR relaxation process (i.e., on the order of kHz rather than MHz) due to processes such as molecular tumbling and exchange (see Section 3.326.2.3.2). The interaction Hamiltonian for B_1 is analogous to that shown in eqn [2] for the Zeeman interaction.

3.326.2.1.4. Direct dipole–dipole interaction

One of the large interactions between nuclei is the mutual through-space coupling of their magnetic dipole moments. In solution, the dipole–dipole interaction is averaged to zero. In the absence of isotropic molecular tumbling, the perturbation of the energy levels, on the order of tens to hundreds of kilohertz, can impart a significant and measurable influence on the NMR signal, and is typically the dominating mechanism for relaxation. The magnitude of the interaction is given by the dipolar coupling constant, d, as shown in eqn [5]:

$$d = -\left(\frac{\mu_0}{4\pi}\right)\frac{\gamma_I\gamma_S\hbar}{r_{IS}^3} \qquad [5]$$

where r is the distance between the point-magnetic dipoles. The manifestation of the dipole–dipole coupling in the NMR signal is orientation-dependent, related to the angle between B_0 and the vector joining the coupled spins.

3.326.2.1.5. Magnetic shielding interaction

The ubiquity of NMR spectroscopy for molecular species identification and structural characterization finds its origin in the sensitivity of the measured frequency to chemical environment. The magnetic shielding interaction gives rise to perturbations of the energy levels which yield frequency shifts related to

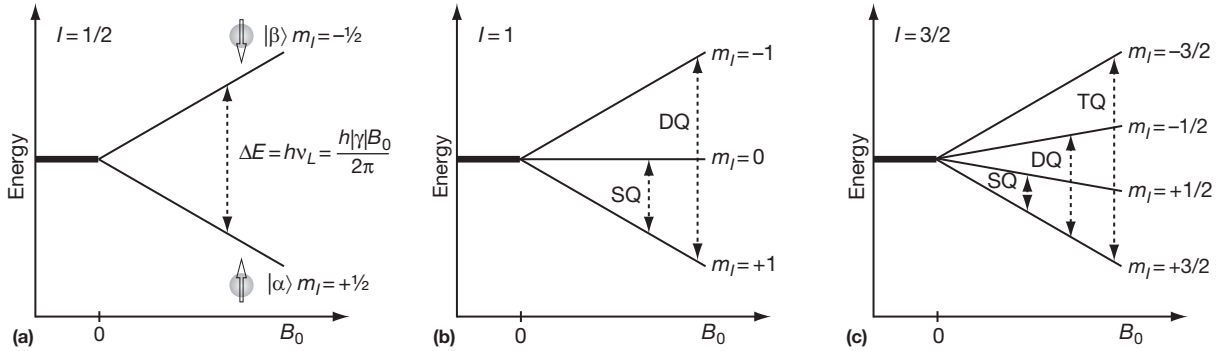

Figure 1 Zeeman energy levels demonstrating the separation of the nondegenerate nuclear spin eigenstates as a function of applied magnetic field, B_0 for (a) a nucleus with $I = 1/2$, (b) $I = 1$, and (c) $I = 3/2$, where SQ, DQ, and TQ are single, double, and triple quantum transitions, respectively.

the specific electronic (and chemical) environment of a nucleus. The interaction Hamiltonian for a spin I in the laboratory frame is described by eqn [6]:

$$\hat{H}_\sigma = -\gamma\hbar B_0\sigma_{iso}\hat{I}_z - \frac{1}{2}\left(3\cos^2\Theta - 1\right)(\sigma_{zz} - \sigma_{iso})\gamma\hbar B_0\hat{I}_z \quad [6]$$

where σ_{iso} is the isotropic shielding value, equal to one-third the trace of the second-rank magnetic shielding tensor, $(\sigma_{zz} - \sigma_{iso})$ is the anisotropic shielding value, and Θ is the angle between B_0 and the principal axis system of the shielding tensor. The angular dependence can be removed by setting Θ to the so-called magic angle ($\sim$54.7°) such that $3\cos^2\Theta = 1$. This technique is often employed in solid-state NMR where samples are spun rapidly (i.e., on the order of kHz) at the magic angle to reduce line-broadening caused by the anisotropic magnetic shielding, quadrupolar, and direct dipolar interactions. In solution, molecular tumbling eliminates the second term in eqn [6] leaving the isotropic shielding value. In practice, magnetic shielding is normalized by measuring the difference in frequency between the sample and a reference Larmor frequency for that nucleus, creating a so-called chemical shift scale which is reported in parts per million and is independent of the applied magnetic field.

3.326.2.1.6. Indirect spin–spin coupling

The indirect spin–spin coupling (also known as scalar or J-coupling) is an interaction between nuclear moments mediated by electrons participating in chemical bonds between the nuclei. The energy of interaction results in small perturbations to the frequency on the order of hertz, ranging from 1 to 10 Hz for homonuclear ^{1}H couplings to hundreds or thousands of hertz for heteronuclear cases involving heavy atoms. Unlike the direct dipolar interaction, J-coupling does not average to zero under conditions of molecular tumbling. This results in a perturbation of the NMR spectrum which is independent of molecular orientation. For an isotropic liquid, the interaction Hamiltonian (in units of Hz) is given by eqn [7]:

$$\hat{H}_J = 2\pi J_{IS}\mathbf{IS} \quad [7]$$

where J_{IS} is the isotropic spin–spin coupling constant, equal to one-third the trace of the J-coupling tensor. For NMR of dilute solutions, J-coupling can provide critical information for analyzing molecular structure, confirmation, and connectivity.

3.326.2.2. Basics of MR Pulse Sequences

3.326.2.2.1. Creating and detecting the MR response

The MR signal generated by an ensemble of nuclei is governed by Boltzmann statistics, which determines the relative populations of the nuclear spin eigenstates. In thermal equilibrium, the net magnetization vector of a sample under study is oriented with the external applied magnetic field and is often denoted M_0. To detect an MR signal, M_0 must be reoriented from the large external applied field. An oscillating magnetic field, B_1, is applied transverse to the z-axis, with frequency that matches ν_L, generally termed an RF pulse. The duration and amplitude of the B_1 field together determine the extent to which the net magnetization vector rotates about the B_1 field away from the z-axis. **Figure 2** shows a schematic of a spin-echo (SE) sequence where the first pulse rotates M_0 by 90°. This orients the magnetization vector along the plane transverse to the external applied field and is often denoted $M_{x,y}$. $M_{x,y}$ continues to precess at the Larmor frequency, creating a detectable signal, called the free-induction decay (FID), the amplitude and phase of which are measured as a function of time. This is the MR signal.

3.326.2.3. Relaxation in MR

NMR relaxation is a general term that is used to describe the phenomena of either the recovery of M_0 or the decay of $M_{x,y}$. The time that is required for the magnetic moments of an ensemble of spins in random orientation to align with an applied magnetic field depends on many variables including material density and molecular motion (e.g., solid, liquid, mobile), and applied field strength. Similarly, the components of $M_{x,y}$ 'dephase' or lose coherence, and the detectable response decays.

3.326.2.3.1. Longitudinal and transverse relaxation

At thermal equilibrium, M_0 is in the direction of B_0 along the z-axis. Application of an RF pulse that rotates the magnetization away from the z-axis and into the x,y plane disturbs the

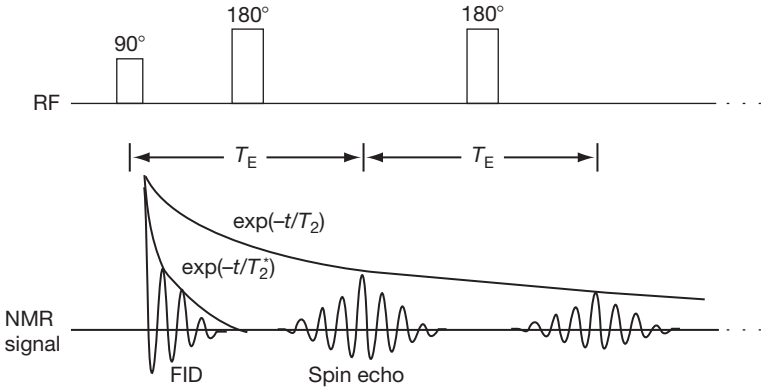

Figure 2 An example of a basic multi spin-echo sequence. The decay of the free-induction decay (FID) can be described as a monoexponential function of characteristic time T_2^*, and the decay of the spin-echo envelop by the spin–spin relaxation time, T_2. The echo time, T_E, is the time between the RF pulse and the peak of the spin-echo.

equilibrium of the spin system. Over time, the equilibrium will be restored, and the magnetization along the z-axis at time t, $M_z(t)$ can be described using the classical equation of motion derived by Bloch, eqn [8][9]:

$$M_z(t) - M_0 = [M_z(0) - M_0] \exp\left(-\frac{t}{T_1}\right) \qquad [8]$$

where $M_z(0)$ is the magnetization remaining along the z-axis after the RF pulse and T_1 is the first-order time constant that describes the recovery of M_0 after the RF pulse. This time constant is generally referred to as the spin-lattice or longitudinal relaxation time. As described by the monoexponential dependence, during a period T_1, approximately 63% of the original equilibrium magnetization recovers, after $3T_1$ approximately 95% recovers, and essentially complete relaxation occurs after $5T_1$. Thus, the number of times that M_z can be tipped (e.g., to signal average) in a particular time period (often called the repetition time, T_R) without saturating the signal is related to T_1 (i.e., a delay of several seconds may be required to reach $M_z = M_0$).

Once the magnetization vector is rotated away from B_0, and into the transverse plane (i.e., $M_z \rightarrow M_{x,y}$), $M_{x,y}$ will decay due to inhomogeneous and random homogeneous interactions and result in no net transverse magnetization. The decay of the FID can typically be described by a monoexponential function with a characteristic time constant $T_2{}^*$ (see **Figure 2**). For molecules in solution, this relaxation process and the transverse magnetization at time t, $M_{x,y}(t)$, can generally be treated using the theory of Bloembergen, Purcell, and Pound[10] and described by eqn [9]:

$$M_{x,y}(t) = M_{x,y}(0) \exp\left(-\frac{t}{T_2}\right) \qquad [9]$$

where $M_{x,y}(0)$ is the transverse magnetization immediately following the RF pulse and T_2 is the spin–spin or transverse relaxation time. In general, $T_2 \leq T_1$. Aqueous or semisolid systems containing water with a homogeneous composition, in the absence of paramagnetic materials, tend to exhibit ^{1}H T_2 values on the order of 10^{-1} s or longer.

In the presence of static magnetic field inhomogeneity, SE-based techniques are often used. After the initial RF pulse to tip the magnetization into the transverse plane, a RF refocusing pulse can be applied to flip $M_{x,y}$ in the transverse plane (i.e., rotate by 180°). This rotation of the magnetization reverses the direction of inhomogeneous dephasing, and results in the formation of an SE. A train of appropriate RF refocusing pulses will yield a series of SEs, the decay envelope of which can be described by a monoexponential function of T_2 (**Figure 2**). This method, referred to as the Carr–Purcell–Meiboom–Gill (CPMG) experiment, is often used to measure T_2.[11,12]

3.326.2.3.2. Rotating frame relaxation

The NMR relaxation processes discussed above require magnetic field fluctuations on the order of megahertz, which often correlates well with molecular tumbling. As originally described by Ailion and Slichter, slower relaxation processes can be probed by measuring the relaxation of the magnetization vector in the transverse plane during application of the B_1 field, which is typically on the order of kilohertz.[13] After an initial 90° RF pulse is applied to place the magnetization in the transverse plane, the phase of the RF pulse is changed so that it is aligned with the transverse magnetization. This technique is called a spin-lock; the transverse magnetization is unable to precess away from this axis for the duration of the spin-lock pulse, and the magnetization decays approximately exponentially. Repeating the procedure for several values of the spin-locking time provides a series of FIDs with a characteristic decay time, denoted $T_{1\rho}$, the spin-lattice relaxation time constant in the rotating frame. In practice, the spin-lock is implemented as a composite pulse termed a rotary-echo to compensate for B_1 inhomogeneity.[14]

Recent developments in spectrometer hardware have facilitated the implementation and application of amplitude and phase-modulated pulses in modern imaging and spectroscopy techniques.[15] Much research has been completed to understand relaxation processes that occur during the application of adiabatic pulses,[16] and to obtain novel contrast in MRI related to tissue pathology.[17,18] Application of an adiabatic full passage (AFP) RF pulse with appropriate parameters such that the sample magnetization vector remains aligned with the applied field will provide $T_{1\rho}$ relaxation contrast. $T_{1\rho}$ contrast is sensitive to water–protein interactions, and research shows that this may be an indicator of neuronal loss in some neurological disorders and of cartilage degeneration.[19,20] If the magnetization vector is placed in the transverse plane prior to application of the AFP RF pulse, the magnetization remains approximately perpendicular to the applied field. This yields contrast related to transverse relaxation in the rotating frame, $T_{2\rho}$. $T_{2\rho}$ contrast has been shown to be sensitive to diffusion and to exchange of water protons in environments with different local magnetic susceptibilities, which is postulated to reflect local iron content.[21]

3.326.2.4. Diffusion in MR

In the presence of a magnetic field gradient, $M_{x,y}$ will dephase in a predicable manner, and can be refocused with an equal gradient of opposite sign. However, if the ensemble of spins is subject to diffusion, the two magnetic fields experienced by the spins will be of different magnitude, and an attenuation of the transverse magnetization will result. Stejskal and Tanner demonstrated that this principle could be applied to obtain the bulk rate of diffusion, D, of the molecular species giving rise to the NMR signal.[22] In the absence of other relaxation mechanisms (i.e., T_2), the attenuated transverse magnetization due to unrestricted translational diffusion, as measured by a pulsed field gradient SE experiment, can be expressed by eqn [10][23,24]:

$$M_{x,y}(t) = M_{x,y}(0) \exp\left[-\gamma^2 G^2 D \delta^2 \left(\Delta - \frac{\delta}{3}\right)\right] \qquad [10]$$

where G is the strength of the applied gradient, δ is the duration of the gradient pulse, and Δ is the time between application of the two gradient pulses.

3.326.2.5. Magnetic Resonance Imaging

3.326.2.5.1. Magnetic field gradients

According to the Larmor equation (eqn [2]), the NMR frequency of a nucleus is related directly to the magnitude of the external applied magnetic field. The application of

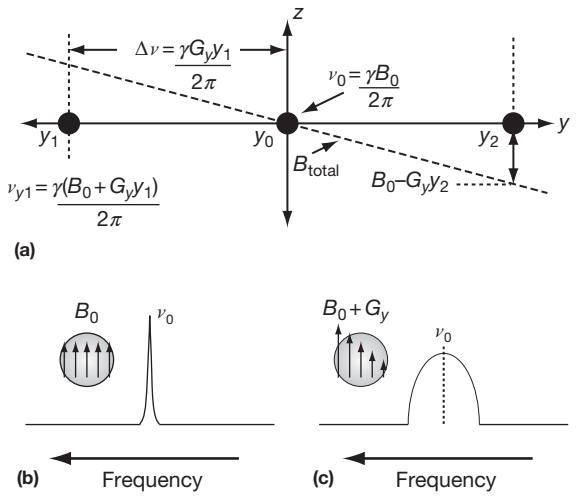

Figure 3 (a) A magnetic field gradient along the *y*-axis, G_y, modulates the magnitude of the total applied magnetic field along the *z*-axis, B_{total}. The change in magnetic field is related to the strength of the gradient and the distance from the origin of the axis along which the gradient is applied such that $B_{total} = B_0 + G_y y$. The resulting resonance frequency, ν_y, can be related to position in space with respect to the gradient axis. (b) A sample placed in a uniform B_0 will exhibit a single peak with frequency centered at ν_0. (c) Application of G_y across the sample introduces a spatial dependence of the frequency, and results in a peak shape representative of the projection of the sample profile.

well-defined and controlled pulsed magnetic field gradients can make the frequency and phase of the NMR signal vary as a function of space. Figure 3(a) shows the relation between a magnetic field gradient along the *y*-axis, G_y, applied onto B_0, and the resulting well-defined spatial dependence of frequency. Note that the magnetic field created is in the *z*-direction, the subscript *y* denotes the axis along which the magnitude of the field varies. The corresponding change in resonance frequency, $\Delta\nu$, can be described as a function of the applied field gradient and therefore of position in space, *y*, by $\Delta\nu(y) = \gamma G_y y / 2\pi$. For example, Figure 3(b) shows a sample experiencing a uniform magnetic field B_0, which results in a single peak at frequency ν_0. In comparison, if a magnetic field gradient, G_y, is applied across the sample as shown in Figure 3(c), the total magnetic field experienced by nuclei varies with respect to their position within the applied gradient.

3.326.2.5.2. NMR signal and k-space

The amplitude of the NMR signal is acquired as a function of time and is denoted $S(t)$. In MRI, the frequency of the signal from a volume of spins at position **r**, that is, the spin density, $\rho(\mathbf{r})$, is a function of the position with respect to the magnetic field gradient vector, **G**. The signal integrated over volume has the form of a Fourier transform (FT) and assuming mixing with a reference frequency, can be expressed as[23]:

$$S(t) = \iiint \rho(\mathbf{r}) \exp[i\gamma \mathbf{G} \mathbf{r} t] d\mathbf{r} \qquad [11]$$

Mansfield introduced the concept of a reciprocal space vector, **k**[25–27]:

$$\mathbf{k} = \frac{\gamma \mathbf{G} t}{2\pi} \qquad [12]$$

which shows that **k**-space can be traversed by gradient magnitude or by time. Shown in eqns [13] and [14] is the fundamental relationship of MRI, that is, the signal, $S(\mathbf{k})$, and $\rho(\mathbf{r})$ are an FT pair:

$$S(\mathbf{k}) = \iiint \rho(\mathbf{r}) \exp[i2\pi \mathbf{k} \mathbf{r}] d\mathbf{r} \qquad [13]$$

$$\rho(\mathbf{r}) = \iiint S(\mathbf{k}) \exp[-i2\pi \mathbf{k} \mathbf{r}] d\mathbf{k} \qquad [14]$$

Subjecting **k**-space to a multidimensional FT converts the data into an image, that is, a map of signal intensity as a function of frequency, and therefore physical space.

3.326.2.5.3. Image contrast

The contrast of an MR image is related to numerous factors including the volume and spin density of the sample, relaxation mechanisms, and local magnetic field variations. To obtain an image with contrast that represents only one of the factors, the data must be collected in a manner to isolate the contribution, or corrected with knowledge of the other parameters. For example, T_1-weighted contrast can be obtained by acquiring images with varied T_R values ($<5T_1$). This results in different amounts of magnetization saturation. To obtain an image with T_2-weighted contrast only, T_1 weighting is removed by adjusting the T_R value to prevent saturation of the magnetization (i.e., $T_R > 5T_1$). Images with contrast related to T_2 can be obtained by acquiring images at a series of different echo times (see Figure 2). This is generally facilitated using multi-echo experiments.

3.326.2.5.4. Example of MRI sequence

An example of a typical slice-selective SE MRI sequence is shown in Figure 4. Slice selection can be performed to obtain an image from a defined region by simultaneous application of an appropriate RF pulse shaped in the time domain (such that the frequency profile is approximately square) and a magnetic field gradient, G_x, in the direction of the slice thickness. The echo time, T_E, is the period between the first RF pulse applied to perturb the magnetization vector, and the peak of the SE that results from application of a refocusing pulse. To allow for T_1 relaxation processes, a delay, referred to as the repeat time, T_R, is implemented between applications of subsequent excitation pulses. One dimension of an image is often encoded by applying a magnetic field gradient, G_y, during acquisition of the signal, a process called frequency encoding. Higher-order dimensions are obtained in a series of experiments by imparting a phase shift in the signal prior to acquisition by incrementing a magnetic field gradient, G_z, that is applied for a fixed time period, in a process called phase encoding. If phase encoding is used to select a defined region and a gradient is not applied during the acquisition time (i.e., no frequency encoding), the FID recorded can be flourier transformed to yield an NMR spectrum corresponding to the selected region; this is referred to as magnetic resonance spectroscopy (MRS). As indicated in Figure 4, multiple refocusing RF pulses can be implemented following a single excitation pulse. The echoes can be phase encoded differently to cover **k**-space more quickly, summed to increase the SNR, or used to create a series of images that have contrast related to T_2 relaxation. In addition, by appropriately changing the T_R and T_E values, contrast with good specificity to tissue pathology can often be obtained.

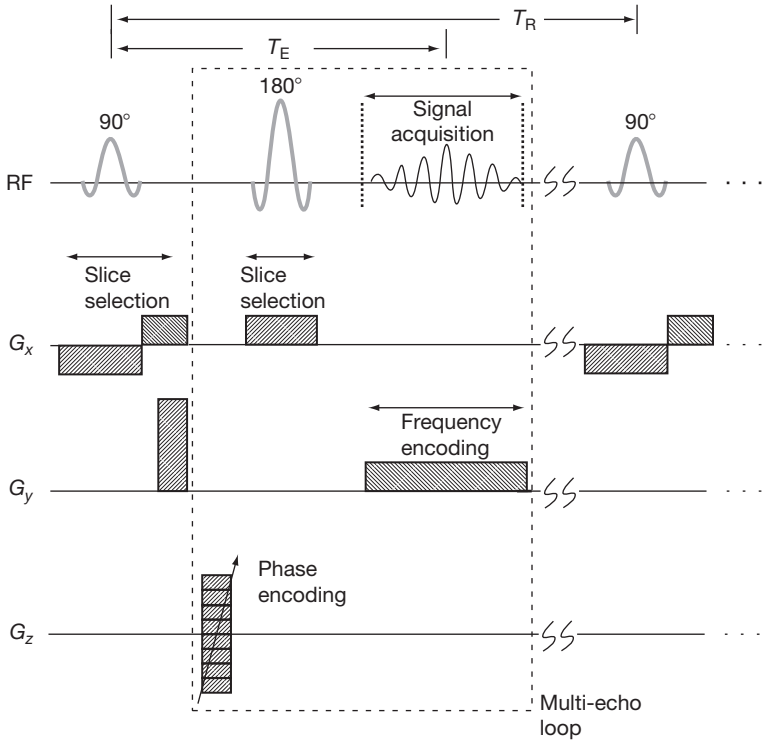

Figure 4 (a) An example of a two-dimensional (2D) spin-echo imaging sequence with slice-selective 90° and 180° radio frequency (RF) pulses along the *x*-axis, followed by frequency encoding along *y*, and phase encoding implemented along the *z*-axis. T_R is the repetition time between 90° RF pulses that perturb the magnetization along *z*.

3.326.2.6. Application to Imaging and Diagnosis of Biological Markers

The multitude of magnetic-field-perturbing NMR interactions enables nuclei to be very sensitive to their local and long-range environment. In solution, the identification of various molecular species relies predominantly on the magnetic shielding and indirect spin–spin coupling interactions, which under rapid molecular tumbling average to isotropic values. Solution NMR techniques are used extensively for *ex vivo* identification and quantification of biological markers.[28–31] MRI exploits the direct dependence of the NMR frequency on applied magnetic field to obtain spatially resolved information. Identification of biological markers with MRI relies on variation in tissue properties to impart contrast related to parameters including NMR relaxation characteristics, susceptibility changes, restricted motion, and diffusion. In the absence of rapid rotational molecular motion (i.e., in solids), the orientational dependence of NMR interactions is evident, which may reveal significant information about the local and long-range molecular environment. Solid-state NMR techniques are often applied on *ex vivo* samples, but *in vivo*, the presence of orientation-dependent interactions (e.g., quadrupolar, direct dipolar) can provide valuable information.

3.326.2.7. Summary

This section introduces the fundamental interactions and concepts of NMR which, over the decades, have facilitated the development and application of diverse and robust MR-based techniques. The various interactions by which MR-active nuclei can be perturbed enable sensitive and specific information to be obtained from appropriate experiments. Recognizing and understanding the influence of the NMR parameters can facilitate development, implementation, and use of MR-based techniques for imaging and diagnosis of biological markers.

3.326.3. Viable Molecules, Nuclei, and Experiments for MR Studies

Of all the biological molecules that can serve as markers for disease, only some can feasibly be studied using MR techniques. The molecules chosen must be in sufficient concentration to yield a strong MR signal; the typical concentration of detectable solutes ranges from 1 to 1000 mmol, depending on the nucleus being studied. This is particularly important for imaging experiments where the signal is spread out over a wide range of frequencies to create the spatially resolved images; MRI requires much higher concentrations to attain images in reasonable amounts of time. For this reason, *ex vivo* studies using NMR spectroscopy or microimaging are often the first step in developing new techniques and often can provide useful diagnostic tools because the number of molecules and nuclei that can be studied is much larger.[32,33]

Each NMR active isotope has unique properties that affect the feasibility of MR studies including the Larmor frequency, the natural abundance, and the nuclear spin number. The receptivity of a nucleus is an important factor when considering which biological markers to use. Of the top 10 occurring

Table 1 NMR properties of the most commonly used nuclei for MR imaging and diagnosis[8]

	Frequency 2.35 T (MHz)	*Natural abundance (%)*	*Receptivity with respect to proton*
^{1}H ($I = 1/2$)	100	99.9	100
^{13}C ($I = 1/2$)	25.14	1.07	0.017
^{23}Na ($I = 3/2$)	26.45	100	9.27
^{31}P ($I = 1/2$)	40.48	100	6.65

elements in the human body, only three have NMR properties that make them amenable to MRI studies (Table 1); while challenging, particularly for *in vivo* studies, ^{13}C can be used in certain cases. This section briefly reviews the nuclei that have found use for MR studies of different classes of biological markers.

3.326.3.1. ^{1}H Magnetic Resonance

Protons are the most commonly used nuclei for imaging and diagnosis. Current medical MRI is based on the fact that the human body is 80% water by mass and ^{1}H is the most receptive nucleus for MR studies. Water is therefore the biological molecule in most routine MRI scans and many reviews and books can be found on MRI methodology and application in medicine.[34–36] Here, we will focus on some of the unconventional methods of harnessing the MR properties of protons to employ different biomarkers.

3.326.3.1.1. Water

Water is abundant in biological systems, and dominates the ^{1}H MR signal. Thus, using water as a specific biological marker can be difficult if the condition of interest is responsible for only a small fraction of the water signal. For example, trying to monitor water tightly bound to large biological molecules such as collagen using basic techniques is all but impossible because of the massive signal from liquid water in most tissues. One way to overcome these challenges is to harness the dipolar interaction to differentiate between water molecules in the body that experience different degrees of restricted motion. The dipolar coupling is an anisotropic interaction, which means that its magnitude is orientationally dependent, Section 3.326.2.1.4. When water is free to move isotropically, the dipolar interaction averages to zero; however, if the water is not moving freely, the dipolar coupling may not completely average. This leads to a nonzero coupling between the two protons, called the residual dipolar coupling, which has a magnitude that can be related to the degree of motional restriction. By employing specific NMR pulse sequences, one can collect spectra that differentiate the water protons with different residual dipolar couplings.[37]

Another way that water can be used as a more specific biological marker is to use MR relaxation times that are sensitive to dynamics on different orders of magnitude than the T_1 and T_2 relaxation mechanisms. An example of this is the use of $T_{1\rho}$ imaging of cartilage where the $T_{1\rho}$ of water is affected by motional frequencies appropriate for studying the interaction of water with large molecules such as collagen and proteoglycan (PG).[38,39]

MR techniques are an ideal way of measuring the bulk diffusion of liquids. In a biological context, this means measuring the diffusion of water in different tissues. Using magnetic field gradients, one can obtain diffusion coefficients (either average values or full diffusion tensors) for each pixel or voxel of an image. Diffusion-weighted imaging (DWI) is particularly useful for identifying areas of increased or irregular blood flow, while tensor-weighted imaging (TWI) has been used to map neuronal tracts. DWI has been applied to the detection of many different cancers and brain injuries and diseases.[40–43]

3.326.3.1.2. Fats

Fats are primarily formed from long hydrocarbons and are amenable to study by ^{1}H MR techniques. Fats also have proton chemical shifts that are well separated from water protons. This has led to the development of fat or water suppression techniques.[44] When applied to imaging, water suppressed techniques provide fat density images that can be used to complement water density images. The separation in chemical shifts has also led to the use of ^{1}H MRS, where ^{1}H NMR spectra are acquired for each pixel or voxel in an image to determine the relative amounts of water and fat on the basis of the NMR peak intensity. As examples, ^{1}H MRI has been used to probe fatty tissue, and fat deposits on arteries and in the liver.[45]

3.326.3.1.3. Direct detection of small molecule metabolites

The use of MR in the field of metabolomics is a rapidly expanding area of research. Studies are clearly showing the relationship between many metabolites in the human body and disease, and that NMR can provide a robust way of analyzing metabolite samples. *Ex vivo* MR studies of blood, stool, and urine are proving to be powerful diagnostic tools.[30,46–48]

The main drawback to using small molecules as markers for imaging is that their concentrations are often low. In the case of ^{1}H MRS, further complexity results because of the relatively small chemical shift range of protons. Complicated spectra of metabolites with many overlapping peaks are common in MR metabolomics and most researchers use high magnetic field strengths ($B_0 > 14.1$ T) to obtain the higher resolution. ^{1}H MRS can be used to monitor metabolites in specific regions but resolution and experimental time constraints can make this challenging. Continued developments in MRS imaging software and hardware bode well for eventual clinical integration of the methodology.[49,50] Chemical shift imaging (CSI) of specific molecules can sometimes be performed if a marker molecule is in high enough concentration and has unique proton chemical shift that can be used as a marker peak; this is analogous to fat imaging discussed in Section 3.326.3.1.2.

3.326.3.2. ^{31}P MR

The MR properties of ^{31}P make phosphorous MR relatively easy to perform. ^{31}P NMR spectroscopy is a well-developed field and much is known about the relationship between the ^{31}P NMR parameters and the local environment around the P nucleus. For diagnosis, this means that *ex vivo* studies can yield a great deal of information. ^{31}P is also used extensively by materials researchers to characterize the molecular structure of phosphorous containing biomaterials.

The primary challenge when employing ^{31}P NMR spectroscopy on a biological marker is that many of the phosphorous containing molecules in the body are chemically very similar; that is, they are phosphates (Table 2). Therefore, despite the fact that ^{31}P has a chemical shift range greater than 1800 ppm, most of the important biological markers have ^{31}P chemical shifts between −25 and 10 ppm. Another challenge when using phosphorous MR imaging is that many interesting phosphorous containing small molecules have low concentrations. The larger phosphorous containing molecules, phospholipids, polynucleotides, and hydroxyapatite (HAp) are more abundant, but generally yield broad lines due to their lack of motion. This makes them difficult to observe using standard imaging sequences; examples of using ^{31}P MR to study bones are discussed in Section 3.326.5.

Due to the general low occurrence of phosphorus (i.e., compared to protons), *in vivo* ^{31}P MR studies typically focus on targeted regions for MRS. Using MRS, it is possible to obtain spectra from specific voxels to reveal information regarding the presence and relative quantities of phosphorous-containing molecules. These molecules can be classified into energy-related molecules and molecules used in the synthesis of phospholipids. Studies have investigated the concentrations of these molecules in healthy tissues as well as different diseases.[52,53] For example, the phosphorous biological markers that are related to phospholipid synthesis provide measures of cell health in a tissue or organ. These can be useful markers for studying cancer, genetic diseases, neurological diseases, and infectious diseases.[52] Typically, the energy-related biological markers are used to determine if a muscle is functioning properly. Figure 5 shows an example of ^{31}P MRS spectra acquired of two human hearts, a healthy patient on the left and a patient who has had heart failure on the right. The ratios of ATP and phosphocreatine can be used to assess the loss of function due to the heart failure.[54] These same biological markers can be used to study brain activity.[55]

Table 2 Commonly used phosphorous containing biological markers

Biological molecule	*Primary function*	*Approximate ^{31}P chemical shift*[a] *(ppm)*
Phosphomonoesters	Phospholipid synthesis	3.5–4.2[b]
Phosphodiesters	Phospholipid synthesis	0.3–1.2[c]
Phosphoethanolamine	Phospholipid synthesis	3.7[b]
Phosphocholine	Phospholipid synthesis	3.2[b]
Glycerophosphoethanolamine	Phospholipid synthesis	0.4[b]
Glycerophosphocholine	Phospholipid synthesis	−0.1[b]
Nucleotide triphosphates	Energy storage and regulation	$\alpha = -9.7$ to -12.7[c] $\beta = 20.7$ to -21.3[c] $\gamma = -5.3$ to -6.0[c]
Phosphocreatine	Energy storage and regulation	−3.3
Inorganic phosphate		1.5

[a]Chemical shifts are referenced to 85% H_3PO_4. Many researchers reference their spectra to phosphocreatine. Others do not state their reference compound. Additionally, chemical shifts are pH and temperature dependent.
[b]Henderson *et al.*[51]
[c]Arias-Mendoza and Brown.[52]

3.326.3.3. ^{23}Na Magnetic Resonance

Sodium ion concentrations throughout the body are relatively high compared to other metal ion species and the favorable NMR properties make ^{23}Na imaging feasible.[56] In general, the sodium concentration is ten times higher in the extracellular matrix than in the cells. However, this can change depending on the health of the tissue.[57] While the measurement of ^{23}Na MR in physiological samples is decades old,[58] the application of ^{23}Na imaging in medicine using medical imagers is relatively recent. In the past 5 years, the number of studies employing ^{23}Na imaging for diagnosis of disease or for the study of molecular level changes has increased significantly. ^{23}Na MR can be harnessed in two ways, concentration imaging and imaging based on specific MR parameters.

3.326.3.3.1. Na^+ concentration for diagnosis

The concentration of Na^+ in different tissues can be measured simply on the basis of the intensity of the MR signal. Sodium ion concentration can be used as a probe of cell health and cellular energy metabolism in many tissues in the body. It is important to be aware that ^{23}Na concentration imaging can be complicated by the quadrupolar spin dynamics of ^{23}Na.[58,59] ^{23}Na is a spin $I = 3/2$ quadrupolar nucleus and therefore, there are three different SQ transitions ($\Delta m_I = \pm 3/2 \leftrightarrow \pm 1/2$ and $\Delta m_I = 1/2 \leftrightarrow -1/2$; see Figure 1(c)). When measuring concentrations using MR signal intensity, variations in relaxation between sodium ions that are in the fast exchange versus the slow exchange regimes must be accounted for. In the fast exchange regime, $\omega_0\tau_c \ll 1$ (ω_0 = the Larmor frequency in radians per second and τ_c is the characteristic correlation time), all the sodium signal intensity is contained in a sharp peak with a monoexponential relaxation rate. However, in the slow exchange regime, $\omega_0\tau_c \geq 1$, the relaxation becomes biexponential for sodium ions that experience a single chemical environment; one rate for the $\Delta m_I = \pm 3/2 \leftrightarrow \pm 1/2$ transitions, for example T_{2f}, and one for the $\Delta m_I = 1/2 \leftrightarrow -1/2$ transition, for example T_{2s}. If there are multiple chemical environments that are not exchange-averaged, then multiexponential relaxation will be observed. This can complicate the interpretation of Na^+ concentration images.[59,60]

Sodium concentrations have been shown to correlate to many aspects of disease. Sodium ions are an important part of maintaining the ionic gradient between the extra and intra cellular matrices. In healthy tissue, the concentration can vary by as much as an order of magnitude across the cell membrane. In diseased cells, the gradient often decreases and the ratio of sodium inside and outside of the cell changes. These changes can result in either an increase or a decrease in the total amount of sodium in the tissue which can be detected using ^{23}Na MRI. Recently ^{23}Na imaging studies have been performed on the heart,[61,62] kidneys,[63] muscle,[57] and cartilage[64–67] while the diseases that have been investigated include different cancers[68] and Alzheimer's.[60]

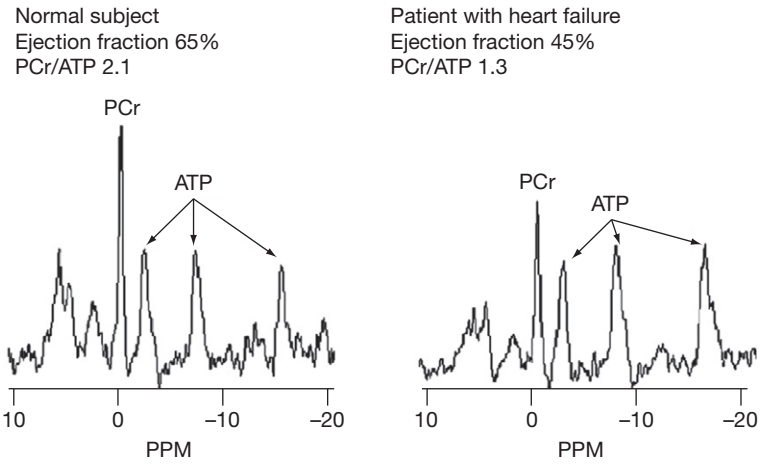

Figure 5 An example of two ^{31}P magnetic resonance spectra of the heart for a normal subject (left) and a subject that has experienced heart failure. It is clear that the phosphocreatin (PCr) levels have dropped in the patient with heart failure. Reproduced from Holloway, C.; Clarke, K. *Heart Lung Circ*. **2010**, *19*, 154–160.

3.326.3.3.2. ^{23}Na NMR parameters as biological markers for diagnosis

A second way that ^{23}Na MR can be used as a specific biological marker is to take advantage of the NMR properties that are sensitive to the local chemical environment that the sodium ions are found in. Using MR techniques that are sensitive to molecular structure can often provide valuable information about the biochemistry that is occurring during disease or as a result of treatment. As mentioned above, the relaxation can be multiexponential. If the different relaxation parameters can be extracted, either using a multiexponential fitting routine or by performing experiments that allow multisite fits of the experimental data, valuable information on the differences in intra- and extracellular volume or sodium coordination to large molecules can be obtained. For example, changes in the charge balance across the cell membrane or changes in the extra- and intracellular volumes can dramatically affect the average relaxation rates observed. This can complement the basic concentration data discussed in Section 3.326.3.3.1. Relaxation-based techniques have been used in many of the studies cited in Section 3.326.3.3.1.[69]

Another parameter that can probe the molecular level changes caused by disease or treatment is the quadrupolar coupling of the sodium. Because sodium is a spin $I = 3/2$ nucleus, there is a quadrupolar coupling between the nucleus and any external EFGs. While rapid motion of sodium in fluid environments often averages this parameter to a small, undetectable value, in some cases residual quadrupolar couplings can be detected. By measuring these couplings, analyzing them with respect to relaxation rates and concentrations, and understanding the biochemistry of the tissue, correlations between the parameters, biochemistry, and disease state can be made.[64,70,71]

3.326.3.4. ^{13}C Magnetic Resonance

The primary role of ^{13}C NMR in biological imaging and spectroscopy is as a probe of metabolites and larger biological molecules such as collagen. While NMR or MRS studies of these types of molecules are often more easily performed using ^{1}H NMR spectroscopy, ^{13}C NMR can sometimes be a more useful technique. One key advantage to ^{13}C NMR over ^{1}H NMR is the larger chemical shift range of ^{13}C. With a chemical shift range around 200 ppm, ^{13}C spectra are often much less crowded than ^{1}H spectra which can aid the identification of peaks specific to the biological molecule of choice. ^{13}C NMR spectroscopy is a well-developed field and *ex vivo* studies have become routine for solution and solid samples, as well as microimaging applications. The main problem with ^{13}C MR for imaging or MRS studies is the low natural abundance of ^{13}C, and therefore the low signal intensity.[72] Recent advances in using hyperpolarized ^{13}C MR of small molecules as contrast agents may greatly increase the utility of ^{13}C for imaging and diagnosis.[73,74]

3.326.3.5. Other Nuclei

Nearly every element on the periodic table has an NMR active isotope. While most are not relevant from a biochemical perspective, the potential to develop techniques to study other biologically important ions and molecules does exist and researchers continually work on applying the knowledge developed in chemical NMR to imaging and diagnostics.

^{2}H is an NMR active isotope of hydrogen that is quadrupolar with a nuclear spin $I = 1$. While the natural abundance of ^{2}H is low, it is relatively inexpensive to obtain isotopically labeled D_2O for *ex vivo* studies. The addition of the quadrupolar interaction and quadrupolar-induced relaxation mechanism can add an additional level of information about local structure to the data obtained from H_2O measurements.[37,75]

Inert gases such as ^{3}He and ^{129}Xe, although not biological species, can be used in imaging experiments. These gasses have been used to image the void space in lungs to detect lung diseases.[76] Xe, which can pass through the blood brain barrier, has also been used for brain imaging.[77] Experiments with ^{3}He and ^{129}Xe are often conducted using hyperpolarized gasses which yield MR signal enhancements on the order of 10 000 compared to standard experiments. Xe has also been proposed

as a biosensor by trapping Xe in cage molecules such as cryptophanes, and then functionalizing the cryptophan to target specific physiological receptors or binding sites.[78,79] Binding of these sensors affects the ^{129}Xe chemical shift and can be detected using MR techniques.[80]

The primary isotope of nitrogen is ^{14}N which is a spin $I = 1$ quadrupole nucleus that has a relatively large quadrupole moment. This makes using ^{14}N very difficult in biological systems. Typically ^{14}N is avoided by labeling molecules with ^{15}N, which is a spin $I = 1/2$ nucleus. While this is practical in synthetic chemistry and biology it is impractical from a diagnostic and imaging perspective. Similarly, ^{17}O is the potentially useful isotope of oxygen for MR experiments but has a very low natural abundance; ^{16}O is not NMR active. As these nuclei are often on organic molecules with hydrogen and carbon atoms, the ^{1}H and ^{13}C MR techniques provide similar information. However, the potential development of these isotopes for imaging and diagnostics may increase as signal enhancement techniques and higher magnetic fields are developed.

3.326.3.6. Summary

To date, MR of protons is the most developed and widely used technique for diagnosis and imaging. The ability to perform a wide range of experiments on conventional MR scanners means that the potential exists for researchers to test new imaging and diagnosis methods without purchasing or building new hardware. The future of ^{1}H imaging will involve using the NMR parameters of ^{1}H, such as chemical shifts and $T_{1\rho}$ relaxation rates, to develop more specific diagnostic tools. ^{23}Na has entered a phase where *in vivo* diagnosis and imaging are possible. While this requires modification of conventional MRI scanners, the ability to use a very simple species, Na^{+}, as a diagnostic marker is very attractive and could greatly compliment ^{1}H imaging of water. Finally the use of ^{31}P and ^{13}C has been limited to NMR and MRS studies. While these show a great deal of promise for understanding the chemistry and biochemistry of different molecules, wide scale applicability to diagnosis and imaging has not been well established. Despite this, the use of these nuclei, particularly ^{31}P, should be studied further as the information they can reveal about cell metabolism could be extremely powerful from a diagnostic perspective.

3.326.4. Case Study: Biological Markers for the Diagnosis of DDD

Degenerative disc disease (DDD) is a leading cause of back pain. Degeneration occurs when the molecular structure of the spinal disc changes with age leading to disc compression and greater structural rigidity. Severe degeneration can cause a loss of mobility and pain for patients.[81] MRI techniques have been used extensively to diagnose spinal disc injuries. The majority of these techniques have employed T_1 and T_2 relaxation methods to diagnose injuries such as herniated discs. These acute injuries can be readily diagnosed because they involve changes in the size or shape of the disc which can be imaged on the basis of the location and concentration of water. However, in cases where the damage does not significantly affect the dimensions of the disc, standard MRI techniques have been unreliable for assessing the stage of DDD.[82–85]

The degeneration caused by DDD is slow, beginning as early as the mid-teens in some patients, and in many cases may be asymptomatic in the early stages.[85] Patients often do not report discomfort until the disease is in its latter stages when treatment options are limited and often invasive. An ideal diagnostic technique for DDD should identify biochemical changes in the disc that are associated with early disc degeneration, thus providing patients with the greatest variety of surgical and nonsurgical treatment options. The same technique would also help monitor the spinal disc tissue after treatment. For example, one potential treatment method currently being explored is the injection of hydrogels into the disc tissue.[86] Currently, this methodology is used after discectomy to replace extracted tissue.[87–89] Recent efforts have focused on matching the chemistry of these hydrogels to the biochemistry of the disc tissue.[88,89] These types of studies and the resulting treatment methods require imaging and diagnostic techniques that can properly report on the biochemical changes within the disc upon treatment. The first step in developing reliable MRI-based diagnostic tools is to determine biological molecules and MR techniques that can be used as markers of DDD (See also **Chapter 5.524, Biomaterials for Replacement and Repair of the Meniscus and Annulus Fibrosus**; **Chapter 6.615, Intervertebral Disc**; **Chapter 6.612, Biomaterials for Intervertebral Disc Regeneration**; and **Chapter 6.613, Nucleus Replacement**).

3.326.4.1. Molecular Changes During DDD

The spinal disc is composed of two regions: the outer annulus fibrosus which provides the structural rigidity of the disc tissue, and the spongy inner nucleus pulposus, which exhibits the greatest changes due to DDD. Both regions primarily contain water, collagen, and PG which compose between 70 and 80% of the disc mass.[85] The primary molecular level change during DDD is the loss of PG. PG contains a protein core to which negatively charged sulfated glycosaminoglycan chains are attached. The negative charge of the PG is balanced by a high concentration of sodium ions in the disc tissue, up to 0.3 M.[85] The loss and degradation of the aggrecan are accompanied by a loss of sodium ions and, due to osmotic forces, the loss of water in the disc tissue.[81,90] PG, sodium ions, and water are all potential biological markers that can be used as probes of DDD (See also **Chapter 2.216, Collagen–GAG Materials**).

The challenges for conventional T_1- and T_2-based MRI experiments relate to the nature of water in disc tissue. The local environments of water vary depending on the biomolecules that the water interacts with during the MRI experiment.[75] As a result, different water molecules can experience different NMR relaxation rates, leading to multiexponential relaxation behavior which can be difficult to analyze. Significantly, the water molecules that would provide the highest degree of diagnostic sensitivity would be those that interact most with PG. These molecules will be a small fraction of the total water in the disc and will have the shortest relaxation times, making them difficult to observe. This is likely one of the reasons that relaxation-based MRI techniques have had difficulties detecting DDD, particularly in the early stages of the disease.

3.326.4.2. ^{2}H Double Quantum Filtered NMR Studies

As discussed in Section 3.326.2, there are many ways that the MR experiment can be employed to measure different interactions and relaxation rates. To provide a robust diagnostic technique, an experiment and molecule must be chosen that can provide information about the specific problem. In the case of DDD the changes in PG, sodium ion and water concentration at a molecular level. One option is to probe the way different molecules interact with each other as the disease progresses. This can be monitored by measuring the dipolar or quadrupolar interactions that are sensitive to the local geometry and not specifically dependent on changes in chemical bonding.

In solution, where water molecules tumble isotropically, the dipolar and quadrupolar interactions are averaged to their isotropic values of zero; these interactions do not affect the NMR frequencies but do cause relaxation. If the water molecules experience restricted motion due to interaction with large biological molecules, the interactions will not average to zero but to some residual value, the size of which will depend on the local structure and exchange dynamics of the water. Typically, these residual interactions are small and can be difficult to detect using standard SQ pulse sequences. In fact, the residual dipolar couplings for water in spinal disc tissues are so small that even experimental techniques designed to detect small couplings have difficulty measuring them.[75]

To harness the quadrupolar interaction to diagnose disc degeneration, the H_2O in the disc must be substituted for D_2O; using the residual ^{2}H quadrupolar interaction in water is an *ex vivo* diagnostic technique. To measure the small quadrupolar interaction, a double quantum filtered (DQF) NMR experiment can be performed that is sensitive to D_2O molecules that are experiencing restricted motion; water molecules that are moving freely are not measured in the DQF experiment.[91] Using this experimental approach, D_2O can be used as a biological marker to monitor the variations in hydration caused by molecular level changes in the collagen and PG. This application of ^{2}H DQF as a biological marker was demonstrated in joint cartilage by numerous groups,[37,92–95] and was recently applied to spinal disc tissue.[75]

The ^{2}H DQF line shapes observed in the spinal disc tissue experiments demonstrated a trend of increasing line width as degeneration occurred.[75] The line width in the DQF spectra is dominated by the magnitude of the residual quadrupolar coupling and therefore is a probe of the motional restriction of the water molecules. At high degeneration, the disc tissue is significantly dehydrated compared to a young healthy tissue and the water molecules interact more with the PG and collagen molecules leading to the larger residual quadrupolar couplings and larger ^{2}H DQF line widths.[75,81]

A simple analysis of the DQF build up curves revealed a correlation between the degree of degeneration and the time of maximum DQF signal intensity, denoted τ_{max}.[75] This parameter is affected by the magnitude of the residual quadrupolar interaction and the T_2 relaxation of the water molecules that experience restricted motion. The correlation was particularly sensitive at low levels of disc degeneration and therefore could be used to develop a diagnostic technique for early stages of disc degeneration.[75]

3.326.4.3. ^{1}H $T_{1\rho}$ Studies of Water to Assess DDD

Another way to use the power of MR for diagnosis and imaging of DDD is to take advantage of relaxation measurements other than T_1 and T_2. One such promising technique is to measure the ^{1}H spin-locked relaxation times, $T_{1\rho}$, of water in the spinal disc tissue.[38,39,96] As mentioned in Section 3.326.2.3.2, $T_{1\rho}$ is sensitive to low-frequency interactions and thus can be used to measure the exchange of water between different environments in the disc tissue.[39] This result is complementary to the data measured using ^{2}H DQF techniques.

Studies using $T_{1\rho}$ have been performed on a wide range of cartilage tissues and have shown a remarkable ability to measure changes in the biochemistry of such tissues.[38,39,96–99] The same properties that affected the ^{2}H DQF spectra also play a role in the $T_{1\rho}$ studies; water molecules that interact differently with the large biological molecules yield different $T_{1\rho}$ values. It has been shown that PG in particular plays a large role in determining the $T_{1\rho}$ values of water in cartilage.[100] Therefore, water $T_{1\rho}$ measurements act as an indirect biological marker for the amount and quality of the PG molecules and by extension the amount of degeneration. *In vivo* $T_{1\rho}$ weighted images of spine sections have been performed and have demonstrated that the measured $T_{1\rho}$ relaxation values correlated reasonably to the degenerative grade of the spinal discs.

3.326.4.4. Na^{+} Concentration Studies to Assess DDD

As mentioned in Section 3.326.4.1, another important species that changes in concentration as a result of DDD is sodium ions. The concentration of Na^{+} in the spinal disc tissue is high, ~0.3 M, in order to balance the negative charge of the PG and maintain high tissue hydration through osmotic forces. During degeneration of the disc, PGs degrade and the concentration decreases resulting in a loss of sodium ions. As outlined in Section 3.326.3.3, the ^{23}Na nucleus is well-suited for NMR and MRI experiments. ^{23}Na NMR of sodium ions holds potential for use in diagnosis and imaging of DDD.

There have been a number of researchers working on sodium MRI of various cartilage tissues. While most have been *ex vivo*, there have been *in vivo* studies of porcine osteoarthritis,[101] and human wrist cartilage.[101] Since the feasibility of ^{23}Na spinal disc imaging was demonstrated,[102] it has been shown that the concentration of Na^{+} as measured by ^{23}Na MRI is strongly correlated to the amount of PG determined by standard methods.[103] Using these correlations, researchers showed that low Na^{+} concentrations could be detected *in vivo* in a young symptomatic subject.

3.326.4.5. ^{23}Na Multiple Quantum Filtered NMR Studies

The same principles outlined for ^{2}H DQF NMR of D_2O in spinal disc tissues can be applied to sodium; the experiment must be modified to account for the fact that sodium is a spin $I = 3/2$ quadrupolar nucleus.[104–106] Using multiple quantum filtered (MQF) NMR experiments, signal can be selected from only those sodium atoms that do not undergo isotropic motion. It is expected that these sodium ions primarily interact with PG and therefore the ^{23}Na DQF signal can act as a specific probe of changes in the PG content and structure of the disc.

^{23}Na MQF experiments have been performed extensively on cartilage tissue.[104,106–109] Other examples of ^{23}Na MQF studies include the analysis of blood cells,[110] brain imaging,[111] and, more recently, spinal disc tissue affected by DDD.[71] The application of ^{23}Na MQF to spinal disc tissue combined two different multiple quantum techniques to measure all the water in the spinal disc samples and then fit the data to a multisite model using analytical expressions. The results clearly show that multiple sodium environments can be observed in the same sample and that the experimentally measured parameters, residual quadrupolar couplings and T_{2f} and T_{2s} relaxation times can be correlated to the hydration level of the specimen. Experiments on healthy disc tissue, which has a higher hydration, produced smaller residual quadrupolar coupling constants as well as longer T_2 relaxation times, whereas degraded samples showed larger couplings and shorter relaxation times. The differences were most clearly seen in the nucleus pulposus where disc degeneration has its greatest effect on molecular and mechanical properties.

The signal intensity of the ^{23}Na MQF experiments as a function of the experimentally controlled mixing time, τ, could be used as a probe of hydration. Signal intensities reach a maximum at shorter τ values for less hydrated tissue and at longer τ values for more hydrated tissues. This characteristic was harnessed to prove that ^{23}Na MQF could be used as an imaging technique for spinal disc tissue.[112] One-dimensional, spatially resolved ^{23}Na images were recorded as a function of τ and revealed contrast could be obtained using a triple quantum filter (TQF) which provides greater signal than a DQF (Figure 6). The τ-maps showed the ability to differentiate the annulus fibrosus and the nucleus pulposus on the basis of their different hydration levels using the TQ signal behavior.

3.326.4.6. Conclusions

The development of new MR-based diagnosis and imaging techniques for studying DDD is being advanced by the combined understanding of the biochemistry, fundamental principles of NMR, and the ability to design MR experiments that can probe the properties of different biological molecules. While this section has focused on diagnosing spinal disc degeneration, the same principles apply to monitoring the interaction of tissues with biomaterials and to monitoring the efficacy of biomaterial treatments.[89] The development of techniques for probing specific biological markers will aid biomaterial researchers as they continue to develop new materials for medical applications.

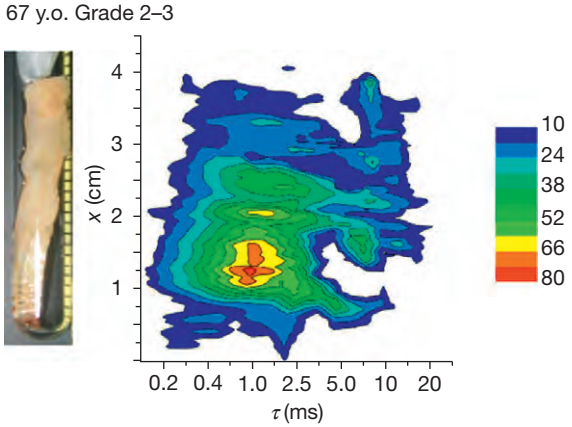

Figure 6 A ^{23}Na triple quantum filtered (TQF) τ-map. The signal intensity in the annulus fibrosus, the lower half of the sample, builds up faster and has a higher maximum signal intensity due to lower hydration. The nucleus pulposus, top half of the sample, shows the opposite trend, longer signal buildup times and lower maximum intensities. Reproduced from Ooms, K. J.; Cannella, M.; Vega, A. J.; Marcolongo, M.; Polenova, T. *J. Magn. Reson.* **2008**, *195*, 112–115.

3.326.5. Case Study: MR for Diagnosing Bone Disease and Treatment

Recent evidence demonstrates that orthopedic conditions, such as osteoporosis, osteoarthritis, and bone tumors are increasingly prevalent. As a result of bone weakening, these orthopedic conditions often result in increased susceptibility to bone fractures and breaks. Sources within Canada, the United States, and Europe cite dramatic increases in bone-related surgeries as well as the hospitalization costs associated with these orthopedic conditions and treatments.[113,114] As a result of the growing patient numbers affected by bone-related disease, there is a need for innovative treatments that strengthen existing bone in degenerated regions and promote the regrowth of bone tissue.

Throughout all stages of diagnosis and treatment of orthopedic conditions, MR techniques are proving to be an effective characterization tool. There are a variety of MR detectable biological markers within the bone that can be correlated with bone health. By understanding changes in bone due to disease, MR techniques can be implemented for diagnostic purposes. MR techniques have also been critical for characterizing synthetic biomaterials. Finally, biomaterial-based treatments can be monitored and studied using MR techniques and provide insights into the functionality and biocompatibility of the new materials. In this section, different biological molecules are identified for studying different parts of bone and MR techniques being used to study these molecules are discussed.

3.326.5.1. Bone Structure and Markers of Disease

Bone is a complex endoskeletal organ that is constantly remodeled and organized through a dynamic process of absorption and resorption which allows for flexibility and bone growth. A variety of bone cells play a role in this process: osteoblasts produce bone collagen and are involved in bone mineralization; osteoclasts are responsible for bone resorption into the circulatory system; and osteocytes, the primary bone cells, are involved in waste exchange, nutrient exchange, and other aspects of bone metabolism.[115] These cellular components all work to maintain the appropriate balance of molecules in the bone (See also Chapter 2.210, Bone as a Material).

The key to employing MR-based imaging and diagnostic techniques lies in determining what molecules serve as biological markers for the bone diseases. There are several components of bone which can be studied: inorganic mineralized portions of bone, organic collagenous tissue, marrow, water

within cortical bone pores, and several other components.[116] With a clear understanding of these components of bone and the changes that occur as a result of disease and treatment, novel MR techniques can provide unique information about the bone.

The solid phase of the bone is a hybrid material composed of an organic component, collagen I, and an inorganic component, calcium HAp that provides the structural rigidity and strength required for proper bone function. The densest region of the solid phase is in the outer portion of the bone which is referred to as the compact bone while the inner part of the bone, the trabecular bone, is much more porous. The inorganic portion of the bone matrix results from the biomineralization of calcium and phosphate by osteoblasts to form HAp nanocrystals. These nanocrystals form among the bone collagen creating a hybrid material that gives bone its strength. Aging is accompanied by a loss of bone mass as the fraction of compact bone decreases. Many bone diseases, such as osteoporosis, result in an increased loss of collagen and HAp, leading to unusually low bone density and the loss of mechanical stability. It has been shown that the chemical structure of both the inorganic and organic components of the solid bone experience changes due to disease; these changes are detectable and significant.

Within the pore spaces of the trabecular bone are the marrow and blood vessels. The marrow is found in two forms, yellow and red. Yellow marrow is primarily adipose and hence has a high lipid content. Red marrow contains primarily hemopoietic tissue, the body's chief site of blood cell production, and blood vessels. Red marrow therefore has a higher amount of water, with the water in the blood vessels being far more mobile than that in the cellular components. As the marrow fills the inner space of bone, and often fills growing porous space within the bone, irregular patterns of marrow development can be used to indicate changing porous space in the bone. As changing and increasing porous space is associated with bone loss, analysis of marrow for irregular changes or growth can be correlated to degenerative bone disease. This provides an indirect, yet vital probe that complements direct measurements of collagen and HAp.

3.326.5.2. Diagnosis of Bone Disease Using MR Techniques

As musculoskeletal conditions are one of the leading causes of disability, technologies for early diagnosis are essential in preventing additional health difficulties.[117] As a result of the relationship between orthopedic conditions and resulting susceptibility to further bone damage, it is essential that innovative techniques, such as MR, are employed to accurately characterize bone tissue and indicate potential for damage. A further prevalent bone condition is cancer, most commonly occurring within the bone as a result of metastasis from cancers in other areas of the body. Conventional bone cancer diagnosis, X-ray imaging, is limited in detecting early bone tumors, as it often cannot detect them until they are 1 cm in size.[118] As a rapid, noninvasive technique, requiring no pretreatment or ionizing radiation, MR is an appealing method for bone analysis. Four main biological markers have been used for studying bone degeneration: collagen and HAp in the solid phases of the bone, and fat and water in the porous regions of the bone.

3.326.5.2.1. Collagen imaging

While conventional methods of diagnosing bone degeneration analyze the density of mineralized bone using X-ray radiation, recent research indicates that a more effective method of diagnosing bone degeneration also involves analysis of collagen in bone.[116,119] MR techniques can potentially detect the presence and density of collagen; however, the use of MR to study solids is complicated by the lack of rapid molecular motion. In the solid, anisotropic NMR interactions can cause broadening of the signal leading to low signal intensities and challenges in image reconstruction. Molecules in the solid state also tend to have much shorter T_2 relaxation times than molecules in liquid phases making complex multipulse experiments challenging. While short T_2s can lead to technical challenges when acquiring spectra of collagen, they can also be used as a contrast mechanism. ^{1}H NMR signal from the bone with fast relaxation times can be separated from the more fluidic components which have longer T_2 relaxation times. Since collagen is the primary source of proton signal in the solid phase, an experiment that can differentiate ^{1}H signal based on T_2 can be used to select only protons from the collagen, leading to an image based on collagen density.[116,119,120] Using these types of techniques, researchers have shown that proton images from the collagen in the bone can be observed and be useful for quantifying bone density.[116]

3.326.5.2.2. Studies of HAp

The chemical formula of synthetic HAp is $Ca_{10}(OH)_2(PO_4)_6$. While natural HAp in bones is similar in structure to synthetic HAp it is not a pure structural phase, existing in a nonstoichiometric, disordered, nanocrystalline state.[121] For example, it has been shown that carbonates substitute for phosphate ions in natural bone so that between 5 and 8 wt% carbonate is achieved. While MR studies of calcium and oxygen are extremely difficult, ^{31}P MR provides an ideal probe for using the phosphate component as a biological marker to measure the density of HAp and its chemical structure.[122]

Solid-state ^{31}P NMR has been used for identifying different HAp phases and stoichiometric compositions. Because the ^{31}P isotropic chemical shifts are similar for the different structural phases of HAp,[123] typically yielding a single or overlapping ^{31}P NMR peak, the anisotropy in the chemical shift has been employed in many studies by analyzing the spinning sideband patterns observed under magic angle spinning conditions.[124,125] ^{1}H–^{31}P cross-polarization and two-dimensional correlation experiments have also been used to study the structure of different HAp phases[122] Another key study was performed to identify the presence of hydroxyl radicals in HAp; the presence of hydroxyl ions in HAp had been the focus of a decades-old controversy.[121] All these studies have been important steps to understanding the structure of HAp and illustrate how NMR spectroscopy is sensitive to the chemical structure of the different HAp phases. These differences could provide valuable tools for development of future diagnostic techniques that monitor the health of solid bone. From a materials perspective, it is vital to develop an understanding of the different structural forms of HAp present in bone so that new biomaterials can be designed with higher degrees of biocompatibility (See also **Chapter 1.112, Calcium Phosphate Coatings**).

Bone density is controlled by the balance between bone production and bone degradation, and therefore studies have been undertaken using ^{31}P NMR to understand mechanisms and structures involved in the formation and decomposition of HAp. The transformation of octacalciumphosphate, a HAp precursor, into synthetic HAp, has been studied using ^{31}P MR, revealing a possible mechanism of HAp formation.[126,127] Complementing these formation studies have been studies that look at the degradation of HAp; for example, ^{31}P NMR spectroscopic signatures have been identified for calcium deficient HAp[128] (See also **Chapter 3.323, Magnetic Resonance of Bone Microstructure and Chemistry**).

Bone mineral density (BMD) tests are performed using X-ray radiation. The feasibility of using ^{31}P MR to measure biological bone mineral densities in conjunction with collagen imaging has recently been demonstrated *ex vivo*.[120] Along with *ex vivo* NMR analysis, simple imaging studies using ^{31}P have been performed.[129,130] Despite these initial studies, very few other ^{31}P imagings have been done on bone. However, as imaging instrumentation is developed for multinuclear studies, the application of ^{31}P MRI may become a valuable tool for the diagnosis of bone conditions.

3.326.5.2.3. MRS of marrow fat

While direct measurements of bone density, either through BMD or potentially through MR measurements of collagen and HAp, are important for diagnosing bone degeneration diseases, recent studies have demonstrated that osteoporosis bone depletion is also connected to factors such as marrow quality, trabecular architecture, and trabecular connectivity. As bone degrades a greater percent of the total bone becomes porous. The new porous regions become filled mostly with yellow marrow; the ratio of yellow and red marrow changes as bone degradation occurs during normal aging or as a result of bone degeneration diseases. As mentioned above, the yellow marrow is full of lipids, while the red marrow contains a higher volume of water. The amount of fat in the bone marrow can be quantified using ^{1}H MRS, where spectra are acquired for specific regions of the bone and the intensity of the ^{1}H water peak is compared to the ^{1}H aliphatic (CH_2, CH_3) peak to determine relative water/lipid ratios.[131–134] It has been shown, for example, that people with osteoporosis have a higher amount of fat in their bones than normal patients based on the ^{1}H MRS.[134] Using MRS measurements of fatty marrow content, researchers have estimated that increases in marrow fat from 0% to 100% correspond to a BMD decrease of $0.16\,g\,cm^{-2}$ in men and $0.14\,g\,cm^{-2}$ in women.[135] This quantitative measure of bone changes due to osteoporosis has been viewed as a more accurate measure of bone density and degradation than BMD measurements.[134]

3.326.5.2.4. Diffusion imaging of water in marrow

As aging and bone degradation occur, the amount of yellow marrow increases and the amount of red marrow decreases. As the red marrow has a far greater degree of vascularization, changes in the amounts of red and yellow marrow will affect the overall vascularization of the marrow in the porous regions of the bone. Researchers speculate that degraded portions of bone, affected by osteoporosis, are filled with adipose tissue and thus have low degrees of vascularization. As a result, the degree of marrow vascularization in some regions of the bone may drop with age or disease.

This change in vascularization has a significant effect on the average mobility of water in the marrow, which can be characterized on the basis of the diffusion coefficient, see **Section 3.326.2.4**. Water in blood vessels will diffuse faster and over longer distances than water in the adipose tissue. MR techniques have been developed that provide image contrast related to the diffusion of water (i.e., DWI) or that aim to measure the magnitude and direction of diffusion (i.e., diffusion tensor imaging, DTI). These MR techniques have significant potential for improving and opening new possibilities in bone diagnostics.[136–140] In recent studies, diffusion techniques have been combined with MRS of water and fats to obtain a more complete picture of the structure of the marrow.[131–134] Investigating changes due to disease with complimentary techniques that rely on unique biomarkers (e.g., diffusion of water and MRS of fat) can provide corroborative information that may lead to more robust diagnosis and a better understanding of specific biochemical changes.

Changes in the porous regions of the bone marrow can also be a useful probe of bone cancer. Bone cancer most commonly occurs when cancer located elsewhere in the body metastasizes to the bone. Bone metastases, observed in higher rates with cancer of the thryroid, breast, lung, and prostate, may result in bone tumors as the cancerous tumor cells clump when traveling through bone via the Haversian canals.[141,142] Identifying metastatic disease can be difficult as bone X-ray computed tomography (CT) scans lack the specificity necessary for definite early stage diagnoses. MR imaging is a far more favorable approach than other techniques for diagnosis, as cancerous cells are detectable with MRI prior to visibility using CT scans.[143] Just as DWI can be used to study the biochemical changes in the marrow due to degenerative disease, it can also report the location of bone cancer tumors. Cancers are far more likely to occur in regions of the bone with high concentrations of red marrow and can lead to regions of even higher vascularization than normal. This elevated vascularization can be detected as an increase in the diffusion of water as measured by DWI.

Other important MR techniques used in the analysis of bone tumors are *in vivo* dynamic contrast-enhanced (DCE) MRI and *in vivo* ^{1}H MRS of metabolites.[144] DCE MRI can assess regions of blood vessel development within bone and as a result can demonstrate even slight changes in tissue vascularization related to tumor development. In the context of bone tumor diagnosis, MRS is also effective; specific metabolic markers such as choline, a constituent of the phospholipid cell membrane, can be identified using MRS and used to determine the changing biochemistry of tumor cells.[145] Using ^{1}H MRS, benign and malignant bone tumors can be distinguished with 89% accuracy, in a noninvasive way.[145] MR techniques have demonstrated a great deal about the nature of bone metastases diagnosis and research.[146]

3.326.5.3. Developing and Assessing Biomaterial Treatments

The strength of healthy bone tissue is essential to human wellness considering the enormous forces that act on bones

even in daily activities. As a result, there is great need for biomaterials that are capable of providing powerful reinforcement for weakened, diseased, or fractured bone tissue. Understanding the structure and chemical characteristics of biomaterials is essential as these properties determine the interaction of a material with bone tissue. In many of the same ways that MR is used to study healthy and diseased bone tissue, it can be used to assess the efficacy of different material implants and their incorporation into the bone (See also **Chapter 6.610, Trends in Materials for Spine Surgery** and **Chapter 1.120, Synthetic Bone Grafts: Clinical Use**).

3.326.5.3.1. Bioinert and resorbable bone materials

In cases of severe bone injury or degradation, synthetic bone implants may be necessary to replace the damaged region. Bioinert materials, those that minimally interact with surrounding tissue, are effective in providing mechanical support and bone retention. These materials are typically magnesium alloys, titanium alloys, or stainless steel. Commonly used to provide weight-bearing support in regions such as the spine; these materials act as replacements for damaged bones while allowing surrounding bone growth to continue.[147] Other forms of bioinert materials include metal bone screws, used to secure damaged joints, such as knee or ankle joints.[148] These forms of bone implants are effective in providing musculoskeletal support and allowing bone fusion.

In general, these implants cannot be imaged directly using MR because of their metallic components. Differences in magnetic susceptibility between materials used in implants and surrounding biological tissue result in dramatic MR frequency shifts and rapid MR signal relaxation (i.e., on the order of microseconds). Conductive materials also effectively attenuate RFs, which prevents both perturbation of the magnetization vector with an applied B_1 field and detection of the MR signal. In addition, the pulsed RF and magnetic field gradients can induce high voltages and eddy currents in conductive components. These factors can either prevent acquisition of MR images, or at the least, impart significant artifacts.[147]

Because MR is such a valuable technique, alternatives to metallic implants have been sought. Researchers have demonstrated the effectiveness of carbon-fiber-reinforced polymers that do not cause image artifacts in the surrounding tissue. Structural support or bone fixation can also be provided by biosorbable biomaterials.[148] These resorbable materials are commonly made up of compounds such as polyglycolic acid (PGA), poly-L-lactic acid (PLLA), poly-D-lactic acid (PDLLA), and polyparadioxanone (PDS) and can be imaged using MR without the interference seen with metal implants. Following the implantation of these biomaterials, *in vivo* MRI can be used to demonstrate the level of biocompatibility between the implant and surrounding tissues.[148] Most studies have used ^{1}H NMR of water; for example, the absorption of bioabsorbable screws has been monitored after implantation using T_1 and T_2 weighted images of water surrounding the implant.[148,149] In addition to monitoring the dimensions of the screws, the surrounding tissue could be monitored for damage caused when implanting the screws. Osteolysis could be detected using imaging techniques that could not be detected using CT methods.[148]

3.326.5.3.2. Bioactive bone implants

The development of bone substitutes with osteoconductive and biologically active properties has played a large role in the effectiveness of bone biomaterials. The central feature of these bioactive materials is their biomimetic properties that ideally result in their full integration with natural bone tissue.[150] Additionally, these biomaterials are intended to promote healthy bone metabolism, bone regrowth, and the development of osteoblast-induced bone mineralization.[151] These materials are often composed of nanophase particles.[152] Several forms of bioactive materials that are used in orthopedic treatments include polymers, glasses, synthetic HAp crystals, and bioactive bone cements.[150,153] Calcium phosphate ceramics, in particular, have been widely used since the 1980s due to their similarity to natural compact bone HAp crystals.[151]

The study of the effects of bioactive materials on osteoformation involves several types of MR analysis. *In vivo* DCE MRI has been effective in clinical studies in demonstrating the development of blood vessels and bone growth following biomaterial use.[154] In research settings, ^{31}P solid-state NMR of biomaterial implants is routinely used to determine the rate of HAp formation and the structure of the new HAp along the tissue implant interface.[155] The feasibility of ^{31}P MRI to differentiate between natural and synthetic HAp has also been demonstrated.[130]

Proton NMR is similarly vital in demonstrating the interaction of surrounding fluids with the gradually forming HAp structures on the material. An additional method of analyzing the effectiveness of bioactive bone substitutes is ^{13}C solid-state NMR, which is useful in demonstrating the production of extracellular matrix in biomaterials.[156] With the ability to demonstrate molecular level characteristics of the resulting HAp crystal and surrounding tissue, MR is invaluable in the development of safe and effectual bioactive biomaterials.

3.326.5.3.3. Hybrid bone biomaterials

In cases of orthopedic damage where bone tissue integration along with strong mechanical support is required, hybrid bone materials are most effective. These synthetic bone analogs involve both structural support, typically using a metal implant coated with bioactive material which promotes attachment, and interaction of the implant with surrounding tissue.[150] MR studies are important for the development and medical application of these novel materials.

HAp coatings on metal implants, such as titanium alloys, chromium cobalt alloys, and stainless steel, significantly improve their biocompability and enhance ingrowth of regenerated bone. Specifically, nanophase HAp coatings are effective as they promote the precise growth of mineralized bone regions with strength similar to that of natural bone.[151] In a recent example, HAp nanoparticles derived from a water-based sol–gel process using triethyl phosphate and a variety of calcium precursors were used as bioactive coatings on 316L stainless steel implants.[151] ^{31}P NMR analysis was essential in characterizing the molecular structure of the HAp as it formed during the sol–gel synthesis.[151]

Following successful implantation of hybrid biomaterials, it is essential that materials are monitored to determine their interaction with natural tissue and their promotion of bone regrowth. The integration of resorbable porous β-tricalcium

phosphate (β-TCP) cylindrical scaffolds containing osteogenically differentiated mesencymal stem cells 3 months following implantation in rabbits has been analyzed using ^{31}P and ^{13}C NMR spectroscopy. Results demonstrated that new bone was formed and that NMR could quantitatively detect both the inorganic calcium HAp and the collagen of the new bone on the implants.[156]

3.326.5.4. Conclusions

This section has described the current need for innovative orthopedic treatments and the necessity of clear diagnostic methods. MR is a technique with a wide range of applications in orthopedics, as it is capable of characterizing healthy bone tissue, diagnosing areas of bone degeneration and weakness, demonstrating structural characteristics of bone biomaterials, and testing the biocompatibility of implanted materials. As MRI hardware improves and multinuclear capabilities become available on medical scanners, the application of novel biological marker imaging techniques will greatly aid doctors and researchers in the diagnosis and treatment of bone diseases. These developments will be greatly facilitated by stronger interdisciplinary research between medical researchers, materials scientists, and MR specialists.

3.326.6. Summary and Future of Imaging and Diagnosis of Biological Markers

This chapter has focused on providing a broad overview of the ideas and considerations behind the use of MR techniques for imaging and diagnosis of biological markers. The two case studies highlighted are meant to provide a framework that demonstrates that by using multiple biological molecules, nuclei, and MR experiments, information about biological markers can be gained. MR techniques are some of the most powerful and noninvasive diagnostic and characterization techniques modern science has at its disposal. The past decade has seen an incredible advance in the implementation of MR for imaging and diagnosis. In many ways, the current clinical applications are akin to the chemists' use of proton NMR; while extremely powerful, it represents only a small part of the potential of MR. While newer techniques such as diffusion-weighted imaging, MRS of ^{1}H, ^{13}C, and ^{31}P containing molecules, and ^{23}Na imaging are proving useful in research, they are only slowly penetrating the diagnostic community. The need for new diagnostic techniques will only increase as biomaterials researchers seek to tailor materials for specific functions to treat disease and injury. To meet these future needs research must be done with an understanding of the biochemistry of disease, the chemistry of novel biomaterials and their interaction with the body, and the fundamental NMR theory that makes the development of novel MR techniques feasible. If approached as a multidisciplinary project between medical, materials, and MR specialists, the future of MR for diagnosis and imaging is extremely bright.

References

1. Tesch, G.; Amur, S.; Schousboe, J. T.; Siegel, J. N.; Lesko, L. J.; Bai, J. P. F. *Am. Assoc. Pharm. Sci. J.* **2010**, *12*, 243–253.
2. Ernst, R. R. *Angew. Chem. Int. Ed. Engl.* **1992**, *31*, 805–823.
3. Abragam, A. *Principles of Nuclear Magnetism*; Oxford University Press: Oxford, 1962.
4. Levitt, M. *Spin Dynamics: Basics of Nuclear Magnetic Resonance*, 2nd ed.; John Wiley & Sons: Chichester, 2008.
5. Mason, J. *Multinuclear NMR*; Plenum Press: New York, 1987.
6. Slichter, C. *Principles of Magnetic Resonance*; Springer-Verlag: Berlin, 1990.
7. Zeeman, P. *Nature* **1897**, *55*, 347–351.
8. Harris, R. K.; Becker, E. D.; De Menezes, S. M. C.; Goodfellow, R.; Granger, P. *Pure Appl. Chem.* **2001**, *73*, 1795–1818.
9. Bloch, F. *Phys. Rev.* **1946**, *70*, 460–474.
10. Bloembergen, N.; Purcell, E. M.; Pound, R. V. *Phys. Rev.* **1948**, *73*, 679–712.
11. Carr, H.; Purcell, E. *Phys. Rev.* **1954**, *94*, 630–638.
12. Meiboom, S.; Gill, D. *Rev. Sci. Instrum.* **1958**, *29*, 688–691.
13. Ailion, D.; Slichter, C. P. *Phys. Rev. Lett.* **1964**, *12*, 168–171.
14. Solomon, I. *Phys. Rev. Lett.* **1959**, *2*, 301–302.
15. Garwood, M.; DelaBarre, L. *J. Magn. Reson.* **2001**, *153*, 155–177.
16. Sorce, D. J.; Michaeli, S.; Garwood, M. *Curr. Anal. Chem.* **2007**, *3*, 239–251.
17. Michaeli, S.; Sorce, D. J.; Garwood, M. *Curr. Anal. Chem.* **2008**, *4*, 8–25.
18. Sepponen, R. E.; Pohjonen, J. A.; Sipponen, J. T.; Tanttu, J. I. *J. Comput. Assist. Tomogr.* **1985**, *9*, 1007–1011.
19. Akella, S. V. S.; Regatte, R. R.; Wheaton, A. J.; Borthakur, A.; Reddy, R. *Magn. Reson. Med.* **2004**, *52*, 1103–1109.
20. Michaeli, S.; Sorce, D. J.; Springer, C. S.; Ugurbil, K.; Garwood, M. *J. Magn. Reson.* **2006**, *181*, 135–147.
21. Michaeli, S.; Grohn, H.; Grohn, O.; *et al. Magn. Reson. Med.* **2005**, *53*, 823–829.
22. Stejskal, E. O.; Tanner, J. E. *J. Chem. Phys.* **1965**, *42*, 288–292.
23. Callaghan, P. T. *Principles of Nuclear Magnetic Resonance Microscopy*; Clarendon Press: Oxford, 1991.
24. Kimmich, R. *NMR: Tomography, Diffusometry, Relaxometry*; Springer: Berlin, 1997.
25. Mansfield, P.; Grannell, P. K. *J. Phy. C Solid State Phys.* **1973**, *6*, L422–L426.
26. Mansfield, P. *Contemp. Phys.* **1976**, *17*, 553–576.
27. Mansfield, P.; Grannell, P. K. *Phys. Rev. B* **1975**, *12*, 3618–3634.
28. Bezabeh, T.; Somorjai, R.; Dolenko, B.; *et al. NMR Biomed.* **2009**, *22*, 593–600.
29. Bezabeh, T.; Ijare, O. B.; Albiin, N.; Arnelo, U.; Lindberg, B.; Smith, I. C. P. *Magn. Reson. Mater. Phys. Biol. Med.* **2009**, *22*, 267–275.
30. Bezabeh, T.; Somorjai, R. L.; Smith, I. C. P. *Magn. Reson. Chem.* **2009**, *47*, S54–S61.
31. Smith, I. C. P.; Baert, R. *IUBMB Life* **2003**, *55*, 273–277.
32. Smith, I. C. P.; Blandford, D. E. *Biochem. Cell Biol. Biochim. Biol. Cell.* **1998**, *76*, 472–476.
33. Smith, I. C. P.; Stewart, L. C. *Prog. Nucl. Magn. Reson. Spectrosc.* **2002**, *40*, 1–34.
34. Brown, M.; Semelka, R. C. *MRI: Basic Principles and Applications*, 4th ed.; Wiley-Blackwell/John Wiley & Sons: Hoboken, NJ, 2010.
35. Hashemi, R. H.; Bradley, W. G., Jr.; Lisanti, C. J. *MRI: The Basics*, 3rd ed.; Lippincott Williams & Wilkins: Philadelphia, 2010.
36. Liney, G. *MRI from A to Z: A Definitive Guide for Medical Professionals*; Cambridge University Press: New York, 2005.
37. Navon, G.; Shinar, H.; Eliav, U.; Seo, Y. *NMR Biomed.* **2001**, *14*, 112–132.
38. Gold, G. E.; Chen, C. A.; Koo, S.; Hargreaves, B. A.; Bangerter, N. K. *Am. J. Roentgenol.* **2009**, *193*, 628–638.
39. Johannessen, W.; Auerbach, J. D.; Wheaton, A. J.; *et al. Spine* **2006**, *31*, 1253–1257.
40. Brooks, D. J. *J. Nucl. Med.* **2010**, *51*, 596–609.
41. Duckworth, J. L.; Stevens, R. D. *Curr. Opin. Crit. Care* **2010**, *16*, 92–97.
42. Razek, A. A. K. A.; Gaballa, G.; Denewer, A.; Tawakol, I. *Acad. Radiol.* **2010**, *17*, 382–386.
43. Sugita, R.; Ito, K.; Fujita, N.; Takahashi, S. *World J. Gastroenterol.* **2010**, *16*, 832–836.
44. Bley, T. A.; Wieben, O.; Francois, C. J.; Brittain, J. H.; Reeder, S. B. *J. Magn. Reson. Imaging* **2010**, *31*, 4–18.
45. Taouli, B.; Ehman, R. L.; Reeder, S. B. *Am. J. Roentgenol.* **2009**, *193*, 14–27.
46. Madsen, R.; Lundstedt, T.; Trygg, J. *Anal. Chim. Acta* **2010**, *659*, 23–33.
47. Nordstrom, A.; Lewensohn, R. *J. Neuroimmune Pharmacol.* **2010**, *5*, 4–17.
48. Wishart, D. S. *Trends Anal. Chem.* **2008**, *27*, 228–237.
49. Suvichakorn, A.; Ratiney, H.; Bucur, A.; Cavassila, S.; Antoine, J. P. *Meas. Sci. Technol.* **2009**, *20*, 104029.
50. Suvichakorn, A.; Ratiney, H.; Bucur, A.; Cavassila, S.; Antoine, J. In *2008 30th Annual International Conference of the IEEE Engineering in Medicine and Biology Society*, 2008; Vols 1–8, pp 2681–2684.

51. Henderson, T. O.; Costello, A. J.; Omachi, A. *Proc. Natl. Acad. Sci. USA* **1974**, *71*, 2487–2490.
52. Arias-Mendoza, F.; Brown, T. R. *Dis. Markers* **2003**, *19*, 49–68.
53. Chance, B.; Im, J.; Nioka, S.; Kushmerick, M. *NMR Biomed.* **2006**, *19*, 904–926.
54. Holloway, C.; Clarke, K. *Heart Lung Circ.* **2010**, *19*, 154–160.
55. Trksak, G. H.; Jensen, J. E.; Plante, D. T.; *et al. Drug Alcohol Depend.* **2010**, *106*, 79–91.
56. Steidle, G.; Graf, H.; Schick, F. *Magn. Reson. Imaging* **2004**, *22*, 171–180.
57. Constantinides, C. D.; Gillen, J. S.; Boada, F. E.; Pomper, M. G.; Bottomley, P. A. *Radiology* **2000**, *216*, 559–568.
58. Cope, F. W. *Proc. Natl. Acad. Sci. USA* **1965**, *54*, 225–227.
59. Rooney, W. D.; Springer, C. S. *NMR Biomed.* **1991**, *4*, 209–226.
60. Mellon, E. A.; Pilkinton, D. T.; Clark, C. M.; *et al. Am. J. Neuroradiol.* **2009**, *30*, 978–984.
61. Lamb, H. J.; van der Meer, R. W.; de Roos, A.; Bax, J. J. *Eur. J. Nucl. Med. Mol. Imaging* **2007**, *34*, S99–S104.
62. Ouwerkerk, R.; Bottomley, P. A.; Solaiyappan, M.; *et al. Radiology* **2008**, *248*, 88–96.
63. Rosen, Y.; Lenkinski, R. E. *Acad. Radiol.* **2009**, *16*, 886–889.
64. Borthakur, A.; Shapiro, E. M.; Akella, S. V. S.; Gougoutas, A.; Kneeland, J. B.; Reddy, R. *Radiology* **2002**, *224*, 598–602.
65. Rong, P.; Regatte, R. R.; Jerschow, A. *J. Magn. Reson.* **2008**, *193*, 207–209.
66. Shinar, H.; Navon, G. *NMR Biomed.* **2006**, *19*, 877–893.
67. Wang, L.; Wu, Y.; Chang, G.; *et al. J. Magn. Reson. Imaging* **2009**, *30*, 606–614.
68. Ouwerkerk, R.; Jacobs, M. A.; Macura, K. J.; *et al. Breast Cancer Res. Treat.* **2007**, *106*, 151–160.
69. Jacobs, M. A.; Ouwerkerk, R.; Kamel, I.; Bottomley, P. A.; Bluemke, D. A.; Kim, H. S. *J. Magn. Reson. Imaging* **2009**, *29*, 649–656.
70. Insko, E. K.; Kaufman, J. H.; Leigh, J. S.; Reddy, R. *Magn. Reson. Med.* **1999**, *41*, 30–34.
71. Ooms, K. J.; Cannella, M.; Vega, A. J.; Marcolongo, M.; Polenova, T. *Magn. Reson. Med.* **2008**, *60*, 246–252.
72. Terreno, E.; Castelli, D. D.; Viale, A.; Aime, S. *Chem. Rev.* **2010**, *110*, 3019–3042.
73. Golman, K.; in't Zandt, R.; Lerche, M.; *et al. Cancer Res.* **2006**, *66*, 10855–10860.
74. Mansson, S.; Johansson, E.; Magnusson, P.; *et al. Eur. Radiol.* **2006**, *16*, 57–67.
75. Perea, W.; Cannella, M.; Yang, J.; Vega, A. J.; Polenova, T.; Marcolongo, M. *Magn. Reson. Med.* **2007**, *57*, 990–999.
76. Fain, S. B.; Korosec, F. R.; Holmes, J. H.; O'Halloran, R.; Sorkness, R. L.; Grist, T. M. *J. Magn. Reson. Imaging* **2007**, *25*, 910–923.
77. Ziegler, A.; Hyacinthe, J. N.; Choquet, P.; *et al. Imaging Biol. Res. A* **2004**, *385*, 149–165.
78. Spence, M. M.; Ruiz, E. J.; Rubin, S. M.; *et al. J. Am. Chem. Soc.* **2004**, *126*, 15287–15294.
79. Taratula, O.; Dmochowski, I. J. *Curr. Opin. Chem. Biol.* **2010**, *14*, 97–104.
80. Berthault, P.; Huber, G.; Desvaux, H. *Prog. Nucl. Magn. Reson. Spectrosc.* **2009**, *55*, 35–60.
81. Urban, J. P. G.; Roberts, S. *Arthritis Res. Ther.* **2003**, *5*, 120–130.
82. Carragee, E. J. *Spine J.* **2009**, *9*, 778–779.
83. Carrino, J. A.; Lurie, J. D.; Tosteson, A. N. A.; *et al. Radiology* **2009**, *250*, 161–170.
84. Lurie, J. D.; Tosteson, A. N. A.; Tosteson, T. D.; *et al. Spine* **2008**, *33*, 991–998.
85. Urban, J. P. G.; Winlove, C. P. *J. Magn. Reson. Imaging* **2007**, *25*, 419–432.
86. Yang, X.; Li, X. *Eur. Spine J.* **2009**, *18*, 1564–1572.
87. Allen, M. J.; Schoonmaker, J. E.; Bauer, T. W.; Williams, P. F.; Higham, P. A.; Yuan, H. A. *Spine* **2004**, *29*, 515–523.
88. Berlemann, U.; Schwarzenbach, O. *Eur. Spine J.* **2009**, *18*, 1706–1712.
89. Nakashima, S.; Matsuyama, Y.; Takahashi, K.; *et al. Biomed. Mater. Eng.* **2009**, *19*, 421–429.
90. Urban, J. P. G.; Mcmullin, J. F. *Spine* **1988**, *13*, 179–187.
91. Sharf, Y.; Eliav, U.; Shinar, H.; Navon, G. *J. Magn. Reson. B* **1995**, *107*, 60–67.
92. Keinan-Adamsky, K.; Shinar, H.; Navon, G. *Magn. Reson. Mater. Phys. Biol. Med.* **2005**, *18*, 231–237.
93. Keinan-Adamsky, K.; Shinar, H.; Navon, G. *J. Orthop. Res.* **2005**, *23*, 109–117.
94. Shinar, H.; Seo, Y.; Ikoma, K.; Kusaka, Y.; Eliav, U.; Navon, G. *Magn. Reson. Med.* **2002**, *48*, 322–330.
95. Tsoref, L.; Eliav, U.; Seo, Y.; Shinar, H.; Navon, G. *J. Magn. Reson. Imaging* **2000**, *11*, 336–341.
96. Auerbach, J. D.; Johannessen, W.; Borthakur, A.; *et al. Eur. Spine J.* **2006**, *15*, S338–S344.
97. Wheaton, A. J.; Borthakur, A.; Charagundla, S. R.; Reddy, R. *Magn. Reson. Med.* **2004**, *51*, 362–369.
98. Wheaton, A. J.; Borthakur, A.; Kneeland, J. B.; Regatte, R. R.; Akella, S. V. S.; Reddy, R. *Magn. Reson. Med.* **2004**, *52*, 1453–1458.
99. Wheaton, A. J.; Casey, F. L.; Gougoutas, A. J.; *et al. J. Magn. Reson. Imaging* **2004**, *20*, 519–525.
100. Duvvuri, U.; Goldberg, A. D.; Kranz, J. K.; *et al. Proc. Natl. Acad. Sci. USA* **2001**, *98*, 12479–12484.
101. Wheaton, A. J.; Borthakur, A.; Dodge, G. R.; Kneeland, B.; Schumacher, H. R.; Reddy, R. *Acad. Radiol.* **2004**, *11*, 21–28.
102. Insko, E. K.; Clayton, D. B.; Elliott, M. A. *Acad. Radiol.* **2002**, *9*, 800–804.
103. Wang, C.; McArdle, E.; Fenty, M.; *et al. Spine* **2010**, *35*, 505–510.
104. Eliav, U.; Navon, G. *J. Magn. Reson. B* **1994**, *103*, 19–29.
105. Eliav, U.; Navon, G. *J. Chem. Phys.* **1991**, *95*, 7114–7118.
106. Eliav, U.; Shinar, H.; Navon, G. *J. Magn. Reson.* **1992**, *98*, 223–229.
107. Boada, F. E.; Tanase, C.; Davis, D.; *et al.* In *Proceedings of the 26th Annual International Conference of the IEEE Engineering in Medicine and Biology Society*, 2004; Vols 1–7; pp 5238–5241.
108. LaVerde, G.; Nemoto, E.; Jungreis, C. A.; Tanase, C.; Boada, F. E. *Magn. Reson. Med.* **2007**, *57*, 201–205.
109. Navon, G.; Eliav, U.; Demco, D. E.; Blumich, B. *J. Magn. Reson. Imaging* **2007**, *25*, 362–380.
110. Shinar, H.; Knubovets, T.; Eliav, U.; Navon, G. *Biophys. J.* **1993**, *64*, 1273–1279.
111. Hancu, I.; Boada, F. E.; Shen, G. X. *Magn. Reson. Med.* **1999**, *42*, 1146–1154.
112. Ooms, K. J.; Cannella, M.; Vega, A. J.; Marcolongo, M.; Polenova, T. *J. Magn. Reson.* **2008**, *195*, 112–115.
113. Dennison, E.; Cole, Z.; Cooper, C. *Curr. Opin. Rheumatol.* **2005**, *17*, 456–461.
114. Papadimitropoulos, E. A.; Coyte, P. C.; Josse, R. G.; Greenwood, C. E. *Can. Med. Assoc. J.* **1997**, *157*, 1357–1363.
115. Netter, F. H. The CIBA collection of Medical Illustrations CIBA-GEIGY Corporation: West Caldwell, NJ, 1987.
116. Wu, Y.; Hrovat, M. I.; Ackerman, J. L.; *et al. J. Magn. Reson. Imaging* **2010**, *31*, 954–963.
117. Melton, L. J.; Thamer, M.; Ray, N. F.; *et al. J. Bone Miner. Res.* **1997**, *12*, 16–23.
118. Eckstein, F.; Cicuttini, F.; Raynauld, J.-P.; Waterton, J. C.; Peterfy, C. *Osteoarthritis Cartilage* **2006**, *14*, A46–A75.
119. Wu, Y.; Ackerman, J. L.; Chesler, D. A.; Graham, L.; Wang, Y.; Glimcher, M. J. *Magn. Reson. Med.* **2003**, *50*, 59–68.
120. Cao, H.; Nazarian, A.; Ackerman, J. L.; *et al. Bone* **2010**, *46*, 1582–1590.
121. Cho, G. Y.; Wu, Y. T.; Ackerman, J. L. *Science* **2003**, *300*, 1123–1127.
122. Kaflak-Hachulska, A.; Samoson, A.; Kolodziejski, W. *Calcif. Tissue Int.* **2003**, *73*, 476–486.
123. Rothwell, W. P.; Waugh, J. S.; Yesinowski, J. P. *J. Am. Chem. Soc.* **1980**, *102*, 2637–2643.
124. Roberts, J. E.; Bonar, L. C.; Griffin, R. G.; Glimcher, M. J. *Calcif. Tissue Int.* **1992**, *50*, 42–48.
125. Roberts, J. E.; Heughebaert, M.; Heughebaert, J. C.; Bonar, L. C.; Glimcher, M. J.; Griffin, R. G. *Calcif. Tissue Int.* **1991**, *49*, 378–382.
126. Tsai, T. W. T.; Chou, F.; Tseng, Y.; Chan, J. C. C. *Phys. Chem. Chem. Phys.* **2010**, *12*, 6692–6697.
127. Tseng, Y. H.; Mou, C. Y.; Chan, J. C. C. *J. Am. Chem. Soc.* **2006**, *128*, 6909–6918.
128. Rodriguez-Lorenzo, L. M. *J. Mater. Sci. Mater. Med.* **2005**, *16*, 393–398.
129. Wu, Y.; Ackerman, J. L.; Chesler, D. A.; *et al. Calcif. Tissue Int.* **1998**, *62*, 512–518.
130. Wu, Y. T.; Chesler, D. A.; Glimcher, M. J.; *et al. Proc. Natl. Acad. Sci. USA* **1999**, *96*, 1574–1578.
131. Fanucci, E.; Manenti, G.; Masala, S.; *et al. Radiol. Med.* **2007**, *112*, 208–223.
132. Griffith, J. F.; Yeung, D. K. W.; Antonio, G. E.; *et al. Radiology* **2005**, *236*, 945–951.
133. Griffith, J. F.; Yeung, D. K. W.; Antonio, G. E.; *et al. Radiology* **2006**, *241*, 831–838.
134. Tang, G. Y.; Lv, Z. W.; Tang, R. B.; *et al. Clin. Radiol.* **2010**, *65*, 377–381.
135. Blake, G. M.; Griffith, J. F.; Yeung, D. K. W.; Leung, P. C.; Fogelman, I. *Bone* **2009**, *44*, 495–501.
136. Hatipoglu, H. G.; Selvi, A.; Ciliz, D.; Yuksel, E. *Am. J. Neuroradiol.* **2007**, *28*, 1934–1937.
137. Rossi, C.; Capuani, S.; Fasano, F.; Alesiani, M.; Maraviglia, B. *Magn. Reson. Imaging* **2005**, *23*, 245–248.
138. Sigmund, E. E.; Cho, H.; Chen, P.; *et al. Magn. Reson. Med.* **2008**, *59*, 28–39.
139. Sigmund, E. E.; Cho, H.; Song, Y. Q. *NMR Biomed.* **2009**, *22*, 436–448.
140. Ueda, Y.; Miyati, T.; Ohno, N.; *et al. J. Magn. Reson. Imaging* **2010**, *31*, 632–635.
141. Rodan, G. A. *Cancer* **2003**, *97*, 726–732.
142. Taoka, T.; Mayr, N. A.; Lee, H. J.; *et al. Am. J. Roentgenol.* **2001**, *176*, 1525–1530.

143. Downey, S. E.; Wilson, M.; Boggis, C.; Baildam, A. D.; Howell, A.; Bundred, N. J. *Br. J. Surg.* **1997**, *84*, 1093–1094.
144. Kwee, T. C.; Takahara, T.; Klomp, D. W. J.; Luijten, P. R. *J. Intern. Med.* **2010**, *268*, 120–132.
145. Wang, C. K.; Li, C. W.; Hsieh, T. J.; Chien, S. H.; Liu, G. C.; Tsai, K. B. *Radiology* **2004**, *232*, 599–605.
146. Lucic, S.; Nikoletic, K.; Peter, A.; Lucic, M. A.; Jovanovic, D. *Vojnosanit. Pregl.* **2010**, *67*, 453–458.
147. Ernstberger, T.; Buchhorn, G.; Heidrich, G. *Cent. Eur. J. Med.* **2009**, *4*, 496–500.
148. Drogset, J. O.; Grontvedt, T.; Myhr, G. *Am. J. Sports Med.* **2006**, *34*, 1164–1169.
149. Bach, F. D.; Carlier, R. Y.; Elis, J. B.; *et al*. *Radiology* **2002**, *225*, 541–550.
150. Alves, N. M.; Leonor, I. B.; Azevedo, H. S.; Reis, R. L.; Mano, J. F. *J. Mater. Chem.* **2010**, *20*, 2911–2921.
151. Natarajan, U. V.; Rajeswari, S. *J. Cryst. Growth* **2008**, *310*, 4601–4611.
152. Zhang, L.; Rakotondradany, F.; Myles, A. J.; Fenniri, H.; Webster, T. J. *Biomaterials* **2009**, *30*, 1309–1320.
153. Beachley, V.; Wen, X. *Prog. Polym. Sci.* **2010**, *35*, 868–892.
154. Sauerbier, S.; Palmowski, M.; Vogeler, M.; *et al*. *Tissue Eng. C Methods* **2009**, *15*, 455–462.
155. Legrand, A. P.; Sfihi, H.; Bouler, J. M. *Bone* **1999**, *25*, 103S–105S.
156. Schulz, J.; Pretzsch, M.; Khalaf, I.; *et al*. *Calcif. Tissue Int.* **2007**, *80*, 275–285.

3.322. Infrared and Raman Microscopy and Imaging of Biomaterials

N B Kavukcuoglu and N Pleshko, Temple University, Philadelphia, PA, USA

© 2011 Elsevier Ltd. All rights reserved.

3.322.1.	**Introduction**	366
3.322.1.1.	Principles of Vibrational Spectroscopy	366
3.322.1.1.1.	Mid-IR spectroscopy	366
3.322.1.1.2.	Raman scattering	366
3.322.1.2.	Mapping and Imaging	366
3.322.2.	**Instrumentation, Sampling, and Data Processing**	367
3.322.2.1.	IR Microscopy Instrumentation	367
3.322.2.2.	IR Imaging Instrumentation	367
3.322.2.3.	FTIR Microscopy and Imaging Sampling	367
3.322.2.4.	Raman Microscopy Instrumentation	368
3.322.2.5.	Confocal Raman Microscopy	368
3.322.2.6.	FT-Raman Microscopy	369
3.322.2.7.	Raman Mapping and Imaging	369
3.322.2.7.1.	Mapping	369
3.322.2.8.	Raman Microscopy and Imaging Sample Preparation	369
3.322.2.9.	Spectral Data Processing	370
3.322.3.	**Applications to Biomaterials**	370
3.322.3.1.	IR Microscopy Applications	370
3.322.3.2.	IR Imaging Applications	370
3.322.3.3.	Raman Microscopy and Imaging Applications	371
3.322.3.3.1.	Raman microscopy	374
3.322.3.3.2.	Raman imaging	376
3.322.4.	**Conclusions**	377
References		377

Glossary

Absorbance Units used to measure the amount of infrared radiation absorbed by a sample; it is linearly proportional to concentration of the component giving rise to the molecular vibration.

Attenuated total reflectance (ATR) An infrared sampling technique, where a sample contacts a crystal with a high refractive index. The infrared radiation undergoes internal reflection, but makes at least one pass through the sample surface along the crystal via an evanescent waveform and gives rise to an infrared spectrum.

CCD detector A charge-coupled device detector used to detect Raman scattering.

Diffuse reflectance Occurs when infrared radiation reflects off a rough surface. The light is scattered and reflected by the surface. The light approaches the surface from one direction, but leaves the surface in all directions.

Interferogram The fundamental measurement obtained by an FTIR spectrometer, which is essentially a plot of infrared detector response versus optical path difference. Interferograms are Fourier transformed to convert to infrared spectra.

Laser Acronym for 'light amplification by stimulated emission of radiation'; a device that produces an intense monochromatic beam of coherent light.

MCT detector A mercury cadmium telluride photoconductive infrared detector that requires liquid nitrogen cooling.

Raman intensity A measure of the amount of Raman scattering; intensity is usually displayed in arbitrary units.

Raman scattering The inelastic scattering of photons at frequencies different from that of the incident photon. The energy, and hence the frequency, of the incident light shifts due to the vibrational energy that is gained or lost in the molecule.

Spatial resolution A measure of the ability of the spectrometer to distinguish the spatial separation (distance) of two points.

Transmission sampling A sampling method where the infrared beam passes through the sample prior to detection.

Wavenumber The commonly used units of frequency for infrared and Raman spectra. The units of wavenumbers are cm^{-1} (1/wavelength), where $2.5\,\mu m = 4000\,cm^{-1}$.

Abbreviations

ATR	Attenuated total reflectance
CCD	Charge-coupled device
FPA	Focal plane array
FTIR	Fourier transform infrared
He–Ne	Helium–neon
MCT	Mercury cadmium telluride
Nd:YAG	Neodymium:yttrium–aluminum–garnet

3.322.1. Introduction

Vibrational spectroscopy has been utilized for the characterization of polymers and other materials since the 1940s[1–3] and soon thereafter was applied to the characterization of biological tissues and their components.[4–12] Variations in the environment of molecular components of materials and tissues are reflected in shifts in absorbance band intensities and positions in vibrational spectra. The spectrum of a material therefore provides insight into the chemical composition of a substance and how it might be altered during processing, or as a result of *in vivo* implantation. The most common vibrational spectroscopic techniques utilized for assessment of biomaterials are mid-infrared (mid-IR) and Raman spectroscopy. Both techniques have been widely applied to evaluate polymers, biomaterials, and tissues, with the choice of technique dependent on the particular problem under investigation. In general, IR techniques require specific sample preparations but have excellent signal-to-noise capabilities, and Raman techniques require minimal sample preparation but with somewhat lower signal to noise.

3.322.1.1. Principles of Vibrational Spectroscopy

3.322.1.1.1. Mid-IR spectroscopy

Molecules absorb radiation in the mid-IR spectral range, 4000–400 cm^{-1} (cm^{-1} is the unit of frequency) and it is converted into energy of molecular vibrations and rotations. The frequency of the vibrations is characteristic of the specific bonds involved and therefore can be utilized to identify chemical species. There are two general types of vibrations, stretching and bending, and a change in overall dipole moment must occur during the vibration for a molecule to absorb IR radiation.

3.322.1.1.2. Raman scattering

When light encounters a molecule or atom, most photons are elastically scattered, also known as Rayleigh scattering. The scattered photons have the same energy (wavelength) as the incident photons. A small proportion of the photons are scattered inelastically at frequencies different from that of incident photon. This is called Raman scattering where the energy, and hence the frequency, of the incident light shifts due to the vibrational energy that is gained or lost in the molecule.[13] The Raman scattering process from the ground vibrational state leads to absorption of energy by the molecule and its promotion to a higher energy state, called Stokes scattering (**Figure 1**). However, some molecules may be present in an excited state. Scattering from these states to the ground state is called anti-Stokes, which is a very weak scattering that involves transfer of energy to the scattered photon. Raman scattering occurs with a change in vibrational, rotational, or electronic energy of a molecule and is presented as the Stokes spectrum.

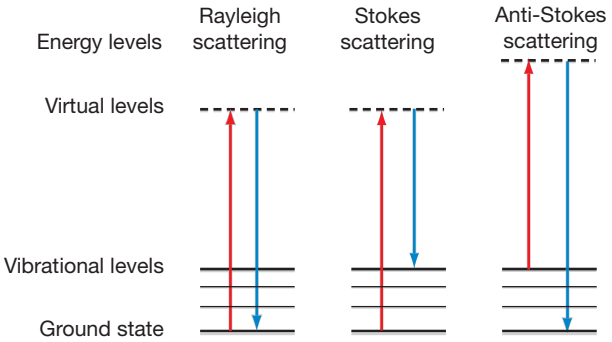

Figure 1 Schematic representation of Raman and Rayleigh scattering. Raman scattering occurs upon inelastic scattering of light and Rayleigh scattering occurs upon elastic scattering of light.

This is given as a shift in energy from the energy of the laser beam and is obtained by subtracting the scattered energy from the laser energy.[13,14] The frequency shift (cm^{-1}) due to the Raman scattering is recorded with respect to the intensity of the light. Therefore, individual peaks at different frequencies provide information on the vibrational states of molecules and ions. Any parameter altering the scattering process can result in a change in the position, intensity, and shape of the Raman bands.

3.322.1.1.2.1. IR spectroscopy versus Raman scattering

The question often arises as to which spectroscopic technique is better for evaluation of a specific sample. Molecular species can have vibrations that are only IR active and/or only Raman active. In contrast to IR, if a molecular vibration does not have an overall change in dipole moment it will be Raman active. Interference from the large water absorbances in the IR spectral regions can be a significant issue to overcome with IR analyses, while with Raman, fluorescence can be a problem. An organic sample, or impurities in the sample, can absorb laser light and reemit a strong fluorescence band that masks the Raman spectra.[13] Therefore, the use of both techniques in a complementary fashion is sometimes required to get the complete vibrational spectrum of a substance.

3.322.1.2. Mapping and Imaging

A major advance in spectroscopic analysis occurred with the coupling of a light microscope to an IR spectrometer,[15] a technology which was first applied to biological tissues with a Fourier transform IR (FTIR) microscope in the 1980s.[16] The coupling of a Raman spectrometer to a microscope was first demonstrated in 1975,[17] followed by biological applications in the 1980s,[18–20] and development of systems capable of single-point analysis and imaging. These techniques enabled

point-by-point mapping of samples and allowed investigators to assess the spatial location of different chemical species at high spatial resolution, on the order of microns.[19,21,22] Data collection by microscopic mapping requires the sample to be moved a specified distance for each point analyzed until the entire region of interest has been mapped. A further advance in these techniques was the coupling of an FTIR microscope with an array detector, FTIR imaging, or 'hyperspectral imaging' which was a true paradigm shift for data collection and processing. With FTIR imaging technology, an image of the sample is focused onto an array detector, and the intensity of radiation passing through the sample is measured at each pixel simultaneously. Thus, entire millimeter sections of tissue samples can be scanned and analyzed at ~6.25 μm pixel resolution in relatively short periods of time.[23,24] Similarly, Raman imaging can be performed with a Raman spectrometer coupled to a charged-coupled device (CCD) detector,[25] with many CCD–Raman spectrometers having the major advantage of a confocal design as well.[26]

3.322.2. Instrumentation, Sampling, and Data Processing

3.322.2.1. IR Microscopy Instrumentation

IR microscopy combines identification of chemical components by vibrational spectroscopy with high spatial resolution microscopy. The use of FTIR microscopes has grown considerably over the past 20 years, with several different models now commercially available. The two most common modes of sampling are transmission and reflectance, and most models are able to interchange between the two quite easily. The most widespread IR source is a globar, an incandescent silicon carbide rod with black-body radiation characteristics. The IR radiation originates from the globar spectrometer source and is directed to the microscope stage through a series of mirrors and lenses. In transmission mode, the radiation passes from beneath the stage through the sample to the detector. In reflectance mode, the radiation passes from above the sample, penetrates the sample and either reflects back to the detector, or scatters inside the sample (diffuse reflectance) and then reflects back toward the detector. The sampling size is controlled through an adjustable microscope aperture that typically spans 5–200 μm. In general, the smaller the aperture size, the less energy is passed through the sample. Further, the radiation that passes through the aperture is diffraction limited, so the minimum practical aperture is on the order of ~10 μm. Spectral resolution is user-defined and generally ranges between 2 and 16 cm^{-1}, dependent on the specific sample parameters. Another sampling mode available on FTIR microscopes is attenuated total reflectance (ATR). In ATR mode, a crystal with a high refractive index, such as germanium, contacts the sample surface and IR radiation passes through the sample surface along the crystal via an evanescent waveform. Sampling resolution is enhanced in ATR mode such that data can be collected at ~1.5–3 μm pixel resolution.[27] With respect to detectors, most laboratory-grade FTIR spectrometers are equipped with deuterated triglycine sulfate (DTGS) detectors that operate at room temperature. However, DTGS detectors are not sensitive enough for microscopy data and therefore,1 FTIR microscopes are generally equipped with the more sensitive mercury cadmium telluride (MCT) detector that requires liquid nitrogen cooling.

3.322.2.2. IR Imaging Instrumentation

IR imaging spectrometers enable acquisition of spatially resolved component maps of biomaterials and tissues over regions millimeters to centimeters in size with relatively short scan times. Hyperspectral images are produced where the *x*- and *y*-axes are the spatial coordinates of the material being imaged, and the *z*-axis is the parameter measured, such as intensity at a specific frequency. There are two types of instrumentation, those equipped with a focal plane array (FPA) detector such as the Varian 620-IR, and those equipped with a linear array detector, such as the Perkin Elmer Spotlight 400. An FTIR imaging spectrometer with an FPA detector will have a defined maximum number of detector elements and a defined maximum field of view for imaging, on the order of 128 × 128 elements with ~5 × 5 mm total imaging field. The Perkin Elmer Spotlight 400 equipped with a linear array detector (**Figure 2**), permits imaging of somewhat larger sample regions and more flexible sample sizes due to its data collection configuration. Both types of imaging spectrometers support ATR attachments that enable high spatial resolution data collection, on the order of 1.5 μm, and larger pixel sizes for data collection in transmittance and reflectance, from 6.25 to 50 μm. In general, larger pixels for sampling are utilized when large regions of tissues or materials are being evaluated. The IR sources used can be the same as those utilized for IR microscopy, typically globars, and MCT detector elements are very common in imaging spectrometers as well.

3.322.2.3. FTIR Microscopy and Imaging Sampling

Preparation of samples for FTIR microscopy and imaging is similar and is determined based on the mode of data acquisition. For data collection in transmittance, flat, thin sections on the order of 2–10 μm thick, similar to those utilized for histological assessments, are required. The specific method of thin sample preparation is dependent on the sample. Mineralized materials typically need to be embedded in a plastic such as polymethyl methacrylate, Epon or Spurr to facilitate sectioning.[28] Soft biomaterial samples and tissues can either be cryosectioned, or embedded in paraffin and then sectioned.[29] It is important to note that most embedding materials also absorb in the IR and can interfere with the component spectrum of interest. It is possible to chemically remove the media from the thin section prior to data collection to alleviate the interference problem, or alternatively, one can spectrally subtract the contribution of the embedding media during the data processing step.[29]

Until very recently, most tissues and materials were sectioned onto salt windows that are IR transmissive, such as KBr, CaF_2, and BaF_2. However, a lower cost substrate is now available, a low-e IR reflective slide by Kevley Technologies. The 'MirrIR' slide is optically transmissive but has a coating that reflects IR radiation. Thin tissue sections are prepared for sectioning onto these slides in a similar fashion as for the salt substrates, but the data is collected in reflectance mode. Use of

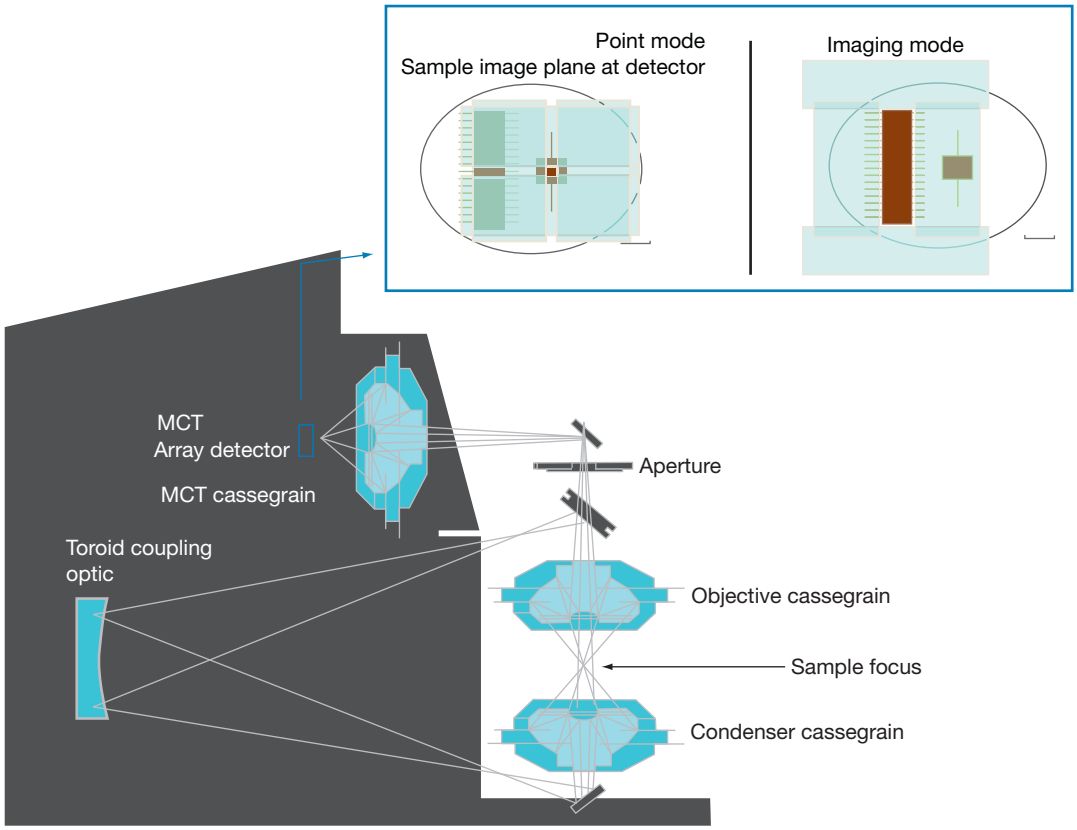

Figure 2 The Perkin Elmer Spotlight 400 with Cassegrain optics. The infrared beam is focused onto the sample which sits on a motorized stage. The transmitted light is collected by the objective, goes through a switched 4× magnifier, passes through a set of motorized aperture blades and gets refocused onto the MCT detector. There is no optical beam switching to alternate between the array detector and the point detector, as the sample image falls across the entire detector plane. Adapted with permission from Perkin Elmer.

these slides permits histological assessments on the same sample utilized for IR data collection. Another substrate has recently been described that permits culture, differentiation and fixing of cells followed by IR imaging on the same substrate, an inexpensive Si_3N_4 membrane.[30] The authors report strong adherence of the cells to the membranes, and visually normal proliferative and phenotypic cell growth. It is also possible to collect data in reflectance from intact or polished samples, such as from the surface of metal implants or from bone.[31] However, scattering artifacts can occur at times, a challenge for data interpretation.

With ATR imaging, contact between the sample and the ATR crystal is critical. For polymer samples, this can mean that high pressure is exerted onto the material to obtain optimal contact. ATR data can be obtained from an intact sample provided that the morphology of the material fits the geometric constraints of the ATR sampling fixture. For biological tissues, they are generally required to be hydrated to obtain good contact with the crystal. If adequately hydrated, the contact pressure can be minimized so that negligible damage to the tissue occurs.

3.322.2.4. Raman Microscopy Instrumentation

Micro-Raman spectroscopy or Raman microscopy, the most extensively utilized type of Raman spectroscopy, involves the pairing of an optical microscope with a Raman spectrometer. This coupling provides enormous power in sampling regions with high spatial resolution, on the order of 1 μm.[14] **Figure 3** shows a Raman microscopy setup, where the laser beam passes through a high numerical aperture microscope objective and focuses on the sample. Types of lasers include continuous wave (CW), such as argon (351.1–514.5 nm), krypton (337.4–676.4 nm), and He–Ne (632.8 nm). More recently diode lasers operating at 785, 810, or 830 nm, and also pulsed lasers such as Nd:YAG (1064 nm) have been used. The scattered light from the sample is then passed through the monochromator that is used to disperse the collected radiation onto multichannel detector. Among the detectors, intensified diode arrays or CCD are the most common type that allow simultaneous detection of a large spectral range.[32]

3.322.2.5. Confocal Raman Microscopy

Traditional Raman microscopes suffer from limited resolution along the optical axis due to the conventional microscope coupling. Improvement in resolution has been achieved with integration of a confocal-designed microscope with a Raman spectrometer. In confocal microscopy, an adjustable pinhole is applied to obstruct the out-of-focus signals from above and below the focal plane. This also reduces the background signals

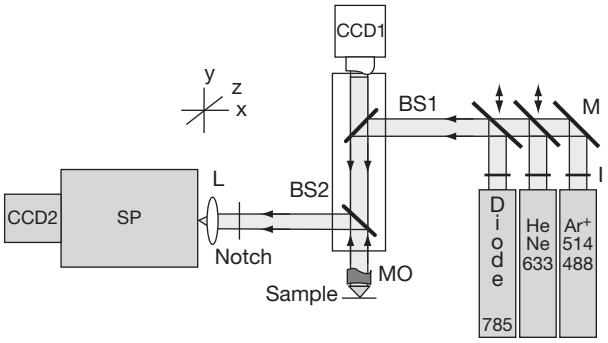

Figure 3 Schematic of a micro-Raman setup featuring different types of laser for the excitation; I, interference filter; M, mirror; BS1 and BS2, beam splitters; MO, microscope objective; CCD1, camera for sample observation; L, lens; SP, spectrometer; OMA, optical multichannel array; CCD2, Peltier-cooled camera for recording of the spectra. Reproduced from Petry, R.; Schmitt, M.; Popp, J. *ChemPhysChem* **2003**, *4*, 14–30, with permission from John Wiley & Sons.

significantly, and a fluorescence-free spectrum with sharper images can be obtained.[32,33] The *z*-axis resolution for confocal Raman is on the order of 1 μm.

3.322.2.6. FT-Raman Microscopy

The FT-Raman technique is the coupling of a Raman accessory with an FTIR instrument that contains an interferometer. The Raman effect is measured by a Nd:YAG laser (emission wavelength of 1064 nm). The scattered light is collected and passed to an interferometer head before focusing onto a liquid nitrogen cooled detector. The most important advantage of this technique is the reduction of the fluorescence effect as a result of working in a near-IR (NIR) higher frequency region. This is particularly important in the application of Raman spectroscopy in medicine and biology. Another advantage is that a higher spectral resolution can be obtained with excellent wavelength accuracy compared to conventional Raman spectroscopy. Further, unlike conventional Raman spectroscopy, FT-Raman simultaneously measures the intensity of light at many frequencies. There are still drawbacks to this technique, however. In particular, sampling at elevated temperatures could be problematic since dark samples strongly absorb and may heat-up considerably, even to the point of degrading the sample. Above 250 °C black-body emission could also occur and mask the Raman signal.[34]

3.322.2.7. Raman Mapping and Imaging

Chemical maps and images of samples are produced by combining Raman microspectroscopy with automated focusing and automated *xyz* movement of the stage. These techniques have been widely applied in the investigation of nonhomogenous samples, especially in the field of biomaterials where the investigation of the distribution of various components is essential. There are several different modes of data acquisition for Raman microscopes. In point mode, a laser is focused on a single point chosen under the microscope and the spectrum is measured by a single channel detector system. A second mode is an imaging technique where the sample is illuminated with a line focus (line-imaging). This system requires a monochromator and a multichannel detector. The scattered light is first split into different frequencies by the monochromator and then focused as a line on the CCD where individual frequencies are detected along each point of line. Another mode is the global illumination (wide-field imaging) mode where a two-dimensional CCD detector is used to measure the spectrum of an entire area under illumination. As the image of the sample is focused onto an array detector, the beam passing through each region is measured at each pixel.[35,36]

3.322.2.7.1. Mapping

During mapping, the laser is focused on the point of interest of the sample and the spectrum of a single point is then dispersed across the CCD. The sample is moved under the focused beam and spectrum is acquired at each point until the whole region is scanned. If the sample is moved in one direction (x or y) it is termed line mapping. If the sample is moved in both x and y directions the data is similar to that obtained while imaging, and the same methodology is applied during the analysis.[36] Regardless of the specific method, each pixel on the image represents a spectrum measured at each spatial location on the sample.

Both Raman mapping and imaging require the use of CCD array detectors. Mapping is a slower process since measurement of spectroscopic data is done point by point, or pixel by pixel. The advantage of mapping is that the entire spectrum is recorded and better spatial resolution can be obtained. Imaging, on the other hand, can be much faster since it uses a multichannel detector to collect data from different spatial regions simultaneously.[14] However, it is limited to the collection of one spectral frequency at a time per image.

3.322.2.8. Raman Microscopy and Imaging Sample Preparation

One of the major advantages of both Raman and FT-Raman microscopy is the minimal sample preparation required. Data can be acquired from samples in the form of solids, liquids, polymers, or vapor. In the visible excitation range glass sample holders or substances dissolved in water can be used since water and glass exhibit only very weak Raman signals. In the UV excitation range quartz sample holders can be used. Crystalline samples can sometimes exhibit orientation effects that arise from the angle of samples with respect to the scattered beam. However, sample rotation can average out orientation-related effects. Another common problem that could arise as previously mentioned is sample degradation, or burning, due to high energy absorbance. Reducing data collection time or moistening the sample when possible can minimize this undesirable effect. A final consideration with respect to sample preparation is penetration depth. The spatial resolution of a Raman microscope depends upon the optics of the system, and the penetration depth will also depend on the laser and specific sample being evaluated. Thus, penetration depth has to be evaluated experimentally, and has traditionally been done using polished Si wafer samples as standards.[37]

3.322.2.9. Spectral Data Processing

Both IR and Raman spectral data are amenable to processing with similar methods and software. Integrated areas and/or peak heights of IR absorbance bands or Raman intensities are generally proportional to the quantity of a specific component present. These univariate analyses often require preprocessing of the spectra, such as baseline correction, but can yield significant information about a sample with minimal computation required. Concomitant with the advances in mapping and imaging instrumentation is the requirement for more efficient analysis of the vast data files generated; thus, multivariate data processing methods are increasingly utilized. Application of these methods to spectral imaging data sets are reviewed in Wang and Mizaikoff.[38]

3.322.3. Applications to Biomaterials

IR and Raman microscopy and imaging are increasingly utilized in biomedical, pharmaceutical, and biomaterials applications to provide information on the quantity, distribution, and quality of sample components at the molecular level. The techniques are sensitive to organic and mineral components, can be applied to intact samples with little preparation, or to samples prepared for histologic evaluation. An overview and examples of applications in the biomaterials field are presented below.

3.322.3.1. IR Microscopy Applications

IR microscopy has been applied to a multitude of interesting and challenging problems in biomaterials, including assessment of polymer composition and degradation, evaluation of composition of tissue-engineered constructs and dental materials, and characterization of drug delivery systems.[39–64] These studies are either performed to assess small quantities of components that can't be detected using FTIR of bulk samples, or to evaluate composition at specific microscopic locations.

Ultra-high-molecular-weight polyethylene (UHMWPE), a material commonly used in orthopedic implants, has been evaluated by several investigators using FTIR microscopy. These studies typically involve assessment of microtomed slices of implants retrieved from surgeries to evaluate oxidation, crystallinity, transvinylene index (TVI),[45,58,59] or in one case, assessment of organic components diffused into the material.[44] The use of FTIR to assess UHMWPE oxidation, based on the area of the carbonyl peak centered near 1720 cm^{-1}, and to assess the amount of unsaturation (trans-vinyls, TVI) based on the area of the peak near 965 cm^{-1} are in fact ASTM methods widely utilized in the orthopedic community.[58]

Shibata and Tomita[60] utilized FTIR microscopy to evaluate whether α-tocopherol, an antioxidant added to UHMWPE, would improve oxidative resistance and crystallinity in γ-irradiated implants. Fifty micron thick slices were obtained from γ-irradiated implants with and without the addition of α-tocopherol, and FTIR microscopy was data acquired over a 50×10 mm region using a 50×50 μm aperture. Oxidation was significantly lower, and crystallinity (based on absorbances related to the crystalline and amorphous UHMWPE phases at 1897 and 1305 cm^{-1}, respectively) significantly higher, in the α-tocopherol samples compared to control γ-irradiated implants. These data also correlated with improved fatigue resistance in the α-tocopherol samples. Thus, the FTIR microscopy studies enabled elucidation of the molecular and structural changes that correlated with changes in material properties of the UHMWPE.

FTIR microscopy characterization of polymers fabricated for novel biomaterial applications continues to be widely applied. Ekblad *et al.*[46] fabricated charged polymer gradients and characterized protein adsorption behavior using FTIR microscopy. In these experiments, they prepared a bilayer of polymers having opposing charges using UV-initiated free-radical polymerization. A 12×12 mm^2 glass slide was coated with a 45 nm thick gold layer as the substrate. First cationic poly (2-aminoethyl methacrylate hydrochloride) was laid down followed by a layer of anionic poly(2-carboxyethyl acrylate). Adsorption from protein solutions and human blood plasma was investigated by FTIR microscopy. FTIR microscopy data were collected in reflectance using a 150 μm aperture along the polymer gradient (*x*-axis). In **Figure 4**, it can clearly be seen that protein adsorption based on the amide bond vibrations, specifically amide I, the carbonyl stretching frequency centered near 1660 cm^{-1}, and amide II, a combination stretching–bending vibration centered near 1560 cm^{-1}, was found in regions where one of the polymers dominated the composition, and that a minimum of protein absorption was found at the interface of the two oppositely charged proteins, where the charge was neutral. These data show the feasibility of creating a protein-resistant surface by balanced material charges.

3.322.3.2. IR Imaging Applications

Applications of IR imaging to assess materials, cells, and tissues have grown considerably over the last decade.[29,65–78] The ability to obtain images of molecular environments has provided insight into spatial variation of material structure and correlates with other properties, such as mechanical strength.[74] Researchers have utilized FTIR imaging to evaluate the composition of engineered tissues such as bone and cartilage,[29,70,72] and degradation, dissolution, and phase separation of biomaterials.[66,71,76]

One challenge in the biomaterials field is the development of polymer blends with a range of properties such as mechanical, biological, degradation, and drug permeability, and the ability to tailor these to specific applications. Malheiro *et al.*[74] utilized FTIR imaging to evaluate a new synthesis method for poly(ε-caprolactone)/chitosan fiber blends (PCL/CHT). The goal of the study was to develop fibers that combined the superior biological properties of chitosan, including CHT being biodegradable, nontoxic, hydrophilic, and having a high protein affinity, with improved mechanical performance provided by the PCL. Fibers were prepared by wet spinning from blend solutions, using a formic acid/acetone 70:30 vol% mixture as common solvent and methanol as coagulant. Varying amounts of PCL and CHT were added to the solvent mixture in order to obtain 0, 25, 50, 75, and 100 wt% CHT in the PCL/CHT blends. FTIR imaging was performed on 10 μm slices of pure components (**Figure 5**) and fiber blends embedded in epoxy resin. The integrated area of the CHT amide I absorbance centered at 1650 cm^{-1} was utilized to map

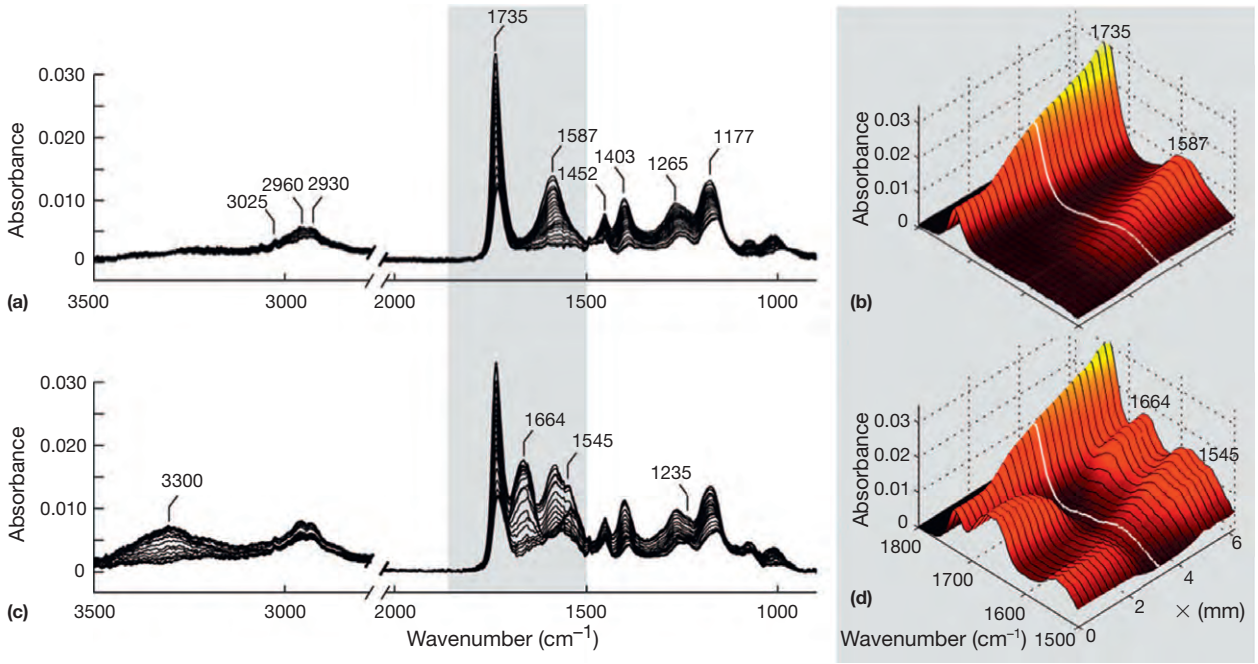

Figure 4 Stacked IR spectra measured along the same line of a gradient surface before (a and b) and after (c and d) incubation in lysozyme/pepsin mixture (0.5 mg ml^{-1} of both in HBS-N, pH 7.4). These spectra are, respectively, plotted against position along the gradient (x) in the 1800–1500 cm^{-1} region in (b) and (d). Note the gradually increasing carbonyl peak at 1735 cm^{-1} and the COO− peak at 1587 cm^{-1} (from the polymer). After protein incubation, two new peaks appeared at 1664 and 1545 cm^{-1}, respectively, both typical for vibrations in the amide bond of proteins. Reproduced from Ekblad, T.; Andersson, O.; Tai, F. I.; Ederth, T.; Liedberg, B. *Langmuir* **2009**, *25*, 3755–3762, with permission from American Chemical Society.

the CHT distribution, and the integrated area of the PCL carbonyl stretching absorption at 1730 cm^{-1} was use to map the PCL distribution (Figure 6). The IR images visualized the even distribution of the two components in the mixtures at all three blend concentrations. Further, FTIR spectra did not display frequency shifts of the signature functional groups of PCL and CHT, indicative of no chemical reaction occurring between the two components in the blends. Dynamic mechanical analysis found that the storage modulus of the blends correlated with component concentration, and also that some interaction exists between the fibers. Together, these data demonstrated the potential for tailoring the properties of PCL/CHT fiber blends for specific tissue engineering applications.

Discussion of a final application of FTIR imaging concerns the assessment of a polymer coated, drug eluting metallic coronary stent.[73] The drug delivery characteristics and stability of coatings are of prime interest for these clinical applications. In the Lewis study, the stent was coated with a phosphorylcholine (PC)-based polymer that either contained the cell migration inhibitor batimastat (loaded) or was unloaded. Stents were implanted in a porcine coronary artery model, removed after 6 months, ATR spectroscopy applied to assess the chemical nature of the stent coating, and FTIR reflectance imaging applied to assess the uniformity of distribution of the PC coating. Figure 7 shows characteristic ATR spectra that arise from the unloaded PC coating (a), the loaded PC coating (b), and from a harvested loaded stent (c). The most prominent absorbance from the PC coating is the carbonyl stretching absorbance at ~1730 cm^{-1}. This absorbance is present in all three spectra. An additional absorbance from the batimastat can be seen in (b) at ~1628 cm^{-1}. The spectrum from the loaded stent harvested after 6 months of *in vivo* implantation is very similar to the unloaded PC-coated, with no evidence of the batimastat absorbance band. This was expected, as drug delivery had previously been shown to occur over the first month of implantation.

Next, IR images of the explanted loaded stent were acquired in reflectance, and the PC carbonyl stretch at 1730 cm^{-1} utilized to image the distribution of the coating (Figure 8). The high intensity spot in the image (Figure 8(d)) corresponds to a pit in the stent surface (Figure 8(c)), and indicates a pooling of the PC solution during the dip-coating process. Overall, the nonuniformity of the coating can be visualized. Although not demonstrated in this study, an advantage of the noninvasive IR reflectance imaging technique is the potential for comparison of coating distribution on the same stent before and after implantation.

3.322.3.3. Raman Microscopy and Imaging Applications

Biomaterial applications of Raman microspectroscopy and imaging have focused on surface wear of synthetic biomaterials, failure analysis of artificial joints (mainly ceramic oxides), dental implants, joint implants, drug delivery systems, tissue engineering, surface engineering, and biocompatibility of biologically inspired materials. There is also an increasing amount of research on medical and clinical applications which include diagnostic applications such as atherosclerosis, breast cancer,

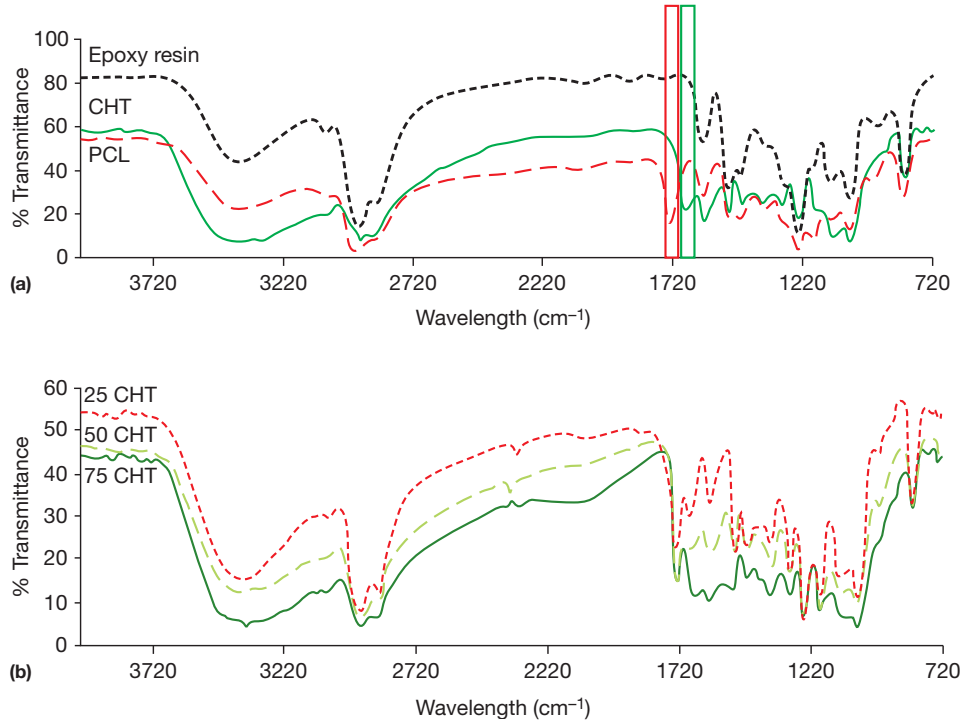

Figure 5 FTIR spectra of the pure PCL (dashed lines), CHT (solid lines), and epoxy-based resin (dotted lines) (a) and of the blend fibers (b). The colored bands identify the regions that have been selected for the integration procedure used to obtain the images of **Figure 6** (red for PCL, green for CHT). Reproduced from Malheiro, V. N.; Caridade, S. G.; Alves, N. L. M.; Mano, J. O. F. *Acta Biomater.* **2010**, *6*, 428, with permission from Elsevier.

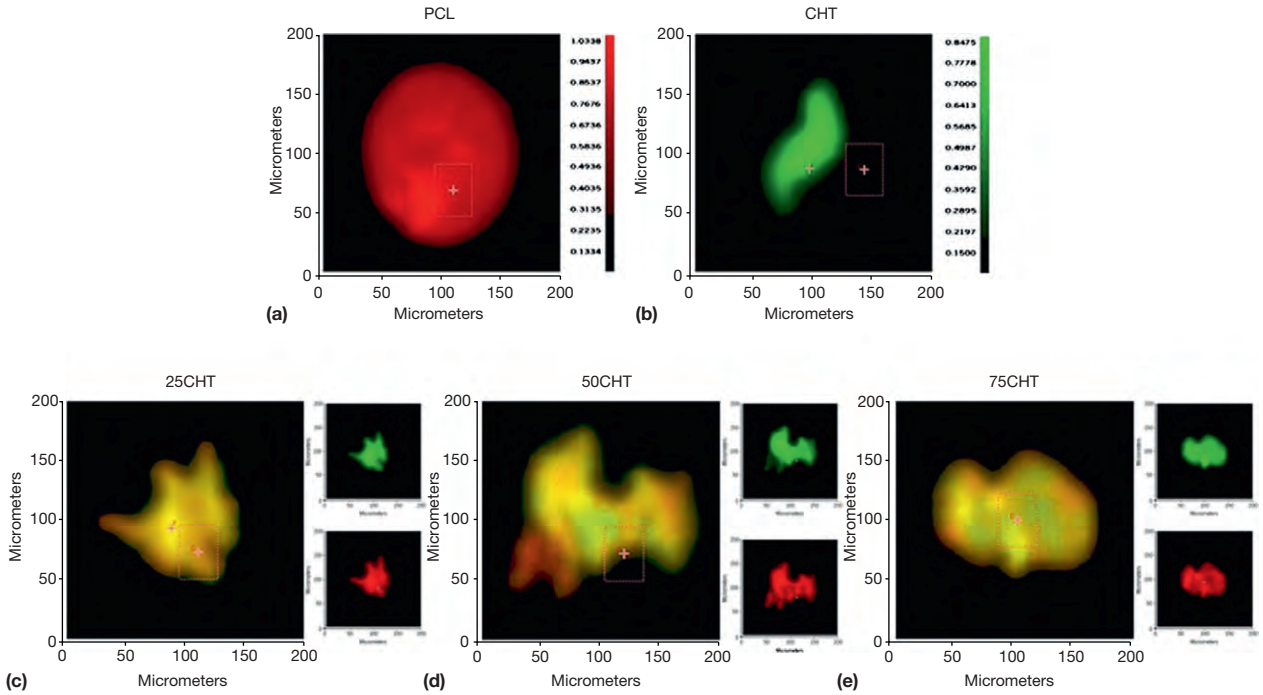

Figure 6 Chemical maps of five discrete compositions of the fiber cross-sections. Note that the existence of regions in the cross-sections with different intensities can be an indication of differences in thickness. For the chemical map, red indicates the presence of PCL, green the presence of CHT, and black corresponds to the epoxy resin. The inset images individualize the presence of the pure polymers in the blends. Reproduced from Malheiro, V. N.; Caridade, S. G.; Alves, N. L. M.; Mano, J. O. F. *Acta Biomater.* **2010**, *6*, 428, with permission from Elsevier.

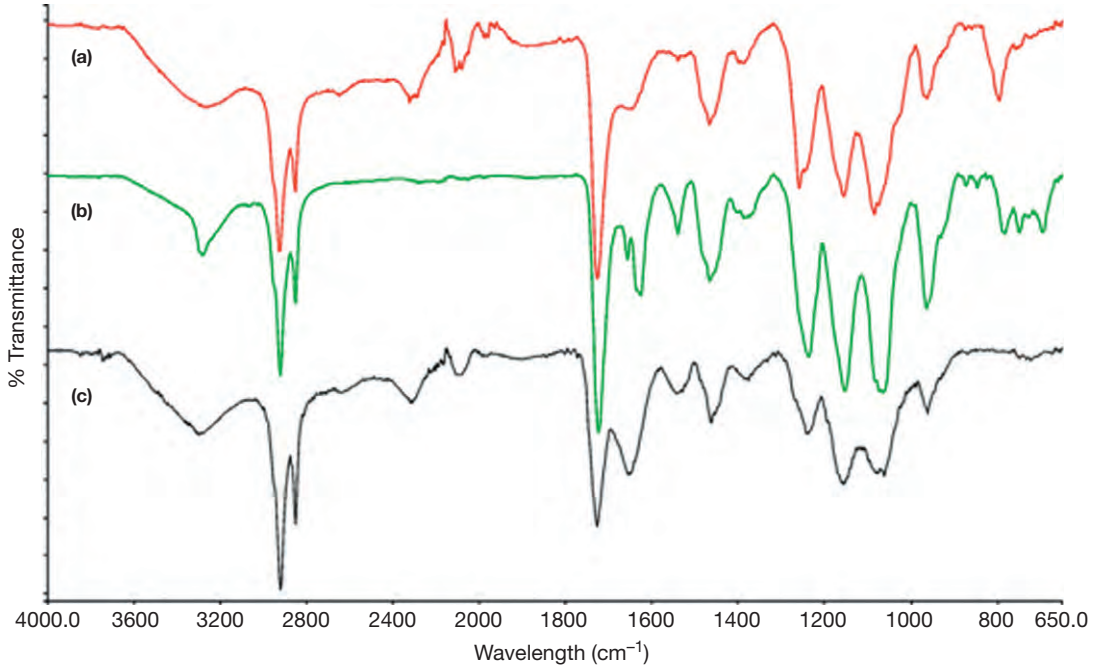

Figure 7 FTIR spectra of (a) an control unloaded PC-coated stent; (b) a batimastat-loaded PC-coated stent; and (c) an explanted PC-coated stent. Reproduced form Lewis, A. L.; Willis, S. L.; Small, S. A.; Hunt, S. R.; O'Byrne, V.; Stratford, P. W. *Biomed. Mater. Eng.* **2004**, *14*, 70, with permission from IOS Press.

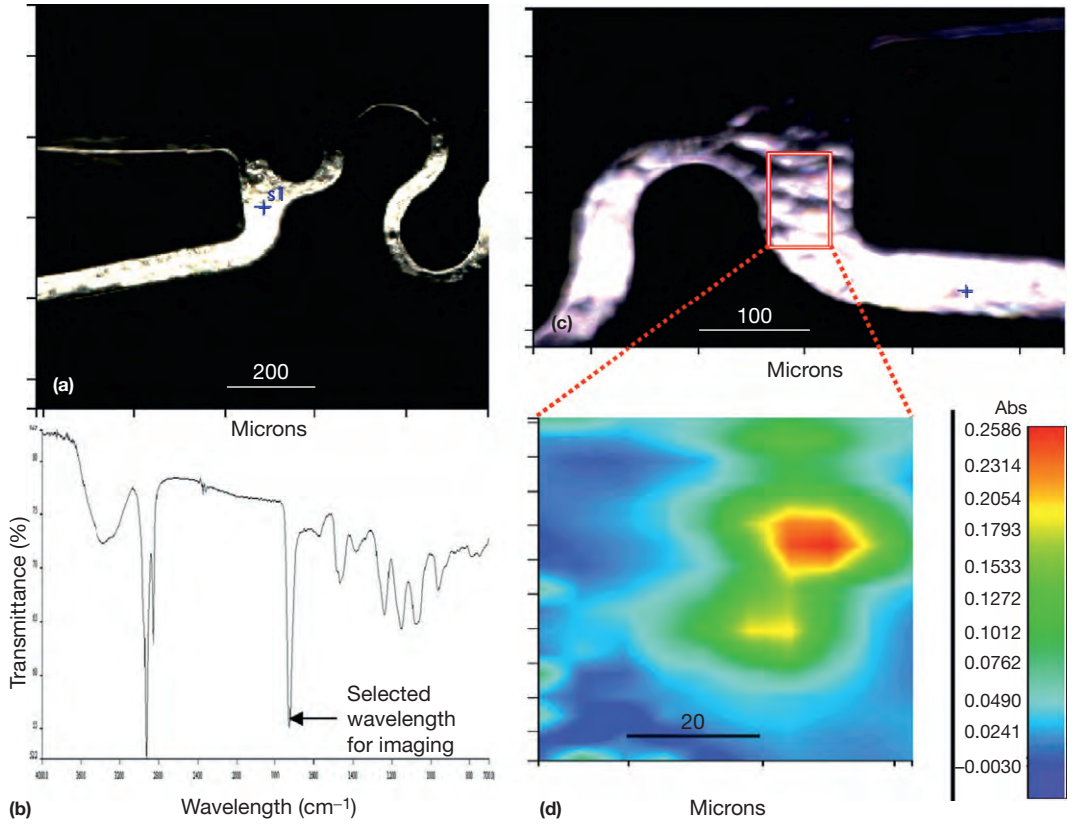

Figure 8 (a) Image of PC-coated stent strut through IR optics; (b) FTIR point spectrum from the PC-coated stent using the imaging system; (d) mapped image of a coated area (c) with color representing intensity of the C=O str. at 1730 cm^{-1}. Reproduced from Lewis, A. L.; Willis, S. L.; Small, S. A.; Hunt, S. R.; O'Byrne, V.; Stratford, P. W. *Biomed. Mater. Eng.* **2004**, *14*, 70, with permission from IOS Press.

Alzheimer's disease, blood analyses, skin studies, and identification of pathogenic microorganisms.[32,79–95] Some recent applications to biomaterials are discussed below.

3.322.3.3.1. Raman microscopy

Synthetic hydroxyapatites (HA) and other calcium phosphates are used as bone implants and prostheses in the medical and dental fields, and characteristics of the coatings of the implant are especially important in terms of biocompatibility. Surface characterization, composition, and mineralization of implant coatings such as HA, bioactive glass, ceramic materials, carbons, and bone cement have been investigated with Raman microscopy.[80,96] Comparison of the Raman vibrational bands of pure components can be utilized to assess whether a chemical reaction between the components took place. These analyses also provide information on the crystallinity and identify of different phases in the coating.[97,98]

Dippel *et al.*[99] investigated the integration of bone into a HA-coated implant via FT-Raman microscopy.[99] They assessed canine and human specimens with hip or knee joint prosthesis (uncoated and HA coated) where the samples were removed 6 and 18 months after implantation. The specimens were then dehydrated, embedded in PMMA and cut into 200 µm slices followed by polishing down to 50 µm. Raman measurements were conducted using a NIR FT-Raman spectrometer coupled to an inverted microscope with a Nd:YAG laser ($\lambda = 1064$ nm). After 18 months of implantation with an HA-coated implant, the canine samples showed that the HA coating was separated from the prosthesis forming a gap which was filled with bone ingrowth (**Figure 9**).

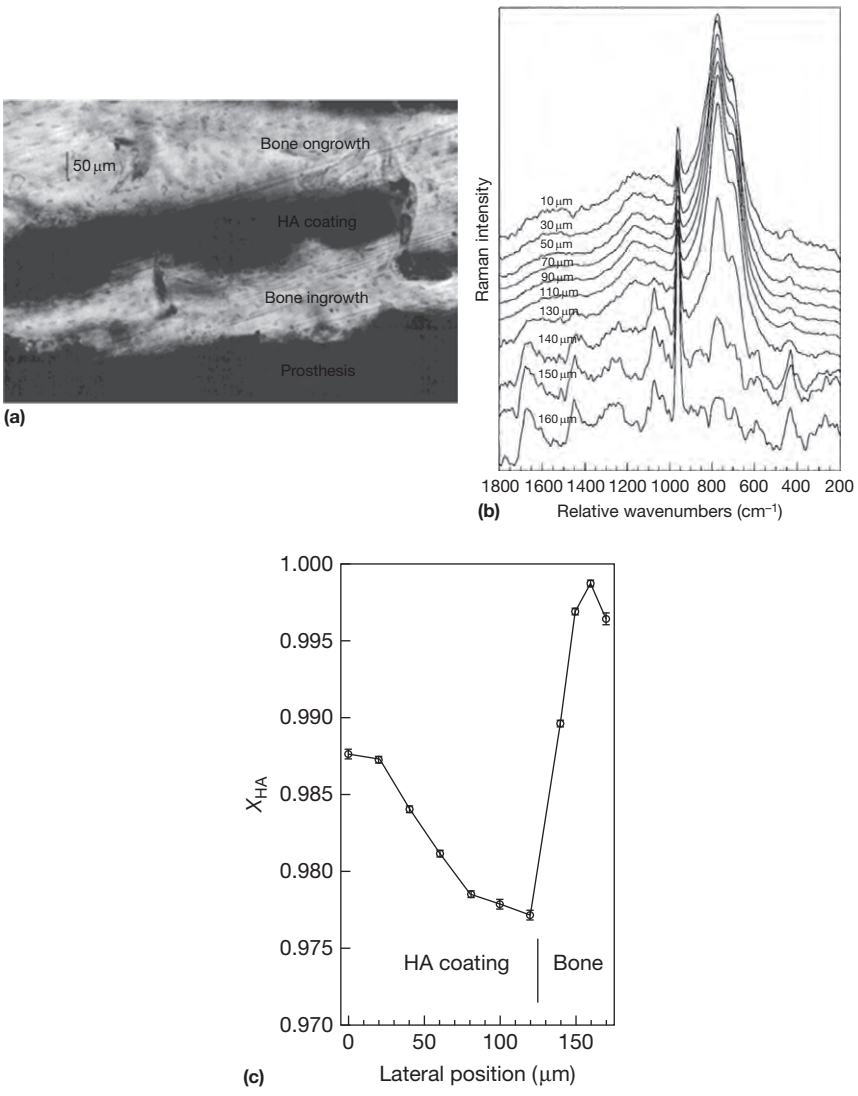

Figure 9 (a) Canine microscopic section 18 months after implantation of a coated implant. The HA coating was separated from the prosthesis. The resulting gap was filled with bone (bone ingrowth). Additionally, bony integration of the HA coating (bone ongrowth) is observed. (b) Series of Raman spectra showing the progression from implant coating (top) to ongrown bone (bottom). (c) HA content (*x*HA) at different lateral positions from the prosthesis. Reproduced form Dippel, B.; Mueller, R. T.; Pingsmann, A.; Schrader, B. *Biospectroscopy* **1998**, *4*, 403–412, with permission from John Wiley & Sons.

They also observed a bony integration (bone ongrowth) with direct contact to the HA coating. A series of Raman measurements were taken from different locations along the coating to the ongrown bone at ~10 μm increments (Figure 9(b)). Figure 9(b) shows that the spectra from the implant HA coating, in addition to the characteristic HA PO-symmetric stretching absorbance at 962 cm^{-1}, have additional dominating bands at 695 and 773 cm^{-1}, probably from POP vibrations of calcium polyphosphates. After the lateral position of 130 μm, the intensities of the organic matrix bands (amide I at 1660 cm^{-1}, and the δ(CH) vibrations at 1445 cm^{-1}), increase, indicative of mineralized protein containing tissue, while the 695 and 773 cm^{-1} bands decrease. This indicates the HA of bone starts to dominate while the calcium polyphosphates decrease. This was quantified by calculation of a mineralization factor, X_{HA}, based on the ratio of the HA and collagen Raman intensities at different lateral positions. Figure 9(c) indicates that the HA which is in direct contact to the implant decreased in mineralization from 98.5% to 97.7% toward the periphery of the coating and increased to 100% at the site of the ongrown bone. Together, the results of this study indicate that FT-Raman spectroscopy can be useful in analysis of compositional changes in HA coatings, along with assessment of the integration of the implant coating with surrounding tissue.

There are a number of Raman studies relevant to dental research including the analysis of synthetic minerals, enamel, dental calculus,[93] dental adhesive resins, and dental implants.[100] Lemor *et al.*[101] utilized Raman microspectroscopy to assess whether chemical reactions were taking place at the surfaces of the dental-amalgam interface that might contribute to adhesion failure, and Miyazaki *et al.*[102] applied Raman microscopy to investigate the chemical composition and demineralization at a dentin–resin interface. In that study, an adhesive system was prepared with a self-etching primer system, Mac Bond II/Palfique Estelite, and a one-bottle adhesive system, Single Bond/Z100. The adhesives were prepared and applied to bovine tooth surfaces, the specimens were sectioned parallel to dentinal tubules and polished. Raman measurements were conducted with a He–Ne laser (wavelength = 632.8 nm) Raman microscope coupled with a CCD camera. The spatial resolution was 0.6–0.8 μm, and spectra were obtained across the dentin–adhesive interface with a 0.2 μm step size.

Figure 10(a) shows the Raman spectrum of bovine dentin without resin. The peak at 960 cm^{-1} arises from the P–O stretching vibration in the mineral component and the bands at 1242, 1450, and 1669 cm^{-1} are associated with the organic phase of dentin. The Raman spectrum of the adhesive is shown in Figure 10(b), where peaks at 640 cm^{-1} (aromatic ring group of Bis-GMA) and 1450 cm^{-1} (C–H alkyl group) were chosen as a measure of resin adhesive. The intensities of selected bands associated with the mineral, aromatic ring, and organic components were plotted across the dentin–resin interface for the different adhesive systems (Figure 11). Transitional changes in the HA and resin were clearly observed at the interface. These changes in the intensity of the Raman peaks suggested that the depth of dentin demineralization was 1.8–2.2 μm for Mac Bond II, and that penetration of Bis-GMA through the entire depth of demineralized dentin occurred.

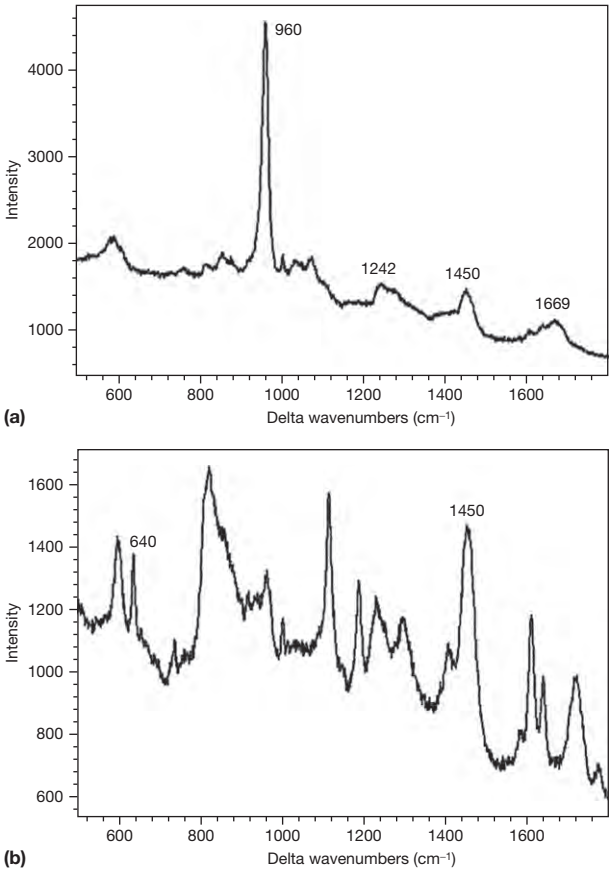

Figure 10 The Raman spectrum of bovine dentin (a) and Single Bond adhesive (b) in the region of 500–1800 cm^{-1}. Reproduced from Miyazaki, M.; Onose, H.; Moore, B. K. *Dent. Mater.* **2002**, *18*, 576–580, with permission from Elsevier.

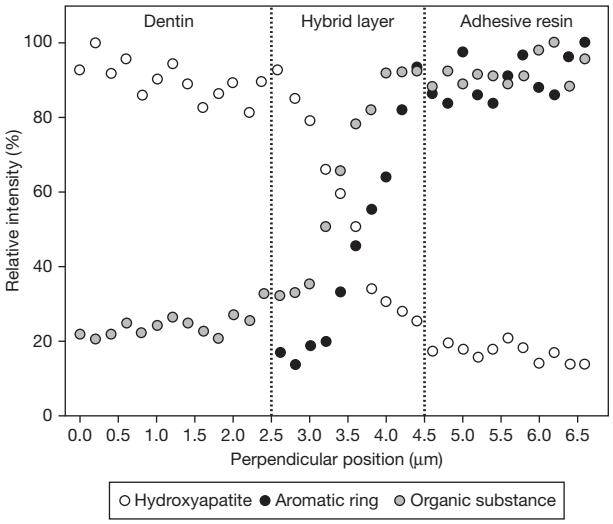

Figure 11 Representative line scans across the resin ± dentin interface of Mac Bond II adhesive system. Reproduced from Miyazaki, M.; Onose, H.; Moore, B. K. *Dent. Mater.* **2002**, *18*, 576–580, with permission from Elsevier.

3.322.3.3.2. Raman imaging

Raman imaging has been employed to monitoring the growth of human cells on scaffolds, to investigate autologous cell culture systems and to evaluate stem cell biology. Several recent studies used this technique to observe real-time cellular interactions with bioactive materials[103] and to detect changes or variation among the cells.[89,104,105] Raman imaging data have been successfully collected from live cells in a nondestructive and noninvasive manner, and different types of cells used in tissue engineering have been recognized based on spectral features.

Applications of Raman imaging in the pharmaceutical industry to characterize drug formulations and kinetics of drug delivery systems have increased in recent years.[83,85,106–108] Information on the degradation of nanoparticulate drug carriers

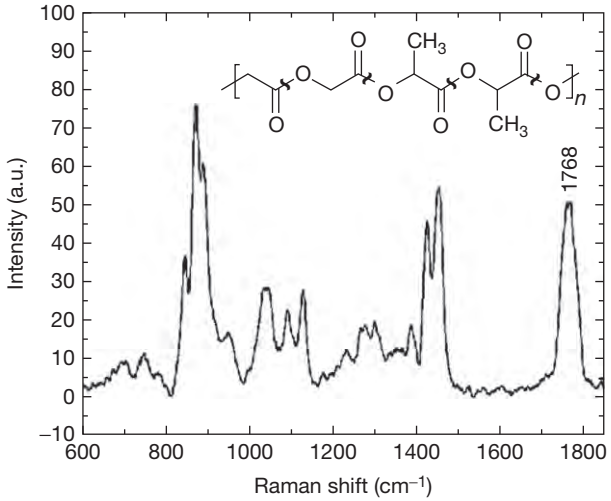

Figure 12 Raman spectrum and chemical structure of PLGA. In the structure, two glycolic acid units are shown on the left, whereas lactic acid units are displayed on the right. The ester bonds (marked '∼'), which are hydrolyzed upon degradation, are characterized by a carbonyl stretching vibration at 1768 cm^{-1}. Reproduced from Van Apeldoorn, A. A.; Van Manen, H. J.; Bezemer, J. M.; De Bruijn, J. D.; Van Blitterswijk, C. A.; Otto, C. *J. Am. Chem. Soc.* **2004**, *126*, 13226–13227, with permission from American Chemical Society.

such as poly(ε-caprolactone) (PCL) and poly(lactic-*co*-glycolic acid) (PLGA) have been assessed based on the decrease of the characteristic spectral peaks of PCL and PLGA. In one recent study, it was found that as the particles integrated into the cell body, shifts in Raman peak heights and ratios occurred that could be indicative of the physical processes that occurred.[83]

Raman imaging also provides information on the degradation of drug carriers *in vivo* and *in vitro*. Van Apeldoorn *et al.*[94] used both confocal Raman microscopy and Raman imaging to assess the degradation of PLGA microspheres inside macrophages *in vitro*. The microspheres were prepared by a salting-out procedure and added to a macrophage cell line. The cells were then cultured on poly-L-lysine coated CaF_2 slides and Raman imaging conducted on samples in PBS. An intracellular area of $7.5 \times 7.5\,\mu m^2$ was scanned with a 647.1 nm laser excitation.

Figure 12 is the Raman spectrum of the pure PLGA, and Figure 13 shows the light microscopy and Raman imaging results of macrophages containing phagocytosed beads. Figure 13(a) reveals a cavity-like structure in the center of the microspheres indicating the degradation of PLGA, as confirmed by Raman imaging as well. Raman images were created using the 1768 cm^{-1} band that is associated with the ester group of PLGA (Figure 13(b)). The image reveals a lower intensity at the center of particles, which means the loss of PLGA ester bonds from these regions. The image also shows a collapsed microsphere in the top right corner.

In another recent study, carbon nanotubes (CNTs) used in drug delivery systems were explored via Raman imaging in order to assess their tumor targeting ability.[109] Single-walled nanotubes (SWNT) have a few strong, distinctive Raman peaks that do not get affected by the fluorescence background and are therefore suitable for Raman imaging. It was shown that isotopically modified SWNTs present shifted G-band (tangential mode) peaks. This feature of SWNTs enables them to be used as color contrast agents in Raman imaging.[110] Figure 14 shows the multicolor confocal Raman imaging of cancer cells that were labeled with three different isotopes of 'colored' SWNT's conjugated with different targeting ligands such as Herceptin (anti-Her2), Erbitux (anti-Her1), and an RGD peptide. These results demonstrate the potential of using SWNT's for biological detection and imaging.

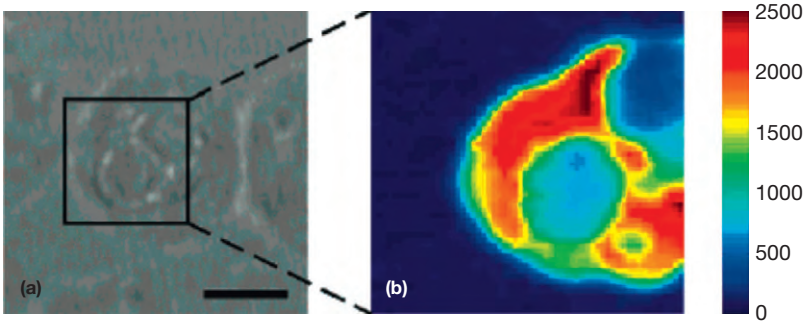

Figure 13 (a) Light micrographs of macrophages containing phagocytosed beads cultured for 1 week (scale bar 5 μm). The Raman image of these beads is shown in (b). The scale in (b) shows the relative intensity of the 1768 cm^{-1} band used for imaging (specific for PLGA ester bonds). Reproduced from Van Apeldoorn, A. A.; Van Manen, H. J.; Bezemer, J. M.; De Bruijn, J. D.; Van Blitterswijk, C. A.; Otto, C. *J. Am. Chem. Soc.* **2004**, *126*, 13226–13227, with permission from American Chemical Society.

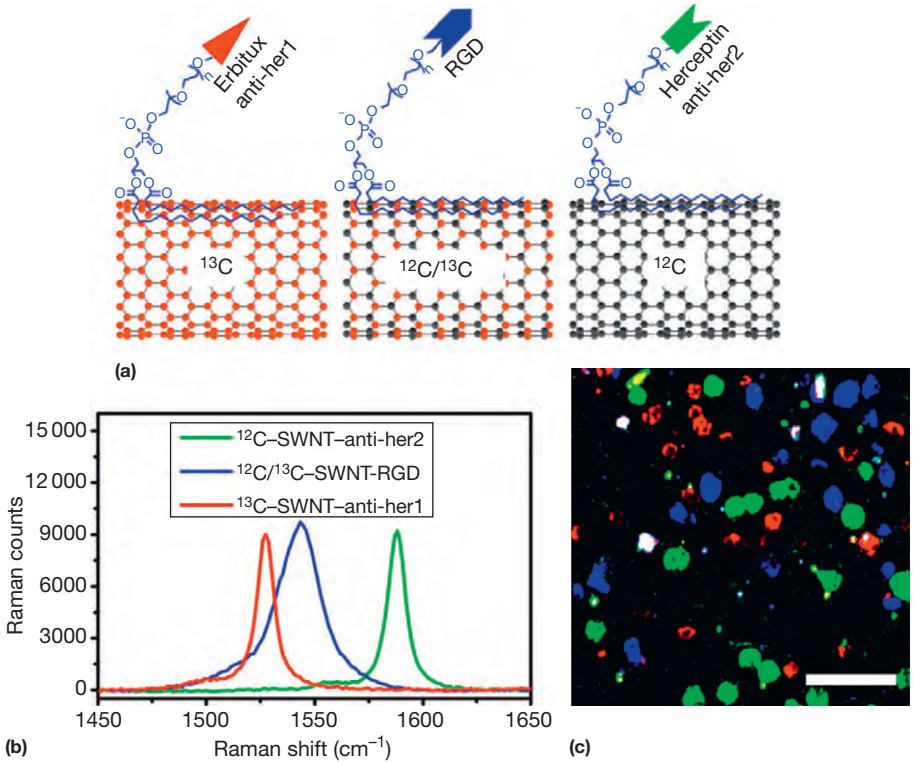

Figure 14 Multicolor Raman imaging with isotopically modified SWNTs. (a) Schematic illustration of SWNTs with three different isotope compositions (13C-SWNT, 12C12/13C-SWNT, 12C-SWNT) conjugated with different targeting ligands. (b) Solution phase Raman spectra of the three SWNT conjugates under 785 nm laser excitation. Different G-band peak positions were observed. (c) A deconvoluted confocal Raman spectroscopy image of a mixture of three cell lines with different receptor expressions incubated with the three-color SWNT mixture. Scale bar = 100 μm. Reproduced from Liu, Z.; Li, X.; Tabakman, S. M.; Jiang, K.; Fan, S.; Dai, H. *J. Am. Chem. Soc.* **2008**, *130*, 13540–13541, with permission from American Chemical Society.

3.322.4. Conclusions

The spatially heterogeneous nature of many biomaterials makes the use of imaging modalities an essential component of analyses, and vibrational spectroscopic techniques can provide a substantial amount of information. Applications of IR and Raman microscopy and imaging to assess biomaterials have greatly increased in recent years, and the field is still maturing. In particular, we anticipate that applications to evaluate cell phenotype and cellular interactions with biomaterials will become essential tools in characterization of the biocompatibility of materials. The ability to obtain images of molecular environments utilizing these methods will greatly enhance correlations of composition with mechanical strength and cell interactions, with the ultimate goal of optimization of *in vivo* material properties.

References

1. Krishnan, R. S. *Nature* **1947**, *159*, 230.
2. Thompson, H. W. *J. Chem. Soc.* **1947**, 289–297.
3. Thompson, H. W.; Torkington, P. *Proc. R. Soc. Lond. A Math. Phys. Sci.* **1943**, *184*, 3–20.
4. Guy, J.; Deltour, G. H.; Weinmann, S. H. *Ann. Biol. Clin. (Paris)* **1955**, *13*, 43–48.
5. Hirano, K. *Bull. Chem. Soc. Jpn* **1968**, *41*, 731–732.
6. Katz, J. J. *Science* **1955**, *121*, 642–644.
7. Lenormant, H. *C. R. Seances Soc. Biol. Fil.* **1953**, *147*, 406–409.
8. Morales, M. F.; Laki, K.; Gergely, J.; Cecchini, L. P. *J. Cell. Physiol.* **1951**, *37*, 477–485.
9. Penati, F.; Borello, E.; Turco, G. L.; Lovisetto, P. *Haematologica* **1955**, *39*, 341–348.
10. Schwarz, H. P. *Adv. Clin. Chem.* **1960**, *3*, 1–34.
11. Schwarz, H. P.; Dreisbach, L.; Childs, R.; Mastrangelo, S. V. *Ann. N. Y. Acad. Sci.* **1957**, *69*, 116–130.
12. Tobin, M. C. *Science* **1968**, *161*, 68–69.
13. Ferraro, J. R.; Nakamoto, K.; Brown, C. W. In *Introductory Raman Spectroscopy*, 2nd ed.; Academic Press: San Diego, CA, 2003; pp 1–94.
14. Lewis, I. R.; Edwards, H. G. M. *Handbook of Raman Spectroscopy: From the Research Laboratory to the Process Line*; CRC Press: Boca Raton, FL, **2001**, 1–94.
15. Barer, R.; Cole, A. R.; Thompson, H. W. *Nature* **1949**, *163*, 198–201.
16. Mendelsohn, R.; Hassankhani, A.; Dicarlo, E.; Boskey, A. *Calcif. Tissue Int.* **1989**, *44*, 20–24.
17. Delhaye, M.; Dhamelincourt, P. *J. Raman Spectrosc.* **1975**, *3*, 33–43.
18. Cavagnat, R.; Cruege, F.; Huong, P. V. *Biochimie* **1981**, *63*, 927–929.
19. De Mul, F. F.; Hottenhuis, M. H.; Bouter, P.; Greve, J.; Arends, J.; Ten Bosch, J. J. *J. Dent. Res.* **1986**, *65*, 437–440.
20. Plouvier, S. R.; Huong, P. V. *Biorheology Suppl.* **1984**, *1*, 345–347.
21. Bot, A. C.; Huizinga, A.; De Mul, F. F.; Vrensen, G. F.; Greve, J. *Exp. Eye Res.* **1989**, *49*, 161–169.
22. Huizinga, A.; Bot, A. C.; De Mul, F. F.; Vrensen, G. F.; Greve, J. *Exp. Eye Res.* **1989**, *48*, 487–496.
23. Lewis, E. N.; Treado, P. J.; Reeder, R. C.; *et al. Anal. Chem.* **1995**, *67*, 3377–3381.
24. Marcott, C.; Reeder, R. C.; Paschalis, E. P.; Tatakis, D. N.; Boskey, A. L.; Mendelsohn, R. *Cell. Mol. Biol. (Noisy-le-grand)* **1998**, *44*, 109–115.
25. Goldstein, S. R.; Kidder, L. H.; Herne, T. M.; Levin, I. W.; Lewis, E. N. *J. Microsc.* **1996**, *184*, 35–45.
26. Puppels, G. J.; De Mul, F. F.; Otto, C.; *et al. Nature* **1990**, *347*, 301–303.

27. Kazarian, S. G.; Chan, K. L. A. *Biochim. Biophys. Acta – Biomembr.* **2006**, *1758*, 858–867.
28. Aparicio, S.; Doty, S. B.; Camacho, N. P.; *et al*. *Calcif. Tissue Int.* **2002**, *70*, 422–429.
29. Boskey, A.; Pleshko Camacho, N. *Biomaterials* **2007**, *28*, 2478.
30. Carter, E. A.; Rayner, B. S.; Mcleod, A. I.; *et al*. *Mol. Biosyst.* **2010**, *6*(7), 1316–1322.
31. Boyan, B. D.; Bonewald, L. F.; Paschalis, E. P.; *et al*. *Calcif. Tissue Int.* **2002**, *71*, 519–529.
32. Petry, R.; Schmitt, M.; Popp, J. *ChemPhysChem* **2003**, *4*, 14–30.
33. Williams, K. P. J.; Pitt, G. D.; Batchelder, D. N.; Kip, B. J. *Appl. Spectrosc.* **1994**, *48*(1), 167–278.
34. Ferraro, J. R.; Nakamoto, K.; Brown, C. W. In *Introductory Raman Spectroscopy*, 2nd ed.; Academic Press: San Diego, CA, 2003; pp 95–146.
35. Ferraro, J. R.; Nakamoto, K.; Brown, C. W. In *Introductory Raman Spectroscopy*, 2nd ed.; Academic Press: San Diego, CA, 2003; pp 147–206.
36. Smith, E.; Dent, G. *Modern Raman Spectroscopy: A Practical Approach*; Wiley-Interscience: New York, 2005.
37. Yamaguchi, H.; Eda, G.; Mattevi, C.; Kim, H.; Chhowalla, M. *ACS Nano* **2010**, *4*, 524–528.
38. Wang, L.; Mizaikoff, B. *Anal. Bioanal. Chem.* **2008**, *391*, 1641–1654.
39. Al-Assaf, K.; Chakmakchi, M.; Palaghias, G.; Karanika-Kouma, A.; Eliades, G. *Dent. Mater.* **2007**, *23*, 829–839.
40. Bonnier, F.; Rubin, S.; Debelle, L.; *et al*. *J. Biophotonics* **2008**, *1*, 204–214.
41. Boylston, E. K.; Morris, N. M. *Biotech. Histochem.* **1997**, *72*, 213–222.
42. Centeno, J. A.; Kalasinsky, V. F.; Johnson, F. B.; Vinh, T. N.; O'leary, T. J. *Lab. Investig.* **1992**, *66*, 123–131.
43. Chesnick, I. E.; Avallone, F. A.; Leapman, R. D.; Landis, W. J.; Eidelman, N.; Potter, K. *Bone* **2007**, *40*, 904–912.
44. Costa, L.; Bracco, P.; Brach Del Prever, E.; Luda, M. P.; Trossarelli, L. *Biomaterials* **2001**, *22*, 307–315.
45. Costa, L.; Luda, M. P.; Trossarelli, L.; Brach Del Prever, E. M.; Crova, M.; Gallinaro, P. *Biomaterials* **1998**, *19*, 659–668.
46. Ekblad, T.; Andersson, O.; Tai, F. I.; Ederth, T.; Liedberg, B. *Langmuir* **2009**, *25*, 3755–3762.
47. Eliades, T.; Eliades, G.; Watts, D. C. *Eur. J. Orthod.* **1999**, *21*, 649–658.
48. Ende, M. T.; Peppas, N. A. *Pharm. Res.* **1995**, *12*, 2030–2035.
49. Garidel, P.; Boese, M. *Microsc. Res. Tech.* **2007**, *70*, 336–349.
50. Gotter, B.; Faubel, W.; Neubert, R. H. H. *Eur. J. Pharm. Biopharm.* **2010**, *74*(1), 14–20.
51. Greenbaum, E. S.; Burroughs, B. B.; Harris, W. H.; Muratoglu, O. K. *Biomaterials* **2004**, *25*, 4479–4484.
52. Jayasuriya, A. C.; Kibbe, S. *J. Mater. Sci. Mater. Med.* **2010**, *21*(2), 393–398.
53. Jayasuriya, A. C.; Shah, C.; Ebraheim, N. A.; Jayatissa, A. H. *Biomed. Mater.* **2008**, *3*, 015003.
54. Kakoulides, E. P.; Smart, J. D.; Tsibouklis, J. *J. Control. Release* **1998**, *54*, 95–109.
55. Liu, K. Z.; Dixon, I.; Mantsch, H. H. *Cardiovasc. Pathol.* **1999**, *8*, 41–47.
56. Mattinen, M. L.; Kruus, K.; Buchert, J.; Nielsen, J. H.; Andersen, H. J.; Steffensen, C. *FEBS J.* **2005**, *272*, 3640–3650.
57. Mccarthy, S. J.; Meijs, G. F.; Mitchell, N.; *et al*. *Biomaterials* **1997**, *18*, 1387–1409.
58. Medel, F. J.; Rimnac, C. M.; Kurtz, S. M. *J. Biomed. Mater. Res. A* **2009**, *89*, 530–538.
59. Muratoglu, O. K.; Delaney, J.; O'connor, D. O.; Harris, W. H. *Biomaterials* **2003**, *24*, 2021–2029.
60. Shibata, N.; Tomita, N. *Biomaterials* **2005**, *26*, 5762.
61. Van De Weert, M.; Van't Hof, R.; Van Der Weerd, J.; *et al*. *J. Control. Release* **2000**, *68*, 31–40.
62. Wiggins, M. J.; Wilkoff, B.; Anderson, J. M.; Hiltner, A. *J. Biomed. Mater. Res.* **2001**, *58*, 302–307.
63. Yang, Y. Y.; Shi, M.; Goh, S. H.; Moochhala, S. M.; Ng, S.; Heller, J. *J. Control. Release* **2003**, *88*, 201–213.
64. Zhao, L.; Tsuchiya, K.; Inoue, Y. *Macromol. Biosci.* **2004**, *4*, 699–705.
65. Bonwell, E. S.; Wetzel, D. L. *J. Agric. Food Chem.* **2009**, *57*, 10072.
66. Coutts-Lendon, C. A.; Wright, N. A.; Mieso, E. V.; Koenig, J. L. *J. Control. Release* **2003**, *93*, 248.
67. Gulley-Stahl, H. J.; Bledsoe, S. B.; Evan, A. P.; Sommer, A. J. *Appl. Spectrosc.* **2010**, *64*, 22.
68. Kazarian, S. G.; Chan, K. L.; Maquet, V.; Boccaccini, A. R. *Biomaterials* **2004**, *25*, 3931–3938.
69. Kazarian, S. G.; Martirosyan, G. G. *Int. J. Pharm.* **2002**, *232*, 81–90.
70. Kim, M.; Foo, L.; Lyman, S.; *et al*. *Tissue Eng. Part C Methods* **2010**, *16*(3), 355–364.
71. Koenig, J. *Adv. Mater.* **2002**, *14*, 457–460.
72. Leone, G.; Delfini, M.; Di Cocco, M. E.; Borioni, A.; Barbucci, R. *Carbohydr. Res.* **2008**, *343*, 327.
73. Lewis, A. L.; Willis, S. L.; Small, S. A.; Hunt, S. R.; O'Byrne, V.; Stratford, P. W. *Biomed. Mater. Eng.* **2004**, *14*, 70.
74. Malheiro, V. N.; Caridade, S. G.; Alves, N. L. M.; Mano, J. O. F. *Acta Biomater.* **2010**, *6*, 428.
75. Steiner, G.; Tunc, S.; Maitz, M.; Salzer, R. *Anal. Chem.* **2007**, *79*, 1316.
76. Vogel, C.; Wessel, E.; Siesler, H. W. *Biomacromolecules* **2007**, *9*, 523–527.
77. Wang, Y.; Yao, X.; Parthasarathy, R. *J. Biomed. Mater. Res. A* **2008**, *91*, 251–262.
78. Wilson, D. J.; Chenery, D. H.; Bowring, H. K.; *et al*. *J. Biomater. Sci. Polym. Ed.* **2005**, *16*, 449–472.
79. Amer, M. S. *Raman Spectroscopy for Soft Matter Applications*; Wiley: New York, 2009.
80. Bertoluzza, A.; Fagnano, C.; Monti, P.; *et al*. *Clin. Mater.* **1992**, *9*, 49–68.
81. Carden, A.; Rajachar, R. M.; Morris, M. D.; Kohn, D. H. *Calcif. Tissue Int.* **2003**, *72*, 166–175.
82. Caspers, P. J.; Lucassen, G. W.; Puppels, G. J. *Biophys. J.* **2003**, *85*, 572–580.
83. Chernenko, T.; Matthaäàus, C.; Milane, L.; Quintero, L.; Amiji, M.; Diem, M. *ACS Nano* **2009**, *3*, 3552–3559.
84. Choo-Smith, L. P.; Edwards, H. G. M.; Endtz, H. P.; *et al*. *Biopolymers* **2002**, *67*, 1–9.
85. Davies, M. C.; Binns, J. S.; Melia, C. D.; *et al*. *Int. J. Pharm.* **1990**, *66*, 223–232.
86. Hanlon, E. B.; Manoharan, R.; Koo, T. W.; *et al*. *Phys. Med. Biol.* **2000**, *45*, R1–R59.
87. Morgan, R. L.; Hill, M. J.; Barham, P. J.; *et al*. *Polymer* **2001**, *42*, 2121–2135.
88. Ogawa, M.; Harada, Y.; Yamaoka, Y.; Fujita, K.; Yaku, H.; Takamatsu, T. *Biochem. Biophys. Res. Commun.* **2009**, *382*, 370–374.
89. Owen, C. A.; Notingher, I.; Hill, R.; Stevens, M.; Hench, L. L. *J. Mater. Sci. Mater. Med.* **2006**, *17*, 1019–1023.
90. Penel, G.; Delfosse, C.; Descamps, M.; Leroy, G. *Bone* **2005**, *36*, 893–901.
91. Pezzotti, G. *Anal. Bioanal. Chem.* **2005**, *381*, 577–590.
92. Timlin, J. A.; Carden, A.; Morris, M. D.; Rajachar, R. M.; Kohn, D. H. *Anal. Chem.* **2000**, *72*, 2229–2236.
93. Tsuda, H.; Arends, J. *Adv. Dent. Res.* **1997**, *11*, 539–547.
94. Van Apeldoorn, A. A.; Van Manen, H. J.; Bezemer, J. M.; De Bruijn, J. D.; Van Blitterswijk, C. A.; Otto, C. *J. Am. Chem. Soc.* **2004**, *126*, 13226–13227.
95. Walton, A. G.; Deveney, M. J.; Koenig, J. L. *Calcif. Tissue Res.* **1970**, *6*, 162–167.
96. Krajewski, A.; Ravaglioli, A.; Bertoluzza, A.; *et al*. *Biomaterials* **1988**, *9*, 528–532.
97. Bertoluzza, A.; Fagnano, C.; Tinti, A.; *et al*. *J. Biomed. Mater. Res.* **1989**, *23*, 523–528.
98. Bertoluzza, A.; Simoni, R.; Tinti, A.; Morocutti, M.; Ottani, V.; Ruggeri, A. *J. Biomed. Mater. Res.* **1991**, *25*, 23–38.
99. Dippel, B.; Mueller, R. T.; Pingsmann, A.; Schrader, B. *Biospectroscopy* **1998**, *4*, 403–412.
100. Zinelis, S.; Thomas, A.; Syres, K.; Silikas, N.; Eliades, G. *Dent. Mater.* **2010**, *26*(4), 295–305.
101. Lemor, R. M.; Kruger, M. B.; Wieliczka, D. M.; Swafford, J. R.; Spencer, P. *J. Biomed. Optics* **1999**, *4*, 22–27.
102. Miyazaki, M.; Onose, H.; Moore, B. K. *Dent. Mater.* **2002**, *18*, 576–580.
103. Georgakoudi, I.; Rice, W. L.; Hronik-Tupaj, M.; Kaplan, D. L. *Tissue Eng. B Rev.* **2008**, *14*, 321–340.
104. Boyd, A.; Burke, G.; Meenan, B. *J. Mater. Sci. Mater. Med.* **2010**, *21*(8), 2317–2324.
105. Van Manen, H.-J.; Kraan, Y. M.; Roos, D.; Otto, C. *Proc. Natl. Acad. Sci. USA* **2005**, *102*, 10159–10164.
106. Davies, M. C.; Binns, J. S.; Melia, C. D.; Bourgeois, D. *Spectrochim. Acta A* **1990**, *46*, 277–283.
107. Tudor, A. M.; Melia, C. D.; Binns, J. S.; Hendra, P. J.; Church, S.; Davies, M. C. *J. Pharm. Biomed. Anal.* **1990**, *8*, 717–720.
108. Wartewig, S.; Neubert, R. H. H. *Adv. Drug Deliv. Rev.* **2005**, *57*, 1144–1170.
109. Liu, Z.; Tabakman, S.; Welsher, K.; Dai, H. *Nano Res.* **2009**, *2*, 85–120.
110. Liu, Z.; Li, X.; Tabakman, S. M.; Jiang, K.; Fan, S.; Dai, H. *J. Am. Chem. Soc.* **2008**, *130*, 13540–13541.

Relevant Websites

www.spectroscopyNow.com

3.328. Biosensors Based on Sol–Gel-Derived Materials

S N Tan, Nanyang Technological University, Singapore
W Wang, Nanyang Technological University, Singapore; Yancheng Institute of Technology, Yancheng, People's Republic of China
L Ge, Nanyang Technological University, Singapore

© 2011 Elsevier Ltd. All rights reserved.

3.328.1.	**Introduction**	471
3.328.2.	**Sol–Gel Bioencapsulation**	472
3.328.2.1.	Sol–Gel Immobilized Biorecognition Elements	472
3.328.2.1.1.	Enzymes	472
3.328.2.1.2.	Antibodies	473
3.328.2.1.3.	Whole cells	473
3.328.2.2.	Stability of Biorecognition Elements in Sol–Gel Matrix	474
3.328.2.3.	Interactions Between Sol–Gel Matrix and Analytes	474
3.328.3.	**Applications of Sol–Gel Biosensors**	475
3.328.3.1.	Electrochemical Biosensors	475
3.328.3.2.	Optical Biosensors	483
3.328.3.3.	Biosensors Based on Other Transducing Principles	486
3.328.4.	**Conclusions and Future Trends**	486
References		487

Abbreviations

AchE	Acetylcholinesterase
ALP	Alkaline phosphatase
BOD	Biochemical oxygen demand
BPEI	Branched polyethyleneimine
bR	Bacteriorhodopsin
CCEs	Ceramic composite electrodes
ChOx	Cholesterol oxidase
CMOS	Complementary metal oxide semiconductor
CNTs	Carbon nanotubes
cyt c	Cytochrome *c*
FITC	Fluorescene isothiocyanate
GO	Galactose oxidase
GOx	Glucose oxidase
Hb	Hemoglobin
HRP	Horseradish peroxidase
Mb	Myoglobin
MB	Meldola blue
MBCPs	Multiblock copolymers
NADH	Adenine dinucleotide
NO	Nitric oxide
ormosil	Organically modified silicate
pDNA	Plasmid DNA
PEG	Polyethylene glycol
PVA-*g*-PVP	Poly(vinyl alcohol)-grafted-poly(4-vinylpyridine)
$Ru(dpp)_3$	Ru(II)-tris(4, 7-diphenyl-1, 10-phenanthroline)
SOD	Superoxide dismutase
SWNT	Single-walled carbon nanotubes
TEOS	Tetraethoxysilane
TMOS	Tetramethoxysilane
XO	Xanthine oxidase

3.328.1. Introduction

Sol–gel processing technique, first reported by Ebelman in the mid-eighteenth century, historically used for fabricating decorative and constructional materials, was extensively developed in the last century for applications such as glasses, ceramics, catalysts, coatings, composites, and fibers.[1] In general, the sol–gel process involves the transition of a system from a liquid 'sol' (mostly colloidal) into a solid 'gel' phase. Because of the special properties of sol–gel materials (e.g., optical transparency, porosity and high surface area, chemical inertness), sol–gel technology has been gradually extended to the encapsulation of specific biorecognition elements, such as enzymes, antibodies, oligonucleotides, or even whole cells and tissues.[2,3] The immobilized biological recognizing elements in sol–gel matrix exhibit structural integrity, very often full biological functions and also significant stability to resist chemical and thermal deactivation.[4,5] Moreover, the sol–gel matrix provides the advantages of good biocompatibility and large immobilization capacity.[3,6] As a result, sol–gel materials offer a suitable and versatile platform for the fabrication of biosensors.[7–9]

A biosensor is a device capable of providing selective quantitative or semiquantitative analytical information using a biological recognition element, by converting a biochemical event into a detectable signal via a transducer and a processor.[8–10] Typically, the biosensor is a self-contained analytical device capable of detecting an analyte which consists of a selective biorecognition element (bioreceptor) and a transducer which converts the changes in the physicochemical properties during the detection of an analyte into a suitable

analytical signal. Biosensors can be classified according to the transduction element (e.g., electrochemical, optical, piezoelectrical, thermometric, or magnetic biosensor) or the biorecognition principle (e.g., enzymatic, immunoaffinity recognition, or whole-cell biosensor). Since the first introduction of the word 'biosensor' by Clark and Lyons,[11] numerous exciting biosensor designs have been proposed in several reports during the past few decades. Nevertheless, simple, low cost, and reliable methods for bioreceptor immobilization are still required for the further development of biosensors, as immobilization is the key step in the fabrication of biosensors.

Several excellent book chapters[9,12] and reviews[7,8] on the applications of sol–gel process for the development of various biosensors for a wide range of applications have been published. Through an exhaustive survey of literatures, it has been shown that a significant number of recent papers clearly illustrate the growing interest on the sol–gel process to develop biosensors.

This chapter, therefore, summarizes a variety of currently available biosensors based on sol–gel-derived materials. Section 3.328.2 gives an overview of current developments in the various sol–gel bioencapsulation techniques, classified according to the immobilized biorecognition elements, stability of biorecognition elements, and interactions between sol–gel matrix and analytes; Section 3.328.3 describes the different classes of sol–gel biosensors, including electrochemical biosensors, optical biosensors, and biosensors based on other transducing principles in detail; and Section 3.328.4 outlines the concluding remarks, challenges, and future prospects of biosensors based on sol–gel-derived materials.

3.328.2. Sol–Gel Bioencapsulation

Sol–gel processing is a soft-chemistry method and high purity method to obtain functionalized materials at low temperature and mild chemical conditions. These materials' hosting and recognition properties, as well as their flexible chemical structures containing many easily accessible active sites, make them particularly attractive for analytical purposes.

Immobilization of biological recognizing elements (e.g., proteins, enzymes, antibodies, DNA, and whole cells) by entrapment in the sol–gel materials has become a research area of intense interest.[2,4,8,13,14] Braun *et al.*[15] first reported that a purified enzyme, alkaline phosphatase (ALP), can maintain some of its biological activity while being entrapped in a tetramethoxysilane (TMOS)-derived sol–gel matrix. Later, Ellerby *et al.*[16] modified this approach to improve on the stability of biomolecules during encapsulation. Bioencapsulation in sol–gel matrices typically involves hydrolysis of tetraalkoxysilanes in an acidic or alkaline medium followed by the addition of biomolecules in the presence of a buffer (pH 7), which initiates condensation of the hydrolyzed precursors around the biomolecules that become physically entrapped in an active form within the porous silicate network.

Since these pioneering studies, many enzymes and proteins have been immobilized in a functional state, and quite a few of them have been protected against degradation by the sol–gel network and have exhibited better activity and longer lifetime than free soluble enzymes. By entrapment in (surfactant modified) silica sol–gel matrices, ALP, naturally with an optimum pH of 9.5, was kept active at extreme acidic environment as low as pH 0.9 and acid phosphatase, naturally with an optimum activity at pH 4.5, was kept functioning at extreme alkaline environment up to pH 13.0. It was found that the protection of the enzymes against harsh pH conditions is dependent on the nature of the surfactant in the sol–gel matrix.[17] Recently, researchers have attempted to optimize this process by controlling the porosity of bioencapsulates and chemical environment of trapped species to avoid the too constrained motions of encapsulated proteins, and to obtain the necessary conformational changes for binding and release of substrates. Investigators have also proposed alternative synthetic routes to avoid enzyme denaturation due to release of alcohol during the hydrolysis and condensation of the tetraalkoxysilanes in a typical sol–gel process. Notably, avoiding denaturation requires the use of biocompatible silane precursors, aqueous silicate starting materials, protein-stabilizing additives, such as charged polymers, or sugars and amino acids.[17,18]

Bioencapsulation via sol–gel processing enables the conversion of labile biological materials into reusable and physicochemically robust (nano)composites that can be interfaced with spectroscopic and electrochemical platforms to generate different analytical useable biosensing devices.[19] The porous structure of the silica matrix ensures an effective biomolecule entrapment while enabling analytes to access the bioactive centers and the diffusion of product(s) from the reaction site. To ensure that the biosensor can achieve the best possible performance, one must provide suitable transduction of the biological recognition event into a measurable physical signal, and one must enhance both the accessibility of the analytes to entrapped biorecognition elements and the mass-transfer rates to improve the biosensor sensitivity.

3.328.2.1. Sol–Gel Immobilized Biorecognition Elements

3.328.2.1.1. Enzymes

Since the emerging report of sol–gel bioencapsulation, enzymes have been widely studied due to their well-known biochemical mechanisms, commercial availability in good purity, wide applications, good solubility in water, good stability, and simple molecules compared with animal, plant, or microorganisms. Dickery[20] demonstrated for the first time bioencapsulation with partial activity of urease and catalase in the sol–gel matrix, but muscle adenylic acid deaminase completely lost its activity. After three decades, considerable attention has resurfaced toward the bioencapsulation using sol–gel glasses. Braun *et al.*[15] successfully encapsulated ALP in silica gel, which retained its activity up to 2 months with improved thermal stability. Furthermore, Shtelzer *et al.*[21] sequestered trypsin within a binary sol–gel-derived composite using tetraethoxysilane (TEOS) and polyethylene glycol (PEG). Ellerby *et al.*[16] also entrapped other proteins, cytochrome *c* (cyt *c*) and myoglobin (Mb), in TEOS sol–gel. Later studies on bioencapsulation were well recorded by other groups, and several proteins, such as Mb, hemoglobin (Hb), cyt *c*, lactate oxidase, glucose oxidase (GOx), ALP, Cu–Zn superoxide dimutase, urease, bacteriorhodopsin (bR), horseradish peroxidase (HRP), and acetylcholinesterase (AchE) were immobilized into various sol–gel matrices. Other studies have included the

various aspects of sol–gel entrapped biomolecules in various properties, such as conformation, dynamics, accessibility, reaction kinetics, activity, and stability.

3.328.2.1.2. Antibodies

The specificity and sensitivity of antigen recognition by antibodies or enzyme-labeled antibodies immobilized in sol–gel materials have been exploited to design affinity biosensors and immunoassays.[22] An acid-labile temperature-responsive sol–gel reversible polymer for enhanced gene delivery to the myocardium and skeletal muscle cells was reported; multiblock copolymers (MBCPs) synthesized from pluronic (R) and di-(ethylene glycol) divinyl ether were used as a delivery vehicle for controlled and sustained release of plasmid DNA (pDNA) in *in vitro* as well as *in vivo* experiments. The nonionic MBCP/pDNA complex showed remarkable transfection efficiencies against the myocardium cells as well as muscle cells *in vivo*, which is otherwise very difficult to achieve by using cationic polymers. In *in vitro* experimental settings, this intelligent stimuli-responsive polymer was shown to improve the transfection efficiency of branched polyethylenimine (BPEI)/pDNA complex when used together. The rapid sol–gel transition of MBCP under thermal stimuli with concomitant release of pDNA under acidic stimulation has potential for site specific, efficient, and controlled transfection of therapeutic gene.[23] The schematic was shown in Figure 1.

In addition to the obvious applications of these designs, namely determining biologically relevant species and detecting diseases, they have also been used for environmental monitoring, for example, detecting contaminants that alter the biosensor response.[24] Although some optical detectors have been reported (e.g., on the basis of antifluorescein antibodies), the key transduction method has mostly involved electrochemical methods, namely potentiometry, amperometry, and conductometry. Sol–gel-derived electrochemical immunosensors based on enzyme-labeled antibodies have experienced advances similar to those described in Section 3.328.2.1.1 and Section 3.328.2.1.2, including improvements in charge-transfer reactions, mass transport of analytes, and the durable immobilization of all components onto the electrode surface. Aptamers are oligonucleic acid or peptide molecules that bind to a specific target molecule, usually created by selecting them from a large random sequence pool, and have been developed to specifically capture the toxic target molecules.[25] Notably, these improvements have allowed us to take advantage of the chemistry of organosilane reagents to enhance the analytical performance and operational stability of the devices[26] and to use nanoparticles assembled in three-dimensional sol–gel networks to enhance the sensitivity of amperometric immunosensors.[27]

3.328.2.1.3. Whole cells

Whole cells (e.g., *Escherichia coli*) have been encapsulated in sol–gel materials in a way that blocks their proliferation and prevents bacterial death upon entrapment,[18,28] which are necessary prerequisites for biosensor development. Most biosensors based on sol–gel entrapment of whole cells employ optical detection modes that exploit the excellent transparency of the silica matrix. Recent examples include fluorescence detection of herbicides with immobilized *Chlorella vulgaris*[29] and naphthalene determination from the bioluminescence response of the bacterial bioreporter *Pseudomonas fluorescens* HK44.[30] Liu *et al.*[31] reported on an organic–inorganic hybrid material, which consisted of silica and copolymer of poly (vinyl alcohol)-grafted-poly(4-vinylpyridine) (PVA-*g*-PVP), and employed to immobilize *Trichosporon cutaneum* strain 2.570 cells. It revealed that arthroconidia produced in the

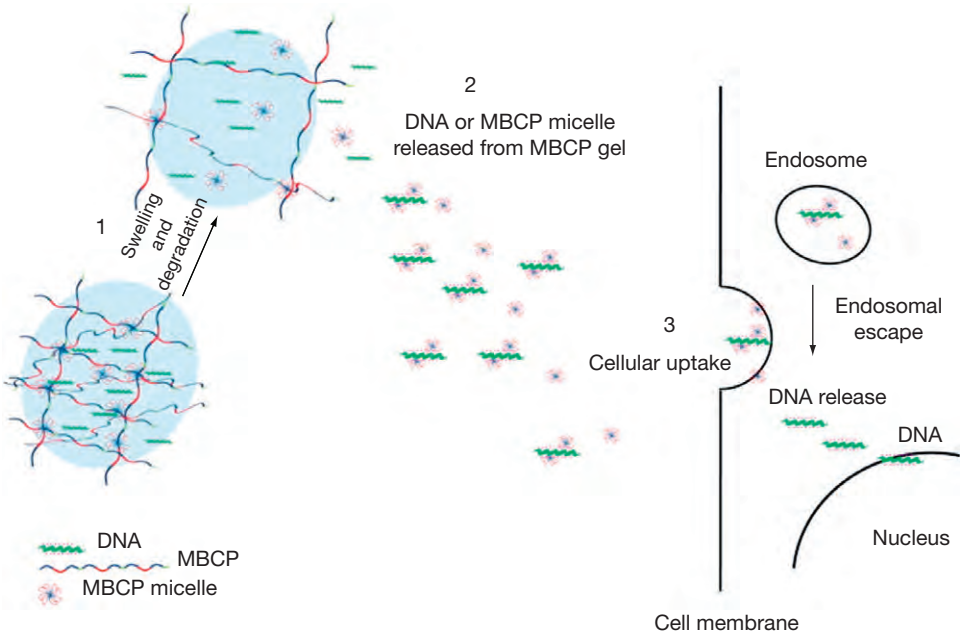

Figure 1 Schematic diagram of MBCP-mediated gene delivery. By swelling and degradation of MBCP gel (1), DNA or MBCP micelles are released into the medium and form complex (2), finally complexes enter into the cells by endocytosis (3). Adapted from Namgung, R.; Nam, S.; Kim, S. K.; *et al. Biomaterials* **2009**, *30*, 5225–5233, with permission.

extracellular material played an important role in keeping the long-term viability of the immobilized microorganism. Other detection methods are based on piezoelectric or surface plasmon resonance measurements. In addition to bacteria, other microorganisms can be used for biosensing applications.[32]

3.328.2.2. Stability of Biorecognition Elements in Sol–Gel Matrix

Leaching of biorecognizing elements from the sol–gel matrix is one of the problems of the immobilization method and this is due to the porosity of the matrix. The decrease in concentration of entrapped species can be observed because these entrapped species are able to migrate out of the matrix resulting in contamination of the media and degradation performance of the biosensor. Direct bonding of molecules to inorganic network is difficult due to relative inertness of the surface, for example, silica matrix has only siloxane and silanol groups.[33] However, such materials can be activated via surface modification, that is, via functional group immobilization which allows the formation of covalent bond. Unfortunately, covalent immobilization may alter the structural and optical properties of the sensing reagent leading to a loss of biosensing properties. In some applications, increasing the hydrophobicity of the network can also prevent leaching. In this case, hydrophobicity allows the increase of sensitivity because water, which decreases the gas permeability, cannot penetrate into the matrix. Another opportunity to increase the chemical stability of the biosensor is preparation of organic–inorganic copolymer using, for instance, using poly(vinyl alcohol) and silica.[34]

The conformational structures of entrapped proteins have been examined. Conformational studies have indicated that proteins tend to retain a native conformation immediately upon entrapment, although some proteins, such as Mb, may undergo substantial conformational changes during entrapment.[35] Aging of the sol–gel matrix can induce significant structural changes in the entrapped proteins. For example, fluorescence measurements for the acrylodan-labeled proteins were consistent with partial unfolding of a fraction of the entrapped protein as aging continued. These structural changes resulted from the changes in internal solvent composition (owing to loss of water and solvent molecules) and subsequent protein–silica interactions, which lead to undesirable changes in the protein conformation. Studies have indicated that the conformational motions of large proteins, such as bovine serum albumin, can be substantially restricted in the sol–gel media, and that in certain cases inactive conformations may end up 'trapped' in the sol–gel matrix.[36] On the other hand, small proteins, such as cyt *c* and parvalbumin, appear to retain their full conformational flexibility upon entrapment and are only moderately affected by aging of the matrix. The inability of larger proteins to fully unfold within the silica-based glasses indicates that the small pore sizes provide insufficient free volume to accommodate the fully unfolded protein as typical pore diameters in aged silicates are 5–20 nm.

Denaturation studies have also indicated that the entrapment of proteins often leads to the need for higher temperatures or denaturant levels to induce protein unfolding.[37,38] Entrapment can also stabilize proteins against other denaturing forces, for example, in the case of catalase, the silica gel stabilises the encapsulated enzyme to higher methanol concentrations. Oxidation of either HRP or Mb by peroxide can also be minimized by immobilization of the proteins in the silicate matrix. The enhanced stability of entrapped proteins has been related to a 'molecular confinement' process, wherein the protein is restricted in its ability to undergo conformational changes and therefore requires a higher energy input before it can unfold. Studies have suggested that increased thermal stability may in fact be transient and that continued aging of the matrix can result in slow denaturation of the protein and loss of conformational integrity. These studies have also indicated that the unfolding of entrapped proteins in most cases is irreversible, predominantly owing to adsorption of the unfolded protein onto the solvent–silica interface. However, reversible denaturation has been reported in the case of the anionic Ca(II)-binding protein oncomodulin,[39] likely owing to unfavorable electrostatic interactions between the protein and the silicate surface.

3.328.2.3. Interactions Between Sol–Gel Matrix and Analytes

The interactions between sol–gel matrices and analytes include electrostatic, hydrogen bonding, and hydrophobic interactions.[40,41] They play key roles in the accessibility of analytes to the entrapped biomolecules even though the pore sizes are large enough for the analytes to pass though the matrices and are important in determining the accessibility of analytes to entrapped proteins. For cases in which repulsive or attractive interactions exist between the glass and analytes, the sol–gel matrices take up the analytes either partially or excessively.[19,42] The study of these interactions is very important because they affect the diffusional properties significantly. Collinson[43] revealed that diffusion is governed by interactions between the entrapped cationic guest and the negatively charged walls of the sol–gel host. Specifically, negatively charged molecules reside in the center of the fluid-filled pore and move at rates similar to the rates at which they move in solution. Positively charged molecules, however, electrostatically interact with the walls of the matrix (silica has a p*I* of −2 and therefore the walls are negatively charged under these conditions) and do not move as rapidly. Diffusional rates slow down as the gel dries and shrinks because the entrapped reagents are closer to the pore walls. The results were supported by strategically modifying the walls of the silica host with organoalkoxysilanes. The most convincing evidence comes from hybrid gels prepared using *N*-trimethoxysilylpropyl-*N*,*N*,*N*-trimethyl trimethylammonium chloride or a polyamine (N^+) polymer. In these gels, it was shown that $Co(bpy)_3^{2+}$, a large positively charged ion, diffused at the same rate as it did in the sol and maintained that rate during a 3-week drying period. In contrast, $Fe(CN)_6^{3-}$ showed an order of magnitude drop in its apparent diffusion coefficient during a few days of drying period. In either case, internal and external concentrations of the ion are unequal even after equilibrium is reached.[44] The protein entrapped in TEOS gels completely showed accessibility to the neutral quenchers, perhaps partial accessibility or repulsion in case of negatively charged quenchers.[45]

3.328.3. Applications of Sol–Gel Biosensors

By far, the most widespread applications of biological recognizing elements doped sol–gel materials have been the development of biosensors. A number of review articles have been published in the general field of sol–gel-based biosensing.[8,14,42,46–48] Such biosensors rely on the intimate interfacing of a biorecognition element to a physical transducer that converts the biological reaction into a measurable signal. Typical transduction schemes in biosensors include electrochemical, optical, piezoelectrical, thermometric, and magnetic methods. However, most sol–gel-based biosensors have relied on electrochemical and optical transduction schemes, for example, amperometric, potentiometric, fluorescent, and absorbent modes.

In the case of biosensors, the key attributes that can be optimized include response time, initial and long-term biological activity, analytical range, sensitivity, selectivity, detection limit, and reproducibility. To a certain extent, many of these parameters are determined by the biorecognition element itself on the basis of its binding constant to the analyte of interest and by the specific detection method employed. Substantial changes in analytical performance can, therefore, be derived from changes in these parameters. A great effort has been made to understand short- and long-term interactions between the biorecognition elements and the evolving sol–gel matrix.[7,49,50] Typically, reduced accessibility or activity leads to poorer sensitivity and detection limits and may alter the analytical range. Furthermore, analyte–matrix interactions can lead to an expanded analytical range, but lower sensitivity, although this can be controlled to some degree by the addition of charged polymers. Other advantages include the ability to make the matrices either electrochemically active or optically transparent, the ability to achieve high protein loading, to tune the polarity and porosity of the matrix to selectively modulate enzyme activity, the potential to modulate the material composition to maximize the biocompatibility of the matrix, and the reduced leaching of biomolecules.

While sol–gel-based biosensors have several advantages, they also suffer from a number of disadvantages. For example, it is generally difficult to predict the final properties of the sol–gel matrix. Aging of sol–gel materials is also a problem, as this process can take up to several months. As the matrix ages, the analytical parameters of merit also change; hence, there is a need for continual recalibration of the biosensor. Denaturation of entrapped biorecognition elements with time can also lead to problems with calibration, and may even result in a loss of biosensor function overtime. Furthermore, pore diameters must be carefully controlled to allow facile transport of analytes into the matrix and diffusion of products away from the reaction site, while preventing leaching of entrapped biorecognition elements. Finally, cracking and shrinkage of the matrix during aging can lead to serious problems with biosensor responses and, in some extreme cases, can lead to removal of the bioreceptor from the biosensor surface.

Sol–gel bioencapsulation has been widely used to immobilize enzymes onto the surface of an electrode or an optical biosensor. The development of biological-based rapid glucose assays has centered on the development of glucose biosensors.[51] Many of the sol–gel-based biosensors typically focus on glucose biosensing as a test case, mainly due to the inherent stability of GOx, the diversity of sensing parameters for glucose, and the clinical importance of this analyte. Glucose biosensors rely on entrapment of GOx, which catalyzes the oxidation of glucose to gluconic acid, and the simultaneous generation of hydrogen peroxide (H_2O_2). The GOx enzyme has been entrapped into a wide variety of sol–gel-derived materials, including silica, metallosilicates, ormosils, and composites which have been formed as monoliths, fibers, layers, thin films, or microarrays. Detection strategies for glucose have relied on the measurement of oxygen levels, H_2O_2 concentration, pH, or changes in the emission properties of the flavin moiety of GOx using electrochemical, absorbent, or fluorescent transduction schemes. Such methods typically provide sensitivity over the physiologically relevant range, rapid response times, and good stability.

In addition to GOx and HRP, biomolecules such as urease, AchE (for pesticide detection), cholesterol oxidase (ChOx), lactate oxidase and lactate dehydrogenase, monoamine oxidase, tyrosinase, catalase, and other oxidoreductases and even whole cells have been developed based on sol–gel-derived biosensors. Bienzymatic immobilization has also been applied to improve the performance of such biosensors.[52] These include substrates, cofactors, effectors, and inhibitors of enzymes, antigens, and haptens that bind to antibodies and gaseous molecules such as O_2, CO, and NO that bind to heme-containing transport proteins. The majority of biosensors fabricated by the sol–gel method have demonstrated reasonable performance with good detection limits, useful analytical ranges, and in many cases excellent long-term stability.

3.328.3.1. Electrochemical Biosensors

Sol–gel-derived materials have attracted the attention of many electrochemists because they provide a versatile way to prepare modified electrodes.[7,8,19,42,53,54] One of the major advantages that sol–gel technology offers to the electrochemical biosensor is that the composition of sol–gel hybrid materials can be easily varied to develop electrodes with different configurations. The slow diffusion of the electroactive species within the sol–gel matrix causes a long response time, hence for the improvement of conductivity, it is possible to prepare electrodes that contain conducting species, organosilanes or polymer additives, redox mediators, and several enzymes, each of which can be used to finetune the properties of the electrode. Typical conducting species including graphite, gold, palladium, iridium, ormosils, and polymers are generally used to modulate enzyme activity. For example, it has been demonstrated that the incorporation of polycationic polymers into the sol–gel materials could improve the performance of flavoproteins,[55,56] while Wang *et al.*[57] demonstrated that the incorporation of copolymers into silica-based glasses can improve the activity of entrapped GOx for amperometric detection of glucose. Gavalas *et al.*[58] have doped carbon nanotubes (CNTs) as conductive materials into alkoxysilane sol–gels, and L-amino oxidase was encapsulated into CNT sol–gel through and an aqueous sol–gel process. The added particles improved

morphology of the composite surface and electrochemical response characteristics.

Most sol–gel-derived electrochemical biosensors reported to date have mainly relied on one of the two basic configurations: conductive ceramic composites and thin sol–gel film coating on the electrode surface. Since the pioneering work of Glezer and Lev,[59] sol–gel-derived composite carbon electrodes have been widely used to develop all kinds of amperometric biosensors.[60–62] The first configuration utilizes a bulky monolith that is doped with conducting materials to create a conducting bioceramic. This is typically achieved by dispersion of carbon or metal powders or colloids (the conductor) together with biomolecules and mediators (when necessary) into the sol before gelation occurs.[63–65] This protocol yields rigid, porous, conducting biocomposites that can be molded in glass tubes to obtain a disk electrode. In particular, this type of biocomposites is suitable for microfabrication. The second configuration involves formation of thin films by spin or dip coating or simply spreading of a sol containing biomolecules and mediators on top of the conventional electrode surfaces.[66–71] This configuration usually avoids the need for dispersion of a conductive component, and is most useful for electrochemical biosensors because of its short diffusion pathway. Three main approaches for the electrodes dependent on the convenience, stability, and response are as follows: single-layer, bilayer, and sandwich configurations (Figure 2). Along with entrapment inside the sol–gel matrix, a few studies have been carried out by covalently linking the active biomolecules on the surface of the sol–gel functionalized matrices.[72,73] Another important factor in developing biosensors is the thickness of gel film. In most cases, thin films exhibit quicker response than the thick layers due to the good diffusion properties.[74–76] With increasing gel thickness, the signal decays and diffusion of analytes to a biomolecule active site becomes slow; eventually these factors lead to poor response. Homogeneous distribution of enzymes is possible in sol–gel films compared with regular carbon paste electrodes; hence, it allows the homogeneous electron transfer and larger current response in amperometric sensing.

Figure 2 illustrates the three most commonly used thin film configurations employed in sol–gel-derived electrochemical biosensors. In the single-layer configuration, the bioreceptor-doped sol–gel film is directly deposited onto the electrode surface. For mediated electrochemical biosensors, mediators can be entrapped together with the bioreceptor in the sol–gel film or may be present in the solution phase, if it is soluble. In the bilayer configuration, initial sol–gel layer is first deposited on the electrode surface and the bioreceptor is then attached either by simple adsorption or by covalent binding via functional groups such as thiol or amine groups present on the sol–gel surface. In this case, the bioreceptor solution can be directly deposited on the surface of an electrode such as a carbon paste electrode, after which a sol–gel film is deposited as a protective layer to prevent the leaching of bioreceptor. For mediated biosensing, the mediator layer is first deposited on the electrode surface and a layer of a bioreceptor-doped sol–gel film is then deposited on top of the mediator layer. For the deposition of the mediator layer, the mediator can be dissolved in an organic solvent or added in the sol before application on the top of the electrode surface.

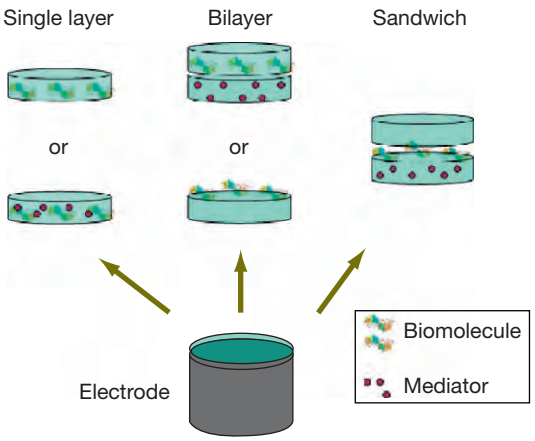

Figure 2 Configurations used to interface sol–gel-derived thin films to electrochemical biosensors.

In the sandwich configuration,[77,78] the mediator-doped sol–gel layer is first deposited on the electrode surface. The bioreceptor layer can be formed by spreading either an enzyme solution or an enzyme containing sol on top of the mediator layer. Another layer of sol–gel-derived material is then added as a protective layer, which prevents bioreceptor leaching and microbial attack. The key advantage of the sandwich configuration is that the methods used to form the first layer and second layer, and the thicknesses, polarity, and porosity of these layers can be different, permitting some control over the final properties of the sandwich films. The two sol–gel layers have great influence on the performance of the glucose biosensor.[63] This configuration provides good sensitivity, low detection limits, and fast response times compared to the use of a bulky monolith for electrochemical measurements. Pauliukaite *et al.*[78] reported protective polymer coatings used to enhance the retention of enzymes in sol–gel films. Carbon film electrodes were electrochemically modified with poly (neutral red). These electrodes were coated with sol–gel films incorporating GOx and an outer coating of carboxylated poly(vinyl chloride) or polyurethane (PU) with and without Aliquat-336 or isopropyl myristate plasticizer. The membranes without plasticizer extend the lifetime of the biosensor to more than 2 months, when PU is used as an outer membrane.

The typical electrochemical biosensors based on sol–gel matrices are listed in Table 1. As shown in Table 1, among the numerous enzymes studied, GOx and HRP have been widely used in sol–gel entrapment studies. The sol–gel immobilized GOx exhibits high thermal stability in terms of half-life mainly due to the favorable local polymer–protein interaction between the positive charges on the GOx and the negatively charged silicate matrix. Tatsu *et al.*[163] prepared TEOS-derived silica gel doped with GOx and responded to glucose of physiological concentration in a flow-injection analytical system. Metal alkoxides are more attractive matrices because they provide good conductivity and the possibility of manipulation of polarity, rigidity, pore size and distribution, and electronic conductivity. Taking into consideration the advantages of metal alkoxides, Glezer and Lev[59] prepared platinum electrodes coated with vanadium pentoxide sol–gel film doped with GOx. Wang *et al.*[71] reported a glucose biosensor based on immobilization

Table 1 Typical electrochemical biosensors based on bioreceptors encapsulated in sol–gel matrices

Biorecognition element(s)	*Analyte(s)*	*Sol–gel precursors*	*Principle of detection*	*Linear range/detection limit*	*References*
Acetylcholinesterase	Paraoxon	ZnO	Amperometry	0.035–1.38 ppm	65
Acetylcholinesterase	Chlorpyriphos-ethyl-oxon	Al_2O_3	Amperometry	2.5×10^{-10} M	79
Alcohol dehydrogenase	Alcohol	Pd–Ormosil	Amperometry	0.04 mM	80
Alcohol dehydrogenase	Alcohol	CNT–Ti_2O_3	Amperometry	1.0×10^{-5} M/3.0×10^{-3} M	81
Aldehyde dehydrogenase	Acetaldehyde	MTMOS/Meldola's blue	Amperometry	10–260 μM	82
L-Amino acid oxidase	L-Phenylalanine	Ormosil	Electrochemical method		60
L-Amino acid oxidase	L-phenylalanine	PTMOS/sodium silicate/carbon nanotubes	Cyclic voltammetry	0.02–10 mM/0.02 mM	58
Catalase	H_2O_2	TMOS	Voltammetry	1–30 μM/0.4 μM	83
Cholesterol oxidase	Cholesterol	TMOS	Amperometry	60 μM–3 mM	84
Cholesterol oxidase	Cholesterol	TEOS/Prussian blue	Cyclic voltammetry	1×10^{-6}–8×10^{-5} M/1.2×10^{-7} M	85
Cholesterol esterase/cholesterol oxidase	Cholesterol oleate	TEOS/chitosan/multiwalled carbon nanotubes	Cyclic voltammetry	10–500 mg dl^{-1}	86
Cholesterol oxidase/HRP	Cholesterol	TEOS	Amperometry	2–10 mM/0.5 mM	87
Choline oxidase	Choline	TEOS	Amperometry	5×10^{-6}–1×10^{-4} M/1×10^{-7} M	88
Choline oxidase	Choline	TEOS/CNT	Cyclic voltammetry	4.0×10^{-6}–1.0×10^{-4} M/1.4×10^{-6} M	89
Complement 3 antiserum	Complement 3	MTrMOS	Amperometry	1.17–35.1 μg ml^{-1}/0.56 μg ml^{-1}	90
Creatininase and creatinase	Creatinine	Ormosil	Cyclic voltammetry	100 μM	91
Creatinine MIP	Creatinine	TEOS/MIP	Differential pulse, cathodic stripping voltammetric	1.23–100 μg ml^{-1}/0.37 μg ml^{-1}	92
Cytochrome P450 $_{cam}$	Camphor	MTEOS/DDAB	Electrochemical method	0.01–0.25 mM	66
D- and L-3,4-dihydroxyphenylalanine MIP	D- and L-3,4-dihydroxyphenyl-alanine	TMOS/PTMOS	Square wave voltammetry	1 nM	93
DNA	DNA	MPTMS/GPTMS	Differential pulse voltammetry	2.51×10^{-9}–5.02×10^{-7} M/8.57×10^{-10} M	94
DNA	DNA	MPTMS/colloidal Ag	Electrochemical impedance spectroscopy	8.0×10^{-9}–1.0×10^{-6} M/4.0×10^{-9} M	95
Galactose oxidase	Galactose	TMOS	Amperometry	20 μM–4 mM	84
GOx	Glucose	TMOS/Prussian blue	Amperometry	0–4–75 mM/0.02 mM	96
GOx	Glucose	Ormosil/ferrocenemonocarboxylic acid	Amperometry	0–35 mM	97
GOx	Glucose	TEOS	Electrochemical method	5–30 mM/0.2 mM	98
GOx	Glucose	TEOS/PVA-*g*-PVP	Electrochemical method	0–14 mM	57
GOx	Glucose	Ormosil	Electrochemical method	0–4.6 mM/$<$0.1 mM	69
GOx	Glucose	MTrMOS	Amperometry	0–15 mM	99
GOx	Glucose	MTrMOS	Amperometry	0.1–9.6 mM/40 μM	100
GOx	Glucose	Al(i-PrO_3)	Amperometry	40 μM–21.9 mM/10 μM	101
GOx	Glucose	MTEOS	Amperometry	2.0–31 mM/0.5 mM	102
GOx	Glucose	Pd–Ormosil	Amperometry		103
GOx	Glucose	Ormosil	Amperometry		69
GOx	Glucose	Ormosil	Amperometry		70
GOx	Glucose	TMOS	Amperometry	2 μM–2 mM	84
GOx	Glucose	MTrMOs	Amperometry	0–10 mM/0.05 mM	104
GOx	Glucose	Titanium isopropoxide/PVA-*g*-PVP	Amperometry	0–9 mM	105

(*Continued*)

Table 1 (Continued)

Biorecognition element(s)	*Analyte(s)*	*Sol–gel precursors*	*Principle of detection*	*Linear range/detection limit*	*References*
GOx	Glucose	MTMOS/polyurethane	Amperometry	0–60 mM	106
GOx	Glucose	MPTMS/copper nitrate/ graphite powder	Amperometry	4.0×10^{-5}–5.6×10^{-3} M/ 1.8×10^{-5} M	107
GOx	Glucose	MTMOS/APTMOS	Cyclic voltammetry	0.1–27 mM/26 μM	73
GOx	Glucose	APTMS/EETMS	Amperometry/ flow-injection analysis	1×10^{-4}–5×10^{-3} M	108
GOx & HRP	Glucose	MTMOS	Amperometry	8.0×10^{-5}–1.3×10^{-3} M	109
GOx	Glucose	Zn-APTMS/TEOS-PEG	Amperometry	4×10^{-6}–1×10^{-3} M/ 2.0 μM	110
GOx	Glucose	Titanium isopropoxide	Cyclic voltammetry	0.07–15 mM	111
GOx	Glucose	MTMOS/CNT	Amperometry	1–25 mM	112
GOx	Glucose	MTMOS/ferrocene	Amperometry	3.2×10^{-4}–3.5×10^{-2} M/ 0.3 mM	113
GOx	Glucose	TEOS/PVA	Cyclic voltammetry	0–4.13 mM/9.8 μM	114
GOx	Glucose	GOx–CNT–PtNP–chitosan–MTOS	Cyclic voltammetry	1.2×10^{-6}–6.0×10^{-3} M/ 3.0×10^{-7} M	115
GOx	Glucose	TEOS	Linear sweep voltammogram	0–10 mM/0.01 mM	116
GOx	Glucose	Al_2O_3	Amperometry	4.00×10^{-5}–2.19×10^{-2} M/ 1×10^{-5} M	101
GOx	Glucose	MTMOS/carbon powder/ vinylferrocene	Amperometry	1×10^{-4}–9.6×10^{-3} M/ 4×10^{-5} M	100
GOx	Glucose	TEOS	Amperometry	0–500 mg dl^{-1}	117
GOx	Glucose	Al_2O_3/BSA/polyurethane	Amperometry	0–40 mM/5.2 mM	118
GOx	Glucose	TEOS/APTMOS/Prussian blue (PB)	Amperometry	0.01–5.8 mM/0.94 μM	72
GOx	Glucose	TMOS/Prussian blue (PB)	Amperometry	0–4.75 mM/0.02 mM	96
Gonorrhoea DNA	Gonorrhoea	ZnO	Amperometry	0.000524 fmol–0.524 nmol	119
Hemoglobin	H_2O_2	Titanium isopropoxide	Amperometry	5.0×10^{-7}–5.4×10^{-5} M/ 1.2×10^{-7} M	120
Hemoglobin	H_2O_2	TEOS/glycerol	Cyclic voltammetry	1×10^{-6}–2.8×10^{-4} M	121
Hepatitis B surface antibody	Hepatitis B surface antigen	MPTMS	Potentiometry	4–960 ng ml^{-1}/1.9 ng ml^{-1}	122
HRP	Cyanide	MTEOS	Amperometry	0.004–0.04 mM/0.5 μM	123
HRP	H_2O_2	TMOS/CTAB	Amperometry	3–57 μM/0.6 μM	77
HRP	H_2O_2	MTrMOS	Amperometry	0.9 μM–0.2 mM/50 μM	104
HRP	H_2O_2	TEOS/PVA-*g*-PVP	Amperometry	0.5 μM–1.6 mM/0.1 μM	124
HRP	H_2O_2	TEOS/PVA-*g*-PVP	Amperometry	0.1–3.4 mM/0.5 μM	125
HRP	H_2O_2	Ormosil/PVA-*g*-PVP	Amperometry	0–0.6 mM/0.9 μM	126
HRP	H_2O_2	TMOS/chitosan	Amperometry	0.25–3.4 mM/3 μM	127
HRP	H_2O_2	TMOS/CTAB	Amperometry	20 μM–2.6 mM	128
HRP	H_2O_2	MTEOS	Amperometry	0.01–2.7 mM/0.005 mM	129
HRP	H_2O_2	MPTMS	Amperometry	5×10^{-6}–4×10^{-3} M/ 2×10^{-6} M	130
HRP	H_2O_2	TEOS/PVA-*g*-PVP	Amperometry	0–1.3 mM/2.5×10^{-7} M	131
HRP	H_2O_2	MTMOS/polypyrrole/ ferrocenecarboxylic acid	Amperometry	9.0×10^{-7}–2×10^{-4} M/ 5.0×10^{-5} M	104
HRP	H_2O_2	MTEOS	Amperometry	0.01–2.7 mM/0.005 mM	129
HRP	H_2O_2	Chitosan/APTES	Chronoamperometry	3.5×10^{-6}–1.4×10^{-3} M/ 8.0×10^{-7} M	132
HRP	H_2O_2	TMOS	Amperometry	1.6–3.2 mM/0.5 μM	133
HRP	H_2O_2	MPTMS	Amperometry	5.0 μM–10.0 mM/2.0 μM	134
HRP	Cyanide	MTEOS	Amperometry	0.004–0.04 mM/0.5 μM	123
HRP	H_2O_2	APMDMOS/chitosan	Amperometry	5.0×10^{-9}–1.0×10^{-7} M/ 2×10^{-9} M	135
HRP/Catalase	H_2O_2	Al_2O_3/methylene blue	Amperometry	0.01–0.1 mM	136
HRP	H_2O_2	MTMOS/MPTMS	Amperometry	0–0.6 mM/9×10^{-7} M	126

(*Continued*)

Table 1 (Continued)

Biorecognition element(s)	*Analyte(s)*	*Sol–gel precursors*	*Principle of detection*	*Linear range/detection limit*	*References*
HRP	H_2O_2	TEOS/$BMIM^+BF_4^-$	Amperometry	0.02–0.26 mM/1.1 μM	137
HRP	Phenols	MTEOS	Amperometry	1 μM	138
Human chorionic gonadotrophin antibody	Human chorionic gonadotrophin	APTMOS	Differential pulse voltammetry	0.5–50 mIU ml^{-1}/ 0.3 mIU ml^{-1}	81
Lactate dehydrogenase	Lactate	TEOS/polyaniline/ indium-tin-oxide (ITO)	Amperometry	1–4 mM	139
Lactate dehydrogenase	Lactic acid	MTEOS/PVA/TiO_2	Cyclic voltammetry	1.0–20 mM/0.4 μM	140
Lactate oxidase	Lactate	TMOS/poly(ethyleneimine)	Amperometry	0.5–2.0 mM/0.03 mM	141
Monoamine oxidase	Benzydamine	Ormosil/graphite powder/ polyethylene glycol	Amperometry	At platinum: 0.05–2.5 mM; At carbon paste electrode, 0.1–2.5 mM	142
Moraxella spp. cells	organophosphates	TMOS	Amperometry		143
Phenol hydroxylase	Phenol	TMOS	Amperometry	2.5–400 μM	144
Soybean peroxidase	H_2O_2	TEOS/PVA-*g*-PVP	Amperometry	0.02–2.6 mM/5×10^{-7} M	71
Streptavidin (STA)	hepatitis C virus (HCV) RNA	IsoTrEOS/O,O′ bis (2-aminopropyl)poly (propylene oxide)	Cyclic voltammetry		145
Superoxide dismutase	Superoxide anion	Na_2SiO_3/PVA	Amperometry	0.2–1.6 μM/0.1 μM	146
Trichosporon cutaneum and *Bacillus subtilis*	BOD	TEOS/PVA-*g*-PVP	Amperometry	1.0–60.0 mg l^{-1}/0.5 mg l^{-1}	32
Tyrosinase	Dopamine	Pd–Ormosil	Amperometry	0–5 mM/50 μM	147
Tyrosinase	Phenols	Al(i-PrO_3)	Amperometry	1.5 nM–0.35 mM/0.2 nM	148
Tyrosinase	Phenols	Al(i-PrO_3)	Amperometry	0.1 μM–0.25 mM/50 nM	148
Tyrosinase	Phenols	TMOS/CTAB	Amperometry	Catecho: 2×10^{-7}–2.6×10^{-5} M; Phenol: 4×10^{-7}–2×10^{-5} M; *p*-cresol: 4×10^{-7}–1.5×10^{-5} M; *m*-cresol: 4×10^{-7}–1.5×10^{-5} M	149
Tyrosinase	Phenols	TiO_2	Amperometry	1×10^{-8} M	150
Tyrosinase	Phenols	TiO_2/PVA	Amperometry	Catechol: 0–14 mM/0.5 μM; *p*-cresol: 0–2.0×10^{-5} M/ 0.2 μM; phenol: 0–14 mM/ 0.9 μM	151
Tyrosinase	Phenols	TiO_2	Amperometry	Catechol: 0.15–0.003 mM; phenol: 0.17–0.008 mM; *p*-cresol: 0.21–0.004 mM	152
Tyrosinase	Phenols	Al_2O_3	Amperometry	$5\ 10^{-9}$–3.5×10^{-4} M/0.2 nM	148
Tyrosinase	Phenols	3-mercaptopropionic acid/ Glutaraldehyde	Amperometry	Catechol: (2.0–1000)$\times 10^{-7}$ M/0.11 μM; *p*-cresol: (6.0–800)$\times 10^{-7}$ M/ 0.23 μM; 4-chloro-3-methylphenol: 0.2–20 μM/94 nM; 4-chlorophenol: 0.4–40 μM/ 0.15 μM; phenol: 0.2–200 μM/8 nM	153
Tyrosinase	Phenols	Aluminum isopropoxide	Amperometry	Phenol: 0.1–250 μM/ 5.0×10^{-8} M	148
Tyrosinase	Phenols	TMOS/Nafion	Amperometry	Catechol: 1–100 μM/ 0.35 μM; phenol: 5–100 μM/1.0 μM; *p*-cresol: 1–50 μM/ 0.34 μM; 4-chlorophenol: 5–50 μM/0.67 μM; 4-acetamidophenol: 5–50 μM/5.0 μM	154
Tyrosinase	Phenols	MTMOS/TEOS/PVA-*g*-PVP	Amperometry		155

(*Continued*)

Table 1 (Continued)

Biorecognition element(s)	*Analyte(s)*	*Sol–gel precursors*	*Principle of detection*	*Linear range/detection limit*	*References*
				Catechol: 1×10^{-7}–1×10^{-4} M/ 0.04 μM; *p*-cresol: 1×10^{-7}–2.3×10^{-4} M/ 0.05 μM; phenol: 2×10^{-7} –1.6×10^{-4} M/ 0.1 M	
Urease	Urea	Ormosil	Potentiometry	20 μM	156
Urease	Urea	TMOS	Conductometry	0.03–2.5 mM/30 μM	157
Urease	Urea	TMOS	Conductometry	0.2–50 mM	158
Urease/glutamate dehydrogenase	Urea	TiO_2–CeO_2	Chronoamperometry	0.166 μM	159
Xanthine oxidase	Hypoxanthine	TMOS/graphite	Amperometry	1×10^{-6}–1×10^{-3} M/ 3.8×10^{-7} M	160
–	Adenine	MTMOS/carbon	Differential pulse stripping adsorption	2×10^{-7}–1×10^{-6} M	161
–	Parathion	TEOS/OH-TSO/PMHS	Chronoamperometry	5.0×10^{-9}–1.0×10^{-4} M/ 1.0×10^{-9} M	162
–	Transferrin	Al_2O_3/gold nanoparticles	Capacitive detection	1–75 ng ml^{-1}/0.05 ng ml^{-1}	75

TEOS, tetraethoxysilane; MTMOS, methyltrimethoxysilane; MPTMS, 3-mercaptopropyltrimethoxysitoxane; OH-TSO, hydroxyterminated silicone oil; PMHS, polymethylhydrosiloxane; IsoTrEOS, 3-(isocyanatopropyl)triethoxysilane; $BMIM^+BF_4^-$, 1-butyl-3-methylimidazolium tetrafluoroborate; MPTMS, 3-mercaptopropyltrimethoxysilane; Ormosil, 3-aminopropyltrimthoxy silane, 2-(3,4-epoxycyclohexyl)-ethyltrimethoxy silane, polyethyleneglycol; PTMOS, propyltrimethoxysilane; GPTMS, 3-glycidoxypropyltrimethoxysiloxane; MTMOS, methyltrimethoxysilane; APTMOS, 3-aminopropyltrimethoxysilane; EETMS, 2-(3,4-epoxycyclohexyl)-ethyltrimethoxy silane; APMDMOS, aminopropylmethyldimethoxysilane; APTES, 3-aminopropyltriethoxysilane; PVA-*g*-PVP, poly(vinyl alcohol)-grafted-poly(4-vinylpyridine); DDAB, didecyldimethylammonium bromide; CTAB, cetyl trimethylammonium bromide.

of enzyme in alumina (aluminum isopropoxide) sol–gel films on a platinized glassy carbon electrode. At the GOx/sol–gel/platinized glassy carbon electrode, glucose response started at +0.20 V and approached a maximum value at +0.60 V. The low operating potential greatly reduced the interference from coexisting electroactive species. Liu *et al.*[164] immobilized HRP in the ZrO_2 sol–gel matrix to develop a biosensor for the H_2O_2 determination. A simple vapor-deposition method was introduced to immobilize HRP, GOx, and other biomolecules in titania sol–gel, which retained their catalytic activity and exhibited good response on electrode surface.[111,165,166] The uniform porous structure of the titania sol–gel matrix has very low mass transport barrier, a high catalytic activity, and a fast response. The advantages of room temperature (or lower) processing conditions, chemical inertness, negligible swelling effects, tuneable porosity, and the high purity of sol–gel-derived glasses make them ideal for many types of biosensing applications. Narang *et al.*[167] developed a glucose biosensor by immobilizing GOx between two sol–gel layers (sandwich). GOx was immobilized in/on a thin TEOS sol–gel film using physisorption, microencapsulation, and a new sol–gel: GOx:sol–gel sandwich configuration for amperometric detection of glucose. The results clearly demonstrate that the sandwich configuration exhibits a fast response and high enzyme loading.

Mediated biosensors have gained wide attention for probing redox enzyme catalyzed reactions. The participation of redox mediator in signal transduction leads to the development of second generation biosensors. Mediators such as ferrocene and its derivatives, osmium complexes, quinone salts, and ruthenium complexes have been employed in biosensors. Biosensors in which the mediator is coimmobilized with enzyme on electrode will not require the addition of the former to the test solution, thereby eliminating many practical challenges. The immobilized mediator catalyzes the redox reactions of biomolecules and shuttles the electrons more efficiently between enzyme and electrode to greatly enhance the sensing performance, and operating potential of the biosensor is typically lowered. On the other hand, the inclusion of electrocatalytically active graphite-supported palladium, platinum, and ruthenium or gold nanocrystals allows the construction of mediator-free electrodes that are highly sensitive, selective, and stable. However, the incorporation of a redox mediator within sol–gel network may provide strongly diminished electrochemistry in dried xerogel samples due to the restricted mobility in a dried sol–gel structure. Mediatorless amperometric biosensors have been reported by coupling GOx with HRP or soybean peroxidases, which mediate the reduction of H_2O_2.

The fundamental problem arising in the construction of an amperometric glucose biosensor is the selectivity of the substrate detection. The often-used detection approach is electrochemical oxidation of the liberated H_2O_2 through the enzymatic reaction, and requires a relatively high working potential. At such a potential, endogenous or exogenous compounds present in biological samples (e.g., urate, ascorbate, or paracetamol) can be electrochemically oxidized, leading to a high level of interference and false results in the quantification of glucose concentration. To overcome this limitation, Wang *et al.*,[168] and Sampath and Lev[169] took advantage of the catalytic

properties of palladium-modified carbon particles to detect glucose at lower potentials (+0.30, +0.50 V) via a screen-printing process or by molding the porous organically modified silica in a glass capillary. A type of sol–gel-derived, inert metal-modified, composite, amperometric biosensor is developed. The electrodes are composed of a dispersion of biochemically and chemically modified graphite powder in a porous, organically modified silicate (ormosil) network. The percolating carbon dispersion provides electrical conductivity; oxidoreductase enzymes are used for biocatalysis, metallic palladium is used for electrocatalysis of the biochemical reaction product; and the porous organically modified silica provides a rigid skeleton.

The hydrophobicity of this composite material guarantees that only a limited section of the electrode is wetted by the aqueous analyte, thus providing a controlled-thickness reactive layer. Coche-Guerente *et al.*[170] reported a mediatorless amperometric bienzymatic glucose biosensor. This mediatorless sensor was made by the simultaneous immobilization of graphite microparticles and two enzymes (HRP and GOx) in a silica gel matrix. The amperometric detection of glucose was assayed by applying a potential of 0 V versus SCE in order to reduce the catalytically generated H_2O_2. The active graphite particles evenly dispersed within the silica gel matrix establish an efficient electrical communication between the electrode surface and the HRP active center. By taking advantage of the direct electrochemistry of HRP, reagentless immunosensors have been developed for the detection of carcinoma antigen 125 and HCG. These kinds of reagentless immunosensors are quite useful for medical applications because the use of fewer reagents in clinical assays leads to less interference and more accuracy, especially in the analysis of real biological samples. Abad *et al.*[171] presented a strategy for establishing electrical contact to the metal center of a redox metalloenzyme, galactose oxidase (GO), by coordination of a linker attached to a monolayer-protected gold cluster. The cluster–enzyme hybrid system was prepared in solution, and the electrochemical communication between a gold electrode and GO was achieved by first modifying the electrode surface with a biphenyl dithiol self-assembled monolayer followed by reaction with gold clusters capped with thioctic acid. GO was then immobilized by replacement of the water molecule at exogenous site by coordination of a carboxylate-terminated gold cluster. This chemical attachment ensures the electrical contact between the redox center and the electrode, leading to direct mediatorless electron transfer to the protein.

Exploiting the encapsulation ability of sol–gel, many other nanomaterials were immobilized onto the electrode surface, such as CNTs,[172–174] carbon nanofibers,[175] and graphene[176] demonstrating that sol–gel nanocomposites can provide new capabilities for the development of nanobased materials for electrochemical biosensors. Arvinte *et al.*[172] prepared a meldola blue (MB)-single-walled carbon nanotubes (SWNT)-sol–gel nanocomposite material by the sol–gel process incorporating a redox mediator and CNTs. The electrocatalytic properties of the nanomaterial-based biosensor toward nicotinamide adenine dinucleotide (NADH) oxidation were studied. Significant enhancement of oxidation current is obtained at electrodes modified by MB-SWNT-sol–gel in comparison with the analogous carbon black and/or graphite composite modified electrode. Analytical parameters of D-lactate biosensors with and without SWNT in the hybrid film were compared demonstrating that performance of the biosensor was significantly improved when SWNT was incorporated. Zhu *et al.*[177] fabricated surface renewable and mechanical rigid CNT ceramic composite electrodes (CCEs) by dispersion of multiwall CNTs in sol–gel solution. Nanotube CCEs provide better reversibility with substantial decreased over working potential, better defined peak shape, and higher sensitivity compared with carbon (graphite) CCEs. In addition, CNTs and graphite ceramic electrodes were employed as H_2O_2 and NADH probes. Watcharotone *et al.*[176] fabricated transparent and electrically conductive composite silica films on glass and hydrophilic SiOx/silicon substrates by incorporation of individual graphene oxide sheets into silica sols followed by spin-coating, chemical reduction, and thermal curing.

To improve on the hydrophilic nature and to reduce the cracking and swelling problems of silica matrix, Tsionsky *et al.*[178] reported some composite ceramic–carbon materials with incorporated surfactants. Modified porous composite carbon–silica electrodes can exhibit hydrophobic or hydrophilic surface characteristics and can serve as an indicator (inert) electrode, as a potentiometric (selective or reference) electrode, and in amperometric sensing and biosensing. The electrodes offer higher stability than carbon paste electrodes, and they are more amenable to chemical modification than monolithic and (organic) composite carbon electrodes. And grafting copolymer, PVA-*g*-PVP has been incorporated into the sol–gel (i.e., TEOS) and entrapped GOx to improve the hydrophilic nature. It prevents the cracking of conventional sol–gel-derived glasses and eliminates the swelling of the hydrogel. The biosensor exhibited a series of good properties of high sensitivity (600 nA $mmol^{-1}\,l^{-1}$), short response time (11 s), and remarkable long-term stability (at least 5 months). PVA-*g*-PVP polymer provides hydrophilic–hydrophobic properties and large amount of hydrogen bonds within the sol–gel matrix, hence the enzyme retains its active conformation.[105] The composite material merged the best properties of the inorganic species, titanium oxide, and the organic copolymer, PVA-*g*-PVP. The GOx entrapped in the composite matrix retained its bioactivity. The response time of the biosensor was less than 20 s. In hybrid sol–gel matrices, organic components contribute to the formation of defect-free inorganic membranes and make it less brittle, and an inorganic phase can improve the chemical and temperature stability of organic membranes.[179] Similarly, to obtain improved properties, pure silica sol–gels have been doped with natural polymers such as chitosan. Miao and Tan[127] fabricated silica sol–gel/organic hybrid composite material consisting of sol–gel and chitosan for amperometric H_2O_2 biosensor. The composite film was used to immobilize HRP on a carbon paste electrode. Hexacyanoferrate (II) was present in the solution as an electron donor. The biosensor had a fast response of less than 10 s. In another study, chitosan was cross-linked with (3-aryloxypropyl) dimethoxymethylsilane, in which HRP was sequestered for the construction of H_2O_2 biosensor. Chen *et al.*[180] fabricated a glucose biosensor by encapsulating the GOx in MTMOS and natural polymer chitosan composite matrix, and using ferrocene as a mediator. All the cases of biomolecules encapsulated in sol–gel hybrid materials showed improved stability and good analytical response due to the improved characteristics of sol–gel matrix. Solanki *et al.*[86] immobilized cholesterol esterase and ChOx onto

sol–gel-derived silica (SiO_2)/chitosan/multiwalled CNTs-based nanobiocomposite film, which is shown in **Figure 3** and which shows the response time of 10 s and shelf-life of about 10 weeks.

Sampath and Lev[169] reported a renewable GOx entrapped glucose biosensor by the addition of hydrophilic PEG into the hydrophobic ormosil (present on the electrode surface). Li *et al.*[100] reported a renewable glucose biosensor based on a sol–gel-derived carbon composite material. GOx and mediator vinylferrocene were immobilized within the porous, rigid, and organically modified silicate network in the composite material. The organic group in the silicate network controls the hydrophobicity of the electrode surface and thus limits the wettability of the electrode surface. The glucose biosensor can be renewed easily in a reproducible manner by a simple polishing step and has a long operational lifetime. Thionin was covalently immobilized to construct a bulk modified, leak-free composite electrode. This renewable composite electrode provides stable immobilization matrix for thionin via glutaraldehyde cross-linking. In the electrode composition, the sol–gel precursor 3-aminopropyltrimethoxy silane serves as the host for immobilization of thionin, thereby preventing its leakage. An additional precursor methyl trimethoxy silane provided the hydrophobicity and limits the wetting section of electrode.[181] Low-cost, screen-printed materials are often used as disposable biosensors.[182] The renewable or screen-printed sensors were highly convenient for application and low cost. In order to circumvent limitations such as microbial adhesion and growth on the surface, recently nitric oxide (NO)-releasing sol–gel particles have been reported;[106] the hybrid sol–gel/PU glucose biosensor consisted of a platinum electrode coated with four polymeric membranes including the following: (1) sol–gel with immobilized GOx; (2) PU to protect the enzyme; (3) NO donormodified sol–gel particle-doped PU; and (4) PU. For the hybrid sol–gel/PU biosensor, sol–gel particles were first modified with the NO donor and then incorporated into a PU layer that was coated onto the preimmobilized GOx electrode. In that manner, the GOx layer was not exposed to the harsh conditions necessary to impart NO release ability to the biosensor. Nitric oxide is a potential antimicrobial agent,[183] if it is released slowly from the matrix adhesion and the growth of microbes can be controlled. NO-releasing glucose biosensors prepared by doping diazeniumdiolate-modified sol–gel particles in a PU membrane exhibit high sensitivity, reproducibility, and fast response. To reduce both enzyme inactivation by NO (by minimizing NO exposure) and sol–gel particle leaching, PU membranes are coated as a layer.

A major advantage of sol–gel-based electrochemical sensors is that they are not limited to the use of silica as the metal center since the films do not need to be optically clear. Hence, sol–gel coatings can be fabricated from alumina, aluminosilicate, vanadium, or titanium to alter both the electrical and material properties and to improve chemical inertness. This also leads to the ability to perform measurements in turbid or opaque samples, as is often the case for *in vivo* sensing. Another advantage of sol–gel composite electrodes

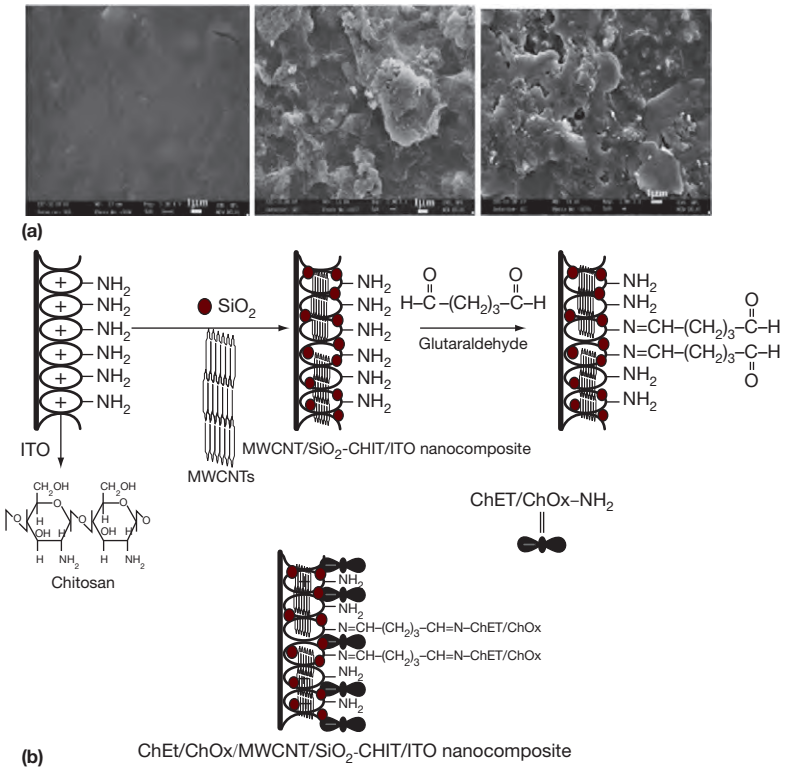

Figure 3 (a) SEM image of chitosan/indium–tin–oxide (ITO) electrode multiwalled carbon nanotubes (MWCNT)/SiO_2–chitosan/ITO electrode and cholesterol esterase (ChEt)–cholesterol oxidase (ChOx)/MWCNT/SiO_2–chitosan/ITO bioelectrode, respectively. (b) Proposed mechanism for preparation of ChEt–ChOx/MWCNT/SiO_2–chitosan/ITO bioelectrode. Adapted from Solanki, P. R.; Kaushik, A.; Ansari, A. A.; Tiwari, A.; Malhotra, B. D. *Sens. Actuators B* **2009**, *137*, 727–735, with permission.

is that they tend to be more homogeneous than regular carbon paste electrodes, leading to homogeneous electron transfer kinetics and larger current responses in amperometric sensing. Of course, the ultimate sensitivity of the electrode is determined by background noise, but it is relatively easy to prepare shielded electrodes to improve on sensitivity and detection limits.

3.328.3.2. Optical Biosensors

The good sol–gel optical transparency with diverse chemistries and configurations for the entrapment of many biorecognition elements enables the development of various optical biosensors.[7,184] Rather than measuring current response as in the case of electrochemical biosensors, optical biosensors normally measure the photons. More specifically, optical biosensors operate based on the measurement of absorbance, reflectance, or fluorescence emissions that occur in the ultraviolet, visible, or near-infrared. Fluorescence spectroscopy is by far the method most widely applied and comes in a variety of schemes.[10] Fluorescence is considered as the ideal technique to monitor sol–gel hybrid systems as it can address both the host matrix and the guest biomolecule and enables the visualization of molecular diffusion down to single-molecule level.[185]

Similar to electrochemical biosensors, the bioreceptor used for recognition is normally immobilized on the surface of optical biosensors as a single-layer, double-layer, and sandwich configurations.[8,10,186] Three different configurations of oxygen transducer and sol–gel immobilized GOx have been investigated by Wolfbeis *et al.*[187]. In the first configuration, GOx was sandwiched between a sol–gel layer doped with Ru(II)-tris(4,7-diphenyl-1,10-phenanthroline) ($Ru(dpp)_3$) and a second pure sol–gel layer. Such configuration provided the highest enzyme activity and the widest dynamic range (0.1–15 mM) but suffered from a distinct decrease in sensitivity upon prolonged use. Secondly, a sol–gel layer doped with $Ru(dpp)_3$ was covered with sol–gel-entrapped GOx, which provided the fastest response time (>50 s). In the third configuration, both the oxygen-sensitive sol–gel powder and the sol–gel powder containing GOx were incorporated into a single sol–gel phase, which provided the best operational lifetime. Three types of immobilization modes (i.e., physisorption, microencapsulation, and sol–gel sandwich) have also been compared in terms of their response profiles to glucose by Narang *et al.*[167] The results indicated that the sandwich configuration (sol–gel:GOx:sol–gel) was most promising for future biosensor operation. Since the diffusion of the analyte proceeded through the sol–gel top layer, its thickness was adjusted to 0.10 μm in order to obtain the shortest response time (30 s).

There has been widespread and growing interest in recent years in the development of optical biosensors for a wide variety of analytes.[188–190] Recent advances in the design and application of optical biosensors assays were extensively reviewed.[10,12,184,191–193] Available data of typical optical biosensors based on sol–gel matrices have been reported and summarized in **Table 2**. In most cases, the optical biosensors are sensitive, robust, rapid in response, cheap, and easily miniaturized.

As shown in **Table 2**, the most frequently used precursors in optical biosensors are based on TMOS and TEOS sol–gel matrices. The sensing material is generally obtained by controlled hydrolytic polycondensation of TEOS to give a fairly inert inorganic glassy matrix, in which porosity and size of pore network can be varied by polymerization conditions.[214] The tailor ability was demonstrated for oxygen-sensitive sol–gel films doped with the $Ru(dpp)_3$ complex and were fabricated using different ratios of TEOS and methyltriethoxysilane precursors.[215] Furthermore, hydroxyethyl carboxymethyl cellulose and TEOS hybrid polymer could improve on the stability of entrapped GOx (up to 3 years).[216]

Generally, optical biosensors can be divided into two main categories based on their bioactivity: biocatalysts (e.g., enzymes and cells) and bioaffinity molecules (e.g., antibodies, receptors, and nucleic acids).[217] Like electrochemical biosensors, most works on sol–gel optical biosensor development have focused on the immobilization of enzymes. Besides their unique biocatalytic properties and specificity for a substrate or a group of substrates, enzymes allow a wide range of analyte recognition processes by using different combinations of enzymes or enzyme-transducer systems. Changes in absorbance and fluorescence of the colored or luminescent substances for enzymatic reactions enable the direct detection using an optical biosensor. If the enzymatic reaction does not involve such substances, optochemical transduction is obligatory for indirect detection.[218] Actually, as most enzymes do not have intrinsic optical properties that undergo a change when they interact with the analyte(s), most of these biosensors rely on the use of a chemical transducer and its analytical signal which can be related to the concentration of the analyte of interest.[184] Following the first report for the successful encapsulation of a purified enzyme (i.e., ALP) in a TMOS-based sol–gel material,[15] a wide variety of enzymes have been immobilized in sol–gel-based optical biosensors which have been employed for the monitoring of pesticides, pharmaceuticals, hydrogen peroxide, sugars, lactate, urea, cholesterol, nitrates, nitrites, etc. (**Table 2**).

Among the various enzymes, the most well-studied enzyme in the sol–gel context biosensors is GOx, which mediates the air oxidation of glucose with generation of H_2O_2. Different biosensing schemes based on sol–gel doped with GOx have been proposed. For instant, de Marcos *et al.*[204] immobilized GOx, firstly covalently bonded to a fluorescein derivative, in a TMOS-based sol–gel film, as the basis of an optical biosensor. During the enzymatic reaction, glucose reacts with the labeled GOx. When the oxygen dissolved in the solution is consumed, an increase in fluorescence intensity is recorded.

Besides GOx, there are many papers reporting the immobilization of other enzymes within sol–gel matrices. Biosensors based on AchE and cholinesterase inhibition have been proposed for screening of organophosphates and carbamates, two major classes of pesticides with widespread uses in agriculture activities. A pH-sensitive fluorescent biosensor was reported for the detection of acetylcholine and praoxon, in which fluorescene isothiocyanate (FITC)-dextran conjugate and AChE were coimmobilized in TMOS sol–gel.[219] A portable optical fiber biosensor for the detection of the pesticides carbaryl and dichlorvos was developed on the basis of a three-layer sandwich scheme. The enzyme cholinesterase was immobilized on the outer layer, a hydrophilic modified polyvinylidenefluoride membrane, which was in contact with a sol–gel film doped

Table 2 Typical optical biosensors based on bioreceptors encapsulated in sol–gel matrices

Biorecognition element(s)	*Analyte(s)*	*Sol–gel precursors*	*Principle of detection*	*Linear range/detection limit*	*References*
AChE and bromothymol blue	Chlorpyrifos	TEOS	Absorption	0.05–2.0 mg l^{-1}/0.04 mg l^{-1}	189
AChE (+FITC-dextran)	Paraoxon	TMOS	Fluorescence	152 ppb (30% inhibition)	218
AChE and a lipophilic chromoionophore	Dichlorvos	TEOS	Absorption	0.5–7 mg l^{-1}/0.5 mg l^{-1}	194
Bacillus licheniformis, *Dietzia maris*, *Marinobacter marinus*	BOD	TMOS + DiMe-DMOS (+PVA)	Fluorescence	0.2–40 mg l^{-1}/0.2 mg l^{-1}	195
Bacillus subtilis (+$Ru(dpp)_3$)	BOD	TMOS (+PVA-*g*-PVP)	Luminescence	0–25 mg l^{-1}	196
Carbonic anhydrase (+cresol red)	Acetazolamide	TMOS	Absorption	1.0–10.0 mM/0.2 mM	197
Cholesterol oxidase + HRP	Colesterol	TEOS	Absorption	2–10 mM	87
Cholinesterase (+bromocresol purple)	Carbaryl dichlorvos	TEOS + PTMOS	Absorption	0.11–0.8 ppm/108 ppb 5.0–30 ppm/5.2 ppb	198
Concanavalin-A labeled with FITC	Bacterial endotoxins	TEOS + APTES	Luminescence	–	199
Cytochrome *c*	NO and CO	TMOS	Absorption	–	200
Cytochrome *c*	NO	TMOS	Absorption	1–25 ppm/1 ppm	201
Cytochrome cd_1 nitrite reductase	NO_2^-	TMOS	Absorption	3.4–57 ppb/3.4 ppb	202
Escherichia coli (recombinant)	DDT, aldicarb, malathion	TMOS	Luminescence	–	18
GOx	Glucose	TEOS	Absorption	5–35 mM/0.2 mM	167
GOx	Glucose	1.0 ml of TMOS and 1.8 ml of DiMe-DMOS	Fluorescence	0.00–0.50 mM and 0.50–3.00 mM/ 3.6×10^{-6} M	203
GOx labeled with fluorescein	Glucose	TMOS	Fluorescence	0.55–55 mM	204
GOx (+$Ru(dpp)_3$)	Glucose	TMOS + PTMOS/ MTMOS	Fluorescence	0.1–15 mM[a]	187
GOx (+DPO)	Glucose	TEOS/ TEOS + APTES	Fluorescence	0.1–15 mM	205
Glutamate dehydrogenase	Glutamate	TiO_2, glycerol, and PVA	Fluorescence	0.04–10 mM/5.5 μM (water sample) 0.02–10 mM/6.7 μM (biological samples)	188
Glutathione *S*-transferase (+bromocresol green)	Atrazine	TEOS + PTMOS	Absorption	2.52–125 μM/0.84 μM	206
Hemoglobin	NO and CO	TMOS	Absorption	–	200
HRP	H_2O_2	TEOS	Chemiluminescence	8×10^{-3}–2 mM	207
HRP or HRP/GOx	H_2O_2 and glucose	TEOS/PDMS Ormosil	Luminescence	0.05–20 mM H_2O_2 and 0.5–20 mM glucose	208
Lactate dehydrogenase (+NADH)	L-Lactate	TMOS	Fluorescence	0.1–1.0 mM	209
Lactate dehydrogenase	Piruvate	TEOS	Absorption	0–1.5 mM/5×10^{-5} M	210
Myoglobin	NO and CO	TMOS	Absorption	–	200
Nitrate reductase	NO_3^-	TMOS	Absorption	0–1.5 μM/0.125 μM	201
Pseudomonas fluorescens	Naphthalene; salicylate	TMOS	Bioluminescence	1.2 mg l^{-1}/0.5 mg l^{-1}	30
SOD and SOD dismutase–peroxidase enzymes	Superoxide radical	TEOS	Fluorescence	0–1.2 μM/20 nM	211
Urease	Urea	TEOS	Absorption	0.05 mM	167,212
Urease	Cu(II), Cd(II), Zn(II), Ni(II), Pb(II), and Cr(III)	TMOS	Fluorescence	10–230 μM/10 μM for Cu(II) and Cd(II) Detection limit: 40 μM for Zn(II), 100 μM for Ni(II), 100 μM for Pb (II), and 300 μM for Cr (III)	213

(*Continued*)

Table 2 (Continued)

Biorecognition element(s)	*Analyte(s)*	*Sol–gel precursors*	*Principle of detection*	*Linear range/detection limit*	*References*
Xanthine oxidase, superoxide dismutase and peroxidase	Xanthine	TEOS	Fluorescence	0–3.5 μM/20 nM	190

AChE, acetylcholinesterase; BOD, biochemical oxygen demand; DiMe-DMOS, dimethyldimethoxysilane; DDT, dichloro-diphenyl-trichloroethane; DPO, 4-[*p*-*N*,*N*-dimethylamino) benzylidene]-2-phenyloxazole-5-one; FITC, fluorescein isothiocyanate; GGA, glucose–glutamic acid solution; MTMOS, methyltrimethoxysilane; NADH, nicotinamide adenine dinucleotide; PTMOS, phenyltrimethoxysilane; PVA, polyvinyl acetate; PVA-*g*-PVP, poly(vinyl alcohol)-grafted-poly(4-vinylpyridine); $Ru(dpp)_3$, ruthenium(II)-tris(4,7-diphenyl-1, 10-phenanthroline); SOD, superoxide dismutase.

[a]0.1–15 mM (sandwich); 0.1–8 mM (two-layer); 0.1–4 mM (powder configuration).

with bromocresol purple, deposited on an inner glass disk.[198] Andreou and Clonis[206] also proposed the same biosensing scheme for the determination of the herbicide atrazine, using the enzyme gluthatione *S*-transferase and bromocresol green. After deterioration, the bioactive sandwich could be easily replaced on the terminal of the probe. **Figure 4** shows the experimental setup and electrode construction.

Carbonic anhydrase was employed in the enzyme sol–gel film for developing optical biosensor for determination of the antiglaucoma agent acetazolamide, suitable for diagnosis and pharmaceutical control purposes.[197] Ferretti *et al.*[202] encapsulated cytochrome *cd1* nitrite reductase between two sol–gel thin films, which enabled the determination of nitrite in environmental waters with detection limits below the levels established by the European Union and response times of 5 min. Sol–gel encapsulation of the enzyme lactate dehydrogenase in thin films was employed by Li *et al.*[209] and Ramanathan *et al.*[210] to develop optical biosensors for L-lactate and piruvate, respectively. Urease had also been entrapped in sol–gel films for the development of biosensors for urea detection.[212]

Multienzymatic entrapment in the same sol–gel matrix allows for sequential reactions to occur in a confined space and lead to high conversion efficiencies due to the proximity of analytes and intermediates to the enzymes' active sites.[19,190] Pastor *et al.*[211] developed a fluorescent biosensor to determine superoxide radical based on the coupled reaction of the enzymes superoxide dismutase (SOD) and HRP, together with the use of the probe *N*-acetyl-dihydroxyphenoxazine (Amplex red). Within this biosensor, SOD catalyzes the dismutation reaction of generated superoxide radical with the release of H_2O_2 which, in the presence of HRP, reacts stoichiometrically with the nonfluorescent Amplex red to generate the red-fluorescent oxidation product resorufine. An array-based optical biosensor for the simultaneous determination of urea, acetylcholine, and heavy metals has been reported.[220] Urease and AChE were coentrapped with FITC-dextran in the sol–gel matrix and fixed on a sensing probe. Coimmobilizion of three enzymes, xanthine oxidase (XO), SOD, and HRP, in a single sol–gel matrix was used to prepare a fluorescent biosensor for the accurate determination of xanthine.[190] In this case, the enzymatic system included XO which catalyzes the oxidation of xanthine to uric acid and superoxide radical. More recently, the ability of three sol–gel immobilized multienzymatic systems coupled with the indicator Amplex red to determine superoxide radical and evaluated the scavenging capacity of several antioxidant compounds was investigated.[221] In the first system, the enzymes SOD and HRP were immobilized in a single sol–gel slide, while in other systems, the enzyme XO was also immobilized either in the same slide (system 2) or in a different slide (system 3). Results indicated that the three systems could be used to quantify superoxide radical, but only systems 1 and 3 were able to detect scavenging capacity.

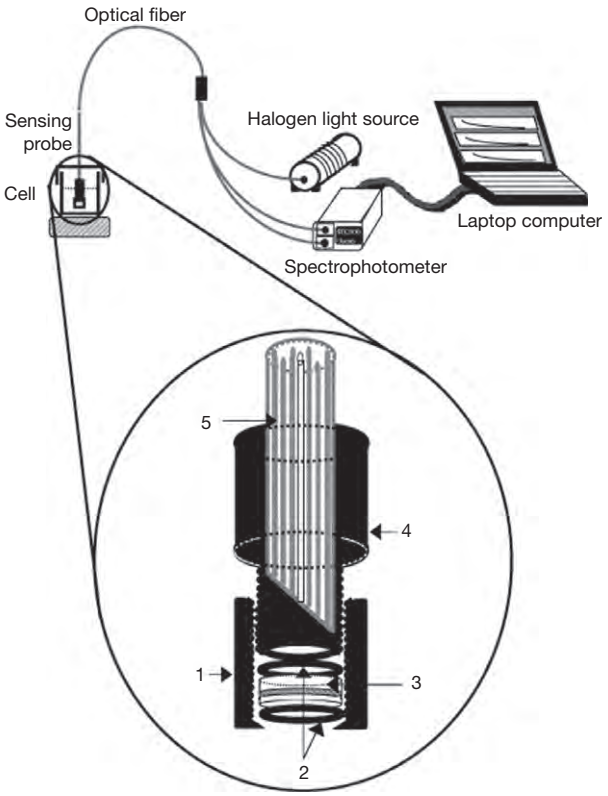

Figure 4 Experimental setup for atrazine analysis showing the optic fiber fitted with the probe at its end: (1) screwable terminal holding ring, (2) sealing 'O' rings, (3) biosensing sandwich (bottom to top: Durapore® membrane with immobilized enzyme, middle sol–gel/indicator layer, supporting glass disk), (4) probe tip, and (5) multielement (six illumination, one read) optical fiber. Adapted from Andreou, V. G.; Clonis, Y. D. *Anal. Chim. Acta* **2002**, *460*, 151–161, with permission.

Another way of using enzymes is through whole cells rather than the purified enzymes, which has been successfully applied in sol–gel films-based optical biosensors for

biochemical oxygen demand (BOD) determination. Lin *et al.*[195] proposed a biosensing film consisting of an organically modified silicate film embedded with tri(4,7-diphenyl-1,10-phenantroline) ruthenium(II) perclorate and three kinds of seawater microorganisms (*Bacillus licheniformis*, *Dietzia maris*, *Marinobacter marinus*) immobilized on a polyvinyl alcohol sol–gel matrix. The coimmobilized microorganisms maintained their activity even if kept for 1 year at 4 °C, and the stored biosensing film could be employed for BOD measurement after 1 day's reactivation. Kwok *et al.*[196] constructed a biosensing device for parallel multisample determination of BOD by immobilizing activated sludge and *Bacillus subtillis* on oxygen-sensing films placed on the bottom of glass sample vials. The microorganisms were entrapped in a sol–gel-derived film of silica and PVA-*g*-PVP copolymer. The oxygen film contained $Ru(dpp)_3$ immobilized in a silicone rubber.

The most important factor in the construction of whole cells biosensors is the immobilization of living cells. Premkumar *et al.*[222] immobilized recombinant luminous bacteria into TEOS sol–gel to study the effect of sol–gel conditions on the cell response (luminescence). The entrapped and free cells showed almost the same intensity of luminescence (little lower), but the entrapped cells were more stable than the free cells (4 weeks at 4 °C). It revealed that the encapsulated recombinant bacteria maintained their physiological ability to synthesize a fully functional luciferase and sufficient substrate to generate luminescence.

Due to the biocompatibility and chemical inertness of sol–gel materials, it was also used for designing optical biosensors for monitoring biological species. For example, Kishen *et al.*[223] developed an evanescent wave biosensor for the monitoring of mutans *streptococci* in human saliva. This sensor employed bromophenol blue entrapped in a porous sol–gel film coated on the unclad portion of an optical fiber, which enabled real-time monitoring of pH variations in saliva produced by the reactivity of mutans *streptococci* with sucrose.

The optical biosensors have been incorporated in lab-on-a-chip (biochip) device.[10] A novel, miniature optical biosensor was developed by integrating the complementary metal oxide semiconductor (CMOS) photosensor, the sol–gel technique and the chemilumminescence detection method.[208] The detection area of chip is only 0.5 mm × 0.5 mm. This miniature CMOS-based optical biosensor not only exhibits high detection capability, short detection time and high reproducibility, but also requires only a small sample. With these characteristics, the miniature optical biosensor has great potential in the future development of a simple portable biosensing system for rapid screening and in-field/on-site monitoring. A more sophisticated, powerful, miniature optical biosensor system is expected to be easily fabricated for future biochip development.

3.328.3.3. Biosensors Based on Other Transducing Principles

Piezoelectricity is the ability of some materials (notably crystals and certain ceramics, including bone) to generate an electric field or electric potential[224] in response to applied mechanical stress. Piezoelectric sensors utilize crystals which undergo an elastic deformation when an electrical potential is applied to them. An alternating potential produces a standing wave in the crystal at a characteristic frequency. This frequency is highly dependent on the elastic properties of the crystal, such that if a crystal is coated with a biological recognition element, the binding of a (large) target analyte to a receptor will produce a change in the resonance frequency, which gives a binding signal. In a mode that uses surface acoustic waves, the sensitivity is greatly increased. This is a specialized application of the Quartz crystal microbalance as a biosensor.[225] Recently, microdiaphragm piezoelectric-based biosensors have been successfully applied as a biological diagnostic tool in air and liquid media.[226]

Thermometric- and magnetic-based sol–gel biosensors are seldom being reported and very few publications could be found in Web of Science. Ramanathan *et al.*[227] reported a sol–gel-based glucose biosensor using thermometric measurement. Enzymes such as GOx and catalase were entrapped on the surface of reticulated vitreous carbon cylinder using sol–gel as a binder. The cartridge was placed within the column of an enzyme thermistor device. Injection of various glucose concentrations resulted in changing the heat content of the circulating buffer, recorded as a thermometric peak by a sensitive thermistor. Wu *et al.*[228] reported a kinetic assay of trypsin with a wireless magnetoelastic sensor. A wireless magnetoelastic trypsin biosensor was fabricated by first coating a magnetoelastic ribbon-like sensor with a pH-sensitive polymer and then upon it a layer of trypsin. In response to an externally applied time-varying magnetic field, the magnetoelastic sensor mechanically vibrates at a characteristic frequency that is inversely dependent upon the mass of the attached film. As the magnetoelastic sensor is magnetostrictive, the mechanical vibrations of the sensor launch magnetic flux that can be detected remotely from the sensor using a pickup coil.

3.328.4. Conclusions and Future Trends

The development of novel biosensor devices is currently the subject of extensive research in areas such as clinical diagnosis, food technology, biomedical, defense science and environmental analysis.[10,229–231] Exciting biosensor designs have been proposed in several reports during the past few decades and numerous approaches for effective biosensor systems have also been demonstrated in laboratories.

The selection of appropriate (and stable) materials probably is the most challenging task in biosensor development.[10] The biocompatible and versatile sol–gel process offers a flexible approach for the fabrication of various biosensors with different configurations to suit different applications.[7–9] Typically, those sol–gel materials possess physical rigidity, chemical inertness, high photochemical biodegradation, and negligible swelling in aqueous and organic solutions.[232]

As previously stressed, the enormous versatility of the sol–gel chemistry enables the production of robust hybrids at low temperatures with remarkably new and improved material properties that can be used to enhance the stability of bioreceptors. Bioencapsulation in mineral/hybrid sol–gel hosts has been successfully attempted with a great variety of biological entities including numerous enzymes, antibodies, microorganisms, and even whole cells.[8,9] Another major reason for the popularity of sol–gels results from the fact that the activity of bioreceptors is retained over a long time.[10] As a result, the

investigation of sol–gel hybrid systems has progressed dramatically over the past two decades for biosensing proposes.

An emerging area for sol–gel biosensors is the incorporation of nanomaterials in the sol–gel matrix. In addition to the molecular inorganic–organic hybrid network, the physical, electronic, optical, or catalytic properties of nanomaterials resulting from the inorganic crystalline, glassy, or metallic properties also can be tailored to suit a particular application.[233–235] Nanomaterials exhibit a number of special properties relative to the bulk materials. Two of the major factors in the special properties are the increase in the ratio of surface area to volume, and the size of the particle moving into the realm where quantum effects predominate.

However, even though some other precursors have been introduced, sol–gel matrices are mainly prepared by TMOS or TEOS as precursor.[232] The poor water solubility of such precursors usually involves enzyme immobilization in organic cosolvents. Therefore, development of enzyme biosensors based on biocompatible silica sol–gel matrix has attracted increasing attention recently. Despite the effects of designing new precursors with improved water solubility and biocompatibility,[236,237] silica-based organic–inorganic hybrids are adopted as attractive materials for biosensor fabricating.[238,239] It is expected that the new hybrid sol–gel materials and/or methods could improve biocompatibility and activity, and also provide less brittle nature matrices.

Furthermore, despite the promising studies, only a few biosensors are commercially available.[240] Some critical issues still need to be considered and resolved, in order to make mass production and commercialization viable. A significant number of sensing devices reported exhibit one or more limitations that hinder their continuous use, and some of them (except when specified) were not applied to real samples or practical situations. Many of the works referred, although describing optimization and, sometimes, showing preliminary results, present insufficient data concerning analytical performance. It is desirable to fabricate sol–gel biosensors with high stability that can be used as everyday analytical tools.

As shown in the reports assembled in this chapter, rapid advances have been made in improving immobilization protocols and overcoming many hurdles of sol–gel technology in the recent years. Novel configurations, such as miniaturized devices and integrated sensors based on planar waveguides, are currently employed and provide high sensitivity, fast response and low costs, as well as an enlarged range of possible applications. It is also expected that microfabrication techniques, such as soft lithography and photo pattern ability, will enable the production of the new generation of microbiosensors.

References

1. Wright, J. D.; Sommerdijk, N. A. J. M. *Sol–Gel Materials: Chemistry and Applications*. Taylor & Francis: London, 2001.
2. Gill, I. *Chem. Mater.* **2001**, *13*, 3404–3421.
3. Gill, I.; Ballesteros, A. *TIBTech* **2000**, *18*, 282–296.
4. Avnir, D.; Coradin, T.; Lev, O.; Livage, J. *J. Mater. Chem.* **2006**, *16*, 1013–1030.
5. Bukowski, R. M.; Ciriminna, R.; Pagliaro, M.; Bright, F. V. *Anal. Chem.* **2005**, *77*, 2670–2672.
6. Doong, R. A.; Shih, H. M.; Lee, S. H. *Sens. Actuators B* **2005**, *111*, 323–330.
7. Gupta, R.; Chaudhury, N. K. *Biosens. Bioelectron.* **2007**, *22*, 2387–2399.
8. Kandimalla, V. B.; Tripathi, V. S.; Ju, H. *Crit. Rev. Anal. Chem.* **2006**, *36*, 73–106.
9. Kandimalla, V. B.; Tripathi, V. S.; Ju, H. X. Biosensors based on immobilization of biomolecules in sol–gel matrices. In *Electrochemical Sensors, Biosensors and Their Biomedical Applications*, Elsevier: New York, 2008; Chapter 16, pp 503–529.
10. Borisov, S. M.; Wolfbeis, O. S. *Chem. Rev.* **2008**, *108*, 423–461.
11. Clark, L. C.; Lyons, I. R. *Ann. N.Y. Acad. Sci.* **1962**, *102*, 29–45.
12. Wang, E. *Analyt. Chem.* **2006**, *47*, 755–775.
13. Besanger, T. R.; Brennan, J. D. *J. Sol Gel Sci. Technol.* **2006**, *40*, 209–225.
14. Walcarius, A.; Collinson, M. M. *Annu. Rev. Anal. Chem.* **2009**, *2*, 121–143.
15. Braun, S.; Rappoport, S.; Zusman, R.; Avnir, D.; Ottolenghi, M. *Mater. Lett.* **1990**, *10*, 1–5.
16. Ellerby, L. M.; Nishida, C. R.; Nishida, F.; *et al. Science* **1992**, *255*, 1113–1115.
17. Frenkel-Mullerad, H.; Avnir, D. *J. Am. Chem. Soc.* **2005**, *127*, 8077–8081.
18. Premkumar, J. R.; Sagi, E.; Rosen, R.; Belkin, S.; Modestov, A. D.; Lev, O. *Chem. Mater.* **2002**, *14*, 2676–2686.
19. Jin, W.; Brennan, J. D. *Anal. Chim. Acta* **2002**, *461*, 1–36.
20. Dickery, F. H. *J. Phys. Chem.* **1955**, *58*, 695–707.
21. Shtelzer, S. S.; Rappoport, D.; Avnir, M.; Ottolenghi, M.; Braun, S. *Biotechnol. Appl. Biochem.* **1992**, *15*, 227–235.
22. Fang, X. Q.; Tan, O. K.; Tse, M. S.; Ooi, E. E. *Biosens. Bioelectron.* **2010**, *25*, 1137–1142.
23. Namgung, R.; Nam, S.; Kim, S. K.; *et al. Biomaterials* **2009**, *30*, 5225–5233.
24. Livage, J.; Coradin, T.; Roux, C. *J. Phys. Condes. Matter* **2001**, *13*, 673–691.
25. Ahn, J.; Cho, M.; Lee, S.; *et al. Mol. Cell. Toxicol.* **2008**, *4*, 100–105.
26. Tan, F.; Yan, F.; Ju, H. X. *Biosens. Bioelectron.* **2007**, *22*, 2945–2951.
27. Liang, R.; Qiu, J.; Cai, P. *Anal. Chim. Acta* **2005**, *534*, 223–229.
28. Meunier, C. F.; Dandoy, P.; Su, B. L. *J. Colloid Interface Sci.* **2010**, *342*, 211–224.
29. Nguyen-Ngoc, H.; Tran-Minh, C. *Anal. Chim. Acta* **2007**, *583*, 161–165.
30. Trogl, J.; Ripp, S.; Kuncova, G.; *et al. Sens. Actuators B* **2005**, *107*, 98–103.
31. Liu, L.; Shang, L.; Guo, S. J.; *et al. Biosens. Bioelectron.* **2009**, *25*, 523–526.
32. Jia, J.; Tang, M.; Chen, X.; Qi, L.; Dong, S. *Biosens. Bioelectron.* **2003**, *18*, 1023–1029.
33. Jal, P. K.; Patel, S.; Mishra, B. K. *Talanta* **2004**, *62*, 1005–1028.
34. Cajlakovic, M.; Lobnik, A.; Werner, T. *Anal. Chim. Acta* **2002**, *455*, 207–213.
35. Edmiston, P. L.; Wambolt, C. L.; Smith, M. K.; Saavedra, S. S. *J. Colloid Interface Sci.* **1994**, *163*, 395–406.
36. Wambolt, C. L.; Saavedra, S. S. *J. Sol Gel Sci. Tech.* **1996**, *7*, 53–57.
37. Flora, K.; Brennan, J. D.; Baker, G. A.; Doody, M. A.; Bright, F. V. *Biophys. J.* **1998**, *75*, 1084–1096.
38. Zheng, L. L.; Reid, W. R.; Brennan, J. D. *Anal. Chem.* **1997**, *69*, 3940–3949.
39. Zheng, L.; Flora, K.; Brennan, J. D. *Chem. Mater.* **1998**, *10*, 3974–3983.
40. Dunn, B.; Zink, J. I. *Chem. Mater.* **1997**, *9*, 2280–2291.
41. Gilliland, J. W.; Yokoyama, K.; Yip, W. T. *J. Phys. Chem. B* **2005**, *109*, 4816–4823.
42. Dave, B. C.; Dunn, B.; Valentine, J. S.; Zink, J. I. *Anal. Chem.* **1994**, *66*, 1120A–1127A.
43. Collinson, M. M. *Acc. Chem. Res.* **2007**, *40*, 777–783.
44. Shen, C.; Kostic, N. M. *J. Am. Chem. Soc.* **1997**, *119*, 1304–1312.
45. Flora, K.; Brennan, J. D. *Chem. Mater.* **2001**, *13*, 4170–4179.
46. Lev, O.; Tsionsky, M.; Rabinovich, L.; *et al. Anal. Chem.* **1995**, *67*, 22–30.
47. Lin, J.; Brown, C. W. *Trac-Trend Anal. Chem.* **1997**, *16*, 200–211.
48. MacCraith, B. D.; McDonagh, C.; McEvoy, A. K.; Butler, T.; O'Keeffe, G.; Murphy, V. *J. Sol Gel Sci. Technol.* **1997**, *8*, 1053–1061.
49. Badjic, J. D.; Kostic, N. M. *Chem. Mater.* **1999**, *11*, 3671–3679.
50. Fang, J.; Zhou, J. C.; Lan, E. H.; Dunn, B.; Zink, J. I. *J. Sol Gel Sci. Technol.* **2009**, *50*, 176–183.
51. Choi, M. M. F.; Pang, W. S. H.; Xiao, D.; Wu, X. *Analyst* **2001**, *126*, 1558–1563.
52. Ghica, M. E.; Pauliukaite, R.; Marchand, N.; Devic, E.; Brett, C. M. A. *Anal. Chim. Acta* **2007**, *591*, 80–86.
53. Gill, I.; Ballesteros, A. *J. Am. Chem. Soc.* **1998**, *10*, 8587–8598.
54. Walcarius, A. *Chem. Mater.* **2001**, *13*, 3351–3372.
55. Chen, Q.; Kenausis, G. L.; Heller, A. *J. Am. Chem. Soc.* **1998**, *120*, 4582–4585.
56. Heller, J.; Heller, A. *J. Am. Chem. Soc.* **1998**, *120*, 4586–4590.
57. Wang, B. Q.; Li, B.; Deng, Q.; Dong, S. J. *Anal. Chem.* **1998**, *70*, 3170–3174.
58. Gavalas, V. G.; Law, S. A.; Ball, J. C.; Andrews, R.; Bachasa, L. G. *Anal. Biochem.* **2004**, *329*, 247–252.
59. Glezer, V.; Lev, O. *J. Am. Chem. Soc.* **1993**, *115*, 2533–2534.
60. Sampath, S.; Lev, O. *Electroanalysis* **1996**, *8*, 1112–1116.
61. Sampath, S.; Lev, O. *J. Electroanal. Chem.* **1998**, *446*, 57–65.
62. Wang, J.; Park, D. S.; Pamidi, P. V. A. *J. Electroanal. Chem.* **1997**, *434*, 185–189.
63. Li, J.; Chia, L. S.; Goh, N. K.; Tan, S. N.; Ge, H. *Sens. Actuators B* **1997**, *40*, 135–141.
64. Maduraiveeran, G.; Ramaraj, R. A. *Electrochem. Commun.* **2007**, *9*, 2051–2055.

65. Sinha, R.; Ganesana, M.; Andreescu, S.; Stanciu, L. *Anal. Chim. Acta* **2010**, *661*, 195–199.
66. Iwuoha, E. I.; Kane, S.; Ania, C. O.; Smyth, M. R.; de Montellano, P. R. O.; Fuhr, U. *Electroanalysis* **2000**, *12*, 980–986.
67. Maldonado, A.; Tirado-Guerra, S.; Cazares, J. M.; Olvera, M. de. la. L. *Thin Solid Films* **2010**, *518*, 1815–1820.
68. Ozasa, K.; Nemoto, S.; Li, Y. Z.; Hara, M.; Maeda, M.; Mochitate, K. *Surf. Interface Anal.* **2008**, *40*, 579–583.
69. Pandey, P. C.; Upadhyay, S.; Pathak, H. C. *Sens. Actuators B* **1999**, *60*, 83–89.
70. Pandey, P. C.; Upadhyay, S.; Pathak, H. C. *Electroanalysis* **1999**, *11*, 59–64.
71. Wang, B. Q.; Li, B.; Wang, Z. X.; Xu, G. B.; Wang, Q.; Dong, S. J. *Anal. Chem.* **1999**, *71*, 1935–1939.
72. Liang, R. P.; Jiang, J. L.; Qiu, J. D. *Electroanalysis* **2008**, *20*, 2642–2648.
73. Yang, X. H.; Hua, L.; Gong, H. Q.; Tan, S. N. *Anal. Chim. Acta* **2003**, *478*, 67–75.
74. Jiang, D.; Tang, J.; Liu, B.; Yang, P.; Kong, J. *Anal. Chem.* **2003**, *75*, 4578–4584.
75. Yin, T. J.; Wei, W. Z.; Yang, L.; Gao, X. H.; Gao, Y. P. *Sens. Actuators B* **2006**, *117*, 286–294.
76. Zhou, J. C.; Chuang, M. H.; Lan, E. H.; Dunn, B.; Gillman, P. L.; Smith, S. M. *J. Mater. Chem.* **2004**, *14*, 2311–2316.
77. Lin, S.; Li, J.; Tan, S. N. *Analyst* **1997**, *122*, 1431–1434.
78. Pauliukaite, R.; Schoenleber, M.; Vadgama, P.; Brett, C. M. A. *Anal. Bioanal. Chem.* **2008**, *390*, 1121–1131.
79. Zejli, H.; De Cisneros, J. L. H. H.; Naranjo-Rodriguez, I.; Liu, B. H.; Temsamani, K. R.; Marty, J. L. *Talanta* **2008**, *77*, 217–221.
80. Pandey, P. C.; Upadhyay, S.; Tiwari, I.; Tripathi, V. S. *Anal. Biochem.* **2001**, *288*, 39–43.
81. Choi, H. N.; Lyu, Y. K.; Han, J. H.; Lee, W. Y. *Electroanalysis* **2007**, *19*, 1757–1763.
82. Noguer, T.; Tencaliec, A.; Calas-Blanchard, C.; Avramescu, A.; Marty, J. L. *J. AOAC Int.* **2002**, *85*, 1382–1389.
83. Di, J. W.; Zhang, M.; Yao, K. A.; Bi, S. P. *Biosens. Bioelectron.* **2006**, *22*, 247–252.
84. Yao, T.; Takashima, K. *Biosens. Bioelectron.* **1998**, *13*, 67–73.
85. Li, J.; Peng, T.; Pengc, Y. *Electroanalysis* **2003**, *15*, 1031–1037.
86. Solanki, P. R.; Kaushik, A.; Ansari, A. A.; Tiwari, A.; Malhotra, B. D. *Sens. Actuators B* **2009**, *137*, 727–735.
87. Kumar, A.; Malhotra, R.; Malhotra, B. D.; Grover, S. K. *Anal. Chim. Acta* **2000**, *14*, 43–50.
88. Song, Z.; Huang, J. D.; Wu, B. Y.; Shi, H. B.; Anzai, J. I.; Chen, Q. *Sens. Actuators B* **2006**, *115*, 626–633.
89. Shi, Q. C.; Peng, T. Z.; Zhu, Y. N.; Yang, C. F. *Electrophoresis* **2005**, *17*, 857–861.
90. Liu, G. D.; Zhong, T. S.; Huang, S. S.; Shen, G. L.; Yu, R. Q. *Fresenius J. Anal. Chem.* **2001**, *370*, 1029–1034.
91. Pandey, P. C.; Mishra, A. P. *Biosens. Bioelectron.* **2004**, *99*, 230–235.
92. Patel, A. K.; Sharma, P. S.; Prasad, B. B. *Electroanalysis* **2008**, *20*, 2102–2112.
93. Fireman-Shoresh, S.; Turyan, I.; Mandler, D.; Avnir, D.; Marx, S. *Langmuir* **2005**, *21*, 7842–7847.
94. Li, F.; Chen, W.; Zhang, S. S. *Biosens. Bioelectron.* **2008**, *24*, 781–786.
95. Fu, Y. Z.; Yuan, R.; Xu, L.; *et al. J. Biochem. Biophys. Methods* **2005**, *62*, 163–174.
96. Li, T.; Yao, Z. H.; Ding, L. *Sens. Actuators B* **2004**, *101*, 155–160.
97. Pandey, P. C.; Upadhyay, S.; Shukla, N. K.; Sharma, S. *Biosens. Bioelectron.* **2003**, *18*, 1257–1268.
98. Narang, U.; Prasad, P. N.; Bright, F. V. *Chem. Mater.* **1994**, *6*, 1596–1598.
99. Pankratov, I.; Lev, O. *J. Electroanal. Chem.* **1995**, *393*, 35–41.
100. Li, J.; Chia, L. S.; Goh, N. K.; Tan, S. N. *J. Electroanal. Chem.* **1999**, *460*, 234–241.
101. Liu, Z. J.; Liu, B. H.; Zhang, M.; Kong, J. L.; Deng, J. Q. *Anal. Chim. Acta* **1999**, *392*, 135–141.
102. Park, T. M.; Iwuoha, E. I.; Smyth, M. R.; MacCraith, B. D. *Anal. Commun.* **1996**, *339*, 271–273.
103. Pandey, P. C.; Upadhyay, S. *Sens. Actuators B* **2001**, *76*, 193–198.
104. Tian, F. M.; Xu, B.; Zhu, L. D.; Zhu, G. Y. *Anal. Chim. Acta* **2001**, *443*, 9–16.
105. Chen, X.; Dong, S. *Biosens. Bioelectron.* **2003**, *18*, 999–1004.
106. Shin, J. H.; Marxer, S. M.; Schoenfisch, M. H. *Anal. Chem.* **2004**, *76*, 4543–4549.
107. Shankaran, D. R.; Uehara, N.; Kato, T. *Biosens. Bioelectron.* **2003**, *18*, 721–728.
108. Couto, C. M.; Araujo, A. N.; Montenegro, M. C.; Rohwedder, J.; Raimundo, I.; Pasquini, C. *Talanta* **2002**, *56*, 997–1003.
109. Tian, F. M.; Zhu, G. Y. *Anal. Chim. Acta* **2002**, *451*, 251–258.
110. Prieto-Simon, B.; Armatas, G. S.; Pomonis, P. J.; Nanos, C. G.; Prodromidis, M. I. *Chem. Mater.* **2004**, *16*, 1026–1034.
111. Yu, J. H.; Liu, S. Q.; Ju, H. X. *Biosens. Bioelectron.* **2003**, *19*, 401–409.
112. Yang, M. H.; Yang, Y. H.; Liu, Y. L.; Shen, G. L.; Yu, R. Q. *Biosens. Bioelectron.* **2006**, *21*, 1125–1131.
113. Niu, J.; Lee, J. Y. *Sens. Actuators B* **2002**, *82*, 250–258.
114. Zuo, S. H.; Teng, Y. J.; Yuan, H. H.; Lan, M. B. *Sens. Actuators B* **2008**, *133*, 555–560.
115. Kang, X. H.; Mai, Z. B.; Zou, X. Y.; Cai, P. X.; Mo, J. Y. *Talanta* **2008**, *74*, 879–886.
116. Jia, W. Z.; Wang, K.; Zhu, Z. J.; Song, H. T.; Xia, X. H. *Langmuir* **2007**, *23*, 11896–11900.
117. Yang, S.; Lu, Y.; Atanossov, P.; Wilkins, E.; Long, X. *Talanta* **1998**, *47*, 735–743.
118. Chen, X.; Hu, Y.; Wilson, G. S. *Biosens. Bioelectron.* **2002**, *17*, 1005–1013.
119. Ansari, A. A.; Sumana, G.; Malhotra, B. D. *Analyst* **2009**, *134*, 997–1002.
120. Yu, J.; Ju, H. X. *Anal. Chim. Acta* **2003**, *486*, 209–216.
121. Wang, Q. L.; Lu, G. X.; Yang, B. J. *Sens. Actuators B* **2004**, *99*, 50–57.
122. Tang, D. P.; Yuan, R.; Chai, Y. Q.; Zhong, X.; Liu, Y.; Dai, J. Y. *Clin. Biochem.* **2006**, *39*, 309–314.
123. Park, T. M.; Iwwuoha, I.; Smyth, M. R. *Electroanalysis* **1997**, *9*, 1120–1123.
124. Wang, B. Q.; Dong, S. J. *Talanta* **2000**, *51*, 565–572.
125. Wang, B. Q.; Zhang, J. Z.; Cheng, G. J.; Dong, S. J. *Anal. Chim. Acta* **2000**, *407*, 111–118.
126. Zhang, J. Z.; Li, B.; Wang, Z. X.; Cheng, G. J.; Dong, S. J. *Anal. Chim. Acta* **1999**, *388*, 71–78.
127. Miao, Y.; Tan, S. N. *Anal. Chim. Acta* **2001**, *437*, 87–93.
128. Li, J.; Tan, S. N.; Ge, H. *Anal. Chim. Acta* **1996**, *335*, 137–145.
129. Park, T. M. *Anal. Lett.* **1999**, *32*, 287–298.
130. Shankaran, D. R.; Shim, Y. B. *Electroanalysis* **2002**, *14*, 704–707.
131. Chen, D. D.; Liu, B. H.; Liu, Z. J.; Kong, J. L. *Anal. Lett.* **2001**, *34*, 687–699.
132. Li, W. J.; Yuan, R.; Chai, Y. Q.; Zhou, L.; Chen, S. H.; Li, N. *J. Biochem. Biophys. Methods* **2008**, *70*, 830–837.
133. Di, J. W.; Shen, C. P.; Peng, S. H.; Tu, Y. F.; Li, S. J. *Anal. Chim. Acta* **2005**, *553*, 196–200.
134. Jia, J. B.; Wang, B. Q.; Wu, A. G.; Cheng, G. J.; Li, Z.; Dong, S. J. *Anal. Chem.* **2002**, *74*, 2217–2223.
135. Wang, G.; Xu, J. J.; Chen, H. Y.; Lu, Z. H. *Biosens. Bioelectron.* **2003**, *18*, 335–343.
136. Chen, X.; Cheng, G. J.; Dong, S. J. *Analyst* **2001**, *126*, 1728–1732.
137. Liu, Y.; Shi, L. H.; Wang, M. J.; Li, Z. Y.; Liu, H. T.; Li, J. H. *Green Chem.* **2005**, *7*, 655–658.
138. Kane, S. A.; Iwuoha, E. I.; Smyth, M. R. *Analyst* **1998**, *123*, 2001–2006.
139. Chaubey, A.; Pande, K. K.; Malhotra, B. D. *Anal. Sci.* **2003**, *19*, 1477–1480.
140. Cheng, J. J.; Di, J. W.; Hong, J. H.; *et al. Talanta* **2008**, *76*, 1065–1069.
141. Cox, J. A.; Hensley, P. M.; Loch, C. L. *Microchim. Acta* **2003**, *142*, 1–5.
142. De Jesus, D. S.; Couto, C. M.; Araujo, A. N.; Montenegro, M. C. B. S.M. *J. Pharm. Biomed. Anal.* **2003**, *33*, 983–990.
143. Yu, D.; Volponi, J.; Chhabra, S.; Brinker, C. J.; Mulchandani, A.; Singh, A. K. *Biosens. Bioelectron.* **2005**, *20*, 1433–1437.
144. Metzger, J.; Reiss, M.; Hartmeier, W. *Biosens. Bioelectron.* **1998**, *13*, 1077–1082.
145. Riccardi, C. D.; Dahmouche, K.; Santilli, C. V.; da Costa, P. I.; Yamanaka, H. *Talanta* **2006**, *70*, 637–643.
146. Di, J. W.; Bi, S. P.; Zhang, M. *Biosens. Bioelectron.* **2004**, *19*, 1479–1486.
147. Pandey, P. C.; Upadhyay, S.; Tiwari, I.; Singh, G.; Tripathi, V. S. *Sens. Actuators B* **2001**, *75*, 48–55.
148. Liu, Z. J.; Deng, J. Q.; Li, D. *Anal. Chim. Acta* **2000**, *407*, 87–96.
149. Li, J.; Chia, L. S.; Goh, N. K.; Tan, S. N. *Anal. Chim. Acta* **1998**, *362*, 203–211.
150. Zhang, T.; Tian, B. Z.; Kong, J. L.; Liu, B. H. *Anal. Chim. Acta* **2003**, *489*, 199–206.
151. Chen, X.; Wang, B.; Dong, S. *Electroanalysis* **2001**, *13*, 1149–1152.
152. Yu, J. H.; Ju, H. X. *Electrophoresis* **2004**, *16*, 1305–1310.
153. Campuzano, S.; Serra, B.; Pedrero, M.; de Villena, F. J. M.; Pingarron, J. M. *Anal. Chim. Acta* **2003**, *494*, 187–197.
154. Kim, M. A.; Lee, W. Y. *Anal. Chim. Acta* **2003**, *479*, 143–150.
155. Wang, B. Q.; Dong, S. J. *J. Electroanal. Chem.* **2000**, *487*, 45–50.
156. Pandey, P. C.; Singh, G. *Talanta* **2001**, *55*, 773–782.
157. Lee, W. Y.; Kim, S. R.; Kim, T. H.; Lee, K. S.; Shin, M. C.; Park, J. K. *Anal. Chim. Acta* **2000**, *404*, 195–203.
158. Lee, W. Y.; Lee, K. S.; Kim, T. H.; Shin, M. C.; Park, J. K. *Electroanalysis* **2000**, *12*, 78–82.
159. Ansari, A. A.; Sumana, G.; Pandey, M. K.; Malhotra, B. D. *J. Mater. Res.* **2009**, *24*, 1667–1673.
160. Niu, J. J.; Lee, J. Y. *Anal. Commun.* **1999**, *36*, 81–83.

161. Teh, H. F.; Yang, X. H.; Gong, H. Q.; Tan, S. N. *Electrophoresis* **2004**, *16*, 769–773.
162. Li, C. Y.; Wang, C. F.; Guan, B.; Zhang, Y. Y.; Hu, S. H. *Sens. Actuators B* **2005**, *107*, 411–417.
163. Tatsu, Y.; Yamashita, K.; Yamaguchi, M.; Yamamura, S.; Yamamoto, H.; Yoshikawa, S. *Chem. Lett.* **1992**, *36*, 1615–1618.
164. Liu, B.; Cao, Y.; Chen, D.; Kong, J.; Deng, J.; Liu, Z. *Anal. Chim. Acta* **2003**, *478*, 59–66.
165. Lu, H.; Jing, Y.; Rusling, J. F.; Hu, N. *Electroanalysis* **2006**, *18*, 379–390.
166. Yu, J.; Ju, H. X. *Anal. Chem.* **2002**, *74*, 3579–3583.
167. Narang, U.; Prasad, P. N.; Bright, F. V.; *et al*. *Anal. Chem.* **1994**, *66*, 3139–3144.
168. Wang, J.; Pamidi, P. V. A.; Park, D. S. *Anal. Chem.* **1996**, *68*, 2705–2708.
169. Sampath, S.; Lev, O. *Anal. Chem.* **1996**, *68*, 2015–2021.
170. Coche-Guerente, L.; Cosnier, S.; Labbe, P. *Chem. Mater.* **1997**, *9*, 1348–1352.
171. Abad, J. M.; Gass, M.; Bleloch, A.; Schiffrin, D. J. *J. Am. Chem. Soc.* **2009**, *29*, 10229–10236.
172. Arvinte, A.; Sesay, A. M.; Virtanen, V.; Bala, C. *Electroanalysis* **2008**, *20*, 2355–2362.
173. Gavalas, V. G.; Andrews, R.; Bhattacharyya, D.; Bachas, L. G. *Nano Lett.* **2001**, *1*, 719–721.
174. Lim, J.; Malati, P.; Bonet, F.; Dunn, B. *J. Electrochem. Soc.* **2007**, *154*, A140–A145.
175. Niedziolka, J.; Murphy, M. A.; Marken, F.; Opallo, M. *Electrochim. Acta* **2006**, *51*, 5897–5903.
176. Watcharotone, S.; Dikin, D. A.; Stankovich, S.; *et al*. *Nano Lett.* **2007**, *7*, 1888–1892.
177. Zhu, L. D.; Tian, C. Y.; Zhai, J. L.; Yang, R. L. *Sens. Actuators B* **2007**, *125*, 254–261.
178. Tsionsky, M.; Gun, G.; Giezer, V.; Lev, O. *Anal. Chem.* **1994**, *66*, 1747–1753.
179. Zoppi, R. A.; Neves, S.; Nunes, S. P. *Polymer* **2000**, *41*, 5461–5470.
180. Chen, X.; Jia, J.; Dong, S. *Electroanalysis* **2003**, *15*, 608–612.
181. Thenmozhi, K.; Narayanan, S. S. *Biosens. Bioelectron.* **2007**, *23*, 606–612.
182. Alvarez-Icaza, M.; Bilitewski, U. *Anal. Chem.* **1993**, *65*, 525A–533A.
183. Nablo, B. J.; Chen, T. Y.; Schoenfisch, M. H. *J. Am. Chem. Soc.* **2001**, *123*, 9712–9713.
184. Jeronimo, P. C. A.; Araujo, A. N.; Montenegro, M.; Conceicao, B. S. M. *Talanta* **2007**, *72*, 13–27.
185. Zurner, A.; Kirstein, J.; Doblinger, M.; Brauchle, C.; Bein, T. *Nature* **2007**, *450*, 705–708.
186. Tripathi, V. S.; Kandimalla, V. B.; Ju, H. X. *Sens. Actuators B* **2006**, *114*, 1071–1082.
187. Wolfbeis, O. S.; Oehme, I.; Papkovskaya, N.; Klimant, I. *Biosens. Bioelectron.* **2000**, *15*, 69–76.
188. Doong, R.; Shih, H. *Biosens. Bioelectron.* **2006**, *22*, 185–191.
189. Kuswandi, B.; Chulaifah, I. F.; Gani, A. A. *Talanta* **2008**, *74*, 613–618.
190. Salinas-Castillo, A.; Pastor, I.; Mallavia, R.; Reyes, M. C. *Biosens. Bioelectron.* **2008**, *24*, 1053–1056.
191. Ligler, F. S. *Anal. Chem.* **2009**, *81*, 519–526.
192. MacCraith, B. D.; McDonagh, C. M.; O'Keeffe, G.; McEvoy, A. K.; Butler, T.; Sheridan, F. R. *Sens. Actuators B* **1995**, *29*, 51–57.
193. Wong, F. C. M.; Ahmad, M.; Lee, Y. H.; Lim, B. P. *Talanta* **2006**, *69*, 888–893.
194. Lin, L.; Xiao, L.; Huang, S.; *et al*. *Biosens. Bioelectron.* **2006**, *21*, 1703–1709.
195. Kwok, N. Y.; Dong, S.; Lo, W.; Wong, K. Y. *Sens. Actuators B* **2005**, *110*, 289–298.
196. Jeronimo, P. C. A.; Araujo, A. N.; Conceicao, M.; Montenegro, B. S. M.; Satinsky, D.; Solich, P. *Analyst* **2005**, *130*, 1190–1197.
197. Andreou, V. G.; Clonis, Y. D. *Biosens. Bioelectron.* **2002**, *17*, 61–69.
198. Hreniak, A.; Maruszewski, K.; Rybka, J.; Gamian, A.; Czyzewski, J. *Opt. Mater.* **2004**, *26*, 141–144.
199. Blyth, D. J.; Aylott, J. W.; Richardson, D. J.; Russell, D. A. *Analyst* **1995**, *120*, 2725–2730.
200. Aylott, J. W.; Richardson, D. J.; Russell, D. A. *Chem. Mater.* **1997**, *9*, 2261–2263.
201. Ferretti, S.; Lee, S. K.; MacCraith, B. D.; *et al*. *Analyst* **2000**, *125*, 1993–1999.
202. Wang, X.; Zhou, T.; Chen, X.; Wong, K. Y.; Wang, X. *Sens. Actuators B* **2008**, *129*, 866–873.
203. de Marcos, S.; Galindo, J.; Sierra, J. F.; Galban, J.; Castillo, J. R. *Sens. Actuators B* **1999**, *57*, 227–232.
204. Ertekin, K.; Cinar, S.; Aydemir, T.; Alp, S. *Dyes Pigm.* **2005**, *67*, 133–138.
205. Andreou, V. G.; Clonis, Y. D. *Anal. Chim. Acta* **2002**, *460*, 151–161.
206. Wang, K. M.; Li, J.; Yang, X.; Shen, F.; Wang, X. *Sens. Actuators B* **2000**, *65*, 239–240.
207. Ho, W. J.; Chen, J. S.; Ker, M. D.; *et al*. *Biosens. Bioelectron.* **2007**, *22*, 3008–3013.
208. Li, C. L.; Lin, Y. H.; Shih, C. L.; Tsaur, J. P.; Chau, L. K. *Biosens. Bioelectron.* **2002**, *17*, 323–330.
209. Ramanathan, K.; Kamalasanan, M. N.; Malhotra, B. D.; Pradhan, D. R.; Chandra, S. *J. Sol Gel Sci. Technol.* **1997**, *10*, 309–316.
210. Pastor, I.; Esquembre, R.; Micol, V.; Mallavia, R.; Reyes, M. C. *Anal. Biochem.* **2004**, *334*, 335–343.
211. Ulatowska-Jarza, A.; Podblieska, H. *Opt. Appl.* **2002**, *32*, 685–690.
212. Tsai, H.; Doong, R.; Chiang, H.; Chen, K. *Anal. Chim. Acta* **2003**, *481*, 75–84.
213. Knobbe, E. T.; Dunn, B.; Gold, M. *Proc. SPIE* **1988**, *906*, 39–41.
214. MacCraith, B. D.; McDonagh, C. *J. Fluoresc.* **2002**, *12*, 333–342.
215. Wu, X. J.; Choi, M. M. F. *Anal. Chim. Acta* **2004**, *514*, 219–226.
216. Jenna, L.; Rickus, B. D.; Jeffrey, I. Z. In *Optical Biosensors: Present and Future*; Ligler, F. S., Taitt, C. A. R., Eds.; Elsevier: Amsterdam, 2002; p 427.
217. Kuswandi, B.; Andres, R.; Narayanaswamy, R. *Analyst* **2001**, *126*, 1469–1491.
218. Doong, R. A.; Tsai, H. C. *Anal. Chim. Acta* **2001**, *434*, 239–246.
219. Tsai, H.; Doong, R. *Biosens. Bioelectron.* **2007**, *23*, 66–73.
220. Pastor, I.; Salinas-Castillo, A.; Esquembre, R.; Mallavia, R.; Mateo, C. R. *Biosens. Bioelectron.* **2010**, *25*, 1526–1529.
221. Premkumar, J. R.; Lev, O.; Rosen, R.; Belkin, S. *Adv. Mater.* **2001**, *13*, 1773–1775.
222. Kishen, A.; John, M. S.; Lim, C. S.; Asundi, A. *Biosens. Bioelectron.* **2003**, *18*, 1371–1378.
223. Holler, F. J.; Skoog, D. A.; Crouch, S. R. *Principles of Instrumental Analysis*, 6th ed.; Cengage Learning: New Delhi, 2007; Chapter 1, p 9.
224. Muralt, P. *J. Micromech. Microeng.* **2000**, *10*, 136–146.
225. Olfatnia, M.; Xu, T.; Ong, L. S.; Miao, J. M.; Wang, Z. H. *J. Micromech. Microeng.* **2010**, *20*, 015007. doi:10.1088/0960-1317/20/1/015007.
226. Ramanathan, K.; Jonsson, B. R.; Danielsson, B. *Anal. Chim. Acta* **2001**, *427*, 1–10.
227. Wu, S.; Cai, Q.; Grimes, C. A. *Sens. Lett.* **2006**, *4*, 160–164.
228. Rich, R. L.; Myszka, D. G. *J. Mol. Recognit.* **2007**, *20*, 300–366.
229. Velasco-García, M.; Mottram, T. *Biosyst. Eng.* **2003**, *84*, 1–12.
230. Xu, Z.; Guo, Z.; Dong, S. *Biosens. Bioelectron.* **2005**, *21*, 455–461.
231. Li, F.; Chen, W.; Tang, C.; Zhang, S. *Talanta* **2009**, *77*, 1304–1308.
232. Keeling-Tucker, T.; Brennan, J. D. *Chem. Mater.* **2001**, *13*, 3331–3350.
233. Menaa, B.; Menaa, F.; Aiolfi-Guimaraes, C.; Sharts, O. *Int. J. Nanotechnol.* **2010**, *7*, 1–45.
234. Schmidt, H.; Jonschker, G.; Goedicke, S.; Mennig, M. *J. Sol Gel Sci. Technol.* **2000**, *19*, 39–51.
235. Sui, X.; Cruz-Aguado, J. A.; Chen, Y.; Zhang, Z.; Brook, M.; Brennan, J. D. *Chem. Mater.* **2005**, *17*, 1174–1182.
236. Wang, G. H.; Zhang, L. M. *J. Phys. Chem. B* **2006**, *110*, 24864–24868.
237. Du, D.; Chen, S. Z.; Cai, J.; Zhang, A. D. *Talanta* **2008**, *74*, 766–772.
238. Tian, X. C.; Li, M. J.; Cai, P. X.; Luo, L. J.; Zou, X. Y. *Anal. Biochem.* **2005**, *337*, 111–120.
239. Mehrvar, M.; Abdi, M. *Anal. Sci.* **2004**, *20*, 1113–1126.
240. Liu, Z. J.; Liu, B. H.; Kong, J. L.; Deng, J. Q. *Anal. Chem.* **2000**, *72*, 4707–4712.

3.325. Imaging Mineralized Tissues in Vertebrates

B Misof and P Roschger, Ludwig Boltzmann Institute of Osteology at Hanusch Hospital of WGKK and AUVA Trauma Centre Meidling, 4th Medical Department Hanusch Hospital, Vienna, Austria
P Fratzl, Max Planck Institute of Colloids and Interfaces, Potsdam, Germany

© 2011 Elsevier Ltd. All rights reserved.

3.325.1. Introduction 408
3.325.2. Structure of Mineralized Tissues 408
3.325.2.1. Bone 408
3.325.2.1.1. Hierarchical structure of bone 408
3.325.2.1.2. Lamellar bone 410
3.325.2.1.3. Woven and plexiform bone 410
3.325.2.2. Tooth 411
3.325.2.3. Calcified Cartilage 411
3.325.2.4. Calcified Tendon 412
3.325.3. Heterogeneity of Mineral Content and the Need for Imaging Techniques 412
3.325.4. Estimates of Total Bone Mineral Content 413
3.325.4.1. Ash Weight Analysis 413
3.325.4.2. Density Fractionation 413
3.325.4.3. Neutron Activation 413
3.325.4.4. Bone Mineral Density 414
3.325.5. Imaging of Mineralized Tissues 414
3.325.5.1. Light Microscopy and Morphometry 414
3.325.5.2. X-Ray Microradiography 415
3.325.5.3. Phase-Contrast and Dark Field X-Ray Imaging 416
3.325.5.4. Microcomputed X-Ray Tomography and Synchrotron Radiation Microtomography 416
3.325.5.4.1. X-ray tomography for structural analysis 416
3.325.5.4.2. X-ray tomography for quantitative analysis of the mineral content 417
3.325.5.5. Magnetic Resonance Imaging 417
3.325.5.6. Transmission Electron Microscopy 417
3.325.6. Property Mapping in Mineralized Tissues 418
3.325.6.1. Vibrational Spectroscopy 418
3.325.6.1.1. Fourier transform infrared imaging 418
3.325.6.1.2. Raman spectroscopy 418
3.325.6.2. Secondary Electron and Back-Scattered Electron Imaging 419
3.325.6.3. Scanning Small Angle X-Ray Scattering and Diffraction 420
3.325.6.4. Mapping of Elastic Properties 421
3.325.6.4.1. Scanning acoustic microscopy 421
3.325.6.4.2. Nanoindentation 421
3.325.6.5. Mapping of Elemental Composition 422
3.325.6.5.1. X-ray fluorescence 422
3.325.6.5.2. Secondary ion mass spectrometry 423
3.325.6.6. Scanning Surface Topography with AFM 423
3.325.7. Conclusions 423
References 424

Abbreviations

AFM	Atomic force microscopy
BE	Backscattered electrons
BMC	Bone mineral content
BMD	Bone mineral density
BMDD	Bone mineralization density distribution
BMU	Bone multicellular unit
BSUs	Bone structural units
CT	Computed tomography
DXA	Dual X-ray absorptiometry
EDX	Energy dispersive X-ray
ERF	Electron induced Roentgen fluorescence
ESRF	European Synchrotron Radiation Facility
FTIRI	Fourier transform infrared imaging
IR	Infrared radiation
ITD	Intertubular dentin
MRI	Magnetic resonance imaging
MTLT	Mineralized turkey leg tendon

NAA	Neutron activation analysis
PCT	Peripheral computed tomography
PMMA	Polymethylmethacrylate
PTD	Peritubular dentin
qBEI	Quantitative backscattered electron imaging
QCT	Quantitative computed tomography
SAM	Scanning acoustic microscopy
SAXS	Small angle X-ray scattering
SE	Secondary electrons
SEM	Scanning electron microscope
SIMS	Secondary ion mass spectrometry
SRμCT	Synchrotron radiation microtomography
TEM	Transmission electron microscopy
WAXS	Wide angle X-ray scattering
WDX	Wavelength dispersive X-ray
XRD	X-ray diffraction
XRF	X-ray induced Roentgen fluorescence
μCT	Microcomputed X-ray tomography

3.325.1. Introduction

The functions of important organs, such as bone and teeth, are determined by the biomechanical properties of the mineralized tissues they are made of.[1,2] In addition, bone is the ion reservoir in our body, a central organ for calcium and phosphate homeostasis[3] and is considered to be an endocrine organ.[4] Its mineral content has a decisive influence on the mechanical properties,[5] and methods for a quantitative characterization of mineral content and characteristics are clearly needed. The difficulty is that virtually all biological materials, including mineralized tissues, are hierarchically structured, which means that they are inhomogeneous over many length scales.[6] Imaging using different techniques and covering many scales is, therefore, needed to fully characterize mineralized tissues.

In recent years, imaging methodologies have been developed on the basis of various probes, diffraction, and spectroscopy using photons or electrons, absorption imaging, as well as scanning probe microscopy techniques and more. For example, the use of synchrotron radiation has rapidly developed in recent years and allows insight into the nanoscale properties of mineralized tissue. The goal of the present chapter is to summarize the characterization possibilities offered by various approaches. This is preceded by a description of the hierarchical structure of mineralized tissues, and in particular of bone. A better understanding of the structure–function relation in mineralized tissues might lead to new strategies for treatment of patients with bone fragility. The systematic use of imaging techniques will thus help to improve our arsenal in fighting such diseases with high socioeconomic impact and influence on quality of life.

3.325.2. Structure of Mineralized Tissues

In vertebrates, several types of mineralized tissues can be found. In this article, we will focus on tissues which mineralize in normal physiologic conditions, such as bone, teeth, mineralized cartilage, and calcified tendon. Many of them have a complex structure and are hierarchically organized. It is important to study their normal occurrence for the understanding of their development. Deviations from their normal structure (for instance changes in osteoporosis) might give not only information on pathological processes occurring in specific diseases but also insights into normal tissue development. It should be mentioned that there are also many different forms of calcified deposits which develop from pathologic processes and occur in tissues which normally do not mineralize (mineralized valves, mineral deposits in muscles, renal or urinary stones, and so on). In many cases, imaging these deposits might give important information on the pathological processes and conditions of their history of formation. However, the description of this is beyond the scope of this chapter. Moreover, we will not touch other classes of mineralized tissues, for example, those based on silicate or calcium carbonates, as found in molluscs or sponges.

3.325.2.1. Bone

Bone is a living organ with outstanding mechanical properties. This is due to the complex structure and the material properties of bone, which is a composite of protein and mineral. In addition, one has to bear in mind that bone cells are actively remodeling it (replacing old and building new bone material) throughout the lifetime of an individual. Bone can grow, it can adapt to changing mechanical loading conditions, and it can heal.[1] Bone fulfils both mechanical and metabolic functions. Indeed, the skeleton enables locomotion and protects vital structures, but bone is also the site of hematopoiesis (blood synthesis) and acts as a calcium and phosphate reservoir for maintaining the required ionic levels in the serum. The amazing mechanical properties of bone are achieved by an adaptation at various levels: not only its form (shape of the bone) but also the material itself varies according to needs, leading to a complex, hierarchically organized structure; see **Figure 1**.[6–10]

Generally, bone is the umbrella term for many different types of materials found in various forms in vertebrates (including lamellar bone, parallel-fibered bone, woven bone).[1] All these variants of bone tissue are complex materials, which have in common their basic building block – the mineralized collagen fibril.[7]

3.325.2.1.1. Hierarchical structure of bone

Starting with the macroscopic visible bone structure (organ level, in **Figure 1**), that is, the shape of the bone, one can distinguish between long (such as in our limbs), short (such as the vertebra), and flat bones (such as the scapula). The optimization for mechanical loading at this macroscopic level is most obviously seen in the long bones. Their circular to ellipse-shaped cross-sections with the central canal of the bone marrow reveal a distribution of the bone material optimized for maximum bending properties at a minimum use of

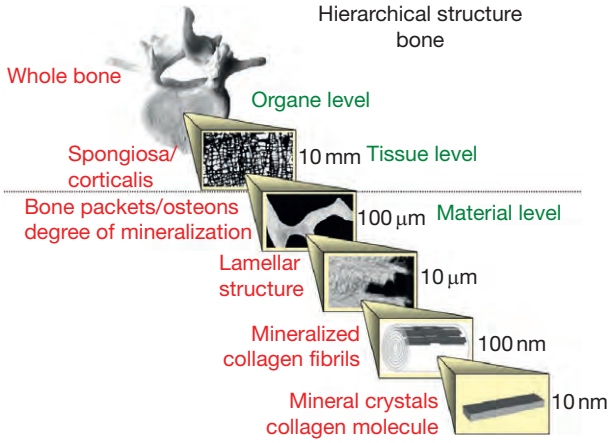

Figure 1 Hierarchical structure of bone shown in a human vertebra. The interior is a porous bony structure (spongiosa) within a dense cortical shell. Each of the struts (trabeculae) of the spongy structure consists of bone packets synthesized at different moments in time because of the permanent remodeling of the structure. At the micron level, bone tissue is lamellar, on the basis of mineralized collagen fibrils arranged in a plywood-like pattern. At the nanoscale, finally, the mineralized fibrils are on the basis of parallel collagen molecules reinforced with thin calcium phosphate mineral platelets.

bone material. As the fourth power of the outer radius is dominating the moment of inertia, the bending stiffness of long bones is highly dependent on the outer diameter of their cross-section.

At the next lower structural level (tissue level in Figure 1), most generally two types of bone architecture can be seen: an outer cortical compact bone is enclosing an inner cancellous (or trabecular) bone. The compact bone dominates in long bones, such as in the midshaft of the femur, for instance, where the cortex has a thickness of several millimeters. Looking closer at cortical bone, one sees that it has a porosity of only about 5–8%. The pores mainly contain blood vessels and nerves. In the human skeleton, about 80% of the total bone is compact bone while the remaining is cancellous (or trabecular) bone. Cancellous bone is found at the metaphyses of long bones, between the cortical plates of flat bones (iliac crest, for example) and essentially in the vertebrae. It exhibits porosity from 30 to 85%. Cancellous bone consists of struts (trabeculae) which are some hundreds of microns in size. Characteristic for cancellous bone is its highly organized trabecular network. Connectivity of the trabeculae is an important prerequisite for mechanical competence of cancellous bone.[11] More than a century ago Wolff compared the architecture in the femoral head with the architecture of a gothic cathedral, where the struts follow the principle load directions.[12] The architecture of the trabecular network is observed to be oriented according to mechanical demands.[13] In the vertebrae, which are mainly loaded in compression, the trabeculae are preferentially arranged in vertical and horizontal direction. During the development of the human lumbar spine vertebra, the structural changes at several size scales were observed.[14] The trabeculae were seen to change from an originally radial pattern in the fetus to a pattern with predominantly vertical and horizontal directions in the adult vertebra. Generally, rod- and plate-like structures can be identified in the trabecular network. With aging, specifically, the rod-like structures get thinned and finally vanish totally from the network[15] causing a significant decrease in mechanical competence (failure due to buckling) of the whole vertebra.

With the next lower hierarchical level, we reach the material level of bone which is divided further into four hierarchical sub levels (material level in Figure 1). We can find that the bone material is not homogenously formed, but composed of so-called bone structural units (BSUs) which are the bone packets in the trabecular and the osteons (here the bone packets have a cylindrical shape surrounding an haversian canal) in the cortical motifs. This BSU bone matrix is formed during remodeling by a bone multicellular unit (BMU) within 180 days involving all types of bone cells. Each of the BSUs has a certain mineral content corresponding to its tissue age[16] and they reveal a uniform lamellar arrangement of mineralized collagenous fibrils. Further they are connected among themselves via a noncollagenous mineralized surface layer (cement surfaces/lines). In that way, a remarkable heterogeneity is introduced into the bone material with respect to mineral content and orientation of bone lamellae.[17,18]

The arrangement of the fibrils can differ depending on the type of bone. Plywood-like and parallel organization can be found in lamellar bone (see Section 3.325.2.1.2) and a less ordered organization of the fibrils is seen in woven bone (see Section 3.325.2.1.3).

The mineralized collagen fibril itself has a diameter of about 0.1 μm.[19] It is the main building block of all types of bone and is composed of a collagenous scaffold into which the nanosized mineral (calcium phosphate) particles are embedded. The exact arrangement of the mineral particles has not been measured directly, and different forms of arrangements have been proposed with parallel[20] or staggered mineral plates.[21] The material at this level can be considered as a composite with the organic components being the elastic part which is stiffened by the calcium phosphate particles. The collagen (type I in bone) is deposited by the osteoblasts which are the bone forming cells. They excrete collagen molecules into the extracellular space, which subsequently assemble into fibrils. These fibrils have a characteristic pattern with adjacent molecules staggered along the axial direction by a specific distance of about 67 nm. This generates zones in which the molecules overlap and zones containing holes.[22,23] When the collagen becomes mineralized, the mineral particles grow in these holes and overlap zones.[24,25] The nucleation, growth, and the final size of these mineral particles are essentially controlled by the collagen[26] and by noncollagenous proteins.[27] The mineral particles are flat with a few nanometers in thickness[7,28] and elongated (nearly 100 nm in length).[25,29] As the mineralized collagen fibril is the basic building block of bone, the understanding of its mechanical function is of specific interest. In a mechanical model, it was demonstrated that under tensile loading, the mineral particles carry the load while the organic matrix transfers the load between the particles via shear.[21] The shape of mineral particles and their large aspect ratio were shown to compensate for the high elasticity of the organic component. An advantage of the small thickness of the particles is that at this size scales the particles become insensitive to flaws.[30] Generally, it can be expected that the amount of

the mineral platelets incorporated into the elastic collagen fiber tunes the stiffness and hardness of the whole structure. Increasing the mineral density will increase the stiffness but also brittleness of the material.[5,31] There are extensive attempts to elucidate the structure of the nanocomposite material (specifically the interface between the mineral particles with the collagen matrix) and to relate this structure to the mechanical properties, the deformation mechanism in mineralized tissues.[32–34]

The lowest level of structural hierarchy represents the components of the nanocomposite material. The collagen I molecule is a large protein consisting of a sequence of amino acids based on –Gly–X–Y– with Gly being glycine, and X and Y being often proline and hydroxyproline.[35,36] The bone mineral is a poorly crystalline hydroxyapatite ($Ca_5(PO_4)_3OH$) having a hexagonal crystal lattice with *a*, *b* being 9.432 Å and *c* being 6.881 Å.[37] However, the mineral is not a static moiety, and ion substitutions for both Ca and phosphate ions are abundant.[38]

3.325.2.1.2. Lamellar bone

The lamellar organization is the most frequent organization of mature bone tissue at the micron and submicron levels (Figure 2). The collagen fibrils are arranged in parallel bundles which are further organized to form a lamellar structure. Slightly different models of fibril arrangement have been suggested for the lamellar bone structure surrounding a blood vessel within cortical bone (osteon): a plywood-like pattern where parallel fibrils are arranged in layers with a rotation of fibril orientation in the direction perpendicular to the layers (similar to a cholesteric liquid crystal[39]) accompanied by a rotation of the fibrils around their own axis resulting in a rotated plywood structure.[40] Alternatively, the structure has been described as alternating dense and loosely packed fibrils which only give the impression of lamellae.[41] The helocoidal structure of the collagen fibrils arranged in a spiral around the blood vessel makes the osteons extensible and compressible during *in vivo* mechanical loading.[42]

Light-microscopy of bone sections or scanning electron microscopic images reveals small holes (10 μm in width) within the lamellar bone matrix. These represent osteocyte lacunae which are occupied by specific bone cells (osteocytes) in the living bone material and which are connected via canaliculi. These cells and their network are assumed to play an important role in the detection of the mechanical load and in transmitting this load signal to the other bone cells.

The orientation of the lamellae is introducing anisotropy in the mechanical properties of the bone material.[43] Such a heterogeneity in material properties is advantageous for crack stopping, but might favor crack initiation too.[17,44] Generally, much higher energies are needed to force a crack perpendicular to the collagen orientation through the material[45,46] compared to parallel collagen orientation. The reason is that a crack propagating in a direction perpendicular to the lamellae has to follow a tortuous path (Figure 2). Furthermore, large variations in elasticity and hardness have been reported from nanoindentation experiments depending on the angle between indentation and the long axis of the mineralized collagen fibrils.[47,48]

3.325.2.1.3. Woven and plexiform bone

The term woven bone is commonly used for bone tissue, which clearly differs from lamellar bone in the organization of its collagen fibrils. It has no regular lamellar structure and the collagen fibrils lie irregularly,[7] not preferentially oriented as can be visualized by polarized light microscopy. Additionally, this tissue is characterized by a huge number of large irregular shaped osteocyte lacunae. It has been suggested[49] that this tissue type is the result of recruitment and activity of specific, not yet polarized osteoblasts synthesizing the extracellular matrix in all directions of free tissue space. Thus, these osteoblasts soon become entrapped in their matrix and become osteocytes living in large, irregularly shaped osteocyte lacunae. This woven bone forms the first scaffold in which regular bone matrix can be apposed by normal polarized 'surface' osteoblasts. This process is called direct or intramembranous ossification as found in the fetal and postnatal growth stage of flat bones (e.g., scull) and also during fracture healing and callus formation. The rapid growth is also characteristic of woven bone which is deposited during bone development enabling lamellar bone formation or during fracture healing (see Figure 3) when a rigid scaffold has to bridge the fracture region very rapidly.[50] In general, woven bone is subsequently remodeled into highly organized lamellar bone. Despite the

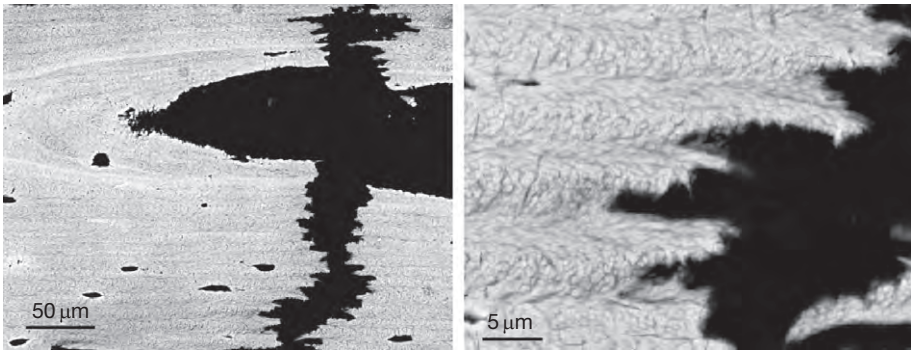

Figure 2 Lamellar bone – example of lamellar organization of mineralized fibrils surrounding a haversian canal (osteon) (backscattered electron image). A crack is propagating perpendicular to the bone lamellae performing a zigzag path because of the changing fibril orientation between the lamellae; right image shows an enlarged detail of the left. Reproduced from Peterlik, H.; Roschger, P.; Klaushofer, K.; Fratzl, P. *Int. J. Fract.* **2006**, *139*, 395–405.

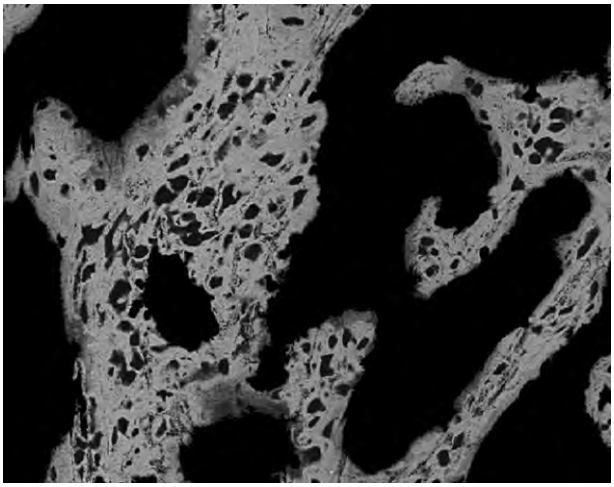

Figure 3 Woven bone – example of intramembranous ossification during bone healing (callus formation). Note the irregularly formed and enlarged osteocyte lacunae (backscattered electron image).

differences in collagen arrangement, transmission electron microscopy (TEM) has shown that the morphology of the mineral particles in woven bone is similar to that in lamellar bone.[51] The mineral particles were found associated with the collagen surface, distributed in extrafibrillar and intrafibrillar collagen regions. Remarkable is that this tissue, when it gets older mineralizes to a higher degree of mineral content than a regular lamellar bone.[52]

Plexiform bone can be found in fast growing animals (such as cows or sheep for instance), where the outer diameter of long bones have to grow rapidly to fulfill their mechanical function.[1] The rapid periosteal growth is accomplished by the repeated formation of a vascular network (plexus) around the bone surface with the generation of parallel buds of bone matrix (woven bone) between them, which provide a huge surface for further bone deposition. Consequently, the increase in bone volume and bone strength can occur more rapidly than in normal lamellar compact bone.[53] This type of bone contains plates of parallel-fibered bone with cores of woven bone.[1] The bone plates are subsequently interconnected in which lamellar bone circumference the blood vessels of the vascular plexus. The mineral particle sizes in these types of bone have been found to be in the same range as in lamellar bone.[29,54]

3.325.2.2. Tooth

Tooth is like bone a highly specialized tissue; however, the essential difference is that it is not remodeled once it has been formed and fully mineralized.[55,56] It consists mainly of dentin, which forms the body of the root and crown, while a thin layer of enamel covers the surface of the crown. Dentin is composed of a network of mineralized collagen I fibrils having hydroxyapatite particles with a thickness comparable to that of bone.[57] It can therefore be considered as one special type of bone.[58] In contrast, enamel is an extremely hard material containing mainly hydroxyapatite (98%) and only small amounts of proteins revealing a structure of huge columns of hydroxyapatite crystallites.

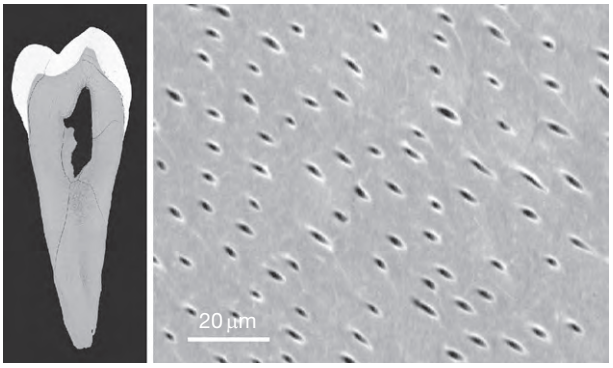

Figure 4 Tooth (overview + zoom-in) (backscattered electron image) obliquely cut tubuli – peritubular dentin lights up because of high mineral content.

Looking closer at dentin, one recognizes different zones: tubules surrounded by the peritubular dentin (PTD) (see Figure 4) and the intertubular dentin (ITD). However, the arrangement of these is variable within dentin from the dentin–enamel-junction towards the pulp which is likely associated with the tooth's mechanical properties.[59,60] Differences between the mineral content of PTD and ITD can be observed (see Figure 4), but the crystal organization in PTD is similar to that found in ITD and bone.[61]

Strong compressive and shear forces act on the tooth during chewing, thus making a specialized structure necessary.[62,63] The construction of a tough bulk material (dentin in the tooth) covered by a hard wear-resistant coating (enamel) is also known from engineering structures. However, one problem of such materials is that they are not resistant to fracture propagation. Once a fatigue crack is generated near to the surface it can propagate easily and catastrophically into the bulk material which is relatively softer than the surface layer. A strategy for reducing this problem is to design the bulk material to have a graded microstructure and mechanical properties (e.g., stiffness) near to the interface to the hard surface layer. This is exactly what is found in the tooth: while the thickness of the mineral crystals increased, the mineral content, hardness, and elastic modulus were found to decrease towards the dentin–enamel interface.[57]

3.325.2.3. Calcified Cartilage

Calcified cartilage plays an important role in the development and growth of long and short bones (e.g., femur, vertebra, etc.). For instance at the metaphyseal growth plate, growth cartilage becomes mineralized, forming the first scaffold for bone apposition by 'surface' osteoblasts. This process is called endochondral ossification. Subsequently, this combination of mineralized cartilage and primary bone apposition gets remodeled into highly organized lamellar bone. Its other prominent role is at the interface of cartilage and bone in joints.

Unlike bone, which contains collagen type I solely, cartilage is comprised of different types of collagen. Types II, IX, and XI are specific for cartilage where type II builds the basic framework for the cartilage material. Unmineralized articular cartilage contains collagens, proteoglycans, and a high amount

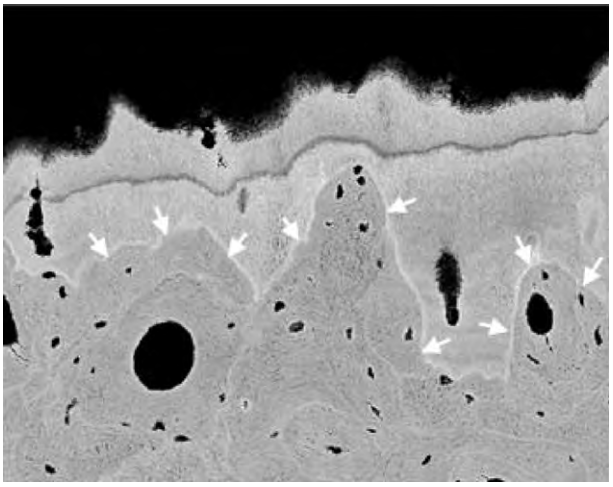

Figure 5 Backscattered electron image of calcified cartilage at the interface between bone (gray) and cartilage (black). Note the cement line which separates bone and calcified cartilage (white arrows). It is also interesting to see the negative gradient of mineral concentration towards the unmineralized cartilage.

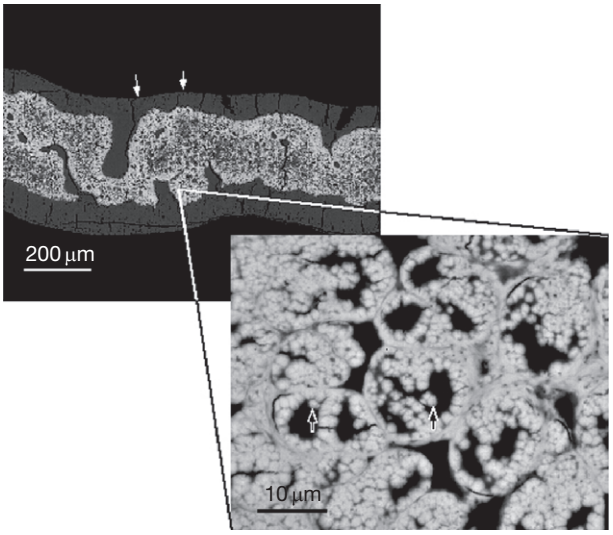

Figure 6 Mineralized turkey leg tendon cross-section (backscattered electron image). Note the heterogeneity of mineral deposition which is important for mechanical behavior.

of water (up to 75%). Structurally, zones of different fibril orientation can be distinguished from parallel to the articular surface in the superficial to a perpendicular orientation in the deep and calcified zones.[64] In the zone of mineralized cartilage in the joint (which is a rather small, about 200-μm-thick region between unmineralized cartilage and bone), the water is replaced by hydroxyapatite mineral particles. Anchoring of cartilage in bone by mineralized cartilage is mechanically important for the load transfer from unmineralized cartilage to the subchondral bone region. It was shown that the relationships between mineral and local mechanical properties such as stiffness and hardness were different in mineralized cartilage and bone. The subchondral bone requires less mineral content to gain the same stiffness and hardness than the mineralized cartilage. Generally, the calcified cartilage was found to be higher mineralized than subchondral bone[65] (see also **Figure 5**). An important aspect in view of microcrack propagation is the varying mechanical properties of the mineralized cartilage: alternating zones with lower and higher stiffness were observed lying parallel to the interface with bone.[66] Such structures of varying stiffness were shown to resist crack propagation and have also been found in other mineralized tissues (for instance in the tooth).

3.325.2.4. Calcified Tendon

In the human skeleton, tendons are normally not mineralized. Extensive tendon mineralization in humans occurs only in pathological conditions or after injury. However, in some species, some of the tendons mineralize also in normal physiologic conditions. Among these, the Achilles tendon of the turkey is the most prominent and an often studied model as it has a more simple structure than bone with parallel collagen fibrils in which the mineral particles are embedded (see **Figure 6**). The mineralized turkey leg tendon (MTLT) is a large, cylindrically shaped, thick tendon which is extending from the claws to the insertion points in two major hip muscles of the animal. Distally, it is a single segment, while proximally it bifurcates into two smaller and more flattened segments. Mineralization occurs near to this bifurcation and proceeds in a distal to proximal direction. As mineralization is rather slow in the tendon, it has been studied extensively.[67–69]

The morphology of the MTLT has some similarities to those of mineralized cartilage and bone. The tendon-forming cells, the tendonoblasts can be found arranged in columnar arrangements parallel to one another and to the long axis of the tendon. These cells synthesize and secrete the organic components of the tendon which is mainly collagen type I but consists also of collagen types V and XII and specific non-collagenous proteins. The collagen molecular packing in the tendon and its relation to mineralization and biomechanical function have been reported in detail.[70,71] *In situ* tensile tests and X-ray diffraction (XRD) experiments were used to measure the fibril deformation, with applied external strain giving evidence for an inhomogeneous elongation at larger strains in the MTLT.[72] Generally, the mineral particles were described to have a plate-like shape[73] and consist of poorly crystalline hydroxyapatite.[72] The reason that avian tendon, such as the long Achilles tendon in the turkey, gets partly mineralized is to reduce the elongation of the tendon and to increase tensile strength and stiffness. Mechanical models have been suggested for the estimation of the effect of the mineral on the energy storage in the tendon.[75] Tensile tests of samples with gradually increasing mineral content showed gradually increasing stiffness and yield strength together with gradually reduced plastic deformation.[31]

3.325.3. Heterogeneity of Mineral Content and the Need for Imaging Techniques

To study the trabecular architecture of bone, standard imaging tools (in particular light microscopy) have a sufficient resolution and, especially, micro computed X-ray tomography allows

a three-dimensional (3D) characterization and helps to estimate the fracture risk for the patient, sometimes in conjunction with finite element (FE) modeling.[76–80] However, imaging techniques are not only needed to study the bone architecture but also the material it is composed of. Most of the biological mineralized tissues are spatially inhomogeneous. Specifically, bone is not only a spatially but also temporally inhomogeneous tissue because of bone modeling and remodeling activities.[6] These are occurring throughout the lifetime of the individual and should maintain the bone mass, remove bone damage, and control the homeostasis of the phosphocalcic metabolism. For instance, a total of about 10% of bone mass is renewed per year in the human skeleton.[81] This percentage varies depending on the location (cancellous, intracortical, etc.). However, it means that the average lifetime of the BSUs is 10 years, resulting in a completely renewed bone tissue after this time period. Bone remodeling takes place at the bone multicellular units (BMUs) at the surfaces of trabecular bone or in the osteons of cortical bone involving all types of bone cells. During the remodeling cycle, preexisting bone packets are resorbed and replaced by new bone. This new bone is first deposited as collagen fibrils which get mineralized after a specific mineralization lag time. During the primary mineralization process, most of the mineral (about 70%) is deposited in the collagen matrix very rapidly (during a few days).[82] The remaining mineral (up to bone's final mineral content) is placed in the matrix during the subsequent secondary mineralization which lasts much longer, having a time scale of several months to years.[83,84] Therefore, the mineral content of the bone material is dependent on two processes, the bone turnover (how much of the bone is renewed in a specific time period) and the kinetics of mineralization of the newly formed bone. These two processes cause a distribution of bone areas having a specific tissue age,[85] being the reason why bone is not a homogeneously mineralized bulk material but has a characteristic pattern of bone mineralization. The deposition rate of newly mineralized bone matrix can be visualized and quantified by fluorescence labeling (see **Section 3.325.5.1**). Using this latter technique, the properties of the bone material of a specific tissue age or age range can be studied and compared between different individuals. Bone turnover is not constant during life but undergoes changes during growth or aging. Together with the speed of the mineralization of the newly formed collagen, it can be affected in diseases and/or by treatment. The pattern of mineral properties (including calcium concentration, mineral:matrix ratio, intensity of the phosphate bands, etc.) contains therefore important information on the present physiologic status of the individual, and on the history of eventual pathophysiological processes. Although average mineral properties are important (such as the bone mineral density (BMD) determined noninvasively and used frequently to estimate the fracture risk of an individual patient), diagnostic techniques with a higher spatial resolution are necessary if the mineral distribution within the bone material is to be assessed.

Moreover, for the evaluation of treatment effects imaging techniques are required. Generally, agents for treatment affect bone turnover (e.g., bisphosphonates reduce[86] and teriparatide increases bone turnover[87]) and some of these agents also become incorporated into the bone mineral (fluoride or strontium for instance[88–91]). Therefore, in many cases, the effect of the treatment can be seen in the new bone material formed during the treatment period.

3.325.4. Estimates of Total Bone Mineral Content

This section discusses techniques which measure the bone sample or the skeleton as a whole but do not provide any spatial information. It has to be mentioned that many of the imaging techniques which will be described in the following section were previously used (sometimes are still used) on powder samples which are also lacking any spatial information on the tissue studied. However, the latter will not be described further.

3.325.4.1. Ash Weight Analysis

Determination of the ratio ash weight to dry weight is a common method to assess the average mineral content of a mineralized tissue.[92] For this purpose, the bone tissue sample is defatted by chloroform and subsequently dried at 80 °C for 4 days and the weight of dried bone is determined. This dried bone sample is placed in crucibles and is heated to 550 °C for 24 h to remove the organic constituents. Subsequently the weight of the ashed bone is determined. The ash fraction is calculated by dividing the weight of the ashed bone by the weight of the dried bone.

The average elemental composition of the bone mineral is also measured by inductively coupled plasma optical emission spectrometry (ICPOES), which requires ashed whole bone tissue.[91]

3.325.4.2. Density Fractionation

Density fractionation separates particles of powdered bone into more homogenous fractions of various densities, thus providing some information on the heterogeneity of the mineralization in the sample. For this purpose bone is ground and sieved to a small particle size (<50 μm). The bone particles are then centrifuged in organic solvents to separate them by specific gravity. The higher the density, the higher is the mineral content in a given volume of organic matrix. The lower density represents the least mineralized fraction.[93]

3.325.4.3. Neutron Activation

If a sample is placed into a neutron beam, the elements within the sample will form radioactive isotopes. As the radioactive emission and the radioactive decay paths are well known in general, the emission spectra from the samples can be analyzed for the elements occurring in the samples (neutron activation analysis, NAA). NAA is a very accurate and nondestructive method for measuring the elemental composition of a mineralized tissue sample, although one disadvantage is that the samples become radioactive and a fairly large amount of material is needed. The method requires a nuclear reactor or another source of neutrons. An advantage of this method is that it is sensitive to the nuclei of the elements and is independent of the chemical compounds in which the elements are present in the sample (for instance ^{49}Ca counts representative for the amount of calcium[94]).Generally, the

γ-ray emission of the elements is collected using scintillation or semiconductor detectors. The parameters which can be varied in NAA are the energy of the neutrons (low energy or thermal neutrons versus high energy neutrons), and the time delay of spectrum acquisition (prompt gamma spectra or delayed gamma spectra).[94–96]

3.325.4.4. Bone Mineral Density

In the clinical routine, bone mineral density (BMD) is measured *in vivo* by absorption of X-rays and is used as an indictor of the patient's bone mass. During lifetime, the BMD is not constant but increases during early life, reaching a maximum value and decreasing in the later lifespan. In particular, BMD is used to diagnose osteoporosis and osteopenia as well as to monitor effects of osteoporosis treatment. However, it has to be emphasized that BMD is a surrogate parameter describing the apparent mineral density of bone at organ level which is dependent on the bone volume (bone volume per tissue volume) as well as the amount of mineral within the bone material (degree of mineralization) of the patient.[97] To distinguish between subtle changes occurring in bone volume and/or in mineralization, a second measurement is necessary, giving the degree of bone matrix mineralization at tissue level (for instance obtained from transiliac bone biopsy samples).[98] The BMD is also influenced by changes in mineral average atomic number, such as in patients treated with strontium ranelate, where strontium atoms are incorporated into the bone material and increase the attenuation of the X-rays, apart from having eventual effects on bone volume.[99]

For the measurement of areal BMD and volumetric BMD, dual X-ray absorptiometry (DXA) and computed tomography (CT), respectively, are widely used. The DXA method is on the basis of unidirectional transmission of the body with X-rays of two different energies and projection of an absorption image on a 2D-detector. Both X-ray energies are differentially absorbed by the different tissues, thus making the discrimination between bone and soft tissue possible. The resulting areal BMD is a 2D-variable (mainly given in grams per square millimeter) which makes several geometrical corrections necessary or is limited to comparison of bone features with similar 3D sizes. Typically, the areal BMD of a specific patient is compared to the maximum BMD of the healthy population and its deviation is given by the T-score (which is the number of standard deviations from the normal value) or it is compared to age-matched normal values and this deviation is given by the Z-score. T- and/or Z-scores are used as important indicators for fracture risk and diagnosis of bone diseases, and are important for treatment decisions.[100]

Volumetric BMD is on the basis of multidirectional transmission of the body with X-rays by CT-scans (quantitative CT, QCT). The attenuation of the X-rays by the sample results in voxels with different gray scales. To transform these into bone mineral equivalents (in grams per cubic centimeter) appropriate bone mineral phantoms have to be used. Generally, such mineral content measurements at organ level can be done *in vivo* (using whole body CT-scanners) or also in *in vitro* samples. Dedicated peripheral CT-scanners (pCT or pQCT) have been developed, which allow the measurement of bone mineral content (BMC) in radius or tibia, either in total or separately within trabecular and cortical compartments.[101] Moreover, high-resolution micro-CT-scanners have been developed for measuring bone microarchitecture in peripheral skeletal sites in humans and in animals (see **Section 3.325.5.4**). However, up to now, DXA is more commonly used than QCT, as it is faster and uses lower doses of ionizing radiation.[101]

3.325.5. Imaging of Mineralized Tissues

Generally, one can distinguish between techniques which produce a full field image of a specific structure such as transmission light or electron microscopy and those in which the specimen is imaged by scanning in a point-by-point mode. Depending on the scanning probe and the produced signal, a property map with a specific spatial resolution of the specimen is generated (for latter see **Section 3.325.6**). In both imaging and mapping, the result is a 2D image of the sample. In certain cases, tomographic techniques utilize 2D projections which are further mathematically processed for a 3D map or images of mineral properties.

For most of the 2D imaging techniques, tissue samples have to be taken and have to be embedded in plastic without decalcifying. Most commonly, polymethylmethacrylate (PMMA)[102] is used because it penetrates well into the tissue, and because of its low viscosity. Such embedding is necessary to perform thin tissue sections or bulk samples with plano-parallel flat surfaces. Additionally, for backscattered electron imaging, the embedded samples require electrical coating (carbon or gold) to avoid a build-up of charge at the surface. In contrast, CT, magnetic resonance imaging (MRI), micro-CT, Raman, scanning acoustic microscopy (SAM), atomic force microscopy (AFM), and nanoindentation can be applied using native samples.

3.325.5.1. Light Microscopy and Morphometry

Histochemical staining of bone and other mineralized tissues is used to generate a selective light absorption contrast. Von Kossa staining is often used to differentiate between soft and calcified tissue. This staining technique uses the chemical reaction between the calcium phosphate and the reagents of a silver nitrate solution. The mineralized tissue will then appear as a black to dark brown color. It can localize mineral in the tissue as well as in bone cell cultures, but it cannot provide additional information on other properties of the mineral such as amount of mineral within the collagen or mineral maturity.[103] As the Von Kossa stained sections reveal a high contrast between the mineralized and the unmineralized tissues, they offer the prerequisite for automated histomorphometrical analyses of the images. Another technique which provides also such a high contrast and therefore suitable for automated histomorphometry is backscattered electron imaging (see **Section 3.325.6.2**).

The analysis of the 2D morphometry of the mineralized tissues has been done for a long time and specifically transiliac bone biopsies from patients are used for clinical management to assess bone quality.[104] Among the variables of interest are the structural indices of trabecular compartment (bone

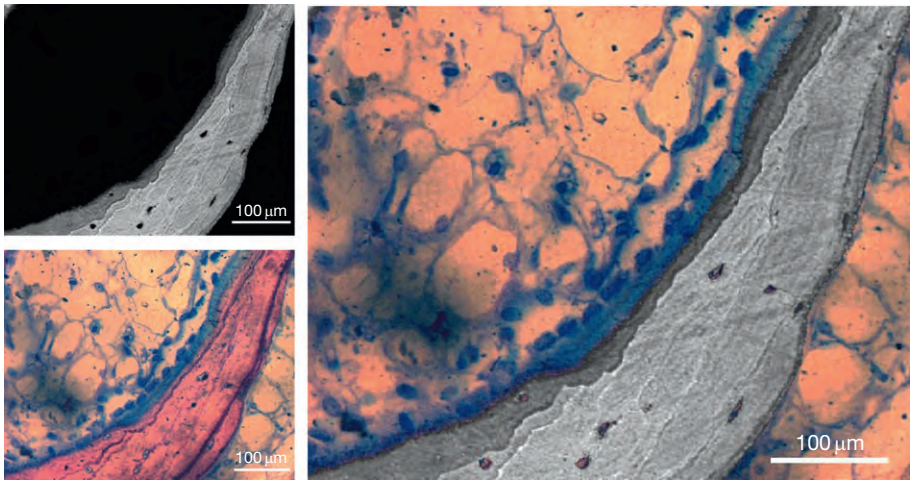

Figure 7 Surface stained (Giemsa) ground section of a trabecular feature combined with mineral map of the identical surface using backscattered electron imaging. Note that the osteoblasts are forming osteoid which starts to mineralize and form a new bone packet of lower mineral content compared to the adjacent old bone packet.

volume fraction, thickness, separation, and number and connectivity of trabeculae) as well as of cortical bone (width and porosity).[105] Further, variables of static bone formation and resorption like osteoid surface, volume and thickness, osteoblast and osteoclast surface as well as eroded surface are assessed. For these variables, staining techniques like trichrome Goldner or Giemsa are applied, to visualize the osteoid, mineralized bone and the cells (see **Figure 7**). Variables of dynamic bone formation like mineralizing surface and mineral apposition rate can be determined, if fluorescence labeling has been applied *in vivo* by administration of tetracyline in a certain time schedule (e.g., 3 days tetracycline, 12 days pause, 3 days tetracycline, and 5 days pause before bone biopsy). The tetracycline is incorporated selectively into the mineralizing front of forming bone packets and can be observed under UV-light. In general, histomorphometric data reveal quite large variations even for healthy individuals and therefore only relatively large deviation from normal can be identified in pathologically altered tissue. This circumstance is mainly caused by the high biological variability at the biopsy site[106] and because 2D histomorphometry using only few or even a single section is a poor representation of the 3D situation.

In the context of histomorphometrical analysis of bone sections, it should be mentioned that sometimes information on the collagen orientation is required[107] which can be obtained from polarized light microscopy.[108] The arrays of collagen fibrils have a highly anisotropic structure, thus causing birefringence of these structures in visible light. Consequently, linearly polarized light[109] and circularly polarized light[110] can be used for the determination of the collagen fibril orientations.

3.325.5.2. X-Ray Microradiography

Microradiography is a technique which utilizes unidirectional X-ray projection and absorption in thin slices of mineralized tissues for imaging and quantifying differently mineralized areas in the sample.[111] This method was developed in the 1950s for studying bone samples[112] and was the first to reveal the heterogeneous pattern of mineralization in bone.

In general, the local X-ray attenuation is measured by photographic films, which are directly in contact with the sample slice. The gray levels generated on the photographic film, which reflect the X-ray intensities transmitted through the bone slice, are evaluated by microdensitometric methods. Samples have to be prepared by embedding the undecalcified tissue into plastic (usually PMMA) which is nearly transparent for X-rays. The embedded samples are then cut into 150-µm-thick slices which are subsequently ground manually to the required thickness (about 100 µm for bone[113]).

As the volume for X-ray absorption within the samples is low, the X-ray energy for illumination has to be relatively low to receive a high contrast between differently mineralized areas in the sample. For bone, a wavelength of about 1.5 Å (nickel-filtered copper K-alpha radiation) is often used.[114] The X-rays penetrating the sample are then absorbed according to the atomic number of the constituents of the sample material. The intensity of the X-ray beam is decreased exponentially with sample depth and dependent on the mass absorption coefficient of the elements in the sample. Therefore, it is crucial that the thickness of the sample is uniform. Moreover, it is highly important that the bone area is illuminated by a homogeneous X-ray field.

For the quantification of the mineral content within the specific sample area, the differences in X-ray attenuation have to be related to the corresponding degrees of mineralization within the tissue. This is usually done using an aluminum step-wedge (thin foils of aluminum of known thickness) reference, which is imaged together with the bone slice. In consequence, the absorption of the sample can be expressed in terms of equivalent thickness of aluminum and can be further transformed to hydroxyapatite density values in grams per cubic centimeter.[114]

Microradiographic studies were extensively done on normal and diseased bone and were used for the detection of osteoporotic treatment effects on the bone material.[91,115]

A limitation of the microradiographic technique is the fact that it is a transmission technique which implies an averaging of the calcium content over the thickness of the sample (i.e., over 100 μm) which seriously limits the resolution of the technique. Indeed, features of mineralized tissues, such as a trabeculum might not be filling the whole thickness of the sample section, thus leading to an erroneous estimate of the mineral content in this particular trabeculum. Specifically, in cancellous bone, which has a relatively large internal surface area, this might lead to significant errors in the resulting mineral content.[16]

3.325.5.3. Phase-Contrast and Dark Field X-Ray Imaging

Conventional X-ray imaging is on the basis of the absorption contrast of the studied object and is limited to tissues which reveal differences in the absorption contrast of their components. In analogy to phase-contrast imaging in light microscopy, where the phase contrast is revealed by inserting a $\lambda/4$ plate into the diffraction plane, for X-ray imaging, a new technique with a grating interferometer has been introduced.[116] The experimental setup consists of a series of three gratings, a source grating placed near to the X-ray source (creating an array of coherent linear X-ray sources), and two other gratings, one being directly in front of the detector. Phase-contrast X-ray imaging is also possible using the coherent X-ray light from synchrotron sources.[117] The advantage is that this contrast may reveal features hardly visible in absorption contrast, particularly in soft tissue. The disadvantage is that it is difficult to evaluate quantitatively the contrast (which typically enhances at interfaces between features in the specimen). Finally, setups using diffraction gratings may also be used for phase-contrast dark field imaging of mineralized tissues.[118]

3.325.5.4. Microcomputed X-Ray Tomography and Synchrotron Radiation Microtomography

3.325.5.4.1. X-ray tomography for structural analysis

Similar to clinical CT-scanners, the microcomputed X-ray tomography (μCT) scanner measures the multidirectional attenuation of the X-ray beam by the sample and allows a structural 3D analysis of the mineralized tissue, but with a spatial resolution in the micrometer range.[119] The microfocus X-ray source illuminates the rotating sample in hundreds of different angles and the projection images are collected by a planar X-ray detector. Numerical algorithms are necessary to reconstruct 3D images from these data. Once the 3D images have been reconstructed, the sample can be viewed in arbitrary virtual cross-sections. The energy of the X-ray source is variable in most instruments (typically 20–100 kV) which enable the study not only of bone but also titanium implants in bone, to give just one example. The typical spatial resolutions for the micro-CT-scanners vary from 10 to 50 μm. Scans with better spatial resolution (down to 1 μm) are possible, but take much longer for the image reconstruction process if the specimen size is not reduced at the same time, and powerful computers are necessary for handling of large amounts of data.

Bone architecture has been investigated for a long time on the basis of histological staining (see Section 3.325.5.1). A big disadvantage of the approach is the use of 2D sections. 3D analysis of the sample not only provides unbiased measurement of architecture[120] but also keeps the sample intact for further (for instance, mechanical) investigation. During recent years, micro-CT has become a commonly used, powerful technique for the assessment of trabecular (see Figure 8) and/or cortical architecture[121] and for the evaluation of human bone biopsy samples after treatment.[122] Micro-CT data also provide the possibility of setting up FE models to estimate strength and stiffness of the whole bone sample, on the basis of its trabecular microarchitecture.[123,124]

High-resolution μCT cannot be applied *in vivo* because of the high dosage needed for obtaining useful images. However, the increasing sensitivity of CCD-cameras has now led to the development of the first *in vivo* CT-scanners. They are used for monitoring local changes in bone architecture with growth or treatment in animal models (typically, mice and rats).[125–127]

Generally, beam hardening, noise, and partial volume effects are challenging problems. Beam hardening can be reduced by using physical filters during scanning and by corrective algorithms during reconstruction. Another option is to work with monochromatic X-ray radiation, as available at synchrotron sources. Similarly, noise can be reduced by applying filters. A crucial parameter in the evaluation of micro-CT images is the segmentation of the raw images – that is, the decision whether a voxel corresponds to bone or to marrow.[128] When the voxel size is not much smaller than the typical feature size (e.g., trabeculae in cancellous bone), this segmentation has a large influence on the outcome of morphometric analyses. Indeed, voxels only partially filled with bone may lead to an over- or underestimation of the bone volume. A simple geometrical consideration shows that imaging rod-like trabecular motifs (of a diameter of 200 μm) using a voxel size of 10 μm will result in 20% of voxels showing a wrong gray level due to the partial volume effect.[16] Global thresholding with a single gray level (selected visually or by analyzing the histogram of μCT bins) is most widely used, but may result in

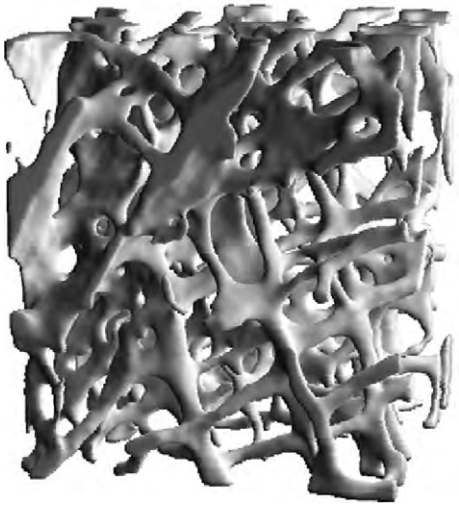

Figure 8 Cancellous bone structure obtained from microcomputed tomography imaging. Reproduced from van Lenthe, G. H.; Hagenmüller, H.; Bohner, M.; Hollister, S. J.; Meinel, L.; Müller, R. *Biomaterials* **2007**, *28*, 2479–2490.

the loss of thin trabeculae or in an overestimation of thicker ones. Segmentation is also very important for extracting cortical from trabecular bone. If the real volume of a sample is known by previous Archimedes testing[124] the binary data set can be forced to have the same volume as determined experimentally. To overcome the errors occurring with global thresholds, more than one threshold value may be used,[129,130] or use of local[131] thresholding algorithms based on the analysis of the histogram of the local neighborhood of a voxel is a possible approach. However, the efficacy of these methods is limited by lower scan resolution and the heterogeneity of the studied materials.

3.325.5.4.2. X-ray tomography for quantitative analysis of the mineral content

A recently developed technique for the quantification of the mineral content of a mineralized tissue at the bone packet level is synchrotron radiation microtomography (SRμCT)[132,133] based on the multidirectional projection and absorption of a focused, monochromatic X-ray beam. The aforementioned difficulties with the segmentation also apply to the SRμCT analysis, but their effect is smaller, because of the generally better spatial resolution of the technique and the higher X-ray beam intensity which improves the signal to noise ratio.

SRμCT can be used with a voxel size of 5 μm or even better and is well suited for the investigation of single trabeculae. The information obtained from the 3D measuring technique is combined with an imaging processing method that derives bone mineralization density distribution (BMDD) from analysis of voxels which are representing the mineral content in units of grams per cubic centimeter. Because of the long time needed for data acquisition and the huge amount of data to be handled, the analyzed volume is usually in the range of few cubic millimeters at the most. This method is rather new and still in development. One difficulty in this method is to avoid artifacts in the 3D reconstruction, but there is rapid progress in this field.[134]

There are also attempts to use normal (laboratory) μCT techniques to record mineral content at tissue level. However, X-ray fluxes in laboratory sources are low which makes the use of a polychromatic beam necessary, resulting in beam hardening effects, which are difficult to correct. Furthermore, the signal to noise ratio is lower than that at the synchrotron, thus reducing the capability to resolve differences in mineral contents. Additionally, it was shown that the effects of varying imaging parameters, such as tube voltage, current, integration time, object to X-ray source distance, projection number, detector array size, and imaging media (surrounding the specimen) have a strong influence on the relationship between equivalent tissue density and its linear attenuation coefficient.[135]

3.325.5.5. Magnetic Resonance Imaging

Magnetic resonance imaging (MRI) techniques are highly sophisticated methods which make use of the magnetic properties of atomic nuclei (spin relaxation time) in a magnetic field irradiated with a radio frequency (RF) pulse. MRI is a noninvasive method which measures the structure of mineralized bone tissue indirectly *in vivo* or *in vitro*. The outcome of MRI is an image of the distribution and state of protons bound in water and fat in the different body tissues. As bone has a relatively low water content, the surrounding bone marrow is visualized while the mineralized bone appears dark in the MRI.

The hardware of an MRI instrument consists of the imaging magnet (which generates the static magnetic field), three weak magnets (providing the gradient magnetic fields for the *xyz*-localization of the signal), transmitter, and receiver RF coils (which transfer energy to the sample and detect the MR signals). In conventional MRI the spatial resolution is too low for the imaging trabecular features; however, there have been attempts to image trabecular bone architecture using high-resolution MR instruments (with a static magnetic field of about 1.5 T for clinical use). Spatial resolutions of about $100 \times 100 \times 300$ μm have been achieved and MR-deduced histomorphometric parameters have been shown to be more or less correlated (depending on the type of studied bone) with those obtained from other methods.[136] MRI has the advantage that it does not need ionizing radiation; however, spatial resolution is still far below that of CT imaging.

3.325.5.6. Transmission Electron Microscopy

TEM provides high-resolution imaging and is used for studying small areas or even single mineral platelets selectively. The TEM can be operated at different electron energies (often 100 keV for conventional TEM and 1 MeV for high-resolution imaging). The contrast of the TEM images is dependent on several factors, mainly on the difference in electron density of the structures in the sample (difference in organic matrix and mineral electron density), the thickness and the density of the sample, the diameter of the objective aperture, and on the energy of the electrons. Another parameter which can be varied is the usage of either bright or dark field imaging. The advantages of dark field imaging in TEM applied to mineral crystals have been discussed.[137]

For viewing the material with TEM, ultrathin sections of the plastic (mainly Spurr's resin or Epon) embedded samples of about 70–100 nm[54,138] have to be prepared. Sections can be left unstained or enhanced by contrast with uranyl acetate and lead citrate.[138] Another preparation technique is cryo-sectioning.[139]

TEM has mainly been used for the characterization of the lamellar structure[39,140] and for studying the arrangement of the mineral particles in the collagen matrix of normal and diseased bone,[141] dentin,[142] enamel,[143] and MTLT.[144,145] One specific interest was also the shape (needle- or plate-like) of the single mineral particle.[73,146]

Although transmission electron tomography is a rather exotic technique for studying bone, it should be mentioned here that TEM analysis can be also used for 3D information. For this purpose, the sample has to be viewed in many directions. In the literature 2° tilt series over a minimum range of $\pm 60°$ is described. The volume of mineralized tissues studied by TEM tomography is rather small. Generally, it is used for viewing the interface between the collagen fibrils and the mineral or for the shape of single mineral particles.[145,147]

The TEM instrument can also be used for the observation of the diffraction pattern of a mineralized tissue sample. One of the specific features here is the selected area electron diffraction (SAD or SAED). Application of lenses enables to image the

diffraction pattern of a very small area (micron to submicron range). This can be used for studying the crystal properties of single bone mineral particles.[148]

3.325.6. Property Mapping in Mineralized Tissues

3.325.6.1. Vibrational Spectroscopy

The molecular bonds of any mineralized material are not stationary but undergo twisting, bending, rotation, and vibration. When irradiated with light, there is absorption and/or inelastic scattering at specific wavelengths, which can be attributed to specific structures and environments of the molecules. Vibrational spectroscopy (infrared and Raman spectroscopy) give access to the basic components of mineralized tissues. The utility of vibrational spectroscopy has been accelerated by the development of optic fibers and by the extension of the previous microprobe technique to spectroscopic imaging.[149–151] The strength of vibrational spectroscopy in the context of mineralized tissues is that it allows the simultaneous mapping of properties of the mineral and of the organic matrix. For instance, collagen cross-link ratios are one of the matrix properties which are clinically relevant, because of their implication for the mechanical performance of bone.[152–155]

3.325.6.1.1. Fourier transform infrared imaging

Infrared radiation (IR) is absorbed at specific wavelengths depending on the molecular bonds and their modes of vibration. Absorbance spectra can be obtained in reflection mode or in transmission mode. The former has the advantage that the surface of a bulk bone sample can be studied, but this is generally more difficult. This makes the combination with other imaging techniques done on the same surface of the bulk sample material easier and more convenient.[57] Attenuated total reflection (ATR) is another possible reflection mode which has been developed recently[156] and is used for studying spectra from aqueous solutions[157] for instance.

For the IR-transmission mode, the common setup consists of a broadband radiation source, a microscope, an automated translation stage for scanning the regions of interest and an Fourier transform infrared (FTIR) spectrometer interfaced to single-channel or a focal plane array detector. The typical spatial resolution of FTIR imaging (FTIRI) is about 10 μm with the laboratory instrument and better (down to 1.3 μm) at the synchrotron.[158] The typical spectral resolution is 8 cm^{-1}.[155] For calcified tissues such as bone, 2–4-μm-thick sections from resin (PMMA) embedded mineralized tissue have to be prepared. Consequently, the spectral contribution of the resin has to be subtracted from each individual spectrum. This is most crucial for poorly mineralized tissues where resin penetration is extensive and less crucial for higher mineralized samples (such as older bone areas) where the resin penetration is much lower.[158]

The infrared absorption spectrum of bone reveals broad absorbance peaks, which are the sum of many smaller subbands. They mirror the collagen (amide bands and cross-links) and the carbonated hydroxyapatite crystals (phosphate and carbonate groups) of the bone mineral. For fast automated evaluations of IR spectra (especially in area scans), the intensities at the wavelength of the band maximum of interest are determined. For more accurate analysis (e.g., in line scans) the broad IR-bands can be deconvoluted into subbands, the contributions of which (peak height) are evaluated by curve fitting. The integrated area under the individual subbands reflects the relative amount of this chemical bond in the sampled volume (voxel). To minimize errors due to heterogeneity in sample thickness (absorbance volume) and surface topography (reflection), FTIR absorbance values are generally given in peak ratios and not in absolute values: mineral to matrix, phosphate to carbonate and, as a measure of cross-link maturity, the pyridinium (an older, trivalent collagen cross-link) to dehydrodihydroxylysinonorleucine (a younger, divalent, and freshly synthesized collagen cross-link) ratio. For a correct interpretation of these variables, it has to be noted that changes in both the numerator and denominator have an influence on changes of the ratio. It was shown that FTIRI mineral to matrix ratios correlated well with ash weight measurements.[159] Mineral to matrix ratios have been extensively studied in normal[160,161] and diseased bone, and have proven to be a powerful tool in monitoring treatment effects.[150] Their usage has been reviewed for the examination of biological tissues in general[157] and for mineralized tissues in particular.[158,162] The collagen cross-link ratios, which reflect collagen maturity or aging and play a pivotal role in mechanical properties of the collagen scaffold, have also been successfully studied,[163–165] to give just some examples).

3.325.6.1.2. Raman spectroscopy

In Raman spectroscopy, the sample is irradiated by monochromatic laser light and the inelastically scattered light from the specimen is measured. While the IR technique has usually a superior signal to noise ratio, Raman spectroscopy has other advantages, such as its easy use in reflectance mode and its higher spatial resolution in 1 μm range. Furthermore, the obtained vibrational bands are very sharp in many cases and, therefore, even small band-shifts can be detected.

The Raman spectrometer consists of a laser which acts as an intense and monochromatic polarized light source, a device that separates the elastically scattered light from the inelastic Raman scattering, a spectrograph, and a detector. A challenging feature with the typically used laser wavelength of 532 nm is the high autofluorescence of the biological samples. One method to avoid this problem is photobleaching prior to Raman imaging[166] or the usage of near infrared laserlight[151] or of UV-laser light which, however, bears the risk of inducing photodegradation damage in the sample.[157] Laser light in the deep UV (about 200 nm wavelength) can also be used to enhance the vibrational intensities of specific parts of the proteins of the organic component in the studied tissue.[167] Moreover, Raman spectroscopy was shown to be compatible with commonly used staining techniques.[168] Fluorescence bands from labeled bone specimens for instance can be identified easily giving access to the tissue age of the studied bone packets in the sample. Minimal or even no sample preparation is necessary for Raman microspectroscopy. Native or embedded samples can be used.[169] If Raman spectroscopy is used in reflectance mode on polished samples, it can be easily combined with other techniques visualizing the same sample surface.

The most prominent band for minerals is the ν1 phosphate band at 961 cm^{-1}. Carbonate substitution in the apatite mineral can be seen at the 1075 cm^{-1} band. Amide collagen bands are

visible at higher frequencies.[151] A characteristic feature of Raman microscopy is that the intensity of the Raman light is strongly dependent on the relative orientation between the polarization plane of the laser light and the bond axis of the molecular group. Thus, Raman intensities have to be interpreted with caution, because they can be due to compositional as well as to orientational contrast. It was shown that the bands have different polarization behavior, which makes some band intensities dependent on the longitudinal axis of the collagen fibrils and/or the apatite crystal *c*-axis orientation in bone (**Figure 9**). For example, using the polarization information one can obtain information on fibril orientation and composition simultaneously.

The high spatial resolution of about 0.5–1 μm makes Raman spectroscopy a powerful tool for dental research,[170] or for the investigation of small sized features in bone, such as the lamellar structure of osteons in cortical bone.[171,172] In disease-related alterations[173] and changes due to mechanical deformation, the breakage of collagen cross-links have been identified using Raman microspectroscopy.[174] Raman microspectroscopy can be used in confocal geometry, thus making information from a specific depth in the sample available[175] (for instance, reviewed by Gamsjäger *et al.*[151]).

3.325.6.2. Secondary Electron and Back-Scattered Electron Imaging

In the scanning electron microscope (SEM), the interaction of the beam electrons with the target material leads to the emission of secondary electrons (SE) with low energy and backscattered electrons (BE) with high energy. In general, the SE and BE signal intensities are highly influenced by the topography of the sample surface. Especially the SE electrons, which are emitted from only a few nanometer thick surface layer, are used for studying topographic features of bone surfaces.[40,176,177] Specific techniques including low voltage imaging and high-resolution imaging have been developed and described in detail.[178,179]

The intensity of the BE signal coming from below the sample surface up to a depth of about 1.5 μm,[180] is related to the average atomic number of the target material. Hence, in bone tissue calcium is dominating the material contrast because of its relatively high atomic number ($Z = 20$), provided that any topographic contrast is excluded by plane surface preparation. This can be done by grinding and polishing or by micromilling of PMMA embedded samples. The pixel gray levels of the BE images, therefore, provide information on the local variation of the mineral content throughout the bone tissue.[181,182] The general rule is that the brighter the gray level of a pixel is, the higher is the concentration of calcium. Thus, soft tissue and PMMA exhibit the lowest gray level in the image. After proper calibration of the gray levels, they can be transferred to calcium concentration values to quantify the local calcium content in the sample (quantitative backscattered electron imaging, qBEI).[16,183] From such calibrated BE images, the frequency distribution of calcium concentration (histogram) can be deduced and is usually referred to as the BMDD. A bin width resolution of 0.17 wt% Ca has been described for qBEI by Roschger *et al.*[16] For statistical analyses and comparison of the different BMDDs, five parameters have been introduced[16]: the average calcium content in the bone volume of investigation (Ca_{MEAN}), the most frequent calcium content (the peak position of the BMDD, Ca_{PEAK}), the width of the calcium content distribution (Ca_{WIDTH}), the amount of low mineralized bone areas (Ca_{LOW}), and the amount of highly mineralized bone areas (Ca_{HIGH}) (see **Figure 10**). These parameters were found to be an effective way of quantifying differences between BMDD curves. Another approach of BMDD evaluation consists in reducing the histogram to only a few bins by including multiple gray levels in one bin.

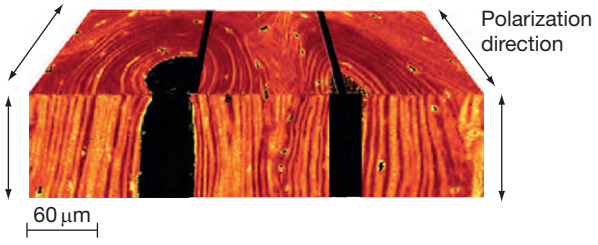

Figure 9 Raman imaging of two orthogonal planes within cortical bone using the intensity ratios of the ν_1 PO_4/amide I vibrations. Same lamellae show different contrast, depending on polarization direction of the beam in panel. Reproduced from Kazanci, M.; Wagner, H. D.; Manjubala, N. I.; *et al*. *Bone* **2007**, *41*, 456–461.

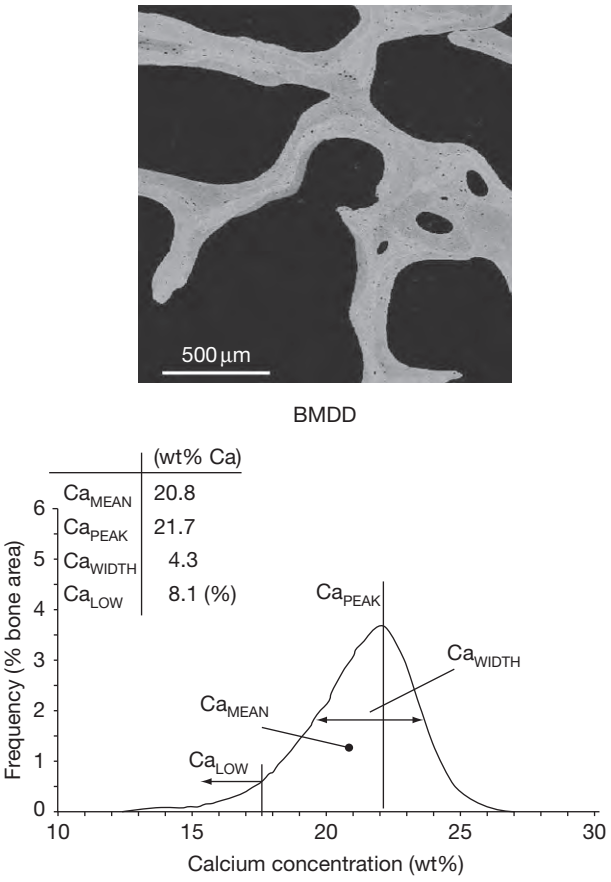

Figure 10 Quantitative backscattered electron imaging revealing trabecular bone mineralization density distribution (BMDD) and corresponding BMDD variables. Reproduced from Roschger, P.; Paschalis, E. P.; Fratzl, P.; Klaushofer, K. *Bone* **2008**, *42*, 456–466.

This allows comparison of BMDD curves on a bin-to-bin basis, by introducing bins with very low, low, intermediate, high, and very high mineral content.[184]

The sensitivity and quality of the BMDD analysis are crucially dependent on the reproducibility of the BMDD acquisition and its resolution in mineral content. For qBEI, an inter-assay variance of 0.3% CV (coefficient of variance) for the mean Ca-content was achieved.[183] The stability of the instrument, especially constant beam intensities, calibration procedures using suitable reference materials, and minimizing the beam damage effects are required to maximize the resolution of differences in the Ca-content. An important parameter which generally limits the resolution is the signal to noise ratio influencing the counting statistics of the detection of the BE signal. A peak broadening of only 5% could be achieved.[16,183] In contrast to other techniques, such as microradiography, for instance, the partially filled volume effect is not a problem in qBEI, as the penetration distance of the electrons is very small. The typical lateral resolution is in the range of 1–4 μm and, thus much smaller than the thickness of a bone trabecula, for example.[16] Caution in interpretation of BE-gray levels is necessary, when the composition of bone mineral is expected to deviate strongly from normal, as it is the case in patients treated with strontium (Sr) ranelate. In this case, one can not differentiate between true changes in the mineralization density and the incorporation of Sr into the bone mineral.[89]

The shape of the BMDD histograms reflects two processes, the mineralization kinetics of formed bone packets and the bone turnover rate.[85] For normal human adult trabecular bone, the BMDD was found to have a specific shape with relatively minor variations. Hence, even small deviations from this normal BMDD in diseased bone were shown to have a biological meaning and, thus, provide an interesting tool for differential diagnosis.[16]

3.325.6.3. Scanning Small Angle X-Ray Scattering and Diffraction

When an X-ray beam hits a target, various processes of interaction of the X-ray electromagnetic wave with the sample electrons, atoms, crystal lattice, and structural components take place. In the present section, the scattered intensities are of interest. These can give information on the crystal lattice and/or on small structures of differing electron densities within the sample. In bone, the difference in electron density between the mineral and organic phase of the composite material produces small angle X-ray scattering (SAXS) and provides information on the collagen-mineral composite material.[28]

In scanning-SAXS, the scattered X-ray intensities within angles not larger 1° with respect to the direction of the incident beam are measured and evaluated. They correspond to scattering vectors of 0.1–5 nm^{-1} and, thus, objects between 1 and 50 nm size can be detected within the sample. The diameter of the primary X-ray beam is about 200–100 μm at laboratory X-Ray sources and down to the submicron range at undulator synchrotron sources, such as the European Synchrotron Radiation Facility (ESRF). During the measurement, the sample is moved in *xy*-directions perpendicular to the primary beam. For each measurement position, the 2D scattering pattern is collected by a 2D X-ray detector. The scattering intensities are analyzed for parameters such as the mineral particle thickness, the predominant orientation of the mineral particles, and their degree of orientation.[185]

These parameters were shown to be a powerful tool for the characterization of healthy bone and for the detection of deviations from normal. The shape of the mineral platelets was studied in human bone[186] and bone from different species.[28,187–189] The thickness of the mineral particles was shown to increase rapidly within the first 5 years, to subsequently reach a plateau level,[16] and to be in the range of 2.5–4 nm in the normal adult human trabecular bone.[186] Scanning SAXS was also used for the evaluation of the effect on the collagen-mineral composite in the most commonly used osteoporosis treatments.[88] In addition, mineral particle characteristics were also measured in teeth, in mineralized cartilage, and in the MTLT.[185]

The usage of a microfocus beamline at the synchrotron provides high photon flux and high brilliance, and enables higher spatial resolution compared to a laboratory device. Scanning-SAXS studies at the synchrotron have been done for characterizing archaeological bone samples,[190] for studying the interface of articular cartilage and subchondral bone,[191,192] for the structure of the mineral particles in the MTLT,[193] for investigation of the lamellar fibril arrangement in osteons,[194] and for examination of the bone mineral particle characteristics after strontium ranelate treatment.

In contrast to SAXS, scanning X-ray diffraction (XRD) measures the scattered X-ray intensities under wide angles (typically larger than 5°) with respect to the direction of the incident beam. This gives information about the crystal structure of the mineral particles, as well as the lattice parameter. The intensity and width of the Bragg reflections also give useful information on the crystallinity and on the crystal dimensions, respectively. Generally, a strong reflection (002 reflection) comes from the longest (the *c*-axis) of the hydroxyapatite crystals. As the hydroxyapatite c-axis is parallel to the collagen fibril axis (as also known from SAXS and TEM analysis), this reflection can also be used for imaging the collagen fibril orientation in mineralized tissues and has been used for the pole figure analysis of the crystal texture. For this purpose, a rotation of the sample is necessary to obtain the 3D-information about the orientation of the crystal axis. Such pole figure analyses for texture were done on femoral bovine bone[195] and on single trabeculae[196] (using X-rays from laboratory sources) and on human osteonal bone with a 1 μm beam at the ESRF.[194] The width of the 002 reflection can additionally be used for the analysis of the longer dimensions of the mineral particles.[197]

Texture analysis of normal bone,[198] disease-related deviations from normal apatite crystal characteristics,[199] and changes in the crystal lattice parameters in the presence of therapeutic agents like strontium ranelate[90,200] were reported. Strontium, for instance, was found to be incorporated into the hydroxyapatite lattice, thus increasing the crystal lattice constant correspondingly. Recent developments in high-resolution area detectors make the simultaneous detection of XRD (wide angle X-ray scattering, WAXS) and the SAXS intensities with one single detector possible (see **Figure 11**). Applications of this combination of methods in mineralized tissues have been reviewed recently.[201] Limitations of the XRD as well as of SAXS technique are generated by beam damage effects which have not yet been systematically studied.

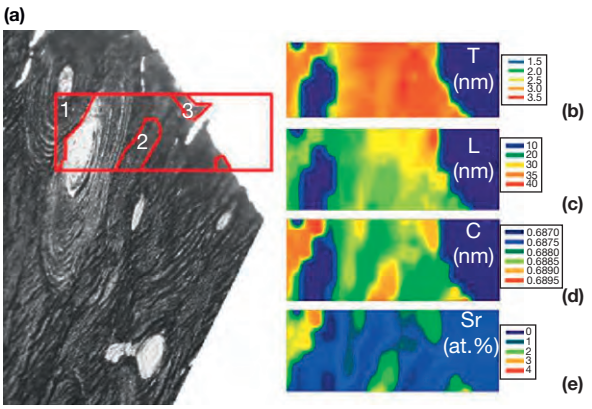

Figure 11 Mapping of bone mineral characteristics in a bone biopsy section of a patient treated with strontium ranelate: (a) light microscopic image of a 10 μm thin bone section with indicated regions of interest, (b) corresponding mapping of mineral thickness parameter (*T*) as obtained by SAXS, (c) mineral crystal length (*L*) using XRD signal, (d) crystal lattice distance (*c*) in *c*-axis direction using XRD signal, and (e) incorporation of atomic percentage of Sr into the cyrstal deduced by the increase of *c*. Regions 1, 2, and 3 indicate newly formed bone under strontium ranelate treatment. Reproduced from Li, C.; Paris, O.; Siegel, S.; Roschger, P.; Paschalis, EP.; Klaushofer, K.; Fratzl, P. *J. Bone Miner. Res.* **2010**, *25*(5), 968–975.

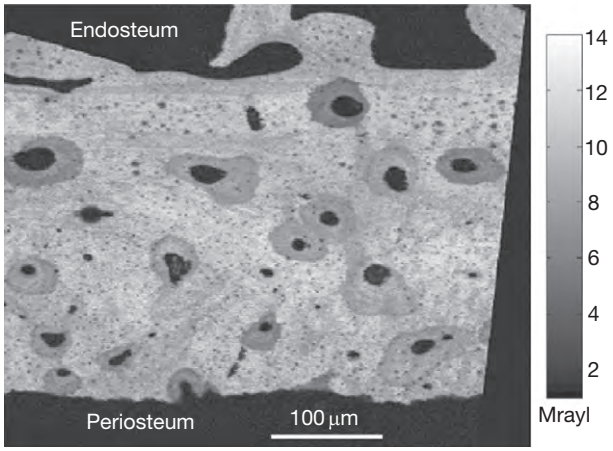

Figure 12 Calibrated acoustic impedance image of osteonal bone from the cross-section of the distal part of the human radius using a 200 MHz acoustic lens. Interstitial bone (high mineral content) has brighter gray levels than secondary osteons (low mineral content) indicating the relationship between mineral content and acoustic/mechanical properties. Reproduced from Raum, K.; Leguerney, I.; Chandelier, F.; *et al. Phys. Med. Biol.* **2006**, *51*, 733–746.

3.325.6.4. Mapping of Elastic Properties

3.325.6.4.1. Scanning acoustic microscopy

In scanning acoustic microscopy (SAM), the inherent contrast mechanism arises from the elastic interaction of high-frequency acoustic waves with the target material. SAM is based on generation and focusing of high-frequency acoustic waves (longitudinal/compressional waves) to a target followed by the detection of the echo signals. The amplitude and the timing of the echo pulses allow mapping local mechanical (elastic) properties of the specimen with spatial resolution up to 1 μm (see **Figure 12**).[202–205]

Three different approaches can be used for assessing elastic properties of bone.[205] (1) Time of flight measurements of pulse echoes from the frontal and backside sample surface in thin tissue sections. If the section thickness is known, the compressional wave velocity can be determined. (2) Measurement of the confocal reflection amplitude in thick sections; the acoustic impedance can be derived. (3) Generation of surface acoustic waves in thick sections by a series of increasing negative defocus of the sound field and detection of the resulting amplitude of the pulse echoes; surface acoustic wave velocities can be derived.

In general, the acoustic lens of the SAM is a piezo-based transducer mounted on a sapphire rod, which has a concave depression on the front side for focusing the emitted sound waves. This lens is scanned mechanically over the specimen using distilled water as the coupling medium between lens and sample surface. The same lens is used to detect the incoming echoes with the transducer working in detection mode. The resolution and pixel of the image depends on the working frequency of the transducer.[206] Frequencies of 400 MHz and 1 GHz are commonly used, providing a resolution of 3–1 μm.[202,207] The frequency of 2 GHz (2000 MHz), being the highest practical frequency available, results in a resolution of about 0.4 μm. For sample preparation, it is crucial that the surface roughness is smaller than the wave length of the acoustic probe, because scratches and local inclination will change the propagation of the incident waves. Further, the reflected amplitude is a maximum, when the focus of the sound beam is coinciding with the sample surface. Thus, the distance between acoustic lens and sample surface should be constant. Native and plastic embedded tissue can be used. Micromilling and grinding following polishing are the methods to manufacture suitable sample surfaces.

Previous studies using frequencies between 50 MHz and 1 GHz revealed new insights into the microstructural and anisotropic elastic properties at various hierarchical levels of the bone structure.[205] A strong correlation was obtained between acoustic impedance and nanoidentation modulus.[207] The strength of SAM is to enable a microelastic imaging of mineralized tissue. However, for interpreting the acoustic contrast properly, SAM has to be combined with other methods providing complementary information like qBEI, SAXS, Raman, etc.

3.325.6.4.2. Nanoindentation

The atomic force microscope (AFM) can be operated at different modes (see **Section 3.325.6.6**). In one of these, the tip of the AFM can be used as a nanosized indenter for measuring the local elastic response of the sample in the submicron range. In a controlled deformation experiment, a diamond tip (in most cases a three-sided pyramid Berkovich tip) is pushed into the sample (block or thick section) and the load displacement curve is recorded, from which the indentation modulus as well as the hardness can be derived.[208]

Nanoindentation is done under wet, dry, and resin-embedded conditions of the mineralized tissue. It has to be emphasized, that under hydrated (physiological) conditions, the values of the indentation outcomes are remarkably lower than under dry conditions.[209] To control the reliability of the

indentation experiments, the formed indents can be imaged directly by AFM in the tapping mode or by SEM. Indents too close to cracks and to edges of bone surface, haversian canals, and osteocytes lacunae can be excluded in this way. To calibrate the instrument, a fused silica sample with a known elastic modulus is commonly used.[210] Typically, the complete loading and unloading cycle of the indenter tip consists of five steps: (1) loading to the maximum force, (2) followed by a holding period, (3) subsequent decrease of the load, and (4) a second holding period, before (5) final unloading. Elastic modulus and hardness are extracted from the first unloading curve, using the Oliver and Pharr method.[210] By measuring the load, the indentation depth, and the projected indentation area (contact area) and by using an empirical indenter shape factor, the reduced elastic modulus can be evaluated, which is the combination of the elastic modulus and Poisson ratio of both the indenter and the sample. The commercially available add-on nanoindentation devices have an instrumental force and displacement resolution of respectively 100 nN and 0.2 nm. Indents are done in a quasi load-controlled mode (i.e., without feed-back control for the loading force).

In nanoindentation studies of bone, a general correlation of the elastic modulus and hardness with the mineral content has been observed; however, the nanoindentation values show quite large variation at a specific mineral content[47] and reveal a high anisotropy of the bone material depending on the direction of the lamellar structure.[211] The latter gives evidence for a relatively strong influence of the organic component (orientation and composition) on the elastic properties of bone which might be a limitation of nanoindentation in characterizing the mineral of the material. Commonly, nanoindentation studies are performed in combination with other spatially resolved techniques which measure for instance the amount of mineral[48,57,66] (see **Figure 13**) and/or the properties of the organic matrix[212,213] at the indentation site.

3.325.6.5. Mapping of Elemental Composition

3.325.6.5.1. X-ray fluorescence

Excitation of characteristic X-ray fluorescence lines in a target material can be done by an electron beam in the SEM (electron induced roentgen fluorescence, ERF) or by an X-ray beam (X-ray induced roentgen fluorescence, XRF). The emitted X-ray spectra, which are specific for each element, are analyzed by an energy dispersive X-ray (EDX) or a wavelength dispersive X-ray (WDX) detection method. The former works with a semiconductor (e.g., germanium detector) sensitive to the energy of the incoming X-ray photons and the latter with crystal Bragg reflections for wave length analysis of the X-rays prior detection. In general, XRF mapping is done on thin or bulk sections in reflection mode.

For the elemental analysis of biological tissue such as bone in the SEM, the beam current of the electron beam has to be carefully chosen to provide sufficient counting statistics for the spectral analysis on one hand, and also to avoid beam damage to the sample on the other hand. Beam damage is the crucial limiting factor for quantifying and mapping elements of low concentration by SEM. As the WDX method needs relatively large XRF signals, it cannot be used in many cases. Studies on dentin[214] and bone[215] can be found in the literature. However, the need for high electron beam intensities makes this technique prone to beam damage. For studying bone with EDX, a 20 keV beam energy, a probe current of 0.220 nA and a data acquisition time of 500 s for small area scans (10 μm × 10 μm) have proven to be successful in quantifying the elemental composition of single bone packets.[89,183] It has to be emphasized that elemental mapping of large areas will require acquisition times of many hours under these conditions because of the low X-ray count rates achieved by this method. Special correction methods for elemental quantification have to be applied for block samples as used in the SEM. For instance, the ZAF method corrects for effects of atomic number (Z), absorption (A) and X-ray fluorescence (F) within the material on the emitted X-ray intensities. Prior to analysis, reference standards with known composition have to be measured which are near or similar to the mineralized tissue of interest.[89,216] The ERF detection method is limited to element concentration of about 0.1–0.5 wt%.[95]

In contrast, XRF in the laboratory or at the synchrotron enables a much more sensitive detection of elements in bone tissue. Trace elements in concentration down to the femtogram range can be detected.[217,218] This is due to the much higher

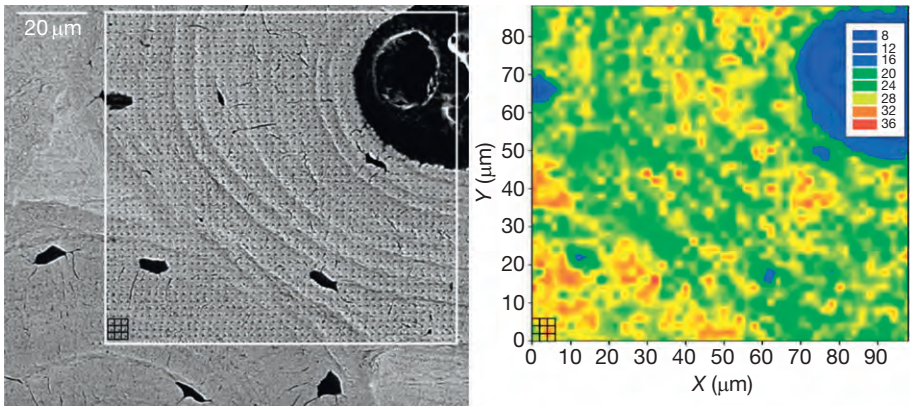

Figure 13 Indentation modulus mapping around a quadrant of an osteon. Left: scanning electron microsopic image with the region of interest after indentation; Right: 2D interpolated color plot of the reduced indentation modulus, showing a clear modulation along the lines of the lamellae inside an osteon. Reproduced from Gupta, H. S.; Stachewicz, U.; Wagermaier, W.; Roschger, P.; Wagner, H. D.; Fratzl, P. *J. Mater. Res.* **2006**, *21*, 1913–1921.

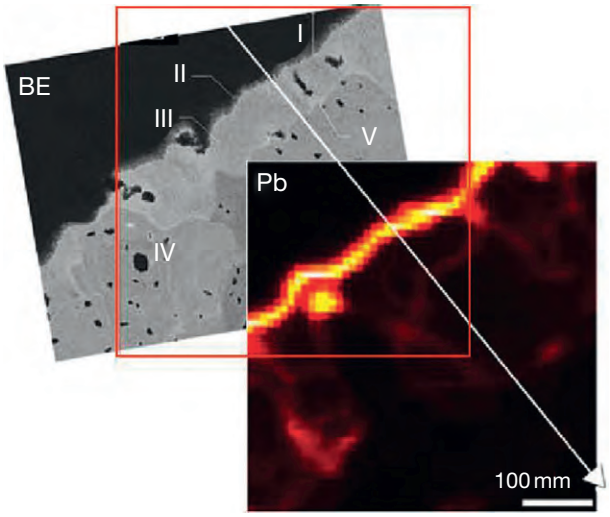

Figure 14 Elemental mapping of Pb concentration using SR μXRF: (BE) Backscattered electron image from a chondral/subchondral region of a patella; Noncalcifed cartilage (I), tidemark (II) calcifed cartilage (III), subchondral bone (IV), and cement-lines (V) can be clearly identifed. (Pb) Pb signal intensity maps of the corresponding region revealing a high accumulation of Pb in the tide mark (II). Modified after Zoeger, N.; Roschger, P.; Hoefstaetter, J. G.; *et al*. *OsteoArth. Carti*. **2006**, *14*, 906–913.

efficiency of the X-ray in exciting elemental X-ray fluorescence compared to electrons. The depth to which the element- and matrix-specific information can be obtained varies with the energy and self absorption of the induced X-rays of the different elements ranging from 40 μm for calcium to 600 μm for strontium.[217]

Synchrotron radiation-induced micro-XRF (SR-μXRF) has the advantage of a higher photon flux, natural collimation, polarization, and tuneable primary photon energy compared to convential XRF. Furthermore, high spatial resolution of typically $10 \times 10 \times 10\ \mu m^3$ can be achieved in bulk samples by a confocal experimental setup[217] (see **Figure 14**). This was used, for example, to study the accumulation of the element Pb in the tide mark of articular cartilage or the local distribution of the element zinc.[219] Strontium could be detected in young bone packets of strontium ranelate-treated patients and experimental animals.[220]

3.325.6.5.2. Secondary ion mass spectrometry

Another powerful technique for microanalytical and -structural analysis of mineralized tissues is secondary ion mass spectrometry (SIMS) which provides a high sensitivity of elemental/isotopic detection combined with a high spatial resolution. SIMS is on the basis of the (1) sputtering (gradual erosion) of the superficial atomic layers of a sample with primary ions, (2) the generated secondary ions from the sample are then separated according to their mass-to-charge ratios and are (3) subsequently collected as mass-spectra, as in-depth or along-surface concentration profiles, or as element distribution images of the studied sample surface.[221,222]

The SIMS technique requires ultra-high vacuum, because the collision of the high energy primary ions is needed to generate and detect the secondary ions from the sample surface. Therefore, the mineralized tissue has to be embedded in plastic. The sensitivity of elemental detection of the SIMS instruments is dependent on the ionization rate of the atoms in the sample and on the transmission of the system, which is the ratio between the number of ions formed and the number of ions detected. The maximum spatial resolution achieved in the instruments today is dependent on the type of the primary ions used and is about 50 nm for Cs and 150 nm for oxygen in the commercially available instruments.[222]

Advantages of SIMS are that the analysis is fast and also sensitive to most elements, including also the light ones. SIMS can be used with a very high mass resolution which however reduces the sensitivity. Nowadays, up to five ion images can be collected in parallel from the same sample volume.[222] As the lateral resolution of SIMS is far behind that of TEM, complementary information can be obtained as done on hydroxyapatite agglomerates during mineralization from the combination of both.[222]

3.325.6.6. Scanning Surface Topography with AFM

In AFM, a sharp tip attached to a small cantilever is used to scan the sample surface. Various surface tip-interactions, such as mechanical contact, atomic-scale friction, and magnetic and electric field sensing, can be used for imaging. The imaging of the surface topography coupled with its usage for nanoindentation has been the main application of AFM in mineralized tissues.[223]

For this purpose, the AFM instrument is operated in the constant-force mode, where the contact force between the tip and the sample is held constant or in the tapping mode, where the cantilever is oscillating closer to the sample than in contact mode, so that it intermittently taps the sample surface. The tapping mode has the advantage that the shear forces can be reduced compared to contact mode. The axial movement of the tip is a direct function of the surface height and is used to visualize for mapping the topography of the sample.

AFM imaging of bone has been done on native samples, as well as on dried and/or embedded specimens for viewing the mineral particles which have been observed to have a plate-like shape,[69,224] for the arrangement of the mineralized collagen fibrils in dentin,[225] and for viewing the Haversian systems in osteonal bone. By using AFM, evidence for the glue-like phase in the nanocomposite material of bone was reported.[226] There have also been attempts to increase the scanning speed of AFM.[227]

3.325.7. Conclusions

Biological mineralized tissues are heterogeneous materials and require imaging techniques which give information on structural and compositional properties on different hierarchical size levels. During recent years, new techniques have emerged (e.g., nanoindentation, Raman spectroscopy, SAM) and already established techniques have been modified to improve spatial resolution to the submicron range (such as SAXS, XRD, XRF, μCT at the synchrotron sources). When bone is investigated, most of the imaging techniques cannot be used *in vivo* but require biopsies (or necropsies). Future developments will increase the feasibility of *in vivo* imaging.

Micro-CT is already used for monitoring the time course of changes in trabecular architecture during treatment and there is promising progress in noninvasive Raman imaging. Phase-contrast imaging with X-rays is not limited to use at synchrotron sources and might become a common setup to improve clinical radiography. Future directions will also include tomographic viewing at high spatial resolution, for instance at the synchrotron. Finally, there is advancement in the combination of techniques providing complementary information from identical sample features. Thus, for example, mechanical/elastic properties combined with the measurements of the mineral components and of the properties of the collagenous and noncollagenous proteins will provide the basis for a better understanding of the structure–function relation of the mineralized tissue at the micron or submicron range. This will lead to a better prediction of fracture risk – a prerequisite for prevalence and treatment of bone fragility.

References

1. Currey, J. *The Mechanical Adaptations of Bone*; Princeton University Press: Princeton, NJ, 1984.
2. Currey, J. D. *J. Biomech.* **2003**, *36*, 1487–1495.
3. Taylor, J. G.; Bushinsky, D. A. *Blood Purif.* **2009**, *27*, 387–394.
4. Fukumoto, S.; Martin, T. J. *Trends Endocrinol. Metabol.* **2009**, *20*, 230–236.
5. Currey, J. D. *J. Biomech.* **1969**, *2*, 1–11.
6. Fratzl, P.; Weinkamer, R. *Progr. Mater. Sci.* **2007**, *52*, 1263–1334.
7. Weiner, S.; Wagner, H. D. *Annu. Rev. Mater. Sci.* **1998**, *28*, 271–298.
8. Katz, J. L. *Symp. Soc. Exp. Biol.* **1980**, *34*, 137–168.
9. Weiner, S.; Traub, W. *Faseb J.* **1992**, *6*, 879–885.
10. Sharir, A.; Barak, M. M.; Shahar, R. *Vet. J.* **2008**, *177*, 8–17.
11. Dempster, D. W. *J. Bone Miner. Res.* **2000**, *15*, 20–23.
12. Wolff, J. J. *Das Gesetz der Transformation der Knochen*; Hirschwald: Berlin, Germany, 1892.
13. Weinans, H.; Odgaard, A. In *Bone Structure and Remodeling*; Odgaard, A.; Weinans, H.; Eds. World Scientific: Singapore, 1995.
14. Roschger, P.; Grabner, B. M.; Rinnerthaler, S.; *et al. J. Struct. Biol.* **2001**, *136*, 126–136.
15. Stauber, M.; Müller, R. *Osteoporos. Int.* **2006**, *17*, 616–626.
16. Roschger, P.; Paschalis, E. P.; Fratzl, P.; Klaushofer, K. *Bone* **2008**, *42*, 456–466.
17. Koester, K. J.; Ager, J. W., 3rd; Ritchie, R. O. *Nat. Mater.* **2008**, *7*, 672–677.
18. Gupta, H. S.; Zioupos, P. *Med. Eng. Phys.* **2008**, *30*, 1209–1226.
19. Weiner, S.; Traub, W. *FEBS Lett.* **1986**, *206*, 262–266.
20. Wagner, H. D.; Weiner, S. *J. Biomech.* **1992**, *25*, 1311–1320.
21. Jäger, I.; Fratzl, P. *Biophys. J.* **2000**, *79*, 1737–1746.
22. Hodge, A. J.; Petruska, J. A. In *Aspects of Protein Structure*; Ramachandran, G. N., Ed.; Academic Press: New York, 1963; pp 289–300.
23. Fratzl, P.; Ed. *Collagen – Structure and mechanics; Springer*: New York, 2008; p 504, ISBN: 978–0–387–73905–2
24. Glimcher, M. J. *Instr. Course Lect.* **1987**, *36*, 49–69.
25. Landis, W. J.; Hodgens, K. J.; Arena, J.; Song, M. J.; McEwen, B. F. *Microsc. Res. Tech.* **1996**, *33*, 192–202.
26. Landis, W. J.; Silver, F. H. *Cells Tissues Organs* **2009**, *189*, 20–24.
27. Boskey, A. L. *Connect. Tissue Res.* **1996**, *35*, 357–363.
28. Fratzl, P.; Groschner, M.; Vogl, G.; *et al. J. Bone Miner. Res.* **1992**, *9*, 1651–1655.
29. Arsenault, A. L.; Grynpas, M. D. *Calcif. Tissue Int.* **1988**, *43*, 219–225.
30. Gao, H.; Ji, B.; Jäger, I. L.; Arzt, E.; Fratzl, P. *Proc. Natl. Acad. Soc. USA* **2003**, *100*, 5597–5600.
31. Landis, W. J.; Librizzi, J. J.; Dunn, M. G.; Silver, F. H. *J. Bone Miner. Res.* **1995**, *10*, 859–867.
32. Fratzl, P.; Gupta, H. S.; Paschalis, E. P.; Roschger, P. *J. Mater. Chem.* **2004**, *14*, 2115–2123.
33. Gupta, H. S.; Wagermaier, W.; Zickler, G. A.; *et al. Nanoletters* **2005**, *5*, 2108–2111.
34. Gupta, H. S.; Seto, J.; Wagermaier, W.; Zaslansky, P.; Boesecke, P.; Fratzl, P. *Proc. Natl. Acad. Soc. USA* **2006**, *103*, 17741–17746.
35. Prockop, D. J.; Kivirikko, K. I. *New Engl. J. Med.* **1984**, *311*, 376–396.
36. Yamauchi, M. In *Calcium and Phosphorus in Health and Disease*; Anderson, J. J. B.; Garner, S. C.; Eds. CRC Press: New York, 1996; pp 127–141.
37. Kay, M. I.; Young, R. A.; Posner, A. S. *Nature* **1964**, *204*, 1050–1052.
38. Posner, A. S. *J. Biomed. Mater. Res.* **1985**, *19*, 241–250.
39. Giraud-Guille, M. M. *Calcif. Tissue Int.* **1988**, *42*, 167–180.
40. Weiner, S.; Traub, W.; Wagner, H. D. *J. Struct. Biol.* **1999**, *126*, 241–255.
41. Marotti, G.; Muglia, M. A.; Palumbo, C. *Clin. Rheumatol.* **1994**, *13*, 63–68.
42. Wagermaier, W.; Gupta, H. S.; Gourrier, A.; Burghammer, M.; Roschger, P.; Fratzl, P. *Biointerphases* **2006**, *1*, 1–5.
43. Ziv, V.; Wagner, H. D.; Weiner, S. *Bone* **1996**, *18*, 417–428.
44. Fratzl, P. *Nat. Mater.* **2008**, *7*, 610–612.
45. Peterlik, H.; Roschger, P.; Klaushofer, K.; Fratzl, P. *Nat. Mater.* **2006**, *5*, 52–55.
46. Peterlik, H.; Roschger, P.; Klaushofer, K.; Fratzl, P. *Int. J. Fract.* **2006**, *139*, 395–405.
47. Oyen, M. L.; Ferguson, V. L.; Bembey, A. K.; Bushby, A. J.; Boyde, A. *J. Biomech.* **2008**, *41*, 2585–2588.
48. Gupta, H. S.; Stachewicz, U.; Wagermaier, W.; Roschger, P.; Wagner, H. D.; Fratzl, P. *J. Mater. Res.* **2006**, *21*, 1913–1921.
49. Shapiro, F. *Eur. Cell. Mater.* **2008**, *15*, 53–76.
50. Uthgenannt, B. A.; Kramer, M. H.; Hwu, J. A.; Wopenka, B.; Silva, M. J. *J. Bone Miner. Res.* **2007**, *22*, 1548–1556.
51. Su, X.; Sun, K.; Cui, F. Z.; Landis, W. J. *Bone* **2003**, *32*, 150–162.
52. Pritchard, J. J. In *The Biochemistry and Physiology of Bone*, 2nd ed.; Bourne, G. H., Ed.; Academic Press: New York, 1972; pp 1–20.
53. Martin, R. B.; Burr, D. B. Raven, New York, 1989.
54. Hong, S. I.; Hong, S. K.; Kohn, D. H. *J. Mater. Sci. Mater. Med.* **2009**, *20*, 1419–1426.
55. Zaslansky, P. In *Collagen – Structure and Mechanics*; Fratzl, P., Ed.; Springer: New York, 2008; Chapter 15, pp 421–446.
56. Zaslansky, P.; Weiner, S. In *Handbook of Biomineralization: Medical and Clinical Aspects*; Epple, M.; Bauerlein, E.; Eds. Wiley-VCH: Weinheim, 2007; pp 183–202.
57. Tesch, W.; Eidelman, N.; Roschger, P.; Goldenberg, F.; Klaushofer, K.; Fratzl, P. *Calcif. Tissue Int.* **2001**, *69*, 147–157.
58. Weiner, S.; Wagner, H. D. *Annu. Rev. Mater. Sci.* **1998**, *28*, 271–298.
59. Zaslansky, P.; Friesem, A. A.; Weiner, S. *J. Struct. Biol.* **2006**, *153*, 188–199.
60. Zaslansky, P.; Zabler, S.; Fratzl, P. *Dent. Mater.* **2010**, *26*(1)
61. Weiner, S.; Veis, A.; Beniash, E.; *et al. J. Struct. Biol.* **1999**, *126*, 27–41.
62. Wang, R. Z.; Weiner, S. *J. Biomech.* **1998**, *31*, 135–141.
63. Zaslansky, P.; Currey, J. D.; Friesem, A. A.; Weiner, S. *J. Biomed. Optic.* **2005**, *10*, 024020.
64. Wong, M.; Carter, D. R. *Bone* **2003**, *33*, 1–13.
65. Ferguson, V. L.; Bushby, A. J.; Boyde, A. *J. Anat.* **2003**, *203*, 191–202.
66. Gupta, H. S.; Schratter, S.; Tesch, W.; *et al. J. Struct. Biol.* **2005**, *149*, 138–148.
67. Landis, W. J.; Silver, F. H. *Comp. Biochem. Physiol. A* **2002**, *133*, 1135–1157.
68. Lees, S.; Page, E. A. *Connect. Tissue Res.* **1992**, *28*, 263–287.
69. Lees, A.; Prostak, S.; Ingle, V. K.; Kjoller, K. *Calcif. Tissue Int.* **1994**, *55*, 180–189.
70. Fratzl, P.; Fratzl-Zelman, N.; Klaushofer, K. *Biophys. J.* **1993**, *64*, 260–266.
71. Wess, T. J.; Hammersley, A. P.; Wess, L.; Miller, A. *J. Struct. Biol.* **1998**, *122*, 92–100.
72. Gupta, H. S.; Messmer, P.; Roschger, P.; Bernstorff, S.; Klaushofer, K.; Fratzl, P. *Phys. Rev. Lett.* **2004**, *93*, 158101.
73. Landis, W.; Moradian-Oldak, J.; Weiner, S. *Connect. Tissue Res.* **1991**, *25*, 181–196.
74. Gadaleta, S. J.; Camacho, N. P.; Mendelsohn, R.; Boskey, A. L. *Calcif. Tissue Int.* **1996**, *58*, 17–23.
75. Freeman, J. W.; Silver, F. H. *Connect. Tissue Res.* **2004**, *45*, 131–141.
76. Keyak, J. H.; Meagher, J. M.; Skinner, H. B.; Mote, C. D., Jr. *J. Biomed. Eng.* **1990**, *12*, 389–397.
77. van Rietbergen, B.; Weinans, H.; Huiskes, R. *Stud. Health Tech. Informat.* **1997**, *40*, 25–32.
78. Ulrich, D.; Rietbergen, B.; Laib, A.; Rüegsegger, P. *Tech. Health Care* **1998**, *6*, 421–427.
79. Eckstein, F.; Kuhn, V.; Lochmüller, E. M. *Ann. Biomed. Eng.* **2004**, *32*, 487–503.
80. Pahr, D. H.; Zysset, P. K. *Comput. Meth. Biomech. Biomed. Eng.* **2009**, *12*, 45–57.
81. Parfitt, A. M. *Bone* **2002**, *30*, 807–809.
82. Misof, B. M.; Roschger, P.; Cosman, R.; *et al. J. Clin. Endocrinol. Metabol.* **2003**, *88*, 1150–1156.

83. Fuchs, R. K.; Allen, M. R.; Ruppel, M. E.; *et al*. *Matrix Biol*. **2008**, *27*, 34–41.
84. Akkus, O.; Polyakova-Akkus, A.; Adar, F.; Schaffler, M. B. *J. Bone Miner. Res*. **2003**, *18*, 1012–1019.
85. Ruffoni, D.; Fratzl, P.; Roschger, P.; Klaushofer, K.; Weinkamer, R. *Bone* **2007**, *40*, 1308–1319.
86. Russell, R. G.; Rogers, M. J.; Frith, J. C.; *et al*. *J. Bone Miner. Res*. **1999**, *14*(Suppl 2), 53–65.
87. Compston, J. *Calcif. Tissue Int*. **2005**, *77*, 65–71.
88. Fratzl, P.; Schreiber, S.; Roschger, P.; Lafage, M. H.; Rodan, G.; Klaushofer, K. *J. Bone Miner. Res*. **1996**, *11*, 248–253.
89. Roschger, P.; Manjubala, I.; Zoeger, N.; *et al*. *J. Bone Miner. Res*. **2010**, *25*(4), 891–900.
90. Li, C.; Paris, O.; Siegel, S.; Roschger, P.; Paschalis, E. P.; Klaushofer, K.; Fratzl, P. *J. Bone Miner. Res*. **2010**, *25*(5), 968–975.
91. Boivin, G.; Farlay, D.; Khebbab, M. T.; Jaurand, X.; Delmas, P. D.; Meunier, P. J.; *Osteoporos. Int*. **2010**, *21*(4), 667–677.
92. Skedros, J. G.; Bloebaum, R. D.; Bachus, K. N.; Boyce, T. M.; Constantz, B. *J. Biomed. Mater. Res*. **1993**, *27*, 57–64.
93. Grynpas, M. *Calcif.Tissue Int*. **1993**, *53*(Suppl 1), S57–S64.
94. Economos, C. D.; Nelson, M. E.; Fiatarone Singh, M. A.; *et al*. *Osteoporos. Int*. **1999**, *10*, 200–206.
95. Akesson, K.; Grynpas, M. D.; Hancock, R. G.; Odselius, R.; Obrant, K. J. *Calcif. Tissue Int*. **1994**, *55*, 236–239.
96. Grynpas, M. D.; Hamilton, E.; Cheung, R.; *et al*. *Bone* **1996**, *18*, 253–259.
97. Rauch, F.; Schoenau, E. *J. Bone Miner. Res*. **2001**, *16*, 597–604.
98. Fratzl, P.; Roschger, P.; Fratzl-Zelman, N.; Paschalis, E. P.; Phipps, R.; Klaushofer, K. *Calcif. Tissue Int*. **2007**, *81*, 73–80.
99. Blake, G. M.; Fogelman, I. *J. Clin. Densitom*. **2007**, *10*, 259–265.
100. Cummings, S. R.; Bates, D.; Black, D. M. *JAMA* **2002**, *288*, 1889–1897.
101. Adams, J. *Eur. J. Radiol*. **2009**, *71*, 415–424.
102. Erben, R. G. *J. Histochem. Cytochem*. **1997**, *45*, 307–313.
103. Bonewald, L. F.; Harris, S. E.; Rosser, J.; *et al*. *Calcif. Tissue Int*. **2003**, *72*, 537–547.
104. Recker, R. R.; Barger-Lux, M. J. In *Primer on the Metabolic Bone Diseases and Disorders of Mineral Metabolism*, American Society for Bone and Mineral Research, 2006; Chapter 24, pp 161–169.
105. Parfitt, A. M.; Drezner, M. K.; Glorieux, F. H.; *et al*. *J. Bone Miner. Res*. **1987**, *2*, 595–610.
106. Parisien, M. V.; McMahon, D.; Pushparaj, N.; Dempster, D. W. *Bone* **1988**, *9*, 289–295.
107. Fratzl-Zelman, N.; Valenta, A.; Roschger, P.; *et al*. *J. Clin. Endocrinol. Metabol*. **2004**, *89*, 1538–1547.
108. Bromage, T. G.; Goldman, H. M.; MCFarlin, S. C.; Warshaw, J.; Boyde, A.; Riggs, C. M. *Anat. Rec. B: New Anat*. **2003**, *274B*, 157–168.
109. Ascenzi, A.; Bonucci, E. *Anat. Rec*. **1968**, *161*, 377–392.
110. Boyde, A.; Riggs, C. M. *Bone* **1990**, *11*, 35–39.
111. Boivin, G.; Baud, C. A. In *Methods of Calcified Tissue Preparation*; Dickson, G. R.; Ed. Elsevier: Amsterdam, 1984; pp 391–411.
112. Amprino, E.; Engstrom, A. *Acta Anat*. **1952**, *15*, 1–22.
113. Boivin, G.; Meunier, P. J. *Osteoporos. Int*. **2003**, *14*(Suppl 5), S22–S28.
114. Boivin, G.; Meunier, P. J. *Calcif. Tissue Int*. **2002**, *70*, 503–511.
115. Boivin, G.; Meunier, P. J. *Osteoporos. Int*. **2003**, *14*(Suppl 3), S19–S24.
116. Pfeiffer, F.; Weitkamp, T.; David, C. *Europhys. News* **2006**, *37*, 13–15.
117. Snigirev, A.; Snigireva, I.; Kohn, V.; Kuznetsw, S.; Schelokov, I. *Rev. Sci. Instrum*. **1995**, *66*, 5486–5492.
118. Pfeiffer, F.; Bech, M.; Bunk, O.; *et al*. *Nat. Mater*. **2008**, *7*, 134–137.
119. Müller, R. *Nat. Rev. Rheumatol*. **2009**, *5*, 373–381.
120. Cohen, A.; Dempster, D. W.; Müller, R.; *et al*. *Osteoporos. Int*. **2010**, *21*, 263–273.
121. Stauber, M.; Müller, R. *Meth. Mol. Biol*. **2008**, *455*, 273–292.
122. Borah, B.; Dufresne, T. E.; Chmielewski, P. A.; Johnson, T. D.; Chines, A.; Manhart, M. D. *Bone* **2004**, *34*, 736–746.
123. Borah, B.; Gross, G. J.; Dufresne, T. E.; *et al*. *Anat. Rec.* **2001**, *265*, 101–110.
124. Chevalier, Y.; Pahr, D.; Allmer, H.; Charlebois, M.; Zysset, P. J. *Biomech*. **2007**, *40*, 3333–3340.
125. Kinney, J. H.; Lane, N. E.; Haupt, D. L. J. *Bone Miner. Res*. **1995**, *10*, 264–270.
126. Holdsworth, D. W.; Thornton, M. M. *Trends in Biotechnol*. **2002**, *20*(Suppl), S34–S39.
127. van Lenthe, G. H.; Hagenmüller, H.; Bohner, M.; Hollister, S. J.; Meinel, L.; Müller, R. *Biomaterials* **2007**, *28*, 2479–2490.
128. Waarsing, J. H.; Day, J. S.; Weinans, H. *J. Musculoskelet. Neuronal interact*. **2005**, *5*, 310–312.
129. Buie, H. R.; Campbell, G. M.; Klinck, R. J.; MacNeil, J. A.; Boyd, S. K. *Bone* **2007**, *41*, 505–515.
130. Davis, K. A.; Burghardt, A. J.; Link, T. M.; Majumdar, S. *Calcif. Tissue Int*. **2007**, *81*, 364–371.
131. Waarsing, J. H.; Day, J. S.; Weinans, H. *J. Bone Miner. Res*. **2004**, *19*, 1640–1650.
132. Nuzzo, S.; Lafage-Proust, M. H.; Martin-Badosa, E.; *et al*. *J. Bone Miner. Res*. **2002**, *17*, 1372–1382.
133. Borah, B.; Ritman, E. L.; Dufresne, T. E.; *et al*. *Bone* **2005**, *37*, 1–9.
134. Schneider, P.; Voide, R.; Stampanoni, M.; Müller, R. *Biomed. Tech. (Be.)* **2009**, *54*, 48–54.
135. Nazarin, A.; Snyder, B. D.; Zurakowski, D.; Müller, R. *Bone* **2008**, *43*, 302–311.
136. Majumdar, S.; Kothari, M.; Augat, P.; *et al*. *Bone* **1998**, *22*, 445–454.
137. Jackson, S. A.; Cartwright, L. S.; Lewis, D. *Calcif. Tissue Res*. **1978**, *25*, 217–222.
138. Landis, W. J.; Paine, M. S.; Glimcher, M. J. *J. Ultra. Res*. **1977**, *59*, 1–30.
139. Wiesmann, H. P.; Tkotz, T.; Joos, U.; *et al*. *J. Bone Miner. Res*. **1997**, *12*, 380–383.
140. Rubin, M. A.; Jasiuk, I. *Micron* **2005**, *36*, 653–664.
141. Rubin, M. A.; Jasiuk, I.; Taylor, J.; Rubin, J.; Ganey, T.; Apkarian, R. P. *Bone* **2003**, *33*, 270–282.
142. Thomas, H. F.; Carella, P. *Arch. Oral Biol*. **1984**, *29*, 641–646.
143. Marshall, A. F.; Lawless, K. R. *J. Dent. Res*. **1981**, *60*, 1773–1782.
144. Traub, W.; Arad, T.; Weiner, S. *Proc. Natl. Acad. Sci. USA* **1989**, *86*, 9822–9826.
145. Landis, W. J.; Hodgens, K. J.; Song, M. J.; *et al*. *J. Struct. Biol*. **1996**, *117*, 24–35.
146. Kim, H. M.; Rey, C.; Glimcher, M. J. *J. Bone Miner. Res*. **1995**, *10*, 1589–1601.
147. Landis, W.; Song, M. *J. Struct. Biol*. **1993**, *110*, 39–54.
148. Li, Z. Y.; Lam, W. M.; Yang, C.; *et al*. *Biomaterials* **2007**, *28*, 1452–1460.
149. Morris, M. D.; Berger, A.; Mahadevan-Jansen, A. *J. Biomed. Optics* **2005**, *10*, 031101.
150. Paschalis, E. P. *Osteoporos Int*. **2009**, doi:10.1007/s00198-009-0857-6.
151. Gamsjäger, S.; Kazanci, M.; Paschalis, E.; Fratzl, P. In *Raman Spectroscopy for Soft Matter Applications*; Amer, M.; Ed. Wiley: Hoboken, NJ, 2009; pp 227–269.
152. Knott, L.; Bailey, A. J. *Bone* **1998**, *22*, 181–187.
153. Boskey, A. L.; Wright, T. M.; Blank, R. D. *J. Bone Miner. Res*. **1999**, *14*, 330–335.
154. Burr, D. B. *Bone* **2002**, *31*, 8–11.
155. Paschalis, E. P.; Shane, E.; Lyritis, G.; Skarantavos, G.; Mendelsohn, R.; Boskey, A. L. *J. Bone Miner. Res*. **2004**, *19*, 2000–2004.
156. Kazarian, S. G.; Chan, K. L. A. *Biochim. Biophys. Acta* **2006**, *1758*, 858–867.
157. Krafft, C.; Steiner, G.; Beleites, C.; Salzer, R. *Review article. J. Biophoton* **2009**, *2*, 13–28.
158. Boskey, A.; Camacho, N. P. *Biomaterials* **2007**, *28*, 2465–2478.
159. Boskey, A. L.; Pleshko, N.; Doty, S. B.; Mendelsohn, R. *Cell. Mater*. **1992**, *2*, 209–220.
160. Paschalis, E. P.; DiCarlo, E.; Betts, F.; Sherman, P.; Mendelsohn, R.; Boskey, A. L. *Calcif. Tissue Int*. **1996**, *59*, 480–487.
161. Paschalis, E. P.; Verdelis, K.; Doty, S. B.; Boskey, A. L.; Mendelsohn, R.; Yamauchi, M. *J. Bone Miner. Res*. **2001**, *16*, 1821–1828.
162. Boskey, A. L.; Mendelsohn, R. *Vib. Spectros*. **2005**, *38*, 107–114.
163. Durchschlag, E.; Paschalis, E. P.; Zoehrer, R.; *et al*. *J. Bone Miner. Res*. **2006**, *21*, 1581–1590.
164. Roschger, P.; Dempster, D. W.; Zhou, H.; *et al*. *J. Bone Miner. Res*. **2007**, *22*, 717–723.
165. Camacho, N. P.; Rinnerthaler, S.; Paschalis, E. P.; Mendelsohn, R.; Boskey, A. L.; Fratzl, P. *Bone* **1999**, *25*, 287–293.
166. Golcuk, K.; Mandair, G. S.; Callender, A. F.; Sahar, N.; Kohn, D. H.; Morris, M. D. *Biochim. Biophys. Acta* **2006**, *1758*, 868–873.
167. Ager, J. W., III; Nalla, R. K.; Balooch, G.; *et al*. *J. Bone Miner. Res*. **2006**, *21*, 1879–1887.
168. Morris, M. D.; Crane, N. J.; Gomez, L. E.; Ignelzi, M. A. *Calcif. Tissue Int*. **2004**, *74*, 86–94.
169. Yeni, Y. N.; Yeramshetty, J.; Akkus, O.; Pechey, C.; Les, C. M. *Calcif. Tissue Int*. **2006**, *78*, 363–371.
170. Tsuda, H.; Arends, J. *Adv. Dent. Res*. **1997**, *11*, 539–547.
171. Kazanci, M.; Roschger, P.; Paschalis, E. P.; Klaushofer, K.; Fratzl, P. *J. Struct. Biol*. **2006**, *156*, 489–496.
172. Kazanci, M.; Wagner, H. D.; Manjubala, N. I.; *et al*. *Bone* **2007**, *41*, 456–461.
173. McCreadie, B. R.; Morris, M. D.; Chen, T.; *et al*. *Bone* **2006**, *39*, 1190–1195.
174. Carden, A.; Rajachar, R. M.; Morris, M. D.; Kohn, D. H. *Calcif. Tissue Int*. **2003**, *72*, 166–175.
175. Wang, C.; Wang, Y.; Huffman, N. T.; *et al*. *J. Biol. Chem*. **2009**, *284*, 7100–7113.
176. Frasca, P.; Harper, R. A.; Katz, J. L. *J. Dent. Res*. **1978**, *57*, 526–533.

177. Sahar, N. D.; Hong, S.; Kohn, D. H. *Micron* **2005**, *36*, 617–629.
178. Boyde, A.; Jones, S. J. *Microsc. Res. Tech.* **1996**, *33*, 92–120.
179. Boyde, A. J. *Anat.* **2003**, *202*, 183–194.
180. Howell, P. G. T.; Boyde, A. *Calcif. Tissue Int.* **2003**, *72*, 745–749.
181. Boyde, A.; Jones, S. J. *Metab. Bone Dis. Rel. Res.* **1983**, *5*, 145–150.
182. Bloebaum, R. D.; Skedros, J. G.; Vajda, E. G.; Bachus, K. N.; Constantz, B. R. *Bone* **1997**, *20*, 485–490.
183. Roschger, P.; Fratzl, P.; Eschberger, J.; Klaushofer, K. *Bone* **1998**, *23*, 319–326.
184. Boyde, A.; Jones, S. J.; Aerssens, J.; Dequeker, J. *Bone* **1995**, *16*, 619–627.
185. Fratzl, P.; Gupta, H. S.; Roschger, P.; Klaushofer, K. In *Nanotechnology*; Vogel, V., Ed.; Nanomedicine; Wiley-VCH: KGaA: Weinheim, 2009; Vol. 5, Chapter 12, pp 345–360, ISBN: 978–3–527–31736–3
186. Rinnerthaler, S.; Roschger, P.; Jakob, H. F.; Nader, A.; Klaushofer, K.; Fratzl, P. *Calcif. Tissue Int.* **1999**, *64*, 422–429.
187. Wachtel, E.; Weiner, S. J. *Bone Miner. Res.* **1994**, *9*, 1651–1655.
188. Fratzl, P.; Schreiber, S.; Boyde, A. *Calcif. Tissue Int.* **1996**, *58*, 341–346.
189. Bünger, M. H.; Foss, M.; Erlacher, K.; *et al. Eur. Cell. Mater.* **2006**, *12*, 81–91.
190. Wess, T.; Alberts, I.; Hiller, J.; Drakopoulos, M.; Chamberlain, A. T.; Collins, M. *Calcif. Tissue Int.* **2001**, *70*, 103–110.
191. Moger, C. J.; Barrett, R.; Bleuet, P.; *et al. Osteoarthr. Cartil.* **2007**, *15*, 682–687.
192. Zizak, I.; Roschger, P.; Paris, O.; *et al. J. Struct. Biol.* **2003**, *141*, 208–217.
193. Gupta, H. S.; Roschger, P.; Zizak, I.; *et al. Calcif. Tissue Int.* **2003**, *72*, 567–576.
194. Wagermaier, W.; Gupta, H. S.; Gourrier, A.; *et al. J. Appl. Crystallogr.* **2006**, *40*, 115–120.
195. Sasaki, N.; Sudoh, Y. *Calcif. Tissue Int.* **1997**, *60*, 361–367.
196. Jaschouz, D.; Paris, O.; Roschger, P.; Hwang, H. S.; Fratzl, P. *J. Appl. Crystallogr.* **2003**, *36*, 494–498.
197. Kazanci, M.; Fratzl, P.; Klaushofer, K.; Paschalis, E. P. *Calcif. Tissue Int.* **2006**, *79*, 354–359.
198. Wenk, H. R.; Heidelbach, F. *Bone* **1999**, *24*, 361–369.
199. Vetter, U.; Eanes, E. D.; Kopp, J. B.; Termine, J. D.; Robey, P. G. *Calcif. Tissue Int.* **1991**, *49*, 248–250.
200. Verberckmoes, S. C.; Behets, G. J.; Oste, L.; *et al. Calcif. Tissue Int.* **2004**, *74*, 405–415.
201. Paris, O. *Biointerphases* **2008**, *3*, FB16–FB26.
202. Qin, L.; Bumrerraj, S.; Leung, K.; Katz, L. *J. Bone Miner. Metabol.* **2004**, *22*, 86–89.
203. Raum, K.; Leguerney, I.; Chandelier, F.; *et al. Phys. Med. Biol.* **2006**, *51*, 733–746.
204. Katz, J. L.; Misra, A.; Spencer, P.; *et al. Mater. Sci. Eng. A Struct. Mater.* **2007**, *27*, 450–468.
205. Raum, K. *IEEE Trans. Ultrason. Ferroelectr. Freq. Control* **2008**, *55*, 1417–1431.
206. Raum, K.; Reisshauer, J.; Brandt, J. *J. Biomed. Mater. Res. A* **2004**, *71*, 430–438.
207. Hofmann, T.; Heyroth, F.; Meinhard, H.; Fränzel, W.; Raum, K. *J. Biomech.* **2006**, *39*, 2282–2294.
208. Lewis, G.; Nyman, J. S. *J. Biomed. Mater. Res. B Appl. Biomater.* **2008**, *87*, 286–301.
209. Zysset, P. K.; Guo, X. E.; Hoffler, C. E.; Moore, K. E.; Goldstein, S. A. *J. Biomech.* **1999**, *32*, 1005–1012.
210. Oliver, W. C.; Pharr, G. M. *J. Mater. Res.* **1992**, *7*, 1564–1583.
211. Rho, J. Y.; Tsui, T. Y.; Pharr, G. M. *Biomaterials* **1997**, *18*, 1325–1330.
212. Donnelly, E.; Boskey, A. L.; Baker, S. P.; van der Meulen, M. C. *J. Biomed. Mater. Res. A* **2010**, *92*(3), 1048–1056.
213. Tai, K.; Dao, M.; Suresh, S.; Plazoglu, A.; Ortiz, C. *Nat. Mater.* **2007**, *6*, 454–462.
214. Akiba, N.; Sasano, Y.; Suzuki, O.; Sasaki, K. *Calcif. Tissue Int.* **2006**, *78*, 143–151.
215. Bang, S.; Baud, C. A. *J. Bone Miner. Res.* **1990**, *1*(5 Suppl), S87–S89.
216. Nicholson, W. A. P.; Dempster, D. W. *Scan. Electron Microsc.* **1980**, *2*, 517–533.
217. Zoeger, N.; Roschger, P.; Hoefstaetter, J. G.; *et al. OsteoArth. Carti.* **2006**, *14*, 906–913.
218. Zoeger, N.; Streli, C.; Wobrauschek, P.; *et al. X-Ray Spectrom.* **2008**, *37*, 3–11.
219. Gomez, S.; Rizzo, R.; Pozzi-Mucelli, M.; Bonucci, E.; Vittur, F. *Bone* **1999**, *25*, 33–38.
220. Fuchs, R. K.; Allen, M. R.; Condon, K. W.; *et al. Osteoporos. Int.* **2008**, *19*, 1331–1341.
221. Lodding, A. *Adv. Dent. Res.* **1997**, *11*, 364–379.
222. Guerquin-Kern, J. L.; Wu, T. D.; Quintana, C.; Croisy, A. *Biochim. Biopyhs. Acta* **2005**, *1724*, 228–238.
223. Thurner, P. J. *Wiley Interdiscip. Rev. Nanomed. Nanobiotechnol.* **2009**, *1*, 624–649.
224. Hassenkam, T.; Fantner, G. E.; Cutroni, J. A.; Waever, J. C.; Morse, D. E.; Hansma, P. K. *Bone* **2004**, *35*, 4–10.
225. Habelitz, S.; Balooch, M.; Marshall, S. J.; Balooch, G.; Marshall, G. W., Jr. *J. Struct. Biol.* **2002**, *138*, 227–236.
226. Fantner, G. E.; Hassenkam, T.; Kindt, J. H.; *et al. Nat. Mater.* **2005**, *4*, 612–616.
227. Fantner, G. E.; Schitter, G.; Kindt, J. H.; *et al. Ultramicroscopy* **2006**, *106*, 881–887.

3.327. Intracellular Probes

S Bhattacharyya and P Ducheyne, University of Pennsylvania, Philadelphia, PA, USA

© 2011 Elsevier Ltd. All rights reserved.

3.327.1.	**Introduction**	448
3.327.2.	**Fluorescence-Based Intracellular Probes**	448
3.327.2.1.	Introduction	448
3.327.2.2.	Physical Principles	448
3.327.2.3.	Fluorescent Molecules for Intracellular Probing	449
3.327.2.3.1.	Design criteria	449
3.327.2.3.2.	Fluorescent dyes	449
3.327.2.4.	FRET-Based Sensing	451
3.327.2.4.1.	Introduction	451
3.327.2.4.2.	Principle of FRET	452
3.327.2.4.3.	Detection	452
3.327.2.4.4.	Applications of FRET	453
3.327.2.4.5.	Problems associated with FRET	453
3.327.2.5.	Nanoplatforms-Based Fluorescent Probes	453
3.327.2.5.1.	Introduction	453
3.327.2.5.2.	Probe embedded by biologically localized encapsulation	454
3.327.2.5.3.	Molecular beacons	456
3.327.3.	**Optical-Label-Free Intracellular Probes**	459
3.327.3.1.	Surface Plasmon Resonance-Based Probes	459
3.327.3.1.1.	Working principle	459
3.327.3.1.2.	SERS nanosensor	460
3.327.3.2.	Quantum Dots as Intracellular Probes	461
3.327.3.2.1.	Introduction	461
3.327.3.2.2.	Synthesis of QDs	461
3.327.3.2.3.	Functionalization of QDs: Solubilization and bioconjugation	462
3.327.3.2.4.	Biological applications	464
3.327.4.	**Conclusion**	467
References		467

Abbreviations

AMC	7-Amino-4-methylcoumarin
BODIPY	Boron difluoride dipyrromethene
CCD	Charge-coupled device
DOX	Doxorubicin
DAPI	4′,6-Diamidino-2-phenylindole
DNA	Deoxyribonucleic acid
DPIBF	1,3-Diphenylisobenzofuran
EDANS	5-((2-Aminoethyl)amino)naphthalene-1-sulfonic acid
FRET	Fluorescence resonance energy transfer
HER	Human epidermal growth factor receptor
HRP	Horseradish peroxidase
ISC	Intersystem crossing
LSPR	Localized surface plasmon resonance
MB	Molecular beacon
MU	4-Methylumbelliferone
NIR	Near-infrared
NR	Nonradiative
PAA	Polyacrylamide
PCR	Polymerase chain reaction
PDMA	Polydecylmethacrylate
PDT	Photodynamic therapy
PeT	Photoinduced electron transfer
PEBBLE	Probes encapsulated by biologically localized embedding
PL	Photoluminescence
PNA	Peptide nucleic acid
PRS	Polarization Raman spectroscopy
PSMA	Prostate-specific membrane antigen
QDs	Quantum dots
RET	Resonance energy transfer
RNA	Ribonucleic acid
ROS	Reactive oxygen species
SERS	Surface-enhanced Raman scattering
SNP	Single-nucleotide polymorphism
SPR	surface plasmon resonance
SPs	Surface plasmons
SQ	super quencher
TMR	Tetramethylrhodamine
TSA	Tyramide signal amplification

3.327.1. Introduction

As research in cell biology, neuroscience, and immunology has progressed from purely structural characterization of cells toward understanding dynamic processes, such as signaling, excitability, growth, and metabolic transport, studies have evolved to include new methodologies applicable to living cells. Organisms comprise a diversity of cells, and these, in turn, contain an enormous variety of biomolecules. The concentrations, chemical modifications, and interactions of these molecules are generally precisely controlled, both spatially and temporally. Deciphering this complex system of interacting molecules inside and among cells is one of the long-term goals of biology. To this end, it is highly valuable to rely on methods that probe the behavior of molecules of interest, and *in vivo* characterization of protein activity, key metabolite expression, or any other important biological functionality has become one of the central quests in molecular cell biology.

The development and application of biomaterials, that is, materials science-based tools, that allow visualization of events in living cells is a highly active and interdisciplinary area of research. Understanding of biological systems is increasingly dependent on the ability to visualize and quantify signaling molecules and events with high spatial and temporal resolution in a cellular context. This represents true biomaterials science, it is state-of-the-art materials science at the interface with biology.

In this chapter, we will review some unique optical techniques for intracellular sensing. We will review fluorescence-based intracellular probes with a brief description of fluorescence phenomena and measurement techniques, and we will describe the use of conventional fluorescent dye molecules for intracellular imaging. Considering the potentially enormous impact of nanomaterials in this field, we will discuss the nanoplatform-based fluorescent probes. In the last section, we will also review optical label-free nanoprobes which can be detected by conventional optical instruments.

3.327.2. Fluorescence-Based Intracellular Probes

3.327.2.1. Introduction

Fluorescence is a widely used optical method for biosensing due to its selectivity and sensitivity. A fluorescence-based device monitors the frequency change of electromagnetic radiation emission stimulated by previous absorption of radiation and subsequent generation of an excited state that only exists for a very short duration of time. Single molecules can be repeatedly excited and detected to produce a bright signal that is easily measured even at the single cell level.

Subsequent to discussing the physical principles, we will describe the most salient applications: (a) Fluorescent molecules for intracellular probing; (b) Fluorescence resonance energy transfer (FRET)-based sensing; and (c) Nanoplatforms-based fluorescent probes. Although there are still other applications, the descriptions of these three fluorescence-based techniques provide an extensive overview of the breadth of options available. All of these probes include the same basic components: biological recognition molecules, a source of excitation light, and an optical readout device capable of discriminating excitation light from emitted fluorescence.

3.327.2.2. Physical Principles

Fluorescence is emission of light from singlet-excited states, in which the electron in the excited orbital is paired (of opposite sign) to the second electron in the ground-state orbital. Return to the ground state is spin-allowed and occurs rapidly by emission of a photon. This emission rate of fluorescence is typically 10^{-8} s, so that a typical fluorescence lifetime is near 10 ns. Fluorescence spectral data are generally presented as emission spectra. Emission spectra vary widely and are dependent upon the chemical structure of the fluorophore and the solvent in which it is dissolved. In this chapter, we will focus on single photon excitation processes, although the analytical use of multiphoton excitation is also an important and vibrant field.[1]

Fluorescence is a quantum mechanical phenomenon and can be best explained by the Jablonsky diagram (Figure 1).

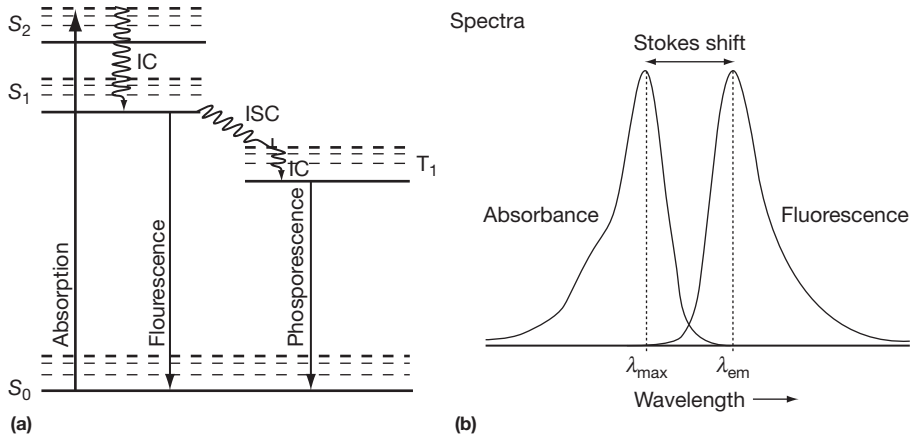

Figure 1 (a) Jablonski diagram of single-photon excitation. The electronic energy levels and their vibrational substructure are shown with horizontal lines, and the physical processes that cause transitions between these levels are depicted by vertical arrows. The singlet ground, first, and second electronic states are labeled S0, S1, and S2, respectively, and the first triplet state is labeled T1. For each of these electronic states, the molecule can exist in a multitude of vibronic states indicated by the dashed lines. (b) Schematic drawing of the absorption and fluorescence emission spectra of a fluorophore. Spectra are normalized to peak absorption and emission, respectively.

For absorption to occur, the energy of the exciting photon has to approximately match the energy difference between the excited state and the ground state (Figure 1). At room temperature, absorption of a photon takes place from the vibrational ground state S0 within $\sim 10^{-18}$ s. Photon absorption excites the molecule to the singlet state S2 from which it undergoes a radiation-less loss of energy by internal conversion to reach S1.

From S1, there are several possible fates. The decay of the excited state can occur with photon emission (i.e., fluorescence) or in a nonradiative (NR) fashion. This 'NR quenching' of the fluorophore excited state can occur through one of a variety of processes, including bond rotation or vibration, molecular collision,[2] and photoinduced electron transfer (PeT).[3] From S1, another possible fate is to emit a phosphorescent photon. In this case, the excited electron undergoes intersystem crossing (ISC) to attain the triplet state, before it exits to the ground state. The lifetime of the excited state in phosphorescence is significantly longer than that in fluorescence and it is in the order of $\sim 10^{-4}$ s to minutes or even hours. The drop to the ground state is accompanied by emission of a photon, also of lower energy than the exciting photon.[4] Another important pathway for decay of the singlet excited state involves FRET to an acceptor molecule. This process is distance-dependent and can be used as a 'spectroscopic ruler' to measure the proximity of labeled entities.[5]

Taking in to account the probabilities of each of these processes, a quantum yield quantifies the relative importance of a given decay pathway. For example, the fluorescence quantum yield gives the efficiency of the fluorescence process. It is defined as the ratio of the number of photons emitted to the number of photons absorbed. The parameters that characterize a molecule's capacity for light absorption and fluorescence emission are the molar extinction ε (measured at peak absorption per mole and cm of optical path-length) and absorption spectrum and the fluorescence quantum yield φ (dimensionless) and emission spectrum, respectively (Figure 1(c)). The brightness of a fluorophore is hence determined by the product $\varepsilon\varphi$.

3.327.2.3. Fluorescent Molecules for Intracellular Probing

When cells are going through physiological activation processes or pathological stresses, their response can be quite heterogeneous in time and space. Conventional physiological and biochemical methods often fail to analyze or describe these parameters in bulk (such as in tissue or cellular suspension), and can often fail to resolve discrete differences in the kinetics and magnitudes of the responses between cells, as well as complex intracellular and subcellular dynamical processes, critical to understanding how cells actually work. Small fluorescent molecules are indispensable tools for these purposes, can be used as biomolecular labels, enzyme substrates, environmental indicators, and cellular stains.[6–17] Given the fact that there are countless fluorescent molecules available either commercially[18] or by modification of existing ones, selection of a suitable fluorophore to visualize a biochemical or biological process can be daunting. Fortunately, the plethora of fluorescent probes has an intrinsic flexibility toward modulation. Attachment of various reactive groups, substrate moieties, chelating components, and other chemical entities to a small number of 'core' fluorophores gives rise to the archive of probes. Overall, these core fluorophores are well-established[14,19] and consist of molecules with excellent spectral characteristics, high chemical stabilities, and facile syntheses. Probe selection and design can, therefore, be simplified by understanding the properties of these core fluorescent compounds. In this regard, some excellent review articles have already appeared in the literature.[20–26]

3.327.2.3.1. Design criteria

In order to apply fluorescent probes to live cells, their design criteria is of utmost importance. In general, four sets of criteria must be kept in mind while designing efficient florescent probes: (i) the physiological and structural integrity of the cells should remain intact during the delivery of the probe; (ii) the probe must be selectively targeted toward ion, molecule, organelle, or other structure; (iii) the spectroscopic characteristics of the probe must be compatible with the instrumentation that is to be used for detection, that is, the fluorescence output of the probe must be sufficient to permit the detection of the target at natural abundance levels; and (iv) probes and target interaction must be detectable through spectroscopic responses such as spatial distribution of fluorescent image or change in fluorescent intensity or a spectral shift.

The specific chemical properties (e.g., reactivity, lipophilicity, pK_a, stability) and photophysical properties (e.g., λ_{max}, λ_{em}, ε, φ, τ) determine the application of a particular fluorophore. For the comparison of spectroscopic properties of different fluorescent molecules we can rely on two parameters, that is, the extinction coefficient (ε) and the quantum yield (φ) and product of them ($\varepsilon\varphi$). A plot of $\varepsilon\varphi$ versus λ_{max} for the major classes of biologically significant fluorescent dyes is shown in Figure 2. Some of those molecules are discussed below in details.

3.327.2.3.2. Fluorescent dyes

Quinine (**1**) was the first naturally occurring fluorescent compound discovered. Subsequently, many other natural compounds were found which exhibit measurable fluorescence.[27] The aromatic amino acids have fluorescence properties that were first described by Weber.[28] While phenylalanine (**2**) and tyrosine (**3**) exhibit weak fluorescence under UV excitation, tryptophan (**4**) is the strongest fluorescent natural amino acid, with a λ_{max} of 280 nm, λ_{em} of 348 nm, extinction coefficient of 6.3×10^3 $M^{-1}\,cm^{-1}$, and a quantum yield of 0.13.[27] Among other naturally occurring fluorophores, reduced nicotinamide cofactors (e.g., nicotinamide adenine dinucleotide; **5**) and Flavin (flavin mononucleotide; **6**) show measurable fluorescence under UV excitation.[27,29,30]

Polycyclic aromatic compounds give a wide variety of useful probes by substitution on its abundant open valencies. A classic example in this category is the naphthalene family. These include the amine-reactive 5-(dimethylamino)naphthalene-1-sulfonyl (dansyl) chloride[31] and other associated fluorophores.[32,33] Another important related naphthalene derivative is 5-((2-aminoethyl)amino)naphthalene-1-sulfonic acid (EDANS). Derivatives of this fluorophore, such as compound (**7**), exhibit a λ_{max} of 336 nm, λ_{em} of 520 nm, extinction coefficient of 6.1×10^3 $M^{-1}\,cm^{-1}$, and a quantum yield of 0.27 in water.[34]

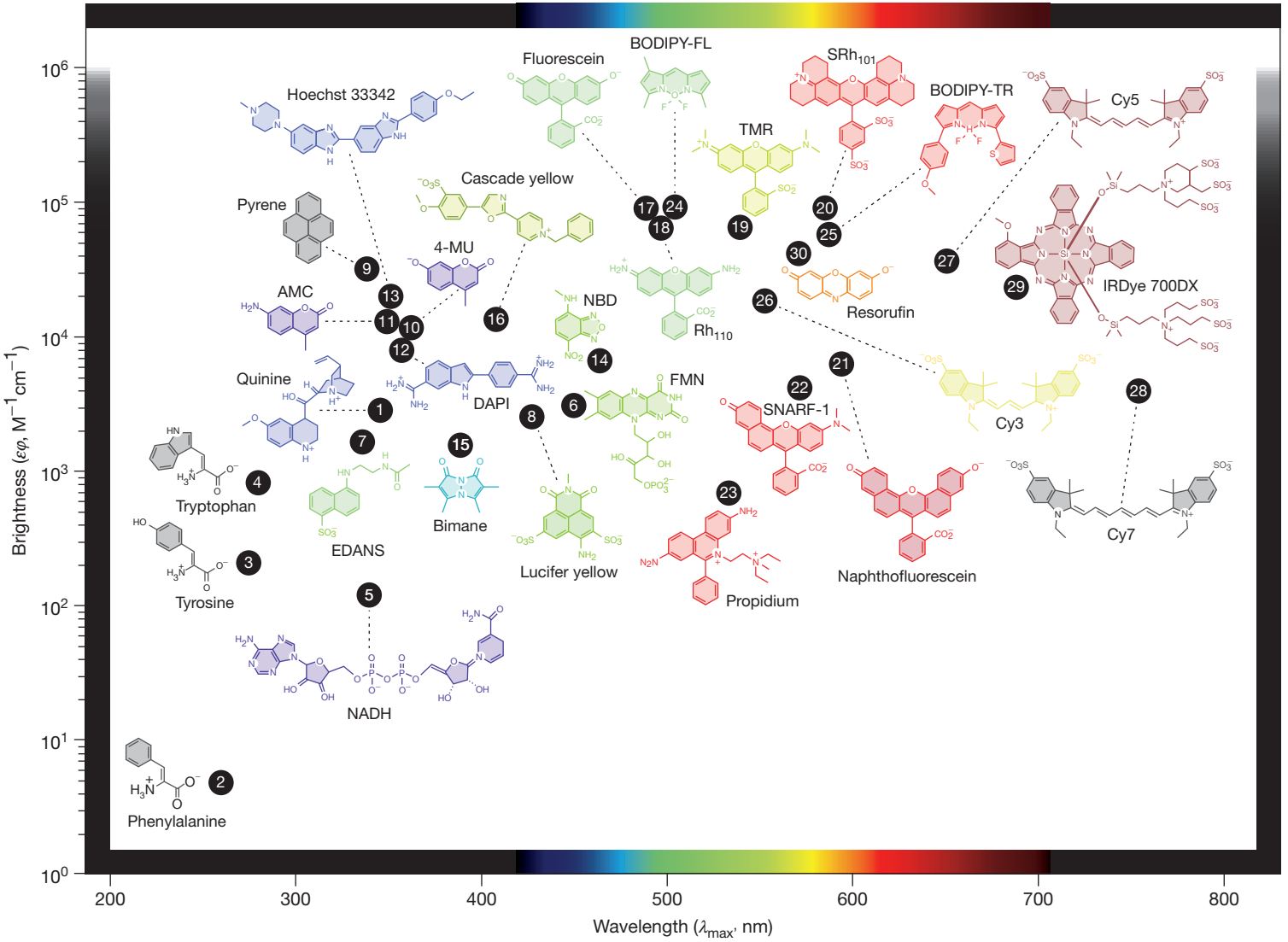

Figure 2 Plot of fluorophore brightness ($\varepsilon\varphi$) versus the wavelength of maximum absorption (λ_{max}) for the major classes of fluorophores. The color of the structure indicates its wavelength of maximum emission (λ_{em}). For clarity, only the fluorophoric moiety of some molecules is shown. Reproduced from Lavis, L. D.; Raines, R. T. *ACS Chem. Biol.* **2008**, *3*, 142–155, with permission from ACS Publications.

Another polycyclic aromatic compound is pyrene. Derivatives of pyrene (**9**) show $\lambda_{max}/\lambda_{em}$ of 340/376 nm, $\varepsilon = 4.3 \times 10^4\ M^{-1}\ cm^{-1}$, and $\varphi = 0.75$.[18,35] It has been shown that environmental sensitivity of this fluorophore can be used to detect the RNA folding.[36] Other polycyclic aromatic molecules such as anthracene, pyrelene, and their derivatives are also used to construct useful fluorescent tools both in water and organic solvent.[37–39]

The naturally occurring compound derivatives of coumarins represent a broad class of fluorophores. A common example is 7-hydroxy-4-methylcoumarin (i.e., 4-methylumbelliferone; 4-MU; **10**), which is derived by heteroatom substitution at position 7 of coumarin.

Other examples include the phenolate form of 4-MU, 7-amino-4-methylcoumarin (AMC; **11**), which exhibits fluorescence under basin condition (>pH 5).[18,40] On of the advantages of coumarins is its versatility due to the possibility of different substitution reactions, which offer to synthesize coumarin dyes with desirable chemical properties, such as higher solubility in aqueous solution and lower sensitivity to pH.[18,40–42] Coumarins are also useful for assembling enzyme substrates. Various derivatives of 7-hydroxycoumarin can be used to assay an assortment of hydrolases[43,44] and dealkylases.[45] Peptidyl derivatives of AMC are widely used to measure protease activity.[46]

Beyond the well-known tryptophan, the derivatives indole fluorophore Indo-1[47] is used as calcium indicator and another notable derivative 4′,6-diamidino-2- phenylindole (DAPI; **12**) is used for staining intracellular DNA.[48] Hoechst AG developed a dye Hoechst 33342 (**13**) very similar to DAPI and it is cell permeable and can be used in live cell for staining DNA.[49,50]

Fluorescein (**17**), the most widely utilized fluorophore in modern biochemical, biological, and medicinal research, is a heterocyclic compound and was first synthesized by Baeyer in 1871.[51] Fluorescein can exist in seven prototropic forms, the most fluorescent and biological relevant form of fluorescein is the dianion form with a λ_{max} of 490 nm, λ_{em} of 514 nm, extinction coefficient of $9.3 \times 10^4\ M^{-1}\ cm^{-1}$, and a quantum yield of 0.95.[15,18] The monoanion form is also used for biological purposes.[52]

The structure of fluorescein can be modified to tune the acid dissociation constant or pK_a values and to increase its photostability. One such example is 2′,7′-difluorofluorescein (i.e., Oregon green), it has fluorescein-like wavelengths, less basic (pK_a 4.6) than fluorescein, and has better photostability relative to fluorescein.[53]

Because of the pH-sensitive fluorescent properties, fluorescein was used as a pH sensor[54] and also used as an index to report on the status of fluorescein-labeled biomolecules.[52]

Another widely used fluorophore is Rhodamine, which is an isologue of fluorescein. Main advantages of this dye are its low pH sensitivity, better photostability, and tunable spectroscopic properties. Different N-alkyl substitution patterns on the rhodamine core can modify spectral characteristics. The most commonly used members in this family are rhodamine 110 (Rh110; **18**; λ_{max}= 496 nm, λ_{em}=517 nm, ε=$7.4 \times 10^4\ M^{-1}\ cm^{-1}$, and φ=0.92 in aqueous solution) and tetramethylrhodamine (TMR; **19**; $\lambda_{max}/\lambda_{em}$ of 540/565 nm, but a lower quantum yield $\varphi = 0.68$).[8,55,56] Rhodamine labels are very useful for FRET-based experiments along with fluorescein derivatives due to efficient energy transfer between these xanthene compounds.[18]

Some important features such as the insensitivity of the spectral properties to the environment, the small Stokes shift, and the overall lipophilicity make the boron difluoride dipyrromethene (BODIPY) dye and its derivatives very useful fluorescent labels and other probes.[18,57,58] The base-sensitive core structure of BODIPY is the main drawback of this dye for its application particularly in solid phase peptide synthesis.[59] The mostly used form BODIPY **24** shows fluorescein-like parameters with $\lambda_{max} = 505$ nm, $\lambda_{em} = 511$ nm, $\varepsilon = 9.1 \times 10^4\ M^{-1}\ cm^{-1}$, and $\varphi = 0.94$ and is commonly called BODIPY-FL.[8,18]

Here we have discussed some of the important small molecule fluorescent dyes and there are also some other important dyes such as cyanine, phthalocyanine, and oxazine dye families which also have important applications in biology. These well known small-molecule fluorophores have a wide range of spectral and chemical properties. Elaboration of these core structures has provided numerous probes for assaying biological systems. Nonetheless, extraordinary opportunities remain, because to deliver deeper insight into complex biochemical and biological phenomena will require ever more sophisticated and tailored probes.

3.327.2.4. FRET-Based Sensing

3.327.2.4.1. Introduction

The applications of Förster or fluorescence resonance energy transfer (FRET) have been extensively studied in the last 25 years,[60–69] but only with recent technical advances has it become feasible to apply FRET to biomedical research.[70–83] In this section, we describe the general principles of FRET microscopy and provide a brief overview of its potential application in the biomedical field. There are various excellent reviews about FRET that can be suggested for further readings; these reviews also provide many of the earlier references.[61,66,67,69,84–94]

FRET is unique in generating fluorescence signals sensitive to molecular conformation, association, and separation in the 1−10 nm range. Thus, FRET is capable of resolving molecular interactions and conformations with a spatial resolution far exceeding the inherent diffraction limit (~λ/2) of conventional optical microscopy, yet is also compatible with super-resolution techniques.

The FRET mechanism involves a donor fluorophore in an excited electronic state, which may transfer its excitation energy to a nearby acceptor chromophore in a nonradiative fashion through long-range dipole–dipole interactions. The theory supporting energy transfer is based on the concept of treating an excited fluorophore as an oscillating dipole that can undergo an energy exchange with a second dipole having a similar resonance frequency. In this regard, resonance energy transfer is analogous to the behavior of coupled oscillators, such as a pair of tuning forks vibrating at the same frequency. In contrast, radiative energy transfer requires emission and reabsorption of a photon and depends on the physical dimensions and optical properties of the specimen, as well as the geometry of the container and the wavefront pathways. Unlike radiative mechanisms, resonance energy transfer can yield a significant amount of structural information concerning the donor–acceptor pair.

3.327.2.4.2. Principle of FRET

In the process of FRET, initially a donor fluorophore absorbs the energy due to the excitation by incident light and transfer the excitation energy to a nearby chromophore, the acceptor.

$$D + h\upsilon \rightarrow D^*$$

$$D^* + A \rightarrow D + A^*[D \rightarrow \text{donor}, A \rightarrow \text{Acceptor}]$$

$$A^* \rightarrow A + h\upsilon'$$

Energy transfer results in decrease or quenching of the donor fluorescence and a reduction of excited state lifetime accompanied also by an increase in acceptor fluorescence intensity.

FRET is a quantum mechanical process in which direct radiationless transfer of energy from a donor (D) to an acceptor (A) molecule occurs.

For FRET to occur between a donor and acceptor, the following four conditions must be fulfilled: (i) there must be an overlap between fluorescence emission spectrum of the donor molecule and the absorption or excitation spectrum of the acceptor chromophore (Figure 3). The degree of overlap is expressed by overlap integral (J). (ii) In order to fulfill the above condition the two fluorophore molecules (donor and acceptor) must be in the close proximity to one another (typically 1–10 nm). (iii) The donor emission dipole moment and the acceptor absorption dipole moment must be approximately parallel to each other. (iv) The fluorescence lifetime of the donor molecule must be of sufficient duration to allow the FRET to occur.

The extent of resonance energy transfer is determined by the distance between the donor and acceptor and the extent of spectral overlap. For convenience the spectral overlap is described as in terms of the Förster distance, R_0, which is defined as the distance at which the resonance energy transfer (RET) is 50% efficient (Figure 4). The rate of energy transfer between the donor–acceptor pair, $k_T(r)$ is given by:

$$k_T(r) = \frac{1}{\tau_D}\left(\frac{R_0}{r}\right)^6$$

where r is the distance between the donor and the acceptor, and τ_D is the lifetime of the donor in the absence of energy transfer. Hence the rate of transfer is equal to the decay rate of the donor in the absence of the acceptor. At the Förster distance, the donor emission would be decreased to one-half of its intensity in the absence of acceptor. The efficiency of energy transfer for a single donor–acceptor pair at a fixed distance is

$$E = R_0^6/\left(R_0^6 + r^6\right)$$

The Förster radius (R_0) depends on the fluorescence quantum yield of the donor in the absence of acceptor (f_d), the refractive index of the solution (η), the dipole angular orientation of each molecule (K_2), and the spectral overlap integral of the donor–acceptor pair (J) and is given by

$$R_0 = 9.78 \times 10^3\left(\eta^{-4} f_d J\right)^{1/6} A^0$$

In summary, the FRET rate depends upon the extent of spectral overlap between the donor–acceptor pair, the quantum yield of the donor, the relative orientation of the donor–acceptor transition dipole moments, and the distance separating the donor–acceptor chromophore. Any event or process that affects the distance between the donor–acceptor pair will affect the FRET rate, consequently allowing the phenomenon to be quantified, provided that the artifacts can be controlled or eliminated. As a result, FRET is often referred to as a 'spectroscopic/molecular ruler,' for example, to measure the distance between two active sites on a protein that have been labeled with suitable donor–acceptor chromophores, and therefore to monitor the conformational changes through the amount of FRET between the fluorophores.

3.327.2.4.3. Detection

The detection and quantitation of FRET can be made in a number of different ways. Simply the phenomenon can be

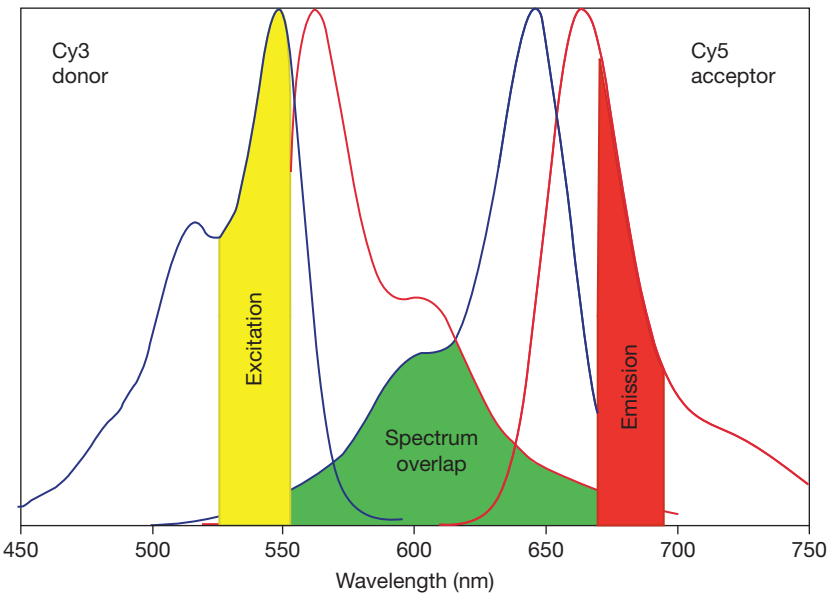

Figure 3 Schematic representation of the spectral overlap integral.

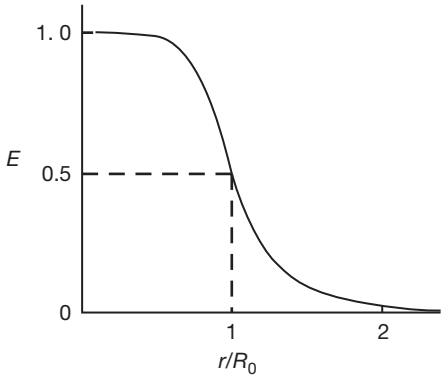

Figure 4 The dependence of the efficiency of energy transfer as a function of distance between fluorophores.

observed by exciting a specimen containing both the donor and acceptor molecules with light emitted at wavelengths centered near the emission maximum of the acceptor. Because FRET can result in both a decrease in fluorescence of the donor molecule as well as an increase in fluorescence of the acceptor, a ratio metric determination of the two signals can be made.

These ratiometric approaches give the true FRET efficiency, which quantifies the fraction of excited donor molecules whose energy is transferred to an acceptor molecule via resonance. The advantage of this method is that a measure of interaction can be made that is independent of the absolute concentration of the sensor. Because not all acceptor moieties are fluorescent, they can be used as a means to quench fluorescence. In these instances, those interactions that result in a fluorescent donor molecule coming in close proximity to such a molecule would result in a loss of signal. Inversely, reactions that remove the proximity of a fluorescent donor to a quencher molecule would result in an increase in fluorescence. One such example involves protease assays. These assays usually involve a fluorescent moiety on one terminus and a quenching molecule on the other terminus separated by a peptide containing the protease cleavage sequence.

3.327.2.4.4. Applications of FRET

The strong distance-dependence of the FRET efficiency has been widely utilized in studying the structure and dynamics of proteins and nucleic acids, in the detection and visualization of intermolecular association, and in the development of intermolecular binding assays.[95]

FRET is a particularly useful tool in molecular biology as the fraction, or efficiency, of energy that is transferred can be measured[94] and depends on the distance between the two fluorophores. The distance over which energy can be transferred is dependent on the spectral characteristics of the fluorophores, but is generally in the range 10–100 nm. Thus, if fluorophores can be attached to known sites within molecules, measurement of the efficiency of energy transfer provides an ideal probe of inter- or intramolecular distances over macromolecular length scales. Indeed, fluorophores used for this purpose are often called 'probes.' Techniques for measuring FRET are becoming more sophisticated and accurate, making them suitable for a range of applications.[94] FRET has been used for measuring the structure,[96–98] conformational changes,[99] and interactions between molecules,[100,101] and as a powerful indicator of biochemical events.[102] Further applications can be found in the reviews of Van der Meer *et al.*,[66] Lakowicz,[62] or Selvin.[103] Although the challenges of labeling molecules with fluorophores and making accurate measurements of the fluorescence emitted by them are being overcome, a number of difficulties still remain when examining real-life systems.

3.327.2.4.5. Problems associated with FRET

When designing FRET experiments, there are a number of issues that need to be considered. The most obvious and important issue is the matter of close proximity of donor and acceptor molecules. Depending on the assay design, close proximity will either be established or removed during the assay, resulting in a change in signal that can be measured. Appropriate donor–acceptor pairs need to be selected. There should be enough spectral overlap for pairs in order to ensure efficient energy transfer along with enough difference in spectra as to be distinguishable from one another. The most common problem is the detection of spectral overlap of donor spectral bleed-through signal in the acceptor channel. The spectral bleed-through results from a combination of both the acceptor fluorophore excited by the donor excitation light, plus the donor emission detected in the acceptor channel. As a result, one would get a high and variable background signal from which a weak FRET-based acceptor emission must be extracted. In addition, it is important to implement correction for the concentration or expression level of the fluorophore labeled to the proteins. These corrective measures would improve the accuracy in the calculation of the distance between the proteins involved in energy transfer. Moreover, there are other problems encountered in FRET microscopy imaging such as autofluorescence, detector, and optical noise, photobleaching, and spectral bleed-through signal. It is important to implement the correction in order to quantitate the FRET signal or in calculating the distance between the two proteins.[81,104]

3.327.2.5. Nanoplatforms-Based Fluorescent Probes

3.327.2.5.1. Introduction

There is a growing interest in the development of optochemical sensing devices that sense down to the submicron scale. This interest arises because in order to decrease typical response time down to the millisecond time scale, miniaturization of the sensors to nano-dimensions is the only option. With nanometer dimensions, the penetration volume is reduced to a few cubic micrometers and the sensors exhibit a spatial resolution at the nanometer scale. Nanoparticle sensors have been successfully applied to noninvasive real-time measurements of analytes, fields in cells and in rodents, with excellent spatial, temporal, physical, and chemical resolution.

This section covers major developments in the area of fluorescence-based nanosensors over the last decade; here we will only describe the fabrication and application of particle-based nanosensors for intracellular analysis. Nanoparticles-based sensors encompass a vast area of research, as a result of which we limit ourselves to two well-defined concepts that clearly illustrate the principles involved. Thus, we will describe probes encapsulated by biologically localized embedding (PEBBLE), and molecular beacons (MBs).

3.327.2.5.2. Probe embedded by biologically localized encapsulation

Fluorescent molecular probes have played a major role in intracellular sensing and imaging.[18,105–107] The fast response time, intense signal against relatively low background noise, and relatively simple instrumentation have made the molecular-probe-based fluorescence technique an ideal platform for real-time measurements in cells. Still, molecular probes suffer from several limitations that affect the reliability of the intracellular measurements.[108,109] The cell impermeability of probe molecules often requires proper derivatization of the molecules whereby their function might be affected. Other common problems are the cytotoxicity of available dyes or the chemical interference of the molecules with the cell's internal processes. Intracellular measurements are often skewed by sequestration to specific organelles inside the cell or by nonspecific binding to proteins and other cell components. Furthermore, the dye is usually not ratiometric (i.e., it has only a single spectral peak), which requires technologically more demanding techniques, such as picoseconds lifetime resolution and phase-sensitive detection, to be implemented. We have to keep in mind that merely loading a separate reference dye into the cell for ratiometric measurements will not solve the above problem because of the aforementioned sequestration and nonspecific binding.

The aforementioned drawbacks become more severe in the case of *in vivo* applications. Only a very few of the molecular probes can reach a specific location of interest within the body, which is also a challenge for other systems such as drug delivery. This is also true for crossing biological barriers, such as the blood–brain barrier. Moreover, for *in vivo* optical methods, photons can only penetrate tissue to a limited depth. For deep-tissue imaging (millimeters to centimeters), one must use near-infrared (NIR) light in the spectral range of 650–900 nm, which is separated from the major absorption peaks of blood and water.[110–112] The biggest advantage of NIR region is that it is free from autofluorescence of cellular components and therefore can be used for intracellular measurements. Note that most of the currently available molecular probes have visible absorption/emission wavelengths. Nanoparticle probes can be easily tailored for the NIR spectral range.

Advances in nanotechnology have made many types of nanoparticles available as platforms for constructing new types of bioanalytical sensors. The nanoparticles range from 1 to 1000 nm in size, thus causing minimal physical interference to cells. For example, a single spherical nanoparticle measuring 500 nm in diameter is at least four orders of magnitude smaller in volume than is a typical mammalian cell,[113] and a 20-nm particle is eight orders of magnitude smaller. Because of the nontoxic properties of most of the nanoparticle matrices the nanoparticles do not cause chemical interference to cells. Moreover, the nanoparticles can be delivered into cells or animals via standard delivery methods.

3.327.2.5.2.1. Design and synthesis

PEBBLE is a generic term to describe nanofabrication techniques that utilize biologically inert polymers to manufacture nanometer-sized spherical optical sensing devices capable of *in vitro* measurements. PEBBLEs are specifically designed to be minimally invasive, facilitating analyte monitoring in viable single cells or cell cultures without perturbing normal cellular functions. PEBBLEs use the same highly selective fluorescent probes normally used in biological monitoring.

For example, probes such as the Alexa Fluor® series of dyes or Oregon Green are often used as reference dyes, paired with an active fluorescent probe for analyte recognition such as fluo-4 for calcium or Ru[dpp($SO_3Na)_2$]$_3$[ruthenium(II) tris (4,7-diphenyl-1,10-phenanthroline disulfonic acid) disodium salt] for oxygen. The paired probes are encased in a permeable biologically inert matrix, which can be thought of as a sensing platform. The reference fluorophore is chosen specifically to complement the analyte-sensitive probe to ensure that ratiometric analysis can be achieved in either the excitation or emission modes.

The sensing mechanism involves two important steps: permeation of analytes into the nanoparticle matrix; the selective interaction of analytes with sensing components, which results in signal changes. The important properties of sensors, such as sensitivity, dynamic range, selectivity, reversibility, and stability, depend mostly on the incorporated sensing components. However, the nanoparticle matrix also plays an important role: The properties of the matrix, such as pore size, hydrophobicity, and charge, determine the permeability and solubility of the analytes as well as the loading efficiency of the sensing probes.[109] For example, polyacrylamide (PAA) nanoparticles have served as good matrices for ion sensors[114–118] due to their neutral and hydrophilic nature, whereas hydrophobic nanoparticle matrices are better suited for oxygen sensors.[119–121] A wide variety of nanoparticle matrices have been used as sensor platforms, including polymer nanoparticles made of organic, inorganic, or organic–inorganic hybrid materials; polymer-capped liposomes or micelles; semiconductor nanoparticles; and metallic (metal or metal-shell) nanoparticles. The pores of the nanoparticle matrix are sufficiently large to allow diffusion of the smaller analyte ions or molecules (so that the matrix can bind with the molecular probes located inside the nanoparticle), but the pores are still small enough to exclude the diffusion of larger proteins into the core matrix. This exclusion of macromolecules is quite significant because many 'naked-molecule' dyes change their fluorescence properties in the presence of proteins. However, the nanoparticle sensors containing these same dyes are not affected by the presence of proteins.[114,116,120,122]

The sensing components of a nanoparticle typically include indicator and reference dyes or a combination of reporter dyes and analyte-specific ligands/biological receptors. Loading of the sensing components into the nanoparticles is performed either during synthesis or after the formation of the nanoparticles by encapsulation, covalent linkage, bioaffinity interaction such as that between streptavidin and biotin, or physical adsorption through charge–charge or hydrophobic interaction. The covalent linkage is typically made via simple coupling reactions between the nanoparticle functionalized with amine, carboxyl, or thiol groups and the molecules containing similar functional groups. Biological molecules such as antibodies, DNAs, and peptides have been used as receptors because of their highly selective biological interactions. These biomolecular receptors have also been utilized as targeting moieties, enabling nanoparticles to perform real-time tracking of target biomolecules in cells[123] as well as tumor-targeted delivery of drugs or

image-contrast agents in rodents.[124,125] If targeting moieties are added to nanoparticle sensors, the sensors can even detect specific analytes in a spatially localized target area.[126]

3.327.2.5.2.2. Biological applications

3.327.2.5.2.2.1. Ion sensors Most of the nanoparticle sensors in this category are polymer-based PEBBLEs sensors. Nanoparticle sensors based on this design comprise the fluorescent indicator and reference dyes are loaded into the polymeric nanoparticle core or its surface-coated layer, and there is no interaction between the dyes (**Figure 5(a)**). For example, Almdal *et al.* and Brown *et al.* synthesize a pH nanoparticle sensor using a PAA nanoparticle with covalent linked dyes,[127] and a K^+ nanoparticle sensor was made by loading the sensing dye into the surface-coated layer polyelectrolytes instead of into the nanoparticle itself.[128] PEBBLE sensors have also made successful intracellular measurements for pH, Mg^{2+}, and Ca^{2+}.[114,115,129,130]

3.327.2.5.2.2.2. Dissolved oxygen sensors The first nanoparticle sensor for dissolved oxygen was the silica-based PEBBLE sensor, which was prepared by embedding $[Ru(dpp)3]^{2+}$ (a ruthenium oxygen indicator dye) and reference dyes into silica nanoparticles.[121] The sensor successfully imaged intracellular oxygen in live C6 glioma cells. Oxygen PEBBLE sensors with enhanced sensitivity and dynamic range were developed embedding the more sensitive platinum-based oxygen dyes, as well as reference dyes, into a hydrophobic matrix such as organically modified silica (ormosil)[119] or polydecylmethacrylate (PDMA).[120] Oxygen sensors have also been created by embedding ruthenium dyes into the polyelectrolyte layers on commercial fluorescent nanoparticle surfaces[131] or into polymerized phospholipid vesicles (liposomes).[132] However, the sensitivities of these sensors were only 60% for polyelectrolyte-coated nanoparticle sensors and 76% for polymerized liposome sensors. The different types of sensors used for dissolved oxygen species are summarized in **Table 1**.

3.327.2.5.2.2.3. Reactive oxygen species sensors Ratiometric PEBBLE sensors were developed for reactive oxygen species (ROS), singlet oxygen, H_2O_2, and hydroxyl radical using irreversible molecular probes. A singlet oxygen PEBBLE sensor was prepared by incorporating the singlet oxygen-sensitive 9,10-dimethyl anthracene or the singlet oxygen-insensitive octaethylporphine into ormosil nanoparticles.[133] The nanoparticle matrix enhances the selectivity of the indicator dye to singlet oxygen by blocking the entry of short-lived polar ROS such as OH and superoxide radicals. These nanoprobes have been used to monitor the singlet oxygen produced by dynamic nanoplatforms, which were developed for photodynamic therapy (PDT).[124] Another singlet oxygen PEBBLE sensor was constructed with ormosil nanoparticles incorporating 1,3-diphenylisobenzofuran (DPIBF). The intracellular concentration of singlet oxygen within C6 glioma cells during PDT was measured with the DPIBF sensors.[134] A PEBBLE sensor for H_2O_2 was prepared by embedding 2′,7′-dichlorofluorescin diacetate into ormosil nanoparticles. The PEBBLE sensors successfully detected H_2O_2 within a macrophage at a low-nanomolar concentration.[134,135]

A PEBBLE sensor for detecting the OH radical was created by covalently attaching the hydroxyl indicator dye, coumarin-3-carboxylic acid, onto the PAA nanoparticle surface while encapsulating the reference dye deep within the sensor.[136]

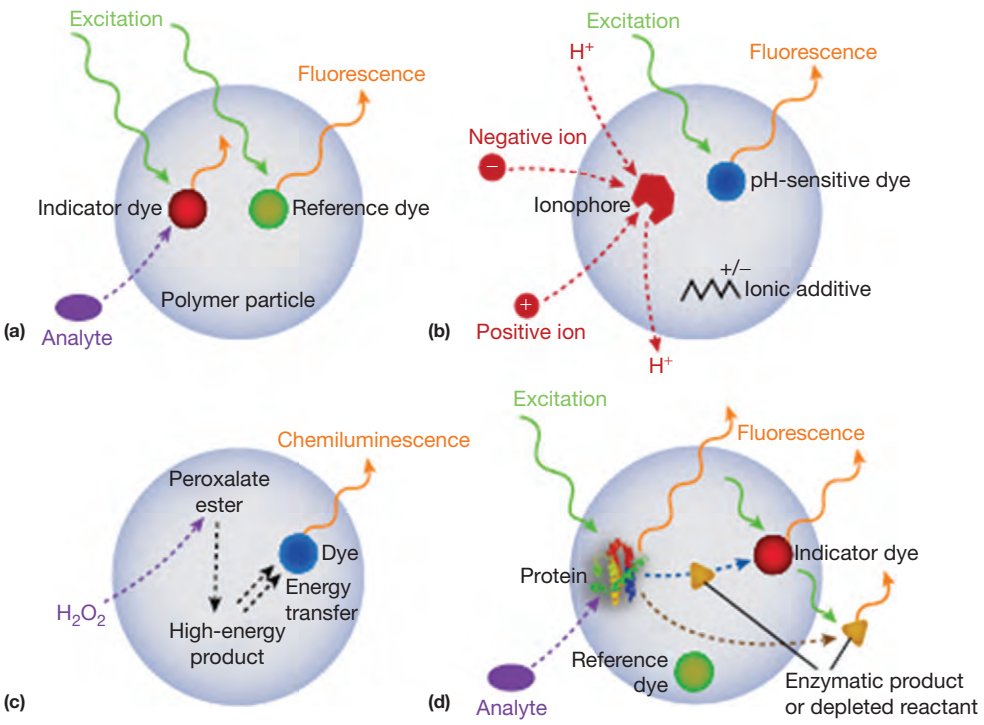

Figure 5 Schematic diagrams of various designs of luminescent nanoparticle sensors. (a) Polymer nanoparticle sensor with fluorescent indicator dyes. (b) Ion-correlation nanoparticle sensor. (c) Chemiluminescence nanoparticle sensor. (d) Polymer nanoparticle sensor with encapsulated protein. Reproduced from Koo Lee, Y.-E.; Smith, R.; Kopelman, R. *Annu. Rev. Anal. Chem.* **2009**, *2*, 57–76, with permission from ACS Publications.

Table 1 The list of different types of sensors used to detect dissolved oxygen species

Matrix	*Size*	*Oxygen indicator*	*Optical signal*	*QDO (%)*	*Reference(s)*
Silica	20–300 nm	Ru(II)-tris(4,7-diphenyl-1, 10-phenanthroline) dichloride	Fluorescence intensity Fluorescence ansotropy	80 N/A	49 43
Ormosil	120 nm	Pt(II) octaethylporphine ketone	Fluorescence intensity	97	10 xxx
Ormosil	120 nm	Pt(II) octaethylporphine	Fluorescence intensity	97	10
PDMA	150–250 nm	Pt(II) octaethylporphine ketone	Fluorescence intensity	97.5	42
Commercial fluorophore coated with polyelectrolyte layers	100 nm	Ru(II)-tris(4,7-diphenyl-1, 10-phenanthroline) dichloride	Fluorescence intensity	60	50
Polymerized liposome	150 nm	Ru(II)-tris(4,7-diphenyl-1, 10-phenanthroline) dichloride	Fluorescence intensity	76	51
Polystyrene	300 nm to 1 μm	Pt(II)-tetra-pentafluorophenyl-porphyrin	Fluorescence lifetime	N/A	52,53

Source: Koo Lee, Y.-E.; Smith, R.; Kopelman, R. *Annu. Rev. Anal. Chem.* **2009**, *2*, 57–76.

This design circumvents two potential problems posed by the hydroxyl radical, the most reactive ROS: (a) its inability to penetrate significantly into any matrix without being destroyed and (b) its ability to oxidize (and photobleach) most potential reference dyes. This nanoprobe demonstrated a proof of principle of a ratiometric hydroxyl radical probe and showed good sensitivity and reversibility.

3.327.2.5.2.2.4. Electric field sensors The E-PEBBLE, a nanosensor designed to measure electric fields, was fabricated by encasing the fast-response, voltage-sensitive fluorescent dye di-4-ANEPPS inside silane-capped (polymerized) micelles.[137] The hydrophobic core of the micelle provides a uniform environment for the molecules and thus allows for universal calibration. It also allows for fast orientation of these dye molecules, which shortens the response time. The E-PEBBLEs were introduced into immortalized astrocyte cells (DITNC) by endocytosis, and – for the first time – enabled complete three-dimensional electric-field profiling throughout the entire volume of living cells (not merely inside membranes)

3.327.2.5.2.2.5. Chemiluminescence sensors Chemiluminescence has been utilized to design sensors for H_2O_2 (**Figure 5(c)**).[138] Such sensors are made of peroxalate ester nanoparticles and encapsulated fluorescent dyes. The sensing mechanism occurs as follows: H_2O_2 reacts with the peroxalate ester groups, generating a high-energy dioxetanedione that then chemically excites encapsulated fluorescent dyes, leading to chemiluminescence. These sensors have nanomolar sensitivity and excellent specificity (over other ROS) for H_2O_2. The chemiluminescence wavelength can be tuned by changing the encapsulated fluorescent dyes. In one study,[138] peroxalate particles containing perylene, rubrene, and pentacene emitted light at wavelengths of 460, 560, and 630 nm, respectively. The nanoparticle sensors with encapsulated pentacene were applied for *in vivo* imaging of H_2O_2 and were externally injected as well as endogenously produced in the peritoneal cavity of mice during lipopolysaccharide-induced inflammatory response.[138]

3.327.2.5.2.2.6. Sensors with encapsulated proteins Two types of nanosensors operating on different sensing mechanisms have been developed using an encapsulated-protein design (**Figure 5(d)**). The first type incorporates an encapsulated protein that behaves as a fluorescent molecular probe. Nanoparticle sensors for copper and phosphate ions are two examples. The $Cu^{+/2+}$ sensor was constructed by incorporating DsRed, red fluorescent protein, and a reference dye into PAA nanoparticles.[117] The detection range for Cu^{+} and Cu^{2+} was 0.2–5 μM. The phosphate sensor was made of PAA nanoparticles and embedded fluorescent phosphate-sensing proteins and had a micromolar detection range.[139] In the second type of sensor, the encapsulated protein is an enzyme that catalyzes the reaction involved with analytes. The enzymatic reaction leads to a change in fluorescence, either by fluorescence product or by coembedded fluorescent indicator dye for depleted reactant. Examples include a glucose sensor and two H_2O_2 sensors.[140–142]

PEBBLE technology is defining a new type of ionic nanoprobe designed specifically for intracellular applications. Single-cell analysis can diagnose disease at an early stage, when tissue-level changes are not yet evident but chemical changes within cells are observable.[143] Obtaining chemical or physical information from a single cell or a specific location within a single cell is an important future application of nanoparticle sensors. The PEBBLE sensors are reversible and dye leaching is limited for the relevant experimental time scales, that is, the lifetime of a cell on a microscope stage. Several PEBBLEs have been optimized for ionic measurements, including PEBBLEs optimized for hydrogen, calcium, potassium, sodium, magnesium, zinc, copper, and chloride ions. By marrying emerging technologies with ion-sensing PEBBLEs (i.e., MOONs, optical tweezing, and targeting), one can enhance signal and/or direct placement of the PEBBLE within the cell for localized ion sensing.

3.327.2.5.3. Molecular beacons

With the continued advances in gene and protein function studies, the need for high-sensitivity, high-affinity molecular biological probes for qualitative and quantitative detection, is increasingly pressing. The methods available for genetic analysis have expanded enormously, mainly because the genetic data thus generated is being utilized not only by biologists but also by the scientific communities such as statisticians (to explore the population genomics) and computational chemists. Over the last decade, there is increasing evidence to suggest that RNA molecules have a wide range of functions in living cells, from physically conveying and interpreting genetic information through essential catalytic roles and providing structural support for molecular machines to gene silencing. These functions are realized through control of their expression level, turnover rates, and through their spatial distribution.

The ability to image specific RNAs in living cells in real-time promises to provide information on RNA synthesis, processing, transport, and localization; this information should offer new opportunities for advancement in molecular biology, disease pathogenesis, drug discovery, and medical diagnostics.

Accurately imaging endogenous or nonengineered RNA in live cells is not an easy task. In the early days, fluorescent methods of DNA analysis were highly dependent on fluorescent dyes that could complex the duplex DNA by means of noncovalent forces. Then, nucleoside building blocks containing different kinds of fluorophores (covalently linked) were used exclusively. Later on, especially in the post-genomic era, sequence-specific complementary binding of short synthetic oligonucleotides containing fluorescent tags have been used in DNA analysis.

MB technology is set up based on FRET and the complementary pairing principles. These fluorescent molecular probes, which are very highly specific and sensitive, have now become one important tool in medical and biological researches. In this section, we will discuss the MB's structure, principle and its application in imaging RNA inside living cells. For additional reading on yet other aspects of MBs, one can consult various other publications.[144–148]

3.327.2.5.3.1. Structure and principle of operation

MB is a fluorescent-labeled oligonucleotide chain, typically has 25–35 nucleotides, and is constructed by three parts: the loop portion, the stem portion, and the fluorescence groups.[149] The loop is generally constructed by 15–30 nucleotides and specifically binds with target molecules. The stem portion comprises 5–8 base pairs. During the binding process of the MBs with target molecules, this portion is reversibly dissociated. Thermodynamic analysis of hybridization of linear and stem-loop (MB) DNA probes demonstrated significantly higher specificity than the conventional linear probe. Finally, the fluorescence groups connected to 5′ end and quenching groups in 3′ end (Figure 6).

Fluorophore/quencher pairs, the signaling elements, produce the on/off signals depending on the conformational state of MBs. When a donor fluorophore is in its excited state, the energy is transferred via a nonradiative long-range dipole–dipole coupling mechanism to an acceptor quencher in close proximity (typically <10 nm), known as FRET, which we have already discussed in detail. On the contrary, the fluorescence signal is freely produced when the quencher is in far distance. Stems made of four to seven base pairs function as lockers to maintain the closed hairpin structures and bring a quencher nearby a fluorophore in a few nanometers' distance without hybridization to the complementary targets. Thus, the quencher turns off fluorescence with high quenching efficiency via FRET. Loops are recognizing elements that, upon hybridization to their complementary targets, induce a conformational change in MBs. This change increases the physical distance between the fluorophore and the quencher, resulting in fluorescence. The unique on/off signal mechanism has been very useful in the field of detecting DNA and RNA targets.

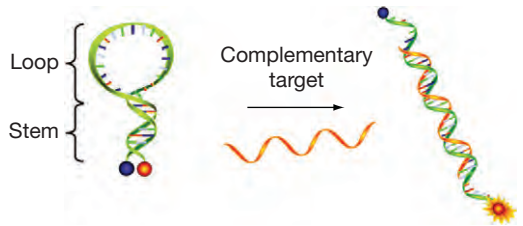

Figure 6 Diagram of an MB in a hybridized and unhybridized state. While the MB remains in free form without its target, it forms hairpin structure with quenched fluorescence. Once it binds to its target, the fluorophore restores the fluorescence signal due to the far distance from the quencher. Adapted from Kim, Y.; Sohn, D.; Tan, W. *Int. J. Clin. Exp. Pathol.* **2008**, *1*, 105–116, with permission from IJCEP.

The conventional MB, which was first designed and developed by Tyagi and coworkers, produces fluorescence without having to separate probe–target hybrids from excess probes in hybridization assays.[149,150] The unique hairpin structure and signaling mechanism endow the MBs with several advantages. First of all, the light-up signaling mechanism allows MBs to perform highly sensitive detection and monitoring of nucleic acids in real time. The unbound MBs stay with quenched fluorescence. Only hybridized MBs, whose amount is proportional to that of the target can produce a high fluorescence signal. Such a detection-without-separation property is particularly useful in situations where it is either impossible or undesirable to extract the probe–target hybrids from an excess of the unbound probes. Another advantage of MBs is their relatively high signal-to-background ratio, providing higher sensitivity of detection. Upon hybridization to its target, a well-designed MB can generate as high as 200-fold fluorescence enhancement under optimal conditions.[150] This provides the MBs with a significant advantage over other fluorescent probes in ultra-sensitive analysis. In addition to its sensitivity, MBs offer excellent selectivity. They are extraordinarily target-specific, and are able to differentiate as low as single-mismatched base pair sequences. The selectivity of MBs is a direct result of their hairpin conformation, as the stem hybrid acts as an activation energy barrier to the loop–target hybrid. The remarkable selectivity provided by the hairpin conformations has been demonstrated in a variety of biological environments where a number of different nucleic acid sequences and enormous amount of non-targets are present.

Due to these unique features in sensitivity and selectivity, the applications of MBs have been explored in many research fields since they were first created in 1996. The conventional MB introduced in the mid 1990s was modified by a number of research groups to improve its function, resulting in a range of modified MBs with varied designs, fluorophores, and quenchers. Some of the important changes are depicted in Figure 7. The functions considered for improvement include eliminating false signals, increasing specificity of the MB toward the target, and enhanced detection limit. It is reported that the background fluorescence intensity could be reduced significantly by using super quenchers (SQs) in place of normal quenchers (**2**; Figure 7).[151] An array of three quencher molecules is assembled at molecular level to produce SQs with a quenching efficiency of 99.7% and the signal to background ratio is also enhanced significantly. It has been shown that the original design constraint of a nucleobasepaired stem is not compulsory. Such 'stemless beacons' (**3**; Figure 7) possess sufficient signal-to-noise (S/N) ratio for some *in vivo* applications.[152]

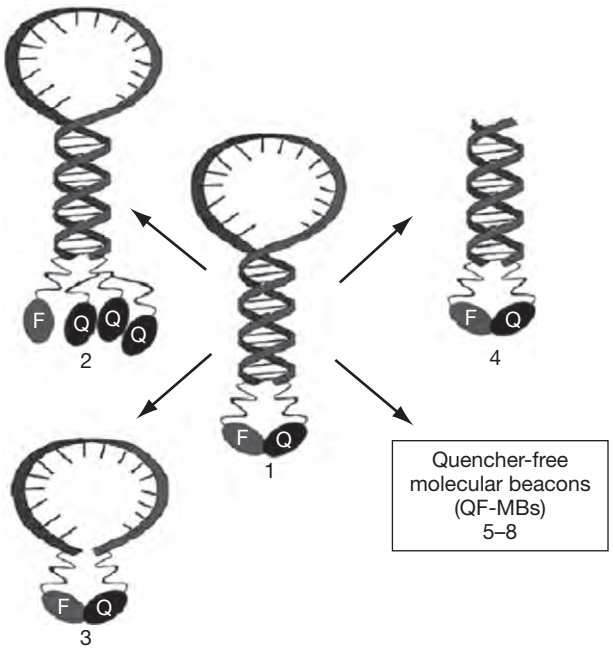

Figure 7 Modification of conventional MB. Adapted from Venkatesan N.; Seo, Y. J.; Kim, B. H. *Chem. Soc. Rev.* **2008**, *37*, 648–663, with permission from Royal Society of Chemistry.

Similar to conventional MB, the quenching of fluorophore in stemless beacon occurs through FRET. Hence, for better activity, the fluorophore and quencher should be chosen in such a way that there is maximum spectral overlap.[153]

3.327.2.5.3.2. Biomedical application

In recent years, real-time intracellular monitoring of gene expression has been developed rapidly. Many scientists used MB technology to detect gene, and achieved some initial results, such as detecting liquid phase hybridization,[154] effectively reducing cross-contamination of nucleic acids[155] and real-time nuclear acid detection.[156,157] Because of the high specificity and sensitivity,[158] it has been increasingly applied in large-scale automated detection[159] and even dynamic detection of nucleic acid *in vivo*.[160]

One of the initial applications of MB technology was to analyze concentration of target by real-time quantitative PCR.[161] On the basis of conventional PCR, corresponding MB probes were added. In every cycle of the PCR process, MBs combined with amplified products, fluorescence, and quenching groups separated and fired fluorescent, but it did not affect the accumulation of PCR products index. Only the DNA template which can combine with MBs can produce fluorescence signal during amplification. Therefore, the fluorescence intensity is proportional to the amount of specific amplification products, and it is the direct markers of template amplified by PCR. Compared with conventional methods, containing of the operation effectively eliminated the cross-contamination of DNA. It is real-time, quantitative, highly sensitive, and highly specific.

Currently, there are many methods used for the detection of mutation, SNP, allele, and multiple ingredients, but only those methods based on the real-time PCR are very effective. Compared with the linear oligonucleotide probes, stem-loop structure MBs have higher specificity. Even a single-base mismatch of target sequences or insertion mutations can be detected. Hence the real-time PCR system along with multicolor MB provides accurate determination of gene mutation, SNP, allele, multiple ingredients.[159,162–164]

Unlike RNA, DNA is the double helix structure and it is very difficult to detect with conventional methods. Peptide nucleic acid (PNA) combines double-stranded DNA complementarily and noncomplementary strand can be replaced and dissociated into single-chain, known as P-loop structure.[165] Dissociated double-stranded DNA can combine with the MBs to give fluorescence. Because of the advantages of MB for the analysis of nucleic acid, it can be used as the DNA probe as biochips and biosensors. This has been achieved with MBs marked with different fluorescent molecules in the form of bioepiderm and fixed to the surface of silicon wafers and used as the MB chips. Typical advantages of MB chips over the other types of DNA chips are low fluorescence background, obligated to remove redundant probes, and can be used multiple times.[166]

One of the marked achievements of MB technology is the dynamic analysis of the process of biological macromolecules metabolism *in vivo*. MBs are successfully employed for dynamic analysis of mRNA transcription process and other changes inside the cells. Perlette *et al*. designed and synthesized an MB specific for β-actin mRNA and microinjected it into the cytoplasm of single living kangaroo rat kidney cells (PtK2 cells). The results showed that MBs can be used for effective and real-time detection of RNA in living cells and understanding the process of RNA/DNA hybridization.[167] Matsuo studied intracellular bFGFmRNA metabolism with MBs.[168] They designed and synthesized MBs of complementary analyte target mRNA sequence and control MBs, respectively, and intake by the cells with liposomes. Using laser scanning confocal microscope or fluorescence microscopy, the results showed that the fluorescence of experimental group cells was much higher than that of control cells. Extended incubation time, fluorescence of the control group would be gradually enhanced. MBs can be hydrolyzed by nucleases and thus emit fluorescence. PNA MBs can effectively avoid being hydrolyzed by DNA enzyme, so that the fluorescence intensity can accurately reflect the metabolism of mRNA *in vivo*.

With the completion of the human genome project, the research interest has shifted focus on utilizing the genetic information for prediction and discovery. Since its inception, because of the high specificity and sensitivity characteristics, MB technology has been quickly adopted in biology, basic medicine, clinical medicine, and other related researches. Their unique property of detection without separation makes them even more attractive in the research areas where the purification step is almost impossible to perform or a major cause of low signal to background ratio. Their great sensitivity due to the excellent quenching efficiency is always advantageous. As a result, a number of nucleic acid-probing systems with close resemblance to the MBs are being reported from time to time. Used with nanotechnology, laser scanning confocal technology and other advanced technology, it will certainly promote the MB technology amendment. With the

development of MB technology and emergence of new MBs, MBs will definitely be applied in gene diagnosis, gene therapy, and new drug researches wider and wider.

3.327.3. Optical-Label-Free Intracellular Probes

3.327.3.1. Surface Plasmon Resonance-Based Probes

One of the main advantages in using optical microscopy for biological imaging is that optical microscopes allow us to observe a sample in living conditions. Another advantage of optical microscopy is that the spectrum of the signal light provides a multitude of information regarding the material in the sample. This allows us to investigate biological molecules in cells and tissues without chemical labeling. The concept of surface plasmons (SPs) traces back to the 1960s and observable phenomena have been known since the beginning of the twentieth century. An SP is a charge density oscillation (transverse magnetic electromagnetic wave) that can exist at the interface between a free electron metal and a dielectric layer.[169–172] Surface plasmon resonance (SPR) is a label-free detection method capable of high sensitivity, monitoring the biointeractions at molecular levels real-time.

Initial application of SPR-based biosensors mainly comprise extracellular measurement.[173–185] The enormous development of nanoparticle synthesis and its surface functionalization procedure along with the development of Raman scattering instrumentation give SPR-based probes a huge boost for using it intracellularly. In this section, we will briefly discuss the principle and application of surface-enhanced Raman scattering tools as intracellular probe. Comprehensive review papers have already appeared in the literatures containing detailed overviews on this topic.[186–191]

3.327.3.1.1. Working principle

The most common technique for studying the intracellular behavior of nanocarriers is to encapsulate a fluorophore or a fluorophore-labeled drug derivative and subsequently image the system using fluorescence microscopy. The information provided from this analysis, however, is limited due to the potential of the fluorophore to leak out of the system and the extent of its interference with the biochemical behavior of the labeled molecule. Furthermore, this method does not provide information regarding nanocarrier/payload association and dissociation patterns, which is the ultimate purpose for the carrier system and a crucial issue in nanotechnology. Low contrast, autofluorescence, and photobleaching also confound fluorescent microscopy, compromising the continuous monitoring of the same sample. Raman spectroscopy in combination with optical microscopy provides a novel noninvasive and a label-free method to assess image-cellular processes based on their biochemical changes.[192–194]

In principle, spectroscopic techniques that deliver sensitive molecular structural information, such as Raman spectroscopy, have the potential to address this issue. Since more than a decade ago it has repeatedly been proven that the fingerprint-like information in Raman microspectra can add to our understanding of the biochemical background of various regular, induced, or pathological changes in eukaryotic cells.[195]

Raman spectroscopy is a highly specific technique used to detect and identify molecules on the basis of their unique vibrational energy levels and corresponding Raman fingerprints. In Raman scattering, photons are scattered inelastically, either losing energy (Stokes shift) or gaining energy (anti-Stokes shift) equal to the molecular vibration of the probed material. Figure 8 illustrates the Raman scattering process in a molecular-level scheme; for a general overview on Raman scattering see Kneipp *et al.*[196] Depending on whether photons interact with a molecule in its vibrational ground or first excited vibrational state, the scattering signals appear at the low-energy side (Stokes: $h\nu_S = h\nu_L - h\nu_M$) or high-energy side (anti-Stokes: $h\nu_{aS} = h\nu_L + h\nu_M$) of the excitation laser. The scattering signal power PRS of a Raman line depends on excitation intensity I_L and the Raman cross-section σ_R, where σ_R is determined by the polarizability derivative of the molecular vibration. In general, anti-Stokes Raman scattering results in much lower scattering signals as compared with Stokes scattering, because only a small fraction of molecules, as determined by the Boltzmann population, is in an excited vibrational state and can contribute to anti-Stokes Raman scattering.

When molecules adsorb onto a plasmonic nanoparticle or move to within a few nanometres of its surface, the local electromagnetic fields around the nanoparticle can enhance the Raman scattering by a factor of 10^6–10^8 for an ensemble of molecules,[197,198] and by as much as 10^{14}–10^{15} for single molecules.[199–201] This phenomenon, known as surface-enhanced Raman scattering (SERS), results in a highly specific and sensitive method for molecular identification.[202] Figure 9 shows a schematic of SERS, where molecules are in the close vicinity of a metal nanostructure. In the schematic, this nanostructure is a small aggregate built from spherical gold nanoparticles.

Two effects might be operative in SERS: (1) An electromagnetic enhancement factor arises because LSPR modes in the metal nanoparticles focus the incident light energy at the nanoparticle surface and also increase the density of states at Stokes-shifted wavelengths. The electromagnetic enhancement factor is typically 10^5–10^8 for nanoprisms, but simulations indicate

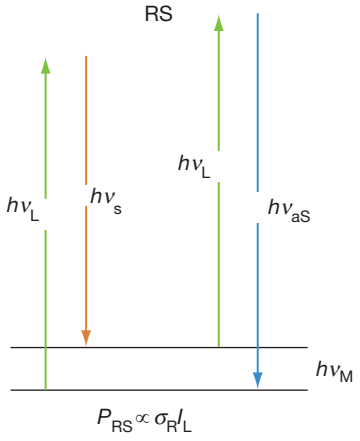

Figure 8 Raman (RS) in a molecular level scheme. Adapted from Kneipp, J.; Kneipp, H.; Kneipp, K. *Chem. Soc. Rev.* **2008**, *37*, 1052–1060, with permission from Royal Society of Chemistry.

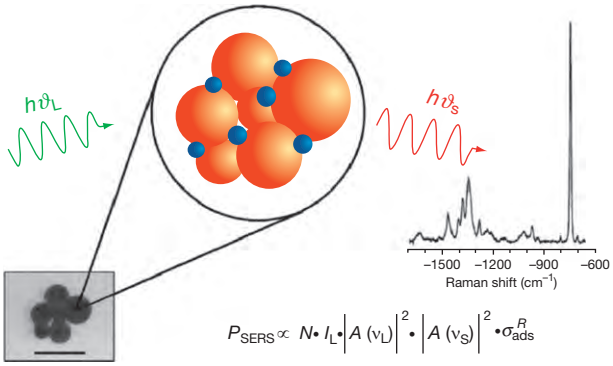

Figure 9 Schematic of surface-enhanced Raman scattering (SERS). Molecules (blue dots) are attached to silver or gold nanoparticles (orange balls). For comparison, the transmission electron micrograph shows SERS-active gold nanoaggregate. Adapted from Kneipp, J.; Kneipp, H.; Kneipp, K. *Chem. Soc. Rev.* **2008**, *37*, 1052–1060, with permission from Royal Society of Chemistry.

that it can be as large as 10^{13} for structures such as arrays of nanoprism dimmers.[203] (2) Chemical enhancement factors arise from changes in the molecular electronic state or resonant enhancements from either existing molecular excitations or newly formed charge transfer states. When molecules are excited by light resonant with an electronic absorbance, an additional enhancement factor of $\sim 10^1$–10^3 is observed in comparison with nonresonant excitation.

3.327.3.1.2. SERS nanosensor

The nanostructures which can provide a high level of electromagnetic field enhancement are the essential component for designing the hybrid SERS nanosensors for biological applications.[204–206] This is the mandatory property of the reporter for exhibiting an intense and stable spectroscopic signature but also for an efficient and sensitive Raman probe of the cellular environment. Moreover, the nanostructures should be small enough to cross cell membranes, and they should allow probing of cells without inducing any perturbation or toxicity.[204] Thus far, silver and gold have been the metals that provide the highest enhancement observed in SERS experiments. Even though silver shows a much better enhancement than gold using visible excitation, aggregates of both metals show comparably good SERS enhancement with NIR excitation, yielding enhancement factors up to 14 orders of magnitude.[207] Reporter molecules permit detection and imaging of the sensor based on their specific SERS spectrum. Potential reporters should be biocompatible molecules showing a strong and specific SERS spectrum.

3.327.3.1.2.1. Intracellular chemical probing

The first key to any successful intracellular SERS experiment is to introduce metal nanoparticles into the cellular matrix. The most common approach is through cellular uptake of fully formed nanoparticles in an external solution; however, as we shall see, there are several examples in which the cell can directly synthesize the nanoparticles *in vivo*. When considering cellular uptake, there are several issues of note: (1) size of the nanoparticle relative to the entry pathways of the cell; (2) mechanism of uptake by the cell; and (3) toxicity. Toxicity of nanoparticles, in particular, is a field of active research and ranges from studies on single cell viability for laboratory-based experiments to the environmental impact of nanoparticles on living tissue.[208–211] Gold nanoparticles have been tools of the trade in cell biology because of their favorable physical and chemical properties and biocompatibility. Once silver or gold nanoparticles are internalized within the cell, the next step is to measure the SERS spectrum that originates from molecules that are in close proximity to the enhanced electromagnetic field at the nanoparticle surface. Many different biological molecules offer strong Raman scattering signatures.[190]

Until now the study of the chemical composition of endosomes has involved fractionation and purification (i.e., *in vitro* approaches). Gold nanoparticles can serve as biocompatible mobile nanosensors and deliver chemical information by providing the enhanced Raman spectra of intrinsic cellular molecules in their vicinity eliminating the need of fractionation and purification steps.[204,205,212–216]

In one of the earliest examples of SERS spectroscopy within cells, the interaction of doxorubicin (DOX) with cancer cells was monitored as a function of cell location SERS for probing internal cellular structure and dynamics.[217] In this case, the SERS spectrum of free DOX and DNA-bound DOX was characterized *in vitro*, and specific bands were identified as being associated with different conformations of the molecule. Cells were then incubated with DOX followed by silver nanoparticles, or in solutions where DOX was preadsorbed onto the silver nanoparticles. In the former case, the drug was largely trafficked into the nucleus of the cell, where it was able to interact with DNA prior to the introduction of the nanoparticles, while in the latter case, the DOX–nanoparticle hybrid remained in the cytoplasm, unable to penetrate the nuclear membrane. Interestingly, the SERS spectra revealed distinct differences between the two scenarios: the DOX in the nuclei exhibited SERS spectra consistent with the drug bound to DNA, while the DOX–nanoparticle hybrid did not. Unlike studies of native biomolecules in cells, this work benefited from the introduction of a SERS-active analyte with a distinct spectrum that exhibited differences between two conformations, that is, DOX bound to DNA versus unbound.[217]

Another type of experiment involves the introduction of a chemical that can stimulate a specific response in the cell, and then using SERS to monitor changes in the environment of the nanoparticle. In one example, ionomycin (a drug that triggers Ca^{2+} release by the cell) was introduced to Chinese hamster ovary cells, and the changes in the SERS spectra from the CHO cell were monitored.[218] A new peak emerged at 1643 cm^{-1}, which is assigned to the amide I mode; this peak showed a fast rise in intensity, and then a steady fall over time. This result is qualitatively consistent with other studies in which Ca^{2+} is monitored via a fluorescent probe, although the two time scales appear to show some differences, with the SERS data showing a faster response to the drug than the fluorescence data.[218,219] In both experiments, Ca^{2+} flux is measured indirectly via a secondary reporter; however, in the SERS experiments, the reporter is a molecule that is native to the cell, providing additional insight into how the cell responds to the introduction of the ionomycin.

During recent years, it has been demonstrated that SERS labels offer exciting new capabilities, particularly also for applications in living cells.[214,215,220–224] Compared to fluorescence tags, SERS labels can provide several advantages. The optical

signature of a SERS label comprises several sharp Raman lines distributed over a spectral range comparable to the spectral width of a fluorescence dye. Because of this high specificity of a Raman spectrum, spectral overlap between different labels is very unlikely, even when their molecular structures are very similar. Spectral correlation techniques using different SERS lines can improve the contrast of an SERS label relative to the cellular background.[220] An important strategy for generating a specific response from nanoparticles internalized by the cell is to functionalize the nanoparticle surface directly with a molecule that has a known SERS spectrum. This can be used for simple location analysis of the nanoparticle aggregates, or can even be used for sensing within cells. In the former case, researchers have tagged nanoparticles with a variety of SERS active probes, each of which has its own unique spectroscopic signature.[220,223] This approach allows researchers to find exactly where the nanoparticles have localized in the cell without competition from non-surface-enhanced Raman bands.[220,223]

The final application of the use of functionalized nanoparticles as SERS probes is for intracellular pH measurements.[215,225] Determining intracellular pH with subcellular resolution is of particular importance for a better understanding of a broad range of physiological and metabolic processes. These include trafficking, recycling, and recruitment of intra- and extracellular molecules.[226–228] This goal can be addressed by using a 'pH sensitive' reporter. In this case, 4-mercaptobenzoic acid is attached to the nanoparticle surface. The protonated and deprotonated forms of this molecule have different relative intensities between the 1430 and 1590 cm^{-1} bands in their SERS spectra; as such, measuring the ratio between the two intensities is an excellent measure of pH.[215,225] 4-Mercaptobenzoic acid has a pK_a of around 5.8, which means that it should be most sensitive to pH changes in the range of 5–7, which is within the range of biological relevance. In the first study of this system, the pH surrounding the nanoparticles in the lysosome was measured to be less than 6, which is expected based on other reports.[225] The second study of this system mapped the pH of the entire cell and found that the pH varied by more than one pH unit depending on the location within the cell.[215] These studies provide unique insight into a particular property of the intracellular environment based on the SERS response of a functionalized probe.

To sum up, SERS represents an attractive technique, which advances hand in hand with nanoscience and nanotechnology, to offer solutions for a diverse array of biomedical applications. Nanomaterials can be engineered for individual and multimodal applications in SERS, including biomolecular recognition and characterization, ultrasensitive diagnosis and biodetection, and biomedical imaging. Although SERS has already been used for a wide range of applications both *in vitro* and *in vivo*, full realization of its potential requires addressing a number of open issues, including nanoparticle stability in biological fluids, single-event recognition detection, label-free analysis and classification, quantification of the analytes of interest, and acute and long-term health effects of nanomaterials.

3.327.3.2. Quantum Dots as Intracellular Probes

3.327.3.2.1. Introduction

Quantum dots (QDs) are semiconductor nanocrystals that have unique fluorescent properties (for review, see Alivisatos *et al.*,[229] Pinaud *et al.*,[230] and Michalet *et al.*[231]). Their photophysical properties are highly dependent on the chemical composition, shape, and size, all of which can be controlled during synthesis. The intrinsic photophysical properties of organic and genetically encoded fluorophores, which generally have broad absorption/emission profiles (**Figure 10(a)**) and low photobleaching thresholds, have limited their effectiveness in long-term imaging and 'multiplexing' (simultaneous detection of multiple signals) without complex instrumentation and processing. The seminal publications describing the first biological uses of QD-fluorophores foresaw that their unique properties could overcome these issues.[232,233] Compared with molecular dyes, two properties in particular stand out: the unparalleled ability to size-tune fluorescent emission as a function of core size (for binary semiconductor materials), and the broad excitation spectra, which allow excitation of mixed QD populations at a single wavelength far removed (>100 nm) from their respective emissions (**Figure 10(b)** and **10(c)**). In the past 10 years, the progress in synthesis and optimization of QDs for biological environments has opened the doors to an expanding variety of biological applications such as serving as specific markers for cellular structures and molecules, tracing cell lineage, monitoring physiological events in live cells, measuring cell motility, and tracking cells *in vivo*. In this section, we will briefly discuss the synthesis, surface bioconjugation, and intracellular applications. For a comprehensive review on this section, you should see the review papers that have appeared in the literature.[229,230,234–237]

3.327.3.2.2. Synthesis of QDs

The synthesis of monodisperse semiconductor nanocrystals, such as CdSe, CdS, or CdTe, can be achieved by injecting liquid precursors into hot (300 °C) coordinating organic solvent.[238,239] Adjusting the amount of precursors and crystal growth time generates QDs of specific sizes.[239] The quantum yield of the nanocrystal core synthesized as above is relatively low (<10%).[238,240] In order to overcome that problem CdSe core was over coated with a layer of wider band gap semiconductor such as ZnS and CdS.[241–243] The ZnS layer passivates the core surface, protects it from oxidation, prevents leeching of the Cd/Se into the surrounding solution and also produces a substantial improvement in the PL yield.[240,244] Even though thin ZnS (1–2 monolayers) shells often produce the highest PL yields, thicker ZnS shells (4–6 monolayers) provide more core protection against oxidation and the harsher conditions presented by biological media (e.g., acidic buffers and cellular organelles). Colloidal QDs made of ZnS, CdS, ZnSe, CdTe, and PbSe, emitting from the UV to the infrared have been prepared[238,240,243,245–257]; however, these are not as common in biological assays.

The real breakthrough in synthesizing high-quality colloidal QDs came when the Bawendi group reported[238] that the use of high-temperature growth solvents/ligands (mixture of trioctyl phosphine/trioctyl phosphine oxide, TOP/TOPO), combined with pyrolysis of organometallic precursors, yielded CdSe QDs with highly crystalline cores and size distributions of 8–11%. The same reaction combined with appropriate organometallic precursors was further used to overcoat the native CdSe core with a layer of wider-band gap semiconducting

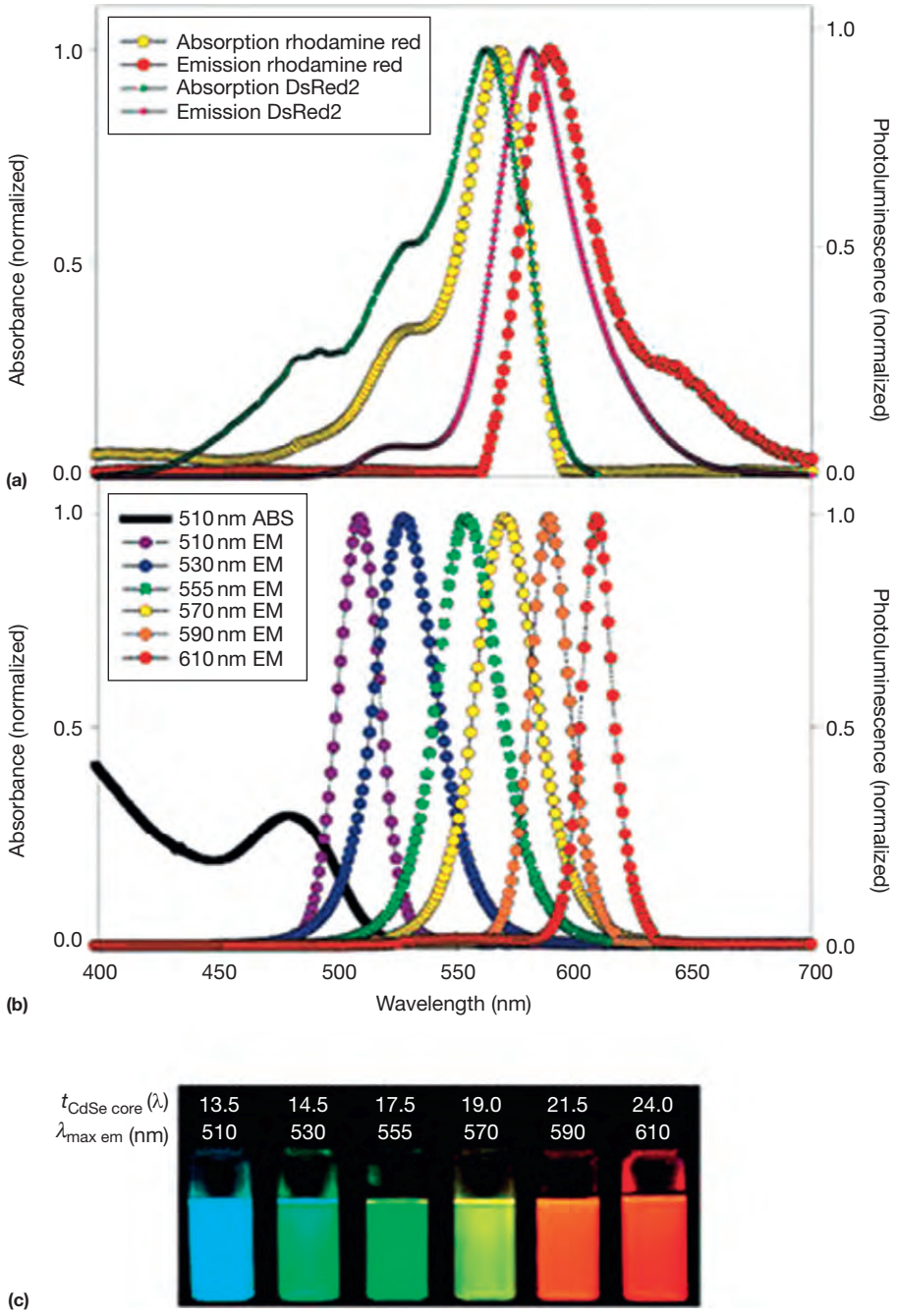

Figure 10 Comparison of rhodamine red/DsRed2 spectral properties to those of QDs highlighting how multiple narrow, symmetric QD emissions can be used in the same spectral window as that of an organic or genetically encoded dye. (a) Absorption (Abs) and emission (E_m) of rhodamine red, a common organic dye and genetically encoded DsRed2 protein. (b) Absorption and emission of six different QD dispersions. The black line shows the absorption of the 510-nm-emitting QDs. Note that at the wavelength of lowest absorption for the 510-nm QD, ~450 nm, the molar extinction coefficient is greater than that of rhodamine red at its absorption maxima (~150 000 vs. 129 000 M^{-1} cm^{-1}). (c) Photo demonstrating the size-tunable fluorescence properties and spectral range of the six QD dispersions plotted in b versus CdSe core size. All samples were excited at 365 nm with a UV source. For the 610-nm-emitting QDs, this translates into a Stokes shift of ~250 nm. Reproduced from Medintz, I. L.; Konnert, J. H.; Clapp, A. R.; *et al. Proc. Natl. Acad. Sci. USA* **2004**, *101*, 9612–9617. © National Academy of Sciences, USA.

material (e.g., ZnS and CdS).[240,243,244] Fine-tuning this synthetic scheme highlighted the importance of the high-temperature solvent/ligand mixtures, along with using less pyrophoric salt precursors (CdO and Cd-acetate), for preparing reproducible high-quality nanocrystals.[245,258]

3.327.3.2.3. Functionalization of QDs: Solubilization and bioconjugation

3.327.3.2.3.1. Solubilization

The core and core-shell QDs synthesized as described are only soluble in nonpolar solvents because of their hydrophobic

surface layer. For QDs to be useful probes for examination of biological specimens, the surface must be hydrophilic. They need to be biofunctionalized in order to meet four key requirements[62,259]:

(a) increased stability in water for long period,
(b) presence of sterically accessible functional groups for bioconjugation,
(c) biocompatibility and non immunogenicity in living systems,
(d) lack of interference with the nanoparticles native properties.

This problem has been solved by replacing the surfactant layer or by coating with an additional layer introducing either electric charge or hydrophilic polymers for mediating solubility in water. Coulomb repulsion between nanocrystals with surface charge of the same polarity prevents aggregation in water. The easiest approach is to exchange the hydrophobic surfactant molecules with bifunctional molecules, which are hydrophilic on one side and hydrophobic on the other side, which bind to the ZnS shell. Most often, thiols (–SH) are used as anchoring groups on the ZnS surface, and carboxyl (–COOH) groups are used as the hydrophilic ends. Many biological applications of QDs have been achieved by using mercaptohydrocarbonic acids (SH–. . .–COOH) to make QDs water soluble.[260–266] The long-term stability of the QDs depends on the bond between thiol and ZnS, which is not strong although it can be enhanced by using two thiol groups instead of one.[254,267] Therefore, the water solubility of the core–shell QDs capped in mercaptocarbonic acids is limited (**Figure 11**).

An alternative approach is based on the growth of a hydrophilic silica shell around the nanocrystals, through a process known as surface silanization.[268–274] A first step involves a ligand exchange to substitute the original hydrophobic surfactant covering the nanocrystal surface. This process involves exchanging the surface ligand with thiol-derived silane such as mercapto-trimethoxysilane (MPS). The trimethoxysilane groups can be cross-linked by the formation of siloxane bonds. In this way, the surfactant shell around the nanocrystal becomes cross-linked and has improved stability toward disintegration. To render the silica shell hydrophilic in the next step, molecules bearing methoxysilane groups at one and hydrophilic groups at the other end are incorporated in the shell again by the formation of siloxane bonds, resulting finally in a multilayer shell.

Recently other solubilization methods have been reported, one of which involves coating the surface with amphiphilic polymers.[275,276] Instead of exchanging the hydrophobic surfactant, the particles in this case are coated with a cross-linked amphiphilic polymer. In this approach the hydrophobic tails of the polymer intercalate the hydrophobic surfactant molecules on the nanocrystal surface and thus form an additional coating. The water solubility of polymer-coated nanocrystals is ensured by hydrophilic groups of the polymer which self-assemble on the outside of the polymer shell. In order to further stabilize the polymer shell around the nanocrystal, the individual polymer chains are cross-linked. Although this is a general method for nanocrystals grown in different organic solvents, the final size of the particles after coating is rather large. For CdSe/ZnS QDs, the diameter is between 19 and 25 nm,[276] which could place restrictions on many biological applications. Other approaches, such as coating the QDs with phospholipid micelles,[277] dithiothreitol,[278] organic dendron,[279,280] and oligomeric ligands,[281] have also been reported.

3.327.3.2.3.2. *Biomolecule conjugation*

In order to apply QDs in various biological systems, certain biological molecules need to be attached to the surface of these dots without any damage to the properties of the

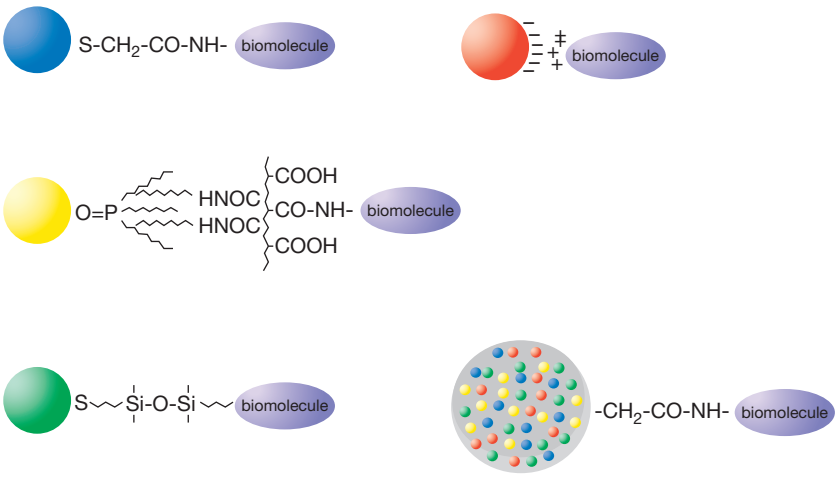

Figure 11 A schematic illustrating different approach of conjugation of QDs to biomolecules: (a) Use of a bifunctional ligand such as mercaptoacetic acid for linking QDs to biomolecules. (b) TOPO-capped QDs bound to a modified acrylic acid polymer by hydrophobic forces. (c) QD solubilisation and bioconjugation using a mercaptosilane compound. (d) Positively charged biomolecules linked to negatively charged QDs by electrostatic attraction. (e) Incorporation of QDs into microbeads and nanobeads. Reproduced from Chan, W. C. W.; Maxwell, D. J.; Gao, X. H.; Bailey, R. E.; Han, M. Y.; Nie, S. M. *Curr. Opin. Biotechnol*. **2002**, *13*, 40–46, with permission from ACS Publications.

molecules.[282] Owing to its finite size (comparable to or slightly larger than that of many proteins), a single QD can be conjugated to several proteins simultaneously. The QD thus acts as a nanoscaffold for attachment of several proteins, or other biomolecules, creating a multifunctional nanoparticle–biological hybrid.

Several successful approaches have been used to link biological molecules to QDs, including adsorption, electrostatic interaction, mercapto (–SH) exchange, and covalent linkage. It has been reported that simple small molecules, such as oligonucleotides[283,284] and various serum albumins,[285] are readily adsorbed to the surface of water-soluble QDs. This adsorption is nonspecific and depends on ionic strength, pH, temperature, and the surface charge of the molecule.

Mattoussi and coworkers presented a method of conjugating proteins to QD surfaces using electrostatic interactions. The protein of interest was engineered to fuse with a positively charged domain, which in turn interacted electrostatically with the negatively charged surface of the QD. The protein–QD conjugates prepared in this way were very stable and the fluorescence yield was even higher than that from the nonconjugated dots.[254,267]

Biological molecules containing thiol groups can be conjugated to the QD surface through a mercapto exchange process.[262,265,266,282,286,287] Unfortunately, the same problem of using thiol as anchoring group on a ZnS surface occurs because the bond between Zn and thiol is not very strong and is dynamic. As a result, biomolecules can readily detach from the surface, causing QDs to precipitate from the solution.

In an alternative method, biological molecules are covalently linked to the QD surface on their outer hydrophilic shell. Most simply, biological molecules can be adsorbed to the hydrophilic shell in a nonspecific way.[284,285] In a more specific way, molecules can be adsorbed to the hydrophilic shell by electrostatic interaction. Most colloidal QDs are negatively charged and therefore positively charged biological molecules stick to their surface. In the case of proteins, it is also possible to genetically engineer a positive zipper to one end of the protein, with which the protein then is electrostatically adsorbed to the QD surface.[267,288–290] Finally, biological molecules can also be covalently attached to the QDs by means of cross-linker molecules.[232,233,260,266,268,275,277,278,287,291,292] This requires hydrophilic surfactant shells with reactive groups, such as –COOH, $-NH_2$, or –SH. Since most biological molecules bear these functional groups or can be easily modified with them, a covalent linkage between functional groups on the QD surface and functional groups of the biological molecule can be formed. Typical procedures include carbodiimide activation of carboxylic acid groups on one entity followed by amide bond formation to amino groups on the other entity or the linkage of thiol and amino groups using bifunctional cross-linkers such as SMCC (4-(*N*-maleimidomethyl) cyclohexane-1-carboxylic acid *N*-hydroxysuccinimide ester).[293] A huge variety of suitable cross-linking reactions can be found in textbooks.[293]

3.327.3.2.3.3. *Toxicity/biocompatibility*

Since constituents of colloidal QDs such as cadmium[294] or selenium[295] are toxic to many cells, harmful effects can be expected, especially when the hydrophilic shell around the QDs is not stable they might dissolve under the release of toxic ions.

Cytotoxicity of QDs has been observed in a large number of *in vitro* studies,[235,271,296–299] affecting cell growth and viability.[300] The extent of cytotoxicity has been found to be dependent upon a number of factors including size, capping materials, color, dose of QDs, surface chemistry, coating bioactivity, and processing parameters.[299,301,302] Even if not inducing significant alterations in cell physiology, QDs can produce subtle alterations of function which may affect the quality of data derived from their use.[298,303,304]

A number of mechanisms have been postulated to be responsible for QD cytotoxicity. These include desorption of free Cd (QD core degradation),[235,271] free radical formation, and interaction of QDs with intracellular components. Examination of QD toxicity in a hepatocyte culture model showed that exposure of core CdSe to an oxidative environment causes decomposition and desorption of Cd ions. Such exposure during synthesis and processing played an important role in subsequent toxicity.

However, when properly capped by both ZnS and hydrophilic shells, no acute and obvious CdSe QD toxicity has been detected in studies of cell proliferation and viability in live cells[270,271,287,288] and animal[282,305] models. The most sensitive environment in which to test QD toxicity is that of the live embryo because even slight cellular perturbances are manifested as measurable biological phenotypes. The toxicity of QDs was examined in *Xenopus* embryos,[277] where injection of low concentrations of QDs had no negative effects. Although some abnormalities were noted with increasing concentrations, it was not clear whether they resulted from the QDs or changes in the osmotic equilibrium of the cell. In another case, primary hepatocyte cultures were examined because the liver is the major target of cadmium injury.[271] Under standard conditions of synthesis and water solubilization, QDs were not toxic. However, cytotoxicity was observed when Cd^{2+} was released.[271] This happened when the QD surface coating was not stable, exposing the CdSe to oxidization by air or UV damage. Therefore, strategies to protect the QD surfaces from oxidative environments are critical for live cell and animal experiments. Coating the QD surface with ZnS eliminates toxicity owing to air exposure but provides only partial protection of the core from UV exposure. Larger molecules, such as bovine serum albumin (BSA) and polymer/streptavidin, further slow down the photooxidation process. However, the potential effect of Cd^{2+} release over time has not been examined. There remains a pressing need for further investigations into QD toxicity in live animals and safety for diagnostic applications.

3.327.3.2.4. Biological applications

3.327.3.2.4.1. *Immunolabeling:* In vitro

The use of QDs for sensitive and multicolor cellular imaging has seen major advances due to significant improvements in QD synthesis, surface chemistry, and conjugation. Fluorescence immunolabeling is widely used in cell biology for probing structure and locating signal-transduction-related molecules. Owing to their robust optical properties, QDs are ideal probes in this area. Their application is in principle very similar to that of organic fluorophores.

Biologically conjugated QDs have shown great promise as multiwavelength fluorescent labels for on-chip bioassays and eukaryotic cells. Since the first experiment by Alivisatos *et al.*,

where semiconductor CdSe/ZnS nanocrystals were used to stain F-actin in fixed cells,[232] investigators have performed a variety of experiments in which QDs have been used to localize molecules in cells and tissues, both in live and fixed specimens.

Nowadays high-quality images such as the dual-color labeling can be obtained with standardized procedures. If antibodies are used as ligands, typically a two-step reaction is used. First, a primary antibody is reacted with the target. Then QDs conjugated with a secondary antibody, which targets the primary antibody, are added.[275,292] Since more than one secondary antibody can bind to each primary antibody, such cascade reactions amplify the fluorescence signal. However, the direct conjugation of antibodies to QDs is laborious; often biotinylated secondary antibodies are used, which are finally labeled by streptavidin–QD conjugates via biotin–avidin interaction.[273,306] This strategy is advantageous, because it involves only one universal conjugation of QDs with streptavidin, and most antibodies are commercially available with an attached biotin group. Further signal amplification can be achieved with the so-called TSA enzyme amplification technique. Here the secondary antibody is conjugated with horseradish peroxidase (HRP) and QDs are conjugated to tyramide (e.g., via biotin–avidin interaction). Horseradish peroxidase converts tyramide to a very reactive oxidized intermediate, which rapidly binds to all proteins in close proximity. In this way, the whole local environment of the secondary antibody is labeled with fluorescent QDs.[306] QD labeling of inner and outer structures of fixed cells has been used for a variety of receptors.

All these studies show that QDs have moved beyond the demonstration stage and are excellent probes with enhanced signal-to-noise ratio, extremely high stability, and improved specificity suitable for studying important biological problems.

3.327.3.2.4.2. Within living cells

Because QDs are extremely bright and photostable, they can be used as cell markers for long-term studies such as cell–cell interactions, cell differentiation, and cell lineage tracking. Most experiments conducted to date have shown that QDs do not interfere with normal cell physiology and cell differentiation.[270,277,307]

The idea of using QDs as cell markers is started when the Nie group reported that QDs are incorporated by living cells.[233] QDs can be internalized by cells, by either receptor-mediated[233] or nonspecific endocytosis.[231,270,285,288] The exact pathway of incorporating QDs into cells under endocytosis is not understood. However, after QDs enter cells, they accumulate in vesicles in the perinuclear region.[270,285,288] Perinuclear vesicles filled with nanocrystals were first seen by multiphoton microscopy.[270] Later, with the use of an endosome-specific marker, such as fluorescein-labeled dextran[285] or pECFP,[288] it was confirmed that QDs were indeed accumulated in the endosomes or lysosomes and not coating them on the basis of colocalization of QDs and endosome markers. Once internalized, QDs divided with the daughter cells at cell division.[270,277,285]

Internalized QDs are powerful probes for long-term studies within live cells. By virtue of their optical properties, QDs can highlight cells and subcellular structures above the surrounding background; in other words, they add contrast to a material that otherwise provides little contrast under visible light observation; in yet other words, they can communicate to the observer an image of a biological structure of interest.

To demonstrate multicolor labeling of live cells, endocytic uptake and selective labeling of cell surface proteins were used with antibody conjugated QDs, and then QD emission was followed for over a week as cellular development was monitored, showing that cells tolerate QDs for extended periods of time.[277,288,308] By using antibody-linked QDs, both the Her2 breast cancer marker and specific intracellular proteins were labeled in both live and fixed cancer cells, demonstrating that QD-probes can cross into cells and specifically bind their intended intracellular targets.[275] QDs can also be useful markers for tracking cellular movement, differentiation, and fate.[277,288,308] Cancer cells seeded on top of QDs engulf them and leave behind a fluorescence-free phagokinetic trail.[308] Using several cell lines, the size and shape of trails were shown to correlate well with potential invasiveness, providing a novel assay for this property.[308] Micelle stabilized QDs injected into *Xenopus* embryos demonstrated cell lineage-tracing during the complex developmental process spanning the embryo–tadpole stage and equal transfer of QDs from mother to daughter cells, again showing long-term cellular compatibility even with $>10^9$ QDs per cell.[277] By exploiting QD photobleaching resistance, previously onerous cellular physiology questions have been investigated on the single-molecule level. These include tracking the diffusion dynamics of individual glycine receptors in neuronal cells over long periods of time (min), which provided unique information on single-protein movement, and interestingly, the authors used blinking to identify single QDs and differentiate them from aggregates.[309] Additionally, the specific erbB/HER cellular receptor-mediated fusion and internalization process has been observed in single cells.[310] These publications mark the transition from 'proof-of-concept' to a useful tool as these complex cellular processes could not be tracked continuously with photolabile organic fluorophores.

3.327.3.2.4.3. In vivo *applications*

Imaging tissue with far red/NIR excitation overcomes some problems due to indigenous tissue autofluorescence, and QD spectroscopic properties can be exploited here to achieve somewhat deeper penetration than the available NIR dyes.[286,311,312] This was demonstrated by synthesizing NIR emitting QDs (840–860 nm) and applying them to sentinel lymph-node mapping in cancer surgery of animals.[70] Using only 5 mW cm^{-2} excitation, they imaged lymph nodes 1 cm deep in tissue, where lymphatic vessels were clearly visualized draining QD solutions into the sentinel nodes.[312]

Colloidal semiconductor nanocrystals have a two-photon cross-section that is 2–3 orders of magnitude greater than organic dyes.[305] A two-photon process requires about twice the excitation wavelength of a single-photon excitation. Longer wavelengths, extending into the infrared region, can be utilized to excite chromophores in a single quantum event. Therefore, multiphoton microscopy enables the imaging of structures deep within biological tissues with minimum photobleaching and photodamage. The high two-photon cross-section of QDs allows for more efficient probing of thick specimens and *in vivo* imaging when using multiphoton excitation microscopy. This makes them suitable for *in vivo* deep-tissue imaging

using two-photon excitation at low intensities.[305,313] Using this technique to excite green-emitting QDs in the near infrared allowed imaging of mice capillaries hundreds of micrometres deep and subcellular resolution of mouse brain.[305,313]

Recently, Gao *et al.* reported *in vivo* cancer targeting and imaging using QDs.[314] They conjugated QDs to the antibody specific for the prostate cancer cell marker PSMA. After injection into mice that had been transplanted with human prostate cancer cells, the QD-tagged PSMA antibodies recognized and bound at the tumor site and were clearly imaged *in vivo*. Owing to the QDs' large absorption coefficient and long lifetime, *in vivo* imaging of QDs was much brighter and more sensitive than imaging with green fluorescence protein (GFP), which was totally buried in autofluorescence and background.

Most recently, self-illuminating QD was conjugated as new probes for *in vivo* imaging. Specific immunofluorescent probes were synthesized by linking QDs to α-fetoprotein AFP antibody for specific recognization of AFP, an important marker for hepatocarcinoma cell line HCCLM6. *In vivo*, active tumor targeting and sensitive spectroscopic hepatoma imaging was achieved with an integrated fluorescence imaging system. The inhomogeneous distribution of the QD probes in tumor by using a site by site measurement method was investigated to test their ability for distribution studies of cancer cells in tumor. These results demonstrate the potential of QD probes as attractive immunofluorescent probes for cancer detection (Figure 12).[315]

Summarizing the above, there is no doubt about the great potential of QDs as labels or contrast agents in life sciences and medical diagnostics. Will QDs replace fluorescent dyes? No, – rather they will complement dye deficiencies in particular applications such as *in vivo* imaging. Moreover, adapting QDs for biological use will teach us critical lessons about creating future inorganic–biological hybrids with direct relevance to many other materials. Future studies will have to characterize the dose–response relationships of QDs. Dose–response in this case means not only evaluating which minimal dose is needed to obtain the desired optical signal as a response but also which dose is acceptable in terms of undesired side effects, which are a type of response as well. The existing literature gives some hints that at least in short-term studies toxicity may not be a limiting problem. Medical application in humans will however require an unequivocal assessment of the potential long-term effects of administered QDs. Together with other interdisciplinary developments of modern science, the optimization and application of QDs in biology and medicine may revolutionize what we know and what we think about biological processes.

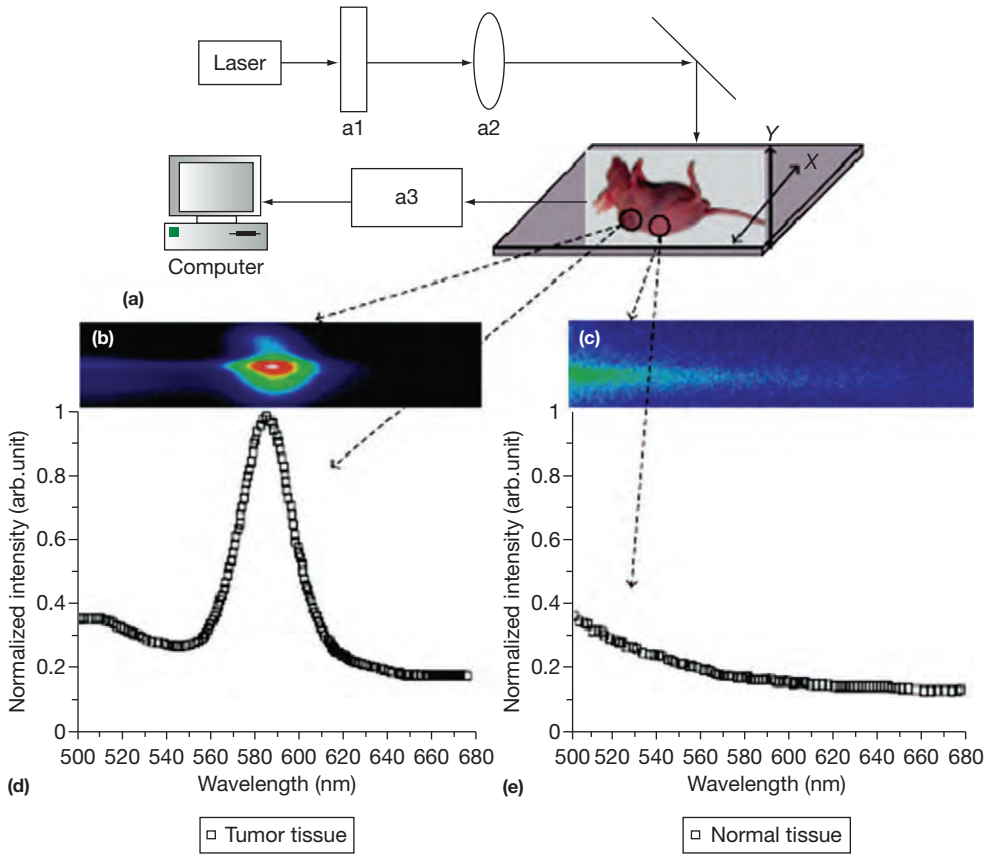

Figure 12 A Simple optical layout of fluorescence imaging system: (a1) optical frequency double system, (a2) lens, and (a3) liquid-nitrogen cooled CCD-array spectrophotometer. Spectroscopic imaging of (b) QDs-tagged tumor tissue and (c) normal tissue. Emission spectrum of (d) QDs-tagged tumor tissue and (e) normal tissue. All the images and the spectrums were captured from a nude mouse with the same exposure time. Reproduced from Yu, X.; Chen, L.; Li, K.; *et al. J. Biomed. Opt.* **2007**, *12*, 014008, with permission from SPIE.

3.327.4. Conclusion

The successful development of new systems and techniques which enable monitoring of individual biological macromolecules or individual biological cells in their natural (aqueous) environment will lead to a better understanding of the microdynamics of living systems. Such systems would, for example, allow real-time monitoring of the functioning of fluorescently tagged drugs absorbed into individual biological cells or their substructures. Nanotechnology combined with optical science will allow the realization of optical-based nanosensors suitable for the tasks described above. So far, research conducted has demonstrated the viability of constructing optical-based sensors allowing intracellular sensing with submicron resolution. Nonetheless, extraordinary opportunities remain, because delivering deeper into biochemical and biological phenomena will require ever more sophisticated and tailored probes.

References

1. Svoboda, K.; Yasuda, R. *Neuron* **2006**, *50*, 823–839.
2. Zelent, B.; Kusba, J.; Gryczynski, I.; Johnson, M. L.; Lakowicz, J. R. *Biophys. Chem.* **1998**, *73*, 53.
3. de Silva, A. P.; Gunaratne, H. Q. N.; Gunnlaugsson, T.; *et al*. *Chem. Rev.* **1997**, *97*, 1515–1566.
4. McGlynn, S. P.; Daigre, J.; Smith, F. J. *J. Chem. Phys.* **1963**, *39*, 675–679.
5. Sapsford, K. E.; Berti, L.; Medintz, I. L. *Angew. Chem. Int. Ed.* **2006**, *45*, 4562–4588.
6. Petit, J.-M.; Denis-Gay, M.; Ratinaud, M.-H. *Biol. Cell* **1993**, *78*, 1–13.
7. Waggoner, A.; Kenneth, S. *Methods Enzymol.* **1995**, *246*, 362–373.
8. Johnson, I. *Histochem. J.* **1998**, *30*, 123–140.
9. Boonacker, E.; Van Noorden, C. J. F. *J. Histochem. Cytochem.* **2001**, *49*, 1473–1486.
10. Zhang, J.; Campbell, R. E.; Ting, A. Y.; Tsien, R. Y. *Nat. Rev. Mol. Cell Biol.* **2002**, *3*, 906–918.
11. Valeur, B. *Molecular Fluorescence: Principles and Applications*. Wiley-VCH: Weinheim, 2002.
12. Frangioni, J. V. *Curr. Opin. Chem. Biol.* **2003**, *7*, 626–634.
13. Goddard, J.-P.; Reymond, J.-L. *Curr. Opin. Biotechnol.* **2004**, *15*, 314.
14. Giepmans, B. N. G.; Adams, S. R.; Ellisman, M. H.; Tsien, R. Y. *Science* **2006**, *312*, 217–224.
15. Lakowicz, J. R. *Principles of Fluorescence Spectroscopy*, 3rd ed.; Springer: New York, 2006.
16. Sadaghiani, A. M.; Verhelst, S. H. L.; Bogyo, M. *Curr. Opin. Chem. Biol.* **2007**, *11*, 20–28.
17. Johnsson, N.; Johnsson, K. *ACS Chem. Biol.* **2007**, *2*, 31–38.
18. Haugland, R. P.; Spence, M. T. Z.; Johnson, I. D.; Basey, A. *The Handbook: A Guide to Fluorescent Probes and Labeling Technologies*, 10th ed.; Molecular Probes: Eugene, OR, 2005.
19. Waggoner, A. *Curr. Opin. Chem. Biol.* **2006**, *10*, 62–66.
20. Lavis, L. D.; Raines, R. T. *ACS Chem. Biol.* **2008**, *3*, 142–155.
21. Terai, T.; Nagano, T. *Curr. Opin. Chem. Biol.* **2008**, *12*, 515–521.
22. Suzuki, T.; Matsuzaki, T.; Hagiwara, H.; Aoki, T.; Takata, K. *Acta Histochem. Cytochem.* **2007**, *40*, 131–137.
23. Domaille, D. W.; Que, E. L.; Chang, C. J. *Nat. Chem. Biol.* **2008**, *4*, 168–175.
24. Rao, J.; Dragulescu-Andrasi, A.; Yao, H. *Curr. Opin. Biotechnol.* **2007**, *2007*, 1817–1825.
25. Day, R. N.; Davidson, M. W. *Chem. Soc. Rev.* **2009**, *38*, 2887–2921.
26. Zhang, J.; Campbell, R. E.; Ting, A. Y.; Tsien, R. Y. *Nat. Rev. Mol. Cell Biol.* **2002**, *12*, 906–918.
27. Wolfbeis, O. S. In *Molecular Luminescence Spectroscopy: Methods and Applications—Part 1*; Schulman, S. G., Ed.; Wiley: New York, 1985; pp 167–317.
28. Teale, F. W.; Weber, G. *Biochem. J.* **1957**, *65*, 476–482.
29. Weber, G. *Nature* **1957**, *180*, 1409.
30. Whitby, L. G. *Biochem. J.* **1953**, *54*, 437–442.
31. Weber, G. *Biochem. J.* **1952**, *51*, 155–167.
32. Daniel, E.; Weber, G. *Biochemistry* **1966**, *5*, 1893–1900.
33. Weber, G.; Farris, F. J. *Biochemistry* **1979**, *18*, 3075–3078.
34. Hudson, E. N.; Weber, G. *Biochemistry* **1973**, *12*, 4154–4161.
35. Karpovich, D. S.; Blanchard, G. J. *J. Phys. Chem.* **1995**, *99*, 3951–3958.
36. Smalley, M. K.; Silverman, S. K. *Nucleic Acids Res.* **2006**, *34*, 152–166.
37. Gunnlaugsson, T.; Glynn, M.; Tocci, G. M.; Kruger, P. E.; Pfeffer, F. M. *Coord. Chem. Rev.* **2006**, *250*, 3094.
38. Suβmeier, F.; Langhals, H. *Eur. J. Org. Chem.* **2001**, *2001*, 607–610.
39. Kohl, C.; Weil, T.; Qu, J.; Mullen, K. *Chem. Eur. J.* **2004**, *10*, 5297–5310.
40. Sun, W. C.; Gee, K. R.; Haugland, R. P. *Bioorg. Med. Chem. Lett.* **1998**, *8*, 3107–3110.
41. Grandberg, I. I.; Denisov, L. K.; Popova, O. A. *Chem. Heterocycl. Compd.* **1987**, *23*, 117–142.
42. Panchuk-Voloshina, N.; Haugland, R. P.; Bishop-Stewart, J.; *et al*. *J. Histochem. Cytochem.* **1999**, *47*, 1179–1188.
43. Gee, K. R.; Sun, W. C.; Bhalgat, M. K.; *et al*. *Anal. Biochem.* **1999**, *273*, 41–48.
44. Babiak, P.; Reymond, J. L. *Anal. Chem.* **2005**, *77*, 373–377.
45. Yamazaki, H.; Inoue, K.; Mimura, M.; Oda, Y.; Guengerich, F. P.; Shimada, T. *Biochem. Pharmacol.* **1996**, *51*, 313.
46. Zimmerman, M.; Ashe, B.; Yurewicz, E. C.; Patel, G. *Anal. Biochem.* **1977**, *78*, 47–51.
47. Grynkiewicz, G.; Poenie, M.; Tsien, R. Y. *J. Biol. Chem.* **1985**, *260*, 3440–3450.
48. Larsen, T. A.; Goodsell, D. S.; Cascio, D.; Grzeskowiak, K.; Dickerson, R. E. *J. Biomol. Struct. Dyn.* **1989**, *7*, 477–491.
49. Crissman, H. A.; Hirons, G. T. *Methods Cell Biol.* **1994**, *41*, 195–209.
50. Mozdziak, P. E.; Pulvermacher, P. M.; Schultz, E.; Schell, K. *Cytometry* **2000**, *41*, 89–95.
51. Baeyer, A. *Ber. Dtsch. Chem. Ges.* **1871**, *4*, 555–558.
52. Lavis, L. D.; Rutkoski, T. J.; Raines, R. T. *Anal. Chem.* **2007**, *79*, 6775–6782.
53. Sun, W. C.; Gee, K. R.; Klaubert, D. H.; Haugland, R. P. *J. Org. Chem.* **1997**, *62*, 6469–6475.
54. Graber, M. L.; Dilillo, D. C.; Friedman, B. L.; Pastorizamunoz, E. *Anal. Biochem.* **1986**, *156*, 202–212.
55. Lavis, L. D.; Chao, T.-Y.; Raines, R. T. *ACS Chem. Biol.* **2006**, *1*, 252–260.
56. Drexhage, K. H. In *Dye Lasers*, 2nd ed.; Schaer, F. P., Ed.; Springer: Berlin, 1977; pp 144–193.
57. Loudet, A.; Burgess, K. *Chem. Rev.* **2007**, *107*, 4891–4932.
58. Karolin, J.; Johansson, L. B. A.; Strandberg, L.; Ny, T. *J. Am. Chem. Soc.* **1994**, *116*, 7801–7806.
59. Lumbierres, M.; Palomo, J. M.; Kragol, G.; Roehrs, S.; Müller, O.; Waldmann, H. *Chem. Eur. J.* **2005**, *11*, 7405–7415.
60. Förster, T. H. In *Modern Quantum Chemistry*; Sinanoglu, O., Ed.; Academic: New York, 1965; Vol. 3, pp 93–137.
61. Stryer, L. *Annu. Rev. Biochem.* **1978**, *47*, 819–846.
62. Lakowicz, J. R. *Principles of Fluorescence Spectroscopy*, 2nd ed.; Plenum: New York, 1999.
63. Jovin, T. M.; Arndt-Jovin, D. J. *Annu. Rev. Biophys. Biophys. Chem.* **1989**, *18*, 271–308.
64. Dale, R. E.; Eisinger, J.; Blumberg, W. E. *Biophys. J.* **1979**, *26*, 161–194.
65. Wu, P.; Brand, L. *Anal. Biochem.* **1994**, 218, 1–13.
66. Van Der Meer, W. B.; Coker, G.; Chen, S.-Y. S. *Resonance Energy Transfer: Theory and Data*. VCH: New York, 1994.
67. Cheung, H. C. In *Topics in Fluorescence Spectroscopy*; Lakowicz, J. R., Ed.; Plenum: New York, 1991; Vol. 3, pp 127–176.
68. Jurgens, L.; Arndt-Jovin, D.; Pecht, I.; Jovin, T. M. *Eur. J. Immunol.* **1996**, *26*, 84–91.
69. Clegg, R. M. In *Fluorescence Imaging Spectroscopy and Microscopy*; Wang, X. F., Herman, B., Eds.; Chemical Analysis Series; Wiley: New York, 1996; Vol. 137, pp 179–251.
70. Periasamy, A.; Day, R. N. *J. Biomed. Opt.* **1998**, *3*, 154–160.
71. Periasamy, A.; Day, R. N. *Methods Cell Biol.* **1999**, *58*, 293–314.
72. Heim, R.; Tsien, R. Y. *Curr. Biol.* **1996**, *6*, 178–182.
73. Sullivan, K. F.; Kay, S. A. *Green Fluorescent Proteins*; Academic Press: New York, 1999; Vol. 58.
74. Periasamy, A. *Proc. SPIE* **1998**, *3260*, 106–114.
75. Gordon, G. W.; Berry, G.; Liang, X. H.; Levine, B.; Herman, B. *Biophys. J.* **1998**, *74*, 2702–2713.
76. Kam, Z.; Volberg, T.; Geiger, B. *J. Cell. Sci.* **1996**, *108*, 1051–1062.
77. Day, R. N. *Mol. Endocrinol.* **1998**, *12*, 1410–1419.
78. Varma, R.; Mayor, S. *Nature (London)* **1998**, *394*, 798–801.
79. Kenworthy, A. K.; Edidin, M. *J. Cell Biol.* **1998**, *142*, 69–84.
80. Periasamy, A. *Proc. SPIE* **2000**, *3921*, 299–304.

81. Periasamy, A.; Elangovan, M.; Wallrabe, H.; *et al*. In *Methods in Cellular Imaging*; Periasamy, A., Ed.; Oxford University Press: New York, 2001; pp 295–308.
82. Guo, C.; Dower, S. K.; Holowka, D.; Baird, B. *J. Biol. Chem.* **1995**, *270*, 27562–27568.
83. Periasamy, A. *Methods in Cellular Imaging*. Oxford University Press: New York, 2001.
84. Agranovich, V. M.; Galanin, M. D. *Electronic Excitation Energy Transfer in Condensed Matter*. North-Holland: Amsterdam, 1982.
85. Andrews, D. L., Demidov, A. A., Eds.; In *Resonance Energy Transfer*; Wiley: Chichester, 1999.
86. Bennett, G.; Kellogg, R. *Prog. React. Kinet.* **1967**, *4*, 215–238.
87. Clegg, R. M. *Methods Enzymol*. **1992**, *211*, 353–358.
88. Förster, T. H. *Fluoreszenz Organischer Verbindungen*. Vandenhoeck & Ruprecht: Göttingen, 1951.
89. Selvin, P. *Fluorescence Resonance Energy Transfer*. Academic Press: San Diego, 1995.
90. Wu, P.; Brand, L. *Anal. Biochem.* **1994**, *218*, 1–13.
91. Periasamy, A. *J. Biomed. Opt*. **2001**, *6*, 287–291.
92. Clegg, R. M. In *Laboratory Techniques in Biochemistry and Molecular Biology*; Gadella, T. W. J., Ed.; Academic press: Burlington, 2009; Vol. 33, pp 1–57.
93. Medintz, I. L. *Trends Biotechnol* **2006**, *24*, 539–542.
94. Jares-Erijman, E. A.; Jovin, T. M. *Nat. Biotechnol*. **2003**, *21*, 1387–1395.
95. Willard, D. M.; Carillo, L. L.; Jung, J.; Orden, A. V. *Nano Lett*. **2001**, *1*, 469–474.
96. Haas, E.; Wilchek, M.; Katchalski-Katzir, E.; Steinberg, I. Z. *Proc. Natl. Acad. Sci. USA* **1975**, *72*, 1807–1811.
97. Lakowicz, J. R.; Gryczynski, I.; Wiczk, W.; Laczko, G.; Prendergast, F. C.; Johnson, M. L. *Biophys. Chem.* **1990**, *36*, 99–115.
98. Chapman, E. R.; Alexander, K.; Vorherr, T.; Carafoil, E.; Storm, D. R. *Biochemistry* **1992**, *31*, 12819–12825.
99. Heyduk, T. *Curr. Opin. Biotechnol*. **2002**, *13*, 292–296.
100. Hink, M. A.; Bisselin, T.; Visser, A. J. *Plant Mol. Biol*. **2002**, *50*, 871–883.
101. Parsons, M.; Vojnovic, B.; Ameer-Beg, S. *Biochem. Soc. Trans*. **2004**, *32*, 431–433.
102. Bunt, G.; Wouters, F. S. *Int. Rev. Cytol*. **2004**, *237*, 205–277.
103. Selvin, P. R. *Nat. Struct. Biol*. **2000**, *7*, 730–734.
104. Elangovan, M.; Periasamy, A. *Proc. SPIE* **2001**, *4262*, 177–182.
105. Bucka, S. M.; Xua, H.; Brasuel, M.; Philbert, M. A.; Kopelman, R. *Talanta* **2004**, *63*, 41–59.
106. Koo Lee, Y.-E.; Smith, R.; Kopelman, R. *Annu. Rev. Anal. Chem.* **2009**, *2*, 57–76.
107. Webster, A.; Coupland, P.; Houghton, F. D.; Leese, H. J.; Aylott, J. W. *Biochem. Soc. Trans*. **2007**, *35*, 538–543.
108. Buck, S. M.; Koo, Y. E. L.; Park, E.; *et al*. *Curr. Opin. Chem. Biol*. **2004**, *8*, 540–546.
109. Koo, Y. E. L.; Agayan, R.; Philbert, M. A.; Rehemtulla, A.; Ross, B. D.; Kopelman, R. In *New Approaches in Biomedical Spectroscopy*; Kneipp, K., Aroca, R., Kneipp, H., Wentrup-Byrne, E., Eds.; American Chemical Society: New York, 2007; Vol. 14, pp 200–218.
110. Cheong, W. F.; Prahl, S. A.; Welch, A. J. *IEEE J. Quant. Electron*. **1990**, *26*, 2166–2185.
111. Delpy, D. T.; Cope, M. *Philos. Trans. R. Soc. Lond. B* **1997**, *352*, 649–659.
112. Ntziachristos, V.; Bremer, C.; Weissleder, R. *Eur. Radiol*. **2003**, *13*, 195–208.
113. Woods, L. A.; Powell, P. R.; Paxon, T. L.; Ewing, A. G. *Electroanalysis* **2005**, *17*, 1192–1197.
114. Park, E. J.; Brasuel, M.; Behrend, C.; Philbert, M. A.; Kopelman, R. *Anal. Chem.* **2003**, *75*, 3784–3791.
115. Clark, H. A.; Hoyer, M.; Philbert, M. A.; Kopelman, R. *Anal. Chem.* **1999**, *71*, 4831–4836.
116. Sumner, J. P.; Aylott, J. W.; Monson, E.; Kopelman, R. *Analyst* **2002**, *127*, 11–16.
117. Sumner, J. P.; Westerberg, N.; Stoddard, A. K.; Fierke, C. A.; Kopelman, R. *Sens. Actuators B* **2005**, *113*, 760–767.
118. Sumner, J. P.; Kopelman, R. *Analyst* **2005**, *130*, 528–533.
119. Koo, Y. E. L.; Cao, Y.; Kopelman, R.; Koo, S. M.; Brasuel, M.; Philbert, M. A. *Anal. Chem.* **2004**, *76*, 2498–2505.
120. Cao, Y.; Koo, Y. L.; Kopelman, R. *Analyst* **2004**, *129*, 745–750.
121. Xu, H.; Aylott, J. W.; Kopelman, R.; Miller, T. J.; Philbert, M. A. *Anal. Chem.* **2001**, *73*, 4124–4133.
122. Horvath, T.; Monson, E.; Sumner, J.; Xu, H.; Kopelman, R. *Proc. SPIE (Int. Soc. Photonic Eng.)* **2002**, *4626*, 482–492.
123. Kumar, S.; Harrison, N.; Richards-Kortum, R.; Sokolov, K. *Nano Lett*. **2007**, *7*, 1338–1343.
124. Reddy, G. R.; Bhojani, M. S.; McConville, P.; *et al*. *Clin. Cancer Res*. **2006**, *12*, 6677–6686.
125. Koo, Y. E. L.; Reddy, G. R.; Bhojani, M.; *et al*. *Adv. Drug Deliv. Rev*. **2006**, *58*, 1556–1577.
126. Myc, A.; Majoros, I. J.; Thomas, T. P.; Baker, J. R. *Biomacromolecules* **2007**, *8*, 13–18.
127. Almdal, K.; Sun, H. H.; Poulsen, A. K.; *et al*. *Polym. Adv. Technol*. **2006**, *17*, 790–793.
128. Brown, J. Q.; McShane, M. J. *IEEE Sens. J*. **2005**, *5*, 1197–1205.
129. Clark, H. A.; Hoyer, M.; Parus, S.; Philbert, M. A.; Kopelman, R. *Mikrochim. Acta* **1999**, *131*, 121–128.
130. Clark, H. A.; Barker, S. L. R.; Brasuel, M.; *et al*. *Sens. Actuators B* **1998**, *51*, 12–16.
131. Guice, K. B.; Caldorera, M. E.; McShane, M. J. *J. Biomed. Opt*. **2005**, *10*, 064031.
132. Cheng, Z. L.; Aspinwall, C. A. *Analyst* **2006**, *131*, 236–243.
133. Cao, Y.; Koo, Y. E. L.; Koo, S.; Kopelman, R. *Photochem. Photobiol*. **2005**, *81*, 1489–1498.
134. Kim, G. Ph.D. Thesis, University of Michigan, Ann Arbor, 2008, 151pp.
135. Kim, G.; Koo, Y. E. L.; Xu, H.; Philbert, M. A.; Kopelman, R. *Anal. Chem*. **2010**, *82*, 2165–2169.
136. King, M.; Kopelman, R. *Sens. Actuators B* **2003**, *90*, 76–81.
137. Tyner, K. M.; Kopelman, R.; Philbert, M. A. *Biophys. J*. **2007**, *93*, 1163–1174.
138. Lee, D.; Khaja, S.; Velasquez-Castano, J. C.; *et al*. *Nat. Mater*. **2007**, *6*, 765–769.
139. Sun, H. H.; Scharff-Poulsen, A. M.; Gu, H.; *et al*. *ACS Nano* **2008**, *2*, 19–24.
140. Xu, H.; Aylott, J. W.; Kopelman, R. *Analyst* **2002**, *127*, 1471–1477.
141. Poulsen, A. K.; Scharff-Poulsen, A. M.; Olsen, L. F. *Anal. Biochem.* **2007**, *366*, 29–36.
142. Kim, S. H.; Kim, B.; Yadavalli, V. K.; Pishko, M. V. *Anal. Chem.* **2005**, *77*, 6828–6833.
143. Soper, S. A.; Brown, K.; Ellington, A.; *et al*. *Biosens. Bioelectron.* **2006**, *21*, 1932–1942.
144. Goulko, A. A.; Li, F.; Le, X. C. *Trends Anal. Chem*. **2009**, *28*, 878–892.
145. Li, Y.; Zhou, X.; Ye, D. *Biochem. Biophys. Res. Commun*. **2008**, *373*, 457–461.
146. Santangelo, P. J. *WIREs Nanomed. Nanobiotechnol*. **2010**, *2*, 11–19.
147. Kim, Y.; Sohn, D.; Tan, W. *Int. J. Clin. Exp. Pathol*. **2008**, *1*, 105–116.
148. Venkatesan, N.; Seo, Y. J.; Kim, B. H. *Chem. Soc. Rev*. **2008**, *37*, 648–663.
149. Tyagi, S.; Kramer, F. R. *Nat. Biotechnol*. **1996**, *14*, 303–308.
150. Tyagi, S.; Bratu, D. P.; Kramer, F. R. *Nat. Biotechnol*. **1998**, *16*, 49–53.
151. Yang, C. J.; Lin, H.; Tan, W. *J. Am. Chem. Soc*. **2005**, *127*, 12772–12773.
152. Gifford, L. K.; Jordan, D.; Pattanayak, V.; *et al*. *Anal. Biochem*. **2005**, *347*, 77–88.
153. Johansson, M. K.; Fidder, H.; Dick, D.; Cook, R. M. *J. Am. Chem. Soc*. **2002**, *124*, 6950–6956.
154. Poddar, S. K. *J. Virol. Methods* **1999**, *82*, 19–26.
155. Lee, D. H.; Mathew, J.; Pfahler, W.; *et al*. *J. Clin. Microbiol*. **2005**, *43*, 5111–5116.
156. Sandhya, S.; Chen, W.; Mulchandani, A. *Anal. Chim. Acta* **2008**, *614*, 208–212.
157. Takács, T.; Jeney, C.; Kovács, L.; Mózes, J.; Benczik, M.; Sebe, A. *J. Virol. Methods* **2008**, *149*, 153–162.
158. Jung, J.; Chen, L.; Lee, S.; *et al*. *Anal. Bioanal. Chem*. **2007**, *387*, 2609–2615.
159. Shi, M. M. *Clin. Chem*. **2001**, *47*, 164–172.
160. Sokol, D. L.; Zhang, X.; Lu, P.; Gewirtz, A. M. *Proc. Natl. Acad. Sci. USA* **1998**, *95*, 11538–11543.
161. Vet, J. A.; Marras, S. A. *Methods Mol. Biol*. **2005**, *288*, 273–290.
162. Balashov, S. V.; Gardiner, R.; Park, S.; Perlin, D. S. *J. Clin. Microbiol*. **2005**, *43*, 214–222.
163. Petersen, K.; Vogel, U.; Rockenbauer, E.; *et al*. *Mol. Cell. Probes* **2004**, *18*, 117–122.
164. Wabuyele, M. B.; Farquar, H.; Stryjewski, W.; *et al*. *J. Am. Chem. Soc*. **2003**, *125*, 6937–6945.
165. Kuhn, H.; Demidov, V. V.; Coull, J. M.; Fiandaca, M. J.; Gildea, B. D.; Frank-Kamenetskii, M. D. *J. Am. Chem. Soc*. **2002**, *124*, 1097–1103.
166. Tan, W.; Wang, K.; Drake, T. J. *Curr. Opin. Chem. Biol*. **2004**, *8*, 547–553.
167. Perlette, J.; Tan, W. *Anal. Chem*. **2001**, *73*, 5544–5550.
168. Matsuo, T. *Biochim. Biophys. Acta* **1998**, *1379*, 178–184.
169. Kretschmann, E.; Reather, H. *Z. Naturforsch*. **1968**, *23a*, 2135–2136.
170. Pockrand, I. *Surf. Sci*. **1978**, *72*, 577–588.
171. Otto, A. *Z. Phys*. **1968**, *216*, 398–410.
172. Wendler, L.; Haupt, R. *Phys. Stat. Sol. B* **1987**, *143*, 131–148.
173. Grosjean, L.; Cherif, B.; Mercey, E.; *et al*. *Anal. Biochem*. **2005**, *347*, 193–200.
174. Lee, H. J.; Nedelkov, D.; Corn, R. M. *Anal. Chem*. **2006**, *78*, 6504–6510.
175. Yuk, J. S.; Jung, S.-H.; Jung, J.-W.; *et al*. *Proteomics* **2004**, *4*, 3468–3476.
176. Yuk, J. S.; Hong, D.-G.; Jung, H.-I.; Ha, K.-S. *Sens. Actuators B* **2006**, *119*, 673–675.

177. Piliarik, M.; Vaisocherová, H.; Homola, J. *Biosens. Bioelectron.* **2005**, *20*, 2104–2110.
178. Pho, H. B.; Shin, Y. B.; Kim, M. G.; Yoon, H. C. *Langmuir* **2005**, *21*, 166–171.
179. Lee, H. J.; Yan, Y.; Marriott, G.; Corn, R. M. *J. Physiol.* **2005**, *563*, 61–71.
180. Guedon, P.; Livache, T.; Martin, F. *Anal. Chem.* **2000**, *72*, 6003–6009.
181. Rella, R.; Spadavecchia, J.; Manera, M. G.; Siciliano, P.; Santino, A.; Mita, G. *Biosens. Bioelectron.* **2004**, *20*, 1140–1148.
182. Liu, J.; Tian, S.; Tiefenauer, L.; Nielsen, P. E.; Knoll, W. *Anal. Chem.* **2005**, *77*, 2756–2761.
183. Wark, A. W.; Lee, H. J.; Corn, R. M. *Anal. Chem.* **2005**, *77*, 3904–3907.
184. Wolf, L. K.; Fullenkamp, D. E.; Georgiadis, R. M. *J. Am. Chem. Soc.* **2005**, *127*, 17453–17459.
185. Spadavecchia, J.; Manera, M. G.; Quaranta, F.; Siciliano, P.; Rella, R. *Biosens. Bioelectron.* **2005**, *21*, 894–900.
186. Zhang, X.; Yonzon, C. R.; Young, M. A.; Stuart, D. A.; Van Duyne, R. P. *IEE Proc. Nanobiotechnol.* **2005**, *152*, 195–205.
187. Alvarez-Puebla, R. A.; Liz-Marzán, L. M. *Small* **2010**, *6*, 604–610.
188. Kneipp, J.; Kneipp, H.; Wittig, B.; Kneipp, K. *Nanomedicine: NBM* **2010**, *6*, 214–226.
189. Anker, J. N.; Hall, W. P.; Lyandres, O.; Shah, N. C.; Zhao, J.; Duyne, R. P. V. *Nat. Mater.* **2008**, *7*, 442–453.
190. Willets, K. A. *Anal. Bioanal. Chem.* **2009**, *394*, 85–94.
191. Swain, R. J.; Stevens, M. M. *Biochem. Soc. Trans.* **2007**, *35*, 544–549.
192. Nijssen, A.; Koljenovic, S.; Bakker Schut, T.; Caspers, P.; Puppels, G. *J. Biophoton.* **2009**, *2*, 29–36.
193. Ellis, D.; Goodacre, R. *Analyst* **2006**, *131*, 875–885.
194. Keren, S.; Zavaleta, C.; Cheng, Z.; de la Zerda, A.; Gheysens, O.; Gambhir, S. *Proc. Natl. Acad. Sci. USA* **2008**, *105*, 5844–5849.
195. Puppels, G. J.; Mul, F. F. M. D.; Otto, C.; *et al. Nature* **1990**, *347*, 301–303.
196. Kneipp, K.; Kneipp, H.; Itzkan, I.; Dasari, R. R.; Feld, M. S. *J. Phys. Condens. Matter.* **2002**, *14*, R597–R624.
197. Jeanmaire, D. L.; Van Duyne, R. P. *J. Electroanal. Chem. Interf. Electrochem.* **1977**, *84*, 1–20.
198. McFarland, A. D.; Young, M. A.; Dieringer, J. A.; Van Duyne, R. P. *J. Phys. Chem. B* **2005**, *109*, 11279–11285.
199. Nie, S.; Emory, S. R. *Science* **1997**, *275*, 1102–1106.
200. Dieringer, J. A.; Ii, R. B. L.; Scheidt, K. A.; Van Duyne, R. P. *J. Am. Chem. Soc.* **2007**, *129*, 16249–16256.
201. Kneipp, K.; Wang, Y.; Kneipp, H.; *et al. Phys. Rev. Lett.* **1997**, *78*, 1667–1670.
202. Van Duyne, R. P. In *Chemical and Biochemical Applications of Lasers*; Moore, C. B., Ed.; Academic: New York, 1979; pp 101–184.
203. Zou, S.; Schatz, G. C. *Chem. Rev. Lett.* **2005**, *403*, 62–67.
204. Kneipp, J. In *Surface-Enhanced Raman Scattering: Physics and Applications*; Kneipp, K., Moskovits, M., Kneipp, H., Eds.; Springer Series Topics in Applied Physics; Springer: Berlin, 2006; Vol. 103, pp 335–349.
205. Kneipp, J.; Kneipp, H.; Kneipp, K. *Chem. Soc. Rev.* **2008**, *37*, 1052–1060.
206. Kneipp, K.; Kneipp, H.; Kneipp, J. *Acc. Chem. Res.* **2006**, *39*, 443–450.
207. Kneipp, K.; Kneipp, H.; Manoharan, R.; Hanlon, E. B.; Itzkan, I.; Dasari, R. R. *Appl. Spectrosc.* **1998**, *52*, 1493–1497.
208. Murphy, C. J.; Gole, A. M.; Stone, J. W. *Acc. Chem. Res.* **2008**, *41*, 1721–1730.
209. Tarantola, M.; Schneider, D.; Sunnick, E.; *et al. ACS Nano.* **2009**, *3*, 213–222.
210. Carlson, C.; Hussain, S. M.; Schrand, A. M.; *et al. J. Phys. Chem. B.* **2008**, *112*, 13608.
211. Marquis, B. J.; McFarland, A. D.; Braun, K. L.; Haynes, C. L. *Anal. Chem* **2008**, *80*, 3431–3437.
212. Premasiri, W. R.; Moir, D. T.; Klempner, M. S.; Krieger, N.; Jones, G.; Ziegler, L. D. *J. Phys. Chem. B* **2005**, *109*, 312–320.
213. Kim, J. H.; Kim, J. S.; Choi, H.; *et al. Anal. Chem.* **2006**, *78*, 6967–6973.
214. Hu, Q.; Tay, L. L.; Noestheden, M.; Pezacki, J. P. *J. Am. Chem. Soc.* **2007**, *129*, 14.
215. Kneipp, J.; Kneipp, H.; Wittig, B.; Kneipp, K. *Nano Lett.* **2007**, *7*, 2819–2823.
216. Dijkstra, R. J.; Scheenen, W.; Dam, N.; Roubos, E. W.; ter Meulen, J. J. *J. Neurosci. Methods* **2007**, *159*, 43–50.
217. Nabiev, I. R.; Morjani, H.; Manfait, M. *Eur. Biophys. J.* **1991**, *19*, 311–316.
218. Zhang, X.; Yin, H.; Cooper, J. M. *Anal. Bioanal. Chem.* **2008**, *390*, 833–840.
219. Zhang, X.; Yin, H.; Cooper, J. M. *Electrophoresis* **2006**, *27*, 5093–5100.
220. Kneipp, J.; Kneipp, H.; Rice, W. L.; Kneipp, K. *Anal. Chem.* **2005**, *77*, 2381–2385.
221. Wabuyele, M. B.; Yan, F.; Griffin, G. D.; Vo-Dinh, T. *Rev. Sci. Instrum.* **2005**, *76*, 063710.
222. Martin, M. E.; Wabuyele, M. B.; Chen, K.; *et al. Ann. Biomed. Eng.* **2006**, *34*, 1061–1068.
223. Wang, Y.; Li, D.; Li, P.; *et al. J. Phys. Chem. C* **2007**, *111*, 16833–16839.
224. Kneipp, J.; Kneipp, H.; Rajadurai, C.; Redmond, R.; Kneipp, K. *J. Raman Spectrosc.* **2009**, *40*, 1–5.
225. Talley, C. E.; Jusinski, L.; Hollars, C. W. *Anal. Chem.* **2004**, *76*, 7064–7068.
226. Maranda, B.; Brown, D.; Bourgoin, S.; *et al. J. Biol. Chem.* **2001**, *276*, 18540–18550.
227. Zhang, A. S.; Sheftel, A. D.; Ponka, P. *Blood* **2005**, *105*, 368–375.
228. Yates, R. M.; Hermetter, A.; Russell, D. G. *Traffic* **2005**, *6*, 413–420.
229. Alivisatos, A. P.; Gu, W. W.; Larabell, C. *Ann. Rev. Biomed. Eng.* **2005**, *7*, 55–76.
230. Pinaud, F.; Michalet, X.; Bentolila, L. A.; *et al. Biomaterials* **2006**, *27*, 1679–1687.
231. Michalet, X.; Pinaud, F. F.; Bentolila, L. A.; *et al. Science* **2005**, *307*, 538–544.
232. Bruchez, M., Jr; Moronne, M.; Gin, P.; Weiss, S.; Alivisatos, A. P. *Science* **1998**, *281*, 2013–2016.
233. Chan, W. C. W.; Nie, S. *Science* **1998**, *281*, 2016–2018.
234. Parak, W. J.; Pellegrinol, T.; Plank, C. *Nanotechnology* **2005**, *16*, R9–R25.
235. Medintz, I. L.; Konnert, J. H.; Clapp, A. R.; *et al. Proc. Natl. Acad. Sci. USA* **2004**, *101*, 9612–9617.
236. Jamiesona, T.; Bakhshia, R.; Petrovaa, D.; Pococka, R.; Imanib, M.; Seifaliana, A. M. *Biomaterials* **2007**, *28*, 4717–4732.
237. Chang, Y.-P.; Pinaud, F.; Antelman, J.; Weiss, S. *J. Biophoton.* **2008**, *1*, 287–298.
238. Murray, C. B.; Norris, D. J.; Bawendi, M. G. *J. Am. Chem. Soc.* **1993**, *115*, 8706–8715.
239. Peng, X. G.; Wickham, J.; Alivisatos, A. P. *J. Am. Chem. Soc.* **1998**, *120*, 5343–5344.
240. Hines, M. A.; Guyot-Sionnest, P. *J. Phys. Chem.* **1996**, *100*, 468–471.
241. Ozkan, M. *Drug Discov. Today* **2004**, *9*, 1065–1071.
242. Murphy, C. J. *Anal. Chem.* **2002**, *74*, 520A–526A.
243. Peng, X.; Schlamp, M. C.; Kadavanich, A. V.; Alivisatos, A. P. *J. Am. Chem. Soc.* **1997**, *119*, 7019–7029.
244. Dabbousi, B. O.; Rodriguez-Viejo, J.; Mikulec, F. V.; *et al. J. Phys. Chem. B* **1997**, *101*, 9463–9475.
245. Peng, Z. A.; Peng, X. *J. Am. Chem. Soc.* **2001**, *123*, 183–184.
246. Bailey, R. E.; Nie, S. *J. Am. Chem. Soc.* **2003**, *125*, 7100–7106.
247. Gu, H.; Ho, P.-L.; Tsang, K. W. T.; Wang, L.; Xu, B. *J. Am. Chem. Soc.* **2003**, *125*, 15702–15703.
248. Gu, H.; Zheng, R.; Zhang, X.; Xu, B. *J. Am. Chem. Soc.* **2004**, *126*, 5664–5665.
249. Pinaud, F.; King, D.; Moore, H.-P.; Weiss, S. *J. Am. Chem. Soc.* **2004**, *126*, 6115–6123.
250. Tsay, J. M.; Pflughoefft, M.; Bentolila, L. A.; Weiss, S. *J. Am. Chem. Soc.* **2004**, *126*, 1926–1927.
251. Xu, C. J.; Xu, K.; Gu, H.; *et al. J. Am. Chem. Soc.* **2004**, *126*, 3392–3393.
252. Murray, C. B.; Kagan, C. R.; Bawendi, M. G. *Ann. Rev. Mater. Sci.* **2000**, *30*, 545–610.
253. Xu, C. J.; Xu, K.; Gu, H.; *et al. J. Am. Chem. Soc.* **2004**, *126*, 5664–5665.
254. Mattoussi, H.; Mauro, J. M.; Goldman, E. R.; *et al. J. Am. Chem. Soc.* **2000**, *122*, 12142–12150.
255. Hines, M. A.; Guyot-Sionnest, P. *J. Phys. Chem. B* **1998**, *102*, 3655–3657.
256. Suyver, J. F.; Wuister, S. F.; Kelly, J. J.; Meijerink, A. *Nano Lett.* **2001**, *1*, 429–433.
257. Artmeyev, M. V.; Gaponenko, S. V.; Germanenko, I. N.; Kapitonov, A. M. *Chem. Phys. Lett.* **1995**, *243*, 450–455.
258. Reiss, P.; Bleuse, J.; Pron, A. *Nano Lett.* **2002**, *2*, 781–784.
259. Brooks, R. A.; Moiny, F.; Gillis, P. *Magn. Reson. Med.* **2001**, *45*, 1014–1020.
260. Chan, W. C. W.; Maxwell, D. J.; Gao, X. H.; Bailey, R. E.; Han, M. Y.; Nie, S. M. *Curr. Opin. Biotechnol.* **2002**, *13*, 40–46.
261. Chen, C. C.; Yet, C. P.; Wang, H. N.; Chao, C. Y. *Langmuir* **1999**, *15*, 6845–6850.
262. Mitchell, G. P.; Mirkin, C. A.; Letsinger, R. L. *J. Am. Chem. Soc.* **1999**, *121*, 8122–8123.
263. Sun, B.; Xie, W.; Yi, G.; Chen, D.; Zhou, Y.; Cheng, J. *J. Immunol. Methods* **2001**, *249*, 85–89.
264. Aldana, J.; Wang, Y. A.; Peng, X. G. *J. Am. Chem. Soc.* **2001**, *123*, 8844–8850.
265. Willard, D. M.; Carillo, L. L.; Jung, J.; Van Orden, A. *Nano Lett.* **2001**, *1*, 469–474.
266. Zhang, C. Y.; Ma, H.; Nie, S. M.; Ding, Y.; Jin, L.; Chen, D. Y. *Analyst* **2000**, *125*, 1029–1031.
267. Mattoussi, H.; Mauro, J. M.; Goldman, E. R.; Green, T. M.; Anderson, G. P. *Phys. Stat. Sol. B* **2001**, *224*, 277–283.
268. Parak, W. J.; Gerion, D.; Zanchet, D.; *et al. Chem. Mater.* **2002**, *14*, 2113–2119.
269. Goldman, E. R.; Balighian, E. D.; Kuno, M. K.; Labrenz, S.; Tran, P. T. *Phys. Stat. Sol. B* **2002**, *229*, 407–414.
270. Parak, W. J.; Boudreau, R.; Le Gros, M.; *et al. Adv. Mater.* **2002**, *14*, 882–885.

271. Derfus, A. M.; Chan, W. C. W.; Bhatia, S. N. *Nano Lett*. **2004**, *4*, 11–18.
272. Kaul, Z.; Yaguchi, T.; Kaul, S. C.; Hirano, T.; Wadhwa, R.; Taira, K. *Cell Res.* **2003**, *13*, 503–507.
273. Tokumasu, F.; Dvorak, J. *J. Microsc.* **2003**, *211*, 256–261.
274. Minet, O.; Dressler, C.; Beuthan, J. *J. Fluoresc.* **2004**, *14*, 241–247.
275. Wu, X.; Liu, H.; Liu, J.; Haley, K. N.; Treadway, J. A. *Nat. Biotechnol*. **2003**, *21*, 41–46.
276. Pellegrino, T.; Manna, L.; Kudera, S.; *et al*. *Nano Lett*. **2004**, *4*, 703–707.
277. Dubertret, B.; Skourides, P.; Norris, D. J.; Noireaux, V.; Brivanlou, A. H.; Libchaber, A. *Science* **2002**, *298*, 1759–1762.
278. Pathak, S.; Choi, S. K.; Arnheim, N.; Thompson, M. E. *J. Am. Chem. Soc.* **2001**, *123*, 4103–4104.
279. Wang, Y. A.; Li, J. J.; Chen, H. Y.; Peng, X. G. *J. Am. Chem. Soc.* **2002**, *124*, 2293–2298.
280. Guo, W.; Li, J. J.; Wang, Y. A.; Peng, X. G. *Chem. Mater*. **2003**, *15*, 3125–3133.
281. Kim, S.; Bawendi, M. G. *J. Am. Chem. Soc.* **2003**, *125*, 14652–14653.
282. Åkerman, M. E.; Chan, W. C. W.; Laakkonen, P.; Bhatia, S. N.; Ruoslahti, E. *Proc. Nat. Acad. Sci. USA* **2002**, *99*, 12617–12621.
283. Lakowicz, J. R.; Gryczynski, I.; Gryczynski, Z.; Nowaczyk, K.; Murphy, C. J. *Anal. Biochem.* **2000**, *280*, 128–136.
284. Mahtab, R.; Harden, H. H.; Murphy, C. J. *J. Am. Chem. Soc.* **2000**, *122*, 14–17.
285. Hanaki, K.; Momo, A.; Oku, T.; Komoto, A.; Maenosono, S. *Biochem. Biophys. Res. Commun.* **2003**, *302*, 496–501.
286. Rosenthal, S. J.; Tomlinson, A.; Adkins, E. M.; *et al*. *J. Am. Chem. Soc.* **2002**, *124*, 4586–4594.
287. Winter, J. O.; Liu, T. Y.; Korgel, B. A.; Schmidt, C. E. *Adv. Mater*. **2001**, *13*, 1673–1677.
288. Jaiswal, J. K.; Mattoussi, H.; Mauro, J. M.; Simon, S. M. *Nat. Biotechnol*. **2003**, *21*, 47–51.
289. Goldman, E. R.; Anderson, G. P.; Tran, P. T.; Mattoussi, H.; Charles, P. T.; Mauro, J. M. *Anal. Chem*. **2002**, *74*, 841–847.
290. Goldman, E. R.; Balighian, E. D.; Mattoussi, H.; *et al*. *J. Am. Chem. Soc.* **2002**, *124*, 6378–6382.
291. Kloepfer, J. A.; Mielke, R. E.; Wong, M. S.; Nealson, K. H.; Stucky, G.; Nadeau, J. L. *Appl. Environ. Microbiol*. **2003**, *69*, 4205–4213.
292. Sukhanova, A.; Venteo, L.; Devy, J.; *et al*. *Lab. Investig.* **2002**, *82*, 1259–1261.
293. Hermanson, G. T. *Bioconjugate Techniques*. Academic: San Diego, CA, 1996.
294. Kondoh, M.; Araragi, S.; Sato, K.; Higashimoto, M.; Takiguchi, M.; Sato, M. *Toxicology* **2002**, *170*, 111–117.
295. Shen, H.-M.; Yang, C.-F.; Ong, C.-N. *Int. J. Cancer* **1999**, *81*, 820–828.
296. Kirchner, C.; Liedl, T.; Kudera, S.; Pellegrino, T.; Javier, A. M.; Gaub, H. E. *Nano Lett*. **2005**, *5*, 331–338.
297. Clarke, S. J.; Hollmann, C. A.; Zhang, Z.; *et al*. *Nat. Mater*. **2006**, *5*, 409–417.
298. Hsieh, S. C.; Wang, F. F.; Hung, S. C.; Chen, Y.; Wang, Y. J. *J. Biomed. Mater. Res. B Appl. Biomater*. **2006**, *79B*, 95–101.
299. Lovric, J.; Bazzi, H. S.; Cuie, Y.; Fortin, G. R. A.; Winnik, F. M.; Maysinger, D. *J. Mol. Med*. **2005**, *83*, 377–385.
300. Chen, F. Q.; Gerion, D. *Nano Lett* **2004**, *4*, 1827–1832.
301. Shiohara, A.; Hoshino, A.; Hanaki, K.; Suzuki, K.; Yamamoto, K. *Microbiol. Immunol*. **2004**, *48*, 669–675.
302. Hardman, R. *Environ. Health. Perspect*. **2006**, *114*, 165–172.
303. Zhang, T. T.; Stilwell, J. L.; Gerion, D.; *et al*. *Nano Lett*. **2006**, *6*, 800–808.
304. Mansson, A.; Sundberg, M.; Balaz, M.; *et al*. *Biochem. Biophys. Res. Commun.* **2004**, *314*, 529–534.
305. Larson, D. R.; Zipfel, W. R.; Williams, R. M.; *et al*. *Science* **2003**, *300*, 1434–1436.
306. Ness, J. M.; Akhtar, R. S.; Latham, C. B.; Roth, K. A. *J. Histochem. Cytochem.* **2003**, *51*, 981–987.
307. Mattheakis, L. C.; Dias, J. M.; Choi, Y. J.; *et al*. *Anal. Biochem.* **2004**, *327*, 200–208.
308. Pellegrino, T.; Parak, W. J.; Boudreau, R.; *et al*. *Differentiation* **2003**, *71*, 542–548.
309. Dahan, M.; Lévi, S.; Luccardini, C.; Rostaing, P.; Riveau, B.; Triller, A. *Science* **2003**, *302*, 442–445.
310. Lidke, D. S.; Nagy, P.; Heintzmann, R.; *et al*. *Nat. Biotechnol*. **2004**, *22*, 198–203.
311. Levene, M. J.; Dombeck, D. A.; Kasischke, K. A.; Molloy, R. P.; Webb, W. W. *J. Neurophys*. **2004**, *91*, 1908–1912.
312. Kim, S.; Lim, Y. T.; Soltesz, E. G.; *et al*. *Nat. Biotechnol*. **2004**, *22*, 93–97.
313. Voura, E. B.; Jaiswal, J. K.; Mattoussi, H.; Simon, S. M. *Nat. Med*. **2004**, *10*, 993–998.
314. Gao, X.; Cui, Y.; Levenson, R. M.; Chung, L. W. K.; Nie, S. *Nat. Biotechnol*. **2004**, *22*, 969–976.
315. Yu, X.; Chen, L.; Li, K.; *et al*. *J. Biomed. Opt*. **2007**, *12*, 014008.

3.329. Hydrogels in Biosensing Applications

F Topuz, D Buenger, and D Tanaka, RWTH Aachen University, Aachen, Germany
J Groll, RWTH Aachen University, Aachen, Germany; University Hospital Würzburg, Würzburg, Germany

© 2011 Elsevier Ltd. All rights reserved.

3.329.1.	**Introduction**	491
3.329.1.1.	Sensors: General Definition and Classification	491
3.329.1.2.	Biosensors	492
3.329.1.3.	Hydrogels: Definitions and Theoretical Aspects	493
3.329.1.4.	Hydrogels for Biosensors	494
3.329.1.5.	Structure of the Chapter	494
3.329.2.	**Physicochemical Sensing Mechanisms**	495
3.329.2.1.	Temperature Sensitivity	495
3.329.2.2.	Ion Strength and pH	496
3.329.2.3.	Gas and Humidity	498
3.329.2.3.1.	Gas	498
3.329.2.3.2.	Humidity	499
3.329.3.	**Biochemical Sensing Mechanisms**	500
3.329.3.1.	Molecular Interactions	500
3.329.3.1.1.	Enzyme–substrate interaction	500
3.329.3.1.2.	Antibody–antigen	501
3.329.3.1.3.	DNA and oligonucleotides	503
3.329.3.1.4.	Other binding mechanisms	506
3.329.3.2.	Living Sensors	510
3.329.3.2.1.	Bacteria	510
3.329.3.2.2.	Cells	511
3.329.4.	**Summary**	513
References		514

Glossary

Free radical polymerization A method of polymerization by which a polymer is formed from the successive addition of free radical building blocks.

Hydrogels Hydrogels are three-dimensionally cross-linked hydrophilic polymeric networks capable of imbibing considerable amounts of water or biological fluids without undergoing dissolution.

Photonic crystals Periodic optical nanostructures that are designed to affect the motion of photons in a similar way that periodicity of a semiconductor crystal affects the motion of electrons.

Quartz crystal microbalance (QCM) A quartz crystal microbalance measures a mass per unit area by measuring the change in frequency of a quartz crystal resonator.

3.329.1. Introduction

3.329.1.1. Sensors: General Definition and Classification

In general, the term sensor is derived from the Latin word *sensus*, which directly translated means *sense*, or to *sense something*. If one thinks about a *sense*, the first idea that comes up is the traditional five human senses: sight, hearing, taste, smell, and touch. The senses give the human body the ability to receive signals or stimuli from the environment and to react or respond to them. If a sense gives the ability to receive and to respond to a signal, we can transfer this to the technical level and define a sensor as follows:

A sensor is a device that receives and responds to signals and stimuli from the environment. Furthermore, the human senses give a first hint of how sensors can be classified. Sight, hearing, and touch have one thing in common, that is they sense physical stimuli, namely light, in the form of electromagnetic waves, acoustic waves, and pressure. Smell and taste respond to chemical stimuli, like odor and taste molecules. Accordingly, sensors can be divided into two big classes: physical and chemical sensors. In 1991, the IUPAC defined the terms physical and chemical sensor with the following definitions[1]:

> A physical sensor is a device that provides information about a physical property of the system.
>
> A chemical sensor is a device that transforms chemical information, ranging from the concentration of a specific sample component to total composition analysis, into an analytically useful signal.

Now that the term sensor is defined and a first classification, corresponding to the sensed stimulus, is made, a closer look at the general structure of sensors can be taken. Again,

the human senses lead the way to this structure: whenever receptor cells in the human body receive certain stimuli, for example, an electromagnetic wave hits a photoreceptor cell in the retina, a chemical reaction is triggered and then transduced, in the form of an electrical signal, to the brain. Deductive sensors consist of two basic parts, namely, a receptor and a transducer part. Technically speaking, the receptor part of a sensor receives a chemical or physical stimulus and transforms it into a form of energy. The transducer part is then capable of transducing this energy into a useful analytical signal, which can be processed and displayed. Figure 1 illustrates the general sensor structure.

At the technical level, there are many ways to classify sensors, for example, according to the measuring effect, given analyte, receptor principle, field of application, mode of application, and so on. The most established way is the one following the principles of signal transduction, committed by the IUPAC 1991 for chemical sensors[1]:

1. Optical sensors, based on absorbance, reflectance, luminescence, fluorescence, index of refraction, optothermal effect, and light-scattering effects.
2. Electrochemical sensors, based on voltammetric, including amperometric and potentiometric effects, chemically sensitized field effect transistors (CHEMFET), and potentiometric solid electrolyte gas sensors.
3. Electrical sensors, based on metal oxide semiconductors and organic semiconductors.
4. Mass-sensitive sensors, based on piezoelectric and surface acoustic wave effects.
5. Magnetic sensors, based on paramagnetic gas properties.
6. Thermometric sensors, based on heat effects of specific chemical reaction or adsorption.
7. Radiation-sensitive sensors, based on absorbance, or emission of X-, β-, or γ-radiation that is used for the determination of a chemical composition.

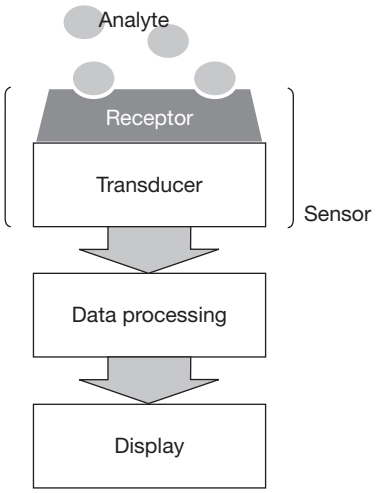

Figure 1 General sensor structure comprising a receptor that interacts with the analyte and a transducer. Beyond that core sensing unit, data processing and display are important parts of complete sensor systems.

As the classification shows, the IUPAC draws no clear line between chemical and physical sensors and counts physical sensors that measure, for example, a chemical state, reaction, or composition as chemical sensors. This shows that a general approach to classification is difficult, as chemical and physical sensing almost always go hand in hand. Hence, more generally, sensors can be defined as devices that determine selectively and reversibly the concentration of analyte molecules by amplifying the signal resulting from an interaction between the analyte and the receptor without the need for any other instrument and additional reagents.[2]

3.329.1.2. Biosensors

If a physical sensor is a device that provides information about the physical property of a system and a chemical sensor is a device that transforms chemical information into an analytically useful signal, a biosensor consequently must work in a similar way. Actually, the class of biosensors can be counted as a cross of both physical and chemical sensors. They can be devices that provide information about a biophysical property of a system and/or transform biochemical information into an analytically useful signal. What is more important is the fact that biosensors have a biological recognition element that enables the analysis of relevant biological information. This concept corresponds with the definition for biosensors given by the IUPAC in 1999[3]:

> A biosensor is an integrated receptor–transducer device, which is capable of providing selective quantitative or semi-quantitative analytical information using a biological recognition element.

A classification of biosensors can be done after one of the following principles:

1. Following the principle of signal transduction, for example, electrochemical, optical, mass sensitive, and so on.
2. Depending on the biological recognition element, for example, biological ionophores, enzymes, antigens/antibodies, whole cells, membrane receptors, plant and animal tissue, protein receptors and channels, oligonucleotides, specific ligands, etc.
3. Classified after the sensed analyte, for example, glucose, DNA, enzymes, toxins, certain drugs, and so on.

From the first biosensor invention filed by Leland C. Clark in 1962 that concerned a potentiometric enzyme electrode developed to measure concentration of glucose,[4] numerous biosensors with different specificities have been developed. During the last decade, much work was devoted to downsize the laboratory workspace toward small and versatile biosensor devices. However, indispensable requirements, including fast responsibility, reproducibility, reliability, and stability, remained the same. Crucial parameters in designing biosensors with high performance are (i) immobilization of biomolecules in their native conformation (ii) accessibility of receptors to the targets, and (iii) specific adsorption to the support.[5–7] Especially regarding these demands, hydrogels offer specific advantages for biosensors. As this chapter is dedicated to hydrogels in biosensing applications, the next paragraph gives a brief theoretical introduction into main properties and definitions.

3.329.1.3. Hydrogels: Definitions and Theoretical Aspects

Hydrogels are three-dimensionally cross-linked hydrophilic polymeric networks capable of imbibing considerable amounts of water or biological fluids without dissolving.[8] The cross-linking degree in hydrogel networks is described as the density of junctions joining the chains into a permanent form defining the mesh size.[9] The mesh size, ξ, is an important term used to define the distance between two adjacent cross-links and provides a measurable space available between the macromolecular chains for diffusion of particles[10] (**Figure 2**).

The swelling process of hydrogels with water consists of three main steps: first, diffusion of water molecule through the gel matrix, then relaxation of polymer chains via hydration, and lastly, expansion of the polymer network into surrounding bulk water upon relaxation.[11] The stretching of the polymer chains increases the elastic refractive force as a counteract for the network expansion. When balance between these two forces becomes equal, the network expansion due to swelling will stop and come to equilibrium volume. Several parameters like nature of the polymer and ionic groups[12,13] contribute to the swelling of the polymer network. For example, an increase of the ionic content inside the network results in an osmotic pressure between the gel matrix and its surrounding, thus exhibiting faster swelling and higher equilibrium degree of swelling.

One of the most widely used theories for swelling of neutral hydrogels is the equilibrium swelling theory of Flory and Rehner.[14,15] They modeled this theory as assuming Gaussian distribution of polymer chains. In this theory, the swelling of the polymer network is a function of elastic forces of the polymer chains and the thermodynamics compatibility of the polymer and water molecules. According to this theory, the free energy of a neutral hydrogel (ΔG) can be expressed as

$$\Delta G = \Delta G_{el} + \Delta G_{mix} \quad [1]$$

where ΔG_{el} represent the contribution of elastic refractive forces and ΔG_{mix} is the thermodynamic compatibility of the polymer and the swelling agent. The incorporation of ionic groups through the matrix will create the term, ΔG_{ionic}, which is the total free energy contribution of ionic groups in the network.

$$\Delta G = \Delta G_{el} + \Delta G_{mix} + \Delta G_{ionic} \quad [2]$$

This equation can be rewritten by means of chemical potentials, and the equilibrium conditions' total chemical potential (μ) will be equal to zero:

$$\mu = \mu_{el} + \mu_{mix} + \mu_{ionic} = 0 \quad [3]$$

In the absence of solvent, Flory and Rehner's theory leads to an expression for molecular weight between cross-links ($\bar{M}_C$) shown in eqn [4]:

$$\frac{1}{\bar{M}_C} = \frac{2}{\bar{M}_N} - \frac{(\bar{v}/V_1)\left[\ln(1-v_{2,s}) + v_{2,s} + \chi_1 v_{2,s}^2\right]}{v_{2,s}^{1/3} - \frac{v_{2,s}}{2}} \quad [4]$$

where $\bar{M}_N$ is the average molecular weight of polymer chains prepared in the absence of a cross-linking agent. $\bar{v}$ and v_1 are the specific volume of water and the molar volume of the water, respectively. $v_{2,r}$ and $v_{2,s}$ refer to the polymer volume fraction in the relaxed, the state of the polymer immediately after cross-linking, and fully swollen states, respectively.

Upon incorporation of ionic groups into the network, the swelling equilibrium of the swelling matrix becomes more complicated. The two new terms, ionic strength, I, and dissociations constants, K_a and K_b, have to be added to eqn [4]. The equivalent expression for anionic and cationic gels is shown in eqns [5] and [6], respectively.[16]

$$\frac{V_1}{4I}\left(\frac{v_{2,s}^2}{\bar{v}}\right)\left(\frac{K_a}{10^{-pH} - K_a}\right) = \left[\ln(1-v_{2,s}) + v_{2,s} + \chi_1 v_{2,s}^2\right] + \left(\frac{V_1}{\bar{v}\bar{M}_C}\right)\left(1 - \frac{2\bar{M}_C}{\bar{M}_N}\right)v_{2,r}\left[\left(\frac{v_{2,s}}{v_{2,r}}\right)^{1/3} - \left(\frac{v_{2,s}}{2v_{2,r}}\right)\right] \quad [5]$$

$$\frac{V_1}{4I}\left(\frac{v_{2,s}^2}{\bar{v}}\right)\left(\frac{K_b}{10^{pH-14} - K_a}\right) = \left[\ln(1-v_{2,s}) + v_{2,s} + \chi_1 v_{2,s}^2\right] + \left(\frac{V_1}{\bar{v}\bar{M}_C}\right)\left(1 - \frac{2\bar{M}_C}{\bar{M}_N}\right)v_{2,r}\left[\left(\frac{v_{2,s}}{v_{2,r}}\right)^{1/3} - \left(\frac{v_{2,s}}{2v_{2,r}}\right)\right] \quad [6]$$

Mesh size, ξ (i.e., correlation length) based on values for the cross-linking density or molecular weight between cross-links, can be described using the following equation:

$$\xi = v_{2,s}^{1/3}(\bar{r}_o^2)^{1/2} = Q^{1/3}(\bar{r}_o^2)^{1/2} \quad [7]$$

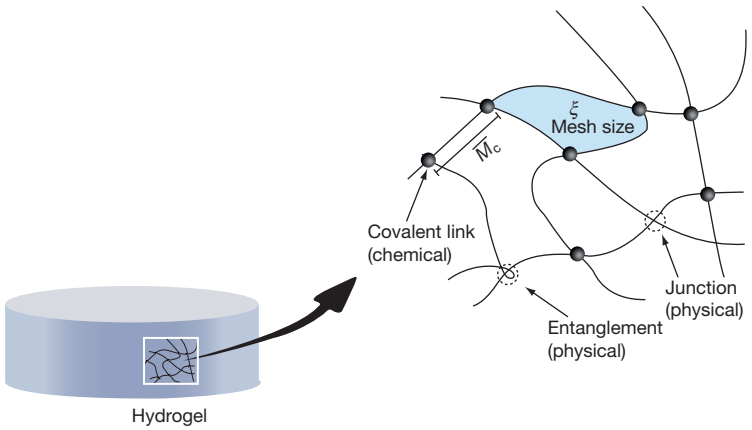

Figure 2 Scheme of a cross-linked hydrogel structure. ξ is the mesh size of the network and $\bar{M}_C$ is the molecular weight between two cross-linking points.

where α is the elongation of the polymer chains in any direction and $(\bar{r}_o^2)^{1/2}$ is the end-to-end distance of the polymer chains between cross-linking points in the unperturbed state. Assuming isotropic swelling of the gels, the end-to-end distance and the pore size of a swollen polymeric network can be calculated using the following equation:

$$\xi = \upsilon_{2,s}^{-1/3} \left(\frac{2\, C_N\, \bar{M}_C}{M_r} \right)^{1/2} \iota \qquad [8]$$

where ι is the length of the bond along the backbone chain and C_N and M_r are the Flory characteristic ratio (ratio of the square of the unperturbed distance to the square of the random flight end-to-end distance) and the molecular weight of the repeating units, respectively.

By changing such factors like mesh size or the molecular weight between cross-links, hydrogel with particular thermal, diffusive, or mechanic properties can be obtained.[17] Moreover, it becomes clear that analyte-induced changes in the characteristics of the network such as the cross-linking density, content of ionic species, or chemical nature of the polymer backbone will result in macroscopic effects such as altered swelling behavior. Such changes can result from physicochemical stimuli such as changes in temperature, pH, or ion strength, or they may originate from biochemical recognition events. Both effects are, among others, used in biosensing applications. The following paragraph gives a brief overview of the different applications of hydrogels in biosensing.

3.329.1.4. Hydrogels for Biosensors

The high water content and hydrophilic nature of hydrogel is similar to the void-filling component of the extracellular matrix and renders them intrinsically biocompatible. Hydrogels are thus used for a wide range of biomedical applications such as soft contact lenses[18] and controlled drug delivery systems.[19] Hence, a straightforward application of hydrogels in biosensors is a protection and coating function of sensor parts to prevent undesired interaction with biological molecules or cells. Their open porous structure and hydrophilic environment allows diffusion of analytes through the hydrogel. However, diffusion of larger molecules such as proteins may be prevented by an increased cross-linking density, and cells are usually not able to penetrate unless the gel structure is biodegradable.

Beyond simple protection, hydrogels can be used as an immobilization matrix for the biosensing elements. Hydrogels provide excellent environments for enzymes and other biomolecules to hold them in their thermodynamically stable form.[20] Also, cells are commonly immobilized in hydrogel matrices for various purposes.[21] Recognition in hydrogel-based sensors is provided by interaction between an analyte and sensing element by volume changes in response to target molecules. As a result of recognition, volumetric change creates a new kind of sensing system instead of the classical biosensor based on the electrochemical way. The prominent point in designing sensors with high selectivity and sensitivity mainly depends on receptors that have to be immobilized in their native conformation to be able to specifically interact with the analyte while support material should be resistant to unspecific adsorption. Furthermore, the quality of sensing mainly depends on accessibility and activity of the immobilized sensing molecules inside the hydrogel network, determining the sensitivity level. As hydrogels may easily be tailored in their properties, they form an ideal platform for this purpose, and extensive work has been carried out with a variety of analytes such as proteins, ions, carbohydrates, and nucleic acids.[22–24]

Hydrogels may also act as active sensing material. For this purpose, the so-called smart gels or stimuli-responsive gels are especially interesting. Such gels are sensitive to small changes in the environment and give the response to physical stimuli (temperature,[25] light,[26] pressure,[27] electric fields,[28] ionic strength,[29] and magnetic field[30]), chemical stimuli (pH,[31] ions[32]), or biological stimuli (glucose,[33] enzyme,[34] and antigen[35]) through volume changes. The response rate is dependent on the hydrogel composition, shape, and size and can be increased by several proposed techniques such as reducing the size,[36] decreasing the cross-linking density,[37] and increasing both ionic groups[38] and pore size.[39] In the presence of these stimuli, the hydrogels undergo phase transition by the sensing molecules and simultaneously translate this sense into a macroscopic event. In this way, the conversion of hydrogel swelling to an electrical output is possible with various techniques like light transmission measurement,[40] conductometry,[41] and pressure generated by the gel swelling.[42]

Hydrogels may be prepared in aqueous solutions by UV[43] or thermoinitiated radical polymerization,[44] addition reaction,[45] self-assembly of recognition motifs such as coiled-coils,[46,47] peptides,[48–50] hydrogen-bridges,[51] or DNA.[52–55] They can be formed by *in situ* gelation from low-viscosity solutions and thus be injected into small voids or complex fluidic and microfluidic devices. This predisposition to miniaturization and integration into the microsystem in desired geometry broadens their analytical applications. Hydrogels may thus be formed by *in situ* patterning on desired devices.[56]

3.329.1.5. Structure of the Chapter

In the last decade, remarkable efforts have been achieved to manifold sensitivity and selectivity of hydrogel-based biosensors. By using different gel combinations, various systems with different specificities have been prepared, leading to better sensor performance. This chapter gives an overview of the use of hydrogels in biosensors, not only actively acting as sensing material themselves but also used for immobilization of molecules that cause the sensing stimulus in the presence of the analyte. We have structured the following detailed discussion strictly according to the sensing mechanism. **Section 3.329.2** comprises examples for physicochemical sensing where the signal is generated as response to changes in parameters such as temperature, pH, ion strength, gas, and humidity. Importantly, no biochemical recognition process is involved in these sensing mechanisms. Studies where the sensing mechanism is based on such processes, either through molecular interaction or by reaction of bacteria or cells toward the analyte, are presented and discussed in **Section 3.329.3**. Molecular interactions may be based on enzyme–substrate interaction, where a chemical reaction is catalyzed and causes the effect that may be sensed, or on binding/debinding events caused by the presence of the analyte that causes changes in the hydrogel network. Antibody–analyte interaction, peptide–peptide bonding, or

streptavidin/biotin are examples for such selective binding systems with high analyte affinity. Also, chemical moieties that mimic biological ligand binding, such as the binding of glucose to phenylboronic acids, are included in Section 3.329.3.

3.329.2. Physicochemical Sensing Mechanisms

An excellent and detailed overview of stimulus-sensitive hydrogels used in sensor and actuators was published by van der Linden *et al.* in 2003.[57] Hence, this chapter presents the basic mechanisms that build the basis for sensing and focuses on the advances achieved in the last decade.

3.329.2.1. Temperature Sensitivity

Temperature sensing is significant in many fields of biotechnology.[58] Detection of temperature via sensors can be achieved in a variety of ways. One of the most convenient ways is the use of thermoresponsive polymers as sensing agents. These temperature-sensitive polymers respond to temperature by volume changes. Poly(*N*-isopropylacrylamide) (PNIPAm) is a widely used polymer for its temperature-induced reversible volume–phase transition behavior, showing between 20 and 40 °C.[59] The underlying sensing mechanism is based on the free energy of the network that comprises hydrophobic side groups. At lower temperatures, hydration of the polymer backbones is dominant. With rising temperature, the motion of the water molecules increases. At the critical solution temperature, the entropy gained by the release of the water molecules together with the energy gained by hydrophobic interaction and clustering of the hydrophobic moieties surpasses the free energy of the hydrated state. Hence, the network collapses. The swelling/shrinking of thermoresponsive-based hydrogel can be monitored by following the thickness and refractive index of the hydrogel layer via the spectroscopic ellipsometric technique in changing temperatures. For that aim, the hydrogel has to be immobilized on the solid support. In this context, also the patterning of PNIPAM-based hydrogels has been used by different groups.[60,61] In one case, a temperature sensor construct was fabricated from PNIPAM-*g*-PEG-based micropatterned hydrogel film by Schmaljohann and colleagues.[62] They used ellipsometry to monitor the changes in the layer of interest due to swelling of hydrogel as a function of temperature on a micrometer scale. PNIPAM-*g*-PEG-based hydrogel was immobilized and micropatterned using photolithography. After confirmation of patterning through imaging ellipsometry in dry state, detection of temperature was performed by changing the volume of the hydrogel in deionized water using the localized nulling node as well as the three-dimensional (3D) profiles of the thickness-sensitive ellipsometric angle.

Intelligent polymerized crystalline colloidal arrays (IPCCAs) are one of the alternative approaches for temperature sensing. IPCCAs consist of a crystal colloidal array of polymer spheres polymerized in a hydrogel matrix. The array of colloidal spheres acts similar to photonic crystal and diffracts the light, giving rise to intense color. With incorporation of a temperature-sensitive hydrogel, the IPCCA structure becomes an ideal candidate for temperature sensing. Upon temperature change, the volume transition of the hydrogel induces color changes by means of change in diffraction properties.[63] The diffraction through PCCA particles follows Bragg's law, which is formalized thus:[64]

$$m\lambda = 2nd\sin\theta \qquad [9]$$

where d is the diffraction order, λ is the wavelength of light in vacuum, and n and d refer to refractive index of system and diffracting phase spacing, respectively. θ is the Bragg glancing angle. Hence, when the hydrogel volume increases upon temperature change, the distance between the colloidal spheres increases and so, the Bragg peak of the diffracted light is shifted to longer wavelengths. In one case, a temperature sensing construct based on IPCCA particles was designed by cross-linking acrylamide (AAm) and *N*-isopropylacrylamide (NIPA) with bisacrylamide in the presence of the UV photoinitiator 2,2-diethoxyacetophenone (DEAP) around a face-centered cubic (fcc) array of monodisperse, ~100-μm diameter highly negatively charged polystyrene colloidal particles.[65] These particles diffract visible light because the (111) planes of the fcc polystyrene colloidal particle array have ~200-nm lattice constant. This NIPAM–IPCCA is swollen in cold water but collapses with increasing temperature, resulting in a blue shift of the diffraction. The change in diffraction wavelength is shown in Figure 3. The diffraction wavelength is monitored at a defined angle relative to the incident light.

A different methodology for sensing temperature was established by Borisov *et al.*[66] They use europium(III) complexes as luminescent temperature indicators within hydrogel-coated microbeads. These complexes exhibit strong brightness when excited at 405 nm. When the excitation is turned off, the luminescence decay time is temperature-dependent, so that an optical readout for temperature is possible. A similar temperature sensor with optical readout based on a PVA/borax hydrogel was reported by Lee *et al.*[67] They used 2-naphthol as a fluorescence indicator probe in the hydrogel with excitation at

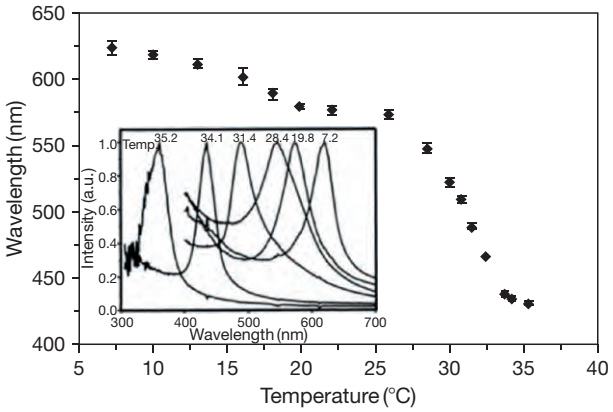

Figure 3 Temperature dependence of diffraction spectrum of *N*-isopropylacrylamide intelligent polymerized crystalline colloidal array particle dispersion. The diffraction is measured in back-scattering. As the temperature increases, the wavelength blue shifts. Reproduced from Reese, C. E.; Baltusavich, M. E.; Keim, J. P.; Asher, S. A. Anal. Chem. **2001**, *75*(21), 5038–5042, with permission from American Chemical Society.

365 nm and a maximum of the emission at 426 nm. Upon temperature increase, the fluorescence emission intensity of 2-naphthol increases linearly in the temperature range of 30–80 °C.

3.329.2.2. Ion Strength and pH

pH-sensitive hydrogels change their volume, mass, and elasticity reversibly in response to a change in the pH value.[68] The pH-sensitive character of hydrogels[69–76] makes them promising materials for a broad range of applications as microsensors[68–71] and microactuators in MEMS devices. The principles for swelling-dependent pH value detection can be various: changes of the holographic diffraction wavelength in optical Bragg grating sensors,[74] shifts of the resonance frequency of a quartz crystal microbalance in microgravimetric sensors,[75] a bending of micromechanical bilayer cantilevers,[76] as well as a deflection of silicon membranes in piezoresistive pressure sensors.[73,76] Before we give some detailed examples for pH sensors based on hydrogels, we advise the reader to have a closer look at the comprehensive review about hydrogel-based pH sensors and microsensors published by Richter *et al.* in 2008.[77] This review introduces the physical background of the special properties of pH-responsive hydrogels and gives a good overview of transducers, which are able to convert the changes of the physical properties of stimuli-responsive hydrogels into electrical signals.

An example for the use of pH-sensitive hydrogels based on an IPCCA was developed by Reese *et al.*[65] Through partial hydrolysis of the acrylamide hydrogel with NaOH, the hydrogel network was endowed with carboxylate groups. As described previously, this hydrogel was polymerized around a fcc array of monodisperse, ~100-μm diameter highly negatively charged polystyrene colloidal particles. Hence, change in pH induced swelling/deswelling of the hydrogel due to protonation/deprotonation of the particle surface and the hydrogel. The resulting color change was measured according to the temperature-sensitive IPCCA described earlier.

The group of Gerald Gerlach used the strong swelling ability of pH-responsive hydrogels[76] to develop a sensor which combines piezoresistive-responsive elements as mechanoelectrical transducers and the phase transition behavior of hydrogels as a chemomechanical transducer. They demonstrated the operational principle of chemical and pH sensors based on the swelling behavior of hydrogels.[78] For the realization of pH sensors, poly(vinyl alcohol)/poly(acrylic acid) (PAA/PVA) hydrogels with a pH value-dependent swelling behavior were used as chemomechanical transducers for a piezoresistive sensor setup. A similar setup but with PNIPAM has been applied and investigated for pH sensors as well. From the same group, Trinh *et al.* reported a simulation and design study of the system.[79] To optimize the sensor design, Sorber *et al.* investigated the swelling effect of the mentioned (PAA/PVA) hydrogel system by Fourier transform infrared (FT-IR) attenuated total reflection spectroscopic imaging under *in situ* conditions.[80] The results of the FT-IR spectroscopic images rendered an improved chemical sensor possible and demonstrated that *in situ* FT-IR imaging is a powerful method for the characterization of molecular processes within chemically sensitive materials.

Lee *et al.* observed the transformations of pH-sensitive hydrogel-based inverse opal photonic sensors from a fcc to a L11-like crystal structure.[81] By directly imaging a Rhodamine B (RhoB)-labeled inverse opal hydrogel, using two-photon laser scanning fluorescence microscopy, it was possible to characterize the mesostructure evolution of the pH-sensitive sensors during swelling. Along with the expected swelling normal to the substrate, they found that the template inverse opal structure undergoes a number of unique structural transformations upon swelling, including a transformation from fcc to an L11-like crystal structure.

An interesting optical sensing system utilizing the stimuli-responsive swelling character of a hydrogel lens system was published by Dong *et al.*[82] The central component of their lens system was a stimuli-responsive hydrogel integrated into a microfluidic system that served as the container for a liquid droplet (Figure 4). The hydrogel simultaneously sensed the presence of stimuli and actuated adjustments to the shape –

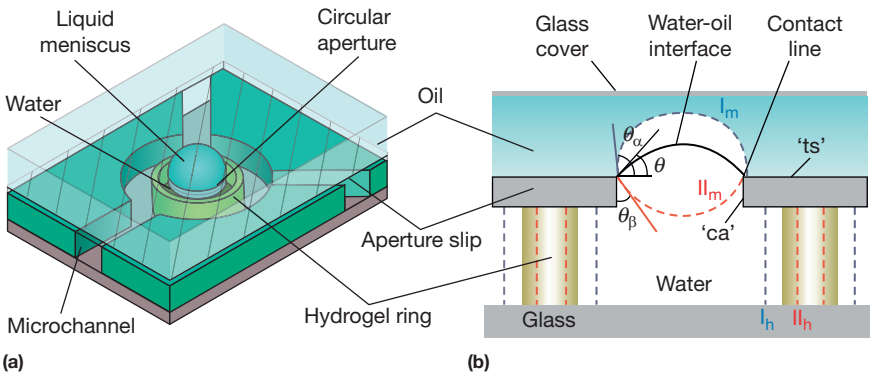

Figure 4 Smart microlens using a pinned liquid–liquid interface. (a) The water–oil interface forms the liquid microlens. The microchannels allow the flow of fluids to the microlens structure. (b) Smart variable-focus mechanism. The hydrophilic sidewall and bottom surface ('ca') and hydrophobic top surface ('ts') of the aperture pin the water–oil meniscus along the contact line 'ca–ts'. The expansion and contraction of the hydrogel regulates the shape of the liquid meniscus by changing the angle ν of the pinned water–oil interface. The blue dashed lines show the expanded state of the hydrogel ring ('Ih') and the corresponding divergent microlens ('Im') at $\theta = \theta_\alpha$. The red dashed lines show the contracted state of the hydrogel ring ('IIh') and the corresponding convergent microlens ('IIm') at $\theta = -(90^\circ - \theta_\beta)$. Reproduced from Dong, L.; Agarwal, A. K.; Beebe, D. J.; Jiang, H. *Nature* **2006**, *442*, 551–554, with permission from Nature Group.

and hence the focal length – of the droplet. The group demonstrated two systems: a pH-sensitive liquid microlens, using an acrylic acid-based hydrogel, and a temperature-sensitive liquid microlens, using a NIPA hydrogel.

An easy and biologically inspired method for sensing a pH value was presented by Kim *et al.*[83] The method is based on elastic instabilities of bipolymer swelling hydrogels: two different bipolymer gel stripes were fixed in such a way together that their differential response in swelling, induced by a designated stimulus, caused the strip to bend. On account of the fixation of the bipolymer gel stripes, the swelling energy released in an explosive elastic instability. One example was a setup with an acid-responsive dimethylaminoethyl methacrylate (DMAEMA)/hydroxyethyl methacrylate (HEMA)-based hydrogel on one side and an acrylic acid (AA)/HEMA-based hydrogel on the other side. In contact with a base or buffer, the bipolymer stripe delaminated in a rapid motion (**Figure 5**).

Sannino *et al.* used a quartz crystal microbalance (QCM) to recognize even very small changes in pH.[84] They established a spin coating method to coat QCM plates with cellulose-based superabsorbent hydrogels to obtain hydrogel-based fast sensors. The hydrogel network was obtained by cross-linking hydroxyethyl cellulose (HEC) and carboxymethyl cellulose (CMC) by the difunctional divinylsulfone (DVS). Owing to the polyelectrolyte CMC, the hydrogels displayed sensitivity to variations of ionic strength and pH of the water solution in which they were immersed. The change in mass resulted in a change of the oscillating frequency of the quartz plate with a fast response and a final accuracy on the weight variation of the order of nanograms.

A hydrogel-based method to recognize a local pH distribution by a change in color was developed by Maruyama *et al.*[85]

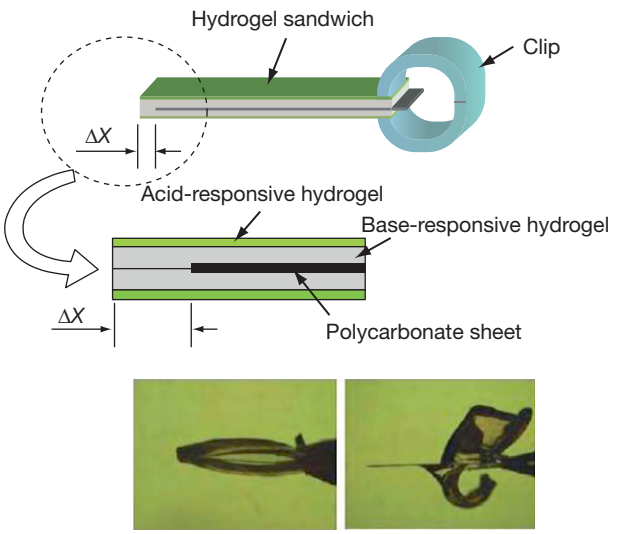

Figure 5 A hydrogel sandwich for explosive fracture motion. The hydrogel sandwich is composed of acid, and base-responsive hydrogels bond together in a certain way that an outward bending is created by stimuli like base and buffer. Once the elastic force overcomes the bonding force, the gels delaminate in a rapid motion. Reproduced from Kim, D.; Beebe, D. J. A sensing method based on elastic instabilities of swelling hydrogels. In *International Conference on Medical Biology*, Japan, 2006; pp 292–294.

They found a novel and easy technique to investigate local pH distribution on a chip using hydrogel films patterned by photolithography. To make the hydrogels sensitive to pH changes, they were functionalized with a pH-indicator, for example, Bromocresol Green (BCG). The local pH was measured from the color of the hydrogel impregnated with BCG based on the calibrated color information in YCrCb color space.

Ion-sensitive hydrogels generally work in a fashion similar to pH-sensitive systems. Guenther *et al.* proposed an online analytical system to monitor metal ions using gels as chemomechanical transducers.[86]

In this case, they improved the rheochemical sensor based on piezoresistive pressure sensor chips. This sensor was constructed from two piezoresistive sensor chips (chemical and viscosity sensors) mounted on a socket with an integrated capillary. A combination of these sensors makes it possible to obtain information about the investigated solutions. A piezoresistive Wheatstone bridge has been used as a mechanoelectrical transducer for the transformation of the plate deflection ω into electrical output signal U_{out}. Hydrogel is composed of a chemically cross-linked PNIPAAm, cross-linker BAA as well as photo-cross-linkable co- and terpolymer of NIPAAm, 2-(dimethyl maleimide)-*N*-ethylacrylamide (DMIAAm) as chromophore, and poly(2-vinylpyridine) (P2VP) (or *N*,*N*-dimethyl acrylamide (DMAAm), respectively), used as chemomechanical transducers. A thin layer of the photo-cross-linkable hydrogel has been deposited onto the back of the bending plate and irradiated with UV light. The aqueous solution has induced the volume change of hydrogel. These volumetric changes were monitored by integrated Wheatstone bridge inside a rectangular silicon plate. The plate deflection caused a stress state change inside the plate and therefore a resistivity change of the resistors affecting proportionally the output voltage of the sensor. An increase of this output voltage corresponded to the hydrogel swelling, whereas a reduction of electrical output voltage corresponded to the shrinkage of the gel.

As mentioned earlier, intelligent polymerized crystalline array (IPCCA)-based sensors can be used to detect pH changes. The same system can be modified for detection such as Pb^{2+} in high ionic-strength solution as well as in body fluids. Therefore, crown ether groups that chelate Pb^{2+} with high specificity were incorporated into the hydrogel network between the spheres, either by functionalization of the hydrogel with crown ether[87] or by direct copolymerization of vinyl-crown ether into the hydrogel matrix. When chelation of Pb^{2+} with crown ether occurred, the hydrogel started to swell driven by osmotic pressure. On account of this swelling, the distance between the spheres increased and red-shift of the diffracted light occurred proportional to the Pb^{2+} concentration. The detection limit of Pb^{2+} was lower than 0.5 $\mu mol\,l^{-1}$.

Also, hydrogel-modified microcantilevers have been used for ion sensing. They provide an excellent dynamic response even to small amounts of analyte by bending upon analyte adsorption on one side of the cantilever due to change in surface tension. CrO_4^{2-} ion can be sensed using microcantilever based on self-assembled monolayer (SAM) of a triethyl-12-mercaptododecylammonium.[88] The detection limit of this sensor is as low as 10^{-9} M; however, this sensor gradually loses its sensitivity over one week because of instability of the layer. Hence, a more stable coating is required for long-

time monitoring purposes. Hence, Zhang *et al.* used a hydrogel layer based on acrylamide and (3-acrylamidopropyl) triethyl ammonium chloride instead of SAM.[89] When this microcantilever is exposed to CrO_4^{2-} ions, deflection occurs as a function of CrO_4^{2-} concentration. This microcantilever shows higher specificity to CrO_4^{2-} compared to other ions like Br^-, HPO_4^{2-}, and NO_3^{2-} with a sensitivity as low as 10^{-11} M.

A different methodology was used to detect ionic strength and pH with hydrogel-based sensor arrays with perforated piezoresistive diaphragms.[90] The sensor was constructed with three components: the piezoelectric detectors, the pH-sensitive hydrogel sensor composed of hydroxypropyl methacrylate (HPMA), *N*,*N*-dimethylaminoethyl methacrylate (DMA), and the crosslinker tetraethylene glycol dimethacrylate (TEGMA), and a backing plate. Diffusion pores were comprised to allow analyte flow to the hydrogel. Alternatively, the backing plate was perforated. Swelling/deswelling of the hydrogel because of changes in ion strength induces pressure changes onto the piezoelectric sensors that are directly converted into electric signals.

3.329.2.3. Gas and Humidity

3.329.2.3.1. Gas

In the field of gas-sensing, hydrogels are mainly used for three purposes. Owing to their antiadhesive and protein-repellent character, hydrogels can be used just as a passive protection coating for a sensor/electrode.[91] Alternatively, hydrogels can be modified by gas-sensitive molecules, for example, special fluorescent dyes[92] which renders them sensitive for certain gases. Finally, the stimuli-responsive swelling character can be used for sensing, mainly for sensing carbon dioxide after the Severinghaus principle.[93,94] This strategy utilizes the pH change resulting from CO_2 diffusion into an electrolyte solution which can then be sensed by a pH-sensitive hydrogel.

One example for use as a protective layer is the internal hydrogel separation layer of the planar ultramicroelectrode nitric oxide (NO) sensor developed by Oh *et al.* to measure local NO surface concentrations.[95] The sensor array consists of a platinized working electrode and a silver paint reference electrode coated with a thin silicone rubber gas-permeable membrane. The working electrode and the gas-permeable membrane were separated by an internal hydrogel layer. They could demonstrate that the NO-selective ultramicroelectrode is an appropriate tool for determining accurate steady-state surface NO concentrations.

A hydrogel gas sensor from the second sub class was described by Zguris *et al.*[96] They developed a possible nitric oxide, hydrogel biosensor that utilized 4-amino-5-methylamino-2′,7′-difluorofluorescein (DAF-FM) entrapped in poly(ethylene glycol) (PEG) hydrogel microstructures. By utilizing the NO-sensitive fluorescence of the dye and bioinert character of the hydrogel matrix, it was possible to create a disposable biosensor that is applicable for nitric oxide production in certain mammalian cells. The sensor has a lower detection range of 0.5 μM of nitric oxide in solution. Owing to the irreversibility of the dye, it is a nondynamic system.

An example for a hydrogel sensor for the detection of carbon dioxide, based on the Severinghaus principle, was developed by Herber *et al.*[97] Therefore, a pH-sensitive hydroxyethyl methacrylate (HEMA)-*co*-dimethylaminoethyl methacrylate (DMAEMA) hydrogel disk, which swelled and deswelled in response to pH changes, was clamped between a silicon pressure sensor chip and a porous metal screen together with a bicarbonate solution. CO_2 reacts with the bicarbonate solution resulting in a pH change, which was converted into a pressure by the enclosed hydrogel. This pressure was a measure for the partial pressure of CO_2. A more sophisticated hydrogel biosensor based on the Severinghaus principle was described by Ter Steege *et al.*[98] They developed the prototype of a continuous hydrogel CO_2 sensor as an alternative and improvement to standard air tonometry. The work follows up on the previous work of Herber *et al.*[99] The sensor consisted of a pH-sensitive, dimethylaminoethyl methacrylate (DMAEMA) and comonomer 2-hydroxyethyl methacrylate (HEMA)-based hydrogel in a bicarbonate solution mounted on a catheter-tip pressure sensor. It is covered by a gas-permeable membrane (**Figure 6**). The swelling/shrinking of the hydrogel is dependent on the CO_2 concentration, which leads to a change in volume and pressure reflected by the pressure sensor.

The sensor enabled continuous measurement of luminal CO_2 and fast detection of sudden and gradual changes in pCO_2 in a clinical significant range. On account of the handmade assembly, the sensor lacked the temperature stability to meet clinical demands, but the authors gave a positive outlook for automated assembly system.

A crossover of the principles could be described in the work of Kocinova *et al.*[100] They presented an interesting method for noninvasive, simultaneous optical monitoring of oxygen and pH during bacterial cultivation in 24-well microplates by using an integrated dual sensor for dissolved oxygen and pH values. The dual sensor was based on oxygen-sensitive organosilica microparticles and pH-sensitive microbeads from a polymethacrylate derivative embedded into a polyurethane hydrogel. The readout was based on a phase-domain fluorescence lifetime. The sensor was used for monitoring the growth of *Pseudomonas putida* bacterial cultures (**Figure 7**).

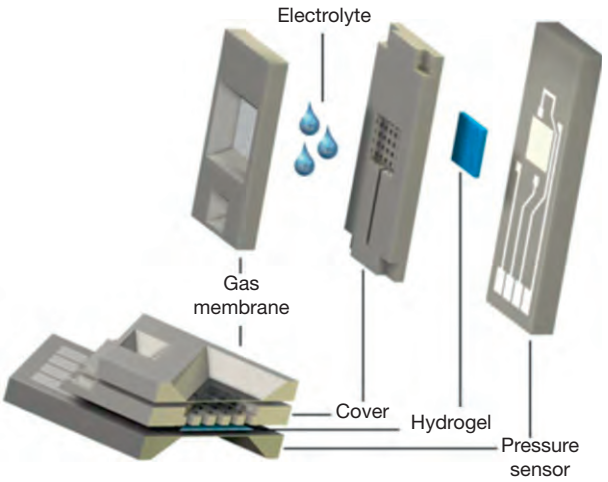

Figure 6 Exploded view of all parts and assembly drawing of the final hydrogel-based CO_2 sensor. Reproduced from ter Steege, R. W. F.; Herber, S.; Olthuis, W.; Bergveld, P.; van den Berg, A.; Kolkman, J. J. *J. Clin. Monit. Comput.* **2007**, *21*(2), 83–90, with permission from Springer.

3.329.2.3.2. Humidity

Humidity sensing is important in numerous industries such as food, petroleum, textiles, ceramics, and many others.[101] Optical-based detection via color change offers the most attractive way for detection of humidity without complex system configuration and tuning in comparison to other sensing mechanisms.[102] Photonic crystals fabricated by the colloidal method form a cubic close packed ordered structure. As the structure diffracts light, it exhibits a stop band in its transmission spectrum. Photonic crystal (PC) hydrogels are widely used in optical-based sensing devices due to the high sensitivity.[103–105] The color change feature of PC hydrogels to water endowed it as a promising candidate to act as a humidity sensor.

A humidity-sensitive PC hydrogel was prepared by infiltrating acrylamide (AAm) solution into a P(St–MMA–AA) PC template and subsequent photopolymerizing.[103] Owing to the intrinsic humidity-sensitive property of acrylamide, a broad range of humidity (from 20 to 100%) could be observed by obvious color changes. This was attributed to the humidity sensitivity of the sample's stopband. The color changes and optical properties were also investigated by UV–vis spectroscopy. The stopbands of the PC hydrogels shift to different values with regard to exposed humidity (Figure 8).

A different photonic crystal-based sensing system was reported by Kang and colleagues.[106] They prepared responsive photonic crystal hydrogel based on amphiphilic poly styrene-*b*-quaternized poly(2-vinyl pyridine) block-copolymers. This structure forms a single 1D periodic lamellar structure resulting in a responsive photonic crystal gel structure. The glassy hydrophobic layer forces expansion of the hydrophilic layer along the layer normal, yielding extremely large optical tunability through the changes in both layer thickness and index of refractions. The wavelength for this system was changed 575% (λ_{peak}= 350–1600 nm) in the position of the stopband.

Barry and coworkers reported the detection of humidity via polyacrylamide-based inverse opal hydrogels (IOH).[107] These smart materials have the capacity to respond to humidity changes by shifting its optical reflection peak noticeably within the visible wavelength range due to interlayer swelling and shrinking of the structures. With increasing humidity, equilibrium-swollen hydrogels absorb more water from air to restore equilibrium conditions. This volume change results in shifting the refractive spectrum. These IOH structures exhibited reflectance spectra with highly differentiable peaks due to their layered structure and Bragg reflection properties.

Galindo and coworkers reported another optical-based system for humidity detection.[108] They encapsulated fluorescent flavylium salts in a poly(2-hydroxylethyl methacrylate) (PHEMA) network matrix. Synthetic flavylium salts are a family of compounds possessing almost the same backbone as that

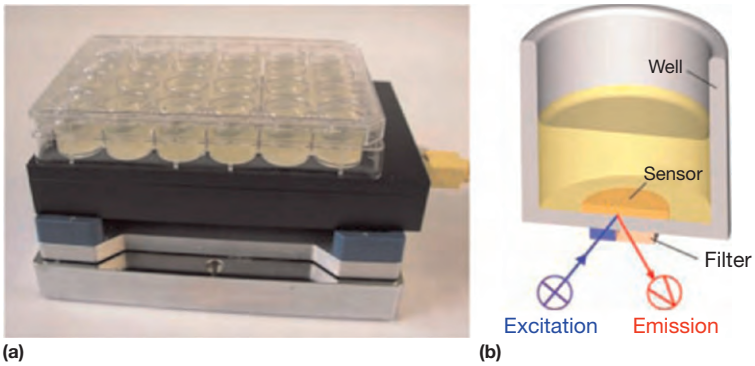

Figure 7 24-channel SensorDish® Reader on the shaker (a) and cross-section of a well of a microplate with included sensor at its bottom (b). Excitation and detection of the emission is performed through the bottom of the plate. Reproduced from Kocincova, A. S.; Nagl, S.; Arain, S.; Krause, C.; Borisov, S. M.; Arnold, M.; Wolfbeis, O. S. *Biotechnol. Bioeng.* **2008**, *100*(3), 430–438.

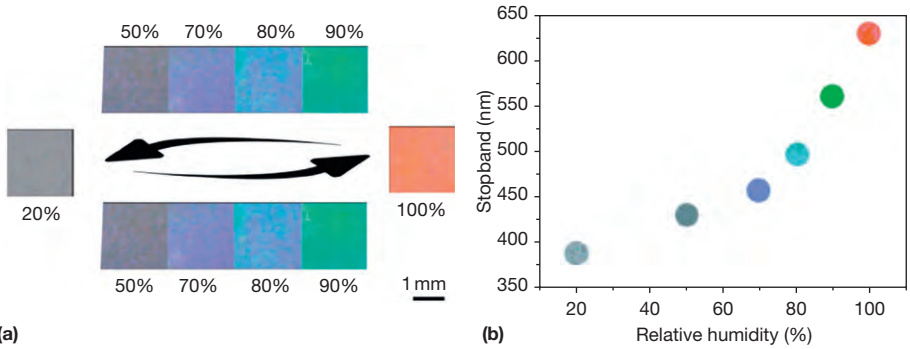

Figure 8 Photographs of poly(acrylic acid)–P(St–MMA–AA) hydrogels corresponding to relative humidity (a) and color/stopband changes of PC hydrogel as a function of humidity (b). Redrawn from Tian, E.; Wang, J.; Zheng, Y.; Song, Y.; Liang, L.; Zhu, D. *J. Mater. Chem.* **2008**, *18*, 1116–1122, with permission from The Royal Society of Chemistry.

of anthocyanin which is the pigment responsible for plant coloration. Flavylium salts are strongly colored and display a fluorescence emission that is quenched by water for synthetic flavylium salts possessing hydroxyl substituents. This is due to the presence of efficient intermolecular excited state proton transfer (ESPT) to water and opens the use of these molecules for humidity sensing. By this, swelling and deswelling of hydrogels at relative humidities between 7% and 100% could be measured by fluorescence decay times of the flavylium salts.

3.329.3. Biochemical Sensing Mechanisms

This paragraph concerns sensing based on biochemical mechanisms. At first, sensing based on molecular interactions is discussed, followed by a paragraph about 'living' sensors where bacteria or cells that are immobilized in or on hydrogels generate the signal that is used for sensing.

3.329.3.1. Molecular Interactions

3.329.3.1.1. Enzyme–substrate interaction

Enzymes are highly specific and efficient in their reaction with substrates. They act as catalysts by lowering the activation energy of chemical reactions. Therefore, in first approximation, the substrate is in a first step forming a complex with the enzyme by docking into the highly selective active pocket of the enzyme. This enzyme–substrate complex represents the reactive transition state of the reaction in which the substrate is activated. After the subsequent chemical reaction, the product is released and the enzyme is restored in its functional conformation. If the concentration of the substrate is sufficiently high, the catalyst is saturated with substrate and the reaction is only determined by the rate of conversion from the substrate to the product. This results in a pseudo-first-order kinetic of the reaction with regard to the concentration of the enzyme according to eqn [10] (Michaelis–Menton equation), where v is the rate of the reaction, k_{cat} the rate constant of the catalyzed reaction, K_m a constant that comprises k_{cat} and the rate constant for the enzyme–substrate complex formation, $[E_0]$ the starting concentration of the enzyme, and [S] is the concentration of the substrate.

$$v = \frac{k_{cat} \cdot [E_0] \cdot [S]}{K_m + [S]} \qquad [10]$$

In reality, often more complex reaction schemes such as multiple binding and allosteric rearrangements occur, in which the affinity and enzymatic activity is different for the consecutive binding events. However, the mathematical description of these processes is comparable. In any case, this brief introduction into enzyme activity and enzyme kinetic shows that enzymatic activity may be used for precise determination of analyte concentrations. In the following sections, a variety of different analytes that have been detected through enzyme substrate interaction in hydrogel matrices are presented and discussed.

3.329.3.1.1.1. Alcohol

Wu *et al.* developed an organic-phase alcohol biosensor by coentrapping alcohol oxidase and horseradish peroxidase within an ionotropic polymer hydrogel matrix fabricated from silica gel particles.[109] By entrapping the enzymes into the hydrogel matrix, it was possible to maintain a biocatalytic reaction at high and stable rates for an online detection of methanol in *n*-hexane under flow operation mode. The analytical working range of the sensor was 2.3–90 mM methanol in *n*-hexane with an operational biosensor-lifetime of more than 45 assays and a shelf lifetime longer than 2 weeks.

3.329.3.1.1.2. Amino acids

An L-glutamate sensor based on a bienzyme redox PVI19-dmeOs/poly(ethylene glycol)(400)diglycidyl ether (PEGDGE) hydrogel was developed by In Castillo *et al.*[110] The sensor was capable of detecting the release of this excitatory neurotransmitter from adherently growing HN10 and C6 cell cultures upon stimulation. Monitoring was utilized using an electrode modified with the bienzyme redox hydrogel at an applied potential of −50 mV versus the internal Ag reference electrode. The detection limit, 0.5 μM, and the response time of the sensor, 35 s, satisfied the experimental requirements of cell culture base experiments.

3.329.3.1.1.3. Ammonia

Kwan *et al.* constructed a bienzyme sensor for the amperometric determination of ammonium (NH_4^+) by immobilizing glutamate oxidase and glutamate dehydrogenase on a clark-type oxygen electrode.[111] To guarantee the catalytic activity, the enzymes were entrapped in a poly(carbamoyl) sulfonate hydrogel matrix. The sensor has fast response (2 s) and short recovery times (2 min), a linear detection range between 10 and 300 μM ammonium and a detection limit of 2.06 μM.

3.329.3.1.1.4. Glucose

On account of the increasing numbers of diabetes patients, the demand for smart glucose sensing systems has grown more and with this the effort to utilize hydrogels for glucose sensing applications. Before concentrating in more detail on hydrogel-biosensor systems that are used for glucose sensing, we would like to draw the reader's attention to the review 'Chemically controlled closed-loop insulin delivery' by Ravaine *et al.* published in 2008.[112] This review focuses on glucose-responsive hydrogels and gives a good overview of the hydrogel systems that are either modified, for example, by glucose oxidase, lectin, and phenylboronic acid moiety, release insulin, or swell/shrink in the presence of glucose. Thus, we want to focus on the major strategies for enzyme-based glucose sensing and on some recently published studies.

One of the most conventional methods to detect glucose levels is the use of enzyme systems like glucose oxidase (GOX)[113,114] or glucose dehydrogenase.[115] For example, when glucose oxidase is immobilized in a pH-sensitive hydrogel matrix, the oxidation reactions from glucose to gluconic acid will force the hydrogel to swell. The swelling of the hydrogel can then be sensed by mass-sensitive magnetoelastic sensors.[116] Kim *et al.* described a micropatterning technique to immobilize proteins on the surface of 3D PEG-based hydrogel microstructures that could be used for hydrogel-biosensor applications.[117] Therefore, hydrogel microstructures were fabricated by replica molding using a poly(dimethylsiloxane) (PDMS) replica as a molding insert and photolithography. Bovine serum albumin

(BSA), a model protein, was covalently immobilized to the otherwise protein-repellant surface of the hydrogel structures. The empty space inside hydrogel microstructures could be occupied by different proteins, and sequential bienzymatic reaction of glucose oxidase and peroxidase (POD) could be demonstrated in a hydrogel microstructure by immobilizing the GOX on the surface of the POD-entrapping hydrogel microstructure.

In 2009, Merchant *et al.* built a high-sensitivity reagentless amperometric biosensor based on ferrocene-modified linear poly(ethylenimine).[118] A double function biosensor for glucose and hydrogen peroxide has been built by immobilizing GOX and horseradish peroxidase (HRP) in cross-linked films of ferrocene-modified linear poly(ethylenimine). Ferrocene was involved as a mediator of electron transfer to the electrode surface. Current densities ~4 times higher than those obtained with other ferrocene-based redox polymers could be achieved. This sensor generated a limiting catalytic density of 1.2 mA cm^{-2} which is the highest known density ever reported for redox polymers with GOX at pH 7. Owing to the very high sensitivity (73 nA cm^{-2} μM^{-1}) of the system, it was possible to detect glucose concentrations in the micromolar range.

3.329.3.1.1.5. Hydrogen peroxide

Hydrogen peroxide is the product of reactions of oxidative metabolism catalyzed by oxidases and its detection is prominent in environmental, clinical, and biological studies due to its applications in many industrial processes as an oxidizing, bleaching, and sterilizing agent.[119] A lot of work has been done for the determination of hydrogen peroxide via different methods like titrimetry, electrochemistry, and UV spectrophotometry.[120] Peroxidases (POD) are generally used in these constructions to convert hydrogen peroxide into radicals. The sensitivity of the determination of hydrogen peroxide via peroxidase enzyme depends on the ability of the immobilizing matrix to retain the functional conformation of the enzyme for a long time. Through the last decade, an impressive number of inventive designs for hydrogen peroxide determination have appeared. Here, we focus on some illustrative example studies of hydrogel-based hydrogen peroxide detection, generally based on the electrochemical sensing system.

The detection of H_2O_2 is based on the intracellular optical sensor reported by Kim *et al.*[121] They established optical nanosensor based on PEG hydrogel spheres containing the enzyme horseradish peroxidase (HRP) for hydrogen peroxide detection. HRP was encapsulated in PEG hydrogel spheres by reverse emulsion photopolymerization without losing activity. Afterward, the fluorescence emission response of these hydrogel spheres changed as a function of H_2O_2 concentration in the presence of Amplex Red, and no leaching of HRP was observed from the spheres. The HRP-loaded hydrogel spheres were introduced via phagocytosis inside macrophages and were found to respond to both exogenous and endogenous sources of oxidative stress.

Varma and Mattiasson developed a simple amperometric biosensor for the detection of hydrogen peroxide in aqueous and organic solvents.[122] Therefore, they entrapped catalase in 30% polyacrylamide gels and created a two-electrode system. By studying the kinetics of the catalase-modified electrode by cyclic voltammetry (CV) and coupling it to a flow injection analysis (FIA) setup, it was possible to create a sensing system that could monitor a broad range of hydrogen peroxide concentrations (0.5–100 mM) in different solvents. As mentioned previously, amperometric detection of H_2O_2 has been achieved via immobilization of HRP in cross-linked films of ferrocene-modified linear poly(ethylenimine).[118] When a small amount of H_2O_2 was added to the solution, oxidation peaks disappeared and reduction peaks increased due to an increase in redox polymer mediation of the HRP-catalyzed reduction of H_2O_2.

A new-type sol–gel/hydrogel composite-based hydrogen peroxide biosensor based on silica sol and a graft copolymer of poly vinyl alcohol with 4-vinyl pyridine was fabricated by Wang *et al.*[123] The film was characterized by FT-IR spectroscopy and optimum analytical performance was obtained depending on the pH and electrochemical behavior of the biosensor using potassium hexacyanoferrate(II) as a mediator. This system exhibited high sensitivity (15 $\mu A\,mM^{-1}$) and a low detection limit of 5×10^{-7} M.

Optical-based local detection of H_2O_2 secreted by stimulated macrophages was performed using an enzyme-based biosensor by Yan *et al.*[124] Photolithographic patterning of hydrogel based on PEG with incorporation of horseradish peroxidase (HRP) applied to construct microstructures, use as sensing agent (**Figure 9**). They used a special organic molecule, called Amplex Red, which became fluorescent in the presence of H_2O_2 and HRP, and was either immobilized inside hydrogel elements alongside enzyme molecules or added into the cell culture media during cell activation. The production of H_2O_2 after mitogenic stimulation of macrophages resulted in the appearance of fluorescence in the HRP-containing hydrogel microstructures.

3.329.3.1.2. Antibody–antigen

Antibody–antigen-based sensors are affinity-based devices with a coupling of immunochemical reactions.[125] The general working principle of this sensor is based on the specific immunochemical recognition of antibodies (or antigens) immobilized on a transducer to antigen (or antibodies), which produce signals that depend on the centration of the analyte. Antibody–antigen-based detection of target molecules has gained attention in the last three decades due to its high specificity and low detection limit.[126] Antibody–antigen sensing has become an increasingly practical and useful tool in biotechnology.[127]

Detection in antibody–antigen sensing system can be performed in different ways. One of the widely used techniques is quartz crystal microgravimetry with dissipation (QCM-D) which provides real-time immunoassay capability. QCM is a detection method that quantifies the decrease of the resonant frequency of the crystal when the mass increases when antigen binds to immobilized antibodies. Dissipation measurement provides additional information about the viscoelasticity of the surface, which can increase with antigen binding. This technique is widely used in immunoassay applications because of high sensitivity. Tabrizian and coworkers prepared and used low-molecular-weight polyethylneimine (PEI) and carboxymethylcellulose (CMC), and covalently immobilized antibody by cross-linking between carboxymethyl groups of CMC and succinimide esters generated on the antibody.[128] This hydrogel-interface has been evaluated with detection of cytokines rhIL-1ra, rhIL-6, and rhiL-18BPa antigens. Increasing the

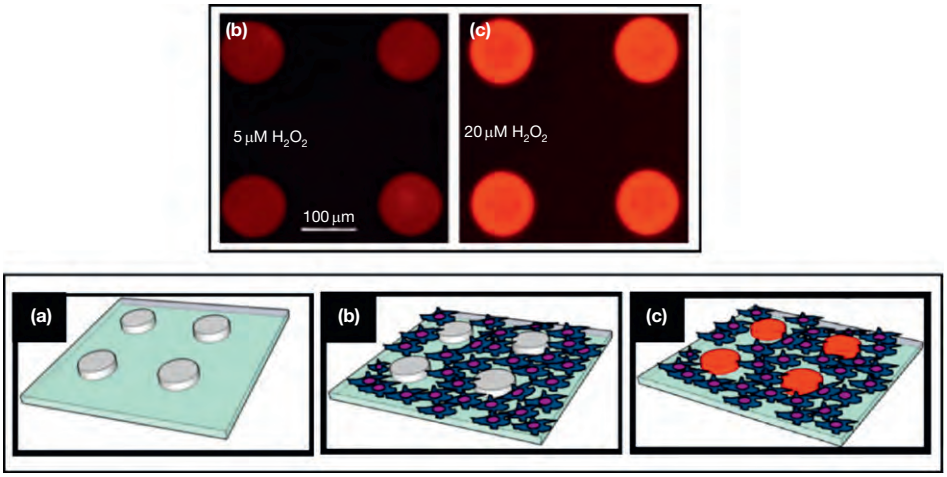

Figure 9 Top: Fluorescence images of hydrogel microstructures after 5 min incubation with 5 μM H_2O_2 (b) and 20 μM H_2O_2 (c) in the presence of Amplex Red. Bottom: Culturing cells with sensing hydrogel micropatterns. HRP-containing PEG hydrogel micropatterns are fabricated on glass substrate (a), encapsulation of enzyme molecules does not diminish cell-resistive properties of PEG hydrogel. When incubated with micropatterned substrates, macrophages attach next to sensing hydrogel structures (b) and macrophages release H_2O_2 upon mitogenic stimulation (c). Reproduced from Yan, J.; Sun, Y.; Zhu, H.; Marcu, L.; Revzin, A. *Biosens. Bioelectron.* **2009**, *24*(8), 2604–2610, with permission from Elsevier.

CMC concentration leads to higher antibody immobilization with decreasing nonspecific binding. At optimum conditions, this system gives a detection limit as low as 400 ng ml^{-1} for a 44 kDa antigen. Another study was performed by the same group using specific antibody capture ligands such as protein A, protein G, and anti-IgG Fc for oriented antibody immobilization and higher frequency QCM-D crystals to increase the detection limit.[129] In this case, the detection limit with the new technique increased to 25 ng ml^{-1} on 5 MHz crystals. Reduction of nonspecific adhesion for this method was shown with incorporation of PEG into this biointerface.[130] A different methodology used by Chen and colleagues is based on the periodate-oxidized dextran layer.[131] *Staphylococcus aureus* protein A (SpA) was immobilized on the poly-L-lysine-modified piezoelectric crystal surface to improve its stability, activity, and binding specificity with human immunoglobulin G (igG) in flow injection assays. The prepared sensing crystal shows best sensitivity and reusability at a flow rate of 140 μl min^{-1} with a detection limit as low as 0.2 nM with the proposed system.

Similar in function to QCM, surface plasmon resonance (SPR) is an established method for the label-free detection of biomacromolecular interactions. SPR uses evanescent waves to examine the surface. Analyte binding leads to a change in refractive index at the sensing surface influencing resonant angle and shifting to generate real-time signal.[132] SPR allows measurements in real time with high precision and repeatability and provides some advantages over other techniques. These are (i) The amount of complex at equilibrium is measured in the presence of unbound reactant without disturbing the reaction equilibrium, (ii) the stability of the immobilized ligand can be monitored by tracing the surface binding capacity and the baseline stability, and (iii) the low amount of material for analysis.[133] As for QCM, the surface of SPR sensors should be antiadhesive to unwanted compounds and interact specifically, and hydrogels have been used for this purpose.

Guidi and coworkers studied the detection of insulin-like growth factor-1 (IGF-1), a suspected carcinogen, in cow milk via SPR-based sensing system.[134] Hyperimmune polyclonal anti-IGF-1 antibodies were immobilized to detect IGF-1 due to its specific binding capacity. The amount of native IGF-1 in fresh raw milk was detected down to 4 ng ml^{-1} which is parallel to the study of Collier *et al.*[135] Another SPR-based sensing was used for the detection of prostate-specific antigen.[136] Anti--PSA antibodies were coupled covalently to the gel sensor disk that can detect PSA molecules with a concentration of 0.15 ng in 1 ml, which is a sufficient detection of physiological (<4 ng ml^{-1}) and clinical (4–10 ng ml^{-1}) PSA levels. A different study was reported for the detection of apolipoprotein B100 sensitivity to ten different monoclonal antibodies (mAbs, all IgG_1). Sensitivity was evaluated in terms of different structure recognition. The detection of recombinant human interferon-γ (IFN-γ) with SPR in plasma was reported by Stigter *et al.*[137] To test nonspecific adsorption of plasma components, numbers of SPR coatings were evaluated. Nonmodified dextran-coated SPR disks were the best candidates for the detection of IFN-γ in plasma with a lower detection limit of 150 ng ml^{-1}.

SPR-based sensors are also used for the detection of steroids. In a typical sensor, real-time detection of pair steroids, cortisol and cortisone, in saliva and urine was carried out using surface plasmon resonance-based immunosensor.[138] A polycarboxylate-based hydrogel layer was used for immobilization of the antibodies, anticortisol, and anticortisone. These antibodies are very specific for cortisol and cortisone and contribute to high specificity of the sensor without binding other steroids like testosterone, epitestosterone, and corticosterone. The layer exhibited a high degree of stability over time during repeated regenerations. Saliva and urine sources were selected due to the presence of a low amount of cortisol and cortisone in comparison to the 100-fold higher concentration in the blood. The detection limit of both steroids in saliva and urine samples was less than 10 μg l^{-1} which is sufficient sensitivity for both clinical and forensic use.

A novel immunosensing system for determination of human α-ferroprotein (AFP) was established using a

boronate immunoaffinity column via flow injection chemoluminescence. Sugar boronic acid was used to immobilize AFP antigen through the sepharose matrix. The mixture of the analyte AFP and horseradish peroxidase-labeled AFP antibody (HRP–anti-AFP) was injected into the column. The free HRP–anti-AFP was trapped by the immobilized antigen in the column and detected via chemoluminescence due to its sensitivity effects on the reaction of luminol and hydrogen peroxide.[139]

As a different method, 3D hydrogel thin films were used to protein binding (antigenicity) and antibody functionality in a microarray format.[140] Protein antigenicity was evaluated using the protein toxin, staphylococcal enterotoxin B (SEB). Cy3-labeled antimouse IgG (capture antibody) was microarrayed onto the hydrogel surfaces and interrogated with the corresponding Cy5-labeled mouse IgG (antigen). Lee *et al.* introduced an elastic and hydrophilic composite mold, which enables the transfer of hydrophilic polar ink such as polyelectrolyte multilayer.[141] The mold is composed of a urethane-related commercial polymer and PEG diacrylate (PEGDA), which forms a hydrogel upon its reaction with a photoinitiator. The group established a simple strategy for immobilizing antibodies exclusively inside the microreservoirs of the patterned composite mold, which made the system suitable for biosensing applications. A first try regarding the detection of *Escherichia coli* O157:H7 was explored.

Electrochemical-based sensing is also used in antibody–antigen sensors for the detection of IgG. In one case, a redox hydrogel-coated carbon electrode with avidin incorporated into the hydrogel was employed.[142] Avidin was conjugated with biotin-labeled antirabbit IgG. After exposure the tested solution to capture of IgG, the sandwich-assay was completed by conjugation of horseradish peroxidase (HRP)-labeled antilabeled IgG. Electrical contact between the HRP and the electrode-bound hydrogel resulted in formation of an electrocatalyst for the electroreduction of H_2O_2 to water. The detection limit with this method was as low as $3\,ng\,ml^{-1}$. The other electrochemical-based sensing was performed by using a 3D porous chitosan network as a matrix for hepatitis B surface antibody (HBsAb).[143] The porous network was prepared by electrodepositing a designer nanocomposite chitosan solution with an encapsulated silica nanoparticle as a hybrid film on an ITO electrode, followed by removal of the silica nanoparticles with HF solution. HBsAb was covalently immobilized to the hydrogel network for the detection of hepatitis B surface antigen. A novel label-free electrochemical detection method of ractomine was developed by Shen *et al.*[144] Ractopamine-bovine thyroglobulin antigen was incorporated into an agarose hydrogel film on a glassy carbon electrode. The $K_3Fe(CN)_6/K_4Fe(CN)_6$ redox probe system was used to translate the binding to an electrochemical signal with addition of the polyclonal antibody against ractopamine. Using a similar mechanism and a same hydrogel layer with a different antibody, the detection of the ferritin molecule was performed by immobilizing the ferritin antibody (FeAb) on the electrode.[145] CV and differential pulse voltammetry (DPV) were used for the conversion of signal to electrical output. The detection limit of ferritin with this method was $1.5 \times 10^{-5}\,g\,l^{-1}$ and the linear range was $5–50 \times 10^{-5}\,g\,l^{-1}$.

3.329.3.1.3. DNA and oligonucleotides

The detection of nucleic acids has become increasingly prominent in diagnostics systems due to its crucial role in a wide range of areas, including genetic diagnostics, monitoring of infectious bacteria, forensics, and basic research.[146] Besides simplicity, DNA-sensing systems require high selectivity to be able to detect single-nucleotide polymorphism (SNPs) and high sensitivity to enable sensing of only a few hybridization events of corresponding small amounts of target DNA fragments.[147,148]

Many groups dedicated their work on the detection of DNA via electro- or optical DNA sensors.[149–153] Generally, DNA-sensors work in three main steps: (i) immobilizing the oligonucleotide probes on the substrate, (ii) hybridizing with incorporation of target sequences through base-pairing interactions, and (iii) readout.[154,155] Fluorescence, electrochemical,[156,157] optical,[158] electrical,[159] and microgravimetric-based systems[158] are widely used for the detection of DNA concentrations down to 10^{-18} M. The key factor of high-throughput DNA analysis technologies, such as DNA microarrays, is the efficiency of the immobilization of nucleic acid fragments. This efficiency plays an important role in determining the accuracy and sensitivity of the detection. On account of their hydrophilic 3D nature and flexible structure, hydrogels can mimic the native environment of nucleic acid fragments and can keep them thermodynamically more stable. These characteristics offer important advantages for capturing probes in comparison to 2D rigid substrates and self-assembled monolayers. Here, we present the currently used hydrogel-based techniques for the detection of DNA and oligonucleotides by outlining some of the key studies. For general DNA-sensing methods including non-hydrogel-based systems, we would like to draw the reader's attention to the reviews 'Recent advances in DNA sensors' by Cosnier *et al.* in 2008,[160] 'Electrochemical DNA sensors' by Drummond *et al.* in 2003,[161] and 'Target-responsive structural switching for nucleic acid-based sensors' by Li *et al.* in 2010.[162]

Cantilevers are a widely used example for sensors that detect DNA with high sensitivity and selectivity. A cantilever is a small rectangular monocrystalline silicon tip of less than $1\,\mu m$ thickness.[163] By applying a thin hydrogel layer, it is possible to immobilize the sensing molecules for a long time without denaturing the structure as well as preventing nonspecific adhesion. These microstructure-based sensing systems can be used in various environmental conditions such as vacuum, liquid, and air having high sensitivity and direct transduction mechanism without the need for any labeling. The immobilization of target-selective receptors on the cantilever makes it possible to identify analyte molecules by means of changes in surface tension. The change in surface tension will lead to a bending of the cantilever and can be sensed by optical laser detection or capacitance changes.[164] This sensing method is widely used to detect DNA using hybridization assays with high sensitivity, as illustrated in **Figure 10**. Each cantilever is coated with an oligonucleotide-functionalized hydrogel layer. Subsequently, hybridization is performed by incorporation of complementary sequences, resulting in bending of the cantilever because of changes in surface tension. As a last step, after rinsing the oligonucleotides with an unbinding agent, the cantilever turns its first place and an optical detection system is used for detecting the bending of the cantilever.

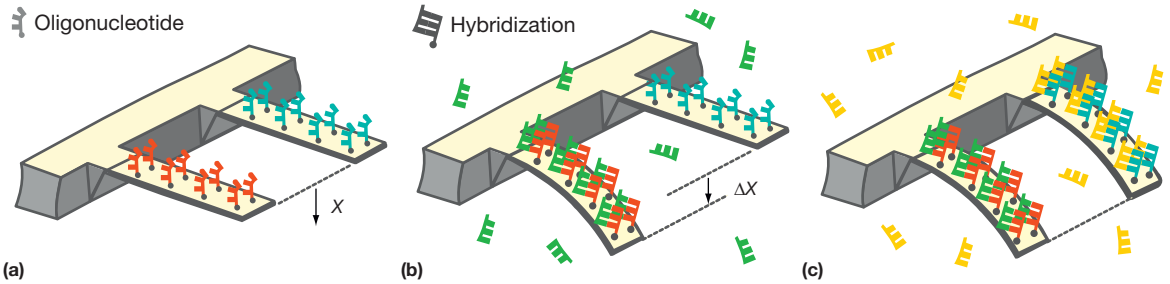

Figure 10 Scheme of the cantilever-array DNA sensor. (a) Refers to the immobilization of ssDNA probes to the cantilevers, (b) refers to hybridization of ssDNA probes with incorporation of the first complementary target strands, and (c) refers to injection of the second complementary oligonucleotide, respectively. Reproduced from Fritz, J.; Baller, M. K.; Lang, H. P.; *et al*. *Science* **2000**, *288*, 316–318, with permission from Science.

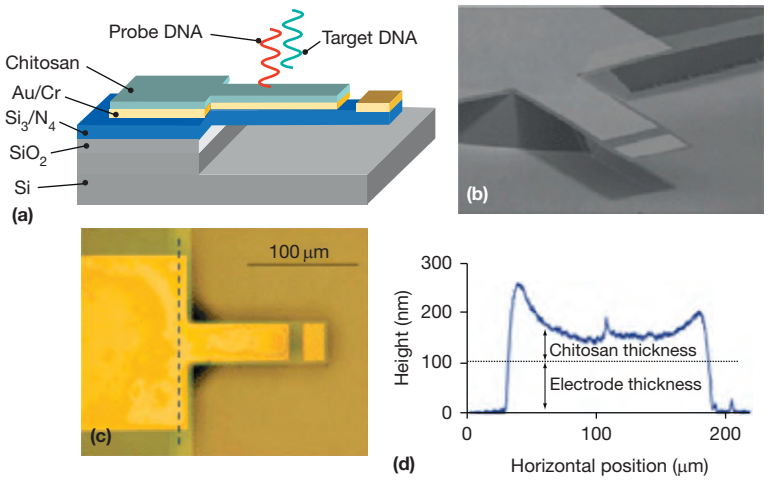

Figure 11 Cartoon illustration (a), scanning electron microscopy (b), and optical microscopy (c) photos of microcantilever construction after chitosan electrodeposition and contact profiler scan of chitosan film along dashed line in (c) (d). Reproduced from Koev, S. T.; Powers, M. A.; Yi, H.; *et al*. *Lab on Chip* **2007**, *7*(1), 103–111, with permission from The Royal Society of Chemistry.

In one case, chitosan film electrodepositing onto cantilever was reported for the detection of nucleic acid hybridization in solution (static) and air (dynamic).[165] Therefore, an electrodeposited chitosan film was biofunctionalized with oligonucleotides. These probes then detected target DNA hybridization by static mode (in solution) and dynamic mode (resonant frequency shift in air) on a cantilever construction, as illustrated in Figure 11.

For the dynamic mode, the resonant frequency shift was measured in air before and after the bimolecular detection event and in the presence of the analyte. In the static mode, the bending of the cantilever was measured in solution before and after the bimolecular event and then in the presence of the analyte. Static measurements in solution demonstrated the DNA hybridization on the chitosan-bound complementary probe. The dynamic measurements in air revealed that the surface density of oligonucleotides was two orders of magnitude larger than the comparable results obtained by probes tethered to SAMs. This was a result of the higher probe concentration in the 3D hydrogel network structure in comparison to the 2D self-assembly monolayer.

The detection of oligonucleotides can also be performed via very simple methods like bioactive papers. Biomolecule-modified papers are used for the detection of biomolecules with a simple mechanism. On account of their inexpensive, sensitive, and robust structure, they are used for detection assays that do not require any instrumentation. A simple bioactive paper-based detection of DNA was reported by Su and colleagues.[166] They used paper stripes printed with carboxylic PNIPAm microgels modified by either an antibody or DNA aptamer. The modification of PNIPAm microgels with vinyl acetic acid groups makes them possible candidates for bioconjugation. Therefore, DNA aptamers were coupled with the carboxylic groups by bioconjugation and then immobilized on the bioactive papers without losing biorecognition activity. The immobilized microgels were used as biosensing elements to detect the target molecule. The working principle of the proposed technique is illustrated in Figure 12.

Another method, used for the detection of adenosine triphosphate (ATP), utilized a structure-switching fluorescent DNA aptamer. The selectivity of the method has been proved by a higher fluorescence level for ATP compared to that of guanosine triphosphate (GTP). The simplicity of the system makes it attractive for a wide range of sensing applications. A novel methodology was developed for the detection of fluorometric DNA hybridizations and was based on noncovalent coupling of DNA to a water-soluble zwitterionic polythiophene derivative.[167] Therefore, 3-[(*S*)-5-amino-5-carboxyl-

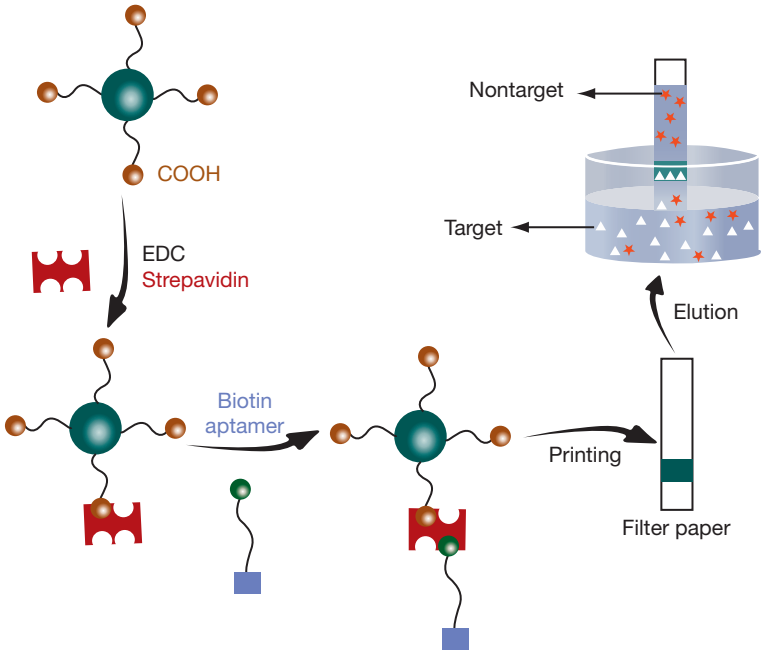

Figure 12 The systematic exhibition of paper-based detection system proposed by Su *et al*. Redrawn from Su, S.; Ali, M.; Filipe, C. D. M.; Li, Y.; Pelton, R. *Biomacromolecules* **2008**, *9*(3), 935–941, with permission from American Chemical Society.

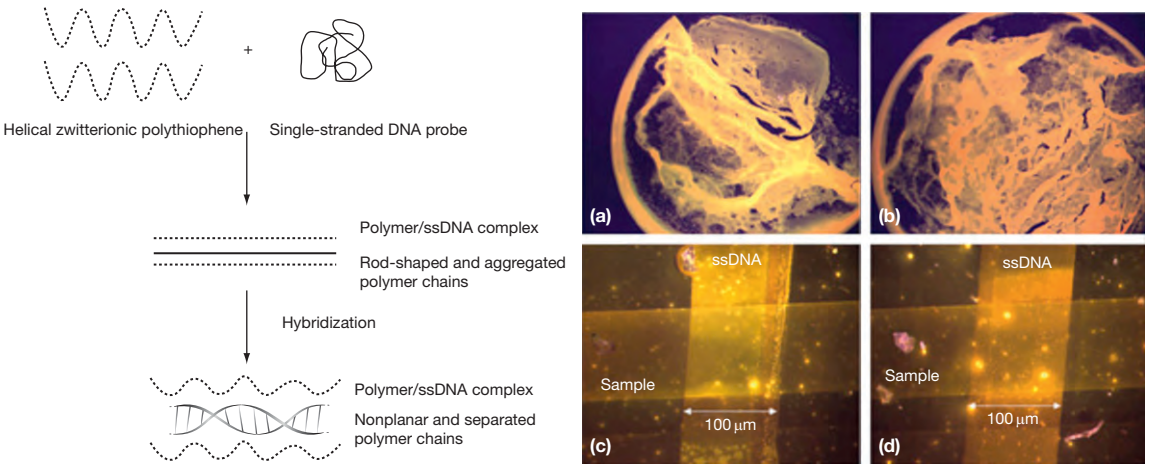

Figure 13 The formation scheme of (left) and fluorescence images (right) of POWT/DNA complexes. Reproduced from Nilsson, K. P. R.; Inganas, O. *Nat. Mater.* **2003**, *2*, 419–424, with permission from Nature Group.

3-oxapentyl]-2,5-thiophenylene hydrochloride (POWT) hydrogel has been cross-linked with cross-linker ssDNA on a polystyrene surface. POWT is the first polyampholytic conjugated polythiophene example, used for the detection of biospecific interactions.[168–171] The zwitteronic side chain of polythiophene forms a complex with polyelectrolytes like DNA via hydrogen bridges exhibiting the anionic or cationic behavior upon pH. In this method, the incorporation of complementary ssDNA fragments resulted in a planar polymer and an aggregation of the polymer chains. This induced a decrease in intensity and a red-shift of the fluoresecence. The proposed method can detect a single-base mismatch in five minutes by means of fluorescence without any denaturation step. The schematic illustration of the POWT/dsDNA complex formation and fluorescence picture of POWT/DNA complex are illustrated in Figure 13. This method has a lower detection limit for DNA hybridization of 10^{-11} M.

DNA microarrays, integrated into optofluidic hybridization systems, are widely used in the field of DNA detection. In one case, a DNA hybridization construct was designed based on microchannels in combination with UV-cross-linked hydrogels and photolithography-defined weirs.[172] ssDNA probes modified microbeads were immobilized in the microchambers and used to capture the complementary target sequences. The transport of complementary DNA target solution was provided by an electrophoretic transport (hydrogel switch open). Subsequently, hybridized DNA targets could be isolated via the weirs using pump-driven pressure (hydrogel switch

closed). Biotin-labeled ssDNA probes were immobilized on the microbeads and coated with strepavidin. Hybridization reactions were conducted by moving the targets across the array of probe-containing microchambers by electrophoresis. The hybridization of flourescein-labeled ssDNA targets to complementary probes was observed by fluorescence microscopy. In 1 min, 90% of the DNA were captured and could sequentially be released and recovered. A different approach in which encoded hydrogel particles were used to detect DNA hybridization has been studied.[173] Encoded particles, consisting of a semi-interpenetrating PEG network with tunable porosity, were prepared by UV cross-linking. The particles were fabricated using flow lithography and then immersed into a solution containing oligonucleotides at unknown concentrations. The dispersion was scanned for fluorescence in a flow-through device and the corresponding fluorescent targets were quantified. Meiring and colleagues used a sensor array platform to detect DNA hybridization.[154] The proposed method was based on a multianalyte sensor array platform which consisted of analyte-specific features that were indexed by shape. The array has been fabricated by soft-lithography using a PEG acrylate hydrogel. Fluorescently tagged methacrylamide-modified oligonucleotides were copolymerized into the hydrogel matrix. The covalent attachment of the ssDNA probes to the matrix was verified by two different DNAs, with and without a polymerizable methaacrylamide group. Each target sequence was dyed with a different fluorophore and retained the ability to hybridize selectively to the designated targets because of the nonadhesive nature of the PEG. Each hydrogel array contained different DNA probes and was incubated in the solution of three-different target sequence mix. After the hybridization, the hydrogels were rinsed with buffer to remove the unbound samples. One bright field and three fluorescence micrographs were captured; each micrograph was obtained using a specific optical filter set for one of the three-different target fluorophores (**Figure 14**).

By using surface-immobilized DNA structures with appropriate redox labels, it is possible to monitor the target-induced structural switching of DNA or aptamer-specific small molecule probes. This is done by measuring electrochemical currents which are directly associated to the distance between the redox label and the electrode.[146] In one case, an enzyme-amplified amperometric DNA hybridization was performed by Hajdukiewicz and colleagues.[174] The proposed method is based on solution-phase ferrocemethanol mediation of glucose oxidase. The carboxlymethylated dextran layer, containing ssDNA probes, was attached to the surface via amine groups. Using a ferrocenemethanol electron mediator, the hybridization of ssDNA probes to biotinylated-ssDNA and addition of glucose oxidase–avidinD conjugate led to a signal current. To analyze the signal current, the group used cyclic voltammetry and achieved a detection limit of 0.2 nmol in a 500-µl sample utilizing a graphite electrode. Most hydrogel-based electrochemical DNA sensors are based on nanoscale interactions between targets in solution, the recognition unit, and a hydrogel-coated electrode surface.

DNA sensors can also be used to detect gene mutations. One example for this application is the highly sensitive detection of a K-ras point mutation in codon 12, pancreatic cancer, based on DNA-carrying hydrogel microspheres.[175] The G–G mismatch in codon 12 of the *K-ras* gene leads to a mutation and seems to be a reason for pancreatic cancer. Hence, the detection of a single mismatch has crucial importance for early diagnosis of genetic disorders. The detection of this single mismatch was performed using hydrogel microspheres, which provided a high flexibility to DNA fragments. The hydrogel microspheres were synthesized by precipitation polymerization. To detect the mutation in the sequence, a hydrogel-enhanced sandwich method of a SPR assay was used. The use of the DNA-carrying microspheres enhanced the SPR response as a result of an increased dielectric constant.

3.329.3.1.4. Other binding mechanisms

3.329.3.1.4.1. Biotin–streptavidin

Responsive hydrogel-based microlenses can change their optical properties upon volume phase transitions in the presence of stimuli. They can be easily constructed in simple and rapid fashion with high sensitivity.[176] In hydrogel microlenses, the stimulus induced phase transition changes the focal lengths that causes a focusing or defocusing of the projected image.[177] Most studies in the literature concerning hydrogel microlenses

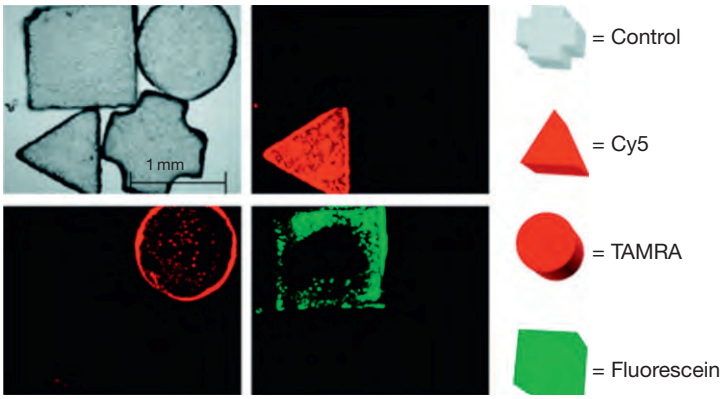

Figure 14 Micrographs of the DNA detection assay demonstrating the successful detection of each of the complementary target sequences with high signal and negligible cross-hybridizational noise. Reproduced from Meiring, J. E.; Schmid, M. J.; Grayson, S. M.; *et al*. *Chem. Mater*. **2004**, *16*(26), 5574–5580, with permission from American Chemical Society.

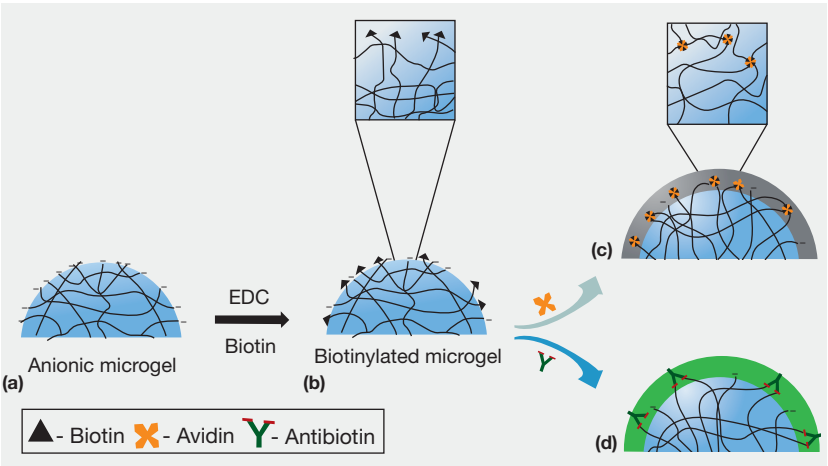

Figure 15 Cartoon representation of the hydrogel microlens assay. Redrawn from Kim, J.; Nayak, S.; Lyon, L. A. *J. Am. Chem. Soc.* **2005**, *127*(26), 9588–9592, with permission from American Chemical Society.

for biosensing have been performed by Lyon and coworkers. In one case, a bioresponsive hydrogel construct was developed to investigate the specific and nonspecific adsorption.[178] Poly(*N*-isopropylacrylamide-*co*-acrylic acid) (PNIPAM-*co*-AAc)-based bioresponsive microgels were prepared by incorporation of both biotin and aminobenzophenone (ABP) as a photoaffinity label via carboimide chemistry. Functionalization with ABP allows for photochemical tethering of antibiotin after it is associated to the microlens through native antibody–antigen association. Hydrogel microlenses were generated by electrostatic assembly of anionic microgels on positively charged, silane-modified glass substrates. Two different routes were used for determination of the specific and unspecific binding. In the first route, the hydrogel microparticles were functionalized with biotin with EDC coupling, whereas in the second route, these particles were functionalized with biotin-ABP via EDC and DCC coupling. With a secondary IgG exposure, specific/ancillary binding effects were investigated via bright-field and fluorescence microscopy. Biotin and polyclonal anti-biotin-sensitive hydrogel microlenses were constructed using the same microlens approach as shown in Figure 15.[176]

First, PNIPAm-*co*-AAc hydrogel particles were prepared by the free-radical precipitation polymerization method (Figure 15(a)). Then, biotin was incorporated into hydrogel particles via EDC coupling (Figure 15(b)), followed by formation of cross-links in the hydrogel by multivalent binding of avidin to biotin and antibiotin to biotin provided on the hydrogel microlenses (Figure 15(c) and 15(d)), respectively). Multivalent binding of both avidin and polyclonal antibiotin was determined by monitoring the optical properties via a bright-field optical microscopy. The same group developed a new method, label-free biosensing by combining antibody–antigen cross-linked hydrogel microlenses, to use for the detection of small molecules with a tunable sensitivity.[179]

Piezoelectric biosensors have widely been used for affinity interaction.[180] In one case, hydrogel-coated streptavidin piezochips were used for the physical and chemical immobilization of streptavidin molecules. Subsequent biosensing of biotinylated bovin serum albumin (BSA) revealed a higher binding capacity for the covalently immobilized streptavidin. Another PZ sensor was used for the detection of poly His-tagged proteins using nitrilotriacetic (NTA) captured oxidized dextran hydrogel layer.[181] The binding of chelating ions, Co^{2+}, Cu^{2+}, and Ni^{2+} was investigated with regard to binding to poly His-tag proteins. Ni^{2+} exhibited the highest binding capability to detect poly His-tag-gel proteins.

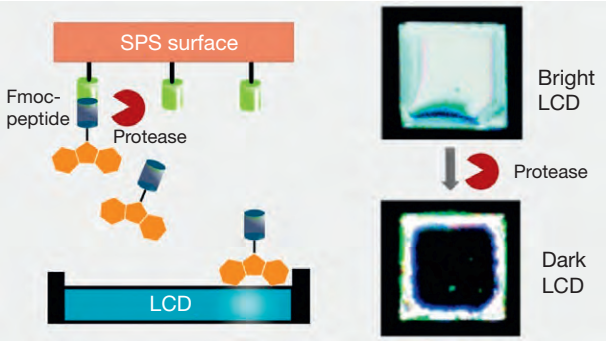

Figure 16 Schematic representation of the sensor chamber in combined SPS–LCD protease. Redrawn from Birchall, L. S.; Ulijn, R. V.; Webb, S. J. *Chem. Commun.* **2008**, 2861–2863, with permission from The Royal Society of Chemistry.

A hydrogel-based sensor for monitoring protease activity has been constructed by combining a versatile solid-phase synthesis (SPS) with the simplicity of liquid crystal display (LCD).[182] In this study, PEG acrylamide (PEGA) was used as SPS support for immobilization of peptide sequences that are specifically recognized and cleaved by proteases. In the presence of proteases, the respective peptides were cleaved with high specificity, resulting in their release from the hydrogel and interaction with the LC surface. This leads to a realignment in the liquid crystalline layer and thus to optical changes from bright to dark. Hence, this method offers the screening of protease specificity by the eye without the need for any special complex instrumentation (Figure 16).

Lee *et al.* created a micropattern on the PEG hydrogels through graft polymerization and photolithography for the

detection of strepavidin binding to an avidin-modified hydrogel layer.[183] Surface modification of the antiadhesive PEG hydrogel layer was performed by grating PAA via photoinduced surface-initiated polymerization with benzophenone as photoinitiator. Biotinyl-3,6,9-dioxaoctanediamine (biotin–NH_2) was coupled to the PAA micropattern via EDC/NHS-coupling. Specific binding between biotin and streptavidin was used for evaluation of new PAA-modified PEG surface.

3.329.3.1.4.2. Calmodulin-based sensing

Daunert and coworkers reported a new hydrogel microlens system that can change optical properties via ligand exchange.[184] Protein calmodulin (CaM) was used as a model hinge-motion binding protein for the chemical tunability of the microlenses. CaM was chemically bound to the hydrogel network as well as its low-affinity ligand phenothiazine. The recognition between CaM and phenothiazine led to a further increase in cross-linking density. However, in the presence of a high-affinity CaM ligand like chlorpromazine (CPZ), an exchange between phenothiazine ligand and CPZ occurs and thus leads to a decrease in cross-linking. In consequence, the hydrogel is swelling and the refractive index decreases. This ability of volume change in response to a (bio)chemical stimulus allows its uses as chemically tunable microlenses.

3.329.3.1.4.3. Carbohydrate recognition by boronic acids

Besides the already mentioned enzyme receptors, synthetic glucose receptors like phenylboronic acids have also been intensively studied for glucose sensing.[185–188] The sensing effect of phenylboronic acid is based on the fact that the molecule becomes negatively charged upon sugar binding, which then can generate an osmotic pressure due to the resulting Donnan potential.[189] This results in a swelling of the hydrogel that can be easily sensed. Asher's group worked intensively on this field and did some pioneering work by applying a crystalline colloidal readout between glucose and phenylboronic acid.[186,190] When an analyte selectively binds to the hydrogel matrix, the binding will result in a change in the osmotic pressure and by that in the swelling of the gel. On account of the swelling, the separation between the colloidal spheres increases and the Bragg peak of the diffracted light will be shifted to longer wavelengths (**Figure 17**).

Ben-Moshe *et al.*, from Asher's group, for example, developed a fast responsive crystalline colloidal array photonic crystal glucose sensor based on hydrogels that embed an array of ~100-nm-diameter monodisperse polystyrene colloids that Bragg diffract light in the visible spectral region.[191] The hydrogels changed volume as the glucose concentration varies. The changes in the lattice spacing changed the wavelength of the diffracted light. The sensor had a full response rate within 90 s to the average glucose concentrations found in blood (5 mM) and within 300 s to the average glucose concentrations found in tear fluid (0.15 mM). They demonstrated that the sensor is responsive to ~0.15 mM glucose concentrations in artificial tear fluid solution.

Another sensing method based on phenylboronic acid was presented by Worsley *et al.*[192] in their work about continuous blood glucose monitoring using a thin-film optical sensor. The sensor is based on holography and made of an acrylamide

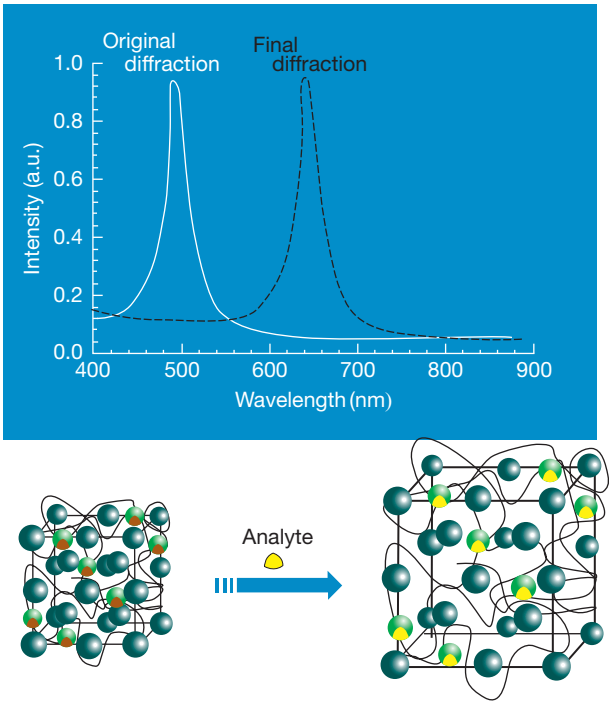

Figure 17 Typical diffraction from intelligent polymerized crystalline colloidal array particle dispersions. Redrawn from Asher, S. A.; Alexeev, V. L.; Goponenko, A. V.; *et al. J. Am. Chem. Soc.* **2003**, *125*(11), 3322–3329, with permission from American Chemical Society.

hydrogel thin-film containing phenylboronic acid receptors. Utilizing the sensor, it was possible to measure glucose in human blood plasma *in vitro*.

Lapeyre *et al.*[193] reported the synthesis of monodispersed PNIPAm submicrometric microgels, modified with a phenylboronic acid (PBA) derivative. The particles were glucose-responsive at a pH close to the pK_a of the PBA derivative, with a swelling degree proportional to the concentration of glucose. Owing to their characteristics, the particles might serve as building blocks for the design of colorimetric sensors based on the light diffraction of colloidal crystals.

3.329.3.1.4.4. Fluorescence-based glucose sensing

Here, we make a short digression for fluorescence-based glucose sensing in combination with hydrogel systems. In this context, three terms need to be mentioned because they are the main components of many fluorescence-based glucose sensors: the fluorescence (or Förster) resonance energy transfer (FRET), Concanavalin A, and dextran labeled with fluorescein isothiocyanate (FITC). FRET involves the nonradiative (i.e., no photons are passed) energy transfer from a fluorescent donor molecule to an acceptor molecule in close proximity (which needs not be fluorescent), and is usually brought about by dipole–dipole interactions. The signal in FRET is a decrease in fluorescence intensity and lifetime of the donor. Concanavalin A (Con A) is a plant lectin, extracted from the jack bean, which has four binding sites for glucose per molecule of the protein. Finally, dextran is a complex, branched glucan (polysaccharide), in this case, labeled with fluorescein isocyanate, a fluorescence dye. These are the three ingredients needed to form a

fluorescence-based glucose sensor involving Con A. Such sensors are based on the competitive binding to the lectin of either glucose or a labeled carbohydrate derivative such as dextran. At this point, we do not want to go more into detail and would like to advise the reader to have a closer look at the review of Pickup *et al.*[194] about fluorescence-based glucose sensors. This review gives the most important background information about the topic, as well as the use of PEG-based hydrogels to improve the biocompatibility of implanted sensors. One example for a hydrogel biosensor based on these three ingredients is the work of Chaudhary *et al.*[195] The group investigated the feasibility of dissolved-core alginate-templated fluorescent microspheres as glucose biosensors in simulated interstitial fluid (SIF). The sensor worked on the principle of competitive binding and fluorescence resonance energy transfer and consisted of multilayer thin film-coated alginate microspheres incorporating dye-labeled glucose receptor and competing ligand within the partially dissolved alginate core. Further, it was possible to combine the visible sensing assay (FITC-dextran-TRITC-Con A/FITC-dextran-TRITC-apo-GOx) with a near infrared sensing assay (AF-647-dextran amino-QSY-21-apo-GOx), co-encapsulated inside polymeric hydrogel microspheres. The incorporation of long wavelength NIR dyes enables more efficient excitation through scattering tissue, which effectively improves the odds of successful use *in vivo*. The system exhibited a maximum response time of 120 s and a sensitivity of 0.94% mM^{-1} glucose with a response in the range of 0–50 mM glucose.

3.329.3.1.4.5. Peptide-modified hydrogels for toxin screening

In comparison to 2D surfaces, the 3D network of hydrogels offers a variety of benefits if used for biosensing applications where the immobilization of receptor molecules, for example, antibody or enzyme, is an important factor. If such a kind of biomolecule is immobilized on a 2D surface, it can denature and lose activity and affinity to antigens.[196–198] The explanation for this is easy: If the molecule binds to a 2D limited surface, it will undergo structural deformations in the binding region or even in the protein structure itself, which will have a negative impact on the activity, binding kinetics, or even inhibit the complete binding process. A 3D hydrogel network, swollen to its equilibrium water content, on the other hand, can preserve the protein structure and simulate a solution-phase environment while also granting multidirectional access for ligand binding.[199] Further, the hydrogel structure allows an easy penetration of large biomolecules and therefore an access to the active binding sites.

Charles *et al.* made use of these benefits that 3D hydrogels offer when they developed a galactose polyacrylate-based hydrogel scaffold for the detection of cholera toxin (CT) and staphylococcal B (SEB) in a sandwich immunoassay format.[199] On account of the galactose polyacrylate backbone and a selected binding chemistry, they succeeded in creating a hydrogel system that provided enhanced sensitivity with low nonspecific binding characteristics. By utilizing a PDMS microchannel template, they patterned arrays of the immobilized antibodies for the development of a sandwich immunoassay (**Figure 18**).

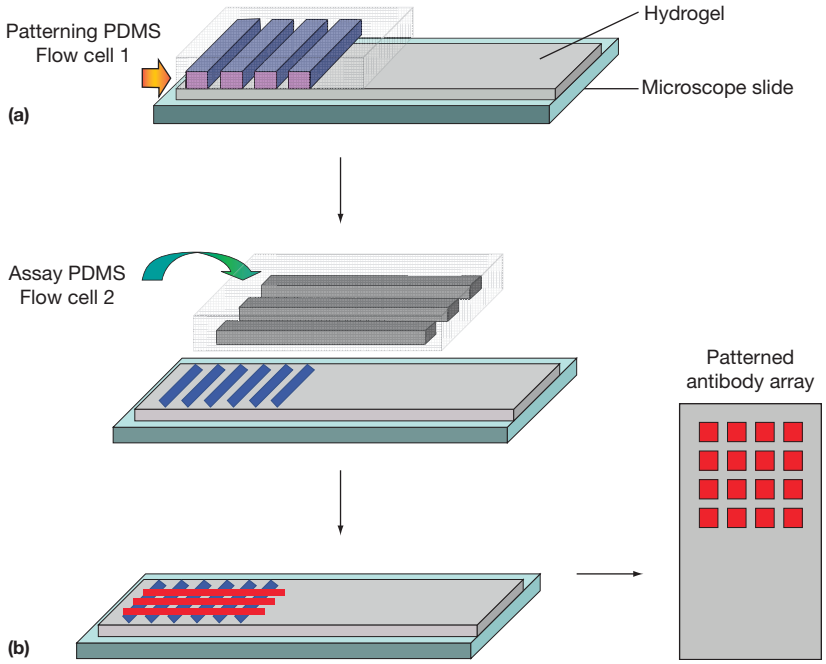

Figure 18 Array patterning template for the immobilization of capture antibodies and application of assay reagents. (a) The poly(dimethylsiloxane) (PDMS) patterning module, containing six channels for fluid flow that run in a perpendicular direction of the slide. When placed in contact with hydrogel, cross-linkers and capture antibodies are applied into each lane and allowed to incubate. Repetitive cycles of cross-linkers and antibodies were performed to optimize immobilization of the biomolecule. (b) Assay template for application of toxin (i.e., cholera or staphylococcal enterotoxin B (SEB)) and tracer antibody (Cy3-anti-SEB or Cy3-anti-CT). The PDMS assay module contains six channels which are placed parallel to the patterned capture antibodies on the hydrogel slide forming the patterned array. Different concentrations of antigen can be applied to each lane to determine detection limits. Reproduced from Charles, P. T.; Velez, F.; Soto, C. M.; *et al*. *Anal. Chim. Acta* **2006**, *578*(1), 2–10, with permission from Elsevier.

Fluorescence and 3D imaging by confocal microscopy and laser scanning confocal microscopy of Cy3-labeled anti-CT and/or Cy3-anti-SEB tracer molecules provided qualitative and quantitative measurements on the efficiency of protein immobilization, detection sensitivity, and signal-to-noise ratios. With the established system, they were able to achieve low limits of detection for SEB and cholera toxins ($1.0\ ng\ ml^{-1}$).

Besides the integration of active biomolecules, it is also possible to create hydrogels that are cross-linked by peptides, which dissolve in the presence of certain stimuli, like reducing agents or enzymes.[200,201] The cross-linking system can be designed in such a way that the hydrogel can act as a self-sacrificing biosensor for enzymatic active analytes. This 'sacrificing' hydrogel can be used for sensing toxins that possess enzymatic activity, such as botulinum neurotoxin type A. A hydrogel system utilizing this system was described by Frisk *et al.*[202] They created peptide-modified hydrogels for sensing the enzymatic activity of botulinum neurotoxin type A (BoNT/A). Using so-called SNAP (synaptosome-associated protein)-modified hydrogels in combination with microfluidics, they were able to generate autonomous sensors that simply required a visual readout (Figure 19). Using microfluidics, they were able to simply introduce ~20 µl of toxin-laden solution and observe degradation without the need for detectors, pumps, or valves, thus making microfluidic-based biosensors promising as toxin-screening vehicles.

3.329.3.2. Living Sensors

This section gives an overview of the combination of hydrogels with living cells and microorganisms to form living cell–polymer composites for biosensing applications. The use of microorganisms and cells as biological sensing elements in biosensors is well established, and microorganisms offer advantages of ability to detect a wide range of chemical substances, amenability to genetic modification, and broad operating pH and temperature range, making them ideal as biological sensing materials. They have been integrated with a variety of transducers such as amperometric, potentiometric, calorimetric, conductimetric, colorimetric, luminescence and fluorescence to construct biosensor devices. Here, we do not want to cite paper over paper and would just like to draw the reader's attention to the short but comprehensive reviews about 'Microbial biosensors' and 'Whole cell biosensors' published by Lei *et al.*[203] and Luc Bousse.[204] The review of Lei *et al.* concentrates on the advantages of using microorganisms as biosensing elements, the immobilization of microorganisms, electrochemical, amperometric, potentiometric, conductimetric, optical, bioluminescence, fluorescence, and colorimetric microbial biosensors as well as microbial fuel cell type biosensors, fluorescent protein-based biosensors, and O_2-sensitive fluorescent material-based biosensors. Luc Bousse also concentrates on the field of biosensors in which the biological component consists of living cells and points out some of the most important reasons for using living cells, that is, to obtain functional information about the effects of a stimuli on a living system.

Our focus should be the use of living cell biosensors utilizing hydrogel networks for biosensing applications. The immobilization of cells in different hydrogel types for biosensing applications is reported: polyacrylamide[205,206] polyurethane-based hydrogels,[207] photo-cross-linkable resins[207,208] and polyvinyl alcohol,[209–213] polyacrylonitrile membranes[214] and PEG hydrogel,[215] alginate,[216–218] carrageenan,[206] low-melting agarose,[219] chitosan[220] and proteinic matrix.[221]

One of the main benefits hydrogels have is their high water content and the 3D polymer network, which allows a high gas exchange rate and transport of nutrients to cells immobilized in the polymer network. These characteristics, in combination with their biocompatibility, make it possible to even cultivate cells or bacteria inside of hydrogels and to use the cell–polymer composites for biosensing applications.

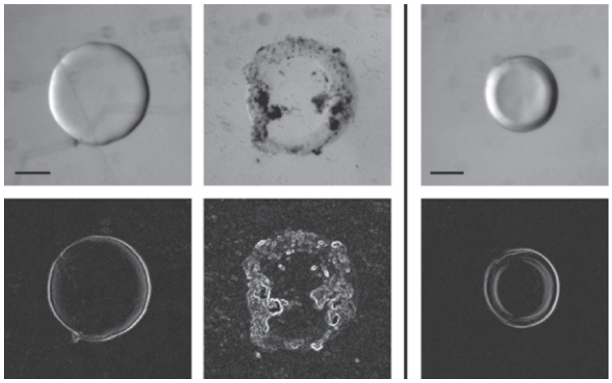

Figure 19 Fifteen micrograms per milliliter BoNT/A degrades posts in cream. (a) Initial 425 µm synaptosome-associated protein peptide post in 1× PBS, $t = 0$ h; (b) after 48 h exposure to BoNT/A in cream; (c) 325 µm control post with BoNT/A-insensitive cross-linker after 48 h toxin exposure. Corresponding images directly below a–c are edge-outlined using ImageJ software for better visualization of degraded hydrogels. Scale bars = 150 µm. Reproduced from Frisk, M. L.; Tepp, W. H.; Lin, G.; Johnson, E. A.; Beebe, D. J. *Chem. Mater.* **2007**, *19*(24), 5842–5844, with permission from American Chemical Society.

3.329.3.2.1. Bacteria

Utilizing the mentioned cell-supporting characteristics, it is possible to create biosensors that use bacterial cells as biological recognition elements. One example for this sensor type is a biosensor for the rapid determination of the concentration of biodegradable pollutants in wastewater, developed by Renneberg *et al.*[222] The sensor consisted of salt-tolerant yeast *Arxula adeninivorans* LS3 cells immobilized in a poly(carbamoyl)sulfonate (PCS) hydrogel, on a Clark-type oxygen electrode. The group claimed that the sensor made it possible to get comparable results for the so-called standard 5-day biochemical oxygen demand (BOD5) method, employed as a pollution index, in just 5 min (Figure 20).

Another example for yeast cells in a hydrogel matrix are the fiber-optic biosensors based on luminescent yeast cells entrapped in calcium alginate, or polyvinyl alcohol (PVA) hydrogels, constructed by Fine *et al.*[223] The entrapped genetically modified *Saccharomyces cerevisiae* cells contained the estrogen receptor α-mediated expression of the *luc* reporter gene and enabled a novel approach for estrogenic endocrine disrupting chemical (EDC) biodetection. Owing to the protective hydrogel matrix that formed a protective environment for the entrapped cells, it was possible to operate even under

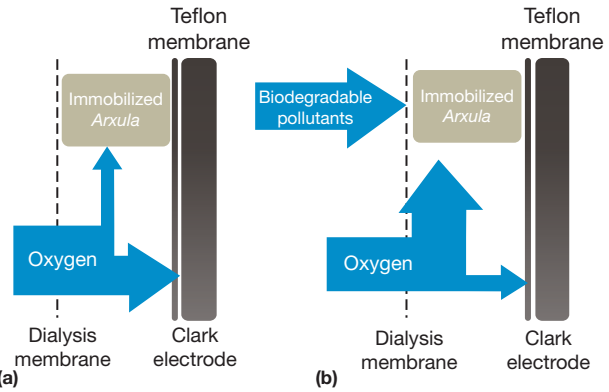

Figure 20 Schematic diagram of the *Arxula adeninivorans* LS3 microbial sensor. It illustrates the microbial consumption of dissolved oxygen (a) before and (b) after the addition of biodegradable pollutants. Redrawn from Renneberg, T.; Kwan, R. C. H.; Chan, C.; Kunze, G.; Renneberg, R. *Microchim. Acta* **2004**, *148*(3–4), 235–240, with permission from Springer.

nonsterile conditions. Further, Martinez *et al.* described a fast method to study cell metabolic characteristics immobilizing yeast cells (*S. cerevisiae*) in a microbial biosensor-like device.[224] Main components of the sensor where *S. cerevisiae*, for example, entrapped in a poly(carbamoylsulfonate) hydrogel membrane, and a carbon dioxide electrode. The sensor device allowed the calculation of Michaelis–Menten parameters related to the kinetics of transport and degradation of several carbohydrates (i.e., glucose, fructose, galactose, sucrose, and xylose, with $K_{m(app)}$ of 6.0, 5.8, 0.9, 2.0, and 147 mM, respectively), and the study of the kinetics of expression of nonconstitutive proteins related to the transport and degradation of galactose.

Köster *et al.* made use of an immobilized *Staphylococcus* type to create an amperometric, microbial respiration-based microbiosensors for the quantification of available dissolved organic carbon (ADOC) instantaneously respired by microorganisms.[225] Therefore, they immobilized aerobic seawater microorganisms, closely related to *Staphylococcus warneri*, in a polyurethane hydrogel sensing membrane. The group focused on biochemical and physiological properties of respiration-based ADOC microbiosensors that measure all of the dissolved organic carbon compounds that are instantaneously respired by the immobilized cells. The sensor had a detection limit equivalent to about 6–10 μM glucose and a 90% response time of 1–5 min. The shelf lives of individual sensors were up to 2 weeks.

With *E. coli*, Fresenko *et al.* used one of the most popular bacteria strains for their hydrogel microchip. They developed a cell–hydrogel system for biosensing and monitoring of cell populations using a polyacrylamide-based hydrogel bacterial microchip (HBMChip).[226] The microchip represented an array of hemispherical gel elements that contained live immobilized *E. coli* cells. They were able to measure and monitor intracellular metabolism using vital fluorescent stains, engineered constructs encoding bioluminescent or fluorescent reporters. It was possible to monitor the dynamics of nucleic acids in growing *E. coli* cells using vital fluorescent stain SYTO 9. Further, they made use of the biosensing opportunities the cell-chip offered and illustrated the detection of antibiotics and sodium meta-arsenite by quantitative analysis.

3.329.3.2.2. Cells

The same characteristics that make hydrogels preferable candidates for bacterial biosensors count as well for cell-based biosensors. Besides the already mentioned biocompatibility and the high diffusion rate for nutrients, gas, etc., hydrogels have a structural similarity to the macromolecular-based components in the human body, which offers applications *in vivo* and *in vitro*. To get a better overview of human cell–hydrogel composites, we advise the reader to have a closer look at the review 'Hydrogels for tissue engineering' written by Lee and Mooney.[227] Further, Hynd *et al.* published a comprehensive review about hydrogels in applications for neural cell engineering.[228] The review gives a overview of acrylate-based polymers and their derivatives, used in biomedical applications, including drug delivery, tissue engineering, cell encapsulation, and as templates for directed cell growth, attachment, and proliferation. In the following sections, we focus on hydrogels used in the field of cell-based biosensors.

3.329.3.2.2.1. Hydrogel coatings and influence of the third dimension

In the field of cell-based biosensors, hydrogels preferably are used in two different shapes: either as coating material for recognition elements like electrodes, implantable sensors etc., or as a 3D-Matrix for cells that are utilized as biological recognition element themselves. Hydrogels that are used as sensor coatings in most cases play a passive role; they, for example, support gas transportation, ion-exchange etc., or make it possible to immobilize cells on sensor surfaces. An example for the immobilization of cells on a sensor surface is the work of Ding *et al.*[229] They prepared a nanocomposite by neutralizing a solution of chitosan encapsulated gold nanoparticles formed by reducing *in situ* tetrachloroauric acid in chitosan. The gel was designed for immobilization and electrochemical study of cells, monitoring their adhesion, proliferation, and apoptosis on electrodes. The nanocomposites gel showed improved immobilization capacity for K562 leukemia cells, as a model cell line, and good biocompatibility for preserving their activity on glassy carbon electrodes. Another example came from the same group when Hao *et al.* combined the biocompatibility of chitosan (CS) and conductivity of carbon nanofiber (CNF).[230] By an electrodeposition of soluble CNF-doped CS colloidal solution, they were able to form a robust CNF-CS nanocomposite film with good biocompatibility for the immobilization and cytosensing of K562 cells on an electrode.

The biocompatibility of hydrogels can be increased by modifying them with certain biomolecules that support the immobilization of cells or decrease the inflammation of tissue in case the sensor is implanted. Norton *et al.* examined the release of vascular endothelial growth factor (VEGF) and dexamethasone (DX) from nonfouling hydrogel-based sensor coatings and their effect on the foreign body response.[231] The hydrogels were prepared from 2-hydroxyethyl methacrylate, *N*-vinyl pyrrolidinone, and PEG. The study revealed that VEGF-releasing hydrogel-coated fibers increased vascularity and inflammation in the surrounding tissue after 2 weeks

of implantation compared to hydrogel-coated fibers. DX-releasing hydrogel-coated fibers reduced inflammation compared to hydrogel-coated fibers and had reduced capsule vascularity compared to VEGF-releasing hydrogel-coated fibers. Owing to the fact that after 6 weeks there were no detectable differences between drug-releasing hydrogel-coated fibers and control fibers, it could be concluded that the drug depot was exhausted.

Apart from immobilizing cells on hydrogel coatings, they can be embedded in the coating as well. In this case, the hydrogel has a passive but important role because it supports the cells by forming a cell-friendly 3D environment and cells can be cultivated as close as possible to the sensor surface. Klueh *et al.*, for example, reported the uses of tissue-interactive biohydrogels, such as fibrin, to enhance gene delivery at sites of sensor implantation.[232] Therefore, cells genetically engineered to overexpress the angiogenic factor (AF) vascular endothelial cell growth factor (VEGF) were incorporated into an *ex ova* chicken embryo chorioallantoic membrane (CAM)-glucose sensor model. The VEGF-producing cells were delivered to sites of glucose sensor implantation on the CAM using a tissue-interactive fibrin biohydrogel as a cell support and activation matrix. This VEGF–cell–fibrin system induced significant neovascularization surrounding the implanted sensor and significantly enhanced the glucose sensor function *in vivo*.

Desai *et al.* demonstrated different behavior of cells cultured on a 2D coating or in a 3D network.[233] When they used SH-SY5Y human neuroblastoma cells, cultured in 3D collagen hydrogel, confocal microscopy, and immunofluorescence staining, to assess the merit of the system as a functional, cell-based biosensor, they were able to show the depolarization-induced differences in intracellular calcium release when cultured using a 2D versus a 3D matrix. Similar results regarding the difference in 2D or in 3D substrates could be shown by Wu *et al.*[234] They fabricated a packed Cytodex 3 microbead array as a simple 3D cell-based biosensing format. Resting membrane potentials and voltage-gated calcium channel (VGCC) function of SH-SY5Y human neuroblastoma cells cultured on the microbead array versus collagen-coated flat (2D) substrates were evaluated by confocal microscopy with a potentiometric dye and a calcium fluorescent indicator. The exaggerated 2D cell calcium dynamics, in comparison with those of 3D cells, were consistent with previous 2D/3D comparative studies. The study established the rationale and feasibility of the microbead array format for 3D cell-based biosensing.

3.329.3.2.2.2. Cell preservation in 3D hydrogels

As a next step, we highlight some results regarding the influence of entrapping cells into hydrogels and possibilities to preserve them over longer times in *in vitro*. Here, we would like to draw the reader's attention to the short but interesting review about preservation methods to keep biosensor microorganisms alive and active, published by Bjerketorp *et al.*[235] That cells can survive the entrapment into hydrogels is known from literature and was already mentioned in the introduction. That it is even possible to immobilize cells in a hydrogel matrix, by photopolymerization, without a loss of activity has been shown by Zguris *et al.*[236] They demonstrated the ability to entrap human microsomes in PEG hydrogel microstructures without loss of activity, during the photopolymerization process, by reference to the activity of cytochrome P450. Further, they developed two photopolymerization methods for the fabrication of heterogeneous PEG hydrogel structures containing multiple phenotypes of mammalian cells.[237] Besides a two-step photoreaction injection molding process, they described a novel method for one-step fabrications of stacked hydrogel microstructures using a microfluidic mold. In addition to hydrogels containing fluorescent dyes, they were able to create differing extracellular matrixes, unmodified or modified with the cell adhesion promoter RGD, within one hydrogel microstructure and to generate patterns of hydrogels containing multiple phenotypes. The studies revealed new promising opportunities for cell-based hydrogel biosensors.

Preservation of cells for certain time periods in a hydrogel matrix has been shown by Itle *et al.* when they entrapped cells into PEG hydrogel microstructures for biosensing applications.[238] In their work on 'Hepatocyte viability and protein expression within hydrogel microstructures,' they reported the entrapment of mammalian hepatocytes in hydrogels of varying PEG compositions. They were able to maintain cell viability for 7 days in free structures and in structures contained in microfluidic channels. The production of protein by cells in hydrogels decreased with increasing PEG concentration, suggesting mass transfer limitations in hydrogels with higher PEG compositions. Following up on this topic, they reported the fabrication of mammalian cell-containing PEG hydrogel microarrays by a 'stage-down' freezing process for potential applications in drug screening and pathogen detection.[239] The work revealed possibilities of fabricating cell-containing microdevices and cryopreserving them for later use. Their work resulted in the fabrication of whole mammalian cell biosensors for the optical monitoring of cell viability and response to two model chemotoxins: sodium hypochlorite and sodium azide, and one model biotoxin, concanavalin A.[240] Therefore, the cells were entrapped either in PEG microspheres or in array format. It was possible to detect sodium azide in micromolar quantities in fewer than 30 min.

3.329.3.2.2.3. Pathogen

On account of their big impact on the human health system, we briefly highlight a few results regarding pathogen detection with hydrogel biosensors. One example is the work of Kim *et al.* who examined the potential of a sensing strategy based on live T cell–B cell interactions in a biosensor chip format which could be used in pathogen detection.[241] They developed an approach to fabricate patterned PEG dimethacrylate (PEGDMA) hydrogel microwells functionalized at their bases with antibodies to promote specific immobilization of lymphocytes. The microwells were used to array single T cells in a regular pattern on a substrate. A sensing platform was created by overlaying arrayed T cells with a confluent layer of antigen-capturing B cells. Utilizing the hydrogel/lymphocyte sensing chip, it was possible to detect a model peptide analyte within minutes, with dose-dependent linear signals over the concentration range 0.05–5 μM (**Figure 21**).

Another example for the detection of pathogens was published by Banerjee *et al.*[242] They developed a multiwell plate-based biosensor containing B cell hybridoma, Ped-2E9,

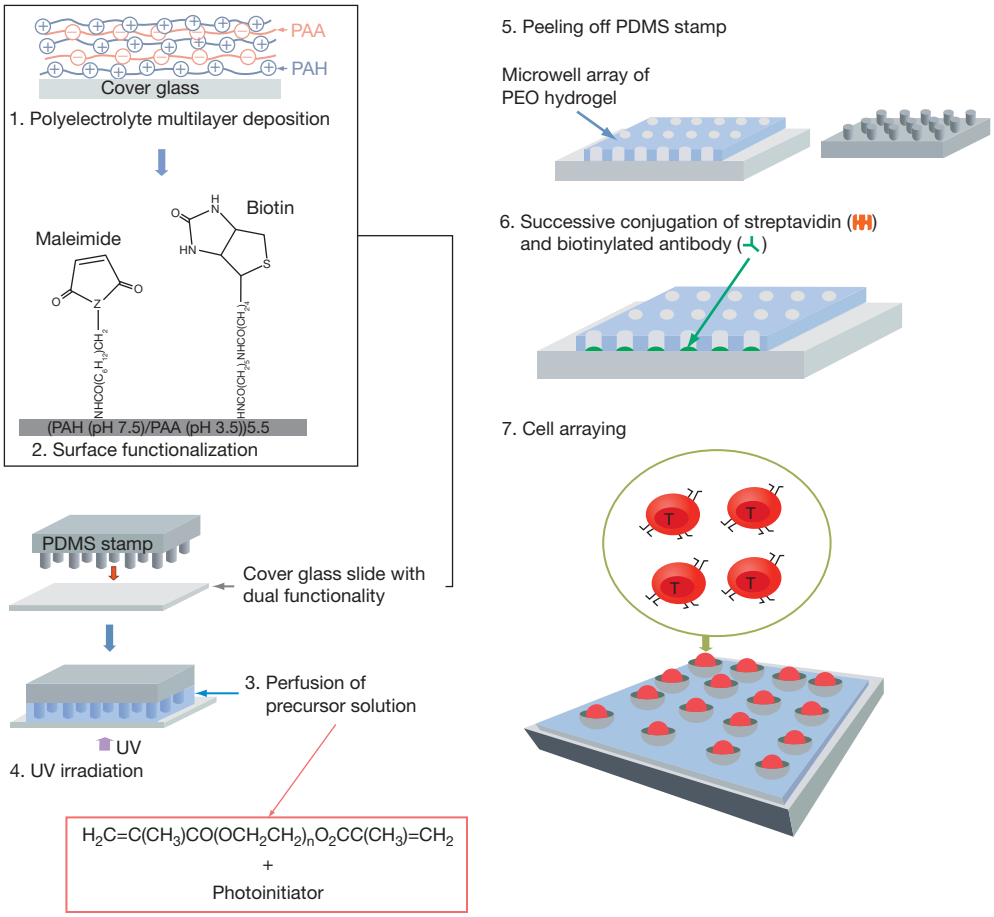

Figure 21 Schematic illustration of poly(ethylene glycol) dimethacrylate (PEGDMA) hydrogel microwell array fabrication and T cell arraying. PAH, poly(allylamine hydrochloride); PAA, poly(acrylic acid); PEO, poly(ethylene oxide). Reproduced from Kim, H.; Cohen, R. E.; Hammond, P. T.; Irvine, D. J. *Adv. Funct. Mater.* **2006**, *16*(10), 1313–1323, with permission from Wiley.

encapsulated in type I collagen matrix, was developed for rapid detection of viable cells of pathogenic *Listeria*, the toxin listeriolysin O, and the enterotoxin from *Bacillus* species. This sensor measured the alkaline phosphatase release from infected Ped-2E9 cells colorimetrically and gave an example of a cell-based sensing system using collagen-encapsulated mammalian cells for rapid detection of pathogenic bacteria or toxin.

3.329.3.2.2.4. Nitric oxide/glutamate

Another interesting field for hydrogel biosensors is the detection of nitric oxide and/or glutamate. Castillo *et al.* presented the simultaneous detection of nitric oxide and glutamate using an array of individually addressable electrodes, which were modified with a sensitive nitric oxide sensing chemistry and a glutamate oxidase/redox hydrogel-based glutamate biosensor.[243] The first working electrode was covered with a positively charged Ni porphyrin, entrapped into a negatively charged electrodeposition paint, and the second working electrode by a bienzyme sensor architecture based on cross-linked redox PEG diglycidyl ether (PEGDGE) hydrogels with entrapped peroxidase and glutamate oxidase. Adherently growing C6-glioma cells were grown on membrane inserts and placed in close distance to the modified sensor surfaces. The current responses recorded at each electrode after stimulation of glutamate and NO release by means of K^+ and bradykinin demonstrated the ability of the individual electrodes in the array to detect the analyte without interference from the neighboring electrode or other analytes present in the test mixture (Figure 22).

From the same group, Wartelle *et al.* reported test results from a compact, biocompatible, hydrogel-based, electrochemical sensing device for the detection of nitric oxide released from C6 glioma cells.[244] Owing to the use of an ionically conducting κ-carrageenan hydrogel membrane, in combination with the integrated electrode setup, used by Castillo *et al.* as well, it was possible to create a living cell-based device for NO detection.

3.329.4. Summary

This chapter gave an overview of the use of hydrogels in biosensing. As highlighted in the introduction, many intrinsic properties of hydrogels predetermine their use in this field of application. The most important points are their high water content that renders them biocompatible and allows diffusion of water-soluble compound through the polymer network as well as their chemical diversity and the ability to tune their

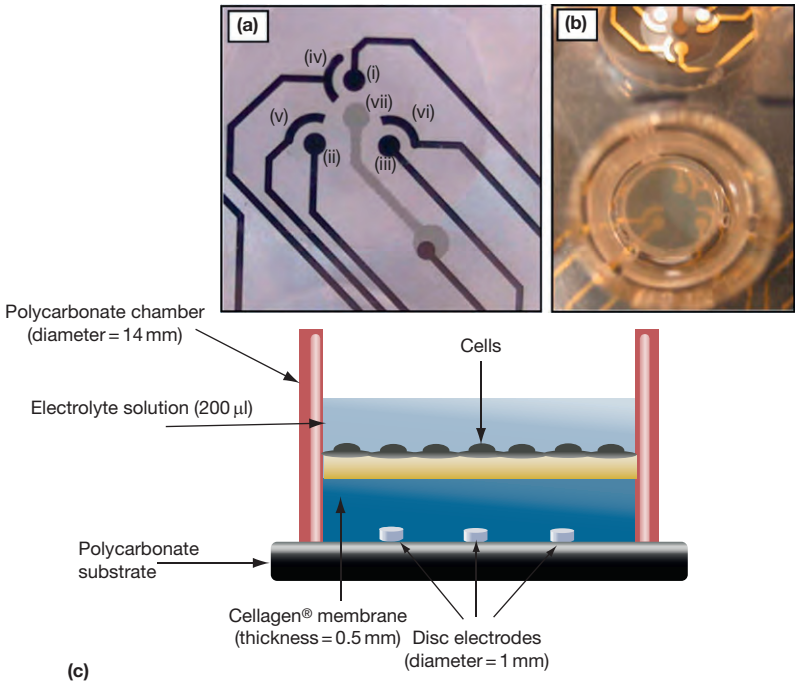

Figure 22 (a) Representation of the array of electrode employed in this study: i, ii, and iii are working electrodes; iv, v, and vi are counter electrodes; and vii is the reference electrode. (b) Photograph and (c) schematic representation of the well plate with and without the membrane insert positioned over the integrated electrodes on the bottom. Redrawn from Castillo, J.; Isik, S.; Bloechl, A.; *et al*. *Biosens. Bioelectron*. **2005**, *20*(8), 1559–1565, with permission from Elsevier.

properties both regarding the chemical nature of the polymer backbone and the introduction of (functional) side groups. This allows the generation and design of stimuli-sensitive hydrogels that may act as sensors themselves, for example, by introduction of hydrophobic groups for temperature sensitivity or protic groups for pH sensitivity. It also enables functionalization of the hydrogel with moieties that act as sensors. The range of molecules that can be and has been used for this purpose is very broad and comprises (fluorescence) dyes, luminescent compounds, enzymes, biochemical recognition sites such as oligonucleotides, antibodies, lectins, and very specific recognition mechanisms.

Hydrogels may be prepared in aqueous solutions through a variety of mechanisms. Most prominently, either UV- or temperature-initiated radical polymerization techniques are used. The gelation from low viscous solutions to gels allows application-specific preparation of the gels in desired geometries and is compatible with miniaturization and microfluidic applications. Moreover, hydrogels can be prepared by preparation methods that are compatible with living cells or bacteria so that these can be encapsulated and may serve as sensors in the hydrogel network.

Recently, especially multifunctionalization of the gels, the combination of hydrogels and other intelligent materials and advances in sensor design has led to advances. Examples are combinations of responsive hydrogels that react with volume changes to stimuli and piezoelectric readout. Also, optical readout through microsphere arrays embedded in a responsive hydrogel matrix is an elegant approach. Double modification of hydrogels with enzymes such as peroxidase and glucose oxidase allows sequential bienzymatic reactions in the hydrogel. Aside of application-specific sensor design, microfabrication techniques are more commonly used to miniaturize and parallelize sensing. The versatile nature of hydrogels, their compatibility with biomolecules, and preservation of their specific activity together with the possibility to tailor the hydrogel preparation process according to application-specific demands make them ideal materials for biosensing.

References

1. Hulanicki, S.; Glab, S.; Ingman, F. *Pure Appl. Chem.* **1991**, *63*(9), 1247–1250.
2. Harsanyi, G. *Sensors in Biomedical Applications: Fundamentals, Technology and Applications*. CRC Press: Boca Raton, FL, 2000.
3. Thevenot, D. R.; Toth, K.; Durst, R. A.; Wilson, G. S. *Pure Appl. Chem.* **1999**, *71*(12), 2333–2348.
4. Clark, L. C.; Lyon, C. *Ann. NY Acad. Sci*. **1962**, *102*, 29–45.
5. Marx, K. A. In *Smart Biosensor Technology*; Knopf, G. K., Bassi, A. S., Eds.; CRC Press: Boca Raton, FL, 2007.
6. Lowe, C. R. In *Handbook of Biosensors and Biochips*; Marks, R. S., Lowe, C. R., Cullen, D. C., Wetall, H. H., Karube, I., Eds.; Wiley: New York, 2007.
7. Kahn, K.; Plaxco, K. W. In *Recognition Receptors in Biosensors*; Zourob, M., Ed.; Springer: Heidelberg, 2010.
8. Hoare, T. R.; Kohane, D. S. *Polymer* **2008**, *49*, 1993–2007.
9. Peppas, N. A.; Wood, K. M.; Blanchette, J. O. *Expert Opin. Biol. Ther.* **2004**, *4*(6), 881–887.
10. Singhal, R.; Tomar, R. S.; Nagpal, A. K. *Int. J. Plast. Technol.* **2009**, *13*, 22–37.
11. Yoshida, R.; Kaneko, Y.; Sakai, K.; *et al*. *J. Control. Release* **1994**, *32*(1), 97–102.
12. Xue, W.; Champ, S.; Huglin, M. B. *Polymer* **2001**, *42*(8), 3665–3669.
13. Okay, O.; Sariisik, S. B.; Zor, S. D. *J. Appl. Polym. Sci.* **1998**, *70*(3), 567–575.
14. Flory, P. J.; Rehner, J. *J. Chem. Phys.* **1943**, *11*, 521–526.
15. Flory, P. J. *J. Chem. Phys.* **1950**, *18*, 108–111.

16. Slaughter, B. V.; Khurshid, S. S.; Fisher, O. Z.; Khademhosseini, A.; Peppas, N. A. *Adv. Mater.* **2009**, *21*, 3307–3329.
17. Rivest, C.; Morrison, D. W. G.; Ni, B.; *et al*. *J. Mech. Mater Struct.* **2007**, *2*(6), 1103–1119.
18. Nicolson, P. C.; Vogt, J. *Biomaterials* **2001**, *22*(24), 3273–3283.
19. Ta, H. T.; Dass, C. R.; Larson, I.; Choong, P. F. M.; Dunstan, D. E. *Biomaterials* **2009**, *30*(27), 4815–4823.
20. Feng, L.; Wang, L.; Hu, Z.; Tian, Y.; Xian, Y.; Jin, L. *Microchim. Acta* **2009**, *164*(1–2), 49–54.
21. Jen, A. C.; Wake, M. C.; Mikos, A. G. *Biotechnol. Bioeng.* **1996**, *50*(4), 357–364.
22. Hong, W.; Hu, X.; Zhao, B.; Zhang, F.; Zhang, D. *Adv. Mater.* **2010**, doi:10.1002/adma.201002512.
23. Disley, D. M.; Morril, P. R.; Sproule, K.; Lowe, C. R. *Biosens. Bioelectron.* **1999**, *14*(5), 481–493.
24. Asher, S. A.; Alexeev, V. L.; Lednev, I. K.; Sharma, A. C.; Wilcox, C. S. U.S. Patent 7,105,352, 2006.
25. Yoshida, R.; Uchida, K.; Kaneko, Y.; *et al*. *Nature* **1995**, *374*, 240–242.
26. Irie, M. *Adv. Polym. Sci.* **1993**, *110*, 49–65.
27. Lee, K. K.; Cussler, E. L.; Marchetti, M.; McHugh, M. A. *Chem. Eng. Sci.* **1990**, *45*(3), 766–767.
28. Bohon, K.; Krause, S. *J. Polym. Sci. B Polym. Phys.* **1998**, *36*, 1091–1094.
29. Horkay, F.; Tasaki, I.; Basser, P. J. *Biomacromolecules* **2000**, *1*(1), 84–90.
30. Cao, X.; Lai, S.; Lee, L. J. *Biomed. Microdevices* **2001**, *3*, 109–118.
31. Zhao, B.; Moore, J. S. *Langmuir* **2001**, *17*(16), 4758–4763.
32. Ju, X. J.; Chu, L. Y.; Liu, L.; Mi, P.; Lee, Y. M. *J. Phys. Chem. B* **2008**, *112*(4), 1112–1118.
33. Hassan, C. M.; Doyle, F. J.; Peppas, N. A. *Macromolecules* **1997**, *30*(20), 6166–6173.
34. Aimetti, A. A.; Machen, A. J.; Anseth, K. S. *Biomaterials* **2009**, *30*(30), 6048–6054.
35. Miyata, T.; Asami, N.; Uragami, T. *Nature* **1999**, *399*, 766–769.
36. Heijl, J. M. D.; Du Prez, F. E. *Polymer* **2004**, *45*(20), 6771–6778.
37. Oh, K. S.; Oh, J. S.; Choi, H. S.; Bae, Y. C. *Macromolecules* **1998**, *31*(21), 7328–7335.
38. Atta, A. M.; Arndt, K.-F. *Polym. Adv. Technol.* **2005**, *16*(6), 442–450.
39. Topuz, F.; Okay, O. *React. Funct. Polym.* **2009**, *69*(5), 273–280.
40. Ding, Z.; Ziaie, B. *Transducers* **2009**, 493–496.
41. Grimshaw, P. E.; Nussbaum, J. H.; Grodzinsky, A. J.; Yarmush, M. L. *J. Chem. Phys.* **1990**, *93*, 4462–4472.
42. Chou, K. F.; Lin, Y. C.; Chen, H. Y.; Huang, S. Y.; Lin, Z. Y. *IFMBE Proc.* **2009**, *23*(2), 855–858.
43. Nguyen, K. T.; West, J. L. *Biomaterials* **2002**, *23*(22), 4307–4314.
44. Biswal, D.; Hilt, J. Z. *Polymer* **2006**, *47*(21), 7355–7360.
45. Dalton, P. D.; Hostert, C.; Albrecht, K.; Moeller, M.; Groll, J. *Macromol. Biosci.* **2008**, *8*(10), 923–931.
46. Kopecek, J.; Yang, J. *Acta Biomater.* **2009**, *5*(3), 805–816.
47. Vandermeulen, G. W. M.; Tziatzios, C.; Duncan, R.; Klok, H. A. *Macromolecules* **2005**, *38*(3), 761–769.
48. Toledano, S.; Willams, R. J.; Jayawarna, V.; Ulijn, R. V. *J. Am. Chem. Soc.* **2006**, *128*(4), 1070–1071.
49. Galler, K. M.; Aulisa, L.; Regan, K. R.; D'Souza, R. N.; Hartgerink, J. D. *J. Am. Chem. Soc.* **2010**, *132*(9), 3217–3223.
50. Lin, C. C.; Metters, A. T.; Anseth, K. S. *Biomaterials* **2009**, *30*(28), 4907–4914.
51. Dankers, P. Y.; Harmsen, M. C.; Brouwer, L. A.; van Luyn, M. J.; Meijer, E. W. *Nat. Mater.* **2005**, *4*(7), 568–574.
52. Topuz, F.; Okay, O. *Macromolecules* **2008**, *41*(22), 8847–8854.
53. Topuz, F.; Okay, O. *Biomacromolecules* **2009**, *10*(9), 2652–2661.
54. Um, S. H.; Lee, J. B.; Park, N.; Kwon, S. Y.; Umbach, C. C.; Luo, D. *Nat. Mater.* **2006**, *5*, 797–801.
55. Horkay, F.; Basser, P. J. *Biomacromolecules* **2004**, *5*(1), 232–237.
56. Kloxin, A. M.; Kasko, A. M.; Salinas, C. N.; Anseth, K. S. *Science* **2009**, *324*, 59–63.
57. van der Linden, H. J.; Herber, S.; Olthuis, W.; Bergveld, P. *Analyst* **2003**, *128*(4), 325–331.
58. Chuppa, S.; Tsai, Y. S.; Yoon, S.; *et al*. *Biotechnol. Bioeng.* **2000**, *55*(2), 328–338.
59. Schild, H. G. *Prog. Polym. Sci.* **1992**, *17*(2), 163–249.
60. Kuckling, D.; Hoffmann, J.; Ploetner, M.; *et al*. *Polymer* **2003**, *44*(16), 4455–4462.
61. Harmon, M. E.; Tang, M.; Frank, C. W. *Polymer* **2003**, *44*(16), 4547–4556.
62. Schmaljohann, D.; Nitschke, M.; Schulze, R.; Eing, A.; Werner, C.; Eichorn, K.-J. *Langmuir* **2005**, *21*(6), 2317–2322.
63. Asher, S. A.; Holtz, J.; Liu, L.; Wu, Z. *J. Am. Chem. Soc.* **1994**, *116*(11), 4997–4998.
64. Weissman, J. M.; Sunkara, H. B.; Tse, A. S.; Asher, S. A. *Science* **1996**, *274*, 959–963.
65. Reese, C. E.; Baltusavich, M. E.; Keim, J. P.; Asher, S. A. *Anal. Chem.* **2001**, *75*(21), 5038–5042.
66. Borisov, S. M.; Wolfbeis, O. S. *Anal. Chem.* **2006**, *78*(14), 5094–5101.
67. Lee, S. M.; Chung, W. Y.; Kim, J. K.; Suh, D. H. *J. Appl. Polym. Sci.* **2004**, *93*(5), 2114–2118.
68. Arndt, K.-F.; Richter, A.; Ludwig, S.; *et al*. *Acta Polym.* **1999**, *50*(11–12), 383–390.
69. Kuckling, D.; Richter, A.; Arndt, K.-F. *Macromol. Mater. Eng.* **2003**, *288*(2), 144–151.
70. Richter A. Quellfähige polymernetzwerke als aktor-sensor-systeme für die fluidtechnik. VDI-Verlag Fortschrittberichte 2002;(8)944.
71. Beebe, D. J.; Moore, J. S.; Bauer, J. M.; *et al*. *Nature* **2000**, *404*, 588–590.
72. Bashir, R.; Hilt, J. Z.; Elibol, O.; Gupta, A.; Peppas, N. A. *Appl. Phys. Lett.* **2002**, *81*(16), 3091–3093.
73. Guenther, M.; Suchaneck, G.; Sorber, J.; Gerlach, G.; Arndt, K.-F.; Richter, A. *Fine Mech. Opt.* **2003**, *48*, 320–322.
74. Marshall, A. J.; Blyth, J.; Davidson, C. A. B.; Lowe, C. R. *Anal. Chem.* **2003**, *75*(17), 4423–4431.
75. Richter, A.; Bund, A.; Keller, M.; Arndt, K.-F. *Sens. Actuat. B Chem.* **2004**, *99*(2–3), 579–585.
76. Gerlach, G.; Guenther, M.; Suchaneck, G.; Sorber, J.; Arndt, K.-F.; Richter, A. *Macromol. Symp.* **2004**, *210*(1), 403–410.
77. Richter, A.; Paschew, G.; Klatt, S.; Lienig, J.; Arndt, K.-F.; Adler, H.-J. P. *Sensors* **2008**, *8*, 561–581.
78. Gerlach, G.; Guenther, M.; Sorber, J.; Suchaneck, G.; Arndt, K.-F.; Richter, A. *Sens. Actuat. B Chem.* **2005**, *111–112*(11), 555–561.
79. Trinh, Q. T.; Gerlach, G.; Sorber, J.; Arndt, K.-F. *Sens. Actuat. B Chem.* **2006**, *117*(1), 17–26.
80. Sorber, J.; Steiner, G.; Schulz, V.; *et al*. *Anal. Chem.* **2008**, *80*(8), 2957–2962.
81. Lee, Y.-J.; Heitzman, C. E.; Frei, W. R.; Johnson, H. T.; Braun, P. V. *J. Phys. Chem. B* **2006**, *110*(39), 19300–19306.
82. Dong, L.; Agarwal, A. K.; Beebe, D. J.; Jiang, H. *Nature* **2006**, *442*, 551–554.
83. Kim, D.; Beebe, D. J. In *International Conference on Medical Biology*, Japan, 2006 pp 292–294.
84. Sannino, A.; Pappada, S.; Giotta, L.; Valli, L.; Maffezzoli, A. *J. Appl. Polym. Sci.* **2007**, *106*(5), 3040–3050.
85. Maruyama, H.; Matsumoto, H.; Fukuda, T.; Arai, F. *Microelectronech. Syst.* **2008**, 224–227.
86. Guenther, M.; Gerlach, G.; Corten, C.; Kuckling, D.; Sorber, J.; Arndt, K.-F. *Sens. Actuat. B Chem.* **2008**, *102*(2), 471–476.
87. Asher, S. A.; Peteu, S. F.; Reese, C. E.; Lin, X.; Finegold, D. *Anal. Bioanal. Chem.* **2002**, *373*(7), 632–638.
88. Ji, H. F.; Thundat, T.; Dabestani, R.; Brown, G. M.; Britt, P. F.; Bonnesen, P. V. *Anal. Chem.* **2001**, *73*(7), 1572–1576.
89. Zhang, Y.; Ji, H. F.; Brown, G. M.; Thundat, T. *Anal. Chem.* **2003**, *75*(18), 4773–4777.
90. Orthner, M. P.; Lin, G.; Avula, M.; *et al*. *Sens. Actuat. B Chem.* **2010**, *145*(2), 807–816.
91. Hart, J. P.; Abass, A. K. *Anal. Chim. Acta* **2005**, *342*(2–3), 199–206.
92. Kojima, J.; Nakayama, Y.; Takenaka, M.; Hashimoto, T. *Rev. Sci. Instrum.* **1995**, *66*(8), 4066–4072.
93. Gumbrecht, W.; Schelter, W.; Lang, S. U.S. Patent 5,376,255, 1994.
94. Severinghaus, J. W.; Bradley, A. F. *J. Appl. Physiol.* **1958**, *13*(3), 515–520.
95. Oh, B. K.; Robbins, M. E.; Schoenfisch, M. H. *Analyst* **2006**, *131*(1), 48–54.
96. Zguris, J.; Pishko, M. V. *Sens. Actuat. B Chem.* **2006**, *115*(1), 503–509.
97. Herber, S.; Olthuis, W.; Bergveld, P.; van den Berg, A. *Sens. Actuat. B Chem.* **2004**, *103*, 284–289.
98. ter Steege, R. W. F.; Herber, S.; Olthuis, W.; Bergveld, P.; van den Berg, A.; Kolkman, J. J. *J. Clin. Monit. Comput.* **2007**, *21*(2), 83–90.
99. Herber, S.; Bomer, J.; Olthuis, W.; Bergveld, P.; van den Berg, A. *Biomed. Microdevices* **2005**, *7*(3), 197–204.
100. Kocincova, A. S.; Nagl, S.; Arain, S.; *et al*. *Biotechnol. Bioeng.* **2008**, *100*(3), 430–438.
101. Rhin, J.-W. *Food Sci. Biotechnol.* **2000**, *13*(4), 528–535.
102. Garcia-Golding, F.; Giallorenzo, M.; Moreno, N.; Chang, V. *Sens. Actuat. A Phys.* **1995**, *47*(1–3), 337–341.

103. Tian, E.; Wang, J.; Zheng, Y.; Song, Y.; Liang, L.; Zhu, D. *J. Mater. Chem.* **2008**, *18*, 1116–1122.
104. Walker, J. P.; Kimble, K. W.; Asher, S. A. *Anal. Bioanal. Chem.* **2007**, *389*(7–8), 2115–2124.
105. Tian, E.; Ma, Y.; Cui, L.; Wang, J.; Song, Y.; Jiang, L. *Macromol. Rapid Commun.* **2009**, *30*(20), 1719–1724.
106. Kang, Y.; Walish, J. J.; Gorishnyy, T.; Thomas, E. L. *Nat. Mater.* **2007**, *6*, 957–960.
107. Barry, R. A.; Wiltzius, P. *Langmuir* **2006**, *22*(3), 1369–1374.
108. Galindo, F.; Lima, J. C.; Luis, S. V.; Melo, M. J.; Parola, A. J.; Pina, F. *J. Mater. Chem.* **2005**, *15*, 2840–2847.
109. Wu, X. J.; Choi, M. M.; Chen, C. S.; Wu, X. M. *Biosens. Bioelectron.* **2005**, *22*(7), 1337–1344.
110. Castillo, J.; Bluechl, A.; Dennison, S.; Schuhmann, W.; Csoeregi, E. *Biosens. Bioelectron.* **2005**, *20*(10), 2116–2119.
111. Kwan, R. C. H.; Hon, P. Y. T.; Renneberg, R. *Sens. Actuat. B Chem.* **2005**, *107*(2), 616–622.
112. Ravaine, V.; Ancla, C.; Catargi, B. *J. Control. Release* **2008**, *132*(1), 2–11.
113. Malitesta, C.; Palmisano, F.; Torsi, L.; Zambonin, P. G. *Anal. Chem.* **1990**, *62*(24), 2735–2740.
114. Hale, P. D.; Boguslavsky, L. I.; Inagaki, T.; *et al. Anal. Chem.* **1991**, *63*(7), 677–682.
115. Zhang, M.; Smith, A.; Gorski, W. *Anal. Chem.* **2004**, *76*(17), 5045–5050.
116. Cai, Q.; Zeng, K.; Ruan, C.; Desai, T. A.; Grimes, C. A. *Anal. Chem.* **2004**, *76*(14), 4038–4043.
117. Kim, D. N.; Lee, W.; Koh, W. G. *Anal. Chim. Acta* **2008**, *609*(1), 59–65.
118. Merchant, S. A.; Tran, T. O.; Meredith, M. T.; Cline, T. C.; Glatzhofer, D. T.; Schmidtke, D. W. *Langmuir* **2009**, *25*(13), 7736–7742.
119. Aizawa, M.; Karube, I.; Suziki, S. *Anal. Chim. Acta* **1974**, *69*(2), 431–437.
120. Xiao, Y.; Ju, H.-X.; Chen, H.-Y. *Anal. Chim. Acta* **1999**, *391*(1), 73–82.
121. Kim, S. H.; Kim, B.; Yadavalli, V. K.; Pishko, M. V. *Anal. Chem.* **2005**, *77*(21), 6828–6833.
122. Varma, S.; Mattiasson, B. *J. Biotechnol.* **2005**, *119*(2), 172–180.
123. Wang, B.; Zhang, J.; Cheng, G.; Dong, S. *Anal. Chim. Acta* **2000**, *407*(1–2), 111–118.
124. Yan, J.; Sun, Y.; Zhu, H.; Marcu, L.; Revzin, A. *Biosens. Bioelectron.* **2009**, *24*(8), 2604–2610.
125. Fowler, J. M.; Wong, D. K. Y.; Halsall, H. B.; Heineman, W. R. In *Electrochemical Sensors, Biosensors, and Their Biomedical Applications*; Zhang, X., Ju, H., Wang, J., Eds.; Elsevier: Amsterdam, 2008.
126. Laschi, S.; Franek, M.; Mascini, M. *Electroanalysis* **2000**, *12*(16), 1293–1298.
127. Jin, X.-Y.; Jin, X.-F.; Ding, Y.-J.; Jiang, J.-H.; Shen, G.-L.; Yu, R.-Q. *Chin. J. Chem.* **2008**, *26*(12), 2191–2196.
128. Carrigan, S. D.; Scott, G.; Tabrizian, M. *Biomaterials* **2005**, *26*(35), 7514–7523.
129. Carrigan, S. D.; Scott, G.; Tabrizian, M. *Langmuir* **2005**, *21*(13), 5966–5973.
130. Carrigan, S. D.; Tabrizian, M. *Langmuir* **2005**, *21*(26), 12320–12326.
131. Lu, H.-S.; Chen, H.-M.; Lin, Y.-S.; Lin, J.-W. *Biotechnol. Prog.* **2000**, *16*(1), 116–124.
132. Scarano, S.; Mascini, M.; Turner, A. P. F.; Minunni, M. *Biosens. Bioelectron.* **2010**, *25*(5), 957–966.
133. Myszka, D. G.; Rich, R. L. *Pharm. Sci. Technol. Today* **2000**, *3*(9), 310–317.
134. Guidi, A.; Laricchia-Robbio, L.; Gianfaldoni, D.; Revoltella, R.; Del Bono, G. *Biosens. Bioelectron.* **2001**, *16*(9–12), 971–977.
135. Coiller, R. J.; Miller, M. A.; Hildebrandt, J. P.; *et al. J. Dairy Sci.* **1991**, *74*(9), 2905–2911.
136. Besselink, G. A.; Kooyman, R. P.; van Os, P. J.; Engbers, G. H.; Schasfoort, R. B. *Anal. Biochem.* **2004**, *333*(1), 165–173.
137. Stigter, E. C.; de Jong, G. J.; van Bennekom, W. P. *Biosens. Bioelectron.* **2005**, *21*(3), 474–482.
138. Frasconi, M.; Mazzarino, M.; Botre, F.; Mazzei, F. *Anal. Biochem.* **2009**, *394*(8), 2151–2159.
139. Wu, Y.; Liu, S. *Analyst* **2009**, *134*, 230–235.
140. Charles, P. T.; Goldman, E. R.; Rangasammy, J. G.; Schauer, C. L.; Chen, M.-S.; Taitt, C. R. *Biosens. Bioelectron.* **2004**, *20*(4), 753–764.
141. Lee, N. Y.; Lim, J. R.; Lee, M. J.; Park, S.; Kim, Y. S. *Langmuir* **2006**, *22*(18), 7689–7694.
142. Zhang, Y.; Heller, A. *Anal. Chem.* **2005**, *77*(23), 7758–7762.
143. Liang, R.; Peng, H.; Qui, J. *J. Colloid Interface Sci.* **2008**, *320*(1), 125–131.
144. Shen, L.; He, P. *Electrochem. Commun.* **2007**, *9*(4), 657–662.
145. Zhang, X.; Wang, S.; Hu, M.; Xiao, Y. *Biosens. Bioelectron.* **2006**, *21*(11), 2180–2183.
146. Wu, Z.-S.; Jiang, J.-H.; Shen, G.-L.; Yu, R.-Q. *Hum. Mutat.* **2007**, *28*(6), 630–637.
147. Liu, B.; Bazan, G. C. *J. Mater. Chem.* **2004**, *16*(23), 4467–4476.
148. Dominguez, E.; Rincon, O.; Narvaez, A. *Anal. Chem.* **2004**, *76*(11), 3132–3138.
149. Palecek, E. *Nature* **1960**, *188*, 656–657.
150. Palecek, E. *Anal. Biochem.* **1988**, *170*(2), 421–431.
151. Singhal, P.; Kuhr, W. G. *Anal. Chem.* **1997**, *69*(23), 4828–4832.
152. Jelen, F.; Yosypchuk, B.; Kourilova, A.; Novotny, L.; Palecek, E. *Anal. Chem.* **2002**, *74*(18), 4788–4793.
153. Wang, J.; Kawde, A. N. *Analyst* **2002**, *127*(3), 383–386.
154. Meiring, J. E.; Schmid, M. J.; Grayson, S. M.; *et al. Chem. Mater.* **2004**, *16*(26), 5574–5580.
155. Homola, J. *Anal. Bioanal. Chem.* **2003**, *377*(3), 528–539.
156. Wang, J. *Biosens. Bioelectron.* **2006**, *21*(10), 1887–1892.
157. Odenthal, K. J.; Gooding, J. J. *Analyst* **2007**, *132*(7), 603–610.
158. Mannelli, I.; Minunni, M.; Tombelli, S.; Wang, R.; Spiriti, M. M.; Mascini, M. *Bioelectrochemistry* **2005**, *66*(1–2), 129–138.
159. Kinsella, J. M.; Ivanisevic, A. *Nat. Nanotechnol.* **2007**, *2*, 596–597.
160. Cosnier, S.; Mailley, P. *Analyst* **2008**, *133*(8), 984–991.
161. Drummond, T. G.; Hill, M. G.; Barton, J. K. *Nat. Biotechnol.* **2003**, *21*, 1192–1199.
162. Li, D.; Song, S.; Fan, C. *Acc. Chem. Res.* **2010**, *43*(5), 631–641.
163. Lang, H. P.; Hegner, M.; Gerber, C. *Mater. Today* **2005**, *8*(4), 30–36.
164. Xiao-Mei, Y.; Da-Cheng, Z.; Cong-Shun, W.; Xian-Feng, D.; Xiao-Bao, W.; Yong, R. *Chin. J. Chem.* **2003**, *20*(9), 1637–1640.
165. Koev, S. T.; Powers, M. A.; Yi, H.; *et al. Lab Chip* **2007**, *7*(1), 103–111.
166. Su, S.; Ali, M.; Filipe, C. D. M.; Li, Y.; Pelton, R. *Biomacromolecules* **2008**, *9*(3), 935–941.
167. Nilsson, K. P. R.; Inganas, O. *Nat. Mater.* **2003**, *2*, 419–424.
168. Wang, J.; Wang, D.; Miller, E. K.; Moses, D.; Bazan, G. C.; Heeger, A. J. *Macromolecules* **2000**, *33*(14), 5153–5158.
169. Wang, D.; Gong, X.; Heeger, P. S.; Rininsland, F.; Bazan, G. C.; Heeger, A. J. *Proc. Natl. Acad. Sci. USA* **2002**, *99*(1), 49–53.
170. Chen, L.; McBranch, D. W.; Wang, H.-L.; Helgeson, R.; Wudl, F.; Whitten, D. G. *Proc. Natl. Acad. Sci. USA* **1999**, *96*(22), 12287–12292.
171. Ho, H. A.; Boissinot, M.; Bergeron, M. G.; *et al. Angew. Chem. Int. Edn.* **2002**, *41*(9), 1548–1551.
172. Seong, G. H.; Zhan, W.; Crooks, R. M. *Anal. Chem.* **2002**, *74*(14), 3372–3377.
173. Pregibon, D. C.; Doyle, P. T. *Anal. Chem.* **2009**, *81*(12), 4873–4881.
174. Hajdukiewicz, J.; Boland, S.; Kavanagh, P.; Leech, D. *Biosens. Bioelectron.* **2010**, *25*(5), 1037–1042.
175. Sato, Y.; Ikegaki, S.; Suziki, K.; Kawaguchi, H. *J. Biomater. Sci. Polym. Ed.* **2003**, *14*(8), 803–820.
176. Kim, J.; Nayak, S.; Lyon, L. A. *J. Am. Chem. Soc.* **2005**, *127*(26), 9588–9592.
177. Hendrickson, G. R.; Lyon, L. A. *Soft Matter* **2009**, *5*, 29–35.
178. Kim, J.; Singh, N.; Lyon, L. A. *Biomacromolecules* **2007**, *8*(4), 1157–1161.
179. Kim, J.; Singh, N.; Lyon, L. A. *Angew. Chem. Int. Edn.* **2006**, *45*(9), 1446–1449.
180. Chen, H.-M.; Lin, C.-W. *Biotechnol. Prog.* **2007**, *23*, 741–748.
181. Chen, H.-M.; Wang, W.-C.; Chen, S.-H. *Biotechnol. Prog.* **2004**, *20*(4), 1237–1244.
182. Birchall, L. S.; Ulijn, R. V.; Webb, S. J. *Chem. Commun.* **2008**, 2861–2863.
183. Lee, W.; Choi, D.; Lee, Y.; Kim, D.-Y.; Park, J.; Koh, W.-G. *Sens. Actuat. B Chem.* **2008**, *129*(2), 841–849.
184. Ehrick, J. D.; Stokes, S.; Bachas-Daunert, S.; *et al. Adv. Mater.* **2007**, *19*(22), 4024–4027.
185. Mader, H. S.; Wolfbeis, O. S. *Microchim. Acta* **2008**, *162*(1–2), 1–34.
186. Asher, S. A.; Alexeev, V. L.; Goponenko, A. V.; *et al. J. Am. Chem. Soc.* **2003**, *125*(11), 3322–3329.
187. Kabilan, S.; Marshall, A. J.; Sartain, F. K.; *et al. Biosens. Bioelectron.* **2005**, *20*(8), 1602–1610.
188. Lee, Y.-J.; Pruzinsky, S. A.; Braun, P. V. *Langmuir* **2004**, *20*(8), 3096–3106.
189. Matsumoto, A.; Kurata, T.; Shiino, D.; Kataoka, K. *Macromolecules* **2004**, *37*(4), 1502–1510.
190. Alexeev, V. L.; Das, S.; Finegold, D. N.; Asher, S. A. *Clin. Chem.* **2004**, *50*(12), 2353–2360.
191. Ben-Moshe, M.; Alexeev, V. L.; Asher, S. A. *Anal. Chem.* **2006**, *78*(14), 5149–5157.
192. Worsley, G. J.; Tourniaire, G. A.; Medlock, K. E. S.; *et al. J. Clin. Chem.* **2007**, *53*(10), 1820–1826.
193. Lapeyre, V.; Gosse, I.; Chevreux, S.; Ravaine, V. *Biomacromolecules* **2006**, *7*(12), 3356–3363.
194. Pickup, J. C.; Hussain, F.; Evans, N. D.; Rolinski, O. J.; Birch, D. J. S. *Biosens. Bioelectron.* **2005**, *20*(12), 2555–2565.

195. Chaudhary, A.; Raina, M.; Harma, H.; Hanninen, P.; McShane, M. J.; Srivastava, R. *Biotechnol. Bioeng.* **2009**, *104*(6), 1075–1085.
196. Haab, B. B.; Dunham, M. J.; Brown, P. O. *Genome Biol.* **2001**, *2*, 2.
197. Chang, I.-T.; Herron, J. N. *Langmuir* **1995**, *11*(6), 2083–2089.
198. Yeung, C.; Leckband, D. *Langmuir* **1997**, *13*(25), 6746–6754.
199. Charles, P. T.; Velez, F.; Soto, C. M.; *et al. Anal. Chim. Acta* **2006**, *578*(1), 2–10.
200. Lutolf, M. P.; Hubbell, J. A. *Nat. Biotechnol.* **2005**, *23*(1), 47–55.
201. Plunkett, K. N.; Berkowski, K. L.; Moore, J. S. *Biomacromolecules* **2005**, *6*(2), 632–637.
202. Frisk, M. L.; Tepp, W. H.; Lin, G.; Johnson, E. A.; Beebe, D. J. *Chem. Mater.* **2007**, *19*(24), 5842–5844.
203. Lei, Y.; Chen, W.; Mulchandani, A. *Anal. Chim. Acta* **2006**, *568*(1–2), 200–210.
204. Bousse, L. *Sens. Actuat. B Chem.* **1996**, *34*(1), 270–275.
205. Deshpande, A.; D'Souza, S. F.; Nadkarni, G. B. *J. Biosci.* **1987**, *11*(1–4), 137–144.
206. Peter, J.; Hutter, W.; Stoellnberger, W.; Hampel, W. *Biosens. Bioelectron.* **1996**, *11*(12), 1215–1219.
207. Koenig, A.; Zaborosch, C.; Spener, F. In *Field Screening Europe*, Proceedings of the First International Conference on Strategies and Techniques for the Investigations and Monitoring of Contaminated Sites; Gottlieb, J., Hoetzl, H., Huck, K., Niessner, R., Eds.; Kluwer Academic: Boston, MA, 1997.
208. Fukui, S.; Sonomoto, K.; Tanaka, A. *Meth. Enzymol.* **1987**, *135*, 230–252.
209. Yang, Z.; Sasaki, S.; Karube, I.; Suzuki, H. *Anal. Chim. Acta* **1997**, *357*(1–2), 41–49.
210. Rouillon, R.; Sole, M.; Carpentier, R.; Marty, J.-L. *Sens. Actuat. B Chem.* **1995**, *27*(1–3), 477–479.
211. Rouillon, R.; Tocabens, M.; Carpentier, R. *Enzyme Microb. Tech.* **1999**, *25*(2–3), 230–235.
212. Uhlich, T.; Ulbricht, M.; Tomaschewski, G. *Enzyme Microb. Tech.* **1996**, *19*(2), 124–131.
213. Tag, K.; Lehmann, M.; Chan, C.; Renneberg, R.; Riedel, K.; Kunze, G. *Sens. Actuat. B Chem.* **2000**, *67*(1–2), 142–148.
214. Ulbricht, M.; Papra, A. *Enzyme Microb. Tech.* **1997**, *20*(1), 61–68.
215. D'Urso, E. M.; Fortier, G. *Enzyme Microb. Tech.* **1996**, *18*(7), 482–488.
216. Nomura, Y.; Ikebukuro, K.; Yokoyama, K.; *et al. Anal. Lett.* **1994**, *27*(15), 3095–3108.
217. Schmidt, A.; Standfuss-Gabisch, C.; Bilitewski, U. *Biosens. Bioelectron.* **1996**, *11*(11), 1139–1145.
218. Smidsord, O.; Skjak-Braek, G. *Trends Biotechnol.* **1990**, *8*(3), 71–78.
219. Mulchandani, A.; Kaneva, I.; Chen, W. *Anal. Chem.* **1998**, *70*(23), 5042–5046.
220. Peter, J.; Hutter, W.; Stoellnberger, W.; Karner, F.; Hampel, W. *Anal. Chem.* **1997**, *69*(11), 2077–2079.
221. D'Souza, S. F.; Marolia, K. Z. *Biotechnol. Tech.* **1999**, *13*(6), 375–378.
222. Renneberg, T.; Kwan, R. C. H.; Chan, C.; Kunze, G.; Renneberg, R. *Microchim. Acta* **2004**, *148*(3–4), 235–240.
223. Fine, T.; Leskinen, P.; Isobe, T.; *et al. Biosens. Bioelectron.* **2006**, *21*(12), 2263–2269.
224. Martínez, M.; Hilding-Ohlsson, A.; Viale, A. A.; Corton, E. *J. Biochem. Biophys. Meth.* **2007**, *70*(3), 455–464.
225. Koester, M.; Gliesche, C. G.; Wardenga, R. *Appl. Environ. Microbiol.* **2006**, *72*(11), 7063–7073.
226. Fesenko, D. O.; Nasedkina, T. V.; Prokopenko, D. V.; Mirzabekov, A. D. *Biosens. Bioelectron.* **2005**, *20*(9), 1860–1865.
227. Lee, K. Y.; Mooney, D. J. *Chem. Rev.* **2001**, *101*(7), 1869–1880.
228. Hynd, M. R.; Turner, J. N.; Shain, W. *J. Biomater. Sci. Polym. Edn.* **2007**, *18*(10), 1223–1244.
229. Ding, L.; Hao, C.; Xue, Y.; Ju, H. *Biomacromolecules* **2007**, *8*(4), 1341–1346.
230. Hao, C.; Ding, L.; Zhang, X.; Ju, H. *Anal. Chem.* **2007**, *79*(12), 4442–4447.
231. Norton, L. W.; Koschwanez, H. E.; Wisniewski, N. A.; Klitzman, B.; Reichert, W. M. *J. Biomed. Mater. Res. A* **2007**, *81*(4), 858–869.
232. Klueh, U.; Dorsky, D. I.; Kreutzer, D. L. *Biomaterials* **2005**, *26*(10), 1155–1163.
233. Desai, A.; Kisaalita, W. S.; Keith, C.; Wu, Z.-Z. *Biosens. Bioelectron.* **2006**, *21*(8), 1483–1492.
234. Wu, Z.-Z.; Zhao, Y.-P.; Kisaalita, W. S. *Biosens. Bioelectron.* **2006**, *22*, 685–693.
235. Bjerketorp, J.; Hakansson, S.; Belkin, S.; Jansson, J. K. *Curr. Opin. Biotechnol.* **2006**, *17*(1), 43–49.
236. Zguris, J. C.; Itle, L. J.; Hayes, D.; Pishko, M. W. *Biomed. Microdevices* **2005**, *7*(2), 117–125.
237. Zguris, J. C.; Itle, L. J.; Koh, W.-G.; Pishko, M. V. *Langmuir* **2005**, *21*(9), 4168–4174.
238. Itle, L. J.; Koh, W.-G.; Pishko, M. V. *Biotechnol. Prog.* **2005**, *21*(3), 926–932.
239. Itle, L. J.; Pishko, M. V. *Biotechnol. Prog.* **2005**, *21*(3), 1004–1007.
240. Itle, L. J.; Pishko, M. V. *Anal. Chem.* **2005**, *77*(24), 7887–7893.
241. Kim, H.; Cohen, R. E.; Hammond, P. T.; Irvine, D. J. *Adv. Funct. Mater.* **2006**, *16*(10), 1313–1323.
242. Banerjee, P.; Lenz, D.; Robinson, J. P.; Rickus, J. L.; Bhunia, A. K. *Lab Invest.* **2008**, *88*, 196–206.
243. Castillo, J.; Isik, S.; Bloechl, A.; *et al. Biosens. Bioelectron.* **2005**, *20*(8), 1559–1565.
244. Wartelle, C.; Schuhmann, W.; Bloechl, A.; Bedioui, F. *Electrochim. Acta* **2005**, *50*(25–26), 4988–4994.
245. Fritz, J.; Baller, M. K.; Lang, H. P.; *et al. Science* **2000**, *288*, 316–318.

3.330. Carbon Nanotube-Based Sensors: Overview

M G Schrlau, Drexel University, Philadelphia, PA, USA

© 2011 Elsevier Ltd. All rights reserved.

3.330.1.	**Introduction**	519
3.330.2.	**CNTs and Related Carbon-Based Nanostructures**	519
3.330.2.1.	Brief Perspective	520
3.330.2.2.	Fabrication	520
3.330.2.3.	Properties	520
3.330.3.	**Manufacturing Devices from Carbon Nanostructures**	521
3.330.3.1.	Devices with Randomly Oriented CNTs	521
3.330.3.2.	Devices from Vertically Aligned CNTs and CNFs	521
3.330.3.3.	Carbon Nanostructure-Tipped Devices	522
3.330.3.4.	Enhancement and Selectivity	523
3.330.4.	**Sensing Applications of Carbon Nanostructures**	524
3.330.4.1.	Electrochemical Sensors	524
3.330.4.2.	Detection of Gases and Vapors	524
3.330.4.3.	Detection of Biomolecules	525
3.330.4.4.	Single-Cell Probes and Sensors	526
3.330.5.	**Future Opportunities**	526
References		526

Glossary

Atomic Force Microscopy (AFM) A microscope that uses a tiny probe mounted on a cantilever to scan the surface of an object. The probe is extremely close to, but does not touch the surface. As the probe traverses the surface, attractive and repulsive forces arising between it and the atoms on the surface induce forces on the probe that bend the cantilever. The amount of bending is measured and recorded, providing a surface map with near atomic detail.

Carbon nanotubes (CNTs) Carbon nanotubes are allotropes of carbon with a cylindrical nanostructure.

Chemical Vapor Deposition (CVD) CVD is a chemical reaction which transforms gaseous molecules, called precursors, into a solid material in the form of thin film or powder on the surface of a substrate.

Field-effect Transistor (FET) A transistor in which the voltage on one terminal (the gate) creates a field that allows or disallows conduction between the other two terminals (the source and drain).

3.330.1. Introduction

In the first two decades since their discovery, carbon nanotubes (CNTs) and their derivatives have proven to be one of the most versatile nanostructures in engineering, science, and medicine. Carbon-based nanomaterials have made broad and significant societal impacts, from providing unique material composites and enabling nanoscale electronics to facilitating effective treatments for disease and the development of novel biological probes. The properties of CNTs are what make them attractive and versatile for many applications: CNTs are nanoscopic in size, have high length-to-width aspect ratio, have a high surface-to-volume ratio, have hollow geometry, are chemically inert but can be easily modified to possess different surface chemistry, are mechanically robust, have conducting or semiconducting properties, and have unique optical properties.

In terms of sensing, combinations of these properties have been attractive for a variety of sensing platforms, including optical, electrical, thermal, mechanical, and so on. For example, the high surface-to-volume ratio and electrical conductivity of CNTs have been used to enhance electrode surfaces and improve sensitivity for electrochemical detection applications. The nanoscopic size, high aspect ratio, hollow geometry, and mechanical robustness have been attractive for probing single living cells. Independent of the desired combination of properties, carbon-based nanomaterials have been widely studied and utilized for a wide range of sensing applications. In this chapter, we discuss the development of CNT-based sensors and their utilization in various biological sensing applications.

3.330.2. CNTs and Related Carbon-Based Nanostructures

Over the past century, carbon fiber research has progressed from carbon fibers and filaments to carbon nanofibers (CNFs) and nanotubes.[1] On the smaller side of things, the field has progressed from hollow graphitic nanofibers to

the higher-ordered structure of CNTs. In the first decade after the discovery of multiwalled CNTs (MWCNTs) in 1991,[2] the majority of research focused on the fabrication, characterization, and determination of properties for CNTs and related structures. In the twenty-first century, one of the main focuses has been on applying their unique qualities as sensors. This section briefly introduces CNTs and related carbon-based nanostructures and, in the context of sensors, describes how these nanostructures are fabricated and explains their distinct properties.

To simplify our discussion of a broad field, we adopt earlier proposed nomenclature[3] to describe all hollow tube-like carbon structures with at least one dimension of 100 nm or less as CNTs. Likewise, we will describe all solid fiber-like carbon structures with at least one dimension of 100 nm or less as CNFs. However, the reader should note where indicated that distinct differences in CNT structure give distinguishing properties.

3.330.2.1. Brief Perspective

One of the first CNTs discovered was produced in vapor-growth carbon fiber processes.[4] These nanotubes, termed graphitic CNTs, had nanoscopic diameters on the order of 10 nm. In 1991, similar structures were observed with a much higher degree of structural perfection,[2] later referred to as MWCNTs. These resemble graphene sheets seamlessly rolled into concentric cylinders spaced apart at distance slightly larger than the interlayer distance in single-crystal graphite (0.34 nm as opposed to 0.335 nm). Although each sheet is highly ordered, the layers are rotationally disordered with respect to one another. The diameters of MWCNTs are typically in the range of 2–25 nm. In 1993, single-walled CNTs (SWCNTs) were discovered.[5,6] Similar to MWCNTs, SWCNTs are also made from a single sheet of graphene seamlessly rolled into a cylinder having a uniform diameter (1–2 nm). SWCNTs and MWCNTs form a distinct class of nanotubes called fullerene CNTs.

Continued carbon fiber research throughout the 1990s led to the development of template-synthesized CNTs[7,8] and CNFs.[9,10] Although the structures of template-synthesized CNTs and CNFs are typically disordered, these carbon nanostructures can be annealed to increase the degree of order and can be formed in a wide range of tube sizes (tens of nanometers to tens of micrometers), geometries (cylinders and cones), and unique material compositions (pristine, nanoparticle-embedded, and so on).

Although all CNTs and CNFs are made of carbon, they have distinguishing characteristics, properties, and capabilities that differentiate them from one another. These distinctions have been reviewed in detail.[11] The first major distinction is the differences in structure. Fullerene CNTs have a known and uniform molecular structure throughout each CNT and between CNTs, which enables near-precise theoretical predictions to be made about their behavior and properties. In contrast, CNTs synthesized from templates or traditional carbon fiber methods (e.g., extrusion, vapor deposition) have nonuniform molecular morphology and structure throughout each CNT and between CNTs. These structural variations hinder precise theoretical predictions of their behaviors and result in large deviations in experimentally determined property values.

The second major distinction is the differences in manufacturing. Fullerene CNTs of various diameters and chirality can be produced in mass by electric arc discharge and laser ablation. The CNTs produced need to be filtered and separated from the highly impure raw material that results from such processes. Decomposing hydrocarbon gases onto catalyzed surfaces can, instead, produce fullerene CNTs. These chemical vapor deposition (CVD) processes produce CNTs of higher purity with narrowed dimensions. In contrast, CNTs synthesized from templates are manufactured in high yield and purity to desired configurations. Template synthesis allows one to manufacture CNTs with prescribed outer diameters, wall thicknesses, and lengths, and even customize the nanostructures with embedded objects or unique geometries and shapes.

3.330.2.2. Fabrication

CNTs of various diameters, lengths, and structure can be fabricated using different methods, including electric arc discharge,[5,12–14] laser ablation,[15,16] catalytic CVD (C-CVD),[17] catalytic plasma-enhanced CVD,[18] and template-based CVD.[7,8,19] Electric arc discharge and laser ablation are very efficient methods for producing high-quality SWCNTs and MWCNTs in large quantities. Useful nanotubes are obtained by removing unwanted carbon particles and other material through complex purification and filtering processes. CNTs made in this fashion are free to be suspended and utilized in random dispersions. CNTs are also produced in quantity by CVD methods. In general, CVD involves the decomposition of hydrocarbon gases to controllably synthesize CNTs and CNFs. In C-CVD, the size of catalyst particle controls the uniform diameter of the carbon products. Catalyst particles can be prefabricated into patterned arrays to produce well-aligned CNT assemblies.[20,21] The location, alignment, geometry, and structure of CNTs and CNFs can be controlled during synthesis with C-PECVD.

As an extension of CVD processing, CNTs and CNFs can be produced by depositing carbon inside porous substrates like alumina membranes and glass capillaries. The template is removed to get aligned arrays,[19,22] individual nanotubes, or single integrated nanostructures.[23–25] Template-synthesis processing allows CNTs to be produced in various dimensions, geometries, and shapes, as well as produce customized nanotubes with wall-embedded nanoparticles[26] or nanoparticle-filled inner bores.[27]

3.330.2.3. Properties

The unique mechanical, electrical, chemical, thermal, and optical properties of CNTs and CNFs are well reviewed[11,18,19] and will not be discussed here in great detail. In addition to these properties, CNTs and CNFs have extremely large length-to-diameter aspect ratios and high surface-to-volume ratios. Their characteristics depend primarily on their structure and can vary significantly between the type and the origin of the carbon material.

CNTs exhibit high tensile strength, stiffness, and ductility. For instance, SWCNTs have tensile strengths as high as 100 times that of steel, making them the strongest known material.[28] CNTs also behave elastically. When pushed against a

hard surface, CNTs bend and buckle without fracture and return to their original shape when force is removed.[24,29] CNTs and related structures exhibit a wide range of electrical characteristics. For example, SWCNTs can be metallic and semiconducting depending on their helicity, whereas MWCNTs exhibit a range of electronic behavior (metallic, semiconducting, and semimetallic).[11] CNTs with defect sites, such as those grown using template-based synthesis methods, are good electrical conductors yet can be annealed to further improve conductivity.[30] Additionally, the reactivity of carbon surfaces varies greatly with surface microstructure, cleanliness, and functional groups.[31] Thus, carbon nanostructures provide a diverse platform to attach biomolecules for a variety of sensing applications.

3.330.3. Manufacturing Devices from Carbon Nanostructures

CNT-based sensors come in many configurations depending on the desired transduction and application. Configurations include electrodes with nanotubes, randomly dispersed nanotubes on their surfaces, substrates, or electrodes consisting of aligned nanotube arrays or forests, probes tipped with individual or bundled nanotubes, transistors made up of a single nanotube or networks of nanotubes, or even three-dimensional nanotube-based electromechanical devices.[32] This section will highlight the variety of CNT-based devices and sensing platforms available.

3.330.3.1. Devices with Randomly Oriented CNTs

Several sensor configurations are manufactured from randomly oriented CNTs, from conductive CNT films and CNT-coated electrode surfaces to transistor-based sensors. CNT films and composites are well suited for macro- and microscale sensing platforms, such as smart wearable fabrics[33] and lab-on-chip devices,[34] where concentrations of analytes are above μM. Smaller electrodes, with tips ranging from hundreds of nanometers to hundreds of micrometers, have been coated with CNTs to enhance their sensitivity.

SWCNTs (**Figure 1(a)**) were coated onto flame-etched carbon fiber nanoelectrodes and utilized as electrochemical sensors (**Figure 1(b)**).[35] The CNT-modified electrode, with tips ranging from 100 to 300 nm, exhibited overall detection capabilities in the nanomolar range, an order of magnitude lower than conventional carbon fiber electrodes of similar geometry. These small electrodes would be well suited for electrochemical applications in ultralow fluid volumes or biological systems such as tissue or cells.

The size and high sensitivity of CNT-based field-effect transistor (FET) sensors make them well suited to detect trace analytes in restricted spaces. FETs, first developed in 1998,[36,37] have been made either by depositing or by growing SWCNTs onto a SiO_2/Si substrate, then patterning connective electrodes or, in reverse order, patterning electrodes and depositing SWCNTs over top. The former is the more common method and has been used extensively by a few research groups. In this method, semiconducting SWCNTs are grown on SiO_2/Si substrates by CVD from catalyst particles or islands.

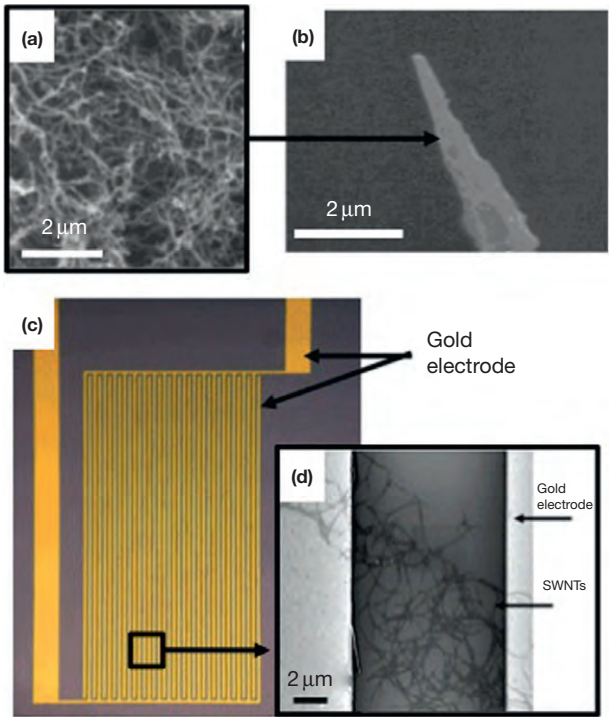

Figure 1 Devices with randomly oriented carbon nanotubes (CNTs). (a, b) CNT-coated carbon fiber nanoelectrode. Adapted from Chen, R. J.; Bangsaruntip, S.; Drouvalakis, K. A.; *et al. Proc. Natl. Acad. Sci. USA*, **2003**, *100*, 4984–4989; Chen, R. S.; Huang, W. H.; Tong, H.; Wang, Z. L.; Cheng, J. K. *Anal. Chem.* **2003**, *75*, 6341–6345, with permission. (c, d) CNT-based field-effect transistor. Adapted from Li, J.; Lu, Y. J.; Ye, Q.; Cinke, M.; Han, J.; Meyyappan, M. *Nano Lett.* **2003**, *3*, 929–933; Li, J.; Ng, H. T.; Cassell, A.; *et al. Nano Lett.* **2003**, *3*, 597–602, with permission.

The result produces randomly oriented nanotubes across the substrate. Electrical contacts are then patterned over the nanotube dispersion using shadow mask evaporation or electron beam or photolithographic processes. The resulting sensor can consist of either single[38,39] or networked[40] CNT-based FET sensors. The latter method has been used to create larger interdigitated electrode (**Figure 1(c)**) with reproducible performance, where, as shown in **Figure 1(d)**, networks of randomly dispersed nanotubes lay on the electrodes to bridge the fingers.

3.330.3.2. Devices from Vertically Aligned CNTs and CNFs

Sensing devices have been made from vertically aligned (normal to the substrate) CNT and CNF forests and patterned arrays. The multiple detection sites of vertically aligned CNT arrays improve the signal-to-noise ratios and temporal responses orders of magnitude better than conventional flat electrodes of similar size and material.[41] When grown in patterns, vertically aligned arrays enable deterministic spatial resolution for a variety of sensing applications, for example, plated living cells.

Although different substrates and growth methods are used, vertically aligned CNT or CNF devices are manufactured using a similar strategy, as shown in **Figure 2**. The device occasionally utilizes nonconducting substrates such as SiO_2/Si but

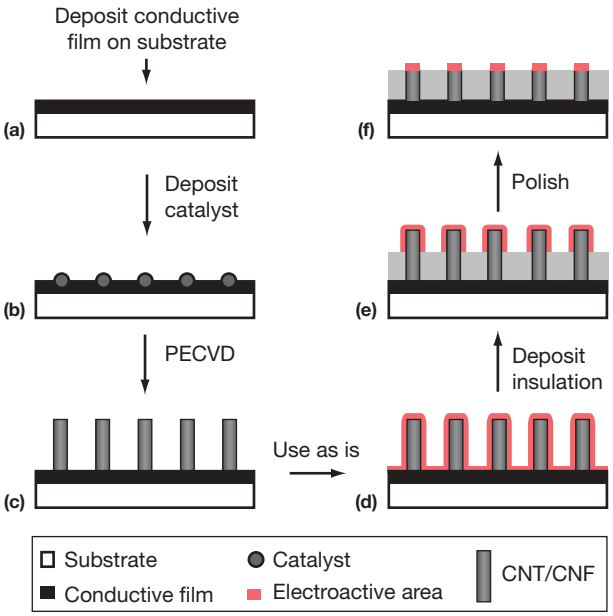

Figure 2 Fabrication of vertically aligned carbon nanotube arrays and device configurations.

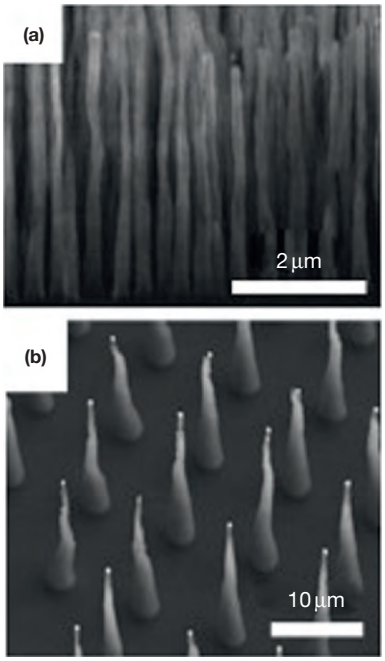

Figure 3 Vertically aligned arrays of carbon nanostructures. (a) Carbon nanotube array. Adapted from Ren, Z. F.; Huang, Z. P.; Wang, D. Z.; *et al*. *Appl. Phys. Lett.* **1999**, *75*, 1086–1088, with permission. (b) Patterned carbon nanofiber array. Adapted from Melechko, A. V.; McKnight, T. E.; Hensley, D. K.; *et al*. *Nanotechnology* **2003**, *14*, 1029–1035, with permission.

typically utilizes a conducting substrate, either in the form of a metal wire, sheet, or plate or a substrate with a deposited metal film (Figure 2(a)). Catalysts such as Fe or Ni films or nanoparticles are then deposited on the substrate (Figure 2(b)). For deterministic arrays, the catalyst films are patterned. PECVD is used to grow the CNTs or CNFs from the catalyst and vertically orient the tubes on the substrate (Figure 2(c)). These devices can be used as is so that the substrate and nanotubes act as the sensor (Figure 2(d)) or embedded in an insulating film to only expose the ends of the nanotubes. In the latter, the insulating layer can be applied such that the nanotube tips protrude (Figure 2(e)) or polished so the tips are flush (Figure 2(f)).

Methods were developed to grow vertically aligned CNTs from Fe nanoparticles embedded into the pores of mesoporous silica[20] and CNFs from Ni films sputtered onto glass.[42] These methods produced large-scale, well-aligned vertical carbon nanostructures that were isolated from one another. Methods were developed to grow vertically aligned CNTs and CNFs arrays at predetermined locations by patterning the catalyst on substrates (Figure 3(a)).[43,44] These methods have since been utilized to produce an assortment of vertically aligned carbon nanostrucutures using PECVD for applications ranging from nanoelectrode ensembles for biosensing to needle arrays for the parallel delivery of reagents to multiple single cells.

As shown in Figure 3(b), arrays of conically shaped CNFs (200 nm tip diameter, 6–20 µm long, deterministic nanofiber separation) were produced from Ni catalyst dots deterministically patterned on Si substrates.[45] The planar arrangement, vertical alignment, and small dimensions of the CNFs made them well suited to penetrate multiple cells simultaneously and deliver surface-adsorbed DNA into the cells.[46] A similar technique was later utilized to produce a nanoelectrode array of CNFs (30–160 nm diameter, ~5 µm long, deterministic nanofiber separation) from patterned Ni catalyst dots on Cr-coated Si wafer.[41]

CNT electrode ensembles consisting of a dense array of CNTs (15–80 nm diameter, 30–100 µm long, 100–200 nm nanotube separation) were produced from an ion-sputtered Fe catalyst film on an Al-coated Si wafer.[47] As depicted in Figure 2(d), the CNTs and the conducting substrate act as the electrode and increase the electroactive surface area. Nanoelectrodes were made from carbon nanopipettes (CNPs) (10–15 nm tip diameter, several micrometers long) on Pt substrates[48] and low-density arrays of vertically aligned CNTs (50–80 nm diameter, 10–12 µm long, >5 µm nanotube separation) from electrodeposited Ni nanoparticles on a Cr-coated Si substrate.[49] To limit the electroactive area to the tips of the CNTs or CNFs, these arrays can be coated with an epoxy to insulate the conductive substrate to expose needle-like tips or surface-polished to expose only the ends of the nanotubes.

3.330.3.3. Carbon Nanostructure-Tipped Devices

In contrast to CNT arrays, devices tipped with a single CNT or bundle of CNTs can deterministically interrogate a single feature on a substrate or a region of interest such as a single cell or intracellular location, with high spatial resolution. Carbon nanostructure-tipped devices have been utilized in several applications including scanning probe microscopy (SPM), nanoscale electrochemistry, and cellular and intracellular studies. Their utilizations differ from other CNT-based devices in that they provide remote manipulation with nanoscale resolution and precise positioning of the sensor.

MWCNTs have been attached to the tips of atomic force microscope (AFM) cantilevers to take advantage of the

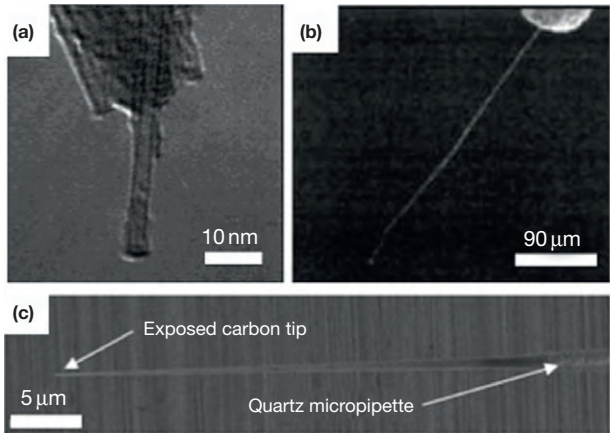

Figure 4 Probes tipped with carbon nanostructures. (a) Carbon nanotube (CNT)-tipped atomic force microscopic probe. Adapted from Hafner, J. H.; Cheung, C. L.; Oosterkamp, T. H.; Lieber, C. M. *J. Phys. Chem. B* **2001**, *105*, 743–746, with permission. (b) CNT-tipped electrode. Adapted from Kaempgen, M.; Roth, S. *Synth. Met.* **2005**, *152*, 353–356, with permission. (c) Carbon nanopipette. Adapted from Schrlau, M. G.; Falls, E. M.; Ziober, B. L.; Bau, H. H. *Nanotechnology* **2008**, *19*, with permission.

precise manipulation capabilities of the AFM (Figure 4(a)). By bringing the tip into contact with an adhesive and then a bundle of tubes dispersed on a surface, CNTs can be adhered onto the surface of the tip.[29] These devices, tipped with CNTs ranging from 5 to 200 nm diameters, were used for SPM of surfaces[50–54] and probing and delivering cargo to cells.[55,56] CNTs have also been grown directly onto the tips of AFM cantilevers.[57] Although CNT-tipped AFM probes are relatively easy to use and have high spatial resolution due to the AFM, they are limited by fabrication, equipment, sensing, and delivery capabilities.

Instead of AFM tips, CNTs have been attached to the tips of thin wires using similar contact assembly methods. One of the earliest examples of such a probe was made by bringing the tip of a micron-sized Pt wire, coated with Ag-conducting epoxy, into contact with aligned MWCNTs (Figure 4(b)).[58] The conductive surfaces were insulated with polyphenol. Afterward, a 1 V negative potential in electrolyte was applied to expose only the CNT tip of the probe. It was demonstrated that these MWCNT bundle-tipped probes could be used as electrochemical nanoelectrodes.

AC electric fields were used to capture bundles of CNTs at the tips of tungsten microelectrodes to form nanoprobes with a macroscopic handle.[59] Two tungsten microelectrodes were submerged in aqueous solutions containing either SWCNT or MWCNTs, so that their tips opposed each other. By applying an AC field across the two electrodes, CNTs were attracted to the regions with high field intensity to form narrow bundles at the electrode tip. Instead of AC fields, magnetic forces have been employed to position ferromagnetic CNTs at the tips of glass micropipettes.[60] Magnetic CNTs placed inside a glass micropipette were driven to its tip by magnetic fields, upon where the protruding CNT was fixed in place by epoxy.

Glass micropipettes have also been used as templates for forming CNPs. Using CVD, a carbon film was deposited onto all the surfaces of the glass micropipettes[23] or preferentially on the inner surfaces with catalyst[24] and CVD process controls.[25] After the glass was selectively removed from the pipette tip, an integrated CNT-like structure remained at the tip of the larger glass micropipette (Figure 4(c)). Diameters as small as 10 nm have been achieved with this technique.

3.330.3.4. Enhancement and Selectivity

Several strategies have been developed to enhance the sensing capabilities of carbon nanostructures. Their surfaces can be functionalized, modified, and customized to selectively detect molecules, chemicals, and biological materials in liquid or gas phases. Noncovalent attachment can be utilized to preserve the structure of CNTs by adsorbing material onto their surface. Covalent attachment needs the surface of CNTs to have defect sites, often requiring the surface to be chemically activated in order to bind molecules to their surface. Alternatively, CNTs can be embedded or filled with material.

Surfaces of CNTs can be modified by noncovalent attachment. A simple method is to deposit material onto CNTs through incubation or drying steps. For example, CNT-coated glassy carbon electrodes were incubated in a combination of proteins and surfactants to enhance interfacial electron transfer[61], while single-stranded DNA were deposited and left to dry on top of CNT-based FETs in order to detect vapors.[62]

A more elegant method is to use adsorption of aromatic compounds. In general, this strategy involves first attaching linker molecules to hydrophobic surfaces of CNTs via pi–pi stacking. Subsequently, nanoparticles, molecules, or proteins are then attached to linker molecule. For example, this method was used to selectively bind to streptavidin.[63] The surfactant poly(ethylene glycol) (PEG) was used to bind to hydrophobic CNTs to prevent the nonspecific binding of proteins to their surface. However, when CNTs were coated with diamino-PEG, amine-reactive protein reagents (in their case, amine-reactive biotin) could be bound to the CNTs. This gave the CNT selectivity by only permitting selective binding to high-affinity molecules, in this case streptavidin. These methods were used with several different linker molecules and selective reagents (proteins, receptors, and even chemicals) to enhance the selectivity of FETs and chemical sensors.[34,38,64]

Covalent functionalization is accomplished by chemically attaching molecules to the CNT surface and is reviewed in detail.[65] In general, CNTs that lack defect sites need to undergo processes, such as sonication, acid treatment, electrochemical oxidation, or plasma treatment to activate their surface and provide hydrophilic surface functional groups for covalent attachment. CNTs and CNFs that have defect sites, such as those grown from template-based synthesis methods, will have binding sites but often still require a degree of surface activation.

A common approach is to use two linker molecules to covalently attach biomolecules to the surface of CNTs. CNTs are first activated by acid, electrochemistry, or other means to produce carboxyl functional groups on their surface. CNTs are then incubated in standard coupling agents, such as 1-ethyl-3-(3-dimethylaminopropyl) carbodiimide (EDC) and derivatives of *N*-hydroxysuccinimide (NHS) or 2(*N*-morpholina)ethane sulfonic acid (MES). The combination of the linker molecules allows biomolecules to bind to

the CNT surface by forming linkages between the biomolecule amine groups and CNT carboxyl groups. This functionalization method has been successful in many applications, for instance, attaching peptide nucleic acid to CNTs to preferentially bind to DNA sequences,[66] attaching DNA to the surface of magnetic CNTs for intracellular delivery,[67] and binding glucose oxidase to CNTs for the electrochemical detection of glucose.[68]

Several methods have been developed to make CNT-nanoparticle hybrids. The tips of CNT-based nanoelectrodes were coated with Au, Fe, and Ag nanoparticles using short-pulse, nonthermal corona discharge in liquids containing metal-salt solutions.[69] Metal nanoparticles can also be attached to CNT surfaces through electrostatic interactions. A positively charged polyelectrolyte was used to attach negatively charged Au nanoparticles to the negatively charged surface of acid-treated nitrogen-doped MWCNTs.[70]

Besides attachment to CNT surfaces, nanoparticles can be embedded into CNTs or filled inside. For instance, CNTs grown by C-PECVD contain ferromagnetic nanoparticles enclosed in their tips. It was demonstrated how vertically aligned CNTs grown from Ni could be manipulated by external magnetic forces and be directed to spear cells.[67] Similar capabilities were demonstrated by embedding iron oxide nanoparticles into the walls of CNTs[26] or filling them with magnetic nanoparticles[27] during template-based CNT synthesis processes.

3.330.4. Sensing Applications of Carbon Nanostructures

The unique properties of CNTs and other carbon nanostrucutures make them well suited for a broad range of sensing applications. For example, the mechanical properties of CNTs enable them to be used, among other things, as strain gauges,[71,72] pressure transducers,[73–75] torsional sensors,[76,77] textile-based sensors,[78] atomic mass sensors,[79] fluid flow sensors,[80] and displacement sensors.[81] The thermal responses of CNTs can be used as thermometers,[82,83] environmental monitors,[84,85] and infrared sensors,[86] while their optical properties have found uses as strain gauges,[87] pressure gauges,[88] and photodetectors.[89] This section mainly focuses on the biological sensing applications of CNTs and other carbon-based nanostructures. Reviews of additional CNT-based biological sensors can be found in literature.[90–92]

3.330.4.1. Electrochemical Sensors

Whether randomly dispersed or grown onto conductive surfaces, the electrical properties and modifiable surfaces of CNTs enable them to be used as electrochemical sensors. Compared to conventional electrodes, CNT-based electrochemical sensors offer higher surface area-to-volume ratio that increases the signal-to-noise ratio for sensitive detection. CNT-based electrodes can be further modified by surface activation to enhance interfacial electron transfer, selectively detect analytes, or attach reagents that prevent nonspecific binding but allow specific binding of analytes. Additional information on chemical sensing with other nanostructured materials is available.[93]

Randomly dispersed CNT films can be used as electrochemical sensors. For instance, ferrocene was noncovalently attached to acid-treated SWCNT films to detect glutamate.[34] The combination of SWCNTs and ferrocene provided enhanced surface area, direct electron transfer, and catalytic effect. Electrodes can also be coated with CNTs to enhance the performance. As described in a previous section, CNT-coated carbon nanoelectrodes outperformed conventional carbon fiber electrodes of similar geometry.[35]

CNT coating with CNTs can also enhance other electrodes, such as glassy carbon and Pt microelectrodes. It was found that CNT-coated glassy carbon electrodes offered superior performance to noncoated electrodes.[94] The same group later showed that direct electrochemistry of microperoxidase immobilized on the surface of CNT-coated Pt microelectrodes catalyzed the reduction of O_2 and H_2O_2.[95]

CNT arrays, as depicted in **Figure 2(e)** and **2(f)**, can be used directly as electrochemical sensors. The Ren group developed an electrochemical sensor (similar to **Figure 2(f)**) from an array of CNTs (50–80 nm diameter, 10–12 μm long) grown from electrodeposited Ni nanoparticle catalyst on a Cr-coated Si substrate.[49] The low-density array exhibited sigmoidal behavior during cyclic voltammetry and provided high signal-to-noise ratio. The electrochemical sensor was used to detect glucose (as well as ascorbic acid, uric acid, and acetaminophen) by attaching glucose oxidase to the CNT surface through the EDC/sulfo-NHS linker moiety.[68] The sensor was later used to detect lead in low-electrolyte conditions[96] and trace cadmium (II) and lead (II) at sub-ppb level (detection limit of 0.04 $\mu g l^{-1}$).[97]

Electrochemical sensors have also been developed from arrays of CNTs that protrude an insulating surface, as depicted in **Figure 2(e)**. Starting with CNPs grown on a Pt-wire substrate (**Figure 3(c)**),[98] a nanoelectrode array with protruding conical carbon tips (**Figure 3(d)**) was produced that exhibited sigmoidal electrochemical behavior.[48] By oxidizing the protruding nanoscopic tips, the sensor was able to electrochemically distinguish between ascorbic acid (oxidation-shifted peak) and dopamine. Electrochemical sensors of a similar configuration using PECVD-grown CNT arrays have also been reported.[99]

3.330.4.2. Detection of Gases and Vapors

The conductance of SWCNT- and MWCNT-based FETs is significantly affected by changes on or near their surface and as such provides attractive sensors for detecting gases and vapors with high sensitivity. Although manufactured in various ways as described previously in this chapter, CNT-based FETs consist of a nanotube or network of nanotubes that bridge the gap between two electrodes (**Figure 5**). Semiconducting CNTs are

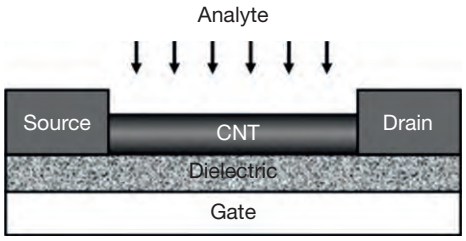

Figure 5 Configuration of a typical carbon nanotube-based field-effect transistor.

attractive for FET applications as their conductance is highly sensitive to the environment and varies significantly with changes in electrostatic charges and surface adsorption of molecules.

The resistance of semiconducting SWCNT-based FETs operating at room temperature dramatically changes when exposed to gaseous molecules such as nitrogen dioxide, ammonia, and oxygen.[39] Due to their sensitivity, SWCNT-based FETs had an order of magnitude faster response than solid-state sensors. Similar SWCNT-based FETs were later used to detect butylamine and 3′-(aminopropyl)-triethoxysilane in vapor phase.[100] The work was extended to detect low levels of NO_2 (44 ppb) and nitrotoluene (262 ppb) using a network of semiconducting SWCNTs connecting interdigitated electrodes (**Figure 1(c)** and **(d)**).[40]

CNT-based FETs were used as 'electronic noses' to detect odors.[62] Metal electrodes were patterned over CVD-grown CNTs on an SiO_2/Si substrate with e-beam lithography to form the FET. To enhance the detection and provide selectivity, single-stranded DNA was deposited and dried on the device (**Figure 6(a)**). The sensor was used to detect and distinguish between methonal and propionic acid, as shown in **Figure 6(b)**, as well as other odors such as trimethylamine, dinitrotoluene, and dimethyl methylphosphonate.

Gas ionization sensors were developed from vertically aligned MWCNTs arrays to overcome argued limitations of CNT-based FETs, such as poor diffusion kinetics, inability to identify gases with low adsorption energies, low capacity to distinguish between gases and gas mixtures, and high susceptibility to changes in moisture, temperature, and gas-flow velocity.[101] These sensors utilized differences in breakdown voltage to distinguish between mocromolar concentrations of distinct gases, measurements that were unaffected by moisture, temperature, and gas-flow.

Acoustic and optical gas sensors, respectively, were developed by coating CNTs onto quartz crystal microbalances (QCMs) and silica optical fibers (SOFs).[102] As shown in **Figure 6(c)**, CNT-coated QCMs were roughly one to two orders of magnitude more sensitive than uncoated QCMs. It was demonstrated that CNT-coated SOFs had similar low limits of detection and enhanced sensitivity.

3.330.4.3. Detection of Biomolecules

CNT-based sensors are attractive for detecting biomolecules commonly found in aqueous environments. For instance, researchers at the NASA Ames Research Center utilized vertically aligned CNT arrays[47] to bind DNA to the surface of CNTs,[103] detected RNA, DNA, and DNA PCR amplicons in solution,[41,104,105] and even delivered DNA plasmids into cells.[46] For the detection applications, CNT-based devices similar to those depicted in **Figure 2(f)** were manufactured and DNA probes were covalently attached to the ends of CNTs using the EDC/sulfo-NHS method. When combined with the $Ru(bpy)_3^{2+}$-mediated guanine oxidation method, the CNT-based sensor was capable of detecting less than a few

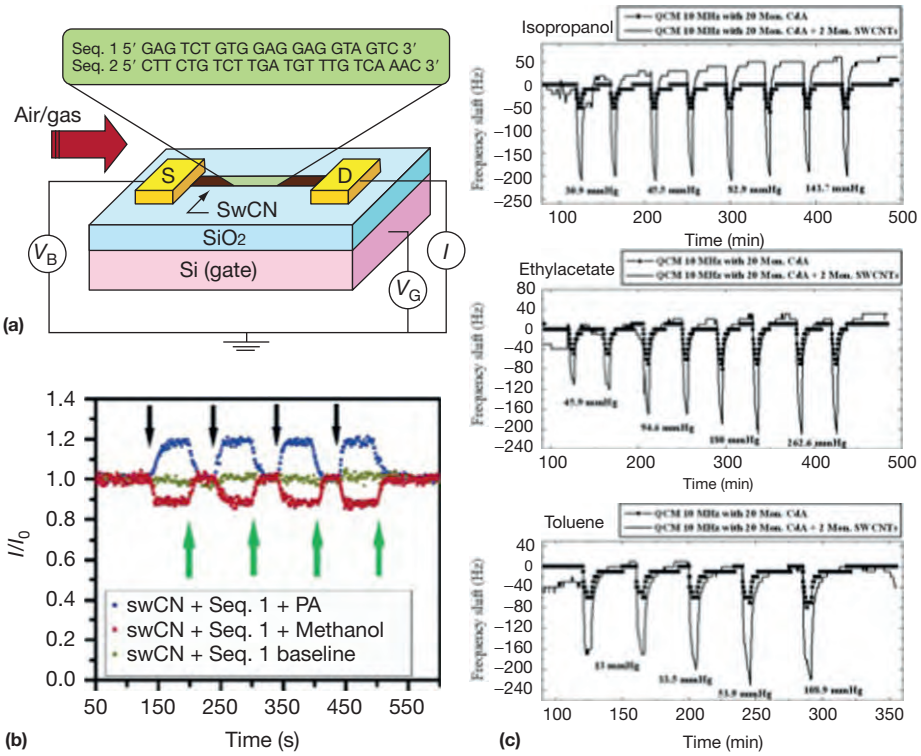

Figure 6 Carbon nanotube-based gas and vapor sensing. (a, b) Odor sensing with field-effect transistor. Adapted from Staii, C.; Johnson, A. T.; Chen, M.; Gelperin, A. *Nano Lett*. **2005**, *5*, 1774–1778, with permission. (c) Gas sensing by microbalance. Adapted from Penza, M.; Cassano, G.; Aversa, P.; *et al*. *Nanotechnology* **2005**, *16*, 2536–2547, with permission.

attomoles of oligonucleotide targets, showing orders of magnitude improvement in sensitivity over other electrochemical detection of DNA immobilization,[105] as well as detecting low number of PCR amplicon targets comparable to fluorescence-based DNA microarray techniques.[104] These detection capabilities were later summarized.[41] The electronic platform facilitates DNA and RNA detection and makes it possible to be integrated into handheld microfluidic lab-on-chip devices.

Although their sensing capabilities were first demonstrated with the detection of gases and vapors, CNT-based FETs were soon utilized in electrolytes[106] to detect chemicals and biomolecules in aqueous environments. The development of such SWCNT-based FETs with the selective binding and recognition of target proteins was reported.[38] FETs were manufactured by dispersing a network of polyethylene oxide (PEO)-functionalized SWCNTs between two electrodes. The PEO coating, noncovalently bound to the CNT surface by pi–pi stacking, strongly prevented nonspecific binding. However, when its hydroxyl termini were activated, the receptors of specific targets could be conjugated to the PEO-coated CNTs to enable selective binding of target proteins. CNT-based FETs conjugated with staphylococcal protein A (SpA) were extremely sensitive to the addition of a protein that has a high affinity to SpA (i.e., IgG protein) but showed negligible response to others. Additional sensors were developed for streptavidin–biotin and U1A-mAbs 10E3 to demonstrate their usefulness in disease detection and proteomics.

The Strano group developed SWCNT-based near-infrared sensors to detect biomolecules *in situ*. These optical sensors detect the presence of specific targets by monitoring the fluorescence of functionalized SWCNTs at wavelengths that are transparent to biological tissue (900–1600 nm). In one application, a porous vessel containing glucose oxidase-coated SWCNTs was implanted beneath a human epidermal tissue sample.[107] The implanted sensor was capable of distinguishing between slight variations in local glucose concentration within the range of blood glucose. In contrast to flux-measuring electrochemical glucose sensors, concentration-measuring optical sensors were less prone to biofouling and significantly more stable over longer periods.[108] The group later reported detecting DNA hybridization and conformational polymorphism in cells with similar sensors.[109,110]

3.330.4.4. Single-Cell Probes and Sensors

CNT-tipped probes offer the ability to probe small aqueous environments, such as ultralow volumes of liquids or single living cells. In contrast to CNT arrays or planar configurations, CNT-tipped probes are needle-like configurations, like those shown in **Figures 1(b)** and 4, things as fluid droplets, single cells, or living tissue.

As discussed earlier, CNT-tipped AFM cantilevers were some of the first CNT-tipped probes to be developed.[29] With high spatial resolution and precise manipulation, CNT-tipped AFM cantilevers were used in SPM applications[50–54] and were able to probe and deliver surface-bound cargo to cells.[55,56] Despite their relatively easy use and high spatial resolution, these CNT-tipped probes were limited by laborious fabrication and inadequately suited for fluid delivery to and electrical sensing of discrete fluid volumes. In contrast, the development of CNT-tipped pencil-shaped probes and their utilization in biological sensing have progressed more rapidly. This is mostly due to their ability to readily fit standard cell physiology equipment such as optical microscopes, micromanipulators, cell injection systems, and electrophysiology amplifiers.

One of the earliest CNT-tipped biological sensors reported was an SWCNT-coated carbon fiber nanoelectrode (100–300 nm tip diameter, as shown in **Figure 1(b)**).[35] Using cyclic voltammetry, the CNT-tipped electrode could detect dopamine, epinephrine, and norepinephrine at concentrations of an order of magnitude lower than that of noncoated probes. The demonstration was significant because the dimensions of the CNT-tipped probe would make it possible to study the functions of living cells and tissue with minimal intrusion. Additionally, the pencil-like shape of the probe readily fit standard cell physiology equipment and facilitated its use.

Several pencil-shaped probes tipped with a single or bundle of CNTs were developed afterwards. Of note, it was reported that a probe tipped with a bundle of MWCNTs could be used as an electrochemical sensor.[58] This demonstration helped inspire the development of CNT-based probes to measure intracellular signals.[111] Referred to earlier as CNPs, these CNT-tipped probes were used to penetrate the membrane of single living cells and electrically measure changes in their transmembrane potential upon extracellular chemical and pharmacological stimuli. It was later shown that a CNT-tipped probe was capable of electrically stimulating and measuring intracellular and extracellular responses more efficiently than the electrolyte-filled glass micropipettes typically used in cell electrophysiology.[112]

3.330.5. Future Opportunities

As illustrated in this chapter, the diversity in size, shape, structure, and configuration of carbon nanostructures enables a broad range of capabilities for biological sensing. Over the past two decades, research related to CNTs and carbon nanostructures has grown from discovery, fabrication, and characterization to utilization and application. However, the later is still in its infancy. Over the next few decades, the applications of CNTs and carbon nanostructures, especially sensing applications, should be expected to grow exponentially into industrial applications, clinical usage, and consumer products.

References

1. Saito, R.; Dresselhaus, G.; Dresselhaus, M. S. *Physical Properties of Carbon Nanotubes*. World Scientific: London, 1998.
2. Iijima, S. *Nature* **1991**, *354*, 56–58.
3. Martin, C. R.; Kohli, P. *Nat. Rev. Drug Discov.* **2003**, *2*, 29–37.
4. Dresselhaus, M. S. *Graphite Fibers and Filaments*. Springer-Verlag: Berlin, New York, 1988.
5. Bethune, D. S.; Kiang, C. H.; Devries, M. S.; *et al*. *Nature* **1993**, *363*, 605–607.
6. Iijima, S.; Ichihashi, T. *Nature* **1993**, *364*, 737 –737.
7. Kyotani, T.; Tsai, L. F.; Tomita, A. *Chem. Mater.* **1995**, *7*, 1427–1428.
8. Martin, C. R. *Science* **1994**, *266*, 1961–1966.
9. Che, G. L.; Lakshmi, B. B.; Martin, C. R.; Fisher, E. R. *Langmuir* **1999**, *15*, 750–758.
10. Rodriguez, N. M. *J. Mater. Res.* **1993**, *8*, 3233–3250.

11. Ajayan, P. M. *Chem. Rev.* **1999**, *99*, 1787–1799.
12. Colbert, D. T.; Zhang, J.; Mcclure, S. M.; *et al. Science* **1994**, *266*, 1218–1222.
13. Ebbesen, T. W.; Ajayan, P. M. *Nature* **1992**, *358*, 220–222.
14. Journet, C.; Maser, W. K.; Bernier, P.; *et al. Nature* **1997**, *388*, 756–758.
15. Guo, T.; Nikolaev, P.; Rinzler, A. G.; Tomanek, D.; Colbert, D. T.; Smalley, R. E. *J. Phys. Chem.* **1995**, *99*, 10694–10697.
16. Thess, A.; Lee, R.; Nikolaev, P.; *et al. Science* **1996**, *273*, 483–487.
17. Amelinckx, S.; Zhang, X. B.; Bernaerts, D.; Zhang, X. F.; Ivanov, V.; Nagy, J. B. *Science* **1994**, *265*, 635–639.
18. Melechko, A. V.; Merkulov, V. I.; McKnight, T. E.; *et al. J. Appl. Phys.* **2005**, *97*.
19. Che, G.; Lakshmi, B. B.; Martin, C. R.; Fisher, E. R.; Ruoff, R. S. *Chem. Mater.* **1998**, *10*, 260–267.
20. Li, W. Z.; Xie, S. S.; Qian, L. X.; *et al. Science* **1996**, *274*, 1701–1703.
21. Terrones, M.; Grobert, N.; Olivares, J.; *et al. Nature* **1997**, *388*, 52–55.
22. Che, G. L.; Lakshmi, B. B.; Fisher, E. R.; Martin, C. R. *Nature* **1998**, *393*, 346–349.
23. Kim, B. M.; Murray, T.; Bau, H. H. *Nanotechnology* **2005**, *16*, 1317–1320.
24. Schrlau, M. G.; Falls, E. M.; Ziober, B. L.; Bau, H. H. *Nanotechnology* **2008**, *19*.
25. Singhal, R.; Bhattacharyya, S.; Orynbayeva, Z.; Vitol, E.; Friedman, G.; Gogotsi, Y. *Nanotechnology* **2010**, *21*, 015304.
26. Mattia, D.; Korneva, G.; Sabur, A.; Friedman, G.; Gogotsi, Y. *Nanotechnology* **2007**, *18*, 155305.
27. Korneva, G.; Ye, H. H.; Gogotsi, Y.; *et al. Nano Lett.* **2005**, *5*, 879–884.
28. Ruoff, R. S.; Qian, D.; Liu, W. K. *Comptes Rendus Phys.* **2003**, *4*, 993–1008.
29. Dai, H. J.; Hafner, J. H.; Rinzler, A. G.; Colbert, D. T.; Smalley, R. E. *Nature* **1996**, *384*, 147–150.
30. Mattia, D.; Rossi, M. P.; Kim, B. M.; Korneva, G.; Bau, H. H.; Gogotsi, Y. *J. Phys. Chem. B* **2006**, *110*, 9850–9855.
31. Chen, P. H.; McCreery, R. L. *Anal. Chem.* **1996**, *68*, 3958–3965.
32. Hayamizu, Y.; Yamada, T.; Mizuno, K.; *et al. Nat. Nanotechnol.* **2008**, *3*, 289–294.
33. Shim, B. S.; Chen, W.; Doty, C.; Xu, C. L.; Kotov, N. A. *Nano Lett.* **2008**, *8*, 4151–4157.
34. Huang, X. J.; Im, H. S.; Lee, D. H.; Kim, H. S.; Choi, Y. K. *J. Phys. Chem. C* **2007**, *111*, 1200–1206.
35. Chen, R. S.; Huang, W. H.; Tong, H.; Wang, Z. L.; Cheng, J. K. *Anal. Chem.* **2003**, *75*, 6341–6345.
36. Martel, R.; Schmidt, T.; Shea, H. R.; Hertel, T.; Avouris, P. *Appl. Phys. Lett.* **1998**, *73*, 2447–2449.
37. Tans, S. J.; Verschueren, A. R. M.; Dekker, C. *Nature* **1998**, *393*, 49–52.
38. Chen, R. J.; Bangsaruntip, S.; Drouvalakis, K. A.; *et al. Proc. Natl. Acad. Sci. USA* **2003**, *100*, 4984–4989.
39. Kong, J.; Franklin, N. R.; Zhou, C. W.; *et al. Science* **2000**, *287*, 622–625.
40. Li, J.; Lu, Y. J.; Ye, Q.; Cinke, M.; Han, J.; Meyyappan, M. *Nano Lett.* **2003**, *3*, 929–933.
41. Koehne, J.; Li, J.; Cassell, A. M.; *et al. J. Mater. Chem.* **2004**, *14*, 676–684.
42. Ren, Z. F.; Huang, Z. P.; Xu, J. W.; *et al. Science* **1998**, *282*, 1105–1107.
43. Merkulov, V. I.; Lowndes, D. H.; Wei, Y. Y.; Eres, G.; Voelkl, E. *Appl. Phys. Lett.* **2000**, *76*, 3555–3557.
44. Ren, Z. F.; Huang, Z. P.; Wang, D. Z.; *et al. Appl. Phys. Lett.* **1999**, *75*, 1086–1088.
45. Melechko, A. V.; McKnight, T. E.; Hensley, D. K.; *et al. Nanotechnology* **2003**, *14*, 1029–1035.
46. McKnight, T. E.; Melechko, A. V.; Griffin, G. D.; *et al. Nanotechnology* **2003**, *14*, 551–556.
47. Li, J.; Cassell, A.; Delzeit, L.; Han, J.; Meyyappan, M. *J. Phys. Chem. B* **2002**, *106*, 9299–9305.
48. Lowe, R. D.; Mani, R. C.; Baldwin, R. P.; Sunkara, M. K. *Electrochem. Solid State Lett.* **2006**, *9*, H43–H47.
49. Tu, Y.; Lin, Y. H.; Ren, Z. F. *Nano Lett.* **2003**, *3*, 107–109.
50. Akita, S.; Nishijima, H.; Nakayama, Y.; Tokumasu, F.; Takeyasu, K. *J. Phys. D Appl. Phys.* **1999**, *32*, 1044–1048.
51. Hafner, J. H.; Cheung, C. L.; Lieber, C. M. *J. Am. Chem. Soc.* **1999**, *121*, 9750–9751.
52. Hafner, J. H.; Cheung, C. L.; Oosterkamp, T. H.; Lieber, C. M. *J. Phys. Chem. B* **2001**, *105*, 743–746.
53. Patil, A.; Sippel, J.; Martin, G. W.; Rinzler, A. G. *Nano Lett.* **2004**, *4*, 303–308.
54. Yenilmez, E.; Wang, Q.; Chen, R. J.; Wang, D. W.; Dai, H. J. *Appl. Phys. Lett.* **2002**, *80*, 2225–2227.
55. Chen, X.; Kis, A.; Zettl, A.; Bertozzi, C. R. *Proc. Natl. Acad. Sci. USA* **2007**, *104*, 8218–8222.
56. Vakarelski, I. U.; Brown, S. C.; Higashitani, K.; Moudgil, B. M. *Langmuir* **2007**, *23*, 10893–10896.
57. Hafner, J. H.; Cheung, C. L.; Lieber, C. M. *Nature* **1999**, *398*, 761–762.
58. Kaempgen, M.; Roth, S. *Synth. Met.* **2005**, *152*, 353–356.
59. Kouklin, N. A.; Kim, W. E.; Lazareck, A. D.; Xu, J. M. *Appl. Phys. Lett.* **2005**, *87*, 173901.
60. Freedman, J. R.; Mattia, D.; Korneva, G.; Gogotsi, Y.; Friedman, G.; Fontecchio, A. K. *Appl. Phys. Lett.* **2007**, *90*, 103108.
61. Yan, Y. M.; Zheng, W.; Zhang, M. N.; Wang, L.; Su, L.; Mao, L. Q. *Langmuir* **2005**, *21*, 6560–6566.
62. Staii, C.; Johnson, A. T.; Chen, M.; Gelperin, A. *Nano Lett.* **2005**, *5*, 1774–1778.
63. Shim, M.; Kam, N. W. S.; Chen, R. J.; Li, Y. M.; Dai, H. J. *Nano Lett.* **2002**, *2*, 285–288.
64. Chen, R. J.; Zhang, Y. G.; Wang, D. W.; Dai, H. J. *J. Am. Chem. Soc.* **2001**, *123*, 3838–3839.
65. Bahr, J. L.; Tour, J. M. *J. Mater. Chem.* **2002**, *12*, 1952–1958.
66. Williams, K. A.; Veenhuizen, P. T. M.; de la Torre, B. G.; Eritja, R.; Dekker, C. *Nature* **2002**, *420*, 761.
67. Cai, D.; Mataraza, J. M.; Qin, Z. H.; *et al. Nat. Meth.* **2005**, *2*, 449–454.
68. Lin, Y. H.; Lu, F.; Tu, Y.; Ren, Z. F. *Nano Lett.* **2004**, *4*, 191–195.
69. Bhattacharyya, S.; Staack, D.; Vitol, E. A.; *et al. Adv. Mater.* **2009**, *21*, 4039–4044.
70. Jiang, K. Y.; Eitan, A.; Schadler, L. S.; *et al. Nano Lett.* **2003**, *3*, 275–277.
71. Grow, R. J.; Wang, Q.; Cao, J.; Wang, D. W.; Dai, H. J. *Appl. Phys. Lett.* **2005**, *86*, 093104.
72. Li, Z. L.; Dharap, P.; Nagarajaiah, S.; Barrera, E. V.; Kim, J. D. *Adv. Mater.* **2004**, *16*, 640–643.
73. Hierold, C.; Jungen, A.; Stampfer, C.; Helbling, T. *Sens. Actuators A Phys.* **2007**, *136*, 51–61.
74. Stampfer, C.; Helbling, T.; Obergfell, D.; *et al. Nano Lett.* **2006**, *6*, 233–237.
75. Wood, J. R.; Frogley, M. D.; Meurs, E. R.; *et al. J. Phys. Chem. B* **1999**, *103*, 10388–10392.
76. Cohen-Karni, T.; Segev, L.; Srur-Lavi, O.; Cohen, S. R.; Joselevich, E. *Nat. Nanotechnol.* **2006**, *1*, 36–41.
77. Meyer, J. C.; Paillet, M.; Roth, S. *Science* **2005**, *309*, 1539–1541.
78. Laxminarayana, K.; Jalili, N. *Text. Res. J.* **2005**, *75*, 670–680.
79. Jensen, K.; Kim, K.; Zettl, A. *Nat. Nanotechnol.* **2008**, *3*, 533–537.
80. Ghosh, S.; Sood, A. K.; Kumar, N. *Science* **2003**, *299*, 1042–1044.
81. Hall, L. J.; Coluci, V. R.; Galvao, D. S.; *et al. Science* **2008**, *320*, 504–507.
82. Shi, L.; Yu, C. H.; Zhou, J. H. *J. Phys. Chem. B* **2005**, *109*, 22102–22111.
83. Wood, J. R.; Zhao, Q.; Frogley, M. D.; *et al. Phys. Rev. B* **2000**, *62*, 7571–7575.
84. Kawano, T.; Chiamori, H. C.; Suter, M.; Zhou, Q.; Sosnowchik, B. D.; Lin, L. W. *Nano Lett.* **2007**, *7*, 3686–3690.
85. Liu, L. T.; Ye, X. Y.; Wu, K.; Han, R.; Zhou, Z. Y.; Cui, T. H. *Sensors* **2009**, *9*, 1714–1721.
86. Pradhan, B.; Kohlmeyer, R. R.; Setyowati, K.; Owen, H. A.; Chen, J. *Carbon* **2009**, *47*, 1686–1692.
87. Frogley, M. D.; Zhao, Q.; Wagner, H. D. *Phys. Rev. B* **2002**, *65*, 113413–113416.
88. Amer, M. S.; El-Ashry, M. M.; Maguire, J. F. *J. Chem. Phys.* **2004**, *121*, 2752–2757.
89. Khairoutdinov, R. F.; Doubova, L. V.; Haddon, R. C.; Saraf, L. *J. Phys. Chem. B* **2004**, *108*, 19976–19981.
90. Kim, S. N.; Rusling, J. F.; Papadimitrakopoulos, F. *Adv. Mater.* **2007**, *19*, 3214–3228.
91. Merkoci, A.; Pumera, M.; Llopis, X.; Perez, B.; del Valle, M.; Alegret, S. *TrAC Trends Anal. Chem.* **2005**, *24*, 826–838.
92. Sinha, N.; Ma, J. Z.; Yeow, J. T. W. *J. Nanosci. Nanotechnol.* **2006**, *6*, 573–590.
93. Huang, X. J.; Choi, Y. K. *Sens. Actuators B Chem.* **2007**, *122*, 659–671.
94. Wang, J. X.; Li, M. X.; Shi, Z. J.; Li, N. Q.; Gu, Z. N. *Anal. Chem.* **2002**, *74*, 1993–1997.
95. Wang, M. K.; Zhao, F.; Liu, Y.; Dong, S. J. *Biosens. Bioelectron.* **2005**, *21*, 159–166.
96. Tu, Y.; Lin, Y. H.; Yantasee, W.; Ren, Z. F. *Electroanalysis* **2005**, *17*, 79–84.
97. Liu, G. D.; Lin, Y. H.; Tu, Y.; Ren, Z. F. *Analyst* **2005**, *130*, 1098–1101.
98. Mani, R. C.; Li, X.; Sunkara, M. K.; Rajan, K. *Nano Lett.* **2003**, *3*, 671–673.
99. Miserendino, S.; Yoo, J.; Cassell, A.; Tai, Y. C. *Nanotechnology* **2006**, *17*, S23–S28.
100. Kong, J.; Dai, H. J. *J. Phys. Chem. B* **2001**, *105*, 2890–2893.
101. Modi, A.; Koratkar, N.; Lass, E.; Wei, B. Q.; Ajayan, P. M. *Nature* **2003**, *424*, 171–174.
102. Penza, M.; Cassano, G.; Aversa, P.; *et al. Nanotechnology* **2005**, *16*, 2536–2547.
103. Nguyen, C. V.; Delzeit, L.; Cassell, A. M.; Li, J.; Han, J.; Meyyappan, M. *Nano Lett.* **2002**, *2*, 1079–1081.
104. Koehne, J.; Chen, H.; Li, J.; *et al. Nanotechnology* **2003**, *14*, 1239–1245.

105. Li, J.; Ng, H. T.; Cassell, A.; *et al*. *Nano Lett*. **2003**, *3*, 597–602.
106. Kruger, M.; Buitelaar, M. R.; Nussbaumer, T.; Schonenberger, C.; Forro, L. *Appl*. *Phys*. *Lett*. **2001**, *78*, 1291–1293.
107. Barone, P. W.; Baik, S.; Heller, D. A.; Strano, M. S. *Nat*. *Mater*. **2005**, *4*, 86–92.
108. Barone, P. W.; Parker, R. S.; Strano, M. S. *Anal*. *Chem*. **2005**, *77*, 7556–7562.
109. Heller, D. A.; Jeng, E. S.; Yeung, T. K.; *et al*. *Science* **2006**, *311*, 508–511.
110. Jeng, E. S.; Moll, A. E.; Roy, A. C.; Gastala, J. B.; Strano, M. S. *Nano Lett*. **2006**, *6*, 371–375.
111. Schrlau, M. G.; Dun, N. J.; Bau, H. H. *ACS Nano* **2009**, *3*, 563–568.
112. de Asis, E. D.; Leung, J.; Wood, S.; Nguyen, C. V. *Appl*. *Phys*. *Lett*. **2009**, *95*.

3.331. Conjugated Polymers for Biosensor Devices

J Bai, S Beyer, and D Trau, National University of Singapore, Singapore

© 2011 Elsevier Ltd. All rights reserved.

3.331.1.	**Conjugated Polymers (CPs): History and Perspectives**	530
3.331.1.1.	Introduction	530
3.331.1.2.	Synthetic Strategies and Processability of CPs	532
3.331.1.3.	Doping Reactions to Facilitate Conductivity and Specific Tasks	533
3.331.1.4.	Properties of CPs	534
3.331.1.4.1.	Electric conductivity	534
3.331.1.4.2.	UV/VIS absorption and fluorescence	534
3.331.1.4.3.	Signal amplifying properties	534
3.331.1.5.	Electrochemical Biosensors	534
3.331.1.5.1.	Amperometric biosensors	534
3.331.1.5.2.	Potentiometric biosensors	534
3.331.1.5.3.	Conductometric biosensor	535
3.331.1.6.	Optical Biosensors and Bioassays	535
3.331.1.6.1.	Colorimetric, fluorescence, and superquenching-based biosensors	535
3.331.2.	**Using CPs for Electrochemical Biosensor Devices**	536
3.331.2.1.	Introduction	536
3.331.2.2.	Immobilization Strategies for Biological Sensing Elements (BSEs) onto CP-Coated Electrodes	538
3.331.2.2.1.	Physical entrapment	542
3.331.2.2.2.	Ion exchange/physical adsorption	542
3.331.2.2.3.	Covalent attachments	542
3.331.2.2.4.	Affinity interactions	542
3.331.2.2.5.	BSE-functionalized CP monomer	543
3.331.2.3.	Choice of Entrapment Approach	543
3.331.2.4.	Current Research Directions of Electrochemical CP-based Biosensors	543
3.331.3.	**Using CPs for Optical Biosensor Devices**	544
3.331.3.1.	Introduction	544
3.331.3.2.	BSE-Functionalized Liposome CPs	544
3.331.3.3.	BSE/CP Complexes	544
3.331.3.3.1.	DNA biosensing using DNA probe/CP complexes	545
3.331.3.3.2.	Protein biosensing using BSE/CP complexes	548
3.331.3.4.	CP Covalently Modified with BSE	552
References		553

Abbreviation

AuNP	Gold nanoparticles
BSA	Bovine serum albumin
BSE	Biological sensing element
CNT	Carbon nanotubes
CP	Conjugated polymer
dsDNA	Double-stranded DNA
DNA	Deoxyribonucleic acid
EDC	1-ethyl-3-(3-dimethylaminopropyl) carbodiimide
ELISA	Enzyme-linked immune sorbent assay
EP	Electropolymerization
FRET	Förster resonance energy transfer
GOx	Glucose oxidase
HRP	Horseradish peroxidase
LbL	Layer-by-layer
LOD	Limit of detection
MBP	Maltose-binding protein
MV-B	Methylviologen-labeled biotin
NTA	Nitrilotriacetic acid
PANI	Polyanline
PDA	Polydiacetylene
PPO	Polyphenol oxidase
PPY	Polypyrrole
PSA	Prostate-specific antigen
PTP	Polythiophene
QCM	Quartz crystal microbalance
RNA	Ribonucleic acid
SPR	Surface plasmon resonance
ssDNA	Single-stranded DNA
ssPNA	Single-stranded peptide nucleic acid
SEM	Scanning electron microscopy

3.331.1. Conjugated Polymers (CPs): History and Perspectives

3.331.1.1. Introduction

Biosensors based on conjugated polymers (CPs) have attracted much attention from the research community during the last 20 years. The definition of biosensors can be summarized from a discussion on biosensors published by IUPAC.[1,2] In reference to these publications, biosensors are a subclass of chemical sensors and devices that recognize selective and reversible chemical substances or ions and produce a concentration dependent continuous signal. Further refinements of this definition and definition of terms are in accordance with the standard article on chemical and biochemical sensors by Renneberg and coworkers published as part of *Ullmann's Encyclopedia of Industrial Chemistry*.[3] The signal that is generated can be in principle electric, calorimetric, or optical. This definition might be extended by the assumption that either the analyte that is to be detected by the sensor or the principle of detector–analyte interaction is derived from biological systems (Figure 1).

This definition appears to be a good measure for technologies that can be easily applied in research or in medicine. In addition, stability, selectivity, shelf life, and cost must be considered for a widely used tool in R&D and medicine. Applying this strict definition for biosensors, sensoric systems based on CPs and biorecognition molecules, described in a major part of the literature, cannot be regarded as biosensors, because they lack the direct contact of the biorecognition component with the transducer, reversibility, selectivity, a continuous signal, or a combination of those.[4] However, even though the definition of a biosensor is not met, it does not mean that the sensoric system cannot be used for analytical purposes. But the technology is rather to be described as a bioassay in analogy to the terms dosimeter or indicator in the field of chemosensors.[5] This chapter aims to give an overview of technologies based on CPs that are used to detect selectively specific analytes and to explain the principles of detection behind these technologies. The focus lies on sensoric systems that meet the definition of a biosensor, though bioassays are important as analytical tools and can sometimes be converted into a biosensor by changing the design and are therefore not, in principle, excluded from this chapter. The selectivity of a sensoric system is further defined by the accuracy of the result in terms of the interference by other substances to the measurement. In detail, selectivity is the ratio of the sensitivity of an interfering substance to the sensitivity measured for the analyte. The sensitivity of a biosensor or a bioassay is the slope of the calibration curve of the analyte and is expressed in signal units per concentration. Sensitivity is the change in signal observed with a change in analyte concentration and should not be confused with the limit of detection (LOD) which expresses the smallest detectable concentration of the analyte. Especially for biosensors that reversibly detect analytes, stability is a very important parameter. Stability describes the variation of the signal with time and often decreases toward the end of the lifetime of a sensor system. To create a biosensor or a bioassay, based on CPs that achieves good properties within the above specifications, the CP, and the sensor or assay design need to be fine-tuned for the employed detection mechanism and the analyte that is to be detected. To see the possibilities and to understand the challenges for tailoring the CPs and sensor and bioassay designs, a short introduction to the properties of CPs will be given, followed by an introduction to electrochemical and optical detection systems. Electrochemical biosensors and optical biosensors and bioassays employing CPs, detecting deoxyribonucleic acid (DNA), small biomolecules, and proteins, will be discussed. Biosensor and bioassays employing CPs is a relatively new discipline that emerged from two different research areas, biosensor/bioassay research and the discovery of specific properties of conductive polymers. It is noteworthy that both research areas needed many decades to advance and to produce such sophisticated materials, methods, and devices that will be discussed in this chapter. Bioassay research dates back to at least the middle of the nineteenth century when Fehling[6] published his method to detect glucose in the urine of diabetic patients in 1848. Biosensors in terms of the definition made above had their dawn in 1962 when Clark reported on an 'electrode' that can continuously and reversibly measure glucose concentration in blood during cardiovascular

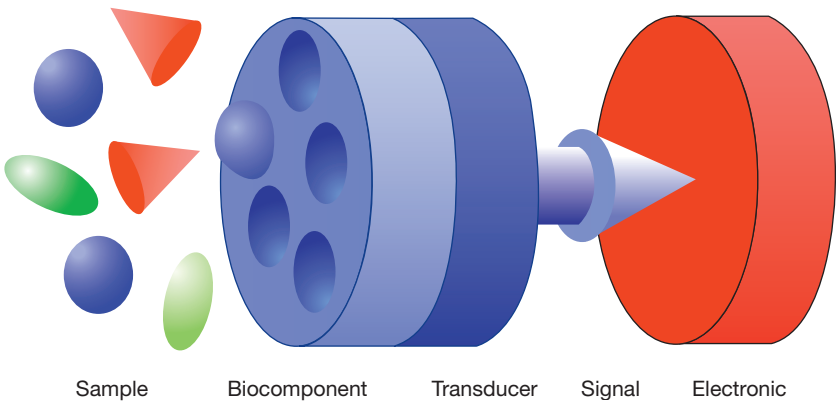

Figure 1 A generalized schematic of a biosensor. The sample contains the analyte that interacts with the biocomponent, which leads to a physical or chemical change that is 'transduced' by the transducer into a signal. This signal is finally detected by the electronic component and displayed or recorded. Reprint with permission from Trau D. Thesis, 2004.

surgery.[7] Since then, biosensors and bioassays have advanced much, and detection of drugs, metabolites, toxins, small molecules, ions DNAs, ribonucleic acids (RNAs), proteins, and polysaccharides is possible nowadays.[8,9] The development of biosensors can be described in three stages, the first, second, and third generation of biosensors.[10–13] In the first generation of biosensors, as, for example, the Clark electrode to detect glucose, the naturally occurring product of the enzymatic reaction diffuses to the transducer and generates the electrical response.[10–12] Biosensors of the second generation use a mediator interacting with the reaction product and the electrode to generate an improved response.[10–12] Biosensors of the third generation, however, do not rely on the diffusion process of reaction products or mediators.[10–12] The enzymes are immobilized together with the mediator very close to the electrode surface, and sometimes there may even be direct electrical contact between the electrode and the enzyme.[14–16] Many of today's biosensors relying on electrochemical transduction mechanism fall into the second or third generation category and can detect various analytes.[11,12,17] In today's biosensor and bioassay research, the major challenges are to create multiplex systems with high selectivity and sensitivity and good LOD without false positive or negative analytical readings. Selectivity of a biosensor or bioassay is especially challenging when real samples such as tissue homogenates, blood, urine, saliva, or sweat are to be analyzed.[4,17] Furthermore, the LOD and the ability to distinguish different concentrations are challenging in real samples. Bioassays that fulfill the above criteria and are commercially available and widely employed in research and medicine are for example: enzyme-linked immune sorbent assays (ELISA), lateral flow assays such as pregnancy tests or CardioDetect® – a bioassay to detect heart attacks in patients. Biosensors that fulfill the above definition and are commercially available are reviewed in the literature[18,19]; the most prominent ones are glucose biosensors in medicine and surface plasmon resonance (SPR), and quartz crystal microbalance (QCM) biosensors as research instruments. CPs are promising candidates to facilitate a new generation of biosensors and bioassays with ultra low limits of detection and high sensitivity due to their signal amplifying properties.[5,20] Research on CPs is ongoing for more than 130 years as extensively pointed out by Gyorgy Inzelt in his book *Conjugated Polymers – Historical Background* (or: There is nothing new under the sun).[21] In fact, the first report about polyacetylene by Adolf von Baeyer entitled *On Polyacetylene Compounds*.[22] dates back to 1885. Reports on polyaniline (PANI) produced by electrochemical oxidation are even older[23] and is unlike the polyacetylenes at that time, very similar to our today's PANI that is frequently used in biosensors.[21] CPs that are frequently used for biosensor and bioassay application are depicted in **Figure 2**.

CPs can serve two major purposes in biosensor devices. They are used either as passive supporting and structuring material on which the sensory biomolecule system can be easily immobilized or as an active component.[8] CPs are able to combine the properties of the very high conductivity of metals with chemical modifiability and properties of polymers.[24] They are therefore also referred to as synthetic metals.[25] Due to the diversity of CPs, many possibilities are available to couple analyte receptor interactions to convert them into an

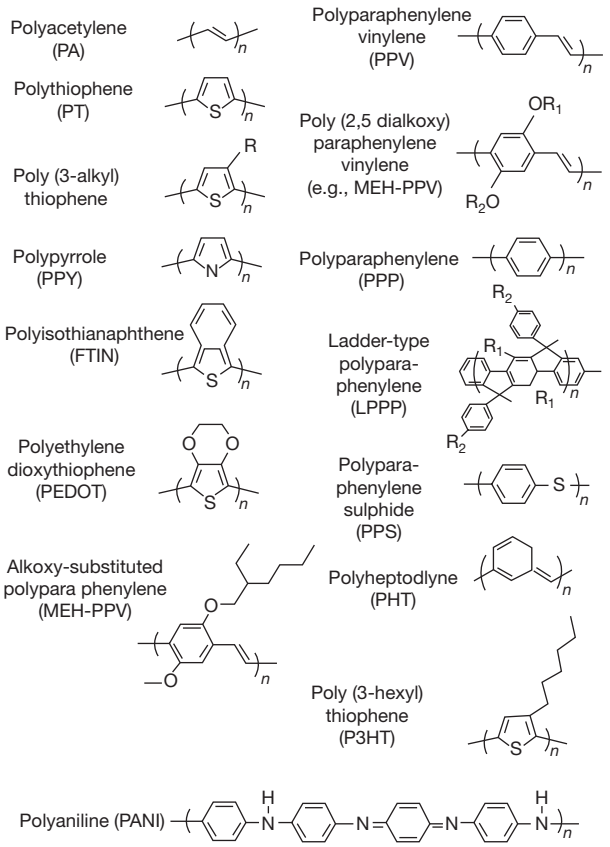

Figure 2 A selection of conjugated polymers that are frequently used for biosensor and bioassay applications. Noteworthy is the occurrence of conjugated double bounds within the polymer backbones, creating a conjugated π-electron system that equips the conjugated polymer with its 'electric conductive' property. Reprinted with permission from Saxena, V.; Malhorta, B. D. *Curr. Appl. Phys.* **2003**, *3*, 293–305.

observable signal. In cases where CPs are used as active component, they often serve as the transducer, mediating the signal upon analyte interaction. One of the main advantages of the use of CPs in biosensor devices over simple small molecule sensor elements is the signal amplifying property of CPs.[5] In biosensor devices using CPs, the sensory system is very sensitive to minor perturbations upon analyte interaction which leads to a dramatic improvement of the LOD compared to biosensors using small molecule sensor elements.[20] For biosensor devices employing CPs, two general classes of transducible signals can be generated: (1) electrical signals, which could be a change in resistivity, in electrical current, or in potential[19,26] and (2) optical signals, manifested in a change of fluorescence wavelength or intensity, in quenching of fluorescence, or change in color or intensity in nonfluorescent systems.[27–29] The signal amplifying properties of CPs are mainly due to their charge and 'signal transport' properties. The backbone of the CP, which consists of a conjugated π-electron system, allows a fast migration of 'signals.' Those signals are electrical charges or energy states that are also responsible for the CPs' high conductivity.[30] It needs to be noted that those energy states and charges create the electrical conductivity unlike in classical semiconductors such as silicon where electrons or holes are transported.

3.331.1.2. Synthetic Strategies and Processability of CPs

The methods to synthesize CPs are extremely versatile and there is often more than one way that leads to the same CP.[31,32] However, the plasticity and processability of the polymer can change dramatically with the procedure that is used for synthesis.[32] Processability is one of the most important properties of CPs when it comes to fabrication of a biosensor device, and the most suitable way of polymerization must be chosen for the desired application. In general, synthetic strategies for the polymerization might be chosen from classical polymer chemistry methods such as coordination polymerization on specific catalysts,[33] common polymer organic chemistry methods,[34,35] or electrochemistry methods.[23,36]

It should be pointed out that most non-modified CPs are insoluble in water and most organic solvents, and often cannot be melted without degradation, and thus, to obtain solubility in organic solvents or water, further processing is necessary.[32] To obtain solubility, side chain modifications of CPs are conducted. Different functionalities can be introduced depending on desired properties.[37] To obtain water solubility, either hydrophilic oligomers such as polyethylene glycols or charged groups such as acid or amine functions, which render the polymer a water-soluble polyelectrolyte, can be introduced. To obtain good solubility in organic solvents, aliphatic or other hydrocarbon chains are introduced.[32] Furthermore, special side chains can be introduced to allow specific interactions or binding with analytes or biomolecules to bring the sensoric system close to the polymer backbone.[28,29,38] In some cases and especially for electrochemical biosensors, the CP is polymerized directly on the surface of the electrode while simultaneously physically entrapping the biomolecular detection system (e.g., enzymes). In this case, the biomolecule is present with polymer monomers in aqueous solution when a certain potential is applied at the electrode on which the CP shall be precipitated (usually by an oxidation reaction). Electrochemical polymerization can, in general, be done by three different methods: (1) the current between the electrodes can be held constant to obtain polymerization under galvanostatic conditions, (2) the potential between the electrodes can be held constant to allow polymerization under potentiostatic conditions, or (3) the scanning or sweeping of the potential can be used to alter the polymer properties obtained during polymerization.[34,36] To polymerize the polymers directly on an electrode surface, usually a divided cell containing a working electrode, a counter electrode, and a reference electrode is used. This method works with most conducting electrode materials and is thus a widely employable method for various biosensor designs. The obtained polymer does not need to be solution processible, but side chain modification can dramatically increase the sensing ability or facilitate polymerization under mild conditions.[39] Special attention is attributed to heterocyclic CPs such as polypyrroles (PPYs), polythiophenes (PTPs), and PANIs because of their importance for biosensor and bioassay systems. PPYs and PTPs can be polymerized by electrochemical oxidation direct on an electrode surface, by oxidizing chemicals, or by other synthetic strategies.[34,35] PANIs are mostly polymerized by direct oxidation on an electrode. For heterocyclic CPs such as PTPs, a side chain modification is necessary to render them water or solvent soluble. Due to the nonsymetric nature of thiophene molecules, four different couplings are possible as depicted in **Figure 3(a)**.

The properties of CPs change significantly from one regioisomer to another, and hence the correct method for synthesis needs to be chosen (**Figure 3(b)**).[31] The chemistry for PPYs is partially similar to that of PTPs, and care must be taken to choose the correct polymerization method.[36,40–42] PANI in its neutral form can exist in different oxidation states (**Figure 4(a)** to **Figure 4(d)**), the least oxidized form called leucoemeraldine base, the semioxidized form called emeraldine base, and the most oxidized form called pernigraniline base.[25] The most practical way to synthesize PANI in its different states is to synthesize the emeraldine base, which is the only form stable at room temperature and air and to reduce or oxidize it to the other forms. The emeraldine base can be obtained by oxidation of aniline in aqueous media by oxidizing agents such as $(NH_4)_2S_2O_8$, KJO_3, $K_2Cr_2O_7$, and others or by electrochemical oxidation in acidified solutions by sulfuric or hydrochloric acid (**Figure 4**).[23]

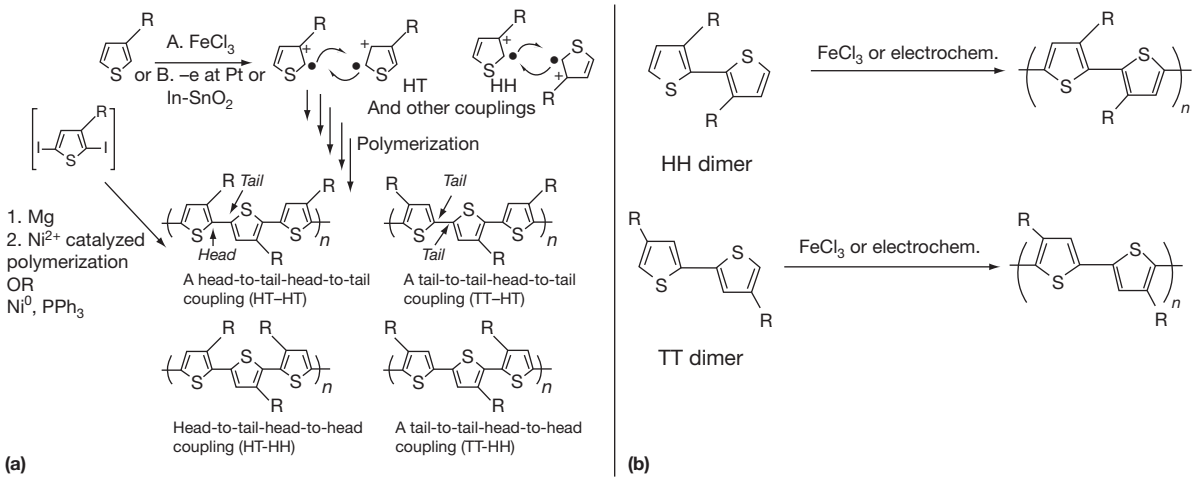

Figure 3 (a) Random chemical or electrochemical polymerization leads to different regioisomers. (b) Electrochemical or chemical oxidation of dimers leads to control over regioisomers. Reprinted with modifications from McCullough, R. D. *Adv. Mater.* **1998**, *10*(2), 93–116.

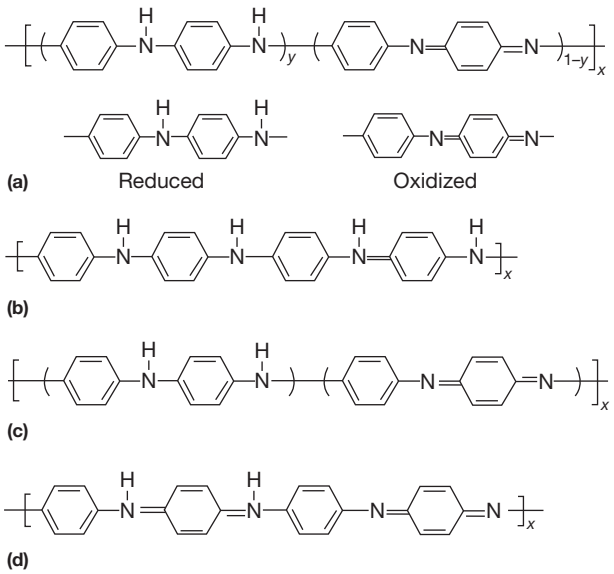

Figure 4 (a) Generalized structure of polyaniline indicating completely reduced and completely oxidized substructures. (b) Depicts the completely reduced polymer while (c) shows the half-oxidized and, (d) the fully oxidized polymer. Reprinted with permission from MacDiarmid, A. G. *Angew. Chem.* **2001**, *40*, 2581–2590.

Excellent reviews describing synthetic strategies for PTPs,[31,35] poly(pyrroles),[41,42] poly(anilines),[23] other CPs suitable for biosensors[43–45] as well as processability of CPs[32] are available and therefore are not further reviewed in this chapter.

3.331.1.3. Doping Reactions to Facilitate Conductivity and Specific Tasks

CPs are usually stated to be 'semiconductors with a wide band gap' in their pristine (not doped) state and exhibit low conductivity properties. However, CPs can be made electrically conductive by doping. The term doping in the chemistry of CPs originates from semiconductor physics. In semiconductor physics, atoms of a material framework are replaced to generate free electrons (e.g., phosphorus atoms in a silicon framework) or electron holes (e.g., boron atoms in a silicon framework), which is referred to as n-type doping and p-type doping, respectively. In CPs, the doping process, however, refers to oxidation (p-doping) or reduction (n-doping) of the σ-electronic structure of the polymer backbone. This fundamental discovery,[46] mainly made by Alan G. MacDiarmid, Hideki Shirakawa, and Alan J. Heeger during their research on the partial oxidation of polyacetylene, earned them the Nobel prize in Chemistry in 2000.

Doping of CPs can be divided into mainly four methods, chemical doping, electrochemical doping, photochemical doping, and interfacial doping.[25,47] One of the most studied chemical doping mechanisms is the doping of PANI by acid base chemistry. The doping of PANI is depicted in **Figure 5**. The emeraldine base is converted into the emeraldine salt upon addition of acid. This mechanism leads to one unpaired spin per repeat unit; however, the electron number per repeat unit does not change.

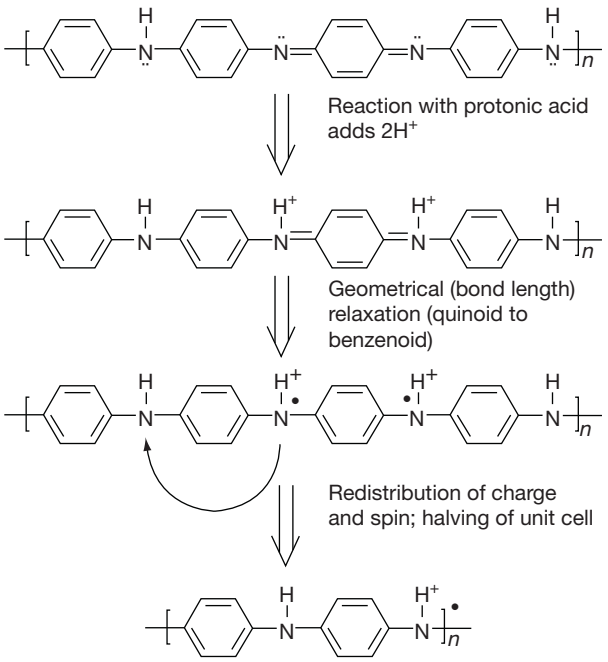

Figure 5 Doping of polyaniline by acid base chemistry changes the properties from insulating to electric conductive without changing the number of electrons in the backbone. Reprinted with permission from Heeger, A. J. *Angew. Chem.* **2001**, *40*, 2591–2611.

A more generalized mechanism for chemical doping is that of charge transfer redox doping in which CPs are either oxidized (p-type doping) or reduced (n-type doping). Oxidation of CPs is often accomplished by exposure of the polymer to halogens such as iodine, bromine, or chlorine leading to partial oxidation of the backbone.[46] Reduction of CPs can be achieved by compounds with a strong reduction potential such as sodium organic compounds.[25] The principle of electrochemical doping is essentially the same as that of chemical doping, except that the redox potential is supplied by an electrode. The extent to which the CP is doped directly depends on the potential and can thus be precisely controlled. The charges that are created during this process are compensated from counter ions from the surrounding electrolyte solution.[36] Electrochemical doping is the most widely used doping mechanism for CPs in biosensor devices and is depicted in **Figure 6**.

During photodoping, the CP becomes locally oxidized and reduced, which creates a charge separation and thereby induces conductivity.[48,49] Interfacial doping of CPs is mainly reported by charge injection at a metal–CP interface.[50] Electrons and holes can be injected from a metallic contact into the π^* and π gaps of the polymer. In this process, electrons are either removed from the band gap (oxidized polymer) or electrons are added into the band gap (reduced polymer). This process is fundamentally different from that of chemical doping because of the fact that no counter ions are present to those charges.[47] The polymerization of pyrrole or thiophene by electrochemical oxidation leads to their doped (oxidized) state.[32,40]

Heterocyclic CPs differ significantly in their properties when they are not doped. PPY is highly reactive and reacts with the smallest amounts of oxygen whereas neutral PTP is stable under ambient conditions.[32]

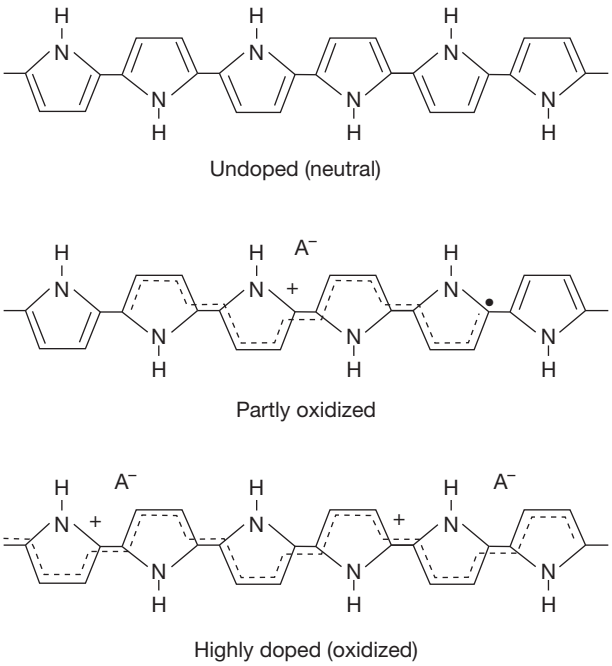

Figure 6 Electronic structure of polypyrrole after electrochemical or chemical oxidation. The charges created are compensated by counterions from the surrounding environment. Reprinted with permission from Smela, E. *Adv. Mater.* **2003**, *15*(6), 481–494.

3.331.1.4. Properties of CPs

3.331.1.4.1. Electric conductivity

During the doping procedure in which the CP is oxidized or reduced, local charge carriers are generated. Those carriers can exist in different variations such as anion, anion radical, dianion or cation, cation radical, and dication.[51] Due to the conjugated π-electron system in the backbone of the polymer, those charge carriers are not isolated and immobile. The surrounding environment is able to interact directly with the charge carriers, which allows relaxation in close proximity to the charge carriers. The result of this relaxation is distortions of different species such as solitons, polarons, and bipolarons. Those distortions are able to migrate through the polymer and thereby mediate electrical conductivity. The electrical conductivity can be best imagined as migration of energy waves through the polymers instead of jumping electrodes in classical conductors. Additionally, the interpolymer chain migrations of electric charges is another very important factor for the very high electric conductivity, especially for films of CPs. The above description is only a very condensed summary of relatively complex physical phenomenons for which excellent reviews are available.[34,52,53]

3.331.1.4.2. UV/VIS absorption and fluorescence

Analogous to molecular spectroscopy, the π-electrons can be excited by an ambient wavelength.[54,55] The relaxation of the electron to its ground state can generally occur by two different mechanisms, by radiative recombination in which the energy difference between the higher state and the ground state is released as light (luminescence or fluorescence) or by a nonradiative mechanism. In general, the assumption can be made that more polarizable polymers in which the π-electrons are more delocalized, such as polyacetylene or PTPs, will exhibit a very weak luminescence, whereas other classes of CPs, for example, poly(phenylenevinylene) or poly(paraphenylene) exhibit a very high luminescence quantum efficiency.[47] For the design of biosensor devices, only the final property of the CP is of importance. Though, detailed theoretical explanations to group CPs in classes of good luminescence and in classes of poor luminescence as well as band gap engineering are available[56], these properties of CPs have direct influence on the design of a biosensor device. If a biosensor or a bioassay is to be designed which uses fluorescence superquenching as detection approach, soluble poly(phenylenevinylene) or poly(paraphenylene) derivatives are often used,[28,29] whereas if an electrochemical transducer principle is employed, soluble PTP, PANI, or PPY derivatives are often used.[26]

3.331.1.4.3. Signal amplifying properties

The surrounding environment can induce hypsochromic or bathochromic effects as well as hypochromic or hyperchromic effects. In the typical case in molecular spectroscopy, however, the surrounding environment interacts with only one separated fluorescent molecule. The signal that can be obtained from one molecule is relatively low, and many interactions need to occur at the same time in order to obtain a measurable signal. This means the concentration of an interacting molecule (e.g., the analyte) needs to be high to be detected. In the case of CPs, one environmental molecule interacts with many monomer units of the CP due to the conjugated π-system. Therefore, in the case of CPs, the concentration of interacting molecules (e.g., analyte) in the environment can be very low and still lead to a large signal. This phenomenon is referred to as signal amplification in CP-based biosensor devices using optical transducer systems.[5,9,20]

3.331.1.5. Electrochemical Biosensors

3.331.1.5.1. Amperometric biosensors

Amperometric biosensors measure the current flow between electrodes when a redox reaction takes place. The most investigated amperometric biosensor system is probably the glucose biosensor. In this system, glucose oxidase (GOx) catalysis the reaction of glucose with oxygen to gluconolacton and hydrogen peroxide. The signal is usually depicted as current (ampere) against concentration of glucose caused by a redox reaction of a mediator or hydrogen peroxide at the working electrode. Noteworthily, most CP-based amperometric biosensors are biosensors of the third generation where the enzyme and the mediator are directly immobilized on the transducer. Thus, the detection of the signal does not rely on the diffusion of reaction products or the mediator. An excellent review of PPY-based biosensors and general electron transfer principles was published by Singh *et al.*[11,12] and Habermüller *et al.*,[57] respectively (**Figure 7**).

3.331.1.5.2. Potentiometric biosensors

In potentiometric biosensors, the CP is immobilized on a measurement electrode, and the electrochemical potential relative to a reference electrode (without a current flow) is

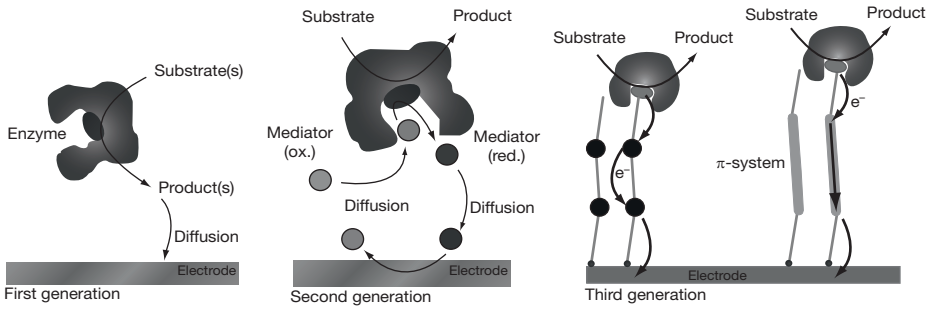

Figure 7 Different principles of amperometric redox enzyme-based biosensors. Left: direct measurement of the current generated by the redox reaction (first generation biosensor). Middle: using a mediator that transfers the signal from the enzyme to the electrode by diffusion (second generation biosensor). Right: transfer of the electron from the enzyme to the electrode by a conjugated π-system or "molecular wire" (third generation biosensor). Adapted with permission from Habermüller, K.; Mosbach, M. *Fresenius J. Anal. Chem.* **2000**, *366*, 560–568.

measured.[16] The mechanism behind those biosensors is the change of the electrochemical potential of the electrode coating materials.[58] The electrode coating can only comprise either the CP or the CP with specific biomolecules.[59] The analyte might bind to the biomolecule that is bound to the CP and thereby change the electrochemical potential of the CP, or the CP might be sensitive to reaction products of the analyte with a bound enzyme (e.g., pH).[60]

3.331.1.5.3. Conductometric biosensor

Biosensor devices based on CP can be designed in such a way that the signal is displayed by a change in electrical conductivity. This can be done relatively easily by connecting a 'source' and 'drain' electrode with a film of CPs.[61,62] The conductivity or resistivity is then measured against the analyte concentration. In general, the applied potential can be either constant or sweeping during this measurement. As the nature of the CPs is to obtain high conductivity only when the polymer is charged, those measurements are very sensitive to processes in which a change of the doping state occurs.[63,64] This needs to be especially considered when the pH affects the doping status. Furthermore, the charges that are created within the backbone of the CP are able to interact with the surrounding environment and thus change the conductivity of the CP.

3.331.1.6. Optical Biosensors and Bioassays

3.331.1.6.1. Colorimetric, fluorescence, and superquenching-based biosensors

Biosensors of the strict definition made above based on optical transducer systems mainly employ SPR or other evanescent wave-based technologies.[65] So far the possibilities of creating optical biosensors using evanescent wave technologies together with CPs have been poorly investigated. Most reports on CP-based optical biosensing focus on homogeneous or surface-immobilized bioassays that are often not reversible.[28,29,66]

The difference between optical transducer systems based on colorimetric change or change of fluorescence is that a colorimetric change refers to a change in absorption wavelength and fluorescence refers to changes in emitted light. Analogous to the principles of molecular spectroscopy, the absorption and emission characteristics of CPs depend on the local electronic structure and the environment. An excellent review of the fluorescence phenomena, fluorescence spectroscopy, and Förster resonance energy transfer (FRET) can be found in 'Principles of fluorescence spectroscopy' by Lakowicz.[67] Transduction principles in optical bioassays based on CPs rely mostly on the following mechanism: quenching (FRET) or main chain conformational perturbation of the CP.[38,68] The fluorescence of CPs can be quenched by FRET. Many CPs exhibit a very high-fluorescence quantum yield attributed to many repeating conjugated monomer units. A single analyte molecule can cause a significant reduction of fluorescence because, in theory, one quencher molecule is able to quench the fluorescence of a whole polymer molecule. This signal amplification by CPs can be in the magnitude of millionfold compared to corresponding molecular excited states.[27] Bioassays based on quenching principles can be based, in general, on increased fluorescence by removing the quencher from the polymer upon analyte interaction or by decreasing fluorescence, bringing the analyte close to the polymer and causing quenching. Both mechanisms are depicted in **Figure 8** on the example of DNA sensing.

In addition to quenching or FRET-based bioassay systems, other mechanisms that generate readable optical signals are used. One possibility is to use CPs that are able to undergo backbone conformational changes upon interaction with the analyte as depicted in **Figure 8(b)**. Suitable polymers (such as PTP derivatives) for this mechanism usually exhibit a relatively low π-electron delocalization while in twisted conformation. As described earlier, the more the π-electrons are delocalized, the weaker is the fluorescence of a CP. In this type of assay, the negatively charged DNA probes interact with the cationic CP to form a duplex in which the polymer has a planar conformation. When the target DNA interacts with the DNA probe, which is attached to the CP, a triplex is formed in which the CP has a twisted conformation. The interaction of the target DNA with the probe-CP duplex restores thereby the initial fluorescence. Bioassays using optical readout signals based on CPs have been introduced for DNA, protein, and polysaccharide sensing.[4,69–71] Bioassays with extremely low LOD (zeptomolar) for DNA and very good selectivity (e.g., single nucleotide mismatch in DNA) have been described ideal samples (solutions of analyte in buffer). However, when it comes to real samples such as cell lysates, body fluids, or cell culture media, those assays often lack specificity and reversibility in general.

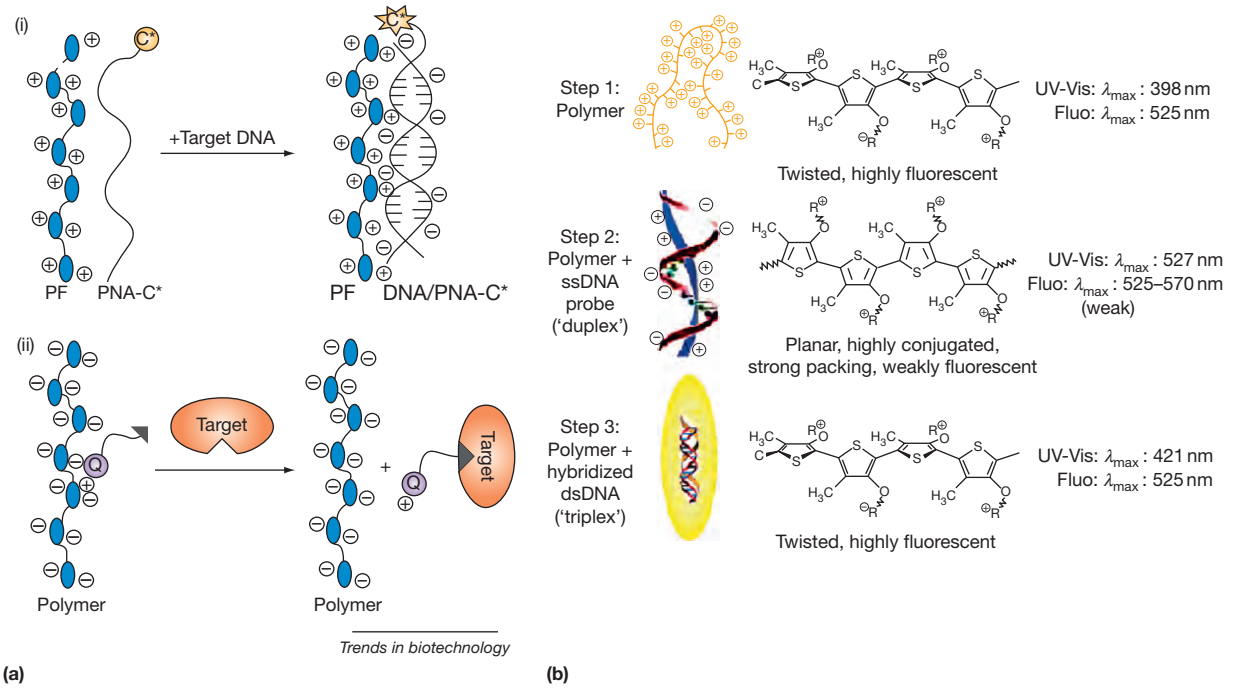

Figure 8 (a) Generalized mechanism on Förster resonance energy transfer-based bioassays. (b) Mechanism for bioassays using backbone conformational changes. Reprinted with permission from Dubus, S.; Gravel, J. F.; LeDrogoff, B.; Nobert, P.; Veres, T.; Boudreau, D. *Anal. Chem.* **2006**, *78*, 4457–4465; Fan, C.; Plaxco, K. W.; Heeger, A. J. *Trends Biotechnol.* **2005**, *23*, 186–192.

3.331.2. Using CPs for Electrochemical Biosensor Devices

3.331.2.1. Introduction

After the establishment of the first electrochemical glucose biosensor, the immobilization techniques of biological sensing elements (BSEs) onto electrodes for subsequent electrochemical biosensors began to evolve as a means to improve the sensitivity and detection limits of these biosensors. Electrochemical biosensors began to utilize associations of these elements, with the electrodes (transducers), through various methods such as direct adsorption, cross-linking, covalent bonding, and gel entrapment. The direct interaction of BSEs with the electrodes, rather than using a dialysis membrane, effectively reduced proximity-related issues and resulted in a better exchange of electrochemical signals and electroanalytical response between these two entities. However, the mentioned approaches were not ideal as there were possibilities of immobilized BSEs getting detached (binding forces are susceptible to changes in pH, temperature, or ionic strength), limiting available surface area for the immobilization of BSEs, and the use of covalent cross-linking chemicals might be too harsh for the BSEs.

Immobilization of BSEs onto electrodes fortunately took a revolutionary transformation after the initial demonstration that stable CPs layers can be deposited onto electrodes with strong adhesion properties.[72] By simply adopting an electropolymerization procedure, which can be performed under mild conditions, with good reproducibility, and onto electrodes of any geometry, BSEs such as DNA,[73] enzymes,[74,75] antibodies,[76,77] and cells[78,79] can be immobilized within the electropolymerized CPs and be in close proximity to the electrodes. In addition, these BSEs can retain their bio-functionality. Electrochemical biosensors were thus revolutionized and two possible CP-based electrochemical biosensor configurations have since been realized. Most works have retained the original Clark and Lyons configuration (Figure 9(a)) for biosensing applications while an alternative miniaturized bioelectrochemical transistor configuration had also been demonstrated (Figure 9(b)).

Currently, the most applied configuration for CP-based electrochemical biosensors is the Clark and Lyons configuration (Figure 9(a)), where the BSEs and CPs are deposited onto the working electrode and various electroanalytical methods, such as amperometric and impedimetric, have been adopted for the detection of the respective analytes. In this setup, the CPs serve as excellent electronic conduits that convey biophysical or biochemical reactions occurring at the biosensing interface as electrical information to the underlying electrodes. Examples include the interaction of antibodies and antigens or an enzymatic reaction that induces a change in the CPs' electronic properties. In contrast, CP-based electrochemical biosensors using the miniaturized bioelectrochemical transistor configuration involves the switching 'on' or 'off' of the conductivity of the deposited CPs (between two electrodes: a 'source' and a 'drain') as depicted in Figure 9(b). For example, at a given source-drain voltage and using GOx as the BSE, introduction of glucose has resulted in a corresponding increase of drain current (i.e., the CP is converted into a better conducting state as a result of chemical interaction of GOx with glucose).[61,62,80,81] On the other hand, the use of horseradish peroxidase (HRP) as BSE caused a decrease in drain current when hydrogen peroxide was introduced (i.e., the CP was

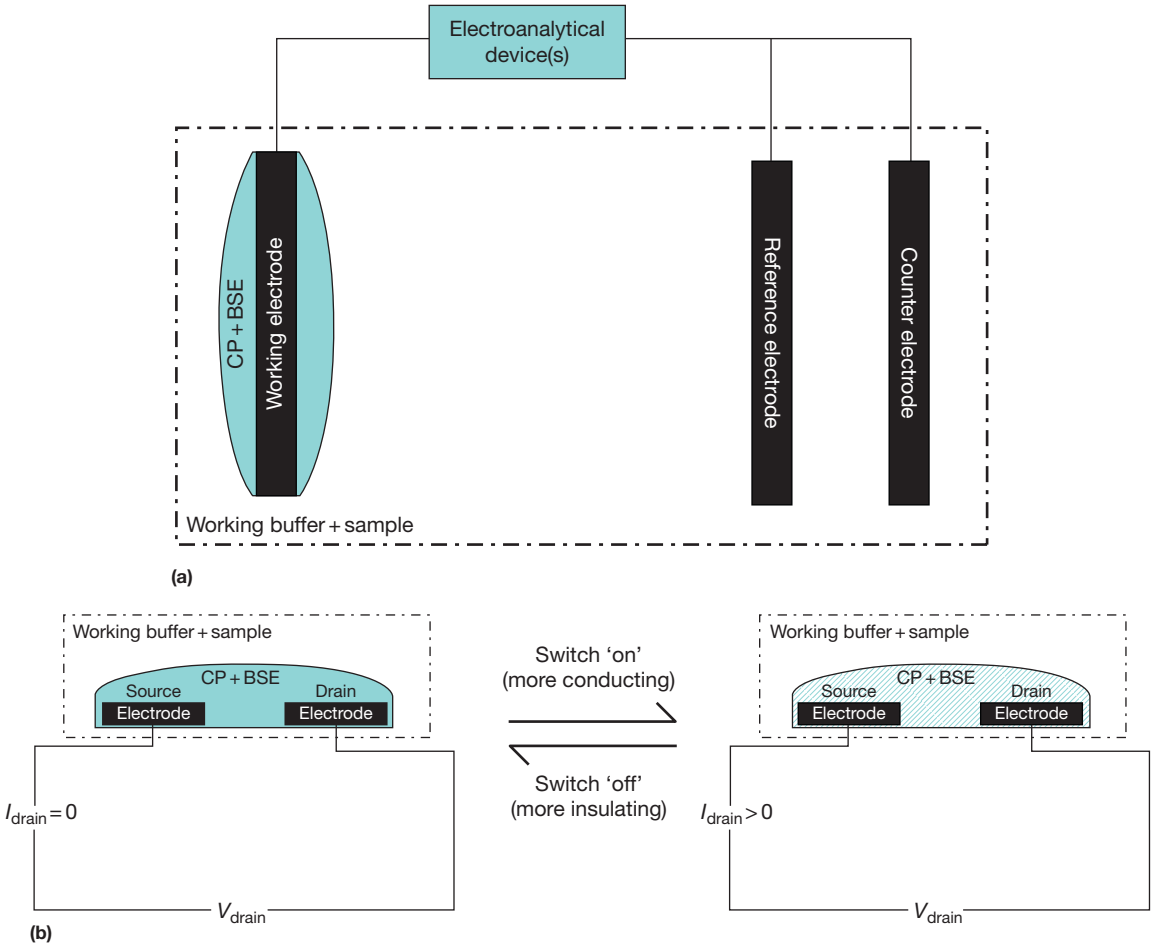

Figure 9 (a) Simplified conjugated polymer-based 'Clark and Lyons' configuration electrochemical biosensors and (b) simplified CP-based miniaturized bioelectrochemical transistor configuration electrochemical biosensors.

converted into a more insulating state).[63,64] Current progress in this area encompasses the use of CP nanowires[82,83] or microtubules[84] as bridges between the 'source' and 'drain' electrodes (**Figure 10**) rather than CP films as the high surface-to-volume ratio of these structures can create strong electrochemical signals in the presence of low analyte concentrations.[85] Advantages of using CPs in these electrochemical biosensors include possible controlled localization of biological materials within defined CP film layers on working electrodes,[86] immobilization of different enzymes onto closely spaced working electrodes through manipulation of the applied potentials,[87] and chemical flexibility in modification of the CPs for association with BSEs[88–90] or redox mediators.[57,91,92] In view of focus to the discussion of CP-based electrochemical biosensors and due to the uncertainties clouding the exact mechanisms, the various biosensing mechanisms via CP-based electrochemical means will not be discussed. Also, subsequent sections will discuss only CP-based biosensors designed through the Clark and Lyons biosensor configuration.

Deposition of CP layers on electrodes is mainly performed either through potentiostatic or galvanostatic techniques, and the thickness of the film can be tuned[93,94] by varying either the potential or current with time. Thicker films have been reported to exhibit electrochemical responses of increasing magnitude with increment of CP layer thickness[95] whilst thinner films, although with lesser sensing elements, produce biosensors with higher sensitivities[58,93,94] and faster response times[96,97] as diffusion of analytes within these thinner films

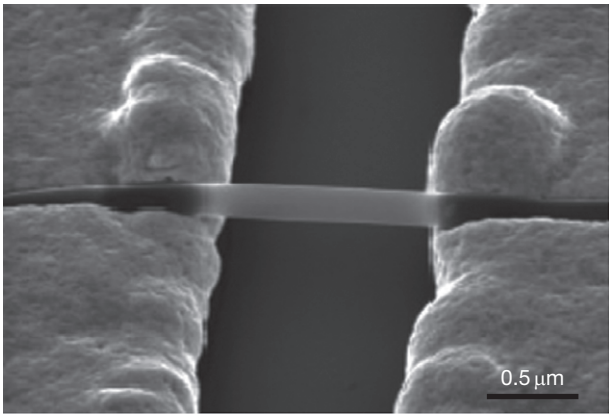

Figure 10 Scanning electron microscope image of a polypyrrole nanowire electrodeposited and partially anchored between the 'source' and 'drain' electrodes. Reproduced from Bangar, M. A.; Shirale, D. J.; Chen, W.; Myung, N. V.; Mulchandani, A. *Anal. Chem.* **2009**, *81*, 2168–2175.

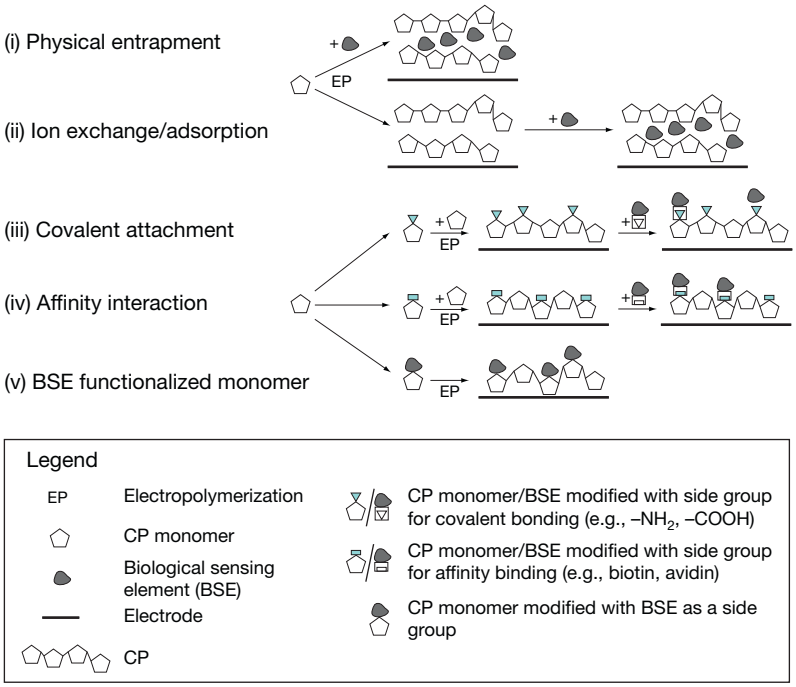

Figure 11 Schematic representation of five general approaches adopted for immobilization of BSEs with conjugated polymer electrochemical biosensors: (i) physical entrapment, (ii) ion exchange or physical adsorption, (iii) covalent attachment, (iv) affinity interaction, and (v) BSE-functionalized CP monomer. It is worth noting that (ii), (iii), and (iv) are post-EP immobilization strategies.

are easier. Supporting electrolytes are usually included during the electropolymerization process as a means to increase the electroconductivity of the CP monomer solution and to compensate the charge of the growing CP layers. Unfortunately, these electrolytes also tend to compete with the BSEs for the polymer doping sites, in the case of physical entrapment technique, and thus reduce the quantity of BSEs incorporated. Therefore, BSEs, such as GOx,[59] α-human serum albumin,[76] and single-stranded DNA (ssDNA),[73] have been substituted as counterions during the growth of the CP layers to allow for more efficient entrapment. Interestingly, deposition of CPs has been demonstrated to be possible via the layer-by-layer (LbL) technique as well.[98,99] In the next section, the incorporation of BSEs during the fabrication phase of electrochemical CP-based biosensors will be described.

3.331.2.2. Immobilization Strategies for Biological Sensing Elements (BSEs) onto CP-Coated Electrodes

PPY is currently one of the most extensively used CPs in the fabrication of CP electrochemical biosensors, as compared to the other CPs such as PANI and PTP. The popularity of PPY stems from the mild conditions required for the one-step simultaneous electropolymerization of pyrrole monomers and entrapment of BSEs. Only mildly oxidative conditions and an aqueous neutral medium are necessary for its electropolymerization onto an electrode, thereby resulting in minimal disturbance to the native properties of the many BSEs that are to be entrapped during the electropolymerization process.[11,12,100] PANI and PTP, on the other hand, require acidic conditions and extreme oxidation potential, respectively, during the electropolymerization process to yield highly conducting CPs, and both conditions are not favorable to many BSEs that are to be entrapped within the CP layers during the electropolymerization process.[11,12,100] Therefore, BSE immobilization strategies involving PANI and PTP, are in general, approached by post-electropolymerization (EP) immobilization strategies. Figure 11 categorizes the five general approaches adopted for immobilization of BSE in CP-based electrochemical biosensors: (1) physical entrapment, (2) ion exchange or physical adsorption, (3) covalent attachment, (4) affinity interaction, and (5) BSE-functionalized CP monomer. (NB: (2), (3), and (4) are post-EP immobilization strategies). In the following section, only brief details of the immobilization protocols are given. Readers are referred to excellent reviews in Table 1 for further elaborations and Table 2 for immobilization examples.

Table 1 Recommended reviews written by other authors

Title	*References*
Recent advances in biological sensors based on electrogenerated polymers: a review	101
Conducting polymers for electrochemical DNA sensing	102
Application of conducting polymers to biosensors	15
Conducting polymer nanostructures and their application in biosensors	103
Electrochemical sensors based on conducting polymer-polypyrrole	100
Polypyrrole-based amperometric glucose biosensors	11,12
Biomolecular immobilization on conducting polymers for biosensing applications	14
Microelectrochemical enzyme transistors	104
Affinity biosensors based on electropolymerized films	105

Table 2 List of CP-based electrochemical biosensors

Biological sensing element (BSE)	*Target of interest (analyte)*	*Immobilization strategy*	*CP used*	*Detection approach*	*Sensitivity*	*Dynamic response range*	*Limit of detection (LOD)*	*References*
Enzymes								
GOx	Glucose	Ion exchange/physical adsorption	PANI	Amperometric	12.2 mA M^{-1} cm^{-2}	0.01–12 mM	0.01 mM	106
Horseradish peroxidase	H_2O_2	Ion exchange/physical adsorption	PANI	Amperometric	–	–	–	107
Uricase	Uric acid	Ion exchange/physical adsorption	PANI	Amperometric	–	0.0036–1.0 mmol dm^{-3}	–	108
GOx	Glucose	Covalent (gluteraldehyde)	PANI	Amperometric	2.3 mA M^{-1}	1×10^{-6} to 8×10^{-4} mol l^{-1}	5×10^{-7} M	109
Glutamate oxidase	Glutamate	Covalent (EDC)	5,2′:5′2″-terthiophene-3′-carboxylic acid	Amperometric	− 14 nA μM	0.2–100 μM	0.1 μM	110
Pyruvate oxidase	Phosphate	Covalent (EDC)	5,2′:5′2″-terthiophene-3′-carboxylic acid	Amperometric	− 0.67 nA μM	1.0–100 μM	0.3 μM	111
PPO	Catechol	Covalent (gluteraldehyde)	PANI	Amperometric	–	0.2–80 μmol dm^{-3}	–	112
GOx	Glucose	Covalent (EDC)	PPY–NH_2	Amperometric	–	–	5 μM	113
GOx	Glucose	Covalent (EDC)	Polyazulene–NH_2	Amperometric	–	–	–	114
GOx	Glucose	Covalent (light irradiation)	PPY–benzophenone	Amperometric	–	–	–	90
GOx-biotin/ PPO-biotin	Glucose/catechol	Affinity (avidin bridge)	PPY–biotin	Amperometric	65 mA M^{-1} cm^{-2} (catechol)	–	2×10^{-7} M (catechol)	89
GOx-biotin/alkaline phosphatase-avidin	Glucose/ phenylphosphate	Affinity (avidin bridge where necessary)	PPY–biotin	Amperometric	0.79 mA M^{-1} cm^{-2} (glucose)/ 1 mA M^{-1} cm^{-2} (phenylphosphate)		40 μM (glucose)/ 0.2 μM (phenylphosphate)	88
GOx-biotin	Glucose	Affinity (avidin bridge)	PPY–biotin	Scanning electrochemical microscopy (amperometric)	–	–	–	115
GOx-histidine	Glucose	Affinity	PPY-nitriloacetic acid/Cu^{2+}	Amperometric	–	–	–	116
Nitroreductase-maltose binding protein	2,4-Dinitrotoluene/ 2,4,6-trinitrotoluence (DNT/TNT)	Affinity	PPY–pyridine	Cyclic voltammetry	205 nA μM^{-1} (TNT)/ 222 nA μM^{-1} (DNT)	–	2 μM (DNT and TNT)	117
GOx	Glucose	BSE-functionalized CP monomer	PPY-GOx	Amperometric	–	–	–	118
GOx	Glucose	Physical entrapment	PANI	Amperometric	–	–	–	74
GOx	Glucose	Physical entrapment	PPY	Potentiometric	–	0.06–10 mM	–	59
Glucose dehydrogenase	Glucose	Physical entrapment	PPY–osmium	Amperometric	–	–	–	57
Quinohemoprotein alcohol dehydrogenase	Ethanol	Physical entrapment	PPY	Amperometric	2.07 nA mM^{-1}	–	–	119
GOx	Glucose	Physical entrapment	PPY	Potentiometric	38.3 mV per decade	1–10 mM	–	58

(*Continued*)

Table 2 (Continued)

Biological sensing element (BSE)	*Target of interest (analyte)*	*Immobilization strategy*	*CP used*	*Detection approach*	*Sensitivity*	*Dynamic response range*	*Limit of detection (LOD)*	*References*
GOx/galactose oxidase/xanthine oxidase	Glucose/galactose/ hypoxanthine	Physical entrapment	PPY-hydrophilic aderivative	Amperometric	21.5/14.7/ 130.0 mA M^{-1} cm^{-2}	1×10^{-6}–3×10^{-3}/ 5×10^{-7}–2×10^{-3}/ 5×10^{-7}–4.5×10^{-6} M	–	120
GOx	Glucose	Physical entrapment	3,4-Ethylenedioxythiophene	Amperometric	15.2 mA M^{-1} cm^{-2}	0.2–8 mM	4×10^{-5} M	121
Urease	Urea	Covalent (EDC)	PPY with embedded BSA	Potentiometric	17.3 mV per decade	6.6×10^{-6}–7.5×10^{-4} M	–	96
GOx	Glucose	Physical entrapment	PPY	Amperometric	–	–	–	75
Antibodies								
α-Rabbit IgG	Rabbit IgG	Physical adsorption	Pyrrole-cyano	Impedimetric	4.4 μg^{-1} ml	600–900 ng ml^{-1}	10 ng ml^{-1}	122
α-Apolipoprotein B-100	Apolipoprotein B-100	Physical adsorption	AuNP-AgCl@PANI	Impedimetric			0.34 pg ml^{-1}	123
α-Bisphenol A	Bisphenol A	Covalent (EDC)	5,2′:5′2″-terthiophene-3′-carboxylic acid	Impedimetric	0.005 Ω (ng ml^{-1})	1–100 ng ml^{-1}	0.3 ng ml^{-1}	124
α-Human IgG-biotin	Human IgG	Affinity (avidin bridge)	PPY–biotin	Impedimetric	–	10–80 ng ml^{-1}	10 pg ml^{-1}	125
α-Neuron-specific enolase	Neuron-specific enolase	Affinity (avidin bridge)	PANI–biotin	Impedimetric	–	1–50 pg ml^{-1}	0.5 pg ml^{-1}	126
α-Human serum albumin	Human serum albumin	Physical entrapment	PPY	Cyclic voltammetry	–	–	–	76
α-Human serum albumin	Human serum albumin	Physical entrapment	PPY	Pulsed amperometric	–	–	1 ppm (pretreated urine sample)	127,128
α-Human serum albumin	Human serum albumin	Physical entrapment	PPY	Impedimetric	–	–	–	77
α-Rabbit IgG	Rabbit IgG	Physical entrapment	PPY	Pulsed amperometric	–	–	1.56 μg ml^{-1}	129
α-BSA	BSA	Physical entrapment	PPY	Pulsed amperometric	–	0–50 mg l^{-1}	–	130
α-BSA	BSA	Physical entrapment	PPY	Impedimetric	–	0–75 ppm	–	131
α-Cyanazine/ α-sheep IgG	Cyanazine-BSA/ sheep IgG	Physical entrapment	PPY	Impedimetric	–	0.1 ppb to 20 ppm (cyanazine-BSA)/ 0.4–3.5 ppm (sheep IgG)	0.01 ppb (cyanazine-BSA)/0.1 ppm	132
α-*Listeria*	*Listeria*	Physical entrapment/ covalent (scission of disulphide bond)	PPY	Cyclic voltammetry	–	–	–	133
Cells								
Banana cells (polyphenol oxidase)	Dopamine	Physical entrapment	PPY	Amperometric	–	–	–	79
Erythrocytes (rhesus (D) antigens)	α-Rhesus (D)	Physical entrapment	PPY	Cyclic resistometry	–	–	–	78
		Physical entrapment	PPY-alginate	Amperometric	2 mA M^{-1} cm^{-2}	–	–	134

Algal *Chlorella vulgaris* cells (alkaline phosphatase)	*p*-Nitrophenyl phosphate							
Gluconobacter oxydans bacterium	Glucose/ethanol	Entrapment via dialysis membrane	4-(2,5-Di(thiophen-2yl)-1H-pyrrol-1-yl) benzenamine	Amperometric	0.415 $\mu A\,cm^{-2}\,mM^{-2}$ (glucose)/ 0.163 $\mu A\,cm^{-2}\,mM^{-2}$ (ethanol)	0.1–2.5 mM (glucose)/ 0.1–5.0 mM (ethanol)	–	135
ssDNA								
ssDNA	Spermidine	Physical adsorption	PPY	Differential pulse voltammetry	–	0.05–1.0 μM	0.02 μM	136
ssDNA–NH_2	ssDNA	Covalent (passive)	PPY–*N*-hydroxyphthalimide	Cyclic voltammetry and amperometric	1 $\mu A\,nmol^{-1}$ (amperometric)	–	10×10^{-2} nmol (amperometric)	137
ssDNA–NH_2	ssDNA	Covalent (passive)	PPY–*N*-hydroxyphthalimide	Cyclic voltammetry and amperometric	1 $\mu A\,nmol^{-1}$ (amperometric)	–	10×10^{-2} nmol (amperometric)	138
ssDNA–NH_2	ssDNA	Covalent (EDC)	PPY–COOH	Cyclic voltammetry, impedimetric and amperometric	10.5, 3.0, 1.7 $\mu A\,cm^{-1}\,nM^{-1}$ for film thickness of 23, 57, 114 nm, respectively (amperometric)	–	–	94
ssDNA–NH_2	ssDNA	Covalent (passive)	PPY–*N*-hydroxyphthalimide	Cyclic voltammetry and amperometric	–	–	10×10^{-11} mol (50 nm thick film) (amperometric)	93
ssDNA–PO_4	ssDNA	Covalent (EDC)	PANI	Differential pulse voltammetry	$-9.659\,\mu A\,pM^{-1}$	–	10×10^{-12} mol l^{-1}	139
ssDNA–COOH	ssDNA	Covalent (EDC)	PANI	Differential pulse voltammetry	–	3.759–755.7 fM	1.0 fM	140
ssDNA–biotin	ssDNA (*N. gonorrhoeae*)	Affinity	PANI–avidin	Differential pulse voltammetry	–	–	0.5×10^{-15} M	11,12
ssDNA	ssDNA	Physical entrapment	PPY	Amperometric	–	–	–	73
dsDNA								
dsDNA	2-Aminoantharcene/ *o*-chlorophenol	Ion exchange/physical adsorption	PPY-polyvinyl sulphonate	Amperometric	–	0.01–15 ppm/ 0.1–25 ppm	–	141
Others								
Peptide	Carboxypeptidase A	BSE-functionalized CP monomer	PPY–peptide	Cyclic voltammetry	–	–	–	142
Peptide	Copper ion	Covalent (EDC)	Poly(3-thiopheneacetic acid)	Square wave voltammetry	–	0.02–20 μM	–	143
Lactose-biotin	Peanut (*Arachis hypogaea*) agglutin	Affinity (avidin bridge)	PPY–biotin	Impedimetric	–	–	–	144

GOx, glucose oxidase; PPO, polyphenol oxidase; BSA, bovine serum albumin; PPY, polypyrrole; PANI, polyaniline; EDC, 1-ethyl-3-(3-dimethylaminopropyl) carbodiimide.

3.331.2.2.1. Physical entrapment

By far, this is the most straightforward BSE immobilization strategy for CP-based electrochemical biosensors and can be achieved in a single step. Physical entrapment of enzymes,[74,75] antibodies,[76,77], DNA,[73] and cells[78,79] has been achieved during the electropolymerization of CP monomers onto electrodes. A solution of CP monomers and BSEs is first prepared and the monomers are subsequently subjected to electrochemical oxidation to create a matrix of CP strongly adhered to the surface of the electrodes that also encapsulates nearby BSE within the matrix. Advantages of this strategy include the possibility of controlling the amount of entrapped biomolecules simply by controlling the thickness of the CP layer that is being polymerized and the ability to entrap different enzymes simultaneously[145] or in a layered fashion.[86] Unfortunately, physical entrapment of BSEs via direct electropolymerization requires a high concentration of monomer and BSEs, which might not be especially suitable for costly BSEs.

3.331.2.2.2. Ion exchange/physical adsorption

An alternative measure for immobilization of BSEs within CP layers can be achieved via a postpolymerization approach as depicted in Figure 11(ii). Such a method is especially suitable when using CPs, such as PANI or PTP, where the polymerization conditions for fabrication of the CP layers are not favorable to maintain the biofunctionality of BSEs. Immobilization of BSEs by physical adsorption is simply performed through the interactions of oppositely charged BSEs and CPs. An ion exchange step can be first performed through manipulation of the redox states of the CPs to realize physical adsorption of BSEs. Depending on the redox states, CPs can exist in the charged or uncharged state, thus affecting the mobility of dopant ions into and out of the polymerized CP layers. By electrochemically changing the CPs into the uncharged state, ions can be expelled from the CP layer and recovery of the charged state will attract and cause oppositely charge BSEs to be adsorbed onto the polymerized CP layers. For example, GOx (pI = 4.2) was successfully adsorbed onto PANI-polyisoprene layers that had been prepared on platinum electrode. Adsorption was achieved through reduction (using a negative potential) of the PANI copolymer layer to remove dopant anions followed by reoxidation (using a positive potential) of the CP layer and immersion of the electrode into a GOx solution (pH = 6.5).[106]

3.331.2.2.3. Covalent attachments

Although immobilization via physical entrapment and absorption are simple procedures, there are also certain drawbacks. Physically adsorbed BSEs are susceptible to desorption should changes in the environment arise (e.g., pH or ionic strength), and biosensors fabricated with entrapped BSEs are likely to experience problems associated with inaccessibility of the embedded BSEs and diffusion hurdles for the analyte (e.g., antigens). To improve the stability and efficiency of interaction between BSEs and CP layers, these BSEs can be covalently attached to the working electrode by a postpolymerization immobilization strategy (Figure 11(iii)). Interfacial localization of these BSEs allows ease of interaction with their respective analytes, especially when considering analytes of large molecular weight. Covalent immobilization of BSEs is commonly carried out by initial preparation of functionalized monomers such as carboxylated pyrrole,[94] carboxylated thiophene monomer[110,111,124] or pyrrole monomers with an amino side group.[113] Electro-oxidative polymerization of these functionalized monomers is subsequently carried out to fabricate CP layers with interfacial attachable side groups. These attachable groups can then be covalently bounded to BSEs containing the corresponding groups (e.g., CP–COOH with NH_2-BSE) through the use of cross-linkers if necessary (e.g., 1-ethyl-3-(3-dimethylaminopropyl) carbodiimide, EDC). PANI, on the other hand, requires no prefunctionalization as the secondary amino groups present within the CP skeletal backbone can be utilized for covalent attachment of BSEs. This can be performed through bifunctional cross-linkers such as gluteraldehyde with BSEs containing an amino side group.[109,112] However, harsh conditions associated with the use of covalent cross-linkers have provided an impetus for researchers to synthesize functionalized monomers containing easy leaving groups such as *N*-hydroxyphthalimide[93,138] which do not require the use of cross-linkers. Work has also been presented that demonstrated the use of benzophenone-functionalized pyrrole monomers that, after polymerization, can be covalently attached to GOx through the use of light irradiation.[90]

3.331.2.2.4. Affinity interactions

Affinity binding systems, such as biotin/avidin, have been employed for immobilization of BSEs onto CP layers as well. Currently, the biotin/avidin affinity pair is the most frequently utilized affinity system in immobilization of BSEs onto CP layers, and stems from the commercial availability of biotinylated enzymes, ssDNA probes, and antibodies. Other possible systems utilized are the nitrilotriacetic acid (NTA)-cation/histidine pair,[116] pyridine/maltose binding protein (MBP) pair,[117] and adamantane/β-cyclodextrin pair.[146] In the biotin/avidin system, the general immobilization approach consists of creating either a biotinylated CP interface (e.g., polymerization of pyrrole-biotin monomer[88,89,125]) or an avidin-CP interface (e.g., postmodification of PANI layer with avidin[11,12]) first. CP layer formation with biotinylated pyrrole monomers unfortunately requires a copolymerization process with unmodified pyrrole monomers due to the poor electropolymerization ability of these biotin derivatives.[89] It follows that if the interface had been biotinylated, the subsequent binding of avidin-modified BSEs (e.g., avidin–alkaline phosphatase[88]) or biotinylated BSEs (e.g., biotin-GOx,[88,89] biotin–antibody[125]), through an avidin bridge, can take place on these biotinylated CP layers. If the interface consists of avidin, following binding of biotinylated BSEs can take place. For the NTA-cation/histidine and pyridine/MBP pair, addition of histidine or MBP tags onto either the C′ or N′ end of proteins was required and performed via mutagenesis to allow binding to their respective binding partners, where these partners had already been modified onto the CP layers. In the last system, GOx and pyrrole monomer were covalently bonded to β-cyclodextrin and adamantane respectively for the fabrication of a glucose electrochemical biosensor. Unlike covalent bonding, affinity interactions can provide the same strong and stable interactions while allowing only a single linkage, through regioselective modification of the BSEs, between the BSEs and CP layer. Multiple linkages are undesirable as

the active site for analyte interaction might become sterically hindered and thus affect the response of the biosensor.

3.331.2.2.5. BSE-functionalized CP monomer

A last and novel approach for the fabrication of CP electrochemical biosensors involves the prefunctionalization of the CP monomer with the desired BSE prior to polymerization. This was first demonstrated with GOx covalent attached to pyrrole monomers in 1992.[118] Polymerization of the GOx-modified pyrrole resulted in a CP layer that demonstrated good stability of the modified enzymes and was used to generate a glucose-sensitive biosensor. This was performed in the presence of the unmodified monomers due to steric problems associated with the dimerization of the GOx-functionalized PPY monomer. Subsequently, only a handful of similar works utilizing this same approach was demonstrated and used for the immobilization of peptides[142,147] and ssDNA[148,149] onto CP films; however, the electrochemical approach for detection of their respective bioanalytes was not used in most works.

3.331.2.3. Choice of Entrapment Approach

As has been described, the immobilization of BSEs will result in two spatial possibilities: either within the CP layers or at the surface of the CP layers. The choice of immobilization approach is dependent on the type of BSE in consideration and the size of the analyte to be detected. For example, immobilization of oxidoreductases (e.g., GOx) is preferentially done via entrapment within the CP layers due to the ease of electron transfer from the enzyme's redox centre to the bulk of the surrounding CP or due to rapid redox reaction of electroactive species (e.g., H_2O_2) resulting from the enzymatic catalysis. In addition, the enzymatic analytes (e.g., glucose) are usually small and are able to diffuse easily within the CP. On the other hand, antibodies and ssDNA are preferentially immobilized on the exterior surface of the CP layers due to the ease of access between these BSEs and their respective target of interest. This was exemplified by the immobilization of antibodies for prostate-specific antigen (PSA) within PANI layers via physical entrapment and onto the exterior surface using the biotin–avidin affinity system. Upon introduction of PSA, the latter affinity biosensor exhibited detection limits that were ~1000 times lower than that of PSA biosensors fabricated using the physical entrapment approach.[126,150]

3.331.2.4. Current Research Directions of Electrochemical CP-based Biosensors

The discovery and application of CPs as an underlying matrix support and conduit for BSEs in electrochemical biosensors has indisputably enhanced the performance and reliability of electrochemical biosensors since its introduction in 1979. Unfortunately, although many significant improvements have been reported, the application of CPs for electrochemical biosensors is still plagued with certain compatibility issues. One issue pertains to the hydrophobic nature of CPs, which provides an unfavorable environment for entrapped BSEs and thus results in biosensors with reduced analytical responses.[120,151] Various methods can be employed to counterbalance this hydrophobic nature of the organic CP and include the use of laponite clay,[151] hydrogels (poly (2-hydroxyethyl methacrylate)[97,152] and alginate[134,153,154]), and hydrophilic pendant groups[120] within the CP layers. Incorporation of hydrophilic functionality within CP layers is likely to improve swelling and thereby increase the percentile of aqueous content within the CP layer. This permits a more efficient diffusion of water-soluble analytes and reaction end-products within the CP layer, and also provides a more favorable environment for the entrapped BSEs.

Gold nanoparticles (AuNPs)[109,123,155] and carbon nanotubes (CNTs)[98,145,156–158] have been utilized in the design of CP-based electrochemical biosensors as a means to enhance the electroconductivity and electroproperties of these biosensors. Incorporation of AuNP has been demonstrated through aqueous electropolymerization of pyrrole monomers in the presence of chloroauric acid[159] (where the chloroauric acid oxidizes into AuNP) or via direct physical entrapment of AuNPs within polypyrrole–pyrrolepropulic acid layers.[160] In both these examples, AuNPs within the CP layers resulted in biosensors of improved sensitivity during analyte detection. Another advantage of utilizing AuNP is the conversion of PANI, where the native form is only electroactive in acidic conditions, to an electroactive form at neutral pH,[123,155] thus extending the range of BSEs that can be incorporated into PANI-based biosensors. Inclusion of CNTs within the CP-based electrochemical biosensor can be achieved using CNT surface-modified electrodes,[145,156] alternate deposition of CP and CNT via the LbL technique[98] or electropolymerization of CP with CNT.[157,158] CNT surface-modified electrodes have been demonstrated to possess higher surface area due to the introduced nanometer-sized CNT and hence allowing an increased quantity of CPs and ssDNA probes to be deposited onto the electrode.[156] Electropolymerization of PPY with CNT was demonstrated to result in biosensors of improved sensitivity[145,157,158] and response times.[157] Lastly, the oxidation potential utilized for glucose detection, through the incorporation of CNTs, could be performed at potentials lower than 0.7 V,[98,158] thereby avoiding possible noise signals from common interfering substances such as ascorbate, urate, acetaminophen.

A final approach pertains to the formation of CP nanostructures rather than using films of CP onto the electrodes. Such nanostructures include nanoparticles,[107,110,124,161] nanofibers,[136] and nanoelectrode arrays.[140,162–166] With a bigger surface area to volume ratio, as opposed to a planar CP film, this allows for a higher capacity of BSEs loading via surface immobilization and an improved diffusion of target analyte to the immobilized BSEs. PANI nanoparticles, doped with dodecylbenzenesulfonic acid, have been fabricated via polymerization and electrodeposited onto the surface of glassy carbon working electrodes.[107] Adsorption of HRP onto these deposited PANI nanoparticles via an ion exchange process resulted in a hydrogen peroxide electrochemical biosensor with improved signal-to-background ratio and an improved response time. Alternatively, CP nanoparticles can be directly synthesized onto electrodes as reported with the use of a thiophene-derivative monomer.[110,124] An advantage of these thiophene nanoparticles, as reported, is the use of a reduced oxidative potential for the sensing of H_2O_2.[110,111] PPY nanofibers have been fabricated onto platinum electrodes through the introduction of a series of potential pulses, and subsequent physical absorption of double-stranded DNA

(dsDNA) resulted in an electrochemical biosensor that can detect a wide linear range of spermidine and with improved LOD.[136] CP-based nanoelectrode arrays can be fabricated either through direct polymerization of CPs onto the exterior of existing nanoelectrodes[162,166] or within the pores of a membrane template.[140,163–165] For example, CP-based nanoelectrode glucose electrochemical biosensors have been fabricated through either the electropolymerization of PPY and GOx onto carbon postmicroarray or physical absorption of GOx within the pores of PPY nanotubes that had been prepared with a porous membrane, and both works demonstrated the fabrication of a glucose biosensor of improved sensitivity.

3.331.3. Using CPs for Optical Biosensor Devices

3.331.3.1. Introduction

In the following section, the optical biosensing of DNAs, proteins, and small organic biomolecules with the use of CPs will be described. Many excellent reviews describing the optical detection of DNAs, protein, and small organic biomolecules with the use of CPs are available[9,28,38,167–172]; and this chapter is different in that the focus will underline 'biosensor' applications and the general detection mechanisms (performed through the use of CPs as transducers) involved in the identification of these different groups of bioanalytes. CPs have also been exploited for the detection of metal ions, but most of the reported works describes the use of CPs as chemosensors rather than biosensors.[8,9] The optical biosensing of metal ions using CPs also appears to be limited (potassium ions using ssDNA/CP liposomes[173,174] and mercury ions using papain/CP complexes,[175] sugar modified CPs[176] or aptamer/CP liposomes)[177] and hence will not be discussed. In addition, experimental specifics will be brief (e.g., synthesis or the exact structure of CPs used, temperature, buffer system, and sequence of DNA used in analysis are intentionally left out) so as to not to 'overload' the readers with information. By providing these general mechanisms, it is hoped that readers will gain insightful information and knowledge regarding the use of CPs in optical biodetection and further apply them for use in biosensor devices.

The exploitation of CPs, for the optical biosensing of biological targets has seen remarkable progress after its proof-of-concept demonstration in the early 1990s.[178] In 1993, a blue colored Langmuir–Blodgett film consisting of ultraviolet polymerized bilayer assembly of polydiacetylene (PDA) functionalized with an analog of sialic acid was prepared for the biosensing of influenza virus.[179] Sialic acid serves as a recognition ligand for the influenza virus hemagglutinin, and the subsequent introduction of target virus resulted in a blue to red color change of the PDA film. Liposomes fabricated from the same functionalized PDA also demonstrated the same colorimetric changes upon incubation with the influenza virus.[180] Two possible mechanisms for the observed colorimetric changes have been suggested.[181] Firstly, the binding of the large multivalent virus is likely to have caused a significant conformational change in the polymer side chains, which progressively affected the main conformational shape of the conjugated backbone, thus resulting in the colorimetric change. The colorimetric change has also been attributed to a possible virus insertion into the bilayer film followed by a disruption of the initial conformational shape of the CPs.

After its initial demonstration, biosensing based on CPs has been further advanced by many researchers and is classified into three subclasses in this section for ease of references for the readers: (1) the use of liposomal CPs functionalized with BSE, (2) the use of BSE/CP complexes, and (3) CP covalently modified with BSE.

3.331.3.2. BSE-Functionalized Liposome CPs

Liposomes, lipid-based microcapsules, are an interesting class of vesicles that have been commonly used for gene or drug delivery therapeutics as they share common properties with cellular membranes. Interestingly, liposomes can be fabricated with CPs (Figure 12) as well and have been utilized for biosensing applications. It is worth noting that functionalizing of liposomal CPs with BSEs for biosensing applications is a critical component of the biological sensing ability and can be carried out by various approaches. For example, the probes can be either initially covalently modified onto the CP monomers prior to assembly into liposomes[179,180,182] or postmodified onto the surface architecture of the liposomes. Postmodification can be carried out covalently[183–185] or by physical insertion into the bilayer assembly.[74,186]

Generally, the biosensing of target species through the use of liposome CPs functionalized with biological probes employs a common transduction mechanism that produces a colorimetric response and can be used to identify the presence of the target of interest. Upon interaction of the probe and target of interest, regardless of whether the interaction is a chemical or physical reaction, the conformational shape of the CP backbone is disturbed and results in a colorimetric response. For example, the interfacial catalysis of phospholipids by phospholipases[187,188] results in hydrolysis products that do not retain within but leave the liposome membrane. The loss of these phospholipids results in pits and cracks within the membrane[187] and perturbs the CPs conformational backbone. Table 3 summarizes a nonexhaustive list of the different types of target and corresponding probes that have been detected with the use of liposomal CPs.

However, for the development of CP-based optical biosensor devices, it is preferred that the demonstration of target detection is performed on a solid support as stable and repeatable analyte monitoring in solution phase (susceptible to concentration variations caused by evaporation) is very unlikely to be achievable. Using solid-support biosensing has an additional advantage of allowing multiplex detection of desired targets. Solid-support liposomal CPs have been demonstrated and this was achieved either by trapping the liposomal CPs in hybrid sol–gel materials[196] or via covalent attachment onto a surface-modified planar substrate.[173,174,177,197] By associating different antibodies with liposomal CPs, solid-support arrays of these differently modified lipsosomal CPs have been fabricated and were shown to be capable of multiplexed detection of proteins[196] or bacteria.[197]

3.331.3.3. BSE/CP Complexes

Aside from optical biosensing via the use of liposomal CPs, optical biosensing of desired targets can also be achieved

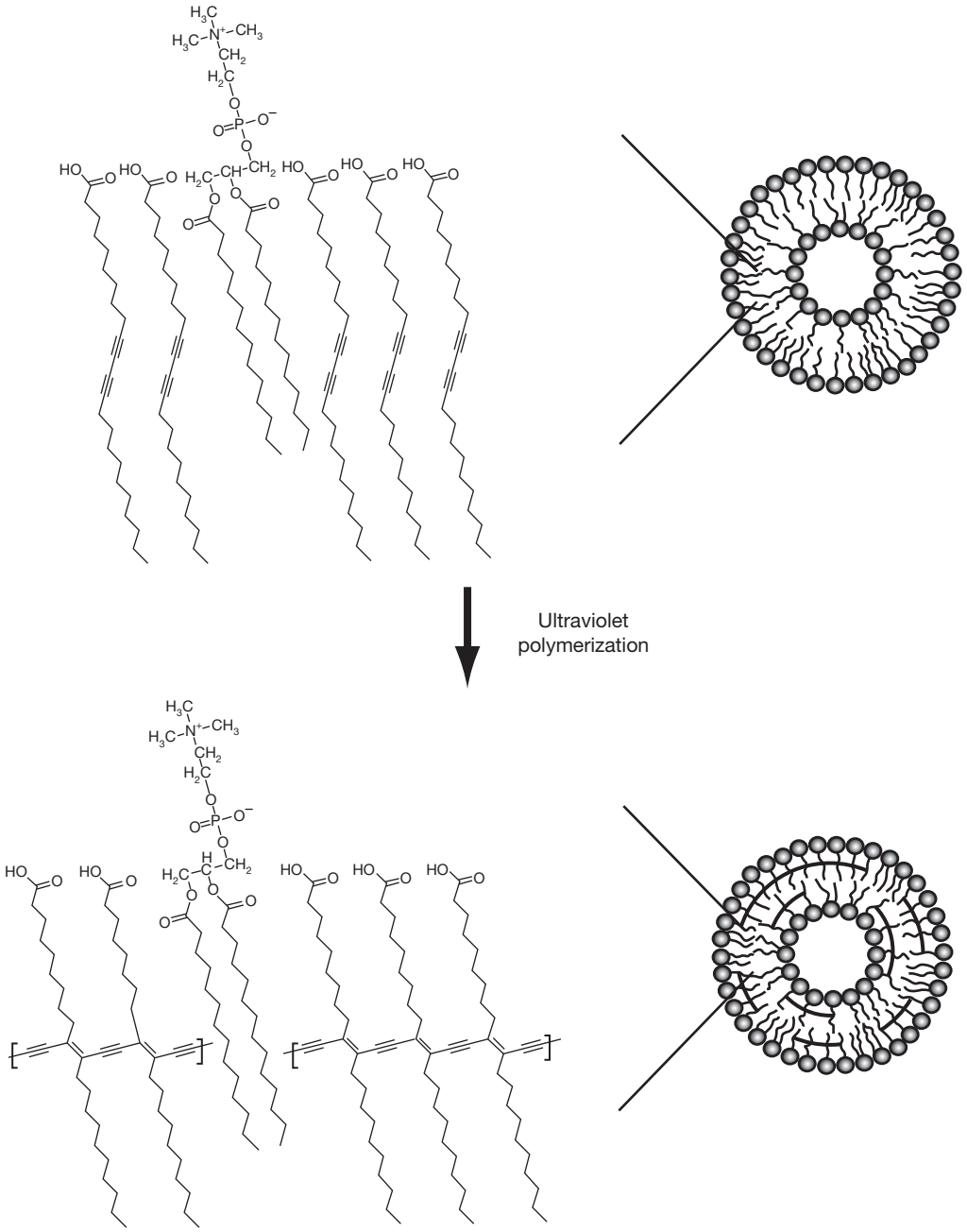

Figure 12 Schematic representation of a typical approach for the fabrication of lipid(dimyristoylphosphatidylcholine in this case)/polydiacetylene liposomes. Reproduced from Okada, S. Y.; Jelinek, R.; Charych, D. *Angew. Chem. Int. Ed.* **1999**, *38*, 655–659.

through the use of BSE/CP complexes. For example, biodetection of ssDNA and enzymes can be achieved through the use of ssDNA probe/CP and enzymatic substrate/CP complexes, respectively. For simplification of target detection, the following section will be split into (1) DNA and (2) protein optical biosensing through the use of BSE/CP complexes.

3.331.3.3.1. DNA biosensing using DNA probe/CP complexes

Intercalating dyes are a conventional and commonly used tool in the detection of dsDNA as these dyes increase in fluorescence quantum yield after intercalating between base pairs of dsDNA. Therefore, intercalating dyes can also serve as transducers for the detection of specific DNA sequences through intercalation of dsDNA that were hybridized from sample ssDNA and a probe ssDNA of predetermined sequence. Unfortunately, the detection efficiency of dsDNA using intercalating dyes has not been as desired but can be significantly enhanced[163,164,198–200] when combined with the use of CPs; where efficient FRET can occur from the excellent light-harvesting CP to the intercalating dyes. Recently, CPs have seen immense applications in the field of DNA sequence

Table 3 A nonexhaustive list of the different types of BSEs and corresponding targets that have been detected through the use of liposomal CPs

Target of interest (analyte)	*Biological sensing element (BSE)*	*Functionalization method*	*References*
Influenza virus	Sialic acid	Precovalent modification of CP monomer	180,181
Ions	Ionophores (valinomycin, monensin)	Physical insertion	189
Escherichia coli	Glycolipid (dioctadecyl glyceryl ether-β-glucosides)	Physical insertion	74
Antibody	Peptide antigen	Physical insertion	186
Streptavidin	Biotin	Precovalent modification of CP monomer	182
Potassium ions	G-Rich ssDNA	Postsurface modification of CP liposome	173,174
Mercury (II) ions	T-Rich aptamers	Postsurface modification of CP liposome	177
Cryptosporidium parvum	Antibody	Postsurface modification of CP liposome	183,184
Phospholipases	Phospholipid	Physical insertion	187,188
Human immunoglobulin	Antibody	Postsurface modification of CP liposome	185
Bacteria (*Escherichia coli*, *Pseudomonas aeruginosa*, *Salmonella enteriditis*, *Salmonella Minnesota*, and *Shigella flexneri*)	Typtophan and tyrosine	Precovalent modification of CP monomer	190
Catecholamines (noradrenaline and dopamine)	Specially designed synthetic receptors	Physical insertion	191
Pore forming toxins (streptolysin O)	Lipid constituents (glycine-terminated diacetylene monomer, 1,2-bis (10,12-tricosadiynoyl)-*sn*-glycero-3-phosphocoline and cholesterol)	Physical insertion and precovalent modification of CP monomer	192
ssDNA	ssDNA	Physical insertion	193
Sphingomyelinase/galactosidase	Sphingomyeline/cerebroside	Physical insertion	194
Cholera toxin	G_{m1} ganglioside	Precovalent modification of CP monomer	195
Antigens (α-fetoprotein, β-galactosidase, bovine serum albumin, and phosphatase)	Antibody	Postsurface modification of CP liposome	196
Bacteria (*Cryptosporidium parvum*, *Giardia lamblia*, *Escherichia coli*, *Salmonella typhimurium*, *Shigella flexneri*, *Encephalitozoon intestinalis*)	Antibody	Postsurface modification of CP liposome	197

optical detection[201–203] and have also been applied in single nucleotide polymorphisms (SNPs) detection,[169,170,204–207] DNA lesion detection,[208–211] and quadruplex-to-duplex transition of G-rich oligonucleotides.[212] RNA optical detection with the use of proteins and CP has been demonstrated[213] but will not be discussed here. An advantage that CP-based optical detection of DNA sequence holds over conventional laboratory methods of DNA detection is the likely elimination of a polymerase chain reaction (PCR) step as the excellent light-harvesting properties and efficient electron/energy transfer properties of CPs allows DNA to be detectable at the zeptomolar (10^{-21} M) range.[205,214] Similar to most DNA detection protocols, DNA sequence optical detection through the use of CPs emphasizes on the need of specific and stable Watson–Crick base pairing of nucleic acids. The sensitive biological elements responsible for specific DNA sequence detection are ssDNA or single-stranded peptide nucleic acid (ssPNA) probes. CPs do not partake in the detection (i.e., not the recognition element) but are exploited as transducers that emit a unique optical response upon interaction with double-stranded helixes.

Using the works of Ho *et al.*[205] as an example, a fluorescence-labeled ssDNA was utilized as a probe for a specific DNA sequence while a cationic PTP derivative was used as a light-harvesting tool to excite the fluorescence-labeled ssDNA via FRET. The use of neutral fluorescence-labeled PNA probes is also possible and has been demonstrated,[29,215,216] but this probe cannot be categorized as a biosensor due to lack of spatial contact between the PNA and CP. A cationic CP is necessary for this approach as the positively charged polymer serves as a counterion for, and allows duplex formation with, the negatively charged DNA to form supramolecular aggregates.[217] A solution of this labeled probe/CP complex gives a red color with an accompanying quenched fluorescence from the probe. However, a new higher-order triplex (dsDNA/CP) structure (**Figure 13**) that possesses fluorescence emission spectra overlapping with the excitation spectra of the labeled dye is established when this probe/CP complex is presented with its complementary ssDNA. This higher-order structure is a result of hybridization occurring between the ssDNA probe and complementary ssDNA. Therefore, fluorescence emission from the labeled probe (excited via FRET from the CP) can be observed in the presence of a complementary ssDNA while no fluorescence is observed at all upon addition of noncomplementary ssDNA. The minimum detection limit determined by this approach was 3 zM, and this approach could also distinguish sequences having two or even one mismatches. As described by the authors, the detection of ssDNA at such low concentrations through their approach is very likely to be attributed to both the large optical density of the polymer and a fast and efficient energy transfer from the CPs to many neighboring labeled probes (a process that was described as 'superlighting' or 'fluorescence chain reaction' (FCR)).

Instead of going through the hassle of labeling DNA probes or using an intercalating dye for DNA detection, DNA biosensing using cationic CPs only is possible. This was well demonstrated by the different colorimetric and fluorescence responses that a PTP derivative had with either ssDNA or

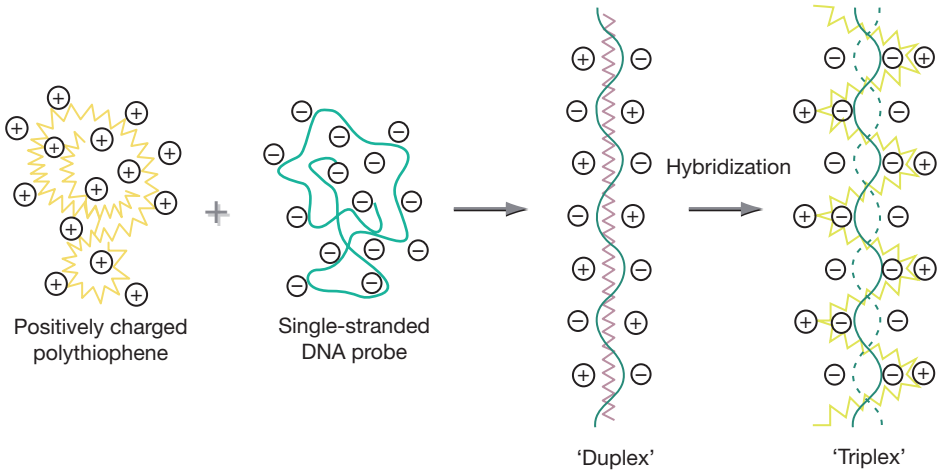

Figure 13 Schematic representation of the formation of polythiophene/single-stranded DNA duplex for the detection of a complementary ssDNA. Reproduced from Ho, H. A.; Boissinot, M.; Bergeron, M. G.; *et al*. *Angew. Chem. Int. Ed*. **2002**, *41*, 1548–1551.

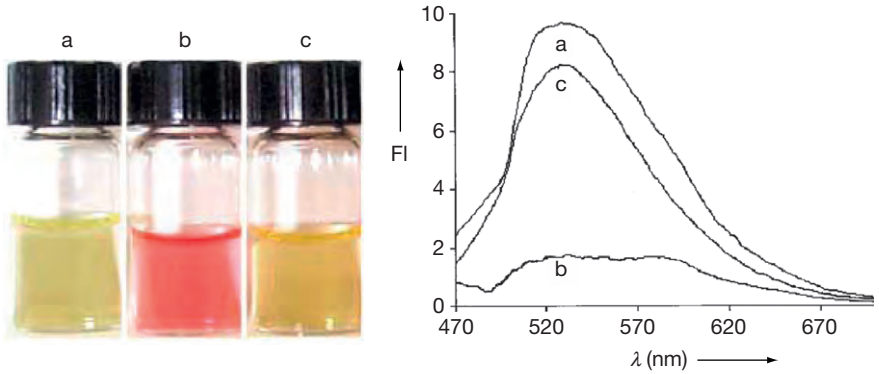

Figure 14 (*Left*) colorimetric images and (*Right*) fluorescence spectrum (FI, fluorescence intensity) of (a) polythiophene derivative, (b) polythiophene derivative/ssDNA duplex, and (c) polythiophene derivative/dsDNA triplex. Reproduced from Ho, H. A.; Boissinot, M.; Bergeron, M. G.; *et al*. *Angew. Chem. Int. Ed*. **2002**, *41*, 1548–1551.

dsDNA (Figure 14)[218] and is attributed to the different conformations[219] adopted by the CPs when interacting with ssDNA or dsDNA. The CP adopts a random coil when in solitude and is highly fluorescent but adopts a highly conjugate, planar conformation upon formation of a duplex with ssDNA that is less fluorescent and with a red-shifted absorbance. In the presence of a complementary ssDNA, a triplex (CP/dsDNA) structure (less conjugated and in a nonplanar conformation) is formed, and the fluorescence is recovered with the absorbance maxima shifted back to the blue region. In summary, the different responses of cationic CPs with either ssDNA or dsDNA allows the possibility of CPs as suitable transducers in biosensor devices.

Many solid-support DNA sequence detection methods using CPs[173,174,183,184,209,220–222] have been demonstrated, but only works describing DNA biosensing by addition of only unlabeled DNA sample will be mentioned. Using a planar polystyrene platform, hydrogel spots of a PTP derivative (formed through cross-linking of the PTP derivative with an ssDNA solution) were created and could demonstrate different results when incubated with either noncomplementary ssDNA or complementary ssDNA.[223] The emitted fluorescence from a hydrogel spot incubated with noncomplementary ssDNA was observed to be more red-shifted compared to the spot incubated with complementary ssDNA (Figure 15). This difference in observed fluorescence is caused by a conformational transition of the polymer backbone when the CP/ssDNA binds with the complementary DNA. Interaction of the CP with cross-linking ssDNA forces the CP coil to become stretched, whereas interaction with dsDNA formed through hybridization with

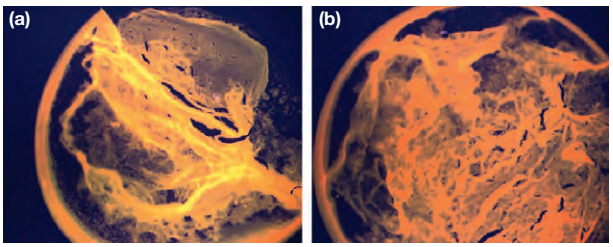

Figure 15 Fluorescence images of hydrogel spots fabricated from polythiophene derivative/single-stranded DNA after incubation with (a) complementary DNA and (b) noncomplementary DNA. Reproduced from Nilsson, K. P. R.; Inganäs, O. *Nat. Mater*. **2003**, *2*, 419–424.

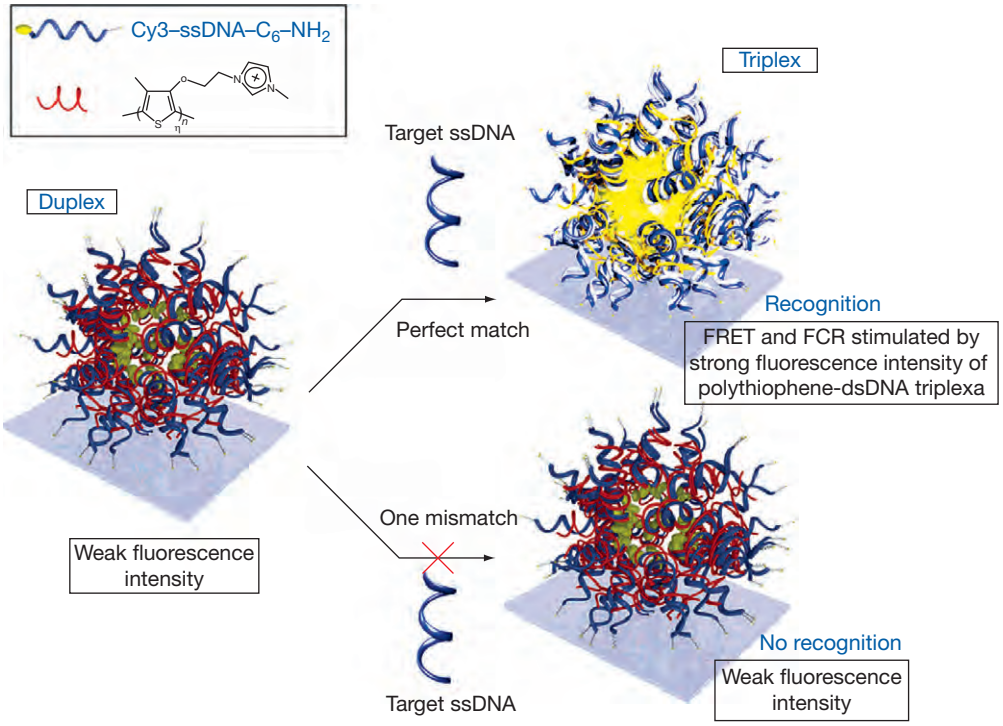

Figure 16 Schematic representation of the specific recognition of target single-stranded DNA by duplex aggregates onto glass slides and of the signal amplification mechanism based on a conformation change of the cationic conjugated polymer transducer and fast energy transfer within the micelle. FCR, fluorescence chain reaction. Reproduced from Najari, A.; Ho, H. A.; Gravel, J.; Nobert, P.; Boudreau, D.; Leclerc, M. *Anal. Chem.* **2006**, *78*, 7896–7899.

complementary ssDNA caused the CP to adopt a more helical conformation. The stretched form of the CP backbone is planar with an emission maximum occurring at longer wavelengths while the helical conformation is nonplanar with an emission maximum occurring at shorter wavelengths.[219]

Alternatively, arrays of labeled DNA capture probe/CP complexes could be created for the detection of DNA. The DNA probe could first be complexed with PTP and subsequently covalently attached unto a surface-treated glass slide.[224] In this model (Figure 16), the CP backbone is more planar with fluorescence intensity that is red-shifted as it has complexed with the Cy3-ssDNA probe. Therefore, no FRET can occur between and the CP and the Cy3 (whose excitation is in the blue wavelength region). Upon formation of the triplex with complementary ssDNA, the fluorescence emission of the CP becomes blue-shifted and will be able to excite (i.e., FRET can occur) the many neighboring Cy3-ssDNA probes (i.e., FCR can occur). This method has also been demonstrated to be capable of quantifying the DNA of interest and of differentiating samples with single nucleotide mismatches (Figure 17).

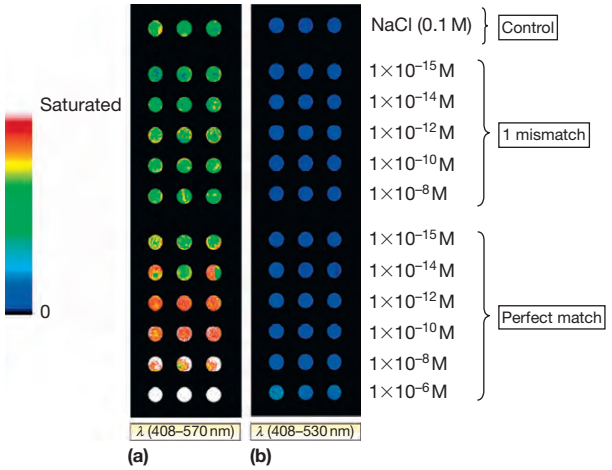

Figure 17 Fluorometric detection and quantification of specific DNA hybridizations on arrays of conjugated polymer/DNA probe aggregates. (a) Excitation at 408 nm, emission at 570 nm, and (b) excitation at 408 nm, emission at 530 nm. Reproduced from Najari, A.; Ho, H. A.; Gravel, J.; Nobert, P.; Boudreau, D.; Leclerc, M. *Anal. Chem.* **2006**, *78*, 7896–7899.

3.331.3.3.2. Protein biosensing using BSE/CP complexes

Detection of proteins through the use of CPs began in the late 1990s[27,188,195] and the number of works involving protein detection using CPs has grown tremendously in the last decade. Metalloproteins are, by a minimal definition, proteins that contain a metal ion cofactor and have been demonstrated to be capable of complex formation with and 'superquenching' of CPs.[225–228] The complex formation process is electrostatically driven between oppositely charged CPs and proteins, and complex formation is thereby highly dependent on the pH and pI of the buffer and protein used, respectively. This observed fluorescence 'superquenching' phenomenon of CPs by metalloproteins is a likely result of an electron transfer mechanism from the CPs to the proteins' metal ion cofactor[225,229] upon excitation of the CPs and is hence likely to be

applicable only for detection of metalloproteins. However, by using an array of 6 different CPs, individual signal signatures were obtained for 17 different proteins, thus providing the conceptualization of using CPs for specific identification of proteins.[230] Aside from detection of proteins, direct interactions between proteins and CPs have also been used for the detection of protein conformation changes (formation of fibrous protein amyloids[231] or negative CP[232] and conformational changes of calmodulin upon binding with calcium ions[233,234]). Although CPs have been demonstrated to be effective in detection or sensing of proteins and protein conformational changes, it is worth noting that no BSEs were employed during these sensing processes and therefore they cannot be categorized as biosensors, but may likely be applied or extended to biosensor devices with the introduction of suitable BSEs. Generally, the strategies of protein biosensing are different compared with those applied for the biosensing of DNA via probe/CP complexes; while DNA biosensing utilized only ssDNA as the BSE, protein biosensing uses various possible BSEs such as protein-specific aptamers[235] and oligonucleotides of random sequences.[236] In addition, it is worth noting that there has been no demonstration of amino acid mutation detection or of specific amino acid sequences within proteins.

Aptamers are DNA or RNA oligonucleotides (16–60 monomers) that bind to specific proteins and have also been utilized with CPs for the detection of proteins.[235,237,238] Being an oligonucleotide, aptamers are negatively charged (in physiological conditions) and therefore capable of forming higher-order complexes with cationic CPs, which exhibit different fluorescence characteristics. The aptamer also changes its conformational shape from an unfolded to a folded (G-quadruplex) structure in the presence of bound protein, and this conformational change likewise affects the conformational shape and optical properties of the closely associated cationic CPs (i.e., the backbone orientation of the CP transducer will differ depending on whether the aptamer is bound with the protein of interest). Fluorescence spectrum of the CPs will therefore be different in the absence (planar, red-shifted) or presence (nonplanar, blue-shifted) of the aptamer's corresponding binding protein. Nonspecific oligonucleotides too can be utilized

Table 4 Nonexhaustive list of works involving CPs used as bioanalytical assays and in biosensing of enzymes

Enzyme of interest	*Enzyme substrate*	*Mechanism*	*References*
Bioanalytical			
Trypsin	BSA	Product chelates CP fluorescence quencher (Cu^{2+})	239,241
Kinase (protein kinase A, protein kinase Cα, interleukin-I receptor-associated kinase 4)	Peptides (refer to reference for exact sequence), myelin basic protein, histone H1, phosphorylated heat- and acid-stable protein	Phosphorylated substrate binds to and quenches Ga^{3+} associated CP coated microspheres or quenches these microspheres via a competitive quenching strategy	248,252
β-Galactosidase	β-Galactopyranoside derivative	Conversion of substrate with another coupled enzyme into a CP fluorescence quencher	208–211
Nucleases (S1, B*am*HI, E*co*RI) and methyltransferases (E*co*RI methylase)	Fluorescently labeled ssDNA and dsDNA	Cleaving away of fluorescence dye from DNA substrates and resulting in reduced FRET or inhibition of cleaving mechanism by methyltransferases	245
Adenylate kinase	ATP	Conversion of substrate from a strong sequestering compound, of a CP fluorescence quencher (Cu^{2+}), into a weaker sequestering compound	251
Alkaline phosphatase	Pyrophosphate	Conversion of substrate from a strong sequestering compound, of a CP fluorescence quencher (Cu^{2+}), into a weaker sequestering compound	247
Bio-sensing			
Alkaline phosphatase/trypsin	ATP/Arg_6 peptide	CPs/substrate aggregates separation upon substrate cleavage by enzymes	246
Protease (trypsin, pepsin)	BSA	Enzymatic cleavage of surfactant substrate that results in CP aggregation	244
Proteases (enterokinase, caspases 3/7, β-secretase)	Peptides (refer to reference for exact sequence)	Cleaving away of quencher from peptide-quencher substrates attached to CP coated microspheres	240
Tyrosinase	Phenol derivative	Conversion of substrate into a CP fluorescence quencher	208–211
Proteases (papain, peptidase, thrombin)	Peptides (refer to reference for exact sequence)	Cleaving away of quencher from peptide-quencher substrates associated with CP or conversion of substrate associated with CP into a quencher	242
Acetylcholinesterase	Modified acetylcholine	Cleaving away of quencher from peptide-quencher substrates associated with CP	250
Endonucleases (HaeIII, Pvu II, EcoRV)	Fluorescence-labeled Y-DNA	Cleaving away of fluorescence dye from DNA substrates associated with CP and resulting in reduced FRET	208
Phospholipase C	1,2-Didecanoyl-*sn*-glycero-3-phosphocholine	Enzymatic cleavage of substrate associated with CP that results in CP aggregation	249
Trypsin	Peptides (refer to reference for exact sequence)	Cleaving away of quencher from peptide substrate covalently associated with CP	243

for the detection of specific proteins.[236] However, the differentiation of protein identity in this case requires the concerted use of a cationic CP along with ssDNA of different random sequence and length to generate a fingerprint identity of the proteins. By using five different ssDNA/CP complexes, it was successfully demonstrated that proteins (of different local hydrophobic and charged domains) could generate distinct and different fluorescence intensities from each of ssDNA/CP complex that, when combined and analyzed, would allow for fingerprinting of the detected proteins.

Another class of proteins that have been detected via the use of CPs are enzymes and include:

1. *Hydrolases* that cleave
   - peptide (proteases[239–244])
   - phosphodiester (nucleases[208,245])
   - phosphoester (phosphatases[246–248] and phospholipase C[249])
   - ester (acetylcholinesterase[250])
   - ether bonds (β-galactosidase[208–211])
2. *Kinases*[248,251,252]

Enzymes are a unique class of proteins as they possess the catalytic ability of converting substrates into a product. One example of such catalysis involves the cleaving of chemical bonds within the substrate to form smaller components of the original substrate (e.g., proteins into amino acids), and researchers have taken advantage of this particular property and coupled it with CPs for the detection of hydrolases. **Table 4** summarizes a nonexhaustive list of works involving CPs used in bioanalytical assays and biosensing of enzymes.

An example of enzyme biosensing using enzymatic substrate/CP complexes is depicted in **Figure 18** and involves (1) the cleaving off of a noncharged quencher from a positively charged peptide (closely interacting with a negatively charged CP) or (2) the conversion of the substrate into a quencher by proteases.[242] With reference to the former principle, the close proximity of the substrate quencher with the CP (prior to substrate cleavage) turns on the 'superquenching' effect of the CP but is rapidly turned off after the quencher has been cleaved off and separated away from the CP/peptide complex. Cleavable fluorescent dyes can also be utilized and result in reduced FRET from the CPs to the cleaved fluorescence dyes.[208] Alternatively, as depicted in the latter principle, an enzymatic substrate that is interacting closely with the CP can be converted into a quencher[208–211,242] in the presence of the enzyme and resulting in 'superquenching' of the CPs.

A third type of BSE/CP complexes are the ligand/CP complexes where the protein of interest would interact with the ligand (e.g., avidin/biotin[27,253] or antibody/antigen[254]) and cause a corresponding response from the closely associated CP. An important requirement of such a strategy is an ability of the ligand to interact closely with both the CP and protein of interest but with a higher affinity for the protein such that the ligand is sequestered. **Figure 19** illustrates the identification of avidin through interaction with a methylviologen-labeled biotin (MV-B)/CP complex. Prior to interaction, the fluorescence of the CP is 'superquenched' due to the close association with MV-B. However, this 'superquenching' effect is turned off upon introduction of avidin (having a higher affinity) which sequesters away the MV-B, resulting in a recovery of the strong fluorescence of the CP.

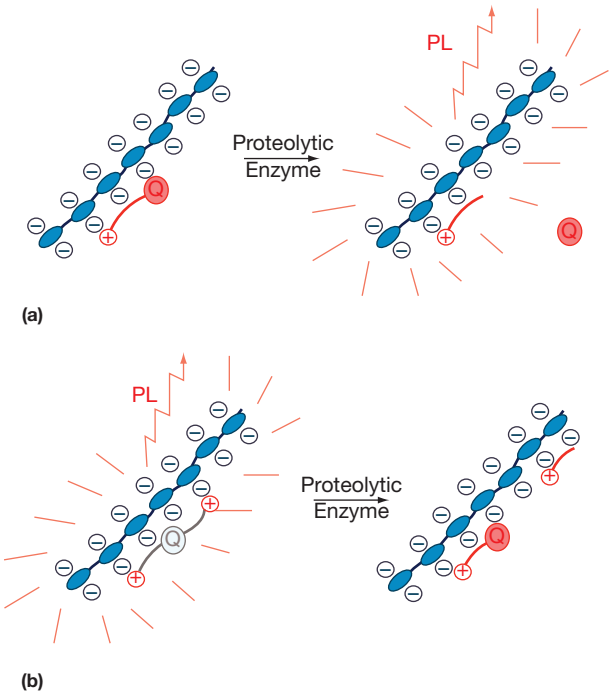

Figure 18 Schematic representation of (a) the cleaving off of a noncharged quencher from an enzymatic substrate and (b) conversion of an enzymatic substrate into a quencher for the detection of proteases. Reproduced from Pinto, M. R.; Schanze, K. S. *Proc. Natl. Acad. Sci. USA* **2004**, *101*, 7505–7510.

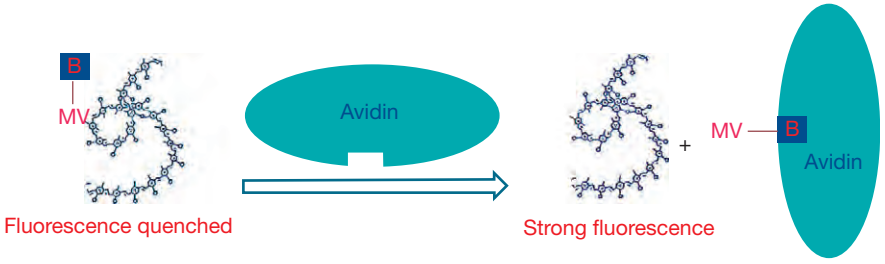

Figure 19 Schematic representation of protein detection via utilizing specific protein–ligand interactions, which sequesters away the quencher-like ligand from the ligand/conjugated polymer complex. Reproduced from Chen, L.; McBranch, D. W.; Wang, H.; Helgeson, R.; Wudl, F.; Whitten, D. G. *Proc. Natl. Acad. Sci. USA* **1999**, *96*, 12287–12292.

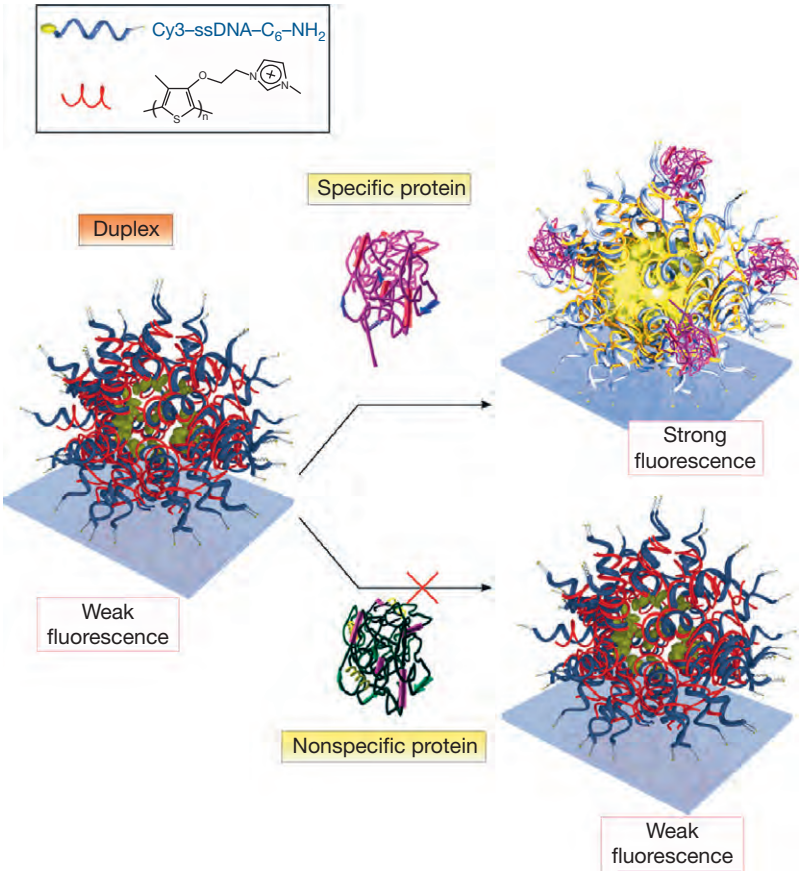

Figure 20 Schematic representation of the specific detection of target proteins by the use of single-stranded DNA aptamer and cationic conjugated polymer duplex aggregates covalently attached on glass slides. Reproduced from Abérem, M. B.; Najari, A.; Ho, H. A.; *et al*. *Adv*. *Mater*. **2006**, *18*, 2703–2707.

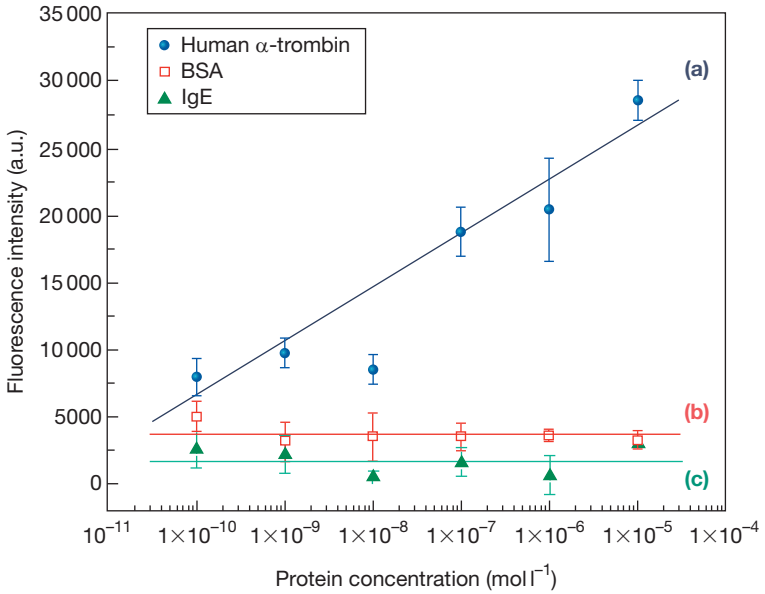

Figure 21 Fluorescence intensity as a function of the concentration of (a) human α-thrombin, (b) bovine serum albumin, and (c) immunoglobulin E measured from arrays fabricated by single-stranded DNA aptamer and cationic conjugated polymer duplex aggregates covalently attached on glass slides. Reproduced from Abérem, M. B.; Najari, A.; Ho, H. A.; *et al*. *Adv*. *Mater*. **2006**, *18*, 2703–2707.

Conventionally, the specific detection of proteins on solid supports is achieved by the ELISA technique. However, although protein detection via ELISA is simple and requires easily accessible laboratory equipments, it is a time-consuming and material-wasting process. Sensitive and specific detection of proteins without the need of excessive washing is desired and has been demonstrated through the use of CPs/aptamers complexes immobilized onto a glass slide.[235] Duplexes of a PTP derivative/Cy3-ssDNA human α-thrombin aptamer were first prepared before being covalently attached onto surface-treated glass slides, where the duplexes exhibited weak FRET fluorescence (Figure 20). However, binding of human α-thrombin with the aptamers causes a subsequent conformation change of both aptamer and accompanying CP that transcends into strong FRET fluorescence exhibited by the duplexes. The weak FRET fluorescence initially observed (i.e., without human α-thrombin) is due to the formation of neutral rigid-rod moieties between the CPs and aptamers that further assembles into nanoaggregates, thus resulting in significant fluorescence quenching of the CP. The strong fluorescence of the PTP derivative after DNA aptamer–protein interaction was described to be due to the partial hindrance of aggregation and planarization of the CP due to the interaction with the protein of interest. In addition, this solid-support array approach also demonstrated the possible differentiation of different concentrations of human α-thrombin from different concentrations of bovine serum albumin (BSA) and immunoglobulin E (IgE) (Figure 21).

3.331.3.4. CP Covalently Modified with BSE

A third possible strategy of developing CP-based optical biosensors is via covalent attachment of the BSEs onto to the pendant chains of CPs, which results in a subsequent optical response when the corresponding target of interest interacts with these modified CPs. Hexokinases, as the BSE of a glucose sensing



Figure 22 Schematic representation of interaction of glucose with hexokinase on the polydiacetylene monolayer. It is not necessary for the enzyme to be consistently oriented in the same manner with respect to the polymer film since glucose will be able to bind to the enzyme in almost any orientation, and it is the conformational change that induces the color change. Reproduced from Cheng, Q.; Stevens, R. C. *Adv. Mater.* **1997**, *9*, 481–483.

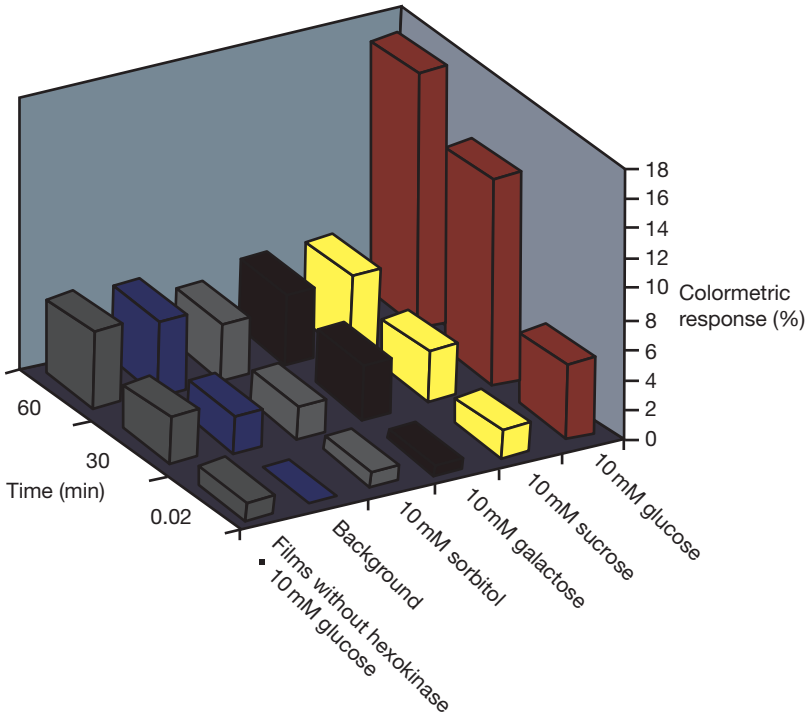

Figure 23 Colorimeric response of the hexokinase-immobilized polydiacetylene sensors for glucose and other compounds used as controls. The first column on the left represents the glucose agitation on the PDA monolayers without immobilized hexokinase. Reproduced from Cheng, Q.; Stevens, R. C. *Adv. Mater.* **1997**, *9*, 481–483.

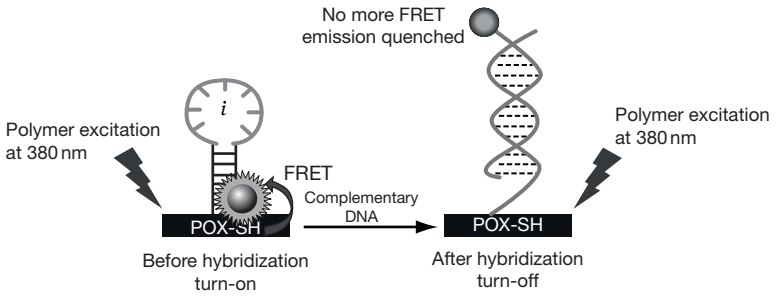

Figure 24 Schematic representation of the detection of DNA sequence by combining a fluorescent dye with a molecular beacon. CP used was POX-SH, a poly(oxadiazole) derivative. Reproduced from Lee, J.; Jun, H.; Kim, J. *Adv. Mater.* **2009**, *21*, 3674–3677.

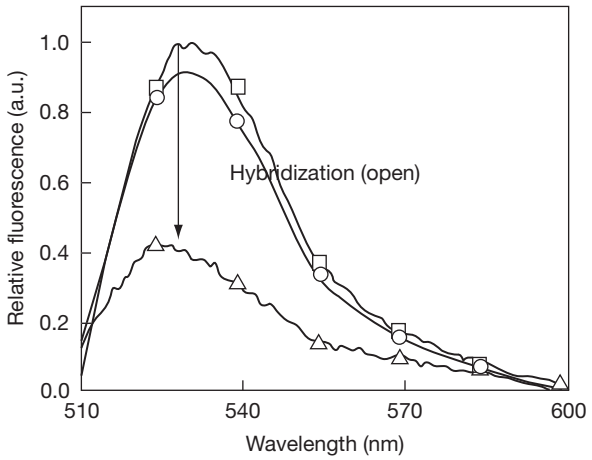

Figure 25 Fluorescence spectrum of POX-SH before (square) and after hybridization with the complementary DNA (triangle) and random noncomplementary DNA (circle). Reproduced from Lee, J.; Jun, H.; Kim, J. *Adv. Mater.* **2009**, *21*, 3674–3677.

platform, have been covalently attached to the side chains of a PDA Langmuir–Blodgett layer deposited on a solid support.[255] Upon binding to glucose, the hexokinases undergo a large conformational change and this creates a mechanical force that affects the conformational shape of the attached PDA layer as well (Figure 22). A concomitant colorimetric response (absorbance increase at 550 nm) over time was observed for this biosensing platform upon glucose incubation but not for sorbitol, galactose, or sucrose incubation (Figure 23). A key contribution of this physical transduction approach is the possibility of capitalizing and incorporation of other biological materials, which also undergo similar conformation changes, into CP-based biosensing devices of small biomolecules.

Using direct on-chip oligonucleotide synthesis methods, ssDNA probe were immobilized onto a layer of polyoxadiazole derivative (possessing amine group and thiol groups).[177] In this model (Figure 24), fluorescently (fluorescein or HEX) labeled synthesized ssDNA probe exists as the closed form in the absence of complementary ssDNA and causes the fluorescent dye to be located close to the POX-SH CP layer. The close proximity allows efficient FRET to occur from the immobilized layer of polyoxadiazole derivative and produces an amplified emission from the fluorescence-labeled dye (Figure 25). Selective hybridization of the ssDNA probes with complementary ssDNA opens up the closed structure of the probe and increases the distance between the fluorescence dye and CP, resulting in a decreased fluorescence emission from the dye as no efficient FRET can take place.

Table 5 Examples of CPs modified with BSEs and their respective target of interest

Target of interest (analyte)	*Biological sensing element (BSE)*	*References*
Avidin	Biotin	257–260
Escherichia coli	Mannose, galactose	261
Influenza virus/*Escherichia coli*	Sialic acid/mannose	262
Lectins (*Concanavalin A*, wheat germ agglutinin)	Glucose	256
ssDNA	Oligonucleotide probe	177
Glucose	Hexokinase	255

Aside from enzymes and ssDNA, glucose[256] and biotin[257–260] moieties have been covalently attached to CPs, and upon binding with lectins and avidin respectively, various types of optical response can be observed. Depending on the optical detection approach adopted, modified CPs were observed either to have a blue-shifted absorbance maxima corresponding to a nonplanar configuration of the CP backbone or an observation of FRET if the target was prelabeled with fluorescence. Further examples of CPs modified with BSEs and their respective target of interest can be found in Table 5.

References

1. Hulanicki, A.; Glab, S.; Ingamn, F. *Pure Appl. Chem.* **1991**, *63*(9), 1247–1250.
2. Thévenot, D. R.; Toth, K.; Durst, G. W. *Pure Appl. Chem.* **1999**, *71*(12), 2333–2348.
3. Cammann, K.; Ross, B.; Katerkamp, A.; Reinbold, J.; Grundig, B.; Renneberg, R. In *Ullmann's Encyclopedia of Industrial Chemistry*; Wiley-VCH Verlag GmbH: Weinheim, 2001.
4. Kim, I. B.; Dunkhorst, A.; Bunz, U. H. F. *Langmuir* **2005**, *21*, 7985–7989.
5. Swager, M. T. *Acc. Chem. Res.* **1998**, *31*, 201–207.
6. Fehling, H. *Archiv Für Physiologische Heilkunde* **1848**, *7*, 64–73.
7. Clark, L. C.; Lyons, C. *Ann. N. Y. Acad. Sci.* **1962**, *102*, 29–45.
8. McQuade, D. T.; Pullen, A. E.; Swager, T. M. *Chem. Rev.* **2000**, *100*, 2537–2574.
9. Thomas, S. W., III; Joly, G. D.; Swager, T. M. *Chem. Rev.* **2007**, *107*, 1339–1386.
10. Habermüller, K.; Mosbach, M. *Fresenius J. Anal. Chem.* **2000**, *366*, 560–568.
11. Singh, M.; Kathuroju, P. K.; Jampana, N. *Sens. Actuators B* **2009**, *143*, 430–443.
12. Singh, R.; Prasad, R.; Sumana, G.; *et al. Biosens. Bioelectron.* **2009**, *24*, 2232–2238.
13. Scheller F. 19XX.
14. Ahuja, T.; Mir, I. A.; Kumar, D.; Rajesh, K. *Biomaterials* **2007**, *28*, 791–805.
15. Gerard, M.; Chaubey, A.; Malhotra, B. D. *Biosens. Bioelectron.* **2002**, *17*, 345–359.

16. Wallace, G. G.; Smyth, M.; Zhao, H. *Trends Anal. Chem.* **1999**, *18*(4), 245–251.
17. Heeger, P. S.; Heeger, A. J. *Proc. Natl. Acad. Sci. USA* **1999**, *96*(22), 12219–12221.
18. Newman, J. D.; Turner, A. P. F. *Biosens. Bioelectron.* **2005**, *20*, 2435–2453.
19. Ronkainen, N. J.; Halsall, H. B.; Herneman, W. R. *Chem. Soc. Rev.* **2010**, *39*, 1747–1763.
20. Qin, Z.; Swager, T. M. *J. Am. Chem. Soc.* **1995**, *117*, 12593–12602.
21. Inzelt, G. In *Conducting Polymers – A New Era in Electrochemistry*; Scholz, F., Ed.; Springer: Berlin Heidelberg, 2008; p 256.
22. Baeyer, A. *Ber. Dtsch. Chem. Ges.* **1885**, *452*, 2269–2281.
23. Genies, E. M.; Boyle, A.; Lapkowski, M.; Tsintavis, C. *Synth. Met.* **1990**, *36*, 139–182.
24. Leclerc, M.; Najari, A.; Beuapré, S. *Can. J. Chem.* **2009**, *87*, 1201–1208.
25. MacDiarmid, A. G. *Angew. Chem.* **2001**, *40*, 2581–2590.
26. Rahman, M. A.; Kumar, P.; Park, D. D.; Shim, Y. B. *Sensors* **2008**, *8*, 118–141.
27. Chen, L.; McBranch, D. W.; Wang, H.; Helgeson, R.; Wudl, F.; Whitten, D. G. *Proc. Natl. Acad. Sci. USA* **1999**, *96*, 12287–12292.
28. Liu, B.; Bazan, G. C. *Chem. Mater.* **2004**, *16*, 4467–4476.
29. Liu, B.; Bazan, G. C. *J. Am. Chem. Soc.* **2004**, *126*, 1942–1943.
30. Hideki, S. *Angew. Chem. Int. Ed.* **2001**, *90*, 2574–2580.
31. McCullough, R. D. *Adv. Mater.* **1998**, *10*(2), 93–116.
32. Pron, A.; Rannou, P. *Prog. Polym. Sci.* **2002**, *27*, 135–190.
33. Babudri, F.; Farinola, G. M.; Naso, F. *J. Mater. Chem.* **2004**, *14*, 11–34.
34. Groenendaal, L. B.; Zotti, G.; Aubert, P. H.; Waybright, S. M.; Reynolds, J. R. *Adv. Mater.* **2003**, *15*(11), 855–879.
35. Roncali, J. *Chem. Rev.* **1992**, *92*, 711–738.
36. Sadki, S.; Schottland, P.; Brodi, N.; Sabouraud, G. *Chem. Soc. Rev.* **2000**, *29*, 283–293.
37. Higgens, S. J. *Chem. Soc. Rev.* **1997**, *26*, 247–257.
38. Fan, C.; Plaxco, K. W.; Heeger, A. J. *Trends Biotechnol.* **2005**, *23*, 186–192.
39. Sung, W. J.; Bae, Y. H. *Biosens. Bioelectron.* **2002**, *18*, 1231–1239.
40. Smela, E. *Adv. Mater.* **2003**, *15*(6), 481–494.
41. Vernitskaya, T. V.; Efimov, O. N. *Russ. Chem. Rev.* **1997**, *66*(5), 443–457.
42. Wang, L. X.; Li, X. G.; Yang, Y. L. *React. Funct. Polym.* **2001**, *42*, 125–139.
43. Bunz, U. H. F. *Chem. Rev.* **2000**, *100*(4), 1605–1644.
44. Huang, F.; Wang, X.; Wang, D.; Yang, W.; Cao, Y. *Polymer* **2005**, *46*, 12010–12015.
45. Saxena, V.; Malhorta, B. D. *Curr. Appl. Phys.* **2003**, *3*, 293–305.
46. Hideki, S.; Louis, E. J.; MacDiarmid, A. G.; Chiang, C. K.; Heeger, A. J. *J. Chem. Soc. Chem. Commun.* **1977**, 578–855.
47. Heeger, A. J. *Angew. Chem.* **2001**, *40*, 2591–2611.
48. Graupner, W.; Mauri, M.; Stampfl, J.; Leising, G. *Solid State Commun.* **1994**, *91*(1), 7–12.
49. Baumgarten, M.; Mullen, K. In *Topics in Current Chemistry*; Springer: Berlin, 1994; pp 1–103.
50. Bharathan, J. M.; Yang, Y. *J. Appl. Phys.* **1998**, *84*(6), 3207–3211.
51. Nicolini, C. In *Nanobiotechnology and Nanobioscience*; PAN-Stanford: Singapore, 2008; pp 17–34.
52. Jaiswal, M.; Menon, R. *Polym. Int.* **2006**, *55*, 1371–1384.
53. Kaiser, A. B. *Rep. Prog. Phys.* **2001**, *64*, 1–49.
54. Bässler, H.; Schweitzer, B. *Acc. Chem. Res.* **1999**, *32*(2), 173–182.
55. Soos, Z. G.; Galvao, D. S.; Etemad, S. *Adv. Mater.* **1994**, *6*(4), 280–287.
56. Mullekom, H. A. M.; Vekemann, J. A. J. M.; Havinga, E. E.; Meijer, E. W. *Mater. Sci. Eng.* **2001**, *32*, 1–40.
57. Habermüller, K.; Ramanavicius, A.; Laurinavicius, V.; Schuhmann, W. *Electroanalysis* **2000**, *12*, 1383–1389.
58. Trojanowicz, M.; Hitchman, M. L. *Electroanalysis* **1996**, *8*, 263–266.
59. Adeloju, S. B.; Moline, A. N. *Biosens. Bioelectron.* **2001**, *16*, 133–139.
60. Karyakin, A. A.; Bobrova, O. A.; Lukachova, L. V.; Karyakina, E. E. *Sens. Actuators B* **1996**, *33*, 34–38.
61. Forzani, E. S.; Zhang, H.; Nagahara, L. A.; Amlani, I.; Tsui, R.; Tao, N. *Nano Lett.* **2004**, *4*, 1785–1788.
62. Hoa, D. T.; Suresh Kumar, T. N.; Punekar, N. S.; Srinivasa, R. S.; Lal, R.; Contractor, A. Q. *Anal. Chem.* **1992**, *64*, 2645–2646.
63. Bartlett, P. N.; Birkin, P. R.; Wang, J. H. *Anal. Chem.* **1998**, *70*, 3685–3694.
64. Raffa, D.; Leung, K. T.; Battaglini, F. *Anal. Chem.* **2003**, *75*, 4983–4987.
65. Choi, M. M. F. *Michrochim. Acta* **2004**, *148*, 107–132.
66. Yang, X.; Zhao, X.; Zuo, X.; Wang, K.; Wen, J.; Zhang, H. *Talanta* **2009**, *77*, 1027–1031.
67. Lakowicz, J. R. *Principles of Fluorescence Spectroscopy*; Springer: New York, 2006.
68. Dubus, S.; Gravel, J. F.; LeDrogoff, B.; Nobert, P.; Veres, T.; Boudreau, D. *Anal. Chem.* **2006**, *78*, 4457–4465.
69. Guan, H.; Zhou, P.; Zeng, S.; Zhou, X.; Wang, Y.; He, Z. *Talanta* **2009**, *79*, 153–158.
70. Shi, J.; Pu, K. Y.; Zhan, R.; Liu, B. *Macromol. Chem. Phys.* **2009**, *210*, 1195–1200.
71. Song, H.; Sun, B.; Gu, K. J.; Yang, Y.; Zhang, Y.; Shen, Q. D. *J. Appl. Polym. Sci.* **2009**, *114*, 1278–1286.
72. Diaz, A. F.; Kanazawa, K. K. *Chem. Commun.* **1979**, *14*, 635–636.
73. Wang, J.; Jiang, M.; Fortes, A.; Mukherjee, B. *Anal. Chim. Acta* **1999**, *402*, 7–12.
74. Ma, Z.; Li, J.; Liu, M.; *et al. J. Am. Chem. Soc.* **1998**, *120*, 12678–12679.
75. Umaña, M.; Waller, J. *Anal. Chem.* **1986**, *58*, 2979–2983.
76. John, R.; Spencer, M.; Wallace, G. G.; Smyth, M. R. *Anal. Chim. Acta* **1991**, *249*, 381–385.
77. Sargent, A.; Sadik, O. A. *Electrochim. Acta* **1999**, *44*, 4667–4675.
78. Campbell, T. E.; Hodgson, A. J.; Wallace, G. G. *Electroanalysis* **1999**, *11*, 215–222.
79. Deshpande, M. V.; Hall, E. A. H. *Biosens. Bioelectron.* **1990**, *5*, 431–448.
80. Bartlett, P. N.; Birkin, P. R. *Anal. Chem.* **1993**, *65*, 1118–1119.
81. Bartlett, P. N.; Birkin, P. R. *Anal. Chem.* **1994**, *66*, 1552–1559.
82. Bangar, M. A.; Shirale, D. J.; Chen, W.; Myung, N. V.; Mulchandani, A. *Anal. Chem.* **2009**, *81*, 2168–2175.
83. Xie, H.; Luo, S.; Yu, H. *Small* **2009**, *5*, 2611–2617.
84. Kanungo, M.; Kumar, A.; Contractor, A. Q. *Anal. Chem.* **2003**, *75*, 5673–5679.
85. Wanekaya, A. K.; Chen, W.; Myung, N. V.; Mulchandani, A. *Electroanalysis* **2006**, *18*, 533–550.
86. Llaudet, E.; Botting, N. P.; Crayston, J. A.; Dale, N. *Biosens. Bioelectron.* **2003**, *18*, 43–52.
87. Sangodkar, H.; Sukeerthi, S.; Srinivasa, R. S.; Lal, R.; Contractor, A. Q. *Anal. Chem.* **1996**, *68*, 779–783.
88. Cosnier, S.; Galland, B.; Gonfran, C.; Pellec, A. L. *Electroanalysis* **1998**, *10*, 808–813.
89. Cosnier, S.; Stotycheva, M.; Senillou, A.; Perrot, H.; Furriel, R. P. M.; Leone, F. A. *Anal. Chem.* **1999**, *71*, 3692–3697.
90. Cosnier, S.; Senillou, A. *Chem. Commun.* **2003**, *3*, 414–415.
91. Fould, N. C.; Lowe, C. R. *Anal. Chem.* **1988**, *60*, 2473–2478.
92. Xue, C.; Chen, Z.; Luo, F.; *et al. Biomacromolecules* **2005**, *6*, 1810–1815.
93. Kouri-Youssoufi, H.; Yassar, A. *Biomacromolecules* **2001**, *2*, 58–64.
94. Peng, H.; Soeller, C.; Vigar, N.; *et al. Biosens. Bioelectron.* **2005**, *20*, 1821–1828.
95. Mu, S.; Xue, H.; Qian, B. *J. Electroanal. Chem.* **1991**, *304*, 7–16.
96. Ahuja, T.; Mir, I. A.; Kumar, D.; Rajesh, K. *Sens. Actuators B* **2008**, *134*, 140–145.
97. Brahim, S.; Narinesingh, D.; Guiseppi-Elie, A. *Anal. Chim. Acta* **2001**, *448*, 27–36.
98. Qu, F.; Yang, M.; Jiang, J.; Shen, G.; Yu, R. *Anal. Biochem.* **2005**, *344*, 108–114.
99. Ram, M. K.; Adami, M.; Paddeu, S.; Nicolini, C. *Nanotechnology* **2000**, *11*, 112–119.
100. Ramanavičius, A.; Ramanavičiene, A.; Malinauskas, A. *Electrochim. Acta* **2006**, *51*, 6025–6037.
101. Cosnier, S. *Anal. Lett.* **2007**, *341*, 1–11.
102. Peng, H.; Zhang, L.; Soeller, C.; Travas-Sejdic, J. *Biomaterials* **2009**, *30*, 2132–2148.
103. Xia, L.; Wei, Z.; Wan, M. *J. Colloid Interface Sci.* **2010**, *341*, 1–11.
104. Bartlett, P. N.; Astier, Y. *Chem. Commun.* **2000**, *2*, 105–112.
105. Cosnier, S. *Electroanalysis* **2005**, *19*, 1701–1715.
106. Xue, H.; Shen, Z.; Li, Y. *Synth. Met.* **2001**, *124*, 345–349.
107. Morrin, A.; Ngamna, O.; Killard, A. J.; Moulton, S. E.; Smyth, M. R.; Wallace, G. G. *Electroanalysis* **2005**, *17*, 423–430.
108. Kan, J.; Pan, X.; Chen, C. *Biosens. Bioelectron.* **2004**, *19*, 1635–1640.
109. Xian, Y.; Hu, Y.; Liu, F.; Xian, Y.; Wang, H.; Jin, L. *Biosens. Bioelectron.* **2006**, *21*, 1996–2000.
110. Rahman, M. A.; Kwon, N.; Won, M.; Choe, E. S.; Shim, Y. *Anal. Chem.* **2005**, *77*, 4854–4860.
111. Rahman, M. A.; Park, D.; Chang, S.; McNeil, C. J.; Shim, Y. *Biosens. Bioelectron.* **2006**, *21*, 1116–1124.
112. Wang, P.; Liu, M.; Kan, J. *Sens. Actuators B* **2009**, *140*, 577–584.
113. Schuhmann, W.; Lammert, R.; Uhe, B.; Schmidt, H. L. *Sens. Actuators B* **1990**, *1*, 537–541.
114. Schuhmann, W.; Huber, J.; Mirlach, A.; Daub, J. *Adv. Mater.* **1993**, *5*, 124–126.
115. Evans, S. A. G.; Brakha, K.; Billon, M.; Mailley, P.; Denuault, G. *Electrochem. Commun.* **2005**, *7*, 135–140.
116. Haddour, N.; Cosnier, S.; Gondran, C. *J. Am. Chem. Soc.* **2005**, *127*, 5752–5753.
117. Naal, Z.; Park, J.; Bernhard, S.; Shapleigh, J. P.; Batt, C. A.; Abruña, H. D. *Anal. Chem.* **2002**, *74*, 140–148.

118. Wolowacz, S. E.; Yon Hin, B. F. Y.; Lowe, C. R. *Anal. Chem.* **1992**, *64*, 1541–1545.
119. Ramanavičius, A.; Habermüller, K.; Csöregi, E.; Laurinavicius, V.; Schuhmann, W. *Anal. Chem.* **1999**, *71*, 3581–3586.
120. Coche-Guerente, L.; Cosnier, S.; Innocent, C.; Mailley, P. *Anal. Chim. Acta* **1995**, *311*, 23–30.
121. Fabiano, S.; Tran-Minh, C.; Piro, B.; Dang, L. A.; Pham, M. C.; Vittori, O. *Mater. Sci. Eng. C* **2002**, *21*, 61–67.
122. Ouerghi, O.; Senillou, A.; Jaffrezic-Renault, N.; Martelet, C.; Ouada, H. B.; Cosnier, S. *J. Electroanal. Chem.* **2001**, *501*, 62–69.
123. Yan, W.; Chen, X.; Li, X.; Feng, X.; Zhu, J. *J. Phys. Chem. B* **2008**, *112*, 1275–1281.
124. Rahman, M. A.; Shiddiky, M. J. A.; Park, J.; Shim, Y. *Biosens. Bioelectron.* **2007**, *22*, 2464–2470.
125. Ouerghi, O.; Touhami, A.; Jaffrezic-Renault, N.; Martelet, C.; Ouada, H. B.; Cosnier, S. *Bioelectrochemistry* **2002**, *56*, 131–133.
126. Barton, A. C.; Davis, F.; Higson, S. P. J. *Anal. Chem.* **2008**, *80*, 9411–9416.
127. Sadik, O. A.; Wallace, G. G. *Anal. Chim. Acta* **1993**, *279*, 209–212.
128. Sadik, O. A.; Wallace, G. G. *Anal. Chim. Acta* **1998**, *376*, 125–131.
129. Gooding, J. J.; Wasiowych, C.; Barnett, D.; Hibbert, D. B.; Barisci, J. N.; Wallace, G. G. *Biosens. Bioelectron.* **2004**, *20*, 260–268.
130. Grant, S.; Davis, F.; Pritchard, J. A.; Law, K. A.; Higson, S. P. J.; Gibson, T. D. *Anal. Chim. Acta* **2003**, *495*, 21–32.
131. Grant, S.; Davis, F.; Law, K. A.; *et al. Anal. Chim. Acta* **2005**, *537*, 163–168.
132. Sadik, O. A.; Xu, H. *Anal. Chem.* **2002**, *74*, 3142–3150.
133. Minett, A. I.; Barisci, J. N.; Wallace, G. G. *Anal. Chim. Acta* **2003**, *475*, 37–45.
134. Ionescu, R. E.; Abu-Rabeah, K.; Cosnier, S.; Durrieu, C.; Chovelon, J.; Marks, R. S. *Electroanalysis* **2006**, *11*, 1041–1046.
135. Tuncagil, S.; Odaci, D.; Yildiz, E.; Timur, S.; Toppare, L. *Sens. Actuators B* **2009**, *137*, 42–47.
136. Ghanbari, Kh.; Bathaie, S. Z.; Mousavi, M. F. *Biosens. Bioelectron.* **2008**, *23*, 1825–1831.
137. Garnier, F.; Kouri-Youssoufi, H.; Srivastava, P.; Mandrand, B.; Delair, T. *Synth. Met.* **1999**, *100*, 89–94.
138. Kouri-Youssoufi, H.; Garnier, F.; Srivastava, P.; Godillot, P.; Yassar, A. *J. Am. Chem. Soc.* **1997**, *2*, 58–64.
139. Zhu, N.; Chang, Z.; He, P.; Fang, Y. *Electrochim. Acta* **2006**, *51*, 3758–3762.
140. Chang, H.; Yuan, Y.; Shi, N.; Guan, Y. *Anal. Chem.* **2007**, *79*, 5111–5115.
141. Arora, K.; Chaubey, A.; Singhal, R.; *et al. Biosens. Bioelectron.* **2006**, *21*, 1777–1783.
142. Garnier, F.; Kouri-Youssoufi, H.; Srivastava, P.; Yassar, A. *J. Am. Chem. Soc.* **1994**, *116*, 8813–8814.
143. Lin, M.; Cho, M. S.; Choe, W. S.; Lee, Y. *Biosens. Bioelectron.* **2009**, *25*, 28–33.
144. Dubois, M.; Gondran, C.; Renaudet, O.; *et al. Chem. Commun.* **2005**, *34*, 4318–4320.
145. Zhu, L.; Yang, R.; Zhai, J.; Tian, C. *Biosens. Bioelectron.* **2007**, *23*, 528–535.
146. Holzinger, M.; Bouffier, L.; Villalonga, R.; Cosnier, S. *Biosens. Bioelectron.* **2009**, *24*, 1128–1134.
147. Heiduschka, P.; Göpel, W.; Beck, W.; Kraas, W.; Kienle, S.; Jung, G. *Chem. Eur. J.* **1996**, *2*, 667–672.
148. Livache, T.; Roget, A.; Dejean, E.; Barthet, C.; Bidan, G.; Téoule, R. *Nucl. Acids Res.* **1994**, *22*, 2915–2921.
149. Livache, T.; Bazin, H.; Caillat, P.; Roget, A. *Biosens. Bioelectron.* **1998**, *13*, 629–634.
150. Barton, A. C.; Davis, F.; Higson, S. P. J. *Anal. Chem.* **2008**, *80*, 6198–6205.
151. Da Silva, S.; Shan, D.; Cosnier, S. *Sens. Actuators B* **2004**, *103*, 397–402.
152. Brahim, S.; Narinesingh, D.; Guiseppi-Elie, A. *Biosens. Bioelectron.* **2002**, *17*, 53–59.
153. Abu-Rabeah, K.; Polyak, B.; Ionescu, R. E.; Cosnier, S.; Marks, R. S. *Biomacromolecules* **2005**, *6*, 3313–3318.
154. Ionescu, R. E.; Abu-Rabeah, K.; Cosnier, S.; Marks, R. S. *Electrochem. Commun.* **2005**, *7*, 1277–1282.
155. Yan, W.; Feng, X.; Chen, X.; Hou, W.; Zhu, J. *Biosens. Bioelectron.* **2008**, *23*, 925–931.
156. Cai, H.; Xu, P.; He, P.; Fang, Y. *Electroanalysis* **2003**, *15*, 1864–1870.
157. Tsai, Y.; Li, S.; Liao, S. *Biosens. Bioelectron.* **2006**, *22*, 495–500.
158. Wang, J.; Musameh, M. *Anal. Chim. Acta* **2005**, *539*, 209–213.
159. Njagi, J.; Andreescu, S. *Biosens. Bioelectron.* **2007**, *23*, 168–175.
160. Chen, W.; Lu, Z.; Li, C. M. *Anal. Chem.* **2008**, *80*, 8485–8492.
161. Ramanavičius, A.; Kaušaite, A.; Ramanavičiene, A. *Sens. Actuators B* **2005**, *111–112*, 532–539.
162. Gao, M.; Dai, L.; Wallace, G. G. *Electroanalysis* **2003**, *15*, 1089–1094.
163. Liu, B.; Dan, T. T. T.; Bazan, G. C. *Adv. Funct. Mater.* **2007**, *17*, 2432–2438.
164. Liu, L.; Jia, N.; Zhou, Q.; Yan, M.; Jiang, Z. *Mater. Sci. Eng. C* **2007**, *27*, 57–60.
165. Mala Ekanayake, E. M. I.; Preethichandra, D. M. G.; Kaneto, K. *Biosens. Bioelectron.* **2007**, *23*, 107–113.
166. Xu, H.; Malladi, K.; Wang, C.; Kulinsky, L.; Song, M.; Madou, M. *Biosens. Bioelectron.* **2008**, *23*, 1637–1644.
167. Achyuthan, K. E.; Bergstedt, T. S.; Chen, L.; *et al. J. Mater. Chem.* **2005**, *15*, 2648–2656.
168. Ambade, A. V.; Sandanaraj, B. S.; Klaikherd, A.; Thayumanavan, S. *Polym. Int.* **2007**, *56*, 474–481.
169. Feng, F.; He, F.; An, L.; Wang, S.; Li, Y.; Zhu, D. *Adv. Mater.* **2008**, *20*, 2959–2964.
170. Feng, X.; Duan, X.; Liu, L.; An, L.; Feng, F.; Wang, S. *Langmuir* **2008**, *24*, 12138–12141.
171. Herland, A.; Inganäs, O. *Macromol. Rapid Commun.* **2007**, *28*, 1703–1713.
172. Ho, H. A.; Najari, A.; Leclerc, M. *Macromol. Acc. Chem. Res.* **2008**, *41*, 168–178.
173. Lee, K.; Maisel, K.; Rouillard, J.; Gulari, E.; Kim, J. *Chem. Mater.* **2008**, *20*, 2848–2850.
174. Lee, J.; Kim, H.; Kim, J. *J. Am. Chem. Soc.* **2008**, *130*, 5010–5011.
175. Kim, I.; Bunz, U. H. F. *J. Am. Chem. Soc.* **2006**, *128*, 2818–2819.
176. Kim, I.; Erdogan, B.; Wilson, J. N.; Bunz, U. H. F. *Chem. Eur. J.* **2004**, *10*, 6247–6254.
177. Lee, J.; Jun, H.; Kim, J. *Adv. Mater.* **2009**, *21*, 3674–3677.
178. Spevak, W.; Nagy, J. O.; Charych, D. H. *Adv. Mater.* **1995**, *7*, 85–89.
179. Charych, D. H.; Nagy, J. O.; Spevak, W.; Bednarski, M. D. *Science* **1993**, *261*, 585–588.
180. Reichert, A.; Nagy, J. O.; Spevak, W.; Charych, D. H. *J. Am. Chem. Soc.* **1995**, *117*, 829–830.
181. Charych, D.; Cheng, Q.; Reichert, A.; *et al. Chem. Biol.* **1996**, *3*, 113–120.
182. Jung, Y. K.; Park, H. G.; Kim, J. *Biosens. Bioelectron.* **2006**, *21*, 1536–1544.
183. Lee, K.; Rouillard, J.; Pham, T.; Gulari, E.; Kim, J. *Angew. Chem. Int. Ed.* **2007**, *46*, 4667–4670.
184. Lee, S. W.; Kang, C. D.; Yang, D. H.; *et al. Adv. Funct. Mater.* **2007**, *17*, 2038–2044.
185. Su, Y.; Li, J.; Jiang, L. *Colloids Surf. B* **2004**, *38*, 29–33.
186. Kolusheva, S.; Kafri, R.; Katz, M.; Jelinek, R. *J. Am. Chem. Soc.* **2001**, *123*, 417–422.
187. Jelinek, R.; Okada, S.; Norvez, S.; Charych, D. *Chem. Biol.* **1998**, *5*, 619–629.
188. Okada, S. Y.; Jelinek, R.; Charych, D. *Angew. Chem. Int. Ed.* **1999**, *38*, 655–659.
189. Kolusheva, S.; Shahal, T.; Jelinek, R. *J. Am. Chem. Soc.* **2000**, *122*, 776–780.
190. Rangin, M.; Basu, A. *J. Am. Chem. Soc.* **2004**, *126*, 5038–5039.
191. Kolusheva, S.; Molt, O.; Herm, M.; Schrader, T.; Jelinek, R. *J. Am. Chem. Soc.* **2005**, *127*, 10000–10001.
192. Ma, G.; Cheng, Q. *Langmuir* **2005**, *21*, 6123–6126.
193. Wang, C.; Ma, Z.; Su, Z. *Sens. Actuators B* **2006**, *107*, 1339–1386.
194. Rozner, S.; Kolusheva, S.; Cohen, Z.; Dowhan, W.; Eichler, J.; Jelinek, R. *Anal. Biochem.* **2003**, *319*, 96–104.
195. Pan, J. J.; Charych, D. *Langmuir* **1997**, *13*, 1365–1367.
196. Gill, I.; Ballesteros, A. *Angew. Chem. Int. Ed.* **2003**, *42*, 3264–3267.
197. Park, C. H.; Kim, J. P.; Lee, S. W.; Jeon, N. L.; Yoo, P. J.; Sim, S. J. *Adv. Funct. Mater.* **2009**, *19*, 3703–3710.
198. Pu, K.; Liu, B. *Adv. Funct. Mater.* **2009**, *19*, 1371–1378.
199. Pu, K.; Liu, B. *Adv. Funct. Mater.* **2009**, *19*, 277–284.
200. Ren, X.; Xu, Q. *Langmuir* **2009**, *25*, 43–47.
201. He, F.; Feng, F.; Duan, X.; Wang, S.; Li, Y.; Zhu, D. *Anal. Chem.* **2008**, *80*, 2239–2243.
202. Jiang, G.; Susha, A. S.; Lutich, A. A.; Stefani, F. D.; Feldmann, J.; Rogach, A. L. *ACS Nano* **2009**, *3*, 4127–4131.
203. Zheng, W.; He, L. *J. Am. Chem. Soc.* **2009**, *131*, 3432–3433.
204. Gaylord, B. S.; Massie, M. R.; Feinstein, S. C.; Bazan, G. C. *Proc. Natl. Acad. Sci. USA* **2005**, *102*, 34–39.
205. Ho, H. A.; Doré, K.; Boissinot, M.; *et al. J. Am. Chem. Soc.* **2005**, *127*, 12673–12676.
206. Li, K.; Liu, B. *Anal. Chem.* **2009**, *81*, 4099–4105.
207. Tian, N.; Tang, Y.; Xu, Q.; Wang, S. *Macromol. Rapid Commun.* **2007**, *28*, 729–732.
208. Feng, F.; Duan, X.; Wang, S. *Macromol. Rapid Commun.* **2009**, *30*, 147–151.
209. Feng, F.; Liu, L.; Wang, S. *Macromol. Chem. Phys.* **2009**, *210*, 1188–1193.
210. Feng, X.; Duan, X.; Liu, L.; *et al. Angew. Chem. Int. Ed.* **2009**, *48*, 5316–5321.
211. Feng, X.; Xu, Q.; Liu, L.; Wang, D. *Langmuir* **2009**, *25*, 13737–13741.
212. He, F.; Tang, Y.; Yu, M.; *et al. J. Am. Chem. Soc.* **2006**, *128*, 6764–6765.
213. Wang, S.; Bazan, G. C. *Adv. Mater.* **2003**, *15*, 1425–1428.

214. Doré, K.; Dubus, S.; Ho, H. A.; *et al*. *J. Am. Chem. Soc.* **2004**, *126*, 4240–4244.
215. Baker, E. S.; Hong, J. W.; Gaylord, B. S.; Bazan, G. C.; Bowers, M. T. *J. Am. Chem. Soc.* **2006**, *128*, 8484–8492.
216. Gaylord, B. S.; Heeger, A. J.; Bazan, G. C. *Proc. Natl. Acad. Sci. USA* **2002**, *99*, 10954–10957.
217. Doré, K.; Neagu-Plesu, R.; Leclerc, M.; Boudreau, D.; Ritcey, A. M. *Langmuir* **2007**, *23*, 258–264.
218. Ho, H. A.; Boissinot, M.; Bergeron, M. G.; *et al*. *Angew. Chem. Int. Ed*. **2002**, *41*, 1548–1551.
219. Leclerc, M. *Adv. Mater.* **1999**, *11*, 1491–1498.
220. Kushon, S. A.; Ley, K. D.; Bradford, K.; Jones, R. M.; McBranch, D.; Whitten, D. G. *Langmuir* **2002**, *18*, 7245–7249.
221. Liu, B.; Bazan, G. C. *Proc. Natl. Acad. Sci. USA* **2005**, *102*, 589–593.
222. Sun, C.; Gaylord, B. S.; Hong, J. W.; Liu, B.; Bazan, G. C. *Nat. Protoc.* **2007**, *2*, 2148–2151.
223. Nilsson, K. P. R.; Inganäs, O. *Nat. Mater.* **2003**, *2*, 419–424.
224. Najari, A.; Ho, H. A.; Gravel, J.; Nobert, P.; Boudreau, D.; Leclerc, M. *Anal. Chem.* **2006**, *78*, 7896–7899.
225. Cheng, F.; Zhang, G. W.; Lu, X. M.; *et al*. *Macromol. Rapid Commun.* **2006**, *27*, 799–803.
226. Fan, C.; Plaxco, K. W.; Heeger, A. J. *J. Am. Chem. Soc.* **2002**, *124*, 5642–5643.
227. Liu, M.; Kaur, P.; Waldeck, D. H.; Xue, C.; Liu, H. *Langmuir* **2005**, *21*, 1687–1690.
228. Zhang, Y.; Liu, B.; Cao, Y. *Chem. Asian J.* **2008**, *3*, 739–745.
229. Sandanaraj, B. S.; Demont, R.; Aathimanikandan, S. V.; Savariar, E. N.; Thayumanavan, S. *J. Am. Chem. Soc.* **2006**, *128*, 10686–10687.
230. Miranda, O. R.; You, C.; Phillips, R.; *et al*. *J. Am. Chem. Soc.* **2007**, *129*, 9856–9857.
231. Herland, A.; Nilsson, K. P. R.; Olsson, J. D. M.; Hammarström, P.; Konradsson, P.; Inganäs, O. *J. Am. Chem. Soc.* **2005**, *127*, 2317–2323.
232. Nilsson, K. P. R.; Herland, A.; Hammarström, P.; Inganäs, O. *Biochemistry* **2005**, *44*, 3718–3724.
233. Åsberg, P.; Nilsson, K. P. R.; Inganäs, O. *Langmuir* **2006**, *22*, 2205–2211.
234. Nilsson, K. P. R.; Inganäs, O. *Macromolecules* **2004**, *37*, 9109–9113.
235. Abérem, M. B.; Najari, A.; Ho, H. A.; *et al*. *Adv. Mater.* **2006**, *18*, 2703–2707.
236. Li, H.; Bazan, G. C. *Adv. Mater.* **2009**, *21*, 964–967.
237. Ho, H. A.; Leclerc, M. *J. Am. Chem. Soc.* **2004**, *126*, 1384–1387.
238. Wang, J.; Liu, B. *Chem. Commun.* **2009**, *17*, 2284–2286.
239. An, L.; Liu, L.; Wang, S. *Biomacromolecules* **2009**, *10*, 454–457.
240. Kumaraswamy, S.; Bergstedt, T.; Shi, X.; *et al*. *Proc. Natl. Acad. Sci. USA* **2004**, *101*, 7511–7515.
241. Lou, X.; Zhang, L.; Qin, J.; Li, Z. *Langmuir* **2010**, *26*, 1566–1569.
242. Pinto, M. R.; Schanze, K. S. *Proc. Natl. Acad. Sci. USA* **2004**, *101*, 7505–7510.
243. Wosnick, J. H.; Mello, C. M.; Swager, T. M. *J. Am. Chem. Soc.* **2005**, *127*, 3400–3405.
244. Zhang, T.; Fan, H.; Zhou, J.; Liu, G.; Feng, G.; Jin, Q. *Macromolecules* **2006**, *39*, 7839–7843.
245. Feng, F.; Tang, Y.; He, F.; *et al*. *Adv. Mater.* **2007**, *19*, 3490–3495.
246. An, L.; Tang, Y.; Feng, F.; He, F.; Wang, S. *J. Mater. Chem.* **2007**, *17*, 4147–4152.
247. Liu, Y.; Schanze, K. S. *Anal. Chem.* **2008**, *80*, 8605–8612.
248. Rininsland, F.; Xia, W.; Wittenburg, S.; *et al*. *Proc. Natl. Acad. Sci. USA* **2004**, *101*, 15295–15300.
249. Liu, Y.; Ogawa, K.; Schanze, K. S. *Anal. Chem.* **2008**, *80*, 150–158.
250. Feng, F.; Tang, Y.; Wang, S.; Li, Y.; Zhu, D. *Angew. Chem. Int. Ed.* **2007**, *46*, 7882–7886.
251. Liu, Y.; Schanze, K. S. *Anal. Chem.* **2009**, *81*, 231–239.
252. Rininsland, F.; Stankewicz, C.; Weatherford, W.; McBranch, D. *BMC Biotechnol.* **2005**, *5*, 16–21.
253. Zhao, D.; Du, J.; Chen, Y.; Ji, X.; He, Z.; Chan, W. H. *Macromolecules* **2008**, *41*, 5373–5378.
254. Wang, D.; Gong, X.; Heeger, P. S.; Rininsland, F.; Bazan, G. C.; Heeger, A. J. *Proc. Natl. Acad. Sci. USA* **2002**, *99*, 49–53.
255. Cheng, Q.; Stevens, R. C. *Adv. Mater.* **1997**, *9*, 481–483.
256. Takasu, A.; Iso, K.; Dohmae, T.; Hirabayashi, T. *Biomacromolecules* **2006**, *7*, 411–414.
257. Faïd, K.; Leclerc, M. *Chem. Commun.* **1996**, *24*, 2761–2762.
258. Mouffouk, F.; Higgins, S. J.; Brown, S. J.; Sedghi, N.; Eccleston, B.; Reeman, S. *Chem. Commun.* **2004**, *20*, 2314–2315.
259. Wilson, J. N.; Wang, Y.; Lavigne, J. J.; Bunz, U. H. F. *Chem. Commun.* **2003**, *14*, 1626–1627.
260. Zheng, J.; Swager, T. M. *Chem. Commun.* **2004**, *24*, 2798–2799.
261. Disney, M. D.; Zheng, J.; Swager, T. M.; Seeberger, P. H. *J. Am. Chem. Soc.* **2004**, *126*, 13343–13346.
262. Baek, M.; Stevens, R. C.; Charych, D. H. *Bioconjug. Chem.* **2000**, *11*, 777–778.

4.401. The Concept of Biocompatibility

M Spector, VA Boston Healthcare System, Boston, MA, USA

© 2011 Elsevier Ltd. All rights reserved.

4.401.1.	**Introduction**	1
4.401.1.1.	Criteria for Assessing Biocompatibility	1
4.401.1.2.	Factors Affecting Biocompatibility	2
4.401.1.3.	Examples of Biocompatible and Adverse Tissue Responses	2
4.401.2.	**Wound-Healing Responses Underlying Biocompatibility**	2
4.401.2.1.	Fundamental Stages of the Wound-Healing Response to Implantation Surgery: Acute Phase	2
4.401.2.2.	Repair Versus Regeneration	3
4.401.2.3.	The Chronic Response: Macrophages and Fibroblasts – Synovium	3
4.401.2.4.	Historical Perspective on Observations on the Tissue Response to Implants	3
4.401.3.	**Characteristic Features of Tissue Around Implants: Emerging Insights**	4
4.401.3.1.	Fibroblasts: Expression of α-Smooth Muscle Actin	4
4.401.3.2.	Presence of Lubricin in the Tissue Around Loose Orthopedic Prostheses	4
4.401.4.	**Summary and Considerations for the Future**	5
References		5

Glossary

Arthroplasty Surgery to relieve pain and restore range of motion by realigning or reconstructing a joint.

Inflammation A complex biological response of vascular tissues to harmful stimuli, such as pathogens, damaged cells, dead tissue, foreign bodies, or other irritants.

Phagocytosis The cellular process of engulfing solid particles by the cell membrane to form an internal phagosome by phagocytes and protists.

4.401.1. Introduction

Biocompatibility is a condition met by a biomaterial or medical device usually based on the tissue response elicited by an implant in an animal model. If the material releases noxious agents or degrades biological molecules coming in contact with its surface, the response in the tissue is obvious – necrosis and persistent acute inflammation – and the material is clearly judged nonbiocompatible. Biocompatible materials include those which are chemically inert and 'bioactive' materials that present certain reactive chemical groups to the surrounding tissue or undergo changes in their chemical composition *in vivo*, often releasing certain agents to achieve a specific biological response. Nonabsorbable bioactive materials may selectively adsorb specific biological molecules or release select agents to favor a particular tissue response. Absorbable biomaterials (e.g., scaffolds for tissue engineering) are, in effect, bioactive materials whose action is temporary.

Determinants of the tissue response to biomaterials, and the subsequent assessment of biocompatibility, reside in the intrinsic wound-healing process in the particular tissue or organ (structure comprising two or more tissues) into which the biomaterial has been implanted. This wound-healing process, initiated by the surgical trauma of implantation, can be modified: by the physical presence of the device, and its porosity and modulus of elasticity; and the chemical composition of the material and agents released by the biomaterial. The tissue response to a biomaterial is, therefore, a characteristic of the host tissue's wound-healing process as well as being a characteristic of the biomaterial. There is often an implication that a biomaterial which displays a favorable (biocompatible) response in a particular test (i.e., tissue) has met the condition of biocompatibility for all applications in which it may be used. In light of the above, the tissue response to the same biomaterial might be quite different depending on the tissue in which it is implanted. Biocompatibility is not, therefore, an invariant property of a biomaterial.

The objectives of this chapter are to: provide a basis for interpreting the tissue response to implants in the context of biocompatibility, with specific attention to the roots of the tissue response in wound-healing processes; provide examples of the types of tissue responses elicited by select biomaterials in certain tissues; and describe specific features of the cellular make up and extracellular matrix composition of the tissue surrounding implants in the context of understanding to what degree the tissue response can be controlled therapeutically, postimplantation.

4.401.1.1. Criteria for Assessing Biocompatibility

The term 'biocompatible' is employed to describe a wide variety of (generally, *in vivo*) findings, from a benign tissue response to a biomaterial in an animal model to the successful clinical implementation of a medical device. Moreover, the

term is also often used to generally describe biomaterials which have met certain standards of safety and efficacy in select situations. While there is convenience in using the term biocompatibility to convey a general assessment of a biomaterial or medical device, its nonspecific use can be misleading. Its use should be qualified with respect to the specific conditions under which the biomaterial/device is being evaluated. The device should be considered biocompatible only in the context of the criteria used to assess the acceptability of the tissue response in relation to the required function of the device.

In this regard, each study involving the assessment of tissue compatibility should provide its own working definition of biocompatibility. For example, biomaterials and devices implanted into bone would be expected to become enveloped by the regenerating osseous tissue, and thus be considered compatible with bone regeneration. However, altered bone remodeling around a modulus-mismatched device due to its alteration of the strain distribution in the bone, with a net loss of bone mass (i.e., osteopenia), could lead to the assessment that a material or device is not compatible with normal bone remodeling.

In situations in which an implant is surrounded by fibrous tissue, macrophages on the surface of the material might be the expected response to the dead space produced by the physical presence of the implant. The cellular array of fibroblasts and macrophages resembles synovium which might then be considered an acceptable chronic response relative to the chemical compatibility of the material with tissue. Utilization of the thickness of the fibrous scar capsule around an implant alone as a measure of biocompatibility is problematic because the formation of scar tissue can be influenced by movement of the tissue at the site relative to the implant. Thicker fibrous capsules may not, therefore, reflect the degree to which a material displays biocompatibility.

4.401.1.2. Factors Affecting Biocompatibility

The biological processes comprising tissue response are affected by implant-related factors, including

1. the 'dead space' created by the presence of the implant;
2. soluble agents released by the implant (e.g., ions or molecular fragments);
3. insoluble particulate material released from the implant (e.g., wear debris);
4. chemical interactions of biological molecules with implant surface; and
5. alterations in the strain distribution in tissue due to the mismatch in modulus of elasticity between the implant and surrounding tissue, or the movement of the implant relative to adjacent tissue as a result of the absence of mechanical coupling.

There are, however, numerous examples of adverse responses to medical devices that have failed to perform properly due to factors unrelated to the biomaterial, including

1. the intrinsic capability of the tissue to heal by repair (scar) or regeneration;
2. problems associated with implantation of the device, including improper positioning and excessive surgical trauma; and
3. host disease.

4.401.1.3. Examples of Biocompatible and Adverse Tissue Responses

Nonbiocompatible responses to biomaterials and medical devices can include the following: persistent acute inflammatory responses and attendant pain; cytotoxicity and necrosis; and tissue changes that are incompatible with, and interfere, with the performance of the device. Examples of the first two of these nonbiocompatible responses to medical devices in human subjects are rare because of the extensive preclinical testing performed on the biomaterials and device before they are introduced into clinical use. Biomaterials and devices that elicit acute adverse biological responses can generally be readily detected in animal studies.

There are many cases of devices such as total joint replacement prostheses, which initially function successfully, relieving pain and restoring joint motion. However, due to premature breakdown of the materials (e.g., wear) particulate debris is generated, which elicits a cellular response (viz., macrophage phagocytic response) that results in the loss of surrounding tissue (e.g., osteolysis). There are other examples of tissue responses to devices that may be benign in some situations, but in other applications result in failure of the device. For example, a relatively benign fibrous capsule around a device in some applications is inconsequential, but for other devices such as a silicone breast implant can lead to scar contracture, pain, and loss of function of the implant to provide the desired effect.

4.401.2. Wound-Healing Responses Underlying Biocompatibility

4.401.2.1. Fundamental Stages of the Wound-Healing Response to Implantation Surgery: Acute Phase

The surgical trauma associated with the preparation of the implant site initiates a cascade of physiological processes which comprise wound healing (Figure 1). This healing process ensues in the gaps between the implant and surrounding, surviving tissue. In vascularized tissue, in which implants are most often placed, surgery initially induces a vascular response in intact vessels surrounding the implant site resulting in the leakage of fluid (edema) and blood proteins. Blood

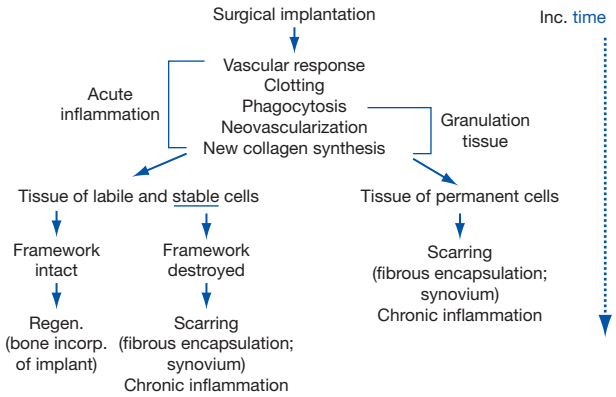

Figure 1 Sequence of physiological processes comprising wound healing.

elements from the cut vessels lead to the formation of a fibrin clot, which serves as a provisional scaffold into which cells can migrate. Phagocytic cells, polymorphonuclear neutrophils first and then macrophages, infiltrate into the surgical site and begin to ingest the cellular and extracellular matrix debris. Endothelial cell migration and the formation of new blood vessels follow. Fibroblasts invade the fibrin clot and synthesize more robust scaffolding made up of types I and III collagen. The tissue comprising phagocytic cells, newly forming blood vessels and fibroblasts, which forms within the first days (acute phase) of healing, is referred to as granulation tissue. Thereafter, the parenchymal cells of the surrounding tissue begin to infiltrate the newly forming stroma.

4.401.2.2. Repair Versus Regeneration

In order for tissue to regenerate in a defect it is necessary for the surrounding cells to divide and migrate into the wound site. The fundamental question, then, regarding the intrinsic capability of the tissue to heal through regeneration or repair with the formation of scar tissue is answered by the potential of the parenchymal cells to divide: Is the tissue made up of labile, stable, or permanent cells? Labile cells are those which are undergoing mitosis, albeit at a low rate, continually. Stable cells are those that can be stimulated to divide, and permanent cells are those which never undergo cell division. Prior dogma instructed that defects in tissues in which the parenchymal cells were incapable of division would never regenerate. However, we now know that many such tissues contain progenitor cells (viz., stem cells) that have the capability of proliferating in response to injury; migrating to the site of injury; and differentiating into the parenchymal cell type. Studies are also revealing the many antagonists that interfere with intrinsic progenitor/stem cell-driven regenerative processes.

There are conditions that can interfere with regeneration, even in tissues with the intrinsic capability to do so, such as bone. Fractures normally heal by bony union of the bone ends, through the process of endochondral and intramembranous ossification in the fracture gap. However, movement of the bone ends and excessive strain in the gap of unstable fractures result in a fibrous (scar) union. An analogous process occurs in the tissue around implants in bone. As expected in a regenerative tissue, bone forms up to the surface of implants (osseointegration) which are mechanically stable. In contrast, fibrous tissue is found encapsulating unstable implants which undergo movement in the bony bed. Explanations for the roles of excessive strains in interfering with bone formation include (1) destruction of the stroma necessary for osteoprogenitor cell migration into the gap, but permissive of opportunistic fibroblasts and (2) induction of differentiation of progenitor cells into fibroblasts instead of osteoblasts.

4.401.2.3. The Chronic Response: Macrophages and Fibroblasts – Synovium

The macrophages that initially invade the gaps between the implant and surrounding tissue to ingest debris can be found to remain indefinitely on the surface of implants in soft tissues. The very presence of the implant provides a dead space in tissue that attracts macrophages to the implant–tissue interface.[1] These macrophages, along with fibroblasts of the scar, often form a definable layer of cells that surrounds the implant. The tissue displays the characteristics of synovium,[2] and can be considered the chronic response to implants (unless the device is directly apposed to osseous tissue, i.e., osseointegrated). This process is often termed 'fibrous encapsulation,'[3,4] highlighting the fibrous tissue component. It is, however, the presence of regulatory cells such as macrophages at the implant–tissue interface that can profoundly influence the host response to a device because these cells have the potential to release proinflammatory mediators[5] if they are irritated by the movement of the device or substances released from the biomaterial. The inflammatory response of the tissue around implants is comparable to the inflammation that can occur in the synovium lining any bursa (e.g., bursitis); hence, the response to implants has also been termed 'implant bursitis.'[2]

While macrophages may be expected to remain on the surface of the implants in soft tissue, even after long periods of implantation, studies investigating the tissue response around devices may not find such cells. One explanation for this could relate to the methodology employed for the experimental studies. Because of the difficulty in sectioning implants, the devices are often removed prior to the histological processing of the resected samples. Macrophages adherent to the device would thus not be revealed in the histological sections.

For implants in bone which have become osseointegrated, there are no macrophages found on the surface of the device. Because macrophages were likely present at the implant site earlier in the healing process, the question arises as to why they did not persist on the surface of the biomaterial. The answer may relate to the inability of the nonmitotic macrophages to recruit monocytes from the circulation. This may be due to the inability of chemoattractants released from the macrophages to penetrate the mineralized matrix, and/or the inability of monocytes to migrate through the osseous tissue.

4.401.2.4. Historical Perspective on Observations on the Tissue Response to Implants

That the macrophage plays a central role in the tissue response to implants focuses attention on the early studies of Ilya (Elie) Metchnikoff (1845–1916),[6,7] a noted Russian zoologist, pathologist, and infection biologist. Metchnikoff spent most of his professional life focusing on his 'phagocytosis theory.' In one of his experiments in 1882, Metchnikoff inserted a splinter into the transparent body of the starfish larva. He observed amoeboid-appearing cells attempting to ingest the splinter. The small ones he referred to as 'microphages' and the large ones 'macrophages,' using as the suffix the Greek term, phage, meaning to ingest. We now refer to microphages as polymorphonuclear neutrophils, while macrophage remains the name of the same cell type. While Metchnikoff's interest was in revealing mechanisms underlying the host defense to invading organisms, he inadvertently made a discovery that should serve as the foundation of the tissue response to implants: the persistence of macrophages around a foreign body. In 1908, Metchnikoff shared the Nobel Prize in Physiology or Medicine with Paul Ehrlich.

A few decades later in 1923 in Boston, Marius Nygaard Smith-Peterson, an orthopedic surgeon, attended to one of his patients who presented with a shard of glass in the fleshy part of the back. By the time the patient had come to see Smith-Peterson the glass shard had been embedded in the tissue for 1 year. When Smith-Peterson resected the shard of glass, he found that it was surrounded by a glistening synovial sac, which contained a few drops of clear yellow fluid. Smith-Peterson reasoned that the glass must have induced the formation of synovium which secreted synovial fluid. He then set out to produce glass cups to fit over the femoral head of his patients with arthritis (in a procedure that came to be known as cup arthroplasty). His supposition was that the glass would induce the formation of a new synovial capsule in the hip joint of his arthritic patients. While the mechanical properties of glass proved unsuccessful for this application, Smith-Peterson's observation is important in the context of that of Metchnikoff. Synovium is a tissue comprising macrophage-like cells ('type A' cells) and fibroblast-like cells ('type B' cells). Smith-Peterson's findings parallel those of Metchnikoff in that macrophages were found on the surface of a foreign body after a long time period (i.e., a chronic response).

Additional insights into the presence of macrophages at the leading edge of wounds and around implants can be found in the work of several investigators employing the rabbit ear chamber model, dating from the late 1930s.[8–10] In the more recent of these studies, Ian A. Silver, a British researcher, studied wound healing in holes punched in the ears of rabbits.[11] The chamber is constructed over the hole in order to observe microscopically the healing of the injuries. Silver found that the leading edge of the tissue filling in the hole was always lined by macrophages, supporting prior findings.[8] In a related work, Silver employed a microelectrode to measure the oxygen tension within the hole and in the surrounding tissue. He found, as expected, low oxygen tension within the 'dead space' of the hole, and an increasing gradient of oxygen proceeding into the vascularized tissue surrounding the hole. Silver reasoned that the macrophages were attracted by the hypoxic environment of the dead space, and so migrated to the leading edge of the hole along the oxygen gradient. Once at the leading edge of the hole, they remained. Silver followed up this work with an experiment in which he placed a plastic coupon into the hole thus demonstrating more directly that macrophages persist at the surface of implants, likely due to the hypoxic environment.

There is much yet to be learned about the behavior of the 'implant macrophage.' The heterogeneity of the macrophage has long been recognized, with macrophages in different tissues displaying dramatically different properties.[12–14] While there is general agreement that marrow-derived cells in the circulation (viz., monocytes) are the source of the tissue macrophage, the specific characteristics of macrophages in different conditions remain in question with respect to their function, longevity, and turnover. While the results of some investigations indicated that the macrophage in chronic inflammatory conditions may persist for only 1–2 weeks,[14] other studies provided evidence that macrophages may persist in granulomatous tissue for up to 3 months without dividing, dying, or being replaced.[15] In general the supposition is that macrophages cannot divide, but there are data that demonstrate the capability of macrophages to undergo mitosis.[16] The indefinite (chronic) persistence of macrophages at an implant surface is generally understood to be the result of the influx of monocytes from peripheral blood into the tissue.

4.401.3. Characteristic Features of Tissue Around Implants: Emerging Insights

Recent studies have revealed characteristic features of the synovium-like layer and the underlying fibrous tissue that comprise the chronic response to implants. These features have been found in the tissue surrounding implants in soft tissue, and also in the tissue that forms around devices in bone which have loosened.

4.401.3.1. Fibroblasts: Expression of α-Smooth Muscle Actin

Generally the focus on the ubiquitous fibrous tissue capsule that surrounds implants is on its thickness which has been considered a reflection of the degree of biocompatibility, but which was noted above to be potentially erroneous. Recent studies have demonstrated that fibroblasts within the fibrous capsule around implants in soft tissue[17] and around prostheses in bone[18] which have loosened, express the gene for the contractile actin isoform, α-smooth muscle actin (α-SMA). These fibroblasts, which have the characteristic of myofibroblasts, resemble the cells seen in contracting skin wounds. Contraction of skin wounds may be beneficial in facilitating closure of the wound, but its adverse effect is in creating a dysfunctional and disfiguring scar. Contracture of fibrous capsules around prostheses, such as silicone breast implants, may result in pain and disfigurement. Contraction of SMA-expressing fibroblasts around orthopedic prostheses may contribute to densification of the fibrous tissue, making it more resistant to remodeling.

4.401.3.2. Presence of Lubricin in the Tissue Around Loose Orthopedic Prostheses

Given that synovial tissue can be found around devices, reflecting the chronic response to implants, the question arises as to the behavior of the synovial cells in the context of the normal physiological function of synovium (viz., in diarthrodial joints). Recent studies have found that the tissue around loose orthopedic prostheses which had previously been described as synovium contains lubricin, which forms a discrete layer on the surfaces of folds in the fibrous tissue comprising the capsule.[18]

Lubricin, a molecule discovered in joint fluid,[19,20] and later found to be synthesized by synovial cells,[21,22] has been shown to play an important role in joint lubrication.[23,24] Later work found that a protein synthesized by superficial zone chondrocytes,[25] superficial zone protein, was homologous to megakaryocyte stimulating factor[26] and to lubricin,[20] both protein products of the megakaryocyte stimulating factor gene (*msf*).[20] Proteoglycan 4 (PRG4) is the name collectively given to these homologous glycoproteins encoded by 12 exons of the gene, which is also known as *Prg4*.[27]

A recent study[28] employing cDNA array technology to screen periprosthetic tissue from five total knee arthroplasty

patients for the expression of over 800 immunologically relevant genes found that the strongest overexpression in aseptic cases (three patients) of all genes was for *msf*. The potential importance of identifying lubricin in periprosthetic tissue is that it may interfere with cell adhesion[29] and integrative repair processes[27] vital to the remodeling and ultimate resorption of periprosthetic tissue.

A single theory could explain the presence of both α-SMA and lubricin in periprosthetic tissue, and help to explain why they are ubiquitous findings. The micromovement of a prosthesis, which is not fixed by bone apposition or ingrowth, stimulates the expression of α-SMA and lubricin directly in the capsule as a result of mechanical stimulation of selected cells, and indirectly by inducing elevated levels of transforming growth factor (TGF-β) which is known to stimulate expression of α-SMA[30] and lubricin.[31] Moreover, of importance is a recent study that demonstrated that myofibroblast (i.e., α-SMA-expressing fibroblast) contraction activates latent TGF-β1 from extracellular matrix.[32] Particulate debris further acts to increase α-SMA and lubricin levels by promoting a cytokine cascade that also results in the upregulation of TGF-β and other molecules that stimulate α-SMA and lubricin synthesis. α-SMA and lubricin could synergistically serve to interfere with reparative and remodeling processes that restore the integrity of the implant–bone interface tissue. According to this theory, it would be expected that some degree of α-SMA and lubricin expression would be found in all periprosthetic tissue.

α-SMA and lubricin may contribute to prosthetic failure by interfering with processes that would result in the reduction of periprosthetic tissue, and this would allow for an ever-widening radiolucent zone around the unstable implant. Human studies to demonstrate such an association would require periprosthetic tissues from arthroplasties displaying varying degrees of loosening and radiolucent zone thickness. Moreover, the finding of α-SMA and lubricin in periprosthetic tissue 6 months postimplantation in one patient raises the question of the time course of expression of these proteins, in order to separate expression related to the response to surgery from the prosthetic loosening process, further complicating the procurement of control tissues. Another issue to be dealt with is that α-SMA expression is known to be transient,[33–35] and lubricin expression may prove to be the same. Therefore, accounting for all the α-SMA and lubricin associated with a periprosthetic tissue of measured thickness may prove to be impossible. Animal studies to prove cause (α-SMA and lubricin) and effect (increasing width of the periprosthetic tissue zone) would require an animal model for a loose prosthesis, which has been reported, and agents which can be administered to selectively downregulate the expression of these proteins in the periprosthetic tissue, which have not yet been developed. Alternative *in vivo* approaches using mice in which α-SMA or lubricin has been knocked out would be interesting to consider, but interpretation of the results would likely be confounded by the multiple critical physiological roles that these two proteins play. *In vitro* models which could be employed to study the relationships between α-SMA and lubricin and the development and persistence of prosthetic tissue and loosening have not yet been developed and would be challenged to account for the many factors, including the mechanical environment, that contribute to the problem.

The direct association between α-SMA and lubricin expression and prosthetic performance (viz., implant-related pain) is unclear. It is possible that α-SMA-enabled contracture of periprosthetic tissue may be related to pain in the same way that contractures of fibrotic lesions in other organs are related to painful conditions. The role of lubricin in pain mechanisms has not yet been studied.

4.401.4. Summary and Considerations for the Future

Despite the fact that the tissue response to implants has been investigated for decades there is much yet to learn the etiology of the response; its effects on device performance; and therapeutic approaches which will enable its regulation. That the response to implants and determinations of biocompatibility are tissue-specific raises questions about the roles of various cells (viz., resident progenitor/stem cells) in the intrinsic wound-healing response that is a principal determinant of the assessment of biocompatibility.

Acknowledgment

The author is supported by a Career Scientist Award from the Department of Veterans Affairs.

References

1. Silver, I. A. In *Wound Healing and Wound Infection*; Hunt, T. K., Ed.; Appleton-Century-Crofts: New York, 1984; pp 11–28.
2. Spector, M.; Shortkroff, S.; Hsu, H. P.; *et al*. *Semin. Arthritis Rheum.* **1992**, *21*(5), 335–344.
3. Coleman, D. L.; King, R. N.; Andrade, J. D. *J. Biomed. Mater. Res.* **1974**, *8*, 199–211.
4. Laing, P. G.; Ferguson, A. B.; Hodge, E. S. *J. Biomed. Mater. Res.* **1967**, *1*, 135–149.
5. Anderson, J. M.; Miller, K. M. *Biomaterials* **1984**, *5*(1), 5–10.
6. Tauber, A. I. *Nat. Rev. Mol. Cell Biol.* **2003**, *4*(11), 897–901.
7. Chang, Z. L. *Biol. Cell* **2009**, *101*(12), 709–721.
8. Cliff, W. J. *Philos. Trans. R. Soc. Lond. Biol. Sci.* **1963**, *246*, 305–325.
9. Cliff, W. J. *Q. J. Exp. Physiol. Cogn. Med. Sci.* **1966**, *51*(2), 112–119.
10. Ebert, R. H.; Florey, H. W. *Br. J. Exp. Pathol.* **1939**, *20*, 342–354.
11. Silver, I. A. In *Wound Healing and Wound Infection*; Hunt, T. K., Ed.; Appleton-Century-Crofts: New York, NY, 1980; pp 11–28.
12. Gordon, S.; Taylor, P. R. *Nat. Rev. Immunol.* **2005**, *5*(12), 953–964.
13. Witsell, A. L.; Schook, L. B. *Proc. Natl. Acad. Sci. USA* **1991**, *88*(5), 1963–1967.
14. Naito, M. *Arch. Histol. Cytol.* **1993**, *56*(4), 331–351.
15. Spector, M.; Shortkroff, S.; Hsu, H.-P.; Lane, N.; Sledge, C. B.; Thornhill, T. S. *Clin. Orthop.* **1990**, *261*, 140–152.
16. Ryan, G. B.; Spector, W. G. *Proc. R. Soc. Lond. B Biol. Sci.* **1970**, *174*(1040), 269–292.
17. Wolfram, D.; Rainer, C.; Niederegger, H.; Piza, H.; Wick, G. *J. Autoimmun.* **2004**, *23*(1), 81–91.
18. Funakoshi, T.; Martin, S. D.; Wolf, B. T.; Schmid, T. M.; Thornhill, T. S.; Spector, M. J. *Biomed. Mater. Res. A* **2010**, *93*, 515–527.
19. Swann, D. A.; Silver, F. H.; Slayter, H. S.; Stafford, W.; Shore, E. *Biochem. J.* **1985**, *225*(1), 195–201.
20. Jay, G. D.; Tantravahi, U.; Britt, D. E.; Barrach, H. J.; Cha, C. J. *J. Orthop. Res.* **2001**, *19*(4), 677–687.
21. Berthelot, J. M. *Med. Hypotheses* **2004**, *62*(6), 894–897.
22. Rhee, D. K.; Marcelino, J.; Baker, M.; *et al*. *J. Clin. Invest.* **2005**, *115*(3), 622–631.
23. Swann, D. A.; Slayter, H. S.; Silver, F. H. *J. Biol. Chem.* **1981**, *256*(11), 5921–5925.
24. Jay, G. D.; Torres, J. R.; Warman, M. L.; Laderer, M. C.; Breuer, K. S. *Proc. Natl. Acad. Sci. USA* **2007**, *104*(15), 6194–6199.

25. Schumacher, B. L.; Block, J. A.; Schmid, T. M.; Aydelotte, M. B.; Kuettner, K. E. *Arch. Biochem. Biophys.* **1994**, *311*(1), 144–152.
26. Flannery, C. R.; Hughes, C. E.; Schumacher, B. L.; *et al. Biochem. Biophys. Res. Commun.* **1999**, *254*(3), 535–541.
27. Englert, C.; McGowan, K. B.; Klein, T. J.; Giurea, A.; Schumacher, B. L.; Sah, R. L. *Arthritis Rheum.* **2005**, *52*(4), 1091–1099.
28. Morawietz, L.; Gehrke, T.; Frommelt, L.; *et al. Virchows Arch.* **2003**, *443*(1), 57–66.
29. Rees, S. G.; Davies, J. R.; Tudor, D.; *et al. Matrix Biol.* **2002**, *21*(7), 593–602.
30. Desmouliere, A.; Geinoz, A.; Gabbiani, F.; Gabbiani, G. *J. Cell Biol.* **1993**, *122*, 103–111.
31. Jones, A. R. C.; Flannery, C. R. *Eur. Cells Mater.* **2007**, *13*, 40–45.
32. Wipff, P. J.; Rifkin, D. B.; Meister, J. J.; Hinz, B. *J. Cell. Biol.* **2007**, *179*(6), 1311–1323.
33. Darby, I.; Skalli, O.; Gabbiani, G. *Lab. Invest.* **1990**, *63*, 21–29.
34. Hastreiter, D.; Chao, J.; Wang, Q.; Ozuna, R. M.; Spector, M. *Wound Repair Regen.* **2004**, *12*(4), 430–438.
35. Sappino, A. P.; Schürch, W.; Gabbiani, G. *Lab. Invest.* **1990**, *63*(2), 144–161.

Relevant Websites

http://ocw.mit.edu/courses/biological-engineering/20-441j-biomaterials-tissue-interactions-fall-2009/ – MIT Open CourseWare for the subject, Biomaterials-Tissue Interactions.

4.402. Biocompatibility and the Relationship to Standards: Meaning and Scope of Biomaterials Testing

J M Anderson, Case Western Reserve University, Cleveland, OH, USA

© 2011 Elsevier Ltd. All rights reserved.

4.402.1.	**Introduction**	8
4.402.2.	**Biocompatibility**	8
4.402.3.	**Materials for Medical Devices**	8
4.402.4.	***In Vitro* Tests for Biocompatibility**	9
4.402.5.	***In Vivo* Tests for Biocompatibility**	10
4.402.5.1.	Sensitization, Irritation, and Intracutaneous (Intradermal) Reactivity	12
4.402.5.2.	Systemic Toxicity (Acute Toxicity) and Subacute and Subchronic Toxicity	12
4.402.5.3.	Genotoxicity	12
4.402.5.4.	Implantation	13
4.402.5.5.	Chronic Toxicity	13
4.402.5.6.	Carcinogenicity	13
4.402.5.7.	Reproductive and Developmental Toxicity	13
4.402.5.8.	Biodegradation	13
4.402.6.	**Inflammation, Wound Healing, and the Foreign-Body Response**	13
4.402.6.1.	Overview	14
4.402.6.2.	Acute Inflammation	15
4.402.6.3.	Chronic Inflammation	16
4.402.6.4.	Granulation Tissue	17
4.402.6.5.	Foreign-Body Reaction	18
4.402.6.6.	Fibrosis/Fibrous Encapsulation	19
4.402.7.	**Hemocompatibility**	19
4.402.8.	**Immune Responses**	20
4.402.9.	**Summary and Conclusion**	24
References		25

Abbreviations

ASTM	American Standards for Testing and Materials
APC	Antigen presenting cells
CTL	Cytotoxic lymphocytes
ECM	Extracellular matrix
EDTA	Ethylenediamine tetraacetic acid
EGF	Epithelial growth factor
ELISA	Enzyme-linked immunoassay
ePTFE	Expanded polytetrafluoroethylene
FBGC	Foreign body giant cell
FDA	Food and Drug Administration
FGF	Fibroblast growth factor
FpA	Fibrinopeptide A
FXIIA	Activated Hageman factor
G-CSF	Granulocyte colony-stimulating factor
GM-CSF	Granulocyte monocyte colony-stimulating factor
H_2C_2	Hydrogen peroxide
IgA	Immunoglobulin A
IgE	Immunoglobulin E
IgG	Immunoglobulin G
INF-γ	Interferon-γ (gamma)
IL-##	Interleukin-##, for example, IL-1, IL-2, IL-3, IL-4, IL-5, IL-6, IL-8, IL-10, IL-12, IL-13, IL-15
ISO	International Standards Organization
LTB_4	Leukotriene-B4
MAC	Complement membrane attack complex
MCF	Monocyte chemoattractant factor
MCP	Monocyte chemoattractant protein
MIF	Migration inhibitory factor
MIP	Monocyte inflammatory protein
MPS	Mononuclear phagocytic system
MTT	[3-(4,5-Dimethylthiazol-2-yl)-2,5-diphenyltetrazolium bromide] assay for cell growth
NK	Natural killer cell
PDGF	Platelet-derived growth factor
PF-4	Platelet factor-4
PMN	Polymorphonuclear leukocyte
PT	Prothrombin time
PTT	Partial thromboplastin time
RANTES	A CC chemokine that is a member of the interleukin 8 superfamily of cytokines
RBC	Red blood cell erythrocyte
RES	Reticuloendothelial system
TAT	Thrombin–antithrombin complex
TCC	Terminal complement complex
TGF-α	Transforming growth factor-alpha
TGF-β	Transforming growth factor-beta

Th1	Thymus-derived type 1 helper lymphocyte	**tPA**	Tissue plasminogen activator
Th2	Thymus-derived type 2 helper lymphocyte	**TT**	Thrombin time
TNF	Tumor necrosis factor	**USP**	United States Pharmacopeia

4.402.1. Introduction

In identifying the biocompatibility of a biomaterial, medical device, or prosthesis, numerous approaches may be taken. The approach presented in this chapter is a practical one, based on regulatory requirements and standards to a great extent. The goal of this chapter is to provide a practical pathway or roadmap for the identification of the fundamental biological requirements, that is, biological response evaluation, for biomaterials, medical devices, or prostheses. Therefore, the chapter is compartmentalized into eight sections: biocompatibility; materials for medical devices; *in vitro* tests for biocompatibility; *in vivo* tests for biocompatibility; inflammation, wound healing, and the foreign-body reaction; hemocompatibility; immune responses; and summary. Perspectives are presented throughout the chapter to provide insight into the ways in which regulatory agencies may view certain aspects and issues regarding the various topic areas. Numerous caveats are presented to provide a perspective on the ways in which the fundamental biological requirements of a biomaterial, medical device, or prosthesis might be viewed by regulatory agencies.

As the intended use of a biomaterial, either alone or in combination with other biomaterials in medical devices or prostheses, is to assist in maintaining or improving the health and welfare of humans, governmental regulation of the biomaterial or medical device is required to ensure appropriate and adequate safety and efficacy of the biomaterial or medical device. In this regard, it is noteworthy that the Food and Drug Administration (FDA) does not regulate biomaterials, but rather regulates the 'as-used' medical device or product intended for clinical application in humans. It is important to understand that the FDA does not regulate nor approves biomaterials, but rather, the FDA regulates the use of biomaterials in the end-stage 'as-used' medical device, that is, product.

In considering the fundamental biological requirements of a biomaterial for clinical application, it must be remembered that the biological requirements in one application may be different from those required in another application, even if the same biomaterial is being used. From this perspective, the intended application of the biomaterial or medical device dictates the biological requirements necessary to ensure safety and efficacy of the medical device or product. In turn, the biological requirements or biological design criteria dictate the types of tests required to determine biocompatibility.

4.402.2. Biocompatibility

The most commonly used term to describe the appropriate biological requirements of a biomaterial or biomaterials used in a medical device is 'biocompatibility.' A simple definition of biocompatibility of materials is 'the quality of not creating any adverse tissue reactions.' A more helpful definition of biocompatibility is 'the ability of a material to perform with an appropriate host response in a specific application.'[1,2] This definition is helpful in linking material properties or characteristics with performance, that is, biological requirements, with a specific application, a specific medical device, or biomaterial used as a medical device. The 'appropriate host response' implies identification and characterization of tissue reactions and responses that could prove harmful to the host and/or lead to ultimate failure of the biomaterial, medical device, or prosthesis through biological mechanisms. Viewed from another perspective, the 'appropriate host response' implies identification and characterization of the tissue reactions and responses critical to the successful use of the biomaterial or medical device. Biocompatibility assessment is considered to be a measure of the magnitude and duration of the adverse alterations in homeostatic mechanisms that determine the host response.[3] Safety assessment of a biomaterial or medical device is generally considered to be synonymous with its biocompatibility assessment.

4.402.3. Materials for Medical Devices

In the selection of biomaterials to be used in device design and manufacture, the first consideration must be the fitness for purpose with regard to characteristics and properties of the biomaterial(s). These include chemical, toxicological, physical, electrical, morphological, and mechanical properties. Relevant to the overall *in vivo* assessment of tissue compatibility of a biomaterial or medical device is knowledge of the chemical composition of the materials, including the conditions of tissue exposure as well as the nature, degree, frequency, and duration of exposure of the device and its constituents to the intended tissues in which it will be used. Table 1 presents a list of biomaterial components and characteristics that may affect the overall biological response of the medical device. Knowledge of the presence and quantity of these components in the medical device, that is, final product, is necessary. The range of potential biological hazards is broad and may include short-term effects, long-term effects, or specific toxic effects, which should be considered for every material and medical device. However, this does not imply that testing for all potential hazards will be necessary or practical.

Table 1 Biomaterials and components

The material(s) of manufacture
Intended additives, process contaminants, and residues
Leachable substances
Degradation products
Other components and their interactions in the final product
The properties and characteristics of the final product

Although the biomaterials and components listed in Table 1 are only superficially, if at all, considered in the research and development of new biomaterials, they become exceedingly important as the biomaterial moves from the R&D stage to the product stage of development. The components of biomaterials may play unexpected roles in the biocompatibility of the material or materials under consideration for a given medical device. Low molecular weight materials such as intended additives, process contaminants, residues, leachable substances, and degradation products may migrate and diffuse from the material and coat the surface of the material, potentially leading to different biological interactions than that intended with the original material. Examples of this phenomenon that have been identified in the past include processing aids that have coated the metal components of heart valves and wax extrusion aids that have ultimately coated the surfaces of polyurethane pacemaker leads. These examples illustrate how the material surfaces at the tissue–implant interfaces were of different chemistry than that intended by the manufacturer. Thus, the knowledge of the components and the composition of the materials of manufacture are important in predicting biological responses, both intended and unintended responses. There is also a possibility that these low molecular weight components, having diffused to the surface of the material in contact with tissue, may ultimately be released into the tissue, leading to modified or undesirable tissue reactions. Short-term biological assessment of the biomaterial may not identify these possibilities as the diffusion from the bulk of a material to its surface requires time. Therefore, long-term *in vivo* assessment and accelerated *in vitro* procedures to identify these possibilities may be necessary.

As final product or 'as-used' medical devices are generally made available in the sterilized state, the effect of sterilization and sterilization technique must be considered. Steam sterilization, radiation sterilization, or ethylene oxide sterilization may lead to modifications in the surface and bulk properties of the material and this may have a potential impact on biocompatibility. Radiation sterilization may crosslink or degrade polymers, leading to property changes. Ethylene oxide residuals are known to have an adverse reaction on *in vitro* toxicity tests. For these reasons, characterization of the final product following sterilization is necessary.

As stated earlier, testing for all potential hazards may not be necessary or practical. If a material and its components are well known and its manufacturing, processing, and sterilization procedures have been characterized with regard to potential changes in the material or biocompatibility, testing may not be necessary.

4.402.4. *In Vitro* Tests for Biocompatibility

The most common type of biocompatibility assay is the use of cell culture systems to identify cytotoxicity, cell adhesion, cell activation, or cell death. Cell culture assays are used extensively in biocompatibility studies of new biomaterials and are being required in biocompatibility assessment programs for products, that is, biomaterials, medical devices, and prostheses[4–6] (Table 2).

Table 2 *In vitro* cytotoxicity tests

Tests on extracts
– L929 elution test
– Neutral red uptake test
– Colony formation test
– MTT and related tests
Direct contact test
Indirect contact test
– Agar diffusion test
– Filter diffusion

Three types of cell culture assays are commonly used for evaluating biocompatibility. These are extract dilution, direct contact, and agar diffusion. Direct contact cell culture is most commonly used by investigators studying the biocompatibility of new biomaterials. In this type of assay, the investigator can use the cell type for which the biomaterial under investigation is intended for clinical use. For example, biomaterials intended for devices such as prosthetic heart valves, vascular grafts, and other cardiovascular devices will use human or animal endothelial cells to investigate biocompatibility as well as to investigate the capability of this cell type to proliferate and present the appropriate endothelial cell phenotype when in contact with the biomaterial. Studies involving inflammation and the foreign-body response use primary cells from blood or macrophage cell lines available through biological suppliers or cell banks. Materials intended for hard tissue or orthopedic application are commonly studied with osteoblasts or osteoblast cell lines. This type of assay permits the investigator to use the specific cell type in investigating the cell interaction and biocompatibility of the biomaterial for an intended application in an organ or tissue. This is a distinct advantage of this type of assay. Using appropriate negative and positive control materials as well as other biomaterials intended for similar application, new biomaterials can be assayed for a wide variety of types of cell interactions using this assay system.

The extract dilution type of cell culture assay requires a solvent extraction of the biomaterial under consideration and testing of this extract, most commonly at various dilutions, for evidence of cytotoxicity and cellular interaction. This type of cell culture assay finds its most common use in providing information for regulatory compliance. As identified in the preceding Materials for Medical Devices section and in Table 1, small molecular weight extractables are of concern regarding biocompatibility. The extraction assay, carried out with a series of solvents that are hydrophilic and hydrophobic, permits examination of the potential cytotoxicity of extracts and the identification of materials within a biomaterial that may be cytotoxic. These types of assays ultimately permit identification and characterization of cytotoxic materials within biomaterials or the lack of cytotoxicity, providing correlation with *in vivo* assays such as sensitization, irritation, intracutaneous (intradermal) reactivity, and other tests where the *in vivo* injection of extracts is required.

For regulatory purposes, the direct contact test commonly involves the development of a near-confluent monolayer of L-929 mammalian fibroblast cells on a culture plate. Biomaterial specimens under investigation are carefully placed on

these cell layers with fresh culture medium and incubated for 24 h at 37 °C. The culture medium and specimens are removed and the cells are fixed and stained with appropriate histological stains. Light microscopic evaluation is then used to identify cells adherent to the culture plate. Other cellular morphological characteristics can also be identified using this technique. Unlike that used for research purposes, regulatory cell culture assays most commonly use established cell lines. The use of established cell lines such as the L-929 mammalian fibroblast cell line offers the advantage of less assay repeatability, reproducibility, and efficiency. In addition, cell lines are more commonly available than are primary cells. For research, the most common practice is to culture cells directly on the new biomaterial surface.

In vitro cytotoxicity assays are the initial biocompatibility screening tests for a wide variety of biomaterials used in medical devices and prostheses. After the cytotoxicity profile of a candidate biomaterial has been determined, more application-specific tests may be performed to assess the biocompatibility of the biomaterial under end-use conditions. In general, biomaterials identified as nontoxic in *in vitro* assays will be nontoxic in *in vivo* assays. Biomaterials identified as toxic in *in vitro* assays must be further investigated for clinical acceptability. There are examples in which low levels of toxicity are present with biomaterials but this does not preclude or obviate their use in medical devices. An excellent example of this is glutaraldehyde-fixed porcine valves that produce adverse effects *in vitro* because of low residues of glutaraldehyde. In spite of the negative *in vitro* findings, this material is still used in the development of prosthetic heart valves for clinical use. This is an example of where the risk of low levels of toxicity is outweighed by the clinical advantage of the use of this material.

Two common problems may occur in *in vitro* cytotoxicity tests. The first problem occurs when the test cell culture is of too short a duration, that is, hours to a few days. In this case, sufficient time may not have been allowed to determine cell proliferation adequately, an important parameter, or cell death by necrosis, apoptosis, or anoikis (surface detachment). The second problem lies in the choice of cell type for the test. Commonly, immortalized cell lines derived from rodent or human tumors are used with virtually no understanding of the positive or negative attributes of phenotype expression by the respective immortalized cell line when compared to the primary cell intended for biological response and cytotoxicity evaluation. For example, primary macrophages derived from human blood-borne monocytes should be utilized to evaluate biomaterial-dependent cytotoxicity and macrophage activation. However, for macrophages, the more commonly used cell lines are HL-60 (human promyelocytic leukemia), U937 (human histiocytic lymphoma), RAW and RAW264.7 (mouse transformed lymphoma), and J774 (mouse histiocytic lymphoma). Rarely is any justification other than convenience given for the use of these tumor-derived cell lines.

4.402.5. *In Vivo* Tests for Biocompatibility

From a practical perspective, the *in vivo* assessment of the biocompatibility of biomaterials and medical devices is carried out to determine that the device performs as intended, that is, designed, and presents no significant harm to the patient or user (Table 3). Thus, the goal of the *in vivo* assessment of biocompatibility is to predict whether a medical device presents potential harm to the patient or user by evaluation under conditions simulating clinical use.

Recently, extensive efforts have been made by government agencies, that is, FDA, and regulatory bodies, that is, ASTM, ISO, and USP, to provide procedures, protocols, guidelines, and standards (Tables 4 and 5) that may be used in the *in vivo* assessment of the tissue compatibility of medical devices.[7–12] This chapter draws heavily on the ISO 10993 standard, Biological Evaluation of Medical Devices (Table 4), in presenting a systematic approach to the *in vivo* assessment of tissue compatibility of medical devices.

Table 3 *In vivo* tests for biocompatibility

Sensitization
Irritation
Intracutaneous reactivity
Systemic toxicity (acute)
Subacute/subchronic toxicity
Genotoxicity
Implantation
Hemocompatibility
Chronic toxicity
Carcinogenicity
Reproductive toxicity
Biodegradation
Toxicokinetics
Immunotoxicity

Table 4 ISO 10993: Biological evaluation of medical devices

Part 1: Evaluation and testing within a risk management process
Part 2: Animal welfare requirements
Part 3: Tests for genotoxicity, carcinogenicity, and reproductive toxicity
Part 4: Selection of tests for interactions with blood
Part 5: Tests for *in vitro* cytotoxicity
Part 6: Tests for local effects after implantation
Part 7: Ethylene oxide sterilization residuals
Part 9: Framework for identification and quantification of potential degradation products
Part 10: Tests for irritation and skin sensitization
Part 11: Tests for systemic toxicity
Part 12: Sample preparation and reference materials
Part 13: Identification and quantification of degradation products from polymeric medical devices
Part 14: Identification and quantification of degradation products from ceramics
Part 15: Identification and quantification of degradation products from metals and alloys
Part 16: Toxicokinetic study design for degradation products and leachables
Part 17: Establishment of allowable limits for leachable substances
Part 18: Chemical characterization of materials
Part 19: Physicochemical, morphological and topographical characterization of materials (Technical Specification)
Part 20: Principles and methods for immunotoxicology testing of medical devices (Technical Specification)

Table 5 ASTM standards and tests for biocompatibility

F 895	Agar diffusion cell culture screening for cytotoxicity
F 2382	Assessment of intravascular medical device materials on partial thromboplastin time (PTT)
E 1397	*In Vitro* rat hepatocyte DNA repair assay
E 1398	*In Vivo* rat hepatocyte DNA repair assay
F 1983	Assessment of compatibility of absorbable/resorbable biomaterials for implant applications
F 981	Assessment of compatibility of biomaterials for surgical implants with respect to effect of materials on muscle and bone
F 756	Assessment of hemolytic properties of materials
F 1027	Assessment of tissue and cell compatibility of orofacial prosthetic materials and devices
F 1877	Characterization of particles
F 813	Direct contact cell culture evaluation of materials for medical devices
F 749	Evaluating material extracts by intracutaneous injection in the rabbit
F 750	Evaluating material extracts by systemic injection in the rabbit
F 2148	Evaluation of delayed contact hypersensitivity using the murine local lymph node assay (LLNA)
F 1906	Evaluation of immune responses in biocompatibility testing using ELISA tests, lymphocyte proliferation, and cell migration
F 619	Extraction of medical plastics
F 2147	Guinea pig: split adjuvant and closed patch testing for contact allergens
F 748	Selecting generic biological test methods for materials and devices
F 1905	Selecting tests for determining the propensity of materials to cause immunotoxicity
F 763	Short-term screening of implant materials
F 1408	Subcutaneous screening test for implant materials
F 719	Testing biomaterials in rabbits for primary skin irritation
F 1903	Testing for biological responses to particles *in vitro*
F 720	Testing guinea pigs for contact allergens: guinea pig maximization test
F 2065	Testing for alternative pathway complement activation in serum by solid materials
F 2567	Testing for classical pathway complement activation in serum by solid materials
F 1984	Testing for whole complement activation in serum by solid materials
F 1904	Testing the biological responses to particles *in vivo*
E 1263	Conduct of micronucleus assays in mammalian bone marrow erythrocytes
E 1202	Development of micronucleus assay standards
E 1262	Performance of Chinese hamster ovary cell/hypoxanthine guanine phosphoribosyl transferase gene mutation assay
E 1439	Performance of lifetime bioassay for the tumorigenic potential of implant materials
E 1280	Performing the mouse lymphoma assay for mammalian cell mutagenicity

In vivo tests for the assessment of biocompatibility are chosen to simulate end-use applications. To facilitate the selection of appropriate tests, medical devices with their component biomaterials can be categorized by the nature of body contact of the medical device and by the duration of contact of the medical device. Table 6 presents medical device categorization by body contact and contact duration. The tissue contact categories and subcategories as well as the contact duration categories have been derived from standards, protocols, and guidelines utilized in the past for safety evaluation of medical devices. Certain devices may fall into more than one category, in which case testing appropriate to each category should be considered.

Two perspectives may be considered in the *in vivo* assessment of the biocompatibility of biomaterials and medical devices. The first perspective involves the utilization of *in vivo* tests to determine the general biocompatibility of newly developed biomaterials for which some knowledge of the tissue compatibility is necessary for further research and development. In this type of situation, manufacturing and other processes necessary for the development of a final product, that is, medical device, have not been carried out. However, the *in vivo* assessment of biocompatibility at this early stage of development can be used to evaluate the general tissue responses of the biomaterial as well as provide additional information relating to the proposed design criteria in the production of a medical device. While it is generally recommended that the identification and quantification of extractable chemical entities of a medical device should precede biological evaluation, it is quite common to carry out preliminary *in vivo* assessments to determine whether there are unknown chemical entities that produce adverse biological reactions. Utilized in this fashion, early *in vivo* assessment of a biomaterial may provide insight

Table 6 Medical device categorization by tissue contact and contact duration

Tissue contact
Surface devices
Skin
Mucosal membranes
Breached or compromised surfaces
External communicating devices
Blood path, indirect
Tissue/bone/dentin communication
Circulating blood
Implant devices
Tissue/bone
Blood
Contact duration
Limited, $\leq$24 h
Prolonged, $>$24 h and $<$30 days
Permanent, $>$30 days

into the biocompatibility of a material and may facilitate further development of a biomaterial into a medical device. Obviously, adverse reactions observed at this stage of development for a biomaterial would require further efforts to improve the biocompatibility of the biomaterial and identify the agents responsible for the adverse reactions.

The second perspective regarding the *in vivo* assessment of medical devices focuses on the biocompatibility of the final product, that is, the medical device and its component materials in the condition in which it is implanted. While medical devices in their final form and condition are commonly implanted in carefully selected animal models to determine function as well as biocompatibility, it may not be appropriate to carry out all of the recommended tests necessary for regulatory approval on the final device. In these situations, some tests may be carried out on biomaterial components of devices that have been prepared under manufacturing and sterilizing conditions and other processes utilized in the final product development.

In this section, brief perspectives on the general types of *in vivo* tests (Table 3) are presented. Details regarding these tests are found in the references. The ultimate selection of tests for *in vivo* biocompatibility assessment is based on the characteristics and end-use application of the device or biomaterial under consideration. Table 4 provides a list of types of tests to be considered for biological response evaluation under ISO 10993 and Table 5 provides a list of ASTM standards that can be used for biocompatibility evaluation.

4.402.5.1. Sensitization, Irritation, and Intracutaneous (Intradermal) Reactivity

Exposure to or contact with even minute amounts of potential leachables in medical devices or biomaterials can result in allergic or sensitization reactions. Sensitization tests estimate the potential for contact sensitization of medical devices, materials, and/or their extracts; are usually carried out in guinea pigs; and should reflect the intended route (skin, eye, mucosa) and nature, degree, frequency, duration, and conditions of exposure of the biomaterial in its intended clinical use. Emphasis is placed on utilizing extracts of the biomaterials to determine the irritant effects of potential leachables. Intracutaneous (intradermal) reactivity tests determine the localized reaction of tissue to extracts of medical devices, biomaterials, or prostheses in the final product form. Irritation and intracutaneous tests may be applicable where determination of irritation by dermal or mucosal irritation tests is not appropriate – albino rabbits are most commonly used.

Since these tests focus on determining the biological response of leachables that may be present in biomaterials, their extracts in various solvents are utilized to prepare the injection solutions. Critical to the conduct of these tests is the preparation of the test material and/or extract solution and the choice of solvents that must have physiological relevance.

4.402.5.2. Systemic Toxicity (Acute Toxicity) and Subacute and Subchronic Toxicity

Systemic toxicity tests estimate the potential harmful effects of either single or multiple exposures, during a period of <24 h, to medical devices, biomaterials, and/or their extracts. These tests evaluate the systemic toxicity potential of medical devices that release constituents into the body. These tests also include pyrogenicity testing.

In these tests, the form and area of the material, the thickness, and the surface area to extraction vehicle volume are critical considerations in the testing protocol. Appropriate extraction vehicles, that is, solvents, should be used to yield a maximum extraction of leachable materials to conduct the testing. Mice, rats, or rabbits are the usual animals of choice for these tests, and depending on the intended application of the biomaterial, oral, dermal, inhalation, intravenous, intraperitoneal, or subcutaneous application of the test substance may be used. Acute toxicity is considered to be the adverse effect that occurs after administration of a single dose or multiple doses of a test sample within 24 h. Subacute toxicity (repeat dose toxicity) focuses on adverse effects occurring after administration of a single dose or multiple doses of a test sample per day for a period of 14–28 days. Subchronic toxicity is considered to be the adverse effect occurring after the administration of a single dose or multiple doses of a test sample per day during a part of the lifespan, usually 90 days but not exceeding 10% of the lifespan of the animal.

Pyrogenicity (fever producing) tests are also included in the systemic toxicity category to detect material-mediated pyrogenic reactions of extracts of medical devices or materials. It is noteworthy that no single test can differentiate pyrogenic reactions that are material-mediated from those due to endotoxin contamination.

4.402.5.3. Genotoxicity

In vivo genotoxicity tests are carried out (Table 7) if potential genotoxicity is indicated by the chemistry and/or composition of the biomaterial (see Table 1) or by *in vitro* test results. Initially, at least three *in vitro* assays should be carried out and two of these assays should utilize mammalian cells. The initial *in vitro* assays should cover the three levels of genotoxic effects: DNA effects, gene mutations, and chromosomal aberrations. *In vivo* genotoxicity tests include the micronucleus test, the *in vivo* mammalian bone marrow cytogenetic tests – chromosomal analysis, the rodent dominant lethal tests, the mammalian germ cell cytogenetic assay, the mouse spot test, and the mouse heritable translocation assay. Not all of the *in vivo* genotoxicity tests need to be performed and the most common test is the rodent micronucleus test. Genotoxicity

Table 7 Tests for genotoxicity, carcinogenicity, and reproductive toxicity

Genotoxicity
– Bacterial reverse mutation assay
– *In vitro* mouse lymphoma tk assay
– Chromosomal aberation in mammalian cells
Carcinogenicity
– Syrian hamster embryo (SHE) cell transformation assays
– Balb/c 3T3 focus transformation assay
– rasH-2 mouse model
Reproductive toxicity
– Embryonic stem cell test

tests are performed with appropriate extracts or dissolved materials using appropriate media as suggested by the known composition of the biomaterial.

4.402.5.4. Implantation

Implantation tests assess the local pathological effects on living tissue of a sample of a material or final product that is surgically implanted or placed into an implant site or tissue appropriate to the intended application of the biomaterial or medical device. Evaluation of the local pathological effects is carried out at both the gross level and the microscopic level. Histological (microscopic) evaluation is utilized to characterize various biological response parameters. For short-term implantation evaluation of about 12 weeks, mice, rats, guinea pigs, or rabbits are the usual animals utilized in these studies. For longer-term testing in subcutaneous tissue, muscle, or bone, animals such as rats, guinea pigs, rabbits, dogs, sheep, goats, pigs, and other animals with relatively long-life expectancy are suitable. If a medical device is to be evaluated, larger species may be utilized. For example, substitute heart valves are usually tested in sheep, while calves are usually the animal of choice for ventricular assist devices and total artificial hearts.

Implant retrieval and evaluation plays a significant role in determining biocompatibility, factors and mechanisms of medical device failure or success, and new biological design criteria for next-generation devices.[13,14]

4.402.5.5. Chronic Toxicity

Chronic toxicity tests determine the effects of either single or multiple exposures to medical devices, materials, and/or their extracts during a period of at least 10% of the lifespan of the test animal, for example, over 90 days in rats. Chronic toxicity tests may be considered an extension of subchronic (subacute) toxicity testing and both may be evaluated in an appropriate experimental protocol or study.

4.402.5.6. Carcinogenicity

Carcinogenicity tests determine the tumorigenic potential of medical devices, materials, and/or their extracts from either single or multiple exposures or contacts over a period of the major portion of the lifespan of the test animal (Table 7). A new carcinogenicity test using a transgenic mouse assay is currently under investigation.[15] This assay is less time-consuming and less expensive than the two animal life-time assays. Carcinogenicity tests should be conducted only if data from other sources suggest a tendency for tumor induction. In addition, both carcinogenicity (tumorigenicity) and chronic toxicity may be studied in a single experimental study. With biomaterials, carcinogenicity studies focus on the potential for solid-state carcinogenicity, that is, the Oppenheimer effect. In carcinogenicity testing, controls of a comparable form and shape should be included; polyethylene implants are a commonly used control material. The use of appropriate controls is imperative as animals may spontaneously develop tumors and statistical comparison of the test biomaterial/device and the controls is necessary.

4.402.5.7. Reproductive and Developmental Toxicity

These tests evaluate the potential effects of medical devices, materials, and/or their extracts on reproductive function, embryonic development (teratogenicity), and prenatal and early postnatal development (Table 7). The application site of the device must be considered and tests and/or bioassays should only be conducted when the device has a potential impact on the reproductive potential of the subject.

4.402.5.8. Biodegradation

Biodegradation tests determine the effects of a biodegradable material and its biodegradation products on the tissue response. They focus on the amount of degradation during a given period of time (the kinetics of biodegradation), the nature of the degradation products, the origin of the degradation products (impurities, additives, corrosion products, bulk polymer, etc.), and the qualitative and quantitative assessment of degradation products and leachables in adjacent tissues and in distant organs. The biodegradation of biomaterials may occur through a wide variety of mechanisms, which in part are biomaterial-dependent, and all pertinent mechanisms related to the device and the end-use application of the device must be considered.[16–18] Test materials comparable to degradation products may be prepared and studied to determine the biological response of degradation products anticipated in long-term implants. An example of this approach is the study of metallic and polymeric wear particles that may be present with long-term orthopedic joint prostheses.

4.402.6. Inflammation, Wound Healing, and the Foreign-Body Response

Inflammation, wound healing, and foreign-body reaction are generally considered as parts of the tissue or cellular host responses to injury.[19] Table 8 lists the sequence/continuum of these events following injury. Overlap and simultaneous occurrence of these events should be considered; for example, the foreign-body reaction at the implant interface may be initiated with the onset of acute and chronic inflammation. From a biomaterials perspective, placing a biomaterial in the *in vivo* environment requires injection, insertion, or surgical implantation, all of which injure the tissues or organs involved.

The placement procedure initiates a response to injury by the tissue, organ, or body and mechanisms are activated to maintain homeostasis. The degrees to which the homeostatic mechanisms are perturbed and the extent to which

Table 8 Sequence/continuum of host reactions following implantation of medical devices

Injury
Blood–material interactions
Provisional matrix formation
Acute inflammation
Chronic inflammation
Granulation tissue
Foreign-body reaction
Fibrosis/fibrous capsule development

pathophysiologic conditions are created and undergo resolution are a measure of the host reactions to the biomaterial and may ultimately determine its biocompatibility. Although it is convenient to differentiate homeostatic mechanisms as blood–material or tissue–material interactions, it must be remembered that the various components or mechanisms involved in homeostasis are present in both blood and tissue and are a part of the physiologic continuum. Furthermore, it must be noted that host reactions may be tissue-dependent, organ-dependent, and species-dependent. Obviously, the severity of injury varies with the implantation procedure.

4.402.6.1. Overview

Inflammation is generally defined as the reaction of vascularized living tissue to local injury. Inflammation serves to contain, neutralize, dilute, or wall off the injurious agent or process.[20] In addition, it sets into motion a series of events that may heal and reconstitute the implant site through the replacement of the injured tissue by regeneration of native parenchymal cells, formation of fibroblastic scar tissue, or a combination of these two processes.

Immediately following injury, there are changes in vascular flow, caliber, and permeability. Fluid, proteins, and blood cells escape from the vascular system into the injured tissue in a process called exudation. Following changes in the vascular system, which also include changes induced in blood and its components, cellular events occur and characterize the inflammatory response. The effect of the injury and/or biomaterial *in situ* on plasma or cells can produce chemical factors that mediate many of the vascular and cellular responses of inflammation.

Blood–material interactions and the inflammatory response are intimately linked, and in fact, early responses to injury involve mainly blood and vasculature. Regardless of the tissue or organ into which a biomaterial is implanted, the initial inflammatory response is activated by injury to vascularized connective tissue (Table 9). Since blood and its components are involved in the initial inflammatory responses, blood clot formation and/or thrombosis also occur. Blood coagulation and thrombosis are generally considered humoral responses and may be influenced by other homeostatic mechanisms such as the extrinsic and intrinsic coagulation systems, the complement system, the fibrinolytic system, the kinin-generating system, and platelets. Thrombus or blood clot formation on the surface of a biomaterial is related to the well-known Vroman effect, in which a hierarchical and dynamic series of collision, absorption, and exchange processes, determined by protein mobility and concentration, regulate early time-dependent changes in blood protein adsorption. From a wound-healing perspective, blood protein deposition on a biomaterial surface is described as provisional matrix formation. Blood interactions with biomaterials are generally considered under the category of hematocompatibility.

Injury to vascularized tissue in the implantation procedure leads to immediate development of the provisional matrix at the implant site. This provisional matrix consists of fibrin, produced by activation of the coagulation and thrombosis systems, and inflammatory products released by the complement system, activated platelets, inflammatory cells, and endothelial cells. These events occur early, within minutes to hours of implantation of a medical device. Components within or released from the provisional matrix, that is, fibrin network (thrombosis or clot), initiate the resolution, reorganization, and repair processes such as inflammatory cell and fibroblast recruitment. The provisional matrix appears to provide both structural and biochemical components to the process of wound healing. The complex three-dimensional structure of the fibrin network with attached adhesive proteins provides a substrate for cell adhesion and migration. The presence of mitogens, chemoattractants, cytokines, and growth factors within the provisional matrix provides for a rich milieu of activating and inhibiting substances for various cellular proliferative and synthetic processes. The provisional matrix may be viewed as a naturally derived, biodegradable, sustained release system in which mitogens, chemoattractants, cytokines, and growth factors are released to control subsequent wound-healing processes. In spite of the increase in our knowledge of the provisional matrix and its capabilities, our knowledge of the control of the formation of the provisional matrix and its effect on subsequent wound-healing events is poor. In part, this lack of knowledge is due to the fact that much of our knowledge regarding the provisional matrix has been derived from *in vitro* studies, and there is a paucity of *in vivo* studies that provide for a wider perspective. Little is known regarding the provisional matrix which forms at biomaterial and medical device interfaces *in vivo*, although attractive hypotheses have been presented regarding the presumed ability of materials and protein-adsorbed materials to modulate cellular interactions through their interactions with adhesive molecules and cells.

The predominant cell type involved in the inflammatory response varies with the age of the inflammatory injury (Figure 1). In general, neutrophils predominate during the first several days following injury and then are replaced by monocytes as the predominant cell type. Three factors account for this change in cell type: neutrophils are short-lived and disintegrate and disappear after 24–48 h; neutrophil

Table 9 Cells and components of vascularized connective tissue

Intravascular (blood) cells
Erythrocytes (RBC)
Neutrophils (PMNs, polymorphonuclear leukocytes)
Monocytes
Eosinophils
Lymphocytes
Plasma cells
Basophils
Platelets
Connective tissue cells
Mast cells
Fibroblasts
Macrophages
Lymphocytes
Extracellular matrix components
Collagens
Elastin
Proteoglycans
Fibronectin
Laminin

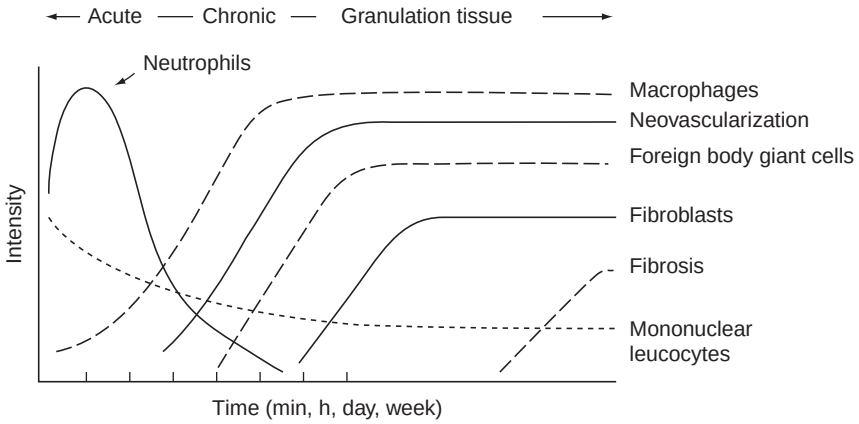

Figure 1 The temporal variation in the acute inflammatory response, chronic inflammatory response, granulation tissue development, and foreign-body reaction to implanted biomaterials. The intensity and time variables are dependent upon the severity of injury created in the implantation and the size, shape, topography, and chemical and physical properties of the biomaterial.

Table 10 Important chemical mediators of inflammation derived from plasma, cells, or injured tissue

Mediators	*Examples*
Vasoactive agents	Histamines, serotonin, adenosine, endothelial-derived relaxing factor (EDRF), prostacyclin, endothelin, thromboxane α_2
Plasma proteases	
Kinin system	Bradykinin, kallikrein
Complement system	C3a, C5a, C3b, C5b–C9
Coagulation/fibrinolytic system	Fibrin degradation products, activated Hageman factor (FXIIA), tissue plasminogen activator (tPA)
Leukotrienes	Leukotriene B_4 (LTB_4), hydroxyeicosatetranoic acid (HETE)
Lysosomal proteases	Collagenase, elastase
Oxygen-derived free radicals	H_2O_2, superoxide anion
Platelet activating factors	Cell membrane lipids
Cytokines	Interleukin 1 (IL-1), tumor necrosis factor (TNF)
Growth factors	Platelet-derived growth factor (PDGF), fibroblast growth factor (FGF), transforming growth factor (TGF-α or TGF-β), epithelial growth factor (EGF)

emigration from the vasculature to the tissues is of short duration; and chemotactic factors for neutrophil migration are activated early in the inflammatory response. Following emigration from the vasculature, monocytes differentiate into macrophages and these cells are very long-lived (up to months). Monocyte emigration may continue for day to weeks, depending on the severity of the injury and the type of the implanted biomaterial, and chemotactic factors for monocytes are activated over longer periods of time. In short-term (24 h) implants in humans, administration of both H1 and H2 histamine receptor antagonists greatly reduced the recruitment of macrophages/monocytes and neutrophils on polyethylene terephthalate surfaces.[21] These studies also demonstrated that plasma-coated implants accumulated significantly more phagocytes than did serum-coated implants.

The temporal sequence of events following implantation of a biomaterial is illustrated in Figure 1. The size, shape, and chemical and physical properties of the biomaterial may be responsible for variations in the intensity and duration of the inflammatory or wound-healing process. Thus, intensity and/or time duration of the inflammatory reaction may characterize the biocompatibility of a biomaterial.

While injury initiates the inflammatory response, the chemicals released from plasma, cells, or injured tissues mediate the inflammatory response. Important classes of chemical mediators of inflammation are presented in Table 10. Several points must be noted in order to understand the inflammatory response and how it relates to biomaterials. First, although chemical mediators are classified on a structural or functional basis, different mediator systems interact and provide a system of checks and balances regarding their respective activities and functions. Second, chemical mediators are quickly inactivated or destroyed, suggesting that their action is predominantly local (i.e., at the implant site). Third, generally the lysosomal proteases and the oxygen-derived free radicals produce the most significant damage or injury. These chemical mediators are also important in the degradation of biomaterials.[22]

4.402.6.2. Acute Inflammation

Acute inflammation is of a relatively short duration, lasting for minutes to days, depending on the severity of the injury. Its main characteristics are the exudation of fluid and plasma proteins (edema) and the emigration of leukocytes

(predominantly neutrophils). Neutrophils (polymorphonuclear leukocytes, PMNs) and other motile white cells emigrate or move from the blood vessels to the perivascular tissues and the injury (implant) site. Leukocyte emigration is assisted by 'adhesion molecules' present on the leukocyte and endothelial surfaces. The surface expression of these adhesion molecules can be induced, enhanced, or altered by inflammatory agents and chemical mediators. White cell emigration is controlled, in part, by chemotaxis, which is the unidirectional migration of cells along a chemical gradient. A wide variety of exogenous and endogenous substances have been identified as chemotactic agents. Specific receptors for chemotactic agents on the cell membranes of leukocytes are important in the emigration or movement of leukocytes. These and other receptors also play a role in the transmigration of white cells across the endothelial lining of vessels and activation of leukocytes. Following localization of leukocytes at the injury (implant) site, phagocytosis and the release of enzymes occur following activation of neutrophils and macrophages. The major role of the neutrophil in acute inflammation is to phagocytose microorganisms and foreign materials. Phagocytosis is seen as a three-step process in which the injurious agent undergoes recognition and neutrophil attachment, engulfment, and killing or degradation. In regard to biomaterials, engulfment and degradation may or may not occur, depending on the properties of the biomaterial.

Although biomaterials are not generally phagocytosed by neutrophils or macrophages because of the disparity in size (i.e., the surface area of the biomaterial is greater than the size of the cell), certain events in phagocytosis may occur. The process of recognition and attachment is expedited when the injurious agent is coated by naturally occurring serum factors called 'opsonins.' The two major opsonins are immunoglobulin G (IgG) and the complement-activated fragment, C3b. Both of these plasma-derived proteins are known to adsorb to biomaterials, and neutrophils and macrophages have corresponding cell membrane receptors for these opsonization proteins. These receptors may also play a role in the activation of the attached neutrophil or macrophage. Other blood proteins such as fibrinogen, fibronectin, and vitronectin may also facilitate cell adhesion to biomaterial surfaces. Owing to the disparity in size between the biomaterial surface and the attached cell, frustrated phagocytosis may occur. This process does not involve engulfment of the biomaterial but does cause the extracellular release of leukocyte products in an attempt to degrade the biomaterial.

Henson has shown that neutrophils adherent to complement-coated and immunoglobulin-coated nonphagocytosable surfaces may release enzymes by direct extrusion or exocytosis from the cell.[23] The amount of enzyme released during this process depends on the size of the polymer particle, with larger particles inducing greater amounts of enzyme release. This suggests that the specific mode of cell activation in the inflammatory response in tissue depends upon the size of the implant and that a material in a phagocytosable form (i.e., powder, particulate, or nanomaterial) may provoke an inflammatory response of a degree different from that of the same material in a nonphagocytosable form (i.e., film). In general, materials >5 μm are not phagocytosed, while materials <5 μm, that is, nanomaterials, can be phagocytosed by inflammatory cells.

Acute inflammation normally resolves quickly, usually in <1 week, depending on the severity of the injury at the implant site. However, the presence of acute inflammation (i.e., PMNs) at the tissue–implant interface at time periods beyond 1 week (i.e., weeks, months, or years) suggests the presence of an infection.

4.402.6.3. Chronic Inflammation

Chronic inflammation is histologically less uniform than acute inflammation. In general, chronic inflammation is characterized by the presence of macrophages, monocytes, and lymphocytes, with the proliferation of blood vessels and connective tissue. Many factors can modify the course and histologic appearance of chronic inflammation.

Persistent inflammatory stimuli lead to chronic inflammation. While the chemical and physical properties of the biomaterial in themselves may lead to chronic inflammation, motion in the implant site by the biomaterial or infection may also produce chronic inflammation. The chronic inflammatory response to biomaterials is usually of a short duration and is confined to the implant site. The presence of mononuclear cells, including lymphocytes and plasma cells, is considered chronic inflammation, whereas the foreign-body reaction with the development of granulation tissue is considered the normal wound-healing response to implanted biomaterials (i.e., the normal foreign-body reaction). Chronic inflammation with the presence of collections of lymphocytes and monocytes at extended implant times (weeks, months, years) may also suggest the presence of a long-standing infection. The prolonged presence of acute and/or chronic inflammation also may be due to toxic leachables from a biomaterial.[24]

The following example illustrates this point. *In vivo* subcutaneous implantation studies were carried out in rats and rabbits with naltrexone sustained release preparations that included placebo (polymer-only) beads and naltrexone-containing beads.[18] Histopathological tissue reactions utilizing standard procedures and light microscopic evaluation to the respective preparations were determined at days 3, 7, 14, 21, and 28. The only significant histological finding in both rats and rabbits at any time period was the persistent chronic inflammation that occurred focally around the naltrexone-containing beads. The focal inflammatory cell density in both rats and rabbits was higher for the naltrexone beads than for the placebo beads at days 14, 21, and 28. This difference in inflammatory response between naltrexone beads and placebo beads increased with increasing time of implantation. Considering the resolution of the inflammatory response for the placebo beads with implantation time in both rats and rabbits, it is suggested that the naltrexone drug itself is identified as the causative agent of the focal chronic inflammation present surrounding the naltrexone beads in the implant sites.

The important lesson from this case study is the necessary use of appropriate control materials. If no negative control, that is, placebo polymer-only material, had been used, the polymer in the naltrexone-containing beads would have also been considered as a causative agent of the extended chronic inflammatory response. Similar chronic inflammatory responses have been identified with drugs, polymer plasticizers and other

additives, fabrication and manufacturing aids, and sterilization residuals. Each case presents its own unique factors in a risk assessment process necessary for determining safety (biocompatibility) and benefit versus risk in clinical application.

Lymphocytes and plasma cells are involved principally in immune reactions and are key mediators of antibody production and delayed hypersensitivity responses. Although they may be present at the sites of nonimmunologic injuries and inflammation, their roles in such circumstances are largely unknown.[25,26] Little is known regarding humoral immune responses and cell-mediated immunity to synthetic biomaterials. The role of macrophages must be considered in the possible development of immune responses to synthetic biomaterials. Macrophages and dendritic cells process and present the antigen to immunocompetent cells and thus are key mediators in the development of immune reactions.

Monocytes and macrophages belong to the mononuclear phagocytic system (MPS), also known as the reticuloendothelial system (RES). These systems consist of cells in the bone marrow, peripheral blood, and specialized tissues. **Table 11** lists the tissues that contain cells belonging to the MPS or RES. The specialized cells in these tissues may be responsible for systemic effects in organs or tissues secondary to the release of components or products from implants through various tissue–material interactions (e.g., corrosion products, wear debris, degradation products) or the presence of implants (e.g., microcapsule or nanoparticle drug-delivery systems).

The macrophage is probably the most important cell in chronic inflammation because of the great number of biologically active products it can produce. Important classes of products produced and secreted by macrophages include neutral proteases, chemotactic factors, arachidonic acid metabolites, reactive oxygen metabolites, complement components, coagulation factors, growth-promoting factors, cytokines, and acid. Phagolysosomes in macrophages can have acidity as low as a pH of 4 and direct microelectrode studies of this acid environment have determined pH levels as low as 3.5. Moreover, only several hours are necessary to achieve these acid levels following the adhesion of macrophages.[27–31]

Growth factors such as platelet-derived growth factor (PDGF), fibroblast growth factor (FGF), transforming growth factor-β (TGF-β), TGF-α/epidermal growth factor (EGF), and interleukin-1 (IL-1) or tumor necrosis factor (TNF-α) are important for the growth of fibroblasts and blood vessels and the regeneration of epithelial cells. Growth factors released by activated cells can stimulate production of a wide variety of cells; initiate cell migration, differentiation, and tissue remodeling; and may be involved in various stages of wound healing.

Table 11 Tissues and cells of MPS and RES

Tissues	*Cells*
Implant sites	Inflammatory macrophages
Liver	Kupffer cells
Lung	Alveolar macrophages
Connective tissue	Histiocytes
Bone marrow	Macrophages
Spleen and lymph nodes	Fixed and free macrophages
Serous cavities	Pleural and peritoneal macrophages
Nervous system	Microglial cells
Bone	Osteoclasts
Skin	Langerhans' cells
Lymphoid tissue	Dendritic cells

4.402.6.4. Granulation Tissue

Within 1 day following implantation of a biomaterial (i.e., injury), the healing response is initiated by the action of monocytes and macrophages. Fibroblasts and vascular endothelial cells in the implant site proliferate and begin to form granulation tissue, which is the specialized type of tissue that is the hallmark of healing inflammation. Granulation tissue derives its name from the pink, soft granular appearance on the surface of healing wounds, and its characteristic histologic features include the proliferation of new small blood vessels and fibroblasts. Depending on the severity of injury, granulation tissue may be seen as early as 3–5 days following implantation of a biomaterial.

The new small blood vessels are formed by budding or sprouting of preexisting vessels in a process known as neovascularization or angiogenesis.[32,33] This process involves proliferation, maturation, and organization of endothelial cells into capillary vessels. Fibroblasts also proliferate in developing granulation tissue and are active in synthesizing collagen and proteoglycans. In the early stages of granulation tissue development, proteoglycans predominate but later collagen, especially type III collagen, predominates and forms the fibrous capsule. Some fibroblasts in developing granulation tissue may have the features of smooth muscle cells, that is, actin microfilaments. These cells are called myofibroblasts and are considered to be responsible for the wound contraction seen during the development of granulation tissue. Macrophages are almost always present in granulation tissue. Other cells may also be present if chemotactic stimuli are generated.

The wound-healing response is generally dependent on the severity of injury or defect created by the implantation procedure[34–38]. Wound healing by primary union or first intention is the healing of clean, surgical incisions in which the wound edges have been approximated by surgical sutures. Healing under these conditions occurs without significant bacterial contamination and with a minimal loss of tissue. Wound healing by secondary union or second intention occurs when there is a large tissue defect that must be filled or there is extensive loss of cells and tissue. In wound healing by secondary intention, regeneration of parenchymal cells cannot completely reconstitute the original architecture and much larger amounts of granulation tissue are formed that result in larger areas of fibrosis or scar formation. Under these conditions, different regions of tissue may show different stages of the wound-healing process simultaneously.

Granulation tissue is distinctly different from granulomas, which are the small collections of modified macrophages called epithelioid cells. Langhans' or foreign-body-type giant cells may surround nonphagocytosable particulate materials in granulomas. Foreign-body giant cells (FBGCs) are formed by the fusion of monocytes and macrophages in an attempt to phagocytose the material.

4.402.6.5. Foreign-Body Reaction

The foreign-body reaction to biomaterials is composed of FBGCs and the components of granulation tissue (e.g., macrophages, fibroblasts, and capillaries in varying amounts, depending upon the form and topography of the implanted material[39]). Relatively flat and smooth surfaces such as that found on breast prostheses have a foreign-body reaction that is composed of a layer of macrophages of one to two cells in thickness. Relatively rough surfaces such as those found on the outer surfaces of expanded poly tetrafluoroethylene (ePTFE) or Dacron vascular prostheses have a foreign-body reaction composed of macrophages and FBGCs at the surface. Fabric materials generally have a surface response composed of macrophages and FBGCs, with varying degrees of granulation tissue subjacent to the surface response.

As previously discussed, the form and topography of the surface of the biomaterial determine the composition of the foreign-body reaction. With biocompatible materials, the composition of the foreign-body reaction in the implant site may be controlled by the surface properties of the biomaterial, the form of the implant, and the relationship between the surface area of the biomaterial and the volume of the implant. For example, high-surface-to-volume implants such as fabrics, porous materials, particulate, or microspheres will have higher ratios of macrophages and FBGCs in the implant site than smooth-surface implants, which will have fibrosis as a significant component of the implant site.[40–44]

The foreign-body reaction consisting mainly of macrophages and/or FBGCs may persist at the tissue–implant interface for the lifetime of the implant (Figure 1). Generally, fibrosis (i.e., fibrous encapsulation) surrounds the biomaterial or implant with its interfacial foreign-body reaction, isolating the implant and foreign-body reaction from the local tissue environment. Early in the inflammatory and wound-healing response, the macrophages are activated upon adherence to the material surface.[45]

Although it is generally considered that the chemical and physical properties of the biomaterial are responsible for macrophage activation, the subsequent events regarding the activity of macrophages at the surface are not clear. Tissue macrophages, derived from circulating blood monocytes, may coalesce to form multinucleated FBGCs. It is not uncommon to see very large FBGCs containing large numbers of nuclei on the surface of biomaterials. While these FBGCs may persist for the lifetime of the implant, it is not known whether they remain activated, releasing their lysosomal constituents, or become quiescent.[46]

Figure 2 demonstrates the progression from circulating blood monocyte to tissue macrophage to FBGCs development that is most commonly observed. Indicated in the figure are biological responses that are considered to play an important role in FBGC development. Material surface chemistry may control adherent macrophage apoptosis (i.e., programmed cell death) that renders potentially harmful macrophages nonfunctional, while the surrounding environment of the implant remains unaffected. The level of adherent macrophage apoptosis appears to be inversely related to the surface's ability to promote diffusion of macrophages into FBGCs, suggesting a mechanism for macrophages to escape apoptosis.

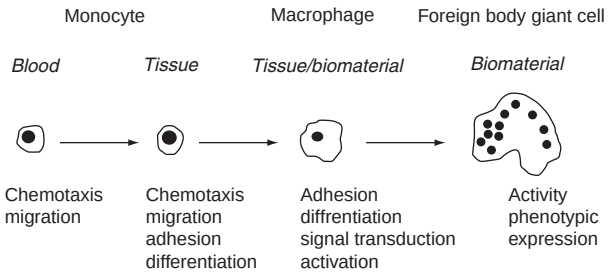

Figure 2 *In vivo* transition from blood-borne monocyte to biomaterial adherent monocyte/macrophage to foreign-body giant cell (FBGC) at the tissue–biomaterial interface. Little is known regarding the indicated biological responses, which are considered to play important roles in the transition to FBGC development.

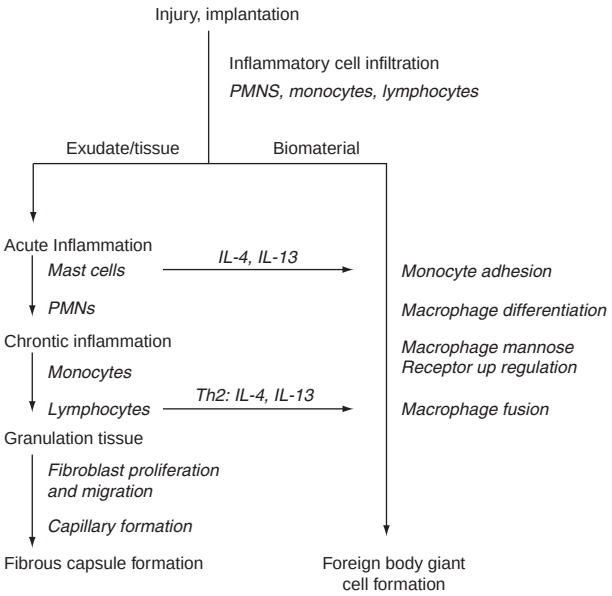

Figure 3 Sequence of events involved in inflammatory and wound-healing responses leading to foreign-body giant cell formation.

Figure 3 demonstrates the sequence of events involved in inflammation and wound healing when medical devices are implanted. In general, the PMN predominant acute inflammatory response and the lymphocyte/monocyte predominant chronic inflammatory response resolve quickly (i.e., within 2 weeks) depending on the type and location of the implant. Studies using IL-4 or IL-13 demonstrate the role for Th2 helper lymphocytes and/or mast cells, respectively, in the development of the foreign-body reaction at the tissue–material interface.[47,48] Integrin receptors of IL-4-induced FBGC are characterized by the early constitutive expression of $\alpha V\beta 1$ and the later induced expression of $\alpha 5\beta 1$ and $\alpha X\beta 2$, which indicate potential interactions with adsorbed complement C3, fibrin(ogen), fibronectin, Factor X, and vitronectin.[48–56] Interactions through indirect (paracrine) cytokine and chemokine signaling have shown a significant effect in enhancing adherent macrophage/FBGC activation at early times, whereas interactions via direct (juxtacrine)

cell–cell mechanisms dominate at later times.[57–59] Th2 helper lymphocytes have been described as 'antiinflammatory' based on their cytokine profile, of which IL-4 is a significant component.

4.402.6.6. Fibrosis/Fibrous Encapsulation

The end-stage healing response to biomaterials is generally fibrosis or fibrous encapsulation. However, there may be exceptions to this general statement (e.g., porous materials inoculated with parenchymal cells or porous materials implanted into bone). As previously stated, the tissue response to implants is in part dependent upon the severity of injury or defect created in the implantation procedure and the amount of provisional matrix.

The ultimate goal of tissue engineering and regenerative medicine is replacement of injured tissue by cells that reconstitute normal tissue and organ structures. Numerous approaches, including stem cells, scaffolds, growth factors, etc., are currently being investigated. However, the relatively rapid responses of inflammation, wound healing, and the foreign-body reaction, as well as other significant factors in tissue regeneration, present major challenges to the successful achievement of this goal.

Repair of implant sites can involve two distinct processes: regeneration, which is the replacement of injured tissue by parenchymal cells of the same type, or replacement by connective tissue that constitutes the fibrous capsule. These processes are generally controlled by either (1) the proliferative capacity of the cells in the tissue or organ receiving the implant and the severity of injury as it relates to the destruction, or (2) persistence of the tissue framework of the implant site.

The regenerative capacity of cells allows them to be classified into three groups: labile, stable (or expanding), and permanent (or static) cells. Labile cells continue to proliferate throughout life; stable cells retain this capacity but do not normally replicate; and permanent cells cannot reproduce themselves after birth. Perfect repair with restitution of normal structure can theoretically occur only in tissues consisting of stable and labile cells, whereas all injuries to tissues composed of permanent cells may give rise to fibrosis and fibrous capsule formation with very little restitution of the normal tissue or organ structure. Tissues composed of permanent cells (e.g., nerve cells and cardiac muscle cells) most commonly undergo an organization of the inflammatory exudate, leading to fibrosis. Tissues of stable cells (e.g., parenchymal cells of the liver, kidney, and pancreas); mesenchymal cells (e.g., fibroblasts, smooth muscle cells, osteoblasts, and chondroblasts); and vascular endothelial and labile cells (e.g., epithelial cells and lymphoid and hematopoietic cells) may also follow this pathway to fibrosis or may undergo resolution of the inflammatory exudate, leading to restitution of the normal tissue structure.

The condition of the underlying framework or supporting stroma of the parenchymal cells following an injury plays an important role in the restoration of normal tissue structure. Retention of the framework with injury may lead to restitution of the normal tissue structure, whereas destruction of the framework most commonly leads to fibrosis. It is important to consider the species-dependent nature of the regenerative capacity of cells. For example, cells from the same organ or tissue but from different species may exhibit different regenerative capacities and/or connective tissue repair.

Following injury, cells may undergo adaptations of growth and differentiation. Important cellular adaptations are atrophy (decrease in cell size or function), hypertrophy (increase in cell size), hyperplasia (increase in cell number), and metaplasia (change in cell type). Other adaptations include a change by cells from producing one family of proteins to another (phenotypic change), or marked overproduction of protein. This may be the case in cells producing various types of collagens and extracellular matrix proteins in chronic inflammation and fibrosis. Causes of atrophy may include decreased workload (e.g., stress-shielding by implants), and diminished blood supply and inadequate nutrition (e.g., fibrous capsules surrounding implants).

Local and systemic factors may play a role in the wound-healing response to biomaterials or implants. Local factors include the site (tissue or organ) of implantation, the adequacy of blood supply, and the potential for infection. Systemic factors may include nutrition, hematologic derangements, glucocortical steroids, and preexisting diseases such as atherosclerosis, diabetes, and infection.

Finally, the implantation of biomaterials or medical devices may be best viewed at present from the perspective that the implant provides an impediment or hindrance to appropriate tissue or organ regeneration and healing. Given our current inability to control the sequence of events following injury in the implantation procedure, restitution of normal tissue structures with function is rare. Current studies directed toward gaining a better understanding of the modification of the inflammatory response, stimuli providing for appropriate proliferation of permanent and stable cells, and the appropriate application of growth factors may provide keys to the control of inflammation, wound healing, and fibrous encapsulation of biomaterials.

4.402.7. Hemocompatibility

Hemocompatibility tests evaluate effects on blood and/or blood components by blood-contacting medical devices or materials.[60,61] *In vivo* hemocompatibility tests are usually designed to simulate the geometry, contact conditions, and flow dynamics of the device or material in its clinical application. From the ISO standards perspective, five test categories are indicated for hemocompatibility evaluation: thrombosis, coagulation, platelets, hematology, and immunology (complement and leukocytes) (**Table 12**).

Several issues are important in the selection of tests for hemocompatibility of medical devices or biomaterials. *In vivo* testing in animals may be convenient; however, species differences in blood reactivity must be considered and these may limit the predictability of any given test in the human clinical situation. While species differences may complicate hemocompatibility evaluation, the utilization of animals in short- and long-term testing is considered to be appropriate for evaluating thrombosis and tissue interaction. European community law prohibits the use of nonhuman primates for blood compatibility and medical device testing even though blood values and reactivity between humans and nonhuman primates are very

similar. Hemocompatibility evaluation in animals is complicated by the lack of appropriate and adequate assay materials; for example, appropriate antibodies for immunoassays. Use of human blood in hemocompatibility evaluation implies *in vitro* testing, which usually requires the use of anticoagulants which are not usually present with the device in the clinical situation, except for perhaps the earliest implantation period. The use of anticoagulants or antithrombotics may complicate *in vitro* and *in vivo* hemocompatibility evaluation. For example, the calcium chelator EDTA is commonly used to anticoagulate whole blood but EDTA also inhibits activation of the complement system that, in turn, may reduce leukocyte adhesion to surfaces.

In vitro flow systems such as flow cells and recirculating flow tubes are usually of short duration, minutes to hours, and thus may not adequately assess blood component interactions with test materials. Flow is an important parameter that must be designed into each test model utilized for hematocompatibility. In additions, *in vitro, ex vivo,* and *in vivo* test systems must also consider and, if possible, evaluate the extent of thromboembolization that occurs. In the past, clean test surfaces have been considered blood compatible when, in fact, significant thrombus formation has occurred with thromboembolization under flow leading to the so-called 'clean' surface and interpretation of blood compatibility. Nonadherence of blood components does not necessarily imply hematocompatibility.

Table 12 Hemocompatibility: test methods for implant devices

Test category	*Evaluation method*
Thrombosis	Scanning electron microscopy (platelet adhesion and aggregation); platelet and leukocyte morphology; fibrin
	Percent occlusion
	Flow reduction
	Labeled antibodies to thrombotic components
	Autopsy of devices (gross and microscopic); histopathology
	Autopsy of distal organs (gross and microscopic); histopathology
Coagulation	Specific coagulation factor assay; FPA, D-dimer, F_{1+2}, PAC-1, S-12, TAT
	PTT (nonactivated), PT, TT; plasma fibrinogen; FDP
Platelets	PF-4, β-TG, thromboxane B2
	Platelet activation markers
	Platelet microparticles
	Gamma imaging of radiolabeled platelets, ^{111}In-labeled platelet survival
	Platelet function analysis
	Platelet count/adhesion
	Platelet aggregation
Hematology	Leukocyte count with or without differential
	Leukocyte activation
	Hemolysis
	Reticulocyte count; activation-specific release products of peripheral blood cells (i.e., granulocytes)
Complement system	C3a, C5a, TCC, Bb, iC3b, C4b, SC5b-9, CH 50, C3 convertase, C5 convertase

Low flow *in vivo* venous models have been suggested for hematocompatibility evaluation. However, these systems are not appropriately and adequately justified for use in assessing the long-term biocompatibility required for cardiac and cardiovascular implants.

4.402.8. Immune Responses

Immune response evaluation is not a component of the standards currently available for *in vivo* tissue compatibility assessment. However, ASTM, ISO, and the FDA currently have working groups developing guidance documents for immune response evaluation where pertinent and technical reports have been produced. The need for immune response evaluation is clearly understood in the case of modified natural tissue implants such as collagen, which has been utilized in a number of different types of implants. The Center for Devices and Radiological Health of the FDA has released a draft immunotoxicity testing guidance document, the purpose of which is to provide a systematic approach to evaluating potential adverse immunological effects of medical devices and constituent materials.[12] Immunotoxicity is any adverse effect on the function or structure of the immune system or other systems as a result of an immune system dysfunction. Adverse or immunotoxic effects occur when humoral or cellular immunity needed by the host to defend itself against infections or neoplastic disease (immunosuppression) or unnecessary tissue damage (chronic inflammation, hypersensitivity, or autoimmunity) is compromised.

With the advent of tissue engineering, the importance of immune response and immunotoxicity evaluation has increased significantly.[62–66] Immune response evaluation is an especially challenging area given the unique nature of the respective medial devices and the latency or time delay in the presentation of a response. Differences between animal and human immune responses provide additional complexity to this issue. The following presents an overview of and guidance to immune response evaluation.

The inflammatory (innate) and immune (adaptive) responses have common components. It is possible to have only inflammatory responses with no adaptive immune response. In this situation, both humoral and cellular components that are shared by both types of responses may only participate in the inflammatory response. Table 13 indicates the common components of the inflammatory (innate) and immune (adaptive) responses. Macrophages and dendritic cells are known as

Table 13 Common components in the inflammatory (innate) and immune (adaptive) responses

Components
Complement cascade components
Immunoglobulins
Cellular components
Macrophages
NK (natural killer) cells
Dendritic cells
Cells with dual phagocytic and antigen-presenting capabilities

professional antigen-presenting cells (APCs) responsible for the initiation of the adaptive immune response.

The acquired or adaptive immune system acts to protect the host from foreign agents or materials and is usually initiated through specific recognition mechanisms and the ability of humoral and cellular components to recognize the foreign agent or material as being 'nonself.'[67] Generally, the adaptive immune system may be considered as having two components: humoral or cellular. Humoral components include antibodies, complement components, cytokines, chemokines, growth factors, and other soluble mediators. These components are synthesized by cells of the immune response and, in turn, function to regulate the activity of these same cells and provide for communication between different cells in the cellular component of the adaptive immune response. Cells of the immune system arise from stem cells in the bone marrow (B lymphocytes) or the thymus (T lymphocytes) and differ from each other in morphology, function, and in the expression of cell surface antigens. They share the common features of maintaining cell surface receptors that assist in the recognition and/or elimination of foreign materials. Regarding tissue-engineered devices, the adaptive immune response may recognize the biological components, modifications of the biological components, or degradation products of the biological components, commonly known as antigens, and initiate immune response through humoral or cellular mechanisms.

Components of the humoral immune system play important roles in the inflammatory responses to foreign materials. Antibodies and complement components C3b and C3bi adhere to foreign materials, act as opsonins, and facilitate phagocytosis of the foreign materials by neutrophils and macrophages that have cell surface receptors for C3b. Complement component C5a is a chemotactic agent for neutrophils, monocytes, and other inflammatory cells and facilitates the immigration of these cells to the implant site. The complement system is composed of classic and alternative pathways that eventuate in a common pathway to produce the membrane attack complex (MAC), which is capable of lysing microbial agents. The complement system, that is, complement cascade, is closely controlled by protein inhibitors in the host cell membrane that may prevent damage to host cells. This inhibitory mechanism may not function when nonhost cells are used in tissue-engineered devices.

T (thymus-derived) lymphocytes are significant cells in the cell-mediated adaptive immune response and their cell adhesion molecules play a significant role in lymphocyte migration, activation, and effector function. The specific interaction of cell membrane adhesion molecules, sometimes also called ligands or antigens, with APCs produce specific types of lymphocytes with specific functions. Table 14 indicates cell types and function in the adaptive immune response. Obviously, the functions of these cells are more numerous than that indicated in Table 14, but the major function of these cells is provided to indicate similarities and differences in the interaction and responsiveness of these cells. Effector T cells (Table 15) are produced when their antigen-specific receptors and either the CD4 or the CD8 co-receptors bind to peptide–MHC (major histocompatibility complex) complexes. A second, co-stimulatory signal is also required, and this is provided by the interaction of the CD28 receptor on the T cell and the B7.1 and B7.2 glycoproteins of the immunoglobulin superfamily present on APCs. B lymphocytes bind soluble antigens through their cell surface immunoglobulin and thus can function as professional APCs by internalizing the soluble antigens and presenting peptide fragments of these antigens as MHC:peptide complexes. Once activated, T cells can synthesize the T cell growth factor interleukin-2 and its receptor. Thus, activated T cells secrete and respond to interleukin-2 to promote T cell growth in an autocrine fashion.

Cytokines are the messenger molecules of the immune system. Most cytokines have a wide spectrum of effects, reacting with many different cell types, and some are produced by several different cell types. Table 16 presents common categories of cytokines and lists some of their general properties. It should be noted that while cytokines can be subdivided into functional groups, many cytokines such as IL-1, TNF-α, and

Table 14 Cell types and function in the adaptive immune system

Cell type	*Function*
Macrophages (APC)	Process and present antigen to immunocompetent T cells Phagocytosis Activated by cytokines (i.e., IFN-γ) from other immune cells
T cells	Interact with APCs and are activated through two required cell membrane interactions Facilitate target cell apoptosis Participate in transplant rejection (type IV hypersensitivity)
B cells	Form plasma cells that secrete immunoglobulins (IgG, IgA, and IgE) Participate in antigen–antibody complex mediated tissue damage (type III hypersensitivity)
Dendritic cells (APC)	Process and present antigen to immunocompetent T cells Utilize Fc receptors for IgG to trap antigen–antibody complexes
NK cells (non-T, non-B lymphocytes)	Innate ability to lyse tumor, virus infected, and other cells without previous sensitization Mediates T and B cell function by secretion of IFN-γ

Table 15 Effector T lymphocytes in adaptive immunity

Th1 helper cells	CD4+ Proinflammatory Activation of macrophages Produces IL-2, interferon-γ (IFN-γ), IL-3, TNF-α, GM-CSF, macrophage chemotactic factor (MCF), migration inhibitor factor (MIF) Induce IgG2a
TH2 helper cells	CD4+ Antiinflammatory Activation of B cells to make antibodies Produces IL-4, IL-5, IL-6, IL-10, IL-3, GM-CSF, and IL-13 Induce IgG1
Cytotoxic T cells (CTL)	CD8+ Induce apoptosis of target cells Produce IFN-γ, TNF-β, and TNF-α Release cytotoxic proteins

Table 16 Selected cytokines and their effects

Cytokine	*Effect*
IL-1, TNF-α, INF-γ, IL-6	Mediate natural immunity
IL-1, TNF-α, IL-6	Initiate nonspecific inflammatory responses
IL-2, IL-4, IL-5, IL-12, IL-15, and TGF-β	Regulate lymphocyte growth, activation, and differentiation
IL-2 and IL-4	Promote lymphocyte growth and differentiation
IL-10 and TGF-β	Downregulate immune responses
IL-1, INF-γ, TNF-α, and MIF	Activate inflammatory cells
IL-8	Produced by activated macrophages and endothelial cells Chemoattractant for neutrophils
MCP-1, MIP-α, and RANTES	Chemoattractant for monocytes and lymphocytes
GM-CSF and G-CSF	Stimulate hematopoiesis
IL-4 and IL-13	Promote macrophage fusion and FBGC formation

Table 17 Potential immunological effects and responses

Effects
Hypersensitivity
Type I – anaphylactic
Type II – cytotoxic
Type III – immune complex
Type IV – cell-mediated (delayed)
Chronic inflammation
Immunosuppression
Immunostimulation
Autoimmunity
Responses
Histopathological changes
Humoral responses
Host resistance
Clinical symptoms
Cellular responses
T cells
Natural killer cells
Macrophages
Granulocytes

IFN-γ are pleotropic in their effects and regulate, mediate, and activate numerous responses by numerous cells.

Immunotoxicity is any adverse effect on the function or structure of the immune system or other systems as a result of an immune system dysfunction.[12] Adverse or immunotoxic effects occur when humoral or cellular immunity needed by the host to defend itself against infections or neoplastic disease (immunosuppression) or unnecessary tissue damage (chronic inflammation, hypersensitivity, or autoimmunity) is compromised. Potential immunological effects and responses that may be associated with one or more of these effects are presented in Table 17. Hypersensitivity responses are classified on the basis of the immunologic mechanism that mediates the response. There are four types: type I (anaphylactic), type II (cytotoxic), type III (immune complex), and type IV cell-mediated (delayed) hypersensitivity. Hypersensitivity is considered to be increased reactivity to an antigen to which a human or animal has been previously exposed, with an adverse rather than a protective effect.[68] Hypersensitivity is a synonym for allergy. Type I (anaphylactic) reactions and type IV (cell-mediated delayed hypersensitivity) reactions are the most common. Types II and III reactions are relatively rare and are less likely to occur with medical devices and biomaterials; however, with tissue-engineered devices containing potential antigens, that is, proteins, extracellular matrix (ECM) components, and/or cells, types II and III reactions must be considered in biological response evaluations.

Type I (anaphylactic) hypersensitivity reactions are mediated by IgE antibodies which are cytotropic and affect the immediate release of basoactive amines and other mediators from basophils and mast cells followed by recruitment of other inflammatory cells. Type IV cell-mediated (delayed) hypersensitivity responses involve sensitized T lymphocytes that release cytokines and other mediators that lead to cellular and tissue injury. Type IV hypersensitivity (cell-mediated) reactions are initiated by specifically sensitized T lymphocytes. This reaction includes the classic delayed-type hypersensitivity reaction initiated by CD4+ T cells and direct cell cytotoxicity mediated by CD8+ T cells. The less common type II (cytotoxic) hypersensitivity involves the formation and binding of IgG and/or IgM to antigens on target cell surfaces that facilitate phagocytosis of the target cell or lysis of the target cell by activated complement components. Type II hypersensitivity (cytotoxic) is mediated by antibodies directed toward antigens present on the surface of cells or other tissue components. Three different antibody-dependent mechanisms may be involved in this type of reaction: complement-dependent reactions, antibody-dependent cell-mediated cytotoxicity, or antibody-mediated cellular dysfunction. Type III immune complex hypersensitivity is present when circulating antigen–antibody complexes activate complement the components of which are chemotactic for neutrophils that release enzymes and other toxic moieties and mediators leading to cellular and tissue injury.

Immunological reactions that occur with organ transplant rejection also offer insight into potential immune responses to tissue-engineered devices. Mechanisms involved in organ transplant rejection include T cell-mediated reactions by direct and indirect pathways and antibody-mediated reactions. Immune responses may be avoided or diminished by using autologous or isogeneic cells in cell/polymer scaffold constructs. The use of allogeneic or xenogenic cells incorporated into the device requires prevention of immune rejection by immune suppression of the host, induction of tolerance in the host, or immunomodulation of the tissue-engineered construct. The development of tissue-engineered constructs by immunoisolation using polymer membranes and the use of nonhost cells have been compromised by immune responses. In this concept, a polymer membrane is used to encapsulate nonhost cells or tissues thus separating them from the host immune system. However, antigens shed by encapsulated cells were released from the device and initiated immune responses.[69–71]

Although exceptionally minimal and superficial in its presentation, the previously discussed humoral and cell-mediated immune responses demonstrate the possibility that any known tissue-engineered construct may undergo immunologic tissue

injury. To date, our understanding of immune mechanisms and their interactions with tissue-engineered constructs is markedly limited. One of the obvious problems is that preliminary studies are generally carried out with nonhuman tissues and immune reactions result when tissue-engineered constructs from one species are used in testing the device in another species. Ideally, tissue-engineered constructs would be prepared from cells and tissues of a given species and subsequently tested in that species. While this approach does not guarantee that immune responses will not be present, the probability of immune responses in this type of situation is markedly decreased.

The following examples provide insight into these issues. They further demonstrate in detail the approach that must be taken to appropriately and adequately evaluate tissue-engineered constructs or devices and their potential adverse responses.

The inflammatory response considered to be immunotoxic is persistent chronic inflammation. With biomaterials, controlled release systems, and tissue-engineered devices, potential antigens capable of stimulating the immune response may be present and these agents may facilitate a chronic inflammatory response that is of extended duration (weeks, months). Regarding immunotoxicity, it is this persistent chronic inflammation that is of concern as immune granuloma formation and other serious immunological reactions such as autoimmune disease may occur. Thus, in biological response evaluation, it is important to discriminate between the short-lived chronic inflammation that is a component of the normal inflammatory and healing responses versus long-term, persistent chronic inflammation that may indicate an adverse immunological response.

Immunosuppression may occur when antibody and T cell responses (adaptive immune response) are inhibited. Potentially significant consequences of this type of response are frequent and serious infections resulting from reduced host defense.

Immunostimulation may occur when unintended or inappropriate antigen-specific or nonspecific activation of the immune system is present. From a biomaterials and controlled release system perspective, antibody and/or cellular immune responses to a foreign protein may lead to unintended immmunogenicity. Enhancement of the immune response to an antigen by a biomaterial with which it is mixed ex vivo or in situ may lead to adjuvancy, which is a form of immunostimulation. This effect must be considered when biodegradable controlled release systems are designed and developed for use as vaccines.

Autoimmunity is the immune response to the body's own constituents, which are considered in this response to be autoantigens. An autoimmune response, indicated by the presence of autoantibodies or T lymphocytes that are reactive with host tissue or cellular antigens, may, but not necessarily, result in autoimmune disease with chronic, debilitating, and sometimes life-threatening tissue and organ injury.[72]

Representative tests for the evaluation of immune responses are given in Table 18. Table 18 is not all-inclusive and other tests may be applicable. The examples presented in Table 18 are only representative of the large number of tests that are currently available.[67] Table 18 is informative but incomplete as in the future direct and indirect markers of immune response may be validated and their predictive value documented thus providing new tests for immunotoxicity. Direct measures of immune system activity by functional assays are the most important types of test for immunotoxicity. Functional assays are generally more important than tests for soluble mediators, which are more important than phenotyping. Signs of illness may be important in *in vivo* experiments but symptoms may also have a significant role in studies of immune function in clinical trials and postmarket studies.

Table 18 Representative tests for the evaluation of immune responses

Functional assays	*Soluble mediators*
Skin testing	Antibodies
Immunoassays (e.g., ELISA)	Complement
Lymphocyte proliferation	Immune complexes
Plaque-forming cells	Cytokine patterns (T cell subsets)
Local lymph node assay (LLNA)	Cytokines (IL-1, IL-1ra, TNF-α, IL-6, TGF-β, IL-4, IL-13)
Mixed lymphocyte reaction	Chemokines
Tumor cytotoxicity	Basoactive amines
Antigen presentation	
Phagocytosis	
Degranulation	*Signs of illness*
Resistance to bacteria, viruses, and tumors	Allergy
	Skin rash
	Urticaria
Phenotyping	Edema
Cell surface markers	Lymphadenopathy
MHC markers	

As with any type of test for biological response evaluation, immunotoxicity tests should be valid and have been shown to provide accurate, reproducible results that are indicative of the effect being studied and are useful in a statistical analysis. This implies that appropriate control groups are also included in the study design.

Immunogenicity involving a specific immune response to a biomaterial is an important consideration as it may lead to serious adverse effects. For example, a foreign, nonhuman, protein may induce IgE antibodies that cause an anaphylactic (type I) hypersensitivity reaction. An example of this type of response is latex protein found in latex gloves. Low molecular weight compounds such as chemical accelerators used in the manufacture of latex gloves may also induce a T cell-mediated (type IV) reaction resulting in contact dermatitis. Tests for type I, for example, antigen-specific IgE, and type IV, for example, guinea pig maximization tests, hypersensitivity should be considered for materials with the potential to cause these allergic reactions. In addition to hypersensitivity reactions, a device may elicit autoimmune responses, that is, antibodies or T cells that react with the body's own constituents. An autoimmune response may lead to the pathological consequences of an autoimmune disease. For example, a foreign protein may induce IgG or IgM antibodies that cross-react with a human protein and cause tissue damage by activating the complement system. In a similar fashion, a biomaterial or controlled release system that has a gel or oil constituent may act as an adjuvant leading to the induction of an autoimmune response. Even if an autoimmune response (autoantibodies and/or autoreactive

T lymphocytes) is suggested in preclinical testing, it is difficult to obtain convincing evidence that a biomaterial or controlled release system causes autoimmune disease in animals. Therefore, routine testing for the induction of autoimmune disease in animal models is not recommended.

Babensee and coworkers have tested the hypothesis that the biomaterial component of a medical device, by promoting an inflammatory response, can recruit APCs (e.g., macrophages and dendritic cells) and induce their activation, thus acting as an adjuvant in the immune response to foreign antigens originating from the histological component of the device.[73–78] Utilizing polystyrene and poly(lactic–glycolic acid) microparticles and poly(lactic–glycolic) scaffolds together with their model antigen, ovalbumin, in a mouse model for 18 weeks, Babensee *et al.*, demonstrated that a persistent humoral immune response that was Th2 helper T cell dependent, as determined by the IgG1, was present. These findings indicated that the activation of CD4+ T cells and the proliferation and isotype switching of B cells had occurred. A Th1 immune response, characterized by the presence of IgG2a, was not identified. Moreover, the humoral immune responses for all three types of microparticles were similar indicating that the production of antigen-specific antibodies was not dependent on the chemistry of the material in this model. Babensee suggests that the presence of the biomaterial functions as an adjuvant for initiation and promotion of the immune response and augments the phagocytosis of the antigen with expression of MHC class II and co-stimulatory molecules on APCs with the presentation of antigen to CD4+ T cells.

Babensee and coworkers have identified differential levels of dendritic cell maturation on different biomaterials used in combination products.[79,80] The effect of biomaterials on dendritic cells maturation, and the associated adjuvant effect, is a novel biocompatibility selection and design criterion for biomaterials to be used in combination products in which immune consequences are potential complications or outcomes.

Badylak and colleagues have carried out extensive studies of the utilization of xenogeneic ECM as a scaffold for tissue reconstruction.[81,82] Use of the small intestinal submucosa (SIS) ECM in animals has indicated a restricted Th2-type immune response. The presence of natural antibodies to the terminal galactose-α-1,3-galactose (α-gal) epitope is considered to be a major barrier to xenotransplantation in humans. Cell membranes of all animals except those of the humans express this epitope and naturally occurring antibodies mediate hyperacute or delayed rejection of transplanted organs through complement fixation or antibody-dependent cell-mediated cytotoxicity. While ECM derived from porcine tissues, SIS, contain small amounts of the gal epitope, it appears that the quantity or distribution of this epitope and/or the subtype of immunoglobulin response to the epitope is such that complement activation does not occur.[83] In addition, the resorbable characteristics of this nonchemically cross-linked ECM scaffold demonstrate constructive tissue remodeling and deposition of new matrix, whereas chemically cross-linked ECM leads to active inflammation and eventually scar formation.

The role of Th1 and Th2 lymphocytes in cell-mediated immune responses to xenografts has been examined. Activation of the Th1 pathway leads to macrophage activation, stimulation of complement fixing antibody isotypes, and differentiation of CD8+ cells to a cytotoxic type phenotype that is associated with both allogeneic and xenogeneic transplant rejection. The Th2 lymphocyte response does not activate macrophages and leads to production of noncomplement fixing antibody isotypes and is usually associated with transplant acceptance.

The use of appropriate animal models is important in the safety evaluation of controlled release systems that may contain potential immunoreactive materials.[84–86] A recently published study involving the *in vivo* evaluation of recombinant human growth hormone in poly(lactic-*co*-glycolic acid) (PLGA) microspheres demonstrates the appropriate use of various animal models to evaluate biological responses and the potential for immunotoxicity. Utilizing biodegradable PLGA microspheres containing recombinant human growth hormone (rhGH), Cleland et al. used rhesus monkeys, transgenic mice expression rhGH, and normal control (Balb/C) mice in their *in vivo* studies.[87] Rhesus monkeys were utilized for serum assays in the pharmacokinetic study of rhGH release as well as tissue responses to the injected microcapsule formulation. Placebo injection sites were also utilized and a comparison of the injection sites from rhGH PLGA microspheres and placebo PLGA microspheres demonstrated a normal inflammatory and wound-healing response with a normal focal foreign-body reaction. To further examine the tissue response, transgenic mice were utilized to assess the immunogenicity of the rhGH PLGA formulation. Transgenic mice expressing a heterologous protein have been previously used for assessing the immunogenicity of sequence or structural mutant proteins.[88,89] With the transgenic animals, no detectable antibody response to rhGH was found. In contrast, the Balb/C control mice had a rapid onset of high titer antibody response to the rhGH PLGA formulation. This study points out the appropriate utilization of animal models to evaluate not only biological responses but also one type of immunotoxicity (immunogenicity) of controlled release systems.

4.402.9. Summary and Conclusion

The identification of the fundamental biological requirements of a biomaterial first requires the identification of how the biomaterial is to be used and in what type of implant, medical device, or prosthesis. After the identification of the intended application of the biomaterial, the identification of the tissues that will contact the biomaterial and the implant duration of the biomaterial, medical device, or prosthesis is necessary. Once these parameters have been defined, appropriate *in vitro* and *in vivo* assays can be selected to identify the success or failure of the biomaterial and its intended application. A broad perspective in the selection of *in vitro* and *in vivo* biocompatibility assays is necessary to not only identify adverse reactions but also to identify reactions that indicate the successful function of the biomaterial in its intended application. Adverse tissue responses do not necessarily reject a biomaterial from use in a medical device or prosthesis. Adverse tissue responses do require a risk assessment evaluation in which the risks are weighed against the benefits in the use of the biomaterial. A risk assessment program may involve additional biocompatibility testing in addition to the development

of a rationale and justification for continued use of a biomaterial that may present with adverse tissue reactions. Finally, it must be remembered that appropriate and adequate biocompatibility evaluation requires testing of the material, medical device, or prosthesis in its 'end-use' state, that is, as a product in which manufacturing processes and sterilization procedures have been considered.

This chapter presents biocompatibility evaluation in the context of current standards and guidelines. As such, it must be emphasized that standards and guidelines are constantly changing and evolving as new medical devices and prostheses, and biomaterials are developed for clinical application and new scientific information is obtained that provides new perspectives on the how and why of specific test procedures. The past decade has seen a virtual explosion in the areas of nanomaterials, tissue engineering, and combination products, each of which brings its own unique characteristics to biocompatibility testing and the development of tests that will ensure safety in clinical application. An example of new perspectives on biocompatibility testing is provided by recent efforts to move away from the use of animals and develop cell-culture-based alternative testing methods. Finally, it should be noted that this chapter presents biocompatibility testing from a so-called horizontal perspective, that is, the suggested test methods should be considered for all types of medical devices, prostheses, and biomaterials. Device-specific standards and guidelines, that is, vertical standards, available from ISO, ASTM, and the FDA have not been considered in this chapter.

References

1. Williams, D. F. In *Proceedings of a Consensus Conference of the European Society for Biomaterials,* Chester, England, March 3–5, 1986; Elsevier: Amsterdam, 1987; Vol. 4.
2. Williams, D. F. *Biomaterials* **2008**, *29*, 2941–2953.
3. Anderson, J. M. *Ann. Rev. Mater. Res.* **2001**, *31*, 81–110.
4. Johnson, H. J.; Northup, S. J.; Seagraves, P. A.; *et al*. *J. Biomed. Mater. Res.* **1985**, *19*, 489–508.
5. Northup, S. J. In *Handbook of Biomaterials Evaluation: Scientific, Technical and Clinical Testing of Implant Materials*; von Recum, A. F., Ed.; Macmillan: New York, 1986.
6. U. S. Pharmacopeia. In *U. S. Pharmacopoeia 23*, United States Pharmacopeial Convention: Rockville, MD, 2004; Vol. 27, pp 2173–2175.
7. AAMI Standards and Recommended Practices. Biological Evaluation of Medical Devices, Association for the Advancement of Medical Instrumentation, 1997, 1998, Vol. 4S, Supplement.
8. ASTM. *2008 Annual Book of ASTM Standards*, ASTM International, 2008; Vol. 13.01.
9. Chapekar, M. S. *J. Biomed. Mater. Res. Appl. Biomat.* **1996**, *33*, 199–203.
10. FDA. *Blue Book Memorandum G95-1: FDA-modified version of ISO 10993-Part 1, Biological Evaluation of Medical Devices – Part 1: Evaluation and Testing*, 1995.
11. ISO 10993. Biological Evaluation of Medical Devices.
12. Langone, J. J. In *Immunotoxicity Testing Guidance*, Draft Document, Office of Science and Technology, Center for Devices and Radiological Health, Food and Drug Administration, 1998.
13. Anderson, J. M.; Schoen, F. J.; Brown, S. A.; Merritt, K. In *Biomaterials Science*; Ratner, B. D., *et al*. Eds.; Elsevier/Academic Press: New York, 2004; pp Chapter 9.5, pp 771–782.
14. ISO 12891. Retrieval and Analysis of Implantable Medical Devices.
15. Yamamoto, S.; Urano, K.; Koizumi, H.; *et al*. *Environ. Health Perspect.* **1998**, *106*(Suppl. 1), 57–69.
16. Anderson, J. M.; Christenson, E. M.; Hiltner, A. *Corrosion Eng. Sci. Technol.* **2007**, *42*(4), 312–323.
17. Dadsetan, M.; Christenson, E. M.; Unger, F.; Ausborn, M.; Kissel, T.; Hiltner, A.; Anderson, J. M. *J. Control. Rel.* **2003**, *93*, 259–270.
18. Yamaguchi, K.; Anderson, J. M. *J. Control. Rel.* **1992**, *19*, 299–314.
19. Kumar, V.; Abbas, A. K.; Fausto, N.; Eds. *Robbins and Cotran Pathologic Basis of Disease*, 7th ed.; W. B. Saunders: Philadelphia, PA, 2005; pp 47–118.
20. Gallin, J. I.; Snyderman, R.; Eds. *Inflammation: Basic Principles and Clinical Correlates*, 3rd ed., Raven Press: New York, 1999.
21. Zdolsek, J.; Eaton, J. W.; Tang, L. *J. Transl. Med.* **2007**, *5*, 31–37.
22. Wiggins, M. J.; Wilkoff, B.; Anderson, J. M.; Hiltner, A. *J. Biomed. Mater. Res.* **2001**, *58*, 302–307.
23. Henson, P. M. *J. Immunol.* **1971**, *107*, 1547–1557.
24. Marchant, R. E.; Anderson, J. M.; Dillingham, E. O. *J. Biomed. Mater. Res.* **1986**, *20*, 37–50.
25. Brodbeck, W. G.; MacEwan, M.; Colton, E.; Meyerson, H.; Anderson, J. M. *J. Biomed. Mater. Res. A* **2005**, *74*, 222–229.
26. MacEwan, M. R.; Brodbeck, W. G.; Matsuda, T.; Anderson, J. M. *J. Biomed. Mater. Res.* **2005**, *74*, 285–293.
27. Haas, A. *Traffic* **2007**, *8*, 311–330.
28. Jankowski, A.; Scott, C. C.; Grinstein, S. *J. Biol. Chem.* **2002**, *277*, 6059–6066.
29. Klebanoff, S. J. *J. Leukocyte Biol.* **2005**, *77*, 598–625.
30. Segal, A. W. *Annu. Rev. Immunol.* **2005**, *23*, 197–223.
31. Silver, I. A.; Murrills, R.; Etherington, D. J. *Exp. Cell Res.* **1988**, *175*, 266–276.
32. Browder, T.; Folkman, J.; Pirie-Shepherd, S. *J. Biol. Chem.* **2000**, *275*, 1521–1524.
33. Nguyen, L. L.; D'Amore, P. A. *Int. Rev. Cytol.* **2001**, *204*, 1–48.
34. Broughton, G.; Janis, J. E.; Attinger, C. E. *Plast. Reconstr. Surg.* **2006**, *117*(Suppl.), 12S–34S.
35. Clark, R. A. F.; Ed. *The Molecular and Cellular Biology of Wound Repair*; Plenum Publishing: New York, 1996.
36. Hunt, T. K.; Heppenstall, R. B.; Pines, E.; Rovee, D.; Eds. *Soft and Hard Tissue Repair*; Praeger Scientific: New York, 1984.
37. Mustoe, T. A.; Pierce, G. F.; Thomason, A.; Gramats, P.; Sporn, M. B.; Deuel, T. F. *Science* **1987**, *237*, 1333–1336.
38. Pierce, G. F. *Am. J. Pathol.* **2001**, *159*(2), 399–403.
39. Anderson, J. M.; Rodriguez, A.; Chang, D. T. *Semin. Immunol.* **2008**, *20*, 86–100.
40. Charnley, J. *J. Bone Joint Surg.* **1970**, *53B*, 340–353.
41. Charnley, J.; Kamangar, A.; Longfield, M. D. *Med. Biol. Eng.* **1969**, *7*, 31–39.
42. Ney, A.; Xia, T.; Mädler, L.; Li, N. *Science* **2006**, *311*, 622–627.
43. Revell, P. A. In *Joint Replacement Technology*; Revell, P. A., Ed.; Woodhead: Cambridge, UK, 2008; pp 315–348.
44. Revell, P. A. *J. Roy. Soc. Interface* **2008**, *5*, 1263–1278.
45. Purdue, E. *Autoimmunity* **2008**, *41*(3), 212–217.
46. Brodbeck, W. G.; Anderson, J. M. *Curr. Opin. Hematol.* **2009**, *16*, 53–57.
47. McNally, A. K.; Anderson, J. M. *Am. J. Pathol.* **1995**, *147*, 1487–1499.
48. McNally, A. K.; DeFife, K. M.; Anderson, J. M. *Am. J. Pathol.* **1996**, *149*, 1487–1499.
49. Hynes, R. O. *Cell* **2002**, *110*, 673–687.
50. Hynes, R. O.; Zhao, Q. *J. Cell. Biol.* **2000**, *150*, F89–F96.
51. Jenney, C. R.; Anderson, J. M. *J. Biomed. Mater. Res.* **2000**, *50*, 281–290.
52. McNally, A. K.; Anderson, J. M. *Proc. Natl. Acad. Sci. USA* **1994**, *91*, 10119–10123.
53. McNally, A. K.; Anderson, J. M. *Am. J. Pathol.* **2002**, *160*, 621–630.
54. McNally, A. K.; MacEwan, S. R.; Anderson, J. M. *J. Biomed. Mater. Res.* **2007**, *82A*, 568–574.
55. McNally, A. K.; Jones, J. A.; MacEwan, S. R.; Colton, E.; Anderson, J. M. *J. Biomed. Mater. Res.* **2008**, *86A*(2), 535–543.
56. Nilsson, B.; Ekdahl, K. N.; Mollnes, T. E.; Lambris, J. D. *Mol. Immunol.* **2007**, *44*, 82–94.
57. Anderson, J. M.; Jones, J. A. *Biomaterials* **2007**, *28*, 5114–5120.
58. Chang, D. T.; Colton, E.; Anderson, J. M. *J. Biomed. Mater. Res.* **2009**, *89A*(2), 490–498.
59. Jones, J. A.; Chang, D. T.; Meyerson, H.; Colton, E.; Kwon, I. K.; Matsuda, T.; Anderson, J. M. *J. Biomed. Mater. Res.* **2007**, *83A*, 585–596.
60. Gorbet, M. B.; Sefton, M. V. *Biomaterials* **2004**, *25*, 5681–5703.
61. Hanson, S. R.; Ratner, B. D. In *Biomaterials Science*; Ratner, B. D., *et al*. Eds.; Elsevier/Academic Press: New York, 2004; pp Chapter 5.4, pp 367–377.
62. Jones, K. S. *Tissue Eng. B* **2008**, *14*(4), 407–417.
63. Jones, K. S. *Semin. Immunol.* **2008**, *20*, 130–136.
64. Merritt, K.; Brown, S. A. *Int. J. Dermatol.* **1981**, *20*, 89–94.
65. Merritt, K.; Rodrigo, J. J. *Clin. Orthop.* **1996**, *329S*, S233–S243.

66. Sefton, M. V.; Babensee, J. E.; Woodhouse, K. A.; Eds. *Sem. Immunol*. **2008**, *20*(2).
67. Rose, N. R.; de Mecario, E. C.; Folds, J. D.; Lane, H. C.; Nakamura, R. M.; Eds. *Manual of Clinical Laboratory Immunology*; ASM Press: Washington, DC, 1997.
68. Nebeker, J. R.; Virmani, R.; Bennett, C. L.; *et al*. *J. Am. Coll. Cardiol*. **2006**, *47*, 175–181.
69. Babensee, J. E.; Anderson, J. M.; McIntire, L. V.; Mikos, A. G. *Adv. Drug Deliv. Rev.* **1998**, *33*, 111–139.
70. Brauker, J. *Cell Transplant*. **1992**, *1*, 163.
71. Brauker, J. H.; Carr-Brendel, V. E.; Martinson, L. A.; Crudele, J.; Johnston, W. D.; Johnson, R. C. *J. Biomed. Mater. Res.* **1995**, *29*, 1517–1524.
72. Ochando, J. C.; Homma, C.; Yang, Y.; *et al*. *Nat. Immunol*. **2006**, *7*, 652–662.
73. Babensee, J. E.; Stein, M. M.; Moore, L. K. *Ann. NY Acad. Sci*. **2002**, *961*, 360–363.
74. Jeong, H. J.; Lee, S. A.; Moon, P. D.; *et al*. *Clin. Exp. Allergy* **2006**, *36*, 785–794.
75. Matzell, M. M.; Babensee, J. E. *Biomaterials* **2004**, *25*, 295–304.
76. Yang, D.; Jones, K. S. *J. Biomed. Mater. Res*. **2009**, *90A*, 411–418.
77. Yoshida, M.; Babensee, J. E. *J. Biomed. Mater. Res*. **2006**, *79*, 393–408.
78. Yoshida, M.; Babensee, J. E. *J. Biomed. Mater. Res*. **2004**, *71*, 45–54.
79. Babensee, J. E.; Paranjpe, A. *J. Biomed. Mater. Res*. **2005**, *74A*, 503–510.
80. Bennewitz, N. L.; Babensee, J. E. *Biomaterials* **2005**, *26*, 2991–2999.
81. Allman, A. J.; McPherson, T. B.; Merrill, L. C.; Badylak, S. F.; Metzger, D. W. *Tissue Eng*. **2002**, *8*(1), 53–62.
82. Badylak, S. F. *Transpl. Immunol*. **2004**, *12*, 367–377.
83. McPherson, T. B.; Liang, H.; Record, R. D.; Badylak, S. F. *Tissue Eng*. **2000**, *6*(3), 233–239.
84. Cohen, I. R.; Miller, A.; Eds. *Autoimmune Disease Models: A Guidebook*; Academic Press: New York, 1994.
85. Greenwald, R. A.; Diamond, H. S.; Eds. In *Handbook of Animal Models for the Rheumatic Diseases*; CRC Press: Boca Raton, FL, 1988; Vol. 1.
86. Rose, N. R. In *Handbook of Human Immunology*; Lefell, M. S., Donnenberg, A. D., Rose, N. R., Eds.; CRC Press: Boca Raton, FL, 1997; pp pp 111–123.
87. Cleland, J. L.; Duenas, E.; Daugherty, A.; *et al*. *J. Control. Rel*. **1997**, *49*, 193–205.
88. Stewart, T. A.; Hollinghead, P. G.; Pitts, S. L.; Chang, R.; Martin, L. E.; Oakley, H. *Mol. Biol. Med*. **1989**, *6*, 275–281.
89. Stewart, T. A. *Trends Endocrinol. Metab*. **1993**, *4*, 136–141.

4.403. The Innate Response to Biomaterials

P A Lalor, Histion, LLC, Everett, WA, USA
L C Jones, Johns Hopkins Orthopaedics at Good Samaritan Hospital, Baltimore, MD, USA

© 2011 Elsevier Ltd. All rights reserved.

4.403.1.	**Introduction**	28
4.403.2.	**Biomaterial Changes**	29
4.403.3.	**Inflammation and Biomaterials**	29
4.403.3.1.	Infection	30
4.403.3.2.	Persistent and Chronic Inflammatory Responses	31
4.403.3.2.1.	Nondegradable materials	31
4.403.3.2.2.	Biodegradable materials	32
4.403.4.	**Evasion Innate Immune System Activation**	33
4.403.5.	**Enhancement of Innate Immune System Activation**	34
4.403.6.	**Concluding Remarks**	34
References		35

Glossary

Acquired immune response A learned response by the immune system of nearly all living things that is developed after a primary exposure to a pathogen or irritant. The development of an acquired response by the immune system results in a more rapid and aggressive response to a repeated exposure by the same pathogen.

Adjuvant Any substance added to a vaccine that acts to accelerate, prolong, or enhance antigen-specific, adaptive immune responses.

Chemotaxis The process by which bodily cells, bacteria, and other single-cell or multicellular organisms direct their movements according to upregulation or downregulation of chemicals including cytokines in their environment.

Chronic inflammatory response Inflammatory response that is persistent and lasting over time.

Inflammasome A multiprotein complex consisting of caspase-1, PYCARD, a NALP, and sometimes caspase-5 or caspase-11. The exact composition of an inflammasome is dependent on the activator which initiates inflammasome assembly (e.g., dsRNA will trigger one inflammasome composition and asbestos will induce assembly a different variant). The inflammasome promotes maturation of inflammatory cytokines interleukin-1β and interleukin-18. The inflammasome is responsible for activation of inflammatory processes, and has been shown to induce cell pyroptosis, a process of programmed cell death distinct from apoptosis. http://en.wikipedia.org/wiki/Inflammasome – cite_note-2.

Inflammation Part of a complex biological response to harmful stimuli including pathogens, traumatic or surgical injury, disease, damaged cells, and irritants. Inflammation is a protective attempt by organisms to remove injurious stimuli and to initiate the healing process. Inflammation is a normal, beneficial response, and not considered adverse unless it becomes chronic and does not promote healing over time.

Innate immune response An intrinsic response of the immune system that is essential or inherent. It is the major response or host defense against pathogens in humans and nearly all other living things.

Passivation The process of making a biomaterial innert, usually by the deposition of a layer of oxide on its surface.

Phagocytosis The cellular process of engulfing solid particles by the cell membrane to form an internal phagosome by phagocytes such as macrophages.

Abbreviations

AR3	Aldehyde reductase
BMPs	Bone morphogenetic protein
C3, C4, C5	Complement proteins
C5a	Complement factor 5a
CoCr	Cobalt chromium
DC	Dendritic cells
dsRNA	Double-stranded RNA
GCs	Giant cells
GPIIb-IIIa	Glycoprotein IIb-IIIa
IgG	Immunoglobulin G
IL	Interleukin
INF-γ	Interferon gamma
NALP	Nacht domain-, leucine-rich repeat-, and PYD-containing protein 3
NK	Natural killer cells
NOD-like	Nucleotide-binding oligomerization domain-like
PEEK	Polyether ether ketone
PGA	Poly(gamma-glutamic acid)
PLA	Polylactic acid
PLGA	Polylactic-*co*-glycolic acid
PMNL	Polymorphonuclear leukocytes
PS	Polystyrene

PVA	Polyvinyl acetate	**TiAlV**	Titanium aluminum vanadium
PYCARD	PYRIN and caspase activation and recruitment domains	**TLRs**	Toll-like receptors
		UHMWPE	Ultrahigh molecular-weight polyethylene
SS	Stainless steel		

4.403.1. Introduction

Physical barriers, such as skin, nails, lips, and mucous membranes, are the first line of defense against pathogen invasion and irritants and are fairly effective in our day-to-day, minute-to-minute defense against exposure to microbes. However, the barriers can be compromised by disease or a physical breach (traumatic or surgical). Once they are breached, there are several strategies that can be used by the human body to respond to the presence of the foreign invader. Traditionally, these response methods have been segregated into *innate* (also called nonspecific) and *acquired* (also called adaptive or specific) immune responses.

The innate, or nonspecific immune response, is used against pathogens that have not been previously encountered and irritants that may or may not have been previously encountered. Unlike the acquired immune response, which adapts rapidly to a second or repeated invasion and therefore confers more long-term protection against pathogens, the innate response is more immediate, but generally takes longer to develop because a new strategy must be devised to deal effectively with the novel intruder or irritant. The major functions of the innate system are (1) inflammation with recruitment of immune cells to sites of infection through the production of cytokines; (2) activation of the complement cascade to identify bacteria, activate cells, and to promote clearance of dead cells or antibody complexes; (3) identification and removal of foreign substances present in organs, tissues, blood, and lymph by specialized white blood cells; and (4) activation of an adaptive immune response via antigen presentation. The major functions of the adaptive immune system are (1) rapid recognition of a returning invasive pathogen or antigen; (2) inflammation or recruitment of immune cells to sites of infection through the production of cytokines; (3) rapid production of antibodies specific to the pathogen; and (4) rapid removal of foreign substances present in organs, tissues, blood, and lymph by specialized white blood cells.

Although there are many differences between the two systems (Table 1), more recent investigations have provided evidence that there is considerable overlap. For example, T-lymphocytes may help macrophages to be more effective as phagocytes, whereas macrophages are needed to present antigens to T-lymphocytes to activate the acquired immunity pathways. Therefore, it is possible to view these systems as a continuum rather than as two separate systems, that is, the response to a pathogen begins with the innate response and macrophages phagocytosing the invader. Macrophages are activated to release cytokines. Other macrophages or precursor cells are then exposed to these cytokines. When recruited, macrophages ingest more particles, become antigen-presenting cells, and then play a role in the acquired immune system.

Irrespective of whether the immune system is viewed as a two-compartment or as an integrated system, the human body's defense against microbes and foreign bodies involves an interrelationship among mechanisms associated with wound healing, acute and chronic inflammation, and innate and acquired immunity. These defenses raised against the invader(s) produce a redundancy of feedback mechanisms that, when activated, serve to maintain homeostasis.

Medical devices used for structural repair and/or regeneration of tissues impact the immune system directly because all medical devices are composed of components that are considered foreign by the immune system whether they consist of nonautologous tissues or tissue components, metals, or polymers. Implantation of any biomaterial should therefore be considered a breach of the immune system. As such, the appropriate selection of a biomaterial or combination of biomaterials is critical to ensure a successful application as a reparative or regenerative device or as a drug-delivery vehicle/device. Selection of a biomaterial should be on the basis not only of engineering considerations but also of whether a material changes immediately after introduction into the body or with time as the implant wears or degrades. Chemical and/or physical temporal implant changes will dictate and drive the innate and adaptive responses to the biomaterials to advantage or disadvantage, depending on the biomaterial choice and the application for which it was chosen.

Table 1 Characterization of innate and adaptive immune responses

Parameter	*Innate*	*Adaptive*
Cells	Coordinated effort from many types of cells including eosinophils, neutrophils, macrophages, mast cells, and NK cells	Coordinated effort between antigen-presenting cells, T-cells, B-cells, and plasma cells
Response time	Rapid (<2 days)	Slower (>2 days)
Memory	None	Plasma cells
Circulating molecules	Complement	Antibodies
Effector molecules	Cytokines	Cytokines
Magnitude of the response	Moderate	Exponential

4.403.2. Biomaterial Changes

Upon implantation, immediate exposure of all implant types to bodily fluids can result in changes or modifications at the surface of the implant that will impact the immune response to the implant. These modifications may include physical changes to the implant surface (such as that which occur with passivation) or physical changes associated with preferential protein deposition on the surface of the implant.

Initially, metal, but not other types of implants, can undergo direct material changes, such as passivation or repassivation that can occur if a manufactured passivation layer intended to render the metal inactive to bodily fluids is scraped from the surface during implantation (e.g., implantation of a soft alloy such as a titanium, aluminum vanadium (TiAlV) total hip implant into bone). This type of change is usually rapid and, in and of itself, appears to have no long-term biological impact unless the process repeatedly occurs because of loosening and results in a large deposition of wear debris[1,2] (see a more detailed description of this phenomenon below).

Passivation can also be accomplished by the deposition of proteins that adhere to all implant surfaces, depending on the physical and chemical properties of the biomaterial. Although this type of passivation process has been harnessed to advantage for vascular implants (whereby the adsorbed proteins serve to passivate stent biomaterials), some investigators have shown that adsorbed protein(s) may undergo conformational changes (i.e., changes in tertiary structure) that could render the protein(s) foreign to the immune system.[3–5] This type of process could conceivably induce an autoimmune response whereby an overactive immune response targets self proteins. While there is no definitive evidence to prove that autoimmunity occurs with medical devices, there has been considerable debate over the evidence that suggests an association between specific implants and autoimmunity.[6] However, adsorbed proteins can be problematic, as has been shown with nonpassivated vascular implants that allow for deposition of proteins such as IgG, C3, fibrinogen, and factor XII (FXII), the effect of which is activation of the coagulation, contact, and complement systems that can ultimately lead to deposition of cells such as platelets, polymorphonuclear leukocytes (PMNL), and monocytes and subsequent thrombosis/stenosis.[7,8] Another example of problematic protein deposition occurs with silicone hydrogel contact lenses, in which deposition of proteins such as denatured lysozyme and albumin on the surface of the lenses can cause irritation.[9]

The immediate host response to implantation is therefore dictated, in part, by protein deposition, and may involve immediate self or nonself (i.e., foreign) recognition as the mechanisms directing acute inflammation and wound repair are activated and temporally contribute to the response to the implant. Assuming appropriate surgical placement, the manner in which healing then progresses is based on the configuration and the material composition of the implant (i.e., whether the materials are inert or biodegradable and whether they are present in appropriate configurations and/or concentrations), the site of implantation, and previous exposure of the host to the implant materials. All of these factors will dictate whether the implant is initially considered inert and therefore simply walled off, or is degraded or integrated with time via a dynamic removal and/or integration of the material(s).

Both inert and degradable biomaterials can change chemically and physically with time, producing chemical byproducts that induce a response that is similar to or different from the initial response to the bulk implant. The healing response can also be complicated by the presence of biomaterial particles (caused by physical or chemical breakdown of implants) that increase the surface area of the materials considerably and therefore increase the exposure of the body to the protein-bound surfaces of the materials or, for biodegradable materials, to increased amounts of chemical breakdown products. Inert materials may, with time, age and degrade *in vivo*, or they may be physically abraded against native tissues or other implant materials, resulting in the generation of particles. Therefore, the dynamic changes of both inert and biodegradable biomaterials will also affect the response to the medical device over time.

4.403.3. Inflammation and Biomaterials

Injection or surgical implantation of a medical device always results in a breach of the first lines of defense (i.e., skin and mucous membranes) and in inflammation, irrespective of whether the implant is composed of a metal, a polymer, a substance of biological origin (e.g., organ, tissue, or protein), or a combination of one or more biomaterials, with or without the addition of drugs. Acute inflammation is a necessary step for an appropriate wound-healing response, and therefore a normal and expected early response to biomaterials and medical devices. Steps in the inflammatory process that ultimately lead to functional incorporation of medical devices comprise the following[10,11]:

1. vasodilation and increased permeability of endothelium – release of circulating leukocytes and fluid, containing enzymes and other proteins, into the region of the insult;
2. decreased blood flow, sludging, clotting, and coagulation;
3. cellular invasion – margination, emigration (diapedesis);
4. chemotaxis – migration toward the site of injury or foreign body;
5. activation of phagocytic cells – synthesis and release of specific substances;
6. resolution with remodeling of tissues.

The immediate response to injection or implantation of a device is influenced by the nature (e.g., injection or surgery) and extent (number of tissues and total tissue mass affected) of tissue injury caused by the procedure as well as by the type of affected tissues (e.g., skin, muscle, nerve, and bone). One of the first responses is vasodilation and increased permeability of the blood vessels, which facilitates the release of fluids and circulating leukocytes into the injured area. Important modulators present in the released fluids include histamine, FXII (the Hageman factor), kinins, prostaglandins, leukotrienes, and kallikrein as well as antibacterial proteins such as properdin, lysozyme, β-lysins, immunoconglutinins, C-reactive protein, transferring, complement, and interferon.[11–13] The first cells to arrive at the site of the insult during the acute inflammatory response are neutrophils, followed by eosinophils

and monocytes.[14] Cells migrate within the circulatory system toward the inciting chemoattractant substances by a process called margination whereby phagocytes stick to lining of blood vessels, and then move into the surrounding tissue. In response to signals from the underlying tissue, there is an increase in specific molecules – for example, E-selectins – on the surface of the endothelial cells lining the blood vessels. A coordinated effort of upregulation and attachment between selectins (e.g., P- and E-selectins on endothelial cells; L-selectins on leukocytes) and their ligands results in margination of the cells with rolling of the phagocytes along the vessel wall.[15,16] Diapedesis (emigration) then occurs, whereby phagocytes squeeze between endothelial cells of blood vessels and enter the injured area.[15,17] The cells responding to the injury are directed to the site via chemotaxis. Several substances have been shown to be chemotactic, including the chemical or biochemical composition of the microbe or foreign body, factors released by most bacteria during growth, lymphokines, factors from the responding phagocytic cells, factors generated by the sequential activation of complement, local pH differences, and electrochemical factors.[11,13] Molecules that can coat the infectious agent or foreign body, called opsonins, can also be chemotactic and can enhance phagocytosis of the microbe or material. One example of an opsonin is the activated form of complement factor 5 (C5a).[11] The method in which chemotactic factors interact with leukocytes has been suggested to be via activation of esterases, including PI3 kinases on their surfaces.[13,18]

Once released at the site of injury, phagocytosis of dead cells and tissue components as well as other foreign implant debris ensues, along with activation of the effector mechanisms of the phagocytes. Neutrophils and eosinophils are the primary cells responsible for the removal of the foreign materials at wound sites because they work primarily through phagocytosis and degranulation, which result in the release of chemotactic factors necessary to recruit other cell types to the site. They are generally short-lived and play a primary role in acute inflammation within the first few days of exposure. However, the presence of extensive numbers of live neutrophils in tissue surrounding implants may, in the absence of infection, be interpreted as evidence of continued inflammatory challenge secondary to toxic or irritating breakdown products or particles caused by abrasion or breakdown of the implant.[11] Subsequently, once acute inflammation passes, chronic inflammation may develop if materials requiring phagocytosis are still present, mandating the continued presence of the cells of the mononuclear phagocyte system that include circulating monocytes and tissue-resident macrophage populations. The source of macrophages at sites of chronic inflammation may be local (because of recruitment and proliferation of tissue-resident macrophages) or distant (because of chemotaxis-driven migration of monocytes or macrophage precursors to the affected tissue).

The process of phagocytosis is dictated by chemotaxis and adherence of a microbe or implant particle to the surface of the phagocyte. To be taken up by a macrophage or some other white blood cell, particles must first bind to the phagocytic cell surface and activate one of a variety of surface receptors.[19] These receptors may recognize antibodies, opsonins (molecules that acts as a binding enhancer), or pattern recognition sites (molecular patterns present on a pathogen). When coated with opsonins, there is recognition of the opsonin through binding to an antigen-membrane receptor. The particle or microbe is then ingested via invagination and formation of a phagosome, which is produced as a portion of the cell membrane that surrounds the particle or microbe, thereby creating a host membrane-bound particle/microbe. This membrane-bound particle/microbe is called a secondary lysosome.[11] Fusion of the phagosome or secondary lysosome with a primary lysosome to form a phagolysosome then occurs and is followed by degranulation into the vacuole[11] and digestion (for biodegradable materials; e.g., cross-linked collagen or hyaluronic acid-based biomaterials) or attempted digestion (for inert materials; e.g., particles of polymethylmethacrylate or metals) by enzymes such as phagocytin, lysozyme, cathepsin, acid phosphatase, alkaline phosphatase, nucleosidase, ribonuclease, deoxyribonuclease, and β-glucuronidase[13] contained in the granules. This process is associated with a respiratory burst-producing hydrogen peroxide and superoxide anions that can also degrade materials and can be measured with *in vitro* assays.[20,21] A residual body then forms, containing indigestible material, and waste materials are discharged. Any residual undigested particles are released into the surrounding interstitial tissue, and the phagocytosis cycle begins again until the healing process and/or material removal process is ultimately complete, the endpoint of which is dictated by the functional requirements of the device. An alternative outcome is chronic inflammation that does not resolve and that adversely affects healing.

The inflammatory response to implants or injectable materials is quite variable, ranging from minimal to more extensive and resolves quickly or more slowly over time, depending on the physical and chemical biomaterial properties of the implant and the surrounding tissues and tissue fluids. The extent to which inflammation persists over time in a given biological environment depends on whether the implant is relatively inert, is resorbed or degraded over short or long periods of time, or results in the production of breakdown products or particulates over time. Inflammation does not necessarily constitute an adverse response to biomaterial implants unless the response is too prolonged and/or prevents appropriate healing, results in chronic inflammation or granulation tissue that occludes native tissue repair, is associated with infection of the injection or surgical site, or is associated with an immune response to the implant materials.

4.403.3.1. Infection

The initial breach of the skin or mucous membranes by needles or scalpels creates a portal for infectious agents to migrate into the biologic tissues surrounding the medical implant. The potential for infection is high for implanted medical devices, given that surgical approaches may involve cauterization, multiple incisions, and resection of tissues that may already be compromised by the trauma or diseases that produced the need for the medical device. Deep infection and unresolved superficial infections can have a major impact on the outcome of the surgical procedure and can ultimately cause failure of the device. Iatrogenic infection at an implant site that occurs because of the placement of a nonsterile implant may cause a large inflammatory response and failure of the implant,

particularly in bony sites where infection is associated with aggressive bone loss.[22] Once infected, bacteria can form biofilms that protect the bacteria from attack, making them extremely difficult to treat. In addition, endotoxins produced by the bacteria can also exacerbate the negative impact that bacteria can have on healing and/or implant stability.[23,24]

Infection has been reported as the cause of failure in some instances for most implant types, including total hip[25] and knee[26] replacements; spine fusion,[27] dental,[28] cranial–facial or maxilla–facial,[29] cardiovascular,[30,31] and optical devices[32]; and skin and bone graft substitutes.[33,34] Use of improved aseptic manufacturing and surgical techniques, and more recent improvements in minimally invasive surgical procedures have reduced the incidences of infection, thereby minimizing the adverse septic inflammatory responses that can result in implant failure. However, latent infection that has been attributed to secondary infections by pathogens such as *Staphylococcus aureus* present at sites other than the implant site has also been reported to result in implant failure many years after implantation.[35,36] Latent infection is associated primarily with metallic implants and is believed to be the result of the presence of a preferential environment at the tissue/implant surface.[14,37] It is not known if this process occurs regularly but is resolved in most instances. However, a large inflammatory response can be induced that can result in catastrophic failure of the implants, particularly those used for orthopedic[38,39] and dental[40] applications where infection is known to be associated with severe bone loss. In instances of infection, the inflammatory response is characterized by the presence of PMNL, lymphocytes, plasma cells, and (at bony sites) numerous osteoclasts at the surface of resorbing bone.

4.403.3.2. Persistent and Chronic Inflammatory Responses

In the absence of sepsis, inflammation caused by injection or by implantation of a successful medical device will generally diminish with time as the implant resorbs completely, or becomes incorporated at the implant site, leaving the implant directly apposed or juxtaposed to native tissue or encapsulated by a thin layer of fibrous tissue.[14,41,42] However, inflammation can persist and prolong the normal healing process or can occur at a later date secondary to the presence of breakdown products or mechanical loosening.

Persistent inflammation, characterized predominantly by the presence of macrophages and GCs, can be perceived as chronic and therefore problematic. However, this type of response is typical for resorbable materials and not considered adverse unless healing is prevented over time. Clearly, an undesirable response to an implant is one in which inflammation does not resolve over a relatively short period of time, becomes chronic, and prevents appropriate healing at the implantation site. This type of chronic inflammatory response can be associated with inert or nonresorbable implants as well as resorbable or degradable devices and can occur early or late in the life of an implant. Chronic inflammation usually occurs for a number of reasons, including instances where the implant (1) becomes dislodged, (2) abrades (resulting in the production of numerous particles that cannot be readily removed), (3) degrades or resorbs with deposition of breakdown products that are not readily eliminated, or (4) degrades or resorbs at a later time point (resulting in release of particles or breakdown products that are irritants or toxic). In these instances, the adverse response is often characterized by the presence of a large infiltrate of macrophages and may include other cell types, depending on the cause of the inflammation, that is, toxic breakdown products, particles, or an immunological component, all of which are discussed below in the context of degradable (i.e., implants intended to degrade over a short period of time) and nondegradable (i.e., implants intended to last many years or the lifetime of the patient) devices.

4.403.3.2.1. Nondegradable materials

Implants that are not expected to degrade quickly over time include a variety of metal alloys (such as stainless steel (SS), cobalt chrome (CoCr), TiAlV, and nitinol) and polymers (such as ultra-high-molecular-weight polyethylene (UHMWPE), delrin, and polyether ether ketone (PEEK)) that are used for a variety of orthopedic, dental, maxillofacial reconstructive, and cardiovascular indications. Although termed nondegradable for the purpose of this discussion, all implants age and degrade given sufficient time *in situ* and therefore have the potential to generate inflammatory responses after long-term implantation. Typically, a well fixed or integrated implant can be found directly apposed to native tissue or surrounded by a thin layer of fibrous tissue, with little evidence of any cells other than fibroblasts.

Corrosion and/or abrasion of total joint prostheses,[43–46] fixation devices,[47] pacemaker leads,[48] vascular stents,[49] and dental implants[50] have been documented extensively in the literature, and in all instances have been found to be associated with chronic inflammatory cells including macrophages, GCs, lymphocytes, and (in some instances) plasma cells and occasional PMNL. The macrophages and GCs present in periimplant tissues associated with these types of nondegradable implants often contain particles of implant material, which suggests a cause-and-effect relationship that has been well documented in the literature whereby loosening can cause the generation of wear debris. However, wear particles are not always present in tissue associated with loosened metal prostheses which suggests a role for metal ions in the loosening process. Metal ions released from implants have been shown to impact the behavior of circulating monocytes and tissue-resident macrophages.[51,52] Using a technique developed to examine phagocytosis in live cells, Graham *et al.* observed a significant effect on the phagocytic index of alveolar macrophages exposed to all concentrations of Ni_2^+.[52] Interestingly, Ni_2^+ had a minimal effect on alveolar macrophage viability or cellular lysis. Caicedo *et al.* noted an increase in the interleukin (IL)-1β secretion by human primary monocytes/macrophages exposed to soluble cobalt, chromium, and molybdenum but not nickel.[51] In addition to a potential effect on phagocytic function, metal ions may also stimulate fibrosis and the development of thickened fibrous tissue membranes around intact implants that may ultimately compromise the function of the implant – whether it be with mechanical loading of orthopedic or dental implants or with drug elution from cardiovascular implants.[3]

When particles are present in periprosthetic tissues, the chronic response is usually greater than responses associated with bulk materials, which strongly suggests that particles can

trigger the innate immune system more aggressively than bulk materials, leading to adverse inflammatory responses that impair healing if generated early on or cause and drive the loosening of well-fixed implants and tissue resorption processes. Although it is difficult to simulate the production of the same types of particles generated by corrosion and abrasion processes *in vivo*, many studies have attempted to determine the role particles play in the generation of innate immune responses.[53–60] Studies of human retrieval tissues containing large numbers of particles of nonresorbable materials have shown the presence of macrophages, GCs, lymphocytes, and (in some instances) lymphocytes and plasma cells as well as proinflammatory cytokines such as IL-1, tumor necrosis factor, and interferon-gamma (INF-γ).[59,61–65] One source of these proinflammatory cytokines is the macrophage. They can release cytokines and other molecules such as IL-1 and INF-γ that are proinflammatory as well as leukotrienes, prostaglandins, complement factors, and clotting factors, all of which are also proinflammatory factors.[66,67] In addition, activated macrophages can release angiogenic factors necessary for neovascularization, which is required to promote chronic inflammation. Other factors that can result in local tissue damage can also be released from activated macrophages. These factors include fibrogenesis factor, elastase, collagenase, hyaluronidase, H_2O_2, acid hydrolases, and C3a.

In *in vitro* studies, macrophages have been shown to be activated by ingestion of small particles or by frustrated phagocytosis, in which the particle is too large to be phagocytosed.[11,68] *In vivo* animal studies have shown that macrophages and T-lymphocytes can be recruited to sites containing large numbers of particles and that proinflammatory cytokines (such as IL-1, tumor necrosis factor, and INF-γ) can be induced by cells containing large numbers of particles at these sites.[69–71] Several key *in vivo* studies in animals suggest that the threshold for stimulating an innate response depends on particle type as well as particle size.[72,73] Because the particles used in these studies were not generated in *in vivo* environments, the results cannot be interpreted as definitive responses. This is particularly true given that a variety of *in vitro* studies of particles have produced conflicting results. For example, Lee *et al.* saw no difference *in vitro.*[74] Haynes *et al.* found CoCr alloy to be better[75] than TiAlV at inducing an inflammatory response, but CoCr resulted in greater toxicity. Kaufman *et al.* and Wooley *et al.*[76] also found less inflammatory reaction to CoCr[77] compared to TiAlV. Collectively, these studies serve to illustrate the fact that differences in particle composition, size, and shape will impact the macrophage response to particulates and therefore can impact macrophage activation.

There are different mechanisms of macrophage activation that have been described.[66,78] Traditionally, activation was thought to be associated with the capacity of the macrophage to perform specific functions. Two categories of activation have been used to describe macrophage activation: acute and adaptive.[66] Acute relates to immediate activation of signaling pathways while adaptive requires transcription and translation of specific modulators. As we have increased our understanding of macrophage behavior, it is clear that macrophage activation is complex and involves distinctly different activities regarding responses to specific external stimuli as well as different modulators. For example, macrophages play a significant role in the down-modulation of inflammation and immunity by a process called alternative activation (in contrast to classical activation).[78] Recently, a specific mechanism of macrophage activation resulting in production of an inflammasome (defined as a multiprotein complex, the exact composition of which depends on the activator that initiates the inflammasome assembly). The inflammasome has been identified as being specifically associated with particles[51,58] and is characterized by the production and release of IL-1β, IL-18, and IL-33. The NALP3 inflammasome contains a NOD-like receptor that comprises three domains: a pyrin domain, a NACHT domain, and 11 LRR (leucine-rich repeat) domains.[79] Nalp3 (also called cryopyrin) activates caspase-1 which in turn cleaves prointerleukin-1β to generate active IL-1β.[79,80] The NALP3 inflammasome has been the most studied with respect to particles and is said to have a role in silicosis and asbestosis.[81] It may also play a role in apoptosis through overexpression of activated caspase-1.[82] Some investigators, including Hallab and Jacobs have advocated that the inflammasome is the primary mechanism driving the response to particles.[51,58] However, this definitive concept remains somewhat controversial, given the diversity of particle composition, shape, and size. Irrespective of the mechanism of activation, effector mechanisms of activated macrophages include the release of degradative enzymes (lysozymes) and the synthesis and release of biochemical factors that recruit other macrophages and monocytes, including lymphocytes and fibroblasts as well as foreign-body GCs, and osteoclasts.

Although phagocytosis is a fundamental activity of mononuclear cells, it requires a carefully orchestrated sequence of events that, because of particle-generating failure modes of nondegradable materials and diverse combinations of implant materials, will influence macrophage activation and the subsequent sequence of inflammatory events. Depending on the mechanism of activation, the inflammatory response to particles may lead to the maturation of cells to perform specific functions such as phagocytosis, antigen presentation, cell recruitment, and lymphocyte activation. Therefore, for activation, receptors on macrophages that interact with particles are important and will likely play a role in determining the ultimate response to particles. Several receptors including Toll-like receptors (TLR),[66,83,84] AR3 and Dectin-1 (scavenger receptors), and mannose receptor have been shown to be expressed by macrophages.[14] TLR4 could, when artificially ligated using antibodies, induce the activation of certain genes necessary for initiating an adaptive immune response.[85] As a group, these are called pattern recognition receptors. Different receptors bind to different ligands or patterns. Pattern recognition receptors have been shown to recognize and bind to biomaterials.[86–89] As such, they play a role in macrophage activation and induction of subsequent responses to particles.

4.403.3.2.2. Biodegradable materials

Historically, implant biomaterials were initially intended to last the lifetime of the patient. However, as metals and polymers were shown to degrade and abrade with time, new materials that were intended to degrade over a relatively short (usually within 1 year) period of time and be replaced by native tissue were explored. Implant materials that are intended to degrade over time include polymers (e.g., polylactic

acid (PLA), polylactic-*co*-glycolic acid (PLGA), and polyvinyl acetate (PVA)), silica-based bioglasses, and biologic materials (e.g., hyaluronic acid and type I collagen). These types of implants generally induce a greater acute inflammatory response than materials that are considered inert and nonresorbable and will always induce a persistent inflammatory response while breakdown products are removed from the implant site. Not only will degradation of the implant induce a greater mononuclear infiltrate, it will also often induce the formation of multinucleated GCs to aid removal of particles or pieces of materials that are of a nonphagocytosable size. Therefore, it is important that a resorbable biological or polymeric implant does not break down more quickly and overwhelm the breakdown product removal process, because doing so could lead to induction of an adverse inflammatory response that could impair healing or regeneration of the tissues adjacent to or at the implant site.

Although all degradable materials generate a persistent inflammatory response, there are a number of factors that can either accelerate or slow the material degradation process, which will, in turn, dictate the severity of the innate response to an implant. These factors include the (1) chemical composition of the implant, (2) physical composition of the implant, (3) mechanism of degradation, (4) load applied to the implant at the implant site, (5) pH of the local environment, and (6) the production of degradative enzymes at the implant site. Even small changes in chemical composition or implant design can lead to dramatic changes *in vivo* that may result in either success or failure of a device at a given site. Also, increases in applied load, and increase or decrease in pH or the concentration of degrading enzymes at a given implant site can dramatically alter the degradation rate of a resorbable implant. It is not surprising therefore that innate responses characteristic of any given material at a given site may be altered by the presence of one or more additional materials in a composite implant. For example, BMPs in additional to a carrier such as collagen can accelerate bone regeneration and healing, but can be characterized by the presence of acute inflammation (characterized by polymorphonuclear nuclear cells) as well as inflammatory infiltrates containing macrophages and GCs (present to remove the carrier) that may slow down the healing process.[90] These types of variable processes that result from the presence of different materials and breakdown products may be conflicting but will certainly be driven by similar processes discussed for particles of undegradable materials including macrophage activation, production of inflammasomes, and phagocytosis and for successful implants, will result in incorporation and or replacement of the implant with appropriate native tissues.

4.403.4. Evasion Innate Immune System Activation

Given the inherent foreign nature of biomaterials, the ability to evade activation of the innate immune response is limited and, as expected, dependant on material properties, size, and shape. Although small particles of biomaterials have been shown to activate the innate system, large, bulk implants that have been shown to facilitate healing and incorporation within the surrounding tissues can remain *in situ* for very long periods of time with little or no additional inflammatory response, effectively evading activation of the innate response. Stable, uninfected implants such as uncemented and cemented total hips and knees, spine fusion cages, dental implants, fixation devices, and maxillofacial devices have been shown to have minimal tissue responses once healed and stabilized.[14,91] Tissue apposed to stable bulk implants is usually native or composed predominantly of fibroblasts oriented into a thin fibrous layer that conforms to the geometry of the implant.

Increasing the potential for tissue integration with implant coatings used to stabilize implants has led to successful application for some biomaterials.[92–94] Coating of total hip implants with hydroxyapatite has been shown to enable better integration with direct apposition of implants to bone, thereby increasing the ability of the implant to remain well fixed and 'hidden' from the innate system.[95] Other types of coatings and surface modifications have been used for similar applications. For instance, surface modifying additives to SS will result in the formation of chromium oxide at the surface, which will increase resistance to corrosion[96] and therefore reduce possibility for the generation of corrosion products that will activate the innate system.

Materials used for applications that are inherently more dynamic pose unique challenges to evasion of the innate system. Under these circumstances, materials that are otherwise considered inert can activate the complement system and result in an adverse response. For example, implants used for vascular applications not only are exposed to blood components and proteins, but they are also exposed to shear stresses which may more readily induce conformational changes upon adsorbed proteins than in the case of those proteins that may adsorb to a more rigid surface such as a hydroxyapatite coating on a hip implant that will be present in a less dynamic environment. Therefore, plasma proteins that adsorb to a biomaterial surface such as a polymer, metal, or ceramic used in a dynamic environment (e.g., a vascular stent) may become activated because of the physical contact and shear action of blood flow. Examples of such molecules are IgG (which activates the classical pathway of complement),[97] C3 (which activates the alternative pathway of complement),[98] fibrinogen (which binds to GPIIb-IIIa on platelets), and FXII (which triggers contact activation). The effect of this initial protein adsorption is activation of the coagulation, contact, and complement systems. The subsequent complement activation deposits C3 fragments on top of the plasma protein layer.[99] C3 fragment deposition adds a substantial amount of protein to the initially adsorbed protein mass and can, under favorable conditions, totally cover the original protein layer.[98] After activation by thrombin and the anaphylatoxins C3a and C5a, cells such as platelets, PMNL, and monocytes bind to the protein film on the biomaterial surface. Adsorbed IgG has been shown to initiate the classical complement pathway on biomaterial surfaces[97] and, even though this activation mechanism deposits only minute amounts of C3b on the surface, the deposition is rapid and sufficient to instantaneously trigger the alternative pathway amplification loop. The relative importance of the different activation pathways is illustrated by *in vivo* studies, which have shown that in patients with C4 deficiency (who lack the classical pathway) undergoing hemodialysis, complement activation is much delayed, but eventually reaches the same amplitude as in patients with normal levels of C4.[100] This finding reflects the

fact that regardless of the recognition mechanism, the alternative pathway amplification loop generates the majority of the C3b molecules that bind to the material surface. *In vitro* studies have confirmed this mechanism and shown that the majority of surface-bound C3 fragments are iC3b covalently bound to the surface-adsorbed plasma proteins.[101]

However, it has been possible to evade this innate activation process through innovation. Protein and peptide coatings have been shown to decrease thrombogenicity[102,103] of cardiovascular devices. Specifically, heparin treatment of vascular biomaterials has been shown to promote hemocompatibility by either binding to regulators of the cascade system (the accepted hypothesis for the mechanism of action) or preventing activation of bound components of the cascade system that would otherwise lead to deleterious results, resulting in longer term success of vascular stents.[104] Further innovations, such as the coating of biomaterials and even multilayered coatings of cells with substances such as polyethylene glycol (a process known as PEGylation) have also been used to enable evasion of the innate immune system. Such encapsulated allogenic and xenogenic islet cells have been shown to survive and function for at least 6 months *in vivo*,[105] indicating that this approach could be used successfully to enable long-term evasion of the immune system.

4.403.5. Enhancement of Innate Immune System Activation

Interestingly, so-called adverse responses to biomaterials have more recently been harnessed and used as a means to augment the adaptive immune response, specifically as therapeutic and prophylactic vaccine adjuvants (defined as any substance that acts to accelerate, prolong, or enhance antigen-specific immune responses when used in combination with a specific vaccine antigen[106] http://en.wikipedia.org/wiki/Immunologic_adjuvant – cite_note-2) and as antigen-delivery systems.[107]

Adjuvants are believed to stimulate the immune system and increase the response to a vaccine without having any specific antigenic properties. There are many known adjuvants in widespread use, including oils, aluminium salts, and virosomes (virus particles that contain no active genetic material), although precisely how they work is still not fully understood. However, it is interesting to note that during the early days of commercial vaccine manufacture, an observation was made that large variations in the effectiveness of different batches of the same vaccine were associated with contamination of the reaction vessels used to produce the vaccines. This caveat suggests that irritants can enhance the effect of vaccines. It is not surprising then that, as requirements to ensure a lack of contaminants in commercially manufactured vaccines increased along with use of recombinant proteins as immunogens (which are poorly immunogenic but are increasingly selected to ensure greater purity of the manufactured antigens), additional types of adjuvants were explored. Nanoparticles and microparticles composed of a variety of biomaterials, including some of those typically used as biomaterials for implantable devices (e.g., PLGA, PLG, hyaluronic acid, and chitosan), were investigated in combination with various antigens and were found to boost the immune response to a variety of antigens compared to administration of the antigen alone. For instance, polystyrene (PS) nanoparticles coadministered with a mite allergen were shown to enhance immune responses to the pathogen[108] over the responses induced with the particles alone and the allergen alone in male NC/Nga mice injected intradermally with three different-sized PS nanoparticles (25, 50, or 100 nm). In that study, all particles boosted the immune response to the antigen, and a trend toward increased immunological responses was shown with smaller particles. Other *in vivo* studies have shown that iron oxide (Fe_3O) nanoparticles enhanced the response of an immunotherapeutic cancer vaccine,[109] whereas PLGA particles have been shown to effectively boost immune responses to a hepatitis B vaccine.[110–112] These, and similar studies, using a variety of different biomaterials and vaccine technologies, demonstrate the advantageous boosting potential of biomaterial particles.

The mechanism of action of these small-sized biomaterials as adjuvants has been investigated and appears to have a direct impact on the innate response to coadministered antigens. Small particles, when coadministered with antigen, initially act as delivery systems, providing a direct route of ingress to antigen-presenting cells as particles that are phagocytosed along with antigen (free, adsorbed, bound, or encapsulated) and carried to the lymph nodes. Within the lymph nodes, the macrophages containing the particles and antigen mature into dendritic cells (DCs).[113–115] The antigen is then positioned appropriately to induce a strong immunological response. In one study of poly(gamma-glutamic acid) (PGA) nanoparticles,[116] modulation of gene expression related to TLR signaling has been proposed as the mechanism by which this occurs. Encapsulation of antigen within resorbable nanoparticles has been shown to clearly alter antigen acquisition and processing by antigen-presenting cells and ensuing adaptive immunity.[117–119] The adjuvant activity of particles is thought to be related to the innate immune response to the materials and has recently been described at the molecular level as engaging the Nalp3 inflammasome and complementing the activity of TLR ligands.[119–121] The inclusion of antigen within erodible particles and subsequent delivery to DCs enable antigen-specific cell-mediated immunity and extended antigen presentation with protective outcomes. It is not surprising, then, that the size and dissolution rates of resorbable particles as well as surface chemistry and charge appear to be central in tuning and enhancing adaptive immune responses. According to Rice-Fecht *et al.* the tremendous power of particulate materials to enhance vaccine efficacy has only recently been recognized and used strategically in vaccine design.[119] It will be interesting to follow progress in this field to continue to better understand the body's innate response to biomaterials and also the favorable impact that biomaterials may have on the adaptive immune response to foreign antigens.

4.403.6. Concluding Remarks

Since the first recorded uses of implantable biomaterials, technology and our understanding of biomaterial/host interactions have continued to advance, making the use of novel medical devices increasingly important for therapeutic intervention aimed at increasing or restoring patient function. For all

applications, the drivers for success or failure of any given device are the immediate and subsequent innate responses to the biomaterials which will dictate how well healing and implant integration or removal will proceed with time. It is clear from the afore-mentioned studies and examples that selection of the biomaterial for a given application is critical. However, while it has become clear that the innate response to materials can have detrimental effects to the success of an implant, it is also clear that the innate system can be harnessed to advantage, enabling new applications for well-characterized biomaterials.

References

1. Goldberg, J. R.; Gilbert, J. L. *Biomaterials* **2004**, *25*, 851–864.
2. Khan, M. A.; Williams, R. L.; Williams, D. F. *Biomaterials* **1999**, *20*, 631–637.
3. Dee, K. C.; Puleo, D. A.; Bizios, R. *An Introduction to Tissue-Biomaterial Interactions*; John Wiley & Sons, Inc.: Hoboken, 2002.
4. Liedberg, B.; Ivarsson, B.; Lundstrom, I. *J. Biochem. Biophys. Methods* **1984**, *9*, 233–243.
5. Nojiri, C.; Okano, T.; Koyanagi, H.; Nakahama, S.; Park, K. D.; Kim, S. W. *J. Biomater. Sci. Polym. Ed.* **1992**, *4*, 75–88.
6. Molina, V.; Shoenfeld, Y. *Autoimmunity* **2005**, *38*, 235–245.
7. Erlich, I.; Strauss, B. H.; Butany, J. *Catheter. Cardiovasc. Interv.* **2006**, *68*, 708–712.
8. Knetsch, M. L.; Aldenhoff, Y. B.; Koole, L. H. *Biomaterials* **2006**, *27*, 2813–2819.
9. Luensmann, D.; Jones, L. *Cont. Lens Anterior Eye* **2008**, *31*, 179–187.
10. Anderson, J. M.; Rodriguez, A.; Chang, D. T. *Semin. Immunol.* **2008**, *20*, 86–100.
11. Black, J. *Biological Performance of Materials: Fundamentals of Biocompatibility*; Marcel Dekker, Inc.: New York, NY, 1992.
12. Arturson, G. *Ann. Chir. Gynaecol.* **1980**, *69*, 178–190.
13. Petty, W. In *Musculoskeletal Infection*; Esterhai, J. L., Gristina, A. G., Poss, R., Eds.; American Academy of Orthopaedic Surgeons: Rosemont, IL, 1992; pp 241–253.
14. Anderson, J.; Cook, G.; Costerton, B.; *et al*. In *Biomaterials Science: An Introduction to Materials in Medicine*, 2nd ed.; Ratner, B., Hoffman, A., Schoen, F., Lemons, J., Eds.; Elsevier Academic Press: San Diego, 2004; pp 293–354.
15. Grailer, J. J.; Kodera, M.; Steeber, D. A. *J. Dermatol. Sci.* **2009**, *56*, 141–147.
16. Smith, C. W. *Can. J. Physiol. Pharmacol.* **1993**, *71*, 76–87.
17. Dejana, E. *Nat. Cell Biol.* **2006**, *8*, 105–107.
18. Comer, F. I.; Parent, C. A. *Mol. Biol. Cell* **2006**, *17*, 357–366.
19. Alberts, B.; Bray, D.; Hopkin, K.; *et al*. *Essential Cell Biology*, 3rd ed.; Garland Science: New York, 2010.
20. Avendano, A.; Sales-Pardo, I.; Marin, L.; Marin, P.; Petriz, J. *J. Immunol. Methods* **2008**, *339*, 124–131.
21. Manara, F. S.; Chin, J.; Schneider, D. L. *J. Leukoc. Biol.* **1991**, *49*, 489–498.
22. Maathuis, P. G.; Neut, D.; Busscher, H. J.; van der Mei, H. C.; van Horn, J. R. *Clin. Orthop. Relat. Res.* **2005**, *433*, 136–139.
23. Bi, Y.; Seabold, J. M.; Kaar, S. G.; *et al*. *J. Bone Miner. Res.* **2001**, *16*, 2082–2091.
24. Wilkins, R.; Tucci, M.; Benghuzzi, H. *Biomed. Sci. Instrum.* **2008**, *44*, 459–464.
25. Dale, H.; Hallan, G.; Hallan, G.; Espehaug, B.; Havelin, L. I.; Engesaeter, L. B. *Acta Orthop.* **2009**, *80*, 639–645.
26. Kurtz, S. M.; Ong, K. L.; Lau, E.; Bozic, K. J.; Berry, D.; Parvizi, J. *Clin. Orthop. Relat. Res.* **2010**, *468*, 52–56.
27. Bose, B. *Spine J.* **2003**, *3*, 394–399.
28. Greenstein, G.; Cavallaro, J.; Romanos, G.; Tarnow, D. *J. Periodontol.* **2008**, *79*, 1317–1329.
29. Kirkpatrick, D.; Gandhi, R.; Van Sickels, J. E. *J. Oral Maxillofac. Surg.* **2003**, *61*, 462–466.
30. Antoniou, G. A.; Koutsias, S.; Antoniou, S. A.; Georgiakakis, A.; Lazarides, M. K.; Giannoukas, A. D. *J. Vasc. Surg.* **2009**, *49*, 782–789.
31. Castelli, P.; Caronno, R.; Ferrarese, S.; *et al*. *Surg. Infect. (Larchmt)* **2006**, *7*(Suppl. 2), S45–S47.
32. Baillif, S.; Hartmann, D.; Freney, J.; Kodjikian, L. *J. Fr. Ophtalmol.* **2010**, *33*, 210–221.
33. Hornicek, F. J.; Gebhardt, M. C.; Tomford, W. W.; *et al*. *Clin. Orthop. Relat. Res.* **2001**, *382*, 87–98.
34. Voineskos, S. H.; Ayeni, O. A.; McKnight, L.; Thoma, A. *Plast. Reconstr. Surg.* **2009**, *124*, 298–306.
35. LaPorte, D. M.; Waldman, B. J.; Mont, M. A.; Hungerford, D. S. *J. Bone Joint Surg. Br.* **1999**, *81*, 56–59.
36. Poss, R.; Thornhill, T. S.; Ewald, F. C.; Thomas, W. H.; Batte, N. J.; Sledge, C. B. *Clin. Orthop. Relat. Res.* **1984**, *182*, 117–126.
37. Campoccia, D.; Montanaro, L.; Arciola, C. R. *Biomaterials* **2006**, *27*, 2331–2339.
38. Vastel, L.; Lemoine, C. T.; Kerboull, M.; Courpied, J. P. *Int. Orthop.* **2007**, *31*, 851–857.
39. Younger, A. S.; Duncan, C. P.; Masri, B. A. *J. Bone Joint Surg. Am.* **1998**, *80*, 60–69.
40. Chaffee, N. R.; Lowden, K.; Tiffee, J. C.; Cooper, L. F. *J. Prosthet. Dent.* **2001**, *85*, 109–112.
41. Kozinn, S. C.; Johanson, N. A.; Bullough, P. G. *J. Arthroplasty* **1986**, *1*, 249–259.
42. Low, S. P.; Voelcker, N. H.; Canham, L. T.; Williams, K. A. *Biomaterials* **2009**, *30*, 2873–2880.
43. Athanasou, N. A. *J. Long Term Eff. Med. Implants* **2007**, *17*, 193–206.
44. Betts, F.; Wright, T.; Salvati, E. A.; Boskey, A.; Bansal, M. *Clin. Orthop. Relat. Res.* **1992**, *276*, 75–82.
45. Gruen, T. A.; Amstutz, H. C. *J. Biomed. Mater. Res.* **1975**, *9*, 465–477.
46. McKellop, H. A.; Sarmiento, A.; Schwinn, C. P.; Ebramzadeh, E. *J. Bone Joint Surg. Am.* **1990**, *72*, 512–517.
47. Cartner, J. L.; Haggard, W. O.; Ong, J. L.; Bumgardner, J. D. *J. Biomed. Mater. Res. B Appl. Biomater.* **2008**, *86B*, 430–437.
48. Parsonnet, V.; Villanueva, A.; Driller, J.; Bernstein, A. D. *Pacing Clin. Electrophysiol.* **1981**, *4*, 289–296.
49. Guidoin, R.; Marois, Y.; Douville, Y.; *et al*. *J. Endovasc. Ther.* **2000**, *7*, 105–122.
50. Lugowski, S. J.; Smith, D. C.; McHugh, A. D.; Van Loon, J. C. *J. Biomed. Mater. Res.* **1991**, *25*, 1443–1458.
51. Caicedo, M. S.; Desai, R.; McAllister, K.; Reddy, A.; Jacobs, J. J.; Hallab, N. J. *J. Orthop. Res.* **2009**, *27*, 847–854.
52. Graham, J. A.; Gardner, D. E.; Waters, M. D.; Coffin, D. L. *Infect. Immun.* **1975**, *11*, 1278.
53. *Implant Wear in Total Joint Replacement*. American Academy of Orthopaedic Surgeons: Rosemont, IL, 2001.
54. Al-Saffar, N.; Revell, P. A.; Kobayashi, A. *J. Mater. Sci. Mater. Med.* **1997**, *8*, 641–648.
55. Endres, S.; Bartsch, I.; Sturz, S.; Kratz, M.; Wilke, A. *J. Mater. Sci. Mater. Med.* **2008**, *19*, 1209–1214.
56. Frick, C.; Dietz, A. C.; Merritt, K.; Umbreit, T. H.; Tomazic-Jezic, V. J. *J. Long Term Eff. Med. Implants* **2006**, *16*, 423–433.
57. Goodman, S. B. *Biomaterials* **2007**, *28*, 5044–5048.
58. Hallab, N. J.; Jacobs, J. J. *Bull. NYU Hosp. Jt Dis.* **2009**, *67*, 182–188.
59. Jones, L. C.; Frondoza, C.; Hungerford, D. S. *J. Biomed. Mater. Res.* **1999**, *48*, 889–898.
60. Revell, P. A. *J. R. Soc. Interface* **2008**, *5*, 1263–1278.
61. Esposito, M.; Thomsen, P.; Ericson, L. E.; Lekholm, U. *Int. J. Oral Maxillofac. Implants* **1999**, *14*, 798–810.
62. Lennox, D. W.; Schofield, B. H.; McDonald, D. F.; Riley, L. H., Jr. *Clin. Orthop. Relat. Res.* **1987**, *225*, 171–191.
63. Mirra, J. M.; Amstutz, H. C.; Matos, M.; Gold, R. *Clin. Orthop. Relat. Res.* **1976**, *117*, 221–240.
64. Morawietz, L.; Classen, R. A.; Schroder, J. H.; *et al*. *J. Clin. Pathol.* **2006**, *59*, 591–597.
65. Santavirta, S.; Konttinen, Y. T.; Hoikka, V.; Eskola, A. *J. Bone Joint Surg. Br.* **1991**, *73*, 38–42.
66. Burke, B.; Lewis, C. *The Macrophage*, 2nd ed.; Oxford University press: Oxford, UK, 2002.
67. Roitt, I.; Brostoff, J.; Male, D. *Immunology*; Mosby: Philadelphia, 1998.
68. Nakashima, Y.; Sun, D. H.; Trindade, M. C.; *et al*. *J. Bone Joint Surg. Am.* **1999**, *81*, 603–615.
69. Dowd, J. E.; Schwendeman, L. J.; Macaulay, W.; *et al*. *Clin. Orthop. Relat. Res.* **1995**, 106–121.
70. Jones, L. C.; Frondoza, C.; Hungerford, D. S. *J. Bone Joint Surg. Br.* **2001**, *83*, 448–458.
71. Sacomen, D.; Smith, R. L.; Song, Y.; Fornasier, V.; Goodman, S. B. *J. Biomed. Mater. Res.* **1998**, *43*, 123–130.
72. Goodman, S.; Aspenberg, P.; Song, Y.; Regula, D.; Lidgren, L. *Acta Orthop. Scand.* **1996**, *67*, 599–605.
73. Goodman, S. B.; Fornasier, V. L.; Lee, J.; Kei, J. *J. Biomed. Mater. Res.* **1990**, *24*, 517–524.
74. Lee, S. H.; Brennan, F. R.; Jacobs, J. J.; Urban, R. M.; Ragasa, D. R.; Glant, T. T. *J. Orthop. Res.* **1997**, *15*, 40–49.

75. Haynes, D. R.; Rogers, S. D.; Hay, S.; Pearcy, M. J.; Howie, D. W. *J. Bone Joint Surg. Am.* **1993**, *75*, 825–834.
76. Wooley, P. H.; Morren, R.; Andary, J.; *et al*. *Biomaterials* **2002**, *23*, 517–526.
77. Kaufman, A. M.; Alabre, C. I.; Rubash, H. E.; Shanbhag, A. S. *J. Biomed. Mater. Res. A* **2008**, *84*, 464–474.
78. Goerdt, S.; Politz, O.; Schledzewski, K.; *et al*. *Pathobiology* **1999**, *67*, 222–226.
79. Petrilli, V.; Dostert, C.; Muruve, D. A.; Tschopp, J. *Curr. Opin. Immunol.* **2007**, *19*, 615–622.
80. Sutterwala, F. S.; Ogura, Y.; Szczepanik, M.; *et al*. *Immunity* **2006**, *24*, 317–327.
81. Cassel, S. L.; Eisenbarth, S. C.; Iyer, S. S.; *et al*. *Proc. Natl. Acad. Sci. USA* **2008**, *105*, 9035–9040.
82. Martinon, F.; Tschopp, J. *Cell* **2004**, *117*, 561–574.
83. Blasius, A. L.; Beutler, B. *Immunity* **2010**, *32*, 305–315.
84. Medzhitov, R.; Janeway, C. A., Jr. *Semin. Immunol.* **1998**, *10*, 351–353.
85. Medzhitov, R.; Preston-Hurlburt, P.; Janeway, C. A., Jr. *Nature* **1997**, *388*, 394–397.
86. Grandjean-Laquerriere, A.; Tabary, O.; Jacquot, J.; *et al*. *Biomaterials* **2007**, *28*, 400–404.
87. Pajarinen, J.; Mackiewicz, Z.; Pollanen, R.; *et al*. *J. Biomed. Mater. Res. A* **2010**, *92*, 1528–1537.
88. Rogers, T. H.; Babensee, J. E. *Biomaterials* **2010**, *31*, 594–601.
89. Shokouhi, B.; Coban, C.; Hasirci, V.; *et al*. *Biomaterials* **2010**, *31*, 5759–5771.
90. Yin, W.; Jo, H.; Voit, E. O. *Ann. Biomed. Eng.* **2010**, *38*, 291–307.
91. Morehead, J. M.; Holt, G. R. *Otolaryngol. Clin. North Am.* **1994**, *27*, 195–201.
92. Epinette, J. A.; Manley, M. T. *Hip Int.* **2008**, *18*, 69–74.
93. Mannan, K.; Freeman, M. A.; Scott, G. *J. Bone Joint Surg. Br.* **2010**, *92*, 480–485.
94. Tanzer, M.; Gollish, J.; Leighton, R.; *et al*. *Clin. Orthop. Relat. Res.* **2004**, *424*, 153–160.
95. Browne, M.; Gregson, P. J. *Biomaterials* **2000**, *21*, 385–392.
96. Ratner, B.; Hoffman, A. In *Biomaterials Science: An Introduction to Materials in Medicine*; Ratner, B., Hoffman, A., Schoen, F., Lemons, J., Eds.; Elsevier Academic Press: San Diego, 2004; pp 201–218.
97. Tengvall, P.; Askendal, A.; Lundstrom, I. I. *Colloids Surf. B Biointerfaces* **2001**, *20*, 51–62.
98. Andersson, J.; Ekdahl, K. N.; Larsson, R.; Nilsson, U. R.; Nilsson, B. *J. Immunol.* **2002**, *168*, 5786–5791.
99. Andersson, J.; Ekdahl, K. N.; Lambris, J. D.; Nilsson, B. *Biomaterials* **2005**, *26*, 1477–1485.
100. Lhotta, K.; Wurzner, R.; Kronenberg, F.; Oppermann, M.; Konig, P. *Kidney Int.* **1998**, *53*, 1044–1051.
101. Nilsson, B.; Ekdahl, K. N.; Mollnes, T. E.; Lambris, J. D. *Mol. Immunol.* **2007**, *44*, 82–94.
102. Sefton, M.; Gemmell, C. In *Biomaterials Science: An Introduction to Materials in Medicine*, 2nd ed.; Ratner, B., Hoffman, A., Schoen, F., Lemons, J., Eds.; Elsevier Academic Press: San Diego, 2004; pp 456–470.
103. Werner, C.; Maitz, M.; Sperling, C. *J. Mater. Chem.* **2007**, *17*, 3376–3384.
104. Nilsson, B.; Korsgren, O.; Lambris, J. D.; Ekdahl, K. N. *Trends Immunol.* **2010**, *31*, 32–38.
105. Dufrane, D.; Gianello, P. *Transplantation* **2008**, *86*, 753–760.
106. Sasaki, S.; Okuda, K. In *DNA Vaccines: Methods and Protocols*; Lowrie, D. B., Whalen, R. G., Eds.; Humana Press: Totowa, NJ, 2000.
107. Broos, S.; Lundberg, K.; Akagi, T.; *et al*. *Vaccine* **2010**, *12*, 5075–5085.
108. Yanagisawa, R.; Takano, H.; Inoue, K. I.; Koike, E.; Sadakane, K.; Ichinose, T. *Int. J. Immunopathol. Pharmacol.* **2010**, *23*, 131–141.
109. Liu, H.; Zhanl, D.; Du, Y. *J. Nanosci. Nanotechnol.* **2010**, *10*, 514–519.
110. Clawson, C.; Huang, C. T.; Futalan, D.; *et al*. *Nanomedicine* **2010**, *6*, 651–661.
111. Malyala, P.; Chesko, J.; Ugozzoli, M.; *et al*. *J. Pharm. Sci.* **2008**, *97*, 1155–1164.
112. Mishra, N.; Tiwari, S.; Vaidya, B.; Agrawal, G. P.; Vyas, S. P. Lectin anchored PLGA nanoparticles for oral mucosal immunization against hepatitis B. *J. Drug Target*. Epub ahead of print March 25, 2010.
113. O'Hagan, D. T.; Singh, M.; Ulmer, J. B. *Immunol. Rev.* **2004**, *199*, 191–200.
114. Singh, M.; Fang, J. H.; Kazzaz, J.; *et al*. *Int. J. Pharm.* **2006**, *327*, 1–5.
115. Tabata, Y.; Ikada, Y. *J. Biomed. Mater. Res.* **1988**, *22*, 837–858.
116. Hamasaki, T.; Uto, T.; Akagi, T.; Akashi, M.; Baba, M. *Clin. Vaccine Immunol.* **2010**, *17*, 748–756.
117. Adair, B. M. *Wiley Interdiscip. Rev. Nanomed. Nanobiotechnol.* **2009**, *1*, 405–414.
118. Jones, D. H.; Clegg, J. C.; Farrar, G. H. *Dev. Biol. Stand.* **1998**, *92*, 149–155.
119. Rice-Ficht, A. C.; Arenas-Gamboa, A. M.; Kahl-McDonagh, M. M.; Ficht, T. A. *Curr. Opin. Microbiol.* **2010**, *13*, 106–112.
120. Harris, J.; Sharp, F. A.; Lavelle, E. C. *Eur. J. Immunol.* **2010**, *40*, 634–638.
121. Sharp, F. A.; Ruane, D.; Claass, B.; *et al*. *Proc. Natl. Acad. Sci. USA* **2009**, *106*, 870–875.

4.404. Adaptive Immune Responses to Biomaterials

R J Love and K S Jones, McMaster University, Hamilton, ON, Canada

© 2011 Published by Elsevier Ltd.

4.404.1.	**Introduction**	37
4.404.1.1.	Cells and Structures of Adaptive Immunity	38
4.404.1.1.1.	Organization of the immune system	38
4.404.1.1.2.	Mononuclear phagocytes	38
4.404.1.1.3.	Lymphocytes	38
4.404.1.1.4.	Cellular identification	38
4.404.2.	**Recognition of Biomaterials by the Adaptive Immune System**	39
4.404.2.1.	Indirect Effects on Lymphocytes	39
4.404.2.1.1.	Attraction of leukocytes to the implant site	39
4.404.2.1.2.	Activation of adaptive cells by innate cells activated through biomaterial contact	41
4.404.2.2.	Direct Effects of Lymphocytes	41
4.404.3.	**Consequences of the Adaptive Response**	42
4.404.3.1.	Spectrum of Adaptive Responses to Biomaterials	42
4.404.3.1.1.	Inflammatory responses	42
4.404.3.1.2.	Range of T cell responses (Th1, 2, 17 rejection, tolerance, effect of duration, and magnitude)	43
4.404.3.2.	Effects on Biomaterial-Only Devices (e.g., Probes, Implants, Biological Scaffold Materials)	43
4.404.3.2.1.	Inflammation	43
4.404.3.2.2.	Foreign body response	43
4.404.3.2.3.	Fibrosis	44
4.404.3.2.4.	Angiogenesis	44
4.404.3.2.5.	Autoimmunity	44
4.404.3.2.6.	Infection	44
4.404.3.3.	Effects on Combination Products (i.e., Vaccine or Tissue-Engineering Construct)	44
4.404.3.3.1.	Magnitude of response	44
4.404.3.3.2.	Altered responses	45
4.404.3.3.3.	Tolerance responses	45
4.404.4.	**Approaches to Engineer Adaptive Responses with Biomaterials**	45
4.404.4.1.	Biomaterials as Vaccine Adjuvants and Antigen Carriers	45
4.404.4.2.	Surface Modification	46
4.404.4.3.	Anti-inflammatory Drug Release	47
4.404.5.	**Conclusions**	47
References		47

Glossary

Angiogenesis The physiological process involving the growth of new blood vessels from preexisting vessels.

Fibrosis The formation of excess fibrous connective tissue in an organ or tissue in a reparative or reactive process. This is as opposed to formation of fibrous tissue as a normal constituent of an organ or tissue.

Genotype The genetic makeup of an organism or a group of organisms with reference to a single trait, set of traits, or an entire complex of traits.

Immune system The system of biological structures and processes within an organism that protects against disease by identifying and killing pathogens and tumor cells. It detects a wide variety of agents, from viruses to parasitic worms, and needs to distinguish them from the organism's own healthy cells and tissues in order to function properly.

Inflammatory response A tissue reaction to injury or an antigen that may include pain, swelling, itching, redness, heat, and loss of function. The response may involve dilation of blood vessels and consequent leakage of fluid, causing edema, leukocytic exudation, and release of plasma proteases and vasoactive amines such as histamine.

Phenotype The observable physical or biochemical characteristics of an organism, as determined by both genetic makeup and environmental influences.

4.404.1. Introduction

When foreign materials are implanted in the human body, the immune system responds. The immune response protects us from being taken over by rapidly proliferating adventitious organisms. Mammalian immunity has evolved substantially from that of phylogenetically older animals such as invertebrates. A distinctive component of the immune system of

jawed vertebrates is adaptive immunity, which provides specificity to, and memory of, foreign pathogens. Adaptive immunity is an active component of the immune response to all materials that are implanted in the human body. Depending on the material, lymphocytes, the main cell type of the adaptive immune system, either actively contribute to material destruction and rejection or produce a cytokine milieu that leads to fibrosis or possibly material tolerance. Since biomaterials are increasingly used in combination products (drug delivery devices, gene delivery devices, tissue-engineering constructs, regenerative medicine constructs, etc.), the adaptive response to the material component can be critical to the viability and function of the entire construct. Indeed the other components of such combination products may also alter the adaptive immune response to the material; in fact, some methods of modifying the adaptive response to a biomaterial construct include adding another component to the construct, such as a drug (e.g., a corticosteroid). Knowledge of the baseline immune response to biomaterials provides researchers not only with an understanding of what happens to materials when they are implanted in the body, but also with a starting point by which the immune response can be manipulated to fit the needs of a biomaterial construct.

This chapter explains how the immune system recognizes biomaterials, and the consequences of the adaptive immune response to biomaterials and constructs that are known to contain biomaterials. The final section of the chapter provides an overview of approaches that may be used to alter the adaptive immune response to a material.

4.404.1.1. Cells and Structures of Adaptive Immunity

4.404.1.1.1. Organization of the immune system

The immune system is an integrated network of tissues, cells, and molecules that function together to resist disruption of homeostasis within the human body. Immunity generally refers to defense against infection, but immune cells respond to tissue damage, as well as to the presence of any foreign substances, infectious or noninfectious. The human immune system is loosely divided into two components: innate immunity and adaptive immunity. Innate immunity consists of barrier systems to prevent passage of foreign substances (e.g., epithelia and endothelia), phagocytic cells (neutrophils and macrophages), and blood proteins (such as complement). Adaptive immunity consists primarily of lymphocytes and the proteins that they produce, such as antibodies and cytokines. Though immune responses have been divided into these two categories, there is much overlap between the innate immune system and the adaptive immune system. For example, phagocytic cells of the innate system, such as macrophages, present the proteins contained in their phagosomes to lymphocytes, the cells of the adaptive system. As a result, most immune reactions in the human body involve both arms of the immune system; rarely is there an immune reaction to a pathogen whereby only innate or only adaptive immune cells respond.

The adaptive immune system has been further subdivided into two categories: humoral immunity and cell-mediated immunity. Humoral immunity is the principal defense mechanism against extracellular microbes and involves the production and secretion of antibodies by CD20+ B lymphocytes. Cell-mediated immunity is the principal defense mechanism against intracellular microbes such as viruses, and involves proliferation and response by CD8+ cytotoxic T lymphocytes. CD4+ T cells are involved in both humoral and cell-mediated responses and are responsible for producing cytokines that stimulate effector cell proliferation and maturation, and antigen-presenting cell (APC) maturation. Due to the incredible complexity of the immune system, it is imperative that the specific cells of the immune system are reviewed to permit comprehension of the various adaptive immune responses to biomaterials. Adaptive immune cells fall into two categories, mononuclear phagocytes and lymphocytes. These cell types and their subsets are discussed below.

4.404.1.1.2. Mononuclear phagocytes

Leukocytes that have one nucleus and the capability of phagocytizing large particles or small organisms (bacteria or dead cells) are referred to as mononuclear phagocytes. Among the mononuclear phagocytes, there are three notable, highly prevalent cell types: the monocyte, which is an immature/undifferentiated cell that exists primarily in the blood; the macrophage, which is derived from the monocyte and is particularly good at phagocytosing foreign organisms and damaged tissue, but less proficient at presenting engulfed proteins to lymphocytes; and the dendritic cell (DC), which is also derived from the monocyte, is less adept at phagocytosing foreign and damaged material, but is more capable of presenting foreign proteins to lymphocytes. Both DCs and macrophages express major histocompatibility complex (MHC)-II, on which phagocytosed foreign antigens are presented. These cells are referred to as APCs because of their ability to present foreign antigens, along with a costimulatory signal, to lymphocytes.

4.404.1.1.3. Lymphocytes

The only cells in the human body that have the capability of recognizing specific antigens are lymphocytes and, as a result, they are responsible for giving the human immune system specificity and memory. Lymphocytes are a functionally heterogeneous group of cells with several distinct populations. T lymphocytes (T cells) are the largest group and consist of CD4+ helper T cells and CD8+ effector T cells. Natural killer (NK) cells are often grouped with the T lymphocytes because they frequently express the T cell receptor (TCR) on their surface, a defining characteristic of all T cells, but NK cells also express receptors that are unique to the other lymphocyte populations. B lymphocytes are the cells responsible for producing antibodies and are therefore the principal effector cells of humoral immunity.

4.404.1.1.4. Cellular identification

Finally, regarding reference to the cells of the immune system, students and researchers should get into the habit of identifying immune cells not only by name, but also by the unique proteins that exist on the cell surface. This is because many of the cells of the immune system have a common origin and are differentiated on the basis of function, morphology, and protein expression. However, there is not always a clear distinction between cells, and cells with the same name can do very different things. For example, since macrophages and most DCs originate from monocytes, the distinction between the

Table 1 Details of the CD molecules that are important to the adaptive response to biomaterials

CD number	*Alternate name(s)*	*Expressing cells*	*Function*
CD3 (γ, δ, ε)	TCR complex	T cells, thymocytes	Required for cell surface expression of and signal transduction of the TCR
CD4	T4, L3T4	Class II MHC-restricted T cells, thymocyte subsets, monocytes, and macrophages	Signaling and adhesion coreceptor in class II MHC antigen-induced T cell activation
CD8 (α, β)	T8, Leu-2, Lyt2	Class I MHC-restricted T cells, thymocyte subsets	Signaling and adhesion coreceptor in class I MHC antigen-induced T cell activation
CD11 (a, b, c)	Noncovalently linked to CD18 to form LFA-1/ Mac-1/p150,95 integrins (a/b/c isoforms respectively)	a: all leukocytes b and c: granulocytes, monocytes/ macrophages, NK cells	Cell–cell adhesion
CD14	LPS receptor	Monocytes, macrophages, granulocytes (free in serum)	Binds lipopolysaccharides (LPS) and LPS-binding protein
CD63	Lysosome-associated membrane protein 3 (LAMP-3)	Activated platelets, endothelial cells, neutrophils, monocytes, macrophages	Unknown
CD68	Macrosialin family; LAMP family	Monocytes, macrophages, DCs, granulocytes, activated T cells, some B cells	Scavenger receptor
CD80	B7-1	DCs, macrophages, some B cells	Antigen costimulation
CD86	B7-2	DCs, macrophages, some B cells	Antigen costimulation

three cell types can be confused. Furthermore, a particular type of cell may do very different things, depending on its particular phenotype/genotype. A prime example of this is the division of macrophage cells into 'regulatory,' 'wound-healing,' and 'classical' phenotypes, which we will discuss in more detail in Section 4.404.3.1. Known immune cell surface proteins have each been assigned a 'cluster of differentiation' (CD) number (e.g., CD1, CD2, CD3, etc.). For example, all T lymphocytes have TCRs on their surface. The TCR has been assigned as CD3. Therefore, all T cells are CD3 positive (CD3+). This practice of referring to cells by CD number prevents the misidentification of cells, which may occur from characterizing cells by their cytokine profile or morphology. A summary of surface proteins that are important to immune cell differentiation is provided in Table 1.

4.404.2. Recognition of Biomaterials by the Adaptive Immune System

4.404.2.1. Indirect Effects on Lymphocytes

4.404.2.1.1. Attraction of leukocytes to the implant site

The implantation of a biomaterial results in damage to the superficial vasculature, epithelial tissue, and local muscle tissue. Therefore, the response to the biomaterial is related to the initial wound-healing process that occurs in response to the damage caused by the implantation. It is generally understood that there are three phases to wound healing: inflammation, proliferation, and remodeling/maturation. Lymphocytes peak in the damaged region on day 7, during the proliferation phase, whether a biomaterial is present or not; however, lymphocyte migration commences as soon as wounding occurs. Immediately upon damage to local vasculature, which is inevitable with almost any incision/puncture, damaged endothelial cells vasoconstrict, α-granules of platelets are opened, and a fibrin clot forms. The degranulation of platelets is the initiating event in leukocyte chemotaxis and activation and initiates migration of neutrophils, monocytes, and lymphocytes. The platelet α-granules contain hundreds of soluble proteins that are released at the time of degranulation. The notable factors are listed in Table 2. Of particular relevance to lymphocyte chemotaxis is the release of transforming growth factor-β (TGF-β); however, other factors, such as histamine, prostaglandins, prostacyclin, and thromboxanes, certainly contribute to the migration of all leukocytes as they cause vasodilation of the constricted vessels and extravasation of the leukocytes

Table 2 Contents of platelet α-granules released upon tissue wounding and their function[a]

Molecule	*Function*
Fibrin	Principle component of thrombus formation. Provisional matrix formation
Fibronectin	Cell adhesion
Factor XIII	Chemoattraction and adhesion
Circulatory growth factors	Mitogenesis, fibroplasia, regulation of chemoattraction
Complement	Antimicrobial, chemoattraction
Cytokines (TGF-β)	Chemoattraction, mitogenesis
Chemokines (CXCL1, CXCL4, CXCL5, CXCL7, CXCL8, CXCL12, CCL2, CCL3, CCL5)	Chemoattraction. CXCL4 (also known as platelet factor IV) and CXCL7 are most abundant. These factors are chemotactic for fibroblasts and monocytes, neutralize heparin, and inhibit collagenase
Platelet-activating factor	Platelet aggregation
Thromboxane A_2 (via platelet COX-1)	Vasoconstriction, platelet aggregation, chemotaxis
Serotonin	Induces vascular permeability, chemoattractant for neutrophils
Platelet-derived growth factor (PDGF)	Promotes angiogenesis

that adhere to the vascular endothelium. The fibrin clot that forms in the injured vascular tissue is very similar to the provisional matrix that forms on the exterior of an implanted biomaterial and is composed of collagen, platelets, thrombin, and fibronectin. Both the clot in the vascular tissue and the provisional matrix on the exterior of the biomaterial concentrate release factors that are involved in wound healing and the response to the biomaterial. In fact, the clot and the provisional matrix serve as scaffolds for the migrated cells, neutrophils, monocytes, lymphocytes, fibroblasts, and endothelial cells.[1]

Ultimately, upon damage during biomaterial implantation, acute inflammation ensues with its severity closely related to the following factors: (1) the extent of damage caused by implantation and therefore the magnitude of prostaglandin release; (2) the site into which the material is implanted; and (3) the extent of provisional matrix formation.[2,3] Neutrophils and mast cells make up the majority of the initial extravasating cells and are therefore characteristic of acute inflammation. Mast cells release histamine from their granules, which exacerbates the initial inflammatory response.[4,5] As inflammation progresses to the proliferation phase or foreign body response, monocytes/macrophages extravasate through vascular walls and migrate to the implant site. Such migration of monocytes/macrophages occurs in response to chemokine production. Once macrophages are recruited to the implantation site, they produce tumor necrosis factor (TNF-α), interleukin-6 (IL-6), platelet-derived growth factor (PDGF), granulocyte-colony stimulating factor (G-CSF), and granulocyte macrophage colony stimulating factor (GM-CSF) to recruit additional macrophages to the area.[1,6] Both Rhodes *et al.*[8] and Jones *et al.*[7] have shown that production of CC-chemokines, such as CCL2, CCL4, CCL13, and CCL22, are produced by macrophages (and possibly monocytes or DCs) responding/adhered to biomaterials and are important for lymphocyte recruitment. A different class of chemokines, the CXC chemokine family, specifically those lacking the glutamic acid-leucine-arginine (ELR) motif before the first cysteine of the CXC motif, are primarily responsible for lymphocyte migration in the body. CXCL9 and CXCL10 have been found to be spatially associated with lymphocyte accumulation in cutaneous wounds and are likely important mediators of lymphocyte migration to biomaterial implantation sites.[9] The major source of these chemokines is most likely the myeloid cells (primarily macrophages, but also DCs and monocytes) in the region of an implanted biomaterial. A list of the chemokines involved in the attraction of adaptive cells to a biomaterial implant site is provided in **Table 3**. **Figure 1** illustrates the events leading to material recognition by the adaptive immune system.

Table 3 Chemokines, their receptors, and migrating cells

Receptor	*Ligands*	*Alternative names*	*Target cell*
CXCR1	CXCL1, CXCL2, CXCL3, CXCL5, CXCL6, CXCL7, CXCL8	IL-8R_A, IL-8R-I	Neutrophils, lymphocytes (B and T cells), monocytes/macrophages
CXCR2	CXCL1, CXCL2, CXCL3, CXCL5, CXCL6, CXCL7, CXCL8	IL-8R_B, IL-8R-II	Neutrophils, lymphocytes (B and T cells), monocytes/macrophages, eosinophils
CXCR3	CXCL9, CXCL10, CXCL11	IP-10/MigR, GPR9	Lymphocytes (B and T cells)
CXCR4	CXCL12	HUMSTR, LESTER, fusin, HM89	Lymphocytes (B and T cells)
CXCR5	CXCL13	BNLR-1, MDR15, BLR11	Lymphocytes (B and T cells)
CXCR6	CXCL16	STRL33, BONZO, TYMSTR	Lymphocytes (B and T cells), NK cells, dendritic cells
CCR2	CCL2, CCL13	CD192 CCL2 = MCP-1	Monocytes, memory T cells, DCs
CCR3	CCL5, CCL7, CCL11, CCL13	CCL13 = MCP-4	Monocytes, T cells, eosinophils, basophils
CCR4	CCL2, CCL4, CCL5, CCL22	CCL4 = MIP-1	Monocytes, memory T cells, DCs
CCR5	CCL4, CCL13	–	NK cells, monocytes

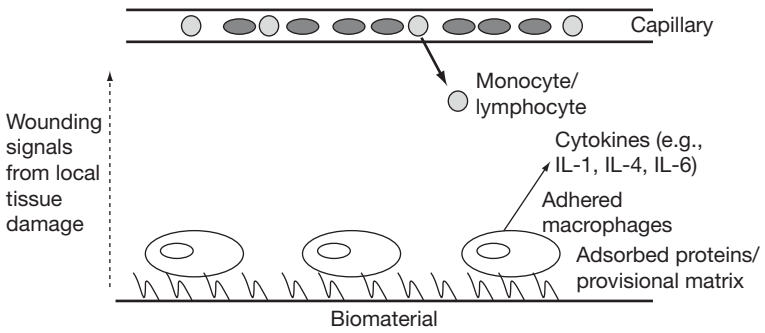

Figure 1 This figure illustrates the biomaterial implantation site following the acute inflammation stage. Macrophages adhering to the protein layer on the biomaterial produce cytokines that direct the lymphocyte response to the material (see **Figure 3** for more detail).

4.404.2.1.2. Activation of adaptive cells by innate cells activated through biomaterial contact

4.404.2.1.2.1. Paracrine/juxtacrine mechanisms

Upon interaction with a biomaterial, macrophages not only attract lymphocytes to the region but also activate the migrated T cells. The activation of lymphocytes by macrophages occurs through both contact and paracrine/juxtracrine mechanisms. The latter is the most common mechanism of lymphocyte activation by macrophages in the response to biomaterials that do not contain proteins. Specifically, material-adherent macrophages produce IL-1, IL-6, and TNF-α that activate local T lymphocytes. The role of the lymphocyte in these responses is yet to be completely determined; however, they are likely responsible for supplementing the production of signaling chemicals and growth factors, which guides the subsequent proliferative response. The form of activation of the responding lymphocytes is critical in the host response as the most prevalent responding lymphocyte, immature CD4+ T cells, can be differentiated into either inflammatory (Th1) or 'helper' (Th2) phenotypes. CD4+ Th1 cells produce IL-2, IFN-γ, and TNF-β, which causes prolongation of the inflammatory phase, and often increased release of nitric oxide and other reactive oxygen species. On the other hand, the 'helper' Th2 cells produce IL-4, IL-5, IL-6, IL-10, and IL-13, with the levels of each cytokine dependent on the specific activation of the T cell. These cells typically promote wound healing, with the exception that cells producing high quantities of IL-10 may inhibit cell proliferation and collagen levels. Since the responding lymphocytes depend on the adherent macrophages for cues, biomaterial surface chemistry, which impacts macrophage and FBGC adhesion and response, indirectly affects lymphocyte activation.[10–12] A reciprocal relationship also exists such that increased lymphocyte stimulation by paracrine/juxtracrine mechanisms can, in turn, result in increased/decreased macrophage stimulation.[10] It is interesting to note that though the Th2 response is typical to implanted biomaterials, B cells are rarely detected at the implantation site. This suggests that though Th2 responses prevail, antibody production at the biomaterial implant site rarely occurs.

4.404.2.1.2.2. Physical macrophage–lymphocyte interactions

Lymphocytes rarely adhere to materials that do not contain proteins, but rather adhere to the macrophage layer. Generally, the contact of lymphocytes with the macrophage layer does not stimulate activation of the cells; rather, juxtacrine cytokine production activates the lymphocytes. However, when the biomaterial contains foreign proteins, APCs (macrophages and DCs) phagocytose the proteins and present the processed peptides to the responding lymphocytes through MHC-II in a physical interaction between the cells. MHC-II presentation of foreign antigens by APCs to lymphocytes requires costimulation through CD80 and CD86. Without physical costimulation of the lymphocyte, activation does not occur, which is one mechanism of ensuring that the adaptive immune system does not respond to self-antigens. Biomaterials, such as poly (lactic-*co*-glycolic acid) and agarose, have been shown to upregulate costimulatory molecule (CD80 and CD86) expression on APCs, one reason biomaterials have been proposed as vaccine adjuvants.[13,14] **Figure 2** provides an illustration of MHC-II-mediated lymphocyte activation. Upon contact with an APC that is presenting a recognized (foreign) antigen on MHC-II with sufficient costimulation, the activated lymphocytes mount a specific response against the particular antigen. Such a response is considered a Th2 response and involves the activation of both CD4+ T lymphocytes and B lymphocytes with concomitant antibody (primarily IgG) production.[15] As a result, the adaptive immune response to the natural biomaterials that contain foreign proteins is often far greater than the response to synthetic biomaterials. Further details of the Th2 response are provided later in this chapter.

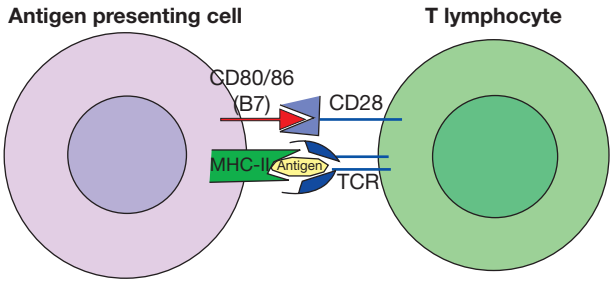

Figure 2 Antigen recognition by T lymphocytes requires proper binding of the host MHC-II protein displaying the recognized antigen with the T cell receptor (TCR). Coactivation involving CD80/86 with CD28 is necessary for activation of the T lymphocyte.

4.404.2.2. Direct Effects of Lymphocytes

It is generally assumed that there is no direct interaction between biomaterials and lymphocytes because, with respect to antigen presentation to T lymphocytes, the TCR, which recognizes the foreign antigen, requires costimulation by the MHC. Since biomaterials do not have or adsorb MHC proteins, T cells are not capable of recognizing the material directly. That is, material components must be internalized by APCs, which 'show' the antigens to the T cells (see **Section 4.404.2.1**). However, direct contact with soluble antigens can stimulate CD20+ B lymphocytes to differentiate into plasma cells and secrete antibodies specific for the antigen. Unlike T lymphocytes, B lymphocytes have the unique ability of recognizing and responding to nonprotein antigens (such as polysaccharides). In fact, activation of B lymphocytes by nonprotein antigens occurs independently of CD4+ T helper cells, whereas activation of B lymphocytes by protein antigens is dependent on costimulation by CD4+ helper T cells. As a result, B cells can recognize a wider range of antigens than T cells, leaving open the possibility that B cells will produce antibodies specific to a biomaterial. Although B cells are rarely detected at biomaterial implant sites, seldom are B lymphocytes suspected to contribute to the adaptive response to biomaterials.

There remains a possibility that T lymphocytes could be directly activated by biomaterials through nonantigen-specific mechanisms that are not currently understood. For example, proteins that adsorb to the material surface in small amounts, such as complement fragments, may cause nonspecific activation of lymphocytes.[16] However, such direct lymphocyte activation is unlikely to make a major difference in the response to a biomaterial as indirect activation of the lymphocyte populations is prevalent.

4.404.3. Consequences of the Adaptive Response

4.404.3.1. Spectrum of Adaptive Responses to Biomaterials

4.404.3.1.1. Inflammatory responses

The differentiation of the adaptive responses occurs during inflammation and is dependent upon the magnitude of damage, the site of implantation, and the material(s) implanted. With respect to adaptive immune responses, inflammation is divided into two segments, acute inflammation and chronic inflammation. Acute inflammation is synonymous with the inflammatory stage of wound healing; as mentioned, platelets degranulate (see Table 1); neutrophils migrate to the damaged tissue, followed by monocytes and lymphocytes. It is notable that acute inflammation can be minimized by limiting tissue damage (e.g., by using minimally invasive techniques) or through the use of certain anti-inflammatory compounds (e.g., glucocorticoids). Chronic inflammation generally coincides with the proliferation phase of wound healing, but the term also encompasses other immune responses that are distinct from wound healing. Unlike acute inflammation, chronic inflammation is quite variable depending on the stimuli encountered during acute inflammation. The presence of certain stimuli, such as pathogen-associated molecular patterns (PAMPs) that are found on bacteria cell walls (e.g., lipopolysaccharides), can be detected by monocytes, DCs, or macrophages, and alter the chronic inflammatory response. During chronic inflammation, APCs are critical mediators in differentiating the adaptive response by producing a cytokine milieu conducive to the formation of a particular lymphocyte response. The differentiation of the chronic inflammatory response is highly dependent on the materials that the infiltrating monocytes phagocytose and the cytokines that predominate in the local environment. An underlying matter to the form of inflammatory response that develops is the specific phenotype of the local matured macrophages and/or DCs. Macrophages have recently been divided into three subcategories, 'classically activated,' 'wound-healing,' and 'regulatory' based on their specific expression of several factors such as cytokines, and intracellular/transmembrane proteins.[17] Similarly, mature DCs have been subdivided into the following two categories: immunogenic DCs and tolerogenic DCs.[18–20] With respect to both macrophages and DCs, most of these cells are derived from the myeloid lineage with monocytes being the precursor of each cell type, plasmacytoid DCs being the exception to this. The specific phenotype of the myeloid cells that populate the biomaterial implant site has significant implications to the future adaptive immune response. Figure 3 illustrates the implications of macrophage phenotype polarization on the lymphocyte response.

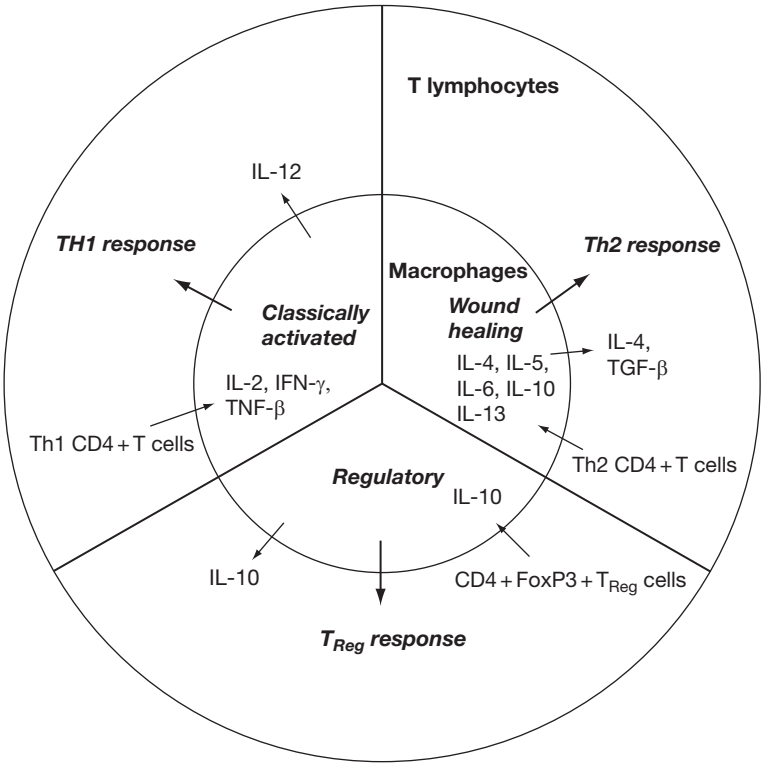

Figure 3 Most leukocytes, such as macrophages and T lymphocytes, have phenotypically diverse populations. Macrophage populations have been likened to colors on a color wheel, illustrating the fact that macrophages can take up a phenotype that is strongly 'wound healing,' 'classically activated,' or 'regulatory,' or one that is a blend of the aforementioned phenotypes. Similarly, T cells, particularly CD4+ T helper cells, display Th1, Th2, and T_{Reg} phenotypes. In this figure, the center of the diagram represents undifferentiated macrophages, known as monocytes. The outer edge of the inner circle represents fully differentiated macrophages separated by the different phenotype classifications. The different macrophage phenotypes produce factors that polarize the adaptive response to its different subsets. Predominant cytokines that cause this polarization are provided. Once the adaptive response has developed, the responding lymphocytes produce cytokines that affect macrophage activity. Therefore a feedback system is created, which permits progression of a specific immune response.

4.404.3.1.2. Range of T cell responses (Th1, 2, 17 rejection, tolerance, effect of duration, and magnitude)

Like innate immune cells, T lymphocytes have been characterized into several different varieties. The three major types of T cells (i.e., CD3+ cells) are CD4+ 'helper' T cells, CD8+ 'effector' T cells, and γδ-T cells. An immense amount of literature on CD4+ T cells has subdivided these cells into Th1, Th2, Th17, and regulatory (T_{Reg}) classifications: Th1 cells produce primarily IFN-γ and IL-12; Th2 cells produce IL-4, IL-5, and TGF-β; Th17 cells produce IL-17; and T_{Reg} cells produce Foxp3 and IL-10. Table 4 contains a breakdown of the different responses and their distinguishing characteristics. With respect to biomaterial–T cell interactions, Th1, Th2, and T_{Reg} cell populations are the most relevant. That is, Th17 cells and γδ-T cells have never been reported as being present at biomaterial implantation sites. However, it is conceivable that Th17 cells and γδ-T cells appear at some biomaterial implantation sites, but their presence has never been assessed.

The difference between Th1 and Th2 T cell responses is critical to defining the amount of matrix production that results on the surface of a biomaterial. If there are foreign proteins present, the Th2 response is expected to prevail. However, if foreign proteins are naturally internal to a cell included in the biomaterial matrix, such as with allogeneic cells, or viruses, the Th1 response is expected to prevail. Complete sterility of biomaterial surfaces, including freedom from endotoxins and any foreign proteins (denatured or not), is critical in biomaterial research to alleviate the possibility of negatively altering the host response to the biomaterial.[21] That is, biomaterial surfaces must be free of any possible contaminants. Otherwise when monocytes adhere to the surface during the initial recognition phase of the host response, they may take up the contaminating element, which would affect the eventual adaptive response. Furthermore, many researchers utilize fetal bovine serum (FBS) in their cell media, which may inadvertently alter the outcome of experiments involving a leukocyte response because of the presence of neoantigens of bovine origin.

Table 4 Characteristics of the various T cell responses

Response	*Cells involved*	*Characteristics*
Th1	CD4+ T cells, CD8+ T cells	Stimulus (foreign protein/antigen from within any cell), found on MHC-I and detected by T cells. IFN-γ, TNF-β, IL-2, and IL-12 are produced. Typically inflammation is prolonged (i.e., chronic inflammation) until the stimulus is no longer present. Macrophages and cytotoxic CD8+ T cells are the effector cells responsible for clearance of the stimulus. Little fibrosis occurs
Th2	CD4+ T cells, B cells	Stimulus found on MHC-II of APCs. IL-4, IL-5, IL-6, IL-10, and IL-13 are produced. Chronic inflammation is often associated with fibrous tissue formation, especially when IL-4 and TGF-β levels are high. B cells produce antibodies that mediate clearance of the stimulus
Th17	CD4+ T cells	IL-17 is strongly upregulated. Th17 cells promote inflammation in autoimmune diseases and in response to some viral infections
Regulation	CD4+, CD25+, Foxp3+ T cells	IL-10 is the predominant cytokine and is responsible for suppressing inflammation and the activity of effector cells (cytotoxic CD8+ T cells, macrophages, and B cells). If TGF-β levels are high, fibrosis occurs

4.404.3.2. Effects on Biomaterial-Only Devices (e.g., Probes, Implants, Biological Scaffold Materials)

4.404.3.2.1. Inflammation

The response to synthetic biomaterial-only devices is relatively straightforward compared to the response to multicomponent devices. As mentioned previously, inflammation occurs immediately upon implantation of a material in the body and defines the future adaptive immune responses. The proper inflammatory response can be critical to the application. For example, some biomaterials have been shown to cause an upregulation of matrix metalloproteinases (MMPs).[22] MMP upregulation is generally welcome in the local environment of artificial joints, catheters, probes, heart monitors, and any other material that is implanted and that does not need a supporting matrix on/around it. However, overproduction of MMPs would likely impair the performance/lifespan of materials that are intended to serve as scaffolds for proliferation of specific cells/tissue. Inflammation is essentially defined as the migration and localization of leukocytes in response to a stimulus that disrupts the homeostasis of the tissue. As a result of cell migration, the tissue becomes swollen and often painful. If the tissue is superficial, inflammation is associated with redness and heat. The inflammatory response can itself be detrimental to the performance of implanted medical devices such as artificial joints, as the migration of leukocytes and subsequently increased local cell density results in reduced mobility of the joint and increased pain. For most medical devices, some inflammation is acceptable, if it is short-lived, but prolonged or severe inflammation precludes proper functioning of the device. The adaptive immune system can prolong inflammation if there are foreign antigens present in the local environment of a medical device. Generally, it is desirable for the inflammatory response following implantation of a material to be very similar to the inflammatory response to a similar surgical procedure without the implantation of a biomaterial component, as the extent and duration of deviation from optimal wound-healing conditions affects the biocompatibility of the device. As a result, it is critical that medical devices should be sterile and also free of foreign antigens or endotoxins.

4.404.3.2.2. Foreign body response

The foreign body response to biomaterials is a well-documented response to materials that occurs due to monocyte/macrophage adherence on the surface of the material and local

production of mediators (such as IL-4), resulting in macrophage fusion. T lymphocytes have been shown to increase monocyte adhesion and macrophage fusion on biomaterial surfaces, enhancing the foreign body response, through indirect (paracrine) signaling.[23] Chang *et al.* have shown that lymphocytes indirectly enhance macrophage and FBGC activation at early time points by producing soluble mediators, and promote sustained activation at later time points through direct cell–cell mechanisms. A bilateral exchange between lymphocytes and macrophages/FBGCs occurs as macrophages/FBGCs actually support the activation of responding lymphocytes. That is, cytokine production by macrophages/FBGCs is correlated with activation of responding lymphocytes, which in turn may cause progression and prolongation of the foreign body response to the material.

4.404.3.2.3. Fibrosis

Fibrosis is a common phenomenon with respect to disease pathology, wound-healing, and material implantation. Soon after placement of a material in the body, myofibroblasts commence production of extracellular matrix (ECM) proteins, which replace the provisional matrix and provide long-term structure for cells to adhere. As mentioned earlier, the antithesis of ECM protein production is the production of MMPs. In fact, constant remodeling of the ECM occurs so that the initial matrix is more elastic and degradable, and becomes stronger through remodeling, such as with replacement of fibronectin and collagen III in the matrix with collagen I. The adaptive immune response certainly affects fibrosis on and around material surfaces by altering the microenvironment. Strong Th2 adaptive responses have been shown to result in strong collagen I-rich scar development, whereas T_{Reg} responses suppress fibrous tissue formation altogether. The fibrotic response to an implanted biomaterial can affect the function and/or lifespan of a medical device. For example, the formation of thick fibrous tissue impedes the function of medical devices in the joints. With respect to drug delivery devices, fibrous tissue development around the construct may act as a barrier and impede nutrient or product diffusion. Acellular tissue engineering scaffolds that are implanted with chemotactic agents for the attraction of desired cells into the scaffold could also be adversely affected by a strong fibrotic response. That is, fibrous tissue may impede the chemomigration of cells into the construct. On the other hand, angiogenesis (see below), a parallel phenomenon to fibrosis, would likely be welcome in acellular tissue-engineering scaffolds. Therefore, appropriate adaptive responses are essential to guiding an appropriate fibrotic response to the medical device.

4.404.3.2.4. Angiogenesis

Angiogenesis occurs simultaneously with fibrosis. Upon implantation of a foreign material, myofibroblasts and endothelial cells migrate to the implant and commence the formation of blood vessels and fibrovascular tissue. Angiogenesis is generally not detrimental in itself, but does permit the development of thicker fibrous tissue. In some situations, such as tissue-engineered constructs and drug delivery devices, angiogenesis on and around the construct may be beneficial, depending on the purpose of the device and the pharmaceutical that is being released.

4.404.3.2.5. Autoimmunity

Autoimmune responses are immune responses against a self-antigen and rarely occur with the implantation of biomaterial-only constructs. It has been suspected that one of the risks of silicone breast implants is an increased risk of rheumatologic disorders (e.g., connective tissue disease, scleroderma, or arthritis), and some studies have found increased autoimmune antibodies in the serum of individuals with implants; however, several epidemiological studies have found no correlation between silicone breast implants and rheumatic diseases. The concern of some researchers is that the silicone implant exposes previously hidden self-protein epitopes (see Section 4.404.2.2), which may occur in some patients without the stimulation of an autoimmune reaction.

4.404.3.2.6. Infection

A general risk of surgery, especially surgeries of invasive nature such as joint replacement, is the possibility of infection. Biomaterials actually increase the risk by providing pathogens (primarily bacterial) with a surface to proliferate and grow. As a result, biofilms form on and around implanted medical devices. It is very difficult for the innate immune system to fight these infections because of the rate at which they grow, the density of the bacteria on the surface of the material implant, and the difficulty faced with phagocytizing the bacteria. Therefore, infected medical devices typically require removal from the body. The only negative consequence of the adaptive immune response to biofilms is the sustainment of inflammation. However, this can hardly be viewed as a downfall of the adaptive response, with the alternative being eventual systemic bacterial infection and possible death of the host.

4.404.3.3. Effects on Combination Products (i.e., Vaccine or Tissue-Engineering Construct)

4.404.3.3.1. Magnitude of response

Combination products elicit an immune response to the biomaterial component as well as to the cellular component. Generally the response to the biomaterial component affects the response to the cellular component and vice versa. Due to the range of potential tissue-engineering constructs, an appropriate response is difficult to define. The maintenance of device function is critical throughout the inflammatory and wound-healing responses, as function is impossible to regain once lost. However, the purpose of an implanted biomaterial combination product is different in peptide-loaded vaccine microparticles and tissue-engineering constructs or cellularized scaffolds intended to supplement the function of an organ/tissue. Without doubt, limiting the magnitude of the response is essential for tissue-engineering constructs, but enhancing the magnitude of the response is desirable for vaccine microparticles.

Biomaterials have been shown to promote immune response to certain antigens, and have therefore been proposed as vaccine adjuvants. As wound healing and fibrovascular tissue formation require a Th2-like response, which normally occurs in response to biomaterial-only constructs, it is not surprising that biomaterials can promote/magnify the response to extracellular proteins. For the desired effect of magnification of a Th2 response to take place against biomaterial-based

vaccines, it is essential that the proteins originate from outside the responding APCs. That is, a biomaterial can be processed to act as a protein carrier as well as an adjuvant, and support a sustained immune response against a cell lysate or a specific protein that has been incorporated into the biomaterial construct.

4.404.3.3.2. Altered responses

The presence of a biomaterial has been shown to alter the immune response to foreign proteins and vice versa. As mentioned, the lymphocyte response to biomaterials is generally a Th2-type response. However, a Th1 response typically develops against allogeneic cells. Therefore, a tissue-engineering construct composed of allogeneic cells and a biomaterial supports competition between Th1 cells and Th2 cells, which have some opposing characteristics (e.g., TGF-β production by Th2 cells). The initial response to such constructs is likely to be against the presence of foreign proteins, so Th1 cells and CD8+ CTLs are likely to dominate at first. Depending on the specific construct, upon clearance of the cells with MHC1 mismatches, the Th2 response against the biomaterial may dominate, resulting in fibrovascular tissue formation.

4.404.3.3.3. Tolerance responses

With respect to a combination product, the term 'tolerance' has different meanings. 'Tolerance' may imply a strong wound-healing response in which the cellular component of the combination product is not harmed; however, others may view 'tolerance' as complete suppression of any immune response. For biomaterial-only components, tolerance may be achieved by simply altering the surface structure of the material, or implanting a drug delivery device that releases anti-inflammatory or antifibrotic compounds locally.[24] That is, upon resolution of the inflammatory response, it is possible to accumulate minimal fibrovascular tissue on and around a biomaterial-only construct. Similarly, cellularized syngeneic combination products are likely to be completely tolerated by the host immune system as no foreign proteins are present. However, achieving tolerance to combination products with foreign proteins is far more elusive, as allogeneic and xenogeneic cells are recognized and destroyed by the host immune system, even when 'hidden' from the APCs and lymphocytes by microencapsulation.[25] The implantation of allogeneic stem cells may be tolerated by the host immune system, but may become immunogenic upon differentiation and maturation. Some immune privileged sites in the human body have been identified including the eyes, the brain, the testicles, and the placenta and fetus.

A method of inducing tolerance to foreign proteins in combination products has yet to be discovered but will inevitably require the induction and proliferation of CD4+Foxp3+ regulatory T cells, and the antigen-specific CD8+ T cells to be rendered anergic. Anergy is a state of unresponsiveness following stimulation with an antigen that is recognized by the cell's TCR. In allotransplantation, immune suppression is generally achieved by lifelong delivery of glucocorticoids, which systemically suppress the entire immune system. Glucocorticoids are naturally produced by the adrenal cortex from cholesterol, with production regulated by the hypothalamic–pituitary–adrenal (HPA) axis. They have long been used in solid organ transplantation because of their nonspecific anti-inflammatory effect, direct effect on lymphocytes (B cells and T cells), and their ability to modulate cellular immune functions.[26] When systemically administered, corticosteroids cause a sequestering of T lymphocytes in the bone marrow, which reduces the number of T lymphocytes that circulate through the vasculature. As glucocorticoids are lipophilic molecules, they are able to freely cross plasma membranes and bind to specific intracellular receptors that belong to a family of transcription factors.[27] Central to their effects on the immune system is their ability to reduce activation of target genes by inhibiting NF-κ by changing confirmation of the protein into a chemically inert form.[28] They also strongly inhibit phosphodiesterase, causing cyclic adenosine monophosphate to accumulate intracellularly, which reduces lymphocyte activation.[26] Production of IL-1 in macrophages and IL-2 in T cells is also inhibited by glucocorticoids, which reduces the generation of CTLs. The anti-inflammatory effect of glucocorticoids results from the suppression of arachidonic acid release and suppression of macrophage phagocytosis. Ultimately, glucocorticoids suppress the immune system and prevent immune response to allotransplants, but as a result, this prevents immune tolerance to the organ/tissue. However, the full potential of glucocorticoid use in medicine may yet be seen as research indicates that glucocorticoids upregulate the formation and proliferation of T_{Reg} cells and tolerogenic DCs. Local sustained glucocorticoid delivery has been achieved through polymeric drug delivery constructs, but has never been used clinically. Therefore, systemic glucocorticoid use may inhibit the immune system and prevent immune responses, but at the same time prevent the induction of tolerance to foreign antigens, while local use suppresses inflammation but promotes tolerance to the foreign proteins. Figure 4 provides a summary of the role of lymphocytes in the various responses to material-only devices and combination products.

4.404.4. Approaches to Engineer Adaptive Responses with Biomaterials

Most work on manipulation of the immune response to biomaterials has been in the area of vaccine research and using biomaterials as adjuvants or delivery vessels, in which the desire has been to amplify the inflammatory response and adaptive immune response. At the same time, efforts have been made to create a biomaterial surface that is tolerated by the body, and not encapsulated with fibrous tissue. Others have incorporated steroidal or nonsteroidal anti-inflammatory drugs into the construct to suppress the initial inflammatory and subsequent foreign body response to the material.

4.404.4.1. Biomaterials as Vaccine Adjuvants and Antigen Carriers

For biomaterials to be effective for use in vaccinations, they must perform three functions: (1) promote the migration of APCs, specifically DCs; (2) activate the DCs to a proinflammatory, antigen-presenting phenotype; and (3) release the antigen such that the responding DCs take it up.[29] Generally, biomaterials acting as vaccine adjuvants are in the form of microparticles, but other designs are likely to be just as effective.

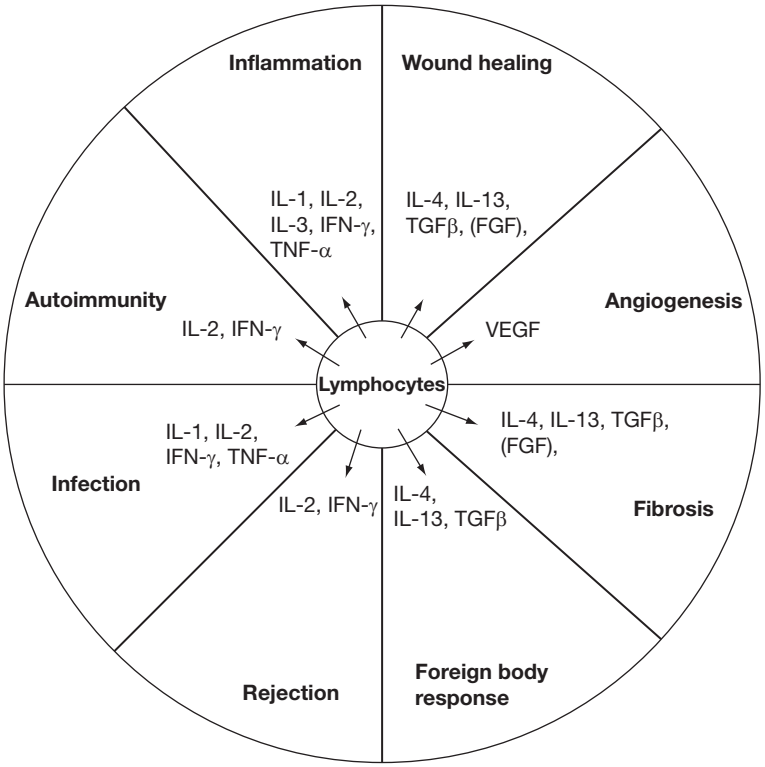

Figure 4 Once activated, lymphocytes affect the subsequent responses to biomaterials. This figure illustrates the specific responses that the adaptive immune system has influence over and lists the predominant protein factors that contribute to signaling of the various responses. With respect to autoimmunity, cell rejection, and the neutralization of infection, lymphocytes are essential contributors. With respect to fibrosis, angiogenesis, foreign body response, inflammation, and wound healing, lymphocytes are not essential, but contribute to the development and end result of each. As shown by the protein factors produced by lymphocytes, substantial overlap of the mediators supporting the different responses exists. In many respects the specificity of the response arises from the specific cell populations involved. For example, foreign body response occurs upon implantation of materials, which provide a surface for attachment of monocytes/macrophages. Since the foreign body response typically occurs concurrent with fibrosis, the cytokine milieu that signals for macrophage fusion is similar to that which signals for fibroblast proliferation and fibrosis. Similarly, autoimmunity, infection, and rejection are generally comparable responses to specific antigens from oneself, a pathogen, or an allogeneic/xenogeneic construct, respectively.

Regardless of the design, the biomaterial should promote inflammation, as inflammation from wounding due to material implantation is not likely a sufficient initiator of a primary response to an antigen. Current adjuvants are based on aluminum salts (hydroxides or phosphates), and act to promote/sustain the inflammatory response so that more antigen is taken up by the responding DCs, which results in an elevated adaptive response. All vaccines used clinically elicit a humoral (Th2) response, are usually composed of live attenuated, killed, or fragmented pathogens, and are typically delivered transdermally.

Biomaterials in the form of microparticles offer the potential of eliciting a Th1 response if they dump their protein contents into the cytoplasm of phagocytizing cells. Antigens within the cytoplasm of the cell are then presented on the surface of the cell by MHC-I, where reactive T lymphocytes recognize the foreign antigens. A delayed cell-mediated Th1 response is then likely to ensue. Such a response would be capable of destroying cells that express the antigen, and could be used to vaccinate against diseases that are currently not curable, such as cancer or AIDS, prior to or following disease induction. For example, most breast cancer tumors produce α-lactalbumin. A vaccination that promotes a strong cell-mediated immune response against cells expressing α-lactalbumin could be capable of destroying all malignant tissue.[30] Biomaterials therefore offer the potential to engineer unique vaccines against diseases that currently have no vaccine.

4.404.4.2. Surface Modification

The greatest body of work in modulation of the host response to biomaterials is in the area of surface modification. Most often, surface modification is intended to change cytocompatibility, as opposed to immunocompatibility. For example, RGD groups or other bioactive molecules are frequently added to the surface of materials to enhance cell adhesion or migration of a particular type of cell. However, modifications to the surface of a material inevitably alter the host immune response to the implant.[31] That is, changing the material surface alters the protein adsorption on the material, thereby affecting the subsequent response. Much of the research on biocompatibility before/after surface modification has involved *in vitro* culture tests, in which the outcome is the observation of cell morphology and differences between materials. Though some information regarding the biosafety of a material can be determined, these assays are poor indicators of

the host response to the material. Better *in vitro* indicators of the host response are derived from mixed leukocyte reactions and simulated foreign body reactions.

4.404.4.3. Anti-inflammatory Drug Release

The release of anti-inflammatory drugs from a biomaterial has been proposed as a potential solution for several medical conditions such as rheumatic diseases, asthma/allergy, fibrotic diseases, and transplant rejection, but has also been proposed as a solution to suppressing a detrimental host response to biomaterial medical devices (e.g., glucose monitors). Anti-inflammatory compounds, particularly glucocorticoids, are incredibly effective at suppressing the formation and release of inflammatory mediators, namely prostaglandins and leukotrienes. As a result, these compounds prevent the migration of inflammatory cells (neutrophils, monocytes, and lymphocytes) by reducing chemotaxis and cell extravasation. Glucocorticoids also suppress fibroblast proliferation, which leads to a significant reduction in fibrovascular tissue formation. Unfortunately, the benefit of anti-inflammatory compounds lasts only as long as the drug is present in the body. For example, once dexamethasone, a glucocorticoid, is completely released from a biomaterial disc, the body begins to recognize the material as a foreign body, and inflammatory and immunogenic reactions commence. This result occurs even if the drug is released over the course of several months. A permanent solution to the foreign body response is yet to be found.

4.404.5. Conclusions

The adaptive response is a component of the host reaction to both implanted biomaterial-only constructs and combination devices. With respect to biomaterial-only constructs, lymphocytes are generally hyporesponsive, but promote monocyte/macrophage adhesion to the material and FBGC formation. The adaptive response is most critical in relation to combination products. Among the list of potential lymphocyte responses, the most relevant to biomaterial devices include Th1 responses, Th2 responses, and regulatory responses. The desired adaptive immune response to a biomaterial device depends on the application. Typically the activation of lymphocytes requires the implantation of foreign (allogeneic or xenogeneic) proteins; however, it may be possible for a synthetic biomaterial-only construct to permit cellular recognition to nontolerated syngeneic protein epitopes, or for syngeneic cells to present nontolerated epitopes on their surface following *in vitro* processing. Biomaterials have recently been proposed as vaccine adjuvants as they permit modulation of adaptive immune responses and promote activation of lymphocytes and inflammation when associated with foreign proteins. In fact, through biomaterial surface modification or drug/protein association, adaptive immune responses can be altered to the benefit of medical devices that have a polymer component.

References

1. Broughton, G., II; Janis, J. E.; Attinger, C. E. *Plast. Reconstr. Surg.* **2006**, *117*, 12S–34S.
2. Anderson, J. M. *Annu. Rev. Mater. Res.* **2001**, *31*, 81–110.
3. Anderson, J. M.; Rodriguez, A.; Chang, D. T. *Semin. Immunol.* **2008**, *20*, 86–100.
4. Tang, L.; Jennings, T. A.; Eaton, J. W. *Proc. Natl. Acad. Sci. USA* **1998**, *95*, 8841–8846.
5. Zdolsek, J.; Eaton, J. W.; Tang, L. *J. Transl. Med.* **2007**, *5*, 31.
6. Rodriguez, A.; Meyerson, H.; Anderson, J. M. *J. Biomed. Mater. Res. A* **2009**, *89*, 152–159.
7. Jones, J. A.; Chang, D. T.; Meyerson, H.; *et al. J. Biomed. Mater. Res. A* **2007**, *83A*, 585–596.
8. Rhodes, N. P.; Hunt, J. A.; Williams, D. F. *J. Biomed. Mater. Res.* **1997**, *37*, 481–488.
9. Gillitzer, R.; Goebeler, M. *J. Leukoc. Biol.* **2001**, *69*, 513–521.
10. Chang, D. T.; Colton, E.; Anderson, J. M. *J. Biomed. Mater. Res. A* **2009**, *89*, 490–498.
11. Chang, D. T.; Colton, E.; Matsuda, T.; Anderson, J. M. *J. Biomed. Mater. Res. A* **2009**.
12. Chang, D. T.; Jones, J. A.; Meyerson, H.; *et al. J. Biomed. Mater. Res. A* **2008**, *87A*, 676–687.
13. Yoshida, M.; Babensee, J. E. *J. Biomed. Mater. Res. A* **2004**, *71A*, 45–54.
14. Yoshida, M.; Babensee, J. E. *J. Biomed. Mater. Res. A* **2006**, *79A*, 393–408.
15. Badylak, S. F.; Gilbert, T. W. *Semin. Immunol.* **2008**, *20*, 109–116.
16. Jones, K. S. *Tissue Eng. B Rev.* **2008**, *14*, 407–417.
17. Mosser, D. M.; Edwards, J. P. *Nat. Rev. Immunol.* **2008**, *8*, 958–969.
18. Morelli, A. E.; Thomson, A. W. *Nat. Rev. Immunol.* **2007**, *7*, 610–621.
19. Steinman, R. M.; Hawiger, D.; Nussenzweig, M. C. *Annu. Rev. Immunol.* **2003**, *21*, 685–711.
20. Thomson, A. W. *Am. J. Transplant.* **2010**.
21. Gorbet, M. B.; Sefton, M. V. *Biomaterials* **2005**, *26*, 6811–6817.
22. Xu, P.; Sefton, M. V. *J. Biomed. Mater. Res. A* **2004**, *71*, 226–232.
23. Brodbeck, W. G.; Macewan, M.; Colton, E.; Meyerson, H.; Anderson, J. M. *J. Biomed. Mater. Res. A* **2005**, *74*, 222–229.
24. Love, R. J.; Jones, K. S. *Crit. Rev. Biomed. Eng.* **2009**, *37*, 259–281.
25. Jones, K. S.; Sefton, M. V.; Gorczynski, R. M. *Transplantation* **2004**, *78*, 1454–1462.
26. Smith, B. T. American Society of Health-System Pharmacists, Inc, 2008.
27. Miner, J. N.; Brown, M. In *Therapeutic Immunology*, 2nd edn.; Austen, K. F., Burakoff, S. J., Rosen, F. S., Strom, T. B., Eds.; Blackwell Science: Winnipeg, 2001.
28. Liden, J.; Rafter, I.; Truss, M.; Gustafsson, J. A.; Okret, S. *Biochem. Biophys. Res. Commun.* **2000**, *273*, 1008–1014.
29. Jones, K. S. *Biotechnol. Prog.* **2008**, *24*, 807–814.
30. Jaini, R.; Kesaraju, P.; Johnson, J. M.; Altuntas, C. Z.; Jane-Wit, D.; Tuohy, V. K. *Nat. Med.* **2010**.
31. Macewan, M. R.; Brodbeck, W. G.; Matsuda, T.; Anderson, J. M. *J. Biomed. Mater. Res. A* **2005**, *74A*, 285–293.

4.405. Leukocyte–Biomaterial Interaction *In Vitro*

J M Curran and J A Hunt, University of Liverpool, Liverpool, UK

© 2011 Elsevier Ltd. All rights reserved.

4.405.1.	**Introduction**	49
4.405.2.	**Characterizing the Inflammatory Response**	50
4.405.2.1.	Protein Adsorption	50
4.405.2.1.1.	Characterizing protein adsorption *in vitro*	52
4.405.2.2.	Cellular Indicators in the Inflammatory Response	52
4.405.2.2.1.	Neutrophil material interactions *in vitro*	53
4.405.2.2.2.	ROS production and measurements *in vitro*	54
4.405.2.2.3.	Cytokine production by neutrophils	54
4.405.2.2.4.	*In vitro* monocyte material interactions	54
4.405.2.2.5.	Monocyte/lymphocyte coculture models	59
4.405.2.2.6.	Foreign body giant cell formation *in vitro*	60
4.405.2.3.	Leukocyte Interactions with Wear Particles	60
4.405.2.3.1.	The role of *in vitro* leukocyte models: Controlling the inflammatory response	61
References		61

Abbreviations

CCL	Chemokine (C–C motif) ligand
CL	Chemiluminescence
ELISA	Enzyme linked immunosorbent assay
FACS	Flow cytometry
FBGC	Foreign body giant cell
FGF	Fibroblast growth factor
GM-CSF	Granulocyte macrophage colony-stimulating factor
IFN	Interferon
IL	Interleukin
MCP-1	Monocyte chemotactic protein-1
MHC	Major histocompatability complex
MIP	Macrophage inflammatory protein
MPO	Myeloperoxidase
PBMC	Peripheral blood mononuclear cells
PDGF	Platelet-derived growth factor
PMN	Polymorphonuclear leukocytes
ROS	Reactive oxygen species
SOD	Superoxide dismutase
TCPS	Tissue culture polystyrene
TGF	Transforming growth factor
TNF	Tumor necrosis factor
VEGF	Vascular endothelial growth factor

4.405.1. Introduction

The key requirement of any implantable material or device is biocompatibility: quite simply, if a material is not biocompatible, it will not be accepted for use *in vivo*, and therefore that material is not suitable as a biomaterial, regardless of its mechanical and esthetic properties. Biocompatibility is defined as the ability of materials to function with an appropriate host response in a specific application.[1] This definition, used in its entirety, is robust and now widely accepted by the biomaterials community. With the expression 'appropriate host response' has evolved a dramatic increase in the number of applications for biomaterials in the field of modern medicine. For a given application, the appropriate host response will change depending on the prespecified functionality of the material that is implanted. An inevitable consequence of the implantation of a material *in vivo* is an inflammatory response, the mechanism by which the body reacts to the process of implantation, that is, surgical cutting of tissues and blood vessels, and the presence of the implanted material. Therefore, based on the fact that the host response will be triggered and some form of inflammatory response will occur when a material is implanted, the events occurring therein need to be modeled and measured; this would lead to a precise understanding of the ensuing inflammatory response, the processes and components involved, the driving forces that dictate the severity and longevity of the response, and their subsequent long-term consequences. With this knowledge, materials and systems can be produced that can control the inflammatory response and thus enhance the efficiency and biocompatibility of implanted devices, thereby further developing and realizing the potential of biomaterials used in tissue engineering processes for regenerative medicine. Can the inflammatory response be classified in terms of cell types and time? Furthermore, can the consequences of the many aspects of an inflammatory response be modeled for their effect on the implanted biomaterial itself? Can the body's innate defense be used to integrate the implanted device rather than let it remain a phase that must be endured towards long-term functional implantation?

The data obtained from *in vitro* models, which have been utilized to assess the ability of a material to induce or sustain certain elements of the inflammatory response have

successfully identified individual parts of this complex host response, making them more cost-effective and accessible compared to *in vivo* models. With the correct choices, these models can be effectively used as preliminary high throughput screens during the development of new materials. It is important to note that to achieve reliable data from *in vitro* systems the right type of models must be established, that is, the right cell type, culture conditions, and time periods. The introduction of a high degree of reproducibility to the models, which comes from careful experimental planning and high levels of control of variables within a system, is crucial, as are benchmark positive and negative reference points and controls.

This chapter discusses the evaluation of the process of an inflammatory response, the cells involved, and the drivers of these cellular responses: all elements that are required to be understood prior to the development of *in vitro* inflammatory models. Based on this, it is possible to develop *in vitro* models that can effectively act as screening tools for quantifying and characterizing the kinetics and the magnitude of the inflammatory response. A major cellular component of the inflammatory response is the leukocyte. This chapter defines leukocytes, their role in inflammation, and the way these cells can be utilized to derive scientifically relevant *in vitro* data that can predict *in vivo* events and device performance. The chapter also investigates their mode of communication and the ramifications of prolonged activity or stimulation of select cell types on the performance of the implanted material. In addition to the introduction of the inflammatory response, *in vitro* models, and the tools of analysis, specific examples highlighting the components of inflammation are also discussed to exemplify the consequences of different inflammatory events on the host and material and their role in determining the success of an implant. One such example would be the aseptic loosening of orthopaedic implants – how can this phenomenon be predicted and evaluated *in vitro* and these data used to develop materials with the correct properties so as to minimize the detrimental aspects of the inflammatory response and increase the longevity and performance of selected implants? As with the inflammatory response itself, the processes of research, data collection, and development of novel materials act as positive feedback and add to the knowledge base; the more the scientifically relevant data, obtained using controlled *in vivo* and *in vitro* models, is disseminated, the deeper becomes the understanding of what drives the cellular response at a fundamental level, thereby increasing the understanding of how certain types of material properties can be used to control and manipulate the cellular response. An important point to note is that the inflammatory response to a material is inevitable due to the process of implantation and should not be considered as a series of negative events that should be avoided or halted completely. Instead, it should be understood in order to harness and tailor it to manipulate the host environment for the efficient integration, or passivation, of the material within the body. The direct effect of a material on the host in terms of inflammation and the direct effect of the leukocytes on the material are critical. However, these events and this interaction have indirect effects on the cells and the surrounding tissue, and also possibly systemic effects. The impact and significance of these indirect effects are introduced, developed, and discussed in this chapter, and pertain to cells such as osteoblasts and stem cells within the host, and to the mediation of the function of these cells by inflammation.

4.405.2. Characterizing the Inflammatory Response

In order to develop relevant *in vitro* models for assessing inflammatory responses such as the breaking down of the leukocyte–biomaterial interaction, a comprehensive perspective of the inflammatory response and its components is required, and this should include the cell types involved, the methods of signaling and the end points in terms of the final tissue state, for example, a common end point is fibrous capsule formation. This section of the chapter discusses the different elements of the inflammatory response and how they can be utilized to develop standardized *in vitro* models. Each sequential element is discussed in chronological order as it occurs after injury *in vivo*, and the methods for *in vitro* experimentation are also discussed. The emphasis is on leukocyte–biomaterial interactions, but along with that, these responses require contextualization in a broader perspective to present some of the other elements that can dictate and affect the specific set of responses. **Table 1** provides a brief overview of the cytokines that are released by cells during the inflammatory process and their subsequent effects. The complexity of the relationships between each cell type is discussed further.

4.405.2.1. Protein Adsorption

Protein adsorption onto the surface of an implanted material is the first phase of the host response; the type, amount, and nature of the protein adsorbed onto the surface can dictate the subsequent cellular responses, a principle that is true for all cell types and not just for leukocytes involved in the inflammatory response.

Any implantation procedure that requires an incision will result in damage to the vascular tissue at the area of implantation, the element involved in hemostasis, which is the mechanism by which the body stops blood loss via the formation of a clot to plug the severed area. The protein systems within the circulating blood, which are involved in the coagulation cascade, play a role in determining the host response, the extent of the response, and the subsequent inflammatory responses as the initial protein adsorption acts as a direct interface and substrate for cell adhesion and signaling. There is a significant complexity in the details of serum protein–biomaterial interactions and the elements of this system, including complement and blood coagulation cascades, and their role in determining biocompatibility are a research area in their own right.[2–4]

When a material is implanted, the first response is the adsorption of the proteins circulating in the blood onto the material's surface, specifically albumin,[5] fibrinogen,[6] fibronectin,[7] vitronectin,[8] and γ-globulin and complement.[9] Detailed analysis of *in vivo* responses to implanted materials has highlighted the relationships between the presence of these proteins and their role in subsequent leukocyte reactions. Briefly, albumin acts as a passivator and has a minimal effect on increased monocyte/macrophage adhesion; it is therefore not generally a marker of a chronic inflammatory response. As it is more a marker of a passive material, it will not be

Table 1 Common cytokines that are used as markers of inflammation during material-induced protein, whole blood and leukocyte interactions *in vitro*

Cytokine	*Nomenclature*	*Description*
Interleukin-1β	IL-1α	Proinflammatory cytokines produced and secreted by monocytes/macrophages. Enable transmigration of inflammatory cells to site of implantation by increasing adhesion receptor expression on endothelial cells
Interleukin-1 receptor antagonist	IL-1β	
Interleukin-2	IL-2	IL-2 binding to T cell receptors stimulates maturation of T cells into antigen selected cytotoxic T cells
Interleukin-3	IL-3	Stimulates differentiation of hematopoietic stem cells to myeloid progenitor cells and stimulates proliferation of myeloid cells (granulocytes and monocytes)
Interleukin-4	IL-4	Stimulates proliferation of T and B cells and induces differentiation of CD4 T cells to Th2 cells and increases production of IL-4. Required for FBGC formation *in vitro*
Interleukin-5	IL-5	Produced by Th2 cells and mast cells and stimulates B cell growth
Interleukin-6	IL-6	Released by T cells and monocytes, stimulates the inflammatory response, also has a role in osteoclast activity
Interleukin-7	IL-7	Released by dendritic and stromal cells stimulates differentiation and proliferation of hematopoietic stem cells into lymphoid progenitor cells, that is, T and B lymphocytes
Interleukin-8	IL-8	CXC chemokine produced by macrophages, chemotactic to neutrophils and granulocytes
Interleukin-9	IL-9	Th2 cytokine, produced by CD4 + ve T cells, stimulates proliferation and prevents apoptosis of T and B cells
Interleukin-10	IL-10	Anti-inflammatory cytokine produced by monocytes and some lymphocytes can inhibit the synthesis of proinflammatory cytokines produced by monocytes and Th1 cells
Interleukin-12	IL-12	Produced by macrophages and stimulates T cells and production of IFN-γ, TNF-α
Interleukin-13	IL-13	Secreted by Th2 cells, required for the formation of FBGC *in vitro* and works with IL-4 in suppressing IFN-γ production by T cells
Interleukin-17	IL-17	Induces production of proinflammatory cytokines from macrophages
Basic fibroblast growth factor	FGF-basic	Growth factor that stimulates angiogenesis and fibroblasts important in wound healing
Granulocyte–macrophage colony stimulating factor	GM-CSF	Secreted by macrophages, T cells, and mast cells. Stimulates the production of monocytes from hematopoietic stem cells. Leads to an increase in monocyte number
Interferon-γ	IFN-γ	Produced by cytotoxic T cells, Th1 cells, increases lysosome activity in macrophages, promotes leukocyte migration to site of implantation
Interferon-γ-induced protein/ chemokine (C–X–C motif) ligand 10	IP-10	Secreted by monocytes, endothelial cells, and fibroblasts when stimulated by IFN-γ, chemotactic for monocytes and T cells and enhances T cell adhesion
Monocyte chemotactic protein-1/ chemokine (C–C motif) ligand 2	MCP-1/CCL2	Chemotactic for monocytes and T cells
Chemokine (C–C motif) ligand 4/ macrophage inflammatory protein	MIP-1/CCL4	Produced by monocytes and activates monocyte recruitment and activation of granulocytes (including neutrophils) to produce IL-1, IL-6, and TNF-α
Macrophage inflammatory protein-2β/ chemokine (C–X–C motif) ligand 3	MIP-2β/ CXCL3	Controls migration and adhesion of monocytes via binding to CXCR2
Platelet-derived growth factor	PDGF	Active in angiogenesis, significant in new tissue formation via fibroblast activation
Transforming growth factor-α	TGF-α	Produced in macrophages and plays a role in wound healing via epithelial cell activation and granulation tissue formation
Tumor necrosis factor-α	TNF-α	Proinflammatory cytokine produced mainly by macrophages but also some lymphocytes, stimulates the release of IL-1 and PGE2
Tumor necrosis factor-β/lymphotoxin	TNF-β	Produced by CD8 cytotoxic T lymphocytes, and similar effects to TNF-α, acts in a paracrine fashion with TNF-α and is inhibited by IL-10
Chemokine (C–C motif) ligand 5	CCL5/ RANTES	Chemotactic to T cells in combination with IL-2 and IFN-γ, induces the proliferation of natural-killer cells, a type of cytotoxic lymphocyte
Vascular endothelial growth factor	VEGF	Activates angiogenesis, the vascularization of new tissue

discussed further as the sole contributor or marker of the inflammatory response.

Studies by Anderson *et al.*[10] have specifically explored the relationship between protein adsorption onto a biomaterial surface and its role in determining the foreign body giant cell (FBGC) response to the material. The exact nature and role of the FBGC in determining the biocompatibility of a material, *in vitro*, are discussed in **Sections 4.405.2.2.4.2** and **4.405.2.2.6.** A direct relationship between fibrinogen adsorption and histamine release has also been reported and used as a marker of a prolonged inflammatory response.[11] Fibrinogen adsorption and histamine release also have a role in increasing vitronectin adsorption, which facilitates monocyte/macrophage adhesion *in vitro*, a phenomenon that will be discussed further in **Section 4.405.2.2.4.2**.

In combination with other components in the blood interacting with the surface, such as platelets, the associated protein systems, and the resultant clot formation, specific plasma protein adsorption onto the surface results in the formation of a provisional matrix[10] which drives the next stages of wound healing and inflammation. The implant biomaterial dictates the levels of protein formation and the conformation of the

proteins adsorbed on the surface, and thus directs the subsequent cellular response by defining the composition of the protein layer. The 'provisional matrix' contains vasodilators, chemoattractants, cell signaling cytokines, and biological agents that can dictate the cellular response via recruitment of the correct inflammatory cell to the interface. In addition to acting as a beacon for specific cell types via the release of cytokines, the conformation of the proteins on the surface can determine how the cells adhere and thus, the subsequent cell signaling events within the specific cell; this results in the control of the activation and duration of a response via the signals presented to the cell through and by the protein layer. The specifics of these events are discussed in the subsequent sections when introducing the different cell types involved in the inflammatory response and the methods of their analysis.

The phenomenon of plasma protein adsorption and its proven role in enhancing (in the case of fibronectin and fibrinogen) or inhibiting (in the case of albumin) the inflammatory response provides a platform for analysis that can act as a very cost-effective and rapid screening technique for the assessment of biomaterials, prior to characterizing the cellular response. Protein adsorption studies can be used as early indicators of the suitability of a material for implantation.

4.405.2.1.1. *Characterizing protein adsorption* in vitro

An array of different *in vitro* studies have been carried out that have characterized protein adsorption onto many different types of biomaterials *in vitro*, in both competitive complex mixtures, usually whole serum, which contains all the proteins,[12–14] or noncompetitive solutions of single or 'spiked' controlled mixtures of specific individual proteins, to form a known solution of specific proteins.[15,16] The *in vitro* analysis of protein deposition onto a surface under a given set of parameters can be achieved qualitatively or quantitatively, and an array of techniques is available to provide information on protein adsorption onto a surface, the stability of that protein on the surface, the probability of protein displacement by other proteins (Vroman effect), the conformation of the protein, and the availability of receptor sites for cell interactions on the surface.

The quantification of the amount of protein adsorbed and the depth of an adsorbed protein layer can be achieved by such methods as scanning angle reflectometry,[17–19] attenuated total reflectance Fourier transform infrared spectroscopy,[14] and quartz crystal microbalance.[20] Other common methods of characterizing the type of protein adsorbed onto a surface can include desorption of proteins from a surface using sodium dodecyl sulphate and characterization of the eluted protein via western blotting. Western blotting and any immunohistochemistry techniques employed to characterize a protein layer allow investigations into the different types of protein adsorbed onto a surface, distribution of a specific protein on a test substrate, and conformational integrity of the protein on the surface and, therefore, its ability to induce specific cellular responses. Such studies have provided information regarding the relationship between vitronectin, fibronectin, and fibrinogen and their role in FBGC formation, an indicator of the inflammatory response and a phenomenon that has been used to develop some of the most widely used *in vitro* models (see **Section 4.405.2.2.4.2**). Therefore, based upon these known relationships, it is possible to use protein adsorption studies as early indicators of the inflammatory potential of a given material.

4.405.2.2. Cellular Indicators in the Inflammatory Response

The initial host response to any implantation could possibly be controlled by protein systems circulating within the blood and in the platelets.[21] The interaction of these systems with the site of injury/implantation results in the formation of a temporary, stabilizing matrix, which is rich in cell signaling factors and proteins that dictate subsequent cellular responses. Due to the process of implantation, the subsequent cellular response is to defend, in the form of the inflammatory response, as the body tries to restore and then maintain homeostasis by reacting to the presence of the foreign body, that is, the biomaterial or implanted device. This is achieved either by integration into a functional tissue or by encapsulation of the device, thus effectively sealing it off from the rest of the body by the formation of a fibrous tissue capsule. The next section of the chapter describes the cellular elements that play a role in determining if a material is integrated, passivated, isolated, or subjected to continuous inflammation defense, the latter ultimately requiring explantation, and thus determining the suitability and efficiency of any implanted device.

Inflammatory responses are often divided into two major phases or types – acute and chronic.[22,23] Acute inflammation is characterized by the presence of polymorphonuclear leukocytes (PMN or PML), predominantly neutrophils and monocytes/macrophages, but can possibly also involve eosinophils and basophils; the term PMN refers to the multilobed morphology of the cell nucleus. Neutrophils, eosinophils, and basophils are collectively also called granulocytes and are characterized by the presence of large numbers of specific and azurophilic granules as well as vesicles in their cytoplasm. If the granule contents are released extracellularly through the processes of 'frustrated' phagocytosis and/or exocytosis, the potent antimicrobial and tissue remodeling molecules such as lysozyme, proteolytic enzymes, and neutral proteases are deposited nonspecifically into the host tissue and stimulate an increase in the magnitude and duration of the acute inflammation. Phagocytosis and frustrated phagocytosis are phenomena associated with the immune cell response to invading material, which is normally microbiological. With respect to biomaterials, this response is conducted by neutrophils and macrophages that are trying to deal with the presence of an implant by killing it and digesting it and thus eliminating the foreign body. Thus, the severity of this process is a good key indicator of the biocompatibility of the implanted substrate. The acute inflammatory response is then followed by the chronic inflammatory response, characterized by the continued and persistent presence of macrophages. The degree of chronic inflammation, ultimately driven by the provisional matrix, will either result in integration of the material and the formation of a fibrous capsule around the material or its rejection by the host. Many models depicting the different stages of inflammation *in vitro* have been developed for screening materials prior to implantation and rely heavily on the thorough characterization of selected cell responses to a material in a controlled environment.

4.405.2.2.1. *Neutrophil material interactions* in vitro

Neutrophils are the most abundant leukocytes in humans and make up ~60% of all white blood cells. At the site of implantation, neutrophils move from the blood, through the blood vessel wall, to the site of injury by the process known as diapedesis or leukocyte extravasation; this phenomenon is driven by the release of chemotactic cues at the site of implantation due to tissue damage and bleeding, and the formation of the provisional matrix. The blood clots and the provisional matrix contain a milieu rich in activated platelets, which release TGF-β (transforming growth factor-β), PDGF (platelet-derived growth factor), CXCL4 (platelet factor 4), LTB4 (leukotriene 4), and IL-1 (interleukin-1),[10] all of which are chemotactic to both neutrophils and monocytes. Neutrophils are the quickest to respond chemotactically to the presence of these molecules and arrive at the site first; the presence of inflammatory cytokines in the local environment also promotes vasodilation, thus facilitating the migration of the inflammatory cells from the blood to the site of implantation. The levels of signaling molecules released into the supernatant by the blood–biomaterial interaction can be quantified *in vitro*, using ELISA (enzyme linked immunosorbent assays) or western blotting techniques. Due to the significance of these chemokines and the intense research activity in the area of inflammation in general, commercial kits for the accurate quantification of these substances are readily available, and the measurements obtained can be used as an early characterization of the level of acute inflammation due to the presence of these chemokines over a sustained period. Higher levels of signaling will result in a greater number of neutrophils being recruited to the site. Due to their predominance and small size, ~10 μm in diameter, neutrophils are the first PMN to reach a site of injury, and for this reason are often studied as markers of acute inflammation. Neutrophils are phagocytes and upon activation can release a series of factors that not only further stimulate neutrophil migration to the site but also act as chemoattractants for monocytes and other cell types. The *in vitro* models aimed at quantifying neutrophil responses to biomaterials often involve quantifying the amount of reactive species produced by the neutrophils when cultured in direct contact with specified test materials, and the quantification of cytokine and chemokine release, which can activate other cell types. As part of the process of phagocytosis, neutrophils undergo a respiratory burst, which is an oxygen-dependent reaction, resulting in the formation of a number of high energy unstable reactive oxygen species (ROS). These play a direct role in defense and the innate nonspecific host response. Neutrophils take up molecular oxygen, which reacts with membrane-bound NADPH oxidase, and this results in the formation of superoxide radicals. These radicals are instantaneously converted to hydrogen peroxide (H_2O_2) by the enzyme SOD (superoxide dismutase). H_2O_2 is a highly reactive compound and reacts with oxygen radicals or trace elements in the local environment to form hydroxyl radicals. In turn myeloperoxidase (MPO) reacts with H_2O_2 to form hypochlorous acid, an agent involved in the destruction of bacteria. As this process is well documented, elements associated with the respiratory burst and formation of ROS are extensively used in *in vitro* studies to assess the levels of activation induced in neutrophils by a test substrate or a microorganism.

To accurately assess neutrophil responses to biomaterials, methods of isolation of neutrophils should minimize induced activation of these cells prior to contact with the test substrate. Therefore, two main models exist for assessing neutrophil activation in response to a stimulus *in vitro*; one uses direct contact with whole blood[24–27] and the other involves culturing the test substrate with purified neutrophils.[28] The preferred source of cells for both models is human adult whole blood donated by healthy volunteers; this is a common source of supply for all human-derived leukocyte cells used in *in vitro* models due to the ease of access and minimal invasion required to derive specific cell types. The process generally involves collection of a volume of blood by venous puncture and heparinization or similar anticoagulation treatment, optional layering on to dextrose to clump and sediment red blood cells, followed by layering of blood onto a density centrifugation medium, and finally, centrifugation. From this point, the protocol becomes more specific for neutrophil activation and requires removal of the sedimented pellet containing red blood cells and neutrophils, lysis of the red blood cells, and further washing and centrifugation steps to separate out an intact and viable neutrophil population.

Culturing with whole blood allows neutrophil activation to be studied with many of the plasma proteins still present, and many of the inflammatory pathways still intact, such as platelet interactions, especially if samples are citrated rather than heparinized in anticoagulation. This is a situation that can be argued to be closer to the *in vivo* environment than a purified single cell type of isolated neutrophils. Data collected from this model usually demonstrate enhanced neutrophil activation due to the presence of the provisional matrix and factors that add to the indirect activation of cells. While, at least in theory, this approach seems extremely relevant and therefore the optimum situation, minimal control over cell number and individual cell type is afforded in these models; as a result, specific relationships between selected material variables and a specific cell response are not easily determined; moreover, reproducibility can also be an issue due to the lack of control over the starting cellular components. Models that use purified neutrophils allow control and consistent reproduction with respect to initial cell number and starting cell populations, thus eliminating not only the indirect interactions between other leukocytes and test substrate, but also the activation of blood proteins that can themselves have an activating effect on leukocytes. This method allows the direct investigation of the role of neutrophil activation, the release of factors associated with the activation, and the development of models and hypothesis relating to material-induced neutrophil activation, and subsequent inflammatory cell responses. In addition, desired levels of neutrophil activation can be induced in the cells prior to and during culture to mimic increased neutrophil activation due to signaling from the provisional matrix. Substances such as PMA[29] or fMLP[30] are often used *in vitro* to induce neutrophil activation, either to act as a positive control in an assay or to validate the *in vitro* models. An important point to note is that, prior to scientific data collection, time must be taken to validate the use of any *in vitro* model; therefore, investigations into the correct type of model and data required must be carried out before data collection. Regardless of the model used, that is, whole blood compared

to purified cells, methods of characterizing the neutrophil response *in vitro* are the same.

4.405.2.2.2. ROS production and measurements in vitro

While it is possible to identify neutrophil adhesion to a substrate via their distinct (PMN) morphological characteristics, the information obtained from these types of basic adhesion studies is subjective and limited in terms of defining the inflammatory potential of a material. These techniques have concentrated on profiling the activation level of neutrophils induced by test substrates and are based on identification and quantification of the products associated with the metabolic respiratory bursts, which is reflective of neutrophil activation, and chemokine and cytokine release. Chemiluminescence (CL) has emerged as a technique for defining the activation state of neutrophils,[31,32] as CL is a natural product of oxygenation activity, that is, neutrophil respiratory burst is directly related to activity. In inflammation, the respiratory bursts refer to the release of ROS such as superoxide and hydrogen peroxide, which are associated with phagocytosis, a characteristic of neutrophils and monocytes as they try to digest foreign body particles. Therefore, the greater the driving force of a material to induce phagocytosis by neutrophils, the greater the stimulation and level of neutrophil activation, as quantified by the release of ROS and the increase in CL. Kits for such assays are commercially available, and these often rely on the addition of luminol[33,34] to increase the sensitivity of the CL and can, therefore, detect even small changes in neutrophil activation.

NADPH oxidase is a membrane-bound enzyme found on phagosomes in neutrophils. NADPH is only activated during the respiratory burst and therefore its production is also used as a direct measure of neutrophil activity.[35–37] NADPH oxidase generates superoxide (ROS), and its activity can also be measured by luminescence in addition to sensitive, commercially available ELISA assays. Another factor that is often measured, due to its role in the neutrophil respiratory burst, is MPO,[38,39] which is found in the granules contained within the neutrophil cytoplasm. Upon activation, MPO produces hydrogen peroxide, H_2O_2, another ROS involved in phagocytosis. MPO production can also be measured via ELISA; therefore quantifying the amount of MPO or NADPH associated with a specific biomaterial and comparing their relative production to subsequent inflammatory responses is a valuable approach. Western blotting techniques can also be used to determine the presence of the enzymes involved in the production of ROS in a semiquantitative or quantitative manner, if electrophoresis is combined with image analysis. Due to the availability of antibodies against MPO and NADPH, immunohistochemistry can also be used as a tool to determine the homogenity of MPO and NADPH, and their production and release in selected areas of the biomaterials and associated cell clusters.

In addition to measurements of ROS production associated with phagocytosis, it is also possible to quantify the release of lysozyme held within the neutrophil granules. Lysozyme production is an oxygen-independent mechanism; its release is known to enhance polymer degradation *in vivo*[32] and is a phenomenon associated with frustrated phagocytosis.[40] Frustrated phagocytosis occurs when the size and dimensions of the materials and associated products, that is, wear debris, are too big for the cells to engulf, internalize, and therefore phagocytose completely, resulting in the cell releasing its hydrolytic enzymes contained within the primary and secondary granules, that is, lysozyme, extracellularly.

4.405.2.2.3. Cytokine production by neutrophils

Another common technique used as an indicator of neutrophil activation, both *in vivo* and *in vitro*, is the measurement of the production and release of cytokines that are chemotactic to PMNs, monocytes, and lymphocytes. The latter cell types are also associated with the second phase of inflammation, that is, chronic inflammation. Neutrophils play a role in the maintenance and severity of an inflammatory response by the release of factors such as IL-10 and IL-12, both of which are chemotactic to both neutrophils and other inflammatory cells, and play a role in determining the longevity of the inflammatory response. This is discussed further in **Section 4.405.2.2.4.3**.

4.405.2.2.4. In vitro monocyte material interactions

Previous sections of this chapter have concentrated on the elements of inflammation associated with acute inflammation, that is, plasma protein adsorption, clot formation, platelet activation, and neutrophil adhesion and activation. The process of acute inflammation normally resolves within 1 week. The level of signaling associated with these events and then further induction over and above the levels associated with the process of implantation and normal wound healing, that is, solely material-induced inflammatory responses, will determine the intensity of the second phase of inflammation, that is, the chronic inflammatory response.[41] The activation of the chronic inflammatory response is characterized by the presence of monocytes and lymphocytes, or mononuclear cells, at the site of implantation.[42–45] For biocompatible materials, the chronic inflammatory response, traditionally, lasts no longer than 2 weeks and is followed by the production of fibrous tissue into which macrophages are embedded, and fibroblasts and other cell types invade, thus resulting in neovascularization of the healing tissue. The specific type of tissue depends on the local environment, that is, osteoblasts or endothelial cells, to name but a few, dependent on the specific application of the implant, that is, bone forming or vascular replacement, and stimuli from the implanted material. It is widely accepted that monocytes and macrophages are the major cellular components that determine the severity and duration of the chronic inflammatory response; therefore, much attention has been paid to developing the correct *in vitro* models for assessing macrophage–material responses, both *in vivo* and *in vitro*. The next sections of the chapter focus on the methods of isolation, purification, and characterization prior to cell seeding onto an implant, and subsequent methods of analysis and markers of interest. The role of lymphocytes in propagating the chronic inflammatory response and the use of coculture models in *in vitro* leukocyte–material interaction models is also discussed.

4.405.2.2.4.1. Monocyte isolation from human whole blood

As stated previously, monocyte/macrophage material interactions have been the focus of much research already, which has been well disseminated and widely published. The available literature indicates that the sources of monocytes can be varied and range from commercially available cell suspensions to

genetically altered, and primary-derived cells. The focus of this chapter is to define cellular responses to biomaterials and the development of *in vitro* models, and in this context, a preferred source or the cell of choice for further discussion is the primary isolated monocyte/macrophage from human whole blood.

As with neutrophil isolation, a major consideration for any isolation technique is to minimize cellular activation in the process of isolation. It is also important to know the starting level of activation for a population of cells at time = 0 as they come into contact with the material for investigation. Therefore, when the cells come in contact with the material, their level of activation is known, and the material-induced cellular responses can be accurately measured and reproduced. Methods of isolation involve venous blood collection, followed by treatment with heparin or another anticoagulation agent, layering onto a density centrifugation medium, centrifugation, and collection of the cloudy PBMC layer.[46] Flow cytometry (FACS) analysis studies have proved that this layer is rich in both lymphocytes (T and B) and monocytes, and the cells collected from this layer are analyzed for their expression of CD3 (T lymphocyte), CD19 (B lymphocyte), CD14 (monocyte marker), and CD45 (generic leukocyte antigen used to label the whole population), and the relative percentage of lymphocytes to monocytes in these cell populations is routinely characterized before experimentation (**Figure 1**). Further isolation steps can be employed to purify either a population of lymphocytes or monocytes from this cell population. Traditionally, simple adherence steps have been used, and these are still routinely being used, to separate the monocytes from lymphocytes, based on the fact that cultured monocytes will adhere to a substrate. Standard tissue culture polystyrene works efficiently, while lymphocytes do not adhere and thus remain in the supernatant. However, subsequent studies have proven that this is not the case and that the monocyte population is contaminated with lymphocytes (**Figure 2**); so the use of adhesion as the sole purification step should be limited and preferably supported with subsequent, more efficient techniques to further purify these cells. Additionally, this technique has limited relevance in studies that are designed to evaluate specific cell–material interactions, as, to do this, one must have control of the starting components and not rely on the efficiency of adherence as a method of determining and purifying the

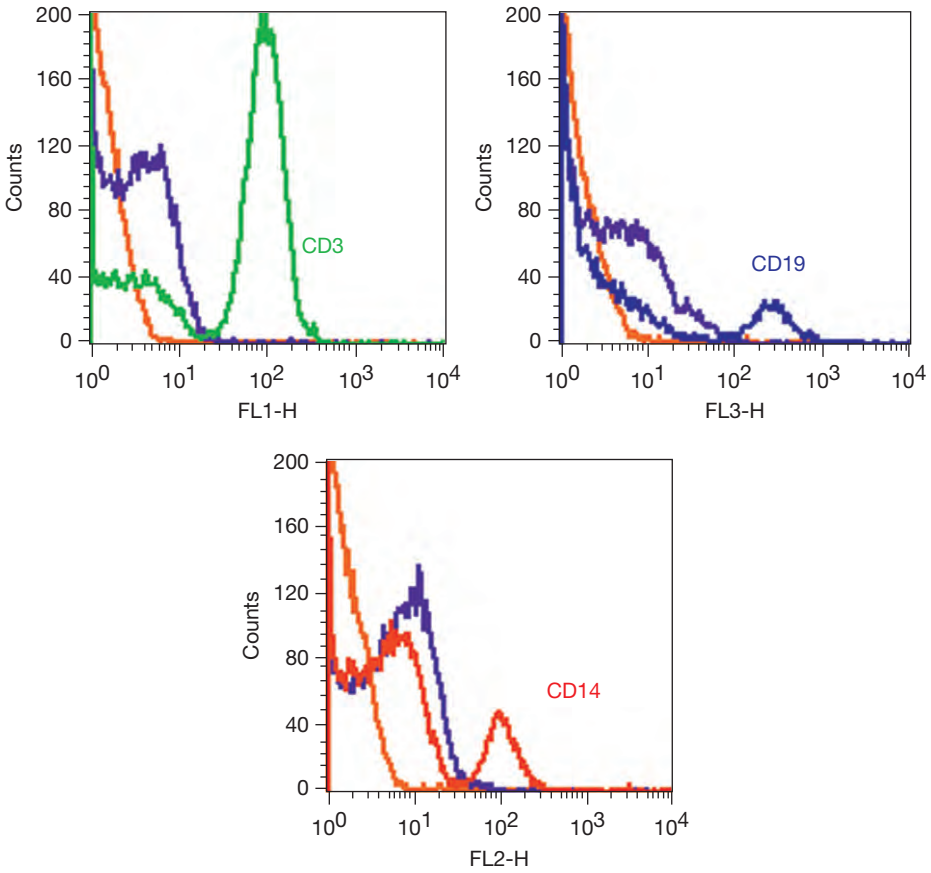

Figure 1 An example of flow cytometry analysis (FACS) of cloudy peripheral blood mononuclear cell (PBMNC) layer obtained from monocyte isolation protocol described in **Section 4.405.2.2.4.1**. Cells were labeled with fluorescein isothiocyanate (FITC)-conjugated CD3 (T cell marker), Cy-5-conjugated CD19 (B cell marker), and PE-conjugated CD14 (monocyte marker). FITC, PE, and Cy-5 are all fluorescent tags that allow detection and quantification of expression by the flow cytometer. Results show that the cloudy layer prior to magnetic purification is a mix of T and B lymphocytes and monocytes; therefore this cell population is not suitable for models focusing on, specific interactions between monocytes and materials, but can be used for coculture models, **Section 4.405.2.2.5**. Purple lines on the histograms are isotype controls (levels of inherent nonspecific staining due to the staining procedure, therefore levels of positive expression are taken above these levels only). The orange lines on all three graphs are measures of the associated autofluorescence associated with the cell population and are used as a negative control and to set the threshold limits of detection by the FACS machine.

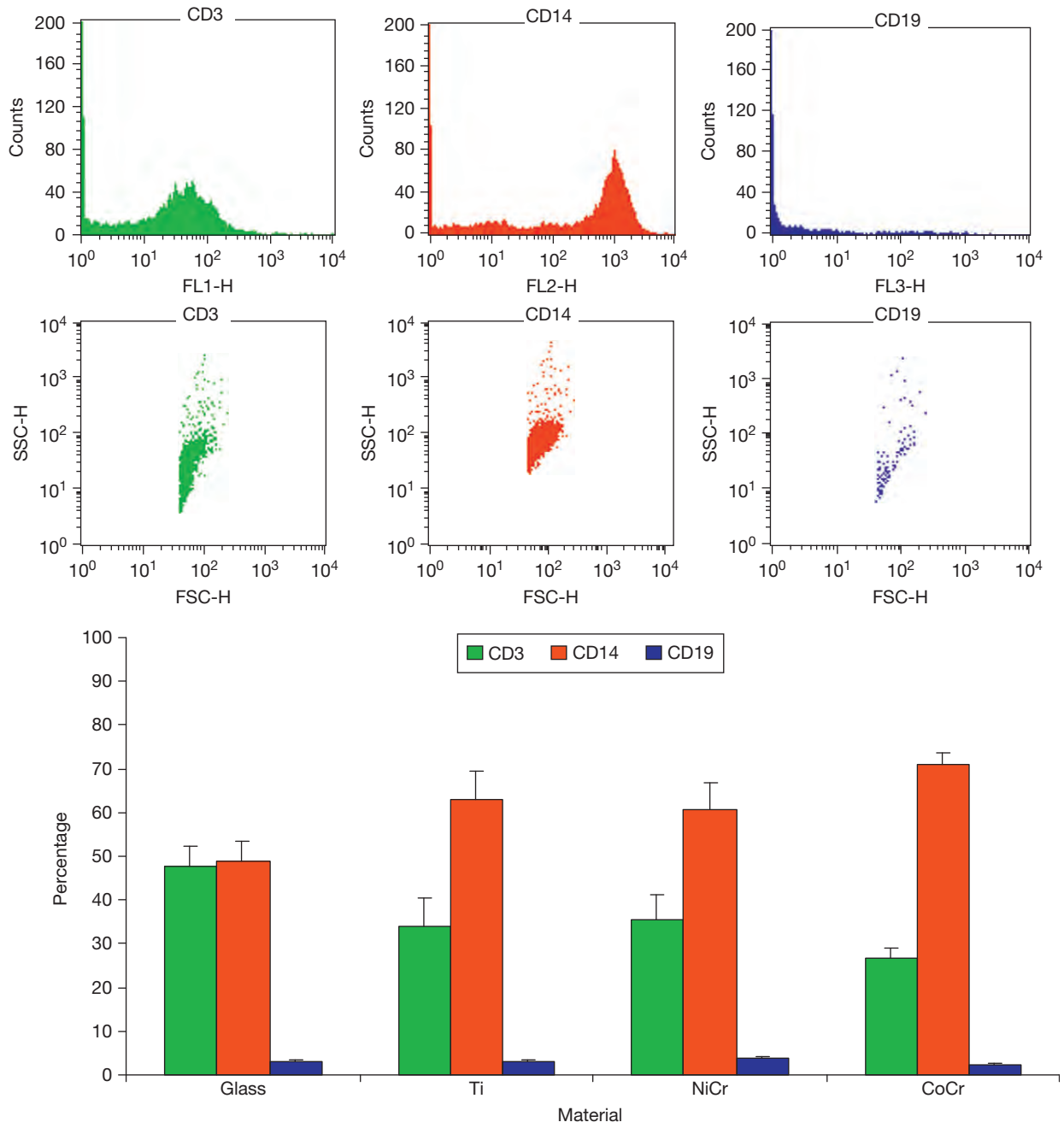

Figure 2 An example of analysis of adherent cell populations to test substrates. Both T lymphocytes and monocytes adhere to all test substrates, but B cells remain in the supernatant. This method can be used as a comparison between materials in terms of levels of supported T lymphocyte and monocyte adhesion as an indicator of a sustained inflammatory response. These results also prove that T lymphocytes adhere to substrates; therefore isolation of monocytes from lymphocytes cannot be ascertained via traditional adherence techniques, **Section 4.405.2.2.4.1**. Reproduced from Muna Khassaf, M. Ph.D. Thesis, Liverpool University, Liverpool, 2004.

starting cell population. This, however, does not suggest that methods of quantifying cell adherence to a material are of no relevance; in fact, it is quite the opposite, and these types of investigations are discussed in more detail in **Section 4.405.2.2.5**, which focuses on the use of monocyte/lymphocyte coculture models *in vitro*.

Further purification and enrichment of either a monocyte or a lymphocyte population from the PBMNC layer can be achieved by using commercially available magnetic bead systems. These systems contain nonphagocytosable magnetic beads, the nonphagocytosable element being important to minimize activation associated with cell/bead interactions. The beads are coated with specific antibodies that target a specific cell type or receptor, that is, CD3, CD19, or CD14, to name but a few. The beads bind to the target cell and can be isolated by positive or negative selection. Positive selection

involves the binding of the beads to the cells of interest, that is, CD14 beads bind to monocytes to positively select the monocyte population for further culture. After binding, the cells are placed in a magnetic field and separated from the nontagged cells by the magnetic field that draws the labeled cells to the side of the tube, immobilizing them in the magnetic field. The untagged cells can then be removed by simply decanting the supernatant by pouring, as the technique relies on the fact that the tagged cells will be pulled to the side of the vessel and held there while within the magnetic field. To culture positively tagged cells requires the inclusion of a detachment protocol, which is also usually a component of the kit, and is designed to detach the beads from the tagged cells with minimal induced activation. An alternative method of isolation that can reduce cell activation and is particularly useful and relevant for monocytes is negative selection. This technique involves using a combination of beads coated with CD3 and CD19 to remove the T and B lymphocyte populations from the PBMNC layer, thus leaving the CD14-rich monocyte layer untagged so that the two fractions can be easily separated when in contact with a magnetic field. Successful implementation of this protocol can result in a >98% pure monocyte cell population.

Highly purified single cell-type solutions are required to carry out specific research projects aimed at understanding how specific material characteristics induce specific changes and levels of activity in certain cell types and their resultant effects, in terms of inflammatory cytokine production and cell viability, and formation of other, more mature, cell types. This single cell-type information can be used as a set of indicators for the biocompatible nature of a material, that is, FBGC. Furthermore, to evaluate the interaction of lymphocytes and monocytes and to study the propagation of material-induced inflammation, simple steps can be taken to eliminate one of the cell types, that is, either T or B lymphocytes from the cell solution, subsequently characterizing the change in cellular response in terms of cytokine production, activation, and adherence of the cell populations. Such studies have highlighted the specific relationship between T lymphocytes and monocytes, the effects of juxtacrine and paracrine signaling on cellular responses, and have demonstrated how these interactions can be used to further investigate biomaterial-induced reactions *in vitro*. This is discussed further in **Section 4.405.2.2.5**.

4.405.2.2.4.2. Characterizing monocyte adhesion in vitro, *indicators of FBGC formation*

As stated earlier, cells respond to the adsorbed protein layer and the provisional matrix. The abundance of ligands, in this case, specific peptide sequences associated with the adsorption of conformationally correct proteins and activated platelets, dictates how the cell interacts with the surface and thus, with subsequent cell signaling. Therefore, levels of cell activation, and, more specifically, monocyte activation can be determined after a short time period by characterizing how monocytes bind and which specific integrins are expressed. Many different studies have been conducted using purified human monocytes from blood with material substrates in direct contact and evaluated the feasibility of the use of expression of integrins to indicate the ability of a material to induce FBGC formation,[47–49] a distinct marker of chronic inflammation.

Initial monocyte/macrophage adhesion occurs through binding of the β_2 integrins, specifically, MAC-1, CD11b/CD18 complexes, to fibronectin, fibrinogen, and the complement proteins. Therefore, the nature of the previously described provisional matrix dictates the levels and type of integrin binding and the subsequent monocyte responses. This relationship between monocyte adhesion and complement proteins provides further evidence for protein adsorption and inflammatory cells being a part of the continuous cascade of events that can be used to develop *in vitro* models and provide standardized tests.

These studies have demonstrated that β_1 integrin is the major indicator of FBGC formation. It is not present to the same extent on immature adherent macrophages, but its expression is increased with activation and fusion of macrophages into FBGC. The roles of β_2, $\alpha_x\beta_2$, $\alpha_5\beta_1$, $\alpha_2\beta_1$, and $\alpha_3\beta_1$ integrins in determining the severity of inflammatory reactions has also been highlighted. *In vitro* integrin expression can be determined and characterized using a number of methods. Polymerase chain reaction, PCR, and real time PCR can be used to measure mRNA expression and changes in mRNA regulation, and they can be determined as a function of increasing time in culture. Differential expression of the integrins of interest can be used to classify specific integrin expression profiles and relate these to cytokine production and levels of activation. Immunohistochemistry, immunogold labeling, and SEM can be used to visualize the formation and distribution of specific integrins on cell membranes, and their presence and distribution mapped to direct spatial cues on the material surface. These types of studies incorporate specific antibodies to a targeted integrin and facilitate data collection on the distribution of specific integrins and its relation to cell function. In addition, these studies provide valuable information on the specific relationships between integrins that can either enhance or inhibit specific aspects of the monocyte response. Using a slightly different antibody-specific surface receptor binding approach, it is also possible to inhibit the action of integrins by blocking the target binding sites on a material. This enables a more in-depth study of either the role of that integrin, or the effects of inhibition of the signaling induced by integrin binding to a surface. This kind of research provides an approach to producing surfaces that minimize inflammatory responses by dictating how the cell binds to the material.[50,51]

Integrin signaling profiles can also be used to elucidate the role of monocytes in prolonging the complement response to an implanted material and in further propagating the inflammatory response. These models can be used as early indicators of the likely severity of the inflammatory response by correlating integrin expression levels with the propensity of the cells to fuse and form FBGCs, as discussed in **Section 4.405.2.2.6**.

4.405.2.2.4.3. Inflammatory cell recruitment: Chemokines and cytokine production

The circulating inflammatory cells respond to stimuli and cues released by the formation of the provisional matrix and the activation of protein systems within the blood. During direct contact in the first phase of localization at a site of injury, invading neutrophils and monocytes adhere to specific ligands and peptides on the surrounding surfaces and this, in turn,

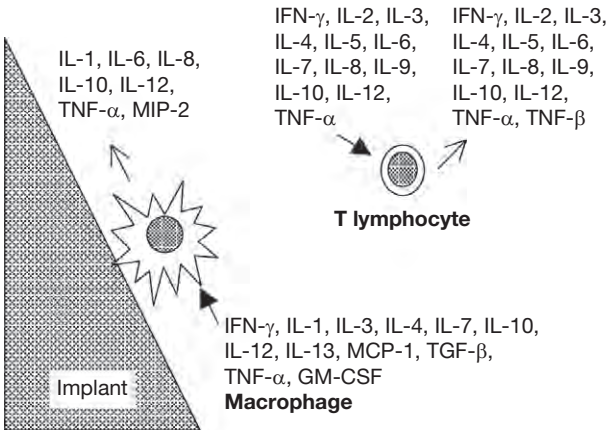

Figure 3 A simplified representation of some of the cytokines and growth factors potentially involved in the inflammatory responses to an implant. IL-1 to IL-13, interleukin-1 to -13; IFN-γ, interferon-γ; G, M, and GM-CSF, granulocyte, macrophage, granulocyte and macrophage colony stimulating factors; TNF-α, tumor necrosis factor-α; TGF-β, transforming growth factor-β; MCP-1, monocyte chemotactic protein-1. Adapted from Rhodes, N. P.; Hunt, J. A.; Williams, D. F. *J. Biomed. Mater. Res.* **1997**, *37*, 481–488.

initiates a level of cellular activity within the inflammatory cells, which results in the production of either pro- or anti-inflammatory cytokines (Figure 3). Chemokines are a family of small cytokines, and as their name suggests, are so called due to their chemotactic effects. Chemokines are often released by a cell upon stimulation by another cytokine: in the case of inflammatory chemokines, from inflammatory cells such as monocytes and neutrophils. Thus, for example, these cells can be stimulated by IL-1 or another cytokine to release chemokines that will recruit other inflammatory cells to the area. There are four main classes of chemokines: CC, CXC, C, and CX_3C, and their classification is dependent on the position of the first two cysteine residues. CC chemokines like MCP-1 (monocyte chemoattractant protein-1) or CCL2 are chemoattractants for monocytes and T cells. CXC chemokines like IL-8 are chemoattractants for neutrophils and some lymphocytes through interactions with CXCR1 and CXCR2 receptors. This subtopic rapidly becomes complex and is filled with detail. For the chemokines to be effective, their binding to a specific receptor on a cell surface is required, that is, CC chemokines bind to CC receptors, CCR and CXC chemokines bind to CXC receptors, CXCR and CX3C chemokines bind to CX3C receptors, CX3CR. Levels of binding dictate intracellular cell signaling, and methods such as traditional ELISA and western blotting methods have been developed that measure not only the levels of chemokine in the supernatant, but also the availability of chemokine receptors on a cell surface when cultured in contact with certain stimuli such as biomaterials.[28,52] This can be achieved using any technique that relies on specific binding of an antibody to its receptor and so can include immunohistochemistry, preferably followed up by quantitative histomorphometry using image analysis, western blotting, FACS, or other quantitative colorimetric assays. Once again, as with integrin binding studies, the knowledge of specific chemokine/receptor interactions has also been used as a tool for developing *in vitro* models that inhibit the binding of selected chemokines by blocking the receptor with an antibody, thus facilitating research into the mechanism of how specific chemokines are responsible for cellular behavior, in both a single and synergistic fashion.[53–56] *In vitro* models have also been used to develop early screening tests that relate the expression of receptors to inflammatory host response outcomes. These studies are extremely relevant when dealing with particulate material and wear debris, and these types of particles are often associated with aseptic loosening of orthopaedic implants as they are localized in the surrounding host tissues. When leukocytes are cultured in direct contact with particulate material, the cells can be analyzed dynamically while in contact with the stimulus to investigate the kinetics of the reaction with increasing time. In addition to providing extremely valuable information on interactions, this research approach is advantageous as it involves minimal loss of activity and cleaving of receptor sites due to processing. These models are discussed further in Section 4.405.2.2.3.

Monocytes/macrophages are the dominant cellular element in the propagation of the inflammatory response, and there is significant scope and potential in research that focuses on utilizing and understanding the roles of this cell type. Thus, for example, determining which chemokines are responsible for inducing monocyte recruitment to a site of implantation and also understanding the effects of these chemokines on subsequent cytokine release and their role in the inflammatory response raises a set of questions, the answers to which could be used to directly control the later phases of inflammation. *In vitro* models that use both primary-derived monocytes from human whole blood and immortalized cell lines with controlled levels of activity have identified an array of proinflammatory and anti-inflammatory cytokines that have specific effects on monocyte and leukocyte recruitment and levels of their activation and induced phagocytosis, that is, proinflammatory, IL-1β, VEGF, IL-8, MCP-1, MIP-1α, tumor necrosis factor-α (TNF-α), interferon-γ (IFN-γ), granulocyte and macrophage colony stimulating factors (GM-CSF), RANTES,[57–59] and anti-inflammatory, IL-4, IL-6, IL-10, IL-11, IL-13, and IL-1 receptor antagonist.[60] Profiling cytokine release, by measuring the amount of cytokines released into the supernatant, has become a common method for assessing the inflammatory and biocompatible properties of an array of test materials, and commercially available kits are now readily accessible that can quantify single or multiple cytokines in one assay, thus allowing direct comparisons of cytokine amounts within a given culture system. The collective data from these studies are still variable and therefore hard to use directly as the sole defining indicators of the biocompatibility of a test material. The variability in data is mostly the result of differences in protocol and differences in experimental parameters. Important variables include differences in starting cell populations, that is, immortalized monocyte cell lines compared to primary-derived monocytes from blood, levels of inherently induced activation either by the process of isolation or by chemical reagents used to stimulate the cells prior to contact with the test materials, and fundamental variables such as different types of medium and serum used in the *in vitro* cell models. Raising experimental variables as an issue in this area of research highlights and exemplifies the

importance of defining and standardizing (where possible) the experimental approach more broadly. The experimental parameters listed earlier highlight just a few of the experimental variables that should be standardized if efficient, reproducible, and translatable *in vitro* models that can be used to predict and define *in vivo* inflammatory responses are to be developed,. It is a complex issue, as levels of inflammation are also controlled by cell–cell signaling, a factor that is influenced not only by the test material, but also by the number and type of cells in the model. Therefore, prior to the introduction of a test material, the effect of the *in vitro* environment on a cellular response should be characterized, and appropriate controls included in any *in vitro* model, that is, profile the cytokine release of an optimized cell number of monocytes cultured in contact with the same area of TCPS as test substrates, with the inclusion of positive controls such as activated monocytes as reference points to normalize or contextualize material-induced data.

Derivation of standardized *in vitro* models will help dissect out important material properties. Thus, key current research questions such as how surface chemistry can control monocyte behavior and ultimately dictate the biocompatibility of a material could be systematically determined. Schutte *et al.*[59] highlighted that there are two opposing schools of thought regarding material chemistry-induced monocyte activation. First, the theory investigated and proposed by Anderson and coworkers[61] stipulates that material chemistry can control cytokine production and subsequent foreign body reactions, while Ratner *et al.* believe that data obtained from other studies[62,63] provide evidence that the inflammatory response to materials with the same surface topography and mass dimensions is the same, regardless of changes in the surface chemistry.

In vitro models that combine purified cell populations in a controlled system can be used to determine if changes in surface chemistry alone can affect monocyte adhesion and subsequent levels of activity, based upon successful data collection from this type of approach. Biomaterials with specific surface chemistries and associated properties, that is, hydrophilicity, could be produced that may be able to induce a controlled level of inflammation and use the associated cytokine profiles to control the induction of other cell subsets. This point is discussed further in **Section 4.405.2.2.5**. The ultimate validation of these hypotheses would come from implantation of materials that can induce specific responses predicted *in vitro*; these should be correlated with the *in vivo* outcome, for example, comparison of one material predicted to be passive and inducing minimal FBGC formation with another one that indicated a strong FBGC reaction, and including characterization of the host response responsible for producing these differences *in vivo*. Full dissemination of the inflammatory and biocompatible nature of a material needs to extend beyond just short-term wound healing and address the effects of the induced inflammatory response on the surrounding environment, and then progress to systemic responses in terms of specific tissue formation and cellular functionality, which is discussed in **Section 4.405.2.2.4**.

4.405.2.2.5. Monocyte/lymphocyte coculture models

As previously discussed, data obtained from *in vitro* models have been extremely useful in terms of identifying specific cellular interactions with biomaterials and subsequent cytokine release and have been used as generic indicators of the propagation and severity of an inflammatory response.[43,64,65] Thus far, many of the *in vitro* models discussed have focused on single monocyte cultures, but realistically, *in vivo*, monocytes interact with and are affected by a range of other cell subsets and systems. Examples include plasma proteins and mast cells that react with fibronectin and release histamine, which in turn recruits more monocytes to the site in addition to releasing IL-4 and IL-13, all of these being known to be essential for monocyte fusion into FBGC. One of the major cell types that plays a role in modulating and/or enhancing a monocyte-driven inflammatory response is the lymphocyte, more specifically, the T lymphocyte. Different subpopulations of T lymphocytes are activated and have been characterized depending on biological cues derived from the provisional matrix and the adherent monocytes and neutrophils.[66,67] CD8 + ve T lymphocytes are cytotoxic T lymphocytes and secrete products that are designed to destroy specifically targeted (by antigen) cells or molecules to which they have bound. CD4 + ve T lymphocytes bind to MHC class II-presenting cells, commonly, activated macrophages and dendritic cells, and produce lymphokines, which are chemotactic to other inflammatory cells. CD4 cells also bind to MHC class II-presenting B cells and further activate them to produce antibodies as part of the humoral response. CD4 +ve T lymphocytes can be further classified into Th1 or Th2, depending on the production of lymphokines. Th1 lymphocytes are characterized by the production of IL-2, IFN-γ, and TNF-β, resulting in further macrophage activation, while Th2 lymphocytes are involved in the production of anti-inflammatory cytokines IL-4 and IL-10, and the propagation of tissue remodeling and acceptance of a material/transplant. When assessing the response induced by a material *in vitro*, it has become apparent that, when cultured in contact with monocytes and lymphocytes as described in **Section 4.405.2.2.4.1**, the lymphocytes adhere in association with the monocytes and not to the material itself.[68,69] The lymphocytes and monocytes use positive feedback mechanisms upon activation, and the presence of lymphocytes increases monocyte adherence to a material and its subsequent fusion to form FBGC; the presence of the monocytes stimulates lymphocyte proliferation and the production of IL-2 and IFN-γ at the material interface. Based upon the sequence of events discussed in this chapter, it is reasonable to suggest that the initial levels of activity are induced by the material itself, or at the very least, the formation of the provisional matrix; the matrix, however, can be controlled by an array of material factors including chemistry, roughness, shape, surface energy, micro- and nanotopography, to name but a few.

Direct material-induced T cell activation has been studied *in vitro* and it has been found that certain polymers can be presented to T cells as mitogens (polymer particles that have been opsonized by specific plasma proteins), which, in turn, could go on to stimulate T cell responses and, therefore, be used as *in vitro* models for assessing the cytotoxic nature of a material.[70] Stimulation by mitogens *in vitro* can be assessed by the expression of CD69 (an early T cell activation marker) and CD25 (IL-2 receptor), and the production of previously

mentioned cytokines. This can be achieved using traditional techniques such as immunohistochemistry or FACS, ELISA, or by developing commercially available quantitative proteomic arrays. The general consensus from these studies, which have isolated T cells and assessed material-induced levels of activation, is that, to accurately assess material-induced inflammatory responses, cocultures of monocytes and lymphocytes are required. Nevertheless, these studies have been invaluable in identifying specific markers expressed by T cells whose levels can be used to measure levels of activation and subsequent cytokine production, and assess their effect on the inflammatory response.

Studies by MacEwam *et al.*[69] have also investigated the role of juxtacrine (cell–cell contact) and paracrine (cells separated by a membrane or matrix) signaling in the relationship between monocytes and lymphocytes that are in contact with biomaterials, and have found that while both types of cell signaling enhanced cellular responses in terms of cytokine production, paracrine signaling, *in vitro*, gave the greatest response in terms of cytokine production and associated monocyte activation. Therefore, one could summarize that the development of these models *in vitro* could lead to more relevant *in vitro* screening processes than either single or direct coculture models. Nevertheless, more work needs to be done to establish the most effective *in vitro* model for accurate modeling of the *in vivo* inflammatory responses.

The data obtained from models to date have established that biomaterials can induce the activation of monocytes and lymphocytes *in vitro*, resulting in differing profiles of cytokine expression, via pathways other than the classical or the alternative pathways of induction.[10] Classical induction refers to the *in vitro* stimulation of monocytes with LPS and the production of proinflammatory cytokines and nitric oxide. Alternative induced-monocyte activation involves stimulation by IL-4 and IL-13 (required for FBGC formation), inhibition of proinflammatory cytokines and the production of anti-inflammatory cytokines, and the upregulation of mannose receptors (a characteristic of FBGC formation). Material-induced stimulation of monocytes can be profiled using the same guidelines, that is, the production of pro-/anti-inflammatory cytokines and the expression of characteristics that indicate FBGC formation and subsequent fibrosis or tissue remodeling and acceptance. A number of the key elements in these processes have been highlighted throughout this chapter, as also the need for standardization of *in vitro* processes, if the data are to be correlated from different studies and an understanding of how material parameters can induce specific elements of cell activity is to be gained. This knowledge of the direct relationships can then be used to develop materials that can induce controlled levels of inflammation and thus bridge the gap between the current characterizations of passive or proinflammatory outcomes based upon *in vitro* models. Currently, *in vitro* models from various research centers are used solely to indicate the possible inflammatory potential of materials. With the development of standardized *in vitro* models, data could be combined, related, and correlated to improve materials, thereby increasing the efficiency of the models and evolving the next generation of 'smart materials' for regenerative medicine.

4.405.2.2.6. *Foreign body giant cell formation* in vitro

FBGC can become a significant component of the chronic inflammatory phase, *in vivo*.[71,72] FBGC are made up of adherent monocytes that have fused together in what is considered to be an attempt to increase their surface area to phagocytose particles that are larger than any single cell can span and engulf. Their analysis, in relation to monocyte culture models, has been discussed in **Section 4.405.2.2.4.2**. FBGC are not efficient phagocytes, but they do play a role in the production and release of ROS, in an attempt to degrade and digest the underlying material. Therefore, they do have a role in material degradation. Their formation, or the potential of adherent monocytes to form FBGC *in vitro*, can be assessed via the analyses of the expression of mannose receptors, the upregulation of β1 integrins and downregulation of β_2 integrins, the up regulation of CD44 and CD47, and the presence of dendritic cell-specific transmembrane protein (DC-STAMP).[10] To form FBGS *in vitro*, cells must be stimulated with IL-4 and IL-13. If FBGC formation was present on a material without the additional stimulation of IL-4 and IL-13, it would be a strong indication of the material's chronic inflammatory potential, without even considering the induction from frustrated phagocytosis. This phenomenon, occurring solely by stimulation from direct contact with a material *in vitro*, has not yet been reported, but continued developments in the knowledge base of *in vitro* leukocyte–biomaterial interactions and the optimization of factors such as cell number could soon lead to the development of such models, and they could be used as a benchmark for the standardization and improvement of current *in vitro* models.

4.405.2.3. Leukocyte Interactions with Wear Particles

One of the most widely used applications of the *in vitro* leukocyte–material models is the assessment of the level of induced inflammation associated with wear particles. The approach is used to simulate, *in vitro*, the *in vivo* situations in which articulating surfaces produce wear debris either by design, deliberate material degradation or by physical abrasion, which are correctly termed wear particles. One of the most widely studied applications comes from the generation of wear particles in total joint replacements, particularly hip joints and total hip arthroplasty. The generation of wear particles associated with these implants can be a constant source of stimuli for inflammatory cells, resulting in fibrous capsule formation around the joint implant caused by the chronic inflammatory response and the associated aseptic loosening, the latter due to poor bone formation around the site of the implant, increased osteoclast activity induced by chronic inflammation, and failure of the implanted device.[64,73–75] To reduce the risk of failure due to aseptic loosening, a significant amount of research effort has focused on generating materials that produce fewer wear particles or generating ones that do not induce significant chronic inflammatory responses. The *in vitro* analyses of induced inflammatory responses have been invaluable in classifying the optimum size range and shape.[76,77] The optimization of the *in vitro* models for the dissemination of clinically relevant data in these circumstances involves optimizing the cell:particulate number ratio to elicit

an optimum response, which must also reflect the *in vivo* environment that is constantly replenishing its source of monocytes from the cardiovascular system. Results from these studies have identified optimal particle sizes, shapes and types of particles (i.e., ion) that are proinflammatory. The *in vitro* models have demonstrated that particles in the size range of 0.24–7.2 μm are the most proinflammatory, and that elongated particles generate a greater proinflammatory response compared with rounder particles. This research is clear proof that data from optimized *in vitro* models can be used to increase the efficiency of biomaterial implants. On the other hand, without these data, *in vivo* studies would need to rely on thorough analysis of failed implants retrieved from patients or *in vivo* models, all of which are costly, time consuming approaches and may be influenced by other host factors such as infection, and underlying disease factors, and are therefore limiting in a short time frame, in terms of optimization of material design.

4.405.2.3.1. The role of in vitro leukocyte models: Controlling the inflammatory response

This chapter has discussed the use of *in vitro* leukocyte models in determining the inflammatory potential of a material and how this has traditionally been used as a marker of biocompatibility. In Section 4.405.1, biocompatibility was defined as "a material's ability to perform with an appropriate host response in a specific application."[1] The term appropriate host response extends far beyond inflammation and refers to the integration of the material/implant and its ability to induce functionality either as cellular responses or as tissue formation at the appropriate site. The inflammatory response is an inevitable event and, as such, should not be viewed as either good or bad. On the contrary, it should be fully understood so that materials can be designed to use the host defense system to induce an inflammatory response that drives the host response toward desired end points. For example, the amount of PGE-2 (prostaglandin E2) released by macrophages should be directed and controlled as, below a certain concentration, PGE2 is stimulatory to osteoblasts (bone-forming cells), but upon saturation and above certain levels, it becomes inhibitory to osteoblasts and induces osteoclasts (bone resorbing cells).

To date, many studies have simply stopped at evaluating the cytokine profiles associated with an inflammatory response to a material *in vitro*, and have based their conclusions on the fact that acute inflammatory responses result in fibrous encapsulation. A passive material and chronic inflammatory responses can also result in a larger fibrous encapsulation due to the activation of fibroblasts. Recent studies have proved that chronic inflammation also plays a role in tissue remodeling and integration of implants *in vivo*, and so, to reflect this, there is the need for *in vitro* models suitable for the investigation of the effect of inflammatory cytokines on functional tissue-forming cell types, that is, osteoblasts for bone contacting application, and epithelial cells for intraocular devices, and stem cells.[78–81] These models are now emerging, and they combine either direct coculture or stimulation of a functional cell type with inflammatory medium (either collected directly from inflammatory cells cultured in contact with a material or artificially supplemented with known concentrations of cytokines). As with the development of *in vitro* inflammatory models, these novel studies still require optimization and standardization if they are to realize their potential. Nevertheless, these kinds of studies are changing the concept of the inflammatory response and are directing our thinking toward the fact that the inflammatory response is a tool that should be used and controlled to enhance the efficiency of an implanted device, mainly by improved integration due to material-induced cellular function from the time of cell/material contact. The derivation and development of these *in vitro* models would not be possible if specific material-induced cell interactions were not already characterized and understood, highlighting the need for constant improvement of our knowledge of these interactions, which can be gained from both purified cell culture models and more comprehensive coculture models ranging from controlled cell phenotypes to whole blood and bone marrow models.

References

1. Williams, D. F. *J. Biomed. Eng.* **1989**, *11*, 185–191.
2. Brash, J. L. *J. Biomater. Sci. Polym. Ed.* **2000**, *11*, 1135–1146.
3. Gorbet, M. B.; Sefton, M. V. *Biomaterials* **2004**, *25*, 5681–5703.
4. Huang, J.; Yue, Y.; Zheng, C. *Sheng Wu Yi Xue Gong Cheng Xue Za Zhi* **1999**, *16*, 371–376.
5. Tang, L.; Eaton, J. W. *Mol. Med.* **1999**, *5*, 351–358.
6. Zdolsek, J.; Eaton, J. W.; Tang, L. *J. Transl. Med.* **2007**, *5*, 31.
7. Schmidt, D. R.; Kao, W. J. *Biomaterials* **2007**, *28*, 371–382.
8. McNally, A. K.; Jones, J. A.; MacEwan, S. R.; Colton, E.; Anderson, J. M. *J. Biomed. Mater. Res. A* **2008**, *86*, 535–543.
9. Remes, A.; Williams, D. F. *Biomaterials* **1992**, *13*, 731–743.
10. Anderson, J. M.; Rodriguez, A.; Chang, D. T. *Semin. Immunol.* **2008**, *20*, 86–100.
11. Tang, L.; Hu, W. *Expert Rev. Med. Devices* **2005**, *2*, 493–500.
12. Courtney, J. M.; Lamba, N. M.; Sundaram, S.; Forbes, C. D. *Biomaterials* **1994**, *15*, 737–744.
13. Roach, P.; Eglin, D.; Rohde, K.; Perry, C. C. *J. Mater. Sci. Mater. Med.* **2007**, *18*, 1263–1277.
14. Tengvall, P.; Lundstrom, I.; Liedberg, B. *Biomaterials* **1998**, *19*, 407–422.
15. Turbill, P.; Beugeling, T.; Poot, A. A. *Biomaterials* **1996**, *17*, 1279–1287.
16. Yang, W.; Chen, S.; Cheng, G.; *et al. Langmuir* **2008**, *24*, 9211–9214.
17. Ladam, G.; Gergely, C.; Senger, B.; *et al. Biomacromolecules* **2000**, *1*, 674–687.
18. Ladam, G.; Schaaf, P.; Decher, G.; Voegel, J.; Cuisinier, F. J. *Biomol. Eng.* **2002**, *19*, 273–280.
19. Lutanie, E.; Voegel, J. C.; Schaaf, P.; Freund, M.; Cazenave, J. P.; Schmitt, A. *Proc. Natl. Acad. Sci. USA* **1992**, *89*, 9890–9894.
20. Welle, A. *J. Biomater. Sci. Polym. Ed.* **2004**, *15*, 357–370.
21. Semple, J. W.; Freedman, J. *Cell. Mol. Life Sci.* **2010**, *67*(4), 499–511.
22. Bridges, A. W.; Singh, N.; Burns, K. L.; Babensee, J. E.; Andrew Lyon, L.; Garcia, A. J. *Biomaterials* **2008**, *29*, 4605–4615.
23. Tang, L.; Ugarova, T. P.; Plow, E. F.; Eaton, J. W. *J. Clin. Invest.* **1996**, *97*, 1329–1334.
24. Eriksson, C.; Lausmaa, J.; Nygren, H. *Biomaterials* **2001**, *22*, 1987–1996.
25. Karlsson, C.; Nygren, H.; Braide, M. *J. Lab. Clin. Med.* **1996**, *128*, 496–505.
26. Nguyen, K. T.; Su, S. H.; Sheng, A.; *et al. Biomaterials* **2003**, *24*, 5191–5201.
27. Sperling, C.; Maitz, M. F.; Talkenberger, S.; Gouzy, M. F.; Groth, T.; Werner, C. *Biomaterials* **2007**, *28*, 3617–3625.
28. Fujiyoshi, K.; Hunt, J. A. *Biomaterials* **2006**, *27*, 3888–3896.
29. Schorr, K.; Rott, A.; Da Costa, F.; Merfort, I. *Biologicals* **2005**, *33*, 175–184.
30. Zhu, L.; Castranova, V.; He, P. *Am. J. Physiol. Heart Circ. Physiol.* **2005**, *288*, H1331–H1338.
31. Jackson, J. K.; Springate, C. M.; Hunter, W. L.; Burt, H. M. *Biomaterials* **2000**, *21*, 1483–1491.
32. Santos, T. C.; Marques, A. P.; Silva, S. S.; *et al. J. Biotechnol.* **2007**, *132*, 218–226.
33. McNally, J. A.; Bell, A. L. *J. Biolumin. Chemilumin.* **1996**, *11*, 99–106.

34. Wettero, J.; Askendal, A.; Tengvall, P.; Bengtsson, T. *J. Biomed. Mater. Res. A* **2003**, *66*, 162–175.
35. Dodd-O, J. M.; Welsh, L. E.; Salazar, J. D.; *et al. Am. J. Physiol. Heart Circ. Physiol.* **2004**, *287*, H927–H936.
36. Edwards, S. W.; Swan, T. F. *Biochem. J.* **1986**, *237*, 601–604.
37. Kim-Park, W. K.; Moore, M. A.; Hakki, Z. W.; Kowolik, M. J. *Ann. NY Acad. Sci.* **1997**, *832*, 394–404.
38. Asberg, A. E.; Videm, V. *Artif. Organs* **2005**, *29*, 927–936.
39. Ono, K.; Ueki, K.; Inose, K.; Tsuchida, A.; Yano, S.; Nojima, Y. *Res. Commun. Mol. Pathol. Pharmacol.* **2000**, *108*, 341–349.
40. Mutasa, H. C. *Cell Tissue Res.* **1989**, *258*, 111–117.
41. Jones, D. A.; Smith, C. W.; Mcintire, L. V. *Biomaterials* **1996**, *17*, 337–347.
42. Baldwin, L.; Hunt, J. A. *J. Biomed. Mater. Res. A* **2006**, *79*, 574–581.
43. Rhodes, N. P.; Bellon, J. M.; Bujan, M. J.; Soldani, G.; Hunt, J. A. *J. Mater. Sci. Mater. Med.* **2005**, *16*, 1207–1211.
44. Rhodes, N. P.; Hunt, J. A.; Williams, D. F. *J. Biomed. Mater. Res.* **1997**, *37*, 481–488.
45. Ziats, N. P.; Miller, K. M.; Anderson, J. M. *Biomaterials* **1988**, *9*, 5–13.
46. Curran, J. M.; Gallagher, J. A.; Hunt, J. A. *Biomaterials* **2005**, *26*, 5313–5320.
47. Anderson, J. M.; Defife, K.; Mcnally, A.; Collier, T.; Jenney, C. *J. Mater. Sci. Mater. Med.* **1999**, *10*, 579–588.
48. McNally, A. K.; Anderson, J. M. *Am. J. Pathol.* **2002**, *160*, 621–630.
49. McNally, A. K.; MacEwan, S. R.; Anderson, J. M. *J. Biomed. Mater. Res. A* **2007**, *82*, 568–574.
50. Chung, A. S.; Gao, Q.; Kao, W. J. *J. Biomater. Sci. Polym. Ed.* **2007**, *18*, 713–729.
51. Patarroyo, M. *Immunobiology* **1994**, *191*, 474–477.
52. Loike, J. D.; Cao, L.; Budhu, S.; Hoffman, S.; Silverstein, S. C. *J. Immunol.* **2001**, *166*, 7534–7542.
53. Bochner, B. S.; Bickel, C. A.; Taylor, M. L.; *et al. J. Allergy Clin. Immunol.* **1999**, *103*, 527–532.
54. Jacques, C.; Gosset, M.; Berenbaum, F.; Gabay, C. *Vitam. Horm.* **2006**, *74*, 371–403.
55. Maus, U. A.; Wellmann, S.; Hampl, C.; *et al. Am. J. Physiol. Lung Cell. Mol. Physiol.* **2005**, *288*, L350–L358.
56. Tominaga, T.; Miyazaki, D.; Sasaki, S.; *et al. Invest. Ophthalmol. Vis. Sci.* **2009**, *50*, 5181–5188.
57. Grignani, G.; Maiolo, A. *Haematologica* **2000**, *85*, 967–972.
58. Li, Y.; Schutte, R. J.; Abu-Shakra, A.; Reichert, W. M. *Biomaterials* **2005**, *26*, 1081–1085.
59. Schutte, R. J.; Parisi-Amon, A.; Reichert, W. M. *J. Biomed. Mater. Res. A* **2009**, *88*, 128–139.
60. Opal, S. M.; DePalo, V. A. *Chest* **2000**, *117*, 1162–1172.
61. Brodbeck, W. G.; Nakayama, Y.; Matsuda, T.; Colton, E.; Ziats, N. P.; Anderson, J. M. *Cytokine* **2002**, *18*, 311–319.
62. Godek, M. L.; Sampson, J. A.; Duchsherer, N. L.; Mcelwee, Q.; Grainger, D. W. *J. Biomater. Sci. Polymer Ed.* **2006**, *17*, 1141–1158.
63. Matzelle, M. M.; Babensee, J. E. *Biomaterials* **2004**, *25*, 295–304.
64. Baldwin, L.; Flanagan, B. F.; Mclaughlin, P. J.; Parkinson, R. W.; Hunt, J. A.; Williams, D. F. *Biomaterials* **2002**, *23*, 3007–3014.
65. Baldwin, L.; Hunt, J. A. *Cytokine* **2008**, *41*, 217–222.
66. Badylak, S. F.; Gilbert, T. W. *Semin. Immunol.* **2008**, *20*, 109–116.
67. Loetscher, P.; Uguccioni, M.; Bordoli, L.; *et al. Nature* **1998**, *391*, 344–345.
68. Chang, D. T.; Colton, E.; Matsuda, T.; Anderson, J. M. *J. Biomed. Mater. Res. A* **2009**, *91A*, 1210–1220.
69. MacEwan, M. R.; Brodbeck, W. G.; Matsuda, T.; Anderson, J. M. Student Research Award in the Undergraduate Degree Candidate category. In *30th Annual Meeting of the Society for Biomaterials*, Memphis, Tennessee, April 27–30, 2005; *J. Biomed. Mater. Res. A* **2005**, *74*, 285–293.
70. Rodriguez, A.; Anderson, J. M. *J. Biomed. Mater. Res.* **2010**, *92*(1), 214–220.
71. Anderson, J. M. *Curr. Opin. Hematol.* **2000**, *7*, 40–47.
72. Xia, Z.; Triffitt, J. T. *Biomed. Mater.* **2006**, *1*, R1–R9.
73. Lassus, J.; Salo, J.; Jiranek, W. A.; *et al. Clin. Orthop. Relat. Res.* **1998**, *352*, 7–15.
74. Otto, M.; Kriegsmann, J.; Gehrke, T.; Bertz, S. *Pathologe* **2006**, *27*, 447–460.
75. Sargeant, A.; Goswami, T. *J. Surg. Orthop. Adv.* **2006**, *15*, 111–112.
76. Hallab, N. J.; Jacobs, J. J. *Bull. Hosp. Joint Dis.* **2009**, *67*, 182–188.
77. Jacobs, J. J.; Hallab, N. J.; Urban, R. M.; Wimmer, M. A. *J. Bone Joint Surg. Am.* **2006**, *88*(Suppl. 2), 99–102.
78. Lacey, D. C.; Simmons, P. J.; Graves, S. E.; Hamilton, J. A. *Osteoarthr. Cartil.* **2009**, *17*, 735–742.
79. Meinel, L.; Hofmann, S.; Karageorgiou, V.; *et al. Biomaterials* **2005**, *26*, 147–155.
80. Prasanna, S. J.; Gopalakrishnan, D.; Shankar, S. R.; Vasandan, A. B. *PLoS One 5*, e9016.
81. Ren, G.; Zhao, X.; Zhang, L.; *et al. J. Immunol. 184*, 2321–2328.

4.406. Protein Interactions with Biomaterials

P Tengvall, University of Gothenburg, Gothenburg, Sweden

© 2011 Elsevier Ltd. All rights reserved.

4.406.1.	**Introduction**	63
4.406.1.1.	Proteins of the Human Body and Relevance for Biomaterials	63
4.406.1.2.	Nonspecific and Specific Surface–Protein Interactions	64
4.406.1.3.	Phenomena Related to Protein Adsorption	66
4.406.1.4.	Nonspecific and Specific Biomaterial Surface–Protein Interactions	66
4.406.2.	**Surface Wettability, Topography, and Protein Adsorption**	67
4.406.2.1.	General	67
4.406.2.2.	Hydrophobic Surfaces	68
4.406.2.3.	Negatively/Positively Charged Surfaces	68
4.406.2.4.	Surface Nano-Roughness and Protein Adsorption	69
4.406.2.5.	Protein Displacement Phenomena	69
4.406.2.6.	Protein-Resistant Surfaces	69
4.406.3.	**Surface-Activated Coagulation**	70
4.406.3.1.	Intrinsic Pathway	70
4.406.3.2.	Tissue Pathway	70
4.406.4.	**Immune Complement at Biomaterials**	70
4.406.4.1.	Prevailing Model of Activator/Inhibitor Surfaces	70
4.406.4.2.	Spontaneous, Classical, and Alternative Complement Activation	71
4.406.5.	**Consequences of Protein Adsorption**	71
4.406.5.1.	Blood Compatibility	71
4.406.5.2.	Inflammation and Wound Healing	72
4.406.5.3.	Adsorbed Proteins and Biomaterials-Related Infection	72
4.406.6.	**Summary and Future Directions**	72
References		73

Glossary

Activation energy The energy that must be overcome in order for a process, such as a chemical reaction or adsorption, to occur.

Anaphylatoxin Molecule able to trigger degranulation of endothelial cells, mast cells, and phagocytes, which produce a local inflammatory response.

Complement system Part of the immune system called the innate immune system that is not adaptable and does not change over the course of an individual's lifetime. However, it can be recruited and brought into action by the adaptive immune system (Wikipedia).

Coulombic interaction Electrostatic interaction between molecules, particles, or bodies. Like charge repels each other and opposite charges attract each other.

Enthalpy change ΔH is equal to the heat absorbed by a chemical reaction.

Entropy change ΔS denotes change in a systems 'disorder.'

Free energy Energy released during a process, such as adsorption or chemical reaction.

Heat capacity Heat capacity is the capacity of a body to store heat.

Nucleophile An electron-rich chemical reactant that is attracted by electron deficient compounds. For instance, water and alcohol are oxygen nucleophiles, amines, and ammonia nitrogen nucleophiles.

Point of zero charge (pzc) The condition when the electrical charge density on a surface is zero. It is usually the pH value at which a solid submerged in an electrolyte exhibits zero net electrical charge on the surface (Wikipedia).

4.406.1. Introduction

4.406.1.1. Proteins of the Human Body and Relevance for Biomaterials

Studies on protein adsorption from blood plasma or whole blood are an accepted method to assess biomaterials, especially in blood-contacting applications. The 20 amino acids in the human body are combined in different ways to build up a huge number, ~100 000, of different proteins. Many of these are found in blood and other body fluids, and some are bound to tissues as frameworks for soft tissues, bone, and hair. It is suggested that proteins make up about 75% of dry body weight.[1] The total protein concentration in native blood is ~70 mg ml^{-1}. High-resolution, two-dimensional electrophoresis shows the

presence of over 150 bands from blood plasma, and it is estimated that more than 5000 different proteins can be observed by this method.[2] However, in the majority of studies related to protein adsorption to biomaterials, only plasma proteins of sufficiently high concentrations are considered, as these are supposed to compete effectively at the interface. Andrade and Hlady limited them to concentrations above $\sim 1\,\mathrm{mg\,ml^{-1}}$, and ended up with a group of plasma proteins named 'The big twelve': albumin, IgG, LDL, HDL, α-macroglobulin, fibrinogen, transferrin, α-antitrypsin, haptoglobulins, C3, IgA, and IgM.[2] However, other proteins outside this narrow group are also of obvious significance, for example, proteins of the coagulation pathways and the complement system. A common denominator for the latter is their surface deposition on top of preadsorbed proteins upon activation of humoral cascade systems that may be at or in the close vicinity of biomaterials. Electrophoresis and Western blots of proteins that were eluted from polyethylene glycol (PEG)-modified liposomes, in one study, revealed adsorption by considerably more than 12 different proteins.[3] However, for practical reasons and based on experience, the analysis of protein adsorption is limited to a relatively few proteins that function as markers of specific binding and activation pathways. For example, deposited fibrinogen predicts the surface binding and activation of platelets and white cells the generation of emboli; surface-bound high molecular weight kininogen (HMWK) is a good marker of activation of the intrinsic pathway of coagulation; and IgG and C3b predict surface activation of the complement system. The identification of specific proteins at surfaces is most commonly performed using immunologic/antibody or protein-labeling techniques and is usually complemented by the analysis of the soluble protein degradation fragments. A selection of analytical techniques to study protein adsorption are listed in **Table 4**.

4.406.1.2. Nonspecific and Specific Surface–Protein Interactions

Proteins in solution accumulate spontaneously at biomaterial and other interfaces, and in the present context, we consider chemically inert surfaces with low solubility in aqueous solutions and blood plasma as examples of such interfaces.

The adsorption process is exothermic (i.e., with spontaneous release of heat)

$$\Delta G = \Delta H - T\Delta S \qquad [1]$$

where, ΔG is the change in Gibbs free energy, ΔH change in enthalpy (generation/loss of bondings), T temperature, and ΔS is the change in entropy.[4] In most cases, a change in system entropy (here, the system includes solution, surface/interface, and the protein that adsorbs from solution) drives the process with an increase in free water that is liberated from between the adsorbent and adsorbing proteins, and an increase in adsorbed protein internal mobility. A part of the liberated energy is needed to partially denature the adsorbing protein, with $\Delta H = \int \Delta c_p \mathrm{d}T$, where $\Delta c_p = c_{p,\,\text{denatured protein}} - c_{p,\,\text{native protein}} > 0$. For some proteins, the adsorption process is driven by enthalpy,[4,5] although such proteins are only exceptions. Adsorbed, that is, partially denatured proteins normally acquire an increase in heat capacity, c_p.[5] As mentioned earlier, proteins change their conformation during the adsorption process, increasing the exposure of hydrophobic protein residues/domains and internal molecular entropy. The degree of denaturation increases upon prolonged contact or residence time. The increase in entropy because of an increase in free water and internal molecular entropy, is suggested to be the main contributor of the driving energy that enables protein adsorption (**Figure 1**). Attractive coulombic protein–surface interactions (interaction force $\sim 1/r^2$, r is distance from surface) are other important contributors to the adsorption process; and once a physical protein–surface interface is established, close range attractive van der Waals interactions (interaction force $\sim 1/r^6$) also help anchor proteins to the surfaces.

Relatively well-understood exceptions to adsorbing artificial surfaces are charge neutral interfaces/surfaces with high water retention and/or high surface mobility, such as surface-immobilized PEGs or sugars, and water–lipid and solid–lipid interfaces. Surfaces inside the human body, for example, the exterior of cell membranes, albumin-associating cell surfaces, extracellular materials such as glucosaminoglycans (GAGs), and mucosae with high oligosaccharide content behave, with respect to spontaneous adsorption, similarly to PEGs. Most internal body surfaces carry a negative net charge at physiological conditions and thus exert repulsive forces between surfaces and macromolecules, that is, proteins, GAGs, and other organic molecules, and macromolecules contribute together with ions of body fluids to retain body water and to keep the biological structures and molecules apart. This also significantly contributes to homeostasis. It should also be pointed out, in this context, that cells and proteins do indeed interact a lot with one another, although such interactions are more specific and largely regulated via receptor–ligand interactions. The description of this is, however, out of the scope of this chapter. Other, more or less specific interactions occur when biomaterials adsorb proteins belonging to the humoral cascade systems and eventually activate them. The intrinsic pathway of coagulation is activated on negatively charged surfaces upon contact with blood or blood plasma.[6,7] The key proteins in these events are HMWK, coagulation factor XII, coagulation factor XI, and prekallikrein.[7,8] The fibrinolytic system may be activated downstream as a consequence of coagulation, but not primarily by the biomaterial itself. The complement system deposits complement factor 3b (C3b or iC3b) and its degradation products onto virtually all types of adsorbing surfaces, especially the nucleophilic ones.[9,10] For a description of the blood cascade systems and biomaterials (see **Sections 4.406.3** and **4.406.4**).

The aforementioned surface properties are often grouped into a simpler classification to separate protein-adsorbing surfaces from protein-resistant surfaces (**Tables 1** and **2**).

Generally, protein adsorption leads to both immediate and delayed effects in the vicinity of the implanted biomaterials.

The rate of single protein adsorption ($R_{\text{adsorption}}$) is Langmuir-like, and proceeds according to equation

$$R_{\text{adsorption}} = \frac{f(\Theta)P}{\sqrt{2\pi MkT}} e^{-E_a/RT} \qquad [2]$$

where k is the rate constant, P molecular pressure ($\mathrm{N\,m^{-2}}$), M mass of one molecule (kg), T temperature (K), Θ fraction of

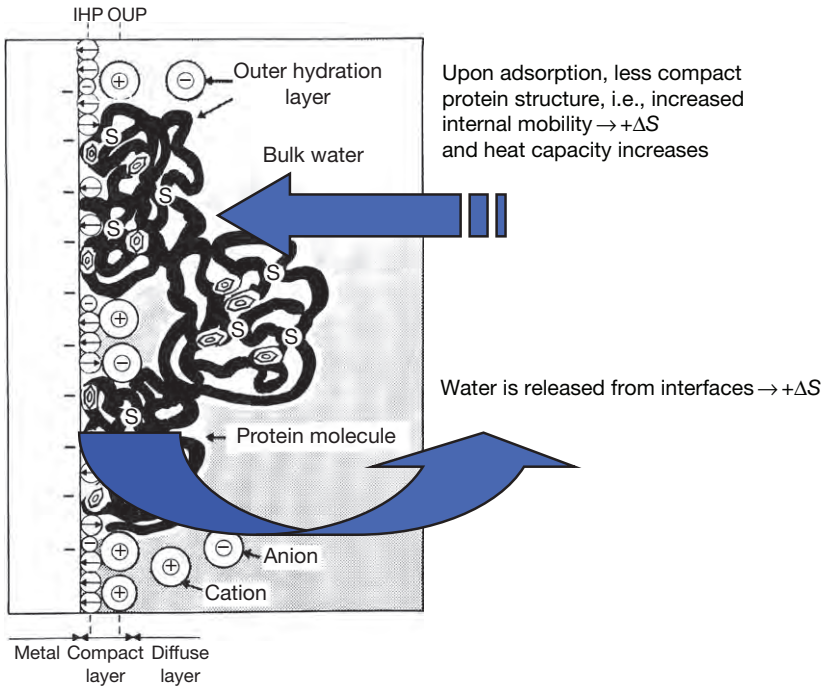

Figure 1 Schematic illustration of the electrochemical double layer at the biomaterial–electrolyte interface. Water molecules shown as individuals, (→), where the arrow symbolizes the dipole moment and as a structured hydration layer. IHP and OHP are inner and outer Helmholtz planes, respectively. A primary strongly adsorbed protein layer with more or less compact molecules and a second loosely held layer consisting of more 'native' molecules are also indicated by (ring molecule) aromatic amino acid, (S) disulphide bridge. Reproduced from Ivarsson, B.; Lundström, I. *CRC Crit. Rev. Biocompat.* **1986**, *2*(1), 1–96.

Table 1 General surface and protein properties that determine adsorption

Surface properties	*Protein properties*
Free energy (hydrophobicity/hydrophilicity)	Overall hydrophobicity
Charge and electric field divergency	Charge and dipole size and localization
Ion binding	Prosthetic groups
Redox/corrosion potential	Ion binding
Hydrogen bonding capacity	Hydrogen bonding residues
Surface water structure/binding strength	Water binding and localization
Acid/base properties (pcz)	pI
Surface impurities	Specific interacting residues
Surface topography at micro- and nanoscale	Quarternary, tertiary, and secondary structure, dipole size and localization
Oxide (thickness, growth, dielectric constant, water, and ion sorption)	Number of internal disulphide bridges
Interactions with small (organic) molecules	Size (molecular weight)

Table 2 Pro- and antiadsorption factors

Proadsorption factors	*Antiadsorption factors*
Dehydration of interfaces	Strong water binding to interfaces
Increase of protein interior mobility	Low protein flexibility
Coulombic interactions	High protein lateral mobility
Dipoles in a divergent electric field	Low net coulombic interactions
Van der Waal interactions at close contact	High surface smoothness

sites occupied (max. 1), $f(\Theta) = 1 - \Theta$, and E_a is activation energy of adsorption.

The balancing rate of single protein desorption ($R_{\text{desorption}}$) is described as

$$R_{\text{desorption}} = -\frac{dN}{dt} = \nu N^{\chi} e^{-E_a^{\text{des}}/RT} \quad [3]$$

where N is the surface concentration of adsorbed proteins, χ kinetic order of desorption, E_a^{des} the activation energy of desorption, and ν is 'attempt frequency' at overcoming the barrier to desorption.

4.406.1.3. Phenomena Related to Protein Adsorption

- Lowered system energy – release of heat
- Coverage Θ – 1 monolayer of adsorbed single proteins equals 50–90% of the total arithmetic area
  - from single protein solutions, 1–5 nm (70–350 ng cm^{-2}), thick film
  - from serum/plasma, 3–20 nm (210–1400 ng cm^{-2}), thick film
  - hydrophobic surfaces tend to adsorb slightly more than hydrophilic surfaces
  - higher protein concentration in solution → thicker protein film
- Firm but not completely irreversible binding – protein exchange processes occur more often on hydrophilic than hydrophobic surfaces.
- Residence time – leads to an increase in conformational changes, with more denaturation on hydrophobic than on hydrophilic surfaces.
- Specific uptake of proteins may take place (e.g., factor XII/IgG).
- Adsorbed fibrinogen may be displaced by other proteins (Vroman effect).
- Cascade reactions may be initiated
  - coagulation, fibrinolytic, and kinin systems
  - complement
- Surfaces become opsonized, that is, they are recognized as foreign bodies by cells.
- Spontaneously generated reactive body C3b* binds to denatured proteins.
- Thickening of the protein layer with time. Both intact and proteolytically fragmented proteins reside at surfaces and in their close vicinity.

The adsorption of proteins to biomaterials would not be interesting or even relevant to study if the adsorbed layer was only a passive bystander or a biologically passive entity. This is, however, not the case. Adsorbed proteins participitate in surface-initiated coagulation with concomitant fibrinolytic activity; generate kallikrein, thrombin, and bradykinin; mediate immune complement activation; and generate biologically active protein degradation products. Also, both cells and bacteria may bind to the adsorbed proteins. Surface–protein interactions lead to the generation of cell-regulating signal molecules such as C3a, C4b, C5a, C5a-des arg, C3d, C3dg, bradykinin, fibrinogen degradation products (FDPs), monomeric fibrin, etc. Last but not least, both surface-bound proteins or protein fragments and soluble fragments interact intensively with the surrounding cells and tissues. This signaling in turn affects local homeostasis via recruitment of specific cells to the site of biomaterial implantation, cell differentiation, wound healing, blood flow and interactions, etc. **Table 3** lists selected protein–cell interactions and indicates, thereby, a strong rationale for research in this area.

4.406.1.4. Nonspecific and Specific Biomaterial Surface–Protein Interactions

Blood proteins and proteins from body fluids adsorb with low specificity and relative unpredictability to biomaterials.

Table 3 Selected protein–cell interactions

Protein	*Major function*	*Cell receptor*	*Cell type*
Serum albumin	Body transport and clearance protein, binds to certain cell surfaces ('passivates'), maintains the osmotic balance	gp30 and gp18	Endothelial, hepatocytes?
Fibrinogen (Fib)	Forms fibrin during blood coagulation	CD11b,c, CD41a, CD51, CD61	Platelet, endothelial, myeloid, NK, osteoclast, tumor
Fibronectin (FNT)	Extracellular matrix protein that binds cells via RGD-sequence	CD49c, d, e, CD41a, CD61	Platelet, B lymphocyte, monocyte, fibroblast, epithelial, keratinocyte, tumor
Immunoglobulin G (IgG)	Opsonizes a nonself cell surface, activates complement	Fc	PMN, macrophage
High molecular weight kininogen (HMWK)	Component of the intrinsic pathway of coagulation, binds to negatively charged surfaces	β1 and β2 receptors	Endothelium, platelets and neutrophils, monocytes, macrophages
Complement factor 1q (C1q)	Binds to IgG and IgM and initiates classical complement activation, related to collagen activation of platelets	cC1q-RI, C1q-Rq, gC1q-R	B lymphocyte, T lymphocyte, monocyte/macrophage, PMN, eosinophil, platelet, fibroblast, endothelial, epithelial, smooth muscle, mesengial
Complement factor 3b (C3b) and C4b	Key adsorbed complement proteins, formed by cleavage of C3 to C3a and C3b, C4 to C4a and C4b	CR1(CD35)	Erythrocyte, phagocyte, B lymphocyte, T lymphocyte, eosinophil
Complement factor 3dg/3d (C3dg,C3d)	Surface-bound complement peptide after proteolytic cleavage of C3b, opsonin	CR2(CD21)	B lymphocyte, T lymphocyte
Complement factor 3bi (C3bi)	Inactivated C3b	CR3 (CD11b and CD18) and CR4 (CD11c)	Monocytes, macrophages, PMNL dendritic cells, myeloid cells, NK, B cells, T cell subset

Protein adsorption to biomaterials can be analyzed by a number of techniques. No single method reveals answers to all questions and many studies seem therefore inconclusive or contradictory, the experiments seem too simplified, and the relevance is questionable in a broader biological context. As body fluids are complex and contain protein-borne humoral systems, only adsorption data from human blood and serum will be discussed in this chapter.

For example, adsorbed albumin has been identified on virtually all types of surfaces in contact with blood serum or plasma. Therefore, the adsorbed protein layer has been called a 'biolayer.' The main reason for this unpredictability is that artificial surfaces lack specific protein receptors, such as those expressed on the exterior or interior of cells, and hence artificial surfaces are simple in a biological context. Nevertheless, different surfaces show some kind of selection that can be related to their different physical/chemical surface properties. For instance, hydrophilic, negatively charged surfaces bind and activate factor XII and HMWK; positively charged surfaces seem not to do that, they may instead bind lipoproteins. Fibrinogen is displaced from hydrophilic negatively charged surfaces but not from hydrophobic. Surfaces with specific IgG uptake are strong complement system activators. When we look more closely into the chemical identity of the surface, there appear some surface selection rules; amine and hydroxyl groups interact strongly with the immune complement system, and negatively charged carboxyl, sulphate, phosphate, and hydroxyls activate the intrinsic pathway of coagulation. No specific chemical groups are, on the other hand, known to activate the tissue pathway of coagulation. What really may be of significance in nonspecific surface binding is the partial denaturation of proteins during long residence times. This makes biomaterials appear as gigantic immune complexes or worn out macromolecules. Now the surrounding proteins, cells, and tissues have to deal somehow with this entity. In a few cases, the impact is positive, while in the majority of cases it is negative. A more complete understanding of the implications of these processes has yet to be achieved.

4.406.2. Surface Wettability, Topography, and Protein Adsorption

4.406.2.1. General

One important physical property of nonsoluble surfaces is their water wettability. This term is coupled to and interchangeable with terms such as surface energy, surface free energy, contact angle, and critical surface tension, although the latter refers to liquids. They all focus, in our context, on the same surface property, its hydrophilicity/hydrophobicity.[11–13] Surface free energy

$$\gamma_{\text{total}} = \gamma_{\text{dispersive}} + \gamma_{\text{polar}} \quad [4]$$

that is, the total surface energy that we normally measure or observe is composed of two components, one describing polar interactions between atoms and materials and the other describing nonpolar interactions. Biomedical metal oxides and bioceramics are designed to be chemically stable and

Table 4 Analytical techniques to study protein adsorption on biomaterials

Technique	*Characteristics*
ELISA	Immunologic technique, single or complex protein solutions, samples with different geometries can be studied, does not require optically reflecting surfaces, quantitation of adsorbed proteins can be difficult, time consuming, cheap
SDS-PAGE	Electrophoretic analysis of desorbed proteins, identification can be made by antibodies, not quantitative, time consuming
Electrophoresis	Analysis of desorbed proteins, identification by antibodies, 2D analysis separates proteins according to molecular weight or charge, very many different proteins can be observed, time consuming
Radiolabeling techniques	Single labeled proteins adsorb from single or complex protein solutions. Can be quantitated accurately in the desorbed or adsorbed state, no restrictions regarding material or surface geometry, not proper for studies on complex cascade reactions at surfaces, Vroman effect can be studied, protein nativity can be impaired by the labeling procedure, nonspecific absorption of ^{125}I may occur
QCM-D	Detects dynamic surface–protein interactions and changes in surface viscoelastic properties, relatively good adsorbed mass quatitation possible in single and complex protein solutions Energy dissipation reveals protein film properties
OWLS	Optical technique, good quatitation, can be combined with immunologic protein identification, commercial availability?
SPR	Quantitative, excellent for studies on dynamics of adsorption and protein–ligand biointeractions, not particularly appropriate for analysis in complex protein solutions
Ellipsometry	Good surface quantitation, no protein labeling required, single and complex protein solutions can be used, adsorbed protein identification by antibody techniques, quick, requires optically reflecting smooth surfaces, complex theory, measurements can be performed in solution or in air
Infrared spectroscopy	Quantitation by protein amide bands, low accuracy, time consuming, single or complex solutions, expensive, protein identification difficult
Spectrophotometry	Quantitation of desorbed proteins or by determination of depleted amounts, mainly single protein solutions, cheap, good accuracy, requires large adsorbing surface areas, not dependent of surface topography or its physical properties
Fluorescence spectroscopy	Detects fluorescing molecules or markers in proteins, high sensitivity, quick measurements but tedious labeling work, single or complex solutions possible, quenching may occur, protein nativity may be disturbed by labeling procedure
AFM	Oscillating mode preferred, measurements in solution or in air possible, appropriate to visualize single adsorbed protein, can be quantitative, labor intense, requires good training for accurate interpretation, protein identification in complex solutions difficult
XPS	Measures signal intensity, for example, N^{1s} (relative to controls), dependent on substrate surface chemistry and the organization of the adsorbed protein film

Table 5 Water contact angles of common biomaterials

Material	*Static water contact angles (°)*	*Surface energy, surface-free energy (mN m^{-1})*	*Critical surface tension (mN m^{-1} or dyn cm^{-1})*	*References*
Metals and ceramics	5–60	High: >40	High: >40	[11–13]
Solid polymeric biomaterials	30–110	Low–medium: 20–45	Nonpolar: 18–33 polar: 22–45	[11–13]

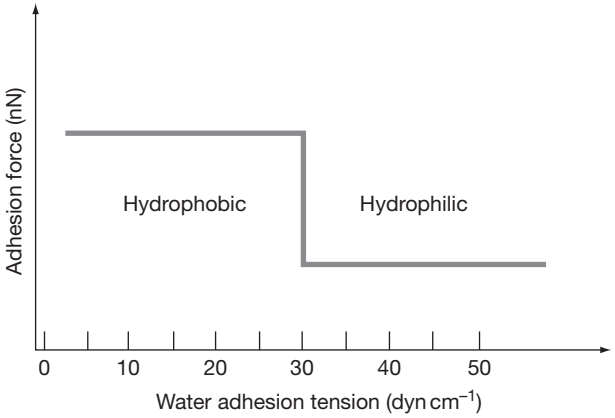

Figure 2 Schematic picture of protein adhesion forces on protein coated tips to surfaces with different water adhesion tension values. In the transition region, the static water contact angle is 55–65°. Reproduced from Lestelius, M.; Liedberg, B.; Tengvall, P. *Langmuir* **1997**, *13*(22), 5900–5908.

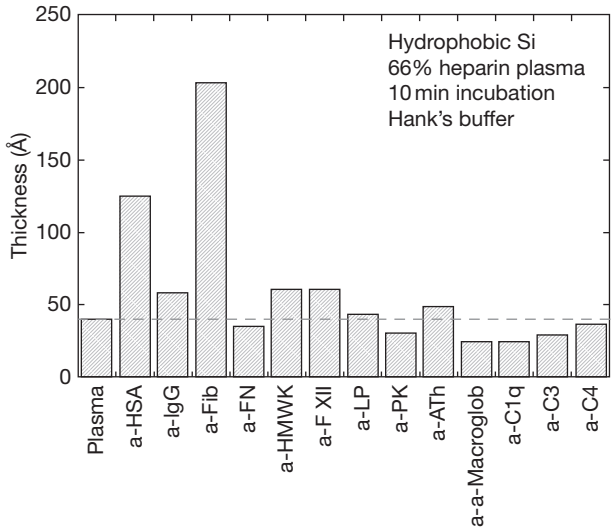

Figure 3 Plasma proteins on hydrophobic silicon silanized with diclorodimethyl (DDS). The dotted line indicates the average heparin plasma layer thickness after 10 min of adsorption in heparin plasma (equals ~450 ng cm^{-2}). Polyclonal antibodies against fibrinogen, human serum albumin, IgG, high molecular weight kininogen, and factor XII bound into the plasma layer. Staple heights below the plasma level indicate a detergency effect by respective antibody solution.

exert, predominantly, polar force interactions on proteins. Polymers possess mixed properties and exert both polar and dispersive (nonpolar) force interactions, that is, they are, commonly, more hydrophobic than metal oxides (Table 5). The structure of the polymer surface is physically less dense than metal or ceramic interfaces, and the outermost molecules may undergo flip-flop rotations, thereby changing character from hydrophilic to hydrophilic and vice versa, which is an adaptation to the environment. The flip-flop process may be instantaneous or take hours, depending on the material and the polarity of the environment or lack of it.

Hydrophobic and hydrophilic surfaces exert different force interactions on proteins when expressed as adhesion forces[13] (see the principle in Figure 2). Hydrophobic surfaces, with structurally more ordered water, attract proteins to a greater extent than hydrophilic surfaces which have less ordered, but more tightly bound, water.

4.406.2.2. Hydrophobic Surfaces

Typical hydrophobic surfaces expose their methyl ($-CH_3$), methylene ($-CH_2-$), methoxy ($-OCH_3$), or trifluoromethyl ester ($-OCF_3$) groups toward the surroundings.[14] Many polymeric biomaterials are hydrophobic, for example, PTFE, PDMS, PET, polyethylene, and polypropylene. The static contact angle is often larger than 80°. In a classical work, Robert Baier suggested that blood compatible materials display a critical surface tension of 20–30 dyn cm^{-1}, that is, they are hydrophobic and have low surface free energy[15] (Table 5).

Hydrophobic surfaces bind to proteins more firmly than hydrophilic surfaces (Figure 2). The main reason for this is the increase in interactions between the hydrophobic surface and hydrophobic protein domains that become exposed during the adsorption process. Interfacial water is then displaced more easily from the contacting hydrophobic surfaces compared to the same process on hydrophilic surfaces with a stronger water binding. The amount of adsorbed protein is then similar to that of electrically conducting materials, such as gold, and antibody mapping of the contents of a blood plasma protein film reveals characteristics that are common to virtually all hydrophobic surfaces. The main proteins exposed on the surface are fibrinogen and albumin (see Figure 3).

4.406.2.3. Negatively/Positively Charged Surfaces

Negatively charged surfaces are surfaces with a negative charge in physiological environments (pH 7). Such surfaces possess an isoelectric point (pI or point of zero charge, pzc) below pH 7.[16–18] Some oxides are strongly acidic, for example, SiO_2 (pzc ~ 1.7–3.5), WO_3 (pzc ~ 0.2–0.5), Ta_2O_5 (pzc ~ 2.7–3), Sb_2O_5 (pzc ~ 0.4–1.9), and Nb_2O_3 (pzc ~ 4.1). Others are amphoteric and include metal and semiconducting oxides such

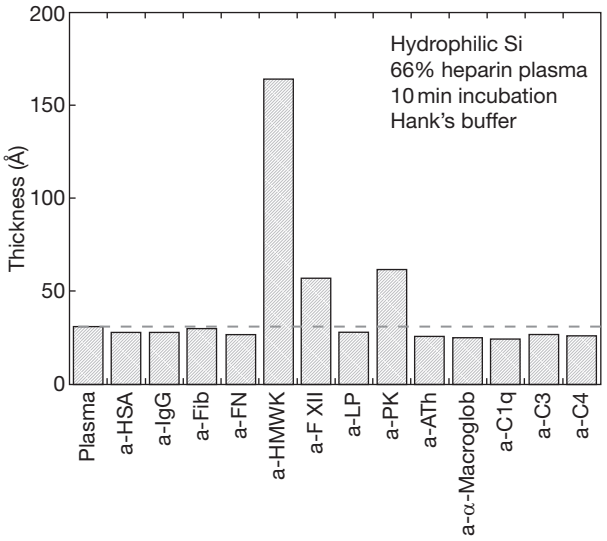

Figure 4 Plasma proteins on negatively charged hydrophilic silicon with pzc ~ 4–5. The dotted line indicates the average heparin plasma layer thickness after 10 min of adsorption from heparin plasma (equals ~400 ng cm^{-2}). Polyclonal antibodies against high molecular weight kininogen, factor XII, and prekallikrein bound into the plasma layer. Staple heights below the plasma level indicate a detergency effect by respective antibody solution.

as TiO_2 (pzc ~ 3.9–8.2), ZrO_2 (pzc ~ 4–11), and Cr_2O_3 (pzc ~ 6.2–8.1). Basic oxides, possessing a positive surface charge at pH 7, include Y_2O_3 (pzc ~ 8.9), α-Fe_2O_3 (pzc ~ 9.4–9), ZnO (pzc ~ 8.7–9.7), and MgO (pzc ~ 12.1–12.7). Al_2O_3 is most often considered basic (pzc ~ 7–9).

Surfaces with a negative charge deposit approximately 400 ng cm^{-2} plasma proteins during short-time incubations and activate the intrinsic pathway of coagulation, but do not retain much fibrinogen after an observed initial adsorption/desorption phenomenon that takes place within seconds. Negative surfaces adsorb and activate plasma proteins such as HMWK, factor XII, and prekallikrein (see Figure 4).[19] During prolonged plasma contact times, at the order of tens of minutes to hours, complement factor 3b is commonly deposited onto previously adsorbed and partially denatured proteins.

4.406.2.4. Surface Nano-Roughness and Protein Adsorption

Increased surface roughness results in increased protein adsorption. The reason is related to both macro- and micro-scale; for ~ $R_a \geq 0.1\,\mu m$, there is an increase in the general surface area, whereas, at the submicron level, $R_a < 0.1\,\mu m$, increased adsorption may result from effects on macromolecules in a divergent electrical field, resulting in an attractive force toward regions with higher field strength (corners, kinks, ..., see Figure 5). This force is the result of a charge-dipole that is induced along the axis of the protein molecule. Thus, the dipole (macromolecule) interacts with an E-field gradient and also polarizes the outermost layers of the surface. As the direction of the induced dipole always opposes the E-field direction, the attractive force is independent of field polarity. One could, therefore, expect protein accumulation at asperities with sizes

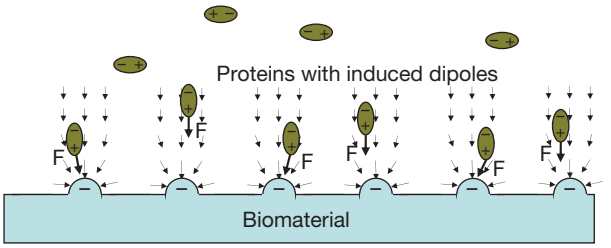

Figure 5 Proteins in divergent electric field. An attractive force toward a denser field section is generated by static or induced macromolecule dipoles. Other attractive or repulsive forces such as columbic, hydrophobic, and van der Waals forces omitted for clarity.

of the order of 1–100 nm, at crystallites; and surface charge may then be used for selecting the direction of molecule adsorption. Exactly how this works out in real life is not well understood and is hard to control, but these phenomena should also induce certain effects at the macro level and be observable during cell spreading, cell motility, and gene expression.

4.406.2.5. Protein Displacement Phenomena

When blood plasma is adsorbed onto negatively charged surfaces such as Ta, Si, and Ti or biopolymers such as polyurethane, proteins adsorb during the early adsorption phase, and become eventually replaced by other plasma proteins. Hydrophobic and positively charged surfaces show no or little protein exchange. The early adsorption of plasma fibrinogen onto negatively charged surfaces and its later displacement by HMWK and other plasma proteins is called the Vroman effect.[20,21] Frequently, the displacement of other plasma proteins in other circumstances are also collectively called 'Vroman effects'[22]; but the distinction between these two is important. The original observation, made way back in the 1960s by Vroman and Adams, was that adsorbed plasma proteins were detectable using antibodies on Ta-oxide in a time-dependent order, viz, albumin, IgG, fibrinogen and fibronectin, and HMWK (Figure 6).[23] The phenomenon has been well described, by the same investigators, for blood plasma adsorption into narrow spaces.[24]

The reasons for plasma protein exchange have not yet been understood in detail but may be as follows. In the early phase, the adsorption of a specific protein increases if its concentration is high, it is structurally flexible, of low molecular weight (quick diffusion), and exerts no columbic repulsions on the surface (pI ~ 7). Albumin fulfils these criteria the best and readily adsorbs from plasma. The adsorbed proteins modify surface electrodynamic conditions, whereby, similar proteins or other proteins with higher surface affinity but lower bulk concentration enter the surface, and the former may be displaced by the entering protein, and so forth.

4.406.2.6. Protein-Resistant Surfaces

Surfaces with low or zero net charge, high water retention capability, and high surface mobility are protein- and hence cell-resistant. Comixtures of surface-immobilized polyethylene glycols or -oxides (PEG or PEO) with the basic structural backbone element $-(-C-C-O-)_m$ are widely used for this purpose

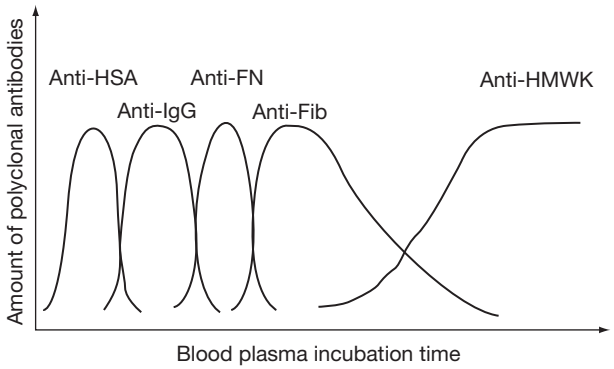

Figure 6 The Vroman plasma protein displacement phenomenon.[22,23] The *x*-axis shows time elapse of incubation of a negatively charged surface, such as glass, Ta-oxide, or Ti-oxide in blood plasma, and the *y*-axis the amount of surface-bound polyclonal antibodies after different plasma incubation times. Observe that this phenomenon reflects antibody access to its surface located antigen, and does not necessarily reflect a true surface displacement of plasma proteins, and may show the antigen accessibility only.

in biotechnology. One consequence of the low surface protein retention is a low cell binding, which may be for good or for bad. The literature indicates that the preferred molecular weight of immobilized PEGs is of the order of 1–5 kD.[25,26] Other protein-resistant molecule classes are, for instance, immobilized natural or artificial hydrogels, proteins (e.g., albumin), polypeptides, sugars, and GAGs, although many of them also have known biological (side) effects, something we avoid whenever possible. One common problem in body fluid-contacting systems is the stability of such surface constructs. It is a relatively easy task to prepare an *in vitro* protein-resistant surface with a molecular pressure equivalent to 1 mg ml^{-1} protein in solution and no chemical reactivity, but a much more complicated task *in vivo* and at 70 mg ml^{-1} protein concentration. Also, the reactive chemistry of human humoral cascade systems, including inflammatory conditions, normal metabolism, and the spontaneous generation of reactive protein cleavage products add to the problem.

4.406.3. Surface-Activated Coagulation

4.406.3.1. Intrinsic Pathway

The intrinsic pathway of coagulation is activated on negatively, but not at positively, charged biomaterial surfaces. An excellent introduction to the initiation of blood coagulation at artificial surfaces was written by Colman *et al.*[27] Hydrophobic surfaces activate coagulation differently, namely, via platelets that interact with the adsorbed fibrinogen.[28] It is in this context that the importance of fibrinogen binding to hydrophobic and electrically conducting surfaces, such as gold,[29] becomes critical and thus explains why it should be avoided.

The physiological role of the intrinsic pathway of coagulation in diseases is, however, obscure as the pathway is not required for the initiation of hemostasis *in vivo*.[30] The significance of factor XII in thrombosis remains controversial, but in mice, a deficiency of factor XII or factor XI attenuates the development of thrombi.[31,32] Furthermore, inhibition or deficiency of factor XII protects mice from ischemic brain injury without causing hemorrhage.[33] In humans, factor XI deficiency may be associated with a hemorrhagic phenotype. Factor XI may also participate in thrombosis in humans, because a deficiency of this protein is associated with a reduced risk of ischemic stroke but not of myocardial infarction.[34] One important physiological role of the intrinsic pathway in tissues may be the amplification of a developing thrombus.[30] One speculation related to negatively charged biomaterial surfaces is, therefore, enhanced fibrin formation when compared to wounds without implants (shams).

4.406.3.2. Tissue Pathway

There is no tissue factor (TF) activity in normal blood, but TF is captured in wounds by platelet P-selectin and PSGL-1, leading to TF accumulation and thrombus formation at the site of injury.[30] Interestingly, the tissue pathway of coagulation was recently connected to complement activation.[35,36] The observations were that both C3 and C5 are necessary for monocyte- and/or granulocyte-mediated release of TF with a concomitant increase in risk of antiphospholipid antibody-mediated thrombophilia,[35] and a risk of C5a for thrombus formation at endothelial surfaces.[34] Hence, the anaphylatoxin C5a appears to be a key molecule for both the complement and the tissue pathway coagulation systems. The implication of this result for implanted biomaterials is that coagulation, and thus wound healing, is probably modulated via both the complement system and the tissue pathway of coagulation. The significance and details of this, however, remain obscure, and it will be of fundamental interest in the forthcoming *in vivo* studies of complement-activating surfaces.

4.406.4. Immune Complement at Biomaterials

4.406.4.1. Prevailing Model of Activator/Inhibitor Surfaces

The contact of blood with a great majority of biomaterials results in complement deposition on the surface and/or activation of the complement system.[10] Findings from the 1980s showed that the use of extracorporeal devices such as cardiopulmonary bypass oxygenators, hemodialysers,[37,38] and heart–lung machines caused significant systemic inflammation. Blood analyses from cardiopulmonary bypass patients revealed that these patients suffered from ~30 min transient leucopenia which generated soluble inflammatory molecules such as thromboxane B_2 and MPAP. The blood reaction was coupled to a large surface area-mediated complement activation that also generated C5a, a potent anaphylatoxin and inflammatory mediator.[9] It was understood at that time that a common denominator for these activating membrane surfaces was a specific surface chemistry and a large contact area. A high level of activation was observed on cuprammonium cellulose; moderate with cellulose acetate and low with polycarbonate or polyacrylonitrile.[9] Based on these observations, Chenoweth proposed a model for complement-activating surfaces.[10] In this model, surface-triggered activation proceeds via the alternative pathway and is mediated by nucleophilic surfaces exposing hydroxyl (−OH) or amine ($-NH_2$) groups. Negatively charged surfaces were suggested to be nonactivators.

A good, state-of-the-art overview of biomaterials-related complement activation and its clinical implications is found in Nilsson.[39]

4.406.4.2. Spontaneous, Classical, and Alternative Complement Activation

The spontaneous tick-over cleavage in plasma of C3 to reactive C3b* and C3a may be the origin of initial surface deposition of C3b at complement-susceptible surface sites, such as adsorbed and partially denatured plasma proteins and nucleophilic sites, that is, complement activation via the alternative pathway. Surface-bound C3b may in turn bind to the complement factor Bb and Properdin, forming the stabilized alternative convertase C3bBbP, which in turn cleaves more C3, and so on (Figures 7 and 8).

Furthermore, experiments with model surfaces suggest modifications in the Chenoweth model, even though it is basically a good complement activation model. It appears that the alternative pathway is not the only pathway involved in surface-mediated complement activation. Immobilized mercaptoglycerol, mercaptoethanol, and IgG, activate the complement via the classical pathway[40–42] in contrast to activation by immobilized IgA via the alternative pathway.[41] One interesting feature of the different pathway model studies was the rapid surface deposition of complement factor 3b (C3b) upon activation via the classical pathway and slow C3b deposition via the alternative pathway. A few, well-known biomaterials demonstrate complement C3b deposition. Thus, hydrated aluminum (pzc∼8–9) in blood plasma activates and rapidly deposits proteins via the classical pathway,[43] spontaneously oxidized titanium (pzc∼5–6) does this in a mixed manner (Figure 9) and silicon (pzc∼2–3) uses the spontaneous or alternative pathway for activation.[44] These model experiments reveal that the complement mainly binds to already adsorbed proteins, but a minor fraction possibly also binds directly to surface groups.[45] The result is not surprising, as the complement is an integral part of the humoral clearance system whose functions include the removal of denatured proteins and debris. The preclinical and clinical significance of complement activation on biomaterials is not well understood, although, in one *in vivo* study, recognized complement activator surfaces recruited more inflammatory cells than nonactivators to the site of subcutaneous implantation in the rat.[46] This reaction is no surprise either, as the complement system also assists the cellular part of the immune system during organ rejection and in autoimmune diseases.

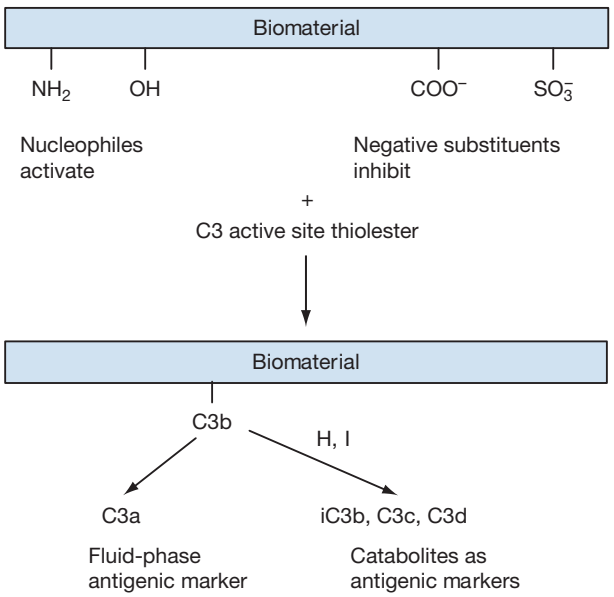

Figure 7 Modified Chenoweth model of complement activation at biomaterial surfaces. Nucleophilic surfaces activate via the alternative pathway and negatively charged surface groups inhibit activation. C3b binds to adsorbed proteins and partly to (material) surface nucleophilic groups.

4.406.5. Consequences of Protein Adsorption

4.406.5.1. Blood Compatibility

Clinical experience indicates that it is very difficult to design a truly blood compatible artificial surface, which, almost without exception, deposits blood proteins. For example, tiny amounts of plasma fibrinogen, $<10\,\mathrm{ng\,cm^{-2}}$ is needed to bind and activate platelets at polystyrene,[47] and all surfaces with hydrophobic character (contact angle in water $>60°$) tend to attract fibrinogen. On the other hand, negatively charged hydrophilic surfaces, comprising the majority of oxide surfaces, activate the intrinsic pathway of coagulation and bind factor XII, HMWK, prekallikrein, C3, and many other proteins; all of these interact more or less with the surrounding cells (Table 3). PEG-like surfaces seem to offer the best compromise with respect to blood compatibility of passive surfaces, the main reason being, of course, the low protein-binding capability, with a concomitant low number of denatured surface-bound proteins and low number of cell-binding sites. Such surfaces are widely used in blood tubings and for biosensor nonfouling prevention. However, platelet and other blood cell activation need not be related to direct platelet binding to surfaces. In one study, circulating and

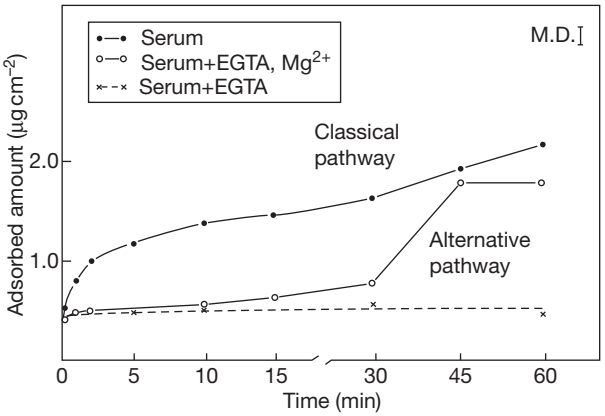

Figure 8 Time course of classical and alternative pathways of complement deposition on model IgG-coated surfaces in whole blood serum, without or with added EGTA or EDTA. Observe the time delay during alternative pathway activation.[40]

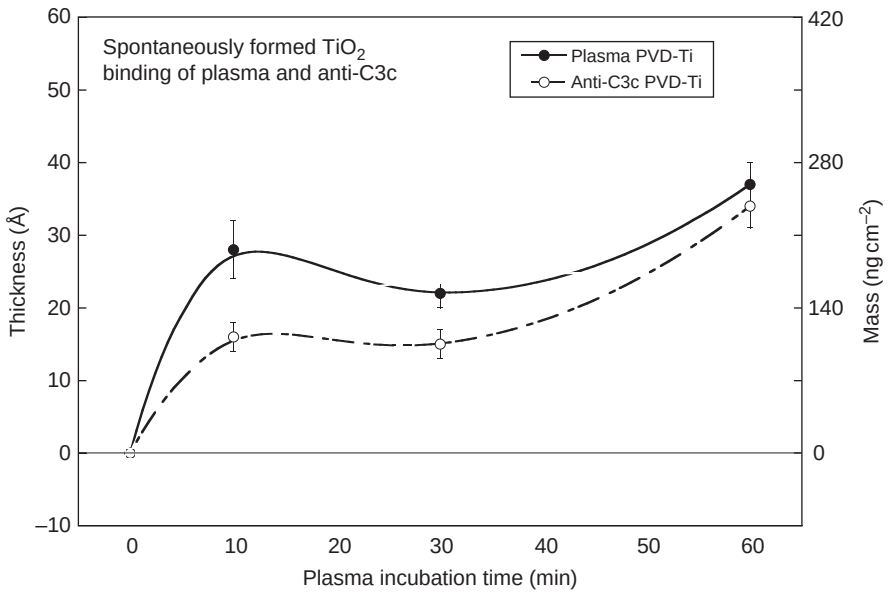

Figure 9 Blood plasma and anti-C3c deposition to spontaneously oxidized titanium that was physically vapor deposited (PVD) to silicon. The plasma value is subtracted from antibody.

surface noncontacted platelets were shown to release their granula contents into the circulation without binding to the test surface.[48] In clinical applications, heparin coatings are often used in blood tubings and large blood-contacting surfaces of heart–lung machines and dialysis apparatus.[49] Immobilized heparin catalyses the degradation of thrombin by the formation of thrombin–antithrombin (TAT) complexes which are subsequently cleared from the circulation. This is, in contrast to PEG, a biologically active surface. Other attempts to mimic low activation or coagulation downregulator surfaces have been made by immobilization of phoshorylcholine[50] and plasminogen to obtain fibrinolytic surface activity via the generation of plasmin.[51]

4.406.5.2. Inflammation and Wound Healing

Adsorbed and partially denatured proteins attract inflammatory cells and redirect, prolong, or enhance the wound healing process around implants. The details of these complex events are not well understood, although it is known that the healing process is different from that at sham sites. Implants in soft tissue become surrounded by a fibrous capsule, more inflammatory cells are recruited to complement-depositing and fibrin-generating interfaces than to sham sites, macrophages and giant cells reside for a long time in tissues outside implants, and the generation of signal molecules is altered during the early healing phase upon the insertion of an implant.[46,52] These changes in the healing process are likely due to changes in communication between implant interfaces and the tissues via adsorbed proteins and activated humoral cascade systems, such as the complement, coagulation, fibrinolytic, and kinin systems, all of which may participitate. The sole presence of a foreign surface is sufficient to change the dynamics of the entire healing process, and can also be observed on the gene level as different materials show quite different gene expressions.[53]

4.406.5.3. Adsorbed Proteins and Biomaterials-Related Infection

Biomaterials-related infection is, according to the traditional Gristina A, 'race for the surface' model, a competition between colonizing bacteria and colonizing tissue cells.[54] Irrespective of the accuracy of this model, adsorbed proteins are sometimes suspected to participitate in bacterial adhesion via host protein-binding adhesins; *S. epidermidis* and *S. aureus* can bind to adsorbed fibrinogen and most likely, also to fibronectin. However, in a recent study on the effect of adsorbed serum proteins and surface colonization via biofilm formation of *S. epidermidis*, it was observed that bacterial biofilm formation was heavily suppressed by adsorbed serum proteins, hydrophobic surfaces were more easily colonized than hydrophilic surfaces, and PEG-coated surfaces resisted biofilm formation very well.[55] The study convincingly shows that adsorbed blood plasma proteins and surface binding strength may assist or resist biomaterials-related infection at the surface, and the response of the surrounding tissue to bacteria is, most likely, much more important in this context.

A recent interesting approach to tissue defense against infection is the identification of antimicrobial peptides (AMPs). The peptides in mammals, defensins, and cathelicidins are expressed by immune and epithelial cells.[56,57] A recent finding shows that many bacteria are killed by the complement anaphylatoxins C3a and C3a-desArg peptide,[58] and C4a.[59] This now opens interesting perspectives, and hypothetically, a sustained short-term tissue infection defense can be an important aspect of complement activation by biomaterials.

4.406.6. Summary and Future Directions

Blood plasma proteins bind to biomaterials. The thickness and composition of the protein film formed vary with surface

chemistry, charge, hydrophilicity/hydrophobicity, water retention capacity, and exposure time. PEG and other hydrogel-like surfaces bind least plasma proteins, and cells often go into apoptosis in such environments. As cells need surface anchorage for proliferation and proper differentiation, this represents an unwanted effect after implantion, but is most often desired in, for example, biosensor applications.

The intrinsic pathway of coagulation is initiated by negatively charged surfaces, and hydrophobic surfaces bind plasma fibrinogen and fibronectin. Complement factor 3b binds to virtually all types of surfaces, although the process may be slow (hours). Cell-surface receptors in turn bind to the adsorbed proteins and change cell expression and activity thereafter.

Future research in this area is needed to increase our understanding of interfacial protein–cell communication, both in the short and the long term. Few studies have until now been devoted to the protein content and biochemistry of the implant-protein film–cell interface, and it is anticipitated that more attention will be given to this aspect in future studies.

References

1. Andrade, J. D.; Hlady, V. *Ann. New York Acad. Sci*. **1987**, *516*, 158–172.
2. Shipman, J.; Wilson, J.; Todd, A. *An Introduction to Physical Science*, 9th ed.; Houghton Mifflin College: Boston, MA, 2001.
3. Price, M. E.; Cornelius, R. M.; Brash, J. L. *Biochim. Biophys. Acta Biomembr.* **2001**, *1512*(2), 191–205.
4. Norde, W. *Adv. Colloid Interface Sci*. **1986**, *25*(4), 267–340.
5. Haynes, C. A.; Norde, W. *J. Colloid Interface Sci*. **1995**, *169*(2), 313–328.
6. Cochrane, C. G.; Griffin, J. H. *Adv. Immunol*. **1982**, *33*, 241–259.
7. Colman, R. W.; Schmaier, A. H. *CRC Crit. Rev. Oncol. Hematol*. **1986**, *5*(I), 57–69.
8. Colman, R. W. *J. Clin. Invest*. **1984**, *73*(5), 1249–1253.
9. Chenoweth, D. E.; Cooper, S. W.; Hugli, T. E.; Stewart, R. W.; Blackstone, E. H.; Kirklin, J. W. *New Engl. J. Med*. **1982**, *304*, 497–503.
10. Chenoweth, D. E. *Ann. New York Acad. Sci*. **1987**, *516*, 306–313.
11. Marchant, R. E.; Wang, I. In *Implantation Biology: The Host Response and Biomedical Devices*; Greco, R. S., Ed.; CRC Press: Boca Raton, FL, 1994; pp 13–38.
12. Spijker, H. T.; Graaff, R.; Boonstra, P. W.; Busscher, H. J.; van Oeveren, W. *Biomaterials* **2003**, *24*, 4717–4727.
13. Xu, L. C.; Siedlecki, C. A. *Biomaterials* **2007**, *28*, 3273–3283.
14. Lestelius, M.; Liedberg, B.; Tengvall, P. *Langmuir* **1997**, *13*(22), 5900–5908.
15. Baier, R. E. *Bull. New York Acad. Med*. **1972**, *48*, 257–272.
16. Kosmulski, M. *Langmuir* **1997**, *13*(23), 6315–6320.
17. Brunelle, J. P. *Pure Appl. Chem.* **1978**, *50*, 1211–1229.
18. http://en.wikipedia.org/wiki/Isoelectric_point, accessed on Nov 15, 2009.
19. Tengvall, P.; Lundstrom, I.; Liedberg, B. *Biomaterials* **1998**, *19*(4–5), 407–422.
20. Wojciechowski, P.; Ten Hove, P.; Brash, J. L. *J. Colloid Interface Sci*. **1986**, *111*(2), 455–465.
21. Scott, C. F. In *The Vroman Effects:* Festschrift in honor of the 75th birthday of Dr. Leo Vroman; Bamford, C. H., Cooper, S. L., Tsuruta, T., Eds.; VSP: Utrecht, 1992; pp 75–83.
22. Andrade, J. D.; Hlady, V. In *The Vroman Effects:* Festschrift in honor of the 75th birthday of Dr. Leo Vroman; Bamford, C. H., Cooper, S. L., Tsuruta, T., Eds.; VSP: Utrecht, 1992; pp 31–42.
23. Vroman, L.; Adams, A. L. *Surf. Sci*. **1969**, *16*, 438–446.
24. Vroman, L.; Adams, A. L. *J. Colloid Interface Sci*. **1986**, 391–402.
25. Nagaoka, S.; Nakao, A. *Biomaterials* **1990**, *11*, 119–121.
26. Hansson, K. M.; Tosatti, S.; Isaksson, J.; *et al*. *Biomaterials* **2005**, *26*(8), 861–872.
27. Colman, R. W.; Scott, C. F.; Schmaier, A. H.; Wachvogel, Y. T.; Pixley, R. A.; Edmunds, L. H. *Ann. New York Acad. Sci*. **1987**, *516*, 253–267.
28. Lindon, J.; Shiba, E.; Kushner, L.; Salzman, E. W. *Arteriosclerosis* **1988**, *8*(5), A725.
29. Kanagaraja, S.; Lundström, I.; Nygren, H.; Tengvall, P. *Biomaterials* **1996**, *17*, 2225–2232.
30. Furie, B.; Furie, B. C. *New Engl. J. Med*. **1992**, *326*, 800–806.
31. Marcus, A. J. *New Engl. J. Med*. **2002**, *347*, 1025.
32. Marmud, J. D. *Circulation* **1996**, *94*, 1226.
33. Massberg, S. *J. Exp. Med*. **2003**, *197*, 41–49.
34. Maynard, J. R. *J. Clin. Investig.* **1975**, *55*, 814.
35. Muhlfelder, T. W.; Niemetz, J.; Kreutzer, D.; Beebe, D.; Ward, P. A.; Rosenfeld, S. I. *J. Clin. Investig*. **1979**, *63*(1), 147–150.
36. Kondo, C.; Mizuno, M.; Nishikawa, K.; Yuzawa, Y.; Hotta, N.; Matsuo, S. *Clin. Exp. Immunol*. **2001**, *124*, 323–329.
37. Hakim, R. M.; Breillatt, J.; Lazarus, J. M.; Port, F. K. *New Engl. J. Med*. **1984**, *311*(14), 878–882.
38. Cheung, A. K.; Henderson, L. W. *Am. J. Nephrol*. **1986**, *6*(2), 81–91.
39. Nilsson, B.; Nilsson Ekdahl, K.; Mollnes, T. E.; Lambris, J. D. *Mol. Immunol*. **2007**, *44*, 82–94.
40. Tengvall, P.; Askendal, A.; Lundstrom, I. *J. Biomed. Mater. Res*. **1996**, *31*(3), 305–312.
41. Tengvall, P.; Askendal, A.; Lundstrom, I. *Biomaterials* **1996**, *17*(10), 1001–1007.
42. Tengvall, P.; Askendal, A.; Lundstrom, I. *J. Biomed. Mater. Res*. **1997**, *35*(1), 81–92.
43. Tengvall, P.; Askendal, A.; Lundstrom, I. *Biomaterials* **1998**, *19*(10), 935–940.
44. Arvidsson, S.; Askendal, A.; Tengvall, P. *Biomaterials* **2007**, *28*(7), 1346–1354.
45. Wettero, J.; Askendal, A.; Bengtsson, T.; Tengvall, P. *Biomaterials* **2002**, *23*(4), 981–991.
46. Kalltorp, M.; Askendal, A.; Thomsen, P.; Tengvall, P. *J. Biomed. Mater. Res*. **1999**, *47*(2), 251–259.
47. Tsai, W. B.; Grunkemeier, J. M.; Horbett, T. A. *J. Biomed. Mater. Res*. **1999**, *44*(2), 130–139.
48. Gemmell, C. H.; Ramirez, S. M.; Yeo, E. L.; Sefton, M. V. *J. Lab. Clin. Med*. **1995**, *125*(2), 276–287.
49. Larm, O.; Larsson, R.; Olsson, P. *Biomater. Med. Dev. Artif. Organs* **1983**, *11* (2–3), 161–173.
50. Kojima, M.; Ishihara, K.; Watanabe, A.; Nakabayashil, N. *Biomaterials* **1991**, *12*(2), 121–124.
51. McClung, W. G.; Clapper, D. L.; Hu, S. P.; Brash, J. L. *J. Biomed. Mater. Res.* **2000**, *49*(3), 409–414.
52. Anderson, J. M. *Annu. Rev. Mater. Res*. **2001**, *31*, 81–110.
53. Awad, H. A.; Wickham, M. Q.; Leddy, H. A.; Gimble, J. M.; Guilak, F. *Biomaterials* **2004**, *25*(16), 3211–3222.
54. Gristina, A. G.; Naylor, P.; Myrvik, Q. *Med. Prog. Technol*. **1988–1989**, *14*(3–4), 205–224.
55. Patel, J. D.; Ebert, M.; Ward, R.; Anderson, J. M. *J. Biomed. Mater. Res. A* **2007**, *80A*(3), 742–751.
56. Ganz, T. *Nat. Rev. Immunol*. **2003**, *3*, 710–720.
57. Zanetti, M. *J. Leukoc. Biol*. **2004**, *75*, 39–48.
58. Andersson Nordahl, E.; Rydengård, V.; Nyberg, P.; *et al*. *Proc. Natl. Acad. Sci. USA* **2004**, *101*(48), 16879–16884.
59. Pasupuleti, M.; Walse, B.; Nordahl, E. A.; Morgelin, M.; Malmsten, M.; Schmidtchen, A. *J. Biol. Chem.* **2007**, *282*(4), 2520–2528.

4.407. Bacterial Adhesion and Biomaterial Surfaces

T F Moriarty, A H C Poulsson, E T J Rochford and R G Richards, AO Research Institute Davos, Davos, Switzerland

© 2011 Elsevier Ltd. All rights reserved.

4.407.1.	**Introduction**	76
4.407.2.	**Laboratory Methods for the Study of Bacterial Adhesion**	79
4.407.2.1.	Static Adhesion Assay	79
4.407.2.2.	Bioreactors	81
4.407.2.3.	Flow Chambers	81
4.407.2.3.1.	Modified Robbins device	81
4.407.2.3.2.	Parallel plate flow chamber	82
4.407.2.4.	Measuring Bacterial Adhesion Forces	82
4.407.3.	**Bacterial Characterization Methods**	83
4.407.3.1.	Structural Characteristics	83
4.407.3.2.	Physicochemical Characteristics	84
4.407.3.2.1.	Bacterial adhesion to hydrocarbons: The BATH test	84
4.407.3.2.2.	Contact angles on bacterial lawns	84
4.407.3.2.3.	Zeta potentials	85
4.407.4.	**Theory and Mechanisms of Bacterial Adhesion**	86
4.407.4.1.	Physicochemical Models of Bacterial Adhesion	86
4.407.4.1.1.	The thermodynamic theory	86
4.407.4.1.2.	The DLVO theory	86
4.407.4.1.3.	The XDLVO theory	86
4.407.4.2.	Forces of Colloidal Adhesion	87
4.407.4.2.1.	Lifshitz–van der Waals: Apolar molecular forces	87
4.407.4.2.2.	Electrostatic forces	87
4.407.4.2.3.	Lewis acid–base: Polar forces	88
4.407.4.3.	Interpreting the Theories	88
4.407.5.	**Mechanisms of Bacterial Adhesion**	89
4.407.5.1.	Nonspecific Adhesion	89
4.407.5.2.	Specific Adhesion	90
4.407.6.	**The Influence of Biomaterial Surface Properties on Bacterial Adhesion**	91
4.407.6.1.	The Influence of Surface Chemistry on Bacterial Adhesion	91
4.407.6.2.	The Influence of Surface Topography on Bacterial Adhesion	92
4.407.7.	**Strategies to Reduce Bacterial Adhesion**	94
4.407.7.1.	Highly Charged Surfaces	94
4.407.7.2.	Low Surface Energy Materials	95
4.407.7.3.	Polymeric Coatings Including Polymer Brushes	95
4.407.7.4.	Bifunctional Polymer Brush-Like Coatings	95
4.407.7.5.	Plasma Activation and Coatings	95
4.407.8.	**Summary and Perspectives**	96
References		98

Glossary

Bacteria Unicellular, prokaryotic (lacking a membrane-bound nucleus) microorganisms that rarely harbor membrane-bound organelles.

Colloid A colloid is defined as nonliving particles dispersed homogeneously within another substance (e.g., milk).

Colonization The presence of bacteria on or in a biomaterial without tissue invasion.

DLVO theory The DLVO theory is a physicochemical equation used to model simplified bacterial adhesion. The theory includes the effects of charge and van der Waals forces.

Electrostatic forces Electrostatic forces arise when two charged surfaces interact. Atoms with opposite charge signs attract while those with similar charge signs repel. The magnitude of this force is dependent on the overall charge of the surfaces and the ion content of the solution surrounding them.

Infection Invasion and multiplication of microorganisms in body tissues.

Lewis acid–base: polar forces Lewis acid–base interactions or polar forces are based on electron-acceptor–electron-donor interactions between polar moieties, in polar media (such as water).

Lifshitz–van der Waals forces Lifshitz–van der Waals (LW) are electrodynamic interactions arising from the attraction or repulsion of molecules due to the unequal distribution of electrons between bound atoms.
Nonspecific bacterial adhesion Bacterial adhesion resulting from a combination of physicochemical forces, excluding specific adhesin bonding.
Opportunistic infection Infection by an organism that does not ordinarily cause disease but becomes pathogenic under certain circumstances, for example host immunosuppression.
Polar forces See Lewis acid–base interactions.
Specific bacterial adhesion Adhesion mediated by highly specific, stereochemical interactions between complementary components on the interacting surfaces such as adhesins.
Surface energy Quantifies the disruption of chemical bonds that occurs when a surface is created.
Thermodynamic theory The thermodynamic theory is a physicochemical equation used to model simplified bacterial adhesion. The theory includes the effects of van der Waals forces and polar interactions.
XDLVO theory The XDLVO theory is a physicochemical equation used to model simplified bacterial adhesion. Like the DLVO theory, the XDLVO theory includes the effects of charge and van der Waals forces. Additionally polar forces are included in the model.

Abbreviations

AFM	Atomic force microscope
ATCC	American Type Culture Collection
BATH	Bacterial Adhesion to Hydrocarbons
CDC – Biofilm reactor	Center for Disease Control and Prevention Biofilm Reactor
cpTi	Commercially pure titanium
cpTi-EP	Commercially pure titanium – electropolished
cpTi-S	Commercially pure titanium – standard microrough
DLVO Theory	Derjaguin, Landau, Verwey and Overbeek theory
ECM	Extracellular matrix
EDL	Electrical double layer
GFP	Green fluorescent protein
MATH test	Microbial adhesion to hydrocarbon
MATS	Microbial adhesion to solvents
MRD	Modified Robbins device
MSCRAMM	Microbial surface components recognizing adhesive matrix molecules
PBS	Phosphate buffered saline
PLL-g-PEG	poly(L-lysine)-graft-poly(ethylene glycol)
PMMA	Polymethyl methacrylate
PPFC	Parallel plate flow chamber
PVC	Polyvinyl chloride
PVD	Plasma vapor deposition
RF	Radio frequency
RGD	arginine-glycine-aspartic acid
X-DLVO	Extended Derjaguin, Landau, Verwey and Overbeek theory

4.407.1. Introduction

One of the most common and serious complications associated with the implantation of any biomaterial into a biological system such as the human body is bacterial infection. Bacterial colonization of a biomaterial through contamination can lead to the development of an infection, which is notoriously difficult to treat. These infections are associated with significant patient morbidity, prolonged treatment times, delays in healing, and in many cases, costly surgical procedures for removal and implantation of a new implant.[1] All biomaterials, ranging from the most simple and commonplace such as sticking plasters, to life-supporting and more complex devices such as cardiac pacemakers, are at risk of bacterial colonization and the subsequent development of an infection. These infections may occur at virtually any stage in the life-cycle of the biomaterial, from pre- or perioperative stages, to months or even years postoperatively. In all instances, however, the presence and growth of bacteria in the vicinity of the biomaterial represents failure of the device, despite the fact that the device may otherwise be free of any material or functional defects.

Many implanted biomaterials are intended for long-term implantation and are designed to be integrated into the tissue of the host. The fate of these biomaterials upon implantation, that is, whether the biomaterial successfully integrates or an infection develops, has been described as the result of the race for the surface.[2] According to this description, the implant becomes primed for cellular adhesion by the formation of a layer of host extracellular matrix proteins immediately upon implantation into the body. Following this conditioning of the surface, both host cells and potentially also bacteria, compete to colonize the available surface. Should the host cells win the race for the surface, any subsequently approaching contaminating bacteria would meet an intact cellular layer that is accessible to the host immune system. In this scenario, successful colonization of the biomaterial surface by bacteria is considered to be much less likely. Conversely, should bacteria win the race for the surface, then the bacteria are afforded an opportunity to adhere to the biomaterial, grow, spread, and fully colonize the implant surface. Once colonized by bacteria, the biomaterial is much more likely to inhibit cellular adhesion, limit tissue integration, and the development of an infection is favored.

Obviously, not all implants develop an infection, and furthermore not all implanted devices are colonized by bacteria (**Chapter 4.410, Sterilization of Biomaterials of Synthetic and Biological Origin**). The factors and processes that can influence the outcome of the race for the surface and determine whether or not a particular biomaterial may become infected or not, arise out of a complex interplay between the competing factors of (1) the contaminating bacteria, (2) the host, and (3) the device/biomaterial itself. These three factors plus their interdependent relationships comprise what is known as the biomaterial-associated infection triangle, shown in **Figure 1**.

The first apex in the biomaterial-associated infection triangle represents the implanted device or the biomaterial of which it is composed. On a fundamental level the surface topography and chemistry of the biomaterial(s) are known to influence the way and the numbers in which contaminating bacteria adhere to the biomaterial. The topic of biomaterial surface chemistry and topography and their influence on bacterial adhesion will be discussed at length in **Section 4.407.6**.

On a practical level, the wide variation in the function, anatomical location, and mechanical impact of the device on the surrounding tissues contribute significantly to the variability in the incidence of infection between different devices (**Chapter 6.609, Orthopedic Implant Use and Infection**). For example, percutaneous devices such as polymeric catheters or metal external fixation pins create a path through the normally protective barrier provided by the skin and are thus particularly prone to infection. Devices which are completely implanted, on the other hand, such as cardiac pacemakers, or intramedullary nails are less susceptible by comparison with percutaneous devices, yet are also susceptible to infection arising out of perioperative contamination or hematogenous seeding. The development of the modern fracture fixation plate serves as an example of the effect of mechanical impact on infection. The original fracture fixation plates bridge the fracture and compress the two bone fragments together and create local periosteal necrosis at the point of contact. In an effort to minimize necrosis, which is an obvious negative aspect of these devices, design modifications were incorporated to protect the periosteum and minimize necrosis. The new devices offered greater protection of the local tissues and this was found to significantly improve resistance to infection.[3] Infections associated with short-term, external implants such as contact lenses[4] or dentures,[5] are also commonplace; however, these are obviously more easily treated, as the colonized biomaterials are easily removed.

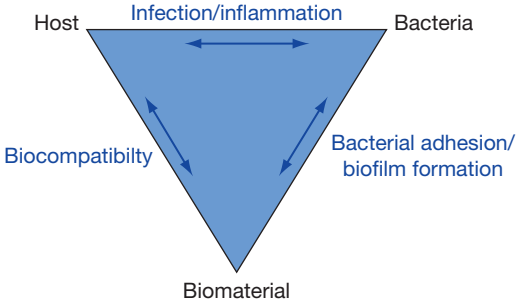

Figure 1 The biomaterial-associated infection triangle.

The second apex in the biomaterial-associated infection triangle represents the host, which plays a very critical role in the development of infection. The factors involved include the medical status of the patient, any comorbidities, wounds, skin lesions, bone fractures, or prior infections.[6] Similarly, the operative conditions in which the device was implanted, the antibiotic prophylaxis administered and postoperative care afforded to the patient will influence the development of infection.[7,8] All these factors can affect susceptibility to infection independent of any interaction with the biomaterial or contaminating bacteria. Aside from these, the host is also involved in crucial interrelationships with the biomaterial. The interaction between the host and the biomaterial is expected to vary somewhat from biomaterial to biomaterial, that is, the host will interact differently with different biomaterials dependent upon the nature of the implanted biomaterial. In general, however, it has been established that the host's ability to clear and eliminate contaminating bacteria is compromised in the vicinity of implanted biomaterials.[9] Frustrated phagocytosis and opsonin deficiency have been observed adjacent to biomaterials.[9,10] The details of the host response to implanted biomaterials and how this impacts upon the development of infection is outside the scope of this chapter and so for further information on this topic, the reader is directed toward some relevant literature.[9–13]

The third and final apex in the biomaterial-associated infection triangle represents the contaminating bacteria and their potential to colonize the biomaterial and/or surrounding tissue. As a brief introduction to the nonbiologist, bacteria are unicellular, prokaryotic (lacking a membrane-bound nucleus) microorganisms that rarely harbor membrane-bound organelles. Bacteria typically range in size from 0.5 to 5 μm in length and the most common physical characteristic used to differentiate bacteria is cell shape or morphology. The most common and simple morphologies include spherical cells (cocci) and elongated rod-shaped cells (bacilli) (**Figure 2**). Bacteria may also be differentiated on the basis of the structure of the cell wall into Gram-positive and Gram-negative (further described in **Section 4.407.3.1**).

Bacteria and eukaryotic cells differ significantly from each other in their growth rate. In a laboratory environment, with optimal nutrient and temperature requirements, the specific growth rate of many commonly encountered bacteria in the

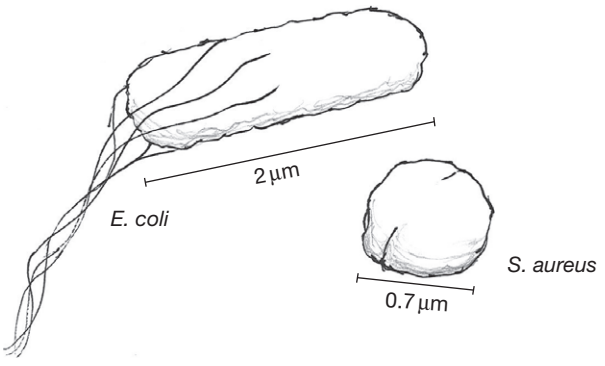

Figure 2 A simplified schematic of two bacterial species *Escherichia coli* (bacillus) and *Staphylococcus aureus* (coccus).

logarithmic phase of growth may be extremely high in comparison with eukaryotic and particularly many mammalian cells. A bacterial species such as *Escherichia coli* may have a cell doubling time as short as 20 min under ideal conditions in the laboratory, while eukaryotic cells may have a doubling time of anywhere between 6 and ~24 h. The growth rate *in vivo* may be significantly reduced, particularly should a sessile community known as a biofilm develop. Another important point to note with respect to bacterial adhesion to biomaterials is the fact that each species of bacteria includes innumerable strains. A bacterial strain is defined as a subset of a bacterial species differing from other bacteria of the same species by some minor, but identifiable difference. Strains within a species may differ slightly from one another in many ways such as their ability to utilize nutrient sources or some minor morphological differences, or as described here, they may also differ with respect to their ability to adhere to host proteins and biomaterials.

The most common bacterial species encountered in biomaterial-associated infections are opportunistic pathogens, that is, bacteria that do not normally cause infections in a healthy host. The bacteria involved are often normal or transient residents of the human skin such as the Gram-positive *Staphylococcus aureus* or *S. epidermidis* and sometimes Gram-negative species such as *E. coli* or *Pseudomonas aeruginosa* (**Figure 3**).

Many of these species are commonly present on the skin of a large percentage of the human population at any given time and it is a combination of decreased host ability to resist infection coupled to the insertion of a biomaterial that can, in a certain percentage of cases, afford these bacteria the opportunity to cause an infection. The contaminating bacteria thus progress from innocent, relatively harmless bystanders, to the agents responsible for the failure of the device, courtesy of implantation of a biomaterial into a host with a localized deficiency, in its ability to fight an infection.

The bacterial species and strains that successfully adhere to a biomaterial and cause an infection do so via the use of numerous virulence factors. Virulence factors may enable bacteria to adhere to biomaterials, surrounding tissue or extracellular matrix proteins, to grow and develop on the cell/biomaterial surface, and resist host defense mechanisms. The single biggest factor in the pathogenesis of bacterial infection associated with biomaterials is the ability of a microorganism or microorganisms to develop a biofilm on the surface of an implanted biomaterial. According to its definition, a biofilm is a sessile bacterial community characterized by cells that are irreversibly attached to a substratum or interface or to each other. These bacteria are embedded in a matrix of extracellular polymeric substances that they have produced, and exhibit an altered phenotype with respect to growth rate and gene transcription.[14] The first step in the development of the biofilm is the initial contact between the contaminating bacterium and implanted biomaterial, and from this first step, infection can develop via the numerous stages of biofilm development (for details see **Figure 4**). Once a biofilm has formed on the device, surrounding tissues may be damaged as a result of the host response to the infection and adjacent tissues may also get infected. In addition, the biofilm is often much more resistant to antibiotic treatment than the free living, individual contaminating bacteria, which had initially adhered to the implant,[15] despite the fact that antibiotic penetration into the biofilm is not necessarily restricted.[16] Faced with an antibiotic-resistant biofilm, the only solution likely to result in successful elimination of the infection is to surgically remove the device, if implanted, followed by antibiotic therapy. The delays in healing, increased patient morbidity and significant costs mean that biomaterial-associated

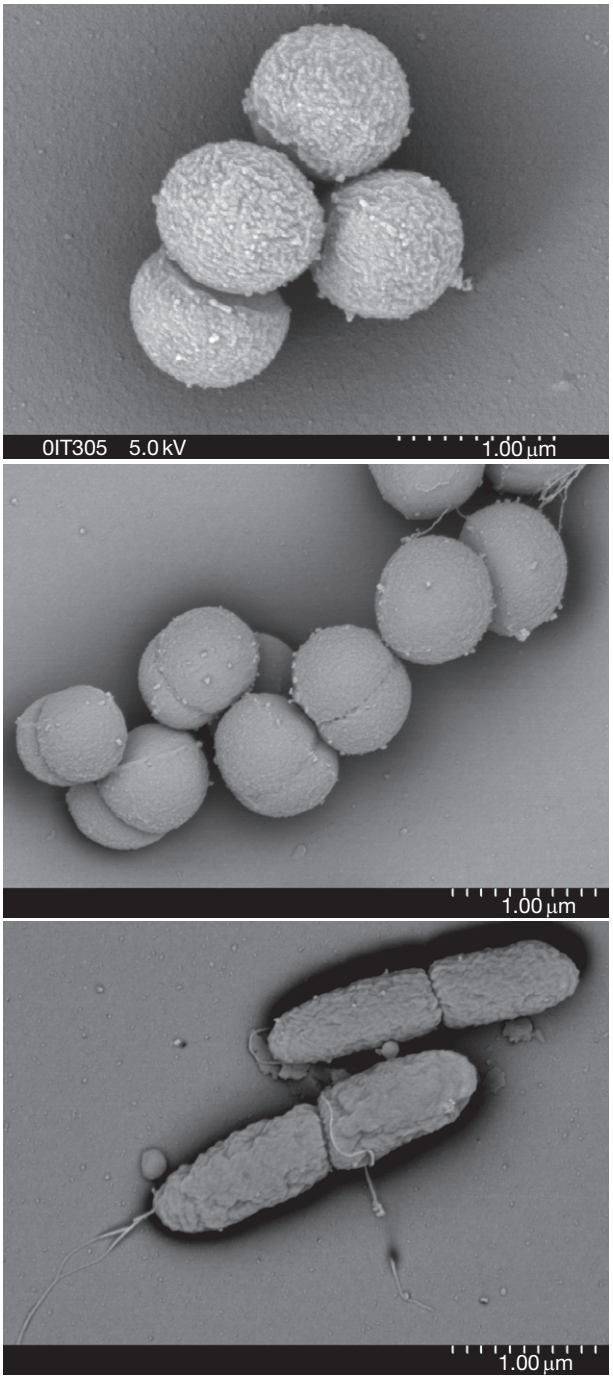

Figure 3 Some commonly isolated bacteria from biomaterial-associated infections. Top to bottom: *Staphylococcus aureus* (~1 µm diameter), *Staphylococcus epidermidis* (~1 µm diameter) and *Pseudomonas aeruginosa* (~0.5 µm wide, 2 µm long).

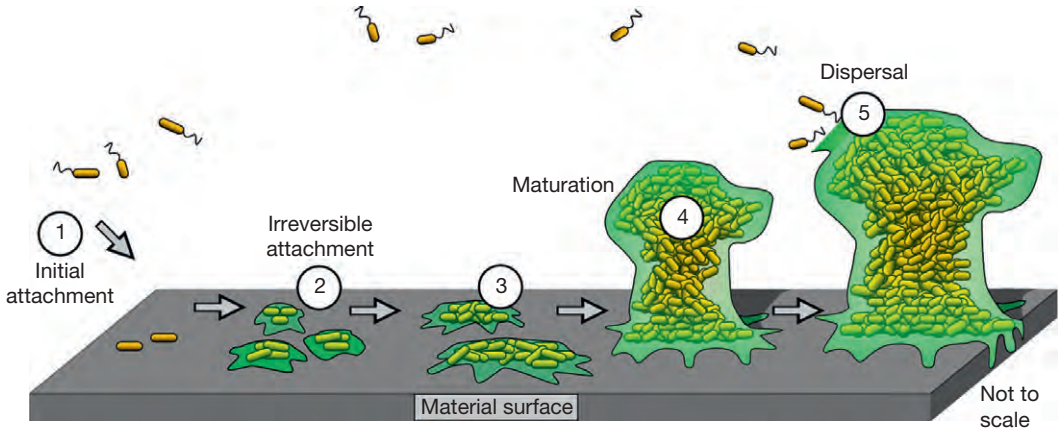

Figure 4 Diagram illustrating the main stages of bacterial biofilm formation.

infections are considered a significant clinical problem. For further details on biofilm formation and associated problems please refer to the published literature where many relevant reviews can be found.[14,17–19]

The significance of bacterial adhesion on biomaterial-associated infection should not be underestimated, considering that the number of adherent bacteria, their ability to grow and spread on the biomaterial surface, and their potential to spread to surrounding tissues and organs, all depend upon this initial interaction between bacterium and biomaterial. The implanted biomaterial will significantly influence these events, and basic research questions involving why contaminating bacteria may adhere more or less abundantly to any particular biomaterial are important fundamental questions that have been extensively investigated by the scientific community. The parameters which influence bacterial adhesion to a biomaterial, the methods used to measure this adhesion, and the theories developed to explain it will all be discussed in this chapter.

A biomaterial is defined as a nonviable material used in a medical device intended to interact with biological systems.[20] This definition has, however, more recently been expanded to include tissue engineered materials,[21] which may also include cells preimplantation. Due to the wide range of biomaterial applications, this chapter will aim to describe bacterial adhesion to a multitude of material types as well as composite materials. Also applicable is a multitude of device types from wound healing plasters, bandages, dentures, and contact lenses, to sutures, catheters, external fixation devices, artificial hips and knees, stents, and cardiac pacemakers. Finally, surface modification has become a major field of work in biomaterial science to improve various aspects of currently available biomaterials, and we will describe the effects of numerous modifications of biomaterial surfaces on bacterial adhesion as well as modifications designed to create so-called bacteria-repellent biomaterials.

4.407.2. Laboratory Methods for the Study of Bacterial Adhesion

The initial adhesion of bacteria to a biomaterial is an important step in the pathogenesis of biomaterial-associated infection. Studies on these initial adhesion events play an important role in the evaluation of a biomaterial, particularly those expected to be exposed to bacterial contamination, such as contact lenses, or those with antiinfective or bacteria-repellent properties, such as polymer brushes or antimicrobial coated surfaces on catheters. Despite the fact that a vast amount of published literature is available characterizing bacterial adhesion to a wide range of biomaterial types, a relatively limited number of techniques are in regular use for the estimation of bacterial adhesion to such surfaces. The laboratory techniques routinely used to measure bacterial adhesion to biomaterial surfaces range from the simple static adhesion assay in which test surfaces are immersed in a bacterial suspension, to the more advanced bioreactors and flow chambers, which can allow measurement of bacterial adhesion under controlled hydrodynamic conditions. The most sophisticated technology currently employed to evaluate bacterial adhesion to biomaterials allows measurement of the strength of adhesion of an individual bacterium to a particular biomaterial surface. This is achieved using modern biophysical approaches such as AFM, optical tweezers, and micromanipulation.

Depending on the actual application of the biomaterial, the choice of technique and experimental approach used to evaluate the interaction between bacterium and biomaterial can, and should, vary. Particularly, the technique used should replicate as much as possible the interaction between bacteria and the surface under the conditions expected to be encountered *in vivo*, particularly with respect to hydrodynamics. Regardless of the biomaterial used, the interpretation of the results of a bacterial adhesion study will be greatly assisted by parallel investigations into bacterial and biomaterial properties and an awareness of the influence each property can have on the interpretation of results (**Box 1**).

4.407.2.1. Static Adhesion Assay

The most commonly reported test method to assess bacterial adhesion to biomaterials is the static adhesion assay. This is because the assay is simple to perform and does not require specialized equipment or advanced personnel training. In a standard static adhesion assay, a sample of the biomaterial to be tested is immersed in a suspension of bacteria for a

Box 1 Important considerations for laboratory procedures investigating bacterial adhesion to biomaterials

Preparation of the biomaterial sample	The preparation protocol should be identical to, or as close as possible to, commercial protocols (if relevant). This includes any cleaning and sterilization protocols and should be replicated exactly for each sample
The physical and chemical properties of the biomaterial	For a full characterization of the biomaterial, the data to be collected should include; surface roughness, surface wettability (hydrophilicity/hydrophobity and surface charge), surface chemical composition and finally whether the surface swells or even dissolves when immersed in fluid. Any changes in these factors can lead to a significant change in the bacterial adhesion profile
Conditioning film	Under *in vivo* conditions the biomaterial is immediately covered by a conditioning film of proteins and solutes. The presence or absence of a conditioning film can have a profound effect on the adhesion of bacteria to the biomaterial and can be an important factor in the evaluation of bacterial adhesion to any biomaterial
Solution choice and molarity	The ionic content of the medium used to suspend the bacteria will have an influence on the results, both in theory (see **Section 4.407.4**) and also in practice. A standard molarity buffer solution such as PBS is most commonly utilized; however, use of physiological fluids, nutritive culture media or changing solution molarity or pH can influence the results of the study
Bacterial species	The choice of the most appropriate bacterial species to be selected is dependent on the biomaterial under investigation and the potential uses of the biomaterial. The most common bacteria used in biomaterials testing include *Staphylococcus epidermidis*, *S. aureus*, *Pseudomonas aeruginosa*, and *Escherichia coli*. Dependent upon application, however, other more relevant organisms should be chosen. For example biomaterials with an intended use in the oral cavity should consider using an oral species of bacteria such as *Streptococcus mutans*
Source and number of bacterial strains	Recently cultured, clinical isolates may provide the most clinically relevant bacterial adhesion data, however, use of a freely available laboratory strain will increase cross reference with other studies performed on the same strain. There is also a recommendation that at least three strains from any given species should be tested to account for the variation observed within strains of the same species
Physical and chemical properties of the bacteria	The bacteria-related characteristics that can influence adhesion should be characterized such as; exopolymer production, presence of a capsule, surface hydrophobicity, surface charge, and bacterial motility should be described when appropriate (see **Section 4.407.3**)
Bacterial inoculum preparation method	The choice of nutritive medium, the density of bacteria added to the sample, the final suspension medium/fluid, number of washes in saline solution and the phase of growth of the bacteria can all have an influence on bacterial adhesion and should be standardized
Bacterial enumeration method	This may be achieved by plating, microscopy, turbidometry, flow cytometry, radiolabeling, fluorescent staining, antibody detection or biomass evaluations. The relative benefits and drawbacks of each of these methods are shown in **Table 1**
Bacterial removal method (if required)	Prior to enumeration of adherent bacteria, it is common for protocols to include steps to allow loosely adherent cells to be removed from the sample. An important consideration for such steps is that it involves the passage of the material through an air liquid interface which can disturb some weakly attached bacteria. If possible, a standardized rinsing procedure should be reported and followed to aid reproduction in other laboratories. In many adhesion protocols, the adherent bacteria are forcibly removed from the surface for subsequent enumeration. The use of sonication has become a common method for such bacterial removal, with methods utilizing chemical removal agents such as Tween or Trypsin sometimes used

Table 1 Bacterial enumeration and visualization methods

Method	*Benefit*	*Drawback*
Sonication followed by agar plating	Reproducible, allows multiple samples to be measured in one experiment	Laborious, requires removal of bacteria from surface and is time consuming
Microscopy	Accurate	Often requires transparent substrate or fixation. Many fields of view must be visualized to obtain a reliable estimation: laborious
Turbidometry/ spectrophotometry	Simple, quick	Measurements of optical density display much reduced sensitivity and accuracy
Fluorescent labeling	May allow microscopy on nontransparent materials	May alter bacterial cell surface and adhesion properties and many fields of view must be visualized to obtain a reliable estimation. Not suitable for autofluorescent biomaterials
Radiolabels	Accurate, sensitive	Safety and cost issues. Requires removal of bacteria from surface, time consuming
Biomass estimation	Simple and quick	Reduced accuracy
Antibody labeling	May be fluorescently labeled to allow visualization on non transparent biomaterials	Laborious and many fields of view must be visualized to obtain a reliable estimation
Flow cytometry	Quick measurement of even mixed populations of bacteria	Laborious, requires removal of bacteria from surface

predetermined period of time, after which the adherent bacteria are enumerated and compared against adhesion to control surfaces. The assay is simple and inexpensive, reliant merely on the availability of the biomaterial in suitable, relatively flat, samples. For example, Harris *et al.*[22] uses the static adhesion assay to assess the effect of surface topography on bacterial adhesion between different orthopedic materials and found that under the conditions of the assay, a smooth surface can result in a reduction in bacterial adhesion for some materials in comparison with microrough equivalents. The static adhesion assay, however, is not standardized and numerous variations in the methodology are common, making comparison between published findings difficult. Static adhesion-type studies also suffer in respect of sampling time, hydrodynamics, and methods for enumeration. Results from a static adhesion assay are measured at a single point in time after a predefined incubation period. Bacterial adhesion at other time points is not measured, which can result in biomaterial-related influences on bacterial adhesion being missed due to reduced sampling times. A second limitation of the static adhesion assay is the fact that the very limited hydrodynamic forces exerted upon the sample are not representative of the clinical situation. A proportion of bacteria adherent on the biomaterial sample will have adhered as a consequence of sedimentation due to gravity; however, sedimentation is expected to contribute minimally to the total amount of bacterial adhesion in many biomaterial applications. For example, in a dynamic fluid such as is present around catheters, any bacteria that approaches the biomaterial, does so in fluid flow rather than sediment through a still solution. The approach of a bacterium to a catheter surface is thus not realistically replicated in static adhesion assays. Finally, to allow enumeration and quantification of the adherent bacteria, the sample coupons are routinely passed through air liquid interfaces and the number of adherent bacteria is determined after serial dilution and plating onto nutrient agars. However, the passage of the coupon through an air liquid interface can potentially cause reproducibility and standardization issues, due to the fact that an unknown amount of bacteria will be removed during each passage through this interface (**Box 1**).

To overcome these issues and provide a better model to investigate bacterial adhesion in more natural environments where hydrodynamics are an important factor, it is increasingly common to see such investigations performed using bioreactors or flow chambers (**Table 1**).

4.407.2.2. Bioreactors

The equipment utilized to perform bacterial adhesion assays under conditions of controlled hydrodynamics broadly fall under two main apparatus types: bioreactors and flow chambers. Bioreactors provide an environment that allows for the controlled interaction between bacteria and biomaterial with the facility for easy sample removal and evaluation of the number of adherent bacteria or the interaction via culture, microscopy, etc. Examples of bioreactors include annular reactors, rotating disc reactors, and the CDC Biofilm reactor. Typically, these reactors are batch apparatus, whereby, bacterial suspension is added to the experiment chamber containing the material samples to be tested, the suspension is then mixed with the samples for a set period of time, and the number of adherent bacteria calculated after this period of time. Typically, bioreactors are used to measure both bacterial adhesion, and subsequent biofilm growth and the results published are generally a combination of these two features (e.g., see Murga *et al.*)[23]

4.407.2.3. Flow Chambers

Flow chambers differ from the bioreactors in ct that, the liquid to which the samples are exposed is continuously refreshed from an external source. Solutions are streamed past the samples at a controlled rate and bacterial adhesion under these conditions can be measured. Flow chambers are particularly useful in modeling *in vivo* flow situation, for example, blood flow. The two most commonly reported flow chambers are the modified Robbins device (MRD) and the parallel plate flow chamber (PPFC).

4.407.2.3.1. Modified Robbins device

The MRD is a multiple sample flow chamber used for quantifying bacterial adhesion after set time periods.[24] In the MRD, samples of biomaterials are placed in series in a fixed position within a chamber and essentially form part of the channel through which the bacteria in suspension is passed (**Figure 5**).

In a standard experiment using an MRD, a bacterial suspension flows through the device for a set period of time usually followed by the passage of a bacteria free solution to remove loosely and nonadhered bacteria. The sample materials are then removed and the adherent bacteria are visualized or enumerated to give the number of adhering bacteria under

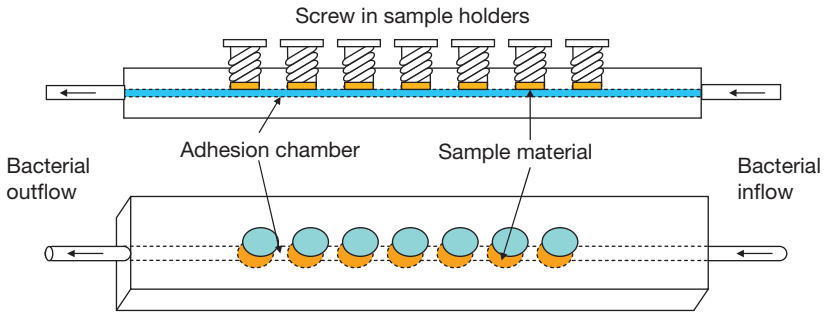

Figure 5 A schematic of a modified Robbins device.

the experimental conditions. The MRD and other similar flow chambers allow fine control of fluid hydrodynamics, are capable of holding multiple samples of biomaterials, and allow quick generation of data. One example of the use of a MRD is the study of bacterial adhesion to cyanoacrylate tissue adhesives, in which adhesion was determined to progress quickly to biofilm formation and there was no or weak bactericidal activity of the material.[25] The use of MRDs has come under scientific scrutiny due to the gradient of conditions along the length of the apparatus, such as a change in temperature and fluid flow rate. Linton *et al.*[26] demonstrate this gradient by illustrating the changing level of adhesion from the proximal to distal samples within the chamber. Despite this, the MRD is still routinely used in laboratories, for example, in the measurement of disinfection efficacy testing of contaminated surfaces.[27]

4.407.2.3.2. Parallel plate flow chamber

Static adhesion assays, bioreactors, and the MRDs are popular due to their ease of use and ability to generate data from multiple samples simultaneously; however, the results are recorded at a single point in time. To generate a continuous dataset of bacterial adhesion, in a non destructive manner, PPFCs are commonly used.[28,29] Numerous flow chambers are commercially available and many custom made versions have also been described in the literature. The construction of PPFCs involves placement of a transparent piece of the sample biomaterial in a chamber, while another piece of transparent material above it seals the chamber to create a channel (**Figure 6**). This setup generates a window through which bacterial adhesion within the channel may be visualized. A pump and tubing system allows a bacterial suspension, or other fluid such as PBS, to flow through the chamber at a controlled rate. Through the use of a microscope and camera, images are regularly captured and the adhesion of bacteria to the material may be monitored. The benefit of the PPFC is that

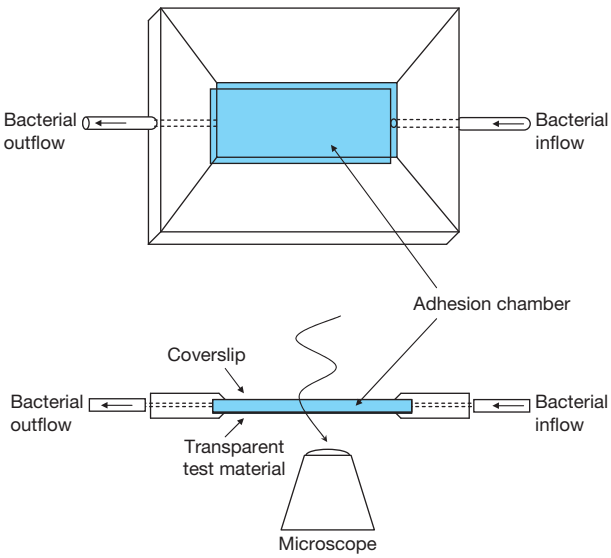

Figure 6 Schematic of a parallel plate flow chamber, top: plan image, bottom: cross-section.

the interaction between bacteria in solution and the biomaterial can be observed in real time and there is no requirement to rinse samples or estimate numbers through plating. Adherent bacteria may then be counted manually or automatically by utilizing computer analysis software on the captured images.

A standard PPFC setup uses light microscopy, therefore, transparent substrates must be used which precludes use of many materials, such as metals, ceramics, or polymers. Various strategies have been employed to overcome this limitation. One such strategy has been to deposit extremely thin films of the material in question onto glass slides. This allows bacterial adhesion to be visualized by light microscopy through the thin coating. This has been achieved, for example, by deposition of titanium onto glass slides.[30] However, coating a glass slide with such a thin film creates a surface that is not chemically or physically identical to the biomaterial one wishes to study, and this may result in a bacterial adhesion pattern that differs from that to the biomaterial under investigation. Another method used to visualize adherent bacteria on nontransparent materials involves the fluorescent labeling of bacteria. However, the fluorescent labeling may influence the surface properties of the bacteria and such an effect could have an impact on the adhesion pattern of the bacteria and should be checked prior to use.[31] Green fluorescent protein (GFP)-labeled bacteria, which have been genetically modified to intrinsically produce a GFP, can also be used to measure bacterial adhesion to nontransparent biomaterials using a fluorescence microscopy and are considered to have a reduced impact on cell surface properties in comparison with fluorescence labeling using a dye. GFP-labeled bacteria are a viable option for testing bacterial adhesion on nontransparent biomaterial surfaces[32]; however, in the case of highly autofluorescent biomaterials, such as most polymers, alternative solutions are required due to the high level of background fluorescence from the material preventing the detection of the fluorescently labeled bacteria.

The PPFC has recently been used to mimic the competition for adhesion between contaminating bacteria and host cells that occurs in a host implanted with a biomaterial in the presence of contaminating bacteria.[33] The adhesion of bacteria to a surface is followed by mammalian cell adhesion, with an ensuing competition for the available surface, that is, the race for the surface as described by Gristina.[2] The outcome of such an experiment can provide an indication of the biomaterial-related factors that influence the race for the surface and may develop into an important tool for biomaterial–bacterial interaction studies, helping to bridge the gap between *in vitro* studies and the clinical situation.

4.407.2.4. Measuring Bacterial Adhesion Forces

In addition to quantifying the number of bacteria adherent to a biomaterial surface, a number of other measurements of interest may also be made. Measurement of dynamic changes during the adhesion of a bacterium to a biomaterial surface may be achieved by the use of a quartz crystal microbalance[34] or surface plasmon resonance.[35] However, these studies have not been extensively used for biomaterial-related investigations into bacterial adhesion as yet. The strength or quality of adhesion of a bacterium to a biomaterial surface may be measured

by methods such as fluid dynamic gauging[36] or jet impingement,[37] although these techniques are rarely cited in the literature. In jet impingement, an incompressible, Newtonian fluid jet impinges on a smooth rigid surface. The resultant pressure forces diminish rapidly away from the jet axis. By directing the jet at a layer of bacterial or mammalian cells, the area from which the cells have been removed provide information as to the detachment strength between the cell and the material.[37] The jet impingement technique allows much variation in jet velocity, exposure time, and the cells and materials that may be used; however, it requires some technical expertise and is not commonly used in experimental studies involving bacterial adhesion.[37] The quality or strength of adhesion is more commonly measured in a PPFC, whereby the number of adherent bacteria can be quantified on a biomaterial surface before and after the passage of an air bubble through the flow chamber. The passage of the bubble through the flow chamber results in detachment force, which will remove a proportion of the adherent bacteria from the biomaterial. The proportion removed is dependent upon the strength of the adhesion.[30]

To directly measure the adhesion strength of a bacterium to a biomaterial surface, critical force techniques such as optical tweezers, atomic force microscopy (AFM), and micromanipulation may be employed. Optical tweezers have been used in a limited capacity to date to measure bacterial adhesion to materials and have centered on measurement of the specific adhesion of bacteria to proteins rather than specifically to biomaterials. Using AFM and related techniques, it is now increasingly common to physically probe biomaterial samples to measure the forces involved in bacteria–material interactions on a nanometer and subnanometer scale.[38–43] Force measurements in the pN to nN range may be detected by AFM and this has been used to measure the interaction between bacterial cell surfaces and biomaterials.[40] AFM probes composed of the biomaterial under investigation are capable of probing bacterial lawns and measuring the forces between the biomaterial and the bacteria. Due to the limited availability of many newer biomaterials in a form suitable to be appended to an AFM tip, an alternative strategy has been developed, whereby the bacteria are actually attached to the AFM tip and used to probe the biomaterial.[41] One example of the use of AFM in bacterial adhesion studies was to show the effect of topography on the resistance of *S. aureus* to removal by physical force.[44] Bacteria on abraded stainless steel surfaces were found to require twice the force to remove than those on polished stainless steel. The use of AFM has allowed for a greater understanding of the interaction forces between bacteria and biomaterials and has immense potential to contribute further understanding and potentiate developments to limit or prevent bacterial adhesion to biomaterials (**Chapter 3.302, Atomic Force Microscopy**).

4.407.3. Bacterial Characterization Methods

As described in **Section 4.407.2**, there are many ways to quantify bacterial adhesion to a surface. However, to gain a better understanding of why bacteria adhere in greater or fewer numbers to any biomaterial one must have an understanding of not only the biomaterial but also the characteristics of the bacteria. Despite the relative simplicity of a bacterial cell, there is a great variety of features expressed by these organisms. The most commonly studied characteristics of bacteria can be divided into two key areas: structural characteristics and physicochemical characteristics. Some of the commonly used methods for determining these features will be summarized in this section.

4.407.3.1. Structural Characteristics

The first and perhaps the most fundamental aspect to characterize bacteria is the cell wall. Bacteria can be divided into two distinct groups depending on the retention of Gram stain due to the cell wall structure. This staining method was originally developed in 1882 by H.C. Gram to distinguish certain bacteria. Bacteria with a thick peptidoglycan layer surrounding the plasma membrane retain the Gram stain and are therefore called Gram-positive. Bacteria with a thin peptidoglycan layer between an outer membrane and the inner plasma membrane lose the Gram stain after washing and are called Gram-negative. For further discussions on the bacterial cell structure the reader is directed to some relevant literature.[45–47] This distinction can be applied to most common bacteria, some examples of which are illustrated in **Table 2** with a summary of the differences between the organisms.

The basic cell wall structure of a bacterium may not influence adhesion directly, however, differences between the adhesion of Gram-positive and Gram-negative species of bacteria to surfaces have been reported.[48] The more complex features,

Table 2 Overview of Gram-positive and Gram-negative bacteria

	Gram-positive	*Gram-negative*
Color after Gram and Safranin counter staining	Dark blue/violet	Red/pink
Characteristics of cell wall	Thick peptidoglycan layer	Thin peptidoglycan layer surrounded by periplasm
	No outer membrane	Outer membrane with lipopolysaccharides and proteins
	Negatively charged teichoic acids are often present	No teichoic acids
Examples	*Staphylococcus aureus*	*Pseudomonas aeruginosa*
	Streptococcus mutans	*Escherichia coli*
	Staphylococcus epidermidis	*Salmonella typhimurium*

Source: Madigan, M. E.; Martinko, J. M.; Parker, J. *Brock Biology of Microorganisms*; Prentice Hall: London, 1997; 8th edn., chap. 3, pp 53–108.

which build upon the cell wall probably affect this difference. Bacterial proteins and cell wall structures fulfill a diverse range of functions, for example, motility, gene transfer, and most importantly in the context of this chapter; adhesion. With the advancement of molecular biology techniques it is now possible to detect the presence of the genes known to code for adhesion enabling proteins and the level of their expression.[49,50] Cell surface appendages such as flagella, cilia, and fibrils are also present on some bacteria species and are also capable of influencing bacterial adhesion to surfaces (further discussed in Section 4.407.5). Electron microscopy is a particularly powerful tool for visualizing adhesion structures and the way they function.[51]

4.407.3.2. Physicochemical Characteristics

Though the surface proteins and surface appendages that may be present on a bacterium have a significant role in bacterial adhesion, physicochemical features must also be considered. A major area of characterization concentrates on the more fundamental aspects of defining the physicochemical features of a bacterium. Commonly, the following aspects of a bacterium are considered: wettability (hydrophilicity/hydrophobicity), electrostatic charge, and intermolecular forces. These characteristics assume particular importance in the application of colloidal theories to the study of bacterial adhesion (discussed in Section 4.407.4). Although appendages and proteins may form strong, specific bonds between the bacterium and a surface, it is believed that it is the physicochemical nature of the bacteria and surface, which exert the initial influences upon whether such bonds form or not. Therefore, measurement of these parameters should form part of the investigative strategy into bacterial adhesion to any biomaterial. There are a wide range of methods to measure physicochemical forces associated with bacteria; the most commonly implemented techniques are described below.

4.407.3.2.1. Bacterial adhesion to hydrocarbons: The BATH test

The BATH test, also known as the MATH test (microbial adhesion to hydrocarbons), was developed to be a rapid and relatively simple test of bacterial hydrophobicity.[52] The test determines the distribution of a bacterial suspension between water and a hydrocarbon, for example hexadecane, octane, or xylene. To perform this test, water, the selected hydrocarbon, and the bacteria are mixed together for a short period of time, typically 120 s. The mixture is then allowed to settle for 15 min, at which point, an emulsion of the hydrocarbon in water will have separated from the bulk of the water due to the hydrophobicity of the hydrocarbon. The location of the bacteria in this partition will depend on the overall hydrophobicity of the organism; hydrophilic bacteria will be located in the water component and hydrophobic organisms will be found associated with the hydrocarbon emulsion. Therefore, by taking a measurement of the optical density of the water component one can determine the relative abundance of bacteria in the water fraction, and thus calculate relative hydrophobicity.[52] A variation on the BATH technique: the microbial adhesion to solvents (MATS) test was developed later with the aim of specifically calculating the Lewis acid–base energy of bacteria by using multiple solvents with different properties.[53]

Despite the simplicity of these tests, these techniques have rarely been used in recent published work due to the problems associated with the method. These problems have been identified as (1) the charge of the hydrocarbons present,[54] (2) the inability to quantify the hydrophilicity of bacteria,[55] and (3) the results are only semiquantitative. More recently, the BATH technique has been largely superseded by the use of contact angles on bacterial lawns.

4.407.3.2.2. Contact angles on bacterial lawns

Contact angles are commonly used as a relatively simple method of estimating the free energy at the surface of a biomaterial. A contact angle refers to the angle made between a solid/liquid/gas interface on a surface. One method of creating a three phase interface is by simply adding a droplet of fluid to a solid surface in air. This produces a measurable, surface-dependant angle as illustrated in Figure 7. By controlling the variables around the three phase interface it is hypothetically possible to calculate both the polar and apolar free energy at a surface. A contact angle is normally measured using a digital goniometer, which photographs the liquid interface and automatically calculates the angle.

To measure a bacterial contact angle, a homogeneous surface of bacteria must be created. Typically, bacteria are grown in suspension to a suitable density and deposited onto filter paper using negative pressure.[56] The contact angle changes as the bacterial lawn dehydrates, so to gain consistent results the lawn must be dried in ambient conditions until the contact angle plateaus and becomes stable, normally after 1–3 h.[57] Despite the broad use of contact angle goniometry, the technique is not ideal for measuring the features of a bacterial lawn as a number of fundamental assumptions about the method must be questioned: for example, is the surface actually smooth and heterogeneous? does the liquid used alter the surface?[21] In measuring bacteria contact angle, the question also arises as to how does the drying affect the bacteria and their interactions with the liquid? Additionally, factors such as the choice of growth medium have also been reported to affect the results generated by this method.[58] Despite doubts about the accuracy of bacterial contact angles, the technique permits relative comparisons between bacteria and is commonly published.[59–70] Contact angles from a large number

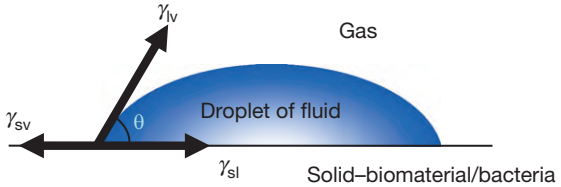

Figure 7 Contact angle (θ) measured between the three phases of the bacterial lawn, the liquid droplet and the surrounding gas. (Liquid–vapor surface tension (γ_{lv}), solid–liquid interfacial tension (γ_{sl}), and solid–vapor interfacial tension (γ_{sv}). Reproduced from Ratner, B. D. In *Biomaterials Science: An Introduction to Materials in Medicine*; Ratner, B. D., Hoffman, A. S., Schoen, F. J., Lemons, J. E., Eds.; Elsevier: Amsterdam, 2004; p 40.

of strains of bacteria have been characterized and whole papers are devoted to documenting the results.[58] In addition to hydrophobicity, bacterial contact angles can also be used to estimate both the polar and apolar energies of a bacterial lawn. To do so three liquids must be used, two polar (e.g., water and formamide) and one apolar (e.g., methylene iodide, cyclohexane, or α-bromonaphthalene). The different types of liquid provide information about how the surface interacts when faced with a polar or apolar liquid. The surface energy of a given material surface or bacterial lawn may then be calculated using the surface energy equations. More detail on the specifics for deriving estimations of free energy from contact angles on bacterial lawns can be found in this review by Sharma.[66]

4.407.3.2.3. Zeta potentials

Zeta potentials are a measure of bacterial surface charge.[57,63,70–75] To understand how the technique works one must first understand the affect of surface charge in a fluid, specifically the formation of an electrical double layer (EDL). When a charged surface, such as the surface of a bacterium, is immersed in an ion-containing fluid, ions of the opposite charge will be electrostatically attracted to the surface. The strength of this attractive force is greatest proximal to the surface and ions with the opposite charge become bound to the particle, or bacterium, forming a feature known as the Stern layer (Figure 8). The electrostatic force then decreases exponentially with increasing distance away from the surface and the concentration of counterions also decreases. The difference in charge between the surface and the bulk fluid creates an electrical potential and the decrease in electrical potential to zero creates a diffuse layer of ions. Together, this diffuse layer of counterions and the charged surface are described as the EDL. In an experimental setup to measure zeta potential, the bacteria moves through the fluid, and as it does so, the proximal adsorbed ions in the Stern layer will move with the surface, while the diffuse layer is more dynamic with ions entering and leaving. This leads to a hypothetical point where on one side ions are immobile and adsorbed, and on the other side ions can slide with the bulk fluid. This is known as the slipping plane and fundamental to the zeta potential theory (Figure 8).

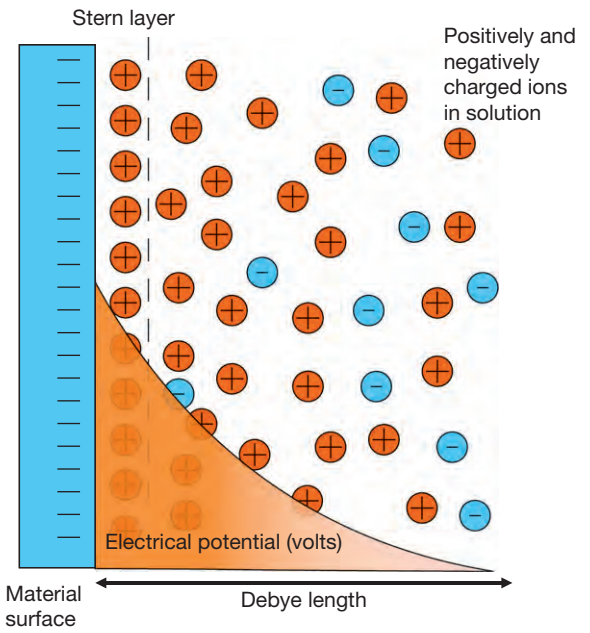

Figure 8 An illustration of an electrical double layer surrounding a negatively charged surface.

The zeta potential technique involves the migration of a charged particle or bacterium in a liquid toward an electrode with the opposite charge, a form of electrophoresis. The speed at which this occurs depends on pH, fluid viscosity, the dielectric constant, the strength of the electrical field around the electrodes, and most importantly the charge of the bacteria. A more highly charged bacterium will move rapidly to the oppositely charged electrode while an uncharged bacterium will remain stationary. The velocity of the particle toward the oppositely charged electrode is measured using a laser and it is this speed which can be substituted into an equation, Smoluchowski's formula,[76] to calculate the zeta potential. The zeta potential is normally expressed in millivolts (mV) and describes the electrical potential between the Stern layer and the bulk fluid, or more concisely the electrical potential at the slipping plane, that is, a measure of charge.

The most commonly used techniques to characterize bacterial physicochemical properties have been summarized (Table 3). However, many of these methods are based on theories, which require critical assumptions that bacteria may not fulfill. This is due to the numerous deviations of bacterial cells from ideal particles with perfect model surfaces. Therefore, the results of these characterizations can only be accurately compared with other bacterial characterization studies when the method utilized is consistent.[77] Additionally, one must always consider that when applying the outcomes of a bacterial characterization analysis the adhesive ability of a bacterium cannot be characterized by physicochemical results alone. For example, contact angles and zeta potentials describe the net characteristics of the bacterial cell surface, omitting individual features such as specific adhesion molecules and cell surface structures. Similarly, only detecting the presence of surface structures, or genes encoding adhesion-related proteins may provide an insight into the adhesive potential of a bacterium; however the actual expression of these features cannot be guaranteed *in vivo* and no information on the physicochemical

Table 3 List of the different characterization techniques discussed and what may be determined from each

Technique	*Use*
Gram staining	Determines the basic structure of the cell wall
Gene/protein analysis	Determines the presence of genes encoding adhesive molecules, surface appendages and the expression of these genes
Microscopy	Visualizes surface structures
BATH/MATH test	Describes hydrophobicity/polar intermolecular forces
Contact angles	Describes wettability, polar, and apolar intermolecular forces
Zeta potentials	Describes surface charge

interaction with the biomaterial is attained. Another important point is that the commonly measured bacterial characteristics are strain and not species dependant.[57] This illustrates the importance of not simply relying on estimating the affects of the aforementioned characteristics on bacterial adhesion, but the need for actual empirical testing for each relevant biomaterial or microorganism. Regardless of the limitations, the proper use of these techniques and a careful interpretation of their significance allow scientists to better interpret bacterial adhesion results and allow hypotheses to be formulated regarding bacterial adhesion to biomaterial surfaces. In the next section, these physicochemical aspects of bacteria will be discussed in relation to bacterial adhesion theories.

4.407.4. Theory and Mechanisms of Bacterial Adhesion

4.407.4.1. Physicochemical Models of Bacterial Adhesion

In order to model and estimate the outcome of bacteria–surface interactions, bacteria may be treated as colloidal particles in a suspension. A colloid is defined as nonliving particles dispersed homogeneously within another substance. By viewing bacteria in a suspension as a colloid it is possible to model bacterial adhesion to a surface as the product of a number of physical or chemical properties of both the bacteria themselves and the biomaterial to which they adhere. These physical and chemical properties may be measured in the laboratory as described in Section 4.407.3. In the study of bacterial adhesion to surfaces, three colloidal models are commonly applied; the thermodynamic theory,[78] the Deryaguin–Landau–Verwey–Overbeek (DLVO) theory,[79,80] and the extended-DLVO (XDLVO) theory.[78]

4.407.4.1.1. The thermodynamic theory

The first theory we will consider is the Thermodynamic Theory, which describes the potential Gibbs free energy change of colloidal adhesion, that is, when the bacteria adheres to a surface. In simple terms, the theory describes the total change in free energy, which is the energy available in a closed system to produce work or a reaction. This is calculated from Lifshitz–van der Waals forces (described in Section 4.407.4.2.1) and Lewis acid–base interactions (described in Section 4.407.4.2.3) when a particle is in contact with a surface, thereby assuming a distance of zero between the particle and the surface. A more detailed review of the thermodynamic theory is described by Morra *et al.*[81]; however, for the purpose of this chapter we shall simplify the theory to eqn [1]

$$\Delta G_{ADH} = \Delta G_{LW} + \Delta G_{AB} \quad [1]$$

ΔG_{ADH} is the Gibbs free energy change of adhesion, ΔG_{LW} is the Gibbs free energy change of the Lifshitz–van der Waals forces, and ΔG_{AB} is the Gibbs free energy change of the Lewis acid–base forces.

The laws of thermodynamics stipulate that a decrease in free energy favors stability. Therefore, when the outcome of eqn [1] is negative, adhesion is favored. The thermodynamic theory of bacterial adhesion is most accurate with uncharged surfaces or in the presence of large quantities of ions.[63,70]

Summary of the thermodynamic theory

Considers Lewis acid–base and Lifshitz–van der Waals forces
Assumes adhesion is always reversible
Distance independent: always calculated for a distance of zero
Does not include the affects of surface charge or the electrolyte concentration of the surrounding fluid

4.407.4.1.2. The DLVO theory

The second commonly used theory is the DLVO theory. The DLVO theory, much like the thermodynamic theory, assumes that adhesion is the product of interfacial energies. The DLVO theory also includes Lifshitz–van der Waals interactions, however, omits the effects of acid–base interactions. Instead, electrostatic forces are included. The interaction between a particle and a surface as predicted by the DLVO theory can be simplified as in eqn [2]:

$$U^{DLVO} = U^{LW} + U^{EL} \quad [2]$$

U^{DLVO} is the total interaction energy, U^{LW} is the Lifshitz–van der Waals interaction energy, and U^{EL} is the electrostatic interaction energy.

The DLVO theory is commonly used to model bacterial adhesion in the literature.[82–86] The DLVO theory is most accurate when electrostatic forces are the predominant interactions and also considers Lifshitz–van der Waals interactions.[63,70] However, the DLVO theory does not incorporate the Lewis acid–base component, which is the ability of a surface to accept or donate electron density to its surroundings. The theory is, therefore, limited in its accuracy because it omits an important aspect of surface chemistry.[63,70,85,86]

Summary of the DLVO theory

Considers Lifshitz–van der Waals and electrostatic interactions
Adhesion can be reversible
Distance dependent: calculated over a range of distances to produce a curve
Does not include the affects of polar interactions

4.407.4.1.3. The XDLVO theory

The most advanced of the theories commonly used for bacterial adhesion is the XDLVO theory. The XDLVO theory combines the features of the thermodynamic and DLVO theories in an attempt to more comprehensively assess colloidal adhesion. The XDLVO was originally devised to model biopolymer adhesion to surfaces,[78] but has since been used in microbial research to more accurately model bacterial adhesion than the existing theories.[63,70,85,86] A simplified version of the XDLVO theory is described in eqn [3]:

$$U^{DLVO} = U^{LW} + U^{EL} + U^{AB} \quad [3]$$

U^{DLVO} is the total interaction energy, U^{LW} is the Lifshitz–van der Waals interaction energy, U^{EL} is the electrostatic interaction energy, and U^{AB} is the Lewis acid–base interaction energy.

Summary of the XDLVO theory

Considers Lifshitz–van der Waals, electrostatic, and Lewis acid–base interactions
Adhesion can be reversible
Distance dependent: calculated over a range of distances to produce a curve

The use of any of the above theories requires some fundamental assumptions about the system to which they are applied to be made:

1. The interacting surfaces are molecularly smooth without a measurable topography.
2. The interacting surfaces are inert and nonreactive under normal conditions.
3. The substance in which the suspension is held is isotropic and maintains bulk properties throughout.

These assumptions must always be considered when applying these theories to bacterial adhesion, as these criteria are often not met by the biomaterial or the bacteria. All of the theories described deal with the free energy of (colloid) bacteria–surface interactions. Bacterial adhesion is hypothetically favorable when the product of the equations associated with the theories is negative. It is important to note that the outcome of these models is always semiquantitative, predicting either an increase or decrease in bacterial adhesion for one set of parameters in comparison with a different set of parameters. For example, for two closed systems otherwise identical, bacterial adhesion will be affected by varying specific parameters such as surface charge or hydrophobicity of the bacteria or the biomaterial.

4.407.4.2. Forces of Colloidal Adhesion

To understand the physicochemical theories applied to microbiological studies, it is important to also understand the forces just mentioned. The three components commonly identified as important in colloidal and bacterial adhesion are Lifshitz–van der Waals, Lewis acid–base, and electrostatic forces. The source of these components will be described in more detail in Section 4.407.4.2.

4.407.4.2.1. Lifshitz–van der Waals: Apolar molecular forces

Lifshitz–van der Waals forces arise from the attraction or repulsion of molecules due to the unequal distribution of electrons between bound atoms.[87] When electrons are unequally distributed between atoms, one atom will gain a net negative charge by having extra electrons, while the other atom will be positively charged due to the excess charge of the nucleus resulting from the loss of electrons. When this arrangement of electrons occurs the atoms are called a dipole. An example of two dipoles interacting is illustrated in Figure 9.

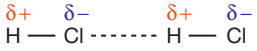

Figure 9 An example of Lifshitz–van der Waals forces between two molecules of hydrogen chloride. The net positive charge of the hydrogen atom attracts the net negative charge of the chlorine atom.

Dipoles can exist due to a number of different reasons[87]:

1. In a molecule such as hydrogen chloride, a dipole is formed due to the higher positive charge of the chlorine nucleus than that of the hydrogen nucleus, this leads to the migration of electrons toward the chlorine nucleus leaving the hydrogen positively charged
2. Alternatively, molecules without this predisposition to form dipoles may temporarily gain a charge differential due to the varying probability of the arrangement of orbiting electrons. This can happen in any atom and creates a very weak- and short-lived intermolecular force
3. A dipole may also be induced by the proximity of another charged molecule. Induced dipoles occur due to the displacement of electrons of one molecule brought about by the attractive or repulsive affect of another. The dipole in this case is formed when a permanent dipole, for example, HCl, interacts with any other atom

Altogether the sum effect of these interactions is called the Lifshitz–van der Waals force. The Lifshitz–van der Waals forces are collectively defined as the apolar energy component. Lifshitz–van der Waals forces are relatively long range and inversely proportional to the distance between the two components. Due to the range of these forces they are often believed to initiate bacterium–biomaterial interactions by either attracting or repelling the bacterial cell at a relatively large distance.

4.407.4.2.2. Electrostatic forces

Electrostatic forces arise from the charge of two interacting surfaces, which can be two solid surfaces, but can also relate to a solid surface and a bacterium. In a liquid, the electrostatic charge of a surface may be caused by the dissociation of surface groups or by the adsorption of charged molecules from the surrounding medium. In nature, most surfaces and bacteria carry a negative charge[88] and therefore, the electrostatic component normally describes a repulsive force.

We have previously encountered electrostatic forces in Section 4.407.3.2. When a surface bearing a charge is submerged in an ion-containing medium, a feature known as the EDL is created, the first part of which is the charged surface itself. The second part of the double layer is the ions carrying the opposite charge which migrate to surround the surface. This layer of complimentary ions is known as the diffuse layer, as the concentration of ions is greatest at the surface and then exponentially decreases with distance away from the surface.[89] The distance to which an electrical potential still exists is known as the Debye length. The presence of ions around a charged surface leads to the dampening of the electrostatic force and therefore a decrease in the Debye length. The distance over which these electrostatic forces can influence bacterial adhesion or repulsion is at zero or equilibrium at the Debye length.

The strength of the force exerted by charged surfaces is dependent on the relative charge of the surfaces, the distance between the surfaces and the number of ions present in the medium around the surfaces. The XDLVO theory predicts that when bacteria and surfaces carry the same charge, adhesion between the two will increase with increasing ionic strength.[63,70] This prediction has been validated experimentally by controlling the ionic strength of the fluid media used in bacterial adhesion experiments.[63,64,70,83,90] The trend of

increased adhesion with increased fluid ionic strength plateaus at ionic strengths greater than ~0.1 M, thus including physiological fluids, which have a concentration of around 0.15 M. At this molarity, the Debye length is too short to cause an observable repulsion.[91] Because the electrostatic force decreases exponentially as a function of ionic strength, liquids with high ion contents, such as physiological fluids (0.15 M), are dominated by the other forces present. As a consequence of the limited influence of electrostatic forces in physiological conditions, bacterial adhesion *in vivo* is influenced more by the effects of the other forces such as Lifshitz–van der Waals forces and Lewis acid–base: polar forces.

4.407.4.2.3. Lewis acid–base: Polar forces

The final parameter, the acid–base interaction, describes the affect of attractive hydrophobicity and repulsive hydration around surfaces. The majority of the acid–base component is brought about by the presence of molecules capable of forming hydrogen bonds. Hydrogen bonds are ~1–2 orders of magnitude stronger than Lifshitz–van der Waals forces and can dominate bacterial adhesion.[92] Hydrogen bond formation requires both a hydrogen bond donor and a hydrogen bond acceptor. The donor is always a hydrogen atom bound to an atom such as oxygen, nitrogen, or fluorine, which strongly attracts the hydrogen electrons; the hydrogen bond acceptor is another oxygen, nitrogen, or fluorine atom bound elsewhere. The hydrogen in the acceptor molecule gains a positive charge due to the relocation of electrons around the bound atom with the more positively charged nucleus. The hydrogen then interacts with the electronegative receptor atom and a strong attractive force is created. Hydrogen bonding is of high importance in water due to the fact that the water molecule is both a hydrogen bond donor and an acceptor. These forces normally make up 90% of all noncovalent interactions in water, and it is the number of hydrogen bonds formed by a surface which influences a characteristic of surfaces known as wettability, the surfaces ability to bond water. When a surface is highly hydrophilic, that is, forms a high density of hydrogen bonds with water, it becomes very difficult for other molecules to approach the surface due to the surface bound water molecules. If however the surface is hydrophobic there is less resistance to adhesion between the surface and colloid or bacteria.

In summary, the three forces discussed in this section and commonly referred to when modeling bacteria as colloids are; Lifshitz–van der Waals, Lewis acid–base, and electrostatic forces (Table 4). The Lifshitz–van der Waals forces act over the longest range; however, the polar Lewis acid–base interactions (hydrogen bonds) are the strongest. The electrostatic forces are highly dependant on the media in which the material is placed and values are therefore not provided.[93] Additionally, the affects of four common functional groups on these forces is illustrated in Table 5. Apolar functional groups can also be described as hydrophobic and polar groups are hydrophilic. The comparisons made in this table are relative and dependant on the environment in which the functional group is found.[94]

Table 4 The range and strength of the intermolecular forces used when modeling bacteria as colloids

Force	*Range (nm)*	*Strength (kJ)*
Lifshitz–van der Waals	0.3–0.4	<2
Hydrogen bond (Lewis acid–base)	0.2–0.3	12–16
Electrostatic forces	Dependant on media	

Stryer, L. Biochemistry. W. H. Freeman: San Francisco, CA, 1975

4.407.4.3. Interpreting the Theories

The application of the DLVO equation can lead to many predicted outcomes for any given particle or bacterial cell, three of which are shown in Figure 10. The patterns illustrated represent three cases within a continuous dataset.

To understand the application of the DLVO theory, graphs of the total free energy as a function of distance between the particle and surface are often generated. Adhesion becomes favorable when the total free energy of adhesion is negative. Figure 11, curve A, shows a situation in which a large energy barrier, possibly caused by strong electrostatic repulsion, prevents bacteria from adhering to the surface. Curve B has a much smaller energy barrier and it is possible for bacteria to adhere in two minima. An expanded version of curve B is illustrated in Figure 11. The proximal minimum or primary minimum is labeled D, and when a bacterium is in this position it is described as irreversibly adhered. The secondary minimum, labeled E in Figure 11, is the distance at which a bacterium maybe reversibly adhered. If a bacterium enters the secondary minimum it may dissociate, translocate, or overcome the energy barrier, and enter the primary minimum.[82] Curve C has no energy barriers and the hypothetical bacteria

Table 5 Four common functional groups with corresponding forces

Functional group	*Polar/apolar*	*Charge*
Methyl ($-CH_3$)	Apolar	Neutral
Hydroxyl ($-OH$)	Polar	Neutral
Amine ($-NH_2$)	Polar	Positive
Carboxyl ($-COOH$)	Polar	Negative

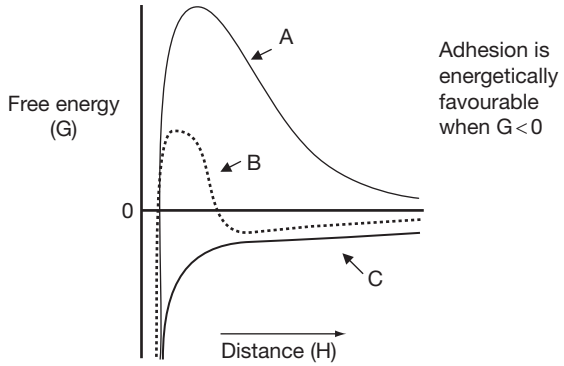

Figure 10 Three possible outcomes of the application of the DLVO theory to a particle approaching a surface with the same charge. The curves are discussed in the main text. Adapted from van Loosdrecht, M. C.; Lyklema, J.; Norde, W.; Zehnder, A. J. *Microbiol. Ecol.* **1989**, *17*, 1–15.

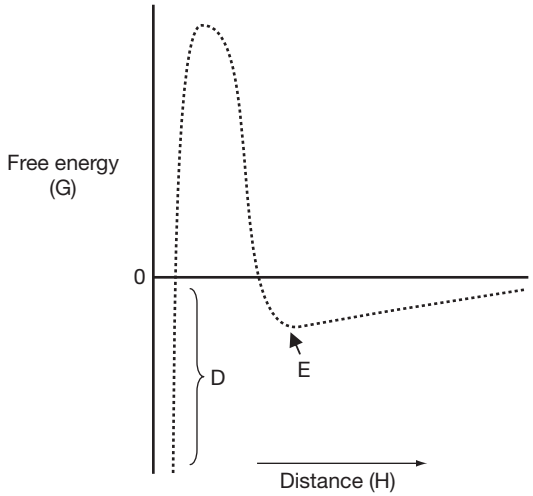

Figure 11 Prediction of the relationship between the free energy of a particle approaching a hydrophobic surface. D is the primary minimum and E is the secondary minimum. Adapted from van Loosdrecht, M. C., Lyklema, J., Norde, W., and Zehnder, A. J. *Microbiol. Ecol.* **1989**, *17*, 1–15.

will be attracted to the surface with increasing force as it approaches the surface. Curve C can be formed when the bacteria and surface are of opposite charges and electrostatic attraction occurs in addition to the attractive Lifshitz–van der Waals forces. The curves shown in Figures 10 and 11 are examples of the possible outcomes of the theory; however, there are an infinite number of curves that may be generated depending on the exact conditions.

Physicochemical theories are often used in bacterial adhesion studies; however, these equations were designed for colloids, not living bacteria. Though accurate when experimental conditions can be controlled, physicochemical modeling will never replace other empirical methods of testing bacterial adhesion. Instead, these theories allow scientists to predict how fundamental forces will affect bacterial adhesion and help explore experimental data. The physicochemical theories provide a good foundation for understanding bacterial adhesion, and in the following section, we shall discuss some of the additional biological aspects of bacterial adhesion.

4.407.5. Mechanisms of Bacterial Adhesion

Broadly speaking, bacteria may adhere to a biomaterial in one of two ways, either directly to the bare biomaterial or indirectly via a conditioning film deposited on the biomaterial. In general, bacteria may be considered to adhere in a nonspecific manner with bare biomaterials and this is largely how the biomaterial–bacterial interaction is investigated *in vitro* and bears closest resemblance to adhesion patterns predicted by the theoretical models. This scenario may be considered analogous to direct bacterial contamination of the biomaterial prior to implantation. However, once the biomaterial is placed in a physiological fluid, after implantation for example, it immediately becomes coated in a conditioning layer of extracellular matrix (ECM) proteins. The presence of a protein layer on the surface of the biomaterial affords contaminating

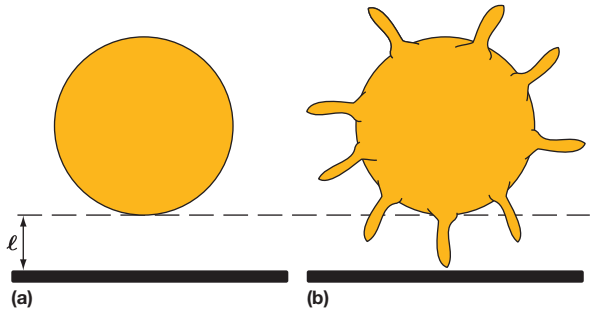

Figure 12 Illustration of the way in which surface structures on bacterium interact with a surface. (a) A spherical particle at the closest approach to a surface (l) and (b) the same spherical particle coated with smaller surface structures. Reproduced from van Oss, C. J. *J. Mol. Recognit.* **2003**, *16*, 177–190.

bacteria the opportunity to adhere in a specific way with the proteins now present on the implant surface. Specific adhesion may be investigated *in vitro* by preconditioning biomaterial samples in defined or complex proteinaceous solutions. However, it is difficult to replicate the exact constitution of the conditioning layer present *in vivo*. Furthermore, it is difficult to separate the relative contribution of nonspecific and specific mechanisms of bacterial adhesion upon infection propagation either *in vitro* or *in vivo*.

4.407.5.1. Nonspecific Adhesion

Many bacteria have surface structures, which function to aid adhesion. These structures can breach the energy barrier, which separates bacteria from a surface. The repulsive force existing between a particle and a surface is a function of distance proportional to the radius of the particle.[89] Therefore, surface structures with a small cross-sectional area allow bacteria to interact with a surface over a decreased distance, which reduces the repulsive energy barrier (Figure 12).

Cell appendages may also aid adhesion through motility, as has been shown for the flagella of *P. aeruginosa*.[95] Increased adhesion to surfaces mediated by the presence of cell structures that do not confer motility has also been described. Ishii *et al.* have shown that a wild-type *Acinetobacter* isolate adhered in greater numbers to surfaces than a surface appendage-deficient mutant. The wild type also became irreversibly attached, something that many of the mutant cells were not able to achieve.[96] The bacteria in the Ishii study were shown to be nonmotile, suggesting that it was not motility, but rather another feature of the cell appendages driving adhesion.[96] A similar trend was also observed using *Listeria monocytogenes*, when the adhesion of flagellum-deficient mutants to stainless steel was reduced 10-fold compared with the wild-type bacteria under conditions preventing motility.[97]

Similar to cell surface structures, the production of exopolymers can also help bridge the energy maximum, allowing irreversible adhesion. Exopolymers are organic substances secreted from the bacterial cell and include bacterial slime, biosurfactants, and proteins, all of which may influence bacterial adhesion. In particular, the slime produced by bacteria is known to increase bacterial adhesion.[98,99] Furthermore, exopolymers can condition material surfaces and affect wettability.

This conditioning has been shown to facilitate an increase in bacterial adhesion, even allowing bacteria to adhere to surfaces that are not predicted to allow adhesion according to the DLVO theory.[85] Some exopolymers have further effects aiding bacterial adhesion, for example, by locally increasing the ion concentrations around a surface to reduce electrostatic repulsion and directly bridge the bacteria to the surface.[100]

In contrast to the production of molecules that increase bacterial adhesion, some bacterial species exude biosurfactants to inhibit adhesion of other bacteria to a surface. Some bacterial species do this as a survival strategy in a competitive environment. A decrease in bacterial adhesion is believed to be achieved via a reduction in water surface tension mediated by the extracellular molecule. A reduction in surface tension increases wettability – which in effect makes the surface relatively more hydrophilic. For example, one biosurfactant, isolated from *Lactobacillus acidophilus*, inhibits over 70% of *Enterococcus faecalis* adhesion to glass.[101] The principle of making an implant surface more hydrophilic to achieve a reduction in bacterial adhesion is a technique, which has been adopted by the biomaterial community to reduce bacterial adhesion (**Section 4.407.6.1**).

4.407.5.2. Specific Adhesion

Analogous to the accepted premise that bacterial adhesion to a biomaterial is the first step in the development of biomaterial-associated infection, bacterial adhesion to tissues, cells, and molecules of their host is the first step in classical infections in which biomaterials are not involved. In these infections, such as osteomyelitis, urinary tract infections or endocarditis, bacterial adhesion proceeds through a specific recognition mechanism that occurs between bacterial surface structures, called adhesins, and molecules present in the host, in a ligand-receptor type interaction. Numerous pathogenic bacteria such as *S. aureus*, *E. coli*, and the Streptococci are known to possess a range of such adhesins, which enable the bacteria to specifically adhere to the host environment, enabling the pathogen to efficiently colonize or infect a certain niche in the host organism.

A large number of adhesins have been identified in many bacterial species. These adhesins may recognize simple or complex carbohydrate structures, membrane proteins or extracellular matrix components of the host and the particular set of adhesins possessed by an individual bacterium depends largely upon the species, but can also vary within strains of the same species. Some of the most extensively studied adhesins include those of the most prominent pathogens such as *S. aureus*, which has been found to express multiple adhesins for target molecules such as collagen, fibrinogen, bone sialoprotein and vitronectin, for example. These are also very important adhesion/binding proteins for eukaryotic cells. These adhesins have been named microbial surface components recognizing adhesive matrix molecules (MSCRAMMs)[102] and evolved as virulence factors in human infections prior to the advent of implanted biomaterials (**Figure 13**).

Despite the fact that there are no adhesins specific for biomaterials, such as metals or polymers, it has been shown that adhesins are capable of mediating specific interactions between bacteria and biomaterials by binding to the extracellular matrix proteins deposited on the device immediately upon implantation (**Figure 14**) (**Chapter 4.406, Protein Interactions with Biomaterials**).

The specific interaction between adhesins and extracellular matrix components deposited on the biomaterial is not accounted for in the physicochemical theory of bacterial adhesion, as the adhesins have not been found to influence any of the bacterial factors present in the physicochemical equations, such as surface free energy or zeta potential. Notwithstanding this fact, it has been shown that when a relevant or suitable protein layer is deposited on the surface of the biomaterial, bacterial adhesion is affected. For example, bacterial adhesion may be significantly enhanced to a protein-conditioned surface when the cognate adhesin is expressed by the tested bacterial strain, and also a reduction in adhesion has been shown when the isogenic mutant lacking in the specific adhesin was tested.[42,103] The actual conformation and composition of the complex protein layer deposited on the biomaterial *in vivo* is influenced by the physicochemical properties of the biomaterial. Therefore, there will be a variable influence on bacterial adhesion, dependent upon biomaterial interaction with the ECM matrix, and the subsequent conformation and composition of the protein layer, as well as the presence or absence of the range of adhesins expressed by the contaminating bacteria.[104]

To quantitatively measure the specific interaction forces between a bacterial cell and a substratum, AFM can be employed. As described already (**Section 4.407.2.4**), the

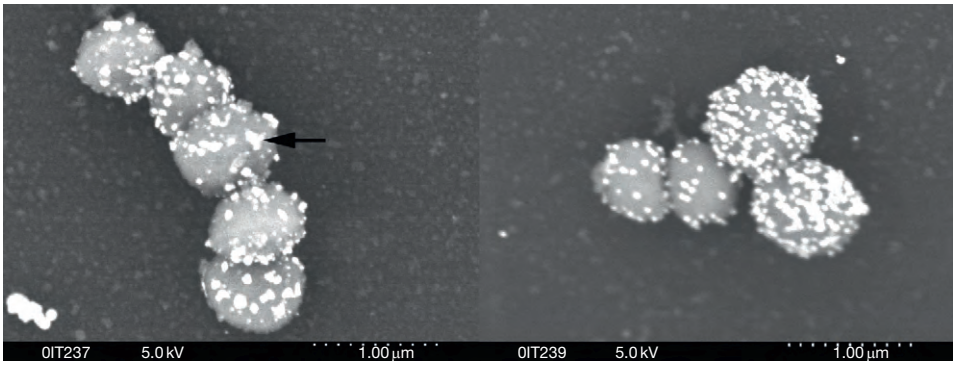

Figure 13 Immunogold labeled *S. aureus* identifying protein A, an MSCRAMM common amongst *S. aureus* isolates. Reproduced from Harris, L. G.; Foster, S. J.; Richards, R. G. *Eur. Cell Mater.* **2002**, *4*, 39–60.

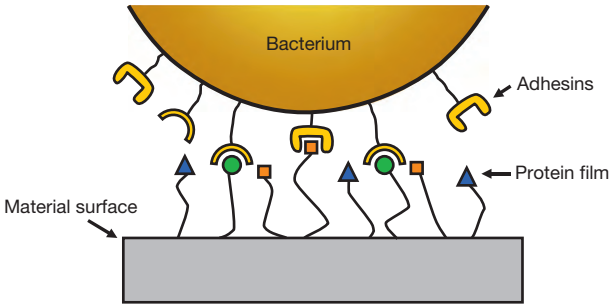

Figure 14 Specific adhesion between a bacterium and biomaterial surface proceeds via adhesins interacting with eukaryotic ECM proteins deposited zupon the biomaterial surface.

interaction forces between a viable bacterial cell (on an AFM tip) and a biomaterial surface measures a so-called real-life interaction.[42] Using this technique AFM has shown that interaction forces of −3 to −5 nN are present when bacteria adhere specifically to protein covered materials. The strength of this interaction is 2–3 times greater than the interaction observed in the absence of a specific interaction, that is, without the adsorbed protein layer on the biomaterial.[105] The strength of this interaction arises from multiple similar interactions between adhesins and host molecules, with each individual binding[106] measured at a few tenths of a nN. The total interaction forces between a bacterium and the protein covered biomaterial are obviously the result of the sum of specific interactions and nonspecific interactions, that is, those interactions described in physicochemical theories. The nonspecific interaction forces contribute relatively minor forces of up to −2 nN.[105] Considering the facts that every implanted biomaterial develops a complex conditioning film of ECM proteins immediately upon implantation, and the majority of bacteria possess numerous ECM recognizing adhesins, the specific interaction between bacteria and biomaterial, via conditioning film proteins, is an extremely important mechanism of bacterial adhesion to implanted biomaterials.

The importance of the adhesins for the progression of infection has inspired attempts at developing vaccines targeted at preventing MSCRAMM-mediated adhesion of Staphylococci to implanted biomaterials.[107] Biomaterial-based strategies to reduce bacterial adhesion *in vivo* may also be developed to take advantage of the specific nature of this type of bacterial adhesion.

4.407.6. The Influence of Biomaterial Surface Properties on Bacterial Adhesion

The success of an implant is to a great extent governed by the bulk properties of the implant material, but upon implantation it is the surface structure and surface chemistry, for example, charge, topography, hydrophobicity, and zeta potential, which determine the biological response. This is true not only for eukaryotic cells, but also prokaryotes. As described in Section 4.407.4, bacterial adhesion occurs as a result of physicochemical interactions. These interactions are influenced by the bacterial strain itself and the surrounding environment, such as pH, ionic concentration or protein concentration, and the biomaterial itself will also influence this process. Biomaterials can generally be defined into metals, ceramics, polymers, natural materials, and composites. It is beyond the scope of this chapter to describe the proposed reasons, influences, mechanisms, or theories put forward as to why certain bacteria adhere in fewer or greater numbers to every available biomaterial; however, this section will describe the bacteria–surface interface from a more fundamental perspective of chemistry and topography.

The surface of a material represents the boundary/exterior of a three-dimensional structure and therefore in general, this surface layer has increased surface energy.[108] This energy is a result of unsaturated or unterminated bonds, that is, the atoms at the surface are not bonded to the maximum number of neighboring atoms and are therefore in a higher energy state than atoms in the interior.[109] The laws of thermodynamics dictate that a material surface in any environment will try to reduce this energy to the state of the lowest free energy. This is hypothetically achieved by, for example, minimizing the total surface area, such as a liquid forming a droplet; however, this is not possible for a solid. A solid will therefore try to react with the surrounding environment, such as the formation of an oxide layer on titanium. Such reactions occur within nanoseconds of the surface being exposed to, for example, air.[108]

The surface of a biomaterial is formed by the individual manufacturing processes for that material and the surface is conferred a specific chemical composition and surface structure or topography. The combination of surface chemistry and topography influences the wettability (hydrophilicity/hydrophobicity) of the biomaterial surface and these three factors are the main influence on bacterial adhesion from the perspective of the biomaterial. The following section will focus on the affect of biomaterial surface chemistry and topography on bacterial adhesion. Bacteria will seldom adhere directly to a biomaterial; a conditioning film always form immediately upon implantation into the body. Therefore, this section shall also briefly describe the fundamental influences on protein adsorption to the surface as this will dictate the cell and bacteria interactions which follow.

4.407.6.1. The Influence of Surface Chemistry on Bacterial Adhesion

When a biomaterial is placed in a biological environment, water is amongst the first molecules to reach the surface. This process occurs within nanoseconds.[110] The orientation of the water molecules on the surface is influenced by its polarity and the wettability of the surface. The subsequent protein interaction is consequently influenced by the orientation of the water molecules.[110,111] The importance of the cascade of molecules absorbing to a surface becomes more apparent when the number and diversity of these molecules is considered. There is an array of more than 200 proteins in plasma, which can interact with the surface and these interactions are influenced by surface chemistry and structure. In turn, this adsorbed protein layer/conditioning film influences pro- and eukaryotic cellular interactions. The surface of a material is therefore integral in controlling the biological reactions.[108,112,113] Protein adsorption occurs within the micro- and millisecond time frame, but can also continue for

longer periods of time.[110,111] The way in which proteins adsorb to a surface is strongly influenced by surface chemistry. Protein adsorption is not fully understood, and proteins are strongly affected by interactions with solid materials.[110] Many proteins contain nonpolar, polar, and charged residues, and the orientation of a protein can therefore change depending on the surroundings.[114] Surfaces which are at neither extreme of hydrophobicity/hydrophilicity are thought to bind protein moderately, allowing reorientation depending on surrounding biomolecules, thus increasing possible interactions with the surroundings.[115] Fibronectin is one of the more influential proteins for eukaryotic cell adhesion and has been shown to adhere strongly to hydrophobic surfaces. However, owing to the conformation caused by this adsorption, the fibronectin is unable to reorientate to aid eukaryotic cell adhesion when the surface is very hydrophobic. When adsorbed onto less hydrophobic surfaces, however, fibronectin can reorientate to aid eukaryotic cell adhesion[115,116] As described in detail in Section 4.407.5 bacteria adhere in a nonspecific and specific manner and surface chemistry will therefore, have an important influence on specific adhesion.

Many studies have focused on the relationship of surface wettability and bacterial adhesion.[74,75,82,117–121] The wettability of both the bacteria and the biomaterial will influence the ability of the bacteria to adhere. Firstly, the wettability of the bacteria; by using contact angles, a simple measure of wettability, it has been shown that more hydrophobic species of bacteria adhere more efficiently to hydrophobic materials, in this case polystyrene.[74,75] More recently, this has been investigated using different strains of the same species. More hydrophobic strains of *S. epidermidis* adhere more readily to polyethylene, also a relatively hydrophobic polymer, at low shear stress in protein-free media, than the more hydrophilic strains.[122] Findings from Li and LoganLi and Logan[64] also identified that bacteria such as *E. coli D21f2*, which are more hydrophobic adhere less readily to more hydrophilic biomaterials than less hydrophobic strains. From the perspective of the wettability of the biomaterial, more hydrophilic surfaces, with wettability between 9° and 22°, had the lowest bacterial adhesion for all the strains tested, and the more hydrophobic surfaces, with wettability between 52° and 68°, had increasing bacterial adhesion. These studies, to a certain extent, confirm the theories described in Section 4.407.4, where colloidal interaction theories are described as a means of predicting bacterial adhesion.

Efforts to alter the surface chemistry of biomaterials to influence the adhesion of bacteria have been shown to successfully do so. For example, poly (ethylene glycol) modification of polyurethane has been shown to decrease hydrophobicity and this dramatically decreased the adhesion of *E. coli* and *S. epidermidis*.[123] Furthermore, it has been reported that surface thiocyanation decreases the hydrophobicity of polyvinylchloride, increasing the wettability from 72° to 50°.[124] The subsequent reduction of *S. epidermidis* and *S. aureus* adhesion by ~90% was identified to be as a result of the increase in surface hydrophilicity and not cytotoxicity.[124] However, surface modification to improve the wettability does not always lead to reduced bacterial adhesion. Cunliffe *et al.* grafted various surface functional groups onto glass substrates to assess the effect of these on protein adsorption and the adhesion of different species of bacteria.[125] The bacteria used were *L. monocytogenes*, *Salmonella typhimurium*, *S. aureus*, and *E. coli* and the grafted surfaces included a wide range of functional groups with varying the wettability, thereby altering surface free energies. In general, the bacteria, the cytochrome C, and bovine serum albumin adhered more readily to hydrophobic surfaces. Both *L. monocytogenes* and *E. coli* followed the same trend as the proteins. However, *S. aureus* and *S. typhimurium* differed, specifically, the hydrophilic surface produced by acetamide functional groups was more susceptible to bacterial adhesion from these two species, than the relatively hydrophobic Krytox perfluoropolymer.[125] Cunliffe *et al.*[125] identified that the surface of the various bacteria, their ability to adhere to bare and protein-conditioned surfaces and their ability to produce exopolymers play an important role in the adhesion to these surfaces, thereby highlighting the importance of characterizing both the biomaterial surface and the bacterial surface before any conclusions can be drawn. More recent work has shown that similar levels of adhesion were achieved by *S. epidermidis* on very hydrophilic surfaces with a water contact angle of 28°, and very hydrophobic surfaces with a water contact angle of 101°.[82] This particular study measured not only adhesion at one time point but also reversible and irreversible bacterial adhesion and the ability of the bacteria to slide along the surface in a form of mobile adhesion. Though the total number of bacteria adhered to each surface was similar, the bacteria were ten times more mobile on the hydrophilic surfaces, where the bacteria were also able to detach from the surface, showing reversible adhesion.[82] For further information on reversible/irreversible and mobile/immobile bacterial adhesion please see relevant literature.[82,126–128]

4.407.6.2. The Influence of Surface Topography on Bacterial Adhesion

To evaluate bacterial interactions with surfaces it is important to have an understanding of not only the surface chemistry and wettability but also surface structure or topography. Titanium implants, for example, can have a titanium oxide (TiO_2) surface layer which can be between 5 and 200 nm thick[129] which results in ~45 at.% surface oxygen, making the surface relatively hydrophilic. However, depending on the manufacturing process this surface can be relatively smooth (R_a of 0.2–0.4 μm) or have micron size surface features, as shown in Figure 15 (see Chapter 6.622, The Effect of Substrate Microtopography on Osseointegration of Titanium Implants).

The interaction of bacteria with these two surfaces of the same chemistry but differing in topography, leads to distinctly different bacterial interactions.[22] Increasing surface roughness has also been identified as a factor leading to increased bacterial adhesion elsewhere.[22,129–131] As previously mentioned, bacterial strains of the same species may differ in their interaction with the same surface due to, for example, different surface charge. However, surface roughness has consistently been reported as one of the major influencing factors, which can lead to increased bacterial adhesion independent of bacterial strains or species investigated.[22,130,132–137]

The affect of surface topography is not included in any of the bacterial adhesion theories described in Section 4.407.4. This is because one of the assumptions the theories are built upon is that the surfaces are perfectly flat that is, no discernable

surface features. Despite being omitted from the theories, the affect of topography has commonly been discussed in work studying the physicochemical aspects of bacterial adhesion. Attempts to understand the affect of topography on the XDLVO theory suggest that increased adhesion to rough surfaces is due to the localized conditions created by surface features, such as peaks. These localized conditions effectively decrease the range of the repulsive components described in the theory,[138] in the same way as bacterial surface appendages do (**Figure 12**), as described in **Section 4.407.5.1**.

Topography has also been identified as a major factor in eukaryotic cell adhesion.[139,140] Topography on the micron scale is purposely incorporated into titanium implants to improve tissue integration,[129] and nanotopography has been shown *in vitro* to influence stem cell differentiation without external stimulus.[141] Ploux *et al.*[142] investigated the adhesion of both a eukaryotic cell type and a bacterial strain in parallel to identify the affect of chemistry and topography. The shape and size of topographical features have been shown to play an influential role in eukaryotic cell adhesion in numerous studies.[139,140,143–153] Fibroblasts were one of the first cell types to be shown to exhibit contact guidance, where the cells react to and align with surface features during adhesion.[139,140,148,150] There is, therefore, a trade-off in designing implantable materials between the need for roughness, for eukaryotic cell adhesion, and limiting the dimensions of these features in order to discourage bacterial adhesion. The influence of surface roughness in relation to bacterial cell adhesion has not only been identified for biomaterials, but also for surfaces used in food preparation areas, where the roughness of stainless steel is monitored for scratches and surface irregularities.[130] Scratches to the surface of dentures have been linked to increased bacterial adhesion, where the crevices created provide the ideal environment for bacteria to adhere and create biofilms[5,134,135] More recently, a few papers have highlighted ordered topographical shapes, including the influence of nanotopographies on bacterial adhesion.[136,142,154,155]

The interpretation of the shape of the surface features and how they would influence bacterial adhesion is often overlooked, and **Figure 16** illustrates why the topography should also be evaluated.

The measures for surface roughness illustrated in **Figure 16** shows R_a, the average roughness, and R_z, the average maximum height profile. Surface topography has been investigated thoroughly in relation to bacterial adhesion,[44,130,136,137,154,156] but without proper evaluation of the surface features, such as those shown in **Figure 16** a full interpretation of the bacterial interaction cannot be made. **Figure 16(a)** shows a surface where the peaks and troughs of the surface permit the bacteria to attach in secluded areas, while **16(b)** shows a surface where this is not possible, and the bacteria will be more exposed. As surface area available for bacterial adhesion has been shown to be important in influencing bacterial retention, the size and shape of surface features are extremely important in influencing bacterial interactions, as shown in **Figure 16**.[136,142,155] Experiments using artificial topographies in flow chambers have shown that adhesion to edges both downstream and upstream were favorable compared to flat control areas. Increased bacterial adhesion was particularly pronounced at the edges when the topographical features were in a similar size range to the adherent organisms, that is, the features accommodated the size of the bacteria.[67,92,156]

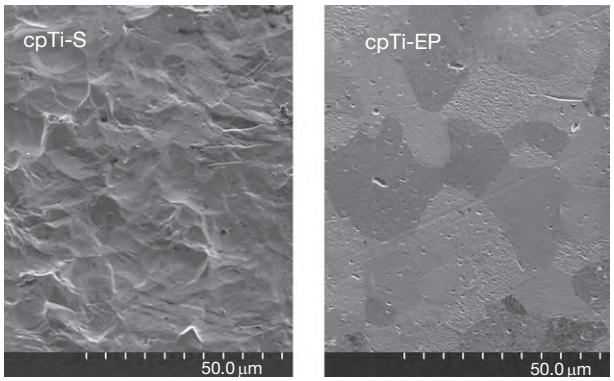

Figure 15 Scanning electron micrographs of standard microrough (cpTi-S) and electropolished titanium (cpTi-EP). Images courtesy of J.S. Hayes.

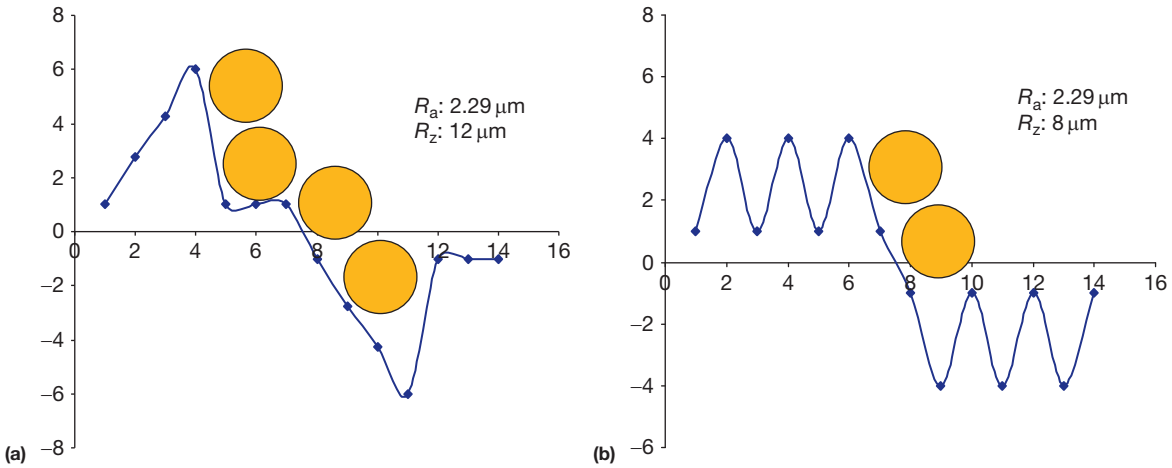

Figure 16 Illustration of the interpretation of surface topography, where two surface with the same roughness (R_a) have very different surface features, (a) one which would allow bacteria to adhere and proliferate, and the other (b) which would not allow adhesion to the same extent.

Topography is one of the major influences on bacterial adhesion and, dependent on the application, the topography of the implant can be manipulated to reduce bacterial adhesion and/or improve tissue biocompatibility. The surface topography can be increased, even made porous or pitted to improve tissue interactions, such as osseointegration, and thereby effectively seal the implant from the surrounding environment, and this is especially important in percutaneous implants.[157] This porous/pitted topography does not necessarily reduce bacterial adhesion, however, the improved soft tissue integration can prevent contaminating bacteria from accessing the subcutaneous tissue-implant interface. On the opposite side of the spectrum the surface can be polished to remove any distinct features, which could propagate bacterial adhesion, as increased roughness has been linked to increased bacterial adhesion.[22,44,130,136,137] Polishing such surfaces may, however, also prevent soft tissue adhesion, leaving liquid filled voids as has been observed surrounding some polished steel orthopaedic implants.[158] Such liquid filled voids could allow bacterial propagation as vascular system and host defence mechanisms may not be able to penetrate the fibrous tissue capsule. The topography of the biomaterial may, therefore, have significant impact on *in vivo* infection rate aside from the impact on bacterial adhesion.

There are many studies which evaluate both the surface chemistry and the topography. Nevertheless, there are few general conclusions which can be drawn, which may stem from the use and understanding of surface characterization techniques, methods used to evaluate the bacterial interactions and finally the wide range of strains investigated. However, two general adhesion patterns have been found; bacterial adhesion to relatively hydrophilic surfaces is normally reduced or the adhesion is weaker than to relatively hydrophobic surfaces, and increased bacterial adhesion is associated with increased surface roughness, although the size of the surface features may also play an influential role in bacterial adhesion.

4.407.7. Strategies to Reduce Bacterial Adhesion

The biomaterial-based strategies developed to reduce or prevent the incidence of infection associated with implanted devices broadly fit into three general categories; those that incorporate an antimicrobial agent to actively kill contaminating bacteria, those that have a modified chemistry to reduce bacterial adhesion, and finally, those with modified surface topographies and surface features to reduce bacterial adhesion (see **Chapter 4.417, Tethered Antibiotics** and **Chapter 4.418, Engineering Interfaces for Infection Immunity**).

Active killing of bacteria is achieved by antimicrobial agents either immobilized on the surface of, or gradually released from, the biomaterial or coating. Those that immobilize antibacterial agents directly on the surface may display a progressive reduction in activity as a consequence of the surface becoming coated with extracellular matrix proteins and host cells, which limit contact between adherent bacteria and the antimicrobial agent. The alternative active antimicrobial strategy: release of the antimicrobial agents from a biomaterial or coating, has largely been limited to the release of antibiotic agents. Suboptimal release profiles of the antibiotic from the biomaterial can lead to the development of resistance, which is an emerging threat to the treatment of infections in general, extending beyond the treatment of biomaterial-associated infections. Devices that are particularly prone to bacterial infection, such as catheters or external fixation pins, are available with numerous antibiotic coatings, such as the rifampin minocycline-impregnated catheters.[159] Nonantibiotic agents have also been incorporated into biomaterials with the same aim of killing adherent bacteria, such as silver,[160] quaternary ammonium compounds,[65] peptides,[60] furanones,[161] nitric oxide,[162] and numerous other molecules making their way through research and into commercial production.[163]

The second strategy to reduce the incidence of infection involves the prevention or reduction of bacterial adhesion to biomaterials. Careful consideration of the physicochemical factors that can increase or decrease bacterial adhesion to a biomaterial may be applied in the manufacturing process of the biomaterial. This is normally achieved by surface modification of biomaterials, which effects a change in protein adsorption, subsequently affecting both bacterial and cellular interactions.

Another biomaterial modification strategy, which will influence the development of infection is the modification of surface topography to reduce bacterial adhesion and/or promote tissue adhesion. Areas where this is of significant interest are percutaneous implants,[157] for which improved tissue integration can reduce the implant susceptibility to infection at the percutaneous region, where any cracks or crevices in the surface would make the implant more susceptible to bacterial colonization. For further information on the effect of topography as a strategy to reduce bacterial adhesion please refer to **Section 4.407.6.2**. In the following section, biomaterial surface modification strategies that aim to reduce or eliminate bacterial adhesion will be briefly described.

4.407.7.1. Highly Charged Surfaces

Bacteria generally possess a net negative surface charge[164] and so, in general, a negatively charged biomaterial surface is expected to display reduced adhesion of bacteria, due to repulsion forces. A biomaterial with positive charge, on the other hand, is expected to encourage bacterial adhesion, and this has been demonstrated in the available literature.[61,62] It has been shown in PPFC experiments that Gram-negative bacteria adhere to a positively charged surface, as expected, in high numbers. However, these adherent Gram-negative bacteria are unable to divide and grow.[48,165] In the same experiments, Gram-positive bacteria did not display an impairment of surface growth on positively charged surfaces. The reason for the observed difference in adhesion and growth patterns of Gram-positive and Gram-negative remains unclear. Overall, the indication is that negatively charged surfaces reduce the chance of bacterial adhesion while positively charged surfaces increase the chance of bacterial adhesion. When one considers the later steps in the development of an infection, such as growth of the bacterium and biofilm formation, then positively charged surfaces, displaying strong electrostatic attraction will limit the growth of the bacteria[48] and thus, perhaps limit biofilm formation, despite the fact that these surfaces display increased initial adhesion. To make a choice between a

biomaterial displaying reduced initial bacterial adhesion or one displaying disrupted biofilm formation is difficult and warrants further investigation to weigh the relative importance of minimizing initial adhesion versus the potential of adherent bacteria to form a biofilm on the surface of the biomaterial. In addition, any initial bacterial adhesion may, over time, develop into a biofilm and as many studies have failed to correlate *in vitro* findings to their *in vivo* findings[166] further elucidation of these processes are necessary. Despite the promise shown by highly charged surfaces, as previously mentioned in **Section 4.407.4.2.2**, the effect of surface charge is highly reduced in ion-containing solutions such as bodily fluids.[91] Thus, some care must be taken when interpreting the results from *in vitro* findings, particularly when an experiment is performed in a solution with a low molarity.

4.407.7.2. Low Surface Energy Materials

Low surface energy polymeric coatings have also been found to inhibit bacterial adhesion to biomaterials by providing a surface to which contaminating bacteria adhere in fewer numbers.[167,168] Tsibouklis *et al.*[168] found reduced bacterial adhesion poly(methylpropenoxyfluoroalkylsiloxane)s and poly(perfluoroacrylates)s, which are low energy surfaces. These polymers contain a flexible linear backbone and the presence of side chains that displayed low molecular interactions. AFM analysis showed that the bacteria were unable to colonize test surfaces films, which was considered to be due to the inability of the bacterial exopolymers to wet or become attached to the low energy surface.

4.407.7.3. Polymeric Coatings Including Polymer Brushes

Many polymeric coatings have been developed over the past decades and many have shown promise in reducing bacterial adhesion.[169–174] Of all the nonfouling surfaces developed, polymer brush coatings have shown the greatest efficacy in reducing bacterial adhesion, with reductions observed in the orders of magnitude.[175] In brief, polymer brushes consist of densely packed polymer chains grafted to a surface, where the average distance between any two attached chains is smaller than the radius of two coiled polymer chains when solvent.[176] Hydrophilic polymer brushes are highly hydrated in aqueous solution and it is hypothesized that the bacteria are hindered in their approach due to the hydrated layer formed with the brushes, which compresses as a result of the bacterial approach and reduces the motility of the polymer brush. Under these conditions the approaching bacterium is repelled and bacterial adhesion either does not occur or is reduced. Numerous examples of polymer brush-like surfaces have been developed and shown in the literature to reduce bacterial adhesion.[175,177,178]

Though polymer brushes are effective at reducing bacterial adhesion, they do not completely eliminate bacteria from material surfaces *in vitro*. The question thus arises as to the utility of such a coating *in vivo*. One commercially available polymer brush has been tested *in vivo* in a mouse model and biofilm formation was reduced in comparison with uncoated controls.[177] It did appear that infections still developed in the surrounding tissues, although biofilm formation on the biomaterial itself was reduced due to the polymer brush coating.[177] As more and more brushes are developed and the stability of these materials is improved, it is anticipated that many such coatings will be developed for future clinical use.

4.407.7.4. Bifunctional Polymer Brush-Like Coatings

The polymer brushes mentioned in the previous section display reduced bacterial adhesion. Moreover, they also display reduced eukaryotic cell adhesion due to a mechanism believed to operate in a similar way to the prevention of bacterial adhesion.[179,180] In order to prepare bifunctional coatings, which prevent microbial adhesion while supporting tissue cell growth, attempts have been made to create a polymer brush-type construct using poly(L-lysine)-graft-poly(ethylene glycol) (PLL-*g*-PEG) copolymers with attached RGD molecules. Additionally, polyelectrolyte multilayers of hyaluronic acid and chitosan have been developed, which also have been modified to display an arginine-glycine-aspartic acid (RGD) peptide sequence toward the exposed surface of the polymer brush.[178,180–182] The RGD peptide sequence is a recognition sequence for integrin receptors through which mammalian cells connect to their ECM molecules. Thus, a polymer brush displaying the RGD sequence may significantly reduce bacterial adhesion, yet not display a reduction in eukaryotic cell adhesion. In an experimental setting, the bifunctional coating did indeed display reduced bacterial adhesion and supported eukaryotic cell adhesion in separate experiments.[178,181,182] More recently, a flow chamber system confirmed this with bacteria and osteoblast cells being cultured in the presence of each other.[183] These bifunctional polymer brushes have significant potential in reducing bacterial adhesion, and the expectation is also that this will translate into a reduced infection rate *in vivo*. The abrasion resistance of these coatings, however, must be suitably tough for the desired use of the material and survive insertion during surgery. In addition, the coatings must also be able to withstand routine sterilization processes such as dry heat-, steam-, gamma-, or ethylene oxide sterilization. These issues represent the challenges faced by polymer brushes to become more readily available in the clinics.

4.407.7.5. Plasma Activation and Coatings

Plasma is the fourth state of matter, and high energy plasma can be used to alter surfaces by changing the chemistry at the surface of a material. There are many different ways in which plasma can be used to modify a surface: it can be direct activation of a surface, coating of the surface with thin polymer films, ion implantation or vapor deposition of, for example, metal or ceramics. Plasma surface modification of polymers to increase the surface energy has been shown to have an effect in reducing bacterial adhesion for several polymers, but the methods of plasma treatment vary and there can be a problem with the stability of the surface modification. In addition, the use of O_2 plasma on devices such as PVC endotracheal tubes could potentially increase eukaryotic cell adhesion, which may consequently cause problems. Finally, where plasma treatments are utilized there may be an etch affect, which could potentially lead to increased bacterial adhesion by increasing the topographical features, and this must therefore also be investigated. Specific examples of plasma activation will briefly be described in this section.

Oxygen plasma glow discharge has been successfully used to reduce bacterial adhesion on polymers such as PVC. Adhesion of *P. aeruginosa* to plasma-treated PVC with ~20–26 at.% surface oxygen was compared to untreated PVC which contains ~10 at.% surface oxygen *in vitro*.[59] These treated surfaces were more hydrophilic than the untreated PVC, and the etching effect of the plasma increasing surface roughness was not found to be significant. *P. aeruginosa* is known to be hydrophobic (negatively charged), and the incorporation of oxygen to the PVC surface leads to an increase in surface energy and therefore, the surface will bond water more easily and repel the hydrophobic bacteria to a greater extent. When *P. aeruginosa* adhesion was quantified, a 70% reduction in the number of bacteria adherent to the plasma-treated PVC was observed.[59] In addition Balazs *et al.* have used radio Frequency (RF) oxygen gas plasma followed by NaOH and $AgNO_3$ treatments to further investigate bacterial adhesion to silver-containing PVC.[184] They found, contradictory to the glow discharge method, that the oxygen plasma alone did not reduce bacterial adhesion. This may be a result of the etching effect of the plasma as the oxygen incorporation was greater with the RF treatment. The surface with silver incorporation was shown to be superhydrophobic. However, no topographical measurements were performed. A 100% reduction in adhesion of viable bacteria was observed with $NaOH/AgNO_3$ with and without oxygen plasma pretreatment.

Constant discharge plasma treatment with 20% O_2 in a He environment was carried out on the polymer PET, and the effect on *S. epidermidis* ATCC 35984 adhesion was investigated.[185] This particular technique aimed to increase the etch affect, but the observed increase in roughness was not correlated to decreased bacterial adhesion: all the plasma-treated surfaces significantly reduced bacterial adhesion. The altered chemistry was hypothesized to be the reason for reduced bacterial adhesion, although no chemical surface analysis was performed. It is believed that the plasma treatment leads to oxygen incorporation and thereby increases surface energy, which would make the surface hydrophilic. This in turn could lead to less bacterial adhesion, especially if the bacteria have a negative surface charge.

CF_4 plasma has also been used to reduce protein adhesion and subsequently inflammatory cells to PMMA intraocular lenses.[186] The use of CF_4–Ar plasma in a postdischarge reactor was investigated on dressings to obtain an antibacterial layer.[187] Various treatment times were investigated with adhesion of *E. coli*, *S. aureus*, *Bacillus subtilis*, and *Candida albicans* (yeast). The exposure to the Ar/CF_4 led to an increase in fluorine with increasing treatment time. After the longest exposure time (80 min), fluorine content was found to be 41 at.% on the wool, 29 at.% on the cotton, and 45 at.% on the polyamide. The antibacterial effect was shown to be greatest with wool, where all the microbes tested were inhibited from adhering, although the effect was reduced with polyamide, irrespective of the atom % fluorine. Additionally, very little effect was shown with cotton. The method in which the fluorine binds to the surface of the dressing is probably the reason why bacterial adhesion was affected differently on the different dressings.

Fluorine has also been the focus when utilizing ion implantation techniques to titanium where, amongst other ions, Ca^+, N^+, and F^+, oxidation, ion plating TiN, ion beam mixing with Ag, Sn, Zn, and Pt with Ar^+ have been examined for their effect on *Porphyromonas gingivalis* and *Actinobacillus actinomycetemcomitans* adhesion.[188] The titanium with F^+ ion implanted surfaces had a significant reduction in bacterial adhesion for both types of bacteria, while none of the other surface treatments had a significant effect. The titanium with F^+ ion implantation surfaces did not affect cell proliferation of L929 cells when incubated for 10 days.

The effect of Ti/Ag plasma vapor deposition onto titanium, on the adhesion of Gram-positive *S. epidermidis* and Gram-negative *Klebsiella pneumoniae*, was investigated by Ewald *et al.*[189] Silver in concentrations from 0.7 to 9% was incorporated utilizing PVD of titanium and a 50% reduction in bacterial adhesion was observed for all the concentrations of silver. The presence of silver was determined, but actual concentration available on the surfaces was not. Cytotoxicity evaluation showed no significant effect of silver on endothelial and osteoblast cells. These results indicate that the presence of a low percentage of silver on a surface could effectively influence bacterial adhesion without having an effect on eukaryotic cells.

The incorporation of silver using these plasma activation processes results in bacterial killing, but silver is also known to have a detrimental effect on eukaryotes.[190] Therefore, the incorporation of silver into any biomaterial must consider potential cytotoxic effects. There are currently many studies evaluating the use silver nanoparticles, however, the cytotoxicity of many such silver nanoparticles are still under investigation.[191–194]

PVD coatings incorporating antimicrobials could also be an effective approach, though for most polymers the temperatures needed would be detrimental to the bulk material and to most antimicrobial agents. In addition, the interface between the bulk material and coating is known to be weak and susceptible to shearing off under pressure/force.

This section has described a range of ways in which to reduce bacterial adhesion, and overall there are a few factors, which should always be taken into consideration; the biomaterial and its bulk properties, the surface chemistry and topography and the environment of the potential application. However, where increased eukaryotic cells adhesion and reduced prokaryotic cells are desirable, some of the techniques described above could be a useful tool, not necessarily hindering bacterial adhesion, but reducing its occurrence.

4.407.8. Summary and Perspectives

Bacterial adhesion to biomaterials is often considered the first in a sequence of events that may culminate in the most feared complication associated with the implantation of a biomaterial into the human body: biomaterial-associated infection. For the cases in which an infection occurs, the first approach of a bacterium to a biomaterial may constitute the biggest single step in the development of an infection. The ability of the contaminating bacterium to adhere to the biomaterial or the surrounding tissue is dependent upon a complex interaction between the contaminating bacterium, the host and the biomaterial itself. Should the bacterium successfully

evade host defenses and adhere to the biomaterial, then a sequence of events unfolds whereby the relatively weak and reversible initial adhesive interactions proceed to stronger, irreversible interactions and ultimately to microcolony formation, and the development of a biofilm. The resultant infection may cause a delay in healing, implant loosening, an increase in morbidity or prolong the duration the patients stay in hospital (see **Chapter 6.609, Orthopedic Implant Use and Infection**).

Given the fact that the number of biomaterial-associated infections is expected to rise in tandem with the expected increase in the use of biomaterials, understanding the basic interactions behind the processes that lead to infection assumes high clinical importance. All stages of the development of a biomaterial-associated infection obviously cannot be studied entirely in one *in vitro* experiment; although the initial adhesion of bacteria to biomaterials is extremely amenable to *in vitro* investigation. *In vitro* experiments have provided the majority of the scientific data available that have furthered our understanding of how biomaterial surface properties influence the bacterial adhesion process. Not only is bacterial adhesion to biomaterials the first step in the infection process, but it is also the only step in the infection process that can be significantly manipulated by a biomaterial scientist to reduce the adhesion of bacteria and thus, reduce susceptibility to infection (antimicrobial activation notwithstanding). Once bacterial adhesion occurs the development of the biofilm is much more dependent upon the virulence factors possessed by the bacteria and the host response, rather than on the biomaterial surface that has been colonized.

This chapter has attempted to give an overview of the available techniques used to study the interaction between bacteria and biomaterials, and in addition, how these techniques have been used to identify how biomaterials of various types influence the process of bacterial adhesion. However, a single, clear, and simple rule of thumb governing the reasons for and influences on the variable adhesion of bacteria to the various biomaterials has not been identified. This difficulty stems from the complexity of a situation involving the adhesion of a wide range of diverse bacterial species and strains to another wide range of diverse biomaterials and manufacturing methods investigated. The variations in methodologies used to experimentally investigate the initial adhesion of a bacterium to biomaterials such as the use of different apparatus or bacterial strains and species or an incomplete physicochemical and topographical analysis of biomaterial and bacteria have all hindered the development of a single overriding theory. Nevertheless, some of the general trends that have come from the literature and may be described include biomaterial surfaces with higher surface energy, that is, more hydrophilic surfaces, generally have less bacterial adhesion and these surfaces are generally those that would promote tissue integration. Polymeric surfaces due to their innate low surface energy are therefore in theory more susceptible to bacterial adhesion, but as these surfaces also limit tissue adhesion, many surface treatments focused on increasing the surface energy are currently being evaluated and some have reached the clinic. Metal surfaces such as titanium are more susceptible from the topographical perspective as the surface energy as a result of the TiO layer is relatively high. This is also true for ceramic materials, and consequently one of the most important factors to consider, when mindful of bacterial adhesion, is a proper evaluation of the topography. Topography has been found to have an overriding effect over chemistry for bacterial adhesion to many biomaterials. It has been postulated that increased bacterial adhesion may be due to increased surface area with increasing roughness, although, topographical features such as cracks, pits, crevices, allow the bacteria to adhere in areas where they are less exposed to factors from the host environment, such as fluid flow and frictional forces, and this is independent of the surface chemistry. Currently, with the increased use of so-called tissue engineered materials, which often encompass composite material, scaffolds with porosity and surface texture to improve not only cellular integration but also promote vascularization, the importance of evaluating these materials for potential bacterial colonization becomes apparent.

These general trends have been largely elucidated from *in vitro* experiments. However, on a very fundamental level, the significance of changing the pattern of bacterial adhesion to biomaterials, as observed *in vitro*, must be carefully weighed when extrapolating to an *in vivo* situation. The limitations of *in vitro* studies, such as the lack of host defenses, conditioning film and specific bacterial adhesion mechanisms serve as the primary justifications for performing *in vivo* experiments. Each of these factors plays a vital role in the outcome of infection, but cannot be replicated to the extent required in an *in vitro* experiment. Adhesion of a bacterium to a biomaterial covered in conditioning layer of proteins may proceed in a specific manner *in vivo* and should adhesin molecules, extracellular polymers, surface structures, and complex conditioning films be incorporated into an *in vitro* bacterial adhesion study, it can allow for a more realistic interpretation of bacterial adhesion to a particular biomaterial. However, these factors can make it virtually impossible to isolate the separate effects of potentially numerous influencing factors on the progression of bacterial adhesion, such as biomaterial physicochemistry versus conditioning film or nonspecific versus specific adhesion effects on bacterial adhesion. A second limitation centers on the actual clinical impact of a reduction in bacterial adhesion that has been achieved *in vitro*. A bacteria-repellent surface may, for example, reduce bacterial adhesion under controlled hydrodynamic conditions by 90% *in vitro*; however, in an *in vivo* situation, with the combined effect of host conditioning layer and perhaps the lack of a hydrodynamic force to remove bacteria from a surface, retention of the same activity cannot be assumed. Furthermore, despite reducing bacterial adhesion, any remaining bacteria may be more than capable of causing an infection, especially considering the rapid growth rate of bacteria means numbers may be replenished within a matter of hours. Potentially, a step forward in attempts to bridge the gap between *in vitro* bacterial adhesion assays and *in vivo* studies is achieved by the progression of the PPFC from exclusively a bacterial adhesion test to incorporate an experimental race for the surface or competitive assay between mammalian cells and bacteria, with serum-containing medium providing a conditioning film. By including cellular interactions in the bacterial adhesion

assay, these coculture competitive-type assays allow for a greater investigation into the potential for standard, modified, antifouling, antimicrobial, or bifunctional surfaces to not only reduce bacterial adhesion, but also provide relevant data for the outcome of the race for the surface.

Ultimately, for biomaterials that are to be implanted into highly infection-susceptible sites, such as intravascular catheters, or devices for the fixation of open fractures of the long bones, antimicrobial activated surfaces are the most successful strategy. Nevertheless, the basic science behind bacterial adhesion to biomaterials still has a role to play in the development of biomaterials. A wealth of information is available with sophisticated methodologies to alter the physicochemical and topographical properties of biomaterials to achieve any one of a number of functions, and altering the surface properties of the biomaterial to reduce bacterial adhesion is a target that is well within the grasp of the biomaterials community. The information gleaned from *in vitro* studies has also provided direction for the development of novel biomaterials such as the bifunctional surfaces that are capable of attracting mammalian cells to the biomaterial surface, while reducing the opportunity for bacterial adhesion and growth on biomaterials. Strategies to reduce bacterial adhesion and encourage host integration are extremely important for all biomaterials. Thus, a combined approach optimizing both aspects is likely to be the focus for future biomaterial-based research into bacteria repellent surfaces.

References

1. Darouiche, R. O. *N. Engl. J. Med.* **2004**, *350*, 1422–1429.
2. Gristina, A. G. *Science* **1987**, *237*, 1588–1595.
3. Arens, S.; Eijer, H.; Schlegel, U.; Printzen, G.; Perren, S. M.; Hansis, M. *J. Orthop. Trauma* **1999**, *13*, 470–476.
4. Elder, M. J.; Stapleton, F.; Evans, E.; Dart, J. K. *Eye (Lond.)* **1995**, *9*(Pt 1), 102–109.
5. Radford, D. R.; Challacombe, S. J.; Walter, J. D. *Crit. Rev. Oral Biol. Med.* **1999**, *10*, 99–116.
6. Harris, L. G.; Richards, R. G. *Injury* **2006**, *37*(Suppl 2), S3–14.
7. Jaeger, M.; Maier, D.; Kern, W. V.; Sudkamp, N. P. *Injury* **2006**, *37*(Suppl 2), S74–S80.
8. Frommelt, L. *Injury* **2006**, *37*(Suppl 2), S87–S94.
9. Elek, S. D.; Conen, P. E. *Br. J. Exp. Pathol.* **1957**, *38*, 573–586.
10. Zimmerli, W.; Waldvogel, F. A.; Vaudaux, P.; Nydegger, U. E. *J. Infect. Dis.* **1982**, *146*, 487–497.
11. Boelens, J. J.; Zaat, S. A.; Murk, J. L.; Weening, J. J.; van der Pool, T.; Dankert, J. *Infect. Immun.* **2000**, *68*, 1692–1695.
12. Kaplan, S. S.; Basford, R. E.; Mora, E.; Jeong, M. H.; Simmons, R. L. *J. Biomed. Mater. Res.* **1992**, *26*, 1039–1051.
13. Zimmerli, W.; Lew, P. D.; Waldvogel, F. A. *J. Clin. Invest.* **1984**, *73*, 1191–1200.
14. Donlan, R. M.; Costerton, J. W. *Clin. Microbiol. Rev.* **2002**, *15*, 167–193.
15. Saginur, R.; Stdenis, M.; Ferris, W.; *et al. Antimicrob. Agents Chemother.* **2006**, *50*, 55–61.
16. Jefferson, K. K.; Goldmann, D. A.; Pier, G. B. *Antimicrob. Agents Chemother.* **2005**, *49*, 2467–2473.
17. Donlan, R. M. *Emerg. Infect. Dis.* **2001**, *7*, 277–281.
18. Donlan, R. M. *Emerg. Infect. Dis.* **2002**, *8*, 881–890.
19. Stewart, P. S. *Antimicrob. Agents Chemother.* **1996**, *40*, 2517–2522.
20. Williams, D. F. In *Progress in Biomedical Engineering*; Williams, D. F., Ed.; Elsevier, 1987.
21. Ratner, B. D. In *Biomaterials Science: An introduction to Materials in Medicine*; Ratner, B. D., Hoffman, A. S., Schoen, F. J., Lemons, J. E., Eds.; Elsevier, 2004; p 40.
22. Harris, L. G.; Meredith, D. O.; Eschbach, L.; Richards, R. G. *J. Mater. Sci. Mater. Med.* **2007**, *18*, 1151–1156.
23. Murga, R.; Miller, J. M.; Donlan, R. M. *J. Clin. Microbiol.* **2001**, *39*, 2294–2297.
24. McCoy, W. F.; Bryers, J. D.; Robbins, J.; Costerton, J. W. *Can. J. Microbiol.* **1981**, *27*(9), 910–917.
25. Olson, M. E.; Ruseska, I.; Costerton, J. W. *J. Biomed. Mater. Res.* **1988**, *22*, 485–495.
26. Linton, C. J.; Sherriff, A.; Millar, M. R. *J. Appl. Microbiol.* **1999**, *86*, 194–202.
27. Sliepen, I.; Van Essche, M.; Quirynen, M.; Teughels, W. *Clin. Oral Investig.* **2009**.
28. Busscher, H. J.; van der Mei, H. C. *Clin. Microbiol. Rev.* **2006**, *19*, 127–141.
29. Sjollema, J.; van der Mei, H. C.; Uyen, H. M.; Busscher, H. J. *FEMS Microbiol. Lett.* **1990**, *57*, 263–269.
30. Koerner, R. J.; Butterworth, L. A.; Mayer, I. V.; Dasbach, R.; Busscher, H. J. *Biomaterials* **2002**, *23*, 2835–2840.
31. Fuller, M. E.; Streger, S. H.; Rothmel, R. K.; *et al. Appl. Environ. Microbiol.* **2000**, *66*, 4486–4496.
32. Vesterlund, S.; Paltta, J.; Karp, M.; Ouwehand, A. C. *J. Microbiol. Meth.* **2005**, *60*, 225–233.
33. Subbiahdoss, G.; Kuijer, R.; Grijpma, D. W.; van der Mei, H. C.; Busscher, H. J. *Acta Biomater.* **2009**, *5*, 1399–1404.
34. Olofsson, A. C.; Hermansson, M.; Elwing, H. *Appl. Environ. Microbiol.* **2005**, *71*, 2705–2712.
35. Jenkins, A. T.; ffrench-constant, R.; Buckling, A.; Clarke, D. J.; Jarvis, K. *Biotechnol. Prog.* **2004**, *20*, 1233–1236.
36. Mohle, R. B.; Langemann, T.; Haesner, M.; *et al. Biotechnol. Bioeng.* **2007**, *98*, 747–755.
37. Bundy, K. J.; Harris, L. G.; Rahn, B. A.; Richards, R. G. *Cell Biol. Int.* **2001**, *25*, 289–307.
38. Fang, H. H.; Chan, K. Y.; Xu, L. C. *J. Microbiol. Meth.* **2000**, *40*, 89–97.
39. Emerson, R. J.; Camesano, T. A. *Appl. Environ. Microbiol.* **2004**, *70*, 6012–6022.
40. Gaboriaud, F.; Dufrene, Y. F. *Colloids Surf. B Biointerfaces* **2007**, *54*, 10–19.
41. Razatos, A.; Ong, Y. L.; Sharma, M. M.; Georgiou, G. *J. Biomater. Sci. Polym. Ed.* **1998**, *9*, 1361–1373.
42. Xu, C. P.; Belt-Gritter, B.; Dijkstra, R. J.; Norde, W.; van der Mei, H. C.; Busscher, H. J. *Langmuir* **2007**, *23*, 9423–9428.
43. Tsang, P. H.; Li, G.; Brun, Y. V.; Freund, L. B.; Tang, J. X. *Proc. Natl. Acad. Sci. USA* **2006**, *103*, 5764–5768.
44. Boyd, R. D.; Verran, J.; Jones, M. V.; Bhakoo, M. *Langmuir* **2002**, *18*, 2343–2346.
45. Beveridge, T. J. *Biotech. Histochem.* **2001**, *76*, 111–118.
46. Beveridge, T. J.; Matias, V. R. F.; Fischetti, V. A. In *Gram-Positive Pathogens*; Fischetti, V. A., Ed.; ASM, 2006; p 1.
47. Costerton, J. W.; Ingram, J. M.; Cheng, K. J. *Bacteriol. Rev.* **1974**, *38*, 87–110.
48. Gottenbos, B.; Grijpma, D. W.; van der Mei, H. C.; Feijen, J.; Busscher, H. J. *J. Antimicrob. Chemother.* **2001**, *48*, 7–13.
49. de Campos, T. A.; Stehling, E. G.; Ferreira, A.; de Castro, A. F. P.; Brocchi, M.; da Silveira, W. D. *Vet. Microbiol.* **2005**, *106*, 275–285.
50. Dalton, H. M.; March, P. E. *Curr. Opin. Biotechnol.* **1998**, *9*, 252–255.
51. Matthysse, A. G.; Holmes, K. V.; Gurlitz, R. H. *J. Bacteriol.* **1981**, *145*, 583–595.
52. Rosenberg, M.; Gutnick, D.; Rosenberg, E. *FEMS Microbiol. Lett.* **1980**, *9*, 29–33.
53. Bellon-Fontaine, M. N.; Rault, J.; van Oss, C. J. *Colloids Surf. B: Biointerfaces* **1995**, *7*, 47–53.
54. Busscher, H. J.; Belt-Gritter, B.; van der Mei, H. C. *Colloids Surf. B: Biointerfaces* **1995**, *5*, 111–116.
55. van der Mei, H. C.; Belt-Gritter, B.; Busscher, H. J. *Colloids Surf. B: Biointerfaces* **1995**, *5*, 117–126.
56. Busscher, H. J.; Weerkamp, A. H.; van der Mei, H. C.; van Pelt, A. W.; de Jong, H. P.; Arends, J. *Appl. Environ. Microbiol.* **1984**, *48*, 980–983.
57. van der Mei, H. C.; Belt-Gritter, B.; Reid, G.; Bialkowska-Hobrzanska, H.; Busscher, H. J. *Microbiology* **1997**, *143*(Pt 12), 3861–3870.
58. van der Mei, H. C.; Bos, R.; Busscher, H. J. *Colloids Surf. B: Biointerfaces* **1999**, *11*, 213–221.
59. Balazs, D. J.; Triandafillu, K.; Chevolot, Y.; *et al. Surf. Interface Anal.* **2003**, *35*, 301–309.
60. Chen, R.; Cole, N.; Willcox, M. D.; *et al. Biofouling* **2009**, *25*, 517–524.
61. Harkes, G.; Feijen, J.; Dankert, J. *Biomaterials* **1991**, *12*, 853–860.
62. Hogt, A. H.; Dankert, J.; Feijen, J. *J. Biomed. Mater. Res.* **1986**, *20*, 533–545.
63. Katsikogianni, M. G.; Missirlis, Y. F. *J. Mater. Sci. Mater. Med.* **2010**.
64. Li, B.; Logan, B. E. *Colloids Surf. B: Biointerfaces* **2004**, *36*, 81–90.
65. Majumdar, P.; Lee, E.; Gubbins, N.; *et al. J. Comb. Chem.* **2009**, *11*, 1115–1127.
66. Sharma, P. K.; Rao, K. H. *Adv. Colloid Interface Sci.* **2002**, *98*, 341–463.

67. Whitehead, K. A.; Colligon, J.; Verran, J. *Colloids Surf. B Biointerfaces* **2005**, *41*, 129–138.
68. Zhang, W.; Chu, P. K.; Ji, J.; *et al*. *Biomaterials* **2006**, *27*, 44–51.
69. Zhao, Q.; Wang, C.; Liu, Y.; Wang, S. *Int. J. Adhes. Adhes.* **2007**, *27*, 85–91.
70. Katsikogianni, M. G.; Missirlis, Y. F. *Acta Biomater.* **2010**, *6*, 1107–1118.
71. Bakker, D. P.; Busscher, H. J.; van der Mei, H. C. *Microbiology* **2002**, *148*, 597–603.
72. Habash, M. B.; van der Mei, H. C.; Reid, G.; Busscher, H. J. *Microbiology* **1997**, *143*(Pt 8), 2569–2574.
73. van Merode, A. E.; van der Mei, H. C.; Busscher, H. J.; Krom, B. P. *J. Bacteriol.* **2006**, *188*, 2421–2426.
74. van Loosdrecht, M. C.; Lyklema, J.; Norde, W.; Schraa, G.; Zehnder, A. J. *Appl. Environ. Microbiol.* **1987**, *53*, 1898–1901.
75. van Loosdrecht, M. C.; Lyklema, J.; Norde, W.; Schraa, G.; Zehnder, A. J. *Appl. Environ. Microbiol.* **1987**, *53*, 1893–1897.
76. Lyklema, J. *Colloids Surf. A Physicochem. Eng. Asp.* **2003**, *222*, 5–14.
77. Hamadi, F.; Latrache, H. *Colloids Surf. B Biointerfaces.* **2008**, *65*, 134–139.
78. van Oss, C. J.; Good, R. J.; Chaudhury, M. K. *J. Colloid Interf. Sci.* **1986**, *111*, 378–390.
79. Derjaguin, B.; Landau, L. *Acta Physico chemica URSS* **1941**, 633.
80. Verwey, E. J. W.; Overbeek, J. Th.G. *Theory of the Stability of Lyophobic Colloids*; Dover: New York, 1948.
81. Morra, M.; Cassinelli, C. *J. Biomater. Sci. Polymer Ed.* **1997**, *9*, 55–74.
82. Boks, N. P.; Kaper, H. J.; Norde, W.; van der Mei, H. C.; Busscher, H. J. *J. Colloid Interf. Sci.* **2009**, *331*, 60–64.
83. Rijnaarts, H. H.; Norde, W.; Lyklema, J.; Zehnder, A. J. *Colloids Surf. B: Biointerfaces* **1999**, *14*, 179–195.
84. Triandafillu, K.; Balazs, D. J.; Aronsson, B. O.; *et al*. *Biomaterials* **2003**, *24*, 1507–1518.
85. Azeredo, J.; Visser, J.; Oliveira, R. *Colloids Surf. B: Biointerfaces* **1999**, *14*, 141–148.
86. Bayoudh, S.; Othmane, A.; Mora, L.; Ben Ouada, H. *Colloids Surf. B: Biointerfaces* **2009**, *73*, 1–9.
87. Garbassi, F.; Morra, M.; Occhiello, E. In *Polymer Surfaces: From Physics to Technology*; Garbassi, F., Morra, M., Occhiello, E., Eds.; Wiley: New York, 1994; p 3.
88. van Loosdrecht, M. C.; Lyklema, J.; Norde, W.; Zehnder, A. J. *Microbiol. Ecol.* **1989**, *17*, 1–15.
89. van Oss, C. J. *J. Mol. Recognit.* **2003**, *16*, 177–190.
90. McWhirter, M. J.; McQuillan, A. J.; Bremer, P. J. *Colloids Surf. B: Biointerfaces* **2002**, *26*, 365–372.
91. Morisaki, H.; Tabuchi, H. *Colloids Surf. B: Biointerfaces* **2009**, *74*, 51–55.
92. Katsikogianni, M.; Missirlis, Y. F. *Eur. Cell Mater.* **2004**, *8*, 37–57.
93. Stryer, L. *Biochemistry*; W. H. Freeman: San Francisco, CA, 1975.
94. Schmidt, D. R.; Waldbeck, H.; Weiyuan, J. K. In *Biological Interactions on Materials Surfaces*; Puleo, A. D., Bizios, R., Eds.; Springer: New York, 2009; p 1.
95. O'Toole, G. A.; Kolter, R. *Mol. Microbiol.* **1998**, *30*, 295–304.
96. Ishii, S.; Unno, H.; Miyata, S.; Hori, K. *Biosci. Biotechnol. Biochem.* **2006**, *70*, 2635–2640.
97. Vatanyoopaisarn, S.; Nazli, A.; Dodd, C. E.; Rees, C. E.; Waites, W. M. *Appl. Environ. Microbiol.* **2000**, *66*, 860–863.
98. Aguilar, B.; Amorena, B.; Iturralde, M. *Vet. Microbiol.* **2001**, *78*, 183–191.
99. Baselga, R.; Albizu, I.; De La, C. M.; Del Cacho, E.; Barberan, M.; Amorena, B. *Infect. Immun.* **1993**, *61*, 4857–4862.
100. Boonaert, C. J. P.; Dufrene, Y. F.; Derclaye, S. R.; Rouxhet, P. G. *Colloids Surf. B: Biointerfaces* **2001**, *22*, 171–182.
101. Velraeds, M. M.; van der Mei, H. C.; Reid, G.; Busscher, H. J. *Appl. Environ. Microbiol.* **1996**, *62*, 1958–1963.
102. Patti, J. M.; Allen, B. L.; McGavin, M. J.; Hook, M. *Annu. Rev. Microbiol.* **1994**, *48*, 585–617.
103. Petersen, F. C.; Assev, S.; van der Mei, H. C.; Busscher, H. J.; Scheie, A. A. *Infect. Immun.* **2002**, *70*, 249–256.
104. Galliani, S.; Cremieux, A.; van der Auwera, P.; Viot, M. *J. Lab Clin. Med.* **1996**, *127*, 71–80.
105. Busscher, H. J.; Norde, W.; van der Mei, H. C. *Appl. Environ. Microbiol.* **2008**, *74*, 2559–2564.
106. Hinterdorfer, P.; Dufrene, Y. F. *Nat. Meth.* **2006**, *3*, 347–355.
107. Rivas, J. M.; Speziale, P.; Patti, J. M.; Hook, M. *Curr. Opin. Drug Discov. Devel.* **2004**, *7*, 223–227.
108. Kasemo, B.; Lausmaa, J. *Environ. Health Perspect.* **1994**, *102*(Suppl 5), 41–45.
109. Callister, W. D. In *Materials Science and Engineering: An Introduction*; Callister, W. D., Ed.; Wiley: New York, 2003; p 451.
110. Kasemo, B. *Surf. Sci.* **2002**, *500*, 656–677.
111. Ratner, B. D. In *Surface Modification of Polymeric Materials*; Ratner, B. D., Castner, D. G., Eds.; Plenum Press: New York, 1996; p 1.
112. Mrksich, M. *Chem. Soc. Rev.* **2000**, *29*, 267–273.
113. Hubbell, J. A. *Trends Polym. Sci.* **1994**, *2*, 20–25.
114. Chinn, J. A.; Horbett, T. A.; Ratner, B. D. *Meth. Cell Sci. J. Tissue Cult. Meth.* **1994**, *16*, 155–159.
115. Altankov, G.; Groth, T. *J. Mater. Sci. Mater. Med.* **1994**, *5*, 732–737.
116. Garcia, A. J.; Keselowsky, B. G. *Crit. Rev. Eukaryot. Gene Expr.* **2002**, *12*, 151–162.
117. Boks, N. P.; Norde, W.; van der Mei, H. C.; Busscher, H. J. *Microbiology* **2008**, *154*, 3122–3133.
118. Bruinsma, G. M.; van der Mei, H. C.; Busscher, H. J. *Biomaterials* **2001**, *22*, 3217–3224.
119. Cerca, N.; Pier, G. B.; Vilanova, M.; Oliveira, R.; Azeredo, J. *Res. Microbiol.* **2005**, *156*, 506–514.
120. Hogt, A. H.; Dankert, J.; de Vries, J. A.; Feijen, J. *J. Gen. Microbiol.* **1983**, *129*, 2959–2968.
121. Miller, M. J.; Ahearn, D. G. *J. Clin. Microbiol.* **1987**, *25*, 1392–1397.
122. Vacheethasanee, K.; Temenoff, J. S.; Higashi, J. M.; *et al*. *J. Biomed. Mater. Res.* **1998**, *42*, 425–432.
123. Ki, D. P.; Young, S. K.; Dong, K. H.; *et al*. *Biomaterials* **1998**, *19*, 851–859.
124. James, N. R.; Jayakrishnan, A. *Biomaterials* **2003**, *24*, 2205–2212.
125. Cunliffe, D.; Smart, C. A.; Alexander, C.; Vulfson, E. N. *Appl. Environ. Microbiol.* **1999**, *65*, 4995–5002.
126. Vigeant, M. A.; Ford, R. M.; Wagner, M.; Tamm, L. K. *Appl. Environ. Microbiol.* **2002**, *68*, 2794–2801.
127. Anderson, B. N.; Ding, A. M.; Nilsson, L. M.; *et al*. *J. Bacteriol.* **2007**, *189*, 1794–1802.
128. Thomas, W. E.; Nilsson, L. M.; Forero, M.; Sokurenko, E. V.; Vogel, V. *Mol. Microbiol.* **2004**, *53*, 1545–1557.
129. Brunette, D. M.; Tengvall, P.; Textor, M.; Thomsen, P. *Titanium in Medicine. Material Science, Surface Science, Engineering, Biological Responses and Medical Applications*; Springer: New York, 2001.
130. Whitehead, K. A.; Verran, J. *Food Bioproducts Process.* **2006**, *84*, 253–259.
131. Bürgers, R.; Gerlach, T.; Hahnel, S.; Schwarz, F.; Handel, G.; Gosau, M. *Clin. Oral Implants Res.* **2010**, *21*, 156–164.
132. Verheyen, C. C. P. M.; Dhert, W. J. A.; de Blieck-Hogervorst, J. M. A.; van der Reijden, T. J. K.; Petit, P. L. C.; de Groot, K. *Biomaterials* **1993**, *14*, 383–391.
133. Edwards, K. J.; Schrenk, M. O.; Hamers, R.; Banfield, J. F. *Am. Mineral.* **1998**, *83*, 1444–1453.
134. Hosoya, N.; Honda, K.; Iino, F.; Arai, T. *J. Dent.* **2003**, *31*, 543–548.
135. Charman, K. M.; Fernandez, P.; Loewy, Z.; Middleton, A. M. *Lett. Appl. Microbiol.* **2009**, *48*, 472–477.
136. Puckett, S. D.; Taylor, E.; Raimondo, T.; Webster, T. J. *Biomaterials* **2010**, *31*, 706–713.
137. Scheuerman, T. R.; Camper, A. K.; Hamilton, M. A. *J. Colloid Interf. Sci.* **1998**, *208*, 23–33.
138. Hoek, E. M.; Agarwal, G. K. *J. Colloid Interf. Sci.* **2006**, *298*, 50–58.
139. Curtis, A. S. G.; Wilkinson, C. D. W. *J. Biomater. Sci. Polym. Ed.* **1998**, *9*, 1313–1329.
140. Manwaring, M. E.; Walsh, J. F.; Tresco, P. A. *Biomaterials* **2004**, *25*, 3631–3638.
141. Dalby, M. J.; Gadegaard, N.; Tare, R.; *et al*. *Nat. Mater.* **2007**, *6*, 997–1003.
142. Ploux, L.; Anselme, K.; Dirani, A.; Ponche, A.; Soppera, O.; Roucoules, V. *Langmuir* **2009**, *25*, 8161–8169.
143. Singhvi, R.; Stephanopoulos, G.; Wang, D. I. *Biotechnol. Bioeng.* **1994**, *43*, 764–771.
144. von Recum, A. F.; van Kooten, T. G. *J. Biomater. Sci. Polym. Ed* **1995**, *7*, 181–198.
145. Berry, C. C.; Campbell, G.; Spadiccino, A.; Robertson, M.; Curtis, A. S. *Biomaterials* **2004**, *25*, 5781–5788.
146. Dalby, M. J.; Giannaras, D.; Riehle, M. O.; Gadegaard, N.; Affrossman, S.; Curtis, A. S. *Biomaterials* **2004**, *25*, 77–83.
147. Wan, Y.; Wang, Y.; Liu, Z.; *et al*. *Biomaterials* **2005**, *26*, 4453–4459.
148. Meredith, D. O.; Eschbach, L.; Wood, M. A.; Riehle, M. O.; Curtis, A. S.; Richards, R. G. *J. Biomed. Mater. Res. A* **2005**, *75*, 541–555.
149. Hamilton, D. W.; Wong, K. S.; Brunette, D. M. *Calcif. Tissue Int.* **2006**, *78*, 314–325.
150. Meredith, D. O.; Riehle, M. O.; Curtis, A. S.; Richards, R. G. *J. Orthop. Res.* **2007**, *25*, 1523–1533.
151. Biggs, M. J. P.; Richards, R. G.; Gadegaard, N.; Wilkinson, C. D. W.; Oreffo, R. O. C.; Dalby, M. J. *Biomaterials* **2009**, *30*, 5094–5103.

152. Biggs, M. J.; Richards, R. G.; McFarlane, S.; Wilkinson, C. D.; Oreffo, R. O.; Dalby, M. J. *J. R. Soc. Interf.* **2008**, *5*, 1231–1242.
153. Poulsson, A. H.; Mitchell, S. A.; Davidson, M. R.; Johnstone, A. J.; Emmison, N.; Bradley, R. H. *Langmuir* **2009**, *25*, 3718–3727.
154. Truong, V. K.; Rundell, S.; Lapovok, R.; *et al*. *Appl. Microbiol. Biotechnol.* **2009**, *83*, 925–937.
155. Decuzzi, P.; Ferrari, M. *Biomaterials* **2010**, *31*, 173–179.
156. Flint, S. H.; Brooks, J. D.; Bremer, P. J. *J. Food Eng.* **2000**, *43*, 235–242.
157. Chehroudi, B.; Brunette, D. M. *Biomaterials* **2002**, *23*, 229–237.
158. Hayes, J. S.; Richards, R. G. *Expert. Rev. Med. Dev.* **2010**, *7*, 131–142.
159. Darouiche, R. O.; Raad, I. I.; Heard, S. O.; *et al*. *N. Engl. J. Med.* **1999**, *340*, 1–8.
160. Martinez-Gutierrez, F.; Olive, P. L.; Banuelos, A.; *et al*. *Nanomedicine* **2010**.
161. Baveja, J. K.; Willcox, M. D.; Hume, E. B.; Kumar, N.; Odell, R.; Poole-Warren, L. A. *Biomaterials* **2004**, *25*, 5003–5012.
162. Hetrick, E. M.; Schoenfisch, M. H. *Biomaterials* **2007**, *28*, 1948–1956.
163. Wu, P.; Grainger, D. W. *Biomaterials* **2006**, *27*, 2450–2467.
164. Noda, Y.; Kanemasa, Y. *Physiol. Chem. Phys. Med. NMR* **1984**, *16*, 263–274.
165. Harkes, G.; Dankert, J.; Feijen, J. *J. Biomater. Sci. Polym. Ed* **1992**, *3*, 403–418.
166. Everaert, E. P.; Belt-Gritter, B.; van der Mei, H. C.; *et al*. *J. Mater. Sci. Mater. Med.* **1998**, *9*, 147–157.
167. Quirynen, M. *J. Dent.* **1994**, *22*(Suppl 1), S13–S16.
168. Tsibouklis, J.; Stone, M.; Thorpe, A. A.; *et al*. *Biomaterials* **1999**, *20*, 1229–1235.
169. Gottenbos, B.; van der Mei, H. C.; Busscher, H. J.; Grijpma, D. W.; Feijen, J. *J. Mater. Sci. Mater. Med.* **1999**, *10*, 853–855.
170. Park, K. D.; Kim, Y. S.; Han, D. K.; *et al*. *Biomaterials* **1998**, *19*, 851–859.
171. Terada, A.; Yuasa, A.; Tsuneda, S.; Hirata, A.; Katakai, A.; Tamada, M. *Colloids Surf. B: Biointerfaces* **2005**, *43*, 99–107.
172. Saldarriaga, F. I.; Mei, H. C.; Metzger, S.; *et al*. *Acta Biomater.* **2010**, *6*, 1119–1124.
173. Fundeanu, I.; van der Mei, H. C.; Schouten, A. J.; Busscher, H. J. *Colloids Surf. B: Biointerfaces* **2008**, *64*, 297–301.
174. Holmes, P. F.; Currie, E. P.; Thies, J. C.; van der Mei, H. C.; Busscher, H. J.; Norde, W. *J. Biomed. Mater. Res. A* **2009**, *91*, 824–833.
175. Nejadnik, M. R.; van der Mei, H. C.; Norde, W.; Busscher, H. J. *Biomaterials* **2008**, *29*, 4117–4121.
176. Leckband, D.; Sheth, S.; Halperin, A. *J. Biomater. Sci. Polym. Ed* **1999**, *10*, 1125–1147.
177. Saldarriaga, F. I.; van der Mei, H. C.; Lochhead, M. J.; Grainger, D. W.; Busscher, H. J. *Biomaterials* **2007**, *28*, 4105–4112.
178. Maddikeri, R. R.; Tosatti, S.; Schuler, M.; *et al*. *J. Biomed. Mater. Res. A* **2008**, *84*, 425–435.
179. Schuler, M.; Trentin, D.; Textor, M.; Tosatti, S. G. *Nanomedicine (Lond)* **2006**, *1*, 449–463.
180. VandeVondele, S.; Voros, J.; Hubbell, J. A. *Biotechnol. Bioeng.* **2003**, *82*, 784–790.
181. Chua, P. H.; Neoh, K. G.; Kang, E. T.; Wang, W. *Biomaterials* **2008**, *29*, 1412–1421.
182. Harris, L. G.; Tosatti, S.; Wieland, M.; Textor, M.; Richards, R. G. *Biomaterials* **2004**, *25*, 4135–4148.
183. Subbiahdoss, G.; Pidhatika, B.; Coullerez, G.; *et al*. *Eur. Cell Mater.* **2010**, *19*, 205–213.
184. Balazs, D. J.; Triandafillu, K.; Wood, P.; *et al*. *Biomaterials* **2004**, *25*, 2139–2151.
185. Amanatides, E.; Mataras, D.; Katsikogianni, M.; Missirlis, Y. F. *Surface and Coatings Technology* **2006**, *200*, 6331–6335.
186. Eloy, R.; Parrat, D.; Duc, T. M.; Legeay, G.; Bechetoille, A. *J. Cataract Refract. Surg.* **1993**, *19*, 364–370.
187. Canal, C.; Gaboriau, F.; Villeger, S.; Cvelbar, U.; Ricard, A. *Int. J. Pharm.* **2009**, *367*, 155–161.
188. Yoshinari, M.; Oda, Y.; Kato, T.; Okuda, K. *Biomaterials* **2001**, *22*, 2043–2048.
189. Ewald, A.; Gluckermann, S. K.; Thull, R.; Gbureck, U. *Biomed. Eng. Online* **2006**, *5*, 22.
190. Atiyeh, B. S.; Costagliola, M.; Hayek, S. N.; Dibo, S. A. *Burns* **2007**, *33*, 139–148.
191. Agarwal, A.; Weis, T. L.; Schurr, M. J.; *et al*. *Biomaterials* **2010**, *31*, 680–690.
192. Hantzschel, N.; Hund, R. D.; Hund, H.; Schrinner, M.; Luck, C.; Pich, A. *Macromol. Biosci.* **2009**, *9*, 444–449.
193. Lee, D.; Cohen, R. E.; Rubner, M. F. *Langmuir* **2005**, *21*, 9651–9659.
194. Vasilev, K.; Sah, V.; Anselme, K.; *et al*. *Nano. Lett.* **2010**, *10*, 202–207.

4.408. Integrin-Activated Reactions to Metallic Implant Surfaces

K B Sagomonyants and G Gronowicz, University of Connecticut Health Center, Farmington, CT, USA

© 2011 Elsevier Ltd. All rights reserved.

4.408.1.	**Introduction**	101
4.408.2.	**Integrins**	102
4.408.2.1.	Integrins Subunits and Adhesion	102
4.408.2.2.	Integrin Structure	102
4.408.3.	**Integrin Function**	103
4.408.3.1.	Cells Adhesion, Survival, Growth, and Differentiation	103
4.408.3.2.	Bone Cells	104
4.408.3.3.	Integrins and Growth Factor Receptors	104
4.408.4.	**Integrin-Signaling Pathways**	105
4.408.4.1.	Intracellular-Signaling Pathways	105
4.408.5.	**Integrin Binding to Biomaterials**	105
4.408.5.1.	Initial Binding of Serum Proteins to Implant Materials	105
4.408.5.2.	Integrin-Mediated Cellular Responses to Implant Materials	107
4.408.5.3.	Inflammatory Responses	108
4.408.6.	**Functionalizing Implant Surfaces Using Adhesion Molecules**	108
4.408.6.1.	General Description of Functionalizing Implant Surfaces	108
4.408.6.2.	*In Vitro* Studies Using Adhesion Molecules on Implant Surfaces	109
4.408.6.3.	*In Vivo* Studies Using Adhesion Molecules on Implant Surfaces	109
4.408.6.4.	Functionalizing Biomaterials with Short Versus Long Peptides	110
4.408.6.5.	Functionalizing Biomaterials with Multiple Peptides	110
4.408.7.	**Conclusions**	111
References		111

Abbreviations

ADAM	A disintegrin and metalloproteinase
BMP2	Bone morphogenetic protein 2
ECM	Extracellular matrix
EGF	Epidermal growth factor
FAK	Focal adhesion kinase
GTPase	Enzyme that can bind and hydrolyze guanosine triphosphate (GTP)
HA	Hydroxylapatite
HY	Hyaluronic acid
iC3b	Inactivated complement C3b
ICAM	Intracellular adhesion molecule
IGF-1	Insulin-like growth factor-1
PDGF	Platelet-derived growth factor
PGE_2	Prostaglandin E_2
RGD	Arginine-glycine-aspartic acid
TCP	Tissue culture plastic
TGF-β	Transforming growth factor-β
Ti	Titanium
VCAM	Vascular adhesion molecule
VEGF	Vascular endothelial growth factor

4.408.1. Introduction

Many biomaterials used in tissue engineering have sufficient mechanical properties with no toxicity and low or no pathological responses. However, one-third to one-half of these implants require replacement within 10–25 years.[1,2] With the current increase in demand for implants in younger patients and in rapidly aging populations, there is a need to improve the functional integration and life span of these implants at the cellular level in order to be able to substitute or augment complex tissues and organs. In many cases, stimulation of the ingrowth of specific, native, or seeded cells to form a continuum with the biomaterial is required. In addition, there are patients in whom aging, disease, or unique tissue responses, due to genetics or environmental issues, compromise the success of the implant. Therefore, novel approaches to tissue engineering are needed to address such specific physiological conditions. For bone implants, the formation of a direct and intimate implant–bone interface called osseointegration is crucial for the biomechanical stability of the implant, the ability to provide load transfer at an optimal level, and biocompatibility.[3] Osseointegration requires an interaction between the cells in the bone and the biomaterial. One of the major pathways by which cells adhere and interact with their extracellular environment is through integrins, which activate intracellular-signaling pathways essential for cell survival, growth, and differentiation. Therefore, understanding the role of integrins in the response to implant materials is essential for the

success of these materials in osseointegration and other tissue interactions. Discussed in this chapter are brief overview of integrins, their cellular functions, their signaling pathways, and biomaterials having integrin-activating surfaces, with particular attention to bone. Our goal is to consider the value of integrin-mediated tissue engineering in addressing some of the issues for long-term implant stability and function.

4.408.2. Integrins

4.408.2.1. Integrins Subunits and Adhesion

The integrins are a superfamily of cell adhesion receptors that bind to the extracellular matrix (ECM) proteins; they also mediate certain cell–cell interactions. Integrins are found only in the metazoans with no known homologs in plants, fungi, or prokaryotes.[4] They are transmembrane receptors composed of a α- and β-heterodimer, and the combination of the α- and β-subunits determines the ligand specificity of the integrin, even though many integrins can bind to the same ligand. In mammals, at least 19 α- and 8 β-integrin subunit genes have been identified and they encode polypeptides forming at least 25 different receptors (**Table 1**).[5,7,8] Alternative splicing of mRNA of some α- and β-subunits and posttranslational modifications in integrin subunits further increase the diversity of the integrin family to 24 α- and 9 β-subunits.[6,9–11] Although more than 20 integrin heterodimers have been identified, the majority of which recognize ECM components, there are also counter receptors on the surface of neighboring cells.[6]

Table 1 Combinations of integrin subunits and their protein ligands

Subunits		*Ligands*
β_1	α_1	Collagens, laminins
	α_2	Collagens, laminins, fibronectin
	α_3	Laminins, fibronectin, collagens, thrombospondin
	α_4	Fibronectin, VCAM, osteopontin
	α_5	Fibronectin, fibrinogen, ADAMs
	α_6	Laminin, ADAMs
	α_7	Laminins
	α_8	Fibronectin, tenascin
	α_9	Tenascin, collagen, osteopontin, laminin, VCAM, ADAMs
	α_{10}	Collagens
	α_{11}	Collagens
	α_v	Fibronectin, vitronectin, thrombospondin
β_2	α_L	ICAMs
	α_M	ICAM, fibrinogen, iC3b
	α_X	Fibrinogen, ICAM, iC3b
	α_D	VCAM, ICAMs
β_3	α_{IIb}	Collagens, fibronectin, vitronectin, von Willebrand factor fibrinogen, thrombospondin, matrix metalloproteinase-2, disintegrins
	α_v	Fibronectin, vitronectin, fibrinogen, thrombospondin, von Willebrand factor, osteopontin, laminin, disintegrins, tenascin, bone sialoprotein, ADAMs
β_4	α_6	Laminins
β_5	α_v	Vitronectin, bone sialoprotein, fibronectin
β_6	α_v	Fibronectin, tenascin
β_7	α_4	Fibronectin, VCAM
	α_E	E-cadherin
β_8	α_v	Collagens, laminins, fibronectin

Subunit–ligand-binding structures were reported by Plow *et al*.[5] and Van der Flier and Sonnenberg.[6]

ICAM, intracellular adhesion molecule; VCAM, vascular adhesion molecule; iC3b, inactivated complement component C3b; ADAM, a disintegrin and metalloproteinase.

The ECM is a complex network of high molecular weight proteins such as laminin, fibronectin and collagens, and polysaccharides. The ECM provides structural support to the cells, acts as a physical barrier or selective filter for soluble molecules, provides a substrate for cell migration, and sequesters growth factors and other molecules that are important for cell activities, growth, and differentiation. According to the specificity of integrin–ligand binding, all mammalian integrins can be grouped in several categories: (1) laminin-binding integrins ($\alpha_1\beta_1$, $\alpha_2\beta_1$, $\alpha_3\beta_1$, $\alpha_6\beta_1$, $\alpha_7\beta_1$, $\alpha_9\beta_1$, $\alpha_v\beta_3$, $\alpha_6\beta_4$, and $\alpha_v\beta_8$); (2) collagen-binding integrins ($\alpha_1\beta_1$, $\alpha_2\beta_1$, $\alpha_3\beta_1$, $\alpha_9\beta_1$, $\alpha_{10}\beta_1$, $\alpha_{11}\beta_1$, and $\alpha_{IIb}\beta_3$); (3) leukocyte integrins ($\alpha_L\beta_2$, $\alpha_M\beta_2$, $\alpha_X\beta_2$, and $\alpha_D\beta_2$), and (4) arginine-glycine-aspartic acid (RGD)-recognizing integrins ($\alpha_5\beta_1$, $\alpha_V\beta_1$, $\alpha_V\beta_3$, $\alpha_V\beta_5$, $\alpha_V\beta_6$, $\alpha_V\beta_8$, and $\alpha_{IIb}\beta_3$) (for review, see Takada *et al*.[12]). RGD was identified as the amino acid sequence in fibronectin and other cell adhesion proteins that could modulate cell attachment.[13] RGD sequences have been found in diverse species such as sea urchins, amoebae, and mammals.[12] Integrins containing the α_4, α_5, α_8, α_{IIb}, and α_v-subunits bind to ECM proteins, mostly fibronectin and vitronectin that contain the RGD sequence. Laminins and collagens also contain RGD sequences but these are often cryptic and inaccessible.[6] In general, integrins on hematopoietic cells bind to counter receptors on other cells (e.g., intercellular adhesion molecules, ICAMs, vascular cell adhesion molecule-1, VCAM-1, and disintegrins/metalloproteinases such as the different ADAMs) or plasma proteins (e.g., fibrinogen) and complement factors (iC3b).[6] Although most integrins are widely expressed in various tissues, some integrins are expressed only in a certain type of cell or tissue. For example, $\alpha_{IIb}\beta_3$ integrin is found in platelets, $\alpha_6\beta_4$ in keratinocytes, $\alpha_E\beta_7$ in T cells, and $\alpha_4\beta_7$ is limited to a subset of memory T cells.[12] The integrin receptors that have been most studied in bone are the vitronectin receptor ($\alpha_v\beta_3$),[14] the type I collagen receptor ($\alpha_2\beta_1$),[15] and the fibronectin receptor ($\alpha_5\beta_1$),[16,17] and they have been found in human osteoblasts.[18,19] Osteoblasts primarily express β_1, while osteoclasts express both β_1 and β_3.[18] Various hormones and growth factors have been shown to modulate integrin levels in osteoblasts and osteocytes.[20,21] The $\alpha_v\beta_3$ integrin is the major integrin involved in osteoclast-mediated bone resorption, although osteoclasts also express $\alpha_2\beta_1$ and $\alpha_v\beta_1$.[22]

4.408.2.2. Integrin Structure

Integrins are composed of noncovalently associated α- and β-subunits; these subunits are type I glycoproteins, consisting of large extracellular and short cytoplasmic domains,[8] and will be briefly described. The length of the α-chain is 1008–1152 amino acids, and it contains a cytoplasmic domain of 22–32 amino acids and a transmembrane domain of 20–29 amino acids. The length of the β-chain is around 770 amino acids, and contains a cytoplasmic domain of 20–50 amino acids (except for cytoplasmic domain of β_4 integrin),[23] and an intramembranous domain of 26–29 amino acids.[24]

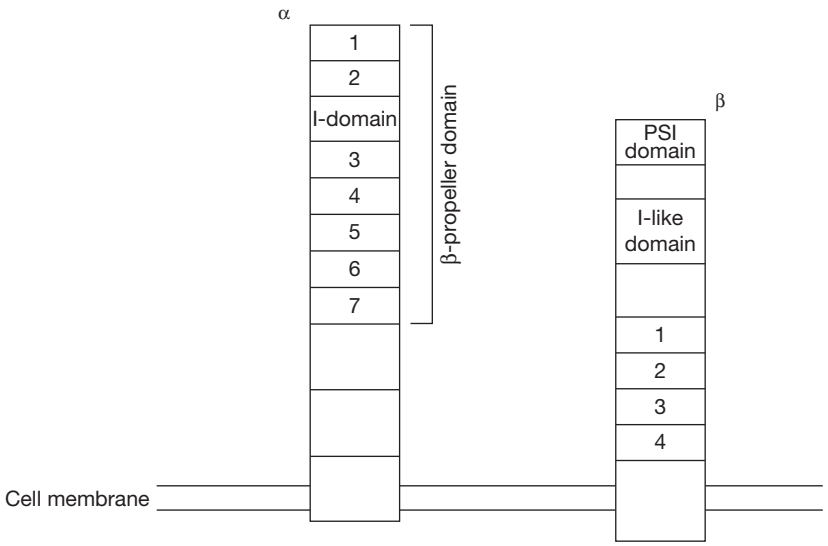

Figure 1 General integrin structure. Organization of the various domains in the of α- and β-subunits. The presence of the I-domain depends on the type of α-subunit. The I-domain is present in seven human α-subunits between β-propeller repeats 2 and 3. The RGD site is located at the interface between the β-propeller domain on the α-subunit and the I-like domain on the β-subunit. All β-integrin subunits contain an I-like domain and EGF-like repeats (1, 2, 3, and 4 on the β-subunit in the diagram). PSI: plexin–semaphorin–integrin domain. The general integrin structure was reported by Takada *et al*.[12] and Takagi and Springer.[25]

The overall shape of the associated integrin subunits can be described by the presence of two, long stalk regions containing C-terminal segments from both α- and β-subunits that connect the extracellular ligand-binding globular headpiece to the transmembrane and cytoplasmic domains (**Figure 1**).[5,6,8,26] The crystal structure of the integrin subunits has been elucidated in great detail in the last decade using various techniques, including electron microscopy, X-ray scattering, site-directed mutagenesis, and computer modeling.[26–31] It has been demonstrated that the extracellular part of the human $\alpha_V\beta_3$[30,31] and $\alpha_{IIb}\beta_3$[29] integrins consists of several domains. The ligand-binding site of integrins is composed of the β-propeller domain of the α-subunit and the I-like domain of the β-subunit. The I-like domain appears to directly bind to ligand in integrins that lack I-domains, and indirectly regulate ligand binding by integrins that contain I-domains. The RGD site is located at the interface between the β-propeller domain on the α-subunit and the I-like domain on the β-subunit.[30] The β-propeller domain contains seven repeats of ~60 amino acids and is folded into a seven-bladed β-propeller structure (corresponding to these repeats) that is similar to the β-subunit of a heterotrimeric G-protein. X-ray scattering and mutagenesis studies have demonstrated that a number of amino acid residues that are critical for ligand binding to the human $\alpha_{IIb}\beta_3$[32] and $\alpha_5\beta_1$ integrins are located within the β-propeller domain.[28]

I-like domains (~200 amino acids) are homologues to the A domain of the von Willebrand factor[33] and contain a metal-ion-dependent adhesive site (MIDAS) and a structurally similar metal-binding motif.[8,30,34] Integrins require divalent cations such as Ca^{2+} or Mg^{2+} for binding to their ligands. Upon ligand binding, the I-like domain undergoes a conformational change from the closed (inactive) to the open (active) state.[25,30,31] Based on the presence of the I-like domain in the α-subunits, mammalian integrins can be grouped into integrins that have the I-like domain (α_1, α_2, α_{10}, α_D, α_E, α_L, α_M, and α_X) and those without it (α_3, α_4, α_5, α_6, α_7, α_8, α_9, α_V, and α_{IIb}).[12] A critical role for the I-like domain of the β_1-subunit[35] and β_2-subunit[36] in ligand binding has been demonstrated.

4.408.3. Integrin Function

4.408.3.1. Cells Adhesion, Survival, Growth, and Differentiation

The binding of ECM proteins to the integrins triggers a series of intracellular signaling events that lead to changes in conformation and cell behavior such as adhesion, proliferation, survival or apoptosis, cell shape, motility, gene expression, and differentiation. Integrins have the ability to transduce signals from the ECM to the cytoplasm and to the nucleus of the cell.[37] Evidence of integrins also being mechanotransducers of force has come from studies in which mechanical stress was applied to cell surface receptors using a magnetic twisting device.[37] The integrin β_1, associated with the cytoskeleton, showed increased stiffening (ratio of stress to strain) which was directly proportional to the stress applied. Integrins and their ligands have a critical role in embryonic development, immune responses, leukocyte homing and activation, bone formation and resorption, clot retraction, cellular responses to mechanical stress, apoptosis, angiogenesis, and hemostasis, and are also involved in cancer and other human diseases, and can be receptors for many viruses and bacteria.[4,7,38–41] The involvement of integrins in these various normal and pathological processes has been demonstrated in several studies using integrin knockout animals. Integrins have been shown to be crucial for development (β_1); immune responses (β_2); cancer, inflammatory responses, and atherosclerosis (β_3 integrins); vasculogenesis (α_V); lymphangiogenesis ($\alpha_9\beta_1$); thrombus formation ($\alpha_{IIb}\beta_3$); and the integrity of the

skin ($\alpha_6\beta_4$) (for review, see De Arcangelis and Georges-Labouesse[42] and Takada *et al.*[12]).

Integrins, particularly $\alpha_5\beta_1$, regulate cell proliferation and apoptosis.[43,44] Overexpression of the α_5-subunit in transformed cell lines suppresses tumorigenicity and anchorage-independent proliferation but promotes anchorage-dependent proliferation. It also upregulates early gene expression of c-fos, c-jun, and jun-B, and this correlates with cell proliferation.[43] In myoblasts, the α_5-subunit promotes anchorage-dependent proliferation,[45] and cell attachment to fibronectin via the α_5-subunit promotes cell survival in Chinese hamster ovary cells.[46] However, in myoblasts, cell attachment alone is not sufficient to protect myoblasts from cell death, unless particular growth factors are present,[45] and thus regulation of cell survival by the α_5-subunit's is cell-type dependent.

The interactions of integrins with the ECM and their other ligands are critical for normal cell function and survival, and integrins have specific, nonredundant, and important functions that are apparent in the phenotypes of the integrin knockout mice. Preimplantation development is blocked by the absence of β_1 while perinatal lethality is found in knockouts of α_3, α_6, α_8, α_v, β_4, or β_8 integrins. Major developmental defects are apparent when α_4, α_5, α_v, or β_8 are absent. Knockouts of α_L, α_M, α_E, β_2, and β_7 have defects in leukocyte function, β_6 in inflammation, α_{IIb}, β_3, and α_2 in hemostasis, β_3 in bone remodeling, and α_1 and β_3 in angiogenesis.[4,47]

4.408.3.2. Bone Cells

Early studies with soluble RGD-containing peptides demonstrated that integrins have an important role in bone formation as these peptides inhibited bone formation and resorption, and decreased the expression of bone matrix proteins.[17,48,49] Conversely, when RGD peptides were bound to a substrate, they stimulated osteoblast proliferation.[50] Since osteoblasts sequentially express specific bone matrix proteins during development (fibronectin, alkaline phosphatase, and type I collagen being early markers of osteoblast differentiation *in vivo*, and osteocalcin being expressed in the later stages[51]) and many of them have RGD sequences, experiments with integrin-perturbing antibodies have shown major effects on bone structure. The $\alpha_5\beta_1$ integrin was shown to be important in mineralization of osteoblast cultures,[52–54] as inhibition of $\alpha_5\beta_1$ in early the osteoblast cultures resulted in the inhibition of mineralization and osteocalcin expression, compared to untreated control cultures.[53] Integrin subunits α_v, α_2, and β_1 have also been shown to mediate human osteoblast adhesion through the generation of focal adhesion sites.[14] Neutralization of α_1- and α_2-integrin subunits and type I collagen has also been shown to inhibit BMP2-induced mineralization and alkaline phosphatase activity in cultured immortalized 2T3 mouse osteoblast cells.[55] In addition, blocking the α_2 integrin with specific inhibitory antibodies in mOG2-luciferase-transfected MC3T3-E1 preosteoblast cells greatly inhibited osteocalcin promoter expression as well as osteocalcin mRNA expression in a dose-dependent manner, while blocking the α_5-subunit did not have any effect.[56] In agreement with this, blocking the α_2-subunit significantly inhibited alkaline phosphatase activity and osteocalcin secretion of rat bone marrow stromal cells.[57] Takeuchi *et al.*[58] demonstrated that blocking of the α_2-subunit with α_2-inhibitory antibodies significantly inhibited alkaline phosphatase activity and disrupted ECM organization in cultured MC3T3-E1 cells, while blocking of the α_5-subunit did not have any effect. Blocking $\alpha_2\beta_1$ integrin with inhibitory antibodies significantly inhibited mineralization in the UMR-106-01-BSP osteosarcoma cell line cultures in a dose-dependent manner.[59] The binding of osteoblast RGDs has been shown to prevent apoptosis.[60] In addition, specific integrins also mediate the response of osteoblasts to fluid-shear stress[61] and the differentiation of human bone marrow stromal cells into the osteoblast lineage.[62,63] In studies with MG-63 human osteoblast-like cells grown on titanium, antibodies to $\alpha_5\beta_1$ reduced osteoblast proliferation but not differentiation. Using siRNA strategy, the α_2-silenced MG-63 human osteoblast-like cells were used to show that $\alpha_2\beta_1$ affected the expression of alkaline phosphatase and osteocalcin, and that the responses of these cells to various hormones and growth factors varied.[64] The RGD sequence is found in numerous bone matrix proteins such as bone sialoprotein, collagens, fibronectin, thrombospondin, vitronectin, decorin, and tenascin.[5]

Other cells in bone are also dependent on integrins for their function. Osteocytes have been shown to bind to the canalicular wall through the β_1-containing integrins and the $\alpha_v\beta_3$ integrin.[20,65] It was also shown that the β_1 integrins on osteocytes mediate specific aspects of mechanotransduction and affect bone geometry in mice undergoing hind limb unloading.[66] Integrins may play a particularly important role in cells of the osteoblast lineage, which are constantly involved in a remodeling process; this process requires the translation of mechanical forces and changes in the extracellular environment into internal biochemical signals which in turn lead to the formation and remodeling of the bony skeleton.[63] Bone resorption by osteoclasts is also dependent on integrin activity, the $\alpha_v\beta_3$ integrin being critical for osteoclast function (see reviews Nakamura *et al.*[22] and Teitelbaum[67]).

4.408.3.3. Integrins and Growth Factor Receptors

In many cases, integrins are necessary for the optimal activity of particular growth factors as cells need to be adherent to the substrate via integrins. The receptors for insulin/insulin-like growth factor-1 (IGF-1), platelet-derived growth factor (PDGF), vascular endothelial growth factor (VEGF), epidermal growth factor (EGF), and thrombin require cell attachment. Integrin clustering and association with cytoskeletal elements and focal adhesion kinase (FAK) promote integrin-growth factor receptor complexes that can partially activate the signaling of these growth factors.[4,68–74] The integrin $\alpha_v\beta_3$ has been immunoprecipitated as a complex with IGF-1, PDGF, and VEGF receptors, and the $\alpha_5\beta_1$ integrin has been shown to be associated with EGF receptors.[68] Signaling through β_1 and β_3 has been implicated in transforming growth factor β (TGF-β) signaling,[75,76] and the RGD peptide has also been shown to stimulate the transcription and secretion of TGF-β upon integrin activation.[77] In addition, TGF-β has been shown to upregulate integrins in epithelial cells and myofibroblasts.[78,79]

Integrins have a critical role in regulating adhesion, proliferation, and differentiation of cells in the osteoblast lineage and in other cells in the bone. Therefore, testing integrin-modulating peptides to stimulate bone formation was a logical

step in tissue engineering of bones. The ultimate design of implant materials with integrin-activating capacity also requires a knowledge of integrin-signaling pathways, and this further complicates our ability to design specific biomaterials that are anabolic to the bone.

4.408.4. Integrin-Signaling Pathways

4.408.4.1. Intracellular-Signaling Pathways

Many integrins are not constitutively active even though they are expressed on the cell surface and require activation to transmit intracellular signals and thus change cell behavior.[4] A major mechanism by which integrins transmit signals intracellularly is through integrin binding and clustering, which results in the formation of focal adhesion sites at which the integrins connect the ECM with the intracellular cytoskeleton (see Danen and Yamada[80] and Van der Flier and Sonnenberg[6] for excellent reviews and diagrams of integrin signaling). Intracellular signals are then propagated by the association of proteins, such as talin, FAK, src, and RAS, with the other components in the focal adhesion site. Talin links integrins to the actin cytoskeleton either directly or indirectly by interacting with vinculin and α-actinin. FAK($pp125^{FAK}$), a tyrosine kinase, binds to the β_1 integrin cytoplasmic tail,[81] and initiates a signaling cascade of autophosphorylation.[82] Intermediate steps involving phosphorylation lead to the transient phosphorylation of mitogen-activated protein kinases (MAP kinase; ERK1 and ERK2) on their threonine and tyrosine residues. Furthermore, ligand binding and tension induce phosphorylation by members of the Src protein kinase family, including c-Src, Csk, and Fyn, at the focal adhesion sites which leads to the recruitment and activation of downstream signaling molecules, for example, Rho-like GTPases, phospholipase-C (PLC), and the ERK- and JNK-signaling cascades[83,84] (**Figure 2**).

The Rho family of GTPases plays an important role in cytoskeletal rearrangement, and its members are active when they are bound to GTP but inactive when bound to GDP.[86] GTP-activation of Rho-like GTPases is regulated by guanidine exchange factors (GEFs), GTPase-activating proteins (GAPs), and guanidine dissociating factors (GDIs). Rho is believed to act upstream of integrin activation[85] and plays a major role in actomyosin-based contractility during the formation of stress fibers and focal adhesions in spread cells.[86] Two other small GTPases that have been located upstream of integrin activation are R-ras[87] and Rap1.[88,89] Ultimately, this signaling cascade leads to cytoskeletal rearrangement, anchorage-dependent entry into the S-phase and gene transcription.[90] Integrin-mediated signaling is characterized by the formation of a signaling complex that is modified and strengthened by multiple interactions between its components which are also linked to numerous other pathways. Such multiple interactions make it difficult to define the primary and crucial regulatory interactions in integrin-mediated signaling.[91]

The nuclear target proteins of MAP kinases include Fos and Jun (members of the AP-1 transcription complex) which control gene expression.[92] Myc is another nuclear regulatory factor involved in transcriptional control of preosteoblastic proliferation,[93] which is also activated. The immediate early genes, c-fos and c-jun, are required for the G0/G1 transition while c-myc is present in measurable quantities throughout the cell cycle and is believed to be involved in the G1 to S transition.[43] AP-1 promoters are found in several bone ECM proteins, such as type I collagen,[94] alkaline phosphatase,[95] osteocalcin,[96,97] and osteopontin.[98] Overexpression of c-fos in transgenic mice results in the development of osteosarcomas[99,100] while mice lacking c-fos develop osteoporosis due to the lack of osteoclast formation even though osteoblast function appears to be normal (probably due to redundant cell-signaling pathways).[100,101] In addition, actively dividing cells express more c-jun than quiescent cells.[102] Mitogens, such as growth factors (EGF and TGF-β) and serum, also induce c-fos and c-jun expression.[93] Osteoblasts that bind to metal implants also induce c-fos and c-jun expression leading to increased cell proliferation.[103]

4.408.5. Integrin Binding to Biomaterials

4.408.5.1. Initial Binding of Serum Proteins to Implant Materials

Previous studies have shown that the surface of the implant material is covered with serum proteins during the first minutes after its implantation into a living tissue.[104,105] This process of protein adsorption is a multistep process that is characterized by distinct events during each stage. Initially, small rapidly diffusing proteins are absorbed onto the implant surface. This stage is then followed by adsorption of larger proteins that mediate cell adhesion (mostly fibronectin and vitronectin).[106] Therefore, it is believed that cells in the adjacent host tissues are never in direct contact with the naked surface of the material and are rather in contact with the absorbed proteins that direct the processes of cell adhesion, proliferation, and further differentiation. However, one study suggests that cells may bind directly to the material using the $\alpha_5\beta_1$ integrin.[107] Adsorption of mineral ions, particularly calcium and inorganic phosphate,[108] also affects cell binding to metals, and due to the presence of an oxide layer on all metals there is spontaneous formation of an apatite layer on some metals,[109] which may partially explain why many metals are very biocompatible with bone (**Figure 3**).

Various substrate properties of the implant, such as surface roughness, surface energy, physicochemical properties of the substrate as well as its local environment (pH, concentration, composition, and functional groups of proteins, strength of solution, temperature) (*Vroman effect*)[110] affect the composition of the absorbed protein layer.[111] Metals and hydroxyapatite have been reported to actively adsorb serum proteins *in vitro*.[112–115] These proteins include fibronectin, vitronectin, and osteopontin, although other proteins and some serum components may contribute to the formation of an organic film on the implant surface immediately upon its exposure to tissue culture medium or to biological fluids. For commercially pure titanium, properties such as surface roughness, chemical composition of the oxide layer and surface wettability may also play an important role in determining the amount of the adsorbed proteins *in vitro*.[114] Both hydrophobic and hydrophilic surfaces are able to adsorb proteins *in vitro*. Even though cells tend to attach better to rough hydrophilic surfaces, these surfaces usually have lower affinity for protein

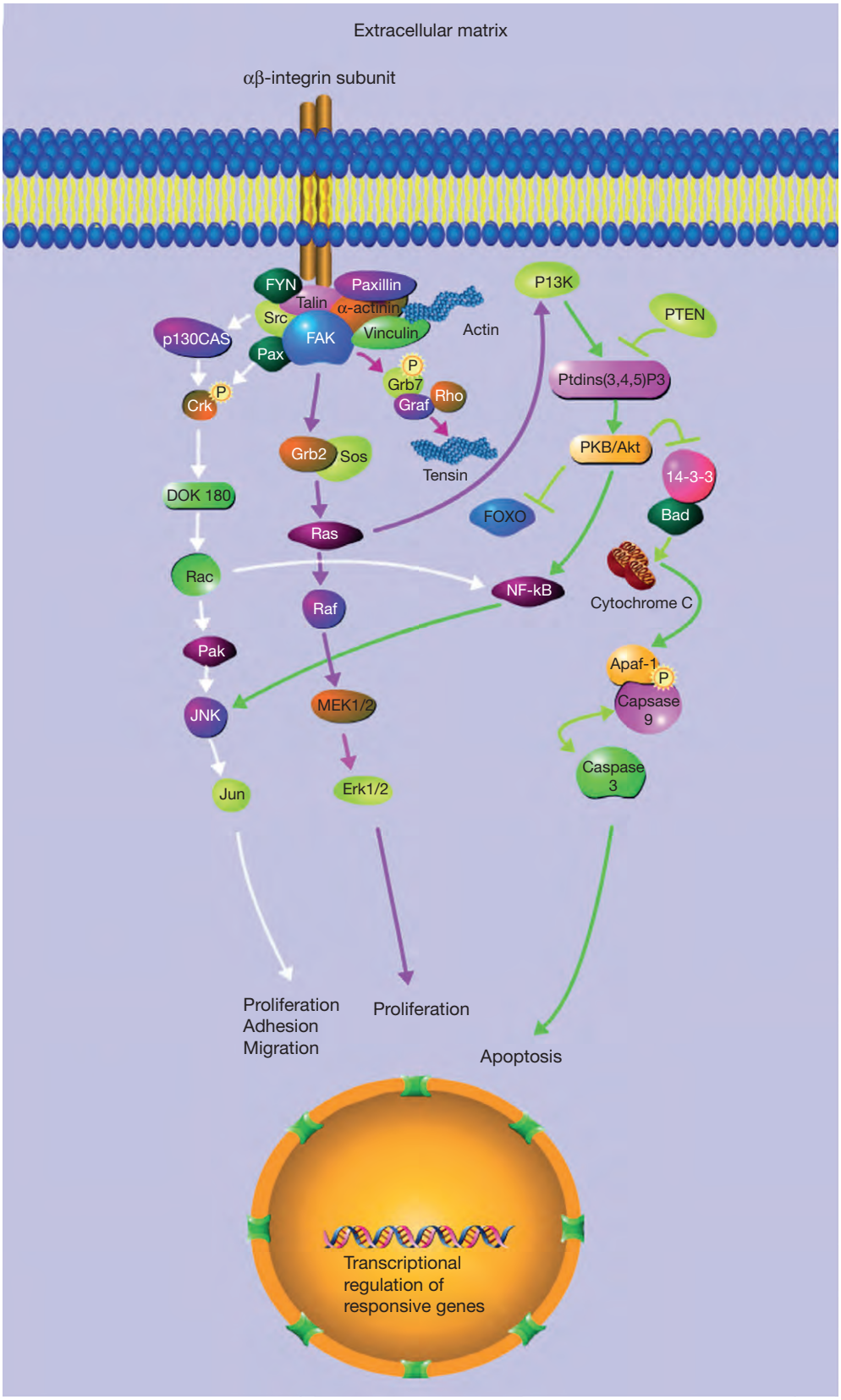

Figure 2 Simplified diagram of integrin-signaling pathways. A major mechanism by which integrins transmit signals intracellularly is through integrin binding and clustering which results in the formation of focal adhesion sites where integrins connect specific extracellular matrix proteins with the actin-based intracellular cytoskeleton and also initiate numerous signaling pathways. These events lead to changes in cell adhesion, migration, cell–cell interations, cell proliferation, apoptosis, and regulation of responsive genes.

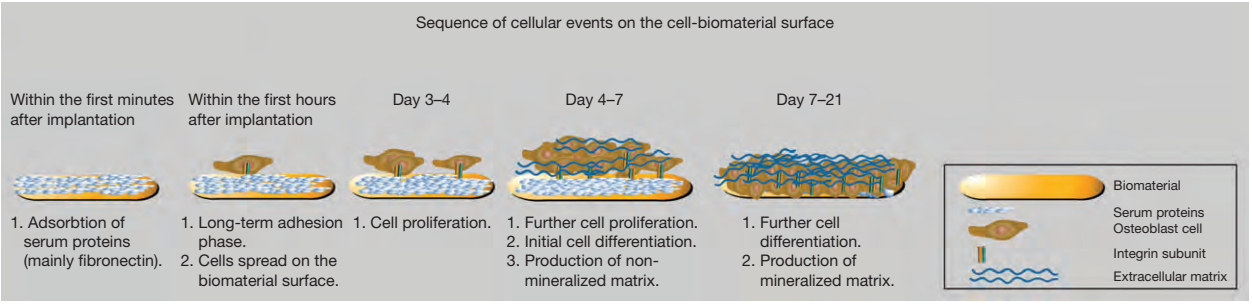

Figure 3 Sequence of events at the cell-biomaterial surface for bone. Within the first few minutes of implanting a biomaterial into a living organism, serum proteins adsorb to the surface of the biomaterial, followed by cell adhesion and spreading that are mediated mostly by integrins. In the next few days, cells begin to proliferate at the surface, and then differentiate by producing an extracellular matrix which subsequently mineralizes.

adsorption.[114,115] However, more fibronectin is adsorbed by a rough Ti–6Al–4V surface compared to the smooth tissue culture polystyrene surface.[115] Interestingly, it has been shown that metal substrates, such as titanium and stainless steel, do not absorb as much serum fibronectin, vitronectin, and albumin as does hydroxyapatite.[112,116,117]

Fibronectin has long been thought to be the principal adhesion-promoting protein both *in vitro* and *in vivo*. However, even though concentrations of fibronectin and vitronectin in the blood are similar, fibronectin has a much lower competitive ability compared to vitronectin.[118,119] Previous studies have demonstrated that cell adhesion is dependent on fibronectin only when its serum concentration is below 3%. At higher concentrations, adsorption of fibronectin declines and vitronectin becomes the predominant adhesive protein.[120,121] It has been suggested that, at higher concentrations, adsorption of fibronectin can be inhibited by other serum proteins, whereas the adsorption of vitronectin may not be affected.[120] *In vitro* studies have also shown that the adhesion of many cell types in culture also depends mostly on vitronectin rather than on fibronectin.[112,118,122,123] Both fibronectin and vitronectin appear to be required for the adhesion of human osteoblast to various substrates (stainless steel, cpTi, and Al_2O_3). However, vitronectin seems to promote cell adhesion better compared to fibronectin; this was demonstrated by depleting these proteins in the culture medium.[122] In addition, tissue culture grade polystyrene adsorbs vitronectin more actively than fibronectin and may therefore promote cell adhesion on its surface.[118] As suggested, the active conformation of fibronectin may be substrate-dependent, whereas it is substrate-independent for vitronectin. Therefore, when adsorbed onto a substrate, vitronectin may have a higher biological activity in enabling increased adhesion of cells *in vitro*.[123,124]

Several lines of evidence demonstrate that, on a nanoscale level, the adsorbance of proteins onto the surface of metal (cpTi) and nonmetal (polyethersulfone) substrates does not depend on the roughness of these materials.[125,126] However, fibrinogen adsorption increased proportionally with an increase in the nanoscale roughness of quartz-deposited tantalum, but the degree of adsorbance was dependent on the nature of the adsorbed proteins with more globular proteins, such as bovine serum albumin, showing little response to nanoscale increases in roughness.[127] Surface roughness has a large effect on cell responses. However, there is little or no substantial evidence of a difference in protein adsorption due to surface roughness. Surface properties do affect osteoblast proliferation and differentiation as differential expression of integrins and osteoblast activities was observed when these cells were cultured on smooth, sandblasted, or plasma-sprayed titanium.[128,129] Cells of the osteoblast lineage respond to surface roughness of the materials in ways that are cell-maturation specific. The MG-63 cells, a human osteoblast-like osteosarcoma cell line, responded to an increasing surface roughness by decreasing proliferation and increasing differentiation with an increase in alkaline phosphatase activity and osteocalcin production.[130] Production of local factors was also modulated by surface roughness with an increase in the production of both TGF-β and PGE_2. On rougher surfaces, MG-63 cells exhibit enhanced responsiveness to 1,25-dihydroxyvitamin D_3. These effects also appeared to be prostaglandin-mediated since indomethacin prevented an increase in the expression of differentiation markers. Osteoblasts appear to be able to detect minute differences in the surface properties of metals, as shown by their differential responses to cpTi Grades 1 and 4.[131]

4.408.5.2. Integrin-Mediated Cellular Responses to Implant Materials

The next development in the sequence of events on the surface of implant materials consists of the consecutive stages of cell adhesion, proliferation, the production of ECM proteins, and differentiation, which in bone is followed by mineralization of the organic scaffold. Adhesion is one of the initial biological responses of cells to implant materials and is one of the indicators of biocompatibility (for review, see Anselme[111]). Two phases of cell adhesion are distinguished, a short-term attachment phase due to simple gravity of the cells (occurs within the first seconds or minutes of contact) and a longer adhesion phase due to specific physicochemical properties of a material (occurs from minutes to several hours).[132] Following adhesion, cells spread out on the surface and adopt a morphology that is characteristic of the cell type and this is influenced by the surface topography and physicochemical properties of the material.[111] Adhesion, therefore, is a prerequisite for the subsequent proliferation and differentiation of cells.

The expression of specific types of integrins varies depending on the stage of cell differentiation, type of the material, and surface properties of the material. Therefore, each cell type and

stage of differentiation displays different arrays of integrin expression. To illustrate some of these differences, bone cells will be used as an example of the complexity of integrin expression. It has been shown that the intracellular signaling pathways of osteoblast adhesion to the metal implant material such as Ti–6Al–4V are similar to integrin-mediated adhesion to ECM proteins which in turn leads to integrin-mediated responses such as increased proliferation.[103] The integrins $\alpha_1\beta_1$, $\alpha_2\beta_1$, $\alpha_5\beta_1$, $\alpha_v\beta_3$, $\alpha_v\beta_5$ but not $\alpha_4\beta_1$ and $\alpha_6\beta_1$, were found to be expressed on normal human osteoblasts by flow cytometry.[129] Primary human osteoblasts express predominantly α_2, α_4, α_v, β_1, and β_3 integrin subunits when grown on Ti–6Al–4V, Co–Cr–Mo, and tissue culture plastic (TCP).[133] Initial adherence of osteoblasts to the surface of metal (including cpTi) substrates and their adherence during stages of osteoblast proliferation and differentiation were shown to be mediated through the $\alpha_5\beta_1$ integrins.[107,128,134] Other studies have shown that osteoblasts growing on TCP predominantly express the $\alpha_5\beta_1$ receptor and shift to the $\alpha_2\beta_1$ when cultured on cpTi or Ti–6Al–4V.[24,64,133] Integrin expression in human osteoblasts also varies depending on degradable polymeric implant materials *in vitro*.[135] Fibronectin, vitronectin, and human osteoblast bone marrow precursor cells bind better to hydroxylapatite (HA) than to metals, suggesting that improved integrin-mediated cell binding may be one of the mechanisms that lead to better clinical bone integration in HA-coated implants.[116]

The expression of the α_2, α_5, β_1, and $\alpha_v\beta_3$ integrins is also substrate-dependent and is enhanced in cells cultured on implant materials with rough surfaces compared to tissue culture plastic.[128,136] However, studies on how topography affects integrin expression and cell behavior are difficult to interpret due to the use of different cell types, integrin antibody sources, and surface topographies prepared by using different methods for *in vitro* studies.[24] TGF-β_1 is upregulated in human osteoblasts growing on rough surfaces and has been shown to stimulate the expression of α_5.[137] On the other hand, α_5 was reduced while α_2 was increased when osteoblast-like cells were treated with 1,25-dihydroxyvitamin D_3. However, it is difficult to directly correlate integrin expression with surface roughness since integrin expression is also dependent on the physicochemical properties of the substrate.[129,133] For example, using MG-63 cells, signaling via the α_5-subunit was shown to be required for DNA synthesis and expression of alkaline phosphatase, but these effects did not appear to be dependent on the surface roughness of chemically polished, grit blasted, and acid-etched titanium, each with different surface microstructures.[134,138] In another study by Mendonca *et al.*,[139] bone-specific mRNAs expression showed a higher increase on surfaces that were nanostructured compared to machined or acid-etched surfaces. *In vivo*, turned and dual acid-etched surfaces, placed in rat femurs, showed that ECM protein synthesis was greatest near the rougher surface which led to an increase in bone–implant contact during the early stages of bone healing.[140]

4.408.5.3. Inflammatory Responses

Following the formation of an adsorbed protein layer, a cascade of inflammatory processes occurs on the biomaterial surface, and their extent depends on the implantation procedure, target tissue/organ, and the properties of the adsorbed protein layer. The presence of specific proteins in the adsorbed layer influences the interaction of inflammatory cells with biomaterials and the subsequent inflammatory responses.[141,142] Inflammatory cells, such as monocytes and macrophages, are among the first cells to arrive at the bone–implant interface. Of the β_1 integrins, in monocytes/macrophages, there are $\alpha_5\beta_1$, $\alpha_4\beta_1$ (bind to fibronectin) and $\alpha_6\beta_1$ (binds to laminin). Of β_2 integrins, they express $\alpha_L\beta_2$ and $\alpha_D\beta_2$ (bind to ICAM), $\alpha_X\beta_2$ and $\alpha_M\beta_2$ (bind to fibronectin). Of the β_3 integrins, monocytes/macrophages express only the $\alpha_V\beta_2$ (bind to vitronectin).[143] It has been demonstrated that initial monocyte adhesion to the implant surface is mediated mainly by the β_1 integrin, and that both β_1 and β_2 are involved in macrophage adhesion, which is followed by its fusion into multinucleated foreign giant cells and further activities.[142,144] These integrin subunits have previously been shown to be involved in the adhesion of monocytes and macrophages to endothelium and their movement to the sites of inflammation.[145] Therefore, expression of the β_1 and β_2 integrins is important for the inflammatory reaction of live tissue to implant insertion and biocompatibility of the biomaterial itself. Indeed, the binding of $\alpha_M\beta_2$ integrin (Mac-1) to P1 and P2 domains of fibronectin adsorbed onto the surface of biomaterials is important for the initial recruitment and accumulation of monocytes/macrophages at the tissue– material interface.[146,147] Interestingly, RGD sequences in fibrinogen were shown not to be involved in fibrinogen-mediated acute inflammatory responses to implanted biomaterials.[146] The recent discovery of numerous resident tissue macrophages (OsteoMacs) on the endosteum and periosteum of bone may impact the bone formation process and is likely to play an important factor in the future design of implant materials for bone.[148]

4.408.6. Functionalizing Implant Surfaces Using Adhesion Molecules

4.408.6.1. General Description of Functionalizing Implant Surfaces

In order to improve physicochemical and mechanical properties of materials and stimulate the biological responses of osteoblast cells on their surfaces, various types of modifications have been proposed. These include, but are not limited to, the generation of new metal alloys, development of their osteoconductive three-dimensional structures (porous tantalum, titanium fiber mesh),[149,150] modification of metal substrates by roughening their surface by acid-etching, grit-blasting, plasma-spraying, anodization, etc.,[151] coating of metal surfaces with HA,[152] and incorporation of growth factors and other biologically active molecules into implants.[153,154]

On the basis of the fact that integrins mediate cell adhesion to substrates, biological modification of implant materials has recently become one of the most interesting approaches in the development of new biomaterials (for review, see Lutolf and Hubbell,[155] Hersel *et al.*,[156] and Kim *et al.*[157]). This strategy mostly focuses on the immobilization of short peptides on the surface of synthetic or natural metallic or nonmetallic materials in order to improve their adhesive

abilities, stimulate osteogenic differentiation of cells, and increase bone healing.[158–165]

4.408.6.2. *In Vitro* Studies Using Adhesion Molecules on Implant Surfaces

In vitro, RGD coating, compared to uncoated substrates, has been shown to increase cell attachment, spreading, proliferation, and differentiation of osteoblasts[158,160,166] and other cell types such as tenocytes[167] and oral epithelial cells.[168] Massia and Hubbell[169] have shown that cellular responses of adhered cells depend on the density of the immobilized RGD peptides. A minimal RGD density of 1 fmol cm^{-2} was enough for complete spreading of the cells; however, the formation of focal contacts and well-organized stress fibers was seen only at a concentration of 10 fmol cm^{-2}. After 3 weeks in culture, surfaces modified with a 15 amino acid peptide containing RGD at a density of 0.62 pmol cm^{-2}, significantly enhanced mineralization in rat calvarial osteoblast cultures compared with a RGD surface density of 0.01 pmol cm^{-2}.[170] Various studies have reported an increase in adhesion, proliferation, and osteogenic differentiation of osteoblast-like cells growing on RGD-coated substrates. Using the KUSA/A1 bone marrow cell line, *in vitro*, Itoh *et al.*[171] have demonstrated a significant increase in adhesion, proliferation, and osteogenic differentiation of cells growing on E_7PRGDT peptide-coated hydroxyapatite discs compared to uncoated discs. Covalently linked RGD peptides on silk increased human osteoblast adhesion, ECM matrix production, and mineralization compared to silk alone or the control peptide, RAD, conjugated to silk.[172] The coating of cpTi grade 2 substrates with fibronectin, but not with vitronectin, significantly increased the initial adhesion of MC3T3-E1 osteoblast-like cells, their subsequent proliferation at day 3 and alkaline phosphatase activity at day 7. Interestingly, significantly more fibronectin adsorbed onto the titanium surface compared to vitronectin, measured colorimetrically by protein adhesion assay, and stimulated MC3T3-E1 proliferation and differentiation.[173] This may indicate that fibronectin adsorbs at higher amounts onto implant surfaces than vitronectin and thus mediates further biological events at the bone–implant interface.

Modifying metal surfaces with a surface-grafted chitosan in conjunction with an RGD peptide reduced bacterial adhesion and promoted osteoblast function of MC3T3-E1 cells.[174] Similar findings were found with MC3T3-E1 on Ti using polyelectrolyte multilayers (PEMs) of hyaluronic acid (HY) and chitosan (CH), coupled with surface-immobilized RGD. The HY/CH PEM-functionalized Ti decreases bacterial adhesion, but the adhesion of osteoblasts is poorer than on Ti. Osteoblast adhesion was significantly improved, along with alkaline phosphatase expression, when the RGD peptide was added to the HY/CH PEM-functionalized Ti.[175] RGD-containing peptides covalently bonded to Ti were shown not only to promote osteoblast attachment but also to promote cell survival when exposed to agents that induce apoptosis.[176] The development of new methods to modify the surface of titanium with oligonucleotide-RGD peptide conjugates[177] or coating titanium implants with a tailor-made cyclic-RGD peptide that binds to specific integrin receptors on the cell surface through multimeric phosphonates[178] may be a promising technology for tissue engineering of metal implants. *In vitro* studies have demonstrated that RGD-coated metal implants have improved early bone formation and biocompatibility compared to non-coated substrates.

4.408.6.3. *In Vivo* Studies Using Adhesion Molecules on Implant Surfaces

In vivo studies using several animal models have reported that implant materials coated with RGD peptides improve early bone formation around implants. Using a rat model, Ferris *et al.*[163] showed that bone formation was significantly higher around RGD-coated smooth titanium implants at 2 and 4 weeks compared to control gold-coated titanium implants. Using a miniature pig model, Germanier *et al.*[179] demonstrated that new bone formation around RGD-coated, sandblasted and acid-etched (SLA) cpTi implants was significantly higher at 2 weeks but not at 4 weeks compared to uncoated control implants. Similarly, a study in canines by Elmengaard *et al.* demonstrated that the coating of plasma-sprayed, porous-coated Ti–6Al–4V implants with cyclic-RGD significantly increased bone formation in the inner gap zone (0–375 μm), surrounding the unloaded RGD-coated implants at 4 weeks. In addition, a push-out test on the mechanical properties of the bone–implant interface showed a significant increase in apparent shear stiffness and much less fibrous tissue surrounding cyclic-RGD-coated implants in both loaded and unloaded models compared to uncoated controls.[180] RGD-Ti fiber mesh implants, inserted into the cranium of a rabbit, showed an increase in bone formation/bone ingrowth compared to porous titanium fiber mesh disks without RGD.[181] Bone–implant contact of screw implants in dog mandibles was increased at earlier time points in an RGD-peptide- and dose-dependent manner in RGD-titanium implants compared to titanium alone. However, volume density of the periimplant bone was similar in collagen-coated or RGD-peptide-coated titanium implants compared to titanium alone.[182] Early bone apposition to a modified, SLA surface coated with an RGD-peptide-modified polymer (PLL-*g*-PEG/PEG-RGD) compared to standard SLA implants was examined in the maxillae of miniature pigs. At 2 weeks, RGD-coated dental implants demonstrated significantly higher percentages of bone-to-implant contact compared to controls (61.68% vs. 43.62%; $p < 0.001$).[179] In another study, titanium screws were coated with type I collagen (Ti/Coll), RGD peptide (Ti/RGD) or type I collagen and chondroitin sulfate (Ti/Coll/CS) and implanted in rat tibiae. Direct contact of the bone with the implant surface was statistically higher with Ti/RGD and Ti/Coll/CS compared to the uncoated Ti implants but was not different between the Ti/RGD and Ti/Coll/CS implants.[183] Similar results were found with a porous titanium (Ti) fiber mesh implant coated with cyclic-RGD peptides and inserted into the cranium of a rabbit. RGD-Ti implants were also compared to porous titanium fiber mesh disks without RGD sequence (Ti) and with an open control defect. Histologic and histomorphometric examinations were performed at 2, 4, and 8 weeks after the operation. A significant increase in bone formation, or bone ingrowth, was seen in the RGD-Ti group compared to the Ti group after 4 and 8 weeks. All control defects stayed open at all the three time points.[181] A comparison of the

results of *in vitro* and *in vivo* studies suggests that the reason for RGD's early anabolic effects on bone formation, *in vivo*, may be due to increased cell adhesion, proliferation, and cell survival combined with the stimulation of early osteoblast differentiation.

In a few studies, early bone formation was not increased with RGD-functionalized implants. The coating of a porous implant with RGD, compared to uncoated screws, demonstrated an increase in the percentage of bone-to-implant contact in the threads of a screw in rabbit femurs at 8 and 12 weeks but not at 4 weeks.[184] Using a canine model, Schliephake *et al*.[185] found no significant difference between alveolar bone formation around RGD-coated and -uncoated Ti–6Al–4V implants at 1 and 3 months, though they observed a significant increase with time in bone formation around RGD-coated implants. Coating metal titanium implants with polymer networks containing rat bone sialoprotein (bsp-RGD(15)), did not enhance bone formation in the periimplant region at 2 or 4 weeks in a rat femoral ablation model.[186] Whether the differences in the responses of bone to RGD peptide implants are due to particular bone applications or the nature of the coating is not known. The technique used to immobilize the peptide coating may also influence the outcome.

4.408.6.4. Functionalizing Biomaterials with Short Versus Long Peptides

There are several reasons for using full-length proteins coated onto material surfaces instead of short peptides.[24,187] In most cases, the biological activity of short peptides is lower compared to that of the full-length protein.[2] Studies by Pierschbacher and Ruoslahti[188] have demonstrated that the adhesion of normal rat kidney cells to a polystyrene surface was considerably higher on fibronectin-coated surfaces compared to those coated with fibronectin-derived short peptides. The presence of a PHSRN (Pro-His-Ser-Arg-Asn) synergy domain enhanced the adhesive activity of the $\alpha_5\beta_1$ integrin compared to that of the RGD alone.[189] Self-assembled monolayers (SAMs) of alkanethiols on gold, functionalized with the FNIII7-10 recombinant fragment presenting RGD and PHSRN adhesive motifs in the correct structural context, exhibited significantly higher osteoblast-like cell adhesion, FAK activation, and proliferation rate than biomaterials presenting an RGD ligand or the RGD–PHSRN. FNIII7-10 functionalized surfaces also displayed specificity for the $\alpha_5\beta_1$integrin while cell adhesion on RGD or RGD–PHSRN was primarily mediated by the $\alpha_v\beta_3$ integrin.[190] As the RGD sequence is recognized by various integrins, it may lead to the nonspecific binding of cells of various types and may therefore attenuate a specific response. The RGD peptide may not be appropriate for all stages of cell differentiation. As full-length proteins usually bind to more than one integrin, different types of cells can adhere to the material. In bone, there is sequential synthesis of matrix proteins *in vivo*[51] and not all the proteins contain the RGD sequence. The RGD-binding integrins may also require the presence of other peptides for adherence to a substrate.[24]

Most of the studies on RGD and other short biomimetic peptides were done *in vitro* where the conditions are different than the conditions *in vivo*, especially in the bone healing models. Therefore, our current knowledge may not be biologically completely accurate and we may not get the desirable effect *in vivo*. However, most of the *in vivo* studies have given results that are comparable to the *in vitro* findings on short and long peptides. Using a goat model, Bernhardt *et al*.[191] showed that the coating of titanium implants with full-length type I collagen resulted in a significant increase in periimplant bone formation at 5 and 12 weeks compared to RGD-coated titanium implants. Other binding peptides have also been shown to influence cell behavior. The GFOGER peptide, compared to collagen-coated or -uncoated titanium, improves binding of the $\alpha_2\beta_1$ integrin, increases periimplant bone formation and osseointegration, as characterized by an increase in bone– implant contact and mechanical fixation, in an *in vivo* rat tibia cortical bone implantation model.[192] In the same publication, *in vitro* studies with the same peptide demonstrated that bone marrow stromal cells displayed enhanced cell adhesion, osteoblast-specific gene expression, and calcification compared to titanium alone. In a different study, collagen-coating alone was not sufficient to accelerate differentiation of rat calvarial osteoblasts on Ti–6Al–4V but it did increase cell adhesion.[193] Interestingly, *in vitro* studies with siRNA directed against the $\alpha_2\beta_1$ integrin have been shown to inhibit osteoblast differentiation and bone formation, suggesting that stimulating this collagen integrin may be anabolic with respect to bone formation.[64] The coating of soluble laminin-5 on titanium implant disks from cell-conditioned medium has been shown to improve cell attachment and production of hemidesmosome proteins in human gingival epithelial cells.[194]

4.408.6.5. Functionalizing Biomaterials with Multiple Peptides

The design of smarter biomaterials that target particular cellular responses and physiological conditions may provide more successful tissue engineering outcomes. Covalently attached RGD and heparin-conjugated fibroblast growth factor 2 (FGF-2) bound to hydrogels increased the survival and growth of primary nerve cells and neural stem cells compared to either agent alone in hydrogel.[195] The application of RGD peptides with other factors in compromised bone situations may also have therapeutic potential. Tetra-cell adhesion molecule (T-CAM) coating, composed of four cell adhesion molecules, an RGD sequence, a PHSRN sequence, a tyrosine-histidine sequence (YH), and a glutamic acid-proline-aspartic acid-isoleucine-methionine (EPDIM) on the rough-surfaced titanium implant, increased periimplant bone formation in rabbit femurs with poor local bone conditions and minimal primary stability.[196]

The development of dental implants that utilize different biomimetic coatings for use at the gingival region and other coatings such as the RGD peptide for bone may also be promising.[197]

The effects of cyclic-RGD-coated implants on tissue integration and implant fixation in two cancellous bone-gap models were examined in canines. Loaded RGD-coated implants with 0.75-mm gap and unloaded RGD-coated implants with 1.5-mm gap were placed into the distal femur and proximal tibia of canines, respectively. Control gap implants, without RGD, were inserted contralaterally. Mechanical implant

fixation was improved in the RGD-coated implants. Unloaded RGD-coated implants showed a significant increase in bone at 4 weeks, and both loaded and unloaded implants showed a significant reduction in fibrous tissue anchorage.[180]

In vitro/*in vivo* experiments that test a particular composite are also helpful in showing the efficacy of a particular implant design. Proliferation, alkaline phosphatase and osteocalcin activity in MC3T3-E1 cells, osteoblast-like cells, was increased when they were cultured on TGF-β_1-loaded collagen/chitosan composite microgranules.[198] The TGF-β_1-loaded microgranules demonstrated a higher capacity for bone regeneration in rabbit calvarial defects after 4 weeks compared to TGF-β_1-unloaded microgranules. Thus, collagen coating did not enhance bone formation in this model, unless coupled with a growth factor.

4.408.7. Conclusions

The crucial role that integrins play in mediating cell–matrix interactions allows them to be key regulators of cell behavior. Therefore, modulation of integrin function has the potential to influence tissue engineering outcomes if integrin activities could be harnessed appropriately for specific biological applications. Due to the fact that integrins are a diverse family of receptors, are large molecules with multiple activities associated with particular peptide regions, and have a complex signaling pathway, our ability to control their function with specifically designed biomaterials is a difficult task. In addition, each cell type and stage of cell differentiation in a tissue expresses different arrays of integrins, so control of their function at one stage of development with a biomaterial may not be appropriate for the next stage in tissue development. However, functionalization of implants with the RGD amino acid sequence has resulted in some success with significant increases in early bone formation both *in vitro* and *in vivo*. In general, *in vitro* studies have been helpful in the design of *in vivo* studies aimed at augmenting bone with integrin-activating peptides or the ligands for integrins, such as specific ECM proteins.

However, our ultimate goal to provide an implant that will last longer in younger patients or for our rapidly aging population still needs to be realized with integrin-activating implants. The outcomes of the majority of the studies have only been tested for several weeks or, at most, a few months. We do not know if integrin modulation will improve the long-term functional integration and life span of these implants. In the future, we may want to consider deactivating particular integrins in certain circumstances, for example, to prevent fibrous tissue growth, but there is little information on this approach in scientific literature. Another possibility is to design implants with sequentially available peptides so that we may provide a better outcome, for example, with an early peptide, stimulating proliferation, and a latter peptide, anabolic for cell differentiation. It is also important to test the particular applications of these functionalized implants. Would these types of implants be more helpful in patients with osteonecrosis or other bone debilitating diseases? These studies are needed to ultimately determine the utility of integrin-modulating peptides in tissue engineering.

References

1. Hench, L. L.; Polak, J. M. *Science* **2002**, *295*, 1014–1017.
2. Vogel, V.; Baneyx, G. *Annu. Rev. Biomed. Eng.* **2003**, *5*, 441–463.
3. Branemark, P. I. *J. Prosthet. Dent.* **1983**, *50*, 399–410.
4. Hynes, R. O. *Cell* **2002**, *110*, 673–687.
5. Plow, E. F.; Haas, T. A.; Zhang, L.; Loftus, J.; Smith, J. W. *J. Biol. Chem.* **2000**, *275*, 21785–21788.
6. Van der Flier, A.; Sonnenberg, A. *Cell Tissue Res.* **2001**, *305*, 285–298.
7. Hynes, R. *Cell* **1992**, *69*, 11–25.
8. Humphries, M. J. *Biochem. Soc. Trans.* **2000**, *28*, 311–339.
9. Fornaro, M.; Languino, L. R. *Matrix Biol.* **1997**, *16*, 185–193.
10. Venter, J. C.; Adams, M. D.; Myers, E. W.; *et al*. *Science* **2001**, *291*, 1304–1351.
11. De Melker, A. A.; Sonnenberg, A. *Bioessays* **1999**, *21*, 499–509.
12. Takada, Y.; Ye, X.; Simon, S. *Genome Biol.* **2007**, *8*, 215.
13. Pierschbacher, M. D.; Ruoslahti, E. *Nature* **1984**, *309*, 30–33.
14. Rezania, A.; Healy, K. *J. Orthop. Res.* **1999**, *17*, 615–623.
15. Ganta, D. R.; Mccarthy, M. B.; Gronowicz, G. A. *Endocrinology* **1997**, *138*, 3606–3612.
16. Horton, M.; Davies, J. *J. Bone Miner. Res.* **1989**, *4*, 803–807.
17. Gronowicz, G.; Derome, M. *J. Bone Miner. Res.* **1994**, *9*, 193–202.
18. Clover, J.; Dodds, R. A.; Gowen, M. *J. Cell Sci.* **1992**, *103*(Pt 1), 267–271.
19. Grzesik, W. J.; Robey, P. G. *J. Bone Miner. Res.* **1994**, *9*, 487–496.
20. Gohel, A.; Hand, A.; Gronowicz, G. *J. Histochem. Cytochem.* **1995**, *43*, 1085–1096.
21. Gronowicz, G.; Mccarthy, M. B. *Endocrinology* **1995**, *136*, 598–608.
22. Nakamura, I.; Duong Le, T.; Rodan, S. B.; Rodan, G. A. *J. Bone Miner. Metab.* **2007**, *25*, 337–344.
23. De Pereda, J. M.; Wiche, G.; Liddington, R. C. *EMBO J.* **1999**, *18*, 4087–4095.
24. Siebers, M. C.; Ter Brugge, P. J.; Walboomers, X. F.; Jansen, J. A. *Biomaterials* **2005**, *26*, 137–146.
25. Takagi, J.; Springer, T. A. *Immunol. Rev.* **2002**, *186*, 141–163.
26. Shimaoka, M.; Takagi, J.; Springer, T. A. *Annu. Rev. Biophys. Biomol. Struct.* **2002**, *31*, 485–516.
27. Arnaout, M. A.; Goodman, S. L.; Xiong, J. P. *Curr. Opin. Cell Biol.* **2007**, *19*, 495–507.
28. Mould, A. P.; Barton, S. J.; Askari, J. A.; Craig, S. E.; Humphries, M. J. *J. Biol. Chem.* **2003**, *278*, 51622–51629.
29. Xiao, T.; Takagi, J.; Coller, B. S.; Wang, J. H.; Springer, T. A. *Nature* **2004**, *432*, 59–67.
30. Xiong, Y. M.; Haas, T. A.; Zhang, L. *J. Biol. Chem.* **2002**, *277*, 46639–46644.
31. Xiong, J. P.; Stehle, T.; Diefenbach, B.; *et al*. *Science* **2001**, *294*, 339–345.
32. Kamata, T.; Tieu, K. K.; Irie, A.; Springer, T. A.; Takada, Y. *J. Biol. Chem.* **2001**, *276*, 44275–44283.
33. Colombatti, A.; Bonaldo, P. *Blood* **1991**, *77*, 2305–2315.
34. Emsley, J.; King, S. L.; Bergelson, J. M.; Liddington, R. C. *J. Biol. Chem.* **1997**, *272*, 28512–28517.
35. Puzon-Mclaughlin, W.; Takada, Y. *J. Biol. Chem.* **1996**, *271*, 20438–20443.
36. Kamata, T.; Wright, R.; Takada, Y. *J. Biol. Chem.* **1995**, *270*, 12531–12535.
37. Wang, N.; Butler, J.; Ingber, D. *Science* **1993**, *260*, 1124–1127.
38. Albelda, S.; Buck, C. *Faseb J.* **1990**, *4*, 2868–2880.
39. Ruoslahti, E. J. *Clin. Invest.* **1991**, *87*, 1–5.
40. Clark, E.; Brugge, J. *Science* **1995**, *268*, 233–239.
41. Mahabeleshwar, G. H.; Feng, W.; Phillips, D. R.; Byzova, T. V. *J. Exp. Med.* **2006**, *203*, 2495–2507.
42. De Arcangelis, A.; Georges-Labouesse, E. *Trends Genet.* **2000**, *16*, 389–395.
43. Varner, J.; Emerson, D.; Juliano, R. *Mol. Biol. Cell* **1995**, *6*, 725–740.
44. Giancotti, F.; Ruoslahti, E. *Cell* **1990**, *60*, 849–859.
45. Sastry, S.; Lakonishok, M.; Thomas, D.; Muschler, J.; Horwitz, A. *J. Cell Biol.* **1996**, *133*, 169–184.
46. Zhang, Z.; Vuori, K.; Reed, J.; Ruoslahti, E. *Proc. Natl. Acad. Sci. USA* **1995**, *92*, 6161–6165.
47. Bouvard, D.; Brakebusch, C.; Gustafsson, E.; *et al*. *Circ. Res.* **2001**, *89*, 211–223.
48. Sato, M.; Sardana, M. K.; Grasser, W. A.; Garsky, V. M.; Murray, J. M.; Gould, R. J. *J. Cell Biol.* **1990**, *111*, 1713–1723.
49. Horton, M. A.; Taylor, M. L.; Arnett, T. R.; Helfrich, M. H. *Exp. Cell Res.* **1991**, *195*, 368–375.
50. Gronowicz, G.; Krause, A.; Mccarthy, M.; Cowles, E. In *The Bone–Biomaterials Interface*; Davies, J. E., Ed.; Em Squared: Toronto, Canada, 2000; Vol. 2, pp 256–267.

51. Cowles, E.; Derome, M.; Pastizzo, G.; Brailey, L.; Gronowicz, G. *Calcif. Tissue Int.* **1998**, *62*, 74–82.
52. Moursi, A. M.; Damsky, C. H.; Lull, J.; *et al. J. Cell Sci.* **1996**, *109*(Pt 6), 1369–1380.
53. Moursi, A. M.; Globus, R. K.; Damsky, C. H. *J. Cell Sci.* **1997**, *110*(Pt 18), 2187–2196.
54. Globus, R. K.; Doty, S. B.; Lull, J. C.; Holmuhamedov, E.; Humphries, M. J.; Damsky, C. H. *J. Cell Sci.* **1998**, *111*(Pt 10), 1385–1393.
55. Jikko, A.; Harris, S. E.; Chen, D.; Mendrick, D. L.; Damsky, C. H. *J. Bone Miner. Res.* **1999**, *14*, 1075–1083.
56. Xiao, G.; Wang, D.; Benson, M. D.; Karsenty, G.; Franceschi, R. T. *J. Biol. Chem.* **1998**, *273*, 32988–32994.
57. Mizuno, M.; Fujisawa, R.; Kuboki, Y. *J. Cell. Physiol.* **2000**, *184*, 207–213.
58. Takeuchi, Y.; Suzawa, M.; Kikuchi, T.; Nishida, E.; Fujita, T.; Matsumoto, T. *J. Biol. Chem.* **1997**, *272*, 29309–29316.
59. Schneider, G. B.; Zaharias, R.; Stanford, C. *J. Dent. Res.* **2001**, *80*, 1540–1544.
60. Grigoriou, V.; Shapiro, I. M.; Cavalcanti-Adam, E. A.; Composto, R. J.; Ducheyne, P.; Adams, C. S. *J. Biol. Chem.* **2005**, *280*, 1733–1739.
61. Lee, D. Y.; Yeh, C. R.; Chang, S. F.; *et al. J. Bone Miner. Res.* **2008**, *23*, 1140–1149.
62. Gronthos, S.; Simmons, P. J.; Graves, S. E.; Robey, P. G. *Bone* **2001**, *28*, 174–181.
63. Ter Brugge, P. J.; Torensma, R.; De Ruijter, J. E.; Figdor, C. G.; Jansen, J. A. *Tissue Eng.* **2002**, *8*, 615–626.
64. Olivares-Navarrete, R.; Raz, P.; Zhao, G.; *et al. Proc. Natl. Acad. Sci. USA* **2008**, *105*, 15767–15772.
65. Mcnamara, L. M.; Majeska, R. J.; Weinbaum, S.; Friedrich, V.; Schaffler, M. B. *Anat. Rec. (Hoboken)* **2009**, *292*, 355–363.
66. Phillips, J. A.; Almeida, E. A.; Hill, E. L.; *et al. Matrix Biol.* **2008**, *27*, 609–618.
67. Teitelbaum, S. L. *Ann. New York Acad. Sci.* **2006**, *1068*, 95–99.
68. Miyamoto, S.; Teramoto, H.; Gutkind, J. S.; Yamada, K. M. *J. Cell Biol.* **1996**, *135*, 1633–1642.
69. Moro, L.; Venturino, M.; Bozzo, C.; *et al. EMBO J.* **1998**, *17*, 6622–6632.
70. Sieg, D. J.; Hauck, C. R.; Ilic, D.; *et al. Nat. Cell Biol.* **2000**, *2*, 249–256.
71. Schneller, M.; Vuori, K.; Ruoslahti, E. *EMBO J.* **1997**, *16*, 5600–5607.
72. Woodard, A. S.; Garcia-Cardena, G.; Leong, M.; Madri, J. A.; Sessa, W. C.; Languino, L. R. *J. Cell Sci.* **1998**, *111*(Pt 4), 469–478.
73. Zheng, B.; Clemmons, D. *Proc. Natl. Acad. Sci. USA* **1998**, *95*, 11217–11222.
74. Soldi, R.; Mitola, S.; Strasly, M.; Defilippi, P.; Tarone, G.; Bussolino, F. *EMBO J.* **1999**, *18*, 882–892.
75. Bhowmick, N.; Zent, R.; Ghiassi, M.; Mcdonnell, M.; Moses, H. *J. Biol. Chem.* **2001**, *276*, 46707–46713.
76. Kanzaki, T.; Otabe, M. *Diabetes* **2003**, *52*, 824–828.
77. Ortega-Velazquez, R.; Diez-Marques, M. L.; Ruiz-Torres, M. P.; Gonzalez-Rubio, M.; Rodriguez-Puyol, M.; Rodriguez Puyol, D. *Faseb J.* **2003**, *17*, 1529–1531.
78. Lai, C.; Feng, X.; Nishimura, R.; *et al. J. Biol. Chem.* **2000**, *275*, 36400–36406.
79. Thannickal, V.; Lee, D.; White, E.; *et al. J. Biol. Chem.* **2003**, *278*, 12384–12389.
80. Danen, E. H.; Yamada, K. M. *J. Cell. Physiol.* **2001**, *189*, 1–13.
81. Schaller, M.; Otey, C.; Hildebrand, J.; Parsons, J. *J. Cell Biol.* **1995**, *130*, 1181–1187.
82. Klawitter, J.; Weinstein, A.; Peterson, L. *J. Dent. Res.* **1977**, *56*, B153–B157.
83. Schlaepfer, D. D.; Hunter, T. *Trends Cell Biol.* **1998**, *8*, 151–157.
84. Aplin, A. E.; Howe, A. K.; Juliano, R. L. *Curr. Opin. Cell Biol.* **1999**, *11*, 737–744.
85. Burridge, K.; Nuckolls, G.; Otey, C.; Pavalko, F.; Simon, K.; Turner, C. *Cell Differ. Dev.* **1990**, *32*, 337–342.
86. Hall, A. *Science* **1998**, *279*, 509–514.
87. Zhang, Z.; Vuori, K.; Wang, H.; Reed, J. C.; Ruoslahti, E. *Cell* **1996**, *85*, 61–69.
88. Katagiri, K.; Hattori, M.; Minato, N.; Irie, S.; Takatsu, K.; Kinashi, T. *Mol. Cell. Biol.* **2000**, *20*, 1956–1969.
89. Reedquist, K. A.; Ross, E.; Koop, E. A.; *et al. J. Cell Biol.* **2000**, *148*, 1151–1158.
90. Boudreau, N.; Bissell, M. J. *Curr. Opin. Cell Biol.* **1998**, *10*, 640–646.
91. Yamada, K. M.; Geiger, B. *Curr. Opin. Cell Biol.* **1997**, *9*, 76–85.
92. Seger, R.; Krebs, E. *Faseb J.* **1995**, *9*, 726–735.
93. Siddhanti, S.; Quarles, L. *J. Cell. Biochem.* **1994**, *55*, 310–320.
94. Monson, J.; Frieam, J.; Mccarthy, B. *Mol. Cell. Biol.* **1982**, *2*, 1362–1371.
95. Matsuura, S.; Kishi, T.; Kajii, T. *Biochem. Biophys. Res. Comm.* **1990**, *168*, 993–1000.
96. Owen, T.; Bortell, R.; Yocum, S.; *et al. Proc. Natl. Am. Soc. USA* **1990**, *87*, 9990–9994.
97. Schule, R.; Umesono, K.; Manelsdorf, D.; Boldo, J.; Pike, J.; Evans, R. *Cell* **1990**, *61*, 497–504.
98. Craig, A.; Denhardt, D. *Gene* **1991**, *100*, 163–171.
99. Grigoriadis, A.; Schellander, K.; Wang, Z.; Wagner, E. *J. Cell Biol.* **1993**, *122*, 685–701.
100. Wang, Z. Q.; Liang, J.; Schellander, K.; Wagner, E.; Grigoriadis, A. *Cancer Res.* **1995**, *55*, 6244–6251.
101. Johnson, R.; Spiegelman, B.; Papaioannou, V. *Cell* **1992**, *71*, 577–586.
102. Angel, P.; Karin, M. *Biochim. Biophys. Acta* **1991**, *1072*, 129–157.
103. Krause, A.; Cowles, E.; Gronowicz, G. *J. Biomed. Mater. Res.* **2000**, *52*, 738–747.
104. Andrade, J. D.; Hlady, V. *Ann. New York Acad. Sci.* **1987**, *516*, 158–172.
105. Nygren, H. *Biophys. Chem.* **1996**, *61*, 73–84.
106. Jager, M.; Zilkens, C.; Zanger, K.; Krauspe, R. *J. Biomed. Biotechnol.* **2007**, 2007, 69036.
107. Gronowicz, G.; Mccarthy, M. *J. Orthop. Res.* **1996**, *14*, 878–887.
108. Ong, J. L.; Prince, C. W.; Lucas, L. C. *J. Biomed. Mater. Res.* **1995**, *29*, 165–172.
109. Hanawa, T. In *The Bone–Biomaterial Interface*; Davies, J. E., Ed.; Em Squared: Toronto, Canada, 1990; pp 49–67.
110. Vroman, L. *Semin. Thromb. Hemost.* **1987**, *13*, 79–85.
111. Anselme, K. *Biomaterials* **2000**, *21*, 667–681.
112. Webster, T. J.; Ergun, C.; Doremus, R. H.; Siegel, R. W.; Bizios, R. *J. Biomed. Mater. Res.* **2000**, *51*, 475–483.
113. Ellingsen, J. E. *Biomaterials* **1991**, *12*, 593–596.
114. Walivaara, B.; Aronsson, B. O.; Rodahl, M.; Lausmaa, J.; Tengvall, P. *Biomaterials* **1994**, *15*, 827–834.
115. Deligianni, D. D.; Katsala, N.; Ladas, S.; Sotiropoulou, D.; Amedee, J.; Missirlis, Y. F. *Biomaterials* **2001**, *22*, 1241–1251.
116. Kilpadi, K. L.; Chang, P. L.; Bellis, S. L. *J. Biomed. Mater. Res.* **2001**, *57*, 258–267.
117. Matsuura, T.; Hosokawa, R.; Okamoto, K.; Kimoto, T.; Akagawa, Y. *Biomaterials* **2000**, *21*, 1121–1127.
118. Underwood, P. A.; Bennett, F. A. *J. Cell Sci.* **1989**, *93*, (Pt 4), 641–649.
119. Bale, M. D.; Wohlfahrt, L. A.; Mosher, D. F.; Tomasini, B.; Sutton, R. C. *Blood* **1989**, *74*, 2698–2706.
120. Knox, P. *J. Cell Sci.* **1984**, *71*, 51–59.
121. Grinnell, F. *Ann. New York Acad. Sci.* **1987**, *516*, 280–290.
122. Howlett, C. R.; Evans, M. D.; Walsh, W. R.; Johnson, G.; Steele, J. G. *Biomaterials* **1994**, *15*, 213–222.
123. Steele, J. G.; Johnson, G.; Underwood, P. A. *J. Biomed. Mater. Res.* **1992**, *26*, 861–884.
124. Mcfarland, C. D.; Mayer, S.; Scotchford, C.; Dalton, B. A.; Steele, J. G.; Downes, S. *J. Biomed. Mater. Res.* **1999**, *44*, 1–11.
125. Cai, K.; Bossert, J.; Jandt, K. D. *Colloids Surf. B Biointerfaces* **2006**, *49*, 136–144.
126. Han, M.; Sethuraman, A.; Kane, R.; Belfort, G. *Langmuir* **2003**, *19*, 9868–9872.
127. Rechendorff, K.; Hovgaard, M. B.; Foss, M.; Zhdanov, V. P.; Besenbacher, F. *Langmuir* **2006**, *22*, 10885–10888.
128. Postiglione, L.; Di Domenico, G.; Ramaglia, L.; *et al. J. Dent. Res.* **2003**, *82*, 692–696.
129. Gronthos, S.; Stewart, K.; Graves, S. E.; Hay, S.; Simmons, P. J. *J. Bone Miner. Res.* **1997**, *12*, 1189–1197.
130. Schwartz, Z.; Lohmann, C. H.; Oefinger, J.; Bonewald, L. F.; Dean, D. D.; Boyan, B. D. *Adv. Dent. Res.* **1999**, *13*, 38–48.
131. Ahmad, M.; Mccarthy, M.-B.; Gronowicz, G. *Biomaterials* **1999**, *20*, 211–220.
132. Bigerelle, M.; Anselme, K. *J. Biomed. Mater. Res. A* **2005**, *75*, 530–540.
133. Sinha, R.; Tuan, R. *Bone* **1996**, *18*(5), 451–457.
134. Keselowsky, B. G.; Collard, D. M.; Garcia, A. J. *Proc. Natl. Acad. Sci. USA* **2005**, *102*, 5953–5957.
135. El-Amin, S. F.; Attawia, M.; Lu, H. H.; *et al. J. Orthop. Res.* **2002**, *20*, 20–28.
136. Raz, P.; Lohmann, C. H.; Turner, J.; *et al. J. Biomed. Mater. Res. A* **2004**, *71*, 217–225.
137. Nesti, L. J.; Caterson, E. J.; Li, W. J.; *et al. J. Cell. Biochem* **2007**, *101*, 348–359.
138. Keselowsky, B. G.; Wang, L.; Schwartz, Z.; Garcia, A. J.; Boyan, B. D. *J. Biomed. Mater. Res. A* **2007**, *80*, 700–710.
139. Mendonca, G.; Mendonca, D. B.; Simoes, L. G.; *et al. Biomaterials* **2009**, *30*, 4053–4062.
140. Ogawa, T.; Nishimura, I. *Int. J. Oral Maxillofac. Implants* **2003**, *18*, 200–210.
141. Jenney, C. R.; Anderson, J. M. *J. Biomed. Mater. Res.* **2000**, *50*, 281–290.
142. Brodbeck, W. G.; Colton, E.; Anderson, J. M. *J. Mater. Sci. Mater. Med.* **2003**, *14*, 671–675.
143. Berton, G.; Lowell, C. A. *Cell. Signal.* **1999**, *11*, 621–635.
144. Mcnally, A. K.; Anderson, J. M. *Am. J. Pathol.* **2002**, *160*, 621–630.
145. Luscinskas, F. W.; Lawler, J. *Faseb J.* **1994**, *8*, 929–938.
146. Tang, L.; Ugarova, T. P.; Plow, E. F.; Eaton, J. W. *J. Clin. Invest.* **1996**, *97*, 1329–1334.

147. Hu, W. J.; Eaton, J. W.; Ugarova, T. P.; Tang, L. *Blood* **2001**, *98*, 1231–1238.
148. Pettit, A. R.; Chang, M. K.; Hume, D. A.; Raggatt, L. J. *Bone* **2008**, *43*, 976–982.
149. Bobyn, J. D.; Poggie, R. A.; Krygier, J. J.; *et al*. *J. Bone Joint Surg. Am.* **2004**, *86A*(Suppl 2), 123–129.
150. Kim, T.; Suzuki, M.; Ohtsuki, C.; *et al*. *J. Biomed. Mater. Res. B Appl. Biomater.* **2003**, *64*, 19–26.
151. Le Guehennec, L.; Soueidan, A.; Layrolle, P.; Amouriq, Y. *Dent. Mater.* **2007**, *23*, 844–854.
152. Oosterbos, C. J.; Rahmy, A. I.; Tonino, A. J.; Witpeerd, W. *Acta Orthop. Scand.* **2004**, *75*, 127–133.
153. Herford, A. S.; Boyne, P. J. *J. Oral Maxillofac. Surg.* **2008**, *66*, 616–624.
154. Freilich, M.; Patel, C.; Wei, M.; *et al*. *Bone* **2008**, *43*, 781–788.
155. Lutolf, M. P.; Hubbell, J. A. *Nat. Biotechnol.* **2005**, *23*, 47–55.
156. Hersel, U.; Dahmen, C.; Kessler, H. *Biomaterials* **2003**, *24*, 4385–4415.
157. Kim, T. I.; Jang, J. H.; Kim, H. W.; Knowles, J. C.; Ku, Y. *Curr. Pharm. Des.* **2008**, *14*, 2201–2211.
158. Kantlehner, M.; Schaffner, P.; Finsinger, D.; *et al*. *Chembiochem* **2000**, *1*, 107–114.
159. Zreiqat, H.; Akin, F. A.; Howlett, C. R.; *et al*. *J. Biomed. Mater. Res. A* **2003**, *64*, 105–113.
160. Huang, H.; Zhao, Y.; Liu, Z.; *et al*. *J. Oral Implantol.* **2003**, *29*, 73–79.
161. Hu, Y.; Winn, S. R.; Krajbich, I.; Hollinger, J. O. *J. Biomed. Mater. Res. A* **2003**, *64*, 583–590.
162. Behravesh, E.; Mikos, A. G. *J. Biomed. Mater. Res. A* **2003**, *66*, 698–706.
163. Ferris, D. M.; Moodie, G. D.; Dimond, P. M.; Gioranni, C. W.; Ehrlich, M. G.; Valentini, R. F. *Biomaterials* **1999**, *20*, 2323–2331.
164. Lutolf, M. P.; Weber, F. E.; Schmoekel, H. G.; *et al*. *Nat. Biotechnol.* **2003**, *21*, 513–518.
165. Eid, K.; Chen, E.; Griffith, L.; Glowacki, J. *J. Biomed. Mater. Res.* **2001**, *57*, 224–231.
166. Cowles, E.; Brailey, L.; Mccarthy, B.; Gronowicz, G. *J. Biomed. Mater. Res.* **2000**, *52*, 725–737.
167. Kardestuncer, T.; Mccarthy, M. B.; Karageorgiou, V.; Kaplan, D.; Gronowicz, G. *Clin. Orthop. Relat. Res.* **2006**, *448*, 234–239.
168. Goto, T.; Yoshinari, M.; Kobayashi, S.; Tanaka, T. *BioMed. Mater. Eng.* **2004**, *14*, 537–544.
169. Massia, S. P.; Hubbell, J. A. *J. Cell Biol.* **1991**, *114*, 1089–1100.
170. Rezania, A.; Healy, K. E. *J. Biomed. Mater. Res.* **2000**, *52*, 595–600.
171. Itoh, D.; Yoneda, S.; Kuroda, S.; *et al*. *J. Biomed. Mater. Res.* **2002**, *62*, 292–298.
172. Sophia, S.; Mccarthy, M.; Gronowicz, G.; Kaplan, D. *J. Biomed. Materials. Res.* **2001**, *54*, 139–148.
173. Ku, Y.; Chung, C. P.; Jang, J. H. *Biomaterials* **2005**, *26*, 5153–5157.
174. Shi, Z.; Neoh, K. G.; Kang, E. T.; Poh, C.; Wang, W. *J. Biomed. Mater. Res. A* **2008**, *86*, 865–872.
175. Chua, P. H.; Neoh, K. G.; Kang, E. T.; Wang, W. *Biomaterials* **2008**, *29*, 1412–1421.
176. Secchi, A. G.; Grigoriou, V.; Shapiro, I. M.; *et al*. *J. Biomed. Mater. Res. A* **2007**, *83*, 577–584.
177. Michael, J.; Schonzart, L.; Israel, I.; *et al*. *Bioconjug. Chem.* **2009**, *20*, 710–718.
178. Auernheimer, J.; Zukowski, D.; Dahmen, C.; *et al*. *Chembiochem* **2005**, *6*, 2034–2040.
179. Germanier, Y.; Tosatti, S.; Broggini, N.; Textor, M.; Buser, D. *Clin. Oral Implants Res.* **2006**, *17*, 251–257.
180. Elmengaard, B.; Bechtold, J. E.; Soballe, K. *J. Biomed. Mater. Res. A* **2005**, *75*, 249–255.
181. Kroese-Deutman, H. C.; Van Den Dolder, J.; Spauwen, P. H.; Jansen, J. A. *Tissue Eng.* **2005**, *11*, 1867–1875.
182. Schliephake, H.; Scharnweber, D.; Dard, M.; Sewing, A.; Aref, A.; Roessler, S. *J. Biomed. Mater. Res. B Appl. Biomater.* **2005**, *73*, 88–96.
183. Rammelt, S.; Illert, T.; Bierbaum, S.; Scharnweber, D.; Zwipp, H.; Schneiders, W. *Biomaterials* **2006**, *27*, 5561–5571.
184. Yang, G. L.; He, F. M.; Yang, X. F.; Wang, X. X.; Zhao, S. F. *J. Biomed. Mater. Res. A* **2009**, *90*, 175–185.
185. Schliephake, H.; Scharnweber, D.; Dard, M.; *et al*. *Clin. Oral. Implants Res.* **2002**, *13*, 312–319.
186. Barber, T. A.; Ho, J. E.; De Ranieri, A.; Virdi, A. S.; Sumner, D. R.; Healy, K. E. *J. Biomed. Mater. Res. A* **2007**, *80*, 306–320.
187. Garcia, A. J.; Reyes, C. D. *J. Dent. Res.* **2005**, *84*, 407–413.
188. Pierschbacher, M. D.; Ruoslahti, E. *Proc. Natl. Acad. Sci. USA* **1984**, *81*, 5985–5988.
189. Aota, S.; Nomizu, M.; Yamada, K. M. *J. Biol. Chem.* **1994**, *269*, 24756–24761.
190. Petrie, T. A.; Capadona, J. R.; Reyes, C. D.; Garcia, A. J. *Biomaterials* **2006**, *27*, 5459–5470.
191. Bernhardt, R.; Van Den Dolder, J.; Bierbaum, S.; *et al*. *Biomaterials* **2005**, *26*, 3009–3019.
192. Reyes, C. D.; Petrie, T. A.; Burns, K. L.; Schwartz, Z.; Garcia, A. J. *Biomaterials* **2007**, *28*, 3228–3235.
193. Becker, D.; Geissler, U.; Hempel, U.; *et al*. *J. Biomed. Mater. Res.* **2002**, *59*, 516–527.
194. Tamura, R. N.; Oda, D.; Quaranta, V.; *et al*. *J. Periodontal Res.* **1997**, *32*, 287–294.
195. Freudenberg, U.; Hermann, A.; Welzel, P. B.; *et al*. *Biomaterials* **2009**, *30*, 5049–5060.
196. Park, J. W.; Lee, S. G.; Choi, B. J.; Suh, J. Y. *Int. J. Oral Maxillofac. Implants* **2007**, *22*, 533–541.
197. Roessler, S.; Born, R.; Scharnweber, D.; Worch, H.; Sewing, A.; Dard, M. *J. Mater. Sci. Mater. Med.* **2001**, *12*, 871–877.
198. Lee, J. Y.; Kim, K. H.; Shin, S. Y.; *et al*. *J. Biomed. Mater. Res. A* **2006**, *76*, 530–539.

4.409. Surfaces and Cell Behavior

L E McNamara, R J McMurray, M J Dalby and P M Tsimbouri, University of Glasgow, Glasgow, UK

© 2011 Elsevier Ltd. All rights reserved.

4.409.1.	**Introduction**	116
4.409.2.	**Manufacturing Surface Topography**	117
4.409.2.1.	Photolithography	117
4.409.2.2.	Laser Holography (LH)	117
4.409.2.3.	Electron-Beam Lithography	117
4.409.2.4.	Colloidal Lithography	117
4.409.2.5.	Polymer Demixing	117
4.409.3.	**History of Differentiated Cell Guidance by Nanostructures**	118
4.409.3.1.	Grooves	118
4.409.3.2.	Pits	118
4.409.3.3.	Pillars	119
4.409.4.	**The History of Stem Cells and Nanotopography**	119
4.409.4.1.	Embryonic Stem Cells	119
4.409.4.2.	Skeletal Stem Cells	120
4.409.4.3.	Neural Stem Cells	120
4.409.5.	**Low Adhesion Materials**	120
4.409.6.	**Nanotopography as a Noninvasive Tool for Cell Biology**	121
4.409.6.1.	Responding to the Cellular Environment	121
4.409.6.2.	Mechanotransduction in the Nucleus	122
4.409.6.3.	Transcriptomic and Proteomic Effects	123
4.409.7.	**Conclusions and Future Perspectives**	124
4.409.7.1.	Orthopedics	124
4.409.7.2.	Stem Cells and Regenerative Medicine	124
4.409.7.3.	Nanotopography for Cell Biology	124
References		125

Glossary

Acetabulum It is a concave surface of the pelvis, where the head of the femur meets with the pelvis forming the hip joint.

Adipocytes These, also known as lipocytes and fat cells, are the cells that primarily compose adipose tissue, specialized in storing energy as fat.

Demixing It refers to the separation of the components of a mixture.

Dexamethasone Dexamethasone is a potent synthetic member of the glucocorticoid class of steroid hormones, is anti-inflammatory, and acts as an immunosuppressant.

Electron-beam lithography It uses electrons to define a pattern and is the most high-fidelity top-down fabrication method.

Electrospining It refers to the use of an electrical charge to draw very fine (typically on the micro or nanoscale) fibers from a liquid.

Etching Wet etching is the process of using strong acid or mordant to cut into the unprotected parts of a metal surface to create a design in intaglio in the metal (in modern manufacturing, other chemicals may be used on other types of material). Dry etching is the use of ion bombardment to etch into a surface.

Focal adhesions FAs (cell–matrix adhesions) are specific types of large macromolecular assemblies through which both mechanical force and regulatory signals are transmitted.

Integrins They are receptors that mediate attachment between a cell and the tissues surrounding it, including other cells or the extracellular matrix (ECM). They are also involved in cell signaling and thereby define cellular shape, mobility, and regulate the cell cycle.

Interference lithography (or holographic lithography) A technique for patterning regular arrays of fine features without the use of complex optical systems or photomasks.

Mesenchymal stem cells (MSCs) MSCs are multipotent stem cells that can differentiate into a variety of cell types, including osteoblasts, chondrocytes, myocytes, adipocytes, endothelia, and β-pancreatic islets cells.

Nanocolloids They are nanoscale colloidal spheres that can be dispersed across a surface and used as an etch mask.

Osteoblast Osteoblast is a mononucleate cell that is responsible for bone formation.

Photo(optical) lithography It is a process used in microfabrication to selectively remove parts of a thin film or the bulk of a substrate. It uses light to transfer a geometric pattern from a photo mask to a light-sensitive chemical photoresist.

Photoresist It refers to a light-sensitive material used in many industrial processes, including photolithography and photoengraving, to form a patterned coating on a surface.

Tribology Tribology is the science and technology of interacting surfaces in relative motion. It includes the study and application of the principles of friction, lubrication, and wear.

Abbreviations

BHK	Baby hamster kidney
Ch	Chromosome
CNT	Carbon nanotube
DiGE	Two dimensional (2D)-fluorescence difference gel electrophoresis
DNA	Deoxyribonucleic acid
EBL	Electron beam lithography
ECM	Extracellular matrix
ERK	Extracellular signal-regulated kinase
ES Cells	Embryonic stem cells
FA	Focal adhesion
FAK	Focal adhesion kinase
GRASP55	Golgi reassembly stacking protein 55
LH	Laser holography
MAPK	Mitogen-activated protein kinase
MARs	Matrix attachment regions
MDCK	Madin-Darby canine kidney
MEF	Mouse embryonic fibroblast
mRNA	Messenger ribonucleic acid
MSC	Mesenchymal stem cell
PAA	Poly(acrylic acid)
PDGF	Platelet-derived growth factor
PL	Photolithography
PLO	Poly-L-ornithine
PMMA	Polymethylmethacrylate
PnBMA	Poly(*n*-butylmethacrylate)
PS-PnBMA	Poly(styrene)-poly(*n*-butylmethacrylate)
Q-PCR	Quantitative-polymerization chain reaction
RNA	Ribonucleic acid
ROCK	Rho kinase
SSCs	Skeletal stem cells
SUN	Sad1 and UNC-84 homology domain

4.409.1. Introduction

Multicellular organisms provide a highly complex environment with many different chemical, physical/mechanical, and geometrical stimuli that affect cell phenotype, differentiation, and development. Researchers have looked at surface chemistry[1–4] growth factors, and mechanical forces[5,6] as factors in cell, and more specifically, stem cell differentiation, but nanotopography and its effects on cell behavior have been studied intensively only in the last decade. Topography varies with different tissues and also within the tissue microenvironment ranging from macro (i.e., bone or ligament) to micro (i.e., shapes of neighboring cells) to nano (i.e., protein folding and collagen binding) (64-nm repeat pattern).[7,8]

The initial study of Carrel in 1911[9] indicating that cells respond to shape opened new directions in the emerging field of cell biology and later, tissue engineering. In 1952, Weiss and Garber[10] first used the term 'contact guidance' to define cell alignment to topography. Since then, many studies of different substrates/biomaterials with different topographies and cell types have emerged.

Photolithography (PL) was the first and most widely used method that allowed the fabrication of micron-scale ($>1\,\mu m$) features (width, diameter) such as grooves or pits with submicron depths (1–0.1 μm).[11] Over the last decade, with the advancement of microfabrication, the effects of microtopography have been documented for several cell types, including changes in cell morphology, adhesion, contact guidance, motility, cytoskeletal organization, apoptosis, macrophage activation, and gene expression in different cell types, including fibroblasts, osteoblasts, osteoclasts, macrophages, endothelial, smooth muscle, epithelial, retinal, neural, and mesenchymal stem cells (MSCs).[12–19]

Current advances in the fabrication techniques, from PL to electron-beam lithography (EBL), have enabled scientists to study cell responses at the nanoscale level ($<0.1\,\mu m$). Interestingly, it was recently demonstrated that many different cell types, including fibroblasts, osteoblasts, osteoclasts, endothelial, smooth muscle, epithelial, epitenon, neural, and MSCs, respond strongly to nanoscale topography and are influenced in a similar way to the microtopography, ranging from morphology and adhesion to genomic regulation.[20–35]

Given that different cell types show different responses to different surface topographies, there is a continuous need for the development of 'next generation' biomaterials and medical implants. The surface properties of biomaterials, that is, porosity[36] or wettability (hydrophilicity/hydrophobicity),[37,38] are important for their application and critical for the adhesion process of adjacent cells in the case of implants. The measurement of the wettability of a material (contact angle in the presence of different liquids) provides us with very useful information about the cytocompatibility of the material. Previous work by Keisler[39] showed that surface roughness may have an effect on contact angle, the increase or decrease of which depended on its initial value. Roughness, measured in Ra, has been increasingly used as a parameter in implant topography. However, roughness is hard to reproduce and the results can be conflicting even for surfaces with similar roughness levels.[40,41]

Consequently, new avenues of scientific inquisition may enable the development of biomaterials that are safe, reliable, and 'smart,' perform ideally in their respective biological environments, and interact appropriately with the tissue type which they interface.

Furthermore, on a basic science level, the use of the recently developed field of nanotopography, in combination with new

biomaterials, will help us to overcome the need for defined media, with patterned surfaces/materials used as noninvasive tools to study cellular function.

4.409.2. Manufacturing Surface Topography

Here, we discuss various methods of nanoscale fabrication.

4.409.2.1. Photolithography

The microchip industry has traditionally used PL to fabricate micron-scale designs. In order to do this, a light-sensitive substrate (photoresist) is spread as a thin film onto silicon wafers. Light can then be directed onto the resist through a patterned mask, exposing the photosensitive layer in a precise pattern. The resist is then developed (analogous with photography), and the nonexposed or exposed area (depending on the resist used) can be removed, thus leaving a topography of resist around areas of exposed silicon. The resist is then baked to make it hard and the substrate is ready for etching.

Etching can be wet (chemical) or dry (reactive ion bombardment), both having the effect of simultaneously removing the hard resist and etching into the substrate. This leaves the samples resist-free and with a topographical pattern. In electronics, doping can take place to give electrical properties to the substrate. For biological purposes, it is desirable to stop after etching and grow cells on the patterned material. It is also possible at this stage to emboss, or cast, the pattern into a polymer suitable for cell growth, such as polycaprolactone or polymethylmethacrylate (PMMA).

While PL was used by many of the pioneers of cell response to microtopography,[16,42,43] its usefulness for producing nanotopography is limited. Thus, alternative fabrication techniques have been sought.

4.409.2.2. Laser Holography (LH)

Clark *et al.*[44] developed an interference technique used to produce ultrafine masks for X-ray printing. Samples coated in photoresist can be exposed to patterns produced in a two-mirror interferometer, producing a linear light pattern whose period is given by: period $= Ll/2\sin\Theta$ ($L = (l =$ light wavelength of light, and $\Theta =$ half angle of the recombination of the beams).

Development of the photoresist (as with PL) results in the formation of an etch mask. Dry etching can then be used to give depth to the pattern. Clark *et al.* successfully produced patterns with a 260-nm groove width and 100–400-nm depth and showed baby hamster kidney (BHK) fibroblast, Madin-Darby canine kidney (MDCK) epithelial, and primary neurite contact guidance.

This technique, however, is still limited in the variety of patterns that can be produced, the smallest size of the dimensions that can be made, and cost.

4.409.2.3. Electron-Beam Lithography

In order to achieve even better resolution, electron beams are now being used as a radiation source for photoresist development to expose the radiation-sensitive polymer resist. In electronics, the smaller the devices can be made, the more engineers can fit on a chip and the faster they can sell; this has led to Moore's law where the density of transistors on a chip has been seen to double every 1.9 years since the 1960s.[45] Thus, there is a massive push at present to develop nanochips. This calls for the use of precision nanofabrication. At present, EBL (e-beam) offers the best precision and resolution (down to 510 nm in *X*- and *Y*-axes, and <1nm in the *Z*-axis). For this technique, computer-aided design software is used to control electron deflection and exposure time onto a radiation-sensitive resist (thus rather than shining a 'block' of light through a mask exposing all areas to be patterned in parallel, the electrons are guided with great precision onto the resist directly, and the pattern written serially). The resist is then developed and etched to produce a topography, as with PL.

This use of EBL in biological applications has been limited due to distortion of the beam when deflected by more than 1 mm, limiting the size of the patterns produced. Recently, techniques using interferometric control have been developed to allow movement of the sample in the e-beam writer and thus stitching of the patterns into large areas (with a stitch accuracy of ~ 20 nm).[11]

E-beam is, however, expensive and time-consuming due to serial exposure to define the pattern, and the more complex the pattern, the more complex the programming, and the more time taken. It is interesting to note that researchers are now also able to produce biomimetic designs using e-beam, such as reproducing collagen banding.[46] However, fabricators are now becoming successful in producing much cheaper nanotopography over larger areas. Such techniques (including colloidal lithography) are potentially very useful to biologists due to their low costs.

4.409.2.4. Colloidal Lithography

This technique uses nanocolloids as an etch mask, and can be used to produce large areas of nanotopography with short-range order. The colloids are dispersed as a monolayer and electrostatically self-assembled on a surface (i.e., the intercolloidal spacing is altered by changing the charge on the particles). The colloids are then etched away, as is the surrounding substrate material, by directed reactive ion bombardment.[47,48] If the etch is directly from above, this technique produces nanocolumns; by altering the angle of etch, nanospheres and nanocones may also be produced.

4.409.2.5. Polymer Demixing

As well as top-down fabrication techniques, some bottom-up methodologies have also been trialled with cells. Polymer demixing relies on the spontaneous phase separation of polymer blends, and the demixing of island topographies allows the production of single chemistry substrates ideal for cell testing as the complexities of mixed surface chemistries can be ignored. The method also allows the production of islands with controlled heights from 10 to 100 nm depending on the polymer blend used.

The surface of a solid amorphous polymer, or polymer mixture, is expected to be smooth and featureless. However, under certain circumstances, marked topography can be

obtained from a spontaneous demixing of the components of a binary blend, that is, in thin films of certain polymer mixtures on selected substrates.

The factors that determine demixing have been extensively studied. Principally, the mutual compatibility of the polymers controls the behavior. The relationship between polymer compatibility and generation of topography in thin films of the blend is illustrated by examining a blend of poly(styrene) with a series of brominated polymers, poly(*p*-bromo$_x$-styrene), where x is the fraction of aromatic rings that are brominated, $1 \geq x \geq 0$. The compatibility of the brominated polymer with poly(styrene) depends on the extent of bromination.[49] When $x = 1$, the polymers are incompatible and the compatibility increases as $x \rightarrow 0$. A measure of the compatibility is the thickness of the interfacial boundary layer between a poly(styrene) film and a poly(*p*-bromo$_x$-styrene) overlayer. Neutron reflectivity data showed a monotonic correlation between the interfacial layer thickness and the extent of bromination of the bromopolymer.[50] Thin films of blends of the bromopolymer and poly(styrene) have smooth surfaces at low values of x. As x increases, topography appears, becoming more marked with increase in x, corresponding to the decreasing compatibility. We have used the fully brominated polymer, $x = 1$, in our studies of cell interactions.

The type of topography depends on the relative amounts of the polymer components of the blend.[49] In the poly(styrene)-poly(*p*-bromostyrene) system, islands of the brominated polymer protrude from a sea of the poly(styrene) when the weight fraction of the bromopolymer is less than $\sim 60\%$. At higher weight fractions, the bromopolymer islands link up to form a sheet with holes that expose the underlying poly(styrene). Similar changes in topography have been observed with other binary polymer mixtures.

The topography can be controlled further by changing the overall thickness of the polymer film. With spin-cast samples, this is readily accomplished by varying the concentration of the polymer blend solution and/or the spin speed. In general, increase in thickness of the cast films results in islands that are higher and wider. A concomitant change in the number density of the features is observed. More subtle control of the topography may be obtained by varying the molecular weights of the polymer components.[51]

From the point of view of producing materials to study cell interactions, it is desirable to reduce the experimental parameters by having the cells exposed to only one chemistry; the poly(styrene)–poly(*p*-bromostyrene) system produces a surface with patches of poly(styrene) and patches of poly(*p*-bromostyrene). In this case, the surface chemistry can be changed by annealing the films.[50] Heating the film to the glass transition temperature of the poly(styrene) causes the poly(styrene) to migrate over the surface, forming an overlayer, thus achieving topography with one chemistry at the surface. The topography is altered by this process, which typically causes the islands to grow in height and width. However, a minimum annealing gives a thin overlayer of poly(styrene) with little change in the topography.

Another polymer mixture, which gives an island topography similar to the above, is poly(styrene)–poly(*n*-butylmethacrylate) (PnBMA).[51] In this system, an overlayer is formed at room temperature. The cast film develops topography that is covered spontaneously by a thin overlayer of the acrylate.

The process of formation of the demixed polymer film is complex, involving the compatibility of the polymer components, their air–polymer and polymer–substrate surface tensions, polymer component molecular weight, solvent used, rate of solvent evaporation, etc. The film is generally also metastable and can change if the temperature is sufficient to allow movement of one, or both, polymer components. These factors have been considered in the papers of Affrossman[50,52] and references therein and the relevant paper for the PS–PnBMA system.[51]

More recently, developments in phase separation with block copolymer systems have allowed the fabrication of nanosurfaces with an order approaching the one achieved by EBL.[53]

4.409.3. History of Differentiated Cell Guidance by Nanostructures

In 1964, Curtis and Varde[54] showed that fibroblast cells orientated themselves in the direction of silica fibers with diameters between 10 and 30 μm. Since this period and over the last 40 years, research has continued to focus on the topographical effects of micron size features; however, more recently, work has begun to focus on the effect of nanotopographical features. This work is driven by the abundance of nanoscale features known to be present within the extracellular matrix (ECM), and to which a cell readily comes into contact within its native environment. Not only have a wide variety of cell types been studied, such as neurons, fibroblasts, smooth muscle cells, and osteoblasts but also a variety of topographic patterns. Nanotopography has also been shown to have an effect on several cellular aspects, including proliferation,[55] morphology, adhesion,[56] and gene expression,[30] which will be discussed further.

4.409.3.1. Grooves

Nanogrooves have been studied extensively in relation to feature size and cell type. Studies have shown that fibroblast, epithelial, endothelial, osteoblast, smooth muscle, and neural cells undergo topographic guidance and have an elongated morphology when cultured on nanogrooved substrates.[13,31,57–60] In relation to feature size, evidence shows that an increase in cell alignment along the groove is inversely proportional to groove width.[31,61] In a recent publication, grooved substrates were also used to identify RACK1, a stabilizer of focal adhesions (FAs), as a modulator of contact guidance.[62] Breast cancer cells that overexpress RACK1 were shown to have a decreased sensitivity to topographical guidance when cultured on nanogrooves. By knocking down RACK1 expression, the authors were able to observe recovery in topographical guidance response with regard to the nanogrooved substrates.

4.409.3.2. Pits

Nanopits of varying degrees of disorder were also shown to influence the morphology and adhesion of osteoblast cells. In a paper by Biggs *et al.*,[29] the authors found that not only did nanopit topographies show a contrast in cell morphology and

adhesion when compared to a flat control, but changes were also observed according to the geometry of the nanopits. It was shown that nanopits with an ordered geometry caused FA length and formation in contrast to nanopit substrates with a slight degree of disorder, which saw an increase in FA length and formation together with increased cell spreading. Similar results regarding adhesion were also obtained when using fibroblast cells.[56]

Lim *et al.*[63] also looked at the effect of varying the depth of nanopits on integrin-mediated FA formation and found that nanopits of < 29 nm increased cell adhesion, various integrin subunits, and phosphorylated focal adhesion kinase (FAK), a protein involved in signal transduction, when compared to a flat control.

4.409.3.3. Pillars

In contrast to low adhesion topographies, nanopillars have been shown to have the opposite effect on cell adhesion. In a study by Milner *et al.*, the effect of different pillar diameters was explored, and results showed that an increase in cell adhesion was observed with a decrease in feature size; however, a decrease in feature size also correlated with a decrease in proliferation. Conversely, nanopillars with larger feature sizes showed a decrease in the initial cell adhesion but with increased proliferation when compared to flat control.[55]

Again, in a second study that looked at nanopillar feature height on the proliferation and adhesion of fibroblasts,[64,65] the authors found that by varying the height of nanopillars over a range of 95 to 13 nm, the level of adhesion could be controlled, with nanopillars of the smallest height inducing the largest increase in cell adhesion and nanopillars of 95 nm having a negative effect on cell adhesion.

4.409.4. The History of Stem Cells and Nanotopography

Until recently, adult and embryonic stem (ES) cells were considered the two main types of stem cells; the former being derived from adult tissues are more accessible, but exhibit less pluripotency than embryonic stem cells. The main drawback of the latter, however, is that they are derived from embryos and therefore involve many ethical issues. The discovery of induced pluripotent stem cells in 2007, whereby a pluripotent stem cell can be produced following viral transfection of a terminally differentiated cell using four key genes, has the potential to address all these issues and provide both pluripotency and accessibility; however, even these stem cells are not void of ethical issues.[66]

In terms of the differentiation of stem cells in normal culture, this is usually induced by the addition of differentiation factors into the medium; for example, in the case of osteogenic differentiation, addition of dexamethasone, for adipogenic differentiation, insulin, and in the case of neural differentiation, retinoic acid. However, several studies over the last decade have shown that nanotopography alone can provide the means to induce differentiation without the need for defined media – an important factor when culturing cells which may ultimately be transplanted into patients.

4.409.4.1. Embryonic Stem Cells

The main drawback of studying ES cells and one possible reason behind the lack of research using ES cells in this field, besides ethical issues, is their requirement for a feeder layer of mouse embryonic fibroblasts (MEFs). In terms of studying the response of ES cells to nanotopography, this is especially significant as any nanotopographical pattern is likely to be masked by the presence of the feeder cell layer. This, however, may change with the recent development of cell culture techniques that no longer require a layer of feeder cells.[67]

Several studies, however, have looked at both differentiation[68,69] and retention of the self-renewal/proliferation capacities of ES cells.[70,71] A study by Gerecht *et al.*[72] investigated the effect of grooved substrates on the morphology and proliferation of ES cells. In line with other similar studies using terminally differentiated cells, changes in morphology and cytoskeletal organization, such as alignment and elongation, were observed in ES cells cultured on nanogrooves. In addition, ES cells cultured on nanogrooves were shown to have reduced proliferation rates when compared to ES cells cultured on flat controls.

In another study by MacFarlin *et al.*,[70] the authors studied the effect of culturing ES cells, which are prone to spontaneous differentiation in culture, on flat culture dishes with a feeder layer, and on grooved substrates in both the presence and absence of a feeder layer. Results of the study showed that when cultured on the grooved substrates with a feeder layer in contrast to a flat control with feeder layer, the rate of spontaneous ES differentiation was significantly reduced. In contrast to this, ES cells cultured on nanogrooves alone showed much higher levels of spontaneous differentiation when compared to a flat substrate with a feeder layer. These results indicate that in the context of a feeder layer, nanotopography can play a synergistic role in the promotion of ES cell self-renewal; however, the mechanism by which it is governed is still not fully understood.

Several studies have looked at the directed differentiation of ES cells into various cell types, including adipocytes[73] and neurons.[74] In the study by Chao *et al.*, the authors examined the neuronal differentiation of human embryonic stem (hES) cells in response to culture upon polymer-grafted carbon nanotubes (CNT). The authors showed that by grafting CNT with poly(acrylic acid) (PAA), a polymer more commonly known for its negative effect on neuronal differentiation, this effect can actually be reversed. The authors observed enhanced neuronal differentiation of the hES cells on PAA-grafted CNT, in comparison to both PAA alone, and poly-L-ornithine (PLO), a common polymer substrate for the neuronal differentiation of hES cells. In addition to enhanced differentiation, similar results were obtained regarding cell viability, with the PAA-grafted CNT results being comparable to those of PLO, in contrast to that of PAA alone.

This study highlights the importance of the context in which a polymer is used. In this case, by grafting a polymer onto a nanotopography such as CNT, its properties have been altered from being unfavorable for neuronal differentiation into a material that can provide an environment more suitable for both cell growth and differentiation of ES cells.

4.409.4.2. Skeletal Stem Cells

Skeletal stem cells (SSCs) have been an exciting target for tissue engineering since their discovery by Freidenstein in 1976,[75] not only because of their accessibility within the bone marrow, but also because they have been shown to differentiate into a variety of cells, including osteoblasts and adipocytes,[76] chondrocytes,[77] smooth muscle cells,[5,78] and neurons.[79]

The differentiation of SSCs into osteoblasts has been observed in two key studies. In the first study, the authors looked at SSC differentiation on a variety of nanopit topographies with varying degrees of order, ranging from a square geometry, near square or semi-disordered geometry and random.[80] Each nanotopography is embossed in PMMA to ensure similar surface chemistry. When cultured on these topographies, SSCs showed increased levels of bone cell markers as identified by immunofluorescence analysis only when grown on topographies with semi-ordered nanopits, in contrast to all other topographies studied. The authors further supported this data by carrying out quantitative PCR and microarray analysis, which identified high levels of genes associated with osteoblast development and comparable to the levels of a positive control.

In a similar study looking at the differentiation of SSCs into osteoblast cells, Oh *et al.*[81] developed a range of CNT topographies with diameters in the range of 30–100 nm. In this study, osteogenic differentiation was observed to occur in SSCs cultured on CNT with a 100-nm diameter. Interestingly, however, this topography was also observed to have the lowest level of cell adhesion. This is in contrast to observations of cell adhesion on the smallest, 30-nm diameter CNT to which a high level of adherent cells could be observed but with no osteogenic differentiation. In this study and other similar studies, these differences in cell adhesion and differentiation have been attributed to the ability of the cell to develop mature FAs, ultimately leading to changes in gene expression.[30]

Neuronal differentiation of SSCs, a process known as transdifferentiation, has been identified in several studies using differentiation factors.[82] Controversially, this has led to SSCs being considered by some as more pluripotent than once thought.

The following study by Yim *et al.*[79] provides an example of SSC differentiation into neurons using nanogrooved surfaces. Neuronal differentiation was observed in SSCs cultured on 350-nm grooves, as identified by the expression of MAP2 and β-tubulin III, in the absence of differentiation factors. This nanotopography alone was also shown to express higher levels of MAP2, as indicated by quantitative PCR, when compared to levels observed in cells cultured on flat controls in the presence of either 1 or 30 μM retinoic acid.

4.409.4.3. Neural Stem Cells

Neural stem cells have the ability to differentiate into three cell types. These include neurons and two nonneural cell types, astrocytes and oligodendrocytes, which act to protect and support neurons.

In two separate papers, neural stem cell differentiation into neurons using nanotopography has been investigated, using electrospinning to produce nanofibers. Yang *et al.*[83] investigated the effect of varying fiber dimensions from microscale to nanoscale and their orientation, that is, aligned or random on neural stem cell differentiation. The authors found that when comparing aligned microfibers and aligned nanofibers, the rates of differentiation were higher on the nanofibers. Consistent with this when comparing the random nanofibers and the random microfibers, differentiation rates were also found to be higher on the random nanofibers.

In a more recent but similar study by Christopherson *et al.*,[84] the authors also studied the effect that fiber diameter has on the differentiation of neural stem cells. In this case, they studied fiber diameters ranging between 283 ± 45, 749 ± 153, and 1452 ± 312 nm. In correlation with the study by Yang *et al.*, the authors of this paper also found that differentiation of the neural stem cells was supported on fiber diameters within the nanoscale range rather than microscale.

As suggested by the authors in Yang *et al.*, both papers indicate that it is the fiber diameter that plays a key role in directing the differentiation of neural stem cells rather than fiber orientation.

4.409.5. Low Adhesion Materials

It is fair to say that in biomaterials research, there has been a major drive to consider how to increase cellular adhesion and proliferation on materials surfaces; however, this is not always the effect desired. There are many applications where low adhesion is required, such as in stents, catheters, heart valves, and acetabulum, where cell migration and tissue formation are problematic. While it is at present difficult to see if topography can have roles where tribological issues are involved, it is possible to foresee that in areas such as catheters and valves topography could play a key role.

Topographies that produce low adhesion in fibroblasts and SSCs have already been patterned inside tubes using polymer demixing to form nanoislands.[85–87] The next step should be the production of the islands on the internal surface in the bulk of the tube polymer. This could perhaps be achieved by embossing the low adhesion shapes and then precision rolling – in a manner similar to that outlined by Seunarine and others.[88] Curved surfaces could be achieved using this method.

Nanoislands produced by polymer demixing are, in fact, tunable to low or high adhesion.[64] Very small islands (< 20 nm) promote adhesion in most cell types tested (endothelial,[21] fibroblastic,[24] and mesenchymal stem[89]). As the islands increase in size, they become less adhesive. Islands produced from a blend of poly(styrene)–poly(butylmethacrylate) were adhesive to fibroblasts at 10-nm in height, but almost completely nonadhesive at 50-nm in height.[90]

Topographies produced by colloidal lithography have shown a similar trend, with very small nanocolumns (11-nm high) producing increased osteoprogenitor response,[89] while larger nanocolumns (160-nm high) produced a significant (but far from complete) reduction in fibroblast adhesion.[91,92] Interesting work has also been done on topographies fabricated through the colloidal route. They first showed 100-nm high columns to reduce epithelial cell adhesion[93] and then went further to show, again in line with the polymer-demixed nanotopographies, that increasing column size decreased epithelial cell adhesion.[94] They then further showed that the 160-nm high nanocolumns imparted properties of low adhesion on osteoblasts.[95]

Using another fabrication method, that of interference lithography, a recent paper further supported these observations of size and adhesion. Choi and others fabricated sharp nanoposts (pointed columns) and nanogratings (very sharp grooves) of different heights. They used three size ranges (50–100, 200–300, and 500–600 nm high) and found decreased adhesion and spreading as size increased.[96]

Nanopits (depth) can also be important, for example, nanopits fabricated in a square array by EBL with diameters of ~100–150 nm and center–center spacing (pitch) in the range of 300 nm. Again, these adhesion effects have been shown to be size-dependent. A study that used three pit sizes (diameter (nm):pitch (nm) – 35:100, 75:200, and 120:300) and fibroblasts as a cell model, showed that as pit diameter increased, filopodial interaction increased, but cell spreading decreased, that is, the interaction of the filopodia with the pits prevented adhesion.[97] A previous study with pit diameters of 150 nm showed almost no epitenon attachment.[22] However, we know that large pits (in the range produced by PL) promote increased cellular response in, for example, SSCs.[98] Thus, there is a large gap in our knowledge of the transition between nonadhesive and adhesive pits.

This is further complicated by pit symmetry being implicated as important. This was originally mooted by Curtis and others in 2004.[99] Subsequent studies have used 120-nm diameter, 300-nm pitch pits in both square and hexagonal arrangement. Both with SSCs[100] and with fibroblasts,[97,101,102] the hexagonal arrangement has been shown to be the least adhesive.

4.409.6. Nanotopography as a Noninvasive Tool for Cell Biology

4.409.6.1. Responding to the Cellular Environment

Cells are responsive to intercellular cues, such as cadherin linkages, and to the constraints of their environmental niche, including its mechanical and chemical properties. The ECM, composed of proteins such as fibronectin and vitronectin, provides protein and mechanical signals for cell attachment,[15,103,104] survival,[15] and differentiation.[5] Nanofeatures can physically direct cells, by processes such as contact guidance[31,57] and direction of filopodia[97,105] (**Figure 1**). Cells interact directly with the protein layer on biomaterial surfaces, and the conformational state,[106] density, and arrangement of these adhesive proteins[15,103,104] and stiffness of the underlying substrate[5] have the potential to influence cell responses. As a result, the ECM is an important factor in cell–material interactions.

FAs are mechanosensitive, multipartite protein assemblies that are the sites of cellular anchorage to the ECM. Chemical signaling cascades can be initiated at these sites in response to a mechanical stimulus by resident and recruited kinases such as FAK and ROCK (Rho kinase), a process known as indirect mechanotransduction. A crucial component of FAs are the integrins, a family of heterodimeric proteins capable of bidirectional signaling. These proteins interact directly with specific amino acid sequences (such as the RGD motif) on their ligands in the ECM. Blocking a β_3 integrin was shown to decrease cytoskeletal nanoimprinting (**Figure 2**) (where the cytoskeleton adapts to the form of the nanofeatures), while the addition of anti-β_1 antibody was shown to enhance nanoimprinting to nanocolloidal substrates.[107] It has been proposed that distension of the plasma membrane may be involved in cellular detection of the topology of nanostructured substrates.[108] In this model, negative features (such as nanogrooves or nanopits) could promote opening of mechanosensitive ion channels, while release of the G-protein Rac may be stimulated by interaction with positive features (such as nanopillars).

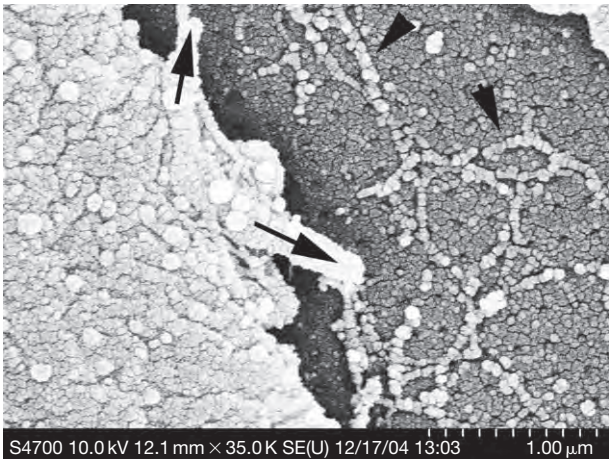

Figure 1 Filopodia and topography. Cells are far larger than nanoscale features – here, a mesenchymal stem cell can be seen cultured on 40-nm diameter pits (originally defined by electron-beam lithography and then imprinted into polymethylmethacrylate). The filopodia (arrows) are used in 'cell sensing' of the surface and are a much closer length scale to the nanofeatures. Note that the scanning electron microscopy image is overexposed to help see the topography and that the cell has produced fibrils of extracellular matrix (arrowheads) on the surface.

Physical tugging on FAs can induce growth of these structures[109] and expose cryptic binding sites. A recent study noted that conformational 'melting' of the FA protein talin allowed it to bind additional vinculin.[110] The cytoskeleton is physically attached to FAs via filamentous (F-)actin, which is partly responsible for the rapid relay of mechanical signals to the nucleus. Direct mechanotransduction involves pulling of the cytoskeleton on the nucleus to effect changes in downstream gene- and protein expression. Biggs *et al.* (2008)[31] noted that the pitch of nanogrooves (the authors examined 10-, 25-, or 100-µm groove spacings, all with a depth of 330 nm) was important for determining the degree of cytoskeletal alignment. The study found that only the 10-µm spacing pitch grooves could induce contact guidance of the cells and align FAs and microtubules along the nanogrooves. On the 25-µm pitch grooves, FAs were primarily localized to regions where the cells were bridging between adjacent grooves and ridges, and on the 100-µm-spaced grooves, the adhesions appeared similar in size, number, and orientation to the planar control, with an analogous cytoskeletal arrangement. Cytoskeletal disorganization can also occur in response to nanosubstrates such as hexagonally arrayed nanopits.[56,102] The tensegrity model[111,112] describes the components of the cytoskeleton in terms of their opposing forces. Actin provides the tensile

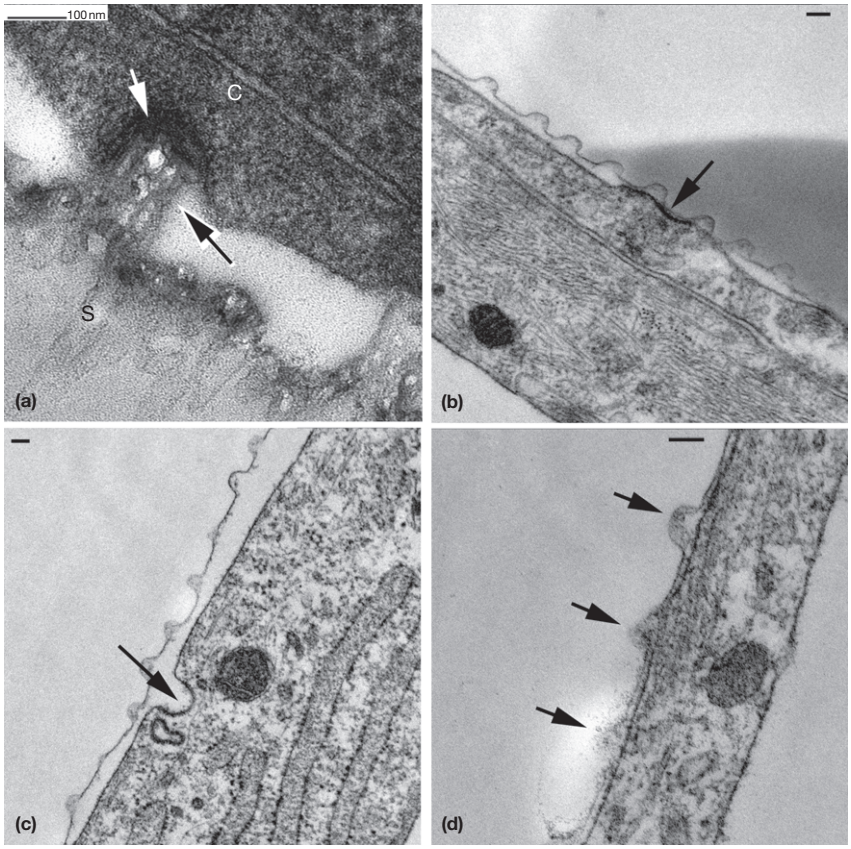

Figure 2 Nanoimprinting. (a) A fibroblast cell (C) is imprinted (white arrow) by a column (black arrow) defined by colloidal lithography in a polymethylmethacrylate (PMMA) substrate (S). Substrates fabricated by Dr Duncan Sutherland (iNano, Denmark). (b) A mesencymal stem cell on a NSQ50 substrate originally defined by electron-beam lithography (120-nm diameter pits with square arrangement (300-nm center–center spacing but with $\pm$50-nm error (highly osteogenic)) embossed into PMMA – arrow shows the start of the formation of a clathrin-coated pit in response to the surface. (c) Shows a more mature endocytosis pit forming (arrow). (d) Shows that nanoimprinting also occurs with the cells trying to fill the pits (arrows, quite rare). All scale bars are 100 nm.

element, with microtubules resisting compression and intermediate filaments generating prestress in the structure. Altered cytoskeletal tension in cells cultured on nanotopographies, most likely generated within the cell as a result of the altered arrangement of FAs, has the potential to alter cellular gene and protein expression through direct mechanotransduction.

4.409.6.2. Mechanotransduction in the Nucleus

Surrounding the nucleus is a meshwork of Type V intermediate filaments, the lamins, which are the major components of the nucleoskeleton, the mechanical bridge between the cytoskeleton and the nucleus. The nuclear lamina is physically associated with actin and vimentin via nesprins and SUN (Sad1 and *UNC*-84 homology domain) proteins[113] (discussed in Wang *et al.*[114]). Micromanipulation experiments have neatly illustrated that transmission of force can occur from the peripheral cytoplasm into the nucleus,[115] demonstrated the mechanical interconnection of chromosomes and nucleoli,[116] and shown the importance of the nuclear lamina in force transmission.[117,118] The structure of the nuclear lamina is shown in Figure 3(a). Compared to micromanipulation, nanotopography has additional advantages of being noninvasive and nondestructive, and can be used as a tool for the investigation of mechanotransduction and cell biology, with surfaces that can be modified to suit the requirements of the study.

Nuclear reshaping has been shown to induce alterations in gene expression.[119] Topography-induced redistribution of chromosomal territories (the space occupied by a given chromosome within the nucleus, reviewed in Cremer and Cremer[120]), or intraterritory loci (the location of particular genes) could affect the cellular transcriptional profile. There are foci of transcriptional activity within the nucleoplasm, where active, transcription-competent RNA polymerase II and transcription factors are clustered. Genes can loop out from chromosome territories to move into these areas, and such repositioning can increase the likelihood of their being transcribed[121,122] (discussed in West and Fraser[123]). Alternatively, movement of genes or territories toward the periphery of the nucleus could promote downregulated transcription. Wang *et al.*[114] suggested a number of models by which tensile forces from FAs could modulate gene expression.[114] It was proposed that the assembly or activity of transcription factor complexes could be affected directly or indirectly by tension-mediated alterations in the nucleoskeleton. In addition, local DNA melting at matrix attachment regions (MARs), where the DNA

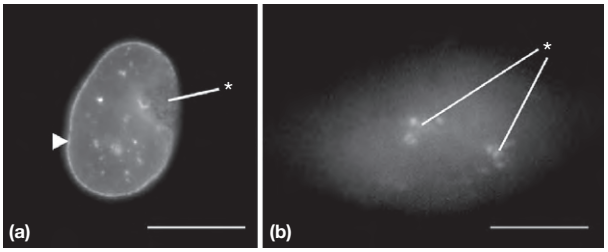

Figure 3 Nuclear lamina and chromosomes. (a) The nucleus has a protective 'skeleton' in the form of a peripheral lamina (arrowhead), which encloses the DNA and other subnuclear components, and can transmit mechanical forces from the cytoskeleton into the nucleus. This nucleus has been immunostained for lamin B, and part of the peripheral lamina is visible covering the nucleus at the focal plane examined (*). (b) Chromosomes can be repositioned in response to mechanical force, such as the cytoskeletal rearrangement induced by culture on topography. This is an example of a fluorescence *in situ* hybridization stained nucleus of a cell on a topographical substrate, stained for chromosome 1 (*). Bars = 10 μm.

is anchored to the lamina, could affect its accessibility for transcription. Furthermore, the authors suggested that gene expression or mRNA transport could also be affected by tension-mediated changes in nuclear pores. Reddy *et al.*[124] elegantly demonstrated that repositioning of a gene to the nuclear lamina could downregulate its transcription and lead to association with lamin B and nuclear envelope proteins.[124] The authors concluded that transcription was being reduced by physically blocking access to transcription factors and by facilitating the assembly of a repressive chromatin architecture.

Nanotopography provides a useful means to investigate mechanotransductive effects on the nucleus. Nanocolumn substrates were shown to induce repositioning of chromosome 3 (Ch 3)[125,126] relative to planar controls. The Ch 3 centromeres were more closely apposed in cells cultured on the nanocolumns, probably as a consequence of the decreased cell spreading and nuclear area. On hexagonally arrayed nanopits, the intercentromeric distance was reduced for both Ch 3 and Ch 11, and the cells were markedly less spread than controls.[126] As the authors noted, the changes were consistent with the tensegrity model. Tension on the cytoskeleton and nucleus should be reduced, which is likely to have lessened the force exerted on chromosomes. **Figure 3(b)** shows an example of Ch 1 territories on a topographical substrate, visualized by fluorescence *in situ* hybridization (FISH).

4.409.6.3. Transcriptomic and Proteomic Effects

To investigate the molecular basis for cell–topography interactions, transcriptomics and proteomics are valuable. These techniques are useful for the large-scale characterization of changes in mRNA and protein abundance between control and test substrata, and the identification of responsive molecules. The study of the transcriptome and the mRNA profile of the cell, using microarray analysis, has the major advantage that the transcript abundance of many thousands of genes can be studied simultaneously. There are additional levels of regulation following transcription, however, and proteomics has the benefit that it permits analysis of the functional effectors.

Culture of mesenchymal stem cells on nanogrooves appeared to stimulate differential expression of genes involved in MAPK (mitogen-activated protein kinase) signaling, which is implicated in key cell processes such as cell growth and differentiation. Interestingly, on 330-nm deep nanogrooved substrates, various transcripts involved in integrin and PDGF (platelet-derived growth factor) signaling were upregulated in cells cultured on 100-μm pitch nanogrooves, whereas transcripts corresponding to these pathways were downregulated in cells cultured on nanogrooved surfaces with a 10-μm pitch.[31] This suggests that there is a transcriptional effect downstream of the changes in size and orientation of FAs on these substrates, which is probably induced by both direct and indirect mechanotransductive pathways. Fibroblasts cultured on a low adhesion hexagonal array of 120-nm wide pits with a depth of 100 nm (spaced 300 nm from center to center) showed downregulation of integrin and fibroblast growth factor signaling. On this surface, including another low adhesion substrate with 10 nm nanocolumns, fibroblasts also showed downregulation of mRNAs encoding ECM proteins and proteins involved in the innate immune response.[102] In contrast, transcripts for signaling proteins were upregulated in fibroblasts cultured on polymer-demixed nanoislands.[27] These observations illustrate that different nanotopographies can induce distinct transcriptional responses as a result of the specific character of the mechanostimulus, which makes such substrates attractive as versatile tools for the study of cell biology.

Some pioneering studies have applied the proteomic technique DiGE (two-dimensional (2D)-fluorescence difference gel electrophoresis) to the study of cellular interactions with nanotopography. This 2D-gel based technique allows the detection of differential protein abundance between control and test states using fluorescent dyes and is discussed in further detail in the context of biomaterials research in Mcnamara *et al.*[127] The basic schema for this technique is shown in **Figure 4**.

On a surface with a partially disordered arrangement of nanopits, DiGE revealed that the cytoskeletal proteins, actin and vimentin, were upregulated in abundance relative to a planar control after 5 weeks of culture.[34] This may have enabled the cells to cope with the demands of cytoskeletal reorganization or altered their capabilities for direct mechanotransduction, which was supported by downregulation of the FA-associated protein zyxin. In addition, Golgi reassembly stacking protein 55 (GRASP55), which is involved in MAPK signaling, was downregulated in cells cultured on the nanopits. In combination with histological results and other differential protein changes, the authors concluded that this was consistent with the tendency toward differentiation rather than proliferation in cells cultured on the nanosurface.

DiGE was also used to examine the temporal response of osteoprogenitors to disordered nanotopography over 6 weeks of culture.[20] The authors noted osteoid nodule formation on the nanotopographical substrate 2 weeks before nodules appeared on the control surface and concluded that the topography had hastened the maturation of these cells. Unlike in the DiGE studies discussed earlier which only examined cellular proteins, in this investigation, an extraction regime that permitted harvest of both intracellular and ECM proteins was used. Compared with controls, vimentin and osteonectin

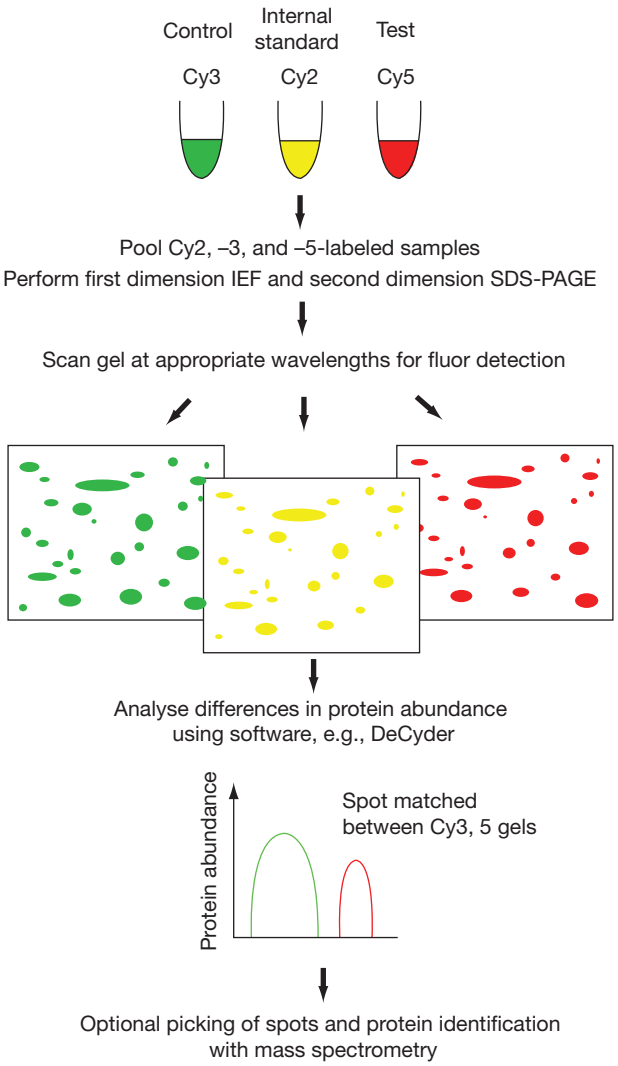

Figure 4 Basic workflow for two-dimensional-fluorescence difference gel electrophoresis, using a three-dye labeling approach (known as minimal labeling). Cy2, -3, and -5-labeled samples are co-resolved on a single gel. The Cy2-labeled samples are used in spot normalization and matching between gels, and differences in protein abundance are quantitated using software. If desired, a picklist can be generated for manual or robotic spot picking and analysis by mass spectrometry, to identify proteins of interest. A modification of this technique, called saturation labeling, is a higher sensitivity approach that is technically challenging but useful for the study of scarce samples such as those typically obtained from cells cultured on small surface areas of nanotopographical substrata. Adapted from Mcnamara, L. E.; Dalby, M. J.; Riehle, M. O.; Burchmore, R. *J. R. Soc. Interface* **2010**, *7*, S107–S118.

(an ECM protein specific to bone lineage cells) were upregulated in cells on the topography following 3 weeks of culture. These proteins are markers of differentiation in this cell type, and interestingly, the abundance of both proteins was not distinguishable from levels in the control cells at later time-points. The authors noted differential regulation of a number of proteins involved in MAPK–ERK (extracellular signal-regulated kinase) signaling, further implicating this pathway as an important regulator of the cellular response to nanotopography. Most of the differential protein regulation occurred before the sixth week (prior to osteoid mineralization), which the authors corroborated with a liquid chromatography-based technique, dimethyl labeling, at the week six time point. This showed minimal changes between the control and nanosurfaces.

4.409.7. Conclusions and Future Perspectives

Nanoscale surfaces will almost certainly find use in several areas of science.

4.409.7.1. Orthopedics

Nanotopography has the potential to improve osteointegration of orthopedic implants. Nanostructuring can be used to promote or discourage cell adhesion and provides the opportunity to generate surfaces that more closely approximate the natural cellular environment. This could be achieved by the introduction of controlled disorder, combinations of feature types and sizes, and tissue-specific architecture. Hardwearing nanostructures that resist denudation from the surface are desirable, such as nanoscale depressions (e.g., nanopits) that can be sunk into the substrate to direct cell behavior. Nanocoatings that can be applied to implant surfaces, such as by vapor deposition,[128] are also advantageous, particularly if these can be utilized to functionalize specific areas of the device with features tailored to induce certain desirable cell responses in that region.

4.409.7.2. Stem Cells and Regenerative Medicine

Topographically patterned substrates currently used in cell culture are more advantageous than the use of defined media in that they allow cell growth and development to be tailored to a specific application without the need to use potentially harmful chemicals within the body. Currently available successful applications of terminally differentiated cells include the generation of skin using keratinocytes and fibroblasts,[129] tissue-engineered airway,[130] and a whole bladder.[131]

Stem cells are a very important tool in tissue engineering. In combination with topography, these cells not only open up the potential to produce patient-specific tissues, reducing the risk for tissue/organ rejection, but through the understanding of material properties that elicit specific responses, they could also allow the formation of complex tissues in the future.

4.409.7.3. Nanotopography for Cell Biology

Nanotopography can provide a tunable stimulus for manipulating cell responses. The ability to produce a variety of feature types with definable size ranges for the noninvasive modulation of cellular architecture, gene expression, and behavior makes nanotopography a valuable tool for fundamental biological research and translational studies. Increasing our understanding of the cell and molecular biology underlying cell–substrate interactions has the potential to revolutionize future materials design for the rational direction of cell responses.

Acknowledgments

The Dalby group is supported by grants from BBSRC, EPSRC, and the Chief Scientist Office.

References

1. Guilak, F.; Cohen, D. M.; Estes, B. T.; Gimble, J. M.; Liedtke, W.; Chen, C. S. *Cell Stem Cell* **2009**, *5*, 17–26.
2. Mcbeath, R.; Pirone, D. M.; Nelson, C. M.; Bhadriraju, K.; Chen, C. S. *Dev. Cell* **2004**, *6*, 483–495.
3. Kilian, K. A.; Burgarija, B.; Lahn, B. T.; Mrksich, M. *Proc. Natl. Acad. Sci. USA* **2009**, *107*, 4872–4877.
4. Alom Ruiz, S.; Chen, C. S. *Stem Cell.* **2008**, *26*, 2921–2927.
5. Engler, A. J.; Sen, S.; Sweeney, H. L.; Discher, D. E. *Cell* **2006**, *126*, 677–689.
6. Saha, K.; Keung, A. J.; Irwin, E. F.; *et al. Biophys. J.* **2008**, *95*, 4426–4438.
7. Curtis, A.; Riehle, M. *Phys. Med. Biol.* **2001**, *46*, R47–65.
8. Curtis, A.; Wilkinson, C. *Trends Biotechnol.* **2001**, *19*, 97–101.
9. Carrel, A.; Burrows, M. *J. Exp. Med.* **1911**, *12*, 571–575.
10. Weiss, P.; Garber, B. *Proc. Natl. Acad. Sci. USA* **1952**, *38*, 264–280.
11. Wilkinson, C. D. W.; Riehle, M.; Wood, M.; Gallagher, J.; Curtis, A. S. G. *Mater. Sci. Eng.* **2002**, *19*, 263–269.
12. Lim, J. M.; Byun, S.; Chung, S.; *et al. Invest. Ophthalmol. Vis. Sci.* **2004**, *45*, 4210–4216.
13. Teixeira, A. I.; Abrams, G. A.; Bertics, P. J.; Murphy, C. J.; Nealey, P. F. *J. Cell Sci.* **2003**, *116*, 1881–1892.
14. Britland, S.; Morgan, H.; Wojiak-Stodart, B.; Riehle, M.; Curtis, A.; Wilkinson, C. *Exp. Cell. Res.* **1996**, *228*, 313–325.
15. Chen, C. S.; Mrksich, M.; Huang, S.; Whitesides, G. M.; Ingber, D. E. *Science* **1997**, *276*, 1425–1428.
16. Clark, P.; Connolly, P.; Curtis, A. S.; Dow, J. A.; Wilkinson, C. D. *Development* **1987**, *99*, 439–448.
17. Dalby, M. J.; Riehle, M. O.; Yarwood, S. J.; Wilkinson, C. D. W.; Curtis, A. S. G. *Exp. Cell Res.* **2003**, *284*, 274–282.
18. Wojciak-Stothard, B.; Curtis, A. S.; Monaghan, W.; Mcgrath, M.; Sommer, I.; Wilkinson, C. D. *Cell Motil. Cytoskeleton* **1995**, *31*, 147–158.
19. Engel, E.; Martinez, E.; Mills, C. A.; Funes, M.; Planell, J. A.; Samitier, J. *Ann. Anat.* **2009**, *191*, 136–144.
20. Kantawong, F.; Burgess, K. E. V.; Jayawardena, K.; *et al. Biomaterials* **2009**, *30*, 4723–4731.
21. Dalby, M. J.; Riehle, M. O.; Johnstone, H.; Affrossman, S.; Curtis, A. S. *Biomaterials* **2002**, *23*, 2945–2954.
22. Gallagher, J. O.; Mcghee, K. F.; Wilkinson, C. D.; Riehle, M. O. *IEEE Trans. Nanobiosci.* **2002**, *1*, 24–28.
23. Berry, C. C.; Campbell, G.; Spadiccino, A.; Robertson, M.; Curtis, A. S. *Biomaterials* **2004**, *25*, 5781–5788.
24. Dalby, M. J.; Riehle, M. O.; Johnstone, H. J.; Affrossman, S.; Curtis, A. S. *Tissue Eng.* **2002**, *8*, 1099–1108.
25. Price, R. L.; Haberstroh, K. M.; Webster, T. J. *Med. Biol. Eng. Comput.* **2003**, *41*, 372–375.
26. Webster, T. J.; Ergun, C.; Doremus, R. H.; Siegel, R. W.; Bizios, R. *Biomaterials* **2001**, *22*, 1327–1333.
27. Dalby, M. J.; Yarwood, S. J.; Riehle, M. O.; Johnstone, H. J.; Affrossman, S.; Curtis, A. S. *Exp. Cell Res.* **2002**, *276*, 1–9.
28. Dalby, M. J.; Berry, C. C.; Riehle, M. O.; Sutherland, D. S.; Agheli, H.; Curtis, A. S. G. *Exp. Cell Res.* **2004**, *295*, 387–394.
29. Biggs, M. J.; Richards, R. G.; Gadegaard, N.; Wilkinson, C. D.; Dalby, M. J. *J. Mater. Sci. Mater. Med.* **2007**, *18*, 399–404.
30. Biggs, M. J.; Richards, R. G.; Gadegaard, N.; Wilkinson, C. D.; Oreffo, R. O.; Dalby, M. J. *Biomaterials* **2009**, *30*, 5094–5103.
31. Biggs, M.; Richards, R.; Mcfarlane, S.; Wilkinson, C.; Oreffo, R.; Dalby, M. *J. R. Soc. Interface* **2008**, *5*, 1231–1242.
32. Biggs, M. J.; Richards, R. G.; Wilkinson, C. D.; Dalby, M. J. *J. Microsc.* **2008**, *231*, 28–37.
33. Biggs, M. J. P.; Richards, R. G.; Gadegaard, N.; *et al. J. Biomed. Mater. Res. A* **2009**, *91*, 195–208.
34. Kantawong, F.; Burchmore, R.; Gadegaard, N.; Oreffo, R. O.; Dalby, M. J. *J. R. Soc. Interface* **2008**, *6*, 1075–1086.
35. Kantawong, F.; Burchniore, R.; Wilkinson, C. D. W.; Oreffo, R. O. C.; Dalby, M. J. *Acta Biomater.* **2009**, *5*, 1137–1146.
36. Brunette, D. M. *Int. J. Oral Maxillofac. Implants* **1988**, *3*, 231–246.
37. Van Wachem, P. B.; Hogt, A. H.; Beugeling, T.; *et al. Biomaterials* **1987**, *8*, 323–328.
38. Ruardy, T. G.; Schakenraad, J. M.; Vandermei, H. C.; Busscher, H. J. *J. Biomed. Mater. Res.* **1995**, *29*, 1415–1423.
39. Keisler, C.; Lataillade, J. L. *J. Adhes. Sci. Technol.* **1995**, *9*, 395–411.
40. Anselme, K.; Bigerelle, M. *Acta Biomater.* **2005**, *1*, 211–222.
41. Schwartz, Z.; Lohmann, C. H.; Sisk, M.; *et al. Biomaterials* **2001**, *22*, 731–741.
42. Clark, P.; Connolly, P.; Curtis, A. S.; Dow, J. A.; Wilkinson, C. D. *Development* **1990**, *108*, 635–644.
43. Dunn, G. A.; Brown, A. F. *J. Cell Sci.* **1986**, *83*, 313–340.
44. Clark, P.; Connolly, P.; Curtis, A. S.; Dow, J. A.; Wilkinson, C. D. *J. Cell Sci.* **1991**, *99*(Pt 1), 73–77.
45. Moore, G. E. *Electronics* **1965**, *38*, 114–117.
46. Gadegaard, N.; Mosler, S.; Larsen, N. B. *Macromol. Mater. Eng.* **2003**, *288*, 76–83.
47. Denis, F. A.; Hanarp, P.; Sutherland, D. S.; Dufrene, Y. F. *Nanoletters* **2002**, *2*, 1419–1425.
48. Hanarp, P.; Sutheraland, D. S.; Gold, J.; Kasemo, B. *Colloid. Surface. A* **2003**, *214*, 23–36.
49. Affrossman, S.; Henn, G.; O'neill, S. A.; Pethrick, R. A.; Stamm, M. *Macromolecules* **1996**, *29*, 5010–5016.
50. Affrossman, S.; O'neill, S. A.; Stamm, M. *Macromolecules* **1998**, *31*, 6280–6288.
51. Affrossman, S.; Jerome, R.; O'neill, S. A.; Schmitt, T.; Stamm, M. *Colloid Polymer Sci.* **2000**, *278*, 993–999.
52. Affrossman, S.; Stamm, M. *Collid Polymer Sci.* **2000**, *278*, 888–893.
53. Krishnamoorthy, S.; Pugin, R.; Brugger, J.; Heinzelmann, H.; Hoogerwerf, A. C.; Hinderling, C. *Langmuir* **2006**, *22*, 3450–3452.
54. Curtis, A.; Varde, M. *J. Natl. Cancer Inst.* **1964**, *33*, 15–26.
55. Milner, K.; Siedlecki, C. *J. Biomed. Mater. Res. A* **2007**, *82*, 80–91.
56. Dalby, M.; Gadegaard, N.; Wilkinson, C. *J. Biomed. Mater. Res. A* **2008**, *84*, 973–979.
57. Loesberg, W.; Te Riet, J.; Van Delft, F.; *et al. Biomaterials* **2007**, *28*, 3944–3951.
58. Barbucci, R.; Pasqui, D.; Wirsen, A.; Affrossman, S.; Curtis, A.; Tetta, C. *J. Mater. Sci. Mater. Med.* **2003**, *14*, 721–725.
59. Yim, E.; Reano, R.; Pang, S.; Yee, A.; Chen, C.; Leong, K. *Biomaterials* **2005**, *26*, 5405–5413.
60. Johansson, F.; Carlberg, P.; Danielsen, N.; Montelius, L.; Kanje, M. *Biomaterials* **2006**, *27*, 1251–1258.
61. Biela, S.; Su, Y.; Spatz, J.; Kemkemer, R. *Acta Biomaterias* **2009**, *5*, 2460–2466.
62. Dalby, M.; Hart, A.; Yarwood, S. *Biomaterials* **2008**, *29*, 282–289.
63. Lim, J.; Dreiss, A.; Zhou, Z.; *et al. Biomaterials* **2007**, *28*, 1787–1797.
64. Dalby, M. J.; Pasqui, D.; Affrossman, S. *IEE Proc. Nanobiotechnol.* **2004**, *151*, 53–61.
65. Dalby, M.; Riehle, M.; Johnstone, H.; Affrossman, S.; Curtis, A. *IEEE Trans. Nanobiosci.* **2002**, *1*, 12–17.
66. Takahashi, K.; Tanabe, K.; Ohnuki, M.; *et al. Cell* **2007**, *131*, 861–872.
67. Bigdeli, N.; Andersson, M.; Strehl, R.; *et al. J. Biotechnol.* **2008**, *133*, 146–153.
68. Smith, L. A.; Liu, X.; Hu, J.; Ma, P. X. *Biomaterials* **2009**, *30*, 2516–2522.
69. Levenberg, S.; Huang, N. F.; Lavik, E.; Rogers, A. B.; Itskovitz-Eldor, J.; Langer, R. *Proc. Natl. Acad. Sci. USA* **2003**, *100*, 12741–12746.
70. Mcfarlin, D. R.; Finn, K. J.; Nealey, P. F.; Murphy, C. J. *Biomim. Biomater. Tissue Eng.* **2009**, *2*, 15–26.
71. Nur, E. K. A.; Ahmed, I.; Kamal, J.; Schindler, M.; Meiners, S. *Stem Cells* **2006**, *24*, 426–433.
72. Gerecht, S.; Bettinger, C.; Zhang, Z.; Borenstein, J.; Vunjak-Novakovic, G.; Langer, R. *Biomaterials* **2007**, *28*, 4068–4077.
73. Kang, X.; Xie, Y.; Powell, H.; *et al. Biomaterials* **2007**, *28*, 450–458.
74. Chao, T.; Xiang, S.; Chen, C.; *et al. Biochem. Biophys. Res. Comm.* **2009**, *384*, 426–430.
75. Friedenstein, A. *Int. Rev. Cytol.* **1976**, *47*, 327–359.
76. Pittenger, M. F.; Mackay, A. M.; Beck, S. C.; *et al. Science* **1999**, *284*, 143–147.
77. Muraglia, A.; Cancedda, R.; Quarto, R. *J. Cell Sci.* **2000**, *113*(Pt 7), 1161–1166.
78. Narita, Y.; Yamawaki, A.; Kagami, H.; Ueda, M.; Ueda, Y. *Cell Tissue Res.* **2008**, *333*, 449–459.
79. Yim, E. K.; Pang, S. W.; Leong, K. W. *Exp. Cell Res.* **2007**, *313*, 1820–1829.
80. Dalby, M. J.; Gadegaard, N.; Tare, R.; *et al. Nat. Mater.* **2007**, *6*, 997–1003.
81. Oh, S.; Brammer, K. S.; Li, Y. S.; *et al. Proc. Natl. Acad. Sci. USA* **2009**, *106*, 2130–2135.
82. Song, L.; Tuan, R. *Faseb J.* **2004**, *18*, 980–982.

83. Yang, F.; Murugan, R.; Wang, S.; Ramakrishna, S. *Biomaterials* **2005**, *26*, 2603–2610.
84. Christopherson, G.; Song, H.; Mao, H. *Biomaterials* **2009**, *30*, 556–564.
85. Berry, C. C.; Dalby, M. J.; Mccloy, D.; Affrossman, S. *Biomaterials* **2005**, *26*, 4985–4992.
86. Gadegaard, N.; Dalby, M. J.; Riehle, M. O.; Curtis, A. S. G.; Affrossman, S. *Adv. Mat.* **2004**, *16*, 1857–1860.
87. Berry, C. C.; Dalby, M. J.; Oreffo, R. O.; Mccloy, D.; Affrosman, S. *J. Biomed. Mater. Res. A* **2006**, *79*, 431–439.
88. Seunarine, K.; Gadegaard, N.; Torman, M.; *et al*. *Nanomedicine* **2006**, *1*, 281–296.
89. Dalby, M. J.; Mccloy, D.; Robertson, M.; *et al*. *Biomaterials* **2006**, *27*, 2980–2987.
90. Dalby, M. J.; Riehle, M. O.; Johnstone, H. J.; Affrossman, S.; Curtis, A. S. *J. Biomed. Mater. Res.* **2003**, *67A*, 1025–1032.
91. Dalby, M. J.; Riehle, M. O.; Sutherland, D. S.; Agheli, H.; Curtis, A. S. *Biomaterials* **2004**, *25*, 5415–5422.
92. Dalby, M. J.; Riehle, M. O.; Sutherland, D. S.; Agheli, H.; Curtis, A. S. *J. Biomed. Mater. Res.* **2004**, *69A*, 314–322.
93. Andersson, A. S.; Backhed, F.; Von Euler, A.; Richter-Dahlfors, A.; Sutherland, D.; Kasemo, B. *Biomaterials* **2003**, *24*, 3427–3436.
94. Andersson, A. S.; Brink, J.; Lidberg, U.; Sutherland, D. S. *IEEE Trans. Nanobiosci.* **2003**, *2*, 49–57.
95. Rice, J. M.; Hunt, J. A.; Gallagher, J. A.; Hanarp, P.; Sutherland, D. S.; Gold, J. *Biomaterials* **2003**, *24*, 4799–4818.
96. Choi, C. H.; Hagvall, S. H.; Wu, B. M.; Dunn, J. C.; Beygui, R. E.; Kim, C. J. *Biomaterials* **2007**, *28*, 1672–1679.
97. Dalby, M. J.; Gadegaard, N.; Riehle, M. O.; Wilkinson, C. D. W.; Curtis, A. S. G. *Int. J. Biochem. Cell Biol.* **2004**, *36*, 2005–2015.
98. Dalby, M. J.; Mccloy, D.; Robertson, M.; Wilkinson, C. D. W.; Oreffo, R. O. C. *Biomaterials* **2006**, *27*, 1306–1315.
99. Curtis, A. S.; Gadegaard, N.; Dalby, M. J.; Riehle, M. O.; Wilkinson, C. D.; Aitchison, G. *IEEE Trans. Nanobiosci.* **2004**, *3*, 61–65.
100. Hart, A.; Gadegaard, N.; Wilkinson, C. D. W.; Oreffo, R. O. C.; Dalby, M. J. *J. Mater. Sci. Mater. Med.* **2007**, *18*, 1211–1218.
101. Dalby, M. J.; Gadegaard, N.; Herzyk, P.; Agheli, H.; Sutherland, D. S.; Wilkinson, C. D. W. *Biomaterials* **2007**, *28*, 1761–1769.
102. Dalby, M. J.; Gadegaard, N.; Wilkinson, C. D. W. *J. Biomed. Mater. Res.* **2007**, *84A*, 973–979.
103. Arnold, M.; Cavalcanti-Adam, E. A.; Glass, R.; *et al*. *ChemPhysChem* **2004**, *5*, 383–388.
104. Lehnert, D.; Wehrle-Haller, B.; David, C.; *et al*. *J. Cell Sci.* **2004**, *117*, 41–52.
105. Dalby, M. J.; Riehle, M. O.; Johnstone, H.; Affrossman, S.; Curtis, A. S. G. *Cell Biol. Int.* **2004**, *28*, 229–236.
106. Smith, M. L.; Gourdon, D.; Little, W. C.; *et al*. *PloS Biol.* **2007**, *5*, e268.
107. Wood, M. A.; Bagnaninchi, P.; Dalby, M. J. *Exp. Cell Res.* **2008**, *314*, 927–935.
108. Vogel, V.; Sheetz, M. *Nat. Rev. Mol. Cell Biol.* **2006**, *7*, 265–275.
109. Riveline, D.; Zamir, E.; Balaban, N. Q.; *et al*. *J. Cell Biol.* **2001**, *153*, 1175–1186.
110. Del Rio, A.; Perez-Jimenez, R.; Liu, R.; Roca-Cusachs, P.; Fernandez, J. M.; Sheetz, M. P. *Science* **2009**, *323*, 638–641.
111. Wang, N.; Naruse, K.; Stamenovic, D.; *et al*. *Proc. Natl. Acad. Sci. USA* **2001**, *98*, 7765–7770.
112. Ingber, D. E. *J. Cell Sci.* **2003**, *116*, 1397–1408.
113. Haque, F.; Lloyd, D. J.; Smallwood, D. T.; *et al*. *Mol. Cell. Biol.* **2006**, *26*, 3738–3751.
114. Wang, N.; Tytell, J. D.; Ingber, D. E. *Nat. Rev. Mol. Cell Biol.* **2009**, *10*, 75–82.
115. Maniotis, A.; Chen, C.; Ingber, D. *Proc. Natl. Acad. Sci. USA* **1997**, *94*, 849–854.
116. Maniotis, A. J.; Bojanowski, K.; Ingber, D. E. *J. Cell. Biochem.* **1997**, *65*, 114–130.
117. Pajerowski, J. D.; Dahl, K. N.; Zhong, F. L.; Sammak, P. J.; Discher, D. E. *Proc. Natl. Acad. Sci. USA* **2007**, *104*, 15619–15624.
118. Martin, C.; Chen, S. B.; Maya-Mendoza, A.; Lovric, J.; Sims, P. F. G.; Jackson, D. A. *J. Cell Sci.* **2009**, *122*, 1551–1562.
119. Thomas, C. H.; Collier, J. H.; Sfeir, C. S.; Healy, K. E. *Proc. Natl. Acad. Sci. USA* **2002**, *99*, 1972–1977.
120. Cremer, T.; Cremer, C. *Nat. Rev. Genet.* **2001**, *2*, 292–301.
121. Osborne, C. S.; Chakalova, L.; Brown, K. E.; *et al*. *Nat. Genet.* **2004**, *36*, 1065–1071.
122. Chambeyron, S.; Da Silva, N. R.; Lawson, K. A.; Bickmore, W. A. *Development* **2005**, *132*, 2215–2223.
123. West, A. G.; Fraser, P. *Hum. Mol. Genet.* **2005**, *14*, R101–R111.
124. Reddy, K. L.; Zullo, J. M.; Bertolino, E.; Singh, H. *Nature* **2008**, *452*, 243–247.
125. Dalby, M. J.; Biggs, M. J. P.; Gadegaard, N.; Kalna, G.; Wilkinson, C. D. W.; Curtis, A. S. G. *J. Cell. Biochem.* **2007**, *100*, 326–338.
126. Dalby, M. J.; Gadegaard, N.; Herzyk, P.; *et al*. *J. Cell. Biochem.* **2007**, *102*, 1234–1244.
127. Mcnamara, L. E.; Dalby, M. J.; Riehle, M. O.; Burchmore, R. *J. R. Soc. Interface* **2010**, *7*, S107–S118.
128. Yang, L.; Sheldon, B. W.; Webster, T. J. *Biomaterials* **2009**, *30*, 3458–3465.
129. Macneil, S. *Nature* **2007**, *445*, 874–880.
130. Macchiarini, P.; Jungebluth, P.; Go, T.; *et al*. *Lancet* **2008**, *372*, 2023–2030.
131. Atala, A.; Bauer, S. B.; Soker, S.; Yoo, J. J.; Retik, A. B. *Lancet* **2006**, *367*, 1241–1246.

4.410. Sterilization of Biomaterials of Synthetic and Biological Origin

Q-Q Qiu, W-Q Sun, and J Connor, LifeCell Corporation, Branchburg, NJ, USA

© 2011 Elsevier Ltd. All rights reserved.

4.410.1.	**Introduction**	128
4.410.2.	**Sterilization Methods**	128
4.410.2.1.	Heat and Pressure	129
4.410.2.2.	Ionization Irradiation	129
4.410.2.3.	Chemical Sterilant	130
4.410.2.3.1.	Ethylene oxide	130
4.410.2.3.2.	Sterilant solutions	130
4.410.2.4.	New Methods	131
4.410.2.4.1.	Supercritical carbon dioxide	131
4.410.2.4.2.	Gas plasma (ionized gas)	131
4.410.2.4.3.	Other	132
4.410.2.5.	Selection Criteria of Sterilization Method for Biomaterials	133
4.410.2.6.	Sterilization Validation	133
4.410.3.	**Sterilization of Biomaterials of Synthetic and Biological Origin**	134
4.410.3.1.	Synthetic Biomaterials	134
4.410.3.1.1.	Metals	134
4.410.3.1.2.	Polymers	135
4.410.3.1.3.	Ceramics/bioactive glasses	136
4.410.3.2.	Materials of Biological Origin	136
4.410.3.2.1.	Soft tissues	136
4.410.3.2.2.	Hard/dense tissues	137
4.410.3.2.3.	Demineralized bone matrix	138
4.410.4.	**Evaluation of Effect of Sterilization on Biomaterials**	139
4.410.4.1.	Selection of Analytical Methods	139
4.410.4.2.	Effect of γ-Irradiation on a Regenerative ECM Matrix: A Case Study	139
References		142

Glossary

Animal model A living animal used to evaluate biomaterials, medical devices, and drugs to be used to treat human diseases, for the purpose of better understanding of the materials and devices' safety, efficacy, and functionality without the added risk of causing harm to human beings during the process.

Bioburden Population of viable microorganisms on a raw material, components, a finished product, and/or a package.

Chemical sterilants Chemicals that are used to destroy all forms of microbiological life, including fungal and bacterial spores.

Disinfectant Substance that is applied to nonliving objects to destroy microorganisms that are living on the objects.

Disinfection A process that eliminates many or all pathogenic microorganisms on inanimate objects with the exception of the bacterial endospore.

Electron beam (e-beam) Continuous or pulsed stream of high-energy electrons.

Ethylene oxide An organic compound with the formula C_2H_4O. It is a colorless flammable gas with a faintly sweet odor. It is used as sterilant.

Extracellular matrix A complex network composed of fibrillar proteins (collagens) and gels of polysaccharide that provides structural support and anchorage for cells and regulates intercellular communication.

Gas plasma Ionized gas contains ions and electrons in about equal number.

In vitro A procedure performed *in vitro* (Latin: within the glass) is performed not in a living organism but in a controlled environment, such as in a test tube or cell culture dish.

In vivo *In vivo* (Latin for 'within the living') is experimentation using a whole, living organism such as animal testing and clinical trials.

Medical device An implant or instrument intended for use in the treatment or to affect the structure or function of the body.

Sterility assurance level A term used in microbiology to describe the probability of a single unit being nonsterile after it has been subjected to the sterilization process.

Sterilization An extreme physical and/or chemical process that effectively inactivates or kills all forms of life, especially microorganisms (e.g., fungi, bacteria, viruses, spore forms, etc.) from a surface, equipment, food or medication, biological culture medium, or medical devices.

Abbreviations

AAMI	Association for the Advancement of Medical Instrumentation
AATB	American Association of Tissue Banks
ACL	Anterior cruciate ligament
AFM	Atomic force microscopy
ANSI	American National Standards Institute
BIS-GMA	Bisphenol A-glycidyl
BPTB	Bone-patellar tendon-bone allografts
CP-Ti	Commercially pure titanium
DBM	Demineralized bone matrix
ECM	Extracellular matrix
EO	Ethylene oxide
EPA	US Environmental Protection Agency
FDA	US Food and Drug Administration
HA	Hydroxyapatite
HP	Hydrogen peroxide
ISO	International Organization for Standardization
PAA	Peracetic acid
PE	Polyethylene
PET	Polyethylene terephthalate
PLA	Polylactic acid
PTFE	Polytetrafluoroethylene
PMMA	Polymethyl methacrylate
PP	Polypropylene
PS	Polystyrene
PVC	Polyvinyl chloride
SAL	Sterility assurance level
SBF	Simulated body fluid
SC-CO_2	Supercritical carbon dioxide
UHMWPE	Ultra-high-molecule-weight polyethylene
UV	Ultraviolet light
XPS	X-ray photoelectron spectroscopy

4.410.1. Introduction

Biomaterials are commonly used to make medical devices or processed to make implants for clinical applications. The biomaterials covered in this chapter include synthetic materials and materials of biological origin that are used to replace or restore function to a body tissue or in contact with body fluid. As they enter sterile body tissues or the vascular system or have contact with blood or other sterile body fluids, they are considered to be critical items. They include orthopedic devices such as total knee and hip replacements, spinal implants, and bone fixation devices; cardiac implants such as artificial heart valves and pacemakers; soft-tissue implants such as acellular dermal matrix for abdominal wall repair and breast reconstruction, and injectable collagen for soft-tissue augmentation; and dental implants to repair teeth and bony tissue in the oral cavity. In general, they are required to be sterilized before use. If sterilization is not feasible, they should be properly disinfected.[1]

Sterilization is the complete elimination of all forms of microbial life, including highly resistant bacterial endospores. Sterilization of medical devices is accomplished by the use of physical or chemical processes that inactivate all forms of microbial life. The effectiveness of a sterilization process is measured by the probability of sterility for each product sterilized (the sterility assurance level or SAL). SAL describes the probability of a single product unit being nonsterile. The sterilization processes used by medical device manufacturers are typically designed to achieve an extremely low probability for any product unit being nonsterile – a chance of one in a million (i.e., a SAL of 10^{-6}), and at the same time to maintain the essential safety and function of the medical devices for intended applications.[2] For certain biological medical devices, FDA considers a SAL of 10^{-3} as an adequate sterility level because harsh sterilization processes may adversely affect the functionality of such biomedical devices (e.g., tissue-based biological meshes and engineered tissue products). Unfortunately, most of the sterilization methods are not suitable for use on biological materials. For example, heat and high doses of γ-irradiation (>30 kGy) used to reach a SAL of 10^{-6} are effective but they denature and weaken the collagen structure.[3]

Disinfection, on the other hand, is to eliminate the recognized pathogenic microorganisms with a chemical or physical procedure, but not necessarily to eliminate all microbial forms on medical devices. High-level disinfection with an FDA-cleared sterilant kills virtually all microorganisms, except bacterial spores. The use of some EPA-registered germicides may only achieve a low-level (some viruses and bacteria) or intermediate-level (mycobacteria, most viruses, and bacteria) disinfection.

In addition to SAL, there are other critical requirements on sterilization method used for a biomaterial or medical device. First, the sterilization should not cause any significant change in the material that would elicit an adverse response from the body. Next, the sterilization should not significantly alter physical and mechanical properties of the material that would compromise the implant's function.

This chapter reviews current sterilization methods used for biomaterials, selection of sterilization methods, and the effects of sterilization treatments on the properties of biomaterials of synthetic and biological origin. The emphasis is given to sterilization of implantable biomedical devices; however, information presented here is also applicable to surgical and diagnostic instruments (e.g., cardiac and urinary catheters). During the past two decades, there has been an increase in medical devices that are made of new biomaterials and require new sterilization methods. The chapter also reviews several novel, low-temperature sterilization systems. For standards and guidance documents for sterilization equipment, process control, and process validation, readers are referred to the ANSI/AAMI/ISO 11737[4,5] documents, which have been developed through a joint effort between academia, medical devices industry, and government regulatory agencies.

4.410.2. Sterilization Methods

Both physical and chemical mechanisms can be used to inactivate microbial life-forms. Physical methods include the use of heat, pressure, filtration, and ionizing radiation, while

chemical methods include the use of various gas and liquid sterilants (e.g., ethylene oxide (EO), gas plasma, phenol, glutaraldehyde, etc.). A brief description on the mode of action for different disinfection and sterilization methods is provided in this section, followed by more comprehensive discussions, in later sections, on their specific application for sterilization of different synthetic and biological materials.

4.410.2.1. Heat and Pressure

The dry-heat sterilization destroys microorganisms by destructive oxidation of cell components. To kill resistant spores by dry heat, it usually requires a temperature of about 160 °C for 2 h. Dry-heat sterilization is suitable for materials that are heat stable, such as metal implants that might be damaged by moist heat, or for those that are impenetrable to moist heat.

Moist heat in the form of saturated steam under pressure is the most wildly used method to sterilize solutions and surgical tools. It inactivates microorganisms by the irreversible coagulation and denaturation of enzymes and structural proteins. To kill resistant bacteria spores by moist heat, it generally requires 121 °C for 15–30 min. Moist heat is commonly used for sterilization of heat and moisture stable materials through which steam can penetrate, such as stainless steel implants and surgical tools. It is not suitable for biomaterials that are heat and moisture sensitive, such as degradable polymers and biological collagen matrix.

An autoclave is a device that uses high-pressure steam to sterilize. The parameters that affect efficacy of sterilization include steam, pressure, temperature, and time. The two common steam sterilizing temperatures are 121 and 132 °C. At constant temperatures, sterilization times vary depending on the type of items as well as the sterilizer type.

4.410.2.2. Ionization Irradiation

Ionizing radiation includes electromagnetic waves (e.g., short wavelength ultraviolet (UV) ray, X-ray, γ-ray), and subatomic particles (e.g., α particle, β particle, neutron) that carry enough energy to ionize atoms or molecules. UV ray, X-ray, γ-ray, and high-energy electron radiation are used for disinfection and sterilization of biomaterials and medical devices.

UV irradiation is used to control airborne microorganisms and surface decontamination for the environment of biomaterial production and processing. An example is the partial contamination control in biological safety cabinets by UV sources with a forced air flow/filtration system. The short wavelength UV light (~254 nm) disrupts the structure of nucleic acids through the formation of thymine dimers and therefore destroys the reproductive capabilities of microorganisms. However, UV radiation alone is not considered to be an effective disinfection or sterilization method because of its poor penetrating power, long treatment time, and the susceptibility to air movement.[1,6] In addition, UV radiation damages many types of plastics. UV radiation may be incorporated as a part of the overall strategy for bioburden control and sterilization during a manufacturing process.

γ-Radiation has been used as a low-temperature sterilization method for over a half-century. γ-Rays are high-energy photons emitted by a ^{60}Co source and have no mass or charge. The wavelengths of γ-rays are less than 10^{-10} m, with frequencies greater than 10^{18} Hz and energies at the 100-keV level. γ-Radiation has far greater penetration power than electron beam (e-beam) (Figure 1). It is a safe, cost-effective sterilization for a wide range of medical products (e.g., tissues for transplantation, pharmaceuticals, medical devices, disposable medical equipments). γ-Radiation kills microorganisms by attacking the DNA molecule through both direct and indirect mechanisms. γ-Sterilization does not leave any chemical residues, and does not impart radioactivity.

X-ray technology for sterilizing medical devices has already been in commercial use for 15 years. X-rays, emitted by electrons, are high-frequency, short-wavelength electromagnetic photons with a very broad energy spectrum. X-rays and γ-radiation differ because of their origins and their energy spectra overlap. X-rays produced by linear accelerators can reach the megavoltage energy level and have higher energy than γ-rays produced by radioactive γ-decay. The maximum photon energy is the same as the kinetic energy of the incident electrons that are used to generate X-rays. Unlike γ-radiation, X-rays are concentrated in the direction of the incident e-beam, and their angular dispersion decreases as the electron energy increases. The high intensity in the forward direction enhances the efficiency of X-ray utilization. The penetration of high-energy X-rays allows one to process large packages and pallet loads of medical devices with very good dose uniformity. The fast process, excellent dose uniformity, and better penetration than γ-rays or e-beam make the X-ray technology an alternative sterilization method for medical devices.

E-beam sterilization uses high-energy e-beam from accelerators to irradiate biomaterials or biomedical devices in their final packages. Unlike photons, fast electrons have both mass and charge. Thus, the range of penetration of high-energy electrons is limited and depends on their energy, the atomic number of the absorbing product, and its density. E-beam inactivates microorganisms by the same mechanisms as γ-radiation does. One of the advantages for e-beam radiation is that its high-energy power can sterilize in seconds instead

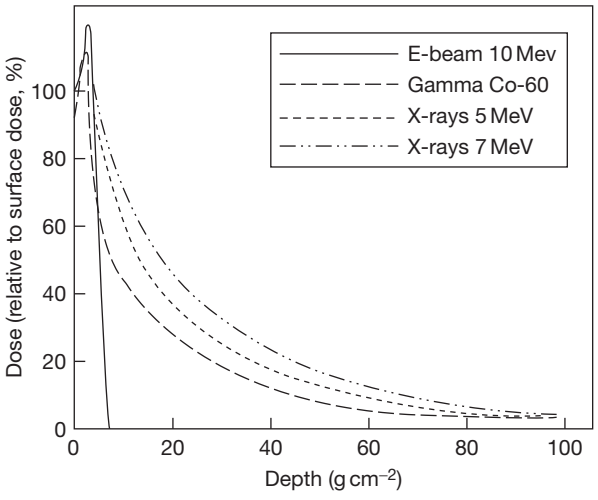

Figure 1 Dose and penetration depth profiles of e-beam, γ-, and X-rays. Note that the penetration depth is a function of both distance and material density. Adapted from Dethier, P.; Bol, J. L.; Mullier, B. *European Medical Device Technology* **2010**, *1*(2) (http://www.emdt.co.uk/article/x-ray-sterilisation-technology-future).

of hours or days compared with other methods. It was shown that bacterial spores show greater sensitivity to e-beam than γ-irradiation.[7] For many polymeric biomaterials, the short exposure time to radiation treatment results in significantly less material degradation than with γ-irradiation. The limitation of e-beam, when compared to γ- or X-rays, is its poor penetration in depth (Figure 1), especially for high-density biomaterials because of the electron's rest mass ($9\,e^{-28}$ g). Depth penetration by e-beam is primarily dependent on kinetic energy. The majority of disposable light density medical products are compatible with e-beam sterilization treatments. E-beam technology has now become a strong competitor to the more traditional γ-irradiation process.[8]

While the primary event of interaction with matter differs among X-rays, γ-irradiation, and electron irradiation, the main interactions with matter are similar, with minor differences. Ionization events under irradiation are initiated by secondary electrons, which then activate chemical reactions and free-radicals-mediated oxidative degradation. The effects of irradiation types on biomaterials are affected by dose rate, exposure time, and penetration depth. γ-Irradiators typically deliver dose rates from between 2 and 10 kGy per hour, whereas electron accelerators can deliver dose rates thousand times higher. The huge dose rate disparity leads to great differences in irradiation exposure times and thermal effects that could alter reaction pathways. A substantial difference in degradation effects between γ-irradiation and e-beam also reflects much higher penetration of γ-irradiation through the polymeric materials.[9]

4.410.2.3. Chemical Sterilant

4.410.2.3.1. Ethylene oxide

EO is bactericidal, sporicidal, and virucidal, and has been widely used as a low-temperature sterilant since the 1950s. EO is a colorless gas that is flammable and explosive.

EO's microbiocidal activity is a result of alkylation of proteins, DNA, and RNA in microorganisms, which prevents normal cellular metabolism and replication and thus renders affected microbes nonviable.[10–12] EO's high reactivity in combination with high diffusivity plays a major role in the inactivation of microorganisms.

In EO sterilization process, the major factors that affect the lethality of sterilization include EO concentration, temperature, humidity, and exposure time.[12,13] The bioburden reduction increases with the increase of EO concentration, exposure time, and temperature. Humidity is another critical variable in EO sterilization. In the range of 30–90% humidity, the humidity does not have significant impact on lethality, and sterilization efficacy decreases markedly below 30% and above 90%. The commonly used operational ranges for EO concentration, temperature, humidity, and exposure time are 450–1200 mg l^{-1}, 29–65 °C, 45–85%, and 2–5 h, respectively.[12]

Besides the major parameters mentioned above, other variables, such as product bioburden, device/package properties, load density, and configuration, should also be considered. In addition, the raw material composition, material diffusion properties, sensitivity to both negative and positive pressure changes, and maximum allowed heat and moisture as well as chemical tolerance to EO should be analyzed to determine if the EO is a suitable sterilization method for the material.

The potential hazards of EO to people and the environment, such as mutagenicity potential and risks associated with handling a flammable gas, have limited its use.[14–16] However, if the recommended practices are followed and current Occupational Safety and Health Administration EO regulations are met, EO can be used safely.

In addition to EO toxicity concerns at work place, it should be noted that EO and EO derived residues in sterilized products also encounter toxicity issues. EO and its derivatives, such as ethylene chlorohydrin, formed in the presence of chloride ions, and ethylene glycol, formed by reaction of EO with water, are toxic residues. The allowable EO residual and its derivatives by categorization of products are specified by International Organization for Standardization.[17] Removal of EO and its derivatives from the EO-sterilized biomaterials to the acceptable level is essential to ensure the safety of the medical device, and the removal process sometimes becomes a challenge.

Despite EO's toxicity and safety concerns, for some sensitive materials, EO is the only acceptable sterilization method.[18] In contrast to irradiations and heat sterilizations that have deleterious effects on biological materials and polymers,[19] EO is compatible with a wide range of materials, and its penetration properties make EO sterilization the most suitable process for the majority of heat- and/or moisture-sensitive medical products.[20]

4.410.2.3.2. Sterilant solutions

In addition to EO, a few other sterilants have also been used for sterilization. They include formaldehyde, hydrogen peroxide (HP), and peracetic acid (PAA)-based systems, as well as other oxidizing agents used in liquid and gaseous processes.

PAA is a strong oxidizing agent, and its oxidation potential is greater than that of chlorine or chlorine dioxide. PAA has bactericidal, fungicidal, virucidal, and sporicidal properties, and has been widely used in medical disinfection processes.[21–24] System 1E (Steris Corp, Mentor, OH) is a liquid chemical sterilant processing system that uses PAA to sterilize heat-sensitive devices such as endoscopes and their accessories.

PAA is a clear and colorless liquid and has a strong pungent acetic acid odor. It is commonly produced by the reaction of acetic acid with HP [I] and therefore PAA solution contains HP (up to 25%) and acetic acid (up to 35%).

$$CH_3-\overset{\overset{O}{\|}}{C}-OH + H_2O_2 \rightarrow CH_3\overset{\overset{O}{\|}}{C}-O-OH + H_2O \qquad [I]$$

PAA oxidizes the outer cell membrane of vegetative bacterial cells, endospores, yeast, and mold spores. A rapid penetration of PAA into microorganisms and the release of oxygen and free radicals critical for the oxidation and destruction of microbial enzymes are likely linked to PAA sterilization efficacy.[24] PAA–methanol mixture could effectively inactivate viruses in bone and porcine intestine.[22,23] It also works synergistically with HP in microorganism inactivation.[25] The efficacy of the PAA sterilization is affected by its ability to access the locations that need to be sterilized, for example, diffusion throughout the matrix or access into the center of the narrow lumen.

PAA's strong oxidation property is critical to its sterilization efficacy. However, this property may also reduce the biological, chemical, and structural integrity of biological materials,

for example, collagen matrix, as oxidation of proteins often renders them inactive, eliminating their bioactive properties.[26] PAA is unstable and readily degrades into acetic acid, oxygen, and water, which helps to alleviate concerns about its residual toxicity.

Similar to PAA, HP also inactivates microorganisms (bacteria, yeasts, fungi, viruses, and spores) through oxidization. It can be converted into highly reactive hydroxyl radicals (OH), which attack membrane lipids, DNA, and other essential cell components to inactivate bacteria. HP is more effective as a sporicide than as a bactericide.[21]

HP appears colorless in dilute solution, and is one of the most powerful oxidizers known. HP is naturally present in milk and honey to preserve them from spoilage. It is also the chemical that the phagocytes use to kill the bacteria that enter the bloodstream. It can be readily decomposed to water and oxygen spontaneously or by enzymes known as peroxidases possessed by living beings.

Formaldehyde is used as a biocide in liquid or gaseous form for sterilization. Because it is toxic, mutagenic, and carcinogenic, its use is limited.

4.410.2.4. New Methods

4.410.2.4.1. Supercritical carbon dioxide

Dense carbon dioxide was firstly found to have the bactericidal effect in the 1950s.[27] The supercritical state is a unique physical state that is reached at a specific temperature and pressure combination defined as the 'critical point' (**Figure 2**). Supercritical carbon dioxide (SC-CO_2) exhibits properties of both the gaseous and liquid physical states. It has the viscosity of a liquid and the transport efficiency of a gas which allow for efficient delivery with high penetration properties. The unique properties of SC-CO_2 make it an appealing medium for sterilization. Its high diffusion characteristics allow for deep penetration into materials. In addition, it is nontoxic and can easily be removed by depressurization and outgassing.

The effectiveness of SC-CO_2 on microorganisms is related to various treatment parameters, which include temperature, pressure, treatment time, and the use of additives.[28–30]

SC-CO_2 can inactivate a variety of microorganisms,[31] but SC-CO_2 alone is not enough to achieve an industrial level of sterilization (SAL 10^{-6}) of some microbes, including bacterial endospores and viruses.[30,31] To enhance the inactivation of microbes, sterilants that contain PAA are commonly used. As described in the previous section, PAA has bactericidal, fungicidal, virucidal, and sporicidal properties and has therefore been used in medical disinfection processes.[23,24,32] When SC-CO_2 is used with additives such as PAA, it can inactivate 6 $\log_{10}$ of bacterial endospores on spore strips.[30,33]

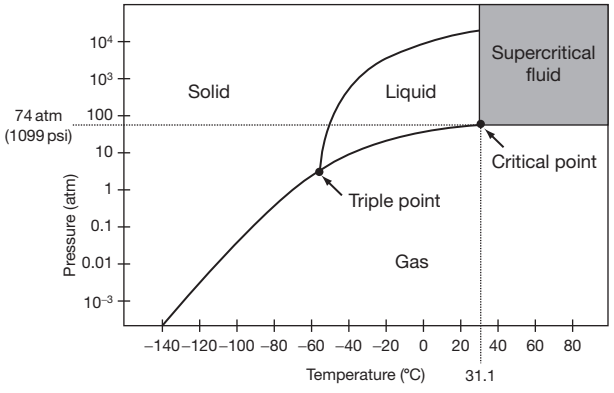

Figure 2 Phase diagram of CO_2.

SC-CO_2 treatment is compatible with many biological materials, including bone and acellular dermal matrix, and it leaves no toxic residues in the treated materials.[34,35] It has been shown that the SC-CO_2–PAA sterilization caused little change in the biochemical and biomechanical properties of acellular dermal matrix.[35]

Nova2200 is an equipment that uses SC-CO_2 with or without sterilant to sterilize heat-, moisture-, and irradiation-sensitive biomaterials. During the Nova2200 process, the CO_2 is pumped into the chamber and the pressure and temperature are modulated until the critical point is surpassed yielding the supercritical state within the chamber. This is the presterilization step. The pressure and temperature are then held constant ($P = 1346$ psi, $T = 35\,^{\circ}C$) within the supercritical phase requirements. The sterilization time is then initiated and the required exposure time is executed (t_{sc}). Following the completion of sterilization exposure phase, the chamber pressure is reversed to allow retrieval of the sterile samples. The complete process of achieving the supercritical phase and its reversal is represented by the total process time (t_{total}).

The sterilant component of the NovaSterilis system consists of a solution containing PAA and H_2O_2. At the onset of the sterilization process, the sterilant is placed into the SC-CO_2 chamber.

The linearity of bioburden reduction as a function of time and the D_{10}-value for the Nova2200 process are determined using the most resistant microorganism, *Bacillus atrophaeus* spores, for this sterilization process.

Tissue samples inoculated with 8 logs of *B. atrophaeus* spores are packaged in the final package configuration. The Nova2200 is run under constant pressure and temperature for increasing supercritical exposure times. The tissue samples are extracted and enumerated to determine the remaining logs of the reporter organism. **Figure 3** displays the results of a validation study using Nova2200.

These validation data demonstrate that the Nova2200 produces a linear sterilization profile over time. The outcome of this data set yields D_{10} values for the Nova2200 sterilization process. On the basis of the ISO 14160 guidance document the following formula is applied to determine the required dose (i.e., supercritical exposure time) to achieve an SAL $= 10^{-6}$ for the Nova2200 process.

$$\text{Exposure time for the sterilization} = D_{10} \times [6 + \log(100 + \text{bioburden})]$$

4.410.2.4.2. Gas plasma (ionized gas)

The low-temperature plasma method is considered to be a promising method for some biomedical materials that are not compatible with heat and chemicals.[36–38] The advantages of the gas plasma method are shorter process cycle and suitability for more complex medical instruments (especially those containing hollow parts for minimal intrusive procedures).

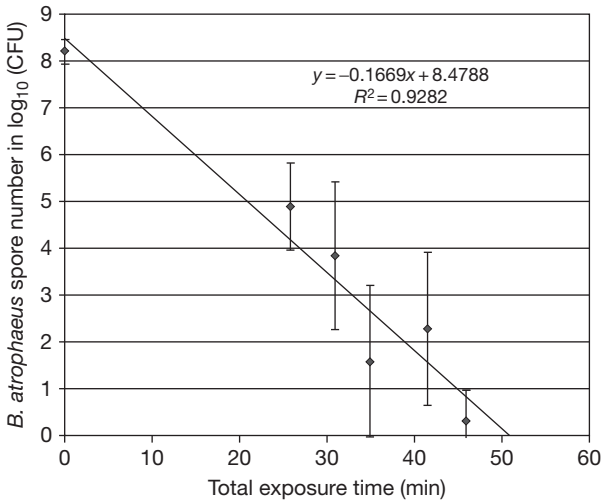

Figure 3 *Bacillus atrophaeus* spore colony forming unit (CFU) reduction by SC-CO_2–PAA as a function of total treatment time. Adapted from Qiu, Q. Q.; Leamy, P.; Brittingham, J.; Pomerleau, J.; Kabaria, N.; Connor, J. *J. Biomed. Mater. Res. B Appl. Biomater.* **2009**, *91*(2), 572–578.

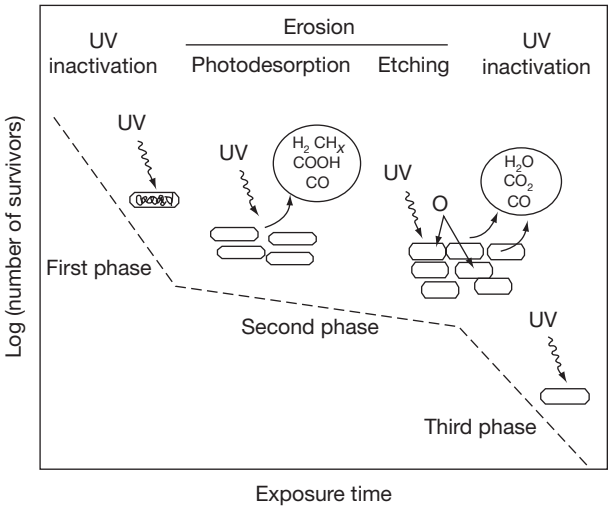

Figure 4 Schematic illustration of killing mechanisms during three phases of gas plasma sterilization. Adapted from Moisan, M.; Barbeau, J.; Crevier, M. C.; Pelletier, J.; Philip, N.; Saoudi, B. *Pure Appl. Chem.* **2002**, *74*(3), 349–358, with permission from IUPAC.

It addresses the issues of prions (the Creutzfeldt–Jakob diseases) and biofilms.

Gas plasmas are generated by exciting gas molecules with radio frequency or microwave to produce charged particles (free radicals). Gas plasma process uses mechanisms combining the action of UV irradiation generated from excited molecules and that of oxygen free radicals (**Figure 4**). UV irradiation causes lesions of DNA strands of microorganisms. Intrinsic photodesorption resulting from UV photons breaks chemical bonds of the other microorganism materials to produce volatile by-products (e.g., CO and CH_x). Reactive species within a plasma field (atomic and molecular radicals or excited molecules in a metastable state) undergo chemical reactions with cell components to initiate spontaneous etching and thereby disrupt the structure and metabolism of microorganisms, yielding the final oxidation products such as CO_2 and H_2O.[37,38]

The type of seed gas is an important variable affecting the effectiveness of the plasma sterilization process. FDA cleared the use of HP plasma sterilizers in the United States. Another gas plasma system uses PAA–acetic acid–HP vapor. The HP gas plasma system typically operates at 37–44 °C and has a cycle time of 50–75 min. The instruments, devices, and materials are placed in a sterilization chamber. Upon evacuation (<10 torr), HP solution is injected into the sterilization chamber where HP is vaporized to diffuse through the entire chamber, exposing all surfaces of the materials to the sterilant. The electrical field that is applied to the chamber creates gas plasma, initiating the inactivation of microorganisms by the combined use of HP gas and the generation of hydroxyl and hydroperoxyl free radicals. The end by-products of the cycle are oxygen and water vapor, and sterilized materials do not contain any toxic residue. The process is able to inactivate a broad range of microorganisms, including resistant bacterial spores. Materials and devices that cannot tolerate high temperatures and humidity, such as some plastics, electrical devices, and corrosion-susceptible metal alloys, can be sterilized by HP gas plasma. This method has been compatible with most medical devices and materials tested (>95%).[39,40] Certain materials (e.g., cellulose products, cotton, certain packaging materials), however, are not compatible with HP plasma units. Cellulosic materials absorb the sterilant, often leading to incomplete sterilization of the device.

The effects of low-temperature gas plasma on some biomaterials of biological origin such as collagens are not well understood. Critical process variables, for example, killing efficacy and mechanisms of action, remain to be investigated further for various plasma species. The weak penetrating power of plasma species severely limits plasma effectiveness in the presence of organic residues and packaging materials. Complex geometries of some biomedical devices may present another challenge to plasma sterilization.[36] Low-temperature HP gas plasma sterilization was found to be unsuitable for sensitive biological materials.[41] The osteoinductive capability of human demineralized bone matrix (DBM) with gas plasma sterilization was evaluated in a rat model. DBM pellets were implanted in soft-tissue pockets at the epaxial musculature. Histological evaluation of explanted materials after 9 weeks of implantation showed that all sites implanted with aseptically harvested DBM contained new bone elements (new bone, cartilage, or bone marrow elements). Gas plasma sterilized DBM sites contained no new bone elements (similar to the steam-sterilized negative controls), suggesting that the osteoinductive ability of DBM was destroyed by low-temperature gas plasma. In another study, exposure of potentially wet ophthalmologic surgical instruments with small bores and brass components to plasma gas led to degradation of the brass to copper and zinc.[42,43]

The STERRAD plasma sterilization system (Advanced Sterilization Products, Irvine, CA) uses a discovered synergism between HP and low-temperature gas plasma for rapid inactivation of microorganisms and the removal of harmful residues.

4.410.2.4.3. Other

A number of other methods have been studied in recent years. They include the use of ozone, chlorine dioxide, high-intensity

visible light, and ultrasonic waves. The effectiveness of these methods and their compatibility with biomaterials of diverse chemistry remain to be evaluated.

4.410.2.5. Selection Criteria of Sterilization Method for Biomaterials

Each sterilization method has its own advantages and limitations, and may have adverse effects on certain types of medical devices and biomaterials being sterilized (Table 1). Before discussing the selection of a suitable sterilization method for a particular medical device or biomaterial, we need to consider several general factors that affect the efficacy of sterilization. The first factor is the natural bioburden of biomaterials and devices. The higher the natural bioburden level is, the stricter the sterilization requirement is. Although contaminating microflora consist primarily of vegetative bacteria, spores are more resistant to sterilization and therefore are the FDA-required test organisms. The second factor is the access by the sterilant. The sterilant (gas or liquid) must come into direct contact with microorganisms during the sterilization process. The presence of biofilms on the biomaterial and device designs that limit the contact will reduce the efficacy of sterilization by impairing exposure of the sterilant to the microbial cells. The third factor is the type of biomaterials used for construction of medical devices. Biomaterials must be compatible with sterilization processes. Certain components, such as salt and organic residues, may compromise the efficacy of sterilization. The last, but not the least important, is the intended use of the biomedical devices or biomaterials. The sterilization process should not alter material properties and stability that are critical to material function.

Despite the extensive research, the selection of an appropriate sterilization method is still an art to some extent. Sterilization of collagen-based medical devices is an excellent example. Collagen gels, foams, tubes, sponges, and extracellular tissue matrices (e.g., demineralized bone, decellularized dermis, and other acellular soft-tissue matrices) are marketed for a wide range of medical applications, such as soft-tissue fillers, wound dressings, conduits of damaged nerves and blood vessels, replacement of heart valves, dura repairs, abdominal wall reconstruction, and breast augmentation. Sterilization methods used for the manufacturing of these collagen-based biomedical devices include glutaraldehyde vapor cross-linking, EO, PAA, e-beam, and γ-irradiation. The selection of one method over others typically represents the optimization for the overall manufacturing process, cost, and performance of the intended clinical applications.

4.410.2.6. Sterilization Validation

The purpose of microbiologic sterilization validation is to assess the microbiologic lethality of a sterilization, while ensuring residue levels in compliance with the requirements.[17] The validation of EO sterilization processes, which will be used as an example in this section, is outlined in ISO 11135.[44]

There are three microbiologic approaches in decreasing order of utilization: (1) overkill method; (2) combined biologic indicator–bioburden method; and (3) bioburden method (Table 2).

The first step is to identify the natural bioburden of the product undergoing sterilization. The second step is to identify which of the native bioburdens has the most resistance to the sterilization process. For EO sterilization, *B. atrophaeus* spores were identified as the most resistant organism and therefore, it is used as the model organism for the sterilization validation. For different sterilization methods, the model organism may be different. For example, for HP plasma process and PAA immersion process the model organism is *B. stearothermophilus*.[45]

The 'overkill method' determines cycle lethality from the half-cycle method, which demonstrates a 6-log reduction in population of biological indicator microorganisms in the half cycle. Using the same process parameters, except exposure time, full sterilization cycle achieves at least a 12-log reduction by doubling the half-cycle time. Because of its simplicity and the robust SAL, it is the most popular approach.

The 'combined biologic indicator/bioburden method' requires a low population of the product bioburden and the microorganism's resistance to be known, as well as a high level of confidence that the bioburden data are representative of

Table 1 Comparison of sterilization technologies

Technology	*Advantage*	*Disadvantage*
Heat/steam (autoclave)	Nontoxic, inexpensive, rapidly microbiocidal, rapid cycle time, good penetration	Deleterious for heat- and/or moisture-sensitive materials
Ethylene oxide (EO)	Compatible with most biomaterials, low-temperature setting for heat- and moisture-sensitive materials, good penetration	Potential hazards to staff and patients; lengthy cycle/aeration time; EO is toxic, a probable carcinogen and flammable
γ-Irradiation	Nontoxic, good penetration	Deleterious to polymers and biological materials
E-beam	Nontoxic, rapid cycle time	Deleterious to polymers and biological materials; penetration distance is limited
Supercritical CO_2	Good for moisture- and heat-sensitive materials, little or no damage on materials	Limited chamber size; sterilant residue in materials
Peracetic acid/ hydrogen peroxide (Steris System I)	No activation required; odor or irritation not significant	Materials compatibility concerns, both cosmetic and functional; limited clinical use, used for immersible instruments/materials only; point-of-use system, no long-term sterile storage
HP or PAA gas plasma (Sterrad 100)	No toxic residues; low temperature setting suitable for heat- and moisture-sensitive materials	Not suitable for cellulose (paper), linens, and liquids; not suitable for devices with lumens

Source: Rutala, W. A.; Weber, D. J. *J. Hosp. Infect.* **1999**, *43*(Suppl.), S43–S55.

Table 2 The differences among ISO methods of establishing sterilization radiation dose for medical products

Terms	*ISO 11137-Method 1*	*ISO 11137-Method 2*	*ISO 13409*
Rationale	Based on bioburden level of the product	Based on the γ-resistance of microorganism population present in the product	An adaptation of ISO11137-Method 1 to substantiate 25 kGy dose
Scope	Normal manufacturing processes	Normal manufacturing processes / Consistent and very low bioburden	Product with bioburden less than 1000 cfu, manufactured less than 1000 units per batch
Sample requirements	Bioburden estimation: 10 Verification dose experiment: 100	Incremental dose experiment: 180 (2A), 160 (2B) Verification dose experiment: 100	Bioburden estimation: 10 Verification dose experiment: 10–90
Verification dose establishment	Estimated bioburden and Table B1 (p. 20 – ISO 11137) used to determine verification dose	Incremental dose series irradiated to samples (20 samples per dose). Then the initial verification dose (D*) chosen among the incremental doses satisfying required conditions	Verification dose $= I + [S \times \log$(average SIP bioburden) where I, S can be found in **Table 3** (p. 6 – ISO 13409)
Verification dose experiment	The verification is accepted if the numbers of positive cultures are $\leq$2/100 performed cultures	The verification dose can be calculated, if the numbers of positive cultures are $\leq$15/100 cultures, by applying formula: D** = DD*kGy + [log(CD*)](DS)kGy, where DD* is actual dose in the experiment; CD* is number of positive sterility tests; DS is the estimated dose required to inactivate 90% of organisms surviving at D** dose	If sample size 10–20: the verification exempted if no more than one positive culture observed If sample size $\geq$ 30: the verification exempted if no more than two positive cultures observed
Dose establishment	Found in Table B1 by matching between the average bioburden and desired SAL	Using formula: sterilization dose = D** + [− log(SAL) − log (SIP) − 2](DS)	If the experiment passed then the dose of 25 kGy is substantiated
Advantages	Following the perception that dose-setting work would be based on the natural presence of microorganism in and on products[116,117,172]		Can be applied for products manufactured in small numbers (less than 1000 product units) and low bioburden levels (less than 1000 cfu)
Disadvantages	Required number of samples was too large compared with bone (tissue) bank production, where the number of product units per batch may be only one, and number of batches is several tens		The radiation sterilization dose could not be reduced less than 25 kGy, if the average bioburden of the grafts is significantly decreased

Source: Adapted from Nguyen, H.; Morgan, D. A.; Forwood, M. R. *Cell Tissue Bank* **2007**, *8*, 81–91.

'worst case' conditions. It requires a validated bioburden recovery method and identification of the microorganisms that are typically found in or on the routine products.[46,47]

The 'bioburden method' is based on inactivation of the microbial population in its natural state.

Besides the half-cycle method, there are two other commonly used methods for calculating cycle lethality: the survivor curve and the fraction-negative method. The survivor curve is the bioburden counts as a function of exposure time with other parameters remaining constant. It should include at least five points. From the curve, the D_{10}-value can be obtained and the EO exposure time required to achieve a specific level of sterility can be determined from the D_{10}-value.[44,48,49] The fraction-negative method is based on the analysis of growth/no growth data from the sterility tests.[44,46,48] The exposure time required to achieve a specified sterility level is calculated from the D-value.

4.410.3. Sterilization of Biomaterials of Synthetic and Biological Origin

Biomaterials can be divided into four categories: metals, polymers, ceramics, and materials of biological origin. A composite is formed when two or more different types of materials are combined. The biomaterials in these four categories are briefly reviewed and the sterilization methods used for these materials are discussed in the following sections.

4.410.3.1. Synthetic Biomaterials

4.410.3.1.1. Metals

Because of their excellent mechanical properties, metals are widely used for load-bearing implants in orthopedic surgery (e.g., joint prostheses for hips and knees), as well as in maxillofacial, cardiovascular, and dental surgeries. Among the

metals used for medical devices, the most commonly employed are stainless steels, titanium and titanium alloys, and cobalt alloys.

For metallic implants, their surface characteristics such as the chemical composition, roughness, and surface energy are important parameters associated with their biocompatibility during the implant–body interactions. Sterilization treatments modify the surfaces of metallic medical devices and therefore, it is critical to select appropriate sterilization method for medical devices that contains metallic component(s).

Metallic devices are commonly sterilized using dry heat, steam autoclaving, γ-irradiation, and EO. E-beam can be used for metallic devices of small sizes only because of its limited penetration distance.

The metals are covered by an oxide layer which can be altered by the sterilization process. The changes in a metal's surface characteristics will modify its corrosion behavior and biocompatibility. Among various sterilization methods, including dry heat, steam autoclaving, EO, PAA, and plasma-based sterilizations, plasma-based sterilization appeared to have less effect on the oxide layer thickness, roughness, and morphology than other methods.[50] A study revealed that steam sterilization affects the oxide film properties of stainless steel, and the oxide film deteriorates as the number of cycles increases.[51] Dry heat, steam autoclave, and EO treatment lead to discoloration on NiTi alloy and titanium surfaces, which have been shown to represent areas of increased thickness of oxide layers or a deposited contaminant.[50,52] The steam autoclave and PAA treatments also cause premature corrosion which leads to cracks and pits on NiTi alloy surfaces. The deterioration of the oxide film and damage of the implant integrity may lead to heavy metal release to the surrounding tissues.

Cell attachment assays showed some correlations between surface change of NiTi alloy from sterilization and cellular responses.[52,53] On EO-sterilized surfaces that showed occasional bluish discoloration and a microscopic particulate contaminant, murine fibroblasts showed modest decreases in cell attachment levels. The autoclaved surfaces that had greatest discoloration and heaviest particulate contamination exhibited a lower level of cell attachment, and the cell spreading was diminished compared with the EO-treated group.

4.410.3.1.2. Polymers

The polymers used as biomaterials include polyvinylchloride (PVC), polyethylene (PE), polypropylene (PP), polymethyl methacrylate (PMMA), polystyrene (PS) and its copolymers, polyesters, polyamides (Nylons), fluorocarbon polymers, rubbers, polyurethanes, polyacetal, polysulfone, polycarbonate, and biodegradable polymers.[54] With a wide range of mechanical, thermal, chemical, and physical properties and ease of manufacturability, synthetic polymers have been used in a wide range of applications including cardiovascular, soft tissue, dental, and orthopedic surgeries.[55] In addition, degradable polymers are used in drug-delivery systems.

As polymers have a wide range of thermal and chemical stabilities and different levels of sensitivity to moisture, heat, and irradiation, the sterilization method selected for a specific polymer should be based on its compatibility with the treatment method.

Steam and dry-heat sterilization use high temperature and high steam pressure. They are not suitable for polymers that have low melting temperature (e.g., PE and PMMA) and are sensitive to moisture (e.g., PVC, polyacetals, PE, polyamides, and PLA). The polymers that can be sterilized by these methods are PTFE and silicone rubber.

EO and chemical sterilization use low temperature and thus are suitable for temperature-sensitive polymers. Because they either use moisture (EO) or the sterilization takes place in solution (chemical sterilization), they are not suitable for moisture-sensitive polymers.

Radiation sterilization can deteriorate polymers as the irradiation causes scission and cross-linking in polymer chains, which lead to brittleness, discoloration, cracking, and degradation of polymer. Their physical properties may continue to deteriorate over time after sterilization.

For example, γ-irradiation, one of the most common sterilization methods used for polymers, has been found to cause degradation of ultra-high-molecular-weight PE (UHMWPE), which led to loosening of the implant, pitting and delamination of the polymer, and the formation of debris particles.[55,56] The sterilization of UHMWPE with γ-irradiation results in a loss in fracture roughness of 50% and a decrease in tearing modulus of 30%.[57] This dramatic reduction could result in a 50% decrease in the residual strength of the components, and maximum permissible crack size under service loading and service life. The time required for a crack to grow from its original size to the maximum permissible size could be decreased by 30%, resulting in earlier failure. However, it was also reported that the sterilization of hydroxyapatite-reinforced PE composites by γ-irradiation at a dose of 25 kGy produced a cross-link structure in the PE matrix in the composite, and this network resulted in the increase in modulus, thereby increasing the creep resistance.[58]

It is well known that γ-radiation generates free radicals which can in turn lead to cross-linking and chain scission of a polymer. The dominance of one of these mechanisms over the other is highly dependent upon the sterilization environment. For example, chain scission is the dominant mechanism when the sterilization of UHMWPE is performed in air, while cross-linking appears to be the principal mechanism when the material is irradiated in nitrogen.[59] The chain scission mechanism is a time-dependent process and is especially important to the structural integrity of the polymer, and could be detrimental to the integrity and performance of the polymer as the material continually evolves with time.[60] Scission is further complicated by the uptake of oxygen. Oxygen is extremely reactive with the free radicals produced by irradiation. Peroxy radicals form, which in turn can break down and lead to further radical production so that the total number of free radicals generated and total extent of chain scission are greatly increased. The dominant response to γ-irradiation appears to be chain scission.

Another commonly used sterilization method for polymers is EO. EO is suitable for polymers that are resistant to moisture and temperature, and not appropriate for moisture- and heat-sensitive polymers. Studies have revealed that EO residue levels and effects are highly dependent on the type of polymer material used.[61] Thus, the effect of EO residues must be evaluated for each type of material or device.

For heat- and moisture-sensitive polymers, HP gas plasma is a sterilization method that may be suitable. Unlike EO sterilization, the materials sterilized by low-temperature HP gas plasma do not need to be outgassed prior to use. The plasma process has been found to induce near-surface cross-linking which improves the polymer's resistance to abrasion and mechanical damage.[62] The low-temperature HP gas plasma process does not alter the bulk properties and in this respect the sample is equivalent to the nonsterile (control) in terms of its structure and fatigue resistance. However, the plasma treatment results in a modified surface which renders it more resistant to abrasive wear than the nonsterile case.

4.410.3.1.3. Ceramics/bioactive glasses

Because of their relative inertness to body fluid, high compressive strength, and esthetically pleasing appearance, bioceramics have been used as restorative materials in dentistry (e.g., crowns, cements, and dentures), as bioactive coatings, and as the ball in the articulating region of a hip joint. On the basis of their ability to maintain chemical, physical, and mechanical properties while in the host, they can be classified as nonabsorbable (inert), bioactive, and biodegradable or resorbable.[63] Inert bioceramics are very stable and can resist corrosion, and are therefore used as structural-support implants. They include alumina, zirconia, silicone nitrides, and carbons and are used in bone plates, bone screws, and femoral heads. They can also be used as drug-delivery devices. Bioactive ceramics include bioactive glasses and hydroxyapatites (HA), and resorbable ceramics include calcium phosphates and calcium aluminates. Biodegradable bioceramics are used as drug-delivery devices, and for bone repair, and regeneration. They also find applications in spinal fusion, and maxillofacial and dental surgeries. Upon implantation in the host, bioactive ceramics and glasses have a series of reactions at the material and host body fluid interface which lead to strong bonding with adjacent tissue.[64–66] They are used in the repair of dental and periodontal defects, small bone defects, and replacement of middle ear ossicles, and as bone plates and screws.[67–71]

In general, ceramics/bioactive glasses are compatible with γ-irradiation and e-beam irradiation. Steam and EO sterilization are compatible with ceramics that are not sensitive to moisture.

The essential requirement for an artificial material to bond to living bone is believed to be the formation of a biologically active apatite-like layer on its surfaces in the body.[72] Bioactive ceramic and glass materials such as bioglass, HA, glass–ceramic A-W, diopside, and pseudowollastonite (psW) are generally known to have the ability to form bone like apatite in the body environment. It was reported that steam autoclaving, HP plasma, EO, and γ-irradiation have no significant effect on psW-coating structure and surface morphology.[73] However, the HA-like layer formed after soaking in the simulated body fluid (SBF) was much thinner on the surface of the samples sterilized with EO, indicating that EO sterilization might affect the bioactivity of the ceramic. It was believed that the residual ethylene gas might have affected the nucleation and crystal growth of HA-like layer.

4.410.3.2. Materials of Biological Origin

Biomaterials that are from biological origin include allografts and biological material derivatives. Allografts are used widely in the surgical practices of sports medicine and orthopedic surgeries including anterior cruciate ligament (ACL) reconstruction,[74,75] meniscal transplantation,[76] and osteoarticular reconstruction.[77,78] The major factors that play a critical role for allograft to be successful in clinical application include sterility, reduction of antigenicity, and preservation of the natural biological and biomechanical properties.

Allografts eliminate the disadvantage associated with autografts, including the perioperative pain and morbidity associated with harvesting the graft, uncertain quality of the graft material, and limited graft shapes and sizes. However, one major drawback to using allograft is the potential risk of disease transmission and infection. To eliminate these potential risks, donor screening, aseptic processing, and storage are important steps.[79] Although allografts are recovered and processed aseptically with use of in-process bactericidal and virucidal steps via physical cleaning and chemical treatments, they do not entirely remove all risk of bacterial and viral contamination. Therefore, following tissue processing, terminal sterilization is used to reach assurance of sterility required for medical devices.

γ- and e-beam irradiations are the most commonly used methods for allograft sterilization. There are important differences of these two sterilization methods. With two-sided irradiation, the acceptable depth-dose distribution is 30 and 8 cm of water for γ- and e-beam irradiation, respectively.[80] For soft-tissue grafts such as skin, pericardium, or tendons that have low thickness and density close to that of water, both sterilization methods provide sufficient penetration depth and thus are appropriate to be used for these tissue grafts. However, for grafts with high density ($>2\,g\,cm^{-3}$), for example, bone, the acceptable thickness of a graft exposed to γ-irradiation is about 10–15 cm and only 3 cm for e-beam.[80] The limited penetration of fast electrons in comparison with γ-rays makes it less favorable, and sometimes an inappropriate method, for bone graft sterilization.

In general, it is believed that there is a dose-dependent effect of irradiation on biological matrix in either hard or soft tissues, and high doses of irradiation adversely affect graft integrity and efficacy. The effect of sterilization on the graft's mechanical and biological properties and their clinical performances are associated with graft type, sterilization parameters (e.g., dose, temperature), preservation condition, bioburden level, etc.

EO was one of the first methods used to sterilize allografts such as soft tissues and bone.[19] As the chemical residues left in allografts by EO sterilization could lead to graft failure and the agent is carcinogenic,[81–83] currently only a few tissue banks use EO for sterilization of allografts.

A major difficulty in developing an effective sterilization method for the materials of biological origin comes from its complex chemistry–structure–function relationship. Multiple functional elements are integrated into molecular complexes that in turn are assembled into higher level structures. It is conceivable that modifications, either chemical or physical, will alter the biological properties. In the following sections, allografts and biological materials in different categories are briefly described, and the sterilization methods used for these materials are reviewed.

4.410.3.2.1. Soft tissues

Soft tissues such as acellular dermal matrix grafts have been increasingly used in tissue repair and regeneration in recent

years, including replacement and solidus or repair of diseased or damaged skin, heart valve, blood vessel, tendon, ligament, abdominal wall reconstruction, and breast augmentation and reconstruction.[84–91] These tissue materials contain structural proteins with proper extracellular architecture and biomechanical properties, and may include signaling proteins that can direct phenotypic expression of in-migrating host cells to repopulate. Upon sterilization, extensive biochemical and structural modifications could decrease the tissue's regenerative capability to be integrated into the patient's own tissues via remodeling.

The commonly used sterilization method for soft tissues is ionizing irradiation. To achieve an SAL of 10^{-6}, a dosage between 10 and 35 kGy is needed for γ, e-beam, or X-ray irradiation for solid matrices, processed tissue extracellular matrices (ECMs) (insoluble collagen of dermis and small intestine submucosa) for cellular tissue grafts (heart valve, skin, meniscus, and tendon). It is well known that ionizing irradiation produced major structural damage at a dosage above 10 kGy.[92,93] Damage to collagen by γ-irradiation included cross-linking and molecular fragmentation or degradation via peptide chain scission,[94–97] which could not only result in the significant modification of mechanical properties[3,98–107] and collagen matrix microstructures,[108–111] but also affect biocompatibility,[110,112–115] and the stability against enzyme degradation and thermal denaturation profiles.[92,100,104,109,110,115]

Nevertheless, successful use of γ-irradiated human soft tissues in patients has been well documented,[116–118] even though there is little basic information available on whether and/or how γ-irradiation alters cell repopulation and tissue matrix remodeling. This is a significant knowledge gap in our understanding about the effect of ionizing radiation on soft-tissue materials (also generally true for all collagen-based medical devices). It is noted that substantial knowledge related to preprocessing before irradiation and the use of radioprotectants against radiation damage does exist, but is kept as the corporate trade secrets from public disclosure. In recent years, a number of tissue matrix products have been approved by FDA, and they are sterilized successfully using γ or e-beam irradiation. These products include Permacol biological implant (Covidien, CT), Strattice reconstructive tissue matrix (LifeCell Corporation, NJ), Veritas collagen matrix (Synovis Surgical, MN), and Xenmatrix surgical graft (Davol Inc., RI).

EO sterilization could cause some damage to the dermal structure, but when combined with mild glycerol treatment beforehand there was very little damage.[93,119] GLY-ETO sterilization gave a dermal matrix with good morphology, pliability, and tensile strength. However, because of its safety concerns related to its reaction products, particularly ethylene chlorohydrins, its use on soft tissues in hydrous state is limited. However, it may be used for freeze-dried or lyophilized soft tissues. For example, the processed skin or small intestinal submucosa (SIS) that are frozen and lyophilized or freeze-dried to produce a dry sheet can be packaged into gas permeable pouches and sterilized with EO gas or irradiation.

It was reported that acellular dermal matrix can be sterilized by SC-CO_2. Biochemical and biomechanical evaluations showed that the SC-CO_2 treatment with PAA sterilant did not cause significant changes in porcine acellular matrix's susceptibility to collagenase digestion, tensile or tear strength, indicating limited alteration of the tissue structure following SC-CO_2 sterilization.[35]

When acellular dermal matrix was sterilized with PAA, it retained the integrity of dermal structure and major components of the basement membrane, and it supported the reconstitution with keratinocytes and fibroblasts.[120]

Glycerol treatment is not a recognized method of sterilization and has issues of clinical acceptability although it has been shown to inactivate viruses, bacteria, and fungi.[93,121–123]

4.410.3.2.2. Hard/dense tissues

When hard/dense tissue allografts are implanted, they need to mimic the mechanical properties of the replaced tissues for a certain time period until the graft incorporates with and be remodeled into host tissue. Therefore, it is critical that they meet the mechanical and biological requirements of the replaced tissues. γ-Irradiation is an effective method for terminal sterilization of biological tissues because of its efficacy against viral and bacterial disease transmission. However, γ-irradiation has deleterious effects on mechanical and biological properties of hard and soft tissues in a dose-dependent manner, especially at high does range (>25 kGy).[105,124–128]

As bone allografts have a large variety in sizes and some are rather large pieces, γ-irradiation is commonly used because it does not have a size limitation on bone graft like e-beam irradiation. γ-Irradiation affects bone mechanical properties, remodeling, osteoinduction, and osteoconduction, and dose-dependent, deleterious effects of conventional γ-irradiation on the biomechanical properties of tissues are well documented.[3,80,124,126,128,129] In general, γ-irradiation adversely affects bone allografts biomechanical properties including maximum load, maximum stress, bending strength, strain energy, and modulus, which are major clinical concerns as bone grafts are used in load-bearing applications. However, it was also found that in a low dose range (<25 kGy), there is no clear correlation between γ dose and mechanical properties, especially when bone allografts are irradiated at low temperature (e.g., on dry ice).[130]

Other dense tissues, such as human bone-patellar tendon-bone (BPTB) allografts, also exhibited a similar dose-dependent manner on biomechanical properties.[3,99,131] It was found that even at a dose of 25 kGy or below, there was a significant reduction in biomechanical properties of human BPTB, and an increase of failure rate of the ACL construction in comparison to nonirradiated allograft. The effect becomes more significant with the increase of the dose.

In addition to dose, the effects of irradiation are also related to other factors, such as bone types, hydration, and preservation solution used. It is believed that cancellous bone is more resistant to γ-irradiation than cortical bone.[124,132] The dose-dependent reduction in mechanical properties positively correlates with the grafts biological performance. The nonunion rate increased with the increase of irradiation dose of the bone allografts with rate increasing from 0 to 12.5 and 33% as the γ-dose increased from 0 to 25 and 75 kGy.[133] Bone induction was eliminated when allografts were irradiated at the doses from 20 to 40 kGy.[134] Moreover, irradiated collagen was much more soluble and the implants were almost resorbed without new bone formation.[134] It was also discovered that degradation of collagen by irradiation of 25 kGy led to a

significant reduction in bone formation when it was implanted with BMP.[135]

The mechanisms of γ-irradiation damage of bone tissues are not clear, but there is evidence showing that the damage is induced by free radical attack on the collagen. It is believed that the collagen phase is more vulnerable to γ-irradiation than the mineral phase of cortical bone tissue,[136] and the integrity of bone's collagen significantly affects the mechanical strength and fracture resistance of bone tissue.[137]

The effects of γ-irradiation on peptide backbone of collagens of bone and tendons have been investigated. It was shown that γ-irradiation led to scission of the peptide backbone,[92] and reduced the concentration of intermolecular cross-links in tendon collagen.[138] Similar destruction of the peptide backbone[92] and reduction in intermolecular cross-link density[139] have also been reported for human femoral cortical bone secondary to γ-irradiation.

The mechanisms of tissue damage by γ-irradiation are different for tissues in dry and wet state.[80,140] In dry state, the irradiation and the free radicals generated in the matrix during the irradiation cause scissions in polypeptide of collagen matrix. The free radicals irradiation may also establish cross-linking of matrix but the extent is limited because of the movement constraint of polypeptide and free radicals in dry state. In wet state, γ-rays and free radicals generated in irradiation also cause scissions in collagen matrix as in dry state. But the cross-linking reaction of collagen matrix could be more significant than in dry state. The free radicals generated in protein matrix and water could cross-link the polypeptides which have less motion constraint. Thus, the scissions and cross-linking occur concurrently during the irradiation and the reaction may cascade even after the irradiation. The structural changes, for example, scissions and cross-linking, alter the mechanical and biochemical properties of collagen matrix, resulting in changes in strength and toughness, and bone defect healing.

In contrast to bone graft, DBM appeared not to be significantly affected by γ-irradiation in terms of its osteoinductivity and higher dose even increased this property.[141–143] As DBM has characteristics that are unique and different from those of bone grafts, the effect on DBM will be reviewed and discussed in a separate section.

The scissions caused by direct irradiations cannot be avoided. However, if the secondary chemistry, for example, generation of free radicals and reactive oxygen species, that occurs during irradiation is minimized, the damaging effects to the tissue could be substantially reduced.[140,144] When treated with a radioprotectant solution, cancellous bone dowels show an ultimate compressive strength and modulus of elasticity equal to irradiated (18 kGy) and nonirradiated control bone grafts.[144] The free radical scavenging solution also alleviates the biomechanical impairment of γ-irradiated femurs.[140]

Similar to bone treated with radioprotectant solution, other dense tissues, for example, tendon, that were treated with a radioprotectant solution (containing propylene glycol, dimethyl sulfoxide, mannitol, and trehalose) and then treated with 50 kGy γ-irradiation at low temperature showed comparable biomechanical properties to the nonirradiated and 18 kGy groups.[145]

4.410.3.2.3. Demineralized bone matrix

DBM is composed of structural proteins, mainly type I collagen, and signaling proteins that regulate cell migration, proliferation, and differentiation. Upon implantation, it can be integrated into host tissue through resorption and remodeling.

Since the discovery of the bone inductive property of DBM,[146] DBM has been used to induce bone formation in various clinical applications, including long bone defects, craniofacial defects, joint surgery, tumor surgery, and spinal fusion.[147–154]

Unlike bone grafts that have to maintain a certain level of mechanical strength for clinical applications, DBM products generally do not have requirements on their mechanical strength. Instead, the osteoinductive potential of DBM is critical for its application. DBM is made through a number of processing steps such as demineralization with acid solution, lip and lipoprotein removal, lyophilization, and sterilization. A variety of combinations of acid, HP, and alcohol have been used by tissue banks for bioburden and viral inactivation.[141] Some of the processing steps have potential effects on osteoinduction.

One of the greatest challenges for DBM products sterilization is to keep their osteoinductivity while ensuring their sterility. Osteoinductivity could be affected by various factors including sterilization method, temperature, moisture level, and storage.

EO has been used for DBM sterilization. The osteoinductive properties of demineralized bone have been shown to be retained following sterilization with EO.[155] As EO requires elevated levels of temperature and humidity to maintain its effectiveness as a sterilization agent, it might affect osteoinductivity depending on the temperature and moisture level used as heat and moisture significantly affect the osteoinductivity of DBM.[156–158] When DBM was in hydrous state, it lost its osteoinductivity more easily than in anhydrous state.[159,160]

Despite the fact that irradiation causes polymer oxidation, chain scission, and the release of free radicals, the effect of irradiation on DBM osteoinductivity has mixed results. Some studies showed γ-irradiation of higher dose increased DBM osteoinductivity.[141–143] Urist reported that processed demineralized bone retained 80% of its activity when irradiated to 40 kGy.[161] Hydration and temperature also play a role in radiation effect on osteoinductivity. For example, 35 or 50 kGy at ambient temperature was shown to inactivate lyophilized decalcified rat bone but had no effect on hydrated material maintained at $-72\,^{\circ}C$.[162] It was reported that the osteoinductivity of hydrated DBM subjected to e-beam irradiation is diminished after 12-month ambient storage, whereas the anhydrous DBM retains its osteoinductivity potential.[159]

Autoclaved demineralized bone produced a foreign body reaction in test animals without any sign of osteoinduction.[163] It was found that 70% alcohol does not destroy osteoinductivity.[141] However, 70% alcohol is not considered as a sterilant for terminal sterilization. Osteoinductivity could also be lost by prolonged exposure to acid, base, acidic alcohol, fixatives, as well as UV radiation and ultrasonic energy. It was reported that exposure to 3%HP abolishes DBM osteoinductive capacity.[164]

Research on methods for terminal sterilization continues to identify effective methods of sterilization that do not inactivate DBM.

Currently, there is no best way to sterilize allograft tissues, and combinations of different sterilization methods are commonly employed to achieve a desired sterility level. For example, Allowash formula (LifeNet, Virginia Beach, VA) uses irradiation (10–13 kGy) in combination with reagents such as detergents, antibiotics, alcohols, and HP to inactivate microorganisms.[165] The BioCleanse tissue sterilization process (Regeneration Technologies, Alachua, FL) uses a low-temperature chemical sterilization process with liquid sterilant and then irradiates the tissue (25 kGy).

The biomaterials reviewed in this chapter, their applications, and the sterilization methods used are summarized in Table 3.

4.410.4. Evaluation of Effect of Sterilization on Biomaterials

Sterilization will alter a biomaterial's properties and thus may affect its clinical performance. *In vitro* and *in vivo* tests are often used to evaluate the impact of sterilization on the safety, efficacy, and functionalities of biomaterials and medical devices. For example, the Instron is used to measure the change of biomechanical strength; X-ray photoelectron spectroscopy (XPS) for chemical analysis of surfaces; atomic force microscopy (AFM) for surface topography analysis; the small animal models (e.g., mouse and rat) are used for biocompatibility, cell repopulation, and revascularization; etc.

4.410.4.1. Selection of Analytical Methods

A quick survey of research literature reveals a large number of analytical methods that have been used to assess the effect of sterilization on biomedical devices or biomaterials. Considering the number of biomaterial types, the number of intended applications, and different sterilization methods, one would not be surprised by the large number of analytical methods used. Instead of reviewing what analytical methods can be used to investigate the sterilization impact for a given biomaterial type, we prefer to discuss here a general framework that may help to establish the correlation between *in vitro* test results and *in vivo* performance expectations.

Among the challenges for evaluation of sterilization impact is that the data from *in vitro* tests on a biomaterial or a biomedical device often could not predict the possible outcomes of *in vivo* performance well. Two biomaterials with similar structures and *in vitro* test results after sterilization could behave differently *in vivo*. The *in vivo* biological performance is affected by so many factors that may interact with any chemical or structural modification caused by sterilization. The *in vitro* tests could not possibly provide all information for one to predict the potential *in vivo* biological outcomes, and each type of *in vitro* test method provides only a snapshot for a certain type of sterilization damage. Various analytical methods may be loosely sorted into four different tiers according to the type of information that the tests provide (Figure 5). The human clinical evaluation is the only first tier method that can fully evaluate the impact of sterilization on biomaterials for implantation. The *in vivo* functional animal models, immunological assay, and *in vivo* degradation kinetics are the second tier methods that can provide data to predict possible outcomes in similar clinical conditions. Biocompatibility tests, toxicity test, and histochemistry belong to the third tier methods. The third tier method may only obtain information of specific biological interactions. The majority of chemical analysis, mechanical test, structural characterization, shelf life stability test, and other biological tests are considered to be the fourth tier methods. While the fourth tier analytical methods may not directly predict clinical outcomes, they provide valuable data for process optimization and critical information for understanding the mechanisms of actions or failures after sterilization.

4.410.4.2. Effect of γ-Irradiation on a Regenerative ECM Matrix: A Case Study

Decellularized soft-tissue matrices of human and animal origin have excellent initial biomechanical properties and extracellular architecture that support the repair and regeneration of diseased human tissues. The native ECM components (e.g., collagen and other signaling proteins) are capable of supporting phenotypic expression of in-migrating host cells to repopulate, to revascularize, and to remodel the implanted ECM into the patient's own tissues without tissue reactivity and rejection after implantation and thus eliminate problems associated with the use of many alloplastic materials. γ-Irradiation was first tested for terminal sterilization of freeze-dried ECM matrix to ensure product safety.

Four methods were initially used to evaluate the effect of γ-irradiation. They are (a) the histological analysis to assess the changes of tissue's ECM structure (the fourth tier method), (b) the tensile test of rehydrated ECM strips to measure the change of strength (the fourth tier method), (c) nude mouse subcutaneous implantation to evaluate the host cell repopulation and revascularization (the third tier method), and (d) a functional abdominal wall reconstruction model (African green monkey) to evaluate tissue regeneration (the second tier method). Histological analysis and tensile test were selected because biomechanical strength and extracellular architecture were important properties for the intended applications. Histological analysis and tensile test of ECM strips rehydrated in 0.9% saline at ambient temperature did not observe significant difference between control ECM material and sterilized ECM material that were γ-irradiated at −80 °C (15 kGy).[166] The nude mouse subcutaneous implantation study showed that both control ECM and γ-sterilized ECM were capable of supporting host cell repopulation and revascularization. However, the primate functional model revealed that γ-irradiated ECM had a very rapid turnover, which prevented the regeneration of functional abdominal wall.[167] In this case, the selected third tier and fourth tier methods did not provide any useful insight for the possible modes of failure in a fully functional model.

In a separate study[168] using the paramagnetic resonance (a forth tier method), it was observed that ionizing irradiation resulted in the accumulation of two long-lived organic free radicals in the sterilized ECM matrix. The transformation (reaction) kinetics of free radicals produced was extremely slow in the nitrogen environment. The presence of oxygen and moisture greatly accelerated free radical reactions in the tissue matrix. The presence of long-lived free radicals in sterilized

Table 3 Biomaterials and corresponding sterilization methods

Material	*Applications*	*Sterilization method*
Metals and alloys		
316L stainless steel	Fracture fixation, stents, surgical instruments	γ, e-beam
CP-Ti, Ti–Al–V, Ti–Al–Nb, Ti–13Nb–13Zr, Ti–Mo–Zr–Fe	Bone and joint replacement, fracture fixation, dental implants, pacemaker encapsulation	γ, e-beam
Co–Cr–Mo, Cr–Ni–Cr–Mo	Bone and joint replacement, dental implants, dental restorations, heart valves	γ, e-beam
Ni–Ti	Bone plates, stents, orthodontic wires	γ, e-beam, gas plasma
Gold alloys	Dental restorations	γ, e-beam
Silver products	Antibacterial agents	γ, e-beam
Ceramics and glasses		
Alumina	Joint replacement, dental implants	γ, e-beam, autoclave
Zirconia	Joint replacement	γ, e-beam, autoclave
Calcium phosphates	Bone repair and augmentation, surface coating on metals	γ, e-beam
Bioactive glasses	Bone replacements	γ, e-beam
Porcelain	Dental restorations	γ, e-beam, autoclave
Carbons	Heart valves, percutaneous devices, dental implants	γ, e-beam
Polymers		
Polyvinychloride	IV sets, dialysis devices, catheter, connectors, and cannulae	Autoclave, γ, e-beam, EO
Polyethylene	Orthopedic implants, catheter	EO
Polypropylene	Sutures, artificial vascular grafts, hernia repair	γ, e-beam, EO
Polyethylenterephthalate	Sutures, artificial vascular grafts, heart valves, meshes	γ, e-beam, EO
Polyamides (Nylon)	Sutures, catheters	γ, e-beam, EO
Polytetrafluoroethylene (Tyflon)	Soft-tissue augmentation, artificial vascular grafts	γ, e-beam, EO, autoclave
Polyurethanes	Blood-contacting devices	γ, e-beam, EO
PVC	Tubing	γ, e-beam, EO
Polymethyl methacrylate	Dental restorations, intraocular lenses, joint replacement (bone cements)	γ, e-beam, EO
Poly(dimethyl siloxane)	Finger joints; heart valves; breast implants; in ear, chin, and nose reconstruction	γ, e-beam, EO
Silicones	Soft-tissue replacement, ophthalmology	γ, e-beam, autoclave
Biodegradable polymers: polylactide, polyglycolide, poly (glycolide-*co*-lactide), poly(dioxanone), poly(trimethylene carbonate), poly(carbonate)	Drug-delivery systems, resorbable sutures	γ, e-beam
Hydrogels	Ophthalmology, drug-delivery systems	γ, e-beam
Composites		
BIS-GMA-quartz/silica filler	Dental restorations	γ, e-beam
PMMA-glass fillers	Dental restorations (dental cements)	γ, e-beam
Materials with biological origin		
Allografts	Orthopedic implants, soft-tissue repair	γ, e-beam, SC-CO_2
Bovine pericardial tissue	Heart valve prosthesis, soft-tissue repair	γ, e-beam
Equine pericardium	soft-tissue repair	Cross-linking and alcohol
DBM	Bone defect repair, spinal fusion	γ, e-beam
Fetal bovine dermis	Bone defect repair	EO
Human dermis	Soft-tissue repair	γ
Porcine dermis	Soft-tissue repair	γ, EO, e-beam
Porcine subintestinal submucosa	Soft-tissue repair	EO

Source: Williams, D. In *Concise Encyclopedia of Medical & Dental Materials*; Williams, D., ed.; Pergamon Press and MIT Press, 1990; pp xvii–xx; Wong, J. Y.; Bronzino, J. D., Eds. *Biomaterials*. CRC Press: Boca Raton, FL, 2006.

ECM matrix suggested the possibility of a time-dependent, oxygen- or moisture-mediated degradation process after sterilization. This type of damage might not be observed if ECM matrix was evaluated immediately after sterilization.

The rapid turnover of ECM matrix observed in the primate model demonstrated that chemical degradation analysis (susceptibility to proteases) and biological stability test (calorimetric analysis) might be more valuable methods. Calorimetric analysis[169] showed that the stability of ECM matrix changed significantly after γ-irradiation. The onset denaturation temperature of type I collagen decreased from 60 to ~35 °C with a dose of 12 kGy (**Figure 6**). Multiple peaks were observed in

γ-irradiated ECM matrix, clearly demonstrating an increase in collagen conformational heterogeneity and collagen destabilization and possible degradation. Further study found that e-beam irradiation caused substantially less damage than γ-irradiation on ECM matrix. ETO sterilization method caused the least amount of change among five sterilization methods (γ-irradiation, e-beam irradiation, ETO, gluteraldehyde cross-linking, and EDC cross-linking) (Figure 7).

There is evidence that the decrease in thermal stability of tissue matrix is correlated to the increased vulnerability to enzyme degradation.[170,171] To understand mechanisms that triggered the rapid *in vivo* degradation of γ-irradiated ECM matrix, four proteolytic enzymes (collagenase, pepsin, trypsin, and proteinase k) were selected for the determination of the susceptibility of ECM matrix to enzyme degradation.[167] The selection of those four enzymes was on the basis of the ECM components and their perceived functions (Figure 8). In all cases, γ-irradiated ECM was digested faster than control ECM. Trypsin assay indicated that γ-irradiation exposed lysine and arginine residues in collagen fibrils, probably via collagen

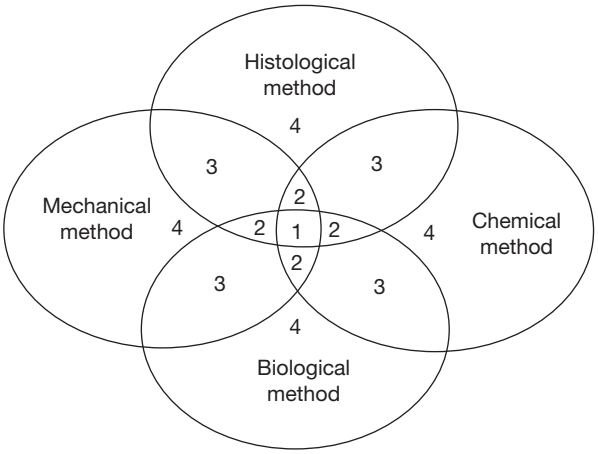

Figure 5 Four tiers of analytical methods for the evaluation of biomaterials.

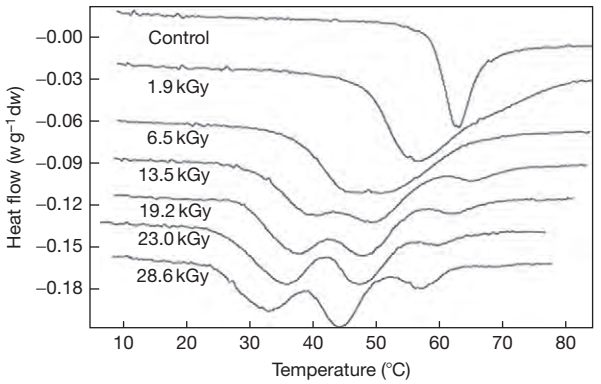

Figure 6 Effect of γ-irradiation on collagen stability in rehydrated ECM matrix tissue matrix. Collagen thermostability was determined using DSC at heating rate of 3°C min^{-1} under constant nitrogen purge. ECM matrix was rehydrated in 0.9% saline before testing. Reproduced from Sun, W. Q.; Leung, P. *Acta Biomater*. **2008**, *4*, 817–826.

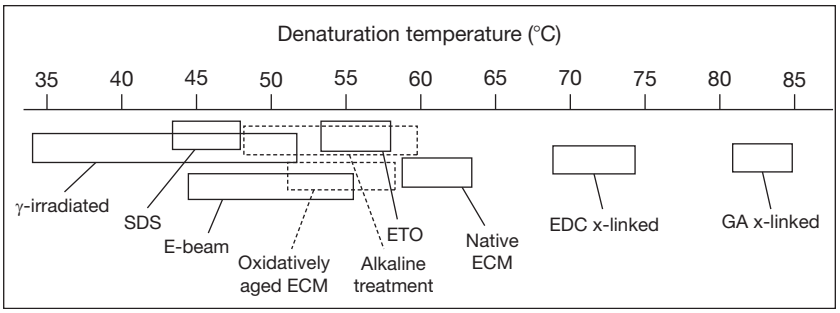

Figure 7 Effects of processes on ECM matrix stability as measured by calorimetric analysis.

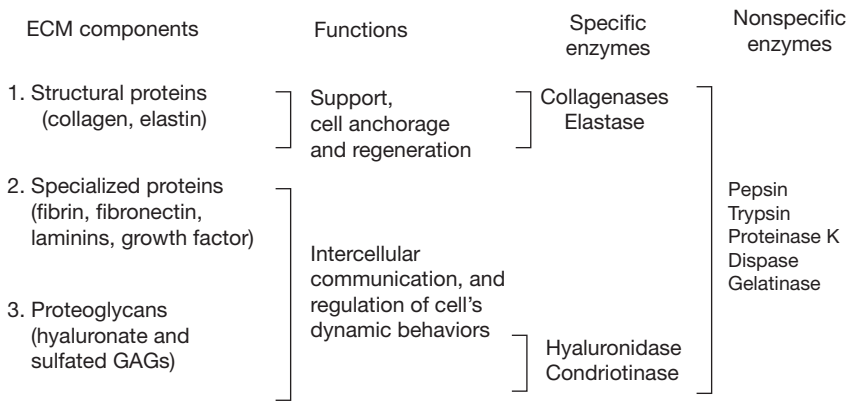

Figure 8 ECM components, their perceived functions, and enzymes selected for the evaluation of sterilization effect by γ-irradiation.

chain scission. Proteinase K assay showed destabilizing collagen conformational changes after γ-irradiation. *In vitro* fibroblast cell culture confirmed the results of ECM matrix degradation upon cell attachment.

The ECM matrix case study demonstrated the importance of selecting the appropriate analytical methods to evaluate the effect of sterilization on biomaterials.

References

1. Rutala, W. A.; Weber, D. J. *Guideline for Disinfection and Sterilization in Healthcare Facilities*. The Healthcare Infection Control Practices Advisory Committee (HICPAC), Center for Disease Control, Department of Health and Human Services, 2008.
2. ANSI/AAMI ST 67, *Sterilization of Health Care Products - Requirements for Products Labeled 'STERILE'*. Association for the Advancement of Medical Instrumentation, 2003.
3. Fideler, B. M.; Vangsness, C. T., Jr.; Lu, B.; Orlando, C.; Moore, T. *Am. J. Sports Med.* **1995**, *23*(5), 643–646.
4. ISO 11737, *Sterilization of Medical Devices - Microbiological Methods - Part 1: Estimation of Population of Microorganisms on Products*. International Standard Organization, 1995.
5. ISO 11737, *Sterilization of Medical Devices - Microbiological Methods - Part 2: Test of Sterility Performed in the Validation of a Sterilization Process*. International Standard Organization, 1998.
6. Quinn, P. J.; Markey, B. K. In *Disinfection, Sterilization and Preservation*, 5th ed.; Block, S. S., Ed.; Lippincott, Williams & Wilkins: Philadelphia, PA, 2001; pp 1069–1103.
7. Blank, G.; Corrigan, D. *Int. J. Food Microbiol.* **1995**, *26*(3), 269–277.
8. Woo, L.; Sandford, C. L. *Radiat. Phys. Chem.* **2002**, *63*, 845–850.
9. Bartonicek, B.; Placek, V.; Hnat, V. *Radiat. Phys. Chem.* **2007**, *76*, 857–863.
10. Bommer, J.; Ritz, E. *Artif. Organs* **1987**, *11*(2), 111–117.
11. Mendes, G. C.; Brandão, T. R.; Silva, C. L. *Am. J. Infect. Control* **2007**, *35*(9), 574–581.
12. Rutala, W. A.; Weber, D. J. *J. Hosp. Infect.* **1999**, *43*(Suppl.), S43–S55.
13. Oxborrow, G. S.; Placencia, A. M.; Danielson, J. W. *Appl. Environ. Microbiol.* **1983**, *45*(2), 546–549.
14. Angerer, J.; Bader, M.; Krämer, A. *Int. Arch. Occup. Environ. Health* **1998**, *71*(1), 14–18.
15. Glaser, Z. R. *J. Environ. Pathol. Toxicol.* **1979**, *2*(5), 173–208.
16. Steenland, K.; Stayner, L.; Deddens, J. *Occup. Environ. Med.* **2004**, *61*(1), 2–7.
17. ISO 10993-7, *Biological Evaluation of Medical Devices. Part 7: Ethylene Oxide Sterilization Residuals*. 2008.
18. Barker, J. *Med. Device Technol.* **1995**, *6*(5), 23–24.
19. Prolo, D. J.; Pedrotti, P. W.; White, D. H. *Neurosurgery* **1980**, *6*(5), 529–539.
20. Baier, R. E.; Meyer, A. E.; Akers, C. K.; Natiella, J. R.; Meenaghan, M.; Carter, J. M. *Biomaterials* **1982**, *3*(4), 241–245.
21. Baldry, M. G. C. *J. Appl. Bacteriol.* **1983**, *54*(3), 417–423.
22. Hodde, J.; Hiles, M. *Biotechnol. Bioeng.* **2002**, *79*, 211–216.
23. Pruss, A.; Kao, M.; Kiesewetter, H.; von Versen, R.; Pauli, G. *Biologicals* **1999**, *27*, 195–201.
24. Pruss, A.; Baumann, B.; Seibold, M.; *et al. Biologicals* **2001**, *29*, 59–66.
25. Lambert, R. J.; Johnston, M. D.; Simons, E. A. *J. Appl. Microbiol.* **1999**, *87*(5), 782–786.
26. Uchiyama, H.; Dobashi, Y.; Ohkouchi, K.; Nagasawa, K. *J. Biol. Chem.* **1990**, *265*(14), 7753–7759.
27. Fraser, D. *Nature* **1951**, *167*, 33–34.
28. Dillow, A. K.; Dehghani, F.; Hrkach, J. S.; Foster, N. R.; Langer, R. L. *Proc. Natl. Acad. Sci. USA* **1999**, *96*, 10344–10348.
29. Kamihira, M.; Taniguchi, M.; Kobayashi, T. *Agric. Biol. Chem.* **1987**, *51*, 407–412.
30. White, A.; Burns, D.; Christensen, T. W. *J. Biotechnol.* **2006**, *123*(4), 504–515.
31. Spilimbergo, S.; Bertucco, A. *Biotechnol. Bioeng.* **2003**, *84*(6), 627–638.
32. Hodde, J.; Hiles, M. *Biotechnol. Bioeng.* **2002**, *79*, 211–216.
33. Hemmer, J. D.; Drews, M. J.; LaBerge, M.; Matthews, M. A. *J. Biomed. Mater. Res. B Appl. Biomater.* **2006**, *80B*, 511–518.
34. Fages, J.; Poirier, B.; Barbier, Y.; *et al. ASAIO J.* **1998**, *44*(4), 289–293.
35. Qiu, Q. Q.; Leamy, P.; Brittingham, J.; Pomerleau, J.; Kabaria, N.; Connor, J. *J. Biomed. Mater. Res. B Appl. Biomater.* **2009**, *91*(2), 572–578.
36. Lerouge, S.; Wertheimer, M. R.; Yahia, L. H. *Plasma Polym.* **2004**, *6*(3), 175–188.
37. Moisan, M.; Barbeau, J.; Moreau, S.; Pelletier, J.; Tabrizian, M.; Yahia, L. H. *Int. J. Pharm.* **2001**, *226*, 1–21.
38. Moisan, M.; Barbeau, J.; Crevier, M. C.; Pelletier, J.; Philip, N.; Saoudi, B. *Pure Appl. Chem.* **2002**, *74*(3), 349–358.
39. Feldman, L. A.; Hui, H. K. *Med. Dev. Diag. Indust.* **1997**, *19*, 57–62.
40. Timm, D.; Gonzales, D. *Surg. Serv. Manage.* **1997**, *3*, 47–49.
41. Ferreira, S. D.; Dernell, W. S.; Power, B. E.; *et al. Clin. Orthop. Relat. Res.* **2001**, *388*, 233–239.
42. Duffy, R. E.; Brown, S. E.; Caldwell, K. L.; *et al. Arch. Ophthalmol.* **2000**, *118*, 1167–1176.
43. Jarvis, W. R. In *Disinfection, Sterilization and Antisepsis: Principles and Practices in Healthcare Facilities*; Rutala, W. A., Ed.; Association for Professional in Infection Control and Epidemiology: Washington, DC, 2001; pp 41–48.
44. ISO 11135-1, *Sterilization of health care products - Ethylene oxide - Part 1: Requirements for the development, validation and routine control of a sterilization process for medical devices*, 2007.
45. Rutala, W. A.; Gergen, M. F.; Weber, D. J. *Am. J. Infect. Control* **1998**, *26*(4), 393–398.
46. AAMI TIR 16, *Process Development and Performance Qualification for Ethylene Oxide Sterilization-microbiological Aspects*. Association for the Advancement of Medical Instrumentation Standard, 2000.
47. ISO(/ANSI/AAMI) 14937, *Sterilization of Health Care Products-general Requirements for Characterization of a Sterilizing Agent and the Development, Validation, and Routine Control of Sterilization Process for Medical Devices*, 2000.
48. ISO 11138-1, *Sterilization of Health Care Products-biological Indicators. Part I: General Requirements*, 2006.
49. ISO 14161, *Sterilization of Health Care Products - Biological Indicators - Guidance for the Selection, Use and Interpretation of Results*, 2000.
50. Thierry, B.; Tabrizian, M.; Savadogo, O.; Yahia, L. *J. Biomed. Mater. Res.* **2000**, *49*(1), 88–98.
51. Shih, C. C.; Su, Y. Y.; Chen, L. C.; Shih, C. M.; Lin, S. J. *Acta Biomater.* **2010**, *6*(6), 2322–2328; Epub 2009 Dec 16.
52. Keller, J. C.; Draughn, R. A.; Wightman, J. P.; Dougherty, W. J.; Meletiou, S. D. *Int. J. Oral Maxillofac. Implants* **1990**, *5*(4), 360–367.
53. Vezeau, P. J.; Koorbusch, G. F.; Draughn, R. A.; Keller, J. C. *J. Oral Maxillofac. Surg.* **1996**, *54*(6), 738–746.
54. Lee, H. B.; Khang, G.; Lee, J. H. In *Biomaterials*; Wong, J. Y., Bronzino, J. D., Eds.; CRC Press: Boca Raton, FL, 2006.
55. Goldman, M.; Pruitt, L. *J. Biomed. Mater. Res.* **1998**, *40*(3), 378–384.
56. Affatato, S.; Bordini, B.; Fagnano, C.; Taddei, P.; Tinti, A.; Toni, A. *Biomaterials* **2002**, *23*(6), 1439–1446.
57. Pascaud, R. S.; Evans, W. T.; McCullagh, P. J.; FitzPatrick, D. P. *Biomaterials* **1997**, *18*(10), 727–735.
58. Suwanprateeb, J.; Tanner, K. E.; Turner, S.; Bonfield, W. *J. Biomed. Mater. Res.* **1998**, *39*(1), 16–22.
59. Streicher, R. *Plast. Rubber Process. Appl.* **1988**, *10*, 221–229.
60. Pruitt, L.; Ranganathan, R. *Mater. Sci. Eng. C* **1995**, *3*, 91–93.
61. Lucas, A. D.; Merritt, K.; Hitchins, V. M.; *et al. J. Biomed. Mater. Res. B Appl. Biomater.* **2003**, *66B*, 548–552.
62. Shen, F. W.; McKellop, H. A.; Salovey, R. *J. Polym. Sci. Polym. Phys.* **1996**, *34*, 1063–1077.
63. Billotte, W. C. In *Biomaterials*; Wong, J. Y., Bronzino, J. D., Eds.; CRC Press: Boca Raton, FL, 2006.
64. Ducheyne, P. *J. Biomed. Mater. Res.* **1985**, *19*, 273–291.
65. Ducheyne, P.; Qiu, Q. *Biomaterials* **1999**, *20*(23–24), 2287–2303.
66. Hench, L. L.; Ethridge, E. C. *Biomaterials: An Interfacial Approach*; Academic Press: New York, 1982; p 147.
67. Ducheyne, P.; McGuckin, J. F., Jr. In *Handbook of Bioactive Ceramics*; Yamamuro, T., Hench, L. L., Wilson, J., Eds.; CRC Press: Boca Raton, FL, 1990; pp 75–86.
68. Feenstra, I.; de Groot, K. In *Bioceramics of Calcium Phosphate*; de Groot, K., Ed.; CRC Press: Boca Raton, FL, 1983; pp 131–141.
69. Hench, L. L. *J. Am. Ceram. Soc.* **1991**, *74*, 1487–1510.
70. Schepers, E.; Ducheyne, P.; De Clercq, M. *J. Biomed. Mater. Res.* **1989**, *23*(7), 735–752.
71. Schepers, E. J.; Ducheyne, P.; Barbier, L.; Schepers, S. *Implant Dent.* **1993**, *2*(3), 151–156.
72. Hench, L. L.; Splinter, R. J.; Allen, W. C.; Greenlee, T. K. *J. Biomed. Mater. Res.* **1971**, *5*(6), 117–141.
73. Zuleta, F. A.; Velasquez, P.; De Aza, P. N. *J. Biomed. Mater. Res. B Appl. Biomater.* **2010**, *94*(2), 399–405.

74. Harner, C. D.; Olson, E.; Irrgang, J. J.; Silverstein, S.; Fu, F. H.; Silbey, M. *Clin. Orthop. Relat. Res.* **1996**, *324*, 134–144.
75. Shelton, W. R.; Treacy, S. H.; Dukes, A. D.; Bomboy, A. L. *J. Am. Acad. Orthop. Surg.* **1998**, *6*(3), 165–168.
76. Cole, B. J.; Dennis, M. G.; Lee, S. J.; *et al. Am. J. Sports Med.* **2006**, *34*(6), 919–927.
77. Czitrom, A. A.; Langer, F.; McKee, N.; Gross, A. E. *Clin. Orthop. Relat. Res.* **1986**, *208*, 141–145.
78. Shasha, N.; Aubin, P. P.; Cheah, H. K.; Davis, A. M.; Agnidis, Z.; Gross, A. E. *Cell Tissue Bank.* **2002**, *3*(3), 175–182.
79. AATB. *Standards for Tissue Banking*; American Association of Tissue Banking: McLean, VA, 2002.
80. Dziedzic-Goclawska, A.; Kaminski, A.; Uhrynowska-Tyszkiewicz, I.; Stachowicz, W. *Cell Tissue Bank.* **2005**, *6*(3), 201–219.
81. Jackson, D. W.; Windler, G. E.; Simon, T. M. *Am. J. Sports Med.* **1990**, *18*, 1–11.
82. Roberts, T. S.; Drez, D., Jr.; McCarthy, W.; *et al. Am. Sports Med.* **1991**, *19*, 35–41.
83. Steenland, K.; Stayner, L.; Greife, A.; *et al. N. Engl. J. Med.* **1991**, *324*, 1402–1407.
84. Badylak, S. F. *Semin. Cell Dev. Biol.* **2002**, *13*, 377–383.
85. Lipman, J.; Medalie, D.; Rosen, M. J. *Am. J. Surg.* **2008**, *195*(1), 84–88.
86. Livesey, S. A.; Herndon, D. N.; Hollyoak, M. A.; Atkinson, Y. H.; Nag, A. *Transplantation* **1995**, *60*, 1–9.
87. Nerem, R. M.; Seliktar, D. *Annu. Rev. Biomed. Eng.* **2001**, *3*, 225–243.
88. Rennekampff, H. O.; Kiessig, V.; Griffey, S.; Greenleaf, G.; Hansbrough, J. F. *J. Burn Care Rehabil.* **1997**, *18*, 535–544.
89. Salzberg, C. A. *Ann. Plast. Surg.* **2006**, *57*(1), 1–5.
90. Schmidt, C. E.; Baier, J. M. *Biomaterials* **2000**, *21*, 2215–2231.
91. Wainwright, D.; Madden, M.; Luterman, A.; *et al. J. Burn Care Rehabil.* **1996**, *17*, 124–136.
92. Cheung, D. T.; Perelman, N.; Tong, D.; Nimni, M. E. *J. Biomed. Mater. Res.* **1990**, *24*, 581–589.
93. Ghosh, M. M.; Boyce, S.; Layton, C.; Freedlander, E.; Mac Neil, S. *Ann. Plast. Surg.* **1997**, *39*(4), 390–404.
94. Bailey, A. J.; Tromans, W. J. *Radiat. Res.* **1964**, *23*, 145–155.
95. Bailey, A. J.; Rhodes, D. N.; Cater, C. W. *Radiat. Res.* **1964**, *22*, 606–621.
96. Bowes, J. H.; Moss, J. A. *Radiat. Res.* **1962**, *16*, 211–223.
97. Davidson, R. J.; Cooper, D. R. *Biochem. J.* **1968**, *107*, 29–34.
98. Butler, D. L.; Gibbons, M. J.; Grood, E. S.; Noyes, F. R. *Tissue Eng. BED ASME* **1989**, *14*, 111–114.
99. Curran, A. R.; Adams, D. J.; Gill, J. L.; Steiner, M. E.; Scheller, A. D. *Am. J. Sports Med.* **2004**, *32*(5), 1131–1135.
100. De Deyne, P.; Haut, R. C. *Connect. Tissue Res.* **1991**, *27*, 51–62.
101. Gibbons, M. J.; Butler, D. L.; Grood, E. S.; Bylski-Austrow, D. I.; Levy, M. S.; Noyes, F. R. *J. Orthop. Res.* **1991**, *9*, 209–218.
102. Haut, R. C.; Powlison, A. C. In *Order of Irradiation and Lyophilization on the Strength of Patellar Tendon Allografts*. Proceedings of the 35th Meeting, Orthopedic Research Society, Orthopedic Transactions 514, 1989.
103. Haut, R. C.; Powlison, A. C. *J. Orthop. Res.* **1990**, *8*, 532–540.
104. Ohan, M. P.; Dunn, M. G. *J. Biomed. Mater. Res. A* **2003**, *67*, 1188–1195.
105. Smith, C. W.; Young, I. S.; Kearney, J. N. *J. Biomech. Eng.* **1996**, *118*(1), 56–61.
106. Smith, C. W.; Kearney, N. J. *J. Mater. Sci. Mater. Med.* **1996**, *7*, 645–650.
107. Yahia, L. H.; Drouin, G.; Zukor, D. *Biomed. Mater. Eng.* **1993**, *3*, 211–221.
108. Inoue, N.; Bessho, M.; Furuta, M.; Kojima, T.; Okuda, S.; Hara, M. *J. Biomater. Sci. Polym. Ed.* **2006**, *17*, 837–858.
109. Liu, B. C.; Harrell, R.; Davis, R. H.; Dresden, M. H.; Spira, M. *J. Biomed. Mater. Res.* **1989**, *23*, 833–844.
110. Noah, E. M.; Chen, J.; Jiao, X.; Heschel, I.; Pallua, N. *Biomaterials* **2002**, *23*, 2855–2861.
111. Shangina, O. R.; Nigmatullin, R. T. *Morfologiia* **2006**, *129*(3), 44–47.
112. Grimes, M.; Pembroke, J. T.; McGloughlin, T. *Biomed. Mater. Eng.* **2005**, *15*, 65–71.
113. Keller, P. F.; Verin, V.; Ziegler, T.; Mermillod, B.; Popowski, Y.; Delafontaine, P. *J. Investig. Med.* **2001**, *49*, 258–264.
114. Kinsner, A.; Lesiak-Cyganowska, E.; Sladowski, D. *Cell Tissue Bank.* **2001**, *2*, 165–171.
115. Lin, X.; Tang, M.; Zhang, X. *Sheng Wu Yi Xue Gong Cheng Xue Za Zhi (J. Biomed. Eng.)* **2006**, *23*, 822–825.
116. IAEA. *Manual on Radiation Sterilization of Medical and Biological Materials*; IAEA: Vienna, 1973.
117. IAEA, *Manual on Radiation Sterilization of Medical and Biological Materials*. Technical Report Series 149 International Atomic Energy Agency: Vienna, 1973; p 327.
118. Vangsness, C. T.; Garcia, I. A.; Mills, C. R.; Kainer, M. A.; Roberts, M. R.; Moore, T. M. *Am. J. Sports Med.* **2003**, *31*, 474–481.
119. Chakrabarty, K. H.; Dawson, R. A.; Harris, P.; *et al. Br. J. Dermatol.* **1999**, *141*(5), 811–823.
120. Huang, Q.; Dawson, R. A.; Pegg, D. E.; Kearney, J. N.; Macneil, S. *Wound Repair Regen.* **2004**, *12*(3), 276–287.
121. Marshall, L.; Ghosh, M. M.; Boyce, S.; *et al. Burns* **1995**, *21*, 356–361.
122. van Baare, J.; Buitenwerf, J.; Hoekstra, M. J.; du Pont, J. S. *Burns* **1994**, *20*(Suppl. 1), S77–S80.
123. van Baare, J.; Cameron, P. U.; Vardaxis, N.; *et al. J. Burn Care Rehabil.* **1998**, *19*(6), 494–500.
124. Anderson, M. J.; Keyak, J. H.; Skinner, H. B. *J. Bone Joint Surg. Am.* **1992**, *74*(5), 747–752.
125. Cornu, O.; Banse, X.; Docquier, P. L.; Luyckx, S.; Delloye, C. *J. Orthop. Res.* **2000**, *18*(3), 426–431.
126. Currey, J. D.; Foreman, J.; Laketić, I.; Mitchell, J.; Pegg, D. E.; Reilly, G. C. *J. Orthop. Res.* **1997**, *15*(1), 111–117.
127. Hamer, A. J.; Strachan, J. R.; Black, M. M.; Ibbotson, C. J.; Stockley, I.; Elson, R. A. *J. Bone Joint Surg. Br.* **1996**, *78*(3), 363–368.
128. Nguyen, H.; Morgan, D. A.; Forwood, M. R. *Cell Tissue Bank.* **2007**, *8*(2), 93–105.
129. Akkus, O.; Belaney, R. M. *J. Orthop. Res.* **2005**, *23*, 1054–1058.
130. Balsly, C. R.; Cotter, A. T.; Williams, L. A.; Gaskins, B. D.; Moore, M. A.; Wolfinbarger, L., Jr. *Cell Tissue Bank.* **2008**, *9*, 289–298.
131. Sun, K.; Tian, S.; Zhang, J.; Xia, C.; Zhang, C.; Yu, T. *Knee Surg. Sports Traumatol. Arthrosc.* **2009**, *17*(5), 464–474.
132. Zhang, Y.; Homsi, D.; Gates, K.; Oakes, K.; Sutherland, V.; Wolfinbarger, L., Jr. *Spine* **1994**, *19*(3), 304–308.
133. Godette, G. A.; Kopta, J. A.; Egle, D. M. *Orthopedics* **1996**, *19*(8), 649–653.
134. Buring, K.; Urist, M. R. *Clin. Orthop. Relat. Res.* **1967**, *55*, 225–234.
135. Ijiri, S.; Yamamuro, T.; Nakamura, T.; Kotani, S.; Notoya, K. *J. Orthop. Res.* **1994**, *12*(5), 628–636.
136. Burstein, A. H.; Zika, J. M.; Heiple, K. G.; Klein, L. *J. Bone Joint Surg.* **1975**, *57A*, 956–961.
137. Wang, X.; Bank, R. A.; TeKoppele, J. M.; Agrawal, C. M. *J. Orthop. Res.* **2001**, *19*, 1021–1026.
138. Salehpour, A.; Butler, D. L.; Proch, F. S.; *et al. J. Orthop. Res.* **1995**, *13*(6), 898–906.
139. Colwell, A.; Hamer, A.; Blumsohn, A.; Eastell, R. *Eur. J. Clin. Invest.* **1996**, *26*, 1107–1114.
140. Akkus, O.; Belaney, R. M.; Das, P. *J. Orthop. Res.* **2005**, *23*, 838–845.
141. Glowacki, J. *Cell Tissue Bank.* **2005**, *6*, 3–12.
142. Hallfeldt, K. K.; Stützle, H.; Puhlmann, M.; Kessler, S.; Schweiberer, L. *J. Surg. Res.* **1995**, *59*(5), 614–620.
143. Wientroub, S.; Reddi, A. H. *Calcif. Tissue Int.* **1988**, *42*(4), 255–260.
144. Grieb, T. A.; Forng, R. Y.; Stafford, R. E.; *et al. Biomaterials* **2005**, *26*(14), 2033–2042.
145. Grieb, T. A.; Forng, R. Y.; Bogdansky, S.; *et al. J. Orthop. Res.* **2006**, *24*(5), 1011–1018.
146. Urist, M. R. *Science* **1965**, *150*, 893–899.
147. Boden, S. D. *Spine* **2002**, *27*(16S), S26–S31.
148. Glowacki, J.; Kaban, L. B.; Murray, J. E.; Folkman, J.; Mulliken, J. B. *Lancet* **1981**, *1*(8227), 959–962.
149. Iwata, H.; Sakano, S.; Itoh, T.; Bauer, T. W. *Clin. Orthop. Relat. Res.* **2002**, *395*, 99–109.
150. Qiu, Q. Q.; Mendenhall, H. V.; Garlick, D. S.; Connor, J. *J. Biomed. Mater. Res. B Appl. Biomater.* **2007**, *81*(2), 516–523.
151. Qiu, Q. Q.; Shih, M. S.; Stock, K.; *et al. J. Biomed. Mater. Res. B Appl. Biomater.* **2007**, *82*(1), 239–245.
152. Russell, J. L.; Block, J. E. *Orthopedics* **1999**, *22*(5), 524–531.
153. Sohn, D. S.; Bae, M. S.; Choi, B. J.; An, K. M.; Shin, H. I. *Oral Surg. Oral Med. Oral Pathol. Oral Radiol. Endod.* **2009**, *108*(5), e30–e35.
154. Urist, M. R.; Iwata, H. *J. Theor. Biol.* **1973**, *38*, 155–167.
155. Zhang, Q.; Cornu, O.; Delloye, C. *Acta Orthop. Scand.* **1997**, *68*(2), 104–108.
156. Aspenberg, P.; Lindqvist, S. B. *Acta Orthop. Scand.* **1998**, *69*(2), 173–176.
157. Han, B.; Yang, Z.; Nimni, M. *J. Orthop. Res.* **2005**, *23*, 855–861.
158. Qiu, Q. Q.; Connor, J. *J. Biomed. Mater. Res. A* **2008**, *87*(2), 373–379.
159. Qiu, Q. Q.; Liu, X. H.; Connor, J. *J. Biomed. Mater. Res. B Appl. Biomater.* **2009**, *91*(1), 401–408.

160. Qiu, Q. Q.; Connor, J. *J. Biomed. Mater. Res. A* **2008**, *87*(2), 373–379.
161. Urist, M. R.; Hernandez, A. *Arch. Surg.* **1974**, *109*, 486–493.
162. Dziedzic-Goclawska, A.; Ostrowski, K.; Stachowicz, W.; Michalik, J.; Grzesik, W. *Clin. Orthop. Relat. Res.* **1991**, *272*, 30–37.
163. Urist, M. R. *Clin. Orthop. Relat. Res.* **1968**, *56*, 37–50.
164. Carpenter, E. M.; Gendler, E.; Malinin, T. I.; Temple, H. T. *Am. J. Orthop.* **2006**, *35*(12), 562–567.
165. Vangsness, C. T., Jr.; Wagner, P. P.; Moore, T. M.; Roberts, M. R. *Arthroscopy* **2006**, *22*(12), 1351–1358.
166. Hayzlett, M.; Griffey, S.; Greenleaf, G. In *Sterilization of Tissues Using Ionizing Radiations*; Kennedy, J. F., Phillips, G. O., Willians, P. A., Eds.; Woodhead Publishing: Cambridge, England, 2005.
167. Gouk, S. S.; Lim, T. M.; Teoh, S. H.; Sun, W. Q. *J. Biomed. Mater. Res. B Appl. Biomater.* **2008**, *84B*, 205–217.
168. Gouk, S. S.; Kocherginsky, N. M.; Kosteski, Y. Y.; *et al. Radiat. Res.* **2005**, *163*, 535–543.
169. Sun, W. Q.; Leung, P. *Acta Biomater.* **2008**, *4*, 817–826.
170. Danielsen, C. C. *Biochem. J.* **1990**, *272*, 697–701.
171. Danielsen, C. C. *Connect. Tissue Res.* **1998**, *38*, 295–307.
172. IAEA, In *Guidelines for Industrial Radiation Sterilization of Disposable Medical Products* (Co-60 γ-Irradiation); IAEA: Vienna, Austria, 1990; pp 12–24.

Relevant Websites

www.wikipedia.org – Wikipedia.
http://www.emdt.co.uk/article/x-ray-sterilisation-technology-future – European Medical Device Technology.

4.411. Peptide- and Protein-Modified Surfaces

N O Enemchukwu and A J García, Georgia Institute of Technology, Atlanta, GA, USA

© 2011 Elsevier Ltd. All rights reserved.

4.411.1.	**Introduction**	146
4.411.2.	**Peptides Versus Proteins**	146
4.411.3.	**Immobilization Strategies**	147
4.411.3.1.	Adsorption	148
4.411.3.2.	Covalent Tethering	149
4.411.3.3.	Affinity or Capture Immobilization	149
4.411.4.	**Functional Parameters**	150
4.411.4.1.	Surface Density	150
4.411.4.2.	Spatial Arrangement	151
4.411.4.3.	Dynamic or Temporal Presentation	152
4.411.4.4.	Biological Activity: Conformation and Orientation	152
4.411.5.	**Sample Applications**	153
4.411.5.1.	Orthopedic Applications	153
4.411.5.2.	Cardiovascular Applications	154
4.411.5.3.	Neural Applications	155
4.411.6.	**Conclusions and Outlook**	156
References		156

Glossary

Cell recognition motifs Short amino acid sequences that are specific recognition sites for cell-surface receptors.

Chemical (surface) conjugation Formation of covalent bonds between functional groups on a surface and reactive groups on a biomolecule.

Differentiation The process in which a less specialized cell becomes more specialized (e.g., bone-marrow-derived stem cell gives rise to red blood cell).

Endothelium A thin layer of flat epithelial cells that lines the heart, serous cavities, lymph vessels, and blood vessels and actively prevents spontaneous blood clotting.

Extracellular matrix (ECM) A gel of polysaccharides and fibrillar proteins, with growth factors, that provides mechanical support as well as chemical signaling for epithelial tissues.

Integrin Member of a family of dimeric transmembrane cell-surface receptors that bind specific amino acid sequences in extracellular proteins and participate in cellular signaling programs.

Moiety A specific segment of a molecule.

Oligo- (prefix) Few; a small number of (e.g., oligopeptide, a molecule composed of ~3–20 amino acids).

Osseointegration The growth action of bone tissue as it assimilates surgically implanted devices or prostheses, as measured by bone–implant surface contact and mechanical fixation.

Amino Acid Abbreviations

A	Alanine
C	Cysteine
D	Aspartic acid
E	Glutamic acid
F	Phenylalanine
G	Glycine
H	Histidine
I	Isoleucine
K	Lysine
L	Leucine
M	Methionine
N	Asparagine
O	Hydroxyproline
P	Proline
Q	Glutamine
R	Arginine
S	Serine
T	Threonine
V	Valine
W	Tryptophan
Y	Tyrosine

Abbreviations

3D	Three-dimensional
AFM	Atomic force microscopy
ATRP	Atom transfer radical polymerization
ePTFE	Expanded PTFE
EC	Endothelial cell
ECGF	Endothelial cell growth factor
ECM	Extracellular matrix
ELISA	Enzyme-linked immunosorbent assay
EPC	Endothelial progenitor cell
FEP	Fluorinated ethylene propylene
FN	Fibronectin
$FNIII_{10}$	Fibronectin tenth type III repeat
$FNIII_{7\text{-}10}$	Fibronectin 7th – 10th type III repeats
FNIIICS	Fibronectin type III connecting segment
IPNs	Interpenetrating polymer networks
LCST	Lower critical solution temperature
LM	Laminin
NGC	Nerve guidance channel
NGF	Nerve growth factor
OEG	Oligo(ethylene glycol)
pNIPAM	Poly(*N*-isopropylacrylamide)
poly(OEGMA)	Poly(oligo[ethylene glycol] methacrylate)
PDMS	Polydimethylsiloxane
PEG	Poly(ethylene glycol)
PET	Poly(ethylene terephthalate)
PLA	Poly(lactic acid)
PNS	Peripheral nervous system
PTFE	Poly(tetrafluoroethylene)
QCM	Quartz crystal microbalance
RGD	Arginine-glycine-aspartic acid
S/V	Surface area-to-volume ratio
SAMs	Self-assembled monolayers
SPR	Surface plasmon resonance
ToF-SIMS	Time-of-flight secondary ion mass spectroscopy
UV	Ultraviolet
VEGF	Vascular endothelial growth factor

4.411.1. Introduction

Proteins and peptides have a myriad of natural functions useful in biotechnology. These functions include cell adhesion ligands, signaling molecules, anticoagulants, high-affinity effectors (e.g., antibodies), and catalysts. Immobilization of proteins and peptides onto surfaces enables powerful devices and analysis platforms including cell culture substrates, bioactive coatings for tissue engineering scaffolds, antithrombogenic surfaces, enzymatic bioreactors, biosensors, diagnostic assays (e.g., enzyme-linked immunosorbent assay, ELISA), and drug delivery devices (Table 1).

Surface-bound biopolymers of diverse biochemistries usually mediate interactions between cells and biomaterials, whether or not the surface modification is intended (Figure 1) (Chapter 4.416, Growth Factors and Protein-Modified Surfaces and Interfaces). Many surface-adsorbed proteins and peptides can interact with cells in many ways, but only a few of the 20 000 known proteins of the human proteome have specific motifs for cell adhesion receptors. These surface-associated proteins may provide anchoring points for specific recognition by cell-surface receptors. Subsequent cell adhesive events trigger signaling programs that regulate cell fate processes including spreading, migration, proliferation, and differentiation.[1,2] In addition, surface-bound enzymes may catalyze local and systemic immune responses *in vivo* (i.e., complement activation, coagulation cascade activation).[3] Consequently, control of cell–material interactions via manipulation of proteins and peptides at interfaces is a critical aim of much work in the field of biomaterials.[4–6]

This chapter discusses various cell-binding proteins and active peptides that might be immobilized on biomaterials and surveys immobilization methodologies available for doing so. We detail several functional parameters (e.g., ligand surface density, spatial arrangement) that directly influence application outcomes. Given the expanse of literature involving engineered cell culture substrates and implantable biomaterials, the examples in this chapter focus on cell adhesion and subsequent cell and tissue behaviors modulated by peptide- and protein-modified surfaces.

Table 1 Functions and applications of immobilized peptides and proteins

Protein/peptide functions	*Immobilized protein/peptide applications*
Cell adhesion ligands	Cell culture substrates Bioactive implant surfaces
Signaling molecules/anticoagulants	Thromboresistant surfaces
High-affinity interactions	Affinity separations Targeted drug delivery Diagnostic assays Biosensors
Enzymatic catalysis	Bioseparations Biosensors Bioreactors Diagnostic assays

Source: Adapted from Hoffman, A. S.; Hubbell, J. A. In *Biomaterials Science*; Ratner, B. D., Hoffman, A. S., Schoen, F. J., Lemons, J. E., eds.; Elsevier Academic Press: San Diego, CA, 2004.

4.411.2. Peptides Versus Proteins

Since Pierschbacher and Ruoslahti showed that the cell attachment activity of fibronectin (FN) could be duplicated with small fragments containing the arginine-glycine-aspartate (RGD) tripeptide, there has been tremendous interest in immobilizing oligopeptides in place of full-length proteins as biomaterial surface modifiers.[7–9] The discovery of integrin family cell-surface receptors and their amino acid binding motifs raised the appeal of peptides for targeting specific receptors to control specific cell responses.[10] Other advantages of

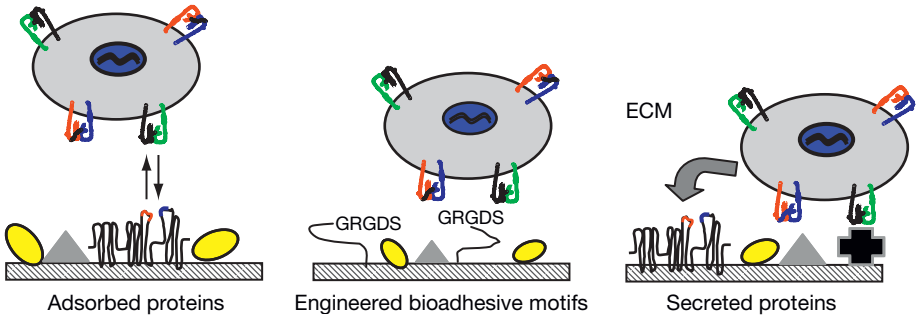

Figure 1 Mechanisms controlling cell adhesion to biomaterials.

Table 2 Design considerations: proteins versus peptides

	Protein	*Peptide*
Ease of immobilization	X	X
Cost		X
Degradability	X	
Nonimmunogenicity		X
Receptor specificity	X	X
Receptor affinity (activity)	X	
Achievable ligand density		X
Stability		X

oligopeptides over full-length proteins include low cost, easy synthesis, high levels (and control) of ligand availability, high achievable signal density, and cell-surface receptor selectivity (Table 2).

Nevertheless, there are some advantages of immobilizing full-length proteins onto biomaterial supports versus oligopeptides. First, the full protein might possibly be presented in its native conformation so as to facilitate native, high-affinity interactions with cell-surface receptors. Second, whereas oligopeptide-modified surfaces typically include only receptor-binding motifs, presentation of the protein exposes cells to the receptor-binding motif as well as other distinct complementary protein domains that modulate responses. Also, the fact that proteins can be simply, and to some extent stably, adsorbed from solution onto surfaces, in addition to covalent and affinity immobilization routes, allows great versatility in their use in surface modification strategies.

The use of full-length proteins on surfaces is, however, limited by difficulties in controlling the activity of the immobilized species with respect to orientation and conformational changes. Also, a protein might include several receptor-binding domains that allow interactions with various cell types or elicit a variety of responses from a given cell type. Similarly, immobilized proteins may provide a relatively low density of any particular binding domain, and thus do not allow enrichment of specific biological responses. Finally, proteins present particular processing challenges for *in vivo* applications. There are difficulties in securing and sterilizing purified natural sources of proteins. In addition, certain proteins have elevated immunogenicity versus a protein-derived oligopeptide.

Limitations associated with use of peptide-modified surfaces include decreased peptide bioactivity relative to native protein, the general requirement of covalent attachment chemistry to produce the bioactive surface, and the absence of domains for cellular modification of the adhesive environment. In spite of generally impressive *in vitro* results with RGD-modified surfaces, careful investigations of bioactivity involving soluble ligand have found peptide bioactivity significantly lower than that involving the native ligand.[8,9,11] These effects are due not only to the absence of protein secondary structures in most peptides but also to the absence of modulatory and complementary domains. As will be discussed in following sections, in the case of matrix protein, FN, robust cell integrin recognition and binding relies on synergistic contributions from disparate peptide domains.[12–14] Nevertheless, recombinant biosynthetic techniques have recently enabled use of protein fragments that present adhesive domains in a correct structural context.[15,16]

Ultimately, the choice of protein versus peptide will be driven by application considerations. For instance, to promote nerve regeneration across critical-sized gaps, full-length laminin (LM) protein has been immobilized within nerve guidance channels (NGCs).[17,18] However, as LM is a large protein with several cell receptor recognition sites, LM-coated scaffolds may facilitate attachment by several cell types *in vivo*, including those involved in scar formation (i.e., glial cells). Therefore, Massia and colleagues have immobilized the LM-derived IKVAV peptide to prepare surfaces that selectively promote neuronal cell attachment with minimal glial cell or fibroblast attachment *in vitro*.[19] Table 3 lists various proteins and peptides used to promote cell adhesion to biomaterial supports.

4.411.3. Immobilization Strategies

Strategies for immobilizing proteins and peptides at surfaces can be classified into three approaches: passive/physical adsorption, affinity/capture, and covalent tethering (Figure 2). These approaches can be further segregated in terms of the physical nature of association, longevity of association, and ease of use. Adsorption and capture are relatively easy but mostly rely on multiple weak and often nonspecific binding interactions (hydrophobic, van der Waals, and electrostatic), although some affinity pairings are quite strong. Covalent tethering involves potentially difficult chemical modifications to the substrate but achieves long-term immobilization. Available covalent tethering techniques offer superior control of molecular orientation.

Table 3 Proteins and peptides for facilitating cell adhesion and signaling on surfaces

Adhesion motif	*Origin*	*Receptor interactions (α/β designations refer to heterodimer receptor subtypes)*	*Functions and applications*	*References*
Fibronectin	Extracellular matrix, blood serum	αVβ3, α5β1, αIIbβ3	Extracellular matrix organization, wound healing	20–23
RGD	Fibronectin 10th type III repeat ($FNIII_{10}$), laminin α1 chain, collagen	αVβ3, α5β1, αIIbβ3, α3β1, αvβ1, α4β1	Cell adhesion, orthopedic implant integration	7–9,24–28
PHSRN	$FNIII_9$	α5β1, αIIbβ3	Cell adhesion to FN, synergy with RGD	13,15,29
REDV	Fibronectin type III connecting segment (FNIIICS)	α4β1	Vascular endothelial cell attachment	30
Type I collagen	Extracellular matrix	α1β1, α2β1	Wound healing, connective tissue, bone matrix	31
GFOGER	Type I collagen α1 chain	α2β1, α1β1	Osteoblast differentiation and orthopedic implant integration	32–35
Laminin-111	Extracellular matrix	α3β1, α6β1, α6β4	Neural cell attachment, neurite extension, epithelial cell polarization	31,36,37
YIGSR	Laminin β1 chain	α1β1, 67 kDa laminin receptor	Vascular endothelial cell attachment and migration, corneal epithelial cell attachment, nerve tissue regeneration	28,38–43
IKVAV	Laminin α1 chain	110 kDa laminin receptor	Selective neuron attachment, neurite outgrowth	19,28,44–46

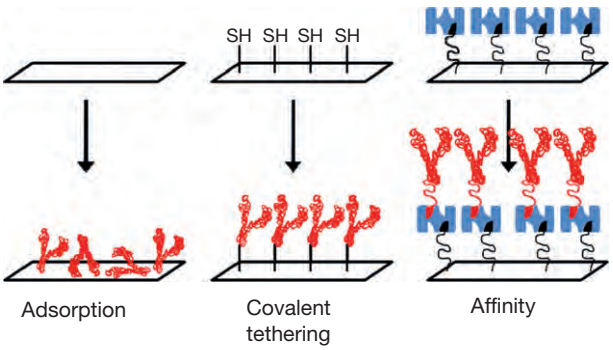

Figure 2 Mechanisms for immobilization of proteins and peptides at surfaces.

The longevity and conformational stability of adsorbed and captured polypeptides depend heavily upon the size and flexibility of the molecule (Table 4).

4.411.3.1. Adsorption

When biomaterials are placed in contact with biological fluids, proteins and other biomacromolecules dynamically adsorb onto the biomaterial surface. This observation has stimulated simultaneous efforts to understand protein adsorption and to exploit the phenomenon for bioactive surfaces. Efforts to intentionally adsorb protein on surfaces to elicit or prevent a biological response date back to the 1950s when purified collagen was adsorbed onto Petri dishes for maintenance and directed differentiation of cultured cells.[47,48] Protein adsorption involves many (i.e., electrostatic and hydrophobic) surface force interactions, and, in some cases, produces protein denaturation.[49–51] Multiple weak interactions between protein and surface produce a metastable or highly stable state of adsorption that is often irreversible under most conditions, even on surfactant rinsing. Although detailed physical relationships are not fully understood, critical surface characteristics modulating adsorption include chemistry, topography, and charge. In addition, the unique size and macromolecular structure of the adsorbent protein will influence the nature of the protein layer.[50,52]

From mixed protein solutions, like blood, plasma, and serum, the composition of an adsorbed protein layer varies over time in a sequence of adsorption, rearrangement, and desorption processes driven by the proteins' ionization states and molecular weights as well as the surface energy.[50,52] Relatively low-molecular-weight proteins that are high in concentration may be the first to adsorb to the surface but can be subsequently displaced by relatively high-molecular-weight proteins that are relatively low in concentration and slower diffusing.[53] Dynamic serum protein adsorption onto implanted biomaterials has been viewed through this paradigm known as the 'Vroman effect.'[4,50,52,54,55] The resulting serum protein layer may impart bioactivity by providing a scaffold for cell attachment. Alternatively, an adsorbed protein film may passivate the surface, rendering it minimally bioactive, as observed with albumin and other proteins that resist subsequent protein adsorption while having minimal cell adhesive properties, if any.[56,57]

In the context of cell adhesion, the earliest studies involved surfaces with proteins adsorbed from pure protein solutions.[58] Substrates coated with collagen, FN, or LM have been employed for fundamental studies of cell adhesion, proliferation, migration, and differentiation for decades.[36,48,58–64] Out of this work has come the discovery of focal adhesions and integrin receptors.[21,22,65] Furthermore, adsorption remains the most straightforward and widely used technique for placing full-length proteins onto surfaces as substrates for studying

Table 4 Protein and peptide immobilization methods

	Adsorption	*Affinity/capture*	*Covalent binding*
Ease	High	Moderate to low	Low
Loading level possible	Low (depends on S/V)	High	Depends on S/V and site density
Leakage/loss	Relatively high	Low to none	Low to none
Cost	Low	Moderate	High

Source: Adapted from Hoffman, A. S.; Hubbell, J. A. In *Biomaterials Science*; Ratner, B. D.; Hoffman, A. S.; Schoen, F. J.; Lemons, J. E., eds.; Elsevier Academic Press: San Diego, CA, 2004.
(S/V = surface area-to-volume ratio)

Table 5 Indirect surface functionalization approaches

Approach	*Substrate interaction*	*Examples*	*References*
Self-assembled monolayer	Chemisorption (–SH–Au) (Si–O)	Integrin-specific coatings	15,72
Polymer-brush/comb copolymer thin film	Physisorption or covalent bond	Nanoscale receptor clustering; titanium implant osseointegration	73–75
Covalent interpenetrating network	Covalent bond	Osteoblast attachment on titanium substrates	76–78

protein interactions, bacterial and mammalian cell adhesion, blood clotting, and tissue engineering methods.

4.411.3.2. Covalent Tethering

Whereas adsorbed proteins are bound to surfaces by multiple but relatively weak and nonspecific interactions, covalent immobilization techniques chemically bond biomolecules to surfaces through specific functional groups. Thus, even small oligopeptides that do not stably adsorb on surfaces can be immobilized permanently to surfaces, sometimes at high density, and, infrequently, in specific orientations. As peptides and proteins share identical amino acid chemistry with the same functional groups, a broad suite of reaction routes are available for covalent tethering of proteins and peptides to diverse biomaterial surfaces (particularly polymers).[7,66,67] Covalent attachment techniques generally require appropriately matched reactive functional groups on both the protein or peptide, and the surface of the biomaterial. These include hydroxyl (–OH), amino ($-NH_2$), carboxyl (–COOH), thiol (–SH), and vinyl ($-CH{=}CH_2$) groups. The polypeptide itself typically has amine, carboxyl, and perhaps thiol or hydroxyl functionalities as part of the canonical amino acid composition. To place reactive groups on inert polymer and metal surfaces that lack them, several chemical modification methods are available.[7,68–71]

Enhanced control of surface density, spacing, and orientation of the immobilized protein or peptides can be achieved using indirect surface functionalization approaches (**Table 5**). For instance, chemisorbed end-functional self-assembled monolayers (SAMs) (e.g., alkanethiols on gold, triethylsiloxanes on metals or ceramics) or physisorbed end-functional polymer-brush thin films may control immobilized surface density through the design of the component molecule or polymer structure.[72–74,79–87] Alternatively, surface-initiated polymer graft preparations and covalently immobilized interpenetrating polymer networks (IPNs) may be used.[76–78]

Further optimization can be achieved using recombinant proteins that limit the number of reactive groups available for linkage to a surface. For instance, limitation of the number of peptide or protein cysteine groups may limit available orientations when immobilized via gold thiolate[88–90] or disulfide bond formation.[91]

4.411.3.3. Affinity or Capture Immobilization

Highly specific molecular recognition between naturally occurring binding pairs is exploited in an alternative strategy for oriented attachment of proteins and peptides on surfaces using affinity recognition adapted from chromatography separations.[92,93] Several distinct affinity methods have been used in many different iterations for decades: the protein A- or protein G-IgG,[94] glutathione-*S*-transferase,[95] and biotin–streptavidin are notable examples.[96–98] A very recent affinity immobilization method involves use of the enzymatic action of HaloTag™ against chloroalkane substrates and use in fusion protein immobilization.[99–101]

The biotin–avidin interaction, the strongest known noncovalent bond (unbinding forces up to 250 pN), has been used extensively to pair various biomolecules and surfaces for applications from chromatography to biosensing.[79,97,98,102–105] Recombinant forms of the protein avidin, including nonglycosylated types with limited nonspecific adsorption, and the bacterial form, streptavidin, are exploited for this use.

There are many variations on the following approach: (1) a (strept)avidin molecule is immobilized on the biomaterial surface by adsorption, (2) the protein or peptide of interest is covalently tagged with a biotin molecule, and (3) the surface is incubated in the solution of biotinylated molecules. Each avidin molecule binds up to four biotin molecules independently with high affinity ($K_d \sim 10^{-15}\,M^{-1}$).[106] This multifunctionality makes avidin–biotin an attractive linking cassette. For instance, molecular adlayers of biotin-derivatized poly(ethylene glycol) (PEG) have provided a useful platform for specific binding of avidin or streptavidin, and subsequent immobilization of biotinylated proteins and peptides. Hydrophilic PEG serves as a flexible linker to present biotin on the surface. Patel *et al.* used adsorbed poly(lactic acid) (PLA)–PEG–biotin on a polystyrene substrate as a base for patterning avidin molecules. Subsequent

incubation of the patterned substrates in a solution of biotinylated RGD- or IKVAV-containing peptides resulted in surfaces that achieved spatially controlled growth of endothelial cells (ECs) or neurons.[44]

Another capture technique is illustrated by degradable hydrogels that covalently incorporate peptide motifs with intrinsic affinity to bind growth factors or other active proteins. A portion of the active protein molecules will be sequestered to the hydrogel surface whereas the internally localized protein may be released as the scaffold is degraded by cell-secreted enzymes. This approach has been illustrated in covalent cross-linking of a factor XIIIa-containing peptide into a fibrin matrix using factor XIIIa transglutaminase cross-linking. The heparin-binding peptide subsequently immobilized heparin in the matrix. The immobilized heparin then interacted with a growth factor to slow its release from the matrix (**Chapter 4.420, Drug Delivery via Heparin Conjugates** and **Chapter 4.427, Cell-Demanded Release of Growth Factors**).[107,108]

4.411.4. Functional Parameters

There are several design considerations involved in rationally designing protein- and peptide-modified surfaces for the purpose of modulating cell–material interactions. Thus, a set of functional parameters by which ligand-presenting surfaces can be evaluated, and cell or tissue interactions, interpreted, is described. These include surface density, spatial arrangement, temporal presentation, and biological activity (i.e., biomolecular orientation and conformation) (**Figure 3**). **Table 6** summarizes the primary effects of these functional parameters on biological responses and major approaches to characterization of these parameters. The biological effects of these parameters are discussed in the context of cell–material adhesion events because of the critical significance of these interactions in biotechnology. However, similar considerations apply to other applications (e.g., biosensing, separations, etc.).

4.411.4.1. Surface Density

The density of tethered peptides or proteins on a surface is a major determinant of biological responses, including cell adhesion and differentiation as well as *in vivo* responses.[16,78,109–111]

In immobilizing proteins or peptides by adsorption or by tethering to functional surfaces, control of surface density is primarily achieved by varying the concentration of protein or peptide in the source solution.[110] In covalent tethering strategies that involve functional interlayers like SAMs, brush polymers, or graft polymers, the variable ratio of functional to nonfunctional end groups allows an extra level of control over the final surface density of immobilized species.

The peculiar relationship between adhesive ligand density and cell migration speed is well documented with RGD-modified surfaces. At low ligand density, cell migration is slow.

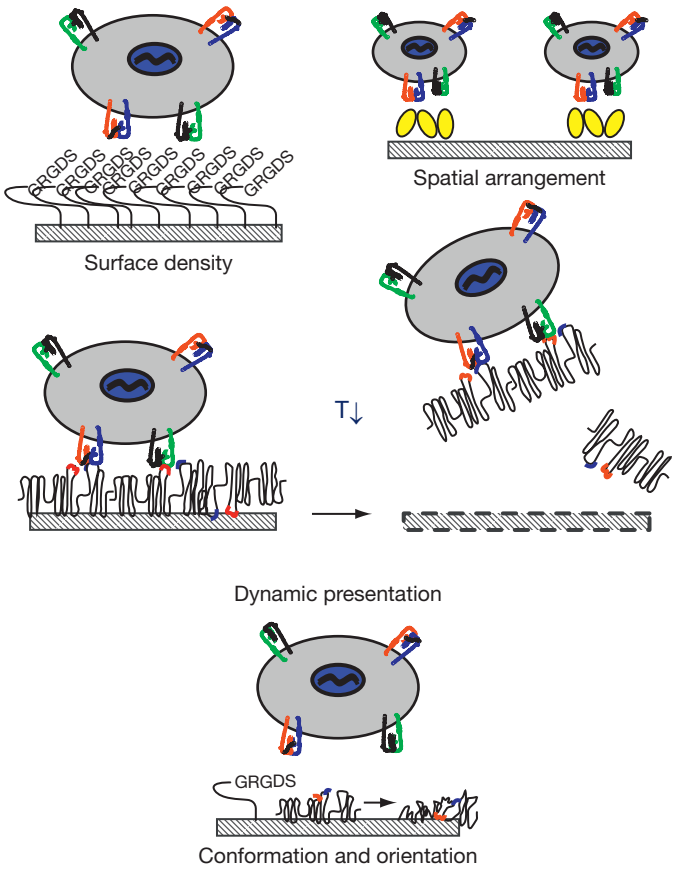

Figure 3 Functional parameters for protein- and peptide-modified surfaces.

Table 6 Design, characterization, and control strategies for protein- and peptide-modified surfaces

Functional parameter	*Primary cell/tissue effects*	*Characterization*	*Control strategy*
Surface density	Adhesion strength Migration efficiency	Radiometry Fluorometry SPR QCM	Solution concentration Surface functionalization Multivalency
Spatial arrangement	Cell–cell contact Cell-shape constraint Receptor clustering	Fluorometry	Lithographic techniques Multivalency
Dynamic presentation	Differentiation Cell-type selectivity	Radiometry Fluorometry SPR QCM	Engineered ligands Tailored degradability
Biological activity (biomolecular orientation and conformation)	Receptor affinity	ELISA ToF-SIMs	Surface chemistry Engineered ligands

With increasing ligand density, cell migration speed increases until a saturation level after which cell migration speed decreases with increasing ligand density.[112] The biphasic behavior illustrates the delicate balance between receptor–ligand attachment and detachment processes in cell migration. Furthermore, this example illustrates the importance of tuning the surface density of immobilized ligands to elicit specific cellular responses.

Techniques for quantifying the surface density of immobilized ligands can be classified in two groups: direct labeling and surface spectroscopy. Radiometry is a direct approach that involves tagging a native protein with a radioactive isotope (e.g., ^{3}H, ^{32}P, ^{35}S, ^{14}C, ^{125}I, or ^{131}I) that does not alter the structure or bioactivity of the protein. After immobilization, the surface radioactivity is compared to a standard solution to yield surface density values with at least 0.01 ng cm^{-2} sensitivity.[110,113,114] An analogous approach using fluorescent tags has increased in popularity.[115–118] In spite of unprecedented analytical sensitivity and adaptability across different biomaterial configurations, the primary drawbacks of radiometry are the safety hazards and regulatory burdens of radioactive materials. Also, it is not clear whether the radioactive labels alter interaction between the protein and the surface. Fluorescence-associated techniques are safe and accessible but limited by fluorophore-surface quenching phenomena and instability that complicate relationships between fluorescence intensity and absolute surface density. Furthermore, fluorescent techniques have lower sensitivity than radiolabeling. Surface plasmon resonance (SPR) spectroscopy and quartz crystal microbalance (QCM) exploit optoelectronic surface phenomena to detect biomolecule deposition and interaction in real time.[119–123] In spite of precise surface density measurements (0.1 ng cm^{-2} sensitivity),[124] the SPR technique is limited to planar metal substrates. QCM offers 1 ng cm^{-2} sensitivity[122] but requires coatings onto the QCM crystal surface and some consideration of solid–fluid phase viscoelastic coupling in analyzing the QCM signal.[125,126]

4.411.4.2. Spatial Arrangement

In living systems, the nano- and microscale organization of adhesive molecules serves to dictate the function of single cells and the cooperation of multicellular assemblies. Specifically, the nanoscale spacing of adhesive motifs is a critical determinant of receptor specificity and signaling amplification[26,75,127–134] while microscale patterns of extracellular matrix (ECM) components serve to maintain tissue architecture.[135] Thus, the spatial arrangements of proteins and peptides on biomaterial surfaces are expected to influence their functions *in vitro* and *in vivo*.

Homo- and heterotypic cell–cell contact is a hallmark of mammalian tissues at all stages of development and has major implications for barrier integrity, signaling, and maintenance. Broadly, the composition of ECM dictates the localization of cell types (e.g., epithelium vs. stroma) over micron length scales. One approach for investigating cell–cell contact-associated signaling *in vitro* involves immobilizing cells on discrete regions of adhesive ECM molecules. Thus, soft lithographic techniques have been used extensively to demonstrate micrometer- and nanometer-scale spatial control of protein adsorption on biomaterial surfaces for detailed studies of constrained single- and multicell behaviors, including visualization of individual focal adhesions.[109,136–142]

The general strategy, termed 'soft lithography,' involves a lithographically patterned relief on which an elastomeric (typically polydimethylsiloxane (PDMS)) precursor is cured, transferring the pattern to the elastomer. This 'stamp' may then be 'inked' in a solution of the protein to be patterned and pressed onto the surface of interest. The proteins are transferred, arraying the adsorbed protein with high fidelity (down to 100 nm features). Coyer *et al.*[138] recently demonstrated a subtractive approach that uses stable features on a silicon template to remove protein from a featureless PDMS stamp, leaving sub-100 nm patterns of protein for transfer onto surfaces. These strategies have been extended to patterning of SAMs, allowing an additional level of control over surface characteristics (e.g., tethering functionality). Furthermore, backfilling with protein-adsorption-resistant molecules (e.g., PEG or oligo(ethylene glycol) (OEG)-terminated alkanethiols) results in robust interfaces for *in vitro* studies. Another application to control the spatial arrangement of peptides or proteins at surfaces is to generate gradients of cell adhesive ligands.[143–146]

Nanoscale clustering of cell-surface receptors is a step in cell adhesion that is critical for adhesion-related intracellular signaling and subsequent cell behaviors.[129,133,134] In some cases, a single growth factor molecule may bind multiple tyrosine

kinase receptors. The induced dimerization of the receptors results in cross-phosphorylation at the cytoplasmic regions of the receptors and initiation of intracellular signaling cascades.[147] Thus, nanoscale ordering of adhesive ligand presentation on biomaterial surfaces may enhance a variety of biological responses. To this end, there has been extensive investigation of the nanoscale geometric arrangements that enrich specific cellular functions. Massia and Hubbell[132] controlled the surface density of RGD peptides on functionalized glass to determine that 440 nm lateral spacing is sufficient to promote fibroblast spreading, whereas 140 nm spacing is required for development of focal contacts and stress fibers. Griffith and colleagues used a polymer linker to independently control surface density and local clustering (50 nm resolution) of five- or nine-headed RGD ligands. Their results indicated that clustering reduced the surface density of ligand required for NR6 fibroblast cell migration. Petrie *et al.*[75] have recently employed multivalent ligands to enhance implant osseointegration, as discussed later.

4.411.4.3. Dynamic or Temporal Presentation

The native ECM dynamically organizes multiple cell types to coordinate tissue development and repair processes through temporally controlled presentation of cell adhesion molecules. The complex of adhesion ligands available at the interface is regulated in time by cell-mediated remodeling (e.g., enzymatic cross-linking and degradation, further matrix deposition) and environmental cues (e.g., temperature, pH).[148] Thus, for biotechnological applications to mimic ECM, it is useful to design protein- and peptide-modified surfaces responsive to cellular and environmental stimuli over time.

'Smart surfaces' for biomedical applications have been designed to modulate the availability or bioactivity of immobilized ligands in response to stimuli including temperature, pH, electric fields, and light[149–151] (**Table 7**). For instance, surfaces grafted with poly (*N*-isopropylacrylamide) (pNIPAM) have been used extensively as thermosensitive cell culture surfaces for control of cell and cell sheet adhesion.[152–154] pNIPAM is a member of a class of polymers that exhibit a lower critical solution temperature (LCST). Above the LCST, these polymers become less solvated and assume a collapsed conformation that promotes adsorption of cell adhesion proteins. Below the LCST, the polymer is hydrated and, like PEG, becomes resistant to protein adsorption. The LCST for pNIPAM is 32 °C and the transition between collapsed and solvated states is fully reversible.[155,156] Thus, cell culture substrates coated with pNIPAM can support serum protein adsorption, cell adhesion, and spreading at 37 °C. Decreasing the temperature below 32 °C causes the pNIPAM transition to the solvated state, triggers desorption of adhesion proteins, and initiates release of adherent cells or sheets of cells.[153,154] Interestingly, the conformational change in pNIPAM is sufficient to alter the affinity of integrins for immobilized RGDS.[157] By adding chemical substituents to modulate LCST and by patterning copolymers, Okano and colleagues have optimized the system for 'cell sheet engineering' with applications including corneal transplants and myocardial patches.[158–162]

Alternatively, photosensitive molecules can be used to modulate the bioactivity of covalently immobilized proteins and peptides. For instance, adding a bulky, photolabile chemical moiety to an oligopeptide cell adhesion motif can prevent its recognition by integrin receptors. In response to ultraviolet (UV) light, the obstructive chemical group can be removed to restore integrin recognition. This approach is facilitated by 'caged' reagents.[163] Various caged RGD molecules have been designed and immobilized to enable photo-triggered cell adhesion.[164–166]

Table 7 Stimuli employed in switchable protein- and peptide-modified surfaces

Energy based	*Chemical based*
Light	pH
Temperature	Ionic strength
Electric field	Solvents
Magnetic field	Metal ions
Ultrasonic radiation	Bio/chemical analytes

Source: Cole, M. A.; Voelcker, N. H.; *et al*. *Biomaterials* **2009**, *30*(9), 1827–1850.

4.411.4.4. Biological Activity: Conformation and Orientation

The three-dimensional (3D) structure of a protein, and even an oligopeptide, is directly linked to its biological activity. In the native ECM, component proteins like FN bind to several other ECM proteins and might adopt several conformational states. Conformational changes in a protein may alter cell and tissue responses by exposing or burying different cell adhesion motifs, exposing cryptic receptor recognition sites, or, in the case of enzymes, disrupting active sites. Meanwhile, the rotational state or orientation of a protein, particularly at an interface, might determine its bioactivity by modulating the accessibility of recognition motifs or active sites. Thus, control of conformation and orientation of surface-immobilized proteins and peptides is a major biomaterials design consideration.

Upon contact with a biomaterial surface, the fate of an interfacing globular protein is highly variable. After initial adsorption, the protein might (1) change orientation, (2) change conformation while retaining biological activity, or (3) conformationally denature and lose activity.[167–169] The dynamics of the protein–surface interaction depend heavily upon surface energy, surface charge, and surface chemistry, as well as the structural characteristics of the protein. Like the affinity of a cell-surface receptor binding an adhesion motif, the affinity of antibody binding to a specific biomolecule antigen is sensitive to changes in the accessibility of the epitope. Thus, antibody-based techniques like ELISA can be used alongside cell culture assays to detect differences in bioactivity of immobilized species with high sensitivity.[170,171] For instance, Grinnell and Feld[172] initially observed substrate-dependent cell spreading and antibody binding on FN-coated substrates. Subsequent studies of adsorbed FN indicated that the extent of molecular unfolding varied across substrates.[173–178] Garcia *et al.* later showed that these substrate-driven conformational differences manifested in altered integrin receptor specificity and correlated to differences in proliferation and differentiation of cells cultured on FN-coated surfaces.[179,180]

Polypeptides immobilized via covalent coupling or high-affinity interactions may avoid conformational changes, especially when linkers or inert interlayers are employed. Control

of protein orientation requires reliable tethering via specifically located functional groups on the protein, and low surface interactions once tethered. As amino or carboxyl moieties may be located at various locations in a protein, coupling through these groups will likely result in a random set of molecular orientations. Even worse, the reactive functional group might be part of a receptor-binding motif or enzymatic active site that would be disrupted by tethering. Alternatively, 'orthogonal coupling chemistry' involves introduction of a less common functional handle at a specific site (e.g., a free cysteine via site-directed mutagenesis) or use of 'click' chemistry reactions to achieve uniform molecular orientation.[143,181,182] Site-specific functionalization, including biotinylation, has been employed to prepare protein microarrays and enzymatic biosensors.[105,183–187]

Many cell adhesion studies involving RGD-containing peptides serve to illustrate the importance of biomolecular design for controlling bioactivity at the interface. Just as RGD's cell adhesive activity was discovered, it was observed that the identities of the amino acids flanking the RGD tripeptide (i.e., primary structure) strongly affect its activity.[8,9] As a result, numerous combinations of amino acids have been substituted (e.g., CGRGDSY) in the flanking sequence to modulate activity or to facilitate immobilization (e.g., cysteine for thiol-mediated immobilization or tyrosine for radiolabeling).[7,188,189] In the context of the full-length FN protein that binds integrin α5β1, the secondary structure of the RGD motif is a (presumably stiff) loop joining two β sheets within the 10th type III domain ($FNIII_{10}$).[190,191] The isolated $FNIII_{10}$ domain, however, is highly flexible and, in this context, RGD targets integrin αVβ3.[192–194] On the hypothesis that the flexibility of the RGD motif controls its binding specificity and affinity, cyclic RGD peptides have been prepared to constrain RGD to a loop and thereby enhance cell attachment.[24,25,195–197] Cell adhesion to FN is a synergistic effect of binding to RGD (on $FNIII_{10}$) and a PHSRN motif located on the neighboring $FNIII_9$ domain. Surfaces presenting mixtures of RGD and PHSRN enhance cell adhesion versus RGD or PHSRN alone. However, surfaces that present a recombinant $FNIII_{7-10}$ fragment include RGD and PHSRN in a 3D orientation and spacing and allow binding of the pair by a single integrin receptor.[29,198] Such surfaces promote superior α5β1 integrin engagement and cell attachment versus an RGD–PHSRN oligopeptide in which the two motifs are linked by a polyglycine tether.[15]

As mentioned earlier, cell culture assays and antibody-based techniques (e.g., ELISA) provide measures of the bioactivity of immobilized peptides and proteins without specifically interrogating conformation or orientation. These details may be directly examined using surface analysis techniques including time-of-flight secondary ion mass spectroscopy (ToF-SIMS), atomic force microscopy (AFM), ellipsometry, and circular dichroism. These techniques are reviewed elsewhere.[199–201]

4.411.5. Sample Applications

4.411.5.1. Orthopedic Applications

The generally desired course of action in implant osseointegration and regeneration of bone tissue includes (1) recruitment of osteoprogenitors to injury/implant sites, (2) adhesion of osteoprogenitors to implant/scaffold surface, and (3) induction of osteoblast-specific cell behaviors including matrix formation and matrix mineralization.

In therapeutic interventions involving implanted materials, much of the above process is mediated by cell–material interactions modulated by immobilized biomolecules on surfaces. Initially, to promote cell adhesion onto orthopedic implants, work focused on the RGD adhesive peptide derived from many of the ECM proteins present during bone development (e.g., bone sialoprotein, osteopontin, thrombospondin, and FN). RGD-modified surfaces enhanced osteogenic cell adhesion, proliferation, and differentiation measured by increased alkaline phosphatase activity, osteocalcin expression, and matrix mineralization *in vitro*.[76,77,202–210] In addition, RGD immobilization on implant surfaces supports bone formation *in vivo*[202,211,212] although the functional significance of this effect to implant performance is debatable.

RGD immobilization on biomaterials remains a popular strategy for driving osteoprogenitor differentiation *in vitro* and implant osseointegration *in vivo*. However, for all of the positive results associated with RGD peptide-presenting surfaces, the approach is limited by three critical factors:[213]

1. Low bioactivity in short adhesive peptide versus complete protein.
2. Limited receptor specificity.
3. Absence of complementary ligands for robust differentiation.

Indeed, independent studies have demonstrated that presentation of RGD on implant surfaces does not enhance implant osseointegration.[16,214–217] Thus, a second generation of peptide- and protein-modified surfaces has emerged to promote integrin-specific cellular recognition to drive robust osteoprogenitor adhesion and differentiation to achieve rapid osseointegration (**Figure 4**). One featured approach is covalent tethering of mixtures of RGD and another peptide that either enhances binding of RGD-binding integrins or targets a non-RGD-binding integrin.[34,35,218,219] Examples include mixtures of RGD and the FN-derived PHSRN synergy site peptide tethered on nonfouling supports.[220,221] In native FN, RGD is located in the 9th type III structural repeat while PHSRN is located in the 10th type III repeat. Independently, each motif scarcely contributes to binding, but together, they synergistically bind to α5β1 for stable adhesion.[29,222] While the mixed surfaces promote integrin binding and cell attachment, their comparability to complete FN is unknown. Furthermore, the synergistic effects require precise spatial orientation that cannot be maintained with short, tethered peptides.[213] However, a recombinant FN fragment (7th to 10th type III repeats, $FNIII_{7-10}$) that presents RGD and PHSRN in the correct spatial orientation retained the synergistic binding effects when tethered to model surfaces via carbodiimide chemistry. Petrie and García conducted detailed characterization of ligand density and bioadhesivity of model surfaces featuring $FNIII_{7-10}$ tethered on a nonfouling SAM background. SPR analysis of ligand tethering and a centrifugation assay for cell adhesion indicated precise control of cell-surface adhesivity. The surfaces also promoted α5β1 integrin ligation while enhancing proliferation and focal adhesion formation versus RGD-presenting surfaces and those presenting an RGD–PHSRN peptide that spaced the

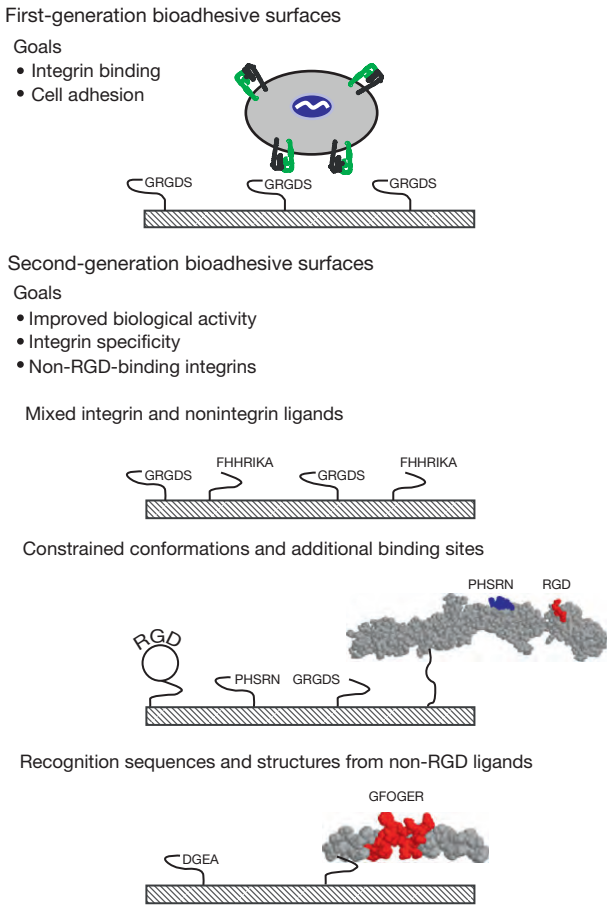

Figure 4 Biomolecular engineering strategies for bioadhesive surfaces. First-generation substrates concentrate on tethering RGD to direct integrin binding and cell adhesion. Second-generation strategies focus on enhancing biological activity, integrin specificity, and binding non-RGD integrins. Reproduced from Garcia, A. J.; Reyes, C. D. *J. Dent. Res.* **2005**, *84*(5), 407–413.

two motifs with a polyglycine linker.[15] Petrie and García demonstrated the benefits of α5β1 integrin-targeting surface treatments *in vivo* by covalently immobilizing $FNIII_{7-10}$ on poly(OEGMA) brushes grown from clinical grade titanium substrates via atom transfer radical polymerization (ATRP). In a rat tibial implant model, the poly(OEGMA)-$FNIII_{7-10}$ surface treatment improved osseointegration, as evidenced by a 70% increase in bone contact area versus clinical standard titanium (Figure 5). The integrin-targeting interface also enhanced mechanical fixation versus implants functionalized with RGD peptide.[16,75]

Protein adsorption remains the simplest approach to conveying bioactivity to a material surface. As simplicity is of great value to the clinical approach, Petrie and García have developed a clinically translatable, single-step passive adsorption strategy for immobilization of $FNIII_{7-10}$ on titanium implants that has enhanced osseointegration in a rat cortical bone defect. Notably, the adsorbed integrin-targeting $FNIII_{7-10}$ fragment enhanced osseointegration versus adsorbed full-length FN.[223]

Whereas little work has focused on biomolecular surface treatments to target non-RGD-binding receptors, García and colleagues have engineered biointerfaces to target α2β1 to promote signals essential for osteoblast differentiation.[34] Characterization of titanium substrates functionalized with a passively adsorbed triple-helical oligopeptide featuring the GFOGER adhesive motif indicated cell adhesion activity and osteoblast-specific gene expression resembling complete type I collagen.[35] Applied *in vivo* for a rat cortical bone–implant model, a facile, single-step application of GFOGER enhanced titanium implant osseointegration versus adsorbed full-length type I collagen.[35] Furthermore, GFOGER coatings passively adsorbed onto polymeric scaffolds, in the absence of exogenous cells or growth factors, significantly accelerated and increased bone formation in nonhealing rat femoral defects compared to uncoated scaffolds and empty defects.[224]

4.411.5.2. Cardiovascular Applications

In cardiovascular conditions where bypass procedures are required, autologous vascular grafts are often unavailable and synthetic substitutes have been developed. These biologically inert materials have proven suitable only as large-diameter blood vessels in specific physiological conditions (i.e., high flow, high shear). However, as small-diameter vascular grafts (diameter < 6 mm), synthetic materials suffer from low patency rates because of thrombotic occlusion. The primary strategy for avoiding thrombus formation is to mimic the anticoagulant characteristics of the lumen of native vasculature.[225] In a healthy blood vessel, a confluent EC layer covers the lumen, interfaces with flowing blood, and actively prevents thrombosis. Therefore, formation of a stable endothelium in small-diameter synthetic vascular grafts has emerged as a major goal in cardiovascular research.[225] Early *in vitro* endothelialization efforts pioneered by Herring revealed that common synthetic graft materials (expanded PTFE (ePTFE), poly(ethylene terephthalate) (PET), polyurethanes) do not promote EC adhesion sufficiently to retain a seeded cell layer under pulsatile flow conditions.[226,227] While certain animal vascular implant models do endothelialize, human implants generally fail.[228] As a result, attention turned to bioactive coatings to enhance EC adhesion to vascular implant materials. Early work involved passive adsorption of FN onto ePTFE grafts and indicated some improvement in EC retention versus untreated grafts.[229] Adsorbed bioactive coatings were found suboptimal compared to covalent immobilization of adhesive proteins and peptides. For instance, covalently immobilized RGD peptides enhanced EC retention versus adsorbed FN.[230] The RGD theme was used in various studies including strategies that incorporated the peptide into the structure of the graft polymer. RGD was paired with the antithrombogenic protein, heparin, toward an EC adhesive surface that will resist thrombosis even in partial endothelialization.[230] Unfortunately, the RGD motif is bound by cell-surface receptors found on various cell types in blood, including platelets. The effects of platelet activation on graft success are thought to be detrimental although they are not completely understood.[225] To target the α4 integrin that is absent from the

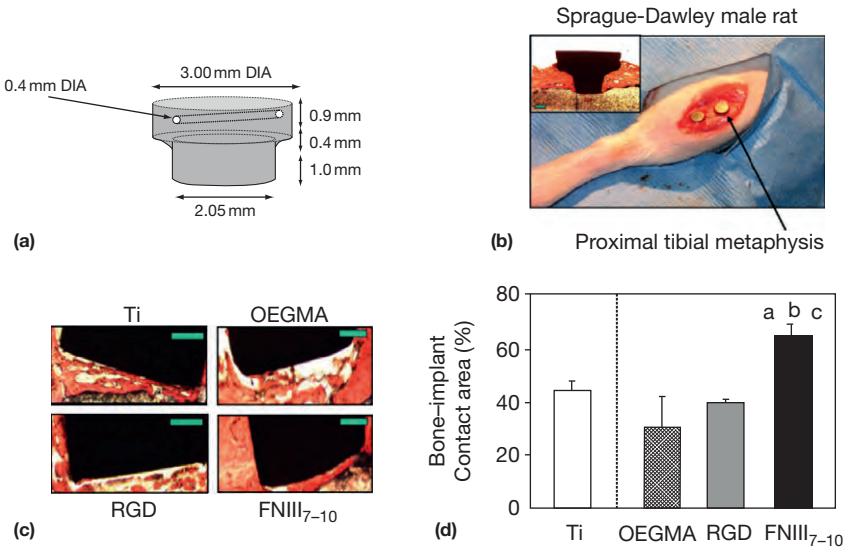

Figure 5 Integrin specificity modulates *in vivo* implant osseointegration. (a) Schematic of tapered titanium implant used in rat tibia implant model. (b) Photograph showing placement of implants in rat tibia. Two implants were placed in each tibia. Inset micrograph is of longitudinal section of entrenched implant after 4-week implantation, stained with Sanderson's rapid bone stain and van Gieson counterstain. (c) Histological sections at 4 weeks postimplantation showing bone (orange)–implant (black) contact (scale bar 0.5 mm). $FNIII_{7-10}$-tethered implant surfaces displayed greater bone tissue formation and connectivity compared to other surface treatments. (d) Bone–implant contact area: a versus RGD ($p < 0.02$); b versus Ti-serum ($p < 0.02$); c versus poly(OEGMA) ($p < 0.02$). Reproduced from Petrie, T. A.; Raynor, J. E.; *et al*. *Biomaterials* **2008**, *29*(19), 2849–2857.

surface of platelets, Massia and Hubbell[231] integrated an FN-derived REDV peptide. Similarly, recombinant FNIIICS-1 has been designed for integrin specificity. In moving to clinical application of *in vitro* endothelialized synthetic grafts, Zilla and colleagues coated ePTFE grafts with fibrin glue prior to seeding with autologously isolated ECs.[232] After culturing to confluence (6–11 days), grafts were anastomosed to vasculature above or below the knee and patients monitored for 7 years. The majority of fibrin-treated grafts remained patent after 7 years.[233] A wider study indicated similar results after 10 years.[234]

In situ endothelialization is an attractive alternative strategy for achieving antithrombogenic, small-diameter synthetic vascular grafts. In this ideal approach, circulating and bone-marrow resident endothelial progenitor cells (EPCs) are recruited to a cell-free synthetic implant where an endothelium forms *in vivo*.[225] Biomolecular surface treatments may be helpful in this approach. Growth factors including vascular endothelial growth factor (VEGF) and EC growth factor (ECGF) are involved in vascular development, induce EPC maturation into EC, and are potent EC mitogens.[235,236] Accordingly, immobilization of VEGF or ECGF in adhesive coating is a promising strategy for localized expansion of ECs at the luminal surface of a synthetic vascular graft. *In vitro* studies with ECGF showed enhanced EC proliferation.[237] *In vitro* experiments involving VEGF immobilization using enzyme-degradable linkers for cell-demanded release showed enhanced EC proliferation and EPC maturation into EC.[238] However, further characterization of growth-factor-associated strategies is required to prevent intimal hyperplasia that has been found in response to VEGF-releasing synthetic grafts *in vivo*.[239,240]

4.411.5.3. Neural Applications

In clinical interventions for peripheral nervous system (PNS) damage, the goal is axon regeneration such that proximal sprouting axons can bridge a defect gap to contact the distal stump.[241,242] The intervention must also prevent scar tissue invasion or other microenvironmental interference. Physical guidance of axons has been accepted as a requirement for nerve repair since the nineteenth century.[241,243] Today, NGCs are made from nondegradable synthetic materials (PTFE and silicone), biodegradable synthetic polymers (PLA, poly(caprolactone), polyurethane), and natural materials (e.g., ECM extracts, fibrin/fibrinogen, and agarose). The ideal NGC is a porous, biodegradable scaffold that can support cell adhesion and delivery of bioactive factors *in vivo*.[241] While the design of characterization of such biomaterials lies outside the scope of this chapter, we discuss the use of peptide- and protein-modified surfaces in development of NGCs.

Like cells in the bone and cardiovascular compartments, neural cell behavior is modulated by specific interactions with ECM proteins and growth factors. Early strategies to probe neural cell-ECM dynamics keyed on immobilization of ECM proteins, particularly LM, to enhance cell adhesion and neurite outgrowth. In the 1980s, LM was identified as an active promoter of neural cell attachment, differentiation, and neurite outgrowth *in vitro*.[244,245] Thus, it was immediately proposed as a bioactive coating to improve performance of NGCs. Later, Kleinman and colleagues identified two cellular recognition domains in LM that specifically bind cell-surface receptors expressed by neural cells. These peptides were YIGSR (from LM β1 chain, bound by a 67-kDa receptor) and IKVAV (from LM α1 chain, bound

by 110 kDa receptor).[246,247] Aebischer and colleagues covalently functionalized fluorinated ethylene propylene (FEP) films with YIGSR, IKVAV, and RGD (also found in LM) and characterized the surfaces with competitive cell attachment assays.[248,249] Using cell lines known to express the 67 or 110 kDa receptors, Raineri *et al.* demonstrated peptide-modified surfaces for receptor-specific neural cell attachment. Other groups employed bioactive surfaces to recreate neural architecture *in vitro* with chemically patterned substrates to control cell attachment and neurite outgrowth.[248,250,251] Toward development of neuron-selective adhesive coatings for NGCs, Hubbell and colleagues immobilized IKVAV peptides on cell adhesion resistant dextran coatings. Culture of PC12 (neuronal), fibroblast, and glial cells indicated that these substrates promoted substantial neuronal attachment with minimal fibroblast and glial cell adhesion.[19] Recently, Gomez and colleagues demonstrated the axon-lengthening effects of locally immobilized nerve growth factor (NGF).[252,253] Together, these *in vitro* studies have identified biomolecular targets for potential clinical applications for neural tissue engineering.[254,255]

4.411.6. Conclusions and Outlook

Interactions between cells and biomaterial surfaces are mediated by surface-immobilized proteins and peptides. Today, the initial state of the interface can be controlled with remarkable precision, owing to contributions from biochemistry, cell biology, synthetic chemistry, and materials science over the last five decades. Purification of the ECM proteins that direct myriad cell behaviors *in vivo* and identification of the peptide motifs involved in specific cell-surface receptor binding have spawned a variety of chemical techniques for immobilizing active, cell adhesion ligands on various biomaterials with precision. Furthermore, fundamental cell biology studies on model substrates have elucidated key functional parameters that may predict performance of host tissues, via cells, to implanted biomaterials. Recently, surfaces featuring rationally designed, integrin-targeting ligands presented with nanoscale spatial order have proven effective in the context of orthopedic implant integration.

Expanded use of orthogonal coupling chemistry for oriented immobilization of integrin-targeting ligands (e.g., 'click' chemistry) along with stimulus-responsive ligand presentation schemes should enable new applications for protein- and peptide-modified surfaces. Implanted dynamic surfaces may be able to withstand the initial assault of the host immune system and synchronize presentation of multiple ligands to the course of wound healing or differentiation programs.

Acknowledgments

AJG gratefully acknowledges support from the National Science Foundation, National Institutes of Health, and the Georgia Tech/Emory Center (GTEC) for the Engineering of Living Tissues and the Atlanta Clinical and Translational Science Institute (ACTSI). NOE is the recipient of a NASA-Harriett G. Jenkins Pre-Doctoral Fellowship and the Georgia Tech Facilitating Academic Careers in Engineering and Science (FACES) Fellowship.

References

1. Giancotti, F. G.; Ruoslahti, E. *Science* **1999**, *285*(5430), 1028–1032.
2. Howe, A.; Aplin, A. E.; Alahari, S. K.; Juliano, R. L. *Curr. Opin. Cell Biol.* **1998**, *10*(2), 220–231.
3. Gorbet, M. B.; Sefton, M. V. *Biomaterials* **2004**, *25*(26), 5681–5703.
4. Anderson, J. M.; Rodriguez, A.; Chang, D. T. *Semin. Immunol.* **2008**, *20*(2), 86–100.
5. Langer, R.; Tirrell, D. A. *Nature* **2004**, *428*(6982), 487–492.
6. Ratner, B. D.; Bryant, S. J. *Annu. Rev. Biomed. Eng.* **2004**, *6*(1), 41–75.
7. Hersel, U.; Dahmen, C.; Kessler, H. *Biomaterials* **2003**, *24*(24), 4385–4415.
8. Pierschbacher, M. D.; Ruoslahti, E. *Nature* **1984**, *309*(5963), 30–33.
9. Pierschbacher, M. D.; Ruoslahti, E. *Proc. Natl. Acad. Sci. USA* **1984**, *81*(19), 5985–5988.
10. Ruoslahti, E.; Pierschbacher, M. D. *Science* **1987**, *238*(4826), 491–497.
11. Hautanen, A.; Gailit, J.; Mann, D. M.; Ruoslahti, E. *J. Biol. Chem.* **1989**, *264*(3), 1437–1442.
12. Aota, S.; Nagai, T.; Yamada, K. M. *J. Biol. Chem.* **1991**, *266*(24), 15938–15943.
13. Aota, S.; Nomizu, M.; Yamada, K. M. *J. Biol. Chem.* **1994**, *269*(40), 24756–24761.
14. Garcia, A. J.; Schwarzbauer, J. E.; Boettiger, D. *Biochemistry* **2002**, *41*(29), 9063–9069.
15. Petrie, T. A.; Capadona, J. R.; Reyes, C. D.; Garcia, A. J. *Biomaterials* **2006**, *27*(31), 5459–5470.
16. Petrie, T. A.; Raynor, J. E.; Reyes, C. D.; Burns, K. L.; Collard, D. M.; Garcia, A. J. *Biomaterials* **2008**, *29*(19), 2849–2857.
17. Itoh, S.; Yamaguchi, I.; Suzuki, M.; *et al. Brain Res.* **2003**, *993*(1–2), 111–123.
18. Madison, R.; Dasilva, C. F.; Dikkes, P.; Chiu, T. H.; Sidman, R. L. *Exp. Neurol.* **1985**, *88*(3), 767–772.
19. Massia, S. P.; Holecko, M. M.; Ehteshami, G. R. *J. Biomed. Mater. Res. A* **2004**, *68A*(1), 177–186.
20. Hynes, R. O.; Yamada, K. M. *J. Cell Biol.* **1982**, *95*(2), 369–377.
21. Pytela, R.; Pierschbacher, M. D.; Ruoslahti, E. *Proc. Natl. Acad. Sci. USA* **1985**, *82*(17), 5766–5770.
22. Pytela, R.; Pierschbacher, M. D.; Ruoslahti, E. *Cell* **1985**, *40*(1), 191–198.
23. Yamada, K. M. *Curr. Opin. Cell Biol.* **1989**, *1*(5), 956–963.
24. Haubner, R.; Gratias, R.; Diefenbach, B.; Goodman, S. L.; Jonczyk, A.; Kessler, H. *J. Am. Chem. Soc.* **1996**, *118*(32), 7461–7472.
25. Kantlehner, M.; Schaffner, P.; Finsinger, D.; *et al. Chembiochem* **2000**, *1*(2), 107–114.
26. Maheshwari, G.; Brown, G.; Lauffenburger, D. A.; Wells, A.; Griffith, L. G. *J. Cell Sci.* **2000**, *113*(10), 1677–1686.
27. Massia, S. P.; Hubbell, J. A. *J. Biomed. Mater. Res.* **1991**, *25*(2), 223–242.
28. Yamada, K. M. *J. Biol. Chem.* **1991**, *266*(20), 12809–12812.
29. Redick, S. D.; Settles, D. L.; Briscoe, G.; Erickson, H. P. *J. Cell Biol.* **2000**, *149*(2), 521–527.
30. Akiyama, S. K.; Olden, K.; Yamada, K. M. *Cancer Metastasis Rev.* **1995**, *14*(3), 173–189.
31. Hynes, R. O. *Cell* **2002**, *110*(6), 673–687.
32. Emsley, J.; Knight, C. G.; Farndale, R. W.; Barnes, M. J.; Liddington, R. C. *Cell* **2000**, *101*(1), 47–56.
33. Knight, C. G.; Morton, L. F.; Peachey, A. R.; Tuckwell, D. S.; Farndale, R. W.; Barnes, M. J. *J. Biol. Chem.* **2000**, *275*(1), 35–40.
34. Reyes, C. D.; Garcia, A. J. *J. Biomed. Mater. Res. A* **2003**, *65A*(4), 511–523.
35. Reyes, C. D.; Garcia, A. J. *J. Biomed. Mater. Res. A* **2004**, *69A*(4), 591–600.
36. Rogers, S. L.; Letourneau, P. C.; Palm, S. L.; McCarthy, J.; Furcht, L. T. *Dev. Biol.* **1983**, *98*(1), 212–220.
37. Timpl, R.; Engel, J.; Martin, G. R. *Trends Biochem. Sci.* **1983**, *8*(6), 207–209.
38. Fittkau, M. H.; Zilla, P.; Bezuidenhout, D.; *et al. Biomaterials* **2005**, *26*(2), 167–174.
39. Graf, J.; Iwamoto, Y.; Sasaki, M.; *et al. Cell* **1987**, *48*(6), 989–996.
40. Iwamoto, Y.; Robey, F. A.; Graf, J.; *et al. Science* **1987**, *238*(4830), 1132–1134.
41. Jun, H. W.; West, J. L. *J. Biomed. Mater. Res. B Appl. Biomater.* **2005**, *72B*(1), 131–139.
42. Maeda, T.; Titani, K.; Sekiguchi, K. *J. Biochem.* **1994**, *115*(2), 182–189.
43. Merrett, K.; Griffith, C. M.; Deslandes, Y.; Pleizier, G.; Sheardown, H. *J. Biomater. Sci. Polym. Ed.* **2001**, *12*(6), 647–671.
44. Patel, N.; Padera, R.; Sanders, G. H. W.; *et al. FASEB J.* **1998**, *12*(14), 1447–1454.
45. Santiago, L. Y.; Nowak, R. W.; Rubin, J. P.; Marra, K. G. *Biomaterials* **2006**, *27*(15), 2962–2969.

46. Tashiro, K.; Sephel, G. C.; Weeks, B.; *et al*. *J. Biol. Chem.* **1989**, *264*(27), 16174–16182.
47. Ehrmann, R. L.; Gey, G. O. *J. Natl. Cancer Inst.* **1956**, *16*(6), 1375–1403.
48. Hauschka, S. D.; Konigsbe, I. R. *Proc. Natl. Acad. Sci. USA* **1966**, *55*(1), 119–126.
49. Roach, P.; Farrar, D.; Perry, C. C. *J. Am. Chem. Soc.* **2005**, *127*(22), 8168–8173.
50. Vogler, E. A. *Adv. Colloid Interface Sci.* **1998**, *74*, 69–117.
51. Vroman, L.; Adams, A. L.; Fischer, G. C.; Munoz, P. C. *Blood* **1980**, *55*(1), 156–159.
52. Wojciechowski, P.; Tenhove, P.; Brash, J. L. *J. Colloid Interface Sci.* **1986**, *111*(2), 455–465.
53. Vroman, L.; Adams, A. L. *Surf. Sci.* **1969**, *16*, 438–446.
54. Horbett, T. A. *Acs Symposium Series* **1987**, *343*, 239–260.
55. Slack, S. M.; Horbett, T. A. *J. Colloid Interface Sci.* **1989**, *133*(1), 148–165.
56. Malmsten, M.; Lassen, B.; Holmberg, K.; Thomas, V.; Quash, G. *J. Colloid Interface Sci.* **1996**, *177*(1), 70–78.
57. Nakanishi, K.; Sakiyama, T.; Imamura, K. *J. Biosci. Bioeng.* **2001**, *91*(3), 233–244.
58. Elsdale, T.; Bard, J. *J. Cell Biol.* **1972**, *54*(3), 626–637.
59. Carbonetto, S.; Gruver, M. M.; Turner, D. C. *J. Neurosci.* **1983**, *3*(11), 2324–2335.
60. Couchman, J. R.; Hook, M.; Rees, D. A.; Timpl, R. *J. Cell Biol.* **1983**, *96*(1), 177–183.
61. Grinnell, F.; Feld, M.; Minter, D. *Cell* **1980**, *19*(2), 517–525.
62. Rubin, K.; Hook, M.; Obrink, B.; Timpl, R. *Cell* **1981**, *24*(2), 463–470.
63. Vlodavsky, I.; Gospodarowicz, D. *Nature* **1981**, *289*(5795), 304–306.
64. Yamada, K. M.; Olden, K. *Nature* **1978**, *275*(5677), 179–184.
65. Grinnell, F. *J. Cell Biol.* **1980**, *86*(1), 104–112.
66. Hermanson, G. T. *Bioconjugate Techniques*; Academic Press: Maryland Heights, MO, 2008.
67. Hoffman, A. S.; Hubbell, J. A. In *Biomaterials Science*; Ratner, B. D., Hoffman, A. S., Schoen, F. J., Lemons, J. E., Eds.; Elsevier Academic Press: San Diego, CA, 2004.
68. Chu, P. K.; Chen, J. Y.; Wang, L. P.; Huang, N. *Mater. Sci. Eng. R Rep.* **2002**, *36*(5–6), 143–206.
69. Hoffman, A. In *Polymers in Medicine*; Springer: Berlin/Heidelberg, 1984; Vol. 57, pp 141–157.
70. Hoffman, A. S.; Gombotz, W. R.; Uenoyama, S.; Dong, L. C.; Schmer, G. *Int. J. Radiat. Appl. Instrum. C Radiat. Phys. Chem.* **1986**, *27*(4), 265–273.
71. Meyer-Plath, A. A.; Schröder, K.; Finke, B.; Ohl, A. *Vacuum* **2003**, *71*(3), 391–406.
72. Lahiri, J.; Isaacs, L.; Tien, J.; Whitesides, G. M. *Anal. Chem.* **1999**, *71*(4), 777–790.
73. Irvine, D. J.; Mayes, A. M.; Griffith, L. G. *Biomacromolecules* **2001**, *2*(1), 85–94.
74. Irvine, D. J.; Ruzette, A. V. G.; Mayes, A. M.; Griffith, L. G. *Biomacromolecules* **2001**, *2*(2), 545–556.
75. Petrie, T. A.; Raynor, J. E.; Dumbauld, D. W.; *et al*. *Sci. Transl. Med.* **2010**, *2*(45), 45ra60.
76. Barber, T. A.; Golledge, S. L.; Castner, D. G.; Healy, K. E. *J. Biomed. Mater. Res. A* **2003**, *64A*(1), 38–47.
77. Bearinger, J. P.; Castner, D. G.; Healy, K. E. *J. Biomater. Sci. Polym. Ed.* **1998**, *9*(7), 629–652.
78. Harbers, G. M.; Gamble, L. J.; Irwin, E. F.; Castner, D. G.; Healy, K. E. *Langmuir* **2005**, *21*(18), 8374–8384.
79. Goddard, J. M.; Hotchkiss, J. H. *Prog. Polym. Sci.* **2007**, *32*(7), 698–725.
80. Groll, J.; Fiedler, J.; Engelhard, E.; *et al*. *J. Biomed. Mater. Res. A* **2005**, *74A*(4), 607–617.
81. Houseman, B. T.; Gawalt, E. S.; Mrksich, M. *Langmuir* **2003**, *19*(5), 1522–1531.
82. Ma, H. W.; Hyun, J. H.; Stiller, P.; Chilkoti, A. *Adv. Mater.* **2004**, *16*(4), 338–341.
83. Nanci, A.; Wuest, J. D.; Peru, L.; *et al*. *J. Biomed. Mater. Res.* **1998**, *40*(2), 324–335.
84. Prime, K. L.; Whitesides, G. M. *Science* **1991**, *252*(5009), 1164–1167.
85. Senaratne, W.; Andruzzi, L.; Ober, C. K. *Biomacromolecules* **2005**, *6*(5), 2427–2448.
86. Tugulu, S.; Arnold, A.; Sielaff, I.; Johnsson, K.; Klok, H. A. *Biomacromolecules* **2005**, *6*(3), 1602–1607.
87. Zhao, B.; Brittain, W. J. *Prog. Polym. Sci.* **2000**, *25*(5), 677–710.
88. Hong, H. G.; Jiang, M.; Sligar, S. G.; Bohn, P. W. *Langmuir* **1994**, *10*(1), 153–158.
89. Jiang, M.; Nolting, B.; Stayton, P. S.; Sligar, S. G. *Langmuir* **1996**, *12*(5), 1278–1283.
90. Wood, L. L.; Cheng, S. S.; Edmiston, P. L.; Saavedra, S. S. *J. Am. Chem. Soc.* **1997**, *119*(3), 571–576.
91. Zhen, G. L.; Eggli, V.; Voros, J.; *et al*. *Langmuir* **2004**, *20*(24), 10464–10473.
92. Cuatreca, P.; Anfinsen, C. B. *Annu. Rev. Biochem.* **1971**, *40*, 259.
93. Phizicky, E. M.; Fields, S. *Microbiol. Rev.* **1995**, *59*(1), 94–123.
94. Akerstrom, B.; Brodin, T.; Reis, K.; Bjorck, L. *J. Immunol.* **1985**, *135*(4), 2589–2592.
95. Smith, D. B.; Johnson, K. S. *Gene* **1988**, *67*(1), 31–40.
96. Diamandis, E. P.; Christopoulos, T. K. *Clin. Chem.* **1991**, *37*(5), 625–636.
97. Wilchek, M.; Bayer, E. A. *Meth. Enzymol.* **1990a**, *184*, 14–45.
98. Wilchek, M.; Bayer, E. A. *Meth. Enzymol.* **1990b**, *184*, 5–13.
99. Hurst, R.; Hook, B.; Slater, M. R.; Hartnett, J.; Storts, D. R.; Nath, N. *Anal. Biochem.* **2009**, *392*(1), 45–53.
100. Los, G. V.; Encell, L. P.; McDougall, M. G.; *et al*. *ACS Chem. Biol.* **2008**, *3*(6), 373–382.
101. Terpe, K. *Appl. Microbiol. Biotechnol.* **2003**, *60*(5), 523–533.
102. Huang, N.-P.; Vörös, J.; De Paul, S. M.; Textor, M.; Spencer, N. D. *Langmuir* **2001**, *18*(1), 220–230.
103. Hyun, J.; Zhu, Y. J.; Liebmann-Vinson, A.; Beebe, T. P.; Chilkoti, A. *Langmuir* **2001**, *17*(20), 6358–6367.
104. Moy, V. T.; Florin, E. L.; Gaub, H. E. *Science* **1994**, *266*(5183), 257–259.
105. Turkova, J. *J. Chromatogr. B* **1999**, *722*(1–2), 11–31.
106. Green, N. M. *Biochem. J.* **1963**, *89*(3), 585–591.
107. Sakiyama-Elbert, S. E.; Hubbell, J. A. *J. Control. Release* **2000a**, *69*(1), 149–158.
108. Sakiyama-Elbert, S. E.; Hubbell, J. A. *J. Control. Release* **2000b**, *65*(3), 389–402.
109. Gallant, N. D.; Michael, K. E.; Garcia, A. J. *Mol. Biol. Cell* **2005**, *16*(9), 4329–4340.
110. Massia, S. P.; Hubbell, J. A. *Anal. Biochem.* **1990**, *187*(2), 292–301.
111. Rezania, A.; Healy, K. E. *J. Biomed. Mater. Res.* **2000**, *52*(4), 595–600.
112. Palecek, S. P.; Loftus, J. C.; Ginsberg, M. H.; Lauffenburger, D. A.; Horwitz, A. F. *Nature* **1997**, *385*(6616), 537–540.
113. Capadona, J. R.; Collard, D. M.; Garcia, A. J. *Langmuir* **2003**, *19*(5), 1847–1852.
114. Nonckreman, C. J.; Rouxhet, P. G.; Dupont-Gillain, C. C. *J. Biomed. Mater. Res. A* **2007**, *81A*(4), 791–802.
115. Barber, T. A.; Harbers, G. M.; Park, S.; Gilbert, M.; Healy, K. E. *Biomaterials* **2005**, *26*(34), 6897–6905.
116. Bullett, N. A.; Whittle, J. D.; Short, R. D.; Douglas, C. W. I. *J. Mater. Chem.* **2003**, *13*(7), 1546–1553.
117. Model, M. A.; Healy, K. E. *J. Biomed. Mater. Res.* **2000**, *50*(1), 90–96.
118. Velzenberger, E.; Pezron, I.; Legeay, G.; Nagel, M. D.; El Kirat, K. *Langmuir* **2008**, *24*(20), 11734–11742.
119. Buttry, D. A.; Ward, M. D. *Chem. Rev.* **1992**, *92*(6), 1355–1379.
120. Jonsson, U.; Fagerstam, L.; Ivarsson, B.; *et al*. *Biotechniques* **1991**, *11*(5), 620–627.
121. Marx, K. A. *Biomacromolecules* **2003**, *4*(5), 1099–1120.
122. O'Sullivan, C. K.; Guilbault, G. G. *Biosens. Bioelectron.* **1999**, *14*(8–9), 663–670.
123. Stenberg, E.; Persson, B.; Roos, H.; Urbaniczky, C. *J. Colloid Interface Sci.* **1991**, *143*(2), 513–526.
124. Homola, J.; Yee, S. S.; Gauglitz, G. *Sens. Actuators B Chem.* **1999**, *54*(1–2), 3–15.
125. Grieshaber, D.; MacKenzie, R.; Voros, J.; Reimhult, E. *Sensors* **2008**, *8*(3), 1400–1458.
126. Rodahl, M.; Hook, F.; Krozer, A.; Brzezinski, P.; Kasemo, B. *Rev. Sci. Instrum.* **1995**, *66*(7), 3924–3930.
127. Arnold, M.; Schwieder, M.; Blummel, J.; *et al*. *Soft Matter* **2009**, *5*(1), 72–77.
128. Geiger, B.; Bershadsky, A.; Pankov, R.; Yamada, K. M. *Nat. Rev. Mol. Cell Biol.* **2001**, *2*(11), 793–805.
129. Geiger, B.; Spatz, J. P.; Bershadsky, A. D. *Nat. Rev. Mol. Cell Biol.* **2009**, *10*(1), 21–33.
130. Huang, J. H.; Grater, S. V.; Corbellinl, F.; *et al*. *Nano Lett.* **2009**, *9*(3), 1111–1116.
131. Koo, L. Y.; Irvine, D. J.; Mayes, A. M.; Lauffenburger, D. A.; Griffith, L. G. *J. Cell Sci.* **2002**, *115*(7), 1423–1433.
132. Massia, S.; Hubbell, J. *J. Cell Biol.* **1991**, *114*(5), 1089–1100.
133. Miyamoto, S.; Akiyama, S. K.; Yamada, K. M. *Science* **1995**, *267*(5199), 883–885.
134. Miyamoto, S.; Teramoto, H.; Coso, O. A.; *et al*. *J. Cell Biol.* **1995**, *131*(3), 791–805.
135. Nelson, C. M.; Tien, J. *Curr. Opin. Biotechnol.* **2006**, *17*(5), 518–523.
136. Christman, K. L.; Enriquez-Rios, V. D.; Maynard, H. D. *Soft Matter* **2006**, *2*(11), 928–939.
137. Christman, K. L.; Requa, M. V.; Enriquez-Rios, V. D.; *et al*. *Langmuir* **2006**, *22*(17), 7444–7450.

138. Coyer, S. R.; Garcia, A. J.; Delamarche, E. *Angew. Chem. Int. Ed.* **2007**, *46*(36), 6837–6840.
139. Kim, J. H.; Kushiro, K.; Graham, N. A.; Asthagiri, A. R. *Proc. Natl. Acad. Sci. USA* **2009**, *106*(27), 11149–11153.
140. Mrksich, M.; Whitesides, G. M. *Annu. Rev. Biophys. Biomol. Struct.* **1996**, *25*, 55–78.
141. Raghavan, S.; Chen, C. S. *Adv. Mater.* **2004**, *16*(15), 1303–1313.
142. Sniadecki, N.; Desai, R. A.; Ruiz, S. A.; Chen, C. S. *Ann. Biomed. Eng.* **2006**, *34*(1), 59–74.
143. Gallant, N. D.; Lavery, K. A.; Amis, E. J.; Becker, M. L. *Adv. Mater.* **2007**, *19*(7), 965–969.
144. Smith, J. T.; Elkin, J. T.; Reichert, W. M. *Exp. Cell Res.* **2006**, *312*(13), 2424–2432.
145. Smith, J. T.; Kim, D. H.; Reichert, W. M. *Comb. Chem. High Throughput Screen.* **2009**, *12*(6), 598–603.
146. Smith, J. T.; Tomfohr, J. K.; Wells, M. C.; Beebe, T. P., Jr.; Kepler, T. B.; Reichert, W. M. *Langmuir* **2004**, *20*(19), 8279–8286.
147. Berg, J. M.; Tymoczko, J. L.; Stryer, L. In *Biochemistry*, W H Freeman: New York, 2002.
148. Kleinman, H. K.; Philp, D.; Hoffman, M. P. *Curr. Opin. Biotechnol.* **2003**, *14*(5), 526–532.
149. Cole, M. A.; Voelcker, N. H.; Thissen, H.; Griesser, H. J. *Biomaterials* **2009**, *30*(9), 1827–1850.
150. Mendes, P. M. *Chem. Soc. Rev.* **2008**, *37*(11), 2512–2529.
151. Mrksich, M. *MRS Bull.* **2005**, *30*(3), 180–184.
152. Kushida, A.; Yamato, M.; Konno, C.; Kikuchi, A.; Sakurai, Y.; Okano, T. *J. Biomed. Mater. Res.* **1999**, *45*(4), 355–362.
153. Okano, T.; Yamada, N.; Sakai, H.; Sakurai, Y. *J. Biomed. Mater. Res.* **1993**, *27*(10), 1243–1251.
154. Yamada, N.; Okano, T.; Sakai, H.; Karikusa, F.; Sawasaki, Y.; Sakurai, Y. *Makromol. Chem. Rapid Commun.* **1990**, *11*(11), 571–576.
155. Heskins, M.; Guillet, J. E. *J. Macromol. Sci. Chem. A2* **1968**, *2*(8), 1441–1455.
156. Plate, N. A.; Lebedeva, T. L.; Valuev, L. I. *Polym. J.* **1999**, *31*(1), 21–27.
157. Ebara, M.; Yamato, M.; Aoyagi, T.; Kikuchi, A.; Sakai, K.; Okano, T. *Biomacromolecules* **2004**, *5*(2), 505–510.
158. Miyahara, Y.; Nagaya, N.; Kataoka, M.; *et al. Nat. Med.* **2006**, *12*(4), 459–465.
159. Nishida, K.; Yamato, M.; Hayashida, Y.; *et al. Transplantation* **2004**, *77*(3), 379–385.
160. Ohashi, K.; Yokoyama, T.; Yamato, M.; *et al. Nat. Med.* **2007**, *13*(7), 880–885.
161. Shimizu, T.; Yamato, M.; Kikuchi, A.; Okano, T. *Biomaterials* **2003**, *24*(13), 2309–2316.
162. Yang, J.; Yamato, M.; Kohno, C.; *et al. Biomaterials* **2005**, *26*(33), 6415–6422.
163. Lee, H. M.; Larson, D. R.; Lawrence, D. S. *ACS Chem. Biol.* **2009**, *4*(6), 409–427.
164. Auernheimer, J.; Dahmen, C.; Hersel, U.; Bausch, A.; Kessler, H. *J. Am. Chem. Soc.* **2005**, *127*(46), 16107–16110.
165. Ohmuro-Matsuyama, Y.; Tatsu, Y. *Angew. Chem. Int. Ed.* **2008**, *47*(39), 7527–7529.
166. Petersen, S.; Alonso, J. M.; Specht, A.; Duodu, P.; Goeldner, M.; del Campo, A. *Angew. Chem. Int. Ed.* **2008**, *47*(17), 3192–3195.
167. Ramsden, J. J. *Q. Rev. Biophys.* **1994**, *27*(1), 41–105.
168. Ramsden, J. J. *Chem. Soc. Rev.* **1995**, *24*(1), 73–78.
169. Wahlgren, M.; Arnebrant, T. *Trends Biotechnol.* **1991**, *9*(6), 201–208.
170. Engvall, E.; Perlmann, P. *Immunochemistry* **1971**, *8*(9), 871–874.
171. Engvall, E.; Perlmann, P. *J. Immunol.* **1972**, *109*(1), 129–135.
172. Grinnell, F.; Feld, M. K. *J. Biol. Chem.* **1982**, *257*(9), 4888–4893.
173. Erickson, H. P.; Carrell, N. A. *J. Biol. Chem.* **1983**, *258*(23), 4539–4544.
174. Iuliano, D. J.; Saavedra, S. S.; Truskey, G. A. *J. Biomed. Mater. Res.* **1993**, *27*(8), 1103–1113.
175. Iwamoto, G. K.; Winterton, L. C.; Stoker, R. S.; Vanwagenen, R. A.; Andrade, J. D.; Mosher, D. F. *J. Colloid Interface Sci.* **1985**, *106*(2), 459–464.
176. Jonsson, U.; Lundstrom, I.; Ronnberg, I. *J. Colloid Interface Sci.* **1987**, *117*(1), 127–138.
177. Narasimhan, C.; Lai, C. S. *Biochemistry* **1989**, *28*(12), 5041–5046.
178. Pitt, W. G.; Spiegelberg, S. H.; Cooper, S. L. In *Proteins at Interfaces*, American Chemical Society 343, 1987; pp 324–338.
179. Garcia, A. J.; Vega, M. D.; Boettiger, D. *Mol. Biol. Cell* **1999**, *10*(3), 785–798.
180. Keselowsky, B. G.; Collard, D. M.; Garcia, A. J. *Proc. Natl. Acad. Sci. USA* **2005**, *102*(17), 5953–5957.
181. Kolb, H. C.; Finn, M. G.; Sharpless, K. B. *Angew. Chem. Int. Ed.* **2001**, *40*(11), 2004–2021.
182. Sun, X. L.; Stabler, C. L.; Cazalis, C. S.; Chaikof, E. L. *Bioconjug. Chem.* **2006**, *17*(1), 52–57.
183. Collioud, A.; Clemence, J. F.; Sanger, M.; Sigrist, H. *Bioconjug. Chem.* **1993**, *4*(6), 528–536.
184. Peluso, P.; Wilson, D. S.; Do, D.; *et al. Anal. Biochem.* **2003**, *312*(2), 113–124.
185. Rao, S. V.; Anderson, K. W.; Bachas, L. G. *Mikrochim. Acta* **1998**, *128*(3–4), 127–143.
186. Rusmini, F.; Zhong, Z. Y.; Feijen, J. *Biomacromolecules* **2007**, *8*(6), 1775–1789.
187. Scouten, W. H.; Luong, J. H. T.; Brown, R. S. *Trends Biotechnol.* **1995**, *13*(5), 178–185.
188. Hirano, Y.; Okuno, M.; Hayashi, T.; Goto, K.; Nakajima, A. *J. Biomater. Sci. Polym. Ed.* **1993**, *4*(3), 235–243.
189. Neff, J. A.; Tresco, P. A.; Caldwell, K. D. *Biomaterials* **1999**, *20*(23–24), 2377–2393.
190. Dickinson, C. D.; Veerapandian, B.; Dai, X. P.; *et al. J. Mol. Biol.* **1994**, *236*(4), 1079–1092.
191. Main, A. L.; Harvey, T. S.; Baron, M.; Boyd, J.; Campbell, I. D. *Cell* **1992**, *71*(4), 671–678.
192. Joshi, P.; Chung, C. Y.; Aukhil, I.; Erickson, H. P. *J. Cell Sci.* **1993**, *106*, 389–400.
193. Leahy, D. J.; Hendrickson, W. A.; Aukhil, I.; Erickson, H. P. *Science* **1992**, *258*(5084), 987–991.
194. Prieto, A. L.; Edelman, G. M.; Crossin, K. L. *Proc. Natl. Acad. Sci. USA* **1993**, *90*(21), 10154–10158.
195. Delforge, D.; Art, M.; Gillon, B.; *et al. Anal. Biochem.* **1996**, *242*(2), 180–186.
196. Ivanov, B.; Grzesik, W.; Robey, F. A. *Bioconjug. Chem.* **1995**, *6*(3), 269–277.
197. Pierschbacher, M. D.; Ruoslahti, E. *J. Biol. Chem.* **1987**, *262*(36), 17294–17298.
198. Cutler, S. M.; Garcia, A. J. *Biomaterials* **2003**, *24*(10), 1759–1770.
199. Castner, D. G.; Ratner, B. D. *Surf. Sci.* **2002**, *500*(1–3), 28–60.
200. Elwing, H. *Biomaterials* **1998**, *19*(4–5), 397–406.
201. Yang, J. T.; Wu, C. S. C.; Martinez, H. M. *Meth. Enzymol.* **1986**, *130*, 208–269.
202. Alsberg, E.; Anderson, K. W.; Albeiruti, A.; Franceschi, R. T.; Mooney, D. J. *J. Dent. Res.* **2001**, *80*(11), 2025–2029.
203. Behravesh, E.; Mikos, A. G. *J. Biomed. Mater. Res. A* **2003**, *66A*(3), 698–706.
204. Dee, K. C.; Rueger, D. C.; Andersen, T. T.; Bizios, R. *Biomaterials* **1996**, *17*(2), 209–215.
205. Hu, Y. H.; Winn, S. R.; Krajbich, I.; Hollinger, J. O. *J. Biomed. Mater. Res. A* **2003**, *64A*(3), 583–590.
206. Itoh, D.; Yoneda, S.; Kuroda, S.; *et al. J. Biomed. Mater. Res.* **2002**, *62*(2), 292–298.
207. Rezania, A.; Johnson, R.; Lefkow, A. R.; Healy, K. E. *Langmuir* **1999**, *15*(20), 6931–6939.
208. Shin, H.; Zygourakis, K.; Farach-Carson, M. C.; Yaszemski, M. J.; Mikos, A. G. *Biomaterials* **2004**, *25*(5), 895–906.
209. Sofia, S.; McCarthy, M. B.; Gronowicz, G.; Kaplan, D. L. *J. Biomed. Mater. Res.* **2001**, *54*(1), 139–148.
210. Zreiqat, H.; Akin, F. A.; Howlett, C. R.; *et al. J. Biomed. Mater. Res. A* **2003**, *64A*(1), 105–113.
211. Eid, K.; Chen, E.; Griffith, L.; Glowacki, J. *J. Biomed. Mater. Res.* **2001**, *57*(2), 224–231.
212. Lutolf, M. R.; Weber, F. E.; Schmoekel, H. G.; *et al. Nat. Biotechnol.* **2003**, *21*(5), 513–518.
213. Garcia, A. J.; Reyes, C. D. *J. Dent. Res.* **2005**, *84*(5), 407–413.
214. Barber, T. A.; Ho, J. E.; De Ranieri, A.; Virdi, A. S.; Sumner, D. R.; Healy, K. E. *J. Biomed. Mater. Res. A* **2007**, *80A*(2), 306–320.
215. Elmengaard, B.; Bechtold, J. E.; Soballe, K. *Biomaterials* **2005**, *26*(17), 3521–3526.
216. Hennessy, K. M.; Clem, W. C.; Phipps, M. C.; Sawyer, A. A.; Shaikh, F. M.; Bellis, S. L. *Biomaterials* **2008**, *29*(21), 3075–3083.
217. Schliephake, H.; Scharnweber, D.; Dard, M.; *et al. Clin. Oral Implants Res.* **2002**, *13*(3), 312–319.
218. Hasenbein, M. E.; Andersen, T. T.; Bizios, R. *Biomaterials* **2002**, *23*(19), 3937–3942.
219. Kam, L.; Shain, W.; Turner, J. N.; Bizios, R. *Biomaterials* **2002**, *23*(2), 511–515.
220. Dillow, A. K.; Ochsenhirt, S. E.; McCarthy, J. B.; Fields, G. B.; Tirrell, M. *Biomaterials* **2001**, *22*(12), 1493–1505.
221. Kao, W. J.; Lee, D.; Schense, J. C.; Hubbell, T. A. *J. Biomed. Mater. Res.* **2001**, *55*(1), 79–88.
222. Garcia, A. J.; Keselowsky, B. G. *Crit. Rev. Eukaryot. Gene Expr.* **2002**, *12*(2), 151–162.
223. Petrie, T. A.; Reyes, C. D.; Burns, K. L.; Garcia, A. J. *J. Cell. Mol. Med.* **2009**, *13*(8B), 2602–2612.
224. Wojtowicz, A. M.; Shekaran, A.; Oest, M. E.; *et al. Biomaterials* **2010**, *31*(9), 2574–2582.

225. de Mel, A.; Jell, G.; Stevens, M. M.; Seifalian, A. M. *Biomacromolecules* **2008**, *9*(11), 2969–2979.
226. Herring, M.; Gardner, A.; Glover, J. *Surgery* **1978**, *84*(4), 498–504.
227. Lindblad, B.; Burkel, W. E.; Wakefield, T. W.; Graham, L. M.; Stanley, J. C. *Acta Chir. Scand.* **1986**, *152*, 653–656.
228. Seifalian, A. M.; Tiwari, A.; Rashid, S. T.; Salacinski, H.; Hamilton, G. *Artif. Organs* **2002**, *26*(2), 209–210.
229. Ramalanjaona, G.; Kempczinski, R. F.; Rosenman, J. E.; Douville, E. C.; Silberstein, E. B. *J. Vasc. Surg.* **1986**, *3*(2), 264–272.
230. Krijgsman, B.; Seifalian, A. M.; Salacinski, H. J.; *et al. Tissue Eng.* **2002**, *8*(4), 673–680.
231. Massia, S. P.; Hubbell, J. A. *J. Biol. Chem.* **1992**, *267*(20), 14019–14026.
232. Zilla, P.; Fasol, R.; Preiss, P.; *et al. Surgery* **1989**, *105*(4), 515–522.
233. Meinhart, J. G.; Deutsch, M.; Fischlein, T.; Howanietz, N.; Froschl, A.; Zilla, P. *Ann. Thorac. Surg.* **2001**, *71*(90050), S327–S331.
234. Deutsch, M.; Meinhart, J.; Zilla, P.; *et al. J. Vasc. Surg.* **2009**, *49*(2), 352–362.
235. Heldin, C. H.; Usuki, K.; Miyazono, K. *J. Cell. Biochem.* **1991**, *47*(3), 208–210.
236. Neufeld, G.; Cohen, T.; Gengrinovitch, S.; Poltorak, Z. *FASEB J.* **1999**, *13*(1), 9–22.
237. Santhosh Kumar, T. R.; Krishnan, L. K. *Biomaterials* **2001**, *22*(20), 2769–2776.
238. Ehrbar, M.; Metters, A.; Zammaretti, P.; Hubbell, J. A.; Zisch, A. H. *J. Control. Release* **2005**, *101*(1–3), 93–109.
239. Randone, B.; Cavallaro, G.; Polistena, A.; *et al. J. Surg. Res.* **2005**, *127*(2), 70–79.
240. Walpoth, B. H.; Zammaretti, P.; Cikirikcioglu, M.; *et al. J. Thorac. Cardiovasc. Surg.* **2007**, *133*(5), 1163–1170.
241. Schmidt, C. E.; Leach, J. B. *Annu. Rev. Biomed. Eng.* **2003**, *5*(1), 293–347.
242. Shin, H.; Jo, S.; Mikos, A. G. *Biomaterials* **2003**, *24*(24), 4353–4364.
243. Kirk, E. G.; Lewis, D. *J. Am. Med. Assoc.* **1915**, *65*, 486–492.
244. Madison, R. D.; Dasilva, C.; Dikkes, P.; Sidman, R. L.; Chiu, T. H. *Exp. Neurol.* **1987**, *95*(2), 378–390.
245. Manthorpe, M.; Engvall, E.; Ruoslahti, E.; Longo, F. M.; Davis, G. E.; Varon, S. *J. Cell Biol.* **1983**, *97*(6), 1882–1890.
246. Kleinman, H. K.; Ogle, R. C.; Little, C. D.; Sweeney, T. M.; Luckenbilledds, L. *Proc. Natl. Acad. Sci. USA* **1988**, *85*(4), 1282–1286.
247. Sephel, G. C.; Burrous, B. A.; Kleinman, H. K. *Dev. Neurosci.* **1989**, *11*(4–5), 313–331.
248. Ranieri, J. P.; Bellamkonda, R.; Bekos, E. J.; *et al. Int. J. Dev. Neurosci.* **1994**, *12*(8), 725–735.
249. Ranieri, J. P.; Bellamkonda, R.; Bekos, E. J.; Vargo, T. G.; Gardella, J. A.; Aebischer, P. *J. Biomed. Mater. Res.* **1995**, *29*(6), 779–785.
250. Saneinejad, S.; Shoichet, M. S. *J. Biomed. Mater. Res.* **1998**, *42*(1), 13–19.
251. Zhang, Z. P.; Yoo, R.; Wells, M.; Beebe, T. P.; Biran, R.; Tresco, P. *Biomaterials* **2005**, *26*(1), 47–61.
252. Gomez, N.; Lu, Y.; Chen, S. C.; Schmidt, C. E. *Biomaterials* **2007**, *28*(2), 271–284.
253. Gomez, N.; Schmidt, C. E. *J. Biomed. Mater. Res. A* **2007**, *81A*(1), 135–149.
254. Dodla, M. C.; Bellamkonda, R. V. *Biomaterials* **2008**, *29*(1), 33–46.
255. Yu, X. J.; Bellamkonda, R. V. *Tissue Eng.* **2003**, *9*(3), 421–430.

4.412. Rational and Combinatorial Methods to Create Designer Protein Interfaces

B H Lui and J R Cochran, Stanford University, Stanford, CA, USA

© 2011 Elsevier Ltd. All rights reserved.

4.412.1.	**Introduction**	162
4.412.2.	**Rational Engineering**	163
4.412.2.1.	Site-Directed Mutagenesis	163
4.412.2.1.1.	Analyzing amino acid sequences	164
4.412.2.1.2.	Applying three-dimensional structures	164
4.412.2.1.3.	Predicting through computational modeling	165
4.412.2.2.	Fusions and Domain Swapping	166
4.412.2.2.1.	Peptide fusions	167
4.412.2.2.2.	Protein fusions	167
4.412.2.3.	Posttranslational Modifications	167
4.412.2.3.1.	Glycosylation	167
4.412.2.3.2.	PEGylation	168
4.412.2.3.3.	Other emerging modifications	168
4.412.3.	**Combinatorial Engineering**	169
4.412.3.1.	Library Creation	169
4.412.3.1.1.	Random mutagenesis	169
4.412.3.1.2.	Directed mutagenesis	170
4.412.3.1.3.	Recombination	171
4.412.3.2.	Screening Platforms	171
4.412.3.2.1.	Plate-based platforms	171
4.412.3.2.2.	Phage display	172
4.412.3.2.3.	Cell surface display	173
4.412.3.2.4.	*In vitro* platforms	174
4.412.4.	**Protein Engineering Considerations for Biomaterials: The Interface Between Proteins and Materials**	175
4.412.4.1.	Protein Encapsulation or Attachment	175
4.412.4.2.	Protein-Based Biomaterials	176
4.412.5.	**Conclusions and Future Directions**	177
References		177

Glossary

Cell surface display A directed evolution technique in which libraries of protein or peptide mutants are displayed on the surface of a cell (typically, a bacteria or yeast cell) and screened to identify variants with desired properties.

Combinatorial protein engineering (directed evolution) An approach to protein engineering where libraries of mutants are created and screened to identify protein variants with desired properties.

Consensus residue The most common residue at a given position when related sequences are aligned.

DNA shuffling A method to create genetic diversity by randomly recombining DNA *in vitro*.

Error-prone PCR A method to create genetic diversity by employing PCR with increased mutation frequencies.

Fluorescence-activated cell sorting (FACS) A technique to sort single cells based on their light scattering or fluorescent characteristics; used to isolate clones from cell surface display and *in vitro* compartmentalization libraries.

Genotype–phenotype linkage The connection between a protein variant and its corresponding DNA sequence, which allows amino acid mutations to be identified following library screening.

Homology The similarity between DNA or protein sequences.

***In vitro* compartmentalization (IVC)** A directed evolution technique in which protein or peptide libraries are encapsulated within cell-like compartments or emulsions, each containing one or more gene(s) and the encoded protein(s).

***In vitro* display** A directed evolution technique which physically links a protein or peptide mutant to the DNA or mRNA encoding for that protein or peptide using *in vitro* transcription and translation.

Phage display A directed evolution technique in which libraries of protein or peptide mutants are displayed on the surface of a bacteriophage and screened to identify variants with desired properties.

Posttranslational modification The modification of a protein after it is translated; describes processes that are

natural (i.e., glycosylation) and artificial (i.e., conjugation to polymers).

Rational protein engineering An approach to engineer proteins by introducing mutations based on knowledge of the protein structure and function.

Site-directed mutagenesis The mutation of a defined site in a gene and its corresponding amino acid mutation in the translated protein.

Structure–function relationship The link between a protein's amino acid sequence and structure and its biological activity.

Abbreviations

^{10}Fn3	10th fibronectin type III domain
APEx	Anchored periplasmic expression
ATP	Adenosine triphosphate
BMP-2	Bone morphogenetic protein 2
BSA	Bovine serum albumin
bZIP	Basic-region leucine zipper
CTA1	Cholera toxin A1
DARPins	Designed ankyrin repeat proteins
dNTPs	Deoxyribonucleotides
ECM	Extracellular matrix
EDTA	Ethylenediaminetetraacetic acid
EGF	Epidermal growth factor
EGFR	Epidermal growth factor receptor
ELISA	Enzyme-linked immunosorbent assay
Fabs	Antibody antigen-binding fragments
FACS	Fluorescence-activated cell sorting
FDA	Food and Drug Administration
FGF-1	Fibroblast growth factor-1
GCSF	Granulocyte-colony stimulating factor
Gβ1	Streptococcal protein G β1 domain
Her2	Human epidermal growth factor receptor 2
HGF	Hepatocyte growth factor
hGH	Human growth hormone
hGHR	Human growth hormone receptor
IFN-β	Interferon beta
IL-12	Interleukin-12
IL-2	Interleukin-2
ITCHY	Incremental truncation for the creation of hybrid enzymes
IVC	*in vitro* compartmentalization
Lpp	Lipoprotein
NESP	Novel erythropoiesis stimulating protein
NMR	Nuclear magnetic resonance
OmpA	Outer membrane protein A
PCR	Polymerase chain reaction
PDB	Protein Data Bank
PDGF	Platelet-derived growth factor
PEG	Polyethylene glycol
PPyCl	Chlorine-doped polypyrrole
PVP	Polyvinylpyrrolidone
RATCHITT	Random chimeragenesis on transient templates
RGD	Arginine-glycine-aspartic acid
scFvs	Antibody single-chain variable fragments
scTCRs	Single-chain T-cell receptors
SOSM	Shotgun ortholog scanning mutagenesis
StEP	Staggered extension process
TCR	T-cell receptor
TGF-α	Transforming growth factor alpha
TNF-α	Tumor necrosis factor alpha
TNFR	Tumor necrosis factor receptor
tPA	Tissue plasminogen activator
uPA	Urokinase plasminogen activator
VEGF	Vascular endothelial growth factor

4.412.1. Introduction

Biomaterials are playing an increasing role in regenerative medicine, serving as medical devices, drug delivery systems, and tissue implants and replacements.[1–3] Early material designs focused on providing mechanical support and proper diffusion of nutrients and waste for cell growth. However, as the field has expanded, it has become clear that these factors alone are not sufficient to promote cell proliferation and differentiation.[4] To help tissue growth and regeneration, biomaterials need to mimic the interactions between cells and their natural environment.

Signals that direct cell fate are mainly received from three sources: the extracellular matrix (ECM), neighboring cells, and soluble factors.[3,5] Protein–protein interactions play a significant role in all these components. For example, the ECM is composed of a meshwork of proteins, such as fibronectin and collagen, which interact with a myriad of cell surface receptors. In addition, neighboring cells communicate through membrane proteins like cadherin and cell adhesion molecules, and families of growth factors and cytokines control cell proliferation and migration by activating signaling pathways through their respective receptors. Thus, biomaterial design must consider and incorporate these protein–protein interactions to provide a customized material interface with the cell surface receptors that mediate these biological functions. This can be accomplished by presenting proteins on the surface of materials or encapsulating proteins inside materials.

Natural proteins, however, are often not ideal for use in biomaterials applications. Many are simply difficult to obtain. Purification from natural sources can be challenging, and the quality or composition can vary significantly from among batches or sources. There is also the risk of disease transfer and immunogenicity from proteins derived from animal sources. Recombinant production can circumvent those problems, but certain proteins, such as silk, collagen, and growth factors, still prove difficult to express in their native forms. Even when a protein can be produced and purified, Nature might not have optimized it for use in biomedical applications.

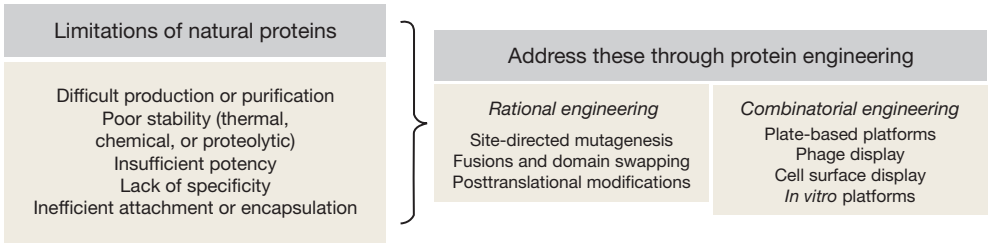

Figure 1 Chapter overview. To promote proliferation and differentiation, biomaterials need to mimic interactions that cells experience in their natural environment. One approach is to create customized materials that interact with and modulate cell surface receptors through protein ligands. Natural proteins, however, are often not optimal for use in biomaterials. In this chapter, we provide an overview of the two main protein engineering approaches that can be used to address these limitations: rational and combinatorial engineering.

For example, the protein of interest may lack the specificity or potency required to obtain a desired biological activity. In addition, many proteins, such as growth factors and cytokines, are not stable in the body due to thermal or proteolytic susceptibility, or possess fast *in vivo* clearance due to their small size. Furthermore, a protein's three-dimensional structure can be denatured upon exposure to chemical or UV-based methods often used for biomaterial incorporation, and attachment to materials can inactivate or reduce a protein's activity due to denaturation or steric constraints.

The principles of protein engineering can be applied to address all of these limitations (Figure 1). Rational protein engineering approaches require some knowledge of the protein's structure and function, but, when this information is available, can enable facile introduction of effective mutations for improved properties. Alternatively, combinatorial engineering approaches, also known as directed evolution, do not require existing knowledge of the protein's structure and function. However, directed evolution requires creation of a diverse library of protein variants and a high-throughput screening method to identify mutants with a desired phenotype. In this chapter, we provide a general overview of protein engineering, including both rational and combinatorial methods. In addition, we discuss specific considerations and challenges in creating proteins for biomaterial applications. Given the large body of work in this field, the chapter is not meant to be comprehensive, but provides key examples within each topic for illustrative purposes.

4.412.2. Rational Engineering

Rational protein engineering is the targeted redesign of a protein based on knowledge of the protein's structure and function. Rational modifications to proteins are most often done through site-directed mutagenesis. The challenge in this approach is to identify appropriate residues for mutation and predict their effects on protein properties. Rational protein engineering methodology varies greatly in complexity. The most basic level of analysis is to simply examine the protein's amino acid sequence, searching for homology with other proteins or unique residues, such as cysteine. If available, three-dimensional structures of proteins can be extremely helpful in guiding mutagenesis. More recently, computational algorithms are being used to employ physics-based modeling to fine-tune predictions.

Despite the plethora of techniques available for predicting the effects of mutagenesis, knowledge of protein structure–function relationships is still limited, making site-directed mutagenesis challenging. An alternative route is to identify protein domains with a known desired function. These domains, which can be peptides or entire proteins, can be fused together to gain enhanced or altered functionality with less uncertainty. However, problems still arise because fusions often alter the protein's spatial orientation and presentation and can be detrimental to activity.

Rational protein engineering also extends beyond amino acid sequence through posttranslational modifications. Natural processes, such as glycosylation, can be controlled to modify protein properties. Synthetic conjugations, notably attachment to polyethylene glycol (PEG), are also common because of established experimental protocols and the biological inertness of certain polymers. However, applications for posttranslation modifications are generally limited to increasing the molecular weight or stability of proteins.

Below, we describe specific techniques and provide examples for each of the three main approaches to rational engineering: site-directed mutagenesis, protein fusions and domain swapping, and posttranslational modifications.

4.412.2.1. Site-Directed Mutagenesis

Site-directed mutagenesis is the mutation of a defined site in a DNA sequence and, consequentially, the corresponding amino acid sequence. It is a common tool in molecular biology to study a protein's structure–function relationship, and many *in vitro* techniques, most of which are based on polymerase chain reaction (PCR), have been developed to efficiently introduce mutations, deletions, or insertions into existing genes by overlap extension (Figure 2(a)).[6] One of the most widely used methods is the QuikChange Site Directed Mutagenesis protocol developed by Stratagene, Inc. (La Jolla, CA)[7,8] (Figure 2(b)). In this protocol, virtually any plasmid can be mutated in just a few simple steps. First, a pair of oligonucleotide primers that are complementary to the plasmid, except for the desired mutation, are extended by PCR. The resulting reaction is treated with the enzyme *Dpn* I, which digests methylated and hemimethylated DNA. Almost all DNA isolated from *Escherichia coli* is methylated, thus the *Dpn* I selects for synthesized DNA containing the mutations. The mixture is then transformed into competent *E. coli* cells for isolation and amplification. This basic technique has been extended to introduce multiple amino acid mutations in addition to single point mutations.[6]

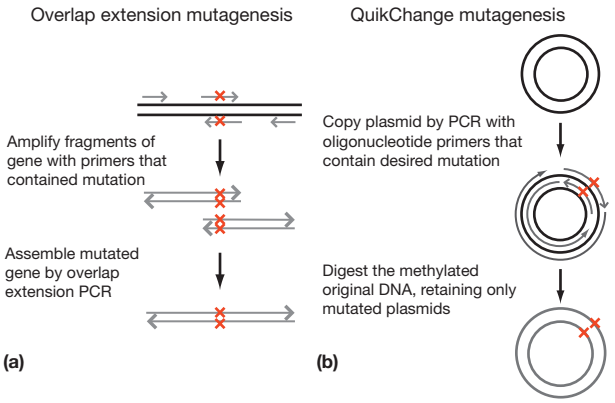

Figure 2 Site-directed mutagenesis methods are well established. Two commonly used techniques are overlap extension and QuikChange mutagenesis. Both employ oligonucleotide primers and PCR and can be used to introduce mutations, deletions, or insertions into target genes.

Because of the plethora of well-practiced mutagenesis techniques, the true challenge for using site-directed mutagenesis to rationally engineer a protein is how to select which residues to mutate and to decide which amino acids they should be mutated to. We describe three main approaches: (1) analyzing a protein's amino acid sequence, (2) extracting information from three-dimensional structures, and (3) employing computational algorithms to model proteins and predict mutations *in silico*.

4.412.2.1.1. Analyzing amino acid sequences

4.412.2.1.1.1. Sequence homology

In some cases, simply knowing the primary structure of a protein can provide sufficient information for rational protein engineering. If structure–function relationships have not been elucidated, comparing a protein's sequence to the sequences of related proteins, such as other species (orthologs) or family members (paralogs), can identify potential sites to mutate. The basic assumption of this approach is that natural evolution has already sampled and selected the optimal amino acids at a given position. When homologous proteins are aligned, the consensus residues (amino acids that appear in the majority of the proteins) have been shown to contribute most favorably to the protein's function.[9,10]

This homology-driven strategy was first applied toward engineering proteins for improved thermostability. One initial report described the improved stability of immunoglobulin variable domains.[10] By aligning sequences from a database of immunoglobulins, Steipe and colleagues assigned free-energy contributions to protein stability based on the frequencies of amino acids in every position. Six out of 10 predicted individual mutations were found to be stabilizing. In a simpler analysis, residues to mutate were identified only by their low occurrence rate among homologs.[11] Sequences of 130 chaperone proteins were aligned, and residues that occurred at a low frequency (<20%) were replaced with the most frequently occurring residue at that position. Out of the 18 mutations identified, 13 were stabilizing: a 72% success rate. Stability of enzymes can also be improved with this method. In one example, a consensus mutant phytase based on 13 fungal enzymes achieved a 15–22 °C increase in unfolding temperature compared to its parental variants.[12]

This consensus mutation concept is now being applied to improve protein properties other than stability. For example, a luciferase protein was aligned with similar proteins from 14 different species.[13] Point mutations were chosen at positions where wild-type differed significantly from the consensus residue and their effects were evaluated individually. Favorable mutations were then combined to create a mutant luciferase that exhibited a fourfold increase in total light output compared to wild-type. Taking this approach even further, a novel fluorescent protein was successfully created by combining consensus mutations from 31 different fluorescent proteins.[14]

4.412.2.1.1.2. Cysteines and disulfide bonds

In two special cases, general knowledge of protein structure and function allows proteins to be engineered without homology information. For this purpose, two handles can be used: cysteine residues (which are able to form disulfide bonds) and glycosylation sites. Glycosylation is a posttranslation modification involving carbohydrate groups and is discussed further in Section 4.412.2.3.1. Cysteine is a unique amino acid as its side chain contains a free thiol group, which often reacts with another thiol (usually another cysteine residue) to form a disulfide bond. If properly formed, disulfide bonds can stabilize proteins and promote stability. However, if incorrectly formed within the protein or between proteins, they can create misfolded protein variants or inactive dimers and oligomers. Thus, cysteine pairs can be introduced into proteins to form disulfide bonds in an attempt to stabilize proteins. Determining the site of disulfide bond insertion usually requires higher order structural information, which is discussed in Section 4.412.2.1.2. In the reverse approach, cysteines can also be removed when they interfere with a protein's stability; this usually occurs when there is an odd number of cysteine residues. Such was the case with both human interferon (IFN-β) and granulocyte-colony stimulating factor (GCSF).[15,16] Free cysteine residues in these proteins were replaced with serine (the amino acid most similar to cysteine), resulting in improvements in thermal and pH stability.

It should be noted that disulfide bonds do not always stabilize proteins. One example of this was found in the case of human fibroblast growth factor-1 (FGF-1),[17,18] which contains three cysteine residues. Two of these cysteine residues are highly conserved, occurring in 11 and 18 out of the 18 FGF family members, and were thought to form a disulfide bond. However, when these two cysteines were both substituted with serine, the protein's half-life at 37 °C increased from 0.26 to 13 h. It was hypothesized that the presence of a disulfide bond in FGF-1 actually destabilizes the protein and is evolutionarily favored to provide more responsive control over FGF-1 levels in the body. For regenerative medicine applications, however, a more stable variant of FGF-1 would be desirable.

4.412.2.1.2. Applying three-dimensional structures

Knowledge of a protein's three-dimensional structure provides significantly more information than the sequence alone, allowing hypothesis-driven mutations to be introduced. There are currently more than 50 000 protein structures in the Protein Data Bank (PDB) (PDB annual report 2009). Structures are

most often determined through X-ray crystallography (~90%) but can also be obtained through nuclear magnetic resonance (NMR) and electron microscopy.

Structural information allows protein visualization and determination of the three-dimensional location of residues; this information can be used for a variety of purposes. One application is to determine which residues are surface-exposed. Residues on the protein surface interact with water, thus it is often more favorable for those residues to be hydrophilic, as hydrophobic residues can decrease protein stability and promote aggregation. This is often a problem when a protein is truncated or a single protein domain is expressed alone for a particular biological application. For example, production of a subunit of cholera toxin A1 (CTA1) maintained the desired adjuvant activity of the full protein, but exhibited poor solubility.[19] However, by mutating two hydrophobic residues located on the newly exposed surface to hydrophilic amino acids, the solubility of the CTA1 subunit was improved threefold over the wild-type subunit.

Another approach where structural information is useful in protein engineering is the introduction of disulfide bonds to increase protein stability (see **Section 4.412.2.1.1.2**). Disulfide bonds are covalent cross-links between cysteine side chains in a protein and can potentially stabilize the protein against unfolding. By analyzing the crystal structure of dihydrofolate reductase, researchers were able to locate a free cysteine in the protein and inserted a cysteine residue in an adjacent protein chain.[20] The formation of this disulfide bond stabilized the reductase, but also resulted in a loss in activity, presumably from restriction of the enzyme's motion. Other disulfide bond introductions have been more successful. For example, a disulfide bond was introduced into the bacteriophage T4 lysozyme, which improved its half-life 2.5-fold over wild-type enzyme.[21,22] However, it is often difficult to predict from structural information alone what locations in proteins will be amenable to modification. As a result, there have been many studies that used model proteins in an attempt to develop more rational guiding frameworks. For example, the stabilities of two proteins, a trypsin inhibitor and a glucoamylase, were characterized after introduction or removal of disulfide bonds and mutation of residues that are known to participate in stabilizing interactions.[23,24] These studies revealed that disulfide bonds can stabilize both folded and unfolded states, and the overall effect on protein stability is a result of many balancing factors.

Structures can also provide information on covalent and noncovalent interfaces between protein domains and between proteins and their ligands. This information can then be used to promote or disrupt these interactions. In one example, insulin normally assembles into dimers or hexamers of protein subunits; an oligomeric state is beneficial for transport and storage, but can slow absorption by the body. In pursuit of a fast-acting insulin, researchers hoped to create a monomeric form of the protein and therefore studied the dimerization interface.[25,26] They pursued two strategies to achieve this goal: (1) introducing charge repulsions by inserting charged amino acids and (2) creating steric clashes by substituting amino acids with larger side chains. With this combined approach, insulin mutants were created that remained monomeric at pharmaceutically relevant concentrations (approximately millimolar) and resulted in two- to threefold improvements in absorption post injection.

Disrupting protein–protein interactions can also be an effective method to engineer receptor antagonists. An early example was the redesign of the human growth hormone (hGH).[27] A single hGH molecule has two interfaces that can bind two separate hGH receptors (hGHRs), inducing receptor dimerization and activation. From the crystal structure of hGH bound to hGHR, a glycine in one of the binding interfaces was identified for substitution with the bulkier amino acid arginine. This mutation disrupted the binding interaction through steric hindrance while leaving the second hGHR-binding interface intact. Thus, the hGH mutant could only bind a single receptor, preventing dimerization and activation of hGHR, thereby acting as an antagonist. In a related approach, a fragment of the hepatocyte growth factor (HGF) was also converted to an antagonist.[28] In this system, one HGF ligand binds to one Met receptor and activation of Met is achieved through ligand-induced dimerization. Through structural analysis, residues in the ligand interface were mutated to prevent dimerization. The resulting HGF fragments retained binding affinity, but no longer dimerized and activated the Met receptor.

Structural knowledge can also be applied to manipulate the specificity of protein interactions. This strategy was employed when researchers introduced a new T-cell receptor (TCR) into cells that already contained endogenous TCRs.[29] TCRs are formed by two subunits (α and β), and undesired hybrids could form between the introduced and endogenous TCR subunits. To prevent this, researchers studied the TCR-α- and TCR-β-chain interface and noticed a complementary steric interaction, where an amino acid in the β-domain fits into a pocket in the α-domain. To obtain specificity with their exogenous TCR, the authors cleverly reversed this interaction, mutating the TCRs such that the amino acid in the α-domain now fit into a pocket in the β-domain. This strategy conferred selective assembly of the introduced TCR chains to each other while maintaining the TCR's antigen-binding capability.

4.412.2.1.3. Predicting through computational modeling

In recent years, many computational algorithms have been developed to model protein folding and behavior, further increasing the ability to rationally choose sites for mutation.[30–33] These methods can estimate the energetic interactions between atoms in the proteins, taking into account steric, solvation, and electrostatic effects. Performing experiments *in silico* enables many more mutations to be considered compared to site-directed mutagenesis, and the power of these methods to engineer proteins for desired properties is rapidly growing. Computational approaches have now been successfully used to improve protein stability,[34] tailor-binding affinity, and cell trafficking,[35] and even create novel protein folds.[36]

Much of the early work in this area was focused on improving protein stability. Using three-dimensional structures as guides, parameters such as side-chain packing and hydrophobic surface area could be optimized. In one example, researchers were able to demonstrate their computational power by analyzing the stability of 10^9 mutants of the streptococcal protein G β1 domain (Gβ1).[37] Variants of Gβ1 were created that remained completely unfolded, formed a

disordered molten globule, or exhibited improved stability over wild-type. The model was also able to specifically target only interior protein residues, leaving surface epitopes alone. This is an important component, as a protein could be engineered for improved stability while leaving its binding interactions and biological function unaffected. Using this approach, 10^{28} mutants of the cytokine GCSF were computationally screened for stability, resulting in a mutant with an extended shelf-life up to 10-fold over wild-type and no deleterious effects on *in vivo* activity[38] (Figure 3).

Another strategy is the design of a protein interaction with its binding partner. This can be performed on a basic level by considering electrostatic interactions between proteins, such as a ligand-receptor interaction. One study by Sarkar and colleagues hoped to improve the biological potency of GCSF by maintaining wild-type affinity of GCSF for its receptor at the cell surface, but reducing the affinity of GCSF for its receptor once it was internalized into acidic components within the cell.[35] It was hypothesized that this differential binding would lower the chance of GCSF being trafficked for degradation. The researchers were able to model the electrostatic interactions between GCSF and its receptor at the cell surface (physiological pH) and inside intracellular compartments (low pH) and found two locations where a histidine residue could be substituted. Histidine's unique pK_a allows it to be neutral at physiological pH and charged at low pH, thereby disrupting any electrostatic interactions and altering binding affinity. As predicted, the two GCSF histidine mutants exhibited reduced intracellular degradation and enhanced cell proliferation by 50–100%, depending on dosage.

Electrostatic interactions are only a part of this complex story. To more fully model protein interactions, properties such as packing, desolvation energy, and the burial of hydrophobic surface area should also be taken into account. All these factors were incorporated into a Poisson–Boltzmann continuum model to improve the binding affinity of two antibodies for their targets by 10- to 140-fold, achieving final dissociation constants of 52 and 30 pM, respectively.[39] In another example, the affinity between integrin lymphocyte function-associated antigen-1 and its ligand intracellular adhesion molecule-1 was improved ~20-fold by also including proper folding as a modeling parameter.[40]

Novel binding specificities have also been achieved by promoting interactions to a desired target while purposefully impairing binding to unwanted proteins.[41] This strategy combining positive and negative design was employed to identify peptides that bound human basic-region leucine zipper (bZIP) transcription factors.[42] Engineered peptides selectively bound their targets over representative bZIPs from all 20 bZIP families, despite the substantial overlap in sequence and structure between the bZIP proteins.

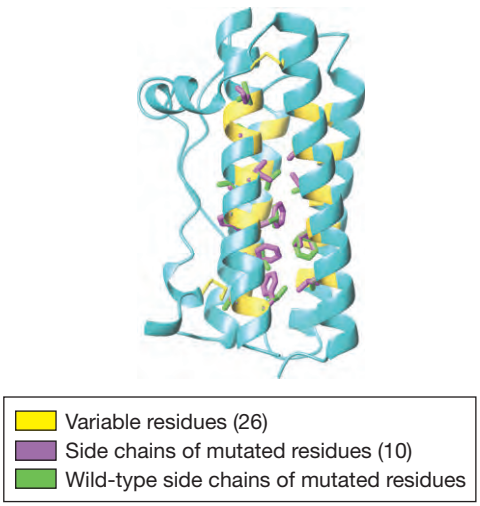

Figure 3 Computational modeling of hydrophobic core packing. Using the structure of bovine granulocyte-colony stimulation factor (GCSF) as a model, the core residues of human GCSF were identified (yellow) and optimized for enhanced packing while minimizing changes in overall protein structure. The resulting GCSF variant had 10 mutations (wild-type side chains in green and substituted side chains in purple) and possessed enhanced thermal stability while retaining full biological activity. Reprinted from Luo, P.; *et al*. *Protein Sci*. **2002**, *11*, 1218–1226, with permission from Wiley.

4.412.2.2. Fusions and Domain Swapping

Despite progress made with site-directed mutagenesis approaches, predicting the effects of mutations remains a great challenge. Alternatively, if a desired property already exists in a different protein, rational engineering can often be accomplished by simply fusing or swapping peptide and protein domains (Figure 4). In certain cases, the introduction of short peptides into a protein framework or 'scaffold' can be sufficient to gain binding capabilities. However, to achieve high binding affinity and specificity, combinations of recognition sequences must often be used and their surrounding residues optimized. Problems with binding specificity and structural context can also be solved by fusing entire proteins or protein domains instead of peptides. Furthermore, protein domain fusions can bring the added benefit of properties besides improved binding affinity, such as increased biological potency and circulation half-life.

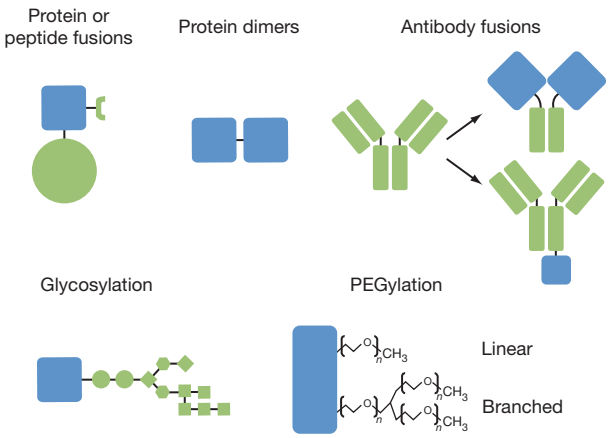

Figure 4 Rational protein engineering through fusions and posttranslational modifications. Besides site-directed mutagenesis, a variety of methods can be used to rationally engineer proteins. Functionality can be added by genetically fusing the target protein to itself to form a dimer or to other proteins and peptides. Natural and synthetic molecules, such as carbohydrates or polyethylene glycol, can also be conjugated posttranslationally to proteins. Blue = protein of interest, Green = fusion partner.

4.412.2.2.1. Peptide fusions

One of the simplest protein recognition sequences is the three amino acid sequence arginine-glycine-aspartic acid (RGD).[43–45] This motif was originally identified as the minimum sequence in fibronectin that maintained recognition for the integrin family of receptors, which are responsible for cell adhesion. RGD was subsequently identified in many different proteins that exist in the ECM, such as vitronectin, collagen, and fibrinogen, and its use was heavily pursued in applications to improve material biocompatibility or to block cell adhesion in cancer. The first approaches focused on the RGD motif, and many RGD-containing peptides were synthesized in a variety of structural contexts – linear and cyclic – with different neighboring amino acids.[46] These peptides were found to be effective in promoting cell adhesion and proliferation[47] and in blocking integrin receptor interactions.[48,49]

Unfortunately, one binding epitope alone is often not sufficient to achieve high affinity or specificity. This was a common limitation to the RGD peptides mentioned above,[50] as many had suboptimal binding affinity for a range of integrin receptor family members. To improve these properties, multiple-binding epitopes can be combined together. Fortunately, several recognition sequences in addition to RGD were discovered in fibronectin and other proteins.[43,51,52] Fusing two or more of these motifs together can result in improved recognition, but the order of the fused epitopes and the linker between them can play a major role on their presentation and often requires optimization. To investigate this, RGD was fused with two other peptides from fibronectin (PHSRN and PRRARV) in different arrangements to find an optimal combination *in vitro*.[53] The selected constructs were then tested in rat models, and the attachment of RGD with the PHSRN motif was found to more effectively elicit macrophage adhesion and activation.[54]

4.412.2.2.2. Protein fusions

The use of short peptide fusions ultimately limits the binding affinity and specificity that can be achieved. This can be overcome by expanding fusion partners to entire proteins or protein domains. Continuing the example of the RGD peptide described above, improved binding specificity to defined integrin receptors has been achieved by replacing the RGD and PHSRN peptides with entire fibronectin domains to better mimic the natural protein structure.[55–57] In addition, protein fusions can enhance biological activity through a variety of other mechanisms. For example, enhanced agonistic chimeras were constructed from epidermal growth factor (EGF) and transforming growth factor α (TGF-α).[58] EGF and TGF-α both bind to and activate EGF receptor (EGFR) but elicit distinct responses due to differences in intracellular trafficking. By fusing truncated versions of EGF and TGF-α, several EGF/TGF-α chimeras were created with optimal binding and cell trafficking properties, resulting in 10-fold improvements in mitogenic activity compared to EGF or TGF-α alone.

Larger proteins can also increase biological potency by extending circulation lifetime in the body. This increased half-life results from an increase in size, as the kidneys rapidly filter out lower molecular weight proteins below a threshold of 60 kDa. A straightforward approach is to create a dimer by genetically fusing two copies of the protein together, as was done with erythropoietin.[59] The erythropoietin dimer had the benefit of improved pharmacokinetics, as well as increased specific activity due to avidity effects. Alternatively, molecular weight can be increased by fusing completely unrelated proteins. Recently, an unstructured polypeptide, XTEN, was developed as a generic fusion partner to increase molecular weight.[60] XTEN was designed to mimic the effect of conjugating proteins to synthetic polymers, such as PEG (see **Section 4.412.2.3.2**), and increased the half-life of a 39-residue peptide, exenatide, by 100-fold.

Besides increasing a protein's molecular weight, certain protein fusions can act as carrier molecules. For example, human serum albumin is the most abundant protein in serum and has an *in vivo* half-life of several weeks.[61] Fusing albumin to a soluble form of CD4, a T-cell membrane protein, was shown to improve the half-life 140-fold over soluble CD4 alone in a rabbit model without any change in activity *in vitro*.[62] Similarly, over a 100-fold increase in circulation half-life was seen after fusing albumin to hirudin, a thrombin inhibitor.[63] Again, the type of fusion can require optimization: fusing albumin to the *C*-terminus of hirudin inhibited its biological activity, whereas fusing it to the *N*-terminus did not. The complications with complete albumin fusions led some researchers to instead fuse albumin-binding peptides. These shorter peptides have been shown to possess the desired effects with examples of half-life improvements of 3-fold with a natural albumin-binding domain taken from streptococcal protein G[64] and 37-fold with an engineered peptide.[65]

Antibody domains are another common protein fusion partner.[66–68] Antibody constant regions can increase a protein's circulation half-life by increasing the molecular weight as well as by promoting interactions with various receptors. Such fusions might also increase the binding avidity of proteins due to the divalent nature of antibodies. Both of these benefits were seen with etanercept, a fusion between the extracellular domain of tumor necrosis factor receptor (TNFR) and the constant region of IgG.[69] The affinity of the fusion increased 50-fold compared to the monomer and resulted in a 5-fold increase in circulation half-life.[70] The divalent antibody structure can also be exploited to join variable domains with different binding specificities, thereby creating bispecific proteins.[71,72] For example, variable domains targeting a tumor-associated antigen and a surface receptor on immune cells, such as EGFR and the T-cell receptor CD3, respectively, can be fused to retarget effector immune cells to cancer cells. High antibody affinity and specificity can be exploited to target cytokines as well, allowing localized delivery of cytokines and reduced systemic toxicity.[73,74] Several fusions between antibodies specific for various tumor markers and immune stimulatory cytokines, such as interleukin-2 (IL-2) and interleukin-12 (IL-12), are currently in clinical trials.

4.412.2.3. Posttranslational Modifications

4.412.2.3.1. Glycosylation

Many modifications, such as phosphorylation, acylation, methylation, and glycosylation, occur naturally after translation to control protein behavior and function. Although of interest from a purely biological standpoint, these processes are also attractive for protein engineering, as they are potential

opportunities to optimize proteins for different applications. Unfortunately, the rules governing most of these modifications are unknown or insufficiently characterized. For example, despite considerable efforts, phosphorylation and *O*-linked glycosylation sites are just beginning to be accurately predicted with accuracies from 70 to 90%.[75–78] Much increase in knowledge is required before these modifications can be inserted rationally into proteins. The exception is *N*-linked glycosylation, which occurs cotranslationally in most cases and is therefore heavily determined by primary structure.[79–81] The consensus sequence required for this modification is the tripeptide sequence asparagine-X-serine/threonine, where X is any amino acid except proline.

Armed with this motif, researchers have pursued *N*-linked glycosylation as a strategy for protein engineering. One major application is to use glycosylation to increase a protein's molecular weight, much like the fusions proteins mentioned above. Erythropoietin was one of the earliest proteins to be altered in this manner. This was an appropriate model system because erythropoietin is already heavily glycosylated – 40% of the native protein's molecular weight is carbohydrate – and its activity is known to be dependent on its three native glycosylation sites.[82] Several dozen glycosylation sites were introduced at locations known not to be involved in the binding of erythropoietin to its receptor.[83] However, only a few of the resulting mutants were successfully glycosylated and retained biological activity. By combining two of these mutants, a novel erythropoiesis stimulating protein (NESP) was created. NESP had five *N*-linked glycosylation chains, retained biological activity *in vivo*, and exhibited a threefold increase in half-life.[84] This strategy has been extended with varying degrees of success. For example, glycosylation sites were identified in tissue plasminogen activator (tPA) that contributed to or detracted from tPA's specificity and clearance.[85] In other work, several glycosylation sites were successfully introduced into more challenging targets: the hormone leptin, which naturally is not glycosylated, and the cytokine megakaryocyte growth and development factor, which normally undergoes *O*-linked glycosylation.[86]

4.412.2.3.2. PEGylation

Despite the existence of a consensus sequence, successful and effective *N*-linked glycosylation remains challenging to predict. An alternative approach is to mimic nature by conjugating proteins with synthetic molecules instead. The most popular polymer for protein conjugation is PEG. PEG is a stable, water-soluble polymer that has been shown to be nontoxic and nonimmunogenic.[87] Conjugation to PEG, also known as PEGylation, has been shown to effectively reduce protein clearance, improve temperature and pH stability, prevent enzymatic degradation, and protect against immunogenicity.[87–89] Most importantly, PEG has been approved by the Food and Drug Administration (FDA), and many PEGylated drugs, such as the asparaginase (Oncaspar) and adenosine deaminase (Adagen), are currently in use in the clinic.

However, PEGylation is not a formulaic procedure. There are several parameters that can affect the outcome, such as the size and type of the PEG polymer, the number of PEGs conjugated, and the type of conjugation. Initial work with asparaginase and adenosine deaminase used low-molecular-weight, single-chain PEG polymers (~5 kDa) and conjugated proteins through their free amino groups on lysines residues and the *N*-terminus.[87,89] Notably, in addition to increasing biological potency by extending half-life, PEGylation also reduced the immunogenicity and incidence of hyperallergic reactions from asparaginase, which is produced in bacteria.[90,91]

Since these early examples, different avenues for PEGylation have been explored to develop protein conjugates that are more homogeneous and efficacious, such as the use of larger or branched PEG molecules. In one case, when IFN-2α was PEGylated with a 5 kDa polymer, no advantage was seen over unconjugated interferon in clinical trials.[87,92] In contrast, conjugation with a 40 kDa branched PEG polymer (Pegasys) reduced renal clearance 100-fold and extended the half-life from 9 to 77 h.

Alternative conjugation methods are also being developed to improve control over the PEGylation reaction.[93] Lysine is one of the most prevalent amino acids; thus when its ε-amino group is used as the PEG attachment site, heterogeneous products result which can block binding and biological activity. By exploiting the slightly lower pK_a of the *N*-terminal amino group over the lysine side chain, specific conjugation at the *N*-terminus can be achieved, as first demonstrated with human GCSF.[94] PEGylation can also be performed through thiol groups on cysteine residues. Thiol chemistry is well established, but free cysteines are generally rare in proteins. Cysteines have been inserted into hGH, GCSF, and interferon for successful site-specific PEGylation.[95] Enzymes have also begun to be used for specific conjugation. For example, transglutaminase was exploited for attaching an amino-PEG molecule to single glutamine residues in IL-2.[96] Enzymes with other amino acid substrates, such as tyrosine, are known and could also potentially be used for specific conjugation in the future.[97]

Site-specific incorporation of nonnatural amino acids offers ultimate control over the point of attachment. Pairs of orthogonal tRNA and tRNA synthetases can insert amino acids with a unique chemical handle at defined locations in proteins, enabling specific conjugation to PEG or other molecules without the risk of nonspecific attachment.[98] This method has been used to effectively reduce the heterogeneity of PEGylated hGH and enabled the creation of variants with single, uniform PEG conjugations.[99] Site-specific conjugation of PEG to hGH using nonnatural amino acids resulted in several promising candidates that exhibited improved half-life over the current commercial formulation.[100]

4.412.2.3.3. Other emerging modifications

The success of glycosylation and PEGylation has sparked research into other potential protein modifications. A survey of different nonionic water-soluble polymers identified polyvinylpyrrolidone (PVP) as a potential PEG alternative.[101] Several polymers had greater circulation lifetime than PEG, but PVP exhibited minimal tissue accumulation. Unlike PEG, PVP can also be polymerized with additional functional groups, potentially allowing more opportunities for targeting and control than PEG. PVP was conjugated to tumor necrosis factor-α (TNF-α) and exhibited a twofold improvement in antitumor activity *in vivo* compared to TNF-α conjugated to a PEG molecule of similar molecular weight.[102]

Outside of synthetic polymers, fatty acids have also been conjugated to proteins. Fatty acids have a weak binding

interaction with albumin and can be used to increase circulation half-life in a similar strategy to the albumin and albumin-binding peptide fusions described above. In one study, chains of 10 to 16 carbon atoms were conjugated to insulin through a lysine amino group and the resulting proteins were screened for binding affinity to insulin receptor and biological activity.[103] Although attachment of a 14-carbon fatty acid chain decreased the affinity to 46% of unconjugated insulin, this acylated analog (Insulin Detemir) resulted in a more stable insulin profile over time with lower variability.[104,105]

4.412.3. Combinatorial Engineering

Although there are many examples of where rational protein engineering has been successful, our understanding of the relationships between protein sequence, structure, and function is far from complete. Thus, many attempts to rationally engineer proteins fail, and introducing complex properties, such as altered enzyme substrate specificity or novel molecular recognition interfaces, is often unachievable. Combinatorial-based methods provide a powerful alternative for protein engineering. Also known as directed or *in vitro* evolution, combinatorial engineering does not require any prior knowledge of protein structure or function. Instead, it mimics the process of natural selection in the laboratory in three steps. First, diversity is introduced into a gene of interest to create a library of DNA sequences. This mutant DNA is then translated into a protein library. Finally, the protein library is screened for a desired property and improved mutants are isolated. This process can be repeated multiple times with additional diversity introduced in each round of evolution. Critical to this process is the maintenance of a genotype–phenotype linkage, meaning that, once a desired protein is identified from the library, its DNA sequence, and hence amino acid sequence, can be determined.

Major advances in molecular biology have allowed directed evolution to become the dominant approach for protein engineering. The technology can be divided in two main parts that are mostly independent: (1) methods to generate library diversity and (2) platforms to express and screen protein libraries. These last two steps in the evolution process are combined because of the requirement to maintain a link between genotype and phenotype.

4.412.3.1. Library Creation

As the first step in the directed evolution process, constructing an appropriate gene library is crucial for overall success. Key decisions are the level of diversity to be introduced and where in the protein to introduce such diversity. High diversity will likely increase the probability of generating an improved mutant; however, this will also increase the number of protein variants that lose their activity. The location of protein mutations is important because the level of diversity that can actually be sampled by current screening platforms is limited. Even the best platforms are limited to screening approximately 10^{14} proteins, which is equivalent to randomizing only 11 amino acids. Therefore, targeting diversity to specific amino acids allows a more thorough library evaluation.

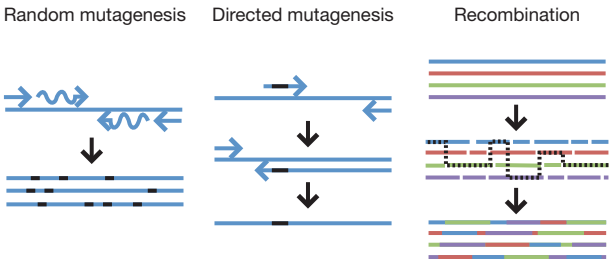

Figure 5 Library creation methods. There are three main approaches to library construction: random mutagenesis, directed mutagenesis, and recombination. Each technique enables different types of mutations to be introduced into a gene such that the optimal method is often a combination of all the three approaches.

On account these factors, trade-offs must be made for different protein engineering applications. To help overcome this dilemma, many different strategies for library creation have been developed. They can be divided into three categories: random mutagenesis, directed mutagenesis, and recombination[106,107] (Figure 5). In random mutagenesis, mutations are created throughout the protein, most commonly by error-prone PCR. This approach is often taken when no previous knowledge of structure–function exists and in attempts to find a protein's 'hot spots.' Directed mutagenesis is the mutation of specific residues in a protein. As mentioned above, limiting the diversity to specific amino acids or regions enables improved sampling of the resulting library. Lastly, recombination introduces diversity by fragmenting a pool of homologous genes and randomly assembling the pieces back into full-length mutants. This increases the likelihood of active proteins in the library and is also a powerful way to combine vastly different sequences. Each of these three methods has its advantages, and a combination of the three is typically used in current combinatorial engineering projects.

4.412.3.1.1. Random mutagenesis

As the name implies, random mutagenesis is the introduction of mutations, insertions, or deletions randomly throughout the entire gene. The predominant methods rely on increasing the error rate in natural DNA copying processes. The earliest techniques were cell-based, using chemical or physical mutagens to introduce errors.[106,108] Specialized bacterial strains were also developed that lack DNA proofreading or editing mechanisms.[109] However, both these approaches have several drawbacks. For example, they lack discrimination: mutations can occur in the gene of interest, the plasmid carrying the gene, or the chromosome of the host. This can result in unwanted alteration of the host or loss of mutator phenotypes. Treated hosts and mutator strains also grow slowly and generally have a low error frequency, requiring several cell divisions for only one or two mutations.

Because of these disadvantages, methods based on PCR have almost completely replaced cell-based methods. PCR is a fast, widespread technique and by nature is specific to the gene of interest. Besides the template sequence and amplifying primers, a PCR reaction is composed of DNA polymerase, deoxyribonucleotides (dNTPs), and buffer. All the three of these components can be exploited to adjust the mutation

frequency of a PCR reaction.[107,110] The simplest component to modify is the buffer. Magnesium chloride ($MgCl_2$) is an important compound in PCR reactions that stabilizes DNA and its interactions with DNA polymerases. Errors can be introduced by stabilizing noncomplementary pairs with higher $MgCl_2$ concentrations.[111] In addition, $MgCl_2$ can be substituted with manganese chloride ($MnCl_2$) to generate even higher error rates.[112]

Unfortunately, manipulating mutation rates with $MgCl_2$ and $MnCl_2$ can severely reduce the efficiency of the PCR reactions. To achieve increased error rates without reducing product, the dNTP composition of the reaction can be changed. Misincorporation can be promoted by lowering the concentrations of certain dNTPs relative to others.[111] For example, by lowering the concentration of dATP, 'wobble' pairs can be formed between G and T, leading to A→G mutations. In the next round of duplication, these can also lead to T→C mutations. Although effective in increasing error rates, simply lowering the level of dATP clearly limits the types of mutations possible. An ideal mutation strategy would allow all point mutations with equal probability. This goal is more approachable using nucleotide analogs, which can be incorporated across different natural bases. In this case, a universal base analog which can pair with all the natural bases equally is desired, and many different analogs have been produced and tested.[107] The best results are often achieved by combining the strengths of different analogs. For example, one analog can be optimized for transition mutations (purine to purine or pyrimidine to pyrimidine) and one can be used to introduce transversion mutations (purine to pyrimidine or vice versa).[113]

Finally, the DNA polymerases themselves can be engineered for increased mutation frequencies. The *Taq* polymerase from *Thermus aquaticus* has a natural high error rate of 8×10^{-6} per bp because it lacks a 3′→5′ proofreading mechanism.[114] This error rate is still not sufficient for most protein engineering applications, but mutation of *Taq* polymerase at its dNTP-binding site allowed a 20-fold higher error rate to be achieved.[115] However, mutational biases still exist as *Taq* polymerase is fourfold more likely to mutate A and T than G and C. As an alternative, a modified *Pfu* polymerase from *Pyroccocus furiosus* can be used, which has been mutated to remove its proofreading ability and hinder its dNTP binding.[116] Proprietary polymerases are also available to achieve balance in mutations. Mutazyme (Stratagene) claims to mutate G and C threefold more than A and T, and a mix of Mutazyme and Taq, called Mutazyme II, is purported to balance their respective biases to produce an even spectrum of mutations.

While much progress has been made in developing technologies for random mutagenesis, PCR-based methods still have an inherent limitation because they generally create only point mutations and rarely perform insertions or deletions. Methods have been developed to insert specific sequences in a random manner, but only more recently has a technique been developed to randomly insert or delete nucleotides.[106,117,118] The random insertion or deletion method is technically challenging, combining several digestion, ligation, and amplification steps with a random Ce(IV) nuclease treatment. But, with this method, up to 16 bases have been successfully inserted and deleted.

4.412.3.1.2. Directed mutagenesis

If some information about the protein's structure (and perhaps function) is known, libraries can also be created by directed mutagenesis, where diversity is generated at specific amino acids within a protein. With the advent of inexpensive and widely available methods for DNA synthesis, the number of amino acids that can be mutated ranges from one to many, and substitutions at particular locations can be controlled. Entire genes, or alternatively, sets of oligonucleotides, can be synthesized by commercial suppliers with nucleotides randomized at defined positions. With careful design to allow sufficient overlap between them, the oligonucleotides can be incorporated into full-length genes using the PCR assembly and overlap extension techniques discussed in **Section 4.412.2.1**.[119]

The most straightforward method to randomize a codon is to replace it with NNN, where N can be any of the four bases (A, T, G, or C) with equal probability. This will result in $4 \times 4 \times 4 = 64$ different codons which encode for all 20 amino acids. One disadvantage of using NNN codons is that redundancy in the genetic code causes biases. For example, certain amino acids, such as serine and arginine, are encoded by six codons, whereas others, such as methionine and tryptophan, are encoded by only a single codon. Thus, an NNN codon is six times more likely to encode a serine than a methionine. A second complication is that the set of all 64 codons includes the three stop codons, resulting in undesired truncations in the protein library.

To limit the effects of this bias, the possible number of codons can be restricted by limiting the variation in the third codon position (**Table 1**). For instance, instead of A, G, C, and T, only two or three nucleotides can be allowed at this position.[106,120] Depending on which combinations are selected, it is possible to completely avoid stop codons. For example, if the third position is limited to only a C or T, no stop codons are included, but the penalty is that only 15 of the 20 amino acids are encoded. Thus, a balance must be made between bias, truncations, and diversity. A common compromise is restricting the third codon to a C or G. The resulting 32 possible codons encode for all 20 amino acids and only 1 stop codon.

Besides amino acid bias and the introduction of stop codons, randomizing individual nucleotides also make it difficult to encode specific subsets of amino acids. For example, one might want to randomize a surface residue with only polar amino acids instead of all 20 possible amino acids. Or one might want to exclude the amino acid cysteine from the library to avoid undesired disulfide scrambling with other residues in the protein. All these challenges can be solved by constructing DNA libraries from defined codon mixtures.[121,122] However, the cost and technical hurdles faced in building these types of

Table 1 Codon bias in library design

	Number of total sequences	*Number of amino acids*	*Number of stop codons*
NNN	64	20	3
NNC/G/T/(NNB)	48	20	1
NNG/T/(NNK)	32	20	1
NNC/G/(NNS)	32	20	1
NNC/T(NNY)	32	15	0

libraries are significant, and thus these methods are not as widely used. Alternative approaches, such as using hybridization to isolate desired codons, are being actively pursued.[123]

4.412.3.1.3. Recombination

DNA recombination is the process of rearranging pieces of DNA, often between homologous regions. This process occurs in natural evolution and has been exploited for combinatorial protein engineering in the past decade with the development of DNA shuffling technology. In this short time period, recombination for DNA library construction has emerged as a strong complement to the random and directed mutagenesis methods described above.[124]

DNA shuffling was the first method to allow simple DNA recombination *in vitro*.[125,126] The starting material is a pool of homologous genes, such as a random library generated through error-prone PCR or genes from related species or family members. This pool is first digested with the enzyme DNAseI, which nonspecifically cleaves the DNA to create small fragments around 50 base pairs long. PCR assembly is then used to randomly reassemble or 'shuffle' the fragments into full-length genes, each composed of pieces from multiple original templates. The PCR assembly process can also be used to introduce additional randomized mutagenesis through error-prone PCR.

Many alternative techniques to perform recombination have followed, each with its own advantages and disadvantages.[124] For example, a slightly simpler method called staggered extension process (StEP) was developed to eliminate the fragmentation stage. In this method, recombination occurs by extending template sequences through extremely short annealing and extension steps, and the entire process occurs in a single tube.[127] Unfortunately, both shuffling and StEP require significant homology between templates for successful recombination. Therefore, alternative methods were developed to perform recombination with lower homology templates. In one method, random chimeragenesis on transient templates (RATCHITT) allowed recombination with only five base pairs of homology.[128] Pushing even further, incremental truncation for the creation of hybrid enzymes (ITCHY) required no homology.[129,130] However, these alternative methods have their concurrent drawbacks, many of them being more technically challenging than the original DNA shuffling protocol.

Despite their differences in recombination, all these techniques begin with the same material: a pool of homologous genes. As mentioned above, a random library created by error-prone PCR is a straightforward option.[131] A more focused approach is to recombine mutations identified from a previous protein engineering screen or selection, thereby increasing the probability of retaining proper protein structure and function. Alternatively, a family of natural genes from one or multiple species can be recombined in a method known as 'family shuffling'; the rationale for this strategy is that Nature has already selected mutations that are ideal for proper protein fold and function through millions of years of evolution.[132]

Bypassing the digestion step, the starting material for recombination can be performed or supplemented with custom-made DNA fragments. For example, primers can be used to introduce diversity into specific regions of genes with error-prone PCR.[133] These sections can then be recombined using the constant primer regions for homology, thereby combining elements of random mutagenesis, directed mutagenesis, and recombination. Completely synthetic oligonucleotides can be used as the source template as well.[134,135] Finally, as a complementary strategy to both family and synthetic oligonucleotide shuffling, orthologous mutations can be doped into a shuffled library to bias mutations toward those that Nature has already selected for folding and function, in a process known as shotgun ortholog scanning mutagenesis (SOSM).[136]

4.412.3.2. Screening Platforms

Once a gene library is constructed, the next step in the combinatorial engineering process is to express and screen the protein library for desired properties. To increase the chances of finding improved protein mutants, the three main objectives of screening platforms are to (1) express the library members in a folded, functional form, (2) reliably screen the library to identify mutants with a relevant phenotype, and (3) screen the highest number of possible proteins. The challenge is to do all of these things while maintaining the genotype–phenotype linkage, as once a protein is isolated from a library, the only way it can be identified is through sequencing the DNA that encoded it.

Screening platforms can be categorized on the basis of their approach to maintaining the genotype–phenotype linkage (**Figure 6**). Plate-based platforms rely on the physical separation of mutants into different wells of microtiter plates. This provides flexibility on the choice of protein expression system and enables a variety of screening readouts such as enzymatic or biological activity. But, depending on the plate density, throughput is limited to $\sim 10^4$–10^6 members. Higher throughput screening can be achieved using phage display and cell surface display (up to 10^{10} members). In these platforms, proteins are displayed on the surface of bacteriophage or cells, which package the encoding DNA inside. These libraries can then be screened by biopanning or flow cytometry to identify proteins with high binding specificity and affinity against a target of interest. Surface display on eukaryotic cells can also take advantage of their protein expression machinery for higher quality library expression. Most recently, *in vitro* techniques have been developed to physically link proteins to the DNA directly or to create artificial cells by emulsification. These platforms achieve the highest throughput, with the potential to screen up to 10^{14} protein variants.

4.412.3.2.1. Plate-based platforms

Perhaps the simplest in concept, plate-based platforms for directed evolution offer great flexibility in protein expression and screening. Unlike the display platforms discussed below, both *in vivo* and *in vitro* protein expression systems can be employed. The key requirement, however, is the ability to isolate sequences in separate wells to maintain the genotype–phenotype linkage described above. For *in vivo* expression, such as in *E. coli*, this can be done by picking colonies individually and inoculating cultures in the wells themselves.[137,138] For *in vitro* expression, a library of DNA templates can be diluted such that there is only one sequence per well.[139,140] These single templates can then be amplified by single-molecule PCR and used for subsequent *in vitro* transcription and translation reactions.

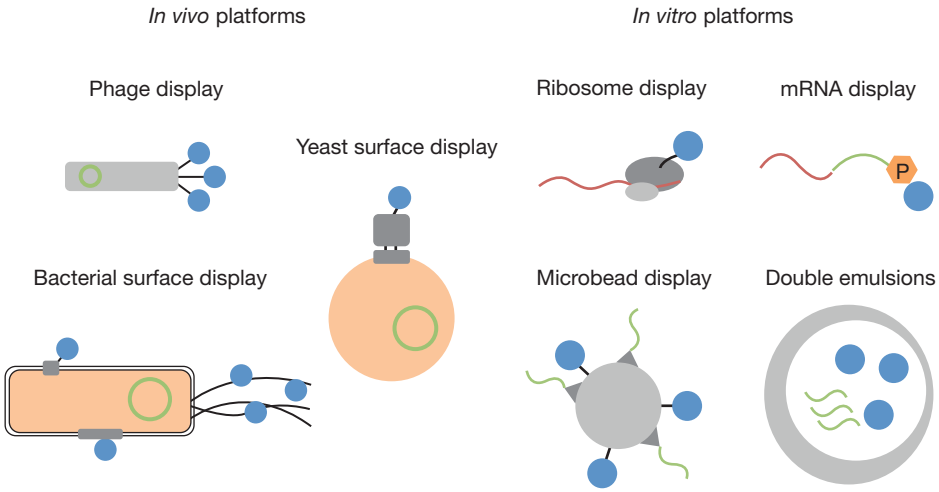

Figure 6 Screening platforms for combinatorial protein engineering. Directed evolution requires the maintenance of a genotype–phenotype linkage while screening for desired protein properties. A variety of *in vivo* and *in vitro* platforms have been developed to fulfill this requirement. Blue = protein to be engineered, Red = RNA, Green = DNA.

The options for screening are also quite diverse, as any assay compatible with a plate-based format can theoretically be used to analyze the protein mutants. One major application is enzyme engineering, where enzymatic activity can be reported through colorimetric or fluorescent readouts.[141,142] For example, the stereoselectivity of an aldolase was altered 100-fold and detected using a dye, which turns purple upon reduction.[138] Protein libraries can also be challenged with increases in temperature to screen for thermal stability, resulting in up to 500-fold increase in half-life at high temperatures.[137] Furthermore, the plate-based format is amenable to more complex assays such as measuring biological responses. For example, a screen was developed to measure the ability of EGF mutants to bind to the EGF receptor and transduce the signal inside the cell, as measured by luciferase expression.[143] In addition, a screen to measure antiviral activity was used to engineer a variant of human IFN-α with 10^2- and 10^5-fold specific activity relative to human IFN-α1 and IFN-α2a, respectively.[144] Recently, we developed a more general platform that enables efficient screening based directly on a cellular readout.[145] We applied this technology to identify EGF mutants that stimulate increased fibroblast cell proliferation over wild-type EGF, but the platform can potentially be combined with any cell-based functional assay.

The limitation of plate-based platforms is their throughput. In most instances, including the examples provided above, 96-well plates are used for expression and screening. This limits the library size that can be reasonably screened to $\sim 10^4$. This number can be improved by using robotic systems or increasing the plate density with 384-, 1536-, or even 6144-well plates.[146] But, the technical requirements and challenges of these methods limit their widespread use.

4.412.3.2.2. Phage display

To increase throughput and the library size that can be screened, display platforms were developed to establish physical genotype–phenotype linkages, removing the need to separate clones into individual microtiter wells. Phage display was the first method developed to accomplish this goal and is still the most widely used evolution platform.[147–150] The original phage-display system fuses peptides to surface-exposed p3 proteins of filamentous bacteriophage M13. *E. coli* are transfected with the phage genome containing this modified fusion protein. The *E. coli* produce phage with peptides displayed on their surface and the genome packaged inside, providing the genotype–phenotype linkage. Screening is accomplished by panning mixtures of phage against an immobilized target and washing to remove nonbinding clones. Phage displaying a peptide that binds a target of interest remains bound during these washes and can be eluted and amplified by reinfecting *E. coli* cultures.

The original phage-display system has been dramatically streamlined since its inception. Phage display is especially convenient for discovering small peptides that bind to desired targets. Peptide cloning systems and linear and cyclic peptide library kits are now commercially available (New England Biolabs, Inc.). Using phage-display technology, peptides have been isolated that bind to a variety of targets, including different integrin receptors, an HIV envelope protein, and even semiconductor surfaces.[151–153] In addition, peptides identified from phage-displayed libraries can be used as custom tags or fusion partners. For example, a phage-displayed peptide library was screened to isolate sequences that bound a model biopolymer, chlorine-doped polypyrrole (PPyCl).[154] PPyCl does not normally support cell growth. However, when it was treated with the identified peptides fused to the adhesive sequence RGD (see **Section 4.412.2.2.1** and **Chapter 4.414, Molecular Biomimetic Designs for Controlling Surface Interactions**), cells were able to attach and proliferate similar to standard tissue-culture-treated surfaces. In another application, a phage-displayed library was screened to identify a peptide that bound to albumin, thereby improving circulation half-life when fused to a protein (see **Section 4.412.2.2.2**).[65]

Variations have also been developed to expand phage display's applicability beyond simple peptides. For example, the spacing and valency (the number of copies of the displayed

protein per phage) can be optimized by controlling the expression levels of the fusion protein or by changing the fusion partner from p3 to one of the other four phage surface proteins, p6, p7, p8, or p9.[149,155] The types of proteins that can be displayed have also been expanded by controlling where the protein folds (cytoplasm vs. periplasm) and the transport mechanism of the fusion protein out of the cell.[156,157]

With these improvements, antibody antigen-binding fragments (Fabs) and single-chain variable fragments (scFvs) have been successfully displayed on phage.[158,159] Nonantibody scaffolds, ranging from the 95-residue 10th fibronectin type III domain (^{10}Fn3) to the 174-residue bilin-binding protein, have also been engineered to bind various targets.[160,161] The affinity maturation of growth factors and cytokines has also been demonstrated. For example, binding affinities of hGH and IFN-α2 to their receptors were increased 400- and 60-fold, respectively.[155,162]

Thus, many different types of proteins can be engineered with phage display, and panning allows very large libraries to be assayed. Library sizes of up to 10^{10} are possible, limited only by the transformation efficiency of *E. coli*.[149] Although phage display has been applied successfully in many cases, the use of *E. coli* as the expression host and the requirement for transport across the cell membranes can make its application to more complex proteins difficult. However, the major drawback of phage display is that the general enzyme-linked immunosorbent assay (ELISA)-based panning protocol does not allow precise control over the binding affinity and cannot differentiate between proteins with minor differences in affinity or kinetics, as is the case with flow cytometry-based screening methods, discussed below.[147] On the other hand, panning affords some flexibility in how the target ligand is presented. Ligands can be presented on myriad solid surfaces, including plates, beads, and even surface-plasmon-resonance chips. Furthermore, phage can be panned against whole mammalian cells to engineer specific cell-targeting sequences[163] or injected into live animals for *in vivo* screening.[164]

4.412.3.2.3. Cell surface display

Alternative combinatorial engineering platforms have been developed to display peptides and proteins as fusions on the surface of cells instead of on phage. This permits the use of fluorescence-activated cell sorting (FACS) to screen libraries. Proteins displayed on the cell surface can be labeled with fluorescent ligands and screened with single-cell resolution based on light scattering and fluorescence intensity.[165,166] Advanced flow cytometers can screen cells at speeds up to 10^9 cells per hour and isolate desired populations in real time. In addition, multiple wavelengths can be measured at the same time, allowing separation based on more than one parameter (i.e., levels of protein expression and target binding). This precise control over the library screening process enables discrimination between proteins with only a twofold difference in binding affinity, which is far superior to what can be achieved with panning-based methods.[167]

Bacterial and yeast surface display platforms have been developed to present proteins on the surfaces of *E. coli* and *Saccharomyces cerevisiae*.[166,168] Display on other bacteria and yeast (such as gram-positive *Streptococcus* or *Pichia pastoris*), insect cells, and mammalian cells is also possible but these are more recent technologies and as a result are not yet as widely used.[169–173]

4.412.3.2.3.1. E. coli *surface display*

E. coli is the most well-characterized microbe, and transformation and protein expression techniques are fully developed. Thus, *E. coli* was the first system to be developed for the engineering of peptides and proteins by cell surface display. Although it is a simple organism, *E. coli* display initially proved to be difficult, with problems of cell toxicity and transport across the inner and outer membranes and the cell wall. Thus, various fusions were used as anchors to present proteins on membrane proteins, lipoproteins, flagella, and pilin,[174,175] and many of these systems were successful in displaying peptides or small proteins. For example, a peptide library was inserted into a loop of the *E. coli* outer membrane protein A (OmpA). Using this system, peptides with 1–10 nM binding affinity were identified to bind various targets such as human serum albumin and the HIV surface protein gp120. In addition, a flagella display system is commercially available (FliTrx, Invitrogen). The FliTrx peptide library was screened against serum from patients with the inflammatory celiac disease to identify common antigenic domains.[176]

The first successful method to display larger proteins on bacteria was the Lpp–OmpA system, a three-part fusion composed of the signal sequence from the major *E. coli* lipoprotein (Lpp), the outer membrane protein OmpA, and the target protein.[177] scFv libraries were successfully displayed on *E. coli* using this system and screened against a model target, the small molecule digoxigenin.[177,178] However, intact antibodies and larger, more complex proteins (such as ones containing disulfide bonds) could not be presented. To overcome these difficulties, more complex techniques were developed to fold and display proteins in the periplasm of *E. coli* and to subsequently remove the outer membrane and cell wall to generate spheroplasts that could be labeled and screened by flow cytometry. Such anchored periplasmic expression (APEx) and E-clonal technologies allow the display of full-length antibodies, but are technically challenging as the spheroplasts are extremely delicate.[179,180] Despite this, full-length antibodies were engineered to bind small model targets with affinities of up to 20 nM.

4.412.3.2.3.2. Yeast surface display

In response to technical difficulties encountered with *E. coli*, yeast surface display was developed as an alternative method for protein engineering.[167,168,181] *S. cerevisiae* is a model eukaryotic microbe. Like *E. coli*, it offers the convenience of well-known experimental methods for transformation and culture. In addition, yeast contains the foldases, chaperones, and translation machinery necessary to properly express eukaryotic proteins. This is a significant advantage over *E. coli* protein expression, which is relied on for both phage and bacterial display. The downside to *S. cerevisiae* as a host is that its transformation efficiency is lower than *E. coli*, reducing the library sizes to 10^7–10^9 members. Larger library sizes could be produced for both bacterial display and yeast display by combining multiple transformations, but screening is limited by the throughput of commercial flow cytometers (10^7–10^9 cells per hour). However, library quality is just as important as library size. For example, when an identical

immune scFv library was presented on the surface of yeast or phage, yeast display identified all of the HIV-gp120 specific scFvs selected by phage display and twice as many novel antibodies.[182]

In contrast to the variety of bacterial display systems, there is one dominant system for yeast surface display. In this system, the protein of interest is fused to the adhesion protein agglutinin Aga2p, which is attached by two disulfide bonds to the cell wall protein Aga1p.[167,181] Approximately 10^5 proteins are displayed on each yeast cell, and short epitope tags are included in the display construct at the *N*- and *C*-terminus of the protein of interest to measure the expression levels. Thus, two-color fluorescent labeling of yeast cells can be performed simultaneously – one label can be directed against the epitope tag and one against the protein to be engineered. This enables library screening against a binding target of interest to be normalized for expression levels. In other words, a protein that exhibits poor yeast expression but binds a high amount of ligand can be distinguished from a protein that is expressed at high levels but binds weakly to a target.

Yeast surface display has been used to successfully screen synthetic and natural scFv libraries.[183,184] As proof of principle, an scFv was isolated with a binding affinity of 53 fM and a dissociation half-life of greater than 5 days.[183] Since then, scFvs have been engineered to bind a wide variety of targets, from neurotoxins to TNF-α.[185,186] Furthermore, a single variable light-chain domain devoid of disulfide bonds was engineered to bind the huntingtin protein htt using yeast surface display, opening the door for potential intracellular targeting.[187] Extremely large, complex proteins have also been amenable to yeast surface display. A few prominent examples are the EGFR extracellular domain, which contains 621 residues and 25 disulfide bonds,[188] single-chain T-cell receptors (scTCRs),[189] and human class II major histocompatibility complexes, displayed as noncovalent heterodimers.[190]

Besides binding affinity, yeast surface display has also been used to engineer proteins with increased thermal stability.[191] In the first example of this approach, scTCRs with increased yeast surface display levels also exhibited increased soluble expression levels and thermal stability. This engineering strategy has been extended to other proteins, particularly receptors that are difficult to express.[192] In addition, we have recently engineered HGF fragments with increased stability. In this example, mutants with increased thermal stability were also displayed at higher levels on the yeast cell surface and exhibited significantly higher soluble expression yields.[193]

The yeast surface display system has also proven to be robust for engineering proteins with therapeutic potential.[194] The human proteins EGF and IL-2 have been engineered for 30- and 150-fold increased binding affinity for their receptors, respectively.[136,195] The engineered EGF mutants, which had faster kinetic on-rates of binding, significantly enhanced EGFR activation, compared to wild-type EGF.[196] The high-affinity IL-2 mutants were able to stimulate persistent T-cell growth while wild-type IL-2 did not, revealing properties of IL-2 receptor subunit binding and consequential cell signaling. In addition, folded cystine-knot (knottin) peptides, named because they contain a constrained disulfide-bonded core, have been recently engineered with high affinities and differing specificities against a variety of integrin receptors, including αvβ3, αvβ5, α5β1, and αiibβ3.[197–199] Given their unique integrin-binding specificities, these engineered peptides have interesting potential applications as ECM mimics for promoting cell adhesion and differentiation.

4.412.3.2.4. In vitro *platforms*

Although phage and cell surface display platforms significantly increase the throughput over plate-based systems, they rely on *in vivo* protein expression and thus their library size is limited by cellular transformation efficiency. To reach even higher library sizes, *in vitro* protein expression methods have been employed, allowing library sizes of up to 10^{14} to be created.[200] In addition, *in vitro* expression allows the production of proteins that otherwise would be toxic to cells and can potentially remove cellular expression biases. *In vitro* systems also do not require cloning, thereby simplifying the library generation process and enabling recursive mutagenesis between each cycle, more closely mimicking true evolution.

To express proteins *in vitro*, transcription and translation machinery is extracted from various ribosome-rich sources, including *E. coli*, wheat germs, and rabbit reticulocytes.[201] Reaction mixtures are typically supplemented with substrates such as amino acids and an energy source. These cell extracts vary in their expression yield and protein quality, as might be expected from prokaryotic versus eukaryotic systems.

There are three major platforms for *in vitro* evolution: ribosome display,[202–205] mRNA display,[206,207] and *in vitro* compartmentalization (IVC).[208,209] Because of their more recent development compared to phage display, the use of these *in vitro* platforms in protein engineering is not as widespread; however, there have been significant contributions as described below.

4.412.3.2.4.1. *Ribosome display*

Ribosome display was the first of the three methods to be introduced.[202,204] In ribosome display, the stop codon is purposely left out of the genetic template, causing the ribosome to pause at the end of the mRNA after protein translation. This forms a noncovalent complex composed of the mRNA, ribosome, and translated protein, which is stabilized by cooling the reaction to 4 °C and adding a magnesium buffer. Attempts to improve the stability of this complex by incorporating additional molecular interactions have been developed, but its noncovalent nature still makes subsequent steps technically challenging. Screening of a library of complexes is performed by panning against immobilized targets, as the complexes are much too small to be sorted by flow cytometry. Bound proteins are eluted by addition of ethylenediaminetetraacetic acid (EDTA), which chelates the magnesium, and individual sequences are recovered by reverse transcription of the mRNA.

The large library sizes afforded by ribosome display allowed the evolution of very high-affinity proteins. For example, a scFv library was screened against insulin, and a clone was recovered with a binding affinity of 82 pM.[202,210] Designed ankyrin repeat proteins (DARPins), a type of nonantibody scaffold, have also been engineered to bind many different targets with ribosome display.[211] A notable achievement was the evolution of a DARPin to bind human epidermal growth factor receptor 2 (Her2) with a binding affinity of 90 pM.[212,213] More recently, ribosome display has been extended to more diverse proteins

and targets. For example, 14-residue peptides that bind copper (II) and zinc finger proteins that bind specific DNA sequences have been isolated.[214,215]

4.412.3.2.4.2. *mRNA display*

mRNA display was developed to provide a covalent genotype–phenotype linkage, eliminating the issue of mRNA and protein dissociation inherent in ribosome display.[200,206,207] Similar to ribosome display, a stop codon is not included in the genetic template; the difference is that, after *in vitro* transcription, the library of mRNA templates is linked to the small molecule puromycin by ligation or hybridization to a short DNA linker.[216] During translation, the ribosome pauses at the RNA–DNA junction and puromycin is actually incorporated by the ribosome into the protein, as if it were an amino acid, to form a covalent mRNA–puromycin–protein fusion. Properly formed complexes are purified and panned against targets, as in ribosome display. Sequences can be recovered by reverse transcription and release of the DNA by RNA hydrolysis.

Like ribosome display, mRNA display has been used to screen extremely large peptide libraries. In one example, completely random peptide libraries of $\sim 10^{13}$ were screened to identify an 88-residue peptide with 5 nM affinity to streptavidin and an 80-residue peptide with 100 nM affinity to adenosine triphosphate (ATP).[217,218] More complex proteins have also been successfully displayed. The 10th domain of fibronectin (^{10}Fn3), which has an immunoglobulin-like fold, was evolved to bind TNF-α with a binding affinity of 20 pM from a starting library of 10^{12}.[219] The ability to express a wide range of proteins and the ease of library construction was further demonstrated by displaying the human proteome from a cDNA library and screening for calmodulin-binding proteins.[220]

4.412.3.2.4.3. In vitro *compartmentalization*

The third *in vitro* evolution platform, IVC, attempts to combine the advantages of *in vitro* display, cell surface display, and plate-based platforms into one system by creating artificial cells.[209,221] The artificial cells are water-in-oil emulsions formed by stirring an *in vitro* transcription and translation mixture with surfactants and oil. Emulsions can also be formed by vortexing, extrusion, or microfluidics; each method produces droplets of varying size (from picoliter to femtoliter volume) and heterogeneity.[208] Analogous to single-molecule PCR used in plate-based platforms (see **Section 4.412.3.2.1**), clones are separated by carefully diluting the template such that each emulsion contains a single mutant sequence. Translation and transcription are then performed inside of the emulsions, and thus the genotype–phenotype linkage is maintained by compartmentalization.

Several systems have been developed to enable library screening by panning or flow cytometry. For panning, a DNA display system was developed in which the template is biotinylated and the proteins are expressed as a fusion to streptavidin.[222] Thus, a DNA–biotin–streptavidin–protein complex is formed in the emulsions and can be panned against immobilized targets. For flow cytometric sorting, microbead display and double emulsion systems have been introduced. In the first system, the DNA and proteins are linked to microbeads, forming DNA–bead–protein complexes large enough to be detected by flow cytometry instrumentation.[223,224] In the second system, water-in-oil emulsions can be re-emulsified into a second aqueous phase.[225,226] The water-in-oil-in-water double emulsions can be sorted as if the droplets were cells. The flexibility of IVC also allows the creation of custom screens. For example, a unique DNA-binding screen was conceived where zinc finger proteins could be screened to bind a target sequence in emulsions.[227]

Most of the IVC screening systems have currently only been demonstrated with model systems. However, the use of IVC for protein engineering has great potential, as it combines the flexibility of plate-based assays with larger library sizes and high-throughput, quantitative screening techniques like flow cytometry. IVC is also starting to be combined with other platforms, such as yeast surface display, to leverage the advantages of each system.[228]

4.412.4. Protein Engineering Considerations for Biomaterials: The Interface Between Proteins and Materials

4.412.4.1. Protein Encapsulation or Attachment

Once a protein has been engineered by the methods described above, the final step is to incorporate the protein inside of or onto the surface of the biomaterial. This can be done by noncovalent or covalent interactions through specific or nonspecific linkages[4,229,230] (**Figure 7**). The challenge in both approaches is to ensure that the process does not inactivate the protein and that the material allows proper access or release of the protein.

Noncovalent protein incorporation can be done through encapsulation or absorption. This is accomplished by combining the protein of interest with the material's precursors before polymerization. After polymerization, the protein can escape

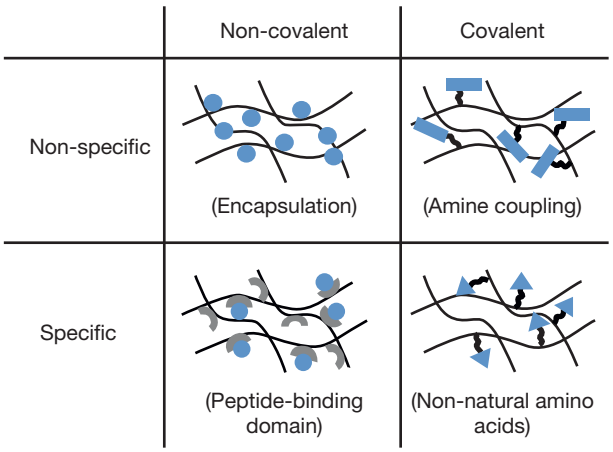

Figure 7 Approaches to protein encapsulation and attachment. Once a protein has been engineered by the methods described in this chapter, it must be incorporated into the biomaterial. This can be done by noncovalent or covalent interactions through specific or nonspecific linkages. An example is shown for each possibility. The challenge in all of these approaches is to ensure that the process does not inactivate the protein and the material allows proper access or release of the protein.

by diffusion out of the material or by degradation of the material over time. Thus, as can be expected, the speed of release is highly dependent on the material's properties. Spheres of dense biodegradable polymers can be used for slower release. Tuning the sphere's size was shown to have a large effect on the diffusion of bovine serum albumin (BSA).[231] In contrast, hydrogels can be used for faster kinetics because of their more porous composition,[232] and enzymatic cleavage sites can be used to increase material degradation or protein release.[4,233] Combinations of these materials can be used to design highly controlled delivery systems.[234] In one example, vascular endothelial growth factor (VEGF) and platelet-derived growth factor (PDGF) were released with distinct kinetics from a hydrogel and were able to stimulate development of mature vasculature, which was an improvement over a material where both were released individually.

Methods to covalently attach proteins to materials overlap with many conjugation techniques discussed in the posttranslational modifications section (**Section 4.412.2.3**). The most basic approach is to attach proteins through their primary amines (the *N*-terminus and the ε-amino group of lysine residues). For example, EGF was coupled to a surface in this manner through a flexible linker.[235] The tethered EGF retained activity similar to that of soluble EGF, while EGF that had been nonspecifically absorbed onto the surface did not. Interestingly, tethered EGF was also shown to enhance differentiation of progenitor cells versus soluble EGF, presumably due to increased local concentrations and protection against internalization and degradation.[236] Other proteins, such as insulin and fibronectin, have also been coupled to surfaces by amine linkages and have improved the attachment and proliferation of fibroblast cells.[237,238] As an alternative, if a protein has a basal level of affinity for a material, general, nonspecific cross-linking by reactive linkers can be used.[239]

Unfortunately, the lack of specificity in these types of conjugation methods results in a risk of the protein becoming inactivated during attachment. Therefore, methods to attach proteins to materials through specific residues or locations are now being pursued. For example, VEGF naturally contains a known collagen-binding domain. VEGF was shown to be retained in a collagen-based material through this domain and activate the VEGF receptor *in vitro*.[240] Extending this to proteins without natural affinities, HGF was genetically fused to a collagen-binding domain from fibronectin. This allowed the growth factor to bind a collagen-based biomaterial and improve endothelial cell proliferation.[241] Another common binding partner, heparin, has been employed successfully for specific protein attachment as well.[239,242,243] Besides protein-binding domains, the use of nonnatural amino acids to site-specifically conjugate proteins to materials through a chemical functional group is emerging as a feasible option.[244]

Regardless of the attachment method, the protein density and presentation has a significant effect on its success as a biomaterial. For example, endothelial cell survival or death has been linked to parameters such as the curvature of the material surface and size of protein patterning.[245] Using RGD peptides as a model system, the clustering of ligands was shown to improve the adhesion of fibroblasts to a surface.[246] Furthermore, changing the level of clustering was shown to affect the behavior of preosteoblast cells.[247] Closely spaced islands of RGD peptides promoted cell spreading, whereas widely spaced islands induced differentiation. The effect of distribution can have opposite effects on different cell types, however, and the true cause of this dependence remains unknown.[248]

4.412.4.2. Protein-Based Biomaterials

In addition to acting as interfaces between materials and tissue, proteins can be used as the materials themselves.[249] Proteins have significantly less polydispersity compared to polymers and their amino acid sequence can be precisely defined. Natural proteins, such as silk, collagen, and ECM proteins, were first investigated for use as biomaterials. However, these proteins are difficult to produce and purify, and do not offer the same material flexibility or tunability compared to synthetic polymers. Therefore, more recently, the protein engineering methods described above have been used to tailor properties such as mechanical strength, degradation rates, and biocompatibility.

For simpler recombinant production, natural proteins have been reduced to shorter, more manageable domains. For example, short collagen fragments were designed with 'sticky ends' that formed disulfide-bonded triple-helices.[250] These fragments can be easily synthesized and were able to assemble into strands of nearly 1 μm in length, much longer than natural collagen which forms fibers ~300 nm in length.

Control over the mechanical properties of natural proteins has also been achieved. For example, altering the β-sheet structure of silk can change the strength of spun fibers.[251] In addition, novel peptides can be designed to self-assemble into a wide range of materials, from hydrogels to nanotubes.[252] The control over amino acid compositions also enables unique features such as reversible polymerization based on environmental pH and divalent ion concentration.[253]

Finally, proteins can be engineered for biocompatibility. For example, known cell interaction domains, such as the RGD peptide, can be easily inserted into protein-based scaffolds. Furthermore, protease sites have been introduced to allow for controlled and localized degradation. In one study, a protein and PEG hydrogel was constructed containing RGD motifs and recognition sites for plasmin and matrix metalloproteinases (proteases involved in the natural bone remodeling process). When bone morphogenetic protein 2 (BMP-2) was encapsulated in this hydrogel system, bone healing in an *in vivo* rat model was observed.[254] In addition, removal of the protease sites prevented healing, highlighting the importance of proper biomaterial degradation for biological activity.

All the parameters described above are now being combined into single biomaterial systems. Recently, an elastin-like protein was constructed with an RGD site for improved cellular adhesion and a urokinase plasminogen activator (uPA) site for localized degradation.[255] Cross-linking could be controlled to form hydrogels with defined mechanical elasticities. In addition, the amino acid sequence of the uPA site could be mutated to produce 200-fold differences in degradation rates. The ability to tailor both the mechanical and biological properties promises to propel engineered proteins to the forefront in the development of biomaterials.

4.412.5. Conclusions and Future Directions

The important role of proteins in biomaterial design is widely recognized; however, to date, the majority of these players are naturally occurring proteins or peptide fragments that have been encapsulated in or attached nonspecifically to natural and synthetic polymers. This has gradually changed as improved methods for covalent attachment have been developed and protein-based biomaterials gain prominence. We expect the marriage between proteins and biomaterials to continue to blossom as the protein engineering methods described in this chapter are further applied to molecules of interest to the regenerative medicine field. An exciting outlook for the future is the role that rational and combinatorial engineering will play in creating customized protein interfaces composed of designer ligands and cell surface receptors. These efforts will generate a toolkit of proteins and peptides beyond those that Nature has provided, resulting in novel molecules for a myriad of biomaterials applications. More specifically, with the help of engineered proteins, biomaterials will be optimized for cellular attachment, proliferation, or differentiation. Computational design and more intricate combinatorial screening methods will also be further developed to streamline protein discovery and characterization. In addition, as more protein candidates are introduced, ligand attachment and presentation will come under even more scrutiny. The focus will turn to techniques that lend more control over the protein density, release, and activity, such as site-specific attachment through specific binding domains or nonnatural amino acids. On the horizon, there are great opportunities for merging the fields of protein engineering and materials science to create biomaterials that will interact and integrate with cells and tissues in a petri dish or in a living organism.

References

1. Chan, G.; Mooney, D. J. *Trends Biotechnol*. **2008**, *26*, 382–392.
2. Langer, R.; Tirrell, D. A. *Nature* **2004**, *428*, 487–492.
3. Lutolf, M. P.; Hubbell, J. A. *Nat. Biotechnol*. **2005**, *23*, 47–55.
4. Vasita, R.; Schanmugam, K.; Katti, D. S. *Curr. Top. Med. Chem*. **2008**, *8*, 341–353.
5. Kleinman, H. K.; Philp, D.; Hoffman, M. P. *Curr. Opin. Biotechnol*. **2003**, *14*, 526–532.
6. Braman, J. *Methods in Molecular Biology:* In vitro *Mutagenesis Protocols*. Humana Press: Totowa, NJ, 2002.
7. Wang, W.; Malcolm, B. A. In *Methods in Molecular Biology:* In vitro *Mutagenesis Protocols*; Braman, J., Ed.; Humana Press: Totowa, NJ, 2002; p 37.
8. Zheng, L.; Baumann, U.; Reymond, J. L. *Nucleic Acids Res*. **2004**, *32*, e115.
9. Lehmann, M.; Pasamontes, L.; Lassen, S. F.; Wyss, M. *Biochim. Biophys. Acta* **2000**, *1543*, 408–415.
10. Steipe, B.; Schiller, B.; Pluckthun, A.; Steinbacher, S. *J. Mol. Biol*. **1994**, *240*, 188–192.
11. Wang, Q.; Buckle, A. M.; Foster, N. W.; Johnson, C. M.; Fersht, A. R. *Protein Sci*. **1999**, *8*, 2186–2193.
12. Lehmann, M.; *et al*. *Protein Eng*. **2000**, *13*, 49–57.
13. Loening, A. M.; Fenn, T. D.; Wu, A. M.; Gambhir, S. S. *Protein Eng. Des. Sel*. **2006**, *19*, 391–400.
14. Dai, M.; *et al*. *Protein Eng. Des. Sel*. **2007**, *20*, 69–79.
15. Arakawa, T.; Prestrelski, S. J.; Narhi, L. O.; Boone, T. C.; Kenney, W. C. *J. Protein Chem*. **1993**, *12*, 525–531.
16. Mark, D. F.; Lu, S. D.; Creasey, A. A.; Yamamoto, R.; Lin, L. S. *Proc. Natl. Acad. Sci*. **1984**, *81*, 5662–5666.
17. Culajay, J. F.; Blaber, S. I.; Khurana, A.; Blaber, M. *Biochemistry* **2000**, *39*, 7153–7158.
18. Lee, J.; Blaber, M. *J. Mol. Biol*. **2009**, *293*, 113–127.
19. Agren, L.; Norin, M.; Lycke, N.; Lowenadler, B. *Protein Eng*. **1999**, *12*, 173–178.
20. Villafranca, J. E.; *et al*. *Science* **1983**, *222*, 782–788.
21. Perry, L. J.; Wetzel, R. *Science* **1986**, *226*, 555–557.
22. Wetzel, R.; Perry, L. J.; Baase, W. A.; Becktel, W. J. *Proc. Natl. Acad. Sci*. **1988**, *85*, 401–405.
23. Li, Y.; Coutinho, P. M.; Ford, C. *Protein Eng*. **1998**, *11*, 661–667.
24. Zavodszky, M.; Chen, C. W.; Huang, J. K.; Zolkiewski, M.; Wen, L.; Krishnamoorthi, R. *Protein Sci*. **2001**, *10*, 149–160.
25. Brange, J.; *et al*. *Nature* **1988**, *333*, 679–682.
26. Walsh, G. *Appl. Microbiol. Biotechnol*. **2005**, *67*, 151–159.
27. Fuh, G.; Cunningham, B. C.; Fukunaga, R.; Nagata, S.; Goeddel, D. V.; Wells, J. A. *Science* **1992**, *256*, 1677–1680.
28. Tolbert, W. D.; *et al*. *Proc. Natl. Acad. Sci*. **2007**, *104*, 14592–14597.
29. Voss, R.; *et al*. *J. Immunol*. **2008**, *180*, 391–401.
30. Hwang, I.; Park, S. *Drug Discov. Today Technol*. **2008**, *5*, e43–e48.
31. Karanicolas, J.; Kuhlman, B. *Curr. Opin. Struct. Biol*. **2009**, *19*, 458–463.
32. Mandell, D. J.; Kortemme, T. *Nat. Chem. Biol*. **2009**, *5*, 797–807.
33. Rosenberg, M.; Goldblum, A. *Curr. Pharm. Des*. **2006**, *12*, 3973–3997.
34. Kuhlman, B.; Baker, D. *Curr. Opin. Struct. Biol*. **2004**, *14*, 89–95.
35. Sarkar, C. A.; Lowenhaupt, K.; Horan, T.; Boone, T. C.; Tidor, B.; Lauffenburger, D. A. *Nat. Biotechnol*. **2002**, *20*, 908–913.
36. Kuhlman, B.; Dantas, G.; Ireton, G. C.; Varani, G.; Stoddard, B. L.; Baker, D. *Science* **2003**, *302*, 1364–1368.
37. Dahiyat, B. I.; Mayo, S. L. *Proc. Natl. Acad. Sci*. **1997**, *94*, 10172–10177.
38. Luo, P.; *et al*. *Protein Sci*. **2002**, *11*, 1218–1226.
39. Lippow, S. M.; Wittrup, K. D.; Tidor, B. *Nat. Biotechnol*. **2007**, *25*, 1171–1176.
40. Song, G.; *et al*. *J. Biol. Chem*. **2006**, *281*, 5042–5049.
41. Bolon, D. N.; Grant, R. A.; Baker, T. A.; Sauer, R. T. *Proc. Natl. Acad. Sci*. **2005**, *102*, 12724–12729.
42. Grigoryan, G.; Reinke, A. W.; Keating, A. E. *Nature* **2009**, *458*, 859–864.
43. Hersel, U.; Dahmen, C.; Kessler, H. *Biomaterials* **2003**, *24*, 4385–4415.
44. Perlin, L.; MacNeil, S.; Rimmer, S. *Soft Matter* **2008**, *4*, 2331–2349.
45. Ruoslahti, E.; Pierschbacher, M. D. *Science* **1987**, *238*, 491–497.
46. Gurrath, M.; Muller, G.; Kessler, H.; Aumailley, M.; Timpl, R. *Eur. J. Biochem*. **1992**, *210*, 911–921.
47. Kantlehner, M.; *et al*. *Chembiochem* **2000**, *1*, 107–114.
48. Dechantsreiter, M. A.; *et al*. *J. Med. Chem*. **1999**, *42*, 3033–3040.
49. van der Pluijm, G.; *et al*. *Cancer Res*. **1996**, *56*, 1948–1955.
50. Garcia, A. J. *Biomaterials* **2005**, *26*, 7525–7529.
51. Aota, S.; Nomizu, M.; Yamada, K. M. *J. Biol. Chem*. **1994**, *269*, 24756–24761.
52. Potts, J. R.; Campbell, I. D. *Matrix Biol*. **1996**, *15*, 313–320.
53. Kao, W. J.; Lee, D.; Schense, J. C.; Hubbell, J. A. *J. Biomed. Mater. Res*. **2001**, *55*, 79–88.
54. Kao, W. J.; Lee, D. *Biomaterials* **2001**, *22*, 2901–2909.
55. Mardilovich, A.; Craig, J. A.; McCammon, M. W.; Garg, A.; Kokkoli, E. *Langmuir* **2006**, *22*, 3259–3264.
56. Petrie, T. A.; Capadona, J. R.; Reyes, C. D.; Garcia, A. J. *Biomaterials* **2006**, *27*, 5459–5470.
57. Reyes, C. D.; Garcia, A. J. *J. Biomed. Mater. Res*. **2003**, *65A*, 511–523.
58. Lenferink, A. E. G.; *et al*. *Biochem. J*. **1997**, *327*, 859–865.
59. Sytkowski, A. J.; Lunn, E. D.; Risinger, M. A.; Davis, K. L. *J. Biol. Chem*. **1999**, *274*, 24773–24778.
60. Schellenberger, V.; *et al*. *Nat. Biotechnol*. **2009**, *27*, 1186–1190.
61. Peters, T. *Adv. Protein Chem*. **1985**, *37*, 161–245.
62. Yeh, P.; *et al*. *Proc. Natl. Acad. Sci*. **1992**, *89*, 1904–1908.
63. Syed, S.; Schuyler, P. D.; Kulczycky, M.; Sheffield, W. P. *Blood* **1997**, *89*, 3243–3252.
64. Makrides, S. C.; *et al*. *J. Pharmacol. Exp. Ther*. **1996**, *277*, 534–542.
65. Dennis, M. S.; *et al*. *J. Biol. Chem*. **2002**, *277*, 35035–35043.
66. Ashkenazi, A.; Chamow, S. M. *Curr. Opin. Immunol*. **1997**, *9*, 195–200.
67. Chamow, S. M.; Ashkenazi, A. *Trends Biotechnol*. **1996**, *14*, 52–60.
68. Marshall, S. A.; Lazar, G. A.; Chirino, A. J.; Desjarlais, J. R. *Drug Discov. Today* **2003**, *8*, 212–221.
69. Goldenberg, M. M. *Clin. Ther*. **1999**, *21*, 75–87.
70. Madhusudan, S.; *et al*. *Clin. Cancer Res*. **2004**, *10*, 6528–6534.
71. Cochran, J. R. *Sci. Transl. Med*. **2010**, *2*, 17ps5.
72. Kriangkum, J.; Xu, B.; Nagata, L. P.; Fulton, R. E.; Suresh, M. R. *Biomol. Eng*. **2001**, *18*, 31–40.
73. Dela Cruz, J. S.; Huang, T. H.; Penichet, M. L.; Morrison, S. L. *Clin. Exp. Med*. **2004**, *4*, 57–64.

74. Gillies, S. D. In *Targeted Cancer Immune Therapy*; Lustgarten, J., *et al*. Eds.; Springer Science: New York, 2009.
75. Chi, A.; *et al*. *Proc. Natl. Acad. Sci*. **2006**, *104*, 2193–2198.
76. Gnad, F.; *et al*. *Proteomics* **2009**, *9*, 4642–4652.
77. Julenius, K.; Molgaard, A.; Gupta, R.; Brunak, S. *Glycobiology* **2004**, *15*, 153–164.
78. Li, S.; Liu, B.; Zeng, R.; Cai, Y.; Li, Y. *Comp. Biol. Chem*. **2006**, *30*, 203–208.
79. Bause, E. *Biochem. J*. **1983**, *209*, 331–336.
80. Hubbard, S. C.; Ivatt, R. J. *Ann. Rev. Biochem*. **1981**, *50*, 555–583.
81. Roitsch, T.; Lehle, L. *Eur. J. Biochem*. **1989**, *181*, 525–529.
82. Yamaguchi, K.; Akai, K.; Kawanishi, G.; Ueda, M.; Masuda, S.; Sasaki, R. *J. Biol. Chem*. **1991**, *266*, 20434–20439.
83. Egrie, J. C.; Browne, J. K. *Nephrol. Dial. Transplant*. **2001**, *16*, 3–13.
84. Fisher, J. W. *Exp. Biol. Med*. **2003**, *228*, 1–14.
85. Thomas, G. R.; *et al*. *Stroke* **1994**, *25*, 2072–2079.
86. Elliott, S.; *et al*. *Nat. Biotechnol*. **2003**, *21*, 414–421.
87. Harris, J. M.; Chess, R. B. *Nat. Rev. Drug Discov*. **2003**, *2*, 214–221.
88. Morar, A. S.; Schrimsher, J. L.; Chavez, M. D. *Biopharm. Int*. **2006**, *19*, 34–49.
89. Veronese, F. M.; Pasut, G. *Drug Discov. Today* **2005**, *10*, 1451–1458.
90. Graham, M. L. *Adv. Drug Deliv. Rev*. **2003**, *55*, 1293–1302.
91. Keating, M. J.; Holmes, R.; Lerner, S.; Ho, D. H. *Leuk. Lymphoma* **1993**, *10*, 153–157.
92. Bailon, P.; *et al*. *Bioconjug. Chem*. **2001**, *12*, 195–202.
93. Roberts, M. J.; Bentley, M. D.; Harris, J. M. *Adv. Drug Deliv. Rev*. **2002**, *52*, 459–476.
94. Kinstler, O. B.; Brems, D. N.; Lauren, S. L.; Paige, A. G.; Hamburger, J. B.; Treuheit, M. J. *Pharm. Res*. **1996**, *13*, 996–1002.
95. Bell, S. J.; *et al*. *Bioconjug. Chem*. **2008**, *19*, 299–305.
96. Sato, H. *Adv. Drug Deliv. Rev*. **2002**, *52*, 487–504.
97. Chen, T.; *et al*. *Langmuir* **2003**, *19*, 9382–9386.
98. Wang, L.; Brock, A.; Herberich, B.; Schultz, P. G. *Science* **2001**, *292*, 498–500.
99. Finn, R. F. In *PEGylated Protein Drugs: Basic Science and Clinical Applications*; Veronese, F. M., Ed.; Birkhauser Verlag: Basel, Switzerland, 2009.
100. Service, R. F. *Science* **2005**, *308*, 44.
101. Kaneda, Y.; *et al*. *Biomaterials* **2004**, *25*, 3259–3266.
102. Kamada, H.; *et al*. *Cancer Res*. **2000**, *60*, 6416–6420.
103. Kurtzhals, P.; *et al*. *Biochem. J*. **1995**, *312*, 725–731.
104. Havelund, S.; *et al*. *Pharm. Res*. **2004**, *21*, 1498–1504.
105. Markussen, J.; *et al*. *Diabetologia* **1996**, *39*, 281–288.
106. Neylon, C. *Nucleic Acids Res*. **2004**, *32*, 1448–1459.
107. Wong, T. S.; Zhurina, D.; Schwaneberg, U. *Comb. Chem. High Throughput Screen*. **2006**, *9*, 271–288.
108. Doudney, C. O.; Haas, F. L. *Proc. Natl. Acad. Sci*. **1959**, *45*, 709–722.
109. Nguyen, A. W.; Daugherty, P. S. In *Methods in Molecular Biology: Directed Evolution Library Creation: Methods and Protocols*; Arnold, F. H., Georgiou, G., Eds.; Humana Press: Totowa, NJ, 2003.
110. Cirino, P. C.; Mayer, K. M.; Umeno, D. In *Methods in Molecular Biology: Directed Evolution Library Creation: Methods and Protocols*; Arnold, F. H., Georgiou, G., Eds.; Humana Press: Totowa, NJ, 2003.
111. Cadwell, R. C.; Joyce, G. F. *Genome Res*. **1992**, *2*, 28–33.
112. Beckman, R. A.; Mildvan, A. S.; Loeb, L. A. *Biochemistry* **1985**, *24*, 5810–5817.
113. Zaccolo, M.; Williams, D. M.; Brown, D. M.; Gherardi, E. *J. Mol. Biol*. **1996**, *255*, 589–603.
114. Cline, J.; Braman, J. C.; Hogrefe, H. H. *Nucleic Acids Res*. **1996**, *24*, 3546–3551.
115. Patel, P. H.; Kawate, H.; Adman, E.; Aschbach, M.; Loeb, L. A. *J. Biol. Chem*. **2001**, *276*, 5044–5051.
116. Biles, B. D.; Connolly, B. A. *Nucleic Acids Res*. **2004**, *32*, e176.
117. Hayes, F.; Hallet, B. *Trends Microbiol*. **2000**, *8*, 571–577.
118. Murakami, H.; Hohsaka, T.; Sisido, M. *Nat. Biotechnol*. **2002**, *20*, 76–81.
119. Georgescu, R.; Bandara, G.; Sun, L. In *Methods in Molecular Biology: Directed Evolution Library Creation: Methods and Protocols*; Arnold, F. H., Georgiou, G., Eds.; Humana Press: Totowa, NJ, 2000.
120. Reetz, M. T.; Kahakeaw, D.; Lohmer, R. *ChemBioChem* **2008**, *9*, 1797–1804.
121. Virnekas, B.; Ge, L.; Pluckthun, A.; Schneider, K. C.; Wellnhofer, G.; Moroney, S. E. *Nucleic Acids Res*. **1994**, *22*, 5600–5607.
122. Yanez, J.; Arguello, M.; Osuna, J.; Soberon, X.; Gaytan, P. *Nucleic Acids Res*. **2004**, *32*, e158.
123. Hughes, M. D.; Nagel, D. A.; Santos, A. F.; Sutherland, A. J.; Hine, A. V. *J. Mol. Biol*. **2003**, *331*, 973–979.
124. Kurtzman, A. L.; Govindarajan, S.; Vahle, K.; Jones, J. T.; Heinrichs, V.; Patten, P. A. *Curr. Opin. Biotechnol*. **2001**, *12*, 361–370.
125. Stemmer, W. P. C. *Nature* **1994**, *370*, 389–391.
126. Stemmer, W. P. C. *Proc. Natl. Acad. Sci*. **1994**, *91*, 10747–10751.
127. Zhao, H.; Giver, L.; Shao, Z.; Affholter, J. A.; Arnold, F. H. *Nat. Biotechnol*. **1998**, *16*, 258–261.
128. Coco, W. M.; *et al*. *Nat. Biotechnol*. **2001**, *19*, 354–359.
129. Lutz, S.; Ostermeier, M.; Moore, G. L.; Maranas, C. D.; Benkovic, S. J. *Proc. Natl. Acad. Sci*. **2001**, *98*, 11248–11253.
130. Lutz, S.; Ostermeier, M.; Benkovic, S. J. *Nucleic Acids Res*. **2001**, *29*, e16.
131. Crameri, A.; Whitehorn, E. A.; Tate, E.; Stemmer, W. P. C. *Nat. Biotechnol*. **1996**, *14*, 315–319.
132. Crameri, A.; Raillard, S. A.; Bermudez, E.; Stemmer, W. P. C. *Nature* **1998**, *391*, 288–291.
133. Hackel, B. J.; Kapila, A.; Wittrup, K. D. *J. Mol. Biol*. **2008**, *381*, 1238–1252.
134. Ness, J. E.; *et al*. *Nat. Biotechnol*. **2002**, *20*, 1251–1255.
135. Zha, D.; Eipper, A.; Reetz, M. T. *ChemBioChem* **2003**, *4*, 34–39.
136. Cochran, J. R.; Kim, Y. S.; Lippow, S. M.; Rao, B.; Wittrup, K. D. *Protein Eng. Des. Sel*. **2006**, *19*, 245–253.
137. Miyazaki, K.; Wintrode, P. L.; Grayling, R. A.; Rubingh, D. N.; Arnold, F. H. *J. Mol. Biol*. **2000**, *297*, 1015–1026.
138. Williams, G. J.; Domann, S.; Nelson, A.; Berry, A. *Proc. Natl. Acad. Sci*. **2003**, *100*, 3143–3148.
139. Koga, Y.; Kato, K.; Nakano, H.; Yamane, T. *J. Mol. Biol*. **2003**, *331*, 585–592.
140. Rungpragayphan, S.; Yamane, T.; Nakano, H. In *Methods in Molecular Biology:* In vitro *Transcription and Translation Protocols*; Grandi, G., Ed.; Humana Press: Totowa, NJ, 2007.
141. Arnold, F. H.; Wintrode, P. L.; Miyazaki, K.; Gershenson, A. *Trends Biochem. Sci*. **2001**, *26*, 100–106.
142. Kaur, J.; Sharma, R. *Crit. Rev. Biotechnol*. **2006**, *26*, 165–199.
143. Souriau, C.; Fort, P.; Roux, P.; Hartley, O.; Lefranc, M. P.; Weill, M. *Nucleic Acids Res*. **1997**, *25*, 1585–1590.
144. Chang, C. J.; *et al*. *Nature* **1999**, *17*, 793–797.
145. Lui, B. H.; Cochran, J. R.; Swartz, J. R. Discovery of improved epidermal growth factor agonists using a novel *in vitro* screening platform. Submitted for publication, 2011.
146. Stockwell, B. R.; Haggarty, S. J.; Schreiber, S. L. *Chem. Biol*. **1999**, *6*, 71–83.
147. Hoogenboom, H. R.; de Bruine, A. P.; Hufton, S. E.; Hoet, R. M.; Arends, J. W.; Roovers, R. C. *Immunotechnology* **1998**, *4*, 1–20.
148. Sidhu, S. S. *Curr. Opin. Biotechnol*. **2000**, *11*, 610–616.
149. Sidhu, S. S.; Koide, S. *Curr. Opin. Struct. Biol*. **2007**, *17*, 481–487.
150. Smith, G. P. *Science* **1985**, *228*, 1315–1317.
151. Ferrer, M.; Harrison, S. C. *J. Virol*. **1999**, *73*, 5795–5802.
152. Koivunen, E.; Gay, D. A.; Ruoslahti, E. *J. Biol. Chem*. **1993**, *268*, 20205–20210.
153. Whaley, S. R.; English, D. S.; Hu, E. L.; Barbara, P. F.; Belcher, A. M. *Nature* **2000**, *405*, 665–668.
154. Sanghvi, A. B.; Miller, K. P. H.; Belcher, A. M.; Schmidt, C. E. *Nat. Mater*. **2005**, *4*, 496–502.
155. Lowman, H. B.; Wells, J. A. *J. Mol. Biol*. **1993**, *234*, 564–578.
156. Paschke, M.; Hohne, W. *Gene* **2005**, *350*, 79–88.
157. Steiner, D.; Forrer, P.; Stumpp, M. T.; Pluckthun, A. *Nat. Biotechnol*. **2006**, *24*, 823–831.
158. Barbas, C. F., III; Kang, A. S.; Lerner, R. A.; Benkovic, S. J. *Proc. Natl. Acad. Sci*. **1991**, *88*, 7978–7982.
159. McCafferty, J.; Griffiths, A. D.; Winter, G.; Chiswell, D. J. *Nature* **1990**, *348*, 552–554.
160. Koide, A.; Bailey, C. W.; Huang, X.; Koide, S. *J. Mol. Biol*. **1998**, *284*, 1141–1151.
161. Schlehuber, S.; Beste, G.; Skerra, A. *J. Mol. Biol*. **2000**, *297*, 1105–1120.
162. Kalie, E.; Jaitin, D. A.; Abramovich, R.; Schreiber, G. *J. Biol. Chem*. **2007**, *282*, 11602–11611.
163. Watters, J. M.; Telleman, P.; Junghans, R. P. *Immunotechnology* **1997**, *3*, 21–29.
164. Pasqualini, R.; Ruoslahti, E. *Nature* **1996**, *380*, 364–366.
165. Daugherty, P. S.; Iverson, B. L.; Georgiou, G. *J. Immunol. Meth*. **2000**, *243*, 211–227.
166. Georgiou, G. *Adv. Protein Chem*. **2000**, *55*, 293–315.
167. Chao, G.; Lau, W. L.; Hackel, B. J.; Sazinsky, S. L.; Lippow, S. M.; Wittrup, K. D. *Nat. Protoc*. **2006**, *1*, 755–768.
168. Wittrup, K. D. *Curr. Opin. Biotechnol*. **2001**, *12*, 395–399.
169. Ernst, W.; Grabherr, R.; Wegner, D.; Borth, N.; Grassauer, A.; Katinger, H. *Nucleic Acids Res*. **1998**, *26*, 1718–1723.
170. Fischetti, V. A.; Medaglini, D.; Pozzi, G. *Curr. Opin. Biotechnol*. **1996**, *7*, 659–666.
171. Ho, M.; Nagata, S.; Pastan, I. *Proc. Natl. Acad. Sci*. **2006**, *103*, 9637–9642.
172. Stahl, S.; Uhlen, M. *Trends Biotechnol*. **1997**, *15*, 185–192.
173. Tanino, T.; Fukuda, H.; Kondo, A. *Biotechnol. Prog*. **2006**, *22*, 989–993.
174. Daugherty, P. S. *Curr. Opin. Struct. Biol*. **2007**, *17*, 474–480.

175. Lee, S. Y.; Choi, J. H.; Xu, Z. *Trends Biotechnol*. **2003**, *21*, 45–52.
176. Zanoni, G.; *et al*. *PLoS Med*. **2006**, *3*, 1637–1653.
177. Francisco, J. A.; Campbell, R.; Iverson, B. L.; Georgiou, G. *Proc. Natl. Acad. Sci*. **1993**, *90*, 10444–10448.
178. Daugherty, P. S.; Olsen, M. J.; Iverson, B. L.; Georgiou, G. *Protein Eng*. **1999**, *12*, 613–621.
179. Harvey, B. R.; Georgiou, G.; Hayhurts, A.; Jeong, K. J.; Iverson, B. L.; Rogers, G. K. *Proc. Natl. Acad. Sci*. **2004**, *101*, 9193–9198.
180. Mazor, Y.; Blarcom, T. V.; Mabry, R.; Iverson, B. L.; Georgiou, G. *Nat. Biotechnol*. **2007**, *25*, 563–565.
181. Boder, E. T.; Wittrup, K. D. *Nat. Biotechnol*. **1997**, *15*, 553–557.
182. Bowley, D. R.; Labrijn, A. F.; Zwick, M. B.; Burton, D. R. *Protein Eng. Des. Sel*. **2007**, *20*, 81–90.
183. Boder, E. T.; Midelfort, K. S.; Wittrup, K. D. *Proc. Natl. Acad. Sci*. **2000**, *97*, 10701–10705.
184. Feldhaus, M. J.; *et al*. *Nat. Biotechnol*. **2003**, *21*, 163–170.
185. Rajpal, A.; *et al*. *Proc. Natl. Acad. Sci*. **2005**, *102*, 8466–8471.
186. Razai, A.; *et al*. *J. Mol. Biol*. **2005**, *351*, 158–169.
187. Colby, D. W.; *et al*. *Proc. Natl. Acad. Sci*. **2004**, *101*, 17616–17621.
188. Kim, Y.; Bhandari, R.; Cochran, J. R.; Kuriyan, J.; Wittrup, K. D. *Proteins* **2006**, *62*, 1026–1035.
189. Shusta, E. V.; Holler, P. D.; Kieke, M. C.; Kranz, D. M.; Wittrup, K. D. *Nat. Biotechnol*. **2000**, *18*, 754–759.
190. Boder, E. T.; Bill, J. R.; Nields, A. W.; Marrack, P. C.; Kappler, J. W. *Biotechnol. Bioeng*. **2005**, *92*, 485–491.
191. Shusta, E. V.; Kieke, M. C.; Park, E.; Kranz, D. M.; Wittrup, K. D. *J. Mol. Biol*. **1999**, *292*, 949–956.
192. Pepper, L. R.; Cho, Y. K.; Boder, E. T.; Shusta, E. V. *Comb. Chem. High Throughput Screen*. **2008**, *11*, 127–134.
193. Jones, D. S.; Tsai, P. C.; Cochran, J. R. Engineering hepatocyte growth factor fragments with high stability and activity as met receptor agonists and antagonists. Submitted for publication, 2011.
194. Gai, S. A.; Wittrup, K. D. *Curr. Opin. Struct. Biol*. **2007**, *17*, 467–473.
195. Rao, B. M.; Driver, I.; Lauffenburger, D. A.; Wittrup, K. D. *Biochemistry* **2005**, *44*, 10696–10701.
196. Lahti, J. L.; *et al*. Engineered epidermal growth factor mutants with faster binding on-rates correlate with enhanced receptor activation. *FEBS Lett*. (*In press*), 2010.
197. Kimura, R. H.; Levin, A. M.; Cochran, F. V.; Cochran, J. R. *Proteins* **2009**, *77*, 359–369.
198. Silverman, A. P.; Levin, A. M.; Lahti, J. L.; Cochran, J. R. *J. Mol. Biol*. **2009**, *385*, 1064–1075.
199. Silverman, A. P.; Kariolis, M. S.; Cochran, J. R. *J. Mol. Recognit*. **2011**, *24*, 127–135.
200. Leemhuis, H.; Stein, V.; Griffiths, A. D.; Hollfelder, F. *Curr. Opin. Struct. Biol*. **2005**, *15*, 472–478.
201. Katzen, F.; Chang, G.; Kudlicki, W. *Trends Biotechnol*. **2005**, *23*, 150–156.
202. Hanes, J.; Pluckthun, A. *Proc. Natl. Acad. Sci*. **1997**, *94*, 4937–4942.
203. He, M.; Taussig, M. J. *Brief. Funct. Genomics Proteomics* **2002**, *1*, 204–212.
204. Mattheakis, L. C.; Bhatt, R. R.; Dower, W. J. *Proc. Natl. Acad. Sci*. **1994**, *91*, 9022–9026.
205. Yan, X.; Xu, Z. *Drug Discov. Today* **2006**, *11*, 911–916.
206. Lipovsek, D.; Pluckthun, A. *J. Immunol. Meth*. **2004**, *290*, 51–67.
207. Roberts, R. W.; Szostak, J. W. *Proc. Natl. Acad. Sci*. **1997**, *94*, 12297–12302.
208. Griffiths, A. D.; Tawfik, D. S. *Trends Biotechnol*. **2006**, *24*, 395–402.
209. Tawfik, D. S.; Griffiths, A. D. *Nat. Biotechnol*. **1998**, *16*, 652–656.
210. Hanes, J.; Schaffitzel, C.; Knappik, A.; Pluckthun, A. *Nat. Biotechnol*. **2000**, *18*, 1287–1292.
211. Stumpp, M. T.; Binz, H. K.; Amstutz, P. *Drug Discov. Today* **2008**, *13*, 695–701.
212. Zahnd, C.; Pecorari, F.; Straumann, N.; Wyler, E.; Pluckthun, A. *J. Biol. Chem*. **2006**, *281*, 35167–35175.
213. Zahnd, C.; *et al*. *J. Mol. Biol*. **2007**, *369*, 1015–1028.
214. Ihara, H.; *et al*. *Biochem. Biophys. Res. Commun*. **2006**, *345*, 1149–1154.
215. Wada, A.; Sawata, S. Y.; Ito, Y. *Biotechnol. Bioeng*. **2008**, *101*, 1102–1107.
216. Kurz, M.; Gu, K.; Lohse, P. A. *Nucleic Acids Res*. **2000**, *28*, e83.
217. Keefe, A. D.; Szostak, J. W. *Nature* **2001**, *410*, 715–718.
218. Wilson, D. S.; Keefe, A. D.; Szostak, J. W. *Proc. Natl. Acad. Sci*. **2001**, *98*, 3750–3755.
219. Xu, L.; *et al*. *Chem. Biol*. **2002**, *9*, 933–942.
220. Shen, X.; Valencia, C. A.; Szostak, J. W.; Dong, B.; Liu, R. *Proc. Natl. Acad. Sci*. **2005**, *102*, 5969–5974.
221. Miller, O. J.; *et al*. *Nat. Meth*. **2006**, *3*, 561–570.
222. Yonezawa, M.; Doi, N.; Kawahashi, Y.; Higashinakagawa, T.; Yanagawa, H. *Nucleic Acids Res*. **2003**, *31*, e118.
223. Griffiths, A. D.; Tawfik, D. S. *EMBO J*. **2003**, *22*, 24–35.
224. Sepp, A.; Tawfik, D. S.; Griffiths, A. D. *FEBS Lett*. **2002**, *532*, 455–458.
225. Bernath, K.; Hai, M.; Mastrobattista, E.; Griffiths, A. D.; Magdassi, S.; Tawfik, D. S. *Anal. Biochem*. **2004**, *325*, 151–157.
226. Mastrobattista, E.; Taly, V.; Chanudet, E.; Treacy, P.; Kelly, B. T.; Griffiths, A. D. *Chem. Biol*. **2005**, *12*, 1291–1300.
227. Sepp, A.; Choo, Y. *J. Mol. Biol*. **2005**, *354*, 212–219.
228. Agresti, J. J.; *et al*. *Proc. Natl. Acad. Sci*. **2010**, *107*, 4004–4009.
229. Crommelin, D. J. A.; Storm, G.; Jiskoot, W.; Stenekes, R.; Mastrobattista, E.; Hennink, W. E. *J. Control. Release* **2003**, *87*, 81–88.
230. Sokolsky-Papkov, M.; Agashi, K.; Olaye, A.; Shakesheff, K.; Domb, A. J. *Adv. Drug Deliv. Rev*. **2007**, *59*, 187–206.
231. Panyam, J.; *et al*. *J. Control. Release* **2003**, *92*, 173–187.
232. Silva, E. A.; Mooney, D. J. *Thromb. Haemost*. **2007**, *5*, 590–598.
233. Gombotz, W. R.; Pettit, D. K. *Bioconjug. Chem*. **1995**, *6*, 332–351.
234. Richardson, T. P.; Peters, M. C.; Ennett, A. B.; Mooney, D. J. *Nat. Biotechnol*. **2001**, *19*, 1029–1034.
235. Kuhl, P. R.; Griffith-Cima, L. G. *Nat. Med*. **1996**, *2*, 1022–1027.
236. Marcantonio, N. A.; *et al*. *Biomaterials* **2009**, *30*, 4629–4638.
237. Ito, Y.; Liu, S. Q.; Imanishi, Y. *Biomaterials* **1991**, *12*, 449–453.
238. Nuttelman, C. R.; Mortisen, D. J.; Henry, S. M.; Anseth, K. S. *J. Biomed. Mater. Res*. **2001**, *57*, 217–223.
239. Wissink, M. J. B.; *et al*. *J. Control. Release* **2000**, *64*, 103–114.
240. Chen, T. T.; Luque, A.; Lee, S.; Anderson, S. M.; Segura, T.; Iruela-Arispe, M. L. *J. Cell Biol*. **2010**, *188*, 595–609.
241. Kitajima, T.; Terai, H.; Ito, Y. *Biomaterials* **2007**, *28*, 1989–1997.
242. Edelman, E. R.; Mathiowitz, E.; Langer, R.; Klagsbrun, M. *Biomaterials* **1991**, *12*, 619–626.
243. Laham, R. J.; *et al*. *Circulation* **1999**, *100*, 1865–1871.
244. de Graaf, A. J.; Kooijman, M.; Hennink, W. E.; Mastrobattista, E. *Bioconjug. Chem*. **2009**, *20*, 1281–1295.
245. Chen, C. S.; Mrksich, M.; Huang, S.; Whitesides, G. M.; Ingber, D. E. *Science* **1997**, *276*, 1425–1428.
246. Koo, L. Y.; Irvine, D. J.; Mayes, A. M.; Lauffenburger, D. A.; Griffith, L. G. *J. Cell Sci*. **2002**, *115*, 1423–1433.
247. Comisar, W. A.; Kazmers, N. H.; Mooney, D. J.; Linderman, J. J. *Biomaterials* **2007**, *28*, 4409–4417.
248. Boontheekul, T.; *et al*. *Faraday Discuss*. **2008**, *139*, 53–70.
249. van Hest, J. C. M.; Tirrell, D. A. *Chem. Comm*. **2001**, *19*, 1897–1904.
250. Kotch, F. W.; Raines, R. T. *Proc. Natl. Acad. Sci*. **2006**, *103*, 3028–3033.
251. Tuele, F.; Furin, W. A.; Cooper, A. R.; Duncan, J. R.; Lewis, R. V. *Mater. Sci*. **2007**, *42*, 8974–8985.
252. Zhao, X.; Zhang, S. *Macromol. Biosci*. **2007**, *7*, 13–22.
253. Hartgerink, J. D.; Beniash, E.; Stupp, S. I. *Proc. Natl. Acad. Sci*. **2002**, *99*, 5133–5138.
254. Rizzi, S. C.; *et al*. *Biomacromolecules* **2006**, *7*, 3019–3029.
255. Straley, K. S.; Heilshorn, S. C. *Soft Matter* **2008**, *5*, 114–124.

4.413. Patterned Biointerfaces

A B Faia-Torres, T Goren, M Textor, and M Pla-Roca, BioInterface Group, Laboratory for Surface Science and Technology, ETH Zurich, Zurich, Switzerland

© 2011 Elsevier Ltd. All rights reserved.

4.413.1.	**Introduction**	182
4.413.2.	**Patterning Techniques**	183
4.413.2.1.	Top-Down Approaches	183
4.413.2.1.1.	Photolithography	183
4.413.2.1.2.	Beam-based lithography	185
4.413.2.1.3.	Embossing	186
4.413.2.1.4.	Soft lithography	186
4.413.2.1.5.	Scanning-probe lithography	188
4.413.2.2.	Bottom-up Approaches	189
4.413.2.2.1.	Colloidal lithography	189
4.413.2.2.2.	Block copolymer micelle nanolithography	190
4.413.2.2.3.	Block copolymers	190
4.413.2.2.4.	DNA templating	190
4.413.3.	**Biointerfacing with Patterned Surfaces**	191
4.413.3.1.	Vesicle and Membrane Patterns	191
4.413.3.1.1.	Vesicle arrays	191
4.413.3.1.2.	Supported membrane arrays	192
4.413.3.2.	Cell Adhesion and Function on Patterned Surfaces	193
4.413.3.2.1.	Cell shape and its impact on cell survival/apoptosis	194
4.413.3.2.2.	Cell adhesion to nanopatterned surfaces	194
4.413.3.2.3.	Cell differentiation on micropatterned surfaces	195
4.413.3.2.4.	Effect of micropatterned surfaces on cytoskeletal architecture	196
4.413.3.2.5.	Cell motility on micropatterned gradients	196
4.413.3.2.6.	Tissue engineering	196
4.413.3.3.	Bacteria at Patterned Interfaces	197
4.413.3.4.	Viruses at Patterned Interfaces	199
References		199

Glossary

Alkylsilanes A class of reactive chemical compounds, often used for their alkyl-derivatized terminal functional groups, which spontaneously form covalent bonds to hydroxylated surfaces.

Alkylthiol A class of chemical compounds containing one or several –SH groups, often used as anchoring groups that spontaneously form a covalent-like bond to several coinage metal surfaces.

Fibronectin A glycoprotein found in the extracellular matrix.

Integrin A class of proteins (receptors) that mediate cell interactions with neighboring cells, tissues, and extracellular matrix proteins.

Lithography A method by which a pattern or design is printed onto a substrate.

Mask A plate consisting of transparent and opaque areas, usually made of glass, quartz, or plastic, which together constitute the design of a given pattern.

Microscale Feature sizes ranging from 0.1 μm to 1 mm.

Nanoscale Feature sizes ranging from 1 to 100 nm.

Polydimethylsiloxane (PDMS) A widely used, transparent silicone elastomeric polymer.

Poly(ethylene glycol) (PEG) (also known as poly (ethylene oxide), PEO) A biocompatible polyether. Surface-grafted PEG is known to resist protein and cell adsorption.

Resist A polymeric film which homogenously coats an underlying substrate. If the polymer is radiation-sensitive, it becomes known as photoresist.

Resolution The smallest possible feature size accurately reproduced from the desired pattern.

RGD A cell-adhesive peptide sequence, Arg-Gly-Asp, known to interact with integrin receptors in cell membranes.

Self-assembled monolayer (SAM) A molecular coating that spontaneously chemi- or physisorbs onto a surface to form a single molecule-thick film.

Streptavidin A tetrameric protein synthesized by *Streptomyces avidinii* bacteria, very tolerant of harsh environments. It has four specific high-affinity binding sites for its ligand, biotin, and is often used as a linker molecule to biotinylated biomolecules.

Throughput A measure of the number of samples that may be processed at a given time.

Abbreviations

AFM	Atomic force microscopy
BSA	Bovine serum albumin
DNA	Deoxyribonucleic acid
DPN	Dip-pen nanolithography
EYFP	Enhanced yellow fluorescent protein
MAPL	Molecular assembly patterning by lift-off
nCP	Nanocontact printing
PEG	Poly(ethylene glycol)
PLL	Poly(L-lysine)
POPC	1-Palmitoyl,2-oleoyl-*sn*-glycero-3-phosphocholine
POPS	1-Palmitoyl-2-oleoyl-*sn*-glycero-3-phospho-L-serine (sodium salt)
SA	Streptavidin
SAM	Self-assembled monolayer
UV	Ultraviolet light
μCP	Microcontact printing

4.413.1. Introduction

The term biointerface refers to the interconnection between a synthetic or natural material and a tissue, microorganism, cell, virus, or biomolecule. The topology, morphology, physical structure, and chemical or biological composition of these interfaces, and their lateral distribution at dimensions ranging from the macro- through the micro- to the nanoscale, strongly influence the behavior of the system. Biointerface science is a highly multidisciplinary field. Scientists and engineers from multiple disciplines work together with the aim of interrogating the mechanistic aspects of interfacial processes, and to develop techniques for the creation of precisely engineered interfaces with the goal of directing biological response to (bio)materials. Biointerface science and engineering is thought to advance our knowledge and capabilities in fields such as biology, biotechnology, bioanalytics, drug delivery, medicine, tissue engineering, and regenerative medicine. One key challenge facing any new biomaterials application is the choice of materials with appropriate bulk properties (e.g., mechanical strength, stability, controlled degradability) and surface functionalities able to direct a favorable biological response in the context of the specific application. The outcome of this focus on the controlled design and tailoring of specific surface properties is a new material that outperforms the conventional bulk material – an advanced material.

The drive to miniaturize devices, thereby rendering the research and development process more efficient and less expensive, has spread from the electronics industry to other fields of science. Now that micro- and nanofabrication have become widely used to tailor surface properties, widespread evidence of the influence of nanoscale physicochemical properties such as surface chemistry, surface energy, and topography of materials on proteins, cells, viruses, and bacteria has emerged. Although it is still unknown how cells ranging from 10 to 100 μm in size identify their spatial position in a multicellular system that ultimately assembles into an organism, the important role played by their substrate and neighboring cells in a laboratory environment has been recognized by the scientific community. Cell–cell and cell–matrix contacts are dynamic, responding and adjusting to protein clusters formed at connection sites. The size and shape of the protein clusters, influenced by the ligands to which they bind on the surface, deeply influence the ability of cells to maintain their function.

Micro- and nanopatterning are used today to achieve not only accurate micro- and nanostructured surfaces, but also biomolecular positioning on the substrate, as reviewed by Blättler *et al.*,[1] which can ultimately influence cellular morphology,[2,3] adhesion,[3,4] proliferation,[5] differentiation,[3,5,6] migration,[3,4] and apoptosis,[4] as well as conformation and functionality of individual proteins attached to the surface.[6]

Micro- and nanopatterning techniques allow researchers to access a new dimension of detail and to thereby recognize and understand surface characteristics that favor the preservation of function of proteins, peptides, and cells, which in turn reflect on the success of the applied patterning strategy. Further studies may also improve our knowledge on how cellular systems integrate physicochemical cues on the surface and how they ultimately translate them into biochemical responses. Additionally, the precise spatial positioning of cells on surfaces greatly promotes the development of cellular and molecular sensors, which are relevant in several fields, from medical diagnosis to lab-on-a-chip applications and biosensing. In this context, we can take advantage of the fact that each cell, as a sensing element, can both express and recognize specific receptors, signaling proteins, and enzymes, which guide the investigation of cell behavior, drug discovery, antibody selection, and RNA interference. Arrays of micropatterned cells can be generated for use as miniature biosensors, allowing the parallel detection of a large number of bioentities and the reduction of the number of samples required, while contributing to the development of more sophisticated detection methods.

As the field of micro- and nanotechnology rapidly evolves, summarizing the drawbacks and advantages of each technique in the context of biointerfaces is a challenging task. Their limitations are constantly being overcome, better scale resolution and less time consumption being two of the most sought-after changes. As technology develops, it commonly seems to be part of the solution to realize the positive characteristics of a key enabling technology by associating it with a second technology that overcomes the technological disadvantages of the first. The final selection of patterning technique will be closely related both to its cost-effectiveness and to the unique aspects of its output, which should match the requirements set by the research project.

The purpose of the first section of this chapter (Section 4.413.2) is to summarize distinct patterning techniques, as depicted in Figure 1, used for the creation of advanced biointerfaces at the micro- and nanoscale in two dimensions, highlighting their main characteristics, advantages, and shortcomings. The techniques are presented separately for top-down and bottom-up processes. In Section 4.413.2, we disclose several examples of the application of those

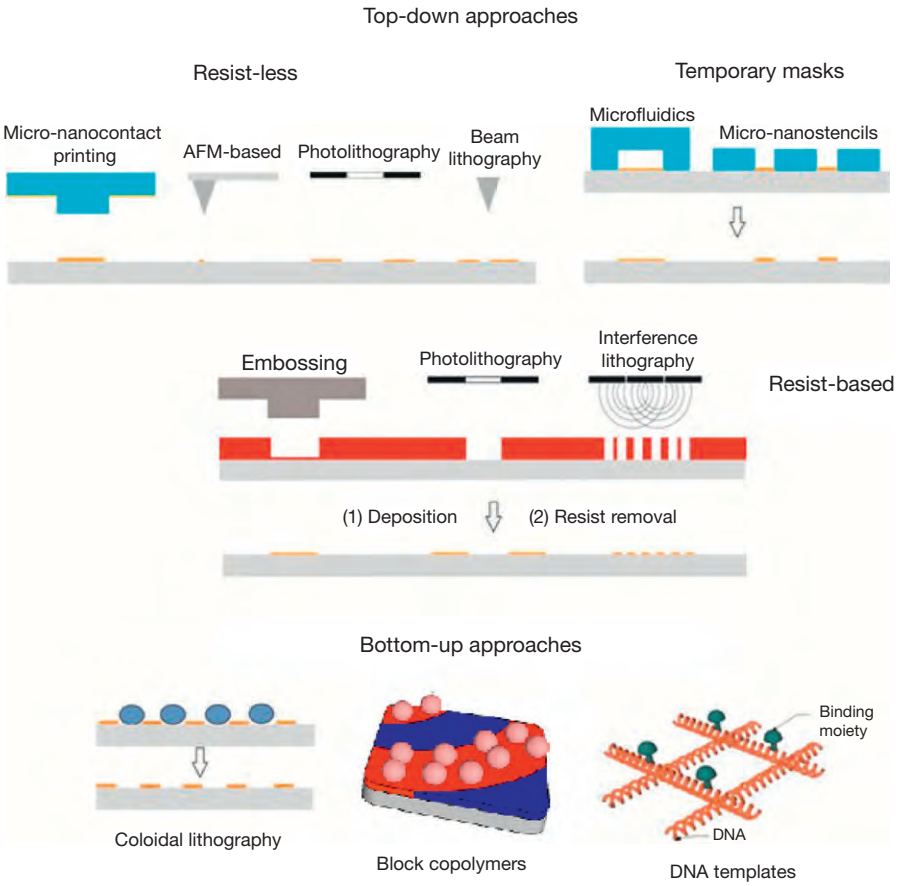

Figure 1 The distinct surface patterning techniques can be classified as bottom-up and top-down approaches. Top-down approaches can be further classified into resist-less, resist-based, and temporary mask-based. The figure summarizes schematically most of the technological strategies that will be presented in the following sections.

technologies toward the production of biopatterns composed of deoxyribonucleic acid (DNA), peptides, proteins, cells, bacteria, and viruses and their (potential) applications in specific fields. Related information on these topics may also be found in **Chapter 4.406, Protein Interactions with Biomaterials**; **Chapter 3.320, Nanostructured Polymeric Films for Cell Biology**; **Chapter 3.321, Microarrays in Biomaterials Research**; **Chapter 4.411, Peptide- and Protein-Modified Surfaces**; **Chapter 4.412, Rational and Combinatorial Methods to Create Designer Protein Interfaces**; **Chapter 4.414, Molecular Biomimetic Designs for Controlling Surface Interactions**; and **Chapter 4.416, Growth Factors and Protein-Modified Surfaces and Interfaces**.

4.413.2. Patterning Techniques

4.413.2.1. Top-Down Approaches

Top-down patterning approaches use large instruments to create smaller features, namely at the micro- and nanoscale, on a given substrate. These approaches can require expensive instrumentation, the quality of which may define the resolution achieved.

4.413.2.1.1. Photolithography

Once the geometrical pattern of interest is decided upon, a CAD software is required to lay it out, after which a physical template – called a (photo-)mask – can be manufactured. The mask and a high-energy beam are the two essential elements of photolithography, a type of projection lithography that transfers the pattern of the mask to the substrate, typically by using ultraviolet light (UV).

The substrate is first coated with a radiation-sensitive organic polymer – known as photoresist – and then selectively exposed to radiation, which shines through the transparent areas of the photomask. Depending on the properties of the photoresist, the polymer chains may either break or become cross-linked in the irradiated areas, making them soluble or insoluble, respectively, to particular solvents – the so-called development solutions. The first kind of resist is known as positive resist, and the second, negative resist. After the substrate is immersed in the resist development solution, the pattern on the surface is either an identical replica of the mask template (if a positive resist was used) or its complimentary geometrical image (if a negative resist was used). If required the photoresist can be removed from the substrate by using suitable chemicals or plasma.

The newly patterned substrate can then be used as a mold to produce polydimethylsiloxane (PDMS) replicas of the original template; these replicas can either serve as a substrate directly or be used as stamps for soft-lithographic processes. The PDMS replicas are produced via a parallel, single-step fabrication mode, which represents one of the main advantages of the technique. For this reason, as well as its high accuracy, photolithography became a major technique for production of patterns from micron to submicron scales on solid-state surfaces. However, photolithographic techniques can require clean rooms, expensive equipment, and high maintenance costs, which may make them inconvenient.

4.413.2.1.1.1. Resist-based patterning (MAPL)

The molecular assembly patterning by lift-off (MAPL)[7] is a technique, which approaches the simplicity of microcontact printing (μCP), to form biofunctionalized patterns on an adsorption-resistant background. This technology (represented in **Figure 2(a)**) relies on an initial step based on photolithography (see **Section 4.413.2.1.1**) to create the desired pattern of resist-protected and -unprotected areas on top of a substrate, typically, glass, silica, or metal oxides. The partially protected wafer is dipped into a solution containing a polycationic bottlebrush copolymer, (poly(L-lysine)-*graft*-poly(ethylene glycol) (PLL-*g*-PEG)), end-functionalized with bioactive molecules such as biotin or RGD. Subsequently, the wafer is exposed to an organic solvent (typically *N*-methylpyrrolidone, NMP) that removes the remaining photoresist while keeping the biofunctional copolymer intact. In a final dip-and-rinse step, nonfunctionalized PLL-g-PEG is adsorbed on the now-bare parts of the wafer, resulting in a pattern of areas that either strongly resist or actively promote biointeraction. The surface density of the bioligands in the bioactive sections can be controlled either by adjusting the fraction of functionalized PLL-g-PEG chains on the copolymer backbone in the synthesis process or by assembling mixed adlayers from solutions containing a defined molar ratio of functionalized to nonfunctionalized PLL-*g*-PEG during the first dip-and-rinse step. The MAPL technique has also been used to create microarrays of vesicles[8] and to pattern polymers on gold surfaces.[9] Recently, Kim *et al.*[10] used a protein-friendly photoresist, called PDMP (poly(2,2-dimethoxy nitrobenzyl methacrylate-*r*-methyl methacrylate-*r*-poly(ethylene glycol) methacrylate)), to pattern multiple proteins on surfaces. The process consists of spin-coating a resist onto a biotin-functionalized surface and, once the photolithographic process is completed, to develop the PDMP resist in near-neutral physiological buffer solution. In a subsequent step, streptavidin (SA) is grafted to the exposed biotinylated surface. The process can be repeated several times, as the development process does not affect the already-patterned proteins.

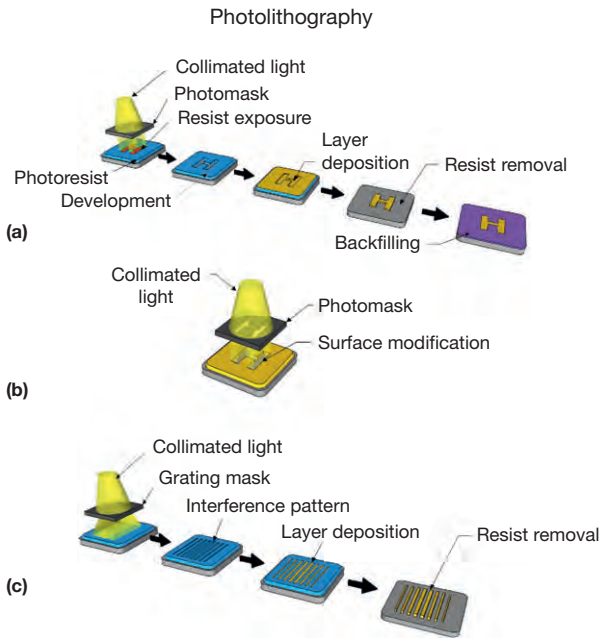

Figure 2 Photolithographic techniques. (a) Resist-based patterning. A beam of light (yellow) is shined through a photomask (gray) onto the photoresist (blue), selectively softening it. Subsequent development removes the softened region, and then deposition and backfilling are used to create the desired surface chemical contrast. (b) Direct patterning. The surface is directly modified by the light beam. (c) Extreme ultraviolet interference lithography (EUVIL). Collimated extreme UV light forms a complex interference pattern upon passing through the grating mask, selectively softening the photoresist.

The control allowed by MAPL over not only the pattern geometry, but also over the type and density of bioligands on the surface, has made it a technique of great relevance. Other advantages of this technology include its simplicity, its noninteractive areas characterized by low nonspecific adsorption of (bio)molecules, the biospecificity of the created interactions, the ease of functionalization of PEG to produce patches composed of multiple types of cell binding sites, and the reproducibility and consistency of the quality of the resulting pattern across the whole wafer (with dimensions around 10 cm), on top of the advantages of photolithographic wafer fabrication, such as variety of form, size, and geometry of the templates. It is also possible to replace the biofunctionalized polymer adsorption step by the assembly of a protein such as fibronectin (which is not adversely affected by the use of the NMP solvent), thus creating a cell-interactive/PEG pattern contrast.

4.413.2.1.1.2. Direct patterning

A chemical pattern can be created on a radiation-sensitive coated surface by selectively exposing regions of it to light via a photomask (as shown in **Figure 2(b)**). Christman and coworkers[11] used this strategy to pattern a surface coated with a pH-reactive polymer, poly(3,3′-diethoxypropyl methacrylate) containing 5% diphenyliodonium-9,10-dimethoxyanthracene-2-sulfonate (DIAS), a molecule that generates protons upon being activated by light. Specifically, upon exposure to a UV light through a photomask, the acetal groups present on the polymer are site-specifically hydrolyzed to aldehydes. These aldehydes can be easily derivatized with molecules of interest as they are highly reactive. By means of a much simpler approach, Xue and coworkers[12] recently created patterns of aldehydes by direct oxidation of an octadecyltrichlorosilane (OTS) monolayer using a UV light source. Anzioned *et al.*[13] employed deep UV light source exposed through a photomask to micropattern a PLL-*g*-PEG-coated glass surface. This caused the protein-repellent PEG chains in the exposed areas to be

selectively cleaved, and thus allowed for the selective adsorption and patterning of fibronectin at the microscale.

4.413.2.1.1.3. Extreme ultraviolet interference lithography

Interference lithography, although closely related to photolithography, is not based on a photomask to selectively expose a surface to be patterned to light. Rather, the principle of interference lithography relies on the use of a light interference pattern projected onto a photoresist, as shown in **Figure 2(c)**. The pattern is created between two or more coherent light beams and consists of a nanometer-spaced periodic series of fringes with minimal and maximal light intensity. For producing the interference pattern, the coherent light source is split by a prism or diffraction grating into two or more waves which, once recombined, generate the desired interference fringes. The typical methods of beam splitting are based on prisms and diffraction gratings.

The main advantage of this methodology, in comparison to e-beam lithography (EBL), is that large areas of photoresist can be nanopatterned. However, the designs that can be generated are limited to the configuration fringes that can be created. Investigators[14,15] have exploited this technique to pattern distinct kinds of resist, including poly(methyl methacrylate) (PMMA) and calixarenes, attaining a pattern resolution of 11 nm. Using several diffraction grating configurations, the resists were patterned in dots, arrays, circles, and rings. Following the same procedure used in the MAPL technique, Städler *et al.*[16] used extreme ultraviolet interference lithography (EUVIL) to selectively nanopattern PMMA coated on Nb_2O_5 surfaces and graft the exposed areas to a PLL-*g*-PEG-biotin polymer. After the PMMA lift-off process, the surface was backfilled with the protein-repellent polymer (PLL-*g*-PEG) and the biotins patterned on the surface used to create SA nanopatterns. Recently, Turachanin and coworkers[17] presented the use of a variant of EUVIL to directly chemically pattern a surface functionalized with a self-assembled monolayer (SAM) of 4′-nitro-1,1′-biphenyl-4-thiol by converting the nitro groups into amino groups upon exposure of the surface to the interference light pattern. Using this approach, chemical patterns with a resolution of 60 nm were achieved.

4.413.2.1.2. Beam-based lithography

There are two main technologies based on the use of a beam to write patterns at the micro- and nanoscale on surfaces, as shown in **Figure 3**.

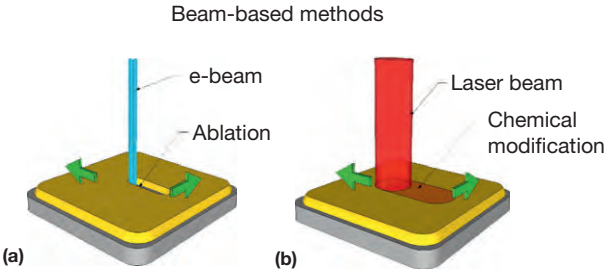

Figure 3 Schematic diagram depicting beam-based lithographic techniques: (a) e-beam-based and (b) laser-based.

4.413.2.1.2.1. Electron beam lithography

Electron beam lithography (E-beam lithography or EBL) (**Figure 3(a)**) is a technique based on the use of a beam of electrons to locally polymerize or remove a resist-coated surface. If starting with an already-polymerized resist, a development step is required in order to remove the unpolymerized polymer film. In a following step, the exposed areas of the surface are usually etched in order to transfer the pattern to the desired surface.

EBL allows the creation of complex nanopatterns on surfaces, although it is time consuming, as large areas must be produced via a stacking methodology. The different techniques that use EBL to create chemical or protein patterns can be classified into resist-based, direct ablation (resist-less), and e-beam-initiated chemical reaction. Further description of EBL may also be found in **Chapter 3.301, Surface Analysis and Biointerfaces: Vacuum and Ambient *In Situ* Techniques**.

- *Resist-based:* High-resolution patterns can be created using EBL on PMMA deposited on surfaces[18] by selective removal of the polymer. Investigators[19] removed areas of PMMA and adsorbed an aminopropyl silane onto the exposed substrate areas. After the lift-off of the remaining PMMA, DNA nanopatterns were created by selective adsorption onto the positively charged aminated surfaces. The grafting of proteins of interest could be easily achieved via functional derivatization of the amino groups.
- *Direct ablation:* Zhang *et al.*[20] used an e-beam to locally remove a perfluorosilane SAM adsorbed on a silicon surface and functionalize the exposed areas with aminosilanes. Derivatization of the amino patterned areas with a biotin linker allowed the investigators to create 100-nm-wide protein patterns of SA and biotinylated GFP. In the same year, Senaratne *et al.*[21] used a similar strategy to pattern dinitrophenyl (DNP) groups on a PEG-modified silicon oxide surface. The DNP patterns were then used to pattern anti-DNP antibodies with a 10-nm lateral resolution. More recently, Pesen *et al.*[22] used EBL to selectively remove bovine serum albumin (BSA) protein adsorbed on a glass surface, and subsequently backfill the newly exposed areas with fibronectin, in order to create patterns with protein contrast. As an alternative strategy to create chemical contrast patterns, the e-beam can be used to selectively remove a thin layer of SiO_2 deposited on TiO_2. In a second step, molecules such as dodecyl phosphate (DDP) can be selectively adsorbed on the exposed TiO_2 surfaces, and finally, the SiO_2 can be coated with PLL-*g*-PEG protein-repellent polymer.[23] Recently, Rundqvist *et al.*[24] presented the use of an e-beam to selectively deactivate a fibronectin-coated surface in order to create a nanoscale pattern of active proteins.
- *E-beam-initiated chemical reaction:* Chemical reactions can be induced directly on surfaces via e-beam exposure. Mendes *et al.*[25] used an electron beam to locally reduce nitro functionalities in SAMs of 3-(4-nitrophenoxy)-propyltrimethoxysilane to amino functionalities, forming chemically well-defined surface patterns on the 100-nm scale. Hong and coworkers[26] utilized an e-beam to locally cross-link thin films of PEG on SiO_2 surfaces and thus create 200-nm diameter spots of hydrogels. More recently, the same

approach was applied to nanopattern eight-armed PEG chains modified with biotin, maleimide, aminooxy, and nitrilotriacetic acid (NTA), in order to create multicomponent protein patterns after sequential e-beam patterning of the distinct polymers.[27] A more sophisticated approach was employed by Winkler *et al.*[28] to create gradients on surfaces of PEG protein-resistant groups. The strategy is based on varying the e-beam exposure time of a dodecanethiol (DDT)-coated gold surface. Whereas the pristine DDT SAM hardly permits any substitution process, the e-beam irradiation induces defects (such as the formation of alkene bonds, which destabilize the SAM) that promote the exchange reaction with a PEG-thiol. Depending on the exposure time, the amount of alkene bonds created on the SAM varies and, thus, the substitution process can be controlled.

4.413.2.1.2.2. Laser beam lithography

A focused laser beam can be utilized to micropattern functionalized surfaces by inducing local photochemical reactions, as represented in **Figure 3(b)**. Jonkheijm and coworkers[29] employed a laser beam to induce a thiol–ene reaction between a thiol-containing surface and a biotinylated olefin, in order to create a micropattern of biotinylated areas. A similar strategy[30] was employed to selectively deprotect a surface coated with carboxylic acid groups, thus creating reactive sites for proteins. More recently, investigators[31] created chemical contrast nanopatterns (up to 110 nm) by utilizing an argon laser beam to selectively desorb 1-hexadecyne SAMs formed on Si surfaces and backfill the fresh Si surfaces with an amine-terminated SAM. Nanoscale resolution was achieved in that case by reducing the lateral distance between the lines written by the laser.

4.413.2.1.3. Embossing

Hoff *et al.*[32] were the first to describe the use of nanoimprint lithography (NIL) for creating chemical contrast on surfaces. As **Figure 4** shows, a nanostructured mold is imprinted into a heated PMMA film spin-coated onto a silicon wafer. Next, a dry etching step converts the topography formed by the variation in PMMA film thickness into a PMMA/silicon oxide contrast by removing the thinner PMMA regions completely. The exposed SiO_2 surface is then passivated with a perfluorosilane layer.

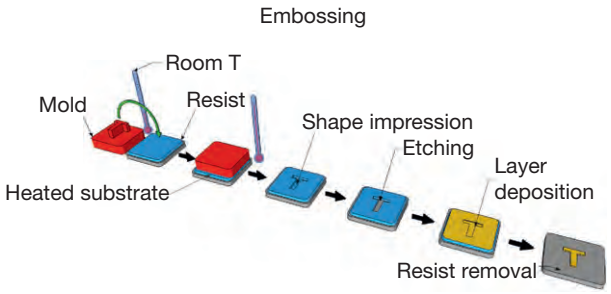

Figure 4 Schematic diagram depicting the embossing technique as used in nanoimprint lithography (NIL) and microimprint lithography (MIL). The substrate coated with resist (blue) is heated up and the target pattern (red) is embossed into the resist film. A subsequent etching step removes the thinner regions of resist entirely, locally exposing the bare substrate.

Finally, the remaining PMMA is stripped away with acetone and the freshly exposed SiO_2 regions are functionalized with an aminosilane. Biotin-succinimidyl ester is then covalently linked to the primary amine of the aminosilane layer in order to create SA patterns on the surfaces, which can be further derivatized with biotinylated biomolecules. Falconnet *et al.*[33] used a similar approach on Nb_2O_5 surfaces to create SA patterns. After the reactive etching process, the fresh oxide areas are derivatized with a biotin-functionalized bottlebrush copolymer, poly(L-lysine)-*graft*-poly(ethylene glycol)-biotin (PLL-*g*-PEG/PEG-biotin). Finally, after the PMMA stripping process, the background is backfilled with protein-resistant PLL-*g*-PEG.

4.413.2.1.4. Soft lithography

Soft lithographic[34] methods are characterized by the use of a chemically modifiable and inexpensive elastomeric material as a stamp to transfer micro- or nanostructured complex patterns from a master, or mold, onto a target material of choice. The elastomeric stamp, typically PDMS, represents an inverted replica of the structure to be produced. Elastomers can generate a conformal contact at the molecular level over large areas of a wide range of substrates of interest, one of the primary advantages of soft lithography. Tight contact is even possible with curved surfaces.[34] The sealing between the target material and the stamp is mediated by van der Waals forces and therefore reversible, so this procedure can be repeated several times using the same mold and stamp.

The Young's modulus of fully cross-linked PDMS, typically in the low MPa range, is suitable to achieve conformability but may reduce the pattern resolution. To obtain high-resolution patterns in the submicrometer range, without any distortions, new types of elastomers were successfully developed, including hard-PDMS,[35] polyolefin plastomers (POPs),[36,37] poly(ethylene)/poly(methyl methacrylate) composite stamps,[38] perfluoropolyethers,[39] domed stamps,[40] and poly(methyl methacrylate) (PMMA) stamps.[41] More information about some of these polymers may also be found in **Chapter 1.122, Structural Biomedical Polymers (Nondegradable)**.

Soft lithography is a low-cost and high-throughput technique that does not require clean rooms to produce high-quality patterned micro- and nanostructures. It avoids the resolution limits imposed upon photolithography by optical diffraction. Furthermore, PDMS samples are suitable for biological applications, as PDMS is stable at temperatures ranging from 37 to 95 °C, chemically inert,[42] optically transparent,[43] minimally autofluorescent, gas-permeable,[44] and biocompatible.[42]

4.413.2.1.4.1. Direct microcontact and nanocontact printing

Microcontact printing (μCP) and nanocontact printing technologies are suitable for directly immobilizing small, surface-active molecules, polymers, or biomolecules onto spatially and geometrically well-defined areas of a material by mechanical contact, as shown in **Figure 5(a)**. This technique entails an inking step of the molecules of interest on a PDMS stamp. The excess solution is dried and the remaining layer at the surface of the stamp is placed in contact with the surface of the required material, for a period of time ranging from a few seconds to minutes, after which the stamp is peeled off, leaving a pattern of the molecules of interest on the surface of the material. The bonds that connect the transferred molecules

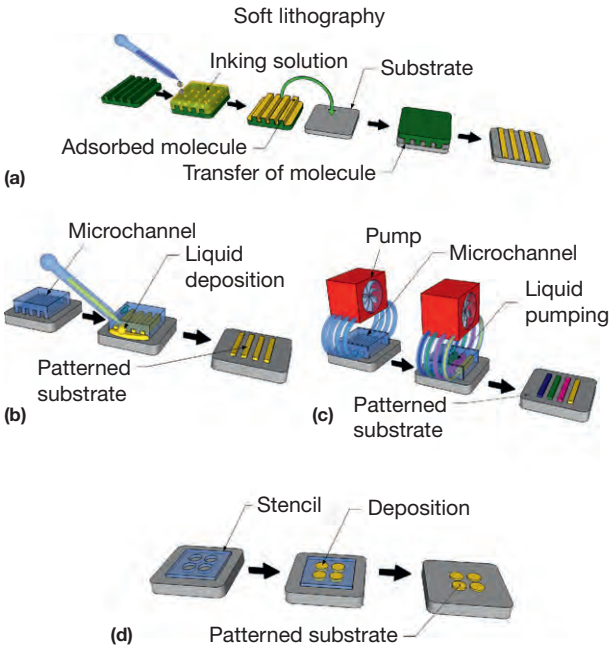

Figure 5 Soft lithographic techniques used to pattern surfaces with chemicals and biomolecules. (a) Direct micro- and nanocontact printing. A flexible stamp (green) is coated with the *ink* (yellow) and pressed onto the surface (gray) to produce the desired transfer pattern. (b) Microfluidic patterning technique based on the use of capillary forces to fill the channels with the solution of interest. (c) Advanced microfluidic patterning technique based on the use of pumps and tubing to address distinct solutions in each channel and thus create multicomponent patterns. (d) Stenciling technique. Micro- or nanostencils (blue) act as temporary masks to create surface patterns (yellow) by site-specific deposition of material through the mask.

and the surface of the material being stamped can be mainly electrostatic or covalent, depending on the species involved. The surrounding unmodified areas may subsequently be backfilled.

Being an additive process, the material wastes incurred in contact printing are minimal, in comparison with techniques such as subtractive printing, described in the following section. Contact printing methods additionally take advantage of the reusability of the photomask and the low cost and flexibility of the stamp to serve as a versatile, cost-effective, high-throughput patterning technique that allows the scientist to work in parallel with cells,[45] proteins,[46–49] oligonucleotide arrays,[50] or gold,[51] on several different materials varying from glass slides[52,53] to polymers,[51] hydrogels,[47,54] and SiO_2.[55]

Most of the methods of patterning proteins discussed in this chapter are restricted to the patterning of planar surfaces. However, Foley and coworkers[56] took advantage of the elastomeric properties of PDMS stamps to integrate biomolecules into nonplanar substrates – namely onto the bottom of microchannels – by deforming them under pressure until they conformed to the microchannel structure. This μCP strategy was shown to work for both flat and three-dimensional (3D) stamps bearing continuous or discontinuous patterns.

The potential drawbacks of microfluidics include mechanical instabilities imposed by the soft stamp – such as lateral collapse or pairing of narrowly spaced features, or sagging of the region between two features widely apart[57] – which limit the pattern geometries that can be produced[37]; blurring of the pattern caused by diffusion of the solution of molecules stamped[58,59]; the risk of contamination of the surface to be patterned by transference of molecules or fragments from the stamp material (e.g., low molecular weight residues when employing PDMS) with consequences for the wetting and adhesion properties of the patterned substrate[60]; and, for applications with multiple printing steps, the difficulty of achieving precise alignment of the stamp with previous printing steps and the resulting pattern inhomogeneity along large surfaces.

To surpass the mechanical stability problems, robust stamp materials and stamp designs have been proposed, such as the ones described in **Section 4.413.2.1.4**.

4.413.2.1.4.2. Subtractive printing

An elegant approach to avoid the loss of patterning resolution due to PDMS nanostructured stamp collapse or instability is the use of subtractive printing. This technique, presented recently by Coyer *et al.*,[61] is based on the use of a nanotemplate (a silicon mold engraved with the pattern of interest) to selectively subtract a protein adsorbed on a flat elastomeric stamp (see the discussion of stamping in **Section 4.413.2.1.4**). The remaining proteins on the stamp form the desired pattern, which can be transferred to the desired surface by direct contact. Combining multiple flat stamp inking processes with subtraction steps allows the fabrication of complex patterned structures of distinct proteins. Until now, this strategy has not, to the best of our knowledge, been used to create chemical nanopatterns.

4.413.2.1.4.3. Microfluidics

Microfluidic patterning is based on the creation of microchannels on the target surface by fabricating the desired geometries on a PDMS stamp, which is then pressed onto the material surface. The stamp can be produced via replication of a master originally produced by photolithography. While the stamp is in contact with the surface, capillary forces (**Figure 5(b)**), pumps (**Figure 5(c)**), or electroosmosis are used to fill the microchannels formed at the interface with a solution of the desired (bio)molecules to be patterned. The compliance and the hydrophobic properties of the PDMS confine the solution to the channels, and the molecules are therefore delivered to the desired areas of the substrate. The bonds between the stamp and the material may be reversible or irreversible. Microfluidic patterning can be particularly useful as an alternative to μCP if a drying step would damage sensitive biomolecules, or when close control over the molecular density of the immobilized component in the material surface is a key requirement.

Microfluidic patterning combines the advantages of being a parallel, additive technique with the unique characteristic of spatially separate microchannels, allowing different solutions to flow over different regions of the same sample to form multimolecule patterns for multiplexed applications. Another interesting attribute is the laminar flow behavior inside the microchannels, meaning that adjacent streams of fluids do not intermix appreciably over macroscopic length scales once they are mutually parallel. This fact allows the concurrent patterning, in a single channel, of different components ('wall-less' microfluidics), which investigators have shown by

organizing multiple ligands and cells within selective patterns, as reviewed by Kane *et al.*[62]

The intrinsic drawback of this technique, when relying on spontaneous capillarity, is its poor speed, which limited its application to large areas in the past. However, the use of external pumping devices with controlled flow rates, down to nanoliters per minute, has successfully addressed this shortcoming. More information about microfluidic techniques may be found in **Chapter 3.309, Fluid Mechanics: Transport and Diffusion Analyses as Applied in Biomaterials Studies**.

4.413.2.1.4.4. Stenciling

Microstencils made of soft silicones, such as PDMS, can be used as temporary masks for surfaces. The softness and elasticity of PDMS microstencils cause them to spontaneously seal to any smooth surface by forming a so-called conformal contact. (**Figure 5(d)**). Once the microstencils are in place, chemicals[63] and proteins[64] can be adsorbed on the unprotected areas or, alternatively, plasma can be used to selectively modify the exposed surfaces.[65] Once the surface modification is accomplished, the microstencil is manually lifted off, yielding a patterned surface. One of the main drawbacks of the PDMS stencils is that they cannot be reused, as they are stretched and deformed during the peel-off process. New materials have been proposed as free-standing alternatives, such as parylene-C stencils[66] or hybrid elastomer metal stencils,[67] allowing them to be reused. Parylene-C stencils, unlike PDMS stencils, are free-standing and rigid, creating regular, well-arranged patterns. However, parylene-C does not form a conformal contact; therefore, the liquid confinement is dependent on the hydrophobicity of both the substrate surface and the stencil. This limits its application to hydrophobic surfaces, preventing, for instance, the use of clean glass as a substrate. To overcome this issue, hybrid stencils,[67] made of steel stencils with micropatterned elastomeric O-gaskets around the stencil apertures, have been proposed as a much more versatile alternative, allowing the creation of protein patterns on both hydrophobic and hydrophilic surfaces.

A nanostencil is a stencil with nanometer-size apertures. Rigid nanostencils made of silicon have been widely used to create patterned nanostructures of distinct materials (i.e., metals, semiconductors) on surfaces.[68–71] The strategy is based on the controlled deposition of such materials through the nanostencil apertures, which act as a 'shadow mask.' There are multiple examples of nanopatterned materials, and the first studies involving chemical or protein patterning have just been presented.[72,73]

4.413.2.1.5. Scanning-probe lithography

Scanning-probe microscopes, such as the tunneling microscope (STM) and atomic force microscope (AFM), are used both to observe surfaces and to fabricate nanoscale structures. Scanning-probe lithography is a powerful mechanical tool to produce nanometer patterns and devices, and to investigate material properties using the scanning tip. A general overview of scanning probe microscopy may be found in **Chapter 3.302, Atomic Force Microscopy**. This technology is mainly serial but multiple probes can be used, thus increasing speed by writing in parallel. Examples of such parallelization include the Millipede, an ultra-high-density, high-date-rate data storage system[74]; the Snomipede, a fusion between the former Millipede concept and scanning near-field photolithography, capable of performing parallel transformations at high resolution over macroscopic areas;[75] and dip-pen nanolithography (DPN) arrays.[76–78] The combination of high spatial resolution, alignment accuracy, throughput, and reproducibility makes scanning-probe lithography a promising technique to produce a wide variety of patterns at the nanoscale.[79]

AFM-based nanolithography is a very flexible and high-resolution technology which easily adapts to different study conditions, including ambient air, liquids, gases, humidity, and temperature differences, making it ideal to match required conditions such as for biomolecules.[80] Its degree of resolution depends on the tip shape, cantilever strength, scan domain, and the number of measurements per scan and, under the appropriate circumstances, enables the manipulation of surfaces at the single-atom level.[81] AFM instrumentation and tips are widely commercially available.

Among the several AFM-based methods used to nanopattern surfaces, nanografting, nanoshaving, anodic oxidation, the Millipede, and the Snomipede are part of a range of techniques that act by chemically or physically modifying the surface to produce a pattern, with subsequent site-specific adsorption of the patterning molecules from the solution. These harsh approaches have an associated handicap regarding the material types that can be micro- and nanopatterned. In contrast, DPN and nanopen are part of the new generation of AFM-based technologies that directly deliver the material to be patterned on the surface of the target substrate without the help of a resist, a stamp, substrate irradiation, or solvents, thereby avoiding surface damage or cross-contamination.

4.413.2.1.5.1. Dip-pen nanolithography

DPN arose from the idea of transforming a common AFM problem into a virtue of a new technology. When an experiment is conducted in air, capillary forces condense the water of the air in between the small distance that separates the tip and the surface sample, influencing imaging approaches. Mirkin and coworkers[82] showed that when the water flows from the tip to the sample surface, multiple nanometer patterns may be formed, as shown in **Figure 6(a)**. This phenomenon allows direct writing on the surface of the samples, opening a new door to the nanopatterning field. DPN, therefore, relies on the spontaneous formation of a meniscus, which acts not only as a conduit for ink transport but also, in some cases, as a reaction vessel. The latter case allows materials precursors on the tip to be synthesized directly on the target material when in contact with the meniscus during the transfer process.[83] The transferred molecules – such as DNA,[84] proteins,[85] or enzymes[86] – act as *ink*, *drawing* (i.e., patterning) the molecules on the substrate via either chemisorption or physisorption. When the velocity of the tip across the surface is increased, the transport of molecules is interrupted and the probe acts as an imaging tool which provides feedback on the pattern characteristics. Progress in this field of molecular printing involving DPN has recently been thoroughly reviewed by Braunschweig and coworkers.[87]

In summary, DPN is an additive technique that allows both hard and soft material to be patterned with minimal material

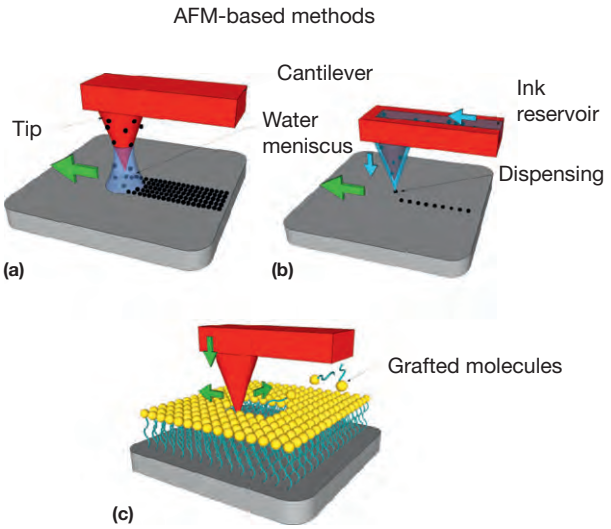

Figure 6 AFM-based patterning methods. (a) Dip-pen nanolithography (DPN). Nanopattern created by an AFM tip (red) previously dipped in the solution of interest (molecules of the solution represented in black). The meniscus formed by condensation of environmental water between the material surface and the AFM tip allows the transport of the molecules from the tip to the surface, which self-assemble, thus creating the pattern. (b) Nanodispensing technique represented by nanofountain probe (in red), characterized by an annular aperture connected to a reservoir containing the solution (or *ink*) of interest following the same principle as DPN. (c) Nanografting. This technique is based on spatially controlled shaving of molecules from the substrate (yellow) with the AFM tip (red), thus creating the pattern.

losses, and there is no need for exposing the substrate to harsh conditions such as radiation or solvents. As the movement of the tip is computer-controlled, the pattern may be easily changed at any point. Molecules are then precisely placed, at will, where needed. An excellent review on the DPN applications was written by Salaita *et al.*[88] As is true for all scanning-probe techniques, DPN has the drawback of being a serial process, which implies low throughput and, therefore, increased cost. This shortcoming has been partially overcome by parallel DPN, making DPN a highly interesting nanoscale patterning technique.

4.413.2.1.5.2. Nanodispensing techniques

Nanopen technology can be interpreted as an improved dip-pen technique. In nanopen lithography, the solution of interest flows through a nanometer pipette-like device – the pen – onto the surface to create the desired pattern, under the control of a nanoscale control tool which spatially manipulates the writing pen.

Among the advantages that nanopen technology retains from its precursor is the ability to achieve nanoscale resolution[89] while still enabling the fabrication of complex pattern geometries. Furthermore, the pipette design is capable of transferring two solutions of interest – also known as inks – onto the substrate,[87] thus allowing a combinatorial approach of molecule-based patterning at the nanoscale.

One shortcoming of nanopen technology is that feature dimensions are limited by the size of the pipette used. This limitation is overcome by nanoscale dispensing,[90] which replaces the pipette with a sharp tip cantilever with a 200-nm hollowed aperture at the apex, allowing for dispensing of volumes down to 5 attoliters with a lateral spacing below 500 nm. A further improvement, represented in **Figure 6(b)**, is the nanofountain probe,[91] which uses an annular aperture at the tip to achieve sub-100-nm resolution. Both of these systems rely on specialized probes, and one can foresee even higher-resolution patterning systems based on further probe refinements.

4.413.2.1.5.3. Nanografting lithography

Nanografting is an AFM nanolithographic technique characterized primarily by spatially controlled nanoshaving of the substrate surface, as shown in **Figure 6(c)**. This operation carefully applies a selected force to a thin film on the substrate, displacing the desired molecules from it. The desorbed molecules are discarded and the free areas are then available for the chemisorption or physisorption of the molecules of interest such as DNA,[92,93] proteins,[94,95] and antibodies.[92]

The highlight of this technique is the selective scratching by controlled manipulation of the AFM tip on the surface, allowing for high-resolution sub-100-nm patterns.[96] However, the energy delivery in this process may be aggressive to the surface, so the materials involved must be selected carefully.

4.413.2.2. Bottom-up Approaches

Bottom-up approaches use molecular entities or particles to build up systems of higher degrees of complexity. Usually, the technologies that are part of this group take advantage of the tendency of the molecules involved to self-assemble into organized structures at the micro- or nanoscale, which would be difficult to achieve by other means.

4.413.2.2.1. Colloidal lithography

Colloidal lithography is based on the use of colloidal particles with sizes ranging typically from 10 to 1000 nm, self-assembled in hexagonally close-packed patterns on a surface, and serving as a temporary mask (**Figure 7(a)**). The self-assembly process can be tuned by varying either the wettability properties of the surfaces and/or the particle chemistry.[97–99] Valsesia *et al.*[100] used colloids to selectively protect a SAM of MHDA (1-mercaptohexadecanoic acid). Upon plasma treatment of the surface and subsequent colloid striping, the ablated areas were backfilled with HDT (*n*-hexadecanethiol) and the MHDA nanopatterns were used to graft proteins at the nanoscale. In contrast, Cai and Ocko[101] used the particles as a mask during a silanization process with a PEG-silane. This procedure allowed them to generate nanopatterned protein-attractive areas surrounded by protein adsorption-resistant PEG-silane. Michel and coworkers,[35] in turn, used colloidal lithography to create pillars of TiO_2 on a SiO_2 background. In this case, the polystyrene colloids, assembled on a silicon wafer coated with a thin film of TiO_2, locally protected the TiO_2 surface during reactive etching that resulted in the exposure of SiO_2 in the unprotected background area. After removal of the colloids, the TiO_2 pillars were selectively functionalized with alkanephosphates, while the SiO_2 background was functionalized with a protein-repellent polymer, PLL-*g*-PEG. Blätter *et al.*[102] added an extra step to the fabrication process

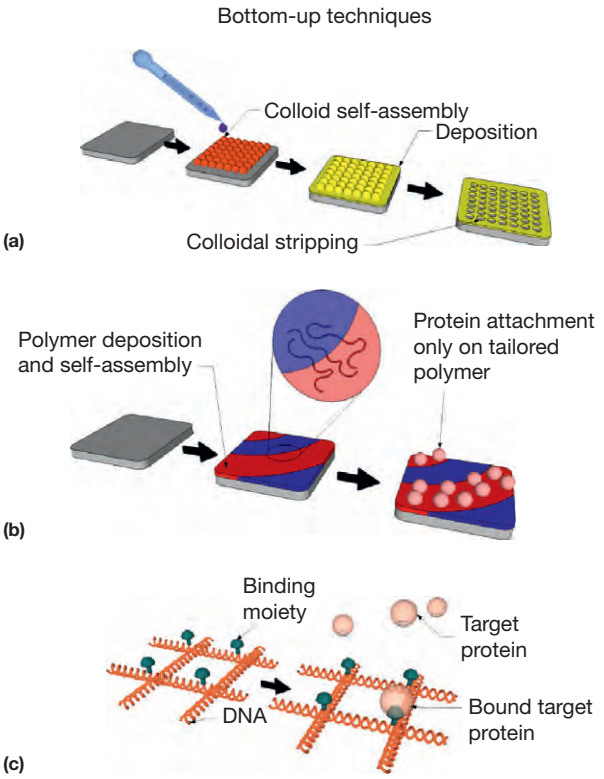

Figure 7 Bottom-up patterning approaches. (a) Colloidal lithography. This method is based on the use of colloidal particles (orange) dispersed in a solution, which self-assemble in hexagonally close-packed patterns on a surface, acting as a temporary mask. The subsequent deposition of a substance of interest (yellow), followed by the removal of the colloids, forms the nanopattern. (b) Block copolymers. Two chemically different polymers (represented in red and blue) covalently bonded at one end self-assemble into ordered structures (represented in Step 2). Their function can include biological activity, represented by the interaction with a biomolecule (pink) in the scheme. (c) DNA templating. DNA-functionalized surfaces (orange) are designed to exhibit binding moieties (green) at intervals of choice, which then bind target proteins from solution to form a protein pattern (pink).

previously described: following the polystyrene colloid assembly, the size of the particles was tailored by shrinking via exposure to an O_2/N_2 plasma for selected etching times. The reduction of the particle diameter by an order of magnitude, from approximately 2000 to 200 nm, allowed the investigators to reduce the size and increase the separation of the patterned features. More recently, Malmström *et al.*[103] used the colloids as a mask during a SiO_2 deposition procedure on a gold-coated surface. After removal of the colloids, the exposed gold areas were selectively functionalized with thiols.

4.413.2.2.2. Block copolymer micelle nanolithography

The ability to create nanoscale arrays of ordered nanoparticles on surfaces is useful in diverse fields, including electronics, optics, and materials development.[104,105] Block copolymer micelle nanolithography is a straightforward strategy to create such ordered nanoparticle structures. This strategy uses micelles of self-assembled block copolymers with a large solubility difference between their hydrophilic and hydrophobic segments.[106,107] In aqueous conditions, the block copolymers assemble into nanoscale double-layered micelles, with a hydrophilic core segregated from the bulk solution by a hydrophobic region. These hydrophilic cores can be loaded with salt precursors (e.g., metal salts or oxides), after which the vesicles are allowed to self-assemble in hexagonally close-packed patterns on surfaces. Once assembled, the salt precursors reduce and yield the desired nanoparticles embedded in the micelle block copolymer matrix. The last step of the process consists of the removal of the block copolymers by means of a hydrogen, oxygen, or argon plasma treatment in order to obtain gold dot patterns on the desired surface. The main advantage of this technology is that the distance between the resulting nanoparticles on the surface can be finely tuned just by varying the molecular weight of the block copolymers. This strategy has been used to create gold[108] and silver[109] nanodot arrays, as well as binary mixtures of gold and iron oxide nanoparticles.[110,111] Applications of self-assembling biomolecules are also discussed in **Chapter 2.207, Extracellular Matrix: Inspired Biomaterials**.

4.413.2.2.3. Block copolymers

Block copolymers consist of at least two chemically different polymers covalently bonded at one end.[112] The engaging characteristic of block copolymers is their intrinsic tendency to self-assemble into ordered domains at the nanoscale (**Figure 7(b)**), which would otherwise require both extreme effort and cost to be recreated by alternative (top-down) techniques.[113] These complex structures are the result of both the interaction energy between the blocks and chain stretching. Chemically different blocks favor phase separation, while the connectivity of the copolymer chains prevents this from happening, leading to spontaneous formation of well-defined structures, limited by the dimensions of the copolymer chain to around 5–50 nm,[113,114] without phase separation at the macroscopic level.[115] The morphology of the resulting nanopatterns depends on the relative volume fraction of each component polymer[114] and their molecular weights. Typically, spherical, cylindrical, or lamellar shapes are observed[113] and known to be thermodynamically stable.[116]

Both the individual blocks and the resulting domains of the copolymers can be modified at will. The size, shape, and arrangement of the nanopattern domains are chemically tunable,[117] while the physical, chemical, electric, and magnetic properties of each block can be additionally tailored via the incorporation of metals, ceramics, and semiconductors, thus equipping the assembled material with additional functionalities. The latter includes biological activity, conductivity, reactivity, or degradability.[112] For all these reasons, block copolymer technology has been extensively used for fabrication of nanomaterials.

4.413.2.2.4. DNA templating

Immobilizing proteins with controlled spacing and precision at the nanometer scale, using a DNA template, offers the opportunity to mimic nature's own biomolecular recognition processes and assembly machinery. Thus, this technique presents a unique way to further study, understand, and exploit fundamental biomolecular interactions, providing vital insights into the field of proteomics, medicine diagnosis, and tissue engineering.

Directed DNA templating uses the intrinsic function of DNA as molecular organizer of the bases adenine, thymine, guanine, and cytosine to create nanostructures with multiple geometries. If one wants to use this methodology, one must define the number, length, and mutual connections between the designed sequences of oligonucleotides, while keeping in mind the intended DNA topology structure. Those parameters play an important role, as the success or failure of the self-assembly strategy is intrinsically determined by their affinity and specificity.

Three specific topologies of DNA seem to be especially relevant in the context of biointerfaces, namely linear, branched, and networked, as reviewed by Campolongo and coworkers.[118] Briefly, the specificity of hybridization (the process of joining two complementary strands of DNA) makes DNA particularly useful for molecular recognition at the nanoscale, such as in pathogen detection as well as in drug delivery and medical diagnostics.

Branched DNA architectures, in turn, present multiple ends available for further functionalization. These systems present higher complexity, can perform 2D or 3D assembly, and are useful in the biosensing field for multiple biomolecule detection.

Finally, the networked topology is characterized by the DNA cross-linking through self-assembly of subunits based on end recognition. In this case, the formed topology can be applied for production of protein arrays and antigen detection.

From a chemical perspective, DNA can not only be conveniently engineered in the laboratory with Angstrom-level accuracy, but also tailored by covalently binding a collection of different functional groups, as represented in **Figure 7(c)**. Additionally, there is a range of enzymes available both to confirm the formation of the desired DNA structure and to modify its structure at will.[119] Excellent reviews about this technique have recently been published by Chhabra *et al.*[119] and Li.[120]

4.413.3. Biointerfacing with Patterned Surfaces

The nature of interfacial phenomena is intrinsically interdisciplinary, encompassing the fields of engineering, physics, chemistry, and biology. To understand the complex relationship between surface chemistry and biological systems, the scientific community has combined the topographical and chemical modification of surfaces to create multifunctional systems that may incorporate biological cues such as vitamins, oligonucleotides, saccharides, peptides, and proteins on solid substrates. The introduction of tissue cells, bacteria, and viruses to these model biointerfaces allows the study and interpretation of their behavior in relation to a biologically significant environment in two and three dimensions. The ability to fabricate biomimetic surfaces intrinsically relates to the development of technology to operate at the micro- and nanoscale in a controlled, precise, and reproducible way. The considerable progress made in the micro- and nanoengineering fields to date has encouraged scientists and engineers to pursue the study of increasingly realistic biological systems, which holds great promise for the fields of tissue engineering and regenerative medicine, immunology, neuroelectronics, biosensors, (targeted) drug delivery, medical imaging, and diagnostic devices for drug discovery and screening.

The concept that cell behavior *in vivo* is governed to a large degree by interactions with neighboring cells and the extracellular matrix (ECM) has become widely accepted by the scientific community. Typical experimental models studying the cell–cell adhesion proteins involved in intercellular connections are based on patterning techniques that provide tight control over the distribution of such ligands on the material surface, and, until 2002, these patterns were restricted to non-membrane proteins. Fang *et al.*[121] reported patterned membrane protein arrays and their use for ligand screening, thereby pointing the way to a new method of compound screening, as membrane-bound proteins are the main targets of modern drugs, and enabling highly parallel studies of the fundamental processes involved in cell−cell communication. Intercellular engagement, however, results from the recruitment and rearrangement of adhesion protein complexes that involve both immobile and laterally mobile proteins.[122] *In vitro* recreation of the lateral mobility of proteins of the cellular membrane is made possible by artificial model membranes, which include Langmuir monolayers, planar bilayers, lipid vesicles (liposomes), and substrate-supported planar bilayers. One important feature of the latter is the potential to generate micropatterned membranes on a solid substrate via microfabrication techniques. Among the technologies described in **Section 4.413.2**, μCP, microfluidics, and scanning-probe microscope techniques follow the principle of spatial control of the deposition or removal of lipid membranes, while photolithographic approaches imply either UV polymerization or deep UV decomposition of lipid bilayers, as reviewed by Morigaki.[123]

In this section, we introduce significant experimental methodologies used to study biologically relevant interfaces via surface patterning down to the nanoscale in the cellular, bacterial, and viral fields. Further discussion of relevant topics may also be found in **Chapter 4.407, Bacterial Adhesion and Biomaterial Surfaces**; **Chapter 4.409, Surfaces and Cell Behavior**; **Chapter 2.207, Extracellular Matrix: Inspired Biomaterials**; and **Chapter 2.220, Extracellular Matrix as Biomimetic Biomaterial: Biological Matrices for Tissue Regeneration**.

4.413.3.1. Vesicle and Membrane Patterns

As the cell membrane is a critical component to understanding the functionality of the cell and investigating its structural and dynamic aspects, artificial bilayer membranes are preferred biomimetic platforms to study, for example, heterogeneities and molecular organization in the bilayer at the submicron scale, for the insertion of transmembrane proteins, and to gain access to both sides of the bilayer if deposited on porous substrates.

4.413.3.1.1. Vesicle arrays

Membrane protein microarrays have the potential to serve as a sensitive and efficient analytical tool for applications in drug discovery and screening.[8,121] While DNA/RNA, and to some extent also protein microarrays, are used routinely, the organization of membrane proteins at surfaces in general, and in an array format in particular, poses a number of specific challenges related to the need to accommodate them

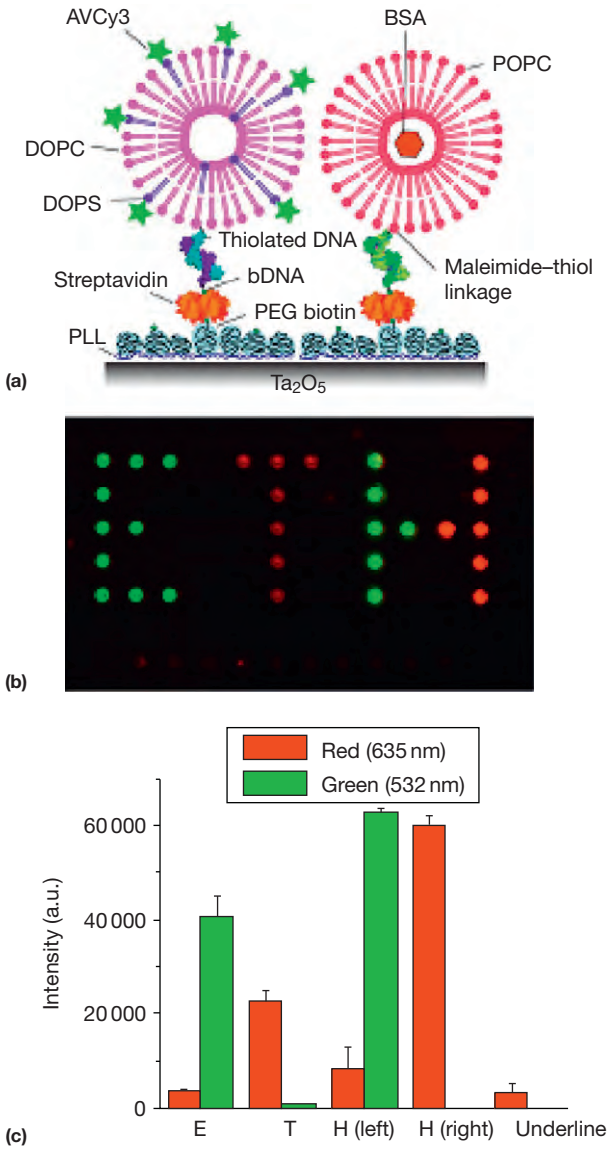

Figure 8 (a) Schematic, (b) microarray fluorescent reader image, and (c) fluorescent intensity signal of the green and red channel of two different surface-immobilized vesicles. A Ta_2O_5 waveguiding chip is coated with PLL-*g*-PEG/PEG-biotin. In a second step, complexes of streptavidin (SA) and biotinylated DNA are spotted onto the chip. Finally, the surface is exposed to a solution of two kinds of functionalized vesicles (Figure b left ('E'): A5Cy3-modified DOPC/DOPS vesicles; right ('T'): BSA647-loaded 1-palmitoyl,2-oleoyl-*sn*-glycero-3-phosphocholine vesicles tagged with DNA via the maleimide-thiol linkage. In addition, controls are included: 'H' (left): SA534; 'H' (right): SA633. The DNA-tagged vesicles selectively decorate the corresponding spots on the surface. Reproduced from Städler, B.; Bally, M.; Grieshaber, D.; *et al. Biointerphases* **2006**, *1*, 142–145, with permission from the American Vacuum Society.

in their natural, lipid-based microenvironment in order to preserve their functionality. In particular, such fragile proteins cannot be spotted and dried for the production of arrays, in contrast with DNA and more stable proteins. To this end, different approaches have been exploited, generally based on solid-supported phospholipid bilayers, liposomes, or polymersomes. In this context, there is an interest in developing patterns of vesicles as a potential carrier of membrane proteins in a heterogeneous array format for multiplexed readouts.

Städler *et al.*[8,124] have proposed an approach that combines conventional microspotting and site-specific immobilization of DNA-tagged nano-objects (lipid vesicles in this specific case) through specific DNA–DNA hybridization. They prepared nonfouling, homogeneous PEGylated surfaces presenting biotin, onto which SA complexed with primary DNA strands was deposited from solution using the pin and ring spotting technique, as shown in Figure 8. For proof of concept, two types of vesicles, each tagged with a different DNA sequence (DNA1 and DNA2), were mixed in solution and exposed to the microarray containing the predefined spots of complementary DNA strands. The vesicles tagged with the complementary DNA1 were functionalized with green-labeled annexin A5 as a representative membrane-binding protein, while the vesicles tagged with complementary DNA2 were loaded with red-labeled BSA. To monitor the sorting of the vesicles to their complementary DNA spots of the microarray chip and judge the selectivity of this process, a fluorescent microarray reader was used.

Control experiments, shown in Figure 9, showed that the presence of the SA was essential in order to provide spots of single-stranded bDNA on the surface for the immobilization of the DNA-tagged vesicles. In Figure 9(aI), Column A represents spotted complexes of SA633 and bDNA1, while B contained only spotted bDNA1. The subsequent immobilization of the DNA-tagged A5Cy3-functionalized vesicles occurred only where the single-stranded DNA was immobilized via SA (Figure 9(aII)). In Column B, less than 1% of the green channel compared to Column A was detectable, demonstrating that no vesicles were surface-immobilized. The results demonstrate the feasibility of solution-based arraying of not only membrane-bound proteins, but also of arraying proteins confined to small compartments that have potential applications in high-throughput studies of enzymatic reactions performed in vesicular nanocontainers.

4.413.3.1.2. Supported membrane arrays

Cell–cell interactions are a key aspect of the development of tissue. Transmembrane cell–cell adhesion proteins, such as the members of the cadherin family, play an important role in the formation and maturation of cell–cell contacts that control paracellular diffusion (tight junctions) and maintain the structural continuum of the epithelium (desmosomes).[125] As the underlying molecular processes in cell membranes are highly dynamic, only platforms that allow for mobility of ligands *in vitro* have a chance to mimic their lateral mobility, recruitment, clustering, and binding, while the commonly used *in vitro* models with proteins immobilized on culture dishes fail to capture this lateral mobility. Supported lipid bilayers, prepared by a fusion of liposomes or proteoliposomes on glass surfaces, have been shown to retain the inherent mobility of incorporated membrane proteins.[126]

Perez *et al.*[122] have described a system for investigating how this lateral mobility influences cadherin-based cell signaling: the GPI-modified E-cadherin protein (hEFG) was tethered to a supported lipid bilayer produced by a fusion of

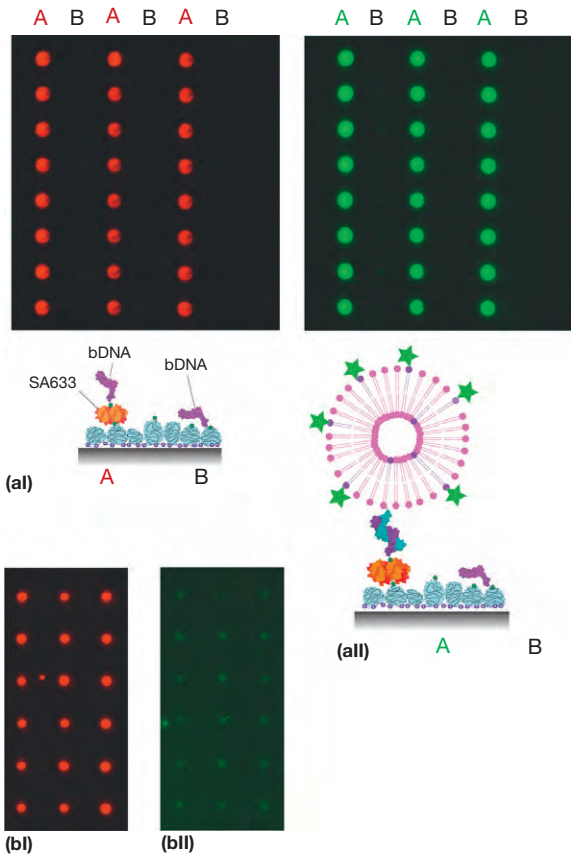

Figure 9 Spotted array of SA633 and bDNA1 complexes (A columns) and bDNA1 alone (B columns) (aI). Subsequent immobilization of the A5Cy3-functionalized DNA-tagged vesicles occurred in Column A, while in Column B, a green signal which is less than 1% compared to Column A is detected (aII). Spotting onto PLL-*g*-PEG without the biotin function leads to smaller spots of SA633 and bDNA1 (bI), and only 2% of vesicles compared to (aII) Column A can be surface-immobilized (bII). Reproduced from Städler, B.; Bally, M.; Grieshaber, D.; *et al*. *Biointerphases* **2006**, *1*, 142–145, with permission from the American Vacuum Society.

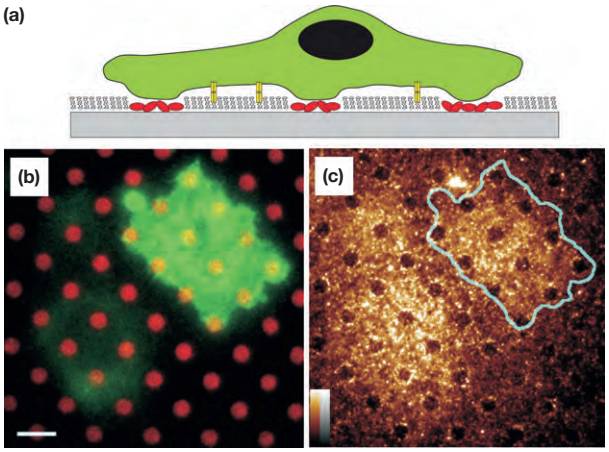

Figure 10 (a) Schematic of cell adhesion to the micropatterned surface, color-coded to correspond to the other panels in this figure. (b) Adhesion of MCF-7 cells (green) onto a hEFG/egg PC bilayer surface, micropatterned with an array of 5 μm diameter fibronectin dots (red). MCF-7 cells were transfected with enhanced yellow fluorescent protein (EYFP)-Mem, yielding a mixed population of cells expressing different levels of this protein. This panel contains three cells which are all detectable at long exposure; the cell visible in the upper right of this lower exposure image expressed the highest level of EYFP. (c) Cy5-hEFG distribution in the same field of view as panel B. Color map is shown in the lower left corner of this panel. The outline of the bright cell shown in panel B is overlaid in light blue. Scale bar = 10 μm. Reproduced from Perez, T. D.; Nelson, W. J.; Boxer, S. G.; Kam, L. *Langmuir* **2005**, *21*, 11963–11968, with permission from American Chemical Society.

proteoliposomes. However, when endothelial (MCF-7) cells were seeded on such functionalized supported membranes, they were found to be unable to spread as a consequence of the mobile nature of membrane-tethered ligands, which prevents cells from being able to exert tensile forces needed for the spread and survival of anchorage-dependent cells. The solution to this problem was found with the approach of using small immobile anchors to allow for cell spreading while facilitating cell interaction with mobile ligands in the bilayer patterns between the adhesion sites (cartoon in Figure 10(a)). The authors used μCP of fibronectin dots of 5 μm diameter that served as integrin-mediated adhesions, allowing the cell to spread across multiple fibronectin adhesion dots (Figure 10 (b)). Apart from being able to spread, cells interacted with ligands presented on the supported lipid bilayer, evidenced by the clustering of hEFG protein, as illustrated in Figure 10(c). There was also evidence that these spread and hEFG protein interacting cells were viable, so the platform used constitutes an appropriate model for studying cell–protein interaction. This study highlights the frequent need for more complex patterns with not just one, but two or more complementary functionalities presented in a spatially controlled manner, in this specific case, the promotion of interaction of cells not with the features themselves but with targets associated with the intervening regions that present membrane-tethered proteins.

4.413.3.2. Cell Adhesion and Function on Patterned Surfaces

The cellular microenvironment is known to be a key aspect of cell adhesion, development, and function, and steers cellular activities such as spreading, apoptosis (programmed cell death), proliferation, differentiation, and motility.[127,128] Cell shape, interactions with neighboring cells and with the extracellular matrix, and substrate rigidity and dimensionality – all affect cell adhesion and function in a complex regulatory process.[129] The emergence of patterning techniques in 2D and 3D has fostered new approaches to study cell adhesion and development in a reductionist format, enabling the quantitative interrogation of the impact of single microenvironmental parameters on cellular function. A plethora of published studies convincingly demonstrate that the presentation of ECM cues in a micropatterned (where the pattern size is comparable to cell dimensions) and nanopatterned (where the pattern size is comparable to the dimension of single adhesion complexes) format steers cell adhesion and development.

In the following section, examples of the use of micro- and nanopatterned substrates are provided, which highlight the importance of pattern geometry on cell adhesion, shape, survival, differentiation, and division. In terms of patterning aspects, a typical approach would be to produce cell-adhesive ECM protein or peptide patterns (consisting of fibronectin, collagen, vitronectin, laminin, or RGD peptide) by a top-down or bottom-up technique on a background that is nonadhesive to proteins and cells, thus confining whole cells or subcellular components to the specific pattern geometry. Varying the size, composition, shape, and spacing between the printed features allows the influence of the individual geometrical/spatial parameters on function and metabolism to be deciphered in a time-resolved manner.

4.413.3.2.1. Cell shape and its impact on cell survival/apoptosis

Chen and coworkers[130] used μCP to create patterns of ECM-coated adhesive islands, and investigated the adhesion, spreading, growth, and survival/apoptosis of human and bovine capillary endothelial cells as a function of ECM pattern shape and size as well as distance (pitch) between the patterns. Figure 11 shows the relationships between the adhesive island area, apoptosis, and DNA synthesis (which correlates with growth). Cells were found to spread on the larger, fibronectin-coated patterns, where they adopted a flat morphology and largely survived. In stark contrast, cells adhering to increasingly smaller patterns retained a more spherical, less spread shape, and increasingly underwent apoptosis. When cells were allowed to spread across small, but closely spaced, adhesive patterns (maintaining the total cell–matrix contact area constant), they again showed high survival rates. Cell shape was thus found to govern whether individual cells grow or die, regardless of the type of matrix protein or antibody to integrin used to mediate adhesion, indicating the fundamental importance of local geometric control of cell growth and viability in the context of developmental regulation within the tissue microenvironment.

4.413.3.2.2. Cell adhesion to nanopatterned surfaces

The presentation of bioligands with tailored surface densities and precisely controlled spatial distribution at the submicrometer to molecular scale is of high interest to the biointerface community, as such designed surfaces have the potential to shed light on many important biological processes. Examples include the formation of multivalent binding (e.g., between carbohydrates and proteins or bacteria), which determine the affinity/avidity and specificity of many biological processes, as well as cell–matrix interactions and cell signaling. Precise control and presentation of biochemical cues at the low nanometer or molecular level remains challenging, however, particularly if large surfaces areas are required for statistically meaningful studies, which cannot cost-effectively be produced by EBL. Bottom-up self-assembly techniques have a clear advantage in this respect.

A successful example of large-scale nanopatterning is the self-assembly of diblock copolymers of polystyrene-*block*-poly(2-vinylpyridine) (PS-*b*-P2VP) incorporating a gold precursor ($HAuCl_4$) into reverse micelles in toluene.[108] Controlled retraction of a substrate from the micellar solution resulted in a uniform and well-ordered monolayer of micelles at the substrate

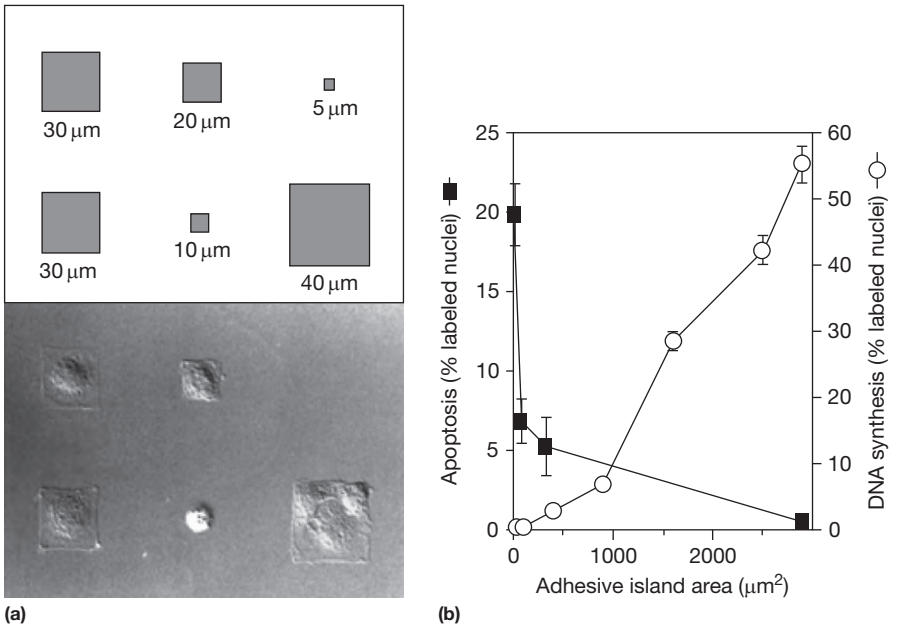

Figure 11 Effect of spreading on cell growth and apoptosis. (a) Schematic diagram showing the initial pattern design containing different-sized square adhesive islands and Nomarski views of the final shapes of bovine adrenal capillary endothelial cells adhered to the microfabricated substrate. Distances indicate lengths of the square's sides. (b) Apoptotic index (percentage of cells exhibiting positive TUNEL staining) and DNA synthesis index (percentage of nuclei labeled with 5-bromode-oxyuridine) after 24 h, plotted as a function of the projected cell area. Reproduced from Chen, C. S.; Mrksich, M.; Huang, S.; Whitesides, G. M.; Ingber, D. E. *Science* **1997**, *276*, 1425–1428, with permission from Science.

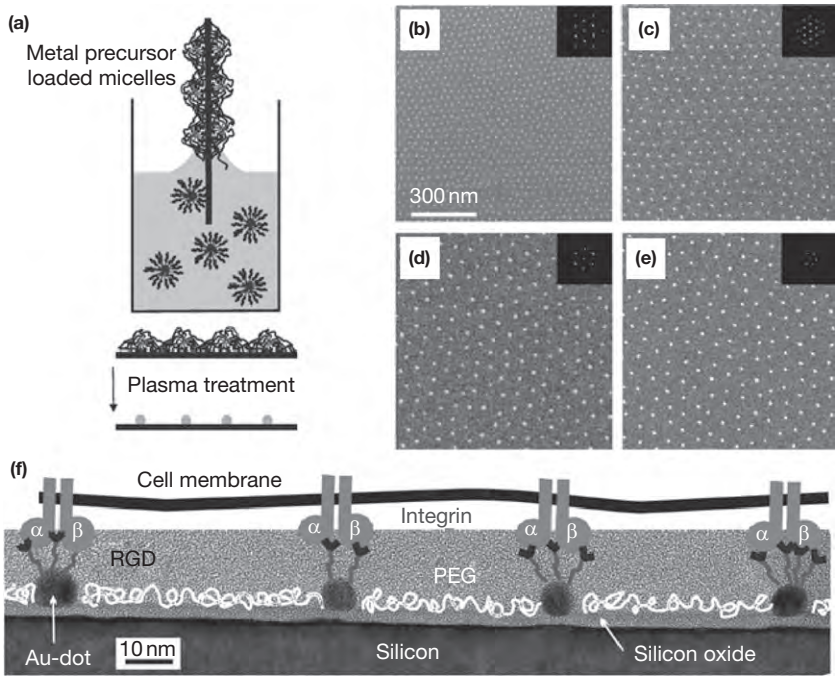

Figure 12 Micellar block copolymer lithography and biofunctionalization. (a) Scheme of diblock copolymer micelle lithography. (b–e) Extended gold (Au) nanodot (3–8 nm in diameter) patterns are displayed by SEM. Variation in the size and separation of the Au nanodots has been achieved by the use of $HAuCl_4$-loaded PS-*b*-PVP with different molecular weights of the polymer components, assembly (a) and reactive plasma treatment. (f) Biofunctionalization of the Au nanodot pattern with integrin-receptor-interactive cyclic RGD-thiols and passivation of the background with PEG. As the gold dot is sufficiently small, it is most likely that only one integrin transmembrane receptor directly interacts with one dot. The Au dots are presented as side view micrographs taken with a high-resolution transmission electron microscope. Reproduced from Spatz, J. P.; Geiger, B. In *Methods in CellBiology*; Wang, Y-L., Discher, D. E., Eds.; Elsevier, 2007; Vol. 83, pp 89–111.

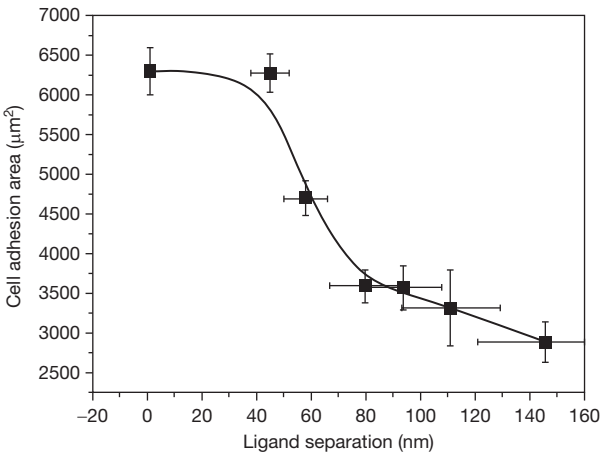

Figure 13 Projected cell adhesion area per cell adhering to different ligand (dot) separation for MC3T3 osteoblasts cultured on integrin-interactive RGD-presenting gold nanodot patterns with a range of different interparticle spacings. Reprinted from Arnold, M.; Cavalacanti-Adam, E.; Glass, R.; *et al*. *ChemPhysChem* **2004**, *5*, 383–388, with permission from Wiley.

surface, as shown schematically in Figure 12(a). Subsequent treatment of these films with reactive gas plasma converted the gold-loaded micellar film into an array of highly regular Au nanoparticles. The size and spacing of the gold nanodots could be controlled by appropriate choice of the molecular weights of the copolymer components (Figure 12(b)–12(e)). Spatz and coworkers[131,132] also demonstrated fabrication of Au nanodot pattern geometries of two different length scales (micro and nano) by the use of inorganic block copolymer micellar monolayers in combination with EBL.

The Au nanodots were subsequently functionalized with cyclic RGD-thiols, a peptide that shows high affinity to $\alpha_v\beta_3$-integrin receptors in the cell membrane (Figure 12(f)). When placed on functionalized Au nanodot patterns separated by varying widths, MC3T3 osteoblasts spread very well and formed focal adhesions (FAs) on patterns if the Au nanodot (and therefore RGD) interparticle spacing was $<\sim$60 nm, comparable to their spreading on uniform RGD- or fibronectin-coated surfaces. In stark contrast, cell spreading on substrates with Au nanodots spaced $>\sim$70 nm was very limited, and FA formation strongly reduced (Figure 13). These findings provide strong evidence that close proximity/clustering of ECM-engaged integrin receptors at the molecular scale is a prerequisite for strong adhesion through FAs and that there is a universal length scale for integrin clustering and activation, as these properties are shared by a variety of cultured cell lines.[133]

4.413.3.2.3. Cell differentiation on micropatterned surfaces

The differentiation of cells into different lineages can be regulated by the local microenvironment. McBeath and coworkers[134] have demonstrated that human mesenchymal stem

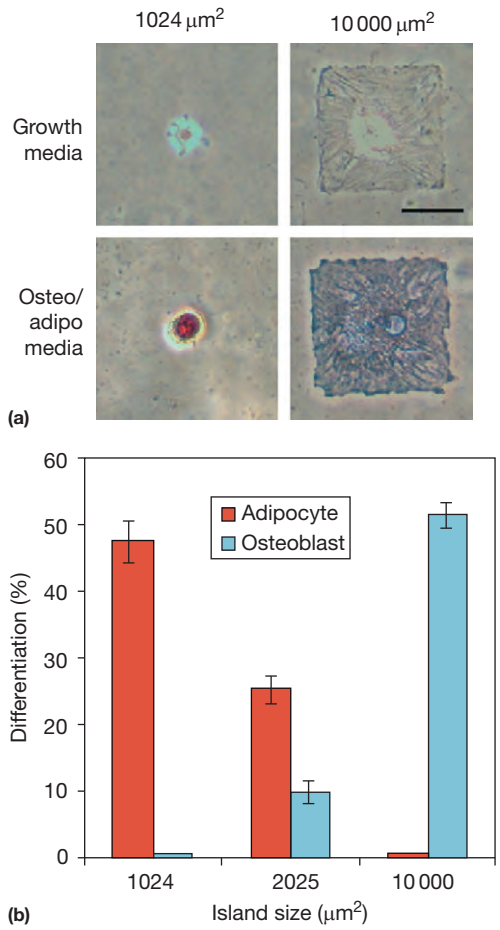

Figure 14 (a) Single hMSCs cells cultured on either small (1024 μm^2) or large (10 000 μm^2) fibronectin patterns after 1 week of growth in mixed media, fixed and stained for both alkaline phosphatase (AP) and lipids. (b) Percentage of differentiation plotted against the island size. hMSC adipogenesis occurred only on the small patterns, osteogenesis occurred on the large ones, and a mixture of both lineages was observed on intermediate-sized patterns. The percentage was determined only for islands containing single cells. Reprinted from McBeath, R.; Pirone, D. M.; Nelson, C.M.; Bhadriraju, K.; Chen, C. S. *Dev. Cell* **2004**, *6*, 483–495, with permission from Science.

cells (hMSCs) can be made to differentiate into adipocytes or osteoblasts by varying the area of the cell adhesive island on which they spread. The micropatterns were created by direct μCP of fibronectin on flat PDMS surfaces. To prevent cell attachment outside the patterns, the surface was backfilled with Pluronics® (PEG–PPO block copolymers).

When cells were confined to a small area, they differentiated into adipocytes, while if they were allowed to spread on an area ten times larger, they differentiated into osteoblasts (Figure 14). The authors showed that cell shape, dictated by the pattern size, regulated the switch in lineage commitment by modulating endogenous RhoA activity. These results also shed light on the close relationship between mechanosensation and commitment of stem cell fate.

4.413.3.2.4. Effect of micropatterned surfaces on cytoskeletal architecture

The shape of the island on which the cell grows affects the internal organization of the cytoskeleton and induces rearrangement of microtubules and actin filaments. This adapted organization affects cell metabolism, especially during the process of cell division. During cell division, cells adopt a more round cell shape while still remaining attached to the surface by means of retraction fibers formed by actin-associated proteins. Thery *et al.*[135] tuned the orientation of the force that these retraction fibers exert over the mitotic cells by changing the design of the ECM micropatterns to which the cells were confined. This study elucidated the effect of the retracting forces on the spindle orientation during the cell division process. Figure 15 shows five distinct patterns produced by μCP of fibronectin and the distinct spindle orientations induced by the corresponding patterns.

4.413.3.2.5. Cell motility on micropatterned gradients

During development of the nervous system, axon growth and neuronal connections are directed by guidance molecules *in vivo*. The guidance molecules create gradient patterns to establish the cell growth cone in the required direction. Further discussion of these and related topics may be found in **Chapter 5.532, Nerve Tissue Engineering**. The signaling environment of the cell can be studied *in vitro* if micropatterned gradients of the guidance molecules are recreated on the surface. von Philipsborn *et al.*[49] used the μCP technique to recreate on a surface a gradient of ephrin A5, a protein known to guide retinal ganglion cells's (RCA) axons. The gradient consisted of an array of patterned features with increasing areas over one direction, in order to generate a unidirectional stepwise increase of ephrin A5 on the surface. Once the retinal ganglion cells were cultured, the axons grew in the direction in which the patterned features were larger, as the surface concentration of ephrin A5 was correspondingly higher. Figure 16(a) shows an axon growth cone of a cell navigating the gradient pattern. The same laboratory later demonstrated the use of a microfluidic patterning strategy to create gradients of the same protein, and demonstrated that the slope of the concentration gradient modulates the growth cones' guidance.[136] Microfluidic patterning allowed for the easy creation of such gradients by loading each subsequent channel with solutions of increasing ephrin A5 concentrations. Upon adsorption of the proteins onto the surface, this process yielded an ephrin A5 concentration that increased unidirectionally along the pattern. Figure 16(b) depicts how growth cone advancement can be tuned depending on the characteristics of the gradient.

4.413.3.2.6. Tissue engineering

The field of tissue engineering uses living cells in a variety of ways to restore, maintain, or enhance tissues and organs.[137] Inside the body, cells lie either in direct contact or in close proximity to other cell types in a tightly controlled architecture that ultimately regulates the resulting tissue function. Tissue engineering strategies to recreate the geometry of tissues will benefit from both the intercellular interactions and the methods to control the local environment. Therefore, patterned coculture models hold the potential to mimic both the local environment

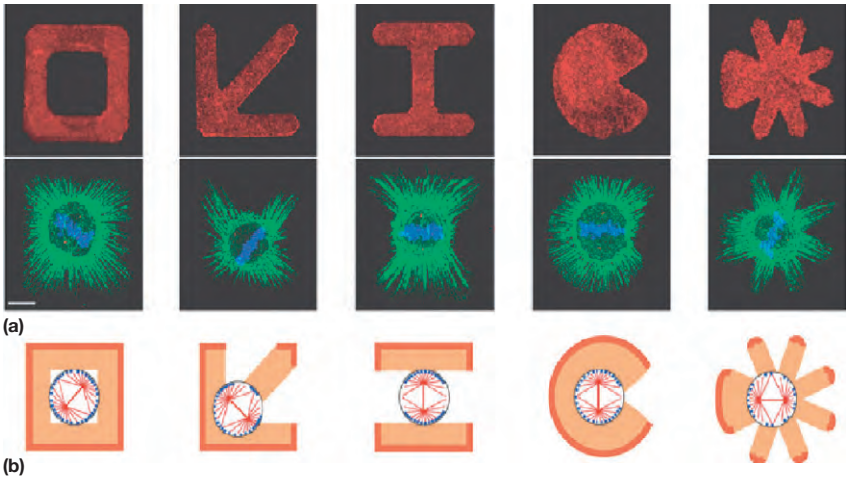

Figure 15 (a) Mitotic single cells growing on five distinct fibronectin micropatterns (red fluorescent staining). Retraction fibers (actin green fluorescent staining) and chromosomes (blue Hoechst staining) indicate the spindle orientation. (b) Schematic micropatterns (orange), anchoring sites for retraction fibers (dark orange), and corresponding distributors of force generators (blue). Adapted from Thery, M.; Jimenez-Dalmaroni, A.; Racine, V.; Bornens, M.; Julicher, F. *Nature* **2007**, *447*, 493–496, with permission from Macmillan Publishers Ltd.

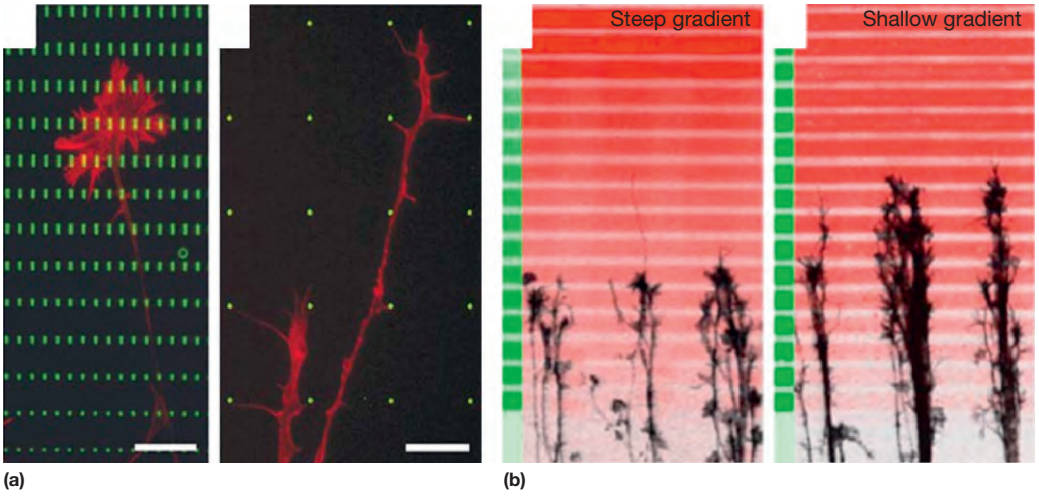

Figure 16 (a) Ephrin A5 protein gradient (green) and retinal ganglion cell (RGC) navigating cones (red) seen with a fluorescence microscope. (b) Temporal RGC axons in gradients produced by μFN. Fluorescence images of a stepwise gradient of ephrinA5 spanning a distance of 320 μm. The stop zone shifts further into a shallow gradient than a steep one. Phalloidin-stained axons are shown in black, antibody-stained ephrin in red. Adapted from von Philipsborn, A.; Lang, S.; Bernard, A.; *et al. Nat. Protoc.* **2006**, *1*, 1322–1328 with permission from Macmillan Publishers Ltd.; Lang, S.; von Philips, A. C.; Bernard, A.; Bonhoeffer, F.; Bastmeyer, M. *Anal. Bioanal. Chem.* **2008**, *390*, 809–816, with permission from Springer.

of tissues, through the location and shape of biological and physical gradients,[138] and the reciprocal regulation and functional relationship between at least two cellular types in the context of tissue formation. For example, Bhatia's laboratory[64] used the microstenciling technique to pattern human liver cell clusters (Figure 17(a)) and study how an environment of fibroblasts affects hepatocyte function (Figure 17(b)). An exhaustive comparison of the gene expression profiles, metabolism, canalicular transport, and susceptibility to hepatoxins was performed between hepatocyte microclusters with and without a fibroblast cell environment. This study may serve as an inspiration to use patterned cocultures instead of cellular purified elements as a tissue model, which could also be useful for the fast screening of drugs. The subject of tissue engineering is further treated in Chapter 5.507, Tissue Engineering and Selection of Cells.

4.413.3.3. Bacteria at Patterned Interfaces

Bacterial adhesion is the first step in the cascade of processes from surface colonization to biofilm formation. The latter is of great medical relevance, as biofilm formation is a key aspect of infection, given the ability of bacteria to protect themselves from the action of drugs, such as antibiotics, by forming a polysaccharide-rich matrix. The underlying molecular

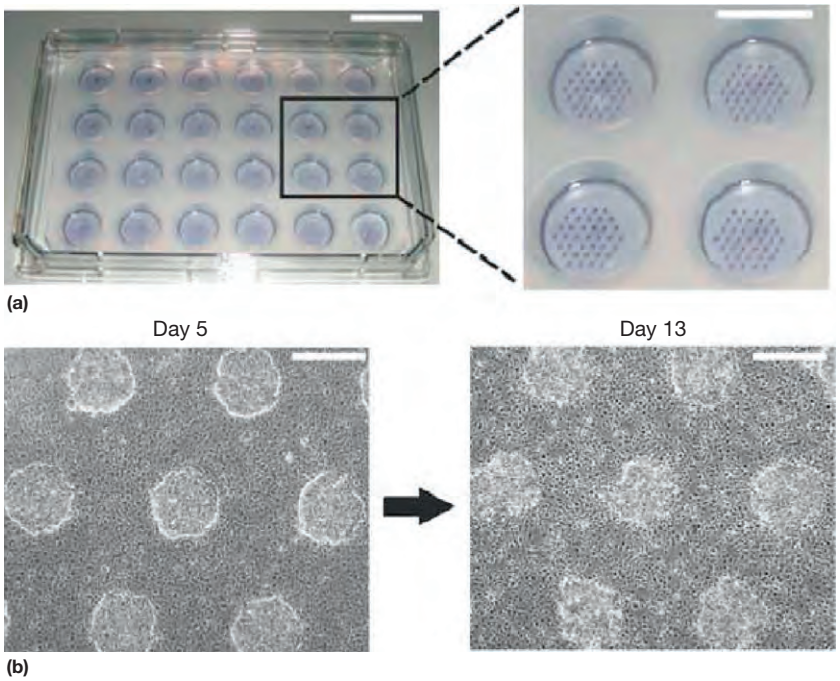

Figure 17 A PDMS microstencil was used to create 400 μm fibronectin islands to study the effect of the fibroblast's environment on the patterned hepatocyte cluster. (a) Photograph of a 24-well device with repeating PDMS microstencils, each with 37 microapertures (insert). (b) Phase-contrast micrographs of cocultures. Once the human hepatocytes adhere to the fibronectin-coated islands, fibroblasts are seeded onto the remaining areas. Images depict pattern fidelity over several weeks of culture. Scale bars are 500 μm. Adapted from Khetani, S. R.; Bhatia, S. N. *Nat. Biotechnol.* **2008**, *26*, 120–126, with permission from Macmillan Publishers Ltd.

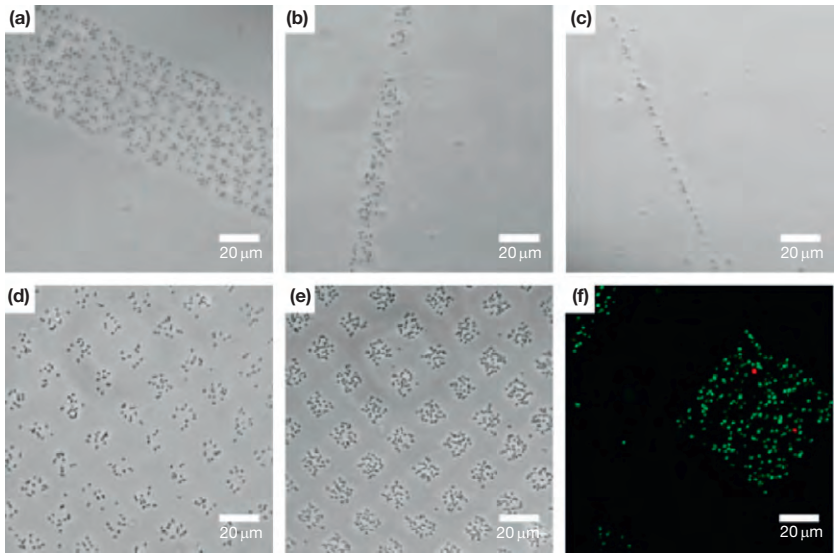

Figure 18 *Escherichia coli* bacteria patterned on PLL-*g*-PEG/PEG-mannoside patterns backfilled with PLL-*g*-PEG. (a–c) Bacteria attached to mannoside-patterned lines of 50, 10, and 2 μm width, respectively (culture time: 30 min). (d–e) The number of cells per patterned square varied depending on the type of mannoside present on the patterns (lower affinity monomannose and higher affinity trimannose, respectively). (f) Fluorescence image of live/dead-stained *E. coli* adhering to $60 \times 60\ \mu m^2$ patterned squares. Live bacteria appear green, dead bacteria red. Most of the bacteria remain alive upon immobilization. Reproduced from Barth, K. A.; Coullerez, G.; Nilsson, L. M.; *et al. Adv. Funct. Mater.* **2008**, *18*, 1459–1469, with permission from John Wiley and Sons.

mechanisms of bacterial colonization and biofilm formation are still poorly understood. For this reason, the study of the nonspecific and specific adhesion mechanisms of pathogens to precisely controlled interfaces has gained increased interest.

Bacterial adhesion to glycoproteins or glycolipids on the surface of eukaryotic cells via specific recognition by bacterial lectins is involved in a plethora of bacterial infections. Bacteria use different types of lectins to target host carbohydrates.[139] For

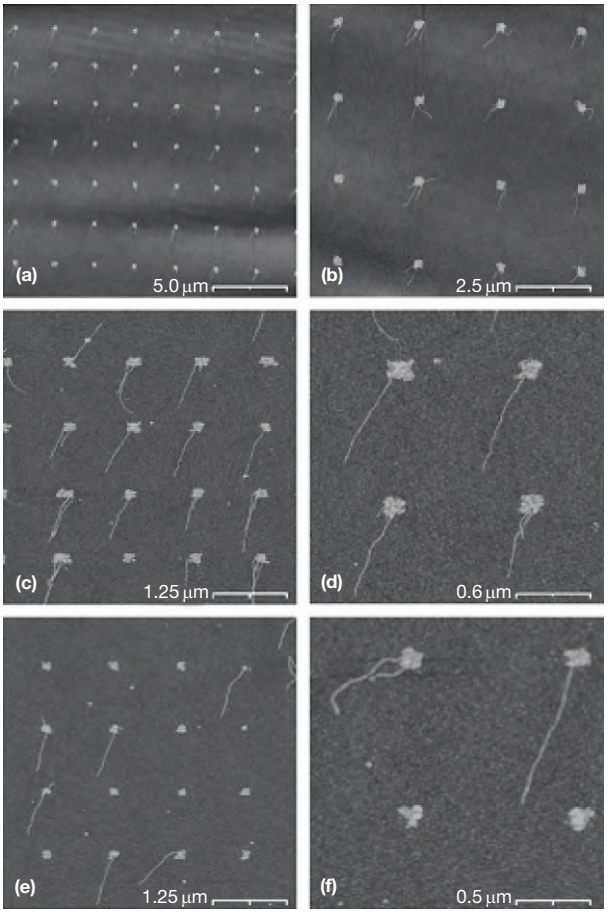

Figure 19 The number of viruses grafted to the antibody nanopatterns varies with the area of the islands. Feature sizes are 240 nm × 240 nm (a,b), 200 nm × 200 nm (c,d), and 90 nm × 90 nm (e, f). The bigger patterns see the majority of sites occupied by two or more phages, while the smaller patterns present only single-cell occupancy, at the cost of having only 20% of the features occupied. The intermediate size presents 21% of the features with two of more viruses and 41% with single virus occupancy. Reproduced from Solis, D. J.; Coyer, S. R.; Garcia, A. J.; Delamarche, E. *Adv. Mater.* **2010**, *22*, 111–114, with permission from John Wiley and Sons.

example, mannoside-containing N-linked glycoproteins are known to be the specific targets of bacterial FimH receptors in *Escherichia coli* bacteria. Barth *et al.*[140] produced surfaces containing PEG brushes presenting distinct oligomannosides (Figure 18), and studied the attachment of *E. coli* bacteria on those surfaces, with the aim of developing surfaces that model host tissues. Micropatterns of PEG-mannoside against a noninteractive background of nonfunctionalized PEG was produced via a resist-based photolithographic technique (MAPL, described in Section 4.413.2.1.1) and used to selectively generate bacteria colonies of different sizes and shapes. Such patterns of well-defined bacterial colonies are of potential interest as model surfaces to study the mechanistic aspects of bacteria communication and the formation of biofilms as well as to mimic controlled defects in antimicrobial coatings at the micron or submicron scale.

4.413.3.4. Viruses at Patterned Interfaces

Arrays of patterned viruses have recently attracted great interest. For example, using nanoscale patterns of antibodies directed against a phage coat protein can provide a strategy for arraying phages, irrespective of their biological diversity, as has been shown by Solis *et al.*[141] (Figure 19). The arrayed phages may subsequently serve as a platform for the presentation of bioligands of interest, and have the potential to elucidate the intricate relationships between spatial organization and resulting functionality in biological systems. Important potential future applications may, therefore, include advanced diagnostic or therapeutic systems. Solis *et al.*[141] used the subtractive printing technique (for details, see Section 4.413.2.1.4) to pattern antibodies directed against the M13 bacteriophage in square nanometric islands (with 90, 200, or 240 nm side length). Incubation of the patterns with bacteriophage suspensions resulted in arrays of viruses. The number of viruses grafted on each island depended on the phage suspension concentration and the size of the nanometric patterns. Using this strategy, large-scale arrays of single identical phages or different phages were created as a platform for the study of interactions with ligands of interest. One can foresee further enlightening studies using this strategy in association with fluorescence microscopy.

Acknowledgments

The authors thank Thomas Michl for rendering the images. A.B.F.-T., T.G., and M.P.-R. gratefully acknowledge financial support from the Portuguese Foundation for Science and Technology (FCT) through grant (SFRH/BD/36476/2007), the Swiss National Science Foundation, and EU-FP7-NMP-ASMENA, respectively.

References

1. Blättler, T.; Huwiler, C.; Ochsner, M.; *et al. J. NanosciNanotechnol.* **2006**, *6*, 2237–2264.
2. Lim, S. H.; Liu, X. Y.; Song, H.; Yarema, K. J.; Mao, H. *Biomaterials* **2010**, *31*, 9031–9039.
3. Liu, W. W.; Chen, Z.; Jiang, X. *Chin. J. Anal. Chem.* **2009**, *37*, 943–949.
4. Ruiz, A.; Buzanska, L.; Gilliland, D.; *et al. Biomaterials* **2008**, *29*, 4766–4774.
5. Jeon, H.; Hidai, H.; Hwang, D. J.; Healy, K. E.; Grigoropoulos, C. P. *Biomaterials* **2010**, *31*, 4286–4295.
6. Yap, F. L.; Zhang, Y. *Biosens. Bioelectron.* **2007**, *22*, 775–788.
7. Falconnet, D.; Koenig, A.; Assi, F.; Textor, M. *Adv. Funct. Mater.* **2004**, *14*, 749–756.
8. Städler, B.; Falconnet, D.; Pfeiffer, I.; Höök, F.; Vörös, J. *Langmuir* **2004**, *20*, 11348–11354.
9. Feller, L.; Bearinger, J. P.; Wu, L.; Hubbell, J. A.; Textor, M.; Tosatti, S. *Surf. Sci.* **2008**, *602*, 2305–2310.
10. Kim, M.; Choi, J.; Jung, H.; Katz, J. S.; Kim, M.; Doh, J. *Langmuir* **2010**, *26*, 12112–12118.
11. Christman, K.; Requa, M. V.; Enriquez-Rios, V. D.; *et al. Langmuir* **2006**, *22*, 7444–7450.
12. Xue, C.; Yang, K. *J. Colloid Interface Sci.* **2010**, *344*, 48–53.
13. Azioune, A.; Storch, M.; Bornens, M.; Thery, M.; Piel, M. *Lab Chip.* **2009**, *9*, 1640–1642.
14. Solak, H. H.; Ekinci, Y. *J. Vac. Sci. Tech. B.* **2007**, *25*, 2123–2127.
15. Solak, H. *J. Phys. D:Appl. Phys.* **2006**, *39*, 171–188.
16. Städler, B.; Solak, H. H.; Frerker, S.; *et al. Nanotechnology* **2007**, *18*, 155306.

17. Turchanin, A.; Schnietz, M.; El-Desawy, M.; Solak, H.; David, C.; Gölzhäuser, A. *Small* **2007**, *3*, 2114–2119.
18. Hang, Q.; Wang, Y.; Lieberman, M.; Bernstein, G. H. *Appl. Phys. Lett.* **2002**, *80*, 4220.
19. Hu, W.; Sarveswaran, K.; Lieberman, M.; Bernstein, G. H. *IEEE Trans. Nanotechnol.* **2005**, *4*, 312–316.
20. Zhang, G.; Tanii, T.; Zako, T.; *et al. Small* **2005**, *1*, 833–837.
21. Senaratne, W.; Sengupta, P.; Harnett, C.; Graighead, H.; Baird, B.; Ober, C. K. *Nanobiotechnology* **2005**, *1*, 23–34.
22. Pesen, D.; Heinz, W. F.; Werbin, J.; Hoh, J. H.; Haviland, D. B. *Soft Matter* **2007**, *3*, 1280.
23. Lussi, J. W.; Tang, C.; Kuenzi, P.; *et al. Nanotechnology* **2005**, *16*, 1781–1786.
24. Rundqvist, J.; Mendonza, B.; Werbin, J. L.; *et al. J. Am. Chem. Soc.* **2007**, *129*, 59–67.
25. Mendes, P. M.; Jacke, S.; Critchley, K.; *et al. Langmuir* **2004**, *20*, 3766–3768.
26. Hong, Y.; Krsko, P.; Libera, M. *Langmuir* **2004**, *20*, 11123–11126.
27. Christman, K.; Schopf, E.; Broyer, R. M.; Li, R. C.; Chen, Y.; Maynard, H. D. *J. Am. Chem. Soc.* **2008**, *131*, 521–527.
28. Winkler, T.; Ballav, N.; Thomas, H.; Zharnikov, M.; Terfort, A. *Angew. Chem. Int. Ed.* **2008**, *47*, 7238–7241.
29. Jonkheijm, P.; Weinrich, D.; Köhn, M.; *et al. Angew. Chem. Int. Ed.* **2008**, *47*, 4421–4424.
30. Alvarez, M.; Best, A.; Pradhan-Kadam, S.; Koynov, K.; Jonas, U.; Kreiter, M. *Adv. Mater.* **2008**, *20*, 4563–4567.
31. Scheres, L.; Klingebiel, B.; Maat, J.; *et al. Small* **2010**, *6*, 1918–1926.
32. Hoff, J. D.; Cheng, L.; Meyhöfer, E.; Guo, L. J.; Hunt, A. J. *Nano Lett.* **2004**, *4*, 853–857.
33. Falconnet, D.; Pasqui, D.; Park, S.; *et al. Nano Lett.* **2004**, *4*, 1909–1914.
34. Xia, Y.; Whitesides, G. M. *Annu. Rev. Mater. Sci.* **1998**, *28*, 153–184.
35. Michel, R.; Reviakine, I.; Sutherland, D.; *et al. Langmuir* **2002**, *18*, 8580–8586.
36. Chow, D. C.; Johannes, M. S.; Lee, W.; Clark, R. L.; Zauscher, S.; Chilkoti, A. *Mater. Today* **2005**, *8*, 30–39.
37. Csucs, G.; Künzler, T.; Feldman, K.; Robin, F.; Spencer, N. D. *Langmuir* **2003**, *19*, 6104–6109.
38. Nakamatsu, K.; Tone, K.; Namatsu, H.; Matsui, S. *J. Vac. Sci. Technol. B Microelectron. Nanometer Struct.* **2006**, *24*, 195–199.
39. Rolland, J. P.; Van Dam, R. M.; Schorzman, D. A.; Quake, S. R.; DeSimone, J. M. *J. Am. Chem. Soc.* **2004**, *126*, 2322–2323.
40. Renault, J. P.; Bernard, A.; Bietsch, A.; *et al. J. Phys. Chem. B* **2003**, *107*, 703–711.
41. Pla-Roca, M.; Fernandez, J. G.; Mills, C. A.; Martinez, E.; Samitier, J. *Langmuir* **2007**, *23*, 8614–8618.
42. Zaytseva, N. V.; Goral, V. N.; Montagna, R. A.; Baeumner, A. J. *Lab Chip* **2005**, *5*, 805–811.
43. Lidstrom, M. E.; Konopka, M. C. *Nat. Chem. Biol.* **2010**, *6*, 705–712.
44. Jiang, X.; Takayama, S.; Chapman, R. G.; Kane, R. S.; Whitesides, G. M. In *Principles of Tissue Engineering*, 3rd ed.; Academic Press: London, UK, 2007; pp 265–278.
45. Stevens, M. M.; Mayer, M.; Anderson, D. G.; Weibel, D. B.; Whitesides, G. M.; Langer, R. *Biomaterials* **2005**, *26*, 7636–7641.
46. Elloumi-Hannachi, I.; Itoga, K.; Kumashiro, Y.; Kobayashi, J.; Yamato, M.; Okano, T. *Biomaterials* **2009**, *30*, 5427–5432.
47. Hynd, M. R.; Frampton, J. P.; Dowell-Mesfin, N.; Turner, J. N.; Shain, W. *J. Neurosci. Meth.* **2007**, *162*, 255–263.
48. Pan, C.; Nie, Y. *Appl. Surf. Sci.* **2010**, *256*, 1878–1882.
49. von Philipsborn, A.; Lang, S.; Bernard, A.; *et al. Nat. Protoc.* **2006**, *1*, 1322–1328.
50. Galeotti, F.; Chiusa, I.; Morello, L.; *et al. Eur. Polym. J.* **2009**, *45*, 3027–3034.
51. Yoon, S. S.; Kim, D. O.; Park, S. C.; *et al. Microelectron. Eng.* **2008**, *85*, 136–142.
52. Bou Chakra, E.; Hannes, B.; Vieillard, J.; *et al. Sens. Actuators B Chem.* **2009**, *140*, 278–286.
53. Das, T.; Mallick, S. K.; Paul, D.; Bhutia, S. K.; Bhattacharyya, T. K.; Maiti, T. K. *J. Colloid Interface Sci.* **2007**, *314*, 71–79.
54. Burnham, M. R.; Turner, J. N.; Szarowski, D.; Martin, D. L. *Biomaterials* **2006**, *27*, 5883–5891.
55. Biasco, A.; Pisignano, D.; Krebs, B.; Cingolani, R.; Rinaldi, R. *Synth. Met.* **2005**, *153*, 21–24.
56. Foley, J.; Schmid, H.; Stutz, R.; Delamarche, E. *Langmuir* **2005**, *21*, 11296–11303.
57. Qin, D.; Xia, Y.; Whitesides, G. *Nat. Protoc.* **2010**, *5*, 491–502.
58. Marzolin, C.; Terfort, A.; Tien, J.; Whitesides, G. M. *Thin Solid Films* **1998**, *315*, 9–12.
59. Wu, Y.; Liao, J.; Weng, C.; Chen, C.; Wang, M.; Zharnikov, M. *J. Vac. Sci. Technol. B Microelectron. Nanometer Struct.* **2007**, *25*, 1729–1736.
60. Glasmästar, K.; Gold, J.; Andersson, A.; Sutherland, D.; Kasemo, B. *Langmuir* **2003**, *19*, 5475–5483.
61. Coyer, S. R.; García, A. J.; Delamarche, E. *Angew. Chem.* **2007**, *119*, 6961–6964.
62. Kane, R. S.; Takayama, S.; Ostuni, E.; Ingber, D. E.; Whitesides, G. M. In *The Biomaterials: Silver Jubilee Compendium*, Elsevier Science: Amsterdam, NL, 2006; pp 161–174.
63. Ostuni, E.; Kane, R.; Chen, C. S.; Ingber, D. E.; Whitesides, G. M. *Langmuir* **2000**, *16*, 7811–7819.
64. Khetani, S. R.; Bhatia, S. N. *Nat. Biotechnol.* **2008**, *26*, 120–126.
65. Tourovskaia, A.; Barber, T.; Wickes, B. T.; *et al. Langmuir* **2003**, *19*, 4754–4764.
66. Wright, D.; Rajalingam, B.; Karp, J. M.; *et al. J. Biomed. Mater. Res. A* **2008**, *85A*, 530–538.
67. Pla-Roca, M.; Leulmi, R. F.; Djambazian, H.; Sundararajan, S.; Juncker, D. *Anal. Chem.* **2010**, *82*, 3848–3855.
68. Brugger, J.; Berenschot, J. W.; Kuiper, S.; Nijdam, W.; Otter, B.; Elwenspoek, M. *Microelectron. Eng.* **2000**, *53*, 403–405.
69. Fostner, S.; Burke, S. A.; Topple, J.; Mativetsky, J. M.; Beerens, J.; Grutter, P. *Microelectron. Eng.* **2010**, *87*, 652–657.
70. Kölbel, M.; Tjerkstra, R. W.; Brugger, J.; *et al. Nano Lett.* **2002**, *2*, 1339–1343.
71. Langford, R. M.; Wang, T. X. *J. Nanosci. Nanotechnol.* **2006**, *6*, 2468–2473.
72. Lee, M. H.; Lin, J. Y.; Odom, T. W. *Angew. Chem. Int. Ed.* **2010**, *49*, 3057–3060.
73. Tan, C. P.; Cipriany, B. R.; Lin, D. M.; Craighead, H. G. *Nano Lett.* **2010**, *10*, 719–725.
74. Vettiger, P.; Brugger, J.; Despont, M.; *et al. Microelectron. Eng.* **1999**, *46*, 11–17.
75. Haq, E.; Liu, Z.; Zhang, Y.; *et al. Nano Lett.* **2010**, *10*, 4375–4380.
76. Bullen, D.; Liu, C. *Sens. Actuators A Phys.* **2006**, *125*, 504–511.
77. Ji, J.; Yang, J.; Larson, D. N. *Biosens. Bioelectron.* **2009**, *24*, 2847–2852.
78. Argwahl, P. B.; Kumar, A.; Saravanan, R.; Sharma, A. K.; Shekhar, C. *Thin Solid Film.* **2010**, *519*, 1025–1027.
79. Choi, I.; Kim, Y.; Yi, J. *Ultramicroscopy* **2008**, *108*, 1205–1209.
80. Kim, S.; Kihm, K. D.; Thundat, T. *Exp. Fluids* **2010**, *48*, 721–736.
81. Custance, O.; Perez, R.; Morita, S. *Nat. Nanotechnol.* **2009**, *4*, 803–810.
82. Piner, R. D.; Zhu, J.; Xu, F.; Hong, S.; Mirkin, C. A. *Science* **1999**, *283*, 661–663.
83. Rosa, L. G.; Liang, J. *J. Phys. Condens. Matter* **2009**, *21*, 483001.
84. Demers, L. M.; Ginger, D. S.; Park, S. J.; Li, Z.; Chung, S. W.; Mirkin, C. A. *Science* **2002**, *296*, 1836–1838.
85. Li, B.; Zhang, Y.; Hu, J.; Li, M. *Ultramicroscopy* **2005**, *105*, 312–315.
86. Li, H.; Carter, J. D.; LaBean, T. H. *Mater. Today* **2009**, *12*, 24–32.
87. Braunschweig, A. B.; Huo, F.; Mirkin, C. A. *Nat. Chem.* **2009**, *1*, 353–358.
88. Salaita, K.; Wang, Y.; Mirkin, C. A. *Nat. Nanotechnol.* **2007**, *2*, 145–155.
89. Liu, G.; Amro, N. A. *Proc. Natl. Acad. Sci. USA* **2002**, *99*, 5165–5170.
90. Meister, A.; Liley, M.; Brugger, J.; Pugin, R.; Heinzelmann, H. *Appl. Phys. Lett.* **2004**, *85*, 6260.
91. Kim, K.; Moldovan, N.; Espinosa, H. D. *Small* **2005**, *1*, 632–635.
92. Bano, F.; Fruk, L.; Sanavio, B.; *et al. Nano Lett.* **2009**, *9*, 2614–2618.
93. Kopf, I.; Grunwald, C.; Bründermann, E.; Casalis, L.; Scoles, G.; Havenith, M. *J. Phys. Chem. C* **2010**, *114*, 1306–1311.
94. Hu, Y.; Das, A.; Hecht, M. H.; Scoles, G. *Langmuir* **2005**, *21*, 9103–9109.
95. Staii, C.; Wood, D. W.; Scoles, G. *J. Am. Chem. Soc.* **2008**, *130*, 640–646.
96. Liu, M.; Amro, N. A.; Liu, G. *Annu. Rev. Phys. Chem.* **2008**, *59*, 367–386.
97. Mukhopadhyay, R.; Al-Hanbali, O.; Pillai, S.; *et al. J. Am. Chem. Soc.* **2007**, *129*, 13390–13391.
98. Pillai, S.; Hemmersam, A. G.; Meyer, R. L.; Moghimi, S. M.; Besenbacher, F.; Kingshoot, P. *Nanotechnology* **2009**, *20*, 025604.
99. Wood, M. A. *J. R. Soc. Interface* **2007**, *4*, 1–17.
100. Valsesia, A.; Mannelli, I.; Colpo, P.; Bretagnol, F.; Rossi, F. *Langmuir* **2008**, *22*, 1763–1767.
101. Cai, Y.; Ocko, B. *Langmuir* **2005**, *21*, 9274–9279.
102. Blättler, T. M.; Binkert, A.; Zimmerman, M.; Vörös, J.; Reimhult, E. *Nanotechnology* **2008**, *19*, 075301.
103. Malmström, J.; Christensen, B.; Jakobsen, H. P.; *et al. Nano Lett.* **2010**, *10*, 686–694.
104. Murray, C. B.; Kagan, C. R.; Bawendi, M. G. *Annu. Rev. Mater. Sci.* **2000**, *30*, 545–610.
105. Sun, S.; Murray, C. B.; Weller, D.; Folks, L.; Moser, A. *Science* **2000**, *287*, 1989–1992.
106. Park, M.; Harrison, C.; Chaikin, P. M.; Register, R. A.; Adamson, D. *Science* **1997**, *276*, 1401–1404.

107. Spatz, J. P.; Sheiko, S.; Möller, M. *Adv. Mater.* **1996**, *8*, 513–517.
108. Glass, R.; Müller, M.; Spatz, J. P. *Nanotechnology* **2003**, *14*, 1153–1160.
109. Sohn, B.; Yoo, S.; Seo, B.; Yun, S.; Park, S. *J. Am. Chem. Soc.* **2001**, *123*, 12734–12735.
110. Kiely, C. J.; Fink, J.; Zheng, J. G.; Brust, M.; Bethell, D.; Schiffrin, D. J. *Adv. Mater.* **2000**, *12*, 640–643.
111. Sohn, B.; Choi, J.; Yoo, S.; *et al. J. Am. Chem. Soc.* **2003**, *125*, 6368–6369.
112. Kim, J. K.; Yang, S. Y.; Lee, Y.; Kim, Y. *Prog. Polym. Sci.* **2010**, *35*, 1325–1349.
113. Stoykovich, M. P.; Nealey, P. F. *Mater. Today* **2006**, *9*, 20–29.
114. Wang, Y. *Cell Mechanics*. Academic Press: London, 2007.
115. Noolandi, J.; Shi, A. *Curr. Opin. Colloid Interface Sci.* **1998**, *3*, 436–439.
116. Hamley, I. W. *Nanotechnology* **2003**, *14*, R39–R54.
117. Darling, S. B. *Prog. Polym. Sci.* **2007**, *32*, 1152–1204.
118. Campolongo, M. J.; Tan, S. J.; Xu, J.; Luo, D. *Adv. Drug Deliv. Rev.* **2010**, *62*, 606–616.
119. Chhabra, R.; Sharma, J.; Liu, Y.; Rinker, S.; Yan, H. *Adv. Drug Deliv. Rev.* **2010**, *62*, 617–625.
120. Li, B. *Biophys. J.* **2009**, *96*, 399a.
121. Fang, Y.; Frutos, A. G.; Lahiri, J. *J. Am. Chem. Soc.* **2002**, *124*, 2394–2395.
122. Perez, T. D.; Nelson, W. J.; Boxer, S. G.; Kam, L. *Langmuir* **2005**, *21*, 11963–11968.
123. Morigaki, K. In *Micropatterned Lipid Bilayer Membranes on Solid Substrates*; Academic Press, 2009; Vol. 9, Chapter 5, pp 107–134.
124. Städler, B.; Bally, M.; Grieshaber, D.; *et al. Biointerphases* **2006**, *1*, 142–145.
125. Frank, M.; Kemler, R. *Curr. Opin. Cell Biol.* **2002**, *14*, 557–562.
126. Groves, J. T.; Wülfing, C.; Boxer, S. G. *Biophys. J.* **1996**, *71*, 2716–2723.
127. Spatz, J. P.; Geiger, B. In *Cell Mechanics*; Academic Press: London, UK, 2007; Vol. 83, pp 89–111.
128. Vogel, V.; Sheetz, M. *Nat. Rev. Mol. Cell Biol.* **2006**, *7*, 265–275.
129. Ochsner, M.; Textor, M.; Vogel, V.; Smith, M. L. *Dimensionality Controls Cytoskeleton Assembly and Metabolism of Fibroblast Cells in Response to Rigidity and Shape. PLoS ONE* **2010**, *5*(3), e9445.
130. Chen, C. S.; Mrksich, M.; Huang, S.; Whitesides, G. M.; Ingber, D. E. *Science* **1997**, *276*, 1425–1428.
131. Glass, R.; Arnold, M.; Blümmel, J.; Küller, A.; Möller, M.; Spatz, J. P. *Adv. Funct. Mater.* **2003**, *13*, 569–575.
132. Spatz, J. P.; Geiger, B. In *Methods in CellBiology*; Wang, Y.-L., Discher, D. E., Eds.; Elsevier, 2007; Vol. 83, pp 89–111.
133. Arnold, M.; Cavalacanti-Adam, E.; Glass, R.; *et al. Chemphyschem* **2004**, *5*, 383–388.
134. McBeath, R.; Pirone, D. M.; Nelson, C. M.; Bhadriraju, K.; Chen, C. S. *Dev. Cell* **2004**, *6*, 483–495.
135. Thery, M.; Jimenez-Dalmaroni, A.; Racine, V.; Bornens, M.; Julicher, F. *Nature* **2007**, *447*, 493–496.
136. Lang, S.; von Philips, A. C.; Bernard, A.; Bonhoeffer, F.; Bastmeyer, M. *Anal. Bioanal. Chem.* **2008**, *390*, 809–816.
137. Griffith, L. G.; Naughton, G. *Science* **2002**, *295*, 1009–1014.
138. Rivron, N. C.; Rouwkema, J.; Truckenmüller, R.; Karperien, M.; De Boer, J.; van Blitterwijk, C. *Biomaterials* **2009**, *30*, 4851–4858.
139. Imberty, A.; Mitchell, E. P.; Wimmerová, M. *Curr. Opin. Struct. Biol.* **2005**, *15*, 525–534.
140. Barth, K. A.; Coullerez, G.; Nilsson, L. M.; *et al. Adv. Funct. Mater.* **2008**, *18*, 1459–1469.
141. Solis, D. J.; Coyer, S. R.; Garcia, A. J.; Delamarche, E. *Adv. Mater.* **2010**, *22*, 111–114.

4.414. Molecular Biomimetic Designs for Controlling Surface Interactions

R E Marchant and J Zhu, Case Western Reserve University, Cleveland, OH, USA

© 2011 Elsevier Ltd. All rights reserved.

4.414.1.	**Introduction**	204
4.414.2.	**Biomaterials' Failure Mechanisms**	204
4.414.2.1.	Protein Adsorption and Thrombus Formation	205
4.414.3.	**Approaches for Controlling Surface Biological Interactions**	206
4.414.3.1.	Rods and Coils	206
4.414.3.2.	Biomimetic Surface Modifications	207
4.414.3.2.1.	Cell membrane biomimetic surface modifications	207
4.414.3.3.	Glycocalyx Biomimetic Models	208
4.414.3.3.1.	Glycocalyx-like biomimetic biomaterials	209
4.414.3.3.2.	Coating blood compatibility	210
4.414.4.	**ECM Biomimetics**	210
4.414.4.1.	ECM-Like Biomimetics	212
4.414.4.1.1.	Integrin-dependent interaction of EC on biomimetic surfactant polymers	212
4.414.4.1.2.	Surface peptide ligand density	213
4.414.4.1.3.	Shear stability of surface-attached cells	214
4.414.4.2.	Biomimetic Modifications of Clinically Relevant Biomaterials	214
4.414.4.2.1.	Cell-selective peptides	214
4.414.5.	**Summary and Outlook**	216
References		216

Glossary

Biomimetic To imitate or copy structure and function from biological macromolecules and assemblies.

Extracellular matrix Interlocking array of proteins and glycosaminoglycans present around cells that often provides anchorage for the cells.

Glycocalyx The carbohydrate-rich glycoprotein–polysaccharide layer that covers a cell surface.

Phosphorylcholine The functional group derived from phosphocholine (choline chloride *O*-(dihydrogen phosphate)).

Plasma coating A thin polymer film created using radiofrequency 'plasma' glow discharge technique.

Saccharide A small carbohydrate molecule such as glucose.

Steric repulsion Dynamic network of associated water molecules (surrounding hydrated molecules) that prevents penetration by large macromolecules such as proteins.

Zwitterion A molecule that contains both a negative and a positive charge on different atoms within the molecule.

Abbreviations

AFM	Atomic force microscopy
APC	Activated protein C
ATIII	Antithrombin III
Dex	Dextran
ePTFE	Expanded polytetrafluoroethylene
EC	Endothelial cell
ECM	Extracellular matrix
FA	Focal adhesion
Fg	Fibrinogen
FN	Fibronectin
G	Generation
GAG	Glycosaminoglycan
Hex	Hexanoyl or Hexanal
HSPG	Heparan sulfate proteoglycan
IC	Ion channel
ID	Internal diameter
MW	Molecular weight
OTS	Octadecyltrichlorosilane
PAI	Plasminogen activator inhibitor
PC	Phosphatidylcholine
PDMS	Polydimethlysiloxane
PEG	Poly(ethylene glycol)
PEO	Poly(ethylene oxide)
PG	Proteoglycan
PGI2	Prostaglandin I2
PLG	Plasminogen
PLM	Plasmin
PMMA	Poly(methyl methacrylate)
PPP	Platelet poor plasma
PRP	Platelet rich plasma
PSFP	Peptide fluorosurfactant polymer

PTFE	Polytetrafluoroethylene	**TAT**	Thrombin-antithrombin complex
PVam	Poly(vinyl amine)	**TF**	Tissue Factor
RGD	Arginine glycine aspartate	**TM**	Thrombomodulin
SEM	Scanning electron micrograph	**TPA**	Tissue plasminogen activator
SP	Surfactant Polymer		

4.414.1. Introduction

Biomaterials are used in biomedical devices that sustain, augment, or completely replace diseased human organs. These include vascular grafts, heart valves, and ventricular assist devices; orthopedic devices; drug delivery systems; extracorporeal systems; and a wide range of invasive treatment and diagnostic systems.[1–4] The use of synthetic materials for biomedical devices has increased considerably in recent years. The principal reasons for this proliferation have been (1) the increasing clinical demand for diverse, improved biomaterials for an aging population and (2) the increasing availability of materials, particularly polymers that possess the appropriate mechanical and physical properties. These materials range from delicate hydrogels for soft contact lenses and tissue engineering scaffolds to tough, ultrahigh molecular weight polyethylene for components of joint prostheses. However, current clinically used biomaterials are still largely based on commodity polymers introduced over 50 years ago, such as polyethylene, polyester fibers, silicones, and polyurethanes. Unfortunately, these and other biomaterials suffer from well-known problems including surface-induced thrombosis, excessive wound healing, and infection.[4,5–7] For example, small-diameter (<6 mm ID) vascular grafts are currently clinically impracticable as they are associated with consistent thrombotic occlusion and intimal hyperplasia.

The interface between a biomaterial and the biological environment is crucial to the solution of these problems because it affects protein and platelet interactions, thrombus formation, infection, fibrosis, calcification, tissue integration, and cell–surface interactions. Consequently, approaches that provide improved blood and tissue biocompatibility would favorably impact medical device performance and facilitate development of devices that are currently not feasible. This chapter considers approaches to the control of surface interactions, with particular emphasis on biomimetic approaches that utilize and adapt structural concepts from Nature to design new interfaces for biomaterials. Although the discussion emphasizes polymeric materials and cardiovascular applications, the approaches presented may be readily adapted to other materials and applications.

4.414.2. Biomaterials' Failure Mechanisms

The principal mechanisms of failure of implanted medical devices include surface-induced thrombosis, excessive wound healing including overproliferation of smooth muscle tissue (e.g., intimal hyperplasia) and fibrosis, calcification, and infection.[3,5–8] Examples are shown in Figure 1. A mechanical heart valve (Figure 1(a)) shows one leaflet completely closed

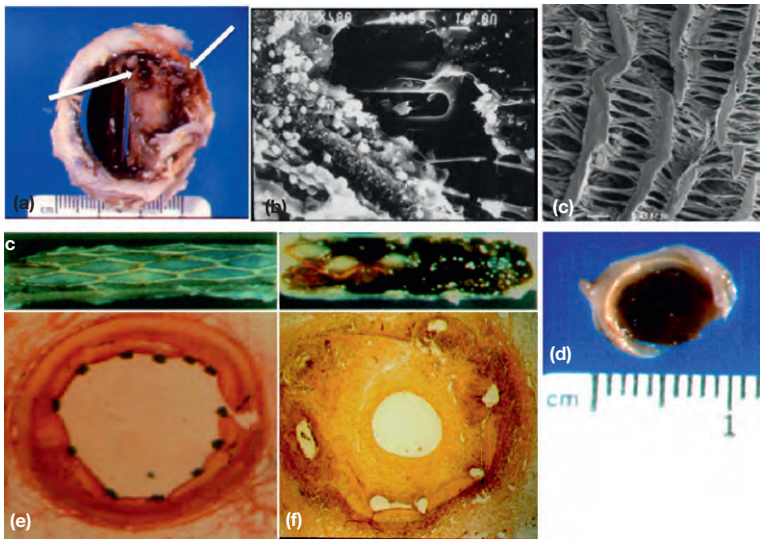

Figure 1 Examples of medical device failure. (a) A mechanical heart valve that shows one leaflet closed from the healing response (fibrous tissue deposition), along with thrombus deposits (arrow) and evidence of infection (arrow). (b) A chamber-type glucose biosensor covered by a thrombus after exposure to canine blood for 2 h *in vivo*. (c) Scanning electron micrograph (SEM) of expanded poly(tetrafluoroetheylene) vascular graft material. (d) Small-diameter vascular graft occluded by a thrombus. (e) Endovascular stent at the time of placement and (f) at 3–6 weeks postimplantation in which restenosis is clearly evident.

from the healing response (fibrous tissue deposition). The valve also shows thrombus deposits (arrow) and evidence of infection (arrow). Figure 1(b) shows a chamber-type glucose biosensor after exposure to canine blood *in vivo* for 2 h covered by a thrombus. Figure 1(c) shows an SEM of expanded poly(tetrafluoroetheylene) (ePTFE) vascular graft material and in Figure 1(d), a small-diameter graft occluded by thrombus. Figure 1 shows an endovascular stent at the time of placement (Figure 1(e)) and at 3–6 weeks postimplantation (Figure 1(f)), in which restenosis is clearly evident. While the majority of biomaterials implanted perform within approved standards, a minority suffer catastrophic failures requiring their removal, and many others do not perform as well as desired. There is substantial opportunity to improve the performance of biomaterials in patients.

4.414.2.1. Protein Adsorption and Thrombus Formation

The host response to biomaterials is largely determined by the surface or interfacial properties of the implanted material. Materials' surface properties have been consistently correlated with various measures of biological interaction such as protein adsorption, thrombosis, and cell and platelet adhesion in blood, and inflammation and wound healing in soft tissue. In addition, this knowledge has led to numerous studies on the application of surface modification methods to improve device and material biocompatibility.[9]

Figure 2 depicts the process of thrombus formation on a biomaterial. The initial adsorption of plasma proteins dominates subsequent coagulation responses (see also Chapter 4.406, Protein Interactions with Biomaterials).[10,11] The composition, conformation, and binding affinity of the adsorbed proteins are critical in determining events leading to thrombus formation, including activation and adhesion of blood platelets, activation of the coagulation cascade, and cell attachment.[10,11] Protein adsorption is governed by all the prevailing intermolecular forces, including van der Waals, electrostatic, and entropic (hydration) forces.[12,13] Many biomaterials are hydrophobic, so entropic forces are important to protein reactions. This invariably results in a net attraction and strong driving forces for protein adsorption from blood, where $>10^4$ different plasma proteins of total concentration $\sim$70 mg ml^{-1} and different individual protein concentration ranges over 10^{11} continually encounter the surface. Controlling these interactions is essential for the achievement of successful blood–materials interface, including the activation and spreading of platelets, and coagulation activation.[2,5,6] The 'ideal' blood–materials interface is the viable vascular endothelium: a typical vascular endothelial cell (EC) undergoes greater than 10^{10} collisions μm^{-2} with plasma proteins every second but is able to manage this barrage using its variety of interfacial structural and metabolic components. Thus, minimizing nonspecific protein adsorption and distinguishing between specific and nonspecific interactions are essential properties of EC function, seldom duplicated in biomaterials to date.

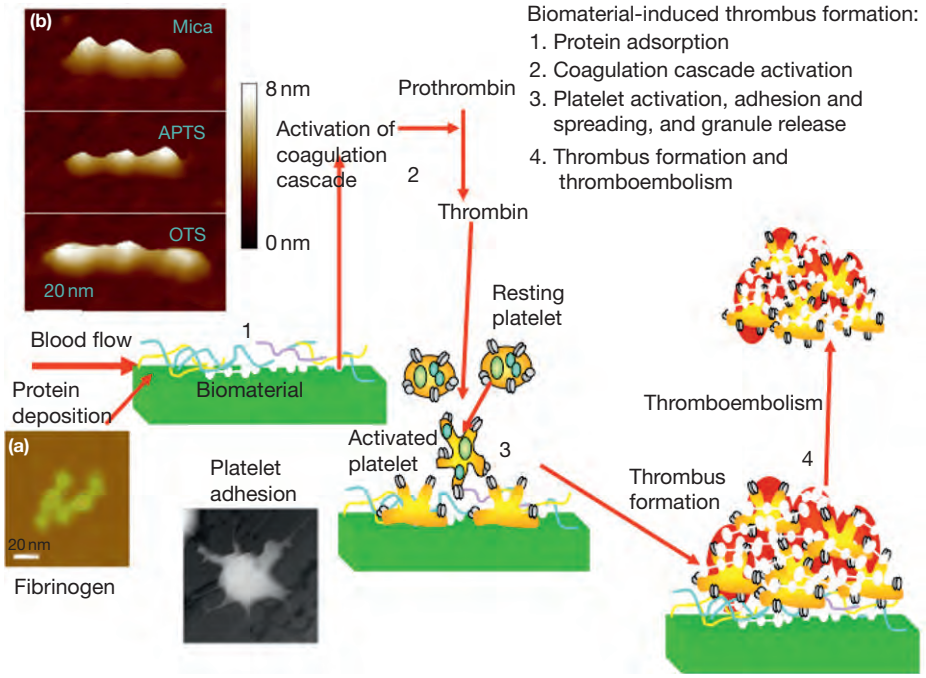

Figure 2 Biomaterial surface-induced thrombus formation is initiated by fast protein adsorption,[1] which will include the coagulation protein fibrinogen (Fg). The AFM image (a) shows Fg's three linked globular domains. The AFM image (b) shows Fg after adsorption on a hydrophilic surface (mica), a positively charged surface (APTS, aminopropyltrichlorosilane), and on a hydrophobic surface (OTS, octadecyltrichlorosilane). Fg undergoes maximum conformational change on the hydrophobic surface, although this actually reduces the ability of Fg to bind platelets. Protein adsorption is followed by the activation of the coagulation cascade[2] and platelet activation, adhesion and spreading, and granule release,[3] leading to thrombus formation, and possibly thromboembolism.[4]

4.414.3. Approaches for Controlling Surface Biological Interactions

Two general strategies are employed for controlling surface interactions with biomaterials: (1) surface modification designed to suppress undesirable protein and cell–surface interactions and (2) approaches designed to enhance favorable interactions such as surface attachment of ECs. This section focuses on approaches, particularly biomimetic approaches, designed to suppress undesirable protein and cell–surface interactions as a way of passivating biomaterials' surface so as to eliminate unwanted biological reactions. This includes surface modifications that passivate surfaces, such as preadsorption of plasma proteins like albumin or suppression of protein adsorption (e.g., use of oligosaccharide- or poly(ethylene oxide)-grafted surfaces). Other approaches, not covered here, include selective adsorption of certain proteins (e.g., plasminogen) with profibrinolytic or anticoagulation properties, or selective adsorption of certain proteins in preferred orientations that reduce platelet interactions.

The surface modification approach is widely used because it has direct applicability to clinical devices: through this strategy, biomaterial bulk and surface properties can be selected and/or modified separately. Numerous surface modification techniques have been developed for the modification of existing clinically used biomaterials.[9] They can be grouped into two broad categories: (1) chemical or physical alteration of the atoms or molecules in an existing biomaterial surface through chemical treatment methods such as wet or plasma etching and chemical modification, and (2) coatings prepared by methods such as solvent casting, covalent chemical grafting, radiation grafting, or thin film deposition by chemical vapor deposition or radiofrequency plasma film formation. Each technique has advantages and disadvantages, and none has completely eliminated surface challenges in biomaterial designs and device function. Surface modifications created by covalent chemical bonding are typically more stable, but usually less reliable or uniform coverage is obtained over surfaces receiving a physisorbed coating. Some materials are not amenable to covalent modification and must be physically coated. Many factors including clinical application and biocompatibility of the material and coating are best considered when choosing the most appropriate modification technique (see also **Chapter 4.402, Biocompatibility and the Relationship to Standards: Meaning and Scope of Biomaterials Testing**; **Chapter 3.301, Surface Analysis and Biointerfaces: Vacuum and Ambient *In Situ* Techniques**; and **Chapter 3.303, Proteomic and Advanced Biochemical Techniques to Study Protein Adsorption**).

Preadsorbing albumin, a protein not involved in coagulation or platelet adhesion, on hydrophobic biomaterials is a simple method that passivates a surface by blocking most surface-binding sites for other adhesive proteins that may initiate adverse surface responses.[10,11] The major disadvantage of this method is that many other adhesive plasma proteins have higher surface affinities and will gradually surface-exchange with the preadsorbed albumin, so this method is not useful for long-term *in vivo* applications.[11] However, this method is very useful for *in vitro* experiments, where the duration of blood–materials interaction is relatively short (i.e., less than a few hours). Many surface modification methods are aimed at creating specific hydrophilic surfaces, such as those bearing carboxylate or hydroxyl groups, or functionalized for immobilization of small hydrophilic molecules. This is based on past observations that hydrophilic polymer surfaces adsorb reduced amounts of proteins.[16] However, proteins that do adsorb will frequently retain their biological functions, so simply making surfaces hydrophilic does not decrease, the risk of thrombogenicity and cell attachment, but increases it. One way to improve this approach is to increase the size of the hydrophilic group. For example, surface attachment of tetraethylene glycol dimethyl ether on polymer surfaces using radiofrequency glow discharge plasma-treated films typically shows very low adsorption of proteins,[14,15] although there is some concern regarding complement activation.[16]

4.414.3.1. Rods and Coils

The relative success of polyethylene oxide (also referred to as poly(ethylene glycol), PEG) as a protein-resistant coating for biomaterials[17–20] has been well explained on the basis of the entropic, or steric, repulsion unique to this tethered hydrated polymer. However, coating molecular architecture such as chain length, surface density, and substrate heterogeneity, all affect the efficacy of the PEG repulsion barrier.[21–25] Regular control of these interfacial coating molecular properties is difficult. An advantage of surface-grafting carbohydrates is that, unlike PEG, they have no amphiphilic or 'surface-active' character and do not exhibit entropic aggregation transitions in water (i.e., no cloud point in solutions).[22,26] Oligosaccharides have well-defined molecular configurations that lead to their molecular structural conformations modeled typically as rigid rods, whereas a PEG molecular structure is dominated by its polymer conformational freedom, modeled as a random coil (**Figure 3**). This one distinction has considerable impact for their different behaviors as coatings for biomaterials. Far greater surface-grafting precision is required in manipulating surface oligosaccharides to achieve an effective hydration barrier on biomaterials. Key properties of molecular architecture (configuration, conformation, chain length, branching, surface density, etc.) and thermodynamic factors that influence local interactions must be addressed to approach an effective glycocalyx-like hydration. At low surface density, the conformational freedom and 'surface activity' of PEG facilitate its spreading over a surface. The surface coating may be thin, but fractional surface defects or uncoated areas will be small due to this property. In contrast, if an oligosaccharide is attached in low density as a rigid rod, only a small fractional surface area will be covered, exposing numerous defect areas where proteins can adsorb. This is the most probable explanation for the wide variability observed for protein resistance of immobilized oligosaccharides.[27] If the immobilization density of oligosaccharides is increased, the observed differences in protein resistance should disappear, and, at high surface coverage, oligosaccharides should become superior in this performance, as PEG undergoes interfacial dehydration and becomes less effective at high density.[28] This hypothesis is difficult to prove because immobilization densities on biomaterials are not easily quantified precisely. However, one quantifiable example is with PEG-coated liposomes, which usually contain ~5 mol%

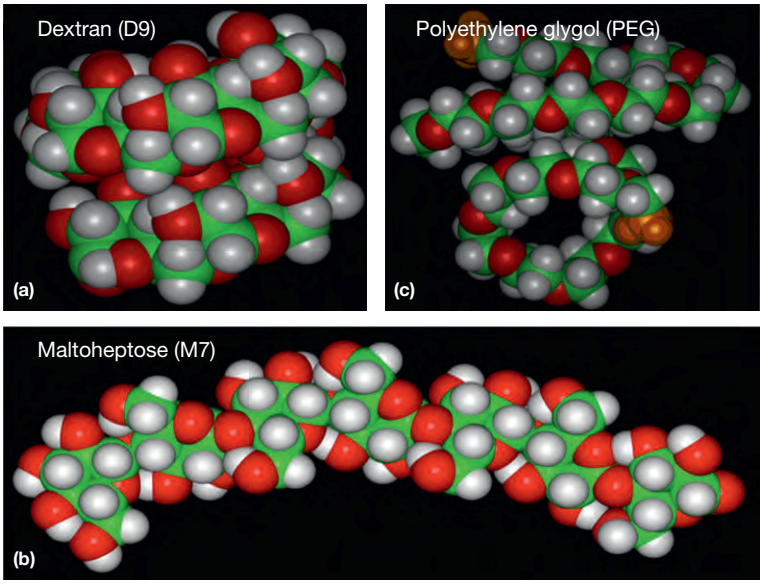

Figure 3 Molecular models of (a) dextran (α-1,6-D-glucose, 9 residues, MW = 1600), (b) maltoheptose (α-1,4-D-glucose, 7 residues, MW = 1152), and (c) poly(ethylene glycol) (PEG, MW= 1500). The 'shape' of the two oligosaccharides depends on their molecular configuration. In dextran, the glucose residues have a 1,6 linked configuration, which generates a helical structure that is relatively short and fat, while in maltoheptose, the glucose residues are 1,4 linked, which generates an extended helical structure. In contrast, PEG is a random coil; its $-CH_2CH_2O-$ repeat units have complete rotational freedom, so the overall molecular shape does not depend on configuration, but on its conformation that will change depending on local molecular and solvent interactions (i.e., the shape for the PEG shown in (b) is arbitrary).

PEG–lipid content. Incorporation of the PEG in liposome formulations increases their blood circulation half-life from 1 h up to ~12–24 h.[19,29] A red blood cell with its dense hydrophilic surface proteoglycan and glycoprotein glycocalyx has a circulation life time of ~120 days.[29] This surface design of the red blood cell glycocalyx has been exploited in synthetic colloids to extend the circulation time of cell–surface-attached polymer nanoparticles used for drug delivery.[31]

4.414.3.2. Biomimetic Surface Modifications

Biomimetic designs represent a common approach for the control of biomaterials' surface interactions. The approach involves the design of interface materials based on the mimicking of the synthetic materials found in Nature on biomaterial surfaces. In particular, the cell lipid membrane or its outer glycocalyx surface, or components of the extracellular matrix (ECM) are all common mimicry foci for biomaterial exploitation. The abundance of complex macromolecular and supramolecular structures within these related systems provides lessons in structural hierarchy that elicit functional efficiency useful as design motifs for creating new biomimetic materials.[30] Also, advances in materials' synthesis provide a scientific basis for the production and manipulation of new macromolecular structures, not just at the level of chemical composition, but at the higher level of structural creation of bioinspired constructs that assemble with hierarchy or supramolecular properties resembling natural systems.[31,32] Combining this knowledge of hierarchical assembly with the lessons from Nature has opened a wealth of new possibilities for new biomaterials and coatings combining both structural hierarchy and programmed biological function.

4.414.3.2.1. Cell membrane biomimetic surface modifications

Biomimetic designs have included utilization of organized phospholipid cell membrane-like coatings seeking to mimic simple cell lipid membrane chemistries, interfaces, and structures.[33–37] Monolayers of phosphatidylcholine (PC) molecules and diacetylene phospholipids, producing films of phosphorylcholine (PC) head groups coated on polymer surfaces, reduced protein adsorption, decreased platelet activation and adhesion, and decreased complement activation.[33,38] Polymers bearing the PC group have also been synthesized and used to modify a variety of hydrophobic polymers, such as polyethylene, showing significant reduction of protein adsorption and improvement in hemocompatibility.[33,38,39] A series of phospholipid polymers having methylene-or oxyethylene-bridging units between the PC group and the backbone was synthesized, and the effects on the mobility of the hydrated polymer chains and the structure of hydration in the polymers on the protein resistance of the polymer surfaces were studied. 2-Methacryloyoxyethyl PC polymers synthesized as biomimetics of the cell membrane structure were reported to reduce protein adsorption and cell adhesion *in vitro* when the polymer was placed in whole blood in the absence of anticoagulants.[39] Despite the observation that a PC lipid bilayer membrane alone is rarely found as a natural biological interface (i.e., actual cell membrane surfaces most often have dense carbohydrate glycocalyx layers), surface modification with PC chemistry and structure is promoted as a promising way to improve blood compatibility of biomaterials.

Polyampholytes – polymers with both positively and negatively charged groups or zwitterions – have been studied for their responsiveness to pH changes and their interactions with

proteins.[39–42] A protein-resistant surface can be achieved when the surface contains a nanometer-scale homogenous mixture of balanced charge groups derived from either zwitterionic or mixed charged groups, since they are strongly hydrated through ionic solvation.[41] Zwitterionic poly(sulfobetaine methacrylate) and poly(carboxybetaine methacrylate) surfaces show resistance to nonspecific fibrinogen adsorption.[42] Two charged compounds (11-mercapto-*N*,*N*,*N*-trimethylammonium chloride and 11-mercaptoundecylsulfonic acid) were shown to self-organize from a wide range of bulk concentrations to achieve a uniform distribution of mixed charged groups at the nanometer scale on a gold substrate, thus forming nonfouling mixed charged SAMs.[41] Another approach similar to creating a protein-resistant surface using balanced charge groups in a self-assembled film can be through the use of natural peptides that are negatively and positively charged such as glutamic acid or aspartic acid and lysine.[41] The protein resistance is reported to be comparable to that achieved with PEG-modified surfaces.[42]

4.414.3.3. Glycocalyx Biomimetic Models

Our own approach to this surface design problem, employing surface-assembling surfactant polymers,[43–48] has focused on biomimetic structures based on the cell's glycocalyx, rather than the lipid bilayer membrane components.

While the lipid bilayer is central to much biological membrane structure, the outer exposed surfaces of nearly all cell membranes bury their lipid headgroups (e.g., PC) beneath a thick layer of hydrated coated polymer – the cell's glycocalyx. The cell's surface is therefore the native glycocalyx (**Figure 4**), which can be as thick as 50 nm,[49,50] as a complex milieu of highly glycosylated molecules dominating the interface between the blood cell lipid bilayer membrane and the extracellular plasma environment.[51,52] An erythrocyte membrane contains ~500 000 glycophorin A proteins (**Figure 4(b)**), a transmembrane glycoprotein with 60% carbohydrate by mass, and ~100 extracellular O- and N-linked saccharides arranged as 16 short (1 nm) chains, facilitating high interfacial solvation.[51,52] Proteoglycans, including heparan sulfate proteoglycans (HSPGs), have received attention because of their roles in anticoagulation and leukocyte interaction.[53] HSPGs comprise a protein core decorated with highly charged polysaccharide side chains of sulfated glycosaminoglycans (GAGs), composed of 1,4 linked residues of uronic acid and glucosamine monomer repeats attached by a conserved tetrasaccharide to the protein core serine residues.[53] The potent anticoagulant properties of heparan sulfate, particularly in the form of its GAG, heparin, have been exploited extensively as a clinical anticoagulant and for immobilization on biomaterials including commercialized, clinically used products.[54]

To minimize nonspecific protein adsorption from more than 20 000 different plasma proteins and to prevent blood coagulation by interfacial activation, the EC glycocalyx relies on carbohydrates. Terminal anionic oligosaccharides produce complex three-dimensional (3D) charge distributions, facilitating an effective electrostatic repulsive (double layer) force. Additional specific ligand recognition sequences provide sufficient attractive forces to overcome the repulsive barrier to

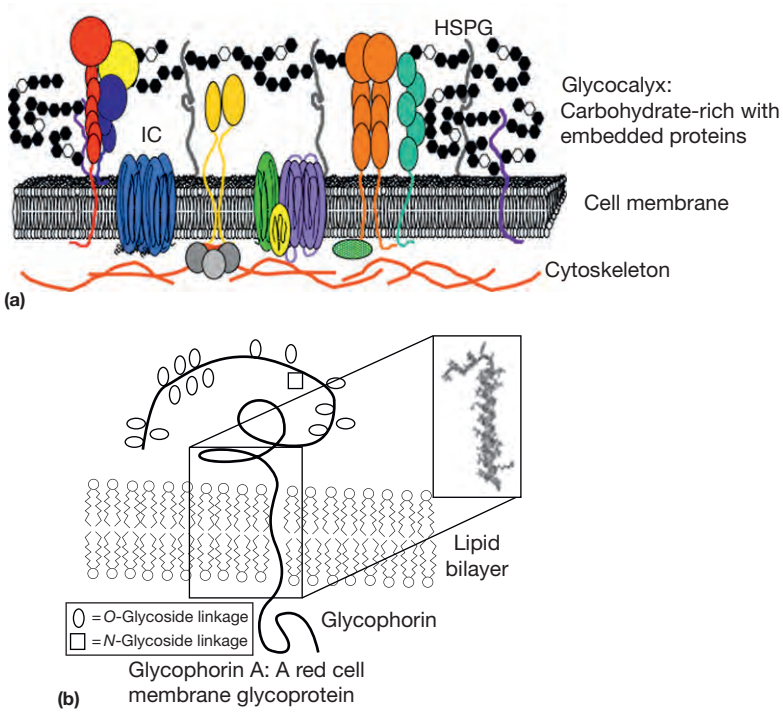

Figure 4 (a) Model of a cell surface glycocalyx that shows the carbohydrate-rich surface with embedded proteins linked to the cell's membrane and the underlying cytoskeleton. The glycocalyx is on the order of 50 nm thick, 10 times the thickness of the cell's bilayer membrane. All structures on the outer membrane surface are glycosylated. (HSPG: heparin sulfate proteoglycan, IC: ion channel). (b) Model of glycophorin A, which is a major red cell glycoprotein with many attached O- and N-linked saccharides.

achieve a highly evolved functional recognition specificity, while nonionic oligosaccharides provide a physical basis for maximizing entropic repulsion that minimizes nonspecific adhesion.[55–57] The glycocalyx is thus capable of both facilitating specific interactions with ligands and minimizing undesirable cell and molecular adhesions. Mimicking the general nonadhesive properties of the cell glycocalyx is a prerequisite for the successful development of biomimetic structures that incorporate bioactive components.

4.414.3.3.1. Glycocalyx-like biomimetic biomaterials

The ability to mimic the nonadhesive properties of the glycocalyx provides a conceptual approach to the solution of important problems with blood-contacting biomaterials related to nonspecific protein adsorption and platelet adhesion (e.g., device and materials thrombosis). An essential consideration in designing suitable modifications is to develop a materials application approach that is simple and inexpensive to implement, yet provides the desired interfacial properties. The commercial Carmeda™ anticoagulant coating represents such a model for biomaterials use.[58–60] The Carmeda coating represents the most successful method used clinically for heparin-based surface modification of blood-contacting medical devices. The innovative feature of this coating was the maximization of heparin's anticoagulant activity by end-point attachment to the biomaterial, rather than the 'side-on' attachment used previously. End-point attachment optimizes heparin's antagonistic interaction with coagulation factors, including thrombin, and involves reductive amination of the aldehyde on the reducing terminal of heparin with amino groups of a polymer layer coating on the biomaterial surface to facilitate covalent immobilization.[60]

Another successful design has been the comb-like surfactant polymer system (**Figure 5**), which provides multiple attachment sites that stabilize surface adhesion of an adsorbed coating.[45–48] The polymers consist of poly(vinyl amine) (PVAm) with both hydrophobic and oligosaccharide branches.[46] The same design may be extended to include different polar groups (carbohydrates, PEG, etc.) and/or peptides to achieve the desired coating interfacial functional properties. Surfactant polymers with glycocalyx-like glycodendrimer designs also have been developed.[47] The hyperbranched dendritic saccharides provide increased surface coverage due to the larger hydrodynamic size of the glycodendron compared with a single pendant saccharide. The spatial arrangement of the glycodendrimer provides a 'canopy' of protective carbohydrate over a biomaterial's surface.[47] Critical factors in the design revolve around two central issues: (i) surface stability and assembly (meaning effective kinetic irreversibility) under conditions expected in physiological environments and (ii) useful and enduring biological function. Multiple factors, both thermodynamic and kinetic, can affect surface stability, including the polymer molecular weight, hydrophobic side chain lengths and density, polar side chain composition and size, the hydrophobic/philic balance, and polymer–polymer and polymer–surface interactions. Given surface stability, biological interfacial function is then largely governed by the density, distribution, and properties of the polar side chains on the surface.

The adhesion stability of surfactant polymers on different biomaterials has been examined using a rotating disk system

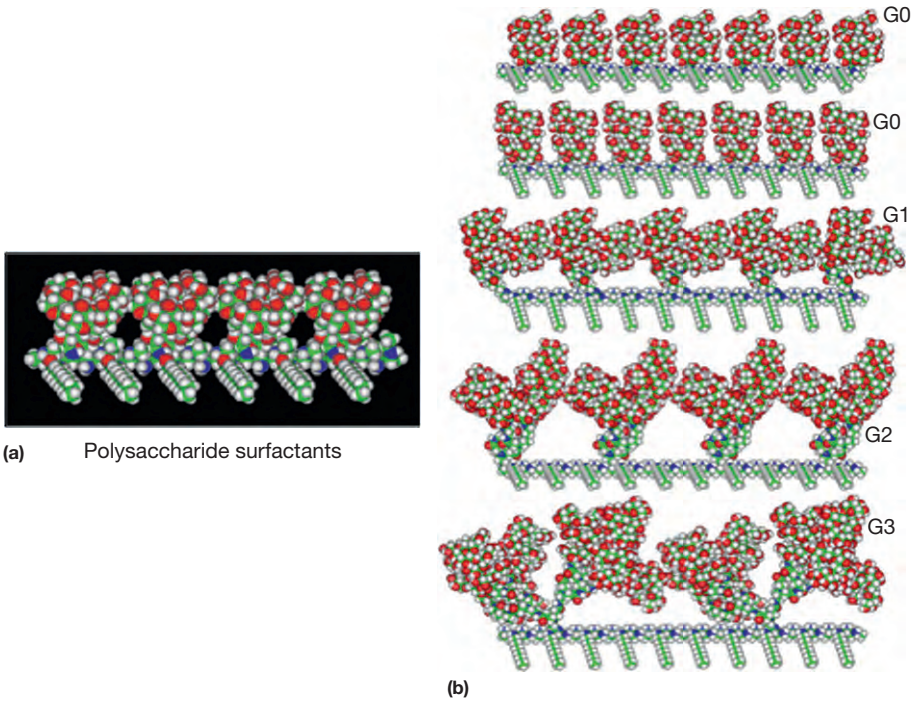

Figure 5 Space-filled model of (a) polysaccharide surfactant consisting of poly(vinyl amine) (PVAm) with both hydrophobic (hexanoyl) and oligosaccharide (dextran) branches (PVAm/hex-Dex). (b). Space-filled model of PVAm/Hex-Dex (top, same as in a) and PVAm/Hex with attached G0, G1, G2, and G3 generation dextran-dendrons (bottom). The number of dextrans/unit PVAm chain length is 16 for both the G2 and G3, even though the spatial arrangement changes.

immersed in PBS at 37 °C.[61] The surfactant polymers undergo spontaneous adsorption with stable adhesion on a diverse range of hydrophobic biomaterials including polyethylene (PE), polydimethylsiloxane (PDMS), polycarbonates, and some polyurethanes. These same surfactant polymers appeared less stable, however, on PTFE. Surfactant polymers readily adsorb on PTFE, but can be desorbed under an applied shear stress. However, if the hydrocarbon side chains are replaced by perfluorocarbons to introduce thermodynamic compatibility between the surfactant and the PTFE surface, stable adhesion on the latter can be achieved.[62]

4.414.3.3.2. Coating blood compatibility

The steric barrier provided by hydrated surface-grafted oligosaccharides is designed to suppress protein adsorption and to minimize platelet adhesion, while the high energy of desorption and low water solubility of the adsorbed surfactant polymer is designed to minimize possible exchange reactions with surface-active plasma proteins and lipids. Protein adsorption from human platelet poor plasma (PPP) and whole human blood is typically suppressed by more than 90% on modified biomaterial surfaces. Platelet interactions were examined for a range of surfactant-modified biomaterials under both static and dynamic flow conditions was reduced significantly.[46,47] For example, polycarbonate (used in blood pumps) was examined with and without a dextran surfactant polymer coating. The polycarbonate was covered by platelets ($>10^4/mm^2$) at 0 dyn cm^{-2}, which decreased at high shear stress with few platelets above ~65 dyn cm^{-2}. In contrast, few to no platelets were seen on the surfactant-modified polycarbonate at 0 dyn cm^{-2} or higher shear stresses. Similar results were obtained using whole human blood containing 3.8% sodium citrate (Figure 6) and a glycodendrimer surfactant polymer-coated octadecyltrichlorosilane (OTS)-glass surface (Figure 7).[47]

4.414.4. ECM Biomimetics

The ideal nonthrombogenic surface is a confluent layer of healthy ECs with a confluent glycoclayx. The EC (Figure 8)

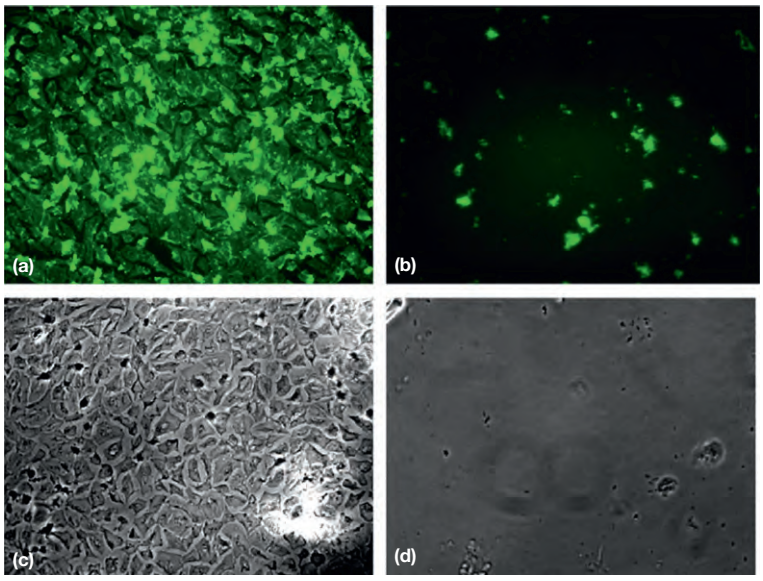

Figure 6 Platelet adhesion from whole human blood (rotating disk experiment). (a) Fluorescent micrographs of adherent platelets on (a) polycarbonate and (b) dextran surfactant polymer-modified polycarbonate at 0 dyn cm^{-2}. (c) Phase contrast of polycarbonate and (d) surfactant polymer-modified polycarbonate at 0 dyn cm^{-2}.

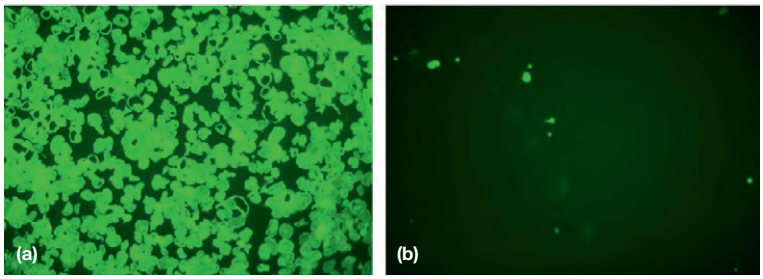

Figure 7 Fluorescent micrographs of platelet adhesion from human platelet-rich plasma (PRP) (rotating disk experiment) on (a) octadecyltrichlorosilane (OTS)-coated glass and (b) dextran surfactant polymer-modified OTS glass.

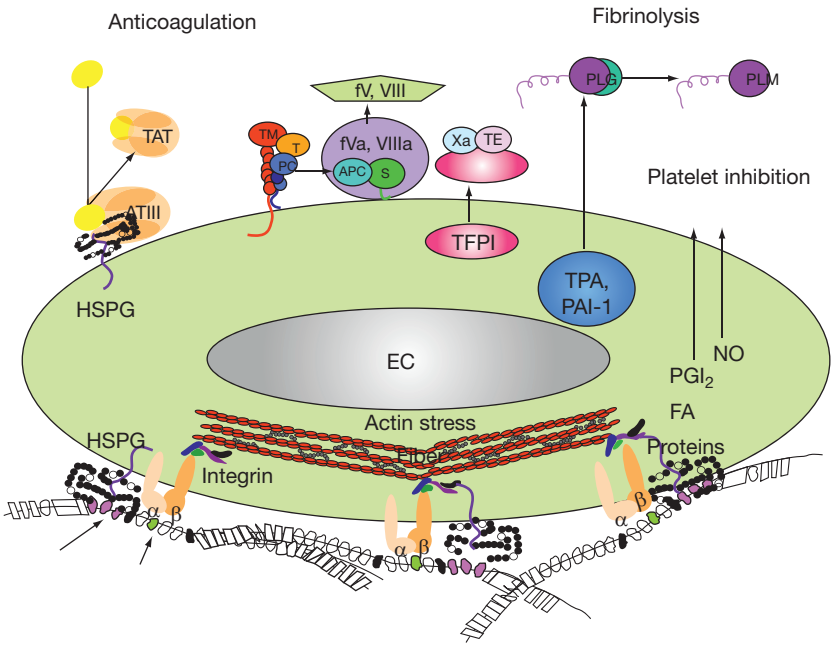

Figure 8 An endothelial cell (EC) with illustration of its anticoagulant functions, including anticoagulation, platelet inhibition, and fibrinolysis. EC integrin–extracellular matrix interactions are also illustrated. TAT, thrombin–antithrombin complex; ATIII, antithrombin III; HSPG, heparin sulfate proteoglycan; TM, thrombomodulin; T, thrombin; PC, protein C; APC, activated protein C; S, protein S; TF, tissue factor; fV, factor V; fVIII, factor VIII; Xa, activated factor X; TPA, tissue plasminogen activator; PAI-1, plasminogen activator inhibitor; PLG, plasminogen; PLM, plasmin; NO, nitrous oxide; PGI2, prostaglandin I2; FA, focal adhesion.

uses both metabolic and interfacial properties to provide several natural anticoagulant functions, regulate fibrinolysis and platelet function, prevent nonspecific adhesion, and interact closely with the ECM. Through its cytoskeletal network, the EC also responds and adapts to changes in shear stress of flowing blood. Consequently, EC seeding of biomaterials such as vascular prostheses has received intense interest as a means to improve thromboresistance with a natural living interfacial barrier.[63–73] Unfortunately, problems including shear stress and/or phenotype-dependent instability and species–species variation in EC seeding responses have limited success with human implants. One approach to addressing this problem in biomaterial surfaces that require cell seeding is creating an interface on these materials that mimics the structure–function properties of the native ECM in order to facilitate improved EC-biomaterial culture and integration (see also **Chapter 4.409, Surfaces and Cell Behavior**).

Like the glycocalyx, the ECM is a complex network of multifunctional biopolymers including collagens, proteoglycans (PGs), and glycosaminoglycans (GAGs) that interact mutually with cells and with each other.[74–76] Much effort has focused on developing biomaterial surfaces that mimic the cell-binding properties of the important ECM protein, fibronectin (FN) (**Figure 9**).[77–79] The central cell-binding domain that spans $FNIII_{8–10}$ is of particular interest because it contains an RGD (Arg-Gly-Asp) sequence, identified as the key cell integrin-binding site present in many ECM proteins including FN, vitronectin, laminin, osteopontin, thrombospondin, and many other ECM glycoproteins.[74–77] Most matrix-dependent cells including EC and smooth muscle cells bind to RGD through integrin interactions such as key EC cell membrane-based receptors, the $\alpha_5\beta_1$ and $\alpha_v\beta_3$ integrins. However, RGD peptide ligands of various forms will also bind the platelet membrane glycoprotein GPIIb/IIIa with high affinity to activate platelets, an important factor to appreciate in designing biomimetic surfaces and colloidal particles for cardiovascular applications.

Figure 9 shows that the RGD sequence is part of a random loop attached to the β-sheet secondary structure of the $FNIII_{10}$ domain. As the RGD sequence is part of a random loop, the small peptide does not require a particular secondary structure in order to maintain its integrin-binding specificity. This presents a significant advantage in using small RGD peptides in biomimetic designs for biomaterials because neither the entire FN domain nor the FN matrix protein is required to produce specific integrin–adhesive cell–surface interactions. However, cell–ligand binding affinity may be reduced relative to the intact whole protein. Two other sequences in FN – PHSRN ($FNIII_9$) and KNEED ($FNIII_8$) – act synergistically with the RGD sequence[80,81] to improve binding. The addition of $FNIII_9$ synergy domain to $FNIII_{10}$ results in ~50% increase in binding affinity, ~60–70% increase in cell adhesion, and ~60–70% increase in cell spreading, compared with $FNIII_{10}$ alone. The EC $\alpha_5\beta_1$ integrin that interacts with the central FN cell-binding domain is upregulated in migrating or shear-exposed EC and involved in early adhesion-dependent cell signaling events.[82–84] Another EC integrin ($\alpha_v\beta_3$) that binds to FN has a role in angiogenesis and shear-induced cytoskeletal alignment.[84,85] Therefore, producing ECM biomimetic surfaces that can bind certain integrin subfamilies and not cross-react with all cell membrane integrin subtypes, or activate platelet receptors represents an attractive area for new developments.

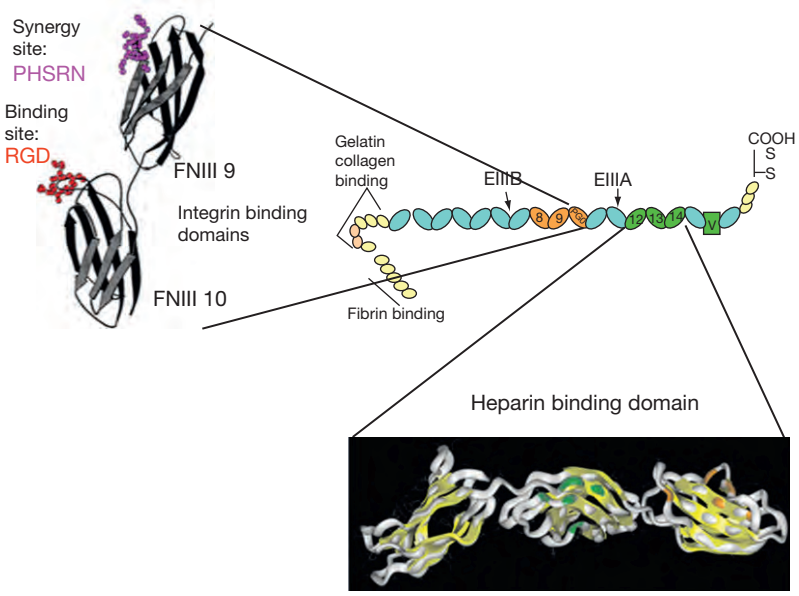

Figure 9 Structure and functional properties of fibronectin (FN). The FNIII 9 and 10 domains are shown expanded in which the RGD is seen located in the random coil loop attached to the β-sheet domain. Similarly, the PHSRN synergy site is located in a random coil loop on the β-sheet FNIII 9 domain. The β-sheet secondary structures in domains 12–14 encompass the heparin (HSPG)-binding region.

4.414.4.1. ECM-Like Biomimetics

Many biomimetic materials have been developed that mimic cell adhesive functions of the ECM, most often FN (*vide supra*), to support a healthy, confluent EC monolayer that remains stable under physiological shear stress conditions (see also **Chapter 2.208, Artificial Extracellular Matrices to Functionalize Biomaterial Surfaces**; **Chapter 4.411, Peptide- and Protein-Modified Surfaces**; **Chapter 4.412, Rational and Combinatorial Methods to Create Designer Protein Interfaces**; **Chapter 4.415, Surface Engineering Using Peptide Amphiphiles**; and **Chapter 4.416, Growth Factors and Protein-Modified Surfaces and Interfaces**). Specific molecular recognition is incorporated into ECM-like biomimetic materials' designs through inclusion of biologically important peptide sequences of many types. To be useful, a selected peptide sequence needs to retain its biological cell signaling specificity, even though it is no longer a part of its larger native protein structure from which it was derived and copied. RGD fulfills this requirement, and is by far the most frequently used ECM-derived peptide for improving the cell adhesiveness of biomaterials.[66,67,70,78,79] Other matrix-derived peptides, such as the REDV sequence derived from FN, or the laminin-derived peptides YIGSR or IKVAV, have also been explored extensively for similar utility on biomaterials.[66,68,69,78] The use of small adhesive peptides has the following advantages: (1) small peptides resist proteolysis from plasma and cellular proteases, (2) they are seldom immunogenic as short sequences, (3) they can be commercially sourced economically at high purity using solid-phase synthetic methods, (4) they enjoy versatile covalent surface tethering strategies with diverse chemistry, and (5) geometrically defined nanoscale peptide patterns can be designed at distinct surface densities that are significantly higher than those achieved with intact matrix proteins.

In designing biomaterials that direct cell behavior, known interactions between cell receptors and ECM protein domains need to be accounted for in designing ECM-like biomimetic surfaces for biomaterials. A wide range of approaches is used to attach RGD or other small peptides to solid surfaces and biomaterials.[86] Most surface grafting, immobilization, and attachment methods, including those using chemical and physical methods discussed previously in this chapter and in related chapters, can be used.[87] RGD-based peptides have been covalently linked to most of the common biomaterials including PLGA, polyacrylamides, titanium, gold, stainless steel, ceramics, and to polyurethanes as well as PTFE. Irrespective of the surface attachment method used, the key factors in any biomimetic design for controlling cell–surface interactions include maintenance of the peptide's biological function and its cell specificity; peptide density on the surface; elimination of nonspecific protein or cell adsorption interference; surface chemistry stability; cell attachment, growth, and migration promotional properties; and for vascular applications, the adherent cell's shear-dependent and phenotypic stability in the presence of flowing blood.

4.414.4.1.1. Integrin-dependent interaction of EC on biomimetic surfactant polymers

An important step in validating a biomimetic surface modification utilizing small peptides like RGD is a demonstration of cell integrin-dependent surface interaction. Importantly, this can be accomplished using a scrambled peptide control (i.e., RDG instead of RGD), excessive free RGD peptide in the assay milieu, or by replacement of a critical amino acid (i.e., RGE in place of RGD). To examine the ability to promote favorable interactions with human EC, RGD peptides were attached to

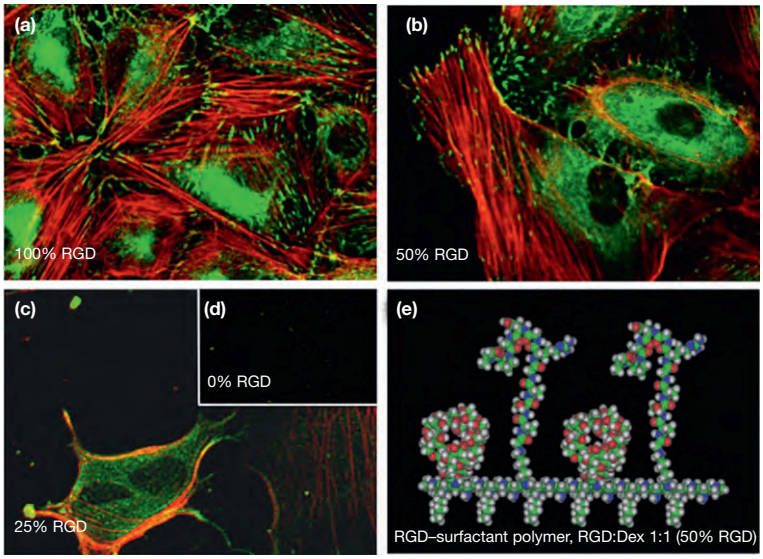

Figure 10 Human pulmonary artery endothelial cell (HPAEC) adhesion and formation of focal adhesions on RGD surfactant polymers (RGD-SP). (a) RGD-SP (100% RGD), (b) RGD-Dex-SP (50% RGD), (c) RGD-Dex-SP (25% RGD), and (d) Dex-SP (0% RGD). HPAEC seeded on these substrates were fixed and fluorescently stained for actin stress fibers (red) and vinculin (green) for focal adhesions after 3 h, and were examined by scanning confocal microscopy (60×). (e) Molecular model of RGD-Dex surfactant polymer (50% RGD), consisting of a poly(vinyl amine) with hexanal, dextran, and peptide branches. The full peptide sequence was –GSSSGRGDSPA–.

a biomimetic surfactant polymer (Figure 10(e)) adsorbed on an OTS-modified glass surface[88–90] *in vitro*. The ECM-like biomimetic polymers consist of a poly(vinyl amine) backbone with hydrophobic alkanal branches and varying ratios of cell adhesive peptide to dextran carbohydrate.[88–91] The RGD-containing peptide was –GSSSGRGDSPA–, in which the –GSSSG– was used as a hydrophilic flexible spacer to move the active cell-binding sequence away from the surfactant polymer backbone. The surfactant polymers (SP) contained increasing molar ratios of RGD:dextran of 0:1, 1:3, 1:1, 3:1, and 1:0, referred to as 0, 25, 50, 75, and 100% RGD, respectively, and were compared to a positive control of FN (1 $\mu g\,cm^{-2}$) coated on glass.[88,90] The pure polysaccharide, dextran (SP, 0% RGD), provided a negative control. After seeding human pulmonary artery ECs (5000 cells cm^{-2} in MCDB 131 basal medium), cell adhesion and growth were quantified by time-dependent phase-contrast microscopy and by a cell MTS proliferation assay. Maximal proliferation was observed with the FN positive controls (0.9 relative absorbance), but comparable results were obtained for surfactant polymers with high RGD content 100% RGD (0.8) > 50% RGD (0.75) >> 25% RGD (0.37) > OTS (0.35) – media only blank. No cells attached to the 0% RGD dextran-SP.

The RGD polymers stimulated EC responses in an integrin-dependent manner. The interaction was specific, as soluble GRGDSP, but not GRGESP, inhibited EC adhesion and spreading. At 3 h, EC attachment and spreading were rapid and comparable on FN and 100% RGD. The cells spread well with sharp spikes of vinculin localized at the termination point of actin stress fibers (Figure 10(a)–10(d)). Cell stress fibers and focal adhesions on the surfactant polymers correlated with the EC spreading pattern and with %RGD in the surfactant polymer. Adherent EC expressed $\alpha_5\beta_1$ integrins all along stress fibers and throughout the cytoskeleton. Substrates coated with a high dextran:RGD ratio (low overall RGD) content exhibited poor cell adhesion, consistent with suppressed protein adsorption, and ECs did not attach or grow on the carbohydrate surfactants. These data also showed the importance of RGD-ligand density in facilitating effective cell attachment and function.

4.414.4.1.2. Surface peptide ligand density

To examine the role of peptide specificity and ligand density, model substrates have been used to determine the dependence of cell adhesion on RGD-ligand density and clustering *in vitro*.[92–96] For the use of GRGDY coupled to glass, adhesion and maximal cell spreading required 6 RGD mm^{-2} or peptide spacing of 440 nm,[94] but a higher peptide density (60 RGD mm^{-2}) was required for focal adhesion formation. This peptide-only density was much lower than that (200–4500 RGD mm^{-2}) reported for FN, FN-fragments, RGD-polyacrylamide, or RGD-albumin.[93,97] Studies using clustered RGD constructs, attached to star-PEO or PMMA–PEO comb polymers, showed increased cell adhesion with increasing RGD cluster density.[12,93,95,96]

Cell migration requires adhesion followed by sufficient receptor/cytoskeleton interactions, cytoskeletal reorganization, and tail end detachment. Ligand-binding affinities, integrin expression levels, and ligand levels dictate cell migration speed, with the average speed displaying a biphasic dependence on adhesive strength, the maximum occurring at an intermediate cell–substrate adhesive strength.[92,98–101] Model surfaces altering substrate ligand density and distribution through use of peptides from the adhesive domains of ECM proteins have shown dependence of cell migration on ligand type and density.[92,101,102] For instance, glass-YIGSRG (derived

from laminin) with peptide clusters (6424 clusters mm^{-2}) showed greater EC locomotion than that on RGDS-glass.[99] Similar results were observed for fibroblasts with peptides at 10 nmol cm^{-2} (60 peptides nm^{-2}).[103] In addition, RGD clustering (1–9 ligands per cluster) with spacing of 6–300 nm enhanced cell motility, attributed to more efficient integrin clustering.[92] Smooth muscle cells showed decreased motility with increasing surface density of RGDS, VAPG, and KQAGDV from 0.2 to 2.0 nmol cm^{-2} (1.2–12 peptides nm^{-2}), providing evidence supporting decreased cell migration with increased adhesivity.[102] Similarly, we have shown decreased motility for human microvascular EC on RGD surfactant polymers with RGD density from 0.2 to 0.6 RGD nm^{-2}, with an inverse correlation between motility and adhesivity.[104] Peptide density affects cellular functions such as growth and migration, with the highest peptide density supporting the most proliferation, but the slowest migration, as determined using a Teflon fence migration assay.[104] Surface RGD peptide density was estimated from a 2D of lattice unit cell model for the surface-assembled surfactant polymer. Peptide surface density for the 100% RGD surfactant polymer was between 0.38 and 0.60 peptides nm^{-2} (i.e., 63–100 pM cm^{-2}). Similarly, surface densities for the 75, 50, and 25% RGD surfactant polymers were estimated to be 0.28–0.44, 0.19–0.30, and 0.095–0.15 peptides nm^{-2}, respectively.

Several studies have demonstrated that the spatial arrangement of cell adhesive peptides as well the surface density are important for controlling cell–surface interactions. When integrin-binding YGRDG peptides are tethered to star-shaped polymers of ~50 nm in size and arranged on inert PEG hydrogels individually or in clusters of between 1 and 9 peptides per cluster (each at low or high overall peptide density), cell adhesion and migration are observed to be supported on surfaces with only one YGRGD peptide per cluster; cell motility increases significantly at a higher peptide density per cluster, whereas nonclustered peptides support neither full spreading nor cell motility. This finding is in accordance with studies by Cavalcanti-Adam *et al.*[101] and supports the notion that peptide spatial arrangement as well as peptide density contribute significantly to the control of cell–surface behavior.

4.414.4.1.3. Shear stability of surface-attached cells

Vascular EC *in vivo* are subjected to physical forces related to blood flow.[104–107] Vascular ECs sense these forces and respond through phenotypic alterations in morphology and alignment, mechanical properties, and signal transduction.[106] Shear stability has also been related to integrin–ligand interaction, although the relationship plateaus at high adhesivity and does not exhibit bimodal behavior. One measure of shear stability is the shear stress at which 50% of cells are detached. This was shown to be greater for cyclic RGD (59 dyn cm^{-2}) than for linear peptide (39 dyn cm^{-2}).[108] It has also been shown that EC shear stability increases with increasing RGD surface density.[89,104] Interpretation of shear stability studies should take into account cell attachment time and the use or otherwise of low-shear preconditioning, its use being known to improve shear stability of attached cells.[109,110]

4.414.4.2. Biomimetic Modifications of Clinically Relevant Biomaterials

Beyond model assay systems, clinically used biomaterials are also modified using immobilized peptides to improve blood and tissue biocompatibility (see also **Chapter 4.402, Biocompatibility and the Relationship to Standards: Meaning and Scope of Biomaterials Testing** and **Chapter 1.128, Fluorinated Biomaterials**). Examples include polyurethanes modified with YIGSR peptides.[68,69] Effective modification of ePTFE, commonly used for small-diameter vascular grafts, has presented a particular challenge. ePTFE is extremely hydrophobic and chemically inert. This makes quantitative modification of its surface very difficult to accomplish. To address this difficulty, a peptide fluorosurfactant polymer (PFSP) modification was developed to facilitate the adhesion and growth of EC on ePTFE vascular graft material.[111–113] The PFSP consisted of a poly(vinyl amine) backbone with integrin-binding RGD peptides for cell engagement, and perfluorocarbon pendant branches to facilitate adsorption and stable adhesion to underlying ePTFE. Aqueous PFSP solution was used to modify the surface of ePTFE fluorocarbon substrates. Following subconfluent seeding, EC adhesion and growth on PFSP were assessed at different time points. Quantification of adherent cell populations demonstrated reduced EC attachment efficiency but increased growth rate on RGD PFSP compared with FN on glass (**Figure 11**). Actin staining revealed a well-developed cytoskeleton for ECs on RGD PFSP indicative of stable adhesion. Uptake of acetylated low-density lipoprotein and positive staining for VE-cadherin confirmed the EC phenotype for adherent cells in these cultures. Production of prostacyclin, a potent antiplatelet agent, was equivalent between ECs on FN and RGD PFSP surfaces. The RGD PFSP provided a simple, quantitative, and effective approach to modify ePTFE and to encourage EC attachment, growth, and function.

4.414.4.2.1. Cell-selective peptides

A biomaterial surface modified with RGD peptides is not suitable as a blood-contacting surface, because in addition to many cell-based integrin receptors, RGD also readily binds the GPIIb/IIIa receptor on platelets, producing platelet binding and activation.[114] As there are many more platelets in blood ($(15–40) \times 10^4$ platelets per microliter) compared with ECs, an RGD-coated surface is essentially highly thrombogenic. To overcome this problem, autologous ECs obtained from the patient can be preseeded and cultured on the graft before implantation. An alternative approach that is much more appealing clinically is to modify the graft with a peptide selective for EC integrins that does not cross-react to bind platelet integrins. This has been shown using RGD-containing peptides with different flanking peptides or cyclic conformations that reduce (but do not eliminate) platelet receptor specificity. As an example, ePTFE was surface modified with an FSP bearing biologically active ligands, including both adhesive peptides and polysaccharide moieties. The goal was to improve graft hemocompatibility by promoting rapid surface endothelialization, while minimizing platelet adhesion. A direct comparison of platelet and EC adhesion to FSPs presents one of three cell adhesion peptides: cyclic Arg-Gly-Asp-D-Phe-Glu (cRGD),

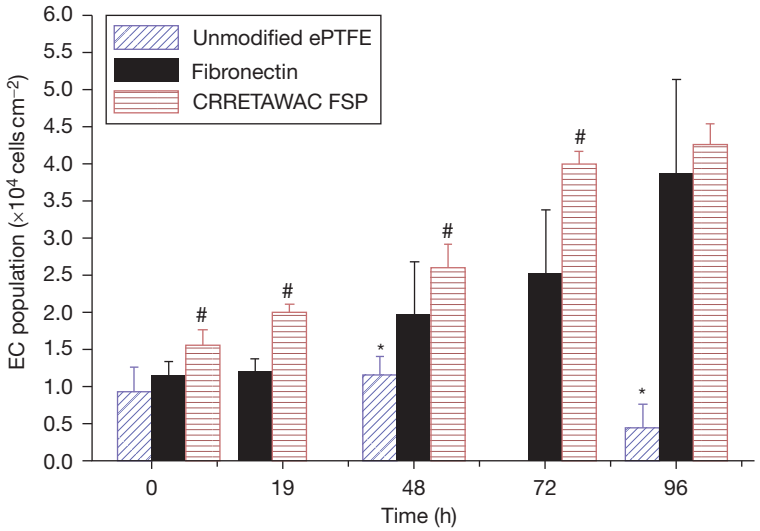

Figure 11 Endothelial cell (EC) attachment and growth on unmodified ePTFE, fibronectin (FN), and –CRRETAWAC– fluorosurfactant polymer (FSP)-modified ePTFE. Cell attachment and growth on CRRETAWAC FSP was higher than on FN and substantially greater than on unmodified ePTFE. #Significantly different ($p < 0.05$) cell population compared with FN and ePTFE surface at the same time point. Significantly different ($p < 0.05$) cell population compared with FN and CRRETAWAC FSP surfaces at the same time point. Bars represent standard deviation.

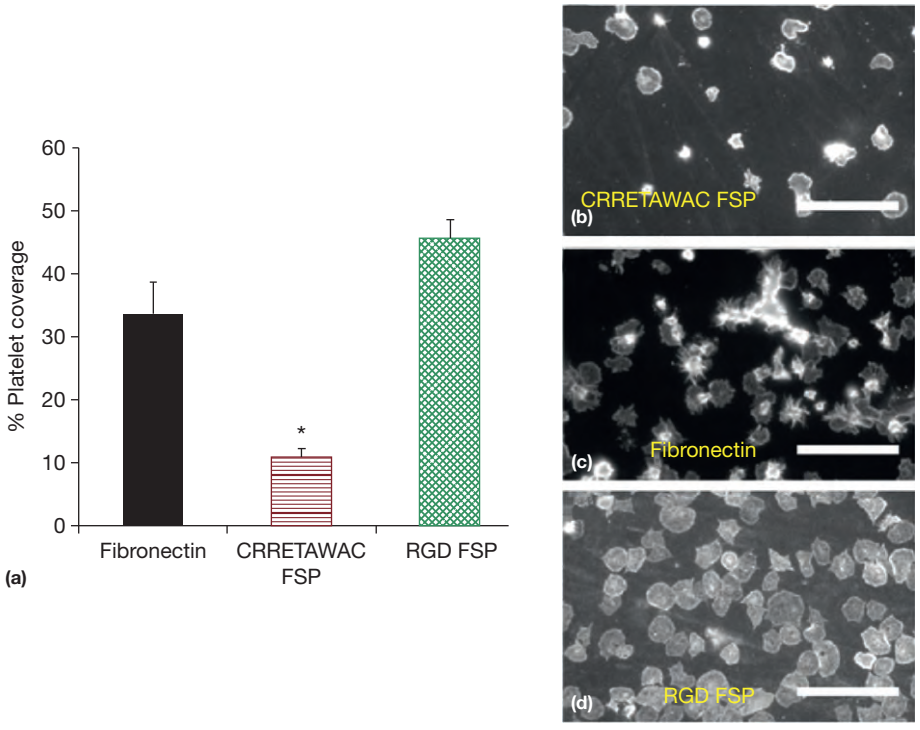

Figure 12 Human platelet adhesion/spreading with CRRETAWAC fluorosurfactant polymer (FSP) surface. (a) Platelet surface coverage on fibronectin (FN), CRRETAWAC FSP, and RGD FSP. Significantly different ($p < 0.05$) platelet surface coverage for CRRETWAC FSP compared with FN and RGD FSP. Bars represent standard deviation. (b) FITC-anti-CD41a-labeled platelets adherent to CRRETAWAC FSP-modified surface. Scale bars for all images are 30 mm. (c) FITC-anti-CD41a-labeled platelets adherent to FN-coated glass. (d) FITC-anti-CD41a-labeled platelets adherent to RGD FSP-modified FSAM.

cyclic *Cys-Arg-Arg-Glu-Thr-Ala-Trp-Ala-Cys* (cRRE, *disulfide bond cyclization), linear Gly-Arg-Gly-Asp-Ser-Pro-Ala (RGD), or simply a polysaccharide moiety, oligomaltose (M-7), the latter designed to prevent plasma protein adhesion. Measurements of soluble peptide–integrin binding indicated that cRRE exhibits very low affinity for the $\alpha_{IIb}\beta_3$ platelet fibrinogen receptor, but high binding affinity for the EC $\alpha_5\beta_1$ integrin.[112,113,115–118] Analysis of static and dynamic platelet adhesion on FSP-modified surfaces demonstrated that both M-7 and cRRE promote significantly less platelet

adhesion compared with RGD and cRGD FSPs, while EC adhesion was similar on all peptide FSPs and minimal on M-7 FSP (Figure 12). The results illustrate the potential for ECM-like peptide ligands presented using an FSP surface modification to selectively adhere ECs with limited platelet attachment.[112,113]

4.414.5. Summary and Outlook

The interface between biomaterial and the biological environment is crucial because it controls protein and platelet interactions, thrombus formation, cell–surface interactions, and the ability of an implant to integrate to perform its intended function in the host. The ability to use biomaterial coating strategies to mimic both the functional and nonadhesive properties of a cell glycocalyx and ECM provides an attractive route to addressing numerous clinical problems with the biomaterial–tissue interface and biocompatibility. ECM biomimetics are also an attractive model for bioadhesive modification for modulation of specific cell responses, in both *in vitro* and *in vivo* model systems. Select peptide sequences derived from ECM proteins, such as FN, laminin, and collagen, have been incorporated onto films, polymer coatings, surfactants, and immobilization methods onto biomaterials to provide versatile biomimetic materials designed to modulate cell functions and potentially guide tissue formation. Several challenges still remain to validate this approach for various scientific and technological goals, including the reliable control over peptide spatial organization and affinity, incorporation of adhesion peptides selective for specific cell types, and the design of different temporally inductive adhesion peptides for time-dependent modulation of cell adhesion or to adhere different cells at different times. For all such strategies, providing a surface that reliably eliminates nonspecific protein and cell interactions while promoting highly specific biological adsorption and cell engagement is critical. Coatings and surface modifications that mix cell-specific ligands into a highly nonfouling chemical matrix are attractive for this purpose. As the fundamental biology of the cellular microenvironment is often the inspiration for material design, the future directions for new biomimetic designs that control surface interactions include innovative strategies for the control of surface architectures, incorporating both spatial and temporal control of ligand presentations, ligand diversities, and subpopulations to target different cell types or phenotypes, controlled cell differentiation and other biofunctional aspects, and dynamic microenvironmental designs that are reliably altered in both space and time at biomaterial surfaces based on biological cues. Materials' design will continue to exploit new discoveries in cell biology (e.g., new peptide ligands, new cell signal molecules, and new cell–surface engagement processes) and tissue physiology (systems integration, cell–cell interactions, communication and differentiation, and cell coculture) to find creative hybrid approaches to biomimetic materials enabling these advanced functions.

Acknowledgments

This work was supported by NIH grant 5RO1EB002067 from the National Institute of Biomedical Imaging and Bioengineering and grant 1RO1HL087843 from the National Heart, Lung and Blood Institute.

References

1. Padera, R. F., Jr.; Schoen, F. J. In *Biomaterials Science – An Introduction to Materials in Medicine*, 2nd edn.; Ratner, B. D., Hoffman, A. S., Schoen, F. J., Lemons, J. E., Eds.; Elsevier Academic: Amsterdam, 2004; pp 470–493.
2. Ghanbari, H.; Viatge, H.; Kidane, A. G.; Burriesci, G.; Tavakoli, M.; Seifalian, A. M. *Trends Biotechnol*. **2009**, *27*(6), 359–367.
3. Galletti, P. M. In *The Biomedical Engineering Handbook*; Bronzino, J. D., Ed.; CRC Press: Boca Raton, FL, 1995; pp 1828–1837.
4. Temenoff, J. S.; Mikos, A. G. In *Biomaterials: The Intersection of Biology and Materials Science;* Prentice Hall: Englewood Cliffs, NJ, 2008; Chapter 1, pp 1–31.
5. Lamba, M. K.; Cooper, S. L. In *Hemostasis and Thrombosis: Basic Principles and Clinical Practice*, 4th edn.; Colman, R. W., Hirsh, J., Marder, V. J., Clowes, A. W., George, J. N., Eds.; Lippincott Williams and Wilkins: Philadelphia, PA, 2001; pp 661–672.
6. Gorbet, M. B.; Sefton, M. V. *Biomaterials* **2004**, *25*, 5681–5703.
7. Anderson, J. M.; Marchant, R. E. In *Infections Associated with Indwelling Medical Devices*, 3rd edn.; Waldvogel, F. A., Bisno, A. L., Eds.; ASM Press: Washington DC, 2000; Chapter 5, pp 89–109.
8. Busuttil, S. J.; Drumm, C.; Plow, E. F. *Vascular* **2005**, *13*(4), 230–235.
9. Ratner, B. D. In *Biomaterials Science – An Introduction to Materials in Medicine*, 2nd edn.; Ratner, B. D., Hoffman, A. S., Schoen, F. J., Lemons, J. E., Eds.; Elsevier Academic: Amsterdam, 2004; pp 40–58.
10. Wu, Y.; Simonovsky, F. I.; Ratner, B. D.; Horbett, T. A. *J. Biomed. Mater. Res.* **2005**, *74A*, 722–738.
11. Horbett, T. A. In *Biomaterials Science – An Introduction to Materials in Medicine*, 2nd edn.; Ratner, B. D., Hoffman, A. S., Schoen, F. J., Lemons, J. E., Eds.; Elsevier Academic: Amsterdam, 2004; pp 237–245.
12. Israelachvili, J. N. In *Intermolecular and Surface Forces*, 2nd edn.; Academic Press: New York, 1991; Chapter 8, pp 122–136.
13. Fisher, L. *J. Chem. Soc. Faraday Trans.* **1993**, *89*, 2567–2582.
14. Ratner, B. D. *Biosens. Bioelectron.* **1995**, *10*, 797–804.
15. Lopez, G. P.; Ratner, B. D.; Tidwell, C. D.; Haycox, C. L.; Rapoza, R. J.; Horbett, T. A. *J. Biomed. Mater. Res.* **1992**, *26*, 415–439.
16. Szott, L. M.; Stein, M. J.; Ratner, B. D.; Horbett, T. A. *J. Biomed. Mater. Res.* **2011**, *96A*, 150–161.
17. Israelachvili, J. N.; Wennerstrom, H. *J. Phys. Chem.* **1992**, *96*, 520–531.
18. Leckband, D. E.; Schmitt, F.-J.; Israelachvili, J. N.; Knoll, W. *Biochemistry* **1994**, *33*, 4611–4624.
19. Lasic, D. D. *Nature* **1996**, *380*, 561–562.
20. Karrer, L.; Duwe, J.; Zisch, A. H.; *et al*. *Int. J. Artif. Organs* **2005**, *28*(10), 993–1002.
21. McPherson, T.; Kidane, A.; Szleifer, I.; Park, K. *Langmuir* **1998**, *14*, 176–186.
22. Kingshott, P.; Thissen, H.; Griesser, H. *J. Biomaterials* **2002**, *23*, 2043–2056.
23. Sheth, S. R.; Leckband, D. *Proc. Natl. Acad. Sci. USA* **1997**, *94*, 8399–8404.
24. Bergstrom, K.; Osterberg, E.; Holmberg, K.; *et al*. *J. Biomater. Sci. Polym. Ed.* **1994**, *6*, 123–132.
25. Irvine, D. J.; Mayes, A. M.; Satija, S. K.; Barker, J. G.; Sofia-Allgor, S. J.; Griffith, L. G. *J. Biomed. Mater. Res.* **1998**, *40*, 498–509.
26. Holland, N. B.; Xu, Z.; Vacheethasanee, K.; Marchant, R. E. *Macromolecules* **2001**, *34*, 6424–6430.
27. Griesser, H. J.; Hartley, P. G.; McArthur, S. L.; McLean, K.; Meagher, L.; Thissen, H. *Smart Mater. Struct.* **2002**, *11*, 652–661.
28. Xu, Z.; Holland, N. B.; Marchant, R. E. *Langmuir* **2001**, *17*, 377–383.
29. Chambers, E.; Mitragotri, S. *Exp. Biol. Med. (Maywood)* **2007**, *232*(7), 958–966.
30. Humphries, M. J.; Newham, P. *Trends Cell Biol.* **1998**, *8*, 78–83.
31. Percec, V.; Ahn, C.-H.; Ungar, G.; Yeardley, D. J. P.; Moller, M.; Sheiko, S. S. *Nature* **1998**, *391*, 161–164.
32. Stupp, S. I.; LeBonheur, V.; Walker, K.; *et al*. *Science* **1997**, *276*, 384–389.
33. Yamasaki, A.; Imamura, Y.; Kurita, K.; Iwasaki, Y.; Nakabayashi, N.; Ishihara, K. *Colloids Surf. B Biointerfaces* **2003**, *28*, 53–62.
34. Iwasaki, Y.; Nakabayashi, N.; Nakatani, M.; Mihara, T.; Kurita, K.; Ishihara, K. *J. Biomater. Sci. Polym. Ed.* **1999**, *10*, 513–529.
35. Chapman, D. *Langmuir* **1993**, *9*, 39–45.
36. Iwasaki, Y.; Ishihara, K. *Anal. Bioanal. Chem.* **2005**, *381*, 534–546.
37. Cheng, G.; Zhang, Z.; Chen, S.; Bryers, J. D.; Jiang, S. *Biomaterials* **2007**, *28*, 4192–4199.

38. Chen, S.; Cao, Z.; Jiang, S. *Biomaterials* **2009**, *30*, 5892–5896.
39. Li, G.; Chang, G.; Xue, H.; Chen, S.; Zhang, F.; Jiang, S. *Biomaterials* **2008**, *29*, 4592–4597.
40. Mi, L.; Bernards, M. T.; Cheng, G.; Yu, Q.; Jiang, S. *Biomaterials* **2010**, *31*, 2919–2925.
41. Chen, S.; Cao, Z.; Jiang, S. *Biomaterials* **2009**, *30*, 5892–5896.
42. Jiang, S.; Cao, Z. *Adv. Mater.* **2010**, *22*, 920–932.
43. Holland, N. B. *Nature* **1998**, *392*, 799–801.
44. Marchant, R. E.; Anderson, E. H.; Zhu, J. In *Structural Diversity and Functional Au15 Versatility of Polysaccharides*; Dimitriu, S., Ed.; Marcel Dekker: New York, 2005; Chapter 45, pp 1055–1085.
45. Ruegsegger, M. A.; Marchant, R. E. *J. Biomed. Mater. Res.* **2001**, *56*, 159–167.
46. Zhu, J.; Gosen, C.; Marchant, R. E. *J. Polym. Sci. Polym. Chem.* **2006**, *44*, 192–199.
47. Zhu, J.; Marchant, R. E. *Biomacromolecules* **2006**, *7*, 1036–1041.
48. Wang, S.; Sen Gupta, A.; Sagnella, S.; Barendt, P. M.; Kottke-Marchant, K.; Marchant, R. E. *J. Biomater. Sci. Polym. Ed.* **2009**, *20*(5–6), 619–635.
49. Evans, W. H.; Graham, J. M. *Membrane Structure and Function*. Oxford University Press: London, 1991.
50. Haldenby, K. A.; Chappell, D. C.; Winlove, C. P.; Parker, K. H.; Firth, J. A. *J. Vasc. Res.* **1994**, *31*, 2–9.
51. MacKenzie, K. R.; *et al*. *Science* **1997**, *276*, 131.
52. Schuster, O.; Klich, G.; Sinnwell, V.; Kranz, H.; Paulsen, H.; Meyer, B. *J. Biomol. NMR* **1999**, *14*, 33–45.
53. Casu, B. In *Heparin: Chemical and Biological Properties, Clinical Applications*; Lane, D. A., Lindahl, U., Eds.; CRC Press: Boca Raton, FL, 1989; pp 25–50.
54. Christensen, K.; Larsson, R.; Emanuelsson, H.; Elgue, G.; Larsson, A. *Biomaterials* **2000**, *22*, 349–355.
55. Varki, A. *Glycobiology* **1993**, *3*, 97–130.
56. Dwek, R. A. *Chem. Rev.* **1996**, *96*, 683–720.
57. Bertozzi, C. R.; Kiessling, L. L. *Science* **2001**, *291*, 2357–2364.
58. Begovac, P. C.; Thomson, R. C.; Fisher, J. L.; Hughson, A.; Gällhagen, A. *Euro. J. Vasc. Endovasc. Surgery* **2003**, *25*(5), 432–437.
59. Heyligers, J. M.; Verhagen, H. J.; Rotmans, J. I.; *et al*. *J. Vasc. Surg.* **2006**, *43*, 587–591.
60. Larm, O.; Larsson, R.; Olsson, P. *Biomater. Med. Devices Artif Organs* **1983**, *11*, 161–173.
61. Vacheethasanee, K.; Marchant, R. E. *J. Biomed. Mater. Res.* **2000**, *50*, 302–312.
62. Wang, S.; Marchant, R. E. *Macromolecules* **2004**, *37*, 3353–3359.
63. Tassiopoulos, A. K.; Greisler, H. P. *J. Biomater. Sci. Polym. Ed.* **2000**, *11*, 1275–1284.
64. Boura, C.; Muller, S.; Vautier, D.; *et al*. *Biomaterials* **2005**, *26*(22), 4568–4575.
65. Chan-Park, M. B.; Shen, J. Y.; Cao, Y.; *et al*. *J. Biomed. Mater. Res. A* **2009**, *88*(4), 1104–1121.
66. Choi, W. S.; Bae, J. W.; Joung, Y. K.; *et al*. *Macromol. Res.* **2009**, *17*(7), 458–463.
67. Choi, W. S.; Bae, J. W.; Lim, H. R.; *et al*. *Biomed. Mater.* **2008**, *3*(4), 044104.
68. Jun, H. W.; West, J. L. *Tissue Eng.* **2005**, *11*(7–8), 1133–1140.
69. Jun, H. W.; West, J. L. *J. Biomed. Mater. Res. B Appl. Biomater.* **2005**, *72*(1), 131–139.
70. Bacakova, L.; Filova, E.; Kubies, D.; *et al*. *J. Mater. Sci. Mater. Med.* **2007**, *18*, 1317–1323.
71. de Mel, A.; Punshon, G.; Ramesh, B.; *et al*. *Biomed. Mater. Eng.* **2009**, *19*(4–5), 317–331.
72. Divya, P.; Krishnan, L. K. *J. Tissue Eng. Regen. Med.* **2009**, *3*(5), 377–388.
73. Filova, E.; Brynda, E.; Riedel, T.; *et al*. *J. Biomed. Mater. Res. A* **2009**, *90*(1), 55–69.
74. Giancotti, F. G.; Ruoslahti, E. *Science* **1999**, *285*, 1028–1032.
75. Boudreau, N. J.; Jones, P. L. *Biochem. J.* **1999**, *339*, 481–488.
76. Plopper, G. In *Cells*; Lewin, B., Cassimeris, L., Lingappa, V., Plopper, G., Eds.; Jones and Bartlett: Sudbury MA, 2007; pp 645–702.
77. Hodde, J.; Record, R.; Tullius, R.; Badylak, S. *Biomaterials* **2002**, *23*, 1841–1848.
78. Kao, W. J.; Lee, D.; Schense, J. C.; Hubbell, J. A. *J. Biomed. Mater. Res.* **2001**, *55*, 79–88.
79. Lateef, S. S.; Boateng, S.; Hartman, T. J.; Crot, C. A.; Russell, B.; Hanley, L. *Biomaterials* **2002**, *23*, 3159–3168.
80. Altroff, H.; van der Walle, C. F.; Asselin, J.; Fairless, R.; Campbell, I. D.; Mardon, H. J. *J. Biol. Chem.* **2001**, *276*, 38885–38892.
81. Wong, J. Y.; Weng, Z.; Moll, S.; Kim, S.; Brown, C. T. *Biomaterials* **2002**, *23*, 3865–3870.
82. Collo, G.; Pepper, M. S. *J. Cell Sci.* **1999**, *112*, 569–578.
83. Urbich, C.; Dernbach, E.; Reissner, A.; Vasa, M.; Zeiher, A. M.; Dimmeler, S. *Arterioscler. Thromb. Vasc. Biol.* **2002**, *22*, 69.
84. Kim, S.; Harris, M.; Varner, J. *Arterioscler. Thromb. Vasc. Biol.* **2002**, *22*, 69.
85. Zheng, D. Q.; Woodard, A. S.; Tallini, G.; Languino, L. R. *J. Biol. Chem.* **2000**, *275*, 24565.
86. Harbers, G.; Grainger, D. W. In *An Introduction to Biomaterials*; Hollinger, J. O., Guelcher, S., Eds.; CRC Press: Boca Raton, FL, 2006; Chapter 5, pp 15–45.
87. Hermanson, G. T. In *Bioconjugate Techniques*, 2nd edn.; Academic Press, Elsevier Inc.: Amsterdam, Netherlands, 2008.
88. Murugesan, G.; Ruegsegger, M. A.; Marchant, R. E.; Kottke-Marchant, K. *Cell Comm. Adhes.* **2002**, *9*, 59–73.
89. Sagnella, S.; Kligman, F. *J. Biomed. Mater. Res. A* **2003**, *67*, 689–701.
90. Anderson, E. H.; Ruegsegger, M. A.; Murugesan, G.; Kottke-Marchant, K.; Marchant, R. E. *Macromol. Biosci.* **2004**, *4*, 760–775.
91. Sagnella, S. M.; Anderson, E. H.; Sanabria, N.; Marchant, R. E.; Kottke-Marchant, K. *Tissue Eng.* **2005**, *11*, 226–236.
92. Maheshwari, G.; Brown, G.; Lauffenburger, D. A.; Wells, A.; Griffith, L. G. *J. Cell Sci.* **2000**, *113*, 1677–1686.
93. Irvine, D. J.; Ruzette, A.-V. G.; Mayes, A. M.; Griffith, L. G. *Biomacromolecules* **2001**, *2*(2), 545–556.
94. Massia, S. P.; Hubbell, J. A. *J. Cell Biol.* **1991**, *114*, 1089–1100.
95. Irvine, D. J.; Mayes, A. M.; Griffith, L. G. *Biomacromolecules* **2001**, *2*, 85–94.
96. Koo, L. Y.; Irvine, D. J.; Mayes, A. M.; Lauffenburger, D. A.; Griffith, L. G. *J. Cell Sci.* **2002**, *115*, 1423–1433.
97. Brandley, B. K.; Schnaar, R. L. *Anal. Biochem.* **1988**, *172*, 270–278.
98. Singer, I. I.; Kawka, D. W.; Scott, S.; Mumford, R. A.; Lark, M. W. *J. Cell Biol.* **1987**, *104*, 573–584.
99. Kouvroukoglou, S.; Dee, K. C.; Bizios, R.; McIntire, L. V.; Zygourakis, K. *Biomaterials* **2000**, *21*, 1725–1733.
100. Palecek, S. P.; Loftus, J. C.; Ginsberg, M. H.; Lauffenburger, D. A.; Horwitz, A. F. *Nature* **1997**, *385*, 537–540.
101. Cavalcanti-Adam, E. A.; Aydin, D.; Hirschfeld-Warneken, V. C.; Spatz, J. P. *HFSP J.* **2008**, *2*(5), 276–285.
102. Mann, B. K.; West, J. L. *J. Biomed. Mater. Res.* **2002**, *60*, 86–93.
103. Olbrich, K. C. *Biomaterials* **1996**, *17*, 759–764.
104. Sagnella, S.; Kligman, F. *Biomaterials* **2004**, *25*, 1249–1259.
105. Grabowski, E. F.; Lam, F. P. *Thromb. Haemost.* **1995**, *74*, 123–128.
106. Davies, P. F.; Barbee, K. A.; Volin, M. V.; *et al*. *Annu. Rev. Physiol.* **1997**, *59*, 527–549.
107. Shyy, J. Y.-J.; Schien, S. *Circ. Res.* **2002**, *91*, 769–775.
108. Chan, B. P.; Chilkoti, A.; Reichert, W. M.; Truskey, G. A. *Biomaterials* **2003**, *24*, 559–570.
109. Xiao, Y.; Trusky, G. A. *Biophys. J.* **1996**, *71*, 2869–2884.
110. Mathur, A. B.; Truskey, G. A.; Reichert, W. M. *J. Biomed. Mater. Res. A* **2003**, *64*, 155–163.
111. Larsen, C. C.; Kligman, F.; Kottke-Marchant, K.; Marchant, R. E. *Biomaterials* **2006**, *27*, 4846–4855.
112. Larsen, C. C.; Kligman, F.; Tang, C.; Kottke-Marchant, K.; Marchant, R. E. *Biomaterials* **2007**, *28*, 3537–3548.
113. Tang, C.; Larsen, C. C.; Kottke-Marchant, K.; Marchant, R. E. *J. Biomed. Mater. Res. A* **2009**, *88*, 348–358.
114. George, J. N.; Colman, R. W. In *Hemostasis and Thrombosis: Basic Principles and Clinical Practice*, 6th edn.; Colman, R. W., Marder, V. J., Clowes, A. W., George, J. N., Goldhaber, S. Z., Eds.; Lippincott Williams and Wilkins: Philadelphia, 2006; pp 437–462.
115. Koivunen, E.; Wang, B.; Ruoslahti, E. *J. Cell Biol.* **1994**, *124*(3), 373–380.
116. Humphries, J. D.; Askari, J. A.; Zhang, X. P.; Takada, Y.; Humphries, M. J.; Mould, A. P. *J. Biol. Chem.* **2000**, *275*(27), 20337–20345.
117. Tomiyama, Y.; Shiraga, M.; Shattil, S. J. In *Platelets in Thrombotic and Nonthrombotic Disorders: Pathophysiology, Pharmacology, and Therapeutics*; Gresele, P., Ed.; Cambridge University Press: Cambridge, New York, 2002; pp 89–109.
118. Meyers, S. R.; Kenan, D. J.; Khoo, X.; Grinstaff, M. W. *Biomacromolecules* **2011**, *12*, 533–539.

4.415. Surface Engineering Using Peptide Amphiphiles

W H Suh, University of California, Berkeley, CA, USA; University of California, Santa Barbara, CA, USA
M Tirrell, University of California, Berkeley, CA, USA

© 2011 Elsevier Ltd. All rights reserved.

4.415.1.	**Introduction**	222
4.415.2.	**The Amphiphilic Nature of Life's Events**	223
4.415.3.	**PAs: Synthesis, Physicochemical Characterization, and Self-Assembly**	223
4.415.3.1.	Synthesis and Characterization of PAs	223
4.415.3.2.	Double-Tailed (Dialkylated) PAs	223
4.415.3.3.	Single-Tailed (Monoalkylated) PAs	226
4.415.4.	**The Multifunctional (Soft) Nanoparticle Concept**	226
4.415.4.1.	Targeting-Enabled PA Spherical Micelles	226
4.415.4.2.	Single-Tailed PAs for Cancer Cell Biology Control	228
4.415.4.3.	*In Vitro* Binding Affinity Control via Native Chemical Ligation	230
4.415.5.	**Protein-Like Structures to 3D Hierarchical Nanostructures**	230
4.415.6.	**Applications in Biomedical Sciences: Tissue and Stem Cell Engineering**	231
4.415.6.1.	Helical Structure and Antibacterial PAs	232
4.415.6.2.	Neural Stem Cell Engineering	233
4.415.6.3.	Bone Marrow Mononuclear Cells	235
4.415.6.4.	Ameoblast Cell Engineering for Tooth Regeneration	235
4.415.6.5.	Heparin-Binding PAs for Regenerative Medicine	237
4.415.6.6.	Human Mesenchymal Stem Cell Engineering	237
4.415.6.7.	Dental Stem Cells	238
4.415.6.8.	Bioactivation of Metallic Surfaces	239
4.415.7.	**Summary and Future Directions**	239
References		243

Glossary

Angiogenesis Growth of new blood vessels from preexisting vessels.

ApoE-null mouse ApoE stands for plasma protein apolipoprotein E, binding to a specific receptor present in liver cells and peripheral cells. It is an essential protein for the normal catabolism of triglyceride-rich lipoprotein constituents. Mice that lack the ApoE gene are either called the ApoE-null or ApoE-knockouts (KO).

Apoptosis The process of programmed cell death involving characteristic changes related to cell morphologies such as blebbing, loss of cell membrane asymmetry, and cell shrinkage.

Astrogliosis An abnormal increase in the number of astrocytes due to the destruction of neurons.

Atherosclerotic plaques Fatty materials such as cholesterol buildup in the arterial wall.

Axon A long, slender projection of a nerve cell (i.e., neuron) that conducts electrical impulses away from the neuron's cell body or the soma.

Ball-and-stick model A molecular model of a chemical structure that aims to display both the 3D positions of the atoms and the bonds.

bFGF Basic fibroblast growth factor is present in the basement membranes and in the subendothelial extracellular matrix of blood vessels. bFGF is involved in the angiogenesis process and, in research, is a critical component in stem cell cultures.

Bioactive A material property based on its interacting ability with cellular organisms and tissues *in vitro* and *in vivo*.

Blastocyst A core–shell structure formed during the early embryogenesis of mammals. The shell is comprised of tropoblasts and the core contains the inner cell mass (ICM or embryoblast) and fluid-filled cavity (blastocoele). Blastocyst, in humans, begin formation 5 days after fertilization.

(Cell) Nucleus A membrane-enclosed cell organelle found in eukaryotic cells. The chromosome inside the nucleus is a complex structure made up of DNA and histone molecules. Gene expression control is done here in the nucleus.

Cell membrane A biological membrane comprised of a phospholipid bilayer with incorporated proteins.

Cell or cellular adhesion The binding of a cell to a surface (i.e., extracellular matrix) or a neighboring cell via adhesion molecules such as integrins, cadherins, and selectins.

Cell signaling A complex system of association that governs cellular activities and coordinates cell actions. The breakdown of the cell signaling pathways can lead to disease formation. Traditionally, focus has been given to exploring individual parts within a cell signaling pathway but, in recent times, systems biology approaches have allowed researchers to investigate multiple pathways and link them together to study a network of genes and proteins.

Centriole A barrel-shaped cell structure found in eukaryotic cells. Microtubules comprise the walls and are arranged perpendicular to the pericentriolar material – this associated pair is called the centrosome.
Circular dichroism (CD) CD refers to the differential absorption of left and right circularly polarized light and is exhibited by optically active chiral molecules such as proteins.
Collagen A family of fibrous proteins rich in glycine and contains hydroxyproline and hydroxylysine. It is found throughout vertebrates and is the most abundant protein in mammals. This protein is a major element in skin, bone, cartilage, teeth, blood vessels, etc.
COMPASS forcefield An *ab initio* forcefield optimized for condensed-phase applications. COMPASS stands for Condensed-phase Optimized Molecular Potentials for Atomistic Simulation Studies.
CREKA A pentapeptide with a sequence of Cysteine-Arginine-Glutamic acid-Lysine-Alanine that preferentially homes to tumor tissue. It was identified via *in vivo* phage display.
Cytoskeleton Internal proteinaceous framework of a eukaryotic cell composed of actin microfilaments, intermediate filaments, and microtubules and giving shape to a cell, and providing support for cell extensions such as villi and axons of nerve cells.
Cytosol The cytoplasm other than the various membrane-bound organelles.
DBU 1,8-Diazabicyclo[5.4.0]undec-7-ene, commonly used in organic synthesis as a nonnucleophilic base.
Dentin A calcified tissue constituting the interior hard part of vertebrate teeth between the enamel and the pulp gum, also written as dentine.
Differentiation (cellular) The cellular process of a less specialized cell transforming into a more specialized (thus differentiated) cell type.
DMEM Dulbecco-modified Eagle's medium utilized to maintain cells. It contains varying amounts of inorganic salts, amino acids, glucose, and vitamins. The most concentrated salt is sodium chloride. Specific media formulations are available from vendors.
DPC Dodecylphosphocholine, a single-C12-tailed phospholipid. CAS No. 29557-51-5.
DPPC 1,2-Dipalmitoyl-*sn*-glycero-3-phosphocholine, a double-C16-tailed phospholipid. CAS No. 63-89-8.
DPPE 1,2-Dipalmitoyl-*sn*-glycero-3-phosphoethanolamine, a double-C16-tailed phospholipid. CAS No. 923-61-5.
DPPG 1,2-Dipalmitoyl-*sn*-glycero-3-phospho-(1'-*rac*-glycerol) (sodium salt), a double-C16-tailed phospholipid. CAS No. 200880-41-7.
DSPE 1,2-distearoyl-sn-glycero-3-phosphoethanolamine, a double-C18-tailed phospholipid. CAS No. 1069-79-0.
Dynamic light scattering (DLS) A light-based physics technique used to determine the size distribution of small particles in liquid solutions undergoing Brownian motion. A monochromatic light source (e.g., fixed wavelength laser) is often utilized and the time-dependent fluctuation of the scattering intensity is monitored.
Endocytosis A membrane-based process for eukaryotic cells taking up foreign materials.
Endoplasmic reticulum (ER) Extensive, convoluted internal membrane in eukaryotic cells, continuous with the outer nuclear membrane and enclosing a continuous internal space (lumen); involved in the synthesis and transport of membrane proteins and lipids, and of proteins destined for secretion from the cell.
Extracellular matrix Macromolecular ground substance of connective tissue, secreted by fibroblasts and other connective tissue cells, generally comprised of proteins, polysaccharides, and proteoglycans.
FAM Carboxyfluorescein, a fluorescent dye molecule often utilized to tag proteins and incorporated into micelles and liposomes. Excitation/emission occurs at 492/517 nm.
Fluorescence Emission of light by a substance that has absorbed electromagnetic radiation often at a lower wavelength. It involves ground-state excitation via absorption, radiationless decay, and then a radiative transition back to the lower electronically excited state and ceases as soon as the source illumination is removed; it is different from phosphorescence.
Fmoc-chemistry 9-Fluorenylmethoxycarbonyl-based synthesis technique. The Fmoc-protecting group attaches to the amine-terminus of an amino acid and is selectively removed by bases such as piperidine and DBU.
Glial scar A reactive cellular process involving astrogliosis that occurs after injury to the CNS (central nervous system) and is the body's mechanism to protect and begin the healing process.
Globular protein A class of proteins that have metastable-folded spherical 3D structures and forms colloidal solutions after aqueous medium dissolution. The other class of proteins are fibrous proteins.
Glycolipid Lipids containing carbohydrate head groups and serving as cellular recognition sites.
Glycoprotein Proteins incorporating carbohydrate chains, ubiquitous in cell membranes and cellular secretions. If they become integral membrane proteins, they are involved in cell–cell interactions. An example is mucin.
Golgi apparatus Stacks of flattened membrane sacs present in eukaryotic cells and are involved in directing membrane lipids and proteins and secretory proteins to their correct destination in the cell.
Growth factor (GF) A general term for specific peptides and proteins required by particular cells for division and/or differentiation. Examples are epidermal growth factor, basic fibroblast growth factor, and nerve growth factor.
Heparin A highly sulfated glycosaminoglycan (polysaccharide) found in mast cells that has anticoagulant activity. This molecule will bind and activate the enzyme inhibitor antithrombin III which then inactivates thrombin and other proteases such as factor Xa.
Hirulogs A group of synthetic peptides designed to inhibit thrombin, leading to anticoagulation.
HOX Homeobox, a DNA sequence found within genes that are involved in the regulation of patterns of anatomical development (morphogenesis) in animals, fungi, and plants.

Hydrophobicity The physical property of molecular species (often nonpolar) being repelled from a mass of water, or forcing the structuring of water as a solvent around this molecule. The tendency to positively interact with or be dissolved by water will be referred to as hydrophilicity.
IKVAV A pentapeptide with a sequence of isoleucine-lysine-valine-alanine-valine that promotes cell adhesion, derived from the extracellular matrix protein laminin.
Inflammation or inflammatory response A complex host-initiated biological process following infection or tissue damage or after a particular immune reaction.
Integral protein A protein assembly that is permanently associated to the biological membrane and is difficult to isolate without the use of detergents or nonpolar solvents.
Integrin receptor (or Integrins) A class of cell receptor molecules that mediate the association between a cell and the surrounding environment (e.g., extracellular matrix, other cells). Integrins are involved in cell signaling processes that often define cell mechanics and regulate the cell cycle.
Ion channel A type of pore-forming integral membrane protein that allows selective flow of ions across the plasma membrane of the cell, thus controlling the electrochemical gradient formed inside and outside the cell.
Iron oxide Inorganic oxides composed of varying degrees of iron and oxygen. The most common iron oxide is Fe_2O_3, rust, and Fe_3O_4, paramagnetic magnetite.
IV-H1 A 15-mer peptide with a sequence of Gly-Val-Lys-Gly-Asp-Lys-Gly-Asn-Pro-Gly-Trp-Pro-Gly-Ala-Pro derived from the extracellular matrix protein collagen known to promote cancer cell adhesion and spreading.
Lipid bilayer A thin membrane composed of two layers of lipid. The cellular membrane is a phospholipid bilayer that incorporated multiple proteins, glycolipids, etc.
Lipidation A covalent addition process of a hydrophobic molecule (e.g., palmitic acid) onto a biomolecule (e.g., protein).
LyP-1 A cyclic nine-amino acid peptide, CGNKRTRGC, that can preferentially bind to tumors.
Lysosome A cellular organelle that contains acid hydrolases capable of breaking up cellular debris (e.g., worn-out organelles, food particles) and waste materials (e.g., engulfed viruses and bacteria). The organelle's pH is below 5.
Magnetic resonance imaging (MRI) A medical imaging technique utilizing an electromagnetic field that allows the visualization of soft tissue based on varying degrees of proton relaxation in different tissues and organs.
Mass spectrometry An analytical technique that measures the mass-to-charge ratio of ionized (thus charged) particles.
Metabolite The intermediates and products of metabolism and is often restricted to small molecules such as ethanol and glutamic acid.
Metallic alloy A partial or complete solid solution of one or more elements in a metallic matrix.
Metallic foam A porous (cellular) structure consisting of a solid metal that incorporates a large volume fraction of gas-filled pores (typically 70–95% porosity).
Micelle An aggregate of surfactant molecules dispersed in a liquid solution. This higher-order structure forms above the critical micelle concentration (CMC), often in the μM range.
Mitochondrion A membrane-enclosed organelle found in most eukaryotic cells and the main source of ATP (adenosine triphosphate), used as a chemical energy source. It also contains nucleic acids.
MSC (mesenchymal stem cell) Bone marrow stromal cells. A population of multipotent adult stem cell cultures discovered from the mesenchyme and the marrow that has been shown to differentiate into osteoblasts, chondrocytes, myocytes, and adipocytes. It is now also identified in nonmarrow tissue such as muscle and the dental pulp.
Nanoparticles Particles that are submicron, often 100 nm or below.
Nanostructure Structure exhibiting significant submicron features.
Native chemical ligation (NCL) A technique that reacts a C-terminal thioester with another peptide (or protein) containing an N-terminal cysteine residue.
Neural progenitor cell (NPC) Progenitor cells have a tendency to differentiate into a specific cell type with a limited amount of division possible. The term is sometimes used in place of neural stem cells, but (neural) stem cells can replicate indefinitely.
Neural stem cell (NSC) Self-renewing, multipotent adult stem cells able to generate the main phenotypes of the nervous system – neurons, astrocytes, and oligodendrocytes.
NiTi (nickel–titanium) A metallic alloy made up of nickel and titanium.
Nuclear magnetic resonance (NMR) A property that magnetic nuclei have in a magnetic field and applied electromagnetic (EM) pulse(s), causing the nuclei to absorb energy from the EM pulse and radiate this energy back out. The energy-radiated back out is at a specific resonance frequency that depends on the strength of the magnetic field and other factors.
Nuclear overhauser effect (NOE) The transfer of spin polarization from one spin population to another via cross-relaxation in NMR spectroscopy. NOE differs from spin coupling in the respect that it is a through-space observation rather than through bonds.
Nuclear transport Macromolecules such as RNA and proteins associate with karyopherins to enter and exit the cell nucleus via the nuclear pore complexes (NPCs), whereas small molecules can be transported without any regulatory process.
Osteogenic differentiation Cellular differentiation into fibroblast cells that, in addition, express the bone sialoprotein (or osteopontin) and osteocalcin.
PBX Pre-B cell leukemia homeobox refers to a family of transcription factors. They act as cofactors in the transcriptional regulation mediated by homeobox proteins during embryonic development and cellular development.
Peptide amphiphile (PA) A molecule that covalently links hydrophobic lipid tails together with hydrophilic peptide head groups. A linker segment (e.g., PEG) can be added in the middle.

Peripheral membrane protein A class of proteins that temporarily associate with the biological membrane either by attaching to integral membrane proteins or penetrating the peripheral region of the lipid bilayer.
Phospholipid A class of lipids comprising fatty acid chains (i.e., diglyceride), a phosphate group, and a small organic molecule such as choline.
Photocurable Polymerization occurring while exposed to a light source.
Posttranslational modification (PTM) The chemical modification of a protein after the translational process. Examples include phosphorylation, ubiquitination, palmitoylation, and acetylation.
Quantum dot A size- and shape-defined semiconductor whose excitons are confined in all three dimensions, often a few nanometers in size.
RGD A tripeptide with a sequence of Arginine-Glycine-Aspartic acid and is derived from the extracellular matrix protein, fibronectin. Peptide, proteins, and materials incorporating the RGD sequence have been shown to promote cellular adhesion.
Ribosome A component within the cell that associates with mRNAs and tRNAs in the cytosol to produce peptides and proteins enzymatically (the translation process).
SC4 A 12-mer bactericidal peptide that forms helical structures that have a sequence of KLFKRHLKWKII.
Self-assembly A term utilized to describe the processes in which a disordered system of preexisting components forms an organized structure or pattern as a consequence of specific, local, and cooperative interaction. If the components are molecules, the process is termed molecular self-assembly.
Self-renewal A cellular process that allows an unlimited number of cell divisions and replications.
Silanize or silanization Surface functionalization via silane molecules such as (3-aminopropyl)-triethoxysilane, (3-mercaptopropyl)-trimethoxysilane, and octadecyltrimethoxysilane.
Spinal cord injury (SCI) An injury to the spinal cord that causes myelopathy (loss of nerve function) or damage to nerve roots or myelinated fiber tracts that mediate signals to and from the brain.
Stem cells Cells that are able to self-renew and differentiate into multiple cell types. Mammalian stem cells are broadly categorized into either embryonic stem cells or adult stem cells.
Theranostic application An application that enables both medical diagnostics and treatment.
Transcription The process of single-stranded DNA being copied into the complementary RNA.
Translation Part of the protein biosynthesis process that involves the production of polypeptides via the association among mRNA, tRNA, and the ribosome.
Transplantation Instillation of an organ from one body to another for the purpose of replacing the recipient's damaged or absent organ. It can also involve the use of cell therapy sources such as stem cells and bone marrow cultures.
Vacuole A membrane-bound cavity in the cytoplasm of eukaryotic cells that contains air, water, cell sap, and digested food. It is present especially in plant and fungal cells while found to a lesser extent in animal and bacterial cells.
Vascular endothelial growth factor (VEGF) VEGF is a signal protein involved in the stimulation of new blood vessel production.
Vesicle A supramolecular assembly made up of lipid bilayers created by double-tailed lipid molecules such as phospholipids. Basically, it is a membrane-enclosed sack that has a hydrophilic core. Artificially prepared vesicles are referred to as liposomes.
Viscosity A measure of the resistance of a fluid being deformed by either shear stress or tensile stress.
W3K A 17-mer peptide with a sequence of WAAAAKAAAAKAAAAKA that is alanine-rich but water-soluble and forms worm-like micelles upon lipidation.
Wound healing An intricate and dynamic process in which tissues and organs repair themselves after sustaining injury.

Abbreviations

DMF Dimethyl formamide, a common solvent used in peptide synthesis.
PEG Poly(ethylene glycol)
SDS Sodium dodecylsulfate, a common anionic C12-alkylated surfactant molecule.
SEM Scanning electron microscopy
TEM Transmission electron microscopy
TFA Trifluoroacetic acid

4.415.1. Introduction

Biomaterials[1–20] can be divided into two different categories: one that exists in nature[21–25] or one that (favorably) mimics nature.[26–32] One facet of applications involving biomaterials is in the field of tissue and bio(medical) engineering. Bioengineers, on a regular basis, prepare biomaterials to influence biological events where genetic codes are transcribed and then translated within a dynamic environment in the *cell*. When taking into account the complexity involving biological systems, it is critical that surface properties are well understood all the way down to a single molecule or even an element. Multiple surface engineering techniques are available depending on the mode and degree of action, meaning the change of

physicochemical properties posttreatment (engineering). Surface cleaning, etching, and depth profiles are often done using radiation (beam) (i.e., plasma treatment[33–35]; electron beam lithography[36,37]; UV[38–41]; ultrasound[16,42]) (Mode 1). Synthetic chemistry-based techniques[43] are used when specific molecules need attachment (i.e., covalent bond formation; self-assembled monolayer) or a passivation of polymeric-networked materials (i.e., layer-by-layer technique[44–47]; core–shell material synthesis[15,48]; polymer coating on glass via photocuring[49,50]) is desired (Mode 2). Spatial positioning of molecules and nanoparticles on extended surfaces with nanometer-level precision can be achieved via printing methods (i.e., microcontact stamping[51–58]; dip-pen lithography printing[59,60]; ink jet printing[61–66] (Mode 3). Intermolecular associative and repulsive forces (interfacial phenomena)[67,68]-induced structuring can be useful as well to achieve well-defined nanostructured surfaces, and this is where self-assembly or cooperative assembly of molecules and (nano)materials[69–72] plays a critical role in the outcome of the final complex structure (Mode 4). (**Figure 1**)

In this chapter, we cover surface engineering efforts performed using peptide amphiphiles (PAs) (see **Chapter 2.205, Self-Assembling Biomaterials**). PAs provide a platform of bioactive nanostructured materials that provide biomaterials with a controlled display of functional and biologically responsive moieties on the periphery of the resulting biomaterial construct; PAs have the potential to mimic nature. The hierarchical two- and three-dimensional (3D) structures formed by PAs via self-assembly processes are spherical vesicles and micelles, lipid layers, and fibrous high-aspect-ratio structures (**Figure 2**).[17,18,74–80] The usual characterization methods for such higher-order structures involve dynamic light scattering (DLS), circular dichroism (CD), fluorescence spectroscopy, and microscopy. One of the key features of a lipidated peptide is that sequences incorporating a distinct secondary structure (i.e., α-helix) will often experience stabilization of the structure over a time domain compatible enough to elicit a cell (signaling) response (i.e., adhesion). We highlight work by several different groups over the past two decades reporting PAs' (nano)structural features as well as biological responses in cellular and animal models. We view 'surfaces' as critical components having unique spatial and temporal domains; they exist over multiple length scales and time domains often bioactive enough to interact with living systems undergoing dynamic changes with varied magnitudes and frequency depending on the type of biosystem. PAs can form surfaces that present bioactive subdomains and physicochemically unique properties that may architecturally and biochemically reproduce materials present in nature (i.e., the cell membrane, subcellular machinery, the extracellular matrix) (see **Chapter 4.406, Protein Interactions with Biomaterials** and **Chapter 2.207, Extracellular Matrix: Inspired Biomaterials**).

4.415.2. The Amphiphilic Nature of Life's Events

The cell membrane (shown in **Figure 3**) comprises multiple amphiphilic and hydrophobicity-controlled structures: lipids, proteins, polysaccharides, and nucleic acids.[15] Among the aforementioned biological entities, proteins interact with other biomolecules in a complex but intricate manner; most importantly, the role and the fate of proteins within a specific cell biology subsystem (i.e., receptor-mediated signaling pathway, cellular adhesion process, cytoskeleton rearrangement, endocytosis, inflammatory response, translation, transcription, ion channeling, posttranslational modification, apoptosis, nuclear transport, differentiation, self-renewal, etc.) will depend strongly on the dynamics associated with the protein's primary and secondary structures – for example, the hydrophobicity and the α-helical propensities will vary in accordance with the incorporated amino acid residue characteristics. We consider a cell membrane as a 2D soft surface that can be mimicked on flat surfaces. In living systems, however, the cell membrane exterior and interior are not interfaced to a hard surface (except in bone) and is, in fact, three-dimensionally responsive through multiple cellular and extracellular signaling pathways that play critical roles in the overall function of cells. In this respect, we can define self-assembly processes occurring in multiple biological systems constituting 3D structural cues and niches – meaning that coassembly of subcomponents are important to produce functionality (see **Chapter 4.401, The Concept of Biocompatibility**).

4.415.3. PAs: Synthesis, Physicochemical Characterization, and Self-Assembly

PAs (or lipopeptides; **Figure 2**) are a class of small molecules that link peptides (as the hydrophilic head group) together with hydrocarbons (hydrophobic tail). Unlike naturally occurring lipids, this platform of materials is synthetically prepared and usually has a molecular weight of 1000–3000. The use of PAs to address biomaterials and bioengineering questions has been developed since the mid-1990's. A highly efficient solid-phase synthesis method was employed by Tirrell and coworkers where dialkyl hydrocarbon chains were covalently bonded to bioactive peptide sequences such as Gly-Val-Lys-Gly-Asp-Lys-Gly-Asn-Pro-Gly-Trp-Pro-Gly-Ala-Pro (denoted as [IV-H1] from here on) derived from the extracellular matrix protein collagen, as shown in **Figure 4**.[80–85] The chemistry behind such PA synthesis is Fmoc-chemistry.[86–89] The motivation to utilize bioactive peptides displaying amphiphilic construct is to mimic aspects of native designs – for instance, the stem cell niche or the tumor microenvironment. The [IV-H1] sequence is a 15-mer biologically proved to promote cancer cell adhesion and spreading while physicochemically observed (via CD, NMR, etc.) to form a triple-helical structure, often the secondary protein structure naturally occurring in collagen (co)assembly.[80,83]

4.415.3.1. Synthesis and Characterization of PAs

The synthesis protocol outline for synthesizing a single-tailed PA is given below (**Figure 5**). Characterization generally involves mass spectrometry, CD, and NMR. Protocols developed by Tirrell and coworkers[80–85] can be easily applied to both dialkylated and monoalkylated PA synthesis.

4.415.3.2. Double-Tailed (Dialkylated) PAs

Double lipidation of cationic peptides often leads to potent antibiotic agents. In the context of surface engineering, double-tailed (low molecular weight) PAs displaying bioactive

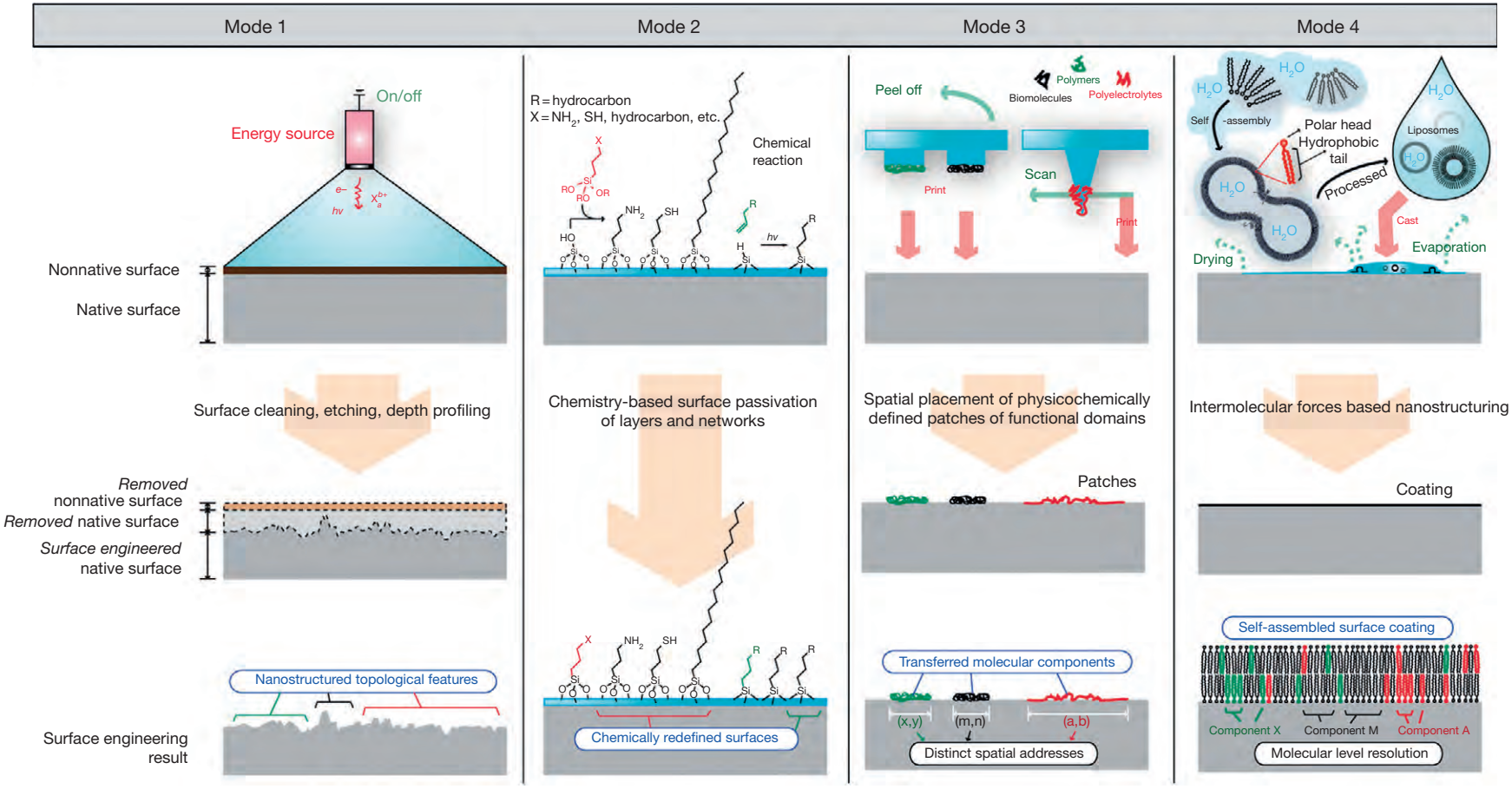

Figure 1 Modes of surface engineering. See main text for details. This review will cover mode 4, in depth. Various combinations of all four modes, however, can lead to unique surfaces with hierarchically, physicochemically, and biologically distinctive properties.

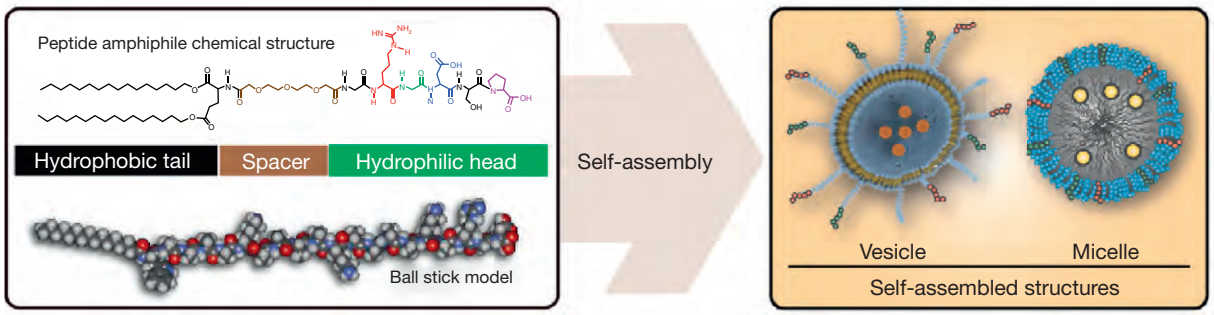

Figure 2 Self-assembled structures of peptide amphiphiles. Based on the degree of lipidation, peptide amphiphiles will form vesicles or micelles. The chemical structure represents the double-tailed peptide amphiphile $(C16)_2$-Glu-C_2-PEG-GRGDSP which is synthesized from covalent linkages among glutamate dialkyl ester 1',3'-dihexadecyl L-glutamate (two hexadecanols attached to glutamic acid; the hydrophobic tail), 3,6,9-trioxaundecanedioic acid (polyethylene oxide spacer), and a 6-mer peptide head group Glu-Arg-Glu-Asp-Ser-Pro (the hydrophilic head).[73] The ball-and-stick model represents the single-tailed peptide amphiphile C16-$WA_4KA_4KA_4$KARGD,[74] created using Accelrys DS Visualization software.

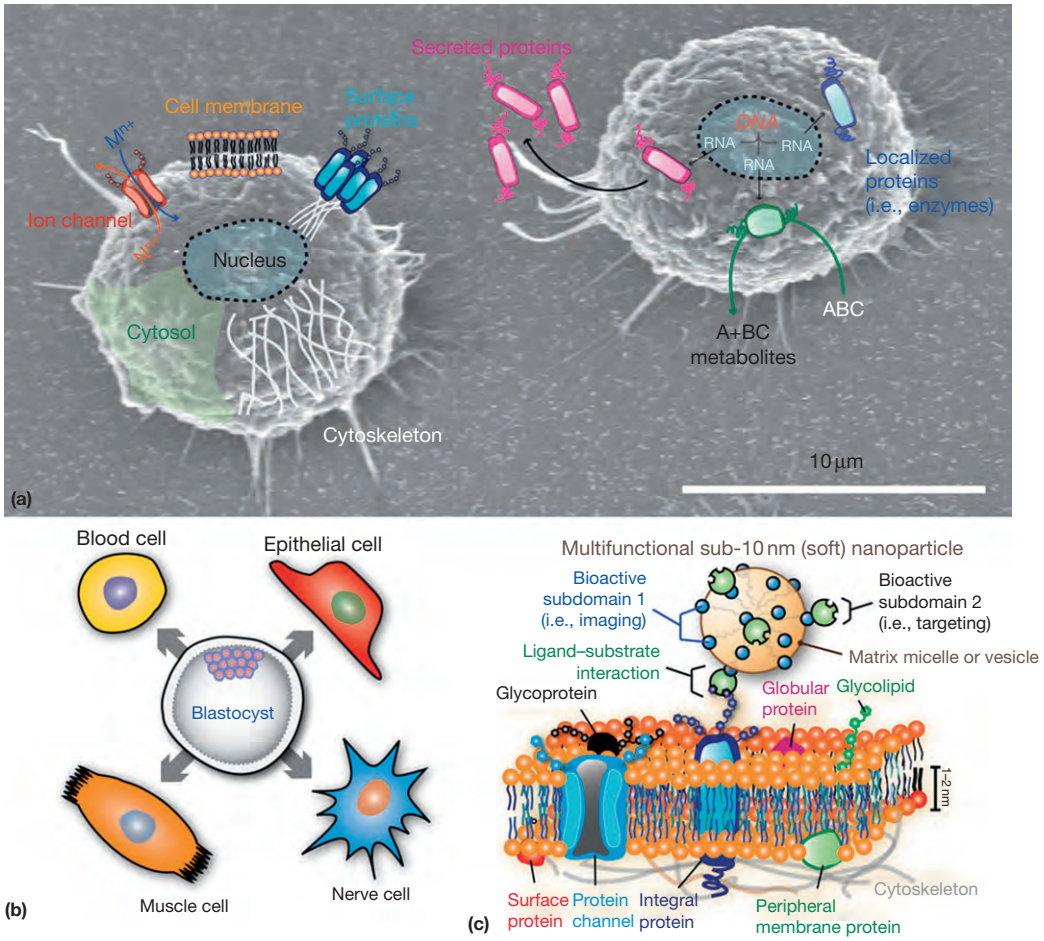

Figure 3 A cell as a multifunctional entity. (a) The breakdown of cellular machinery shows that a mammalian cell is essentially a multifunctional micron-sized particle comprised of internal and external components that function in coordination. The external components are (1) the cell membrane, (2) surface proteins/ion channels, and (3) the cytoskeleton, while the internal components are (4) the cytosolic organelles (i.e., ribosome, endoplasmic reticulum, golgi apparatus, mitochondrion, vacuole, lysosome, and centriole) and (5) the nucleus (which contains nucleic acids). Another major component in a living cell consists of the active biological processes that occur in a hierarchical and consistent fashion. These so-called biological pathways involve proteins, metal ions, nucleic acids, amino acids, external stimuli, and other biomolecules to work in concert with one another. The represented scanning electron microscopic (SEM) image shows two murine BV-2 microglia cells attached to a surface. (b) Multiple cell types exist differing in their function, shape, and size. (c) The cell membrane consists of many functional biomolecules, including multiple forms of functional proteins, displayed carbohydrates, and the lipid bilayer. A bioactive and nanometer-sized material (i.e., multifunctional micelles, liposomes, and inorganic nanoparticles) can directly interact with such biomolecules present on or inside a cell as shown in the illustration. It is important to precisely define the nature of such interactions in order to elicit a biologically definable process through certain types of surface engineering presented in **Figure 1**. Adapted from Suh, W. H.; Suh, Y. H.; Stucky, G. D. *Nano Today* **2009**, *4*, 27–36.

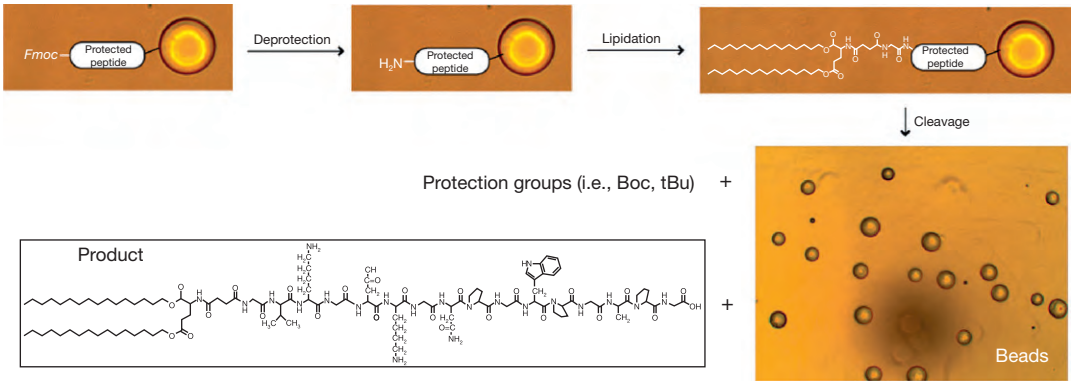

Figure 4 Synthetic outline of peptide amphiphile based on Fmoc-chemistry. A protected peptide is first prepared on a solid polymer bead using a standard peptide synthesizer. The amine-protecting Fmoc group is removed using base reagents (i.e., piperidine, piperidine/DBU, or 4-methylpiperidine in DMF), followed by lipid tail (or linker) addition. After the hydrocarbon tail addition process is complete, the peptide amphiphile and the protecting groups are cleaved under a mild acid condition (i.e., 95% TFA). Adapted from Berndt, P.; Fields, G. B.; Tirrell, M. *J. Am. Chem. Soc.* **1995**, *117*, 9515–9522.

sequences can be embedded into lipid bilayers created by phospholipids via vesicle fusion. This feature allows facile screening of functional molecules that play an intricate role in the cell adhesion process or to probe biomolecular forces in a controlled environment that may provide information crucial for our increased understanding of biological systems such as membrane protein trafficking and protein–biomolecule interactions.

Dialkylated hydrophilic moieties including PAs will form vesicles in liquid media (Figure 6).[91] Depending on the number of lipid bilayers formed and size of the soft spheres, such vesicles (often termed liposomes) can be categorized into small unilamellar vesicles (SUVs, < 100 nm diameter), larger unilamellar vesicles (LUVs, 100–1000 nm), multilamellar vesicles (MLVs, 100 nm to 20 μm), and multivesicular vesicles (MVVs, 100 nm to 20 μm). Generally, when PA-incorporated films are rehydrated and liposomes have formed, it is further purified via extrusion to predominately populate the working solution with SUVs before lipid bilayer experiments are conducted to minimize the heterogeneity of the surface being created (Figure 7) (see Chapter 1.124, Polymer Films Using LbL Self-Assembly).[92]

Peptide amphiphile $(C16)_2$-Glu-C_2-$(GPO)_4$-GVKGDKGNP GWPGAP (herein $(C16)_2$-Glu-C_2-$(GPO)_4$-[IV-H1], where O is hydroxyproline) was constructed by Tirrrell and coworkers and compared to poly(ethylene glycol) (PEG) lipids for its ability to promote melanoma cell adhesion, based on ligand accessibility as a means to control cell responses on a bioactive lipid bilayer.[93] The head group lengths for the studied lipids (neutron reflective data) were 8.8 nm for $(C16)_2$-Glu-C_2-$(GPO)_4$-IV-H1, while for DSPE-PEG-120, -750, -2000, and -5000, the lengths were 1.6, 3.5, 9.0, and 16.8, respectively. When the particular PA was mixed 50:50 with the PEG lipids and spread out as lipid bilayers, melanoma cells M14 clone #5 adhered to only 50% DSPE-PEG-120, -750, and -2000. For DSPE-PEG-5000, the head group length of the PEG lipid (16.8 nm) exceeds the PA head group length (8.8 nm) so the bioactive sequence IV-H1 – a known sequence to promote melanoma cell adhesion – was not accessible and PEG molecules are known antifouling agents,[94–97] hence no cell attachment and proliferation (see Chapter 3.320, Nanostructured Polymeric Films for Cell Biology).

4.415.3.3. Single-Tailed (Monoalkylated) PAs

Monoalkylated amphiphilic constructs self-assemble into spherical micelles with a hydrophobic core and hydrophilic head groups at the periphery of the soft nanoparticle (Figure 8). This is a contrasting feature compared to double-tailed (low molecular weight) amphiphile construct, as liposomes have a hydrophilic core surrounded by a lipid bilayer as mentioned earlier.

Tirrell and coworkers prepared an alanine-rich 17-mer peptide sequence containing single-tailed PA and profiled its conversion from spherical micelles into worm-like fibrous micelles based on modulation of physicochemical properties (i.e., shear induction).[74] The particular PA is C16-$WA_4KA_4KA_4KA$ (C16-W3K herein); above its critical micelle concentration (CMC), the PA molecules form spherical micelles or fibrous structures depending on shear, time, concentration, and temperature, and C16-W3K switches into fibrous structures. Multiple examples of monoalkylated PAs exist and we further examine their physicochemical and biological properties in the later sections of this chapter.

4.415.4. The Multifunctional (Soft) Nanoparticle Concept

Multiple chemically distinctive PAs can comprise different higher-order structures such as liposomes and spherical micelles (Figure 9) with nanometer-scale precision (see Chapter 3.319, Characterization of Nanoparticles in Biological Environments; Chapter 3.319, Characterization of Nanoparticles in Biological Environments; and Chapter 4.429, Ordered Mesoporous Silica Materials). We describe some recent examples of molecular delivery and theranostic applications using multicomponent liposomes and spherical micelles.

4.415.4.1. Targeting-Enabled PA Spherical Micelles

Ruoslahti, Tirrell, and coworkers utilized a double-tailed PEG construct appended with a homing (targeting) peptide sequence (i.e., CREKA, LyP-1) for targeting atherosclerotic plaques or

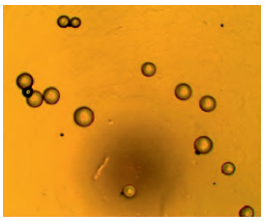

Beads with protected peptides

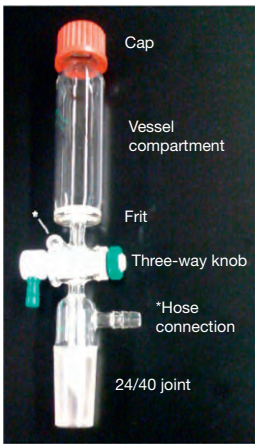

Synthesis vessel

Peptide amphiphile synthesis protocol

0. Calculations (using excel is helpful) and preparation

a. Obtain a clean synthesis vessel.
b. Weigh peptide conjugated beads and calculate the mmol g^{-1}.
c. Calculate how much 4 equivalent carboxylic acid (lipid tail), 4 eq. HOBt (1-hydroxybenzotriazole), 4 equiv. HBTU (2-(1*H*-benzotriazol-1-yl)-1,1,3,3-tetramethyluronium hexafluorophosphate), 8 equiv. DIEA (*N*,*N*-diisopropylethylamine) are needed.

Steps 1 through 12 should be done inside a chemical hood.

1. Swelling

a. Add the pre-weighed beads to the clean synthesis vessel.
b. Add 10–15 ml of DCM (dichloromethane).
c. Shake slowly for 30 min.

2. Washing

a. Stop shaking and empty DCM.
b. Add 10–15 ml of DMF (dimethylformamide) and shake to wash for 5 min.
c. Stop shaking and empty DMF.
d. Repeat step 2(b) and 2(c) twice more.

3. Deprotection (*Fmoc* to free amine)

a. Mix 2% piperidine, 2% DBU, and 96% DMF (recommended final volume 20–30 ml).
b. Add the deprotection solution to the emptied synthesis vessel from 2.
c. Shake moderately (beads are well dispersed during) for 1 h.
d. Stop reaction, empty the *Fmoc* deprotection solution; proceed to the wash step.
**Fmoc* = 9*H*-fluoren-9-ylmethoxycarbonyl

4. Washing

a. Wash 3× DMF (10–20 ml volumes; 5 min/ea).
b. Empty the final washing solution and proceed to either step 5 or 6.

5. (Optional) Amine test

6. Coupling

a. Coupling reagents from 0(b) are dissolved in 20 ml DMF, 2 ml DCM.
b. The coupling solution is added to the dried bead containing synthesis vessel from 4.
c. Shake moderately for, at least, 2–4 h but overnight reaction is also acceptable.
d. Stop reaction, empty the remaining coupling solution; proceed to the wash step.

7. Washing

a. Wash in the following order, first: 2× DMF, 2× DCM, 1× MeOH (10–20 ml volumes).
b. Do the final washing step: 1× DCM, 2× MeOH (also 10–20 ml volumes).
c. Dry under vacuum at room temperature.

8. Cleavage

a. Prepare a clean glassware (100 ml Erlenmeyer flask recommended) to receive the as-prepared peptide amphiphile solution.
b. Mix 2.5% water, 2.5% TIS (triisopropylsilane), and 95% TFA (trifluoroacetic acid) (final vol. 10–20 ml)
c. Add the cleaving solution to the dried bead containing synthesis vessel from 7.
d. Shake slowly for approximately 4 h.
e. Stop reaction and collect the crude PA solution into the precleaned glassware from 8(a) via vaccum filtration or nitrogen gas purging.

9. Evaporation

a. Transfer the collected crude PA in TFA (approximately 10–30 ml) to a 50 ml plastic tube.
b. Evaporate TFA via nitrogen gas purging.
c. After evaporation is complete (usually after overnight purging), the crude PA oil can be stored below −20 °C or undergo the final precipitation step.

10. Precipitation

a. Prepare a cold solution of ether (i.e., diethyl ether).
b. Add 20–30 ml of cold ether into the 50 ml plastic tube containing the PA oil.
c. Hand shake, vortex, and/or sonicate the PA-ether dispersion for approximately 5–10 min until white/ivory colored precipitates are visible.
d. Centrifuge at 1500 rpm for 5 min.
e. Empty the ether supernatant solution.
f. Repeat steps (a) through (e) twice more. Discard ether after product identification.

11. Drying

a. After the final precipitation (/wash) from 10, the collected crude PA pellet/particles are dried under nitrogen gas purging until the ether has visibly evaporated.
b. The crude PA solid is further dried under vacuum for 1–2 h (room temperature).
c. The crude PA is ready for HPLC separation. Store below −20 °C when appropriate.

12. Separation

13. Lyophilization

Figure 5 Peptide Amphiphile Synthesis Protocol. A macrophotograph of the synthesis vessel and the beads with protected peptides are shown on the far left. The optional amine test (Step 5) is usually done using the Kaiser test[90] in which the beads will turn blue if amine groups are exposed.

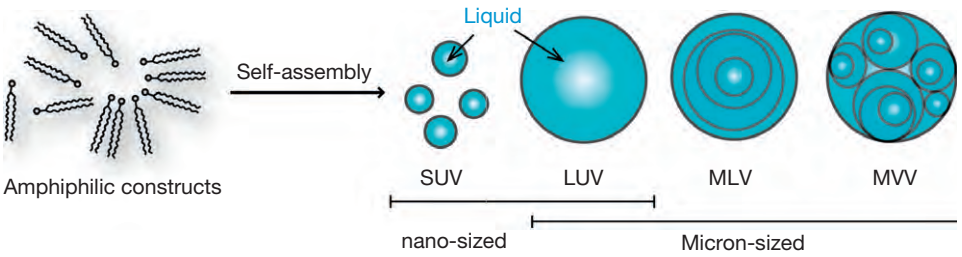

Figure 6 Lipid vesicles. Adapted from Jones, M. N. *Adv. Coll. Interfac. Sci.* **1995**, *54*, 93–128.

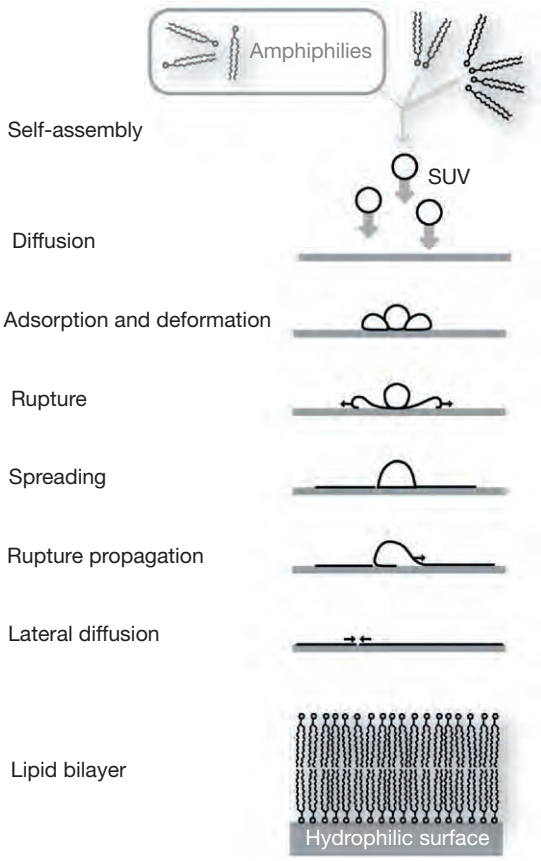

Figure 7 Vesicle fusion mechanism (hypothesis) on a hydrophilic surface. Adapted from Stroumpoulis, D.; Parra, A.; Tirrell, M. *AIChE J.* **2006**, *52*, 2931–2937.

tumors (see **Chapter 3.312, Cell Culture Systems for studying Biomaterial Interactions with Biological Barriers**).[76,98] The resulting spherical micelles have a diameter of ~25–35 nm and their *in vivo* circulation half-life time was 2–3 h. The added feature of the PA was the covalent linkage of either a bioimaging probe or a therapeutic agent; this makes them a multifunctional nanoparticle (type V MFNPS) (**Figure 9**). Synthesis-wise, the anticoagulant peptide hirulog[99] (CF*PRPGGGGNGDFEEIPEEYL where F* is D-Phenylalanine and a cysteine was added to the N-terminus of hirulog for functionalization), CREKA,[100] or LyP-1 (cyclic nine-amino acid peptide CGNKRTRGC)[101,102] were linked to DSPE-PEG2000-maleimide via Fmoc-chemistry methods (**Figure 10**). DSPE-PEG2000-CREKA spherical micelles, in particular, are able to home to the aortic tree of atherosclerotic mice within 3 h of injection (**Figure 10**). Thus, when CREKA-targeted hirulog micelles were injected into ApoE-null mice, the antithrombin activity was significantly higher compared to the wild-type mice or when nontargeted micelles were administered.

4.415.4.2. Single-Tailed PAs for Cancer Cell Biology Control

Hartgerink and coworkers[103] prepared C16-WYPWMKKHH, C16-RQIKIWFQNRRMKWKK, and C16-WYPWMKKHHRQI KIWFQNRRMKWKK to study their effects on cancer cell proliferation and inhibition of growth. The sequence WYPWMKKHH disrupts HOX/PBX/DNA complex formation, while the RQIKIWFQNRRMKWKK sequence allows cargo delivery into cells. The C16 hydrocarbon chain allowed the self-assembly process to occur; the resulting stable population of spherical micelles incorporated stable secondary structures (i.e., α-helix) when embedded in a micelle that predominantly comprised anionic surfactant molecules (i.e., SDS) (**Figure 11**).

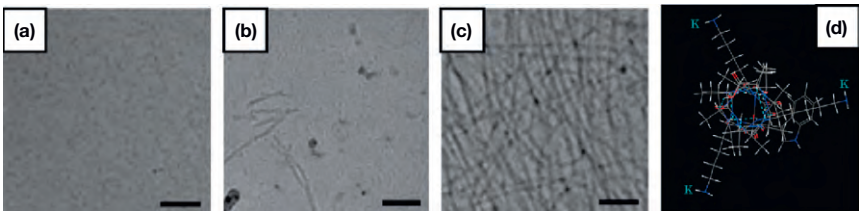

Figure 8 TEM of C16-W3K Peptide Amphiphile. (a) Spherical versus (b, c) fibrous micelles. C16-W3K initially forms spherical micelles (a). However, fibrous micelles are observed after 1 day (b) and highly cross-networked nanofibrous micelles dominate after 3 days (c). (d) Molecular mechanics method optimized W3K structure via the COMPASS Force Field produced by Accelrys Software Inc. The image shows that three lysine residues are evenly distributed along the peptide backbone, presenting no angular and longitudinal asymmetry around the α-helix. Adapted from Shimada, T.; Lee, S.; Bates, F. S.; Hotta, A.; Tirrell, M. *J. Phys. Chem. B* **2009**, *113*, 13711–13714.

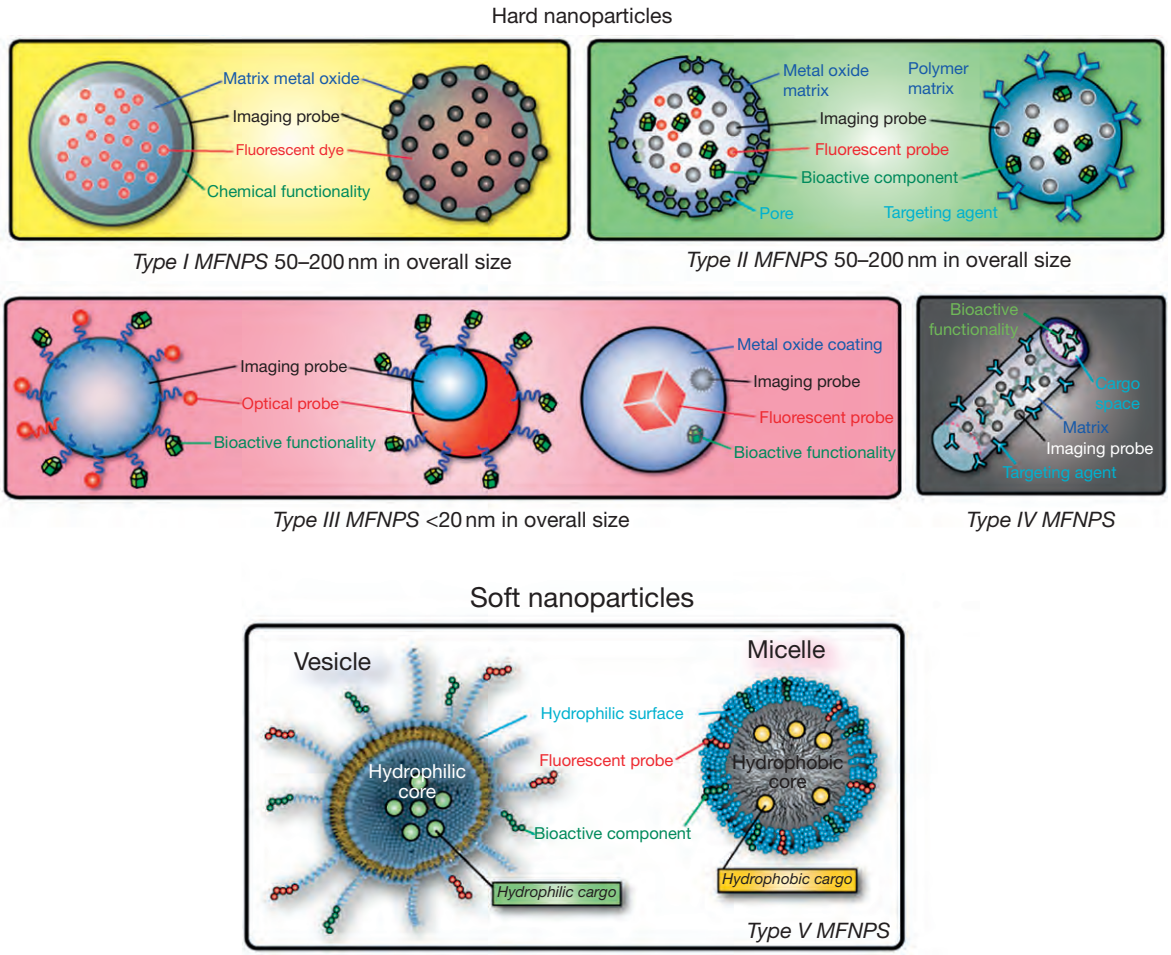

Figure 9 Categorization of multifunctional nanoparticles. Five distinctive multifunctional nanoparticle systems (MFNPS) can be conceptualized based on soft/hardness of the constituting material, core–shell structure, functional subdomains, and size. Adapted and expanded from Suh, W. H.; Suh, Y. H.; Stucky, G. D. *Nano Today* **2009**, *4*, 27–36.

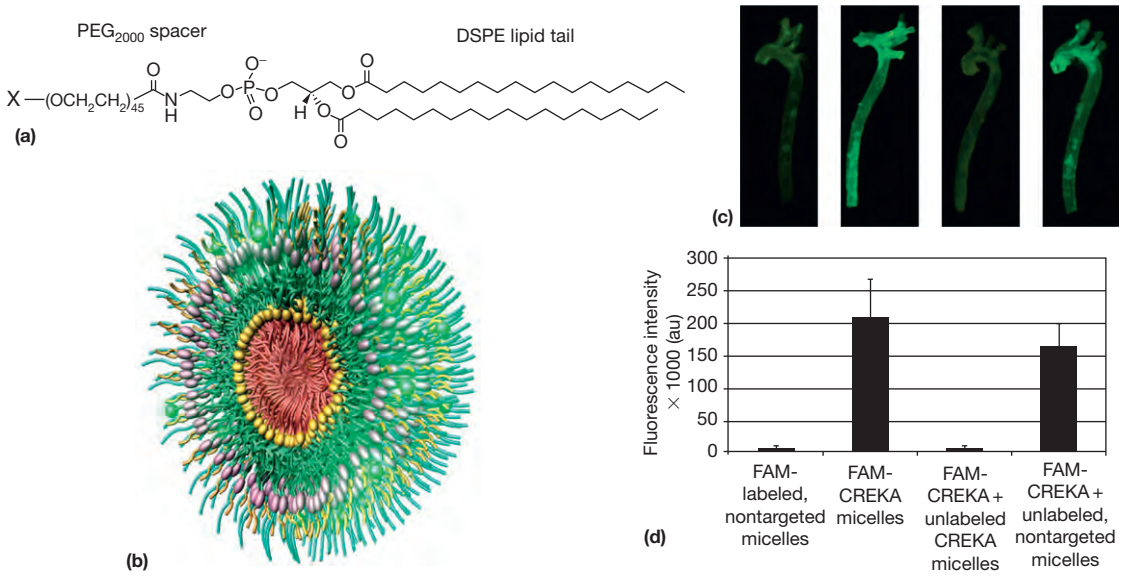

Figure 10 Schematic representation of a modular DSPE-PEG PA-based multifunctional micelle (a, b) and *ex vivo* imaging of the aortic tree of atherosclerotic mice (c, d). Adapted from Peters, D.; Kastantin, M.; Kotamraju, V. R.; *et al*. *Proc. Natl. Acad. Sci. USA* **2009**, *106*, 9815–9819.

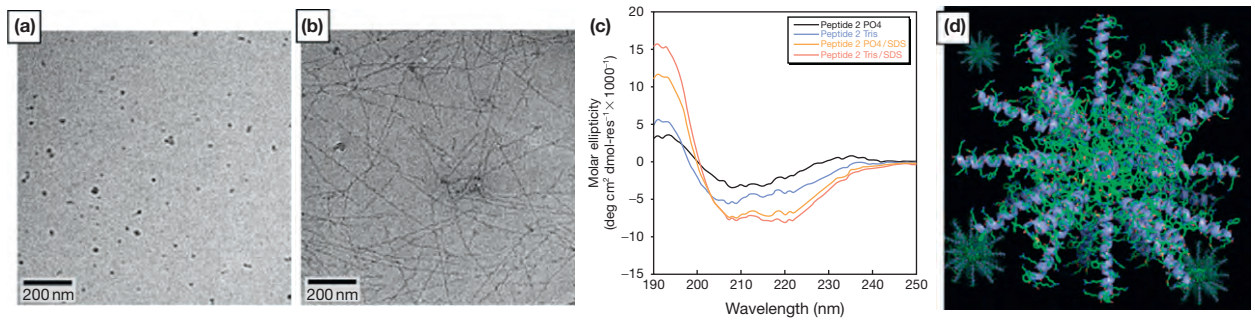

Figure 11 Structural analysis of peptide amphiphile C16-WYPWMKKHH-RQIKIWFQNRRMKWKK via TEM at (a) low concentration (2 mg ml^{-1}, spherical micelles), (b) high concentration (12 mg ml^{-1}, fibrous micelles), and via (c) CD; (d) schematic representation of the α-helix-incorporating spherical micelle of the analyzed PA. Adapted from Aulisa, L.; Forraz, N.; McGuckin, C.; Hartgerink, J. D. *Acta Biomater.* **2009**, *5*, 842–853.[103]

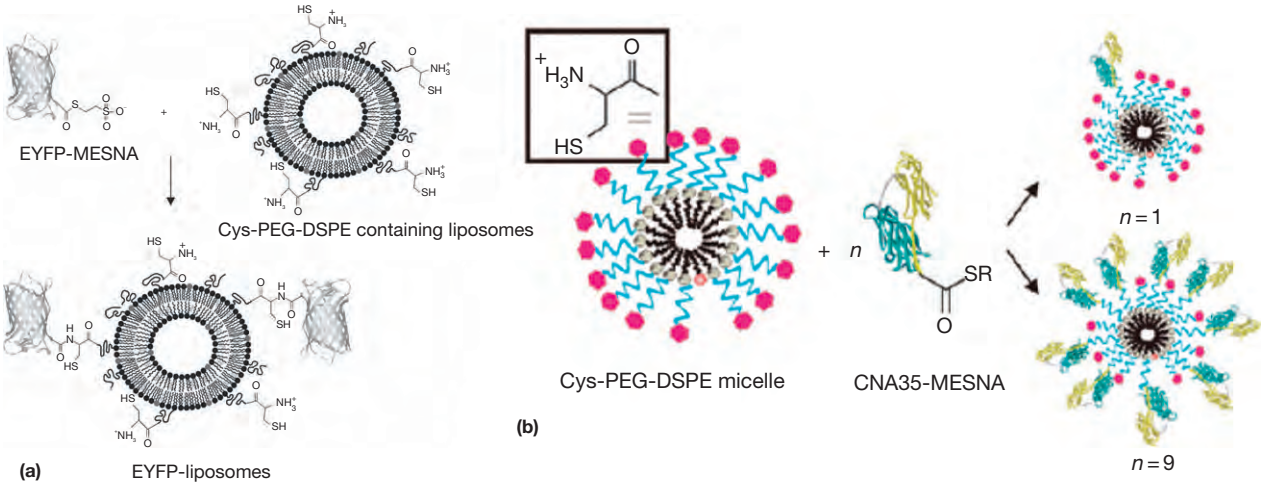

Figure 12 Preparation of multivalent CNA35 (a) vesicles and (b) micelles. Adapted from Reulen, S. W. A.; Brusselaars, W. W. T.; Langereis, S.; Mulder, W. J. M.; Breurken, M.; Merkx, M. *Bioconj. Chem.* **2007**, *18*, 590–596; Reulen, S. W. A.; Dankers, P. Y. W.; Bomans, P. H. H.; Meijer, E. W.; Merkx, M. *J. Am. Chem. Soc.* **2009**, *131*, 7304–7312.

4.415.4.3. *In Vitro* Binding Affinity Control via Native Chemical Ligation

Micelles and vesicles were prepared with a collagen binding protein CNA35 – 35 kDa collagen binding domain present in an adhesion protein from *Staphylococcus aureus* – displayed on the exterior of DSPE-PEG2000 that had moderate collagen binding affinities ($K_{micelle}$ ~0.5 μM, $K_{liposome}$ ~3 ± 1 nM) and allowed facile detection via fluorescence spectroscopy.[104,105] The native chemical ligation (NCL) method[106,107] was employed successfully to create covalent linkages between recombinant proteins and the PEG-conjugated vesicles and micelles; NCL exclusively occurs at the protein C-terminus – often not involved in any binding activities with high specificity. These examples (Figure 12) demonstrate a highly effective instillation of multiple functionalities (i.e., multiple collagen binding sites) into soft nanoparticles that may be necessary for targeting sites with multivalent architectures. The NCL method should be easily expanded to other nanoparticle systems (i.e., iron oxides and quantum dots) coated with peptide moieties.

4.415.5. Protein-Like Structures to 3D Hierarchical Nanostructures

Close to two decades ago, Yamada *et al.*[108] reported that dialkylated PAs made up of C12 and C16 tails along with 14 residues of L-glutamic acid (Figure 13) self-assembled into helical super structures (nanotubes) comprising single-walled PA bilayers. Transmission electron microscopic (TEM) and CD analysis suggested that the PAs formed tube-like nanostructures and also displayed α-helical secondary structures at ~0.1 wt% concentration (Figure 14). During the same period, Kunitake and coworkers also reported identical nanostructures formed from self-assembly of ammonium-based amphiphilic molecules in aqueous media.[109]

In the 1990s, Tirrell and colleagues[80,81,85] realized that controlling the mode of lipidation on PAs instilled with a collagen-model head group enabled the controlled mimicking of protein-like (secondary) structures by conducting an extensive investigation into the relationship between the degree of

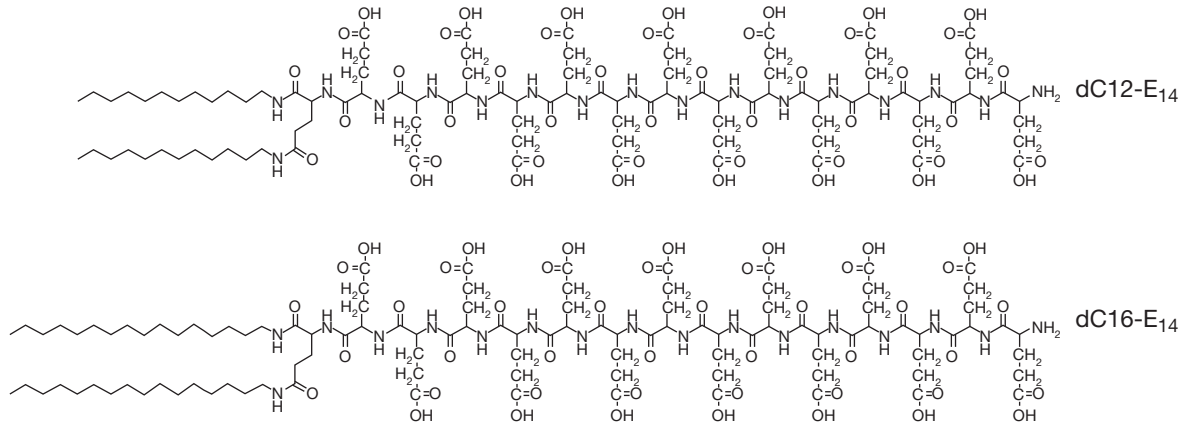

Figure 13 Double-tailed poly(L-glutamic acid) peptide amphiphile chemical structures. Adapted from Yamada, K.; Ihara, H.; Ide, T.; Fukumoto, T.; Hirayama, C. *Chem. Lett.* **1984**, 1713–1716.

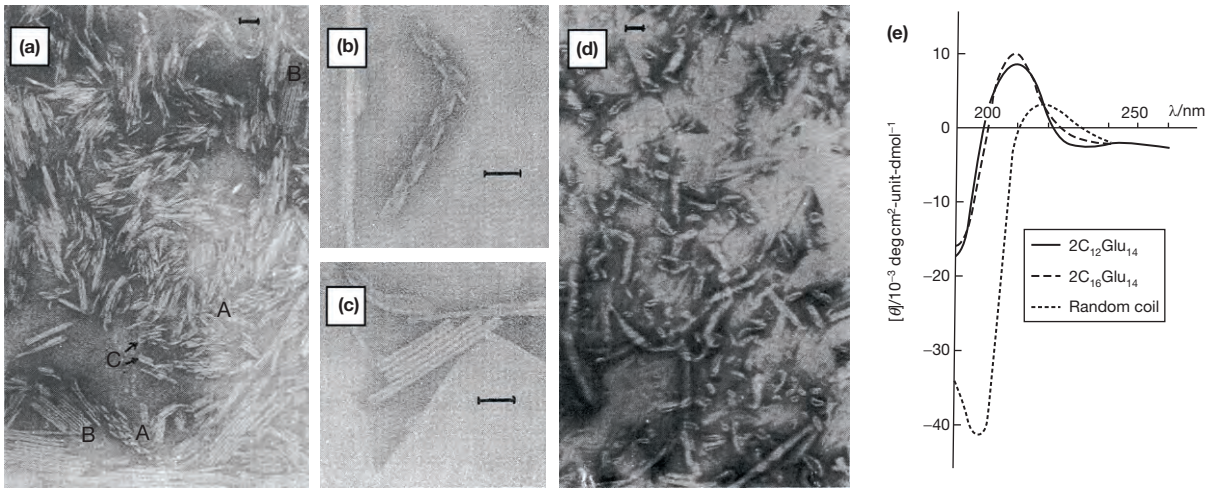

Figure 14 TEM of dC12-E14 (a–c) and dC16-E14 at 0.1 wt% (stained). Scale bar in b, c equals 50 nm. (d) dC16-E14 at 0.1 wt% (stained). Scale bar in b,c equals 50 nm. (e) CD spectra of lipidated Glu14 at pH 9.0, 25 C, 5.0x10^{04} M. Adapted from Yamada, K.; Ihara, H.; Ide, T.; Fukumoto, T.; Hirayama, C. *Chem. Lett.* **1984**, 1713–1716.

alkylation (i.e., chain length, number of chains per molecule) and their secondary structure stabilization. The experiments involved the use of the peptide sequence $(GPO)_4$[IV-H1] $(GPO)_4$ where [IV-H1] is the alpha1(IV)1263-1277 collagen sequence (GVKGDKGNPGWPGAP) and C6, C8, C10, C12, C14, C16, and diC12 tails. Based on multiple CD and NMR analyses, C6-$(GPO)_4$[IV-H1]$(GPO)_4$ can form a triple-helix structure below 30 °C with the [IV-H1] region within the PA being in a triple-helical environment; the PA melting temperature is increased when the monoalkyl chain length is increased. The denaturation temperature for the C16 PA is comparable to the original $(GPO)_4$[IV-H1]$(GPO)_4$ sequence. However, the degree of stabilization differs between mono- (Tm = 55.0 °C) and dialkylated (Tm = 71.2 °C) PAs. All in all, whether a helix-forming peptide sequence is covalently linked to a single hydrocarbon tail or a double tail, synthesized PAs can oligomerize, self-assemble, and form various stable structures that may be crucial in positively (or negatively) influencing biological systems. More recently, Stupp and coworkers prepared 12 different PAs (Table 1) that self-assembled into fibrous structures made up of spherical micelles having exposed bioactive peptide sequences RGD and IKVAV. TEM was utilized as seen in the figures to unmistakably show amphiphilic constructs forming fibrous structures based on pH-tuning; this change in physical property allowed the formation of gel-like macroscopic materials (Figure 15). Table 1 lists single-tailed PAs that form fibrous worm-like 3D structures explored in this work. In Section 4.415.6, we highlight research that utilized mono-lipidated PAs in biomedical applications.

4.415.6. Applications in Biomedical Sciences: Tissue and Stem Cell Engineering

Mode 4 of surface engineering, mentioned earlier in this chapter (Figure 1), can be divided into three subcategories when

bioactive PAs are involved: (1) lipid bilayer embedded bioactive PAs, (2) fibrous PA incorporating bioactive PAs, and (3) 3D gel matrices displaying bioactive PAs and other biomolecules (**Figure 16**) (see **Chapter 4.409, Surfaces and Cell Behavior** and **Chapter 3.312, Cell Culture Systems for studying Biomaterial Interactions with Biological Barriers**).[111] In this section, we highlight the use of PAs to influence biological systems; we consider micelles with high-aspect ratios to be ideal for tissue engineering both on 2D surfaces and on 3D matrices.

4.415.6.1. Helical Structure and Antibacterial PAs

Tirrell, Mayo, and colleagues[112,113] studied single-tailed PAs for their antibacterial ability. In one instance, KLFKRHLKWKII-NH_2 (amidated C-terminus) was monoalkylated with C12 and C18 chains. The particular 12-mer peptide sequence (SC4)[114] is a potent antibacterial peptide that displays activity at nanomolar concentrations against Gram-negative bacterial species and micromolar concentrations against Gram-positive bacteria. SC4 also neutralizes endotoxins while displaying no hemolytic activity sub-100 μM. The bactericidal mechanism appears to be coming from the helix-forming nature of the peptide sequence that can permeabilize through the cell membrane. Lipidation of SC4 resulted in a 30-fold increase of biocidal activity against *Staphylococcus aureus*, *Steptococcus pyogene*, and *Bacillus anthracis* (Gram-positive), but there was little or no increase of antibacterial activity against *Escherichia coli* and *Pseudomonas aeruginosa* (Gram-negative) strains. In addition, lipidated SC4 PAs neutralized lipopolysaccharides (LPS) more than SC4 alone (~3–6 times increased inhibition of LPS activity). Red blood cells were observed to undergo lysis at micromolar PA concentrations (antibacterial activity induction occurs at the sub-1 μM to tens of nanomolar range), whereas endothelial cell toxicity was negligible. The molecular modeling representation based on 2D NMR data (i.e., Nuclear Overhauser Effect) suggests that the monoalkylated SC4 is helical in secondary structure and that has also been validated by CD experiments where the PAs were embedded in liposomes mimicking eukaryotic and bacterial cell membranes (**Figure 17**).

The next study by Tirrell and coworkers[112] showed that lauric acid (C12)-modified YGAA(KKAAKAA)$_2$ (termed AKK PA) had increased antibacterial activity, whereas YG(AKAKAAKA)$_2$ (termed KAK PA) did not in comparison to C12-SC4 PA. Here, the importance of helical structure was once again demonstrated; CD results as well as the helical wheel diagram analysis shown in **Figure 18** suggest that KAK PA does not share structural homology with SC4 PA. However, AKK PA displays a wider hydrophobic region, with cationic regions grouped on one side (similar to the SC4 PA) when an α-helical structure

Table 1 List of PA molecules that form nanofibers via pH control, divalent ion induction, and concentration. The chemical structure of C16-$C_4G_4S^{(PO4)}$RGD (PA 4) is shown in **Figure 15**.

Molecule	*N-terminus*	*Peptide (N to C)*	*Charge pH 7*
1	H	CCCCGGGS$^{(PO4)}$RGD	–2
2	$C_6H_{11}O$	CCCCGGGS$^{(PO4)}$RGD	–3
3	$C_{10}H_{19}O$	CCCCGGGS$^{(PO4)}$RGD	–3
4	$C_{16}H_{31}O$	CCCCGGGS$^{(PO4)}$RGD	–3
5	$C_{22}H_{43}O$	CCCCGGGS$^{(PO4)}$RGD	–3
6	$C_{10}H_{19}O$	AAAAGGGS$^{(PO4)}$RGD	–3
7	$C_{16}H_{31}O$	AAAAGGGS$^{(PO4)}$RGD	–3
8	$C_{16}H_{31}O$	CCCCGGGS$^{(PO4)}$	–3
9	$C_{16}H_{31}O$	CCCCGGGS$^{(PO4)}$KGE	–3
10	$C_{16}H_{31}O$	CCCCGGGS$^{(PO4)}$RGDS	–3
11	$C_{16}H_{31}O$	CCCCGGGSRGD	–1
12	$C_{16}H_{31}O$	CCCCGGGEIKVAV	–1

Adapted from reference.[110]

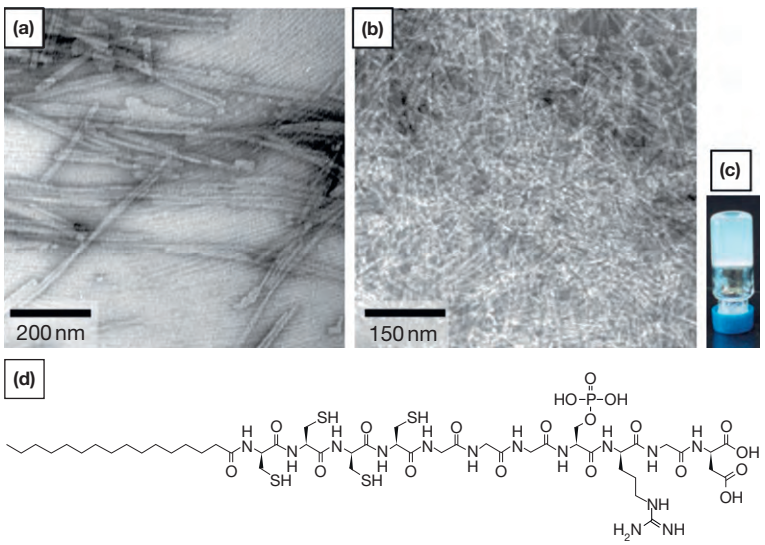

Figure 15 TEM images of nanofibers from PAs 6 and 7 from **Table 1**. Samples were (negatively) stained with phosphotungstic acid. (a) The aspect ratio of the nanofibers is much higher for C10–$A_4G_3S^{(PO4)}$RGD (PA 6) compared C16–$A_4G_3S^{(PO4)}$RGD (PA 7). (b) PA 7 will form a highly networked gel. Macrophotograph of PA 6 gel is provided on the far right (c). (d) Example chemical structure of PA 4 from Table 1. Adapted from Hartgerink, J. D.; Beniash, E.; Stupp, S. I. *Proc. Natl. Acad. Sci. USA* **2002**, *99*, 5133–5138.

is formed (embedded in a bacterial cell membrane mimic). AKK PA also shows reduced hemolytic activity, different from SC4 PA – although the AKK peptide sequence has a strong hydrophobic property, it is less than SC4 peptide. The structure–activity relationship, at least in cytotoxicity, is well demonstrated by Chu-Kung *et al.*[112]

4.415.6.2. Neural Stem Cell Engineering

Palmitic acid (C16) modified A_4G_3-IKVAV (IKVAV-PA) was utilized in Silva *et al.* to create an artificial 3D extracellular matrix (Figure 19) ideal for supporting murine neural progenitor cells (NPCs) at physiological conditions (see Chapter 2.209, Materials

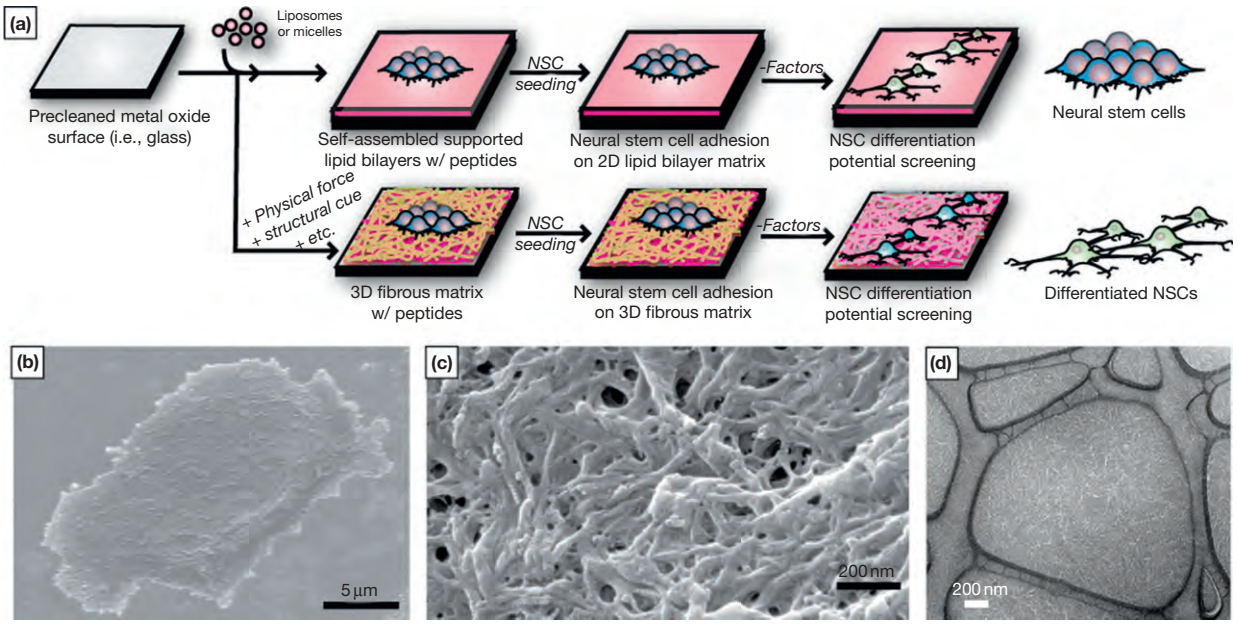

Figure 16 Surface engineering of surfaces using bioactive peptide amphiphiles for tissue engineering applications (schematic a). Electron microscopy images of a 3D peptide amphiphile gel matrix: SEM (b, c) and TEM (d) images. Adapted from Tirrell, M. WFPC Project 4.4.5: Modular, switchable, synthetic, extracellular matrices for regenerative medicine; In *AFIRM Annual Report*; Vandre, R., Ed.; 2009; pp II-53–II-56.

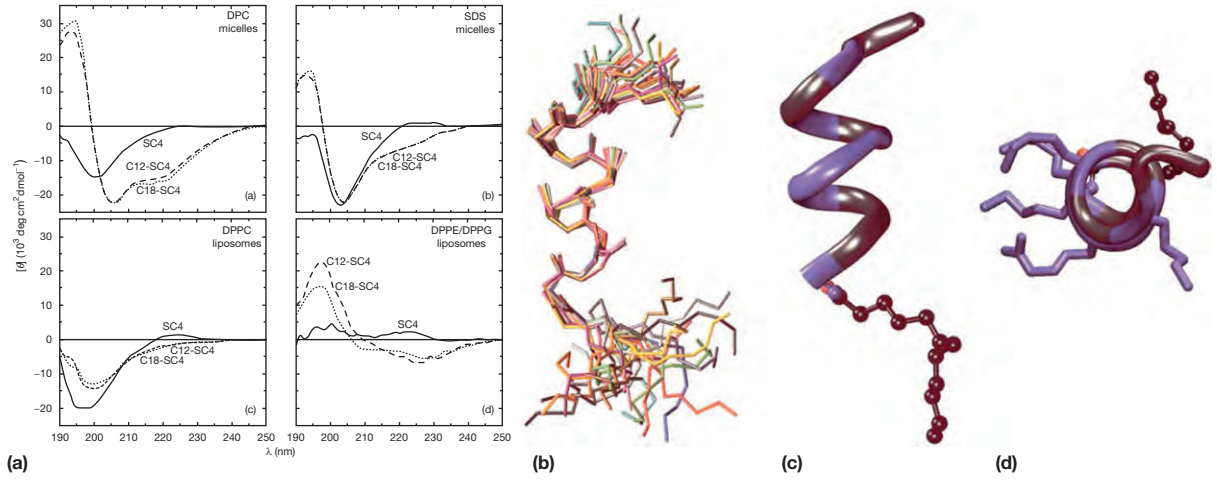

Figure 17 CD spectra of SC4 (unbroken lines), C12-SC4 (dashed lines), and C18-SC4 (dotted lines) in micelle and liposome membrane mimics. In micellar mimics, the SC4 amphiphiles showed spectra consistent with helical conformation in DPC (a-a) and somewhat less helix in SDS (a-b). Liposome membrane mimics showed spectra indicating little SC4 amphiphile structure in DPPC (a-c), the erythrocyte mimic, but a more structured state in bacterial-mimicking DPPE/DPPG liposomes (a-d). The SC4 peptide spectra indicate little structure under any condition. Spectra in water: NOE-derived structures of C12-SC4 in DPC micelles (b) Superposition of the 24 final structures, using residues Lys-1 through Trp-9 for alignment. (c) A ribbon backbone representation of one structure, showing the overall helical fold and a less-ordered C-terminus. Polar residues are shown in blue and apolar residues in gray. The fatty acid tail is shown as a ball-and-stick model. (d) An axial view of the average structure, demonstrating the distribution of charged side chains (arginine and lysine) in an amphipathic helix. The colors are as described in (c) looked similar to those in DPPC liposomes; results at 37°C were similar for all conditions. Adapted from Lockwood, N. A.; Haseman, J. R.; Tirrell, M. V.; Mayo, K. H. *Biochem. J.* **2004**, *378*, 93–103.

as Artificial Stem Cell Microenvironments).[115] The working concentration was 0.5 wt% of PA in NPC medium. The NPC experiment confirmed the utility of PA gels that allowed the survival of NPCs over a 3-week period encapsulated (three-dimensionally) – there was no abnormal cell behavior arising from the use of PA gels versus the poly(D-lysine) control. Differentiation profiling revealed that NPC grown inside the soft, nanofibrous PA gel scaffolds produced an increased population of cells identifiable as neurons compared to laminin and poly(D-lysine) controls; the underlying mechanism, however, is not clear. Additional 2D experiments using self-assembled IKVAV-PA coatings on substrates showed that the 2D PA matrix system works equally well compared to the 3D system in promoting the differentiation of NPCs into neurons; these findings suggested that the degree of bioactive sequence IKVAV displayed on the nanofibrous matrices influenced NPC biology rather than the dimensionality of the prepared extracellular matrices. Back-of-the-envelope calculations (2D surface approximated) show that the density of bioactive epitope IKVAV in the self-assembled nanostructures ($\sim 10^{14}$–$10^{15}\,cm^{-2}$) far exceeds the numbers for naturally occurring laminin ($\sim 10^{11}$–$10^{12}\,cm^{-2}$) by more than 1000-fold. It was also noted that injection of IKVAV-PA gels in animals resulted in no detrimental effects on the host.

Niece *et al.*[116] expanded on the aforementioned work and prepared 7 PAs with distinct functional subdomains: (1) lipid tail, (2) β-sheet inducer, (3) spacer, and (4) bioactive peptide sequence were systematically varied (Figure 20). Nanofibrous gels presenting the IKVAV sequence (highlighted PA box) had the highest NPC viability and, in addition, substantially outperforming the other PAs in promoting neuronal differentiation. The gelation of PAs was modulated by controlling the hydrophobicity instilled into the midpeptide region (subdomains 2, 3) – comparing the kinetic and the turbidity data, the viscosity and the speed of PA gelation was PA1>PA2>PA3.

Tysseling-Mattiace and coworkers[117] utilized the monoalkylated C16-AAAA-GGG-E-IKVAV peptide amphiphile (IKVAV-PA) (Figure 21) to study its efficacy and regenerative potential in a murine spinal cord injury (SCI) model (see Chapter 6.630, Biomaterials for Spinal Cord Repair). The injected PA gels biodegraded *in vivo* in ~4 weeks. Injection of PA gels (0.5 wt %) and controls were monitored up to several months for hindlimb functional recovery; the IKVAV-PA gel-injected mice had the best behavioral recovery – significant enough to categorize as a functional improvement. Immunohistochemical and biochemical analyses revealed that astrogliosis (i.e., glial scarring at the SCI site) and programmed cell death (i.e., apoptosis of oligodendroglial cells after SCI) were both attenuated. In addition, it was found that IKVAV-PA nanofibers foster the regeneration of sensory and motor axons, a goal of high clinical relevance (see Chapter 2.220, Extracellular Matrix as Biomimetic Biomaterial: Biological Matrices for Tissue Regeneration).

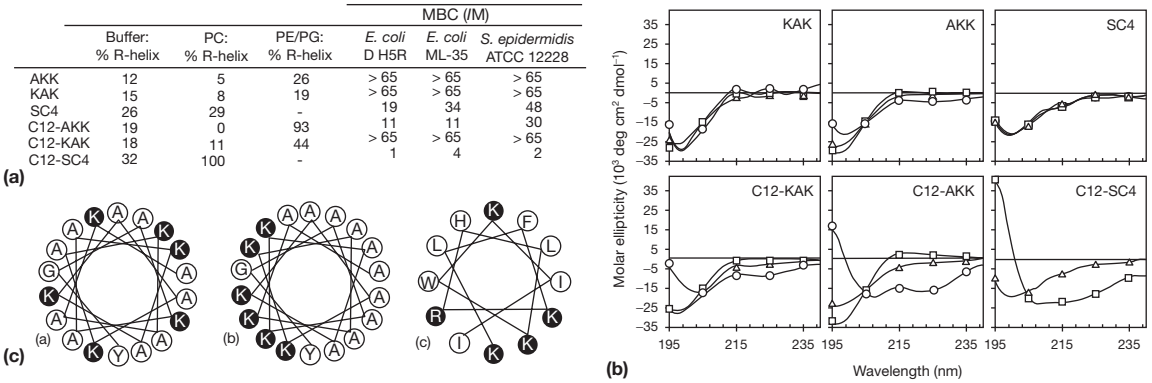

Figure 18 Physical and biological properties of AKK, KAK, SC4 peptides, and their respective peptide amphiphiles. (a) Helicity based on solvent/vesicle conditions and representative minimum bactericidal concentration (MBC) data based on different strains. PC = vesicles from dilauroylphosphatidylcholine and PE/PG = vesicles from dilauroyl phosphatidylethanolamine and dilauroyl phosphatidylglycerol. (b) CD spectra: Sodium phosphate buffer (triangle), PC (square), and PE/PG vesicle (circle). (c) Helical wheel diagrams: (c-a) KAK, (c-b) AKK, and (c-c) SC4. Charged residues are in black. Adapted from Chu-Kung, A. F.; Bozzelli, K. N.; Lockwood, N. A.; Haseman, J. R.; Mayo, K. H.; Tirrell, M. V. *Bioconj. Chem.* **2004**, *15*, 530–535.

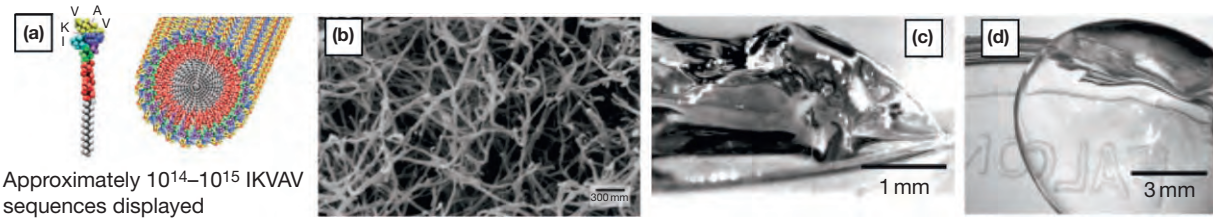

Figure 19 (a) Molecular graphics representation of C16-A_4G_3-IKVAV before and after self-assembly. (b) SEM and (c) macrophotograph of nanofibrous gel prepared in cell medium (DMEM). (d) PA with cerebral spinal fluid. Adapted from Silva, G. A.; Czeisler, C.; Niece, K. L.; *et al*. *Science* **2004**, *303*, 1352–1355.

More recently, Schaffer and coworkers[118] demonstrated that RGD-incorporating peptides could be readily prepared into 2D surfaces for stem cell tissue engineering. GGGNGEPRGDTYRAY (bsp-RGD(15)) and GRGDSP were lipidated and embedded into phospholipid bilayers at fixed mol%. Murine neural stem cells (NSCs) adhered to the RGD-functionalized surfaces and, for bsp-RGD(15) PA, the NSCs had a large fraction of single adherent cells, comparable to the laminin control (Figure 22). NSCs cultured on both 2D PA surfaces differentiated into both neurons and astrocytes.

4.415.6.3. Bone Marrow Mononuclear Cells

Webber *et al.* have demonstrated a dilution-based PA scaffolding approach by mixing bioactive C16-$V_3A_3K_3$RGDS with C16-$V_3A_3R_3$, C16-$V_3A_3K_3$, and C16-$V_3A_3E_3$ to determine the optimum ratio density of the bioactive PA[119] that promotes cell adhesion of bone marrow mononuclear cells (BMNCs) (Figure 23). This study reports that 10% (molar) doping of C16-$V_3A_3K_3$RGDS in C16-$V_3A_3E_3$ allows BMNCs to adhere effectively on fibrous PA structures *in vitro* (Figure 24) (see Chapter 4.411, Peptide- and Protein-Modified Surfaces). However, the degree of 2D surface adhesion that can be considered a dramatic increase was not observed, while the increase in proliferation of encapsulated BMNCs was 6 times more efficient compared to other controls.

4.415.6.4. Ameoblast Cell Engineering for Tooth Regeneration

Arg-Gly-Asp-incorporating PAs were self-assembled into nanofibers under physiological conditions at 1 wt% concentration;

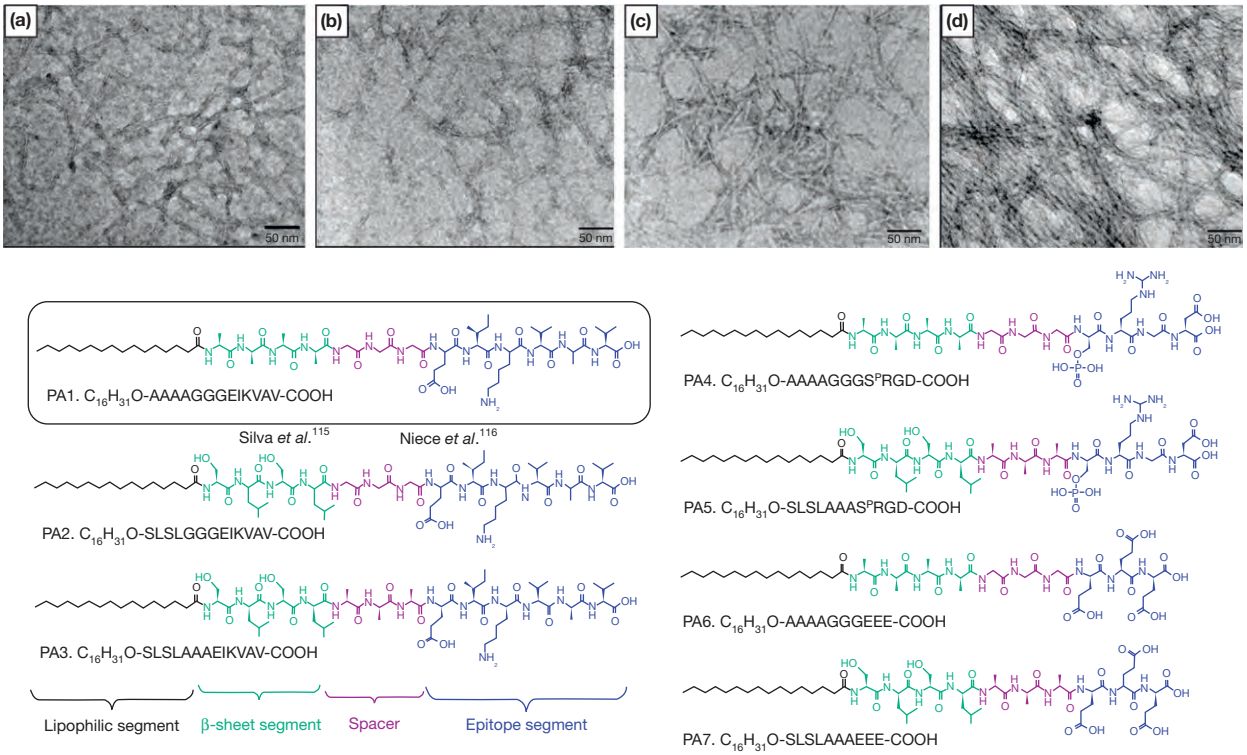

Figure 20 TEM images of self-assembled nanofibers from (a) C16-A_4G_3E-IKVAV, (b) C16-SLSLA_3E-IKVAV, (c) C16-$A_4G_3S^{(PO4)}$-RGD, and (d) C16-SLSL$A_3S^{(PO4)}$-RGD. The studied PA chemical structures are also given. Adapted from Niece, K. L.; Czeisler, C.; Sahni, V.; *et al*. *Biomaterials* **2008**, *29*, 4501–4509.

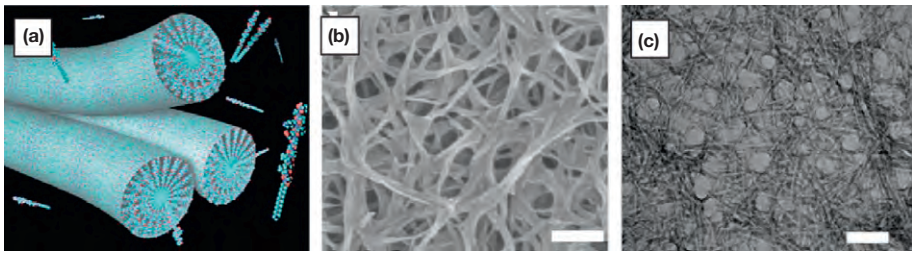

Figure 21 Nanofibrous C16-AAAA-GGG-E-IKVAV peptide amphiphile gel matrix. (a) Schematic representation, (b) SEM of bundled nanofibers (scale bar = 200 nm), and (c) TEM of nanofibers (scale bar = 100 nm). Adapted from Tysseling-Mattiace, V. M.; Sahni, V.; Niece, K. L.; *et al*. *J. Neurosci*. **2008**, *28*, 3814–3823.

ameoblast-like cells (LS8) and primary enamel organ epithelial (EOE) cells were grown inside the 3D PA matrix and injected into the enamel organ epithelia of murine embryonic incisors (*in vitro* organ culture model) **Chapter 6.619, Materials in Dental Implantology**. The peptide sequence is a branched RGD (BRGD-PA, **Figure 25**) and increased the cell proliferation and Ca^{2+} accumulation when cultured with LS8 cells and EOE cells. The microinjection of BRGD-PA into the enamel organ epithelia of incisors resulted in cell proliferation at the site of injection, with the eventual level of amelogenin and

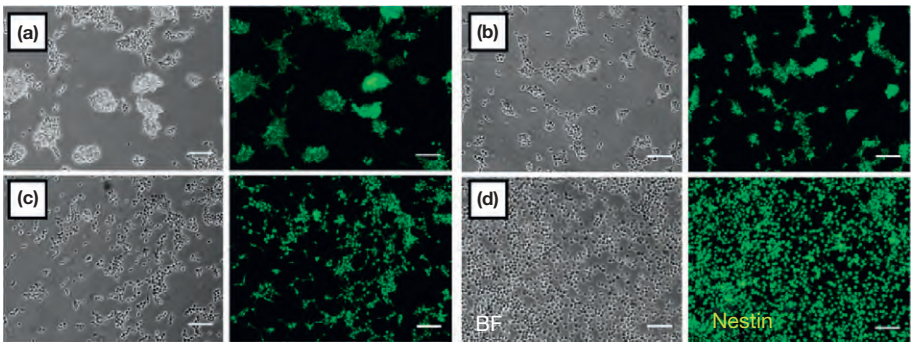

Figure 22 Bright field and immunofluorescence images of NSCs after 5 days. NSCs grown on (a) EggPC, (b) 40% GRGDSP PA, (c) 20% bsp-RGD(15) PA, and (d) Laminin treated surfaces. All NSCs expressed Nestin (green). Cells on EggPC and 40% GRGDSP PA surfaces formed loosely attached aggregates, whereas NSCs on laminin, and to a lesser extent, 20% bsp-RGD(15) PA, grew as monolayer adherent cells. Scale bar = 100 μm. Adapted from Ananthanarayanan, B.; Little, L.; Schaffer, D. V.; Healy, K. E.; Tirrell, M. *Biomaterials* **2010**, *31*, 8706–8715.

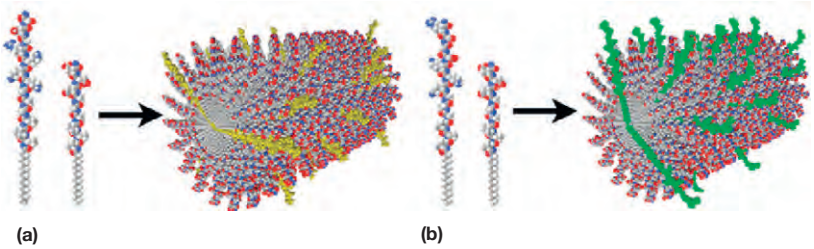

Figure 23 Molecular graphics representation of binary PA fibers assembled from 90% C16-$V_3A_3E_3$ diluent and (a) 10% RGDS PA accented in yellow or (b) 10% DGSR scrambled PA accented in green. Adapted from Webber, M. J.; Tongers, J.; Renault, M.-A.; Roncalli, J. G.; Losordo, D. W.; Stupp, S. I. *Acta Biomater.* **2010**, *6*, 3–11.

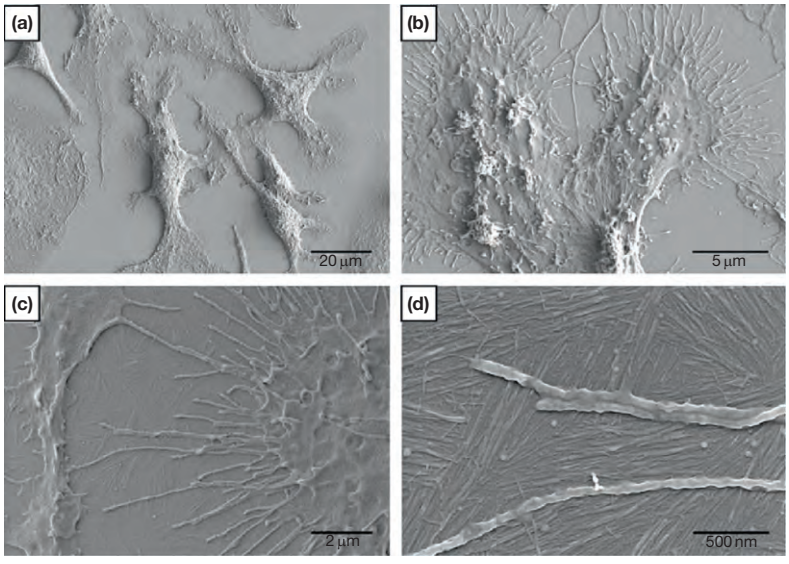

Figure 24 BMNCs cultured on surfaces coated with 10% RGDS PA, exhibiting extensive process formation (a–c) in contact with the PA-coated surface at higher magnification. (d) Scale bars are 20 μm (a), 5 μm (b), 2 μm (c), and 500 nm (d). Adapted from Webber, M. J.; Tongers, J.; Renault, M.-A.; Roncalli, J. G.; Losordo, D. W.; Stupp, S. I. *Acta Biomater.* **2010**, *6*, 3–11.

ameloblastin protein expression (within the extracellular matrix) increasing, which is an indication that a population of cells is undergoing a differentiation process. In this study, multiple control PAs were utilized that consisted of D-amino acid RGD epitope and a rearranged terminal amino acid sequence (still displaying the same charge density) – the controls did not present significant positive responses via *in vitro* experiments.

4.415.6.5. Heparin-Binding PAs for Regenerative Medicine

Rajangam *et al.*[120] prepared two heparin-binding PAs (HBPAs) that self-assembled into bundles of nanofibers (Figure 26). The bioactivities of the PA gels were investigated using an *in vitro* angiogenesis assay using bovine pulmonary arterial endothelial cells sandwiched between two layers of either PA gel. The chemical structure of HBPA is C16-A_4G_3LRKKLGKA and the scrambled PA (SPA) is C16-A_4G_3LLGARKKK. Several different protein growth factors (GFs; i.e., angiogenic heparin binding growth factor, bFGF, VEGF) were supplemented to the PA–heparin gels prepared for *in vitro* assays. HBPA–heparin gel supplemented with GFs outperformed SBA-heparin gel's ability (with or w/o GFs) to form tubules in three dimensions with continuous lumens; this higher bioactivity of HBPA may be due to the stabilization of interactions among the exposed heparin-binding sequences (on the nanofiber matrix) and heparin via specific and nonelectrostatic interactions (Figure 27). *In vivo* angiogenesis studies conducted by Ghanaati *et al.* using HBPA confirmed the potential of HBPA–heparin sulfate nanostructures in vascularization and soft tissue regeneration.[121] Two rodent animal models were utilized that showed no harmful effects (i.e., inflammation, toxicity) arising from PA gel injections. These studies demonstrated that fibrous PA gels displaying bioactive subdomains on the nanofiber surface can potentially find usefulness in the area of wound healing and cell (transplantation) therapy.

4.415.6.6. Human Mesenchymal Stem Cell Engineering

PAs with photo-cross-linkable diacetylene units bearing a bioactive sequence RGD were utilized as silica surface-coating materials to influence human mesenchymal stem cell biology (Figure 28).[122] The studied PA is an extended version of the ones studied by Huang *et al.*[123] mentioned earlier. Peptide sequences KKLLA(K)-$(CH_2)_4$-NH_2 and RGDSKKLLA(K)-$(CH_2)_4$-NH_2 were linked to HOOC-C8-diacetylene-C12 monoalkyl chain. Soft lithography techniques were utilized to prepare nanofibrous PA (micron-sized) patterns that include channels and holes (see Chapter 4.413, Patterned Biointerfaces). The interesting observation noted in this particular study was that bioactive PA nanofibers that were aligned perpendicular to the micron-sized channels promoted hMSC attachment and subsequent alignment (nanofiber alignment:micron channel alignment = 35%:45%) to an identical degree (Figure 29). This example of surface bioactivity and architectural engineering

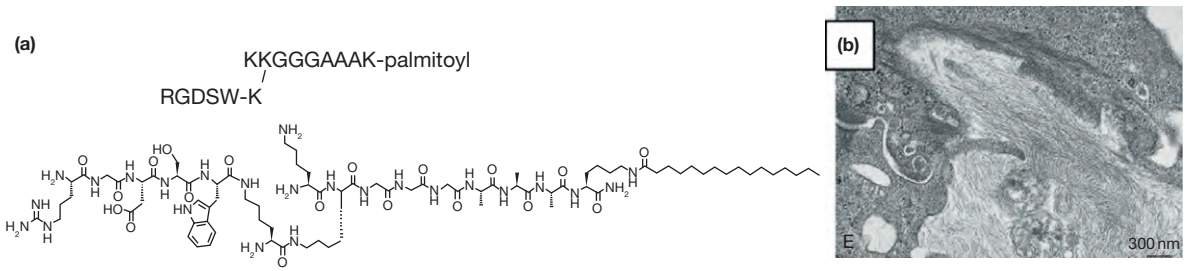

Figure 25 (a) Schematic chemical structure of the branched RGD peptide amphiphile (BRGD-PA). (b) TEM image of BRGD-PA injected incisor primordia 5 days after injection. The PAs assembled into nanofibers within the enamel organ epithelia, with cytoplasm extension into the nanofibers. Adapted from Huang, Z.; Sargeant, T. D.; Hulvat, J. F.; *et al*. *J. Bone Miner. Res*. **2008**, *23*, 1995–2006.

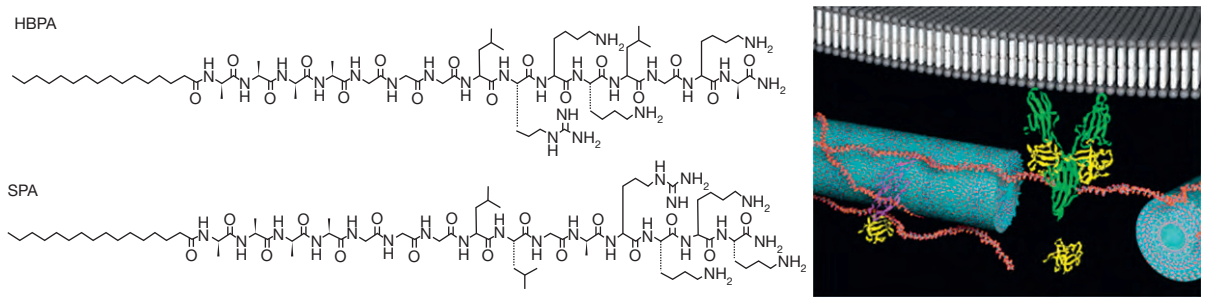

Figure 26 Molecular structures of heparin binding PAs and a schematic representation of heparin–nucleated HBPA nanofibers interacting with GF and receptors. The HBPA nanofibers (blue) are shown with adsorbed heparin chains on them (red). Heparin is known to bind and activate VEGF (purple), FGF-2 (yellow), and FGF receptor (green). The design proposes that the heparin–FGF-2–FGF receptor complex is further stabilized by their anchoring on HBPA nanofibers. For the control PA, it is possible that the absence of heparin stabilization by hydrophobic interactions and via the consensus format in the SPA nanofibers is responsible for the decreased bioactivity seen in SPA–heparin gels. Adapted from Rajangam, K.; Arnold, M. S.; Rocco, M. A.; Stupp, S. I. *Biomaterials* **2008**, *29*, 3298–3305.

via nanofibrous PAs may thus provide an excellent platform of biomaterials capable of influencing cytoskeleton organization and associated cell signaling pathways, leading to controlling key stem cell biology.

Jun and colleagues[124] subsequently reported five different C16-tailed PAs all incorporating (cell-mediated) proteolytically cleavable sequence GTAGLIGQ[125] which should prove useful in future cell encapsulation studies in a 3D nanofiber gel matrix (Figure 30); an additional 1–4-mer terminal head group dictated each PA's modular nature mediating and/or promoting integrin-receptor-based cellular responses by hMSCs. Among the PAs, C16-RGDS PA nanofibrous extracellular matrix (coating; 0.1 wt%) most successfully promoted hMSC adhesion and further osteogenic differentiation (i.e., mineral deposition). The same group further demonstrated that multiple different viscosity-controlled 3D PA gel matrices (1 wt%) (Figure 31) can be prepared via doping bioactive PAs into non-bioactive PAs (C16-GTAGLIGQS)[126] – an approach identical to the work done by Stupp and coworkers[119] to control the cell biology of BMNCs. The terminal 4–5-mer peptide sequences are derived from naturally occurring motifs associated with integrin-mediated binding architecture (RGDS), elastin (VAPG), collagen type I (DGEA), and laminin (YIGSR).

4.415.6.7. Dental Stem Cells

Galler *et al.*[127] prepared a single-tail C16-GTAGLIGQERGDS PA (Figure 32) to create a gel matrix (1 wt%) for dental stem cell (i.e., stem cells from human exfoliated deciduous teeth (SHED), dental pulp stem cells (DPSC)) engineering. Mineral deposition was observed for dental stem cells cultured with osteogenic supplements (i.e., beta-glycerophosphate (betaGP), dexamethasone (dex), KH_2PO_4 (KPh)) (Figure 33). As it turns out, the SHED-PA system showed promising tissue engineering results that suggest its potential application in soft dental tissue regeneration (i.e., dental pulp), whereas the DPSC-PA system may find utility in mineralized dental tissue engineering (i.e., bone, dentin) – mineral deposition tendency was far greater for DPSC than for SHED (see **Chapter 2.208, Artificial Extracellular Matrices to Functionalize Biomaterial Surfaces**).

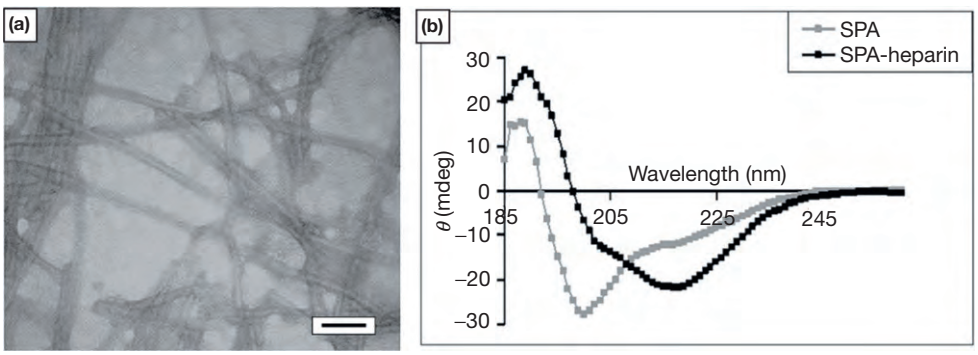

Figure 27 (a) TEM of SPA–heparin nanofibrous gel (stained) and (b) CD spectra showing predominant β-sheet formation for SPA in the presence of heparin (black) compared to predominantly helix formation without heparin (gray). The SPA–heparin spectra have been corrected for contribution by heparin alone. Adapted from Rajangam, K.; Arnold, M. S.; Rocco, M. A.; Stupp, S. I. *Biomaterials* **2008**, *29*, 3298–3305.

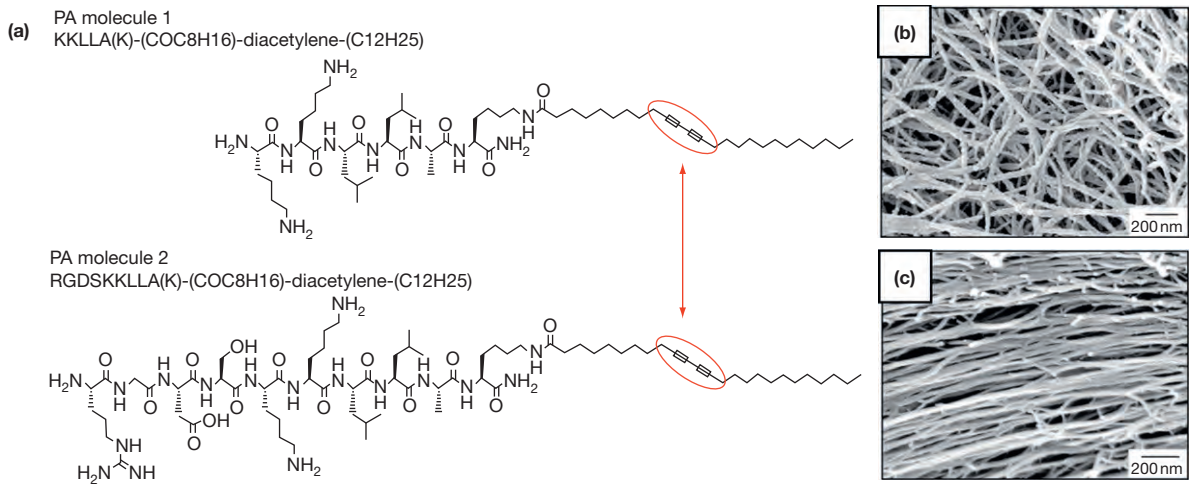

Figure 28 Chemical structure of photocurable and/or bioactive peptide amphiphiles (a) and their SEM images of fibrous nanostructures (randomly oriented, b, and aligned, c). Adapted from Mata, A.; Hsu, L.; Capito, R.; Aparicio, C.; Henrikson, K.; Stupp, S. I. *Soft Matter* **2009**, *5*, 1228–1236.

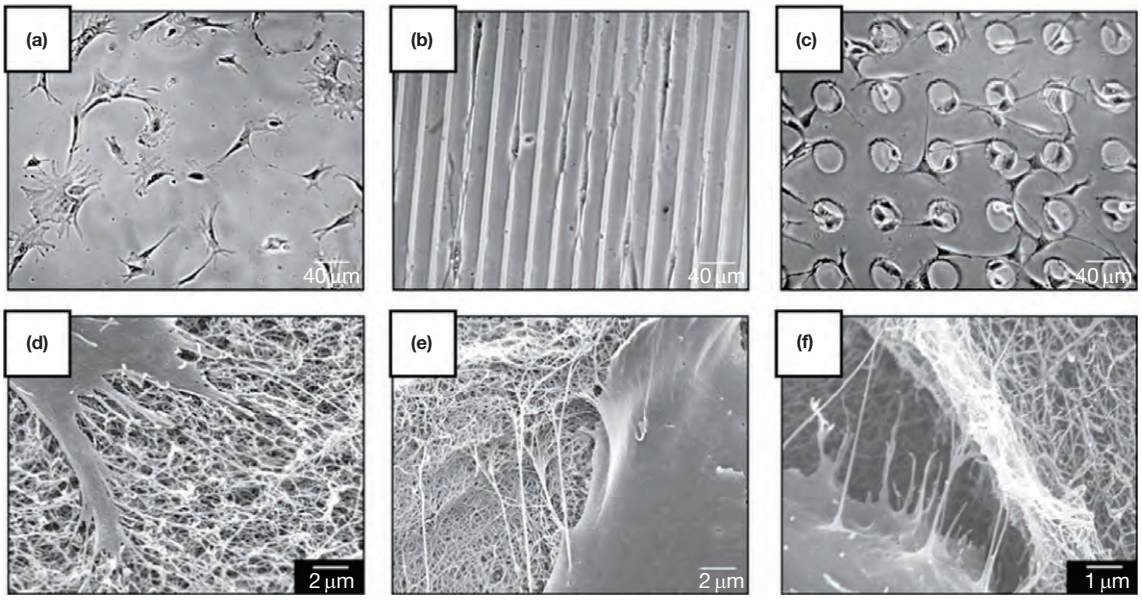

Figure 29 SEM analysis of hMSCs cultured on nanofibrous PA gel surfaces. (a, d) Randomly orientation no micron-sized topology, (b, e) aligned microchannels, and (c, f) 40-μm-sized patterned holes. Adapted from Mata, A.; Hsu, L.; Capito, R.; Aparicio, C.; Henrikson, K.; Stupp, S. I. *Soft Matter* **2009**, *5*, 1228–1236.

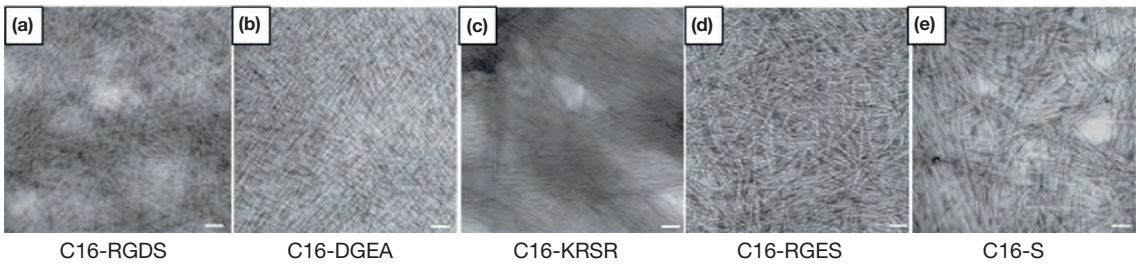

Figure 30 TEM images of nanofibers that form multilayered PA surface coatings of (a) C16-RGDS, (b) C16-DGEA, (c) C16-KRSR, (d) C16-RGES, and (e) C16-S. The PAs were prepared at 0.1 wt% concentrations. Scale bar represents 40 nm. Adapted from Anderson, J. M.; Kushwaha, M.; Tambralli, A.; Bellis, S. L.; Camata, R. P.; Jun, H. W. *Biomacromolecules* **2009**, *10*, 2935–2944.

4.415.6.8. Bioactivation of Metallic Surfaces

Titanium-based metallic implants are popular choices for orthopedic, dental, and bone replacements possessing great biocompatibility and mechanical stability. Stupp and coworkers demonstrated that self-assembling bioactive PAs are suitable surface modifiers for Ti–6Al–4V metallic foams[128,129] and nickel–titanium (NiTi) shape memory metallic alloys (see **Chapter 2.201, Bio-inspired Silica Nanomaterials for Biomedical Applications**).[130] Branched PAs identical to those developed by Guler *et al.*[131,132] were utilized which contained the bioactive sequence RGD (**Figure 34**). NiTi metal sheets were first polished, cleaned, and silanized (using aminopropyltriethoxysilane (APTES)), then a 0.05 wt% PA solution was drop-cast onto the metallic surface. C16-A_3L_3K-ERGDS (BRGD-PA2), in particular, was used to achieve the bioactivation of nonbiologically responsive surfaces. Primary bovine pulmonary artery endothelial cells (CPAE) and mouse calvarial preosteoblastic cells (MC3T3-E1) were cultured on bioactivated metal surfaces to evaluate the efficacy of the surface engineering procedures. Proliferation assays indicated that MC3T3-E1 and CPAE cells grew best on TiNi surfaces silanized and then covalently modified with the branched PA (**Figure 35**).

4.415.7. Summary and Future Directions

Peptides amphiphiles are ideal molecular building blocks that self-assemble into hierarchical bioactive structures with controlled and defined physicochemical properties.[18,133] Two additional promising platforms of amphiphilic biomaterials involving bioactive moieties and nanosized structures described here can be used to explore biomedical applications[6] including regenerative medicine,[134] theranostics,[135] and drug delivery,[136,137] exploiting the stability of the final structures.

The utilization of *polymeric micelles* has been well investigated for multiple biomedical applications,[138–140] and here, we summarize a few recent excerpts. First, MacKay *et al.* formulated a recombinant production of ~62 kD polypeptide that self-assembles into spherical micelles consisting of a

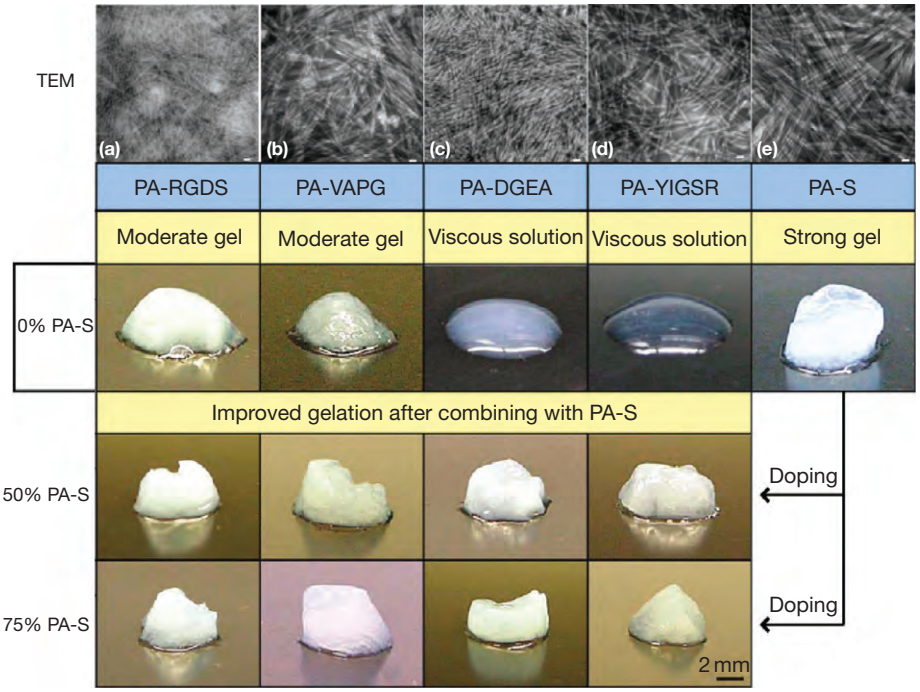

Figure 31 Macrophotographs of viscosity-controlled peptide amphiphile gels (hydrogels). Adapted from Anderson, J. M.; Andukuri, A.; Lim, D. J.; Jun, H. W. *ACS Nano* **2009**, *3*, 3447–3454.[126]

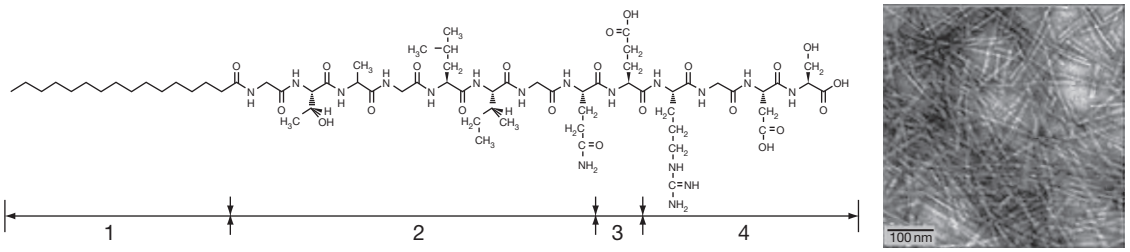

Figure 32 Chemical structure of C16-GTAGLIGQERGDS. The numbering refers to function: (1) hydrocarbon chain, (2) enzyme-cleavable site, (3) calcium binding, and (4) cell adhesion promoting sequence. A representative nanofibrous TEM is given. Adapted from Galler, K. M.; Cavender, A.; Yuwono, V.; *et al*. *Tissue Eng. A* **2008**, *14*, 2051–2058.

core–shell structure[141]; a hydrophobic core incorporating a hydrophobic drug (i.e., doxorubicin) covered with a hydrophilic corona shell made up predominantly of elastin-like protein sequence XGVPG (X = V,A,G) – herein, the PA will be referred to as CP-dox (chimeric polypeptide doxorubicin as coined by the original authors). The main feature of this particular system is that the self-assembled spherical micelles are sub-100 nm and the hydrophobic moiety can be any small molecule with aromatic groups. The second feature is that the attached therapeutic molecule was acid-labile which meant that the anticancer drug, doxorubicin, will release upon cellular uptake and endosomal or lysosomal processing (pH < 6). *In vivo* studies involving the treatment of malignant tumors with CP-dox revealed 96% tumor volume decrease compared to 50% decrease when only treated with doxorubicin. In addition, animal survival rate increased more than twofold when doxorubicin-only control increased 30%. This CP-dox also decreased the accumulation of doxorubicin in the animal's heart, important for overcoming any dose-limiting side effects that may result in cardiomyopathy. Second, Hubbell and coworkers,[142] more recently, developed a polymeric micelle system that incorporates carbon monoxide (CO)-releasing ruthenium (Ru) metal centers. The polymeric backbone comprises hydrophilic PEG, $Ru(CO)_3Cl$ instilled poly(ornithine acrylamide) and hydrophobic poly(*n*-butylacrylamide); it is a triblock copolymer system that self-assembles into 30–40 nm spherical micelles. The CO molecules release in a sustained manner *in vitro* after cysteine introduction (to 80% FBS cell medium) and effectively attenuated the LPS or Toll-like receptor ligand-induced NF-kB (proinflammatory transcription factor) activation of human acute monocytic leukemia cells, THP-1. Third, functional recovery after SCI was achieved via a diblock copolymer monomethoxy poly(ethylene glycol)-poly(D,L-lactic acid) self-assembled into 60 nm spherical micelles. The polymeric micelles, in this case, deterred the spreading of damage caused by the primary SCI process involving the neuronal cell membrane breakage and calcium influx. It is interesting to note that Stupp and coworkers reported the use

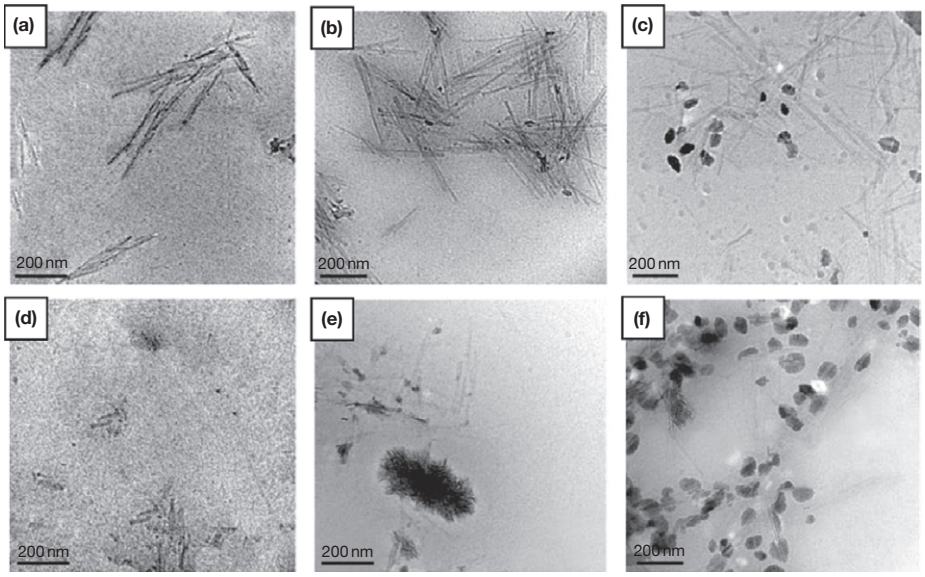

Figure 33 TEM images (cryo-TEM analysis) showing mineral (spherical shapes) deposition for cells treated with osteogenic supplements (4 week culture). (a) SHED control, (b) SHED cultured with betaGP and dex, (c) SHED cultures with KPh and dex, (d) DPSC control, (e) DPSC cultured with betaGP and dex, and (f) DPSC cultured with KPh and dex. Adapted from Galler, K. M.; Cavender, A.; Yuwono, V.; *et al*. *Tissue Eng. A* **2008**, *14*, 2051–2058.

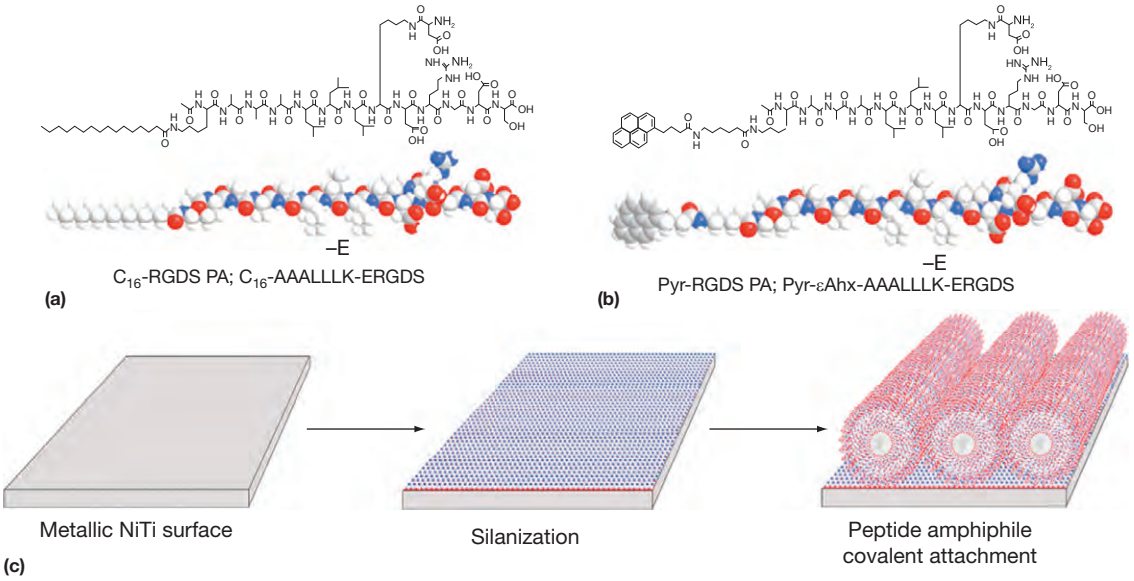

Figure 34 Titanium surface coated with peptide amphiphiles (chemical structure, molecular representation provided in a and b) and their fibrous schematic (c). Adapted from Sargeant, T. D.; Rao, M. S.; Koh, C. Y.; Stupp, S. I. *Biomaterials* **2008**, *29*, 1085–1098.

of a nanofibrous micellar matrix to promote functional recovery after SCI, as highlighted in **Section 4.415.6.2.**[117,143] It will be interesting to see how the SCI rescue process differs between the two micellar systems where one is spherical and the other fibrous. More up-to-date research involving polymeric micelles can be found in reviews by Bae and colleagues,[144] Bae and Kataoka,[145] Park and coworkers,[146] and Hennink and coworkers.[147]

The second platform involves *organic–inorganic nanocomposites* or *multifunctional nanoparticle systems* (MFNPS) (**Figure 9**).[15,148,149] In one example, Ruoslahti and coworkers[100,150] utilized inorganic oxide nanoparticles that were magnetic resonance imaging (MRI)-active and incorporating a targeting feature (i.e., CREKA) to home-in on tumor tissue. The core material is iron oxide, and the surface chemistry is such that different peptides and small molecules can be attached in a facile manner. Second, Labhasetwar and colleagues,[151] more recently, demonstrated image-guided drug therapy to treat xenograft breast tumors in mice utilizing iron oxide nanoparticles (10–25 nm magnetite particles) coated with oleic acid, Pluronic F127, and incorporating hydrophobic near-IR dye molecules (overall hydrodynamic diameter

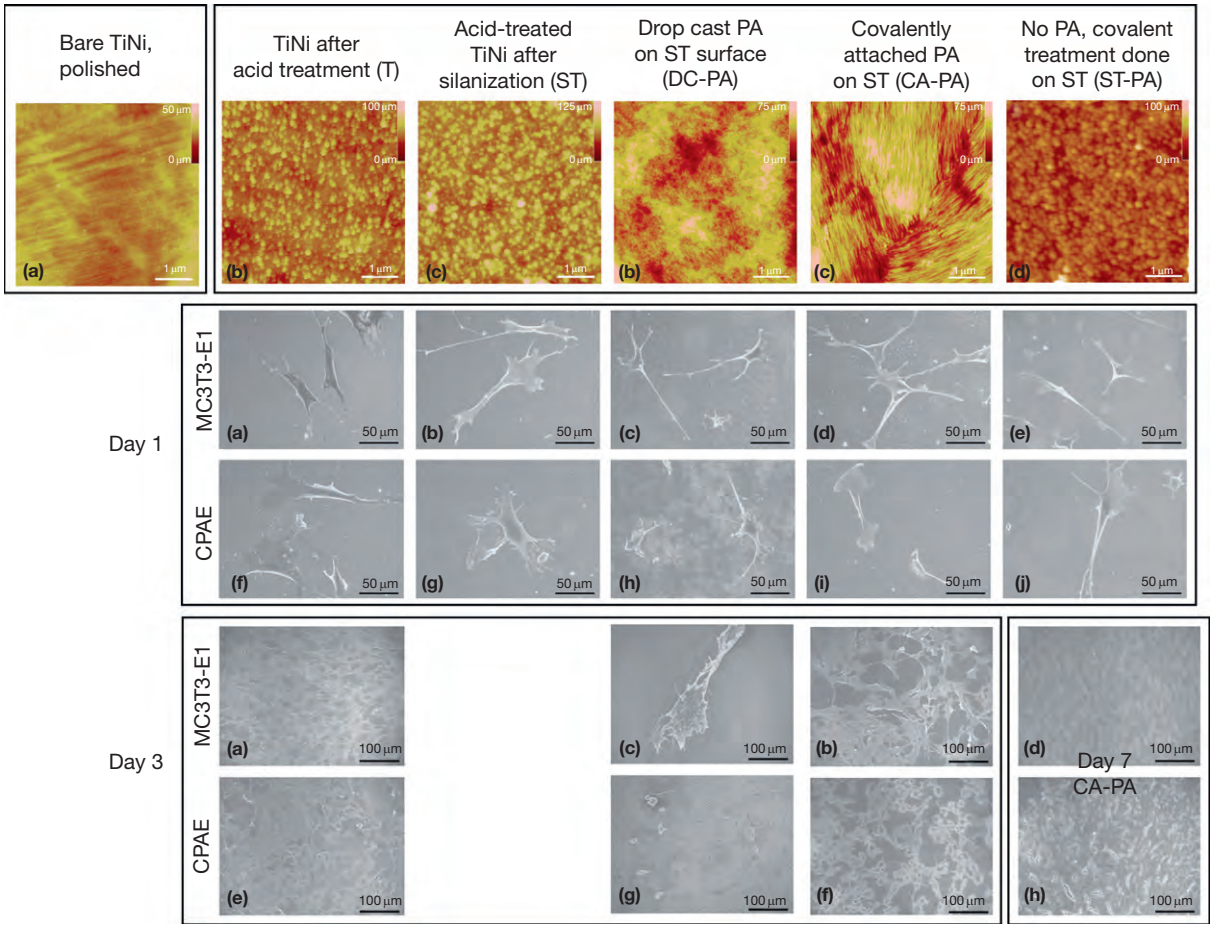

Figure 35 Atomic Force Microscopy analysis of TiNi surfaces with and without peptide amphiphiles (first row). Cells grown on each surface-engineered TiNi material: day 1 (2nd two rows), day 3 (3rd two rows, and day 7 only for TiNi surface with covalently attached peptide amphiphile. Adapted from Sargeant, T. D.; Rao, M. S.; Koh, C. Y.; Stupp, S. I. *Biomaterials* **2008**, *29*, 1085–1098.

determined via DLS was ~240 nm). *In vitro* toxicity testing using MCF7 breast cancer cells revealed no apparent toxicity from the prepared particle system. Inorganic species-incorporating nanomaterials will be useful for detecting small tumors in the body with high precision and sensitivity,[152–157] but the key obstacle will be the body's inability to process highly dense and essentially non-biodegrading inorganic structures[158–161] such as iron oxide, silicon dioxide, and titanium dioxide after prolonged accumulation. Biodistribution studies have shown nanoparticle accumulation in key organs such as the liver, spleen, and kidney[162–164] which can be long-term risk factors for patients. Of course, the patient-to-patient treatment response variations and dose-dependent-toxicity over multiple time domains will be difficult to extensively study on humans,[149] and so, it will be important and crucial to develop *in vitro* cell-based assessment models[163,165] with these particular platforms of biomaterials. Further examples of successful utilization of hard nanoparticles in biomedical applications are recently reviewed.[15,48]

The modulated stability of injectable self-assembled structures made up of amphiphilic constructs that include PAs and copolymers will be key for the development of new biomaterials for biomedical applications. Recently, Tirrell and coworkers[166] explored the internalization mechanism of PAs using an *in vitro* cancer cell model (i.e., SJSA-1). The particular PA consisted of a C16 tail and a peptide sequence derived from p53, a tumor suppressor protein (p5314-29, Pep; LSQETFSDLWKLLPEN). The results point to individual PA monomers (or unimers) being taken up by cells rather than the entire intact self-assembled spherical micelles (soft nanoparticles) being internalized, as often observed in solid inorganic (hard) nanoparticle endocytosis[46,48,161,167]; inorganic oxide nanoparticles, as mentioned earlier, are condensed solids (density of 2–5 g ml^{-1}),[168] and cellular organisms will not be able to process or degrade them using preexisting cellular machineries such as the lysosome or the lysozyme protein.[169–174] Aforementioned monomer dissociation/uptake mechanism will increase the instability of micelles introduced to the body, as multiple biological entities (i.e., proteins, ions, tissues, cells) undergoing dynamic changes are present *in vivo*. Park, Cheng, and colleagues[175] utilized an ~60-nm-sized block copolymer micelle system made from PEG-PDLLA (poly(ethylene glycol)-b-poly(D,L-lactic acid)) to demonstrate that the dynamic instability of polymeric micelles is important for the delivery of hydrophobic small molecules encapsulated inside the micelles to the cell cytosol via membrane-mediated

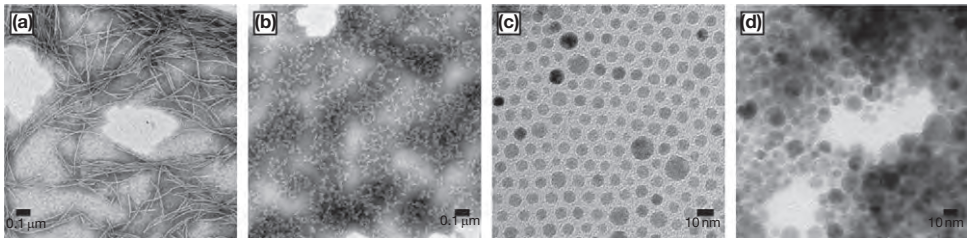

Figure 36 TEM images of C16-W3K-RGD and iron oxide nanoparticles. (a) C16-W3K-RGD peptide amphiphiles showing worm-like fibrous morphologies, negatively stained with PTA (phosphotungstic acid), (b) C16-W3K-RGD fixed and negatively stained, showing globular particle-like morphologies, (c) magnetite iron oxide nanoparticles prepared in organic phase, and (d) aggregated magnetite nanoparticles after phase transfer with C16-W3K-RGD peptide amphiphiles.

transportation. The challenge of self-assembled structure (i.e., micelles, vesicles) instability can be overcome by employing chemistry-based techniques such as cross-linking (via polymerization) of the hydrocarbon chains,[176,177] as demonstrated by Biesalski *et al.*,[178] or utilizing hard nanoparticles such as iron oxides and metallic particles that are magnetically susceptible[153,155,179–184] and surface-engineering the nanoparticles with bioactive functionalities. It will be important, however, to control the degree of polymerization, as extensive cross-linking or fixation will lead to the loss of self-assembling capabilities of PAs that may be crucial for bioactivity control (**Figure 36(a,b)**); moreover, the application-specific development of hybrid nanoparticles will be crucial as aggregations (**Figure 36(c,d)**), and oxidation of the core oxide nanoparticles may lead to decreased magnetic susceptibility and injectability for *in vivo* experiments.

The development of PA-based surface engineering of lipid bilayers, spherical micelles, and nanofibrous micelles has advanced in great quality and quantity in the past three decades, with continued increase in interest and work involving PAs (see **Chapter 5.531, Peripheral Nerve Regeneration** and **Chapter 5.532, Nerve Tissue Engineering**).[81,109,185–188] In particular, many research groups around the world developed multidisciplinary projects linked to translational medicine; regenerative medicine applications such as nerve/bone regeneration, wound healing, stem cell differentiation, and transplantation. In order for such practical applications to further advance the precise understanding of surface engineering principles, stability of assembled structures, biodistribution, and the cell–material interface created by peptide-based materials and living systems will be very important. Two key aspects of PAs' capabilities to control biological systems will be to control protein and nucleic acid function within and outside the cell[103,166,189–194] and to three-dimensionally mimic the naturally occurring extracellular matrices[7,11,73,115,118,195–197] – if these two functions are combined and well defined, then some of the undefined components pertaining to biomedical applications, such as stem cell tissue engineering and targeted drug delivery, can incorporate more quantitative subcomponents.

Acknowledgments

WHS thanks the Otis Williams Postdoctoral Fellowship in Bioengineering, UCSB (sponsored by the Santa Barbara Foundation). In addition, the authors thank the Armed Forces of Regenerative Medicine (AFIRM) and the University of California, Berkeley for funding. The magnetite iron oxide nanoparticles experimented with in **Figure 36** were a kind gift from Dr. Cafer Yavuz.

References

1. Atala, A. *Nat. Clin. Pract. Urol.* **2005**, *2*, 143–149.
2. Castner, D. G.; Ratner, B. D. *Surf. Sci.* **2002**, *500*, 28–60.
3. Dillow, A. K.; Tirrell, M. *Curr. Opin. Solid State Mat. Sci.* **1998**, *3*, 252–259.
4. Griffith, L. G. *Acta Mater.* **2000**, *48*, 263–277.
5. Hench, L. L. *J. Am. Ceram. Soc.* **1998**, *81*, 1705–1728.
6. Langer, R.; Tirrell, D. A. *Nature* **2004**, *428*, 487–492.
7. Little, L.; Healy, K. E.; Schaffer, D. *Chem. Rev.* **2008**, *108*, 1787–1796.
8. Lutolf, M. P.; Hubbell, J. A. *Nat. Biotechnol.* **2005**, *23*, 47–55.
9. Ma, P. X. *Adv. Drug Deliv. Rev.* **2008**, *60*, 184–198.
10. Ratner, B. D.; Bryant, S. J. *Annu. Rev. Biomed. Eng.* **2004**, *6*, 41–75.
11. Saha, K.; Pollock, J. F.; Schaffer, D. V.; Healy, K. E. *Curr. Opin. Chem. Biol.* **2007**, *11*, 381–387.
12. Shin, H.; Jo, S.; Mikos, A. G. *Biomaterials* **2003**, *24*, 4353–4364.
13. Stevens, M. M.; George, J. H. *Science* **2005**, *310*, 1135–1138.
14. Stupp, S. I.; Donners, J.; Li, L. S.; Mata, A. *MRS Bull.* **2005**, *30*, 864–873.
15. Suh, W. H.; Suh, Y. H.; Stucky, G. D. *Nano Today* **2009**, *4*, 27–36.
16. Suslick, K. S.; Price, G. J. *Annu. Rev. Mater. Sci.* **1999**, *29*, 295–326.
17. Tirrell, M.; Kokkoli, E.; Biesalski, M. *Surf. Sci.* **2002**, *500*, 61–83.
18. Tu, R. S.; Tirrell, M. *Adv. Drug Deliv. Rev.* **2004**, *56*, 1537–1563.
19. Ying, J. Y. *Nano Today* **2009**, *4*, 1–2.
20. Zhang, S. G. *Nat. Biotechnol.* **2003**, *21*, 1171–1178.
21. Holten-Andersen, N.; Fantner, G. E.; Hohlbauch, S.; Waite, J. H.; Zok, F. W. *Nat. Mater.* **2007**, *6*, 669–672.
22. Miserez, A.; Schneberk, T.; Sun, C. J.; Zok, F. W.; Waite, J. H. *Science* **2008**, *319*, 1816–1819.
23. Ruoslahti, E. *Annu. Rev. Biochem.* **1988**, *57*, 375–413.
24. Ruoslahti, E. *J. Clin. Investig.* **1991**, *87*, 1–5.
25. Waite, J. H.; Andersen, N. H.; Jewhurst, S.; Sun, C. J. *J. Adhes.* **2005**, *81*, 297–317.
26. Cha, J. N.; Stucky, G. D.; Morse, D. E.; Deming, T. J. *Nature* **2000**, *403*, 289–292.
27. Lee, H.; Dellatore, S. M.; Miller, W. M.; Messersmith, P. B. *Science* **2007**, *318*, 426–430.
28. McKenna, B. J.; Waite, J. H.; Stucky, G. D. *Cryst. Growth Des.* **2009**, *9*, 4335–4343.
29. Pierschbacher, M. D.; Ruoslahti, E. *Nature* **1984**, *309*, 30–33.
30. Ruoslahti, E. *Annu. Rev. Cell Dev. Biol.* **1996**, *12*, 697–715.
31. Ruoslahti, E.; Pierschbacher, M. D. *Science* **1987**, *238*, 491–497.
32. Waite, J. H. *Nat. Mater.* **2008**, *7*, 8–9.
33. Denes, F. S.; Manolache, S. *Prog. Polym. Sci.* **2004**, *29*, 815–885.
34. PoncinEpaillard, F.; Brosse, J. C.; Falher, T. *Macromolecules* **1997**, *30*, 4415–4420.
35. Suh, W. H.; Suslick, K. S. *J. Am. Chem. Soc.* **2005**, *127*, 12007–12010.
36. Frost, F.; Ziberi, B.; Schindler, A.; Rauschenbach, B. *Appl. Phys. A Mater. Sci. Process* **2008**, *91*, 551–559.
37. Lee, E. H.; Lewis, M. B.; Blau, P. J.; Mansur, L. K. *J. Mater. Res.* **1991**, *6*, 610–628.
38. Benson, R. S. *Nucl. Instrum. Methods Phys. Res. Sect. B* **2002**, *191*, 752–757.

39. Fischbach, C.; Tessmar, J.; Lucke, A.; *et al*. *Science* **2001**, *491*, 333–345.
40. Heitz, J.; Gumpenberger, T.; Kahr, H.; Romanin, C. *Biotechnol. Appl. Biochem.* **2004**, *39*, 59–69.
41. Iwaguch, S.; Matsumura, K.; Tokuoka, Y.; Wakui, S.; Kawashima, N. *Colloids Surf. B* **2002**, *25*, 299–304.
42. Bang, J. H.; Suslick, K. S. *Adv. Mater.* **2010**, *22*, 1039–1059.
43. Hermanson, G. T. *Bioconjugate Techniques*. Academic Press: San Diego, CA, 1996.
44. Boettcher, S. W.; Strandwitz, N. C.; Schierhorn, M.; Lock, N.; Lonergan, M. C.; Stucky, G. D. *Nat. Mater.* **2007**, *6*, 592–596.
45. Caruso, F. *Adv. Mater.* **2001**, *13*, 11–22.
46. Suh, W. H.; Jang, A. R.; Suh, Y. H.; Suslick, K. S. *Adv. Mater.* **2006**, *18*, 1832–1837.
47. Toublan, F. J. J.; Boppart, S.; Suslick, K. S. *J. Am. Chem. Soc.* **2006**, *128*, 3472–3473.
48. Suh, W. H.; Suslick, K. S.; Stucky, G. D.; Suh, Y. H. *Prog. Neurobiol.* **2009**, *87*, 133–170.
49. Saha, K.; Irwin, E. F.; Kozhukh, J.; Schaffer, D. V.; Healy, K. E. *J. Biomed. Mater. Res.* **2007**, *81A*, 240–249.
50. Saha, K.; Keung, A. J.; Irwin, E. F.; *et al*. *Biophys. J.* **2008**, *95*, 4426–4438.
51. Bernard, A.; Delamarche, E.; Schmid, H.; Michel, B.; Bosshard, H. R.; Biebuyck, H. *Langmuir* **1998**, *14*, 2225–2229.
52. Bernard, A.; Renault, J. P.; Michel, B.; Bosshard, H. R.; Delamarche, E. *Adv. Mater.* **2000**, *12*, 1067–1070.
53. Chen, C. S.; Mrksich, M.; Huang, S.; Whitesides, G. M.; Ingber, D. E. *Biotechnol. Prog.* **1998**, *14*, 356–363.
54. Kane, R. S.; Takayama, S.; Ostuni, E.; Ingber, D. E.; Whitesides, G. M. *Biomaterials* **1999**, *20*, 2363–2376.
55. Mrksich, M.; Dike, L. E.; Tien, J.; Ingber, D. E.; Whitesides, G. M. *Exp. Cell Res.* **1997**, *235*, 305–313.
56. Smith, R. K.; Lewis, P. A.; Weiss, P. S. *Prog. Surf. Sci.* **2004**, *75*, 1–68.
57. Xia, Y. N.; Whitesides, G. M. *Annu. Rev. Mater. Sci.* **1998**, *28*, 153–184.
58. Zhang, S. G.; Yan, L.; Altman, M.; *et al*. *Biomaterials* **1999**, *20*, 1213–1220.
59. Piner, R. D.; Zhu, J.; Xu, F.; Hong, S. H.; Mirkin, C. A. *Science* **1999**, *283*, 661–663.
60. Salaita, K.; Wang, Y. H.; Mirkin, C. A. *Nat. Nanotechnol.* **2007**, *2*, 145–155.
61. Boland, T.; Xu, T.; Damon, B.; Cui, X. *Biotechnol. J.* **2006**, *1*, 910–917.
62. Calvert, P. *Chem. Mater.* **2001**, *13*, 3299–3305.
63. Delaney, J. T.; Smith, P. J.; Schubert, U. S. *Soft Matter* **2009**, *5*, 4866–4877.
64. Roth, E. A.; Xu, T.; Das, M.; Gregory, C.; Hickman, J. J.; Boland, T. *Biomaterials* **2004**, *25*, 3707–3715.
65. Sirringhaus, H.; Kawase, T.; Friend, R. H.; *et al*. *Science* **2000**, *290*, 2123–2126.
66. Sirringhaus, H.; Shimoda, T. *MRS Bull.* **2003**, *28*, 802–804.
67. Israelachvili, J. N.; Ninham, B. W. *J. Colloid Interface Sci.* **1977**, *58*, 14–25.
68. Leckband, D.; Israelachvili, J. *Q. Rev. Biophys.* **2001**, *34*, 105–267.
69. Euliss, L. E.; Grancharov, S. G.; O'Brien, S.; *et al*. *Nano Lett.* **2003**, *3*, 1489–1493.
70. Israelachvili, J. N.; Mitchell, D. J.; Ninham, B. W. *Biochim. Biophys. Acta* **1977**, *470*, 185–201.
71. Liang, H. J.; Whited, G.; Nguyen, C.; Stucky, G. D. *Proc. Natl. Acad. Sci. USA* **2007**, *104*, 8212–8217.
72. Uskokovic, V. *Adv. Colloid Interface Sci.* **2008**, *141*, 37–47.
73. Stroumpoulis, D.; Zhang, H. N.; Rubalcava, L.; Gliem, J.; Tirrell, M. *Langmuir* **2007**, *23*, 3849–3856.
74. Shimada, T.; Lee, S.; Bates, F. S.; Hotta, A.; Tirrell, M. *J. Phys. Chem. B* **2009**, *113*, 13711–13714.
75. Palmer, L. C.; Stupp, S. I. *Acc. Chem. Res.* **2008**, *41*, 1674–1684.
76. Peters, D.; Kastantin, M.; Kotamraju, V. R.; *et al*. *Proc. Natl. Acad. Sci. USA* **2009**, *106*, 9815–9819.
77. Texter, J.; Tirrell, M. *AIChE J.* **2001**, *47*, 1706–1710.
78. Tirrell, M. V.; Katz, A. *MRS Bull.* **2005**, *30*, 700–704.
79. Tomalia, D. A.; Wang, Z. G.; Tirrell, M. *Curr. Opin. Colloid Interface Sci.* **1999**, *4*, 3–5.
80. Yu, Y. C.; Berndt, P.; Tirrell, M.; Fields, G. B. *J. Am. Chem. Soc.* **1996**, *118*, 12515–12520.
81. Berndt, P.; Fields, G. B.; Tirrell, M. *J. Am. Chem. Soc.* **1995**, *117*, 9515–9522.
82. Rezler, E. M.; Khan, D. R.; Tu, R.; Tirrell, M.; Fields, G. B. Peptide mediated targeting of liposomes to tumor cells. In *Peptide Characterization and Application Protocols*, 2007; pp 269–298.
83. Yu, Y. C.; Pakalns, T.; Dori, Y.; McCarthy, J. B.; Tirrell, M.; Fields, G. B. In *Solid-Phase Peptide Synthesis*; Fields, G. B., Ed.; Academic Press: San Diego, 1997; pp 571–587.
84. Yu, Y. C.; Roontga, V.; Daragan, V. A.; Mayo, K. H.; Tirrell, M.; Fields, G. B. *Biochemistry* **1999**, *38*, 1659–1668.
85. Yu, Y. C.; Tirrell, M.; Fields, G. B. *J. Am. Chem. Soc.* **1998**, *120*, 9979–9987.
86. Chan, W. C.; White, P. D. *Fmoc Solid Phase Peptide Synthesis: A Practical Approach*. Oxford University Press: Oxford and New York, 2000.
87. Fields, G. B.; Noble, R. L. *Int. J. Pept. Protein Res.* **1990**, *35*, 161–214.
88. Fields, G. B.; Tian, Z.; Barany, G. In *Synthetic Peptides: A User's Guide*; Grant, G. A., Ed.; WH Freeman & Co: New York, 1992; pp 77–183.
89. Hachmann, J.; Lebl, M. *J. Comb. Chem.* **2006**, *8*, 149.
90. Kaiser, E.; Colescott, R. L.; Bossinger, C. D.; Cook, P. I. *Anal. Biochem.* **1970**, *34*, 595.
91. Jones, M. N. *Adv. Coll. Interfac. Sci.* **1995**, *54*, 93–128.
92. Stroumpoulis, D.; Parra, A.; Tirrell, M. *AIChE J.* **2006**, *52*, 2931–2937.
93. Dori, Y.; Bianco-Peled, H.; Satija, S. K.; Fields, G. B.; McCarthy, J. B.; Tirrell, M. *J. Biomed. Mater. Res.* **2000**, *50*, 75–81.
94. Prime, K. L.; Whitesides, G. M. *Science* **1991**, *252*, 1164–1167.
95. Prime, K. L.; Whitesides, G. M. *J. Am. Chem. Soc.* **1993**, *115*, 10714–10721.
96. Sigal, G. B.; Mrksich, M.; Whitesides, G. M. *J. Am. Chem. Soc.* **1998**, *120*, 3464–3473.
97. Singhvi, R.; Kumar, A.; Lopez, G. P.; *et al*. *Science* **1994**, *264*, 696–698.
98. Karmali, P. P.; Kotamraju, V. R.; Kastantin, M.; *et al*. *Nanomed. Nanotechnol. Biol. Med.* **2009**, *5*, 73–82.
99. Maraganore, J. M.; Bourdon, P.; Jablonski, J.; Ramachandran, K. L.; Fenton, J. W. *Biochemistry* **1990**, *29*, 7095–7101.
100. Simberg, D.; Duza, T.; Park, J. H.; *et al*. *Proc. Natl. Acad. Sci. USA* **2007**, *104*, 932–936.
101. Laakkonen, P.; Akerman, M. E.; Biliran, H.; *et al*. *Proc. Natl. Acad. Sci. USA* **2004**, *101*, 9381–9386.
102. Laakkonen, P.; Porkka, K.; Hoffman, J. A.; Ruoslahti, E. *Nat. Med.* **2002**, *8*, 751–755.
103. Aulisa, L.; Forraz, N.; McGuckin, C.; Hartgerink, J. D. *Acta Biomater.* **2009**, *5*, 842–853.
104. Reulen, S. W. A.; Brusselaars, W. W. T.; Langereis, S.; Mulder, W. J. M.; Breurken, M.; Merkx, M. *Bioconjug. Chem.* **2007**, *18*, 590–596.
105. Reulen, S. W. A.; Dankers, P. Y. W.; Bomans, P. H. H.; Meijer, E. W.; Merkx, M. *J. Am. Chem. Soc.* **2009**, *131*, 7304–7312.
106. Dawson, P. E.; Muir, T. W.; Clark-Lewis, I.; Kent, S. B. H. *Science* **1994**, *266*, 776–779.
107. Hackeng, T. M.; Griffin, J. H.; Dawson, P. E. *Proc. Natl. Acad. Sci. USA* **1999**, *96*, 10068–10073.
108. Yamada, K.; Ihara, H.; Ide, T.; Fukumoto, T.; Hirayama, C. *Chem. Lett.* **1984**, 1713–1716.
109. Nakashima, N.; Asakuma, S.; Kim, J. M.; Kunitake, T. *Chem. Lett.* **1984**, 1709–1712.
110. Hartgerink, J. D.; Beniash, E.; Stupp, S. I. *Proc. Natl. Acad. Sci. USA* **2002**, *99*, 5133–5138.
111. Tirrell, M. WFPC Project 4.4.5: Modular, switchable, synthetic, extracellular matrices for regenerative medicine. In *AFIRM Annual Report*; Vandre, R., Ed.; 2009; pp II-53–II-56.
112. Chu-Kung, A. F.; Bozzelli, K. N.; Lockwood, N. A.; Haseman, J. R.; Mayo, K. H.; Tirrell, M. V. *Bioconjug. Chem.* **2004**, *15*, 530–535.
113. Lockwood, N. A.; Haseman, J. R.; Tirrell, M. V.; Mayo, K. H. *Biochem. J.* **2004**, *378*, 93–103.
114. Mayo, K. H.; Haseman, J.; Young, H. C.; Mayo, J. W. *Biochem. J.* **2000**, *349*, 717–728.
115. Silva, G. A.; Czeisler, C.; Niece, K. L.; *et al*. *Science* **2004**, *303*, 1352–1355.
116. Niece, K. L.; Czeisler, C.; Sahni, V.; *et al*. *Biomaterials* **2008**, *29*, 4501–4509.
117. Tysseling-Mattiace, V. M.; Sahni, V.; Niece, K. L.; *et al*. *J. Neurosci.* **2008**, *28*, 3814–3823.
118. Ananthanarayanan, B.; Little, L.; Schaffer, D. V.; Healy, K. E.; Tirrell, M. *Biomaterials* **2010**, *31*, 8706–8715.
119. Webber, M. J.; Tongers, J.; Renault, M.-A.; Roncalli, J. G.; Losordo, D. W.; Stupp, S. I. *Acta Biomater.* **2010**, *6*, 3–11.
120. Rajangam, K.; Arnold, M. S.; Rocco, M. A.; Stupp, S. I. *Biomaterials* **2008**, *29*, 3298–3305.
121. Ghanaati, S.; Webber, M. J.; Unger, R. E.; *et al*. *Biomaterials* **2009**, *30*, 6202–6212.
122. Mata, A.; Hsu, L.; Capito, R.; Aparicio, C.; Henrikson, K.; Stupp, S. I. *Soft Matter* **2009**, *5*, 1228–1236.
123. Huang, Z.; Sargeant, T. D.; Hulvat, J. F.; *et al*. *J. Bone Miner. Res.* **2008**, *23*, 1995–2006.
124. Anderson, J. M.; Kushwaha, M.; Tambralli, A.; Bellis, S. L.; Camata, R. P.; Jun, H. W. *Biomacromolecules* **2009**, *10*, 2935–2944.
125. Jun, H. W.; Yuwono, V.; Paramonov, S. E.; Hartgerink, J. D. *Adv. Mater.* **2005**, *17*, 2612.

126. Anderson, J. M.; Andukuri, A.; Lim, D. J.; Jun, H. W. *ACS Nano* **2009**, *3*, 3447–3454.
127. Galler, K. M.; Cavender, A.; Yuwono, V.; *et al*. *Tissue Eng. A* **2008**, *14*, 2051–2058.
128. Sargeant, T. D.; Guler, M. O.; Oppenheimer, S. M.; *et al*. *Biomaterials* **2008**, *29*, 161–171.
129. Sargeant, T. D.; Oppenheimer, S. M.; Dunand, D. C.; Stupp, S. I. *J. Tissue Eng. Regen. Med*. **2008**, *2*, 455–462.
130. Sargeant, T. D.; Rao, M. S.; Koh, C. Y.; Stupp, S. I. *Biomaterials* **2008**, *29*, 1085–1098.
131. Guler, M. O.; Hsu, L.; Soukasene, S.; Harrington, D. A.; Hulvat, J. F.; Stupp, S. I. *Biomacromolecules* **2006**, *7*, 1855–1863.
132. Guler, M. O.; Soukasene, S.; Hulvat, J. F.; Stupp, S. I. *Nano Lett*. **2005**, *5*, 249–252.
133. Stupp, S. I. *MRS Bull*. **2005**, *30*, 546–553.
134. Atala, A. *J. Tissue Eng. Regen. Med*. **2007**, *1*, 83–96.
135. McCarthy, J. R.; Weissleder, R. *Adv. Drug Deliv. Rev*. **2008**, *60*, 1241–1251.
136. Mandal, A. S.; Biswas, N.; Karim, K. M.; *et al*. *J. Control. Release* **2010**, *147*, 314–325.
137. Uhrich, K. E.; Cannizzaro, S. M.; Langer, R. S.; Shakesheff, K. M. *Chem. Rev.* **1999**, *99*, 3181–3198.
138. Allen, T. M.; Cullis, P. R. *Science* **2004**, *303*, 1818–1822.
139. Kataoka, K.; Kwon, G. S.; Yokoyama, M.; Okano, T.; Sakurai, Y. *J. Control. Release* **1993**, *24*, 119–132.
140. Kwon, G. S.; Kataoka, K. *Adv. Drug Deliv. Rev*. **1995**, *16*, 295–309.
141. MacKay, J. A.; Chen, M.; McDaniel, J. R.; Liu, W.; Simnick, A. J.; Chilkoti, A. *Nat. Mater*. **2009**, *8*, 993–999.
142. Hasegawa, U.; van der Vlies, A. J.; Simeoni, E.; Wandrey, C.; Hubbell, J. A. *J. Am. Chem. Soc*. **2010**, *132*, 18273–18280.
143. Tysseling, V. M.; Sahni, V.; Pashuck, E. T.; *et al*. *J. Neurosci. Res*. **2010**, *88*, 3161–3170.
144. Lee, E. S.; Gao, Z. G.; Bae, Y. H. *J. Control. Release* **2008**, *132*, 164–170.
145. Bae, Y.; Kataoka, K. *Adv. Drug Deliv. Rev*. **2009**, *61*, 768–784.
146. Kim, S.; Shi, Y. Z.; Kim, J. Y.; Park, K.; Cheng, J. X. *Expert Opin. Drug Deliv*. **2010**, *7*, 49–62.
147. Oerlemans, C.; Bult, W.; Bos, M.; Storm, G.; Nijsen, J. F. W.; Hennink, W. E. *Pharm. Res*. **2010**, *27*, 2569–2589.
148. Grainger, D. W.; Castner, D. G. *Adv. Mater*. **2008**, *20*, 867–877.
149. Kim, B. Y. S.; Rutka, J. T.; Chan, W. C. W. *N. Engl. J. Med*. **2010**, *363*, 2434–2443.
150. Simberg, D.; Park, J. H.; Karmali, P. P.; *et al*. *Biomaterials* **2009**, *30*, 3926–3933.
151. Foy, S. P.; Manthe, R. L.; Foy, S. T.; Dimitrijevic, S.; Krishnamurthy, N.; Labhasetwar, V. *ACS Nano* **2010**, *4*, 5217–5224.
152. Cheon, J.; Lee, J. H. *Acc. Chem. Res*. **2008**, *41*, 1630–1640.
153. Jun, Y. W.; Lee, J. H.; Cheon, J. *Angew. Chem. Int. Ed*. **2008**, *47*, 5122–5135.
154. Kim, J.; Piao, Y.; Hyeon, T. *Chem. Soc. Rev*. **2009**, *38*, 372–390.
155. Lee, J. H.; Huh, Y. M.; Jun, Y.; *et al*. *Nat. Med*. **2007**, *13*, 95–99.
156. Na, H. B.; Hyeon, T. *J. Mater. Chem*. **2009**, *19*, 6267–6273.
157. Na, H. B.; Song, I. C.; Hyeon, T. *Adv. Mater*. **2009**, *21*, 2133–2148.
158. Bass, J. D.; Grosso, D.; Boissiere, C.; Belamie, E.; Coradin, T.; Sanchez, C. *Chem. Mater*. **2007**, *19*, 4349–4356.
159. Lin, Y. S.; Abadeer, N.; Haynes, C. L. *Chem. Commun*. **2010**, *47*, 532–534.
160. Nel, A.; Xia, T.; Madler, L.; Li, N. *Science* **2006**, *311*, 622–627.
161. Nel, A. E.; Madler, L.; Velegol, D.; *et al*. *Nat. Mater*. **2009**, *8*, 543–557.
162. Barbe, C.; Bartlett, J.; Kong, L. G.; *et al*. *Adv. Mater*. **2004**, *16*, 1959–1966.
163. Gil, P. R.; Oberdorster, G.; Elder, A.; Puntes, V.; Parak, W. J. *ACS Nano* **2010**, *4*, 5527–5531.
164. Jain, T. K.; Reddy, M. K.; Morales, M. A.; Leslie-Pelecky, D. L.; Labhasetwar, V. *Mol. Pharm*. **2008**, *5*, 316–327.
165. Jones, C. F.; Grainger, D. W. *Adv. Drug Deliv. Rev*. **2009**, *61*, 438–456.
166. Missirlis, D.; Khant, H.; Tirrell, M. *Biochemistry* **2009**, *48*, 3304–3314.
167. Maurer-Jones, M. A.; Lin, Y. S.; Haynes, C. L. *ACS Nano* **2010**, *4*, 3363–3373.
168. Brinker, C. J.; Scherer, G. *Sol–Gel Science*. New York: Academic Press, 1990.
169. Arbab, A. S.; Wilson, L. B.; Ashari, P.; Jordan, E. K.; Lewis, B. K.; Frank, J. A. *NMR Biomed*. **2005**, *18*, 383–389.
170. Bareford, L. M.; Swaan, P. W. *Adv. Drug Deliv. Rev*. **2007**, *59*, 748–758.
171. Barratt, G. *Cell. Mol. Life Sci*. **2003**, *60*, 21–37.
172. Gray, J. J. *Curr. Opin. Struct. Biol*. **2004**, *14*, 110–115.
173. Mukherjee, S.; Ghosh, R. N.; Maxfield, F. R. *Physiol. Rev*. **1997**, *77*, 759–803.
174. Unfried, K.; Albrecht, C.; Klotz, L. O.; Von Mikecz, A.; Grether-Beck, S.; Schins, R. P. F. *Nanotoxicology* **2007**, *1*, 52–71.
175. Chen, H. T.; Kim, S. W.; Li, L.; Wang, S. Y.; Park, K.; Cheng, J. X. *Proc. Natl. Acad. Sci. USA* **2008**, *105*, 6596–6601.
176. Mueller, A.; O'Brien, D. F. *Chem. Rev*. **2002**, *102*, 727–757.
177. Nielsen, M. B.; Diederich, F. *Chem. Rev*. **2005**, *105*, 1837–1867.
178. Biesalski, M. A.; Knaebel, A.; Tu, R.; Tirrell, M. *Biomaterials* **2006**, *27*, 1259–1269.
179. Hyeon, T.; Lee, S. S.; Park, J.; Chung, Y.; Bin Na, H. *J. Am. Chem. Soc*. **2001**, *123*, 12798–12801.
180. Murray, C. B.; Sun, S. H.; Doyle, H.; Betley, T. *MRS Bull*. **2001**, *26*, 985–991.
181. Park, J.; An, K. J.; Hwang, Y. S.; *et al*. *Nat. Mater*. **2004**, *3*, 891–895.
182. Puntes, V. F.; Krishnan, K. M.; Alivisatos, A. P. *Science* **2001**, *291*, 2115–2117.
183. Yavuz, C. T.; Mayo, J. T.; Yu, W. W.; *et al*. *Science* **2006**, *314*, 964–967.
184. Yu, W. W.; Falkner, J. C.; Yavuz, C. T.; Colvin, V. L. *Chem. Commun*. **2004**, *20*, 2306–2307.
185. Cui, H. G.; Webber, M. J.; Stupp, S. I. *Biopolymers* **2010**, *94*, 1–18.
186. Deming, T. J. *Nat. Mater*. **2010**, *9*, 535–536.
187. Tirrell, M. *AIChE J*. **2005**, *51*, 2386–2390.
188. Versluis, F.; Marsden, H. R.; Kros, A. *Chem. Soc. Rev*. **2010**, *39*, 3434–3444.
189. Bitton, R.; Schmidt, J.; Biesalski, M.; Tu, R.; Tirrell, M.; Bianco-Peled, H. *Langmuir* **2005**, *21*, 11888–11895.
190. Guler, M. O.; Pokorski, J. K.; Appella, D. H.; Stupp, S. I. *Bioconjug. Chem*. **2005**, *16*, 501–503.
191. Marques, B. F.; Schneider, J. W. *Colloid Surf. B Biointerfaces* **2006**, *53*, 1–8.
192. Neumann, T.; Gajria, S.; Tirrell, M.; Jaeger, L. *J. Am. Chem. Soc*. **2009**, *131*, 3440–3441.
193. Smitthipong, W.; Neumann, T.; Gajria, S.; *et al*. *Biomacromolecules* **2009**, *10*, 221–228.
194. Tu, R. S.; Marullo, R.; Pynn, R.; Bitton, R.; Bianco-Peled, H.; Tirrell, M. V. *Soft Matter* **2010**, *6*, 1035–1044.
195. Dillow, A. K.; Ochsenhirt, S. E.; McCarthy, J. B.; Fields, G. B.; Tirrell, M. *Biomaterials* **2001**, *22*, 1493–1505.
196. Discher, D. E.; Mooney, D. J.; Zandstra, P. W. *Science* **2009**, *324*, 1673–1677.
197. Gupta, N.; Lin, B. F.; Campos, L.; *et al*. *Nat. Chem*. **2009**, *2*, 138–145.

4.416. Growth Factors and Protein-Modified Surfaces and Interfaces

Y Ito, RIKEN Advanced Science Institute, Saitama, Japan

© 2011 Elsevier Ltd. All rights reserved.

4.416.1.	**Introduction**	250
4.416.2.	**Proteins for Surface Immobilization**	250
4.416.2.1.	Cell Adhesion	250
4.416.2.1.1.	ECM–cell interactions	250
4.416.2.1.2.	Cell–cell interactions	251
4.416.2.1.3.	Cell adhesion peptides	252
4.416.2.2.	Cell Growth	253
4.416.2.2.1.	Mechanisms	253
4.416.2.2.2.	Growth factors for immobilization on surfaces	253
4.416.2.3.	Cell Adhesion and Growth	255
4.416.3.	**Protein Immobilization**	255
4.416.3.1.	Immobilization for ECM–Cell Interactions	255
4.416.3.1.1.	Extracellular matrices	255
4.416.3.1.2.	Biomimetic peptides	256
4.416.3.2.	Immobilization for Cell–Cell Interaction	257
4.416.3.2.1.	Cadherin	257
4.416.3.2.2.	Selectin	258
4.416.3.2.3.	Notch ligand	258
4.416.3.2.4.	Ephrin B2	259
4.416.3.2.5.	Sonic hedgehog	259
4.416.3.3.	Surface Immobilization of Growth Factors	260
4.416.3.3.1.	Mechanisms	260
4.416.3.3.2.	Examples of immobilized growth factors	261
4.416.4.	**Summary and Future Directions**	275
References		275

Glossary

Adhesion factors A class of membrane proteins comprising the outer surfaces of cell membranes in the developing nervous system that is thought to be intimately involved in guiding the development during embryonic life.

Autocrine A form of signaling in which a cell secretes a hormone or chemical messenger (called the autocrine agent) that binds to autocrine receptors *on the same cell*, leading to changes in the cell. This can be contrasted with paracrine signaling, intracrine signaling, or classical endocrine signaling.

Binding growth factor Juxtacrine mechanism of growth control and intercellular communication involving specific cell-to-cell contacts that are established by the interaction of membrane-bound forms of growth factors that are normally secreted with receptors on an adjacent cell and thus playing an important role in developmental processes that have spatial restrictions.

Down-regulation Densensitization. It means no response to further stimulation, rapid attenuation of receptor responsiveness due to agonist exposure, or weakening of the signal transmission under long lasting stimulation by hormones, neurotransmitters, or sensory signals. Modes of desensitization include ion channel regulation, ubiquitination, phosphorylation and dephosphorylation, endocytosis and recycling, GTP/GDP exchange, auto inhibition/feedback loop, or mRNA and protein synthesis regulation.

Endocrine A system of glands, each of which secretes a type of hormone into the bloodstream to regulate the body functions. It derives from the Greek words endo (Greek *ένδο*) meaning inside, within, and crinis (Greek *κρινής*) for secrete.

Extracellular matrix The extracellular part of animal tissue that usually provides structural support to the animal cells in addition to performing various other important functions. The extracellular matrix is the defining feature of connective tissue in animals.

Growth factor A naturally occurring substance capable of stimulating cellular growth, proliferation, and cellular differentiation. Usually it is a protein or a steroid hormone. Growth factors are important for regulating a variety of cellular processes. Growth factors typically act as signaling molecules between cells. Examples are cytokines and hormones that bind to specific receptors on the surface of their target cells. They often promote cell differentiation and maturation, which vary with growth factors.

Internalization Essentially three uptake mechanisms (phagocytosis, diffusion, and endocytosis) have been reported in the literature.

Intracrine A hormone that acts inside a cell. Steroid hormones act through intracellular (mostly nuclear) receptors and, thus, are considered to be intracrines. In contrast, peptide or protein hormones, in general, act as endocrines, autocrines, or paracrines by binding to their receptors present on the cell surface.

Juxtacrine A type of intercellular communication that is transmitted via oligosaccharide, lipid, or protein components of a cell membrane and may affect either the emitting cell or the immediately adjacent cells. It occurs between adjacent cells that possess broad patches of closely opposed plasma membrane linked by transmembrane channels known as connexons. Unlike other types of cell signaling (such as paracrine and endocrine), juxtacrine signaling requires physical contact between the two cells involved.

Matricrine Signal transduction of growth factors bound to extracellular matrix. Binding of the growth factors to ECM not only protects them from degradation but also concentrates the growth factors around the responding cells.

Multivalency Multivalency of ligand plays an important role in signal transduction. One unique determinant of effector function is the ability to dimerize or oligomerize receptors. Multivalent ligands can interact with the target receptors through multiple binding modes. The structure of a multivalent ligand determines the favored binding modes. In addition, after complex formation with receptors multivalent ligands prevent lateral diffusion of the activated receptors or complex in the plane of the cell membrane. This enhancement of clustering is considered to lead to a rapid and long-lasting effect.

Paracrine A form of cell signaling in which the target cell is near ('para' = near) the signal-releasing cell. Some signaling molecules degrade very quickly, limiting the scope of their effectiveness to the immediate surroundings.

RGD peptide The single letter code for arginine-glycine-aspartate. This tripeptide motif can be found in proteins of the extracellular matrix. Integrins link the intracellular cytoskeleton of cells with the extracellular matrix by recognizing this RGD motif. Without attachment to the extracellular matrix, cells normally undergo apoptosis ('anoikis'). Soluble RGD peptides induce apoptosis and might be used as drugs against angiogenesis, inflammation, and cancer mestastasis as small soluble peptides containing the RGD motif inhibit cell attachment and consequently induce apoptosis.

Signal transduction Signal transduction comes from the verb to 'transduce' meaning to 'lead across.' In biology, signal transduction is the process by which an extracellular signal molecule activates a membrane receptor that in turn alters intracellular molecules to create a response. Transmembrane receptors span the cell membrane, with part of the receptor outside and part inside the cell. The chemical signal binds to the outer portion of the receptor, changing its shape and conveying another signal inside the cell. Some chemical messengers, such as testosterone, can pass through the cell membrane, and bind directly to receptors in the cytoplasm or nucleus. Sometimes, there is a cascade of signals within the cell. With each step of the cascade, the signal can be amplified, so a small signal can result in a large response. Eventually, the signal creates a change in the cell, either in the expression of the DNA in the nucleus or in the activity of enzymes in the cytoplasm. These processes can take milliseconds (for ion flux), minutes (for protein- and lipid-mediated kinase cascades), hours, or days (for gene expression).

Abbreviations

α_2-PI	α_2-Plasmin inhibitor
aFGF	Acidic FGF
ALK	A peptide sequence ALKRQGRTLYGF
ALK1	Activin receptor-like kinase 1
ALP	Alkaline phosphotase
Ang1	Angiopoietin 1
AV	Arteriovenous
BDNF	Brain-derived neutrotrophin factor
bFGF	Basic FGF
BMHSCs	Bone marrow hematopoetic stem cells
BMP	Bone morphorgenic protein
BMSCs	Bone marrow-derived mesenchymal stem cells
BSA	Bovine serum albumin
BSP	Bone sialoprotein
C2C12	A typical pluripotent mesenchymal precursor cell line
cAMP	Cyclic adenosine monophosphate
CAMs	Cell adhesion molecules
CBD	Collagen-binding domain
CBF-1	C promoter binding factor
CCMBM	Collagen-containing mineralized bone-derived matrix
CD31	Cluster of differentiation 31
CD34	Cluster of differentiation 34
CD44	Cluster of differentiation 44
c-fos	A cellular proto-oncogene belonging to the immediate early gene family of transcription factors
CHO	Chinese hamster ovary
CMCS	Carboxymethyl chitosan
CMP	Collagen mimetic peptide
CNTF	Ciliary neutrophic factor
CSF-1	Colony stimulating factor 1
CT	Computed tomography

CTLL-2	A clone of cytotoxic T cells derived from a C57BL/6 mouse
CXCR3	$G\alpha_i$ protein-coupled receptor in the CXC chemokine receptor family
DBM	Demineralized bone matrix
DGR	A peptide sequence DGRGDSVAYG
DLL4	Delta-like protein 4
DM-GRASP	Dorsal funiculus, ventral midline immunoglobulin-like restricted axonal surface protein
DRG	Dorsal root ganglion
ECM	Extracellular matrix
ECs	Endothelial cells
EDC	Ethylcarbodiimide hydrochloride
EGF	Epidermal growth factor
EGFR	EGF receptor
ELISA	Enzyme-linked immunosorbent assay
Eph	Ephrin
Epo	Erythropoietin
ERK	Extracellular signal-regulated kinase
ES	Embryonic stem
F9	Embryonal carcinoma cell
FXIIIa	Coagulation factor XIII
FAK	Focal adhesion kinase
FBD	Fibrin-binding domain
FGF	Fibroblast growth factor
FGFR	FGF receptor
Flk-2/Flt-3	Fetal liver kinase-2/fetal liver ligand-3
FN	Fibronectin
FP6	Receptor chimeric protein
GDF	Growth differentiation factor
HA	Hydroxyapatite
HB-EGF	Heparin binding-epidermal growth factor
HC-DBM	Heparin-cross-linked DBM
HEK293	Human Embryonic Kidney 293
HEMA	2-Hydroxyethyl methacrylate
HER2	Human EGFR-related 2
HGF	Hepatocyte growth factor
HSCs	Hematopoietic stem cells
HUBECs	Human umbilical vein ECs
IFBMs	Interfacial biomaterials
IFN-γ	Interferon-γ
IgCAM	Immunoglobulin CAM
IGF-1	Insulin-like growth factor
IGFBP	IGF binding proteins
IgG Fc	Immunoglobulin fragment c
IL-2	Interleukin-1
IL-2R	IL-2 receptors
IL-1ra-ELP	Fusion protein of recombinant human IL-1 receptor antagonist and elastin-like peptide
IPN	Interpenetrating polymer network
JNK	c-jun N-terminal kinase
K1	Fibrin-binding peptide Kringle 1
KGF	Keratinocyte growth factor
LCST	Lower critical solution temperature
LIF	Lukemia inhibitory factor
LOCSs	Linear ordered collagen scaffolds
MAPK	Mitogen-activated protein kinase
MBP	Maltose-binding protein
MC3T3-E1	A well-studied osteoblast-like murine-derived cell line
MDCK	Madin-Darby canine kidney
MEF	Mouse embryonic fibroblast
MG-63	Human osteosarcoma cell line
MSCs	Mesenchymal stem cells
mShh	N-terminal Shh
NCAM	Neural CAM
NCD	Nanocrystaline diamond
NGF	Nerve growth factor
NHS	N-hydroxysuccimide
NIH3T3	NIH Swiss mouse embryonic fibroblast cell line. The name 3T3 is from(3 days, transfer, inoculum 3×10^5 cells/50 mm dish)
NMuMG	Mammary gland cell
NSPCs	Neural stem/progenitor cells
NT	Neurotrophin
OCT-1	Osteoblast cell derived from osteocalcin promoter-driven SV-40 T-antigen transgenic mouse calvarias
OP9	A stromal cell line
OPDs	Osteopromotive domains
OPN	Osteopontin
P19	Embryonal carcinoma cell
PC12	A cell line derived from a pheochromocytoma of the rat adrenal medulla
PCL	Poly(ε-caprolactone)
pDCs	Plasmacytoid dendric cells
PDGF	Platelet derived growth factor
PDL	Periodontal ligament
PEG	Polyethylene glycol
PEGDA	Poly(ethylene glycol) diacrylate
PEG-TGF-β2	PEG-attached TGF-β2
PET	Polyethylene terephthalate
PHSRN	A peptide sequence
PLGA	Poly(lactide-*co*-glycolide)
PLA	Polylactide
PPDAs	OPD peptide-amphiphiles
PPy	Polypyrole
PRG	A peptide sequence PRGDSGYRGDS
PSCs	Pancreatic stem cells
PTH(1–34)	Parathyroid hormone (1–34)
Rac 1	Ras-related C3 botulinum toxin substrate 1
RGD	Arginine-glycine-aspartic acid
rhBMP3-C	Recombinant human BMP3 fusion protein
RT-PCR	Reverse transcription-polymerase chain reaction
SAM	Self-assembled monolayer
SCF	Stem cell factor
SCI	Spinal cord injury
SCID	Severe combined immunodeficient
SEM	Scanning electron microscopy
Shh	Sonic hedgehog
SMC	Smooth muscle cell
SPR	Surface plasmon resonance
SRCs	SCID repopulating cells

SRK	A proto-oncogenic tyrosine kinase
STO	A mouse fibroblast cell line (S, SIM; T, 6-thioguanine resistant; O, ouabain resistant)
TGF-β	Transforming growth factor-β
TGFβRII	TGF-β type II receptor
TG-pI-BMP-2	Fusion protein of N-terminal transglutaminase substrate (TG) domain, plasmin substrate (pI) domain, and BMP-2
Ti6Al4V	An α/β titanium base alloy
TKKTLRT	A peptide sequence
TNF-α	Tumor necrosis factor-α
TrkA	A protein that in humans is encoded by the *NTRK1* gene
UT-7/Epo	UT-7 is a cell line established from the bone marrow of a patient with acute megakaryoblastic leukemia. UT-7/Epo is a subline of UT-7 cells established from UT-7 cells maintained for more than six months in the presence of Epo
VCAM	Vascular CAM
VEGF	Vascular endothelial growth factor
vWF	von Willebrand factor
XTT	2,3-bis(2-methoxy-4-nitro-5-sulfony)-2H-tetrazoline-5-carboxanilide

4.416.1. Introduction

Engineering of cellular environments is a valuable tool for guiding cellular activities such as differentiation, spreading, motility, proliferation, or apoptosis, all of which together regulate tissue development in a complex manner. In the field of biomaterials research, the rational control of these cell functions is very important. These functions of cells are considered to be generally regulated by three types of interactions as shown in Figure 1. They are the interactions between cell and extracellular matrix (ECM), between cell and cell (e.g., cadherin), and between cell and soluble biosignals (e.g., cytokines and growth factors). Considering the role of proteins in these interactions, the surface immobilization of proteins is important for the rational engineering of bioactive materials with cells.

Here, various proteins used for surface immobilization to regulate cell functions on biomaterials are reviewed, and various approaches for material designs using immobilization of proteins for regulation of cell functions are discussed.

4.416.2. Proteins for Surface Immobilization

4.416.2.1. Cell Adhesion

Cell adhesion is mediated by cell adhesion molecules (CAMs) located on the cell surface and they are involved in the binding with ECM or with other cells.[1] These proteins are typically transmembrane receptors and are composed of three domains: an intracellular domain that interacts with the internal skeleton, a transmembrane spanning section, and an extracellular domain that interacts either with CAMs of the same kind (homophilic) or with other CAMs or the ECM (heterophilic binding). CAMs account for cell-to-cell or cell-to-ECM interactions and are divided into four major groups: the integrins, the cadherins, the selectins, and the members of the immunoglobulin superfamily as shown in Table 1. These molecules are of paramount importance in the establishment of normal tissue structure and function and participate in a variety of physiological processes such as morphogenesis, embryogenesis, organogenesis, immunological function, wound healing, and inflammation.

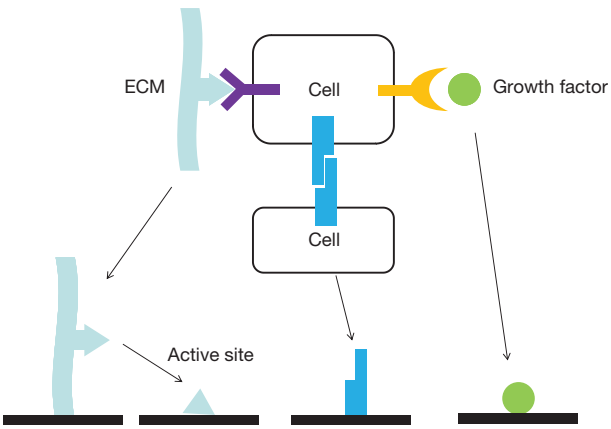

Figure 1 (Top) three types of interactions (cell–ECM, cell–cell, and cell-growth factor) of cells and (bottom) applications for biomaterials.

4.416.2.1.1. ECM–cell interactions

ECM is primarily composed of a complex meshwork of fibrous protein surrounded by space-filling molecules such as glycosaminoglycans as well as mineral deposits in hard tissues such as bone. Many of these components are secreted by resident cells and primarily provide support and anchorage and they also play important roles as tissues boundaries and in the modulation of intracellular and intercellular communication.[2] Moreover, the ECM is not only made but also organized and remodeled by the cells within it. Formation and remodeling of this ECM network is vital for tissue responses such as cell

Table 1 Primary families of cell adhesion molecules (CAMs)

CAMs	*Members*	*Interactions*
Integrins	Heterodimers of α- and β-subunits	Cell-to-ECM and cell-to-cell
Cadherins	Classic: N-, P-, E-, R-, B-cadherin Nonclassic: desmosomal, protocadherins	Homophilic cell-to-cell
Selectins	L-, E-, P-selectin	Heterophilic cell-to-cell
IgCAM superfamily	NCAM, VCAM, ICAM, Mad CAM, PECAM, CD146, CD2, CEA	Homophilic and heterophilic cell-to-cell

migration during tissue formation and repair, growth, wound healing, and fibrotic responses. Cell–matrix interactions can directly modulate cell morphology, survival, proliferation, and differentiation in multiple cell systems. Many of the fibrous proteins that make up the ECM, including collagen, fibronectin (FN), elastin, tenascin, and laminin, have both structural and adhesive functions and are secreted in specific tissues by specialized cells, including fibroblasts (present in most connective tissues), chondroblasts (cartilage), and osteoblasts (bone).

The collagens are the most abundant proteins in mammals, constituting about 25% of the total protein mass. They contribute significantly to the integrity and mechanical properties of tissues such as bone, skin, cartilage, and tendon.[3–5] So far, about 25 distinct collagen α-chains have been identified, each encoded by a separate gene. Different combinations of these genes are expressed in different tissues. Although in principle more than 10 000 types of triple-stranded collagen molecules could be assembled from various combinations of the 25 or so α-chains, only about 20 types of collagen molecules have been found. The main types of collagen found in connective tissues are types I, II, III, V, and XI, type I being the principal collagen of skin and bone and by far the most common. These are the fibrillar collagens, or fibril-forming collagens, with the rope-like structure. After being secreted into the extracellular space, these collagen molecules assemble into higher order polymers called collagen fibrils, which are thin structures (10–300 nm in diameter), many hundreds of micrometers long in mature tissues and clearly visible in electron micrographs. Collagen fibrils often aggregate into larger, cable-like bundles, several micrometers in diameter, which can be seen under the light microscope as collagen fibers.

FN is a complex, multifunctional protein with multiple domains, each with specific binding sites for other matrix macromolecules and for receptors on the surface of cells. FN therefore contributes to both organizing the matrix and helping cells attach to it.[6,7] Among the ECM proteins, FNs as a family of structurally related soluble and matrix glycoproteins have been extensively studied in numerous biological processes including cell adhesion, wound healing, and organogenesis. Following tissue injury, fibroblasts invade the fibrin clot in the wound space where they are activated. This activation to accelerate the wound healing process appears to initiate a switch of the fibroblast cell surface receptors from binding type I collagen to those that bind provisional matrix proteins such as fibrin and FN. Cells producing a sufficient amount of FN can spread on material surfaces in a serum-free medium, whereas cells that do not secrete adequate levels of FN cannot spread even with added FN in the medium. This is one of the many examples showing the important role of FN in mediating the interaction between cells and biomaterials surface.

Elastin is the dominant ECM protein in elastic fibers, a major component of arteries, lungs, and skin.[8,9] Laminin is the major noncollagenous component of the basal lamina, playing a critical role as the 'glue' that holds many body structures together. Osteopontin (OPN) is a soluble protein found in all body fluids; it stimulates signal transduction pathways (via integrins and CD44 variants) similar to those stimulated by components of the ECM. This appears to promote the survival of cells exposed to potentially lethal insults such as ischemia/reperfusion or physical/chemical trauma. OPN is chemotactic for many cell types including macrophages, dendritic cells, and T cells; it enhances B lymphocyte immunoglobulin production and proliferation. In inflammatory situations, it stimulates both pro- and anti-inflammatory processes, which on balance can be either beneficial or harmful depending on what other inputs the cell receives.

Most of these structural proteins also play fundamental roles in promoting cell adhesion and mediating intracellular signals critical to tissue function. In particular, cell adhesion to the ECM is essential for controlling such complex biological processes as embryonic development, wound healing, immune responses, and tissue organization and repair. For example, cell-adhesive interactions with specific ECM proteins regulate bone cell survival, cell cycle progression, differentiation, and matrix formation; at the tissue level, these interactions can play crucial roles in bone remodeling, maintenance, and formation. Moreover, ECM-mediated cell adhesion plays critical roles in animal development, as evidenced by the embryonic lethality of mice that have genetic deletions for particular ECM ligands and receptors. Proteins such as FN are important in guiding cell movements during organism development, including migration of mesodermal cells at different embryonic stages. These ECM components regulate cell behavior by interacting with cell surface receptors to activate particular intracellular signaling pathways, resulting in tissue-specific alterations in cell spreading, migration, cell–cell communication, and differentiation. Hynes[10] reviewed many effects beyond providing structural support.

Although there are many types of cell receptors that facilitate cell–ECM interactions, cells recognize and adhere to ECM ligands primarily via integrins, a widely expressed class of cell surface receptors. Integrins are transmembrane, heterodimeric proteins consisting of a particular combination of two noncovalently associated subunits (α and β), of which 24 specific combinations have been currently identified in humans.[11,12] Integrins interact with the ECM through their extracellular domains, and are linked to cytoskeletal elements and signaling molecules through their intracellular domains, functioning primarily as a bridge between the ECM environment and the cell. Different α and β subunit combinations have the capacity to bind to one or more ECM ligands, whereas many ECM proteins can act as ligands for more than one integrin. For example, FN is a ligand of $\alpha_5\beta_1$, laminin, $\alpha_6\beta_1$, $\alpha_7\beta_1$, $\alpha_6\beta_4$, fibrinogen, and $\alpha_2\beta_3$. Moreover, a wide array of integrins can be expressed, typically in tissue- and development-specific patterns. For example, osteoblasts and osteoprogenitor cells express multiple integrins, including $\alpha_1\beta_1$, $\alpha_2\beta_1$, $\alpha_3\beta_1$, $\alpha_4\beta_1$, $\alpha_5\beta_1$, $\alpha_6\beta_1$, $\alpha_8\beta_1$, $\alpha_v\beta_3$, and $\alpha_v\beta_5$, that can vary in degree of expression with the stage of the osteoblast and bind to numerous ECM components.

4.416.2.1.2. Cell–cell interactions

4.416.2.1.2.1. Cadherins

Cadherins are integral transmembrane single-chain glycoproteins that mediate intercellular cell–cell adhesion thorough homotypic interactions (between molecules of the same types, that is, neural cell adhesion molecule (NCAM) to NCAM in the presence of extracellular Ca^{2+}). The first three cadherins discovered were named according to the main tissues in which they were found: E (epithelial)-cadherin is present on many types of epithelial cells; N (neural)-cadherin on

nerve, muscle, and lens cells; and P (placental)-cadherin on cells in the placenta and epidermis. More than 300 different cadherins have been reported.[13] All are also found in various other tissues; N-cadherin, for example, is expressed in fibroblasts, and E-cadherin is expressed in parts of the brain. These and other classical cadherins are related in sequence throughout their extracellular and intracellular domains. There are also a large number of nonclassical cadherins, with more than 50 expressed in the brain alone. The nonclassical cadherins include proteins with known adhesive function, such as the desmosomal cadherins discussed earlier and the diverse protocadherins found in the brain. The classical and nonclassical cadherin proteins constitute the cadherin superfamily. Tissue-specific expression of cadherin molecules is required for cell sorting and recognition during embryogenesis and for preserving tissue architecture.

4.416.2.1.2.2. Selectins

Selectins are a family of transmembrane proteins containing an amino-terminal lectin domain for binding to ligands, an epidermal growth factor (EGF)-like domain, 2–9 regulatory protein repeats, a transmembrane domain, and a short cytoplasmic tail. This class of CAMs consists of three proteins, namely, E (endothelial)-, L (leukocyte)-, and P (platelet)-selectin, which mediate the adhesion between endothelial cells (ECs), leukocytes, and platelets. Selectins have received considerable attention because of their importance in inflammatory and immune trafficking as well as their role in diseases such as atherosclerosis and cancer metastasis.[14]

4.416.2.1.2.3. Immunoglobulin superfamily

Immunoglobulin CAMs (IgCAMs) are a large group of cell surface glycoproteins, which contain an immunoglobulin-like extracellular domain. Several members of this family have been implicated in malignancies, such as NCAM, vascular CAM (VCAM), intracellular CAM, platelet-endothelial CAM, mucosal addressin CAM, and carcinoembryonic antigen. These molecules are capable of both homotypic and heterotypic (between different types of molecules, i.e., VCAM to $\alpha_4\beta_1$ integrin) adhesions. IgCAMs play multiple roles in many biological processes, including nervous system development and immune response. In some cases, their expression is induced by cytokines, such as tumor necrosis factor α (TNF-α), interleukin-1 (IL-1), and interferon-γ (IFN-γ) and this suggests a link between inflammation and tumorigenesis.

4.416.2.1.2.4. Others

In addition to cadherin, selectins, and immunoglobulin superfamily, other cell–cell interactions include Notch signaling and sonic hedgehog (Shh) as components for stem cell niches.

4.416.2.1.2.5. Notch

Notch proteins are involved in cell–cell signaling pathways essential during embryonic development and in adult self-renewal systems. The molecules involved in the Notch pathway are highly conserved across species and are vital in developmental cell fate decisions such as neural development, epithelial-to-mesenchymal transitions, vascular development, keratinocyte differentiation, as well as hematopoietic and T cell differentiation.[15] The Notch receptor is a single-pass transmembrane protein that is a heterodimer of two subunits. The first subunit consists of a large extracellular segment with EGF repeats – a common repeat found in growth factors and ECM proteins. The second subunit consists of a short extracellular domain, a transmembrane domain, and an intracellular domain.

4.416.2.1.2.6. Sonic hedgehog

Shh signaling is a well-known cell-signaling pathway conserved in many mammals. Shh is one of the best-studied ligands that regulate proliferation and differentiation in many cell types.[15] Shh, upon binding to the Patched-1 receptor, initiates a cascade of molecular signaling involving other molecules. The cascade regulates the receptor transcription and also transcriptional effectors of the Gli family.

4.416.2.1.3. Cell adhesion peptides

Active regions in signal proteins, ECMs and CAMs, or peptides that essentially interact with integrins are known. They are listed in **Table 2**.[35,36]

Most integrins recognize specific binding sites, typically small peptide sequences motifs, such as the ubiquitous arginine–glycine–aspartic acid (RGD) motif present in a variety of ECM proteins.[37–39] Integrin binding to ligands is a dynamic and highly regulated process that requires 'activation' of the integrin and mechanical coupling to the ligand. This activation changes the conformation of the extracellular proteins of the receptor into a more 'high-affinity' structural orientation for ligand binding, although divalent metal ions are also typically needed for functional binding. After integrin–ligand binding, integrins associate with the actin cytoskeleton and begin to aggregate together in clusters forming focal adhesions, distinct structures that form intracellular scaffolds of structural and signaling molecules. Focal adhesion mediates stable adhesion by providing structural links between ECM and cell

Table 2 Peptide sequences concerned with integrin-mediated cell adhesion

Peptide	*Protein*	*Integrin*	*References*
RGD	Collagen, fibronectin, vitronectin, PECAM (IgG superfamily), fibrinogen	$\alpha_1\beta_1$, $\alpha_v\beta_3$, $\alpha_v\beta_6$, $\alpha_{IIb}\beta_3$, $\alpha_3\beta_1$, $\alpha_5\beta_1$	16,17
KQAGDV	Fibrinogen	$\alpha_{IIb}\beta_3$	18,19
RYD		$\alpha_{IIb}\beta_3$	20
KGD		$\alpha_{IIb}\beta_3$	21
RHD	Amyloid peptide	$\alpha_5\beta_1$	22,23
NGR		RGD-directed integrin	24
(S)DGR		RGD-directed integrin	24,25
LDV	Fibronectin	$\alpha_4\beta_1$, $\alpha_4\beta_7$	26–28
DGEA	Collagen I	$\alpha_2\beta_1$	29
YGYYGDALR	Laminin	$\alpha_2\beta_1$	30
FYFDLR	Type IV collagen	$\alpha_2\beta_1$	30
KRLDGS	Fibrinogen	$\alpha_M\beta_2$ (CD11b/CD18)	31
R and D	Type I collagen	$\alpha_1\beta_1$	32
L/IET	ICAMs	β_2	33,34

skeleton to regulate force-associated cell functions such as adhesion, spreading, morphology, and migration. These adhesive structures also activate discrete signaling pathways (mitogen-activated protein kinase (MAPK), c-jun N-terminal kinase (JNK), extracellular signal-regulated kinase (ERK) through accumulation and activation of signaling mediators, such as focal adhesion kinase (FAK) and sarcoma (Src) that can ultimately regulate transcriptional factor activity and direct major cell functions such as migration, proliferation, and differentiation. For example, $\alpha_2\beta_1$-mediated cell attachment to type I collagen stimulates the tyrosine phosphorylation of FAK and, subsequently, the activation of ERK, an MAPK implicated in the control of osteoblast-specific gene expression and matrix mineralization.

On the other hand, many synthetic peptides, especially RGD-containing peptide, have been prepared. Potential to develop RGD-based therapeutics that function either as agonists to promote the interaction of cells and tissues with artificial matrices or as antagonists to control the nature of cell–cell and cell–ECM interactions exists.[40] Many types of linear and cyclic RGD peptides have been developed and also peptidemimetics are chemically investigated.[41]

4.416.2.2. Cell Growth

There are two general types of cells: anchorage-dependent and anchorage-independent. In the case of the former, the cell destiny is determined after adhesion to ECM. In the case of the latter, the density is not dependent on cell adhesion. However, the growth, differentiation, apoptosis, transformation, etc. of both types of cells are regulated by soluble growth factors or cytokines. Advances in developmental molecular and cell biology, biochemistry, and medicine have identified various chemical compounds such as growth factors, cytokines, and chemokines that are produced by cells; these agents act as biosignals in their respective microenvironments, provide essential cues, and regulate crucial events that are necessary for tissue development, repair, and regeneration at the cellular and molecular levels. Such contributions elucidate the fundamental aspects of biology and physiology in both health and disease; research in relevant fields is continuing and breakthrough developments are forthcoming.

4.416.2.2.1. Mechanisms

Development and homeostasis of tissues and organs depend on a fascinating, but complex, interplay and function of their constituent cells with their microenvironment. It is known that there are many types of growth factors, for example, insulin, EGF, nerve growth factor (NGF), bone morphogenic protein (BMP), vascular endothelial growth factor (VEGF), fibroblast growth factor (FGF), insulin-like growth factor 1 (IGF-1), transforming growth factor β1 (TGF-β1), hepatocyte growth factor (HGF), and platelet-derived growth factor (PDGF). The action mechanisms of growth factors are summarized as shown in Figure 2. Diffusible interactions, such as endocrine, paracrine, autocrine, and intracrine, and nondiffusible interactions such as juxtacrine and matricrine are generally known.[42–44] It is also known that each growth factor does not have just one mechanism but multiple mechanisms to act upon cells.

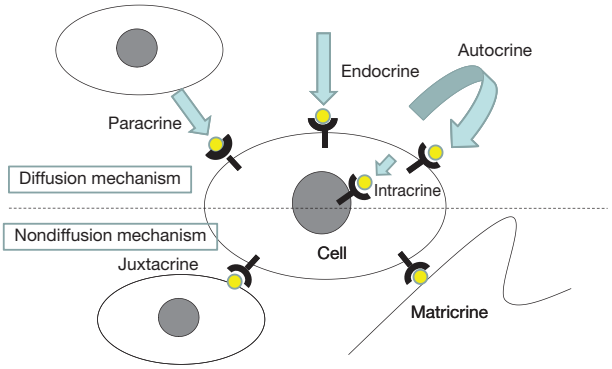

Figure 2 Various action mechanisms of growth factors.

4.416.2.2.2. Growth factors for immobilization on surfaces

Growth factors can be immobilized on solid surfaces for medical applications using different techniques.

4.416.2.2.2.1. Insulin

Insulin is a peptide hormone composed of 51 amino acids and has a molecular weight of 5808 Da. It is produced in the islets of Langerhans in the pancreas. The action of insulin on the human metabolism level includes control of cellular intake of certain substances, most prominently glucose in muscle and adipose tissue (involving about two-thirds of body cells), increase of DNA replication and protein synthesis via control of amino acid uptake, and modification of the activity of numerous enzymes. Many types of nonserum cell culture media include insulin as a supplement.

4.416.2.2.2.2. Insulin growth factor 1

IGFs have high sequence similarity to insulin and are part of a complex system that cells use to communicate with their physiologic environment. The complex system consists of two cell-surface receptors (IGFR1 and IGF2R), two ligands (IGF-1 and IGF-2), a family of six high-affinity IGF binding proteins (IGFBP 1–6), as well as associated IGFBP-degrading enzymes, collectively referred to as proteases. IGF-1 is important for both the regulation of normal physiology and a number of pathological states, including cancer. IGF has been shown to play roles in the promotion of cell proliferation and the inhibition of cell death (apoptosis). IGF-2 is thought to be a primary growth factor required for early development while IGF-1 expression is required for achieving maximal growth. While IGF-2 may be primarily fetal in action, it is also essential for development and function of organs such as the brain, liver, and kidney.

4.416.2.2.2.3. Epidermal growth factor

EGF, a peptide composed of 53 amino acids with a molecular weight of 6045 Da, promotes cellular proliferation, differentiation, and survival. EGF was first purified from the mouse submandibular gland, but since then has been found in many human tissues including submandibular gland and parotid gland. Salivary EGF, which seems also regulated by dietary inorganic iodine, also plays an important physiological role in the maintenance of oroesophageal and gastric tissue

integrity. The biological effects of salivary EGF include healing of oral and gastroesophageal ulcers, inhibition of gastric acid secretion, stimulation of DNA synthesis, as well as mucosal protection from intraluminal injurious factors such as gastric acid, bile acids, pepsin, and trypsin and protection to physical, chemical, and bacterial agents. EGF acts by binding to the EGF receptor (EGFR) on the cell surface and stimulating the intrinsic protein–tyrosine kinase activity of the receptor. The tyrosine kinase activity, in turn, initiates a signal transduction cascade that results in a variety of biochemical changes within the cell – a rise in intracellular calcium levels, increased glycolysis and protein synthesis, and increases in the expression of certain genes including the gene for EGFR – that ultimately lead to DNA synthesis and cell proliferation.

4.416.2.2.2.4. Nerve growth factor

NGF was discovered more than 50 years ago and is one of the neutrophic factors important for neuron survival and neurite growth. NGF 7S is a 130 kDa protein composed of five noncovalently linked subunits (2α, 1β, 2γ). From proteolytic fragmentation studies, the β-subunit is understood to be responsible for the neutrophic activity in the NGF 7S.[45] Studies showed that NGF plays a critical role in nerve injury repair.[46] It is also a factor with chemotactic effects on nerve growth cones. When presented with a concentration gradient of NGF, growth cones guide growing axons to their proper innervating target. In a proof-of-concept study, a well-defined linear concentration gradient of soluble NGF of at least 133 ng (ml mm)$^{-1}$ was required to guide neurites of PC12 cells and/or dorsal root ganglion (DRG) neurons up to 7.5 mm toward the higher end of the concentration gradient.[47] Other members of the neurotrophin (NT) family that are well recognized include brain-derived neurotrophic factor (BDNF), NT-3, and NT-4/5.

4.416.2.2.2.5. Bone morphogenic protein

BMPs consisting of more than 20 isoforms are members of the TGF superfamily. BMPs are powerful stimulators of bone formation and effectors of mesenchymal cell differentiation into bone cells. BMPs are primarily secreted by osteoblasts. There are two types of BMP receptors in cell membranes, both of which are serine–threonine kinases. BMP binding to the type II receptor leads to dimerization of that receptor with a type I receptor and phosphorylation of the type I receptor, which then activates downstream signaling.[48] BMP-2, BMP-4, BMP-6, BMP-7, BMP-9, and BMP-13 growth differentiation factor-6 (GDF-6) are the most important BMPs in promoting the differentiation of pluripotent mesenchymal cells into osteoblasts and lead to increased bone formation. Both *in vitro* and *in vivo*, BMPs promote the fusion of mononuclear hematopoietic cells of the macrophage–granulocyte lineage; this process results in osteoblast formation and activation, leading to increased bone turnover and remodeling in the late stages of bone repair and development.

4.416.2.2.2.6. Vascular endothelial growth factor

VEGF, the most widely studied stimulator of EC migration, proliferation, and differentiation, plays a role in nearly every phase of vascular tissue development and maintenance. The VEGF family (a subset of the PDGF superfamily) includes VEGF-A, VEGF-B, VEGF-C, VEGF-D, and placental growth factor, and VEGF is the primary regulator of vasculogenesis and angiogenesis. The effect of VEGF is conveyed by its interaction with pertinent receptors on the cell membrane. There are two important VEGF receptors expressed on ECs, VEGF-1 (Flk-1) and VEGF-2 (Flk-2).

VEGF is involved in the organization of primitive blood vessel development, guidance of capillary extension, proliferation of ECs, recruitment and commitment of EC precursors, wound healing, and maintenance of healthy blood vessels. Because VEGF critically affects almost every stage of vascular tissue development, repair, and expansion, it is the most important candidate among growth factors for the development of vascular tissue and of vascularized, engineered constructs of other tissues and organs. VEGF alone, even in high doses, is unlikely to lead to functional blood vessel formation: VEGF must be used in conjunction with other important factors.

4.416.2.2.2.7. Fibroblast growth factor

FGFs are secreted by many cells, especially macrophages and tumor cells. There are more than 20 FGFs, but most pertinent to the vasculare are the acidic fibroblast growth factor (aFGF or FGF-1) and basic fibroblast growth factor (bFGF or FGF-2). These growth factors act by activating the tyrosine kinase receptors, FGF receptor 1 (FGFR-1) and FGFR-2, on target cell membranes. FGF affects angiogenesis through both direct and indirect pathways that involves upregulation of receptors specific to other important angiogenetic factors such as VEGF. bFGF stimulates expression of VEGF in ECs and stromal cells. When combined with VEGF, bFGF acts synergetically to increase EC migration and proliferation.

4.416.2.2.2.8. Transforming growth factor β

TGF-β is an important regulator of early vascular development and angiogenesis. The TGF-β superfamily consists of nearly 30 proteins including the BMPs. There are two types of TGF-β receptors on cells, both of which are serine–threonine kinases; type II receptors (such as TGF-βRII) bind the growth factors and then phosphorylate type I receptors (such as activin receptor-like kinase 1 (ALK1)), which activate intracellular signaling cascades. Of all the growth factors and receptors in the TGF-β family, TGF-β1 interacting with TGF-βRII and ALK1 are the most pertinent ones to vascular tissue and fibrosis.

4.416.2.2.2.9. Hepatocyte growth factor

HGF, a mesenchymal-derived protein, has been found to play a central role in liver development and regeneration after injury. As a pleiotropic morphogen, it has been shown to have mitogenic, motogenic, and antiapoptic effects. In addition, HGF is being explored as an antifibrotic agent and may have applications in the treatment of liver fibrosis.[49]

4.416.2.2.2.10. Platelet-derived growth factor

PDGFs, members of the same superfamily as VEGF, are potent mediators of smooth muscle cell (SMC) and pericyte proliferation, migration, and recruitment. There are five PDGFs: PDGF-AA, PDGF-AB, PDGF-BB, PDGF-C, and PDGF-D. The PDGFs act via two receptors, PDGFR-α and PDGFR-β, located in cell membranes. The most prevalent *in vivo* interaction

of PDGFs and PDGFRs pertinent to the vascular system is that of PDGF-BB and PDGFR-β.[48] PDGF regulation of SMCs and pericytes is critical to the formation of blood vessels, as these cell types form the supportive mural layer around mature vessels.

4.416.2.3. Cell Adhesion and Growth

The formation of complex organs, the organization of cells within them, and the expression of tissue-specific genes require a combination of spatial instructions from the ECM and intercellular adhesion, together with temporal signals from soluble factors such as growth factors, hormones, and cytokines. The precise integration of the resulting intracellular signaling networks drives the principal cellular processes of suppression of apoptosis, cell cycle, migration, and differentiation, which are all keys to the morphogenesis and function of tissues. Eliceiri[50] described the importance of crosstalk between integrins and growth factor receptors in signaling mechanism to provide specificity during normal development and pathological processes in vasucular biology. It was shown that integrins directly associate with growth factor receptors and regulate the capacity of integrin–growth factor receptor complexes to propagate downstream signaling. The crosstalk occurs during cell growth, migration, and invasion as well as in ECs during angiogensis. Streuli and Akhtar[51] reviewed the pathways, both activated and coordinated by the integrin class of cell–matrix receptors and other receptor systems. They discuss (1) how β_3 and β_1 integrins work together with growth factors to control angiogenesis; (2) how $\alpha_6\beta_4$ integrin cooperated with receptor tyrosine kinases in normal epithelial function and cancer; (3) the interplay between β_1 integrins and EGFR; (4) signal integration connecting integrins and cytokine receptors for ILs, prolactin, and IFNs; and (5) how integrins and syndocans cooperate in cell migration.

Ivaska and Heino[52] review the present information concerning the role of integrins as assisting growth factor receptors and the interplay between the receptors in cell signaling and in the orchestration of receptor recycling. They summarize some forms of collaboration between integrins and growth factor receptors as follows: (1) Integrins directly bind to latent growth factors and activate them. Subsequently, activated growth factors bind to their signaling receptors. (2) The binding of integrins to ECM proteins activates the same signaling pathways as binding to the receptors does. (3) Receptors can signal when located either on the cell surface or in endosomes. Coendocytosis of integrins and growth factors regulates cellular signaling at multiple levels. (4) Integrins activate growth factor receptors in a collaborative manner. Integrins create an environment in which growth factor receptors can properly interact with the downstream signaling molecules. In the collaborative mechanism, the binding of growth factors to their receptors precedes receptor activation. (5) Integrins activate growth factor receptors in a direct manner. Integrins create an environment in which growth factor receptors can properly interact with the downstream signaling molecules. In the direct mechanism, the growth factor receptors are activated without receptor activation. (6) Integrins activate protein tyrosine phosphatase and suppress signaling by growth factor receptors.

4.416.3. Protein Immobilization (Chapter 2.209, Materials as Artificial Stem Cell Microenvironments; Chapter 4.411, Peptide- and Protein-Modified Surfaces; and Chapter 5.508, Scaffold Materials for hES Cell Culture and Differentiation)

4.416.3.1. Immobilization for ECM–Cell Interactions (Chapter 2.207, Extracellular Matrix: Inspired Biomaterials; Chapter 2.208, Artificial Extracellular Matrices to Functionalize Biomaterial Surfaces; and Chapter 2.220, Extracellular Matrix as Biomimetic Biomaterial: Biological Matrices for Tissue Regeneration)

4.416.3.1.1. Extracellular matrices

Surface modification can modify the interaction between the biomaterials surface and the biological environment and yet preserve the mechanical properties of the base biomaterials.[53] Design of functionalized polymer surfaces for biomaterial applications often relies on immobilization of ECM proteins or peptides to control the integrin-mediated cell attachment. Given the central roles of integrins in cellular processes, ongoing biomaterials research has focused on identifying material surface characteristics that modulate the type, strength, and degree of ECM–integrin binding. Cell adhesion to ECM components or ECM-derived ligands on engineered surfaces governs host responses to implanted devices, integration of biomedical prostheses and tissue-engineered constructs, and the performance of biotechnological supports.

The coating of various biomaterial substrates with full-length ECM proteins modulates integrin-mediated cell function to varying degrees.[2] For instance, FN coatings on polystyrene increase osteoblast expression of α_3 and α_5 and reduce expression of α_2, α_6, and α_v subunits compared with uncoated polystyrene. Stromal cell, calvarial osteoblast, and osteoblast-like cells exhibit enhanced β_1-mediated adhesion, proliferation, and differentiation on FN-coated and type I collagen-coated surfaces compared with that on uncoated glass, polystyrene, or titanium surfaces. It has been postulated that plasma FN-coated implants enhanced early bone formation because of a chemotactic attraction of osteoprogenitors near the ECM-coated implant surface. Although there are conflicting data regarding the functional effects of collagen coating on polystyrene and titanium for various cell types, there is evidence of cell type-specific distinct integrin expression profiles on collagen versus noncollagen-coated surfaces. Osteoblasts upregulate α_3 expression over α_6 on type I collagen-coated polystyrene, whereas type IV collagen coatings mediate greater α_1, α_2, α_3, and β_1 expression and activation. Other bone-specific matrix proteins, including bone sialoprotein (BSP) and OPN, have also been explored as bioactive surface coatings to control β_3-mediated binding and signaling for human osteoblasts and stromal cells. BSP is an acidic, noncollagenous glycoprotein abundantly expressed in mineralized tissues. BSP bound to type I collagen was found to orient in a bioactive orientation that augments β_3 binding and subsequent osteoblast adhesion and differentiation over unmodified interfaces. Implants coated with BSP were found to be fairly osteoconductive *in vitro*, yet supported only minimal functional integration and mechanical fixation *in vivo*.

Vitronectin is another ECM protein that dominates serum-exposed adsorption to polystyrene. Coating vitronectin on polystyrene not only enhances mouse osteoblast expression of $\alpha_v\beta_3$,

but has also been shown to weaken adhesion of murine cells compared with uncoated polystyrene. However, for human osteoblasts, adhesion to vitronectin was found to be primarily $\alpha_{v\beta5}$-mediated and more robust than adhesion to uncoated surfaces. These studies highlight cell type-dependent effects on integrin binding and cell function that surface modifications using natural ECM proteins may elicit.

The ECM adsorption approach is nevertheless highly sensitive to materials surface chemistry. Grinnell and Feld[54] first showed that plasma FN would be adsorbed in higher content but with lower bioactivity on hydrophobic compared to hydrophilic surfaces, a finding subsequently confirmed by other studies[55,56] FN has been immobilized to surfaces using covalent coupling chemistries via the amine, thiol, and aldehyde groups.[57–60] Covalent coupling or conjugation presumably would be more efficient and stable against detachment. A critical issue of the covalent strategy is the conservation of the desired bioactivity of the immobilized FN. The degree of activity depends on the binding procedure and the substrate.[60] A combination of conjugation and adsorption can sometimes produce optimal results. By conjugating FN to the terminals of Pluronic™ F108 adsorbed on polystyrene, Biran *et al.*[58] concluded that the FN was more bioactive than the FN adsorbed directly onto polystyrene as revealed by the neurite adhesion and outgrowth assays.

Zhang *et al.*[61] investigated the bioactivity of FN immobilized on polyethylene terephthalate (PET), one of the most widely studied biomaterials surfaces, using both conjugation and adsorption methods. In the first case, FN was covalently conjugated to an aminated PET surface via glutaraldehyde cross-linking, and then the surface was blocked by ethanolamine. In the second case, FN was physically adsorbed to the ethanolamine-blocked aminated-PET surface without FN conjugation. Adsorption methods preserved the compact conformation of FN, reaching saturation when a monolayer of FN was formed. Covalent conjugation induced FN unfolding and fibrillogenesis, forming multiple layers of FN. Adsorption maintained a more active RGD domain, thereby promoting cell adhesion, whereas conjugation induced fibrollogenesis and blocked the access to RGD, consequently suppressing cell adhesion as the surface density of FN increased. On the other hand, Bramfeldt and Vermette[62] demonstrated that covalent immobilization of FN, fibrinogen, or fibrin resulted in significantly enhanced cell adhesion of poly(ε-caprolactone) (PCL)-polyethylene-glycol (PEG) block copolymers. In addition, they reported that the cell growth was also more enhanced on the covalently immobilized surface than on the one with physisorbed proteins.

Recently, Kohen *et al.*[63] examined the property of some substrata coated with Matrigel™, a blend of ECM proteins derived from murine tumor cells, by culturing human embryonic stem (ES) cells. They observed that human ES cells attached and grew poorly on Matrigel adsorbed on polystyrene, while they proliferate when exposed to Matrigel adsorbed onto glass or oxygen plasma-treated polystyrene (e.g., 'tissue culture' treated polystyrene). Furthermore, human ES cells grown on the Matrigel-coated tissue culture polystyrene are less likely to differentiate than those grown on the Matrigel-coated glass. Matrigel formed a viscoelastic multilayer with similar thickness on all three surfaces; however, the network structures were different, as the adsorbed proteins formed a globular network on polystyrene and fibrillar networks on the hydrophilic substrates. Matrigel networks on glass were denser than those on oxygen plasma-treated polystyrene, suggesting that the density and structure of the Matrigel network affected stem cell differentiation, whereas a denser network promoted uncontrolled human ES cell differentiation and did not maintain the self-renewal phenotype.

OPN, an ECM molecule involved in wound-healing processes, was immobilized onto poly(2-hydroxyethyl methacrylate) (poly(HEMA)) by Martin.[64] The immobilization was confirmed by electron spectroscopy for chemical analysis and time-of-flight secondary ion mass spectroscopy. Iodination of OPN yielded quantitative data supportive of dose-dependent immobilization. Enzyme-linked immunosorbent assay (ELISA) was also used to investigate the presence of OPN on poly(HEMA). The cell-adhesive properties of immobilized OPN were also confirmed by using a bovine aortic EC adhesion assay. Martin *et al.*[65] covalently attached OPN to type I collagen and they confirmed the attachment using surface plasmon resonance (SPR). Radio-iodination of OPN showed that binding to collagen was dose-dependent and maximal in basic conditions. Principal component analysis of time-of-flight secondary ion mass spectrometry data identified differences in OPN immobilized. They showed that adhesion of bovine aortic ECs on immobilized OPN using the affinity coating was significantly enhanced compared to controls.

4.416.3.1.2. Biomimetic peptides (Chapter 4.415, Surface Engineering Using Peptide Amphiphiles)

For promoting cell-specific functions, the functionalization of biomaterials with natural matrix proteins has several drawbacks. As many full-length matrix proteins contain multiple integrin and other biomolecule binding sites, it is likely that these proteins may induce significant binding of more than one integrin, and hence, do not truly support an 'integrin-specific' surface. Moreover, immunogenic and pathogen transmission concerns across species limit widespread use of these ECM-derived protein ligands as bioactive coatings for implants in humans. Furthermore, processing issues including scale-up difficulties and long-term stability may reduce the widespread application of these matrix-functionalized surfaces.

Synthetic biomimetic strategies to promote cell adhesion have primarily focused on presenting short bioactive motifs derived from ECM components onto biomaterial or implant surfaces.[66–70] ECM-derived ligands to control cell adhesion were comprehensively reviewed by Petrie and Garcia[2] and Raynor *et al.*[71] A number of adhesion motifs from ECM components that can be subsequently incorporated in a small synthetic peptide have been identified. These motifs consist of a short linear sequence of amino acids, typically no more than a dozen amino acids in length, that one or more integrin receptors can recognize and bind. These short sequences (**Table 2**) can be easily incorporated into adhesion oligopeptides that can be strategically immobilized in numerous ways on a biomaterial support to promote integrin-mediated adhesive and functional responses. These immobilization schemes include covalent tethering directly onto a biomaterials substrate, using plasma treatment to increase the functional groups on the substrate, or tethering onto polymer coatings functionalized on an underlying substrate. Nonbiofouling

supports (i.e., PEG or alginate) are often used to isolate the activity of these motifs better by utilizing a background with minimal nonspecific protein adsorption.[72]

Carrico *et al.*[73] reported microbial expression of artificial proteins bearing the photosensitive noncanonical amino acid para-azidophenylalanine. The recombinant proteins, designated artificial ECM proteins with aryl azides, belong to a family of engineered proteins designed to exhibit mechanical properties similar to those of native elastin and to support adhesion of mammalian cells through cell-binding domains (CS5 or RGD) derived from FN. Liu and Tirrell[74] presented a method for preparing cross-linked artificial ECM films that are suitable for cell studies, and they demonstrated that cells recognized the RGD sequence within cross-linked, PEG-conjugated (PEGylated) protein films. They varied the density of adhesion ligands by mixing artificial ECM-RGD and artificial ECM-RDG prior to cross-linking, and they examined the role of RGD density in modulating the adhesion, spreading, and migration of human umbilical vein ECs. Zhe *et al.*[75] reported rational design and synthesis of a new type of bioactive poly(ethylene glycol) diacrylate (PEGDA) macromonomers, cyclic RGD-PEGDA, to mimic the cell-adhesive properties of ECM, aiming to create biomimetic scaffolds with controlled spatial organization of ligands and enhanced cell binding affinity for tissue engineering. Petty *et al.*[76] used microfluidic networks to establish a gradient of RGD peptide in contact with a monolayer that presented meleimide groups among tri(ethylene glycol) groups. Foillard *et al.*[77] prepared tetrameric RGD-containing peptide for highly efficient cell adhesion on beads. Perlin *et al.*[78] reviewed RGD functional materials including both synthesis and design strategies. Robertus *et al.*[79] reviewed recent development in the cell adhesion of mammalian cells to RGD-modified self-assembled monolayer (SAM)-modified surfaces, the physical properties of which can be controlled by an external stimulus, for example, by light, electrochemistry, etc.

Hwang *et al.*[80] designed and constructed a hybrid of the mussel adhesive protein with RGD peptide. Meyers *et al.*[81] created multidomain peptides for use as coatings to endow material surfaces with desired biological activities. They termed such peptide-based functional coatings as 'interfacial biomaterials' (IFBMs). Especially, IFBM is a modular peptide containing at least one material binding domain and at least one bioactive functionality. They combined polystyrene-binding peptide with RGD, yielding a bifunctional IFBM; they created spatially resolved patterns of cells on substrates and the patterns retained the border in culture.

Self-assembly of peptides has also been investigated by many researchers. Rexeisen *et al.*[82] showed that single-tailed peptide-amphiphiles formed nanofibers in solution and gels after screening of their electrostatic charges and those containing cell-binding motifs. FN-mimetic peptide sequences were developed, containing both the primary binding domain RGD and the synergy binding domain Proline-Histidine-Serine-Arginine-Asparagine (PHSRN), which has shown superior cell adhesion properties over simple RGD sequences and FN in two-dimensional (2D) culture. Cryo-transmission electron microscopic images of a 100 μM peptide-amphiphile solution showed individual nanofibers with a diameter of ~10 nm and lengths on the order of several micrometers. The peptide-amphiphile gel was monitored by parallel-plate rheometry, and the elastic modulus (G') was greater than the viscous modulus (G''), which indicates that the peptide forms a gel. The shear modulus for a 2-day-old gel was measured to be ~500 Pa, which is within the modulus range for living tissue. Cejas *et al.*[83] also prepared collagen-related peptides which were self-assembly of short, single strands into functional biomaterials of micrometer scale. Horii *et al.*[84] showed a class of self-assembling peptide nanofiber scaffolds having an excellent biological material for three-dimensional cell culture and stimulating cell migration into the scaffold, as well as for repairing tissue defects in animals. They designed a pure self-assembling peptide scaffold RADA16-I by direct coupling to short biologically active motifs. The motifs included osteogenic growth peptide ALK (ALKRQGRTLYGF) bone-cell secreted-signal peptide, OPN cell adhesion motif DGR (DGRGDSVAYG), and 2-unit RGD binding sequence PRG (PRGDSGYRGDS). Compared to pure RAD16 scaffold, they found that these designer peptide scaffolds significantly promoted mouse preosteoblast MC3T3-E1 cell proliferation. Moreover, alkaline phosphatase (ALP) activity and osteocalcin secretion, which are early and late markers of osteoblastic differentiation, were also significantly increased. They demonstrated that the designer, self-assembling peptide scaffolds promoted the proliferation and osteogenic differentiation of MC3T3-E1. Under the identical culture medium condition, confocal images unequivocally demonstrated that the designer PRG peptide scaffold stimulated cell migration into the 3D scaffold. Their results suggest that these designer peptide scaffolds may be very useful for promoting bone tissue regeneration.

The density or spacing of plasma membrane proteins is thought to be crucial for their function; clear-cut experimental evidence, however, is still rare. Therefore, Jaehrling *et al.*[85] examined nanopatterns biofunctionalized with cell adhesion molecule neural CAM DM-GRASP (dorsal funiculus, ventral midline immunoglobulin-like restricted axonal surface protein) with respect to their impact on neuron attachment and neurite growth. Data analysis/modeling revealed that these cellular responses improve with increasing DM-GRASP density, with the exception of one spacing, which does not allow for the anchorage of a cytoskeletal protein (spectrin) to three DM-GRASP molecules.

4.416.3.2. Immobilization for Cell–Cell Interaction

In order to control cell–cell interaction, the investigations on immobilization of CAM proteins such as cadherin, selectin, Notch ligand, Shh, etc. have been reported.

4.416.3.2.1. Cadherin

Nagaoka *et al.*[86] prepared a cadherin-immobilized surface for ES cell culture. Gelatin-coated plates or feeder layers form tight aggregated colonies by the E-cadherin-mediated cell–cell adhesions. They showed that murine ES cells do not make cell–cell contacts or form colonies when cultured on the plate coated with a fusion protein of E-cadherin and IgG fragment crystallizable Fc domain. The cells in culture retain all ES cell features including pluripotency to differentiate into cells of all three germ layers and germ-line transmission after

extended culture. Furthermore, they show a higher proliferative ability, lower dependency on leukemia inhibitory factor (LIF), and higher transfection efficiency than colony-forming conditions. Their results suggested that aggregated colony formation might inhibit diffusion of soluble factors and increase cell–cell communication, which may result in a heterogeneous environment within and between surrounding cells of the colony. This method should enable the more efficient and scalable culture of ES cells, an important step toward the clinical application of these cells.

Nagaoka *et al.*[87,88] also used the E-cadherin fusion protein as an adhesion matrix for the culture of F9 embryonal carcinoma cells which usually form colonies when cultured on gelatin or FN matrices. F9 cells cultured on the E-cadherin fusion protein matrix formed a scattered distribution with a different cytoskeletal organization and E-cadherin-rich protrusions that were regulated by Rac1 activity. The same scattering activity was observed in P19 embryonal carcinoma cells. In contrast, three types of differentiated cells, mouse, NAMRU, mammary gland (NMuMG) cells, Madin-Darby canine kidney (MDCK) kidney epithelial cells, and mouse primary isolated hepatocytes, did not show the scattering activity observed in F9 and P19 cells. These results suggest that migratory behavior on an E-cadherin-immobilized surface is only observed in embryonic cells and that the regulatory mechanisms underlying E-cadherin-mediated cell adhesion vary with the state of differentiation.

4.416.3.2.2. Selectin

Koike *et al.*[89] immobilized P-selectin purified from human platelets to induce monocytes to release TNF-α. The induction of TNF-α release was dependent on the concentration of P-selectin used for the immobilization, and the maximal stimulation was observed when the plate was coated with $0.3\,\mu g\,ml^{-1}$ of P-selectin. Use of either a higher or a lower concentration of P-selectin for the plate-coating was found to elicit less TNF-α release, although the higher concentration of P-selectin caused a stronger adhesion of HL-60 leukemic cells. The expression of mRNA of TNF-α roughly paralleled the TNF-α secretion, as assessed by reverse transcription-polymerase chain reaction (RT-PCR). These results indicate that monocytes are activated by immobilized P-selectin in a density-dependent manner.

Cell rolling is an important physiological and pathological process used to recruit specific cells in the bloodstream to a target tissue. This process may be exploited for biomedical applications to capture and separate specific cell types. A commonly studied protein that regulates cell rolling is P-selectin. P-selectin has been covalently immobilized on glass substrates by Hong *et al.*[90] By coating surfaces with this protein, biofunctional surfaces that induce cell rolling were prepared. Although most immobilization methods have relied on physisorption, chemical immobilization has obvious advantages, including longer functional stability and better control over ligand density and orientation. The chemistry was categorized on the basis of the functional groups on modified glass substrates: amine, aldehyde, and epoxy. The prepared surfaces were first tested in a flow chamber by flowing microspheres functionalized with a cell surface carbohydrate (sialyl Lewis(x)) that binds to P-selectin. Adhesion bonds between P-selectin and sialyl Lewis(x) dissociate readily under shear forces, leading to cell rolling. P-selectin immobilized on the epoxy glass surfaces exhibited enhanced long-term stability of the function and better homogeneity as compared to that for surfaces prepared by other methods and physisorbed controls. The microsphere rolling results were confirmed *in vitro* with isolated human neutrophils. This work was essential for the future development of devices for isolating specific cell types on the basis of cell rolling, which may be useful for hematologic cancers and certain metastatic cancer cells that are responsive to immobilized selectins. Schmidt *et al.*[91] constructed a biophysical simulation of the motion of a rigid microsphere coated with selectin in shearing flow undergoing thermal motion.

Plasmacytoid dendritic cells (pDCs) recognize microbes, viruses in particular, and provide unique means of innate defense against them. The mechanism of pDC tissue recruitment remained enigmatic because the ligands of CXCR3, the cardinal chemokine receptors on pDCs, have failed to induce *in vitro* chemotaxis of pDCs in the absence of additional chemokines. Kohrgruber *et al.*[92] demonstrated that CXCR3 is sufficient to induce pDC migration, however, by a migratory mechanism that amalgamates the features of haptotaxis and chemorepulsion. To mediate 'haptorepulsion' of pDCs, CXCR3 requires the encounter of its cognate ligands immobilized, optimally by heparan sulfate, in the form of a negative gradient. This is the first report of the absolute requirement of chemokine immobilization and presentation for its *in vitro* promigratory activity. The paradigmatic example of pDC haptorepulsion described here may represent a new pathophysiologically relevant migratory mechanism potentially used by other cells in response to other chemokines.

4.416.3.2.3. Notch ligand

Cell–cell interactions mediated by Notch and its ligands are known to affect many cell fate decisions in both invertebrates and vertebrates. However, the mechanisms involved in ligand-induced Notch activation are unknown. Recently, it was shown that, in at least some cases, endocytosis of the extracellular domain of Notch and ligand by the signaling cell is required for signal induction in the receptive cell. These results imply that soluble ligands, (ligand extracellular domains) although capable of binding Notch, would be unlikely to activate it. To test the potential activity of soluble Notch ligands, Varnum-Finney *et al.*[93] generated monomeric and dimeric forms of the Notch ligand Delta-1 by fusing the extracellular domain to either a series of myc epitopes (Delta-1(ext-myc)) or to the Fc portion of human IgG-1 (Delta-1(ext-IgG)). Notch activation, assayed by inhibition of differentiation in C2 myoblasts and by HES1 transactivation in U20S cells, occurred when either Delta-1(ext-myc) or Delta-1(ext-IgG) was first immobilized on the plastic surface. However, Notch was not activated by either monomeric or dimeric ligand in solution (nonimmobilized). Furthermore, both nonimmobilized Delta-1(ext-myc) and Delta-1(ext-IgG) blocked the effect of immobilized Delta. These results indicate that Delta-1 extracellular domain must be immobilized to induce Notch activation in C2 or U20S cells and that nonimmobilized Delta-1 extracellular domain is inhibitory to Notch function. These results imply that ligand stabilization may be essential for Notch activation.

Konno *et al.*[94] immobilized Notch ligand by photoimmobilization and showed that immobilized Notch ligand maintained growth of Notch ligand-dependent cells, such as soluble Notch ligand. The Notch signaling pathway was identified as a key regulator of epithelial differentiation. Utilizing this knowledge, Beckstead *et al.*[95] applied an affinity immobilization scheme designed to attach and orient the Notch ligand, Jagged-1, in an active conformation on a biomaterial surface. When epithelial stem cells were plated on the bound ligand, the Notch/CBF-1 signaling pathway was stimulated and the cells were upregulated by both intermediate- and late-stage differentiation markers. In addition, the ligand promoted tight clustering and extensive stratification. Soluble Jagged-1 showed no Notch/CBF-1 signaling and very little, if any, cell differentiating activity. The high potency of bound Jagged-1 suggests that modification of a surface with a Notch ligand presents a powerful method to control stem cell differentiation at the cell–biomaterial interface.

Thymocyte development takes place in a complex milieu of supportive cells and ECM that are responsible for the proliferation, adhesion, migration, and selection processes that these cells undergo before reaching maturity. In recent years, the role of Notch signaling in lymphocyte development, specifically T cell development, has been extensively characterized. Although Notch-ligand-mediated signals have been shown to be a necessary component of T cell generation from stem cells, high-throughput, synthetic biomaterial-based systems for Notch-directed stem-cell differentiation into lymphocytes are yet to be reported. Taqvi *et al.*[96] reported a microbead-based, artificial Notch signaling system to study stem-cell differentiation into the T cell lineage. Magnetic microbeads were functionalized with the Notch ligand DLL4 using streptavidin-biotin binding and antibody–antigen coupling. Immunohistochemistry and flow cytometry analysis indicated ~65% conjugation efficiency. Efficient Notch signaling through these functionalized microbeads was demonstrated through a myotube inhibition assay in C2C12 myoblasts. Thy1.2(+) early T cells were successfully generated from mouse bone marrow hematopoietic stem cells (BMHSCs) using DLL4 functionalized beads using both insert-based and mixed stromal cell (OP9) coculture conditions, indicating that stem cell–stromal cell physical contact is not necessary for DLL4-directed T cell differentiation. In coculture studies, bead-to-cell ratios of 1:1 generated higher T cell differentiation efficiencies compared to bead-to-cell ratios of 5:1. They demonstrated the promising potential of this biomaterial-based Notch signaling system to generate T cells from stem cells and to elucidate the molecular interactions in T cell development.

Suzuki *et al.*[97] demonstrated efficient *ex vivo* expansion of hematopoietic stem cells (HSCs) measured by long-term severe combined immunodeficient (SCID) repopulating cells (SRCs) from human cord blood CD133-sorted cells using a soluble form of Delta-1. After a 3-week culture on immobilized Delta-1 supplemented with stem cell factor (SCF), thrombopoietin, Flt-3 ligand, IL-3, and IL-6/soluble IL-6 receptor chimeric protein (FP6) in a serum- and stromal cell-free condition, we achieved approximately sixfold expansion of SRCs when evaluated by limiting dilution/transplantation assays. The maintenance of full cell multipotency and self-renewal capacity during culture was confirmed by transplantation to nonobese diabetic/SCID/gammac(null) mice, which showed myeloid, B, T, and natural killer cells as well as CD133(+)CD34(+) cells, and hematopoietic reconstitution in the secondary recipients. Interestingly, the CD133-sorted cells contained ~4.5 times more SRCs than the CD34-sorted cells. The present study provides a promising method to expand HSCs and encourages future trials on clinical transplantation.

Kertész *et al.*[98] showed that prolonged *in vitro* culture (14 days) of murine bone marrow lineage negative cells in a medium supplemented with three early acting cytokines (SCF, Flk-2/Flt-3 ligand, thrombopoietin) and with immobilized Notch ligand, Jagged-1, resulted in robust expansion of serially transplantable HSCs with long-term repopulating ability. They found that the absolute number of marrow cells was increased ~8–14-fold in all cultures containing recombinant growth factors. However, the frequency of high quality stem cells was markedly reduced at the same time, except in cultures containing growth factors and Jagged-1-coated Sepharose-4B beads. The absolute number of hematopoietic cells with long-term repopulating ability was increased ~10–20-fold in the presence of multivalent Notch ligand. These results supported the idea of the role of the combinatorial effects of Notch and cytokine-induced signaling pathways in regulating HSC fate and the potential role of Notch ligand in increasing cell numbers in clinical stem cell transplantation.

4.416.3.2.4. Ephrin B2

Zisch *et al.*[99] developed the natural hydrogel matrix fibrin as platform for extensive interactions and continuous signaling by the vascular morphogen ephrin-B2 that normally resides in the plasma membrane and requires multivalent presentation for ligation and activation of ephrin (Eph) receptors on apposing EC surfaces. Using fibrin and protein engineering technology to induce multivalent ligand presentation, a recombinant mutant ephrin-B2 receptor binding domain was covalently coupled to fibrin networks at variably high densities. The ability of fibrin-bound ephrin-B2 to act as ligand for ECs was preserved, as demonstrated by a concomitant, dose-dependent increase of EC binding to engineered ephrin-B2-fibrin substrates *in vitro*. The therapeutic relevance of ephrin-B2-fibrin implant matrices was demonstrated by a local angiogenic response in the chick embryo chorioallontoic membrane evoked by the local and prolonged presentation of matrix-bound ephrin-B2 to tissue adjacent to the implant. This new knowledge on biomimetic fibrin vehicles for precise local delivery of membrane-bound growth factor signals may help to elucidate specific biological growth factor function and serve as starting point for the development of new treatment strategies.

4.416.3.2.5. Sonic hedgehog

The signaling domain of Shh, a potent upstream regulator of cell fate, has been implicated in osteoblast differentiation from undifferentiated mesenchymal cells in its endogenous form. Therefore, an immobilized form as a means for accelerating differentiation of uncommitted cells to the osteoblast phenotype was investigated by Ho *et al.*[100] A recombinant cysteine-modified N-terminal Shh (mShh) was synthesized, purified, and immobilized onto interpenetrating polymer network

(IPN) surfaces and also grafted with a BSP-derived peptide containing the RGD sequence (BSP-RGD), at calculated densities of 2.42 and 10 pmol cm^{-2}, respectively. The mitogenic effect of mShh was dependent on the mode of presentation, as surfaces with immobilized mShh and BSP-RGD had no effect on the growth rate of rat bone marrow-derived mesenchymal stem cells (BMSCs), while soluble mShh enhanced cell growth compared to a similar surface without mShh supplementation. In conjunction with media supplemented with bone morphogenetic protein-2 and -4, mShh and BSP-RGD-grafted IPN surfaces enhanced the ALP activity of BMSCs compared with tissue culture polystyrene and BSP-RGD-grafted IPN surfaces supplemented with soluble mShh, indicating enhanced osteoblast differentiation. The adhesive peptide BSP-RGD was necessary for cell attachment and proliferation, as well as differentiation in response to immobilized mShh. The addition of immobilized Shh substantially improved the differentiation of uncommitted BMSCs to the osteoblast lineage, and therefore warrants further testing *in vivo* to examine the effect of the stated biomimetic system on peri-implant bone formation and implant fixation.

4.416.3.3. Surface Immobilization of Growth Factors

The effect of immobilized growth factors is expected to be different from immobilized adhesion factors because of intrinsic differences in their cell interaction mechanisms (**Chapter 4.427, Cell-Demanded Release of Growth Factors** and **Chapter 4.412, Rational and Combinatorial Methods to Create Designer Protein Interfaces**).

4.416.3.3.1. Mechanisms

Figure 3 shows the possible cell interaction mechanisms for both diffusible and nondiffusible growth factors. First, growth factor interacts with cognate receptors on cell surfaces to form complexes. Second, the complex moves on the cell surface to be aggregated. At the same time, the interaction induces phosphorylation of intracellular domains of receptors and triggers cell signal transduction within the cell. In the case of diffusible interactions, the aggregates of formed complexes are internalized through clathrin-dependent or -independent mechanisms. The internalized complexes are partially decomposed in lysosomes and are partially recycled back to the cell membrane. In the case of intracrine mechanisms, although the internalization mechanism is not known, the receptor is considered to be located in the cell, but not on the cell membrane. In diffusible actions, with the exception of intracrine functions, the number of factor-specific cell receptors determines the sensitivity of the cell. Internalization of receptors by complex formation downregulates numbers on the cell membrane. This critical downregulation mechanism for cell desensitization reduces excess response to excess exogeneous stimulation.

Nondiffusible mechanisms (juxtacrine) are enabled by discovery of cell membrane-bound growth factors in 1990s. Heparin-binding epidermal growth factor (HB-EGF), TGF-β, TNF-α, colony stimulating factor 1 (CSF-1), and c-kit ligand are known as juxtacrine growth factors as reviewed by Massague and Pandiella[101] and Iwamoto and Mekada.[102]

In the 1990s, chemically immobilized growth factors were devised and investigated (reviewed by Ito[103,104]). The effect of immobilized growth factors has been investigated as either artificial juxtacrine or matricrine. Comparison between diffusible and nondiffusible cell stimulations by growth factors is important to design the combination of growth factor with scaffold and cells. Immobilization of growth factors onto scaffolds is considered to induce some characteristic phenomena with cellular cognate receptors, as shown in Figure 4. Immobilized growth factors stimulate cells with increased potency over soluble factors. It has also been also demonstrated that immobilized growth factors exhibit increased and effective distinct soluble factors because their interaction is not only a ligand–receptor complex formation. These effects of immobilized growth factors are considered to be due to complex, multiple mechanisms.

One difference is the high local density and multivalency on surfaces. The interaction of immobilized biosignal molecules from the substrate due to local density is extremely high and constant. In addition, the importance of mutivalency of immobilized biosignal molecules has been discussed by many researchers. Recently, Kiessling *et al.*[105] considered synthetic multivalent ligands as probes of cell signal transduction. Multivalent ligands can bind avidly to multiple receptors on the cell surface, a process facilitated by the cell's fluid lipid bilayer and the 2D diffusion of membrane receptors. Multivalent ligands can activate signaling pathways if they can cluster signaling

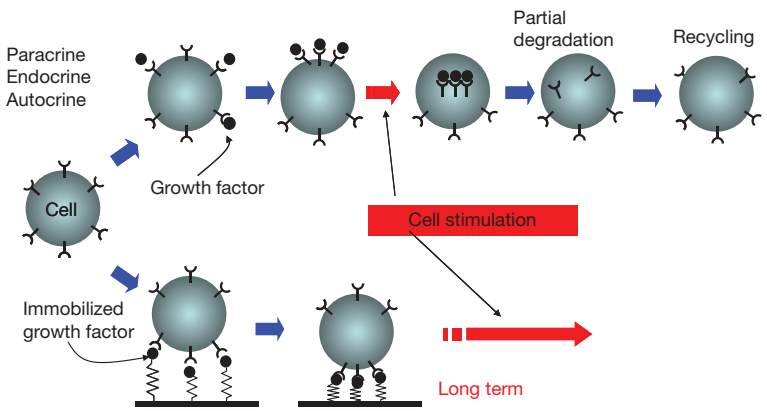

Figure 3 Cell interaction mechanisms with diffusible and nondiffusible growth factors.

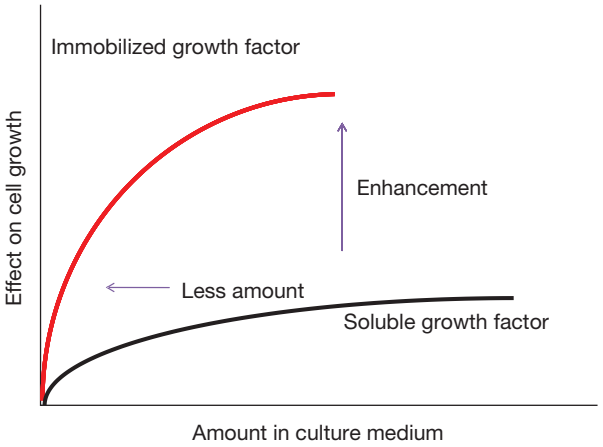

Figure 4 Schematic comparison of the mitogenic effect of immobilized growth factor with that of nonimmobilized growth factor. Immobilized growth factor induces a greater effect than nonimmobilized growth factor. A smaller amount of immobilized growth factor is considered to induce the effect as a result of multivalency and high local concentration. Potentiation of mitogenic effects is considered to be caused by inhibition of downregulation and other factors.

receptors. They discussed the three major concepts critical for application of multivalent ligands as effective probes of signal transduction: (1) Signal transduction cascades are mediated by receptor–receptor interactions and promoting receptor assembly is critical for signaling. (2) Multivalent ligands can interact with the target receptors through multiple binding modes. (3) The structure of a multivalent ligand will determine the favored binding modes. Thus, the structure can be optimized to elicit the desired biological response.

In addition to high local concentration and multivalency, prevention of lateral diffusion of the activated receptors or the receptor–ligand complexes in the plane of the cell membrane must be considered. This equates to stabilization of the aggregates of complexes and thus leads to a long-lasting effect. Inhibition of the cell internalization process should also be considered as shown in Figure 3. In general, cells decompose these biosignal molecules within the cells to reduce their stimulation by a process called downregulation. Factor immobilization inhibits this downregulation and as a result, cell stimulation continues for a long time without reduction. In addition, differences in stimulation between the cells in medium and at the cell–matrix interface should also be distinguished. The specific situation differentially affects various cell functions at surfaces.

4.416.3.3.2. Examples of immobilized growth factors

4.416.3.3.2.1. Insulin

Insulin was immobilized and the effect was investigated by Ito *et al.*[66,67] They immobilized insulin, transferrin, and collagen on the surface of hydrolyzed poly(methyl methacrylate) films using ethylcarbodiimide hydrochloride (EDC) chemistry, and cultured mouse STO (S, SIM; T, 6-thioguanine resistant; O, ouabain resistant) fibroblasts on the protein-immobilized films. They found that insulin remained immobilized without detachment and accelerated cell growth in a more potent manner than free or adsorbed insulin. Subsequently, Ito *et al.*[106] compared the effects with those of proteins such as a cell-growth factor insulin, cell adhesion factors fibrinogen and FN, and serum proteins albumin and γ-globulin. As a result, the insulin-immobilized poly(methyl methacrylate) membrane strongly accelerated the growth and slightly accelerated the adhesion of fibroblast cells and immobilized FN and fibrinogen enhanced cell adhesion and the former also accelerated the cell growth. Immobilized albumin and γ-globulin influenced the adhesion and growth of cells very little. It was found that various proteins specifically influence the adhesion and growth of cells in an immobilized state. Liu *et al.*[107] revealed that cell growth was enhanced by the addition of immobilized insulins that were not internalized. It appears that insulin–receptor binding is enough for the transmission of the cell growth signal to the cell nucleus. The enhanced cell growth by the immobilized insulins compared with free insulin molecules is ascribable to suppression of the cell downregulation, a consequence of intracellular decomposition of the insulin–receptor complex. Liu *et al.*[108] also reported that the growth acceleration by immobilized insulin was enhanced by the introduction of a spacer arm between insulin and the immobilization matrix. The amount of receptor proteins present on the biological membrane of fibroblast cells after culture with insulin immobilized on nondegradable polymer membrane was much higher than that after culture with free insulin, implying suppression of downregulation by immobilized insulin. It was demonstrated that the effects of immobilized growth factors overcome the effect of multivalent soluble growth factors.[109,110]

In order to investigate the signal transduction of immobilized insulin, Chinese hamster ovary (CHO) cells overexpressing human insulin receptors were cultured on polymer film in the absence of serum or soluble proteins.[111,112] Small amounts of immobilized insulin (1–10% of the required amount of free insulin) were sufficient to stimulate cell proliferation. In addition, the maximal mitogenic effect of immobilized insulin was greater than that of free insulin. Immobilized insulin activated the insulin receptor and downstream signaling proteins, and this activation persisted for longer periods than that obtained with free insulin, probably explaining the greater mitogenic effect of the immobilized insulin. In addition, the immobilized-insulin film was usable repeatedly without marked loss of activity. Repeated utilization provides evidence indicating the stable activity of immobilized growth factors. If the immobilized growth factor was released from the surface because of proteolysis or incompleteness of immobilization, the biological activity of surface is not considered to be maintained. Repeated utilization is an advantage of immobilized enzymes for bioreactors useful for mass cell culture.

If the concept of immobilization was applied to other materials[113–119] or to a protein-free cell culture,[120–122] the activity was enhanced by coimmobilization with cell adhesion proteins[113,123–132] for other cells.[122,131–133] Heparin was coimmobilized for enhancement by Kim *et al.*[134] and Sasmazel *et al.*[135] On the other hand, Ito *et al.*[111,112] developed a photoimmobilization method and Ito *et al.*[125,126,128] succeeded in visualization of the cell signal transduction. Spatial regulation of the cell functions was performed on

micropattern-immobilization of insulin. When cell culture was performed on micropatterned growth factors, cell growth was accelerated only on the growth factor-immobilized areas.

In addition to spatial control, temporal control using a temperature-sensitive polymer poly(*N*-isopropylacrylamide) was performed by Chen *et al.*[136] and Hatakeyama *et al.*[137–139] Insulin was immobilized and a thermoresponsive polymer was grafted onto a substrate. They investigated the effect of insulin coupling under lower critical solution temperature (LCST) of the thermoresponsive polymer film, poly(*N*-isopropylacrylamide-*co*-acrylic acid), using polymers that were either ungrafted or coupled with insulin. The insulin conjugates were precipitated from an aqueous solution at high temperatures, but they were soluble at low temperatures. The LCST was not significantly affected by the insulin coupling. The thermoresponsive polymer was grafted to glow-discharged polystyrene film and covalently conjugated with insulin. The surface wettability of the conjugate film was high at low temperatures and low at high temperatures. The amounts of immobilized insulin required to stimulate cell growth were 1–10% of the amount of free insulin required to produce the same effect. The maximal mitogenic effect of immobilized insulin was greater than that of free insulin. About half of the viable cells were detached from the film only by lowering the culture temperature. The recovered cells proliferated normally on new culture dishes.

4.416.3.3.2.2. Insulin-like growth factor 1

Adult stem cells exhibit a much higher differentiation potential than previously expected and the sources within the adult organism seem to be surprisingly abundant. Brose *et al.*[140] investigated adult stem cells isolated from mouse and rat pancreas and showed their potential to differentiate into osteoblasts, chondrocytes, and adipocytes and they also showed that pancreatic stem cells (PSCs) differentiated spontaneously into cell types of all three germ layers. In addition, it was demonstrated that a directed differentiation is also possible and a variety of cytokines are compared as inducers. They applied the soluble differentiation factors for the use of immobilized cytokines. They immobilized IGF-1 to amino- or epoxy-silanized glass or affinity binding of the biotinylated cytokine to neutravidin-coated surfaces. The immobilized IGF-I induced adipogenic differentiation of mouse PSCs. At day 18, the cell cultures were analyzed by Oil red O staining and showed clear formation of oil vesicles. The results show that cytokines could be immobilized functionally, retaining their biological activity to effectively induce stem cell differentiation in long-term cell culture experiments. Miller *et al.*[141] developed an inkjet printing methodology for creating solid-phase patterns of unmodified growth factors on native biological material substrates. They demonstrated this approach by printing gradients of fluorescently labeled BMP-2 and IGF-II bio-inks on fibrin-coated surfaces. Concentration gradients were created by overprinting individual substrate locations using a dilute bio-ink to modulate the surface concentration of deposited growth factor. After inkjet printing, cell culture was performed to evaluate the effect of immobilized growth factors.

Stefonek-Puccinelli and Masters[142] demonstrated cell migration control by coimmobilization of gradient-patterned growth factors. Growth factors, including IGF-1 and EGF, are known to be deficient in chronic wounds; unfortunately, traditional delivery of soluble growth factors to wounds is expensive and complicated by their degradation. Therefore, they attempted to direct and accelerate keratinocyte migration by creating immobilized gradients of EGF. In addition, they optimized EGF gradients for cell migration, synthesized and characterized gradient patterns of IGF-1, and tested for migration synergy upon combination of EGF and IGF-1 patterns. An optimal EGF concentration and pattern was identified, resulting in migration that was almost tenfold of that achieved on unpatterned controls. Immobilization of IGF-1 gradients also accelerated and directed keratinocyte migration ($p < 0.05$); however, no difference in migration was found across various IGF-1 concentrations or gradient patterns. Although combining EGF with IGF-1 patterns did not accelerate migration beyond levels achieved using EGF alone, these methods can be applied to create other types of multicomponent gradients that may ultimately be utilized to create bioactive wound dressings.

Van Lonkhuyzen *et al.*[143] produced a chimeric protein of IGF-1 and vitronectin, the protein associated with IGF-I-binding protein. The complex of fusion protein and IGF-binding protein bound to both the IGF-1 receptor and integrin (thus binds to cells), and stimulated receptor-mediated and integrin-mediated pathways. As a result, the fusion protein complex exhibits a higher cell proliferation activity compared with the nonfusion protein complex.

4.416.3.3.2.3. Epidermal growth factor

Early work by Kuhl and Griffith-Cima[144] covalently tethered EGF to aminosilane-modified glass via star PEG, which allows the ligand to retain significant mobility and active conformation. The tethered EGF was as effective as soluble EGF in eliciting DNA synthesis and cell rounding responses of primary rat hepatocytes under different surface conditions. Ito *et al.*[125,126,128] considered the effect of immobilized EGF as artificial juxtacrine stimulation. Chen *et al.*,[145,146] Ogiwara *et al.*,[147] and Woo *et al.*[148] performed photo-immobilization of EGF and they clearly showed growth enhancement by the immobilized EGF. Coimmobilization of EGF and cell adhesion proteins or peptides was also investigated by Park *et al.*[149] and Tigli and Gumusdereliglu.[150] In addition, to further investigate the interaction of immobilized growth factor, CHO cells overexpressing the cognate receptors were cultured on plates immobilized with growth factors in narrow stripe patterns less than cell size.[151] The contact area (stripes 2 μm in width) between the cells and the immobilized growth factor was stained by antiphosphotyrosine antibody. As free lateral diffusion and internalization of the bound growth factor and the receptor complex were prohibited by immobilization of growth factor, only signal proteins in the interaction regions were activated. This finding also indicates that the biological signal was transduced only to the cell that interacted with immobilized growth factor. Utilization of microbeads immobilized with growth factors is also one of the tools to probe the interaction of cellular receptors with immobilized growth factor. Ichinose *et al.*[152] quantitatively investigated the interaction between immobilized growth factor and cellular receptors at the single molecular level. When immobilized density was only slightly lower than that of receptor dimers, cellular response was dramatically decreased. Receptor molecules bound with the immobilized growth factor were prevented

from lateral diffusion and internalization and maintained their initial surface position and density.

Chen and Ito[153] succeeded in the preparation of gradient micropattern immobilization of EGF to investigate the effect of artificial juxtacrine stimulation. Wang and Bohn[154] prepared surface composition gradients of EGF by adaptating an electrochemical gradient technique. Stefonek and Masters[155] synthesized surfaces covalently modified with gradients of EGF to create a platform that promotes directed cell migration. Under serum-free conditions, human epidermal keratinocytes on immobilized EGF gradients preferentially migrated in the direction of higher EGF concentrations and exhibited unidirectional migration speed and distance that were over fivefold greater than that observed on control surfaces. Treatment of migrating cells with an inhibitor of the EGFR resulted in immediate cessation of migration, thus verifying that the observed migration trends were directly attributable to keratinocyte interactions with immobilized EGF. EGF was also immobilized on polydimethylsiloxane,[156] silica nanoparticles,[157] silicone rubber,[158] and chitosan.[159]

Interestingly, Ito *et al.*[160] found that cellular gene expression is affected by both the kind and mode of growth factor stimulation (diffusive vs. nondiffusive). EGF was pattern-immobilized on a polystyrene plate. Although the growth of the rat phaeochromocytoma cell line PC12 is stimulated by diffusible EGF, and differentiation is stimulated by diffusible NGF, immobilized (nondiffusible) EGF stimulated PC12 differentiation. Immobilized EGF caused a long-lasting stimulation of intracellular signal protein, MAPK (also known as ERK), and p38 (a subfamily of the MAPK superfamily) in cells, as did diffusible NGF. The switching between growth stimulation and differentiation is considered to be due to the duration of the stimulus. The function of the biosignal conjugate was regulated using conjugation methodology.

Fan *et al.*[161] found that immobilized EGF provides a survival advantage to mesenchymal stem cells (MSCs). It is known that MSCs can act as a pluripotent source of reparative cells during injury and therefore have great potential in regenerative medicine and tissue engineering. However, the response of MSC to many growth factors and cytokines is unknown. Therefore, they investigated cellular responses of MSC on a biomaterial surface covalently modified with EGF. They found that surface-tethered EGF promotes both cell spreading and survival more strongly than saturating concentrations of soluble EGF. By sustaining MAPK kinase-extracellular-regulated kinase signaling, tethered EGF increases the contact of MSC with an otherwise moderately adhesive synthetic polymer and confers resistance to cell death induced by the proinflammatory cytokine, Fas ligand. It was concluded that tethered EGF may offer a protective advantage to MSC *in vivo* during acute inflammatory reactions to tissue engineering scaffolds.

Signaling by the EGFR plays a role in cell survival and has been implicated in bone development and homeostasis. Providing EGF in a scaffold-tethered format may sustain local delivery and shift EGFR signaling to prosurvival modes compared to soluble ligand. Marcantonio *et al.*[162] therefore examined the effect of tethered EGF on osteogenic colony formation from human bone marrow aspirates in the context of three different adhesion environments using a total of 39 donors. They found that tethered EGF, but not soluble EGF, increased the numbers of colonies formed regardless of the adhesion background, and that tethered EGF did not impair early stages of osteogenic differentiation. It is known that EGFR-mediated signaling helps regulate bone development and healing through its effects on osteogenic cells. Platt *et al.*[163] showed how EGFR activity and osteogenic differentiation responses in primary human MSCs were influenced by presenting covalently immobilized EGF on the culture substratum, a presentation mode that reduced EGFR internalization and restricted signaling to the cell surface. In both the absence and presence of immobilized EGF, MSCs increased the expression levels of EGFR and its heterodimerization partner HER2 during the course of osteogenic differentiation. Immobilized EGF increased levels of phosphorylated EGFR and phosphorylated ERK compared to control substrata, and these elevations were associated with a twofold enhancement of MSC ALP activity at day 7 and matrix mineralization at day 21. Surprisingly, addition of soluble EGF to cells cultured on immobilized EGF substrata reduced osteogenic differentiation, even though EGFR signaling is more strongly activated in an acute, short-term manner by sEGF treatment than by immobilized EGF treatment. A striking concomitant result of the soluble EGF effects was near-complete downregulation of EGFR and HER2, demonstrating that the immobilized EGF–EGFR interaction was dynamically reversible even though temporally sustained. Taken together, their results showed that enhanced MSC osteogenic differentiation corresponds to a sustained combination of receptor expression and ligand presentation, both of which were maintained by immobilized EGF.

Parallel screening was investigated by many researchers. For example, Nakajima *et al.*[164] prepared parallel and rapid screening of composite biomaterials through assays using cell-based arrays to optimize matrix–growth factor combinations. They employed photo-assisted patterning of an alkanethiol SAM to achieve site-addressable combinatorial immobilization of natural and synthetic matrices incorporated with growth factors including EGF, ciliary neurotrophic factor (CNTF), NGF, and NT-3. Neural stem cell obtained from the rat embryonic striatum was cultured directly on the array to screen for cell adhesion, proliferation, and promotion of neuronal and glial specification. The results showed that a significant number of cells adhered to laminin-1, FN, ProNectin, and poly(ethyleneimine). They found that cells proliferated most extensively on a spot with immobilized EGF among the spots with different matrix–growth factor combinations.

Protein engineering has been employed for the immobilization of growth factors. Nishi *et al.*[165] produced fusion proteins using the collagen-binding domain (CBD) motif from bacterial collagenase fused to EGF and FGF. Both were retained for 5–10 days when subcutaneously injected into rats (5–7 days), which suggests their tight binding to collagen or other ECM components. The EGF fusion protein exhibited only 1/10 of the original EGF activity, while the bFGF fusion protein showed an activity comparable with that of the native molecule. The CBD used may affect the activity of the fusion protein or its binding to the receptor, depending on the growth factors being fused. Hall *et al.*[166] incorporated a high affinity CBD derived from coagulation von Willebrand factor (vWF) to specifically target EGF to colonic lesions. The CBD-EGF fusion proteins bound tightly to collagen matrices under conditions

in which native nontargeted EGF was washed away. In biologic assays, the CBD-EGF fusion protein stimulated NIH3T3 cell proliferation with near wild-type biological activity. *In vivo* binding studies showed that the collagen-targeted EGF, but not the nontargeted EGF, accumulated at areas the where collagen on the luminal surface of the inflamed colon was exposed. A single colonic instillation of the collagen-targeted EGF induced a more rapid regeneration of intestinal crypts 24 h after treatment. These findings indicated that intracolonic delivery of collagen-targeted EGF represents a potentially effective therapeutic strategy for acute or chronic inflammatory bowel disease.

Ishikawa *et al.*[167] established another type of collagen-binding growth factor (CBD-EGF) consisting of EGF and FN CBD. A typical yield of CBD-EGF was $\sim 200\,\mu g\,ml^{-1}$ culture in an *Escherichia coli* expression system. This fusion protein bound to gelatin and fibrillar collagen sponges, and the bound protein was not effectively eluted even with 2 M NaCl. In addition, CBD-EGF bound to type I, II, III, or IV collagen-coated plates, and the specificity of binding was confirmed by competitive inhibition using FN. CBD-EGF substantially stimulated cell growth after binding to collagen-coated culture plates, whereas EGF had no effect, indicating that this fusion protein acted as a collagen-associated growth factor. In an animal model of impaired wound healing, CBD-EGF, but not EGF, was retained with collagen sponges at wound sites 4 days after implantation, and repair of epidermis was observed underneath the sponges. These results suggested that the fusion protein with high collagen affinity would be useful for wound healing. Ishikawa *et al.*[168] investigated the concept that CBD moiety with high collagen affinity may enhance the effective local concentration of EGF at the site of administration in the following tissues: skin wounds, catheter-injured arteries, and hind limb muscles. In an animal model of impaired wound healing, application of CBD-EGF in combination with collagen gel induced granulation tissue formation in the intractable skin wounds of diabetic mice (db/db) because of its sustained retention. It was also shown that CBD-EGF binds to type IV collagen (basement membrane, BM) exposed on the inner surface of blood vessels after balloon-catheter injury. In the injured artery, infused CBD-EGF remained bound to collagen exposed on the injured tissues even after blood circulation was restored. Injection of the fusion protein into the hind limbs revealed that our delivery system was effective for direct administration to muscular tissue. Native EGF did not exhibit these wound healing effects. Kato *et al.*[169] also developed collagen-growth factor composites for use in tissue engineering; chimeric proteins consisting of EGF and collagen binding domains derived from vWF or FN were synthesized by means of recombinant technology. Hall *et al.*[166] showed that collagen-binding EGF (CBD-EGF) dosed into an injured colon without a carrier promotes the repair of the inflamed luminal surface.

Fibrin-binding growth factor was reported by Kitajima *et al.*:[170] a chimeric protein of the FN fibrin-binding domain (FBD) and EGF. This fusion protein (FBD-EGF) binds to fibrin in the absence of the cross-linking enzyme (FXIIIa) and may be suitable for the preparation of fibrin-based scaffolds with EGF activity. The wound-healing potential of FBD-EGF was examined using an *in vitro* culture model of keratinocyte sheets; repair of the injured sheet was enhanced by fibrin-bound FBD-EGF, but not by EGF alone. *In vivo* evaluation of EGF-immobilized material was performed by Choi *et al.*[171] They immobilized human EGF on electrospun nanofibers composed of biodegradable polymers for the purpose of treating diabetic ulcers. Wound healing effects of the EGF nonofibers were confirmed in diabetic animals with dorsal wounds. The expression of keratinocyte-specific genes significantly increased with the application of EGF-conjugated nanofibers. The EGF-nanofibers exerted superior *in vivo* wound healing activities compared to control groups or EGF solutions. Furthermore, immunohistochemical-staining results showed that EGFR was highly expressed in the EGF nanofiber group. This study showed that EGF-conjugated nanofiber could potentially be employed as a novel wound healing material by increasing proliferation and phenotypic expression of keratinocytes.

Ogiwara *et al.*[172] produced an EGF fusion protein coupled with the Fc region of IgG. The Fc region is often used as a fusion tag to allow extracellular domains of large membrane proteins or receptor molecules to adhere nonspecifically to solid surfaces. These authors used the hydrophobicity of the Fc region as a binding domain for hydrophobic artificial substrates, although this type of fusion protein is not considered as a binding growth factor. Similarly, Nakaji-Hirabayashi *et al.*[173–176] demonstrated that human epidermal growth factor carrying a hexahistidine sequence at the C-terminus (hEGF-His) could be anchored to the Ni-chelated surface by coordination and they investigated the immobilization state in detail. Boucher *et al.*[177] immobilized EGF by a new capture system based on *de novo* designed peptides, that is, the E and K coils. The influence of the type of coil (E or K) upon EGF bioactivity, assessed in an *in vitro* cell assay, was compared to that of the Fc domain of immunoglobulin G by monitoring phosphorylation of EGFR upon chimeric EGF exposure. They demonstrated that the type and the location of the tag have a strong impact on growth factor bioactivity (EC50 ranging from 5.5 to 63 nM). Additional SPR-based biosensor experiments were conducted to test the ability of captured chimeric EGF to bind to its receptor ectodomain *in vitro*. These experiments indicated that the oriented coiled-coil-mediated immobilization of EGF was significantly more efficient than a random approach as coil-tagged EGF displayed enhanced affinities for artificially dimerized EGFR ectodomain when compared to Fc-tagged EGF (apparent KD of 5 pM vs. 16 nM). Altogether, they suggested that coil-tagged chimeras represent an attractive avenue for the oriented immobilization of growth factors for tissue engineering applications and that HEK293 cells offer a robust platform for their expression in a bioactive form. In addition, Boucher *et al.*[178] demonstrated that immobilized EGF provided a sustained phosphorylation of A-431 cell surface EGFRs.

Cell-binding growth factors were developed by Kawase *et al.*[179] and Hashi *et al.*[180] by employing the FN cell-binding domain ($\sim$30 kDa, including the RGD sequence). The EGF fusion protein promoted the proliferation of rat kidney fibroblasts. Another type of cell-binding EGF (containing an RGD sequence) was generated via the incorporation of hydrophobic linker sequences[181] and collagen-binding sequences.[182] They constructed a new multifunctional protein that can be easily immobilized onto hydrophobic surfaces, and at the same time can help enhance specific cell adhesion and proliferation onto collagen substrates.

Hayashi *et al.*[183] developed a recombinant technology to confer a mitogenic activity on type III collagen by fusing it to EGF at the collagen's N-terminus. The chimeric protein of EGF-collagen was synthesized in insect cells by the baculovirus-insect cell expression system. The fusion protein was shown to hold the triple helical conformation of collagen and the mitogenic activity of EGF. It was also demonstrated that the chimeric protein can be immobilized on tissue culture dishes as a fibrous form and on collagen fibrils without abolishing the original mitogenic activity of EGF. This fusion protein can be utilized as a biocompatible, biodegradable, and adhesive fibrous mitogen for a variety of purposes in the area of tissue engineering.

4.416.3.3.2.4. Nerve growth factor

Neurons are highly affected by the components of their environment including bioactive molecules such as neutrophic factors, electrical signals, ECM molecules, and cell-to-cell interactions. As a consequence, neuron tissue engineering has focused on how to produce optimal scaffolds by integrating multiple cues to mimic natural nerve tissue. Immobilization of NGF on polystyrene was reported by Ito[184] for the first time. He immobilized NGF on polystyrene to regulate the neurocite growth of pheochromocytoma PC12 cell line. Chen *et al.*[185] immobilized NGF on a gelatin–tricalcium phosphate membrane. Yu *et al.*[47] immobilized NGF on chitosan films either at indistinct areas or as concentration gradients. They found that when neurons were plated on a chitosan film that has distinct immobilized NGF-pattterned areas surrounded by unmodified chitosan, the neurons remained predominantly as single cells in the NGF-patterned regions, but formed aggregates outside of these patterns on the plain chitosan film. The immobilized NGF influenced neuron behavior and can be used to further probe mechanisms of other neuron behaviors such as axon guidance.

Neurotrophic factors that present as concentration gradients are neurotropic cues that direct axonal growth toward their targets. Multiple factors work together *in vivo* to ensure that axons reach the proper targets, likely interacting with one another via intracellular signaling pathways. NGF and NT-3 are NTs known to guide axons as well as promote axonal growth following injury to both the spinal cord and peripheral nerve. These molecules interact with neurons through different tyrosine kinase receptors. Kapur and Schoichet[186,187] immobilized NGF to guide neurite outgrowth. Moore *et al.*[188] showed that the receptors for these growth factors were colocalized on E10 chick DRG cells, providing an opportunity for synergism. Well-defined concentration gradients of NGF and NT-3 were immobilized for the first time in a cell-penetrable, cell-adhesive scaffold of poly(hydroxyethyl methacrylate) PHEMA and poly(L-lysine). An NGF concentration gradient of 310 ng ml^{-1} mm^{-1} was required to guide chick DRG neurites. A lower concentration gradient of 200 ng ml^{-1} mm^{-1} of NGF was shown to elicit guidance when an NT-3 concentration gradient of 200 ng ml^{-1} mm^{-1} was also present, indicating a synergistic response in the DRG neurons. These gradient scaffolds may be useful for guided regeneration following injury to the spinal cord or peripheral nerve and may also elucidate the mechanism for intracellular signaling of neurotrophic factors.

Shibata *et al.*[189] demonstrated that NGF-receptor complexes had two distinct diffusive states, characterized as mobile and immobile phases. The transition between the two diffusive states occurred reversibly with time durations determined by a single rate limiting process. The abrupt transition to the immobile phase often occurred simultaneously with the clustering of NGF-receptor complexes. Immobilization depended on the phosphorylation of the TrkA NGF-receptor. Using dual-color imaging, it was demonstrated that the membrane recruitment of the intercellular signaling protein occurred with NGF-receptor complexes in the immobile phase indicating that signal transduction occurs during this phase. Thus, it was considered that NGF signaling was performed through a repetitive random process to induce formation of signaling complexes.

Bhang *et al.*[190] reported that NGF immobilization on a culture substrate reduced the amount of NGF required for the PC12 cell culture dramatically. They considered several mechanisms explaining the enhancement of immobilized NGF. First, NGF immobilized on substrates bound receptors on cultured cells more efficiently than NGF added to culture media, and triggered signals more efficiently with less or no loss of bioactivity. NGF added to culture medium was evenly distributed throughout medium, so only a small portion reached the cell microdomains to trigger NGF signaling. In addition, NGF suspended in the culture medium may lose bioactivity by denaturing more easily than NGF bound to the surface. Second, downregulated signaling due to NGF internalization into cells may be inhibited by immobilization. Immobilized NGF was considered to sustain the signal protein phosphorylation, which activates signal transduction.

Numerous therapeutic interventions have been also tested to enhance functional recovery after sciatic nerve injuries. NGF was employed to treat the nerve injury repair. Sun *et al.*[46,191–193] constructed a collagen-binding human NGF-β and a polypeptide TKKTLRT as a CBD which could bind to the native collagen utilized. They reported that CBD-NGF-β bound to endogenous collagen on the rat sciatic nerve and maintained NGF activity both *in vitro* and *in vivo*. In the rat sciatic nerve crush injury model, they found that collagen-binding NGF could be retained and concentrated at the nerve injured site to promote nerve repair and enhance function recovery following nerve damage. CBD-NGF-mediated nerve fiber density was approximately twice as much as that observed for native NGF. It also enhanced healing of rabbit dermal ischemic ulcers. Han *et al.*[194,195] constructed an efficient delivery system including collagen-binding BDNF and linear ordered collagen scaffolds (LOCSs). *In vitro* activity assay showed that CBD-BDNF had similar bioactivity in neurite outgrowth of dorsal root ganglia and the survival of PC12 cells. CBD-BDNF was shown to have specific binding activity to collagen. Using the rat hemisection in spinal cord injury model, they found that LOCS loaded with CBD-BDNF significantly improved the recovery evaluated by the Basso, Beattie, and Bresnahan scale and immunohistochemical staining with antineurofilament antibody. Thus, this targeting drug delivery system consisting of CBD-BDNF and LOCS could be an effective strategy for the repair of spinal cord injury (SCI). Nakaji-Hirabayashi *et al.*[175,176] also prepared BDNF carrying histidine groups at the C-terminus by recombinant DNA technology for enhancing cell survival in a hydrogel composed of hyaluronic acid.

Fibrin is an abundant protein present on the surface of injured tissues. In addition, it has been studied as a material for tissue engineering scaffolds. Therefore, growth factors with fibrin-binding affinity are considered useful for tissue regeneration. Sakiyama-Elbert *et al.*[196] produced a fusion protein between NGF and a short polypeptide of the α_2-plasmin inhibitor (α_2-PI); the activated coagulation factor XIII (FXIIIa) mediated the cross-linking of this sequence to fibrin. In addition, a plasmin cleavage sequence was inserted between the α_2-pI sequence and the growth factor. The fusion protein (TG-P-NGF) was incorporated into fibrin clots by FXIIIa and was then released by plasmin when the tissues started to heal. TG-P-NGF was designed to be released 'when cells demand.' The activity of the fusion protein was ~40% of that of native NGF, when assayed by neurite extension in PC12 cells. Unlike collagen-binding growth factors, this fusion protein bound to fibrin covalently. This may relate to the reduced activity observed in an *in vitro* assay. Fibrin-binding NGF (TG-P-NGF) mixed with fibrin gel enhanced neurite extension from chick embryo DRG (organ culture) by 50%, compared to native NGF, and by 350% relative to the fibrin gel alone, in spite of the reduced activity of the fusion construct.

Electrical stimulation plays an important role in inducing cell adhesion and differentiation and reducing inflammation. Incorporating neuroactive molecules, such as neurotrophic factors, ECM components, and topographical features for contact guidance, into electroconductive materials is a key goal in nerve tissue engineering. Polypyrrole (PPy) is known as a conductive polymer that has been widely studied for biomedical applications such as biosensors, drug delivering vehicles, and nerve tissue engineering. Therefore, Lee *et al.*[197–199] incorporated neuroactive molecules into PPy via a specific and stable method. They demonstrated that application of an external electrical potential to NGF-immobilized PPy films did not cause a significant release of NGF nor reduce their neurotrophic activity. The novel scaffold provided electroconductive and neurotrophic activities. Gomez *et al.*[200] reported that immobilized NGF and microtopography had distinct effects on polarization versus axon elongation in hippocampal cells in culture.

Coimmobilization of NGF and ECM proteins was performed by Achyuta *et al.*[45] to enhance neural adhesion and proliferation on surfaces for application in nerve tissue engineering and neuroprosthetic devices. They reported that in the absence of immobilized NGF, neurite growth of PC12 cell line is influenced strongly by the presence of NGF in solution and unaffected significant increases in laminin surface density (18.7–93.5 ng mm^{-2}). However, when both laminin and NGF were immobilized together, the surface density of laminin was an important factor in determining whether or not the neurite outgrowth-promoting effect of NGF can be obtained. Immobilized laminin was shown to play a synergistic role in the induction of neurite extension by NGF. It was considered that this approach may eventually be utilized to engineer surfaces that promote primary neuronal adhesion and proliferation on neural implant surfaces or on nerve tissue engineering scaffolds.

4.416.3.3.2.5. Bone morphogenic protein

Bone formation is one the most widely explored areas of tissue engineering.[201] A variety of biomaterials have been used as scaffolds for bone growth *in vitro* and *in vivo*, ranging from inorganics such as metals and ceramics to natural polymers such as collagen. Osteogenic factors and particularly members of the TGF-β superfamily have a key role in bone formation and repair. BMP-2 is one the most potent members of the BMP family for the induction of bone formation *in vivo*. BMP was immobilized on a variety of biomaterials, ranging from inorganics such as metals and ceramics to organics such as natural and synthetic polymers. Immobilization of BMP on metal surface was performed by several researchers. Adden *et al.*[202] prepared alkyl phosphonic acid monolayer films for immobilization of BMP-2 on titanium (Ti) surfaces. They employed (11-hydroxyundecyl)phosphonic acid or (12-carboxydodecyl)phosphonic acid to the metal surface. For coupling reaction, the former used carbonyldimidazole and the latter *N*-hydroxysuccinimide. Puleo *et al.*[203] immobilized BMP-4 on titanium alloy. Shi *et al.*[204] and Lim *et al.*[205] reported that the surfaces of Ti alloy substrates were functionalized by first covalently grafting carboxymethyl chitosan (CMCS), followed by the conjugation of BMP-2 to the CMCS-grafted surfaces. The modified substrates significantly promoted attachment, alkaline phosphatase activity, and calcium mineral deposition of both osteoblast and BMSCs. On the other hand, Kashiwagi *et al.*[206] created artificial proteins that contained three copies of a Ti-binding motif, and fused them to the N-terminal of BMP-2. The engineered BMP-2 showed reversible binding to Ti surfaces and induced BMP signaling activity.

Schuessele *et al.*[207] immobilized BMP-2 on hydroxyapatite (HA) disks. They employed a novel method using aminobisphosphonate, pamidronate, and alendronate, which are strong calcium ion chelating agents compared with the established silanization technique. Osteoblastic differentiation of C2C12 cells was efficiently induced by immobilized BMP-2. They concluded that the bisphosphonate-based surface modification represented a safe and easy alternative for the attachment of protein to HA surfaces. Kloss *et al.*[208] immobilized BMP-2 on nanocrystaline diamond (NCD). They demonstrated that coating of endosseous implants with NCD allowed stable functionalization by means of physisorption with BMP-2. Strong physisorption was shown to be directly related to the unique properties of NCD, and BMP-2 in its active form interacted strongly when NCD was oxygen-terminated. They indicated that the technical advancement is application in clinical therapies with regard to bone healing, as primary human mesenchymal stromal cells strongly activated the expression of osteogenic markers, while being cultivated on NCD physisorbed with physiological amounts of BMP-2.

BMP was also immobilized onto natural biopolymeric materials. For example, Karageorgiou *et al.*[209] immobilized BMP-2 onto silk fibroin films using carbodimide chemistry. Using cell culture inserts, it was demonstrated that differentiation was induced by the immobilized BMP-2 and not by BMP-2 released into the culture medium. Culture of cells in a medium, apart from immobilized growth factor, is one evidence indicating the activity of immobilized growth factors. Transwell™ substrates composed of semipermeable polyester membranes are a convenient medium-permeable but growth factor-impermeable tool to study the cell stimulating effects of released growth factors. If cell growth on the semipermeable membrane was not enhanced and the growth of cells on

immobilized surface is enhanced, this demonstrates that the immobilized growth factor is active without release. Comparison with similar amounts of medium-supplemented BMP-2, where no additional BMP-2 was added with medium changes, showed that delivery of BMP-2 immobilized on the biomaterial surface was more efficient than soluble delivery. They concluded that BMP-2 covalently coupled on silk biomaterial matrices retained biological function *in vitro* on the basis of the induction of osteogenic markers in seeded bone marrow stromal cells.

Tsujigiwa *et al.*[210,211] and Yamachika *et al.*[212] immobilized BMP-2 on succinylated type I atelocollagen and the immobilized BMP enhanced the osteoblastic differentiation. In addition, the phosphorylation of receptor-activated Smads, part of the signaling pathway activated by BMP-2, was prolonged by immobilized BMP-2. Implantation of immobilized BMP-2 into the backs of rats promoted the formation of mature bone-like structure. They demonstrated that immobilized BMP-2 had higher bioactivity than nonimmobilized BMP-2. Park *et al.*[213] immobilized BMP-2 on nanofibrous chitosan membranes used for guided bone regeneration. The BMP-2-conjugated surface increased osteoblastic cell attachment proportional to the amount of BMP-2 conjugated. In addition, the BMP-2-conjugated chitosan membrane significantly promoted cell proliferation, ALP activity, as well as calcium deposition when compared with BMP-2 adsorbed membrane, indicating a stable localization of BMP-2 at the surface of the chitosan membrane.

Chen *et al.*[214] and Zhao *et al.*[215,216] developed collagen-binding BMP-2. They explored a collagen-containing mineralized bone-derived matrix (CCMBM) from bovine bone tissues, which not only maintains proper mechanical strength but also binds to the collagen-binding recombinant human collagen-binding bone morphogenetic protein-2 (CBD-BMP-2). By analyzing its morphology and composition, they found that CCMBM was porous and mainly composed of calcium compounds. CCMBM could provide mechanical support for bone injury repair. It also showed good biocompatibility and proper degradation rate helpful for bone regeneration. In addition, the intentionally preserved collagen allowed the specific binding of CBD-BMP-2 to CCMBM and resulted in significantly increased osteogenesis *in vivo*. The results indicated that the combination of CCMBM with collagen-binding BMP-2 could emerge as an effective medical device for bone repair. Chen *et al.*[214] subcutaneously implanted demineralized bone matrix (DBM) combined with CBD-BMP-2 and showed ectopic bone formation in rats. They also showed that BMP-2-loaded DBM was effective in the repair of rabbit mandible bone defects, with an efficiency that was 10–20% higher than that of native BMP-2/DBM. Lin *et al.*[217] employed DBM, collagen-based viscous scaffold, but its low mechanical strength and limited BMP-2 binding ability restrict its application in bone repair. They cross-linked heparin to DBM to increase its BMP-2-binding ability. The mechanical strength of DBM was dramatically increased. The compression modulus of heparin-cross-linked DBM (HC-DBM) was improved (sevenfold increased) under wet conditions, which would allow the scaffolds to keep specific shapes *in vivo*. As expected, HC-DBM showed specific binding ability to BMP-2. Additional studies showed that the bound BMP-2 exerted its function to induce cell differentiation on the scaffold. Subcutaneous implantation of HC-DBM carrying BMP-2 showed higher ALP activity (2 weeks), more calcium deposition (4 and 8 weeks), and more bone formation than that of control groups. It was concluded that HC-DBM has increased mechanical properties as well as specific BMP-2 binding ability.

Schmoekel *et al.*[218] prepared fibrin-binding BMP-2 (TG-pI-BMP-2) and its mediated elevation of ALP activity in C3H10T1/2 cells was comparable with that observed for native BMP-2, while its retention in a fibrin gel was higher than that of the native protein (60% vs. 25% of added amount). They examined the effects of TG-pI-BMP-2 in a rat craniotomy defect model and revealed that the healing area was 76% larger than that observed for native BMP-2. In addition to craniofacial bones, this study was extended to the repair of long bones, as assessed by bone bridging.

Immobilization onto synthetic polymers has also been reported. Edlund *et al.*[219] immobilized BMP-2 onto polylactide (PLA) or PCL which were the most commonly used degradable polymers and have been extensively studied for temporary supports. They prepared heparin covalently bonded surfaces and BMP-2 was immobilized in the heparin layer. The coupling scheme involved functionalization of surfaces by grafting in the vapor phase with PLA and PCL films. The biocompatibility of functionalized surfaces was verified by a much improved attachment and proliferation of MSCs. Shen *et al.*[220] reported immobilization of BMP-2 onto polylactone-type polymer scaffolds via plasma treatment. To introduce proper functional groups on the surface of poly(lactide-*co*-glycolide) (PLGA) matrix, PLGA films were treated under different atmospheres. Oxygen plasma-treated PLGA has the strongest binding ability to BMP-2. When mouse OCT-1 cells were cultured on the BMP-2-immobilized PLGA, the immobilized BMP-2 stimulated differentiation of OCT-1 cell and accelerated process of mineralization of OCT-1 cell in the scaffolds. Liu *et al.*[221] used heterobifunctional acrylate-*N*-hydroxysuccinimide PEG as a spacer to tether BMP-2 onto a PLGA scaffold. Use of PEG-tethered BMP-2 was feasible because BMP-2 retained its activity after covalent conjugation. The PEG-tethered BMP-2 conjugate sustained stimulation and retained its mitogenic activity, notably affecting pluripotent stem cell proliferation and differentiation. They seeded the scaffolds with bone marrow-derived mesenchymal stromal cells as progenitor cells to evaluate their morphology and phenotypic expression. They also created bilateral, full-thickness cranial defects in rabbits to investigate the osteogenic effect of cultured mesenchymal stromal cells on bone regeneration *in vivo*. Histomorphometry and histology demonstrated that the PEG-tethered BMP-2 conjugate enhanced *de novo* bone formation after surgery. Winkler *et al.*[222] reported that heating of BMP-2 depots on various materials to 100 °C augmented the intensity of local ALP induction. They considered that the heat treatment generated both soluble pool of BMP-2 and a materials-bound layer of BMP-2 in which the protein is protected against degradation and it appeared useful to locally immobilize BMP-2 on various implant surfaces.

BMP-3 is also a potent osteoinductive growth factor belonging to the TGF-β superfamily. Han *et al.*[223] engineered a recombinant BMP-3 protein to include an auxiliary collagen-targeting domain derived from vWF. The renatured rhBMP3-C fusion protein bound tightly to collagen matrices and inhibited

DNA synthesis in normal rat calvaria cells and in two out of three human osteosarcoma cell lines tested. ALP activity was increased in rat calvarial cells and was decreased in osteosarcoma cells *in vitro* in a dose-dependent manner. Collagen sponges impregnated with rhBMP3-C and implanted subcutaneously in Fischer-344 rats induced dose-dependent dystrophic calcification of the collagen matrix, with no evidence of ectopic bone formation. However, local injection of rhBMP3-C infused in a collagen suspension induced new bone formation on the periosteal surface of rat calvaria. In a rat cranial defect model, surgical implantation of rhBMP3-C arrayed on either collagen sponges or on porous ceramics coated with type I collagen exhibited marked osteoinductive properties. Taken together, these results demonstrate the feasibility of engineering and manufacturing targeted-BMPs, which exhibit an integral gain-of-function that may be exploited to therapeutic advantage in (1) the enhancement of effective local concentrations, (2) the prevention of systemic biodistribution and side effects, and (3) the design of improved osteoinductive matrices.

Oligopeptides derived from BMP-2 and BMP-7 were immobilized on alginate hydrogels and glass, respectively. Suzuki *et al.*,[224] Saito *et al.*,[225] and Kirkwood *et al.*[226] prepared synthetic oligopeptide derived from BMP-2 and demonstrated osteoinduction in immobilized alginate. Recently, Sharon and Puleo[227,228] attempted to control the orientation of bioactive molecules immobilized on a biodegradable substrate to improve their accessibility for binding to cell surface receptors and, therefore, to increase bioactivity. The osteotropic peptide, parathyroid hormone (1–34) (PTH(1–34)) was used to demonstrate the approach. The intrinsic N-terminal serine residue was oxidized to create an aldehyde group that specifically bound to hydrazide-derivatized PLGA under neutral conditions to form a hydrazone bond. Use of dihydrazide spacers significantly increased the amount of peptide immobilized compared to simple adsorption or direct, random attachment. In probing the accessibility of immobilized PTH(1–34), attachment using longer dihydrazide spacers enhanced the binding of an antibody against an epitope in the N-terminal region of the peptide. The longest spacer also increased binding of a C-terminal antibody. Furthermore, substrates with peptide tethered via spacers stimulated intracellular synthesis of cAMP, with activity increasing with dihydrazide length. PTH(1–34) immobilized using the longest spacer was significantly more effective than both random binding and adsorption. Site-directed binding of bioactive peptides to surfaces presents biomolecules for binding with cells so as to enhance interaction with receptors, and therefore the approach may be useful for obtaining preferred localized tissue responses.

Lee *et al.*[197–199] showed that self-assembled nanostructures consisting of BMP receptor-binding peptides, termed osteopromotive domains (OPDs), and hydrophobic alkyl chains were fabricated with the aim of developing 3D scaffolding materials for osteoblastic differentiation. OPD peptide was identified from BMP-2 and had an affinity for BMP receptors thereby inducing differentiation of human bone marrow stromal cells into osteoblastic cells. The peptide-hydrophobic alkyl chain amphiphiles were designed to mimic nanofibrous extracellular structures and to add osteogenic ligands to enhance osteoblastic cell function. The OPD peptide-amphiphiles (OPDAs) that end with the alkylation of the N-terminus of the OPD peptide were synthesized by standard solid phase chemistry. The self-assembly was triggered by mixing OPDA solution with calcium ions. Observation using scanning electron microscopy (SEM) revealed the formation of nanofibrous structures with extremely high aspect ratios and high surface areas. The FT-IR and circular dichroism spectrophotometry demonstrated that self-assembled nanofibers have a β-sheet structure. The activation of Smad, an osteoblastic differentiation marker, was obtained in the cell culture gel of self-assembled OPDA; therefore, they concluded that the intracellular signal transduction for osteogenesis was performed in the same manner as it was done for an OPD peptide. Cell survival was supported in the OPDA gel for 10 days, and osteoblastic differentiation of human BMSCs was evident as demonstrated by calcein staining and ALP activity measurement. These results revealed that self-assembled OPDA maintained osteogenic activity through the surface-exposed OPD peptide. Taken together, the self-assembled OPDA nanofibrous gel can be utilized as a cell culture scaffold in bone regeneration.

4.416.3.3.2.6. Vascular endothelial growth factor

Tissue engineering and tissue regeneration approaches presently suffer from oxygen and nutrient delivery constraints because of the inability of current scaffolds to rapidly and reliably guide the formation of stable and long lasting vascular networks. Cell seeded or residing in the middle of the tissue construct has a limited supply of oxygen and nutrients as blood vessels do not infiltrate at an appreciable rate and the diffusion limit of oxygen is only a few hundred microns. VEGF is a key component in the signaling cascade to form new blood vessels from existing vessels and can trigger proliferation, migration, and survival of cells through a single growth factor–receptor binding event. It is known that VEGF exists as many different isoforms with different affinities for ECM because of alternative splicing.

Immobilization of VEGF has been reported by Taguchi *et al.*[229] They immobilized VEGF onto poly(arylic acid) grafted polyethylene films using (*N*-(3-dimethylaminoprophyl)-*N*′-enthylcarbodiinide hydrochloride) EDC chemistry and found that VEGF and FN coimmobilized surface greatly promoted the growth of human umbilical vein ECs (HUVECs). Ito *et al.*[230] photoimmobilized VEGF with gelatin and showed that the immobilized VEGF greatly enhanced the proliferation and surface coverage of HUVECs. They demonstrated that the specific interaction of immobilized growth factor with the cognate receptor was examined by the antibody against immobilized growth factor. If the effect of immobilized growth factor was inhibited by the antibody, the specific interactions were certified. They showed that adsorption of antibody against immobilized VEGF reduced the effect of immobilized VEGF.

Shen *et al.*[231,232] immobilized VEGF by EDC onto collagen scaffolds. They also found that immobilized VEGF (relative to soluble VEGF) promoted the penetration and proliferation of ECs in the collagen scaffold on the basis of the results of cell density analysis in histological sections, immunehistochemistry, 2,3-bis(2-methoxy-4-nitro-5-sulfony)-2H-tetrazoline-5-carboxanilide (XTT) proliferation assay, glucose consumption, and lactate production. Sharon and Puleo[227,228] employed another chemistry to immobilize VEGF on

biodegradable polymer PLGA. Exposed carboxy groups on acid-terminated PLGA were modified with dihydrazide spacer molecules. The number of hydrazide groups available for subsequent attachment of protein was dependent on dihydrazide length, with shorter molecules presenting a significantly greater surface density. Immobilized VEGF enhanced EC proliferation, with surfaces having the shortest and longest spacers stimulating greater effects.

Anderson *et al.*[233] designed another covalent immobilization of VEGF using its heparin-binding domain to orient the molecule (bind) and secondary functional group to mediate covalent binding (lock). This bind-and-lock approach aimed to allow VEGF to assume a bioactive orientation before covalent immobilization. Surface density of immobilized VEGF was determined by SPR and ELISA. The electrostatically and covalently bound VEGF successfully phosphorylated the receptor VEGFR-2.

Wang *et al.*[234] designed a synthetic collagen mimetic peptide (CMP) $((ProHypGly)_x$; Hyp: hydroxyproline) in contact with collagen and discovered CMP's structure-dependent binding affinity to type I collagen. Therefore, the CMP architecture consisting of multiple anionic charges at peptide's N-terminus is designed to attract VEGF by charge–charge interactions and bind to collagen by CMP–collagen interaction. By VEGF binding, the morphological features of ECs, indicative of tubulogenesis but not equivalent to functional angiogenesis, were enhanced.

Protein engineering for binding VEGF was performed using the $VEGF_{121}$ isoform lacking the fibrin-binding sequence found in the major isoform ($VEGF_{165}$) as reported by Sahni and Francis.[235] Fusion with the α_2-PI sequence enabled the incorporation of $VEGF_{121}$ into a fibrin gel by Zisch *et al.*[236] and Ehrbar *et al.*[237] In addition, the fusion protein (α_2-PI_{1-8}-$VEGF_{121}$) stimulated the growth of ECs on the gel in a dose-dependent manner. Fibrin-binding $VEGF_{121}$ (α_2PI_{1-8}-$VEGF_{121}$) mixed with fibrin exhibits efficacious angiogenic properties, as assessed using a chorioallantoic membrane assay by Ehrbar *et al.*[237]: the blood-vessel density in the presence of fibrin-binding $VEGF_{121}$ was $\sim$1.5 times higher than that induced by native $VEGF_{121}$. In addition, α_2PI_{1-8}-$VEGF_{121}$ induced the formation of nonleaky vessels on a Teflon chamber coated with fibrin and subcutaneously implanted. Backer *et al.*[238] engineered a cysteine tag into VEGF, then conjugated VEGF onto FN-coated surfaces via the cysteine-tag, and observed growth stimulation of VEGFR-2 overexpressing cells. The maltose-binding protein (MBP), which possesses a large number of exposed hydrophobic zones, was used as a link for the immobilization of VEGF by Han *et al.*[194,195] Cell adhesion onto the VEGF-immobilized surface was enhanced and the phosphorylation of VEGFR in cells was observed on the immobilized surface. Ishikawa *et al.*[239] prepared collagen-binding VEGF using CBD found in FN.

In addition to VEGF, the other growth factor coimmobilization has also been carried out. Arkudas *et al.*[240,241] quantitatively assessed the angiogenic effects of different concentrations of VEGF and bFGF immobilized in a fibrin-based drug-delivery system in the arteriovenous (AV) loop model. An AV loop was created in the medial thigh of 60 rats. The loop was placed in a Teflon isolation chamber and embedded in 500 µl of fibrin gel loaded with VEGF and bFGF in four different concentrations (no growth factor, 100 ng ml^{-1} of VEGF, 25 ng ml^{-1} of VEGF and bFGF, 100 ng ml^{-1} pf VEGF and bFGF). The explanation intervals were 1, 2, and 4 weeks after the initial operation for all groups. Specimens were investigated using micro-CT and histological and morphometrical techniques. After 2 weeks, the cross-section area and construct weight were significantly lower with the use of 100 ng ml^{-1} of VEGF and bFGF. Micro-CT and histology showed significantly greater vascular density and number of vessels of the constructs at 2 and 4 weeks when 100 ng ml^{-1} of $VEGF_{165}$ and bFGF were applied than in the growth factor-free specimens. The angioinductive effects were dose-dependent, with best results when 100 ng ml^{-1} of $VEGF_{165}$ and bFGF were used. The greater tissue formation was accompanied by faster resorption of the fibrin matrix.

Chiu and Radisic[242] coimmobilized VEGF and angiopoietin 1 (Ang1) onto 3D porous collagen scaffolds using EDC chemistry. Over both 3 and 7 days *in vitro*, seeded ECs had increased proliferation on scaffolds with immobilized VEGF and/or Ang1 compared to that on unmodified scaffolds with soluble growth factor controls. Notably, the group with coimmobilized VEGF and Ang1 showed significantly higher cell number, higher overall lactate production rate, and higher overall glucose consumption rate at day 3 than its corresponding soluble control for which growth factors were added to culture medium. By day 7, hematoxylin and eosin, live/dead, CD31, and vWF staining all showed improved tube formation by ECs when cultivated on scaffolds with coimmobilized growth factors. Interestingly, scaffolds with coimmobilized VEGF and Ang1 showed increased EC infiltration in the chorioallantoic membrane assay, compared to scaffolds with independently immobilized VEGF/Ang1. They presented an alternative method for promoting the formation of vascular structures, via covalent immobilization of angiogenic growth factors that are more stable than soluble ones and have a localized effect.

Leslie-Barbick *et al.*[243] investigated strategies to facilitate vascularization in scaffold materials, in their case, PEG hydrogels. The hydrogels are hydrophilic and resist protein adsorption and subsequent nonspecific cell adhesion, but can be modified to contain cell-adhesive ligands and growth factors to support cell and tissue function. In addition, the hydrogel matrix can include proteolytically degradable peptide sequences in the backbone of the structure to allow cells to control scaffold biodegradation, allowing 3D migration. VEGF, a potent angiogenic signal, and the cell-adhesive peptide arginine-glysine-aspartic acid-serine (RGDS) were covalently attached to PEG monoacrylate linkers. PEGylated RGDS and VEGF were then covalently immobilized in PEGDA hydrogels in 2D and 3D. Immobilized VEGF increased EC tubulogenesis on the surface of nondegradable PEGDA hydrogels fourfold compared to controls without the growth factor. EC behavior in 3D collagenase-degradable hydrogels modified with RGDS and VEGF was observed using time-lapse confocal microscopy. Bulk immobilization of VEGF in 3D collagenase-degradable RGDS-modified hydrogels increased EC motility 14-fold and cell–cell connections 3-fold. Covalent incorporation of PEGylated VEGF in PEG hydrogels can be a useful tool to promote EC migration, cell–cell contact formation, and tubulogenesis in an effort to produce vascularized tissue-engineered constructs.

4.416.3.3.2.7. Fibroblast growth factor

DeLong *et al.*[244] immobilized bFGF to hydrogel scaffolds with the retention of mitogenic and chemotactic activity. The bFGF was functionalized to incorporate it covalently within PEG hydrogel scaffolds by reaction with acryloyl-PEG-NHS. Hydrogels were formed by exposing aqueous solutions of PEGDA, acryloyl-PEG-RGDS, and acryloyl-PEG-bFGF to long-wavelength ultraviolet light in the presence of a photoinitiator. These bFGF-modified hydrogels with RGD adhesion sites were evaluated for their effect on vascular SMC behavior, and it was found that SMC proliferation increased by ~41% and migration by ~15%. A covalently immobilized bFGF gradient was formed using a gradient maker to pour the hydrogel precursor solutions and then photopolymerizing to lock in the concentration gradient. Silver staining was used to detect the bFGF gradient, which increased linearly along the hydrogel's length. Cells were observed to align on hydrogels modified with a bFGF gradient in the direction of increasing tethered bFGF concentration as early as 24 h after seeding. SMCs also migrated differentially, up the concentration gradient, on bFGF-gradient hydrogels compared to control hydrogels with and without a constant bFGF concentration. These hydrogel scaffolds may be useful for studying protein gradient effects on cell behavior and for directing cell migration in tissue-engineering applications.

Ito *et al.*[160] micropattern-immobilized heparin on a polystyrene plate for adsorption of bFGF and demonstrated that the growth of NIH3T3 cells was enhanced only in the heparin-immobilized regions. This result indicated that gradient-micropattern-immobilized heparin activated bFGF for cell growth. In addition, the growth of cells was found to be affected by the surface density of immobilized heparin. The surface density was regulated by a gap length of 2 μm-width stripes immobilized with heparin. Although a high density (a region having short gap length) of immobilized heparin suppressed the cell growth in the absence of bFGF, it enhanced cell growth in the presence of bFGF. The dependence of cell function on the density of immobilized heparin was visualized by gradient-micropattern-immobilization. Christman *et al.*[245] prepared a heparin-mimicking polymer and micropattern-immobilized the polymer for bFGF or VEGF micropatterned adsorption.

Watanabe *et al.*,[246] Campbell *et al.*,[247] and Miller *et al.*[248] investigated cell behavioral responses to inkjet printed spatial patterns of hormones biologically immobilized on biomimetic substrates, by using the example of preosteoblastic cell response *in vitro* to FGF-2 printed on fibrin films. Concentration-modulated patterns of FGF-2, including continuous concentration gradients, were created by overprinting dilute FGF-2 bioinks with a custom inkjet printer. The immobilized FGF-2 was biologically active and the printed patterns persisted up to 10 days under cell culture conditions. Cell numbers increased in register with printed patterns from an initial random uniform cell distribution across the patterned and nonpatterned fibrin substrate. Pattern-immobilized FGF-2, not cell attachment, directed cell organization because the fibrin substrate was homogeneous. The capability to engineer arbitrary and persistent hormone patterns was relevant to basic studies across various fields including developmental biology and tissue regeneration. MG-63 cells were uniformly seeded onto patterned substrates. Cells were exposed to defined spatial FGF-2 surface concentrations of 1–22 pg mm^{-2}. Cell numbers were observed to increase in register with the printed FGF-2 patterns from an initial random uniform cell distribution across the patterned and nonpatterned regions. Higher surface concentrations did not result in increased cell density. In addition, the cells on the FGF-2 patterns survived longer than the cells off patterns. They demonstrated that the inkjet printing approach permits the systematic study of cellular responses to defined spatial surface concentrations of immobilized growth factors.

Activation of FGFRs requires the formation of a ternary complex between FGFs, FGFRs, and heparan sulfate proteoglycans, which are all located on the cell surface and the BM/ECM. Heparan sulfate proteoglycans appear to stabilize FGFs by inhibiting the rapid degradation of FGFs normally observed in solution. Because of the pivotal role of FGFs in proliferative and developmental pathways, a number of recent studies have attempted to engineer microenvironments to stabilize growth factors for use in applications in tissue culture and regenerative medicine. Nur-E-Kamal *et al.*[249] demonstrated that covalent linkage of FGF-2 to nanofibrillar surfaces (defined as covalently bound FGF-2) composed of a network of polyamide nanofibers resulted in the maintenance of the biological efficacy of FGF-2 when stored dry for at least 6 months at 25 or 4 °C. Moreover, covalently bound FGF-2 was more potent than FGF-2 in solution when measured in cellular assays of proliferation and viability using a variety of cell types. Covalently bound FGF-2 also strongly activated FGFR, ERK1/2, and c-fos. Hence, cell-signaling molecules can be incorporated into synthetic nanofibrillar surfaces, providing a novel means to enhance their stability and biological activity.

Shen *et al.*[231,232] immobilized bFGF on carbon dioxide plasma-treated PLGA films. They found that adhesion and growth of cells on PLGA scaffolds were greatly improved by immobilization of bFGF on them. Mori *et al.*[250] and Ijiri *et al.*[251] immobilized growth factors such as FGF in stable infectious microcrystals called polyhedra which function to protect a certain insect virus after the death of infected larvae. They showed that FGF-2, FGF-7, and EGF immobilized on polyhedra were functional, inducing the growth of fibroblast cells and keratinocytes. In addition to these organic materials, FGFs have been immobilized on metals and ceramics. Ohyama *et al.*[252] immobilized bFGF onto a platinum microcoil to enhance tissue organization in intracranial aneurysms. Ultrathin multiorganic layers were assembled on a platinum coil through successive deposition of cationic polyethylenimine and anionic heparin, and then bFGF was immobilized through an affinity interaction with heparin. bFGF was effectively immobilized on the surface of the platinum coil without deterioration of the coil's mechanical properties. Coil embolization of aneurysms constructed using a canine common carotid artery was performed via the endovascular approach. The aneurysms together with parent arteries were harvested 2 weeks after coil embolization. Platinum coils unmodified, coated with heparin, or immobilized with heparin and bFGF were examined. The percentage of occlusion at the aneurysm orifice in animals treated with bFGF-immobilized coils was significantly greater than that in animals treated with heparin-coated coils or unmodified coils. The histological score of the aneurysms

treated with bFGF-immobilized coils was also significantly greater than the scores in the control group. They indicated that bFGF-immobilized microcoils may be beneficial in the obliteration of aneurysms. Peelen *et al.*[253] immobilized bFGF on gold film for the specific capture of mammalian cells by FGF receptor binding. Kokubu *et al.*[254] investigated the behavior of rat periodontal ligament (PDL) cells cultured on FGF-2-immobilized titanium surfaces treated by oxygen plasma. They used cell disks (15 mm in diameter), and 35-mm culture dishes sputter-coated with titanium. These were treated with oxygen plasma and dipped in FGF-2 solution. The PDL cells were obtained from rat incisors. Proliferation ratio, ALP activity, and expressions of type I collagen and VEGF mRNAs were evaluated. Proliferation ratio and expressions of type I collagen and VEGF mRNAs were significantly higher, whereas ALP activity was significantly lower in FGF-2-immobilized cells than in the control group. These findings suggested that oxygen plasma modification can immobilize FGF-2 onto a titanium surface. Immobilized FGF-2, although inferior to culture medium with FGF-2, influenced the proliferation of PDL cells and might have promoted collagen and vascular synthesis.

Sogo *et al.*[255] reported formation of a FGF-2 and calcium phosphate composite layer on HA ceramic for promoting bone formation. To avoid the risk of FGF-2 denaturation, FGF-2 immobilization was carried out at 25 °C. FGF-2 was successfully immobilized on HA ceramic surfaces by deposition with calcium phosphate to form an FGF-2 and calcium phosphate composite layer. A maximum of $2.72 \pm 0.01\ \mu g\,cm^{-2}$ of FGF-2 was immobilized in the composite layer formed on the HA ceramic under the optimum condition. An FGF-2-immobilized HA ceramic is likely to have the ability to release sufficient amount of FGF-2 to promote bone formation. FGF-2 released from an FGF-2-immobilized HA ceramic maintained its biological activity, as the proliferation of fibroblastic NIH3T3 was promoted. Therefore, the FGF-2-immobilized HA ceramic is expected to be a useful material for promoting new bone formation.

Lee *et al.*[197–199] prepared two synthetic peptides derived from FGF-2, namely residues 36–41 (F36; PDGRVD) and 77–83 (F77; KEDGRLL), and their N-termini were further modified for ease of chitosan surface immobilization. The adhesion of MSCs to the peptide (F36 and F77)-immobilized chitosan membrane was increased in a dose-dependent manner and completely inhibited by soluble RGD (Arg-Gly-Asp) and antiintegrin antibody, indicating the existence of an interaction between F36/F77 and integrin. Peptide-immobilized chitosan supported human bone-marrow-derived mesenchymal-stem-cell differentiation into osteoblastic cells, as demonstrated by alkaline phosphate expression and mineralization.

Andrades *et al.*[256] showed that collagen-binding bFGF dissolved in collagen solution accelerates wound healing, both in normal and in diabetic rats. Implantable scaffolds combined with collagen-binding growth factors have also been studied. Brewster *et al.*[257] generated another collagen-binding bFGF of which the bFGF part was an engineered one that has thrombin resistance. These authors used SPR analysis to show that the binding affinity of the fusion protein was fourfold higher than that of native FGF and the engineered bFGF part alone. collagen binding-bFGF stimulated EC angiogenesis in fibrin gel. However, the advantage of the collagen-binding affinity of the fusion protein during angiogenesis was not clearly shown via comparison with unfused bFGF.

Zhao *et al.*[258,259] developed a fibrin-binding FGF. To endow bFGF with fibrin-targeting ability, a fibrin-binding peptide Kringle1 (K1), derived from human plasminogen, was fused to human bFGF. The recombinant K1bFGF showed high fibrin and plasma-clot-binding ability. When applied to the wound sites with plasma clots, K1bFGF induced robust neovascularization and improved wound healing. To extend the application of K1bFGF to other cases where no plasma clots exist, they developed a fibrin-scaffold/K1bFGF system. This system could induce localized neovascularization by delivery of K1bFGF in a sustained and site-targeting manner, and provide a microenvironment promoting cell growth and tissue regeneration. They successfully used the pathologic environment of fibrin clot as the target for bFGF, on the basis of which bFGF was designed into a targeting agent by the introduction of a fibrin-binding peptide. This provided a potential approach to improve therapeutic neovascularization and wound repair. Zhao *et al.*[258] compared a short polypeptide sequence of vWF with that of human collagenase as the fusion partner for bFGF and found that the latter provides a higher binding affinity to collagen. Considering that the same growth factors fused with different partner polypeptides were synthesized, the properties of these factors were compared by Zhao *et al.*[259] They demonstrated that vessel migration into collagen scaffolds was enhanced by CBD-bFGF, although the collagen-binding affinity did not vary much between native bFGF and CBD-bFGF. The difference in the angiogenic effect between native and engineered bFGFs was apparent at 7 days, but not at 4 days, after implantation.

4.416.3.3.2.8. Transforming growth factor β

TGF-β represents a superfamily of over 30 protein growth factors. Ti and Ti alloys are often used for orthopedic and dental implants. Osseointegration of Ti6Al4V may be improved not only by precoating of the surface with ECM proteins like type 1 collagen but also by additional immobilization of growth factors. Fischer *et al.*[260] immobilized TGF-β, which is known as an inducer of collagen synthesis. It was immobilized adsorptively on uncoated and type 1 collagen coated Ti6Al4V surfaces. TGF-β was found immobilized slightly faster to type 1 collagen-coated than to uncoated Ti6Al4V and released slower from the collagen-coated material. Immobilized TGF-β was biologically active for at least 3 weeks storage at 4 °C. Sterilization by ethylene oxide inactivates immobilized TGF-β. In osteoblasts cultured on implants with adsorptively immobilized TGF-β, mRNA level and specific catalytic activity of ALP as well as accumulation of calcium and phosphate were found reduced, whereas procollagen α1(I) mRNA level and the rate of collagen synthesis were increased.

The downgrowth of corneal epithelial cells at the interface of an artificial cornea and the host eye tissue poses a significant problem to be overcome in developing a successful implant. As a means of inhibiting the proliferation of corneal epithelial cells on the stromal surface of the implant, Merrett *et al.*[261] examined the immobilization of TGF-β2 via a bifunctional PEG spacer to poly(dimethylsiloxane) surfaces.

Biomaterials developed for tissue engineering and wound healing applications need to support robust cell adhesion, yet also need to be replaced by new tissue synthesized by

those cells. In order to maintain mechanical integrity of the tissue, the cells must generate sufficient ECM before the scaffold is degraded. On the other hand, Mann *et al.*[262] found that TGF-β1 can be used in scaffolds to dramatically increase ECM production. Matrix production by vascular SMCs grown on adhesive ligand-modified glass surfaces and in PEG hydrogels containing covalently bound adhesive ligands was increased in the presence of 0.04 pmol ml^{-1} (1 ng ml^{-1}) TGF-β1. TGF-β1 can counteract the effect of these adhesive ligands on matrix production; matrix production could be increased even above that observed in the absence of adhesive peptides. Further, TGF-β1 covalently immobilized to PEG retained its ability to increase matrix production. Tethering TGF-β1 to the polymer scaffold resulted in a significant increase in matrix production over the same amount of soluble TGF-β1.

To overcome rapid diffusion and clearance from the implant site and to increase stability, recombinant TGF-β2 was covalently bound to injectable bovine dermal fibrillar collagen and its activity compared to admixed TGF-β by Bentz *et al.*[263] Covalent binding was achieved in a two-step procedure: First, TGF-β2 was made to react with the difunctional PEG linker, and then the PEG-attached TGF-β2 (PEG-TGF-β2) was bound to the fibrillar collagen. After reaction with injectable fibrillar collagen, extraction of unbound PEG-TGF-β2 and Western blot analysis, using a TGF-β-specific antibody, demonstrated that at least 85% of the TGF-β2 was bound to the fibrillar collagen. The activity of PEG-TGF-β2 was fully stable in phosphate-buffered saline at 4 and 37 °C for at least up to 4 weeks. Unmodified TGF-β2 mixed with fibrillar collagen was completely inactivated after 1 week of incubation, as measured by the mink lung epithelial cell growth inhibition assay. TGF-β2-containing formulations showed the TGF-β typical fibroblastic response at the day 7 time-point. Covalent binding of TGF-β2 to collagen with both difunctional PEG cross-linkers resulted in a significantly stronger and longer lasting TGF-β2 response than that observed with admixed formulations of collagen and TGF-β. The TGF-β response with bound PEG-TGF-β2 lasted up to day 42 but was not seen after day 7 for TGF-β2 admixed to fibrillar collagen. The findings clearly demonstrated that TGF-β2 remains fully active after being covalently bound to collagen via difunctional PEG. In addition, covalent binding potentiates and prolongs *in vivo* TGF-β responses and stabilizes the TGF-β *in vitro*. Their results suggest that this method of formulation could be useful to stabilize and deliver similar peptide growth factors or biologically active agents.

Tuan *et al.*[264] reported biologically active TGF-β1 tripartite fusion proteins consisting of (1) a purification tag, (2) a protease-sensitive linker/collagen binding domain, and (3) a cDNA sequence encoding the active fragment of human TGF-β 1. Purified collagen-binding TGF-β exhibited antiproliferative activities comparable to purified platelet TGF-β1, but at lower specific activities. Coupling of proteins was achieved with TGF-β on collagen gels by the addition of an auxiliary collagen binding domain (WREPSFMALS) by Andrades *et al.*[256] They showed that the result was better access of the protein to the cells because of a longer half-life and slower release, resulting in more potency than TGF-β1 supplied directly in medium.

Chou *et al.*[265] immobilized TGF-β1 onto the surface of the tri-*co*-polymer sponge to suppress undesired cell differentiation during the cartilage growth *in vitro*. Tri-*co*-polymer with the composition of gelatin, hyaluronic acid, and chondroitin-6-sulfate has been used to mimic the cartilage ECM as scaffold for cartilage tissue engineering. The scaffold was synthesized with a pore size in the range of 300–500 μm. TGF-β1 was immobilized on the surface of the tri-*co*-polymer scaffold with EDC as a cross-linking agent. Tri-*co*-polymer scaffolds with and without TGF-β1 were seeded with porcine chondrocytes and cultured in a spinner flask. After culturing for 4 weeks, chondrocytes expressed S-100 protein, Alcian blue, and type II collagen for the scaffold with TGF-β1 immobilization. There was no observed type I and type X collagen expression in the scaffolds by observation of RT-PCR. In addition, in the scaffold without TGF-β1 immobilization, type X collagen could be detected after culture for 2 weeks. Type I collagen was progressively expressed after 4 weeks. They concluded that TGF-β1-immobilized scaffold suppressed chondrocytes toward prehypertrophic chondrocytes and osteolineage cells. TGF-β1 immobilization was considered to be of great potential in cartilage tissue engineering.

On the other hand, Bhatnagar *et al.*[266] reported another type of immobilization for TGF-β. They prepared cross-linked hydrogel features patterned using subtractive lift-off of polymerized hydrogel film. Projection lithography and oxygen plasma etch were used to pattern parylene C polymer film. Molecular self-assembly of polymerizable monolayer was obtained in solution-phase and acrylamide-based hydrogel was polymerized using free-radical polymerization on this substrate. Parylene C film was mechanically lifted off to remove the blanket hydrogel film and microhydrogel features were obtained attached to the predefined patterns in the range from 1 to 60 μm. The microhydrogels were functionalized with aldehyde functional groups, and proteins were coupled to them using Schiff base chemistry followed by reductive amination. Interaction of MSCs with TGF-β1 functionalized features was studied and TGF-β1-was found to retain its tumor suppression activity.

4.416.3.3.2.9. Hepatocyte growth factor

Immobilization of HGF was reported by Kitajima *et al.*[267] for the first time. They prepared a fusion protein consisting of HGF (an angiogenic factor) and CBD polypeptide of FN. The fusion protein (CBD-HGF), produced by a baculovirus expression system, exhibited much stronger collagen binding activity than native HGF in the range of 0.4–6.4 μg ml^{-1}. Its binding at the lowest concentration exceeded that of HGF at the highest concentration. In addition, the collagen-bound CBD-HGF promoted growth of ECs to a greater degree at least 4 days longer than HGF added to the culture medium, and afforded about fivefold greater increase in cell number after 10 days. These findings suggest that the fused CBD moiety not only helped immobilize HGF on collagen but also helped stabilize the fusion molecule, resulting in prolonged activity. The angiogenic activity of CBD-HGF in animal tissues was examined by subcutaneously implanting collagen sponges containing bound CBD-HGF. Blood vessel formation in the sponges after 7 days was 4–6-fold more extensive than in the control sponges without modification. Implanted sponges with native HGF did not show significant differences from control. These results indicate that CBD-HGF is suitable for *in vitro* culture of ECs and that this fusion protein can be used to confer HGF activity on biomaterials for use in tissue engineering.

Jones *et al.*[49] also investigated solid-phase presentation of HGF on microarrays of ECM proteins. In their experiments, HGF was mixed in solution with ECM proteins (types I and IV collagen or laminin) and robotically printed onto silane-modified glass slides. Primary rat hepatocytes were seeded onto HGF–ECM protein microarrays and formed cellular clusters that corresponded in size to the dimensions of individual protein spots (500-μm diameter). Analysis of liver-specific products, albumin and α1-antitrypsin, revealed several fold higher levels of expression of these proteins in hepatocytes cultured on HGF–ECM microarrays compared to cells cultivated on ECM proteins alone. In addition, cultivation of hepatocytes on HGF/ECM protein spots led to spontaneous reorganization of cellular clusters from a monolayer into 3D spheroids. They investigated the effects of surface-tethered HGF on hepatocytes cocultivated with stromal cells and observed a significantly higher level of albumin in cocultures where hepatocytes were stimulated by HGF–ECM spots compared to cocultures created on ECM protein islands without the growth factor. They demonstrated that incorporation of HGF into ECM protein microarrays has a profound and long-lasting effect on the morphology and phenotype of primary hepatocytes.

A recombinant HGF fused to an IgG Fc region was constructed by Azuma *et al.*[268] Almost similar amounts of HepG2 cells adhered to the fusion protein-coated surface compared to collagen-coated controls with large morphological changes. Immobilized fusion protein continuously activated Akt in HepG2 cells whereas Akt activation induced by soluble HGF rapidly decreased with time, indicating that immobilized fusion protein followed different signal transduction pathways from that followed by soluble HGF.

HGF is known to stimulate EC proliferation. However, reendothelialization is not enhanced when the native protein is administered to the injured artery, probably because of the short half-life of HGF at the site of injury. Therefore, the effects of an HGF fusion protein having CBD-HGF on reendothelialization and neointimal formation were studied in the balloon-injured rat carotid artery by Ohkawara *et al.*[269] The left common carotid artery of male Sprague-Dawley rats was injured with an inflated balloon catheter, and then treated with CBD-HGF ($10\,\mu g\,ml^{-1}$), HGF ($10\,\mu g\,ml^{-1}$), or saline (control) for 15 min. After 14 days, the rats were injected with Evans blue and sacrificed. The reendothelialized area was significantly greater in the CBD-HGF-treated rats than in the control or HGF-treated rats. Neointimal formation was significantly more pronounced in the CBD-HGF-treated rats than in other rat groups. Both HGF and CBD-HGF stimulated proliferation of vascular SMCs as well as ECs *in vitro*. Consistent with this, cultured SMCs were shown to express the HGF receptor (c-Met). It was concluded that CBD-HGF accelerates reendothelialization and neointimal formation *in vivo*. CBD fusion protein is a useful vehicle to deliver vascular growth factors to injured arteries.

Ota *et al.*[270] sought to promote myocardial repair using urinary bladder matrix incorporated with a fusion protein CBD-HGF in a porcine model. Urinary bladder matrix incorporated with CBD-HGF was implanted into the porcine right ventricular wall to repair a surgically created defect. Linear local shortening was significantly improved in the CBD-HGF-treated matrix compared with controls, whereas it was inferior to the normal myocardium. Mean electrical activity was statistically greater in the CBD-HGF-treated matrix than that in the control groups and less than in the normal myocardium. Histologic examination showed predominant α-smooth muscle actin positive cells with the CBD-HGF-treated matrix showing the thickest layer, with an endocardial endothelial monolayer. Scattered isolated islands of α-actinin positive cells were observed only in the CBD-HGF-treated matrix, but not in the controls, suggesting the presence of cardiomyocytes. It was concluded that CBD-HGF/urinary bladder matrix patch demonstrated increased contractility and electrical activity compared with urinary bladder matrix alone or Dacron and facilitated a homogeneous repopulation of host cells. Urinary bladder matrix incorporated with CBD-HGF was considered to contribute to constructive myocardial remodeling.

4.416.3.3.2.10. Platelet-derived growth factor

There is a great interest in adult stem cells and their resulting progenitors because of inherent capacity to self-renew and differentiate into multiple cell types, providing promising cell-based therapeutic strategies after tissue loss due to disease or injury. For example, neural stem/progenitor cells (NSPCs) hold great promise in regenerative medicine. However, controlling their differentiation into a desired phenotype within a defined matrix is challenging. To guide the differentiation of NSPCs, Aizawa *et al.*[271] first created a cell-adhesive matrix of agarose modified with glycine-arginine-glycine-aspartic acid-serine and then demonstrated the multipotentiality of NSPCs to differentiate into the three primary cell types of the central nervous system on this matrix: neurons, oligodendrocytes, and astrocytes. They examined whether immobilized PDGF-AA would promote differentiation in a manner similar to the same soluble factor and found similar percentages of NSPCs differentiated into oligodendrocytes. They found that the gene expression of the differentiated oligodendrocytes was similar for 2′, 3′-cyclic nucleotide 3′-phosphodiesterase but different for myelin oligodendrocyte glycoprotein in the presence of soluble PDGF-AA versus immobilized PDGF-AA. Their observation demonstrated for the first time that it is possible to control the differentiation of NSPCs, and specifically to oligodendrocytes, in cell-adhesive matrices with immobilized PDGF-AA.

A short polypeptide sequence of the human collagenase CBD was also employed to construct collagen-binding fusion proteins of PDGF-BB by Lin *et al.*[272] Sun *et al.*[191,193] used the rabbit dermal ischemic ulcer model to study the effects of CBD-PDGF loaded on collagen membranes. Their results revealed that this system maintained a higher concentration and stronger bioactivity of PDGF-BB on the collagen membranes and promoted the reepithelialization of dermal ulcer wounds, the collagen deposition, and the formation of capillary lumens within the newly formed tissue area. It was demonstrated that collagen membranes loaded with collagen-targeting human PDGF-BB could effectively promote ulcer healing.

4.416.3.3.2.11. Keratinocyte growth factor

Exogenous keratinocyte growth factor (KGF) significantly enhances wound healing, but its use is hampered by a short biological half-life and lack of tissue selectivity. Geer *et al.*[273] used a biomimetic approach to achieve cell-controlled delivery

of KGF by covalently attaching a fluorescent matrix-binding peptide that contained two domains: one recognized by factor XIII and the other by plasmin. Modified KGF was incorporated into the fibrin matrix at high concentration in a factor XIII-dependent manner. Cell-mediated activation of plasminogen to plasmin degraded the fibrin matrix and cleaved the peptides, releasing active KGF to the local microenvironment and enhancing epithelial cell proliferation and migration. To demonstrate *in vivo* effectiveness, they used a hybrid model of wound healing that involved transplanting human bioengineered skin onto athymic mice. At 6 weeks after grafting, the transplanted tissues underwent full thickness wounding and treatment with fibrin gels containing bound KGF. In contrast to topical KGF, fibrin-bound KGF persisted in the wounds for several days and was released gradually, resulting in significantly enhanced wound closure. A fibrinolytic inhibitor prevented this healing, indicating the requirement for cell-mediated fibrin degradation to release KGF. In conclusion, this biomimetic approach of localized, cell-controlled delivery of growth factors may accelerate healing of large full-thickness wounds and chronic wounds that are notoriously difficult to heal.

4.416.3.3.2.12. Leukemia inhibitory factor

For the maintenance of pluripotency, mouse ES cells are cultured on a feeder layer of mouse embryonic fibroblast (MEF) or incubated with LIF that is produced by MEF. LIF is a pleiotropic cytokine, which induces the differentiation of leukemia cell lines into macrophages and the expression of acute phase proteins in hepatocytes, as well as inhibits proliferation of ECs. Makino *et al.*,[274] Cetinkaya *et al.*,[275] and Alberti *et al.*[276] reported that chemically immobilized LIF can be effective for the maintenance of mouse ES cells.

On the other hand, Nagaoka *et al.*[87,88] prepared an immobilizable fusion protein composed of LIF and IgG-Fc region, which was used as a model for the matrix-anchored form of LIF to establish a novel system for ES cell culture and to investigate the effect of immobilized LIF on maintenance of ES cell pluripotency. Mouse ES cells maintained their undifferentiated state on the surface coated with LIF-Fc. Furthermore, when cultured on the coimmobilized surface with LIF-Fc and E-cadherin-Fc, mouse ES cells showed characteristic scattering morphologies without colony formation, and they could maintain their undifferentiated state and pluripotency without additional LIF supplementation. The activation by LIF signaling was sustained on the coimmobilized surface. They indicated that immobilized LIF and E-cadherin maintained mouse ES cells efficiently.

4.416.3.3.2.13. Stem cell factor

In vivo, SCF exists in both a bound and soluble isoform. It is believed that the bound form is more potent and fundamentally required for the maintenance of HSCs. This theory is supported by the observation that steel-Dickie mice lacking the bound isoform of SCF are unable to maintain hematopoiesis and by the fact that bound SCF displayed on the surface of transgenic cells is better able to maintain c-kit activation than soluble SCF. Further work has shown that recombinant SCF molecules, which include a surface-binding domain, are more potent than their soluble equivalent. It is generally assumed that such an elegant approach is necessary to provide the correct molecular orientation and avoid the pitfalls of random cross-linking or the denaturation associated with the adsorption of proteins to surfaces. Doran *et al.*[277] demonstrated that SCF physisorbed to tissue culture plastic was not only bioactive, but also more potent than the soluble equivalent.

Cellulose-binding domain-fused protein technology facilitated the binding of bioactive cytokines to cellulose materials and has permitted the analysis of several aspects of cell stimulation by surface-localized growth factors. Doheny *et al.*[278] reported the synthesis and initial characterization of a fusion protein comprising a cellulose binding domain and murine SCF. A significant advantage of the cellulose-binding domain fusion protein system is that it permits the stimulation of factor-dependent cells with localized growth factor, essentially free of nonfactor-derived interactions between the cell and matrix. The long-term stability and bioactivity of cellulose binding SCF adsorbed to microcrystalline cellulose under cell culture conditions were demonstrated by Jervis *et al.*[279] Cellulose-bound SCF was shown to stimulate receptor polarization in the cell membrane and adherence to the cellulose matrix. In addition, cellulose-surface presentation of the cellulose-bound SCF fusion attenuated c-kit dephosphorylation kinetics, potentially modulating the overall response of the cell to the SCF signal.

4.416.3.3.2.14. Erythropoietin

Erythropoietin (Epo) was immobilized on a culture plate and the Epo-dependent human leukemia cell line UT-7/Epo was then cultured upon the plate.[280] A photo-reactive gelatin was mixed with Epo and the mixture was cast on a plate. The plate was then irradiated with ultraviolet light in the presence or absence of a photo-mask. After washing with water, a micropatterned or unpatterned surface was formed. A leukemia cell line dependent on Epo, UT-7/Epo, was cultured on the sample plate. On the micropatterned surface, apoptosis of cells was induced on the surface without Epo, but was not observed on the Epo-immobilized surface. This result demonstrated that Epo stimulated the cells even after immobilization. Although the activity of immobilized Epo was low, the activity was slightly higher than that achieved by soluble Epo at higher concentration. In addition, the immobilized Epo could be repeatedly used for culture of UT-7/Epo cell. The present study provided a convenient immobilization method and indicated that immobilization of cytokines will be useful for creating an artificial cell culture device.

4.416.3.3.2.15. Interleukins

The mouse T cell line cytotoxic T lymphocyte lines-2 (CTLL-2) is known to be dependent on IL-2 for both growth and viability. These cells possess high affinity IL-2 receptors and have been shown to internalize IL-2 after binding. To determine if internalization of IL-2 is required for the mediation of its signal, IL-2 was covalently coupled to an insoluble matrix via glutaraldehyde cross-linking and CTLL-2 cells were incubated with the immobilized lymphokine matrix.[281] This covalent cross-linking prevents the free lateral diffusion and internalization of the bound IL-2 receptors (IL-2R) while still permitting specific binding between the cells and the immobilized ligands. Although only very limited proliferation was observed during the incubation as assessed by ^{3}H-thymidine

incorporation, the viability of the CTLL-2 cells on the immobilized IL-2 matrix was preserved. Cells incubated on the immobilized IL-2 surface could proliferate in response to exogenous soluble IL-2 that was added to the cultures after 36 h whereas control cultures incubated with an immobilized bovine serum albumin (BSA) matrix had died. This indicates that immobilized IL-2 can mediate some of the activity of soluble IL-2 and that internalization of the IL-2 receptor may not be required for at least part of the IL-2-mediated effect.

The expansion of CD34+ HSCs on 2D and 3D polymeric scaffolds, surface-immobilized with hematopoietic growth factors, was investigated by Chai *et al.*[282] The polymeric scaffolds were prepared by functionalizing polyethylene terephthalate film disks and nonwoven disks with carboxy groups by oxidation. SCF and IL-6 were covalently immobilized individually or concomitantly into amide bond formation. It was observed that immobilized IL-6 on 2D PET induced drastic expansion of CD34+ cells, contributed largely by expansion of progenitor cells with multilineage potential.

Kim *et al.*[283] investigated whether immobilized anti-inflammatory cytokines will signal changes in the inflammatory profile of cultured monocytes. A fusion protein of recombinant human IL-1 receptor antagonist and elastin-like peptide (IL-1ra-ELP) was expressed in *E. coli*. THP-1 human monocytes were cultured on either carboxyl-terminated SAMs, or SAMs with either covalently immobilized or soluble IL-1ra-ELP. LPS-stimulated monocytes exposed to either soluble or immobilized IL-1ra-ELP were prevented from cell differentiation, showed attenuated expression of proinflammatory cytokines, and had increased production of anti-inflammatory and pro-wound healing cytokines. These results suggest that immobilized anti-inflammatory cytokines have the potential to be immunomodulatory biomaterials. Novak *et al.*[284] reviewed biomimetic strategies based on viruses and bacteria for the development of immune evasive biomaterials.

4.416.3.3.2.16. Tumor necrosis factor α

TNF-α is a cell-derived inflammatory factor with potent antitumor activity. Photoactive arylazide-4-azidobenzoic acid was modified to TNF-α by Guan *et al.*[285] By photo-immobilization, the modified TNF-α was immobilized on cell culture polystyrene. Both the relation between the amount of TNF-α in the feed and immobilized TNF-α and the influence of different UV irradiation time on photo-immobilization are discussed. In addition, Guan *et al.*[286] coimmobilized TNF-α and interferone γ (IFN-γ) on polystyrene membranes for cell culture to prepare biomaterials and they showed that coimmobilization of IFN-γ and TNF-α had significant inhibitory effect on growth of Hela cells, with inhibitory rates up to 82%, and IFN-γ showing synergistic activity.

4.416.4. Summary and Future Directions

To endow biofunctionality to materials, protein immobilization is a very promising methodology.[287,288] The surfaces of various materials including metals, ceramics, and organics can be modified with proteins and biomimics. In the case of metal and ceramics, organic functional groups or organic layers were introduced and the modified surfaces were further functionalized with bioactive molecules (reviewed here) to render the surfaces bioactive.[289–292] For Ti, its alloys, and stainless steel, surfaces were first functionalized by silane derivatives or stable coating[293–295] by phosphonic acid molecules,[202,296–298] and electrodeposition,[299] electrochemical treatment,[300] or photo-modifications[301,302] were performed before immobilization of biological molecules.

In addition to these methods, as a universal modification method, an unusual amino acid, 3,4-dihydroxyphenylalanine, contained in mussel adhesive protein, was incorporated into surface modifiers for inorganic sufaces directly or as its derivatives.[303–307] The utility of combinatorially selected peptides through viral- or bacterial-displayed peptide libraries has recently proven to be an effective technique for generating polypeptide sequences with specific affinities to a variety of inorganic surfaces.[308–311] In this approach, a pool of random amino acid sequences displayed on the surface of a host organism is exposed to a target inorganic substrate and mutant organisms displaying specific binding sequences are selected. Several groups have applied this approach successfully to identify inorganic binding peptides and utilized them for various applications including making templated conjugates.

Various methods to couple with organic surfaces have also been developed with the progress in protein microarray technologies,[312–317] enzyme immobilization technology,[318,319] and surface grafting technology.[70,71] Not only chemical binding structure but also the spatio-temporal control of immobilized proteins is reported. Recently, in addition to biomedical materials or usual cell culture substrates, niche substrata for stem cells have become important.[320–323] Although the structure of this niche is considered to be very complex, precise spatio-temporal control of specific signal proteins and coimmobilization techniques will enable new capabilities to control cell-surface behaviors of improved biomaterials. Successful extension of many *in vitro* approaches to modifying cell-materials responses to actual *in vivo* scenarios has not yet been undertaken but must be used to validate the utility of immobilized growth factors, cytokines, and proteins for possible clinical applications.

References

1. Alberts, B.; Johnson, A.; Lewis, J.; Raff, M.; Roberts, K.; Walter, P. *Molecular Biology of the Cell*, 5th ed.; Garland Science Textbooks: New York, **2007**.
2. Petrie, T. A.; Garcia, A. J. In *Biological Interactions on Materials Surfaces*; Puleo, D. A., Bizios, R., Eds.; Springer: New York, **2009**; 133–156.
3. Exposito, J. Y.; Valcourt, U.; Cluzel, C.; Lethias, C. *Int. J. Mol. Sci.* **2010**, *11*, 407–426.
4. Gordon, M. K.; Hahn, R. A. *Cell Tissue Res.* **2010**, *339*, 247–257.
5. Kruegel, J.; Miosge, N. *Cell. Mol. Life Sci.* **2010**, *67*, 2879–2895.
6. Pankov, R.; Yamada, K. M. *J. Cell Sci.* **2002**, *115*, 3861–3863.
7. Singh, P.; Carraher, C.; Schwarzbauer, J. E. *Annu. Rev. Cell Dev. Biol.* **2010**, *26*, 397–419.
8. Almine, J. F.; Bax, D. V.; Mithieux, S. M.; *et al. Chem. Soc. Rev.* **2010**, *39*, 3371–3379.
9. Muiznieks, L. D.; Weiss, A. S.; Keeley, F. W. *Biochem. Cell Biol.* **2010**, *88*, 239–250.
10. Hynes, R. O. *Science* **2009**, *326*, 1216–1219.
11. Cabodi, S.; Di Stefano, P.; Leal Mdel, P.; *et al. Adv. Exp. Med. Biol.* **2010**, *674*, 43–54.
12. Dityatev, A.; Schachner, M.; Sonderegger, P. *Nat. Rev. Neurosci.* **2010**, *11*, 735–746.

13. Nollet, F.; Kools, P.; van Roy, F. *J. Mol. Biol.* **2000**, *2999*, 551–577.
14. Makrilia, N.; Kollias, A.; Manolopoulos, L.; Syrigos, K. *Cancer Invest.* **2009**, *27*, 1023–1037.
15. Kim, M. H.; Roy, K. In *Biological Interactions on Materials Surfaces*; Puleo, D. A., Bizios, R., Eds.; Springer: New York, 2009; pp 158–172.
16. Pierschbacher, M. D.; Ruoslahti, E. *Nature* **1984**, *309*, 30–33.
17. Pierschbacher, M. D.; Ruoslahti, E. *J. Biol. Chem.* **1987**, *261*, 17294–17298.
18. Kloczewiak, M.; Timmons, S.; Lukas, T. J.; Hawiger, J. *Biochemistry* **1984**, *23*, 1767–1774.
19. Santoro, S. A.; Lawing, W. J., Jr. *Cell* **1987**, *48*, 867–873.
20. Kodandapani, R.; Veerapandian, B.; Kunicki, T. J.; Ely, K. R. *J. Biol. Chem.* **1995**, *270*, 2268–2273.
21. Plow, E. F.; Pierschbacher, M. D.; Ruoslahti, E.; Marguerie, G. A.; Ginsberg, M. H. *Proc. Natl. Acad. Sci. USA* **1985**, *82*, 8057–8061.
22. Ghiso, J.; Rostagno, A.; Gardella, J. E.; Liem, L.; Gorevic, P. D.; Frangione, B. *Biochem. J.* **1992**, *288*, 1053–1059.
23. Saporito-Irwin, S. M.; Van Nostrand, W. E. *J. Biol. Chem.* **1995**, *270*, 26265–26269.
24. Yamada, K. M.; Kennedy, D. W. *J. Cell. Physiol.* **1987**, *130*, 21–218.
25. Koivunen, E.; Wang, B.; Ruoslahti, E. *J. Cell Biol.* **1994**, *124*, 373–380.
26. Guan, J. L.; Hynes, R. O. *Cell* **1990**, *60*, 53–61.
27. Mould, A. P.; Wheldon, L. A.; Komoriya, A.; Wayner, E. A.; Yamada, K. M.; Humphries, M. J. *J. Biol. Chem.* **1990**, *265*, 4020–4024.
28. Rüegg, C.; Postigo, A. A.; Sikorski, E. E.; Butcher, E. C.; Pytela, R.; Erle, D. J. *J. Cell Biol.* **1992**, *17*, 179–189.
29. Staatz, W. D.; Fok, K. F.; Zutter, M. M.; Adams, S. P.; Rodriguez, B. A.; Santoro, S. A. *J. Biol. Chem.* **1991**, *66*, 7363–7367.
30. Underwood, P. A.; Bennett, F. A.; Kirkpatrick, A.; Bean, P. A.; Moss, B. A. *Biochem. J.* **1995**, *309*, 765–771.
31. Altieri, D. C.; Plescia, J.; Plow, E. F. *J. Biol. Chem.* **1993**, *268*, 1847–1853.
32. Eble, J. A.; Golbik, R.; Mann, K.; Kühn, K. *EMBO J.* **1993**, *12*, 4795–4802.
33. Li, R.; Nortamo, P.; Valmu, L.; *et al. J. Biol. Chem.* **1993**, *268*, 17513–17518.
34. Vonderheide, R. H.; Tedder, T. F.; Springer, T. A.; Staunton, D. E. *J. Cell Biol.* **1994**, *125*, 215–222.
35. Ruoslahti, E. *Annu. Rev. Cell Dev. Biol.* **1996**, *12*, 697–715.
36. Yamada, K. M. *J. Biol. Chem.* **1991**, *266*, 12809–12912.
37. Koenig, A. L.; Grainger, D. W. In *Methods of Tissue Engineering*; Atala, A., Lanza, R., Eds.; Academic Press: San Diego, CA, 2001; pp 751–770.
38. Koenig, A. K.; Grainger, D. W. In *Biomimetic Materials and Design: Interactive Biointerfacial Strategies, Tissue Engineering and Targeted Drug Delivery*; Dillow, A., Lowman, A., Eds.; Marcel-Dekker: New York, 2002; pp 187–250.
39. Maters, K. S.; Anseth, K. S. *Adv. Chem. Eng.* **2004**, *29*, 7–46.
40. Craig, W. S.; Cheng, S.; Mullen, D. G.; Blevitt, J.; Pierschbacher, M. D. *Biopolymers* **1995**, *37*, 157–175.
41. Schaffner, P.; Dard, M. M. *Cell. Mol. Life Sci.* **2003**, *60*, 119–132.
42. Re, R. N. *BioEssays* **2003**, *25*, 401–409.
43. Singh, A. B.; Harris, R. C. *Cell. Signal.* **2005**, *17*, 1183–1193.
44. Wells, A.; Marti, U. *Nat. Rev. Mol. Cell Biol.* **2002**, *3*, 697–702.
45. Achyuta, A. K.; Cieri, R.; Unger, K.; Murphy, S. K. *Biotechnol. Prog.* **2009**, *25*, 227–234.
46. Sun, W.; Sun, C.; Kin, H.; *et al. Biomaterials* **2009**, *30*, 4649–4656.
47. Yu, L. M. Y.; Wosnick, J. H.; Shoichet, M. S. *J. Neurosci. Meth.* **2008**, *171*, 253–263.
48. Gibson, C. C.; Puleo, D. A.; Bizios, R. In *Biological Interactions on Materials Surface*; Springer: New York, 2009; pp 199–224.
49. Jones, C. N.; Tuleuova, N.; Lee, J. Y.; *et al. Biomaterials* **2009**, *30*, 3733–3741.
50. Eliceiri, B. P. *Circ. Res.* **2001**, *89*, 1104–1110.
51. Streuli, C. H.; Akhtar, N. *Biochem. J.* **2009**, *418*, 491–506.
52. Ivaska, J.; Heino, J. *Cell Tissue Res.* **2010**, *339*, 111–120.
53. Cornwell, K. G.; Landsman, A.; James, K. S. *Clin. Podiatr. Med. Surg.* **2009**, *26*, 507–523.
54. Grinnell, F.; Feld, M. K. *J. Biol. Chem.* **1982**, *257*, 4888–4893.
55. Kowalczyńska, H. M.; Nowak-Wyrzykowska, M.; Kołos, R.; Dobkowski, J.; Kamiński, J. *J. Biomed. Mater. Res. A* **2005**, *72*, 228–236.
56. Toworfe, G. K.; Composto, R. J.; Adams, C. S.; Shapiro, I. M.; Ducheyne, P. *J. Biomed. Mater. Res. A* **2004**, *71*, 449–461.
57. Barbucci, R.; Magnani, A.; Chiumiento, A.; Pasqui, D.; Cangioli, I.; Lamponi, S. *Biomacromolecules* **2005**, *6*, 638–645.
58. Biran, R.; Webb, K.; Noble, M. D.; Tresco, P. A. *J. Biomed. Mater. Res.* **2001**, *55*, 1–12.
59. Johansson, S.; Svineng, G.; Wennerberg, K.; Armulik, A.; Lohikangas, L. *Front. Biosci.* **1997**, *2*, 126–146.
60. Zhang, Z.; Yoo, R.; Wells, M.; Beebe, T. P., Jr.; Biran, R.; Tresco, P. *Biomaterials* **2005**, *26*, 47–61.
61. Zhang, Y.; Chai, C.; Jaing, X. S.; Teoh, S. H.; Leong, K. M. *Mater. Sci. Eng. C* **2007**, *27*, 213–219.
62. Bramfeldt, H.; Vermette, P. *J. Biomed. Mater. Res. A* **2008**, *88*, 520–528.
63. Kohen, N. T.; Little, L. E.; Healy, K. E. *Biointerphases* **2009**, *4*, 69–79.
64. Martin, S. M.; Ganapathy, R.; Kim, T. K.; Leach-Scampavia, D.; Giachelli, C. M.; Ratner, B. D. *J. Biomed. Mater. Res.* **2003**, *67A*, 334–343.
65. Martin, S. M.; Schwartz, J. L.; Giachelli, C. M.; Ratner, B. D. *J. Biomed. Mater. Res.* **2004**, *70A*, 10–19.
66. Ito, Y.; Kajihara, M.; Imanishi, Y. *J. Biomed. Mater. Res.* **1991**, *25*, 1325–1337.
67. Ito, Y.; Liu, S. Q.; Imanishi, Y. *Biomaterials* **1991**, *12*, 449–453.
68. Massia, S.; Hubbell, J. *Anal. Biochem.* **1990**, *187*, 292–301.
69. Massia, S.; Hubbell, J. *J. Cell Biol.* **1991**, *144*, 1089–1100.
70. Rezania, A.; Healy, K. E. *Biotechol. Prog.* **1999**, *15*, 19–32.
71. Raynor, J. E.; Capadona, J. R.; Collard, D. M.; Petrie, T. A.; Garcia, A. J. *Biointerphases* **2009**, *4*, FA3–FA16.
72. Harbers, G. M.; Emoto, K.; Greef, C.; *et al. Chem. Mater.* **2007**, *19*, 4405–4414.
73. Carrico, I. S.; Maskarinec, S. A.; Heilshorn, S. C.; *et al. J. Am. Chem. Soc.* **2007**, *129*, 4874–4875.
74. Liu, J. C.; Tirrell, D. A. *Biomacromolecules* **2008**, *9*, 2984–2988.
75. Zhe, J.; Tang, C.; Kottke-Marchant, K.; Marchant, R. E. *Bioconjug. Chem.* **2009**, *20*, 333–339.
76. Petty, R. T.; Li, H. W.; Maduram, J. H.; Ismagilov, R.; Mrksich, M. *J. Am. Chem. Soc.* **2007**, *129*, 8966–8967.
77. Foillard, S.; Dumy, P.; Boturyn, D. *Org. Biomol. Chem.* **2009**, *7*, 4159–4162.
78. Perlin, L.; MacNeil, S.; Rimmer, S. *Soft Matter* **2008**, *4*, 2331–2349.
79. Robertus, J.; Browne, W. R.; Feringa, B. L. *Chem. Soc. Rev.* **2010**, *39*, 354–378.
80. Hwang, D. S.; Sim, S. B.; Cha, H. J. *Biomaterials* **2007**, *28*, 4039–4046.
81. Meyers, S. R.; Khoo, X.; Huang, X.; Walsh, E. B.; Grinstaff, M. W.; Kenan, D. J. *Biomaterials* **2009**, *30*, 277–286.
82. Rexeisen, E. L.; Fan, W.; Pangburn, T. O.; *et al. Langmuir* **2009**, *26*, 1953–1959.
83. Cejas, M. A.; Kinney, W. A.; Chen, C.; *et al. J. Am. Chem. Soc.* **2007**, *129*, 2202–2203.
84. Horii, A.; Wang, X.; Gelain, F.; Zhang, S. *PLoS One* **2007**, *2*, e190.
85. Jaehrling, S.; Thelen, K.; Wolfram, T.; Pollerberg, G. E. *Nano Lett.* **2009**, *9*, 4115–4121.
86. Nagaoka, M.; Koshimizu, U.; Yuasa, S.; *et al. PLoS One* **2006**, *1*, e15.
87. Nagaoka, M.; Hagiwara, Y.; Takemura, K.; *et al. J. Biol. Chem.* **2008**, *39*, 26468–26476.
88. Nagaoka, M.; Ise, H.; Harada, I.; Koshimizu, U.; Maruyama, A.; Akaike, T. *J. Cell. Biochem.* **2008**, *103*, 296–310.
89. Koike, J.; Nagata, K.; Kudo, S.; Tsuji, T.; Irimura, T. *FEBS Lett.* **2000**, *477*, 84–88.
90. Hong, S.; Lee, D.; Zhang, H.; *et al. Langmuir* **2007**, *23*, 12261–12268.
91. Schmidt, B. J.; Papin, J. A.; Lawrence, M. B. *PLoS Comput. Biol.* **2009**, *5*, e1000612.
92. Kohrgruber, N.; Groger, M.; Meraner, P.; *et al. J. Immunol.* **2004**, *173*, 6592–6602.
93. Varnum-Finney, B.; Wu, L.; Yu, M.; *et al. J. Cell Sci.* **2000**, *113*, 4313–4318.
94. Konno, T.; Sakano, S.; Higashida, S.; Ito, Y. *Inflam. Regen.* **2005**, *25*, 426–430.
95. Beckstead, B. L.; Santosa, D. M.; Giachelli, C. M. *J. Biomed. Mater. Res.* **2006**, *79A*, 94–103.
96. Taqvi, S.; Dixit, L.; Roy, K. *J. Biomed. Mater. Res. A* **2006**, *79*, 689–697.
97. Suzuki, T.; Yokoyama, Y.; Kumano, K.; *et al. Stem Cells* **2006**, *24*, 2456–2465.
98. Kertész, Z.; Vas, V.; Kiss, J.; *et al. Cell Biol. Int.* **2006**, *30*, 401–405.
99. Zisch, A. H.; Zeisberger, S. M.; Ehrbar, M.; *et al. Biomaterials* **2004**, *25*, 3245–3257.
100. Ho, J. E.; Chung, E. H.; Wall, S.; Schaffer, D. V.; Healy, K. E. *J. Biomed. Mater. Res.* **2007**, *83A*, 1200–1208.
101. Massague, J.; Pandiella, A. *Annu. Rev. Biochem.* **1993**, *62*, 515–541.
102. Iwamoto, R.; Mekada, E. *Cytokine Growth Factor Rev.* **2000**, *11*, 335–344.
103. Ito, Y. *Soft Matter* **2008**, *4*, 46–56.
104. Ito, Y. In *Biological Interactions on Materials Surface*, Springer: New York, 2009; pp 174–199.
105. Kiessling, L. L.; Gestwicki, J. E.; Strong, L. E. *Angew. Chem. Int. Ed.* **2006**, *45*, 2348–2368.
106. Ito, Y.; Liu, S. Q.; Nakabayashi, M.; Imanishi, Y. *Biomaterials* **1992**, *13*, 789–794.
107. Liu, S. Q.; Ito, Y.; Imanishi, Y. *Biomaterials* **1992**, *13*, 50–58.
108. Liu, S. Q.; Ito, Y.; Imanishi, Y. *J. Biochem. Biophys. Meth.* **1992**, *25*, 139–148.
109. Bromberg, L.; Salvati, L., Jr. *Bioconjug. Chem.* **1999**, *10*, 678–686.
110. Chen, G.; Ito, Y.; Imanishi, Y. *Bioconjug. Chem.* **1997**, *8*, 106–110.
111. Ito, Y.; Chen, G.; Imanishi, Y. *Biotechnol. Prog.* **1996**, *12*, 700–703.

112. Ito, Y.; Zheng, J.; Imanishi, Y.; Yonezawa, K.; Kasuga, M. *Proc. Natl. Acad. Sci. USA* **1996**, *93*, 3598–3601.
113. Ito, Y.; Inoue, M.; Liu, S. Q.; Imanishi, Y. *J. Biomed. Mater. Res.* **1993**, *27*, 901–907.
114. Ito, Y.; Liu, S. Q.; Orihara, T.; Imanishi, Y. *J. Bioact. Compat. Polym.* **1994**, *9*, 170–183.
115. Kang, I. K.; Choi, S. H.; Shin, D. S.; Yoon, S. C. *Int. J. Biol. Macromol.* **2001**, *28*, 205–212.
116. Kellner, K.; Tessmar, J.; Milz, S.; *et al. Tissue Eng.* **2004**, *10*, 429–440.
117. Kim, E. J.; Kang, I. K.; Jang, M. K.; Park, Y. B. *Biomaterials* **1998**, *19*, 239–249.
118. Tessmar, J.; Kellner, K.; Schulz, M. B.; Blunk, T.; Gopferich, A. *Tissue Eng.* **2004**, *10*, 441–453.
119. Tessmar, J.; Mikos, A.; Gopferich, A. *Biomaterials* **2003**, *24*, 4475–4486.
120. Ito, Y.; Uno, T.; Liu, S. Q.; Imanishi, Y. *Biotechnol. Bioeng.* **1992**, *40*, 1271–1276.
121. Liu, S. Q.; Ito, Y.; Imanishi, Y. *Enzyme Microb. Technol.* **1993**, *15*, 167–172.
122. Liu, S. Q.; Ito, Y.; Imanishi, Y. *J. Biomed. Mater. Res.* **1993**, *27*, 909–915.
123. Gumusdrelioglu, M.; Turkoglu, H. *Biomaterials* **2002**, *23*, 3927–3935.
124. Gumusdrelioglu, M.; Karakecili, A. G. *J. Biomater. Sci. Polym. Ed.* **2003**, *14*, 199–211.
125. Ito, Y.; Kondo, S.; Chen, G.; Imanishi, Y. *FEBS Lett.* **1997**, *403*, 159–162.
126. Ito, Y.; Li, J. S.; Takahashi, T.; *et al. J. Biochem.* **1997**, *121*, 514–520.
127. Ito, Y.; Zheng, J.; Imanishi, Y. *Biotechnol. Bioeng.* **1995**, *45*, 144–148.
128. Ito, Y.; Zheng, J.; Imanishi, Y. *Biomaterials* **1997**, *18*, 197–202.
129. Li, J. S.; Ito, Y.; Zheng, J.; Takahashi, T.; Imanishi, Y. *J. Biomed. Mater. Res.* **1997**, *37*, 190–197.
130. Zheng, J.; Ito, Y.; Imanishi, Y. *Biomaterials* **1994**, *15*, 963–968.
131. Zheng, J.; Ito, Y.; Imanishi, Y. *Biotechnol. Prog.* **1995**, *11*, 677–681.
132. Zheng, J.; Ito, Y.; Imanishi, Y. *J. Biomater. Sci. Polym. Ed.* **1995**, *7*, 515–522.
133. Liu, S. Q.; Ito, Y.; Imanishi, Y. *Int. J. Biol. Macromol.* **1993**, *15*, 221–226.
134. Kim, Y. J.; Kang, I. K.; Huh, M. W.; Yoon, S. C. *Biomaterials* **2000**, *21*, 121–130.
135. Sasmazel, H. T.; Aday, S.; Gumusderelioglu, M. *Int. J. Biol. Macromol.* **2007**, *41*, 338–345.
136. Chen, G.; Ito, Y.; Imanishi, Y. *Biotechnol. Bioeng.* **1997**, *53*, 339–344.
137. Hatakeyama, H.; Kikuchi, A.; Yamato, M.; Okano, T. *Biomaterials* **2005**, *26*, 5167–5176.
138. Hatakeyama, H.; Kikuchi, A.; Yamato, M.; Okano, T. *Biomaterials* **2006**, *27*, 5069–5078.
139. Hatakeyama, H.; Kikuchi, A.; Yamato, M.; Okano, T. *Biomaterials* **2007**, *28*, 3632–3643.
140. Brose, C.; Schmidt, D.; von Briesen, H.; Reinmann, M. *Ann. Anat.* **2009**, *191*, 83–93.
141. Miller, E. D.; Phillippi, J. A.; Fisher, G. W.; Campbell, P. G.; Walker, L. M.; Weiss, L. E. *Comb. Chem. High Throughput Screen.* **2009**, *12*, 604–618.
142. Stefonek-Puccinelli, T. J.; Masters, K. S. *Ann. Biomed. Eng.* **2008**, *36*, 2121–2133.
143. Van Lonkhuyzen, D. R.; Hollier, B. G.; Shooter, G. K.; Leavesley, D. I.; Upton, Z. *Growth Factors* **2007**, *25*, 295–308.
144. Kuhl, P. R.; Griffith-Cima, L. G. *Nat. Med.* **1996**, *2*, 1022–1027.
145. Chen, G.; Ito, Y.; Imanishi, Y. *Biochim. Biophys. Acta* **1997**, *1358*, 200–208.
146. Chen, G.; Ito, Y.; Masuda, S.; Sasaki, R. *Cytotechnology* **2001**, *35*, 3–8.
147. Ogiwara, K.; Nagaoka, M.; Cho, C. S.; Akaike, T. *Biochem. Biophys. Res. Commun.* **2006**, *345*, 255–259.
148. Woo, Y. K.; Kwon, S. Y.; Lee, H. S.; Park, Y. S. *J. Orthop. Res.* **2007**, *25*, 73–80.
149. Park, Y.-S.; Seo, Y.-K.; Lee, H.-S.; Kaon, S.-Y.; Park, J.-K. *Macromol. Symp.* **2007**, *249–250*, 124–129.
150. Tigli, R. S.; Gumusdereliglu, M. *Int. J. Biol. Macromol.* **2008**, *43*, 121–128.
151. Ito, Y.; Chen, G.; Imanishi, Y. *Bioconjug. Chem.* **1998**, *9*, 277–282.
152. Ichinose, J.; Morimatsu, M.; Yanagida, T.; Sako, Y. *Biomaterials* **2006**, *27*, 3343–3350.
153. Chen, G.; Ito, Y. *Biomaterials* **2001**, *22*, 2453–2457.
154. Wang, Q.; Bohn, P. W. *Thin Solid Films* **2006**, *513*, 338–346.
155. Stefonek, T. J.; Masters, K. S. *Wound Repair Regen.* **2007**, *15*, 847–855.
156. Klenkler, B. J.; Griffith, M.; Becerril, C.; West-Mays, J. A.; Sheardown, H. *Biomaterials* **2005**, *26*, 7286–7296.
157. Waddell, J. T.; Liesenfeld, B.; Batich, C. D. *Ann. Tech. Conf. ANTEC Conf. Proc.* **2005**, *10*, 19–22.
158. Klenkler, B. J.; Sheardown, H. *Biotechnol. Bioeng.* **2006**, *95*, 1158–1166.
159. Karakecili, A. G.; Satriano, C.; Gumusdereliglu, M.; Marletta, G. *Acta Biomater.* **2008**, *4*, 989–996.
160. Ito, Y.; Chen, G.; Imanishi, Y.; *et al. J. Biochem.* **2001**, *129*, 733–737.
161. Fan, V. H.; Au, A.; Tamama, K.; *et al. Stem Cells* **2007**, *25*, 1241–1251.
162. Marcantonio, N. A.; Boehm, C. A.; Rozic, R. J.; *et al. Biomaterials* **2009**, *30*, 4629–4638.
163. Platt, M. O.; Roman, A. J.; Wells, A.; Lauffenburger, D. A.; Griffith, L. G. *J. Cell. Physiol.* **2009**, *221*, 306–317.
164. Nakajima, M.; Ishimuro, T.; Kato, K.; *et al. Biomaterials* **2007**, *28*, 1048–1060.
165. Nishi, N.; Matsushita, O.; Yuube, K.; Miyanaka, H.; Okabe, A.; Wada, F. *Proc. Natl. Acad. Sci. USA* **1998**, *95*, 7018–7023.
166. Hall, F. L.; Kaiser, A.; Liu, L.; *et al. Int. J. Mol. Med.* **2000**, *6*, 635.
167. Ishikawa, T.; Terai, H.; Kitajima, T. *J. Biochem.* **2001**, *129*, 627–633.
168. Ishikawa, T.; Terai, H.; Yamamoto, T.; Harada, K.; Kitajima, T. *Artif. Organs* **2003**, *27*, 147–154.
169. Kato, K.; Sato, H.; Iwata, H. *Bioconjug. Chem.* **2007**, *18*, 2137–2143.
170. Kitajima, T.; Sakuragi, M.; Hasuda, H.; Ozu, T.; Ito, Y. *Acta Biomater.* **2009**, *5*, 2623–2632.
171. Choi, J. S.; Leong, K. W.; Yoo, H. S. *Biomaterials* **2008**, *29*, 587–596.
172. Ogiwara, K.; Nagaoka, M.; Cho, C. S.; Akaike, T. *Biotechnol. Lett.* **2005**, *27*, 1633–1637.
173. Nakaji-Hirabayashi, T.; Kato, K.; Arima, Y.; Iwata, H. *Biomaterials* **2007**, *2*, 3517–3529.
174. Nakaji-Hirabayashi, T.; Kato, K.; Iwata, H. *Biomaterials* **2008**, *29*, 4403–4408.
175. Nakaji-Hirabayashi, T.; Kato, K.; Iwata, H. *Bioconjug. Chem.* **2009**, *20*, 102–110.
176. Nakaji-Hirabayashi, T.; Kato, K.; Iwata, H. *Biomaterials* **2009**, *30*, 4581–4589.
177. Boucher, C.; St-Laurent, G.; Loignon, M.; Jolicoeur, M.; De Crescenzo, G.; Durocher, Y. *Tissue Eng.* **2008**, *14*, 2069–2077.
178. Boucher, C.; Liberelle, B.; Jolicoeur, M.; Durocher, Y.; De Crescenzo, G. *Bioconjug. Chem.* **2009**, *20*, 1569–1577.
179. Kawase, Y.; Ohdate, Y.; Shimojo, T.; Taguchi, Y.; Kimizuka, F.; Kato, I. *FEBS Lett.* **1992**, *298*, 126–128.
180. Hashi, H.; Hatai, M.; Kimizuka, F.; Kato, I.; Yaoi, Y. *Cell Struct. Funct.* **1994**, *19*, 37–47.
181. Elloumi, I.; Kobayashi, R.; Funabashi, H.; Mie, M.; Kobatake, E. *Biomaterials* **2006**, *27*, 3451–3458.
182. Hannachi Imen, E.; Nakamura, M.; Mie, M.; Kobatake, E. *J. Biotechnol.* **2009**, *139*, 19–25.
183. Hayashi, M.; Tomita, M.; Yoshizato, K. *Biochim. Biophys. Acta* **2001**, *1528*, 187–195.
184. Ito, Y. *Jpn. J. Artif. Organs* **1998**, *27*, 383–394.
185. Chen, P. R.; Chen, M. H.; Lin, F. H.; Su, W. Y. *Biomaterials* **2005**, *26*, 6579–6587.
186. Kapur, T. A.; Schoichet, M. S. *J. Biomater. Sci. Polym. Ed.* **2003**, *14*, 383–394.
187. Kapur, T. A.; Schoichet, M. S. *J. Biomed. Mater. Res.* **2004**, *68A*, 235–243.
188. Moore, K.; MacSween, M.; Shoichet, M. *Tissue Eng.* **2006**, *12*, 267–278.
189. Shibata, S. C.; Hibino, K.; Mashimo, T.; Yanagida, T.; Sako, Y. *Biochem. Biophys. Res. Commun.* **2006**, *342*, 316–322.
190. Bhang, S. H.; Lee, T.-J.; Yang, H. S.; *et al. Biochem. Biophys. Res. Commun.* **2009**, *382*, 315–320.
191. Sun, W.; Lin, H.; Chen, B.; Zhao, W.; Zhao, Y.; Dai, J. *J. Biomed. Mater. Res. A* **2007**, *83*, 1054–1061.
192. Sun, W.; Lin, H.; Chen, B.; *et al. J. Biomed. Mater. Res. A* **2010**, *92*, 887–895.
193. Sun, W.; Lin, H.; Xie, H.; *et al. Growth Factors* **2007**, *25*(5), 309–318.
194. Han, M.; Park, I. S.; Kim, S. H.; Kim, B. S.; Kim, S.-H. *Biotechnol. Lett.* **2009**, *31*, 1677–1684.
195. Han, Q.; Sun, W.; Lin, H.; *et al. Tissue Eng. A* **2009**, *15*, 2927–2935.
196. Sakiyama-Elbert, S.; Panitch, A.; Hubbell, J. A. *FASEB J.* **2001**, *15*, 1300–1302.
197. Lee, J.-Y.; Choo, J.-E.; Choi, Y.-S.; *et al. Biotechnol. Appl. Biochem.* **2009**, *52*, 69–77.
198. Lee, J.-Y.; Choo, J.-E.; Choi, Y.-S.; *et al. Biomaterials* **2009**, *30*, 3532–3541.
199. Lee, J. Y.; Lee, J.-W.; Schmidt, C. E. *J. R. Soc. Interface* **2009**, *6*, 801–810.
200. Gomez, N.; Lu, Y.; Chen, S.; Schmidt, C. E. *Biomaterials* **2007**, *28*, 271–284.
201. Porter, J. R.; Ruckh, T. T.; Popat, K. C. *Biotechnol. Prog.* **2009**, *25*, 1539–1560.
202. Adden, N.; Gamble, L. J.; Castner, D. G.; Hoffmann, A.; Gross, G.; Menzel, H. *Langmuir* **2006**, *22*, 8197–8204.
203. Puleo, D. A.; Kissling, R. A.; Sheu, M. S. *Biomaterials* **2002**, *23*, 2079–2087.
204. Shi, Z.; Neoh, K. G.; Kang, E. T.; Poh, C. K.; Wang, W. *Biomacromolecules* **2009**, *10*, 1603–1611.
205. Lim, T. Y.; Wang, W.; Shi, Z.; Poh, C. K.; Neoh, K. G. *J. Mater. Sci. Mater. Med.* **2009**, *20*, 1–10.
206. Kashiwagi, K.; Tsuji, T.; Shiba, K. *Biomaterials* **2009**, *30*, 1166–1175.
207. Schuessele, A.; Mayr, H.; Tessmar, J.; Goepferich, A. *J. Biomed. Mater. Res.* **2008**, *90A*, 959–971.
208. Kloss, F. R.; Gassner, R.; Preiner, J.; *et al. Biomaterials* **2008**, *29*, 2433–2442.
209. Karageorgiou, V.; Meinel, L.; Hofmann, S.; Malhotra, A.; Volloch, V.; Kaplan, D. *J. Biomed. Mater. Res.* **2004**, *71A*, 528–537.

210. Tsujigiwa, H.; Nagatsuka, H.; Gunduz, M.; *et al*. *J. Biomed. Mater. Res.* **2005**, *75*, 210–215.
211. Tsujigiwa, H.; Nagatsuka, H.; Lee, Y. J.; *et al*. *J. Biomed. Mater. Res.* **2006**, *77A*, 507–511.
212. Yamachika, E.; Tsujigiwa, H.; Shirasu, N.; *et al*. *J. Biomed. Mater. Res. A* **2009**, *88*, 599–607.
213. Park, Y. J.; Kim, K. H.; Lee, J. Y.; *et al*. *Biotechnol. Appl. Biochem.* **2006**, *43*, 17–24.
214. Chen, B.; Lin, H.; Wang, J.; *et al*. *Biomaterials* **2007**, *28*(6), 1027–1035.
215. Zhao, Y.; Chen, B.; Lin, H.; *et al*. *J. Biomed. Mater. Res. A* **2009**, *88*(3), 725–734.
216. Zhao, W.; Han, Q.; Lin, H.; *et al*. *Tissue Eng. A* **2009**, *15*(5), 991–998.
217. Lin, H.; Zhao, Y.; Sun, W.; *et al*. *Biomaterials* **2008**, *29*(9), 1189–1197.
218. Schmoekel, H. G.; Weber, F. E.; Schense, J. C.; Graetz, K. W.; Schwalder, P.; Hubbell, J. A. *Biotechnol. Bioeng.* **2005**, *89*, 253–262.
219. Edlund, U.; Danmark, S.; Albertsson, A. C. *Biomacromolecules* **2008**, *9*, 901–905.
220. Shen, H.; Hu, X.; Yang, F.; Bei, J.; Wang, S. *Biomaterials* **2009**, *30*, 3150–3157.
221. Liu, H. W.; Chen, C. H.; Tsai, C. L.; Lin, I. H.; Hsiue, G. H. *Tissue Eng.* **2007**, *13*, 1113–1124.
222. Winkler, L.; Bingmann, D.; Wiemann, M. *J. Biomed. Mater. Res.* **2006**, *79*, 895–901.
223. Han, B.; Perelman, N.; Tang, B.; Hall, F.; Shors, E. C.; Nimni, M. E. *J. Orthop. Res.* **2006**, *20*, 747–755.
224. Suzuki, Y.; Tanihara, M.; Suzuki, K.; Saitou, A.; Sufan, W.; Nishimura, Y. *J. Biomed. Mater. Res.* **2000**, *50*, 405–409.
225. Saito, A.; Suzuki, Y.; Ogata, S.; Ohtsuki, C.; Tanihara, M. *Biochim. Biophys. Acta* **2003**, *1651*, 60–67.
226. Kirkwood, K.; Rheude, B.; Kim, Y. J.; White, K.; Dee, K. C. *J. Oral Implantol.* **2003**, *29*, 57–65.
227. Sharon, J. L.; Puleo, D. A. *Acta Biomater.* **2008**, *4*, 1016–1023.
228. Sharon, J. L.; Puleo, D. *Biomaterials* **2008**, *29*, 3137–3142.
229. Taguchi, T.; Kishida, A.; Akashi, M.; Maruyama, I. *J. Bioact. Compat. Polym.* **2000**, *15*, 309–320.
230. Ito, Y.; Hasuda, H.; Terada, H.; Kitajima, T. *J. Biomed. Mater. Res.* **2005**, *74*, 659–665.
231. Shen, H.; Hu, X.; Bei, J.; Wang, S. *Biomaterials* **2008**, *29*, 2388–2399.
232. Shen, Y. H.; Shoichet, M. S.; Radisic, M. *Acta Biomater.* **2008**, *4*, 477–489.
233. Anderson, S. M.; Chen, T. T.; Iruela-Arispe, M. L.; Segura, T. *Biomaterials* **2009**, *30*, 4618–4628.
234. Wang, A. Y.; Leong, S.; Liang, Y.-C.; Huang, R. C. C.; Chen, C. S.; Yu, S. M. *Biomacromolecules* **2008**, *9*, 2929–2936.
235. Sahni, A.; Francis, C. W. *Blood* **2000**, *96*(12), 3772–3778.
236. Zisch, A. H.; Schenk, U.; Schense, J. C.; Sakiyama-Elbert, S. E.; Hubbell, J. A. *J. Control. Release* **2001**, *72*, 101–113.
237. Ehrbar, M.; Djonov, V. G.; Schnell, C.; *et al*. *Circ. Res.* **2004**, *94*, 1124–1132.
238. Backer, M. V.; Patel, V.; Jehning, B. T.; Claffey, K. P.; Backer, J. M. *Biomaterials* **2006**, *27*, 5452–5458.
239. Ishikawa, T.; Eguchi, M.; Wada, M.; *et al*. *Arterioscler. Thromb. Vasc. Biol.* **2006**, *26*, 1998–2004.
240. Arkudas, A.; Tjiawi, J.; Bleiziffer, O.; *et al*. *Mol. Med.* **2007**, *13*, 480–487.
241. Arkudas, A.; Pryymachuk, G.; Hoereth, T.; *et al*. *Tissue Eng. A* **2009**, *15*, 2501–2511.
242. Chiu, L. L. Y.; Radisic, M. *Biomaterials* **2010**, *31*, 226–241.
243. Leslie-Barbick, J. E.; Moon, J. J.; West, J. L. *J. Biomater. Sci. Polym. Ed.* **2009**, *20*(12), 1763–1779.
244. DeLong, S. A.; Moon, J. J.; West, J. L. *Biomaterials* **2005**, *26*, 3227–3234.
245. Christman, K. L.; Vázquez-Dorbatt, V.; Schopf, E.; *et al*. *J. Am. Chem. Soc.* **2008**, *130*, 16585–16591.
246. Watanabe, K.; Miyazaki, T.; Matsuda, R. *Zoolog. Sci.* **2003**, *20*, 429–434.
247. Campbell, P. G.; Miller, E. D.; Fisher, G. W.; Walker, L. M.; Weiss, L. E. *Biomaterials* **2005**, *26*, 6762–6770.
248. Miller, E. D.; Fisher, G. W.; Weiss, L. E.; Walker, L. M.; Campbell, P. G. *Biomaterials* **2006**, *27*, 2213–2221.
249. Nur-E-Kamal, A.; Ahmed, I.; Kamal, J.; Babu, A. N.; Schindler, M.; Meiners, S. *Mol. Cell. Biochem.* **2008**, *309*, 157–166.
250. Mori, H.; Shukunami, C.; Furuyama, A.; Notsu, H.; Nishizaki, Y.; Hiraki, Y. *J. Biol. Chem.* **2007**, *282*, 17289–17296.
251. Ijiri, H.; Coulibaly, E.; Nishimura, G.; *et al*. *Biomaterials* **2009**, *30*, 4297–4308.
252. Ohyama, T.; Nishide, T.; Iwata, H.; *et al*. *J. Neurosurg.* **2005**, *102*, 109–115.
253. Peelen, D.; Kodoyianni, V.; Lee, J.; Zheng, T.; Shortreed, M. R.; Smith, L. M. *J. Proteome Res.* **2006**, *5*, 1580–1585.
254. Kokubu, E.; Yoshinari, M.; Matsuzaka, K.; Inoue, T. *J. Biomed. Mater. Res.* **2009**, *91*, 69–75.
255. Sogo, Y.; Onoguchi, M.; Oyane, A.; Tsurushima, H.; Ichinose, N. *Biomed. Mater.* **2007**, *2*, S175–S180.
256. Andrades, J. A.; Han, B.; Becerra, J.; Sorgente, N.; Hall, F. L.; Nimni, M. E. *Exp. Cell Res.* **1999**, *250*, 485–498.
257. Brewster, L. P.; Washington, C.; Brey, E. M.; *et al*. *Biomaterials* **2008**, *29*, 327–336.
258. Zhao, W.; Chen, B.; Li, X.; *et al*. *J. Biomed. Mater. Res. A* **2007**, *82*(3), 630–636.
259. Zhao, W.; Han, Q.; Lin, H. *et al*. *J. Mol. Med.* **2008**, *86*(10), 1081–1083.
260. Fischer, U.; Hempel, U.; Becker, D.; *et al*. *Biomaterials* **2003**, *24*, 2631–2641.
261. Merrett, K.; Griffith, C. M.; Deslandes, Y.; Pleizier, G.; Sheardown, H. *J. Biomed. Mater. Res.* **2003**, *67A*, 981–993.
262. Mann, B. K.; Schmedlen, R. H.; West, J. L. *Biomaterials* **2001**, *22*, 439–444.
263. Bentz, H.; Schroeder, J. A.; Estridge, T. D. *J. Biomed. Mater. Res.* **1998**, *15*, 539–548.
264. Tuan, T. L.; Cheung, D. T.; Wu, L. T.; *et al*. *Connect. Tissue Res.* **1996**, *34*, 1.
265. Chou, C. H.; Cheng, W. T. K.; Lin, C. C.; Chang, C. H.; Tsai, C. C.; Lin, F. H. *J. Biomed. Mater. Res.* **2006**, *77B*, 338–348.
266. Bhatnagar, B.; Nixon, A. J.; Kim, I.; Kameoka, J. *Biomed. Microdevices* **2008**, *10*, 567–571.
267. Kitajima, T.; Terai, H.; Ito, Y. *Biomaterials* **2007**, *28*, 1989–1997.
268. Azuma, K.; Nagaoka, M.; Cho, C. S.; Akaike, T. *Biomaterials* **2010**, *31*, 802–809.
269. Ohkawara, N.; Ueda, H.; Shinozaki, S.; *et al*. *J. Atheroscler. Thromb.* **2007**, *14*, 185–191.
270. Ota, T.; Gilbert, T. W.; Schwartzman, D.; *et al*. *J. Thorac. Cardiovasc. Surg.* **2008**, *136*, 1309–1317.
271. Aizawa, Y.; Leipzig, N.; Zahir, T.; Schoichet, M. *Biomaterials* **2008**, *29*, 4676–4683.
272. Lin, H.; Chen, B.; Sun, W.; Zhao, W.; Zhao, Y.; Dai, J. *Biomaterials* **2006**, *27*(33), 5708–5714.
273. Geer, D. J.; Swartz, D. D.; Andreadis, S. T. *Am. J. Pathol.* **2005**, *167*(6),1575–1586.
274. Makino, H.; Hasuda, H.; Ito, Y. *J. Biosci. Bioeng.* **2004**, *98*, 374–379.
275. Cetinkaya, G.; Torkoglu, H.; Arat, S.; *et al*. *J. Biomed. Mater. Res.* **2007**, *81A*, 911–919.
276. Alberti, K.; Davey, R. E.; Onishi, K.; *et al*. *Nat. Meth.* **2008**, *5*, 645–650.
277. Doran, M. R.; Markway, B. D.; Aird, I. A.; *et al*. *Biomaterials* **2009**, *30*, 4047–4052.
278. Doheny, J. G.; Jervis, E. J.; Guarna, M. M.; Humphries, R. K.; Warren, R. A.; Kilburn, D. G. *Biochem. J.* **1999**, *339*, 429–434.
279. Jervis, E. J.; Guarna, M. M.; Doheny, J. G.; Haynes, C. A.; Kilburn, D. G. *Biotechnol. Bioeng.* **2005**, *91*, 314–324.
280. Ito, Y.; Hasuda, H.; Yamauchi, T.; Komatsu, N.; Ikebuchi, K. *Biomaterials* **2004**, *25*, 2293–2298.
281. Horwitz, J. I.; Toner, M.; Tompkins, R. G.; Yarmuch, M. L. *Mol. Immunol.* **1993**, *30*, 1041–1048.
282. Chai, C.; Feng, Q.; Jaing, X. S.; Leong, K. W.; Mao, H. Q. In *Transactions – 7th World Biomaterials Congress*, Sidney, 2004; p 897.
283. Kim, D. H.; Smith, J. T.; Chilkoti, A.; Reichert, W. M. *Biomaterials* **2007**, *28*, 3369–3377.
284. Novak, M. T.; Breyers, J. D.; Reichers, W. M. *Biomaterials* **2008**, *19*, 5725–5730.
285. Guan, Y.; He, L.; Cai, S.; Zhou, T. *J. Mater. Sci. Technol.* **2006**, *22*, 200–204.
286. Guan, Y.; Zhong, H.; Wang, X.; Zhou, T. *Sheng Wu Yi Xue Gong Cheng Xue Za Zhi* **2006**, *23*, 346–349.
287. Ma, Z.; Mao, Z.; Gao, C. *Colloids Surf. B Biointerfaces* **2007**, *60*, 137–157.
288. Vasita, R.; Shanmugam, K.; Katti, D. S. *Curr. Top. Med. Chem.* **2008**, *8*, 341–353.
289. de Jonge, L. T.; Leeuwenburgh, S. C. G.; Wolke, J. G. C.; Jansen, J. A. *Pharm. Res.* **2008**, *25*, 2357–2369.
290. De Mel, A.; Jell, G.; Stevens, M. M.; Seifalian, A. M. *Biomacromolecules* **2008**, *9*, 2969–2979.
291. Hayes, J. S.; Richards, R. G. *Expert Rev. Med. Devices* **2010**, *7*, 131–142.
292. Morra, M. *Expert Rev. Med. Devices* **2007**, *4*, 361–372.
293. Jewell, C. M.; Zhang, J.; Fredin, N. J.; Wolff, M. R.; Hacker, T. A.; Lynn, D. M. *Biomacromolecules* **2006**, *7*, 2483–2491.
294. Zhang, F.; Kang, E. T.; Neoh, K. G.; Wang, P.; Tan, K. L. *Biomaterials* **2001**, *22*, 1541–1548.
295. Zhang, F.; Zhang, Z.; Zhu, X.; Kang, E. T.; Neoh, K. G. *Biomaterials* **2008**, *29*, 4751–4759.
296. Amalric, J.; Mutin, H.; Guerrero, G.; Ponche, A.; Sotto, A.; Lavigne, J.-P. *J. Mater. Chem.* **2009**, *19*, 141–149.
297. Hanson, E. L.; Schwartz, J.; Nickel, B.; Koch, N.; Danisman, M. F. *J. Am. Chem. Soc.* **2003**, *125*, 16074–16080.

298. Mani, G.; Johnson, D. M.; Marton, D.; *et al*. *Biomaterials* **2008**, *29*, 4561–4573.
299. Oya, K.; Tanaka, Y.; Saito, H.; *et al*. *Biomaterials* **2009**, *30*, 1281–1286.
300. Guo, K. T.; Scharnweber, D.; Schwenzer, B.; Ziemer, G.; Wendel, H. P. *Biomaterials* **2007**, *28*, 468–474.
301. Heydari, M.; Hasuda, H.; Sakuragi, M.; Yoshida, Y.; Suzuki, K.; Ito, Y. *J. Biomed. Mater. Res. A* **2007**, *83*, 906–914.
302. Ito, Y.; Hasuda, H.; Sakuragi, M.; Tsuzuki, S. *Acta Biomater.* **2007**, *3*, 1024–1032.
303. Charlot, A.; Sciannaméa, V.; Lenoir, S.; *et al*. *J. Mater. Chem.* **2009**, *19*, 4117–4125.
304. He, T.; Shi, Z. L.; Fang, N.; Neoh, K. G. E.; Kang, E. T.; Chan, V. *Biomaterials* **2009**, *30*, 317–326.
305. Lee, H.; Dellatore, S. M.; Miller, W. M.; Messersmith, P. B. *Science* **2007**, *318*, 426–430.
306. Westwood, G.; Horton, T. N.; Wilker, J. J. *Macromolecules* **2007**, *40*, 3960–3964.
307. Yin, M.; Yuan, Y.; Liu, C.; Wang, J. *Biomaterials* **2009**, *30*, 2764–2773.
308. Gungormus, M.; Fong, H.; Kim, I. W.; Evans, J. S.; Tamerler, C.; Sarikaya, M. *Biomacromolecules* **2008**, *9*, 966–973.
309. Sarikaya, M.; Tamerler, C.; Jen, A. K.; Schulten, K.; Baneyx, F. *Nat. Mater.* **2003**, *2*, 577–585.
310. Segvich, S. J.; Smith, H. C.; Kohn, D. H. *Biomaterials* **2009**, *30*, 1287–1298.
311. Seker, U. O.; Wilson, B.; Sahin, D.; Tamerler, C.; Sarikaya, M. *Biomacromolecules* **2009**, *10*, 250–257.
312. Huebsch, N.; Mooney, D. J. *Nature* **2009**, *462*, 426–432.
313. Ito, Y. *Biomaterials* **1999**, *20*, 2333–2342.
314. Ito, Y. *Biotechnol. Prog.* **2006**, *22*, 924–932.
315. Jonkheijm, P.; Weinrich, D.; Schröder, H.; Niemeyer, C. M.; Waldmann, H. *Angew. Chem. Int. Ed.* **2008**, *47*, 9618–9647.
316. Rusmini, F.; Zhong, Z.; Feijen, J. *Biomacromolecules* **2007**, *8*, 1775–1789.
317. Tayalia, P.; Mooney, D. J. *Adv. Mater.* **2009**, *21*, 3269–3285.
318. Brady, D.; Jordaan, J. *Biotechnol. Lett.* **2009**, *31*, 1639–1650.
319. Hanefeld, U.; Gardossi, L.; Magner, E. *Chem. Soc. Rev.* **2009**, *38*, 453–468.
320. Dellatore, S. M.; Garcia, A. S.; Miller, W. M. *Curr. Opin. Biotechnol.* **2008**, *19*, 531–540.
321. Derda, R.; Musah, S.; Orner, B. P.; Klim, J. R.; Li, L.; Kiessling, L. L. *J. Am. Chem. Soc.* **2010**, *132*, 1289–1295.
322. Lutolf, M. P.; Blau, H. M. *Adv. Mater.* **2009**, *21*, 3255–3268.
323. Lutolf, M. P.; Gilbert, P. M.; Blau, H. M. *Nature* **2009**, *462*, 433–441.

4.417. Tethered Antibiotics

N J Hickok* **and C Ketonis**, Thomas Jefferson University, Philadelphia, PA, USA
C S Adams, Philadelphia College of Osteopathic Medicine, Philadelphia, PA, USA

© 2011 Elsevier Ltd. All rights reserved.

4.417.1.	**Implant-Associated Infection in Orthopedic Materials**	282
4.417.1.1.	The RANKL Pathway and the Pathogenesis of Osteomyelitis	282
4.417.1.2.	Biofilm Development	283
4.417.2.	**Bacterial Responses to Orthopedic Implants**	284
4.417.2.1.	Metallic Implants	284
4.417.2.2.	Bone Allograft	284
4.417.3.	**Antibiotic Prophylaxis and Treatment of Surgical Infection**	284
4.417.3.1.	Structure of VAN	285
4.417.3.1.1.	VAN's mechanism of action	285
4.417.3.1.2.	Antibiotic resistance to VAN	286
4.417.4.	**Surface Tethering of Antibiotics to Prevent Bacterial Adhesion**	286
4.417.4.1.	Device Surface Preparations for Tethering	287
4.417.4.2.	Properties of Surface-Tethered VAN	288
4.417.4.2.1.	Properties of surface-tethered antibiotics	289
4.417.4.3.	Biocompatibility of Tethered VAN	291
4.417.4.4.	Coupling with Other Technologies	291
References		292

Glossary

Aminopropyltriethoxysilane (APTES) This chemical ideally forms three siloxy bonds (Ti–O–Si–) with the Ti-oxide surface to result in stable linkage of the moiety and exposure of a primary amine for further chemical coupling reactions.

Biofilm bacteria Bacteria adherent to a surface and encased in a polysaccharide matrix; bacteria in this state display reduced metabolism and sensitivity to antibiotics.

Interleukin 1, 6 (IL-1, 6), etc. Cytokines released by osteoblastic cells as inflammatory mediators.

Microbial surface components recognizing adhesive matrix molecules (MSCRAMM) One of the proteins on the bacterial surface used to attach to the extracellular matrix of the host tissue.

Nuclear factor-κB (NF-κB) A transcription factor mediating, among others, signaling through RANK.

Osteoprotegerin (OPG) A soluble RANK inhibitor that binds to RANKL.

Passivation Formation of a metal oxide layer through acid etching or through hydrothermal aging.

Phosphate-buffered saline (PBS) 137 mM NaCl, 2.7 mM KCl, 10 mM Na_2HPO_4, 2 mM NaH_2PO_4, pH 7.4 in water (Fisher Scientific).

Planktonic bacteria Rapidly proliferating, nonadherent bacteria.

Polyethylene glycol (PEG) A common substance used in drug formulations. PEG linkers are available commercially for use in peptide synthesis reactions to provide space between different components.

Prostaglandin E2 (PGE2) An arachidonic acid derivative important in inflammatory responses.

Quorum sensing An interbacterial communication mechanism dependent on population density and associated with marked (more than 50%) changes in protein expression patterns.

Receptor activator of NF-κB (RANK) A TNF-α superfamily transmembrane receptor expressed on osteoclast precursors and mature osteoclasts.

Ti6Al4V A titanium alloy frequently used in the manufacture of orthopedic devices.

Tryptic soy broth (TSB) A dextrose, casein, and soybean meal containing buffered salt medium for growing aerobic bacteria.

Tumor necrosis factor-related apoptosis-inducing ligand (TRAIL) A protein that can block OPG effects and induce osteoclastogenesis.

Vancomycin (VAN) A glycopeptide antibiotic against species of gram-positive bacteria.

Vancomycin coupled to the Ti-oxide surface (VAN-Ti) The actual structure would be Ti–O–APTES–PEG–PEG–VAN. In this case, PEG is 2-(2-amino-ethoxy)-ethoxy-acetic acid (AEEA).

**Conflict of Interest*: Noreen J. Hickok is a part owner of SmartTech which has a commercial interest in the technology described in this manuscript.

Abbreviations

AEEA	2-[(ethoxy)ethoxy]acetic acid
APTES	Aminopropyltriethoxy silane
CFU	Colony forming units
Chromic acid	H_2SO_4/HNO_3
D-Ala-D-Ala	The D conformation of Alanine in a dipeptide
DNA	Deoxyribonucleic acid
HATU	*O*-(7-azabenzo-triazole-1-yl)-1,1,3,3-tetramethyluronium hexafluoride
IL-1, 6, etc.	The cytokines interleukin-1, 6, etc.
MALDI-TOF	Matrix-assisted laser desorption/ionization time of flight mass spectrometry
MIC	Minimum inhibitory concentration
MRSA	Methicillin-resistant *staphylococcus aureus*
MSCRAMM	Microbial surface components regulating adhesive matrix molecules
MW	Molecular weight
NF-κB	Nuclear factor κB
OPG	Osteoprotegrin
PBS	Phosphate buffered saline
PEG	Polyethylene glycol
PGE2	Prostaglandin E2
Piranha Acid	H_2O_2/H_2SO_4
RANK	Receptor activator of NF-κB
RANKL	Ligand for RANK
RGD	The cell binding motif arginine-glycine-aspartic acid
RNA	Ribonucleic acid
SAM	Self-assembled monolayer
Ti6Al4V	The metal alloy 6% aluminium, 4% vanadium with the remainder titanium
TNF	Tumor necrosis factor
TRAIL	Tumor necrosis factor-related apoptosis-inducing ligand
TSB	Tryptic Soy Broth
VAN	Vancomycin
VAN-Ti	Vancomycin bonded to Ti
VRSA	Vancomycin resistant *S. aureus*
VSSA	Vancomycin sensitive *S. aureus*

4.417.1. Implant-Associated Infection in Orthopedic Materials

Perhaps the most insidious complication associated with implants in general, and orthopedic implants specifically, is infection. Approximately 50–70% of all hospital-acquired infections are associated with indwelling biomedical devices.[1] In the context of the skeletal system, such infections can have devastating consequences. The implantation of any foreign material, whether consisting of cadaverous or allogenic tissue or an inert biomaterial of a chemistry or composition, increases the probability of infection.[2] The very properties of material that allow close juxtaposition of bone tissue with the implant to facilitate bone ingrowth are also those that predispose the implant to establishment of infection.[3] When an orthopedic implant is placed, it becomes quickly coated with serum proteins. Poor perfusion and clot formation limit immune system accessibility to the foreign surface. Ideally, as the clot dissolves, new tissue either forms around the implant (spinal fusions, joint arthroplasty) or begins to replace the implant (allograft and autograft). However, if any bacteria are present, a 'race for the surface' begins where both bacteria and osteoblasts attempt to colonize the surface.[4] Unfortunately, bacteria have perhaps an unfair advantage due to their proliferative potential and ability to survive under less than ideal circumstances. Bacterial adhesion and propagation quickly progresses from individual microorganisms to formation of a polysaccharide-rich biofilm that subverts immune surveillance and limits antibiotic efficacy. Importantly, while blood-borne bacteria are readily cleared by a healthy immune system or antibiotic therapy, implant-associated bacteria protected in a biofilm can survive to become a continuing nidus of infection.[5]

4.417.1.1. The RANKL Pathway and the Pathogenesis of Osteomyelitis

Once established, bacterial colonization of an orthopedic implant, whether biomaterial or harvested graft material, results in high local concentrations of bacteria and their released factors/metabolites. These bacterial products can interact with resident cells to result in osteomyelitis and eventually, osteolysis.[6] Osteomyelitis, from the Greek osteon (bone), myelo (marrow), and the suffix -itis (inflammation), is defined as an infection of bone characterized by progressive inflammation and bone destruction (osteolysis). Independent of cause, all factors involved in the pathogenesis of osteolysis are known to act through the regulation of the RANK–RANKL pathway.[7] Receptor activator of NF-κB (RANK) is a TNF-α superfamily transmembrane receptor expressed on osteoclast precursors and mature osteoclasts. Activation of RANK by its ligand, RANKL, initiates a signaling cascade resulting in osteoclast precursor differentiation and mature osteoclast activation. Competitive inhibition of RANK is achieved by the binding of a soluble protein, osteoprotegerin (OPG), secreted by bone marrow stromal cells and osteoblasts, to RANKL.[8] It has also been shown that injections of OPG can block osteoclast-mediated osteolysis.[7]

During an immune response, neutrophils first reach the infectious locus and destroy bacteria via phagocytosis.[9] These neutrophils reside at the infectious locus until macrophages and other inflammatory cells arrive (hours–days), at which point the neutrophils undergo apoptosis. As macrophages and immune cells are recruited to the infected bone area, they, in turn, produce mediators that act on stromal cells and osteoblasts to regulate the RANK–RANKL–OPG pathway. With the infiltration of such immune cells, osteoblasts secrete an array of inflammatory cytokines, colony-stimulating factors, and chemokines.[10,11] One particular proinflammatory cytokine, IL-6, plays a key role in the osteolysis associated with infection.[12] Finally, cytokines such as TNF and IL-1 and IL-6 have also been theorized to play a direct role in osteomyelitis since they are known to regulate RANKL and OPG levels.[13] Cytokines released by interactions between bacteria and resident osteoblasts can amplify the immune response and increase the number of the bone-resorbing osteoclasts. *Staphylococcus aureus*,

responsible for 48.6% of all surgical site infections,[14] is a potent inducer of membrane-bound RANKL. In osteoblasts resident in infected bone, this induction seems to be mediated by a 5–30-fold upregulation of prostoglandin E2 (PGE2); this induction is not observed in cases of aseptic loosening.[15] Importantly, PGE2 induces RANKL expression.[15] When infected by *S. aureus*, osteoblasts also increase tumor necrosis factor-related apoptosis-inducing ligand (TRAIL) expression.[16] TRAIL can bind OPG, blocking its inhibitory effect on RANK, and increasing osteoclast formation and thus bone resorption. In addition, by production of cytokines such as IL-6 and IL-12, bacterially challenged osteoblasts can direct immune responses by infiltrating leukocytes.[17] Finally, the inflammatory process itself leads to tissue destruction, as many inflammatory processes result in compression and obliteration of vascular channels leading to ischemia and bone necrosis. The responsive hyperemia at the infarction edge is associated with increased osteoclastic activity, bone loss, and localized osteoporosis.[18,19] Overall, the role of the RANK–RANKL–OPG pathway in the mediation of osteoclastogenesis and osteoclast activation is one that is manipulated by invading bacteria to alter bone responses.[19,20]

4.417.1.2. Biofilm Development

Despite a robust immune response, implant-associated bacteria still survive. The key to this survival is the formation of biofilm. Biofilms are ubiquitous in the natural world and their control has posed significant challenges not only in medicine but also in geology, the petroleum industries, water distribution systems, and naval and aviation technologies.[21] Biofilm formation on medical devices and transplanted tissues reduces resident bacteria accessibility to immune surveillance, local cellular defense mechanisms, and antibiotic treatment.[5,22–25] The majority of bacterial infections currently treated by physicians in the developed world are considered to involve biofilm formation (**Chapter 4.418, Engineering Interfaces for Infection Immunity**).[5,24]

Establishment of a biofilm is a multistep process involving not only the microorganism, but also the implant and host tissue (**Figure 1**). The initial attachment of a bacterium to the surface of an implant is usually very rapid and mediated by nonspecific surface conditions (e.g., surface tension, hydrophobicity, electrostatic forces), presence of host tissue ligands (e.g., fibronectin, fibrinogen, collagen), and specific bacterial surface proteins.[3] Bacteria express and upregulate several adhesins (e.g., microbial surface components recognizing adhesive matrix molecules (MSCRAMMs)) on their surfaces that facilitate adhesion to elements of the host extracellular matrix and to biomaterials;[2,27] each MSCRAMM interacts with specific extracellular matrix proteins.[28] For example, one MSCRAMM is autolysin that exhibits a vitronectin-binding site and may also have a role in adherence to hydrophobic surfaces.[29] Once attached to the surface, adherent bacteria can commence formation of biofilm. Structural examination of biofilms shows that they are complex structures composed of cells (±15% by volume) embedded in matrix material (±85% by volume).[30,31] The biofilm-embedded, sessile bacteria grow in matrix-enclosed microcolonies interspersed with porous regions important for metabolism and nutrient access. The high level of biofilm organization suggests that these communities are regulated by

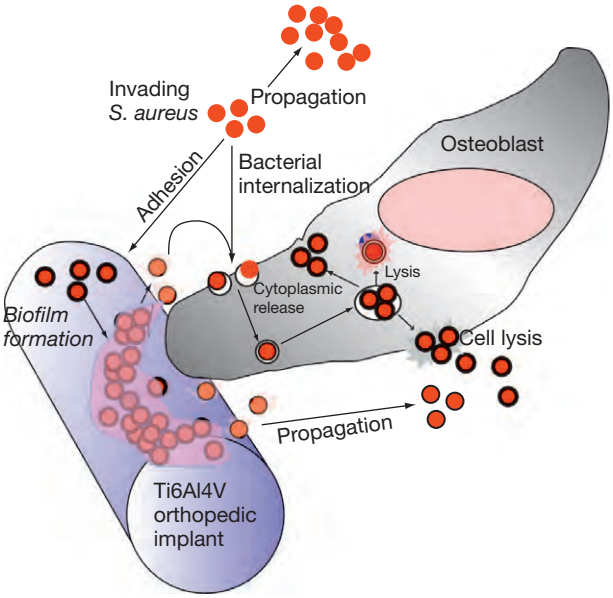

Figure 1 Cartoon of the mechanisms for establishment of infection around an implant. Invading *S. aureus* either continue to propagate or adhere to a surface. The surface can either be the resident bone cells (osteoblasts) that internalize the bacteria and establish intracellular infection,[17] thought to be one of the causes of latent infection, or the bacteria can adhere to the implant surface and make it inhospitable for continued osteoblastic cell growth.[26] Once adherent, metabolic changes occur in the bacteria that make the adherent bacteria relatively insensitive to bathing antibiotics (indicated by thickened black lines on the implant surface). These adherent bacteria propagate and encase themselves in a biofilm slime, further protecting themselves from immune surveillance, as well as bathing antibiotics. This organized biofilm community exists in a protected niche that, upon maturation, can slough off bacteria into the surrounding space. These sloughed off bacteria can then propagate, and exactly akin to the initial invasion, either propagate, seed new areas of the implant, or become internalized into the surrounding bone.

signals analogous to hormones and pheromones that regulate multicellular eukaryotic tissues. This signal system, referred to as 'quorum sensing,' is an interbacterial communication mechanism dependent on population density and associated with marked (i.e., more than 50%) changes in protein expression patterns.[32] During this process of biofilm maturation, bacteria begin to bud from the biofilm, allowing continued seeding of new sites, adherence and internalization of bacteria by adjacent cells, and propagation of infection. The survival of the biofilm is dependent on convective flow through channels that carry bulk fluid into the community, thereby keeping resident bacteria alive; depletion of nutrients and accumulation of waste products in biofilms still occurs. Metabolic waste accumulation induces resident bacteria to enter a slow growth state, or even senescence, rendering them up to a 1000 times more resistant to most antimicrobial agents than their rapidly proliferating, nonadherent planktonic counterparts.[22,33–35]

During maturation, adhesion-associated resistance in biofilm-embedded bacteria does not seem to stem from the familiar mechanisms of antibiotic resistance, such as efflux pumps, modifying enzymes, and target mutations.[35] Even sensitive bacteria without any known genetic basis for resistance can exhibit profoundly reduced susceptibility within a biofilm. For example, a β-lactamase-negative strain of *Klebsiella*

pneumoniae, with a minimum inhibitory concentration of 2 μg ml^{-1} ampicillin in aqueous suspension, is scarcely affected (66% survival) by 5000 μg ml^{-1} ampicillin when entrenched in a biofilm.[36] Even more importantly, when resilient biofilm-encased bacteria are dispersed, they usually rapidly become susceptible to antibiotics. Currently, several hypotheses exist for this resistance to antibiotics imparted by biofilms, including limited penetration of antibiotics in biofilms, partial differentiation of bacteria into a protected phenotypic state, and the altered microenvironment within the depths of the biofilm.[34] Thus, formation of a biofilm on an implant results in a complex microenvironment that cannot be effectively treated by normal pharmacological therapies. The surgical remedy therefore is removal of the infected component. Unfortunately, many treatments that make these implants suitable for osteoblast adhesion could also foster bacterial adhesion.

4.417.2. Bacterial Responses to Orthopedic Implants

4.417.2.1. Metallic Implants

Metal implants have made fracture fixation, joint replacement, and spinal surgery possible and significantly bettered the quality of life for millions of patients. Metal implants have numerous strengths and weaknesses as biocompatible surfaces within a bony environment. However, we focus on their interaction with bone and conditions under which they are colonized by pathogens. In general, any surface that can foster extracellular matrix molecule attachment to induce osteoblast cell population, and by inference, osseointegration, also fosters bacterial adhesion. The consequences of this ready implant colonization have been countered through stringent sterilization procedures and the use of clean-room technology to improve the sterility of the operating field. Some safeguards associated with these measures have decreased surgical infection rates. However, because of perioperative bacterial contamination, patient infection still remains a significant issue for metallic implants.[37–40]

The surfaces of many metallic implants are modified in order to enhance tissue integration. Different levels of microtexturing are used, ranging from anodization of screws, nails, and fracture plates to the creation of deliberate roughness and porosity of hip and knee implants to foster bone ingrowth.[41–44] Additional coatings, including hydroxyapatite, can be applied to foster osseointegration.[45,46] While many studies have addressed the effects of roughness on bacterial colonization, the data remain variable (e.g., Raulio *et al.*,[47] Duarte *et al.*,[48] Riedewald[49]). An examination of the dental literature suggests that surface roughness may retard bacterial colonization (e.g., Yoshinari *et al.*,[50] Duarte *et al.*,[48] Harris and Richards[51]). It appears that the most important determinant is surface hydrophobicity.[52–54] Thus, bacterial colonization, at least *in vitro*, can be lessened, to some degree, by alterations in surface chemistry. However, such modifications can be complicated by the addition of hydroxyapatite. The elevated porosity seen in a hydroxyapatite coating opens up the potential for use as a controlled release system.[55–57] In one application, adsorption of gentamicin to hydroxyapatite results in sufficient antibiotic release to allow short-term prophylaxis.[58,59]

Unfortunately, once infected, the most successful means of eradicating infection is surgical removal of the implant. This removal is accompanied by debridement of the surrounding bone to remove any possible infection, and either replacement (with aggressive antibody treatment)[60] of the infected component or implantation of an antibiotic-eluting spacer to eliminate residual infection followed by subsequent insertion of a new implant, a process that can require up to 6 weeks of antibiotic treatment.[61,62] With both treatments, recurrence of infection after replacement of the implant can occur, with arthrodesis or amputation the only options in difficult cases.[60] This propensity for reinfection underscores the importance of preventing the establishment of infection. Importantly, metal surfaces are prone to bacterial colonization, whether in medical applications or in applications related to their industrial use.[63–66] This propensity for colonization, considering the adaptability of bacteria, is best circumvented by a combination of approaches. While the maintenance of the sterile operating field continues to be the first defense to prevent perioperative contamination, combinations of controlled release systems with implant designs that retard bacterial colonization hold the greatest potential for preventing establishment of implant-associated infection.

4.417.2.2. Bone Allograft

Allograft bone, often used in repairing large bone defects and fostering bone growth around the new implant,[67–70] is also prone to bacterial colonization and biofilm formation.[71–74] These bone grafts are porous, avascular foreign bodies whose porosity provides a haven for bacterial colonization, while their lack of vascularization leads to low perfusion, limited immune surveillance, and inadequate penetration of systemic antibiotics. Furthermore, bacteria often associated with graft infections are notoriously efficient biofilm producers and encase themselves in a thick biofilm matrix that further protects them from environmental challenges. Multiple attempts have been made to combat this problem, and one of the most popular solutions possibly is antibiotic impregnation of grafts to deliver local high concentrations.[75–82] These elution systems, however, are limited by variable elution kinetics, short-term protection, local tissue toxicity,[83] and by the possibility of an increased incidence of microbial resistance.

Despite the clinical success seen with the use of allograft bone,[84–88] there remain a number of complications associated with its use, including infection rates which can reach 20% in massive allograft surgeries.[89–92] Once infection is established, treatment is similar to that of the metal implant. The grafts are removed, the surgical site is extensively debrided, and long antibiotic regimens are administered. Despite all these measures, also complicated by an immunocompromised host or adjuvant chemotherapy, complete eradication of the infection can fail, leading to limb amputation or even death.

4.417.3. Antibiotic Prophylaxis and Treatment of Surgical Infection

Infection rates after orthopedic surgery depend on the surgeon, the patient comorbidity, the procedure, and the implanted material.[90] Risk of perioperative infection is mitigated by routine administration of prophylactic systematic antibiotics intravenously for 2–14 days and orally for up to 16 weeks.[90,93] In an

attempt to ensure therapeutic doses of antibiotics, numerous systems have been designed to locally deliver antibiotics and prevent bacterial attachment.[94] One early attempted local antibiotic delivery system used cancellous bone as an antibiotic carrier in which bone pores were filled with penicillin.[95] Similar systems that depend on passive adsorption/loading have been used in collagen sponges and other porous materials as an adjunct to implantation.[96] In an attempt to ensure that eluting antibiotics kill bacteria before they initiate biofilm, these techniques rely on adsorption of antibiotics prior to implantation akin to the procedure for mixing antibiotic-bearing polymethylmethacrylate cement.[97–101] Other procedures rely on formation of a drug-release coating of a device or formation of an antibiotic-impregnated spacer. Antibiotic release is then achieved through passive diffusion or elution as the biomaterial degrades.

Unfortunately, all drug elution systems suffer shortcomings. Specifically, initial release of high local antibiotic concentrations quickly drops, rendering these implants unprotected beyond a few days. As an example, in an allograft system, ~75% of the adsorbed vancomycin (VAN) and ~99% of netilmicin eluted within 120 h, independent of initial concentrations and the time of impregnation.[102] When release patterns of eight antibiotics impregnated into cancellous bone were assessed by two different *in vitro* methods, agar diffusion and broth elution, only rifampicin (out of benzylpenicillin, dicloxacillin, cephalotin, netilmicin, clindamycin, VAN, ciprofloxacin, and rifampicin) maintained MIC or higher for longer than 21 days.[103] As the majority of periprosthetic infections occur within 4 months of surgical transplantation, this short-term elution may be insufficient to combat infection.[90,92] Thus, even though release of antibiotic from a controlled release system might effectively combat acute infection, biofilms can reestablish as local antibiotic dissipates into the tissue immediately surrounding the implant; this tissue serves as an important reservoir of additional viable bacteria.[104–106] Furthermore, exposure of bacteria to subinhibitory concentrations of antibiotics at the tail end of elution runs the risk of fostering development of resistant strains of bacteria.[5,107] Importantly, after use of gentamicin-loaded beads in patients undergoing two-stage exchange arthroplasty, resistant bacterial subpopulations with extremely high MICs were detected, suggesting that the use of these gentamicin-loaded beads may contribute to the occurrence of reinfection with resistant variants.[107] No consensus exists to date on the ideal concentration of the impregnation solution or the incubation time and drug bioavailability, bioactivity, elution kinetics, and maximum concentration required for efficacy in the postoperative period for any procedure or antimicrobial agent. The duration of antibiotic elution and more importantly the time it takes to reach sub-MIC concentrations can vary significantly and depends on pH, porosity, degradation characteristics, and many other parameters that influence elution.[102] These release parameters can be further complicated *in vivo* by patient and surgical factors such as vascular health, perfusion, local implant site, trauma, and inflammatory conditions.

In combating bacterial infection, the antibiotic itself can have deleterious effects in the bone environment. Specifically, topically applied antibiotic powder (chloramphenicol and methicillin) was detrimental to osteogenesis in fresh corticocancellous isograft;[78] gentamicin also showed toxicity toward osteoblast-like cells *in vitro*.[108] One of the most important antibiotics in clinical use today is the antibiotic VAN. Because of the prevalence of deep infections due to *S. aureus* and the increase in numbers of MRSA, VAN has become the antibiotic of choice in the treatment of deep infections (prior to typing) associated with implants. Since high doses of VAN have been shown to decrease the rate of osteoblast replication and even cause cell death,[109] controlled-release technologies with VAN are less frequent and await more thorough studies to ascertain local and systemic toxicity. *In vitro* studies show that ciprofloxacin at a dose greater than 100 $\mu g\,ml^{-1}$ and VAN and tobramycin at doses greater than 2000 $\mu g\,ml^{-1}$ severely decreased osteoblast-like cellular proliferation.[83] Cytotoxicity has also been demonstrated *in vivo* where 100 g of antibiotic-impregnated cancellous bone impacted in a rabbit femur condyle eluted more than 7000 mg of netilmicin, a dose that can be toxic in humans.[102]

4.417.3.1. Structure of VAN

VAN was first isolated from a *Streptomyces* species, found in soils obtained from Borneo and India. This antibiotic was developed in the 1950s and is the first glycopeptide antibiotic; it has since been synthetically diversified to represent several analogous drugs.[110–112] This class of glycopeptide antibiotics generally comprises a relatively conserved heptapeptide backbone of five to seven aromatic rings and different sugars.[113] VAN specifically contains two hexoses and five aromatic rings.[114] Today, it is commercially produced in cultures of *Amycolatopsis orientalis* (previously designated as *Nocardia orientalis* and *Streptomyces orientalis*). VAN is used as the more soluble hydrochloride salt, and because it is not readily absorbed by the gastrointestinal tract, must be administered intravenously.[115] Over the past 30 years, VAN has been used to treat deep-seated gram-positive bacterial infections and remains the drug of choice for infections caused by *S. aureus*, especially those caused by the increasing numbers of strains resistant to methicillin (MRSA). Its human nephrotoxicity starts at 90 $\mu g\,ml^{-1}$ but many initial accounts of serious nephrotoxicity have been since attributed to early production impurities.[116] Importantly, even many staphylococci responsible for prosthetic infections are now resistant to gentamicin[117] and the reports of VAN-resistant staphylococci remain few;[116,118,119] unfortunately, reports of VAN-resistant organisms are increasing.[120–123]

Importantly, VAN is very well characterized both in terms of its clinical actions and its structure–function relationship.[109] Specifically, its chemical structure, ligand-binding site, and the results of its functionalization on antimicrobial activity have been reported.[124] VAN is stable as a powder, which makes it convenient for use in diverse new delivery formulations and is effective against most gram-positive organisms (especially *S. epidermidis* and *S. aureus*, including MRSA) which are the main culprits in orthopedic infections.[14,125,126] VAN can be coupled to a surface through its carboxylic acid group and through its amines, allowing retention of activity.[127–129]

4.417.3.1.1. VAN's mechanism of action

VAN preferentially targets gram-positive bacteria that typically have a relatively simple external structure. The outer surfaces of these bacteria consist of diverse surface adhesins or

MSCRAMMs (microbial surface components recognizing adhesive matrix molecules), which are used to attach to the extracellular matrix, other bacteria, host cells, and foreign surfaces. Below this layer, a thick peptidoglycan wall gives the cell structural integrity and protects it from internal turgor pressure. This cross-linked peptidoglycan wall terminates in the interior cytoplasmic lipid bilayer membrane. The overall biosynthetic pathway of the bacterial cell wall occurs in three stages: first, the monomeric glycan wall precursors are synthesized with peptides in the cytoplasm; second, peptidoglycan wall monomers are packed in mobile lipid carriers (undecaprenylphosphate) that are transferred to the outer surface of the growing membrane; and finally, monomers are attached to the growing glycan chains in enzymatically controlled processes. Two enzymes located in the cytoplasmic membrane are critical: the first, glycosyltransferase, polymerizes murein (or peptidoglycan) monomers between their amino-sugar moieties to produce nascent peptidoglycan chains; the second, transpeptidase, also known as penicillin-binding protein (PBP), links the newly formed nascent peptidoglycan chains to preexisting peptidoglycan layers of the *S. aureus*, stabilizing both chemistry and membrane mechanical structure.

In contrast to penicillin which directly binds to and inhibits the bifunctional transglycosylases/transpeptidases involved in cell wall biosynthesis, VAN competes with these enzymes for their native substrates.[130] In *S. aureus*, these substrates fall into two classes: the D-alanyl-D-alanine (D-Ala-D-Ala) residues in either the completed peptidoglycan layers or on the nascent peptidoglycan chain, and peptidoglycan monomers located in the cytoplasmic membrane that serve as the substrates for glycosyltransferase. When VAN interacts with a sensitive (dividing) bacterium, large amounts first interact with the ~20 peptidoglycan layers of the cell wall. In this context, the wall acts as an ion-exchange resin where eventually all of the binding sites of the wall become saturated with VAN.[124] As VAN molecules penetrate through the wall, they encounter their second (and most important) target on the outside surface of the membrane: the lipid intermediates containing the disaccharide–pentapeptide wall subunit as it is extruded through the cell membrane.[131] VAN encases the D-Ala-D-Ala terminus of the lipid–PP–disaccharide–pentapeptide, burying it into a cleft of the antibiotic molecule. This large antibiotic–peptidoglycan complex can no longer interact with the transglycosylase enzyme, preventing transfer of the peptidoglycan precursor disaccharide to the growing glycan polymer chain, thereby inhibiting cell wall synthesis.[113]

Inhibition of the transglycosylation reaction results in accumulation of lipid intermediates in the cytoplasm due to the continued biosynthesis of cell wall constituents. With cell wall formation inhibited, the cell cannot increase in diameter, and DNA, RNA, and protein synthesis ultimately cease. Importantly, since gram-positive bacteria have a high osmotic pressure ($10–20 \times 10^5$ Pa), synthesis of this rigid cell wall is vital to prevent the cells from rupturing.[132] In the presence of VAN-mediated inhibition of these enzymes, autolytic enzymes continue to function. In the absence of wall growth, the continued autolytic activity causes lowered cell wall rigidity and these bacteria become susceptible to osmotic lysis.[113,131] Although VAN has been reported to be bactericidal, bacteria are not necessarily killed directly but rather cell death ensues because of the inhibition of cell wall growth. Therefore, this lysis is unlikely to occur as rapidly as with other true bactericidal agents such as β-lactam antibiotics. Furthermore, the stoichiometric 1:1 complex that VAN forms with the peptidoglycan precursor UDP–*N*-acetylmuramylpentapeptide is mediated by weak, multiple hydrogen bonds,[115] making its affinity for its substrate low.

4.417.3.1.2. Antibiotic resistance to VAN

Inevitably, there are reports of gradual reductions in VAN susceptibility among *S. aureus* isolates.[133] The possible mechanisms of resistance to glycopeptide antibiotics include inactivation of antibiotic, modification of the target site, altered accessibility of the target site, and sequestration of antibiotic. Many studies on mechanism of VAN resistance have been performed on the first clinical isolate of VAN-resistant *S. aureus* (VRSA) strain, Mu50.[134–138] A thickened cell wall seems to be the cardinal feature of all the VRSA clinical strains isolated so far. The cell walls of 16 VRSA strains isolated from seven countries are significantly thicker (mean 31.3 nm, SD 2.6 nm) than the average of VAN-susceptible *S. aureus* (VSSA) strains (mean 23.4 nm, SD 1.9 nm). Fundamentally, there are two main ways to increase the thickness of the cell wall peptidoglycan layers. The first is to produce excess amounts of peptidoglycan, as seen in Mu50, and the second is to reduce peptidoglycan turnover. Normally, new peptidoglycan layers are produced on the surface of the cytoplasmic membrane, displacing the older layers outwards so that they are eventually cast off from the cell surface. Autolytic enzymes (peptidoglycan hydrolyzing enzymes) are involved in these shedding processes and have also been found to have a remarkably reduced autolytic activity in certain strains. Overall, it appears likely that recently reported resistance in coagulase-negative staphylococci results either from a *change* in the accessibility of the target site or from a *decreased* amount of antibiotic available at the target site due to its sequestration in a modified wall structure.[134,135]

4.417.4. Surface Tethering of Antibiotics to Prevent Bacterial Adhesion

Overall, the strategy to combat implant-associated infection is complex. Two key considerations are involved: (1) prevent bacterial adhesion and biofilm formation and (2) avoid therapies likely to foster pathogen resistance. Review of the literature shows that the most successful means of combating infections have been achieved using controlled release systems that attain sufficient antibiotic concentrations to eliminate soft-tissue/bone infection. While a large body of literature describes the effects of different surfaces on bacterial colonization, experience suggests that the ideal surface must resist colonization over the long term (months to years). However, as previously stated, these controlled release systems, even without their other drawbacks, have a very finite drug-release life span, and the establishment of hematogenous or reestablishment of homologous infection can occur. To overcome these limitations, one alternative is the use of tethered antibiotics. We have hypothesized that if bacterial adhesion can be minimized, then biofilm formation can be prevented, allowing either immune surveillance or an adjunct-controlled release system to clear the surrounding tissue of infection. Research supports this idea

while emphasizing the importance of a multipronged attack to combat infection without fostering antibiotic resistance.

4.417.4.1. Device Surface Preparations for Tethering

The first consideration in deciding to modify the implant is the existing engineered design of the implant. For metal implants, the shape is critical for function and the surface is highly engineered to influence its interaction with bone. Without further surface complexities resulting from coatings such as hydroxyapatite, the same implant can display different degrees of roughness so as to enhance strength, longevity, and, of course, osseointegration.

Immobilization of substrates on devices has been explored for different metals, as well as bone allograft. Specifically, the adhesion peptide RGD was immobilized to glass,[139] quartz,[140–142] gold,[143] silicone,[144] silica,[145] and titanium[146–148] surfaces, among others to allow enhanced cell adhesion and, by implication, osseointegration.[146] Different linkages have been used on titanium surfaces including phosphonates,[149,150] plasma amination,[151] silanization to reveal active amines,[127,148,152] surface photopolymerization of PEG-acrylamide groups,[153] reaction with *p*-nitrophenyl chloroformate to activate the surface,[154] and, interestingly, titanium-binding peptides to allow PEGylation.[155] Modifications have also been introduced to the titanium surface to allow enhanced physisorption and release of antibiotics.[156–162] Covalent modification of these titanium surfaces with antibiotics has to date focused predominantly on VAN.[153,163–165]

One immobilization strategy relies on initial formation of an amine-rich, reactive surface to allow chemical coupling of linkers and antibiotics. Initially, both Ti and Ti6Al4V, common orthopedic metal materials, were explored, including powdered Ti, Ti and Ti6Al4V wires, and Ti6Al4V foils of different sizes for derivatization, as well as using a modified procedure for bone allograft. On the basis of the properties of titanium in aqueous environments, stable tethering to the implant surface must rely on formation of a covalent bond with Ti oxide, the naturally occurring ambient surface. While a variety of agents that form bonds with this amphoteric Ti oxide have been used (e.g., dopamine[166,167] and phosphonate[168]), aminopropyltriethoxy silane (APTES) that ideally can form three siloxy bonds to the titanium oxide in a self-assembled monolayer (SAM), and can be further cross-linked for added stability,[169] was used. Thus, to allow stable metal oxide bonding of APTES, a rich metal oxide layer is required. Formation of the oxide layer (or passivation) could be achieved either through cleaning of the surface using oxidizing solutions that strongly etched the metal (e.g., chromic acid (H_2SO_4/HNO_3), or piranha acid (H_2O_2/H_2SO_4)) or by other means of oxidation, such as hydrothermal aging.[163,170,171] Both methods yield a very water-wettable polar surface. Importantly, a gentle piranha acid (50:50 H_2O_2/H_2SO_4, 4 °C) increased surface pitting as visualized by scanning electron microscopy; surface pitting was not increased with hydrothermal aging.[170] Hydrothermal aging of the metal surfaces also resulted in increased surface wettability, with little change in surface features as determined by surface angles (**Figure 2**). Therefore, production of a surface oxide layer suitable for further coupling with APTES could be produced with retention of topography.

Production of the APTES layer results in addition of primary amines. These amines can be used to monitor success through either labeling with fluorescamine, followed by imaging with confocal laser scanning microscopy[128,170] (**Figure 3**), or

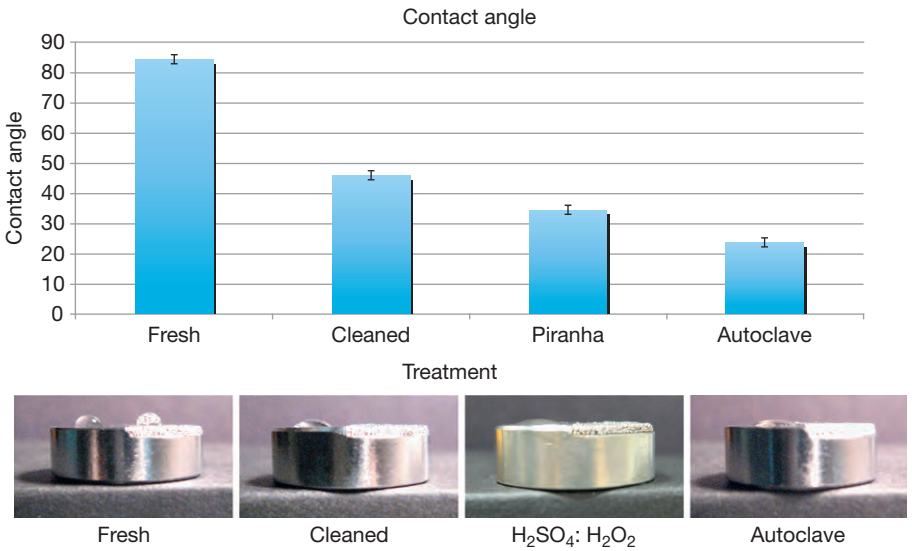

Figure 2 Changes in hydrophobocity as a function of cleaning and passivation. Surface hydrophobicity was assessed as a function of treatment, by placing a 10-μl water drop on disks that were untreated, cleaned, passivated by H_2SO_4/H_2O_2, or passivated by autoclaving. The top panel presents the contact angles measured from pictures of droplets on surfaces; statistical *p*-values between groups are as noted (n.s. = not significant). Representative pictures of the droplets on the surfaces are presented in the bottom panel. The decreasing contact angles obtained for the H_2SO_4/H_2O_2 and autoclaved conditions suggest that these treatments are successful in creating a robust oxide layer. Contact angles measured between all treatments were significantly different ($p < 0.05$). Reproduced from Ketonis, C.; Parvizi, J.; Adams, C. S.; Shapiro, I. M.; Hickok, N. J. *Clin. Orthop. Relat. Res.* **2009**, *467*(7), 1678–1687, with permission from Springer.

measuring spectrophotometrically after performance of the ninhydrin reaction.[127,163] Milligram quantities of powder have sufficient surface area to fall within the detectable range of the assay; with 1-mm wires, 5–10 wires 1.5-cm in length were required.[127,163]

Antibiotics typically target cell wall synthesis, cell wall cross-linking, protein synthesis, and DNA repair. Therefore, any surface-bound antibiotic needs to have an ability to dissolve and extend into the bacterial cell. To achieve this, we sequentially coupled two Fmoc-[2-(2-amino-ethoxy)-ethoxy]-acetic acid (Fmoc-AEEA) linkers to the APTES surface in the presence of *O*-(7-azabenzo-triazole-1-yl)-1,1,3,3-tetramethyluronium hexafluorophosphate (HATU). After deprotection of the second linker, we coupled VAN to the primary amine in the presence of HATU.[163] Others have used a similar scheme with the addition of multiple PEG arms to result in a high density of VAN coupled to the underlying surface.[129,153,164]

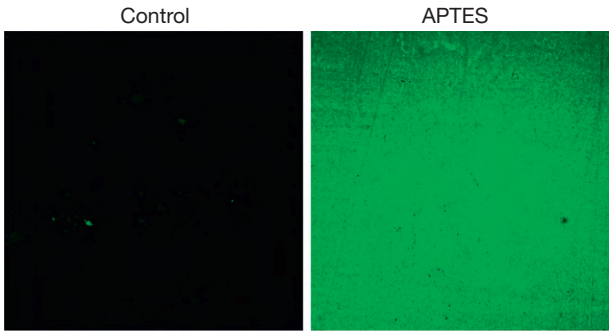

Figure 3 Amine coverage of Ti foil as visualized by staining with fluorescamine. The surface amine content of a control foil or a foil that had been cleaned, passivated, and reacted with APTES was visualized by epifluorescence after reaction with fluorescamine. Control foils showed little fluorescence, whereas the APTES foil showed a bright green fluorescent signal, indicative of a rich surface amine content.

4.417.4.2. Properties of Surface-Tethered VAN

To certify efficacy as an immobilized drug, the antibiotic must be truly bonded to the surface and must remain stable. In initial studies, this question was answered through deliberate bond cleavage at the APTES, collection of the cleaved material, and analysis by MALDI-TOF. The array of molecular ions detected consisted of the predicted structure of vancomycin-Ti (VAN-Ti) illustrated in Figure 4.[163,172] However, it would be possible that, in addition to the necessarily small quantities of surface-bound VAN, larger quantities of physisorbed antibiotic would remain on the surface. To exclude that possibility, VAN-coupled rods were routinely incubated in phosphate-buffered saline for at least 24 h to remove any easily desorbed material. Prolonged elution is sometimes required to solubilize antibiotic adsorbed during the initial synthesis; this elution was complete in the days to several weeks time frame, leaving only surface-coupled antibiotic for analysis as determined by analysis of eluted VAN activity.[173]

In order for the metal surface-coupled antibiotic to retard bacterial adhesion, sufficient antibiotic must be immobilized to the surface to affect bacterial adhesion and proliferation. Surface coupling of antibiotics has been achieved either directly through APTES using short PEG linkers,[163,172] or through multifunctional PEG acrylate linkers;[129,153] other methods of coupling agents and peptides to Ti surfaces have not been used for coupling of antibiotics. VAN that was directly coupled through the APTES via two PEG linkers was visualized through indirect immunofluorescence using a polyclonal anti-VAN antibody. A bright, uniform fluorescence was visible over the surface; this coverage appeared to largely recapitulate that already observed for detection of the APTES using fluorescamine, that is, a uniform, bright coverage that was easily distinguishable from control surfaces (Figure 5).[127,170,174,175] Because VAN (MW 1547.3) comprises multiple rings and thus is larger than the basically straight chain structure for APTES

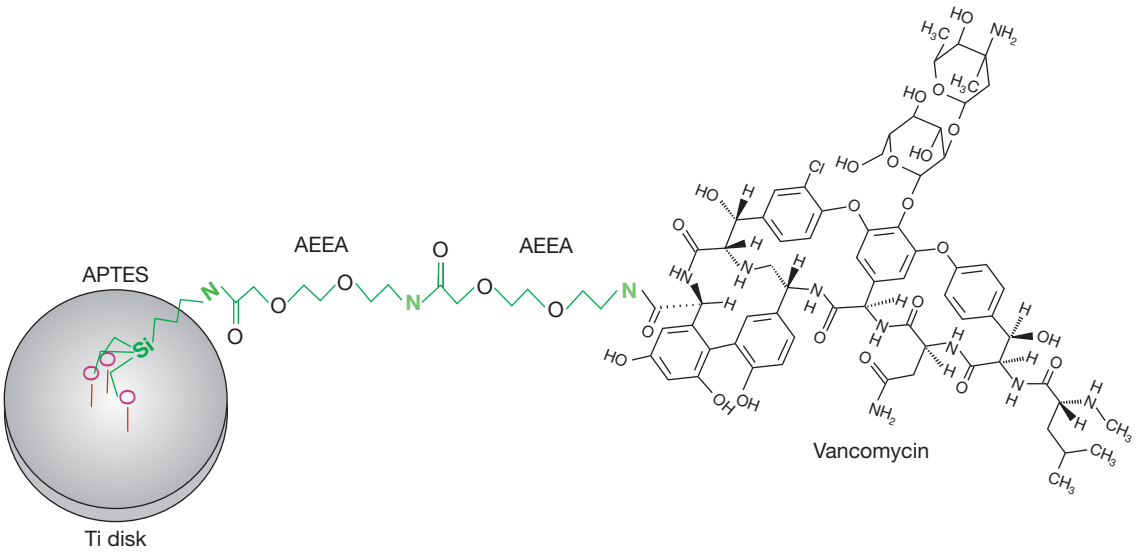

Figure 4 Predicted structure of the vancomycin-modified Ti surface. Vancomycin is bonded to the Ti surface via aminopropylation, followed by the addition of two AEEA linkers. Vancomycin coupling is then achieved through coupling of the carboxylic acid of vancomycin to the exposed linker primary amine. Adapted from Jose, B.; Antoci, V., Jr.; Zeiger, A. R.; Wickstrom, E.; Hickok, N. J. *Chem. Biol.* **2005**, *12*, 1041–1048.

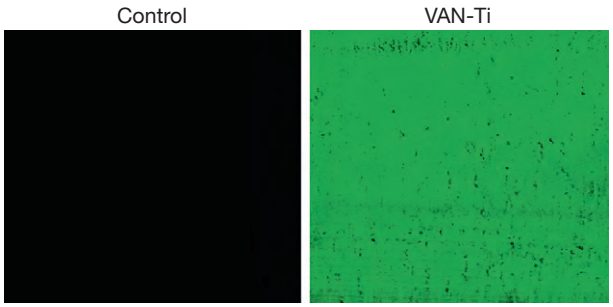

Figure 5 Vancomycin (VAN) can be detected tethered to the surface of Ti. After coupling VAN to the surface of Ti, any adsorbed antibiotic was removed by a 24-h incubation in PBS. Presence of VAN on the surface of the pin was tested by incubation with an anti-VAN antibody, followed by reaction with an Alexafluor488 secondary antibody. Fluorescence was visualized by confocal laser scanning microscopy. Control surfaces (cleaned Ti with reaction with primary and secondary antibody) showed no fluorescence, whereas the VAN-Ti surface showed a bright fluorescence, with some out-of-plane areas showing a darker signal.

(MW 221.37), it is likely that because of steric hindrance, only a subset of the available amines could be used for coupling the much larger VAN. Therefore, VAN coverage was also estimated through recovery of fluorescent antibodies (as compared to a treated, uncoupled surface that underwent the same blocking and incubation with VAN antibodies) and estimated to be 1.8 ng VAN per 1 mm × 1.5 cm Ti6Al4V rod.[175]

Having an estimation of antibiotic amounts on a surface begged the next question – how much antibiotic is sufficient on a two-dimensional surface, when minimum inhibitory concentrations (MIC) for antibiotics are defined on the basis of three-dimensional tests? This question will remain unanswered until more antibacterial surfaces and their accompanying control surfaces are assayed so that a standard can be developed.

The final question associated with any surface derivatization is that of long-term stability. The other major studies of polymerized VAN on surfaces have not measured longevity.[129,153,164] Longevity was measured on the VAN-Ti surfaces as a function of time at 37 °C. For short-term experiments, the surfaces were incubated for 7 days, at 37 °C, in PBS, 10% fetal bovine serum in Dulbecco's modified essential medium, and in the presence of *S. aureus* cultured in tryptic soy broth (TSB). For long-term experiments, antibiotic-modified surfaces were either kept dry or in PBS, at 37 °C for months to years. No changes in VAN coverage of Ti pins were apparent after incubation under any of these conditions for times out to 2 years.[127,174] A similar modification of native allograft bone was stable for at least 10 months by antibody staining and at least 2 months on the basis of activity determinations.[173]

4.417.4.2.1. Properties of surface-tethered antibiotics

Many previous studies for bioimmobilization indicate that it is clearly possible to attach PEG-like linkers to solid supports,[129,155,176–179] and these PEG linkers have the potential to be used for tethering VAN to those linkered supports.[128,163,172] In order to be of utility, however, these tethered antibiotics must retain their ability to either inhibit bacterial proliferation (bacteriostatic) or cause bacterial lysis (bactericidal). The tethering chemistry described for VAN uses the only carboxylic acid

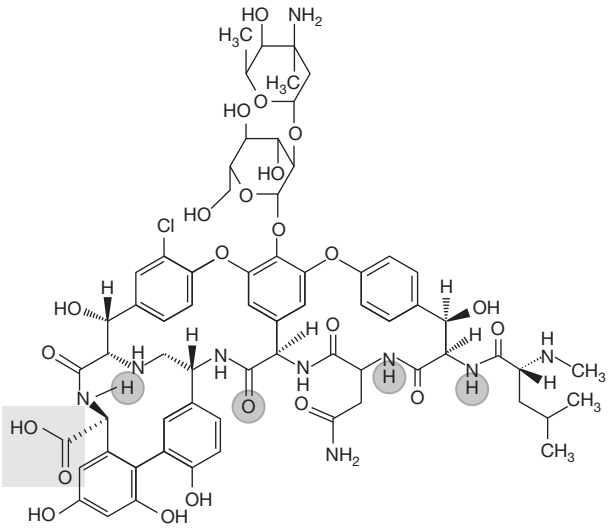

Figure 6 Vancomycin (VAN) structure with substrate interaction sites indicated. The structure of VAN is shown, with the Lys–D-Ala-D-Ala hydrogen bonding sites indicated by circles. The carboxylic acid used for coupling to the Ti surface is indicated by a square.

group present in VAN. Importantly, this carboxylic acid group is not directly part of the substrate interaction site that binds the D-Ala-D-Ala peptidoglycan to inhibit cross-linking of the gram-positive bacterial cell wall[180] (**Figure 6**). On that basis, alone, VAN should retain at least some of its antibacterial activity. Furthermore, the chemistry of VAN is well known and many modifications to its parent structure have been described,[124] as well as their effects on its activity. On the basis of literature reports, addition of chemical moieties to this sole carboxylic acid group appeared to retain bioactivity.[124] Others have used the amines on VAN for tethering with retention of activity.[153,164] Furthermore, it appeared that membrane-anchoring of VAN increased its activity against a VAN-insensitive strain.[181] Interestingly, addition of the AEEA linkers was to facilitate bacterial membrane solubility of the VAN[163] and perhaps increase the efficacy of the antibiotic in the tethered stage. This remains to be tested.

For a surface-bound VAN, antibiotic activity is expected to be only effective against those bacteria in the process of adhering to the surface; as antibiotic elution does not occur from a tethered surface, nonadherent bacteria distal to the surface are expected to be able to continue to proliferate. Measurement of the effects of these tethered antibiotics can be performed by visualization of the adherent bacteria or by recovery of the adherent bacteria through gentle sonication in the presence of detergent, followed by plating and enumeration. Both methods yield important and somewhat different information. Importantly, the magnitude of the effects using the two methods is not necessarily compatible, although both show the same trends.

Adherent bacteria and biofilms can be fluorescently visualized using the commercially available Live/Dead BacLight™ kit (Invitrogen) which relies on the differential membrane permeability of two fluorescent dyes to allow discrimination between viable bacteria and those that have sufficient membrane damage to no longer be viable.[182] Syto9, the first of the

two dyes, is able to enter all bacteria and bind to its DNA, thus causing both viable and nonviable bacteria to fluoresce green. The second dye, propidium iodide, is excluded by the intact membrane of viable bacteria, whereas nonviable bacteria readily allow its internalization and subsequent binding to DNA.[182] Thus, only nonviable bacteria fluoresce red. In examining fields of bacteria, viable bacteria will fluoresce green, whereas nonviable bacteria will fluoresce both red and green. Because the polysaccharide matrix of biofilms can contain free DNA as well as cause retention of dye, biofilms can show staining with both dyes. On VAN-modified surfaces, usually no red fluorescence is apparent, suggesting that nonviable bacteria do not remain sticky.[127,128,174,175,183]

When VAN-modified metal or allograft surfaces are examined using the Live/Dead BacLight™ dyes, little fluorescence is apparent. In contrast, control surfaces (surfaces that have been washed but not taken through subsequent synthetic steps; this surface most closely mimics actual smooth Ti surfaces used clinically), depending on the time of incubation and the bacterial strain used, tend to be heavily colonized by bacteria and show intense green fluorescence with some structures that reproduce those apparent in other published reports of biofilms.[174] The magnitude of this inhibition of bacterial adhesion (which may be the result of facilitated killing of bacteria attempting to adhere, although this analysis cannot distinguish between killing and inhibition) appears to be dependent on the inocula.[184] Importantly, even after incubation with *S. aureus* or *S. epidermidis* for 24 h, when bathing bacterial concentrations are expected to exceed 10^7–10^8 cfu ml^{-1}, statistically fewer bacteria are observed on the VAN-coupled surfaces than on the control, untethered surface (metal or bone allograft).[127,173,174,184] The ability to retard bacterial colonization appears to be stable to exposure to bacteria as the activity of the VAN-coupled Ti rods appears to be retained for at least four to five 24-h rechallenges with *S. aureus*.[127,174,175] *S. aureus*, the major causative organism in deep infections,[14] and *S. epidermidis*, a second frequent contaminant,[185] are studied in this fashion. Because the lab strains adapt fairly quickly to liquid culture *in vitro*, adhesion can be lost and become difficult to regain in strains that are not virulent.

Because these microscopy methods only provide a snapshot of small areas of the surface, the only means to assign a magnitude to the effect of the VAN-coupled surface is through direct recovery of the adherent bacteria from the rod surface. These numbers were determined by incubating either clean, unmodified surfaces or VAN-modified surfaces with *S. aureus* in TSB in static cultures for times out to 24 h. Static cultures allow bacterial adhesion, although some viability may be sacrificed in quickly growing cultures that remain static. It is important to note that bacterial adhesion and biofilm formation occur under both flow conditions and static conditions, although the strength of the adhesion may be different, depending on the fluid stress to which the culture is exposed.[186,187] At the end of the incubation period, surfaces are gently washed approximately six times with PBS to remove loosely adherent bacteria and any nucleic acid contamination from the culturing medium. Again, this washing step is crucial and is probably one of the least defined steps in the procedure. Washing must be gentle enough to not generate sufficient shear force to remove chunks of biofilm, but thorough enough to remove nonadherent bacteria. When examining the surfaces after Live/Dead staining, insufficient washing will result in the appearance of many free-floating bacteria; plating of washes to determine bacterial content as a function of wash conditions and numbers can help to standardize the conditions for the particular laboratory.

After this washing, removal of the bacteria from the surface straddles the fine line between (a) complete removal with accompanying bacterial lysis of at least a subset of the adherent bacteria and (b) partial, reproducible removal, with the remaining adherent bacteria visualized using the Live/Dead stain as described previously. Many papers have detailed methods for sonication in Triton-X, Tween-20, or Tween-80 detergents for amounts of time varying from 5 to 10 min.[188,189] Sonication with PBS containing 0.3% Tween-80 for 5 min was used, and numbers of recovered cfu were statistically lower on the VAN-modified surfaces.[127,173,174,184]

In parallel with these experiments, tethered VAN was assayed to determine if the spectrum of bioactivity described for the parent antibiotic was reproduced, using both the Live/Dead assay and direct colony counting. Specifically, as VAN inhibits cell wall synthesis, a process important for the viability of gram-positive but not gram-negative microorganisms, VAN has little gram-negative coverage.[190] Therefore, if the VAN tethered to the surface retains its native activity, gram-negative organisms ought to be relatively unaffected by its presence. The gram-negative organism *E. coli* readily adhered to the control surfaces (both metal and allograft) at all times tested. When the VAN-coupled surfaces were examined, they were indistinguishable from the control rods, as were the counts retrieved from them.[174,184]

A problem in quantification of adherent bacteria can arise, however, in the characterization of these antibacterial surfaces. If the surfaces are performing as expected, that is, inhibiting bacterial adhesion, then the strength of adhesion may, in fact, be lower on the antibacterial surface than it is on the control surface. Because sonication does not completely remove adherent bacteria, differences in strength of adhesion will skew the results. Specifically, assuming that adhesion is stronger on the control surface than on the antibacterial surface, the difference between numbers of bacteria recovered from the control and from the antibiotic-modified surfaces is smaller than that actually observed with representative fields of Live/Dead staining. Adhesive measurements relying on shear force to detachment or on the force required to remove individual cells using atomic force microscopy could certainly determine if adhesive strength was decreased on antibacterial surfaces.

If these surfaces are to have clinical utility, they must retain their antibacterial character in a physiological environment, that is, in the presence of full plasma, which also contributes to biofilm formation. While *in vitro* modeling necessarily requires a reductionist approach that cannot begin to recapitulate the complexity of the *in vivo* situation, coating with serum or with fibrin can begin to address the effect of host protein adhesion on antibacterial surface and MSCRAMM binding activity. During the performance of all *in vitro* adhesion imaging studies described earlier, 10% fetal bovine serum was routinely used to block the surfaces for prevention of nonspecific antibody binding, suggesting that the VAN remains accessible even with protein coating.[127,174] The final proof was whether or not the surface retained antibacterial activity after serum

coating. This was tested by first coating pins with 10% fetal bovine serum, followed either by confirmation of the presence of serum proteins, specifically fibronectin by immunohistochemistry, or by incubation with *S. aureus*. The tethered VAN continued to inhibit bacterial adhesion, even in the presence of serum proteins.[174]

To determine if these surfaces withstand multiple bacterial challenges, the antibiotic-tethered pins were repeatedly challenged for 24 h with *S. epidermidis* in TSB, followed by removal of the adherent bacteria with sonication in sodium dodecyl sulfate.[127] After washing to remove the residual detergent, the rods were stained again to make certain that adherent bacteria were removed, washed, and incubated with *S. epidermidis* for 24 h. Again, rod colonization was assessed by Live/Dead staining, followed by washing, restaining, etc. By the fifth rechallenge in TSB, some variability was apparent not only in the resistance of the VAN pin to colonization, but also in the ability of the bacteria to colonize the control pins probably due to the presence of the residual detergent.[174] Thus, the presence of the tethered VAN should endow the implant with the ability to resist bacterial colonization not only for the first bacterial assault, but also for several subsequent assaults.

Finally, in dealing with a permanent antibiotic surface, the question of antibiotic resistance must be raised. *S. aureus* was cultured in the presence of VAN-Ti pins for up to 2 months. In order to ensure that any adherent bacteria had sufficient nutrients, the VAN-Ti pins were sterilely moved to fresh TSB medium every 2–3 days. Adherent bacteria were recovered by sonication and antibiotic sensitivity was measured. No changes in the susceptibility of the parent *S. aureus* strain to VAN was detected at the end of the incubation.[175] Of course, this selection for resistance is only being tested under essentially selective metabolic pressure. Resistance often arises in mixed populations of bacteria, especially in biofilms, where transfer of plasmid elements can cause transfer of traits.[191,192] While this most important test will rely on clinical conditions, resistance was not fostered under these ideal conditions. Firstly, bacterial resistance arises because the resistant organism has a selective growth advantage over the growth-suppressed organisms that are sensitive to the drug. This condition of growth advantage is one of the concerns of the controlled release systems because this scenario typically happens as the antibiotic levels deplete to levels near the MIC. In the case of the tethered VAN pin, the level of antibiotic at the surface of the implant is expected to remain fairly constant so that the bacteria that attempt to adhere to the surface will continue to encounter bactericidal levels of antibiotic, thus effectively preventing development of resistance by this mechanism. Importantly, as biofilm formation appears to be retarded on these surfaces, the ability to horizontally transfer plasmids is limited, thus also minimizing the possibility of resistance. Finally, antibiotic resistance is not a frequent event and generally arises in the gut due to the large numbers of bacteria that are actively proliferating at any time. In the infected implant, numbers of bacteria that will see the surface are limited so that the probability of a resistant organism is small. As the bulk of the bacteria (i.e., those not in contact with the surface) will not be experiencing a metabolic pressure, an incidental resistant organism, which is typically slow growing,[191,192] will not have a selective growth advantage and is likely to lose out in the struggle for nutrients. While all of these predictions suggest that resistance due to surface-tethered antibiotics will be very rare, only the simple conditions have been tested to date.

4.417.4.3. Biocompatibility of Tethered VAN

As noted in the introduction, high concentrations of antibiotics can have deleterious effects on bone cell viability. Thus, on an osseointegrating implant surface, even low levels of attached antibiotics can affect host tissue biocompatibility. When osteoblast-like cells are cultured on either Ti or VAN-Ti surfaces, similar morphology, size, and density of cells are apparent (**Figure 7**).[175] In other studies, we have explicitly tested biocompatibility. To date, we have found no significant differences in cell number, viability, or levels of osteoblast maturation markers associated with culturing on VAN-modified allograft surfaces.[173,184] On the basis of these cell adhesion data, we would expect that use *in vivo* would be feasible, with standard tests such as pullout tests determining the strength of the bone-modified implant interface.

4.417.4.4. Coupling with Other Technologies

When describing these antibiotic-coupled surfaces, their strength is also their weakness. Specifically, while the tethered antibiotic may keep the implant from becoming the nidus for future infection, it cannot control infection in the tissue surrounding the implant. The surgeon always tries to minimize the impact of the previous infection by removal of the infected bone by debridement; however, latent infection does exist and is probably due to (1) hematogenously sourced microbes, (2) biofilm formation on bone or adjacent soft tissue surfaces distant from the implant insertion site, or (3) equally challenging, due to the presence of internalized phagocytosed but viable bacteria that can lyse the host cells to reestablish infection.[5,6,193] Any of these possibilities require effective antibiotic therapy. Systemic antibiotic administration is always a possibility, but due to poor penetration into the bone, is often problematic – although in the presence of an implant that actively resists infection, these therapies may become more efficacious. The most successful means to treat infection to date has been through the controlled release systems, especially release of antibiotics from cement spacers used to treat infection.[37,194,195] The ultimate therapy for prevention of

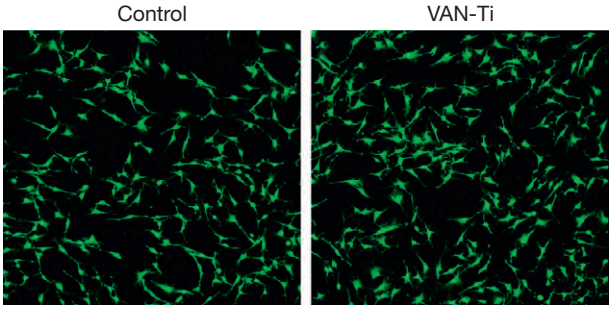

Figure 7 Osteoblastic MC3T3-C1 cells cultured on control or vancomycin (VAN)-Ti surfaces. Cells plated on either control or VAN-modified surfaces for times out to 24 h showed no differences in cell morphology or number as a function of surface modification.

implant-associated infections may well lie with combination therapies. The tethered antibiotic surface could serve as a platform for the application of a controlled release system, such as a sol–gel, for delivery of two therapies over a defined therapeutic window. Similarly, orthopedic implant placement is often accompanied by the use of allograft bone to foster osseointegration – this allograft bone is not only compatible with the tethering chemistry,[128] but is also available as a simple antibiotic elution system.[82,173,196] Together, these combination therapies could better minimize the incidence of implant-related infection and ensure that the costs, pain, repeated surgeries, and sometimes dire consequences of these infections become a less frequent event.

Acknowledgments

The authors thank Stephanie Barr for excellent technical help throughout the work described. They also thank the Musculoskeletal Transplant Foundation for providing samples for this work and for their generous support for these studies. Further, the authors thank the NIH (grants DE-13319, DE-10875, AR-051303, DE019901, and HD061053) and the Department of Defense (grant DAMD17-03-1-0713) for funding these studies. Results presented are not the statement or policy of the funding agencies.

References

1. Centers for Disease Control and Prevention, *MMWR* **2003**, *52*, 1174–1176.
2. Harris, L. G.; Richards, R. G. *Injury* **2006**, *37*(S2), S3–S14.
3. Von Eiff, C.; Peters, G.; Heilmann, C. *Lancet Infect. Dis.* **2002**, *2*, 677–685.
4. Gristina, A. G. *Science* **1987**, *237*, 1588–1595.
5. Costerton, J. W. *Clin. Orthop. Relat. Res.* **2005**, *437*, 7–11.
6. Brady, R. A.; Leid, J. G.; Calhoun, J. H.; Costerton, J. W.; Shirtliff, M. E. *FEMS Immunol. Med. Microbiol.* **2008**, *52*, 13–22.
7. Logar, D. B.; Komadina, R.; Prezelj, J.; Ostanek, B.; Trost, Z.; Marc, J. *J. Bone Miner. Metab.* **2007**, *25*, 219–225.
8. Jiang, Y.; Mehta, C. K.; Hsu, T. Y.; Alsulaimani, F. F. *Infect. Immun.* **2002**, *70*, 3143–3148.
9. Moore, R.; Beredjiklian, P.; Rhoad, R.; *et al. J. Biomed. Mater. Res.* **1997**, *34*, 137–147.
10. Wada, T.; Nakashima, T.; Hiroshi, N.; Penninger, J. M. *Trends Mol. Med.* **2006**, *12*, 17–25.
11. Walsh, M. C.; Kim, N.; Kadono, Y.; *et al. Annu. Rev. Immunol.* **2006**, *24*, 33–63.
12. Marriott, I.; Gray, D. L.; Tranguch, S. L.; *et al. Am. J. Pathol.* **2004**, *164*, 1399–1406.
13. Yoshii, T.; Magara, S.; Miyai, D.; *et al. Cytokine* **2002**, *19*, 59–65.
14. Saadatian-Elahi, M.; Teyssou, R.; Vanhems, P. *Int. J. Surg.* **2008**, *6*, 238–245.
15. Somayaji, S. N.; Ritchie, S.; Sahraei, M.; Marriott, I.; Hudson, M. C. *Infect. Immun.* **2008**, *76*, 5120–5126.
16. Alexander, E. H.; Rivera, F. A.; Marriott, I.; Anguita, J.; Bost, K. L.; Hudson, M. C. *BMC Microbiol.* **2003**, *3*, 5; Doi: 10.1186/1471-2180-3-5.
17. Bost, K. L.; Ramp, W. K.; Nicholson, N. C.; Bento, J. L.; Marriott, I.; Hudson, M. C. *J. Infect. Dis.* **1999**, *180*, 1912–1920.
18. Wagner, E. F.; Eferl, R. *Immunol. Rev.* **2005**, *208*, 126–140.
19. Wright, J. A.; Nair, S. P. *Int. J. Med. Microbiol.* **2010**, *300*, 193–204.
20. Herman, S.; Krönke, G.; Schett, G. *Trends Mol. Med.* **2008**, *14*, 245–253.
21. Costerton, J. W.; Cheng, K. J.; Geesey, G. G.; *et al. Annu. Rev. Microbiol.* **1987**, *41*, 435–464.
22. Donlan, R. M.; Costerton, J. W. *Clin. Microbiol. Rev.* **2002**, *15*, 167–193.
23. Herscu, G.; Wilson, S. E. *Surg. Clin. North Am.* **2009**, *89*, 391–401.
24. Vinh, D. C.; Embil, J. M. *J. Long Term Eff. Med. Implants* **2005**, *15*, 467–488.
25. Wilson, M. *Sci. Prog.* **2001**, *84*, 235–254.
26. Saldarroaga-Fernández, I. C.; Busscher, H. J.; Metzger, S. W.; Grainger, D. W.; van der Mei, H. C. *Biomaterials* **2011**, *32*, 979–984.
27. Hauck, C. R.; Ohlsen, K. *Curr. Opin. Microbiol.* **2006**, *9*, 5–11.
28. Hudson, M. C.; Ramp, W. K.; Frankenburg, K. P. *FEMS Microbiol. Lett.* **1999**, *173*, 279–284.
29. Heilmann, C.; Thumm, G.; Chhatwal, G. S.; Hartleib, J.; Uekötter, A.; Peters, G. *Microbiology* **2003**, *149*, 2769–2778.
30. Costerton, J. W. *J. Ind. Microbiol.* **1995**, *15*, 137–140.
31. Stoodley, P.; Sauer, K.; Davies, D. G.; Costerton, J. W. *Annu. Rev. Microbiol* **2002**, *56*, 187–208.
32. Cvitkovitch, D. G.; Li, Y. H.; Ellen, R. P. *J. Clin. Invest.* **2003**, *112*, 1626–1632.
33. Costerton, J. W.; Stewart, P. S.; Greenberg, E. P. *Science* **1999**, *284*, 1318–1322.
34. Stewart, P. S. *Int. J. Med. Microbiol.* **2002**, *292*, 107–113.
35. Stewart, P. S.; Costerton, J. W. *Lancet* **2001**, *358*, 135–138.
36. Anderl, J. N.; Franklin, M. J.; Stewart, P. S. *Antimicrob. Agents Chemother.* **2000**, *44*, 1818–1824.
37. Cierny, G., III; Dipasquale, D. *Clin. Orthop. Relat. Res.* **2002**, *403*, 23–28.
38. Duggan, J. M.; Georgiadis, G. M.; Kleshinski, J. F. *Infect. Med.* **2001**, *18*, 534–541.
39. Mcpherson, E. J.; Woodson, C.; Holtom, P.; Roidis, N.; Shufelt, C.; Patzakis, M. J. *Clin. Orthop. Relat. Res.* **2002**, *1*, 8–15.
40. Nair, S. P.; Williams, R. J.; Henderson, B. *Rheumatology* **2000**, *39*, 821–834.
41. Buser, D.; Schenk, R. K.; Steinemann, S.; Fiorellini, J. P.; Fox, C. H.; Stich, H. *J. Biomed. Mater. Res.* **1991**, *25*, 889–902.
42. Galante, J. O.; Jacobs, J. *Clin. Orthop. Relat. Res.* **1992**, *276*, 41–49.
43. Lincks, J.; Boyan, B. D.; Blanchard, C. R.; *et al. Biomaterials* **1998**, *19*, 2219–2232.
44. Puleo, D. A.; Nanci, A. *Biomaterials* **1999**, *20*, 2311–2321.
45. Ducheyne, P.; Beight, J.; Cuckler, J.; Evans, B.; Radin, S. *Biomaterials* **1990**, *11*, 531–540.
46. Ducheyne, P.; Hench, L. L.; Kagan, A., II; Martens, M.; Bursens, A.; Mulier, J. C. *J. Biomed. Mater. Res.* **1980**, *14*, 225–237.
47. Raulio, M.; Järn, M.; Ahola, J.; *et al. J. Ind. Microbiol. Biotechnol.* **2008**, *35*, 751–760.
48. Duarte, P. M.; Reis, A. F.; De Freitas, P. M.; Ota-Tsuzuki, C. *J. Periodontol.* **2009**, *80*, 1824–1832.
49. Riedewald, F. *PDA J. Pharm. Sci. Technol.* **2006**, *60*, 164–171.
50. Yoshinari, M.; Oda, Y.; Kato, T.; Okuda, K.; Hirayama, A. *J. Biomed. Mater. Res.* **2000**, *52*, 388–394.
51. Harris, L. G.; Richards, R. G. *J. Mater. Sci. Mater. Med.* **2004**, *15*, 311–314.
52. Boks, N. P.; Kaper, H. J.; Norde, W.; Van Der Mei, H. C.; Busscher, H. J. *J. Colloid Interface Sci.* **2009**, *331*, 60–64.
53. Boks, N. P.; Norde, W.; Van Der Mei, H. C.; Busscher, H. J. *Microbiology* **2008**, *154*, 3122–3133.
54. Kaudhi, H. *Microb. Pathogenesis* **2010**, *49*, 14–22.
55. Buranapanitkit, B.; Srinilta, V.; Ingviga, N.; Oungbho, K.; Geater, A.; Ovatlarnporn, C. *Clin. Orthop. Relat. Res.* **2004**, *424*, 244–252.
56. Rauschmann, M. A.; Wichelhaus, T. A.; Stirnal, V.; *et al. Biomaterials* **2005**, *26*, 2677–2684.
57. Shirtliff, M. E.; Calhoun, J. H.; Mader, J. T. *Clin. Orthop. Relat. Res.* **2002**, *401*, 239–247.
58. Alt, V.; Bitschnau, A.; Osterling, J.; *et al. Biomaterials* **2006**, *27*, 4627–4634.
59. Avés, E. P.; Estévez, G. F.; Sader, M. S.; *et al. J. Mater. Sci. Mater. Med.* **2009**, *20*, 543–547.
60. Winkler, H. *Int. J. Med. Sci.* **2009**, *6*, 247–252.
61. Fink, B. *Int. J. Med. Sci.* **2009**, *6*, 287–295.
62. Sukeik, M.; Haddad, F. S. *Int. J. Med. Sci.* **2009**, *6*, 253–257.
63. De Carvalho, C. C. C. R. *Recent Pat. Biotechnol.* **2007**, *1*, 49–57.
64. Sand, W.; Gehrke, T. *Res. Microbiol.* **2006**, *157*, 49–56.
65. Subramani, K.; Jung, R. E.; Molenberg, A.; Hammerle, C. H. F. *Int. J. Oral Maxillofac. Implants* **2009**, *24*, 616–626.
66. Verran, J.; Whitehead, K. *Int. J. Artif. Organs* **2005**, *28*, 1138–1145.
67. Brubaker, S. M.; Brown, T. E.; Manaswi, A.; Mihalko, W. M.; Cui, Q.; Saleh, K. J. *J. Arthroplasty* **2007**, *22*, 52–56.
68. De Long, W. G., Jr.; Einhorn, T. A.; Koval, K.; *et al. J. Bone Joint Surg. Am.* **2007**, *89*, 649–658.
69. Nishida, J.; Shimamura, T. *Med. Sci. Monit.* **2008**, *14*, RA107–RA113.
70. Oakes, D. A.; Cabanela, M. E. *J. Am. Acad. Orthop. Surg.* **2006**, *14*, 620–628.
71. Biau, D. J.; Larousserie, F.; Thévenin, F.; Piperno-Neumann, S.; Anract, P. *Clin. Orthop. Relat. Res.* **2010**, *468*, 834–845.
72. Dominiak, A.; Interewicz, B.; Swoboda, E.; Olszewski, W. L. *Ann. Transplant.* **2006**, *11*, 30–37.
73. Kappe, T.; Cakir, B.; Mattes, T.; Reichel, H.; Flören, M. *Cell Tissue Bank.* **2010**, *11*, 253–259.
74. Rorabeck, C. H.; Smith, P. N. *Orthop. Clin. North Am.* **1998**, *29*, 361–371.

75. Buttaro, M. A.; González Della Valle, A. M.; Piñeiro, L.; Mocetti, E.; Morandi, A. A.; Piccaluga, F. *Acta Orthop. Scand.* **2003**, *74*, 505–513.
76. Day, R. E.; Megson, S.; Wood, D. *J. Bone Joint Surg. Br.* **2005**, *87*, 1568–1574; erratum appears in *J. Bone Joint Surg. Br.* **2006**, *88*(6), 837.
77. Evans, G. H.; Yukna, R. A.; Sepe, W. W.; Mabry, T. W.; Mayer, E. T. *J. Periodontol.* **1989**, *60*, 491–497.
78. Gray, J. C.; Elves, M. W. *J. Bone Joint Surg. Br.* **1981**, *63*, 441–445.
79. Harris, R. J. *Int. J. Periodontics Restorative Dent.* **2002**, *22*, 381–387.
80. Kanellakopoulou, K.; Sahinides, T.; Tsaganos, T.; Galanakis, N.; Giamarellou, H.; Giamarellos-Bourboulis, E. J. *J. Chemother.* **2008**, *20*, 645–647.
81. Petri, W. H., III; Schaberg, S. J. *J. Oral Maxillofac. Surg.* **1984**, *42*, 699–704.
82. Witso, E.; Persen, L.; Benum, P.; Bergh, K. *Acta Orthop.* **2005**, *76*, 481–486.
83. Antoci, V., Jr.; Adams, C. S.; Hickok, N. J.; Shapiro, I. M.; Parvizi, J. *Clin. Orthop. Relat. Res.* **2007**, *462*, 200–206.
84. Costain, D. J.; Crawford, R. W. *Injury* **2009**, *40*, 1260–1264.
85. Drosos, G. I.; Kazakos, K. I.; Kouzoumpasis, P.; Verettas, D.-A. *Injury* **2007**, *38*(S4), S13–S21.
86. Epstein, N. E. *Surg. Neurol.* **2008**, *69*, 16–19.
87. Haddad, F. S.; Rayan, F. *Orthopedics* **2009**, , *32*, 675–679.
88. Lynch, J. R.; Clinton, J. M.; Dewing, C. B.; Warme, W. J.; Matsen, F. A., III. *J. Shoulder Elbow Surg.* **2009**, *18*, 317–328.
89. Aro, H.; Aho, A. *Ann. Med.* **1993**, *25*, 403–412.
90. Lord, C.; Gebhardt, M.; Tomford, W.; Mankin, H. *J. Bone Joint Surg. Am.* **1988**, *70*, 369–376.
91. Tomford, W.; Starkweather, R.; Goldman, M. *J. Bone Joint Surg. Am.* **1981**, *63*, 244–248.
92. Tomford, W.; Thongphasuk, J.; Mankin, H.; Ferraro, M. *J. Bone Joint Surg. Am.* **1990**, *72*, 1137–1143.
93. Mankin, H.; Doppelt, S.; Tomford, W. *Clin. Orthop. Relat. Res.* **1983**, *174*, 69–86.
94. Buttaro, M. A.; Morandi, A.; Rivello, H. G.; Piccaluga, F. *J. Bone Joint Surg. Br.* **2005**, *87*, 1684–1687.
95. De Grood, M. *Arch. Chir. Neerl.* **1951**, *3*, 128–138.
96. Buttaro, M. A.; Pusso, R.; Piccaluga, F. *J. Bone Joint Surg. Br.* **2005**, *87-B*, 314–319.
97. Humphrey, J. S.; Mehta, S.; Seaber, A. V.; Vail, T. P. *Clin. Orthop. Relat. Res.* **1998**, 218–224.
98. Kanellakopoulou, K.; Giamarellos-Bourboulis, E. J. *Drugs* **2000**, *59*, 1223–1232.
99. Rushton, N. *Eur. J. Surg.* **1997**, *578*, S27–S30.
100. Suh, H.; Suh, S.; Min, B. *ASAIO J.* **1994**, *40*, M406–M411.
101. Wachol-Drewek, Z.; Pfeiffer, M.; Scholl, E. *Biomaterials* **1996**, *17*, 1733–1738.
102. Witsø, E.; Persen, L.; Benum, P.; Bergh, K. *Acta Orthop. Scand.* **2002**, *73*, 199–205.
103. Witso, E.; Persen, L.; Loseth, K.; Bergh, K. *Acta Orthop. Scand.* **1999**, *70*, 298–304.
104. Broekhuizen, C. A. N.; Schultz, M. J.; Van Der Wal, A. C.; *et al. Crit. Care Med.* **2008**, *36*, 2395–2402.
105. Broekhuizen, C. A. N.; Sta, M.; Vandenbroucke-Grauls, C. M. J. E.; Zaat, S. A. J. *Infect. Immun.* **2010**, *78*, 954–962.
106. Kuijpers, A. J.; Engbers, G. H.; Van Wachem, P. B.; *et al. J. Control. Release* **1998**, *53*, 235–247.
107. Neut, D.; Van De Belt, H.; Stokroos, I.; Van Horn, J. R.; Van Der Mei, H. C.; Busscher, H. J. *J. Antimicrob. Chemother.* **2001**, *47*, 885–891.
108. Isefuku, S.; Joyner, C. J.; Simpson, A. H. *J. Orthop. Res.* **2001**, *19*, 950–954.
109. Edin, M.; Miclau, T.; Lester, G.; Lindsey, R.; Dahners, L. *Clin. Orthop. Relat. Res.* **1996**, *454*, 245–251.
110. Axelsen, P. H.; Li, D. *Bioorg. Med. Chem.* **1998**, *6*, 877–881.
111. Eggert, U. S.; Ruiz, N.; Falcone, B. V.; *et al. Science* **2001**, *294*, 361–364.
112. Malabarba, A.; Ciabatti, R. *Curr. Med. Chem.* **2001**, *8*, 1759–1773.
113. Barna, J. C.; Williams, D. H.; Stone, D. J. M.; Leung, T.-W. C.; Doddrell, D. M. *J. Am. Chem. Soc.* **1984**, *106*, 4895–4902.
114. Sheldrick, G. M.; Jones, P. G.; Kennard, O.; Williams, D. H.; Smith, G. A. *Nature* **1978**, *271*, 223–225.
115. Nagarajan, R. *Antimicrob. Agents Chemother.* **1991**, *35*, 605–609.
116. Chohfi, M.; Langlais, F.; Fourastier, J.; Minet, J.; Thomazeau, H.; Cormier, M. *Int. Orthop.* **1998**, *22*, 171–177.
117. Zimmerli, W.; Trampuz, A.; Ochsner, P. E. *N. Engl. J. Med.* **2004**, *351*, 1645–1654.
118. Murray, R. J.; Sieunarine, K.; Ward, P. B.; Pearman, J. W. *Med. J. Aust.* **2004**, *181*, 227–228.
119. Zeller, V.; Kitzis, M. D.; Graff, W.; Mamoudy, P.; Desplaces, N. *Scand. J. Infect. Dis.* **2006**, *38*, 934–938.
120. Bagga, B.; Shenep, J. L. *Pediatr. Infect. Dis. J.* **2010**, *29*, 662–664.
121. Hammerum, A. M.; Lester, C. H.; Heuer, O. E. *Foodborne Pathog. Dis.* **2010**, *7*, 1137–1146.
122. Mirani, Z. A.; Jamil, N. *J. Coll. Physicians Surg. Pak.* **2010**, *20*, 558–559.
123. Vogel, L. *Can. Med. Assoc. J.* **2010**, *182*, E505–E506.
124. Loll, P. J.; Axelsen, P. H. *Annu. Rev. Biophys. Biomol. Struct.* **2000**, *29*, 265–289.
125. Christian, S.; Kraas, J.; Conway, W. F. *Semin. Roentgenol.* **2007**, *42*, 92–101.
126. Sia, I. G.; Berbari, E. F. *Baillieres Best Pract. Res. Clin. Rheumatol.* **2006**, *20*, 1065–1081.
127. Antoci, V., Jr.; King, S. B.; Jose, B.; *et al. J.Orthop.Res.* **2007**, *25*, 858–866.
128. Ketonis, C.; Adams, C. S.; Barr, S.; *et al. Tissue Eng. A* **2010**, *16*, 2041–2049.
129. Lawson, M. C.; Shoemaker, R.; Hoth, K. B.; Bowman, C. N.; Anseth, K. S. *Biomacromolecules* **2009**, *10*, 2221–2234.
130. Kaplan, J.; Korty, B. D.; Axelsen, P. H.; Loll, P. J. *J. Med. Chem.* **2001**, *44*, 1837–1840.
131. Reynolds, P. E. *Eur. J. Clin. Microbiol. Infect. Dis.* **1989**, *8*, 943–950.
132. Hiramatsu, K.; Cui, L.; Kuroda, M.; Ito, T. *Trends Microbiol.* **2001**, *9*, 486–493.
133. Howden, B. P.; Davies, J. K.; Johnson, P. D. R.; Stinear, T. P.; Grayson, M. L. *Clin. Microbiol. Rev.* **2010**, *23*, 99–139.
134. Cui, L.; Murakami, H.; Kuwahara-Arai, K.; Hanaki, H.; Hiramatsu, K. *Antimicrob. Agents Chemother.* **2000**, *44*, 2276–2285.
135. Hanaki, H.; Kuwahara-Arai, K.; Boyle-Vavra, S.; Daum, R. S.; Labischinski, H.; Hiramatsu, K. *J. Antimicrob. Chemother.* **1998**, *42*, 199–209.
136. Hanaki, H.; Labischinski, H.; Inaba, Y.; Kondo, N.; Murakami, H.; Hiramatsu, K. *J. Antimicrob. Chemother.* **1998**, *42*, 315–320.
137. Hiramatsu, K. *Am. J. Med.* **1998**, *104*, 7S–10S.
138. Kuroda, M.; Kuwahara-Arai, K.; Hiramatsu, K. *Biochem. Biophys. Res. Commun.* **2000**, *269*, 485–490.
139. Massia, S. P.; Hubbell, J. A. *Anal. Biochem.* **1990**, *187*, 292–301.
140. Rezania, A.; Healy, K. E. *Biotechnol. Prog.* **1999**, *15*, 19–32.
141. Rezania, A.; Healy, K. E. *J. Biomed. Mater. Res.* **2000**, *52*, 595–600.
142. Rezania, A.; Thomas, C. H.; Branger, A. B.; Waters, C. M.; Healy, K. E. *J. Biomed. Mater. Res.* **1997**, *37*, 9–19.
143. Derda, R.; Wherritt, D. J.; Kiessling, L. L. *Langmuir* **2007**, *23*, 11164–11167.
144. Cavalcanti-Adam, E. A.; Shapiro, I. M.; Composto, R. J.; Macarak, E. J.; Adams, C. S. *J. Bone Miner. Res.* **2002**, *17*, 2130–2140.
145. El-Ghannam, A. R.; Ducheyne, P.; Risbud, M.; *et al. J. Biomed. Mater. Res. A* **2004**, *68*, 615–627.
146. Ferris, D. M.; Moodie, G. D.; Dimond, P. M.; Gioranni, C. W.; Ehrlich, M. G.; Valentini, R. F. *Biomaterials* **1999**, *20*, 2323–2331.
147. Okamoto, K.; Matsuura, T.; Hosokawa, R.; Akagawa, Y. *J. Dental Res.* **1998**, *77*, 481–487.
148. Secchi, A. G.; Grigoriou, V.; Shapiro, I. M.; *et al. J. Biomed. Mater. Res. A* **2007**, *83*, 577–584.
149. Danahy, M. P.; Avaltroni, M. J.; Midwood, K. S.; Schwarzbauer, J. E.; Schwartz, J. *Langmuir* **2004**, *20*, 5333–5337.
150. Heijink, A.; Schwartz, J.; Zobitz, M. E.; Nicole Crowder, K.; Lutz, G. E.; Sibonga, J. D. *Clin. Orthop. Relat. Res.* **2008**, *466*, 977–984.
151. Puleo, D. A.; Kisslinga, R. A.; Sheu, M.-S. *Biomaterials* **2002**, *23*, 2079–2087.
152. Wojcik, S. M.; Puleo, D. A. *Biomed. Sci. Instrum.* **1997**, *33*, 166–171.
153. Lawson, M. C.; Bowman, C. N.; Anseth, K. S. *Clin. Orthop. Relat. Res.* **2007**, *461*, 96–105.
154. Mikulec, L. J.; Puleo, D. A. *J. Biomed. Mater. Res.* **1996**, *32*, 203–208.
155. Khoo, X.; Hamilton, P.; O'Toole, G. A.; Snyder, B. D.; Kenan, D. J.; Grinstaff, M. W. *J. Am. Chem. Soc.* **2009**, *131*, 10992–10997.
156. Brohede, U.; Forsgren, J.; Roos, S.; Mihranyan, A.; Engqvist, H.; Strømme, M. *J. Mater. Sci. Mater. Med.* **2009**, *20*, 1859–1867.
157. Kalicke, T.; Schierholz, J.; Schlegel, U.; *et al. J. Orthop. Res.* **2006**, *24*, 1622–1640.
158. Moojen, D. J.; Vogely, H. C.; Fleer, A.; *et al. J. Orthop. Res.* **2009**, *27*, 710–716.
159. Radin, S.; Ducheyne, P. *Biomaterials* **2007**, *28*, 1721–1729.
160. Stigter, M.; Bezemer, J.; De Groot, K.; Layrolle, P. *J. Control. Release* **2004**, *99*, 127–137.
161. Tang, L.; Zhao, C.; Xiong, Y.; Pan, C.; Wang, A. *Orthopedics* **2009**, *32*, 324–329.
162. Xiao, J.; Zhu, Y.; Liu, Y.; Zeng, Y.; Xu, F. *J. Biomed. Mater. Res. B* **2009**, *89B*, 543–550.
163. Jose, B.; Antoci, V., Jr.; Zeiger, A. R.; Wickstrom, E.; Hickok, N. J. *Chem. Biol.* **2005**, *12*, 1041–1048.
164. Lawson, M. C.; Hoth, K. C.; Deforest, C. A.; Bowman, C. N.; Anseth, K. S. *Clin. Orthop. Relat. Res.* **2010**, *468*, 2081–2091.
165. Parvizi, J.; Wickstrom, E.; Zeiger, A. R.; *et al. Clin. Orthop. Relat. Res.* **2004**, *429*, 33–38.

166. Dimitrijevic, N. M.; Rozhkova, E.; Rajh, T. *J. Am. Chem. Soc.* **2009**, *131*, 2893–2899.
167. Wach, J.-Y.; Malisova, B.; Bonazzi, S.; *et al*. *Chemistry* **2008**, *14*, 10579–10584.
168. Gawalt, E. S.; Avaltroni, M. J.; Danahy, M. P.; *et al*. *Langmuir* **2003**, *19*, 200–204.
169. Lee, M. H.; Brass, D. A.; Morris, R.; Composto, R. J.; Ducheyne, P. *Biomaterials* **2005**, *26*, 1721–1730.
170. Ketonis, C.; Parvizi, J.; Adams, C. S.; Shapiro, I. M.; Hickok, N. J. *Clin. Orthop. Relat. Res.* **2009**, *467*, 1678–1687.
171. Puleo, D. A. *J. Biomed. Mater. Res.* **1997**, *37*, 222–228.
172. Edupuganti, O. P.; Antoci, V., Jr.; King, S. B.; *et al*. *Bioorg. Med. Chem. Lett.* **2007**, *17*, 2692–2696.
173. Ketonis, C.; Barr, S.; Shapiro, I. M.; Parvizi, J.; Adam, S. A.; Hickok, N. J. *Bone* **2010**; doi:10.1016/j.bone.2010.10.171.
174. Antoci, V., Jr.; Adams, C. S.; Parvizi, J.; *et al*. *Biomaterials* **2008**, *29*, 4684–4690.
175. Antoci, V., Jr.; Adams, C. S.; Parvizi, J.; Ducheyne, P.; Shapiro, I. M.; Hickok, N. J. *Clin. Orthop. Relat. Res.* **2007**, *461*, 81–87.
176. Aumsuwan, N.; Mcconnell, M. S.; Urban, M. W. *Biomacromolecules* **2009**, *10*, 623–629.
177. Blanchemain, N.; Haulon, S.; Boschin, F.; *et al*. *Biomol. Eng.* **2007**, *24*, 149–153.
178. Dennes, T. J.; Schwartz, J. *J. Am. Chem. Soc.* **2009**, *131*, 3456–3457.
179. Narayan, R. J.; Adiga, S. P.; Pellin, M. J.; *et al*. *Philos. Transact. A Math. Phys. Eng. Sci.* **2010**, *368*, 2033–2064.
180. Walsh, T. R.; Howe, R. A. *Annu. Rev. Microbiol.* **2002**, *56*, 657–675.
181. Sharman, G. J.; Try, A. C.; Dancer, R. J.; Cho, Y. R.; Staroske, T. *J. Am. Chem. Soc.* **1997**, *119*, 12041–12047.
182. Boulos, L.; Prévost, M.; Barbeau, B.; Coallier, J.; Desjardins, R. *J. Microbiol. Methods* **1999**, *37*, 77–86.
183. Ketonis, C.; Barr, S.; Adams, C. S.; Hickok, N. J.; Parvizi, J. *Clin. Orthop. Relat. Res.* **2010**, *468*, 2113–2121.
184. Ketonis, C.; Barr, S.; Adams, C. S.; Shapiro, I. M.; Parvizi, J.; Hickok, N. J. *Antimicrob. Agents Chemother.* **2011**; doi:10.1128/AAC.00741-10.
185. De Lalla, F. *J. Chemother.* **2001**, *13*(S1), 48–53.
186. Pamp, S. J.; Sternberg, C.; Tolker-Nielsen, T. *Cytometry A* **2009**, *75*, 90–103.
187. Williams, I.; Paul, F.; Lloyd, D.; *et al*. *Microbiology* **1999**, *145*, 1325–1333.
188. Barth, E.; Myrvik, Q. M.; Wagner, W.; Gristina, A. G. *Biomaterials* **1989**, *10*, 325–328.
189. Trampuz, A.; Piper, K. E.; Jacobson, M. J.; *et al*. *N. Engl. J. Med.* **2007**, *16*, 654–663.
190. Walsh, C. T.; Fisher, S. L.; Park, I. S.; Prahalad, M.; Wu, Z. *ChemBiol* **1996**, *3*, 21–28.
191. Sykes, R. *J. Antimicrob. Chemother.* **2010**, *65*, 1842–1852.
192. Wimpenny, J. *Adv. Microbial. Physiol.* **2009**, *56*, 29–84.
193. Ellington, J. K.; Harris, M.; Hudson, M. C.; Vishin, S.; Webb, L. X.; Sherertz, R. *J. Orthop. Res.* **2006**, *24*, 87–93.
194. Diefenbeck, M.; Muckley, T.; Hofmann, G. O. *Injury* **2006**, *37*(S2), S95–S104.
195. Jiranek, W. *Orthopedics* **2005**, *28*(Suppl. 8), S873–S877.
196. Buttaro, M.; Comba, F.; Piccaluga, F. *Clin. Orthop. Relat. Res.* **2007**, *461*, 74–80.

4.418. Engineering Interfaces for Infection Immunity

J D Bryers and K A Woodrow, University of Washington, Seattle, WA, USA

© 2011 Elsevier Ltd. All rights reserved.

4.418.1.	**The Problem**	297
4.418.1.1.	Nosocomial Infections	297
4.418.1.2.	Current Anti-infective Biomaterials Strategies	297
4.418.1.3.	Bacterial Evasion of Host Immune Defenses	298
4.418.1.3.1.	Biofilm–immune cell interactions	298
4.418.1.4.	Thinking Outside the Cube	299
4.418.2.	**Innate and Adaptive Immune Responses**	300
4.418.2.1.	Immunology 101	300
4.418.2.2.	Innate Immune Responses to Biomaterials: 'Anger Management'	301
4.418.2.3.	Adaptive Immune Responses to Biomaterials: Biomaterial Vectors for Transfecting DCs	303
4.418.2.3.1.	Phenotype/characteristics of peripheral versus LN DCs	303
4.418.2.3.2.	Vaccine Adjuvant Design	304
4.418.2.3.3.	Biomaterial vectors for targeted antigen delivery *in vivo*	305
4.418.3.	**Engineering Infection Immunity**	306
4.418.3.1.	Enhanced Innate Response	306
4.418.3.2.	Biomaterials that Vaccinate	307
4.418.4.	**Concluding Remarks**	311
References		312

Glossary

Adaptive immune response It is composed of highly specialized, systemic cells and processes that eliminate or prevent pathogenic challenges. The adaptive immune response provides the vertebrate immune system with the ability to recognize and remember specific pathogens (to generate immunity), and to mount stronger attacks each time that specific pathogen is encountered.

Adjuvants A pharmacological or immunological agent that modifies the effect of other agents (e.g., drugs, vaccines) while having few if any direct effects when given by itself. Adjuvants are often included in vaccines to enhance the recipient's immune response to a supplied antigen.

Antibiotics Broad category of antimicrobial compounds that kill bacteria or inhibit their growth.

B cells Lymphocytes that make antibodies against antigens, perform the role of antigen-presenting cells (APCs), and develop into memory B cells after activation by antigen interaction.

Bacteriophage Any one of a number of viruses that infect bacteria.

Biofilms Adherent bacteria can secrete mostly insoluble gelatinous exopolymers that form a three-dimensional cell: polymer matrix known as a biofilm.

C3b C3b is the larger of two elements formed by the cleavage of complement component 3. C3b covalently bonds to microbial cell surfaces upon invasion of a host. This leads to the production of surface-bound C3 convertase and thus more C3b components. Bound C3b also aids in opsonization of the microbe preparing the microbe for phagocytosis.

Cathelicidins Antimicrobial peptide is a family of polypeptides found in lysosomes in macrophages and polymorphonuclear leukocytes (PMNs).

CD+4 T cell (Th 2 response) A subgroup of lymphocytes that are unusual in that they have no cytotoxic or phagocytic activity. CD4+ T cells are generally treated as having a predefined role as helper T cells within the immune system, although there are known rare exceptions.

CD+8 T cell (Th 1 response) A cytotoxic T cell (also known as TC, CTL, T-Killer cell, cytolytic T cell, CD8+ T cells, or killer T cell) belonging to a subgroup of T lymphocytes (a type of white blood cell) that are capable of inducing the death of infected somatic or tumor cells; they kill cells that are infected with viruses (or other pathogens), or are otherwise damaged or dysfunctional.

CpG Regions of DNA where a cytosine nucleotide occurs next to a guanine nucleotide in the linear sequence of bases along its length. Unmethylated CpG sites can be detected by Toll-like receptor 9 on dendritic cells and B cells in humans; this is used to detect intracellular viral, fungal, and bacterial pathogen DNA.

CR1 Erythrocyte complement receptor 1; in primates, CR1 serves as the main system for processing and clearance of complement opsonized immune complexes.

Cross-presentation (cross-priming) The ability of certain APCs to take up, process, and present extracellular antigens with MHC class I molecules to CD8+ T cells (cytotoxic T cells). Cross-priming describes the stimulation of naïve cytotoxic CD8+ T cells by this process.

DC-SIGN Dendritic cell-specific intercellular adhesion molecule-3-grabbing nonintegrin; DC-SIGN on macrophages recognizes and binds to mannose-type

carbohydrates commonly found on viruses, bacteria, and fungi.

DEC-205 A type I cell surface protein expressed primarily by dendritic cells (DC).

Defensins Small cysteine-rich cationic proteins found in both vertebrates and invertebrates; active against bacteria and fungi; consist of 18–45 amino acids including six to eight conserved cysteine residues.

Disinfectants Chemicals that kill microorganisms.

Endocytosis Process by which cells absorb molecules (such as proteins) by engulfing them.

F(ab′) Fragment antigen-binding (Fab fragment) is a region on an antibody that binds to antigens. It is composed of one constant and one variable domain of each of the heavy and the light chain.

Fc region Fragment crystallizable region (Fc region) is the tail region of an antibody that interacts with cell surface receptors called Fc receptors and some proteins of the complement system.

FimH Mannose-binding adhesin, FimH, component of the Type 1 pili produced by all members of the Enterobacteriaceae family.

Gingipains Extracellular cysteine proteinases of *Porphyromonas gingivalis* constitute the major virulence factor of this periodontopathogenic bacterium.
They are the product of three genes, two coding for an Arg-specific (RgpA and RgpB) and one for a Lys-specific proteinase (Kgp).

Granulocyte–macrophage colony-stimulating factor (GM-CSF) Stimulates stem cells to produce granulocytes (neutrophils, eosinophils, and basophils) and monocytes.

Histatins A group of electrophoretically distinct histidine-rich polypeptides with antimicrobial activity found in human parotid and submandibular gland secretions.

IL-1; IL-10 Fifteen different types of interleukin proteins are known, and they are designated numerically, IL-1 through IL-15.

Immunoglobulin G (IgG) IgG antibodies are large molecules of about 150 kDa composed of four peptide chains. It contains two identical heavy chains of about 50 kDa and two identical light chains of about 25 kDa, thus tetrameric quaternary structure.

Innate immune response Innate immune response comprises the cells and mechanisms that defend the host from infection by other organisms, in a *nonspecific* manner. This means that the cells of the innate system recognize and respond to pathogens in a generic way.

J774 macrophage-like cells An immortalized murine macrophage cell line that exhibits many of the responses of primary acquired macrophage.

Langerhans cells (LCs) Dendritic cells in the epidermis. LCs are normally present in lymph nodes and other organs, including the stratum spinosum layer of the epidermis.

M cells Microfold (M) cells located in the epithelium overlying follicles of the mucosa-associated lymphoid tissue.

Macrophage Phagocytic cells acting in both nonspecific defense (innate immunity) and in specific defense mechanisms (adaptive immunity) of vertebrate animals. Their role is to phagocytose (engulf and then digest) cellular debris and pathogens.

Macropinocytosis A form of endocytosis that accompanies cell surface ruffling. It is distinct in many ways from the better-characterized micropinocytosis, which includes clathrin-coated vesicle endocytosis and small uncoated vesicles. Because macropinosomes are relatively large, they provide an efficient route for nonselective endocytosis of solute macromolecules.

MHC-I Major histocompatibility complex (MHC) I; function of the MHC-I is thus to display to cytotoxic T cells (CTLs), the endogenous (from host cell) antigen fragments.

MHC-II MHC (major histocompatibility complex) class II; antigens presented by class II molecules are derived from extracellular, endogenous proteins.

MyD88 Myeloid differentiation primary response gene (88); a universal adapter protein as it is used by all TLRs (except TLR 3) to activate the transcription factor NF-κB.

Neutrophils A type of white blood cell, specifically a form of granulocyte, that help the cell to kill and digest microorganisms it has engulfed by phagocytosis. The neutrophil has a life span of about 3 days.

Nuclear factor kappa-light-chain-enhancer of activated B cells (NF-KB) A protein complex that controls the transcription of DNA.

Nosocomial infections Infections that are a result of treatment in a hospital or a health-care service unit. Infections are considered nosocomial if they first appear 48 h or more after hospital admission or within 30 days after discharge.

Opsonization An opsonin is any molecule that acts as a binding enhancer for the process of phagocytosis, for example, by coating the negatively charged molecules on the membrane.

OVA Ovalbumin is the main protein found in egg white, making up 60–65% of the total protein.

Phagocytosis Process in which phagocytes engulf and digest microorganisms and cellular debris.

PRRs Proteins expressed by cells of the innate immune system to identify pathogen-associated molecular patterns, or PAMPs, which are associated with microbial pathogens or cellular stress.

Quorum sensing A type of decision-making process used by decentralized groups to coordinate behavior. Many species of bacteria use quorum sensing to coordinate their gene expression according to the local density of their population.

RhII The opportunistic human pathogen *Pseudomonas aeruginosa* possesses two cell density-dependent genetic regulatory systems that control expression of a number of secreted virulence factors. These two systems, the *lasI–lasR* and *rhII–rhIR* gene pairs, are members of the *luxI–luxR* family of quorum-sensing signal generators and signal receptors. The *rhII* gene in *P. aeruginosa* encodes a 201-amino-acid protein that catalyses the synthesis of an autoinducer, butyrylhomoserine lactone.

T cells Belong to a group of white blood cells known as lymphocytes, and play a central role in cell-mediated immunity. They can be distinguished from other lymphocyte types, such as B cells and natural killer cells (NK cells), by the presence of a special receptor on their cell surface called T cell receptors (TCR).
TLRs A class of proteins that play a key role in the innate immune system. They are single, membrane-spanning, noncatalytic receptors that recognize structurally conserved molecules derived from microbes.
TNF-α A cytokine involved in systemic inflammation and is a member of a group of cytokines that stimulate the acute phase reaction.
Transforming growth factor beta (TGF-β) A protein that controls proliferation, cellular differentiation, and other functions in most cells.

Abbreviations

APCs	Antigen-presenting cells (e.g., macrophage, dendritic cells)
BiFPs	Bispecific fusion proteins; used as artificial opsonins
CF	Cystic fibrosis
CT	Cholera toxin
CTL	Cytotoxic T cell
DC	Dendritic cell
ECM	Extracellular matrix
FBGCs	Foreign body giant cells
FcR	Fc receptor on a APC
Lamp1	Lysosomal-associated membrane protein 1
LPS	Lipopolysaccharides
MALT	Mucosa-associated lymphoid tissue
MDP	Synthetic muramyl dipeptide
MPL	Monophosphoryl lipid A
PBMCs	Peripheral blood mononuclear cells
pDNA	Plasmid DNA
PLG	Poly(D,L-lactide-*co*-glycolide)
PLGA	poly(lactic acid-*co*-glycolic acid)
PMNs	Polymorphonuclear leukocytes

4.418.1. The Problem

4.418.1.1. Nosocomial Infections

Biofilms cause a significant amount of all human microbial infections and are particularly problematic in medical device infections. Nosocomial (hospital acquired) infections are the fifth leading cause of death in the United States with 2 million cases annually (or ~10% of American hospital patients) leading to more than $5 billion in added medical cost per annum.[1] About 60–70% of nosocomial infections are associated with some type of implanted medical device, and it is estimated that over 5 million such devices or implants are used per annum in the United States alone. Regardless of the sophistication of the biomedical implant (i.e., catheters vs. a three-dimensional (3D) stem cell-containing polymer scaffold), all medical devices or tissue engineering constructs are susceptible to microbial colonization and infection.[2,3]

Upon adhesion to a surface (inanimate material or tissue), replicating adherent bacteria can secrete mostly insoluble gelatinous exopolymers that form a 3D cell:polymer matrix known as a biofilm (Figure 1). From a medical perspective, both commensal and pathogenic microorganisms form biofilm-like conglomerates that are either associated with the epithelial or endothelial lining; embedded in the lung, intestinal, or vaginal mucus layer; attached to the teeth or medical implant surfaces, or formed intracellularly. Biofilm formation and persistence has profound implications for the patient because microorganisms growing as biofilms are significantly less susceptible to antibiotics and host defenses than are planktonic forms of the same microorganisms. Many biofilm infections are notoriously difficult to resolve and they commonly manifest as chronic or recurrent infections. Biofilm infections constitute a number of clinical challenges, including diseases involving uncultivable species, chronic inflammation, impaired wound healing, rapidly acquired antibiotic resistance, and the spread of infectious emboli.

On account of space constraints, we urge readers to explore the many excellent recent literature reviews of medical biofilms that are directed at such special topics as overall biofilm formation and infection,[4–8] biofilm diagnosis and treatment,[9] general survival strategies of infectious biofilms,[10,11] biofilm antibiotic/antimicrobial resistance,[12–14] quorum-sensing control of biofilm formation,[15–17] and biofilm issues related to specific infections, such as cystic fibrosis (CF),[18] osteomyelitis,[19,20] otitis media,[21,22] dental caries and oral infections,[23–26] and infection immunotherapy.[27]

4.418.1.2. Current Anti-infective Biomaterials Strategies

Since native immunity can be circumvented or compromised (by drugs or disease), the medical profession has naïvely attempted to eradicate biofilm-based infections by resorting to disinfectants and antibiotics. These are mostly synthetic compounds selected primarily for their ability to inactivate or kill *suspended* bacteria but exhibit little efficacy when applied to *biofilm* infections.[14,28] Biofilm-bound bacteria are significantly less susceptible to antibiotics and antimicrobial stressors than planktonic organisms of the same species.[14,29] Recent studies have shown that sublethal doses of antibiotics can actually enhance biofilm formation. Bagge *et al.*[30] report that genes coding for alginate biosynthesis were induced by exposure to the β-lactam antibiotic, imipenem. Exposure to subinhibitory concentrations of imipenem caused structural changes in the biofilm, for example, an increased biofilm mass and alginate polymer matrix. Increased levels of alginate matrix production may be an unintended adverse consequence of imipenem

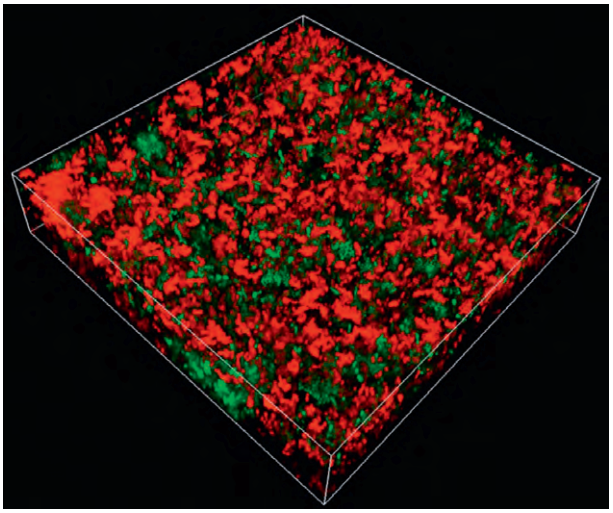

Figure 1 Three-dimensional reconstructed image of a binary culture biofilm collected by confocal laser scanning microscopy. Biofilm *z*-direction 'height' is 15–20 μm. The biofilm comprises the bacterial species, *Klebsiella pneumoniae* (green) and *Psedomonas aeruginosa* (red), which have been visualized using species-specific monoclonal antibody-conjugated quantum dots. Unlike traditional fluorochrome stains, quantum dot luminescence is photostable and size-tunable, allowing for multicolor emitted light from QDs of varying size all with a single excitation wavelength. Here, *K. pneumoniae* is labeled with monoclonal antibody conjugated to CdSe-core, ZnS-shell nanocrystals (green 560 nm emission maxima), and *P. aeruginosa* (red) monoclonal antibody conjugated to CdSe/ZnS nanocrystals (red 600 nm emission maxima).

treatment in CF patients. Similarly, Hoffman *et al.*[31] report that subinhibitory concentrations of aminoglycoside antibiotics (e.g., tobramycin) induced biofilm formation in *Pseudomonas aeruginosa* and *Escherichia coli*. Hoffman's results along with those of Bagge *et al.*, suggest that enhanced biofilm formation in the presence of antibiotics may be one universal defense mechanism of bacteria in avoiding the lethal effects of antibiotics.

The biomaterials community over the past 30 years has attempted to produce anti-infective devices or implants by either (1) designing device alternatives (liquid:air breaks, skin cuffs, antibiotic fills, all for indwelling catheters), (2) tethering anti-infective agents, bound directly to the surface of the material (silver coatings, tethered quaternary ammonium, synthetic antibiotics), or (3) releasing soluble toxic agents (chlorhexidine, antibiotics) into the adjacent surroundings. Mechanical design alternatives have had only marginal success and are applicable for short-term indwelling catheters. Tethered anti-infective agents are inhibitory only to the initial wave of incoming bacteria and provide little residual effects once layers of dead cells accumulate, which are also inflammatory. Finally, regardless of the type of 'drug-release' method used (passive vs. sustained or responsive control), release of a toxic agent from a biomaterial of a soluble anti-infective agent will inevitably stop once the entrapped agent is depleted. Further, as shown earlier, delivery of sublethal dosages of antibiotics can lead to accelerated biofilm formation and induced virulence factor expression.

4.418.1.3. Bacterial Evasion of Host Immune Defenses

The primary defense against infection is the innate immunity provided by neutrophils, macrophages, and dendritic cells (DCs) particularly by activating the complement system. The role of complement activation is to control infections by eliminating microorganisms by opsonization and then clearance from the bloodstream.[32] Components of the complement system also interact with B and T cells to coordinate the adaptive immune response by regulating antigen presentation, promoting the formation of specific antibodies, and maintaining immunological memory.[33,34] Complement evasion by many Gram-positive bacteria involves incorrect binding of complement recognition factors by bacterial cell wall proteins (protein A, G, M).[35] Gram-negative bacteria have also evolved secretory proteins that can degrade complement factors or their binding components, or that prove antichemotactic or toxic to immune cells. For example, *S. aureus* has the ability to thwart neutrophils and macrophages by (a) inhibiting chemotaxis (blocking formylated peptide recognition, blocking C5a binding, secreting leukotoxins, and blocking LFA1-ICAM1-mediated extravasation), (b) negating opsonization (via protein G binding IgG antibody molecules by way of their Fc segments, plasmin degradation of bound IgG and C3b, and blocking C3b binding), and (c) thwarting phagocytosis (cell wall modifications to resist low endosomal pH, enzymatic degradation of endosomes).[10] *Staphylococcus epidermidis*, another Gram-positive bacteria and the main species isolated in the majority of nosocomial infections, avoids the immune system through adhesion and biofilm formation.[36,37] Otto and coworkers[38] have documented that Gram-positive bacteria actually sense antimicrobial peptides released by neutrophils and macrophage and can coordinate a directed defensive response. They discovered an antimicrobial peptide sensor system that controls major specific resistance mechanisms; the sensor contains a classical two-component signal transducer and an unusual third protein, all of which are indispensable for signal transduction and antimicrobial peptide resistance.

Some pathogens obviate the immune response by specifically targeting C-type lectin receptors, particularly DC-specific ICAM-3-grabbing nonintegrins and mannose receptors, which benefits the pathogen by downregulating intracellular signaling, inhibiting maturation, and cytokine secretion.[39] For example, entry of the Gram-negative oral pathogen, *Porphyromonas gingivalis*, into monocyte-derived DCs *in vitro*, leads to suboptimal DC maturation. This process requires *P. gingivalis* to express the major fimbriae, FimA.[40,41] *P. gingivalis* also expresses unique immunosuppressive lipopolysaccharides (LPS)[42–44] and proteolytic gingipains.[45] The lipopolysaccharides of *P. gingivalis*, relative to those of *E. coli*, stimulate DCs to secrete IL-10, but not IL-12 *in vitro*[43] and *in vivo*.[44] These two factors (suboptimal DC maturation and truncated cytokine expression) lead to the induction of a Th2-effector response, which suggests that *P. gingivalis* may target DC C-type lectin receptors (e.g., DC-specific ICAM-3-grabbing nonintegrins) for entry, and for blunting DC maturation.

4.418.1.3.1. Biofilm–immune cell interactions

As indicated above, freely suspended microorganisms have evolved a multitude of ways to avoid the immune system.

One of these mechanisms is to form biofilms. Historically, there have been few studies that have focused on biofilm-bound bacterial cell interactions with the immune system, but this is changing.

For years, one explanation behind a biofilm's resistance to the immune system was that immune cells could not penetrate into the biofilm. However, Leid *et al.*[46] documented such penetration in an *in vitro* study with freshly isolated human leukocytes contacting 2-day-old (early, maturing) and 7-day-old (fully developed) *S. aureus* biofilms under static and flowing fluid conditions that mimic physiological shear. Leukocytes penetrated 7-day-old *S. aureus* biofilms under laminar-shear conditions but do not penetrate 2-day-old *S. aureus* biofilms grown under static conditions. Leukocytes produced a Th1-type response to both the 7-day-old shear and 2-day-old static *S. aureus* biofilms. That leukocytes were able to penetrate biofilms but unable to phagocytose bacteria suggests that other mechanisms may inhibit normal leukocyte function. Leid *et al.*[47] continued this investigation to report that the exopolysaccharide alginate matrix protects *P. aeruginosa* biofilm bacteria from interferon-γ (IFN-γ)-mediated leukocyte killing.

Jesaitis *et al.*[48] exposed *P. aeruginosa* biofilms to neutrophils and then measured *in vitro* oxygen consumption, cell morphology, and host defensive processes. They report that the consumption of oxygen increases in both the bacteria and neutrophils, but with little accumulation of H_2O_2 when leukocytes settled on established biofilm. Neutrophils did not exhibit significant motility or the characteristic polarized morphology of motile cells, but were still able to engage in phagocytosis while retaining a roughly spherical shape and modest membrane ruffling. However, bacteria exhibited increased oxygen consumption and initiated a detachment response that released a cloud of bacteria from the biofilm that eventually enveloped and obscured the settled neutrophils.

Walker *et al.*[49] report that human neutrophils may serve to enhance the initial development of *P. aeruginosa* biofilms. The mechanism of biofilm enhancement by neutrophils was attributed to neutrophil-generated polymers containing actin and DNA. The bacteria bind to F-actin and the free DNA promotes biofilm matrix stability. Disruption of the polymers with DNase results in dispersion of the bacteria and a reduction in biofilm development. The presence of these actin–DNA polymers, with colocalization of *P. aeruginosa*, was confirmed in both neutrophil lysates and CF sputum. Introduction of additional neutrophils after 24 and 48 h further enhanced *P. aeruginosa* biofilm development, while exposure to fewer neutrophils resulted in a lesser degree of biofilm enhancement.

Similarly, Chandra *et al.*[50] showed that peripheral blood mononuclear cells (PBMCs) enhanced the ability of the yeast, *Candida albicans*, to form biofilms and that the majority of PBMCs were localized to the basal and middle layers of the biofilm. They also found that only viable PBMCs enhanced *Candida* biofilm formation and that PBMCs cell surface components did not contribute to this biofilm enhancement; the biofilm-enhancing effect is mediated by a soluble factor released into the medium, and that the supernatant collected from cocultures contained differential levels of pro- and anti-inflammatory cytokines.

Zimmermann *et al.*[51] report that the quorum-sensing molecule *N*-(3-oxododecanoyl)-L-homoserine lactone (3OC12-HSL) synthesized by *P. aeruginosa* induces directed migration (chemotaxis) of neutrophils in an *in vitro* assay. They proposed that this early attraction of polymorphonuclear leukocytes (PMN) could contribute to prevention of biofilm formation, which may be an inaccurate conclusion. It could be possible that these bacterial signals are actually used by adherent bacteria to stimulate an immune cell response that enhances biofilm formation and virulence. In a mini-review, Wagner *et al.*[52] discusse the topic of communication between adherent bacteria and host immune cells. Wu *et al.*[53] demonstrate that IFN-γ binds to an outer membrane protein in *P. aeruginosa*, OprF, resulting in the expression of a quorum-sensing-dependent virulence determinant, the PA-I lectin. To determine whether IFN-γ induced PA-I by activation of the QS signaling system, they measured *rhlI* gene expression in response to IFN-γ. *rhlI* is the gene required for the synthesis of C4-HSL (C4-homoserine lactone), a core QS signaling molecule that plays a central role in the expression of PA-I. IFN-γ induced *rhlI* transcription in PAO1 and C4-HSL synthesis increased significantly after exposure to IFN-γ. Activation of the QS system by IFN-γ also led to the increase of pyocyanin production, which is another quorum-sensing-dependent virulence product. The results by Wu *et al.* and others[17] suggest that adherent bacteria not only actively sense but can also manipulate host immune response.[17,54]

Mittal *et al.*[55] reports that strains of *P. aeruginosa* vary in their ability to induce macrophage response, which affects the composition of secreted products (cytokines, chemokines). Concomitantly, these different compositions of macrophage-secreted products influenced overall biofilm formation and upregulated expression of a litany of virulence factors in a cytokine composition-dependent manner, again indicating the need to study macrophage response to biofilm not planktonic bacteria.

4.418.1.4. Thinking Outside the Cube

Most emerging alternatives to commercial antibiotics are still based upon some mechanism of killing or terminating the target bacteria, for example, bacteriophage,[56] bacteriophage lytic enzymes,[57] probiotics,[58,59] and human antimicrobial peptides such as defensins, cathelicidins, and histatins.[60] This 'kill' philosophy preordains the potential development of resistance in bacteria. An alternative approach is to develop therapies that specifically inhibit bacterial virulence or enhance immune response. Such 'antipathogenic' drugs, in contrast to antibacterial drugs, do not kill bacteria or stop their growth and are assumed not to select for resistant strains. The very elegant 'antivirulence' strategy seeks to inhibit regulatory systems that govern the expression of bacterial virulence phenotype such as antiadhesion therapy (passive antibody therapy[61,62] and synthetic peptide vaccine and antibody therapy[63]), inhibiting or negating cell–cell signaling[64] and upregulation of biofilm detachment promoters (rhamnolipids).[65]

Here, we highlight the prospects and remaining obstacles to generating both a short-term (innate) and a life-long (adaptive) infection immunity that originates from the biomedical device itself. Technologies described here could also have implications outside infection defense in the area of cancer immunotherapy, where current commercial techniques employ *ex vivo* transfection of DCs collected from patients by a tedious

apheresis protocol. Our approach of a surgical implant releasing *in vivo* transfection vectors could also dramatically improve cancer immunotherapy delivery (see Section 4.418.3).

4.418.2. Innate and Adaptive Immune Responses

4.418.2.1. Immunology 101

The immune system has evolved to protect the host from infection in two ways: *innate* and *adaptive* immunity. *Innate immunity* is the ability to produce a response within minutes or hours after infection through the recognition of molecules expressed by pathogens (e.g., bacterial cell wall components, bacterial nucleic acids, formylated peptides, and viral double-stranded RNA). Such molecules are recognized by specialized receptors on cells of the innate immune system, which include DCs, macrophages, neutrophils, natural killer cells, and γ–δ T cells. Binding of microbial components to innate immune cell receptors triggers signaling cascades within the cells that induce phagocytosis and the production of antimicrobial products (Figure 2). Phagocytes also produce growth factors that can regulate adaptive immune responses. While innate immune responses are immediate (and may induce cross-protective immunity[66]), they are typically short-lived.

Although macrophages can eliminate invading pathogens by phagocytosis and then present various antigens, macrophages are not potent activators of naïve T cells. In contrast, DCs are bone marrow-derived leukocytes that are specialized for the uptake and presentation of antigens to naïve T cells.[67–69] In fact, only one DC is required to activate 100–3000 naïve T cells.[70] DCs rapidly circulate the peripheral tissues in their 'immature' form but accumulate very rapidly at sites of injury, device implantation, or infection,[71] suggesting that circulating DC precursors are recruited in response to local inflammatory cues. Immature DCs – characterized by their high phagocytic activity and lack of surface costimulatory B.7 molecules (CD80, CD86)[72] – can capture exogenous antigens via several pathways; including macropinocytosis, receptor-mediated endocytosis, and phagocytosis of particles such as necrotic cell fragments and microbes.[71] DCs can be activated to mature DCs via several different signals (Figure 2), such as interaction with pathogen-related molecules (e.g., LPS), stimulation by cytokines in the local microenvironment (e.g., tumor necrosis factor (TNF), IL-1, IL-10, transforming growth factor beta (TGF-β)), and engagement of other receptors (e.g., mannose receptors, complement receptors).[71,72] Upon capture of antigen, DCs go through phenotypic changes in which their rate of antigen uptake briefly increases and then almost completely stops. DCs then morphologically change, downregulate expression of chemokine receptors responsible for the migration of other immune cell types to the inflammation site, and upregulate expression of receptors that mediate DC translocation to the lymph nodes (LNs). Surface expression by DCs of 'costimulatory' molecules is also upregulated. These costimulatory molecules are required for the activation of T cells, together with presentation of the antigen on major histocompatibility complexes (MHC) Class I and II, which are also upregulated upon 'maturation.' Once in the LNs, where most T cells reside, surface costimulatory and secreted cytokine signals communicate structural information about the antigen that was captured between the DC and T cell. T cells, specific to the peptide–MHC complex, will then proliferate into clones capable of either destroying a target cell that

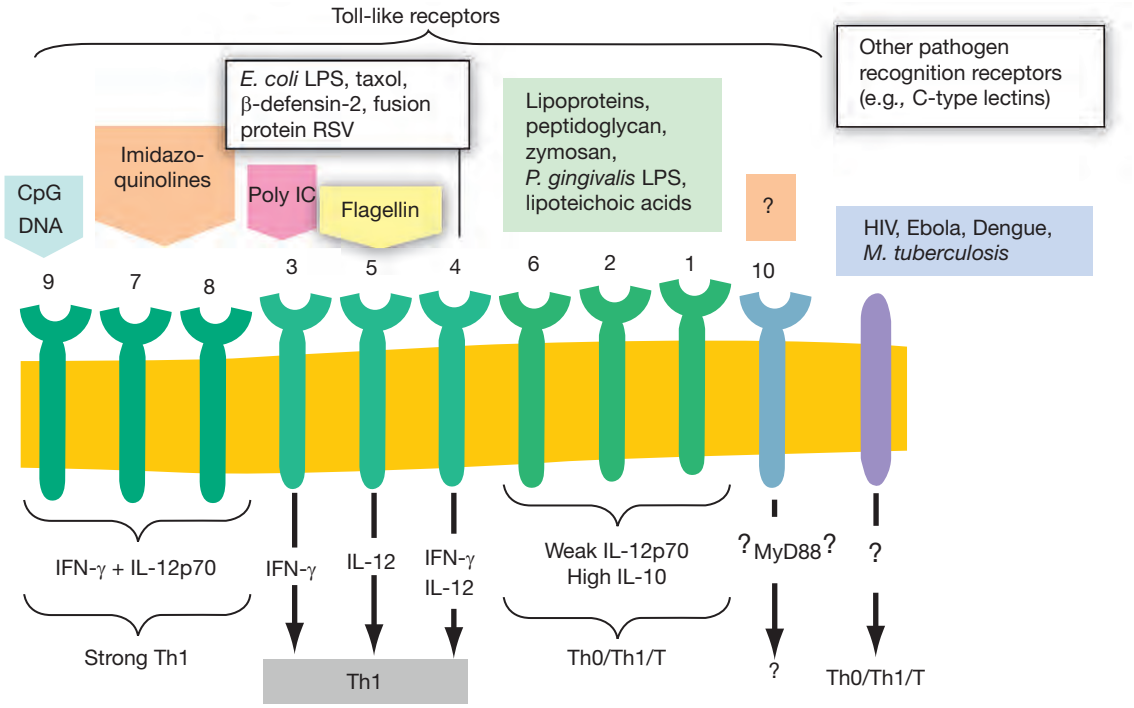

Figure 2 Triggering dendritic cell response through TOL-like receptors and other adaptor proteins results in distinctive dendritic response depending on signal and activated receptor. Adapted from Pulendran, B.; Kumar, P.; Cutler, C. W.; Mohamadzadeh, M.; Van Dyke, T.; Banchereau, J. *J. Immunol*. **2001**, *167*, 5067–5076.

expresses that same complex on its surface (CD8+ T cell) or, in the case of helper T cells (CD4+ Th), capable of secreting soluble signals to B and T cells that direct the immune response required. Cell signaling between lymphocytes can shift the immune response to either a cytotoxic cell-mediated response, called a Th1 response (characterized by secretion of cytokines such as IFN-γ, IL-2, and IL-12 along with IgG2a antibody) or to B cell secretion of antibody, called a Th2 response (characterized by secretion of IL-4 and IL-10 along with IgG1 antibody).

DCs choreograph the innate and adaptive immune systems in response to pathogen invasion. Although DCs and other antigen-presenting cells (APCs) traffic throughout almost every tissue in the body, the sites for strong immunosurveillance activity are concentrated primarily in epithelial and mucosal tissues.[73] These sites form the barriers to the outside world and are the portals of entry for many pathogens. When a pathogen breaches the skin or mucosal barrier, it encounters a phenotypically distinct population of immune cells in a physiological environment that is unique to the route of entry. Therefore, the site of initial antigen challenge sets the stage for the immune response in which DCs play a directing role. Resident DCs at these sites act as immunological sensors that receive signals from microbial components and their local cellular environment to activate and then regulate immunity. In the skin, Langerhans cells (LCs), other DCs, and macrophages are the first to respond to the danger signals and antigens presented by an invading pathogen. Secretion of chemokines attract other immune cells to the site of infection and activated APCs then migrate to draining LNs to condition the adaptive immune response. Most traditional vaccines that are delivered subcutaneously or intramuscularly target these first responders and the resulting immune response consists primarily of IgG antibody and central memory lymphocytes that are disseminated throughout the peripheral lymphatic organs.[74,75] In contrast, antigens presented in the airways, digestive tract, and vagina are collected by microfold (M) cells found in specialized mucosa-associated lymphoid tissues (MALT).[76] Priming the immune response by mucosal antigen delivery leads primarily to production of secretory IgA in mucosal secretions. Locally produced immunoglobulin M (IgM) and IgG, and mucosal cytotoxic T cell (CTLs) can also contribute significantly to mucosal immunity.[73,77] In general, systemic vaccination does not typically induce strong mucosal immunity.[73,78–80] Identifying the signals that promote DC development and function as educators of T and B lymphocytes will lead to improved vaccines and other immunotherapies. Understanding how to modulate the tropism and effectiveness of the adaptive immune response by antigen delivery and presentation to specific DC subsets is particularly important.

4.418.2.2. Innate Immune Responses to Biomaterials: 'Anger Management'

The host response to biomaterials follows a cascade of events initially similar to, but ultimately diverging from, normal wound healing. The initial injury (a wound or the implantation of a medical device) causes a perturbation of the homeostatic mechanisms, setting off the process of healing.[81] The classic view of the host response to biomaterials divides the response into several overlapping phases: blood–material interactions, acute inflammation, chronic inflammation, foreign body reaction, and fibrous encapsulation. The various different cell phenotypes participating in the immune and inflammatory host response are depicted in **Figure 3**.

Inflammatory cell recruitment requires enhanced leukocyte chemotaxis to the implant site, as well as leukocyte transmigration through the endothelium. Various molecular signals at the implant site can act as chemoattractants for the initial recruitment of inflammatory cells. Initial injury from the implantation procedure induces injured cells to release a variety of distress signals such as ATP, uric acid, and bioactive lipids. Activated platelets release several growth factors and activated mast cells likewise release various degranulation products (e.g., histamine, proteoglycans, proteases) and cytokines (e.g., TNF-α and interleukin IL-16).[82] Mast cells can also initiate the production of various other cytokines and chemokines, such as granulocyte–macrophage colony-stimulating factor (GM-CSF), IL-4, IL-6, IL-10, IL-13, macrophage inflammatory protein (MIP)-α, and monocyte chemotactic protein (MCP)-1. As leukocytes arrive at the site of injury, they, too, begin to produce various growth factors and cytokines that attract more inflammatory cells. MIP-1α and MCP-1 have been implicated in phagocyte chemotaxis toward the implant.[83]

Following their chemotaxis toward the medical implant and transmigration through the endothelium, leukocytes adhere to the implant surface and become activated to carry out their functions. Since neutrophils arriving first at the implant site are 'spent' within hours to less than a day,[84] the focus of most cell–biomaterial interaction studies has been the next incoming cell line, macrophages. Macrophages are widely considered the central cell type in directing and determining the outcome of the host response against implanted materials, because they are the predominant cell type found at the tissue–material interface in the later stages of the host response.[85] It is commonly hypothesized that host cells interact with surface-adsorbed proteins, rather than with the biomaterial surface itself.[86,87] Macrophage function is a dynamic process, which is dependent on the modulation of their activation states by either the changing local microenvironment[88,89] or by the macrophages themselves, as they release a wide variety of cytokines, extracellular matrix (ECM) proteins, and growth factors. Presence of adherent infecting bacteria can lead to a chronic inflammatory situation at the device interface. Chronic inflammation is associated with macrophages, lymphocytes, proliferation of connective tissues, deposition of matrix proteins, and capillary neogenesis.[90] Ultimately, macrophages may form foreign body giant cells (FBGCs) in an attempt to 'wall off' the implanted device leading to fibrous encapsulation by recruited fibroblasts.

Monocyte-derived macrophages are key mediators of the inflammatory response, as evidenced by changes in wound healing exhibited by animals with altered macrophages.[91,92] In the setting of inflammation, macrophages can be activated in a polarized manner by local factors such as cytokines and microbial organisms (for review, see Mantovani *et al.*[93] and Mosser[94]). The classic form of the activated macrophages (termed M1) is elicited by cytokines including IFN-γ and TNF, as well as by Gram-negative bacterial cell wall LPS. M1 macrophages generate large amounts of reactive oxygen species and inflammatory cytokines, all of which serve to augment killing of phagocytosed

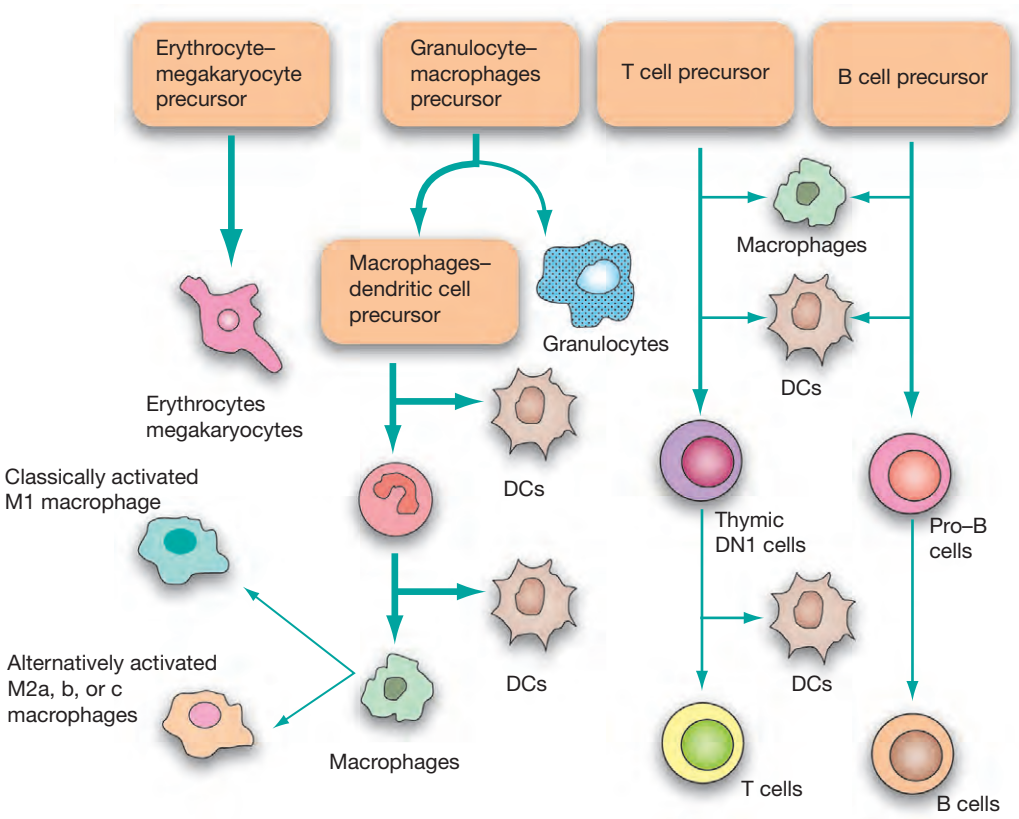

Figure 3 Phenotypes of cells comprising the immune system.

intracellular parasites and local cell-mediated immune response (the Th1 response). While M1 macrophages are critical for the early response to injury and infection, prolonged or aberrant activation of M1 macrophages can also result in undesired tissue destruction and chronic inflammation.

Designation of M2 macrophages is a broad category that encompasses macrophages activated in a manner different from the classic M1 macrophages, and includes macrophages activated by IL-4 and IL-10, immune complexes, and glucocorticoids.[95–97] M2 macrophages promote angiogenesis, tissue remodeling, parasite encapsulation, and can act as immunoregulators by suppressing the inflammatory response. M2 macrophages are generally characterized by low levels of IL-12 and IL-23 along with high levels of IL-10. M1 macrophages can be distinguished from M2 macrophages by the expression of distinct sets of chemokines and chemokine receptors.[97] Polarization of macrophages toward the M2 form can create an environment that is favorable toward wound healing, tissue regeneration, and implantable biomaterials. Consequently, the identification of pathways that can be modified to regulate macrophages polarization will be extremely beneficial for harnessing inflammation in pathologic states.

Wagner and Bryers[98] developed poly(ethylene glycol):poly (acrylate) PEG-*g*-PA copolymers (inherently nonfouling) covalently modified with either cell adhesion peptides (YRGDS, YRGES (negative control), or YEILDV) or F(ab′) fragments of monoclonal antibodies (Mabs) to monocyte integrin receptors (anti-VLA4, anti-β1, and anti-β2, anti-CD64) known to enhance macrophage adhesion and modulate inflammation activation. Monocyte adhesion, phagocytic response (oxidative burst), and cytokine expression were determined for each material. Monocyte/macrophages cytokine expression (TNF-α, IL-1β, IL-6, and IL-8) in response to control, base, and modified materials, was also determined. Tissue culture poly (styrene) (TCPS) mediated the greatest number of adherent monocytes. Both YRGDS and YEILDV peptides tethered to PEG-*g*-PA increased macrophage adhesion versus PEG-*g*-PA controls by a factor of two. However, F(ab′) fragments of all four antibodies promoted enhanced monocyte adhesion (7×) versus PEG-*g*-PA controls. Monocytes adhering to F(ab′) modified surfaces exhibited a lower oxidative burst without the addition of exogenous stimuli (LPS) versus peptide-modified surfaces. Cytokine expression and phagocytosis response by surface adherent macrophages to *S. epidermidis* and *P. aeruginosa* bacteria were also quantified on a per macrophages cell basis. Upon bacterial challenges, peptide-modified materials predisposed adherent macrophages to overexpressed proinflammatory cytokines and exhibited a significant immediate phagocytic response that diminished within 1 h. Conversely, bacterial challenge of materials modified by F(ab′)s exhibited 'per cell' cytokine expression levels that were significantly reduced compared to peptide-modified PEG-*g*-PA. Efficiency of adherent macrophages to ingest and kill both species was determined using radiolabeled and fluorescently labeled bacterial cell ingestion studies as a function of the PEG-*g*-PA surface modification. Macrophages adhering to F(ab′) modified

surfaces exhibited sustained enhanced phagocytic response (>3 h) and 3× higher bacterial killing efficiencies when compared with macrophages on peptide-modified materials.

The Wagner study indicates that signal molecules, either 'surface-decorated' on or 'released from' a biomaterial can directly influence macrophage inflammatory response and subsequent interactions with invading bacteria. In addition, this work may indicate that biomaterial signals could direct the local differentiation of monocytes into either M1- or M2-type macrophages.

4.418.2.3. Adaptive Immune Responses to Biomaterials: Biomaterial Vectors for Transfecting DCs

4.418.2.3.1. Phenotype/characteristics of peripheral versus LN DCs

DCs *in vivo* are present in peripheral tissues and secondary lymphoid organs (i.e., spleen, LNs), and also circulate within the blood. Within these compartments, DCs are composed of subsets with specialized functions and unique MHC class I or MHC class II processing capabilities. Particular DC subsets are dedicated to establishing protective responses against viral infections, whereas other subsets are involved in eliminating bacterial, fungal, and parasitic infections.[99] Priming of T and B cells also requires different DC subsets, as does the induction of immunity versus tolerance.[75] LCs are a DC subset populating mucosal-stratified squamous epithelium and skin epidermis, and overlie interstitial DC (intDC) present in the dermis.[100] LC and intDC are located ideally to capture pathogens that infect humans through the skin or mucosa, and bridge the innate and adaptive immune responses to tailor microbe-specific immunity. LC and intDC show different phenotypes and perform different biological functions. For example, they express distinct pathogen pattern-recognition receptors (PRRs) and exhibit different responses to chemokines. Epidermal LCs express CD1a, Langerin, and E-cadherin, whereas dermal intDCs express DC-SIGN, CD11b, factor XIIIa, and CD14.[101] It has been proposed that LCs preferentially induce cellular immunity, whereas intDCs more efficiently prime humoral immunity.[75] This is based on observations that LCs are particularly efficient at inducing cytotoxic high-avidity CD8+ T and induce CD4+ T polarization into Th1 and Th2 cells.[75] In contrast, intDCs are inefficient at priming CD8+ cells but rather secrete IL-6 and IL-12 to induce differentiation of naïve B cells into IgM-secreting plasma cells.[102] Dermal intDCs are also strong activators of naïve CD4+ T cells but polarize their development to help immunoglobulin production from B cells (Tfh).[103]

Sexually transmitted mucosal pathogens such as HIV, human papillomavirus (HPV), and herpes simplex virus (HSV) – all interact with LC during initial infection of the female genital tract but generate different immune responses depending on the antigens presented and the receptors involved. In human mucocutaneous herpes simplex, HSV infection is typically confined to the stratified squamous epithelium.[104] Langerin receptors on LCs are involved in initial HSV uptake; however, infected keratinoctyes also play a key role in the immune response by secreting specific chemokines, and cytokines proposed to cause apoptosis of infected LCs at the site of infection.[105,106] This outcome is thought to facilitate transfer of HSV antigens to other DC subtypes responsible for activation of HSV-specific CD8+ T cells in the draining LNs.[107] In the sexual transmission of HIV-1, cervicovaginal LCs also play an important but different role. For example, vaginal epidermal DCs express Langerin receptors that bind efficiently to HIV, but the virus largely bypasses this receptor in favor of alternative endocytic routes of LC entry.[108] The result is a distinct fate for the endoctyosed virion. Langerin receptors expressed by epidermal LCs can direct HIV-1 to Birbeck granules for degradation, but Langerin-independent LC entry may protect the virus by trafficking it to endocytic compartments where antigens are preserved for cross-penetration.[109] As a consequence, vaginal LCs migrating into the submucosa have been shown to transmit intact virions to CD4+ T cells,[110] and the *de novo* production of HIV-1 in infected LCs has also been proposed.[111] It is evident that the interaction between LCs and HSV or HIV-1 results in markedly different immune responses. Therefore, knowing the route of pathogen transmission and understanding the mechanisms underlying pathogen infection will lead to the development of novel immunotherapies based on targeting DCs.

Infectious diseases are caused by a broad array of pathogens with differing etiologies. Despite the formidable challenge this poses for vaccine development, pathogens share some commonalities that can be exploited to develop immunotherapies against many types of infections. For example, all viruses and some bacterial and protozoan pathogens are considered *obligate intracellular pathogens*. Therefore, activation of a cellular immune response that identifies and eliminates infected host cells is critical (i.e., MHC class I antigen presentation). However, targeting antigen delivery to DC subsets that will prime specific T cell immunity is a complex problem that requires antigen transport to DC-rich areas (e.g., site of biomedical device implantation, antigen binding to and uptake by DCs, and antigen processing and presentation. Antigen-loaded *ex vivo*-generated DCs and *in vivo* DC targeting are the two approaches being pursued for DC-based immunocancer therapies (e.g., Dendreon's Sipuleucel-T™). *Ex vivo* strategies consist of exposing immature DCs isolated from a patient's blood to specific antigens or other stimuli and then returning the maturated DCs to the donor. This approach has shown that DCs matured with a cocktail of proinflammatory cytokines can induce broad T cell immunity.[112–114] However, the high complexity associated with this procedure makes it economically prohibitive and will possibly prevent its impact on diseases of the developing world. In contrast to *ex vivo* strategies, novel approaches are being developed to target antigens directly to DCs *in vivo*. Multiple DC surface molecules have been identified and used for antigen internalization and processing by MHC I and MHC II pathways. Effective *in vivo* results have been observed using heat-shock proteins, pseudovirions, or protein antigens conjugated to DC-specific antibodies that can lead to DC activation. In the absence of DC activation, studies in mice have shown that antigen targeting to DCs induces tolerance.[115,116] Complete success of this strategy depends on overcoming biological delivery challenges and the weak immunogenicity of many antigens. These challenges are being addressed by biomaterial vectors, which are the next generation of immunotechnologies that target antigen delivery to DCs and are tailored to the specific immunopathology of the pathogen (see **Section 4.418.3**).

4.418.2.3.2. Vaccine Adjuvant Design

Adjuvants are molecules, compounds, or macromolecular formulations that boost the potency and longevity of specific immune response to antigens, but cause minimal toxicity or long-term immune effects themselves. Addition of adjuvants to a vaccine enhances and directs the immune cell response to the antigens, thus reducing the amount of antigen or number of immunizations required and improving the vaccine's efficacy. Traditional 'live vaccines' based on attenuated pathogen cells do not require the addition of adjuvants. Likewise, vaccines based on inactivated viruses or bacteria are often sufficiently immunogenic without added adjuvants, although some are formulated with adjuvants to further enhance the immune response. By contrast, current-generation vaccines increasingly consist of highly purified recombinant proteins or protein subunits, synthetic peptides, or plasmid DNA (pDNA). Such vaccines possess defined compositions and are less reactogenic, making them less toxic and safer but also poorly immunogenic compared to traditional vaccines.[117,118] Therefore, these new vaccines increasingly require a combination with adjuvants that can enhance the quality and magnitude of the adaptive immune response produced from using the specific antigen alone.

Adjuvants can be classified according to their component sources, physiochemical properties, or mechanisms of action. Two main classes of adjuvants commonly found in modern vaccines are the following: (1) *immunostimulants* that directly act on the immune cells to increase responses to antigens (e.g., Toll-like receptor (TLR) ligands, cytokines, saponins, and bacterial exotoxins) and (2) *vehicles* that present vaccine antigens to the immune system in an optimal manner, including controlled release and depot delivery systems to increase the specific immune response to the antigen, for example, mineral salts, emulsions, liposomes, virosomes (nanoparticles made of viral proteins such as influenza hemagglutinin and phospholipids), biodegradable polymer microspheres, and so-called immune-stimulating complexes (i.e., ISCOM™, ISCOMATRIX™). Vehicles can also serve to deliver the aforementioned immunostimulants.

To date and despite decades of research, aluminum-based mineral salts, collectively referred to as 'Alum,' are the only adjuvant approved for human use in the United States by the FDA.[119] Alum is classified among the first generation of adjuvants, which also includes emulsions (e.g., MF59 and Freud's adjuvant), polymeric particles, and liposomes.[120] These first-generation adjuvants are particulate-based and are naturally targeted for uptake by phagocytic macrophage and DCs, because their physical structure and dimensions closely mimic the size and geometry of pathogens. The primary mode of action of particulate adjuvants is to adsorb or encapsulate vaccine antigens to enhance persistency and improve delivery.[117,120] For example, antigens adsorbed onto alum exhibit enhanced stability and persist longer at the site of injection.[120] Alum and MF59 are good vaccine adjuvants for induction of antibody and TH2 responses.[118,121] However, as is the case with all first-generation particulate adjuvants, they only weakly stimulate antibody production to protein subunit antigens and are poor adjuvants for cell-mediated immunity.[122]

Second-generation adjuvants were developed 40–50 years after Alum and MF59. These adjuvants consist of more than one adjuvant component and arise from the addition of immunostimulants to first-generation adjuvants.[120] The most potent immunostimulants often take the form of pathogen-associated molecular patterns and include bacterial products (e.g., LPS), toxins (e.g., cholera toxin, CT), or bacterial nucleic acids (e.g., unmethylated bacterial CpG DNA). These specific immunostimulants induce DC maturation by binding to PRRs on DCs inducing the expression of the costimulatory molecules required to shape the adaptive immune response.[75,123] However, these natural pathogen-associated signals can lead to systemic inflammation and shock, and are considered too toxic for human clinical use.[124] Derivatives of natural immunostimulants, such as the synthetic muramyl dipeptide (MDP) and monophosphoryl lipid A (MPL), are less toxic and are showing promise in second-generation adjuvants. For example, the combination of alum with MPL is licensed in a significant number of countries for use as a vaccine component against HPV[125] and hepatitis B virus.[126] MPL is a TLR4 agonist and its addition to alum has been shown to increase antibody titers and to induce potent and focused T cell responses.[117,120,127] A multicomponent adjuvant that consists of two immunostimulants (MPL and QS21) combined with an oil-in-water emulsion has been shown to induce potent TH1 cellular immune responses and has promise for use as a malaria vaccine candidate.[128]

The components of an ideal adjuvant formulation will include immunostimulants to stimulate the innate immune system and provide the costimulatory signals that shape adaptive immunity, the antigen against which the adaptive immune responses are elicited, and a delivery system that can combine these two components at the place and time to elicit optimal stimulation. Biomaterials are an integral component to the design of these formulations because they can be engineered for localized and targeted delivery of antigens through specific intracellular pathways to control the presentation of antigens to key immune cells.[73] In addition, biomaterials can be designed to control the cytokine environment and influence how T cells perceive antigens.[73,74] Biomaterials that contain hydrophobic domains have been shown to exhibit natural adjuvant behavior.[124,129] For example, the adjuvant activity of block copolymers containing a higher proportion of hydrophobic poly(propylene glycol) compared to hydrophilic poly (ethylene glycol) improved antibody formation against BSA in mice.[130] The hydrophobic portions of these materials might function as danger signals that trigger activation of PRRs, in particular, TLRs. For example, TLR4 binds to a variety of ligands that possess hydrophobic domains such as LPS and bacterial fimbriae.[123,124] Hydrophobic biomaterials have also been shown to induce greater inflammatory responses.[74] In particular, micro- and nanoparticles formulated from biodegradable poly(lactic-*co*-glycolic acid) have been shown to cause lysosomal damage and activate the NAPL3 inflammasome, which stimulates caspase-1 activation and promotes secretion of proinflammatory cytokines.[131] These inflammatory responses are the first indication of pathogen invasion and lead to recruitment of cells to the sites of infections and coordination of systemic immune defenses.[132] Other groups have also demonstrated that the chemical composition of biomaterials can lead to DC maturation. Uto *et al.*[133] showed that γ-PGA nanoparticles induce DC maturation through MyD88-mediated NF-κβ and activation of the p38 MAPK pathways,

which is similar to LPS-mediated maturation of DCs. Poly (lactic acid-*co*-glycolic acid) (PLGA) microparticles and films have also been shown to promote maturation of bone marrow-derived DCs.[134,135] Yoshida and Babensee[136] directly compared DC maturation phenotype reporting that PLGA was a stronger stimulus of DC maturation than agarose, and this maturation was not affected by microparticle phagocytosis. However, agarose-treated DCs showed higher activation of NFκB 24 h after the initial stimulation of DCs.

Although the chemical composition of certain biomaterials may intrinsically provide adjuvant activity, encapsulation or presentation of immunostimulants within or conjugated to the surface of the biomaterials can provide stronger signals required to activate sustained immunity.[73,124] Codelivery of a tumor antigen with LPS or IFN-γ was shown to provide improved immunotherapy and lead to disease-free survival versus delivery of the antigen alone.[137] Other studies show that incorporation of synthetic analogs of bacterial and mycoplasmal lipoproteins within liposomes or conjugated to the surface of lipid vesicles provides highly potent immunoadjuvant activities by binding to TLRs and triggering cell activation and adaptive immune responses.[138,139] Demento *et al.*[140] showed that a recombinant envelope protein antigen incorporated into PLGA nanoparticles, with their surfaces modified with LPS, could provide protection from a lethal challenge from West Nile virus. Recent work by Ali and Mooney demonstrate the potential for designer vaccine and adjuvant formulation using biomaterials. Their work describes the use of porous poly(D,L-lactide-*co*-glycolide) (PLG) matrices engineered to incorporate a combination of inflammatory cytokines, immune potentiators, and antigens as an immunotherapy against large invasive tumors.[141,142] These PLG matrices were formed into discs and engineered to present CpG DNA and corelease both cytokines and tumor antigens. When implanted into tumor-bearing mice, the PLG constructs coordinated the response of multiple DC subtypes that led to a sustained and potent tumor-specific CD8+ CTLs response and inhibition of immunoregulatory pathways.[141] Finally, biomaterials can be engineered to selectively activate aspects of the complement system, which is a series of enzyme-signaling cascades that promote inflammation, macrophage phagocytosis, anaphylaxis, B cell maturation, and T cell responses, and can also enhance antigen presentation by follicular DCs present in lymphoid tissue.[33,129] Polyhydroxylated nanomaterials have been shown to activate LN-resident DCs in mice by stimulating the C3b component of the complement cascade.[129] Complement activation by nonspecific adsorption of complement proteins, antibodies, and opsonins onto polymer particles has also been shown to enhance phagocytosis by macrophages and monocytes.[143,144]

4.418.2.3.3. Biomaterial vectors for targeted antigen delivery in vivo

Biomaterials used commonly for drug delivery are experiencing a new role as antigen delivery vehicles. Drug delivery biomaterials have historically sought to minimize immunological interactions with materials. In contrast, biomaterials for immunotherapy exploit advantages of immunological properties of certain materials for designing new biomaterial vectors that induce specific and desired immune responses. Liposomes, micelles, and polymer micro- and nanoparticles are the commonly used platforms for the design of new DC-based vaccines and immunotherapies. These biomaterials are specifically designed to (1) protect the antigen against degradation before they reach DCs; (2) prolong antigen presentation to DCs by delivering effective and sustained doses; (3) traffic antigens intracellularly into MHC class I or II pathways to induce specific T cell responses; and (4) increase antigen targeting to stimulate LN or peripheral DC maturation. The biomaterial itself can also function as a synthetic adjuvant to enhance the immunogenicity of the delivered antigen. In general, biomaterial vectors provide protracted presentation of intact antigens to increase the opportunity for DC uptake and processing.

Immature DCs sample their antigenic environment and readily internalize exogenous solutes, particles, and necrotic or apoptotic cells by macropinocytosis, receptor-mediated endocytosis, and phagocytosis.[145] The mechanism for antigen uptake by DCs affects the subsequent processing of antigen through MHC class I or MHC class II pathways for presentation to CD8+ and CD4+ T cells, respectively. Cellular immunity is mediated primarily by CD8+ T cells, CD4+ Th1 cells, and natural killer T cells that recognize pathogen-derived antigens presented by MHC class I molecules or CD1-lipid antigen complexes.[74,75,146] However, most exogenous antigens are internalized within endosomes and are processed into the MHC class II pathway to stimulate CD4+ T cell humoral immunity. Cross-presentation, or the presentation of exogenous antigens on MHC class I molecules, is challenging and can limit the quality and magnitude of the cellular immune response achieved by DC-based vaccines. Cross-presentation pathways for antigen presentation by MHC class I molecules can also be exploited to elicit both CD4+ and CD8+ T cell immunity.[147] Therefore, many efforts have focused on enhancing cross-presentation of exogenous antigens delivered by biomaterial vectors. These methods include targeting DC subsets that actively cross-present antigen,[148] employing pH-responsive polymers that facilitate escape of antigens into the cytosol from the endosome,[149] and delivering pDNA encoding the expression of antigens that can be loaded onto MHC class I molecules for presentation.[150]

Several studies have confirmed that liposomes and polymer particles are readily internalized by DCs, and that the physicochemical and biochemical properties of the biomaterial can be altered to control DC uptake and presentation. For example, antigen molecules contained within liposomes coated with mannose are internalized to a greater extent by DCs via receptor-mediated endocytosis and induce a twofold higher proliferation of primed T cells compared to uncoated liposomes or free antigen.[151] Enhancing cellular immunity is improved by targeting specific DC surface receptors such as the C-type lectins DC-SIGN and DEC-205.[152–154] Mouse CD8α+ DCs uniquely express DEC-205 and are specialized to efficiently cross-present antigens via the MHC class I pathway.[147,155] Microparticles surface-modified with a DEC-205 targeting ligand show threefold enhanced uptake *in vivo* by CD8α+ DCs compared to control particles.[148] Inducing cellular immunity through the MHC class I pathway by delivering exogenous antigens formulated within particles can be challenging, since particles are often internalized initially within

endosomes that are then rapidly trafficked to lysosomes, where the particle and antigen can be degraded before being processed and presented. Or, the antigen is processed into the MHC class II pathway to stimulate CD4+ T cell humoral responses. Employing acid-degradable polymers to deliver oligonucleotide and peptide antigens has been shown to evade lysosomal trafficking by destabilization of endosomes and release of the antigens into the cytosolic compartment where they can be processed by the MHC class I pathway.[156–159] Release of DNA inside the cell cytosol of DCs has also been achieved with poly(ortho ester) microspheres and acid-degradable microparticles.[160] Gene delivery of antigen-encoding pDNA promotes processing and presentation by the MHC class I pathway, since gene products are naturally processed to the cytoplasm and endoplasmic reticulum. Therefore, biomaterial vectors that facilitate intracellular gene delivery can enhance the cellular immune response.

Biomaterial vectors have been designed primarily to target peripheral immature DCs, particularly LCs found in the epidermis. However, new approaches in biomaterial technology are being developed to target LN DCs. This has the advantage of avoiding premature antigen presentation by peripheral DCs that can lead to antigen tolerance.[161,162] To overcome the challenge of targeting peripheral DCs, biomaterial vectors are being designed to delay the intracellular bioavailability of their antigen load until DCs reach a LN. The stringency for DC-targeting specificity is also reduced because of the high tissue concentration of phagocytically active DCs present in LNs. Therefore, although the requirement for DC-targeting ligands, such as anti-Dec205, may be necessary to compensate for the low LC numbers in skin, these targeting ligands may not be needed to deliver antigens to LN DCs.[124] Targeting antigen delivery to microfold (M) cells located in the epithelium overlying follicles of the MALT is also an active area of biomaterials design for mucosal vaccines. For example, antigens targeted to M cells present at immune inductive sites located in the nasopharyngeal duct can elicit antigen-specific T and B lymphocyte responses in the respiratory and reproductive tissues by way of the common mucosal immune system.[76] A DNA vaccine against HIV glycoprotein gp160 conjugated to σ1 protein for M cell-targeting was delivered intranasally and effectively produced gp160-specific CTL responses in various mucosa-associated and systemic immune compartments.[163,164]

The targeting challenge then becomes designing biomaterial vectors small enough to be taken into lymphatic vessels and be retained in draining LNs. Several studies have examined the size-dependent trafficking of particles to the draining LNs. In a recent study by Manolova *et al.*,[165] 20–200 nm diameter particles readily migrated to the draining LNs after intradermal injection in mice. These particles were subsequently internalized by the LN-resident DCs. In contrast, the same study showed that LC present in the epidermis internalized 500–2000 nm-diameter particles. These trafficking patterns have consequences of the immune response, since CD8α+ DCs in the LNs more efficiently prime cellular immunity.

A final strategy has been to conjugate molecules to the particle surface that will preferentially interact with DCs. For example, liposomes have been coated with antibodies specific to DCs (e.g., anti-CD11c and anti-DEC-205), which improved DC uptake and resulted in immunity against the surrogate tumor antigen (OVA).[137,166] Similarly, mannose has been used to target receptor-mediated gene delivery to DCs; mannose was coupled to polyethylenimine DNA transfer complexes[167] and chitosan/DNA nanoparticles[168] to improve transfection.

4.418.3. Engineering Infection Immunity

4.418.3.1. Enhanced Innate Response

Opsonization is the process where microorganisms and inanimate colloids (e.g., liposomes, particulates) are coated with host-produced proteins and lipids (immunoglobulins, complement factors), facilitating the binding of the opsonized bacteria or particle to specific receptor molecules present on phagocytes (i.e., neutrophils, macrophage, DCs). IgG antibodies bind to their antigens on the surface of bacteria through coupling of the variable binding sites in the Fab region of the antibody, leaving the Fc region exposed. Phagocytes possess Fc γ receptors and therefore can bind to the Fc-coated bacteria or particles and internalize them. Complement fragment, C3b, also specifically binds to surface proteins or polysaccharides on microorganisms, thus mediating binding to C3b receptors on the phagocytes. Unfortunately, bacteria have evolved numerous ways to avoid opsonization by IgG and complement and thus avoid phagocytic elimination.

An alternative antibiofilm biomaterials defense is one where the biomaterial would release factors that enhance macrophage phagocytosis of bacteria. Currently, we are developing small molecules, called 'artificial opsonins,' that are designed to uniquely bind to both target bacteria and macrophage, thus enhancing phagocytosis. There are a number of reports of synthetically derived 'opsonins' enhancing bacterial phagocytic clearance.

Whitesides' group[169] describes the application of a bifunctional polyacrylamide molecule containing both vancomycin and fluorescein groups, which recognized the surfaces of four species of Gram-positive bacteria (*S. aureus*, *S. epidermidis*, *Streptococcus pneumoniae*, and *Enterococcus faecalis*). The vancomycin group binds to replicating bacterial cell wall component peptides terminated in D-Ala–D-Ala. Fluorescein groups allow for the imaging of the bound opsonin, plus the fluorescein group is recognized by antifluorescein Mabs, the Fc portion of which promotes binding to macrophage. Flow cytometry revealed that bifunctional polyacrylamide molecule-labeled *S. aureus* and *S. pneumoniae* were opsonized by antifluorescein Mabs 20-fold more than were untreated bacteria and promoted subsequent *in vitro* phagocytosis of *S. aureus* bacteria by cultured J774 macrophage-like cells ~twofold more efficiently than in control groups.

The Taylor group, in a series of elegant papers, reports the use of several different *bispecific fusion proteins* (BiFPs) that enhanced phagocytosis by macrophage of various pathogens, including *E. coli*,[170] *P. aeruginosa*,[171] and *S. aureus*.[172] In all cases, BiFPs consisted of (1) a molecule that recognizes a surface marker on the pathogen that was chemically coupled with (2) a Mab that is specific to the complement receptor 1 (CR1) present on primate erythrocytes. In *in vitro* and *in vivo* studies, a series of works from the Taylor group has shown that BiFPs promote binding of the target pathogen first to

circulating erythrocytes, which then enhances macrophage phagocytosis of the bacteria. BiFP-mediated phagocytosis did not apparently harm the erythrocyte, as verified in both *in vitro* and *in vivo* experiments.[170]

Kobayashi *et al.*[173] reports improved *in vivo* and *in vitro* phagocytosis of a periodontal pathogen, *P. gingivalis*, using a BiFP composed of two monoclonal antibody fragments; one against (a) the hemagglutinin domain of *P. gingivalis* (anti-r130k-HMGD antibody) and (b) the PMN FcαRI (CD89) receptor (FcR). The Kobayashi work selectively targeted Fc receptors that were dominant on PMNs collected from gingival crevicular fluid of chronic periodontitis patients versus Fc receptors dominant on peripheral blood PMNs. Data show that PMNs exhibited a higher capacity to phagocytose and kill *P. gingivalis* opsonized with the BiFP targeting *P. gingivalis* r130k-HMGD to leukocyte Fc RI as compared to opsonizing the bacteria with only the anti-r130k-HMGD antibody.

A novel biomedical device would thus release artificial opsonins upon implantation to exploit the surge in macrophage numbers at the site of injury, thus promoting a short-term enhanced innate immune response. The bacterial or macrophage recognition moieties forming the BiFP opsonin could be a variety of different molecules, including synthetic cell structure recognition molecules (vancomycin, lectins), complete poly- or monoclonal antibodies, $F(ab')_2$ or $F(ab')$ fragments of antibodies, genetically constructed diabodies, or surface structure recognizing aptamers. Note, however, that the aforementioned examples use entire Mabs or fragments of Mabs and are very specific to their target bacterium. Thus, multiple BiFPs would need to be generated to protect against mixed strain or species infections. Currently, we are developing a class of small molecules as the bacterial-recognition portion of BiFPs that would provide broad-spectrum protection against any Gram-positive species.

4.418.3.2. Biomaterials that Vaccinate

While artificial BiFP opsonins may enhance an innate short-term immune response against device-colonizing microbes, literature indicates that most indwelling biomedical devices are susceptible to infections sometimes decades after implantation (e.g., late-stage endocarditis of heart valves).

The goal of any vaccine is to produce a long-term protective immune response against a pathogen. For most bacteria, initial attachment to a eukaryotic cell surface or ligand-coated biomedical device leads to biofilm formation, and then upregulation of virulence factors leads to infection. Both an innate and an induced adaptive antibody response could prevent attachment and abrogate pathogen colonization. The ideal antigens to promote both levels of immune response would be the very surface proteins (i.e., bacterial 'adhesins') that mediate specific bacterial cell adhesion to ligands present on host tissue or device surfaces.[174] Given that bacterial-specific adhesion can trigger expression of many virulence factors leading to acute and chronic inflammation, a vaccine approach that effectively blocks bacterial adhesion would have multiple advantages.

Our research group is developing a biomaterial platform to engineer infection immunity by releasing in multiple waves, vaccines that have as antigen target those bacterial surface structures used for bacterial-specific adhesion. Recent research has greatly expanded the molecular details of the specific adhesin: ligand couples (Table 1) employed by Gram-positive bacteria (*S. epidermidis*, *S. aureus*, Group A and B *Streptococcus*, *E. faecalis*), Gram-negative bacteria (*P. aeruginosa*, *Klebsiella pneumoniae*, *P. gingivalis*, *E. coli*), and yeast (*Candida* spp.) to colonize and infect living tissue and implanted biomedical devices.[174] Thus, the concept of biomaterials designed to engineer infection immunity, targeting specific adhesins, could be applied to numerous situations. Many of these cell-bound molecules have served as antigens in vaccines that have been evaluated *in vivo* (Table 2) for their ability to prevent systemic infections.

There are essentially three ways to activate a DC to present antigen, with the subsequent immune response being dependent upon the form of the antigen (Figure 4): direct antigen presentation (e.g., whole attenuated pathogen, isolated antigen molecule, recombinant protein), DNA vaccine (i.e., pDNA encoding for the antigen protein), and mRNA vaccine (i.e., RNA encoding for the antigen protein). Exogenously acquired protein antigens are processed by late endosomes into MHC-II complexes that initiate CD+4 T cell activation and then activate B cell antibody secretion. Endogenously acquired antigen (e.g., viral infection; DNA/mRNA vaccine) is tagged with ubiquitin, then partially degraded in the proteosome, transported next to the endoplasmic recticulum, and presented on the DC's surface as a MHC-I complex, thus activating an immediate (but short-lived) cytotoxic CD8+ T cell response. In contrast to protein vaccines, DNA- or RNA-based vaccines can provide the ability to potentially generate both a strong CTL response and humoral response.

Upon internalization of a pDNA vaccine carrier by DCs, the carrier must escape endosomal entrapment or be degraded, the carrier must release the pDNA into the cytoplasm, and finally, the pDNA must be incorporated into the DC nucleus for expression. Subsequently expressed antigen can be processed as aforementioned into MHC-I complexes to initiate priming of CD8+ T cell, or the antigen can be secreted. The secreted antigen can be taken up exogenously by the same or other DCs and presented by the MHC-II pathway to CD4+ T cells, which can secrete soluble cytokine signals in T or to B cells to induce antibody secretion. In DCs, in a process known as 'cross-priming,' endogenously expressed antigen could be routed to the MHC-II complex.

DNA vaccines have certain advantages over protein antigens, including (a) DNA can serve as a natural adjuvant by including unmethylated CpG motifs; (b) by coding for multiple gene expression, DNA vaccines can also induce costimulatory molecules; (c) pDNA can target expression to certain cellular locations, thus fine-tuning the immune response; and (d) pDNAs allow the possibility of multiple antigen expression. Disadvantages of DNA vaccines include (a) incorporated CpG motifs can lead to overstimulation and toxicity;[192,193] (b) the required large amounts of highly characterized pDNA require processing with antibiotics and antibiotic-resistance markers; (c) pDNA contain sequences meant to control gene expression (e.g., promoters, polyA signals, introns) that may deregulate gene expression after integration into the genome; and (d) genome-incorporated pDNA can result in uncontrolled duration and strength of antigen expression.

RNA vaccines offer the same advantages as DNA vaccines versus protein antigens, but RNA vaccines have several added

Table 1 Potential targets for anti-infection immunotherapy

Microbial species	*Common venue of infection*	*Molecular target/role*	*Molecule (accession no.; Swiss-Prot. no.)*	*Molecule gene (GeneID; Locus Tag)*
Staphylococcus epidermidis	Cardiovascular biomaterials, intravascular catheters, vascular prostheses, pacemaker leads, defibrillator systems, prosthetic heart valves, and left ventricular assist devices	AltE and Aae; autolysins, mediate adhesion	YP-188221; Q5HQB9	GeneID: 3241348; SERP0636
		SdrG; fibronigen (FGN)-binding protein	YP-187803; Q5HRI6	GeneID: 3242987; SERP0207
		GehD; collagen-binding protein	YP-189935.1; Q5HKF8	GeneID: 3241026; SERP2388
	Ventriculoperitoneal cerebrospinal fluid shunts and continuous ambulatory Peritoneal dialysis	icaC; polysaccharide intercellular adhesin (PIA)	YP-189846.1; Q5HKP7	GeneID: 3242232; SERP2296
		Aap; accumulation association protein	YP-189945.1; Q5HKE8	GeneID: 3242404; SERP2398
Staphylococcus aureus	Cardiovascular biomaterials; contact lenses; intraocular lenses, breast implants, indwelling catheters; fracture-fixation devices, ventricular shunts, inflatable penile implants; orthopedic devices	SAR2040 autolysin	YP-041411.1; Q6GFB1	GeneID: 2861487; SAR2040
		fnbA and fnbB; fibronectin (FN) receptors	fnbA [YP-495075.1; Q2FE03] fnbB [YP-495074.1; Q2FE04]	fnbA [GeneID: 3913735; SAUSA300-2441] fnbB [GeneID: 3913823; SAUSA300-2440]
		SdrD, SdrE, SdrG; FGN-binding protein	YP-493249.1; Q2FJ79	GeneID: 3914310; SAUSA300-0546
		CnA; collagen-binding receptor	YP-042111.1; Q6GDB2	GeneID: 2859239; SAR2774
		Bap; biofilm-associated protein		
		icaC; polysaccharide intercellular adhesin (PIA)	YP-042088.1; Q6GDD5	GeneID: 2859657; SAR2750
Candida albicans	Catheters; hemodialysis grafts; peritoneal dialysis Catheters; VADs; penile implants	Ala5 adhesin	XM-712914.1 → XP-718007.1; Q5A8L3	GeneID: 3640334; CaO19.13158
Pseudomonas aeruginosa	Contact lenses; intraocular lenses; urinary catheters; orthopedic implants; tracheal lavage tubes	lecB fucose-binding lectin PA-IIL	NP-252051.1; Q9HYN5	GeneID: 882528; PA3361
		oprF, major porin and FN-binding protein	NP-250468.1; P13794	GeneID: 878442; PA1777
		Adhesin LapA	NEWENTRY 175	GeneID: 3760128; NEWENTRY 176
		Asialo GM1		
Enterococcus faecalis	Cardiovascular materials; cardiovascular devices; intravascular catheters; transjugular intrahepatic portosystemic shunt devices; urinary catheters	Collagen type 4 binding Ace	NEWENTRY	GeneID: 2828057
		Endocarditis- and biofilm-associated pilus (ebp) genes (ebpA,B, and C)	NP-814823.1; Q836L8	GeneID: 1199995; EF1093
		Sortase A (SrtA)	NP-816668.1; Q82ZJ9	GeneID: 1201902; EF3056
		Alt autolysin	NP-814543.1; P37710	GeneID: 1199693; EF0799
Porphyromonas gingivalis	Dental biomaterials	Arg-specific (RgPA) proteases	YP-001930085.1; B2RM93	GeneID: 6330747; PGN-1970
		Lys-specific (KgP) proteases	YP-001929844.1; B2RLK2	GeneID: 6330196; PGN-1728

Microbial cell surface molecules involved in cellular adhesion or adherent cell biofilm formation.

benefits versus DNA vaccines.[194] Owing to RNA's smaller size, a larger amount can be delivered per carrier, thus in general being more efficient. Since RNA does not require nuclear incorporation, expression of antigen in transfected cells occurs much faster than with pDNA. Potentially dangerous side effects are reduced, since eukaryotic promoters needed for pDNA are not present in RNA constructs. mRNAs are relatively easy to manufacture in high amounts, to purify to homogeneity, and to characterize. Finally, RNA does not persist in the organism, and RNA is not incorporated into the genome.

One main drawback of both DNA and RNA vaccines is that the efficiency of naked oligonucleotide transfection is very low (compared to viral systems) due to lack of protection from systemic nucleases, inability to migrate through cell membranes, or entrapment and degradation within endosomes. Consequently, nonviral gene constructs typically require some type of polymer delivery system. The reader is directed to a number of excellent reviews on the subject of polymer gene delivery.[195–199]

Currently, we are developing a platform of polymer constructs that would release condensed RNA vaccines meant to transfect DCs arriving upon implantation of a biomedical device. Our polymer constructs will release nanoparticles of condensed DNA or mRNA vaccine that will target a selected adhesion protein employed by the microorganism to initiate colonization. Such targets could be the fibronectin-binding

Table 2 Existing vaccines that target microbial adhesin or biofilm formation virulence factors (**Table 1**)

Microbial species	*Antigen selected*	*Results*	*References*
Staphylococcus aureus	Immunization with four antigens (iron-regulated surface determinant protein = IsdA, iron-regulated heme-iron binding protein = IsdB, SdrD, and SdrE)	In contrast to individual protein antigens, immunization with the combined vaccine afforded complete protection against a lethal challenge with *S. aureus* Newman. Survival analysis revealed that the combined vaccine afforded significant protection against lethal challenge (10^9 cfu ml^{-1}) with any one of the five clinical *S. aureus* isolates	177
	Collagen-binding protein (CNA); CNA-based DNA vaccine	Vaccine produced hi titer (64 000) antibody and evidence of a cell-mediated immune response (CMI). The anti-CNA antibodies recognized intact bacteria and prevented binding to collagen *in vitro*. However, the vaccination did not protect against bacterial challenge using the intraperitoneal route of infection	178
	Multivalent polyprotein DNA vaccine; vaccines expressed clumping factor A (ClfA), fibronectin-binding protein A (fnbA), and the enzyme Sortase (Srt) as single proteins or combined as a polyprotein	All animals produced mixed Th1 and Th2 response including functional antigen-specific, mostly IgG2a antibodies, sustained production of IFN-γ, and a predominantly CD8+ T cell response. Upon virulent *S. aureus* isolate challenge, after 21 days, 55% of the multigene vaccinated mice survived infection compared to only 15% of control groups	179
	Four adhesion factors (fibrinogen-binding protein-SdrD), fnbA, clumping factor A-ClfA, and collagen adhesin-CnA as targets in a DNA vaccine	Intranasal immunization with a pDNA mixture coding the four adhesins, triggered significant levels of specific serum and mucosal Ig that inhibited *S. aureus* adhesion to cow mammary gland epithelial cells *in vitro*. Splenocytes of immunized mice challenged *in vitro* with *S. aureus* extracts showed a strong proliferative response. Finally, immunized mice were significantly protected against intramammary challenge with *S. aureus*	180
	Aurexis® (tefibazumab), a humanized monoclonal antibody anti- to clumping factor A, ClfA	Preclinical *in vivo* testing revealed that a single administration of Aurexis® significantly protected against an IV Challenge with a methicillin-resistant *S. aureus* (MRSA) strain in murine septicemia and rabbit-infective endocarditis (IE) models	181
	Surface polysaccharide poly-*N*-acetyl-β-(1-6)-glucosamine (PNAG) and a deacetylated form of the antigen (dPNAG; 15% acetylation) were conjugated to the carrier protein diphtheria toxoid (DT) and used to immunize animals	Immunization of animals with a conjugate vaccine of dPNAG elicit antibodies that mediated opsonic killing and protected against *S. aureus* infection	182
Staphylococcus epidermidis	mAbs against Aap and against surface-exposed lipoteichoic acid (LTA) were used for passive immunization of mice	Neither anti-Aap nor anti-LTA mAbs showed protection *in vivo*, although *in vitro*, anti-Aap, and anti-LTA did show binding to *S. epidermidis*	183
	Active immunization (AI) using a major immunogenic polysaccharide determinant of slime (20-kDa PS) as antigen, and passive immunization (PI) after administration of specific antibodies toward 20-kDa PS	Clinical grading showed that both AI and PI rabbits had a significantly less corneal damage as compared with infected nontreated rabbits	184
Enterococcus faecalis	Enterococcal aggregation substance (AS) is a large (137-kDa) surface-expressed protein encoded by pheromone-responsive, conjugative plasmids	Antibodies specific for AS were opsonic for *E. faecalis* expressing AS *in vitro*. New Zealand White rabbits immunized with AS were challenged intravenously with *E. faecalis* cells constitutively expressing AS in the rabbit model of experimental endocarditis. Highly immune animals did not show significant differences in clearance of organisms in comparison with nonimmune animals	185
Porphyromonas gingivalis	Immunized BALB/c mice with rgpA DNA vaccine via the abdomen with a Gene Gun or via the nasal cavity weekly for 6 weeks	Immunization elicited IgG responses against *P. gingivalis* in both groups. Nasal immunization also induced sIgA against *P. gingivalis*, although Gene Gun immunization did not. Reduction of alveolar bone loss was observed in both groups at 42 days following initial infection	186

(*Continued*)

Table 2 (Continued)

Microbial species	*Antigen selected*	*Results*	*References*
	An unnamed 40-kDa outer membrane protein of *P. gingivalis* (40-kDa OMP) was nasally administered with a nontoxic chimeric adjuvant (combination of A subunit of mutant cholera) Toxin and pentameric B subunit of heat-labile enterotoxin *E. coli*	Mice given nasal OMP adjuvant showed a significant reduction of alveolar bone loss caused by oral infection with *P. gingivalis* even 1 year after the immunization compared to unimmunized mice	187
	The ability of eight recombinant protein fragments corresponding to domains/regions of the RgpA–Kgp proteinase–adhesin complex to attenuate *P. gingivalis* infection, when used as a vaccine, in the murine lesion model was determined	The A1 adhesin portions of either the RgpA or Kgp complexes gave the best protection. Immunization with catalytic portions of the RgpA–Kgp proteinase–adhesin complex had no effect on *P. gingivalis* infection	188
Porphyromonas gingivalis	IgG generated by immunization with plasmids encoding for either the catalytic domain of Kgp or Arg-gingipain (Rgp) used to vaccinate mice	Immunized mice were challenged by intraperitoneal inoculation with *P. gingivalis*. All nonimmunized mice died within 72 h. Vaccination with either pDNA prevented inflammatory responses and prolonged the survival rate of immunized mice by 43 and 27%, respectively	189
	RgpA–Kgp complex and synthetic ABM and proteinase active site peptides conjugated to diphtheria toxoid	Protected against *P. gingivalis* induced periodontal bone loss in a murine periodontitis model. When RgpA–Kgp complexes or active site peptides are used as a vaccine, they induce a Th2 response that blocks function of the RgpA–Kgp complex	190
Pseudomonas aeruginosa	Compared the formation of antibodies in lower airways induced by systemic and mucosal vaccination strategies. Immunized 48 volunteers in six vaccination groups with either a systemic, a nasal, or four newly constructed oral live vaccines based on attenuated live *Salmonella* strains, followed by a systemic booster vaccination. All vaccines were based on a recombinant fusion protein of the highly conserved *P. aeruginosa* outer membrane proteins OprF and OprI as antigen	While systemic and mucosal vaccines induced a comparable rise of serum antibody titers, a significant rise of IgA and IgG antibodies in the lower airways was noted only after nasal and oral vaccinations	191

receptors on *S. aureus* used to bind to surface-immobilized fibronectin; cell surface Arg-specific (RgpA) and Lys-specific (Kgp) proteinases (designated the RgpA–Kgp complex) used by the oral pathogen, *P. gingivalis*, the major cause of chronic periodontitis; Group B *Streptococcus* to immobilized fibronectin; *Steptococcus mutans* and *S. sangiuns* to mucin-coated dental devices; *P. aeruginosa* binding to a G4 glycolipid on cornea and contact lenses; or *E. coli* FimH binding to mannose-coated catheters.

One distinct advantage of nucleotide transfection of DCs (vs. direct antigen protein) is that one can modify the DNA or mRNA with targeting signals to better control MHC class I and class II presentation. For example, incorporation of ubiquitin mRNA with the target antigen will result in an enhanced formation of peptides for MHC class I presentation,[200–202] whereas targeting sequences from the invariant chain (Ii) or lysosome-associated membrane protein (Lamp1) will lead to presentation of the antigen in the context of both MHC class I and class II, thus providing antigen-specific help.[203–206] Currently, we are developing mRNA vaccines against the *S. epidermidis* fibronectin-binding receptors used to colonize fibronectin-coated cardiovascular devices. *S. epidermidis* upregulate these fibronectin-binding receptors once exposed to serum at high shear stresses, which distinguishes infecting strains from benign *S. epidermidis* skin flora.

One might ask "Why transfect DCs from the medical device rather than simply vaccinate the patient prior to implantation?" Why not vaccinate patients systemically with antigen or mRNA vaccines coupled with a proven adjuvant? As reported previously, most systemic vaccine formulations consist of the antigen or a nucleotide molecule destined to express the antigen plus an adjuvant concoction meant to stimulate and heighten immune response. Typically, vaccine formulations seek to capitalize on immune cell phagocytosis by employing adjuvants in particulate form with or without additional immunostimulants. Even proven vaccine adjuvant formulations require multiple doses to achieve protective immunity.

Circumstantial evidence is emerging that biomedical implants may serve as the ideal vaccine adjuvant when designed properly. Classical vaccine/adjuvant combinations are notoriously inefficient at transfecting DCs. While the injection of naked pDNA in mice can induce an immune response, including the generation of antibodies and CTLs, high doses of DNA were needed to reach protective titers. Adjuvants have reduced the required DNA dose, but their design is mostly art. Only recently, because of the needs of cancer immunotherapies, has the biomaterials/gene delivery community begun to develop new strategies for adjuvant engineering. Bennewitz and Babensee[207] incorporated a model protein

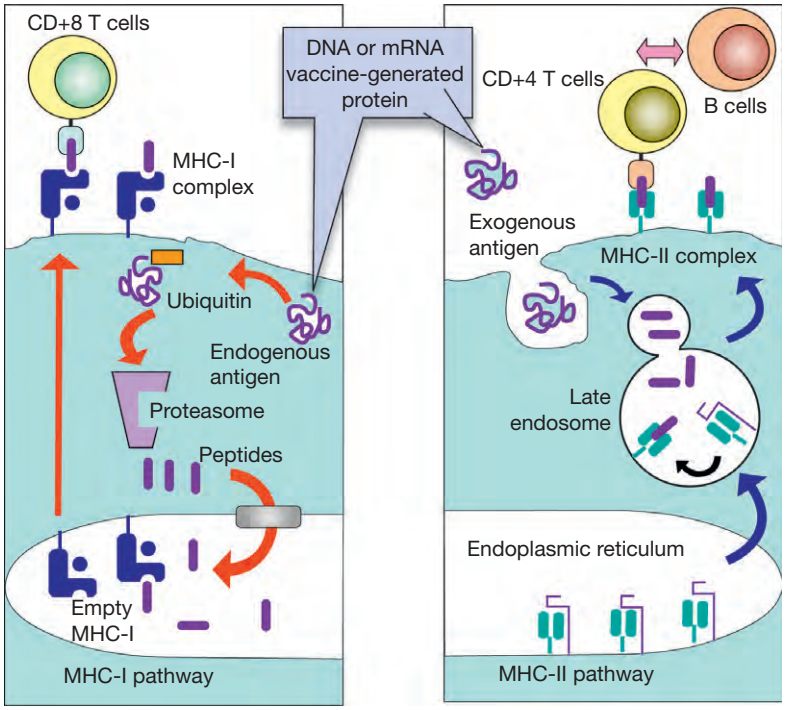

Figure 4 Antigen presentation and pathways of vaccine response. Plasmid DNA or mRNA is taken up by dendritic cells for intracellular expression of antigen. Antigen can be secreted (not shown) and subsequently taken up by other DCs as an exogenous antigen. Antigen expressed intracellularly by a dendritic cell or taken up through cross-priming is presented by MHC-I to CD8+ T cells (cytotoxic leukocytes; CTLs). Antigen taken in exogenously or directed by DNA or mRNA trafficking signals are processed by the MHC-II pathway and presented to CD4+ TH cells, which can subsequently secrete soluble cytokine signals (e.g., IL-12) back to the dendritic cell, proliferative signals (e.g., IL-2 and IFN-γ) to Tc cells, or signals directed toward B cells (e.g., IL-4) to induce B cell proliferation and antibody secretion.

antigen ovalbumin (OVA) into PLGA carriers; carriers were either microparticles (diameter = 3.5 μm) or porous scaffolds (0.7 cm dia. × 0.2 cm thick discs; pores ~400 μm). Carriers with antigen were then injected (particles) or surgically implanted (scaffolds) into mice and the resulting systemic humoral immune response to the released OVA was assessed by following the OVA-specific IgG concentration and isotypes. The total amount of polymer and antigen delivered was kept constant, as well as the antigen release rates. Humoral immune response was higher and sustained for antigen released from implanted scaffolds with associated tissue damage but was lower and transient when the same amount of polymer/antigen was delivered by particles, which were minimally invasively delivered by injection. Results implicate 'danger signals' associated with the implantation of the scaffolds because of tissue injury, and may prime the system for an enhanced immune response. Localized DC cell counts reported were significantly higher around the surgically implanted scaffolds versus particle injections.

Ali *et al.*[141,142] developed porous poly[lactide-*co*-glycolide] polymeric scaffolds to first release a cytokine (GM-CSF) to recruit and house host DCs, and subsequently present cancer antigens (melanoma tumor lysates) and danger signals (bacterial CpG oligonucleotide sequences) to activate the resident DCs and markedly enhance their homing to LNs. The ability of the scaffolds to recruit DCs and program an immune response was evaluated *in vivo* in a murine melanoma tumor model. The vaccine provided significant protection, with the level of protection correlating with CpG dose. Animal survival increased from 23 to 50% and 90% at CpG doses of 0, 10, and 100 μg, respectively. Scaffolds presenting CpG-ODN with antigen alone resulted in only a 20% survival, indicating the benefit of recruiting DCs with GM-CSF. The failure of vaccine formulations consisting of bolus systemic injections of antigen, CpG-ODN, with and without 3000 ng of GM-CSF, demonstrated the benefit of the scaffold, providing a local residence for recruited DCs while they are programmed with CpG. Similar to the work of Bennewitz and Babensee[207] earlier, injecting GM-CSF-loaded PLG nonporous microspheres that provided sustained GM-CSF delivery but not porous structure to provide a residence for recruited cells, with bolus injections of CpG-ODN and tumor lysate, resulted in little immune protection, and animals did not survive past 35 days.

4.418.4. Concluding Remarks

As engineered biomaterials and tissue regenerative medicine advance, an increasing portion of the population will receive one or multiple biomedical devices, ranging from disposable contact lenses, dental implants, orthopedic implants, and vascular grafts to tissue-engineered livers, small-diameter vascular grafts that promote stem cells differentiation into endothelial cells, and a polymer transfection system that delivers microRNA knockout therapy to control chronic inflammation. Current biomaterials approaches to prevent infections of such

implants will do little to reduce the current nosocomial infection epidemic, thus seriously compromising the use of the advanced devices and tissue constructs currently under development. Newer approaches are required to prevent device-based infections; approaches that, like tissue engineering, direct the human immune system against biofilm-forming microorganisms with biologically specific programming.

Here, we have highlighted the prospects and remaining obstacles to generating both a short-term (innate) and a lifelong (adaptive) host infection immunity that originates from the biomedical device itself. Technologies described here could also have implications outside infection defense; in the areas of vaccine delivery or cancer immunotherapy.

References

1. Wenzel, R. P. *Clin. Infect. Dis.* **2007**, *45*(Suppl. 1), S85–S88.
2. Bryers, J. D.; Ratner, B. D. *ASM News* **2004**, *70*, 232–237.
3. Castelli, P.; Caronno, R.; Ferrarese, S.; *et al. Surg. Infect.* **2006**, *7*(Suppl. 2), s45–s47.
4. Donlan, R. M. *Emerg. Infect. Dis.* **2002**, *8*(9), 881–890.
5. Hall-Stoodley, L.; Costerton, J. W.; Stoodley, P. *Nat. Rev. Microbiol.* **2004**, *2*(2), 95–108.
6. Hall-Stoodley, L.; Stoodley, P. *Trends Microbiol.* **2005**, *13*(1), 7–10.
7. Parsek, M. R.; Singh, P. K. *Annu. Rev. Microbiol.* **2003**, *57*, 677–701.
8. Reisner, A.; Høiby, N.; Tolker-Nielsen, T.; Molin, S. *Contrib. Microbiol.* **2005**, *12*, 114–131.
9. Fux, C. A.; Stoodley, P.; Hall-Stoodley, L.; Costerton, J. W. *Expert Rev. Anti Infect. Ther.* **2003**, *1*(4), 667–683.
10. Foster, T. J. *Nat. Rev. Microbiol.* **2005**, *3*, 948–958.
11. Fux, C. A.; Cost-a-ton, J. W.; Stewart, P. S.; Stoodley, P. *Trends Microbiol.* **2005**, *13*(1), 34–40.
12. Döring, G.; Conway, S. P.; Heijerman, H. G.; *et al. Eur. Respir. J.* **2000**, *16*(4), 749–767.
13. Mah, T. F.; O'Toole, G. A. *Trends Microbiol.* **2001**, *9*(1), 34–39.
14. Stewart, P. S. *Int. J. Med. Microbiol.* **2002**, *292*, 107–113.
15. Bjarnsholt, T.; Givskov, M. *Philos. Trans. R. Soc. Lond. B Biol. Sci.* **2007**, *362*(1483), 1213–1222.
16. Harraghy, N.; Kerdudou, S.; Herrmann, M. *Anal. Bioanal. Chem.* **2007**, *387*(2), 437–444.
17. Smith, R. S.; Iglewski, B. H. *Curr. Opin. Microbiol.* **2003**, *6*(1), 56–60.
18. Høiby, N. *J. Cyst. Fibros.* **2002**, *1*(4), 249–254.
19. Brady, R. A.; Leid, J. G.; Calhoun, J. H.; Costerton, J. W.; Shirtliff, M. E. *FEMS Immunol. Med. Microbiol.* **2007**, *52*(1), 13–22.
20. Wagner, C.; Obst, U.; Hänsch, G. M. *Int. J. Artif. Organs* **2005**, *28*(11), 1172–1180.
21. Bakaletz, L. O. *Pediatr Infect. Dis. J.* **2007**, *26*(Suppl. 10), S17–S19.
22. Post, J. C.; Hiller, N. L.; Nistico, L.; Stoodley, P.; Ehrlich, G. D. *Curr. Opin. Otolaryngol. Head Neck Surg.* **2007**, *15*(5), 347–351.
23. Bryers, J. D.; Ratner, B. D. *BMC Oral Health* **2006**, *6*(Suppl. 1), S15.
24. Offenbacher, S.; Barros, S. P.; Singer, R. E.; Moss, K.; Williams, R. C.; Beck, J. D. *J. Periodontol.* **2007**, *78*(10), 1911–1925.
25. Selwitz, R. H.; Ismail, A. I.; Pitts, N. B. *Lancet* **2007**, *369*(9555), 51–59.
26. Slayton, R. L.; Bryers, J. D.; Milgrom, P. *BMC Oral Health* **2006**, *6*(Suppl. 1), S1.
27. Otto, M. *BioDrugs* **2008**, *22*(1), 27–36.
28. Stewart, P. S.; Costerton, J. W. *Lancet* **2001**, *358*, 135–138.
29. Gilbert, P.; Allison, D. G.; McBain, A. J. *J. Appl. Microbiol.* **2002**, *92*(Suppl.), 98S–110S.
30. Bagge, N.; Schuster, M.; Hentzer, M.; *et al. Antimicrob. Agents Chemother.* **2004**, *48*(4), 1175–1187.
31. Hoffman, L. R.; D'Argenio, D. A.; MacCoss, M. J.; Zhang, Z.; Jones, R. A.; Miller, S. I. *Nature* **2005**, *436*(25), 1171–1175.
32. Wagner, E.; Frank, M. M. *Nat. Rev. Drug Discov.* **2010**, *9*(1), 43–56.
33. Carroll, M. C. *Nat. Immunol.* **2004**, *5*(10), 981–986.
34. Kemper, C.; Atkinson, J. P. *Nat. Rev. Immunol.* **2007**, *7*(1), 9–18.
35. Rooijakkers, S. H.; van Strijp, J. A. *Mol. Immmunol.* **2007**, *44*(1–3), 23–32.
36. Sun, D.; Accavitti, M. A.; Bryers, J. D. *Clin. Diagn. Lab. Immunol.* **2005**, *12*, 93–100.
37. Vuong, C.; Kocianova, S.; Voyich, J. M.; *et al. J. Biol. Chem.* **2004**, *279*, 54881–54886.
38. Li, M.; Lai, Y.; Villaruz, A. E.; Cha, D. J.; Sturdevant, D. E.; Otto, M. *Proc. Natl. Acad. Sci. USA* **2007**, *104*(22), 9469–9474.
39. van Kooyk, Y.; Geijtenbeck, T. B. *Nat. Rev. Immunol.* **2003**, *3*, 697–709.
40. Evans, R. T.; Klausen, B.; Sojar, H. T.; *et al. Infect. Immun.* **1992**, *60*, 2926–2935.
41. Jotwani, R.; Cutler, C. W. *Infect. Immun.* **2004**, *72*, 1725–1732.
42. Cohen, N.; Morisset, J.; Emilie, D. *J. Dent. Res.* **2004**, *83*, 429–433.
43. Jotwani, R.; Pulendran, B.; Agrawal, S.; Cutler, C. W. *Eur. J. Immunol.* **2003**, *33*, 2980–2986.
44. Pulendran, B.; Kumar, P.; Cutler, C. W.; Mohamadzadeh, M.; Van Dyke, T.; Banchereau, J. *J. Immunol.* **2001**, *167*, 5067–5076.
45. Potempa, J.; Sroka, A.; Imamura, T.; Travis, J. *Curr. Protein Pept. Sci.* **2003**, *4*, 397–407.
46. Leid, J. G.; Shirtliff, M. E.; Costerton, J. W.; Stoodley, A. P. *Infect. Immun.* **2002**, *70*(11), 6339–6345.
47. Leid, J. G.; Willson, C. J.; Shirtliff, M. E.; Hassett, D. J.; Parsek, M. R.; Jeffers, A. K. *J. Immunol.* **2005**, *175*(11), 7512–7518.
48. Jesaitis, A. J.; Franklin, M. J.; Berglund, D.; *et al. J. Immunol.* **2003**, *171*(8), 4329–4339.
49. Walker, T. S.; Tomlin, K. L.; Worthen, G. S.; *et al. Infect. Immun.* **2005**, *73*(6), 3693–3701.
50. Chandra, J.; McCormick, T. S.; Imamura, Y.; Mukherjee, P. K.; Ghannoum, M. A. *Infect. Immun.* **2007**, *75*(5), 2612–2620.
51. Zimmermann, S.; Wagner, C.; Müller, W.; *et al. Infect. Immun.* **2006**, *74*(10), 5687–5692.
52. Wagner, V. E.; Frelinger, J. G.; Barth, R. K.; Iglewski, B. H. *Trends Microbiol.* **2006**, *14*(2), 55–58.
53. Wu, L.; Estrada, O.; Zaborina, O.; *et al. Science* **2005**, *309*(5735), 774–777.
54. Tateda, K.; Ishii, Y.; Horikawa, M.; *et al. Infect. Immun.* **2003**, *71*(10), 5785–5793.
55. Mittal, R.; Sharma, S.; Chhibber, S.; Harjai, K. *Comp. Immunol. Microbiol. Infect. Dis.* **2006**, *29*, 12–26.
56. Sulakvelidze, A.; Alavidze, Z.; Morris, J. G., Jr. *Antimicrob. Agents Chemother.* **2001**, *45*(3), 649–659.
57. Fischetti, V. A. *Trends Microbiol.* **2005**, *13*(10), 491–496.
58. Hong, H. A.; Ducle, H.; Cutting, S. M. *FEMS Microbiol. Rev.* **2005**, *29*(4), 813–835.
59. Persson, G. R. *J. Clin. Periodontol.* **2005**, *32*(Suppl. 6), 39–53.
60. de Smet, K.; Contreras, R. *Biotechnol. Lett.* **2005**, *27*(18), 1337–1347.
61. Casadevall, A.; Dadachova, E.; Pirofski, L. A. *Nat. Rev. Microbiol.* **2004**, *2*(9), 695–703.
62. Martinez, L. R.; Casadevall, A. *Infect. Immun.* **2005**, *73*(10), 6350–6362.
63. Cachia, P. J.; Hodges, R. S. *Biopolymers* **2003**, *71*(2), 141–168.
64. Otto, M. *FEMS Microbiol. Lett.* **2004**, *241*, 135–141.
65. Boles, B. R.; Thoendel, M.; Singh, P. K. *Mol. Microbiol.* **2005**, *57*, 1210–1223.
66. Schmid, D.; Dengjel, J.; Schoor, O.; Stevanovic, S.; Münz, C. *J. Mol. Med.* **2006**, *84*, 194–202.
67. Hart, D. *Blood* **1997**, *90*, 3245–3287.
68. Matzinger, P. *Annu. Rev. Immunol.* **1994**, *12*, 991–1045.
69. Steinman, R. *Annu. Rev. Immunol.* **1991**, *9*, 271–296.
70. Banchereau, J.; Steinman, R. M. *Nature* **1998**, *392*, 245–252.
71. Banchereau, J.; Briere, F.; Caux, C.; *et al. Annu. Rev. Immunol.* **2000**, *18*, 767–811.
72. Janeway, C. J.; Travers, P.; Walport, M.; Shlomchik, M. *Immunobiology: The Immune System in Health and Disease*, 6th ed.; Garland Science Publishing: New York, 2005.
73. Hubbell, J. A.; Thomas, S. N.; Swartz, M. A. *Nature* **2009**, *462*(7272), 449–460.
74. Look, M.; Bandyopadhyay, A.; Blum, J. S.; Fahmy, T. M. *Adv. Drug Deliv. Rev.* **2010**, *62*(4–5), 378–393.
75. Ueno, H.; Klechevsky, E.; Morita, R.; *et al. Immunol. Rev.* **2007**, *219*, 118–142.
76. Kiyono, H.; Fukuyama, S. *Nat. Rev. Immunol.* **2004**, *4*(9), 699–710.
77. Holmgren, J.; Czerkinsky, C. *Nat. Med.* **2005**, *11*(Suppl. 4), S45–S53.
78. Belyakov, I. M.; *et al. Nat. Med.* **2001**, *7*(12), 1320–1326.
79. Kuznetsov, A. V.; Avramenko, A. A. *Math. Biosci.* **2009**, *218*(2), 142–152.
80. Belyakov, I. M.; Ahlers, J. D. *Trends Immunol.* **2008**, *29*(11), 574–585.
81. Anderson, J. M. *Annu. Rev. Mater. Res.* **2001**, *31*, 81–110.
82. Mekori, Y.; Metcalfe, D. *Immunol. Rev.* **2000**, *173*, 131–140.
83. Tang, L.; Jennings, T.; Eaton, J. *Proc. Natl. Acad. Sci. USA* **1998**, *95*, 8841–8846.
84. Savill, J. *Biochem. Soc. Trans.* **1996**, *24*, 1065–1069.

85. Schwartz, B.; Karsan, A.; Bombeli, T.; Harlan, J. *J. Immunol.* **1999**, *162*, 4842–4848.
86. Hu, W.; Eaton, J.; Tang, L. *Blood* **2001**, *98*, 1231–1238.
87. Wilson, C.; Clegg, R.; Leavesley, D.; Pearcy, M. *Tissue Eng.* **2005**, *11*, 1–18.
88. Stout, R. D.; Jiang, C.; Matta, B.; Tietzel, I.; Watkins, S. K.; Suttles, J. *J. Immunol.* **2005**, *175*, 342–349.
89. Stout, R.; Suttles, J. *J. Leukoc. Biol.* **2004**, *76*, 509–513.
90. Shankar, R.; Greisler, H. P. In *Implantation Biology*; Greco, R. S., Ed.; CRC Press: Boca Raton, FL, **1994**.
91. Leibovich, S. J.; Ross, R. *Am. J. Pathol.* **1975**, *78*, 71–100.
92. Martin, P.; D'Souza, D.; Martin, J.; *et al. Curr. Biol.* **2003**, *13*, 1122–1128.
93. Mantovani, A.; Sozzani, S.; Locati, M.; Allavena, P.; Sica, A. *Trends Immunol.* **2002**, *23*, 549–555.
94. Mosser, D. M. *J. Leukoc. Biol.* **2003**, *73*, 209–212.
95. Goldmann, O.; von Köckritz-Blickwede, M.; Höltje, C.; Chhatwal, G. S.; Geffers, R.; Medina, E. *Infect. Immun.* **2007**, *75*(8), 4148–4157.
96. Mantovani, A.; Sica, A.; Sozzani, S.; Allavena, P.; Vecchi, A.; Locati, M. *Trends Immunol.* **2004**, *25*, 677–686.
97. Mosser, D. M. *J. Leukoc. Biol.* **2003**, *73*(2), 209–212.
98. Wagner, V. E.; Bryers, J. D. *J. Biomed. Mater. Res. A* **2004**, *69*(1), 79–90.
99. Liu, N. *Lymphat. Res. Biol.* **2003**, *1*(1), 67–70.
100. Valladeau, J.; Saeland, S. *Semin. Immunol.* **2005**, *17*(4), 273–283.
101. Nestle, F. O.; Turka, L. A.; Nickoloff, B. J. *J. Clin. Investig.* **1994**, *94*(1), 202–209.
102. Caux, C.; Massacrier, C.; Vanbervliet, B.; *et al. Blood* **1997**, *90*(4), 1458–1470.
103. Dubois, B.; *et al. J. Immunol.* **1998**, *161*(5), 2223–2231.
104. Cunningham, A. L.; Turner, R. R.; Miller, A. C.; Para, M. F.; Merigan, T. C. *J. Clin. Investig.* **1985**, *75*(1), 226–233.
105. Mikloska, Z.; *et al. J. Infect. Dis.* **1998**, *177*(4), 827–838.
106. York, I. A.; Roop, C.; Andrews, D. W.; Riddell, S. R.; Graham, F. L.; Johnson, D. C. *Cell* **1994**, *77*(4), 525–535.
107. Cunningham, A. L.; Carbone, F.; Geijtenbeek, T. B. H. *Eur. J. Immunol.* **2008**, *38*(9), 2377–2385.
108. de Witte, L.; Nabatov, A.; Pion, M.; *et al. Nat. Med.* **2007**, *13*(3), 367–371.
109. Hladik, F.; McElrath, M. J. *Nat. Rev. Immunol.* **2008**, *8*(6), 447–457.
110. Hu, Q. X.; *et al. J. Exp. Med.* **2004**, *199*(8), 1065–1075.
111. Kawamura, T.; *et al. J. Immunol.* **2008**, *180*(5), 3297–3304.
112. Dhodapkar, M. V.; *et al. J. Exp. Med.* **2001**, *193*(2), 233–238.
113. Dhodapkar, M. V.; *et al. J. Clin. Investig.* **1999**, *104*(2), 173–180.
114. Schuler, G.; Schuler-Thurner, B.; Steinman, R. M. *Curr. Opin. Immunol.* **2003**, *15*(2), 138–147.
115. Hawiger, D.; *et al. J. Exp. Med.* **2001**, *194*(6), 769–779.
116. Kretschmer, K.; *et al. Nat. Immunol.* **2005**, *6*(12), 1219–1227.
117. Guy, B. *Nat. Rev. Microbiol.* **2007**, *5*(7), 505–517.
118. Singh, M.; O'Hagan, D. *Nat. Biotechnol.* **1999**, *17*(11), 1075–1081.
119. Clements, C. J.; Griffiths, E. *Vaccine* **2002**, *20*, S24–S33.
120. O'Hagan, D. T.; De Gregorio, E. *Drug Discov. Today* **2009**, *14*(11–12), 541–551.
121. Herbert, W. J. *Immunology* **1968**, *14*(3), 301–318.
122. Gupta, R. K. *Adv. Drug Deliv. Rev.* **1998**, *32*(3), 155–172.
123. Akira, S.; Takeda, K. *Nat. Rev. Immunol.* **2004**, *4*(7), 499–511.
124. Reddy, S. T.; Swartz, M. A.; Hubbell, J. A. *Trends Immunol.* **2006**, *27*(12), 573–579.
125. Harper, D. M.; Franco, E. L.; Wheeler, C. M.; *et al. Lancet* **2006**, *367*(9518), 1247–1255.
126. Boland, G.; Beran, J.; Lievens, M.; *et al. Vaccine* **2004**, *23*(3), 316–320.
127. Garcon, N.; Chomez, P.; Van Mechelen, M. *Expert Rev. Vaccin.* **2007**, *6*(5), 723–739.
128. Vandepapeliere, P.; Horsmans, Y.; Moris, P.; *et al. Vaccine* **2008**, *26*(10), 1375–1386.
129. Reddy, S. T.; van der Vlies, A. J.; Simeoni, E.; *et al. Nat. Biotechnol.* **2007**, *25*(10), 1159–1164.
130. Hunter, R.; Strickland, F.; Kezdy, F. *J. Immunol.* **1981**, *127*(3), 1244–1250.
131. Ogura, Y.; Sutterwala, F. S.; Flavell, R. A. *Cell* **2006**, *126*(4), 659–662.
132. Iwasaki, A.; Medzhitov, R. *Nat. Immunol.* **2004**, *5*(10), 987–995.
133. Uto, T.; Wang, X.; Sato, K.; *et al. J. Immunol.* **2007**, *178*(5), 2979–2986.
134. Allemann, E.; Gravel, P.; Leroux, J. C.; Balant, L.; Gurny, R. *J. Biomed. Mater. Res.* **1997**, *37*(2), 229–234.
135. Ross, T. M.; Xu, Y.; Green, T. D.; Montefiori, D. C.; Robinson, H. L. *AIDS Res. Hum. Retroviruses* **2001**, *17*(9), 829–835.
136. Yoshida, M.; Babensee, J. E. *J. Biomater. Sci. Polym. Ed.* **2006**, *17*(8), 893–907.
137. van Broekhoven, C. L.; Parish, C. R.; Demangel, C.; Britton, W. J.; Altin, J. G. *Cancer Res.* **2004**, *64*, 4357–4365.
138. Espuelas, S.; Roth, A.; Thumann, C.; Frisch, B.; Schuber, F. *Mol. Immunol.* **2005**, *42*(6), 721–729.
139. Roth, A.; Espuelas, S.; Thumann, C.; Frisch, B.; Schuber, F. *Bioconjug. Chem.* **2004**, *15*(3), 541–553.
140. Demento, S. L.; Eisenbarth, S. C.; Foellmer, H. G.; *et al. Vaccine* **2009**, *27*(23), 3013–3021.
141. Ali, O. A.; Emerich, D.; Dranoff, G.; Mooney, D. J. *Sci. Transl. Med.* **2009**, *1*(8), 8ra19.
142. Ali, O. A.; Huebsch, N.; Cao, L.; Dranoff, G.; Mooney, D. J. *Nat. Mater.* **2009**, *8*(2), 151–158.
143. Leroux, J. C.; Dejaeghere, F.; Anner, B.; Doelker, E.; Gurny, R. *Life Sci.* **1995**, *57*(7), 695–703.
144. Owens, D. E.; Peppas, N. A. *Int. J. Pharm.* **2006**, *307*(1), 93–102.
145. Lanzavecchia, A. *Curr. Opin. Immunol.* **1996**, *8*(3), 348–354.
146. Bouvet, J. P.; Decroix, N.; Pamonsinlapatham, P. *Trends Immunol.* **2002**, *23*(4), 209–213.
147. Lin, M. L.; *et al. Immunol. Cell Biol.* **2008**, *86*(4), 353–362.
148. Kwon, Y. J.; *et al. Proc. Natl. Acad. Sci. USA* **2005**, *102*(51), 18264–18268.
149. Flanary, S.; Hoffman, A. S.; Stayton, P. S. *Bioconjug. Chem.* **2009**, *20*(2), 241–248.
150. Minigo, G.; *et al. Vaccine* **2007**, *25*(7), 1316–1327.
151. Copland, M. J.; Baird, M. A.; Rades, T.; *et al. Vaccine* **2003**, *21*(9–10), 883–890.
152. Bonifaz, L. C.; Bonnyay, D. P.; Charalambous, A.; *et al. J. Exp. Med.* **2004**, *199*(6), 815–824.
153. Caminschi, I.; Lahoud, M. H.; Shortman, K. *Eur. J. Immunol.* **2009**, *39*(4), 931–938.
154. Tacken, P. J.; *et al. Blood* **2005**, *106*(4), 1278–1285.
155. Benko, S.; Benko, S.; Magyarics, Z.; Szabo, A.; Rajnavolgyi, E. *Biol. Chem.* **2008**, *389*(5), 469–485.
156. Jones, R. A.; *et al. Biochem. J.* **2003**, *372*, 65–75.
157. Lackey, C. A.; *et al. Bioconjug. Chem.* **1999**, *10*(3), 401–405.
158. Murthy, N.; *et al. J. Control. Release* **1999**, *61*(1–2), 137–143.
159. Seki, K.; Tirrell, D. A. *Macromolecules* **1984**, *17*(9), 1692–1698.
160. Shedlock, D. J.; Weiner, D. B. *J. Leukoc. Biol.* **2000**, *68*(6), 793–806.
161. Pack, D. W. *Nat. Mater.* **2004**, *3*(3), 133–134.
162. Probst, H. C.; *et al. Immunity* **2003**, *18*(5), 713–720.
163. Wu, L.; Yuan, Z. H.; Liu, F.; Waters, J. A.; Wen, Y. M. *Viral Immunol.* **2001**, *14*(4), 359–367.
164. Wang, X.; Hillemeyer, P.; Pascual, D. W. *Viral Immunol.* **2003**, *16*(4), 525–539.
165. Manolova, V.; *et al. Eur. J. Immunol.* **2008**, *38*(5), 1404–1413.
166. Altin, J. G.; van Broekhoven, C. L.; Parish, C. R. *Expert Opin. Biol. Ther.* **2004**, *4*, 1735–1747.
167. Diebold, S. S.; Plank, C.; Cotten, M.; Wagner, E.; Zenke, M. *Somat. Cell Mol. Genet.* **2002**, *27*, 65–74.
168. Kim, T. H.; Nah, J. W.; Cho, M. H.; Park, T. G.; Cho, C. S. *J. Nanosci. Nanotechnol.* **2006**, *6*, 2796–2803.
169. Krishnamurthy, V. M.; Quinton, L. J.; Estroffa, L. A.; *et al. Biomaterials* **2006**, *27*, 3663–3674.
170. Kuhn, S. E.; Nardin, A.; Klebba, P. E.; Taylor, R. P. *Immunology* **1998**, *160*, 5088–5097.
171. Lindorfer, M. A.; Nardin, A.; Foley, P. L.; *et al. J. Immunol.* **2001**, *167*, 2240–2249.
172. Gyimesi, E.; Bankovich, A. J.; Schuman, T. A.; Goldberg, J. B.; Lindorfer, M. A.; Taylor, R. P. *Immunol. Lett.* **2004**, *95*, 185–192.
173. Kobayashi, T.; Takauchi, A.; van Spriel, A. B.; *et al. Vaccine* **2004**, *23*, 585–594.
174. Wizemann, T. M.; Adamou, J. E.; Langermann, S. *Emerg. Infect. Dis.* **1999**, *5*, 395–403.
175. Newell, P. D.; Monds, R. D.; O'Toole, G. A. *Proc. Natl. Acad. Sci. USA* **2009**, *106*(9), 3461–3466.
176. Hazlett, L. D.; Masinick, S.; Barrett, R.; Rosol, K. *Infect. Immun.* **1993**, *61*(12), 5164–5173.
177. Stranger-Jones, Y. K.; Bae, T.; Schneewind, O. *Proc. Natl. Acad. Sci. USA* **2006**, *103*(45), 16942–16947.
178. Therrien, R.; Lacasse, P.; Grondin, G.; Talbot, B. G. *Vaccine* **2007**, *25*(27), 5053–5061.
179. Gaudreau, M. C.; Lacasse, P.; Talbot, B. G. *Vaccine* **2007**, *25*(5), 814–824.
180. Castagliuolo, I.; Piccinini, R.; Beggiao, E.; *et al. Vaccine* **2006**, *24*(20), 4393–4402.
181. Patti, J. M. *Vaccine* **2004**, *22S*, S39–S43.
182. Maira-Litrán, T.; Kropec, A.; Goldmann, D. A.; Pier, G. B. *Infect. Immun.* **2005**, *73*(10), 6752–6762.
183. Broekhuizen, C. A.; de Boer, L.; Schipper, K.; *et al. Biomaterials* **2009**, *30*(32), 6444–6450.

184. Georgakopoulos, C. D.; Exarchou, A. M.; Gartaganis, S. P.; *et al*. *Curr*. *Eye Res*. **2006**, *31*(2), 137–146.
185. McCormick, J. K.; Hirt, H.; Waters, C. M.; Tripp, T. J.; Dunny, G. M.; Schlievert, P. M. *Infect*. *Immun*. **2001**, *69*(5), 3305–3314.
186. Miyachi, K.; Ishihara, K.; Kimizuka, R.; Okuda, K. *J*. *Dent*. *Res*. **2007**, *86*(5), 446–450.
187. Momoi, F.; Hashizume, T.; Kurita-Ochiai, T.; Yuki, Y.; Kiyono, H.; Yamamoto, M. *Infect*. *Immun*. **2008**, *76*(6), 2777–2784.
188. Frazer, L. T.; O'Brien-Simpson, N. M.; Slakeski, N.; *et al*. *Vaccine* **2006**, *24*(42–43), 6542–6554.
189. Kuboniwa, M.; Amano, A.; Shizukuishi, S.; Nakagawa, I.; Hamada, S. *Infect*. *Immun*. **2001**, *69*(5), 2972–2979.
190. O'Brien-Simpson, N. M.; Pathirana, R. D.; Paolini, R. A.; *et al*. *J*. *Immunol*. **2005**, *175*(6), 3980–3989.
191. Bumann, D.; Behre, C.; Behre, K.; *et al*. *Vaccine* **2010**, *28*(3), 707–713.
192. Heikenwalder, M.; Polymenidou, M.; Junt, T.; *et al*. *Nat*. *Med*. **2004**, *10*, 187–192.
193. Zhao, H.; Hemmi, H.; Akira, S.; Cheng, S. H.; Scheule, R. K.; Yew, N. S. *Mol*. *Ther*. **2004**, *9*, 241–248.
194. Gilboa, E.; Vieweg, J. *Immunol*. *Rev*. **2004**, *199*, 251–263.
195. Dang, J. M.; Leong, K. W. *Adv*. *Drug Deliv*. *Rev*. **2006**, *58*(4), 487–499.
196. Gao, Y.; Gu, W.; Chen, L.; Xu, Z.; Li, Y. *J*. *Control*. *Release* **2007**, *118*(3), 381–388.
197. Keegan, M. E.; Saltzman, W. M. *Methods Mol*. *Med*. **2006**, *127*, 107–113.
198. Little, S. R.; Langer, R. *Adv*. *Biochem*. *Eng*. *Biotechnol*. **2005**, *99*, 93–118.
199. Pack, D. W.; Hoffman, A. S.; Pun, S.; Stayton, P. S. *Nat*. *Rev*. *Drug Discov*. **2005**, *4*(7), 581–593.
200. Tobery, T.; Siliciano, R. F. *J*. *Immunol*. **1999**, *162*, 639–642.
201. Tobery, T. W.; Siliciano, R. F. *J*. *Exp*. *Med*. **1997**, *185*, 909–920.
202. Varshavsky, A.; Turner, G.; Du, F.; Xie, Y. *Biol*. *Chem*. **2000**, *381*, 779–789.
203. Bonini, C.; Lee, S. P.; Riddell, S. R.; Greenberg, P. D. *J*. *Immunol*. **2001**, *166*, 5250–5257.
204. Lin, K. Y.; Guarnieri, F. G.; Staveley-O'Carroll, K. F.; *et al*. *Cancer Res*. **1996**, *56*, 21–26.
205. Thomson, S. A.; Burrows, S. R.; Misko, I. S.; Moss, D. J.; Coupar, B. E.; Khanna, R. *J*. *Virol*. **1998**, *72*, 2246–2252.
206. Wu, T. C.; Guarnieri, F. G.; Staveley-O'Carroll, K. F.; *et al*. *Proc*. *Natl*. *Acad*. *Sci*. *USA* **1995**, *92*, 11671–11675.
207. Bennewitz, N. L.; Babensee, J. L. *Biomaterials* **2005**, *26*, 2991–2999.

4.419. Vaccine and Immunotherapy Delivery

D J Irvine, Massachusetts Institute of Technology, Cambridge, MA, USA; Ragon Institute of MGH, MIT and Harvard, Boston, MA, USA; Howard Hughes Medical Institute, Chevy Chase, MD, USA
C M Jewell, Massachusetts Institute of Technology, Cambridge, MA, USA; Ragon Institute of MGH, MIT and Harvard, Boston, MA, USA

© 2011 Elsevier Ltd. All rights reserved.

4.419.1.	**Introduction**	316
4.419.2.	**The Paradigm of Immune Responses in Infection Versus Vaccination**	317
4.419.3.	**Biomaterials as Delivery Vehicles for Vaccines and Immunomodulators**	319
4.419.3.1.	Vaccine Delivery Across Mucosal Barriers and Skin	319
4.419.3.2.	Controlling Vaccine Delivery at the Tissue/Organ Level	319
4.419.3.2.1.	Creation of antigen depots	320
4.419.3.2.2.	Targeting and 'reverse targeting' of APCs	321
4.419.3.2.3.	Lymph node targeting	322
4.419.3.3.	Controlling Vaccine Delivery at the Cellular Level	323
4.419.3.3.1.	Cross-presentation of antigen to $CD8^+$ T cells	323
4.419.3.3.2.	B cell activation and humoral responses	324
4.419.4.	**Biomaterials as Immunostimulators and Carriers of Immunostimulatory Adjuvants for Vaccines**	324
4.419.4.1.	Intrinsic Adjuvant Activity of Biomaterials	324
4.419.4.1.1.	Activation of the inflammasome	324
4.419.4.1.2.	Role of TLRs in immune cell response to biomaterials used as vaccine carriers	325
4.419.4.1.3.	Complement-activating biomaterials	326
4.419.4.1.4.	Biomaterial-mediated adjuvant mechanisms not yet elucidated	327
4.419.4.2.	Biomaterials as Carriers of Adjuvant Molecules	327
4.419.4.2.1.	Delivery of PAMPs, DAMPs, and related immunostimulatory molecules	327
4.419.4.2.2.	Delivery of immunoregulatory cytokines	329
4.419.5.	**Future Directions**	329
4.419.6.	**Conclusions**	330
References		330

Glossary

Adjuvant Any material used to augment the immune response to an antigen during vaccination.
Antigen Molecule derived from a pathogen that is the molecular target of a T cell or antibody response.
Antigen-presenting cells (APC) Cells capable of displaying peptide antigens bound to major histocompatibility complex (MHC) molecules on their surface, enabling the activation of antigen-specific T cells.
Chemokine Host protein secreted by stromal or immune cells to attract immune cells (or other cells) to a tissue site by the process of chemotaxis.
CpG DNA Short single-stranded oligonucleotides containing specific patterns of unmethylated C-G motifs, which are PAMP signatures of bacterial DNA and ligands for TLR9.
Cross-presentation Process of APC internalization of extracellular antigens, and processing and loading of these antigens onto class I MHC molecules for presentation to $CD8^+$ T cells.
DAMPs Danger-associated molecular patterns; endogenous molecular signatures of tissue damage/cell death, which are recognized by immune cells as 'danger' signals.
DNA vaccine Vaccine based on the delivery of nucleic acids that encode for antigens of interest, enabling *in situ* production of antigen in tissue to drive an immune response.
PAMPs Pathogen-associated molecular patterns; conserved molecular motifs that the immune system has evolved to recognize as signatures of pathogenic microbes.
Toll-like receptor agonist (TLRa) Ligand for a Toll-like receptor.
Toll-like receptors A set of ten different protein receptors, both cell surface and endolysosomal, expressed by immune cells and some stromal cells, which recognize PAMPs and stimulate the activation of immune defenses.

Abbreviations

APC	Antigen-presenting cell
BALT	Bronchus-associated lymphoid tissue
DAMP	Danger-associated molecular pattern
DC	Dendritic cell
GALT	Gut-associated lymphoid tissue
GI	Gastrointestinal

GM-CSF	Granulocyte/macrophage colony-stimulating factor
GMP	Good manufacturing process
HA	Hyaluronic acid
HMW	High molecular weight
HyAp	Hydroxyapatite
hyppos	Hydrophobic portions/moieties
IL	Interleukin
LPS	Lipopolysaccharide
mAb	Monoclonal antibody
MHC	Major histocompatibility complex
MPLA	Monophosphoryl lipid A
NALP3	Nacht domain, leucine-rich repeat, and pyrin domain-containing protein 3
NALT	Nasal-associated lymphoid tissue
NKT	Natural killer T cell
NLR	NOD-like receptor
OVA	Ovalbumin
PAMP	Pathogen-associated molecular pattern
PCR	Polymerase chain reaction
PE	Polyethylene
PEG	Polyethylene glycol
PEO	Polyethylene oxide
PEVAc	Polyethylene-*co*-vinyl acetate
PLGA	Polylactide-*co*-glycolide
PPO	Polypropylene oxide
PPS	Polypropylene sulfide
RIG	Retinoic acid-inducible gene
TLR	Toll-like receptor
TLRa	Toll-like receptor agonist
TT	Tetanus toxoid

4.419.1. Introduction

Biomaterials designed for drug delivery have had a major clinical impact and are likely to become even more important in a broad range of such applications in the near future. Of particular practical and scientific importance is the application of biomaterials for vaccine delivery and related immunotherapy strategies. Vaccines are often cited as the biomedical advance with the greatest impact on public health ever devised.[1] Vaccines against polio and smallpox have largely eradicated these diseases, and vaccines against seasonal influenza, measles, hepatitis B, and typhus (to name a few) have greatly reduced morbidity and mortality from these infectious agents.[2] However, great challenges remain as vaccines for pathogens that establish persistent chronic infections in unimmunized individuals, which are often highly mutable and fail to elicit protective neutralizing antibody responses, remain an unsolved challenge. Examples of these vaccine challenges include HIV,[3] hepatitis C,[4] tuberculosis,[5] and malaria,[6] which affect millions of people worldwide. In addition to these prophylactic vaccine challenges, therapeutic vaccines against cancer have long been sought but remain in the preclinical and clinical study stage. Here, some of the key challenges include the difficulty in eliciting immune responses against poorly immunogenic tumors that produce a variety of immunosuppressive factors, overcoming tolerance of the immune system against 'self' antigens expressed by tumor cells, and exhaustion of the immune system due to continuous unresolved antigen stimulation over time.[7,8] Finally, vaccines have been pursued as novel therapeutic strategies aimed at redirecting unwanted immune responses triggered by allergens[9] and promoting tolerance against self antigens to reverse autoimmune disease,[10] or as interventions to block pathological processes such as amyloid fiber deposition in Alzheimer's disease.

Vaccines are traditionally viewed as consisting of an antigen, the molecular target against which the immune response must be primed, and an adjuvant, which is generically defined as any component added to the vaccine to enhance the immune response to the antigen. The goal of prophylactic vaccination is to elicit a population of memory lymphocytes (T cells and B cells) capable of (1) maintaining antibodies directed against the antigen(s) in the systemic circulation and/or at mucosal portals of pathogen entry and (2) rapidly responding with new antibody production, regulation of innate immune defense, and killing of infected cells if a pathogen bearing the target antigen(s) enters the host. Therapeutic vaccines have the more challenging goal of eliciting such responses in the face of an ongoing infection/insult. The earliest vaccines were prepared from live attenuated (passaged *in vitro* to generate less virulent forms of the original microbe) or whole-killed (chemically fixed or denatured) pathogens. These approaches elicit extremely potent, often lifelong, immunity as essentially every potential molecular target of the immune response is used in the vaccine (the entire microbe), and the immune system has evolved explicitly for the recognition and elimination of microbes. However, in many cases, live attenuated vaccines are not considered safe (such as HIV), and in some cases, live attenuated/whole-killed vaccines are not feasible due to a lack of viable *in vitro* culture strategies (such as in *vivax* malaria[11]). Further, the whole-killed vaccine approach fails in instances of pathogens that are extremely mutable such as HIV, where a potent immune response raised against a given molecular clone of the virus is not sufficiently cross-reactive to provide protection against the numerous quasispecies circulating in the population. Finally, the cost, time, and complexities involved in producing GMP quality whole pathogens/split pathogen vaccines are a significant issue (e.g., the 6-month-long chicken egg-based production of the seasonal influenza vaccines). These considerations in concert with the molecular biology revolution of the 1970s have led to the pursuit of a broad variety of 'subunit' vaccine strategies – vaccines where a subset of antigens (in some cases, only one) from the pathogen of interest are prepared using recombinant DNA technology and delivered in the form of DNA, recombinant proteins, or safe viral or bacterial vectors.

One of the key drivers in the development of biomaterials for vaccine delivery has been this move toward subunit vaccines, which are generally much less immunogenic than live

attenuated or whole-killed pathogen vaccines. In addition, our expanding understanding of immunology has led to a desire to rationally shape the immune response and the resulting immunological memory elicited by vaccines. For the purposes of this review, we *define biomaterial vaccine adjuvants broadly as any materials combined with antigens to enhance vaccines that are not purely derived from biological components*. Biomaterials can serve several functions in vaccine delivery (**Table 1**): they can promote entry of antigen/adjuvant molecules into mucosal sites that are the critical portals of entry for pathogens, they can promote trafficking of antigen to the lymph nodes and other secondary lymphoid organs where primary immune responses are initiated, they can codeliver inflammatory molecules or directly elicit controlled local inflammation to promote fully functional immune memory, or they can exploit the immune system's evolved capacity to respond efficiently to particulate microbes by delivering antigen/adjuvant signals in a particulate (micron- or submicron-sized) form. A diverse array of biomaterials have been explored as adjuvants for vaccines, including aluminum salt gels (alum), oil-in-water or water-in-oil emulsions, liposomes and solid lipid particles, polymer particles, and antigen-conjugated soluble polymers.[12] These materials may encapsulate/adsorb antigen or alternatively may be mixed and coinjected without significant physical interactions with the antigen, and may codeliver immunostimulatory compounds (e.g., molecular adjuvants such as Toll-like receptor agonists (TLRas)). Despite extensive preclinical and clinical research, only two adjuvant materials are approved for use in the United States, the aluminum salts (alum), and one vaccine employing alum mixed with the TLRa monophosphoryl lipid A (MPLA) (although several additional candidates are in late stage clinical trials). This discrepancy arises due to both the arduous and often empirical nature of vaccine research and the extremely stringent safety requirements for adjuvants used in prophylactic vaccines, especially those used routinely in pediatric populations. Importantly, although safe and often effective, alum is far from ideal as a vaccine adjuvant, as it elicits antibody isotypes largely associated with Th2 immune responses and poor cellular immune responses, poorly adsorbs some vaccine antigens, and is associated with injection site reactions due to the long-lived granulomas formed at the injection site in a fraction of recipients.[13–15]

The field of vaccine delivery is both established and growing, and an exhaustive analysis of the existing knowledge is well outside the scope of any single review. This chapter provides instead a general perspective on our current understanding of how licensed biomaterial adjuvants already in the clinic and new biomaterials in preclinical development work in diverse ways to enhance vaccine delivery, with a particular emphasis on the conceptual and immunological rationale for designing biomaterials for vaccine delivery. In the following two sections, we break this field down broadly into considerations of (i) physical delivery, transporting antigen/adjuvant molecules to target immune cells, and (ii) provision of adjuvant signals, either by the intrinsic composition of biomaterials themselves or via codelivery of adjuvant molecules. Additional excellent reviews are also available overviewing current biomaterials vaccine strategies,[16–20] particle delivery materials for vaccines,[21–23] and the preparation, properties, and historical development of licensed aluminum[13,14,24–26] and oil–water emulsion-based[27] adjuvants.

4.419.2. The Paradigm of Immune Responses in Infection Versus Vaccination

Although vaccinology has its roots in empiricism, modern vaccine design is increasingly motivated and guided by immunology and our growing understanding of the functions of the immune system at a genetic/molecular level. It is no accident that, among the different classes of vaccines, live attenuated vaccines generally give the strongest immune responses. Because the immune system has evolved to deal with infections, vaccines that closely mimic actual infections tend to give the strongest immune responses and subsequent immune memory. The paradigm of how the immune system deals with local infections is thus useful in understanding the goals of vaccination and the design of better vaccines.

In response to infection by viral or bacterial pathogens at a local portal of entry (e.g., skin, mucosa, etc.), infected cells are triggered to release inflammatory cytokines such as interferons and interleukin-1β, which in turn trigger the local release of inflammatory chemoattractants. These attractant signals are displayed on local inflamed endothelium, and promote the entry of early innate immune responders such as neutrophils as well as monocytes and dendritic cells (DCs) from the blood (**Figure 1**). DCs are an important subtype of antigen-presenting cells (APC). DCs are critical initiators of adaptive immune responses,[28] as they sample antigens and dying infected cells at the infection site, become activated, and alter their chemokine receptor expression to permit homing to local lymphatics and from there to the draining secondary lymphoid tissue.[29] Monocytes recruited from blood can enter tissues and differentiate into DCs in response to cues in the inflammatory site as well.[30]

Table 1 Roles for biomaterials in vaccine delivery

Materials characteristic	*(Proposed) function(s) in vaccine delivery*
Penetration of mucosal/skin barriers	Promote antigen/adjuvant deposition at important portals for immune protection
Penetration of tissue/lymphatics	Transport of antigen/adjuvant molecules to secondary lymphoid organs where primary immune responses are initiated
Slow-release depot of antigen	Sustain immune response and development of fully functional memory cells
Elicit local inflammatory signals	Promote fully functional immune memory
Codelivery of antigen with immunostimulatory adjuvant molecules	Promote fully functional immune memory
Particulate presentation of antigen	Drive cross-presentation of antigen to $CD8^+$ T cells and promote B cell response

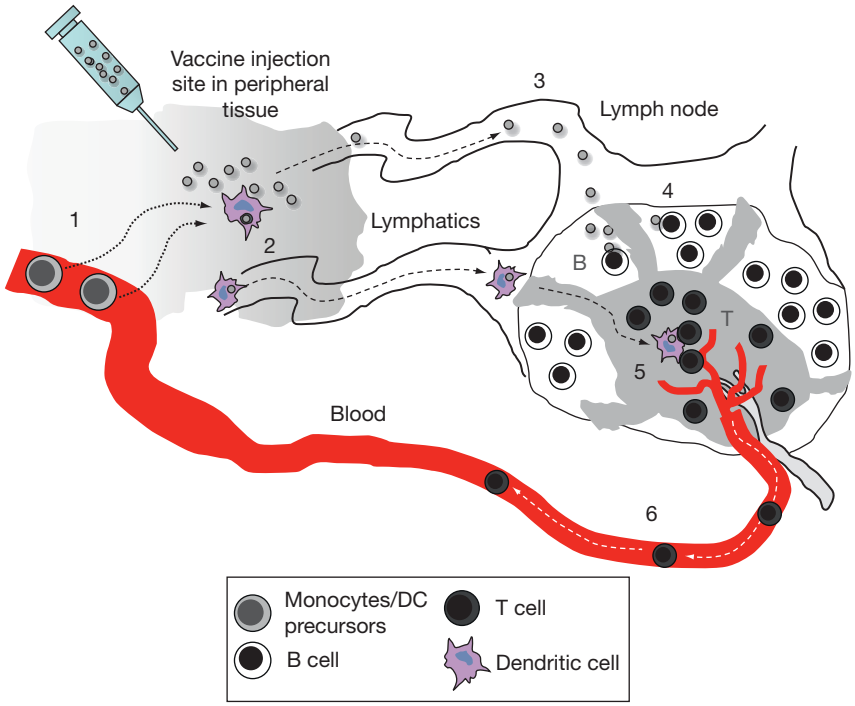

Figure 1 Early steps in the immune response to vaccination or infection. Shown here is a simplified view of the cascade of events that typically accompany immunization or infection: (1) inflammatory cells, including dendritic cell precursors, are recruited to the injection/infection site; (2) encounter with pathogen- or tissue damage-derived 'danger signals' activates recruited dendritic cells, and triggers their migration to lymph nodes. (3) Soluble antigen or small particles can drain directly to lymph nodes, where (4) B cells can be activated in the follicles. (5) Activated dendritic cells acquiring soluble or particle-associated antigen migrate to the T-cell areas of lymph nodes, where antigen-specific $CD4^+$ and $CD8^+$ T-cell activation commences, followed by (6) emigration of activated effector cells to the periphery.

Cell-free pathogens and pathogen debris are also transported by lymph flow to the draining lymph nodes, where B cells and DCs in the LN can acquire and process these antigens directly (Figure 1). Thus, antigen reaches the draining lymph nodes either carried by DCs or transported by lymph.

As they sample antigen at a site of activation of DCs infection or vaccination is critical for the generation of functional memory T and B cell responses. Activation (or maturation) of DCs is mediated by a host of pathogen- and danger-recognition sensors in these sentinel cells, receptors that recognize conserved pathogen-associated molecular patterns (PAMPs) or danger-associated molecular patterns (DAMPs), respectively.[31] PAMPs are molecular motifs evolutionarily conserved in pathogens but absent from host tissue; examples include bacterial cell wall components (lipopolysaccharide (LPS), peptidoglycans), double-stranded RNA (a viral signature), or unmethylated CpG DNA sequences (characteristic of bacterial genomes). DCs recognize PAMPs through cell surface and endolysosomal TLRs and cytosolic nucleic acid sensors such as the retinoic acid-inducible gene (RIG)-I-like receptor family of proteins and NOD-like receptors (NLRs).[32] There are ten identified TLRs to date, which recognize a broad range of PAMP molecules. DAMPS, on the other hand, are molecular signatures of tissue damage, for example, uric acid, ATP, HMGB1 proteins, or hyaluronan fragments. DC activation by DAMPS and PAMPS leads to the production of proinflammatory cytokines such as IL-12 and TNF-α and upregulation of costimulatory receptors required for the activation of naïve T cells (e.g., CD80, CD86, CD40), and triggers a transition in DC antigen processing functions, from 'uptake' to 'presentation,' with internalized antigens being degraded to short peptide fragments that are loaded into the clefts of major histocompatibility complex (MHC) molecules for display at the cell surface. In the absence of these many alterations in DC functional phenotype that accompany maturation, productive T cell and antibody responses are severely compromised. As mentioned above, a last critical change in maturing DCs is the alteration of chemokine receptor expression, which causes the activated cells to begin migrating to draining lymph nodes.

The secondary lymphoid tissues, where naïve T and B lymphocytes reside, are regional control centers for adaptive immune responses, consisting of lymph node-like structures with distinct features depending on the anatomic site. Nasal-associated lymphoid tissue (NALT), bronchus-associated lymphoid tissue (BALT), and gut-associated lymphoid tissue (GALT) are located in the nasal passages, airways, and GI tract, respectively. Regional lymph nodes drain essentially all other peripheral tissue sites, and the spleen acts as a filtration center for immunologic monitoring of the blood. DCs are believed to be the only APCs capable of priming naïve T cells under normal circumstances,[33] and thus are critical controllers of antibody (through regulation of helper T-cell activation, and possibly through direct interactions through B cells[34,35]) and cytotoxic T cell responses. Once in the lymph node, DC-bearing antigen will activate $CD4^+$ helper T cells and

$CD8^+$ cytotoxic T cells, triggering massive proliferation of antigen-specific T cells (Figure 1). B cells, by contrast, are thought to be capable of directly binding antigen transported to lymph nodes;[36,37] cross-linking of cell surface immunoglobulins triggers activation of these cells and the first steps toward antigen-specific antibody production. A fraction of helper T cells may engage antigen-triggered B cells at T cell zone-follicular borders of lymph nodes to promote B-cell proliferation and differentiation toward antibody-producing plasma cells or cells that will enter germinal centers to begin the process of somatic hypermutation/antibody affinity maturation.[38,39] In parallel, activated effector T cells leave the lymph nodes to patrol the peripheral tissues for infected cells (Figure 1). Activated DCs have a short lifespan of only a few days, and as antigen is cleared, stimulation of T cells and B cells wanes, the expanded T-cell population contracts, and a long-lived population of memory T and B cells develops, which can be sustained by homeostatic expansion over many years. Prophylactic vaccines aim at achieving long-lived, highly responsive memory cell populations, while therapeutic vaccines may aim at eliciting a mix of immediate potent effector cells and memory to sustain responses in the long term. All these responses depend on intricate spatial and temporal interactions between immune cells and tissues; thus, the fundamental immune activation scheme outlined here is conventionally termed the 'geographical' view of immunity. Importantly, many of these steps are similar in the response to immunization (Figure 1), as discussed in detail below.

Memory T cells have complex tissue-homing phenotypes that are still under active investigation, defined in part by the specific chemokine and adhesion receptors they express that determine their ability to enter different tissue sites. These memory cells can be roughly compartmentalized into central memory and effector memory cells, based on whether they express CCR7 and CD62L (chemokine and adhesion receptors required for lymph node entry) or lack these receptors (instead expressing homing molecules leading to peripheral tissues).[40] Memory lymphocytes can be 'addressed' to specific sites such as the gut, skin, or bone marrow, and some of these cells may be long-lived and permanently resident within the peripheral tissues,[41] serving as sentries for rapid response upon pathogen challenge at portals of entry. Because provision of rapidly responding effector memory cells directly at sites of entry or sites where pathogen propagation (e.g., the gut in HIV infection[42]) could be important for providing protection against infection, understanding how these tissue-homing phenotypes are established during vaccination is of great interest.

4.419.3. Biomaterials as Delivery Vehicles for Vaccines and Immunomodulators

As in other drug delivery applications, biomaterials can play a key role in the physical delivery of vaccine antigen and adjuvant molecules to the proper organ, tissue, or cell-level locations with appropriate timing to promote immune responses. The biological responses to vaccination follow a geographical/temporal order that closely parallels the immune response to infection outlined above in many cases: (1) antigen/adjuvant is deposited at a peripheral tissue site, (2) antigen is transported to draining lymph nodes, (3) lymphocyte priming commences, (4) effector and, subsequently, memory lymphocytes are generated, and (5) memory cells home to distinct sites throughout the body. We review the challenges and materials strategies for controlling physical delivery aspects following this geographical/temporal order, exploring sequentially the barriers faced by vaccines from their initial entry into the body to the final delivery of molecular cues to immune cells at key tissue sites.

4.419.3.1. Vaccine Delivery Across Mucosal Barriers and Skin

Although the majority of currently licensed vaccines are given via intramuscular or subcutaneous injection, much of the research focus in recent years has been directed toward mucosal delivery. This emphasis is motivated by the finding that the homing of memory lymphocytes can be directed to match the site of origin of an immune response,[43] and the route of immunization can have a dramatic effect on the imprinting of memory homing phenotypes. Thus, oral delivery of vaccines to the GALT preferentially promotes gut IgA antibody responses and T cell homing to the Peyer's patches and mesenteric lymph nodes; skin immunization promotes skin-homing memory T cells; airway immunization promotes memory lymphocytes with airway tropism. In addition to this immunological motivation, skin and mucosal vaccine delivery approaches may offer other advantages. Traditional needle-based vaccine delivery, in addition to contributing to reduced speed, ease, and compliance in administration, has been shown to contribute to reduced overall safety due to needle reuse and needle-based injuries.[44] Although each target mucosal tissue site presents its own unique physiological barriers to vaccine delivery, mucosal vaccine delivery in general faces the challenge of providing transport of antigen/adjuvant molecules through an epithelial barrier to reach the underlying mucosal tissue. A broad range of biomaterials (microparticles, nanoparticles etc.) and delivery strategies (gels, microneedles, etc.) are being developed to overcome these barriers and deposit antigens into tissues, but covering the range of issues unique to each mucosal site is beyond the scope of this review (see also **Chapter 1.115, Calcium Phosphates for Cell Transfection**; **Chapter 4.430, Silica-Based Mesoporous Nanospheres**; **Chapter 4.424, Nanoparticles for Nucleic Acid Delivery**; and **Chapter 4.434, Hybrid Magnetic Nanoparticles for Targeted Delivery**). We refer the interested reader to recent reviews of mucosal and skin vaccine delivery.[22,45–47]

4.419.3.2. Controlling Vaccine Delivery at the Tissue/Organ Level

Once entry into a local tissue site is achieved, via needle injection or transmucosal delivery through one of the routes discussed above, antigen and adjuvant signals must still be transported to draining lymph nodes to initiate primary adaptive immune responses, as naïve T and B lymphocytes recirculate among the secondary lymphoid organs but do not normally enter peripheral tissues. (Direct intra-lymph node injections have been utilized in some cancer vaccine trials guided by ultrasound,[48,49] but would be difficult to translate to mass vaccination settings.) Thus, injection site-to-lymphoid

organ transport becomes the second geographical barrier in vaccination. At least three distinct biomaterial strategies have been explored for vaccine delivery: generation of injection site depots that enable release of soluble antigen over time, strategies to recruit APCs to the site of injection to enhance cell-mediated transport of antigen to lymphoid organs, and direct delivery of antigen to lymph nodes via transport on very small particles that can passively diffuse through the tissue and enter lymphatics.

4.419.3.2.1. Creation of antigen depots

Soluble proteins injected subcutaneously or intramuscularly are rapidly cleared from the tissue by convection and lymph flow, flushing the majority of material through the draining lymph nodes within a few hours.[13,36,50] Thus, the duration of antigen exposure for B cells and DCs to acquire soluble antigen is often very limited. This issue was recognized very early in vaccinology, and the concept of creating 'depots' of antigen that would be released over time to draining lymphoid organs has been explored for many years, particularly in the context of the humoral immune response. The concept of single-shot vaccines that could elicit robust immune responses following a single injection has also been proposed, with the idea that antigen depots or materials releasing staggered bursts of antigen *in vivo* might obviate the need for booster injections.[51–53] Such approaches would be very attractive for vaccines needed in the developing world, where compliance rates with multi-shot vaccination schedules over many months may be poor.

Aluminum-based mineral salts such as aluminum phosphate and aluminum hydroxide – frequently referred to as alum – comprise the oldest and most common class of vaccine adjuvants. First discovered in 1926 as a means of increasing antigen immunogenicity by precipitating diphtheria toxin,[54] alum until very recently was the only clinically approved adjuvant in the United States.[26] Alum was believed to act by reversibly adsorbing/trapping antigen on alum particles, which prolonged their retention at the injection site and provided a slow release of the antigen over time.[55] However, responding B cells are not detected after a few weeks following alum immunization in draining lymph nodes, and excision of the alum injection site 14 days after immunization has no impact on antibody responses.[25,56] Interestingly, alum is resorbed very slowly and generates a granuloma at the injection site; alum particles excised from injection sites after several weeks can be used to successfully immunize naïve animals.[25,57] Together these data suggest that intact antigen is retained for very long periods in alum depots, but release of antigen from the granuloma is very limited after a few days and antigen retained in the peripheral tissue is unable to further promote the antibody response.[58] As discussed in detail below, the importance of long-term depot effects for alum has also been called into question by very recent studies,[24,59] and currently it is recognized that the licensed aluminum hydroxide alum adjuvants have multiple immunostimulatory effects beyond simple antigen retention.[25,60–62]

Notably, oil-in-water emulsions and liposomes, which are the two other most prominent examples of licensed biomaterial vaccine adjuvants, do not necessarily act as long-lived antigen depots either. MF59, composed of nanoscale droplets (~170 nm diameter) of squalene oil stabilized by surfactants, does not alter the tissue clearance of proteins with which it is mixed and coinjected.[27,50] Proteins injected parenterally in saline have the same serum clearance kinetics as that injected in (incomplete) Freund's adjuvant, the classic experimental mineral oil adjuvant.[63] Although liposomes can encapsulate protein antigens in their aqueous core, they are also rapidly destabilized by interactions of high-density lipoprotein particles and other serum components with their lipid bilayer surfaces,[64,65] and thus generally do not have long lifetimes at parenteral injection sites.

Although the slow-release properties of alum and lipid/emulsion adjuvants may be transient, polymer matrix- and microsphere-based delivery systems have convincingly shown an ability to retain and release antigen over periods up to several weeks (see also **Chapter 4.430, Silica-Based Mesoporous Nanospheres**; **Chapter 4.424, Nanoparticles for Nucleic Acid Delivery**; and **Chapter 4.434, Hybrid Magnetic Nanoparticles for Targeted Delivery**). Preis and Langer demonstrated that solid poly(ethylene-*co*-vinyl acetate) (PEVAc) slow-release matrices loaded with protein antigens and implanted s.c. in mice could elicit antibody responses sustained over many weeks and comparable to two injections of the same antigens with complete Freund's adjuvant.[66] PEVAc matrices have also been shown to promote mucosal immunity when used in the form of vaginal rings, releasing antigen in contact with the vaginal epithelium.[67] For safe injectable vaccines, biodegradable poly(lactide-*co*-glycolide) (PLGA) microspheres with encapsulated protein antigens have been shown to elicit sustained retention and slow release of antigen from sites of injection lasting several weeks,[68] and such microsphere delivery agents achieve enhanced antibody titers compared to alum.[69,70] DNA vaccine plasmids encapsulated in PLGA microparticles are detectable by PCR analysis of tissue homogenates from i.m. or s.c. injection sites for up to approximately 60 days, while naked DNA injected at the same sites is undetectable after such long times (see also **Chapter 4.424, Nanoparticles for Nucleic Acid Delivery** and **Chapter 4.425, Delivery of Nucleic Acids and Gene Delivery**).[71] However, the buildup of an acid environment within PLGA particles as they degrade, and their generally hydrophobic interior, has been shown to lead to protein denaturation and aggregation within particles over time,[72,73] and strategies to overcome this issue have had mixed success.[23,74] Antigen aggregation/denaturation may particularly be a problem for obtaining protective antibody responses against conformational epitopes of proteins. Thus, although PLGA microparticle/nanoparticle technology is well established, PLGA particles with encapsulated antigens have received very limited testing in nonhuman primates[75] and no clinical trials have been run using PLGA-encapsulated vaccines to date.[23] An alternative strategy is to adsorb protein antigens or DNA-encoding vaccine antigens onto the surface of charged biodegradable particles.[76] For example, PLGA particle surfaces modified with the cationic surfactant cetyl trimethylammonium bromide allow electrostatic adsorption of DNA vaccine plasmids or recombinant protein antigens.[77] This approach was pioneered at Chiron Corporation (now Novartis), and avoids antigen damage during encapsulation processes, while eliciting equivalent or superior immune responses. Like other depot strategies, DNA adsorbed on cationic PLGA particles is

retained upto at least 7 days at i.m. injection sites, while naked DNA is undetectable in muscle at this time.[78] Although PLGA is attractive for its long record of safety in humans, alternative bioresorbable polymers that can avoid some of the limitations of PLGA are under development and might offer a viable approach for encapsulated vaccine delivery. Examples include the development of polymers that degrade to uncharged or net neutral products that do not acidify their environment, such as poly(ortho esters)[79] or polyketals.[80,81] However, in relation to all particulate antigen depots, it must be remembered that most tissue sites for vaccination are not static beds of extracellular matrix, but rather contain a dynamic inflammatory infiltrate responding to the injection, and interactions of host cells with foreign particles must be considered to understand the mechanisms of the ensuing immune response. This is examined further in the next section.

4.419.3.2.2. Targeting and 'reverse targeting' of APCs

The particulate nature of microbes is itself a motif used by innate immune cells to recognize foreign material, and monocytes recruited to sites of inflammation internalize particles and carry them to draining lymph nodes.[30] Particles of a size small enough for phagocytosis (~5–10 μm and smaller) but too large for endocytosis by stromal cells are thus 'naturally targeted' to phagocytes (**Figure 1**). However, neutrophils, macrophages, monocytes, and DCs are all phagocytic, and neutrophils and macrophages typically greatly outnumber DCs (or monocytes that might differentiate into DCs *in situ*) early in the host response at injection sites. Flow cytometric analyses of cells infiltrating the peritoneum following PLGA microsphere vaccine injection have found that the vast majority of cells internalizing particles exhibit a macrophage-like phenotype (60–70% at 48 h, vs. 5–8% DCs[82,83]). For particles with mean sizes of a few microns, a small but detectable population of microsphere$^+$ cells can be found in draining lymph nodes 24–48 h after immunization, although these small particle$^+$ populations likely represent a tiny fraction of the total injected dose, which was 1 or more milligrams in these studies.[82,83] Thus, such 'natural targeting' may be inefficient in directing antigen-carrying particles to the DCs most critical for initiating adaptive immune responses. Interestingly, although these studies describe the persistence of fluorescently tagged vaccine particles at injection sites for prolonged periods, no reports have attempted to quantify the fraction of particles that are internalized by phagocytes at the injection site over time – information which could provide significant insight into the ability of released antigen to reach draining lymph nodes. In relation to these issues, recent work exploring the role of particle geometry on macrophage phagocytosis has suggested that it may be possible to engineer phagocytosis-resistant particles purely on the basis of shape considerations, which could be an interesting area for exploration in vaccine delivery.[84]

An alternative to relying on passive processes of phagocytosis is to functionalize particle vaccine carriers with antibodies targeting specific APCs, in order to deliver antigen to APCs via binding of particles to specific receptors. Conjugates of protein antigens with a monoclonal antibody to the DEC-205 lectin receptor expressed by DCs were shown to elicit extremely potent T cell responses following vaccination with minute doses of antigen.[85] Following on this discovery, it was shown that liposome-like plasma membrane vesicles prepared from tumor cells could be targeted to DCs for enhanced internalization by functionalizing the surface of these vesicles with antibody fragments targeting CD11c (a canonical DC surface marker) or DEC-205.[86] Frechet's group demonstrated that anti-DEC-205-functionalized hydrogel microparticles carrying protein antigens triggered enhanced phagocytosis of these particles *in vitro* and an approximately threefold enhanced uptake of particles into DCs following s.c. injection *in vivo*, with a coincident improvement in cytotoxicity and cytokine secretion by antigen-specific T cells.[87] Macrophages and DCs express scavenger receptors, such as the mannose receptor, which promote internalization of pathogens. Thus, in a similar vein, functionalization of DNA vaccine-loaded liposomes with monoclonal antibodies directed against the mannose receptor has been shown to enhance *in vivo* transfection of splenic DCs by ~10-fold following i.p. injection and concomitantly, the generation of cytotoxic T cells.[88]

A final approach for enhancing delivery of antigens into APCs is to use biomaterials for 'reverse targeting'–attracting APCs to antigen depots instead of targeting particulate antigen to cells. Inflammation at sites of infection triggers the release of a host of chemoattractants that recruit monocytes and DCs from the blood;[89,90] these cells can take up antigen and transport it to draining lymph nodes to prime T and B cells.[29] Mimicking this natural response to infection is another strategy to enhance the function of antigen depot vaccine delivery systems. Using PEVAc polymer matrices very similar to that first reported by Langer for vaccine depot generation, Kumamoto prepared implantable rods that released both a protein antigen and a chemoattractant, CCL19 (see also **Chapter 5.522, Bone Tissue Engineering: Growth Factors and Cytokines**).[91] Notably, CCL19 is an attractant for mature (activated) DCs, not immature (resting/unactivated) DCs, and binds the same receptor (CCR7) as the chemokine CCL21 produced by lymphatic vessels that attracts activated DCs to lymph nodes. By applying a topical inflammatory stimulus over the implant site, these authors were able to activate DCs locally at the implant and then trap them locally for sustained periods, by providing a competing chemoattraction gradient that slowed DC trafficking to CCL21-producing lymphatics. This local trapping provided a greater time window for DCs to accumulate and internalize antigen released from the implanted rods, and thereby enhanced T cell and antitumor responses elicited by the vaccine. In an approach more closely resembling the response to infection, attractants for immature DCs have been encapsulated in PLGA microspheres, allowing the generation of local chemoattraction gradients around collections of microspheres that potently chemoattract resting DCs.[92] Singh *et al.*[93] have shown that *in situ* cross-linkable hydrogels can be loaded with chemoattractants to draw DCs to DNA vaccine depots. One of the most promising antitumor vaccines (presently in clinical trials) is based on the injection of irradiated autologous tumor cells, which are transfected to produce the cytokine granulocyte/macrophage colony-stimulating factor (GM-CSF).[94] GM-CSF is an attractant for DC precursors, and also triggers the differentiation of these cells into potent APCs, which leads to strong immune responses elicited by attracting and differentiating

DCs *in situ*. Recently, Ali *et al.*[95] demonstrated that this process can be mimicked by designing implantable biodegradable PLGA scaffolds carrying GM-CSF and tumor lysates (as a source of antigen), which provides a substantial advantage as no live cells are used in the therapy (see also **Chapter 5.522, Bone Tissue Engineering: Growth Factors and Cytokines**). Notably, immunostimulatory TLRas could be coreleased from these scaffolds to provide additional 'danger' signals promoting the immune response.

4.419.3.2.3. Lymph node targeting

In the approaches described above, especially those employing implanted matrices or polymer microparticles, most of the 'targeting' of APCs likely occurs in the peripheral tissue injection site, as these materials will have poor, if any, direct access into the lymphatics and downstream lymph nodes. These strategies thus rely on the activation of targeted APCs and the subsequent trafficking of these cells to the lymph nodes to initiate immune responses. Alternatively, vaccines might aim for direct transport to lymph nodes, to allow direct delivery to lymph node-resident DCs and B cells. Although particles draining through lymph were long thought to be largely scavenged by macrophages lining the subcapsular sinus of lymph nodes, recent studies have revealed that viral particles,[96] immune complexes,[97] and synthetic antigen-displaying nanoparticles[98] are transferred through the floor of the lymph node subcapsular sinus by macrophages to B cells scanning for antigen, providing a potential mechanism for B cells to directly acquire particulate antigen. Particles small enough to diffuse through the interstitial matrix at an injection site pass between lymphatic endothelial cell junctions to enter lymphatics, then drain to downstream lymph nodes, and pass through the subcapsular sinus into the lymph node cortex; they could potentially achieve direct delivery to both DCs and B cells. Numerous studies have explored relationships between particle properties and lymph node draining following subcutaneous, intradermal, or intramuscular injection.[99–101] A wide variety of materials have been used in these studies, ranging from lipid-stabilized oil emulsions to solid polymer particles, and potential differences in the stability and elastic properties of these nanoparticles may be relevant to understanding the results obtained in any particular system. However, several general trends emerge: smaller particles, particularly those less than 100 nm in size, are transported more efficiently to lymph nodes from injection sites.[101,102] For rigid polymer particles, sizes under ~50 nm appear to be required for efficient diffusion through tissue matrix in intradermal sites (**Figure 2**),[101] but liposomes of substantially larger diameters are capable of draining to lymph nodes,[100] perhaps reflecting the deformable nature of these elastic vesicles. Attachment of poly(ethylene glycol) (PEG) chains to the surfaces of liposomes or polymer particles reduces interactions of the particles with ECM and adsorption of serum opsonins to the particles,[103] enabling enhanced lymphatic draining.[104,105] Small particles reaching lymph nodes can access

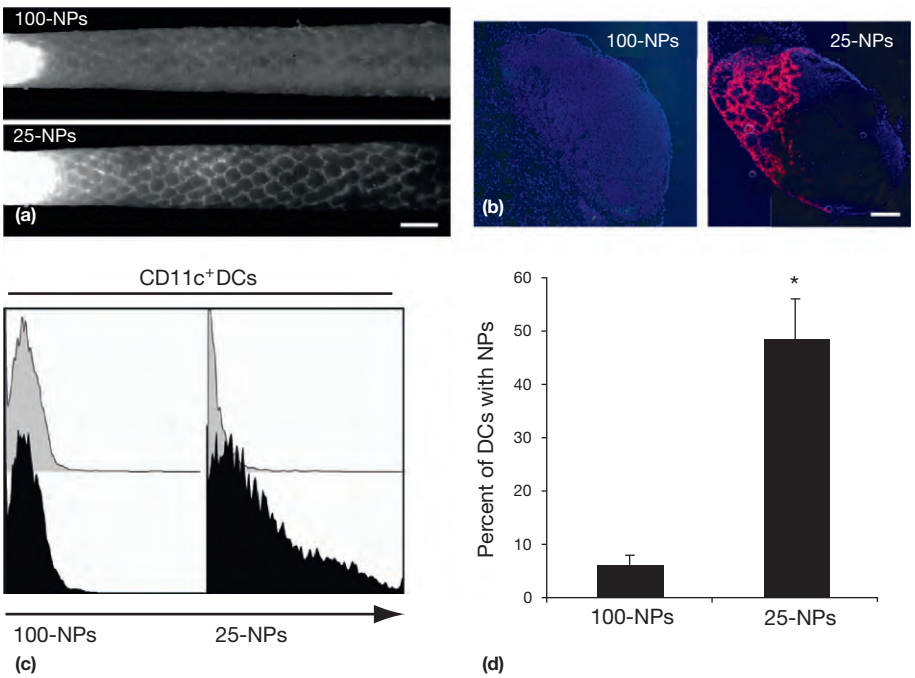

Figure 2 Lymph node-targeting, complement-activating polymer nanoparticles accumulate in lymph nodes after intradermal injection and induce antigen-specific adaptive immune responses in a size-dependent manner. (a) Fluorescence microlymphangiographs demonstrating more efficient draining of fluorescent 25 nm polymer nanoparticles compared with 100 nm nanoparticles through lymphatics in a mouse tail (lymphatic capillaries all drain in one direction), (b) 25 nm, but not 100 nm, nanoparticles are visible in mouse lymph node sections 24 h after injection. (c) Flow cytometry histograms show $CD11c^+$ dendritic cells isolated from draining lymph nodes after intradermal coinjection of fluorescently labeled 100 and 25 nm nanoparticles (black) or phosphate-buffered saline (PBS) control (gray). (d) Quantification of preferential targeting of lymph node DCs by 25 nm nanoparticles compared with 100 nm. Adapted from Reddy, S. T.; van der Vlies, A. J.; Simeoni, E.; *et al*. *Nat. Biotechnol*. **2007**, *25*(10), 1159–1164.

not only macrophages in the subcapsular sinus but also CD11c$^+$ and DEC-205$^+$ DCs in the lymph nodes.[101,106] Lymph node targeting requires not only transport through the lymphatics but also retention in the node, and particles of smaller size and PEGylation can in fact pass through the draining lymph nodes to reach the bloodstream – thus, particles with optimal lymph node accumulation are not necessarily the smallest/most hydrophilic compositions. Functionalization of PEGylated nanoparticles with targeting agents such as antibodies may enhance retention of vaccine particles specifically by DCs.[107]

Only a few studies have directly explored the impact of particle size on lymph node targeting coupled to vaccine responses. Plebanski and colleagues showed that nanoparticle vaccines composed of protein antigen or minimal peptide epitopes covalently linked to monodisperse polystyrene particles were capable of eliciting strong CD8$^+$ T cell and antibody responses.[106,108] Testing a range of particle sizes from 20 nm up to 2 μm, they found that both antibody and CD8$^+$ T cell responses were maximal for particles 40 nm in diameter. In these studies, no specific molecular adjuvant was included, so the nature of the 'danger' signals promoting these responses is not clear, and the clinical translatability of nondegradable polystyrene as a vaccine carrier is uncertain. Reddy *et al.*[101] developed biodegradable nanoparticles based on poly(propylene sulfide), which could similarly display surface-tethered, antigens, and demonstrated that PPS particles of ~25 nm were capable of much more efficient lymph node transport than particles 45 or 100 nm in diameter (**Figure 2**). They further found that display of hydroxyl-terminated PEG at the surface of these particles could be used to activate complement, providing an *in situ* adjuvant signal at the particle surface following injection.[109] These lymph node-targeting and complement-activating particles elicited strong CTL and antibody responses *in vivo* that were comparable to injections of antigen with LPS,[109] a very strong adjuvant in mice that is too toxic to be used safely in humans. Notably, 100 nm particles of the same composition and carrying the same antigen dose gave much weaker immune responses, suggesting that lymph node targeting can substantially amplify the immune response to particulate vaccines.

4.419.3.3. Controlling Vaccine Delivery at the Cellular Level

Vaccine antigens and any associated adjuvant signals must be delivered into tissue sites, transported to either DCs in the tissue or to B cells/DCs in draining lymph nodes, and finally, taken up by individual DCs and B cells. Vaccine materials can play a critical role in modulating this final key step of vaccine delivery. The most studied concept in controlling immune responses at the single-cell level is the use of particulate delivery agents to 'target' antigens to phagocytic APCs (DCs, macrophages, and B cells), which are capable of internalizing particles greater than 1 μm in size with greater efficiency than other cell types. Using alum as the classic example, Mannhalter *et al.*[110] demonstrated that tetanus toxoid (TT) antigen adsorbed to aluminum hydroxide particles induced significant increases in T cell proliferation, mediated by an increase in macrophage/T cell interactions. A more recent report demonstrated that for a model antigen (alpha casein), uptake by DCs *in vitro* was increased fourfold relative to soluble antigen when the protein was adsorbed onto aluminum hydroxide.[111] These findings support the ability of aluminum-based adjuvants to target antigen-presenting DCs by 'particulating' soluble antigens. Similar results have been found for a broad range of particulate biomaterial vaccines, including a range of polymer particles and liposomes.[23] Recent studies have begun to explore additional strategies to exploit such APC-targeted uptake, for example, via the delivery of antigen-loaded polyelectrolyte multilayer-based microcapsules to monocytes and DCs in whole blood.[112] Beyond this simple strategy of preferential internalization by APCs, particulate antigens have been explored for enhancing CD8$^+$ T cell responses and B cell responses by additional mechanisms, as outlined in the following sections.

4.419.3.3.1. Cross-presentation of antigen to CD8$^+$ T cells

Much work has focused on controlling antigen uptake and activation of DCs, due to their central role in regulating naïve CD4$^+$ and CD8$^+$ T cell priming. A key challenge facing subunit vaccines is the elicitation of CD8$^+$ T cell responses, as exogenous antigens internalized by DCs are effectively processed and loaded onto class II MHC molecules for presentation to CD4$^+$ T cells (for induction of Ab responses), but only very inefficiently processed for loading into MHC I molecules for presentation to CD8$^+$ T cells (for generation of cellular immunity). Predominantly, antigen presented on class I MHC derives from proteins processed in the cytosol of DCs (e.g., proteins from a virus that has infected the cell) (see also **Chapter 4.424, Nanoparticles for Nucleic Acid Delivery** and **Chapter 4.425, Delivery of Nucleic Acids and Gene Delivery**). However, it was shown in the early 1990s that particulate forms of antigen trigger 'cross-presentation,' the loading of exogenous antigens onto class I MHC.[113,114] Although the mechanisms underlying cross-presentation remain controversial,[115] the finding that antigen attached to or encapsulated within particles ranging in size from a few tens of nanometers to several microns is cross-presented with up to 1000-fold greater efficiency has inspired the exploration of a broad range of biodegradable particle carriers for vaccine delivery, including liposomes,[116,117] PLGA particles,[118–120] and hydrogel particles.[121,122] Notably, particle-delivered antigen elicits strong CD4$^+$ T cell responses *in vivo* as well.[118] Although relatively stable materials such as polystyrene or iron oxide particles with surface-attached antigen promote cross-presentation of antigen and subsequent CD8$^+$ T cell responses *in vitro* and *in vivo*,[106,113] another approach that has been explored is the design of particles that disrupt phagosomes/endolysosomes, allowing direct transport of antigen into the cytosol where it can be proteolyzed by the classical MHC I antigen processing pathway. For example, acid-responsive microparticles and nanoparticles that quickly break down in phagosomes[122,123] or swell in response to acidification of these compartments[124] have been used to osmotically disrupt the phagosomal membrane, delivering antigen into the cytosol and eliciting enhanced cross-presentation. DCs are also known to be capable of storing antigen for prolonged periods in their endosomal/phagosomal compartments,[125] and biodegradable particles that slowly release antigen over time in these vesicles or within the cytosol may also be able to prolong antigen presentation.[120] A third strategy to promote CD8$^+$ T cell responses is

to deliver plasmid DNA-encoding antigens directly into DCs so that they produce antigens endogenously, and biodegradable microparticles and nanoparticles capable of endosome/phagosome disruption have been used for such DNA vaccines.[126,127] Although PLGA is not traditionally viewed as an acid-responsive polymer, a few studies have suggested that PLGA particles may also disrupt phagosomes.[120,128] Perhaps employing this mechanism in part, cationic PLGA microparticles with surface-adsorbed antigen-encoding DNA have been shown to enhance $CD8^+$ T cell responses in both mice and nonhuman primates.[77,129,130]

4.419.3.3.2. B cell activation and humoral responses

B cells are triggered by antigen-mediated cross-linking of cell surface Ig receptors. It has long been appreciated that antigen receptor recognition of repetitive surface structural motifs common in microbes efficiently triggers B cell signaling, and such repetitive structures may act intrinsically as danger signals for humoral responses.[131] B cells that bind to organized surface proteins or polysaccharides on viral particles or bacteria are robustly activated.[132] Thus, synthetic vaccine particles displaying many copies of surface-conjugated antigen are efficient triggers of antibody responses.[106,109,133] The most extreme example of the importance of particulate display for humoral responses comes from studies of minimal epitope vaccines: When short peptides are used as defined B cell antigens, display of the peptides on the surface of liposomes triggers robust antibody responses while soluble peptides or peptides encapsulated in liposomes fail to elicit humoral immunity.[133,134] Similar to the case of antigen delivery to DCs, maximal B cell responses might require the codelivery of antigen and accessory danger signals in the same particle.[135]

4.419.4. Biomaterials as Immunostimulators and Carriers of Immunostimulatory Adjuvants for Vaccines

As outlined in Section 4.419.2, antigens must be acquired by the immune system in the context of danger signals to promote the generation of a productive immune response. Biomaterials can thus play a key role not only in vaccine antigen delivery, but also in the codelivery of appropriate danger cues that prime protective immunity to the delivered antigens rather than tolerance. Two strategies for provision of danger signals using biomaterial delivery agents have been explored: (1) biomaterials that intrinsically provide danger signals to responding innate immune cells, and (2) biomaterials as cocarriers of antigens and defined molecular danger signals, such as PAMPs, DAMPs, and cytokines.

4.419.4.1. Intrinsic Adjuvant Activity of Biomaterials

Many biomaterials developed for vaccine delivery have been thought of primarily as passive physical delivery agents, controlling the kinetics and localization of antigen during immunization to promote the immune response. However, our expanding understanding of how the immune system detects danger has led to recent revelations about the complex interaction biomaterials have with the immune system and unexpected danger cues elicited by materials previously viewed as immunologically inert antigen depots. In this context, a discussion of the most established and well-studied adjuvant, alum, and recent discoveries about the role of the inflammasome in mediating biomaterial adjuvant effects is introduced. Then other ways in which danger-sensing pathways may be triggered by biomaterials under development for vaccine delivery are discussed. Together, these recent developments are paving the way for viewing biomaterials themselves as agents for actively shaping immune responses.

4.419.4.1.1. Activation of the inflammasome

As discussed in Section 4.419.4.2.1, alum was traditionally thought to function primarily by providing sustained antigen release from the injection site, but conflicting data existed regarding the actual depot function of alum and its importance in the immune response.[59] In addition, a number of clear biological events occur in response to alum/antigen injections. Coadministration of alum and antigen induces chemokine production and recruitment of monocytes, granulocytes, and macrophages to the injection site.[136,137] Alum also induces secretion of cytokines and the differentiation of monocytes toward a DC phenotype.[62,110,137,138] Alum was also found to trigger antigen-independent proliferation of splenic B cells, which coincides with accumulation of $Gr1^+$ IL-4-producing cells in the spleen, indicating a previously unappreciated role for alum in B cell priming and expansion.[62] Together, these observations suggest a potentially important role for alum in mediating innate immune responses that bridge to adaptive immunity.

Recently, new mechanistic insights have emerged regarding the pathways by which alum triggers this suite of responses *in vivo*, via a danger/pathogen-sensing signaling pathway known as the inflammasome.[60,61,139–141] As highlighted in Section 4.419.2, DCs and other innate immune cells express PAMP and DAMP sensors, which can be cell surface receptors (e.g., TLR2, TLR4 and TLR6) or intracellular proteins (e.g., NLRs). Inflammasomes are cytosolic, multiprotein complexes that play key roles in mediating innate immunity through the induction of inflammatory cytokines in response to bacterial pathogens.[142,143] While several distinct inflammasome complexes have been described, a common downstream event is the production of inflammatory cytokines. For example, activation of the caspase-1 inflammasome leads to production of active caspase-1, which cleaves the inactive precursor forms of two potent proinflammatory cytokines (pro-IL-Iβ and pro-IL-18) to generate active IL-1β and IL-18. IL-1β and IL-18 – along with another inflammasome-inducible cytokine, IL-33 – increase cell migration, induce secretion of interferon-γ, promote differentiation of T_h17 cells, and enhance humoral immune responses (via IL-5 and IL-13). Another inflammasome complex, NALP3 (NAcht domain-, leucine-rich repeat-, and Pyrin domain-containing protein 3), is indicated in sensing and generating proinflammatory responses against bacterial toxins using a similar pathway.[32] *In vitro* studies in mouse and human cells using MyD88-deficient cells (a key adaptor protein required for signaling through TLRs) indicated that alum induces secretion of IL-1β and IL-18 independently of TLR signaling.[140] In mice, IL-1β, IL-18, and IL-33 secretion

by alum was dependent on the NALP3 inflammasome. The mechanism by which alum is capable of triggering the NALP3 inflammasome is still a subject of debate: Alum has been indicated in the induction of uric acid, a known DAMP released from necrotic cells;[139] uric acid crystals can trigger inflammasome activation. An alternative theory suggests the ability of alum to induce phagocytic uptake is critical for inflammasome activation, holding that the danger signal is potassium efflux resulting from rupture of alum-containing endosomes and lysosomes.[60,61] Using alum-containing vaccine formulations administered to NLRP3-deficient mice (mice lacking the NALP3 inflammasome), antigen-specific antibody production was greatly reduced, further supporting the key role of inflammasome activation in alum's adjuvant activity.[60]

These findings regarding the classic adjuvant alum appear to have relevance for a range of vaccine biomaterials, and perhaps for the host response to biomaterials in general. For example, PLGA, one of the most ubiquitous resorbable biomaterials, also activates the NALP3 inflammasome when incubated with immune cells in particulate form. PLGA microparticles have been shown to greatly enhance secretion of IL-1β and IL-18 when incubated with DCs in the presence of LPS, which on its own is a weak inducer of IL-1β.[144,145] This behavior is true for PLGA coadministered with a number of other TLRas that act through intracellular or extracellular TLRs. While PLGA-induced inflammasome activity was found to be dependent on coincubation with TLRas *in vitro*, *in vivo*, inflammasome activation as well as proinflammatory cytokine secretion was induced in the absence of LPS or other TLRas,[145] suggesting that PLGA may serve as, or induce, a second signal for inflammasome activation. IL-1β induction by PLGA particles is NALP3 dependent, and interestingly, inflammasome activation by PLGA is dependent on uptake of particles by DCs, lysosome acidification, and efflux of intracellular potassium ions. Administration of PLGA microparticles with ovalbumin (OVA) leads to increased production of antigen-specific antibodies compared with soluble antigen and this effect persists in NALP3-deficient mice. In contrast, PLGA-induced enhancement of cellular immunity through proliferation of $CD11b^{+}Gr1^{-}$ cells and IL-6 production was absent in NALP3-deficient mice.[145] Thus, PLGA appears to confer adjuvant activity by antigen-independent inflammasome activation, as well as two antigen-dependent mechanisms, namely, enhancement of antibody-specific responses and a yet-to-be-determined route requiring NALP3 inflammasome activation for mediating cellular immunity through induction of $CD11b^{+}Gr1^{-}$ cell populations and upregulation of IL-6. Similarly, particles of chitosan, a biodegradable polysaccharide, have been shown to induce activation of the NALP3 inflammasome and IL-1/IL-18 secretion through a caspase-1-dependent mechanism similar to that of alum.[141] These findings suggest that other nominally nondegradable microparticles (polystyrene, silica) also trigger inflammasomes,[61] and indicate a common route through which particulate biomaterials may confer adjuvant activity.

4.419.4.1.2. Role of TLRs in immune cell response to biomaterials used as vaccine carriers

In addition to inflammasome activation, a variety of biomaterials have recently been implicated in the activation of DCs and PAMP-mediated TLR pathways. Many of these findings have their origins in the study of biopolymers or synthetic polymers for implantable devices and are known to elicit certain anti-inflammatory or inflammatory responses depending on the stability of degradation products postimplantation (see also **Chapter 5.501, Scaffolds: Flow Perfusion Bioreactor Design**; **Chapter 5.502, Engineering Scaffold Mechanical and Mass Transport Properties**; **Chapter 5.520, Bioactive Ceramics and Bioactive Ceramic-Composite-Based Scaffolds**; **Chapter 5.503, Biomaterials and the Microvasculature**; **Chapter 5.504, Effect of Substrate Modulus on Cell Function and Differentiation**; **Chapter 5.506, Effects of Mechanical Stress on Cells**; **Chapter 5.522, Bone Tissue Engineering: Growth Factors and Cytokines**; **Chapter 5.507, Tissue Engineering and Selection of Cells**; and **Chapter 5.508, Scaffold Materials for hES Cell Culture and Differentiation**).

Naturally occurring polysaccharide biopolymers such as alginate, hyaluronic acid (HA), chitin/chitosan, and heparin have all been recently implicated as triggers of TLRs under certain conditions. HA is a polysaccharide component of the extracellular matrix and widely studied as a component of topical and implantable biomedical materials. *In vivo*, HA is enzymatically degraded by hyaluronidase to oligosaccharides containing glucuronic acid and acetylglucosamine. While high molecular weight (HMW) endogenous HA is essentially inert, low molar mass fragments of HA have recently been shown to activate DCs and macrophages.[146–148] HA degradation products (glycosaminoglycan hyaluronan) produced after lung tissue injury initiate inflammatory responses dependent on both MyD88 and TLR-2/TLR-4 pathways. Interestingly, overexpression of HMW HA was found to be protective against lung injury.[149] Activation is mediated through TLR-4 signaling as indicated by abrogation of these effects in the presence of anti-TLR-4-mAb, or in mice lacking functional TLR-4.[147] Further evidence of the involvement of the TLR-4 pathway is suggested by the upregulation of key TLR-4 signaling components (e.g., p38/p42/44 MAP-kinases) associated with treatment of DCs and macrophages with HA fragments, but not with HMW HA. Similarly, DC activation has also been demonstrated for heparin-containing materials, through activation of NF-κβ and TLR-4.[150–152] An important implication of this work is the demonstration of an endogenous material inert in its native polymeric form, but inflammatory upon specific chemical modification (e.g., breakdown by inflammatory enzymes) – such materials might be very useful as safe, biodegradable vaccine adjuvants. Particles of hydroxyapatite (HyAp), which forms the basis of commercial calcium phosphate vaccine adjuvants, have recently been shown to induce secretion of inflammatory cytokines (e.g., TNF) through activation of the TLR-4 pathway, as well as NF-κβ.[153] Analogous to the case of HA fragments, this response may have evolved as a danger response for damaged bone and other hard tissues, where HyAp particles may be produced.

Polysaccharides derived from pathogens also tend to trigger TLR signaling in a manner that may reflect evolved recognition of multivalent, particulate microbes. For example, the naturally occurring polysaccharide chitin, a component of fungi and parasitic nematodes,[154] elicits size-dependent immune responses in macrophages, stimulating TNF-α production with polymer fragments ranging in size from 2 to 70 μm.[155] Intermediate fragments (40–70 μm) function through the TLR-2, dectin-1,

and NF-κβ pathways, whereas smaller fragments (2–10 μm) were found to mediate immune responses through activation of both TLR-2-dependent and TLR-2-independent dectin-1 pathways involving the mannose receptor and spleen tyrosine kinases. Additionally, only these smaller fragments induced secretion of the anti-inflammatory cytokine, IL-10.[155] Similarly, covalent linking of low molecular weight mannuronic acid polymers (representative of fragments of bacterial alginate polymers) to magnetic particles triggered a robust TNF-α production, whereas soluble forms of these low MW fragments did not.[156] These intriguing findings suggest a plausible mechanism for endogenous immune regulation: large/particulate polysaccharide fragments that are a signature of intact invading pathogens activate *inflammatory* pathways (e.g., TLRs), whereas low MW fragments representative of degraded pathogens activate *anti-inflammatory* cytokines such as IL-10.

In the last few years, a number of synthetic polymers traditionally associated with biomedical devices have also been identified as TLRas, suggesting that even completely nonbiological materials may be capable of modulating immune responses relevant for vaccination. Alkane and alkyl polymers such as polyethylene (PE) are commonly employed as components of biomedical implants. PE in the traditional ultra HMW form used in prosthetic implants is immunologically inert. *In vivo*, however, PE is oxidized such that the concentration of hydroxyl and carboxyl functional groups increases over time.[157] Using oxidized PE purified from implant sites and chemically modified PE with defined levels of hydroxyl and carboxyl groups, Maitra *et al.*[157] recently demonstrated that these materials mediate inflammatory responses by activating TLR-1 and TLR-2 pathways. Polymers induced NF-κβ signaling and activated DCs, leading to secretion of proinflammatory cytokines such as IL-12. Molecular docking experiments indicate that alkane oxidation confers specificity for interactions between oxidized PE and TLR-1/TLR-2 receptors. Clearly, the immune system has not evolved to protect the host from biomedical implants, and this has led to the suggestion that the patterns recognized by the host immune system may in some instances relate to very basic physicochemical properties. One recent theory points out that PAMPs and DAMPs have in common the presence of hydrophobic moieties (hyppos), which might serve as a universal danger signature.[158] For example, HA has already been described as inert – and lacking obvious hyppos – in the polymeric form, but becomes inflammatory upon degradation to oligosaccharide subunits. However, during degradation, hydrophobic portions of HA become exposed,[158] possibly serving as a conformation-specific trigger for TLR activation, similar to that described for PE. Another recent study focused on ionic charge as a core property required for activating T cells and APCs through TLR-mediated pathways.[159] Many zwitterionic bacterial polysaccharides activate T cells and APCs. By introducing cationic charge into naturally occurring anionic polysaccharides through chemical modification, these materials are able to activate monocytes and DCs in a manner similar to wild-type zwitterionic polysaccharides.[159] The ability of natural and synthetic biomaterials to activate TLR pathways through presentation of common physical and chemical properties could provide the foundation for designing new hybrid adjuvants that elicit defined immunological responses. Recently, polyamidoamine dendrimers modified with glucosamine (a prevalent component of exoskeletons, crustacean, and fungi) have been reported.[160] Interestingly, these materials blocked TLR-4 activation by LPS and the production of TNF-α, IL-1β, and IL-6. However, they allowed upregulation of costimulatory molecules including CD25, CD80, CD83, and CD86. Thus, hybrid materials that contain both natural and synthetic components, may allow tailored immunogenic profiles with both pro- and anti-inflammatory character to be elicited *in vivo*.

4.419.4.1.3. Complement-activating biomaterials

The complement pathway is a component of innate immunity that functions to enhance the clearance of antigens by antibodies in the blood stream. Depending on the type of activating signal, complement can be called into action through any of three biochemical pathways (classical, alternative, and lectin), or can be stimulated by the adaptive immune system. When antigen is present in the blood, a biochemical cascade activates a series of precursor proteins – synthesized in the liver and circulating in the blood – to assemble into complement proteins that enhance antigen clearance. These proteins act through several mechanisms, including coating or 'opsonization' of antigens to increase phagocytosis, pore formation on foreign cell membranes to induce lysis, and recruitment of macrophages and neutrophils. Biomedical engineers have long known of the abilities of a range of biomedical polymers to activate inflammatory and complement pathways, but the specific mechanisms by which these materials elicit such responses are only recently being explored at a more basic level.[16,161] Gold surfaces functionalized with defined thiol-containing groups have been investigated, and these studies suggest that mercaptoglycerol- and mercaptoethanol-containing surfaces generate the strongest inflammatory responses.[162] Using complement-depleted animals, this response was found to be generated through a surface-mediated complement activation mechanism. Pluronics, a versatile class of triblock copolymers composed of alternating hydrophilic PE oxide (PEO) blocks and hydrophilic polypropylene oxide (PPO) blocks, have been explored extensively as potential vaccine adjuvants. These block copolymers have recently been implicated in the stimulation of several immune pathways including complement activation through the recognition of terminal hydroxyls, and in the enhancement of CTL and Ab responses.[163–165] Pluronic F108 (PF108) grafted to glass surfaces induces complement activation, whereas PEO homopolymer does not.[163] As with some of the other examples described in this section and previously,[158] this finding suggests that the hydrophobic portion (i.e., PPO repeat units) serves as a distinct chemical functionality involved in activating immune pathways linked to the complement cascade. As discussed in **Section 4.419.3.2.3**, Hubbell and coworkers employed a 25 nm nanoparticles surface modified with pluronic to activate complement *in situ* following parenteral injection.[109] These materials were able to activate DCs, generate danger signals, and, upon conjugation to OVA, mediate cellular and humoral immunity. Thus, new biomaterial adjuvants may find utility in activating TLR and inflammasome pathways as well as by exhibiting intrinsic complement-activating capacity.

4.419.4.1.4. Biomaterial-mediated adjuvant mechanisms not yet elucidated

As described above, the last few years have witnessed a number of exciting discoveries demonstrating the potential of biomaterials to serve as more integral vaccine components. However, many questions still surround the key mechanisms through which the existing biomaterials adjuvants function. Of note, MF59, a widely employed oil-in-water emulsion approved for clinical use in Europe, also shares many of the immunological properties of alum. Both of these adjuvants are able to induce the secretion of multiple cytokines involved in cell migration (CCL2, CCL3, CCL4, CXCL8), enhance monocyte differentiation to DCs, and ultimately facilitate adaptive immune responses by facilitating migration of activated DCs to draining lymph nodes.[137] However, a number of differences exist between the responses elicited by alum and MF59. MF59 has been found to upregulate CD83 and CCR7 on differentiating monocytes compared with the levels observed using alum, and it also appears to act on granulocytes, macrophages, and monocytes, whereas alum acts primarily on only the latter cell populations. This example illustrates characteristic 'immunological profiles' induced by adjuvants, and further studies of MF59 and other new adjuvants will be required to ascertain whether they function through activation of the inflammasome, or through other mechanism(s) distinct from that of alum or PLGA.[166]

Another series of reports describing the ability of biomaterials to induce Th2 helper T cells also raises interesting questions. Scaffold or microparticle forms of PLGA or polystyrene used as adjuvants for immunization with adsorbed OVA enhanced humoral immune responses by supporting Th2 helper T cell development. This effect was sustained for at least 18 weeks, but was not dependent on the specific polymer chemistry (e.g., PLGA composition).[167] Subsequent work has demonstrated that while both scaffold and particle polymer forms generate adjuvant effects, scaffolds induce a higher and more sustained humoral response. Is this finding linked to danger signals resulting from a more invasive implantation of scaffolds that increases tissue damage and necrosis,[168] or is another physical mechanism at play? A range of biomaterials appear to induce differential maturation of DCs depending on the specific composition.[169] When DCs are cultured *in vitro* with PLGA, chitosan, or agarose, the corresponding levels of CD86, CD40, and HLA-DQ (human MHC molecules) increase in a manner similar to that of LPS.[170] In contrast, when DCs are cultured with HA or alginate, these same phenotypes decrease; thus these results suggest chemistry-dependent interactions that exert distinct maturation effects on DCs. How these findings correlate to *in vivo* settings, or the mechanism through which these effects are achieved, is yet to be determined. Recent findings that binding of particulate materials to the membrane of DCs can induce lipid sorting at the cell surface and trigger receptor-independent activation of kinases suggest that much remains to be learned about the pathways by which immune cells can sense materials in their environment.[171] Are there common physical and chemical properties – molecular weight, fragment size, hydrophobicity, physical form, or inflammatory degradation products – that determine the ability of different biomaterials to elicit specific immune responses? Despite these open questions, the intrinsic ability of biomaterials to induce a range of immune responses is a promising feature that holds significant potential in the design of new materials functioning both as carriers and adjuvants.

4.419.4.2. Biomaterials as Carriers of Adjuvant Molecules

As discussed in the previous section, biomaterials are capable of directly activating inflammatory pathways, maturing DCs, and inducing inflammatory cytokine secretion. However, the use of biomaterials as carriers to codeliver defined immunoregulatory molecules (e.g., DAMPs, PAMPs, or regulatory cytokines) together with antigens is a second strategy for providing suitable danger signals during vaccination and regulating the developing immune response. Incorporation of one or multiple adjuvant components, controlled and sustained release, targeting, enhanced uptake, and cargo protection are just some of the performance characteristics biomaterial-based carriers offer for vaccination and immunotherapy.

4.419.4.2.1. Delivery of PAMPs, DAMPs, and related immunostimulatory molecules

Because of their potent ability to drive the development of long-lived, effective immunological memory, the use of molecularly defined PAMPs and DAMPs especially TLRas as adjuvants in vaccines has been of obvious interest. In the simplest setting, mixing antigens delivered by biomaterials adjuvants such as alum, MF59, or PLGA particles with soluble TLRas has been shown to enhance serum antibody levels, T cell proliferation, and interferon-γ production by T cells in response to subunit vaccine antigens.[172,173] Administration of MF59 alone or in the presence of CpG or the TLR4 agonist E6020 has also been reported to elicit similar T cells responses, but addition of the TLRas shifts the antibody isotypes toward a Th1-biased immune response.[174] Thus, simple mixing of TLRas with biomaterials designed to regulate delivery of antigens can enhance vaccine responses. However, coformulation of both antigen and PAMP/DAMP molecules in biomaterials for vaccine delivery has several potential benefits: (i) encapsulated danger signal molecules have been shown to have substantially increased potency, allowing 10–100-fold lower doses of these molecules to be used, potentially reducing side effects;[175–177] (ii) codelivery of antigen and danger signals into the same phagosomal/endosomal compartment within DCs may be important for regulating optimal presentation of antigen to T cells;[178] (iii) particles carrying both antigen and 'helper' ligands to ensure codelivery into antigen-specific cells trigger optimal antibody responses from B cells;[135] and (iv) sustained release of danger signals from controlled-release biomaterials may promote persistent TLR signaling, which has been implicated in breaking tolerance to tumor antigens.[179] Formulation of TLRas by adsorbing or encapsulating these components on or within various biomaterials has been used to enhance immune responses induced by antigens associated with a number of diseases including influenza, meningitis, streptococcus, and HIV, as well as cancer.[176]

Liposome-based vaccines for both cancer and infectious diseases have been explored for many years and provide the earliest examples of codelivering antigen with immunostimulatory molecules via vaccine biomaterials. While only a brief

survey of the work is presented in this chapter, the reader is referred to recent reviews for liposome-mediated TLR delivery.[180,181] Reports from the early 1990s have demonstrated that TLRas incorporated into antigen-carrying liposomes could enhance antibody and T cell responses.[134,182] These studies demonstrated that TLR4 agonist derivatives of LPS incorporated directly into the membrane of liposomes provided strong adjuvant effects, and biased antibody production from IgG1a to more potent IgG2a isotypes. In another strategy, oligonucleotide TLRas such as unmethylated CpG oligos (TLR9 ligands) have been encapsulated in liposomes, providing protection for these compounds from nucleases and prolonging immune responses.[183] Coencapsulation with OVA antigen enhances IFN-γ production and substantially increases IgG responses compared with equivalent antigen and TLRa doses administered in soluble form. In the case of cancer immunotherapy, TLRas – at least in the case of CpG – have also been shown to achieve these effects largely through a potent activation of cytotoxic T lymphocytes.[184,185] Liposomes containing CpG and HER-2/neu-derived peptide – a self tumor antigen – also increased IFN-γ (∼100-fold compared with antigen only); in addition, these materials have been shown to induce significant $CD8^+$ T cell responses.[186] Hepatitis antigen delivered with CpG in liposomes also enhances antibody responses, induces IL-12 production, and drives a Th1-biased immune response compared with the Th2 response observed in control groups immunized with free peptide.[187] Cationic liposomes improve uptake of antigen and CpG oligos into $CD11c^+$ DCs and activate natural killer T (NKT) cells to produce IFN-γ in a TLR-9-dependent manner.[188] This approach has also been recently extended to Leishmania vaccines to increase IgG2a titers.[189]

Although TLR4 and TLR9 agonists have been most widely studied, several additional TLRas have also been explored in the context of liposomal vaccination. Liposomes complexed with CpG or poly(I:C) (double-stranded RNA mimic, TLR3 ligand) and an antigen, trigger cross-priming of $CD8^+$ T cells and also elicit $CD4^+$ T cell responses.[190] In studies involving antigens for melanoma (trp2) or mycobacterium tuberculosis (ESAT-6), these antigen/TLRa complexes controlled tumor growth and offered protective immunity, respectively. Another TLRa, 3M-019 (TLR-7), dramatically improves antibody responses to the model antigen OVA.[191] Coadministration of OVA liposomes and 3M-019 increased levels of IgG2a and IgG2b 625-fold and 3000-fold, respectively, which were further increased when liposomes contained both OVA and 3M-019. A similar trend was observed with cellular immunity, and these observations suggest a potent synergy for codelivery of antigen and TLRas to the same APCs.

PLGA microparticles and nanoparticles have also been extensively studied as carriers for codelivery of antigen and PAMP molecules. One of the early reports of biomaterials as carriers of TLRas described the enhancement of both cellular and humoral immune responses by adsorbing CpG oligonucleotides (ligands for TLR-9) and HIV-associated antigens to separate populations of charged PLGA microparticles, leading to enhanced serum IgG titers and CTL generation.[192] Using PLGA nanoparticles to coencapsulate TT with CpG oligos, Diwan *et al.* demonstrated increased DC activation and enhanced antibody and T cell responses compared to soluble TT/CpG immunizations.[193,194] PLGA microparticles have been used to codeliver hepatitis B core antigen (HBcAg) with the TLR4 agonist MPLA.[195] Particle codelivery enhanced both $CD4^+$ and $CD8^+$ immune responses *in vitro* and *in vivo*.[118,196] *In vitro*, microparticles encapsulating OVA protein along with CpG or the TLR7 agonist imiquimod are phagocytosed by DCs and activate TLR pathways. These materials stimulate proliferation of primary and secondary $CD4^+$ and $CD8^+$ T cells *in vivo*, and elicit levels of cross-priming comparable to those induced by live microbe vectors.[196] An interesting variation of this approach is the addition of a TLR4 agonist (LPS) to the outer surface of PLGA nanoparticles using a double emulsion synthesis technique.[144] In comparison to unmodified nanoparticles, these particles are preferentially internalized and are able to elicit both humoral and cellular immune responses in mice, and were ultimately able to provide protection against West Nile encephalitis. In wild-type mice, IL-1β production is also increased, but this effect was abrogated in the absence of endocytosis and lysosomal fusion, suggesting inflammasome-mediated responses. Additional immune potentiators, including MPLA and RC539, have also been explored using PLGA microparticle-based delivery strategies.[197] In these studies, MPLA and RC539 significantly enhanced antibody-mediated immunity compared with soluble CpG, although the effect on cellular immunity was not described. Together, the observations discussed here suggest that PAMPs carried in biomaterials mediate activation of TLR pathways, and perhaps in many cases, of the inflammasome activation. While codelivery of PAMPs and antigen with biomaterials generally seems to have a positive enhancing effect on immune response, the specific response characteristics vary somewhat among different carrier systems. In the case of anthrax and meningitis studies, for example, PLGA-adsorbed CpG significantly enhanced antibody-mediated immunity and survival compared with soluble CpG.[198,199] In contrast, soluble and surface-adsorbed CpG had similar enhancing effects when administered using PLGA/chitosan microparticles, although encapsulated CpG still produced a marked improvement compared to these formulations.[198] The examples above demonstrate the growing body of literature focused on exploiting the delivery of PAMPs as adjuvants to enhance and direct the immune response, but DAMPs could also provide a complementary approach to enhancing vaccination following similar technical strategies. Because DAMPs function through alternate cell signaling pathways, these materials could serve as complementary adjuvants for new and existing vaccination and immunotherapy studies.

Most of the discussion above has focused on peptide and protein-based antigens, but biomaterials have also been used as a platform for enhancing DNA vaccination, and recently, several approaches have exploited TLRas to increase control over the magnitude and type of immune response associated with these materials.[19,176] As with the case for TLR enhancement of protein-based antigens described above, most of the DNA-based TLR work has also focused on encapsulation or adsorption of TLRas such as CpG on or within polymers and liposomes. Cross-linked polyacrylamide microparticles have been employed to deliver plasmid DNA encoding both a model antigen (β-galactosidase) and CpG immunostimulatory DNA, and these materials were internalized by phagocytic

macrophages, inducing a 40-fold increase in IL-6 secretion.[200] Recently, agonists for TLR-1, TLR2, TLR3, TLR4, TLR6, TLR7, and TLR9 were explored in the context of tumor therapy by injecting tumors with nanoparticles containing both TLRas and plasmid DNA-encoding CD40L.[201] TLR treatments containing CpG and/or poly(I:C) enhanced tumor therapy compared with treatment of plasmid only, activating DCs and inducing an influx of $CD8^+$ T cells. These reports demonstrate the potential for enhancing DNA vaccination through synergistic effects with one or more TLRas, and this is an area that will certainly be further explored in the near future.

In addition to these liposomal and PLGA particle canonical vaccine carriers, several other classes of materials have been employed as carriers of TLRas, including MF59,[173] alum,[202,203] alginate,[204] chitosan,[204,205] and protamine.[206] Each of these materials serves as an additional carrier of PAMPs or DAMPs and the reader is referred to recent reviews for additional background information and references.[16,176] In addition to TLRas, novel molecular danger signals are also being explored as potential adjuvants for biomaterial vaccine delivery. For example, α-galactosylceramide is an NKT cell ligand that has been shown to have potent adjuvant activity for a range of viral, parasitic, protein, and DNA vaccines.[207] This molecule has been formulated in poly(lactic acid) biodegradable nanoparticles for immunotherapy.[177] This and other molecules that act through distinct mechanistic pathways could provide opportunities to address particular immunological gaps, or act synergistically with other antigens and adjuvant molecules.

4.419.4.2.2. Delivery of immunoregulatory cytokines

Cytokines represent an interesting class of molecules that are being explored as adjuvant drug candidates for delivery using a range of biomaterials, providing additional control to shape the nascent immune response beyond the inflammatory signals provided by TLRas and related PAMP/DAMP molecules (see also **Chapter 5.522, Bone Tissue Engineering: Growth Factors and Cytokines**). Some of the signaling pathways of greatest interest include GM-CSF, which promotes the differentiation of DCs at an immunization site, IL-2, which drives T cell proliferation and effector functions, and IL-12, which promotes cytotoxic T cell differentiation and Th1-biased immunity. For example, influenza antigen (H3N2) can be efficiently loaded into liposomes with IL-2 and/or GM-CSF, and these materials are stable for several months.[208] As with other liposomal vaccines, antibody responses to antigen-encapsulated H3N2 are superior to responses to free antigen, and coadministration of soluble cytokines further enhances this effect. Of particular note, liposomes loaded with antigen and cytokines are even more potent compared with soluble antigen alone, or soluble cytokines administered with antigen-containing liposomes. Antigen- and cytokine-loaded liposomes conferred 100% seroconversion with upto a tenfold reduction in antigen dose, and a marked improvement in protective capacity compared with animals receiving antigen and alum as an adjuvant. GM-CSF has also been used to enhance vaccination using microparticles formed from natural or synthetic materials.[209,210] Albumin-heparin microparticles containing GM-CSF administered along with plasmid DNA-encoding HIV gag induce enhanced Ab, CTL, and T helper responses compared with antigen alone.[210] This result is sustained for at least 1 month, although subsequent boosts do not improve immune response. Interestingly, microparticles encapsulating protein antigen and cytokine serve as effective boost formulations to the DNA/cytokine prime injection, and CTL response can be further enhanced using this regimen. Sustained exposure of DCs *in vitro* to both plasmid-based antigens and GM-CSF has also recently been shown to dramatically increase gene expression using a model antigen *in vitro*.[209] Using PLGA scaffolds loaded with GM-CSF and PEI-condensed plasmid-encoding luciferase, gene expression was increased 20-fold and persisted for 10 days. While this study did not investigate the immunological implications, these findings could be promising for the development of new strategies utilizing biomaterials to concurrently present cytokines and DNA protein antigens, and the use of a scaffold could have some interesting implications for new strategies involving the combination of 'implantable' vaccines that could allow sustained release, reduce the number of injections, and improve patient compliance.

Cytokine-containing liposomes have also been explored in the enhancement of cancer therapies. IFN-γ facilitates tumor immunotherapy when encapsulated in liposomes and administered in conjunction with irradiated B16 cells.[211] Radiolabeling experiments suggest that one of the mechanisms of this enhancement is through an increase in the cytokine residence time *in vivo*, compared with that of soluble IFN-γ. A similar approach has been reported for the codelivery of OVA antigen and recombinant IL-2 by encapsulation of one or both components in liposomes.[212] Compared to formulations containing soluble or liposomal antigen, liposomes containing antigen and IL-2 led to a significant enhancement in antibody and $CD8^+$ T cell responses, as well as increases in protective capacity. Thus, cytokine delivery by biomaterials can lead to enhanced immune responses by coupling increased persistence with physical colocalization of antigen and cytokine signals.

4.419.5. Future Directions

The finding that several natural and synthetic polymers are immunologically inert in one form (polymerized) but active in another – during degradation or at low molecular weights – suggests a new approach for vaccines based on functionally responsive carriers, a topic of great interest more broadly in drug delivery. Perhaps new biomaterial adjuvants can be designed to 'sense' and respond to specific conditions, such as tumor microenvironments, or increases in particular small-molecule concentrations or cell populations. Such materials would thus represent a class of stimuli-responsive formulations that are inert or anti-inflammatory under one set of conditions, but become immunologically active in other conditions or upon receipt of specific environmental cues.

In addition to exploiting native signaling pathways triggered by pathogens, vaccines may also make use of other regulatory strategies to shape immune responses, such as signaling pathway inhibition with small-molecule drugs or via RNA interference. For example, CpG was recently conjugated to siRNA targeting a key immunosuppressive transcription factor active both in tumor cells and immune cell in the tumor environment, STAT-3. Administration of these

materials *in vivo* leads to targeting of specific cells populations (TLR-9$^+$ myeloid cells and B cells), silencing of STAT3, and activation of TLR-mediated antitumor effects.[213] This multifunctional approach illustrates an intriguing idea, based on the simultaneous activation of favorable immune pathways with concurrent silencing, or inactivation of suppressive or negative regulatory pathways. Several recent studies describe promising tumor immunotherapies based on codelivery of tumor antigens and inhibition of stat3 using a synthetic small molecule, JSI-124, and these approaches have employed a variety of polymer micelle, lipid, and particulate biomaterials for delivery.[214,215] Of note, some early variations of this approach have already started to appear that focus on codelivering DNA and anticancer drugs such as doxorubicin.[216–218] One logical expansion is to extend this dual prong approach of enhancing favorable pathways and suppressing 'unfavorable' pathways to other vaccination targets. Another example of interest for vaccination is the recent finding that retinoic acid plays a key role in imprinting particular gut-homing phenotypes to T cells during their activation by DCs.[219,220] Retinoic acid has also been incorporated in nanoparticles formed from synthetic copolymers and this system exhibits many of the basic advantages of biomaterials.[221] While these materials were not studied in the context of vaccination, it appears that the stage is set for an approach in which one activates DCs with an antigen of choice while simultaneously delivering retinoic acid to direct the destination of armed T cells to a particular tissue site – perhaps the site of a budding viral infection. The basic immunology and biological signal literature holds numerous such examples of key pathways involved in mediating particular immunological behavior, such as directing cell migration or constraining an immune response, and one could imagine that any of these pathways could serve as potential future targets for enhancing antigen-induced immune response by simultaneously silencing or inhibiting select pathways. The ability of biomaterials to provide sustained, targeted immune cell delivery of small-molecule regulators that may have poor solubility and very short half-lives may enable many powerful but inexpensive drugs to be considered as adjuvant components in vaccines. Thus, the importance of biomaterials as vaccine delivery agents is likely to grow in the coming years.

4.419.6. Conclusions

Biomaterials have clearly had a major impact on the development of new strategies for vaccination and immunotherapy. Many of the themes discussed in this chapter have highlighted the utility of biomaterials in addressing particular barriers to delivery, at both the organism and cellular level. These materials have also played a key role in facilitating vaccination through classical mechanisms such as sustained delivery and protection of biological cargos. Of particular relevance to vaccination, biomaterials have also recently been exploited for their intrinsic adjuvant activities and served as carriers not only of antigens, but also of a variety of vaccine-enhancing components including PAMPs, DAMPs, and cytokines. The ability of biomaterials, especially biodegradable microparticles and nanoparticles, to shape both humoral and cellular immune responses is providing new and exciting opportunities for the development of safe and effective vaccines/immunotherapies against infectious disease and cancer.

Acknowledgment

This work was supported in part by the NSF (award 0348259), the NIH (AI073165), and the Ragon Institute of MGH, MIT, and Harvard. CMJ is supported by a postdoctoral fellowship from the Ragon Institute. DJI is an investigator of the Howard Hughes Medical Institute.

References

1. Roush, S. W.; Murphy, T. V. *JAMA* **2007**, *298*, 2155–2163.
2. Plotkin, S. A.; Orenstein, W. A. *Vaccines*, 3rd ed.; W.B. Saunders: New York, 1999.
3. Virgin, H. W.; Walker, B. D. *Nature* **2010**, *464*, 224–231.
4. Stoll-Keller, F.; Barth, H.; Fafi-Kremer, S.; Zeisel, M. B.; Baumert, T. F. *Expert Rev. Vaccines* **2009**, *8*, 333–345.
5. Rook, G. A.; Dheda, K.; Zumla, A. *Nat. Rev. Immunol.* **2005**, *5*, 661–667.
6. Wang, R.; Smith, J. D.; Kappe, S. H. *Expert Rev. Mol. Med.* **2009**, *11*, e39.
7. Boon, T.; Coulie, P. G.; Van den Eynde, B. J.; van der Bruggen, P. *Annu. Rev. Immunol.* **2006**, *24*, 175–208.
8. Mantovani, A.; Romero, P.; Palucka, A. K.; Marincola, F. M. *Lancet* **2008**, *371*, 771–783.
9. Holgate, S. T.; Polosa, R. *Nat. Rev. Immunol.* **2008**, *8*, 218–230.
10. Harrison, L. C. *Immunol. Cell Biol.* **2008**, *86*, 139–145.
11. Yadava, A.; Sattabongkot, J.; Washington, M. A.; *et al. Infect. Immun.* **2007**, *75*, 1177–1185.
12. Guy, B. *Nat. Rev. Microbiol.* **2007**, *5*, 505–517.
13. Gupta, R. K. *Adv. Drug Deliv. Rev.* **1998**, *32*, 155–172.
14. Lindblad, E. B. *Vaccine* **2004**, *22*, 3658–3668.
15. Singh, M.; O'Hagan, D. *Nat. Biotechnol.* **1999**, *17*, 1075–1081.
16. Hubbell, J. A.; Thomas, S. N.; Swartz, M. A. *Nature* **2009**, *462*, 449–460.
17. Jones, K. S. *Biotechnol. Prog.* **2008**, *24*, 807–814.
18. Mallapragada, S. K.; Narasimhan, B. *Int. J. Pharm.* **2008**, *364*, 265–271.
19. Nguyen, D.; Green, J.; Chan, J.; Langer, R.; Anderson, D. *Adv. Mater.* **2009**, *21*, 847–867.
20. Peek, L. J.; Middaugh, C. R.; Berkland, C. *Adv. Drug Deliv. Rev.* **2008**, *60*, 915–928.
21. Bramwell, V. W.; Perrie, Y. *Crit. Rev. Ther. Drug Carrier Syst.* **2005**, *22*, 151–214.
22. Mutwiri, G.; Bowersock, T. L.; Babiuk, L. A. *Expert Opin. Drug Deliv.* **2005**, *2*, 791–806.
23. Singh, M.; Chakrapani, A.; O'Hagan, D. *Expert Rev. Vaccines* **2007**, *6*, 797–808.
24. De Gregorio, E.; Tritto, E.; Rappuoli, R. *Eur. J. Immunol.* **2008**, *38*, 2068–2071.
25. Marrack, P.; McKee, A. S.; Munks, M. W. *Nat. Rev. Immunol.* **2009**, *9*, 287–293.
26. Mosca, F.; Tritto, E.; Muzzi, A.; *et al. Proc. Natl. Acad. Sci. USA* **2008**, *105*, 10501–10506.
27. Ott, G.; Barchfeld, G. L.; Chernoff, D.; Radhakrishnan, R.; van Hoogevest, P.; Van Nest, G. *Pharm. Biotechnol.* **1995**, *6*, 277–296.
28. Banchereau, J.; Steinman, R. M. *Nature* **1998**, *392*, 245–252.
29. Randolph, G. J.; Angeli, V.; Swartz, M. A. *Nat. Rev. Immunol.* **2005**, *5*, 617–628.
30. Randolph, G. J.; Inaba, K.; Robbiani, D. F.; Steinman, R. M.; Muller, W. A. *Immunity* **1999**, *11*, 753–761.
31. Iwasaki, A.; Medzhitov, R. *Science* **2010**, *327*, 291–295.
32. Takeuchi, O.; Akira, S. *Cell* **2010**, *140*, 805–820.
33. Steinman, R. M.; Banchereau, J. *Nature* **2007**, *449*, 419–426.
34. Qi, H.; Egen, J. G.; Huang, A. Y.; Germain, R. N. *Science* **2006**, *312*, 1672–1676.
35. Wykes, M.; Pombo, A.; Jenkins, C.; MacPherson, G. G. *J. Immunol.* **1998**, *161*, 1313–1319.
36. Pape, K. A.; Catron, D. M.; Itano, A. A.; Jenkins, M. K. *Immunity* **2007**, *26*, 491–502.
37. Pape, K. A.; Kouskoff, V.; Nemazee, D.; *et al. J. Exp. Med.* **2003**, *197*, 1677–1687.
38. Garside, P.; Ingulli, E.; Merica, R. R.; Johnson, J. G.; Noelle, R. J.; Jenkins, M. K. *Science* **1998**, *281*, 96–99.

39. Okada, T.; Miller, M. J.; Parker, I.; *et al*. *PLoS Biol*. **2005**, *3*, e150.
40. Sallusto, F.; Lenig, D.; Forster, R.; Lipp, M.; Lanzavecchia, A. *Nature* **1999**, *401*, 708–712.
41. Masopust, D.; Choo, D.; Vezys, V.; *et al*. *J. Exp. Med*. **2010**, *207*, 553–564.
42. Brenchley, J. M.; Schacker, T. W.; Ruff, L. E.; *et al*. *J. Exp. Med*. **2004**, *200*, 749–759.
43. Woodland, D. L.; Kohlmeier, J. E. *Nat. Rev. Immunol*. **2009**, *9*, 153–161.
44. Pruss-Ustun, A.; Rapiti, E.; Hutin, Y. *Sharps Injuries: Global Burden of Disease from Sharps Injuries to Health Care Workers*; *WHO Environmental Burden of Disease Series;* World Health Organization: Geneva, Switzerland, 2003.
45. Brayden, D. J.; Baird, A. W. *Microbes Infect*. **2001**, *3*, 867–876.
46. Mitragotri, S. *Nat. Rev. Immunol*. **2005**, *5*, 905–916.
47. Vyas, S. P.; Gupta, P. N. *Expert Rev. Vaccines* **2007**, *6*, 401–418.
48. Gilliet, M.; Kleinhans, M.; Lantelme, E.; Schadendorf, D.; Burg, G.; Nestle, F. O. *Blood* **2003**, *102*, 36–42.
49. Spaner, D. E.; Astsaturov, I.; Vogel, T.; *et al*. *Cancer* **2006**, *106*, 890–899.
50. Dupuis, M.; McDonald, D. M.; Ott, G. *Vaccine* **1999**, *18*, 434–439.
51. Cleland, J. L.; Lim, A.; Barron, L.; Duenas, E. T.; Powell, M. F. *J. Control. Release* **1997**, *47*, 135–150.
52. Gupta, R. K.; Singh, M.; O'Hagan, D. T. *Adv. Drug Deliv. Rev*. **1998**, *32*, 225–246.
53. Kipper, M. J.; Wilson, J. H.; Wannemuehler, M. J.; Narasimhan, B. *J. Biomed. Mater. Res. A* **2006**, *76*, 798–810.
54. Glenny, A. T.; Pope, C. G.; Waddington, H.; Wallace, U. *J. Pathol. Bacteriol*. **1926**, *29*, 38–45.
55. Glenny, A. T.; Buttle, G. A. H.; Stevens, M. F. *J. Pathol. Bacteriol*. **1931**, *34*, 267–275.
56. Holt, L. B. In *Developments in Diphtheria Prophylaxis*; William Heinemann Medical Books: London, England, 1950; pp 1–181.
57. Harrison, W. T. *Am. J. Pub. Health* **1935**, *25*, 298–300.
58. White, R. G.; Coons, A. H.; Connolly, J. M. *J. Exp. Med*. **1955**, *102*, 73–82.
59. Brewer, J. M. *Immunol. Lett*. **2006**, *102*, 10–15.
60. Eisenbarth, S. C.; Colegio, O. R.; O'Connor, W.; Sutterwala, F. S.; Flavell, R. A. *Nature* **2008**, *453*, 1122–1126.
61. Hornung, V.; Bauernfeind, F.; Halle, A.; *et al*. *Nat. Immunol*. **2008**, *9*, 847–856.
62. Jordan, M. B.; Mills, D. M.; Kappler, J.; Marrack, P.; Cambier, J. C. *Science* **2004**, *304*, 1808–1810.
63. Cohen, S.; Bernstein, H.; Hewes, C.; Chow, M.; Langer, R. *Proc. Natl. Acad. Sci. USA* **1991**, *88*, 10440–10444.
64. Allen, T. M. *Biochim. Biophys. Acta* **1981**, *640*, 385–397.
65. Damen, J.; Regts, J.; Scherphof, G. *Biochim. Biophys. Acta* **1981**, *665*, 538–545.
66. Preis, I.; Langer, R. S. *J. Immunol. Meth*. **1979**, *28*, 193–197.
67. Wyatt, T. L.; Whaley, K. J.; Cone, R. A.; Saltzman, W. M. *J. Control. Release* **1998**, *50*, 93–102.
68. Gupta, R. K.; Chang, A. C.; Griffin, P.; Rivera, R.; Siber, G. R. *Vaccine* **1996**, *14*, 1412–1416.
69. Moore, A.; McGuirk, P.; Adams, S.; *et al*. *Vaccine* **1995**, *13*, 1741–1749.
70. Uchida, T.; Martin, S.; Foster, T. P.; Wardley, R. C.; Grimm, S. *Pharm. Res*. **1994**, *11*, 1009–1015.
71. Lunsford, L.; McKeever, U.; Eckstein, V.; Hedley, M. L. *J. Drug Target*. **2000**, *8*, 39–50.
72. Singh, M.; Chesko, J.; Kazzaz, J.; *et al*. *Pharm. Res*. **2004**, *21*, 2148–2152.
73. Zhu, G.; Mallery, S.; Schwendeman, S. *Nat. Biotechnol*. **2000**, *18*, 52–57.
74. Fu, K.; Klibanov, A.; Langer, R. *Nat. Biotechnol*. **2000**, *18*, 24.
75. Cleland, J. L.; Lim, A.; Daugherty, A.; *et al*. *J. Pharm. Sci*. **1998**, *87*, 1489–1495.
76. Singh, M.; Kazzaz, J.; Ugozzoli, M.; Chesko, J.; O'Hagan, D. T. *Expert Opin. Biol. Ther*. **2004**, *4*, 483–491.
77. Singh, M.; Briones, M.; Ott, G.; O'Hagan, D. *Proc. Natl. Acad. Sci. USA* **2000**, *97*, 811–816.
78. Denis-Mize, K. S.; Dupuis, M.; Singh, M.; *et al*. *Cell. Immunol*. **2003**, *225*, 12–20.
79. Yang, Y. Y.; Wan, J. P.; Chung, T. S.; Pallathadka, P. K.; Ng, S.; Heller, J. *J. Control. Release* **2001**, *75*, 115–128.
80. Heffernan, M. J.; Kasturi, S. P.; Yang, S. C.; Pulendran, B.; Murthy, N. *Biomaterials* **2009**, *30*, 910–918.
81. Heffernan, M. J.; Murthy, N. *Bioconjug. Chem*. **2005**, *16*, 1340–1342.
82. Newman, K. D.; Elamanchili, P.; Kwon, G. S.; Samuel, J. *J. Biomed. Mater. Res*. **2002**, *60*, 480–486.
83. Peyre, M.; Fleck, R.; Hockley, D.; Gander, B.; Sesardic, D. *Vaccine* **2004**, *22*, 2430–2437.
84. Champion, J. A.; Mitragotri, S. *Proc. Natl. Acad. Sci. USA* **2006**, *103*, 4930–4934.
85. Bonifaz, L. C.; Bonnyay, D. P.; Charalambous, A.; *et al*. *J. Exp. Med*. **2004**, *199*, 815–824.
86. van Broekhoven, C. L.; Parish, C. R.; Demangel, C.; Britton, W. J.; Altin, J. G. *Cancer Res*. **2004**, *64*, 4357–4365.
87. Kwon, Y. J.; James, E.; Shastri, N.; Frechet, J. M. *Proc. Natl. Acad. Sci. USA* **2005**, *102*, 18264–18268.
88. Lu, Y.; Kawakami, S.; Yamashita, F.; Hashida, M. *Biomaterials* **2007**, *28*, 3255–3262.
89. McWilliam, A. S.; Nelson, D.; Thomas, J. A.; Holt, P. G. *J. Exp. Med*. **1994**, *179*, 1331–1336.
90. Ravindran, R.; Rusch, L.; Itano, A.; Jenkins, M. K.; McSorley, S. J. *Proc. Natl. Acad. Sci. USA* **2007**, *104*, 12075–12080.
91. Kumamoto, T.; Huang, E. K.; Paek, H. J.; *et al*. *Nat. Biotechnol*. **2002**, *20*, 64–69.
92. Zhao, X.; Jain, S.; Benjamin Larman, H.; Gonzalez, S.; Irvine, D. J. *Biomaterials* **2005**, *26*, 5048–5063.
93. Singh, A.; Suri, S.; Roy, K. *Biomaterials* **2009**, *30*, 5187–5200.
94. Dranoff, G.; Jaffee, E.; Lazenby, A.; *et al*. *Proc. Natl. Acad. Sci. USA* **1993**, *90*, 3539–3543.
95. Ali, O. A.; Huebsch, N.; Cao, L.; Dranoff, G.; Mooney, D. J. *Nat. Mater*. **2009**, *8*, 151–158.
96. Junt, T.; Moseman, E. A.; Iannacone, M.; *et al*. *Nature* **2007**, *450*, 110–114.
97. Phan, T. G.; Green, J. A.; Gray, E. E.; Xu, Y.; Cyster, J. G. *Nat. Immunol*. **2009**, *10*, 786–793.
98. Carrasco, Y. R.; Batista, F. D. *Immunity* **2007**, *27*, 160–171.
99. Hawley, A.; Davis, S.; Illum, L. *Adv. Drug Deliv. Rev*. **1995**, *17*, 129–148.
100. Oussoren, C.; Storm, G. *Adv. Drug Deliv. Rev*. **2001**, *50*, 143–156.
101. Reddy, S. T.; Rehor, A.; Schmoekel, H. G.; Hubbell, J. A.; Swartz, M. A. *J. Control. Release* **2006**, *112*, 26–34.
102. Ikomi, F.; Hanna, G. K.; Schmid-Schonbein, G. W. *Lymphology* **1999**, *32*, 90–102.
103. Vonarbourg, A.; Passirani, C.; Saulnier, P.; Benoit, J. P. *Biomaterials* **2006**, *27*, 4356–4373.
104. Hawley, A. E.; Illum, L.; Davis, S. S. *Pharm. Res*. **1997**, *14*, 657–661.
105. Moghimi, S. M. *FEBS Lett*. **2003**, *540*, 241–244.
106. Fifis, T.; Gamvrellis, A.; Crimeen-Irwin, B.; *et al*. *J. Immunol*. **2004**, *173*, 3148–3154.
107. Moghimi, S. M. *Biomaterials* **2006**, *27*, 136–144.
108. Fifis, T.; Mottram, P.; Bogdanoska, V.; Hanley, J.; Plebanski, M. *Vaccine* **2004**, *23*, 258–266.
109. Reddy, S. T.; van der Vlies, A. J.; Simeoni, E.; *et al*. *Nat. Biotechnol*. **2007**, *25*(10), 1159–1164.
110. Mannhalter, J. W.; Neychev, H. O.; Zlabinger, G. J.; Ahmad, R.; Eibl, M. M. *Clin. Exp. Immunol*. **1985**, *61*, 143–151.
111. Morefield, G. L.; Sokolovska, A.; Jiang, D.; HogenEsch, H.; Robinson, J. P.; Hem, S. L. *Vaccine* **2005**, *23*, 1588–1595.
112. De Rose, R.; Zelikin, A. N.; Johnston, A. P. R.; *et al*. *Adv. Mater*. **2008**, *20*, 4698–4703.
113. Kovacsovics-Bankowski, M.; Clark, K.; Benacerraf, B.; Rock, K. L. *Proc. Natl. Acad. Sci. USA* **1993**, *90*, 4942–4946.
114. Reis e Sousa, C.; Germain, R. N. *J. Exp. Med*. **1995**, *182*, 841–851.
115. Amigorena, S.; Savina, A. *Curr. Opin. Immunol*. **2010**, *22*, 109–117.
116. Alving, C. R. *J. Immunol. Meth*. **1991**, *140*, 1–13.
117. Zhou, F.; Rouse, B. T.; Huang, L. *J. Immunol*. **1992**, *149*, 1599–1604.
118. Hamdy, S.; Elamanchili, P.; Alshamsan, A.; Molavi, O.; Satou, T.; Samuel, J. *J. Biomed. Mater. Res. A* **2007**, *81*, 652–662.
119. Kazzaz, J.; Neidleman, J.; Singh, M.; Ott, G.; O'Hagan, D. T. *J. Control. Release* **2000**, *67*, 347–356.
120. Shen, H.; Ackerman, A. L.; Cody, V.; *et al*. *Immunology* **2006**, *117*, 78–88.
121. Jain, S.; Yap, W. T.; Irvine, D. J. *Biomacromolecules* **2005**, *6*, 2590–2600.
122. Murthy, N.; Xu, M.; Schuck, S.; Kunisawa, J.; Shastri, N.; Frechet, J. M. *Proc. Natl. Acad. Sci. USA* **2003**, *100*, 4995–5000.
123. Lynn, D. M.; Amiji, M. M.; Langer, R. *Angew. Chem. Int. Ed*. **2001**, *40*, 1707–1710.
124. Hu, Y.; Litwin, T.; Nagaraja, A. R.; *et al*. *Nano Lett*. **2007**, *7*, 3056–3064.
125. Delamarre, L.; Pack, M.; Chang, H.; Mellman, I.; Trombetta, E. S. *Science* **2005**, *307*, 1630–1634.
126. Little, S. R.; Lynn, D. M.; Ge, Q.; *et al*. *Proc. Natl. Acad. Sci. USA* **2004**, *101*, 9534–9539.
127. Wang, C.; Ge, Q.; Ting, D.; *et al*. *Nat. Mater*. **2004**, *3*, 190–196.
128. Panyam, J.; Zhou, W. Z.; Prabha, S.; Sahoo, S. K.; Labhasetwar, V. *FASEB J*. **2002**, *16*, 1217–1226.
129. Kasturi, S. P.; Sachaphibulkij, K.; Roy, K. *Biomaterials* **2005**, *26*, 6375–6385.
130. Otten, G. R.; Schaefer, M.; Doe, B.; *et al*. *J. Virol*. **2005**, *79*, 8189–8200.

131. Dintzis, H. M.; Dintzis, R. Z.; Vogelstein, B. *Proc. Natl. Acad. Sci. USA* **1976**, *73*, 3671–3675.
132. Bachmann, M. F.; Rohrer, U. H.; Kundig, T. M.; Burki, K.; Hengartner, H.; Zinkernagel, R. M. *Science* **1993**, *262*, 1448–1451.
133. Guan, H. H.; Budzynski, W.; Koganty, R. R.; *et al. Bioconjug. Chem.* **1998**, *9*, 451–458.
134. Friede, M.; Muller, S.; Briand, J. P.; Van Regenmortel, M. H.; Schuber, F. *Mol. Immunol.* **1993**, *30*, 539–547.
135. Barral, P.; Eckl-Dorna, J.; Harwood, N. E.; *et al. Proc. Natl. Acad. Sci. USA* **2008**, *105*, 8345–8350.
136. Goto, N.; Kato, H.; Maeyama, J.; *et al. Vaccine* **1997**, *15*, 1364–1371.
137. Seubert, A.; Monaci, E.; Pizza, M.; O'Hagan, D. T.; Wack, A. *J. Immunol.* **2008**, *180*, 5402–5412.
138. Rimaniol, A. C.; Gras, G.; Verdier, F.; *et al. Vaccine* **2004**, *22*, 3127–3135.
139. Kool, M.; Soullie, T.; van Nimwegen, M.; *et al. J. Exp. Med.* **2008**, *205*, 869–882.
140. Li, H.; Nookala, S.; Re, F. *J. Immunol.* **2007**, *178*, 5271–5276.
141. Li, H.; Willingham, S. B.; Ting, J. P.; Re, F. *J. Immunol.* **2008**, *181*, 17–21.
142. Mariathasan, S.; Monack, D. M. *Nat. Rev. Immunol.* **2007**, *7*, 31–40.
143. Martinon, F.; Mayor, A.; Tschopp, J. *Annu. Rev. Immunol.* **2009**, *27*, 229–265.
144. Demento, S. L.; Eisenbarth, S. C.; Foellmer, H. G.; *et al. Vaccine* **2009**, *27*, 3013–3021.
145. Sharp, F. A.; Ruane, D.; Claass, B.; *et al. Proc. Natl. Acad. Sci. USA* **2009**, *106*, 870–875.
146. Scheibner, K. A.; Lutz, M. A.; Boodoo, S.; Fenton, M. J.; Powell, J. D.; Horton, M. R. *J. Immunol.* **2006**, *177*, 1272–1281.
147. Termeer, C.; Benedix, F.; Sleeman, J.; *et al. J. Exp. Med.* **2002**, *195*, 99–111.
148. Tesar, B. M.; Jiang, D.; Liang, J.; Palmer, S. M.; Noble, P. W.; Goldstein, D. R. *Am. J. Transplant.* **2006**, *6*, 2622–2635.
149. Jiang, D.; Liang, J.; Fan, J.; *et al. Nat. Med.* **2005**, *11*, 1173–1179.
150. Boros, P.; Bromberg, J. S. *Am. J. Transplant.* **2006**, *6*, 652–658.
151. Yan, M.; Peng, J.; Jabbar, I. A.; *et al. Virology* **2004**, *324*, 297–310.
152. Yan, M.; Peng, J.; Jabbar, I. A.; *et al. Immunol. Cell Biol.* **2005**, *83*, 83–91.
153. Grandjean-Laquerriere, A.; Tabary, O.; Jacquot, J.; *et al. Biomaterials* **2007**, *28*, 400–404.
154. Zhu, Z.; Zheng, T.; Homer, R. J.; *et al. Science* **2004**, *304*, 1678–1682.
155. Da Silva, C. A.; Chalouni, C.; Williams, A.; Hartl, D.; Lee, C. G.; Elias, J. A. *J. Immunol.* **2009**, *182*, 3573–3582.
156. Berntzen, G.; Flo, T. H.; Medvedev, A.; *et al. Clin. Diagn. Lab. Immunol.* **1998**, *5*, 355–361.
157. Maitra, R.; Clement, C. C.; Crisi, G. M.; Cobelli, N.; Santambrogio, L. *PLoS ONE* **2008**, *3*, e2438.
158. Seong, S. Y.; Matzinger, P. *Nat. Rev. Immunol.* **2004**, *4*, 469–478.
159. Gallorini, S.; Berti, F.; Parente, P.; *et al. J. Immunol.* **2007**, *179*, 8208–8215.
160. Shaunak, S.; Thomas, S.; Gianasi, E.; *et al. Nat. Biotechnol.* **2004**, *22*, 977–984.
161. Nilsson, B.; Ekdahl, K. N.; Mollnes, T. E.; Lambris, J. D. *Mol. Immunol.* **2007**, *44*, 82–94.
162. Tang, L.; Liu, L.; Elwing, H. B. *J. Biomed. Mater. Res.* **1998**, *41*, 333–340.
163. Kidane, A.; Park, K. *J. Biomed. Mater. Res.* **1999**, *48*, 640–647.
164. Lanier, J. G.; Newman, M. J.; Lee, E. M.; Sette, A.; Ahmed, R. *Vaccine* **1999**, *18*, 549–557.
165. Todd, C. W.; Pozzi, L. A.; Guarnaccia, J. R.; *et al. Vaccine* **1997**, *15*, 564–570.
166. Tritto, E.; Mosca, F.; De Gregorio, E. *Vaccine* **2009**, *27*, 3331–3334.
167. Matzelle, M. M.; Babensee, J. E. *Biomaterials* **2004**, *25*, 295–304.
168. Bennewitz, N. L.; Babensee, J. E. *Biomaterials* **2005**, *26*, 2991–2999.
169. Babensee, J. E. *Semin. Immunol.* **2008**, *20*, 101–108.
170. Babensee, J. E.; Paranjpe, A. *J. Biomed. Mater. Res. A* **2005**, *74*, 503–510.
171. Ng, G.; Sharma, K.; Ward, S. M.; *et al. Immunity* **2008**, *29*, 807–818.
172. Vajdy, M.; Selby, M.; Medina-Selby, A.; *et al. J. Gen. Virol.* **2006**, *87*, 2253–2262.
173. Wack, A.; Baudner, B. C.; Hilbert, A. K.; *et al. Vaccine* **2008**, *26*, 552–561.
174. Baudner, B. C.; Ronconi, V.; Casini, D.; *et al. Pharm. Res.* **2009**, *26*, 1477–1485.
175. Diwan, M.; Elamanchili, P.; Cao, M.; Samuel, J. *Curr. Drug Deliv.* **2004**, *1*, 405–412.
176. Malyala, P.; O'Hagan, D. T.; Singh, M. *Adv. Drug Deliv. Rev.* **2009**, *61*, 218–225.
177. Thapa, P.; Zhang, G.; Xia, C.; *et al. Vaccine* **2009**, *27*, 3484–3488.
178. Blander, J. M.; Medzhitov, R. *Nature* **2006**, *440*, 808–812.
179. Yang, Y.; Huang, C.; Huang, X.; Pardoll, D. *Nat. Immunol.* **2004**, *5*, 508–515.
180. Altin, J. G.; Parish, C. R. *Methods* **2006**, *40*, 39–52.
181. Wilson, K. D.; de Jong, S. D.; Tam, Y. K. *Adv. Drug Deliv. Rev.* **2009**, *61*, 233–242.
182. Glenn, G. M.; Rao, M.; Richards, R. L.; Matyas, G. R.; Alving, C. R. *Immunol. Lett.* **1995**, *47*, 73–78.
183. Gursel, I.; Gursel, M.; Ishii, K. J.; Klinman, D. M. *J. Immunol.* **2001**, *167*, 3324–3328.
184. Jerome, V.; Graser, A.; Muller, R.; Kontermann, R. E.; Konur, A. *J. Immunother.* **2006**, *29*, 294–305.
185. Wakita, D.; Chamoto, K.; Zhang, Y.; *et al. Int. Immunol.* **2006**, *18*, 425–434.
186. Sullivan, N. J.; Geisbert, T. W.; Geisbert, J. B.; *et al. Nature* **2003**, *424*, 681–684.
187. Jiao, X.; Wang, R. Y.; Qiu, Q.; Alter, H. J.; Shih, J. W. *J. Gen. Virol.* **2004**, *85*, 1545–1553.
188. Suzuki, Y.; Wakita, D.; Chamoto, K.; *et al. Cancer Res.* **2004**, *64*, 8754–8760.
189. Badiee, A.; Jaafari, M. R.; Samiei, A.; Soroush, D.; Khamesipour, A. *Clin. Vaccine Immunol.* **2008**, *15*, 668–674.
190. Zaks, K.; Jordan, M.; Guth, A.; *et al. J. Immunol.* **2006**, *176*, 7335–7345.
191. Johnston, D.; Zaidi, B.; Bystryn, J. C. *Cancer Immunol. Immunother.* **2007**, *56*, 1133–1141.
192. Singh, M.; Ott, G.; Kazzaz, J.; *et al. Pharm. Res.* **2001**, *18*, 1476–1479.
193. Diwan, M.; Elamanchili, P.; Lane, H.; Gainer, A.; Samuel, J. *J. Drug Target.* **2003**, *11*, 495–507.
194. Diwan, M.; Tafaghodi, M.; Samuel, J. *J. Control. Release* **2002**, *85*, 247–262.
195. Chong, C. S.; Cao, M.; Wong, W. W.; *et al. J. Control. Release* **2005**, *102*, 85–99.
196. Heit, A.; Schmitz, F.; Haas, T.; Busch, D. H.; Wagner, H. *Eur. J. Immunol.* **2007**, *37*, 2063–2074.
197. Kazzaz, J.; Singh, M.; Ugozzoli, M.; Chesko, J.; Soenawan, E.; O'Hagan, D. T. *J. Control. Release* **2006**, *110*, 566–573.
198. Malyala, P.; Chesko, J.; Ugozzoli, M.; *et al. J. Pharm. Sci.* **2008**, *97*, 1155–1164.
199. Xie, H.; Gursel, I.; Ivins, B. E.; *et al. Infect. Immun.* **2005**, *73*, 828–833.
200. Goh, S. L.; Murthy, N.; Xu, M.; Frechet, J. M. *Bioconjug. Chem.* **2004**, *15*, 467–474.
201. Stone, G. W.; Barzee, S.; Snarsky, V.; *et al. PLoS ONE* **2009**, *4*, e7334.
202. Mullen, G. E.; Aebig, J. A.; Dobrescu, G.; *et al. Vaccine* **2007**, *25*, 5343–5347.
203. Qian, F.; Rausch, K. M.; Muratova, O.; *et al. Vaccine* **2008**, *26*, 2521–2527.
204. Borges, O.; Cordeiro-da-Silva, A.; Tavares, J.; *et al. Eur. J. Pharm. Biopharm.* **2008**, *69*, 405–416.
205. Zhao, Z. Z.; Zhang, H. B.; Chen, Q.; *et al. Comp. Immunol. Microbiol. Infect. Dis.* **2009**, *32*, 191–205.
206. Kerkmann, M.; Lochmann, D.; Weyermann, J.; *et al. Oligonucleotides* **2006**, *16*, 313–322.
207. Cerundolo, V.; Silk, J. D.; Masri, S. H.; Salio, M. *Nat. Rev. Immunol.* **2009**, *9*, 28–38.
208. Babai, I.; Samira, S.; Barenholz, Y.; Zakay-Rones, Z.; Kedar, E. *Vaccine* **1999**, *17*, 1223–1238.
209. Ali, O. A.; Mooney, D. J. *J. Control. Release* **2008**, *132*, 273–278.
210. Song, R.; Liu, S.; Adams, R. J.; Leong, K. W. *J. Interferon Cytokine Res.* **2006**, *26*, 380–389.
211. van Slooten, M. L.; Storm, G.; Zoephel, A.; *et al. Pharm. Res.* **2000**, *17*, 42–48.
212. Johnston, D.; Reynolds, S. R.; Bystryn, J. C. *Cancer Immunol. Immunother.* **2006**, *55*, 412–419.
213. Kortylewski, M.; Kujawski, M.; Herrmann, A.; *et al. Cancer Res.* **2009**, *69*, 2497–2505.
214. Mahmud, A.; Patel, S.; Molavi, O.; Choi, P.; Samuel, J.; Lavasanifar, A. *Biomacromolecules* **2009**, *10*(3), 471–478.
215. Molavi, O.; Mahmud, A.; Hamdy, S.; *et al. Mol. Pharm.* **2010**, *7*(2), 364–374.
216. Qiu, L. Y.; Bae, Y. H. *Biomaterials* **2007**, *28*, 4132–4142.
217. Wang, Y.; Gao, S.; Ye, W. H.; Yoon, H. S.; Yang, Y. Y. *Nat. Mater.* **2006**, *5*, 791–796.
218. Zhu, C.; Jung, S.; Luo, S.; *et al. Biomaterials* **2010**, *31*, 2408–2416.
219. Mora, J. R.; Cheng, G.; Picarella, D.; Briskin, M.; Buchanan, N.; von Andrian, U. H. *J. Exp. Med.* **2005**, *201*, 303–316.
220. Mora, J. R.; von Andrian, U. H. *Trends Immunol.* **2006**, *27*, 235–243.
221. Li, Y.; Qi, X. R.; Maitani, Y.; Nagai, T. *Nanotechnology* **2009**, *20*, 55106.

4.420. Drug Delivery via Heparin Conjugates

S E Sakiyama-Elbert, Washington University, St. Louis, MO, USA

© 2011 Elsevier Ltd. All rights reserved.

4.420.1.	**Rationale for Using Heparin Conjugates for Drug Delivery**	334
4.420.2.	**Methods for Heparin Immobilization**	335
4.420.2.1.	Covalent Heparin Immobilization on Beads (Sepharose)	335
4.420.2.2.	Noncovalent Immobilization of Heparin	335
4.420.2.3.	Covalent Immobilization of Heparin by EDC/NHS Chemistry	336
4.420.2.4.	Covalent Immobilization of Heparin via Generation of Aldehyde Groups	336
4.420.2.5.	Covalent Immobilization of Heparin via Methacrylate Groups	336
4.420.2.6.	Covalent Immobilization of Heparin via Thiol Groups	337
4.420.2.7.	Covalent Immobilization of Heparin via Maleimide Groups	337
4.420.2.8.	Covalent Immobilization of Heparin Via Hydrazide Groups	337
4.420.2.9.	Covalent Immobilization of Heparin as a Gelation Agent	337
4.420.3.	**Use of Heparin Mimetic Molecules for Delivery of Heparin-Binding Growth Factors**	337
4.420.4.	**Summary**	337
References		338

Glossary

Affinity-based delivery system Drug delivery system that employs specific, noncovalent interactions to immobilize and stabilize biomolecules within a matrix to sustain bioactivity and slow diffusion-based release.

Covalent immobilization Method used to incorporate drug delivery system components via covalent linkages (e.g., hydrogels formed via Michael-type additions with thiolated glycosaminoglycans and PEG diacrylate).

Cross-linking Formation of chemical bonds between polymer chains promoting the arrangement of a three-dimensional network (e.g., hydrogel delivery systems formed with heparin and amine PEG-star polymers via EDC/NHS chemistry).

Fibrin Fibrous protein network formed in blood coagulation that is used as a scaffold material for drug delivery systems to achieve controlled release of biomolecules.

Growth factor Proteins capable of promoting cellular growth, cellular differentiation, and regulation of cellular processes (e.g., basic fibroblast growth factor, neurotrophic factor-3, vascular endothelial growth factor).

Heparin Linear polysaccharide used for affinity-based delivery systems that are capable of interacting with proteins via electrostatic interactions, the hydrophobic effect, and hydrogen bonding. They are highly sulfated and also contain carboxylic acids, which contribute to an overall net negative charge.[12] Heparin polymer chains are made up of repeating disaccharides, primarily uronic acid and glucosamine.

Hydrogel Three-dimensional, water-swollen polymeric network capable of promoting controlled release of biomolecules.

Michael-type addition Addition reaction between olefins (alkene containing compounds) and nucleophiles, such as thiols (commonly used with diacrylates to form cross-linked networks).

Microspheres/nanospheres Particulate delivery systems with diameters in the micrometer/nanometer scale that encapsulate biomolecules and promote controlled release.

Neurotrophic factor Protein capable of promoting the growth, differentiation, and survival of neurons in the peripheral and central nervous systems.

Noncovalent immobilization Method used to incorporate components of a drug delivery system via noncovalent linkages (e.g., heparin cross-linked in a fibrin matrix using a bidomain peptide containing a heparin-binding site and factor XIIIa substrate).

Transglutaminase Enzyme that catalyzes covalent cross-linking between glutamine and lysine resides (e.g., factor XIIIa, which cross-links fibrin after noncovalent self-assembly).

Abbreviations

bFGF	Basic fibroblast growth factor
BDNF	Brain-derived neurotrophic factor
BMP2	Bone morphogenetic protein 2
DMA	Dimethacrylate
DTT	Dithiothreitol
EDC	1-Ethyl-3-(3-dimethylaminopropyl) carbodiimide
EGF	Epidermal growth factor
FRET	Förster resonance energy transfer
GAG	Glycosaminoglycan
GDNF	Glial-derived neurotrophic factor
hGH	Human growth hormone
HA	Hyaluronic acid
HIP	Heparin interacting peptide

HSV	Herpes simplex virus
MSC	Mesenchymal stem cell
NGF	Nerve growth factor
NHS	*N*-hydroxysuccinimide
NT-3	Neurotrophin-3
PDGF	Platelet-derived growth factor
PEG	Poly(ethylene glycol)
PF4	Platelet factor 4
PLGA	Poly(lactide-*co*-glycolide)
RGD	Arginine-glycine-aspartic acid
SBA	Succinimidyl butanoic acid
Shh	Sonic hedgehog
tBoc	*Tert*-butoxycarbonyl
TGF	Transforming growth factor
TNF	Tumor necrosis factor
UV	Ultraviolet
VEGF	Vascular endothelial growth factor

4.420.1. Rationale for Using Heparin Conjugates for Drug Delivery

Many types of drug delivery systems benefit different biomedical applications.[1] However, for delivery of protein drugs, such as recombinant growth factors, there are many advantages in using an affinity-based delivery system. Affinity-based delivery systems rely on the use of noncovalent but specific interactions, such as electrostatic interactions, to immobilize and stabilize proteins within a matrix, sustain effective bioactivity, and slow their diffusion-based release. These noncovalent interactions can also protect protein drugs from degradation by proteases and denaturation. In some cases, these interactions may also facilitate the binding of the drug (growth factor) to the cell-surface receptor, as has been observed for basic fibroblast growth factor (bFGF) and heparin.[2] The interactions between protein drugs and affinity-based delivery systems mimic those that commonly occur within the native extracellular matrix between growth factors and cell-surface heparin sulfate proteoglycans, and can provide a repository of drug for controlled release.

Several methods for the direct covalent attachment of growth factors to biomaterials scaffolds have been developed.[3]

> Although intelligent, this approach requires permanent modification of growth factors that may not be desirable due to the potentially decreased protein bioactivity after structural modification and an enhanced immunogenicity once these modified proteins are released *in vivo*.[4]

Further advances in polymeric drugs and inorganic/hybrid controlled release systems are described in **Chapter 4.423, Polymeric Drug Conjugates by Controlled Radical Polymerization**. Additionally, some growth factors may require internalization for complete cell signaling pathway activation, and this is not possible if they are permanently attached to the biomaterial scaffold. Thus, affinity-based drug delivery offers an attractive alternative approach for growth factors, because the growth factor is sequestered in its native form and released by dissociation from the affinity-binding site, followed by diffusion from the biomaterial scaffold. This process can be modulated by using scaffolds that are hydrolytically or enzymatically degradable, providing an additional mechanism for controlling release. In the case of enzymatic degradation, drug release can be controlled by cellular activation of the enzyme (e.g., cellular activation of plasminogen during neurite extension), allowing a cell-mediated mechanism of release.

The most commonly used molecule for the binding site in affinity-based delivery systems is heparin, which has a high degree of similarity to heparan sulfate found in proteoglycans. Because a large number of growth factors bind to heparin with either moderate or high affinity, heparin-binding systems can be used to deliver a broad variety of growth factors for a number of different applications (**Figure 1**).[5] These growth factors include some of the most well-studied heparin-binding growth factors, such as bFGF and vascular endothelial growth factor (VEGF), as well as members of transforming growth factor (TGF, e.g., BMPs), platelet-derived growth factor (PDGF), epidermal growth factor (EGF), and hepatocyte growth factor families.[6–9] Additionally, many morphogens, such as sonic hedgehog (Shh), and pathogens, such as *Bordetella pertussis*, herpes simplex virus (HSV), and *Plasmodium falciparum*, have also been found to bind to heparin.[10,11]

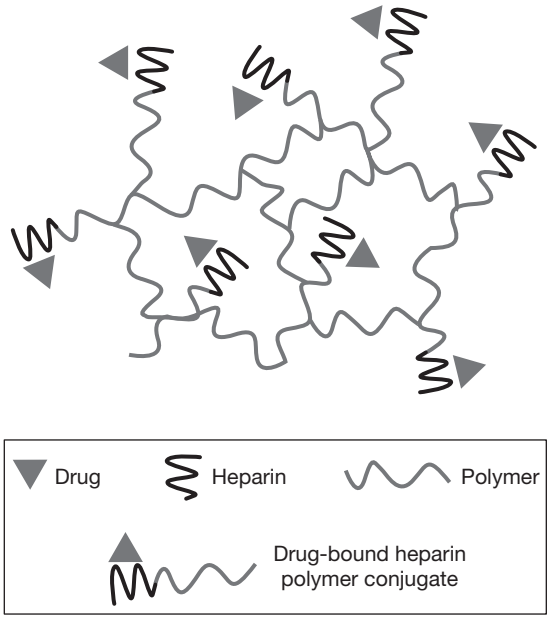

Figure 1 Schematic of heparin conjugate drug delivery system. Heparin is immobilized to a natural or synthetic polymer scaffold by covalent or noncovalent interactions. The heparin serves as a binding site to immobilize heparin-binding proteins (e.g., growth factors) by electrostatic interactions, sequestering them within the scaffold and protecting them from degradation. Drug release can occur by dissociation from the heparin and diffusion from the scaffold or degradation of the polymer scaffold.

Heparin and heparin sulfate are linear polysaccharides. They are highly sulfated and also contain carboxylic acids, which contribute to an overall net negative charge.[12] Heparin polymer chains are made up of repeating disaccharides, primarily uronic acid and glucosamine. While their interactions with proteins are largely electrostatic, there are clear contributions from hydrophobic effects and hydrogen bonding as well, imparting some selectivity and specificity. In addition to binding to growth factors, heparin also binds to a number of enzymes (e.g., antithrombin III), plasma proteins (platelet factor 4), and extracellular matrix protein (e.g., fibronectin, laminin).[13,14] In some cases, specific heparin sulfation codes have been identified that facilitate binding with growth factors (e.g., bFGF) or enzymes (e.g., antithrombin III).[15,16]

Thus, heparin conjugation to biomaterials was originally used as a method to generate nonthrombogenic materials through ionic immobilization in the 1960s[17,18] and covalent coupling in the 1980s.[19] More recently, heparin conjugation has been used for affinity-based delivery of growth factors for roughly three decades. Initially, a lack of flexible methods for heparin incorporation within biomaterial scaffolds limited this approach. However, since 2000, several new methods for heparin conjugation have led to more widespread use of heparin-based drug delivery systems. The next sections will outline the different approaches to heparin immobilization within drug delivery systems. Advancements in carbohydrate polymers and extracellular matrix-inspired biomaterials are described in **Chapter 2.207, Extracellular Matrix: Inspired Biomaterials**, respectively.

4.420.2. Methods for Heparin Immobilization

4.420.2.1. Covalent Heparin Immobilization on Beads (Sepharose)

Following the early heparin-immobilization work focused on biomaterial-induced coagulation mitigation, the seminal work demonstrating the utility of heparin-based delivery systems was performed by Edelman and Langer. They used heparin-conjugated Sepharose beads to immobilize bFGF within alginate microspheres. The initial *in vitro* studies demonstrated controlled release of active growth factor for at least 2 weeks, and growth factor activity was greater in the presence of heparin under a variety of environmental conditions than in the absence of heparin.[20] A later *in vivo* study demonstrated that bFGF delivered from heparin–Sepharose beads in alginate microcapsules was biologically active, and stimulated both angiogenesis and neointimal proliferation in a rat carotid artery model.[21] A Phase I clinical trial using this approach demonstrated that bFGF improves revascularization after coronary artery bypass grafts in a small cohort of patients.[22] In a later Phase II trial, improved revascularization was observed with bFGF treatment, with a trend toward improved left ventricular ejection fraction.[23] This work demonstrates that heparin-based delivery systems can be used to provide sustained release of biologically active growth factors in a clinical model.

4.420.2.2. Noncovalent Immobilization of Heparin

Sakiyama-Elbert and Hubbell developed a novel method for immobilization of heparin within biomaterial scaffolds by using noncovalent (primarily electrostatic) interactions rather than covalent immobilization. This three-component delivery system consists of a heparin-binding peptide covalently immobilized on the biomaterial scaffold, heparin, and the heparin-binding growth factor of interest. To demonstrate the feasibility of this approach, they cross-linked a peptide containing a modified version of the heparin-binding domain of antithrombin III into fibrin matrices via the transglutaminase activity of factor XIIIa and demonstrated that bFGF could be released in a controlled manner from this delivery system.[24] They went on to demonstrate that this approach can also be used with growth factors that possess only moderate heparin-binding affinity ($K_D \sim 10^{-6}$) via short basic domains that are accessible on protein surfaces, such as nerve growth factor (NGF), neurotrophin 3 (NT-3), and brain-derived neurotrophic factor (BDNF).[25]

Other studies have shown that this approach can be expanded to other scaffold materials, such as polyethylene glycol (PEG) hydrogels, for the delivery of heparin-binding growth factors. Pratt *et al.*[26] demonstrated that bone morphogenetic protein 2 (BMP2) delivered from plasmin-degradable PEG hydrogels via a heparin-binding peptide–heparin complex could promote improved bone healing in a rat cranial defect model. This approach has also been used for delivery of PDGF-BB to enhance gliding after midsubstance injury in a canine flexor tendon model.[27–29]

In this type of delivery system, three mechanisms control the rate of growth factor release: (1) the concentration of binding sites for the drug, (2) the affinity of the binding sites for the drug, and (3) the rate of degradation of the scaffold/delivery system. Increasing the concentration of binding sites has been found to increase the rate of release up to the limit of incorporation of the binding sites into the delivery system.[30,31] The effect of binding site affinity on the rate of release has also been explored. To identify peptide sequences with a broader range of affinities for heparin, a phage display library was screened to identify sequences with varying affinity for heparin.[32] The role of heparin-binding affinity on peptide-mediated heparin retention was evaluated for electrostatic immobilization of heparin, and increasing heparin-binding affinity has been shown to provide a longer duration of release.[33] For additional work in cell-demanded release of growth factors, refer to **Chapter 4.427, Cell-Demanded Release of Growth Factors**.

This approach for delivery of heparin-binding growth factors has proved useful in a number of applications. Delivery of NGF and glial-derived neurotrophic factor (GDNF) using fibrin scaffolds containing heparin-binding delivery systems has been found to enhance peripheral nerve regeneration in a rat sciatic nerve injury model at both 6 (number of nerve fibers) and 12 weeks (muscle force generation and prevention of muscle atrophy).[34,35] Advancements and recent work in peripheral nerve regeneration and nerve tissue engineering are further described in **Chapter 5.531, Peripheral Nerve Regeneration** and **Chapter 5.532, Nerve Tissue Engineering**, respectively. This approach has also been used for the delivery of NT-3 and was found to promote neural fiber sprouting after acute and subacute (2-week delayed) treatment of rat spinal cord injury.[36,37] More recently, this approach has also been used to deliver NT-3 and PDGF-AA to direct the differentiation and survival of embryonic stem cell-derived neural progenitor cells

in vitro and *in vivo* after spinal cord injury, demonstrating the broad utility of this approach.[38,39]

More recently, novel methods have been developed to assess the interaction of growth factors with affinity-binding peptides in scaffolds. Lin and Anseth used Förster resonance energy transfer (FRET) to assess how the architectures of affinity peptides in cross-linked hydrogels affect their binding to diffusible proteins[4] in thiol–acrylate photopolymerized PEG hydrogels. They incorporated bFGF-binding peptides and used these to control release of bFGF from PEG gels *in vitro*. In **Chapter 1.131, Superporous Hydrogels for Drug Delivery Systems**, additional work involving hydrogels for drug delivery systems is described.

4.420.2.3. Covalent Immobilization of Heparin by EDC/NHS Chemistry

Another early approach to immobilizing heparin within a scaffold was covalently attaching it to a protein, such as albumin or collagen, using 1-ethyl-3-(3-dimethylaminopropyl) carbodiimide (EDC).[40] Albumin–heparin conjugates were then emulsified to form microspheres and cross-linked with glutaraldehyde.[41] This approach can also be used to cross-link heparin covalently to collagen matrices to provide controlled delivery of bFGF, and this method was found to enhance endothelial cell proliferation *in vitro*.[42,43] Delivery of bFGF from similar matrices also demonstrated increased vascularization for up to 3 weeks *in vivo* in a rat subcutaneous implant model.[44,45]

Other groups utilized this method to couple heparin to other biomaterial scaffolds, such as alginate, decellularized tissue, and PEG. Tanihara *et al.*[46] used heparin-alginate gels to deliver bFGF and demonstrated effects both *in vitro* (fibroblast proliferation) and *in vivo* (increased angiogenesis) in a rat subcutaneous implant model. Conklin *et al.* decellularized pig carotid arteries and reacted the tissue with heparin and EDC to immobilize heparin on the vascular graft surface. The grafts were then coated with bFGF, and this approach was found to increase endothelial cell density and adhesion under perfusion culture conditions for both human microvascular endothelial cells and canine peripheral blood endothelial progenitor cells.[47] Further work in cardiovascular and heart valve tissue engineering is described in **Chapter 5.527, Cardiovascular Tissue Engineering**.

A similar approach was used for immobilization of heparin onto poly(L-lactide-*co*-glycolide) (PLGA)-based materials. Jeon *et al.* developed heparin-conjugated PLGA nanospheres. They synthesized amine-terminated PLGA by reacting PLGA with t-Boc-protected glycine and then deprotected the t-Boc group. Nanospheres of PLGA were formed using an oil–water emulsion and reacted with heparin in the presence of EDC/*N*-hydroxysuccinimide (NHS).[48] They demonstrated controlled release of bFGF over 28 days *in vitro* and increased cell proliferation. In a mouse ischemic limb model, they observed increased capillary density with bFGF and the PLGA nanospheres versus controls. Similar heparin-conjugation methods can also be used with salt-leached porous PLGA scaffolds for delivery of heparin-binding growth factors, such as BMP2. Delivery of BMP2 using this approach was found to increase bone formation in an ectopic bone formation (mouse hind limb muscle) model compared to PLGA scaffolds lacking heparin.[49]

This approach can be expanded to develop scaffolds that consist primarily of heparin through the addition of functional groups that allow polymerization of the heparin. Nakamura *et al.*[50] developed a method for generating photopolymerizable heparin hydrogels cross-linked using UV light. Controlled release of bFGF from these gels was observed *in vitro* and increased capillary number was found *in vivo* with heparin–bFGF gels at 2 weeks in a rat subcutaneous implant model. Additional studies involving biomaterials and the microvasculature are described in **Chapter 5.503, Biomaterials and the Microvasculature**.

This approach can be expanded to heparin along with another polymer as the base material for the scaffold. Freudenberg used amine-terminated PEG-star polymers to form hydrogels for growth factor delivery with heparin using EDC/NHS cross-linking. They also coupled arginine-glycine-aspartic acid (RGD) peptides to the heparin to enhance cell adhesion to the scaffolds. The addition of bFGF and RGD promoted improved cell survival and differentiation of mesencephalic neural stem cells from embryonic day 13.5 mice.[51] This broad body of work demonstrates that this approach is versatile and easy to implement for a variety of biomaterial scaffolds.

4.420.2.4. Covalent Immobilization of Heparin via Generation of Aldehyde Groups

Oxidation of heparin can be used to generate aldehyde groups (e.g., using sodium periodate).[52] The aldehyde groups can then be used to couple heparin to other macromolecules via reductive amination.[19] Liu *et al.*[53] modified hyaluronic acid (HA) to contain amine groups (using periodate and then added amine groups using ethylenediamine in the presence of cyanoborohydride) and then reacted this with heparin-aldehyde via reductive amination. They demonstrated controlled release of bFGF from HA scaffolds via enzymatic degradation of the HA and biological activity of the released bFGF (cell proliferation).

4.420.2.5. Covalent Immobilization of Heparin via Methacrylate Groups

Addition of unsaturated bonds (e.g., polymerized acrylate groups) can also be used to add unique reactive functionality to heparin for incorporation into biomaterial scaffolds. Benoit *et al.* synthesized heparin methacrylate[54] and cross-linked it into PEG dimethacrylate (DMA) hydrogels by photopolymerization. The heparin was used to deliver bFGF, which was found to increase human mesenchymal stem cell (MSC) proliferation and also to sequester proteins for cell adhesion.[55] These gels were also tested in combination with RGD peptides (attached via PEG acrylate) and the greatest differentiation was observed on gels containing both RGD and heparin.[56] Heparin methacrylate has also been photopolymerized with pluronic diacrylate to form hydrogels for bFGF delivery and stimulated neovascularization in a subcutaneous rat implant model.[57] This approach shows a great deal of potential for incorporating heparin-binding growth factors into PEG hydrogels for a broad variety of tissue engineering applications.

4.420.2.6. Covalent Immobilization of Heparin via Thiol Groups

The addition of thiol groups can also be used to give an additional reactive functionality to heparin, which reacts with many existing polymer end groups (e.g., acrylates, vinyl sulfones). The Prestwich lab developed a method for thiolation of glycosaminoglycans (GAGs), such as HA and heparin,[58] by reacting them with EDC and dithiothreitol (DTT). They reacted the thiolated GAGs (HA and heparin) with PEG diacrylate via Michael-type addition to generate PEG–HA–heparin hydrogels.[59] The release of growth factor from these gels was dependent on hyaluronidase for gels containing HA (as part of the GAG component) and bFGF release was sustained for at least 28 days *in vitro*. Delivery of bFGF from these scaffolds was also found to promote neovascularization *in vivo* in a mouse subcutaneous implant model.

Tae *et al.*[60] adapted this approach for use with PEG diacrylate hydrogels in the absence of HA and demonstrated that fibroblasts could be encapsulated within these gels. This approach can also be used for delivery of human growth hormone (hGH) from hydrogels formed from thiolated heparin and PEG diacrylate by Michael-type addition, rather than by photopolymerization.[61] Delivery of osteoprotegerin, a proangiogenic factor from the tumor necrosis factor (TNF) superfamily, from these hydrogels was shown to promote increased vascularization in a subcutaneous mouse implant model.[62] This thiolation method also shows great potential for a broad variety of applications and the thiol chemistry is somewhat more selective because of the relatively low incidence (1–4% frequency) of thiols (cysteines) in protein sequences.[63]

4.420.2.7. Covalent Immobilization of Heparin via Maleimide Groups

Addition of maleimide groups provides another unique functionality to react with polymer end groups and allows conjugation of heparin to biomaterial scaffolds. Heparin-containing PEG hydrogels were made by reacting PEG-tetrathiol with low molecular weight heparin-maleimide. The PEG–heparin conjugates were then reacted with PEG-tetraHIP (heparin-interacting peptide)[64] and these gels were shown to sequester bFGF. This approach can also be modified to react PEG-dithiol with high molecular weight heparin-maleimide and controlled bFGF can be obtained from these gels as well.[65] This approach can be modified to work well with the thiol-based approaches discussed in the previous section.

4.420.2.8. Covalent Immobilization of Heparin Via Hydrazide Groups

Another method for modification of heparin by several groups is the addition of hydrazide groups. The carboxylic acid groups on heparin can be modified to hydrazide groups for covalent attachment to polymers using a method developed by Bulpitt and Aeschlimann.[66] Tae *et al.* used this method to react hydrazide-modified heparin with NHS ester of PEG–bis-butanoic acid (SBA-PEG-SBA) to form hydrogels. They demonstrated sustained VEGF release *in vitro* and increased angiogenesis *in vivo* in a subcutaneous mouse implant model.[67]

4.420.2.9. Covalent Immobilization of Heparin as a Gelation Agent

Others have used the ability of heparin to bind basic peptides and polymer to design materials that self assemble when mixed with heparin. Seal and Panitch demonstrated the ability to form self-assembling PEG hydrogels, by coupling heparin-binding peptides to each arm of PEG tetravinyl sulfone and mixing the PEG with heparin.[68] Zhang *et al.* built upon this approach and used a four-arm PEG modified with either heparin-binding peptides from PF4 or low molecular weight heparin (as described in **Section 4.420.2.7**)[64] to form gels that assemble noncovalently and can deliver bFGF.[69] Rajangam *et al.*[70] used a similar approach to generate self-assembling materials from basic peptide amphiphiles and heparin. They were able to show controlled bFGF release *in vitro* and increase angiogenesis with bFGF delivery *in vivo* in a rat corneal implant model. Some caution must be used with this approach, as the hydrogels formed using this method are generally weak mechanically, but may be useful for applications that require materials to gel after injection in the absence of any cross-linking agent. For further information on growth factor and protein modified surfaces and interfaces, refer to **Chapter 4.416, Growth Factors and Protein-Modified Surfaces and Interfaces**. Additional work involving self-assembling biomaterials is covered in **Chapter 2.205, Self-Assembling Biomaterials**.

4.420.3. Use of Heparin Mimetic Molecules for Delivery of Heparin-Binding Growth Factors

Because of the heterogeneity of heparin, it may be desirable to develop a synthetic analog that can bind to heparin-binding growth factors, but over which there is more selective synthetic control. Toward this goal, Maynard *et al.*[71] used sulfated amino acids and combinatorial chemistry to identify artificial peptide sequences that function as heparin mimetics and are capable of heparin-binding growth factor sequestration. They found a tetrapeptide sequence of sulfated amino acids that can bind to VEGF with micromolar affinity. This approach can be extended for nanopatterning applications using e-beam lithography to provide patterns of heparin-binding growth factors on a surface.[72] This approach holds great potential for developing sequences that are selective for an individual growth factor and that could potentially be resistant to degradation by heparinases.

4.420.4. Summary

In summary, heparin conjugates can be attached to biomaterial scaffolds using the various methods described and have been found to deliver biologically active growth factors in a controlled manner in a number of *in vitro* and *in vivo* models. Thus far, most groups using this approach have delivered model heparin-binding growth factors, such as bFGF and VEGF, often in subcutaneous implant angiogenesis models. However, more recent studies have demonstrated that this approach can be useful in bone, peripheral nerve, spinal

cord, and flexor tendon regeneration models. Because of the large number and wide variety of growth factors that bind to heparin, delivery systems developed using heparin sequestration of growth factors hold great potential for use in many different tissue regeneration applications (Figure 1).

References

1. Langer, R. *Nature* **1998**, *392*, 5–10.
2. Ornitz, D. M.; Yayon, A.; Flanagan, J. G.; Svahn, C. M.; Levi, E.; Leder, P. *Mol. Cell. Biol.* **1992**, *12*, 240–247.
3. Kuhl, P. R.; Griffith-Cima, L. G. *Nat. Med.* **1996**, *2*, 1022–1027.
4. Lin, C. C.; Anseth, K. S. *Adv. Funct. Mater.* **2009**, *19*, 2325–2331.
5. Cardin, A. D.; Jackson, R. L.; Sparrow, D. A.; Sparrow, J. T. *Ann. N. Y. Acad. Sci.* **1989**, *556*, 186–193.
6. Klagsbrun, M. *Curr. Opin. Cell Biol.* **1990**, *2*, 857–863.
7. Lin, L. F.; Zhang, T. J.; Collins, F.; Armes, L. G. *J. Neurochem.* **1994**, *63*, 758–768.
8. Lyon, M.; Rushton, G.; Gallagher, J. T. *J. Biol. Chem.* **1997**, *272*, 18000–18006.
9. Tessler, S.; Rockwell, P.; Hicklin, D.; *et al. J. Biol. Chem.* **1994**, *269*, 12456–12461.
10. Lee, J. J.; Ekker, S. C.; Von Kessler, D. P.; Porter, J. A.; Sun, B. I.; Beachy, P. A. *Science* **1994**, *266*, 1528–1537.
11. Rostand, K. S.; Esko, J. D. *Infect. Immun.* **1997**, *65*, 1–8.
12. Lodish, H.; Berk, A.; Kaiser, C.; *et al. Molecular Cell Biology.* W.H. Freeman: New York, 2008.
13. Edgar, D.; Timpl, R.; Thoenen, H. *EMBO J.* **1984**, *3*, 1463–1468.
14. Rogers, S. L.; McCarthy, J. B.; Palm, S. L.; Furcht, L. T.; Letourneau, P. C. *J. Neurosci.* **1985**, *5*, 369–378.
15. Choay, J.; Petitou, M.; Lormeau, J. C.; Sinay, P.; Casu, B.; Gatti, G. *Biochem. Biophys. Res. Commun.* **1983**, *116*, 492–499.
16. Ishihara, M.; Shaklee, P. N.; Yang, Z.; *et al. Glycobiology* **1994**, *4*, 451–458.
17. Gott, V. L.; Whiffen, J. D.; Dutton, R. C. *Science* **1963**, *142*, 1297–1298.
18. Grode, G. A.; Anderson, S. J.; Grotta, H. M.; Falb, R. D. *Trans. Am. Soc. Artif. Intern. Organs* **1969**, *15*, 1–6.
19. Larm, O.; Larsson, R.; Olsson, P. *Biomater. Med. Devices Artif. Organs* **1983**, *11*, 161–173.
20. Edelman, E. R.; Mathiowitz, E.; Langer, R.; Klagsbrun, M. *Biomaterials* **1991**, *12*, 619–626.
21. Edelman, E. R.; Nugent, M. A.; Smith, L. T.; Karnovsky, M. J. *J. Clin. Invest.* **1992**, *89*, 465–473.
22. Laham, R. J.; Sellke, F. W.; Edelman, E. R.; *et al. Circulation* **1999**, *100*, 1865–1871.
23. Ruel, M.; Laham, R. J.; Parker, J. A.; *et al. J. Thorac. Cardiovasc. Surg.* **2002**, *124*, 28–34.
24. Sakiyama-Elbert, S. E.; Hubbell, J. A. *J. Control. Release* **2000**, *65*, 389–402.
25. Sakiyama-Elbert, S. E.; Hubbell, J. A. *J. Control. Release* **2000**, *69*, 149–158.
26. Pratt, A. B.; Weber, F. E.; Schmoekel, H. G.; Muller, R.; Hubbell, J. A. *Biotechnol. Bioeng.* **2004**, *86*, 27–36.
27. Gelberman, R. H.; Thomopoulos, S.; Sakiyama-Elbert, S. E.; Das, R.; Silva, M. J. *J. Hand Surg. Am.* **2007**, *32*, 373–379.
28. Thomopoulos, S.; Das, R.; Silva, M. J.; *et al. J. Orthop. Res.* **2009**, *27*, 1209–1215.
29. Thomopoulos, S.; Zaegel, M.; Das, R.; *et al. J. Orthop. Res.* **2007**, *25*, 1358–1368.
30. Sakiyama-Elbert, S. E.; Das, R.; Gelberman, R. H.; Harwood, F.; Amiel, D.; Thomopoulos, S. *J. Hand Surg. Am.* **2008**, *33*, 1548–1557.
31. Taylor, S. J.; McDonald, J. W., III; Sakiyama-Elbert, S. E. *J. Control. Release* **2004**, *98*, 281–294.
32. Maxwell, D. J.; Hicks, B. C.; Parsons, S.; Sakiyama-Elbert, S. E. *Acta Biomater.* **2005**, *1*, 101–113.
33. Wood, M. D.; Sakiyama-Elbert, S. E. *J. Biomed. Mater. Res. A* **2008**, *84*, 300–312.
34. Lee, A. C.; Yu, V. M.; Lowe, J. B., III; *et al. Exp. Neurol.* **2003**, *184*, 295–303.
35. Wood, M. D.; Moore, A. M.; Hunter, D. A.; *et al. Acta Biomater.* **2009**, *5*, 959–968.
36. Johnson, P. J.; Parker, S. R.; Sakiyama-Elbert, S. E. *Biotechnol. Bioeng.* **2009**, *104*, 1207–1214.
37. Taylor, S. J.; Rosenzweig, E. S.; McDonald, J. W., III; Sakiyama-Elbert, S. E. *J. Control. Release* **2006**, *113*, 226–235.
38. Johnson, P. J.; Tatara, A.; McCreedy, D. A.; Shiu, A.; Sakiyama-Elbert, S. E. *Soft Matter* **2010**, *6*, 5127–5137.
39. Willerth, S. M.; Rader, A.; Sakiyama-Elbert, S. E. *Stem Cell Res.* **2008**, *1*, 205–218.
40. Hennink, W. E.; Feijen, J.; Ebert, C. D.; Kim, S. W. *Thromb. Res.* **1983**, *29*, 1–13.
41. Cremers, H. F.; Kwon, G.; Bae, Y. H.; *et al. Biomaterials* **1994**, *15*, 38–48.
42. Wissink, M. J.; Beernink, R.; Poot, A. A.; *et al. J. Control. Release* **2000**, *64*, 103–114.
43. Wissink, M. J.; Beernink, R.; Scharenborg, N. M.; *et al. J. Control. Release* **2000**, *67*, 141–155.
44. Pieper, J. S.; Hafmans, T.; van Wachem, P. B.; *et al. J. Biomed. Mater. Res.* **2002**, *62*, 185–194.
45. van Wachem, P. B.; Plantinga, J. A.; Wissink, M. J.; *et al. J. Biomed. Mater. Res.* **2001**, *55*, 368–378.
46. Tanihara, M.; Suzuki, Y.; Yamamoto, E.; Noguchi, A.; Mizushima, Y. *J. Biomed. Mater. Res.* **2001**, *56*, 216–221.
47. Conklin, B. S.; Wu, H.; Lin, P. H.; Lumsden, A. B.; Chen, C. *Artif. Organs* **2004**, *28*, 668–675.
48. Jeon, O.; Kang, S. W.; Lim, H. W.; Hyung Chung, J.; Kim, B. S. *Biomaterials* **2006**, *27*, 1598–1607.
49. Jeon, O.; Song, S. J.; Kang, S. W.; Putnam, A. J.; Kim, B. S. *Biomaterials* **2007**, *28*, 2763–2771.
50. Nakamura, S.; Ishihara, M.; Obara, K.; *et al. J. Biomed. Mater. Res. A* **2006**, *78*, 364–371.
51. Freudenberg, U.; Hermann, A.; Welzel, P. B.; *et al. Biomaterials* **2009**, *30*, 5049–5060.
52. Hermanson, G. *Bioconjugate Techniques*. Academic Press: San Diego, CA, 1996.
53. Liu, L. S.; Ng, C. K.; Thompson, A. Y.; Poser, J. W.; Spiro, R. C. *J. Biomed. Mater. Res.* **2002**, *62*, 128–135.
54. Smeds, K. A.; Pfister-Serres, A.; Miki, D.; *et al. J. Biomed. Mater. Res.* **2001**, *54*, 115–121.
55. Benoit, D. S. W.; Anseth, K. S. *Acta Biomater.* **2005**, *1*, 461–470.
56. Benoit, D. S. W.; Durney, A. R.; Anseth, K. S. *Biomaterials* **2007**, *28*, 66–77.
57. Yoon, J. J.; Chung, H. J.; Park, T. G. *J. Biomed. Mater. Res. A* **2007**, *83*, 597–605.
58. Shu, X. Z.; Liu, Y.; Luo, Y.; Roberts, M. C.; Prestwich, G. D. *Biomacromolecules* **2002**, *3*, 1304–1311.
59. Cai, S. S.; Liu, Y. C.; Shu, X. Z.; Prestwich, G. D. *Biomaterials* **2005**, *26*, 6054–6067.
60. Tae, G.; Kim, Y. J.; Choi, W. I.; Kim, M.; Stayton, P. S.; Hoffman, A. S. *Biomacromolecules* **2007**, *8*, 1979–1986.
61. Choi, W. I.; Kim, M.; Tae, G.; Kim, Y. H. *Biomacromolecules* **2008**, *9*, 1698–1704.
62. Mcgonigle, J. S.; Tae, G.; Stayton, P. S.; Hoffman, A. S.; Scatena, M. *J. Biomater. Sci. Polym. Ed.* **2008**, *19*, 1021–1034.
63. Mccaldon, P.; Argos, P. *Proteins* **1988**, *4*, 99–122.
64. Yamaguchi, N.; Kiick, K. L. *Biomacromolecules* **2005**, *6*, 1921–1930.
65. Nie, T.; Baldwin, A.; Yamaguchi, N.; Kiick, K. L. *J. Control. Release* **2007**, *122*, 287–296.
66. Bulpitt, P.; Aeschlimann, D. *J. Biomed. Mater. Res.* **1999**, *47*, 152–169.
67. Tae, G.; Scatena, M.; Stayton, P. S.; Hoffman, A. S. *J. Biomater. Sci. Polym. Ed.* **2006**, *17*, 187–197.
68. Seal, B. L.; Panitch, A. *Biomacromolecules* **2003**, *4*, 1572–1582.
69. Zhang, L.; Furst, E. M.; Kiick, K. L. *J. Control. Release* **2006**, *114*, 130–142.
70. Rajangam, K.; Behanna, H. A.; Hui, M. J.; *et al. Nano Lett.* **2006**, *6*, 2086–2090.
71. Maynard, H. D.; Hubbell, J. A. *Acta Biomater.* **2005**, *1*, 451–459.
72. Christman, K. L.; Vazquez-Dorbatt, V.; Schopf, E.; *et al. J. Am. Chem. Soc.* **2008**, *130*, 16585–16591.

4.421. Self-Assembled Prodrugs

P K Vemula and N R Campbell, Harvard Medical School, MA, USA; Harvard-MIT Division of Health Sciences & Technology, Harvard, MA, USA; Harvard Stem Cell Institute, Harvard, MA, USA
F Zhao and B Xu, Brandeis University, Waltham, MA, USA
G John, The City College of the City University of New York, NY, USA
J M Karp, Harvard Medical School, MA, USA; Harvard-MIT Division of Health Sciences & Technology, Harvard, MA, USA; Harvard Stem Cell Institute, Harvard, MA, USA

© 2011 Elsevier Ltd. All rights reserved.

4.421.1.	**Introduction**	340
4.421.1.1.	Molecular Versus Polymeric Gelators: Perspectives in Hydrogels	340
4.421.1.1.1.	An introduction to hydrogels	340
4.421.1.1.2.	Polymeric hydrogels	340
4.421.1.1.3.	Molecular hydrogels	341
4.421.2.	**Challenges and Opportunities of Hydrogels in Drug Delivery**	341
4.421.2.1.	Delivery of Hydrophobic Drugs	341
4.421.2.2.	Challenges and Opportunities	341
4.421.3.	**Self-Assembled Prodrugs**	342
4.421.3.1.	Motivation to Design Self-Assembling Prodrugs as Biomedical Gelators	342
4.421.3.2.	Structure-Based Self-Assembled Prodrugs	342
4.421.3.3.	General Strategy to Design Self-Assembled Prodrugs	343
4.421.3.3.1.	Acetaminophen-based self-assembled prodrugs	344
4.421.3.3.2.	Amygdalin-based self-assembled prodrugs	345
4.421.3.3.3.	Ibuprofen-based self-assembled prodrugs	346
4.421.3.3.4.	Paclitaxel-based self-assembled prodrugs	346
4.421.3.4.	Morphology-Based Self-Assembled Prodrugs	347
4.421.3.4.1.	Self-assembled nanoparticles from prodrugs	347
4.421.3.4.2.	Self-assembled vesicles from prodrugs	348
4.421.3.4.3.	Self-assembled micelles from prodrugs	348
4.421.4.	**Self-Assembled Irreversible Prodrug-Based Hydrogels**	350
4.421.4.1.	Paclitaxel-Based Self-Assembled Hydrogels	351
4.421.4.2.	Vancomycin-Based Self-Assembled Hydrogels	351
4.421.4.3.	Glucosamine-Based Self-Assembled Hydrogels	352
4.421.5.	**Conclusions and Outlook**	353
References		354

Glossary

Amphiphile Molecule containing a polar hydrophilic group chemically connected to nonpolar hydrophobic group.
Bioavailability The amount of drug or bioactive substance actually absorbed from a given systemic dose.
Critical micelle concentration (CMC) A phase change characterized by the minimum concentration of amphiphilic (surfactant) molecule required to spontaneously aggregate into micelles in solution.
Gel A semisolid matrix incorporating much more swelling solvent than solute, resulting in a material with mechanical properties between liquids and viscous solids.
Gelator A low-molecular-weight or polymeric molecule that induces gel formation in both polar and nonpolar solvents.
Hydrogel A gel formed by solutes in aqueous solution.
Lipid An amphiphilic molecule or surfactant comprising a polar hydrophilic headgroup and one or more nonpolar hydrophobic chains.
Micelle An aggregate of amphiphilic molecules in water with nonpolar parts in the interior and the polar parts forming a corona exposed to water.
Organogel A gel formed by solutes in an organic solvent.
Prodrug A therapeutic agent precursor intrinsically inactive pharmacologically, but capable of being transformed into one or more active metabolites *in vivo* that exhibit therapeutic efficacy.
Surfactant A surface-active molecule, synonymous with an amphiphilic molecule.

Abbreviations

^{1}H-NMR	Proton nuclear magnetic resonance
3D-networks	Three-dimensional networks
ACS	American Chemical Society
CIMIT	Center for Integration of Medicine and Innovate Technology
CMC	Critical micellar concentration
DSC	Differential scanning calorimetry
FDA	Food and Drugs Administration
FTIR	Fourier transform infrared
HIV	Human immunodeficiency virus
HPLC	High-performance liquid chromatography or high-pressure liquid chromatography
IOP	Intraocular pressure
MGC	Minimum gelation concentrations
MRSA	Methicillin-resistant *Staphylococcus aureus*
NMR	Nuclear magnetic resonance
NSAID	Non steroidal anti-inflammatory drug
PAA	Polyacrylic acid (PAA)
P_{app}	Apparent permeability coefficient
PBS	Phosphate buffer saline
PEG	Polymers including polyethylene glycol
pH	Potential of hydrogen
PHEMA	Poly(2-hydroxyethyl methacrylate)
p*Ka*	Logarithmic measure of the acid dissociation constant
POM	Polarized optical microscopy
PVA	Polyvinyl alcohol
PVP	Polyvinylpyrrolidone
SEM	Scanning electron microscopy
TC_{50}	Toxic concentration 50, that is, concentration during 50% of toxicity
TEM	Transmission electron microscopy
T_{gel}	Gel melting temperature
TLC	Thin-layer chromatography
USD	United States dollar
UV	Ultraviolet
VRE	Vancomycin-resistant enteroccoci
XRD	X-ray diffraction

4.421.1. Introduction

4.421.1.1. Molecular Versus Polymeric Gelators: Perspectives in Hydrogels

4.421.1.1.1. An introduction to hydrogels

The term 'gel' applies to states of matter between liquids and solids (more viscous than liquids and more elastic than solids): a 'hydrogel' is formed through gelation of a solute in an aqueous solution, while an 'organogel' gelates solutes in an organic solvent. In general, the term 'gelator' depicts a molecule (either polymer or low-molecular-weight molecule) that forms three-dimensional (3D) networks in a given solvent, either through covalent cross-linking or noncovalent intermolecular interactions, resulting in the formation of a gel phase where typically the amount of imbibed solvent exceeds the solid dry mass of the gelator network by up to several hundred percent. Hydrogels consist of elastic networks with interstitial spaces that contain as much as 90–99% (w/w) water.[1,2] Most gels are formed from fibrous nanostructures that entangle or are chemically cross-linked into 3D networks, providing a semiwet environment for molecular-level biological interactions.[3–5] Gels find wide range of applications in cosmetics, drug delivery, sensors, biotechnology separations, wound closure materials, contact lenses, and food processing, to name a few, representing a major part of USD $80 billion drug delivery, contact lens, and wound closure market.

4.421.1.1.2. Polymeric hydrogels

Polymeric hydrogels exhibit the ability to swell in water or various aqueous solutions by forming an enlarged gel phase that, in the case of cross-linked systems, cannot dissolve, regardless of the solvent.[6] There are many different types of hydrogels classified according to their physicochemical properties and their preparation methods.[7] Hydrogels can be generated using either natural polymers (proteins, polysaccharides, and deoxyribonucleotides) or synthetic polymers (from appropriate synthetic monomers). In general, natural polymer-based hydrogels have superior biocompatibility; however, synthetic polymers are well known for inclusion of desired functionality. Thus, logically, a third category could be hybrid hydrogels, generated from the combination of natural polymers (i.e., for desired biocompatibility) and synthetic polymers (i.e., for specific functionality).[8,9]

Primarily, strong interactions between polymeric chains lead to formation of 3D networks that induce gelation. If these networks of chains are connected (i.e., cross-linked) through strong covalent bonds, they are called chemical gels, whereas those connected through noncovalent interpolymeric chain interactions (i.e., physical polymer chain entanglements and self-assembled gels via formation of disordered 3D networks) are called physical gels.[5] With their high water content and ease of modulation of physical and chemical properties through subtle changes in monomer structure and polymer molecular weight, polymeric hydrogels can be both biocompatible and user-friendly.[2,10–14] Biodegradable and biocompatible hydrogels have been designed both based on natural polymers that are susceptible to enzyme degradation and using synthetic polymers that consist of hydrolyzable moieties.[15] For instance, hydrogels using the natural polymer, chitosan, have received a great deal of attention because of their well-documented biocompatibility, low toxicity, and degradability by human enzymes.[16–18] Custom-made hydrogels could be prepared according to need. Bioadhesive properties could be obtained by promoting interchain bridges between the hydrogel polymer's functional groups and mucus glycoproteins.[19,20] Polymers including polyethylene glycol (PEG), polyvinyl alcohol (PVA), poly(2-hydroxyethyl methacrylate) (PHEMA), and polyacrylic acid (PAA) are used in the preparation of hydrogels that have mucoadhesive and bioadhesive properties to enhance drug residence time and tissue permeability.[19,21] Polyvinylpyrrolidone

(PVP) is popular in ophthalmic, drug tablet, and wound healing applications.

4.421.1.1.3. Molecular hydrogels

In addition to conventional polymer gels, low-molecular-weight organogels and hydrogels have been developed that self-assemble into polymer-like fibers, forming the so-called 'self-assembled,' 'supramolecular,' 'low-molecular-weight,' or 'molecular' gels.[22–36] In particular, small molecule hydrogels are promising because of both their compatibility with rational design using nanostructures, and their spontaneous gelation and rapid degradation. Thus, biodegradation of molecular hydrogels might have certain advantages compared to traditional polymeric hydrogels. Importantly, the pool of diverse functional groups benefits the design and synthesis of custom-made molecular gelators according to need. Typically, gelation is a delicate balance between solubility and aggregation; thus, gels are formed by dissolving minute amounts of gelator (~0.1–10%, w/v) in hot solution, while cooling below the gel melting temperature (T_{gel}), the gelator self-assembles into 3D networks that immobilize the complete volume of solvent, supporting their own weight without collapsing the gel structure. A schematic representation of the typical gelation process is illustrated in Figure 1.

The inherent morphology of hydrogels can be characterized using various microscopy techniques, such as polarized optical microscopy (POM), scanning electron microscopy (SEM), and transmission electron microscopy (TEM). The stability of a gel can be delineated by analyzing both thermal properties (often with differential scanning calorimetry, DSC),[37–40] and physical state.[37–39,41] In addition, gels can be characterized through various spectroscopic techniques, such as nuclear magnetic resonance (NMR),[38,42,43] ultraviolet (UV),[43,44] circular dichroism (CD),[40,42,45] and fluorescence spectroscopy.[40,45] In addition, the mechanical properties of gels can be investigated through a series of rheology experiments.[46–51] A range of amphiphiles with great structural diversity could be tailored to form nanofibrous 3D networks in aqueous solution, which typically initiates the gelation in water (i.e., hydrogelation). Hydrogelation is readily visually observed as a macroscopic change and acts as a quick and simple test for the formation of a nanofibrous network. Given that such a simple process is required for testing gelation, a large group of molecules (i.e., both low- and high-molecular-weight candidates) could be tested for formation of molecular nanofibers and hydrogels in a relatively short time period.

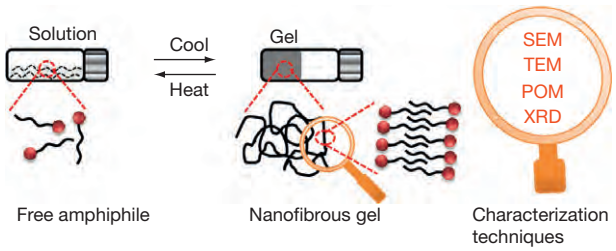

Figure 1 Schematic representation of gelation of solvent through self-assembly of amphiphilic molecules. The majority of self-assembled gels are thermoreversible.

4.421.2. Challenges and Opportunities of Hydrogels in Drug Delivery

4.421.2.1. Delivery of Hydrophobic Drugs

The field of hydrogel-based drug delivery has expanded over the past few decades to significantly improve the bioavailability of water-insoluble drugs, which otherwise exhibit attractive therapeutic potential.[52] Drug discovery efforts within the pharmaceutical industry currently provide a large number of active candidate compounds that could serve as therapeutic agents, yet new drug approval rates have been low (i.e., single-digit) for the better part of the past decade. Most new, potent therapeutic candidates are poorly soluble in aqueous media, limiting possibilities for their formulation and dosing via oral or parenteral administration.[53] In order to overcome this limitation, novel drug delivery systems such as hydrogels, micelles, vesicles, and nanoparticles are continually developed to solubilize and improve drug administration, dosing, and bioavailbility (Figure 2). In general, these nano/micron-sized carriers contain hydrophobic domains to help solubilize poorly water-soluble drugs and stabilize them in dosage forms. Upon administration, they could potentially improve drug therapeutic efficacy through reliable controlled release of the dose while reducing their toxicity profile.

4.421.2.2. Challenges and Opportunities

Although an overwhelming number of hydrogel-based drug delivery formulations and model systems are reported, the field still faces major challenges. Primarily, improvements in both the versatility of clinical usage and drug dosing and release kinetics of such systems for both hydrophobic and hydrophilic drugs remain obstacles.[54] On the front of clinical usage, several factors are at play. First, hydrogels typically have a relatively low tensile strength, making them poorly suited for load-bearing applications. In some cases, this also means that applications of hydrogel-derived medication can be washed away too easily, a problem often solved by subcutaneous injection to form depots.[54] Secondly, although hydrogels are deformable, a property that allows them to conform to the location of their application, they are often not viscous enough so as to allow for simple injection. As a result, methods of *in situ* generated hydrogels have been explored as a possible solution using several strategies. However, photocurable *in situ* gels introduce problems of potential toxicity from methods such as ultraviolet (UV) irradiation or the use of cross-linkers.[54] On the front of release kinetics, hydrogels often produce rapid release of their drug payload because of their large pore size and high water content.[55] Clinical control over dose dumping of hydrophilic drugs or insufficient release of hydrophobic drugs is a problem (see Chapter 4.422, pH-Responsive Polymers for the Intracellular Delivery of Biomolecular Drugs; and Chapter 4.426, Electrospun Fibers for Drug Delivery).

Rewards for overcoming significant challenges in use of hydrogels in drug delivery are substantial. Hydrogel uses with stem cells[56] and developing micro- and nanohydrogels to facilitate faster response[57] are emerging areas. Innovation and creative technical ingenuity are improving capabilities of hydrogels in drug delivery to address some of its most difficult challenges and provide new capabilities.

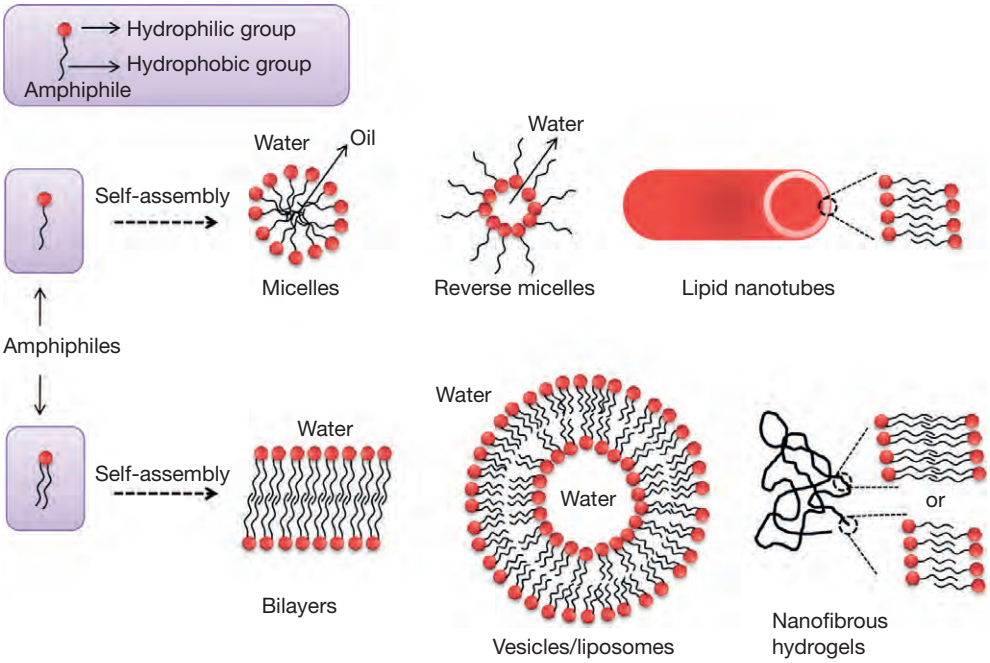

Figure 2 Various self-assembled nanomaterials potentially useful to deliver either lipophobic or lipophilic drugs. Amphiphiles have two distinct regions (hydrophobic/hydrophilic) in their structure, which drives them to self-associate in a given solvent (lyotropic assembly). In general, on the basis of the hydrophilic/hydrophobic ratio, most amphiphiles undergo self-assembly to generate various nanostructures such as micelles, nanofibers, and vesicles.

4.421.3. Self-Assembled Prodrugs

4.421.3.1. Motivation to Design Self-Assembling Prodrugs as Biomedical Gelators

To date, the majority of drug delivery systems load drugs through encapsulation, with inherent limitations such as low drug loading capacity, drug leakage during encapsulation, and inefficient preservation.[58] Another routinely encountered hurdle is the degradation of carriers under *in vivo* conditions before reaching the targeted site. Thus, designing amphiphilic prodrugs to undergo self-assembly to form hierarchical gel nanostructures would eliminate the use of an external gel carrier. It is well established that surfactant-like amphiphiles self-assemble into ordered lyotropic nanomaterial phases, including micelles, vesicles, liquid crystals, hexacosomes, cubosomes, fibers, helices, and nanotubes (Figure 2). Hence, converting known or desired drugs into surfactant-like prodrug structures using synthesis would enable the generation of self-gelling drugs. Such drugs could exhibit diverse formulations and controlled release under either chemical hydrolytic control or phase disassembly control and overcome issues with administration of gels. Herein, we discuss a few key examples of the design and synthesis of self-assembled prodrugs from our and others' research efforts.

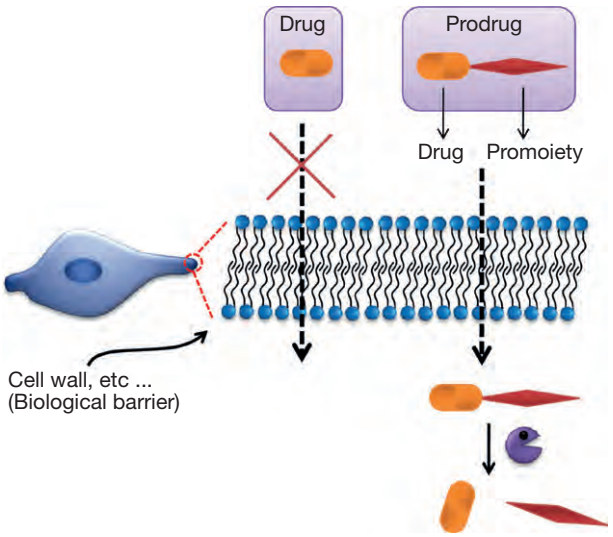

Figure 3 A prodrug is a conjugate of a known drug and a promoiety. In general, a prodrug is an inactive form of the drug; however, its chemistry helps to overcome certain inherent hurdles of the parent therepeutic agent, and could significantly contribute to optimal pharmacokinetics. For instance, a prodrug may facilitate crossing of biological barriers, enhancing distribution in either blood or tissue which otherwise might not be possible with the parent drug.

4.421.3.2. Structure-Based Self-Assembled Prodrugs

Prodrugs are therapeutic agent precursors that may be intrinsically largely inactive, but are transformed within the host into one or more active metabolites *in vivo* that exhibit therapeutic efficacy (Figure 3). The term 'prodrug' was introduced by Albert in 1958[59] to describe molecules that undergo biotransformation prior to exhibiting their pharmacological effects. This transformation usually refers to a chemical change in the prodrug, usually with chemical removal of a specific prodrug component, to yield the active drug form. This can be enzymatically triggered or simply a general hydrolytic event. The use of prodrugs is now the most welcomed strategy for improving the physicochemical and pharmacokinetic

properties of pharmacologically active compounds, increasing the utility of a prospective drug.[60–65] Prodrugs can be categorized on the basis of chemical classes and/or mechanism of activation. Carrier-linked prodrugs, macromolecular prodrugs, labile esters, phosphorylated prodrugs, and antibody–drug conjugates are all examples of chemical classes. In general, most prodrugs are chemical derivatives, synthesized through chemical group transformation, which subsequently require a one- or two-step enzyme-mediated or chemical transformation to produce the potent parent drug. Often, the prodrug approach seems to surmount several hurdles, such as chemical instability, poor water solubility, rapid presystemic metabolism, inadequate absorption, and toxicity.[66] Interestingly, approximately 15% of all new drugs approved in 2001 and 2002 were prodrugs,[62,63] a number expected to increase in the future.

Despite the growth of prodrugs, several inherent problems still exist. For example, once released from an injection site, prodrugs are usually converted into their active drug form rapidly, thus limiting the potential of prodrugs to exhibit extended release. To overcome these challenges, 'self-assembled prodrugs' were designed to achieve (i) maximum drug loading efficiency, and (ii) controlled, prolonged release kinetics (Figure 4). To expand further, avoiding use of an external carrier by turning prodrugs into their own self-deliverable carriers would increase the deliverable dosage fraction of parent drugs per formulation. In addition, the self-assembled (nanovehicular, networked) form of prodrug amphiphiles may undergo much slower degradation (either enzyme- or hydrolysis-mediated) compared to the free (unassembled) molecular prodrug form, enhancing controlled delivery for longer periods of time (sustained/controlled drug delivery).

Self-assembly is an integral part of biological form and function, playing pivotal roles in integrated cellular functions.[67] Intermolecular interactions such as hydrogen bonding, van der Waals interactions, π–π stacking, and strong ionic interactions govern supramolecular chemistry in biology and materials sciences.[68] Prodrug chemistry can be custom tailored to produce drug amphiphiles that assemble into aggregates and become bioactive at different rates.

4.421.3.3. General Strategy to Design Self-Assembled Prodrugs

Despite explosive growth in the development of diverse low-molecular-weight hydrogels, their dependability in drug delivery must address the unknown toxicity of *in situ*-generated metabolites and fragments produced from degradation of the host amphiphilic gelator. Often, the metabolic pathway of those fragments is a 'black box,' and considered one of the major hurdles in low-molecular-weight hydrogel-based drug delivery. This uncertainty can be diminished to some extent by designing amphiphilic prodrugs from clinically approved drugs; thus, the degradation products from the prodrug will be a known drug and a promoiety that could be potentially less toxic. Thus, we have developed a general design approach, that is, selecting the known, clinically approved drugs whose

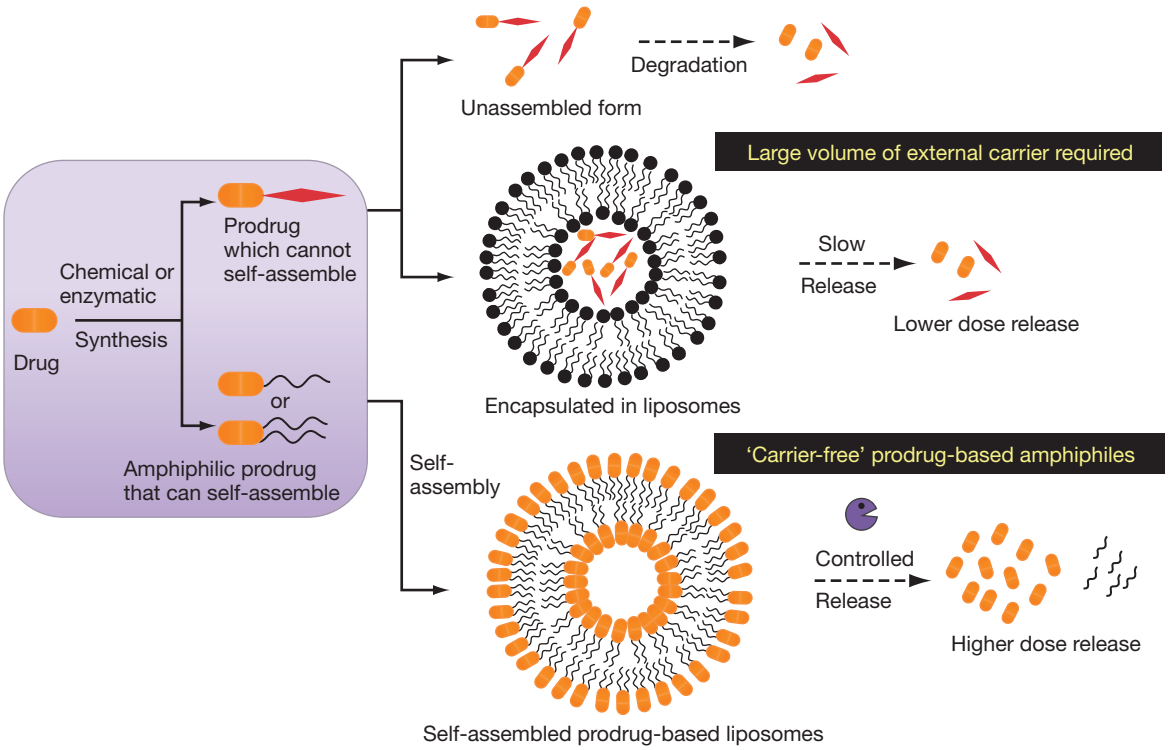

Figure 4 Self-assembled prodrug-based delivery concept. This scheme demonstrates the advantage of self-assembled prodrug-based carriers over traditional encapsulation of drug within an external carrier. In Path 1, either unmodified drug or prodrug that does not self-assemble is encapsulated in an external carrier. However, this approach suffers with low encapsulation ability of additional drugs. Path 2 depicts the superior nature of self-assembled prodrug-based drug delivery. Advantages of this approach are (i) manifold increase in drug loading efficiency, (ii) nonrequirement of external carrier, and (iii) versatile opportunities for controlled release.

metabolic pathways are well documented, followed by attaching a biocompatible promoiety through covalent modification (Figure 5). Consequently, such prodrug amphiphiles could be capable of undergoing self-assembly in aqueous solutions and in a variety of other solvents, and remain susceptible to enzymatic and hydrolytic degradation to produce their active forms. Importantly, self-assembly in water could exploit formation of stable hydrophobic domains, which could be further used to encapsulate other hydrophobic therapeutics. Thus, this approach could enable multiple drugs to be delivered simultaneously (Figure 5) as new combination therapies.

In designing chemical derivatives of known drugs to produce amphiphilic prodrugs, several key factors must be carefully examined, including (i) availability of appropriate functional groups in parent drugs amenable to routine functional-group transformation reactions under mild conditions; (ii) promoiety that ideally should not promote adverse effects, and facilitate stable and reliable prodrug self-assembly in physiological conditions; (iii) linker functional group that should release the parent drug under either enzyme-mediated or hydrolytic degradation; and (iv) degradation by-products that should not generate ancillary bioactivity or toxicity.

4.421.3.3.1. Acetaminophen-based self-assembled prodrugs

To demonstrate this concept keeping the above parameters as a guideline, we have designed and synthesized a series of amphiphilic prodrugs from the clinically approved drug, acetaminophen, *N*-(4-hydroxyphenyl)acetamide, popularly known as paracetamol (Figure 6).[69] Acetaminophen is a common analgesic and antipyretic drug used for the relief of fever and headache. Esters are the most common prodrugs used, and it is estimated that 49% of all marketed prodrugs are activated by enzymatic hydrolysis.[61] Thus, a series of amphiphiles and bolaamphiphiles (**Apn-Prodrugs**) have been synthesized from acetaminophen by appending a biocompatible fatty acid covalently attached through an ester bond susceptible to both esterase-mediated and possible hydrolytic degradation to produce the parent drug (Figure 6). Without an enzyme present, those gels exhibited hydrolytic stability over months.

The amphiphilic acetaminophen prodrugs underwent self-assembly in water to form hydrogels, with minimum gelation concentrations (MGCs) between 0.4 and 1.5% (w/v), and unprecedented thermal and temporal stabilities. As anticipated, acetaminophen prodrug-based amphiphiles formed branched or fibrous/sheet-like networks at the microscopic level, as seen through SEM and TEM (Figure 6). The average thickness of the fibers was in the range of 50–400 nm, with lengths on the order of several microns. Intriguingly, investigation of these hydrogels by X-ray diffraction (XRD) measurements, *ab initio* calculations, and Fourier transform infrared (FT-IR) experiments revealed that lamellar structures were formed by self-assembly of amphiphilic prodrugs (Figure 7). Subsequently, the possibility of single and multiple drug delivery using self-assembled prodrugs has been investigated. The well-studied potential chemotherapeutic drug, curcumin,[70–74] has been utilized as a model hydrophobic drug to encapsulate within self-assembled nanofibers formed by **Apn-Prodrug** amphiphiles. Hydrogels of Apn-Prodrug were found to encapsulate up to 0.5 mM concentration of curcumin, possibly because of efficient localization of hydrophobic curcumin within the hydrophobic nanofibrous prodrug 3D network. Subjected to lipase (an esterase) at 37 °C in phosphate buffer saline (PBS), degradation of the curcumin-encapsulating hydrogel was triggered, and after 48 h the hydrogel was completely degraded to release the parent drug acetaminophen and the encapsulated curcumin (followed using absorbance spectra). On the contrary, in the absence of enzyme, the **Apn-Prodrug** hydrogels showed excellent hydrolytic stability in PBS over the course of a few months. This stability could be due to the presence of tightly self-associated prodrugs, protecting ester bonds in hydrophobic segments and reducing the

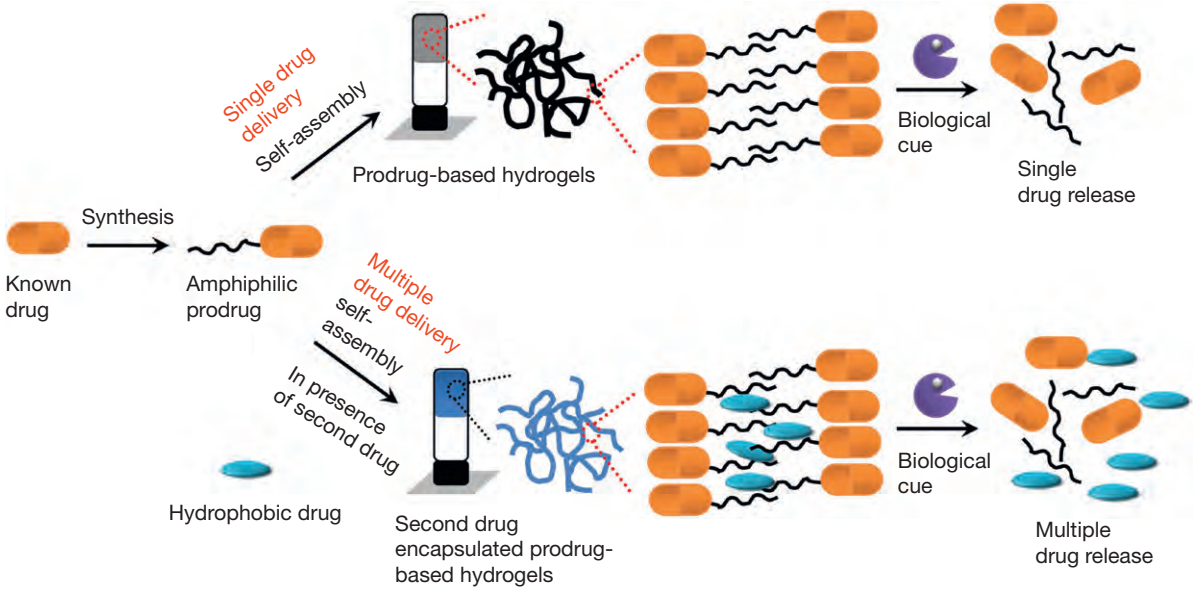

Figure 5 Cartoon presentation of general approach for the synthesis of amphiphilic prodrugs that could self-assemble to form hydrogels. Synthesis and self-assembly of amphiphilic prodrugs, encapsulation of a hydrophobic drug, and triggred multiple drug-delivery are illustrated.

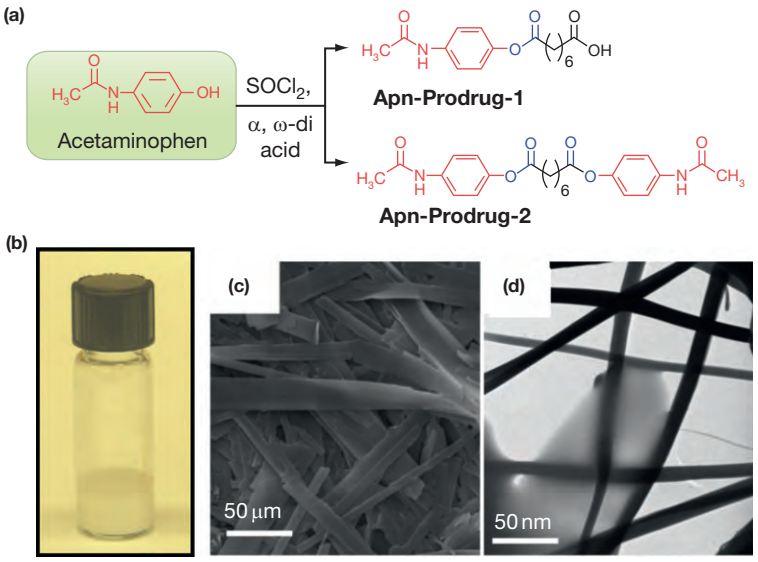

Figure 6 (a) Synthesis of **Apn-Prodrugs** by attaching a fatty acid through an ester link. (b) Image of hydrogel of **Apn-Prodrug-1**, and characterization of the gel through (c) scanning electron microscopy and (d) transmission electron microscopy. Electron microscopy images clearly show the presence of self-assembled fibers.

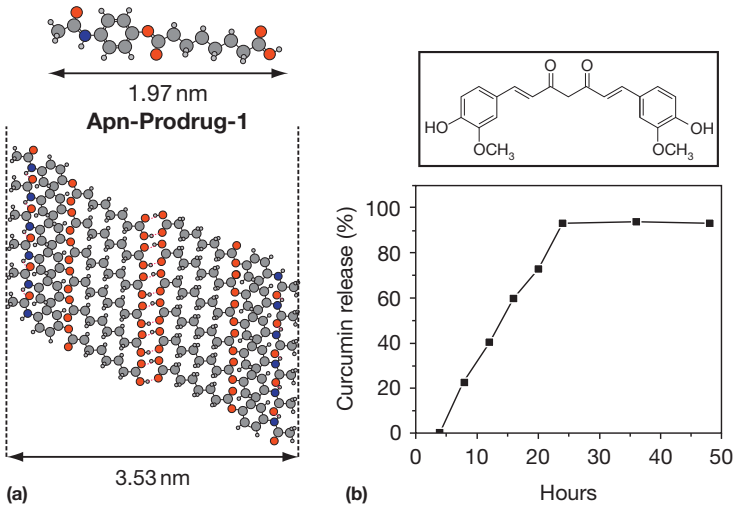

Figure 7 (a) Schematic representation of molecular packing of **Apn-Prodrug-1** into a prodrug hydrogel. (b) Top: curcumin structure; bottom: absorbance maxima of curcumin that was released from hydrogel of **Apn-Prodrug-1** by lipase-mediated gel degradation. Reproduced from Vemula, P. K.; Cruikshank, G. A.; *et al*. *Biomaterials* **2009**, *30*(3), 383–393. Copyright 2009, Elsevier.

accessibility of water molecules compared to the dissolved molecular form. A distinction of the self-assembled prodrug approach is attenuation of the burst release of drug (Figure 7 (b)), a major hurdle in hydrogel-based release of hydrophobic drugs. Another interesting observation was that although the sustained release of the drug occurred over a period of 2 days, the enzyme concentration ($100\,U\,ml^{-1}$) in those experiments was significantly higher than physiological concentrations of esterases (e.g., cholesterol esterase, $7\,U\,ml^{-1}$).[75] Thus, the anticipated release under *in vivo* conditions may provide sustained release for several days, if not months. However, the presence of multiple enzymes, serum, and plasma – the complex biological environment that alters the kinetics of gel degradation *in vivo* – has not been addressed.

4.421.3.3.2. Amygdalin-based self-assembled prodrugs

Amygdalin, an anticancer agent, belongs to cyanogenic glycoside family.[76,77] D-Amygdalin, [*O*-β-glucopyranosyl-(1→6)-β-D-glucopyranosyloxy]benzeneacetonitrile (Figure 8), is a by-product of the processing of apricots, almonds, peaches, and cherries,[78] and its rigid sugar backbone is rich in directional hydroxyl groups. The primary hydroxyl group on amygdalin was selected as a site to generate amphiphilic prodrugs by tethering natural fatty acids with an enzyme-cleavable ester linker.[79] Interestingly, the extremely regioselective esterification ability of lipase has been utilized as a tool to synthesize amygdalin-prodrug amphiphiles (**Amy-Prodrugs**) in quantitative yields (Figure 8). **Amy-Prodrugs** underwent self-assembly to form nanofiber-rich nanoarchitectures in a wide range of

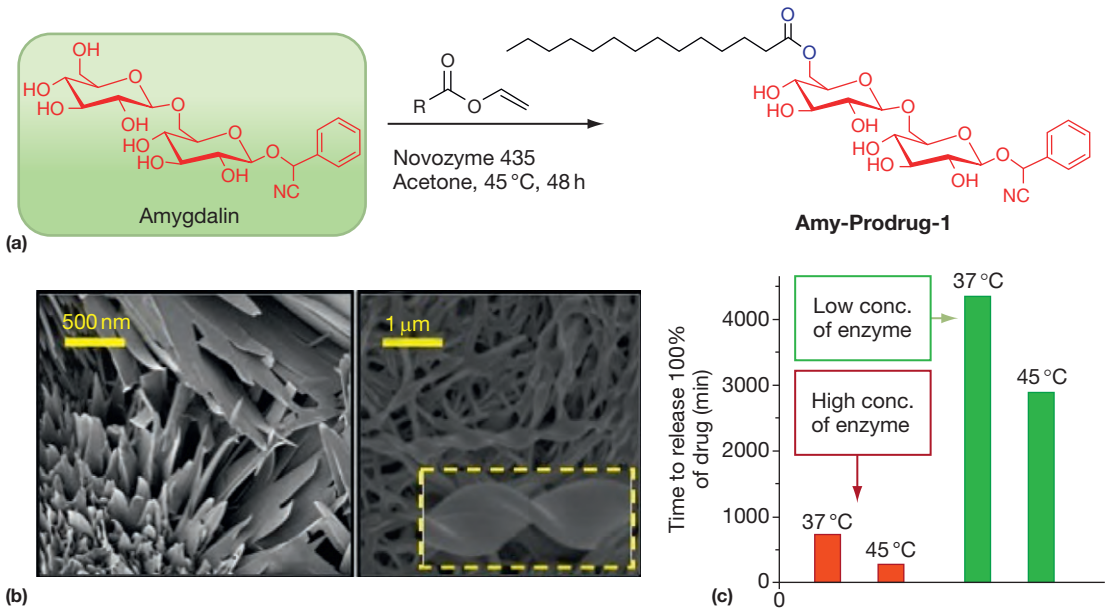

Figure 8 (a) Enzyme-mediated regioselective synthesis of amygdalin-based amphiphilic prodrug, **Amy-Prodrug-1**, which could form both hydro- and organogels at lower concentration. (b) Scanning electron microscopy images of organogel (left) and hydrogel (right), which show sheet-like and helical fibers, respectively. (c) Effect of enzyme concentration (10 and 100 U ml^{-1}) and incubation temperature on gel degradation/encapsulated drug release. By modulating either temperature or enzyme concentration, the drug release kinetics from the networks are modulated. Reproduced from Vemula, P. K.; Li, J.; *et al. J. Am. Chem. Soc.* **2006**, *128*(27), 8932–8938. Copyright 2006, American Chemical Society.

solvents including aqueous solutions, and both polar and nonpolar organic solvents at extremely low MGC values (0.05–0.2%, w/v) revealed the presence of helical fibers and sheet-like structures (Figure 8(b)). Furthermore, to evaluate the ability of **Amy-Prodrug** gels to deliver multiple drugs simultaneously, akin to acetaminophen prodrugs, curcumin has also been encapsulated within the **Amy-Prodrug**-based hydrogels. The ester-based **Amy-Prodrug** amphiphiles were susceptible to lipase, causing an esterase-mediated enzymatic degradation, and therefore, a detailed investigation was carried out to achieve controlled drug delivery. The inherent hydrophobic domains within the self-assembled fibers were utilized for enhanced encapsulation, as in this manner, hydrogels have the potential to increase the bioavailability of water-insoluble drugs. Interestingly, in the absence of esterase enzyme, **Amy-Prodrug**-based hydrogels exhibited unprecedented temporal stability, with no drug leakage occurring under physiological conditions (PBS, pH 7.4, and 37 °C). In addition, we demonstrated controlled gel degradation, allowing drug release through modulation of either enzyme concentration and/or incubation temperature (Figure 8(c)). Interestingly, **Amy-Prodrug**-based hydrogels also did not exhibit any detectable burst release profile, akin to hydrogels made from **Apn-Prodrugs**.

As discussed earlier, it is equally important to understand the by-products formed after enzyme-mediated prodrug-based hydrogel degradation. Conventional thin-layer chromatography (TLC) was performed to characterize the components formed after gel degradation; tetradecanoic acid was shown by ^{1}H NMR spectroscopy. Subsequently, further TLC analysis of the solution demonstrated the presence of amygdalin and curcumin. Taken together, the formation of amygdalin and fatty acid suggests that prodrug degradation occurred as expected at the ester bond of amygdalin prodrugs by lipase (esterase) enzyme.

4.421.3.3.3. Ibuprofen-based self-assembled prodrugs

As a widely used nonsteroidal anti-inflammatory drug (NSAID), ibuprofen is administered as an analgesic and to relieve the symptoms of fever, arthritis, and primary dysmenorrhea.[80] Kim and coworkers incorporated a dipeptide glycine–glycine backbone into (*S*)-(+)-ibuprofen and successfully transformed it into molecular prodrug-based hydrogelator ibuprofen–glycine–glycine (**Ibu-Prodrug**, Figure 9(a)) with an MGC of 0.9% (w/v; 28 mM).[81] To delineate structure–function relationships, ibuprofen was covalently connected to several dipeptides such as glycine–glycine, glycine–alanine, glycine–serine, glycine–phenylalanine, and glycine–histidine (Figure 9(a)); however, only the glycine–glycine derivative could self-assemble to form nanofibrous hydrogels (Figure 9(b)). Extensive spectroscopic studies suggested that hydrogen bonding of amide and carboxylic groups and π–π interactions were the driving forces for efficient self-assembly. This could be efficient peptide motif for gel assembly. Furthermore, on the basis of HPLC retention times, the authors concluded that the hydrolysis product of this hydrogelator was ibuprofen, after incubation with the carboxypeptidase for 24 h. This work is one example of a drug successfully modified into a hydrogelator by a simple peptide motif. The knowledge gained from modification of ibuprofen with simple structures will be insightful and instructive for the modification of more expensive or complicated therapeutic agents.

4.421.3.3.4. Paclitaxel-based self-assembled prodrugs

Paclitaxel, a well-known novel anticancer chemotherapeutic agent originally isolated from the American Pacific yew tree (*Taxus brevifolia*),[82] exhibits an important *in vivo* antitumor activity.[83] However, because of taxol's extreme hydrophobicity,

its poor water solubility ($<5 \times 10^{-6}$ M) still remains as a large hurdle for effective *in vivo* delivery. To overcome this obstacle, various delivery vehicles such as nanoparticles, colloids, and liposomes have been developed.[84–87] In addition, numerous taxol-based prodrugs have been synthesized.[88] Nicolaou *et al.* synthesized the methylpyridinium acetate derivative at the 2′ hydroxyl group of taxol (**Tax-Prodrug-1**, Figure 10),[89] which showed enhanced bioavailability of paclitaxel. Although its water solubility was high, at >20 mM, **Tax-Prodrug-1** underwent self-assembly to form colorless transparent hydrogels.[89] **Tax-Prodrug-1** was found to form several types of assemblies, including regular helices and micelles, depending on the nature of the media. TEM of the hydrogels revealed the presence of fibrillar nanostructures with helices, which exhibited varied lengths around 80 nm, but a consistent diameter of approximately 10 nm. The molecular structure of **Tax-Prodrug-1** is sufficient to promote intermolecular interactions, as it contains a defined polar headgroup, with paclitaxel serving as a hydrophobic chiral backbone, while the hydroxyl and amide groups promote hydrogen bonding.

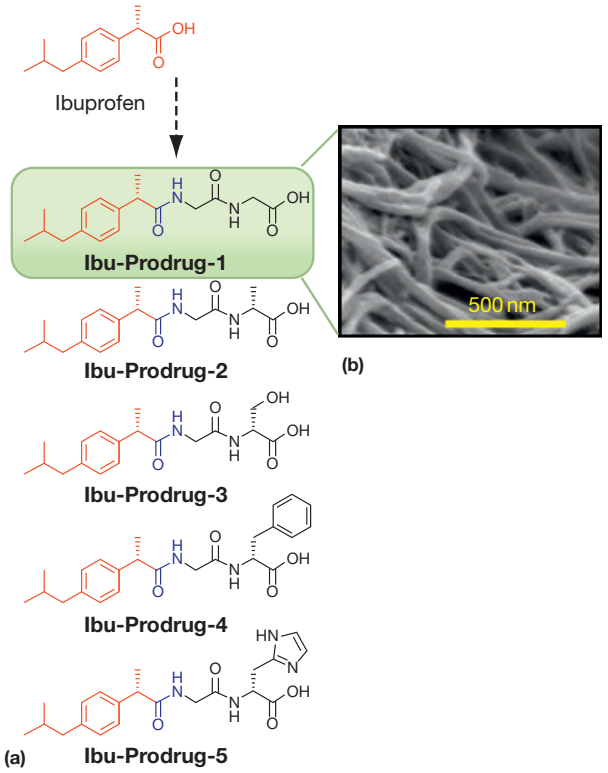

Figure 9 (a) Synthesis of ibuprofen-based self-assembled prodrugs, **Ibu-Prodrugs**. Among various dipeptide-based prodrugs, **Ibu-Prodrug-1** could self-assemble to form nanofibrous hydrogels, (b) scanning electron microscopy image. Reproduced from Bhuniya, S.; Seo, Y. J.; *et al. Tetrahedron Lett.* **2006**, *47*(40), 7153–7156. Copyright 2006, Elsevier.

4.421.3.4. Morphology-Based Self-Assembled Prodrugs

In addition to self-assembled nanofibrous hydrogels, other classes of ordered lyotropic supramolecular phases such as micelles, vesicles, hexacosomes, cubosomes, fibers, helices, and nanotubes were developed by introducing subtle structural modification into known drugs.

4.421.3.4.1. Self-assembled nanoparticles from prodrugs

Acyclovir is a nucleoside antiviral agent against herpes simplex virus (HSV) with low oral bioavailability, typically <20%, and a short circulation half-life, $t_{1/2} = 2.5$ h.[90] Jin *et al.* have synthesized a series of long-chained alkylated derivatives of acyclovir and characterized their ability to self-assemble in aqueous solutions.[91] As it is amphiphilic, the single-chain lipid derivative **Acyclovir-Prodrug-1** (Figure 11(a)) predictably self-assembled at the air–water interface. In general, bulk-phase hydrophobic interactions and hydrogen bonding lead the neutral single alkyl chain derivatives to aggregate layer-by-layer into nanoparticles, while the charged derivatives form self-assembled vesicles based on hydrophobic interactions (Figure 11(b)).[92] The self-assembly behavior of long-chain alkyl derivatives of nucleoside analogs in a given solvent media is determined by the number of alkyl chains and the resulting charged state. Self-assembled nanoparticles formed through **Acyclovir-Prodrug-1** had an average size of 83 nm, with a negatively charged surface.[91] *In vitro* and *in vivo* stability, interaction with cells, pharmacokinetics, and tissue distribution after intravenous (i.v.) administration in animals have been

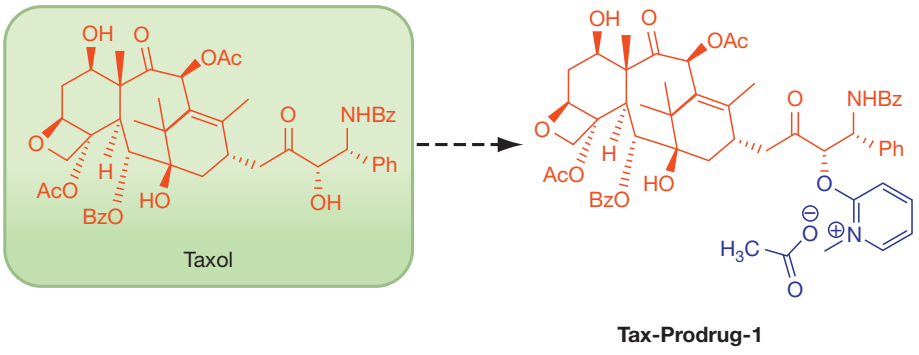

Figure 10 Methylpyridinium salt derivative of taxol (**Tax-Prodrug-1**) forms transparent hydrogels, and under physiological hydrolytic conditions, the parent potent drug, paclitaxel, could be generated. Reproduced from Nicolaou, K. C.; Guy, R. K.; *et al. Angew. Chem. Int. Ed. Engl.* **1994**, *33*(15/16), 1583–1587. Copyright 1994, Wiley-VCH.

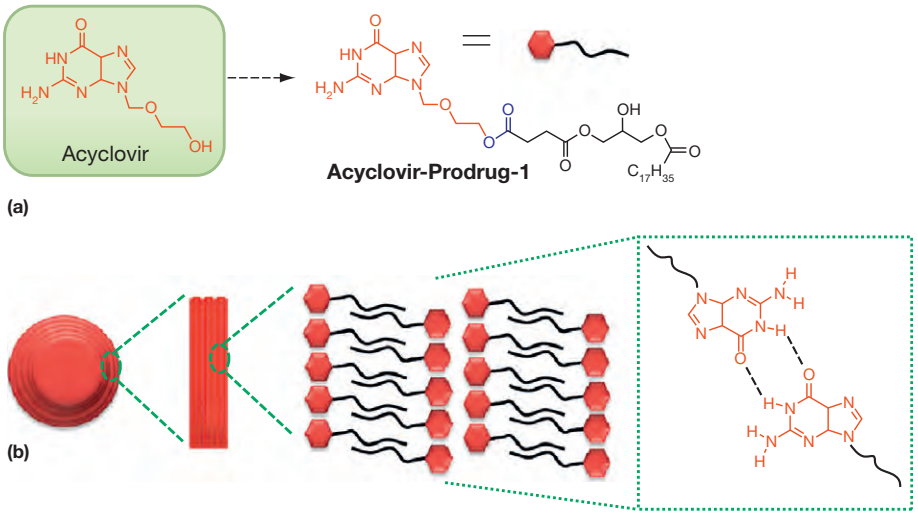

Figure 11 (a) Single-chain amphiphilic prodrugs (**Acyclovir-Prodrug-1**) were prepared from antiviral agent acyclovir. (b) Formation of self-assembled nanoparticles from **Acyclovir-Prodrug-1**. Hydrophobic interactions between lipid chains, and strong hydrogen bonding between nucleobase headgroups stabilize the self-assembled nanoparticles. Reproduced from Jin, Y.; Qiao, Y.; *et al*. *Colloids Surf. B Biointerfaces* **2005**, *42*(1), 45–51. Copyright 2005, Elsevier.

reported.[91] **Acyclovir-Prodrug-1** nanoparticles are degraded by rabbit plasma and pig liver carboxylesterase with half-lives of 25 and 4.5 h, respectively, to release the parent drug, acyclovir.

Clearly self-assembled prodrug-based nanostructures are attractive options for development, yet it is important to consider interactions between nanostructures and organisms/cells before advancing to the clinic. For instance, nanoparticles of **Acyclovir-Prodrug-1** showed slight toxicity to Vero cells with TC_{50} of 1126 μM. On the contrary, acyclovir did not show any toxicity at over 4000 μM. This 'toxicity window' was attributed to the interaction between self-assembled nanoparticles and erythrocytes, with the strong cell-membrane insertion of amphiphilic **Acyclovir-Prodrug-1** a likely primary reason for cell toxicity.

4.421.3.4.2. Self-assembled vesicles from prodrugs

Diverse nucleoside analogs are known to serve as potential anticancer[93] and antiviral[94] therapeutics. Careful inspection of the chemical structure of these agents revealed that derivatization by simple chemical functional group transformation would provide a library of amphiphilic-prodrugs. Antiviral nucleoside analogs have either purine-type (i.e., guanine in **AntiVir-Prodrug-1**, hypoxanthine in **AntiVir-Prodrug-2** and **AntiVir-Prodrug-3**) or pyrimidine-type nucleobase heads (thymine in **AntiVir-Prodrug-4** and **AntiVir-Prodrug-5**), and are conjugated to a steroid-based cholesterol through a dicarboxylic acid (Figure 12) that could promote the formation of self-assembled nanoparticles and vesicles. Jin *et al*. synthesized five cholesterol derivatives of antiviral nucleoside analogues containing representative nucleobase groups, and both their physiochemical properties and their nature of self-assembly have been reported.[95,96]

AntiVir-Prodrug-2 and **AntiVir-Prodrug-3** were synthesized from didanosine, and **AntiVir-Prodrug-4** and **AntiVir-Prodrug-5** were synthesized from zidovudine. In 1991, the FDA approved didanosine as a first-generation anti-HIV agent. Its bioavailability is in the range of 20–40% depending on the formulation used. Various lipid-derivative prodrugs were made from didanosine to improve the bioavailability for direct lymphatic delivery against HIV.[97–99] Didanosine-based vesicles were able to attain longer *in vivo* circulation with twofold enhanced drug bioavilability.[100]

Self-assembly of purine- and pyrimidine-based prodrugs in aqueous solution produced nanosized monodispersed vesicles.[95,96] Schematic representation for self-assembly of **AntiVir-Prodrugs** is illustrated in Figure 13. To initiate vesicle formation, prodrugs were dissolved in tetrahydrofuran, and then added to water, which initiated hydrophobic interactions and intermolecular hydrogen bonding, with promoiety groups and nucleobase headgroups, respectively. The **AntiViral-Prodrugs** self-assembled into bilayers in water, with the polar headgroups outside and the hydrophobic tails inside, to avoid contact with aqueous solution. Furthermore, bending in bilayers (i.e., curvature) resulted in the formation of closed vesicles.

Though self-assembled prodrug-based delivery systems have promising efficiency, there is always room for surprises. For instance, despite producing stable self-assembled nanoparticles, **AntiVir-Prodrug-2** and **AntiVir-Prodrug-3** do not demonstrate effective pharmacokinetics, metabolism, and therapeutic utility.[95] Although **AntiVir-Prodrug-2** and **AntiVir-Prodrug-3** consist of appropriate molecular structures that could promote stable self-assembly, they failed to undergo degradation in physiological media to deliver the parent drug (Figure 13). However, reasons for nondegradability of these prodrugs are unknown. These examples demonstrate that obtaining self-assembly and good stability is not sufficient if active parent drugs are difficult to release via a desired mode in targets. Thus, self-assembled prodrugs should be designed and modified carefully and extensively to accomplish all objectives of self-assembly, stability, and degradation performance.

4.421.3.4.3. Self-assembled micelles from prodrugs

Dynamic colloidal dispersions, micelles, are typically formed through self-assembly of amphiphiles or surface-active molecules

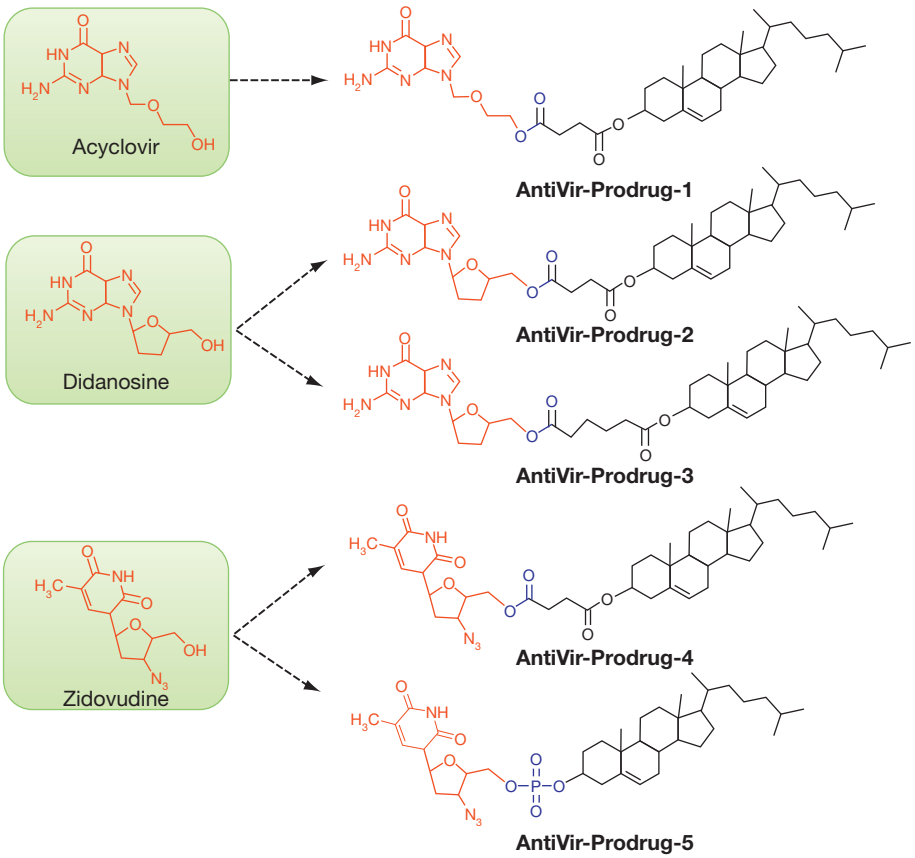

Figure 12 A series of amphiphilic prodrugs prepared from nucleobase-antiviral agents acyclovir, didanosine, and zidovudine. Steroidal cholesterol conjugation has been used to promote strong intermoelcular interactions, while headgroups provide hydrogen bonding. Adapted from Jin, Y.; Xin, R.; *et al*. *Int*. *J*. *Pharm*. **2008**, *350*(1–2), 330–337; Jin, Y.; Ai, P.; *et al*. *Int*. *J*. *Pharm*. **2009**, *368*(1–2), 207–214.

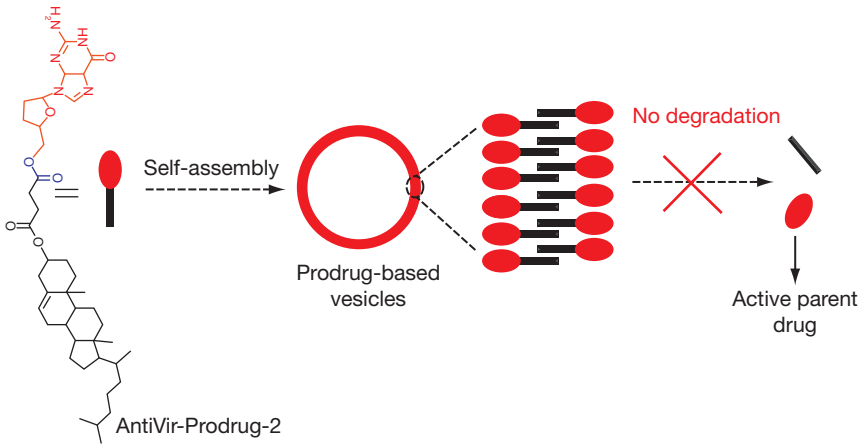

Figure 13 Schematic representation for formation of strong vesicles through self-assembly of **AntiVir-Prodrug-2**. Although efficient self-assembly and impressive stability are observed, they do not undergo degradation (either through biological or chemical cues), and thus fail to regenerate active parent drug. Thus, it is equally important to have a balance between self-assembly, stability, and dispersion characteristics versus degradation to release the parent drug. Reproduced from Jin, Y.; Ai, P.; *et al*. *Int*. *J*. *Pharm*. **2009**, *368*(1–2), 207–214. Copyright 2008, Elsevier.

(surfactants). Below the minimum association concentration, amphiphilic molecules are freely diffusing (unassociated monomers) in a given media; however, as the concentration of amphiphiles increases, self-assembly into molecular aggregates occurs – producing an equilibrium between free prodrug molecules and micelle aggregates at the critical micellar concentration (CMC); however, temperature, pH, and ionic strength influence the CMC and ability to form micelles. Hydrophobic regions of amphiphilic molecules form the core of a micelle, while hydrophilic regions form the micelle's surface/shell.[101]

CS-088, 4-[1-hydroxy-1-ethylmethyl]-2-propyl-1-[4-[2-[tetrazole-5-yl]phenyl]phenyl] methylimidazole-5-carboxylic acid monohydrate (**Figure 14**), is an angiotensin AT1 receptor antagonist known to reduce intraocular pressure (IOP) in rabbits.[102] This IOP reduction is caused by a small increase in uveoscleral outflow, with no changes in aqueous inflow or outflow facility observed when **CS-088** was topically applied to rabbits.[103,104] However, **CS-088** permeability across rabbit corneal membrane decreased at higher concentrations, prompting Kikuchi *et al.* to investigate the self-assembling properties of **CS-088** in aqueous solution.[105] Various characterization techniques such as those based on surface tension and dye encapsulation have been utilized to calculate the CMC of **CS-008**. Above 10 mg ml^{-1} concentration, **CS-088** was found to form micellar aggregates with hydrodynamic radii in the range of 1 nm. The apparent permeability coefficient (P_{app}) of **CS-088** through the corneal membrane was constant in the unassociated state; however, P_{app} significantly decreased as self-assembled structures formed. This demonstrates the importance of thorough characterization of each new self-assembled system for the intended application.

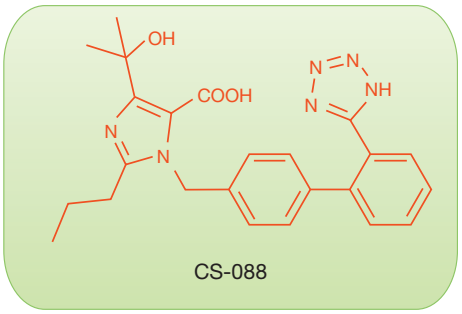

Figure 14 Molecular structure of **CS-088** which could generate micelles. Reproduced from Inoue, T.; Yokoyoma, T.; *et al. Curr. Eye Res.* **2001**, *23*(2), 139–143; Inoue, T.; Yokoyoma, T.; *et al. Curr. Eye Res.* **2001**, *23*(2), 133–138.

In addition, Boury *et al.* demonstrated that a trivial modification of the known drug amiodarone could yield micelles.[106] Amiodarone (**Figure 15(a)**) is an antianginal and antiarrhythmic therapeutic agent widely used in the treatment of heart diseases.[107–109] Amiodarone is poorly water soluble at room temperature; however, low pH produced a cationic amphiphile (**Amid-Prodrug**), with the ability to undergo self-assembly to form micellar aggregates. **Amid-Prodrug** is a nonchiral amphiphilic molecule when protonated at low pH below the pK_a of the amine (but it is reversible with increasing pH). **Amid-Prodrug** is highly lipophilic in its unprotonated form, and has a high partition coefficient (>16500) in the presence of biological membranes such as phospholipid bilayers.[110] Like any surfactant, **Amid-Prodrug** associates at air–water interfaces, with apolar moieties toward the air phase, resulting in surface film (**Figure 15(b)**) that equilibrates with bulk phase spherical micelles (as long as pH is low). In addition, they have also studied the effect of counter ions on micellar self-assembly.

4.421.4. Self-Assembled Irreversible Prodrug-Based Hydrogels

In some of the above discussed examples, selective key steps are (i) converting drug into amphiphilic prodrug by attaching an appropriate promoiety, (ii) generating self-assembled ordered nanocarriers, and subsequently (iii) *generating parent drug* back into the system through cleaving prodrug. On the contrary, we have designed another class of hydrogels: self-assembled irreversible prodrug-based hydrogels. In this approach, initially known drugs could be converted into prodrugs by attaching an appropriate promoiety, and allowing them to undergo self-assembly to form hydrogels. Interestingly, without

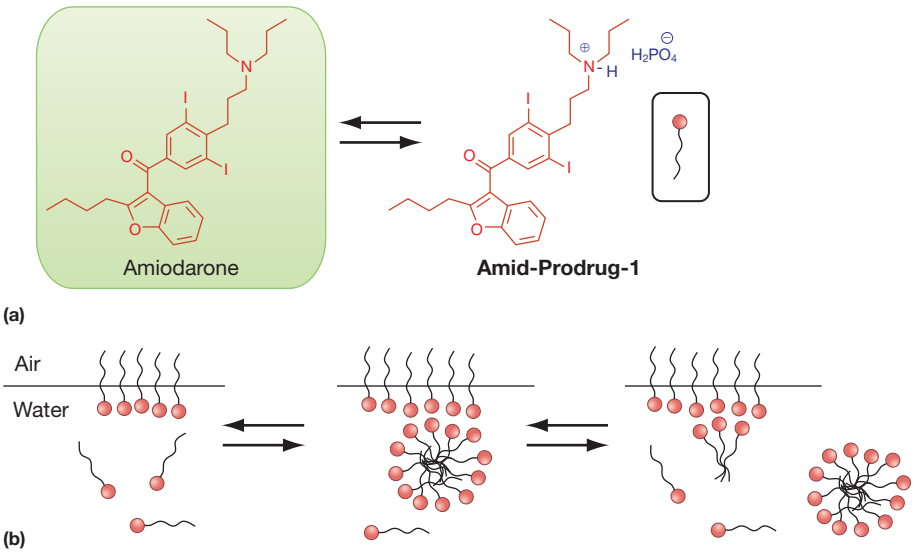

Figure 15 (a) Cationic salts of amiodarone obtain amphiphilic characteristics; thus, (b) at air–water interface **Amiod-Prodrug-1** self-associates to form monolayers at the surface, which subsequently form regular micellar structures. Reproduced from Chatelain, P.; Laruel, R. *J. Pharm. Sci.* **1985**, *74*(7), 783–784. Copyright 1985, Wiley-Liss, Inc.

regenerating the parent drug (absence of prodrug degradation), modified drugs retain their bioactivity in their self-assembled form. For eventual therapeutic use, this mandates development of this fully new molecular entity as a new drug in terms of complete safety and efficacy equivalence testing, and regulatory approval.

4.421.4.1. Paclitaxel-Based Self-Assembled Hydrogels

Recently, modification of paclitaxel with a hydrogelator motif yielded a hydrogel of a paclitaxel derivative with therapeutic bioactivity.[111] In addition, to connect paclitaxel covalently with a motif that tends to self-assemble, while allowing for enzyme cleavage, we have synthesized a drug-based precursor for gelator, **Tax-Prodrug-2** (Figure 16(a)), with enhanced aqueous solubility compared to that of paclitaxel, by attaching a phosphate derivative. Interestingly, the dephosphorylated form (**Tax-Prodrug-3**) could not undergo self-assembly to form a hydrogel directly by changing either temperature or pH, because of its extreme insolubility in water. However, unlike previous examples, an alkaline phosphatase enzyme triggers biotransformation of **Tax-Prodrug-2** into the dephosphorylated form, **Tax-Prodrug-3** *in situ*, triggering self-assembly to form a hydrogel (Figure 16(b)) that consists of nanofibers a few nanometers in width and a few microns in length.[111] A cytotoxicity test (Figure 16(c) and 16(d)) showed a conservation of bioactivity for the paclitaxel-based prodrug. Interestingly, even in its hydrogel form, **Tax-Prodrug-3** exhibited anticancer activity against HeLa cells comparable to that of unmodified paclitaxel. It is possible for fibers endocytosed and dissociated in endosomes/cytoplasm to act as a drug. This demonstrates the possibility of creating nanofibers of therapeutic molecules with a dual role as both the delivery vehicle and drug itself.[112]

4.421.4.2. Vancomycin-Based Self-Assembled Hydrogels

Vancomycin, a broad-spectrum glycopeptidic antibiotic against Gram-positive bacteria, remains one of the most important antibiotics because of its ability to inhibit methicillin-resistant *Staphylococcus aureus* (MRSA),[113] a virulent and highly contagious pathogen spreading in hospitals and communities.[114] Vancomycin has a strong tendency to form multiple hydrogen bonds with itself in aqueous solution, making it an ideal drug in which to introduce a promoiety to generate a prodrug capable of efficient self-assembly to form hydrogels. To validate this

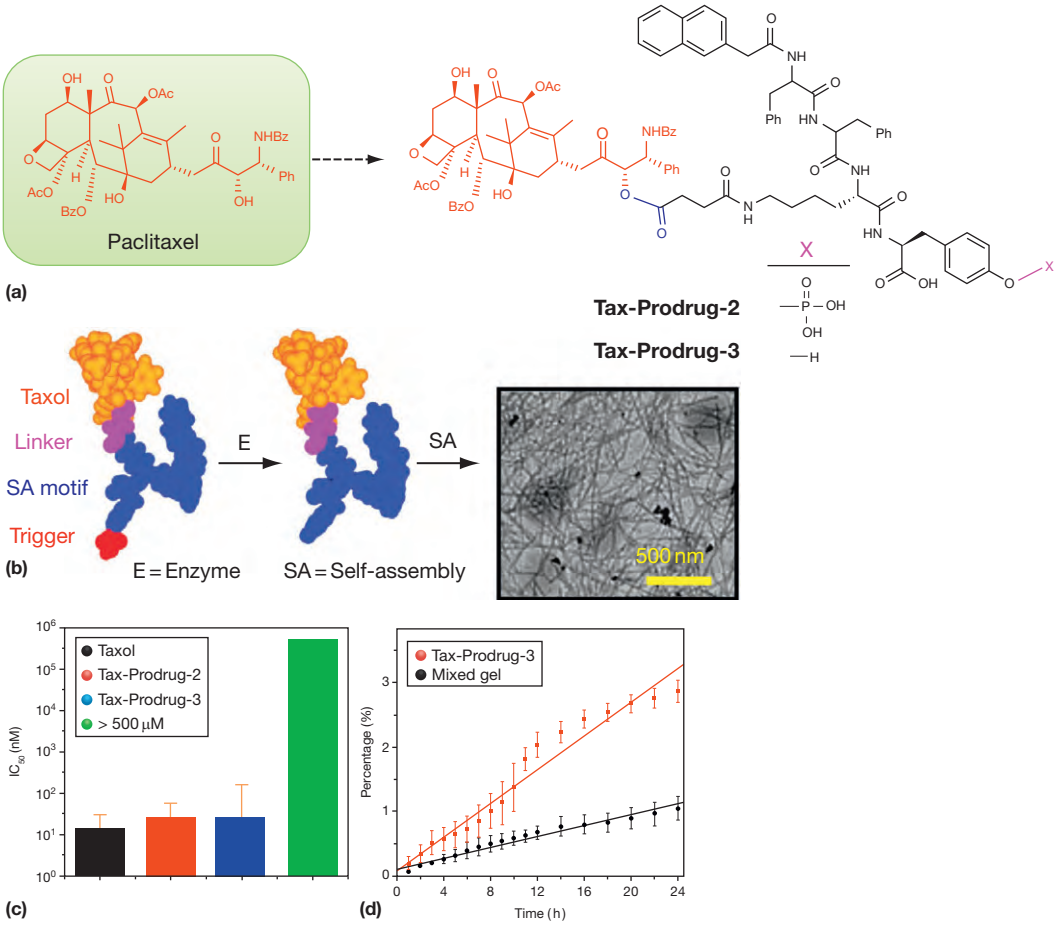

Figure 16 (a) Covalent modification of taxol by attaching peptide-promoiety, to promote self-assembly. (b) Schematic representation of enzyme-triggered hydrogelation of **Tax-Prodrug-3,** and its TEM image. (c) Cytotoxicity (*y*-axis in $\log_{10}$ scale) of taxol, **Tax-Prodrug-2**, **Tax-Prodrug-3**, and the self-assembly motif (green bar) after incubation with HeLa cells for 48 h, and (d) cumulative drug release profile of two types of paclitaxel gels in 100 mM buffer. Reproduced from Gao, Y.; Kuang, Y.; *et al. J. Am. Chem. Soc.* **2009**, *131*(38), 13576–13577. Copyright 2009, American Chemical Society.

hypothesis, Xu and coworkers modified vancomycin by introducing a pyrene group to the C-terminal of the backbone of vancomycin, and serendipitously turned vancomycin into the hydrogelator vancomycin-pyrene (**Van-Prodrug-1**), which formed a hydrogel (Figure 17(a)) with an MGC of 0.36% (w/v; 2.2 mM).[115] According to spectroscopic analysis, π–π interactions between pyrenes and the hydrogen bonding between vancomycin moieties drove the self-assembly of **Van-Prodrug-1** in water (Figure 17(b)). Further, TEM study (Figure 17(c)) suggested that **Van-Prodrug-1** self-assembled to afford supramolecular networks that aggregated further into nanofibers as the matrices of the hydrogel. In contrast to most of the structural modifications of commercial drugs that usually cause a loss of activity, **Van-Prodrug-1** exhibited unusual potency, nearly three-orders of magnitude more potent than vancomycin against vancomycin-resistant enteroccoci (VRE).[115] Further investigation indicated that the enhanced efficacy might have resulted from the adsorption of **Van-Prodrug-1** onto surfaces of the bacteria cells.[116] Vancomycin is known to form key H-bonding with D-Ala–D-Ala peptide moieties of bacterial cell wall. Although the generality of this proposed mechanism requires further validation, it is consistent with the work of Tiller and coworkers, in which they showed an excellent example of a molecular hydrogelator that formed a hydrogel on a surface with a concentration 50 times below the MGC.[117] Although the modified vancomycin showed promising potency, the toxicity of this modified drug toward mammalian cells remains to be evaluated. Nevertheless, pyrene is highly toxic itself. Thus, a more attractive design would involve other small molecules such as amino acid analogs that are nontoxic and promote self-assembly.

4.421.4.3. Glucosamine-Based Self-Assembled Hydrogels

D-Glucosamine, one of the most abundant monosaccharides, is used as an oral supplement for the management of mild osteoarthritis with limited efficacy. Glucosamine also plays a role in the process of wound healing, and Shaunak and coworkers have demonstrated that a polyvalent dendrimer of glucosamine conjugates prevented scar tissue formation.[118] Plant *et al.* demonstrated that polymeric hydrogels incorporating glucosamine increased the adhesion with neural tissue of the host, improved vascularization, and enhanced infiltration of nonneural cells of the host.[119] Therefore, glucosamine in/as supramolecular hydrogel may exhibit similar effects and serve as a novel self-assembled drug-based hydrogel. Xu *et al.* proposed that glucosamine-based hydrogel may assist wound healing and prevent the formation of scars.[120] Encouraged by this preliminary work, and based on other low-molecular-weight gelators made from carbohydrates,[121] Xu and coworkers transformed glucosamine into

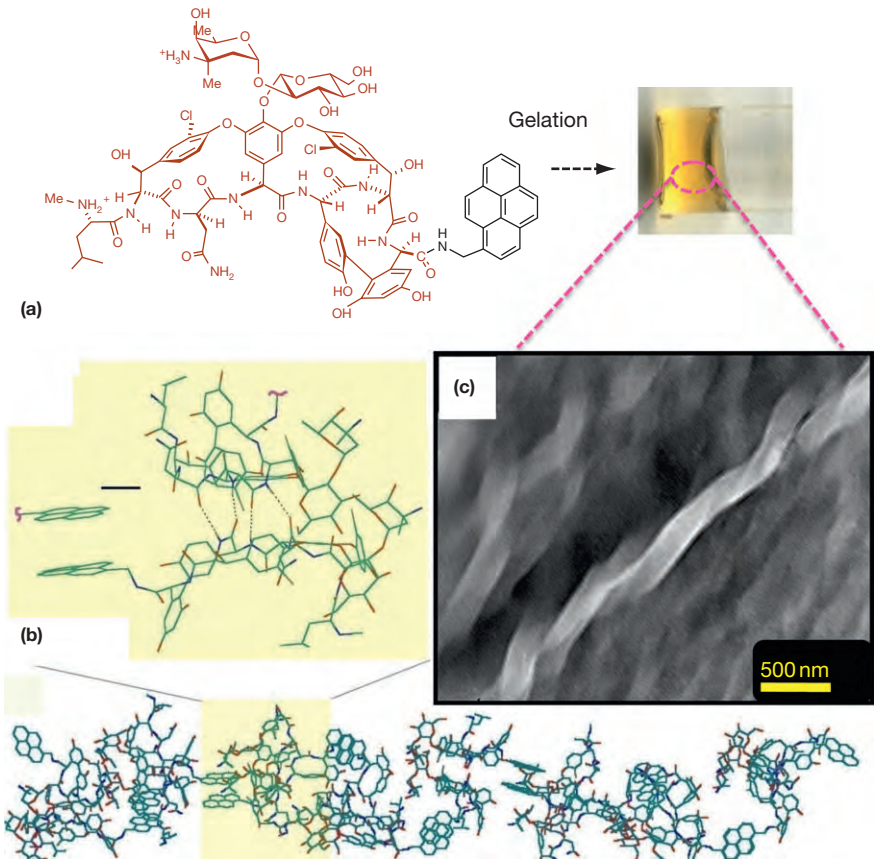

Figure 17 (a) Molecular structure of vancomycin-pyrene (**Van-Prodrug-1**) with the optical image of the hydrogel at 0.36 wt%. (b) The noncovalent interactions involved in the self-assembly of **Van-Prodrug-1**. (c) TEM image of the helical nanofibers of **Van-Prodrug-1**. Reproduced from Xing, B.; Yu, C. W.; *et al. J. Am. Chem. Soc.* **2002**, *124*(50), 14846–14847. Copyright 2002, American Chemical Society.

molecular gelators, linking either napthyl-L-phenylalanine (**Glu-Prodrug-1**) or napthyl-D-phenylalanine (**Glu-Prodrug-2**, Figure 18).[120] The cell toxicity of these glucosamine prodrugs was thoroughly investigated, and **Glu-Prodrug-2** exhibited better cell tolerance than **Glu-Prodrug-1**. Thus, **Glu-Prodrug-2** was evaluated for its ability to reduce the scar tissue at wound sites on a mice dermal model. The hydrogel of **Glu-Prodrug-2** promoted both significantly faster wound healing and less scarring than was observed in an untreated control group.

4.421.5. Conclusions and Outlook

While prodrugs are routine and significant, self-assembled prodrugs are the 'new kids in the block', and have potential benefits for specific aspects of drug delivery. They are shown to circumvent inherent hurdles routinely encountered in traditional drug delivery methods such as external carrier-based issues. Prodrugs for generating self-deliverable vehicles must have the ability to undergo self-assembly to form stable and hierarchical nanostructures in physiological conditions, and they should be programmed to degrade at the molecular level to release the parent drug at a controllable rate in response to biological cues, preferably at targeted tissue/cells, with acceptable efficacy and toxicity.

During the design process to produce amphiphilic prodrugs, several key factors should be carefully examined, including (i) choice of an appropriate parent drug which has functional groups amenable to routine conjugation reactions under mild conditions; (ii) safety of the promoiety, and its ability to promote self-assembly of resultant prodrugs; (iii) ability of the linker-functional group to undergo reversible defunctionalization to release the parent drug in response to either biological or chemical cues; and (iv) safety of the degradation by-products, and avoidance of the generation of unwanted or toxic moieties *in situ*.

In the early stages of research, most attention is given to both introducing self-assembling ability into the amphiphilic prodrugs and improving stability of the self-assembled nanomaterials. However, the field of drug delivery demands more than the stability of nanomaterials, that is, efficient self-assembly and stability of the materials are insufficient to complete the drug delivery development cycle. These self-assembled prodrugs should have the ability to degrade at targeted locations in response to biological cues to consistently produce the parent potent drug with the desired kinetic rate profile. However, a deep understanding of the mechanism of both drug action and its interaction with the microenvironment and biomolecules such as enzymes and proteins is vital to the ideal design of self-assembled prodrug-based

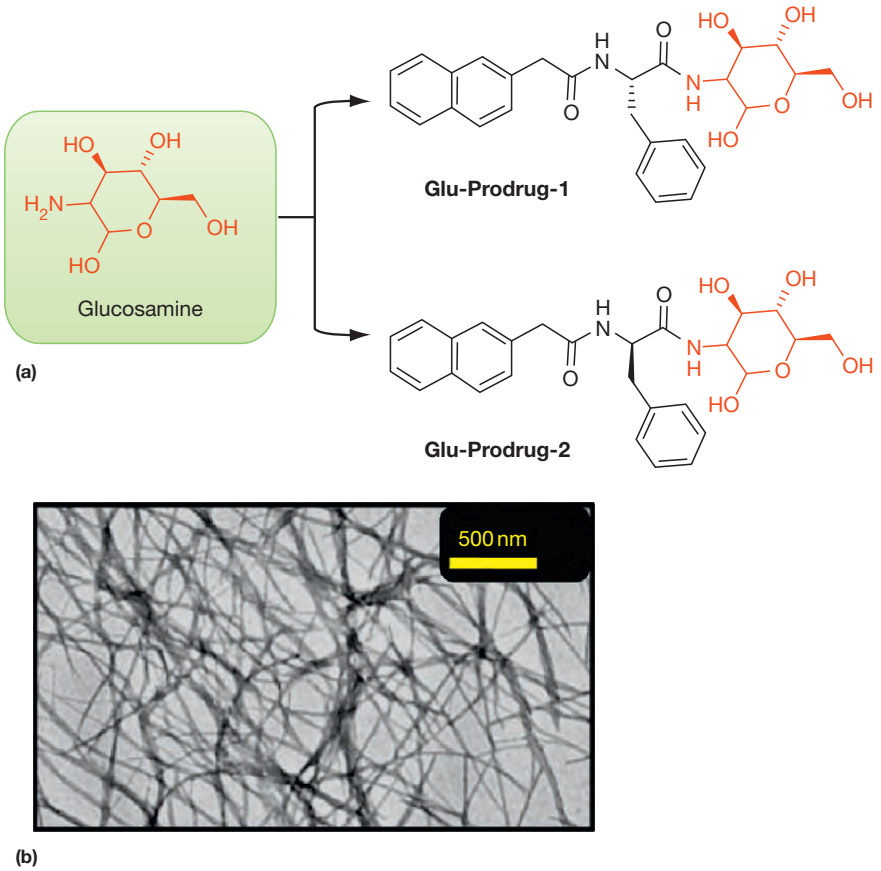

Figure 18 (a) Molecular structures of glucosamine prodrugs, **Glu-Prodrug-1** and **Glu-Prodrug-2,** which have the ability to form hydrogels. (b) TEM image of the nanofibers from the hydrogel of **Glu-Prodrug-2**. Reproduced from Yang, Z.; Liang, G.; *et al. Chem. Commun. (Camb.)* **2007**, *8*, 843–845. Copyright 2007, The Royal Society of Chemistry.

biomaterials. Despite the significant advantages of self-assembled nanostructures for achieving controlled drug delivery, the possible adverse effects due to interactions between nanostructures and organelles, cells, enzymes, and proteins must be fully tested, although given the relatively weak mechanical properties, this is not anticipated to present significant issues. Self-assembly, stability, and degradation must simultaneously be considered. Thus, incorporation of multiple disciplines, such as organic chemistry, medicinal chemistry, supramolecular chemistry, nanosciences, pharmaceutics, and clinical science, should accelerate and enhance the design and development of ideal self-assembling drug delivery vehicles. With this awareness, we believe future research will enable the development of such smart systems to benefit certain therapeutic regimes.

Acknowledgments

JMK would like to thank the Center for Integration of Medicine and Innovate Technology (CIMIT) for generously supporting this work. GJ thanks the ACS Petroleum Research Fund (Grant GCI-PRF #48124-GCI) for generously supporting this work. BX thanks Human Frontier Science Program for financial support and Brandeis University EM facility for technical support.

References

1. Peppas, N. A.; Hilt, J. Z.; *et al*. *Adv. Mater*. **2006**, *18*(11), 1345–1360.
2. Wichterle, O.; Lim, D. *Nature* **1960**, *185*, 117–118.
3. Corkhill, P. H.; Hamilton, C. J.; *et al*. *Biomaterials* **1989**, *10*(1), 3–10.
4. Ratner, B. D.; *et al*. *Biomaterials Science: An Introduction to Materials in Medicine*. Elsevier/Academic Press: London, UK, 2004.
5. Zhang, S. *Nat. Mater*. **2004**, *3*(1), 7–8.
6. Hoffman, A. S. *Adv. Drug Deliv. Rev*. **2002**, *54*(1), 3–12.
7. Jeong, S. H.; Huh, K. M.; *et al*. *Polymers in Drug Delivery*. Taylor & Francis: Boca Raton, FL, 2005.
8. de la Torre, P. M.; Torrado, S. *Biomaterials* **2003**, *24*(8), 1459–1468.
9. Kumashiro, Y.; Huh, K. M.; *et al*. *Biomacromolecules* **2001**, *2*(3), 874–879.
10. Bae, Y. H.; Kim, S. W. *Adv. Drug Deliv. Rev*. **1993**, *11*(1), 109–135.
11. Lee, K. Y.; Mooney, D. J. *Chem. Rev*. **2001**, *101*(7), 1869–1879.
12. Lendlein, A.; Kelch, S. *Angew. Chem. Int. Ed. Engl*. **2002**, *41*(12), 2035–2057.
13. Pelton, R. *Adv. Colloid Interface Sci*. **2000**, *85*(1), 1–33.
14. Schild, H. G. *Prog. Polym. Sci*. **1992**, *17*, 163–249.
15. Bhattarai, N.; Gunn, J.; *et al*. *Adv. Drug Deliv. Rev*. **2010**, *62*(1), 83–99.
16. Hirano, H. S. S.; Akiyama, I.; *et al*. *Progress in Biomedical Polymers*. Plenum: New York, 1990.
17. Knapczyk, L. K. J.; Krzck, J.; *et al*. *Chitin and chitosan: Sources, Chemistry, Biochemistry. Physical Properties and Applications*. Elsevier: London, 1989.
18. Muzzarelli, R. A. A. *Cell. Mol. Life Sci*. **1997**, *53*, 131–140.
19. Peppas, N. A.; Sahlin, J. J. *Biomaterials* **1996**, *17*(16), 1553–1561.
20. Salamat-Miller, N.; Chittsang, M.; *et al*. *Adv. Drug Deliv. Rev*. **2005**, *57*(11), 1666–1691.
21. Peppas, N. A.; Bures, P.; *et al*. *Eur. J. Pharm. Biopharm*. **2000**, *50*(1), 27–46.
22. Bhattacharya, S.; Acharya, S. N. G. *Chem. Mater*. **1999**, *11*, 3504–3511.
23. Drapeau, G. R.; Boily, Y.; *et al*. *J. Biol. Chem*. **1972**, *247*(20), 6720–6726.
24. Estroff, L. A.; Hamilton, A. D. *Angew. Chem. Int. Ed. Engl*. **2000**, *39*(19), 3447–3450.
25. Hamachi, I.; Kiyonaka, S.; *et al*. *Chem. Commun. (Camb.)* **2000**, 1281–1282.
26. Kiyonaka, S.; Shinkai, S.; *et al*. *Chem. Eur. J*. **2003**, *9*(4), 976–983.
27. Kiyonaka, S.; Sugiyasu, K.; *et al*. *J. Am. Chem. Soc*. **2002**, *124*(37), 10954–10955.
28. Kiyonaka, S.; Zhous, S.-L.; *et al*. *Supramol. Chem*. **2003**, *15*, 521–528.
29. Kunitake, T. *Angew. Chem. Int. Ed. Engl*. **1992**, *31*, 709–726.
30. Lottenberg, R.; Christensen, U.; *et al*. *Methods Enzymol*. **1981**, *80*(Pt C), 341–361.
31. Makarevic, J.; Jokic, M.; *et al*. *Chemistry* **2001**, *7*(15), 3328–3341.
32. Masaki, T.; Fujihashi, T.; *et al*. *Biochim. Biophys. Acta* **1981**, *660*(1), 51–55.
33. Masaki, T.; Tanabe, M.; *et al*. *Biochim. Biophys. Acta* **1981**, *660*(1), 44–50.
34. Oda, R.; Huc, I.; *et al*. *Angew. Chem. Int. Ed. Engl*. **1998**, *37*(19), 2689–2691.
35. Stryer, L. *J. Mol. Biol*. **1965**, *13*(2), 482–495.
36. Surewicz, W. K.; Mantsch, H. H.; *et al*. *Biochemistry* **1993**, *32*(2), 389–394.
37. Abdallah, D. J.; Weiss, R. G. *Langmuir* **2000**, *16*(2), 352–355.
38. Aoki, M.; Nakashima, K.; *et al*. *J. Chem. Soc. Perkin Trans*. **1993**, *2*, 347–354.
39. Hafkamp, R. J. H.; Feiters, M. C.; *et al*. *J. Org. Chem*. **1999**, *64*(2), 412–426.
40. Lin, Y.-C.; Weiss, R. G. *Macromolecules* **1987**, *20*(2), 414–417.
41. Tan, H.; Moet, A.; *et al*. *Macromolecules* **1983**, *16*(1), 28–34.
42. Amanokura, N.; Yoza, K.; *et al*. *J. Chem. Soc. Perkin Trans*. **1998**, *2*, 2585–2592.
43. Maitra, U.; Kumar, P. V.; *et al*. *Chem. Commun. (Camb.)* **1999**, 595–596.
44. Kimura, T.; Shinkai, S. *Chem. Lett*. **1998**, *27*(10), 1035–1036.
45. Lin, Y.-C.; Kachar, B.; *et al*. *J. Am. Chem. Soc*. **1989**, *111*(15), 5542–5551.
46. Aggeli, A.; Bell, M.; *et al*. *J. Mater. Chem*. **1997**, *7*, 1135–1145.
47. Clausen, T. M.; Vinson, P. K.; *et al*. *J. Phys. Chem*. **1992**, *96*(1), 474–484.
48. Gradzielski, M.; Bergmeier, M.; *et al*. *J. Phys. Chem. B* **1997**, *101*(10), 1719–1722.
49. Hoffman, H.; Thunig, C.; *et al*. *Langmuir* **1994**, *10*(11), 3372–3981.
50. Ikeda, S.; Foegeding, E. L.; *et al*. *Langmuir* **1999**, *15*(25), 8584–8589.
51. Terech, P.; Weiss, R. G. *Chem. Rev*. **1997**, *97*(8), 3133–3160.
52. Breimer, D. D. *J. Control Release* **1999**, *62*, 3–6.
53. Kidane, A.; Bhatt, P. P. *Curr. Opin. Chem. Biol*. **2005**, *9*(4), 347–351.
54. Hoare, T. R.; Kohane, D. S. *Polymer* **2008**, *49*, 1993–2007.
55. Huang, X.; Brazel, C. S. *J. Control. Release* **2001**, *73*(2–3), 121–136.
56. Schmidt, J. J.; Rowley, J.; *et al*. *J. Biomed. Mater. Res. A* **2008**, *87A*(4), 1113–1122.
57. Raemdonck, K.; Demeester, J.; *et al*. *Soft Matter* **2009**, *5*, 707–715.
58. Barenholz, Y. *Curr. Opin. Colloid Interface Sci*. **2001**, *6*, 66–77.
59. Albert, A. *Nature* **1958**, *182*(4633), 421–422.
60. Beaumont, K.; Webster, R.; *et al*. *Curr. Drug Metab*. **2003**, *4*(6), 461–485.
61. Ettmayer, P.; Amidon, G. L.; *et al*. *J. Med. Chem*. **2004**, *47*(10), 2393–2404.
62. Stella, V. *Optimizing the 'Drug-Like' Properties of Leads in Drug Discovery*. Springer: New York, 2006.
63. Stella, V. J. *Expert Opin. Ther. Pat*. **2004**, *14*, 277–280.
64. Stella, V. J.; Nti-Addae, K. W. *Adv. Drug Deliv. Rev*. **2007**, *59*(7), 677–694.
65. Testa, B. *Biochem. Pharmacol*. **2004**, *68*(11), 2097–2106.
66. Rautio, J.; Kumpulainen, H.; *et al*. *Nat. Rev. Drug Discov*. **2008**, *7*(3), 255–270.
67. Qi, S. Y.; Groves, J. T.; *et al*. *Proc. Natl. Acad. Sci. USA* **2001**, *98*(12), 6548–6553.
68. Lehn, J.-M. *Angew. Chem. Int. Ed. Engl*. **1990**, *29*(11), 1304–1319.
69. Vemula, P. K.; Cruikshank, G. A.; *et al*. *Biomaterials* **2009**, *30*(3), 383–393.
70. Dahl, T. A.; Bilski, P.; *et al*. *Photochem. Photobiol*. **1994**, *59*(3), 290–294.
71. Duvoix, A.; Blasius, R.; *et al*. *Cancer Lett*. **2005**, *223*(2), 181–190.
72. Hergenhahn, M.; Soto, U.; *et al*. *Mol. Carcinog*. **2002**, *33*(3), 137–145.
73. Jovanovic, S. V.; Boone, C. W.; *et al*. *J. Am. Chem. Soc*. **2001**, *123*(13), 3064–3068.
74. Shim, J. S.; Kim, J. H.; *et al*. *Chem. Biol*. **2003**, *10*(8), 695–704.
75. Christenson, E. M.; Patel, S.; *et al*. *Biomaterials* **2006**, *27*(21), 3920–3926.
76. Syrigos, K. N.; Rowlinson-Busza, G.; *et al*. *Int. J. Cancer* **1998**, *78*(6), 712–719.
77. Turczan, J. W. *Anal. Chim. Acta* **1977**, *92*(1), 123–128.
78. Jones, D. A. *Phytochemistry* **1998**, *47*(2), 155–162.
79. Vemula, P. K.; Li, J.; *et al*. *J. Am. Chem. Soc*. **2006**, *128*(27), 8932–8938.
80. Brooks, P. M.; Day, R. O. *N. Engl. J. Med*. **1991**, *324*(24), 1716–1725.
81. Bhuniya, S.; Seo, Y. J.; *et al*. *Tetrahedron Lett*. **2006**, *47*(40), 7153–7156.
82. Wani, M. C.; Taylor, H. L.; *et al*. *J. Am. Chem. Soc*. **1971**, *93*(9), 2325–2327.
83. Rowinsky, E. K.; Onetto, N.; *et al*. *Semin. Oncol*. **1992**, *19*(6), 646–662.
84. Crosasso, P.; Ceruti, M.; *et al*. *J. Control Release* **2000**, *63*, 19–30.
85. Bae, K. H.; Lee, Y.; *et al*. *Biomacromolecules* **2007**, *8*(8), 650–656.
86. Tarr, B. D.; Sambandan, T. G.; *et al*. *Pharm. Res*. **1987**, *4*, 162–165.
87. Kan, P.; Chen, Z. B.; *et al*. *J. Control Release* **1999**, *58*, 271–278.
88. Nicolaou, K. C.; Riemer, C.; *et al*. *Nature* **1993**, *364*(6436), 464–466.
89. Nicolaou, K. C.; Guy, R. K.; *et al*. *Angew. Chem. Int. Ed. Engl*. **1994**, *33*(15/16), 1583–1587.
90. de Miranda, P.; Blum, M. R. *J. Antimicrob. Chemother*. **1983**, *12*(Suppl. B), 29–37.
91. Jin, Y.; Qiao, Y.; *et al*. *Colloids Surf. B Biointerfaces* **2005**, *42*(1), 45–51.
92. Menger, F. M. *Proc. Natl. Acad. Sci. USA* **2002**, *99*, 4818–4822.
93. Lech-Maranda, E.; Korycka, A.; *et al*. *Mini Rev. Med. Chem*. **2006**, *6*(5), 575–581.
94. Simons, C.; Wu, Q.; *et al*. *Curr. Top. Med. Chem*. **2005**, *5*(13), 1191–1203.
95. Jin, Y.; Ai, P.; *et al*. *Int. J. Pharm*. **2009**, *368*(1–2), 207–214.
96. Jin, Y.; Xin, R.; *et al*. *Int. J. Pharm*. **2008**, *350*(1–2), 330–337.

97. Lalanne, M.; Andrieux, K.; *et al*. *Int. J. Pharm.* **2007**, *344*(1–2), 62–70.
98. Lalanne, M.; Paci, A.; *et al*. *Bioorg. Med. Chem. Lett.* **2007**, *17*(8), 2237–2240.
99. Manouilov, K. K.; Xu, Z. S.; *et al*. *Antiviral Res.* **1997**, *34*(3), 91–99.
100. Dipali, S. R.; Lin, Y.-J.; *et al*. *Int. J. Pharm.* **1997**, *152*, 89–97.
101. Lasic, D. D. *Nature* **1992**, *355*(6357), 279–280.
102. Wang, R. F.; Podos, S. M.; *et al*. *Exp. Eye Res.* **2005**, *80*, 629–632.
103. Inoue, T.; Yokoyoma, T.; *et al*. *Curr. Eye Res.* **2001**, *23*(2), 139–143.
104. Inoue, T.; Yokoyoma, T.; *et al*. *Curr. Eye Res.* **2001**, *23*(2), 133–138.
105. Kikuchi, T.; Ito, N.; *et al*. *Int. J. Pharm.* **2005**, *299*(1–2), 100–106.
106. Boury, F.; Gautier, J.; *et al*. *Colloids Surf. B Biointerfaces* **2001**, *20*(3), 219–227.
107. Gill, J.; Heel, R. C.; *et al*. *Drugs* **1992**, *43*(1), 69–110.
108. Marcus, F. I.; Fontaine, G. H.; *et al*. *Am. Heart J.* **1981**, *101*(4), 480–493.
109. Singh, B. N.; Nademanee, K. *Am. Heart J.* **1983**, *106*(4 Pt 2), 857–869.
110. Chatelain, P.; Laruel, R. *J. Pharm. Sci*. **1985**, *74*(7), 783–784.
111. Gao, Y.; Kuang, Y.; *et al*. *J. Am. Chem. Soc.* **2009**, *131*(38), 13576–13577.
112. Zhao, F.; Ma, M. L.; *et al*. *Chem. Soc. Rev.* **2009**, *38*(4), 883–891.
113. Walsh, C. *Antibiotics: actions, origins, resistance*. ASM Press: Washington, DC, 2003.
114. Klevens, R. M.; Morrison, M. A.; *et al*. *JAMA* **2007**, *298*(15), 1763–1771.
115. Xing, B.; Yu, C. W.; *et al*. *J. Am. Chem. Soc.* **2002**, *124*(50), 14846–14847.
116. Xing, B.; Ho, P. L.; *et al*. *Chem. Commun. (Camb.)* **2003**, (17), 2224–2225.
117. Bieser, A. M.; Tiller, J. C. *Chem. Commun. (Camb.)* **2005**, (31), 3942–3944.
118. Shaunak, S.; Thomas, S.; *et al*. *Nat. Biotechnol.* **2004**, *22*(8), 977–984.
119. Plant, G. W.; Woerly, S.; *et al*. *Exp. Neurol.* **1997**, *143*(2), 287–299.
120. Yang, Z.; Liang, G.; *et al*. *Chem. Commun. (Camb.)* **2007**, (8), 843–845.
121. Kiyonaka, S.; Sada, K.; *et al*. *Nat. Mater.* **2004**, *3*(1), 58–64.

4.422. pH-Responsive Polymers for the Intracellular Delivery of Biomolecular Drugs

D S W Benoit, University or Rochester, Rochester, NY, USA
W Gray and N Murthy, Georgia Institute of Technology and Emory University Parker H. Petit Institute for Bioengineering and Bioscience, Atlanta, GA, USA
H Li and C L Duvall, Vanderbilt University, Nashville, TN, USA

© 2011 Elsevier Ltd. All rights reserved.

4.422.1.	**Introduction**	358
4.422.2.	**Acid–Base Equilibria and pH-Responsive Chemistries**	359
4.422.3.	**Anionic pH-Responsive Polymers**	360
4.422.3.1.	Poly(alkylacrylic acid)s	362
4.422.3.2.	Poly(styrene-*alt*-maleic anhydride)	362
4.422.4.	**Acid-Degradable Delivery Vehicles**	363
4.422.4.1.	Encrypted Polymers	363
4.422.4.2.	Buchwald Coupling-Based Vehicles	364
4.422.4.3.	Acid-Cleavable Lipid Drug Delivery Vehicles	364
4.422.5.	**Osmotically Disruptive Cationic Polymers**	364
4.422.5.1.	Poly(L-lysine)	365
4.422.5.2.	Polyethyleneimine	365
4.422.5.3.	Poly(amidoamine) Dendrimers and Polymers	366
4.422.5.4.	Poly(β-amino esters)	367
4.422.5.5.	Chitosan	367
4.422.6.	**Histidine- and Imidazole-Containing Copolymers**	367
4.422.7.	**Fusogenic Peptides**	369
4.422.7.1.	GALA	369
4.422.8.	**Future Perspectives**	371
References		372

Glossary

Amphipathic A molecule that contains both polar (water-soluble, hydrophilic) and nonpolar (not water-soluble, hydrophobic) components in its structure. (synonym to amphiphilic).

Biomacromolecule A polymer consisting of natural monomers (e.g., amino acids or nucleic acids) forming a large molecular weight molecule (e.g., proteins, DNA, carbohydrates).

Block polymer A polymer comprising two or more compositionally distinct subunits linked by covalent bonds. Block polymers with two or three distinct blocks are called diblock polymers and triblock polymers, respectively.

Buffering capacity A measure of the ability of a solution (i.e., containing a pH-responsive polymer) to resist pH change when a small amount of acid or base is added. It can be quantitatively defined as the molarity of strong acid or base that must be added to change pH by one unit, and it is important to recall that buffering capacity is highest when $pH = pK_a$.

Chemoselective The preferential reaction with one functional group (e.g., incorporated onto a polymer terminus) in the presence of others (e.g. pendant groups on the polymer backbone).

Controlled, living radical polymerization A chain growth polymerization that proceeds with negligible termination or chain transfer steps and where the rate of chain initiation is much larger than the rate of propagation. The polymerization proceeds by first order kinetics, and the molecular weight increases linearly with conversion. The degree of polymerization can be predetermined, and the polymers produced are relatively monodispersed. The radical polymerization can be stopped and reinitiated under external control, allowing facile formation of block polymers (see definition above). Chain ends are preserved and can be predefined based on the chemistry of polymer precursors.

Dendrimers Monodispersed, symmetric structures consisting of highly branched architectures that are synthesized through stepwise addition of branched monomers. Each sequentially added layer of branched monomer is known as a dendrimer 'generation'.

Encrypted In this chapter, this refers to a membrane disruptive polymer that is masked by an outer shield consisting of a more inert polymer. The inert polymer is linked to the membrane disruptive polymer by covalent bonds that are broken upon exposure to the more acidic environment in endolysosomes. Removal of the inert polymer shield exposes the core polymer and enables its membrane disruptive activity.

Endocytosis The process by which materials are internalized by a cell without diffusing through the cell

membrane. The material localizes to the cell surface where an invagination is formed that fuses and buds off inside the cell, enclosing the material within an intracellular vesicle. This process can be specific (e.g., receptor-mediated endocytosis) or nonspecific (e.g., pinocytosis or phagocytosis).

Endolysosome The product of the fusion of an endosome and a lysosome during endocytosis.

Endosomolytic Having the capacity to disrupt the integrity of endosomal membranes in response to the acidic pH present inside the endosomal environment.

Enhanced permeation and retention (EPR) The process by which nanoparticles, liposomes, or other macromolecular drugs nonspecifically accumulate in tumors as a result of their leaky vasculature and poor lymphatic drainage.

Lipid A fat, oil, or wax organic compound that is soluble in nonpolar organic solvents (e.g., ether) but not in polar solvents (e.g., water). Many lipids are amphipathic (see definition above), which triggers them to self-assemble into micelles, liposomes, or membranes in polar solvents. The cell membrane and other biological vesicles are composed of self-assembled lipid bilayers, and synthetic lipids can be used to encapsulate drugs into liposomal vesicles for drug delivery.

Proton-sponge effect A process leveraged by pharmaceutical scientists where proton-accepting polymers buffer the microenvironment in endosomes and lead to their eventual disruption. The basic, amine-containing polymers inhibit acidification of the endosomal compartment and lead to continued, abnormal influx of protons and their counter ions. This increases osmotic pressure in the endosome and causes water influx, swelling, and disruption.

Random copolymer A copolymer consisting of more than one monomer heterogeneously incorporated into a polymer with no regular repeating pattern. A random copolymer usually results from the copolymerization of two or more monomers in the presence of a free-radical initiator.

Smart polymers Polymers that respond in a dramatic way to a very slight change in their environment (e.g., pH, temperature, ionic strength, etc.).

4.422.1. Introduction

The underutilized potential of proteins, peptides, DNA, and RNA as therapeutics is widely recognized, and the lack of effective strategies for intracellular delivery of these biologics is the primary barrier hindering their ability to improve therapies for a plethora of human diseases. For example, increased target specificity and disruption of barriers and interfaces currently considered 'undruggable' could be achieved using proteins, antibodies, and peptides as pharmaceutically active inhibitors. Such antagonists could be applied in pathologies where intracellular signaling pathways have gone awry (i.e., cancer). The once 'hot' but now more stagnant field of gene therapy could also benefit from development of efficient nonviral carriers that can escape endolysosomal fates (see **Chapter 4.425, Delivery of Nucleic Acids and Gene Delivery**). Synthetic systems that can effectively deliver DNA into the cell would likely trigger a dramatic increase in gene therapy clinical activity considering that safety of (highly efficient) viral vector-based approaches is a major concern.[1–3] In addition, short interfering RNA (siRNA) has recently emerged as a class of therapeutics that, if efficiently delivered, may offer a platform technology capable of specific knockdown of any desired protein target.[4,5] Similar to the other classes of biologics, siRNA is hindered by limited endosomal escape because it must access cellular gene silencing machinery and mRNA targets located in the cytoplasm to achieve mRNA degradation. Finally, endosomal escape and cytoplasmic delivery of antigen to dendritic cells constitute a rigorously studied component in vaccine development.[6–29] This is because cytoplasmic delivery to antigen-presenting cells enables processing and presentation through the MHC-I pathway, which leads to activation of cytotoxic T-lymphocytes (CTLs). Importantly, CTLs have the ability to directly identify and destroy foreign cells that express the antigen, making them an important component of a robust, therapeutically effective immune response.

Although the potential pharmaceutical impact is high, there has been minimal clinical translation of intracellular-acting biologic drugs because they have large molecular weights and are hydrophilic and polar compared to small molecule drugs. These properties present a substantial delivery challenge because it is energetically unfavorable for biomacromolecules to diffuse through the nonpolar core of membrane lipid bilayers. Therefore, their internalization must proceed via cell engulfment and internalization processes of various types, generally endocytosis or pinocytosis, producing drug sequestration and degradation in endolysosomes, or exocytosis out of the cell (see **Figure 1**). Thus, even when pharmaceutical strategies are employed for targeting the cell surface and triggering internalization, the endolysosomal escape of biotherapeutics to molecular targets in the cytoplasm presents a formidable challenge.

A key characteristic of intracellular trafficking from the extracellular space through early endosomes, late endosomes, and lysosomes is that the therapeutic is exposed to significant variations in environmental pH ranging from 7.4 in the extracellular space to approximately 5 in the lysosomes (**Figure 1**). This pH gradient provides an environmental stimulus that pharmaceutical scientists have learned to exploit in order to 'activate' carriers, including colloids, lipids, particles, and polymers, to disrupt and escape from endosomal compartments. Specifically, polymers that are membrane-disruptive at acidic pH relevant to endolysosomal trafficking (pH ~5–7) and are inert at pH 7.4 have found numerous applications for intracellular delivery because they have low toxicity and high efficacy. Finely tuned membranolytic activity in this range has been achieved by a variety of anionic and cationic polymers whose pH-dependent protonation states drive physicochemical transitions that trigger this 'switch'. 'Encrypted' membrane-disruptive polymers that are 'unmasked' by acidic conditions have also been developed. The remainder of this chapter reviews the mechanisms of activity of these endosomally disruptive

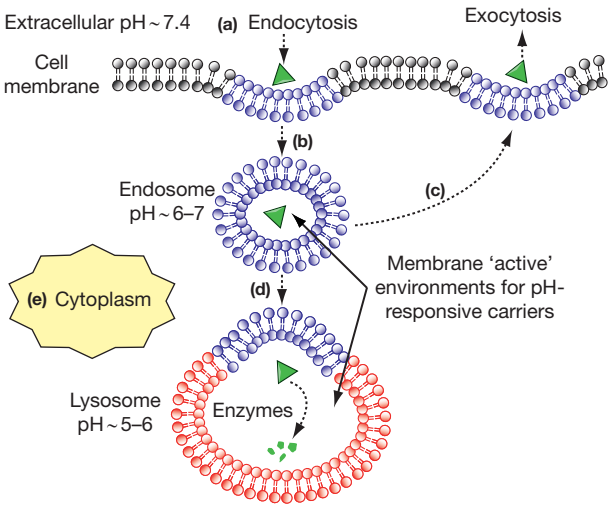

Figure 1 Internalization and trafficking pathways that serve as barriers against biomacromolecular drug intracellular delivery. (a) Biotherapeutics are internalized by endocytosis or pinocytosis into intracellular vesicles (b). Subsequently, the biomolecule is routed toward (c) exocytotic recycling to the extracellular space or (d) trafficking into lysosomes, an environment rich with degradactive enzymes. Endolysosomal membranes maintain localized acidic environments that can be leveraged to activate pH-responsive carriers to enable delivery to the cytoplasm (e) where the biomolecule is able to exert its desired bioactivity.

polymers and discusses some of the most promising advances from each of these classes of pH-responsive drug carriers. It should be noted that potent, pH-responsive lipid-based formulations have a substantial record of development and promise for drug delivery (see Buse and El-Aneed,[30] Jabr-Milane *et al.*,[31] MacEwan *et al.*,[32] Sebiakin Iu and Budanova[33]), but this chapter focuses solely on polymeric delivery systems (see Chapter 4.424, Nanoparticles for Nucleic Acid Delivery).

4.422.2. Acid–Base Equilibria and pH-Responsive Chemistries

The physicochemical behavior of pH-responsive polymers is on the basis of classical acid–base equilibria involving weak acids and bases in buffered physiological systems. All reversible pH-responsive lipid or polymer systems known comprise functional groups that are weakly acidic or basic and respond to local biochemically driven pH changes in physiological systems near pH 7. A weak acid, denoted by 'HA', is capable of acting reversibly as a proton donor (eqn [1]), and its conjugate base (A^-) can serve as a proton acceptor. Both of these actions depend on the local pH and the strength of the acid. Many carboxylic acids (RCOOH) are classical weak acids exhibiting this behavior. These acid groups reside on amino acids (e.g., aspartate), or are products of the Krebs cycle (e.g., malic or succinic acid), phosphates, sulfites, nitrites, and natural metabolites (fatty acids, e.g., oleic acid). Therefore, they are biologically endogenous and their equilibria are common to physiological systems. Additionally, carboxylic acids are common to many water-soluble natural and synthetic polymers of interest as biomaterials (e.g., carboxymethylcellulose, alginate, heparins, nucleic acids, polyacrylic acids, polyamino acids), facilitating their involvement in these host acid–base equilibria processes if introduced appropriately as biomaterials. Matching the pH-responsive polymer's acid–base equilibria to that of the host microenvironment being targeted for delivery is the key to this biomaterial performance.

For a given weak acid dissolved in water, a characteristic equilibrium will be achieved between the concentrations of the acid in its protonated and dissociated forms. The capacity of an acid to dissociate to release protons (i.e., its 'strength') can be quantitatively defined by the acid dissociation constant, K_a (eqn [2]). The logarithmic form (pK_a, eqn [3]) is often used to represent this value as K_a values vary over many orders of magnitude, and the convention is such that strong acids have lower pK_a values than weak acids.

$$[HA] \rightleftharpoons [A^-]\ [H^+] \qquad [1]$$

$$K_a = \frac{[A^-]\ [H^+]}{[HA]} \qquad [2]$$

$$pK_a = -\log K_a = -\log \frac{[A^-]\ [H^+]}{[HA]} \qquad [3]$$

Similar relationships exist for weak bases as common proton acceptors in water. When a base 'B' accepts protons from water, it converts water molecules into hydroxide anions. This equilibrium between the protonated (BH^+) and deprotonated (B) form of the weak base can be described by an analogous set of equations for quantitatively characterizing the degree of basicity with an expression for pK_b (eqn [4]). As with acids, stronger bases have lower values for pK_b. Natural weak bases of physiologic relevance include primary and secondary amines (ammonia, alkylamines) as metabolic by-products, amino acids arginine, lysine, and histidine, and nucleotide bases with pK_b values near pH 7. Chitosan is an important naturally existing basic polymer, and synthetic pH-responsive polymers with weak base chemistry include polyethyleneimine (PEI), poly(lysine), poly(arginine), poly(histidine), poly(amidoamines), and various copolymers. Importantly, water (recall: 55 M concentration in its bulk state) can act either as a weak acid or weak base, depending on the conjugate acid–base chemistry present.

$$pK_b = -\log K_b = -\log \frac{[BH^+]\ [OH^-]}{[B]} \qquad [4]$$

By rearranging eqn [2] to solve for $[H^+]$ and substituting $pH = -\log[H^+]$, the well-known Henderson–Hasselbalch equation is derived (eqn [5a]). An equivalent version of the equation is shown in the base representation (eqn [5b]).

$$pH = pK_a + \log\left\{\frac{[A^-]}{[HA]}\right\} \qquad [5a]$$

$$pOH = pK_b + \log\frac{[BH^+]}{[B]} \qquad [5b]$$

A simplified way to conceptualize the reversible equilibria relationships for weak acids and bases is that, in the case of an acid, when the local pH is equivalent to the pK_a, $\log([A^-]/[HA])$ equals zero (see eqn [5a]). This means that when pH is equal to the pK_a, the ratio $[A^-]/[HA]$ is equal to 1; thus, equivalent concentrations of the protonated (HA) and deprotonated (A^-) forms of the acid coexist. If the local pH is

below the pK_a, the protonated form becomes the dominant species. This central concept is important to this chapter because understanding pH-responsive delivery systems requires correlating the relationship between the local environmental pH and the ionization state(s) of acidic or basic moieties present on larger molecules (e.g., pH-responsive polymers) applied as drug delivery vehicles. This is because many of the pH-responsive polymers discussed in this chapter possess acidic (e.g., –COOH) or basic (e.g., $-NR_2$) moieties that accept or donate protons based upon the pH of their local environment. Significantly, as pH-responsive polymers respond to local physiological pH, these polymer systems increase or decrease the protonation states of their acidic or basic groups, altering their solubility, conformation, size, susceptibility to enzymatic or receptor recognition, target binding, or membrane interactions. These pH-driven, reversible responses from polymer acidic and basic groups produce the effects that can be exploited in their use as biomaterials.

Because protonation/deprotonation is accompanied by requisite changes in ionization, dramatic transformations in the physical properties of the polymer can result from acid–base equilibria. For example, ionization of compounds (e.g., polymers) increases their solubility in water while lack of ionic charges makes molecules more hydrophobic, effectively changing their partition coefficient (as exploited in acidic-gradient chromatography, for example) or their water solubility. Such changes in the polymer hydrophilic–hydrophobic balance can induce conformational changes and phase transitions driven primarily by the association with or repulsion of solvating water. For example, a polymer containing –COOH units donates protons in media with a pH above its pK_a. The resulting ionized $-COO^-$ chemistry increases polymer solubility via solvation with water. With a decrease in local pH, the protonated –COOH form dominates and the more hydrophobic state of this uncharged polymer is unable to solvate sufficiently with water, forcing collapse into a compact polymer globular conformation (partial or complete insolubility). This increased polymer hydrophobicity produces greater lipophilic behavior and increased partitioning into lipid bilayer membranes (e.g., cell membranes, cell organelles). By contrast, polymers containing weakly basic $-NR_2$ moieties accept protons, become ionized (e.g., as $-HN^+R_2$), and are more water soluble in environments with local pH below their pK_b. This means that these basic polymers can absorb acidic proton influx when the pH is near their pK_b, allowing them to buffer the local microenvironment against pH change as they equilibrate. In this regard, it is important to note that such amine-containing weak bases exhibit the strongest buffering capacity at a pH near their pK_b. This property is most relevant to the mechanism of activity for 'proton-sponge' polymers that are discussed subsequently in this chapter. Thus, pH-responsive phase transitions of carboxylated polymers and buffering of environmental pH by polyamines are vital to the membrane activity and endosomal-disruptive mechanisms described herein. The environmental pH at which these activities occur depends on the pK_a or pK_b of the relevant groups, and as discussed, pK_a and pK_b of the acidic/basic groups can often be tuned on the basis of the overall chemistry of the polymer in order to formulate drug delivery systems that are finely tuned to respond in the endosomal environment.

A further important consideration is that biological systems are buffered, and physiological pH is generally buffered between pH 7 and 7.4 in most tissues using two important biological buffer systems based on distinct phosphate and bicarbonate acid–base equilibria. These equilibria can compete with, neutralize, or complicate intended pH-responsive changes in biomaterials. Any pH change in or pH response from introduced agents must respond to these buffers and their pH influence if different from their pK values, or attempt to overwhelm the local physiological buffering capacity to produce sustained pH-responsive dynamics or reversible behavior. Multiple simultaneous polyequilibria, including Donnan effects, metal ion-induced complexation, and solution deviations from the Henderson–Hasselbalch equation, are more complicated, advanced topics beyond the scope of this chapter.

4.422.3. Anionic pH-Responsive Polymers

Anionic, amphiphilic polymers containing a polycarboxylic acid segment are pH-responsive membrane disruptive agents that, because of the protonation of their carboxyl groups and resulting increased hydrophobicity at acidic pH, possess membrane-partitioning behavior. Polymers with these properties can be achieved by synthesizing homopolymers of alkylacrylic acids (i.e., poly(methylacrylic acid) (PMAA), poly(ethylacrylic acid) (PEAA), poly(propylacrylic acid) (PPAA), etc.),[34–37] copolymers of acrylic acid and alkyl acrylates,[37–39] or alkylacrylic acids and other hydrophobic monomers,[40] or alkylamide modification of poly(styrene-*alt*-maleic anhydride)[41,42] (**Figure 2**). Collectively, these polymer families have shown great versatility for intracellular delivery of a multitude of biomacromolecules including peptides, proteins, siRNA, and DNA. In addition, they are amenable toward synthesis via controlled-polymerization techniques, including reversible addition–fragmentation chain transfer (RAFT) (see **Chapter 4.423, Polymeric Drug Conjugates by Controlled Radical Polymerization**).[43] Anionic polymers also enhance drug circulation times and are well-suited for *in vivo* delivery because of their cytocompatibility,[44] but one disadvantage is their inability to complex electrostatically with anionic nucleic acids. Thus, additional components such as cationic polymers/lipids or conjugation sites are needed for packaging/attachment and incorporation of targeting moieties as may be necessary to ensure endocytotic uptake.

Mechanistically, the carboxylate protonation of anionic polymers that occurs in more acidic environments tips their hydrophilic–hydrophobic balance toward an uncharged, net hydrophobic state, triggering the polymer to transition from an extended soluble form into a more compact, less soluble, and globular state that could be membrane disruptive (**Figure 3**). The mechanism of this transition and its role on lipid bilayer disruption have been studied most rigorously for the poly (alkylacrylic acids), and much of this work was pioneered by the Tirrell group with a focus on PEAA disruption of lipid vesicles.[35,36] In 1987, Tirrell *et al.* demonstrated via calorimetry that PEAA transitioned from an ionized, expanded conformation at higher pH into a collapsed, hydrophobic globular coil in acidic conditions with a transition midpoint at approximately pH 6.2,[45] and similar results were later shown with quasielastic light scattering (QELS).[46] This was also analogous

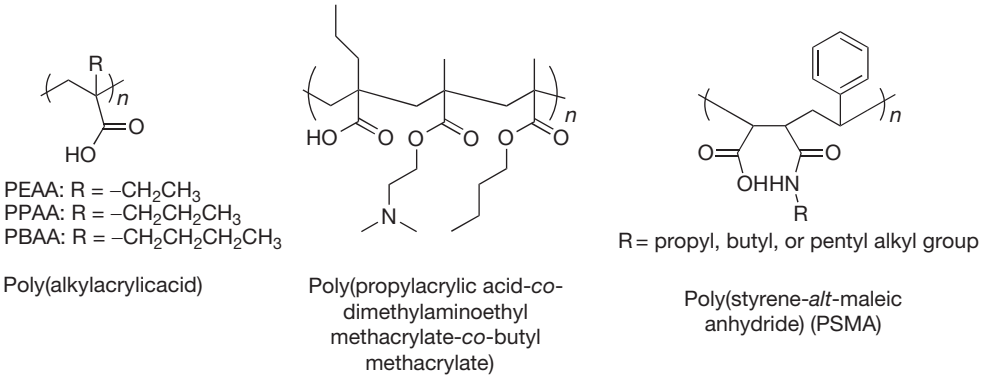

Figure 2 Structures of anionic, pH-responsive polymers useful toward intracellular delivery of biomacromolecules.

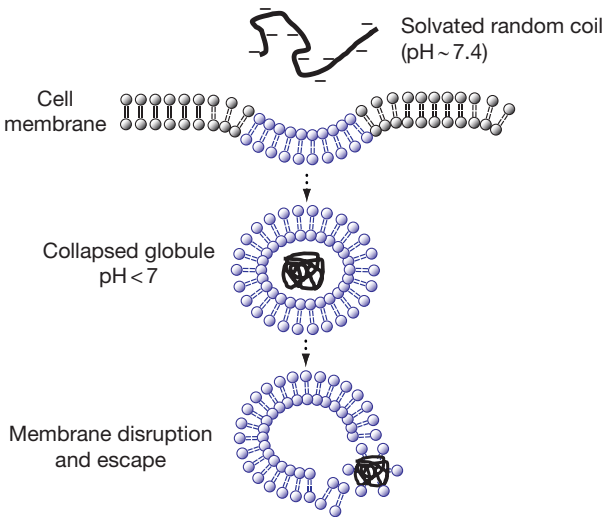

Figure 3 Schematic illustration of pH-driven coil-to-globule transition of poly(alkylacrylic acid) systems used for endosomolytic activity in drug delivery applications.

to behavior previously shown by Chen and Thomas for PMAA, which shows a similar transition at pH < 5.[47] Importantly, this change in polymer morphology correlates with the ability of these polymers to disrupt lipid bilayers. As PEAA and similar polymers are synthetic, polydispersed, and stereoirregular, it is unlikely that the membrane disruptive behavior is dependent on acquisition of any specific (i.e., pore-forming) secondary structure. In fact, Thomas and Tirrell have presented evidence that the membrane disruptive behavior is instead a hydrophobically driven process where the less soluble polymer initially binds to a membrane surface and then disrupts the vesicle bilayer by penetration and formation of mixed polymer/lipid micelles (Figure 3).[36]

Tirrell's studies focused on functionalization of liposomes with PEAA for triggered disruption and release of the contents of these vesicles as opposed to disruption and escape from endolysosomal membranes. Nevertheless, his studies in simplified, well-defined model systems yielded insight into mechanisms of membrane disruption by anionic polymers. The red blood cell (RBC) hemolysis assay has been predominantly used for subsequent studies on more complex biological membranes. This assay provides a relatively simple initial screen, and although its usefulness as an overall predictor for carrier *in vivo* performance may be overstated, past results have indicated that pH-dependent RBC hemolysis correlates with the ability of polymers to disrupt endosomal compartments.[48] Jones and coauthors compared PMAA, PEAA, and PPAA hemolytic profiles, and found that shifts in the pH-dependent hemolytic activity exist that correlate to Tirrell's findings on pH-dependent polymer conformational changes.[34] Their studies found that PPAA created hemolysis just under physiologic pH (7.4), PEAA at pH < 6.2, and PMAA showing no activity in the physiologically relevant range tested. Murthy, Cheung, and coworkers also found that PPAA (Figure 2) was ~15× more membrane disruptive than PEAA and showed maximum membrane disruption at pHs relevant for endosomal trafficking (pH ~6.0).[49–51] The increased activity was attributed to higher pK_a value because of one additional CH_2 group, and this motivated the investigation of poly(butylacrylic acid) (PBAA, Figure 2), where the pK_a was expected to increase yet again. For PBAA, membrane disruption at physiological pH was observed, a characteristic undesirable for ensuring biocompatibility on the basis of the polymer remaining inert in the extracellular environment. In addition to the important balance between pH responsiveness and polymer hydrophobicity, the membranolytic activity of PPAA is dependent upon regularly spaced acid and hydrophobic groups. For example, the membrane-disruptive behavior of PPAA was significantly higher at acidic pHs compared to that of a random copolymer of propyl acrylate (PA) and acrylic acid (AA).[50,52] It was presumed that PPAA can penetrate into the lipid bilayer more efficiently than the random copolymer because of the more regular spacing of the hydrophobic alkyl chains.[50,53] Murthy *et al.* also found that PEAA hemolysis was partially inhibited by addition of osmolytes such as dextran into the buffered solutions, indicating that a colloid osmotic mechanism may contribute to hemolytic activity of these polymers.[37] Colloid osmotic hemolysis results from an osmotic imbalance that occurs when small solutes (i.e., buffer salts) equilibrate across the membrane while larger macromolecules present in the cytoplasm of the RBC are not able to cross transmembrane pores because of size.[54] This creates a net osmotic imbalance, leading to water influx, swelling, and further damage to the lipid bilayer membrane. It is uncertain how much this effect contributes in the endosome, but it is conceivable that the macromolecular

osmotic gradient would be less significant across the endolysosomal membranes relative to this model system. Although the exact mechanism of disruption of these less homogenous biological membranes is not as clearly elucidated, strong evidence remains that the more hydrophobic polymer state at lower pHs leads to partitioning of the polymer into the core of the lipid bilayer, leading to bilayer disruption and solute permeability.

The literature contribution from Jones and coauthors demonstrated one of the most thorough and informative investigations to date on the mechanism of endolysosomal vesicle disruption of poly(2-alkylacrylic acid)s in living cells.[34] Their studies indicated that in human U937 myelomonocytic transformed secondary cells (i.e., cells with a highly phagocytic phenotype), all three 2-alkylacrylic acid polymers tested were able to achieve escape of small molecules and cathepsin B fused with green fluorescent protein from endolysosomal pathways into the cytosol. Furthermore, the pH-driven nature of this activity was validated by experiments showing that agents that inhibit the acidification of endosomes abrogate polymer-mediated endolysosomal release into the cytoplasm. On the basis of experiments using fixed-cell immunocytochemistry and live-cell intracellular stains, the authors found that 2-alkylacrylic acid polymers altered distribution and morphology of late endosomes, but not early endosomes or lysosomes. The polymers may have exerted their effects prior to reaching the lysosomes, or it could be speculated that the lack of change in lysosome morphology may have been related to differences in the compositional integrity of the lysosomal membrane or polymer precipitation (and thus loss of the amphiphilicity required for activity) in this highly acidic environment.

4.422.3.1. Poly(alkylacrylic acid)s

Because PPAA exhibited the optimal pH-responsive membrane destabilization behavior in mechanistic studies, it has been extensively studied for cytosolic delivery of biomolecular drugs. Simple linkage of PPAA to a protein (e.g., streptavidin) did not affect the pH-dependent conformational change of the polymer chains nor its pH-responsive membrane-destabilizing activity.[55] In addition, PPAA conjugation aids in antibody cytosolic delivery, where ~73% of the total antibody was measured cytoplasmically when delivered following PPAA conjugation versus ~0% for free antibody.[55] More recently, PPAA was conjugated to a model antigen, ovalbumin, and used to treat macrophages *in vitro* as a first step toward a polymeric vaccine delivery system. This treatment resulted in increased cellular major histocompatibility complex class 1 presentation and ovalbumin-specific cytotoxic T cell activation, results that require cytosolic delivery and processing of antigen.[56] In a follow-up study using the EG.7-OVA mouse tumor protection model, PPAA was also shown to produce a functionally significant prophylactic effect *in vivo*. In this study, PPAA-based delivery of ovalbumin as a model protein antigen facilitated an 8-fold increase in antigen-specific CTL production and an approximately 3.5-fold increase in the length of tumor-free survival relative to vehicle controls following inoculation with mouse EG.7-OVA thymoma cells.[7]

In addition to these protein delivery applications, PPAA has also proven to be useful in gene therapy approaches. Introduction of PPAA into a mixture dioleoyltrimethylammonium propane (DOTAP), a cationic lipid traditionally used for gene delivery, enhanced plasmid DNA gene expression (20-fold) and serum stability.[49] Further exploration of this delivery system was performed in a murine model of wound healing, showing that when PPAA was added to the formulation, expression of TSP2 was enhanced in TSP2-null mice compared to control formulations.[57] In an analogous ternary system, enhanced gene expression was obtained using a combination of chitosan, DNA, and PPAA in HeLa cells.[58] These studies also showed a lack of colocalization of PPAA and a lysosomal dye, providing mechanistic evidence that PPAA enhanced transfection efficiency by enabling endosomal escape of DNA prior to lysosomal degradation.[57]

Copolymers with diblock architectures that exploit the pH-responsive activity of PAA have also been synthesized and explored for macromolecular intracellular drug delivery. Typically, diblock copolymers have been designed with twofold delivery characteristics in mind – for example, long circulation times or drug complexation and protection, in addition to endosomal escape. One copolymer designed specifically for siRNA delivery is a block copolymer consisting of poly(dimethylaminoethyl methacrylate)-*b*-poly(propylacrylic acid-*co*-butyl methacrylate-*co*-dimethylaminoethyl methacrylate) (pDMAEMA-*b*-p(PAA-*co*-BMA-*co*-DMAEMA)).[59] This diblock copolymer was designed to complex and protect the siRNA, which is negatively charged, and to enable endosomal escape. Therefore, a cationic first block (to condense and protect siRNA) and a terpolymer second block containing PAA (see **Figure 2**) were synthesized (for endosomolysis). Delivery of siRNA using the diblock copolymer resulted in gene product knockdown of up to 30% of untreated cells and resulted in no detectable cytotoxicity,[59] and further optimization through adjusting relative block sizes produced even higher levels of knockdown.[60] Another carrier was developed using the same pH-responsive block but with different delivery requirements. In particular, the polymer poly(*N*-(2-hydroxypropylmethacrylamide))-*b*-poly(propylacrylic acid-*co*-butyl methacrylate-*co*-dimethylaminoethyl methacrylate) (pHPMA-*b*-p(PAA-*co*-BMA-*co*-DMAEMA) was utilized to confer long circulation times (pHPMA block) and endosomal escape (terpolymer block containing PAA, **Figure 2**) to an intracellular-acting proapoptotic peptide.[61] The peptide was conjugated through disulfide exchange using a pyridyl disulfide polymer chain end functionality incorporated through a RAFT-based synthetic procedure. Peptide–polymer conjugates increased HeLa cervical carcinoma cell apoptotic activity over free peptide and resulted in 50% tumor cell death in cultures after 6 h of treatment.[61] Data gathered using these polymer delivery systems indicate that cytosolic delivery is enhanced using PAA functionalities even when incorporated into a diblock copolymer – opening up new and exciting avenues for delivery systems requiring multiple functionalities to overcome diverse delivery hurdles.

4.422.3.2. Poly(styrene-*alt*-maleic anhydride)

Another class of anionic, pH-responsive membrane-destabilizing polymers are copolymers of styrene and maleic anhydride (poly(styrene-*alt*-maleic anhydride), PSMA). Styrene and maleic anhydride are known to produce alternating copolymers[62] that have been used in a variety of applications. Generally, PSMA has many desirable attributes for use as a polymer therapeutic. It enhances drug circulation half-life and lipid solubility, and it

binds noncovalently with albumin during systemic circulation, thereby reducing polymer clearance.[63] The initial use of PSMA was to exploit these properties, and Maeda and coworkers first used low molecular weight PSMA copolymers (<6 kDa) clinically to deliver an antitumor protein, neocarzinostatin (NCS).[64–66] The polymer–protein conjugate (SMANCS)[64–66] significantly improved the pharmacological properties of NCS and has been clinically effective in treating liver cancer. The SMANCS conjugate is also known to accumulate in tumor tissue and the lymphatic system through the proposed enhanced permeation and retention (EPR) effect.[64–66] Additional research by Maeda *et al.* indicated that PSMA enhanced NCS uptake by increasing cell binding. They also speculated that PSMA enhanced translocation of NCS across the endosomal membrane by increasing the interactions between NCS and the membrane at acidic pH.[67] However, in more recent work, PSMA has been thoroughly evaluated as a pH-dependent membrane-destabilizing polymer, and this property is likely the reason for enhanced cytosolic NCS delivery. Specifically, Henry *et al.* found PSMA to be endosomolytic, particularly upon modification of the maleic anhydride with alkyl chains (see **Figure 2**).[68] Results showed that varying the length of alkyl chain used in the modification, the percent modification of PSMA, and the overall molecular weight of PSMA can be utilized to tune the pH-dependent membrane-destabilizing activity of these derivatives.[68] PSMA has also been further developed and optimized for the delivery of siRNA.[69] The pH-responsive complexes were used to deliver siRNA against polo-like kinase 1 (plk1), a gene upregulated in many cancers and responsible for cell cycle progression. Treating cells using the complexes resulted in approximately 50% reduction of plk1 gene expression in NCI/ADR-RES and OVCAR8 ovarian cancer cell lines.[69]

4.422.4. Acid-Degradable Delivery Vehicles

Another class of endosomal-disruptive delivery vehicles has been developed based on the use of acid-degradable chemical linkages. These linkages have been used to fabricate delivery vehicles that hydrolyze at the acidic pH of the endosome and, in turn, generate membrane disruptive molecules that allow escape to the cytoplasm. Two linkages have been extensively used for these applications, the acetal/ketal linkage and the orthoester linkage. The rate of hydrolysis of acetals is first order relative to the concentration of the hydronium ion, and therefore, per unit decrease in pH, the rate of hydrolysis increases by a factor of ten. It is worth noting that the rate of hydrolysis can be tuned according to the structure of the acetal,[70] which can be useful for tuning the point at which hydrolysis occurs during endolysosomal trafficking. Similarly, the rate of hydrolysis of orthoesters also increases with the hydronium ion concentration, but the relationship is not first order and is therefore more difficult to predict. Highly potent disruptive polymers can be 'masked' with more inert carriers using these classes of linkages. One shortcoming is the potential toxicity due to the lack of reversibility relative to an anionic polymer that would revert to a more hydrophilic conformation following endosomal escape.

4.422.4.1. Encrypted Polymers

Murthy *et al.* developed one of the first designs of an endosomal-disruptive polymer drug delivery vehicle based on acid-degradable linkages, termed 'encrypted polymers.'[71,72] In this approach, the polymer contains a membrane-disruptive backbone connected to the other molecular species via acid-labile acetal linkers. A disulfide bond connects the acid-degradable linker to either PEG grafts or a therapeutic molecule. A targeting ligand for endocytosis can be attached to the PEG chains (**Figure 4**). In cases where the drug is not conjugated via a disulfide bond, ionic groups can be incorporated at the PEG terminus to complex with charged drugs (i.e., nucleic acids). In the intact polymeric configuration, PEG chains 'mask' the membrane disruptive potential of the backbone. However, once the pH of the maturing endosome drops, hydrolysis of the acid-degradable linker 'unmasks'

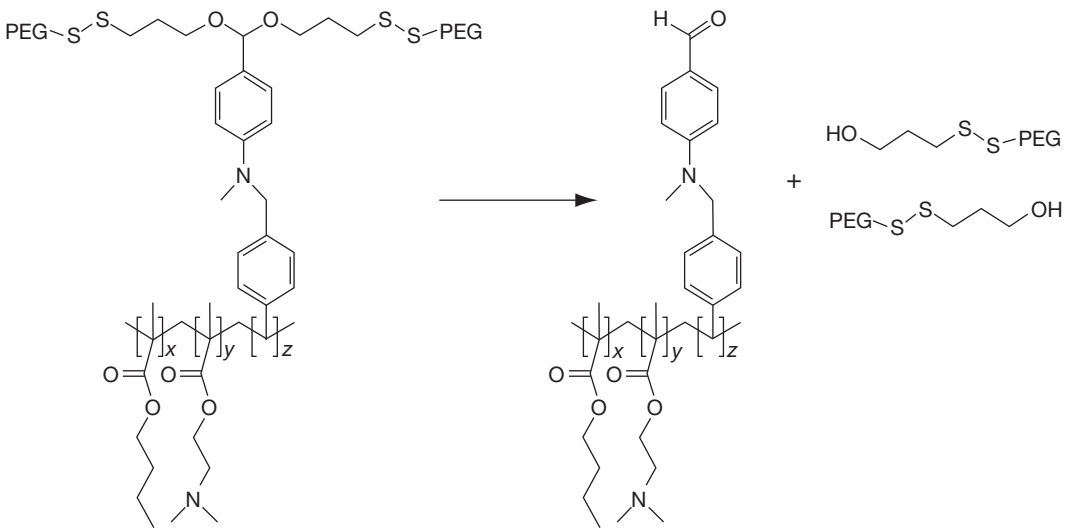

Figure 4 Chemical structure of encrypted polymers. Before hydrolysis, the membrane-disruptive backbone is 'masked' by PEG grafts through an acid-labile acetal linkage. As the pH drops, hydrolysis of the acetal 'unmasks' the backbone, leading to disruption of the endosome.

the backbone which disrupts the endosome and allows the drug to diffuse into the cytoplasm. Importantly, this design enables the development of polymers that are significantly more effective at membrane disruption compared to anionic pH-responsive polymers, because of the greater hydrophobicity and cationic content that can be incorporated into the polymer backbone. However, the synthesis of polymers containing acetal linkages is fairly challenging and limits the type of molecules that can be generated with the encrypted polymer strategy.

4.422.4.2. Buchwald Coupling-Based Vehicles

Knorr *et al.* developed an elegant strategy for generating endosomal-disruptive drug delivery vehicles, composed of polyethyleneimine (PEI) polyplexes, on the basis of the Buchwald coupling reaction.[73] Polyplexes of PEI with negatively charged DNA have been widely used because of their ability to shield DNA from serum degradation, stimulate endocytosis, and create the 'proton-sponge' effect to trigger endosomal escape (discussed in detail below). However, in order to achieve high gene transfer activity, an excess of cationic PEI is needed, which leads to toxicity. Knorr *et al.* were able to alleviate these side effects by neutralizing the polyplex surface using PEG chains incorporated into the formulation through acid-degradable acetal linkages. Similar to the previous encrypted polymers, the acetal link between the PEG and the PEI allows for removal of PEG units from the polyplexes as the pH drops, facilitating efficient endosomal disruption. The synthesis of the key intermediate needed to generate these complexes is shown in Figure 5 and uses the Buchwald–Hartig coupling reaction to substitute a PEGylated aromatic bromine with a protected piperazine. This key step also generates an aniline type acetal, which has rapid hydrolysis kinetics at acidic pHs.[70]

4.422.4.3. Acid-Cleavable Lipid Drug Delivery Vehicles

Natural lipids known as the plasmalogens contain vinyl ether linkages in their alkyl regions that are hydrolyzable at acidic pH. Plasmalogens can be utilized to achieve triggered release of liposomal contents at endosomal pH, and have been explored for over a decade for applications in drug and gene delivery.[74–76] Several newer synthetic types of lipids have also been developed that incorporate acid-degradable linkages. These lipids are designed to be stable at pH 7.4 but decompose at the acidic pH of the endosome to generate products that are membrane disruptive. For example, Guo *et al.* synthesized a PEGylated lipid that contains an orthoester linkage, via the route shown in Figure 6.[77] This lipid is stable in pH 7.4 buffer at 37 °C, but degrades at pH 5 within one hour, generating a lipid byproduct that is membrane disruptive. At pH 5.5, liposomes containing 10 mol% of this lipid released most of their contents within 30 min.[77]

4.422.5. Osmotically Disruptive Cationic Polymers

Another approach to achieve intracellular delivery has been the use of cationic, amine-containing polymers thought to facilitate endosomal release through osmotic disruption (e.g., the hypothesized 'proton-sponge' effect[78–82] first proposed by Behr and coworkers[78,79]). During normal endosomal trafficking, endolysosomes are acidified by the action of an ATPase-driven proton pump in the vesicle membrane (see Figure 7). If present within the vesicle, proton-accepting polymers buffer the acidic microenvironment and inhibit the normal drop in pH. This leads to a continued, abnormal influx of protons and their counter ions. The higher ion concentration increases osmotic pressure inside the vesicle, leading to water influx, swelling and disruption of the endosome, and release of its contents into the cytoplasm (see Figure 7). Although it is efficient for gaining cytosolic entry for therapeutics, proton-sponge-mediated endosomolysis has the potential to induce cytotoxicity because of release of endolysosomal enzymes along with therapeutic. Thus, there is a poorly understood, but critical balance that must be achieved between efficient therapeutic escape and the potential negative side effects of endolysosomal disruption (e.g., more escape may not always be 'better'). Nonetheless, a distinct requirement for endosomal disruption via the proton-sponge effect is buffering capacity of

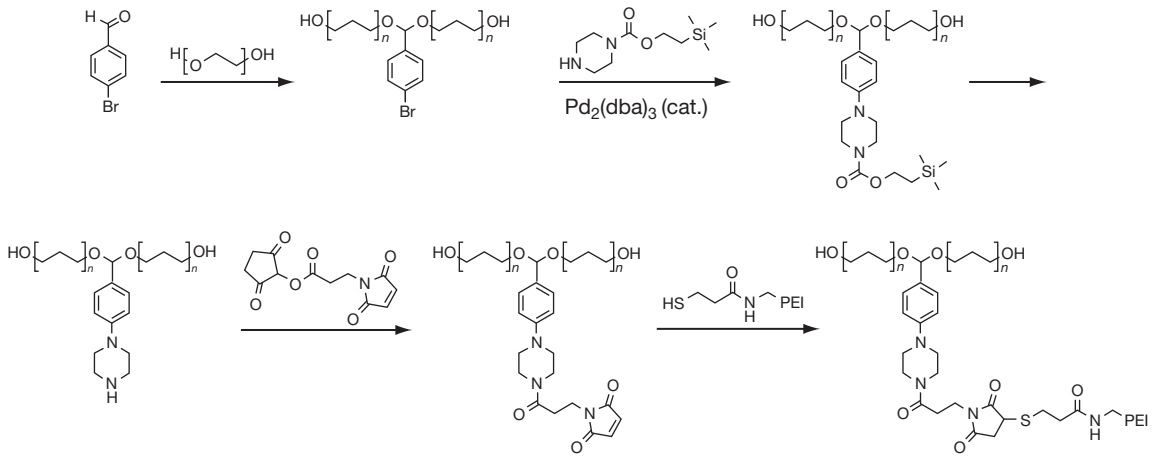

Figure 5 Buchwald–Hartig coupling for synthesis of an acid-cleavable PEI polyplex.

the polymer that matches the range of pH values present during endolysosomal trafficking (e.g., pH 7.4 to 5.0). Therefore, secondary, tertiary, and some quaternary amines are capable of mediating 'proton-sponge' endosomolysis. Primary amines (e.g., of poly(L-lysine) and PEI) are not considered to be active via this mechanism ($pK_a > 8.0$), but modifications to the architecture of these polymers can performed to lower the pK_a of the amines and render them endosomolytic.[83]

Cationic polymers whose mechanism is on the basis of the 'proton-sponge effect' have demonstrated efficient intracellular delivery of nucleic acid drugs[84–86] and proteins.[87–90] Somewhat serendipitously, these polymers were initially investigated as they were available commercially and able to complex negatively charged nucleic acids into readily internalized particles. These particles are overall positively charged and associate electrostatically with negatively charged plasma proteins, platelet and erythrocyte membranes, and glycosaminoglycans located on cell surfaces to permit nonspecific cell endocytosis.[91] However, the major drawbacks limiting therapeutic development of cationic polymers are their intrinsic cytotoxicity and serum instability *in vivo*. Therefore, current advances in cationic polymer development include development of chemical compositions that reduce or eliminate cytotoxic side effects while enhancing *in vivo* stability.

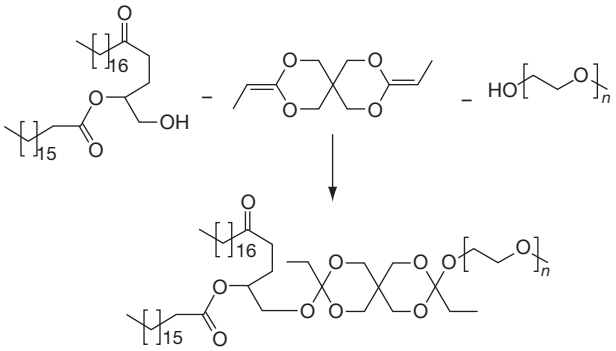

Figure 6 Synthetic scheme used by Guo *et al.*[77] for preparation of a lipid containing an acid-cleavable orthoester linkage.

4.422.5.1. Poly(L-lysine)

One of the first cationic polymers used for DNA delivery was poly(L-lysine).[92] Although poly(L-lysine) is able to complex DNA, its transfection activity is very low, requiring addition of endosomolytic agents such as chloroquine to modulate gene expression (see **Figure 8(a)**). Therefore, poly(L-lysine) has been relegated to use in mechanistic studies. However, these mechanistic studies have led to noteworthy contributions to the understanding of DNA/polymer complex formation,[92] targeting strategies,[93–105] and endolysosomal escape.[92,94]

4.422.5.2. Polyethyleneimine

PEI is the current gold standard cationic polymer for intracellular DNA delivery because of its proven efficacy. A variety of different polymers and copolymers of linear and branched architectures of PEI (see **Figure 8(b)** and **8(c)**) have been synthesized and utilized for biotherapeutic delivery. Branched PEI (bPEI) is highly endosomolytic because of its high density of primary, secondary, and tertiary amines, of which only 15–20% are protonated at physiological pH[106,107] (primary amine $pK_a \sim 9.0$, secondary amine $pK_a \sim 8.0$, and tertiary amine $pK_a \sim 6–7$), making it a buffering agent to weak acids and powerful proton sponge. However, linear PEI (lPEI) contains mostly secondary amines and is 90% protonated at physiological pH, limiting its ability to mediate 'proton-sponge' endosomolysis. Literature covering the use of PEI as a delivery agent is vast (see Lungwitz *et al.*,[84] Morille *et al.*,[108] Park *et al.*[109]); recent advances (published within the past ~10 years) are summarized herein.

PEI polymers have been used to effectively deliver oligonucleotides,[106,110] plasmid DNA (pDNA),[107,111,112] and Epstein-Barr virus-based plasmid vectors[113–117] as well as RNA, siRNA,[118,119] and intact ribozymes.[120] Not only has PEI had great success for *in vitro* macromolecular drug delivery, but it has also been utilized *in vivo* to deliver DNA to a variety of tissues, including the central nervous system,[121,122] kidney,[123] lung,[122,124] and tumors.[125] As detailed above, the amine-rich structure of PEI generates its endosomolytic activity. However,

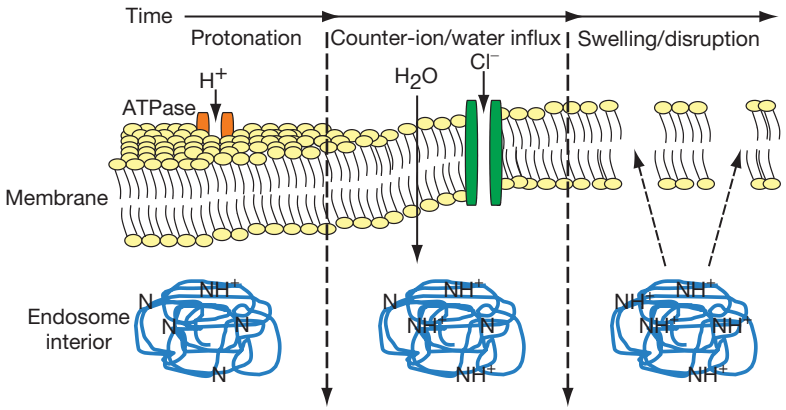

Figure 7 The 'proton sponge' effect. Upon endosomal uptake, ATPases pump protons (H^+) in to acidify the compartments, but secondary and tertiary amines on the proton-sponge polymers prevent acidification, leading to continued ion import. Concomitant counter-ion (Cl^- and others) influx into the endolysosomal vesicle creates an osmotic gradient, triggering water influx, vesicle swelling, and membrane rupture, releasing the polymer and drug cargo into the cytosol.

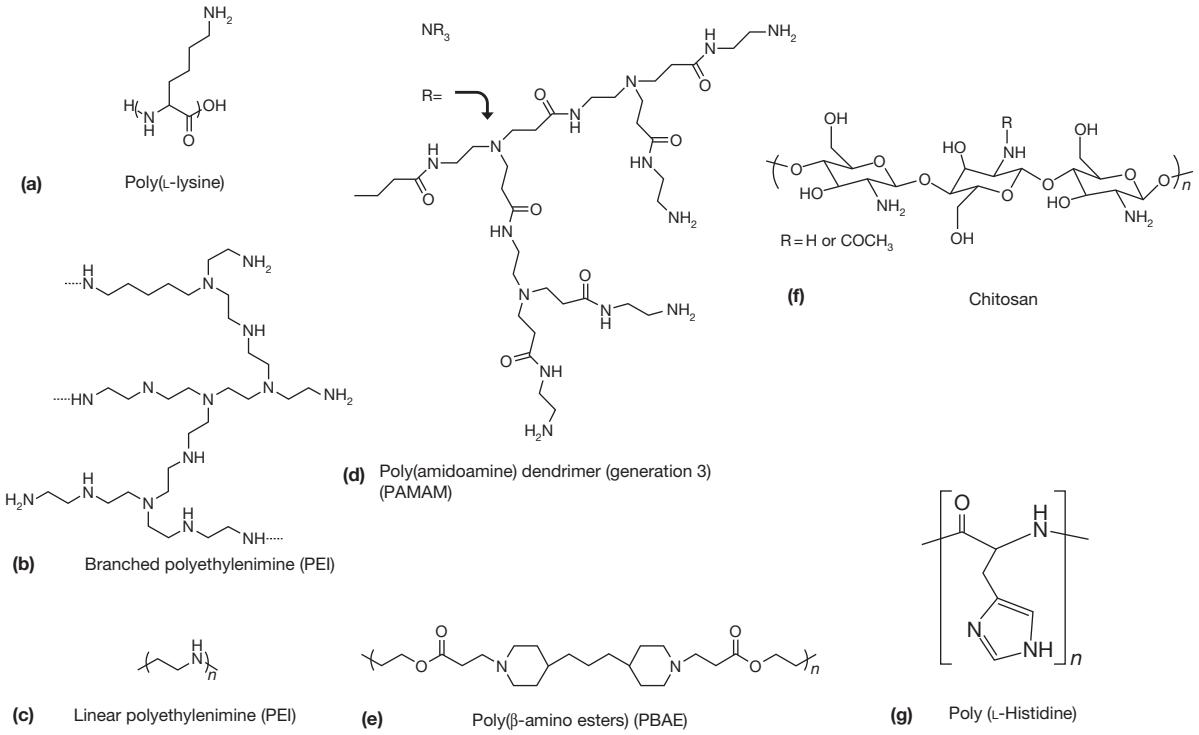

Figure 8 Structures of amine-containing, 'proton-sponge' polymers useful toward intracellular delivery of biomacromolecules.

the amines of PEI are also exploited for electrostatically condensing drug cargo (nucleic acids or anionic proteins) and to enhance uptake. More recent work has also exploited PEI's primary amines to conjugate macromolecular drugs[126] and/or other molecules that enhance endosomal escape or enable tissue-specific targeting.[28,98,127–130]

Linear PEI, as described above, contains mostly secondary amines that are protonated at extracellular pH and do not buffer the pH range present in endocytosis pathways. On the basis of this observation, one would hypothesize that bPEI would outperform lPEI for cytosolic delivery because it is a much better 'proton sponge' in the relevant pH range. However, gene delivery studies utilizing lPEI (MW = 22 kDa) showed greater transfection efficiencies and lower cytotoxicity compared to bPEI (MW = 25 kDa).[131,132] The greater efficiency of lPEI is hypothesized to be due to inherent kinetic instability of lPEI complexes under physiological salt conditions.[133] Efficient gene therapy using lPEI (MW = 22 kDa) has also been verified *in vivo* by a study showing significant and long-lasting (15 days or longer) expression of a reporter gene following injection directly into solid tumors using micropumps.[125]

Although remarkably potent with respect to intracellular drug delivery both *in vitro* and *in vivo*, PEI suffers from high levels of cytotoxicity, which has limited its translation into clinical use. Cytotoxicity associated with PEI is primarily attributed to necrosis and mitochondrial apoptosis activation.[134] In addition, *in vivo* experiments have revealed that free and bPEI/DNA complexes activate genes in the Th1/Th2 immune response and adaptive immune response.[135] Moreover, systemic administration of unshielded bPEI (800 kDa) was lethal in animal models.[136] Therefore, much of the recent developments in the arena of PEI polymer therapeutics are focused on abrogating cytotoxicity. For example, cytotoxicity can be moderated through the use of low molecular weight PEIs (5–48 kDa),[137–139] but increased overall polymer concentrations are needed to achieve comparable efficacy. Importantly, the lower molecular weight PEIs (~25 kDa) used at greater concentrations also improved serum stability relative to higher molecular PEIs, increasing their probability for success for *in vivo* therapeutic delivery.[138] Alternatively, many studies have explored conjugation of low molecular weight PEIs with degradable linkages such as amides, acetals, esters, and disulfides. This approach produces a polymer with lower toxicity and relatively high gene transfection efficiency, as well as long-term safety.[140–143] Others have altered the amines to contain other molecules, such as poly(ethylene glycol), imidazole, or peptides to reduce toxicity of PEI while maintaining effective intracellular delivery.[82,118,144,145]

4.422.5.3. Poly(amidoamine) Dendrimers and Polymers

Dendrimers are synthetic, spherical, highly branched macromolecules of nanometer dimensions (see **Figure 8(d)**). The size and the charge of these polymers are controlled by varying the number of generations or branches in the polymer synthesis.[146] Because of the large number of secondary and tertiary amines on the polymer, poly(amidoamine) (PAMAM) dendrimers, in particular, are potent weak bases and proton sponges. Haensler and Szoka originally reported the use of PAMAM dendrimers for gene delivery.[147] They found that the sixth generation dendrimer was better at gene delivery than higher and lower generations by 10-fold. Because of their relatively high gene delivery efficiency, PAMAM dendrimers have recently been used in several *in vivo* gene delivery

studies.[148–151] However, there are conflicting reports regarding their biological safety.[152,153] The cytotoxicity of PAMAM dendrimers is similar to PEI: necrosis and mitochondrial apoptosis activation. To reduce these unintended side effects, Wang *et al.* decorated PAMAM with poly(ethylene glycol) (PEG) chains, resulting in 12–105-fold increases in the IC50 values with PEG versus undecorated PAMAM.[154] The level of cytotoxicity was inversely related to the molecular weight of the PEG conjugated to the dendrimers, but longer PEG had a negative effect on cellular uptake. For example, greater than 90% of the cells internalized dendrimers functionalized with 2 kDa PEG compared to only ~60% when 5 kDa PEG was used. This finding again highlights the critical balance between activity and cytotoxicity of cationic macromolecular carriers and serves further motivation to pursue systems actively targeted for receptor-mediated endocytosis. In addition, PAMAM dendrimers have been partially degraded at their amide bonds and found to be more effective DNA delivery polymers (> 50-fold enhancement of transfection activity)[155] compared to intact dendrimers. PAMAM dendrimers have also been modified with 3.5 kDa PEG containing a mannose or galactose unit for cell surface receptor targeting.[156] These hybrid polymers self-assembled with DNA and presented the targeting moiety on the outer shell, which enabled improved transfection over PEI. Although the authors did not posit a reason for enhanced activity, the hybrid, multifunctional nature of the dendrimers provided facile means to tune carrier properties to optimize blood stability, cellular targeting, DNA binding, and endosomal buffering capacity.

4.422.5.4. Poly(β-amino esters)

Poly(β-amino esters) (PBAEs) are very recent additions to the growing list of pH-responsive polymers. PBAE are structurally similar to the PAMAM polymers discussed above and have been formulated into hyperbranched dendrimer structures as well.[157] Formulations of PBAE polymers have been used for intracellular delivery of nucleic acids, including siRNA[158] and DNA.[159–172] PBAE have very interesting and unique properties that make them favorable toward drug delivery. PBAE are insoluble at physiological pH and can be formulated into micron-sized particles for drug delivery. On the basis of their size, PBAE particles accumulate in the tumor microenvironment through either vascular filtration or extravasated via the EPR effect. Although PBAEs are not soluble at physiological pH, they rapidly dissolve upon exposure to a slightly acidic pH of 6.5, and once solubilized, PBAEs (shown in **Figure 8(e)**) have tertiary amines that serve as powerful proton sponges. PBAEs are also desirable because they decompose into cytocompatible, low molecular weight degradation products, diols and bis(β-amino acids), and, therefore, are significantly less toxic than PEI and poly(L-lysine).[81] A library of PBAE polymers has been screened to find molecular parameters that support efficient transfection.[159–161] Although effective compositions were identified, no clear design criteria were identified, and the role of some key factors (i.e., molecular weight and charge density) were not comprehensively investigated. For example, the top 5% most effective carriers of the 486 compositions examined for delivery of a luciferase reporter gene to COS-7 cells ranged in molecular weight from ~5 to ~50 kDa. All of these carriers condensed DNA into sub-150 nm particles with positive surface charges. Moreover, the top nine performers had very similar structures, providing a framework with which PBAE carriers can be further modified to fulfill other design criteria required for *in vivo* delivery of nucleic acid drugs (circulation time, targeting, dosing).[173]

4.422.5.5. Chitosan

Chitosan, a naturally derived polysaccharide obtained by deacetylation of chitin, is composed of two subunits, D-glucosamine and *N*-acetyl-D-glucosamine, linked by a 1-4 glycosidic linkage (see **Figure 8(f)**). Chitosan is a nontoxic, biodegradable, and renewable polymer with a long history of use in drug delivery for the entrapment of enzymes[174,175] and controlled release of proteins.[176–179] In addition, because of its disaccharide composition, chitosan contains several primary and secondary amines capable of endosomolysis via the 'proton-sponge' effect. Therefore, chitosan has been examined as a pH-responsive drug delivery polymer,[180–185] mostly for nucleic acid-based therapeutics. In particular, low molecular weight chitosan (LMWC) has been most extensively explored because high molecular weight chitosan polymers are insoluble in aqueous solutions at physiological pH. LMWC interacts with DNA to form complexes that efficiently protect it from degradation by DNase I. Chitosan also exhibits greater gene delivery efficiency and lower cytotoxicity than PLL.[109] However, even LMWC suffers from relatively poor solubility in physiological buffers and lower endosomolytic activity compared with PEI. To augment its drug delivery activity, modification of chitosan with a variety of chemical moieties has been a recent area of interest to provide better endosomal escape and solubility. For example, PEI has been conjugated to chitosan to enhance endosomal escape properties, enabling 10–100-fold increases in transfection efficiency in a variety of cell lines.[186] Chitosan has also been modified with lactose through reductive amidation to target drug uptake through the asialoglycoprotein receptor of hepatocytes. However, lactosylated chitosan failed to enhance transfection of a hepatocyte cell line, which was attributed to insufficient cell membrane interaction needed for ligand–receptor binding because of reduced surface charge of the modified carrier.[187] Imidazole-functionalized chitosan (MW = 130 kDa) resulted in a more potent pDNA and siRNA carrier, largely attributed to increased solubility at physiological pH and 'proton-sponge' capability due to introduction of additional secondary and tertiary amines within the polymer backbone.[188] Imidazole-functionalized chitosan was further modified with PEG to inhibit serum-induced aggregation *in vivo*.[189] The PEGylated imidazole-chitosan was found to be highly efficient in delivering bioactive siRNA in a mouse model, resulting in up to 50% gene silencing in lung and 40% gene silencing in liver. Importantly, this carrier exhibited minimal cytotoxicity or other adverse side effects *in vivo*, indicating great promise for further development into a clinically relevant nucleic acid delivery system.

4.422.6. Histidine- and Imidazole-Containing Copolymers

Histidine (His) is an amino acid with an imidazole side chain containing a secondary amine that makes His a weak base

(Figure 8(g)). Protonation of this amine on poly(His) or synthetic imidazole-containing polymers in acidic environments provides membrane fusogenic properties with negatively charged liposomes[190] and makes it useful as a biocompatible drug delivery tool because of its 'proton-sponge' activity.[191] Like the other proton-sponge polymers, poly(His) was initially sought for its ability to enhance cytoplasmic access of pDNA for gene therapy. With the aim of achieving biocompatible systems made of natural amino acids, lysine (Lys) and His have been utilized in numerous successful combinations because the high pK_b of the primary amines on Lys makes it cationic and efficient at condensing nucleic acids at physiologic pH, while the lower pK_b of His provides endosomal buffering.

Midoux, Monsigny, and coauthors made some of the earliest advances toward improving poly(Lys)–DNA complex transfection efficiencies using a histidine-rich peptide[192] or by delivery using a poly(L-lysine) (degree of polymerization = 190) partially substituted with histidine residues.[193] In the later study, substitution with 72 ± 9 histidyl residues (38% substitution of the Lys primary amines) was found to produce the best transfection, and these carriers were also found to maintain their activity in the presence of up to 20% serum. Approximately 1.5 times better transfection efficiency and significantly higher biocompatibility (~90% versus ~40% viability) have also been achieved in 293 T cells using poly(His) grafted to poly(Lys) relative to poly(Lys) alone (20:1 polymer:DNA weight ratio for both). However, chloroquine increased transfection efficiency for both polymers, indicating that even grafting of His polymers did not produce optimal endosomal escape.[194] Langer and coauthors have also explored imidazole-containing systems for gene delivery. One approach incorporated glycosylated poly(His) (glycosylation was performed to increase water solubility at physiologic pH) into ternary complexes with DNA and transferrin-functionalized poly(Lys) used for complexation and receptor-mediated uptake.[195] They also synthesized both poly(His)–PEG block polymers and polymer combs of PEG grafted to a poly(His) backbone.[196] Although they did show promise, none of these carriers resulted in transfection efficiencies equivalent to control formulations using 25 kDa PEI. However, in another study similar to the earlier approach by Midoux *et al.*, 73.5, 82.5, and 86.5 mol% imidazole substitution of the primary amines was performed on a 34 kDa poly(Lys). This same approach was utilized to optimize the balance between cationic content and endosomal escape functionality, and the most substituted polymers (86.5 mol% imidazole content) produced similar protein expression as PEI in several cell lines *in vitro* with significantly less cytotoxicity (e.g., ~100% viability for modified polymer versus <25% viability for PEI for the median polymer concentration tested using an MTT viability assay).[197] Mixson and coauthors have also explored a variety of histidine–lysine (HK) copolymers with varying branching and H/K ratio, and they have found that optimal polymer architecture (linear vs. branched) may vary based on cell type because of differences in the pH of endocytotic vesicles.[198,199] Mixson's group more recently derived highly branched HK polymers that were efficient siRNA carriers,[200] and effective siRNA delivery has also been shown in hepatocytes using a His-containing reducible polycation designed to effectively unpackage the siRNA in the reducing environment of the cytoplasm.[201] Histidine has also been used to modify chitosan through reducible disulfide bonds[202] and covalent amide linkages[203] to enhance endosomal escape and increase transfection efficiency.

Use of poly(His) to facilitate delivery of small molecule drugs is a relatively unique application compared to other proton-sponge polymers. In a chemotherapeutic drug delivery application, paclitaxel was successfully delivered intracellularly using *N*-acetyl histidine-conjugated chitosan self-assembled nanoparticles.[204] Histidines have also been extensively used in micelle carriers, and Bae's group has prolifically contributed to poly(His) applications in this context. Their initial effort was aimed at micelles that release their payload in the slightly acidic extracellular environment common to hypoxic solid tumors. In this application, a 5 kDa poly(His) was coupled to a 2 kDa PEG to form a diblock polymer. This polymer was found to produce stable micelles at pH 8 that were destabilized below 7.4 as the imidazoles in the micelle core became increasingly protonated and hydrophilic.[205] A follow-up study focused on intracellular delivery of chemotherapeutics using a mixed micelle carrier composed of a diblock polymer with 5 kDa poly(His) and 2 kDa PEG and a diblock polymer with 3 kDa poly(L-lactic acid) (PLLA) and 2 kDa PEG.[206] The poly(PEG-*b*-PLLA) was employed in conjunction with poly(PEG-*b*-His) to increase the hydrophobicity of the micelle core, and the PEG end of the poly(PEG-*b*-PLLA) was conjugated to folate to target the micelles for receptor-mediated endocytosis in cancer cells that overexpress the folate receptor. It was determined that the mixed micelles with 25 wt% poly(PEG-*b*-PLLA) and 75 wt% poly(PEG-*b*-His) had optimal pH-responsive properties. This formulation shifted the pK_b of the His imidazole to be better tuned to respond in the lower pH of the endosomes while also increasing micelle stability at pH 7.4, which is key for *in vivo* systemic delivery applications. Further physicochemical characterization verified that progressive protonation in acidic environments increases hydrophilicity and electrostatic repulsion of imidazole rings, which overwhelms the hydrophobic interactions in the core of the micelle.[207] Scale-up and clinical applicability of this micelle system were also shown to be feasible on the basis of the stability and activity of reconstituted particles lyophilized in the presence of 33 wt% Pluronic F127 copolymer as an excipient.[208]

The folate-targeted mixed micelle was subsequently applied in numerous studies aimed at chemotherapeutic delivery to multidrug resistant (MDR) cancer cells. These cells overexpress drug efflux pumps, and targeted uptake of drugs via endocytosis (i.e., the folate receptor pathway) is believed to circumvent this delivery challenge. Thus, the combination of folate targeting with poly(His) proton-sponge activity was the key approach for efficient intracellular delivery. In an initial application, this strategy produced more than 90% cytotoxicity in doxorubicin resistant MCF-7 cells at 10 μg ml^{-1}, while free doxorubicin had no effect on viability of MCF7s at this dose. In an *in vivo* tumor inhibition study, the folate-targeted pH-responsive mixed micelles produced 2.7-times smaller tumors than free doxorubicin and 1.9-times smaller than non-pH-responsive poly(PEG-*b*-PLLA) control micelles. The targeted micelles produced 20-times greater doxorubicin accumulation in the tumor relative to free doxorubicin and also

decreased body weight loss relative to free drug, indicating decreased systemic toxicity.[209] In a subsequent mechanistic study examining drug retention, MDR cells pulsed with the pH-responsive doxorubicin micelles for 30 min *in vitro* retained 80% of the drug after 24 h while control micelles without the pH-responsive component retained only 40% of the drug.[210] Subsequent studies verified the ability of the folate-targeted, pH-sensitive mixed micelles to inhibit MDR ovarian A2780/DOX^R xenograft tumors, which were fivefold smaller than free doxorubicin controls after 27 days.[211]

Bae and coauthors recently developed a second generation mixed micelle carrier composed of poly(PEG-*b*-(His-*co*-phenylalanine (Phe))) and poly(folate-PEG-*b*-PLLA). Relative block sizes were the same as in the first generation system, but further control over the pH buffering range of the histidine was achieved through varying the ratio of His and Phe in the copolymer block. In this study, it was found that a copolymer with 16 mol% Phe buffered the pH range from 7.6 to 4.7 and produced optimal *in vitro* results.[212] In an *in vivo* study, mixed micelles with 80 wt% poly((His-*co*-Phe)-*b*-PEG) (5 kDa His-*co*-Phe and 3 kDa PEG) and 20 wt% poly(folate-PEG-*b*-PLLA) (2 kDa PEG and 3 kDa PLLA) were tested in an MDR ovarian tumor xenograft model. Three IV injections of 10 mg kg^{-1} doxorubicin were given at 3-day intervals, and the mice delivered this dose using the pH-responsive micelles (loaded at 20 wt% doxorubicin) had an average tumor size of 300 mm^3 at day 50. The free doxorubicin controls, on the other hand, were euthanized on day 27 because tumor sizes had reached approximately 3000 mm^3.[213] Finally, other authors have recently developed histidine-containing mixed micelle systems that achieve pH-sensitive drug release and proton-sponge activities.[214–216] Tsai and coauthors developed one of the most noteworthy, comparable systems using mixed micelles composed of poly(HEMA-*co*-histidine)-*g*-PLA and the diblock copolymer PEG–PLA. In an *in vivo* study, an equivalent dose of 5 mg kg^{-1} doxorubicin was given three times at 5 day intervals using these micelles with folate targeting. This treatment inhibited tumor volume by up to 80% relative to untreated controls at day 25 while free doxorubicin inhibited tumor growth by only 40%.[216]

4.422.7. Fusogenic Peptides

Naturally occurring peptide sequences derived from bacterial toxins and viruses and synthetic analogues of these peptides have also been rigorously exploited as pH-responsive, endosomal-disruptive agents. Design cues from natural systems are logical to follow because, although intracellular biomolecular drug delivery has proven to be an immense challenge for pharmaceutical scientists, microorganisms have evolved over millennia to possess efficient mechanisms for transport of peptide toxins and genetic material into eukaryotic cells. One example is the diphtheria toxin produced by *Corynebacterium diphtheria*, which possesses a pH-responsive fragment that forms transmembrane pores in endosomes that enable entry of a disulfide-linked toxin fragment into the cytosol.[217–225] Other examples include the melittin peptide derived from bee venom[226] and the influenza viral protein hemagglutinin, which can mediate pH-dependent fusion of the virus with the endosomal membrane to enable delivery of the viral genetic material into the cytoplasm.[227–233] A multitude of other fusogenic proteins have also been tested, including synthetic hemagglutinin derivatives, model amphipathic peptides (MAPs), β-amyloid transmembrane protein derivatives, and a family of fusion-associated small transmembrane (FAST) proteins (i.e., the p10 avian reovirus, the p14 reptilian reovirus, and the p15 baboon reovirus).[48,234–238]

Another class of peptides called cell-penetrating peptides (CPPs) has some overlap with the pH-responsive, fusogenic category. The initial discovery that the trans-activating transcriptional factor (TAT) of HIV-1 can penetrate cell membranes[239,240] was followed shortly thereafter by the description of the *Drosophilia*-derived antennapedia (also known as penetratin)[241] that triggered the development of a new research field focused on development of CPPs for intracellular drug delivery. The fact that CPPs can cross biological membranes at physiologic pH has motivated exploration of their ability to transport cargo such as pDNA, siRNA, antisense oligonucleotides, proteins, antibodies, peptides, small molecule drugs, nanoparticles, and contrast agents into cells (see recent CPP reviews[242,243]). CPPs are composed of a diversity of peptide sequences, some of which are highly cationic while others are amphipathic structures, and their precise mechanism of internalization is controversial. Strong evidence suggests that there are, in fact, multiple modes of uptake including membrane fusion and translocation directly into the cytosol in addition to vesicular pathways such as endocytosis or macropinocytosis, which can lead to entrapment in endosomes.[243,244] In this vein, it has been demonstrated that low levels of cytosolic activity of drug cargo are achievable using CPPs alone. However, bioactivity suffers from vesicular sequestration, which is supported by evidence that endosome-releasing polymers and peptides can increase cytosolic delivery of CPP conjugates and fusion proteins.[61,245–249] Alternatively, Lundberg and coauthors have shown that it is possible to directly increase the endosomal escape potential of the CPP itself in order to circumvent the need for additional drug components. Using this promising strategy, they made a synthetic analogue of penetratin called EB1 that was strategically substituted with His amino acids to achieve pH-responsive endosomolysis. This synthetic variant was found to significantly improve the therapeutic efficacy of siRNA compared to other CPPs tested.[250]

4.422.7.1. GALA

Because the peptide GALA is one of the most extensively characterized synthetically engineered fusogenic peptides,[251] a more in-depth discussion will be dedicated to this model peptide. The thorough mechanistic understanding of the pH-responsive membrane activity of GALA can be used as a model to lend insight into the biophysical properties of other less well-characterized fusogenic peptides. GALA is a 30-amino acid (AA) sequence (WEAALAEALAEALAEHLAEALAEALEALAA) possessing repeats of glutamic acid-alanine-leucine-alanine (Glu-Ala-Leu-Ala or EALA). The Glu-Ala-Leu-Ala repeating structure was innovatively engineered by Szoka *et al.* to possess a combination of charged/acidic (Glu), spacer (Ala), and hydrophobic (Leu) AAs that impart pH-dependent structure–function properties that mimic fusogenic viral proteins to form pores in

membranes under acidic conditions.[252–254] Near neutral pH, Glu residues exist predominantly in an ionized state, making GALA hydrophilic and creating intramolecular charge repulsion that causes the peptide to adopt an extended state. When exposed to the slightly acidic endosomal environment, Glu residues ($pK_a \sim 6$) are protonated, which transforms GALA into a more hydrophobic state with decreased anionic charge density and triggers the peptide to adopt an amphipathic α-helical structure[254] (**Figure 9**). Within this helix, the Glu residues form a hydrophilic α-helical face, and the Leu residues localize to the opposing, nonpolar face.[252] This amphipathic helix is able to interact with lipid bilayers in an orientation parallel to the membrane, and it subsequently self-aggregates and reorients into a pore perpendicular to the membrane surface once a critical number of approximately 10 peptide chains have oligomerized.[255–257] These pores, which generate pH-dependent lipid vesicle leakage, are lined on the interior with hydrophilic Glu residues while the more hydrophobic amino acids associate with the alkyl chains that constitute the interior of the lipid bilayer.[252,253,255] One potential limitation of GALA is that cholesterol content and some phospholid compositions can reduce pore formation.[258,259] However, more recently, new derivatives of GALA have been created that are activated earlier in the endosomal pathway at a higher pH (i.e., pH 6–7 versus pH < 6 for GALA), and these variants have also improved performance in cholesterol-containing membranes.[260]

GALA has been predominantly applied as a constituent of nonviral vectors for nucleic acid delivery, and Haensler and Szoka were the first to apply GALA for pDNA delivery.[147] GALA was conjugated to cationic PAMAM dendrimers (10–13 GALA per dendrimer used in a 1:1 ratio with unmodified dendrimer) to enhance endosomal escape of plasmids electrostatically complexed with PAMAM. Using a luciferase plasmid as a reporter system, the authors found that inclusion of GALA on the dendrimers improved transfection for all seven cell types tested. For some cells (i.e., fibroblast (CV-1), leukemia (K562), and hepatocyte (HepG2) cell lines), luciferase activity increased by four orders of magnitude in GALA-containing dendrimers relative to unmodified PAMAM. Subsequently, Simoes and coauthors used cationic liposomes to electrostatically complex GALA (anionic due to Glu residues) into ternary (lipid/GALA/DNA) and quaternary (lipid/GALA/DNA/transferrin) systems.[261–263] They initially developed a ternary system formed by cationic lipids complexed with GALA followed by plasmid condensation to form a net negatively charged carrier, and it was found that this approach produced a fourfold increase in luciferase production relative to controls.[261] A follow-up, mechanistic study found that GALA enhancement of transfection was inhibited by bafilomycin, a drug that inhibits endosomal acidification, verifying the key contribution of pH-dependent GALA activity.[262] Subsequently, a quaternary system that also included the targeting ligand transferrin was developed and shown to successfully transfect human macrophages, a particularly difficult target for nonviral gene therapy due to their potent lysosomal degradative activity.[263] The quaternary complex performed better than two control ternary systems (lipid/DNA/transferrin and lipid/GALA/DNA) and better than an alternative quaternary complex containing the influenza-derived fusogenic peptide, HA-2, as an alternate to GALA. However, a primary shortcoming of using multiple, electrostatically complexed components was exemplified by the significant falloff in activity observed in the presence of serum.

The Harishima laboratory has produced the most recent advances in the use of GALA in liposomal drug delivery.[264–269] An early application involved mixing GALA with commercially available cationic liposomes. This resulted in as much as a fivefold increase in transfection efficiency in some conditions tested, further illustrating the efficacy of GALA for enhancing cytoplasmic delivery.[265] In other studies, GALA was derivatized with cholesterol (chol-GALA) in order to anchor GALA to the surface of the liposome. Chol-GALA efficiently mediated diffusion of the model molecule rhodamine from the liposomal carrier into the cytosol of treated cells (while GALA encapsulated within the liposomal aqueous interior did not).[264] In subsequent iterations of this carrier, transferrin was covalently linked to the liposome surface to target the liposomes for cell uptake. This targeted system effectively delivered nucleic acids (plasmid and siRNA) and the antitumor peptide, mastoparan.[267–269] Enhanced *in vivo* circulation time and production of smaller, more homogeneous particles were also achievable through carrier surface PEGylation. Not surprisingly, it was found that attachment of PEG chains to the liposomal surface inhibited activity of GALA anchored in

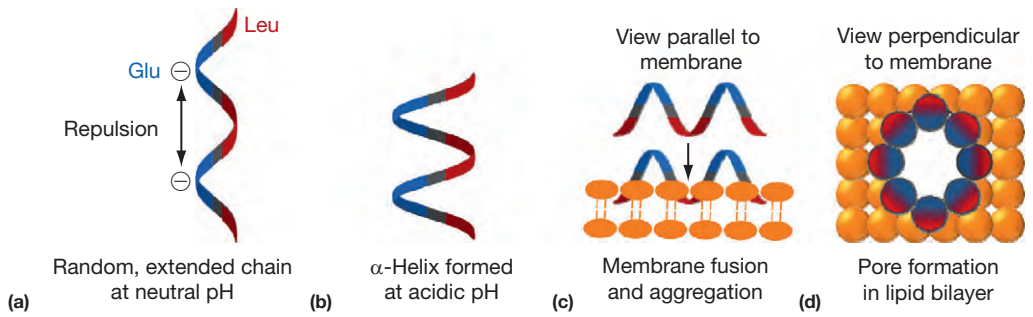

Figure 9 Schematic illustration of GALA pH-dependent activation. (a) The Glu residues in GALA extend the peptide backbone at neutral pH but are protonated at acidic pH, triggering the peptide to adopt an alpha helix structure (b). The GALA alpha helix is amphipathic in nature and (c) initially interacts and aggregates parallel to the lipid bilayer. (d) When a critical number of peptides aggregate (estimated to be 10), they self-assemble into a transmembrane channel with polar Glu residues lining an aqueous pore that allows biomacromolecule diffusion across the bilayer.

the membrane.[267] However, activity could be restored when GALA functionalization was present both on the lipid membrane and on the free PEG chain ends[267] or by using reversible PEG attachments removed in matrix metalloproteinase-rich environments.[268]

GALA peptides have also been utilized for delivery of therapeutic proteins. One of the first applications was by Anderson and coworkers who covalently conjugated GALA to the Fab fragments of an antitumor antibody with the goal of enhancing cell–surface interactions, tumor retention time, and therapeutic functionality.[270] Although their application did not exploit the pH-responsive properties of GALA for cytoplasmic delivery, it did prolong cell-surface antibody retention of the protein in human melanoma cells (although this effect was not as apparent in a similar colon carcinoma application). More recently, Kuehne and Murphy conjugated GALA to OKT9, an antibody against the transferrin receptor, with the ultimate goal of targeted, intracellular delivery of cancer-killing immunotoxins.[271] Optimal performance was achieved with 2–3 GALA peptides per therapeutic antibody, although a sevenfold greater concentration of GALA in the OKT9 conjugate form was required to cause 50% leakage compared to free GALA. Inclusion of a flexible PEG spacer between GALA and OKT9 did not rescue pH-dependent activity, although the potential negative effect of the hydrophilic linker on membrane interactions was not addressed. In a recent study, Kobayashi *et al.* tested the ability of biotinylated GALA to achieve cytoplasmic delivery of avidin (serving here as a model protein) and quantum dots (QDs) surface functionalized with streptavidin.[272] Cellular uptake for these systems was enhanced by electrostatic formulation with a commercially available cationic liposome transfection agent. Four GALA peptides per avidin improved cytosolic delivery of the model protein, and GALA functionalization of the QDs decreased their colocalization with lysosomes. However, QD staining remained punctate, and it was not apparent whether decreased presence in lysosomes was due to altered intracellular trafficking or the inability of QDs to escape through small GALA-formed pores in the endolysosomal membranes. Thus, additional work will be needed to further elucidate and develop GALA-induced cytosolic delivery of QD imaging probes.

The most recent developments incorporating GALA functionality have involved its incorporation into genetically engineered proteins. Wang and coauthors recently engineered a biomimetic protein consisting of GALA, a DNA-condensing set of histone H2A repeats, a cathepsin cleavable motif (that separates the targeting ligand and its potential steric hindrances once the full construct reaches the cathepsin-containing endosomes), and a HER2 receptor cancer cell surface targeting motif.[273] This novel application showed the importance of GALA activity in achieving gene transfer using this approach and serves as a starting point for development of future biosynthetic vectors with perfectly defined, monodispersed compositions and architectures that may prove to be advantageous to the chemosynthetic approaches utilized previously. Another recent, novel approach employed GALA as a component in an engineered protein designed to produce pH-sensitive 'nanocages' that, after further development, may serve as a new type of acid-induced molecular switch.[274]

4.422.8. Future Perspectives

Significant promise exists for expanding the number of pharmaceutically druggable targets using peptide-, protein-, and nucleic acid-based macromolecular therapeutics to overcome classic delivery challenges presented by small molecule drugs. However, application of these high molecular weight and polar molecules is precluded by substantial delivery hurdles. As we have reviewed in this chapter, primary delivery goals include providing mechanisms for cellular uptake and endosomal escape. Although pharmaceutical scientists have developed innovative pH-responsive polymers that can overcome these hurdles, numerous other design criteria must be optimized before these technologies can be translated into the clinic. Major limitations to the clinical translation of pH-responsive polymers include low transfection efficiency, toxicity, lack of stability and desirable pharmacokinetics *in vivo*, and difficulty with scaling up the complex synthesis and purification procedures required for incorporating drug, pH-responsive polymer, and targeting agents.

Because delivery efficiency of polymer systems still remains very low compared to that of viruses, endosomolytic carriers must be developed that are exquisitely potent in achieving biomolecule cytoplasmic delivery. For example, if one assumes that a single drug carrier is internalized into a spherical endosome of 200 nm diameter,[275] the pH-responsive agent would need to be activated by a modest environmental change of approximately 2 pH units to produce endosomal disruption at a concentration of less than 400 nM. This 'thought exercise' only accentuates one of the primary challenges in these applications; pH-responsive carriers must be sufficiently potent to robustly and reliably produce activity under these conditions while avoiding carrier-induced toxicity, immunogenicity, serum instability, and steric hindrance of biomolecule activity.

Multiple carriers have approached virus-like potency, but there is often a correlation between their activity and toxicity. PEI is a good example that has encountered great difficulties in balancing the trade-off between toxicity and transfection efficiency. Recently, a zwitterionic, biodegradable delivery system has been developed that exhibits similar activity to PEI, but this carrier hydrolytically degrades into completely nontoxic byproducts.[276] This approach and others are generating new promise that potent, nontoxic synthetic delivery systems are achievable for delivery of nucleic acids.

The complex but necessary chemistry involved in assembling endosomal-disruptive agents with the targeting agent and drug involves either assembling a micelle or nanoparticle that contains all components or performing sequential conjugation reactions between three independent macromolecules. Both approaches are technically challenging and can have difficulty in characterizing and purifying, making the production of well-defined, monodispersed formulations one of the major challenges in pharmaceutical development. Fortunately, controlled radical polymerization techniques such as a RAFT[43] and atom transfer radical polymerization (ATRP)[277,278] have enhanced the ability of polymer chemists to achieve precise molecular weight control, monodispersity, well-defined (i.e., block and other) architectures, and incorporation of site-specific, chemoselective conjugation chemistries. Furthermore,

there are a number of new, selective, orthogonal chemistries, that is, site-specific 'click' chemistries[279–282] that enable rapid and precise conjugation of constituent parts of the polymer therapeutic with high efficiency. These tightly controlled and highly efficient approaches can improve quality of the final product and decrease the number of synthetic steps required, making mass production more feasible.

Finally, although pH-responsive carriers address intracellular delivery of therapeutics *in vitro*, they often do not account for the multitude of new challenges that are present *in vivo*. Delivery systems must be equipped to perform in the harsh *in vivo* environment, which is more chemically complex and biologically diverse than *in vitro* cultures. For systemic intravenous delivery, drugs must be equipped to effectively modulate their interactions with thousands of different blood proteins. For example, binding of serum proteins 'marks' drug carriers for removal from the body through the macrophages of the reticuloendothelial system (i.e., liver).[283,284] PEG functionalization is the primary method used to reduce protein adsorption and subsequent carrier clearance. In a promising new approach, Huang *et al.* recently found that optimally sized (~100 nm), stable liposomes could be generated using PEG functionalization and that high density but 'sheddable' surface PEGylation may be key to improving tumor accumulation. In these studies, a previously unprecedented 70–80% injected dose per gram of tissue biodistributed to xenograft tumors, and effective silencing of tumor genes was achieved at impressively low (i.e., $<1\ mg\ kg^{-1}$) siRNA doses.[285–287] Although the generalized applicability is clearly limited, another approach has been to design systems that promote interactions with serum proteins (i.e., apolipoprotein E) in order to use them as endogenous targeting ligands to improve targeting and uptake in the liver.[288] In addition to opsonization in the blood, electrostatically complexed drugs (e.g., nucleic acids) can also be quickly replaced with other anionic molecules (heparin, glycosaminoglycans, etc.) in the extracellular environment. These competing interactions can destroy the integrity of the formulation and produce 'naked' drug delivery that leads to very little therapeutic efficacy, thus making the microenvironment within the targeted tissue another important consideration.[289]

The complexity of diverse *in vivo* delivery barriers further underscores the importance of controlled-polymerization strategies to provide novel synthesis of well-defined chemoselective conjugation chemistries that might better address challenges. Because these chemistry techniques enable synthesis of highly reproducible and controlled (e.g., monodispersed) polymer therapeutics, they are expected to lead to more reliable and predictable structure–function relationships that may enhance the probability of improved performance both *in vitro* and *in vivo*. As synthetic advancements continue to emerge in this area, it will also be vital that great emphasis is placed on assembling interdisciplinary teams (e.g., pathologists, medicinal chemists, polymer chemists, oncologists, clinicians, etc.) well equipped to identify and solve the diversity of drug delivery challenges. With this more comprehensive approach, a complete set of design criteria can be carefully identified and incorporated into carriers during the initial development stages. This will lead to biomacromolecular drugs better optimized for specific medical applications and will aid in the continued evolution of pH-responsive polymer therapeutics toward clinical reality.

References

1. Marshall, E. *Science* **1999**, *286*(5448), 2244–2245.
2. Hacein-Bey-Abina, S.; von Kalle, C.; Schmidt, M.; *et al*. *N. Engl. J. Med*. **2003**, *348*(3), 255–256.
3. Thomas, C. E.; Ehrhardt, A.; Kay, M. A. *Nat. Rev. Genet*. **2003**, *4*(5), 346–358.
4. Whitehead, K. A.; Langer, R.; Anderson, D. G. *Nat. Rev. Drug Discov*. **2009**, *8*(2), 129–138.
5. Castanotto, D.; Rossi, J. J. *Nature* **2009**, *457*(7228), 426–433.
6. Flanary, S.; Hoffman, A. S.; Stayton, P. S. *Bioconjug. Chem*. **2009**, *20*(2), 241–248.
7. Foster, S.; Duvall, C. L.; Crownover, E. F.; Hoffman, A. S.; Stayton, P. S. *Bioconjug. Chem*. **2010**.
8. Altin, J. G.; Parish, C. R. *Methods* **2006**, *40*, 39–52.
9. Chikh, G.; Schutze-Redelmeier, M.-P. *Biosci. Rep*. **2002**, *22*(2), 339–353.
10. Haining, W. N.; Anderson, D. G.; Little, S. R.; *et al*. *J. Immunol*. **2004**, *173*, 2578–2585.
11. Tacken, P. J.; Torensma, R.; Figdor, C. G. *Immunobiology* **2006**, *211*, 599–608.
12. Maloy, K. J.; Donachie, A. M.; O'Hagan, D. T.; Mowat, A. M. *Immunology* **1994**, *81*, 661–667.
13. Shen, H.; Ackerman, A. L.; Cody, V.; *et al*. *Immunology* **2006**, *117*, 78–88.
14. Panyam, J. *FASEB J*. **2002**, *16*, 1217–1226.
15. Newman, K. D.; Kwon, G. S.; Miller, G. G.; Chlumecky, V.; Samuel, J. *J. Biomed. Mater. Res*. **2000**, *50*, 591–597.
16. Lutsiak, M. E. C.; Robinson, D. R.; Coester, C.; Kwon, G. S.; Samuel, J. *Pharm. Res*. **2002**, *19*(10), 1480–1487.
17. Partidos, C. D.; Vohra, P.; Jones, D.; Farrar, G.; Steward, M. W. *J. Immunol. Methods* **1997**, *206*, 143–151.
18. Bennewitz, N. L.; Babensee, J. E. *Biomaterials* **2005**, *26*, 2991–2999.
19. Mundargi, R. C.; Babu, V. R.; Rangaswamy, V.; Patel, P.; Aminabhavi, T. M. *J. Control. Release* **2008**, *125*, 193–209.
20. Newman, K. D.; Elamanchili, P.; Kwon, G. S.; Samuel, J. *J. Biomed. Mater. Res*. **2002**, *60*, 480–486.
21. Harding, C. V.; Song, R. *J. Immunol*. **1994**, *153*, 4925–4933.
22. Kovacsovics-Bankowski, M.; Clark, K.; Benacerraf, B.; Rock, K. L. *Proc. Natl. Acad. Sci. USA* **1993**, *90*, 4942–4946.
23. Thiele, L.; Merkle, H. P.; Walter, E. *Pharm. Res*. **2003**, *20*(2), 221–228.
24. Yoshikawa, T.; Okada, N.; Oda, A.; *et al*. *Biochem. Biophys. Res. Commun*. **2008**, *366*, 408–413.
25. Yoshikawa, T.; Okada, N.; Oda, A.; *et al*. *Vaccine* **2008**, *26*, 1303–1313.
26. Murthy, N.; Xu, M.; Schuck, S.; Kunisawa, J.; Shastri, N.; Frechet, J. M. J. *Proc. Natl. Acad. Sci. USA* **2003**, *100*(9), 4995–5000.
27. Kwon, Y. J.; Standley, S. M.; Goh, S. L.; Frechet, J. M. J. *J. Control. Release* **2005**, *105*, 199–212.
28. Standley, S. M.; Kwon, Y. J.; Murthy, N.; *et al*. *Bioconjug. Chem*. **2004**, *15*, 1281–1288.
29. Bachelder, E. M.; Beaudette, T. T.; Broaders, K. E.; Paramonov, S. E.; Dashe, J.; Frechet, J. M. *Mol. Pharm*. **2008**, *5*(5), 876–884.
30. Buse, J.; El-Aneed, A. *Nanomedicine (Lond)*. **2010**, *5*(8), 1237–1260.
31. Jabr-Milane, L.; van Vlerken, L.; Devalapally, H.; *et al*. *J. Control. Release* **2008**, *130*(2), 121–128.
32. MacEwan, S. R.; Callahan, D. J.; Chilkoti, A. *Nanomedicine (Lond)*. **2010**, *5*(5), 793–806.
33. Sebiakin Iu, L.; Budanova, U. A. *Bioorg. Khim*. **2006**, *32*(5), 453–458.
34. Jones, R. A.; Cheung, C. Y.; Black, F. E.; *et al*. *Biochem. J*. **2003**, *372*(Pt 1), 65–75.
35. Thomas, J.; Tirrell, D. A. *Acc. Chem. Res*. **1992**, *25*, 336–342.
36. Thomas, J. L.; Barton, S. W.; Tirrell, D. A. *Biophys. J*. **1994**, *67*(3), 1101–1106.
37. Murthy, N.; Robichaud, J. R.; Tirrell, D. A.; Stayton, P. S.; Hoffman, A. S. *J. Control. Release* **1999**, *61*(1–2), 137–143.
38. Murthy, N.; Chang, I.; Stayton, P. S.; Hoffman, A. S. *Macromol. Symp*. **2001**, *172*, 49–55.
39. El-Sayed, M. E.; Hoffman, A. S.; Stayton, P. S. *J. Control. Release* **2005**, *104*(2), 417–427.
40. Convertine, A. J.; Benoit, D. S.; Duvall, C. L.; Hoffman, A. S.; Stayton, P. S. *J. Control. Release* **2009**, *133*(3), 221–229.
41. Henry, S. M.; El-Sayed, M. E.; Pirie, C. M.; Hoffman, A. S.; Stayton, P. S. *Biomacromolecules* **2006**, *7*(8), 2407–2414.
42. Benoit, D. S.; Henry, S. M.; Shubin, A. D.; Hoffman, A. S.; Stayton, P. S. *Mol. Pharm*. **2010**, *7*(2), 442–455.

43. Chiefari, J.; Chong, Y. K.; Ercole, F.; *et al*. *Macromolecules* **1998**, *31*(16), 5559–5562.
44. Nicolazzi, C.; Mignet, N.; de la Figuera, N.; *et al*. *J. Control. Release* **2003**, *88*(3), 429–443.
45. Borden, K. A.; Eum, K. M.; Langley, K. H.; Tirrell, D. A. *Macromolecules* **1987**, *20*(2), 454–456.
46. Eum, K. M.; Langley, K. H.; Tirrell, D. A. *Macromolecules* **1989**, *22*(6), 2755–2760.
47. Chen, T. S.; Thomas, J. K. *Influence of the Conformational State of Polymethacrylic Acid on the Photophysical Properties of Pyrene in Aqueous Solution: A Fluorescent Probe and Laser Photolysis Study*. Wiley: New York, 1979.
48. Plank, C.; Oberhauser, B.; Mechtler, K.; Koch, C.; Wagner, E. *J. Biol. Chem.* **1994**, *269*(17), 12918–12924.
49. Cheung, C. Y.; Murthy, N.; Stayton, P. S.; Hoffman, A. S. *Bioconjug. Chem.* **2001**, *12*(6), 906–910.
50. Murthy, N.; Chang, I.; Stayton, P.; Hoffman, A. *Macromol. Symp.* **2001**, *172*, 49–55.
51. Murthy, N.; Stayton, P.; Hoffman, A. *Abstr. Pap. Am. Chem. Soc.* **2000**, *219*, U448–U.
52. Murthy, N.; Robichaud, J. R.; Tirrell, D. A.; Stayton, P. S.; Hoffman, A. S. *J. Control. Release* **1999**, *61*(1–2), 137–143.
53. Murthy, N.; Campbell, J.; Fausto, N.; Hoffman, A. S.; Stayton, P. S. *J. Control. Release* **2003**, *89*(3), 365–374.
54. Tosteson, M. T.; Holmes, S. J.; Razin, M.; Tosteson, D. C. *J. Membr. Biol.* **1985**, *87*(1), 35–44.
55. Lackey, C. A.; Murthy, N.; Press, O. W.; Tirrell, D. A.; Hoffman, A. S.; Stayton, P. S. *Bioconjug. Chem.* **1999**, *10*(3), 401–405.
56. Flanary, S.; Hoffman, A. S.; Stayton, P. S. *Bioconjug. Chem.* **2009**, *20*(2), 241–248.
57. Kyriakides, T. R.; Cheung, C. Y.; Murthy, N.; Bornstein, P.; Stayton, P. S.; Hoffman, A. S. *J. Control. Release* **2002**, *78*(1–3), 295–303.
58. Kiang, T.; Bright, C.; Cheung, C. Y.; Stayton, P. S.; Hoffman, A. S.; Leong, K. W. *J. Biomater. Sci. Polym. Ed.* **2004**, *15*(11), 1405–1421.
59. Convertine, A. J.; Benoit, D. S.; Duvall, C. L.; Hoffman, A. S.; Stayton, P. S. *J. Control. Release* **2009**, *133*(3), 221–229.
60. Convertine, A. J.; Diab, C.; Prieve, M.; *et al*. *Biomacromolecules* **2010**, *11*(11), 2904–2911.
61. Duvall, C. L.; Convertine, A. J.; Benoit, D. S. W.; Hoffman, A. S.; Stayton, P. S. *Mol. Pharm.* **2010**, *7*(2), 468–476.
62. Ha, N. T. H.; Fujimori, K. *Acta Polym.* **1998**, *49*(8), 404–410.
63. Mu, Y.; Kamada, H.; Kaneda, Y.; *et al*. *Biochem. Biophys. Res. Commun.* **1999**, *255*(1), 75–79.
64. Maeda, H. *Adv. Drug Deliv. Rev.* **2001**, *46*(1–3), 169–185.
65. Maeda, H.; Sawa, T.; Konno, T. *J. Control. Release* **2001**, *74*(1–3), 47–61.
66. Maeda, H.; Ueda, M.; Morinaga, T.; Matsumoto, T. *J. Med. Chem.* **1985**, *28*(4), 455–461.
67. Oda, T.; Sato, F.; Maeda, H. *J. Natl. Cancer Inst.* **1987**, *79*(6), 1205–1211.
68. Henry, S. M.; El-Sayed, M. E. H.; Pirie, C. M.; Hoffman, A. S.; Stayton, P. S. *Biomacromolecules* **2006**, *7*(8), 2407–2414.
69. Benoit, D. S. W.; Henry, S. M.; Shubin, A. D.; Hoffman, A. S.; Stayton, P. S. *Mol. Pharm.* **2010**, *7*(2), 442–455.
70. Gillies, E. R.; Goodwin, A. P.; Frechet, J. M. *Bioconjug. Chem.* **2004**, *15*(6), 1254–1263.
71. Murthy, N.; Campbell, J.; Fausto, N.; Hoffman, A. S.; Stayton, P. S. *Bioconjug. Chem.* **2003**, *14*(2), 412–419.
72. Murthy, N.; Campbell, J.; Fausto, N.; Hoffman, A. S.; Stayton, P. S. *J. Control. Release* **2003**, *89*(3), 365–374.
73. Knorr, V.; Allmendinger, L.; Walker, G. F.; Paintner, F. F.; Wagner, E. *Bioconjug. Chem.* **2007**, *18*(4), 1218–1225.
74. Gerasimov, O. V.; Schwan, A.; Thompson, D. H. *Biochim. Biophys. Acta* **1997**, *1324*(2), 200–214.
75. Rui, Y.; Wang, S.; Low, P. S.; Thompson, D. H. *J. Am. Chem. Soc.* **1998**, *120* (44), 11213–11218.
76. Boomer, J. A.; Thompson, D. H. *Chem. Phys. Lipids* **1999**, *99*(2), 145–153.
77. Guo, X.; Szoka, F. C. *Bioconjug. Chem.* **2001**, *12*(2), 291–300.
78. Behr, J. P. *Med. Sci.* **1996**, *12*(1), 56–58.
79. Behr, J. P. *Chimia* **1997**, *51*(1–2), 34–36.
80. Boussif, O.; Lezoualc'h, F.; Zanta, M. A.; *et al*. *Proc. Natl. Acad. Sci. USA* **1995**, *92*(16), 7297–7301.
81. Lynn, D. M.; Langer, R. *J. Am. Chem. Soc.* **2000**, *122*(44), 10761–10768.
82. Pack, D. W.; Putnam, D.; Langer, R. *Biotechnol. Bioeng.* **2000**, *67*(2), 217–223.
83. Yamagata, M.; Kawano, T.; Shiba, K.; Mori, T.; Katayama, Y.; Niidome, T. *Bioorg. Med. Chem.* **2007**, *15*(1), 526–532.
84. Lungwitz, U.; Breunig, M.; Blunk, T.; Gopferich, A. *Eur. J. Pharm. Biopharm.* **2005**, *60*(2), 247–266.
85. Min, S. H.; Lee, D. C.; Lim, M. J.; *et al*. *J. Gene Med.* **2006**, *8*(12), 1425–1434.
86. Pietersz, G. A.; Tang, C. K.; Apostolopoulos, V. *Mini Rev. Med. Chem.* **2006**, *6*(12), 1285–1298.
87. Kitazoe, M.; Futami, J.; Nishikawa, M.; Yamada, H.; Maeda, Y. *Biotechnol. J.* **2010**, *5*(4), 385–392.
88. Kitazoe, M.; Murata, H.; Futami, J.; *et al*. *J. Biochem.* **2005**, *137*(6), 693–701.
89. Murata, H.; Futami, J.; Kitazoe, M.; *et al*. *J. Biosci. Bioeng.* **2008**, *105*(1), 34–38.
90. Murata, H.; Futami, J.; Kitazoe, M.; *et al*. *J. Biochem.* **2008**, *144*(4), 447–455.
91. Poon, G. M.; Gariepy, J. *Biochem. Soc. Trans.* **2007**, *35*(Pt 4), 788–793.
92. Wagner, E.; Ogris, M.; Zauner, W. *Adv. Drug Deliv. Rev.* **1998**, *30*(1–3), 97–113.
93. Cotten, M.; Wagner, E.; Birnstiel, M. L. *Methods Enzymol.* **1993**, *217*, 618–644.
94. Cotten, M.; Wagner, E.; Zatloukal, K.; Phillips, S.; Curiel, D. T.; Birnstiel, M. L. *Proc. Natl. Acad. Sci. USA* **1992**, *89*(13), 6094–6098.
95. Ferkol, T.; Perales, J. C.; Mularo, F.; Hanson, R. W. *Proc. Natl. Acad. Sci. USA* **1996**, *93*(1), 101–105.
96. Harbottle, R. P.; Cooper, R. G.; Hart, S. L.; *et al*. *Hum. Gene Ther.* **1998**, *9*(7), 1037–1047.
97. Hashida, M.; Takemura, S.; Nishikawa, M.; Takakura, Y. *J. Control. Release* **1998**, *53*(1–3), 301–310.
98. Leamon, C. P.; Weigl, D.; Hendren, R. W. *Bioconjug. Chem.* **1999**, *10*(6), 947–957.
99. Perales, J. C.; Ferkol, T.; Beegen, H.; Ratnoff, O. D.; Hanson, R. W. *Proc. Natl. Acad. Sci. USA* **1994**, *91*(9), 4086–4090.
100. Suh, W.; Chung, J. K.; Park, S. H.; Kim, S. W. *J. Control. Release* **2001**, *72*(1–3), 171–178.
101. Wadhwa, M. S.; Knoell, D. L.; Young, A. P.; Rice, K. G. *Bioconjug. Chem.* **1995**, *6*(3), 283–291.
102. Wu, C. H.; Wilson, J. M.; Wu, G. Y. *J. Biol. Chem.* **1989**, *264*(29), 16985–16987.
103. Wu, G. Y.; Wu, C. H. *J. Biol. Chem.* **1987**, *262*(10), 4429–4432.
104. Wu, G. Y.; Wu, C. H. *J. Biol. Chem.* **1988**, *263*(29), 14621–14624.
105. Zatloukal, K.; Wagner, E.; Cotten, M.; *et al*. *Ann. N. Y. Acad. Sci.* **1992**, *660*, 136–153.
106. Boussif, O.; Zanta, M. A.; Behr, J. P. *Gene Ther.* **1996**, *3*(12), 1074–1080.
107. Kichler, A.; Leborgne, C.; Coeytaux, E.; Danos, O. *J. Gene Med.* **2001**, *3*(2), 135–144.
108. Morille, M.; Passirani, C.; Vonarbourg, A.; Clavreul, A.; Benoit, J. P. *Biomaterials* **2008**, *29*(24–25), 3477–3496.
109. Park, T. G.; Jeong, J. H.; Kim, S. W. *Adv. Drug Deliv. Rev.* **2006**, *58*(4), 467–486.
110. Bandyopadhyay, P.; Ma, X.; Linehan-Stieers, C.; Kren, B. T.; Steer, C. J. *J. Biol. Chem.* **1999**, *274*(15), 10163–10172.
111. Breunig, M.; Lungwitz, U.; Liebl, R.; *et al*. *Biochem. Biophys. Acta* **2007**, *1770*(2), 196–205.
112. Oh, Y. K.; Suh, D.; Kim, J. M.; Choi, H. G.; Shin, K.; Ko, J. J. *Gene Ther.* **2002**, *9*(23), 1627–1632.
113. Durocher, Y.; Perret, S.; Kamen, A. *Nucleic Acids Res.* **2002**, *30*(2), E9.
114. Geisse, S.; Fux, C. In *Guide to Protein Purification*, 2nd edn.; Methods in Enzymology; Elsevier: Amsterdam, 2009; Vol. 466, pp 223–238.
115. Iwai, M.; Harada, Y.; Tanaka, S.; *et al*. *Biochem. Biophys. Res. Commun.* **2002**, *291*(1), 48–54.
116. Kim, J.; Chen, C. P.; Rice, K. G. *Gene Ther.* **2005**, *12*(21), 1581–1590.
117. Pham, P. L.; Kamen, A.; Durocher, Y. *Mol. Biotechnol.* **2006**, *34*(2), 225–237.
118. Creusat, G.; Rinaldi, A. S.; Weiss, E.; *et al*. *Bioconjug. Chem.* **2010**, *21*(5), 994–1002.
119. Segura, T.; Hubbell, J. A. *Bioconjug. Chem.* **2007**, *18*(3), 736–745.
120. Aigner, A.; Fischer, D.; Merdan, T.; Brus, C.; Kissel, T.; Czubayko, F. *Gene Ther.* **2002**, *9*(24), 1700–1707.
121. Abdallah, B.; Hassan, A.; Benoist, C.; Goula, D.; Behr, J. P.; Demeneix, B. A. *Hum. Gene Ther.* **1996**, *7*(16), 1947–1954.
122. Goula, D.; Benoist, C.; Mantero, S.; Merlo, G.; Levi, G.; Demeneix, B. A. *Gene Ther.* **1998**, *5*(9), 1291–1295.
123. Boletta, A.; Benigni, A.; Lutz, J.; Remuzzi, G.; Soria, M. R.; Monaco, L. *Hum. Gene Ther.* **1997**, *8*(10), 1243–1251.
124. Ferrari, S.; Pettenazzo, A.; Garbati, N.; Zacchello, F.; Behr, J. P.; Scarpa, M. *Biochim. Biophys. Acta* **1999**, *1447*(2–3), 219–225.
125. Coll, J. L.; Chollet, P.; Brambilla, E.; Desplanques, D.; Behr, J. P.; Favrot, M. *Hum. Gene Ther.* **1999**, *10*(10), 1659–1666.
126. Merdan, T.; Callahan, J.; Peterson, H.; *et al*. *Bioconjug. Chem.* **2003**, *14*(5), 989–996.

127. Kwon, E. J.; Bergen, J. M.; Pun, S. H. *Bioconjug. Chem.* **2008**, *19*(4), 920–927.
128. Kwon, E. J.; Liong, S.; Pun, S. H. *Mol. Pharm.* **2010**, *7*(4), 1260–1265.
129. Leamon, C. P.; Low, P. S. *Drug Discov. Today* **2001**, *6*(1), 44–51.
130. Saito, G.; Swanson, J. A.; Lee, K. D. *Adv. Drug Deliv. Rev.* **2003**, *55*(2), 199–215.
131. Bonnet, M. E.; Erbacher, P.; Bolcato-Bellemin, A. L. *Pharm. Res.* **2008**, *25*(12), 2972–2982.
132. Zou, S. M.; Erbacher, P.; Remy, J. S.; Behr, J. P. *J. Gene Med.* **2000**, *2*(2), 128–134.
133. Wightman, L.; Kircheis, R.; Rossler, V.; *et al. J. Gene Med.* **2001**, *3*(4), 362–372.
134. Moghimi, S. M.; Symonds, P.; Murray, J. C.; Hunter, A. C.; Debska, G.; Szewczyk, A. *Mol. Ther.* **2005**, *11*(6), 990–995.
135. Regnstrom, K.; Ragnarsson, E. G.; Koping-Hoggard, M.; Torstensson, E.; Nyblom, H.; Artursson, P. *Gene Ther.* **2003**, *10*(18), 1575–1583.
136. Gharwan, H.; Wightman, L.; Kircheis, R.; Wagner, E.; Zatloukal, K. *Gene Ther.* **2003**, *10*(9), 810–817.
137. Fischer, D.; Bieber, T.; Li, Y.; Elsasser, H. P.; Kissel, T. *Pharm. Res.* **1999**, *16*(8), 1273–1279.
138. Kunath, K.; von Harpe, A.; Fischer, D.; *et al. J. Control. Release* **2003**, *89*(1), 113–125.
139. Turunen, M. P.; Hiltunen, M. O.; Ruponen, M.; *et al. Gene Ther.* **1999**, *6*(1), 6–11.
140. Ahn, C. H.; Chae, S. Y.; Bae, Y. H.; Kim, S. W. *J. Control. Release* **2002**, *80*(1–3), 273–282.
141. Gosselin, M. A.; Guo, W. J.; Lee, R. J. *Bioconjug. Chem.* **2001**, *12*(6), 989–994.
142. Petersen, H.; Merdan, T.; Kunath, K.; Fischer, D.; Kissel, T. *Bioconjug. Chem.* **2002**, *13*(4), 812–821.
143. Tang, G. P.; Guo, H. Y.; Alexis, F.; *et al. J. Gene Med.* **2006**, *8*(6), 736–744.
144. Meyer, M.; Philipp, A.; Oskuee, R.; Schmidt, C.; Wagner, E. *J. Am. Chem. Soc.* **2008**, *130*(11), 3272.
145. Putnam, D.; Gentry, C. A.; Pack, D. W.; Langer, R. *Proc. Natl. Acad. Sci. USA* **2001**, *98*(3), 1200–1205.
146. Tomalia, D. A.; Naylor, A. M.; Goddard, W. A. *Angew. Chem. Int. Ed. Engl.* **1990**, *29*(2), 138–175.
147. Haensler, J.; Szoka, F. C., Jr. *Bioconjug. Chem.* **1993**, *4*(5), 372–379.
148. Harada, Y.; Iwai, M.; Tanaka, S.; *et al. Cancer Gene Ther.* **2000**, *7*(1), 27–36.
149. Maruyama-Tabata, H.; Harada, Y.; Matsumura, T.; *et al. Gene Ther.* **2000**, *7*(1), 53–60.
150. Rudolph, C.; Lausier, J.; Naundorf, S.; Muller, R. H.; Rosenecker, J. *J. Gene Med.* **2000**, *2*(4), 269–278.
151. Tanaka, S.; Iwai, M.; Harada, Y.; *et al. Cancer Gene Ther.* **2000**, *7*(9), 1241–1250.
152. Malik, N.; Wiwattanapatapee, R.; Klopsch, R.; *et al. J. Control. Release* **2000**, *65*(1–2), 133–148.
153. Roberts, J. C.; Bhalgat, M. K.; Zera, R. T. *J Biomed. Mater. Res.* **1996**, *30*(1), 53–65.
154. Wang, W.; Xiong, W.; Wan, J.; Sun, X.; Xu, H.; Yang, X. *Nanotechnology* **2009**, *20*(10), 105103.
155. Tang, M. X.; Redemann, C. T.; Szoka, F. C., Jr. *Bioconjug. Chem.* **1996**, *7*(6), 703–714.
156. Wood, K. C.; Little, S. R.; Langer, R.; Hammond, P. T. *Angew. Chem. Int. Ed. Engl.* **2005**, *44*(41), 6704–6708.
157. Wu, D. C.; Liu, Y.; Jiang, X.; He, C. B.; Goh, S. H.; Leong, K. W. *Biomacromolecules* **2006**, *7*(6), 1879–1883.
158. Vanden-Broucke, R. E.; De Geest, B. G.; Bonne, S.; *et al. J. Gene Med.* **2008**, *10*(7), 783–794.
159. Anderson, D. G.; Akinc, A.; Hossain, N.; Langer, R. *Mol. Ther.* **2005**, *11*(3), 426–434.
160. Anderson, D. G.; Lynn, D. M.; Langer, R. *Angew. Chem. Int. Ed. Engl.* **2003**, *42*(27), 3153–3158.
161. Anderson, D. G.; Peng, W. D.; Akinc, A.; *et al. Proc. Natl. Acad. Sci. USA* **2004**, *101*(45), 16028–16033.
162. Arote, R.; Kim, T. H.; Kim, Y. K.; *et al. Biomaterials* **2007**, *28*(4), 735–744.
163. Arote, R. B.; Hwang, S. K.; Yoo, M. K.; *et al. J. Gene Med.* **2008**, *10*(11), 1223–1235.
164. Arote, R. B.; Jere, D.; Jiang, H. L.; Kim, Y. K.; Choi, Y. J.; Cho, C. S. *Biomed. Mater.* **2009**, *4*(4), 044102.
165. Arote, R. B.; Lee, E. S.; Jiang, H. L.; *et al. Bioconjug. Chem.* **2009**, *20*(12), 2231–2241.
166. Green, J. J.; Langer, R.; Anderson, D. G. *Acc. Chem. Res.* **2008**, *41*(6), 749–759.
167. Green, J. J.; Shi, J.; Chiu, E.; Leshchiner, E. S.; Langer, R.; Anderson, D. G. *Bioconjug. Chem.* **2006**, *17*(5), 1162–1169.
168. Green, J. J.; Zhou, B. Y.; Mitalipova, M. M.; *et al. Nano Lett.* **2008**, *8*(10), 3126–3130.
169. Green, J. J.; Zugates, G. T.; Tedford, N. C.; *et al. Adv. Mater.* **2007**, *19*(19), 2836.
170. Greenland, J. R.; Liu, H. N.; Berry, D.; *et al. Mol. Ther.* **2005**, *12*(1), 164–170.
171. Lin, C.; Zhong, Z. Y.; Lok, M. C.; *et al. Bioconjug. Chem.* **2007**, *18*(1), 138–145.
172. Zhong, Z. Y.; Song, Y.; Engbersen, J. F. J.; Lok, M. C.; Hennink, W. E.; Feijen, J. *J. Control. Release* **2005**, *109*(1–3), 317–329.
173. Anderson, D. G.; Akinc, A.; Hossain, N.; Langer, R. *Mol. Ther.* **2005**, *11*(3), 426–434.
174. Ghanem, A.; Skonberg, D. *J. Appl. Polym. Sci.* **2002**, *84*(2), 405–413.
175. Wentworth, D. S.; Skonberg, D.; Donahue, D. W.; Ghanem, A. *J. Appl. Polym. Sci.* **2004**, *91*(2), 1294–1299.
176. Bugamelli, F.; Raggi, M. A.; Orienti, I.; Zecchi, V. *Arch. Pharm. (Weinheim)* **1998**, *331*(4), 133–138.
177. Chandy, T.; Sharma, C. P. *Biomaterials* **1992**, *13*(13), 949–952.
178. Colinet, I.; Dulong, V.; Mocanu, G.; Picton, L.; Le Cerf, D. *Int. J. Biol. Macromol.* **2010**, *47*(2), 120–125.
179. Inouye, K.; Machida, Y.; Nagai, T. *Drug Des. Deliv.* **1987**, *1*(4), 297–305.
180. de Martimprey, H.; Bertrand, J. R.; Fusco, A.; *et al. Nucleic Acids Res.* **2008**, *36*(1), e2.
181. Gao, S.; Chen, J.; Dong, L.; Ding, Z.; Yang, Y. H.; Zhang, J. *Eur. J. Pharm. Biopharm.* **2005**, *60*(3), 327–334.
182. Katas, H.; Alpar, H. O. *J. Control. Release* **2006**, *115*(2), 216–225.
183. Pille, J. Y.; Li, H.; Blot, E.; *et al. Hum. Gene Ther.* **2006**, *17*(10), 1019–1026.
184. Roy, K.; Mao, H. Q.; Huang, S. K.; Leong, K. W. *Nat. Med.* **1999**, *5*(4), 387–391.
185. Roy, K.; Wang, D.; Hedley, M. L.; Barman, S. P. *Mol. Ther.* **2003**, *7*(3), 401–408.
186. Jiang, H. L.; Kim, T. H.; Kim, Y. K.; Park, I. Y.; Cho, M. H.; Cho, C. S. *Biomed. Mater.* **2008**, *3*(2), 025013.
187. Jiang, H. L.; Kwon, J. T.; Kim, E. M.; *et al. J. Control. Release* **2008**, *131*(2), 150–157.
188. Ghosn, B.; Kasturi, S. P.; Roy, K. *Curr. Top. Med. Chem.* **2008**, *8*(4), 331–340.
189. Ghosn, B.; Singh, A.; Li, M.; *et al. Oligonucleotides* **2010**, *20*(3), 163–172.
190. Wang, C. Y.; Huang, L. *Biochemistry* **1984**, *23*(19), 4409–4416.
191. Pichon, C.; Gonçalves, C.; Midoux, P. *Adv. Drug Deliv. Rev.* **2001**, *53*(1), 75–94.
192. Midoux, P.; Kichler, A.; Boutin, V. R.; Maurizot, J.-C.; Monsigny, M. *Bioconjug. Chem.* **1998**, *9*(2), 260–267.
193. Midoux, P.; Monsigny, M. *Bioconjug. Chem.* **1999**, *10*(3), 406–411.
194. Benns, J. M.; Choi, J.-S.; Mahato, R. I.; Park, J.-S.; Kim, S. W. *Bioconjug. Chem.* **2000**, *11*(5), 637–645.
195. Pack, D. W.; Putnam, D.; Langer, R. *Biotechnol. Bioeng.* **2000**, *67*(2), 217–223.
196. Putnam, D.; Zelikin, A. N.; Izumrudov, V. A.; Langer, R. *Biomaterials* **2003**, *24*(24), 4425–4433.
197. Putnam, D.; Gentry, C. A.; Pack, D. W.; Langer, R. *Proc. Natl. Acad. Sci. USA* **2001**, *98*(3), 1200–1205.
198. Chen, Q.-R.; Zhang, L.; Stass, S. A.; Mixson, A. J. *Nucleic Acids Res.* **2001**, *29*(6), 1334–1340.
199. Chen, Q.-R.; Zhang, L.; Luther, P. W.; Mixson, A. J. *Nucleic Acids Res.* **2002**, *30*(6), 1338–1345.
200. Leng, Q.; Scaria, P.; Zhu, J.; Ambulos, N.; Campbell, P.; Mixson, A. J. *J. Gene Med.* **2005**, *7*(7), 977–986.
201. Stevenson, M.; Ramos-Perez, V.; Singh, S.; *et al. J. Control. Release* **2008**, *130*(1), 46–56.
202. Chang, K.-L.; Higuchi, Y.; Kawakami, S.; Yamashita, F.; Hashida, M. *Bioconjug. Chem.* **2010**, *21*(6), 1087–1095.
203. Moreira, C.; Oliveira, H.; Pires, L. R.; Simões, S.; Barbosa, M. A.; Pêgo, A. P. *Acta Biomater.* **2009**, *5*(8), 2995–3006.
204. Park, J. S.; Han, T. H.; Lee, K. Y.; *et al. J. Control. Release* **2006**, *115*(1), 37–45.
205. Lee, E. S.; Shin, H. J.; Na, K.; Bae, Y. H. *J. Control. Release* **2003**, *90*(3), 363–374.
206. Lee, E. S.; Na, K.; Bae, Y. H. *J. Control. Release* **2003**, *91*(1–2), 103–113.
207. Yin, H.; Lee, E. S.; Kim, D.; Lee, K. H.; Oh, K. T.; Bae, Y. H. *J. Control. Release* **2008**, *126*(2), 130–138.
208. Oh, K. T.; Lee, E. S.; Kim, D.; Bae, Y. H. *Int. J. Pharm.* **2008**, *358*(1–2), 177–183.
209. Lee, E. S.; Na, K.; Bae, Y. H. *J. Control. Release* **2005**, *103*(2), 405–418.
210. Mohajer, G.; Lee, E.; Bae, Y. *Pharm. Res.* **2007**, *24*(9), 1618–1627.
211. Kim, D.; Lee, E.; Park, K.; Kwon, I.; Bae, Y. *Pharm. Res.* **2008**, *25*(9), 2074–2082.
212. Kim, D.; Lee, E. S.; Oh, K. T.; Gao, Z. G.; Bae, Y. H. *Small* **2008**, *4*(11), 2043–2050.
213. Kim, D.; Gao, Z. G.; Lee, E. S.; Bae, Y. H. *Mol. Pharm.* **2009**, *6*(5), 1353–1362.
214. Yang, S. R.; Lee, H. J.; Kim, J.-D. *J. Control. Release* **2006**, *114*(1), 60–68.
215. Chang, G.; Li, C.; Lu, W.; Ding, J. *Macromol. Biosci.* **2010**, *10*(10), 1248–1256.
216. Tsai, H.-C.; Chang, W.-H.; Lo, C.-L.; *et al. Biomaterials* **2010**, *31*(8), 2293–2301.
217. Collier, R. J.; Kandel, J. *J. Biol. Chem.* **1971**, *246*(5), 1496–1503.
218. Sandvig, K.; Olsnes, S. *J. Cell Biol.* **1980**, *87*(3 Pt 1), 828–832.

219. Donovan, J. J.; Simon, M. I.; Draper, R. K.; Montal, M. *Proc. Natl. Acad. Sci. USA* **1981**, *78*(1), 172–176.
220. Kagan, B. L.; Finkelstein, A.; Colombini, M. *Proc. Natl. Acad. Sci. USA* **1981**, *78*(8), 4950–4954.
221. Sandvig, K.; Olsnes, S. *J. Biol. Chem.* **1981**, *256*(17), 9068–9076.
222. Hu, V. W.; Holmes, R. K. *J. Biol. Chem.* **1984**, *259*(19), 12226–12233.
223. Zalman, L. S.; Wisnieski, B. J. *Proc. Natl. Acad. Sci. USA* **1984**, *81*(11), 3341–3345.
224. Blewitt, M. G.; Chung, L. A.; London, E. *Biochemistry* **1985**, *24*(20), 5458–5464.
225. Bennett, M. J.; Choe, S.; Eisenberg, D. *Protein Sci.* **1994**, *3*(9), 1444–1463.
226. Ogris, M.; Carlisle, R. C.; Bettinger, T.; Seymour, L. W. *J. Biol. Chem.* **2001**, *276*(50), 47550–47555.
227. White, J.; Kartenbeck, J.; Helenius, A. *EMBO J.* **1982**, *1*(2), 217–222.
228. Wharton, S. A.; Ruigrok, R. W.; Martin, S. R.; *et al. J. Biol. Chem.* **1988**, *263*(9), 4474–4480.
229. Skehel, J. J.; Bayley, P. M.; Brown, E. B.; *et al. Proc. Natl. Acad. Sci. USA* **1982**, *79*(4), 968–972.
230. Maeda, T.; Kawasaki, K.; Ohnishi, S. *Proc. Natl. Acad. Sci. USA* **1981**, *78*(7), 4133–4137.
231. Gray, C.; Tamm, L. K. *Protein Sci.* **1998**, *7*(11), 2359–2373.
232. Bullough, P. A.; Hughson, F. M.; Skehel, J. J.; Wiley, D. C. *Nature* **1994**, *371*(6492), 37–43.
233. Durrer, P.; Galli, C.; Hoenke, S.; *et al. J. Biol. Chem.* **1996**, *271*(23), 13417–13421.
234. Turk, M. J.; Reddy, J. A.; Chmielewski, J. A.; Low, P. S. *Biochim. Biophys. Acta* **2002**, *1559*(1), 56–68.
235. Van Rossenberg, S. M.; Sliedregt-Bol, K. M.; Meeuwenoord, N. J.; *et al. J. Biol. Chem.* **2002**, *277*(48), 45803–45810.
236. Top, D.; de Antueno, R.; Salsman, J.; *et al. EMBO J.* **2005**, *24*(17), 2980–2988.
237. Pillot, T.; Goethals, M.; Vanloo, B.; *et al. J. Biol. Chem.* **1996**, *271*(46), 28757–28765.
238. Efremov, R. G.; Nolde, D. E.; Volynsky, P. E.; Chernyavsky, A. A.; Dubovskii, P. V.; Arseniev, A. S. *FEBS Lett.* **1999**, *462*(1–2), 205–210.
239. Frankel, A. D.; Pabo, C. O. *Cell* **1988**, *55*(6), 1189–1193.
240. Green, M.; Loewenstein, P. M. *Cell* **1988**, *55*(6), 1179–1188.
241. Derossi, D.; Joliot, A. H.; Chassaing, G.; Prochiantz, A. *J. Biol. Chem.* **1994**, *269*(14), 10444–10450.
242. Fonseca, S. B.; Pereira, M. P.; Kelley, S. O. *Adv. Drug Deliv. Rev.* **2009**, *61*(11), 953–964.
243. Heitz, F.; Morris, M. C.; Divita, G. *Br. J. Pharmacol.* **2009**, *157*(2), 195–206.
244. Sugita, T.; Yoshikawa, T.; Mukai, Y.; *et al. Br. J. Pharmacol.* **2008**, *153*(6), 1143–1152.
245. Wadia, J. S.; Stan, R. V.; Dowdy, S. F. *Nat. Med.* **2004**, *10*(3), 310–315.
246. Albarran, B.; To, R.; Stayton, P. S. *Protein Eng. Des. Sel.* **2005**, *18*(3), 147–152.
247. Flynn, C. R.; Cheung-Flynn, J.; Smoke, C. C.; *et al. J. Pharm. Sci.* **2009**, *99*(7), 3100–3121.
248. Al-Taei, S.; Penning, N. A.; Simpson, J. C.; *et al. Bioconjug. Chem.* **2006**, *17*(1), 90–100.
249. Duvall, C. L.; Convertine, A. J.; Benoit, D. S.; Hoffman, A. S.; Stayton, P. S. *Mol. Pharm.* **2010**, *7*(2), 468–476.
250. Lundberg, P.; El-Andaloussi, S.; Sütlü, T.; Johansson, H.; Langel, U. *FASEB J.* **2007**, *21*(11), 2664–2671.
251. Li, W.; Nicol, F.; Szoka, F. C., Jr. *Adv. Drug Deliv. Rev.* **2004**, *56*(7), 967–985.
252. Subbarao, N. K.; Parente, R. A.; Szoka, F. C., Jr.; Nadasdi, L.; Pongracz, K. *Biochemistry* **1987**, *26*(11), 2964–2972.
253. Parente, R. A.; Nir, S.; Szoka, F. C., Jr. *J. Biol. Chem.* **1988**, *263*(10), 4724–4730.
254. Parente, R. A.; Nadasdi, L.; Subbarao, N. K.; Szoka, F. C., Jr. *Biochemistry* **1990**, *29*(37), 8713–8719.
255. Parente, R. A.; Nir, S.; Szoka, F. C., Jr. *Biochemistry* **1990**, *29*(37), 8720–8728.
256. Choi, H. S.; Huh, J.; Jo, W. H. *Biomacromolecules* **2006**, *7*(1), 403–406.
257. Goormaghtigh, E.; De Meutter, J.; Szoka, F.; Cabiaux, V.; Parente, R. A.; Ruysschaert, J. M. *Eur. J. Biochem.* **1991**, *195*(2), 421–429.
258. Nicol, F.; Nir, S.; Szoka, F. C., Jr. *Biophys. J.* **1996**, *71*(6), 3288–3301.
259. Nir, S.; Nicol, F.; Szoka, F. C., Jr. *Mol. Membr. Biol.* **1999**, *16*(1), 95–101.
260. Haas, D. H.; Murphy, R. M. *J. Pept. Res.* **2004**, *63*(1), 9–16.
261. Simoes, S.; Slepushkin, V.; Gaspar, R.; de Lima, M. C.; Duzgunes, N. *Gene Ther.* **1998**, *5*(7), 955–964.
262. Simoes, S.; Slepushkin, V.; Pires, P.; Gaspar, R.; de Lima, M. P.; Duzgunes, N. *Gene Ther.* **1999**, *6*(11), 1798–1807.
263. Simoes, S.; Slepushkin, V.; Pretzer, E.; *et al. J. Leukoc. Biol.* **1999**, *65*(2), 270–279.
264. Kakudo, T.; Chaki, S.; Futaki, S.; *et al. Biochemistry* **2004**, *43*(19), 5618–5628.
265. Futaki, S.; Masui, Y.; Nakase, I.; *et al. J. Gene Med.* **2005**, *7*(11), 1450–1458.
266. Yamada, Y.; Shinohara, Y.; Kakudo, T.; *et al. Int. J. Pharm.* **2005**, *303*(1–2), 1–7.
267. Sasaki, K.; Kogure, K.; Chaki, S.; *et al. Anal. Bioanal. Chem.* **2008**, *391*(8), 2717–2727.
268. Hatakeyama, H.; Ito, E.; Akita, H.; *et al. J. Control. Release* **2009**, *139*(2), 127–132.
269. Akita, H.; Kogure, K.; Moriguchi, R.; *et al. J. Control. Release* **2010**, *143*(3), 311–317.
270. Anderson, D. C.; Manger, R.; Schroeder, J.; *et al. Bioconjug. Chem.* **1993**, *4*(1), 10–18.
271. Kuehne, J.; Murphy, R. M. *Bioconjug. Chem.* **2001**, *12*(5), 742–749.
272. Kobayashi, S.; Nakase, I.; Kawabata, N.; *et al. Bioconjug. Chem.* **2009**, *20*(5), 953–959.
273. Wang, Y.; Mangipudi, S. S.; Canine, B. F.; Hatefi, A. *J. Control. Release* **2009**, *137*(1), 46–53.
274. Choi, S. H.; Choi, K.; Chan Kwon, I.; Ahn, H. J. *Biomaterials* **2010**, *31*(19), 5191–5198.
275. Kulkarni, R. P.; Castelino, K.; Majumdar, A.; Fraser, S. E. *Biophys. J.* **2006**, *90*(5), L42–L44.
276. Carr, L. R.; Jiang, S. *Biomaterials* **2010**, *31*(14), 4186–4193.
277. Kato, M.; Kamigaito, M.; Sawamoto, M.; Higashimura, T. *Macromolecules* **1995**, *28*(5), 1721–1723.
278. Wang, J.-S.; Matyjaszewski, K. *Macromolecules* **1995**, *28*(23), 7901–7910.
279. Baskin, J. M.; Prescher, J. A.; Laughlin, S. T.; *et al. Proc. Natl. Acad. Sci. USA* **2007**, *104*(43), 16793–16797.
280. Kolb, H. C.; Finn, M. G.; Sharpless, K. B. *Click Chemistry: Diverse Chemical Function from a Few Good Reactions*. Wiley-VCH: New York, 2001.
281. Kolb, H. C.; Sharpless, K. B. *Drug Discov. Today* **2003**, *8*(24), 1128–1137.
282. Tornøe, C. W.; Christensen, C.; Meldal, M. *J. Org. Chem.* **2002**, *67*(9), 3057–3064.
283. Opanasopit, P.; Nishikawa, M.; Hashida, M. *Crit. Rev. Ther. Drug Carrier Syst.* **2002**, *19*(3), 191–233.
284. Owens, D. E., III; Peppas, N. A. *Int. J. Pharm.* **2006**, *307*(1), 93–102.
285. Li, S.-D.; Chen, Y.-C.; Hackett, M. J.; Huang, L. *Mol. Ther.* **2007**, *16*(1), 163–169.
286. Li, S.-D.; Huang, L. *Biochim. Biophys. Acta* **2009**, *1788*(10), 2259–2266.
287. Li, S.-D.; Huang, L. *J. Control. Release* **2010**, *145*(3), 178–181.
288. Akinc, A.; Querbes, W.; De, S.; *et al. Mol. Ther.* **2010**, *18*(7), 1357–1364.
289. Burke, R. S.; Pun, S. H. *Bioconjug. Chem.* **2008**, *19*(3), 693–704.

4.423. Polymeric Drug Conjugates by Controlled Radical Polymerization

S-H Kim, T H Nguyen, and H D Maynard, University of California, Los Angeles, CA, USA

© 2011 Elsevier Ltd. All rights reserved.

4.423.1.	**Introduction**	377
4.423.2.	**Overview of Controlled Radical Polymerization**	379
4.423.2.1.	Reversible Addition-Fragmentation Chain Transfer Polymerization	379
4.423.2.2.	Atom Transfer Radical Polymerization	380
4.423.2.3.	Nitroxide-Mediated Polymerization	380
4.423.3.	**Examples of Polymer Conjugates Synthesized by Controlled Radical Polymerization**	380
4.423.3.1.	Polymer–Small Molecule Drug Conjugates	380
4.423.3.2.	Polymer–Protein Drug Conjugates	382
4.423.3.3.	Polymer–Peptide Drug Conjugates	384
4.423.4.	**Prospects and Challenges**	385
References		386

Abbreviations

AIBN	Azobisisobutyronitrile	**NMP**	Nitroxide-mediated polymerization
ATRP	Atom transfer radical polymerization	**OEGA**	Oligo(ethylene glycol) acrylate
BSA	Bovine serum albumin	**PDI**	Polydispersity index
CPT	Camptothecin	**PEG**	Poly(ethylene glycol)
CRP	Controlled radical polymerization	**PEGMA**	Poly(ethylene glycol) methacrylate
CTA	Chain transfer agent	**RAFT**	Reversible addition–fragmentation chain transfer
DOX	Doxorubicin	**RGD**	Arginine-glycine-aspartic acid
EPR	Enhanced permeability and retention	**SAv**	Streptavidin
HPMA	*N*-(2-Hydroxypropyl)methacrylamide	**SDS-PAGE**	Sodium dodecyl sulfate-polyacrylamide gel electrophoresis
LCST	Lower critical solution temperature	**SPPS**	Solid-phase peptide synthesis
NHS	*N*-Hydroxysuccinimide	**TEMPO**	2,2,6,6-Tetramethylpiperidinyloxy
NIPAAM	*N*-Isopropylacrylamide		

4.423.1. Introduction

Synthetic polymers have been utilized broadly in biomedicine, including temporary assisting materials such as sutures, dressing grafts, tissue regeneration scaffolds, permanent implants, and drug delivery vehicles. Polymeric materials used in such applications share common properties, for example, biocompatibility, low immunogenicity, renal clearance without causing kidney failure, and stability in physiologic conditions.[1–5] Ever since Ringsdorf established the concept of polymers as pharmacologically active drug carriers,[6] many have focused on designing macromolecules as drug delivery matrices. Colloidal encapsulants (liposomes, microspheres, nanospheres, micelles), polymeric complexes, polymer–drug conjugates, and polymers as prodrugs are classes of matrices already reported (**Figure 1**). These polymers improve the drug-loading efficiency, solubility, specificity, and constancy of serum concentration of drugs, as well as the circulation time of biomolecular drugs (i.e., protein/peptides, DNA, and RNA) (see **Chapter 4.403, The Innate Response to Biomaterials**).

The first polymer–drug conjugate was reported by Jatzkewits in 1955, in which he demonstrated a sustained release of mescaline from a copolymer of *N*-vinylpyrrolidone and peptamine, opening a new era of polymer conjugate research.[6–8] In many cases, the presence of a polymer can solubilize hydrophobic drugs (many market-available anticancer drugs such as doxorubicin (DOX) and paclitaxel are hydrophobic,[9–11]) aiding in their formulation and lowering their toxicity. The pharmacokinetics of drug substances can be modified by attaching high molecular weight polymers to elongate the blood circulation time. In addition, polymers help target tumors by the enhanced permeability and retention (EPR) effect[12] due to their large size.

Ever since Abuchowski and coworkers introduced the pharmaceutical advantage of poly(ethylene glycol) (PEG) conjugation to a protein, that is, lowered immunogenicity,[13] a great deal of work has also been reported on improving the therapeutic effect of protein drugs via polymer conjugation.[14–18] It has consequently been shown that PEG increases the circulation time of protein and peptide drugs by preventing protease degradation, and reducing immunogenicity and antigenicity by hindering antigenic determinants.[16,19–21] The nonreactive chemical property of the PEG minimizes unwanted reaction and chemical interference with functional drugs when used as a drug delivery platform. Synergistically combining the properties of drugs with those of synthetic polymers has become a well-accepted strategy to improve the pharmacological and biological effects of the therapeutic agents.

Much effort has also been focused on exploiting functional synthetic polymers for delivering drugs in a target-directed or stimuli-responsive manner (Figure 2).[3,22–24] The release rate of drugs and/or degradation of polymer matrices can be tuned by introducing hydrolytically or enzymatically degradable chemical linkages.[8] The polymer–drug conjugate can facilitate endocytotic cellular entry in select cases, for instance, by masking adverse interactions of highly charged drugs with cell membranes.[25] Thermosensitive conjugates, which exhibit a lower critical solution temperature (LCST), enable entrapment of drugs, followed by penetration through biological barriers after undergoing a phase transition.[26,27] Polymer conjugates with tumor-specific antibodies or ligands can be used as homing devices for targeted delivery of anticancer

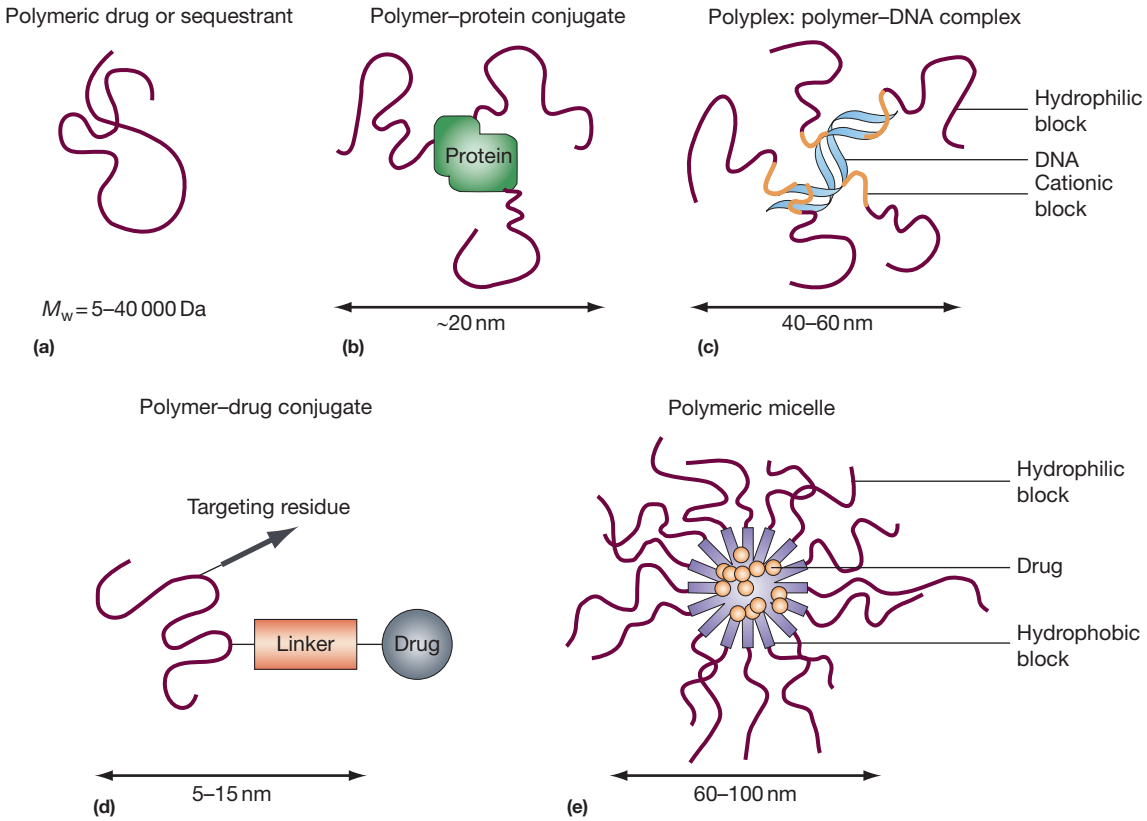

Figure 1 Therapeutic application of polymers. Reprinted with permission from Duncan, R. *Nat. Rev. Drug Discov.* **2003**, *2*(5), 347–360. © 2003 Nature Publishing Group.

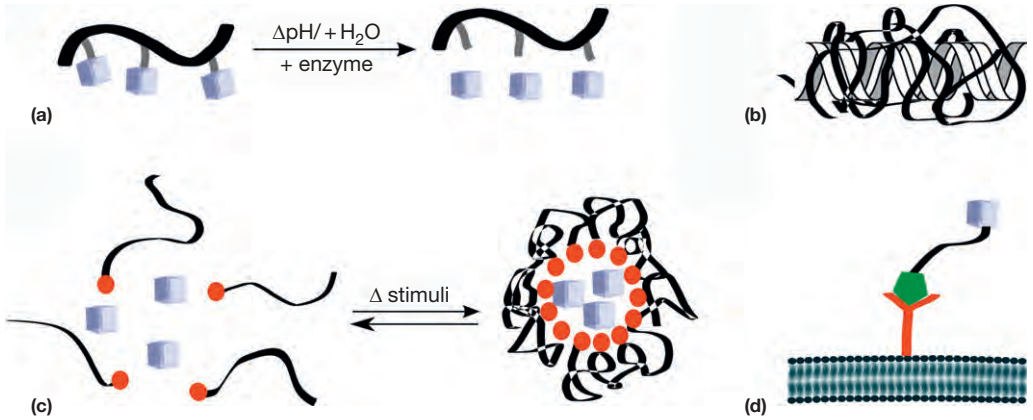

Figure 2 Examples of polymers as drug delivery vehicles. (a) Polymer conjugates with side chains that release drugs via hydrolysis, change in pH, or enzyme action; (b) masking of highly charged drugs (such as DNA) with polymers; (c) stimuli-responsive (such as temperature, pH, light, current, and mechanical stimuli) encapsulation of drugs; (d) target-directed therapy via polymeric conjugates with a specific homing molecule (such as antibodies).

drugs or contrast agents, enabling visualization of tumor sites (see **Chapter 4.421, Self-Assembled Prodrugs**; **Chapter 4.422, pH-Responsive Polymers for the Intracellular Delivery of Biomolecular Drugs**; **Chapter 4.425, Delivery of Nucleic Acids and Gene Delivery**; **Chapter 5.510, Engineered Bioactive Molecules**; and **Chapter 1.123, Degradable Polymers**).[8,24,28]

Although polymeric conjugates by and large have the many advantages mentioned earlier, challenges still remain: only a few polymer conjugates have been tested for clinical use. Heterogeneity with respect to polymer molecular weight, composition, or structure can be problematic, as it often causes batch-to-batch and/or lab-to-lab variations. This can lead to unpredictable pharmacokinetic and pharmacodynamic behavior, reduction in bioactivity, or unreliable release kinetics. Polymerization techniques that provide well-defined polymer chains with reactive moieties for site-specific conjugation can overcome these limitations. Controlled radical polymerizations (CRPs) meet these requirements, and this chapter will focus on synthetic strategies by CRP to prepare polymer–drug conjugates.

4.423.2. Overview of Controlled Radical Polymerization

Polymers with predetermined molecular weights, complex architectures, and functional end groups are attainable with CRPs. Reversible addition–fragmentation chain transfer (RAFT) polymerization,[29] atom transfer radical polymerization (ATRP),[30] and nitroxide-mediated polymerization (NMP)[31] are widely used CRP techniques. Different from living cationic and anionic polymerizations, CRPs have high tolerance to many functional groups such as alcohols, esters, amides, and carboxylates; yet similar to these approaches, the molecular weight distributions are narrow.[32] The strategies can be used to form block,[33,34] branched,[35–37] star,[38–43] comb/graft[40] copolymers, as well as architectures desired for polymer–drug conjugations (see **Chapter 1.121, Polymer Fundamentals: Polymer Synthesis**).

4.423.2.1. Reversible Addition-Fragmentation Chain Transfer Polymerization

RAFT polymerization, invented by Rizzardo, Moad, and Thang, is a facile and versatile CRP technique that is compatible with a wide range of monomers (acrylates, methacrylates, acrylamide, methacrylamide, styrene, and vinyl acetate).[44,45] Moreover, controlled polymerization of cationic,[46] anionic,[47,48] and zwitterionic[49] monomers are made possible in aqueous media via RAFT polymerization. RAFT polymerization takes advantage of a reversible chain transfer agent (CTA) to produce low polydispersity index (PDI) polymers. A number of thiocarbonylthio-based CTAs, including dithioesters,[29] trithiocarbonates,[50] dithiocarbamates,[51,52] and xanthates,[53,54] have been studied. The mechanism of RAFT polymerization first proposed by its inventors at the Commonwealth Scientific and Industrial Research Organization (CISRO)[29] and studied by others,[55–57] is depicted in **Figure 3**. An important feature is reversible addition of the growing polymer radical to the reactive C=S of the CTA, followed by rapid fragmentation to form the stable radical R•. Selection of an appropriate R group is important to achieve controlled polymerization for a specific set of specific monomers because the chosen R group must be stable enough to be

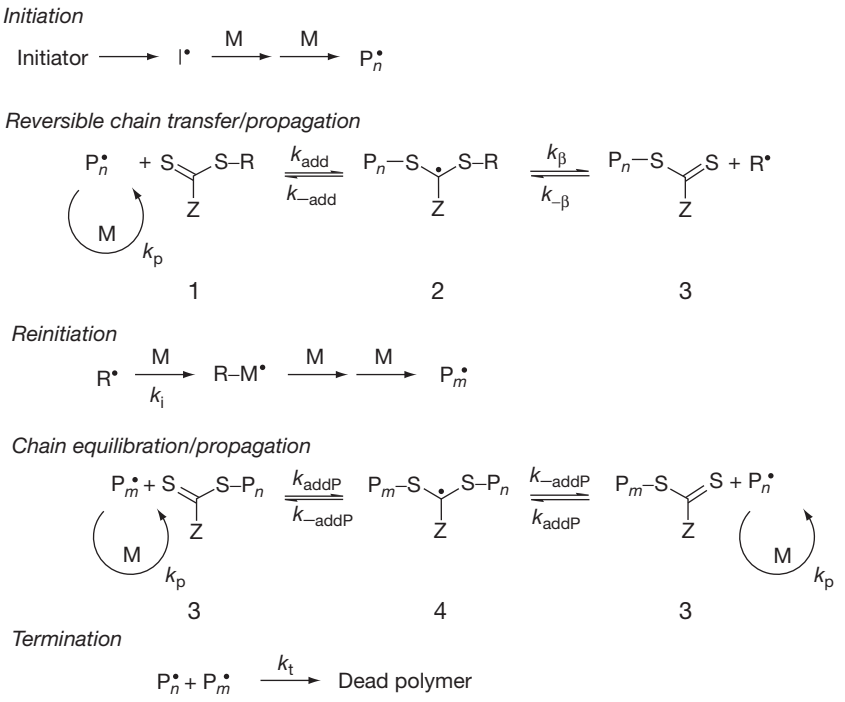

Figure 3 Generally accepted mechanism for reversible addition–fragmentation chain transfer polymerization. Reprinted with permission from Moad, G.; Rizzardo, E.; Thang, S. H. *Aust. J. Chem.* **2006**, *59*, 24. © 2006 CSIRO Publishing.

fragmented as a radical, yet reactive enough to reinitiate the polymerization. The equilibrium between the propagating polymeric radical and dormant RAFT agent–polymer adduct results in uniform chain growth and low PDI for the resultant polymer.

4.423.2.2. Atom Transfer Radical Polymerization

ATRP, also termed transition metal-mediated living polymerization or transition metal-catalyzed living free-radical polymerization, is another popular CRP technique that was first reported by Matyjaszewski[30,58–60] and Sawamoto.[61] Like RAFT polymerization, ATRP is tolerant to many functional groups, allowing a broad range of monomer choices, including styrenyls, alkyl (meth)acrylates, acrylonitrile, and (meth)acrylamides. Control is gained in the ATRP process by a reversible termination reaction, shown in Figure 4.[60] The radicals are generated through a reversible redox process (±1 change in oxidation state of the metal), catalyzed by a transition metal (such as copper, ruthenium, iron, or nickel) complex. The equilibrium between activation (k_{act}) and deactivation (k_{deact}) is important. Owing to fast initiation and reversible deactivation, ATRP results in a uniform chain growth, and thus well-controlled molecular weight.

4.423.2.3. Nitroxide-Mediated Polymerization

Nitroxide-mediated living free-radical polymerization (NMP) is another well-studied CRP technique that involves using reversible termination of the growing polymer chain to reduce the overall concentration of the propagating radical chain end.[31] Stabilized nitroxides, such as 2,2,6,6-tetramethylpiperidinyloxy (TEMPO), are introduced to trap carbon-centered free radicals generated from the addition of initiator to vinyl monomers. Solomon, Rizzardo, and Moad first reported the concept of NMP, in which a standard free-radical polymerization of methyl acrylate or styrene monomers in the presence of TEMPO produced low molecular weight polymers.[63–65] Georges *et al.* reported a bulk polymerization of styrene with a bimolecular initiation process at high temperature (130 °C) in a molar ratio of benzoyl peroxide:styrene:TEMPO of 1:3:1 to result in a linear

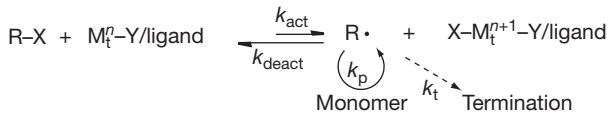

Figure 4 Reversible termination in atom transfer radical polymerization. Reprinted with permission from Matyjaszewski, K.; Xia, J. *Chem. Rev.* **2001**, *101*(9), 2921–2990. © 2001 American Chemical Society.

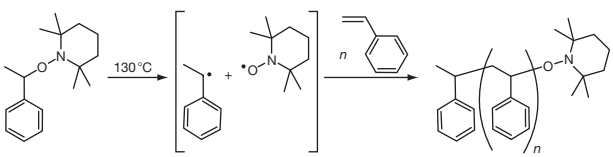

Figure 5 Nitroxide-mediated living free radical polymerization of styrene via unimolecular initiation. Reprinted with permission from Hawker, C. J.; Bosman, A. W.; Harth, E. *Chem. Rev.* **2001**, *101*(12), 3661–3688. © 2001 American Chemical Society.

conversion with PDIs between 1.2 and 1.3.[66] Unimolecular initiators for NMP, developed by Hawker and coworkers, allowed better control over molecular weight and architecture.[67,68] A representative NMP reaction is shown in Figure 5. Upon heating, the alkoxyamine derivative initiator heterolytically cleaves to form a methylbenzyl radical that initiates the polymerization of styrene, as well as the mediating nitroxide radical, in a 1:1 stoichiometry.

Synthetic polymers produced by CRP have increasingly been employed in materials for biotechnology, biomedical, nanotechnology, and pharmaceutical use.[2,69,70] In the following sections, polymer conjugates of synthetic drugs and biomolecules (proteins and peptides) prepared using CRP techniques are discussed. Because biomedical applications of polymers synthesized via CRPs have been extensively reviewed,[23,62,71–73] the following sections are not comprehensive but rather provide an overview of the field.

4.423.3. Examples of Polymer Conjugates Synthesized by Controlled Radical Polymerization

4.423.3.1. Polymer–Small Molecule Drug Conjugates

As already discussed, polymer conjugation often improves drug efficacy by aiding solubility and suppressing toxicity. Drugs can be conjugated to the ends of the polymer chain or to the side chains (Figure 6). The latter allows the drug loading to be regulated by varying the conjugation density along the polymer backbone, either via postpolymerization side-chain modification or copolymerization of monomers with different dangling side chains. This feature may be suitable for small molecule drug conjugation, while the chain-end conjugation is typically more appropriate for larger molecules such as proteins and peptides. Certain drugs must be released to function; in such cases, the release rate can be finely tuned by introducing a cleavable linkage between the drug and the polymer backbone. As a result, the polymer–drug conjugation technique has been extensively utilized for drug delivery and tissue-engineering applications. Some have already been investigated in clinical trials, including anticancer drugs such as DOX and paclitaxel (Taxol) conjugated to poly(*N*-(2-hydroxypropyl)methacrylamide) (pHPMA) or poly(L-glutamic acid).[74–76] Historically, polymer–drug conjugates have been prepared by conventional radical polymerization. Implementation of CRP provides better control over the production of polymer–drug conjugates. Polymers with desired molecular weight and narrow polydispersity can be achieved reliably and reproducibly. Polymer architecture can be manipulated at the molecular level, which offers the design of higher-order macromolecular assemblies.[77]

Godwin *et al.* introduced the use of CRP to produce a polymer with activated ester side chains and narrow polydispersity indices for potential application in polymer–drug conjugates.[78] They polymerized *N*-hydroxysuccinimide (NHS) methacrylate via copper-mediated ATRP in the presence of 2,2′-bipyridine to give various molecular weights with PDIs <1.20. They conjugated *p*-nitroanilide as a model drug in various ratios to demonstrate the potential to produce polymer–drug conjugates in a well-controlled manner. In subsequent studies, the synthesis of polymers with a wide range of side-chain functional groups have been reported via ATRP, including NHS ester,[79,80]

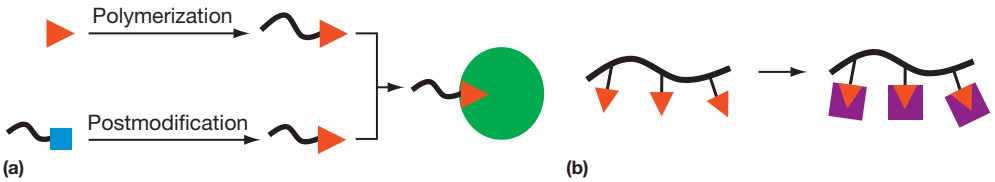

Figure 6 Polymer conjugate architectures. (a) Chain-end conjugation by chemoselective initiator/chain transfer agent (upper route) or by postmodification of polymer chain-end (lower route). (b) Conjugation via reactive functional groups along the polymer side chain.

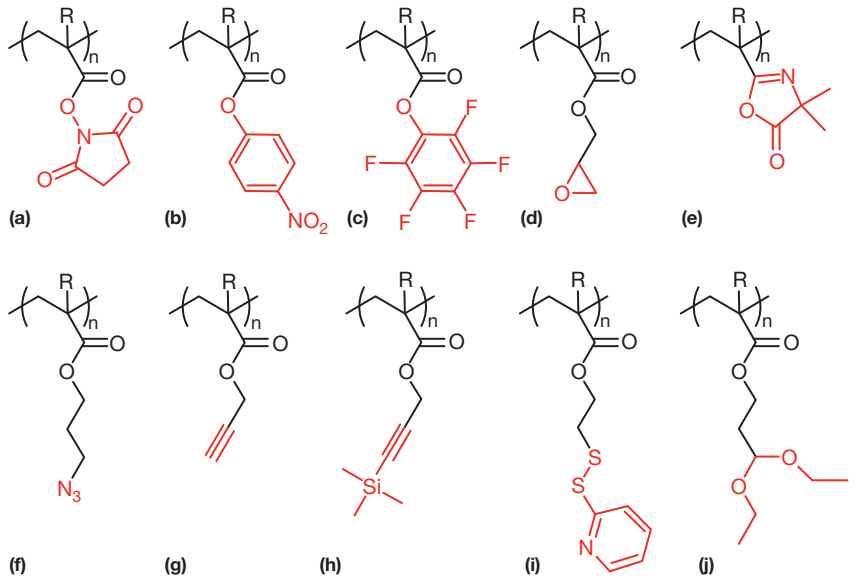

Figure 7 Reactive side chains of polymers by controlled radical polymerization for drug conjugation: (a) *N*-hydroxysuccinimide ester, (b) *p*-nitrophenyl ester, (c) pentafluorophenyl ester, (d) epoxide, (e) oxazolone, (f) azide, (g) alkyne, (h) trimethylsilyl propargyl, (i) pyridyl disulfide, (j) acetals which are easily converted to reactive aldehydes.

2,4,5-trichlorophenol ester,[81] and *p*-nitrophenyl ester.[82] Activated polyesters can react with primary amines under mild conditions (pH and temperature) resulting in stable amide bonds in relatively high yield. While the activated esters are most commonly used for polymer–drug conjugate synthesis, polymers with other side-chain functional groups have also been reported. These include epoxides,[83,84] oxazolones,[85] and acetal[86] functional groups. Click chemistry has drawn much attention in recent years because it results in high reaction yields in the presence of other functional groups without side reactions, making it suitable for many biologically active drugs.[87] Polymers with the click reaction partners, either azides[88] or alkynes,[89] have been prepared. RAFT polymerization has also been utilized to produce polymers with narrow PDI that are functionalized with reactive side chains such as activated esters,[90–95] disulfides,[96,97] protected alkynes,[98–100] and acetals/aldehydes.[90,101] Polymers with reactive side chains that are prepared via NMP have also been reported, including alkynes,[102,103] oxazolones,[104] and epoxides.[105,106] The reactive side chains of polymers that could be potentially used for polymer–drug conjugation are summarized in Figure 7.

Anticancer drugs have been particularly targeted by researchers for polymer conjugation, because large molecules passively target some solid tumors via the EPR effect. While the direct use of CRP techniques in anticancer drug conjugation is still in the initial stages, recent efforts have been promising. Rickert *et al.* was the first to report polymer conjugation of tamoxifen, a breast cancer drug (Figure 8(a)).[107] They prepared a polyester by polymerizing NHS methacrylate via CuBr-mediated ATRP in the presence of 2,2′-bipyridine (polymer molecular weight 12 500 Da and PDI 1.07) and conjugated a 4-hydroxytamoxifen derivative with 50% substitution. Antagonistic activity to the estrogen receptor (ER) was improved compared to protein-based conjugates as indicated by IC_{50} values obtained from a radiolabeled estradiol competition assay. Chen *et al.* demonstrated camptothecin (CPT)–polymer conjugates in two different architectures: CPT-terminated polymer and CPT as side-chain pendant groups (shown in Figure 8(b)).[108] They polymerized biocompatible poly(methacryloyloxyethyl phosphorylcholine) (polyMPC) either by using a CPT-modified ATRP initiator to make CPT-terminated polyMPC or by copolymerizing MPC and trimethylsilyl propargyl methacrylate with azidyl CPT via ATRP in one-pot to make polyMPC-*graft*-CPT. Hydrolytically degradable ester linkages were introduced and the *in vitro* cytotoxicity was tested on three different cancer cell lines: human breast (MCF7), ovarian (OVCAR-3), and colon (COLO 205) adenocarcinoma cells. The conjugates were potent as anticancer drugs, although the IC_{50} values were higher than CPT due to the slow release of CPT from the polymers. This study demonstrated feasibility of controlling the drug loading and

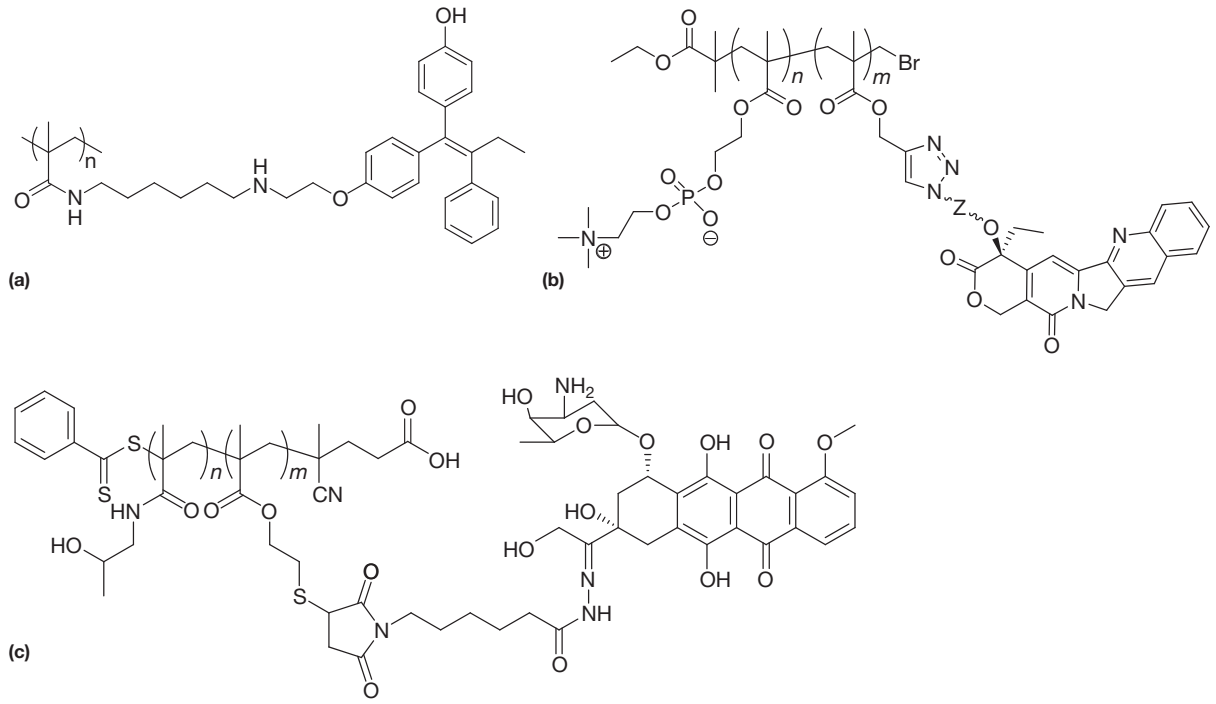

Figure 8 Structure of polymer conjugates of (a) tamoxifen,[107] (b) camptothecin,[108] and (c) doxorubicin.[109]

release rate in polymers with precisely designed molecular weights and narrow molecular distribution, as well as variable choice of degradable linker arms. Jia *et al.* reported conjugation of Dox to an amphiphilic block copolymer of HPMA and a thiol-reactive monomer 2-(2-pyridyl disulfide)ethyl methacrylate (PDSM) synthesized via RAFT polymerization using 4-(cyanopentanoic acid)-4-dithiobenzoate as the CTA (**Figure 8(c)**).[109] Maleimide hydrazone-modified Dox was then conjugated to the pyridyl disulfide pendant group at 32% substitution. The remaining reduced thiol groups were oxidized to disulfides to form cross-linked miscellular particles. Study of the pH-dependent release of Dox via cleavage of the acid-susceptible hydrazone linkage showed 3.6-fold faster liberation of Dox at lower pH (pH 5.0) than the physiological pH. These results are promising for targeting acidic tumors.

4.423.3.2. Polymer–Protein Drug Conjugates

The global protein drug market, which includes growth hormones, insulin, cytokines, plasma proteins, vaccines, and monoclonal antibodies, is rapidly increasing. However, delivering protein-based pharmaceutics is challenging because of their short circulation times and lack of stability in media, as well as enzymatic and cellular (i.e., endothelial) barriers *in vivo*. As discussed previously, polymeric conjugation to such protein drugs mitigates these issues, vastly improving clinic usability. With polymer chains attached, protein drugs need to be administered (injected) less often, increasing patient compliance.

PEGylation is the most implemented method for delivering protein therapeutics, since the nontoxic and low-immunogenic PEGs have been shown to enhance efficacy by protecting proteins from environmental and enzymatic degradation. Use of linear PEG, either PEG-diol or monomethoxy PEG (mPEG), in protein conjugation poses potential problems owing to the heterogeneous products that result.[18,110] An end-group-functionalized linear PEG can be straightforwardly conjugated to the amine side chain of lysine residues, the N-terminus, or the thiol side chain of cysteines. However, an electrophilically modified PEG can react with multiple residues on proteins, resulting in mixtures of PEG isomers per protein. This heterogeneity is problematic for drug manufacturing processes, regulatory approvals, and clinical use. Another possible problem of conventional linear PEGylation is that the residual diol-PEG in mPEG may cause cross-linking of conjugate products, lowering the overall yield.[16] Moreover, recently increasing evidence has been reported on PEG's immunogenicity, contrarily to the conventional assumption, which may impact clinical application of PEGylated therapeutics.[111]

CRP techniques provide a route to polymers for conjugation to proteins that circumvent some of the issues associated with PEGylation, in that monofunctionalized polymers that are well defined are readily synthesized. Other polymers, besides those that are PEGylated, are readily accessed, allowing a greater functionality space to be explored. In addition, hydrophobic polymer protein conjugates can be synthesized. This leads to materials that self-assemble such as miscelles for potential drug delivery applications.[112] Polymers synthesized by CRP that target natural and unnatural amino acids have been reviewed.[62,71–73] Some examples of polymers that target amine or thiol residues are given below.

The Haddleton and Maynard groups independently reported a way to utilize CRP to generate in one step end-functionalized polymers that react with proteins.[113,114] The general approach is to utilize a protein-reactive ATRP initiator or RAFT CTA in the controlled polymerization (**Figure 9**). Haddleton polymerized poly(ethylene glycol) methyl ether methacrylate (mPEGMA)

monomers using *N*-succinimidyl-2-bromo-2-methylpropionate as an initiator in the presence of Cu(I)Br/*N*-(ethyl)-2-pyridylmethanimine catalyst to yield a monofunctionalized brush PEG polymer with a narrow PDI (<1.15).[113] They showed that a complete conjugation was achievable by using the polymer prepared by initiation with N-succinimidyl 2-bromopropionate, in their lysozyme model system. An average 6–7 polymer molecules were observed, which were in good agreement with the number of free amine residues in the lysozyme. In another report, they also studied an α-aldehyde-terminated PEGMA by using acetal-functionalized ATRP initiator.[115] The acetal group was deprotected to give an aldehyde and conjugated to amine groups of lysozyme via reductive amination (**Figure 10**). Use of PEGMA with well-controlled molecular weight and functional groups provides an alternative PEGylation method that may allow further protection from proteolysis compared to that of linear PEG.[116] Maynard reported a cysteine-targeting polymer by utilizing a pyridyl disulfide-functionalized 2-bromo-2-methylpropionate ATRP initiator to polymerize 2-hydroxyethyl methacrylate (HEMA). The obtained polymers with various molecular weights had PDIs <1.25 and retained 85–91% of the end group. Conjugation to bovine serum albumin (BSA), which contains 45–50% free Cys34 residue, was demonstrated, and the sodium dodecyl sulfate-polyacrylamide gel electrophoresis (SDS-PAGE) analysis showed a band shift to higher molecular weight in conjugates. Other studies employing cysteine-reactive maleimide[89] and pyridyl disulfide[117] ATRP initiators were reported. RAFT polymerization was also used to produce reactive end groups

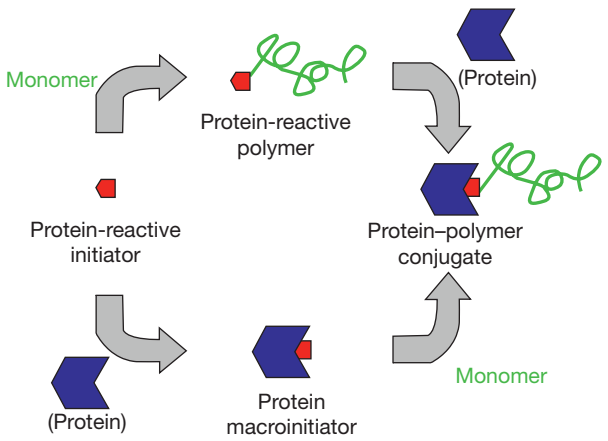

Figure 9 Routes to protein–polymer conjugates. Reprinted with permission from Heredia, K. L.; Maynard, H. D. *Org. Biomol. Chem.* **2007**, *5*(1), 45–53. © 2007 RSC Publishing.

for protein conjugation, such as pyridyl disulfide,[41,109,118–120] maleimide,[121,122] vinyl sulfone,[123,124] and thiozolidine.[125] In some cases, the functional group was incorporated directly into the CTA. In other cases, postpolymerization modification, such as aminolysis/reduction of thiocarbonylthio or heating with a protein-reactive azo initiator, was carried out to give thiol-reactive polymers.

The Maynard group first reported a novel approach to prepare protein–polymer conjugates that involves using the protein as a macroinitiator for polymerization, as illustrated in **Figure 9**.[126] Streptavidin (SAv) was activated with a biotinylated 2-bromoisobutyrate ATRP initiator, and *N*-isopropylacrylamide (NIPAAM) was polymerized in the presence of CuBr/2,2′-bipyridine catalyst at room temperature.[126] The result demonstrated a new method of site-specific polymer conjugation to protein; furthermore, the protein retained its bioactivity. In this route, the removal of unconjugated polymer is not necessary. On subsequent study, the *in situ* polymeric conjugation of BSA and T4 lysozyme by using the proteins as active ATRP initiators was described (**Figure 11**).[127] The free Cys residue of proteins was activated by using thiol-reactive, either a 2-pyridyl disulfidyl or a maleimidyl 2-bromoisobutyrate ATRP initiator and subsequently, NIPAAM was polymerized. Both conjugates showed higher molecular weight shifts by SDS PAGE. The enzymatic activity of lysozyme–pNIPAAM conjugate was the same as unmodified lysozyme. This study confirmed the versatility of the 'grafting-from' polymer conjugation method. Others have also reported the synthesis of protein–polymer conjugates utilizing 'grafting-from' ATRP. These include BSA–polystyrene giant amphiphiles[128] and chymotrypsin–p(MPEG-methacrylate)s.[129] Recently, several researchers have utilized this 'grafting-from' approach to prepare PEGylated proteins with improved therapeutic effects. Caliceti *et al.* demonstrated *in situ* PEGylation human growth hormone[130] and Chilkoti of myoglobin.[131] For the latter, the resulting myoglobin-polymer conjugate showed 40 times improved pharmacokinetic property compared to the unmodified version ($t_{1/2\alpha}$= 2 h compared to $t_{1/2\alpha}$ = 3 min). In a subsequent study, the same group also utilized ATRP to polymerize OEGMA from a modified C-terminus of green fluorescent protein (GFP).[132] The conjugate demonstrated 20 times improved pharmacokinetic property (i.e., from $t_{1/2\alpha}$ = 0.1 h to $t_{1/2\alpha}$ = 4 h) and 50 times greater tumor accumulation than did unmodified GFP. These latest results demonstrate the applicability of using the 'grafting-from' approach to generate conjugates for use *in vivo*.

Protein-mediated RAFT polymerizations were also reported.[133,134] The Centre for Advanced Macromolecular

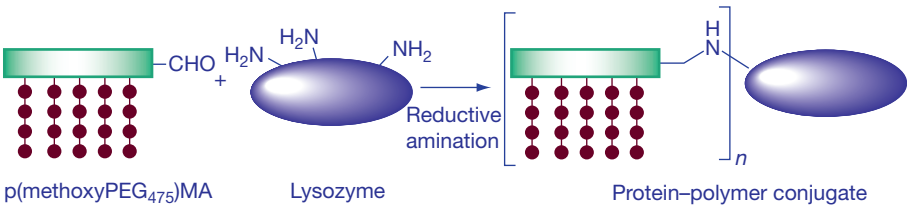

Figure 10 PEGylation of lysozyme by atom-transfer radical polymerization prepared poly(ethylene glycol) methacrylate via reductive amination. Reprinted with permission from Tao, L.; Mantovani, G.; Lecolley, F.; Haddleton, D. M *J. Am. Chem. Soc.* **2004**, *126*, 13220–13221. © 2004 American Chemical Society.

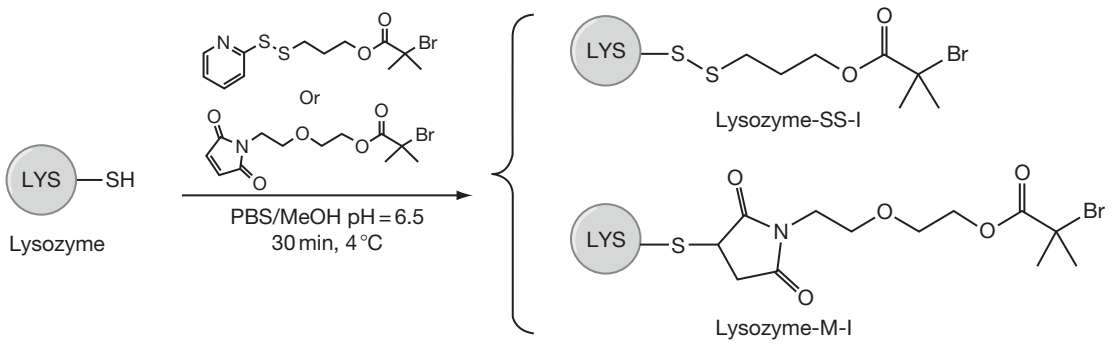

Figure 11 *In situ* protein–polymer conjugate formation. Reprinted with permission from Heredia, K. L.; Bontempo, D.; Ly, T.; Byers, J. T.; Halstenberg, S.; Maynard, H. D. *J. Am. Chem. Soc.* **2005**, *127*(48), 16955–16960. © 2005 American Chemical Society.

Design (CAMD) group modified the free cysteine of BSA using a pyridyl disulfide-functionalized trithiocarbonate CTA and polymerized NIPAAM in a phosphate buffer at 25 °C in the presence of azobisisobutyronitrile (AIBN).[133] They attained high molecular weight BSA–pNIPAAM conjugates (up to M_n~200 000) with increasing monomer conversion and were able to retain narrow PDIs (<1.20) below 50% monomer conversion (M_n~100 000). Sumerlin also reported a BSA-*grafted*-pNIPAAM conjugate by modifying BSA with a maleimide-functionalized trithiocarbonate.[134]

Exploitation of external stimuli-responsive materials, those that respond to temperature, pH, enzyme, and magnetic field, is at the forefront of biomaterials. Incorporation of these smart polymers into protein–polymer conjugate systems provides tools for making conjugates with tailored therapeutic properties and actuation. For example, pNIPAAM has been widely studied in drug delivery since it exhibits a thermoresponsive phase transition behavior (LCST); the polymer goes through a hydrophobic transition and becomes less soluble above the LCST.[135] This feature can be used for facilitating the localization of anticancer drugs or surface modifiers for control of cellular adhesion.[136] Various applications of protein-pNIPAAM, such as control of biorecognition, triggered release, and actuation, have been demonstrated.[136–139] Recently, Maynard and coworkers,[43,122,126,140–143] and Sumerlin and coworkers[134,144] have described a series of synthetic methods to produce BSA– or SAv–pNIPAAM conjugates via controlled radical polymerization. It is anticipated that stimuli-responsive polymeric conjugates with a well-defined structure will be increasingly used in biomedical research.

In summary, protein–polymer conjugates synthesized using CRPs, by either the 'graft-to' or 'grafting-from' approach, are promising as therapeutics. A homogeneous product may lead to increased therapeutic efficacy, and easy routes to these materials are provided via CRP techniques. Conjugates synthesized using ATRP or RAFT polymerization may find use in a myriad of applications, including as-targeted delivery of anticancer drugs by using tumor-specific antibodies,[145] immunodiagnostics,[146] and signal enhancement of immunoassays.[147] It is possible that this fast-developing field will soon be applied to clinical use.

4.423.3.3. Polymer–Peptide Drug Conjugates

Functional peptides that mimic the specific secondary structures and biological roles of their native proteins are applied as cell-permeation agents,[148–150] antimicrobials,[151] bioadhesives,[152] and molecular imaging tools.[153] Polymer conjugation may further stabilize and solubilize peptides and improve their efficiency.[154] Thus, well-defined functional peptide–polymer conjugate materials have enormous potential in biomedicine.

Different routes for preparing peptide–polymer conjugates have been reported. Polymers that are synthesized via CRPs with reactive initiators/CTAs[155] or side chains[90] can be conjugated to a specific amino acid of peptides in a postpolymerization approach. Peptide–polymer conjugates have also been produced by utilizing peptidyl monomers[78,156] or peptide-modified ATRP initiators.[157] Solid-phase peptide synthesis (SPPS) methodology offers facile production of oligopeptides in high purity, yield, and reproducibility.[158] Taking advantage of SPPS, peptide–polymer conjugates have also been prepared on solid phase by activating the resin-bound peptides with ATRP (**Figure 12**) and NMP initiators[151,159] or RAFT agents.[160]

Peptides that interact with cell surface receptors are exploited in tissue-engineering scaffolds. One such peptide, Agr-Gly-Asp (RGD), is the most investigated peptide for cell adhesion; the sequence derives from many extracellular matrix (ECM) proteins, including fibronectin. Mei *et al.* reported a solid-phase synthesis of peptide–polymer hybrid GRGDS-pHEMA using ATRP.[161] The GRGDS peptide was synthesized via standard fluorenylmethyloxycarbonyl (Fmoc) solid-phase synthesis using a Wang resin.[158] The peptidyl initiator was prepared by adding 2-bromopropionyl bromide; the initiator was used to polymerize HEMA in the presence of copper(I) chloride. The peptide–polymer conjugate was then liberated from the solid resin to give a polymer with a PDI of 1.47. Hentschel *et al.* reported another method for preparation of an RGD–polymer conjugate.[160] The GGRGDS sequence was synthesized by standard Fmoc solid-phase synthesis on a 2-chlorotrityl chloride resin, and a trithiocarbonate RAFT CTA was introduced. The peptide–CTA conjugate was then cleaved and used for polymerization of *n*-butyl acrylate (*n*BA), NIPAAM, and oligo(ethylene glycol) acrylate (OEGA) to yield PDIs between 1.1 and 1.2. Both studies showed that cells adhere specifically to the RGD–polymer materials, demonstrating a versatile methodology to produce well-defined peptide–polymer materials. Maynard reported a polymer with RGD as a pendant group.[90] Poly(diethoxypropyl methacrylate) (pDEPMA) was polymerized via RAFT using cumyl dithiobenzoate (CDB) as the CTA in the presence of AIBN (M_n 14 400 and PDI 1.26). The protected side chain was then

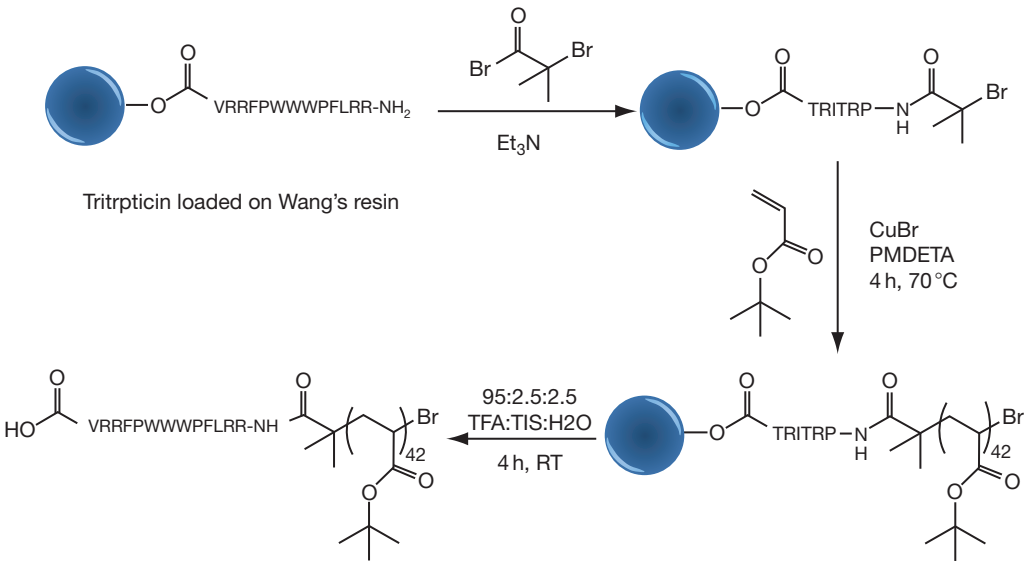

Figure 12 Synthetic strategy for peptide–polymer conjugate via solid-phase atom-transfer radical polymerization. Reproduced with permission from Becker, M. L.; Liu, J.; Wooley, K. L. *Biomacromolecules* **2004**, *6*(1), 220–228. © 2005 American Chemical Society.

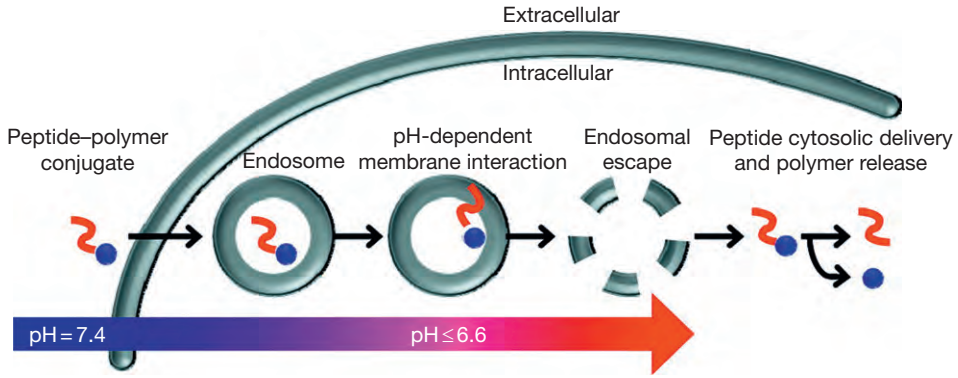

Figure 13 Intracellular delivery of a proapoptotic peptide via conjugation to a reversible addition–fragmentation chain transfer synthesized endosomolytic polymer. Reprinted with permission from Duvall, C. L.; Convertine, A. J.; Benoit, D. S. W.; Hoffman, A. S.; Stayton, P. S. *Mol. Pharmacol.* **2010**, *7*(2), 468–476. © 2010 American Chemical Society.

deprotected in a 1:1 mixture of trifluoroacetic acid:H_2O to give an aldehyde side chain. Aminooxy-functionalized RGD was conjugated to this polymer via oxime chemistry with a targeted 15% substitution.

Similar to nonbiologic drug conjugates described earlier, the peptide density along the polymer backbone can be finely tuned. This feature is advantageous in biomedical applications where multivalency is required. For example, a copolymer of poly(HPMA-*co*-*N*-methacryloyloxysuccinimide), prepared via RAFT, has been reported: the polymer was subsequently conjugated with a bioactive oligopeptide, HTSTYWWLDGAPK.[162] It was demonstrated that this polyvalent peptide conjugate improved, by three orders of magnitude, inhibition of anthrax toxin, compared to monovalent peptide.

A polymeric conjugate with a proapoptotic peptide derived from homology domain BH3 of B cell lymphoma 2 was recently reported by Hoffman and Stayton.[155] A Cys-terminated fusion peptide of BH3 with a cell-permeating peptide Antp[163] was prepared and conjugated to a pyridyl disulfide-functionalized RAFT polymer. The polymer was composed of two modules: pHPMA to increase solubility and circulation time and a copolymer of dimethylaminoethyl methacrylate (DMAEMA), butyl methacrylate (BMA), and propylacrylic acid (PAA) to trigger pH-dependent cytosolic release of the therapeutic peptide. A pyridyl disulfide-functionalized trithiocarbonyl CTA was used to polymerize HPMA, and the polymer was, in turn, employed as a macro-CTA to construct the second block of poly(PAA-*co*-BMA-*co*-DMAEA). The result showed that the pH-dependent block assisted the homogeneous endosomal distribution of internalized peptide, and the peptide–polymer conjugate exhibited apoptotic functionality (**Figure 13**).

4.423.4. Prospects and Challenges

Synthetic polymeric materials offer tremendous opportunities to improve drug efficacy. It has been proved that polymers enhance the performance of biological drugs, such as therapeutic proteins and peptides, by protecting them from degradation, increasing circulation time, and facilitating cell

internalization. Numerous polymeric materials have been investigated for medicinal purposes, and some of them have made it to the clinic. However, problems inherent in the heterogeneity of the polymer and conjugation site need to be circumvented. Recent progress in controlled radical polymerization has enabled remarkable improvement in controlling molecular weights, polydispersities, architectural structures, and placement of functional groups in polymers for these applications.

There are some important considerations that should be taken into account when designing polymeric conjugates. The polymeric component (chain ends, functional pendant groups, and degradation products) should have minimal interaction with the host (i.e., no toxicity or minimal immunogenicity). The polymer should be excreted from the body in a timely manner without accumulating in any organs. If a degradable site is introduced to achieve this, the degradation should occur in a predictable manner with controlled kinetics, and the by-products should be inert to the body. CRP conjugation products often contain unwanted impurities such as copper catalyst from ATRP or released 2-pyridyl thione from pyridyl disulfide-functionalized polymers. These should be completely removed prior to administration.[164]

Advancement in the rapidly emerging interdisciplinary study of system biology, materials characterization, and imaging technologies promises a better understanding of pharmacokinetics and pharmacodynamics, as well as host responses, of administered polymeric conjugates. One can design an optimized polymeric conjugate that provides both medical effects and requirements as biomaterials, and expect minimized undesirable side effects and maximized therapeutic effects. Controlled radical polymerizations will certainly play an increasing role in designing small molecule, protein, and peptide–drug polymer conjugates of this description in the future.

Acknowledgments

The authors thank the National Science Foundation (CHE-0809832) and the Alfred P. Sloan Foundation (HDM) for financial funding.

References

1. Dhal, P. K.; Holmes-Farley, S. R.; Huval, C. C.; Jozefiak, T. H. In *Advances in Polymer Science*, Springer: Heidelberg, 2006; pp 9–58.
2. Duncan, R. *Nat. Rev. Drug Discov.* **2003**, *2*(5), 347–360.
3. Duncan, R.; Ringsdorf, H.; Satchi-Fainaro, R. In *Advances in Polymer Science*, Springer: Heidelberg, 2006; pp 1–8.
4. Kiick, K. L. *Science* **2007**, *317*(5842), 1182–1183.
5. Liu, S.; Maheshwari, R.; Kiick, K. L. *Macromolecules* **2009**, *42*(1), 3–13.
6. Ringsdorf, H. *J. Polym. Sci. Polym. Symp.* **1975**, *51*(1), 135–153.
7. Jatzkewitz, H. *Z. Naturforsch.* **1955**, *10b*, 27–31.
8. Hoste, K.; De Winne, K.; Schacht, E. *Int. J. Pharm.* **2004**, *277*(1–2), 119–131.
9. Marupudi, N. I.; Han, J. E.; Li, K. W.; Renard, V. M.; Tyler, B. M.; Brem, H. *Expert Opin. Drug Saf.* **2007**, *6*(5), 609–621.
10. Plosker, G. L. *Drugs* **2008**, *68*, 2535–2551.
11. Tan, M. L.; Choong, P. F. M.; Dass, C. R. *J. Pharm. Pharmacol.* **2009**, *61*, 131–142.
12. Maeda, H.; Wu, J.; Sawa, T.; Matsumura, Y.; Hori, K. *J. Control. Release* **2000**, *65*(1–2), 271–284.
13. Abuchowski, A.; van Es, T.; Palczuk, N. C.; Davis, F. F. *J. Biol. Chem.* **1977**, *252*(11), 3578–3581.
14. Arakawa, T.; Timasheff, S. N. *Biochemistry* **1985**, *24*(24), 6756–6762.
15. Harris, J. M. *Poly(Ethylene Glycol) Chemistry: Biotechnical and Biomedical Applications*. Plenum: New York, 1997.
16. Harris, J. M.; Chess, R. B. *Nat. Rev. Drug Discov.* **2003**, *2*(3), 214–221.
17. Harris, J. M.; Zalipsky, S. *Poly(Ethylene Glycol) Chemistry and Biological Applications*. The American Chemical Society: New York, 1992.
18. Roberts, M. J.; Bentley, M. D.; Harris, J. M. *Adv. Drug Deliv. Rev.* **2002**, *54*(4), 459–476.
19. Joralemon, M. J.; McRae, S.; Emrick, T. *Chem. Comm.* **2010**, *46*(9), 1377–1393.
20. Ryan, S. M.; Mantovani, G.; Wang, X.; Haddleton, D. M.; Brayden, D. J. *Expert Opin. Drug Deliv.* **2008**, *5*(4), 371–383.
21. Webster, R.; Didier, E.; Harris, P.; *et al*. *Drug Metab. Dispos.* **2007**, *35*(1), 9–16.
22. Maeda, H.; Seymour, L. W.; Miyamoto, Y. *Bioconjug. Chem.* **1992**, *3*(5), 351–362.
23. Thordarson, P.; Le Droumaguet, B.; Velonia, K. *Appl. Microbiol. Biotechnol.* **2006**, *73*(2), 243–254.
24. Vicent, M. J.; Dieudonné, L.; Carbajo, R. J.; Pineda-Lucena, A. *Expert Opin. Drug Deliv.* **2008**, *5*, 593–614.
25. Neuse, E. W. *Met. Based Drugs* **2008**, *2008*, 1–19.
26. Ding, Z.; Fong, R. B.; Long, C. J.; Stayton, P. S.; Hoffman, A. S. *Nature* **2001**, *411* (6833), 59–62.
27. Schmaljohann, D. *Adv. Drug Deliv. Rev.* **2006**, *58*(15), 1655–1670.
28. Duncan, R. *Nat. Rev. Cancer* **2006**, *6*(9), 688–701.
29. Chiefari, J.; Chong, Y. K.; Ercole, F.; *et al*. *Macromolecules* **1998**, *31*(16), 5559–5562.
30. Wang, J.-S.; Matyjaszewski, K. *J. Am. Chem. Soc.* **1995**, *117*(20), 5614–5615.
31. Hawker, C. J.; Bosman, A. W.; Harth, E. *Chem. Rev.* **2001**, *101*(12), 3661–3688.
32. Moad, G.; Rizzardo, E.; Thang, S. H. *Aust. J. Chem.* **2005**, *58*, 379–410.
33. Gemici, H.; Legge, T.; Whittaker, M.; Monteiro, M.; Perrier, S. *J. Polym. Sci. Polym. Chem.* **2007**, *45*(11), 2334–2340.
34. Liu, J. Q.; Liu, H. Y.; Boyer, C.; Bulmus, V.; Davis, T. P. *J. Polym. Sci. Polym. Chem.* **2009**, *47*(3), 899–912.
35. Dong, Z. M.; Liu, X. H.; Tang, X. L.; Li, Y. S. *Macromolecules* **2009**, *42*(13), 4596–4603.
36. Rosselgong, J.; Armes, S. P.; Barton, W.; Price, D. *Macromolecules* **2009**, *42*(16), 5919–5924.
37. Tao, L.; Liu, J. Q.; Tan, B. H.; Davis, T. P. *Macromolecules* **2009**, *42*(14), 4960–4962.
38. Angot, S.; Murthy, K. S.; Taton, D.; Gnanou, Y. *Macromolecules* **2000**, *33*(20), 7261–7274.
39. Liu, J. Q.; Tao, L.; Xu, J. T.; Jia, Z. F.; Boyer, C.; Davis, T. P. *Polymer* **2009**, *50*(19), 4455–4463.
40. Quinn, J. F.; Chaplin, R. P.; Davis, T. P. *J. Polym. Sci. Polym. Chem.* **2002**, *40*(17), 2956–2966.
41. Setijadi, E.; Tao, L.; Liu, J. Q.; Jia, Z. F.; Boyer, C.; Davis, T. P. *Biomacromolecules* **2009**, *10*(9), 2699–2707.
42. Stenzel, M. H.; Davis, T. P. *J. Polym. Sci. Polym. Chem.* **2002**, *40*(24), 4498–4512.
43. Tao, L.; Kaddis, C. S.; Loo, R. R. O.; Grover, G. N.; Loo, J. A.; Maynard, H. D. *Macromolecules* **2009**, *42*(21), 8028–8033.
44. Moad, G.; Rizzardo, E.; Thang, S. H. *Aust. J. Chem.* **2006**, *59*, 24.
45. Moad, G.; Rizzardo, E.; Thang, S. H. *Aust. J. Chem.* **2009**, *62*, 1402–1472.
46. Vasilieva, Y. A.; Thomas, D. B.; Scales, C. W.; McCormick, C. L. *Macromolecules* **2004**, *37*(8), 2728–2737.
47. Mitsukami, Y.; Donovan, M. S.; Lowe, A. B.; McCormick, C. L. *Macromolecules* **2001**, *34*(7), 2248–2256.
48. Sumerlin, B. S.; Donovan, M. S.; Mitsukami, Y.; Lowe, A. B.; McCormick, C. L. *Macromolecules* **2001**, *34*(19), 6561–6564.
49. Donovan, M. S.; Sumerlin, B. S.; Lowe, A. B.; McCormick, C. L. *Macromolecules* **2002**, *35*(23), 8663–8666.
50. Mayadunne, R. T. A.; Rizzardo, E.; Chiefari, J.; *et al*. *Macromolecules* **2000**, *33*(2), 243–245.
51. Mayadunne, R. T. A.; Rizzardo, E.; Chiefari, J.; Chong, Y. K.; Moad, G.; Thang, S. H. *Macromolecules* **1999**, *32*(21), 6977–6980.
52. Schilli, C.; Lanzendorfer, M. G.; Muller, A. H. E. *Macromolecules* **2002**, *35*(18), 6819–6827.
53. Francis, R.; Ajayaghosh, A. *Macromolecules* **2000**, *33*(13), 4699–4704.
54. Ladavière, C.; Dörr, N.; Claverie, J. *Macromolecules* **2001**, *34*(16), 5370–5372.
55. Barner-Kowollik, C.; Quinn, J.; Nguyen, T.; Heuts, J.; Davis, T. *Macromolecules* **2001**, *34*(22), 7849–7857.
56. Barner-Kowollik, C.; Quinn, J. F.; Morsley, D. R.; Davis, T. P. *J. Polym. Sci. Polym. Chem.* **2001**, *39*(9), 1353–1365.
57. Monteiro, M. J.; de Brouwer, H. *Macromolecules* **2001**, *34*(3), 349–352.

58. Wang, J.-S.; Matyjaszewski, K. *Macromolecules* **1995**, *28*(22), 7572–7573.
59. Wang, J.-S.; Matyjaszewski, K. *Macromolecules* **1995**, *28*(23), 7901–7910.
60. Matyjaszewski, K.; Xia, J. *Chem. Rev.* **2001**, *101*(9), 2921–2990.
61. Kato, M.; Kamigaito, M.; Sawamoto, M.; Higashimura, T. *Macromolecules* **1995**, *28*(5), 1721–1723.
62. Nicolas, J.; Mantovani, G.; Haddleton, D. M. *Macromol. Rapid Commun.* **2007**, *28*(10), 1083–1111.
63. Rizzardo, E.; Solomon, D. *Polym. Bull.* **1979**, *1*(8), 529–534.
64. Moad, G.; Rizzardo, E.; Solomon, D. H. *Macromolecules* **1982**, *15*(3), 909–914.
65. Solomon DH, Rizzardo E, Cacioli P. Polymerization process and polymers produced thereby. US Patent 4,581,429, **1986**.
66. Georges, M. K.; Veregin, R. P. N.; Kazmaier, P. M.; Hamer, G. K. *Macromolecules* **1993**, *26*(11), 2987–2988.
67. Hawker, C. J. *J. Am. Chem. Soc.* **1994**, *116*(24), 11185–11186.
68. Hawker, C. J.; Barclay, G. G.; Orellana, A.; Dao, J.; Devonport, W. *Macromolecules* **1996**, *29*(16), 5245–5254.
69. Langer, R.; Tirrell, D. A. *Nature* **2004**, *428*, 487–492.
70. Whitesides, G. M. *Small* **2005**, *1*(2), 172–179.
71. Heredia, K. L.; Maynard, H. D. *Org. Biomol. Chem.* **2007**, *5*(1), 45–53.
72. Gauthier, M. A.; Gibson, M. I.; Klok, H. A. *Angew. Chem. Int. Ed. Engl.* **2009**, *48*(1), 48–58.
73. Boyer, C.; Bulmus, V.; Davis, T. P.; Ladmiral, V.; Liu, J.; Perrier, S. B. *Chem. Rev.* **2009**, *109*(11), 5402–5436.
74. Chipman, S. D.; Oldham, F. B.; Pezzoni, G.; Singer, J. W. *Int. J. Nanomed.* **2006**, *1*(4), 375–383.
75. Duncan, R.; Vicent, M. J. *Adv. Drug Deliv. Rev.* **2010**, *62*(2), 272–282.
76. Li, C.; Wallace, S. *Adv. Drug Deliv. Rev.* **2008**, *60*(8), 886–898.
77. Hawker, C. J.; Wooley, K. L. *Science* **2005**, *309*(5738), 1200–1205.
78. Godwin, A.; Hartenstein, M.; Müller, A. H. E.; Brocchini, S. *Angew. Chem.* **2001**, *113*(3), 614–617.
79. Hu, Z. C.; Liu, Y.; Hong, C. Y.; Pan, C. Y. *J. Appl. Polym. Sci.* **2005**, *98*(1), 189–194.
80. Shunmugam, R.; Tew, G. N. *J. Appl. Polym. Sci. A Polym. Chem.* **2005**, *43*(23), 5831–5843.
81. Theato, P.; Kim, J. U.; Lee, J. C. *Macromolecules* **2004**, *37*(15), 5475–5478.
82. Liu, Y.; Wang, L. X.; Pan, C. Y. *Macromolecules* **1999**, *32*(25), 8301–8305.
83. Matyjaszewski, K.; Coca, S.; Jasieczek, C. B. *Macromol. Chem. Phys.* **1997**, *198*(12), 4011–4017.
84. De La Fuente, J. L.; Canamero, P. F.; Fernandez-Garcia, M. *J. Appl. Polym. Sci. A Polym. Chem.* **2006**, *44*(6), 1807–1816.
85. Fournier, D.; Pascual, S.; Fontaine, L. *Macromolecules* **2004**, *37*(2), 330–335.
86. Li, R. C.; Broyer, R. M.; Maynard, H. D. *J. Polym. Sci. Polym. Chem.* **2006**, *44*(17), 5004–5013.
87. Inglis, A. J.; Barner-Kowollik, C. *Macromol. Rapid Commun.* **2010**, *31*, 1247–1266. doi:10.1002/marc.200900924.
88. Sumerlin, B. S.; Tsarevsky, N. V.; Louche, G.; Lee, R. Y.; Matyjaszewski, K. *Macromolecules* **2005**, *38*(18), 7540–7545.
89. Ladmiral, V.; Mantovani, G.; Clarkson, G. J.; Cauet, S.; Irwin, J. L.; Haddleton, D. M. *J. Am. Chem. Soc.* **2006**, *128*(14), 4823–4830.
90. Hwang, J. Y.; Li, R. C.; Maynard, H. D. *J. Control. Release* **2007**, *122*(3), 279–286.
91. Schilli, C. M.; Muller, A. H. E.; Rizzardo, E.; Thang, S. H.; Chong, Y. K. In *Advances in Controlled/Living Radical Polymerization*, ACS Symposium Series; Oxford University Press: New York, 2003; Vol. 854, pp 603–618.
92. Vosloo, J. J.; Tonge, M. P.; Fellows, C. M.; D'Agosto, F.; Sanderson, R. D.; Gilbert, R. G. *Macromolecules* **2004**, *37*(7), 2371–2382.
93. Hu, Y. C.; Liu, Y.; Pan, C. Y. *J. Appl. Polym. Sci. A Polym. Chem.* **2004**, *42*(19), 4862–4872.
94. Favier, A.; D'Agosto, F.; Charreyre, M. T.; Pichot, C. *Polymer* **2004**, *45*(23), 7821–7830.
95. Savariar, E. N.; Thayumanavan, S. *J. Appl. Polym. Sci. A Polym. Chem.* **2004**, *42*(24), 6340–6345.
96. Wong, L. J.; Boyer, C.; Jia, Z. F.; Zareie, H. M.; Davis, T. P.; Bulmus, V. *Biomacromolecules* **2008**, *9*(7), 1934–1944.
97. Ghosh, S.; Basu, S.; Thayumanavan, S. *Macromolecules* **2006**, *39*(17), 5595–5597.
98. Krieg, A.; Becer, C. R.; Richard, H.; Schubert, U. S. *Macromol. Symp.* **2009**, *275–276*(1), 73–81.
99. O'Reilly, R. K.; Joralemon, M. J.; Hawker, C. J.; Wooley, K. L. *Chemistry* **2006**, *12*(26), 6776–6786.
100. Mellon, W.; Rinaldi, D.; Bourgeat-Lami, E.; D'Agosto, F. *Macromolecules* **2005**, *38*(5), 1591–1598.
101. Sun, G.; Cheng, C.; Wooley, K. L. *Macromolecules* **2007**, *40*(4), 793–795.
102. Sessions, L. B.; Miinea, L. A.; Ericson, K. D.; Glueck, D. S.; Grubbs, R. B. *Macromolecules* **2005**, *38*(6), 2116–2121.
103. Malkoch, M.; Thibault, R. J.; Drockenmuller, E.; *et al. J. Am. Chem. Soc.* **2005**, *127*(42), 14942–14949.
104. Tully, D. C.; Roberts, M. J.; Geierstanger, B. H.; Grubbs, R. B. *Macromolecules* **2003**, *36*(12), 4302–4308.
105. Benoit, D.; Chaplinski, V.; Braslau, R.; Hawker, C. J. *J. Am. Chem. Soc.* **1999**, *121*(16), 3904–3920.
106. Jones, R. G.; Yoon, S.; Nagasaki, Y. *Polymer* **1999**, *40*(9), 2411–2418.
107. Rickert, E. L.; Trebley, J. P.; Peterson, A. C.; Morrell, M. M.; Weatherman, R. V. *Biomacromolecules* **2007**, *8*(11), 3608–3612.
108. Chen, X.; McRae, S.; Parelkar, S.; Emrick, T. *Bioconjug. Chem.* **2009**, *20*(12), 2331–2341.
109. Jia, Z. F.; Wong, L. J.; Davis, T. P.; Bulmus, V. *Biomacromolecules* **2008**, *9*(11), 3106–3113.
110. Zalipsky, S. *Adv. Drug Deliv. Rev.* **1995**, *16*(2–3), 157–182.
111. Ganson, N. J.; Kelly, S. J.; Scarlett, E.; Sundy, J. S.; Hershfield, M. S. *Arthritis Res. Ther.* **2006**, *8*(1), R12.
112. Reynhout, I. C.; Cornelissen, J. J. L. M.; Nolte, R. J. M. *J. Am. Chem. Soc.* **2007**, *129*(8), 2327–2332.
113. Lecolley, F.; Tao, L.; Mantovani, G.; Durkin, I.; Lautru, S.; Haddleton, D. M. *Chem. Comm.* **2004**, *18*, 2026–2027.
114. Bontempo, D.; Heredia, K. L.; Fish, B. A.; Maynard, H. D. *J. Am. Chem. Soc.* **2004**, *126*(47), 15372–15373.
115. Tao, L.; Giuseppe, M.; Lecolley, F.; Haddleton, D. M. *J. Am. Chem. Soc.* **2004**, *126*, 13220–13221.
116. Veronese, F. M. *Biomaterials* **2001**, *22*(5), 405–417.
117. Vazquez-Dorbatt, V.; Tolstyka, Z. P.; Chang, C. W.; Maynard, H. D. *Biomacromolecules* **2009**, *10*(8), 2207–2212.
118. Liu, J.; Bulmus, V.; Barner-Kowollik, C.; Stenzel, M. H.; Davis, T. P. *Macromol. Rapid Commun.* **2007**, *28*(3), 305–314.
119. Heredia, K. L.; Nguyen, T. H.; Chang, C. W.; Bulmus, V.; Davis, T. P.; Maynard, H. D. *Chem. Comm.* **2008**, *28*, 3245–3247.
120. Tao, L.; Liu, J. Q.; Davis, T. P. *Biomacromolecules* **2009**, *10*(10), 2847–2851.
121. Bays, E.; Tao, L.; Chang, C.-W.; Maynard, H. D. *Biomacromolecules* **2009**, *10*(7), 1777–1781.
122. Tao, L.; Kaddis, C. S.; Loo, R. R. O.; Grover, G. N.; Loo, J. A.; Maynard, H. D. *Chem. Comm.* **2009**, (16), 2148–2150.
123. Alconcel, S. N. S.; Grover, G. N.; Matsumoto, N. M.; Maynard, H. D. *Aust. J. Chem.* **2009**, *62*(11), 1496–1500.
124. Grover, G. N.; Alconcel, S. N. S.; Matsumoto, N. M.; Maynard, H. D. *Macromolecules* **2009**, *42*(20), 7657–7663.
125. Tao, L.; Liu, J. Q.; Xu, J. T.; Davis, T. P. *Org. Biomol. Chem.* **2009**, *7*, 3481–3485.
126. Bontempo, D.; Maynard, H. D. *J. Am. Chem. Soc.* **2005**, *127*(18), 6508–6509.
127. Heredia, K. L.; Bontempo, D.; Ly, T.; Byers, J. T.; Halstenberg, S.; Maynard, H. D. *J. Am. Chem. Soc.* **2005**, *127*(48), 16955–16960.
128. Le Droumaguet, B.; Velonia, K. *Angew. Chem. International Edition* **2008**, *47*(33), 6263–6266.
129. Lele, B. S.; Murata, H.; Matyjaszewski, K.; Russell, A. J. *Biomacromolecules* **2005**, *6*(6), 3380–3387.
130. Magnusson, J. P.; Bersani, S.; Salmaso, S.; Alexander, C.; Caliceti, P. *Bioconjug. Chem.* **2010**, *21*(4), 671–678.
131. Gao, W.; Liu, W.; Mackay, J. A.; Zalutsky, M. R.; Toone, E. J.; Chilkoti, A. *Proc. Natl. Acad. Sci. USA* **2009**, *106*(36), 15231–15236.
132. Gao, W.; Liu, W.; Christensen, T.; Zalutsky, M. R.; Chilkoti, A. *Proc. Natl. Acad. Sci. USA* **2010**, *107*(38), 16432–16437.
133. Boyer, C.; Bulmus, V.; Liu, J. Q.; Davis, T. P.; Stenzel, M. H.; Barner-Kowollik, C. *J. Am. Chem. Soc.* **2007**, *129*(22), 7145–7154.
134. De, P.; Li, M.; Gondi, S. R.; Sumerlin, B. S. *J. Am. Chem. Soc.* **2008**, *130*(34), 11288–11289.
135. Heskins, M.; Guillet, J. E. *J. Macromol. Sci. Chem.* **1968**, *2*(8), 1441–1455.
136. Noriko, Y.; Teruo, O.; Hideaki, S.; Fumiko, K.; Yoshio, S.; Yasuhisa, S. *Makromol. Chem. Rapid Commun.* **1990**, *11*(11), 571–576.
137. Chen, G.; Hoffman, A. S. *Bioconjug. Chem.* **1993**, *4*(6), 509–514.
138. Ding, Z.; Long, C. J.; Hayashi, Y.; Bulmus, E. V.; Hoffman, A. S.; Stayton, P. S. *Bioconjug. Chem.* **1999**, *10*(3), 395–400.
139. Stayton, P. S.; Shimoboji, T.; Long, C.; *et al. Nature* **1995**, *378*(6556), 472–474.
140. Bontempo, D.; Li, R. C.; Ly, T.; Brubaker, C. E.; Maynard, H. D. *Chem. Comm.* **2005**, *37*, 4702–4704.
141. Heredia, K. L.; Tolstyka, Z. P.; Maynard, H. D. *Macromolecules* **2007**, *40*(14), 4772–4779.

142. Heredia, K. L.; Grover, G. N.; Tao, L.; Maynard, H. D. *Macromolecules* **2009**, *42*(7), 2360–2367.
143. Heredia, K. L.; Tao, L.; Grover, G. N.; Maynard, H. D. *Polym. Chem.* **2010**, *1*(2), 168–170.
144. Ming, L.; Priyadarsi, D.; Sudershan, R. G.; Brent, S. S. *Macromol. Rapid Commun.* **2008**, *29*(12–13), 1172–1176.
145. Hoffman, A. S.; Stayton, P. S. *Prog. Polym. Sci.* **2007**, *32*(8–9), 922–932.
146. Torchilin, V. P.; Trubetskoy, V. S.; Narula, J.; Khaw, B. A.; Klibanov, A. L.; Slinkin, M. A. *J. Control. Release* **1993**, *24*(1–3), 111–118.
147. Khaw, B. A.; Narula, J. U.S. Pat. 380,168, 1999.
148. Kim, K.; Lee, M.; Park, H.; *et al. J. Am. Chem. Soc.* **2006**, *128*(11), 3490–3491.
149. Nori, A.; Jensen, K. D.; Tijerina, M.; Kopeckov, P.; Kopecek, J. *J. Control. Release* **2003**, *91*(1–2), 53–59.
150. Nori, A.; Jensen, K. D.; Tijerina, M.; Kopečková, P.; Kopeček, J. *Bioconjug. Chem.* **2002**, *14*(1), 44–50.
151. Becker, M. L.; Liu, J.; Wooley, K. L. *Biomacromolecules* **2004**, *6*(1), 220–228.
152. Dalsin, J. L.; Hu, B.-H.; Lee, B. P.; Messersmith, P. B. *J. Am. Chem. Soc.* **2003**, *125*(14), 4253–4258.
153. Lee, S.; Xie, J.; Chen, X. *Chem. Rev.* **2010**, *110*(5), 3087–3111.
154. Ohm, D. K.; Kristi, L. K. *Pept. Sci.* **2010**, *94*(1), 32–48.
155. Duvall, C. L.; Convertine, A. J.; Benoit, D. S. W.; Hoffman, A. S.; Stayton, P. S. *Mol. Pharm.* **2009**, *7*(2), 468–476.
156. Ayres, L.; Vos, M. R. J.; Adams, P. J. H. M.; Shklyarevskiy, I. O.; van Hest, J. C. M. *Macromolecules* **2003**, *36*(16), 5967–5973.
157. Broyer, R. M.; Quaker, G. M.; Maynard, H. D. *J. Am. Chem. Soc.* **2008**, *130*(3), 1041–1047.
158. Chan, W. C.; White, P. D. *Fmoc Solid Phase Peptide Synthesis: A Practical Approach*, 1st ed.; Oxford University Press: New York, 2000.
159. Becker, M. L.; Liu, J.; Wooley, K. L. *Chem. Comm.* **2003**, *2*, 180–181.
160. Hentschel, J.; Bleek, K.; Ernst, O.; Lutz, J.-F.; Borner, H. G. *Macromolecules* **2008**, *41*(4), 1073–1075.
161. Mei, Y.; Beers, K. L.; Byrd, H. C. M.; VanderHart, D. L.; Washburn, N. R. *J. Am. Chem. Soc.* **2004**, *126*(11), 3472–3476.
162. Yanjarappa, M. J.; Gujraty, K. V.; Joshi, A.; Saraph, A.; Kane, R. S. *Biomacromolecules* **2006**, *7*(5), 1665–1670.
163. Holinger, E. P.; Chittenden, T.; Lutz, R. J. *J. Biol. Chem.* **1999**, *274*(19), 13298–13304.
164. Chang, C.-W.; Bays, E.; Tao, L.; Alconcel, S. N. S.; Maynard, H. D. *Chem. Commun.* **2009**, 3580–3582.

4.424. Nanoparticles for Nucleic Acid Delivery

S G Spain, University of Nottingham, Nottingham, UK
G Yaşayan, University of Nottingham, Nottingham, UK; Marmara University, Haydarpaşa, İstanbul,Turkey
M Soliman, University of Nottingham, Nottingham, UK; Ain Shams University, Cairo, Egypt
F Heath, University of Nottingham, Nottingham, UK
A O Saeed, University of Nottingham, Nottingham, UK; National University of Ireland, Galway, Ireland
C Alexander, University of Nottingham, Nottingham, UK

© 2011 Elsevier Ltd. All rights reserved.

4.424.1. Introduction 390
4.424.1.1. Therapeutic Opportunities for Nucleic Acids 390
4.424.1.1.1. DNA therapies 390
4.424.1.1.2. Antisense and small-interfering RNA therapies 390
4.424.1.2. Formulation Issues for Nucleic Acid Therapeutics 391
4.424.1.2.1. Barriers to nucleic acid delivery 391
4.424.2. General Classes of Nucleic Acid Delivery Systems 391
4.424.2.1. Viral Vectors for Nucleic Acid Delivery 393
4.424.2.2. Nonviral Vectors for Nucleic Acid Delivery 393
4.424.3. Classes of Nonviral Vectors 393
4.424.3.1. Cationic Lipids and Liposomes 393
4.424.3.1.1. Cytocompatibility of cationic lipids and liposomes 395
4.424.3.2. Synthetic Peptides 395
4.424.3.2.1. Lysine-containing peptides 395
4.424.3.2.2. Arginine-containing peptides (CPPs) 396
4.424.3.2.3. Histidine-containing peptides (endosomal escape peptides) 396
4.424.3.2.4. Cysteine-containing peptides 396
4.424.3.3. Chitosan and Derivatives 396
4.424.3.4. Synthetic Polymer/Polyplex Carriers 397
4.424.3.4.1. Polycations for condensing nucleic acids 398
4.424.3.4.2. Polymers for nucleic acid encapsulation 400
4.424.3.4.3. Polymer micelles and vesicles as NP nucleic acid delivery systems 402
4.424.4. Opportunities and Challenges in NP Therapeutics: Biological Barriers to Nucleic Acid Delivery 403
4.424.4.1. Systemic Barriers 403
4.424.4.2. Cellular Barriers to Uptake of Nucleic Acids 404
4.424.4.3. Overcoming Systemic and Local Biological Barriers: Surface Coating of NPs with Hydrophilic Polymers and Targeting Agents 405
4.424.4.3.1. Sterically stabilized PEGylated polyplexes 405
4.424.4.3.2. Overcoming local biological barriers: surface modification of NPs with targeting ligands 406
4.424.4.3.3. Chimeric/hybrid NPs for overcoming systemic barriers gene delivery 406
4.424.4.4. Formulation Issues for Nucleic Acid Therapeutics – Binding Between Vector and Nucleic Acid: A Balancing Act 407
4.424.5. Conclusions 407
References 407

Abbreviations

DOPE	Dioleoylphosphatidylethanolamine
DOTMA	Dioleyloxypropyl trimethylammonium chloride
DPA	2-(Diisopropylamino)ethyl methacrylate
MPC	2-(Methacryloyloxy)ethyl phosphorylcholine
PAMM	Poly(amidoamine)
p[DMAEMA]	Poly[2-(*N*,*N*′-dimethylamino)-ethyl methacrylate]
PEG	Poly(ethylene glycol)
PEI	Poly(ethyleneimine)
pHPMA	Poly[*N*-(2-hydroxypropyl)methacrylamide]
PLGA	Poly(lactic acid-*co*-glycolid acid)
Polyplex	Polymer–nucleic acid complex
RPC	Reducible polycation
siRNA	Short-interfering RNA
Tf	Transferrin

4.424.1. Introduction

Gene therapy employs nucleic acids to treat or prevent disease. The nucleic acids may be entire genes, partial genes, oligonucleotides, and synthetic analogs of DNA and RNA such as morpholino-oligonucleotides and peptide nucleic acids. There is great clinical interest in using gene therapy for treating a wide range of diseases, including single gene disorders, such as cystic fibrosis and Duchenne muscular dystrophy, and complex, multifactorial diseases such as neurodegeneration and cancers. At present, over 2000 trials in gene therapy are recruiting, in progress, or completed (clinicaltrials.gov), yet only two treatments have received worldwide approval: gendicine,[1] an adenovirus engineered to express p53 for the treatment of head and neck carcinoma, has been approved in China and Vitravene (Fomivirsen), a synthetic oligonucleotide, has FDA approval for the treatment of cytomegalovirus retinitis in human immunodeficiency virus (HIV)/AIDS patients but has been removed from the market by its manufacturer.[2] There are many factors that have limited the translation of gene therapy from the bench to the bedside, not least the relative youth of the field and the complex nature of the therapeutics compared to traditional small molecules. One particularly important problem that has hampered clinical acceptance is the inherent difficulty in delivering nucleic acids specifically to a target site, at a therapeutic dose and with a practical administration regime. The human body is a hostile place for unknown nucleic acids with multiple barriers to delivery and the requirements for an efficient delivery vehicle; protection from degradation, delivery into cells, and subsequent release of the delivered material into the cytosol are challenging. If effective methodologies for the delivery of nucleic acids can be achieved, then gene therapy may finally live up to the promise it has offered.

This chapter focuses on nanoparticles (NPs) for delivering nucleic acids, a field that has attracted an ever-increasing interest in the last 20 years. The challenges for biomaterials to deliver DNA, RNA effectively and reliably , and related therapeutics remain significant, but the therapeutic opportunities are enormous.

4.424.1.1. Therapeutic Opportunities for Nucleic Acids

Gene therapies may be loosely divided into two classes: gene addition/replacement and gene silencing. Gene addition/replacement is the best known of these and involves the replacement of a gene that is mutated, resulting in lost or incorrect function, by delivery of a normal allele. Hemophilia B, for example, is a hereditary disorder characterized by a mutation in the gene that encodes for the protein factor IX which is, in part, responsible for blood coagulation. In severe cases, where circulatory levels of factor IX are <1% of normal, this leads to episodes of spontaneous bleeding which can prove fatal. Gene replacement therapy for hemophilia B involves the introduction of a normal gene for factor IX resulting in restoration of blood coagulation activity.[3] Genes that do not normally exist in the target cells may also be introduced, a strategy that is often used in potential cancer treatments by introduction of a viral genome; once introduced, virus is produced in the cell resulting in its destruction. Gene silencing therapies, typified by antisense methodologies, allow for the removal of a gene that is upregulated as part of disease pathology. For example, the antiapoptopic protein Bcl-2 is upregulated in many multi-drug-resistant cancers;[4,5] silencing the gene that encodes for Bcl-2 may result in improved tumor susceptibility to apoptosis-inducing chemotherapeutics such as doxorubicin.

4.424.1.1.1. DNA therapies

DNA therapies are used for gene addition/replacement. Those under development include treatments for hereditary genetic disorders, such as hemophilia B, cystic fibrosis, and the retinal disorder Leber's congenital amaurosis (LCA), that are caused by single mutated genes, as well as multifactorial diseases such as cancer. The replacement of malformed factor IX in hemophilia B has been demonstrated in a canine model using a recombinant adeno-associated viral (rAAV) vector to deliver the normal gene. Therapeutic levels of factor IX were achieved and sustained for long periods (>2 years) postadministration, but expression was limited to weeks when assessed at clinical trial.[3] LCA is a degenerative disorder of the retina that begins in childhood and results in complete blindness by adulthood. Mutation of any one of a number of genes can result in LCA, with research to date focusing on mutation in the gene RPE65. Phase I clinical trials for the treatment of LCA with rAAV vectors delivering normal RPE65 have demonstrated some restoration of sight in patients.[6,7] A later trial found that younger patients, with less degeneration prior to treatment, could regain sufficient sight to negotiate a maze in low light conditions.[8] Gene replacement is also the basis of action for gendicine in the treatment of cancers with a mutation of the tumor suppressor gene TP53 that encodes the tumor suppressor protein p53. The introduction of antiangiogenic genes, that inhibit the production of tumor vasculature and consequent blood supply, allows tumors to be starved of nutrients and also prevents removal of waste products from the tumor, resulting in necrosis. Additional genes have been added to improve the spread through tumors. Alleles encoding for fusogenic membrane proteins, proteins that cause cells to fuse into a large multinuclear *syncytia*, allow a single infected cell to fuse with many neighboring cells; as these syncytia grow, they become nonviable and die via necrosis.[9]

4.424.1.1.2. Antisense and small-interfering RNA therapies

Antisense oligonucleotides are a family of short (<50 bp), noncoding oligonucleotides that bind to RNA via Watson–Crick base pair matching, resulting in modulation of RNA function.[10] Although RNA function may be affected by several mechanisms, for therapeutics, two of the most heavily studied are RNA interference (RNAi) and RNase H-mediated degradation.[10,11] RNAi is a cellular gene regulatory process that involves the binding of oligonucleotides, for example, small-interfering RNA (siRNA) and microRNA (miRNA), to posttranscriptional messenger RNA (mRNA) as part of an RNA-induced silencing complex (RISC).[12] When siRNA base pair matching is complete, the mRNA is then cleaved by RISC, resulting in the silencing of the target gene. For miRNA, where some mismatching is typical, mRNA translation is disrupted, resulting in downregulation of the target gene. The ability to silence genes has made siRNA-induced RNAi an invaluable tool in

determining gene function. RNase H-mediated cleavage is a nuclear process that is responsible for removal of the RNA primer during DNA replication.[13] Its degradation can be induced by introducing an antisense oligonucleotide for the RNA target.

Several therapeutic targets exploiting these mechanisms have been identified and several therapies are in various phases of clinical trial.[10,14,15] Antisense phase III trials currently include oblimersen (in conjunction with fludarabine and rituximab), which targets the antiapoptotic Bcl-2 protein, for the treatment of various cancers, including non-Hodgkin's lymphoma;[16] Aganirsen, which targets insulin receptor substrate-1 reducing angiogenesis, for the prevention of corneal graft rejection;[17] and Bevasiranib, which targets vascular endothelial growth factor, for the treatment of age-related macular degeneration/diabetic macular edema.[18] Fomivirsen (Vitravene) binds to mRNA responsible for the production of protein IE2 which is essential for replication of cytomegalovirus.[2]

4.424.1.2. Formulation Issues for Nucleic Acid Therapeutics

A number of formulation constraints for nucleic acid drugs are common to those of all controlled drug delivery systems. For any drug that is especially potent, or unstable under certain conditions, delivery systems are needed that can control the rate of drug release such that steady plasma levels are obtained. In addition, there is the desire for a low dosage volume, a need to avoid toxicity, and an ability to target the drug to the disease sites. Accurate and efficient dosing leads to improved patient compliance and enhanced therapeutic outcome – this is particularly important for cancer therapies where the aim is to selectively kill the cancer cells while leaving healthy cells intact. Many controlled drug delivery systems have accordingly been developed, and in a variety of formats, including emulsions, micelles, micro- and nanocapsules, micro- and nanospheres, and molecular complexes/conjugates.

However, in contrast to more common small molecule drugs, biopolymer drugs such as DNA and RNA have further requirements in terms of formulation and delivery on account of their much higher molecular weights. Although some mechanical delivery routes, such as microneedle injections, gene guns, electroporation, and hydrodynamic techniques, have been developed for direct introduction of unprotected nucleic acids, these have had limited success. Being large molecules, ranging from 13 kDa for a siRNA duplex to several million Dalton for a typical DNA plasmid, they are subject to physical shear forces, which are often important in an encapsulation process. In addition, owing to their biological origin, they are susceptible to *in situ* degradation by enzymes, capture (opsonization), and eventual destruction by the immune system. Delivery systems are thus required not only to protect DNA and RNA therapeutics from chemical and physical degradation before reaching their target site, but also to effect release once they have reached the target site. Again, the polymeric and charged nature of the nucleic acids renders the release and (intra) cellular uptake processes more problematic than for small lipophilic drugs. An outline description of the hurdles to gene delivery is given in the next section, followed by the evaluation of the classes of NP delivery systems developed to protect, transport, and release nucleic acids. More detailed considerations of key biological barriers en route to the desired therapeutic outcome are included for specific NP systems as these can vary with the type and function of each delivery system.

4.424.1.2.1. Barriers to nucleic acid delivery

For any drug to exert a therapeutic effect, it must reach its physiological target, which is in the nucleus or mitochondria for DNA and in the cytoplasm for RNA. Adequate adsorption and access to the target sites are important attributes of nanoparticulate nucleic acid delivery systems, as are prevention of nonspecific distribution in the body, premature metabolism, and premature excretion. The efficiency of naked DNA delivery is significantly hampered because of the existence of many extracellular and intracellular barriers. However, long-term gene expression is possible if the target cell is muscle (postmitotic) or hepatocytes (slowly mitotic). Therefore, to improve the delivery efficacy, nucleic acid therapeutics must be condensed to a small size and protected from serum and intracellular nucleases. The nucleic acid must be delivered to the target cell, cross the external cell membranes passively or actively, leave any subcellular organelles (such as endosomal compartments), avoid degradative enzymes, and then must escape traffic to the digesting lysosomes. Furthermore, if the biopolymer is DNA, it must cross into the nucleus ready for transcription. NP carriers must thus protect the nucleic acids and help transport them across all these cell barriers, yet ensure release at the correct time. In addition, for an injectable delivery formulation, the carriers with encapsulated/complexed nucleic acids must be capable of extended circulation in the bloodstream in order to have a chance to reach their cellular target (**Figure 1**).

NPs are inherently of the correct size range to gain access to tissues and cells (<250 nm in diameter is preferable), and can be stabilized to enhance circulation time by charge or by coating with a hydrophilic polymer such as poly(ethyleneglycol) (PEG). For commercial development, it is also desirable for a nucleic acid carrier to have adaptable functionality, so that one 'platform carrier' can be adapted for application across a wide range of disease targets with reliable chemical and formulation properties. Above all, the NPs must be safe, that is, nontoxic, nonimmunogenic, and fully cleared from the body after drug delivery.

4.424.2. General Classes of Nucleic Acid Delivery Systems

A variety of nucleic acid delivery systems (often termed 'vectors') are being developed. In general, these are in the submicron size range and hence fit broadly into the accepted definitions of NPs. It should be noted, however, that for pulmonary delivery of nucleic acids, particles in the 1–5 μm size range may be used for the initial delivery to the desired physiological site, and implantable biodegradable matrices of much larger size ranges are also under consideration for controlled release applications. Nevertheless, most DNA delivery vectors have been designed to accomplish the function of protecting their delicate biopolymer cargo through condensing and compacting the DNA into particles smaller than 1 μm in diameter.

For this chapter, we consider NPs to be colloidal species with submicron diameters among which the most widely

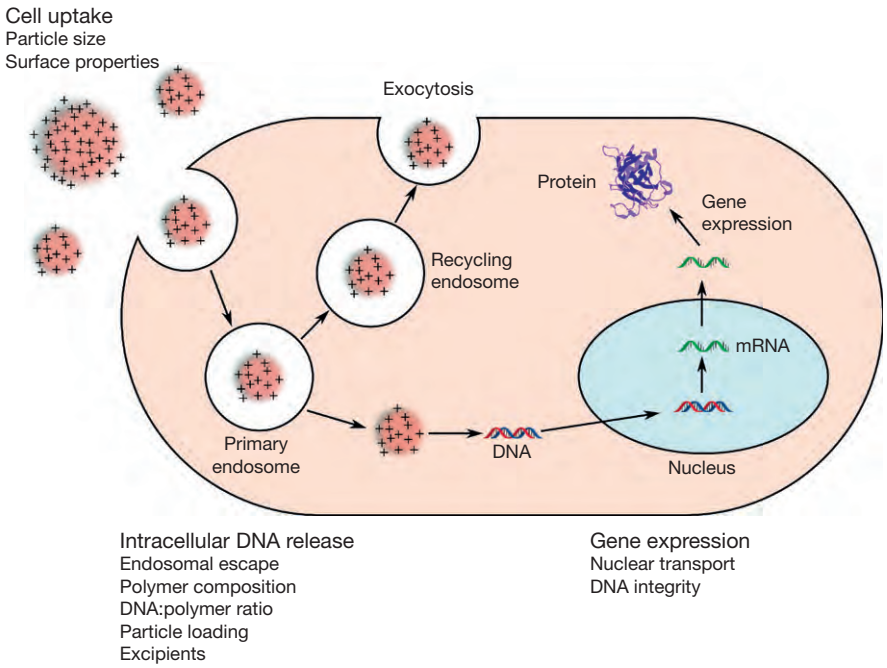

Figure 1 Formulation factors affecting the delivery of nucleic acids.

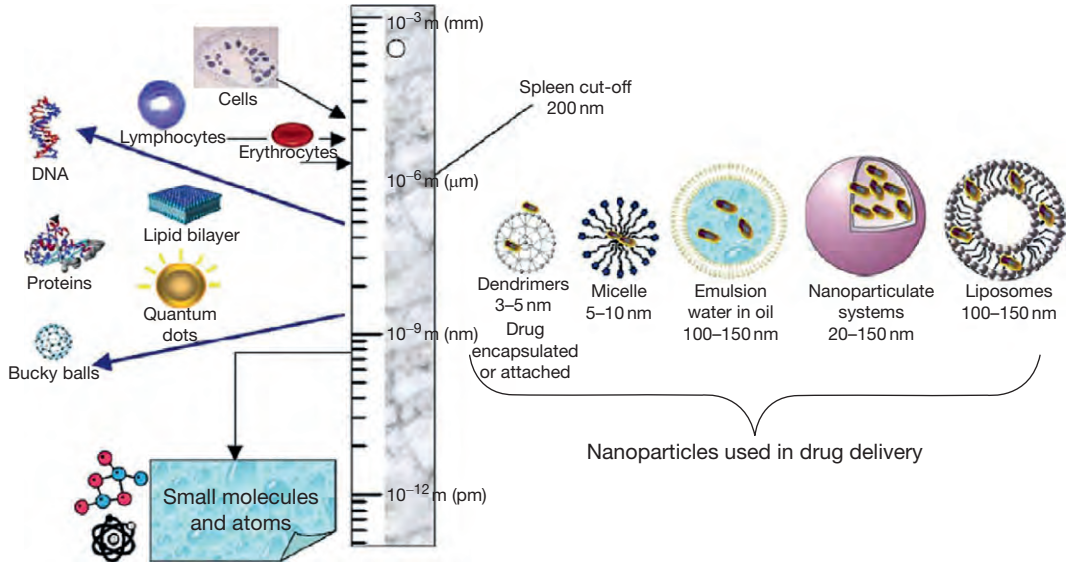

Figure 2 Classes of nanoparticles and carriers for drug delivery applications. Reprinted from Arruebo, M.; Fernández-Pacheco, R.; Ibarra, M. R.; Santamaría, *J. Nanotoday* **2007**, *2*, 22–32.

explored for biomedical applications are those between 10 and 500 nm in diameter. This class of materials is being investigated as carriers both for conventional drugs and biopolymer therapeutics, such as peptides, proteins, and enzymes, as well as nucleic acids.[19] They can be prepared from biodegradable or nonbiodegradable, inorganic, organic, and biological materials. Many components ranging from lipids, natural polymers such as albumin, gelatine, and derivates of alginate, through to a host of synthetic polymers have been evaluated (Figure 2).[20,21]

As noted previously, DNA and RNA are large, negatively charged, hydrophilic macromolecules that do not cross biological membranes efficiently. Compaction and protection inside a nanoscale carrier is a means by which the transport of nucleic acids can be enhanced, as particles in this size range can be taken up into biological tissue and subcellular organelles by a variety of processes. Classes of NP vectors for gene delivery fall broadly into two types: viral and nonviral, but irrespective of their classification, an ideal gene delivery vector needs to meet the following requirements:

- Ability to transport nucleic acids of varying sizes
- Ability to transduce cells

- Ability to target a specific cell type and/or subcellular organelle
- Controlled release of nucleic acid at target site
- Low toxicity and immunogenicity.

In addition, nucleic acid vectors need to be able to cross biological barriers without adverse interaction with other cells, blood components, or the reticuloendothelial system (RES).[22]

4.424.2.1. Viral Vectors for Nucleic Acid Delivery

Nature has solved the problem of nucleic acid delivery with its own nanoscale vehicles: viruses. Viruses are prototypical gene therapy agents that have evolved to fulfill many of the roles required of a gene therapy vector (see **Chapter 2.202, Engineering Viruses For Gene Therapy**). It is, therefore, unsurprising that much research has focused on the production of viruses as gene therapy vectors, several of which have been extensively reviewed recently and to which the reader is referred for a more detailed coverage of the topic.[23–26] Viral vectors have several advantages over their nonviral counterparts, including established mechanisms for cell entry, nucleic acid release and nuclear transport, and long-term gene expression through sustained replication (e.g., adeno-associated virus) or gene integration into the host genome (e.g., retroviruses). Despite their prevalence, more than two-thirds of gene therapy clinical trials to date have used viral vectors (http://www.wiley.co.uk/genmed/clinical), there are still outstanding barriers to the widespread use of viral vectors. First and foremost are safety concerns regarding the immunogenicity, toxicity, and mutagenicity of viral vectors. Adenovirus serotype 5 (Ad5), the most widely used vector in clinical trials, has been linked to severe immune response resulting in a patient fatality.[27,28] Gene integration has also been linked to leukemia-like disease in children treated with murine leukemia virus for severe combined immunodeficiency disorder.[29] These problems have been alleviated to some extent through modification of viral vectors to remove the gene(s) responsible for pathogenicity or improve target selectivity. The other disadvantages of viral vectors may be summarized as a lack of versatility and the resulting cost of development, regulatory clearing, and manufacture. No virus is universally applicable to gene therapy due to the aforementioned safety concerns, packaging capacity (the size of a genome that can be contained within a virus), and their compatibility with the desired administration route. Continuing the Ad5 example, stability has been demonstrated to be sensitive to both increases and decreases in genome length, limiting the size of genes that may be added or removed as required. Additionally, systemic (intravenous) delivery is complicated by Ad sequestration by erythrocytes[30] and commonality of anti-Ad neutralizing antibodies.[31,32] The genetic modifications required to tailor a viral vector to a disease and the resulting procedures to demonstrate its regulatory safety and subsequent manufacture make viral gene therapy financially very costly. Synthetic nonviral NPs offer a simpler, cheaper method of nucleic acid delivery that may be applicable to a wider range of diseases.

4.424.2.2. Nonviral Vectors for Nucleic Acid Delivery

Nonviral vectors are potentially advantageous compared to viral vectors due to the possibilities of enhanced stability, ease of modification, low acute toxicity, low cost, standardized production, better (bio)safety profile, and higher flexibility. Although nonviral vectors can be derived from inorganic materials, synthetic or natural lipids and polymers, dendrimers, and combinations of these, for this chapter, we concentrate on organic and polymeric materials, as inorganic vectors have been the subject of a number of recent reviews.[33–35] The resultant vectors can be in the form of liposomes, micelles, vesicles, or polyelectrolyte complexes, but nearly all are generated as NPs with various degrees of structural rigidity. The association of many of these carriers with DNA or RNA is via charge–charge interaction, utilizing cations in a lipid or polymer to form polyelectrolyte complexes with the polyanionic nucleic acid. Complexes of nucleic acids with cationic lipids are often described as lipoplexes, while those with polymers are generally referred to as polyplexes.[22,36–39] Other NP delivery systems encapsulate DNA or RNA without charge interactions by kinetically trapping the nucleic acid in a polymeric matrix or reservoir, for example, inside the hydrophilic core of a vesicle or polymersome. In general, nonviral vectors are less immunogenic than viral systems and can therefore be administered repeatedly to the patient without leading to severe immune responses.[40,41] Another major advantage is greater flexibility regarding the size of the delivered transgenes compared to viral delivery. For example, the titers of recombinant adenoviruses are heavily reduced when the genome is either too short or too long.[42] However, it should be noted that to date, nonviral vectors have shown low overall transfection efficiency, and the resultant gene expression has often been of short duration. Some nonviral vectors have also been shown to be toxic.

4.424.3. Classes of Nonviral Vectors

4.424.3.1. Cationic Lipids and Liposomes

Cationic lipids are amphiphilic molecules in which the water-soluble group is positively charged. Generally, they may be considered to be composed of three sections: a hydrophobic lipid group, or anchor, which may be either one or two fatty acid or alkyl moieties or a cholesterol moiety, a hydrophilic amino head group, and a linker that connects these moieties. Lipid anchors have typically been chosen for their ability to facilitate lipoplex fusion with the cell membrane and to aid in destabilization of intracellular barriers such as endosomal compartments[43] while the amino moieties bind the nucleic acid electrostatically serving to condense it.[44,45] The electrostatic interaction between lipids in cationic liposomes and anionic biopolymers results in a polyelectrolyte interaction as the self-assembled cationic lipids behave, in effect, as a polycation. The resulting materials are able to associate into a range of different structures with nucleic acids, including DNA/RNA adsorbed onto the surface of cationic liposomes, encapsulated within the interior of the liposome itself or the nucleic acid absorbed between the lamellae of multilamellar structures.[46,47]

Focused methodical research into lipid-mediated DNA delivery *in vitro* can be considered to have started in 1987, with the discovery that high transfection levels could be obtained with DNA complexed to dioleyloxypropyl trimethylammonium chloride:dioleoylphosphatidylethanolamine (DOTMA:DOPE) liposomes in the JZ-1 cell line.[48] (A 1:1 mixture

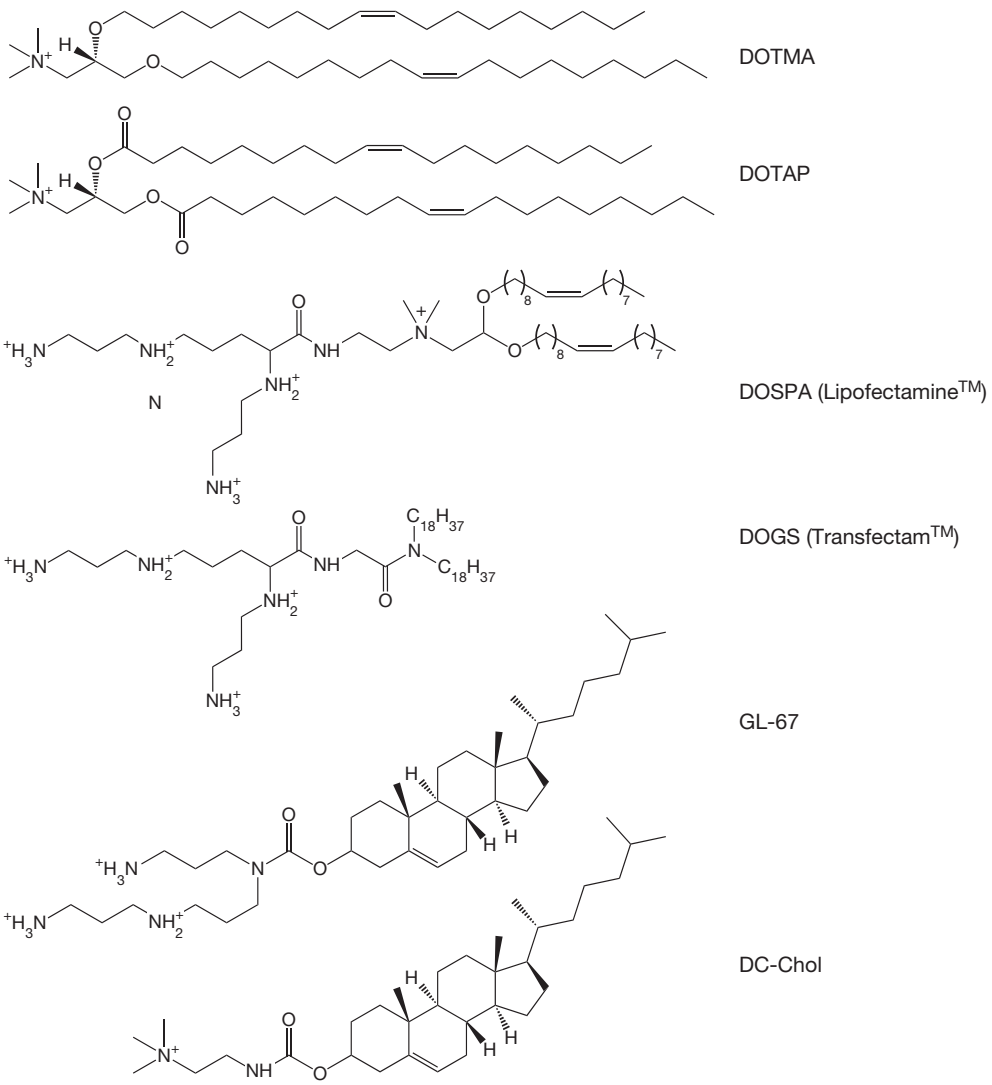

Figure 3 Example structures of cationic lipids. *N*-[1-(2,3-dioleyloxy)propyl]-*N*,*N*,*N*-trimethylammonium chloride (DOTMA). 1,2-bis(oleoyloxy)-3-(timethylammonio)propane (DOTAP). DOSPA, dioctadecyl amino glycyl spermine (DOGS). *N*-4-spermine cholesteryl carbamate (GL-67). 3-β-[*N*-(*N*′,*N*′-dimethylaminoethane)-carbamoyl] cholesterol (DC-Chol).

of DOTMA:DOPE has since been commercialized as Lipofectin (GIBCO-BRL).) In this example, DNA was simply mixed with the cationic lipids as opposed to the encapsulation of DNA into the liposome. Since this groundbreaking work, many other cationic lipids have been extensively studied as nonviral gene carriers.[48] In addition to DOTMA and DOPE, common examples include 1,2-bis(oleoyloxy)-3-(trimethylammonio)propane (DOTAP),[49] dioctadecylamidospermine (DOGS, Transfectam™),[50] 3-β-[*N*-(*N*′,*N*′-dimethylaminoethane)-carbamoyl] cholesterol (DC-Chol),[51] and GL-67[52] (see **Figure 3** for structures). In general, these have been used in the form of liposomal systems, as these have been demonstrated to reduce extracellular degradation by DNase, resulting in increased transfection efficiency.[53]

Structure–activity relationship studies have demonstrated that even subtle differences in the head group structure, such as a change from alanine to its isomer β-alanine, can cause significant differences in transfection efficiencies of certain cell lines.[54] Postmitotic cells are considered to be more difficult to transfect than dividing cells, as many transfection reagents rely on the breakdown of the nuclear envelope in order to take up the therapeutic DNA (usually in the form of a plasmid, or pDNA). Lipofectamine 2000, a widely used commercially available vector, has been found to be efficient in the transfection of postmitotic neuronal cells (rat embryonic cortical and hippocampal tissues)[55] and is able to facilitate the delivery of DNA through intact nuclear membranes.[56] Lipoplexes formulated with a high positive charge have shown charge-related toxicity and therefore, *in vivo* applications of these gene delivery agents require them to be administered as close to the target site as possible.[57] This administration preference has recently been demonstrated in several *in vivo* studies. Experiments conducted by Saada *et al.* involved the instillation of a transfection solution of bis-guanidinium-tren-cholesterol/dioleoylphosphatidylethanolamine (BGTC/DOPE) cationic liposomes into sheep fetus airways, combined with tracheal occlusion, to treat lung hypoplasia associated with congenital diaphragmatic

hernia (CDH). The gene therapy strategy required dosing of keratinocyte growth factor to the airways to improve the development of type II alveolar cells, which are found to be of reduced abundance in CDH cases treated purely with tracheal occlusion. The tracheal occlusion maintained the transfection reagent in contact with the target region, and the liposomes used were found to mediate efficient transfection into the sheep airways.[58] A preliminary study involving a single patient involved treatment of hereditary inclusion body myopathy by intramuscular injection of 1,2-dioleoyl-3-trimethylammonium-propane (DOTAP) and cholesterol liposomes carrying the therapeutic gene. An improvement in muscle function was observed in some of the muscle groups treated, and limited toxicity was noted.[59]

Lipids featuring polycationic spermine head groups, such as DOGS, and GL-67, have been demonstrated to form lipoplexes with better defined, more compact (50–100 nm), structures compared to other cationic lipids and promote more efficient escape from endosomal compartments.[60] GL-67:DOPE liposomes have been demonstrated to yield a 1000-fold increase in transfection compared to naked DNA and 100-fold compared to other cationic lipids in a murine model via nasal delivery to lungs.[52]

Careful design of formulation has enabled lipoplexes to be produced using anionic lipids, in which ternary complexes of endogenous-occurring nontoxic anionic lipids (e.g., DOPG/DOPE mixtures), combined with Ca^{2+} ions (to provide cation content), and nucleic acids were found to impart high transfection efficiency and low toxicity.[61–63] It has been proposed that excess Ca^{2+} ions associated with the lipoplex surface could be responsible for its interaction with the cell surface, thus facilitating cellular uptake.[61]

4.424.3.1.1. Cytocompatibility of cationic lipids and liposomes

Despite their widespread use in lab-based studies, there are still some concerns for liposomal delivery vectors. As with many other nonviral vectors, cell toxicity, poor nucleic acid loading, instability, and inefficient entry to the cell (and for DNA to the nucleus) still represent major hurdles to their intended application.[46,64–67] It has also been found that DNA lipoplexes can display increased cytotoxicity compared to the cationic lipid alone, resulting in cellular apoptosis.[68] In an attempt to overcome these hurdles, other groups that target the lipoplexes to specific cells or subcellular compartments may be coupled with cationic lipid surfaces. The transactivating transcriptional (TAT) activator peptide from HIV has been reported to enhance cell entry by a nonendocytotic pathway.[69] TAT peptide–liposome–DNA complexes have been shown to possess both improved efficiency of gene delivery and reduced toxicity as compared to cationic lipids alone.[70] Antibody-recognizing cell surface molecules and tissue-specific ligands such as asialoglycoprotein and transferrin (Tf) have also been attached to the surface of liposomes. Accordingly, it is possible that enhanced targeted liposomal formulations may yet prove advantageous in practical nucleic acid delivery. In addition, it is worth considering that specific modalities in nucleic acid delivery can be more or less important for classes of cationic lipids and other vectors dependent on the particular application. Thus, transfection by cationic lipids is widely used for *in vitro* cell culture experiments, where toxicity is less of a problem, whereas for *in vivo* therapies or *ex vivo* transfection and reinfusion, cation-induced toxicity is much more problematic.

4.424.3.2. Synthetic Peptides

Peptides and novel polypeptides are an important class of nucleic acid vectors. Some polypeptides are inherently favorable for delivery in the cytosol as they possess specific amino acid sequences that can destabilize cellular and subcellular membranes.[71,72] Several peptide sequences have been shown to have pH-selective endosomolytic effects,[73] while peptides rich in basic residues, such as lysine and/or arginine, exhibit the ability to efficiently condense large nucleic acids into small, compact particles.[74,75] Additionally, there are cargo proteins containing nuclear localization signals (NLS), which can be recognized by import carriers (such as importin-β), in the cytoplasm that have been found to be essential for nuclear translocation capability.[76,77] In recent years, the design of polypeptides capable of responding to environmental changes or stimuli (e.g., the redox potential gradient) by alteration of their properties and behavior has begun to be exploited for improving the efficacy of the delivery process. Redox-sensitive polyplexes based on such cationic peptides represent a promising option because of the possibility of combining DNA condensation capability with an inherent biological activity of the peptides.[78,79] Various basic amino acids have been utilized in the manufacture of synthetic peptide vectors, primarily lysine, arginine, and histidine (pK_a values of ~10.5, 12.5, and 6, respectively), often combined with the thiol-functional amino acid cysteine.

4.424.3.2.1. Lysine-containing peptides

Lysine has a well-documented efficacy in polyplex formation due to the efficient anion-binding capability of its positive side chains, which are fully protonated at physiological pH (pK_a ~10.5). This in turn increases extracellular stability of polyplexes and their cellular uptake via endocytosis due to the electrostatic binding to proteoglycans on cell surfaces. Lysine has generally been converted to the homopolymer, poly-L-lysine (PLL), which is the most commonly used polypeptidic gene delivery vector. PLL is a biodegradable material that can mediate gene delivery both *in vitro* and *in vivo*.[80,81] PLL is commercially available in various molecular weights ranging from approximately 1 to 300 kDa. Its pK_a value is ~10 which is relatively high compared to other polypeptidic vectors. This property enables it to package nucleic acids into nanoparticulate complexes, masking the negative charge of DNA and RNA and shielding against enzymatic and hydrolytic degradation. High-molecular-weight PLL has a greater net positive charge and therefore forms tighter, smaller, and more stable complexes than the low-molecular-weight PLL[82,83]; however, high-molecular-weight PLL has shown high levels of cytotoxicity.[74] In general, PLL has been regarded as quite inefficient in terms of endosomal escape and transfection efficiencies,[46] and is less potent than poly(ethyleneimine) (PEI).[84] The poor gene expression observed *in vitro* when PLL was used alone necessitated the concomitant addition of endosomolytic reagents such as chloroquine or a fusogenic peptide.[81,85,86] PLL has been enhanced as a vector by direct modification, such as the

incorporation of cleavable bonds in the backbone or side chains, to reduce *in vivo* toxicity and to enhance transfection efficiency due to facilitated release of nucleic acid. It has also been possible to attach targeting ligands, such as sugars, folic acid derivatives, antibodies, and proteins (e.g., Tf), allowing receptor-mediated gene delivery to be achieved.[87] Transfection efficacy of PLL has also been improved by conjugation to other peptides such as fusogenic or cell-penetrating peptides (CPPs) or modification with histidine to enhance endosomal escape.[88]

4.424.3.2.2. Arginine-containing peptides (CPPs)

Arginine-containing peptides are highly cationic and hydrophilic, and have been shown to be promising biological transport systems. This has been attributed to the arginine residues causing translocation of vectors to the cell membrane, allowing access to the cellular interior and leading to efficient internalization of cargo.[89] Certain specific arginine-based systems are strongly membrane-permeabilizing and have come to be referred to as protein transduction domains (PTDs) or CPPs. Examples of these peptides are TAT, the transcription activating factor of the HIV,[69,90] and the drosophila homeodomain protein-derived penetration.[91] The TAT peptide has been the most frequently investigated protein-derived CPP, and its translocation efficiency seems to be due to a small cluster of basic amino acids (GRKKRRQRRR) containing mainly arginines and lysines[90,92]; cell surface binding of TAT residues is not dependent on specific receptors.[93,94] TAT has been widely exploited for the intracellular uptake of different size cargoes in different cell types both *in vitro* and *in vivo*[95,96]; studies have also reported facilitated delivery of TAT-conjugated protein into live mice tissue following intraperitoneal injection.[97–99]

4.424.3.2.3. Histidine-containing peptides (endosomal escape peptides)

Histidine-based peptides have also been explored for gene delivery studies due to their biocompatibility and lack of toxicity.[100] The imidazole side chain of histidine has a pK_a of ~6.0[81,101] and thus becomes cationic in a slightly acidic medium. These histidine-rich peptides are able to buffer effectively at endosomal pH, resulting in an influx of counterions into the endosomal compartments (the proton sponge hypothesis[102]) as well as form strong electrostatic interactions with the subcellular membranes when protonated, allowing the endosomal escape of DNA.[103]

A peptide containing several histidines, H5WYG (GLFHAIAHFIHGGWHGLIHGWYG), was designed by Midoux and coworkers and was shown to efficiently permeabilize cell membranes at pH 6.4. H5WYG also increased the expression of genes transferred to cells and was resistant to protein adsorption due to its neutral charge at physiological pH.[103,104] Polyhistidine, containing a high density of imidazole groups, has been investigated as a gene vector but, due to its insolubility at physiological pH (at pH > 6.0), it has required covalent conjugation to more water-soluble components, such as to gluconic acid (glycosylated polyhistidine), for formation of complexes with nucleic acids.[105] Polylysine conjugated to the Tf has been added to DNA/poly-L-histidine polyplexes to achieve DNA condensation and to provide targeting for receptor-mediated endocytosis. The resultant complexes were shown to have desirable physicochemical properties for gene delivery and were essentially nontoxic.[100]

Benns and colleagues synthesized *N*-Ac-poly(L-histidine)-graft-poly(L-lysine) (PLH-*g*-PLL) by grafting poly(L-histidine) to PLL in order to make use of the dual properties of both polymers for efficient gene transfer (extracellular DNA binding and endosomal escape).[106] Similarly, Pichon and coworkers designed histidylated polylysine molecules that yielded a transfection of 3–4.5 orders of magnitude higher than polylysine alone.[107]

4.424.3.2.4. Cysteine-containing peptides

Cysteine, possessing side-chain sulfhydryl (thiol) groups, has been exploited as a useful tool for the introduction of disulfide bridges between cationic polymer chains to form thiopolycations.[74] The disulfide bond (–S–S–) between cysteine side chains forms readily upon oxidation in biological conditions. Furthermore, two advantageous characteristics render this bond attractive in the context of gene delivery vectors. These are (i) the reversibility of thiol-disulfide conversion within the cell and (ii) the relative stability of disulfide links in plasma.[108] Disulfide bonds have been investigated extensively in the design of (bio)reducible polycations (RPCs), by utilizing the presence of a high redox potential difference between the oxidizing extracellular space and the reducing intracellular space.[109] RPCs can form stable complexes with nucleic acids in the extracellular oxidative environment, while allowing for triggered DNA or RNA release intracellularly via cleavage of the disulfide bonds by glutathione (GSH), which is located in both cytoplasmic and nuclear compartments; consequently, gene expression is enhanced and cytotoxicity is significantly reduced.[71,74,109] Oupický and colleagues developed a synthetic vector based on an RPC prepared by oxidative polycondensation of the peptide Cys–Lys_{10}–Cys, enabling reduced toxicity and efficient DNA release.[110] Addition of DOTAP to these RPCs yielded up to a 187-fold higher level of gene expression compared with nonreducible PLL.[111]

4.424.3.3. Chitosan and Derivatives

Chitosan is a heteropolysaccharide, derived from the natural product chitin, consisting of 2-acetamido-2-deoxy-*N*-D-glucose (*N*-acetylglucosamine) and 2-amino-2-deoxy-*N*-D-glucose (glucosamine) linked by β-1→4-glycosidic bonds, and arranged in a random manner.[112] The pK_a of the glucosamine amino groups has been reported to be ~6.5.[113,114] Chitosan is prepared by alkaline N-deacetylation of chitin, which is mainly derived from crustacean shells.[112,115] Owing to low immunogenicity, minimal toxicity, biocompatibility, and biodegradability, chitosan has been considered as a suitable candidate for nonviral gene delivery.[116] However, some chitosans have shown cytotoxicity, which was dependent on their molecular weight, degree of deacetylation, and salt form.[117] Chitosan cell compatibility has been enhanced by separating and purifying low-molecular-weight fractions.[118] The degree of deacetylation has also been found to be important in terms of transfection efficiency, as it affects zeta potential, cellular uptake, and *in vitro* and *in vivo* transfection of its complexes.[119]

The strength by which chitosan can complex nucleic acids can be controlled by changing the fraction of positively charged monomer (i.e., by changing the degree of chitin

deacetylation). The degree of acetylation must not exceed 35% to obtain stable chitosan polyplexes.[120] Transfection efficiency is unaffected by chitosan molecular weight in the 20–200 kDa range,[121,122] but high molecular weights lead to low solubility at physiological pH[123] and high viscosity.[120] However, complexes between small multivalent cations, including chitosan oligomers, and DNA are not stable under physiological conditions.[60,124] Hence, chitosan fractions have been chosen specifically to have backbones long enough to form stable polyplexes, but sufficiently short to be soluble at neutral pH with minimal viscosity modification, as well as forming complexes that are easily dissociated and less prone to aggregation.[105,124] Moreover, shorter polycations have displayed reduced toxicity, including decreased complement activation and platelet aggregation, compared to their high molecular weight counterparts.[125,126] Chitosan–DNA complexes were found to be less compact than other polyelectrolyte complexes due to the rigidity and low cation density of the chitosan backbone; this may result in DNA degradation due to increased exposure to extracellular nucleases.[127]

Chemical modification of chitosan has been utilized to improve these properties. Solubility at physiological pH has been increased while reducing viscosity by conjugation of a lactobionic acid, to yield galactosylated chitosan.[128] Modification with histidine[129] or deoxycholic acid has resulted in amphiphilic chitosan that self-associates into 100–300 nm aggregates depending on molecular weight and on the level of incorporation of the hydrophobic moiety. Deoxycholic acid-modified chitosan polyplexes were shown to transfect COS-1 cells *in vitro*, but no comparison to a commercial transfection reagent or unmodified chitosan was shown (**Figure 4**).[130]

4.424.3.4. Synthetic Polymer/Polyplex Carriers

In addition to the biomimetic and naturally derived polymers described earlier, many synthetic polymers have been investigated (see **Chapter 1.121, Polymer Fundamentals: Polymer Synthesis**; **Chapter 1.130, Electroactive Polymeric Biomaterials**; **Chapter 1.131, Superporous Hydrogels for Drug Delivery Systems**; **Chapter 4.422, pH-Responsive Polymers for the Intracellular Delivery of Biomolecular Drugs**; **Chapter 4.425, Delivery of Nucleic Acids and Gene Delivery**; and **Chapter 1.123, Degradable Polymers**). Synthetic polymers are advantageous compared to peptides and polysaccharides as they may be synthesized with relative ease and in large quantities. Properties such as molecular weight and side-chain functionality may also be finely tuned to the desired application. Synthetic polymeric NPs for nucleic acid delivery can be split into three broad subtypes: those that condense DNA or RNA into NPs via polyelectrolyte interactions, those that encapsulate the nucleic acid into the core of a capsule or matrix, and those that complex with DNA or RNA on a surface of a preformed NP (**Figure 5**).

Important parameters for all polymeric nucleic acid delivery systems are the molar mass of polymer, composition, viscosity,

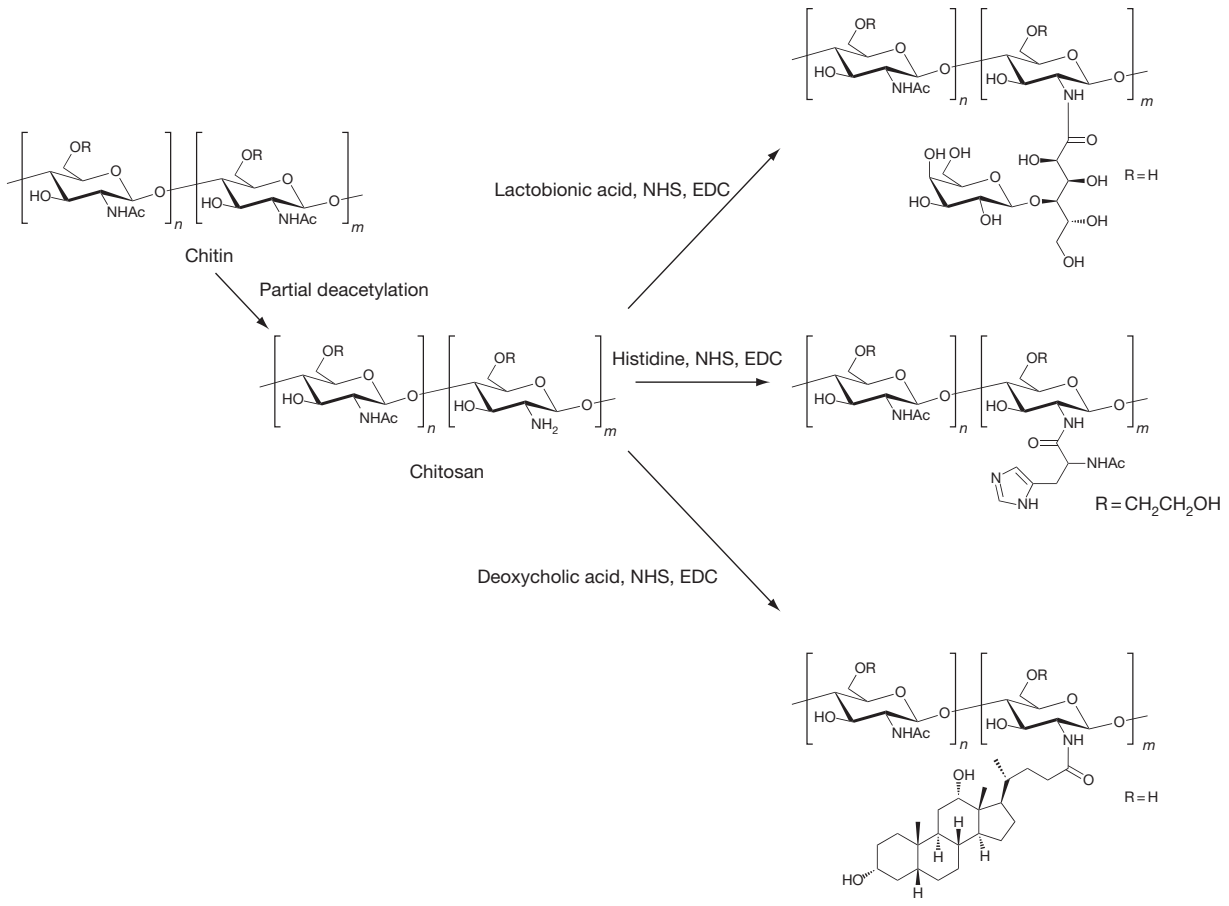

Figure 4 Chitosan derivatives for nucleic acid delivery (polyplex carriers).

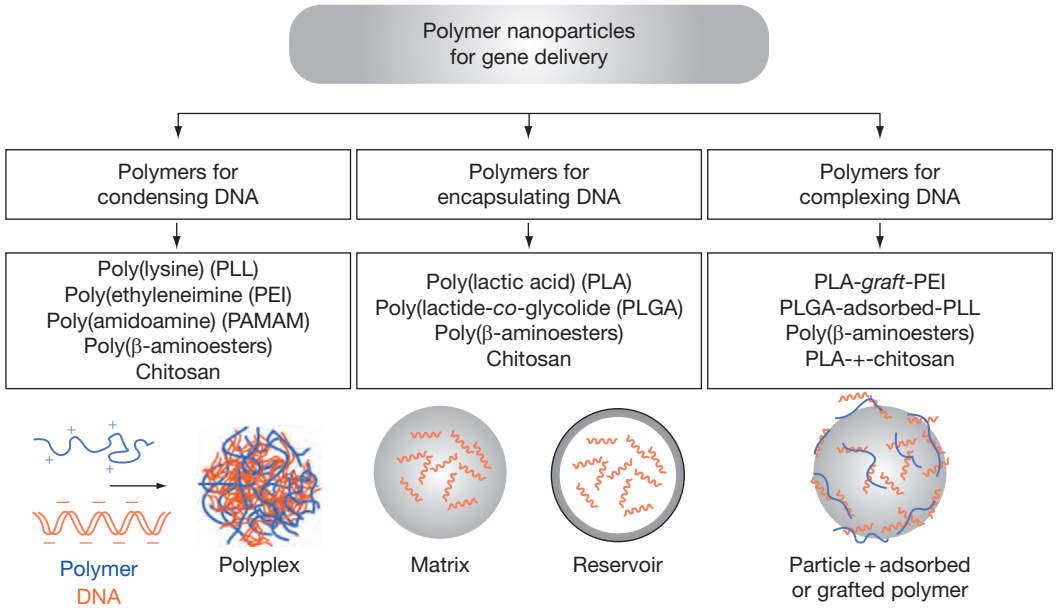

Figure 5 Categories of polymeric nanoparticles used for gene delivery.

and biocompatibility or degradability. Other factors such as emulsifying capabilities and charge of the polymer can affect interactions with, or loading of, nucleic acids, as well as change other properties such as the overall size of the NP, its surface functionality, cellular uptake, and release of cargo.

4.424.3.4.1. Polycations for condensing nucleic acids

The field of polymeric cationic nucleic acid delivery vectors is an intensively researched and highly competitive area. Many natural and synthetic polycations have been used for delivery of nucleic acids, with the focus mostly on DNA delivery until the potential of siRNA became apparent. These include histones (H1, H3, or H4), polylysine, histidylated polylysine, polyornithine, polyarginine, high-mobility group protein (HMG) 1 and 17, modified chitosans, cationized human serum albumin, PEI, polypropyleneimine (PPI), cationic dendrimers, poly(2-(dimethylamino) ethyl methacrylate) (PDMAEMA), polyallylamine derivatives, diethylaminoethyl (DEAE)-dextran, and poly(*N*-alkyl-4-vinylpyridinium) salts.[131–138] Efficiency of gene delivery can be improved by chemical modification as well as adding targeting ligands and nuclear localizing sequences to these polycations.[22,84,139,140] One almost universal feature of these delivery agents is the ability of the vector to condense large nucleic acids such as plasmid DNA into particles that are in the 50–250 nm size range. This size, akin to that of virus particles, enables endocytosis of the particle to overcome the cellular membrane barrier. The condensed structure also provides protection of the nucleic acid from *in vivo* enzymatic degradation. Condensation of the polyanion is achieved through electrostatic interactions and subsequent loss of charge–charge repulsion as the negatively charged phosphate groups of the nucleic acid backbone interact and are neutralized by the cations of the polymer carrier. Polymeric DNA delivery, although far less efficient than viral DNA delivery, offers advantages in terms of size of DNA that can be delivered, improved safety profiles, and ease of production.

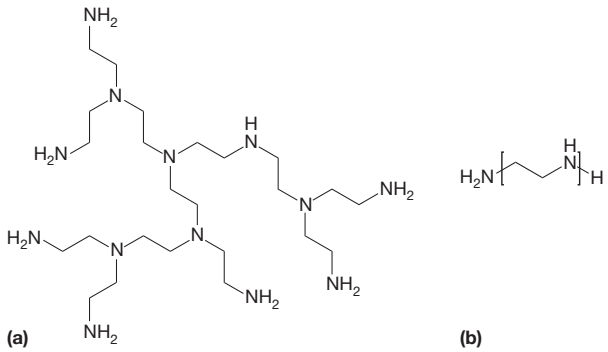

Figure 6 Polyethyleneimine (PEI) structures: (a) branched PEI and (b) linear PEI.

4.424.3.4.1.1. DEAE–dextran

DEAE–dextran was one of the first polycations to be used in gene delivery studies. In 1965, Vaheri *et al.* used DEAE–dextran for *in vitro* delivery of infectious viral nucleic acids and in 1984, Lopata *et al.* performed transfection studies with DEAE–dextran. However, compared to other polymers, DEAE–dextran has been found to be toxic and nonbiodegradable, and its transfection efficiency is low. These properties have limited its usage as a gene carrier system.[141,142]

4.424.3.4.1.2. Polyethyleneimine

PEI is a linear or branched cationic polymer (Figure 6), available in different molecular weights (e.g., 700 Da, 2, 25, 50, 70, 800 kDa), that condenses DNA by electrostatic interactions and displays high transfection efficiency *in vitro* and *in vivo*. Every third atom of PEI is an amine group, and protonation can increase from ~20% at pH 7 to ~45% at pH 5.[143] This in turn facilitates its interaction with negatively charged cell membranes via heparan sulfate proteoglycans, resulting in improved cellular uptake.[144]

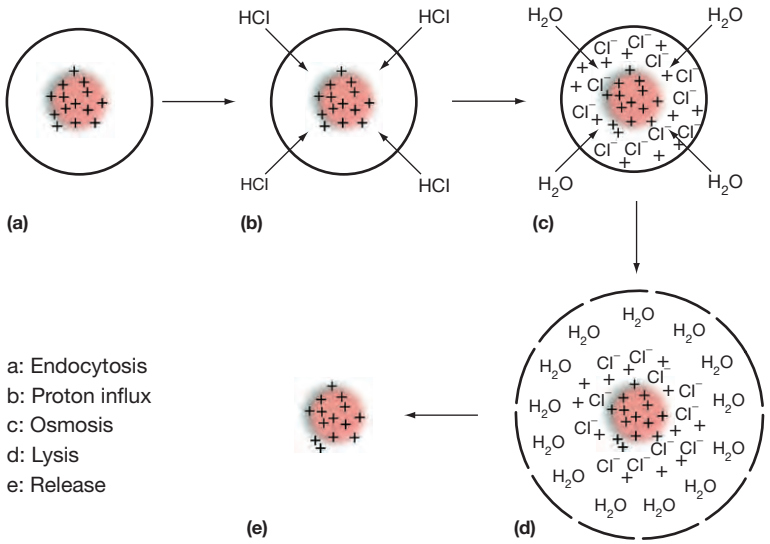

Figure 7 The proposed proton sponge mechanism of endosomal escape: (a) polyplexes enclosed in an endosome after endocytosis (b) due to the pH buffering in the endosome, the protons are continued to pump in the vesicle resulting in Cl^- influx and increase in the osmolarity inside the endosomal vesicle. (c) Because of the osmolarity increase, water passes into the endosomal vesicle. (d) The increase in water volume results in the swelling of the endosomal compartment until it ruptures to (e) release the polyplex into the cytoplasm which leads to nuclear uptake of DNA.

Use of PEI as a DNA delivery vector was initially proposed in 1995 by Boussif *et al.*[131] Promising results were obtained *in vitro* and since then the polymer has been extensively studied in attempts to improve the efficiency and reduce its toxicity. PEI is regarded as a prototypical vector material on account of its high density of amine groups and its potential to buffer endosomes aiding escape of the DNA from degradation in the lysosome. The high buffering capacity of PEI contributes significantly to its high transfection efficiency specifically via the proton sponge effect (**Figure 7**).[60,131,145,146] After cellular uptake of PEI polyplexes, via endocytosis, acidification of the endosome begins, and PEI induces very high accumulation of protons, leading to the passive influx of chloride ions accompanied by water. The increase in osmotic pressure results in swelling and eventually rupture of the endosomal vesicle and efficient DNA release.[131,147]

Akinc *et al.* explored in detail the effect of PEI as a proton sponge and the resulting enhanced release of PEI/pDNA complexes. When endosomal acidity was reduced using a proton pump inhibitor (bafilomycin), transfection was reduced by two orders of magnitude. A similar reduction in transfection efficiency was seen when the ability of PEI to become increasingly protonated was removed through N-quaternization. Both these results suggested that the effectiveness of PEI resulted, in part, from its ability to confer escape of polymer–DNA complexes from endosomes and thus avoid degradation of DNA in subsequent digesting lysosomes.[102]

PEI polyplexes have the advantage of being less toxic and more efficient than lipoplexes *in vitro*[148] and *in vivo*.[131,149] They are also more efficient than PLL and do not require endosomal escape agents (e.g., chloroquine).[150] The DNA condensing ability of PEI has been found to be critical for transfection efficiency.[84] For example, 2 kDa PEI, which condensed pDNA into large aggregates (2 μm in size), yielded poorer transgene expression than 25 kDa PEI that formed small compact particles (80–100 nm).[151,152]

Despite being very efficient in transfecting cells, the main disadvantage of PEI is its high cationic charge density and nonbiodegradability. This has resulted in some toxicity compared to otherwise similar but biodegradable polycations.[135,153–156] Lower molecular weight PEI (800 Da) shows less toxicity but also a reduction in transfection efficiency.[143,157] Therefore, much research has been focused upon polymerizing the lower molecular weight species using degradable linkages to enable higher transfection efficiency with reduced toxicity.[157–159]

4.424.3.4.1.3. Amino-functionalized methacrylates and methacrylamides

(Meth)acrylate and (meth)acrylamide polymers have attracted attention as gene delivery vectors due to their biocompatibility, relative ease of synthesis, and availability of functional monomers with different positive charge-bearing moieties. Cationized polymers previously tested as gene delivery include poly[2-(dimethylamino)-ethyl methacrylate] (p[DMAEMA]); poly[3-(dimethylamino)-propyl methacrylate] (poly[DMAPMA]); poly[2-(dimethylamino)-ethyl methacrylamide] (p[DMAEMAm]); poly[3-(dimethylamino) propyl methacrylamide] (p[DMAPMAm]); poly[2-(trimethylamino) ethyl methacrylate chloride] (p[TMAEMA]); poly[2-(diethylamino)ethyl methacrylate], (p[DEAEMA]); and poly[2-(dimethylamino)ethyl acrylate], (p[DMAEA]). Of these, p[DMAEMA] has been shown to have the best transfection efficiency.[160] p[DMAEMA] is a water-soluble synthetic polycation that can strongly bind nucleic acids through electrostatic interactions forming small and compact particles. However, p[DMAEMA]/DNA ratio was found to determine both the size and charge of the condensed polyplexes. Moreover, the weakly basic secondary amines in the p[DMAEMA] side chains are partly (~50%) protonated at physiological pH (pK_a ~7.5), hence are expected to confer some endosomal escape properties through buffering and osmolysis of acidic endosomal vesicles. However, p[DMAEMA] has demonstrated cytotoxic effects, which

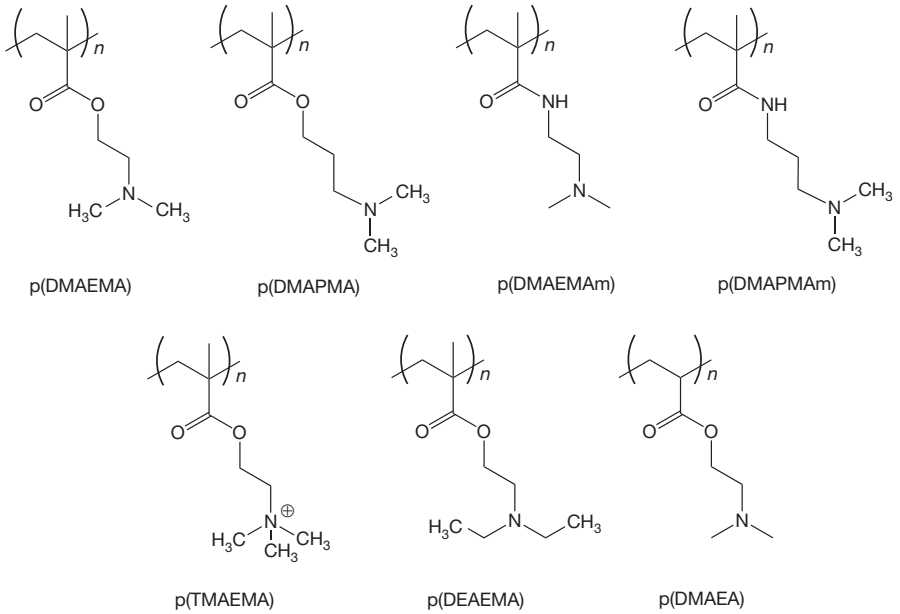

Figure 8 Structures of (meth)acrylate and (meth)acrylamide polymers tested as nucleic acid delivery vectors.

are thought to be due to late endosome or lysosome bursting, leading to undesired enzymatic activity in the cytosol. The observed p[DMAEMA] cytotoxicity and nonbiodegradability have limited its usage in gene delivery, irrespective of its efficiency to transfect cells (Figure 8).[160–162]

4.424.3.4.1.4. Dendrimers

Dendrimers are highly branched, spheroidal, cascade polymer molecules that are synthesized either by divergent or convergent methodologies, forming tree-like architectures.[163] Polyamidoamine (PAMAM) (Starburst) dendrimers, synthesized from an ammonia or ethylenediamine core by successive addition of methyl acrylate and ethylenediamine, have been evaluated extensively as gene delivery vectors.[164–168] PAMAM dendrimers showed high buffering capacity[169] and significantly higher transfection efficiency than PEI for a variety of cell lines.[170,171] Such dendrimers have multiple terminal primary amines with pK_a of approximately 9 (i.e., protonated at physiological pH) and interior tertiary amines with pK_a of 5.5.[166,172] For these systems, it is considered that nucleic acids interact with primary amines on the dendrimer surface while the internal tertiary amines act as buffers exploiting the proton sponge mechanism of endosomal escape. Once endocytosed, the internal tertiary nitrogens of the PAMAM–nucleic acid complexes are protonated in the acidic endosome causing swelling and eventual lysis of the endosome with subsequent release of the polynucleotide into the cytoplasm.[173,174] However, certain cationic dendrimers have been found to be hemolytic and cytotoxic depending on their molecular weight (or generation, see Figure 9) and the number of surface amine groups.[175]

Transfection efficiency of PAMAM dendrimers has been enhanced by adding endosomolytic agents, and also by preparing partially degraded or fractured dendrimers. The improved gene transfer properties of the latter have been partially attributed to their higher aqueous solubility and resistance to aggregation.[22]

Many other dendrimer-based systems have been prepared, with promising recent data on the *in vivo* efficacy of

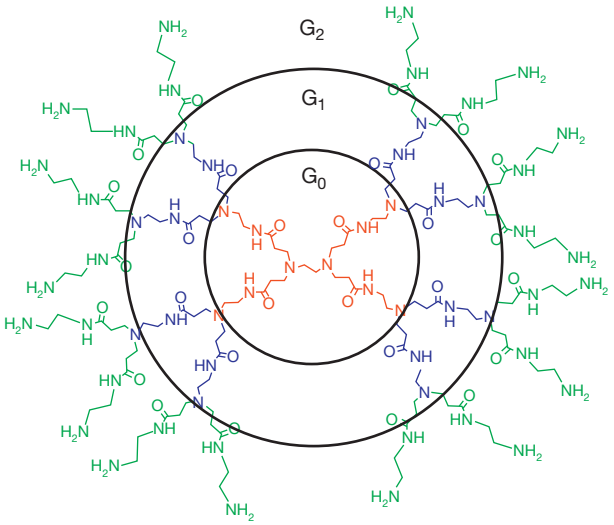

Figure 9 Structure of polyamidoamine (PAMAM) dendrimer. (The core is shown in red (G0). Primary (G1) and secondary (G2) generations are shown in blue and green, respectively.)

poly(propyleneimine) (PPI) dendrimers. Lower-generation (e.g., G2) PPI dendrimers have been found to be the most effective gene carriers compared to higher generation analogs, and these vectors have also been used for efficient delivery of oligodeoxynucleotides (ODNs).[139]

4.424.3.4.2. Polymers for nucleic acid encapsulation

A second class of polymeric gene delivery system utilizes polymers in matrix or encapsulant form. Nanospheres or nanocapsules are obtained according to the preparation method. Nanocapsules are vesicular systems in which the drug is entrapped in the core, whereas nanospheres are usually regarded as matrix systems in which the drug is dispersed.[21]

4.424.3.4.2.1. Micro- and nanoparticle-based gene delivery

Polymer-based micro- and nanoparticles provide several advantages for the delivery of macromolecules such as DNA and RNA. Polymeric delivery systems provide protection against nuclease degradation by encapsulation of the drug and macromolecules in the polymeric matrix.[176] Control over the release of biopolymer into a particular tissue or organ can be achieved via careful tailoring and choice of the polymers and by adjusting parameters such as nucleic acid:polymer ratio, polymer molecular weight, porosity, and functionality. Incorporation of plasmid DNA and oligonucleotides into a matrix of either polymer microparticles or NPs has been investigated widely. Various natural and synthetic polymers can be formulated as matrices and microspheres.[177,178] The structures of some polymers that have been used in microparticle formation for DNA delivery are shown in **Figure 10**.

Poly(lactic acid-*co*-glycolid acid) (PLGA)-based polymers have been widely used in developing microparticles/NPs for encapsulating therapeutic molecules for controlled release applications due to their inherent advantage over conventional devices, including extended release rates from days to months.[179–182] Macromolecules such as proteins, peptides, plasmid DNA, and human growth hormone factor have been successfully incorporated into PLGA-based microparticles/NPs.[183–185] Microparticles with diameters larger than 1 μm are internalized mainly through phagocytosis preferentially by antigen-presenting cells (such as macrophages and dendritic cells), but not by other cells. As a consequence, biodegradable microparticles have been especially investigated for (DNA) vaccination purposes against viruses and tumors, as antigen-presenting cells play a pivotal role in initiation of immune responses. Conversely, submicron-sized particles offer important advantages over microparticles as their cellular uptakes are relatively higher; studies have shown that NPs of 100-nm diameter have 2.5-fold greater cellular uptake when compared to 1 μm and sixfold greater when compared to 10-μm microparticles in Caco-2 cell lines.[186] Similar results were also obtained in a rat *in situ* intestinal loop model; efficiency of uptake of 100-nm-size particles was 15–250-fold greater than larger-sized (1 and 10 μm) microparticles.[187]

4.424.3.4.2.2. Fabrication of nucleic acid-loaded PLGA NPs: challenges and opportunities

A number of approaches are described for encapsulating plasmid DNA or RNA within PLGA-based NPs, including spray drying, phase separation methods, and double emulsion techniques.[188–191] Initially, these approaches were used for encapsulation of peptide and proteins within the PLGA particles but have now been extended to incorporate nucleic acids. The double emulsion technique refers to a process where the aqueous cargo is dispersed in the organic phase to make a water-in-oil emulsion using homogenization or sonication. In the phase separation method, the particles are produced by extracting the organic solvent or adding nonsolvent to induce coacervation, while in spray-drying techniques, particle formulation is achieved by atomizing the emulsion through a stream of hot air to induce rapid solvent evaporation. In addition to the approaches mentioned previously, plasmid DNA can also be coated on the surface of PLGA particles.

4.424.3.4.2.3. Double emulsion techniques for matrix NP nucleic acid delivery

Double emulsions of nucleic acids have typically been formed by mixing or dispersing of an aqueous solution of DNA or RNA with a solution of PLGA dissolved in an organic solvent. The dispersion of the nucleic acid solution is usually performed by using sonication or homogenization techniques. This results in the formation of a first, or primary emulsion in which the aqueous droplets containing nucleic acid are suspended in the organic phase. The size of the droplet formed by sonication or homogenization can be optimized by adjusting the amount of shear force used during the dispersion process. The primary emulsion is then mixed with a second aqueous solution that contains surfactants to prevent the aggregation of water-in-oil droplets (coalescence). The addition of primary emulsion with the solution of surfactant results in precipitation of polymer around the aqueous droplets and finally, the evaporation of the organic solvents leads to the formation of solid particles in which the nucleic acid is embedded and trapped in the polymeric matrix of the particles. PLGA-based particles are sensitive to moisture and undergo hydrolysis upon contact with water; therefore, it is important to keep the final particles free of moisture. Drying of the particles can usually be done by lyophilization for long-term storage. Cryoprotective sugar, usually sucrose or glucose, may be added to the formulation to preserve the tertiary structure (e.g., DNA supercoiling) during the drying process.[192]

One drawback of the double emulsion technique is the shear force used to disperse the aqueous solution of nucleic acid in the organic phase. The energy input through shear force can damage the biopolymer reducing its integrity and, eventually, biological activity. Additionally, contact of nucleic acid with the organic phase can adversely affect the tertiary structure. There are some methods that have been used to minimize nucleic acid damage during the dispersion process. Condensation of DNA with cationic polymers such as PLL has been carried out as described earlier to reduce the size of the DNA and make it less exposed to shear force while preserving

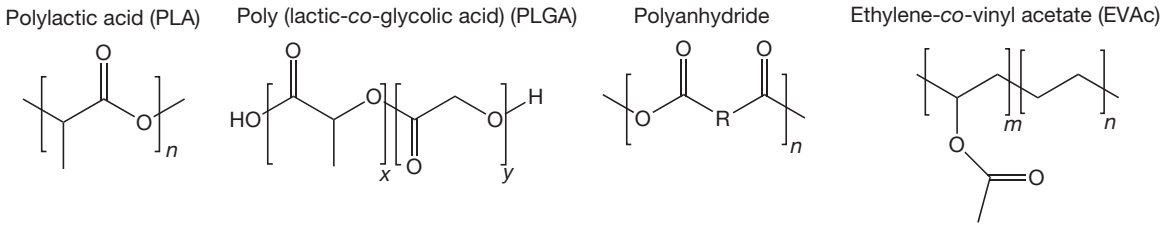

Figure 10 Structure of selected polymeric materials used for gene delivery in nanoparticles.

supercoiling and retaining its biological activity.[193,194] Another technique that has been adopted to reduce the damage by shear force has been to conduct the dispersion of the DNA solution in organic phase of PLGA at reduced temperature. This generated a more viscous solution that was less affected by shear force during the dispersion process.[192] One remaining issue for double emulsion techniques has been low-reported encapsulation efficiencies of the therapeutic biopolymer in the particles. The key problem is that of dose as sufficient therapeutic needs to be incorporated for efficacy. Even for potent biopolymers, such as siRNA, encapsulation of the nucleic acid has often been reported to be inefficient. For example, encapsulation efficiencies of less than 50% have been described for siRNA in PLGA NPs prepared by the double emulsion route, equating to $\sim 3\,\mu g\,mg^{-1}$ loadings on the delivery system.[195]

4.424.3.4.2.4. Spray-drying techniques for matrix NP nucleic acid delivery

Nucleic acid-loaded particles have been produced by combining emulsification steps with spraying via an atomizer through a steam of hot air. Initially, the nucleic acid solution is mixed with a solution of polymer, for example, PLGA in organic solvents using shear force to form droplets of DNA or RNA in the bulk (organic/polymer) phase. Finally, the particles are formed by spraying the suspension of nucleic acid droplets in PLGA solution through an atomizer in the presence of hot air. During spraying of the suspension through the hot air, the organic solvent and water evaporate, resulting in the formation of dried solid particles loaded with nucleic acid. Spray-drying techniques have enabled control of nucleic acid carrier particle size by factors such as the flow rate through the atomizer, temperature of the air, and size of the nucleic acid aqueous droplets.[196] The advantage of this process over the double emulsion technique has been that the addition of primary emulsion into a second aqueous phase is absent, thus reducing nucleic acid loss. However, the mechanical and thermal stresses have not been eliminated from spray-drying techniques, affecting DNA supercoiling.

4.424.3.4.2.5. Adsorption of nucleic acids on PLGA particle surfaces

In this technique, particles have been made by double emulsion techniques in the absence of nucleic acids to produce empty PLGA particles, and in the second aqueous phase stage, the particles have been suspended in solutions of cationic agents which coat the outer surface. Examples have been reported of nucleic acid binding to the external surface through electrostatic interaction, although for this type of procedure, usually the loading efficiency of the biopolymer has been limited to 1% (w/w).[197]

4.424.3.4.2.6. Challenges associated with matrix particles as nonviral gene delivery systems

Generally, nonviral gene delivery systems have been significantly less efficient in comparison to viral vectors. For matrix particles to be considered for practical gene delivery systems in future, they will need to be able to carry a higher amount of the therapeutic biopolymer than has been achieved to date. Secondly, as has been mentioned earlier, the integrity of the nucleic acid such as the supercoiled structure of DNA needs to be preserved during matrix particle formulation, that is, all the detrimental conditions of high shear forces and thermal stress should be avoided or reduced.[198] Considering the *in vivo* transfection efficiency, matrix particles based on PLGA have demonstrated protection of DNA from extracellular nucleases, but have also shown undesirable 'burst release' profiles, as adsorbed DNA has been prematurely lost from the surface of the particles. Another problem particularly associated with PLGA NPs has been the effect of hydrolysis of the PLGA backbone during biodegradation. The hydrolysis process generates lactic and glycolic acid units and may lead to substantial reduction in pH in the PLGA matrix where nucleic acids have been embedded. This in turn has been reported to cause degradation of DNA, compromising its therapeutic effect.[191,199] For RNA therapeutics, similar problems of stability can occur, but with the further complication of rapid degradation of RNA via RNAses. In addition, the short, rigid siRNA chains are difficult to condense compared to large DNA plasmids. This may seem counterintuitive, but in fact better condensation of siRNA into particles has been obtained by linking several siRNA molecules via short flexible linkers, such that multipolymer complexes with polycations are formed. This is most likely a result of connected siRNA 'rods' folding back on each other bridged by polycations, forming a tightly packed complex overall, whereas unconnected siRNA units adopt a more loose arrangement when complexed with the same polycations.[200]

4.424.3.4.3. Polymer micelles and vesicles as NP nucleic acid delivery systems

Polymeric micelles and vesicles form another important class of delivery agent, with some features similar to the nucleic acid condensing vectors, and other properties resembling those of the matrix NP systems. Block copolymers with a cationic segment and a noncharged hydrophilic block have been widely investigated for their ability to self-assemble with polyanionic DNA or RNA to form core–shell structures with high stability and reduced interaction with blood components (**Figure 11**).[201]

Polymeric micelles have a number of other advantages for application in gene delivery.[202] Assembly may be controlled by variation in polymer block length, functionality, and external stimuli, while the chemistry of the external block may be varied to increase steric shielding or add targeting ligands. The general principles behind the use of polymeric micelles are similar to those for other polymer systems used in gene delivery, that is, a cationic segment is often used to condense the nucleic acid, while PEG and other hydrophilic polymers are used to confer protection against nucleases as well as extend residence time in the bloodstream to allow passive targeting. There are now a number of excellent reviews that cover the detailed and more specialist aspects of polymer micelles for nucleic acid delivery.[203–205] Disadvantages of these systems include low drug payload, poor stability in serum in some cases, and potential issues with cost and scale-up.

4.424.3.4.3.1. Stimuli-responsive polymersomes

Polymersomes are vesicular structures, analogous to liposomes, formed by the self-assembly of amphiphilic block copolymers in solution. Due to their higher stability and tuneable size compared to liposomes, they have garnered great interest as potential drug delivery vehicles.[206] In particular,

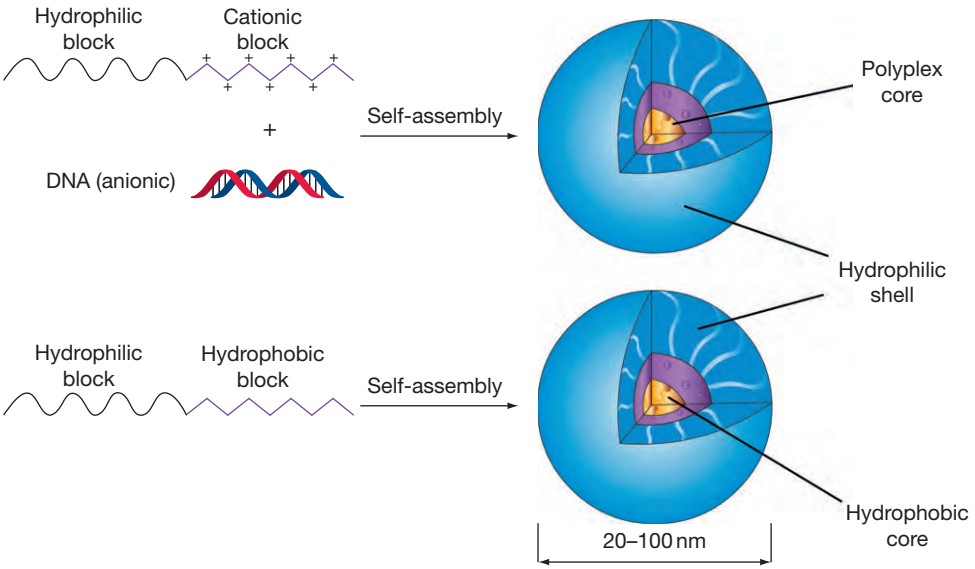

Figure 11 Formation of polymeric micelles.

polymersomes have the ability to trap nucleic acids inside their core (in the 'waterpool'), or in charged components in their membranes. In addition, through control of polymer–polymer interactions, this class of vesicles can reversibly self-associate. This versatility enables further control of nucleic acid binding and release, and several exciting examples of polymersomal gene delivery agents have been reported in recent years. Block copolymers of hydrophilic 2-(methacryloyloxy)ethyl phosphorylcholineMPC (MPC) and pH-responsive 2-(diisopropylamino)ethyl methacrylate (DPA) have been demonstrated to reversibly form polymersomes with a transition at pH ≈ 6.[54,207,208] Dissolution of the polymer with plasmid DNA at pH 6, followed by an increase to pH 7.5, resulted in polymersomes containing DNA with an encapsulation efficiency of ~20%. *In vitro* cell viability and transfection efficiency were assayed in comparison to Lipofectamine TD and $CaCl_2$; poly [MPC-*block*-DPA] polymersomes were found to have high transfection efficiency with reduced toxicity compared to controls.[209] Further study also determined the absence of any proinflammatory/immunogenic response to the polymersomes *in vitro*.[210]

4.424.4. Opportunities and Challenges in NP Therapeutics: Biological Barriers to Nucleic Acid Delivery

Although NP systems have been shown to be effective for many gene delivery experiments in cell culture, the extension to *in vivo* efficacy remains problematic. This is because circulation and uptake of NPs varies in different parts of the body and with healthy compared to diseased tissue. In healthy tissues, distribution of NPs through the body and their removal is size-dependent as shown in **Table 1**.

However, in some cases, selective removal of NPs can be advantageous, as it results in accumulation at a site that may be a therapeutic target. Passive targeting of NPs can occur in cancerous regions, because the microvasculature is highly permeable and leaky in these sites, while efflux mechanisms can be less efficient. The accumulation of polymers and NPs in the cancer tissues or cells is known as the enhanced permeation and retention (EPR) effect.[211] In addition, because of the sizes of the capillaries, passive targeting is possible to the mononuclear phagocyte system (MPS) organs (liver, spleen, and bone marrow). For delivering NPs and their cargo to other organs, active targeting (e.g., via a cell surface affinity ligand) is necessary.

In active targeting, functional groups that recognize the specific cell epitopes or receptors are attached to the carrier systems. These may be low molecular weight ligands (folic acid, thiamine, sugars), peptides (RGD, LHRD), or higher molecular mass weight moieties such as proteins (transferrin, antibodies, lectins) and polysaccharides (hyaluronic acid). In addition, active targeting can be achieved by introducing functionality on the carrier that will evoke a change of structure, conformation, or nucleic acid binding/release in response to an external stimulus, such as temperature, pH, electric charge, light, sound, and magnetism, or to a biological trigger such as reducing potential or pH.[20,212]

4.424.4.1. Systemic Barriers

Even with active targeting systems, a number of other factors must be considered. For the therapeutic nucleic acid to reach its site of action within the cell nucleus, it must negotiate a plethora of biological barriers, which vary with the administration route and desired target.[213] If the intended route of administration is intravenous, into the systemic circulation, then one of the first challenges presented is that of the blood. Typically, synthetic DNA delivery vectors are cationic and, when used in excess to DNA to form stable particles, the overall complex assumes a positive charge. Therefore, these DNA complexes bind to the cell surface via charge–charge interactions with the negatively charged proteoglycans of the cell membrane. This in turn facilitates their internalization by different

Table 1 Relevant sizes regarding particle distribution through and removal from the capillaries of the human vascular system.

		Size	*System/organ*
Particle removal[a]	Tight-junction capillaries	<1 nm	Central nervous system, blood–brain barrier
	Continuous capillaries	~6 nm	Tissues such as muscle, skin, and lung
	Fenestrated capillaries	~50–60 nm	Kidney, intestine, and some endocrine and exocrine glands
	Sinusoidal capillaries	~100–1000 nm	Liver, spleen, and bone marrow
Particle delivery	Arteriole radius	0.005–0.07 mm	Circulatory system. Particles supplied by intravenous administration. Elimination involves opsonization and removal by monocytes in the blood
	Artery radius	0.08–7.5 mm	
	Venule radius	8–100 μm	

Soruce: Arruebo, M.; Fernández-Pacheco, R.; Ibarra, M. R.; Santamaría, J. *Nanotoday* **2007**, *2*, 22–32.

[a]In this table, only the morphological pores contributing to diffusive permeability are listed. Actual transcapillary exchanges can be modified by active transport mechanisms, which are able to internalize particles with sizes from 20 to 200 nm.

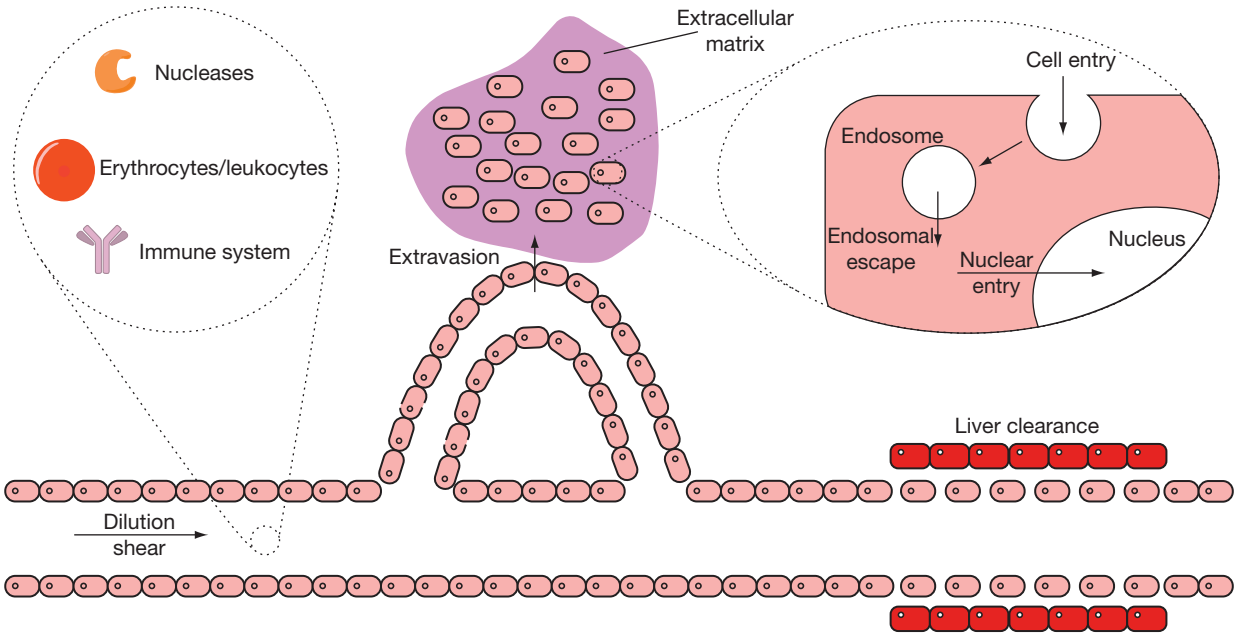

Figure 12 Biological barriers to DNA delivery, both extracellular and intracellular.

endocytic mechanisms.[214,215] However, while vector–DNA complexes with an overall positive charge are known to be suitable for transfecting cells *in vitro*, this effect does not necessarily translate *in vivo*. The condensation of DNA into colloidal polyplexes that can be taken up by cells through endocytosis in cell culture cannot guarantee their passage through different barriers *in vivo* and subsequently, the transfection efficiencies vary between different types of systems.[216]

The net positive charge makes the lipo-/polyplex delivery systems susceptible to interactions with negatively charged proteins present in plasma.[217] Complexes between DNA and the polycation poly(ethylenimine) (PEI) have been shown to interact with immunoglobulin M, fibrinogen, fibronectin, and complement C3. Interactions with these proteins (opsonization) can lead to activation of the complement system and removal of complexes out of the bloodstream via the RES.[218] Organs of the RES, including the liver, spleen, adrenal gland, and bone marrow, have discontinuous capillaries with pores enabling uptake of particles ~50 nm in diameter.[213] It has been found that coating vector/DNA complexes with neutral hydrophilic polymers such as PEG can minimize interactions with proteins in the plasma,[217] thus reducing opsonization and prolonging circulation time. However, it should be noted that RES filtration efficiencies often approach 95% of the administered dose.

Another area that can hinder NP-associated nucleic acids reaching their target site is the capillary bed in the lungs; aggregated polyplexes or lipoplexes can become trapped in the fine capillaries of the lung. Several polymeric gene delivery vectors have been found to localize initially within the lung, sometimes aggregated with erythrocytes, which has resulted in enhanced transfection of this organ.[143,219] Shielding of positively charged complexes between DNA and PEI by covalently attaching the cell-binding ligand Tf has been shown to decrease nonspecific interactions between the complex and the erythrocytes, alongside reducing gene expression in the lungs and directing gene expression to subcutaneous Neuro2a tumors (**Figure 12**).[220]

4.424.4.2. Cellular Barriers to Uptake of Nucleic Acids

If the delivery vector overcomes the hurdles encountered in the bloodstream and reaches its target tissue (<5% of dose,

typically), it must then negotiate the cellular membrane to gain entry into the cell. As noted earlier, nucleic acids are large negatively charged molecules which cannot passively transport across the hydrophobic interior of the cell membrane. Delivery vectors that can condense the nucleic acids to nanometer-sized particles can exploit the uptake pathways of endocytosis. Broadly speaking, the process of endocytosis may be defined as the means by which material can be taken into the cell and includes phagocytosis and pinocytosis. Many different types of endocytic mechanisms have been characterized, including both those involving clathrin-coated pits, which involve some of the most widely adopted receptor-mediated endocytosis pathways, and those that are clathrin-independent, such as the caveolae route.[221–223]

Many nucleic acid delivery systems have employed targeting ligands to direct the therapeutic to a particular tissue type, for example, Tf targeting to tumor cells[220] and galactose ligands targeting to liver cells.[224] These ligands ensure the uptake of the nucleic acid–vector complex using receptor-mediated endocytosis, which has been found to result in higher transfection efficiencies than ligand-free complexes.[217] Following endocytosis, the nucleic acid–vector complexes become enclosed within endosomes. Some endosomes are classified as sorting endosomes that are responsible for recycling receptors back to the membrane surface. When a receptor–ligand complex is taken up into the cell, the acidity within the endosome can release the ligand from the receptor. Materials that are not recycled back to the cell surface become susceptible to degradation within the late endosome where the pH is lowered to pH 5–6. The late endosome eventually fuses with the lysosome where hydrolase enzymes further digest the introduced materials. Consequently, NP delivery vectors require mechanisms to escape the endosomal environment in order to avoid degradation of their delicate biopolymer cargo. Polymers exhibiting buffering between pH 7 and 5, such as PEI and PAMAMs, have been proposed and proceed to intracellular targets to enable endosomal escape through the 'proton sponge mechanism' as described previously. Increased chloride ion accumulation in buffered endosomes was found to occur prior to swelling and lysis of the endosomes.[225] Non-buffering poly(amines), such as poly(lysine), did not show as much chloride ion accumulation and were less likely to escape the endosomal compartments. This has been suggested to account for the lower transfection efficiency of poly(lysine) compared to PEI vectors. Indeed, grafting of imidazole groups (pK_a 6.5) to poly(lysine) increased its transfection efficiency, indicating that the imidazole units acted as endosomal escape moieties. DNA delivery systems that lack endosomal escape mechanisms have shown improved transfection efficiency when applied with a separate endosomal buffering agent such as chloroquine.[102,135,213]

Once released into the cytoplasm, DNA delivery systems must find a way to transport DNA and gain entry into the nucleus through the nuclear envelope. A proportion of complexes between PEI and DNA, in a similar way to adenoviruses, have been seen to migrate through the cell under active transport mechanisms along microtubules, either as free complexes or within endosomal compartments. This motor protein-driven transport localized the complexes to the perinuclear region of the cell. Transport of the complexes was hypothesized to take place along the microtubules to the microtubule organizing center of the cell, which resides close to the nucleus.[226] Entry of macromolecules into the cell nucleus is regulated, with the nuclear pore complex limiting access to materials greater than 40 kDa. Species of larger size require a nuclear localization signal in order to be actively transported into the nucleus. Nuclear localization signals generally comprise a peptide of four cationic residues. Researchers have explored the attachment of these signals to complexes and DNA in order to improve uptake into the nucleus.[227]

4.424.4.3. Overcoming Systemic and Local Biological Barriers: Surface Coating of NPs with Hydrophilic Polymers and Targeting Agents

Although cationic lipids and polymers can condense nucleic acids efficiently to form NPs, the presence of a high overall positive charge can result in nonspecific interactions with body components and/or toxicity (see **Chapter 3.319, Characterization of Nanoparticles in Biological Environments**). Coating or functionalizing the surfaces of NPs has been reported by many groups, using a number of methods:

1. *PEG shielding of polyplexes*. The most popular shielding agent is PEG, which can form an extended swollen hydrated layer, thus effectively masking the positive charge of polycation/DNA complex NPs. The overall positive zeta potentials of the complexes have been reduced by this method, leading to decreased interactions with other body components, lower toxicity of the complexes, and increased circulation time.[228]
2. *Poly[N-(2-hydroxypropyl)methacrylamide] (pHPMA) shielding*. Like shielding with PEG, toxicity of the complex and interaction with other body components has been reduced by attachment of this hydrophilic polymer.[229]
3. *Ligand attachment*. Ligands such as Tf have been covalently attached to polycations, leading to a decreased zeta potential, as well as active uptake. In this way, nonspecific interactions have been lessened and toxicity has been reduced.[22]

4.424.4.3.1. Sterically stabilized PEGylated polyplexes

As described previously, the positively charged surface of the polyplexes can lead to undesired nonspecific interactions with blood components,[230,231] rapid elimination by the RES, aggregation,[232] and serum complement system activation.[218] This results in reduced circulation times and can cause significant toxicity and/or poor transfection efficiency.[233] PEG has been used to shield cationic DNA polyplexes, where the polycation has been PEI,[234–236] PLL,[83] and PAMAM,[237] incorporated either by condensing DNA with PEG-polycation copolymers (pre-PEGylation) or by coupling a PEG layer onto the surface of preformed polyplexes (post-PEGylation). Surface neutralization by PEGylation has formed sterically stabilized polyplexes with increased solubility, enhanced stability, reduced toxicity, and prolonged circulation times. Ogris and coworkers prepared PEGylated PEI/DNA complexes that exhibited improved plasma circulation and reduced *in vivo* toxicity, and resulted in high-level gene expression in tumors after systemic administration into tumor-bearing mice.[217]

Although PEG shields have improved the characteristics of polycation/DNA complex NPs in the extracellular compartment and increased their systemic delivery to target cells, overstabilization of this shield (stable and irreversible) has negatively affected the subsequent desired intracellular steps of polyplex internalization into the cell and endosomal release, thus reducing overall transfection efficiency.[238–240] This overstabilization by the shielding PEG layer has been overcome by forming pH-sensitive PEG coatings for polyplexes: these systems have exhibited enhanced transfection efficiency,[241–243] with up to 100-fold higher gene transfer activity reported for pH-sensitive PEGylated DNA complexes compared to stable PEG-shielded polyplexes.[243]

4.424.4.3.2. Overcoming local biological barriers: surface modification of NPs with targeting ligands

Target cell specificity of polyplexes has been achieved by the incorporation of cell-binding ligands into the surfaces of nanoparticulate vectors, most notable for polymer–DNA complexes. A variety of targeting ligands have been attached covalently or noncovalently to polycations such as Tf, epithelial growth factor (EGF), folate, galactose-containing ligands, low-density lipoprotein (LDL), basic fibroblast growth factor (bFGF), and antibodies.[224,244–251]

Tf, an iron-binding glycoprotein, is a common ligand that is recognized by and binds to Tf receptors on cell surfaces. Tf has been used as a tumor-targeting ligand for several drug delivery systems, and Tf-based gene delivery has been termed 'transferrinfection.'[250] For example, Tf–PLL–DNA conjugates were designed and revealed efficient delivery systems for gene transfer into many cell lines.[252,253] Also, there have been numerous reports on tumor-selective gene transfection by Tf–PEI–DNA complexes.[230,254–256] After their intravenous injection, gene expression in the tumors was approximately 100-fold higher than in other tissues.

Combining the two surface modification strategies by attaching both ligand (e.g., Tf and EGF) and hydrophilic polymers (e.g., PEG and HPMA) was found to have beneficial outcome on the *in vivo* use of polyplexes. It was found that the attachment of both PEG and Tf to modify the surface of PEI/DNA complexes either before or after complex formation not only decreased polyplex toxicity and increased its solubility and stability to freeze drying but also increased polyplex circulation time.[217,257] Moreover, intravenous injection of a shielded PEG–PEI–Tf system containing DNA encoding for tumor necrosis factor-α(TNF-α) was shown to inhibit tumor growth in murine tumor models.[257] Tf targeting of both PEG-coated and noncoated PEI/DNA complexes enabled gene delivery into distant subcutaneous neuroblastoma tumors of syngeneic A/J mice.[217,220,257] In a similar study, it was also found that EGF–PEG-coated PEI/DNA polyplexes efficiently targeted human hepatocellular carcinoma xenografts in SCID mice showing 10–100-fold higher localization in the xenografts compared to other organ tissues.[258]

4.424.4.3.3. Chimeric/hybrid NPs for overcoming systemic barriers gene delivery

An innovative approach to highly targeted gene delivery has been the development of chimeric vectors, which are hybrid combinations of viral and nonviral gene carriers. One study employed DNA-loaded liposomes fused with ultraviolet (UV)-inactivated HVJ (hemagglutinating virus of Japan; Sendai virus) to obtain fusogenic viral liposomes. These carriers were reported to be able to protect DNA from endosomal and lysosomal degradation[37,259] (**Figure 13**).

Similar approaches have involved solubilization of influenza virus A with detergent followed by mixing with a cationic lipid (dioleoyldimethylamonium chloride:DODAC) to form cationic virosomes capable of complexation with DNA. The HIV envelope proteins, gp120 and gp41, have been attached

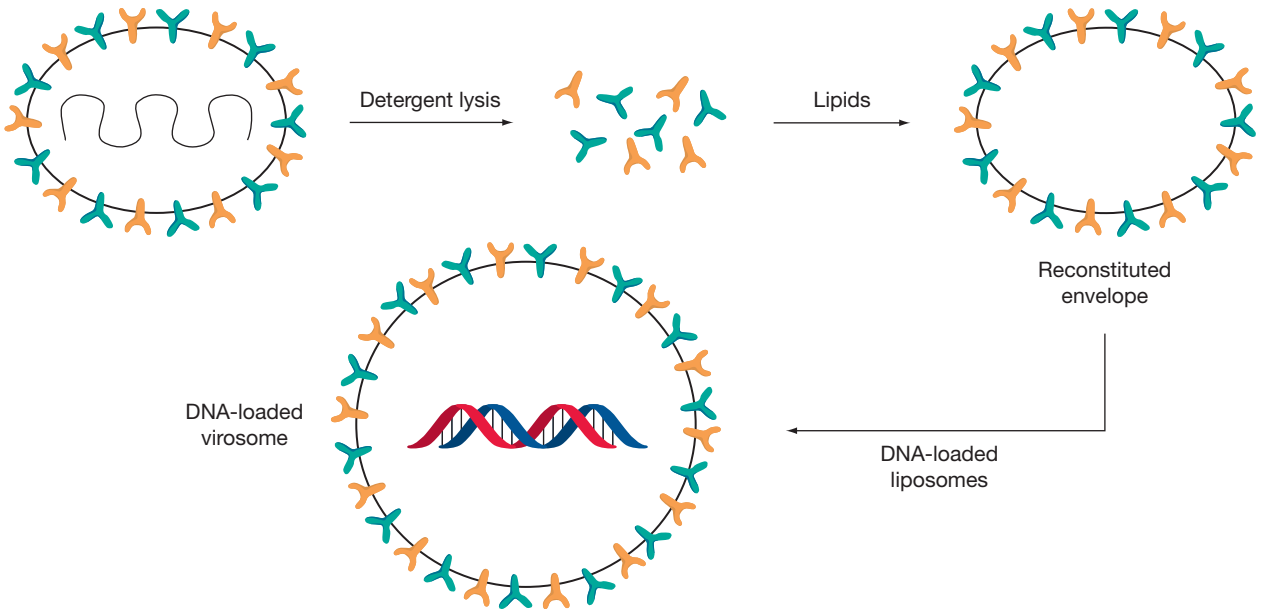

Figure 13 Virosome formation. Envelope viruses are lysed by detergent and then mixed with lipids to form a reconstituted envelope presenting viral proteins. Addition of a DNA-loaded liposome results in fusion to yield a DNA-loaded virosome.

to liposomes to form gene carriers with similar cell recognition and entry properties to HIV but without pathogenicity. In addition, HVJ–liposomes have been prepared using both cationic and anionic lipids. Studies showed that HVJ–anionic liposomes achieved greater penetration and wider distribution compared to cationic ones; however, transfection efficiencies were lower. The authors thus suggested that anionic HVJ–liposomes should be used for gene transfer across a range of tissues, while cationic ones should be used for restricted regions or surface areas.[259] These data are analogous with those for cationic and anionic liposomes, and indicate the balance between systemic and local effects, and potency and side effects.

4.424.4.4. Formulation Issues for Nucleic Acid Therapeutics – Binding Between Vector and Nucleic Acid: A Balancing Act

Although NP systems have been shown to be very effective in protecting nucleic acids from biodegradation, a balance needs to be achieved between sufficient protection while allowing adequate release such that the vector can release the nucleic acid.[133] Several studies have revealed that vector unpackaging presents a significant barrier for DNA delivery. Schaffer *et al.* conducted a detailed study into the ability of a variety of different lengths of poly(lysine) to mediate DNA delivery. It was found that the larger polymers led to less efficient delivery due to a reduced tendency to dissociate from the DNA within the nucleus. Lower molecular weight polymers showed enhanced transgene expression, which was correlated to a reduced inhibition of transcription in the nucleus. A similar effect was seen with PEI (25 kDa) where the larger polycation inhibited transcription of the transgene to a greater extent than the 2 kDa sized polymer.[105] Glover *et al.*[260] showed that although PEI showed higher amounts of plasmid DNA–polymer complex uptake into cell nuclei, higher levels of transgene were achieved by fewer plasmids delivered by lipofectamine as it dissociates from the DNA before entering the nucleus.

Attempts to strike the most effective balance in binding between polymer and DNA have been made by several groups. Kurisawa *et al.*[261] explored the incorporation of hydrophobic butyl methacrylate (10%) into poly[*N*-isopropyl acrylamide-*co*-DMAEMA] copolymers using lower amounts of the cationic DMAEMA (20%) and found the transfection efficiency to be twofold higher than that of the p[DMAEMA] homopolymer. Similarly, Park and Healy[134] investigated the effect of polycation content in polymers of poly[lysine-*graft*-poly(lactide-*block*-ethylene glycol)] in order to achieve enhanced DNA release from the controlled release formulation.

Many stimuli- or environmentally responsive polymers and NPs have been investigated for nucleic acid delivery, and this field has been very extensively reviewed in recent years. However, the common concept in all of these studies is a change in NP behavior or properties, which enable targeting and/or release of the nucleic acid cargo. These changes in the delivery system can be a conformational switch, exposure of a binding group, cleavage of a side chain linked to a binding group, such that the affinity of the carrier NP with the nucleic acid changes. Even with the stimuli-responsive systems, to date no single gene vector fulfills all the desirable characteristics of protection, targeting, and delivery of the nucleic acid, and each has its own advantages and limitations. The optimization of a vector system, thus, has to be individualized according to each clinical setting, leaving both challenges and opportunities for researchers in the gene delivery field.

4.424.5. Conclusions

Large numbers of nanoparticulate nucleic acid delivery systems have now been evaluated in the laboratory, and several drugs have progressed to clinical trials. However, in addition to therapeutic efficacy, a major question that needs to be answered is the *in vivo* fate of NPs, whether of natural or synthetic origin. Any material introduced into the body must either degrade to harmless fragments or be excreted unchanged once it has fulfilled its therapeutic use. This is one reason why only a relatively small number of gene delivery vectors have been used in the clinic and, in turn, is due to difficulty, time, and expense of conducting full toxicological studies of biological and synthetic materials, to determine the ultimate fate of all vector, and vector-derived fragments in the body.

There also remain many challenges for the biomaterials scientist in developing better materials for biomedical applications. True precision in the engineering and modification of viruses or in the generation of synthetic architectures, placement of functionality, and ease of conjugation or complexation with a nucleic acid are all necessary for optimum biomaterial formulations. In addition, 'intelligent,' controlled behavior is likely to be required in these materials in order that an injected, inhaled, or even ingested NP can carry the nucleic acid to a disease site or repair a defective gene.

Finally, it is important to recognize that the trade-off between what is achievable in a research context and what is affordable as a medicine, and for nucleic acid delivery in particular, many hurdles are still to be overcome. The challenge for biomaterials scientists is to devise materials that best combine nucleic acid binding and release in a format that can readily be manufactured, administered, and monitored to produce a safe, effective human therapeutic. If this can be done in a cost-effective and safe manner, the long-promised benefits of gene therapy might be realized.

Acknowledgments

This work was supported by research grants from the UK Engineering and Physical Sciences and Biotechnology and Biological Sciences Research Councils (Grants EP/H005625/1, EP/G042462/1, EP/D022347/1, D021847/1, and BB/F01855X/1) and the University of Nottingham, UK, and by scholarships to GY and MS from the Turkish and Egyptian Governments, respectively.

References

1. Pearson, S.; Jia, H.; Kandachi, K. *Nat. Biotechnol.* **2004**, *22*, 3–4.
2. Mercorelli, B.; Sinigalia, E.; Loregian, A.; Palù, G. *Rev. Med. Virol.* **2008**, *18*, 177–210.
3. High, K. A. *Trans. Am. Clin. Climatol. Assoc.* **2009**, *120*, 331–359.

4. Allouche, M.; Bettaieb, A.; Vindis, C.; Rousse, A.; Grignon, C.; Laurent, G. *Oncogene* **1997**, *14*, 1837–1845.
5. Stavrovskaya, A. A. *Biochemistry (Mosc)* **2000**, *65*, 95–106.
6. Bainbridge, J. W. B.; Smith, A. J.; Barker, S. S.; *et al*. *N. Engl. J. Med*. **2008**, *358*, 2231–2239.
7. Maguire, A. M.; Simonelli, F.; Pierce, E. A.; *et al*. *N. Engl. J. Med*. **2008**, *358*, 2240–2248.
8. Maguire, A. M.; High, K. A.; Auricchio, A.; *et al*. *Lancet* **2009**, *374*, 1597–1605.
9. Higuchi, H.; Bronk, S. F.; Bateman, A.; Harrington, K.; Vile, R. G.; Gores, G. J. *Cancer Res*. **2000**, *60*, 6396–6402.
10. Bennett, C. F.; Swayze, E. E. *Annu. Rev. Pharmacol. Toxicol*. **2010**, *50*, 259–293.
11. Fire, A.; Xu, S.; Montgomery, M. K.; Kostas, S. A.; Driver, S. E.; Mello, C. C. *Nature* **1998**, *391*, 806–811.
12. Pratt, A. J.; Macrae, I. J. *J. Biol. Chem*. **2009**, *284*, 17897–17901.
13. Cerritelli, S. M.; Crouch, R. J. *FEBS J*. **2009**, *276*, 1494–1505.
14. Kling, J. *Nat. Biotechnol*. **2010**, *28*, 295–297.
15. Tiemann, K.; Rossi, J. J. *EMBO Mol. Med*. **2009**, *1*, 142–151.
16. Robak, T.; Jamroziak, K.; Robak, P. *Drugs* **2009**, *69*, 2415–2449.
17. Al-Mahmood, S.; Colin, S.; Farhat, N.; Thorin, E.; Steverlynck, C.; Chemtob, S. *J. Pharmacol. Exp. Ther*. **2009**, *329*, 496–504.
18. Barakat, M. R.; Kaiser, P. *Expert Opin. Investig. Drugs* **2009**, *18*, 637–646.
19. Kim, D. K.; Dobson, J. *J. Mater. Chem*. **2009**, *19*, 6294–6307.
20. Arruebo, M.; Fernández-Pacheco, R.; Ibarra, M. R.; Santamaría, J. *Nanotoday* **2007**, *2*, 22–32.
21. Schmidt, C.; Lamprecht, A. In *Nanotherapeutics, Drug Delivery Concepts in Nanoscience*, Pan Stanford Publishing Pte. Ltd: Singapore, 2009; pp 3–30.
22. Wightman, L.; Kircheis, R.; Wagner, E. In *Pharmaceutical Gene Delivery Systems*, Marcel Dekker: New York, 2003; pp 109–125.
23. Bouard, D.; Alazard-Dany, N.; Cosset, F. L. *Br. J. Pharmacol*. **2009**, *157*, 153–165.
24. Escors, D.; Breckpot, K. *Arch. Immunol. Ther. Exp*. **2010**, *58*, 107–119.
25. Heilbronn, R.; Weger, S. In *Drug Delivery*; Schäfer-Korting, M., Ed.; Springer: Berlin, Heidelberg, 2010; pp 143–170.
26. Pluta, K.; Kacprzak, M. M. *Acta Biochim. Pol*. **2009**, *56*, 531–595.
27. Marshall, E. *Science* **1999**, *286*, 2244–2245.
28. Marshall, E. *Science* **2000**, *287*, 565–567.
29. Cavazzana-Calvo, M.; Fischer, A. *J. Clin. Investig*. **2007**, *117*, 1456–1465.
30. Carlisle, R. C.; Di, Y.; Cerny, A. M.; *et al*. *Blood* **2009**, *113*, 1909–1918.
31. Ganly, I.; Kirn, D.; Eckhardt, G.; *et al*. *Clin. Cancer Res*. **2000**, *6*, 798–806.
32. Nemunaitis, J.; Cunningham, C.; Buchanan, A.; *et al*. *Gene Ther*. **2001**, *8*, 746–759.
33. Bhakta, G.; Mitra, S.; Maitra, A. *Biomaterials* **2005**, *26*, 2157–2163.
34. Son, S. J.; Bai, X.; Lee, S. B. *Drug Discov. Today* **2007**, *12*, 650–656.
35. Zhi, P. X.; Qing, H. Z.; Gao, Q. L.; Ai, B. Y. *Chem. Eng. Sci*. **2006**, *61*, 1027–1040.
36. Ho, R. J. Y.; Gibaldi, M. *Biotechnology and Biopharmaceuticals – Transforming Proteins and Genes into Drugs*, Wiley: Hoboken, NJ, 2003; pp 395–396.
37. Huang, L.; Viroonchatapan, E. In *Nonviral Vectors for Gene Therapy*; Huang, L., Hung, M-.C., Wagner, E., Eds.; Academic Press: San Diego, CA, 1999; pp 7–10.
38. Mahato, R. I., Ed.; In *Biomaterials for Delivery and Targeting of Proteins and Nucleic Acids*; CRC Press (Taylor and Francis): Boca Raton, FL, 2004.
39. Vasir, J. K.; Labhasetwar, V. *Nanoparticulate Drug Delivery Systems*, Informa Healthcare: New York, 2007; pp 291–305.
40. Corsi, K.; Chellat, F.; Yahia, L.; Fernandes, J. C. *Biomaterials* **2003**, *24*, 1255–1264.
41. Kreiss, P.; Cameron, B.; Rangara, R.; *et al*. *Nucleic Acids Res*. **1999**, *27*, 3792–3798.
42. Kennedy, M. A.; Parks, R. J. *Mol. Ther*. **2009**, *17*, 1664–1666.
43. Liu, F.; Huang, L. *J. Control. Release* **2002**, *78*, 259–266.
44. Brown, M. D.; Schätzlein, A. G.; Uchegbu, I. F. *Int. J. Pharm*. **2001**, *229*, 1–21.
45. El-Aneed, A. *J. Control. Release* **2004**, *94*, 1–14.
46. Elouahabi, A.; Ruysschaert, J.-M. *Mol. Ther*. **2005**, *11*, 336–347.
47. Safinya, C. R. *Curr. Opin. Struct. Biol*. **2001**, *11*, 440–448.
48. Felgner, P. L.; Gadek, T. R.; Holm, M.; *et al*. *Proc. Natl. Acad. Sci. USA* **1987**, *84*, 7413–7417.
49. Simberg, D.; Weisman, S.; Talmon, Y.; Barenholz, Y. *DOTAP (and Other Cationic Lipids): Chemistry, Biophysics, and Transfection*. ETATS-UNIS, Begell House: New York, NY, 2004.
50. Behr, J. P.; Demeneix, B.; Loeffler, J. P.; Perez-Mutul, J. *Proc. Natl. Acad. Sci. USA* **1989**, *86*, 6982–6986.
51. Gao, X.; Huang, L. *Biochem. Biophys. Res. Commun*. **1991**, *179*, 280–285.
52. Lee, E. R.; Marshall, J.; Siegel, C. S.; *et al*. *Hum. Gene Ther*. **1996**, *7*, 1701–1717.
53. Crook, K.; Mclachlan, G.; Stevenson, B. J.; Porteous, D. J. *Gene Ther*. **1996**, *3*, 834–839.
54. Du, J.; Tang, Y.; Lewis, A. L.; Armes, S. P. *J. Am. Chem. Soc*. **2005**, *127*, 17982–17983.
55. Ohki, E. C.; Tilkins, M. L.; Ciccarone, V. C.; Price, P. J. *J. Neurosci. Meth*. **2001**, *112*, 95–99.
56. Dalby, B.; Cates, S.; Harris, A.; *et al*. *Methods* **2004**, *33*, 95–103.
57. Dass, C. R. *J. Mol. Med*. **2004**, *82*, 579–591.
58. Saada, J.; Oudrhiri, N.; Bonnard, A.; *et al*. *J. Gene Med*. **2010**, *12*, 413–422.
59. Nemunaitis, G.; Maples, P. B.; Jay, C.; *et al*. *J. Gene Med*. **2010**, *12*, 403–412.
60. Blessing, T.; Remy, J. S.; Behr, J. P. *Proc. Natl. Acad. Sci. USA* **1998**, *95*, 1427–1431.
61. Patil, S. D.; Rhodes, D. G.; Burgess, D. J. *AAPS J*. **2004**, *6*, e29.
62. Patil, S. D.; Rhodes, D. G.; Burgess, D. J. *BBA Biomembr*. **2005**, *1711*, 1–11.
63. Srinivasan, C.; Burgess, D. J. *J. Control. Release* **2009**, *136*, 62–70.
64. Allison, S. D.; Molina, M. D. C.; Anchordoquy, T. J. *BBA Biomembr*. **2000**, *1468*, 127–138.
65. Filion, M. C.; Phillips, N. C. *Int. J. Pharm*. **1998**, *162*, 159–170.
66. Gao, X.; Kim, K.-S.; Liu, D. *AAPS J*. **2007**, *9*, E92–E104.
67. Li, B.; Li, S.; Tan, Y.; *et al*. *J. Pharm. Sci*. **2000**, *89*, 355–364.
68. Nguyen, L. T.; Atobe, K.; Barichello, J. M.; Ishida, T.; Kiwada, H. *Biol. Pharm. Bull*. **2007**, *30*, 751–757.
69. Frankel, A. D.; Pabo, C. O. *Cell* **1988**, *55*, 1189–1193.
70. Torchilin, V. P.; Levchenko, T. S.; Rammohan, R.; Volodina, N.; Papahadjopoulos-Sternberg, B.; D'souza, G. G. M. *Proc. Natl. Acad. Sci. USA* **2003**, *100*, 1972–1977.
71. Nasanit, R.; Iqbal, P.; Soliman, M.; *et al*. *Mol. Biosyst*. **2008**, *4*, 741–747.
72. Soliman, M.; Nasanit, R.; Allen, S.; *et al*. *Soft Matter* **2010**, *6*, 2517–2524.
73. Plank, C.; Oberhauser, B.; Mechtler, K.; Koch, C.; Wagner, E. *J. Biol. Chem*. **1994**, *269*, 12918–12924.
74. Mckenzie, D. L.; Kwok, K. Y.; Rice, K. G. *J. Biol. Chem*. **2000**, *275*, 9970–9977.
75. Wadhwa, M. S.; Collard, W. T.; Adami, R. C.; Mckenzie, D. L.; Rice, K. G. *Bioconjug. Chem*. **1997**, *8*, 81–88.
76. Bremner, K. H.; Seymour, L. W.; Logan, A.; Read, M. L. *Bioconjug. Chem*. **2003**, *15*, 152–161.
77. Zanta, M. A.; Belguise-Valladier, P.; Behr, J.-P. *Proc. Natl. Acad. Sci. USA* **1999**, *96*, 91–96.
78. Ogris, M.; Carlisle, R. C.; Bettinger, T.; Seymour, L. W. *J. Biol. Chem*. **2001**, *276*, 47550–47555.
79. Soundara Manickam, D.; Bisht, H. S.; Wan, L.; Mao, G.; Oupicky, D. *J. Control. Release* **2005**, *102*, 293–306.
80. Duguid, J. G.; Li, C.; Shi, M.; *et al*. *Biophys. J*. **1998**, *74*, 2802–2814.
81. Martin, M.; Rice, K. *AAPS J*. **2007**, *9*, E18–E29.
82. Adami, R. C.; Collard, W. T.; Gupta, S. A.; Kwok, K. Y.; Bonadio, J.; Rice, K. G. *J. Pharm. Sci*. **1998**, *87*, 679–683.
83. Männistö, M.; Vanderkerken, S.; Toncheva, V.; *et al*. *J. Control. Release* **2002**, *83*, 169–182.
84. Thomas, M.; Klibanov, A. M. *Appl. Microbiol. Biotech*. **2003**, *62*, 27–34.
85. Khalil, I. A.; Kogure, K.; Akita, H.; Harashima, H. *Pharmacol. Rev*. **2006**, *58*, 32–45.
86. Read, M. L.; Singh, S.; Ahmed, Z.; *et al*. *Nucleic Acids Res*. **2005**, *33*, e86.
87. Yamasaki, Y.; Jang, W.-D.; Nishiyama, N.; Kataoka, K. *Non-viral Gene Therapy – Gene Design and Delivery*, Springer-Verlag: Tokyo, 2005; pp 51–62.
88. Lee, M.; Kim, S. W. In *Polymeric Gene Delivery – Principles and Application*; Amiji, M. M., Ed.; CRC Press: Boca Raton, FL, 2005; pp 89–90.
89. Melikov, K.; Chernomordik, L. *Cell. Mol. Life Sci*. **2005**, *62*, 2739–2749.
90. Vives, E.; Brodin, P.; Lebleu, B. *J. Biol. Chem*. **1997**, *272*, 16010–16017.
91. Derossi, D.; Joliot, A. H.; Chassaing, G.; Prochiantz, A. *J. Biol. Chem*. **1994**, *269*, 10444–10450.
92. Fawell, S.; Seery, J.; Daikh, Y.; *et al*. *Proc. Natl. Acad. Sci. USA* **1994**, *91*, 664–668.
93. Lundberg, M.; Wikstrom, S.; Johansson, M. *Mol. Ther*. **2003**, *8*, 143–150.
94. Ziegler, A.; Seelig, J. *Biophys. J*. **2004**, *86*, 254–263.
95. Snyder, E.; Dowdy, S. *Pharm. Res*. **2004**, *21*, 389–393.
96. Torchilin, V. P. *Adv. Drug Deliv. Rev*. **2008**, *60*, 548–558.
97. Dietz, G. P.; Kilic, E.; Bahr, M. *Mol. Cell. Neurosci*. **2002**, *21*, 29–37.
98. Kilic, E.; Hermann, D. M.; Kügler, S.; *et al*. *Ann. Neurol*. **2002**, *52*, 617–622.
99. Kilic, U.; Kilic, E.; Dietz, G. P. H.; Bahr, M. *Stroke* **2003**, *34*, 1304–1310.
100. Pack, D. W.; Putnam, D.; Langer, R. *Biotechnol. Bioeng*. **2000**, *67*, 217–223.
101. Bechinger, B. *J. Mol. Biol*. **1996**, *263*, 768–775.
102. Akinc, A.; Thomas, M.; Klibanov, A. M.; Langer, R. *J. Gene Med*. **2005**, *7*, 657–663.
103. Midoux, P.; Kichler, A.; Boutin, V.; Maurizot, J.-C.; Monsigny, M. *Bioconjug. Chem*. **1998**, *9*, 260–267.
104. Midoux, P.; Monsigny, M. *Bioconjug. Chem*. **1999**, *10*, 406–411.

105. Schaffer, D. V.; Fidelman, N. A.; Dan, N.; Lauffenburger, D. A. *Biotechnol. Bioeng.* **2000**, *67*, 598–606.
106. Benns, J. M.; Choi, J.-S.; Mahato, R. I.; Park, J.-S.; Kim, S. W. *Bioconjug. Chem.* **2000**, *11*, 637–645.
107. Pichon, C.; Gonçalves, C.; Midoux, P. *Adv. Drug Deliv. Rev.* **2001**, *53*, 75–94.
108. Saito, G.; Swanson, J. A.; Lee, K.-D. *Adv. Drug Deliv. Rev.* **2002**, *55*, 199–215.
109. Saito, G.; Amidon, G. L.; Lee, K. D. *Gene Ther.* **2003**, *10*, 72–83.
110. Oupicky, D.; Parker, A. L.; Seymour, L. W. *J. Am. Chem. Soc.* **2002**, *124*, 8–9.
111. Read, M. L.; Bremner, K. H.; Oupický, D.; Green, N. K.; Searle, P. F.; Seymour, L. W. *J. Gene Med.* **2003**, *5*, 232–245.
112. Vårum, K. M.; Anthonsen, M. W.; Grasdalen, H.; Smidsrød, O. *Carbohydr. Res.* **1991**, *217*, 19–27.
113. Anthonsen, M. W.; Smidsrød, O. *Carbohydr. Polym.* **1995**, *26*, 303–305.
114. Domard, A. *Int. J. Biol. Macromol.* **1987**, *9*, 98–104.
115. Vårum, K. M.; Ottøy, M. H.; Smidsrød, O. *Carbohydr. Polym.* **2001**, *46*, 89–98.
116. Mumper, R. J.; Wang, J.; Claspell, J. M.; Rolland, A. P. In *Proceedings of the International Symposium of Controlled Release Bioactive Materials*; Seattle, WA, USA, 1995 pp 178–179.
117. Mao, S.; Shuai, X.; Unger, F.; Simon, M.; Bi, D.; Kissel, T. *Int. J. Pharm.* **2004**, *281*, 45–54.
118. Richardson, S. C. W.; Kolbe, H. V. J.; Duncan, R. *Int. J. Pharm.* **1999**, *178*, 231–243.
119. Kiang, T.; Wen, J.; Lim, H. W.; Leong, K. W. K. W. *Biomaterials* **2004**, *25*, 5293–5301.
120. Koping-Hoggard, M.; Guan, I. T.; Edwards, K.; Nilsson, M.; Varum, K. M.; Artursson, P. *Gene Ther. Mol. Biol.* **2001**, *8*, 1108–1121.
121. Lee, M.; Nah, J. W.; Kwon, Y.; Koh, J. J.; Ko, K. S.; Kim, S. W. *Pharm. Res.* **2001**, *18*, 427–431.
122. Maclaughlin, F. C.; Mumper, R. J.; Wang, J.; *et al. J. Control. Release* **1998**, *56*, 259–272.
123. Vårum, K. M.; Ottøy, M. H.; Smidsrød, O. *Carbohydr. Polym.* **1994**, *25*, 65–70.
124. Bloomfield, V. A. *Biopolymers* **1997**, *44*, 269–282.
125. Fischer, D.; Bieber, T.; Li, Y. X.; Elsasser, H. P.; Kissel, T. *Pharm. Res.* **1999**, *16*, 1273–1279.
126. Plank, C.; Tang, M. X.; Wolfe, A. R.; Szoka, F. C., Jr. *Hum. Gene Ther.* **1999**, *10*, 319–332.
127. Guillem, V. M.; Alino, S. F. *Gene Ther. Mol. Biol.* **2004**, *8*, 369–384.
128. Il'ina, A.; Varlamov, V. *Appl. Biochem. Microbiol.* **2007**, *43*, 73–77.
129. Park, J. S.; Han, T. H.; Lee, K. Y.; *et al. J. Control. Release* **2006**, *115*, 37–45.
130. Kim, Y. H.; Gihm, S. H.; Park, C. R.; *et al. Bioconjug. Chem.* **2001**, *12*, 932–938.
131. Boussif, O.; Lezoualc'h, F.; Zanta, M. A.; *et al. Proc. Natl. Acad. Sci. USA* **1995**, *92*, 7297–7301.
132. Hinrichs, W. L. J.; Schuurmans-Nieuwenbroek, N. M. E.; Wetering, P. V. D.; Hennink, W. E. *J. Control. Release* **1999**, *60*, 249–259.
133. Kurisawa, M.; Yokoyama, M.; Okano, T. *J. Control. Release* **2000**, *69*, 127–137.
134. Park, S.; Healy, K. E. *J. Control. Release* **2004**, *95*, 639–651.
135. Putnam, D.; Gentry, C. A.; Pack, D. W.; Langer, R. *Proc. Natl. Acad. Sci. USA* **2001**, *98*, 1200–1205.
136. Twaites, B. R.; Alarcon, C. D.; Cunliffe, D.; *et al. J. Control. Release* **2004**, *97*, 551–566.
137. Twaites, B. R.; Alarcon, C. D. L. H.; Lavigne, M.; *et al. J. Control. Release* **2005**, *108*, 472–483.
138. Zheng, F.; Shi, X.-W.; Yang, G.-F.; *et al. Life Sci.* **2007**, *80*, 388–396.
139. Arima, H. In *Non-viral Gene Therapy – Gene Design and Delivery*; Niidome, T., Taira, K., Kataoka, K., Eds.; Springer-Verlag: Tokyo, 2005; pp 75–85.
140. Uherek, C.; Winfried, W. *Adv. Drug Deliv. Rev.* **2000**, *44*, 153–166.
141. De Smedt, S. C.; Demeester, J.; Hennink, W. E. *Pharm. Res.* **2000**, *17*, 113–126.
142. Lopata, M. A.; Cleveland, D. W.; Sollner-Webb, B. *Nucleic Acids Res.* **1984**, *12*(14), 5707–5717.
143. Wightman, L.; Kircheis, R.; Rössler, V.; *et al. J. Gene Med.* **2001**, *3*, 362–372.
144. Zou, S.-M.; Erbacher, P.; Remy, J.-S.; Behr, J.-P. *J. Gene Med.* **2000**, *2*, 128–134.
145. Behr, J. P. *Chimia* **1997**, *51*, 34–36.
146. Kichler, A.; Leborgne, C.; Coeytaux, E.; Danos, O. *J. Gene Med.* **2001**, *3*, 135–144.
147. Merdan, T.; Kunath, K.; Fischer, D.; Kopecek, J.; Kissel, T. *Pharm. Res.* **2002**, *19*, 140–146.
148. Gebhart, C. L.; Kabanov, A. V. *J. Control. Release* **2001**, *73*, 401–416.
149. Bragonzi, A.; Dina, G.; Villa, A.; *et al. Gene Ther.* **2000**, *7*, 1753–1760.
150. Klemm, A. R.; Young, D.; Lloyd, J. B. *Biochem. Pharmacol.* **1998**, *56*, 41–46.
151. Petersen, H.; Kunath, K.; Martin, A. L.; *et al. Biomacromolecules* **2002**, *3*, 926–936.
152. Thomas, M.; Klibanov, A. M. *Proc. Natl. Acad. Sci. USA* **2002**, *99*, 14640–14645.
153. Godbey, W. T.; Wu, K. K.; Mikos, A. G. *Biomaterials* **2001**, *22*, 471–480.
154. Gosselin, M. A.; Guo, W.; Lee, R. J. *Bioconjug. Chem.* **2001**, *12*, 989–994.
155. Regnstrom, K.; Ragnarsson, E. G. E.; Koping-Hoggard, M.; Torstensson, E.; Nyblom, H.; Artursson, P. *Gene Ther.* **2003**, *10*, 1575–1583.
156. Wolfert, M. A.; Dash, P. R.; Nazarova, O.; *et al. Bioconjug. Chem.* **1999**, *10*, 993–1004.
157. Knorr, V.; Russ, V.; Allmendinger, L.; Ogris, M.; Wagner, E. *Bioconjug. Chem.* **2008**, *19*, 1625–1634.
158. Knorr, V.; Ogris, M.; Wagner, E. *Pharm. Res.* **2008**, *25*, 2937–2945.
159. Neu, M.; Sitterberg, J.; Bakowsky, U.; Kissel, T. *Biomacromolecules* **2006**, *7*, 3428–3438.
160. Wetering, P.; Moret, E. E.; Schuurmans-Nieuwenbroek, N. M. E.; Steenbergen, M. J.; Hennink, W. E. *Bioconjug. Chem.* **1999**, *10*, 589–597.
161. Jones, R. A.; Poniris, M. H.; Wilson, M. R. *J. Control. Release* **2004**, *96(3)*, 379–391.
162. You, Y. Z.; Manickam, D. S.; Zhou, Q. H.; Oupický, D. *J. Control. Release* **2007**, *122*(3), 217–225.
163. Sadler, K.; Tam, J. P. *Rev. Mol. Biotech.* **2002**, *90*, 195–229.
164. Arima, H.; Kihara, F.; Hirayama, F.; Uekama, K. *Bioconjug. Chem.* **2001**, *12*, 476–484.
165. Dufès, C.; Uchegbu, I. F.; Schätzlein, A. G. *Adv. Drug Deliv. Rev.* **2005**, *57*, 2177–2202.
166. Haensler, J.; Szoka, F. C. *Bioconjug. Chem.* **1993**, *4*, 372–379.
167. Kihara, F.; Arima, H.; Tsutsumi, T.; Hirayama, F.; Uekama, K. *Bioconjug. Chem.* **2002**, *13*, 1211–1219.
168. Svenson, S. *Eur. J. Pharm. Biopharm.* **2009**, *71*, 445–462.
169. Lin, C.; Blaauboer, C.-J.; Timoneda, M. M.; *et al. J. Control. Release* **2008**, *126*, 166–174.
170. Christensen, L. V.; Chang, C. W.; Kim, W. J.; *et al. Bioconjug. Chem.* **2006**, *17*, 1233–1240.
171. Christensen, L. V.; Chang, C. W.; Yockman, J. W.; *et al. J. Control. Release* **2007**, *118*, 254–261.
172. Maiti, P. K.; Cagan, T.; Lin, S.-T.; Goddard, W. A. *Macromolecules* **2005**, *38*, 979–991.
173. Dennig, J.; Duncan, E. *Rev. Mol. Biotech.* **2002**, *90*, 339–347.
174. Tang, M. X.; Redemann, C. T.; Szoka, F. C. *Bioconjug. Chem.* **1996**, *7*, 703–714.
175. Malik, N.; Wiwattanapatapee, R.; Klopsch, R.; *et al. J. Control. Release* **2000**, *65*, 133–148.
176. Langer, R. *Nature* **1998**, *392*, 5–10.
177. Jong, Y. S.; Jacob, J. S.; Yip, K. P.; *et al. J. Control. Release* **1997**, *47*, 123–134.
178. Shea, L. D.; Smiley, E.; Bonadio, J.; Mooney, D. J. *Nat. Biotech.* **1999**, *17*, 551–554.
179. Bilati, U.; Allemann, E.; Doelker, E. *J. Microencapsul.* **2005**, *22*, 205–214.
180. Govender, T.; Stolnik, S.; Garnett, M. C.; Illum, L.; Davis, S. S. *J. Control. Release* **1999**, *57*, 171–185.
181. Jain, R. A. *Biomaterials* **2000**, *21*, 2475–2490.
182. Kim, D. H.; Martin, D. C. *Biomaterials* **2006**, *27*, 3031–3037.
183. Bala, I.; Hariharan, S.; Kumar, M. *Crit. Rev. Ther. Drug Carrier Syst.* **2004**, *21*, 387–422.
184. Bittner, B.; Ronneberger, B.; Zange, R.; Volland, C.; Anderson, J. M.; Kissel, T. *J. Microencapsul.* **1998**, *15*, 495–514.
185. Kumar, M.; Bakowsky, U.; Lehr, C. M. *Biomaterials* **2004**, *25*, 1771–1777.
186. Desai, M. P.; Labhasetwar, V.; Amidon, G. L.; Levy, R. J. *Pharm. Res.* **1996**, *13*, 1838–1845.
187. Desai, M. P.; Labhasetwar, V.; Walter, E.; Levy, R. J.; Amidon, G. L. *Pharm. Res.* **1997**, *14*, 1568–1573.
188. Freitas, S.; Merkle, H. P.; Gander, B. *J. Control. Release* **2005**, *102*, 313–332.
189. Hsu, Y. Y.; Hao, T.; Hedley, M. L. *J. Drug Target.* **1999**, *7*, 313–323.
190. Sah, H.; Bahl, Y. *J. Control. Release* **2005**, *106*, 51–61.
191. Walter, E.; Moelling, K.; Pavlovic, J.; Merkle, H. P. *J. Control. Release* **1999**, *61*, 361–374.
192. Ando, S.; Putnam, D.; Pack, D. W.; Langer, R. *J. Pharm. Sci.* **1999**, *88*, 126–130.
193. Capan, Y.; Woo, B. H.; Gebrekidan, S.; Ahmed, S.; Deluca, P. P. *J. Control. Release* **1999**, *60*, 279–286.
194. Capan, Y.; Woo, B. H.; Gebrekidan, S.; Ahmed, S.; Deluca, P. P. *Pharm. Dev. Technol.* **1999**, *4*, 491–498.
195. Patil, Y.; Panyam, J. *Int. J. Pharm.* **2009**, *367*, 195–203.
196. Takashima, Y.; Saito, R.; Nakajima, A.; *et al. Int. J. Pharm.* **2007**, *343*, 262–269.
197. O'hagan, D.; Singh, M.; Ugozzoli, M.; *et al. J. Virol.* **2001**, *75*, 9037–9043.
198. Luten, J.; Van Nostruin, C. F.; De Smedt, S. C.; Hennink, W. E. *J. Control. Release* **2008**, *126*, 97–110.

199. Wang, D. Q.; Robinson, D. R.; Kwon, G. S.; Samuel, J. *J. Control. Release* **1999**, *57*, 9–18.
200. Mok, H.; Lee, S. H.; Park, J. W.; Park, T. G. *Nat. Mater.* **2010**, *9*, 272–278.
201. Kakizawa, Y.; Kataoka, K. *Adv. Drug Deliv. Rev.* **2002**, *54*, 203–222.
202. Kataoka, K.; Harada, A.; Nagasaki, Y. *Adv. Drug Deliv. Rev.* **2001**, *47*, 113–131.
203. Lee, Y.; Kataoka, K. *Soft Matter* **2009**, *5*, 3810–3817.
204. Mahmud, A.; Xiong, X. B.; Aliabadi, H. M.; Lavasanifar, A. *J. Drug Target.* **2007**, *15*, 553–584.
205. Van Dongen, S. F. M.; De Hoog, H. P. M.; Peters, R.; Nallani, M.; Nolte, R. J. M.; Van Hest, J. C. M. *Chem. Rev.* **2009**, *109*, 6212–6274.
206. Lo, P. C.; Lomas, H.; Massignani, M.; Smart, T.; Battaglia, G. *J. Mater. Chem.* **2009**, *19*, 3576–3590.
207. Giacomelli, C.; Le Men, L.; Borsali, R.; *et al*. *Biomacromolecules* **2006**, *7*, 817–828.
208. Lomas, H.; Du, J.; Canton, I.; *et al*. *Macromol. Biosci.* **2010**, *10*, 513–530.
209. Lomas, H.; Canton, I.; Macneil, S.; *et al*. *Adv. Mater.* **2007**, *19*, 4238–4243.
210. Lomas, H.; Massignani, M.; Abdullah, K. A.; *et al*. *Faraday Discuss.* **2008**, *139*, 143–159.
211. Matsumura, Y.; Maeda, H. *Cancer Res.* **1986**, *46*, 6387–6392.
212. Cammas-Marion, S. In *Nanotherapeutics, Drug Delivery Concepts in Nanoscience*; Lamprecht, A., Ed.; Pan Stanford: Singapore, 2009; pp 67–86.
213. Pouton, C. W. In *Advanced Gene Delivery from Concepts to Pharmaceutical Products*; Rolland, A., Ed.; Harwood Academic: Amsterdam, 1999; pp 66–102.
214. Erbacher, P.; Remy, J. S.; Behr, J. P. *Gene Ther.* **1999**, *6*, 138–145.
215. Kawakami, S.; Hashida, M. *Drug Metab. Pharmacok.* **2007**, *22*, 142–151.
216. Tang, M. X.; Szoka, F. C. *Gene Ther.* **1997**, *4*, 823–832.
217. Ogris, M.; Brunner, S.; Kircheis, R.; Wagner, E. *Gene Ther.* **1999**, *6*, 595–605.
218. Plank, C.; Mechtler, K.; Szoka, F. C.; Wagner, E. *Hum. Gene Ther.* **1996**, *7*, 1437–1446.
219. Remaut, K. *Mater. Sci. Eng.* **2007**, *58*, 117–161.
220. Kircheis, R.; Wightman, L.; Schreiber, A.; *et al*. *Gene Ther.* **2001**, *8*, 28–40.
221. Mayor, S.; Pagano, R. E. *Nat. Rev. Mol. Cell. Biol.* **2007**, *8*, 603–612.
222. Mousavi, S. A.; Malerød, L.; Berg, T.; Kjeken, R. *Biochem. J.* **2004**, *377*, 1–16.
223. Mukherjee, S.; Ghosh, R. N.; Maxfield, F. R. *Physiol. Rev.* **1997**, *77*, 760–803.
224. Sagara, K.; Kim, S. W. *J. Control. Release* **2002**, *79*, 271–281.
225. Sonawane, N. D.; Szoka, F. C. J.; Verkman, A. S. *J. Biol. Chem.* **2003**, *278*, 44826–44831.
226. Suh, J.; Wirtz, D.; Hanes, J. *Proc. Natl. Acad. Sci. USA* **2003**, *100*, 3878–3882.
227. Ludtke, J. J.; Zhang, G.; Sebestyen, M. G.; Wolff, J. A. *J. Cell Sci.* **1999**, *112*, 2033–2041.
228. Pasut, G.; Veronese, F. M. *Adv. Drug Deliv. Rev.* **2009**, *61*, 1177–1188.
229. Satchi-Fainaro, R.; Duncan, R.; Burnes, C. M. In *Polymer Therapeutics II: Polymers as Drugs, Conjugates and Gene Delivery Systems*; Satchi-Fainaro, R., Duncan, R., Eds.; Advances in Polymer Science; Springer: Berlin Heidelberg, 2006; Vol. 193, pp 1–65.
230. Kircheis, R.; Wightman, L.; Wagner, E. *Adv. Drug Deliv. Rev.* **2001**, *53*, 341–358.
231. Maruyama, K.; Iwasaki, F.; Takizawa, T.; *et al*. *Biomaterials* **2004**, *25*, 3267–3273.
232. Dash, P. R.; Read, M. L.; Barrett, L. B.; Wolfert, M. A.; Seymour, L. W. *Gene Ther.* **1999**, *6*, 643–650.
233. Chollet, P.; Favrot, M. C.; Hurbin, A.; Coll, J.-L. *J. Gene Med.* **2002**, *4*, 84–91.
234. Banerjee, P.; Weissleder, R.; Bogdanov, A. *Bioconjug. Chem.* **2006**, *17*, 125–131.
235. Mao, S.; Neu, M.; Germershaus, O.; *et al*. *Bioconjug. Chem.* **2006**, *17*, 1209–1218.
236. Zhong, Z.; Feijen, J.; Lok, M. C.; *et al*. *Biomacromolecules* **2005**, *6*, 3440–3448.
237. Rackstraw, B. J.; Martin, A. L.; Stolnik, S.; *et al*. *Langmuir* **2001**, *17*, 3185–3193.
238. Erbacher, P.; Bettinger, T.; Belguise-Valladier, P.; *et al*. *J. Gene Med.* **1999**, *1*, 210–222.
239. Ogris, M.; Walker, G.; Blessing, T.; Kircheis, R.; Wolschek, M.; Wagner, E. *J. Control. Release* **2003**, *91*, 173–181.
240. Oupicky, D.; Ogris, M.; Seymour, L. W. *J. Drug Target.* **2002**, *10*, 93–98.
241. Choi, J. S.; Mackay, J. A.; Szoka, F. C. *Bioconjug. Chem.* **2003**, *14*, 420–429.
242. Li, W.; Huang, Z.; Mackay, J. A.; Grube, S.; Szoka, F. C., Jr. *J. Gene Med.* **2005**, *7*, 67–79.
243. Walker, G. F.; Fella, C.; Pelisek, J.; *et al*. *Mol. Ther.* **2005**, *11*, 418–425.
244. Cristiano, R. J.; Roth, J. A. *Cancer Gene Ther.* **1996**, *3*, 4–10.
245. Ferkol, T.; Perales, J. C.; Eckman, E.; Kaetzel, C. S.; Hanson, R. W.; Davis, P. *J. Clin. Invest.* **1995**, *95*, 10.
246. Nishikawa, M.; Yamauchi, M.; Morimoto, K.; Ishida, E.; Takakura, Y.; Hashida, M. *Gene Ther.* **2000**, *7*, 548–555.
247. Perales, J. C.; Ferkol, T.; Beegen, H.; Ratnoff, O. D.; Hanson, R. W. *Proc. Natl. Acad. Sci. USA* **1994**, *91*, 4086–4090.
248. Sosnowski, B. A.; Gonzalez, A. M.; Chandler, L. A.; Buechler, Y. J.; Pierce, G. F.; Baird, A. *J. Biol. Chem.* **1996**, *271*, 33647–33653.
249. Wagner, E.; Curiel, D.; Cotten, M. *Adv. Drug Deliv. Rev.* **1994**, *14*, 113–135.
250. Wagner, E.; Zenke, M.; Cotten, M.; Beug, H.; Birnstiel, M. L. *Proc. Natl. Acad. Sci. USA* **1990**, *87*, 3410–3414.
251. Zhao, X. B.; Lee, R. J. *Adv. Drug Deliv. Rev.* **2004**, *56*, 1193–1204.
252. Dash, P. R.; Read, M. L.; Fisher, K. D.; *et al*. *J. Biol. Chem.* **2000**, *275*, 3793–3802.
253. Fisher, K. D.; Ulbrich, K.; Subr, V.; *et al*. *Gene Ther.* **2000**, *7*, 1337–1343.
254. Kircheis, R.; Schuller, S.; Brunner, S.; *et al*. *J. Gene Med.* **1999**, *1*, 111–120.
255. Ogris, M.; Steinlein, P.; Kursa, M.; Mechtler, K.; Kircheis, R.; Wagner, E. *Gene Ther.* **1998**, *5*, 1425–1433.
256. Wightman, L.; Patzelt, E.; Wagner, E.; Kircheis, R. *J. Drug Target.* **1999**, *7*, 293–303.
257. Kursa, M.; Walker, G. F.; Roessler, V.; *et al*. *Bioconjug. Chem.* **2003**, *14*, 222–231.
258. Wolschek, M. F.; Thallinger, C.; Kursa, M.; *et al*. *Hepatology* **2002**, *36*, 1106–1114.
259. Kaneda, Y. In *Pharmaceutical Gene Delivery Systems*; Rolland, A., Sullivan, S. M., Eds.; Marcel Dekker: New York, 2003; pp 137–146.
260. Glover, D. J.; Leyton, D. L.; Mosely, G. W.; Jans, D. A. *J. Gene Med.* **2010**, *12*, 77.
261. Kurisawa, M.; Yokoyama, M.; Okano, T. *J. Control. Release* **2000**, *68*, 1–8.

4.425. Delivery of Nucleic Acids and Gene Delivery

H Akita, H Hatakeyama, I A Khalil, Y Yamada, and H Harashima, Hokkaido University, Hokkaido, Japan

© 2011 Elsevier Ltd. All rights reserved.

4.425.1.	**Introduction**	413
4.425.2.	**Packaging Concept**	413
4.425.2.1.	Nucleic Acids	413
4.425.2.1.1.	Plasmid DNA	414
4.425.2.1.2.	Oligodeoxyribonucleotide	415
4.425.2.1.3.	Small interfering RNA and microRNAs	415
4.425.2.2.	Carrier Systems	416
4.425.2.2.1.	Liposomes	416
4.425.2.2.2.	Polymers	418
4.425.2.2.3.	Polymeric micelles	419
4.425.2.2.4.	Multifunctional envelope-type nanodevice	420
4.425.3.	**Pharmacokinetics**	422
4.425.3.1.	Factors Governing the PK of a Carrier System	422
4.425.3.1.1.	Carrier charge	423
4.425.3.1.2.	Carrier size	423
4.425.3.2.	Passive Carrier Targeting	423
4.425.3.2.1.	Strategy for addressing the PEG dilemma	425
4.425.3.3.	Endothelial Barriers	425
4.425.4.	**Intracellular Trafficking**	425
4.425.4.1.	Routes of Cell Uptake	425
4.425.4.2.	Endosomal Escape	427
4.425.4.3.	Cytoplasmic Transport	429
4.425.4.4.	Nuclear Delivery	429
4.425.4.5.	Intranuclear Disposition	431
4.425.4.6.	Heterogeneity in Transfection	431
4.425.5.	***In Vivo* Applications**	432
4.425.5.1.	*In Vivo* Delivery of pDNA	432
4.425.5.1.1.	Cancer	432
4.425.5.1.2.	Liver	432
4.425.5.1.3.	Lung	435
4.425.5.1.4.	Kidney	435
4.425.5.1.5.	Muscle	435
4.425.5.2.	*In Vivo* Delivery of siRNA	436
4.425.5.2.1.	Chemical modification, bioconjugation and targeted *in vivo* siRNA delivery	436
4.425.5.2.2.	Lipid-based *in vivo* siRNA delivery	436
4.425.5.2.3.	Polymer-mediated *in vivo* siRNA delivery	437
4.425.5.2.4.	Other delivery systems	437
4.425.5.2.5.	Clinical trials of siRNA therapeutics	438
References		439

Glossary

Endocytosis The cellular uptake of macromolecules and solutes into membrane-bound vesicles derived by the invagination and pinching-off of pieces of the plasma membrane.

Enhanced permeability and retention (EPR) effect A theory used to explain how long-circulating macromolecules, including PEGylated liposomes and colloids 200 nm in diameter and below, can passively accumulate in tumor tissue and sites of inflammation after systemic administration. Such particle accumulation is attributed to changes in tissue capillary vascular permeability in inflammatory sites, including discontinuous or absent basement membranes, lack of an effective lymphatic drainage system, and altered fenestrations and tight junctions.

Lipoplexes Complexes formed between DNA and cationic lipids, which are used mainly in the form of cationic liposomes.

Liposome A spherical vesicle with a membrane composed of a phospholipids bilayer used to deliver drugs or genetic materials into a cell.

Micelles A collection of amphiphilic surfactant molecules that spontaneously aggregate in water into a spherical vesicle. The center of the micelle is hydrophobic and therefore can sequester hydrophobic drugs.
Octaarginine (R8) A peptide that consists of eight arginine residues and possesses membrane translocation activity.
Polyethyleneimine (PEI) A cationic polymer that can condense DNA and possess a buffering capacity (proton sponge mechanism) to allow cytosolic release.
Polyplexes Complexes formed spontaneously when a cationic polymer is mixed with DNA.
Reticulo-endothelial system (RES) The reticuloendothelial system (RES), part of the immune system, consists of phagocytic cells, primarily monocytes and macrophages, that are located in reticular connective tissue. These cells accumulate in lymph nodes and the spleen. The Kupffer cells of the liver and tissue histiocytes are also part of the RES system.
RNA-induced silencing complex (RISC) A multiprotein complex that incorporates one strand of an siRNA. RISC uses the siRNA as a template for recognizing complementary mRNA. When it finds a complementary strand, it activates RNase and cleaves the RNA.
Small fragment homologous replacement (SFHR) A method for gene therapy. The method involves the introduction of small fragments of exogenous DNA into regions of endogenous genomic DNA, which is virtually homologous to the exogenous DNA. The exogenous DNA fragments contain sequence modifications that correct mutations in the endogenous DNA or introduce mutations that alter a cellular or an infecting pathogen phenotype.

Abbreviations

AAV	Adeno-associated virus
AKI	Acute kidney injury
ApoB	Apolipoprotein B
ASGPr	Asialoglycoprotein receptor
asODN	Antisense synthetic ODN
BBB	Blood–brain barrier
BMD	Becker muscular dystrophy
Bmpr1a	Bone morphogenetic protein receptor type 1 A
BSA	Bovine serum albumin
caALK6	Constitutively active activin receptor-like kinase 6
CFTR	Cystic fibrosis transmembrane conductance regulator
CHEMS	Cholesteryl hemisuccinate
CNS	Central nervous system
CMV	Cytomegalovirus
DGF	Delayed graft function
DMD	Duchenne muscular dystrophy
DME	Diabetic macular edema
DOPC	1,2-Dioleoyl-*sn*-glycero-3-phosphocholine
DOPE	1,2-Dioleoyl-*sn*-glycero-3-phosphoethanolamine
DOTAP	1,2-dioleoyl-3-trimethylammonium-propane
DOTMA	*N*-[1-(2,3,-dioleyoxy)propyl]-*N*,*N*,*N*-trimethylammonium
DOX	Doxorubicin
DTS	DNA nuclear targeting sequence
EPR	Enhanced permeability and retention
EPO	Erythropoietin
FACS	Fluorescence-activated cell sorter
FGF	Fibroblast growth factor
FH	Familial hypercholesterolemia
FRET	Fluorescence resonance energy transfer
GalNac	*N*-acetylgalctosamine
GFP	Green fluorescent protein
HGF	Hepatocyte growth factor
HIV	Human immunodeficiency virus
His-PLL	Histidylated PLL
HPV	Human papillomavirus
HSPGs	Heparan sulfate proteoglycans
HSV	Herpes simplex virus
HVJ	Hemagglutinating virus of Japan
IL	Interleukin
JNK-1/-2	c-Jun *N*-terminal kinase-1/-2
LDL	Low-density lipoprotein
LPD	Liposome–polycation–DNA
LPLL	Lipo-PLL
MEND	Multifunctional envelope type nanodevice
miRNAs	MicroRNAs
MMP	Matrix metalloproteinase
MTOC	Microtubule-organizing center
MPS	Mononuclear phagocytic system
MRI	Magnetic resonance imaging
MVD	Microvessel density
NLS	Nuclear localization signal
N/P	Nitrogen to phosphorus
NPC	Nuclear pore complex
ODN	Oligodeoxyribonucleotides
PAsp	Poly(aspartate)
PCR	Polymerase chain reaction
PEG	Poly(ethylene glycol)
PEG-PAsp	PEG-*b*-poly(aspartate)
PEG-PAsp(DET)	PEG–polyaspartamide with an ethylenediamine unit as a side chain
PEG-Plys	PEG–poly(lysine)
PEI	Polyethylenimine
PIV	Parainfluenza virus
PK	Pharmacokinetics
PLL	Poly-(L-lysine)
PMPA	Poly[(3-morpholinopropyl) aspartamide]
PPD	PEG-peptide-DOPE
R8	Octaarginine

RES	Reticuloendothelial system	**SPLP**	Stabilized plasmind–lipid particle
RISC	RNA-induced silencing complex	**STR-R8**	Stearylated octaarginine
RNAi	RNA interference	**TAT**	Transcriptional transactivator
Runx2	Runt-related transcription factor 2	**TLR**	Toll-like receptor
RSV	Respiratory virus	**Tf**	Transferrin
siRNA	Small interfering RNA	**TNFs**	Tumor necrosis factors
SCAD	Short-chain acyl-CoA dehydrogenase	**TRAIL**	TNFrelated apoptosis-inducing ligand
α-SMA	α-smooth muscle actin	**VEGF**	Vascular endothelial growth factor
S/MAR	Scaffold matrix attachment region	**Wet-AMD**	Wet-age-related macular degeneration
SNALP	Stable nucleic acid lipid particle		

4.425.1. Introduction

Gene therapy has long been proposed as a new therapeutic strategy for directly treating diseases at the level of genes. In this therapy, nucleic acids themselves play an important role as a drug and they need to be delivered safely to a site of action, such as the cytosol and nucleus. Therefore, it is essential for these molecules to be able to pass through the plasma and nuclear membranes to efficiently reach the target sites. As the plasma membrane is composed of a lipid bilayer, only low-molecular-weight and lipophilic compounds are able to pass through via diffusion. As nucleic acids are high-molecular-weight, negatively charged molecules, a safe and efficient gene delivery system is needed for them to reach their target.[1] Both viral or nonviral gene delivery systems are used to circumvent these problems. Viral vectors are the ultimate gene delivery system, especially from the view point of efficiency. However, nonviral vectors have advantages over viral vectors particularly from the viewpoints of safety and commercial production. Therefore, much effort has been expended to improve the performance of nonviral vectors, and we will discuss the major carrier systems that have been developed to date for use as gene therapy. These systems generally involve the use of cationic liposomes or cationic polymers to control DNA/RNA intracellular trafficking as well as pharmacokinetics (PK) after their systemic administration.[2] We also describe a newly developed multifunctional envelope-type nanodevice (MEND) based on the concept of programmed packaging, in which multifunctional devices are integrated into a nanocarrier system according to the program designed to overcome all of the barriers during the course of biodistribution as well as intracellular trafficking.[3]

Once in the blood circulation after systemic administration, carrier systems should be sufficiently stable in the blood circulation and be able to avoid immunological recognition to reach a target tissue. The EPR (enhanced permeability and retention) effect, a key concept in passive drug targeting, is introduced, especially for tumor targeting. The concept of active targeting for the selective delivery of nucleic acids to a target cells via receptor-mediated endocytosis, which leads to controlled intracellular trafficking, is also discussed. Vascular endothelial cells are absolute barriers to the passage of nanoparticles from circulation to targets. A breakthrough technology designed to overcome endothelial barriers will also be introduced.

In most cases, both viral and nonviral vectors enter cells via a type of endocytosis, which is a common cell system for macromolecular uptake.[4] Once in endosomes after endocytosis, gene delivery systems must then escape from endosomes to reach the cytosol. Otherwise, they will be degraded by fusion with lysosomes. The cytosol is a major site of action in terms of controlling the function of mRNA, but plasmid DNA (pDNA) must be delivered to the nucleus for transcription. Therefore, the nuclear membrane is a major barrier for high-molecular-weight pDNA. Functional devices need to be introduced to overcome these intracellular barriers such as the endosomal and nuclear membranes. The appropriate design of a nonviral gene vector requires an in-depth understanding of both the characteristics of the vectors themselves as well as mechanisms by which they interact with cellular components.[5]

In this chapter, a nonviral gene delivery system is discussed from several important view points, including the packaging concept, PK, intracellular trafficking, and *in vivo* applications.

4.425.2. Packaging Concept

4.425.2.1. Nucleic Acids

Gene therapy is an attractive approach for treating causes of disease rather than the symptoms.[6] There are many types of candidate nucleic acids for gene therapy (**Table 1**).

Table 1 Summary of candidate nucleic acids for gene therapy

Candidates	*Structure*	*Function*	*Target site*
pDNA	dsDNA	Gene expression	Nucleus
ODN	ssDNA	Gene silencing by antisense technology	Cytosol
		Gene correction	Nucleus
siRNA	dsRNA	Gene silencing by RNA interference	Cytosol
miRNA	ssRNA	Gene silencing by RNA interference	Cytosol

ds, double stranded; ss, single stranded.

For example, pDNA is a candidate for gene-complement therapy. In this strategy, pDNA needs to be delivered to the nucleus for cellular expression of a therapeutic protein. In the case of oligodeoxyribonucleotides (ODN), they must be delivered to the cytosol or nucleus depending on their intended therapeutic use. Gene silencing using antisense synthetic ODN (asODN) can be applied to the suppression of specific genes for tumor growth and virus replication.[7–15] This strategy can be achieved by the cytosolic delivery of asODN to target cells, because asODN inhibits target mRNA in the cytosol for gene silencing. On the other hand, gene-correction therapy requires the delivery of therapeutic ODN to the interior of the nucleus, where the sequence of a disease-causing gene is converted to the normal sequence by the ODN. Strategies for silencing human diseases using RNA interference (RNAi) have attracted attention as an innovative gene therapy. RNAi-mediated gene silencing requires the cytosolic delivery of small RNAs, which include small interfering RNA (siRNAs) and microRNAs (miRNAs).

The main requirement for successful gene therapy is that the therapeutic nucleic acids must pass through the plasma membrane and reach their intracellular targets. The DNA (or RNA) molecule, which is a basic element of a therapeutic nucleic acid, is a hydrophilic, negatively charged, high-molecular-weight molecule. The addition of naked DNA molecules to cells is not likely to result in significant internalization because the DNA cannot pass through the lipophilic plasma membrane. Therefore, a gene vector is needed to carry the DNA to the target site.[4] Vectors can be divided into viral and nonviral vector categories. They differ primarily in the process used for their assembly. A viral vector is assembled in a cellular production system,[16] whereas a nonviral vector is constructed in a test tube.[2,3,17–20]

To achieve efficient gene delivery using a nonviral vector, it is first necessary to efficiently package the nucleic acid cargo into the vector. Second, the vectors must be efficiently targeted and internalized by specific cell types. Finally, sophisticated regulation of intracellular trafficking is needed to release the vector from the endosome and deliver it to its final destination (Figure 1). For example, siRNA should be delivered to the cytosol, where siRNA digests the target mRNA for gene silencing, whereas pDNA should be delivered to the nucleus for gene expression. Thus, the final destination is dependent on each cargo, and vectors must be designed with the specific target site appropriate to the cargo in mind. Here, we describe target sites and therapeutic effects of nucleic acid candidates in detail, as this information can be helpful in the development of nonviral vectors.

4.425.2.1.1. Plasmid DNA

For gene-complement therapy, the gene sequence encoding the therapeutic protein should be delivered to the nucleus for gene expression. pDNA, which is a closed circular DNA molecule containing sequences that allow the gene to be grown in bacteria, is one candidate for realizing gene-complement therapy. pDNA usually carries only one or a few genes representing the genetic therapeutic instructions for the host and has a single origin of replication. The molecular weight is >1 MDa and the hydrodynamic diameter in aqueous suspension is >100 nm. pDNA is very convenient as a material for gene therapy because it can be easily prepared in large quantities using bacterial production system and harvest. Examples of some candidate diseases for gene-complement therapy are described below.

Inherited diseases are typically caused by a single gene mutation or deletion. Therefore, pDNA containing a particular normal gene for a deficient protein could be used if reliably delivered for therapeutic replacement. Examples of candidate-inherited diseases for gene therapy are summarized in Table 2.[21–26] For example, familial hypercholesterolemia (FH) is a genetic disorder caused by the lack of a receptor for

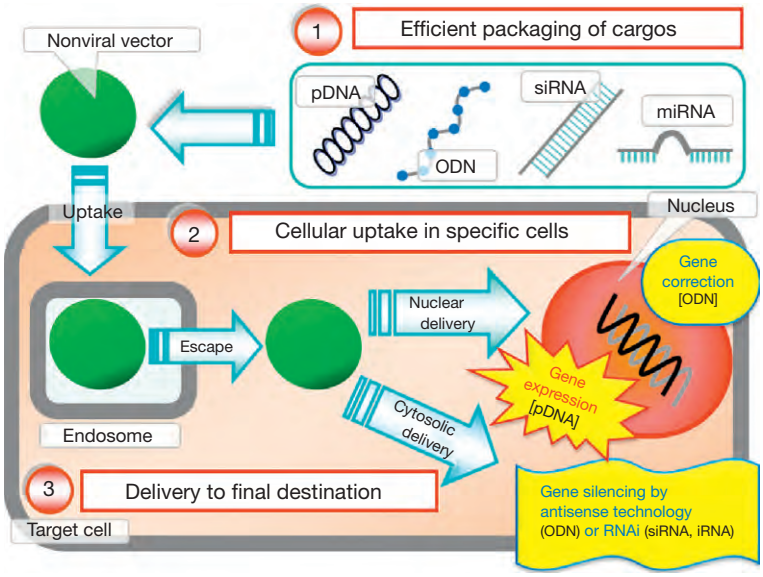

Figure 1 Schematic diagram of gene delivery using nonviral vector. To achieve efficient gene delivery by nonviral vectors, efficient packaging of cargos into the vectors must first be achieved (1). Second, the vectors must be efficiently targeted and internalized by specific cell types (2). Finally, the vector should be delivered to the final destination of each cargo (3).

Table 2 Candidate diseases for gene therapy

Disease	*Defect*	*Target*
A. Inherited diseases		
SOID	AD	T cells
CF	CFTR	Lung
Gaucher's disease	Glucocerebrosidase	Liver
Hernoglobinopathies	Globins	RBC precursors
Hemophilia	Clotting factors VIII and IX	Liver and muscle
Familial hypercholesterolemia	LDL receptor	Liver
Muscular dystrophy	Dystrophin	Muscles
B. Acquired diseases		
Cancer	Defect in tumor supressors and/or presence of oncogenic factors	Variable
Neurological diseases	Defect in doparnine synthesis	CNS
Cardiovascular diseases	Defect in blood vessels	Arteries
Infectious diseases	Suppressed immune system (HIV) or liver destruction (HBV)	T cells, liver, macrophages

SCID, severe combined immunodeficiency; AD, adenosine deaminase; CF, cystic fibrosis; CFTR, cystic fibrosis transmembrane conductance regulator; RBC, red blood cell; LDL, low-density lipoprotein; CNS, central nervous system; HIV, human immunodeficiency virus; HBV, hepatitis B virus.

low-density lipoprotein (LDL), resulting in circulation of LDL particles in the bloodstream, a condition referred to as hypercholesterolemia.[24] Cholesterol contributes to the accelerated formation of atherosclerotic plaques in blood vessel walls. The transfection of patient liver cells with a gene for the LDL receptor represents a strategy for eliminating this condition.

Acquired diseases can also be amenable to treatment by gene-complement therapy. Although no single gene can be identified as the only cause of the disease in acquired diseases, the expression of a single gene in target cells can potentially lead to the elimination of the disease state. Examples of acquired diseases amenable to gene therapy are summarized in Table 2.[27–35]

For these therapies to be successful, vectors are needed to deliver pDNA to the nucleus of target cells. Nonviral vectors are quite attractive for this because of their excellent safety profile, even though their transgene expression efficiency is low in comparison to viral vectors. It is obvious that the intracellular DNA trafficking, particularly nuclear entry in nondividing cells, is a very important issue for high transgene expression. Moreover, the controlled intranuclear disposition of the delivered DNA is also an important issue in terms of achieving practical gene therapy. For example, transgene expression with nonviral vectors is generally transient and of short duration. To overcome these problems, efficient and practical gene therapy using nonviral vectors is required.

4.425.2.1.2. Oligodeoxyribonucleotide

ODNs are predicted to be useful tools for gene therapy mediated by gene silencing and gene correction. In the case of pDNA, its final destination is only the nucleus for gene expression, whereas ODNs must be delivered to the cytosol or nucleus, depending on the therapeutic strategy. In antisense technology, the use of an antisense sequence can inhibit gene expression (gene silencing). In this strategy, asODN must be delivered to the cytosol in target cells, because asODN inhibits target mRNA in the cytosol. On the other hand, gene correction requires the delivery of therapeutic ODN to the nucleus in target cells, because gene correction by ODN occurs in the nucleus. The details of these strategies are described below.

Gene silencing mediated by cytosolic asODN delivery has various advantages, such as technical simplicity, high stability, and temporal effects. This strategy has already been applied to the suppression of specific genes for growth of tumor and virus replication.[7–15] The concept underlying antisense technology involves the use of a sequence that is complementary to a specific host mRNA, which inhibits this mRNA expression thereby inducing a blockade in the transfer of genetic information from DNA to protein. Translation is inhibited by blocking the attachment of mRNA to a ribosome, inhibition of mRNA splicing, or RNase-mediated cleavage of the target mRNA with a DNA/RNA heteroduplex.[31,36] Many antisense sequences showed beneficial therapeutic effects in reducing tumor growth. These include antisense against the human papillomavirus (HPV) E7 protein, fibroblast growth factor-2 (FGF-2),[37] and c-Jun *N*-terminal kinase-1/-2 (JNK-1/-2).[38]

Gene correction (nucleotide sequence conversion) using therapeutic ODN is also an attractive strategy for gene therapy and biotechnology.[39–47] Conversion of the mutations to the normal sequence (gene correction) and disruption (knockout) of disease-related genes would be achieved when the therapeutic ODN is delivered to the nucleus. Single-stranded oligonucleotides, chimeric 2′-*O*-methyl-RNA/DNA oligonucleotides, and triplex-forming oligonucleotides have been examined as chemically synthesized nucleic acids for gene correction. Heat-denatured 400−800 bp double-stranded polymerase chain reaction (PCR) fragments containing the normal sequences have also been examined for their gene correction abilities by the small-fragment homologous replacement method. It has recently been reported that gene correction efficiency with a single-stranded DNA fragment, prepared by the digestion of single-stranded phagemid DNA with a restriction enzyme, is higher than that with a conventional PCR fragment.[48–50]

4.425.2.1.3. Small interfering RNA and microRNAs

During recent decades, RNAi is found to be a natural mechanism for reducing the production of a specified protein via cleavage of mRNA.[51,52] The key therapeutic advantage of using RNAi lies in its ability to specifically and potently

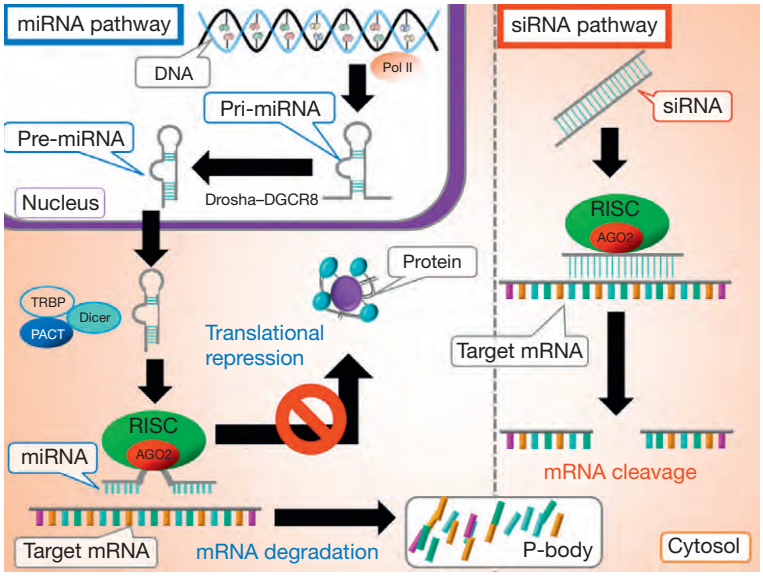

Figure 2 Different mechanisms of RNA interference for siRNA and miRNA. As shown in the pathway on the right, siRNAs are loaded into Argonaute 2 (AGO2) and the RNA-induced silencing complex (RISC). The siRNA guide strand recognizes target sites to direct mRNA cleavage, which is carried out by the catalytic domain of AGO2. As shown in the pathway on the left, endogenously encoded primary microRNA transcripts (pri-miRNAs) are transcribed by RNA polymerase II (Pol II) and initially processed by Drosha–DGCR8 (DiGeorge syndrome critical region gene 8) to generate precursor miRNAs (pre-miRNAs). These precursors are exported to the cytoplasm and subsequently bind to the Dicer–TRBP–PACT complex, which processes the pre-miRNA for loading into AGO2 and RISC. The mature miRNA recognizes target sites in the 3′ untranslated region (3′ UTR) of mRNAs to direct translational inhibition and mRNA degradation in processing (P)-bodies that contain the decapping enzymes.

knock down the expression of disease-causing genes. Gene silencing mediated by an RNAi requires the cytosolic delivery of small therapeutic RNAs including siRNAs and miRNAs. The major role played by small noncoding RNAs in regulating gene expression has recently been recognized.[53–55] siRNAs are produced from long double-stranded RNA that is exogenously introduced artificially by either nonviral or viral transfection. It is thought that the function of siRNAs is to defend cells against unwelcome genetic elements, such as viruses, as shown in Figure 2.

In contrast, miRNAs are encoded by genomes and are evolutionarily conserved among species. miRNAs are intended to act as key regulators of cellular processes as diverse as developmental timing, cell proliferation, cell death, apoptosis, fat metabolism, morphogenesis, and cell differentiation. Both siRNAs and miRNAs act by means of a protein–small RNA complex, the RNA-induced silencing complex (RISC) that silences target gene expression. Via the RISC, siRNAs can direct the cleavage of an mRNA at any single binding site to which they are highly complementary, whereas miRNAs usually act as translational repressors by binding to partially complementary binding sites of their target mRNAs.

4.425.2.2. Carrier Systems

4.425.2.2.1. Liposomes

Liposomes are self-closed colloidal particles in which bilayer membranes composed from self-aggregated lipid molecules encapsulate a fraction of the medium in which they are suspended into their interior.[56–58] Liposomes are formed spontaneously when phospholipids are dispersed in aqueous media, giving rise to a population of vesicles ranging from 10 nm to 10 μm in diameter. They are highly promising as a carrier or sustained release system for the encapsulated molecules. Liposomes have several other advantages such as their biocompatibility, biodegradability, low toxicity, and immunogenicity. In addition, they can incorporate various molecules at high concentrations, and the lipid bilayer can protect the biologically active molecules from damage by chemicals or enzymes. The surface of liposomes can be easily modified with various functional devices such as targeting ligands or other specific devices for optimization.

Conventional liposomes that are not modified with any specific entities were first used as delivery systems to deliver DNA into cells mainly because of their ability to enhance intracellular accumulation of these large and charged molecules across cell membranes. However, the procedure was not efficient as conventional liposomes do not highly bind to cell surfaces and, as a result, they are not highly internalized.[58] Improvements were achieved by using pH-sensitive liposomes,[59] but the use of liposomes in transfection in gene therapy was revived mainly with the emergence of cationic liposome–nucleic acid complexes (lipoplexes). Cationic liposomes can condense and compact DNA. Such complexes can be several orders of magnitude more efficient in transfection than other approaches.[60,61] Gene transfer using cationic liposomes can also be achieved *in vivo* using localized or systemic administration (especially in the lung endothelial cells).[62] Cationic liposomes used for gene delivery are normally formed from cationic lipids along with a neutral lipid such as dioleoylphosphatidylethanolamine (DOPE) or cholesterol. DOPE is frequently used because of its ability to fuse with other lipids when exposed to a low pH, such as in endosomes, which aids in the release of associated DNA into the cytosol.[63,64]

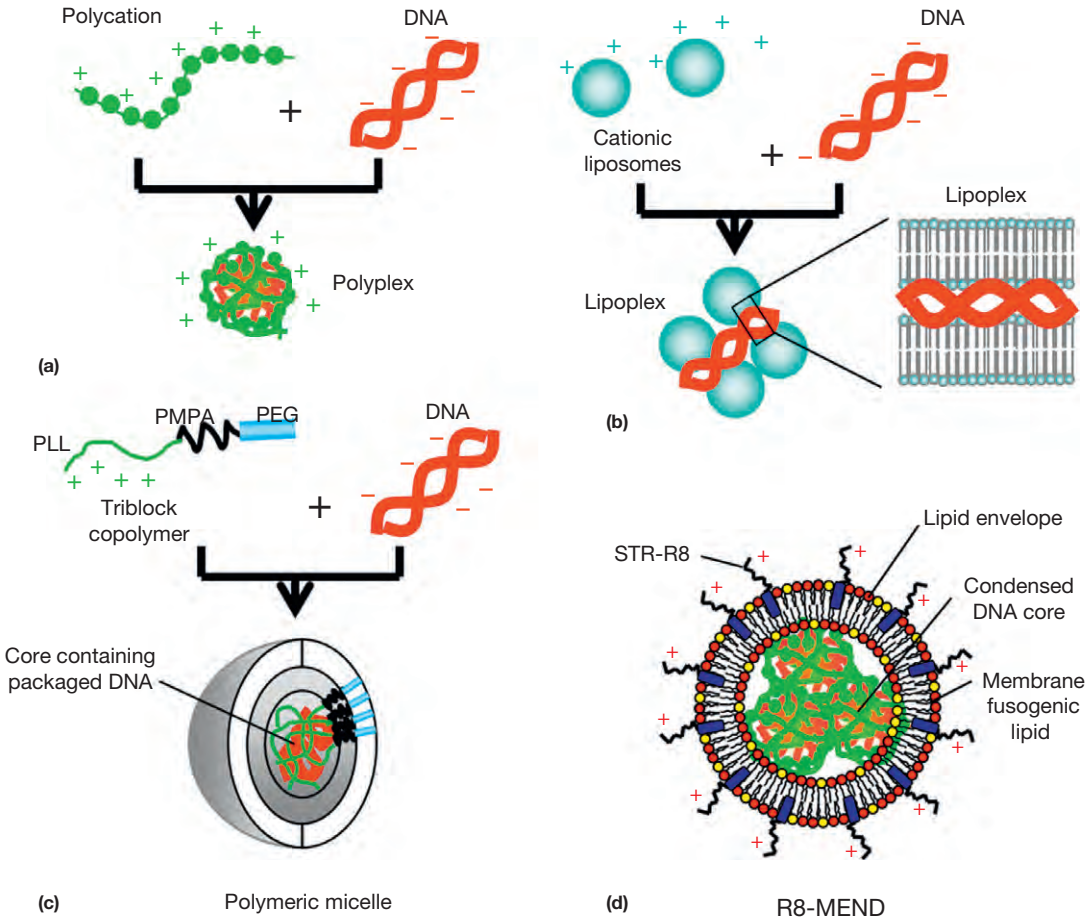

Figure 3 Schematic diagram of different gene carriers. (a) Polyplexes are formed spontaneously by mixing a polycation and DNA. (b) Lipoplexes are complexes formed between DNA and cationic liposomes. The formation of lipoplexes is generally difficult to control and different structures are produced. The interaction involves the formation of multilamellar structures consisting of DNA sandwiched between lipid bilayers. (c) An example of polymeric micelle formed between DNA and a triblock copolymer. This copolymer consists of: a PEG segment for biocompatibility, a PMPA segment to enhance endosomal escape and a PLL segment for DNA binding. (d) Octaarginine-modified multifunctional envelope-type nanodevice (R8-MEND) for gene delivery. It consists of a condensed DNA core covered with a lipid envelope that contains fusogenic lipids and the surface is modified with stearylated R8 for enhancing cellular uptake as well as endosomal escape.

Cholesterol provides structural stability and protection, and there is evidence that it can influence targeting *in vivo* via scavenger receptors.[65,66]

Lipoplexes are typically formed by direct mixing between cationic lipids and DNA solutions. Positively charged lipids bind to negatively charged phosphate molecules on the DNA backbone through electrostatic interactions as shown in Figure 3. Generally, complexes are formed with an excess positive charge to permit the interaction with the negatively charged cell surface. The ratio between the cationic charge of the liposome and the negative charge of the DNA usually are factors that control the lipoplex size.[67] At high positive or negative charge ratios, relatively small complexes are formed, while, larger aggregates are usually formed when the net charge is close to neutrality.[67,68] Cationic liposomes used are typically small (around 100 nm) before adding to DNA; however, complexes formed with DNA exhibit diameters that range from as small as 200 nm to structures as large as 2 μm.[69] Formation of lipoplexes is generally difficult to control, and different structures are produced in the same lipoplex preparation. The proposed model for describing the interaction between cationic liposomes and DNA involves a compaction of DNA and charge neutralization followed by aggregation and formation of heterogeneous multilamellar structures of different shapes consisting of DNA sandwiched between lipid bilayers. Finally, it is proposed that DNA affects the liposomes, inducing lipid mixing and rearrangement resulting in the fusion of the multilamellar structures to form large DNA/lipid complexes.[70]

Usually, positively charged lipoplexes lead to more efficient gene expression by virtue of ionic interactions with the negative cell surface constituents.[71] In addition to the compaction and neutralization of DNA, cationic liposomes provide a protective role against cellular nucleases. This can be attributed to the compaction and covering of DNA by the lipid bilayers.[68] However, the positive charge of lipoplexes makes them susceptible to interaction with the negative components in blood circulation, including hundreds of plasma proteins, platelets, and blood cells, after *in vivo* administration.[18,72,73] Although

smaller-sized lipoplexes would be expected to be more efficiently internalized via endocytosis, larger lipoplexes have been reported to improve transfection efficiency.[74] This may be due to the greater ability of the larger particles to sediment onto the cell surface. However, the *in vivo* transfection ability of larger complexes is weak, mainly due to their inability to reach the target cells because of their large size, which also renders them more susceptible to interaction with extracellular components.

Unless a specific targeting ligand is incorporated in the system, the binding of lipoplexes to cell surfaces is the result of random, nonspecific ionic interactions between cationic complexes and anionic cell surfaces and biopolymers. Negatively charged cell surface constituents, such as heparan sulfate proteoglycans (HSPGs) and integrins, play an important role in the cellular binding of positively charged lipoplexes.[75] For example, in proteoglycan-deficient mutant cells, the cellular binding of lipoplexes and polyplexes is reduced.[75] The presence of soluble heparin and heparan sulfate in the medium competitively inhibits the binding. At this point, the HSPGs may act as nonspecific receptors for cationic macromolecules, but their exact role in mediating cellular uptake is not clear. There is some evidence to show that the transmembrane proteins, syndecans, may cluster to form focal points at the plasma membrane during binding to cationic particles and this clustering induces their interaction with the actin cytoskeleton, probably resulting in the formation of tension fibers. This tension provides the energy required to engulf the particles.[76]

The main disadvantage of lipoplexes as gene delivery systems is their nonspecificity.[72] They can bind to all cell types, as well as hundreds of plasma proteins and biopolymers, owing to nonspecific electrostatic interactions with negative components. An alternative is specific liposomes, which carry surface-attached targeting ligands or antibodies and have the capability to interact specifically with tissues and cells based on the ligand attached to the surface. For example, hepatocytes exclusively express large numbers of high-affinity cell-surface receptors that bind to and subsequently internalize asialoglycoproteins.[77] Introducing a galactose moiety into a gene delivery system can achieve liver-parenchymal-cell-specific gene transfection. Mannose-receptor-mediated gene transfection is another approach for targeting macrophages, which overexpress mannose receptors on their surface.[78] Transferrin (Tf), an iron-binding glycoprotein, has been used as a tumor-targeting ligand for gene delivery systems.[79,80] Tf receptors are overexpressed in rapidly dividing cells because of the increased cellular need for iron. The folate receptor is another example of receptors overexpressed in tumor cells and it can be used for tumor targeting.[81,82] Despite the potential of targeted liposomes as specific gene delivery systems, most of the currently used ligands are internalized by clathrin-mediated endocytosis, and the poor intracellular trafficking associated with this pathway significantly limits the transfection activities of the systems.[83–85] Therefore, functional devices that increase the cytosolic delivery of genes are needed. For example, the intracellular fate of Tf liposomes was largely improved by adding GALA (glutamic acid-analine-leucine-alanine), a pH-sensitive fusiogenic peptide, which enhances the endosomal escape in response to the low pH in endosomes.[79,86,87]

Cationic liposomes, with their high fraction of cationic lipids, can produce cell toxicity. A recent approach to decrease this known cell toxicity includes replacing cationic lipids with a cationic peptide such as arginine-rich peptides. Torchilin *et al.* reported liposome modification with a peptide derived from the transcriptional transactivator (TAT) protein of human immunodeficiency virus (HIV-1).[88] TAT-modified liposomes were rapidly and efficiently internalized into cells. These liposomes were able to bind to DNA and internalize them efficiently with lower cytotoxicity compared to liposomes containing cationic lipids.[89] Other reports showed efficient internalization of TAT-, penetratin-, and octaarginine-modified liposomes.[90–94] We have previously shown a rapid and efficient internalization of liposomes modified with both low- or high-density octaarginine (R8).[95] We used a simple and versatile strategy to attach R8 to liposomes, using the stearylation of R8. Stearylated R8 (STR-R8) was mixed with other lipids during the formation of liposomes, exploiting stearyl groups to be anchored into the lipid bilayer thus leaving the R8 freely attached at the surface. The prepared R8-modified liposomes were around 100–150 nm in diameter and were positively charged.[95] The liposomes are rapidly and efficiently internalized into different cell lines as judged by flow cytometry and confocal microscopy. Both hydrophilic and lipophilic model drugs were efficiently internalized when encapsulated in R8-liposomes without any remarkable cytotoxicity. When double-labeled liposomes were added to cells, high intracellular fluorescence could be detected inside cells and both labels were highly localized, indicating that the liposomes are internalized as intact vesicles.[95,96] These results showed that R8-liposomes are highly promising drug delivery systems with little or no cytotoxicity, which prompted us to investigate the applicability of R8-liposomes in gene delivery, as will be explained later.

4.425.2.2.2. Polymers

One main class of nonviral gene delivery vectors extensively investigated comprise complexes of cationic polymers and DNA, termed polyplexes.[97,98] Cationic polymers without hydrophobic moieties can condense DNA more efficiently, resulting in smaller DNA condensed particles as shown in **Figure 3**. Among the many cationic polymers available, those most frequently used in gene delivery are poly-L-lysine (PLL) and polyethylenimine (PEI). Upon mixing with DNA, electrostatic interactions occur between the polymer cations and DNA anions, forming particles as small as 20–40 nm in some cases.[99–102] Polyplexes form spontaneously by mixing aqueous solutions of DNA and cationic polymers at appropriate nitrogen/phosphorous (N/P) ratios. Polyplex size and charge depend to a greater extent on the ratio between the cationic polymer and DNA than on the polymer properties.[99]

DNA compaction with cationic polymers provides several advantages including size reduction, charge neutralization, and DNA protection against nucleases and other enzymes. However, polyplexes formed with PLL are generally less efficient than cationic lipids, and a ligand is usually attached to PLL polyplexes to increase their cell internalization.[103] Furthermore, these polyplexes have low ability to escape from intracellular endocytic compartments. The more recently introduced PEI polymer produces more efficient cell DNA internalization and endosomal escape.[101] The latter ability is attributed to a theorized proton sponge effect that causes swelling and disruption of

endosomes under vesicle acidification. Polyplexes formed between PEI and plasmid DNA at the proper NP ratio produce highly efficient gene expression *in vitro*. However, both branched and linear PEI used for gene delivery generally produce toxicity. Linear PEI is generally preferred for *in vivo* applications because of its lower toxicity. However, branched PEI is more suitable for modification due to the presence of a higher percentage of primary amines. Examples of modifications include incorporation of targeting ligands to increase specificity, labeling the polymer with fluorophore for intracellular trafficking, or the addition of poly(ethylene glycol) (PEG) to increase polyplex stability. Incorporation of PEG reduces interaction with blood components, resulting in decreased uptake by the organ-based reticuloendothelial system, and resulting in prolonged circulation times for PEGylated polyplexes. However, PEGylation also reduces cellular uptake by cells, which in turn reduces the transfection efficiency.

Short, positively charged peptides such as TAT and oligoarginines also have the ability to condense DNA.[104–107] TAT peptide was shown to be able to compact and stabilize DNA, and the complexes were superior to PEI.[107] In addition, PLL-linked TAT was efficient as a transfection reagent.[105] Octaarginine (R8) was shown to have the ability to condense DNA and the complexes were as efficient as PLL polyplexes.[104] In addition, the *N*-terminal stearylation of R8 greatly improved its transfection ability.[108] This was attributed to the improved condensation of DNA by R8 by both the hydrophobic stearyl group and cationic peptide, producing both ionic and hydrophobic binding with the DNA. Stearylated R8 polyplexes showed improved cellular binding and internalization, resulting in transfection activities as efficient as the commercially available cationic lipid transfection reagent lipofectamine.[104,108]

Similar to lipoplexes, cationic polymer–DNA complexes bind to cell surfaces through ionic interactions with negatively charged cell surface constituents. Cellular binding of polyplexes to proteoglycan-deficient mutant cells is highly reduced.[75] In the addition, the presence of soluble heparin or heparan sulfate also prevented cellular binding and uptake of polyplexes. Uptake of PEI polyplexes was proposed to occur through actin-mediated phagocytosis mechanisms as a result of the adhesion of polyplexes to syndecan molecules followed by their clustering in lipid rafts.[109] The exact role of negative cell surface constituents in mediating cellular uptake of polyplexes remains unclear.

The term 'lipopolyplex' has been introduced recently and involves the condensation of DNA using a polycation followed by entrapping the polyplexes within anionic or neutral liposomes.[110–112] The charge ratio between DNA and cationic polymers can be controlled to produce negatively charged complexes that can be further complexed or entrapped in cationic liposomes.[110] Lipoplyplexes are generally more efficient in cell transfection than lipoplexes or polyplexes.[113] This method combines the high compaction of polyplexes and the facilitated endosomal escape of lipoplexes. In addition, it provides more protection to DNA, and the complex surface can be easily modified with functional ligands for targeting or for long circulation.

4.425.2.2.3. Polymeric micelles

A micelle is generally defined as a collection of amphiphilic surfactant molecules that spontaneously aggregate in water in a concentration-dependent manner to produce a metastable aggregate. The core of the micelle is hydrophobic and therefore can sequester hydrophobic drugs. Conventional micelles are formed from small surface-active molecules that have a polar head group and a hydrophobic tail (amphiphiles). However, micelles can also be formed from large amphiphilic block copolymers. In aqueous media, amphiphilic block copolymers, which have a large solubility difference between hydrophilic and hydrophobic segments, spontaneously form polymeric micelles with a core–shell structure in which a hydrophobic inner core is surrounded by a hydrophilic shell or corona.[114] In contrast to micelles from small surfactant molecules, polymeric micelles are generally more stable and can retain the loaded drug for a prolonged period.[115,116] Biocompatible PEG is often used as the hydrophilic segment to improve water solubility and to provide a 'stealth' corona to decrease nonspecific interactions, leading to increased blood circulation time.[117–119] Such polymeric micelles are usually large enough to escape renal excretion (15–30 nm). However, their size is controlled below 100 nm to allow extravasation and tumor accumulation, even though drug loading efficiencies at this size are generally low. These characteristics facilitate tumor accumulation by the EPR effect.[120]

One example of polymeric micelles used in drug delivery is the anticancer drug doxorubicin (Dox). Dox-conjugated PEG-*b*-poly(aspartate) (PEG–PAsp) block copolymers spontaneously form polymeric micelles in aqueous media.[121–123] Dox was covalently conjugated to the side chains of the poly(aspartate) (PAsp) segment. This conjugation provided sufficient hydrophobicity in the PAsp segment due to Dox's hydrophobicity, thus forming a stable inner core of polymeric micelles. A Dox molecule can be physically entrapped in the micellar core by hydrophobic interactions. This physically entrapped Dox exerts the major cytotoxic function, while the conjugated Dox works mainly to increase micelle stability.[124] The PEG–PAsp(Dox) micelle showed prolonged blood circulation times and effective accumulation into a subcutaneous ectopic solid tumor (murine colon adenocarcinoma (C-26)).[125,126]

Following the same concept, polymeric micelles were used for gene delivery. A polymeric micelle containing nucleic acids is formed by complexation between DNA or RNA and a block copolymer having a hydrophilic segment and a cationic segment. Complexation of plasmid DNA with PEG–poly(lysine) (PEG–PLys) occurs spontaneously.[127,128] The PEG shell promotes extended systemic circulation and thus tumor accumulation by the alleged EPR effect. Polyplex micelles containing pDNA indeed exhibited efficient gene introduction in cultured cells, achieving prolonged blood circulation.[129] These results demonstrate that polymeric micelles might also serve as promising gene carriers in gene therapy.

Polymeric micelles can be regarded as a first-generation system, as they are mostly monofunctional.[130] Supramolecular multifunctional nanodevices prepared with smart multifunctional polymeric micelles designed with stimuli-responsive properties may provide promising systems with increased targeting ability and reduced toxicity.[130] For example, active targeting using specific ligands can increase gene delivery efficiency and reduce side effects. Antibodies and their fragments, transferrin, folate, sugars, and peptides are commonly used to achieve active tumor site targeting.[131] One example of

such targeted smart nanocarriers is the polymeric micelle encapsulating pDNA targeted to hepatocytes bearing abundant ASGP receptors bind lactose moieties.[132] The transfection of these micelles in HepG2 cells showed that lactose-bearing micelles were significantly more efficient at transfection than micelles lacking lactose.[133] Another example involves targeting vascular cells near tumors to inhibit formation of new blood vessels, thus cutting off the nutritional supply to cancer cells. The cyclic RGD peptide (c(RGDfK)), which specifically target integrin receptors on vascular cells, was conjugated to PEG–PLys block copolymers,[134] showing increased transfection efficiency *in vitro* compared to ligand-free polyplex micelles.

A second approach to prepare smart multifunctional polymeric micelles involves the use of stimuli-responsive biodegradable micelles. Nanocarriers must be sufficiently stable to resist extracellular degradation and dissociation. However, they must also release their nucleic acid payload near their intended site of action. One class relies on acid-dependent degradation of polymeric micelles. Nanocarriers internalized through endocytosis experience a pH drop in endosomes. Thus, drug carriers with pH-sensitive linkages based on hydrazone, *cis*-aconityl, or acetal groups that degrade at low pH can be prepared. Such carriers are stable at physiologic pH but degrade under acidic conditions inside cells. As an example of acid-sensitive micelles, a triblock copolymer was designed for micelle formation by two cationic segments in a single polymer strand.[135] In this triblock copolymer, each segment has its own distinctive role: a PEG segment for biocompatibility, a second segment composed of low pK_a amines (poly[(3-morpholinopropyl) aspartamide] (PMPA)) for buffering capacity to enhance endosomal escape, and a third segment composed of high pK_a amines (PLys segment) for DNA payload binding. The transfection activity of the triblock system exhibited one order of magnitude higher transfection compared with the PEG–PLys block copolymer with similar PLys unit length. This transfection efficiency is comparable with that of the well-known PEI/pDNA polyplex, but with a remarkably lower cytotoxicity.

To find a suitable cationic segment, PEG block copolymers with a series of cationic side chains were synthesized. A polymer library was prepared, from which it was found that PEG–polyaspartamide with an ethylenediamine unit as a side chain (PEG–PAsp(DET)) had high transfection efficiency as well as low cytotoxicity.[136] This polymeric micelle provided gene expression in primary cells as well as in *in vivo* disease models with low toxicity. The polyplex micelle prepared with PEG–PAsp(DET) and pDNA was also applied to vascular lesions with good results.[137] The micelle was instilled intravascularly into rabbit carotid arteries with neointima, exhibiting appreciable reporter gene transfer into vascular lesions without any vessel occlusion by thrombus. The PEG–PAsp(DET) polyplex system was also applied for *in vivo* gene transfer in a bone-defect model of mouse skull bone.[138] The polyplex micelle was mixed with a calcium phosphate cement scaffold and installed into the bone defect. Sustained release of PEG–PAsp (DET) from the scaffold and transfection of surrounding cells were observed. Transfection of constitutively active activin receptor-like kinase 6 (caALK6) and runt-related transcription factor 2 (Runx2) induced osteogenic differentiation in mouse calvarial cells with no signs of inflammation.

In a similar way, stimuli-responsive smart nanocarriers can be prepared with a disulfide bond, which is known to be stable in the extracellular environment yet readily cleaved inside the cell due to the increased concentrations of glutathione. In this regard, bioresponsive smart polymeric micelles that dissociate inside cells in response to chemical stimuli were designed. The inner core of the micelle was cross-linked through disulfide bonds for cleavage inside the cell, increasing the stability of the micelle. At the same time, the efficient release of packaged pDNA was demonstrated in response to reducing reagent (dithiothreitol), mimicking the intracellular environment.[139] Gene transfection was higher by an order of magnitude than that of the non-cross-linked system, with the cross-linked micelle exhibited appreciable gene expression in parenchymal cells of the mouse liver through intravenous injection.[140] The disulfide cross-linking micelle maintained the original transfection capacity even after freeze–thaw treatment without the use of any protective reagents, while the non-cross-linked micelles showed significantly lower transfection efficiency after the same treatment.

4.425.2.2.4. Multifunctional envelope-type nanodevice

Recently, we developed a multifunctional envelope-type nanodevice (MEND) as a novel nonviral gene delivery system based on a new packaging concept termed 'programmed packaging'.[110] Programmed packaging was proposed to develop a rational nonviral gene delivery system equipped with various functional devices, including ligands for specific receptors, pH-sensitive fusogenic peptides for endosomal escape, and a nuclear localization signal (NLS) for enhanced nuclear delivery, to overcome several barriers in the process of gene delivery to the nucleus of target cells.[141] Simple mixing of these functional devices is not sufficient to have each function exerted at the appropriate time and correct place, and therefore an innovated nanotechnology is required to assemble these multiple components. The concept of programmed packaging consists of three components: (1) a program to overcome all barriers; (2) designs of several functional devices to overcome different barriers; and (3) technology to assemble all the pieces into a nanosize single structure.[3]

The MEND system mimics an envelope-type virus. It consists of a condensed DNA core covered with a lipid envelope. DNA is condensed with a polycation to control size for facilitated lipid coating and to protect DNA from degradation. The lipid envelope is equipped with various functional devices to avoid various extracellular and intracellular barriers. The MEND was constructed using a lipid film hydration method.[110] This method is based on packaging in three consecutive steps: (i) DNA condensation with polycations to form positive or negative polyplexes; (ii) hydration of the lipid film, which carries an opposite charge for electrostatic binding of condensed DNA; and (iii) sonication to self-assemble liposomes or lipid envelopes and packing the condensed DNA within the envelope. A typical MEND was prepared by using PLL/DNA positive polyplexes of ~100 nm in size. The lipid film contained a negatively charged lipid such as cholesteryl hemisuccinate (CHEMS) and hydrated with an aqueous solution containing positive DNA/PLL particles. Packaging of the PLL/DNA particles into a lipid bilayer was achieved by sonication in a bath-type

sonicator. The diameter and ζ-potential of the MEND were around 300 nm and −40 mV, respectively. DNA encapsulation efficiency was greater than 70%.[110]

As we had previously shown that R8 had a great potential for enhancing cellular uptake of liposomes,[4,95,96] we investigated the applicability of the R8 peptide to MEND internalization. We found that the cell internalization and transfection efficiency of MEND was greatly improved by R8 modification.[110,141] The internalization of MEND via nonclassical pathways, which can avoid lysosomal degradation, probably plays an important role in the R8-mediated improvement.[95] The R8-MEND consisting of EPC/Chol showed higher transfection activities than PLL/DNA complexes.[141] Substitution of EPC with the fusogenic lipid DOPE increased the transfection activities by more than 4 orders of magnitude compared to negatively charged PLL/DNA particles. Furthermore, the transfection activity was increased further by replacing cholesterol with the negatively charged fusogenic lipid CHEMS.[141] DOPE and CHEMS may enhance the cell internalization efficiency into the cytoplasmic space by their fusogenic properties, thus facilitating nuclear delivery of DNA. Thus, the transgene delivery ability of R8-MEND could be improved by about 2 orders of magnitude by optimization of the lipid envelope.

Moreover, the R8-MEND was examined for its ability to deliver siRNA expression plasmids.[142] The pDNA encoding anti-luciferase siRNA was condensed by PLL and packaged into the R8-MEND. The silencing effect of the R8-MEND(PLL) exhibited a 96% level of inhibition of luciferase activities in the co-transfection study without any detectable toxicities. The silencing effect was maintained at more than 60% even under conditions of a 100-fold dilution. In luciferase-transformed cells, however, the R8-MEND(PLL) did not show the same high silencing effect (only 10%), suggesting heterogeneity in the transfection by the R8-MEND(PLL).[142] To solve this problem, the DNA condensing agents were optimized by comparing PLL, STR-R8, and the spermatozoal peptide protamine. While there was no difference in the silencing effect among these R8-MENDs in the co-transfection study, the R8-MEND (protamine) showed a 70% silencing effect in the transformed cells. Thus, the transgene ability of R8-MEND was further improved by optimization of the DNA condensing agent.[142]

The transfection activity of the optimized R8-MEND was further compared with that of an adenovirus, one of the most potent viral vectors, in human cervical cancer HeLa cells, and in a human lung epithelial carcinoma cell line A549.[141] These cells display receptors for adenovirus serotype 5, such as coxsackie and adenovirus receptor (CAR) and integrin receptors. In both cell lines, the transfection activities of the adenovirus increased with increasing dose up to 1×10^5 particles per cell, above which toxicity appeared and the transfection activities then decreased. The transfection activities of R8-MEND were as high as those of the adenovirus using 1×10^5 particles per cell. As judged from the protein content in cell lysates after transfection, the R8-MEND showed no significant cytotoxicity, while higher doses of the adenovirus produced significant cytotoxicity (~50% loss of protein content).[141] The optimized R8-MEND did not contain cationic lipids, and this may explain its low cytotoxicity. The transfection activity of R8-MEND was strongly inhibited by amiloride (~95%). This indicates that macropinocytosis is the major pathway mediating the efficient transgene delivery of R8-MEND. As will be explained in a later section, the uptake by macropinocytosis involves the formation of large and heterogeneous macropinosomes (>1 μm), which appear to be leaky and fuse with lysosomes to a lesser extent. As macropinosomes are large, macropinocytosis readily explains the efficient internalization of the relatively large R8-MEND (>300 nm), which is somewhat larger than clathrin-coated vesicles (~150 nm) and caveolae (~50 nm).

The R8-MEND was particularly useful for *in vivo* gene delivery into hair follicles after topical application to the skin of a 4-week-old ICR mouse.[141] Gene expression was observed in the hair shafts and follicle cells treated with R8-MEND encapsulating LacZ- or green fluorescent protein (GFP)-encoding plasmid DNA. The gene transfer efficiency of R8-MEND was significantly higher than that of lipoplexes made of the commercially available reagent Lipofectamine and DNA. In a further experiment, R8-MEND containing DNA encoding bone morphogenetic protein receptor type 1 A (Bmpr1a), which is involved in the hair growth cycle, was applied to the mouse skin. The R8-MEND formulated Bmpr1a gene was able to extend the hair growth period.[141]

Further applications of R8-MEND include successful delivery of antisense ODNs, which can inhibit the function of mRNA in the cytosolic space. For delivery of ODN, ODN-encapsulated R8-MEND (ODN-MEND) packaged using protamine as a condenser showed a 90% antisense effect 8 h after transfection, and a persistent antisense effect of over 75% for up to 48 h, which was much more effective than that of LipofectAmine2000 (LA2000).[142,143] These results suggest that R8-MENDs are able to deliver encapsulated nucleic acids to the cytosol as well as to the nucleus, and that protamine can also function as an efficient decondenser not only in the nucleus but in the cytosol as well.

The R8-MEND was also expected to be an efficient and safe delivery system of siRNA. However, it was unclear whether the siRNA could be packaged well into the MEND, because the structure and physicochemical characteristics (i.e., persistence length) of double-stranded RNA (siRNA) differ from those of plasmid DNA and ODN. Thus, a polycation able to compact siRNA as a nanoparticle was screened by measuring the size and ζ-potential of complexes formed between siRNA and polycations PLL, STR-R8, and protamine.[144] Only STR-R8 was able to compact siRNA to form nanosized particles (<100 nm), whereas all three polycations were able to condense pDNA or ODN. The hydrophobic stearyl moiety, which is not contained in PLL or protamine, may be critical in aiding compaction of siRNA into small particles. The silencing effect of siRNA-encapsulated R8-MEND (siRNA-MEND) was compared with that of LA2000. The siRNA-MEND inhibited luciferase activity by more than 80% in HeLa cells stably expressing luciferase. In contrast, an absolute silencing effect could not be obtained for LA2000, possibly due to nonspecific enhancement of gene expression by LA2000 treatment. In addition, the R8-MEND-encapsulated siRNA showed no cytotoxicity.[144]

In vitro gene delivery assays, mostly delivery to culture cell monolayers on solid supports (either cell culture plates or 3D scaffolds), often employ serum-free media to prove concept. This condition in the absence of serum proteins is practically irrelevant for all but the most carefully concocted *ex vivo* cell transfections. However, vector transfection performance in

serum-containing media is substantially reduced (i.e., often only 1–10% of cells). Analogously, for effective *in vivo* application of synthetic, nonviral, especially cationically based, gene vectors, a primary drawback is the lowered transfection activity in the presence of plasma, with its many proteins and cells. This is also the case for the vector R8-MEND. Efforts to overcome the very demanding serum protein transfection challenges include optimization of vector charge density, optimization of lipid composition, and grafting of corona polymers that effectively resist plasma component complexation and extend circulation. Our current trials toward improving synthetic vector *in vivo* application and efficacy in trasngene delivery are described in Section 4.425.3.2.1.

4.425.3. Pharmacokinetics

4.425.3.1. Factors Governing the PK of a Carrier System

After a carrier system is administered, its fate in the body is often unknown and difficult to track. Numerous biological barriers exist to protect the human body from invasion by foreign molecules and particles, as shown in Figure 4. These barriers hinder drug delivery and must be overcome in order to effectively deliver the carrier to a target organ. Cationic compounds such as cationic lipids, including DOTAM,[60,61] DOTAP,[145] and natural polymer,[146] or a synthetic polymer including PLL, PEI, and dendrimer are commonly employed as carrier systems, defining lipoplexes and polyplexes. The physicochemical properties of their nucleic acid complexes, such the N/P ratio, surface charge, size and structure of the cationic compounds, have a strong effect on their biodistribution. In addition, the destination of a carrier system in the body would be significantly altered by the route used for its administration. From the viewpoint of practical use, systemic administration would be desired because of the ease of operation. Immediately upon i.v. injection, a carrier system faces a myriad of different biological components in the systemic circulation (e.g., blood proteins, RNAses, DNAses, cells, platelets). For successful gene delivery to a target organ, the carrier needs to avoid nonspecific interactions with this biological milieu. The carrier system also should not be eliminated from the blood circulation by kidney glomerular filtration, lung capillaries, and uptake by the liver and spleen (the reticuloendothelial system (RES)), and should subsequently be delivered to the target organ at sufficient doses to reliably produce therapy. Therefore, in this section, the factors governing the PK of a carrier system are discussed from the viewpoint of the properties of the carrier system such as charge and size after systemic administration.

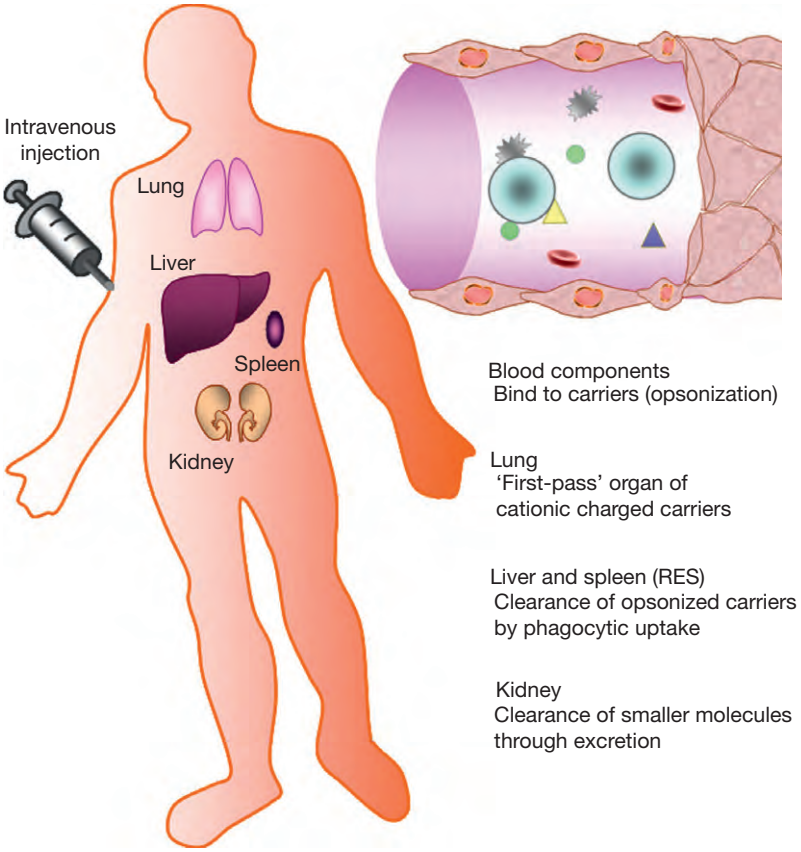

Figure 4 Biological barriers in the human body. Macromolecules with molecular weight smaller than the renal excretion threshold (typically molecular weight <50 kDa, and diameter <10 nm) are eliminated from blood circulation through glomerular filtration in the kidney. After systemic administration, cationic carriers aggregate with blood components (opsonins), which allows accumulation in the lung capillary. The opsonized carriers are finally taken up by liver and spleen, collectively known as the reticuloendothelial system (RES).

4.425.3.1.1. Carrier charge

The surface charge of carrier complexes plays an important role in determining the final destination of the complexes. It is known that the higher cationic charged complexes of DNA with polymers or lipids exhibit a gene expression in the lung that is 10–100-fold higher than in the liver, spleen, or kidney as early as 2 h after intravenous administration.[147,148] The maximum level of expression was maintained in the lung over the first 24 h, followed by a rapid decrease. The remarkably rapid and efficient transgene expression in the lung raises the question of what happens following the systemic administration of positively charged gene carriers. After entering the blood stream, the cationic charged surface immediately interacts with anionic serum proteins and cells in the blood, resulting in the formation of aggregates with sizes of more than 1 μm[149–152] Based on biodistribution analyses, a large fraction of the carrier dose (60–80%) of lipoplexes or polyplexes is found mainly in the lung at early phases within minutes after systemic administration. This is because aggregated complexes are trapped in the small capillaries in the lung due to the fact that pulmonary vasculature is the first capillary bed encountered, the so-called first-pass effect.[150,153] However, as early as 1–2 h post injection, this amount drops to less than half, with increasing amounts shifted to the liver. This phenomenon suggests that binding of serum proteins to complexes might be reversible, which is explained by the displacement of serum proteins from complexes by extracellular proteoglycans, allowing their shift from lung to liver.[154]

Histochemical analyses indicate that cells expressing genes were found in both endothelial cells and pneumocytes.[149] It is possible that vascular endothelial cells are transfected as the result of the direct association of complexes in blood, whereas the mechanism of the translocation of complexes in pulmonary cells through endothelial cells remains unclear. The efficiency and pattern of gene expression in the lung and other organs by the complexes are greatly influenced by the properties of the complexes. For example, in a lipoplex, DOTMA containing an ether linkage exhibits a more efficient gene expression in the lung than DOTAP containing an ester linkage.[148] In general, a higher N/P ratio of complexes tends to lead to a higher transgene activity. As mentioned above, cationic charged complexes are capable of introducing transgene expression in lungs after systemic administration, whereas side effects such as acute cytotoxicity-related liver necrosis and death resulting from a high cationic charge remain to be solved.[155] On the other hand, distinct from lung, the amount of DNA in the liver increases with time up to 24 h post i.v. injection. Even though a large amount of DNA accumulation ultimately occurs in the liver, gene expression in the liver was significantly lower than that in the lung.[148] Why do gene carriers represent less 'lipofectable' results in liver than in lung after systemic administration? To address the underlying mechanism, the features of the liver as a major clearance organ of nanocarriers must be better understood, with an insight into carrier properties, principally size, that carriers should satisfy.

4.425.3.1.2. Carrier size

How does the size of a carrier influence its biodistribution and fate in the body? In general, this depends on its route of administration. But, macromolecules with a lower molecular weight than the renal excretion threshold (typically, molecular weight <50 kDa and diameter <10 nm) are eliminated from circulation through kidney glomerular filtration.[156] Because the complexes considered herein are tens to hundreds of nanometers in diameter, they are not removed through renal excretion. Opsonized complexes are found in lung, and subsequently in liver and spleen, due to uptake by cells of the mononuclear phagocytic system (MPS), including macrophages located in liver and spleen (originally and also still known as the RES), which function as an important host defense mechanism.[157] Therefore, the liver and spleen are the major clearance organs of complexes after intravenous injection. One of the reasons for why the liver is less 'lipofectable' could be the uptake and the degradation of lipoplexes by nonparenchymal Kupffer cells. Additionally, another important role of carrier size should be considered in terms of delivery to parechymal hepatocytes in the Disse space through endothelial capillaries. Blood vessels are responsible for supplying molecules, nutrients, and oxygen and, of course, delivering the systemically administered carriers to organs. On the basis of morphological features of the endothelium, blood vessels have been classified as continuous, fenestrated, or discontinuous.[158] The liver lacks a continuous basement membrane, liver blood vessels contain fenestrae that are 100 nm in diameter on average,[159] and Kupffer cells, the resident liver macrophages, are located in the sinusoidal space,[160] as shown in **Figure 5**.

For successful gene delivery to liver parenchymal cells, the behavior of carrier systems should be controlled, considering the characteristics of liver blood vessels organized by nonparenchymal fenestrated endothelial cells and Kupffer cells. In other words, a diameter of less than 100 nm and escape from Kupffer cell recognition would allow carriers to gain access from the sinusoidal space to hepatocytes thorough the liver fenestrae. Hashida and coworkers reported that delivery of higher amounts of pDNA to parenchymal cells than nonparenchymal cells was achieved using cationic liposomes in which Gal-C4-Chol had been incorporated, because hepatocytes express an abundance of asialoglycoprotein receptors (ASGPr) that selectively recognize galactose and *N*-acetylgalctosamine (GalNac) residues.[161] However, this behavior may not be sufficient for transfection in distant sites (e.g., tumors). In the next section, properties of nanoparticles relevant to evade macrophages to facilitate long circulation in the blood and delivery of a carrier system to a tumor are discussed.

4.425.3.2. Passive Carrier Targeting

In the case of anionically charged complexes, opsonization also occurs, followed by rapid disappearance from the blood circulation by scavenger receptors on macrophages known to be involved in the uptake of a variety of polyanionic molecules or macromolecular complexes.[162] For complexes with a neutral surface, carrier opsonization by thousands of plasma proteins takes place in the blood circulation.[163] To overcome nonspecific interactions of complexes with blood components and nontarget cells, the most common strategy is to shield the surface of complexes with hydrophilic, uncharged polymers such as PEG. In the early 1990s, it was reported that

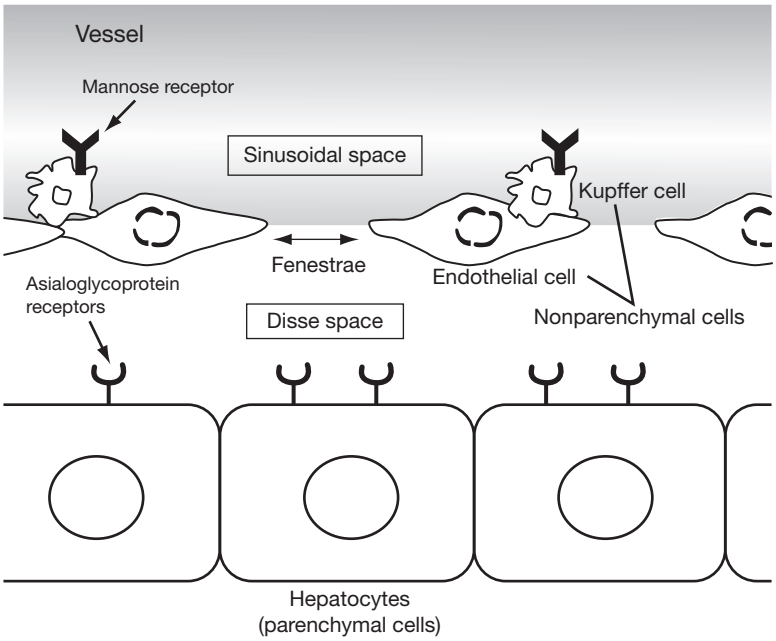

Figure 5 Sinusoidal barriers in liver. Liver blood vessels are organized by nonparenchymal fenestrated endothelial cells containing 100 nm diameter pores and Kupffer cells, lacking a continuous basement membrane. Opsonized carriers are taken up and degraded by the Kupffer cells, reducing transfection efficiency for gene carriers. Therefore, sizes below 100 nm in diameter and with capability to avoid Kupffer cell recognition would allow the carriers to gain liver access from the sinusoidal space to hepatocytes thorough the vascular fenestrae.

modification with PEG allows liposomes to circulate for hours in blood circulation after intravenous administration.[164–166] The PEG moiety forms an aqueous grafted brush layer on the surface of liposomes and provides lipid bilayer stabilization and steric hindrance, which results in inhibition of the plasma protein opsonization.

Cullis and coworkers developed stabilized plasmid–lipid particles (SPLP) composed of a cationic lipid, DOPE, and PEG-CerC20 encapsulating pDNA, which exhibited a long half-life in the systemic circulation.[167] It is well known that long-circulating liposomes (e.g., half-life >6 h) with an average diameter of 100–200 nm accumulate efficiently in tumor tissues.[168] Matsumura *et al.* found that high-molecular-weight (40 kDa or higher), long-circulating macromolecules as well as various long-circulating nanoparticulate pharmaceutical carriers are capable of spontaneously accumulating in solid tumors and inflammation areas via the proposed EPR effect.[169] This effect is based on the empirical observation that the pathological neovasculature of tumor tissue, with its discontinuous or absent basement membrane unlike normal tissues, is 'leaky,' allowing for some molecule extravasation and accumulation in the interstitial tumor space passively if long circulating, as shown in Figure 6. Such carrier accumulation is additionally facilitated by the lack of a lymphatic system, which is normally responsible for the drainage of macromolecules from tissues. This effect is not universal to all tumors but is also common to some inflammatory diseases where vasculature barriers break down.

Advances in the development of long-circulating liposomes that can find tumors via the EPR effect permit an improved use in tumor chemotherapy, such as DOXIL (CAELYX). However,

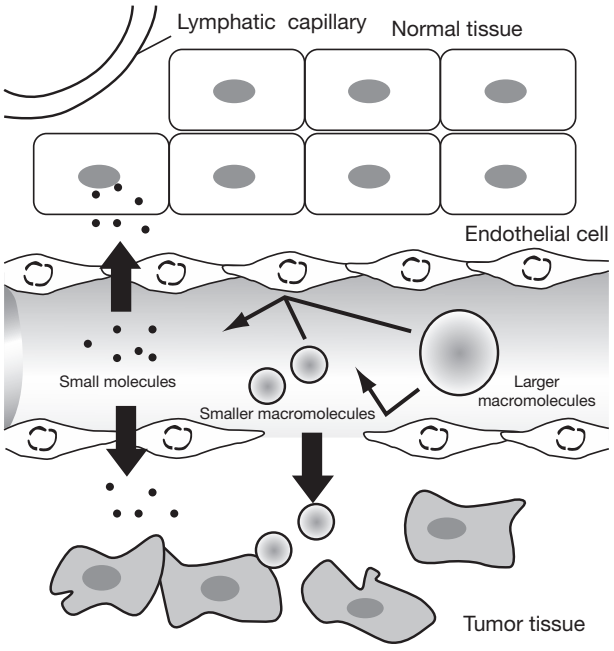

Figure 6 Unique microvasculature of tumor tissue and the EPR effect. Long-circulating nanoparticulate pharmaceutical carriers with <200 nm in diameter are capable of spontaneous accumulations in solid tumors and inflammation areas via the EPR effect. Unlike normal tissue, pathological neovasculature in tumor tissues, such as discontinuous or absent basement membrane, allows for their extravasation and accumulation in an interstitial tumor space passively. The lack of lymphatic system, responsible for the drainage of macromolecules from tissues, also facilitates the carrier accumulation.

the issue of PEGylation is a drawback in *in vivo* applications of such complexes as gene carriers directed to tumors and other organs. PEGylation reduces specific interactions with target tumor cells and results in minimal cellular uptake and poor endosomal escape, yielding a significant loss of bioactivity.[170,171] These issues are currently referred to as the 'PEG dilemma.'

4.425.3.2.1. Strategy for addressing the PEG dilemma

4.425.3.2.1.1. Targeting by specific ligands

One strategy for overcoming the PEG problem is to display affinity ligands on the PEGylated carriers for receptors on targeted cells, which would be expected to improve their selectivity, binding, and uptake of the carriers to targeted cells. Transferrin (Tf) and certain antibodies have been widely investigated as target ligands for gene delivery in targeting to Tf-receptor overexpressed tumor cells.[172,173] Wagner and coworkers developed Tf-linked PEG–PEI for tumor-selective gene delivery.[173] The surface charge of the complexes was shielded by either PEG or a higher density of linked Tf, which was intended to block undesired nonspecific interactions with blood components, followed by selective targeting to tumor cells. One well-characterized target is integrin, a heterodimeric cell-adhesion membrane receptor family, composed of α and β subunits.[174] The arginine-glycine-aspartic acid (RGD) motif has often been used for the targeted delivery of drugs and genes because of its ability to recognize integrins expressed on both tumor cells and tumor endothelial cells,[175] but not expressed on normal cells. Other active targeting to either tumor cells or new blood vessels can be achieved via the use of overexpressed molecules such as the folate receptor.[176–182] Despite their utility in cell monocultures *in vitro*, as tumors *in vivo* are very heterogeneous with multiple cell types with multiple phenotypes, one ligand targeting one cell feature may not be sufficient to produce therapy.

4.425.3.2.1.2. Facilitating endosomal escape

Endosomal release of a cargo such as pDNA or siRNA into the cytoplasm is a critical step in achieving successful gene delivery. Endosomal escape is caused by membrane fusion or the disruption of endosomes.[183] PEGylation, however, confers steric stability to complexes and inhibits their disruption and fusion with the inner endosomal membrane after their uptake. Therefore, valid approaches involve timely removal of the PEG moiety from complexes in the target site in response to the local environment. This would be expected to improve the cellular uptake and subsequent endosomal escape of carriers. The low pH of the endosomal environment is exploited as a trigger for PEG cleavage. Szoka and colleagues constructed pH-sensitive PEG lipids containing an orthoester linkage, and transfection experiments showed a greater luciferase expression of the pH-sensitive lipoplexes as compared to stable PEGylated carriers.[184] Other linkages such as hydrazone linkages, β-thiopropionate, vinyl ester, orthoester, or acetals were also investigated as pH-sensitive PEG system in lipoplexes or polyplexes.[185–189]

Besides the pH gradient, the intracellular reducing environment is considered an alternative stimulating trigger. A PEG-lipid containing disulfide bonds developed by Zalipsky and colleagues accelerated the rate of release of cargo from liposomes compared to a noncleavable PEG-lipid-modified liposome.[190] Hatakeyama *et al.* synthesized an enzymatically cleavable PEG-lipid (PPD) containing a peptide substrate for a matrix metalloproteinase (MMP) present in the extracellular space of tumor tissues.[178,179] Ambegia *et al.* proposed a novel strategy involving the use of exchangeable PEG-lipids, which provides serum stability, long circulation lifetimes, and efficient transgene expression in tumors by using SPLP.[191]

Alternative methods for increasing the endosomal escape of PEGylated carriers are the acceleration of either membrane fusion or deliberate disruption of the endosomal membrane. The pH-sensitive fusogenic membrane peptide GALA was developed on the basis of the endosomal escape mechanism of the influenza virus.[86] GALA undergoes a structural change to an α-helix under acidic conditions. Harashima and colleagues recently demonstrated that a combination of GALA with a PEGylated liposomal formulation containing ether pDNA or siRNA facilitated endosomal release of the cargo and efficient gene expression or knockdown.[192–194] Melittin-PEI-containing carriers showed enhanced gene expression due to their high lytic activity at acidic pH to trigger enhanced membrane destabilization in endosomes.[195] Other peptide derivatives, such as INF7, have also been used.[196] The manipulation of cellular uptake and the endosomal escape of PEGylated carriers using bioreponsive systems should be valuable strategy for overcoming these obstacles and to achieve successful tumor gene delivery.

4.425.3.3. Endothelial Barriers

The continuous vascular capillary is the most ubiquitous type found in the body other than those naturally fenestrated in liver and porous in some tumor tissues, and the resulting transport of molecules and nutrients is strictly regulated by tight junctions and transporters.[158] Therefore, gene delivery to parenchyma over the continuous endothelium is considered to be an ultimate challenge. Because the central nervous system (CNS) beyond the blood–brain barrier (BBB) is connected with related disorders such as Parkinson's disease and Alzheimer's disease, gene therapy for the brain is a highly desirable goal. Pardridge and colleagues demonstrated the liposomal delivery of pDNA and siRNA using particles modified with monoclonal antibodies against insulin or transferrin receptors on the BBB via receptor-mediated endocytosis.[197,198] Kumar *et al.* demonstrated brain delivery of siRNA using RVG, a rabies viral glycoprotein, and an oligoarginine conjugate (RVG-9R).[199] RVG-9R enabled transvascular siRNA delivery to the brain via acetylcholine receptors and the targeted gene knockdown was achieved. However, the efficient delivery of a carrier system through the continuous vascular endothelium is still under development. Despite the remarkable progress made on the development of delivery systems, optimization of target-specific, safe, and efficient carrier systems of nucleic acids remains an ongoing challenge. These barriers will have to be overcome to advance gene and nucleic acid therapeutics to the clinical study stage for crucial diseases.

4.425.4. Intracellular Trafficking

4.425.4.1. Routes of Cell Uptake

The sites of action of gene-based therapeutics are mainly inside cells, either in the cytosol or in the nucleus. Therefore, the

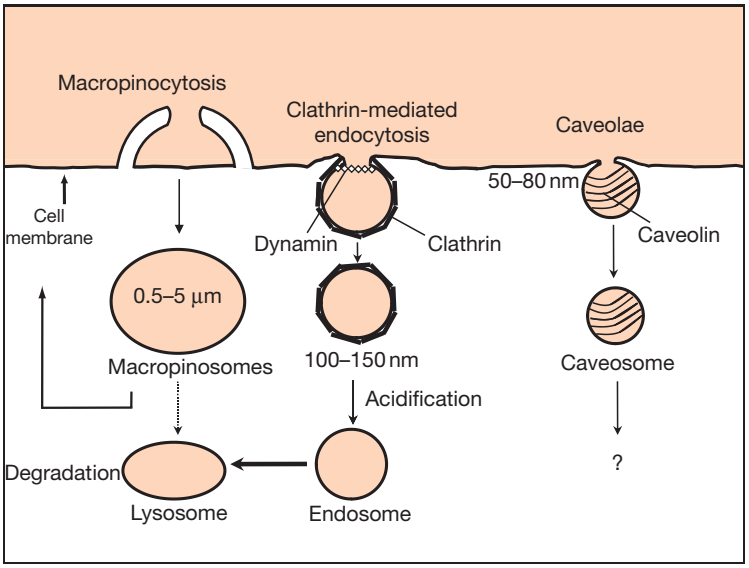

Figure 7 Different endocytic pathways involved in gene delivery. Clathrin-mediated endocytosis is the common and most characterized cell entry pathway. The clathrin coat is removed, and vesicles mature to late endosomes and eventually fuse with lysosomes for degradation. Caveolae are flask-shaped invaginations of the plasma membrane. Caveolae result in the formation of caveosomes. This pathway is generally nonacidic and nondigestive. Macropinocytosis involves the formation of large and heterogeneous macropinosomes that mostly recycle their contents back to the cell surface.

reliable internalization of genes and gene vectors into cells is a prerequisite to efficient transfection. Gene vectors and macromolecules, in general, use different cell internalization pathways for traversing cellular membranes as shown in **Figure 7**. Identifying the specific internalization pathway for a gene vector is critical to effectively optimize the system for efficient transfection. This is due to the fact that the internalization pathway is closely related to the intracellular trafficking and the fate of the internalized molecules. Many distinct pathways and internal endpoints are possible depending on carrier properties, cell type, tissue type, cell cycle, and activation. Selecting these pathways for a particular carrier is currently difficult. Some internalization pathways may favor high lysosomal degradation and endosomal escape is difficult, while other pathways may less efficiently lead to lysosomal degradation and cytosolic delivery is easier.[200] For example, the internalization through clathrin-mediated endocytosis is generally believed to lead to extensive acidic and lysosomal degradation.[201,202] Meanwhile, caveolar endocytosis leads to entrapment of internalized molecules in caveosomes that are not highly acidified and do not fuse with lysosomes.[84,203] Similarly, the internalization through macropincoytosis leads to the entrapment of internalized molecules in large macropinosomes that are generally recycling to the cell surface with low fusion with lysosomes.[204,205]

Actually, while identifying the internalization mechanism is important, directing a certain gene vector into a certain internalization pathway using specific functional device is probably more important as a promising strategy for avoiding lysosomal degradation. Combining internalization through a cell uptake pathway that avoids lysosomal degradation with effective methods to escape endocytic vesicles is expected to lead to high levels of cell transgene expression. For example, we have previously shown that the uptake of lipid vesicles encapsulating different nucleic acids can be directed to macropinocytosis through the proper use of octaarginine peptide.[95,141] Topology control and the density of the attached peptide were shown to be important factors in targeting internalization through macropinocytosis.[95,108] Proper attachment of the peptide to the lipid envelope in a way that the peptide remains free for interaction with cellular membranes was shown to be important for determining the uptake mechanism.[108] In addition, only liposomes modified with a high density of octaarginine were internalized mainly through macropinocytosis, while those modified with a low density of octaarginine were internalized mainly through clathrin-mediated endocytosis.[95] Therefore, these factors, along with others, should be carefully considered while designing a nonviral gene vector. Internalization through macropinocytosis still requires an efficient system for escaping vesicular entrapment. When the system was combined with a highly fusogenic lipid envelope or with a fusogenic peptide, effective cytosolic delivery was achieved as was evident from confocal laser scanning studies. As a result, the R8-MEND system that was described earlier produced highly efficient gene expression and its application extends to oligonucleotide and siRNA delivery.[3]

Regarding the internalization mechanism of lipoplexes in general, available studies show contradicting results. This suggests that complex factors affect the internalization mechanism, including the diameter, charge, composition of the lipoplexes, as well as the physiology of a certain cell type. Early reports of lipoplex internalization suggested that fusion between the lipids and the plasma membrane is responsible for delivering DNA directly to the cytosol.[60,61,206] It was suggested that the interaction between the liposomes and DNA or the cell membrane destabilizes the liposomes, thus facilitating their fusion with each other and with other membranes. However, most of the following experimental evidence supports the involvement of endocytosis as a main cell entrance route. For example, use

of endocytosis inhibitors significantly reduces transgene expression. Furthermore, interference of the endocytic pathway with lysosomotropic reagents such as chloroquine was found to enhance gene expression.[103] The strongest evidence comes from electron microscopy imaging of gold-labeled DNA formulated in lipoplexes, which clearly shows the presence of DNA in intracellular vesicles, typically entering via endocytosis.[207,208] In general, it is currently believed that membrane fusion is important for transfection but that most of the uptake occurs through endocytosis. Membrane fusion occurs as a result of endosome acidification and is responsible for releasing the endosome contents to the cytosol.

The available data regarding the contribution of a certain endocytic pathway in the overall internalization show diverse results. Rejman *et al*. reported that uptake of lipoplexes formed between the cationic lipid DOTAP and DNA is inhibited by chloropromazine and potassium depletion but is unaffected by filipin and genestein, suggesting that the uptake occurs solely by clathrin-mediated endocytosis.[209] Furthermore, they have shown that particles internalized by this pathway are eventually degraded in lysosomes. Earlier, Zhou *et al*. suggested that the uptake of lipo-PLL (LPLL) lipoplexes occurs through clathrin-mediated endocytosis as the presence of the actin-depolymerizing reagent cytochalsin B increased transfection activities.[210] They suggested that clathrin-mediated endocytosis is the most productive pathway for internalization. Zuhorn *et al*. have shown that lipoplex-mediated transfection occurs through cholesterol-dependent clathrin-mediated endocytosis.[211] Cholesterol depletion with methyl-α-cyclodextrin decreased the activities of SAINT-2/DOPE lipoplexes. This is largely indicative of non-clathrin endocytosis. However, inhibitors of caveolae-like filipin and cytochalasin D had only a slight effect on cell internalization. Co-localization with Tf and the inhibition by potassium depletion further confirmed the involvement of clathrin-dependent endocytosis. Matsui *et al*. suggested that the uptake of LipofectACE lipoplexes occurs through phagocytosis in poorly differentiated airway epithelial cells.[212] Similar to the uptake of large (2 μm) microspheres used as markers for phagocytosis, they found that the uptake of lipoplexes was inhibited by cytochalasin B as well as by potassium depletion.

The uptake of polyplexes also occurs through endocytosis, but without fusion with the cell membrane, and similarly shows some diverse results regarding specific uptake pathways. In general, it is believed that the uptake of PLL and PEI complexes occurs through clathrin-mediated endocytosis. Goncalves *et al*. have shown that the uptake of histidylated PLL (His-PLL) occurs through both clathrin-dependent and clathrin-independent pathways, the latter mostly macropinocytosis as it was inhibited by amiloride and stimulated by phorbol esters.[213] Furthermore, they found that macropinocytosis of the polyplexes and the recycling of DNA impaired transfection and concluded that clathrin-mediated endocytosis is the most productive pathway. Rejman *et al*. also suggested that the uptake of PEI-polyplexes occurs through both clathrin-dependent and clathrin-independent pathways. However, they suggested that the latter mechanism involves the caveolae as it was inhibited by filipin and genestein.[209] Another difference arises from the finding that clathrin-mediated endocytosis is less productive as caveolar internalization escapes lysosomes, thus leading to efficient transfection.

Finally, it is worth mentioning that cellular uptake may or may not be a rate-limiting step in transfection with cationic lipoplexes. For example, the binding and cellular uptake in differentiated primary cell cultures were shown to be rate-limiting steps to efficient transfection. These steps were not rate-limiting in some transformed cell lines such as HeLa cells.[214]

4.425.4.2. Endosomal Escape

After internalization via the several possible mechanisms described above, the internalized molecules exist in different types of endocytic vesicles. The contents of these vesicles are considered still outside the cells as they have no direct access to the cytosol or the nucleus. These vesicles either fuse with lysosomes for degradation or recycle their contents back to the cell surface. Therefore, escape from endocytic vesicles is essential for efficient transfection. Actually, entrapment in endocytic vesicles and lysosomal degradation should be regarded as two different barriers to efficient transfection. This is because some endocytic vesicles do not fuse with lysosomes and the contents are not subject to lysosomal degradation. However, they are still distant from their site of action, being entrapped in closed vesicles. In other words, escaping lysosomal degradation does not necessarily lead to efficient cell transfection. Escaping vesicular compartment or enhancing cytosolic delivery is probably the more useful term, which directly reflects improved transfection.

Different gene vectors use different mechanisms to escape from endosomes. The most common mechanism involves the fusion between lipids in lipoplexes with lipids in endosomal membranes under acidic conditions leading to membrane destabilization as shown in **Figure 8**. Lipoplexes containing the pH-sensitive fusogenic lipid DOPE can release the associated DNA into the cytosol.[64] DOPE forms a stable lipid bilayer at physiological pH ~7. However, at an acidic pH 5–6, DOPE undergoes a transition from a bilayer to an inverted hexagonal structure, which is highly unstable and rapidly fuses with and destabilizes the endosomal membrane, releasing the associated DNA to the cytosol.[63] Evidence shows that fusion with the endosomal membrane is essential for DOPE-containing lipoplexes.[215] DOPE seems to cause this pH-dependent membrane fusion as a similar neutral lipid DOPC does not lead to endosomal escape.[210] Another explanation of membrane fusion involves flip of anionic lipids of endosomal membranes from cytoplasmic side to endosomal luminal side.[216] The positive charge of cationic lipids increases under acidic conditions, causing flipping of anionic lipids from the cytoplasmic side to face the endosomal lumen. Interaction between cationic lipids of the lipoplexes and anionic lipids from endosomal membrane leads to the formation of neutral ion pairs, which destabilizes the endosomal membrane. This lipid mixing displaces DNA from cationic lipoplexes and allows its release into the cytoplasm. It is possible that only DNA or the lipoplexes as a whole will be released to the cytosol after fusion. If lipoplexes are released, the dissociation of DNA must occur in the cytosol or even at the nuclear membrane to achieve transfection.

The second mechanism of endosomal escape involves endosome disruption, which is evident with the polycation

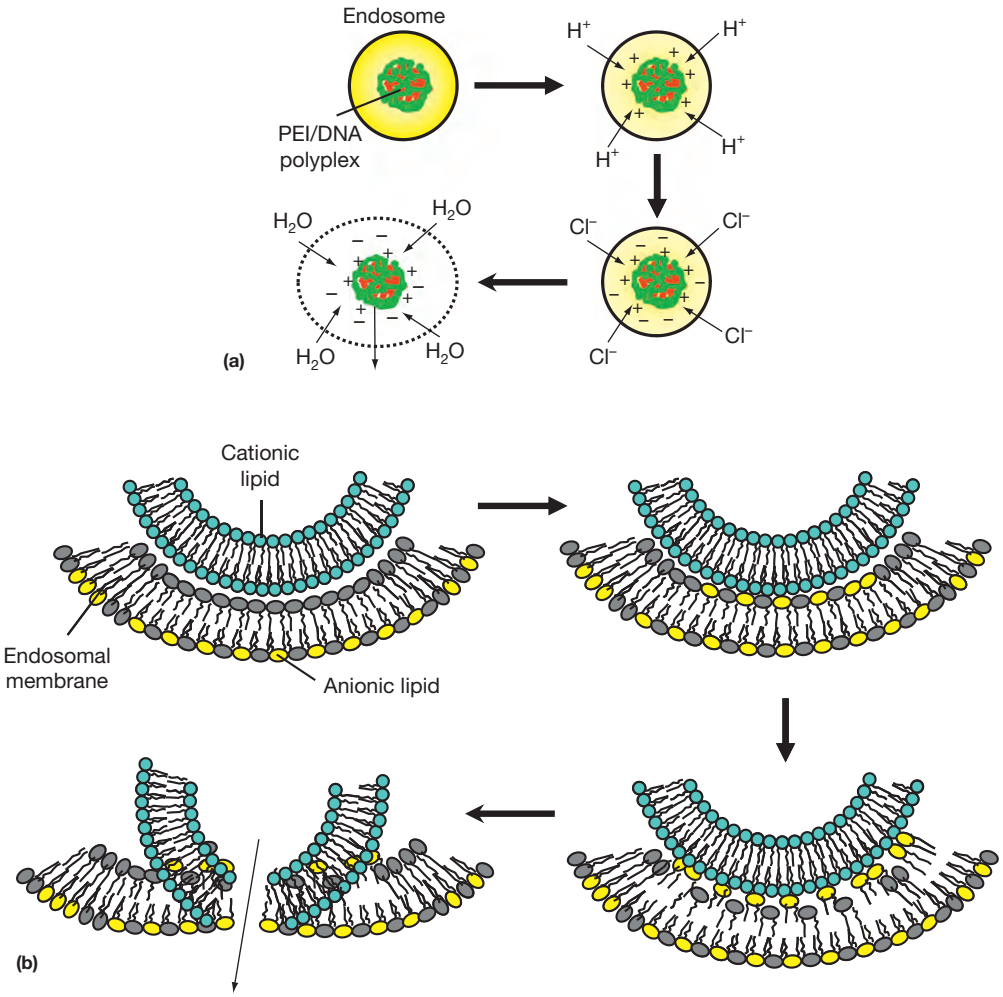

Figure 8 Mechanisms of endosomal escape. (a) Proton sponge mechanism. PEI becomes more protonated at low pH as in endosomes. This protonation triggers an influx of Cl^- ions with protons, leading to a water influx and finally, the swelling and rupturing of the endosomes. (b) The positive charge of cationic lipids increases under acidic conditions, causing flipping of anionic lipids from the cytoplasmic side to face the endosomal lumen. Interaction between cationic lipids of the lipoplexes and anionic lipids from endosomal membrane leads to the formation of neutral ion pairs, which destabilizes the endosomal membrane.

PEI. Transfection with PEI-polyplexes is not improved by fusogenic peptides or chloroquine.[217] The 'proton sponge hypothesis' proposed by Behr *et al*. is frequently used to explain this phenomenon.[97] This hypothesis suggests that PEI becomes more protonated at low pH, as in endosomes, when they actively acidify. PEI acts as a localized buffer within these vesicles, inducing excessive proton pumping into the vesicle. This protonation triggers a co-influx of Cl^- ions with the protons, leading to an osmotically driven water influx and finally the swelling and rupturing of the endosomes.

Pore formation is an additional mechanism of endosomal escape. Certain peptides have the ability to induce membrane pore formation, which facilitates DNA release into the cytosol. These peptides are either derived from viruses, such as the peptide derived from the *N*-terminal sequence of the influenza virus hemagglutinin subunit HA-2, or prepared synthetically such as GALA (WEAALAEALAEALAEHLAEALAEALEALAA) or KALA (WEAKLAKALAKALAKHLAKALAKALKA).[80,218] These peptides undergo conformational changes at low pH in endosomes to interact with and perturb the endosomal membrane. Incorporation of the influenza HA-2 subunit augmented Tf-PLL-mediated gene transfer.[219] Presence of the cholesterol-GALA peptide on the liposomal membrane effectively enhanced the endosomal release of the liposome contents.[79]

Another approach for increasing endosomal escape is the use of lysosomotropic reagents such as chloroquine. It is the weak hydrophobic base that enters the lysosomes and becomes protonated in its acidic environment. As with the proton sponge hypothesis, this presence and buffering capacity triggers a localized swelling of lysosomes and destabilization of their membranes. Chloroquine also inhibits the acidification and maturation of endosomes, thus retarding the lysosomal degradation of genes.[220] Addition of chloroquine to the transfection medium usually favors transfection. This may be due to the destabilization of the endosomal/lysosomal membranes and/or to a slow down in the translocation of DNA to the lysosomes. However, depending on

the system used, chloroquine may also decrease transfection, such as with PEI-polyplexes, by inhibiting endosome acidification required for the release of DNA from endosomes. It is worth mentioning that use of chloroquine and similar lysosomotropic reagents is usually associated with toxicity, which limits their use in actual therapeutic applications.

4.425.4.3. Cytoplasmic Transport

Once released into the cytosol, cytoplasmic transport is also a crucial barrier for macromolecules. Due to the cytoplasmic viscosity, the translation diffusion of dextrans or Ficolls in cytoplasm is 3–4-fold slower than in water.[221] Diffusion of large-sized DNA (>250 bp) is greatly impeded and is dependent on the size of the molecule.[222] This is most likely due to restrictions by actin cytoskeletal filaments.[223] Viruses (i.e., adenoviruses[224,225] and HSV[222,226,227]) have developed a sophisticated machinery for overcoming these biological barriers and are able to successfully deliver their genomes to the nucleus. It is now generally accepted that adenovirus particles are taken up via endocytosis,[204] and then released to the cytosol by disruption of the endosomal membrane via the action of capsid protein VI, which is released from virus particles in response to an acidic pH environment.[228] Adenovirus particles then undergo microtubule-dependent transport to the periphery of the nucleus or to the microtubule-organizing center (MTOC) with the aid of dynein, a microtubule-associated motor protein.[224,229–235] Real-time particle tracking provides new insights into the dynamic transport mechanism of particles in cytoplasm. A detailed particle tracking analysis revealed that the apparent nuclear accumulation of adenovirus results from a dynamic equilibrium involving the more frequent minus end-directed transport toward the nucleus and less frequent plus end-directed transport.[235]

In contrast to viruses, the issue of whether artificial nanoparticles are subject to microtubule-dependent cytoplasmic transport is less well understood. The dynamic transport of PEI-based nanocarriers has been studied.[236–239] An EGF-tagged PEI polyplex[237] showed three-phase dynamics for cytoplasmic transport: (Phase I) a slow directional motion caused by retrograde actin flow; (Phase II) random motion with instantaneous velocity; and (Phase III) directional motion along microtubules. However, the most significant difference between adenovirus and PEI-based carriers is that the directional transport of a PEI-based vector occurs in conjunction with vesicular transport, while adenovirus directly binds to motor proteins.

Another concern is the dissociation of plasmid DNA from the gene carrier. It has been shown that the direct cytoplasmic injection of the lipoplex exhibited a much lower transgene expression compared with the injection of naked DNA.[73,240] In addition, Itaka *et al.* demonstrated that in various types of PEI-mediated transfection the level of transgene expression is correlated with the extent of DNA decondensation in the cytoplasm.[241] Moreover, cytoplasmic translocation of pDNA may be driven by the insertion of specific sequences such as the SV40 enhancer region.[242,243] This region includes consensus sequences for various transcription factors (i.e., AP-1, AP-2, and NF-κB). Therefore, a transcription factor, when bound to the specific sequence of pDNA, may accelerate nuclear delivery. As this accumulation was inhibited by the disruption of microtubules and by the co-injection of anti-dynein antibodies, it is plausible that pDNA accumulates in the nucleus via dynein-mediated transport.[244]

In contrast, data from several studies suggest that the cytoplasmic decondensation of DNA is disadvantageous for transgene expression. Naked DNA is easily degraded by nucleases in the cytoplasm with a half-life of dozens of minutes.[240,245] Furthermore, the diffusion of naked DNA in the cytoplasm is severely limited because of the viscosity of the cytoplasm; the diffusion coefficient of naked DNA > 2000 bp in the cytoplasm is less than 1% of that in water.[222] In fact, pDNA released into the cytosol cannot enter the nucleus and, therefore, has no appreciable transfection activity.[246] Transgene expression was reported to be severely diminished in cell-cycle-arrested (synchronized) cells, suggesting that release of pDNA into the cytoplasm may not facilitate pDNA delivery to the nucleus in nondividing cells.[247] Early release in the cytosol may not be adequate for gene expression. The timing and location (cytosol or nucleus) for the DNA decondensation may be important factors for efficient transgene expression.

4.425.4.4. Nuclear Delivery

In mitotic cells, it is generally thought that pDNA primarily enters the nucleus when the nuclear membrane structure breaks down during the M-phase.[248–251] However, in nondividing cells, the nuclear membrane structure remains intact. Therefore, the nuclear membrane is the ultimate barrier to be overcome for successful nuclear delivery in nondividing cells. The mutual transport of various types of molecules between the cytosol and nucleus occurs via the nuclear pore complex (NPC), which allows the passive transport of gold nanoparticles with sizes of <9 nm.[252] The mechanism for the nuclear localization signal (NLS)-dependent nuclear import of proteins is well characterized.[253] One of the most well-defined NLS signals is the peptide (**PKKKRKV**) derived from the SV40 T-antigen (NLS_{SV40}). Endogenous or chemically modified NLSs bind to importin α and is subsequently recognized by importin β, which facilitates nuclear import of cargo via its efficient interaction with hydrophobic phenylalanine-glycine (FG) rich domains inside of the nuclear pore.[254] One of the most important characteristics of NLS-dependent transport is that the threshold size of the NPC expands to >39 nm in size.[255,256]

Wolff and coworkers investigated the effect of pDNA size on nuclear transport activity using digitonin-permeabilized cells.[257,258] Short DNA (<200 bp) fragments were effectively imported into the nucleus, whereas nuclear import decreased when the size of the pDNA increased and was negligible at a size of >1500 bp. The typical plasmid DNA used (>5 kbp) is too large to pass through the cell's nuclear pore complexes. In fact, microinjection studies demonstrated that more than 100-fold larger amount of pDNA is required to achieve a transgene expression by cytoplasmic microinjection compared to that by nuclear microinjection. This suggests that less than 1% of the cytoplasm-microinjected plasmid DNA reaches the nucleus.[240] Therefore, efficient systems for the nuclear delivery of pDNA would be highly desirable in developing an efficient gene delivery system.

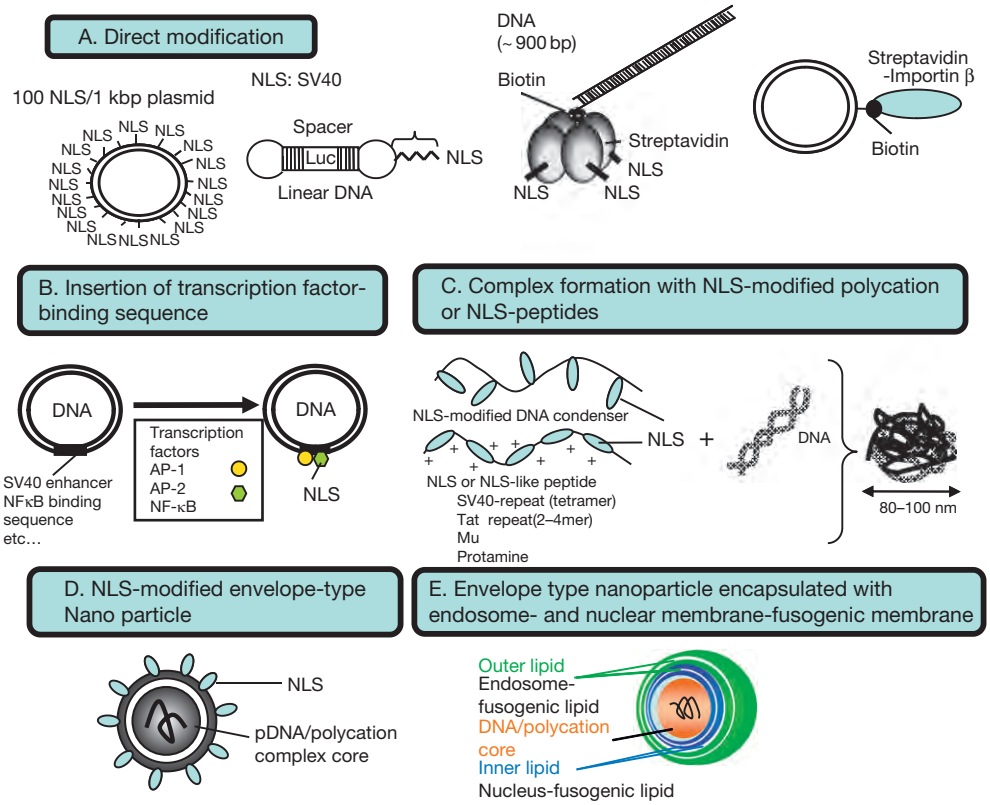

Figure 9 Strategies to overcome a nuclear member barrier. (a) Direct modification of NLS peptides and/or nucleus-targeting proteins to pDNA by chemical linkage or avidin–biotin interaction. (b) Insertion of nuclear-transcription factor-binding sequences (i.e., NF-κB) in the pDNA. (c) Condensation of pDNA with NLS itself or NLS-modified polymers. (d) Surface modification of NLS on the surface of lipid-based particle. (e) Encapsulation of pDNA in NLS-fusogenic lipid envelope.

In the light of these findings, many trials were designed to improve nuclear delivery processes (summarized in Figure 9). First, NLS were chemically linked to the plasmid DNA itself.[259] However, in this strategy, >100 NLS peptides/1 kbp are required to induce the nuclear delivery of pDNA, where transcription is severely inhibited. Similarly, several groups conjugated NLSs on the edge of linearized pDNA. However, microinjection studies[260,261] failed to demonstrate the utility of this strategy. As it uses highly cationic NLS_{SV40}, electrostatic interactions between NLS_{SV40} and DNA may prevent it if being recognized by importins. One excellent strategy for overcoming this issue is to modify the pDNA with an NLS-possessing protein or importin β via avidin–biotin interactions.[258,262] Alternatively, specific DNA sequences can be introduced into the plasmid DNA (i.e., NF-κB binding sequence,[263–266] SV40 enhancer[242,243] and smooth muscle gamma actin promotors,[267] and the oriP sequence derived from the Epstein-Barr virus[268]), which allows the binding of nuclear transcription factors in the cytosol and supports nuclear import. This strategy is advantageous in controlling nuclear import in a signal-dependent and cell-type-dependent manner. Proteomic analysis identified core histone H2B and NM23-H2, a ubiquitous c-Myc transcription-activating nucleotide diphosphate kinase, as a cytoplasmic determinant for nuclear import of a pDNA-containing fragment of the SV40 promoter and enhancer region (*D*NA nuclear *t*argeting sequence, DTS). Insertion of these protein-related sequences (NM23-H2 and Chx10) significantly enhanced gene expression.[269] Moreover, DTS-specific interactions with cytoplasmic cofactors (i.e., importin β1, importin 7, and the small guanosine triphosphatase, Ran) were demonstrated.[270]

A second approach is to condense pDNA with an NLS-modified polycation. One example is an NLS_{SV40}-modified PLL. Condensation of pDNA with this polycation resulted in a slight enhancement in transgene expression compared with nonmodified PLL.[271,272] To avoid electrostatic interactions between NLS and DNA, a novel NLS derived from heterogeneous nuclear ribonucleoprotein-A1 (M9) was conjugated to a cationic peptide (scattered SV40 NLS). Complexes, formed with M9-modified polycations exhibited enhanced transfection activity by lipofection.[235] An alternative approach is to condense pDNA with the NLS peptide itself or NLS-like peptides. Currently, various NLS variants, such as tetramers of SV40 NLS,[273] TAT oligomers,[107] Mu peptide derived from the adenoviral core,[274,275] and protamine,[276,277] are under investigation. DNA condensation with these peptides enhances transgene expression. Of note, cytoplasmic microinjection showed that the transgene expression of pDNA was enhanced by condensation depending on the N/P charge ratio (+/−) when it was condensed with protamine, a peptide containing four possible NLS-like regions consisting of basic amino acid and proline or serine residues.[276] At a low charge ratio, the basic

amino acids of protamine may be largely occupied in the condensation of pDNA, and, as a result, NLS-like function would be limited. By increasing the charge ratio, the protamine displayed on the surface of particles functions as an NLS, allowing the particles to be recognized by nuclear transport-associating proteins. However, it is difficult to control the density of surface-displayed NLS, as it would likely vary with condensation status.

One strategy for controlling topology is to use nuclear transport molecules that are noncationic and water soluble, such as sugars. Sugars as NLS were first reported by Duverger *et al.*[278] They reported that large amounts of sugar-conjugated bovine serum albumin (BSA) accumulated in the cell nucleus. In recent decades, the function of sugar molecules as a nuclear transport signal[279–281] and its mechanism[280,282–285] have been partially clarified. According to these reports, sugar-dependent nuclear transport is mediated by its receptors (i.e., lectins) and occurs in an energy-dependent manner via the NPC. Glycosylated polymers, such as lactosylated polylysine and lactosylated polyethyleneimine, have recently been reported.[286–289] It was recently reported that surface modification of fluorescent nanoparticles (quantum dots) with maltotriose enhanced their nuclear accumulation.[290] Another strategy is to modify the NLS on a pDNA-encapsulating liposome by inserting a lipid derivative of a NLS. The NLS is spontaneously oriented outward from the particles, and results in the effective transfection of nondividing cells (i.e., primary dendritic cell cultures).[291]

The modification of lipid derivatives of sugars on the surface of lipid envelope-type nanoparticles also enhanced gene expression by 10–100-fold in synchronized HeLa cells.[247] In the case of adenovirus (Ad), it first docks to the NPC. Then, the proximity of the Ad capsid to the NPC allows hexon binding to histone H1. The hexon–histone H1 complex is then transported to the nucleus by histone H1 import factors (i.e., importin 7 and importin β). This triggers the nuclear transfer of Ad genomic DNA in conjunction with the disruption of the viral capsid.[292] While the mechanism for nuclear delivery with NLS-modified particles is currently unknown, NLS-modified lipid nanoparticles may mimic this mechanism; the particles first dock to the NPC via the surface-modified NLS, and are subsequently disassembled on the NPC. Meanwhile, a NPC-independent nuclear transport approach has recently been proposed. In this strategy, intracellular membrane barriers are overcome using stepwise membrane fusion. The critical structural elements of the particle are a DNA–polycation condensed core coated with two nuclear membrane–fusogenic inner envelopes and endosome–fusogenic outer envelopes, which are shed in a stepwise fashion as the core is trafficked through the cell.[293]

4.425.4.5. Intranuclear Disposition

It is generally accepted that the most significant obstacle to the clinical use of nonviral vectors is their low transfection activity. Viruses have evolved sophisticated mechanisms to overcome intracellular barriers. Dose–response data for transgene expression showed that, Lipofectamine PLUS (LFN), a lipoplex-based nonviral vector, required 3–4 orders of magnitude more gene copies than the adenovirus to achieve a comparable transgene expression.[294] Therefore, it is important to clarify which intracellular process is responsible for such a large difference in transfection activity. A quantitative comparison of intracellular trafficking between LFN and adenovirus clarified that the nuclear transport efficiency of adenovirus was only twofold greater than that of LFN. Thus, the large difference in transfection efficiency cannot be explained by intracellular trafficking. A comparison of the nuclear delivery of DNA revealed that 3–4 orders of magnitude more gene copies were required when LFN was used to obtain a transfection activity comparable to that of adenovirus. Transcription efficiency was calculated as expression divided by gene copies in the nucleus. As a result, adenovirus was found to be 8100-fold more efficient at nuclear transcription than LFN.[294] This result indicates that a post-nuclear delivery process is critical to the difference in transfection efficiency between LFN and adenovirus. Less efficient nuclear transcription compared to adenovirus was also demonstrated in the case of a PEI-based polyplex.[295]

Transgene expression of nucleus-delivered DNA is limited by both transcription and translation. Transcription efficiency was calculated as mRNA expression divided by nuclear DNA. Similarly, translation efficiency was calculated as transgene expression divided by mRNA expression. Measurements of mRNA products showed that the translation efficiency of adenovirus was approximately 16-fold higher than that of LFN. Collectively, the translation efficiency of adenovirus was 460-fold higher than LFN. Therefore, the 3 orders of magnitude difference in the postnuclear delivery process was attributed to the 1 order of magnitude difference in transcription efficiency and the 2 orders of magnitude difference in translation efficiency.[296]

Imaging of intranuclear DNA using *in situ* hybridization showed that adenoviral DNA was specifically located in the euchromatin region, where transcription activity is relatively high. Moreover, decondensation efficiency was dramatically lower in the case of LFN. Collectively, these results suggest that poor decondensation and poor targeting activity of DNA to the euchromatin region are responsible for the less efficient nuclear transcription with LFN. *In vitro* translation activity was drastically inhibited in the presence of LFN, whereas only a slight inhibition was observed in the case of adenovirus. These data indicate that electrostatic interactions between LFN and mRNA are significant contributors to the difference in translation efficiency between LFN and adenovirus.[296]

4.425.4.6. Heterogeneity in Transfection

Another drawback to the use of the current nonviral gene vectors is heterogeneous transgene expression. As gene expression is achieved when cells pass through the mitosis phase,[248–251] nuclear delivery is considered to be a key process that limits transduction in nonexpressing cells. However, recent imaging studies showed that intranuclear disposition is also a rate-limiting factor for heterogeneous gene expression. Simultaneous visualization of the nuclear delivery of pDNA and transgene expression in an individual cell clarified that nuclear delivery was achieved only in 22.5% of the cells. Moreover, marker gene expression was detected in a portion of the nuclear pDNA-positive cells only, suggesting that the postnuclear delivery process is also a determinant of heterogeneity.[297] This is also supported by results showing a relationship between the amount of nuclear pDNA and marker gene expression. Transfected cells

were separated into three fractions depending on marker gene expression using a fluorescence-activated cell sorter (FACS), and thereafter the nuclear accumulation of DNA was determined. As marker gene expression is related to the nuclear delivery of pDNA, nuclear delivery is one of the determinants for the heterogeneity of gene expression. However, it is noteworthy that a large number of pDNA (700–800 copies) are delivered to the nucleus, even in cells with a low expression.[298] Therefore these data also support the conclusion that intranuclear disposition is important for efficient gene expression. For an examination of the relationship between decondensation and gene expression in living cells, imaging of fluorescence resonance energy transfer (FRET) among donors and acceptors labeled on pDNA is a useful technique.[299] Especially in polyplexes, pDNA decondensation in the nucleus is the major determinant of gene expression.

4.425.5. *In Vivo* Applications

Worldwide trends and status of gene therapy clinical trials were reviewed in 2007 in the *Journal of Gene Medicine*.[300] From the first human gene therapy trial in 1989,[301] the number of clinical trials increased rapidly and peaked in 1999. After the report on the unfortunate fatal adverse effects associated with the use of the adenovirus vector[302] and retrovirus vector-induced oncogeneity,[303] the number of trials decreased in 2003. However, the number is now slowly recovering from 2004 to 2006. Up to 2007, 1340 gene therapy studies have been completed, with viral vectors used in two-thirds of the total 1304 trials, whereas nonviral approaches are becoming increasingly more common. Table 3 summarizes some candidate genes for curing diseases. It is noteworthy that not only in clinical studies but also in animal studies viral vectors are used in most of the trials. The most serious bottleneck for the current use of a nonviral gene carrier appears to be their low transfection efficiency in the presence of plasma proteins and cell media. Upgrading transgene expression efficiency is, therefore, essential if the use of nonviral vectors is to be expanded.

4.425.5.1. *In Vivo* Delivery of pDNA

4.425.5.1.1. Cancer

Gene therapy is a promising strategy for treating some cancers. Strategies for cancer gene therapy include (i) manipulation of the cell cycle and apoptosis, (ii) activation of the immune system, and (iii) inhibition of angiogenesis. Concerning the first approach, tumor suppressor genes such as p53[384–386] and proapoptotic genes bax,[387] caspase 9,[388] and toxins (i.e., diphtheria toxin A[389]) inhibit tumor growth when overexpressed in cancer cells. Tumor necrosis factors (TNFs) such as the TNF-related apoptosis-inducing ligand (TRAIL) is a potent inducer of apoptosis in tumor cells but not in normal cells and tissues.[390,391] Genetic prodrug-activation therapy or suicide gene therapy is an alternative approach to modulate tumor cells to acquire sensitivity to prodrugs (i.e., ganciclovir). The example includes the gene transfer of DNA encoding thymidine kinase combined with a ganciclovir prodrug[392,393] and cytosine deaminase which converts fluocytosine into 5-fluorouracil.[394]

Stimulation of cancer immunotherapy is a second approach. Activation of the immunoresponse against a tumor can be achieved by the topical expression of cytokines such as interleukin 2 (IL-2),[395] interleukin 12 (IL-12),[396,397] and granulocyte-macrophage colony stimulating factors.[398] When a lipoplex is systemically administered, high levels of IL-12 and INF-γ are produced, most probably due to the inflammatory effect of the lipoplex itself, and the innate and adaptive immuneresponses appear, irrespective of the gene expression form of pDNA.[399,400] This side effect of the lipoplex itself may aid in combating pulmonary metastasis.

Finally, inhibition of angiogenesis is a novel approach for limiting tumor growth. The most widely demonstrated approach is the use of soluble vascular endothelial growth factor (VEGF) receptor (soluble FLT1), which antagonizes the binding of VEGF to VEGF receptors, a key player in angiogenesis.[401,402] In the nonviral approach, cationic liposomes modified with inactivated hemagglutinating virus of Japan (HVJ) target gastric cancer. By expressing soluble FLT1, the microvessel density (MVD) is decreased, resulting in a significantly longer survival compared to control mice.[403] Another gene is endostatin, a broad-spectrum angiogenesis inhibitor that may interfere with the pro-angiogenic action of growth factors such as basic fibroblast growth factor (bFGF/FGF-2) and VEGF.[404] Herpes simplex virus encoding endostatin inhibits angiogenesis in colon carcinomas in model mice.[405] A combination of two adenovirus vectors that encode the fusion protein of endostatin/angiostatin, as well as the soluble form of the endothelial cell-specific TEK tyrosine kinase (TIE-2) receptor, a receptor of angiopoetin1, synergistically inhibited tumor growth in a PC-3 prostate xenograft tumor mouse model.[406]

4.425.5.1.2. Liver

The liver plays an important role in the synthesis (i.e., carbohydrates and lipids), filtration, degradation, and storage of various substances, and is a critical sentinel of healthy blood biochemistry. At the same time, the liver protects the whole body from xenobiotics via its strong metabolic bioactivity. Therefore, a loss of liver function leads to the development of a variety of severe pathologies.

Generally, access of nanoparticles from blood to the parenchymal cells is blocked by the continuous endothelium. However, the liver is comprised of a unique thin-walled endothelium (sinusoids) containing small pores called fenestrations. In addition, Kupffer cells (stellate macrophages) are distributed throughout the endothelial cells that line the sinusoids. As a result, the liver is a major clearance organ for nanoparticles as nanosized particles can gain access to hepatocytes, or alternatively can be trapped by Kupffer cells. The liver is a promising organ as a target of viral (adenovirus, lentivirus, and adeno-associated virus; AAV) and nonviral gene delivery carriers via i.v. administration. Avoiding accumulation in the liver of non-liver-targeted vectors is often a critical challenge in systemic administration. Of note, the hydrodynamic i.v. injection of naked DNA resulted in a high transgene expression predominantly in the liver.[407,408] The image-guided insertion of a balloon catheter into the hepatic vein of the selected lobe, followed by an injection of plasmid DNA using a computer-controlled injection device, enables lobe-specific hydrodynamic gene delivery to the liver.[409]

A wide variety of animal models are used in gene delivery studies of liver-derived monogenic disorders.[45]

Table 3 Genes for the cure of disorders

Organ	*Target disease*	*Gene*	*Animals*	*Vector/method*	*Reference*
Liver	Cirrhosis (chronic administration of dimetylnitrosamine)	Hepatocyte growth factor (HGF)	Rat	Electroporation	304
	Growth hormone deficiency (hypophysectomized mouse)	Human growth hormone (hGH)	Mouse	Hydrodynamic	305
	Hemophilia	Factor IX	Mouse	Hydrodynamic	306
			Human	AAV	307
	Wilson disease	ATP7B	Rat	Lentivirus	308
	Cirrhosis (chronic administration of carbon tetrachloride)	Urokinase-type plasmisnogen activator (uPA)	Rat	Adenovirus	309
	Cirrhosis (chronic administration of carbon tetrachloride and bile duct ligation)	Matrix metalloprotease 8	Rat	Adenovirus	310
	Glycogen storage disease type Ia (GSD-Ia)	Glucose-6-phosphatase-α	Mouse	Adeno-associated virus (AAV)	311
	Glycogen storage disease type Ib (GSD-Ib)	Glucose-6-phosphate transporter	Mouse	Adenovirus	312
	Mucopolysaccharidosis type-I (MPS I)	α-L-Iduronidase (IDUA)	Mouse	Lentivirus	313
	Mucopolysaccharidosis type-I (MPS IIIb)	α-*N*-Acetylglucosaminidase (NAGLU)	Mouse	Lentivirus	314
	Mucopolysaccharidosis type-VII (MPS VII)	Canine β-glucuronidase (cGUSB).	Dog	Retroviral vector	315
	Glycogen storage disease type II	α-Glucosidase (GAA; acid maltase)	Mouse	AAV	316
	Hepatic fibrosis (chronic administration of dimetylnitrosamine)	Heme oxygenase-1	Rat	AAV	317
Kidney	Unilateral ureteral obstruction	Smad7	Rat	Ultrasound-microbubble	318
		Egr-1	Rat	Electroporation	319
	Renal fibrosis in a remnant kidney	Smad7	Rat	Ultrasound-microbubble	320
	Chronic renal disease induced by unilateral ureteral obstruction	HGF	Mouse	Hydrodynamic	321,322
Lung	Transplanted lung	Endothelial nitric oxide synthase (ecNOS)	Rat	Adenovirus	323,324
	Hemophilia	Erythropioetin	Mouse	AAV	325
		Factor IX	Mouse	AAV	325
	Transplanted lung	TGF-β	Rat	Lipoplex	326
	Irradiation damage	Manganese superoxide dismutase (MnSOD)	Mouse	Lipoplex	327
	Pulmonary emphysema	α1-Antitrypsin	Cotton rat	Adenovirus	328
			Rabbit	Lipoplex	329
			Human	Lipoplex	330
			Human	Lipoplex	331
	Cystic fibrosis (CF)	Fibrosis transmembrane conductance regulator (CFTR)	Mouse	Adenovirus	332
			Human	Adenovirus	333–336
			Mouse	Lentivirus	337
			Rabbit	AAV2	338
			Nonhuman primate	AAV2	339
			Human	AAV2	340–345
			Mouse	AAV5	346
			Nonhuman primate	AAV5	347
			Mouse	Lipoplex	348,349
			Human	Lipoplex	350–355
			Human	Lipoplex (GL-67)	356,357
			Human	Polyethylene glycol-substituted 30-mer lysine peptides	358

(*Continued*)

Table 3 (Continued)

Organ	*Target disease*	*Gene*	*Animals*	*Vector/method*	*Reference*
	Allergic bronchopulmonary aspergillosis (ABPA) concomitant with CFTR deficiency	CFTR	Mouse	AAV	359
	Allergy in Cftr deficient mouse	IL-10	Mouse	AAV	360
Muscle	Pulmonary emphysema (genetic disorder)	α1-Antitrypsin	Mouse	AAV	361
			Nonhuman primate	AAV	361
	Hemophilia	Factor IX	Human	AAV	362,363
	Fibrosis induced by glomerulonephritis	Decorin	Rat	Naked pDNA	364
	δ-Sarcoglycan (δ-SG)	Muscular dystrophy	Hamsters	AAV	365
	Short-chain acyl-CoA dehydrogenase (SCAD)-deficiency	Short-chain acyl-CoA dehydrogenase (SCAD)	Mouse	AAV	366
	Cardiomyopathy	HGF	Mouse	Adenovirus	367
	Diabetic nephropathy	HGF	mouse	Adenovirus	368
	Duchenne muscular dystrophy (DMD)	Dystrophin	Mouse	Electroporation	369
				Naked pDNA	370
			Human	Naked pDNA	371
	Diabetic hind limb ischemia	Hepatocyte growth factor (HGF)	Rat	Hemagglutinating virus of Japan (HVJ)-liposome	372
Heart	Ischemic heart disease	VEGF	Porcine	Direct myocardial DNA injection	373,374
			Porcine	Adenovirus	375
			Human	Direct DNA injection	376,377
			Rabbit	Water-soluble lipopolymer (WSLP)	378
		VEGF2	Human	Direct DNA injection	379
		FGF-2	Porcine	Direct DNA injection	373
		HGF	Porcine	Direct DNA injection	380
		HGF	Rat	HVJ liposome	381
		Sonic hedgehog	Mouse/rat	Direct myocardial DNA injection	382
		Netrin-1	Rabbit	Water-soluble lipopolymer (WSLP)	383
	Congestive heart failure	δ-SG	Hamsters	AAV	365
	Glycogen storage disease type II	α-Glucosidase (GAA; acid maltase)	Mouse	AAV	316

Some trials are summarized in Table 3. Transduced genes play important roles in hepatocytes for metabolism and transport. Examples include (i) Long–Evans cinnamon rats, a model for Wilson disease, in which copper-transporting ATPase 2 (ATP7B) is hereditarily lacking and (ii) the Gunn rat, a model of Crigler–Najjar syndrome type I, deficient in UDP-glucuronyltransferase. Another category is gene products excreted from liver to circulating blood, which then act in different organs or in the liver itself. Examples include hemophilia,[306,307] α1-antitrypsin deficiency glycogen storage diseases,[311,312,316] and mucopolysaccharidosis.[313–315]

Concerning liver gene therapy, the rapid decrease in transgene expression is an obstacle to be overcome. As the half-life of gene expression is shorter than that of the remaining amount of pDNA, intranuclear inactivation and degradation of pDNA are key factors in the overall decrease in gene expression.[410] Optimized selection of the gene expression cassette is essential for efficient and sustained transgene expression. In liver, a combination of chicken β-actin and cytomegalovirus (CMV) enhancer is one promising candidate for liver gene expression.[411] Moreover, Wooddell *et al.* reported that the optimal expression cassette consists of an albumin promoter combined with an alpha-fetoprotein MERII enhancer, the 5′ intron from the factor IX gene, and the 3′UTR from the albumin gene including intron 14.[412] Addition or removal of specific sequence elements in pDNA is an alternative or supporting strategy for prolonging hepatic gene expression. The scaffold matrix attachment region (S/MAR) is an AT-rich sequence locating in close proximity to promoters, replication origins, and multiple nuclear processes, such as recombination and breakpoint sites, to attach chromosomal DNA to the nuclear scaffold/matrix.[413] The hydrodynamic injection of S/MAR-inserted pDNA showed long-lasting gene expression after the hydrodynamic injection when gene expression was controlled by a liver-specific α1-antitrypsin promoter.[414] Another strategy involves removing plasmid backbones consisting of an antibiotic resistance gene, an origin of replication, and inflammatory sequences that are intrinsic to bacterial DNA (minicircle system; reviewed in Mayrhofer *et al.*[415]). Genomic integration of expression cassette by means of phage phiC31 integrase-mediated recombination is an alternative candidate for achieving long-term gene expression.[416] Improved DNA construction is a factor for future studies directed toward clinical applications.

4.425.5.1.3. Lung

The lung is an important target for gene therapy for curing α1-antitrypsin deficiency and cystic fibrosis. α1-Antitrypsin deficiency is an inherited metabolic disorder in which mutations in the coding sequence of α1-antitrypsin prevent its export from hepatocytes. It results in the loss of circulating α1-antitrypsin, predisposing to early-onset panlobular emphysema. In addition, it causes an abnormal accumulation of the glycoprotein in hepatocytes, resulting in programmed cell death, hepatic inflammation, fibrosis, and cirrhosis (reviewed in Fairbanks and Tavill[417]). Gene therapy related to α1-antitrypsin deficiency has been extensively reviewed.[418]

The cystic fibrosis transmembrane conductance regulator (CFTR) is an anion channel regulated by cAMP-dependent phosphorylation, which is expressed in epithelial cells of a wide variety of tissues including the reproductive tract. In the lung, CFTR plays an important role in ion transport in the conducting pulmonary airways and exocrine glands. Mutations in the gene encoding CFTR causes cystic fibrosis (CF), a common genetic disease in the Caucasian population. Gene delivery for CF has also been reviewed.[419] Nonviral gene therapy for CF has been more extensively reviewed in Pringle *et al.*[420]

Similar to the liver, the short duration of gene expression is also an obstacle in lung-targeted gene therapy. The human polyubiquitin C (UbC) promoter is a promising choice for sustained gene expression in lungs when delivered by electroporation.[421] Moreover, it is likely that the silencing of lung gene expression is closely related to the host immunoreaction in response to gene carriers. The most plausible determinant is an unmethylated CpG sequence in pDNA, a ligand for Toll-like receptor 9 (TLR9) in endosomes.[422,423] The action is enhanced when pDNA is complexed with cationic liposomes.[356,357,424] In the lung, a wide variety of cytokines are produced, including IL12, INFγ, and TNFα.[425] As commonly used viral promoters, such as the CMV immediate/early promoter, are attenuated in response to cytokines (i.e., TNFα and IFNγ) by a transcription-related mechanism,[426,427] inflammatory cytokines produced from macrophages in response to the gene carrier may paracrine-regulate the gene expression in target cells.[428] The complete deletion of CpG motifs from pDNA results in a dramatic reduction in cytokine production, even in the case of lipoplex-based gene carriers, and in sustained gene expression,[429] indicating that CpG-free pDNA is highly beneficial for gene delivery for the lung, and most probably for other tissues.

4.425.5.1.4. Kidney

The simplest method of gene delivery to the kidney is through hydrodynamic injection of plasmid DNA (pDNA). Dai *et al.* injected human pDNA encoding hepatocyte growth factor (hHGF) with a large volume of saline via the tail vein of mice over a span of 5–10 s. The hydrodynamic technique was originally developed for targeting gene delivery to the liver. However, this technique is also promising when the kidney is obstructed, such as during chronic renal fibrosis caused by unilateral ureteral obstruction (UUO).[321] As a result of the injection of pDNA encoding hHGF, hHGF was expressed in >90% of glomeruli, whereas no transgene expression was observed in the tubular compartment.[430] hHGF expression suppresses the renal expression of TGF-β and of the TGF-β receptor, thereby ameliorating renal failure.[321] Similarly, hHGF expression also protects renal epithelial cells from necrosis and apoptosis by inducing the expression of the anti-apoptotic Bcl-xL protein.[430] Another effective route for the administration of naked DNA is retrograde renal vein injection. The injection of erythropoietin (EPO) encoding DNA, increased serum EPO concentrations to a level sufficient for erythropoiesis.[431]

The ultrasound-microbubble system is a promising method for widely distributing DNA to various compartments. Under optimal conditions, FITC-labeled ODN accumulated in all glomerular cells (>95%), vascular and perivascular cells (>90%), and medullary tubular and interstitial cells (70–80%) after ultrasound treatment.[318] In the UUO mouse, endogenous smad 7 expression is reduced in conjunction with Smad 2 and 3 activation, resulting in tubulointerstitial fibrosis. The transfection of pDNA encoding Smad 7 into UUO mice results in Smad 7 expression in as high as 95% of the glomerular cells, all of the capillary endothelial cells, and all of the interstitial fibroblastes/myoblasts, thereby preventing tubulointerstitial fibrosis.[318]

Electroporation is a widely used technique for the transfection of DNA into muscle, skin, liver, and cancer cells. Interstitial cells were targeted by slowly injecting DNA into the ureter while clamping the left renal vein, followed by the delivery of square-wave electric pulses. In UUO rats, the early growth response gene 1 (Egr-1), which increases α-smooth muscle actin (α-SMA) levels, was increased in interstitial cells. The introduction of DNAzyme against Egr-1 blocked the expression of the corresponding gene, with a concomitant reduction in TGF-β, α-SMA, and type I collagen, thereby inhibiting interstitial fibroblasts.[319]

4.425.5.1.5. Muscle

Skeletal muscle is an attractive target not only for viral vectors but also for nonviral vectors. Importantly, in skeletal muscle, plasmid DNA can be administered and used without any special delivery system and persist for long in an extrachromosomal form.[432] Viral vectors such as adenovirus and AAV are also applicable.[433]

Gene delivery to the skeletal muscle is a promising strategy for the production of topically functional proteins, such as dystrophin,[371] as a therapeutic protein for Duchenne muscular dystrophy (DMD) or Becker muscular dystrophy (BMD) patients.[371] HGF is also a highly promising factor for the cure of ischemic diseases, because of its strong angiogenesis activity.[434] Meanwhile, muscle gene delivery is a convenient strategy for supplying various types of proteins that are useful for the total body (i.e., factor IX for hemophilia[362,363]) or other disease-associated organs. Conlon *et al.* demonstrated that intramuscular administration of AAV encoding short-chain acyl-CoA dehydrogenase (SCAD) systemically corrected fatty acid oxidation disorders in SCAD-deficient mouse.[366] Similarly, decorin[364] and HGF[368] expressed in muscles by naked DNA and adenovirus, respectively, are secreted into the bloodstream, and systemically function for the kidney diseases.

For the case of cardiac muscle, the direct injection of pDNA is a major tool for gene transduction. To date, curing ischemic diseases is a major goal of gene delivery. Expert reviews with operative examples are available.[383]

4.425.5.2. *In Vivo* Delivery of siRNA

The field of RNA interference (RNAi) has expanded at a remarkable rate since the discovery in 1998 by Fire, Mello, and colleagues of the ability of double-stranded RNA to silence gene expression in *Caenorhabditis elegans*.[435] Tuschl *et al.* demonstrated that small synthetic interfering RNA (siRNA) consisting of 21–25 nucleotides with a 3′ overhang can achieve sequence-specific gene knockdown in a mammalian cell line.[436,437] RNAi has been widely applied in gene functional analysis and has become a powerful tool for drug target discovery. The first successful use of siRNA for *in vivo* gene silencing in mice was achieved in the liver via rapid injection of a large volume of physiological saline solution containing naked siRNA, so-called hydrodynamic injections, for a hepatitis C virus into the tail vein of mice.[438] Since that report, siRNA-mediated marker gene knockdown in postnatal mice by hydrodynamic injections has been observed by Lewis *et al.*,[439] and Lieberman and colleagues subsequently demonstrated that *Fas* knockdown in the liver by siRNA hydrodynamic injections protects mice from fulminate hepatitis.[440] Given their specific potent RNAi triggering activity, siRNA is considered as a new generation of biopharmaceutical drugs. Gene product inhibition mechanism is triggered by introduction of siRNA into the cytoplasm, where the guide strand of siRNA (usually antisense strand) loaded into RISC binds to its target mRNA and the expression of the target gene is blocked. After normal intravenous injection (not hydrodynamically), siRNA is rapidly eliminated from blood circulation through renal excretion to the urine due to its molecular weight (−13 kDa).[441] On the other hand, from the view point of cellular uptake, its molecular weight as well as polyanionic and hydrophilic nature interrupts the free transport of siRNA across the cell membrane. Furthermore, naked siRNA is subject to degradation by serum RNases within a short period in the body. Therefore, for the *in vivo* use of siRNA, chemical modification can be used to increase their half-life for *in vivo* stability and targetability for specific organs, and cells should be installed by conjugation or the delivery system. In this section, *in vivo* siRNA delivery and its clinical use are discussed.

4.425.5.2.1. *Chemical modification, bioconjugation and targeted* in vivo *siRNA delivery*

Chemical modification of siRNA has been investigated in attempts to prolong its half-life without destroying its biological activity. Stability against nuclease degradation has been achieved by introducing a phosphorothioate (P=S) backbone linkage at the 3′ end for exonuclease resistance and 2′-sugar modification (such as 2′-*O*-methyl or 2′-fluoro) to provide endonuclease resistance.[442] The strategy for improving the therapeutic efficacy of siRNA involves the bioconjugation of functional peptides, lipophilic molecules, or aptamers to one or both strands of the siRNAs. Cholesterol, when covalently conjugated to siRNA, induces significant silencing of the apolipoprotein B (apoB) gene in the liver and jejunum after intravenous administration in mice ($50\,mg\,kg^{-1}$), which resulted in decreased plasma apoB protein levels and the total level of cholesterol, because cholesterol conjugation increases the hydrophobicity and cellular association of the complex.[443] Song *et al.* demonstrated that an antibody-protamine fusion protein is capable of delivering siRNA (80 μg×3) to HIV-infected tumor cells and silencing target genes via either direct or intravenous injection in tumor-bearing mice.[444] Kumar *et al.* demonstrated the brain delivery of siRNA using RVG, a rabies viral glycoprotein, and sn oligoarginine conjugate (RVG-9R) (50 μg × 3).[199] Aptamer–siRNA conjugates showed efficacy in cell-specific knockdown via intraperitoneal administration in tumor xenograft mice (1 nmol × 10).[445] The direct conjugation of vitamin E (α-tocopherol) to siRNA resulted in the efficient delivery of siRNA to the liver and the knockdown of apoB when administrated i.v. in mice ($32\,mg\,kg^{-1}$).[446] As mentioned above, bioconjugation approaches resulted in the tissue- and cell-specific delivery of siRNA and exhibited an *in vivo* therapeutic potential.

4.425.5.2.2. *Lipid-based* in vivo *siRNA delivery*

Various lipid-based delivery systems have been developed for *in vivo* applications of siRNA for diseases of the liver, infectious diseases, or cancer. Stable nucleic acid lipid particle (SNALP) formulations composed of a cationic lipid such DLinDMA and a PEG-lipid derivative have been used for the siRNA-mediated targeting of the Ebola-virus-specific gene in guinea pigs (i.p.; $1\,mg\,kg^{-1}$) or ApoB (i.v.; 1 or $2.5\,mg\,kg^{-1}$) in livers of cynomologus monkeys.[447,448] Systemic administration of SNALP has been demonstrated for siRNA-mediated cancer therapeutics in an intrahepatic tumor model in mice ($2\,mg\,kg^{-1} \times 6$).[449] Vitamin A-coupled liposomes were used in the delivery of siRNA and the resolution of liver fibrosis because of the specific uptake via vitamin A ($0.75\,mg\,kg^{-1} \times 12$).[450] Hashida and colleagues reported that galactosylated cationic liposomes could induce a silencing effect in the liver via targeting parenchymal cells mediated by galactose ($0.18\,nmol\,g^{-1}$).[451] Huang and colleagues developed ligand-targeted liposome–polycation–DNA (LPD) nanoparticles for siRNA delivery.[452] LPD modified with anisamide targeting sigma-receptor-expressing tumor cells showed siRNA-mediated therapeutic efficacy on tumor growth after i.v. injection into tumor-bearing mice ($0.6\,mg\,kg^{-1} \times 3$). Yagi *et al.* developed Wrapsome, which contains siRNA-binding cationic liposomes, as a core completely covered with a PEGylated neutral lipid bilayer.[453] After systemic administration, Wrapsome induced gene silencing in tumor cells of a xenograft mice model, resulting in the inhibition of tumor growth (50 μg × 7). Santel *et al.* designed a vasculature endothelium-targeted liposomal delivery system for siRNA, AtuPLEX, which exhibited knockdown of endothelium markers such as CD31 in a xenograft tumor ($1.88\,mg\,kg^{-1} \times 9$).[454] Antibodies against β_7 integrin-modified liposomes induced siRNA-mediated silencing in leukocytes *in vivo* ($2.5\,mg\,kg^{-1} \times 4$).[455] Natural lipid analogs of cardiolipin have been successful in systemically delivering siRNA to cancer xenografts.[456] Incorporation of siRNA into a neutral liposome instead of a cationic liposome has been investigated based on DOPC.[457] Commercially available cationic liposome reagents have been also used for siRNA delivery via local administration. The vaginal insertion of the Oligofectamine (Invitrogen)/siRNA complex targeting herpes simplex virus (HSV)-2 led to uptake by the epithelial and lamina propria cells in the vagina in mice and protected the mice from lethal infection for periods of up to 9 days (500 pmol).[458] Pretreatment with siRNA (70 μg) using TransIT TKO (Mirus) via intranasal treatment

Table 4 Examples of siRNA delivery for treatment of diseases

Formulation/delivery system	*Target site*	*Target gene*	*Route*	*Dose*	*Reference*
Conjugation or peptide complex					
Cholesterol–siRNA	Liver	ApoB	i.v.	50 mg kg^{-1}	443
Aptamer–siRNA	Tumor/s.c.	Swap	i.p.	1 nmol × 10	445
RVG-R9/siRNA	Viral encephalitis/brain	FvE^{J}	i.v.	50 μg × 3	199
Antibody-protamine/siRNA	Tumor/s.c.	c-Myc, MDM2, VEGF	i.v.	80 μg × 3	444
Antibody-protamine/siRNA	Tumor/lung metastasis	–	i.v.	6 nmol	455
Vitamin E-siRNA	Liver	ApoB	i.v.	2 mg ml^{-1}	446
Cholesterol-R9	Tumor/s.c.	VEGF	i.t.	3.5 μg×6	180
Dynamic PolyConjugates	Liver	ApoB	i.v.	50 μg	460
Liposomes/lipoplexes					
SNALP	Liver	ApoB	i.v.	1.2.5 mg kg^{-1}	448
Galactosylated liposome	Liver	Ubc13	i.v.	0.18 nmol g^{-1}	451
Vitamin A-liposome	Cirrhosis liver	gp46	i.v.	0.75 mg kg^{-1} × 12	450
SNALP	Tumor/intrahepatic	PLK1	i.v.	2 mg kg^{-1} × 6	449
Anisamide-LPD	Tumor/s.c.	EGFR	i.v.	0.6 mg kg^{-1} × 3	452
Wrapsome	Tumor/s.c.	KLF5	i.v.	50 μg×7	453
PEGylated LIC liposome	Tumor/s.c.	B043	i.v.	10 mg kg^{-1} × 10	461
Cardiolipin liposome	Tumor/s.c.	c-raf	i.v.	7.5 mg kg^{-1} × 10	456
AtuPLEX	Tumor endothelium/s.c.	CD31	i.v.	7.88 mg kg^{-1} × 9	454
Neutral liposome (DOPC)	Tumor/peritoneal metastasis	EphaA2	i.v.	150 μg kg^{-1} × 8	457
Immunoliposme	Leukocyte	Cyd1	i.v.	2.5 mg kg^{-1} × 4	455
SNALP	Ebola virus	Polymerase L	i.p.	1 mg kg^{-1}	447
Oligofectamine	HSV-2/vagina	UL27/29	local	500 pmol	458
TransIT TKO	RSV, PIV/lung	P protein	i.n.	70 μg	459
Polymer/polyplexes					
RGD-PEG-PEI	Tumor/s.c.	VEGFR2	i.v.	40 μg×3	175
PEI	Tumor/s.c.	Her2	i.p.	0.6 nmol	462
His-Lys polymer	Tumor/s.c.	Raf-1	i.v.	50 μg×7	463
Tf-OEI-HD	Tumor/s.c.	Ran	i.v.	2.5 mg kg^{-1} × 3	464
iNOPs	Liver	ApoB	i.v.	5 mg kg^{-1}	465
Cyclodextrin-containing polycation	Tumor/s.c.	EWS-FLI1	i.v.	2.5 mg kg^{-1} × 8	172
Others					
Atelocollagen	Tumor/s.c.	VEGF	i.t.	10 μM×4	466
Atelocollagen	Tumor/metastasis	EZH2/p1 10-α	i.v.	50 μg×3	146
Chitosan nanoparticle	Lung	EGFP	i.n.	30 μg×5	467
Chitosan nanoparticle	Tumor/s.c.	RhoA	i.v.	1.5 mg kg^{-1} × 10	468
siRNA-MRI probe	Tumor/s.c.	Survivin	i.v.	440 nmol kg^{-1} × 4	469

protected from respiratory syncytial virus (RSV) and respiratory syncytial virus (PIV) pulmonary infection.[459] Other lipid-based delivery systems are listed in Table 4.

4.425.5.2.3. *Polymer-mediated* in vivo *siRNA delivery*

Cationic polymers have also been investigated for use as siRNA delivery vehicles as well as lipid-based carriers. Of the many cationic polymers used for gene delivery, PEI has also been widely studied for siRNA delivery. Schiffelers *et al.* complexed siRNA with PEGylated PEI, of which the RGD motif was attached to the distal PEG end, known as ICS-283, and is currently undergoing preclinical study.[175] Systemically delivered siRNA for the VEGF receptor 2 (VEGFR2) mediated by RGD-PEG-PEI inhibited protein expression within the tumor, and suppressed both angiogenesis and tumor growth due to RGD recognition of integrin-overexpressed tumor cells and tumor endothelial cells (40 μ × 3). A histidine-lysine rich polymer was shown to systemically deliver siRNA (50 μg × 7) to MDA-MB-435 tumor xenografts and silence Raf-1, followed by the inhibition of tumor growth.[463] Wagner and coworkers demonstrated that transferrin-shielded siRNA OEI-HD polyplexes induced the siRNA-mediated silencing of Ran in an s.c. xenograft neuroblastoma after i.v. injection (2.5 mg kg^{-1} × 3).[464] Hu-Lieskovan *et al.* developed cyclodextrin polymers as siRNA delivery agents.[172] Tumor growth in mice of metastatic Ewing's sarcoma was inhibited by the systemic administration of polycationic cyclodextrin with adamantine-PEG for stabilization and Tf for specific targeting (2.5 mg kg^{-1} × 8). Moreover, cyclodextrin-containing polycation nanoparticles showed promising safety profiles in a nonhuman primate study.[470] A listing of polymer-based siRNA delivery is shown in Table 4.

4.425.5.2.4. *Other delivery systems*

In addition to lipids and polymers, several other delivery systems have been examined. Atellocolagen is a very large protein (300 kDa) derived from pepsin-treated type I collagen from calf dermis and has been used to administer siRNA both locally and systemically in tumor models.[146,466] Medarova *et al.* developed dual-purpose probes for *in vivo* siRNA delivery and the

simultaneous imaging of its accumulation in tumors by means of a magnetic resonance imaging (MRI) probe, in which siRNA was immobilized on the surface.[469] The systemically injected siRNA-MRI probe could be monitored by MRI and the level of targeted human survivin expression was suppressed to below 15% compared to a saline-treated control (440 nmol $kg^{-1} \times 4$). As mentioned above, substantial advances have been made in the field of *in vivo* siRNA delivery. However, numerous challenges and obstacles remain to be solved. The dose-based relationship between the PK of any siRNA delivery system and its pharmacodynamics has not been well defined in most studies. Safety profiles of the delivery systems should be investigated, including off-target effects and immune stimulation. With the further remarkable advancements in siRNA delivery, the potential use of RNAi molecules as therapeutic agents holds great promise.

4.425.5.2.5. Clinical trials of siRNA therapeutics

siRNA therapeutics are currently in progress in clinical trials (Table 5). Most trials rely on forms of localized delivery such as intravitreal or intranasal administration, while trials involving the systemic administration of either siRNA or with delivery agents are now under way. Cand5 or Bevasirnabin, which targets VEGF mRNA by intravitreal injection, developed by Acuity Pharmaceticals (now re-named as Opko Health) became the first ever RNAi therapeutic indicated to treat wet age-related macular degeneration (wet-AMD) to enter into human clinical trials in October 2004. Wet-AMD is caused by the oversecretion pf VEGF, which induces angiogenesis and increases vascular permeability and inflammation, all of which are thought to contribute to the progression of the disease. Phase I and II trials investigating the safety and efficacy of the compound gave satisfactory results. As of early 2006, Cand3 is also being evaluated in a separate phase II trial for efficacy in the treatment of diabetic macular edema (DME). However, it was reported that the silencing of target VEGF by Cand5 in wet-AMD was caused by nonspecific immunostimulation of the TLR3 pathway.[471] This fact led them to terminate the Phase III study of Bevasiranib. In November 2004, immediately after the beginning of Cand5, Sirna Therapeutics (now owned by Merck) initiated a Phase I study of their candidate Sirna-027, a chemically modified siRNA targeting VEGF receptor mRNA and administered by intravitreal injection. Phase I and II dose–escalation trials suggested that Sirna-027 was efficacious. A further Phase II trial was commenced with Allergan (Sirna-027 was renamed AGN211745), but this compound failed to show efficacy. Therefore, Allergan made the decision to terminate this clinical study in May 2009. These issues suggest that further research needs to address the important challenges related to a more effective design, enhanced biological stability, and efficient targeted delivery *in vivo*. Alnylam Pharmaceuticals, a leading company in the siRNA field, has developed several siRNA candidates. ALN-RSV01, a siRNA targeting the virus nucleocapsid N gene, is in a Phase II clinical trial for treatment of respiratory virus (RSV) infections via intranasal inhalation using a nebulizer. In 2009, they conducted a Phase I trial of ALN-VSP, a liposomal formulation of siRNA, in collaboration with Tekmir for the treatment of liver cancer via systemic administration. The first ever siRNA drug candidate to be delivered systemically in humans was Quark's QPI-1002 (formerly AKIi-5) which is in Phase I clinical trials since 2007 for the treatment of either acute kidney injury or delayed graft function. Calando Pharmaceuticals' CCLAA-01 is a cyclodextrin-based polymeric nanoparticle containing siRNA against the M2 subunit of ribonucleotide reductase with Tf targetability for treating a variety of tumors. CCLAA-01 has entered phase I trials in March 2008, and is the first clinical trial using a targeted and systemic siRNA delivery system for cancer treatment. A number of important lessons can be learned from *in vivo* studies with siRNA (Table 4). The RNAi revolution has fundamentally changed our understanding of how gene expression is regulated, and has provided powerful new tools for therapeutic targeting, biological research, and drug discovery. As we learn more about the *in vivo* action of siRNA delivery systems, including their biodistribution, precise

Table 5 siRNA therapeutics currently in clinical trials

Company	*Product*	*Formulation*	*Disease*	*Target gene*	*Route*	*Status*
Opko Health (formerly Acuity Pharmaceticals)	Bevasirnanib (Cand5)	Unmodified siRNA	Wet-AMD	VEGF	Intravitreal	Phase III[a]
			DME	VEGF	Intravitreal	Phase II
Allergan (Sirna Therapeutics/Merck)	AGN211745 (Sirna-027)	Modified siRNA	wet-AMD	VEGFR	Intravitreal	Phase II[a]
Quark/Pfizer	PF-04523655 (RTP801i-14)	Modified siRNA (AtuRNAi)	wet-AMD	PTR801	Intravitreal	Phase II
			DME	PTR801	Intravitreal	Phase II
Qurak	QPI-1002 (Akli-5/15NP)	Modified siRNA (AtuRNAi)	AKI	p53	Intravenous	Phase I
			DGF	p53	Intravenous	Phase I
Alnylam Pharmaceuticals	ALN-RSV01	Modified siRNA	RSV	Nucleocapsid	Intranasal	Phase II
Alnylam Pharmaceuticals/Tekmir	ALN-VSP	Liposomal formulation	Liver cancer	KSP/VEGF	Intravenous	Phase I
Calando Pharmaceuticals	CALAA-01	Cyclodextrin-containing polymer formulation	Solid tumor	M2 subunit	Intravenous	Phase I

Wet-AMD, wet age-related macular degeneration; DME, diabetic macular edema; AKI, acute kidney injury, DGF, delayed graft function; RSV, respiratory virus; TLR3, Toll-like receptor3.

[a]Clinical studies have been called off because medicinal effect is not due to specific gene silencing, but nonspecific immune stimulation via TLR3.

mechanisms, and toxicogenomics, it will be possible to refine delivery strategies for improved efficacy and safety, which will open the way for new types of therapeutics.

Acknowledgments

This work was supported by Grants-in-Aid for Scientific Research (S) from the Ministry of Education, Culture, Sports, Science and Technology of Japan and by grants from the Special Education and Research Expenses of the Ministry of Education, Culture, Sports, Science and Technology of Japan. We would like to thank Dr. Milton Feather for his helpful advice in editing the manuscript.

References

1. Allen, T. M.; Cullis, P. R. *Science* **2004**, *303*(5665), 1818–1822.
2. Niidome, T.; Huang, L. *Gene Ther.* **2002**, *9*, 1647–1652.
3. Kogure, K.; Akita, H.; Yamada, Y.; Harashima, H. *Adv. Drug Deliv. Rev.* **2008**, *60* (4–5), 559–571.
4. Khalil, I. A.; Kogure, K.; Akita, H.; Harashima, H. *Pharmacol. Rev.* **2006**, *58*, 32–45.
5. Kamiya, H.; Akita, H.; Harashima, H. *Drug Discov. Today* **2003**, *21*, 990–996.
6. Mountain, A. *Trends Biotechnol.* **2000**, *18*, 119–128.
7. Brignole, C.; Pagnan, G.; Marimpietri, D.; *et al. Cancer Lett.* **2003**, *197*, 231–235.
8. Matsuno, A.; Nagashima, T. *Med. Electron Microsc.* **2004**, *37*, 158–161.
9. Park, W. S.; Miyano-Kurosaki, N.; Abe, T.; Takai, K.; Yamamoto, N.; Takaku, H. *Biochem. Biophys. Res. Commun.* **2000**, *270*, 953–960.
10. Pastorino, F.; Brignole, C.; Marimpietri, D.; *et al. Ann. N. Y. Acad. Sci.* **2004**, *1028*, 90–103.
11. Robaczewska, M.; Guerret, S.; Remy, J. S.; *et al. Gene Ther.* **2001**, *8*, 874–881.
12. Stuart, D. D.; Kao, G. Y.; Allen, T. M. *Cancer Gene Ther.* **2000**, *7*, 466–475.
13. Wang, M.; Tsou, T. H.; Chen, L. S.; *et al. Hum. Gene Ther.* **2004**, *15*, 1077–1090.
14. Yamanaka, K.; Gleave, M. E.; Hara, I.; Muramaki, M.; Miyake, H. *Mol. Cancer Ther.* **2005**, *4*, 187–195.
15. Yuan, J.; Cheung, P. K.; Zhang, H.; *et al. Lab Invest.* **2004**, *84*, 703–714.
16. Robbins, P. D.; Ghivizzani, S. C. *Pharmacol. Ther.* **1998**, *80*, 35–47.
17. Mahato, R. I.; Takakura, Y.; Hashida, M. *Crit. Rev. Ther. Drug Carrier Syst.* **1997**, *14*, 133–172.
18. Nishikawa, M.; Huang, L. *Hum. Gene Ther.* **2001**, *12*(8), 861–870.
19. Nishiyama, N.; Kataoka, K. *Pharmacol. Ther.* **2006**, *112*, 630–648.
20. Zuber, G.; Dauty, E.; Nothisen, M.; Belguise, P.; Behr, J. P. *Adv. Drug Deliv. Rev.* **2001**, *52*, 245–253.
21. Beutler, E.; Liebman, H.; Gelbart, T.; Stefanski, E. *Acta Haematol.* **2000**, *104*, 103–105.
22. Blau, H. M.; Springer, M. L. *N. Engl. J. Med.* **1995**, *333*, 1204–1207.
23. Dai, Y.; Roman, M.; Naviaux, R. K.; Verma, I. M. *Proc. Natl. Acad. Sci. USA* **1992**, *89*, 10892–10895.
24. Grossman, M.; Raper, S. E.; Kozarsky, K.; *et al. Nat. Genet.* **1994**, *6*, 335–341.
25. Lynn, D. J.; Woda, R. P.; Mendell, J. R. *Clin. Chest Med.* **1994**, *15*, 661–674.
26. Santilli, G.; Thornhill, S. I.; Kinnon, C.; Thrasher, A. J. *Expert Opin. Biol. Ther.* **2008**, *8*, 397–407.
27. Baekelandt, V.; De Strooper, B.; Nuttin, B.; Debyser, Z. *Curr. Opin. Mol. Ther.* **2000**, *2*, 540–554.
28. Crystal, R. G. *Science* **1995**, *270*, 404–410.
29. Hedman, M.; Yla-Herttuala, S. *Drugs Today (Barc)* **2000**, *36*, 609–617.
30. Hsieh, S. S.; Malerczyk, C.; Aigner, A.; Czubayko, F. *Int. J. Cancer* **2000**, *86*, 644–651.
31. Myers, K. J.; Dean, N. M. *Trends Pharmacol. Sci.* **2000**, *21*, 19–23.
32. Navarro, J.; Oudrhiri, N.; Fabrega, S.; Lehn, P. *Adv. Drug Deliv. Rev.* **1998**, *30*, 5–11.
33. Swaans, R. J.; Rondot, P.; Renier, W. O.; Van Den Heuvel, L. P.; Steenbergen-Spanjers, G. C.; Wevers, R. A. *Ann. Hum. Genet.* **2000**, *64*, 25–31.
34. Tomita, N.; Morishita, R.; Kaneda, Y.; Higaki, J.; Ogihara, T. *Drug News Perspect.* **2000**, *13*, 206–212.
35. Rubinstein, A. *Ann. N. Y. Acad. Sci.* **2000**, *918*, 27–35.
36. Qian, C.; Drozdzik, M.; Caselmann, W. H.; Prieto, J. *J. Hepatol.* **2000**, *32*, 344–351.
37. Bost, F.; McKay, R.; Dean, N.; Mercola, D. *J. Biol. Chem.* **1997**, *272*, 33422–33429.
38. Funato, T.; Ishii, T.; Kambe, M.; Scanlon, K. J.; Sasaki, T. *Cancer Gene Ther.* **2000**, *7*, 495–500.
39. Andersen, M. S.; Sorensen, C. B.; Bolund, L.; Jensen, T. G. *J. Mol. Med.* **2002**, *80*, 770–781.
40. Bertoni, C. *Acta Myol.* **2005**, *24*, 194–201.
41. de Semir, D.; Aran, J. M. *Curr. Gene Ther.* **2006**, *6*, 481–504.
42. Gruenert, D. C.; Bruscia, E.; Novelli, G.; *et al. J. Clin. Invest.* **2003**, *112*, 637–641.
43. Igoucheva, O.; Alexeev, V.; Yoon, K. *Curr. Mol. Med.* **2004**, *4*, 445–463.
44. Parekh-Olmedo, H.; Kmiec, E. B. *Gene Ther.* **2007**, *14*, 1675–1680.
45. Richardson, P. D.; Augustin, L. B.; Kren, B. T.; Steer, C. J. *Stem Cells* **2002**, *20*, 105–118.
46. Sangiuolo, F.; Novelli, G. *Cytogenet. Genome Res.* **2004**, *105*, 435–441.
47. Seidman, M. M.; Glazer, P. M. *J. Clin. Invest.* **2003**, *112*, 487–494.
48. Tsuchiya, H.; Harashima, H.; Kamiya, H. *Biochem. Biophys. Res. Commun.* **2005**, *336*, 1194–1200.
49. Tsuchiya, H.; Harashima, H.; Kamiya, H. *J. Gene Med.* **2005**, *7*, 486–493.
50. Tsuchiya, H.; Uchiyama, M.; Hara, K.; *et al. Biochemistry* **2008**, *47*, 8754–8759.
51. Hannon, G. J.; Rossi, J. J. *Nature* **2004**, *431*, 371–378.
52. Venkatesan, A.; Das, S.; Dasgupta, A. *Nucleic Acids Res.* **1999**, *27*, 562–572.
53. Matzke, M. A.; Birchler, J. A. *Nat. Rev. Genet.* **2005**, *6*, 24–35.
54. Meister, G.; Tuschl, T. *Nature* **2004**, *431*, 343–349.
55. Wassenegger, M. *Cell* **2005**, *122*, 13–16.
56. Lasic, D. D. *Trends Biotechnol.* **1998**, *16*, 307–321.
57. Lasic, D. D.; Papahadjopoulos, D. *Curr. Opin. Solid State Mater. Sci.* **1996**, *1*, 392–400.
58. Lasic, D. D.; Templeton, N. S. *Adv. Drug Deliv. Rev.* **1996**, *20*, 221–266.
59. Legendre, J. Y.; Szoka, F. C., Jr. *Proc. Natl. Acad. Sci. USA* **1993**, *90*(3), 893–897.
60. Felgner, P. L.; Gadek, R. R.; Holm, M.; *et al. Proc. Natl. Acad. Sci. USA* **1987**, *82*, 4438–4442.
61. Felgner, P. L.; Gadek, T. R.; Holm, M.; *et al. Proc. Natl. Acad. Sci. USA* **1987**, *84*(21), 7413–7417.
62. Brigham, K. L.; Meyrick, B.; Christman, B.; Magnuson, M.; King, G.; Berry, L. C., Jr. *Am. J. Med. Sci.* **1989**, *298*(4), 278–281.
63. Cullis, P. R.; Hope, M. J.; Tilcock, C. P. *Chem. Phys. Lipids* **1986**, *40*(2–4), 127–144.
64. Farhood, H.; Serbina, N.; Huang, L. *Biochim. Biophys. Acta* **1995**, *1235*(2), 289–295.
65. Allen, T. M.; Chonn, A. *FEBS Lett.* **1987**, *223*(1), 42–46.
66. Hug, P.; Sleight, R. G. *Biochim. Biophys. Acta* **1991**, *1097*(1), 1–17.
67. Almofti, M. R.; Harashima, H.; Shinohara, Y.; Almofti, A.; Baba, Y.; Kiwada, H. *Arch. Biochem. Biophys.* **2003**, *410*(2), 246–253.
68. Eastman, S. J.; Siegel, C.; Tousignant, J.; Smith, A. E.; Cheng, S. H.; Scheule, R. K. *Biochim. Biophys. Acta* **1997**, *1325*(1), 41–62.
69. Wasan, E. K.; Reimer, D. L.; Bally, M. B. *J. Pharm. Sci.* **1996**, *85*(4), 427–433.
70. Radler, J. O.; Koltover, I.; Salditt, T.; Safinya, C. R. *Science* **1997**, *275*(5301), 810–814.
71. Pires, P.; Simoes, S.; Nir, S.; Gaspar, R.; Duzgunes, N.; Pedroso de Lima, M. C. *Biochim. Biophys. Acta* **1999**, *1418*, 71–84.
72. Bally, M. B.; Harvie, P.; Wong, F. M.; Kong, S.; Wasan, E. K.; Reimer, D. L. *Adv. Drug Deliv. Rev.* **1999**, *38*(3), 291–315.
73. Zabner, J.; Fasbender, A. J.; Moninger, T.; Poellinger, K. A.; Welsh, M. J. *J. Biol. Chem.* **1995**, *270*(32), 18997–19007.
74. Liu, Y.; Mounkes, L. C.; Liggitt, H. D.; *et al. Nat. Biotechnol.* **1997**, *15*(2), 167–173.
75. Mislick, K. A.; Baldeschwieler, J. D. *Proc. Natl. Acad. Sci. USA* **1996**, *93*(22), 12349–12354.
76. Woods, A.; Couchman, J. R. *Mol. Biol. Cell* **1994**, *5*(2), 183–192.
77. Perales, J. C.; Grossmann, G. A.; Molas, M.; *et al. J. Biol. Chem.* **1997**, *272*(11), 7398–7407.
78. Kawakami, S.; Hattori, Y.; Lu, Y.; Higuchi, Y.; Yamashita, F.; Hashida, M. *Pharmazie* **2004**, *59*(5), 405–408.
79. Kakudo, T.; Chaki, S.; Futaki, S.; *et al. Biochemistry* **2004**, *43*(19), 5618–5628.
80. Qian, Z. M.; Li, H.; Sun, H.; Ho, K. *Pharmacol. Rev.* **2002**, *54*(4), 561–587.
81. Cho, K. C.; Kim, S. H.; Jeong, J. H.; Park, T. G. *Macromol. Biosci.* **2005**, *5*(6), 512–519.
82. Lee, R. J.; Huang, L. *J. Biol. Chem.* **1996**, *271*(14), 8481–8487.

83. Goldstein, J. L.; Brown, M. S.; Anderson, R. G.; Russell, D. W.; Schneider, W. J. *Annu. Rev. Cell Biol.* **1985**, *1*, 1–39.
84. Lamaze, C.; Schmid, S. L. *Curr. Opin. Cell Biol.* **1995**, *7*(4), 573–580.
85. Stoorvogel, W.; Strous, G. J.; Ciechanover, A.; Schwartz, A. L. *Targeted Diagn. Ther.* **1991**, *4*, 267–304.
86. Li, W.; Nicol, F.; Szoka, F. C., Jr. *Adv. Drug Deliv. Rev.* **2004**, *56*(7), 967–985.
87. Sasaki, K.; Kogure, K.; Chaki, S.; Kihira, Y.; Ueno, M.; Harashima, H. *Int. J. Pharm.* **2005**, *296*(1–2), 142–150.
88. Torchilin, V. P.; Rammohan, R.; Weissig, V.; Levchenko, T. S. *Proc. Natl. Acad. Sci. USA* **2001**, *98*(15), 8786–8791.
89. Torchilin, V. P.; Levchenko, T. S.; Rammohan, R.; Volodina, N.; Papahadjopoulos-Sternberg, B.; D'Souza, G. G. *Proc. Natl. Acad. Sci. USA* **2003**, *100*(4), 1972–1977.
90. Cryan, S. A.; Devocelle, M.; Moran, P. G.; Hickey, A. J.; Kelly, J. G. *Mol. Pharm.* **2006**, *3*(2), 104–112.
91. Fretz, M. M.; Koning, G. A.; Mastrobattista, E.; Jiskoot, W.; Storm, G. *Biochim. Biophys. Acta* **2004**, *1665*(1–2), 48–56.
92. Marty, C.; Meylan, C.; Schott, H.; Ballmer-Hofer, K.; Schwendener, R. A. *Cell. Mol. Life Sci.* **2004**, *61*(14), 1785–1794.
93. Schwarze, S. R.; Dowdy, S. F. *Trends Pharmacol. Sci.* **2000**, *21*(2), 45–48.
94. Tseng, Y. L.; Liu, J. J.; Hong, R. L. *Mol. Pharmacol.* **2002**, *62*(4), 864–872.
95. Khalil, I. A.; Kogure, K.; Futaki, S.; Harashima, H. *J. Biol. Chem.* **2006**, *281*, 3544–3551.
96. Khalil, I. A.; Kogure, K.; Futaki, S.; Harashima, H. *Int. J. Pharm.* **2008**, *354*, 39–48.
97. Boussif, O.; Lezoualc'h, F.; Zanta, M. A.; *et al. Proc. Natl. Acad. Sci. USA* **1995**, *92*(16), 7297–7301.
98. Howard, K. A.; Alpar, H. O. *J. Drug Target.* **2002**, *10*, 143–151.
99. Choosakoonkriang, S.; Lobo, B. A.; Koe, G. S.; Koe, J. G.; Middaugh, C. R. *J. Pharm. Sci.* **2003**, *92*(8), 1710–1722.
100. Dunlap, D. D.; Maggi, A.; Soria, M. R.; Monaco, L. *Nucleic Acids Res.* **1997**, *25*, 3095–3101.
101. Klemm, A. R.; Young, D.; Lloyd, J. B. *Biochem. Pharmacol.* **1998**, *56*(1), 41–46.
102. Ruponen, M.; Yla-Herttuala, S.; Urtti, A. *Biochim. Biophys. Acta* **1999**, *1415*, 331–341.
103. Cotten, M.; Langle-Rouault, F.; Kirlappos, H.; *et al. Proc. Natl. Acad. Sci. USA* **1990**, *87*(11), 4033–4037.
104. Futaki, S.; Ohashi, W.; Suzuki, T.; *et al. Bioconjug. Chem.* **2001**, *12*(6), 1005–1011.
105. Hashida, H.; Miyamoto, M.; Cho, Y.; *et al. Br. J. Cancer* **2004**, *90*(6), 1252–1258.
106. Hyndman, L.; Lemoine, J. L.; Huang, L.; Porteous, D. J.; Boyd, A. C.; Nan, X. *J. Control. Release* **2004**, *99*(3), 435–444.
107. Rudolph, C.; Plank, C.; Lausier, J.; Schillinger, U.; Muller, R. H.; Rosenecker, J. *J. Biol. Chem.* **2003**, *278*(13), 11411–11418.
108. Khalil, I. A.; Futaki, S.; Niwa, M.; *et al. Gene Ther.* **2004**, *11*, 636–644.
109. Kopatz, I.; Remy, J. S.; Behr, J. P. *J. Gene Med.* **2004**, *6*(7), 769–776.
110. Kogure, K.; Moriguchi, R.; Sasaki, K.; Ueno, M.; Futaki, S.; Harashima, H. *J. Control. Release* **2004**, *98*(2), 317–323.
111. Tsai, J. T. *Biotechnol. Appl. Biochem.* **2002**, *36*, 13–20.
112. Yang, J.-P.; Huang, L. In *Self-Assembling Complexes for Gene Delivery*; Kabanov, A. V., Felgner, P. L., Seymour, L. W., Eds.; Wiley: Chichester, 1998.
113. Ibanez, M.; Gariglio, P.; Chavez, P.; Santiago, R.; Wong, C.; Baeza, I. *Biochem. Cell Biol.* **1996**, *74*(5), 633–643.
114. Kataoka, K.; Kwon, G. S.; Yokoyama, M.; Okano, T.; Sakurai, Y. *J. Control. Release* **1993**, *24*, 119–132.
115. Kwon, G.; Naito, M.; Yokoyama, M.; Okano, T.; Sakurai, Y.; Kataoka, K. *Langmuir* **1993**, *9*, 945–949.
116. Soma, C. E.; Dubernet, C.; Bentolila, D.; Benita, S.; Couvreur, P. *Biomaterials* **2000**, *21*, 1–7.
117. Jeon, S. I.; Lee, J. H.; Andrade, J. D.; Degennes, P. G. *J. Colloid Interface Sci.* **1991**, *142*, 149–158.
118. Kabanov, A. V.; Batrakova, E. V.; Melik-Nubarov, N. S.; *et al. J. Control. Release* **1992**, *22*, 141–158.
119. Otsuka, H.; Nagasaki, Y.; Kataoka, K. *Curr. Opin. Colloid Interface Sci.* **2001**, *6*, 3–10.
120. Matsumura, Y. *Adv. Drug Deliv. Rev.* **2008**, *60*, 899–914.
121. Yokoyama, M.; Inoue, S.; Kataoka, K.; Yui, N.; Okano, T.; Sakurai, Y. *Makromol. Chem. Macromol. Chem. Phys.* **1989**, *190*, 2041–2054.
122. Yokoyama, M.; Inoue, S.; Kataoka, K.; Yui, N.; Sakurai, Y. *Makromol. Chem. Rapid Commun.* **1987**, *8*, 431–435.
123. Yokoyama, M.; Miyauchi, M.; Yamada, N.; *et al. J. Control. Release* **1990**, *11*, 269–278.
124. Yokoyama, M.; Sugiyama, T.; Okano, T.; Sakurai, Y.; Naito, M.; Kataoka, K. *Pharm. Res.* **1993**, *10*, 895–899.
125. Kwon, G. S.; Suwa, S.; Yokoyama, M.; Okano, T.; Sakurai, Y.; Kataoka, K. *J. Control. Release* **1994**, *29*, 17–23.
126. Yokoyama, M.; Okano, T.; Sakurai, Y.; Fukushima, S.; Okamoto, K.; Kataoka, K. *J. Drug Target.* **1999**, *7*, 171–186.
127. Katayose, S.; Kataoka, K. *Bioconjug. Chem.* **1997**, *8*, 702–707.
128. Katayose, S.; Kataoka, K. *J. Pharm. Sci.* **1998**, *87*, 160–163.
129. Harada-Shiba, M.; Yamauchi, K.; Harada, A.; Takamisawa, I.; Shimokado, K.; Kataoka, K. *Gene Ther.* **2002**, *9*, 407–414.
130. Osada, K.; James Christie, R.; Kataoka, K. *J. R. Soc. Interface* **2009**, *6*, S325–S339.
131. Davis, M. E.; Chen, Z.; Shin, D. M. *Nat. Rev. Drug Discov.* **2008**, *7*, 771–782.
132. Kataoka, K.; Harada, A.; Wakebayashi, D.; Nagasaki, Y. *Macromolecules* **1999**, *32*, 6892–6894.
133. Wakebayashi, D.; Nishiyama, N.; Yamasaki, Y.; *et al. J. Control. Release* **2004**, *95*, 653–664.
134. Oba, M.; Fukushima, S.; Kanayama, N.; *et al. Bioconjug. Chem.* **2007**, *18*, 1415–1423.
135. Fukushima, S.; Miyata, K.; Nishiyama, N.; Kanayama, N.; Yamasaki, Y.; Kataoka, K. *J. Am. Chem. Soc.* **2005**, *127*, 2810–2811.
136. Kanayama, N.; Fukushima, S.; Nishiyama, N.; *et al. ChemMedChem* **2006**, *1*, 439–444.
137. Akagi, D.; Oba, M.; Koyama, H.; *et al. Gene Ther.* **2007**, *14*, 1029–1038.
138. Itaka, K.; Ohba, S.; Miyata, K.; *et al. Mol. Ther.* **2007**, *15*, 1655–1662.
139. Kakizawa, Y.; Harada, A.; Kataoka, K. *J. Am. Chem. Soc.* **1999**, *121*, 11247–11248.
140. Miyata, K.; Kakizawa, Y.; Nishiyama, N.; *et al. J. Control. Release* **2005**, *109*, 15–23.
141. Khalil, I. A.; Kogure, K.; Futaki, S.; *et al. Gene Ther.* **2007**, *14*, 682–689.
142. Yamada, Y.; Kogure, K.; Nakamura, Y.; *et al. Biol. Pharm. Bull.* **2005**, *28*, 1939–1942.
143. Nakamura, Y.; Kogure, K.; Yamada, Y.; Futaki, S.; Harashima, H. *J. Pharm. Pharmacol.* **2006**, *58*, 431–437.
144. Nakamura, Y.; Kogure, K.; Futaki, S.; Harashima, H. *J. Control. Release* **2007**, *119*, 360–367.
145. Regelin, A. E.; Fankhaenel, S.; Gürtesch, L.; Prinz, C.; von Kiedrowski, G.; Massing, U. *Biochim. Biophys. Acta* **2000**, *1464*, 151–164.
146. Takeshita, F.; Minakuchi, Y.; Nagahara, S.; *et al. Proc. Natl. Acad. Sci. USA* **2005**, *102*, 12177–12182.
147. Goula, D.; Benoist, C.; Mantero, S.; Merlo, G.; Levi, G.; Demeneix, B. A. *Gene Ther.* **1998**, *5*, 1291–1295.
148. Song, Y. K.; Liu, F.; Chu, S.; Liu, D. *Hum. Gene Ther.* **1997**, *8*, 1585–1594.
149. Goula, D.; Becker, N.; Lemkine, G. F.; *et al. Gene Ther.* **2000**, *7*, 499–504.
150. Mahato, R. I.; Anwer, K.; Tagliaferri, F.; *et al. Hum. Gene Ther.* **1998**, *9*, 2083–2099.
151. Semple, S. C.; Chonn, A.; Cullis, P. R. *Adv. Drug Deliv. Rev.* **1998**, *32*, 3–17.
152. Simberg, D.; Weisman, S.; Talmon, Y.; Faerman, A.; Shoshani, T.; Barenholz, Y. *J. Biol. Chem.* **2003**, *278*, 39858–39865.
153. Liu, F.; Qi, H.; Huang, L.; Liu, D. *Gene Ther.* **1997**, *4*, 517–523.
154. Simberg, D.; Weiss, A.; Barenholz, Y. *Hum. Gene Ther.* **2005**, *16*, 1087–1096.
155. Chollet, P.; Favort, M. C.; Hurbin, A.; Coll, J. L. *J. Gene Med.* **2002**, *4*, 84–91.
156. Haraldsson, B.; Nyström, J.; Deen, W. M. *Physiol. Rev.* **2008**, *88*, 451–487.
157. Scherphof, G. L.; Dijkstra, J.; Spanjer, H. H.; Derksen, J. T. P.; Roerdink, F. H. *Ann. N. Y. Acad. Sci.* **1985**, *446*, 368–384.
158. Pugsleya, M. K.; Tabrizchi, R. *J. Pharmacol. Toxicol. Meth.* **2000**, *44*, 333–340.
159. Wisse, E.; Jacobs, F.; Topal, B.; Frederik, P.; De Geest, B. *Gene Ther.* **2008**, *15*, 1193–1199.
160. Bilzer, M.; Roggel, F.; Gerbes, A. L. *Liver Int.* **2006**, *26*, 1175–1186.
161. Nishikawa, M.; Yamauchi, M.; Morimoto, K.; Ishida, E.; Takakura, Y.; Hashida, M. *Gene Ther.* **2000**, *7*, 548–555.
162. da Silva, P. R.; Platt, N.; deVilliers, W. J. S.; Gordon, S. *Biochim. Soc. Trans.* **1996**, *24*, 220–224.
163. Ishida, T.; Harashima, H.; Kiwada, H. *Biosci. Rep.* **2002**, *22*, 197–224.
164. Allen, T. M.; Hansen, C. *Biochim. Biophys. Acta* **1991**, *1068*, 133–141.
165. Blume, G.; Cevc, G. *Biochim. Biophys. Acta* **1990**, *1029*, 91–97.
166. Klibanov, A. L.; Maruyama, K.; Torchilin, V. P.; Huang, L. *FEBS Lett.* **1990**, *268*, 235–237.
167. Tam, P.; Monck, M.; Lee, D.; *et al. Gene Ther.* **2000**, *7*, 1867–1874.
168. Yuan, F.; Leuning, M.; Huang, S. K.; Berk, D. A.; Papahadjopoulos, D.; Jain, K. *Cancer Res.* **1994**, *54*, 3352–3356.
169. Maeda, H.; Sawa, T.; Konno, T. *J. Control. Release* **2001**, *74*, 47–61.
170. Mishar, S.; Webster, P.; Davis, M. E. *Eur. J. Cell Biol.* **2004**, *83*, 97–111.

171. Remaut, K.; Lucas, B.; Braeckmans, K.; Demeester, J.; de Smed, S. C. *J. Control. Release* **2007**, *117*, 256–266.
172. Hu-Lieskovan, S.; Heidel, J. D.; Bartlett, D. W.; Davis, M. E.; Triche, T. J. *Cancer Res.* **2005**, *65*, 8984–8992.
173. Ogris, M.; Walker, G.; Blessing, T.; Kircheis, R.; Wolschek, M.; Wagner, E. *J. Control. Release* **2003**, *91*, 173–181.
174. Ruoslahti, E. *Matrix Biol.* **2003**, *22*, 459–465.
175. Schiffelers, R. M.; Ansari, A.; Xu, J.; *et al. Nucleic Acids Res.* **2004**, *32*, e149.
176. Asai, T.; Shimizu, K.; Kondo, M.; *et al. FEBS Lett.* **2002**, *520*, 167–170.
177. Chono, S.; Li, S. D.; Conwell, C. C.; Huang, L. *J. Control. Release* **2009**, *131*, 64–69.
178. Hatakeyama, H.; Akita, H.; Ishida, E.; *et al. Int. J. Pharm.* **2007**, *342*, 194–200.
179. Hatakeyama, H.; Akita, H.; Kogure, K.; *et al. Gene Ther.* **2007**, *14*, 68–77.
180. Kim, S. H.; Mok, H. J.; Jeong, J. M.; Kim, S. W.; Park, T. G. *Bioconjug. Chem.* **2006**, *17*, 241–244.
181. Mamot, C.; Ritschard, R.; Küng, W.; Park, J. W.; Herrmann, R.; Rochlitz, C. F. *J. Drug Target.* **2006**, *14*, 215–223.
182. Moffatt, S.; Wiehle, S.; Cristiano, R. J. *Gene Ther.* **2006**, *13*, 1512–1523.
183. Hafez, I. M.; Cullis, P. R. *Adv. Drug Deliv. Rev.* **2001**, *47*, 139–148.
184. Li, W.; Huang, Z.; MacKay, J. A.; Grube, S.; Szoka, F. C. *J. Gene Med.* **2005**, *7*, 67–79.
185. Masson, C.; Garinot, M.; Mignet, N.; *et al. J. Control. Release* **2004**, *99*, 423–434.
186. Murthy, N.; Campbell, J.; Fausto, N.; Hoffman, A. S.; Stayton, P. S. *J. Control. Release* **2003**, *89*, 365–374.
187. Oishi, M.; Nagatsugi, F.; Sasaki, S.; Nagasaki, Y.; Kataoka, K. *ChemBioChem* **2005**, *6*, 718–725.
188. Shin, J.; Shum, P.; Thompson, D. H. *J. Control. Release* **2003**, *91*, 187–200.
189. Walker, C. F.; Fella, C.; Pelisek, J.; *et al. Mol. Ther.* **2005**, *11*, 418–425.
190. Zalipsky, S.; Qazen, M.; Walker, J. A.; Mullah, N.; Quinn, M. Y.; Huang, S. K. *Bioconjug. Chem.* **1999**, *10*, 703–707.
191. Ambegia, E.; Ansell, S.; Cullis, P.; Heyes, J.; Palmer, L.; MacLachlan, I. *Biochim. Biophys. Acta* **2005**, *1669*, 155–163.
192. Hatakeyama, H.; Ito, E.; Akita, H.; *et al. J. Control. Release* **2009**, *139*, 127–132.
193. Sakurai, Y.; Hatakeyama, H.; Akita, H.; *et al. Biol. Pharm. Bull.* **2009**, *32*, 928–932.
194. Sasaki, K.; Kogure, K.; Chaki, S.; *et al. Anal. Bioanal. Chem.* **2008**, *391*, 2717–2727.
195. Boeckle, S.; Fahrmeir, J.; Roedl, W.; Ogris, M.; Wagner, E. *J. Control. Release* **2006**, *112*, 240–248.
196. EL-Sayed, A.; Masuda, T.; Khalil, I.; Akita, H.; Harashima, H. *J. Control. Release* **2009**, *138*, 160–167.
197. Zhang, Y.; Boado, R. J.; Pardridge, W. M. *J. Gene Med.* **2003**, *5*, 157–163.
198. Zhang, Y.; Boado, R. J.; Pardridge, W. M. *J. Gene Med.* **2003**, *5*, 1039–1045.
199. Kumar, P.; Wu, H.; McBride, J. L.; *et al. Nature* **2007**, *448*, 39–43.
200. Conner, S. D.; Schmid, S. L. *Nature* **2003**, *422*(6927), 37–44.
201. Brodsky, F. M.; Chen, C. Y.; Knuehl, C.; Towler, M. C.; Wakeham, D. E. *Annu. Rev. Cell Dev. Biol.* **2001**, *17*, 517–568.
202. Takei, K.; Haucke, V. *Trends Cell Biol.* **2001**, *11*(9), 385–391.
203. Parton, R. G.; Joggerst, B.; Simons, K. *J. Cell Biol.* **1994**, *127*(5), 1199–1215.
204. Meier, O.; Greber, U. F. *J. Gene Med.* **2003**, *5*(6), 451–462.
205. Swanson, J. A.; Watts, C. *Trends Cell Biol.* **1995**, *5*(11), 424–428.
206. Felgner, P. L.; Tsai, Y. J.; Sukhu, L.; *et al. Ann. N. Y. Acad. Sci.* **1995**, *772*, 126–139.
207. Friend, D. S.; Papahadjopoulos, D.; Debs, R. J. *Biochim. Biophys. Acta* **1996**, *1278*(1), 41–50.
208. Labat-Moleur, F.; Steffan, A. M.; Brisson, C.; *et al. Gene Ther.* **1996**, *3*(11), 1010–1017.
209. Rejman, J.; Bragonzi, A.; Conese, M. *Mol. Ther.* **2005**, *12*(3), 468–474.
210. Zhou, X.; Huang, L. *Biochim. Biophys. Acta* **1994**, *1189*(2), 195–203.
211. Zuhorn, I. S.; Kalicharan, R.; Hoekstra, D. *J. Biol. Chem.* **2002**, *277*(20), 18021–18028.
212. Matsui, H.; Johnson, L. G.; Randell, S. H.; Boucher, R. C. *J. Biol. Chem.* **1997**, *272*(2), 1117–1126.
213. Goncalves, C.; Mennesson, E.; Fuchs, R.; Gorvel, J. P.; Midoux, P.; Pichon, C. *Mol. Ther.* **2004**, *10*(2), 373–385.
214. Elouahabi, A.; Ruysschaert, J.-M. *Mol. Ther.* **2005**, *11*(3), 336–347.
215. Wrobel, I.; Collins, D. *Biochim. Biophys. Acta* **1995**, *1235*(2), 296–304.
216. Xu, Y.; Szoka, F. C., Jr. *Biochemistry* **1996**, *35*, 5616–5623.
217. Kichler, A.; Leborgne, C.; Coeytaux, E.; Danos, O. *J. Gene Med.* **2001**, *3*(2), 135–144.
218. Simoes, S.; Slepushkin, V.; Pires, P.; Gaspar, R.; de Lima, M. P.; Duzgunes, N. *Gene Ther.* **1999**, *6*(11), 1798–1807.
219. Wagner, E.; Plank, C.; Zatloukal, K.; Cotten, M.; Birnstiel, M. L. *Proc. Natl. Acad. Sci. USA* **1992**, *89*(17), 7934–7938.
220. Mellman, I.; Fuchs, R.; Helenius, A. *Annu. Rev. Biochem.* **1986**, *55*, 663–700.
221. Seksek, O.; Biwersi, J.; Verkman, A. S. *J. Cell Biol.* **1997**, *138*, 131–142.
222. Lukacs, G. L.; Haggie, P.; Seksek, O.; Lechardeur, D.; Freedman, N.; Verkman, A. S. *J. Biol. Chem.* **2000**, *275*, 1625–1629.
223. Dauty, E.; Verkman, A. S. *J. Biol. Chem.* **2005**, *280*, 7823–7828.
224. Leopold, P. L.; Kreitzer, G.; Miyazawa, N.; *et al. Hum. Gene Ther.* **2000**, *11*, 151–165.
225. Subramanian, A.; Ranganathan, P.; Diamond, S. L. *Nat. Biotechnol.* **1999**, *17*, 873–877.
226. Sodeik, B.; Ebersold, M. W.; Helenius, A. *J. Cell Biol.* **1997**, *136*, 1007–1021.
227. Ye, G. J.; Vaughan, K. T.; Vallee, R. B.; Roizman, B. *J. Virol.* **2000**, *74*, 1355–1363.
228. Wiethoff, C. M.; Wodrich, H.; Gerace, L.; Nemerow, G. R. *J. Virol.* **2005**, *79*, 1992–2000.
229. Kelkar, S. A.; Pfister, K. K.; Crystal, R. G.; Leopold, P. L. *J. Virol.* **2004**, *78*, 10122–10132.
230. Kelkar, S.; De, B. P.; Gao, G.; Wilson, J. M.; Crystal, R. G.; Leopold, P. L. *J. Virol.* **2006**, *80*, 7781–7785.
231. Leopold, P. L.; Ferris, B.; Grinberg, I.; Worgall, S.; Hackett, N. R.; Crystal, R. G. *Hum. Gene Ther.* **1998**, *9*, 367–378.
232. Mabit, H.; Nakano, M. Y.; Prank, U.; *et al. J. Virol.* **2002**, *76*, 9962–9971.
233. Nakano, M. Y.; Greber, U. F. *J. Struct. Biol.* **2000**, *129*, 57–68.
234. Suomalainen, M.; Nakano, M. Y.; Boucke, K.; Keller, S.; Greber, U. F. *Embo J.* **2001**, *20*, 1310–1319.
235. Suomalainen, M.; Nakano, M. Y.; Keller, S.; Boucke, K.; Stidwill, R. P.; Greber, U. F. *J. Cell Biol.* **1999**, *144*, 657–672.
236. Bausinger, R.; von Gersdorff, K.; Braeckmans, K.; *et al. Angew. Chem. Int. Ed. Engl.* **2006**, *45*, 1568–1572.
237. de Bruin, K.; Ruthardt, N.; von Gersdorff, K.; *et al. Mol. Ther.* **2007**, *15*, 1297–1305.
238. Suh, J.; Wirtz, D.; Hanes, J. *Proc. Natl. Acad. Sci. USA* **2003**, *100*, 3878–3882.
239. Suh, J.; Wirtz, D.; Hanes, J. *Biotechnol. Prog.* **2004**, *20*, 598–602.
240. Pollard, H.; Remy, J. S.; Loussouarn, G.; Demolombe, S.; Behr, J. P.; Escande, D. *J. Biol. Chem.* **1998**, *273*, 7507–7511.
241. Itaka, K.; Harada, A.; Yamasaki, Y.; Nakamura, K.; Kawaguchi, H.; Kataoka, K. *J. Gene Med.* **2004**, *6*, 76–84.
242. Dean, D. A. *Exp. Cell Res.* **1997**, *230*, 293–302.
243. Wilson, G. L.; Dean, B. S.; Wang, G.; Dean, D. A. *J. Biol. Chem.* **1999**, *274*, 22025–22032.
244. Vaughan, E. E.; Dean, D. A. *Mol. Ther.* **2006**, *13*, 422–428.
245. Lechardeur, D.; Sohn, K. J.; Haardt, M.; *et al. Gene Ther.* **1999**, *6*, 482–497.
246. Cornelis, S.; Vandenbranden, M.; Ruysschaert, J. M.; Elouahabi, A. *DNA Cell Biol.* **2002**, *21*, 91–97.
247. Masuda, T.; Akita, H.; Nishio, T.; *et al. Biomaterials* **2008**, *29*, 709–723.
248. Marenzi, S.; Adams, R. L.; Zardo, G.; Lenti, L.; Reale, A.; Caiafa, P. *Mol. Biol. Rep.* **1999**, *26*, 261–267.
249. Mortimer, I.; Tam, P.; MacLachlan, I.; Graham, R. W.; Saravolac, E. G.; Joshi, P. B. *Gene Ther.* **1999**, *6*, 403–411.
250. Tseng, W. C.; Haselton, F. R.; Giorgio, T. D. *Biochim. Biophys. Acta* **1999**, *1445*, 53–64.
251. Wilke, M.; Fortunati, E.; van den Broek, M.; Hoogeveen, A. T.; Scholte, B. J. *Gene Ther.* **1996**, *3*, 1133–1142.
252. Allen, T. D.; Cronshaw, J. M.; Bagley, S.; Kiseleva, E.; Goldberg, M. W. *J. Cell Sci.* **2000**, *113*(Pt 10), 1651–1659.
253. Stewart, M. *Nat. Rev. Mol. Cell Biol.* **2007**, *8*, 195–208.
254. Ben-Efraim, I.; Gerace, L. *J. Cell Biol.* **2001**, *152*, 411–417.
255. Dworetzky, S. I.; Lanford, R. E.; Feldherr, C. M. *J. Cell Biol.* **1988**, *107*, 1279–1287.
256. Pante, N.; Kann, M. *Mol. Biol. Cell* **2002**, *13*, 425–434.
257. Hagstrom, J. E.; Ludtke, J. J.; Bassik, M. C.; Sebestyen, M. G.; Adam, S. A.; Wolff, J. A. *J. Cell Sci.* **1997**, *110*(Pt 18), 2323–2331.
258. Ludtke, J. J.; Zhang, G.; Sebestyen, M. G.; Wolff, J. A. *J. Cell Sci.* **1999**, *112*(Pt 12), 2033–2041.
259. Sebestyen, M. G.; Ludtke, J. J.; Bassik, M. C.; *et al. Nat. Biotechnol.* **1998**, *16*, 80–85.
260. Nagasaki, T.; Myohoji, T.; Tachibana, T.; Futaki, S.; Tamagaki, S. *Bioconjug. Chem.* **2003**, *14*, 282–286.
261. Tanimoto, M.; Kamiya, H.; Minakawa, N.; Matsuda, A.; Harashima, H. *Bioconjug. Chem.* **2003**, *14*, 1197–1202.

262. Nagasaki, T.; Kawazu, T.; Tachibana, T.; Tamagaki, S.; Shinkai, S. *J. Control. Release* **2005**, *103*, 199–207.
263. Breuzard, G.; Tertil, M.; Goncalves, C.; *et al*. *Nucleic Acids Res*. **2008**, *36*, e71.
264. Kuramoto, T.; Nishikawa, M.; Thanaketpaisarn, O.; Okabe, T.; Yamashita, F.; Hashida, M. *J. Gene Med*. **2006**, *8*, 53–62.
265. Mesika, A.; Grigoreva, I.; Zohar, M.; Reich, Z. *Mol. Ther*. **2001**, *3*, 653–657.
266. Mesika, A.; Kiss, V.; Brumfeld, V.; Ghosh, G.; Reich, Z. *Hum. Gene Ther*. **2005**, *16*, 200–208.
267. Miller, A. M.; Dean, D. A. *Gene Ther*. **2008**, *15*, 1107–1115.
268. Langle-Rouault, F.; Patzel, V.; Benavente, A.; *et al*. *J. Virol*. **1998**, *72*, 6181–6185.
269. Munkonge, F. M.; Amin, V.; Hyde, S. C.; *et al*. *J. Biol. Chem*. **2009**, *284*, 26978–26987.
270. Miller, A. M.; Munkonge, F. M.; Alton, E. W.; Dean, D. A. *Mol. Ther*. **2009**, *17*, 1897–1903.
271. Chan, C. K.; Jans, D. A. *Hum. Gene Ther*. **1999**, *10*, 1695–1702.
272. Chan, C. K.; Senden, T.; Jans, D. A. *Gene Ther*. **2000**, *7*, 1690–1697.
273. Ritter, W.; Plank, C.; Lausier, J.; *et al*. *J. Mol. Med*. **2003**, *81*, 708–717.
274. Akita, H.; Tanimoto, M.; Masuda, T.; *et al*. *J. Gene Med*. **2006**, *8*, 198–206.
275. Keller, M.; Harbottle, R. P.; Perouzel, E.; *et al*. *ChemBioChem* **2003**, *4*, 286–298.
276. Masuda, T.; Akita, H.; Harashima, H. *FEBS Lett*. **2005**, *579*, 2143–2148.
277. Sorgi, F. L.; Bhattacharya, S.; Huang, L. *Gene Ther*. **1997**, *4*, 961–968.
278. Duverger, E.; Carpentier, V.; Roche, A. C.; Monsigny, M. *Exp. Cell Res*. **1993**, *207*, 197–201.
279. Duverger, E.; Pellerin-Mendes, C.; Mayer, R.; Roche, A. C.; Monsigny, M. *J. Cell Sci*. **1995**, *108*(Pt 4), 1325–1332.
280. Monsigny, M.; Rondanino, C.; Duverger, E.; Fajac, I.; Roche, A. C. *Biochim. Biophys. Acta* **2004**, *1673*, 94–103.
281. Rondanino, C.; Bousser, M. T.; Monsigny, M.; Roche, A. C. *Glycobiology* **2003**, *13*, 509–519.
282. Guinez, C.; Morelle, W.; Michalski, J. C.; Lefebvre, T. *Int. J. Biochem. Cell Biol*. **2005**, *37*, 765–774.
283. Menon, R. P.; Strom, M.; Hughes, R. C. *FEBS Lett*. **2000**, *470*, 227–231.
284. Rousseau, C.; Felin, M.; Doyennette-Moyne, M. A.; Seve, A. P. *J. Cell Biochem*. **1997**, *66*, 370–385.
285. Rousseau, C.; Muriel, M. P.; Musset, M.; Botti, J.; Seve, A. P. *J. Cell Biochem*. **2000**, *78*, 638–649.
286. Fajac, I.; Grosse, S.; Briand, P.; Monsigny, M. *Gene Ther*. **2002**, *9*, 740–742.
287. Fajac, I.; Thevenot, G.; Bedouet, L.; *et al*. *J. Gene Med*. **2003**, *5*, 38–48.
288. Grosse, S.; Aron, Y.; Honore, I.; *et al*. *J. Gene Med*. **2004**, *6*, 345–356.
289. Grosse, S.; Tremeau-Bravard, A.; Aron, Y.; Briand, P.; Fajac, I. *Gene Ther*. **2002**, *9*, 1000–1007.
290. Niikura, K.; Sekiguchi, S.; Nishio, T.; *et al*. *ChemBioChem* **2008**, *9*, 2623–2627.
291. Nakamura, T.; Moriguchi, R.; Kogure, K.; *et al*. *Biol. Pharm. Bull*. **2006**, *29*, 1290–1293.
292. Trotman, L. C.; Mosberger, N.; Fornerod, M.; Stidwill, R. P.; Greber, U. F. *Nat. Cell Biol*. **2001**, *3*, 1092–1100.
293. Akita, H.; Kudo, A.; Minoura, A.; *et al*. *Biomaterials* **2009**, *30*, 2940–2949.
294. Hama, S.; Akita, H.; Ito, R.; Mizuguchi, H.; Hayakawa, T.; Harashima, H. *Mol. Ther*. **2006**, *13*, 786–794.
295. Varga, C. M.; Tedford, N. C.; Thomas, M.; Klibanov, A. M.; Griffith, L. G.; Lauffenburger, D. A. *Gene Ther*. **2005**, *12*, 1023–1032.
296. Hama, S.; Akita, H.; Iida, S.; Mizuguchi, H.; Harashima, H. *Nucleic Acids Res*. **2007**, *35*, 1533–1543.
297. Akita, H.; Ito, R.; Kamiya, H.; Kogure, K.; Harashima, H. *J. Gene Med*. **2007**, *9*, 197–207.
298. Cohen, R. N.; van der Aa, M. A.; Macaraeg, N.; Lee, A. P.; Szoka, F. C., Jr. *J. Control. Release* **2009**, *135*, 166–174.
299. Matsumoto, Y.; Itaka, K.; Yamasoba, T.; Kataoka, K. *J. Gene Med*. **2009**, *11*, 615–623.
300. Edelstein, M. L.; Abedi, M. R.; Wixon, J. *J. Gene Med*. **2007**, *9*, 833–842.
301. Rosenberg, S. A.; Aebersold, P.; Cornetta, K.; *et al*. *N. Engl. J. Med*. **1990**, *323*, 570–578.
302. Raper, S. E.; Chirmule, N.; Lee, F. S.; *et al*. *Mol. Genet. Metab*. **2003**, *80*, 148–158.
303. Hacein-Bey-Abina, S.; von Kalle, C.; Schmidt, M.; *et al*. *N. Engl. J. Med*. **2003**, *348*, 255–256.
304. Matsuno, Y.; Iwata, H.; Umeda, Y.; *et al*. *Gene Ther*. **2003**, *10*, 1559–1566.
305. Sondergaard, M.; Dagnaes-Hansen, F.; Flyvbjerg, A.; Jensen, T. G. *Am. J. Physiol. Endocrinol. Metab*. **2003**, *285*, E427–E432.
306. Miao, C. H.; Thompson, A. R.; Loeb, K.; Ye, X. *Mol. Ther*. **2001**, *3*, 947–957.
307. Manno, C. S.; Pierce, G. F.; Arruda, V. R.; *et al*. *Nat. Med*. **2006**, *12*, 342–347.
308. Merle, U.; Encke, J.; Tuma, S.; Volkmann, M.; Naldini, L.; Stremmel, W. *Scand. J. Gastroenterol*. **2006**, *41*, 974–982.
309. Salgado, S.; Garcia, J.; Vera, J.; *et al*. *Mol. Ther*. **2000**, *2*, 545–551.
310. Siller-Lopez, F.; Sandoval, A.; Salgado, S.; *et al*. *Gastroenterology* **2004**, *126*, 1122–1133; discussion 1949.
311. Ghosh, A.; Allamarvdasht, M.; Pan, C. J.; *et al*. *Gene Ther*. **2006**, *13*, 321–329.
312. Yiu, W. H.; Pan, C. J.; Allamarvdasht, M.; Kim, S. Y.; Chou, J. Y. *Gene Ther*. **2007**, *14*, 219–226.
313. Kobayashi, H.; Carbonaro, D.; Pepper, K.; *et al*. *Mol. Ther*. **2005**, *11*, 776–789.
314. Di Natale, P.; Di Domenico, C.; Gargiulo, N.; *et al*. *Biochem. J*. **2005**, *388*, 639–646.
315. Ponder, K. P.; Melniczek, J. R.; Xu, L.; *et al*. *Proc. Natl. Acad. Sci. USA* **2002**, *99*, 13102–13107.
316. Sun, B.; Zhang, H.; Franco, L. M.; *et al*. *Mol. Ther*. **2005**, *11*, 889–898.
317. Tsui, T. Y.; Lau, C. K.; Ma, J.; *et al*. *Hepatology* **2005**, *42*, 335–342.
318. Lan, H. Y.; Mu, W.; Tomita, N.; *et al*. *J. Am. Soc. Nephrol*. **2003**, *14*, 1535–1548.
319. Nakamura, H.; Isaka, Y.; Tsujie, M.; *et al*. *Gene Ther*. **2002**, *9*, 495–502.
320. Hou, C. C.; Wang, W.; Huang, X. R.; *et al*. *Am. J. Pathol*. **2005**, *166*, 761–771.
321. Yang, J.; Chen, S.; Huang, L.; Michalopoulos, G. K.; Liu, Y. *Hepatology* **2001**, *33*, 848–859.
322. Yang, J.; Dai, C.; Liu, Y. *Gene Ther*. **2001**, *8*, 1470–1479.
323. Jeppsson, A.; Pellegrini, C.; O'Brien, T.; Miller, V. M.; Tazelaar, H. D.; McGregor, C. G. *Ann. Thorac. Surg*. **1998**, *66*, 318–324.
324. Jeppsson, A.; Pellegrini, C.; O'Brien, T.; *et al*. *Transpl. Int*. **2000**, *13*(Suppl. 1), S591–S596.
325. Auricchio, A.; O'Connor, E.; Weiner, D.; *et al*. *J. Clin. Invest*. **2002**, *110*, 499–504.
326. Mora, B. N.; Boasquevisque, C. H.; Boglione, M.; *et al*. *J. Thorac. Cardiovasc. Surg*. **2000**, *119*, 913–920.
327. Epperly, M. W.; Guo, H. L.; Jefferson, M.; *et al*. *Gene Ther*. **2003**, *10*, 163–171.
328. Rosenfeld, M. A.; Siegfried, W.; Yoshimura, K.; *et al*. *Science* **1991**, *252*, 431–434.
329. Canonico, A. E.; Conary, J. T.; Meyrick, B. O.; Brigham, K. L. *Am. J. Respir Cell Mol. Biol*. **1994**, *10*, 24–29.
330. Brigham, K. L.; Lane, K. B.; Meyrick, B.; *et al*. *Hum. Gene Ther*. **2000**, *11*, 1023–1032.
331. Stecenko, A. A.; Brigham, K. L. *Gene Ther*. **2003**, *10*, 95–99.
332. Scaria, A.; St George, J. A.; Jiang, C.; Kaplan, J. M.; Wadsworth, S. C.; Gregory, R. J. *J. Virol*. **1998**, *72*, 7302–7309.
333. Crystal, R. G.; Jaffe, A.; Brody, S.; *et al*. *Hum. Gene Ther*. **1995**, *6*, 643–666.
334. Crystal, R. G.; McElvaney, N. G.; Rosenfeld, M. A.; *et al*. *Nat. Genet*. **1994**, *8*, 42–51.
335. Hay, J. G.; McElvaney, N. G.; Herena, J.; Crystal, R. G. *Hum. Gene Ther*. **1995**, *6*, 1487–1496.
336. Zabner, J.; Couture, L. A.; Gregory, R. J.; Graham, S. M.; Smith, A. E.; Welsh, M. J. *Cell* **1993**, *75*, 207–216.
337. Limberis, M.; Anson, D. S.; Fuller, M.; Parsons, D. W. *Hum. Gene Ther*. **2002**, *13*, 1961–1970.
338. Flotte, T. R. *Curr. Opin. Mol. Ther*. **1999**, *1*, 510–516.
339. Conrad, C. K.; Allen, S. S.; Afione, S. A.; *et al*. *Gene Ther*. **1996**, *3*, 658–668.
340. Aitken, M. L.; Moss, R. B.; Waltz, D. A.; *et al*. *Hum. Gene Ther*. **2001**, *12*, 1907–1916.
341. Leung, K.; Louca, E.; Munson, K.; Dutzar, B.; Anklesaria, P.; Coates, A. L. *J. Gene Med*. **2007**, *9*, 10–21.
342. Moss, R. B.; Milla, C.; Colombo, J.; *et al*. *Hum. Gene Ther*. **2007**, *18*, 726–732.
343. Wagner, J. A.; Messner, A. H.; Moran, M. L.; *et al*. *Laryngoscope* **1999**, *109*, 266–274.
344. Wagner, J. A.; Moran, M. L.; Messner, A. H.; *et al*. *Hum. Gene Ther*. **1998**, *9*, 889–909.
345. Wagner, J. A.; Nepomuceno, I. B.; Messner, A. H.; *et al*. *Hum. Gene Ther*. **2002**, *13*, 1349–1359.
346. Sirninger, J.; Muller, C.; Braag, S.; *et al*. *Hum. Gene Ther*. **2004**, *15*, 832–841.
347. Fischer, A. C.; Smith, C. I.; Cebotaru, L.; *et al*. *Mol. Ther*. **2007**, *15*, 756–763.
348. Alton, E. W.; Middleton, P. G.; Caplen, N. J.; *et al*. *Nat. Genet*. **1993**, *5*, 135–142.
349. Hyde, S. C.; Gill, D. R.; Higgins, C. F.; *et al*. *Nature* **1993**, *362*, 250–255.
350. Caplen, N. J.; Alton, E. W.; Middleton, P. G.; *et al*. *Nat. Med*. **1995**, *1*, 39–46.
351. Gill, D. R.; Southern, K. W.; Mofford, K. A.; *et al*. *Gene Ther*. **1997**, *4*, 199–209.
352. Hyde, S. C.; Southern, K. W.; Gileadi, U.; *et al*. *Gene Ther*. **2000**, *7*, 1156–1165.
353. Noone, P. G.; Hohneker, K. W.; Zhou, Z.; *et al*. *Mol. Ther*. **2000**, *1*, 105–114.
354. Porteous, D. J.; Dorin, J. R.; McLachlan, G.; *et al*. *Gene Ther*. **1997**, *4*, 210–218.
355. Zabner, J.; Ramsey, B. W.; Meeker, D. P.; *et al*. *J. Clin. Invest*. **1996**, *97*, 1504–1511.
356. Alton, E. W.; Stern, M.; Farley, R.; *et al*. *Lancet* **1999**, *353*, 947–954.

357. Ruiz, F. E.; Clancy, J. P.; Perricone, M. A.; *et al*. *Hum. Gene Ther*. **2001**, *12*, 751–761.
358. Konstan, M. W.; Davis, P. B.; Wagener, J. S.; *et al*. *Hum. Gene Ther*. **2004**, *15*, 1255–1269.
359. Mueller, C.; Torrez, D.; Braag, S.; *et al*. *J. Gene Med*. **2008**, *10*, 51–60.
360. Mueller, C.; Braag, S. A.; Martino, A. T.; Tang, Q.; Campbell-Thompson, M.; Flotte, T. R. *Gene Ther*. **2009**, *16*, 172–183.
361. Song, S.; Scott-Jorgensen, M.; Wang, J.; *et al*. *Mol. Ther*. **2002**, *6*, 329–335.
362. Jiang, H.; Pierce, G. F.; Ozelo, M. C.; *et al*. *Mol. Ther*. **2006**, *14*, 452–455.
363. Manno, C. S.; Chew, A. J.; Hutchison, S.; *et al*. *Blood* **2003**, *101*, 2963–2972.
364. Isaka, Y.; Brees, D. K.; Ikegaya, K.; *et al*. *Nat. Med*. **1996**, *2*, 418–423.
365. Zhu, T.; Zhou, L.; Mori, S.; *et al*. *Circulation* **2005**, *112*, 2650–2659.
366. Conlon, T. J.; Walter, G.; Owen, R.; *et al*. *Hum. Gene Ther*. **2006**, *17*, 71–80.
367. Esaki, M.; Takemura, G.; Kosai, K.; *et al*. *Am. J. Physiol. Heart Circ. Physiol*. **2008**, *294*, H1048–H1057.
368. Kagawa, T.; Takemura, G.; Kosai, K.; *et al*. *Nephron Physiol*. **2006**, *102*, p92–p102.
369. Ferrer, A.; Foster, H.; Wells, K. E.; Dickson, G.; Wells, D. J. *Gene Ther*. **2004**, *11*, 884–893.
370. Bertoni, C.; Jarrahian, S.; Wheeler, T. M.; *et al*. *Proc. Natl. Acad. Sci. USA* **2006**, *103*, 419–424.
371. Romero, N. B.; Braun, S.; Benveniste, O.; *et al*. *Hum. Gene Ther*. **2004**, *15*, 1065–1076.
372. Taniyama, Y.; Morishita, R.; Hiraoka, K.; *et al*. *Circulation* **2001**, *104*, 2344–2350.
373. Heilmann, C. A.; Attmann, T.; Thiem, A.; Haffner, E.; Beyersdorf, F.; Lutter, G. *Eur. J. Cardiothorac. Surg*. **2003**, *24*, 785–793.
374. Heilmann, C. A.; Attmann, T.; von Samson, P.; *et al*. *Eur. J. Cardiothorac. Surg*. **2003**, *23*, 74–80.
375. Tio, R. A.; Tkebuchava, T.; Scheuermann, T. H.; *et al*. *Hum. Gene Ther*. **1999**, *10*, 2953–2960.
376. Kastrup, J.; Jorgensen, E.; Ruck, A.; *et al*. *J. Am. Coll. Cardiol*. **2005**, *45*, 982–988.
377. Losordo, D. W.; Vale, P. R.; Symes, J. F.; *et al*. *Circulation* **1998**, *98*, 2800–2804.
378. Yockman, J. W.; Choi, D.; Whitten, M. G.; *et al*. *Gene Ther*. **2009**, *16*, 127–135.
379. Losordo, D. W.; Vale, P. R.; Hendel, R. C.; *et al*. *Circulation* **2002**, *105*, 2012–2018.
380. Azuma, J.; Taniyama, Y.; Takeya, Y.; *et al*. *Gene Ther*. **2006**, *13*, 1206–1213.
381. Ueda, H.; Sawa, Y.; Matsumoto, K.; *et al*. *Ann. Thorac. Surg*. **1999**, *67*, 1726–1731.
382. Kusano, K. F.; Pola, R.; Murayama, T.; *et al*. *Nat. Med*. **2005**, *11*, 1197–1204.
383. Yockman, J. W.; Kastenmeier, A.; Erickson, H. M.; *et al*. *J. Control. Release* **2008**, *132*, 260–266.
384. Asgari, K.; Sesterhenn, I. A.; McLeod, D. G.; *et al*. *Int. J. Cancer* **1997**, *71*, 377–382.
385. Nemunaitis, J.; Swisher, S. G.; Timmons, T.; *et al*. *J. Clin. Oncol*. **2000**, *18*, 609–622.
386. Schuler, M.; Herrmann, R.; De Greve, J. L.; *et al*. *J. Clin. Oncol*. **2001**, *19*, 1750–1758.
387. Li, X.; Marani, M.; Yu, J.; *et al*. *Cancer Res*. **2001**, *61*, 186–191.
388. Xie, X.; Zhao, X.; Liu, Y.; *et al*. *Cancer Res*. **2001**, *61*, 6795–6804.
389. Peng, W.; Verbitsky, A.; Bao, Y.; Sawicki, J. *Mol. Ther*. **2002**, *6*, 537–545.
390. Gerspach, J.; Wajant, H.; Pfizenmaier, K. *Results Probl. Cell Differ*. **2009**, *49*, 241–273.
391. Griffith, T. S.; Stokes, B.; Kucaba, T. A.; *et al*. *Curr. Gene Ther*. **2009**, *9*, 9–19.
392. Herman, J. R.; Adler, H. L.; Aguilar-Cordova, E.; *et al*. *Hum. Gene Ther*. **1999**, *10*, 1239–1249.
393. Vile, R. G.; Hart, I. R. *Cancer Res*. **1993**, *53*, 3860–3864.
394. Yoshimura, I.; Ikegami, S.; Suzuki, S.; Tadakuma, T.; Hayakawa, M. *J. Urol*. **2002**, *168*, 2659–2664.
395. Belldegrun, A.; Tso, C. L.; Zisman, A.; *et al*. *Hum. Gene Ther*. **2001**, *12*, 883–892.
396. Diez, S.; Navarro, G.; de Ilarduya, C. T. *J. Gene Med*. **2009**, *11*, 38–45.
397. Suzuki, R.; Namai, E.; Oda, Y.; *et al*. *J. Control. Release* **2010**, *142*(2), 245–250.
398. Simons, J. W.; Mikhak, B.; Chang, J. F.; *et al*. *Cancer Res*. **1999**, *59*, 5160–5168.
399. Dow, S. W.; Elmslie, R. E.; Fradkin, L. G.; *et al*. *Hum. Gene Ther*. **1999**, *10*, 2961–2972.
400. Dow, S. W.; Fradkin, L. G.; Liggitt, D. H.; Willson, A. P.; Heath, T. D.; Potter, T. A. *J. Immunol*. **1999**, *163*, 1552–1561.
401. Pin, R. H.; Reinblatt, M.; Bowers, W. J.; Federoff, H. J.; Fong, Y. *J. Gastrointest. Surg*. **2004**, *8*, 812–822; discussion 822–823.
402. Reinblatt, M.; Pin, R. H.; Bowers, W. J.; Federoff, H. J.; Fong, Y. *Ann. Surg. Oncol*. **2005**, *12*, 1025–1036.
403. Mori, A.; Arii, S.; Furutani, M.; *et al*. *Gene Ther*. **2000**, *7*, 1027–1033.
404. Folkman, J. *Exp. Cell Res*. **2006**, *312*, 594–607.
405. Mullen, J. T.; Donahue, J. M.; Chandrasekhar, S.; *et al*. *Cancer* **2004**, *101*, 869–877.
406. Raikwar, S. P.; Temm, C. J.; Raikwar, N. S.; Kao, C.; Molitoris, B. A.; Gardner, T. A. *Mol. Ther*. **2005**, *12*, 1091–1100.
407. Budker, V. G.; Subbotin, V. M.; Budker, T.; Sebestyen, M. G.; Zhang, G.; Wolff, J. A. *J. Gene Med*. **2006**, *8*, 874–888.
408. Sebestyen, M. G.; Budker, V. G.; Budker, T.; *et al*. *J. Gene Med*. **2006**, *8*, 852–873.
409. Kamimura, K.; Suda, T.; Xu, W.; Zhang, G.; Liu, D. *Mol. Ther*. **2009**, *17*, 491–499.
410. Ochiai, H.; Fujimuro, M.; Yokosawa, H.; Harashima, H.; Kamiya, H. *Gene Ther*. **2007**, *14*, 1152–1159.
411. Nguyen, A. T.; Dow, A. C.; Kupiec-Weglinski, J.; Busuttil, R. W.; Lipshutz, G. S. *J. Surg. Res*. **2008**, *148*, 60–66.
412. Wooddell, C. I.; Reppen, T.; Wolff, J. A.; Herweijer, H. *J. Gene Med*. **2008**, *10*, 551–563.
413. Fiorini, A.; Gouveia Fde, S.; Fernandez, M. A. *Biochemistry (Moscow)* **2006**, *71*, 481–488.
414. Argyros, O.; Wong, S. P.; Niceta, M.; *et al*. *Gene Ther*. **2008**, *15*, 1593–1605.
415. Mayrhofer, P.; Schleef, M.; Jechlinger, W. *Methods Mol. Biol*. **2009**, *542*, 87–104.
416. Calos, M. P. *Curr. Gene Ther*. **2006**, *6*, 633–645.
417. Fairbanks, K.; Tavill, A. *Am. J. Gastroenterol*. **2008**, *103*, 2136–2141.
418. McLean, C.; Greene, C.; McElvaney, N. *Biologics* **2009**, *3*, 63–75.
419. Mueller, C.; Flotte, T. *Clin. Rev. Allergy Immunol*. **2008**, *35*, 164–178.
420. Pringle, I. A.; Hyde, S. C.; Gill, D. R. *Expert Opin. Biol. Ther*. **2009**, *9*, 991–1003.
421. Pringle, I. A.; McLachlan, G.; Collie, D. D.; *et al*. *J. Gene Med*. **2007**, *9*, 369–380.
422. Barton, G. M.; Kagan, J. C. *Nat. Rev. Immunol*. **2009**, *9*, 535–542.
423. Barton, G. M.; Kagan, J. C.; Medzhitov, R. *Nat. Immunol*. **2006**, *7*, 49–56.
424. Kako, K.; Nishikawa, M.; Yoshida, H.; Takakura, Y. *J. Pharm. Sci*. **2008**, *97*, 3074–3083.
425. Freimark, B. D.; Blezinger, H. P.; Florack, V. J.; *et al*. *J. Immunol*. **1998**, *160*, 4580–4586.
426. Qin, L.; Ding, Y.; Pahud, D. R.; Chang, E.; Imperiale, M. J.; Bromberg, J. S. *Hum. Gene Ther*. **1997**, *8*, 2019–2029.
427. Sung, R. S.; Qin, L.; Bromberg, J. S. *Mol. Ther*. **2001**, *3*, 757–767.
428. Bromberg, J. S.; Debruyne, L. A.; Qin, L. *Adv. Immunol*. **1998**, *69*, 353–409.
429. Hyde, S. C.; Pringle, I. A.; Abdullah, S.; *et al*. *Nat. Biotechnol*. **2008**, *26*, 549–551.
430. Dai, C.; Yang, J.; Liu, Y. *J. Am. Soc. Nephrol*. **2002**, *13*, 411–422.
431. Maruyama, H.; Higuchi, N.; Nishikawa, Y.; *et al*. *Hum. Gene Ther*. **2002**, *13*, 455–468.
432. Danko, I.; Wolff, J. A. *Vaccine* **1994**, *12*, 1499–1502.
433. Wells, D. *Curr. Opin. Drug Discov. Devel*. **2006**, *9*, 163–168.
434. Morishita, R.; Nakamura, S.; Hayashi, S.; *et al*. *Hypertension* **1999**, *33*, 1379–1384.
435. Fire, A.; Xu, S.; Montgomery, M. K.; Kostas, S. A.; Driver, S. E.; Mello, C. C. *Nature* **1998**, *391*, 806–811.
436. Elbashir, S. M.; Harborth, J.; Lendeckel, W.; Yalcin, A.; Weber, K.; Tuschl, T. *Nature* **2001**, *411*, 494–498.
437. Elbashir, S. M.; Martinez, J.; Patkaniowska, A.; Lendeckel, W.; Tuschl, T. *EMBO J*. **2001**, *20*, 6877–6888.
438. McCaffrey, A. P.; Meuse, L.; Pham, T. T.; Conklin, D. S.; Hannon, G. J.; Kay, M. A. *Nature* **2002**, *418*, 38–39.
439. Lewis, D. L.; Hagstrom, J. E.; Loomis, A. G.; Wolff, J. A.; Herweijer, H. *Nat. Genet*. **2002**, *32*, 107–108.
440. Song, E.; Lee, S. K.; Wang, J.; *et al*. *Nat. Med*. **2003**, *9*, 347–351.
441. van de Water, F. M.; Boerman, O. C.; Wouterse, A. C.; Peters, J. G.; Russel, F. G.; Masereeuw, R. *Drug Metab. Dispos*. **2006**, *34*, 1393–1397.
442. Behlke, M. A. *Oligonucleotides* **2008**, *18*, 305–319.
443. Soutschek, J.; Akinc, A.; Bramlage, B.; *et al*. *Nature* **2004**, *432*, 173–178.
444. Song, E.; Zhu, P.; Lee, S. K.; *et al*. *Nat. Biothechnol*. **2005**, *23*, 709–717.
445. Dassie, J. P.; Liu, X. Y.; Thomas, G. Whitaker; *et al*. *Nat. Biothechnol*. **2009**, *27*, 839–846.
446. Nishina, K.; Unno, T.; Uno, Y.; *et al*. *Mol. Ther*. **2008**, *16*, 734–740.
447. Geisbert, T. W.; Hensley, L. E.; Kagan, E.; *et al*. *J. Infect. Dis*. **2006**, *15*, 1650–1657.
448. Zimmermann, T. S.; Lee, A. C.; Akinc, A.; *et al*. *Nature* **2006**, *441*, 111–114.
449. Judge, A. D.; Robbins, M.; Tavakoli, I.; *et al*. *J. Clin. Invest*. **2009**, *119*, 661–673.
450. Sato, Y.; Murase, K.; Kato, J.; *et al*. *Nat. Biotechnol*. **2008**, *26*, 431–442.

451. Sato, A.; Takagi, M.; Shimamoto, A.; Kawakami, S.; Hashida, M. *Biomaterials* **2007**, *28*, 1434–1442.
452. Chen, Y.; Sen, J.; Bathula, S. R.; Yang, Q.; Fittipaldi, R.; Huang, L. *Mol. Pharm.* **2009**, *6*, 696–705.
453. Yagi, N.; Manabe, I.; Tottori, T.; *et al. Cancer Res.* **2009**, *69*, 6531–6538.
454. Santel, A.; Aleku, M.; Keil, O.; *et al. Gene Ther.* **2006**, *13*, 1–11.
455. Peer, D.; Park, E. J.; Morishita, Y.; Carman, C. V.; Shimaoka, M. *Science* **2008**, *319*, 627–630.
456. Chien, P. Y.; Wang, J.; Carbonaro, D.; *et al. Cancer Gene Ther.* **2005**, *12*, 321–328.
457. Landen, C. N., Jr.; Chavez-Reyes, A.; Bucana, C.; *et al. Cancer Res.* **2005**, *65*, 6910–6918.
458. Palliser, D.; Chowdhury, D.; Wang, Q. Y.; *et al. Nature* **2006**, *439*, 89–94.
459. Bitko, V.; Musiyenko, A.; Shulyayeva, O.; Barik, S. *Nat. Med.* **2005**, *11*, 50–55.
460. Rozema, D. B.; Lewis, D. L.; Wakefield, D. H.; *et al. Proc. Natl. Acad. Sci. USA* **2007**, *104*, 12982–12987.
461. Sonoke, S.; Ueda, T.; Fujiwara, K.; *et al. Cancer Res.* **2008**, *68*, 8843–8851.
462. Urban-Klein, B.; Werth, S.; Abuharbeid, S.; Czubayko, F.; Aigner, A. *Gene Ther.* **2005**, *12*, 461–466.
463. Leng, Q.; Scaria, P.; Lu, P.; Woodle, M. C.; Mixson, A. J. *Cancer Gene Ther.* **2008**, *15*, 485–495.
464. Tietze, N.; Pelisek, J.; Philipp, A.; *et al. Oligonucleotides* **2008**, *18*, 161–174.
465. Baigude, H.; McCarroll, J.; Yang, C. S.; Swain, P. M.; Rana, T. M. *ACS Chem. Biol.* **2007**, *2*, 237–241.
466. Takei, Y.; Kadomatsu, K.; Yuzawa, Y.; Matsuo, S.; Muramatsu, T. *Cancer Res.* **2004**, *64*, 3365–3370.
467. Howard, K. A.; Rahbek, U. L.; Liu, X.; *et al. Mol. Ther.* **2006**, *14*, 476–484.
468. Pillé, J. Y.; Li, H.; Blot, E.; *et al. Hum. Gene Ther.* **2006**, *17*, 1019–1026.
469. Medarova, Z.; Pham, W.; Farrar, C.; Petkova, V.; Moore, A. *Nat. Med.* **2007**, *13*, 372–377.
470. Heidel, J. D.; Yu, Z.; Liu, J. Y.; *et al. Proc. Natl. Acad. Sci. USA* **2007**, *104*, 5715–5721.
471. Kleinman, M. E.; Yamada, K.; Takeda, A.; *et al. Nature* **2008**, *452*, 591–597.

4.426. Electrospun Fibers for Drug Delivery

W Cui, Shanghai Jiao Tong University, Shanghai, People's Republic of China
J Chang, Shanghai Jiao Tong University, Shanghai, People's Republic of China; Shanghai Institute of Ceramics, Chinese Academy of Sciences, Shanghai, People's Republic of China
P D Dalton, Shanghai Jiao Tong University, Shanghai, People's Republic of China; Queensland University of Technology, Kelvin Grove, QLD, Australia

© 2011 Elsevier Ltd. All rights reserved.

4.426.1. Introduction 446
4.426.1.1. Historical Perspective 446
4.426.1.2. Scope of Electrospun Fiber Use 447
4.426.2. Principles of Electrospinning 448
4.426.2.1. Polymers used in Electrospinning 448
4.426.2.2. Electrospinning Parameters Used to Alter Fiber Morphology 448
4.426.2.3. Permutations of the Electrospinning Process 449
4.426.2.3.1. Rotating collectors 449
4.426.2.3.2. Ring collectors 450
4.426.2.3.3. Dual collectors 450
4.426.2.3.4. Adhesive collectors 450
4.426.2.3.5. Patterned collectors 451
4.426.2.3.6. Electrospinning writing 452
4.426.2.4. Three-Dimensional Scaffolds of Electrospun Fibers 452
4.426.2.4.1. Electrospinning onto ice crystals 453
4.426.2.4.2. Hydrospinning 454
4.426.2.4.3. Simultaneous electrospinning/electrospraying 454
4.426.2.4.4. Electrospinning microfibers 454
4.426.2.4.5. Electrospinning onto scaffold carriers 454
4.426.3. Drug Delivery from Electrospun Fibers 455
4.426.3.1. Drug Inclusion within the Polymeric Solution 455
4.426.3.2. Bioavailability of Drugs at the Fiber Surface 456
4.426.3.2.1. Chemical binding 456
4.426.3.2.2. Drug adsorption 457
4.426.3.2.3. Nanoparticle formation 457
4.426.3.2.4. Multilayer assembly 457
4.426.3.2.5. Surface-segregated chemistry for functionalization 457
4.426.3.3. Release Rates and Bioactivity of Incorporated Drugs 458
4.426.3.4. Coaxial Electrospinning 458
4.426.3.5. Emulsion Electrospinning 459
4.426.3.6. Morphological Variations Affecting Drug Delivery 460
4.426.3.7. Additives to Modify Electrospinning Materials 460
4.426.4. Conclusions and Future Directions 461
References 461

Glossary

Amphiphilic Physical property of a molecule or material that is both hydrophilic and hydrophobic.
Blooming A surface condition where an element of a fiber is exposed after other components are eroded away.
Denaturation Disruption of the natural configuration of a protein.
Electrospinning The electrostatic drawing of fibers.
Glycosaminoglycan A long unbranched polysaccharide that is found extracellularly.
Integrin A major class of adhesion receptors found on the cell membrane.
Ligands A chemical functional group that can be bioactive.
Lysozyme An enzyme that digests and breaks down bacterial cell walls.
Mandrel A collection substrate such as a rod that can be rotated to collect electrospun fibers.
Myoblast A cell that can become a myocyte (also known as a muscle cell).
Nanoscale A material with a dimension below 100 nm in one of the axes.

Neurite A cellular process that projects away from the cell body of a neuron and may transmit electrical signals.
Osteoblast A cell found in bone tissue that is responsible for bone formation.
Spinneret The orifice through which a polymer melt is pushed; often a flat-tipped needle in electrospinning.
Transfection The process of introducing nucleic acids into cells.

Abbreviations

BMP	Bone morphogenetic protein
BSA	Bovine serum albumin
DNA	Deoxyribonucleic acid
FDM	Fused deposition modelling
FITC	Fluoroscein isothiocyanate
HFIP	1,1,1,3,3,3-hexafluoro-2-propanol
MMP	Matrix metalloproteinase
O/W	Oil-in-water
PCL	Poly(ε-caprolactone)
PDLLA	Poly(DL-lactic acid)
PE	Polyelectrolyte
PEG	Poly(ethylene glycol)
PEI	Poly(ethylene imine)
PEO	Poly(ethylene oxide)
PLCL	Poly(L-lactide-*co*-ε-caprolactone)
PLLA	Poly(L-lactic acid)
PVA	Poly(vinyl alcohol)
RGD	Arginine-glycine-aspartic acid
TE	Tissue engineering
UV	Ultraviolet
VEGF	Vascular endothelial growth factor
W/O	Water-in-oil

4.426.1. Introduction

New drug delivery concepts have focused on nanoscale delivery over the past decade to improve release control, levels of dosing, and local delivery for drugs to reduce undesired side effects from systemic delivery.[1,2] As reviewed here, there are numerous manufacturing routes for nanostructured fibers, with electrospinning being one dominant approach used for tissue engineering (TE).[3–5] What distinguishes electrospun TE materials from other controlled release drug systems is that the fiber is also the scaffold/matrix for cells. The traditional concept of drug delivery is also different here – immobilized bioactive molecules are also considered a component of a drug delivery system. Many immobilized bioactive molecules such as growth factors and/or integrin-binding ligands are provided to cells via contact with their nanofiber substrates and are currently exploited in TE.

The term 'nanofiber' has been used widely and should first be defined. Widespread use of the term 'nano' in recent electrospun fiber research is encouraged by focused attention on nanotechnology in general. In a great number of research papers, the term nanofiber is applied to any fiber with diameters below 1000 nm; however, this description is misleading. There have been numerous discussions on 'what is nanotechnology' with widespread agreement within the materials science community – the dominant core of nanotechnology research[6] – that the upper limit for nanotechnology is 100 nm.[7–9] The key point for defining this boundary is the quantum effects and material behavior observed below 100 nm.[10] In contrast, the majority of 'nanofibers' electrospun for TE applications are above this 100-nm boundary.

However, this should not devalue the importance of the scale range of interest for TE applications. Cellular entities do not embrace the SI unit system, and do not prefer fibers that are only below 100 or even 1000 nm! Living tissues require a multitude of conditions for survival and vary from cell type and organ of interest. In relation to the intense focus on electrospinning 'nano' materials, the manufacture of fibers in the dimensions between 1 and 15 μm is not well described in the literature. However, these fibers are the diameters required to achieve the minimum interconnectivity for cellular penetration, which is usually 2 to 3 μm and above. These interconnecting pores facilitate cellular penetration into the scaffold and mass transport for metabolism, while a high surface area is still maintained. Because of their importance in TE, this chapter will focus on electrospun fibers up to 15 μm in scale, but define them on a basis accepted by Reneker, where a fiber with a diameter below 10 μm is termed an 'ultrafine fiber,' while a 'nanofiber' is below 100 nm.[9]

4.426.1.1. Historical Perspective

Electrospinning is now widely used within the TE community where the majority of research articles are available and has attracted significant interest over the last 20 years. Such a rapid rise in development reflects the simplicity, speed, and cost-effectiveness of the process. However, it is important to have a historical perspective on the technology as it can still be regarded as in its infancy. As such, the electrospinning literature is very dynamic: current shortfalls and limitations with the technique could quickly be overcome in a few years and replaced with a new set of challenges. With future developments in surface modification, electrospinning configurations, and writing technologies, electrospinning will be at a different stage in another decade. It is therefore useful to understand the origins of electrospinning to appreciate where we stand regarding electrospun drug delivery systems and applications in TE.

Even though most of the electrospinning literature is recent, solution electrospinning was first demonstrated at the turn of the twentieth century.[11,12] While the technique was primarily

the focus of patents until the mid-twentieth century,[13–15] solution electrospinning was competing with other methods of manufacturing fibers, and issues of scale-up, and with little requirement for making ultrafine fibers in this period, it was overshadowed by mechanical extrusion techniques. During the 1990s, however, Reneker and coworkers showed that solution electrospinning could be used for nanotechnology research – it is inexpensive and simple to perform in the laboratory.[16] The next 15 years generated the vast majority of our knowledge with this technique, with now literally hundreds of different polymers electrospun into nano- and ultrafine fibers. Following a similar path, melt electrospinning was first described in a 1936 patent[14] and in a 1981 series of papers[17–19] before Reneker published a 2001 meeting abstract that involved melt electrospinning polypropylene in vacuum.[20] While there were periods in the twentieth century with no electrospinning reported in the literature, there was significant work performed on electrostatic drawing of fluids. In particular, the understanding how certain fluids break up (due to Raleigh instabilities) and modeling of stable jets were most famously studied by Taylor in the late 1960s.[21] Table 1 shows the number of full-length articles, proceedings papers, and reviews published from 1994 until 2009, and reflects this rapid growth and interest in electrospinning. The challenge for electrospinning within TE through the next decade is to live up to the hype surrounding the process and be used in a clinical setting.

4.426.1.2. Scope of Electrospun Fiber Use

Normally, electrospun fibers drug delivery systems for TE also form the scaffold/matrix upon which cells survive (Figure 1). Therefore, both a high surface area and pores large enough for cell invasion and metabolism transport are crucial properties for a successful TE scaffold. Electrospun fiber meshes have been investigated in most of the different tissues in the body, including vascular grafts, bone, nerve, and cartilage. The straightforward principles and the low cost of setting up electrospinning devices in the laboratory have allowed many laboratories to readily make ultrafine fibers. In turn, these materials have been investigated *in vitro* to determine their biocompatibility with various cells. There is an increasing interest in using electrospun fiber-based systems as substrates for three-dimensional cell culture, where experiments on fundamental cell biology, drug delivery, and cancer research are performed. A range of review articles for different TE organs and tissues are shown in Table 2.

Biological signals are an important component of TE constructs, and both surface-bound and soluble factors are incorporated within the design as drug delivery systems. Mediation of various biological signals can be performed either through signaling molecules (e.g., growth factors, nitric oxide) or compounds that induce a change in biological behavior (e.g., anti-inflammatory steroids). Drugs can be delivered via release systems from the electrospun fibers, or by making these agents available on the surface of the fiber, either free or carried within other nanostructures (Figure 1). In this perspective, electrospun fibers can play a multifunctional role in TE. Firstly, the fiber behaves as a mechanical support for the cell as a substrate, scaffold, or matrix, and even influences cell differentiation. Figure 1 also shows that the flexibility of the material can influence the cell phenotype.[35] Matrix remodeling is also a component of any TE construct, and fiber properties play a role

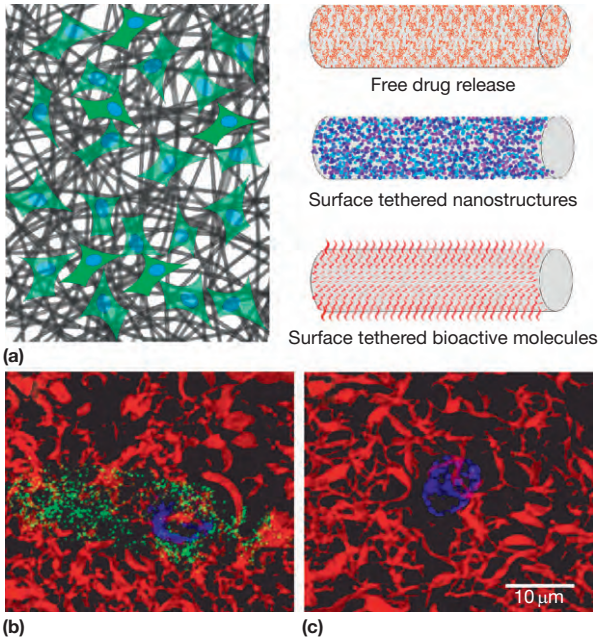

Figure 1 (a) Schematic of a fibrous scaffold for cell support in tissue engineering. Drugs can be released free, via nanostructures or provided on the surface of the fiber. (b, c) Confocal microscope images of human dermal fibroblasts within a collagen scaffold. The different mechanical moduli of the scaffolds affect the alpha-smooth muscle actin in the cell, indicating (c) a shift to a proto-myofibroblast phenotype. (b, c) Reproduced from Ayres, C. E.; Jha, B. S.; Sell, S. A.; Bowlin, G. L.; Simpson, D. G. *Wiley Interdiscip. Rev. Nanomed. Nanobiotechnol.* **2010**, *2*, 20–34.

Table 1 Number of various publications found on sci-finder with the words 'electrospinning' or 'electrospun'

Publication year	*Journal articles*	*Proceedings papers*	*Reviews*
1996/1997	2	0	0
1998/1999	7	5	0
2000/2001	24	5	0
2002/2003	101	10	2
2004/2005	387	38	9
2006/2007	814	92	38
2008/2009	1566	99	80

Table 2 Review papers of electrospinning for various organs, tissues, and cell types

Organ/tissue/cell type	*Reference*
Cartilage	22,23
Bone	23–25
Neural	26,27
Skin	28–30
Corneal	31
Cardiovascular	30,32
Tendon	30,33
Stem cell engineering	34

in how this develops. The surface properties of the electrospun fiber can also be modified to provide cell-anchoring or differentiation signals. Finally, the release of a soluble factor from the fiber, to provide a therapeutic level of drug to cells, is the final challenge of drug delivery. One component of this challenge is to provide a therapeutic level of the drug over the period of time that is biologically relevant. This therapeutic window, well described elsewhere,[36] is a level of dosage that is neither too low nor too high in the context of a specific therapy, and is provided over the timescale of interest.

One of the more significant limitations of electrospinning for TE is that in a majority of studies, the collected material is not a scaffold, but a thin sheet (e.g., a mat) of ultrafine fibers that is not cell invasive. When looking at the collection of the electrospun fibers, this is not surprising – since the fibers are usually below 1 μm in diameter, and when they stack upon one another, the pore sizes between the fibers are also below this value. Furthermore, the electrospun fibers tend to insulate the collector after a certain collection period and therefore, uniform electrospun meshes and mats typically never become thicker than 100 μm in the *z*-direction. Low volumes and cell invasiveness are two clear challenges for electrospun fibers in the future, and research groups are already devising methods to overcome this limitation.

4.426.2. Principles of Electrospinning

Electrospinning was a term coined with the recent interest in nano- and ultrafine fiber fabrication and refers to 'electrostatic spinning,' where an electric field draws a fiber out from a polymer solution or melt. It is a very simple and inexpensive technique to use in the laboratory, and allows researchers to perform 'nanotechnology' studies, although as previously mentioned, applying the term nanofiber to electrospun materials may not be fully correct.

The description of the electrospinning technique is reviewed well elsewhere.[37,38] In particular, the review by Reneker and Yarin provides a good overview of electrostatic jet formation (**Figure 2**).[39] Electrospinning is particularly useful for drug delivery, as soluble release systems can be incorporated by simply adding the drug to the solvent that is electrospun. The drug is incorporated within the fiber during processing, and then later released, according to the structure of the fiber and the nature of the polymer(s). Electrospinning can occur from both polymer solutions and polymer melts; however, as there is little literature for polymer melts, this review will emphasize fiber drug delivery from solution electrospinning (see **Chapter 1.127, Electrospinning and Polymer Nanofibers: Process Fundamentals**).

4.426.2.1. Polymers used in Electrospinning

The number of different polymers electrospun is literally in the hundreds. While it is not necessary to discuss all of them here, extensive lists of electrospun polymers can be found in other articles.[28,40] **Table 3** provides a selected list of electrospun polymers – these are selected since they are often investigated by different groups. By no means comprehensive, this table provides a good place to start for electrospinning with a range of different polymers.

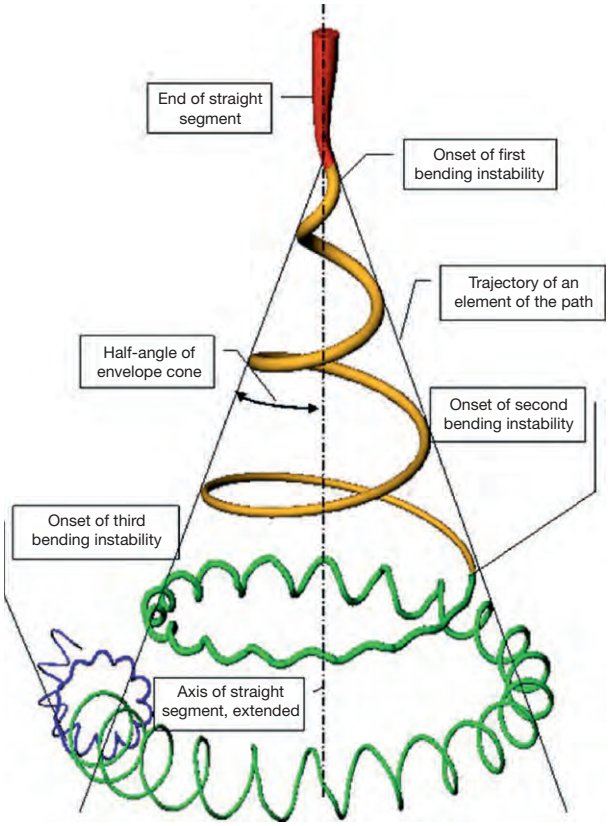

Figure 2 Trajectory of an electrostatically drawn polymer jet, demonstrating the various bending instabilities. Reproduced from Reneker, D. H.; Yarin, A. L. *Polymer* **2008**, *49*, 2387–2425, with permission from Elsevier.

Biologically derived polymers have the advantage of providing biological signals to cells; however, the nature of the actual fiber should be confirmed, since this can be altered by the electrospinning process. For example, collagen can be denatured to gelatin during electrospinning, due to both the solvent used (often 1,1,1,3,3,3-hexafluoro-2-propanol (HFIP)) and the high voltage applied.[46] Silk fibroin is another biologically derived polymer often electrospun; however, it requires some treatment to dissolve the polymer or render it insoluble after electrospinning.[55–57] This is true for many polymers electrospun from aqueous solution – a degree of posttreatment is needed after generating the fiber so that is does not redissolve upon placement in aqueous media. In this way, non-water-soluble polymers have an advantage of incorporating drugs as posttreatment, and an extra step is not necessary.

4.426.2.2. Electrospinning Parameters Used to Alter Fiber Morphology

While the polymer and its properties are an important facet of electrospinning, the conditions used to deliver the solution are also relevant. Most importantly, this includes the applied electrical potential difference between the spinneret and the collector and also the flow rate to the spinneret. In addition, the spinneret–collector distance and the spinneret diameter all

Table 3 Selected polymers for electrospinning

Polymer	*Solvent*	*Use*	*Reference*
Poly(ε-caprolactone) (PCL)	Chloroform/methanol	Heparin-release, cardiomyocyte seeding	41–43
Poly(ethylene oxide) (PEO)	Water	Water-derived electrospun fibers	44,45
Collagen	HFIP	Broad range of TE applications	46–48
PLGA	THF/DMF	Wound healing	49,50
PLL-CL	Chloroform/acetone	Vascular TE	51
Polyurethane	THF/DMF, HFIP, DMF	Vascular TE, skin TE, drug release	52–54
Silk fibroin	Various	Broad range of TE applications	55

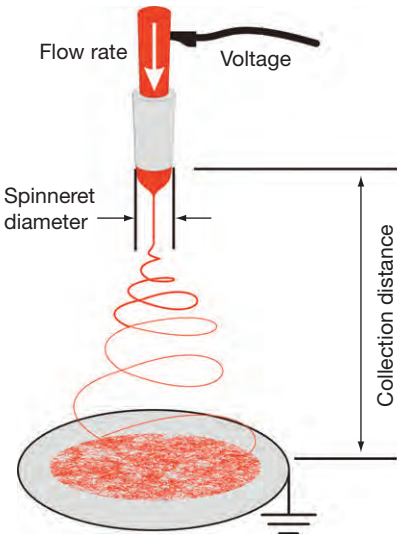

Figure 3 Various instrument parameters that influence the types of fibers collected.

influence the ultimate diameter of the fiber and consequently, the morphology. These parameters are schematically demonstrated in Figure 3 and are well reviewed elsewhere.[37,38,58–60] Many researchers showed that the fiber diameter and the structured morphology depended on processing parameters such as solution viscosity (e.g., concentration and polymer molecular weight), applied electric field strength, solution feeding rate, ionic salt addition, and solvent.[61–64] Although significant work has been done to characterize the properties of fibers as a function of process and material parameters, most of the investigations are not systematic and describe the electrospinning process without quantitative accuracy. Orthogonal experimental methods were used to investigate qualitative and quantitative correlations between fiber characteristics (diameters and morphologies) and the processing and materials parameters by Cui *et al.*[65] Their results showed that both the molecular weight of the polymer and solution concentration significantly influenced the fiber diameters and morphologies, while regression analysis revealed quantitative relations between fiber properties (diameters and beads percent) and electrospinning parameters (polymer molecular weight and solution concentration).

While investigating the various parameters for electrospinning, Son *et al.* found that electrospun poly(ethylene oxide) (PEO) fibers could be obtained, and the average diameters of PEO fibers ranged from 0.36 to 1.96 μm with increasing PEO solution concentration from 3, 4, 7, and 7 wt%. The higher the solvent dielectric constant, the thinner the PEO fiber was.[44] Heikkilä *et al.* investigated the importance of different solution and process parameters on evaluating multinozzle electrospinning of polyamide-6, and the chosen solution parameters were polymer grade, viscosity of solution, salt content and solvent grade and process parameters, voltage, distance, nozzle size and feeding pressure of solution. They found that the viscosity of the solution was the main parameter determining the fiber diameter, and also the salt content and the strength of the electric field had a strong effect on it.[66]

4.426.2.3. Permutations of the Electrospinning Process

Beyond polymeric constitution and instrument parameters, there are numerous configurations of the electrospinning apparatus that result in distinctly different types of fiber morphology. Many of these permutations involve the nature of the collector (Figure 4). While a static single collector is the most widely adopted, this has limitations when used for certain aspects of TE (see Section 4.426.2.4). While the collector is often grounded, this is not necessary and opposing voltages on the spinneret and collector have been employed to generate the potential difference necessary to electrostatically draw the fibers.

4.426.2.3.1. Rotating collectors

The collector has often been configured so that it rotates either rapidly to align the collected fibers or slowly so that a random network of fibers is formed – the latter is also combined with electrospraying or freezing to induce a porous morphology within the electrospun material (see Section 4.426.2.4). If the angular momentum is great enough, fibers will align themselves along an axis, although the efficiency of the alignment does not appear to be at the same level as when using dual collectors (Figure 4). Larger sheets of electrospun fibers can be manufactured this way, and a hollow rotating collector filled with solid carbon dioxide can grow ice crystals off the surface to generate porosity in the electrospun mesh (see Figure 9). When fibers are oriented on a rotating collector, then cells tend to align their actin filaments in the direction of the fibers.[51]

One benefit of using rotating collectors is the ability to incorporate gels and/or cells within the fibrous construct. This was nicely demonstrated by Stankus *et al.*, where two spinnerets were used for a single rotating collector.[67] Gelatin and cells were electrosprayed from one spinneret, while a polymer dissolved in dimethyl sulfoxide was used to electrospin the fiber. Another role for rotating collectors is to fabricate a tubular structure, which is of interest for vascular and applications in the nervous

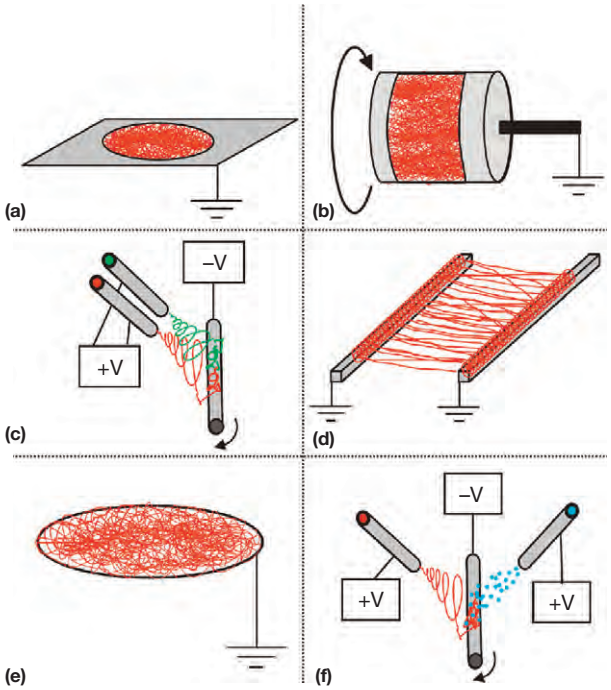

Figure 4 Various collector types for electrospinning. (a) single collector, (b) rotating collector, (c) coelectrospinning onto a rotating collector, (d) dual collectors, (e) ring collector, and (f) simultaneous electrospinning and electrospraying onto a rotating collector.

system in particular. Using different polymers, laminated tubes that consist of collagen and polyurethane have been fabricated.[68] Furthermore, nerve guides made from electrospun fibers have also been manufactured.[69]

4.426.2.3.2. Ring collectors

If there are geometrical gaps within the conductive collector, then the electrospun fibers can bridge this gap and be suspended in the air. This was demonstrated by Vacanti and colleagues,[41,70] where a ring of wire was used to suspend a thin membrane of electrospun material. Cardiomyocytes were seeded on this membrane and then cultured, to create a cell sheet that could be investigated further. The wire ring behaved as a mechanical support for the fragile electrospun mesh and was incorporated within the *in vitro* experiments. However, there are limits with this approach in that above certain air gaps, fibers do not bridge and suspend in the air.

4.426.2.3.3. Dual collectors

Similar to that described in Section 4.426.2.3.2, when the collectors are completely separated by a gap, the fibers are suspended in the air.[42,76] This approach has been used numerous times for making aligned fibers. The significant difference between this approach to align fibers and that of a rotating collector is that the oriented fiber is typically single and suspended without contact with other fibers. This is useful for applications where a dilute concentration of fibers is required on a surface. For example, a series of aligned fibers collected onto a rotating mandrel have morphological similarities to that of a grooved surface. Individual fibers made using dual collectors can be taken out and mechanically tested individually, or placed *in vitro* where single cell–single fiber interactions are observed. One problem with dual collectors is that it is not currently a continuous process, and the fibers start becoming nonuniform as the deposited fibers begin to insulate the collector. Sun *et al*. combined a dual collector with a rotating mandrel and manufactured an oriented sheet with various distances between the fibers. This allowed *in vitro* experiments to determine the diameter and how far apart suspended electrospun fibers need to be before cells can adhere to them.[77]

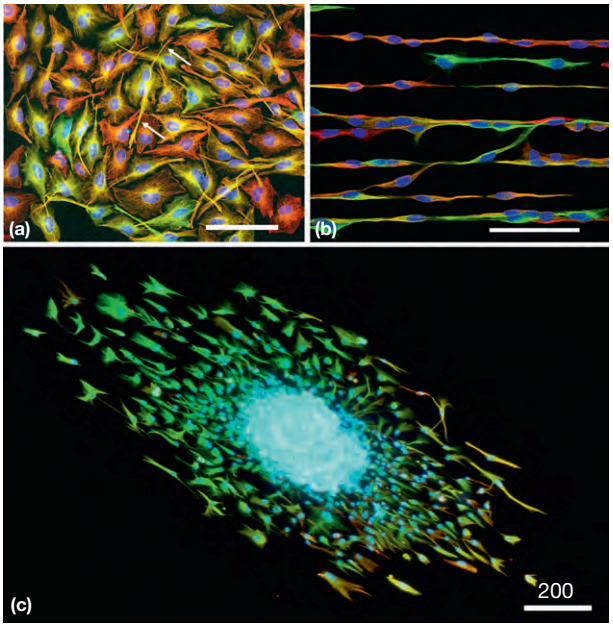

Figure 5 *In vitro* culture of astrocytes on (a) polylysine treated cell culture well and (b, c) aligned electrospun fibers deposited on chemically reactive substrates. The substrates adhere to the fibers and then continue to react with water, resulting in a nonadhesive surface for cells. The only location for cell attachment is on the electrospun fiber. (b) An image of an astrocyte cell line while a pellet of primary astrocytes is placed on the oriented electrospun material (c). Adapted from Gerardo-Nava, J.; Fuhrmann, T.; Klinkhammer, K.; *et al*. *Nanomedicine Uk* **2009**, *4*, 11–30, with permission from Future Medicine Ltd.

4.426.2.3.4. Adhesive collectors

One technical issue with the *in vitro* analysis of ultrafine fibers is that media exchanges can lift off fibers from a substrate. While glues and adhesives can be used, this causes complications with the analysis and may not be very effective. Therefore, electrospinning has been performed on collectors that bind and hold the fibers to a frame, which can then be removed. Similarly, collectors with a parallel gap have been used to create a series of oriented fibers, upon which cells can be seeded and visualized. Parameters such as fiber spacing can then be determined for a range of different cell types and diameters.

Recently, a chemically reactive and nanolayered hydrogel was used to coat glass cover slips, and adhered electrospun fibers, but also continued to react with water to form a protein-resistant surface between the fibers (Figure 5). This allows 'dilute' quantities of fibers to be deposited while providing a neighboring flat surface that is nonadherent to cells.[78,79] Fibers can either be

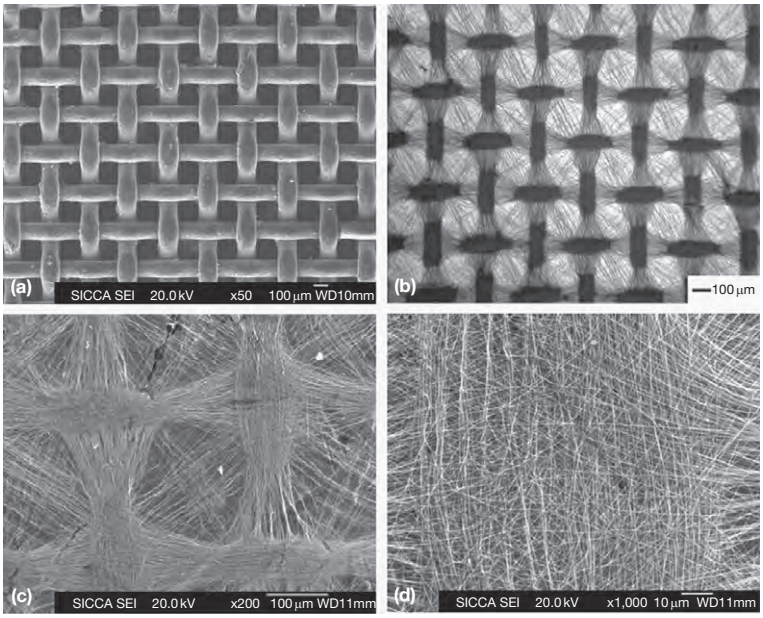

Figure 6 (a) A scanning electron microscopic (SEM) image of a patterned collector and (b) an optical image of an electrospun mesh collected on (a). (c, d) SEM images of electrospun fibers collected on (a). Reproduced from Zhang, D. M.; Chang, J. *Adv. Mater.* **2007**, *19*, 3664–3367, with permission from Copyright Wiley-VCH Verlag GmbH & Co., KGaA.

electrospun directly onto this chemically reactive surface, or collected and then transferred to this substrate. Adhesion and migration assays on RGD (arginine-glycine-aspartic acid)-modified or collagen-blended electrospun fibers have been demonstrated so far.[78] While these hydrogel collectors are not used for TE, they allow confirmation of surface modification and the binding of bioactive peptides to the surface of the electrospun fiber, including qualitative testing of the fibers for protein adsorption.

4.426.2.3.5. Patterned collectors

Ordered microstructures and patterned materials can have specific functions in biomedical applications, and therefore, ordered and structured patterns of electrospun fibers are of interest. As far back as 1966, different patterned electrospun fibers could be obtained by Simons,[80] using a fabric to deposit and collect them. With the development of electrospinning, more collector systems were used to control architectures and patterns, including electroconductive templates, magnetic fields, and dielectric materials. One interesting aspect of patterned collectors is that pore size of the resulting meshes can be altered and increased for cellular penetration.

Zhang *et al.* used electroconductive templates for the patterning of electrospun fibers, and found that the shapes of the collector could greatly affect the structures of the electrospun mats (Figure 6).[81] Neves *et al.* also fabricated patterned electrospun fibers using various shaped collectors with specific dimensions and designs, and they further evaluated the structures of fibers for biomedical applications. The blending polymers of PEO and poly(ε-caprolactone) (PCL) resulted in patterned electrospun fibrous mats, and mechanical properties of fibrous mats depended on the degree of fibers alignment (which could be strained up to 200%), and osteoblasts preferred cell adhesion within certain areas of the patterns.[82]

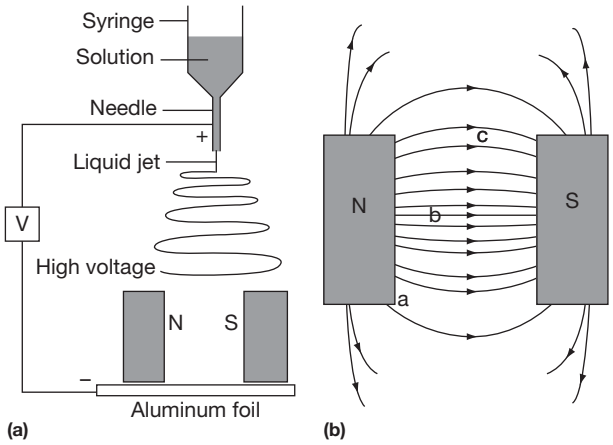

Figure 7 (a) Illustration of the apparatus for magnetic electrospinning to generate aligned fibers. (b) Calculated magnetic field strength vectors in the region between the two magnets. The arrows denote the direction of the magnetic field lines. Reproduced from Yang, D. Y.; Lu, B.; Zhao, Y.; Jiang, X. Y. *Adv. Mater.* **2007**, *19*, 3702–3705, with permission from Copyright Wiley-VCH Verlag GmbH & Co., KGaA.

Wang *et al.* also found that electrospun fabrics with tailored architectures and patterns have potential for TE applications through inducing an ordered cellular organization.[83]

Yang *et al.* used a different approach – magnetic electrospinning – to generate an electrospun pattern (Figure 7) for fabricating well-aligned arrays and multilayer grids fibers.[84] Through prepared magnetized electrospinning solutions and magnetized collectors, the magnetic field caused the magnetized electrospun fibers to align in a parallel fashion along the magnetic field lines. Yan *et al.* collected aligned electrospun ultrafine fibers using dielectric materials, and they studied the relationship between collector relative permittivity

and fibers alignment. They found that well-aligned electrospun fibers could be obtained by manipulating the electric field profile with various dielectric materials as collectors.[85]

4.426.2.3.6. Electrospinning writing

There have been numerous attempts to control the deposition of the electrospun fibers to prevent chaotic deposition.[45] While this is challenging work, some approaches are quite simple. A process called 'near-field electrospinning' was developed, which involves lower voltages (600 V) and smaller collection distances (0.5 mm).[86] This prevents the polymer jet from undergoing significant whipping instabilities, and the fiber can be 'drawn' by moving an *x*–*y* stage or spinneret (Figure 8). Interestingly, the jet can be deposited as a straight fiber above a certain speed – below this, the forces associated with a visco-elastic jet hitting the collector surface results in coiled fiber morphology. One permutation on this concept is to generate a charged drop without a Taylor cone and then mechanically pierce the drop, so that the surface is disrupted and a polymer jet is also drawn out into an electrospun fiber.[87]

Writing of the polymeric jet is also where polymer melts are interesting. Since polymer melts are nonconductive materials, whipping instabilities can occur near the collector surface, or not at all (Figure 8). In a similar manner to near-field electrospinning (but with higher voltages and larger gaps), an *x*–*y* stage can be used to 'write' with the electrospun fiber. Discrete lines of coiled electrospun fibers can be written with melt-electrospun PCL/poly(ethylene glycol-*block*-PCL) blends (Figure 8), and is a promising method for applying electrospun fibers directly onto cells or tissues.[88] Compared to patterning techniques such as fused deposition modelling (FDM) and direct writing, these electrospinning writing techniques are in their infancy.

There are also approaches to control the deposition of electrospun fibers without any movement of the collector. Deitzel *et al*. showed that a metallic ring surrounding the jet, and with a potential difference between that of the spinneret and the collector, was able to 'focus' the deposition area of the fibers.[45] Building on this, Craighead and colleagues devised an 'electrostatic lens,' with four independent electrodes, that formed a ring around the polymer jet.[89] While unable to fully control each deposited fiber, the approach is unique and will undoubtedly be expanded upon in the future.

4.426.2.4. Three-Dimensional Scaffolds of Electrospun Fibers

As previously mentioned, the lack of freely accessible volume or cell invasiveness of electrospun materials has impeded their efficacy as a TE scaffold (Table 4). The low pore size of electrospun meshes is a fundamental issue with the layering of fibers

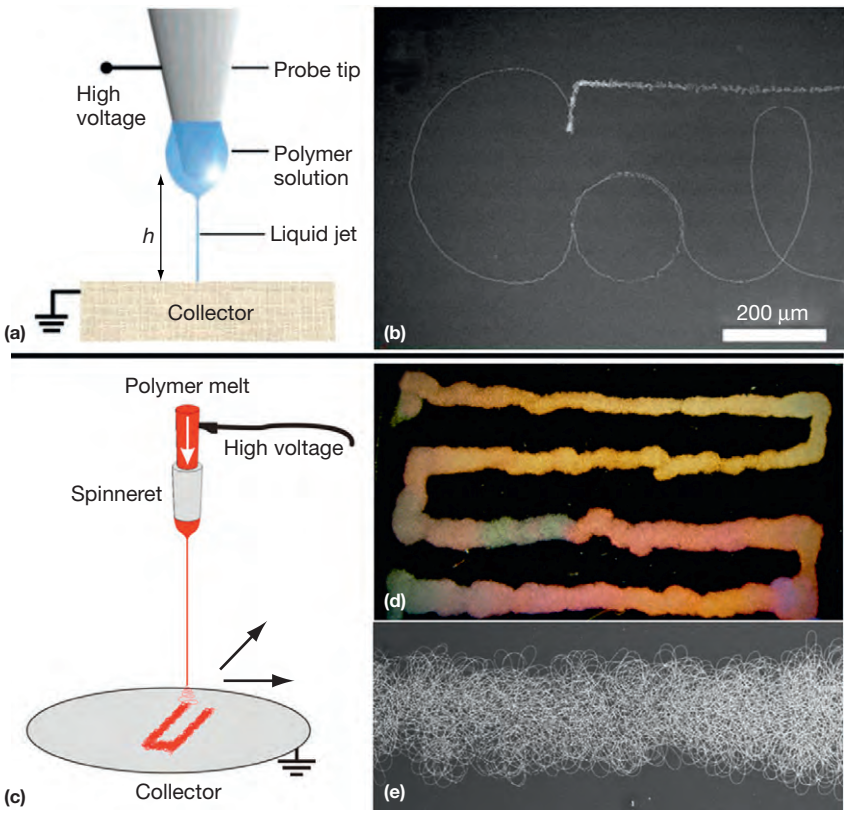

Figure 8 Electrospinning writing onto a substrate. Near-field electrospinning (a) involves close spinneret to collector distances with polymeric solutions and results in writing of the fiber. Electrospinning with a nonconductive material such as a polymer melt (c) results in instabilities just above the collector, allowing writing (d, e) with a moving *x*–*y* stage. (a, b) Reproduced from Sun, D. H.; Chang, C.; Li, S.; Lin, L. W. *Nano Lett*. **2006**, *6*, 839–842, with permission from American Chemical Society. (c, d) Reproduced from Dalton, P. D.; Joergensen, N. T.; Groll, J.; Moeller, M. *Biomed. Mater*. **2008**, *3*, 034109.

Table 4 Summary of electrospun materials combined with micron scale TE scaffolds

Electrospun material	*Carrier*	*Reference*
PLCL (50:50)	Melt-spun PLCL macrofibers (500μm)	71
PCL/collagen	Direct-deposited PCL polymer melt	72
PCL/starch	Fiber-bonded PCL/starch microfibers	73
PCL	Electrospun PCL microfibers	74
PLGA	Melt-electrospun PLGA	75

with diameters below 1 μm. Some mechanism is therefore needed to introduce porosity into and between the fibers. However, there are approaches that respond to this challenge and there are different effective approaches to achieve this, shown in Figure 9. These are electrospinning onto ice crystals, hydrospinning, coelectrospinning/electrospraying, and electrospinning microfibers.

4.426.2.4.1. Electrospinning onto ice crystals

One interesting approach is to electrospin onto ice crystals, as they grow off a surface (Figure 9). This has been done by using a hollow rotating drum filled with solid CO_2, which grows

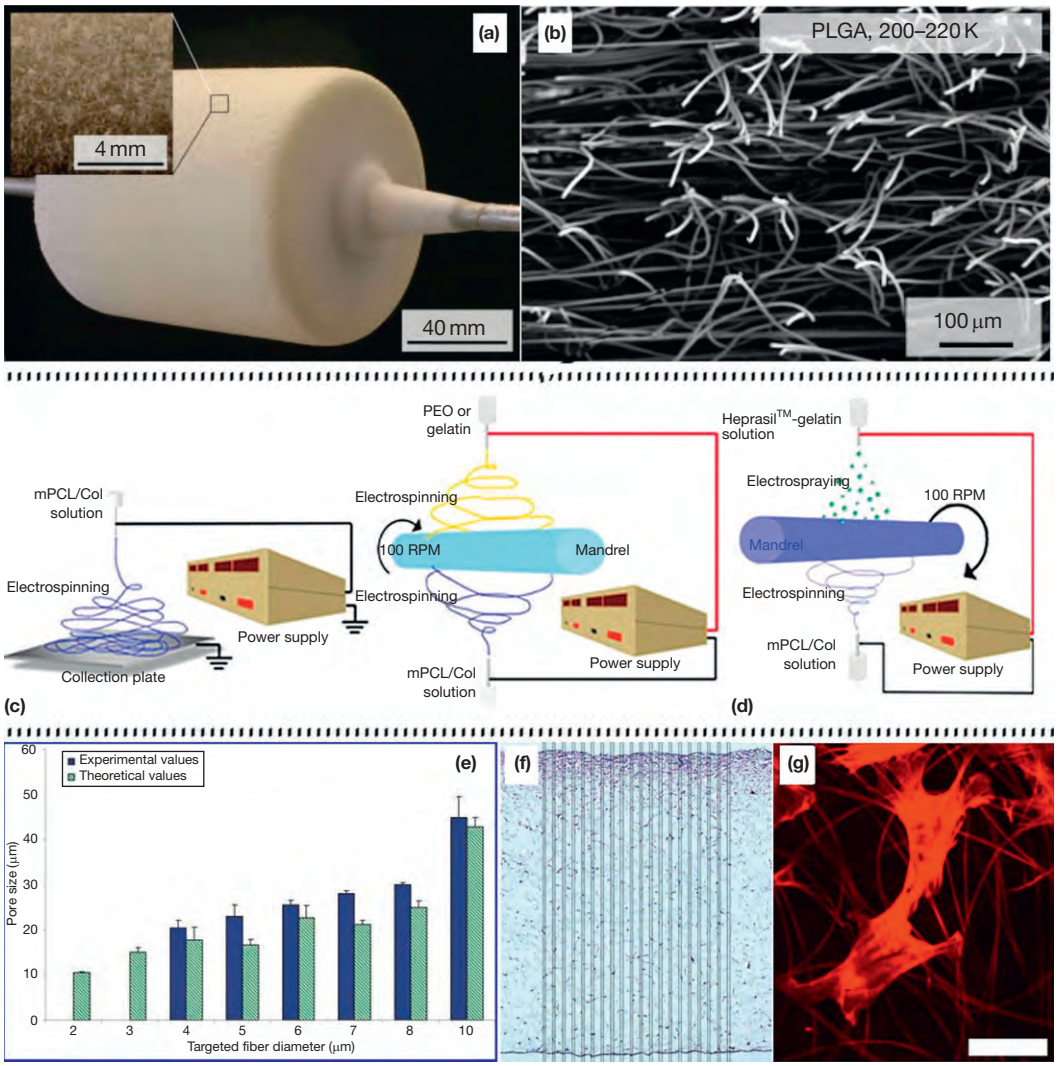

Figure 9 Various approaches to manufacture cell-invasive electrospun fibers. (a) Electrospinning onto ice crystals and the resulting fibers (b) provide a highly porous material. (c) and electrospinning/electrospraying (d) are also methods to improve porosity. The fiber diameter is also important, as shown in (e) where fibers below 2 μm do not provide enough interconnecting porosity for cell penetration (f). Melt-electrospun fibers of this diameter allow cell penetration (g). (a, b) Reproduced from Simonet, M.; Schneider, O. D.; Neuenschwander, P.; Stark, W. *J. Polym. Eng. Sci.* **2007**, *47*, 2020–2026, with permission from Wiley. (c, d) Reproduced from Ekaputra, A. K.; Prestwich, G. D.; Cool, S. M.; Hutmacher, D. W. *Biomacromolecules* **2008**, *9*, 2097–2103, with permission from American Chemical Society. (e, f) Reproduced from Pham, Q. P.; Sharma, U.; Mikos, A. G. *Biomacromolecules* **2006**, *7*, 2796–2805, with permission from American Chemical Society. (g) Reproduced from Dalton, P. D.; Joergensen, N. T.; Groll, J.; Moeller, M. *Biomed. Mater.* **2008**, *3*, 034109.

water crystals off the collector while depositing the fibers.[90] The electrospun fibers are embedded within the ice, which is sublimed away via lyophilization. The consequence is increasing the interconnective pores. Furthermore, the porous fibers can be mechanically pulled and transformed into a material with a consistency of cotton wool.[91]

4.426.2.4.2. Hydrospinning

In this method, electrospun fibers are collected upon water as a film and then transferred to a microscope slide.[92] By repeating this process, multiple layers are generated, and the water is then removed with a vacuum. The resulting scaffolds have considerable volume and are highly porous and cell invasive. Alternatively, the process can be modified to incorporate cells into the process at any stage, which results in a unique method to incorporate cells within a TE scaffold. In the study reported by Levenberg and colleagues, myoblasts were successfully cultured with an equal density throughout the electrospun scaffold.

4.426.2.4.3. Simultaneous electrospinning/electrospraying

Another approach to decrease the fiber density is to simultaneously electrospray and electrospin. In an excellent research Wagner and colleagues electrospun polyurethane while electrospraying a mixture of smooth muscle cells and gelatin.[67] The resulting construct has higher cell survival when cultured in a bioreactor compared to a static culture. In addition, Hutmacher and colleagues electrospun PCL/collagen while electrospraying a thiolated hyaluronic acid solution.[93] The resulting mixed electrospun fibers and gel was infiltrated with human fetal osteoblasts up to 200 μm into the scaffold. In both instances, a rotating collector was used and the spinnerets were positioned at 90° apart from each other. This approach is interesting, as the pore size of the scaffolds is increased and at the same time, a cellular component can be introduced into the material (via electrospraying).

4.426.2.4.4. Electrospinning microfibers

When electrospun fibers are produced with diameters of 2 or 3 μm, the pore size of the resulting scaffold is 10.5±0.1 μm and 14.9±1.0 μm, respectively, and large enough for cellular penetration.[74] This latter point is interesting, as there are only a handful of studies on cellular interactions with fibers with diameters between 2 and 10 μm. With numerous studies investigating submicron-diameter fibers and with lower limits to the diameters of mechanically drawn fibers, this is a notably underinvestigated fiber diameter range. Such micron-diameter fibers were investigated as scaffolds, with mesenchymal stem cells penetrating up to 1200 μm into the scaffold under flow conditions and 300 μm under static. Furthermore, an electrospun mesh was deposited on top of the microporous electrospun material, creating a bimodal scaffold that consisted of 600-nm ultrafine fibers deposited onto a 5-μm PCL mesh. Melt electrospinning, which can readily produce micron-diameter fibers,[94] has been used for this purpose in producing cell-invasive scaffolds in combination with solution electrospinning. Outlined by Kim *et al.*, the same source of PLGA was simultaneously solution- and melt-electrospun onto a rotating mandrel, resulting in a thick cell-invasive mesh.[75] This mesh was 'bimodal,' in that it contained a mixture of ultrafine solution-electrospun fibers with a diameter of 530±240 nm and melt-electrospun microfibers with a diameter of 28.0±2.6 μm. The bimodal scaffold was able to seed a greater number of cells than did a melt-electrospun scaffold alone.

4.426.2.4.5. Electrospinning onto scaffold carriers

Electrospun fibers have also been deposited onto scaffolds typically used for TE, with the larger pores filled with electrospun fibers. Conventional fibers can also be mixed with electrospun fibers, creating a scaffold where the ultrafine electrospun fibers are mechanically supported by the larger structures. This is achieved in one instance by melt-spinning poly(L-lactide-*co*-ε-caprolactone) (PLCL) into a cylindrical structure for vascular TE and then electrospinning onto this.

Notably, an automated scaffold assembly system has been used to construct the scaffold carrier in one study.[72] FDM has become widely used in different TE applications and in this instance, the process was interrupted between each layer to deposit an electrospun PCL/collagen fiber mesh (Figure 10).[72]

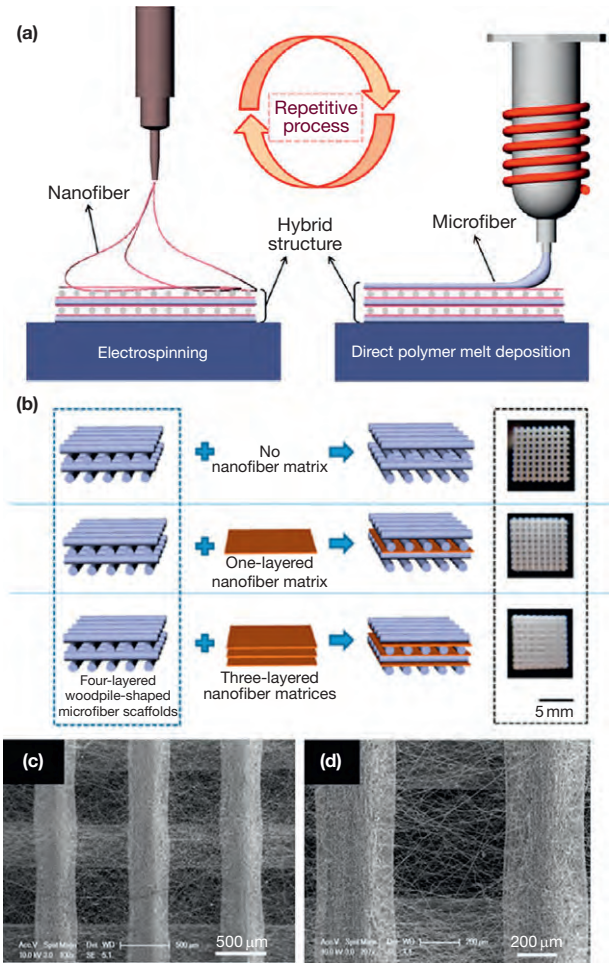

Figure 10 Combining electrospinning with a melt-printing technique to create an electrospun carrier. Reproduced from Park S. H.; Kim, T. G.; Kim, H. C.; Yang, D. Y.; Park, T. G. *Acta Biomater.* **2008**, *4*, 1198–1207, with permission from Elsevier.

The resultant construct had large pores, while the electrospun fibers were structures upon which cells could adhere to. This effectively increases the surface area available for penetrating cells to attach.

4.426.3. Drug Delivery from Electrospun Fibers

The ideal interaction between cellular and fibrous components in a TE construct should initially be controlled. This is why drug delivery should not just be considered as the release of soluble molecules from a degrading biomaterial, but also the availability of bioactive molecules on a scaffolds surface that initiate and perpetuate certain cellular functions. The latter is a complex effort, with protein adsorption potentially fouling the surface to prevent specific cellular signaling. There are excellent and pertinent reviews elsewhere on the subject of protein adsorption on flat surfaces and monolayers (see **Chapter 4.406, Protein Interactions with Biomaterials**);[95–97] however, the inclusion of electrospun fibers in this research is an important translation of fundamental surface chemistry research. Whether a drug is bound or released from a fiber, the drug must be available to the cells or tissue at a suitable concentration for an appropriate length of time for the specific outcome. Drug release from electrospun fibers is therefore a complex component of electrospinning research. However, incorporation of the nonbound drug into electrospun fibers is relatively straightforward – they are simply blended into the solution to be electrospun. As described later, there are issues with this approach such as nonideal mixing, protein denaturation, and blooming of the drug to the fiber surface. Expansion of the range of drugs that can be directly encapsulated within the fibers involves their appropriate dispersal within the electrospinning solution.

Drug release from electrospun fibers could be controlled by various fabrication conditions, for example, the polymer types, fibers diameters, blending of different content, fiber surface coating, drug dispersion, electrospinning models, and so on.[98] However, most biodegradable electrospun fibers directly entrapping drugs exhibited high burst effects with poor controlled release patterns, probably due to incompatibility of drug/polymer/solvent system and slow degradation of biodegradable polymer.[98–100] Therefore, additives to fiber materials that increase both drug solubility and compatibility in the polymer solution have influenced drug release profiles by altering the drug dispersion inside the electrospun fibers.

4.426.3.1. Drug Inclusion within the Polymeric Solution

Simply adding the drug to the electrospinning solution is a rapid method to produce an electrospin-controlled release system. This blends the drugs into the polymeric jet, and evaporation of the solvent results in drug-loaded ultrafine fibers; however, this approach is only suitable for limited drugs with suitable stability and solubility in the solvent. An example of a successful approach is the incorporation of heparin into PCL electrospun fibers.[43] Using a chloroform/methanol solvent mixture, both the PCL and heparin are dissolved and electrospun. The heparin is homogenously dispersed within the electrospun fibers. After an initial burst release, heparin diffuses from the electrospun fibers for 14 days and retains biological activity (**Figure 11**).

By adding drugs to electrospun fibers, an initial burst release is common. Incorporated drugs locate on the fiber surface because of the rapid solvent evaporation and resulting high ionic strength (due to drug phase separation to fiber surface) and polymer in solution. Therefore, fibrous mats prepared by blending drugs into the electrospinning solution will result in a burst effect during the initial stage of drug release (see **Chapter 4.417, Tethered Antibiotics**).[99,101] This could be useful for antibacterial approaches, where the initial burst release is used to eliminate intruding bacteria before they begin to proliferate.[102] For water-soluble, -insoluble, and -microsoluble drugs, the electrospinning solvent is particularly important for fabricating the fibers. For water-soluble drug systems, triethyl benzyl ammonium chloride and poly(L-lactic acid) (PLLA) are dissolved into a solvent of a 2:1 (in volume) mixture of chloroform and acetone.[101] Drugs are capsulated inside the fibers, and drug release in the presence of proteinase K follows nearly zero-order kinetics due to PLLA fiber degradation. Cui *et al*. dissolved water-soluble paracetamol into acetone solution containing PDLLA and found that electrospun fibers with larger diameter exhibited longer periods of nearly zero-order release, and higher drug encapsulation resulted in a more significant burst release.[103] For water-microsoluble drugs, Brewster *et al*. investigated poorly water-soluble drugs (itraconazole and ketanserin) loaded in a water-insoluble, nonbiodegradable polymer.[52] Electrospinning solutions were made by dissolving drug and polymer in dimethylformamide (for itraconazole) and in dimethylacetamide (for ketanserin). The collected nonwoven fabrics were shown to release drugs at various rates and profiles based on the ultrafine fiber morphology and drug content.

Another way of incorporating drugs into electrospun fibers is via emulsion electrospinning, in which two miscible or immiscible components can be conveniently electrospun into a composite fiber with a core layer encapsulated inside a shell. In this way, drugs or their mixture can be enclosed within the polymer outer shell to form a core–shell-type drug delivery device.[104,105] Core–shell electrospun fibers are described in greater detail in **Section 4.426.3.4**.

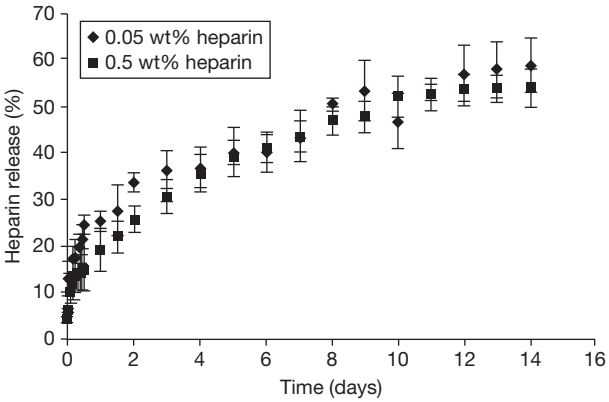

Figure 11 Heparin release from electrospun PCL fibers. Reproduced from Luong-Van, E.; Grondahl, L.; Chua K. N.; Leong, K. W.; Nurcombe, V.; Cool, S. M. *Biomaterials* **2006**, *27*, 2042–2050, with permission from Elsevier.

4.426.3.2. Bioavailability of Drugs at the Fiber Surface

While much drug delivery research with electrospun fibers focuses on mixing the drug before electrospinning, making the drugs available at the surface of the fiber is important for some specific applications such as prevention of bacterial infection.[106] Therefore, postinclusion of drugs has been adopted to coat the electrospun fibers using bioactive molecules, drug and cell recognizable ligands after electrospinning. There are four main approaches for drug loading onto surfaces of electrospun fibers for drug delivery through physical technology, and they are (1) chemical binding, (2) drug adsorption, (3) nanoparticle formation, and (4) multilayer assembly.[3,107] Furthermore, there is recent research into making bioactive electrospun fiber surfaces using surface segregation.

4.426.3.2.1. Chemical binding

Bioactive molecules and drugs can be incorporated after electrospinning using a posttreatment with chemical coupling agents to surface bind the drug of interest. Yao *et al.* developed a novel antibacterial material of electrospun polyurethane fibrous membranes; they modified the fibers with plasma pretreatment, followed by UV-induced graft copolymerization of 4-vinylpyridine and the quaternization of the grafted pyridine groups with hexylbromide.[108] They found that these fibrous membranes possessed effective antibacterial properties. In another example of electrospun fiber chemical modification, Ma *et al.* grafted methacrylic acid onto polysulfone fibers through radical initiation to introduce polymer carboxyl groups, and Cibacron blue F3GA and bovine serum albumin (BSA) were covalently attached on the fiber by using carbodiimide as a coupling agent. They found that the functionalized polysulfone electrospun membranes had a capturing capacity of 22 mg g^{-1} for BSA.[109] Kim *et al.* fabricated amine-functionalized block copolymers (PCL-*block*-PEG-NH_2) (poly(ethylene glycol), PEG), electrospun fibers, and chemically conjugated linear poly(ethylene imine) (PEI) to the fibers surface using matrix metalloproteinase (MMP)-cleavable peptides, and then DNA was electrostatically incorporated onto electrospun fibers (**Figure 12**).[110] They found that DNA and PEI were rapidly released in the presence of MMPs, and the transfection efficiency of the release fractions was influenced by the ratios of the released DNA and PEI.

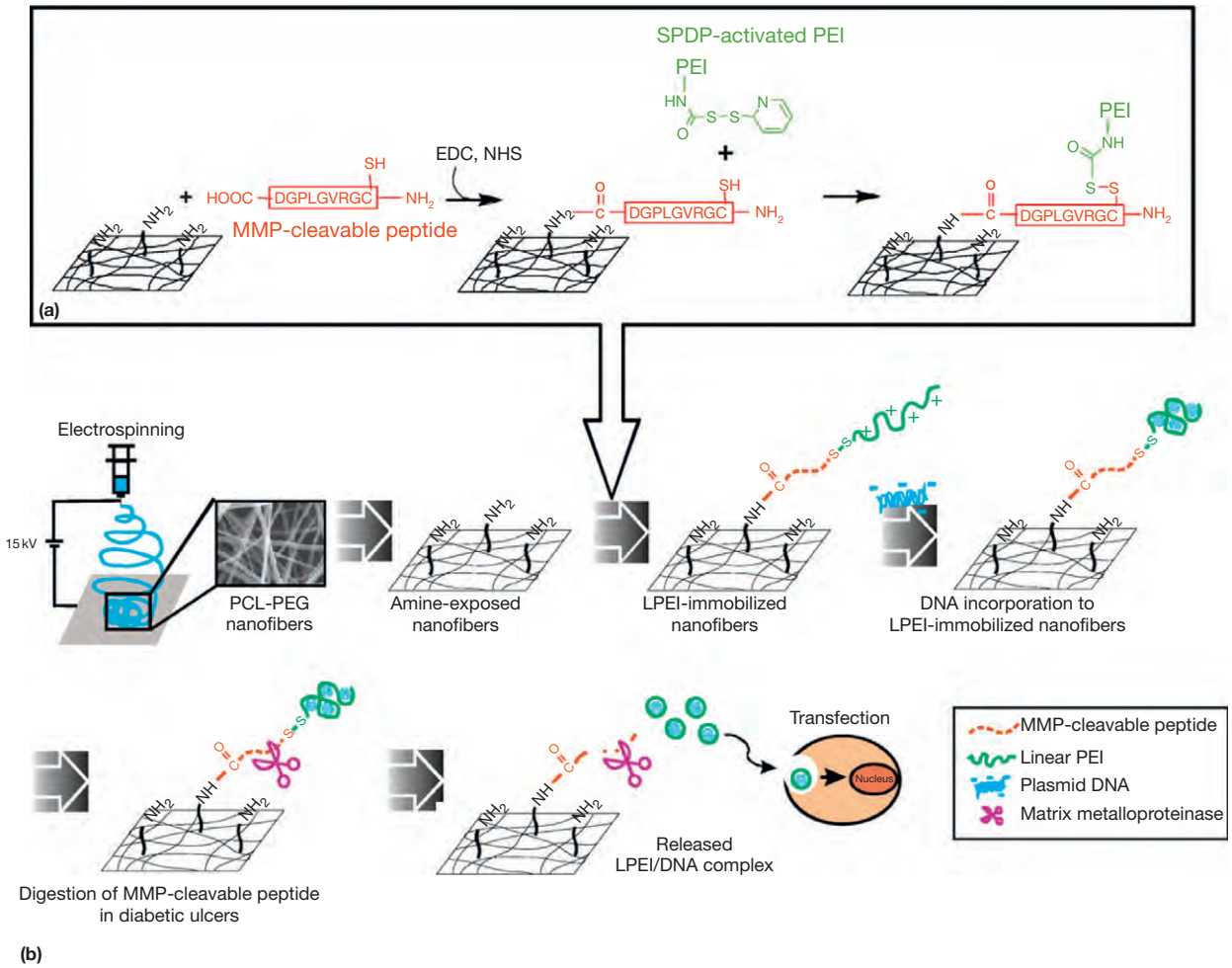

Figure 12 (a) Synthetic scheme of LPEI immobilization on the surface of an electrospun fibrous matrix via a MMP-cleavable linkage. (b) Schematic diagram of an MMP-responsive electrospun material for gene delivery. Reproduced from Kim, H. S.; Yoo, H. S. *J. Control. Release* **2010**, *145*(3), 264–271, with permission from Elsevier.

4.426.3.2.2. Drug adsorption

Some drugs adsorb onto electrospun fibers through simple physical adsorption, using electrostatic interactions, hydrogen bonding, and hydrophobic interactions.[3,111] Patel *et al*. developed aligned and bioactive electrospun scaffolds by immobilizing extracellular matrix protein and growth factor onto ultrafine fibers, which simulated the physical and biochemical properties of native matrix fibrils. Carboxylic groups on the PLLA ultrafine fibers could be obtained through briefly treating the electrospun fibers with a base, with di-NH_2-PEG, and then heparin covalently attached to the carboxylic groups on the PLLA electrospun fibers using cross-linkers 1-ethyl-3-(3-dimethylaminopropyl) carbodiimide hydrochloride and *N*-hydroxysulfosuccinimide. Heparin, a highly sulfated glycosaminoglycan, exhibits strong binding affinity with various growth factors such as fibroblast growth factor, vascular endothelial growth factor (VEGF), heparin-binding epidermal growth factor, and transforming growth factor-β. They found that the immobilized biochemical factors (as efficient as soluble factors) synergized with aligned ultrafine fibers to promote highly efficient neurite outgrowth but had less effect on skin cell migration.[112] Proteins can also adsorb onto hydrophobic surfaces. Ramakrishna *et al*. adsorbed laminin onto electrospun fibers for investigations with neural tissue. Laminin-adsorbed fibers, however, had modest neurite outgrowth compared to laminin/PL-adsorbed glass surfaces. When laminin was included within the electrospinning solution, neurite growth of PC-12 cells was significantly higher compared to electrospun fibers with adsorbed laminin.[113]

4.426.3.2.3. Nanoparticle formation

Therapeutic or biocompatible nanoparticles such as hydroxyapatite and silver (Ag) nanoparticles have been combined with the nanostructured electrospun fibers to functionalize the materials.[3,114,115] Rujitanaroj *et al*. prepared gelatin electrospun fibers containing Ag for wound dressing pads through a gelatin solution containing $AgNO_3$ (Figure 13). They found that cumulative release of Ag^+ ions from fibers *in vitro* occurred rapidly during the first 60 min before leveling off in a typical burst-release profile. Cui *et al*. prepared poly(DL-lactic acid) (PDLLA) electrospun fibers with calcium nitrate entrapment and then incubated in phosphate solution to form *in situ* calcium phosphate nanoparticles on the polymer fibers matrix.[116] They then further grafted gelatin or chitosan on the PDLLA electrospun fibers through an optimized aminolysis process, and the hydroxyapatite nanoparticles could nucleate and grow on these PDLLA electrospun fibers in simulated body fluid.[117] The hydroxyapatite nanoparticles could also be induced to nucleate and grow onto electrospun fibers surface through functional surface groups of electrospun fibers.[118]

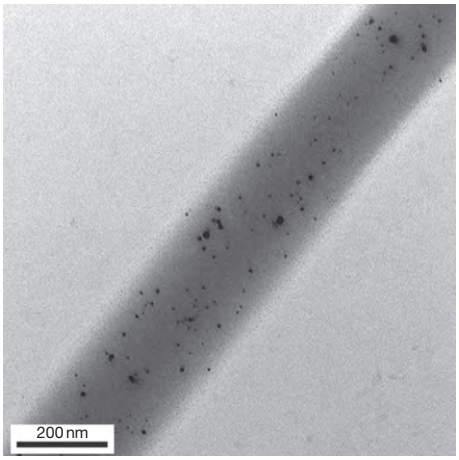

Figure 13 Transmission electron microscopic image of a gelatin electrospun fiber containing $AgNO_3$. Reproduced from Rujitanaroj, P. O.; Pimpha, N.; Supaphol, P. *Polymer* **2008**, *49*, 4723–4732, with permission from Elsevier.

4.426.3.2.4. Multilayer assembly

Layer-by-layer polyelectrolyte (PE) multilayer assembly is an important and versatile surface modification method exploiting electrostatic forces on charged substrates.[119] Muller *et al*. reported layer-by-layer surface functionalization of high-aspect-ratio polystyrene electrospun fibers of various diameters with PEs, deoxyribonucleic acid (DNA) oligonucleotides, and PE/gold nanoparticle composite layers.[120] In this study, PEs were introduced onto polystyrene electrospun fibers through sequential immersion into an aqueous solution of fluorescein isothiocyanate (FITC)-labeled poly(allylamine hydrochloride) and poly-(styrene sulfonate) for 20 min. The DNA was deposited in two steps – firstly, the fibers were treated with sulfuric acid to impart an initial positive charge to the surface, followed by the adsorption of DNA. The PE/Au nanoparticle-coated fibers were prepared by adding a 4-(dimethylamino)-pyridine-stabilized gold nanoparticles dispersion to the PE-coated polystyrene electrospun fibers for 1 day. This study demonstrates that electrospun fibers can be readily modified with various agents by the layer-by-layer assembly approach.

4.426.3.2.5. Surface-segregated chemistry for functionalization

Thermodynamically driven surface segregation is an approach that provides a single-step approach to functionalization of electrospun fibers. Charged amino acid species have been included within the electrospun solution and are concentrated on the surface of the fiber after electrospinning.[121] Studies also show that electrospun fibers can be rendered both protein-resistant and functionalized with a biologically active compound by using amphiphilic polymers. When a PEG-*block*-PCL copolymer is predominantly hydrophilic, and solvent mixtures are used, the resulting fibers are hydrophilic.[122] Furthermore, when end-modified PEG-*block*-PCL is used (e.g., RGD-PEG-*block*-PCL or biotin-PEG-*block*-PCL), the fibers are protein-resistant, hydrophilic, and functionalized. Using a more simplified approach, an amphiphilic and isocyanate star-shaped macromer is used as a reactive additive to a PCL or PLGA solution, creating both a biofunctionalized and hydrophilic fiber.[123,124] Protein-resistant fibers are produced using solutions containing only 7% star-shaped macromer, relative to the PLGA or PCL. Functionalization is through adding a bioactive peptide to the macromer/polymer solution prior to electrospinning with RGDS and RDES-modified electrospun substrates exhibiting distinct differences with cell adhesion.

4.426.3.3. Release Rates and Bioactivity of Incorporated Drugs

Drug release rates and bioactivity from electrospun fibers have been found to depend on a variety of parameters such as the mode of encapsulation, the properties of the encapsulating material, the concentration of the drug encapsulated, and the fibers matrix architecture. This provides sufficient flexibility to control the rate of drug release and maintain drug bioactivity to achieve therapeutically effective doses for the required time period.

In creating electrospun fibers that are drug carriers, Kim *et al*. dissolved model protein lysozyme and polymer into organic solvents for blending fibrous mats, and they observed a high initial burst (45%) with a low controlled release profile, attributed to the presence of lysozyme particles on the fiber surface.[98] The major disadvantages of this type of electrospinning are the severe burst-release phenomenon and the limited effective lifetime of the delivery. To delay the drug release rate, BSA was incubated into PCL electrospun fibers via coaxial electrospinning by Zhang *et al.*, and they found that over 50% of the protein release was observed for fibers with only 0.2% of BSA entrapment.[125] Qi *et al.* encapsulated protein-loaded Ca-alginate microspheres into polymer fibers generating beads-on-string morphologies. The polymer shells around the beads were too thin to modulate protein release, and over 40% of the protein doses were released from the fibers during the initial 12 h.[126] Yang *et al.* incubated lysozyme into PDLLA electrospun fibers prepared by emulsion electrospinning process for core–shell structures, and they found that around 27% of the burst release was detected from fibers with a 1.0% of lysozyme loading, followed by sustained release for 2 weeks.[127]

Another important factor is the maintenance of both structure and bioactivity of the incorporated proteins, which is difficult due to both the complex physical and chemical instabilities inherent in proteins because of the processes of electrospinning, storage, and release. Li *et al.* studied silk fibroin fibers containing bone morphogenetic protein 2 (BMP-2) prepared via electrospinning as a bone TE scaffold. The results suggested that BMP-2 in the electrospun fiber led to higher calcium deposition and upregulation of BMP-2 transcript levels when compared with the control group.[128] Zeng *et al.* obtained electrospun composite fibers through incubating luciferase into poly(vinyl alcohol) (PVA) and poly(*p*-xylylene) (also known as parylene) ultrafine fibers prepared by chemical vapor deposition. Luciferase retained its enzymatic activity after electrospinning and release.[129] However, even though electrospun fiber-based protein delivery systems are in early stages of development, protein structural stability and bioactivity and their controlled release profiles from the fibers require substantial improvements.

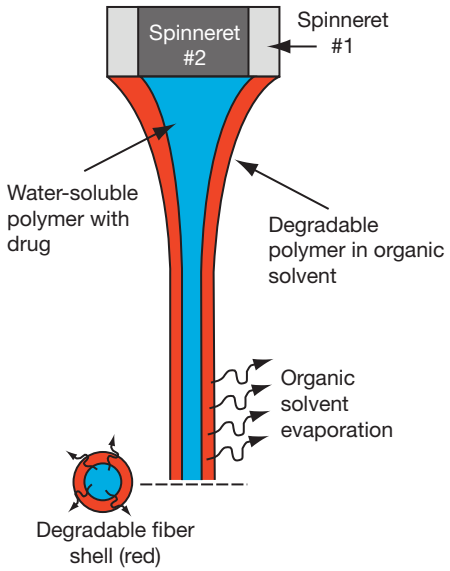

Figure 14 Schematic of coaxial electrospinning showing the core–shell structure of the resulting fiber.

4.426.3.4. Coaxial Electrospinning

One important variation of the electrospinning technique is coaxial electrospinning. This involves using two spinnerets – one inside of another, delivering two polymer solutions that are immiscible with each other (Figure 14). The result of this configuration is that the internal fluid is drawn within the outer fluid in the same Taylor cone, and a two-phase fiber is created with a core and a shell. This fiber can be treated so that the second core phase can be removed to generate a hollow tube – this process provides remarkable continuity in the core–shell structure. Undoubtedly, reiterations in what can be delivered within the polymeric core will influence future drug delivery system designs involving electrospinning.

Zhang *et al.* obtained core–shell-structured electrospun fibers using coaxial electrospinning (Figure 15), with FITC-conjugated

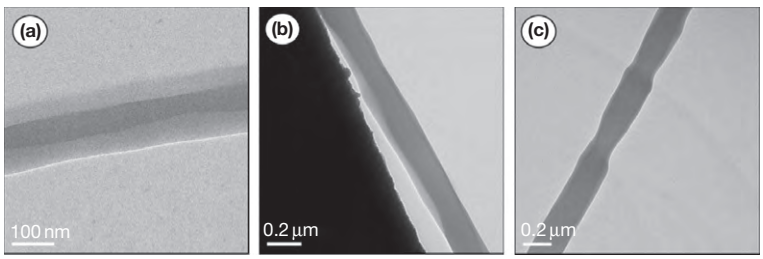

Figure 15 Typical TEM images of coaxially electrospun PCL-r-fitc-BSA/PEG ultrafine fibers produced from varying inner flow rates of 0.2–0.6 ml h^{-1} and with outer flow rate of 1.8 ml h^{-1}. (a) Core component properly located in the center, (b) irregular movement of the core component, and (c) fluctuated fiber shape. Reproduced from Zhang, Y. Z.; Wang, X.; Feng, Y.; Li, J.; Lim, C. T.; Ramakrishna, S. *Biomacromolecules* **2006**, *7*, 1049–1057, with permission from American Chemical Society.

BSA (FITC-BSA) as the core and PCL as the shell. They found that BSA protein in the core–shell-structured electrospun fibers could be released continuously over more than 5 months.[125] Two model proteins – BSA and lysozyme – were incorporated into PCL fibers via coaxial electrospinning by Jiang *et al.*[130] They found that the core thickness could be increased by increasing the feed rate of the inner core material, with more rapid release of core contents. Core–shell electrospun fibers of cationized gelatin-coated PCL were prepared by coaxial electrospinning by Lu *et al.*, and the gelatin was used for immobilizing diverse macromolecular model bioactive agents (FITC-labeled BSA (FITC-BSA), FITC-heparin, or VEGF) to the fibers for release. Sustained release of VEGF could be controlled from heparin-adsorbed electrospun fibers, and the released VEGF maintained its bioactivity.[131] Using coaxial electrospinning, Ahmad *et al.* developed a device with three coaxially arranged needles to obtain multilayer encapsulated fibers (**Figure 16**) for drug delivery.[132] In this regard, coaxial electrospinning is a versatile method for altering how the contents could be released steadily from the multilayered structure.

4.426.3.5. Emulsion Electrospinning

Electrospinning with water-in-oil (W/O) or oil-in-water (O/W) emulsions can yield core–shell fibers.[126] Modified core–shell electrospinning techniques (such as emulsion and coaxial electrospinning) are important to expand the utility of the process. Xu *et al.* electrospun a W/O emulsion containing a PEO solution in water and an oily phase of an amphiphilic poly (ethylene glycol)–poly(L-lactic acid) (PEG-*block*-PLA) di-block copolymer dissolved in chloroform (**Figure 17**).[133] They found that the fiber size and diameter of core and shell could also be changed through adjusting solvent and proportions. Xu *et al.* also prepared core–shell electrospun fibers through W/O emulsion electrospinning, and a water-soluble anticancer agent (doxorubicin hydrochloride) was included into amphiphilic poly(ethylene glycol)-poly(L-lactic acid) (PEG-PLLA) di-block copolymer.[105] They found that drug release in core–shell structure fibers became slower and slower and the accumulated release percentage became steady (**Figure 18**). Yang *et al.*[134] obtained core–shell-structured ultrafine fibers of BSA and PDLLA through emulsion electrospinning as carriers for therapeutic proteins. Release data suggested that emulsion electrospinning can provide a useful core–sheath structure for effective release and protection of bioactive proteins. Yang *et al.* further investigated the structural integrity, bioactivity, and release patterns of lysozyme encapsulated within the core–shell-structured ultrafine fibers prepared by emulsion electrospinning. They found that emulsion electrospinning successfully produced core–shell-structured ultrafine fibers that could significantly delay initial burst release, prolong the release period depending on the protein loading amount, and protect the structural integrity and bioactivity of encapsulated lysozyme during incubation in release medium.[127]

Research performed with emulsion electrospinning has demonstrated that the characteristics of the drug (e.g., solubility and compatibility) are not the defining properties for

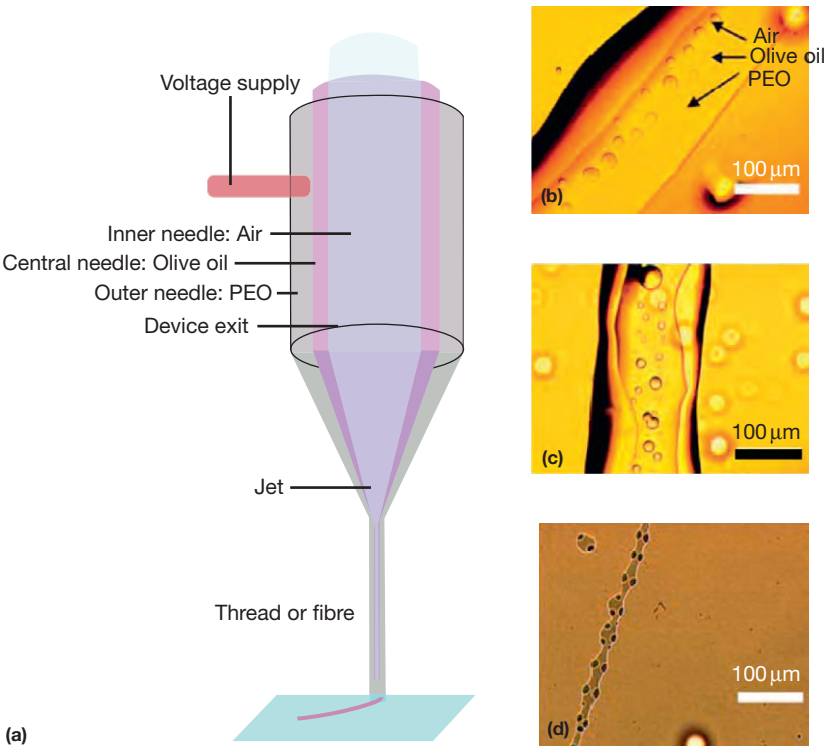

Figure 16 Thread encapsulation. (a) Flow arrangement, (b) air encapsulation in twin-layered thread with olive oil and PEO solution, (c) instabilities during thread formation, and (d) two-needle (third needle switched off) coaxial nonconcentric thread encapsulation using olive oil and PEO solution. Reproduced from Ahmad, Z.; Zhang, H. B.; Farook, U.; Edirisinghe, M.; Stride, E.; Colombo, P. *J. R. Soc. Interf.* **2008**, *5*, 1255–1261.

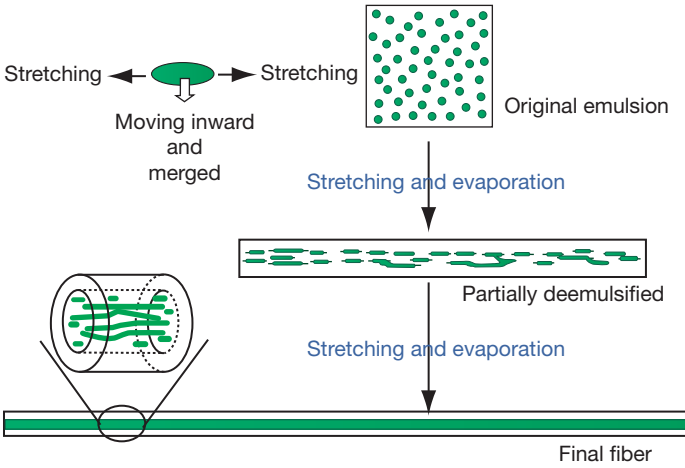

Figure 17 Schematic mechanism for the formation of core–sheath composite fibers during emulsion electrospinning. Reproduced from Xu, X. L.; Zhuang, X. L.; Chen, X. S.; Wang, X. R.; Yang, L. X.; Jing X. B. *Macromol Rapid Comm*. **2006**, *27*, 1637–1642.

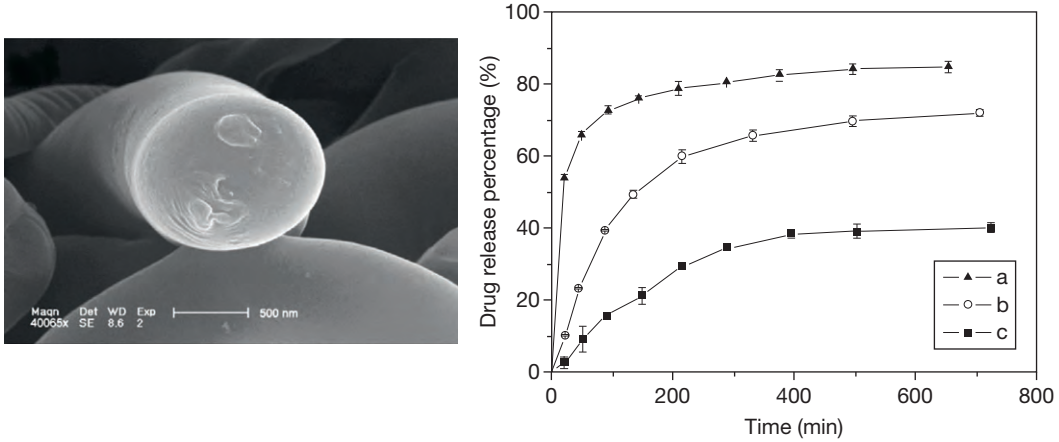

Figure 18 ESEM photographs of cross-sectional view of PEG-PLLA fibers containing 2.06 wt% doxorubicin (left) and release profile (right): (a) suspension-spun doxorubicin /PEG5000-PLLA fibers, (b) emulsion-spun doxorubicin /PLLA fibers, and (c) emulsion-spun Dox/PEG750-PLLA fibers. Reproduced from Xu, X. L.; Yang, L. X.; Xu, X. Y.; *et al*. *J. Control. Release* **2005**, *108*, 33–42, with permission from Elsevier.

electrospinning technology, and that flexible drug formulations within electrospun fibers could be designed and obtained.

4.426.3.6. Morphological Variations Affecting Drug Delivery

One common observation with electrospinning is the formation of 'beads' along the fiber length, long been considered an undesirable phenomenon.[135] However, beads along the fiber could be used as reservoirs for drug or cell inclusion, and could have distinct degradation properties from the fibers. The optimization of bead percent was also necessary to extend such fiber applications in biomedical, biotechnological, and other industrial fields.[65] The possible effects of fiber beads on cellular proliferation, growth, and adhesion are not known. On the positive side, understanding reasons for development of beads provides another parameter for scaffold design.

4.426.3.7. Additives to Modify Electrospinning Materials

Release of pharmaceutical agents can be altered to be immediate, delayed, or pulsed depending on the polymer carriers used and other included additives. Some studies report correlations of additives and drug distribution in the polymer to release profiles and degradation.[136] The addition of additives to electrospinning solutions is an important parameter influencing the fiber morphology because of changes to polymer solution physicochemical properties including the surface tension.[103] Yang *et al*. fabricated core–shell-structured composite electrospun fibers (lysozyme/methyl cellulose/PDLLA) with lysozyme as a model protein, encapsulated into the PDLLA fibers along with methyl cellulose (MC additive).[127] They also obtained BSA and MC in PDLLA core–sheath ultrafine fibers by emulsion electrospinning.[134] The MC additive benefited core–shell electrospun fiber formation and showed no effect on the Amide I FTIR band for both lysozyme and BSA. The protein-specific activity retention of secondary structure through Fourier transform infrared analyses was significantly higher for lysozyme and BSA encapsulated within composite fibers containing additives than free lysozyme and BSA incubated with fibers. The MC additive could quicken protein release. With the additives released from composites leading

to more pores in the fibers, water penetrated into the fiber and promoted faster hydrolysis of the polymer backbone, so that the mass loss of the fiber matrix and molecular weight loss for PDLLA were much more rapid than that of pure PDLLA.

4.426.4. Conclusions and Future Directions

There is an increasing demand for engineered nanostructured polymeric materials and surfaces to improve interfaces in biomedicine, biology, materials science, and nanotechnology. Electrospinning has, in particular, been widely used within laboratories due to its inexpensive convenience and simplicity, and its capacity to deliver bioactive molecules to cells or tissues. Many current forms of fibers, however, are not very cell-conducive for TE use. Controlled drug delivery via these fibers is one component of this growing and burgeoning part of TE. Drugs can be incorporated by simply adding them directly to the electrospinning polymer solution, or bound to the fiber surface using postelectrospinning treatments or single-step processes. While many polymers were electrospun over the past decade, controlling the specific chemistry of the electrospun fiber surface remains a challenge. Ongoing advancements with different electrospun fiber morphologies using different device configurations will fabricate different fiber designs. Various approaches to collect electrospun fiber in distinct solid morphologies are evolving. Relatively little is known about 'microscale' electrospun fibers – those with 2–15-μm diameter range that might yield different porous scaffolds useful for TE.

References

1. Blanco, E.; Kessinger, C. W.; Sumer, B. D.; Gao, J. *Exp. Biol. Med. Maywood* **2009**, *234*, 123–131.
2. Vijayaraghavalu, S.; Raghavan, D.; Labhasetwar, V. *Curr. Opin. Investig. Drugs* **2007**, *8*, 477–484.
3. Yoo, H. S.; Kim, T. G.; Park, T. G. *Adv. Drug Deliv. Rev.* **2009**, *61*, 1033–1042.
4. Nisbet, D. R.; Forsythe, J. S.; Shen, W.; Finkelstein, D. I.; Horne, M. K. *J. Biomater. Appl.* **2009**, *24*, 7–29.
5. Hutmacher, D. W.; Woodfield, T.; Dalton, P. D. In *Tissue Engineering*; Van Blitterswijk, C., Thomsen, P., Lindahl, A., Hubbell, J., Williams, D., Cancedda, R., *et al*. Eds.; Elsevier: Oxford, 2008; pp 403–450.
6. Porter, A. L.; Youtie, J. *J. Nanopart. Res.* **2009**, *11*, 1023–1041.
7. Franks, A. *J. Phys. E Scientific Instrum.* **1987**, *20*, 872–881.
8. Teli, M. K.; Mutalik, S.; Rajanikant, G. K. *Curr. Pharm. Des.* **2010**, *16*, 1882–1892.
9. Reneker, D. H.; Yarin, A. L.; Zussman, E.; Xu, H. *Adv. Appl. Mech.* **2007**, *41*, 43–195.
10. Theis, T.; Parr, D.; Binks, P.; *et al*. *Nat. Nanotechnol.* **2006**, *1*, 8–10.
11. Cooley, J. F. Apparatus for Electrically Dispersing Fluids. U.S. Patent 692,631, Feb 4, 1902.
12. Morton, W. J. Method of Dispersing Fluids. U.S. Patent 705,691, Jul 29, 1902.
13. Formhals, A. Method and Apparatus for Spinning. U.S. Patent 2,349,950, May 30, 1944.
14. Norton, C. L. Method of and Apparatus for Producing Fibrous or Filamentary Material. U.S. Patent 2,048,651, Jul 21, 1936.
15. Formhals, A. Process and Apparatus for Preparing Artificial Threads. U.S. Patent 1,975,504, Oct 2, 1934.
16. Reneker, D. H.; Chun, I. *Nanotechnology* **1996**, *7*, 216–223.
17. Larrondo, L.; Manley, R. S. J. *J. Polym. Sci. B Polym. Phys.* **1981**, *19*, 933–940.
18. Larrondo, L.; Manley, R. S. J. *J. Polym. Sci. B Polym. Phys.* **1981**, *19*, 909–920.
19. Larrondo, L.; Manley, R. S. J. *J. Polym. Sci. B Polym. Phys.* **1981**, *19*, 921–932.
20. Rangkupan, R.; Reneker, D. H. *Development of Electrospinning from Molten Polymers in a Vacuum. New Frontiers in Fiber-Based Products*. The Fiber Society: Raleigh, NC, 2001.
21. Taylor, G. *Proc. R. Soc. Lond.* **1969**, *313*, 453–475.
22. Baker, B. M.; Gee, A. O.; Sheth, N. P.; *et al*. *J. Knee Surg.* **2009**, *22*, 45–59.
23. Bonzani, I. C.; George, J. H.; Stevens, M. M. *Curr. Opin. Chem. Biol.* **2006**, *10*, 568–575.
24. Jang, J. H.; Castano, O.; Kim, H. W. *Adv. Drug Deliv. Rev.* **2009**, *61*, 1065–1083.
25. Ramachandran, K.; Gouma, P. I. *Recent Pat. Nanotechnol.* **2008**, *2*, 1–7.
26. Seidlits, S. K.; Lee, J. Y.; Schmidt, C. E. *Nanomedicine UK* **2008**, *3*, 183–199.
27. Cao, H. Q.; Liu, T.; Chew, S. Y. *Adv. Drug Deliv. Rev.* **2009**, *61*, 1055–1064.
28. Zahedi, P.; Rezaeian, I.; Ranaei-Siadat, S. O.; Jafari, S. H.; Supaphol, P. *Polym. Adv. Technol.* **2010**, *21*, 77–95.
29. Simpson, D. G. *Expert Rev. Med. Devices* **2006**, *3*, 471–484.
30. Kumbar, S. G.; James, R.; Nukavarapu, S. P.; Laurencin, C. T. *Biomed. Mater.* **2008**, *3*, 034002.
31. Wray, L. S.; Orwin, E. J. *Tissue Eng. A* **2009**, *15*, 1463–1472.
32. Sell, S. A.; McClure, M. J.; Garg, K.; Wolfe, P. S.; Bowlin, G. L. *Adv. Drug Deliv. Rev.* **2009**, *61*, 1007–1019.
33. Chen, J.; Xu, J.; Wang, A.; Zheng, M. *Expert Rev. Med. Devices* **2009**, *6*, 61–73.
34. Lim, S. H.; Mao, H. Q. *Adv. Drug Deliv. Rev.* **2009**, *61*, 1084–1096.
35. Ayres, C. E.; Jha, B. S.; Sell, S. A.; Bowlin, G. L.; Simpson, D. G. *Wiley Interdiscip. Rev. Nanomed. Nanobiotechnol.* **2010**, *2*, 20–34.
36. Hubbell, J. A. In *Tissue Engineering*; Van Blitterswijk, C., Thomsen, P., Lindahl, A., Hubbell, J., Williams, D., Cancedda, R., *et al*. Eds.; Elsevier: Oxford, 2008; pp 455–482.
37. Huang, Z. M.; Zhang, Y. Z.; Kotaki, M.; Ramakrishna, S. *Compos. Sci. Technol.* **2003**, *63*, 2223–2253.
38. Teo, W. E.; Ramakrishna, S. *Nanotechnology* **2006**, *17*, R89–R106.
39. Reneker, D. H.; Yarin, A. L. *Polymer* **2008**, *49*, 2387–2425.
40. Wang, Y. K.; Yong, T.; Ramakrishna, S. *Aust. J. Chem.* **2005**, *58*, 704–712.
41. Shin, M.; Ishii, O.; Sueda, T.; Vacanti, J. P. *Biomaterials* **2004**, *25*, 3717–3723.
42. Dalton, P. D.; Klee, D.; Moller, M. *Polymer* **2005**, *46*, 611–614.
43. Luong-Van, E.; Grondahl, L.; Chua, K. N.; Leong, K. W.; Nurcombe, V.; Cool, S. M. *Biomaterials* **2006**, *27*, 2042–2050.
44. Son, W. K.; Youk, J. H.; Lee, T. S.; Park, W. H. *Polymer* **2004**, *45*, 2959–2966.
45. Deitzel, J. M.; Kleinmeyer, J. D.; Hirvonen, J. K.; Tan, N. C. B. *Polymer* **2001**, *42*, 8163–8170.
46. Zeugolis, D. I.; Khew, S. T.; Yew, E. S. Y.; *et al*. *Biomaterials* **2008**, *29*, 2293–2305.
47. Matthews, J. A.; Boland, E. D.; Wnek, G. E.; Simpson, D. G.; Bowlin, G. L. *J. Bioact. Compat. Polym.* **2003**, *18*, 125–134.
48. Matthews, J. A.; Wnek, G. E.; Simpson, D. G.; Bowlin, G. L. *Biomacromolecules* **2002**, *3*, 232–238.
49. Katti, D. S.; Robinson, K. W.; Ko, F. K.; Laurencin, C. T. *J. Biomed. Mater. Res.* **2004**, *70B*, 286–296.
50. Li, W. J.; Laurencin, C. T.; Caterson, E. J.; Tuan, R. S.; Ko, F. K. *J. Biomed. Mater. Res.* **2002**, *60*, 613–621.
51. Xu, C. Y.; Inai, R.; Kotaki, M.; Ramakrishna, S. *Biomaterials* **2004**, *25*, 877–886.
52. Verreck, G.; Chun, I.; Rosenblatt, J.; *et al*. *J. Control. Release* **2003**, *92*, 349–360.
53. Stankus, J. J.; Guan, J. J.; Wagner, W. R. *J. Biomed. Mater. Res.* **2004**, *70A*, 603–614.
54. Khil, M. S.; Cha, D. I.; Kim, H. Y.; Kim, I. S.; Bhattarai, N. *J. Biomed. Mater. Res.* **2003**, *67B*, 675–679.
55. Zhang, X. H.; Reagan, M. R.; Kaplan, D. L. *Adv. Drug Deliv. Rev.* **2009**, *61*, 988–1006.
56. Beglou, M. J.; Haghi, A. K. *Cell Chem. Technol.* **2008**, *42*, 441–462.
57. Min, B. M.; Jeong, L.; Nam, Y. S.; Kim, J. M.; Kim, J. Y.; Park, W. H. *Int. J. Biol. Macromol.* **2004**, *34*, 281–288.
58. Liao, S.; Li, B. J.; Ma, Z. W.; Wei, H.; Chan, C.; Ramakrishna, S. *Biomed. Mater.* **2006**, *1*, R45–R53.
59. Schiffman, J. D.; Schauer, C. L. *Polym. Rev.* **2008**, *48*, 317–352.
60. Sill, T. J.; von Recum, H. A. *Biomaterials* **2008**, *29*, 1989–2006.
61. Zong, X. H.; Kim, K.; Fang, D. F.; Ran, S. F.; Hsiao, B. S.; Chu, B. *Polymer* **2002**, *43*, 4403–4412.
62. Yang, Q. B.; Li, Z. Y.; Hong, Y. L.; *et al*. *J. Polym. Sci. B Polym. Phys.* **2004**, *42*, 3721–3726.
63. Kim, K. W.; Lee, K. H.; Khil, M. S.; Ho, Y. S.; Kim, H. Y. *Fiber Polym.* **2004**, *5*, 122–127.
64. Kim, K.; Kang, M.; Chin, I. J.; Jin, H. J. *Macromol. Res.* **2005**, *13*, 533–537.
65. Cui, W. G.; Li, X. H.; Zhou, S. B.; Weng, J. *J. Appl. Polym. Sci.* **2007**, *103*, 3105–3112.
66. Heikkila, P.; Harlin, A. *Eur. Polym. J.* **2008**, *44*, 3067–3079.
67. Stankus, J. J.; Guan, J. J.; Fujimoto, K.; Wagner, W. R. *Biomaterials* **2006**, *27*, 735–744.
68. Kidoaki, S.; Kwon, I. K.; Matsuda, T. *Biomaterials* **2005**, *26*, 37–46.

69. Bini, T. B.; Gao, S. J.; Wang, S.; Ramakrishna, S. *J. Mater. Sci.* **2006**, *41*, 6453–6459.
70. Ishii, O.; Shin, M.; Sueda, T.; Vacanti, J. P. *J. Thorac. Cardiovasc. Surg.* **2005**, *130*, 1358–1363.
71. Chung, S.; Ingle, N. P.; Montero, G. A.; Kim, S. H.; King, M. W. *Acta Biomater.* **2009**, *6*, 1958–1967.
72. Park, S. H.; Kim, T. G.; Kim, H. C.; Yang, D. Y.; Park, T. G. *Acta Biomater.* **2008**, *4*, 1198–1207.
73. Tuzlakoglu, K.; Bolgen, N.; Salgado, A. J.; Gomes, M. E.; Piskin, E.; Reis, R. L. *J. Mater. Sci. Mater. Med.* **2005**, *16*, 1099–1104.
74. Pham, Q. P.; Sharma, U.; Mikos, A. G. *Biomacromolecules* **2006**, *7*, 2796–2805.
75. Kim, S. J.; Jang, D. H.; Park, W. H.; Min, B. M. *Polymer* **2010**, *51*, 1320–1327.
76. Teo, W. E.; Ramakrishna, S. *Nanotechnology* **2005**, *16*, 1878–1884.
77. Sun, T.; Norton, D.; McKean, R. J.; Haycock, J. W.; Ryan, A. J.; MacNeil, S. *Biotechnol. Bioeng.* **2007**, *97*, 1318–1328.
78. Gerardo-Nava, J.; Fuhrmann, T.; Klinkhammer, K.; *et al. Nanomedicine UK* **2009**, *4*, 11–30.
79. Schnell, E.; Klinkhammer, K.; Balzer, S.; Brook, G.; Klee, D.; Dalton, P. *Biomaterials* **2007**, *28*, 3012–3025.
80. Simons, H. Process and Apparatus for Producing Patterned Nonwoven Fabrics. U.S. Patent 3,280,229, 1966.
81. Zhang, D. M.; Chang, J. *Adv. Mater.* **2007**, *19*, 3664–3667.
82. Neves, N. M.; Campos, R.; Pedro, A.; Cunha, J.; Macedo, F.; Reis, R. L. *Int. J. Nanomed.* **2007**, *2*, 433–448.
83. Wang, Y.; Wang, G.; Chen, L.; *et al. Biofabrication* **2009**, *1*, 015001.
84. Yang, D. Y.; Lu, B.; Zhao, Y.; Jiang, X. Y. *Adv. Mater.* **2007**, *19*, 3702–3705.
85. Yan, H.; Liu, L. Q.; Zhang, Z. *Appl. Phys. Lett.* **2009**, *95*, 143144.
86. Sun, D. H.; Chang, C.; Li, S.; Lin, L. W. *Nano Lett.* **2006**, *6*, 839–842.
87. Chang, C.; Limkrailassiri, K.; Lin, L. W. *Appl. Phys. Lett.* **2008**, *93*, 123111.
88. Dalton, P. D.; Joergensen, N. T.; Groll, J.; Moeller, M. *Biomed. Mater.* **2008**, *3*, 034109.
89. Bellan, L. M.; Craighead, H. G. *J. Vac. Sci. Technol. B* **2006**, *24*, 3179–3183.
90. Simonet, M.; Schneider, O. D.; Neuenschwander, P.; Stark, W. J. *Polym. Eng. Sci.* **2007**, *47*, 2020–2026.
91. Schneider, O. D.; Loher, S.; Brunner, T. J.; *et al. J. Biomed. Mater. Res.* **2008**, *84B*, 350–362.
92. Tzezana, R.; Zussman, E.; Levenberg, S. *Tissue Eng. C Meth.* **2008**, *14*, 281–288.
93. Ekaputra, A. K.; Prestwich, G. D.; Cool, S. M.; Hutmacher, D. W. *Biomacromolecules* **2008**, *9*, 2097–2103.
94. Hutmacher, D. W.; Dalton, P. D. *Chem. Asian J.* **2011**, *6*, 44–56.
95. Ma, Z.; Mao, Z.; Gao, C. *Colloids Surf. B Biointerf.* **2007**, *60*, 137–157.
96. Ratner, B. D.; Bryant, S. J. *Annu. Rev. Biomed. Eng.* **2004**, *6*, 41–75.
97. Mollerup, J. M. *Chem. Eng. Technol.* **2008**, *31*, 864–874.
98. Kim, T. G.; Lee, D. S.; Park, T. G. *Int. J. Pharm.* **2007**, *338*, 276–283.
99. Jing, Z.; Xu, X. Y.; Chen, X. S.; *et al. J. Control. Release* **2003**, *92*, 227–231.
100. Zeng, J.; Yang, L. X.; Liang, Q. Z.; *et al. J. Control. Release* **2005**, *105*, 43–51.
101. Kenawy, E. R.; Bowlin, G. L.; Mansfield, K.; *et al. J. Control. Release* **2002**, *81*, 57–64.
102. Kim, K.; Luu, Y. K.; Chang, C.; *et al. J. Control. Release* **2004**, *98*, 47–56.
103. Cui, W. G.; Li, X. H.; Zhu, X. L.; Yu, G.; Zhou, S. B.; Weng, J. *Biomacromolecules* **2006**, *7*, 1623–1629.
104. Sun, Z. C.; Zussman, E.; Yarin, A. L.; Wendorff, J. H.; Greiner, A. *Adv. Mater.* **2003**, *15*, 1929–1932.
105. Xu, X. L.; Yang, L. X.; Xu, X. Y.; *et al. J. Control. Release* **2005**, *108*, 33–42.
106. Bolgen, N.; Vargel, I.; Korkusuz, P.; Menceloglu, Y. Z.; Piskin, E. *J. Biomed. Mater. Res.* **2007**, *81B*, 530–543.
107. Nisbet, D. R.; Rodda, A. E.; Finkelstein, D. I.; Horne, M. K.; Forsythe, J. S.; Shen, W. *Colloid Surf. B* **2009**, *71*, Cp 1–Cp 12.
108. Yao, C.; Li, X. S.; Neoh, K. G.; Shi, Z. L.; Kang, E. T. *J. Membr. Sci.* **2008**, *320*, 259–267.
109. Ma, Z. W.; Masaya, K.; Ramakrishna, S. *J. Membr. Sci.* **2006**, *282*, 237–244.
110. Kim, H. S.; Yoo, H. S. *J. Control. Release* **2010**, *145*(3), 264–271.
111. Yoshida, M.; Langer, R.; Lendlein, A.; Lahann, J. *Polym. Rev.* **2006**, *46*, 347–375.
112. Patel, S.; Kurpinski, K.; Quigley, R.; *et al. Nano Lett.* **2007**, *7*, 2122–2128.
113. Koh, H. S.; Yong, T.; Chan, C. K.; Ramakrishna, S. *Biomaterials* **2008**, *29*, 3574–3582.
114. Rujitanaroj, P. O.; Pimpha, N.; Supaphol, P. *Polymer* **2008**, *49*, 4723–4732.
115. Dong, H.; Wang, D.; Sun, G.; Hinestroza, J. P. *Chem. Mater.* **2008**, *20*, 6627–6632.
116. Cui, W. U.; Li, X. H.; Zhou, S. B.; Weng, J. *J. Biomed. Mater. Res.* **2007**, *82A*, 831–841.
117. Cui, W. G.; Li, X. H.; Chen, J. G.; Zhou, S. B.; Weng, J. *Cryst. Growth Des.* **2008**, *8*, 4576–4582.
118. Cui, W.; Li, X.; Xie, C.; *et al. Polymer* **2010**, *51*, 2320–2328.
119. Tang, Z. Y.; Wang, Y.; Podsiadlo, P.; Kotov, N. A. *Adv Mater.* **2007**, *19*, 906.
120. Muller, K.; Quinn, J. F.; Johnston, A. P. R.; Becker, M.; Greiner, A.; Caruso, F. *Chem. Mater.* **2006**, *18*, 2397–2403.
121. Sun, X. Y.; Shankar, R.; Borner, H. G.; Ghosh, T. K.; Spontak, R. J. *Adv. Mater.* **2007**, *19*, 87–91.
122. Grafahrend, D.; Calvet, J. L.; Salber, J.; Dalton, P. D.; Moeller, M.; Klee, D. *J. Mater. Sci. Mater. Med.* **2008**, *19*, 1479–1484.
123. Klinkhammer, K.; Bockelmann, J.; Simitzis, C.; *et al. J. Mater. Sci. Mater. Med.* **2010**, *21*, 2637–2651.
124. Grafahrend, D.; Heffels, K. H.; Beer, M.; *et al. Nat. Mater.* **2010**, *10*, 67–73.
125. Zhang, Y. Z.; Wang, X.; Feng, Y.; Li, J.; Lim, C. T.; Ramakrishna, S. *Biomacromolecules* **2006**, *7*, 1049–1057.
126. Qi, H. X.; Hu, P.; Xu, J.; Wang, A. J. *Biomacromolecules* **2006**, *7*, 2327–2330.
127. Yang, Y.; Li, X. H.; Qi, M. B.; Zhou, S. B.; Weng, J. *Eur. J. Pharm. Biopharm.* **2008**, *69*, 106–116.
128. Li, C. M.; Vepari, C.; Jin, H. J.; Kim, H. J.; Kaplan, D. L. *Biomaterials* **2006**, *27*, 3115–3124.
129. Zeng, J.; Aigner, A.; Czubayko, F.; Kissel, T.; Wendorff, J. H.; Greiner, A. *Biomacromolecules* **2005**, *6*, 1484–1488.
130. Jiang, H. L.; Hu, Y. Q.; Li, Y.; Zhao, P. C.; Zhu, K. J.; Chen, W. L. *J. Control. Release* **2005**, *108*, 237–243.
131. Lu, Y.; Jiang, H. L.; Tu, K. H.; Wang, L. Q. *Acta Biomater.* **2009**, *5*, 1562–1574.
132. Ahmad, Z.; Zhang, H. B.; Farook, U.; Edirisinghe, M.; Stride, E.; Colombo, P. *J. R. Soc. Interf.* **2008**, *5*, 1255–1261.
133. Xu, X. L.; Zhuang, X. L.; Chen, X. S.; Wang, X. R.; Yang, L. X.; Jing, X. B. *Macromol. Rapid Comm.* **2006**, *27*, 1637–1642.
134. Yang, Y.; Li, X.; Cui, W.; Zhou, S.; Tan, R.; Wang, C. *J. Biomed. Mater. Res.* **2008**, *86A*, 374–385.
135. Lin, T.; Wang, H. X.; Wang, H. M.; Wang, X. G. *Nanotechnology* **2004**, *15*, 1375–1381.
136. Wang, H.; Song, H.-R.; Chen, X.-S.; Deng, Y.-J. *Polym. Sci.* **2010**, *28*, 417–425.

4.427. Cell-Demanded Release of Growth Factors

A H Zisch, University Hospital Zurich, Zurich, Switzerland; Zurich Center for Integrative Human Physiology, Zurich, Switzerland; Swiss Federal Institute of Technology (ETH), Zurich, Switzerland
M Ehrbar, University Hospital Zurich, Zurich, Switzerland; Zurich Center for Integrative Human Physiology, Zurich, Switzerland

© 2011 Elsevier Ltd. All rights reserved.

4.427.1.	**Introduction**	464
4.427.1.1.	Medical Motivation	464
4.427.1.2.	Technological Motivation for Development of Biomaterial Mimetics of Natural ECM	464
4.427.2.	**Enabling Polymer Hydrogels for Cell-Demanded Release**	465
4.427.2.1.	Collagen Engineering	465
4.427.2.2.	Fibrin Engineering	465
4.427.2.3.	Polysaccharide-Based Semisynthetic Materials	467
4.427.2.4.	Fully Synthetic ECM Mimetic Hydrogels	468
4.427.2.5.	Fully Synthetic Fibrin Mimetic Hydrogels	469
4.427.3.	**Preclinical Evaluation in Angiogenesis**	469
4.427.3.1.	Clinical Need for Angiogenic Therapy	470
4.427.3.2.	Lessons from Embryonic Development and Early Therapeutic Angiogenesis Research	470
4.427.3.3.	Cell-Demanded Release in Vascularization	470
4.427.4.	**Conclusion and Future Directions**	471
References		472

Glossary

Angiogenesis Formation of blood vessels from preexisting ones.
Angiogenic switch Switch of a tumor from an avascular to a vascular state because of the disturbed balance of pro and antiangiogenic signals.
Arteriogenesis The formation of larger arteries from arterioles.
Cell-mediated Activities which are restricted to the cell surface, resulting in a localized effect (here extracellular matrix remodeling).
Haptotaxis The recruitment of cells toward an immobilized signal.
Heparan sulfate A linear charged polysaccharide that is bound to proteins.
Morphogenesis Processes that control the formation of functional shapes and tissues.
Proteoglycan Proteins with a substantial glycosylation.
Transglutaminase An enzyme that catalyzes the reaction between a γ-carboxamid (glutamine) and amine (lysine) groups.
Ulcer An open lesion, for example, in skin or mucosa often maintained by an inflammation and/or an infection.
Vasculogenesis The *de novo* formation of capillaries from angoiblasts.

Abbreviations

2D	Two-dimensional
Ang-1	Angiopoietin-1
bFGF	Basic fibroblast growth factor
BMP-2	Bone morphogenetic protein-2
CAM	Chick chorioallantoic membrane
EC	Endothelial cell
ECM	Extracellular matrix
FXIII	Factor XIII
HA	Hyaluronic acid
HUVEC	Human umbilical cord vein endothelial cell
KGF	Keratinocyte growth factor
L1Ig6	Sixth Ig-like domain of the cell adhesion molecule L1
MMP	Matrix metalloproteinase
NGF	Nerve growth factor
NT-3	Neurotrophin-3
PDGF-BB	Platelet-derived growth factor-BB
PEG	Poly(ethylene glycol)
PTH	Parathyroid hormone
SDF-1α	Stromal cell-derived factor-1 alpha
TGF-β2	Transforming growth factor beta-2
VEGF	Vascular endothelial growth factor
α_2PI_{1-8}	*N*-terminal amino acid sequence (NQEQVSPL) of α2-plasmin inhibitor
α_2PI_{1-8}-Pla-VEGF	α_2PI_{1-8} fused via a plasmin linker to VEGF
α_2PI_{1-8}VEGF	α_2PI_{1-8} fused to VEGF

4.427.1. Introduction

4.427.1.1. Medical Motivation

Polypeptide growth factors and cytokines are key players in normal tissue morphogenesis as well as tissue regeneration in the diseased adult. Intense basic research has led to a great deal of knowledge about the biological characteristics and potency of these factors in triggering specific cellular responses.[1–3] However, the translation of this scientific understanding of growth factor function into pharmacological enhancement of tissue repair in clinical therapies has been rather unsuccessful.[4] For example, one of the more relevant and therefore well-studied needs has been the treatment of chronic wounds, such as diabetic ulcer, pressure ulcer, or venous static ulcer, that are caused by deficient vascular supply. Scores of trials with ulcer patients using growth factors or cytokines have produced disappointing results.[5–7] One likely reason for the poor clinical outcomes with recombinant growth factor therapeutics in the past has been the modes of growth factor delivery, that is, their topical application or injection in soluble form.[8] Without embedment, the soluble factors are very rapidly cleared from the target site by diffusion, or never reach the target in sufficient quantities, or reach it only at extreme dose.[9] To overcome this problem, relatively simple delivery systems such as creams or sprays were tested for sustained release of growth factors or cytokines, but in this context they were inefficient.[5,10] In recent years, research was done to find a biomaterial environment that preserves growth factor activity, entraps growth factors, and permits their controlled, local release into the surrounding tissue.[11,12] This strategy was expected to prevent the rapid clearance from the pharmacological site of application which is often observed. Key questions that need to be addressed for pharmacological intervention with growth factors are the following:

- how do we prevent rapid clearance of a growth factor signal?
- how do we preserve its activity?
- how can we translate a supranormal dose of exogenous growth factor signal into a local, physiological, tiny dose of active factor?
- which dose is optimal for which treatment site?
- how can we achieve this optimal dose?
- how can we maintain it over a prolonged period of time?

The aim of this chapter is to describe materials that are either of biological origin or are fully synthetic and are engineered to address the criterions listed above. Of the myriad of possible materials, promising candidate materials for growth factor delivery strategies would be hydrogels, as they are three-dimensional (3D) cross-linked polymers that are swollen by and typically comprise more than 95% water.[13] They have comparable mechanical properties to the naturally occurring extracellular matrix (ECM), allow the diffusion of nutrition, proteins, and respiratory gases, and can thus be considered good ECM mimetics (see **Chapter 2.207, Extracellular Matrix: Inspired Biomaterials**; **Chapter 2.211, Polymers of Biological Origin**; and **Chapter 2.220, Extracellular Matrix as Biomimetic Biomaterial: Biological Matrices for Tissue Regeneration**).[14,15]

To explain the principles of cell-demanded growth factor presentation, we focus on hydrogel-forming materials that have been extensively studied in the context of engineering growth factor release. Design principles that could potentially be used as 3D matrices, but so far have only been tested in 2D conditions, are not considered. We begin by describing the development of biologically derived and synthetic hydrogel platforms which might be used in different growth factor delivery strategies. Then, the benefit of these release schemes are exemplified in the context of treatment strategies for the induction of new blood vessel formation (angiogenesis).

4.427.1.2. Technological Motivation for Development of Biomaterial Mimetics of Natural ECM

Materials that are degradable by hydrolytic or proteolytic means and therefore only temporarily occupy space, subsequently giving way to in-growing cells, allow the formation of new tissue and mitigate problems with chronic foreign body responses. The use of such implant materials to incorporate bioactive molecules, followed by implanting them at the site of desired administration, is an attractive strategy for localized growth factor delivery. To become effective, this approach demands biomaterial schemes for growth factor administration that emulate biological principles of growth factor function and the cell biological basis that is necessary to produce functional tissue. Alongside their base function to protect the embedded factor from clearance and proteolytic inactivation, these biomaterial delivery vehicles must mimic the *in vivo* release mechanisms and profiles (**Figure 1(a)**).

Initially, clinically approved biomaterials such as α-hydroxy-ester-based polymers or alginates have been adapted for localized growth factor delivery (the reader is referred to other reviews[16,17] and references therein; **Figure 1(b)**). Release of growth factors from such polymer depots is either driven by passive diffusion, or coupled to the material degradation rate via ester hydrolysis, which occurs independently of ongoing biological activity and thus can be out of tune with the actual healing process. Such materials offer to adjust the release kinetics by varying the amount of growth factor admixed to the matrix or by altering the material degradation rate via material composition or structure. However, these measures for dosing often proved insufficient to synchronize growth factor levels with cellular demands at the healing site.[16] Moreover, these polymer preparations provide neither sites for biologically specific molecular interaction with the growth factor molecules embedded in the polymer, nor sites for specific interaction with cells at the target tissue. Thus, growth factor release kinetics and cell–material interactions are often poorly controllable.

In order to match the needs of the treatment site, a reciprocal signal exchange between the material and the recruited cells is desirable. Such a molecular 'dialogue' may be achieved by incorporating into the material biological, active moieties that can directly interact with cells or interpret cell-derived signals, for example, proteolytic activity at the target site.[18,19]

In the last decade, the design of new materials for drug delivery and tissue repair has been inspired by functionalities of natural ECM that provides a tissue repository for storage, protection, and cell-regulated release of growth factors. In essence, the natural ECM is a cell-secreted, protein- and glycosaminoglycan-rich scaffold that not only provides

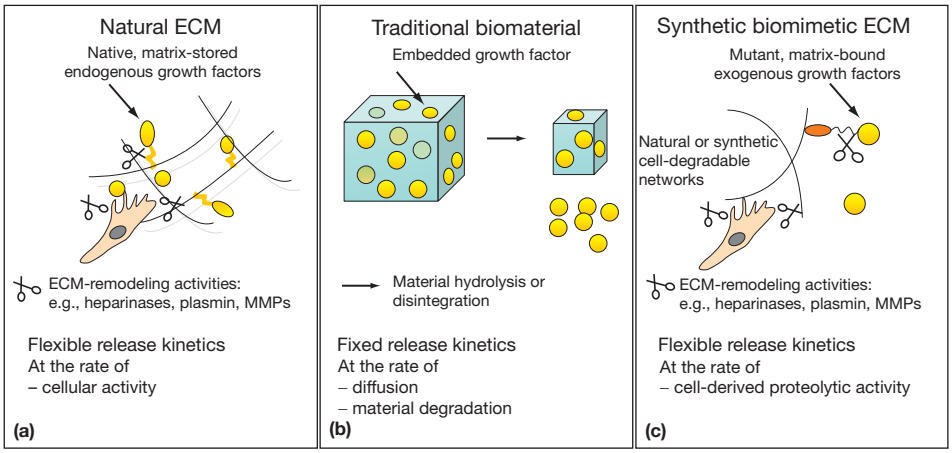

Figure 1 Biomaterials schemes for growth factor administration. (a) Many growth factors in the natural extracellular matrix (ECM) are matrix immobilized and released by local cellular activity. (b) In traditional biomaterials, growth factors are entrapped and released by diffusion and matrix degradation. (c) Matrix and growth factor engineering to control the distribution and release kinetics of growth factors.

mechanical stability but also plays a highly functionalized role in presentation and storage of biological signals, which contributes to tissue homeostasis, remodeling, and regeneration in case of injury. Our current view is that most endogenous polypeptide growth factors are not freely diffusible in tissues but are tightly associated with ECM components, such as heparan sulfate proteoglycans or fibronectin.[20] These assemblies between growth factors and matrix components are critical to stabilize the factors' active conformations, and serve as a depot of growth factors. Degradation of the matrix components by cellular enzymes such as heparinases or proteases then leads to the release of the growth factors in soluble form.[21] The preparation of both natural and completely synthetic materials with biological characteristics of the ECM has become central to tissue engineering approaches that aim to deliver growth factors in a therapeutically efficient mode and by more natural ECM-based mechanisms (**Figure 1(c)**).

4.427.2. Enabling Polymer Hydrogels for Cell-Demanded Release

As stated by Randy Pauch in his famous booklet *'The Last Lecture'* – engineering is not about the perfect solution but about the perfect solution with limited resources.[22] For a long time, the surgical material arsenal for potentially realizing cell-demanded release of growth factors from material implants was indeed very limited. In fact, growth factors were admixed to the bulk of materials or adsorbed onto the surface of scaffolds and were thus released in a largely uncontrolled fashion. For over a decade now, engineering of natural matrices and growth factors has enabled improved cell-instructive, biomimetic matrices.[23]

4.427.2.1. Collagen Engineering

Collagen matrices derived from tissue extracellular matrices have been successfully used in many tissue engineering applications, including improved endothelialization after coating vascular grafts with collagen matrices loaded and heparinized with basic fibroblast growth factor[24] (**Figure 2(a)**). Type I collagen forms highly porous networks with good adhesion and migration properties but exhibits poor binding capability for growth factors (see **Chapter 2.215, Collagen: Materials Analysis and Implant Uses**). However, one of the major limitations of naturally derived matrices like collagen in engineering applications is their inherent biological properties such as susceptibility toward proteolytic enzymes that has hindered their use in clinical settings. In order to prevent rapid degradation of collagen matrices, they are cross-linked by *N*-(3-dimethylaminopropyl)-*N*′-ethylcarbodiimide and *N*-hydroxysuccinimide. The resulting matrices were shown to be noncytotoxic *in vitro*[25] as well as *in vivo*.[26,27] Thrombogenicity of collagen in vascular graft coatings was even shown to be reduced after this cross-linking step.[28] Taking advantage of heparin's anticoagulation activity, protocols for its immobilization during the chemical cross-linking of the matrix were established (see **Chapter 2.216, Collagen–GAG Materials** and **Chapter 4.420, Drug Delivery via Heparin Conjugates**).[29,30] These engineered matrices prevented platelet adhesion and blood coagulation in response to collagen. They were additionally shown to recapitulate some of the retention and presentation properties of the naturally occurring ECMs toward growth factors. These biomimetic matrices have been employed to deliver basic fibroblast growth factor (bFGF) and vascular endothelial growth factor (VEGF) by controlled diffusion and matrix degradation, and in consequence to induce angiogenesis (**Table 1** and references therein). As preparation of these matrices relies on chemical cross-linking of heparin to the collagen fibers, their usage will be restricted to implant materials which are fabricated prior to application.

4.427.2.2. Fibrin Engineering

Fibrin is a natural polymer that forms by polymerization of activated fibrinogen during blood coagulation and plays an important role as provisional matrix in homeostasis and wound healing (see **Chapter 2.217, Fibrin**). In the wound, fibrin serves as a provisional platform for the infiltration of cells from neighboring tissues during the repair process. Fibrin is nontoxic, and various biomedical-grade 'fibrin glues' are

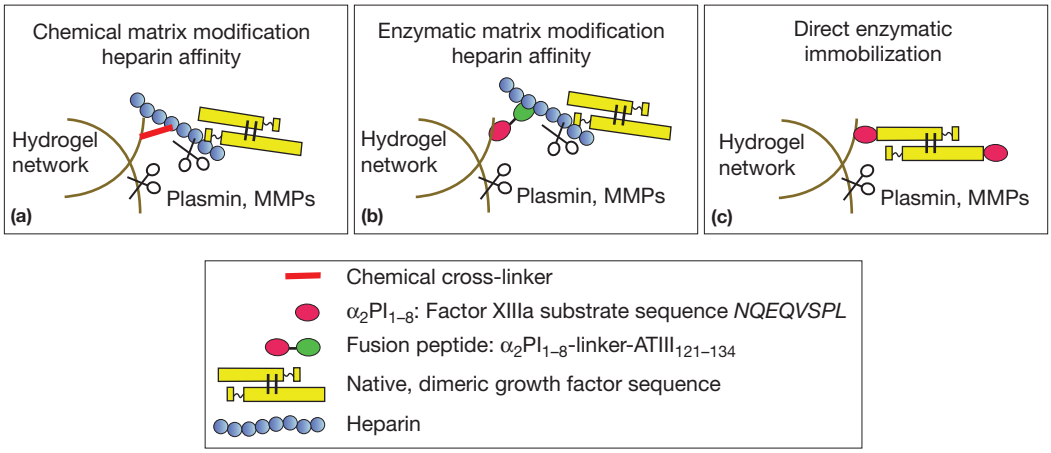

Figure 2 Engineering of biologically derived polymers. Heparin is retained within the matrix (a) by chemical cross-linking or (b) by matrix-bound heparin-binding peptides. (c) Engineered growth factors are covalently tethered to the matrix.

Table 1 Collagen engineering

Growth factor	*Engineering*	*Binding*	*Release*	*Comment*	*References*
$VEGF_{165}$	Immobilized heparin	Affinity	Controlled diffusion/matrix degradation	Chick CAM and subcutaneous tissue vascularization	31
$VEGF_{165}$	Immobilized heparin	Affinity	Controlled diffusion/matrix degradation	HUVEC process formation	32,33
$VEGF_{165}$	Chemical coupling of GF	Covalent	Cell-mediated release	EC spreading and proliferation, Chick CAM	34,35
TGF-β2	Chemical coupling of GF	Covalent	Cell-mediated release	Fibroblastic response in subcutaneous tissue	36
bFGF	Immobilized heparin	Affinity	Controlled diffusion/matrix degradation	HUVEC proliferation, biocompatibility in rats, human platelet adhesion	24,29,37
SDF-1α	Immobilized heparin	Affinity	Controlled diffusion/matrix degradation	Recruitment of hematopoietic cells in mice	38

accepted for clinical application.[39] Fibrin can be applied clinically as an injectable matrix, which can be readily formed by mixing solutions containing fibrinogen, thrombin, and the transglutaminase factor XIII (FXIII) directly at the site of therapeutical need. First, a physically linked gel is formed through thrombin-mediated conversion of soluble fibrinogen to fiber-forming fibrin, which is subsequently stabilized by FXIII-mediated cross-link formation between fibrin fibers. Under physiological conditions, the transglutaminase FXIII is also responsible for tethering of α2-plasmin inhibitor to the fibrin network. While fibrin provides many qualities desired for healing, in its natural form it provides no or low binding affinity for growth factor proteins. Thus, initial success to use fibrin as a matrix to deliver growth factors has been limited to physical growth factor entrapment and release.

In 1999, a new technology was reported that permits cell-demanded release of exogenous bioactive (polypeptide) factors, including growth factors, in the context of the biological matrix fibrin[40–44] (**Figure 2(b)** and **2(c)**). Exogenous peptides or proteins that are produced as fusion peptides or proteins with the specific eight-amino acid substrate sequence NQEQVSPL, derived from α2-plasmin inhibitor (α_2PI_{1-8}), at their N-terminus can be covalently attached to fibrin during the coagulation process through transglutamination by factor XIIIa (FXIIIa) enzymatic action.[43] Fibrin matrices containing these tailored immobilized proteins can then serve as depots, be proteolytically remodeled by invading cells, and thus represent excellent candidate vehicles for the delivery of biologically active proteins prompted by cell invasion and associated enzymatic activity.

The two principally distinct schemes for growth factor incorporation into fibrin are summarized in **Table 2**: the linkage of the heparin-binding growth factors to modified fibrin decorated with heparin (**Figure 2(b)**) and the covalent incorporation of the otherwise diffusible growth factors (**Figure 2(c)**) modified with NQEQVSPL sequence.

The first principle mimics the growth factors' natural presentation modality through heparan sulfate proteoglycans in the ECM (see **Chapter 4.420, Drug Delivery via Heparin Conjugates**). It is on the basis of the affinity-based interaction of heparin (**Figure 2(b)**) with a modified fibrin matrix and an electrostatic interaction of growth factors with natural affinities for heparin.[46,55] To accomplish the heparin immobilization, a synthetic bidomain peptide consisting of a heparin-binding peptide derived from both antithrombin III and the α_2PI_{1-8} domain is covalently incorporated into fibrin during the coagulation process.[41] When heparin is added simultaneously into the mixture before coagulation, a matrix rich in heparin is created. A growth factor entrapped within this matrix would then interact with the incorporated heparin molecules and be

Table 2 Fibrin engineering

Growth factor	*Engineering*	*Binding*	*Release*	*Comment*	*References*
NGF	Bifunctional peptide/heparin	Affinity	Controlled diffusion/ matrix degradation	Neurite extension from dorsal root ganglia *in vitro*, peripheral nerve regeneration in rats	45–47
BMP-2	Recombinant bifunctional GF	Covalent plasmin	Linker cleavage/ matrix degradation	Rat/rabbit critical size, dog patients	48
$VEGF_{121}$	Recombinant bifunctional GF	Covalent	Matrix degradation	HUVEC proliferation, angiogenesis on chick CAM, angiogenesis in mouse implants	44,49,50
$VEGF_{121}$	Recombinant bifunctional GF	Covalent	Linker cleavage/ matrix degradation	EPC differentiation	51
Ang-1 (extracellular domain)	Recombinant bifunctional GF	Covalent	Linker cleavage/ matrix degradation	HUVEC proliferation/adhesion Angiogenesis on Chick CAM	52
Ephrin-B2 (extracellular domain)	Recombinant bifunctional GF	Covalent	Matrix degradation	HUVEC proliferation/adhesion Angiogenesis on Chick CAM	53
KGF	Chemical coupling of peptide and GF	Covalent	Matrix degradation	Wound healing in a hybrid model (human on mouse)	54
bFGF	Bifunctional peptide/ heparin	Affinity	Controlled diffusion/ matrix degradation	Neurite extension from dorsal root ganglia	55
bFGF	Recombinant bifunctional GF	Affinity	Controlled diffusion/ matrix degradation	Neovascularization in subcutaneous implants	56,57
PDGF-BB	Bifunctional peptide/ heparin	Affinity	Controlled diffusion/ matrix degradation	Tendon repair in adult dogs	58
PTH(1-34)	Synthetic bifunctional peptide	Covalent	Linker cleavage/ matrix degradation	Critical size defect in sheep	59
L1Ig6	Recombinant bifunctional protein	Covalent	Matrix degradation	HUVEC process extension, Angiogenesis on Chick CAM, neurite extension of PC12 cells	60–63
NT-3	Bifunctional peptide/ heparin	Affinity	Controlled diffusion/ matrix degradation	Dorsal root ganglia outgrowth *in vitro*, peripheral nerve regeneration in rats, spinal cord injury	64–69
PDGF-BB	Bifunctional peptide/ heparin	Affinity	Controlled diffusion/ matrix degradation	Tendon healing	70,71

retained within the matrix.[46,55] The release of heparin-bound proteins from such engineered fibrin matrices is based on enzymatic matrix degradation by fibrinolysis, heparin degradation by heparinases as well as dissociation from heparin, and subsequent diffusion of the growth factor out of the gel. Using the protein's intrinsic affinity for heparin is an elegant strategy, which however is limited by the highly variable binding efficiency among different growth factors. This strategy has also been employed with other naturally derived polymers, such as gelatine and chitosan,[72] and has been recently extended also to semisynthetic and fully synthetic materials platforms.[73,74]

In the second design, the engineered growth factor molecules are directly linked to the fibrin backbone by the enzymatic activity of FXIII.[40,44] The tethered growth factors are presented to invading, fibrin-remodeling cells and are eventually liberated by bulk matrix degradation (**Figure 3(a)**). The rate of release is dependent on the activity of locally recruited cells, which on their surface secrete and activate fibrinolytic enzymes such as matrix metalloproteinases (MMPs) or plasmin. This mode of growth factor presentation, which relies on the disintegration of the fibrin matrix, can thus be considered a slow and cell-dependent one. Through the introduction of a plasmin-susceptible linker domain between the tether and the growth factor domain, protein release may be achieved not only by the cleavage of the matrix network itself but also by cleavage of the fibrin-coupling domain. As the release will be faster because of two simultaneous mechanisms, it can be considered an accelerated cell-demanded mechanism[51] (**Figure 3(a)**). This differential susceptibility to local proteolysis as a consequence can be applied in materials with different programmable and predictable growth factor release rates, which might be desired for controlled delivery of growth factors in experimental or clinical settings. The direct tethering of growth factors to fibrin, although an appealing and feasible approach, suffers the major limitation that growth factors that are employed to confer the biomaterial with biological activity must use time and labor-intensive procedures to genetically engineer and recombinantly express their modified forms.

4.427.2.3. Polysaccharide-Based Semisynthetic Materials

Polysaccharides, such as hyaluronic acid (HA), heparin, and alginate, are largely nontoxic materials with good biocompatibility that are present in living organisms and used in many different biomaterials design concepts.

Besides fibrous proteins, HA represents a major component of the ECM. HA consists of repeating units of glucuronic acid with *N*-acetyl-D-glucosamine with an average molecular weight between 100 and 5000 kDa[75] and is well known as a highly biocompatible polymer (see **Chapter 2.214, Hyaluronic Acid**). HA by itself has no known functionalities that facilitate the chemical binding and presentation of therapeutic growth

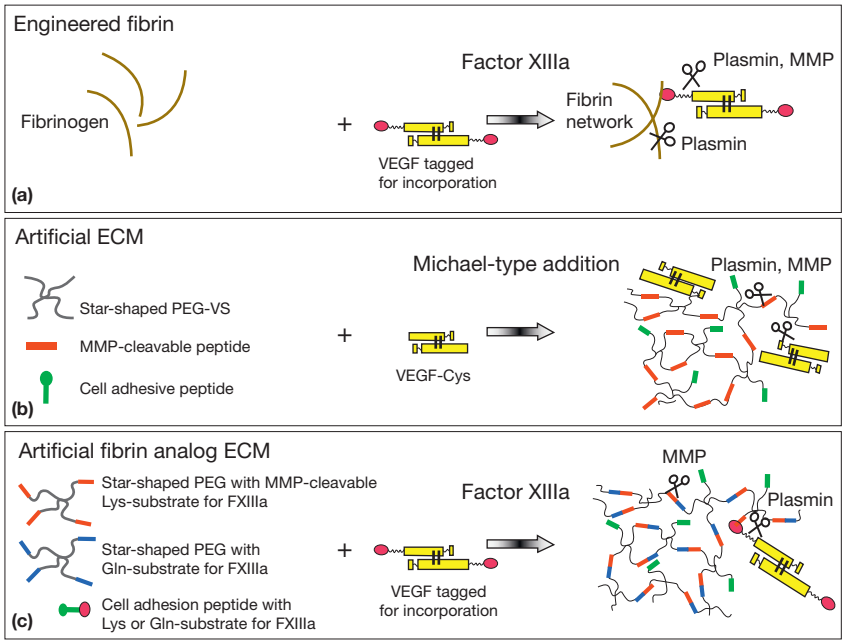

Figure 3 Engineering of synthetic biomaterials. (a) Tethering of engineered growth factors by FXIIIa enzymatic reaction to fibrin. (b) Free cystein (Cys) containing growth factors are chemically immobilized during Michael-type reaction-controlled PEG–hydrogel formation. (c) Artificial fibrin analog, PEG-based matrices are formed by FXIIIa. Engineered growth factors are simultaneously tethered to the matrix.

factors. Introducing known binding functionalities for growth factors would make these sugar-based materials more versatile biomaterials. Many attempts have been made to functionalize HA with chemical groups to modify it with synthetic polymers or bioactive signals (for review see Yadav *et al.*[76]). For example, HA modifications with thiol residues to enable cross-linking with PEG via Michael-type reactions have been described.[77] The same reaction was simultaneously used to decorate the forming HA-PEG hydrogel with biologically active components such as heparin and gelatin in a thiol-specific fashion.[77,78] Trace amounts of heparin were demonstrated to confer the HA-PEG materials with reasonable binding properties for heparin-binding growth factors.[78]

Protein-free scaffolds based on PEG and a noncovalent assembly of peptides with heparin have been used to study the delivery of growth factors. Such materials were formed by blends of heparin-functionalized and ATIII-peptide-functionalized four-arm star PEG polymers.[74,79–81] As these injectable materials form via affinity interactions, they are reversible and might mediate not only the retention but also the activity of growth factor molecules. The advantage of using the heparin affinity to control growth factor delivery is that naturally occurring molecules can be readily employed and time- and cost-intensive protein engineering can be avoided. However, such a system relies on the protein's affinity for heparin which might be limited and highly variable among different growth factors. Semisynthetic release systems relying on heparin binding affinity of growth factors are summarized in **Table 3**.

4.427.2.4. Fully Synthetic ECM Mimetic Hydrogels

As biologically derived polymers are difficult to engineer and bear the risk of disease transmission or induce immunological reactions, they are frequently substituted with fully synthetic materials for tissue engineering. Ideally, such materials are biocompatible and can be engineered toward specific applications, for example, by varying the building block composition. Initially, synthetic materials that interacted only moderately with cells in culture or in the living tissue were employed. A major stride has been made by introducing peptide building blocks or even recombinant proteins into synthetic hydrogels.[86–89] This allowed not only to control the physical and chemical properties of man-made materials but also to instill biological function into them. Introduced functions include integrin binding sites[90,91] and sequences susceptible toward cell surface-localized proteases.[18,19,92] That these materials can recapitulate some properties of the cell-derived polymeric ECM was demonstrated by 3D cell culture experiments. Cell spreading, migration, and proliferation in these fully synthetic matrices relied on the presence of the prototypic integrin binding peptide RGD and also MMP-sensitive linker peptides, proving that cell adhesion and matrix degradation were achieved.[18] The provisional character of the matrix was further demonstrated by its complete remodeling and replacement with native ECM in the context of bone regeneration.[19,93]

Attempts to control growth factor delivery from synthetic, ECM-mimicking materials are summarized in **Table 4**. Initial approaches relied on the incorporation of free cysteine-containing growth factors using thiol-specific Michael-type reactions, which also drive cross-linking of the matrix, to form cell-instructive matrices[98] (see **Figure 3 (b)**). Release of covalently bound growth factors in this system is coupled to the material degradation rate, tuned properly to the local cellular activity and thus considered as cell controlled.

Table 3 Semisynthetic biomimetic materials

Growth factor	*Engineered matrix*	*Binding*	*Release*	*Comment*	*References*
bFGF	PEG, heparin	Affinity	Controlled diffusion/ matrix degradation	hMSC adhesion, proliferation, differentiation *in vitro*, neuronal stem cell differentiation	73,74,79,81,82
$VEGF_{165}$	PEG, heparin	Affinity	Controlled diffusion/ matrix degradation	PAEC proliferation	80
VEGF, KGF, Ang-1, PDGF	PEG, hyaluronic acid, gelatin, heparin	Affinity	Controlled diffusion/ matrix degradation	Implants in ear pinnae of mice, microvascular number and maturity	75
HGF	PEG, hyaluronic acid, gelatin, heparin	Affinity	Controlled diffusion/ matrix degradation	Recruitment of MSCs *in vitro*	83
bFGF	PEG, chondrotinsulfate, heparin	Affinity	Controlled diffusion/ matrix degradation	Wound repair in diabetic mice microvascularization	84
VEGF + Ang-1	PEG, hyaluronic acid, heparin	Affinity	Controlled diffusion/ matrix degradation	Ear pinnas of mice, microvascularization	85
VEGF + bFGF	PEG, hyaluronic acid, gelatin, heparin	Affinity	Controlled diffusion/ matrix degradation	Ear pinnae of mice, microvascularization	78
bFGF	PEG, chondrotinsulfate, heparin	Affinity	Controlled diffusion/ matrix degradation	Subcutaneous pockets in mice, microvascularization	77

Table 4 Synthetic biomimetic materials

Growth factor	*Matrix*	*Engineering*	*Binding*	*Release*	*Comment*	*References*
TGF-β1	PEG	Chemical coupling of GF	Covalent	Cell-mediated release	ECM production by vascular smooth muscle cells *in vitro*	94
bFGF	PEG	Chemical coupling of GF	Covalent	Cell-mediated release	SMC migration	95
SDF-1α	PEGylated fibrinogen	Chemical coupling of GF	Covalent	Cell-mediated release	Recruitment of c-kit pos. Cells to acute myocardial infarcted heart	96
IFN-γ	Methacrylamide chitosan	Chemical coupling of GF	covalent	Cell-mediated release	Neural progenitor cell differentiation *in vitro*	97
$VEGF_{165}$/ $VEGF_{121}$	PEG	Native/recombinant cystein tagged GF	Covalent	Cell-mediated release	HUVEC proliferation, angiogenesis on chick CAM, angiogenesis in rat implants	98
$VEGF_{121}$	PEG	Enzymatic coupling of recombinant bifunctional GF	Covalent	Cell-mediated release	Angiogenesis on chick CAM	99

4.427.2.5. Fully Synthetic Fibrin Mimetic Hydrogels

Formation of matrices and incorporation of growth factors by chemical means might compromise the bioactivity of cell surface molecules and more importantly the protein cargo. Recently, a scheme has been established that relies on cross-linking of synthetic hydrogel matrices under physiological conditions by a FXIIIa-catalyzed enzymatic reaction[100–104] (**Figure 3(c)**). In one example, the material is composed of equimolar blends of star-shaped poly(ethylene glycol) (PEG) precursors that are functionalized with either the FXIIIa-specific substrate Lys (AcFKG)[101] or Gln (NQEQVSPL) sequence.[43] On addition of the enzyme, the matrix is formed, and simultaneously any protein or peptide carrying a FXIIIa-specific sequence can be immobilized within the matrix.[99] This design principle now allows the site-specific tethering of growth factors to the fully defined synthetic matrix as described above for the clinically relevant fibrin. By this scheme not only is the bioactivity of growth factors preserved but the release properties can also be flexibly and reproducibly controlled, namely, by (i) controlling the matrix cross-link density, (ii) engineering the matrix susceptibility toward proteolytic remodeling, and (iii) using different immobilization strategies. As release profiles can thus be tuned almost independently of the physical, chemical, and other biological properties, this new material might be interesting for future clinical applications.

4.427.3. Preclinical Evaluation in Angiogenesis

It is becoming increasingly evident that not only do appropriate biological signals need to be presented, but also that their spatiotemporal mode of presentation and combinations of several signals are necessary for proper induction of new and functional tissues.[15,105] Novel biomaterials concepts, developed to match some of these demands, will have to confirm the beneficial outcome in clinically relevant situations. One demanding application that is at the same time optimal for the rigorous evaluation of controlled growth factor delivery systems is the need to control angiogenesis. As outlined below, disturbed or insufficient angiogenic functions are involved in many diseases and await improved intervention modalities. In most of the sites requiring angiogenesis, the presence of body fluid will contribute to dilution, diffusion,

and eventually proteolytic inactivation of the therapeutically administered growth factor using conventional treatments.

4.427.3.1. Clinical Need for Angiogenic Therapy

Impaired vessel function, disrupting normal blood supply (ischemia), and consequently producing deficient functions of the heart or limbs, as well as hindering chronic wound healing, remains a major medical problems in societies with Western lifestyles and demographic shifts to longer life span. While improved surgical and minimally invasive interventional procedures (e.g., percutaneous transluminal balloon angioplasty or stent application, or the restoration of tissue perfusion pathways, e.g., by coronary artery bypass surgery) to restore blood supply in underperfused regions of the heart or leg have helped to decrease the mortality rates, the prevalence of ischemia has increased.[106] In many patients with tissue ischemia, for example, in the lower extremities in peripheral vascular disease, or in coronary artery disease, the intrinsic capacities for spontaneous tissue repair appear to be severely compromised, for reasons that are not understood at present. Multiple deficits may be responsible for inadequate regeneration of functional vasculature in ischemic patients, including (i) insufficient levels of endogenous angiogenic growth factors; (ii) disease- or age-related changes in cell metabolism, and an imbalanced production of angiogenic growth factors that have complementary functions in the initiation of vessels and their subsequent maturation into a stable vasculature; or (iii) an inability of cells to rebuild an extracellular microenvironment that fulfills its natural function as a site of growth factor-mediated cell signaling. As these causes may be coupled, the ischemic and chronic wound conditions present complex challenges for healing therapies. Therefore, prevention and treatment of ischemia represents an important goal. Tissue engineering has emerged as a significant potential alternative to conventional therapies of tissue or organ failure by surgical repair, transplantation, or mechanical devices.

4.427.3.2. Lessons from Embryonic Development and Early Therapeutic Angiogenesis Research

The establishment of a vascular supply is an important process not only during embryonic development but also in the adult, for wound healing or female reproductive functions.[107,108] Blood vessel formation in development is initiated by an assembly of endothelial progenitor cells (EPCs) into a primitive vascular network (vasculogenesis), which is expanded by sprouting or intussusceptive angiogenesis and finally remodeled by flow-driven mechanisms (arteriogenesis) that are not well understood at this point. These processes are regulated by various families of growth factor ligands that act through paracrine signaling by activating tyrosine kinase receptors, expressed on endothelial cells and supporting vessel wall cells. The most prominent growth factors tested in therapeutic angiogenesis regimens are VEGF-A, placental growth factor (PlGF), angiopoietin 1 (Ang 1), platelet-derived growth factor B (PDGF-B), FGF, and ligands of the ephrin family.

VEGF, initially regarded as the most promising entity, was shown to mediate blood vessel formation by chemotactic recruitment of EPCs or endothelial cells to the sites of neovascularization.[109] It promotes the differentiation of EPCs as well as the proliferation of endothelial cells. In tumors, the secretion of superphysiological levels of VEGF among other proangiogenic factors, in a phenomenon called angiogenic switch, attracts new blood vessels.[110,111] In common with tumors, the administration of superphysiological doses of exogenous VEGF induces the formation of supernumerary vessels. These vessels tend to be malformed and leaky, which in consequence cause edema and compromise the function of the tissue. Recent findings demonstrate a clear relationship between the morphology of newly formed vessels and the rate of VEGF release.[112] Additionally, neovessels are absolutely dependent on continuous long-term VEGF presentation to become patent and lasting.[113,114] On the basis of this knowledge, VEGF seemed to be an ideal candidate to prove the efficiency and functionality of the cell-controlled growth factor delivery.

4.427.3.3. Cell-Demanded Release in Vascularization

Synthetic and fibrin-based implants supplied with angiogenesis-stimulating growth factor signals were explored to promote regeneration of vascular-deficient tissue *in situ*.[115] Such provisional tissue replacement materials, formed directly at the site of therapeutic need, deliver biological signals to stimulate the body's own repair mechanisms to grow its cells into functional tissue, and might be valuable tools for a therapeutic treatment in regenerative medicine known as *in situ* tissue engineering.[116]

To this end, engineered growth factor variants were created with the eight-amino acid N-terminal domain (α_2PI_{1-8}) fused either directly (α_2PI_{1-8}–$VEGF_{121}$)[44,49] or in front of a plasmin-sensitive sequence linker (α_2PI_{1-8}–Pla–$VEGF_{121}$)[51] to the N-terminus of native variant $VEGF_{121}$ (**Figure 4(a)–4(c)**). These modified growth factors were readily incorporated into fibrin or synthetic fibrin analogs, whereas the native protein was unbound and therefore washed out rapidly in an aqueous environment. Biochemical analyses of the $VEGF_{121}$-modified cell-instructive the fibrin matrices, combined with mathematical modeling, confirmed that the release rate is controlled by plasmin susceptibility of the fibrin matrix and the linker peptide.[51] Thus, matrices with predictable and differential $VEGF_{121}$ release profiles could be generated by the use of (i) native $VEGF_{121}$ (burst diffusion-controlled release) (**Figure 4(a)**), (ii) α_2PI_{1-8}–Pla–$VEGF_{121}$ (accelerated, cell-demanded release) (**Figure 4(b)**), or (iii) α_2PI_{1-8}–$VEGF_{121}$ (slow, cell-demanded release) (**Figure 4(c)**). Cell culture and chick chorioallantoic membrane (CAM) experiments demonstrated that neither the method of matrix incorporation nor the plasmin-mediated liberation compromised the growth factor's activity.[49] More importantly, however, the kinetics of VEGF presentation to the CAM resulted in newly formed vascular networks that were (i) tumor like and of chaotic nature, in the case of fast VEGF release, (ii) largely disturbed in the case of intermediate release, and (iii) mostly well formed and with good integrity of the vascular basement membrane when VEGF was presented in a sustained, slow fashion. Subcutaneous murine implants confirmed that the balanced and prolonged presentation of the VEGF protein induced the formation of more mature and leakage-resistant blood vessels compared to the rapidly released factor.[49] This

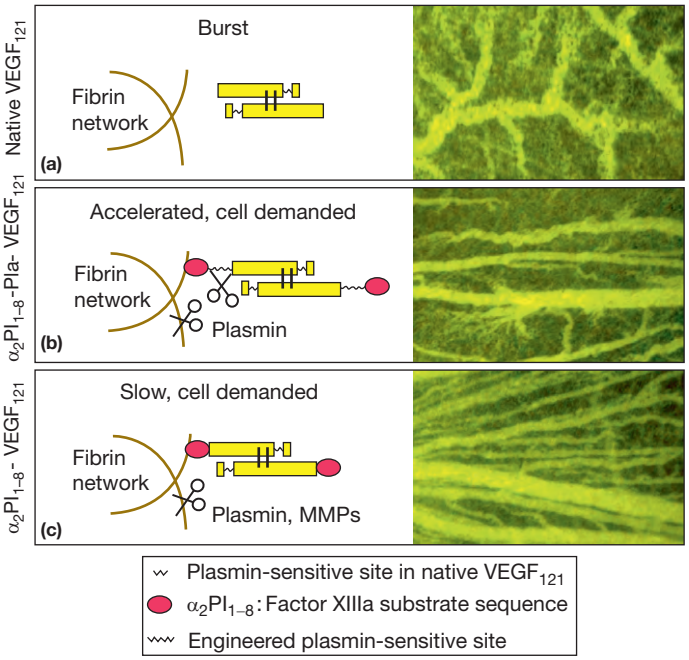

Figure 4 Therapeutic angiogenesis assay on the chick chorioallantoic membrane comparing fibrin scaffolds with different release regimen. (a) Native $VEGF_{121}$ entrapped in fibrin matrices is released by diffusion and induces malformed new vessels. (b) Cell-demanded accelerated release of $VEGF_{121}$ by matrix and linker cleavage results in vessels of better quality. (c) Slow, cell-demanded release of $VEGF_{121}$ by matrix degradation results in higher vessel number of 'good quality.'

observation is most likely because of the more balanced expression and activation of the differentially signaling VEGF receptors VEGFR1(Flt) and VEGFR2 (KDR). In experiments exceeding 3 weeks, slowly delivered VEGF proved to be more efficient in inducing blood vessels that were also more mature.[50] Yet, the newly formed vessels, independently of their stabilization, regressed at later time points, most likely because of a lack of metabolic need. In these experiments, exhaustion of the exogenous VEGF signal cannot be excluded. Thus, materials with a longer lifetime, which provide more rigorous control over VEGF over time, need to be evaluated in therapeutically relevant preclinical settings.

In conclusion, materials that provide sustained low-level presentation of VEGF might be employed to stimulate new blood vessel formation and induce the formation of stable and patent vessels. As their *in vivo* stability might largely influence the biological outcome, systems with a larger freedom to engineer the materials properties with respect to *in vivo* lifetime and growth factor release rate might be desirable.

4.427.4. Conclusion and Future Directions

The release of single growth factors by a relatively simple delivery regimen has been shown to enhance regional revascularization in preclinical and, to some extent, clinical trials. In clinical trials, the only marginal improvement in response to treatment could partially be explained by the nonideal delivery modalities of growth factors. As the biological demand might only be insufficiently matched regarding duration, amount, and activity of the presented growth factor, improved delivery devices and modalities were explored. Besides the elaboration of materials that can be loaded with defined quantities of protein and their release in a diffusion- and material-degradation controlled manner, protein engineering strategies were followed to generate novel classes of materials containing naturally derived and/or synthetic components.

One appealing way to control the release profile of growth factors is the immobilization of growth factors within hydrogel materials by covalent or high-affinity interactions. Such materials platforms have growth factor storage and presentation characteristics comparable to those of the natural ECM. In this context, the immobilization of locally produced factors and their slow but continuous exposure to neighboring cells under homeostatic conditions or in response to tissue remodeling are important. Many of the now-available materials schemes rely on the high-affinity interactions between growth factors and heparin. Through tethering of heparin molecules to the backbone of a matrix, hydrogels are obtained that readily bind several growth factors albeit with different efficiencies. A more reproducible way of immobilizing growth factors in a hydrogel matrix, but at the expense of labor-intensive recombinant protein production, is the covalent tethering of bifunctional factors to the material. Release of the growth factors from such matrices was shown to be controlled by site-directed, cell-mediated proteolysis. Initial studies exploring cell-mediated delivery of angiogenic, neurogenic, and osteogenic growth factors proved that these factors are delivered in a balanced and active manner. In the case of angiogenesis using this regimen, even singular VEGF therapy successfully induced morphologically integer vessels, whereas conventional delivery induced vessels that were malformed and leaky. These findings indicate that

cell-mediated protein delivery might not only improve efficiency but also safety of growth factors treatments, and in the future could be useful for therapeutic applications.

Delivery strategies at this stage are established only for a limited number of growth factors. The binding affinities of many growth factors and cytokines to heparin are not yet known and the fraction of proteins binding with high affinity cannot be estimated. The covalent tethering of growth factors relies on cloning, expression, and purification of every individual protein. For these reasons, it would be valuable to have a more versatile and broadly reliable release regimen available. Materials platforms should be developed, which can be applied to immobilize and present a large spectrum of proteins. Ideally, such platforms would allow the use of commercially available proteins. As biological events are tightly regulated by time and spatially controlled expression of different growth factors, engineering strategies should aim at mimicking such staged or simultaneous release. In order to make protein-presenting hydrogels relevant tools to study fundamental biological questions such as haptotaxis, and composition and function of tissue-specific niches, sequential or even trigger inducible release of factors would be desirable (see **Chapter 2.209, Materials as Artificial Stem Cell Microenvironments**). Furthermore, strategies developed for protein delivery might best be combined with those for gene delivery, or even common shared platforms might be of interest. Because of their high flexibility in design, fully synthetic matrices could be an ideal basis to create both protein and gene delivery platforms to control growth factor and cytokine distribution in time and space.

Acknowledgments

We would like to thank Prof. M.P. Lutolf for fruitful discussions and critically reviewing the manuscript. This work was supported by grants from the Swiss National Science Foundation (No. CR3213-125426/1) and the European Community's Angioscaff Program contract No. 214402.

References

1. Andrae, J.; Gallini, R.; Betsholtz, C. *Genes Dev.* **2008**, *22*, 1276–1312.
2. Carmeliet, P. *Nat. Med.* **2000**, *6*, 389–395.
3. Coultas, L.; Chawengsaksophak, K.; Rossant, J. *Nature* **2005**, *438*, 937–945.
4. Molin, D.; Post, M. J. *Curr. Opin. Pharmacol.* **2007**, *7*, 158–163.
5. Hanft, J. R.; Pollak, R. A.; Barbul, A.; *et al. J. Wound Care* **2008**, *17*, 30–32; 34–37.
6. Hinchliffe, R. J.; Valk, G. D.; Apelqvist, J.; *et al. Diabetes Metab. Res. Rev.* **2008**, *24*(Suppl. 1), S119–S144.
7. Margolis, D. J.; Morris, L. M.; Papadopoulos, M.; *et al. Mol. Ther.* **2009**, *17*, 1822–1829.
8. Eming, S. A.; Smola, H.; Krieg, T. *Cells Tissues Organs* **2002**, *172*, 105–117.
9. Post, M. J. *Ann. N. Y. Acad. Sci.* **2002**, *961*, 249–250.
10. Richard, J. L.; Parer-Richard, C.; Daures, J. P.; *et al. Diabetes Care* **1995**, *18*, 64–69.
11. Breen, A.; O'Brien, T.; Pandit, A. *Tissue Eng. B Rev.* **2009**, *15*(2), 201–214.
12. Chen, R. R.; Mooney, D. J. *Pharm. Res.* **2003**, *20*, 1103–1112.
13. Peppas, N. A.; Huang, Y.; Torres-Lugo, M.; Ward, J. H.; Zhang, J. *Annu. Rev. Biomed. Eng.* **2000**, *2*, 9–29.
14. Drury, J. L.; Mooney, D. J. *Biomaterials* **2003**, *24*, 4337–4351.
15. Lutolf, M. P.; Hubbell, J. A. *Nat. Biotechnol.* **2005**, *23*, 47–55.
16. Babensee, J. E.; Mcintire, L. V.; Mikos, A. G. *Pharm. Res.* **2000**, *17*, 497–504.
17. Quaglia, F. *Int. J. Pharm.* **2008**, *364*, 281–297.
18. Lutolf, M. P.; Lauer-Fields, J. L.; Schmoekel, H. G.; *et al. Proc. Natl. Acad. Sci. USA* **2003**, *100*, 5413–5418.
19. Pratt, A. B.; Weber, F. E.; Schmoekel, H. G.; Muller, R.; Hubbell, J. A. *Biotechnol. Bioeng.* **2004**, *86*, 27–36.
20. Hynes, R. O. *Science* **2009**, *326*, 1216–1219.
21. Whitelock, J.; Mitchell, S.; Graham, L.; Underwood, P. A. *Cell Biol. Int.* **1997**, *21*, 181–189.
22. Pausch, R.; Zaslow, J. *The Last Lecture*. Hyperion: New York, 2008; 224 p.
23. Hubbell, J. A. *Curr. Opin. Biotechnol.* **2003**, *14*, 551–558.
24. Wissink, M. J.; Beernink, R.; Poot, A. A.; *et al. J. Control. Release* **2000**, *64*, 103–114.
25. Van Luyn, M. J.; Van Wachem, P. B.; Damink, L. O.; Dijkstra, P. J.; Feijen, J.; Nieuwenhuis, P. *J. Biomed. Mater. Res.* **1992**, *26*, 1091–1110.
26. Van Luyn, M. J. A.; Van Wachem, P. B.; Dijkstra, P. J.; Damink, L.; Feijen, J. *J. Mater. Sci. Mater. Med.* **1995**, *6*, 288–296.
27. Van Wachem, P. B.; Van Luyn, M. J.; Olde Damink, L. H.; Dijkstra, P. J.; Feijen, J.; Nieuwenhuis, P. *J. Biomed. Mater. Res.* **1994**, *28*, 353–363.
28. Quinones-Baldrich, W. J.; Moore, W. S.; Ziomek, S.; Chvapil, M. *J. Vasc. Surg.* **1986**, *3*, 895–903.
29. Van Wachem, P. B.; Plantinga, J. A.; Wissink, M. J.; *et al. J. Biomed. Mater. Res.* **2001**, *55*, 368–378.
30. Wissink, M. J.; Beernink, R.; Scharenborg, N. M.; *et al. J. Control. Release* **2000**, *67*, 141–155.
31. Steffens, G. C.; Yao, C.; Prevel, P.; *et al. Tissue Eng.* **2004**, *10*, 1502–1509.
32. Grieb, G.; Groger, A.; Piatkowski, A.; Markowicz, M.; Steffens, G. C.; Pallua, N. *Cells Tissues Organs* **2010**, *191*(2), 96–104.
33. Markowicz, M.; Heitland, A.; Steffens, G. C.; Pallua, N. *Int. J. Artif. Organs* **2005**, *28*, 1251–1258.
34. Koch, S.; Yao, C.; Grieb, G.; Prevel, P.; Noah, E. M.; Steffens, G. C. *J. Mater. Sci. Mater. Med.* **2006**, *17*, 735–741.
35. Shen, Y. H.; Shoichet, M. S.; Radisic, M. *Acta Biomater.* **2008**, *4*, 477–489.
36. Bentz, H.; Schroeder, J. A.; Estridge, T. D. *J. Biomed. Mater. Res.* **1998**, *39*, 539–548.
37. Wissink, M. J.; Beernink, R.; Pieper, J. S.; *et al. Biomaterials* **2001**, *22*, 2291–2299.
38. Bladergroen, B. A.; Siebum, B.; Siebers-Vermeulen, K. G.; *et al. Tissue Eng. A* **2009**, *15*, 1591–1599.
39. Spotnitz, W. D. *World J. Surg.* **2010**, *34*, 632–634.
40. Sakiyama-Elbert, S. E.; Panitch, A.; Hubbell, J. A. *FASEB J.* **2001**, *15*, 1300–1302.
41. Sakiyama, S. E.; Schense, J. C.; Hubbell, J. A. *FASEB J.* **1999**, *13*, 2214–2224.
42. Schense, J. C.; Bloch, J.; Aebischer, P.; Hubbell, J. A. *Nat. Biotechnol.* **2000**, *18*, 415–419.
43. Schense, J. C.; Hubbell, J. A. *Bioconjug. Chem.* **1999**, *10*, 75–81.
44. Zisch, A. H.; Schenk, U.; Schense, J. C.; Sakiyama-Elbert, S. E.; Hubbell, J. A. *J. Control. Release* **2001**, *72*, 101–113.
45. Lee, A. C.; Yu, V. M.; Lowe, J. B., III; *et al. Exp. Neurol.* **2003**, *184*, 295–303.
46. Sakiyama-Elbert, S. E.; Hubbell, J. A. *J. Control. Release* **2000**, *69*, 149–158.
47. Wood, M. D.; Sakiyama-Elbert, S. E. *J. Biomed. Mater. Res. A* **2008**, *84*, 300–312.
48. Schmoekel, H. G.; Weber, F. E.; Schense, J. C.; Gratz, K. W.; Schawalder, P.; Hubbell, J. A. *Biotechnol. Bioeng.* **2005**, *89*, 253–262.
49. Ehrbar, M.; Djonov, V. G.; Schnell, C.; *et al. Circ. Res.* **2004**, *94*, 1124–1132.
50. Ehrbar, M.; Zeisberger, S. M.; Raeber, G. P.; Hubbell, J. A.; Schnell, C.; Zisch, A. H. *Biomaterials* **2008**, *29*, 1720–1729.
51. Ehrbar, M.; Metters, A.; Zammaretti, P.; Hubbell, J. A.; Zisch, A. H. *J. Control. Release* **2005**, *101*, 93–109.
52. Weber, C. C.; Cai, H.; Ehrbar, M.; *et al. J. Biol. Chem.* **2005**, *280*, 22445–22453.
53. Zisch, A. H.; Zeisberger, S. M.; Ehrbar, M.; *et al. Biomaterials* **2004**, *25*, 3245–3257.
54. Geer, D. J.; Swartz, D. D.; Andreadis, S. T. *Am. J. Pathol.* **2005**, *167*, 1575–1586.
55. Sakiyama-Elbert, S. E.; Hubbell, J. A. *J. Control. Release* **2000**, *65*, 389–402.
56. Zhao, W.; Han, Q.; Lin, H.; *et al. J. Mol. Med.* **2008**, *86*, 1127–1138.
57. Zhao, W.; Han, Q.; Lin, H.; *et al. Tissue Eng. A* **2009**, *15*, 991–998.
58. Gelberman, R. H.; Thomopoulos, S.; Sakiyama-Elbert, S. E.; Das, R.; Silva, M. J. *J. Hand Surg. Am.* **2007**, *32*, 373–379.
59. Arrighi, I.; Mark, S.; Alvisi, M.; Von Rechenberg, B.; Hubbell, J. A.; Schense, J. C. *Biomaterials* **2009**, *30*, 1763–1771.
60. Hall, H.; Djonov, V.; Ehrbar, M.; Hoechli, M.; Hubbell, J. A. *Angiogenesis* **2004**, *7*, 213–223.
61. Hall, H.; Hubbell, J. A. *Microvasc. Res.* **2004**, *68*, 169–178.
62. Luhmann, T.; Hanseler, P.; Grant, B.; Hall, H. *Biomaterials* **2009**, *30*, 4503–4512.
63. Pittier, R.; Sauthier, F.; Hubbell, J. A.; Hall, H. *J. Neurobiol.* **2005**, *63*, 1–14.

64. Johnson, P. J.; Parker, S. R.; Sakiyama-Elbert, S. E. *Biotechnol. Bioeng.* **2009**, *104*, 1207–1214.
65. Johnson, P. J.; Parker, S. R.; Sakiyama-Elbert, S. E. *J. Biomed. Mater. Res. A* **2010**, *92*, 152–163.
66. Johnson, P. J.; Tatara, A.; Shiu, A.; Sakiyama-Elbert, S. E. *Cell Transplant.* **2010**, *19*(1), 89–101.
67. Taylor, S. J.; McDonald, J. W., III; Sakiyama-Elbert, S. E. *J. Control. Release* **2004**, *98*, 281–294.
68. Taylor, S. J.; Rosenzweig, E. S.; McDonald, J. W., III; Sakiyama-Elbert, S. E. *J. Control. Release* **2006**, *113*, 226–235.
69. Taylor, S. J.; Sakiyama-Elbert, S. E. *J. Control. Release* **2006**, *116*, 204–210.
70. Sakiyama-Elbert, S. E.; Das, R.; Gelberman, R. H.; Harwood, F.; Amiel, D.; Thomopoulos, S. *J. Hand Surg. Am.* **2008**, *33*, 1548–1557.
71. Thomopoulos, S.; Zaegel, M.; Das, R.; *et al. J. Orthop. Res.* **2007**, *25*, 1358–1368.
72. Tanihara, M.; Suzuki, Y.; Yamamoto, E.; Noguchi, A.; Mizushima, Y. *J. Biomed. Mater. Res.* **2001**, *56*, 216–221.
73. Benoit, D. S.; Anseth, K. S. *Acta Biomater.* **2005**, *1*, 461–470.
74. Yamaguchi, N.; Kiick, K. L. *Biomacromolecules* **2005**, *6*, 1921–1930.
75. Hosack, L. W.; Firpo, M. A.; Scott, J. A.; Prestwich, G. D.; Peattie, R. A. *Biomaterials* **2008**, *29*, 2336–2347.
76. Yadav, A. K.; Mishra, P.; Agrawal, G. P. *J. Drug Target* **2008**, *16*, 91–107.
77. Cai, S.; Liu, Y.; Zheng Shu, X.; Prestwich, G. D. *Biomaterials* **2005**, *26*, 6054–6067.
78. Pike, D. B.; Cai, S.; Pomraning, K. R.; *et al. Biomaterials* **2006**, *27*, 5242–5251.
79. Nie, T.; Baldwin, A.; Yamaguchi, N.; Kiick, K. L. *J. Control. Release* **2007**, *122*, 287–296.
80. Yamaguchi, N.; Zhang, L.; Chae, B. S.; Palla, C. S.; Furst, E. M.; Kiick, K. L. *J. Am. Chem. Soc.* **2007**, *129*, 3040–3041.
81. Zhang, L.; Furst, E. M.; Kiick, K. L. *J. Control. Release* **2006**, *114*, 130–142.
82. Freudenberg, U.; Hermann, A.; Welzel, P. B.; *et al. Biomaterials* **2009**, *30*, 5049–5060.
83. Zhao, J.; Zhang, N.; Prestwich, G. D.; Wen, X. *Macromol. Biosci.* **2008**, *8*, 836–842.
84. Liu, Y.; Cai, S.; Shu, X. Z.; Shelby, J.; Prestwich, G. D. *Wound Repair Regen.* **2007**, *15*, 245–251.
85. Riley, C. M.; Fuegy, P. W.; Firpo, M. A.; Shu, X. Z.; Prestwich, G. D.; Peattie, R. A. *Biomaterials* **2006**, *27*, 5935–5943.
86. Kopecek, J. *Biomaterials* **2007**, *28*, 5185–5192.
87. Kopecek, J.; Yang, J. Y. *Acta Biomater.* **2009**, *5*, 805–816.
88. Tibbitt, M. W.; Anseth, K. S. *Biotechnol. Bioeng.* **2009**, *103*, 655–663.
89. Webber, M. J.; Kessler, J. A.; Stupp, S. I. *J. Intern. Med.* **2010**, *267*, 71–88.
90. Drumheller, P. D.; Hubbell, J. A. *Anal. Biochem.* **1994**, *222*, 380–388.
91. Hern, D. L.; Hubbell, J. A. *J. Biomed. Mater. Res.* **1998**, *39*, 266–276.
92. West, J. L.; Hubbell, J. A. *Macromolecules* **1999**, *32*, 241–244.
93. Lutolf, M. P.; Weber, F. E.; Schmoekel, H. G.; *et al. Nat. Biotechnol.* **2003**, *21*, 513–518.
94. Mann, B. K.; Schmedlen, R. H.; West, J. L. *Biomaterials* **2001**, *22*, 439–444.
95. Delong, S. A.; Moon, J. J.; West, J. L. *Biomaterials* **2005**, *26*, 3227–3234.
96. Zhang, G.; Nakamura, Y.; Wang, X.; Hu, Q.; Suggs, L. J.; Zhang, J. *Tissue Eng.* **2007**, *13*, 2063–2071.
97. Leipzig, N. D.; Xu, C.; Zahir, T.; Shoichet, M. S. *J. Biomed. Mater. Res. A.* **2010**, *93*(2), 625–633.
98. Zisch, A. H.; Lutolf, M. P.; Ehrbar, M.; *et al. FASEB J.* **2003**, *17*, 2260–2262.
99. Ehrbar, M.; Rizzi, S. C.; Hlushchuk, R.; *et al. Biomaterials* **2007**, *28*, 3856–3866.
100. Ehrbar, M.; Rizzi, S. C.; Schoenmakers, R. G.; *et al. Biomacromolecules* **2007**, *8*, 3000–3007.
101. Hu, B. H.; Messersmith, P. B. *J. Am. Chem. Soc.* **2003**, *125*, 14298–14299.
102. Sanborn, T. J.; Messersmith, P. B.; Barron, A. E. *Biomaterials* **2002**, *23*, 2703–2710.
103. Sperinde, J. J.; Griffith, L. G. *Macromolecules* **1997**, *30*, 5255–5264.
104. Sperinde, J. J.; Griffith, L. G. *Macromolecules* **2000**, *33*, 5476–5480.
105. Cao, L.; Mooney, D. J. *Adv. Drug Deliv. Rev.* **2007**, *59*, 1340–1350.
106. Laham, R. J.; Garcia, L.; Baim, D. S.; Post, M.; Simons, M. *Curr. Interv. Cardiol. Rep.* **1999**, *1*, 228–233.
107. Ferrara, N.; Alitalo, K. *Nat. Med.* **1999**, *5*, 1359–1364.
108. Risau, W. *Nature* **1997**, *386*, 671–674.
109. Li, B.; Sharpe, E. E.; Maupin, A. B.; *et al. FASEB J.* **2006**, *20*, 1495–1497.
110. Folkman, J. *Nat. Med.* **1995**, *1*, 27–31.
111. Folkman, J.; Hanahan, D. *Princess Takamatsu Symp.* **1991**, *22*, 339–347.
112. Ozawa, C. R.; Banfi, A.; Glazer, N. L.; *et al. J. Clin. Invest.* **2004**, *113*, 516–527.
113. Benjamin, L. E.; Golijanin, D.; Itin, A.; Pode, D.; Keshet, E. *J. Clin. Invest.* **1999**, *103*, 159–165.
114. Dor, Y.; Djonov, V.; Abramovitch, R.; *et al. EMBO J.* **2002**, *21*, 1939–1947.
115. Sun, Q.; Chen, R. R.; Shen, Y.; Mooney, D. J.; Rajagopalan, S.; Grossman, P. M. *Pharm. Res.* **2005**, *22*, 1110–1116.
116. Fischbach, C.; Mooney, D. J. *Biomaterials* **2007**, *28*, 2069–2076.

4.428. Sol–Gel Processed Oxide Controlled Release Materials

H Qu, S Bhattacharyya, and P Ducheyne, University of Pennsylvania, Philadelphia, PA, USA

© 2011 Elsevier Ltd. All rights reserved.

4.428.1.	**Introduction**	476
4.428.2.	**Sol–Gel Process**	477
4.428.2.1.	Overview	477
4.428.2.2.	Hydrolysis	477
4.428.2.3.	Condensation	478
4.428.2.4.	Physicochemical State of Sol–Gels and Incorporated Drugs	478
4.428.2.4.1.	Sol–gel	478
4.428.2.4.2.	Incorporated drugs	478
4.428.2.5.	Ordered Mesoporous Silica	479
4.428.3.	**Drug Release Mechanisms**	479
4.428.3.1.	Diffusion-Controlled Release	479
4.428.3.2.	Degradation-Controlled Release	480
4.428.3.3.	Mixed Release Kinetics	481
4.428.3.4.	Difference Between *In Vitro* and *In Vivo* Kinetics	481
4.428.4.	**Control of Release Kinetics**	481
4.428.4.1.	Effect of pH of the Sol	481
4.428.4.2.	Effect of Water/Alkoxide Molar Ratio	482
4.428.4.3.	Effect of Drying Conditions	483
4.428.4.4.	Effect of Additives	483
4.428.4.4.1.	Polymers	483
4.428.4.4.2.	Organically modified alkoxy silanes	484
4.428.4.4.3.	Surface modification	484
4.428.4.4.4.	Stimuli-responsive delivery	484
4.428.5.	**Biocompatibility and Resorption**	484
4.428.5.1.	Biocompatibility	484
4.428.5.2.	Systemic Biocompatibility of Resorbable Silica-Based Glasses	484
4.428.6.	**Applications**	487
4.428.6.1.	Sol–Gel Application Forms	487
4.428.6.1.1.	Monoliths	487
4.428.6.1.2.	Particle	487
4.428.6.1.3.	Fibers	488
4.428.6.1.4.	Thin films	488
4.428.6.1.5.	Hydrogels	489
4.428.6.1.6.	Mixed oxide sol–gels	489
4.428.6.1.7.	Composites	490
4.428.6.2.	Therapeutic Agents of Various Size	490
4.428.6.2.1.	Small therapeutic agents	490
4.428.6.2.2.	Intermediate sized therapeutic agents (proteins or growth factors)	490
4.428.6.2.3.	Large therapeutic agents (DNA or virus)	491
4.428.6.3.	Clinical Applications	491
4.428.6.3.1.	Pain management	492
4.428.6.3.2.	Bacterial infection control	492
4.428.6.3.3.	Cancer therapy	492
4.428.7.	**Summary**	493
References		493

Glossary

BET analysis An analysis based on the theory proposed by Brunauer, Emmett, and Teller in 1938 to determine the specific surface area of a material.

Biocompatibility The ability of a material to perform its desired function without eliciting any undesirable local or systemic effects.

Burst release A rapid release of more than 50% of drug within 24 h.

Isoelectric point The pH at which a particular molecule or surface carries no net electrical charge.
Mesoporous materials Materials containing pores with diameters between 2 and 50 nm.
Microporous materials Materials containing pores with diameters smaller than 2 nm.
Xerogel A gel dried at a temperature close to room temperature and under atmospheric pressure.

Abbreviations

APTES	Aminopropyl(triethoxy)silane
BSA	Bovine serum albumin
DMDES	Dimethyl(diethoxy)silane
ETES	Ethyl(triethoxy)silane
HLB	Hydrophile–lipophile balance
MTES	Methyl(triethoxy)silane
NMR	Nuclear magnetic resonance
PCL	Poly(caprolactone)
PDMS	Poly(dimethylsiloxane)
PEG	Poly(ethylene glycol)
PEI	Poly(ethyleneimine)
PNIPAAm	Poly(*N*-isopropyl acrylamide)
PTES	Propyl(triethoxy)silane
PVI	Poly(vinylimidazole)
TEOS	Tetraethoxysilane
TGF-β1	Transforming growth factor-β1
TMOS	Tetramethoxysilane

Symbols

C_{max} Maximum safe concentration
C_{min} Minimum effective concentration

4.428.1. Introduction

Therapeutic drugs, once administered, should be present in a concentration between the minimum effective concentration (C_{min}) and the maximum safe concentration (C_{max}) in blood, lest full efficacy is not achieved or side effects may occur. Typical systemic drug administration procedures, such as direct injection, inhalation, or ingestion, usually result in an inefficient bolus delivery and may need multiple administrations to avoid toxic plasma concentrations. Oral delivery and injection, which are the typical routes for drug administration, do not easily allow to control the rate of drug adsorption or do not enable to easily reach the target tissue of therapeutic interest, and are often associated with an immediate and rapid drug concentration spike. Consequently, the initial concentration of the drug in the body peaks above the level of toxicity and then gradually diminishes over time to an ineffective level. The duration of therapeutic efficacy then becomes dependent on the frequency of administration and the half-life of the drug. High dosages of drugs are often administered to achieve an effective blood concentration.

Controlled release systems can maintain the levels of therapeutic agents within the effective range, can reduce spread to undesirable sites, can avoid toxic side effects, and can enable more optimized drug dosage by virtue of increasing bioavailability and therapeutic index of the drug molecule. With these systems, drug levels in blood can follow 'constant' profiles between C_{min} and C_{max} for extended periods of time. Depending on the formulation and the application, this duration can vary from 24 h to 1 month to 5 years (in case of certain implants). This unique aspect of controlled release systems helps reduce the number of drug administrations required during a specific treatment.

One of the first principles underlying controlled drug delivery was to provide for a desirable near constant safe drug concentration at the site of action for prolonged durations. In addition, controlled release also offers numerous other advantages over systemic drug administration, such as protection of fragile drugs and increased patient compliance and convenience. It is also worth mentioning that controlled release systems can be utilized to target the release of the drug to the precise site of action within the body. For example, a drug molecule that acts on a receptor in the brain will not be effective if it is distributed by the patient's blood system without being able to cross the blood–brain barrier. Suitable controlled release materials loaded with such drug molecules and implanted inside the brain will allow drug molecules to be released at site of action.

An ideal drug delivery system must be biocompatible with human tissue, capable of achieving high drug loading, free from accidental leakage, and easy to fabricate. Many biocompatible materials including liposomes,[1] polymers,[2,3] and sol–gels[4,5] have been proposed as controlled release systems. Among these controlled release systems, the sol–gel processed oxides are biodegradable and biocompatible materials. They can also be made in a bioactive form. Unlike polymeric drug carriers, the sol–gel silica only elicits a minimal inflammatory response.[6,7] Also by nature of its simple processing conditions, various therapeutic agents can be homogenously incorporated in the nanoporous sol–gel silica.[7–12]

The nanostructure of sol–gel silica can be extensively and reproducibly varied by careful alteration of various processing related parameters. The variation in structure of sol–gel materials affects the release kinetics of the incorporated drug molecules, which in turn provides excellent control of the release profile.

Since the mid-1980s, when Avnir showed that the sol–gel process could be used to entrap dye molecules, the sol–gel process was first considered as no other than as expensive, fancy

glass making technique, useful to functionalize glass with organic molecules.[13] The same investigators continued to pursue the entrapment or immobilization concept with sol– gel materials. Thus, enzymes were entrapped in the sol–gels, and high retention of activity was reported in the early 1990s.[14–16] When entrapped in the sol–gel material, the enzymes were intended to function as biocatalysts within the sol–gel matrix. The entrapment of living organisms such as cells or bacteria was explored later using the same rationale.[17–20]

The use of sol–gel for the controlled release of incorporated molecules, a conceptually diametrically opposed idea for keeping molecules entrapped, did not emerge until the mid-to-late 1990s.[8,9,21–26] The demand for controlled, prolonged release of therapeutic agents started to pick up in pharmaceutical industry, and the quest for better matrix materials has brought sol–gel materials to the controlled release arena.

Many biocompatible oxides have been synthesized with the sol–gel method and used as controlled release systems. Sol–gel processed titanium dioxide (TiO_2) with porous structure was used to incorporate drug molecules inside the pores first, followed by controlled release thereafter.[27–30] Sol–gel processed TiO_2 containing an anticonvulsant drug (valproic acid) has been tested for the control of epileptic seizures in the temporal lobe of the brain.[29] Also a composite comprising sol–gel-derived TiO_2 and poly(ε-caprolactone) (PCL) was used for controlled drug delivery.[31] Sol–gel processed hydroxyapatite can also be used as a controlled delivery material.[32] Hydroxyapatite can further be coated with sol–gel silica to provide better control on the release of incorporated molecules. A hydroxyapatite/sol–gel silica composite was used to impregnate drug[33,34] and compared with hydroxyapatite and sol–gel silica materials alone. It was found that the composite material prevented rapid release and showed a prolonged release profile.[33] Among many sol–gel processed oxides that have been studied for their potential use as a controlled release carrier, sol–gel processed silica has been most thoroughly explored for applications as a controlled release material.

Herein, we focus extensively on sol–gel processed silica to illustrate the benefits and to elucidate the structure–property–processing relationships of sol–gel oxides as controlled release system. In this chapter, we discuss the general sol–gel process and the biocompatibility of the sol–gel oxides. As a control release system, the release kinetics of the incorporated molecules is discussed. Following the discussion regarding the effect of physical and chemical processing parameters of sol–gel-derived oxides on drug release kinetics, we review the applications potential of these materials in the controlled release arena. In the last section, we also summarize various applications that are being pursued with sol–gel oxides as controlled release system for pharmaceutics and biological molecules.

4.428.2. Sol–Gel Process

4.428.2.1. Overview

Although other sol–gel materials such as titanium oxide or hydroxyapatite have been tried for controlled release application,[35] silica sol–gel has been studied most extensively as a controlled release material in no small reason because it can be processed uniquely at room temperature. While traditional sol–gel processed materials will invariably include a sintering step intended to densify the material and achieve higher strength, the sintering step is conceptually deleterious when sol–gel processed silica would be used for controlled release. In fact, most therapeutically active molecules are unstable at higher temperature. Although mechanical properties are less critical in this application, the very fundamental inclusion of sintering in the classical processing of sol–gels rendered this departure of omitting sintering a nonobvious and failure prone approach.

The sol–gel process has been extensively studied during the 1980s–1990s. In this section, we briefly introduce the sol–gel process for silica used to synthesize controlled release sol–gels. Readers who are interested in more detail about the sol–gel process at large are referred to *Sol–Gel Science* by Brinker and Scherer, which deals with the general physical and chemical principles of sol–gel processing.[36]

In a typical sol–gel process, silica precursors (organosilanes), such as tetramethoxysilane (TMOS, $Si(OCH_3)_4$) or tetraethoxysilane (TEOS, $Si(OC_2H_5)_4$), are subjected to a hydrolysis–condensation reaction to form a colloidal suspension of silica particles, subsequent to which the particles condense in a new gel phase. The hydrolysis reaction, which can be either acid or base catalyzed, replaces alkoxide groups of organosilane with hydroxyl groups. Siloxane bonds (Si–O–Si) are formed during the subsequent condensation reaction. Alcohol and water are byproducts of the condensation reaction and evaporate during drying. In general, drugs are added to the liquid sol after hydrolysis. During condensation, the drugs are homogenously incorporated within the silica xerogel (a xerogel is a sol–gel processed material not or not yet subjected to sintering).

Different reaction rates of hydrolysis and condensation, especially the relative rates of hydrolysis and condensation, influence the silica particle formation. The nanostructure of sol–gel silica can be extensively varied in a controlled manner by selecting different processing parameters, including the pH of the sol and the water/alkoxide molar ratio, and by selecting various additives.[36,37] For example, the silica matrix has a microporous structure with a pore size smaller than 2 nm in case of hydrolysis under acidic conditions, while a mesoporous structure with a pore size range from 2 to 20 nm can be obtained under alkaline catalysis conditions. It is a logical concept to consider that the release kinetics of the drug molecules can be influenced by the variation in nanostructure of silica xerogel thus achieved by varying the processing.[38]

4.428.2.2. Hydrolysis

The hydrolysis occurs by the nucleophilic attack of the oxygen contained in water on the silicon atom of the organosilane. The hydrolysis is most rapid and complete when catalysts are employed. Many researchers have reported that mineral acids are more effective catalysts than an equivalent concentration of base.

Under acidic conditions, the alkoxide group (OR) is protonated, which makes the silicon more electrophilic and susceptible to attack by water. All strong acids behave in a similar way as the hydrolysis is a first-order reaction, while weak acids

require a longer time for the hydrolyzation. In acid-catalyzed reactions, the hydrolysis rate is increased by alkyl groups with less steric hindrance around silicon (i.e., hydrolysis of TMOS is much faster than TEOS).

Under basic conditions it is likely that water dissociates to produce nucleophilic hydroxyl anions in a rapid first step. The hydroxyl anion then attacks the silicon atom and liberates the alcohol. Similar as acid-catalyzed hydrolysis, the steric factor also affect the hydrolysis rate and the base-catalyzed hydrolysis reaction is also dependent on catalyst concentration.

Sonolysis is an alternative method to promote hydrolysis without acid or base catalysts. By subjecting the silica precursor and water mixture to ultrasonic vibration, active radical species are formed. Such active radical species, derived from silica precursors ($(OR)_n(OH)_mSiO^{\bullet}$ and $(OR)_n(OH)_mSi^{\bullet}$ $(m+n=3)$) reacts with an active radical species from water ($H^{\bullet}$ and $^{\bullet}OH$) to form a $Si(OR)_n(OH)_m$ $(m+n=3)$ such as hydrolyzation pruduct.[39] Sol–gels prepared through sonolysis are commonly referred as sonogels. Sonogels have been tested for their feasibility as pharmaceutical delivery systems.[40] However, concern that the ultrasonic irradiation, which is necessary for producing the radical species, may damage the incorporated sensitive drug molecules has limited the pursuit of this processing method to produce controlled release materials.

No matter what condition, the overall hydrolysis reaction is given by the reaction:

$$Si(OR)_4 + 4H_2O \rightarrow Si(OH)_4 + 4ROH \qquad [I]$$

4.428.2.3. Condensation

Condensation is the polymerization process that creates siloxane bonds.

The condensation reaction is as below:

$$Si(OH)_4 \rightarrow SiO_2 + 2H_2O \qquad [II]$$

Under acidic condition, the condensation involves protonated silanol species. The protonation of silanol makes the silicon more electrophilic and thus more susceptible to nucleophilic attack. Under basic condition, the condensation reaction involves the attack of nucleophilic deprotonated silanol on a neutral silicate species.

The condensation rate is highly affected by the pH condition. The maximized condensation rate can be achieved around pH 7.0 where both protonated and deprotonated silanols are highest in concentration, while the minimum condensation rate is found around the isoelectric point (pH ~2.0).

The overall sol–gel process is as follows:

$$nSi(OR)_4 + 2nH_2O \rightarrow nSiO_2 + 4nROH \qquad [III]$$

Condensation reactions (eqn [II]) involving the silanol groups (Si–OH) produce siloxane bonds (Si–O–Si) plus the by-products water or alcohol. Under most conditions, condensation commences before hydrolysis is complete. However, conditions such as, pH, H_2O/Si molar ratio (R), and catalyst can force completion of hydrolysis before condensation begins. Additionally, because water and alkoxides are immiscible, a mutual solvent such as an alcohol is utilized. With the presence of this homogenizing agent, alcohol, hydrolysis is facilitated due to the miscibility of the alkoxide and water. As the number of siloxane bonds increases, the individual molecules are bridged and jointly aggregate in the sol. When the sol particles aggregate, or inter-knit into a network, a gel is formed. Under acidic conditions, the most basic silanol species are most likely to be protonated. Therefore, condensation reaction may occur preferentially between neutral species and protonated silanols situated on the end groups of chains. As the result, the final gel is mostly an extended, weakly branched structure. Under alkaline condition, as most acidic (deprotonated) silanols resides in the middle of the chains, the condensation is directed toward the middles rather the end of the chains, leading to more compact higher branched structures.

The condensation in gels continues long after gelation, due to large amount of unreacted silanol groups. Aging is an extension of the gelation step in which the gel network is reinforced through further condensation. The gel matrix shrinks due to the expulsion of solvent, called syneresis, and this takes place during drying.

Depending on the condensation conditions, the final sol–gels have different structures. Sol–gels that condensed in acidic conditions generally acquire low-porosity microporous (smaller than 2 nm) pore structures and the sol–gels that condensed under basic condition have mesoporous pore structures.

During the hydrolysis of TEOS or TMOS, a significant amount of alcohol is liberated, which may denature the incorporated protein molecules. This problem can be overcome by using aqueous precursors of silica such as sodium silicate, silicic acid, or glycerated silanes.[41,42] This procedure mimics the biogenic silica formation (biosilicification) in aqueous environment with the dilute silicic acidic $Si(OH)_4$ solutions. In such a way, living organisms such as cell and bacteria can be safely encapsulated in the silica matrix.[43]

4.428.2.4. Physicochemical State of Sol–Gels and Incorporated Drugs

4.428.2.4.1. Sol–gel

During the sol–gel process, hydrolysis and condensation reactions determine the states and numbers of Si–O–Si linkages in the sol–gel oxide structure. Ideally, a four-functional metal alkoxide such as TEOS reacts to completion, forming a tetrahedrally bonded glass network. If either the hydrolysis or condensation reactions are incomplete, the tetrahedrally bonded SiO_2 network is not fully formed. The silicon connectivity can be categorized with five degrees: Q^0 denotes a silicon with no Si–O–Si linkages, Q^1 denotes a silicon with one Si–O–Si linkage, Q^2 denotes a silicon with two Si–O–Si linkage, Q^3 denotes a silicon with three Si–O–Si linkage, and Q^4 denotes a silicon with four Si–O–Si linkages.[44] The degree of condensation, defined by Viitala,[45] is $Q^4/(Q^2+Q^3)$. Obviously, the higher degree of condensation, the more silicons have four Si–O–Si linkages. The degree of condensation can be obtained by using solid-state ^{29}Si magic-angle-spinning nuclear magnetic resonance (NMR) measurement.

4.428.2.4.2. Incorporated drugs

Drugs with low volatility (low vapor pressure) will remain inside the silica gel structure during the water and alcohol evaporation. If the drug added in the sol is not as volatile as

water or ethanol, theoretically, the final drug retention within the sol–gel should be 100%. Indeed, many studies have evidenced a close to unit drug retention.

Sol–gel materials are attractive for the delivery of poorly water soluble drugs. It is a major therapeutic challenge to deliver water insoluble drug due to low bioavailability and insufficient dissolution during the gastrointestinal absorption. Hydrophobic drugs with low water solubility, dissolved in organic solvents, can easily be mixed with a hydrolyzed sol. After removal of the organic solvents and byproducts (water and ethanol) through evaporation, drugs are stored inside the sol–gel matrix and ready for delivery. Both the sol–gel process and silica inorganic matrix are robust enough to tolerate many organic solvents.

Further studies also revealed that drugs incorporated in the sol–gel silica pores are in the amorphous state.[46–48] In general, the amorphous form of drugs has a faster dissolution rate and a higher solubility when compared to its crystalline form.[49] This particular phenomenon is very beneficial for the delivery of poorly water soluble drugs.[46,50,51] Both *in vitro* and *in vivo* studies confirmed that drugs with low water solubility are released faster when incorporated in mesoporous silica. In addition, more drugs can be released, thereby increasing the bioavailability.[46]

4.428.2.5. Ordered Mesoporous Silica

Ordered mesoporous silica materials with pore sizes in the range from 2 to 30 nm represent a variant of sol–gel oxides used for controlled drug delivery. Mesoporous silica was first studied by the researchers of Mobil Oil Corporation in 1992.[52] The synthesis methods of mesoporous silica such as MCM (mobile composition of matter) and SBA (Santa Barbara Amorphous) are similar to the regular sol–gel process. The reaction also involves the hydrolysis (eqn [I]) and subsequent condensation (eqn [II]) of silica precursors (organosilanes) such as tetraethoxysilane (TEOS). In this case, a mixture of ethanol, water, aqueous ammonia, and surfactants in basic (pH 10–12) environment is used. The surfactants first self-assemble into a micelle structure when the surfactant concentration reaches the critical micellar concentration. The shape and size of the micelle structure depends on factors, such as chemical and physical properties of the surfactant, surfactant concentration, pH, and temperature. During hydrolysis and condensation, the silica forms at the surface of the surfactants micelle through strong electrostatic interactions. After removing the surfactant either by solvent extraction or calcinations at high temperature, the porous structure remains in the silica material. The surface area and pore size of the mesoporous silica materials can be adjusted by choosing different surfactants and pH values.[53] The drug is incorporated by soaking the mesoporous silica in a highly concentrated drug solution and subsequent drying. Mesoporous silica have unique features such as a stable structure, open pores, and a controlled pore size with narrow pore size distribution. These materials are also promising materials for controlled release.[54] Different drug release kinetics can be achieved by either adjusting the structural properties or modifying the mesoporous silica walls with organic moieties.[55–57] In **Chapter 4.429, Ordered Mesoporous Silica Materials**, the mesoporous silica is discussed in great detail.

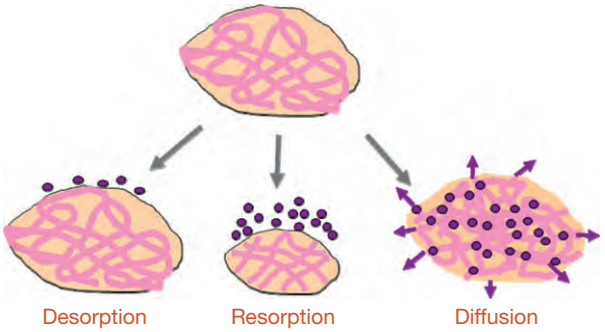

Figure 1 Schematic representation of the drug release mechanisms.

4.428.3. Drug Release Mechanisms

Drugs can generally be released from a matrix in three different ways. **Figure 1** is a schematic representation of the drug release mechanisms. Among the three mechanisms, desorption release accounts for the release of molecules that are superficially absorbed on the surface of the materials. This mechanism is hard to control, but it contributes negligibly to the total drug release. Therefore, the majority of drug released from sol–gel silica is controlled by the diffusion rate of drug molecules from the pores within the silica by the degradation of the silica matrix itself, or by both.

4.428.3.1. Diffusion-Controlled Release

The diffusion-controlled release is the leaching of drug molecules encapsulated in the pores of the silica when liquid penetrates the porous matrix, dissolves the drugs and diffuses into the exterior liquid due to concentration gradient. The drug release is governed by Fick's law of diffusion. One of the most important controlled release equations to describe the release kinetics of molecules in a diffusion-controlled process is called the 'Higuchi equation.' The Higuchi equation has helped define the mathematical perspective of controlled release drug delivery systems since the era of development of sustained release dosage forms.[58] This equation has been applied for diffusion-controlled release from a porous matrix, from which a drug is leached by the bathing fluid that penetrates the matrix through pores and capillaries:

$$Q = \sqrt{\frac{D\varepsilon(2A - \varepsilon C)Ct}{\tau}} \qquad [1]$$

with Q, amount of drug released after time t; D, diffusivity of the drug in the permeating fluid; τ, the tortuosity factor of the capillary system. The tortuosity indicates that the tortuous path of transport of a drug through porous structure. The tortuosity accounts for the complexity of pore geometry; A, the total amount of the drug present in the matrix; C, the solubility of the drug in the permeating fluid; and ε, the porosity of the matrix. The porosity is the fraction of pores in the system that open to the surface.

The above eqn [I] can be expressed in more simple form as:

$$Q = k\sqrt{t} \qquad [2]$$

where k is known as Higuchi dissolution constant. Thus, the cumulative release of drug released is proportional to the square root of time.

Today, the Higuchi equation is one of the most widely used and the most well-known controlled release equations. According to this equation, and as stated, the cumulative release of released drug is proportional to the square root of time. The rate of release can be increased by increasing the drug's solubility (C) in the host matrix, or the inverse, can be decreased by decreasing the solubility.

It is important to note that a few assumptions are made in this Higuchi model. They include (i) the initial drug concentration in the system is much higher than the matrix solubility, (ii) perfect sink conditions are maintained, (iii) the diffusivity of the drug is constant, and (iv) the swelling of the matrix is negligible. The sink conditions are achieved by ensuring the concentration of the released drug in the release medium never reaches more than 10% of its saturation solubility.

It can be seen from the Higuchi equation that the nanostructure structures of sol–gel, such as the pore volume, the specific surface area, and the pore diameter have a major influence on the release phenomena. The pore surface chemistry also can affect the drug molecular release through drug sol–gel interaction.

In addition to the commonly used Higuchi model, other release kinetic models have been proposed to describe the drug release behavior from sol–gel processed xerogels.[59,60] The Higuchi model only considers the drug released from planar/tabular matrix. In reality, the sol–gel oxides can be prepared into various shapes, such as coatings, fibers, and particles. Among these various shapes, sol–gel oxide particles, or powders attracted more attention by virtue of its simple preparation process and easy application. Therefore, studies have been devoted to analyze release kinetics from spherical matrix. Baker and Lonsdale[59,60] developed a model from the Higuchi model and described the drug release from spherical matrices according to the equation:

$$\frac{3}{2}\left[1-\left(1-\frac{M_t}{M_\infty}\right)^{2/3}\right]-\frac{M_t}{M_\infty}=kt \qquad [3]$$

where M_t/M_∞ is the fractional drug released at time t; k, the constant depending on the structural and geometrical characteristics.

To study the release kinetics, data obtained from *in vitro* drug release studies were plotted as $d[(M_t/M_\infty)]/dt$ with respect to the root of time inverse.

In diffusion-controlled release, the pores are large enough to be thought of as 'channels' for diffusion (pore diameter greater than drug molecular), diffusion occurs predominantly through these water-filled pores. However, if the pores are smaller than drug molecules, then the diffusion-controlled mechanism may not be able to account for the kinetics of drug release.

4.428.3.2. Degradation-Controlled Release

When implanted in to body, silica sol–gels gradually degrade over time. The dissolved sol–gel silica is harmlessly excreted in soluble form through the urine, as described below. The sol–gel silica degradation rate is mostly depended on silica's structure. In a normal conditioned body (pH around 7.4 and temperature around 37 °C), the solubility of amorphous silica is around 120–150 ppm while the crystalline silica is ten times less soluble.[61,62] Not only is the solubility, but also the dissolution rate is dependent on the structure. There are two major parameters that one can focus on to vary the sol–gel silica degradation rate: degree of condensation and specific surface area.

Compared with Si–O–Si linkage, the silanol (Si–O–H) group is easier to break through a hydrolysis process. Therefore, the amount of silanol groups is related to the degradation rate. The degradation rate is higher when more silanol groups are present in the silica. When the degree of condensation is low, there are much more free silanol groups in the silica surface.[45,61]

A well-hydrolyzed sol of alkoxides gelled to a low degree of condensation can result in a high number of free silanol groups per surface area. As an example, in a typical silica sol–gel process, a sol with low water-to-TEOS ratios and low pH (pH around 2) near gel point, for example, to $t_{gel}=0.90$–0.98 (0 corresponds to sol preparation, 1.00 to the gel point) can be spun to form fibers. Sol–gel fibers are spun immediately before the condensation process, leaving no time for condensation reactions. The resulting silica fiber having a very low degree of condensation usually degrades within less than a day.[45] Other fast form-giving processes can also form silica with a low degree of condensation, such as freeze drying and spray drying. On the other hand, the regular slow spontaneous gelation process of the same sol gives rise to fully condensed silanol groups. Thus, spontaneously formed silica monoliths dissolve at a much slower rate.

The specific surface area also affects the degradation rate. The higher the specific surface area, the more silanol groups are accessible, such as to be liberated from the surface into the dissolution medium. Therefore, a high surface area makes the silica to degrade faster.[62] Typically, silica hydrogels contain a very high water content, about >90% (w/w) of water and <8% of silica.[63–65] The sols for these hydrogels are generally prepared at high water-to-alkoxide ratios (>50). Silica hydrogels dissolve completely within 2–3 days *in vitro* using sink dissolution conditions.

The mathematical model developed by Hopfenberg describes the idealized kinetics of drug release from a matrix by any erosion/relaxation process regardless of mechanism, and it is assumed that the relaxations are not confounded by diffusion processes.[66] In this model, all mass transfer processes involved in controlling drug release are assumed to add up to a single zero-order process (characterized by a rate constant, k_0) confined to the surface area of the system. This zero-order process can correspond to a single physical or chemical phenomenon, but it can also result from the superposition of several processes, such as dissolution, swelling, and matrix chain cleavage. Good examples for systems where Hopfenberg's model can be applied are surface eroding polymers or sol–gel silica matrices where a zero-order surface detachment of the drug is the rate limiting release step. Hopfenberg derived the following, general equation, which is valid for spheres, cylinders, and slabs:

$$\frac{M_t}{M_\infty}=1-\left(1-\frac{k_0 t}{c_0 a}\right)^n \qquad [4]$$

M_t and M_∞ are the cumulative amounts of drug released at time t and at infinite time, respectively; c_0 denotes the uniform initial drug concentration within the system; a is the radius of a cylinder or sphere or the half-thickness of a slab; n is a 'shape factor' representing spherical ($n=3$), cylindrical ($n=2$), or slab geometry ($n=1$). For sol–gel silica system, the above equation can be approximated (for $n=1$) to:

$$\frac{M_t}{M_\infty} = kt \quad [5]$$

4.428.3.3. Mixed Release Kinetics

From the above discussion, it is evident that the release kinetics controlled by diffusion can be described by Higuchi model. The Higuchi model can be rewritten as:

$$\frac{M_t}{M_\infty} = kt^{0.5} \quad [6]$$

where M_t/M_∞ is the fractional drug released at time t; k, the constant depending on the structural and geometrical characteristics.

Similarly, the release kinetics controlled by degradation can be expressed as:

$$\frac{M_t}{M_\infty} = kt \quad [5]$$

where M_t/M_∞ is the fractional drug released at time t; k, the constant depending on the structural and geometrical characteristics.

Based on Fick's second law of diffusion and assuming that the release experiment proceeds in perfect sink condition and that the drug distribution is homogeneous, Peppas introduced the following simple exponential relationship to describe drug release under mixed release kinetics conditions, including both degradation and diffusion.[67,68]

$$\frac{M_t}{M_\infty} = kt^n \quad [7]$$

where M_t/M_∞ is the fractional drug released at time t; k, the constant depending on the structural and geometrical characteristics; n, the indicator of the mechanism of drug release.

This equation can be used until 60% of the drug has been released. It is shown that exponent values $n<0.5$ are indicative of diffusion-controlled release. $n=1.0$ indicates actually zero-order drug release kinetics, which can be achieved also with degradation-controlled release. The n values between 0.5 and 1.0 are indicative of anomalous transport behavior including both diffusion and degradation. Although the power law has its limitations, it is considered to be more useful in the comparative studies providing explanations for the diffusion-controlled release with consideration of the matrix degradation effect on the release kinetics.

4.428.3.4. Difference Between *In Vitro* and *In Vivo* Kinetics

Considering that one can vary sol–gel processing conditions, that the range of the size of drug molecules is large, and that drug molecules may interact with the silica, drug release from sol–gel silica can be diffusion-controlled, degradation-controlled or both. With such unique property for sol–gel materials, the drug release profile can be readily adjusted for various applications.

Although many models have been proposed to fit *in vitro* drug release behavior, one has to carefully apply the *in vitro* release profiles for the *in vivo* situation, as in fact *in vitro* release profiles often do not completely correlate to the *in vivo* profiles. The *in vivo* degradation rate of silica structures is much slower than *in vitro* degradation rates. For example, it has been found that the *in vitro* degradation rate is about eight to ten times higher than *in vivo* degradation rate for sol–gel silica. Such results indicated the longer degradation period and longer drug release duration *in vivo*.[61,69]

The difference in the behavior between *in vitro* and *in vivo* data likely stem from two origins: difference in fluid flow *in vitro* and *in vivo*, and tissue – sol–gel carrier interaction. When implanted, the fibrous capsule around the drug carrier may reduce the fluid flow around the drug-controlled release material and slow down drug diffusion from the carrier material into the surrounding tissues.[6,69] In case of a situation where there is tissue – sol–gel carrier interaction present, research has shown that serum proteins absorbed on the silica sol–gel result in a 20–30% reduction in dissolution, suggesting a slower degradation *in vivo*.[62]

4.428.4. Control of Release Kinetics

One of the unique properties of sol–gel oxides as drug carriers for controlled release is that the drug release kinetics can be optimized through either physical or chemical alterations of the silica. The silica xerogel structure can be extensively varied in a controlled manner by selecting different processing parameters, such as the pH of the sol, the water/alkoxide molar ratio, and the use of various additives. In addition, chemically modified silica sol–gels can interact with an incorporated drug, and thereby alter the drug diffusion rate. Molecules sensitive to external stimuli such as temperature, light, or pH attached within the pores can further be used to regulate the drug release kinetics.

4.428.4.1. Effect of pH of the Sol

During hydrolysis, all strong acids (e.g., hydrochloride acid, nitric acid, and sulfuric acid) behave similarly as the hydrolysis is a first-order reaction, while weak acids such as acetic acid require a longer time for hydrolysis. Thus, the time to achieve a homogeneous state of hydrolysis is longer for catalysis with weak than strong acids. The size and shape of the silica colloid in the hydrolyzed sol are also different. Therefore by selecting either a strong or a weak acid (which would catalyze the sol at different pH values), it is easy to alter the final structure of gel. Under different pHs, sol–gel silica structures are developed with different porosity.[70,71] During the condensation, the silica colloids in the sol (3–10 nm) will pack differently to yield various xerogel structures ranging from microporous (pore size <2nm) to mesoporous (pore size 2–50 nm) at different synthesis conditions.[36,72] The pH of the colloidal silica particles has a major impact on the packing properties. Therefore,

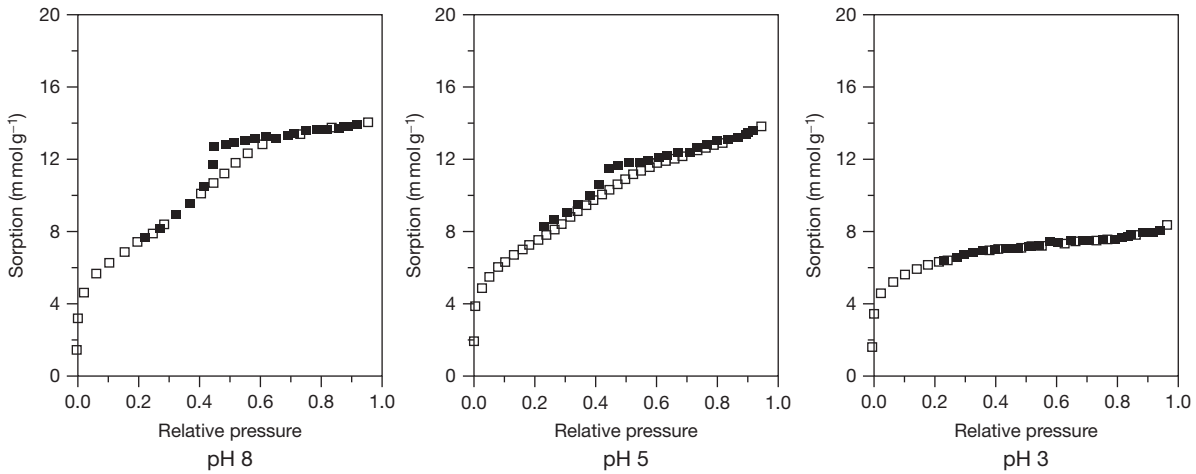

Figure 2 Effect of gelation pH on the microstructure of silica gels. The pore volume of silica increases and the silica clusters become more and more loosely packed as pH increases from low to high. Reproduced from Chu, L.; Tejedor-Tejedor, M. I.; Anderson, M. A. *Microporous Mater.* **1997**, *8*(5–6), 207–213, with permission from Elsevier.

the microstructure of the resulting gels will be different.[70] When sol is prepared at the isoelectric point of the hydrolyzed silica precursor, the silica colloids aggregate easily due to lesser electric compulsive forces. As a result, silica colloids can easily form a densely packed structure and silica sol–gels have the most condensed structure at pH values around the isoelectric point. Above the isoelectric point, the gel results in a more porous structure.

Nitrogen adsorption–desorption isotherms were used to analyze the nanostructure of silica xerogels. It was found that the gelation of sol with same sized silica colloids (~6 nm) at different pH resulted in gels with different pore volumes. Figure 2 shows that when the gelation was carried under pH close to isoelectric point (pH = 3), the resulting gel showed a type I isotherm, and a pore volume of about 30%. When the pH was raised to 5 or higher (pH = 8), the gels formed showed a type 2 isotherm and a pore volume up to 50%.[73] With less pores, release of the drug dexmedetomidine shows a slower diffusion rate from the silica sol–gel prepared near the isoelectric point of the silica than when the sol–gel is prepared at either low (pH = 1) or high pH (pH = 5) (Figure 3).[70]

A procedure known as a 'two-step acid–base catalyzed process' requires less time for the hydrolysis process and gives more freedom on pH selection during the condensation reaction. In fact, when the sol is prepared at low pH (strong acid) the hydrolysis process is very fast. But once homogenous hydrolysis is achieved, the pH of the sol can be adjusted for the condensation reaction. One can add a strong alkaline solution such as NaOH. By doing so, the sol is catalyzed and condensed within a totally different environment. The two-step acid–base-catalyzed sol–gel materials exhibit hierarchical structures that are otherwise difficult to achieve using single step acid-catalyzed or base-catalyzed gels.

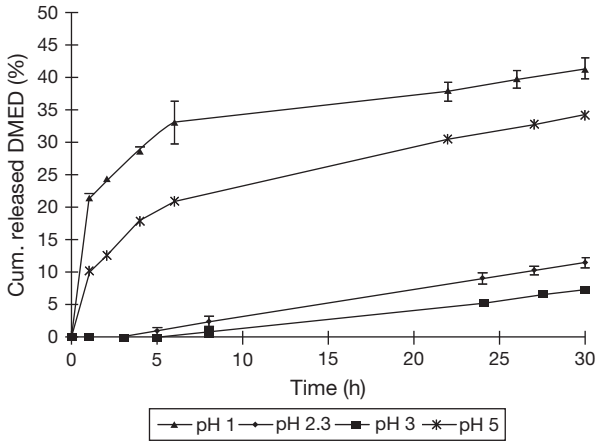

Figure 3 Effect of processing pH on the release rate of dexmedetomidine from silica gel microparticles prepared with water/TEOS ratio 14. The drug (dexmedetomidine) release shows slower rate from the silica sol–gel prepared near the isoelectric point (pH = 2.3–3) of the silica compared to the silica sol–gel prepared at low (pH = 1) or high pH (pH = 5) values. Reproduced from Kortesuo, P.; Ahola, M.; Kangas, M.; *et al*. *Biomaterials* **2002**, *23*(13), 2795–2801, with permission from Elsevier.

4.428.4.2. Effect of Water/Alkoxide Molar Ratio

The water/alkoxide molar ratio (R) in the sol can also affect the xerogel nanostructure. As the water/alkoxide molar ratio increases, pore volume and specific surface area of xerogels increase without a concomitant change in pore size.[11] Higher water/alkoxide ratios are associated with higher surface area and larger pore volume.[38] The corollary of the higher pore volume is that larger amounts of water can penetrate into the sol–gel pores and that diffusional drug release increases. Actually, differences in pore volumes lead to major changes in release kinetics. For example, the release kinetics of vancomycin from xerogels synthesized with the water/TEOS molar ratio $R = 10$ shows a much faster release compared to that from sol–gels prepared at $R = 4$ (Figure 4). It was found that about 90% of the incorporated vancomycin was released from xerogels synthesized with $R = 10$ and

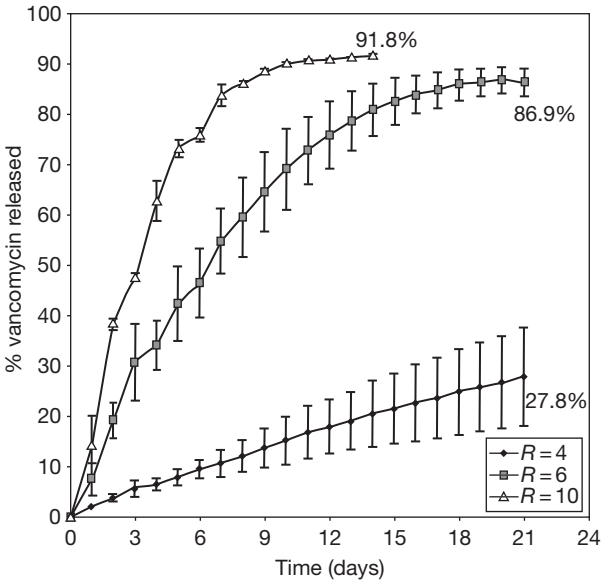

Figure 4 Percent of incorporated vancomycin released from disks of load 20 mg g^{-1} as a function of time and water/TMOS molar ratio (R) ($n = 3$, errors bars represent ± 1 standard deviation). Average total vancomycin amount in water/TMOS molar ratio four disks of load 20 mg g^{-1} was 8.5 mg per disk. Percentage cumulative release of vancomycin from xerogel increases as water/alkoxide molar ratio (R) increases. Reproduced from Aughenbaugh, W.; Radin, S.; Ducheyne, P. *J. Biomed. Mater. Res.* **2001**, *57*(3), 321–326, with permission from Wiley.

$R = 6$ by 14 and 21 days, respectively. In contrast, only 28% of vancomycin was released from xerogels prepared with $R = 4$ after 21 days of immersion.[38]

4.428.4.3. Effect of Drying Conditions

During the drying step, solvents are removed from the silica matrix, thereby giving rise to empty pores in the matrix. When conventional drying or ambient drying in air is used, the gel shrinks due to capillary forces. The final product is called xerogel; it typically has pores with size less than 1.5 nm. When the solvent is removed by freeze drying, the resulting solid material is called cryogel. An aerogel is formed when solvent in the gel is removed by extraction using supercritical drying. Freeze drying and supercritical drying preempts capillary effects, and thereby protects the gel structure from collapse. For cryogels and aerogels, the gel volume remains unchanged and large pores are obtained. It has been demonstrated that after a sol turns into the gel state, and the drying is a supercritical drying using CO_2 at 40 °C, the dried aerogels have a large pore size ranging from 10 to 30 nm. As a result, the drug release rate from aerogels is much faster than from conventionally dried xerogels.[74–76]

In addition to effects resulting from pore structure, the chemical state of the sol–gel surface also controls the drug release rate from aerogels and cryogels. For aerogels and cryogels, the condensation reaction is hindered due to difficulty in silanol movement. A lesser degree of condensation means more unreacted silanol (Si–O–H) groups on the surface. These silanol groups can easily break due to hydrolysis when the sol–gels are present in a physiological milieu. Therefore, a higher amount of residual silanol groups results in a higher rate of degradation. Many researchers have observed that xerogels prepared by a quick drying method such as freeze drying or spray drying have fast release kinetics duo to this higher rate of degradation.[45,61,77,78]

Recently, it has also been found that the drying temperature affects the drug release rate.[71] The reasoning was offered that the decrease of the drug release rate is caused by the decrease in pore size and pore volume of the xerogels. It was concluded that higher drying temperatures cause a faster evaporation rate and results in a higher capillary pressure which results in a denser gel. However, other research found that the drying temperature did not affect the release rate.[79] Such difference suggests that more detailed work is needed to elucidate the effect of drying temperature.

4.428.4.4. Effect of Additives

4.428.4.4.1. Polymers

Controlled amounts of polymers or biopolymers, such as poly(ethylene glycol) (PEG), poly(vinylimidazole) (PVI), poly(ethyleneimine) (PEI), or chitosan, can be added to silica xerogels during the sol–gel process without disturbing the silica formation. When small amounts of soft polymer are added, the polymer additives can reduce the shrinkage of the material by functioning as a 'pore filling' material, and the resulting silica composites have a smaller specific surface area and less pores.[80,81] Due to the lesser number of pores and the 'pore filling' property of the polymers, drug releases becomes slower.[79,82] By adding chitosan to sol–gels, it has been possible to remarkably reduce an initial burst release.[81] Another effect associated with the addition of polymers is the change in mechanical properties of the silica. When chitosan is added to sol–gel silica, the strength, strain to failure, and fracture strength of silica are significantly enhanced.[81]

There are adverse effects associated with adding large amounts of polymers to sol–gels. The silica network formation during the condensation reaction can be severely disturbed. As a result, a weaker silica structure with large pores is formed.[79,83] Swelling of polymer in the sol causes the expansion of silica sol–gel matrix and creates large pores in the sol–gel. Thus, diffusion-controlled drug release would be dominant in such systems. However, the sol–gel matrix degrades faster due to a low degree of condensation caused by polymer interference.[83] As a result of this, it is very difficult to control the drug release kinetics from these materials. Studies have shown that drug release rate were much faster when 8.6–27.4 wt% PEG or 23.7 wt% poly(dimethylsiloxane) (PDMS) were added in the sol–gel during the sol–gel process.[83,84]

Drug release kinetics can also be changed by embedding the silica sol–gel particles in a polymeric matrix.[85] Drug containing silica sol–gels or mesoporous silica particles have been mixed with a polymer matrix for the subtle control of the release kinetics. When silica is surrounded by the polymer matrix, the polymer acts as a barrier to water influx that is necessary to release the drug from the silica sol–gels and thereby reduces the release rate. The polymer–drug interaction through hydrogen bonding or electrostatic interaction also reduces the drug

release rate. Studies with silica sol–gel/tyrosine-poly(ethylene glycol)-derived (ether carbonate) polymer composites revealed that a prolonged drug release profile can be achieved comparable to silica sol–gel alone.[85] Other polymer reactions, namely swelling and bulk erosion can also be effective parameters to adjust drug release kinetics in composite polymer–sol–gel systems.[86,87]

4.428.4.4.2. Organically modified alkoxy silanes

Organically modified alkoxides, such as $RSi(OEt)_3$ $R_2Si(OEt)_2$ (e.g., R=CH_3 or CH_2CH_3) or PDMS ($[Si(CH_3)_2O]_n$), which are derived by the addition of organically modified silanes to TEOS or TMOS-based sol–gels can be used to adjust the drug release kinetics. Many researchers have succeeded in partially substituting TEOS or TMOS with organically modified alkoxy silanes such as dimethyl(diethoxy)silane (DMDES), methyl (triethoxy)silane (MTES), ethyl(triethoxy)silane (ETES), or propyl(triethoxy)silane (PTES) in sol–gel process. It was found that the condensation rate of the alkyl-substituted alkoxysilanes decreases with increasing length of the alkyl chain[36] and the drug release rate from this type of sol–gel silica is slower compared to that from conventional ones. The decrease in the release rate may be due to the hydrophobic nature of the stable CH_3 or CH_3CH_2 groups present in the silica network. These alkyl-groups act in two possible ways: they either prevent the hydrophilic molecules to diffuse out or they prevent water molecules to penetrate into the silica network.[24,37,88–91]

Organically modified silanes using an amide moiety were also synthesized with the goal of controlling the drug release kinetics by taking advantage of electrostatic interactions between protonated aminopropyl groups and carboxylate groups present in the drugs. It was shown that the release rate of ibuprofen could be considerably reduced when the aminopropyl-triethoxysilane was used to functionalize the silica materials.[92]

4.428.4.4.3. Surface modification

Sol–gel oxide to drug interaction can be a useful tool to adjust the drug release kinetics. Various surface modifications have been explored to change this interaction. By way of example, the surface of mesoporous silica particles was coated with magnesium oxide (MgO) using a hydrothermal method. This rendered basic properties to the surface of the silica particles. Such surface characteristics are useful for the controlled release of drug substances with acidic groups such as ibuprofen.[93] In fact, it was observed that the release rate of ibuprofen was considerably reduced in such systems. The extent of rate reduction increased with the amount of MgO coated onto the internal surfaces.[93]

Sol–gel silica itself can also be used to coat mesoporous silica particles for additional control of their release rates. Drug release rates decrease with the increase in the number of coatings. With a judicial organosilane selection and an optimal number of coatings deposited, an initial burst release can be attenuated.[94]

4.428.4.4.4. Stimuli-responsive delivery

Molecules with moveable elements attached to the pore can be used to regulate the drug release through pores. These moving parts respond to external stimuli such as temperature,[95] light,[96–98] pH,[99] and chemical agents.[100] When the right stimuli are present, the movable parts that block the pore on the surface of the silica particle move away from the pore thus allow the drug diffusion through the pores. Thus, the release can also be controlled by external stimuli.

4.428.5. Biocompatibility and Resorption

4.428.5.1. Biocompatibility

Silica glass materials have a favorable tissue response when implanted subcutaneously or in bone.

When implanted subcutaneously, tissue irritation was not observed at the site of implantation and the acute inflammation subsided within a 7-day span, a typical duration for any wound healing. A fibrous capsule was present from around 14 days.[7,70] The xerogels gradually resorbed over time and bulk material breakdown or sol–gel related tissue necrosis was not observed.

In our laboratory, we have extensively studied the tissue response to various xerogels in the subacute implantation phase (up to 4 weeks of implantation). When implanted in bone (iliac crest of New Zealand white rabbit), the implanted silica xerogel showed a minimal inflammatory response and a gradual resorption over time. At 2 weeks of implantation, there was also extensive trabecular bone ingrowth around the silica xerogel. There was no statistical difference in amount of bone formed in empty defects (controls) and bone defects filled with silica granules (**Figure 5**). The size of all granules gradually decreased with implantation time, revealing gradual resorption.[6]

4.428.5.2. Systemic Biocompatibility of Resorbable Silica-Based Glasses

Silicon, next to oxygen, is the most prevalent element on Earth (26%) and crystalline silica in the form of quartz is the most abundant mineral in the Earth's crust. Although silica is a major component in our environment, it is not a major component of our tissues. Mammals, including humans, have evolved mechanisms over time to remove silicon from their bodies in order to maintain trace concentrations of silicon. In animals, silicon is most abundant in connective tissue, hair, feathers, skin, tendons, muscle, and bone. Silicon is a constituent of certain glycosaminoglycans and polyuronides, where it occurs firmly bound to the polysaccharide matrix.[101] In most tissues, silicon concentrations in humans range from 0.6 ppm for serum, to 41 ppm for muscle, and to a high of 57 ppm for lung tissue. In other animals, the silicon concentrations are similar to humans, <1 ppm in serum and 25 ppm in femora of both rats and monkeys.[102–104]

In our laboratory, we performed *in vivo* studies with granules of silica-based glass using rabbits. The granules were implanted in two separate studies. The implantation was either in the tibiae[105] or in the paraspinal muscle[101] of rabbits.

We traced the silicon release from silica glasses and the silicon excretion from the body. In addition, we examined a variety of tissues for silicon accumulation using chemical and histopathological analyses. We also evaluated the kidney function of the rabbits, and to this end, we measured urinary

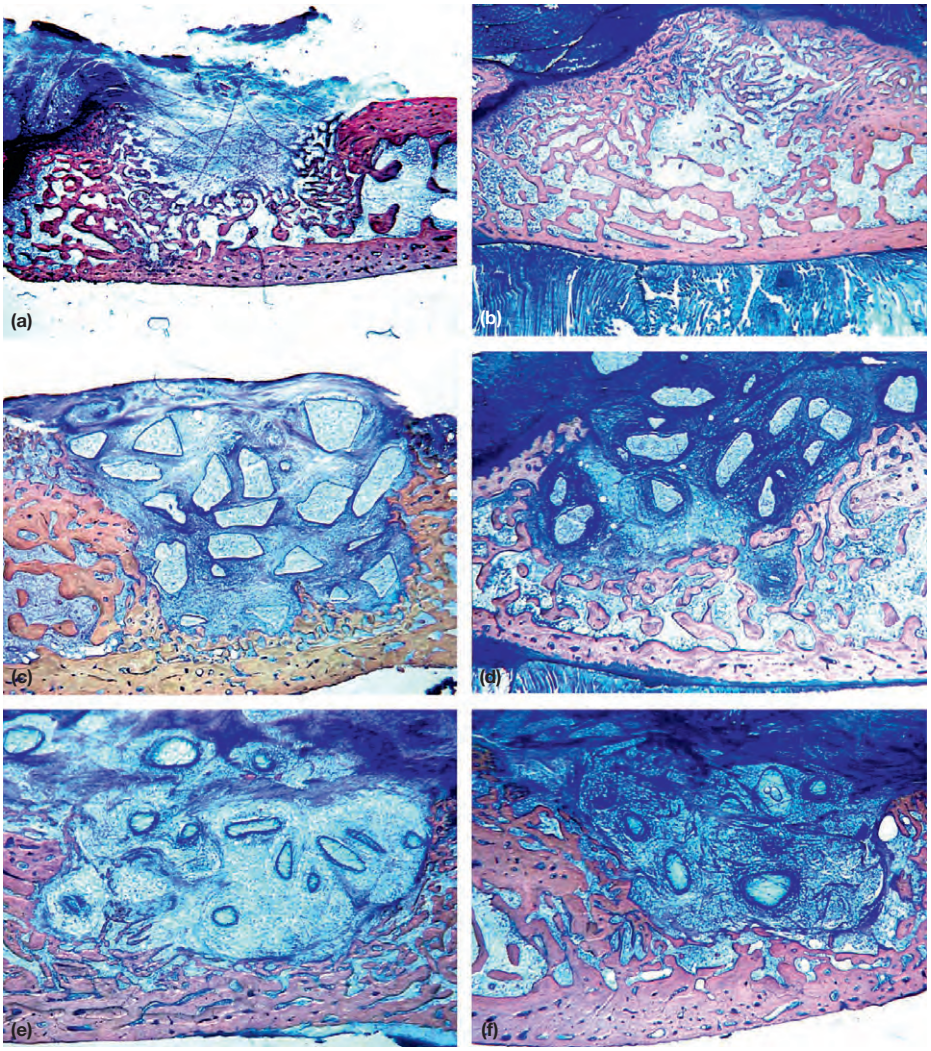

Figure 5 Light micrographs of rabbit bone tissue response to (a, b) control, (c, d) S100, and (e, f) S90V granules without apatite surface layer after implantation into the iliac crest defects: for 2 (a, c, e) and 4 (b, d, f) weeks (phase II of the experiment). Original magnification: 12× (a, e, f) and 10× (b–d). Progressing healing of the defect via trabecular bone growth was observed for both the control and the implant groups. Extensive trabecular bone growth occurred at the opening and the borders of the defects at 2 weeks of implantation. After 4 weeks, the amount and the density of the trabaculae increased for all the experimental groups. S100: pure silica xerogel; S90: xerogel composition 90% SiO_2–5% CaO–5% P_2O_5. Reproduced from Radin, S.; El-Bassyouni, G.; Vresilovic, E. J.; Schepers, E.; Ducheyne, P. *Biomaterials* **2005**, *26*(9), 1043–1052, with permission from Elsevier.

creatinine. Creatinine is a natural metabolite found in the urine that is proportional to the body's muscle mass. Its excretion rate reflects kidney function, with a decreased rate reflecting impairment. We found that the creatinine excretion rates were relatively constant and stable over three different treatment groups sampled at several time points during the experiment. Since creatinine excretion rates were similar for all rabbits, we concluded that the surgical procedure and the increased silicon excretion did not adversely affect kidney function.

For silica implanted in the tibiae, the silicon release was measured in 24-h urine and blood samples for up to 7 months after implantation. Surrounding bone and muscle tissue as well as kidney, liver, lung, lymph nodes, and spleen were resected for chemical and histopathological analyses. The urinary silicon of both implanted groups was significantly higher than in the control group (Figure 6). The calculated average excretion rate was approximately 1.8 mg day^{-1}, and as such, the amount of implanted silicon was excreted within statistical bounds in 24 weeks. Increased concentrations of silicon were not found in any of the organs and the histological appearance of all organs was normal. Since no significant increase in silicon was found in any of the organs including the kidney, the increased silicon excretion rate was within the physiological capacity of rabbits.

In the study with silica implantation in the paraspinal muscle, silicon was traced and the release quantified by obtaining 24-h urine and blood samples for up to 6 months after implantation. In addition, local muscle tissue as well as the same organs as in the previous study were resected for chemical and histopathological analyses. The urinary silicon of the

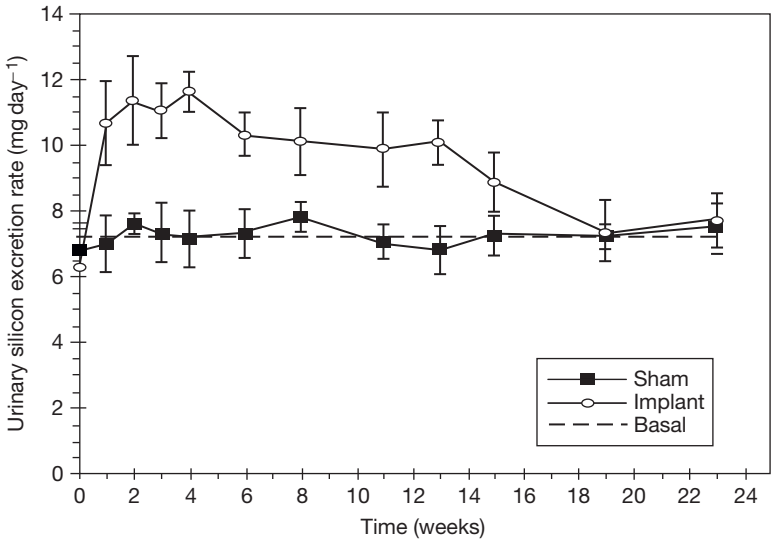

Figure 6 Urinary silicon excretion rates for the long-term study with 'long' implants. Total silicon excreted by the implant rabbits after 19 weeks = 318 mg (100%). $n = 7$ for both sham and implant groups. Basal excretion rate is the average of all sham data points. Week 0 was sampled before surgery and Week 1 was sampled immediately after surgery. Reproduced from Lai, W.; Garino, J.; Flaitz, C.; Ducheyne, P. *J. Biomed. Mater. Res. A* **2005**, *75A*(2), 398–407, with permission from Wiley.

group with implanted granules was significantly higher than in the sham-operated, control group. The average excretion rate was 2.4 mg day^{-1}, and as such, 100% (within statistical bounds) of the implanted silicon was excreted in 19 weeks. No elevated concentrations of silicon were found at the implant sites or in the other organs at sacrifice, that is, 24 weeks. The histological appearance of all organs was normal throughout. The concentrations of silicon measured in the urine were well below saturation and since no significant increase in silicon was found in any organ, including kidney, the increased silicon excretion rate was within the physiological capacity of rabbits.

In both studies, systemic measurable levels of Si were only found in the urine. The Si-release product in the blood must be relatively small in order to pass through kidney filtration. In humans, the size of molecules passing through filtration is approximately 18 Å.[106] The increased urinary Si measured in these studies supports the hypothesis that the silica gel from the reacted silica glass granules is dissolved into the blood stream and removed by the kidney.

Silicic acid, $Si(OH)_4$, in food and beverages has been reported to be readily absorbed across the intestinal wall and rapidly excreted in the urine.[107,108] In plasma and red cells, Baumann found that the concentration of silica was the same (0.4–0.5 ppm) and was present as a monomer. When 50 mg of soluble silica was given to humans in drinking water, it was all excreted in the urine within 10 h; the concentration in urine ranged from 200 to 600 ppm at its peak, depending on urine volume, and it was still all monomeric. The elimination rate was constant when measured as micrograms per minute, regardless of urine volume and the rate was proportional to the amount not yet excreted (first-order rate constant). The concentration in blood reached 2–3 ppm, and if 300 mg of soluble silica was given, it reached 6 ppm. Baumann also showed that monomeric $Si(OH)_4$ penetrates all body liquids and tissues at concentrations less than its solubility (1.7 ppm which is 1% of Si solubility in water). However, Policard *et al.*[109] suggested that polymeric molecules of silicic acid containing up to four to five silicon–oxygen units characterize the transport form of silicic acid in blood.

With a clinically relevant dose, a slow silicon dissolution rate from silica glass and subsequent diffusion into the blood was observed. Under these conditions, the critical concentration at which silicon polymerizes (180 ppm) was never reached.[110] Meanwhile the kidney's ability to excrete the Si resorption product continued and no accumulation of silicon took place.

The systemic accumulation of silicon from Si-containing bioactive ceramics depends on the rate of dissolved silica that diffuses into the tissue and into the blood. Furthermore, the rate of dissolution is dependent on dose, site of implantation, effective surface area, and chemical composition of the silica. Given silicon biology, the rate of dissolution is typically smaller than the rate of excretion. As seen in both studies, the silicon release rates from the silica glass granules were well within physiological tolerances.

When massive amounts of silica-containing bioceramics powder were injected intraperitoneally into rats and mice (5000 mg kg^{-1} body weight), the animals died by nephrosis. Silica deposition in renal tubules was observed, indicating that a large quality of silicon eluted from the powder and accumulated and repolymerized within renal tubules.[111–113] Although a large amount of dissolved silica can be toxic, the adverse effect results from a combination of extreme conditions: ultra high powder load (5000 mg kg^{-1} body weight), fast silica dissolution rate, and abundant blood circulation (peritoneal injection). These conditions are far removed from those in the applications being pursued with sol–gel-controlled release materials.

With knowledge of trace silicon chemistry in the body and the aforementioned bioactive silica glass resorption

studies,[101,105] these studies suggest that the removal pathway of silicon from silica glass *in vivo* can be described as follows: (1) the bioactive silica is constantly reacting with its surroundings, and the silica gel is removed by a combination of silicon dissolution into the circulating interstitial fluid and active degradation by phagocytic action of macrophages contacting the silica matrix surface; (2) the silicon-containing resorption product diffuses into the local tissue and then enters the bloodstream or lymph to be distributed to other parts of the body in soluble form;[107,109,114] (3) since there are no known physiological processes specific for the absorption and metabolism of soluble silicon, the silicon will finally be filtered out of the blood by the kidney;[109,115–117] during this resorption, the silicon concentration in the organs and body fluids remains within physiologically safe ranges.

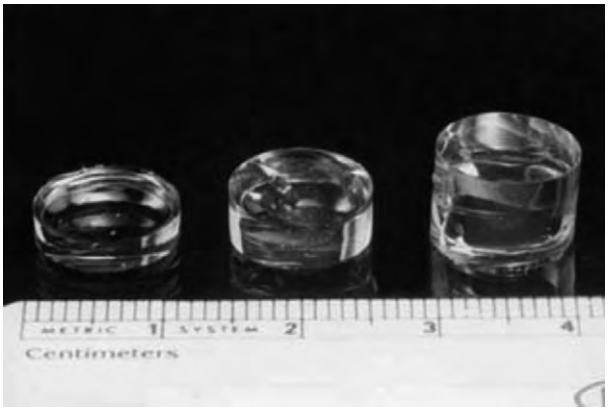

Figure 7 Silica xerogel monoliths. The samples are glassy, transparent, and crack-free. The thickness of samples varies with the amount cast. Reproduced from Radin, S.; Ducheyne, P.; Kamplain, T.; Tan, B. H. *J. Biomed. Mater. Res.* **2001**, *57*(2), 313–320, with permission from Wiley.

4.428.6. Applications

4.428.6.1. Sol–Gel Application Forms

Sol–gel materials can be prepared in a variety of different physical forms, including monoliths, crushed particles, microspheres, nanospheres, fibers, hydrogels, thin films, and composites. Silica sol–gel monoliths or crushed particles were used as implantable or injectable materials.[21,22,24] Spray-drying and emulsification methods were used to prepare silica xerogel microspheres and nanospheres with a narrow particle size range with the goal of excellent control of the release kinetics of various incorporated molecules.[59,118,119] Hydrolyzed silica sols containing drugs were either directly sprayed and dried in air, or mixed and separated by nonpolar organic solvents, in order to form microspheres or nanospheres. Drug-loaded sol–gel films have been produced by applying a solution of liquid sol with drugs onto implant surfaces with the goal of releasing therapeutic agents at the implantation site of devices.[120,121] Silica hydrogels (water content ~90 wt%), which provide, in principle, a viable aqueous environment essential for living organisms, enable the delivery of viruses for gene therapy.[65]

4.428.6.1.1. Monoliths

In case of room temperature synthesis of acid-catalyzed sol–gel-derived silica, the sol starts to gel after hydrolysis. Time to gelation can vary from a few hours to tens of days. The gelation time is determined by synthesis parameters including pH, water/alkoxide ratio, etc. (as described above). After aging in sealed vials for several days, the gels are dried until the gel weight became constant. A major weight loss (75–78%) is typically observed and shrinkage during drying does not lead to cracking of the resulting disks.[11] Figure 7 shows typical sol–gel xerogel monoliths. Monoliths can be processed further, by crushing them into granules or fine powders with a size range upward from 10 μm.

4.428.6.1.2. Particle

4.428.6.1.2.1. Microparticles

4.428.6.1.2.1.1. Emulsion sol–gel process A sol–gel solution is prepared by combining tetramethylorthosilicate (TEOS), an aqueous solution of the active molecule and methanol at the desired pH. The resulting solution is stirred for 30 min at 300 rpm and left to age for 1 day at ambient temperature. In parallel, a surfactant (e.g., sorbitan monoleate) is dissolved in a nonpolar solvent (e.g., cyclohexane) followed by homogenization to form a clear surfactant/solvent solution. The sol–gel solution is then added to the surfactant/solvent solution and the resulting emulsion vigorously stirred. A suspension of microspheres forms and is filtered, washed, and dried.

The condensation and gelation occur inside the water pool and the silica particles form inside this water pool. The size of sol–gel droplets, which eventually become particles, is controlled by the interfacial tension between the water and oil phases. The higher interfacial tension leads to a smaller size of sol–gel droplets and the formation of small silica particles. The nature of surfactant and solvent can be exploited to control the size of sol–gel particles.[119] Figure 8 shows the variation in the size of silica particles obtained by changing the polarity of the organic solvent used as the oil phase, or by changing the nature of the surfactant.

4.428.6.1.2.1.2. Spray-drying sol–gel process In this method, when the acid-catalyzed hydrolysis of the silica precursor has gone to completion, the condensation of the silica sol is stopped before the onset of gelation. The 'close-to-gel' silica sol can be sprayed with a spray dryer to form silica microparticles. The scanning electron microscopy image of Figure 9 shows that spray-dried silica microspheres have a smooth surface and are formed in an aggregated cluster of spheres. Nitrogen adsorption measurements show that spray-dried silica particles have a very low surface area of less than $2\,m^2\,g^{-1}$, indicative of materials that exhibit no or only very small open porosity. The *Q*-values that have been reported ($Q^2 = 19–20\%$, $Q^3 = 39–42\%$, and $Q^4 = 38–42\%$) indicate a low degree of condensation for spray-dried silica. In these materials, the drug release kinetics is predominantly mediated by degradation of the silica matrix.[12]

4.428.6.1.2.2. Nanoparticles

The process of preparing nanosized silica particles with a sol–gel technique is slightly different from that mentioned above for synthesizing micro-sized particles with an emulsion sol–gel

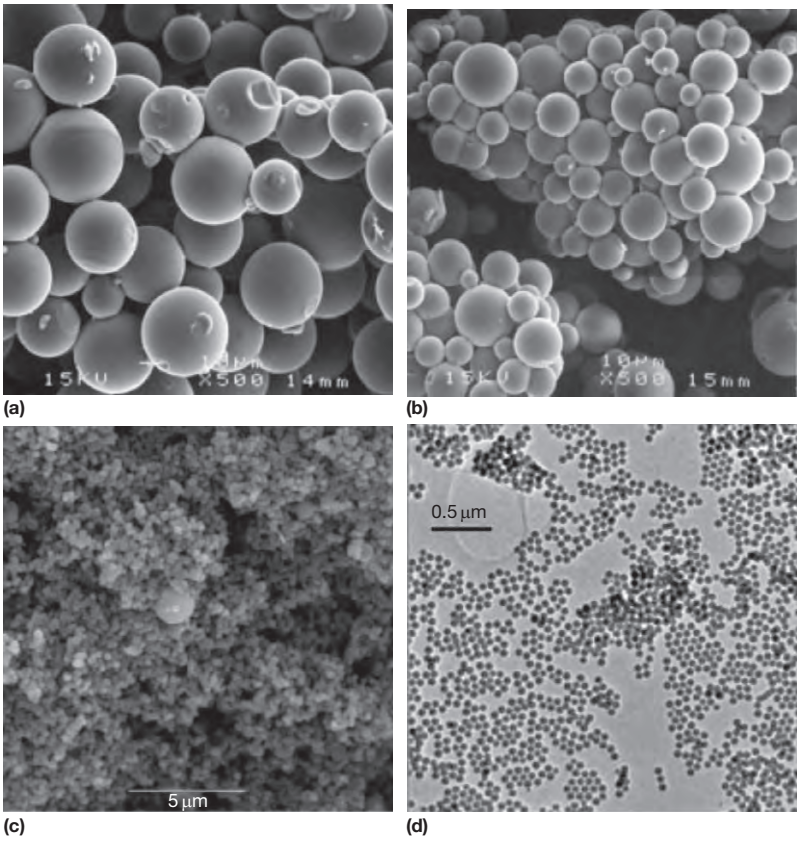

Figure 8 Electron micrographs of silica particles synthesized using (a) SPAN80/kerosene, (b) SPAN80/cyclohexane, (c) AOT/cyclohexane, and (d) NP9/cyclohexane. Both an increase in the polarity of the solvent and a decrease in the surfactant hydrophile–lipophile balance lead to a smaller water droplets and thus, the production of smaller sol–gel particles. Reproduced from Barbe, C.; Bartlett, J.; Kong, L.; *et al*. *Adv*. *Mater*. **2004**, *16*(21), 1959–1966. Copyright Wiley-VCH Verlag GmbH & co. KGaA.

process.[122] In the present case, the silica precursor is introduced in a surfactant/oil solution and slowly diffuses through the surfactant wall into the water droplets, where it is hydrolyzed and condensed. By virtue of this, silica precursor forms the emulsion prior to the gelation. As a result, the hydrolysis and condensation occur simultaneously and a smaller size particle is formed. With respect to the emulsion properties, surfactants with a mid-range HLB (hydrophilic–lipophilic balance) value (between 10 and 15) are suitable for nanoparticle synthesis.

4.428.6.1.3. Fibers

Conventionally, glass fibers are obtained by drawing or blowing a high temperature oxide melt through a small orifice. High temperature processes, however, cannot be used when the goal is to synthesize fibers loaded with drugs. In order to overcome this problem, sol–gel technique including only steps at room temperature has been used to synthesize silica fibers. Specifically, fibrous gels can be drawn from spinnable sols at room temperate and then converted into fibers, again at room temperature.[123]

In this method, the silica sols are prepared from TEOS, water, ethanol, and acid. After hydrolysis, the sols are poured into test tubes and sealed. At this stage drugs can be added to the sol. The test tubes are placed into a water bath and the temperature kept constant at 40 °C. After vigorously stirring for 2 min, the sol is then immediately put back into the water bath. Some ethanol evaporates, which accelerates the reaction kinetics in the sol. After evaporation of ethanol, the sols are cooled to either 20 or 0 °C. The spinning is started when the viscosity of the sol reached a value in the range 2–100 Pa s. To avoid breaking of sol–gel filaments air bubbles have to be removed from the spinning solution under partial vacuum and dry spinning is employed to prepare sol–gel fibers.[124–126] After spinning, the fibers can be dried either in air (or an oven, but this is not desirable given the addition of drugs). **Figure 10** is the representative SEM image of silica fibers prepared by sol–gel technique.

Silica fibers prepared using this process have a very high degree of condensation. The BET surface area of silica fibers prepared by sol–gel is less than 1 $m^2 g^{-1}$, indicating a dense surface of the fibers. Except for a very brief release stage with diffusion control (<1%), the drug release from the fibers is governed by silica degradation.

4.428.6.1.4. Thin films

Dip-coating or spin-coating techniques are commonly used for the deposition of sol–gel thin films onto a variety of substrates. For dip coating, the substrate is dipped and withdrawn at a controlled speed from sol using a dipping device. On the other

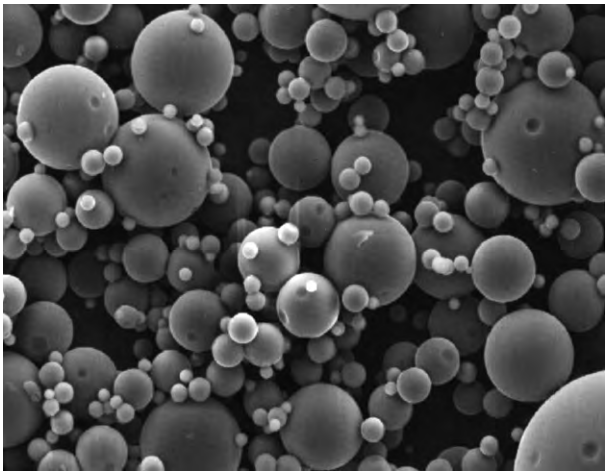

Figure 9 Scanning electron micrograph of sol–gel silica microparticles prepared by spray-drying method. Original magnification ×2500. Reproduced from Kortesuo, P.; Ahola, M.; Kangas, M.; Kangasniemi, I.; Yli-Urpo, A.; Kiesvaara, J. *Int. J Pharm.* **2000**, *200*(2), 223–229, with permission from Elsevier.

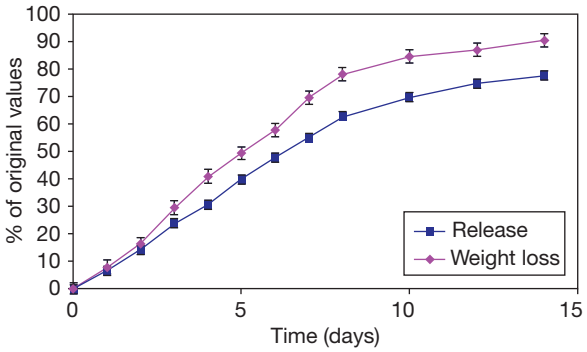

Figure 11 Sol–gel/vancomycin film with release and stability extended up to 14 days: mean cumulative vancomycin release (expressed as % of the original load) and degradation (weight loss, %) as a function of immersion time in PBS. The film was composed of three layers and contained 10% vancomycin. The calculated load in the various films varied from 20 to 22 mg cm^{-2}. The error bars represent the standard deviation ($n = 3$). Reproduced from Radin, S.; Ducheyne, P. *Biomaterials* **2007**, *28*(9), 1721–1729, with permission from Elsevier.

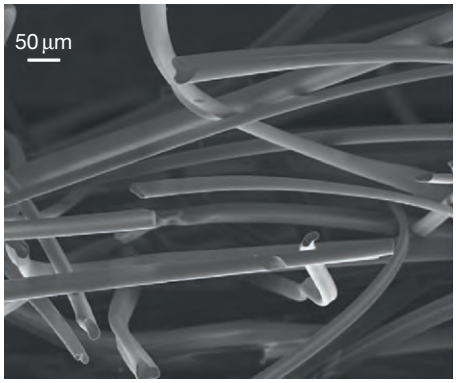

Figure 10 Scanning electron micrograph image of drug (dexmedetomidine hydrochloride) containing silica fiber spun at a sol viscosity of 33–100 Pa s. Reproduced from Czuryszkiewicz, T.; Ahvenlammi, J.; Kortesuo, P.; *et al. J. Non-Cryst. Solids* **2002**, *306*(1), 1–10, with permission from Elsevier.

hand for spin coating, excess amount of sol is dropped on the substrate, which is then rotated at high speed to spread the sol on the substrate by centrifugal force. The thin film coatings are typically air-dried. In order to produce thin film composed of several layers, the dipping or spinning and drying procedures are repeated several times.

During the drying, there is little time for the condensation reaction, resulting in silica coatings with a low degree of condensation. This low degree of condensation, together with a resultant low porosity, the drug release kinetics are primarily controlled by silica degradation and a zero-order release is predominant.[120] Figure 11 shows that the zero-order release profiles of sol–gel dipped coatings that contain vancomycin is associated with a similar degradation rate of the sol–gel films.

4.428.6.1.5. Hydrogels

After hydrolysis and condensation, the sol gradually turns into a gel. There are applications for use of the material in this condition. Thus, unlike when used in monolith form, silica hydrogels are not dried before use. The silica gel, in its gel phase is used as controlled release system. Because of the high water content at this stage (>75 wt%), such silica gel is also called a hydrogel.

The applications with silica hydrogel can be traced back to 1997 when Pope *et al.* encapsulated mouse islet cells into silica hydrogel in order to achieve an *in vivo* secretion of insulin.[17] This research inspired many others for using silica hydrogels in the encapsulation of cells. These gels with cells then served as building blocks for artificial organs and transplants. A prime consideration in these studies was preventing immune response and transplant rejection by walling off the cells in these materials with nanosized pores.[127]

Recently, silica hydrogel was also used for the controlled delivery of virus. The sol–gel process was modified so that the adenoviruses could be added to the liquid sol. After the gel formation, the adenoviruses became encapsulated inside the solid gel structure. Infectivity of the virus was sustained for more than 855 days when stored at 4 °C. Observed linear virus release kinetics correlated to silica dissolution rate suggests that the release mechanism is degradation controlled.[65]

4.428.6.1.6. Mixed oxide sol–gels

Calcium and phosphate containing xerogel composites have been synthesized through a sol–gel procedure by adding calcium precursor (such as calcium methoxyethoxide or calcium chloride) and phosphate precursor (such as triethylphosphate) into the sol.[22] The addition of Ca- and P-oxides affected the physical properties of xerogels, decreasing the surface area and increasing the pore size. When these materials were exposed to physiological fluids, a calcium phosphate

layer quickly formed on their surface. The newly formed calcium phosphate layer was beneficial for new bone formation and provided an excellent surface to stimulate the osteoblastic differentiation of stromal marrow cells.[72] This calcium phosphate layer could dramatically reduce the dissolution rate of xerogel composites and can be used to regulate the degradation-controlled drug release rate from the xerogel.

Calcium only containing xerogel was explored for hemorrhage control. Such an idea stems from the understanding that the Ca ions released from xerogel can induce an accelerated coagulation response.[128]

Owing to the significant antimicrobial properties of copper and silver, sol–gel silica comprising these metal ions have been explored in order to provide for a controlled delivery of copper and silver ions. Mesoporous silica was synthesized through a one-step based catalyzed self-assembly process with cetyltrimethylammonium bromide (CTAB). Silver ions were loaded by soaking silica particles in the silver nitrate solution. Copper-containing xerogels were prepared by adding copper sulfate solution in the sol solution during the one step acid-catalyzed hydrolysis process. After drying, the copper ions were incorporated inside the xerogel. It has been reported that Cu or Ag ions released from xerogels exert a bactericidal action and can be used to aid in wound healing.[129,130]

4.428.6.1.7. Composites

Polymers of synthetic or biological origin can be mixed with sol–gels to form polymer–sol–gel composites. The matrix of the composite can be either the polymer or the sol–gels. Regardless of the matrix, the release kinetics as well as the mechanical properties of the composites can be readily adjusted. Details on polymer–sol–gel composites have been extensive discussed in **Section 4.428.4.4.1**.

4.428.6.2. Therapeutic Agents of Various Size

Because of their controllable structure, sol–gel materials show an efficient and exquisitely tunable delivery of drugs varying in size. Molecules ranging from small (molecular weight of a few hundred Dalton) to large, such as protein molecules (with molecular weight exceeding 50 kDa) can be released at a controlled rate. Recently, very large therapeutic agents such as DNA or virus have been incorporated and released from sol–gel silica in a controlled manner.[65] Cells, which are much larger than viruses, can be delivered with sol–gel system as well. **Chapter 4.431, Encapsulation of Cells (Cellular Delivery) Using Sol–Gel Systems** describes this extensively.

4.428.6.2.1. Small therapeutic agents

Many small drugs, such as dexmedetomidine (MW 200),[37,70,131] steroids (progesterone, estradiol, estrone, and hydrocortisone, MW range 271–362),[26] ibuprofen (MW 206),[132] lidocaine (MW 234),[89] bupivacaine (MW 288),[59] biphosphonates (MW 303),[12] toremifene citrate (MW 598),[7,69,79] and vancomycin (MW 1449)[9,11,133] have been successfully loaded in silica sol–gel oxides using a sol–gel method.

With a size smaller than the pore size of the silica xerogel, the release kinetics of these drugs is mostly diffusion-controlled. The interaction between any drug and the silica sol–gel affects the diffusion rate, though. It has been shown that drugs with fewer hydroxyl and carbonyl groups have a faster diffusion rate, due to less hydrogen bond formation with the silanol groups present in the silica surface.[26] A study on the incorporation of the local anesthetic lidocaine in silica sol–gels suggested that the release of lidocaine can be easily controlled by partially substituting TEOS with organically modified alkoxides (MTES or PTES) or nonionic surfactant.[89]

4.428.6.2.2. Intermediate sized therapeutic agents (proteins or growth factors)

Various proteins and growth factors with molecular weight over several kiloDalton, such as heparin (MW 2–16 kDa), transforming growth factor-β1 (TGF-β1) (MW 25 kDa),[21] trypsin inhibitor (MW 21 kDa),[8] bone morphogenetic protein-2 (BMP-2) (MW 30–32 kDa),[22] bovine serum albumin (BSA) (MW 68 kDa),[45,78] have been incorporated into silica sol–gel and the release kinetics determined *in vitro* and *in vivo*. It was shown that the incorporated proteins maintained their original conformation and were resistant to protease degradation.[63] Depending on the size of protein molecules and pore size of the silica xerogel, the release was diffusion-controlled or degradation-controlled. When pores in the silica sol–gel matrix were not large enough for diffusion of the molecules, the drug release rate was determined by the silica dissolution rate. For example, it has been reported that BSA (MW 66 kDa) was not released in SiO_2-saturated buffer, indicating that the release of large molecule is controlled by SiO_2 matrix dissolution.[45,78]

Heparin is an anticoagulant that is used to overcome the propensity for blood to clot, for instance when it contacts damaged endothelium in a surgical wound. Silica sol–gels have been successfully employed for controlled delivery of heparin to prevent thrombus formation at the site of trauma. Heparin incorporated in sol–gel retains its biological activity before the release.[10] It has been reported that heparin of small molecular weight showed diffusion-controlled release kinetics (<8 kDa), while large size heparins (13–16 kDa) has zero-order release profiles indicative of a dissolution-controlled mechanism.[10,88]

The first report showing the delivery of a biological growth factor from sol–gel based silica was performed in our laboratory and published in 1997.[21] TGF-β1, a 25 kDa homodimeric polypeptide growth factors, which can modulate osteoblast cell activity, including adhesion, proliferation, differentiation, and maturation were incorporated into silica sol–gel oxides. The sol–gel procedure was carried out in acidic condition, as TGF-β1 is highly stable under such conditions. The *in vitro* study demonstrated that sol–gel can provide a sustained release of biologically active TGF-β1 over a 7-day period in a degradation-controlled manner. The released TGF-β1 from silica sol–gel still kept its inhibitory effect on the proliferation of lung epithelial cells, a cell line which is arrested by TGF-β1 in the G1 phase of the cell cycle. On the basis of published TGF-β1 potency, the released amount is capable of eliciting bone tissue reactivity. These findings suggest that the sol–gel oxide loaded with growth factors has potential to serve as an effective bone graft material for the repair of osseous tissue defects.

4.428.6.2.3. Large therapeutic agents (DNA or virus)

Typically, DNA is incorporated into biodegradable polymers for controlled delivery of genes.[134–137] The concept of sol–gel silica mediated gene delivery has not been tested until recently. It was reported that DNA in a silica sol–gel matrix showed good resistance to nuclease and that the DNA release rate could be adjusted chemically by adding linking agent such as aminopropyl(triethoxy)silane (APTES) to the sol–gel precursor.[138] Because of their large size, only small DNA molecule can be released from silica xerogel through diffusion. Pierre *et al*. found that DNA molecules are bonded to the silica network through the P–O–Si link during the encapsulation process. For this reason and by virtue of constraints arising from the small pore size, they found that large DNA molecules remain trapped inside the xerogel and only small DNA molecules (<50 bp or ~17 kDa) can be released from silica xerogel through diffusion mechanism.[139]

Recently, scientists in Finland have demonstrated that recombinant adenoviruses coding for beta-galactosidase (lacZ) can be encapsulated in silica hydrogel for gene delivery[65] (adenovirus genome is double stranded DNA with a size larger than 26 kbp).

They prepared the silica hydrogels at room temperature from TEOS and water. Nitric acid was used as a catalyst. Before virus addition, the pH was adjusted to 6.6 by adding NaOH, The recombinant adenoviruses were added while vigorously mixing. The sols turned into gels within 5–10 min. Water content of the resulting silica gel was 90 ± 3 wt% and silica with adenovirus degraded within 10 days *in vitro*. During the degradation of the silica sol–gels in Tris–HCl buffer, the amount of the virus released from the silica gel increased over time. Viral release kinetics was in accordance with silica hydrogel degradation. Linear release kinetics of the virus suggests that the mechanism is dependent on silica dissolution.[65] Figure 12 shows the degradation, release kinetics from silica hydrogel and its infectivity.

The encapsulated recombinant adenoviruses stayed infective for months at 4 °C. *In vitro* study showed that adenoviruses released from silica gel were able to infect fibroblasts longer than 28 days. It was also reported that this virus incorporated in the silica hydrogel was completely absorbed after 21 days *in vivo*.[64] Furthermore, *in vivo* investigations revealed that antibody induction for silica-adenovirus-implanted mice was slower than for mice treated with virus alone suggesting that the silica matrix provided immuno protection until the virus was released. In needle-injected mice, the highest amount of virus in tumor and liver was seen on day 2, whereas in silica-implanted mice, the amount of virus increased continuously for 2 weeks. This study of antitumor efficacy of oncolytic adenovirus incorporated in silica showed that virus incorporated in silica improved the median survival of mice from 57 to 91 days.[65]

4.428.6.3. Clinical Applications

Because of their excellent biocompatibility and tunable delivery properties, the sol–gel materials have been investigated for treating various clinical conditions, including pain management, bacterial infection control, osteoporosis prevention and bone repair, cancer therapy, hypertension treatment, anticoagulation, and gene therapy (Table 1).

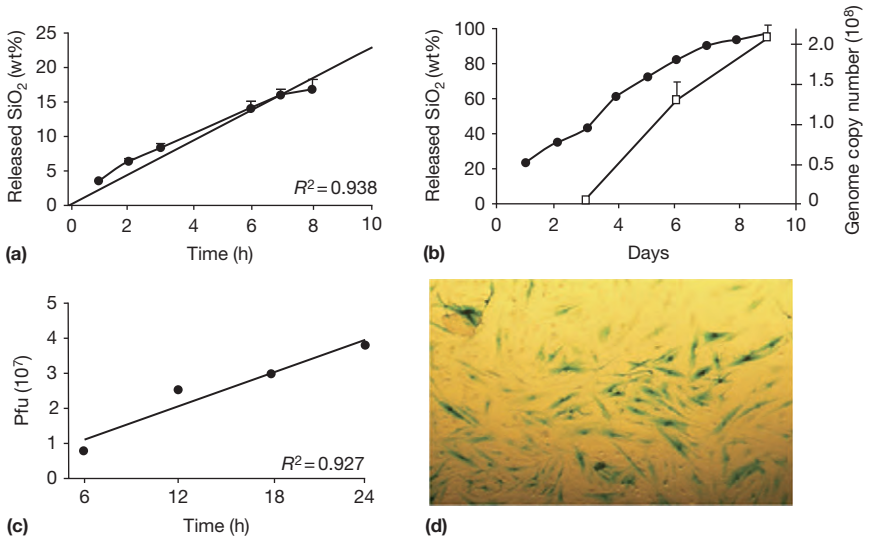

Figure 12 (a) Degradation of the silica gel in 250 ml of 0.05 M Tris–Cl buffer (pH 7.4) at +37 °C and released Si. Release was extrapolated by linear regression ($n = 3$). (b) Silica gel degradation (●) relative to release of adenovirus (□). Gel was dissolved in 250 ml of Tris–Cl buffer, and Si content was measured daily ($n = 4$). The buffer was changed every third day. The release of replication-deficient adenovirus was measured with quantitative PCR. (c) *In vitro* release and infectivity of silica-embedded oncolytic adenovirus Ad5-D24RGD. Silica gels were dialyzed at +37 °C and 106 r.p.m. in 200 ml of growth medium. TCID50 test was performed to quantify the release of functional oncolytic virus/implant. (d) Viability of silica-embedded LacZ-coding adenovirus cultured 3 days on HSF cells after incubating for 229 days at +4 °C. Error bars (a and b) indicate SE HSF, human skin fibroblast. Reproduced from Kangasniemi, L.; Koskinen, M.; Jokinen, M.; *et al*. *Gene Ther*. **2009**, *16*, 103–110, with permission from Nature Publishing Group.

Table 1 Overview of clinical uses of sol-gel materials. Among the uses, several areas stand out, including pain management, bacterial infection control, and cancer therapy

Application fields	*Therapeutic agent*	*Size*	*Physical forms of the sol–gels used in the studies*	*References*
Pain management	Dexmedetomidine	MW 200	Monolith, microparticle, fiber	37,70,125,131
	Diclofenac	MW 296	Monolith	71
	Ibuprofen	MW 206	Monolith, microparticle	34,132
	Lidocaine	MW 234	Monolith	89
	Bupivacaine	MW 288	Microparticle, granule, composite	59,85
	Mepivacaine	MW 246	Composite	85
Bacterial infection control	Vancomycin	MW 1449	Coating, monolith, micoparticle	9,11,133
	Gentamicin	MW 448	Granule, composite	86,140
	Tobramycin	MW 468	Composites	141
	Cu^{2+}	MW 64	Granule	129
	Ag^{+}	MW 108	Microparticle	130
	Nitric oxide	MW 30	Coating	142,143
Cancer therapy	Toremifene citrate	MW 598	Monolith, microparticle	7,69,79
	Cisplatin	MW 300	Granule	83,84,144
	Doxorubicin	MW 543	Granule, microparticle, nanoparticle	62,77,91,119,122,145
Osteoporosis prevention/bone reunion	Biphosphonates	MW 303	Microparticle	12
	BMP-2	MW 32 kDa	Granules	8,22
Hypertension treatment	Nifedipine	MW 346	Micoparticles	24
Anticoagulant	Heparin	MW 2–16 kDa	Monolith, granule	10,88
Hemorrhage control	Ca^{2+}	MW 40	Microparticle, composite	128,146
Growth factors	TGF-β1	MW 25 kDa	Monolith	21
Gene therapy	Recombinant adenoviruses	MW >26 kbp	Hydrogel	65

4.428.6.3.1. Pain management

Sol–gel silica materials containing local anesthetics such as bupivacaine or mepivacaine have been synthesized and their effect to treat pain *in vivo* demonstrated. Before, sustained, controlled release of bupivacaine and mepivacaine from polymer–xerogel composites was shown *in vitro*.[59,85,147]

Dexmedetomidine, an alpha-2-agonists, is widely used in veterinary anesthesia. Dexmedetomidine contained in sol–gel monoliths (rod in shape) was subcutaneously administrated to dogs in a bioavailability study. This *in vivo* study showed that the mean maximum safe concentration of dexmedetomidine (C_{max}) in serum extended over 5 h, much longer than in the control arm with a bolus injection (1 h).[37] After injection, the concentration of dexmedetomidine in serum declined rapidly and was undetectable after 6 h. In contrast, measurable dexmedetomidine concentrations were still found in serum samples taken after 48 h when silica xerogel rods with dexmedetomidine were implanted. This study proved that anesthetic drugs (dexmedetomidine) incorporated in silica xerogel can be released in a sustained way *in vivo*.[37]

Other than the aforementioned drugs, ibuprofen, diclofenac, and lidocaine have also been incorporated in sol-gels.[34,89,132]

4.428.6.3.2. Bacterial infection control

The controlled release of bactericidal drugs from sol–gel materials have been studied. Among them, vancomycin is the typical antibiotic used for treating refractive bone infections caused by Gram-positive bacteria such as *Staphylococci* and *Streptococci*.[32] Room temperature processed sol–gel silica loaded with vancomycin showed a controlled release for up to 4 weeks. A first-order release was observed, suggesting a diffusion-controlled process. By varying sol–gel synthesis parameters, such as water/alkoxide molar ratio and vancomycin concentration, the vancomycin release kinetics were tailored to meet specific therapeutic goals.[11,133] Room temperature processed vancomycin-containing sol–gel silica thin films on titanium implant surfaces were investigated for the treatment of osteomyelitis. The sol–gel/vancomycin thin film showed a long-term sustained release of vancomycin. The bactericidal efficacy of the released vancomycin was retained *in vitro* and *in vivo*.[11,120,121] **Figure 13** shows that vancomycin-containing sol–gel-coated Ti rods exhibit controlled antibiotic release *in vitro* and an effective treatment of virulent infection *in vivo*.

4.428.6.3.3. Cancer therapy

The controlled delivery of antitumor drugs, either directly to the tumor site or via the blood circulation, is a widely studied concept in cancer therapy. Doxorubicin is one of the most potent antitumor agents used in the general treatment of cancer. The continuous release of doxorubicin from xerogel materials has been pursued by implanting xerogel inside the tumor. Prokopowicz proceeded as follows: he synthesized doxorubicin-containing xerogel monoliths, which he then crushed to obtain granules for easy implantation. He found that that this xerogel powder can continuously release the doxorubicin for more than 2 days. He also determined that the release kinetics was diffusion controlled.[91,145]

Another approach for cancer drug delivery is to use silica nanoparticles. Nanoparticles, when administered intravenously,

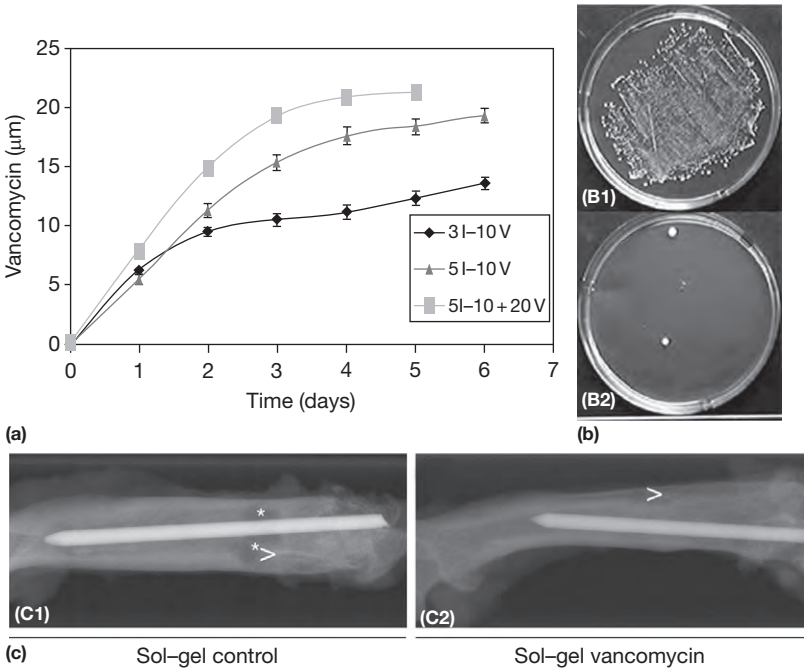

Figure 13 Vancomycin-containing sol–gel-coated Ti rods exhibit controlled antibiotic release and effective microbicidal activity. (a) vancomycin release into PBS for more than 5 days, (b) vancomycin-containing sol–gel-coated Ti rods minimize bacterial adherence *in vivo* for 7 days (B1: sol–gel silica coating alone, B2: vancomycin-containing sol–gel silica coating). Many bacteria were visualized on the control plates (B1), very few colonies were recovered from the vancomycin-containing sol–gel silica-coating rods at 7 days (B2). (c) Radiographic analysis indicates that vancomycin-containing sol–gel-coated Ti rods prevent osteomyelitis. (Control sol–gel (C1) and vancomycin-containing sol–gel (C2) coated Ti rods were implanted into infected rat femora.) The femora were harvested at 28 days. Note that while the sol–gel-coating rods show unmistakable signs of bone infection (periosteal elevation, enlargement of the medullary canal [>], as well as focal cysts [*]), there are minimal changes in the bones treated with vancomycin-containing sol–gel silica-coating rods. Reproduced from Adams, C. S.; Antoci, V. A., Jr; Harrison, G.; *et al. J. Orthop. Res.* **2009**, *27*(6), 701-709, with permission from Wiley.

can travel through the blood circulation and can deliver the antitumor drug to specific target sites. Barbé *et al.* demonstrated that xerogel nanoparticles with doxorubicin incorporated can release this drug in a controlled fashion over several weeks.[119,122]

4.428.7. Summary

The excellent bioresorbable and biocompatible behavior of sol–gel oxides have been well documented *in vivo*. The *in vitro* and *in vivo* drug release rates from sol–gels have also been extensively studied. Kinetics can be easily adjusted by varying sol–gel processing parameters, as well as by modifying their chemical compositions. Not only can the sol–gel process be adjusted for different release kinetics of a particular drug, it is also possible to adjust the sol–gel process for various drugs. Sol–gel oxides have proven to be useful in pharmaceutics industry for the controlled delivery of small drug molecules. What is even more attractive with sol–gel oxides is their potential in biotechnology for the sustained, controlled delivery of large molecules such as proteins, DNA, or virus. Highly sensitive proteins, growth factors, polypeptides, and even virus can be easily encapsulated in the sol–gel oxides. Incorporated biomolecules retain their original conformation and are stable to protease degradation *in vivo* before released. Undoubtedly, sol–gel oxides represent a very promising controlled release carrier material for the next generation of controlled delivery systems.

References

1. Grant, G. J.; Barenholz, Y.; Piskoun, B.; Bansinath, M.; Turndorf, H.; Bolotin, E. M. *Pharm. Res.* **2001**, *18*(3), 336–343.
2. Shikanov, A.; Domb, A. J.; Weiniger, C. F. *J. Control. Release* **2007**, *117*(1), 97–103.
3. Curley, J.; Castillo, J.; Hotz, J.; *et al*. *Anesthesiology* **1996**, *84*(6), 1401–1410.
4. Quintanar-Guerrero, D.; Ganem-Quintanar, A.; Nava-Arzaluz, M. G.; Pinon-Segundo, E. *Expert Opin. Drug Deliv.* **2009**, *6*(5), 485–498.
5. Rigby, S. P.; Fairhead, M.; van der Welle, C. F. *Curr. Pharm. Des.* **2008**, *14*(11), 1821–1831.
6. Radin, S.; El-Bassyouni, G.; Vresilovic, E. J.; Schepers, E.; Ducheyne, P. *Biomaterials* **2005**, *26*(9), 1043–1052.
7. Kortesuo, P.; Ahola, M.; Karlsson, S.; Kangasniemi, I.; Kiesvaara, J.; Yli-Urpo, A. *J. Biomed. Mater. Res.* **1999**, *44*(2), 162–167.
8. Santos, E. M.; Radin, S.; Ducheyne, P. *Biomaterials* **1999**, *20*(18), 1695–1700.
9. Falaize, S.; Radin, S.; Ducheyne, P. *J. Am. Ceram. Soc.* **1999**, *82*(4), 969–976.
10. Roveri, N.; Morpurgo, M.; Palazzo, B.; Parma, B.; Vivi, L. *Anal. Bioanal. Chem.* **2005**, *381*(3), 601–606.
11. Radin, S.; Ducheyne, P.; Kamplain, T.; Tan, B. H. *J. Biomed. Mater. Res.* **2001**, *57*(2), 313–320.
12. Czuryszkiewicz, T.; Areva, S.; Honkanen, M.; Lindén, M. *Colloids Surf. A Physicochem. Eng. Asp.* **2005**, *254*(1–3), 69–74.
13. Avnir, D.; Levy, D.; Reisfeld, R. *J. Phys. Chem.* **1984**, *88*(24), 5956–5959.

14. Braun, S.; Rappoport, S.; Zusman, R.; Avnir, D.; Ottolenghi, M. *Mater. Lett.* **1990**, *10*(1–2), 1–5.
15. Avnir, D.; Braun, S.; Lev, O.; Ottolenghi, M. *Chem. Mater.* **1994**, *6*(10), 1605–1614.
16. Avnir, D. *Acc. Chem. Res.* **1995**, *28*(8), 328–334.
17. Pope, E. J. A.; Braun, K.; Peterson, C. M. *J. Sol-Gel. Sci. Technol.* **1997**, *8*(1), 635–639.
18. Fennouh, S.; Guyon, S.; Livage, J.; Roux, C. *J. Sol-Gel. Sci. Technol.* **2000**, *19*(1), 647–649.
19. Coiffier, A.; Coradin, T.; Roux, C.; Bouvet, O. M. M.; Livage, J. *J. Mater. Chem.* **2001**, *11*(8), 2039–2044.
20. Livage, J.; Coradin, T.; Roux, C. *J. Phys. Condens. Matter* **2001**, *13*(33), R673.
21. Nicoll, S. B.; Radin, S.; Santos, E. M.; Tuan, R. S.; Ducheyne, P. *Biomaterials* **1997**, *18*(12), 853–859.
22. Santos, E. M.; Radin, S.; Shenker, B. J.; Shapiro, I. M.; Ducheyne, P. *J. Biomed. Mater. Res.* **1998**, *41*(1), 87–94.
23. Böttcher, H.; Kallies, K.; Haufe, H. *J. Sol-Gel. Sci. Technol.* **1997**, *8*(1), 651–654.
24. Böttcher, H.; Slowik, P.; Süß, W. *J. Sol-Gel. Sci. Technol.* **1998**, *13*(1), 277–281.
25. Sieminska, L.; Zerda, T. W. *J. Phys. Chem.* **1996**, *100*(11), 4591–4597.
26. Sieminska, L.; Ferguson, M.; Zerda, T. W.; Couch, E. *J. Sol-Gel. Sci. Technol.* **1997**, *8*(1), 1105–1109.
27. Lopez, T.; Sotelo, J.; Navarrete, J.; Ascencio, J. A. *Opt. Mater.* **2006**, *29*(1), 88–94.
28. Lopez, T.; Navarrete, J.; Conde, R.; Ascencio, J. A.; Manjarrez, J.; Gonzalez, R. D. *J. Biomed. Mater. Res. A* **2006**, *78A*(3), 441–448.
29. Lopez, T.; Ortiz, E.; Quintana, P.; Gonzalez, R. D. *Colloids Surf. A Physicochem. Eng. Asp.* **2007**, *300*(1–2), 3–10.
30. Catauro, M.; Raucci, M.; Convertito, C.; Melisi, D.; Rimoli, M. *J. Mater. Sci. Mater. Med.* **2006**, *17*(5), 413–420.
31. Catauro, M.; Raucci, M. G.; de Marco, D.; Ambrosio, L. *J. Biomed. Mater. Res. A* **2006**, *77A*(2), 340–350.
32. Avés, E.; Estévez, G.; Sader, M.; *et al. J. Mater. Sci. Mater. Med.* **2009**, *20*(2), 543–547.
33. Sousa, A.; Souza, K. C.; Sousa, E. M. B. *Acta Biomater.* **2008**, *4*(3), 671–679.
34. Andersson, J.; Areva, S.; Spliethoff, B.; Lindén, M. *Biomaterials* **2005**, *26*(34), 6827–6835.
35. Peterson, A.; Lopez, T.; Islas, E. O.; Gonzalez, R. D. *Appl. Surf. Sci.* **2007**, *253*(13), 5767–5771.
36. Brinker, C. J.; Scherer, G. W. *The Physics and Chemistry of Sol-Gel Processing*. Academic Press: San Diego, CA, 1990.
37. Kortesuo, P.; Ahola, M.; Kangas, M.; *et al. J. Control. Release* **2001**, *76*(3), 227–238.
38. Radin, S.; Ducheyne, P. In *Learning from Nature How to Design New Implantable Materials: From Biomineralization Fundamentals to Biomimetic Materials and Processing Routes*; Reis, R. L., Weiner, S., Eds.; Kluwer Academic Publishers: The Netherland, 2004; pp 59–74.
39. Ocotlán-Flores, J.; Saniger, J. *J. Sol-Gel. Sci. Technol.* **2006**, *39*(3), 235–240.
40. Pinon-Segundo, E.; Ganem-Quintanar, A.; Flores-Flores, J. O.; *et al. Drug Deliv.* **2008**, *15*(6), 399–407.
41. Gill, I.; Ballesteros, A. *J. Am. Chem. Soc.* **1998**, *120*(34), 8587–8598.
42. Finnie, K. S.; Jacques, D. A.; McGann, M. J.; Blackford, M. G.; Barbé, C. J. *J. Mater. Chem.* **2006**, *16*, 4494–4498.
43. Lopez, P. J.; Gautier, C.; Livage, J.; Coradin, T. *Curr. Nanosci.* **2005**, *1*(1), 73.
44. Glaser, R. H.; Wilkes, G. L.; Bronnimann, C. E. *J. Non-Cryst. Solids* **1989**, *113*(1), 73–87.
45. Viitala, R.; Jokinen, M.; Maunu, S. L.; Jalonen, H.; Rosenholm, J. B. *J. Non-Cryst. Solids* **2005**, *351*(40–42), 3225–3234.
46. Mellaerts, R.; Mols, R.; Jammaer, J. A. G.; *et al. Eur. J. Pharm. Biopharm.* **2008**, *69*(1), 223–230.
47. Mellaerts, R.; Aerts, C. A.; Humbeeck, J. V.; Augustijns, P.; Mooter, G. V.; Martens, J. A. *Chem. Commun.* **2007**, *2007*(13), 1375–1377.
48. Tozuka, Y.; Sasaoka, S.; Nagae, A.; Moribe, K.; Oguchi, T.; Yamamoto, K. *J. Colloid Interface Sci.* **2005**, *291*(2), 471–476.
49. Maver, U.; Godec, A.; Bele, M.; *et al. Int. J. Pharm.* **2007**, *330*(1–2), 164–174.
50. Michiel Van, S.; Valery, B.; Thao Do, T.; *et al. J. Pharm. Sci.* **2009**, *98*(8), 2648–2658.
51. Ambrogi, V.; Famiani, F.; Perioli, L.; Marmottini, F.; Di Cunzolo, I.; Rossi, C. *Microporous Mesoporous Mater.* **2006**, *96*(1–3), 177–183.
52. Kresge, C. T.; Leonowicz, M. E.; Roth, W. J.; Vartuli, J. C.; Beck, J. S. *Nature* **1992**, *359*(6397), 710–712.
53. Lin, H.-P.; Mou, C.-Y. *Acc. Chem. Res.* **2002**, *35*(11), 927–935.
54. Horcajada, P.; Ramila, A.; Perez-Pariente, J.; Vallet-Regi, M. *Microporous Mesoporous Mater.* **2004**, *68*(1–3), 105–109.
55. Slowing, I. I.; Vivero-Escoto, J. L.; Wu, C.-W.; Lin, V. S. Y. *Adv. Drug Deliv. Rev.* **2008**, *60*(11), 1278–1288.
56. Kosuge, K.; Singh, P. S. *Microporous Mesoporous Mater.* **2001**, *44–45*, 139–145.
57. Vallet-Regi, M.; Ruiz-Gonzalez, L.; Izquierdo-Barba, I.; Gonzalez-Calbet, J. M. *J. Mater. Chem.* **2006**, *16*(1), 26–31.
58. Higuchi, T. *J. Pharm. Sci.* **1963**, *52*, 1145–1149.
59. Radin, S.; Chen, T.; Ducheyne, P. *Biomaterials* **2009**, *30*, 850–858.
60. Baker, R. W.; Lonsdale, H. K. In *Controlled Release of Biologically Active Agents*; Tanquary, A. C., Lacey, R. F., Eds.; Plenum Press: New York, 1974; pp 15–71.
61. Jokinen, M.; Koskinen, M.; Areva, S. *Key Eng. Mater.* **2008**, *377*, 195–210.
62. Finnie, K.; Waller, D.; Perret, F.; *et al. J. Sol-Gel. Sci. Technol.* **2009**, *49*(1), 12–18.
63. Teoli, D.; Parisi, L.; Realdon, N.; Guglielmi, M.; Rosato, A.; Morpurgo, M. *J. Control. Release* **2006**, *116*(3), 295–303.
64. Koskinen, M. K.; Toriseva, M.; Jokinen, M. J.; Jalonen, H.; Salonen, J. I.; Kahari, V.-M. *Mol. Ther.* **2005**, *11*(S1), S422.
65. Kangasniemi, L.; Koskinen, M.; Jokinen, M.; *et al. Gene Ther.* **2009**, *16*, 103–110.
66. Hopfenberg, H. B. In *Controlled Release Polymeric Formulations*; Paul, D. R., Haris, F. W., Eds.; American Chemical Society: Washington, DC, 1976; pp 26–31.
67. Siepmann, J.; Peppas, N. A. *Adv. Drug Deliv. Rev.* **2001**, *48*(2–3), 139–157.
68. Ritger, P. L.; Peppas, N. A. *J. Control. Release* **1987**, *5*(1), 23–36.
69. Kortesuo, P.; Ahola, M.; Karlsson, S.; Kangasniemi, I.; Yli-Urpo, A.; Kiesvaara, J. *Biomaterials* **2000**, *21*(2), 193–198.
70. Kortesuo, P.; Ahola, M.; Kangas, M.; *et al. Biomaterials* **2002**, *23*(13), 2795–2801.
71. Katarzyna, C.; Joanna, C. *J. Biomed. Mater. Res. B Appl. Biomater.* **2008**, *87B*(1), 114–120.
72. Radin, S.; Falaize, S.; Lee, M. H.; Ducheyne, P. *Biomaterials* **2002**, *23*(15), 3113–3122.
73. Chu, L.; Tejedor-Tejedor, M. I.; Anderson, M. A. *Microporous Mater.* **1997**, *8*(5–6), 207–213.
74. Gorle, B. S. K.; Smirnova, I.; McHugh, M. A. *J. Supercrit. Fluids* **2009**, *48*(1), 85–92.
75. Smirnova, I.; Suttiruengwong, S.; Arlt, W. *J. Non-Cryst. Solids* **2004**, *350*, 54–60.
76. Smirnova, I.; Mamic, J.; Arlt, W. *Langmuir* **2003**, *19*(20), 8521–8525.
77. Prokopowicz, M. *J. Sol-Gel. Sci. Technol.* **2010**, *53*(3), 525–533.
78. Viitala, R.; Jokinen, M.; Rosenholm, J. B. *Int. J. Pharm.* **2007**, *336*(2), 382–390.
79. Ahola, M.; Kortesuo, P.; Kangasniemi, I.; Kiesvaara, J.; Yli-Urpo, A. *Int. J. Pharm.* **2000**, *195*(1–2), 219–227.
80. Baker, G. A.; Jordan, J. D.; Bright, F. V. *J. Sol-Gel. Sci. Technol.* **1998**, *11*(1), 43–54.
81. Lee, E.-J.; Jun, S.-H.; Kim, H.-E.; Kim, H.-W.; Koh, Y.-H.; Jang, J.-H. *J. Mater. Sci. Mater. Med.* **2010**, *21*(1), 207–214.
82. Wang, G.-H.; Zhang, L.-M. *J. Phys. Chem. B* **2007**, *111*(36), 10665–10670.
83. Czarnobaj, K.; Prokopowicz, M.; Lukasiak, J. *Drug Deliv.* **2006**, *13*(5), 339–344.
84. Czarnobaj, K.; Lukasiak, J. *J. Mater. Sci. Mater. Med.* **2007**, *18*(10), 2041–2044.
85. Costache, M. C.; Qu, H.; Ducheyne, P.; Devore, D. I. *Biomaterials* **2010**, *31*(24), 6336–6343.
86. Xue, J. M.; Tan, C. H.; Lukito, D. *J. Biomed. Mater. Res. B Appl. Biomater.* **2006**, *78B*(2), 417–422.
87. Xue, J. M.; Shi, M. *J. Control. Release* **2004**, *98*(2), 209–217.
88. Ahola, M. S.; Säilynoja, E. S.; Raitavuo, M. H.; Vaahtio, M. M.; Salonen, J. I.; Yli-Urpo, A. U. O. *Biomaterials* **2001**, *22*(15), 2163–2170.
89. Wu, Z.; Joo, H.; Gyu Lee, T.; Lee, K. *J. Control. Release* **2005**, *104*(3), 497–505.
90. Wu, Z.; Joo, H.; Ahn, I.-S.; Kim, J.-H.; Kim, C.-K.; Lee, K. *J. Non-Cryst. Solids* **2004**, *342*(1–3), 46–53.
91. Prokopowicz, M. *Acta Biomater.* **2009**, *5*(1), 193–207.
92. Munoz, B.; Ramila, A.; Perez-Pariente, J.; Diaz, I.; Vallet-Regi, M. *Chem. Mater.* **2003**, *15*(2), 500–503.
93. Shen, S.; Chow, P. S.; Chen, F.; Tan, R. B. H. *Chem. Pharm. Bull.* **2007**, *55*(7), 985–991.
94. Wu, Z.; Jiang, Y.; Kim, T.; Lee, K. *J. Control. Release* **2007**, *119*(2), 215–221.

95. Fu, Q.; Rao, G. V. R.; Ista, L. K.; *et al*. *Adv. Mater*. **2003**, *15*(15), 1262–1266.
96. Lu, J.; Choi, E.; Tamanoi, F.; Zink, J. I. *Small* **2008**, *4*(4), 421–426.
97. Nguyen, T. D.; Leung, K. C.-F.; Liong, M.; Liu, Y.; Stoddart, J. F.; Zink, J. I. *Adv. Funct. Mater*. **2007**, *17*(13), 2101–2110.
98. Zhu, Y.; Fujiwara, M. *Angew. Chem. Int. Ed*. **2007**, *46*(13), 2241–2244.
99. Nguyen, T. D.; Leung, K. C. F.; Liong, M.; Pentecost, C. D.; Stoddart, J. F.; Zink, J. I. *Org. Lett*. **2006**, *8*(15), 3363–3366.
100. Lai, C.-Y.; Trewyn, B. G.; Jeftinija, D. M.; *et al*. *J. Am. Chem. Soc*. **2003**, *125*(15), 4451–4459.
101. Lai, W.; Garino, J.; Flaitz, C.; Ducheyne, P. *J. Biomed. Mater. Res. A* **2005**, *75A*(2), 398–407.
102. Dobbie, J.; Smith, M. *Scot. Med. J*. **1982**, *27*(1), 17–19.
103. Hamilton, E. I.; Minski, M. J.; Cleary, J. J. *Sci. Total Environ*. **1973**, *1*(4), 341–374.
104. LeVier, R. R. *Bioinorg. Chem*. **1975**, *4*(2), 109–115.
105. Lai, W.; Garino, J.; Ducheyne, P. *Biomaterials* **2002**, *23*(1), 213–217.
106. Royals, M. A.; Fujita, S. M.; Yewey, G. L.; Rodriguez, J.; Schultheiss, P. C.; Dunn, R. L. *J. Biomed. Mater. Res*. **1999**, *45*(3), 231–239.
107. Baumann, H. *Hoppe Seylers Z. Physiol. Chem*. **1960**, *320*, 11–20.
108. Baumann, H. *Hoppe Seylers Z. Physiol. Chem*. **1960**, *319*, 38–51.
109. Policard, A.; Collet, A.; Daniel-Moussard, H.; Pregermain, S. *J. Urol. Med. Chir*. **1960**, *66*, 585–600.
110. Sauer, F.; Laughland, D. H.; Davidson, W. M. *Can. J. Biochem. Physiol*. **1959**, *37*(2), 183–191.
111. Kawanabe, K.; Yamamuro, T.; Nakamura, T.; Kotani, S. *J. Biomed. Mater. Res*. **1991**, *25*(1), 117–128.
112. Kawanabe, K.; Yamamuro, T.; Kotani, S.; Nakamura, T. *J. Biomed. Mater. Res*. **1992**, *26*(2), 209–219.
113. Nagase, M.; Abe, Y.; Chigira, M.; Udagawa, E. *Biomaterials* **1992**, *13*(3), 172–175.
114. Iler, R. K. *The Chemistry of Silica: Solubility, Polymerization, Colloid and Surface Properties and Biochemistry of Silica*. Wiley: New York, 1979.
115. Policard, A.; Collet, A.; Daniel-Moussard, H.; Pregermain, S. *J. Biophys. Biochem. Cytol*. **1961**, *9*, 236–238.
116. Gye, W.; Purdy, W. *Br. J. Exp. Pathol*. **1922**, *3*, 75–94.
117. Scheel, L.; Fleischer, E.; Klemperer, F. *AMA Arch. Ind. Hyg. Occup. Med*. **1953**, *8*, 564–573.
118. Kortesuo, P.; Ahola, M.; Kangas, M.; Kangasniemi, I.; Yli-Urpo, A.; Kiesvaara, J. *Int. J. Pharm*. **2000**, *200*(2), 223–229.
119. Barbe, C.; Bartlett, J.; Kong, L.; *et al*. *Adv. Mater*. **2004**, *16*(21), 1959–1966.
120. Radin, S.; Ducheyne, P. *Biomaterials* **2007**, *28*(9), 1721–1729.
121. Adams, C. S.; Antoci, V., Jr.; Harrison, G.; *et al*. *J. Orthop. Res*. **2009**, *27*(6), 701–709.
122. Barbé, C.; Kong, L.; Finnie, K.; *et al*. *J. Sol–Gel. Sci. Technol*. **2008**, *46*(3), 393–409.
123. Sakka, S. In *Sol-Gel Technology for Thin Films, Fibers, Preforms, Electronics and Specialty Shapes*; Klein, L. C., Ed.; William Andrew Publishing/Noyes: Park Ridge, NJ, 1988.
124. Jokinen, M.; Peltola, T.; Veittola, S.; Rahiala, H.; Rosenholm, J. B. *J. Eur. Ceram. Soc*. **2000**, *20*(11), 1739–1748.
125. Czuryszkiewicz, T.; Ahvenlammi, J.; Kortesuo, P.; *et al*. *J. Non-Cryst. Solids* **2002**, *306*(1), 1–10.
126. Peltola, T.; Jokinen, M.; Veittola, S.; Rahiala, H.; Yli-Urpo, A. *Biomaterials* **2001**, *22*(6), 589–598.
127. Avnir, D.; Coradin, T.; Lev, O.; Livage, J. *J. Mater. Chem*. **2006**, *16*(11), 1013–1030.
128. Wu, X.; Wei, J.; Lu, X.; *et al*. *Biomed. Mater*. **2010**, *5*(3), 035006.
129. Wu, X.; Ye, L.; Liu, K.; *et al*. *Biomed. Mater*. **2009**, *4*(4), 045008.
130. Dai, C.; Yuan, Y.; Liu, C.; *et al*. *Biomaterials* **2009**, *30*(29), 5364–5375.
131. Kortesuo, P.; Ahola, M.; Kangas, M.; Yli-Urpo, A.; Kiesvaara, J.; Marvola, M. *Int. J. Pharm*. **2001**, *221*(1–2), 107–114.
132. Yilmaz, E.; Bengisu, M. *J. Biomed. Mater. Res. B Appl. Biomater*. **2006**, *77B*(1), 149–155.
133. Aughenbaugh, W.; Radin, S.; Ducheyne, P. *J. Biomed. Mater. Res*. **2001**, *57*(3), 321–326.
134. Shea, L. D.; Smiley, E.; Bonadio, J.; Mooney, D. J. *Nat. Biotechnol*. **1999**, *17*, 551–554.
135. Bonadio, J.; Smiley, E.; Patil, P.; Goldstein, S. *Nat. Med*. **1999**, *5*(7), 753–759.
136. Meilander-Lin, N. J.; Cheung, P. J.; Wilson, D. L.; Bellamkonda, R. V. *Tissue Eng*. **2005**, *11*(3–4), 546–555.
137. Jang, J.-H.; Rives, C. B.; Shea, L. D. *Mol. Ther*. **2005**, *12*(3), 475–483.
138. Satoh, S.; Fugetsu, B.; Nomizu, M.; Nishi, N. *Polym. J*. **2005**, *37*(2), 94–101.
139. Pierre, A.; Bonnet, J.; Vekris, A.; Portier, J. *J. Mater. Sci. Mater. Med*. **2001**, *12*(1), 51–55.
140. Meseguer-Olmo, L.; Ros-Nicolás, M. J.; Clavel-Sainz, M.; *et al*. *J. Biomed. Mater. Res*. **2002**, *61*(3), 458–465.
141. DiCicco, M.; Goldfinger, A.; Guirand, F.; Abdullah, A.; Jansen, S. A. *J. Biomed. Mater. Res. B Appl. Biomater*. **2004**, *70B*(1), 1–20.
142. Nablo, B. J.; Prichard, H. L.; Butler, R. D.; Klitzman, B.; Schoenfisch, M. H. *Biomaterials* **2005**, *26*(34), 6984–6990.
143. Marxer, S. M.; Rothrock, A. R.; Nablo, B. J.; Robbins, M. E.; Schoenfisch, M. H. *Chem. Mater*. **2003**, *15*(22), 4193–4199.
144. Czarnobaj, K.; Lukasiak, J. *Drug Deliv*. **2004**, *11*(6), 341–344.
145. Prokopowicz, M. *J. Pharm. Pharmacol*. **2007**, *59*(10), 1365–1373.
146. Dai, C.; Liu, C.; Wei, J.; Hong, H.; Zhao, Q. *Biomaterials* **2010**, *31*(30), 7620–7630.
147. Qu, H.; Costache, M. C.; Inan, S.; Cowan, A.; Devore, D.; Ducheyne, P. Polymer – xerogel composites for controlled release wound dressings: A rat incisional pain model study. Society for Biomaterials 2010 Annual Meeting; 2010; Seattle, WA, 2010.

4.429. Ordered Mesoporous Silica Materials

M Colilla and M Vallet-Regí, Universidad Complutense de Madrid, Madrid, Spain

© 2011 Elsevier Ltd. All rights reserved.

4.429.1.	**Introduction**	498
4.429.2.	**Ordered Mesoporous Materials: General Remarks**	499
4.429.3.	**Biocompatibility of Mesoporous Materials**	500
4.429.4.	**Mesoporous Materials for Local Drug Delivery**	501
4.429.4.1.	Influence of the Textural Properties	502
4.429.4.1.1.	Pore diameter	502
4.429.4.1.2.	Surface area	502
4.429.4.1.3.	Pore volume	503
4.429.4.2.	Influence of the Matrix Structure	504
4.429.4.3.	Influence of the Particle Morphology	504
4.429.4.4.	Influence of the Matrix Organic Functionalization	504
4.429.4.4.1.	Functionalization with amino groups	505
4.429.4.4.2.	Functionalization with hydrophobic groups	506
4.429.5.	**Bioactivity of Mesoporous Matrices**	506
4.429.5.1.	Incorporation of Phosphorous into Mesoporous Silica Matrices	507
4.429.5.2.	Addition of Small Amounts of Bioactive Glasses	508
4.429.5.3.	Mesoporous Bioactive Glasses	508
4.429.6.	**Hierarchical Macroporous Scaffolds for Bone Tissue Engineering**	510
References		512

Glossary

Bioactive agent Bioactive agents are those substances able to induce an effect on or to stimulate a response in a living tissue.

Biomimetism Reproducing artificially essential properties of one or several biological systems. It finalizes products and processes as they are used in Nature.

Functionalization Functionalization is the addition of functional groups onto the surface of a material by chemical synthesis methods. The functional group added can be subjected to ordinary synthesis methods to attach virtually any kind of organic compound onto the surface.

Local controlled delivery Release of an agent at a controlled rate for an extended time in a specific place to localize agent action.

Macropores Macropores are those pores with diameter larger than 50 nm according to IUPAC pores classification. Biomaterials scientific community traditionally considers macropores as those pores with diameter above 100 μm.

Mesopores Mesopores are those pores with diameter in the range 2–50 nm according to IUPAC pores classification.

Mesoporous bioactive glasses Mesoporous bioactive glasses are materials with chemical compositions similar to those of conventional bioactive sol–gel glasses (SiO_2–CaO–P_2O_5) and the textural properties and ordered mesopore arrangement of ordered mesoporous materials.

Micropores Micropores are those pores with diameter smaller than 2 nm according to IUPAC pores classification. Biomaterials scientific community traditionally considers micropores as those pores with diameter below 10 μm.

Nanoscale The nanoscale has been defined as being of the order of 100 nm or less.

Ordered mesoporous materials A mesoporous material is a material containing pores with diameters between 2 and 50 nm forming ordered arrangements of pore networks. They have high surface areas, great pore volumes, and narrow pore size distributions. These materials are excellent matrices to host different molecules, which make them suitable for numerous applications in catalysis, separation, biomedical field, etc.

Rapid prototyping Rapid prototyping is the name given to a host of related technologies that are used to fabricate physical objects directly from computer-assisted design (CAD) data sources. These methods are unique in that they add and bond materials in layers to form objects. Such systems are also known by the general names solid freeform fabrication and layered manufacturing and offer advantages in many applications compared to classical subtractive fabrication methods such as milling or turning.

Surfactant Short for 'SURFace ACTive AgeNT,' it is a molecule that lowers surface tension. Such molecules contain both hydrophobic and hydrophilic components and are thus semisoluble in both organic and aqueous solvents.

Abbreviations

AL	Alendronate
ACP	Amorphous calcium phosphate
AMS	Anionic surfactant templated mesoporous silica
BSA	Bovine serum albumin
C_8	Octyl chains
C_8TAB	Octyltrimethylammonium bromide surfactant
C_{10}TAB	Decyltrimethylammonium bromide surfactant
C_{12}TAB	Dodecyltrimethylammonium bromide surfactant
C_{16}TAB	Hexadecyltrimethylammonium bromide surfactant
C_{18}	Octadecyl chains
CHA	Carbonate hydroxyapatite
CLCT	Cooperative liquid-crystal template mechanism
cmc	Critical micelar concentration
CTAB	Cetyltrimethylammonium bromide surfactant
DMS	Dimethylsilyl groups
ED	Electron diffraction
EDS	Energy dispersive scattering
FDU	FuDan University
F127	Pluronic® F127 block copolymer surfactant containing poly(ethylene glycol)-block-poly(propylene glycol)-block-poly(ethylene glycol) units ($EO_{100}PO_{65}EO_{100}$)
FSM	Folded sheet materials
FTIR	Fourier transmission infrared spectroscopy
HPLC	High-performance liquid chromatography
KIT	Korean Advanced Institute of Science and Technology
LCT	Liquid-crystal templating mechanism
MBG	Mesoporous bioactive glass
MCF	Mesostructured cellular foam
MCF-NH_2	Mesostructured cellular foam material functionalized with aminopropyl groups
MCM	Mobil composition of matter
MCM-41-DMS	MCM-41 mesoporous material functionalized with dimethylsilyl groups
MCM-41-MS	MCM-41 mesoporous material functionalized with methylsilyl groups
MCM-41-NH_2	MCM-41 mesoporous material functionalized with aminopropyl groups
MCM-41-SH	MCM-41 mesoporous material functionalized with mercaptopropyl groups
MCM-41-TMS	MCM-41 mesoporous material functionalized with trimethylsilyl groups
MS	Methylsilyl groups
MSU	Michigan State University
NMR	Nuclear magnetic resonance
OCP	Octacalcium phosphate
P123	Pluronic® P123 block copolymer surfactant containing poly(ethylene glycol)-block-poly(propylene glycol)-block-poly(ethylene glycol) units ($EO_{20}PO_{70}EO_{20}$)
PTHrP	Parathyroid hormone-related protein
PUF	Polyurethane foam
PVP	Poly(vinylpyrrolidone)
SBA	Santa BArbara
SBA-15-$C_3N^+Me_3$	SBA-15 functionalized with *N*-trimethoxysilylpropyl-*N*,*N*,*N*-trimethyl ammonium chloride
SBA-15-$C_3N^+Me_2C_{18}$	SBA-15 functionalized with octadecyldimethyl (3-trimethoxysilyl-propyl) ammonium chloride
SBA-15-NH_2	SBA-15 mesoporous material functionalized with aminopropyl groups
SBF	Simulated body fluid
SEM	Scanning electron microscopy
SMM	Silica-based ordered mesoporous material
TEM	Transmission electron microscopy
TEOS	Tetraethylorthosilicate
TLCT	True liquid-crystal template mechanism
TMOS	Tetramethylorthosilicate
TMOS-$C_3N^+Me_3Cl$	*N*-trimethoxysilylpropyl-*N*,*N*,*N*-trimethyl ammonium chloride
TMOS-$C_3N^+Me_2C_{18}Cl$	Octadecyldimethyl (3-trimethoxysilyl-propyl) ammonium chloride
TMS	Trimethylsilyl groups
UV–vis	Ultraviolet–visible spectroscopy
XRD	X-ray diffraction

Symbols

D_P	Pore diameter
V_P	Pore volume

4.429.1. Introduction

Since their discovery in 1990s, silica-based ordered mesoporous materials (SMMs) have received much attention from the scientific community because of their outstanding textural and structural properties. During the last few years, SMMs have found many applications in catalysis, sensors, separation, etc.[1,2] Recently, the biomedical research field has shown a growing interest toward these ordered mesoporous materials. These matrices exhibit two principal features: they can act as controlled delivery systems and they have bone-bonding capability through the development of nanoapatites similar to the

biological ones onto their surfaces when in contact with physiological fluids.

It was in 2001 when MCM-41 was proposed for the first time as a controlled delivery system, using ibuprofen as the model drug.[3] Their stable mesoporous structures and well-defined surface properties make SMMs good matrices to host a wide variety of drugs and biologically active species for local controlled delivery applications.[4–13] The structural and textural properties of mesoporous matrices can be tailored depending on the targeted guest molecule. Moreover, there are a number of silanol groups covering the mesoporous silica walls susceptible of undergoing chemical functionalization with organic functions. The different approaches developed up to date to achieve better control over drug loading and release kinetics are tackled in this chapter.

The *in vitro* bioactive behavior of SMMs has been also demonstrated.[8,14] Recently, the synthesis of mesoporous bioactive glasses (MBGs), with chemical compositions similar to those of conventional bioactive sol–gel glasses and the textural properties and ordered mesopore arrangement of SMMs has been reported.[15,16] MBGs exhibit fascinating features such as the fastest bioactive response reported till date for bioceramic materials or biomimetic behavior similar to the *in vivo* bone mineralization process.[17] All these aspects and the different chemical strategies carried out to modulate the time of bioactive response are reviewed within this chapter.

This double scope, controlled delivery capability and *in vitro* bioactivity, makes ordered mesoporous materials promising candidates to be used as bioceramics for bone tissue-regeneration technologies.[4,18–20] In addition, it is also possible to organically modify the external surface of silica walls to graft certain biomolecules such as peptides, proteins, or growth factors that act as signals to enhance or stimulate new bone formation. Considering all these properties the question is: do these materials have good potential to be used as bioceramics in clinical medical practice? Their biocompatibility, bioactivity, capability to regenerate bone, and ability to act as controlled delivery systems of biologically active molecules have been confirmed. Actually, the preliminary *in vitro* and *in vivo* tests performed using SMMs have been favorable. So, the current challenge is to optimize all these properties to the concrete clinical need and to evaluate the performance of SMMs in comparison with that of bioceramics that are widely employed in clinical practice such as bioactive glasses.

4.429.2. Ordered Mesoporous Materials: General Remarks

As previously commented, SMMs were reported for the first time in the early 1990s by Japanese researchers[21,22] and Mobil Oil Corporation scientists,[23] who reported for the first time the synthesis of KSW-n and M41S families of mesostructured materials, respectively. Ordered mesoporous materials represent a new generation of structurally unique materials, which exhibit order at the mesoscopic scale (2–50 nm) and disorder at the atomic scale. The mesoporous channels are divided by amorphous silica walls and arranged periodically on lattices such as artificial atoms or molecules in ordinary crystals. The synthesis of mesoporous materials is based on the use of surfactants that act as templates, that is, structure directing agents, for the assembly and subsequent condensation of inorganic precursors.[24,25]

SMMs are characterized by regular arrays of uniform channels, whose dimensions can be tuned through the chemical nature of the surfactant, additives, and synthesis conditions (pH, temperature, etc.) in the so-called *liquid-crystal templating* (LCT) mechanism.[26] This method is based on the formation of liquid crystals in mixtures of polar solvents and surfactants with a nonpolar tail group. However, different investigations in the formation procedures of SMMs led to suggest two different variations of the LCT mechanism (**Figure 1**).

As per the first mechanism, known as *true liquid-crystal template* (TLCT), the surfactant concentration is so high that under certain conditions of temperature and pH a lyotropic liquid-crystalline phase is formed in absence of the inorganic precursor. According to the TLCT mechanism, the amount of surfactant dissolved in the aqueous solution is above the critical micelar concentration (*cmc*), which allows the surfactant molecules to form aggregates called micelles. These micelles are formed because the hydrophobic tails of the surfactant tend to congregate to minimize contact with water while their

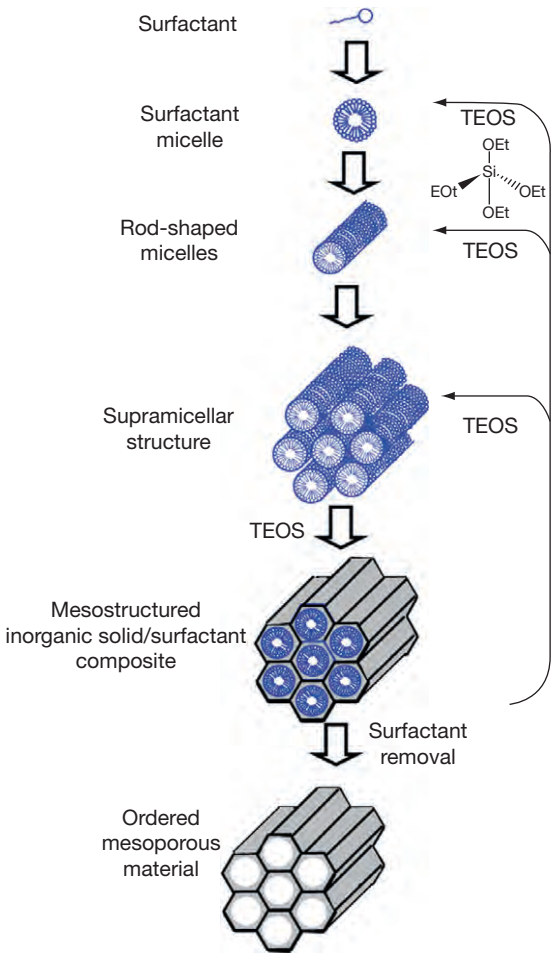

Figure 1 Schematic representation of true liquid-crystal template mechanism and cooperative liquid-crystal template mechanism used to describe the synthesis of silica-based ordered mesoporous materials.

hydrophilic heads orientate to maximize the interaction with the aqueous medium. The shape and size of these micelles depend on the composition and chemical nature of the surfactant and on the solution conditions, such as the surfactant concentration, pH and temperature, presence of cosurfactants, etc. These micelles aggregate themselves forming supramicellar structures with hexagonal, cubic, or laminar geometry depending on the experimental conditions. Thus, the geometry of the resulting mesoporous framework will depend on the geometry of the supramicellar aggregates. Then the silica source, which is normally tetraethylorthosilicate (TEOS) or tetramethylorthosilicate (TMOS), is added, which condenses around the supramicellar structures. The second proposed mechanism is the cooperative liquid-crystal template (CLCT), which suggests that it is also possible that the lyotropic liquid-crystalline phase is formed even at concentrations of surfactant molecules below the *cmc*, existing as a cooperative assembly of the surfactant and the already added silica precursor.

Independently of the synthetic route followed, the last step in the synthesis of SMMs consists in the surfactant removal by calcination or solvent extraction. The surfactant removal leaves a network of cavities within the silica framework that will determine the physical–chemical properties of the resulting materials. These materials exhibit outstanding properties, such as stable mesoporous structure, high surface area ($\sim$1000 $m^2 g^{-1}$), large pore volume ($\sim$1 $cm^3 g^{-1}$), regular and tunable nanopore size (2–50 nm), homogeneous pore morphology (hexagonal or cubic pores), nontoxic and biocompatible behavior, and the possibility of being chemically modified with different organic groups grafted to the silica walls. Different mesoporous structures can be obtained depending on the synthesis pathway, such as MCM (Mobil Composition of Matter) series,[23,26–30] SBA (Santa BArbara) series,[31–33] MSU-n (Michigan State University) series,[34] KIT-n (Korean Advanced Institute of Science and Technology) series,[35] FSM-n (Folded Sheet Materials) series,[36] FDU (FuDan University) series,[37–39] and AMS-n (Anionic surfactant templated Mesoporous Silica) series.[40]

Figure 2 displays the structural models corresponding to different mesoporous structures exhibiting different symmetries. Among them, three well-known mesoporous materials are MCM-41, SBA-15, and MCM-48, whose structural models are displayed in Figure 2. The two MCM-type materials are synthesized by using cationic quaternary ammonium surfactants under basic conditions. They have narrow pore size distributions ranging from 2.5 to 4.0 nm, with 2D-hexagonal *p6mm* structure (MCM-41)[41] and 3D-bicontinuous cubic $Ia\bar{3}d$ structure (MCM-48).[28] SBA-15 mesoporous material is synthesized by using neutral nonionic surfactants (block copolymers) as templates. SBA-15 exhibits large pore sizes in the 6–10 nm range with 2D-hexagonal *p6mm* structure and complementary micropores. These micropores are arranged in a disordered fashion interconnecting adjacent mesopores.[42,43] SBA-15 is currently receiving much attention because of its possible utilization in applications that require materials with easily accessible, uniform, and large-size pores with good stability.[44,45] Besides, different research approaches have allowed the development of new SBA-15-type mesoporous structures with enhanced textural properties to increase the application fields of such matrices. Thus, SBA-15 materials with really large surface areas have been reported.[46]

4.429.3. Biocompatibility of Mesoporous Materials

Bioceramics aimed at bone implant applications must be in contact with physiological fluids. In this sense, long-term biocompatibility, which has been demonstrated to depend on the implantation site, the shape, and size of the material and also on its surface chemistry, is a mandatory requirement that must be satisfied (see Chapter 4.401, The Concept of

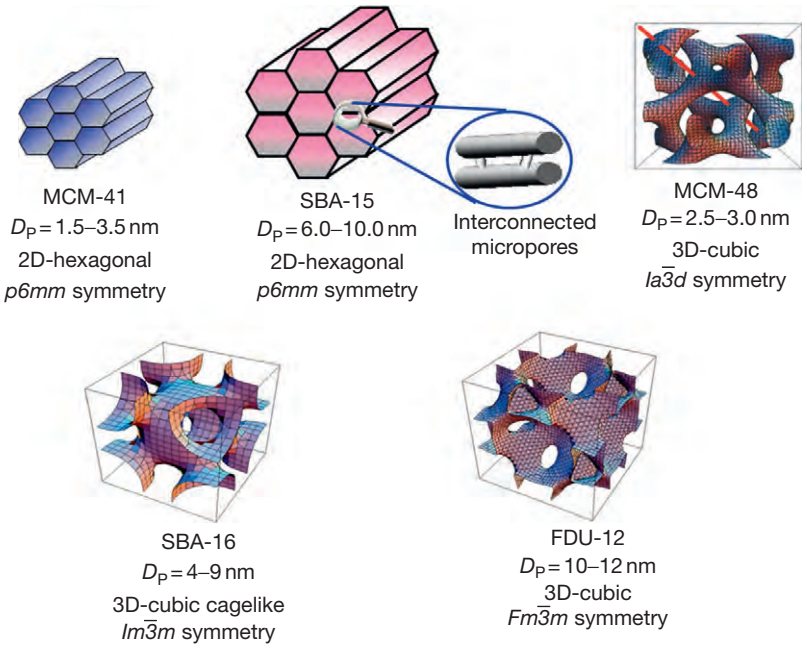

Figure 2 Models of different mesoporous structures, including their pore diameters (D_P) and symmetries.

Biocompatibility and Chapter 4.402, Biocompatibility and the Relationship to Standards: Meaning and Scope of Biomaterials Testing). Among bioceramics, SMMs are good candidates to be used as bone implant materials, because they can host a wide variety of biologically active molecules for the treatment of bone diseases.

Amorphous silica has been generally considered as nontoxic, and it has been reported as biocompatible and degradable in living tissue.[47–49] In fact, amorphous colloidal and porous silica are used as adjuvant in pharmaceutical technology. To date, biocompatibility and degradability with time of different silica materials have been described,[49–52] but few research works have reported the inherent cytotoxicity and biocompatibility of SMMs. The concentration of SMMs has been revealed as an important factor in their *in vitro* toxicity. SMMs showed low toxicity at low concentrations,[53–59] whereas the toxicity increased at high concentrations.[53] It has been also shown that size and concentration of mesoporous silica particles affect the viability of human monocyte-derived dendritic cells as well as the expression of immune regulatory markers by these cells.[60] The results derived from such research showed that mesoporous silica particles have promising properties to serve as immune stimulants/regulants with possible T-cell modulatory properties favorable for vaccine delivery as well as for more neutral drug delivery systems. If intracelullar delivery is the aim in biological applications, it is critical to minimize the particle size of SMM to the nanometer scale. Thus, fluorescein functionalized mesoporous silica nanoparticles, with sizes close to 110 nm have been reported to be internalized into 3T3-L1 fibroblast cells and accumulated into cytoplasm with no apparent cytotoxic effects.[61]

The surface area of an SMM has been also reported as an important factor that causes cell death. Thus, the *in vitro* cytotoxicity of MCM-41 mesoporous material, MCM-41 functionalized with aminopropyl groups (MCM-41-NH_2) and mercaptopropyl groups (MCM-41-SH) and spherical silica nanoparticles (SiO_2), toward human neuroblastoma cells[62] has been investigated. Taking into account that the particles studied were not soluble in aqueous media, authors introduced a new quantity to measure the cytotoxicity of these materials, Q_{50}, which is the number of particles required to inhibit normal cell growth by 50%. This study showed that Q_{50} increased in the order: MCM-41 < MCM-41-SH < MCM-41-$NH_2 \approx SiO_2$. These results would point to MCM-41 as the most cytotoxic of the studied materials. Albeit the chemical basis of the cytotoxic effect of these materials remains unclear, the exposed surface area of the particle could play an important role in cellular death. Therefore, the most toxic mesoporous silica materials were those with the largest surface areas. However, the chemical nature of the attached functional groups should be also considered. Moreover, surface area may not be the origin for cytotoxicity as spherical silica nanoparticles, which exhibited relatively small surface area, displayed cytotoxicity similar to that of MCM-41-NH_2, which had higher surface area. All these findings suggest that cell death could be governed by other factors, such as size and shape.

In vivo studies with rats evidenced low toxicity with small amounts of 1–2 μm SBA-15[63] surgically implanted into the basolateral amygdale of rats. In addition, mesoporous particles (~100 nm) fused with iron oxide and amorphous silica particles exhibited low toxicity when intravenously administrated in mice.[64] Recently, *in vivo* studies using MCM-41, MCM-48, and mesostructured cellular foam (MCF) mesoporous materials have been reported.[65] Histological studies performed after subcutaneous injection of such SMMs at the sciatic nerve in rats evidenced a good biocompatibility at all time points. However, intraperitoneal and intravenous injections in mice resulted in death or euthanasia.

The above-mentioned results clearly show that toxicity of SMMs strongly depends on the administration route to the living body. Therefore, when evaluating the viability of SMMs as biomaterials for bone tissue regeneration, the first step should consist in performing *in vitro* tests with osteoblastic cell cultures. Accordingly, *in vitro* assays with osteoblastic cell culture using several mesoporous materials in the system SiO_2–P_2O_5 with different phosphorus contents have been reported.[66] These preliminary *in vitro* assays indicated that the lowest cellular damage was induced by the sample with the highest P-content (5% in mol). This fact was ascribed to the greatest decrease in the amount of silica leached from matrices with the highest phosphorous content. Recently, the *in vitro* behavior of both unmodified and organically modified SBA-15 materials loaded with osteostatin, which is the sequence 107–111 of the parathyroid hormone-relatedprotein (PTHrP), has been evaluated.[67] The results revealed that the incorporation of osteotatin into the SMMs increased cell proliferation and expression of several osteoblast phenotypic markers (alkaline phosphatase, osteocalcin, osteoprotegerin, receptor activator of nuclear factor-KB ligand, and vascular endothelial growth factor) in mouse MC3T3-E1 osteoblast cell line. Moreover, there was an increase in the matrix mineralization, and the secretion of collagen was stimulated after 12 days. Thus, it has been demonstrated that osteostatin-loaded SBA-15 materials promote osteogenesis in cell culture, which is interesting from the point of view of their potential clinical usage in bone regeneration technologies.

Once these bioceramics successfully passed the *in vitro* tests, they were investigated under *in vivo* conditions.[68,69] Such experiments were performed in healthy and dexamethasone-induced osteoporotic rabbits. Cavitary defects in distal, medial, and lateral condyle were performed and both SBA-15 and SBA-15 loaded with osteostatin were implanted. The histopathological evaluation was carried out after 2 weeks of implantation. The cavitary defects in healthy animals revealed an efficient reparative process, with neoformed bone tissue around the biomaterials after 2 weeks. However, the incorporation of osteostatin into the mesoporous matrices was found to reduce tissue encapsulation, associated with increased cellularity and the appearance of osteoid deposits surrounding the biomaterial. These results open promising expectation for SMMs to be used as bioceramics for bone repair and regeneration technologies.

4.429.4. Mesoporous Materials for Local Drug Delivery

The fascinating structural and textural properties of SMMs made them suitable to act as host systems of a wide range of different drugs for the treatment of bone diseases. This is especially important when dealing with anticancer and

antiosteoporosis drugs for the local treatment of osseous tumors and osteoporosis, respectively. The local administration of therapeutic agents by bioceramic matrices presents advantages over conventional therapies, such as oral intake, because a better control over drug loading and release can be achieved. Moreover, the local sustained administration permits to keep constant drug levels in plasma and to reduce undesired side effects.[70] Sol–gel processed silica controlled release materials were first proposed in 1990s.[52,71–74] Since 2001, when MCM-41 was proposed for the first time as controlled delivery system,[3] several SMMs have been tested as delivery systems of different drugs, such as ibuprofen,[75–82] naproxen,[83] aspirin,[84] piroxicam,[85] gentamicin,[86,87] amoxicillin,[88] erythromycin,[77,89] vancomycin,[90] diflunisal,[90] captopril,[91] nimodipine,[92] itraconazole,[93] alendronate,[94–96] zoledronate,[97,98] ipriflavone,[99] methotrexate,[100] and cisplatin.[101] In addition, SMMs have been also reported as controlled delivery systems of proteins,[5,20,102,103] peptides,[67,104,105] and amino acids.[106]

Molecule adsorption and *in vitro* delivery tests are remarkable steps in the performance of SMMs as controlled delivery systems (**Figure 3**). There are different methods of molecule adsorption, but the most commonly used are impregnation methods, in which the mesoporous carrier is soaked into a concentrated molecule solution. Loading conditions, such as temperature, pH, solvent, etc., must be selected attending to the chemical nature of the targeted molecule.[107] On the other hand, *in vitro* delivery assays are performed by soaking the loaded SMMs into simulated body fluid (SBF)[108] or saline solution at pH 7.4 and 37 °C to try to mimic physiological conditions. Normally, the amount of molecule released is monitored by chromatographic and spectroscopic techniques, such as high-performance liquid chromatography (HPLC) and ultraviolet–visible (UV–vis) spectroscopy.

The research performed since 2001 on ordered mesoporous silica indicates that the textural properties, mesoporous structure, morphology, and organic functionalization of the silica walls are the main factors that govern adsorption and release of molecules from SMMs. All these parameters can be tailored for the design mesoporous matrices, opening many paths in this research field.

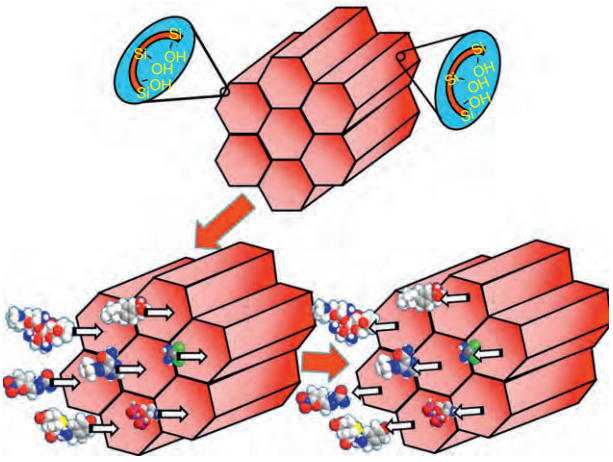

Figure 3 Schematic representation of drug loading and release processes in ordered mesoporous materials.

4.429.4.1. Influence of the Textural Properties

4.429.4.1.1. Pore diameter

The adsorption of molecules into SMMs depends on the mesopore diameter of the host matrix, that is, it follows size-selectivity criteria. Commonly, pore diameters slightly larger than the molecule dimensions (pore/molecule size ratio >1) are enough to allow the adsorption of molecule inside the pores. On the contrary, if the mesopore diameter is smaller than the molecule size, the molecule would adsorb only on the external surface of the material. This molecule-sieve effect is especially remarkable when the adsorption of large-size molecules, such as proteins, is targeted. Some authors have investigated the adsorption of globular proteins on MCM-41 materials.[109] Such studies demonstrated that proteins with dimensions larger than the mesopore diameter were only adsorbed in the outer surface of MCM-41. In addition, adsorption tests into SBA-15 of proteins displaying different dimensions were carried out.[110] These assays also evidenced that only proteins with sizes smaller than the mesopore diameter showed significant adsorption and consequently, that SBA-15 was acting as a molecular sieve.

Among proteins, serum albumins, which are one of the major components in plasma proteins in humans, are of special interest. Albumin is usually composed of a single chain of 582 amino acids with an average length of 10 nm and width of 6 nm.[111,112] Albumins are capable of binding reversibly to a wide variety of ligands. They can also bind different drugs that can be released to sites where the pharmacological action is needed. Therefore, albumins could be employed to store, protect, transport, and deliver different drugs used for the treatment of bone diseases. SBA-15 has been used as host matrix of bovine serum albumin (BSA).[102] However, the size of BSA is quite close to the SBA-15 pore diameter and the diffusion of protein molecules into the mesoporous channels is difficult. For this reason, an attractive strategy would consist in increasing the pore size of SBA-15 by modifying the synthesis conditions, such as using different hydrothermal treatments.[113,114] Recently, Vallet-Regí *et al.* reported BSA adsorption and release tests into SBA-15 with different pore diameters.[103] In such research work, pore diameters ranging from 8.2 to 11.5 nm were obtained for SBA-15 materials synthesized by using hydrothermal treatments ranging from 1 to 7 days. BSA loading tests indicated that there is a direct dependence of protein adsorption on pore size, that is, the greater the pore diameter, the higher is the amount of protein loaded (**Table 1**).

Pore diameter has been also demonstrated to play a key role in molecule release kinetics. This fact was observed when testing MCM-41 matrices of different pore diameters as ibuprofen delivery systems. MCM-41 materials with pore sizes ranging from 2.5 to 3.6 nm were obtained by using short-chain or long-chain cationic surfactants, respectively.[115] Ibuprofen release profiles revealed that the drug release rate was modulated by the pore diameter of SMMs. Thus, the ibuprofen release to the delivery medium was faster as the pore diameter increased, confirming the diffusional nature of drug release.

4.429.4.1.2. Surface area

The adsorption of molecules into mesoporous matrices depends on the adsorptive properties of the silica surface.

Table 1 Pore diameter and amounts of BSA loaded into SBA-15 materials submitted to different hydrothermal treatments ranging from 1 to 7 days

Material	*Time of hydrothermal treatment (days)*	*Pore diameter (nm)*	*Amount of BSA loaded (mg g^{-1})*
SBA-15-1d	1	8.2	151
SBA-15-3d	3	9.5	234
SBA-15-5d	5	10.1	242
SBA-15-7d	7	11.4	270

Table 2 Surface area of MCM-41 materials synthesized using different surfactants and amount of ibuprofen loaded

Surfactant	*Surface area (m^2 g^{-1})*	*Amount of ibuprofen loaded (mg g^{-1})*
85%C_8TAB–15%C_{10}TAB	768	110
70%C_8TAB–30%C_{10}TAB	936	190
C_{12}TAB	1087	230
C_{16}TAB	1157	340

The surfactants used during the synthesis are indicated for each case. C_8TAB, trimethyloctylammonium bromide; C_{10}TAB, decyltrimethylammonium bromide; C_{12}TAB, dodecyltrimethylammonium bromide; C_{16}TAB, hexadecyltrimethylammonium bromide.

Therefore, the chemical interactions between the silanol groups covering the silica surface and the functional groups of the guest molecule will determine the amount of molecule loaded (Figure 3). Surface of SMMs is the textural parameter that indicates the silica surface susceptible of undergoing chemical interactions with the guest molecule and, consequently, it is expected that the higher the surface area, the higher is the amount of molecule loaded. This fact was corroborated when several MCM-41 matrices exhibiting different values of surface area were tested as ibuprofen delivery systems (Table 2).

The same behavior was also observed when carrying out loading and release assays of captopril[91] into several 2D-hexagonal structures with different surface areas. This trend was also confirmed when MCM-41 and SBA-15 matrices, with surface areas of 1157 and 719 m^2 g^{-1}, respectively, were tested as alendronate delivery system.[94] Alendronate is a potent bisphosphonate commonly used for osteoporosis treatments. The maximum loads of alendronate were 139 and 83 mg g^{-1} for MCM-41 and SBA-15, respectively. All these findings demonstrate the direct dependence of the amount of drug loaded on the surface area of the SMM, that is, the highest surface areas promote the greatest amounts of drug loaded.

4.429.4.1.3. Pore volume

The adsorption of molecules into SMMs is a molecule-surface interaction, and consequently, the amount of molecule loaded depends on the pore diameter as the size selective limiting factor, and also on the surface area. However, it has been reported performing successive impregnations of MCM-41 material with ibuprofen solutions is possible, which allows to achieve complete pore filling and leads to higher drug loads.[116] This fact was explained by the increase in the intermolecular ibuprofen interactions, as confirmed by solid-state nuclear magnetic resonance (NMR) spectroscopy measurements.[117] In this case, the amount of ibuprofen adsorbed is limited by the pore volume of the SMM, that is, the larger the pore volume the greater is the amount of drug loaded.

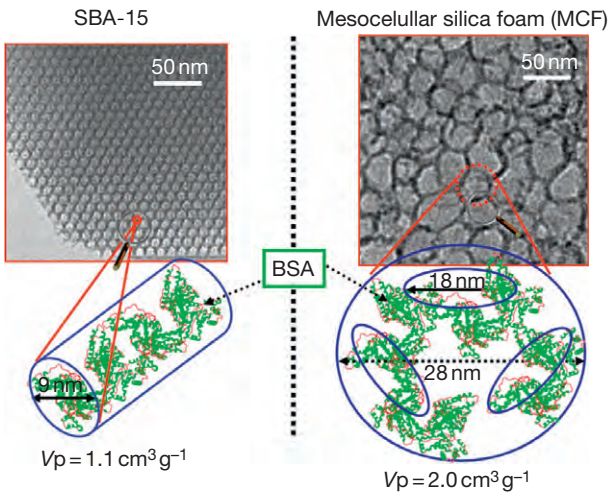

Figure 4 Schematic illustration of host–guest interactions for large-volume molecules, such as bovine serum albumin (BSA) protein, into SBA-15 and mesocelullar silica foam (MCF) matrices.

The pore volume must be also considered when the confinement of large-volume molecules, such as certain proteins, is aimed. With regard to this topic, MCFs have been proposed as host matrices of several enzymes and proteins.[118,119] The synthesis of MCFs is carried out by employing triblock copolymer surfactants and adding a swelling agent, normally trimethylbenzene, into the structure directing template solution.[120,121] For comparison purposes, loading and release tests of BSA were performed on SBA-15 and MCF materials.[4,5] Different transmission electron microscopy (TEM) and N_2 adsorption studies of MCF matrix revealed the existence of spherical cells of around 28 nm with windows of around 18 nm, with the pore volume of 2.0 cm^3 g^{-1} (Figure 4). In the case of SBA-15, such studies indicated the presence of 2D-hexagonal pore networks with pore sizes of around 8 nm, with 1.1 cm^3 g^{-1} as the pore volume (Figure 4). The BSA loading tests indicated that the amount of BSA loaded was higher in MCF (240 mg g^{-1}) than in SBA-15 (150 mg g^{-1}). Certainly, the different BSA loads could be ascribed to the difference in the pore volume, that is, the greater the pore volume, the higher is the amount of BSA loaded. Nevertheless, the contribution of other parameters, such as pore diameter, cannot be overruled. As previously mentioned, the BSA dimensions are very tight to the SBA-15 diameter, which could make the protein adsorption difficult. However, the wide pore size of MCF would be facilitating BSA penetration into the carrier cavities.

4.429.4.2. Influence of the Matrix Structure

The influence of pore connectivity and structure of SMM into drug release kinetics was observed by using different mesostructures as host matrices. Two SMMs with similar pore size, between 2 and 3 nm, and different structures were selected: MCM-41, which contains 2D-hexagonal array of pores, and MCM-48, which consists of a 3D-bicontinuous cubic mesoporous structure with $Ia\bar{3}d$ symmetry (**Figure 2**). Then, loading and release experiments were performed using erythromycin[77] and ibuprofen.[78] MCM-48 matrix exhibits unique penetrating bicontinuous networks of channels that allow easy molecular accessibility and fast molecular transport. As a consequence of this, a faster drug release was observed from cubic matrices than from hexagonal materials, although the release profile was similar from both matrices, which exhibits first-order kinetics.

4.429.4.3. Influence of the Particle Morphology

The particle morphology of the mesoporous matrix represents the extension of the interface between the host material and the body fluid, so the effect on drug release kinetics is predictable. For this reason, MCM-41 was synthesized in the form of irregularly shaped powder and monodispersed spheres ranging from 490 to 770 nm in diameter, and ibuprofen loading and release assays were carried out.[79] Such experiments showed that microsized spheres displayed slower release rate than irregularly shaped powders. In fact, those spherical particles with the smallest sizes exhibited the slowest ibuprofen release kinetics.

The control of the particle morphology of SMMs is also expected to lead to a more reliable and reproducible controlled delivery system. This control has been achieved by employing an aerosol assisted synthesis to obtain different mesoporous structures in the form of micrometric spheres as delivery system of triclosan, a widely used antimicrobial agent.[122]

On the other hand, the use of hollow mesoporous spheres offers the possibility to store higher amounts of guest molecules than conventional SMMs. It has been reported that hollow spheres with mesoporous shells would exhibit more advantages in mass diffusion and transportation compared to conventional hollow spheres of solid shells. Within this porous shell, it is of special interest that porous channels penetrate across the shell for drug storage and delivery systems. This penetrating pore channels can be obtained by using poly(vinylpyrrolidone) (PVP) and cetyltrimethylammonium bromide (CTAB) as co-templates during the synthetic procedure.[123] The authors loaded the hollow spheres with ibuprofen by impregnation, leading to a storage capacity three times higher than that of conventional SMMs, as previously published.[124]

4.429.4.4. Influence of the Matrix Organic Functionalization

The organic modification or functionalization of SMMs using different organic groups has been revealed as the cornerstone to modulate the adsorption and release of molecules from these matrices.[9,125–127] The surface of silica walls contains high density of silanol groups susceptible of organic modification by covalently grafting organic silanes ($(RO)_3SiR'$).[128]

In general, there are two main functionalization methods that are applied to organically modify SMMs for controlled delivery purposes:

(i) *Cocondensation method*: Also known as one-pot route, it involves the addition of the organic group, normally a silane-containing reactive group, such as chloride, methoxy, or ethoxy groups, during the mesoporous synthesis and the entire functionalization process is carried out in a unique way. This route leads to functionalized materials in which the organic groups are grafted to the outer and to the inner surface of the silica walls. For this reason, and to avoid loosening of the mesostructural order, the functionalization degree cannot exceed 40% mol. Two exceptional examples have been given for the vinyl- and thiol-functionalization up to 62 and 50 mol%, respectively, even though the resulting mesoporous silicas were not well-ordered.[129,130] Recently, functionalization up to 60 mol% of SBA-15 with carboxylic acid groups has been also reported.[131]

(ii) *Postsynthesis method*: It involves an organic modification process carried out under anhydrous conditions, once the free-surfactant SMM has been already synthesized. Albeit this method leads to heterogeneous distributions of the functional groups, it results in well-defined structures controlled by the silica matrix. Besides, this route guarantees that the organic groups are placed in the outer surface of mesopore walls, which leads to higher functionalization degrees than that obtained by cocondensation method.

The functionalization method must be selected considering the targeted guest molecule. For instance, MCM-41 organically modified with aminopropyl groups through cocondensation and postsynthesis routes was used as host carrier for ibuprofen.[80] As expected, MCM-41 functionalized by postsynthesis route experienced higher decrease in the textural properties (pore diameter, surface area, and pore volume) than MCM-41 functionalized by cocondensation method. Moreover, ibuprofen release tests on these matrices revealed that drug release rate from MCM-41 functionalized by postsynthesis was smaller than that from MCM-41 functionalized using cocondensation route. This fact can be explained considering that aminopropyl groups are placed in the outer surface of the silica matrix, giving up higher functionalization degree capable of interacting with ibuprofen molecules and promoting higher drug retention. Proton nuclear magnetic resonance (^{1}H NMR) spectroscopy measurements confirmed the existence of ionic interactions between amino groups from modified matrix and carboxylic groups of ibuprofen.[132] More recently, the organic modification of SBA-15 with aminopropyl groups and the two above-mentioned functionalization methods has been reported.[102] For comparison purposes ibuprofen and BSA were chosen as model molecules and loading and *in vitro* release assays were carried out. Such studies indicated that functionalization with aminopropyl groups using postsynthesis route led to the smallest ibuprofen delivery rate, in agreement with the results obtained for MCM-41. Oppositely, the smallest BSA delivery rate was obtained from SBA-15 functionalized by cocondensation. Such behavior was explained by the balance of electrostatic interaction and hydrophilic interaction between BSA and the functionalized SBA-15 matrix that would be more favorable in matrices synthesized by cocondensation synthesis method.

The chemical nature of the matrix-drug host–guest interaction can be modulated by the appropriate choice of the organic groups depending on the targeted molecule and its application. For this purpose, two main approaches have been widely reported. The first strategy concerns the use of different organic groups able to induce attracting interactions with the functional groups of the guest molecule. For this purpose, the influence of host–guest interaction on drug adsorption and release was investigated by functionalizing MCM-41 through postsynthesis method with several organic functional groups (chloropropyl, phenyl, benzyl, mercaptopropyl, cyanopropyl, and butyl) and using ibuprofen as model drug.[133] Because of the different interactions of carboxylic group of ibuprofen with the tested organic functions, diverse load and release behaviors were observed. MCM-41 functionalized with polar groups loaded higher amounts of ibuprofen than MCM-41 functionalized with nonpolar groups. Furthermore, the smallest drug delivery rates resulted from matrices modified with mercapto or amino groups because such functions induced the strongest attracting electrostatic interactions with the carboxylic acid of ibuprofen. The second strategy involves the use of hydrophobic groups to functionalize the mesoporous silica walls. The main aspects concerning both approaches are tackled in the next sections, which are mainly focused on the functionalizations using amino groups and hydrophobic groups.

4.429.4.4.1. Functionalization with amino groups

The organic functionalization of SMMs with amino groups has been widely reported. For instance, MCM-41 and SBA-15 materials functionalized with aminopropyl groups via the postsynthesis route have been proposed as alendronate controlled delivery systems.[94] These research showed that the amount of drug loaded on amino-modified matrices (MCM-41-NH_2 and SBA-15-NH_2) was almost threefold greater than that on unmodified matrices (Table 3). Concerning alendronate release behavior, amino-functionalized matrices exhibited slower release kinetics than that of unmodified materials (Table 3).

Recently, the organic modification of SBA-15 using different aminopropyl functionalization degrees has been reported as a good strategy to modulate alendronate dosage.[96] The functionalization was performed following the postsynthesis route but improved by adding a catalyst during the functionalization process. The results derived from this work pointed to a linear dependence of the amount of drug loaded on the functionalization degree. Besides, the higher the functionalization degree, the smaller the total amount of alendronate released to the delivery medium. For this reason, this gradual functionalization has been demonstrated to allow better control over drug loading and release. These results are of great interest for bone implant technologies, because the high potency of bisphosphonates requires only small local doses.

The organic functionalization of SBA-15 using partially silylated poly(propyleneimine) dendrimers has been also reported as a good strategy to modulate drug dosage.[76] For this purpose, authors employed first, second, and third dendrimer generations and two different nominal degrees of surface functionalization, which led to a wide range of materials with a great variety of amine functionalization and surface coverage. The performance of such systems was tested *in vitro* using ibuprofen as model drug. Such studies revealed that the higher the dendrimer generation, the higher is the host–guest attracting interactions and, consequently, the higher are the drug loads. Moreover, drug delivery patterns exhibit a sustained drug release and the drug dosage is governed by the dendrimer generation.

Amino functionalization of SMMs has been also revealed as a good approach to control adsorption and release of proteins such as BSA.[102,103] As previously commented, SBA-15 materials with different pore diameters, which were synthesized using different hydrothermal treatments, were functionalized by postsynthesis route.[103] It is well-known that organic functionalization following the postsynthesis route always leads to a decrease of pore diameter. In the case of BSA, the protein dimensions are very tight to the SBA-15 mesopore size and consequently, the amount of BSA loaded was smaller in amino-modified matrices than in unmodified materials. Nevertheless, the attracting interactions taking place between amine groups of functionalized matrices and amide groups of BSA strongly influenced protein release behavior (Figure 5).

Table 3 Alendronate (AL) release data from MCM-41 and SBA-15 before and after amine functionalization

Material	*AL loading (mg g^{-1})*	*% AL released after 24 h*	*AL total delivery time (h)*
MCM-41	139.2	58	72
MCM-41-NH_2	366.1	28	264[a]
SBA-15	82.8	56	264
SBA-15-NH_2	223.0	11	264[b]

[a]Incomplete delivery (76%).
[b]Incomplete delivery (69%).

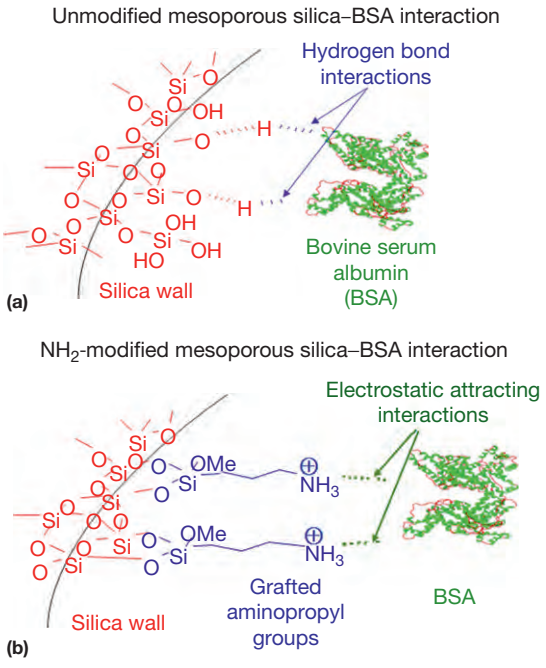

Figure 5 Schematic representation of mesoporous matrix-bovine serum albumin (BSA) host–guest interactions for (a) pure mesoporous silica and (b) aminopropyl-functionalized mesoporous silica.

Thus, the initial burst effect observed in BSA released from unmodified matrices (~90%) was reduced almost three times (~30%) after amino functionalization. Moreover, the BSA release from all SBA-15-NH_2 mesoporous materials was incomplete, whereas the total amount of loaded BSA was released after 192 h from unmodified matrices.

Amino functionalization of large-pore and large-volume MCF materials has also been probed to increase the affinity toward BSA molecule.[4,5] The results revealed that the amount of BSA loaded was higher in amino-modified MCF (MCF-NH_2) than in unmodified MCF (Figure 5). This fact can be easily explained because despite the reduction of pore diameter as a consequence of functionalization, the pore size of MCF-NH_2 (~16 nm) is still big enough to permit the BSA penetration. Regarding BSA release behavior, as expected, functionalization exerts a noticeable effect in BSA delivery patterns. Thus, the initial burst effect of unmodified MCF (~60%) was significantly reduced in MCF-NH_2 (~10%).

All these findings demonstrate that amino functionalization of SMMs is a suitable strategy for the design of controlled delivery systems of many biologically active molecules exhibiting organic groups which are capable of chemically interacting with amino functions.

4.429.4.4.2. Functionalization with hydrophobic groups

The organic modification of SMMs with hydrophobic groups is a commonly used way to control the loading and release of certain molecules. For example, the functionalization of SBA-15 with different alkyl chains, octyl (C_8) and octadecyl (C_{18}), has been carried out and controlled delivery tests of erythromycin, a hydrophobic antibiotic, have been reported.[89] As previously commented, the functionalization always leads to a decrease in the textural properties of SMMs, which in this case, led to a decrease in the amount of erythromycin loaded in SBA-15-C_8 and SBA-15-C_{18} materials, that is, 130 and 180 mg g^{-1}, respectively, compared to unmodified SBA-15 (340 mg g^{-1}). However, erythromycin delivery rate was slower from functionalized matrices than from unmodified SBA-15. This fact can be ascribed to the diminution of the wettability degree of the functionalized surfaces, which makes difficult the penetration of the aqueous release medium inside the mesoporous channels and induces slower drug delivery kinetics.

Tang *et al.* reported the functionalization of MCM-41 matrices with methylsilyl (MS) or dimethylsilyl (DMS) groups and tested their capability as ibuprofen delivery systems.[81] As expected, functionalized materials loaded smaller ibuprofen amounts than unmodified MCM-41. However, MS and DMS groups led to slower drug release caused by the difficult diffusion of the delivery medium inside the mesopore channels. Therefore, the complete drug release was achieved after around 10, 20, or 500 h from MCM-41, MCM-41-MS, and MCM-41-DMS, respectively. These authors also reported the modification of ibuprofen-loaded-MCM-41 using trimethylsilyl (TMS) groups.[82] Again, the *in vitro* release tests revealed that the presence of TMS groups remarkably delayed the drug release compared to unmodified MCM-41 material.

SBA-15 materials functionalized using hydrophobic groups have been also proposed as controlled delivery systems of L-tryptophan (L-Trp),[106] a hydrophobic amino acid present in the 3D structure of many peptides, proteins, and growth factors of interest in bone tissue-regeneration technologies.[134,135] L-Trp exhibits a hydrophobic aromatic indol ring that makes necessary to increase the hydrophobicity of SBA-15, which contains high density of silanol groups. Actually, unmodified SBA-15 loaded less than 5 mg g^{-1} of L-Trp, probably due to the extremely different chemical nature of the hydrophobic amino acid and hydrophilic SBA-15 (Figure 6(a)). Thus, to increase the host–guest interactions, functionalization of SBA-15 using quaternary amines with different alkyl lengths, namely, *N*-trimethoxysilylpropyl-*N*,*N*,*N*-trimethyl ammonium chloride (TMOS-$C_3N^+Me_3Cl$), and octadecyldimethyl (3-trimethoxysilylpropyl) ammonium chloride (TMOS-$C_3N^+Me_2C_{18}Cl$), has been reported. The main forces that governed amino acid adsorption in SBA-15 functionalized with short alkyl chains (~$C_3N^+Me_3$) were coulombic attracting interactions between deprotonated carboxylic groups of amino acid ($-COO^-$) and protonated quaternary amines ($-N^+R_4$) covering the mesoporous surface (Figure 6(b)). In this case, the amount of L-Trp loaded into SBA-15-$C_3N^+Me_3$ matrix increased up to 43 mg g^{-1}. When using long hydrocarbon chains (~$C_3N^+Me_2C_{18}$) two-thirds of the silica surface was functionalized. This high functionalization degree using hydrophobic chains induced strong interactions between mesoporous surface and indol group of L-Trp (Figure 6(c)), leading to L-Trp loading amounts of 82 mg g^{-1} for SBA-15-$C_3N^+Me_2C_{18}$.

4.429.5. Bioactivity of Mesoporous Matrices

When considering any material for biomedical purposes, the first consideration that should be addressed is the interaction between the material and the living body. Thus, the surface of such material must be carefully investigated. SMMs are characterized by exhibiting high surface areas and high surface density of silanol groups (Si–OH). It is well known that the bioactive response of conventional bioactive glasses depends on the presence of silanol groups (see Chapter 1.109, Bioactive Ceramics). In addition, porosity has been evidenced as key factor that modulates the kinetics of formation of the carbonate hydroxyapatite (CHA) layer.[136–141] In this sense, SMMs are expected to induce bioactive response because they exhibit a high density of silanol groups that could act as nucleation sites for CHA. Moreover, these materials exhibit outstanding textural properties that could bring enhanced kinetics of CHA formation.

The first reports on the *in vitro* bioactivity behavior of mesoporous materials involved three well-known structures, MCM-41, MCM-48, and SBA-15.[127,142,143] The evaluation of the bone-bonding capability of bioceramics was performed following accepted *in vitro* protocols at 37 °C by soaking disk-shaped pieces of materials into SBF.[108,144] The modifications of SMM surfaces were monitored using different characterization techniques, such as Fourier transform infrared spectroscopy (FTIR) and X-ray diffraction (XRD). Scanning electron microscopy (SEM) and TEM together with energy dispersive scattering (EDS) and electron diffraction (ED) are also employed. In the case of bioactive materials, all these techniques allow to confirm the formation of a new layer, mainly consisting of CHA, on the materials surfaces. However, MCM-41, MCM-48, and SBA-15 mesoporous materials exhibit different textural and structural features, which induce variations in the rates of

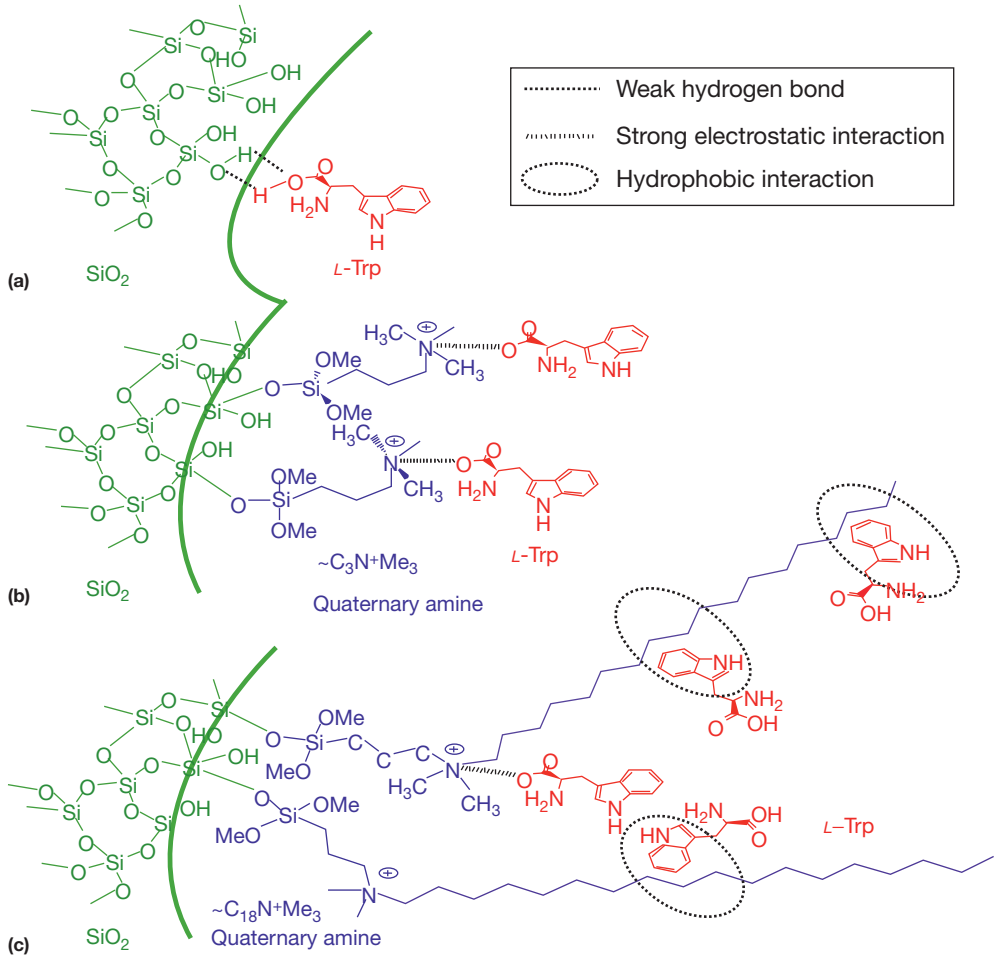

Figure 6 Schematic representation of different chemical interactions between L-Trp and (a) unmodified SB-15: L-Trp is linked by weak hydrogen bond interaction, (b) SBA-15 functionalized with short-chain quaternary amines ($\sim C_3N^+Me_3$), and (c) SBA-15 functionalized with long-chain quaternary amines ($\sim C_{18}N^+Me_3$).

formation of the CHA layer. Thus, SBA-15 and MCM-48 were able to induce the formation of a nanocrystalline CHA layer onto their surfaces after 30 and 60 days of assay, respectively. However, no evidence of formation of such layer was observed on the surface of MCM-41. These different *in vitro* bioactive behaviors could be due to the different concentrations of silanol groups present in each material and their diverse textural and structural properties. In this sense, MCM-41 presents a relatively small silanol density ($\sim$2 mmol Si–OH·m^{-2}) compared to SBA-15 and MCM-48 ($\sim$13 mmol Si–OH·m^{-2}), which could explain its nonbioactive response after 60 days of test. However, SBA-15 and MCM-48, which exhibited similar silanol density, presented very different rates of formation of the CHA layer. Such difference could be related to the different textural and structural properties of the matrices. Hence, mesoporous matrices with large and accessible pore networks should favor the ionic diffusion through the mesoporous framework, which should promote the formation of the CHA layer. This fact is in agreement with the experimental results that indicate that SBA-15, with the greatest pore diameters ($\sim$9 nm) and 2D-hexagonal arrangement of mesopores interconnected by micropores exhibited the fastest bioactive behavior among the three tested materials.

These results clearly indicate that the textural and structural features of SMMs are important factors that are involved in their *in vitro* behavior. However, these are not enough conditions to achieve a timely bioactive behavior to be useful *in vivo* because the formation of the CHA layer on SMMs is much slower than that on conventional sol–gel glasses (around 3 days).[145] Therefore, the chemical composition of materials, mainly the presence of calcium and/or phosphate, has to be also considered. Thus, the next subsections will focus on the different strategies developed to date to accelerate the bioactive response of SMMs.

4.429.5.1. Incorporation of Phosphorous into Mesoporous Silica Matrices

In vitro bioactivity assays performed with bioactive sol–gel glasses revealed that the presence of phosphorous in the glass network affected the formation of the CHA layer.[146] This fact inspired the idea of incorporating small amounts of phosphorous, of around 1% in weight, into the MCM-41 silica network.[147] The structural and compositional characterization of this new material, denoted as P-MCM-41, using XRD,

N_2 adsorption porosimetry, SEM-EDS, and TEM-EDS techniques pointed to the preservation of the 2D-hexagonal *p6mm* mesoporous structure. It was also revealed that the phosphorous content was heterogeneously distributed into the mesoporous silica network and mainly placed in the outer edge of the particles and not in their inner nucleus. The *in vitro* bioactivity assays demonstrated that P-MCM-41 developed a CHA layer on its surface after 15 days of assay. Compared to the bioactive behavior of SBA-15 or MCM-48, the incorporation of phosphorus into the silica network accelerates the bioactive response of SMMs (Table 4).

4.429.5.2. Addition of Small Amounts of Bioactive Glasses

A widely employed strategy to induce bioactivity to different materials consists in preparing biphasic mixtures by incorporating another phase that acts as an accelerator of the CHA nucleation.[148–150] For this purpose, MCM-41 as the main phase (90% in weight) was mixed with a bioactive sol–gel glass in the system SiO_2–CaO–P_2O_5 (10% of weight),[142] which gave rise to the so-called G-MCM-41 material. The *in vitro* bioactivity tests of this material revealed that the formation of the apatite layer started just after 3 h of assay and were completed in 1 day (Table 4). These results indicate that the addition of small amounts of bioactive glasses is a good strategy to reduce the time of bioactive response of SMMs materials to just 1 day.

4.429.5.3. Mesoporous Bioactive Glasses

Recently, another strategy has been developed to accelerate the time of bioactive response. This approach consists in using the synthesis methods of SMMs but with the same compositions of glasses. It was in 2004 when the synthesis of highly ordered MBGs in the system SiO_2–CaO–P_2O_5 was reported for the first time.[16] The synthesis of these MBGs was carried out by using the evaporation-induced self-assembly (EISA) method[151] in the presence of a nonionic triblock copolymer as template (Pluronic® P123, $EO_{20}PO_{70}EO_{20}$) and with the employ of TEOS, triethylphosphate (TEP), and calcium nitrate ($Ca(NO_3)\cdot 4H_2O$) as SiO_2, P_2O_5, and CaO precursors, respectively. The enhanced textural properties of MBGs promoted by the template led to highly bioactive responses compared to conventional bioactive glasses.[152–154] Moreover, it has been demonstrated that the textural and structural properties of MBGs can be modulated by varying the CaO content of the mesoporous glasses.[15] A gradual evolution from 2D-hexagonal to 3D-bicontinuous cubic structure together with an increase in the textural properties was observed when decreasing the CaO content (Figure 7). The possibility of tailoring both structural and textural features of MBGs is an interesting advance toward the development of biomaterials able to fulfill the essential requirements for specific biomedical applications.

The *in vitro* assays carried out in SBF demonstrated that this new family of mesoporous glasses exhibits enhanced bioactive behaviors, with even faster apatite phase formation than

Table 4 Structural characteristics, composition (% in mol), and time of bioactive response of different mesoporous materials

Matrix	*Structure*	*Composition (% in mol)*	*Bioactive*[a]	*Time in SBF*
MCM-41	2D-hexagonal (*p6mm*)	$100SiO_2$	No	60 days
MCM-48	3D-cubic ($Ia\bar{3}d$)	$100SiO_2$	Yes	60 days
SBA-15	2D-hexagonal (*p6mm*)	$100SiO_2$	Yes	30 days
P-MCM41	2D-hexagonal (*p6mm*)	$99SiO_2$–$1P_2O_5$	Yes	15 days
G-MCM41	2D-hexagonal (*p6mm*)	$95.6SiO_2$–4.0CaO–$0.4P_2O_5$	Yes	1 day
MG-S58m	2D-hexagonal (*p6mm*) + wormlike	$58SiO_2$–37CaO–$5P_2O_5$	Yes	1 day
MG-S75m	2D-hexagonal (*p6mm*) + orthorhombic (*p2mm*)	$75SiO_2$–20CaO–$5P_2O_5$	Yes	8 h
MG-S85m	3D-cubic ($Ia\bar{3}d$)	$85SiO_2$–10CaO–$5P_2O_5$	Yes	1 h

[a]Induction time needed for the formation of a carbonate hydroxyapatite (CHA) layer onto the surface of materials.

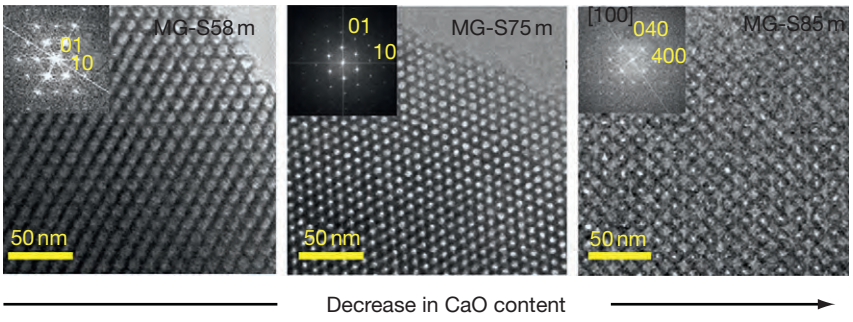

Figure 7 TEM images and their corresponding FT diffractograms of MBGs in the SiO_2–CaO–P_2O_5 system with different CaO contents. TEM images were taken with the electron beam parallel to the pore channels of 2D-hexagonal structures corresponding to mesoporous glasses with compositions (a) $58SiO_2$–37%CaO–5%P_2O_5 and (b) $75SiO_2$–20%CaO–5%P_2O_5, respectively. (c) TEM image taken in the [100] directions of 3D-bicontinuous cubic structure with $Ia\bar{3}d$ symmetry corresponding to a mesoporous glass of $85SiO_2$–10%CaO–5%P_2O_5 composition (see Table 4).

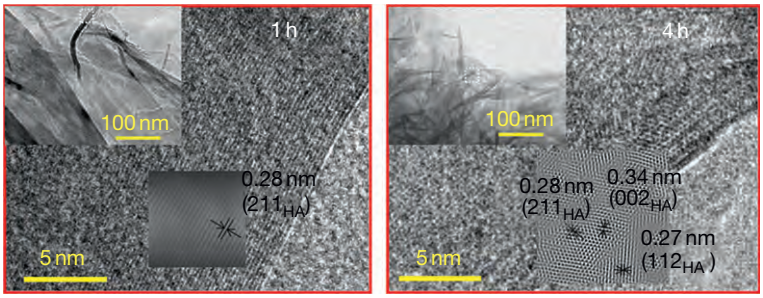

Figure 8 *In vitro* bioactive study in SBF of MG-S85 sample, with 3D-cubic structure by TEM.

conventional bioactive glasses. Hence, it has been revealed that the kinetics of formation of the CHA layer in MBGs is controlled by their textural and structural properties.[155] In this respect, MBGs differ from bioactive glasses, in which the formation kinetics mainly depends on the composition and textural properties.

Thus, the MBG material with the smallest CaO content (MG-S85m) but having 3D-bicontinuous cubic structure and the highest surface area values exhibited faster bioactive response than MBG materials with the greatest CaO content (MG-S58m). FTIR and TEM-ED studies revealed an accelerated bioactive behavior for MG-S85m sample, which was able to form a nanocrystalline CHA layer in just 1 h after coming into contact with SBF[17] (**Figure 8**). In this case, the 3D pore system not only provided high surface area and porosity, but also promoted the ions interchange by increasing mass transport and diffusion processes, which resulted in the fastest bioactive behavior reported till date in silica-based bioactive materials.

Recently, a new property derived from the textural and structural characteristics of MBGs, namely biomimetic behavior, has been reported. This biomimetic mechanism, where there is a sequential transition from amorphous calcium phosphate (ACP) to octacalcium phosphate (OCP) to calcium deficient carbonatehydroxyapatite (CHA) maturation, similarly to the *in vivo* biomineralization process, has been observed for the first time.[17–19]

Many bioceramics develop a CHA phase *in vitro* through the direct crystallization of previously precipitated ACP,[156] without the prior formation of OCP phase which is formed in natural bone biomineralization process.[157–159] OCP is a metastable phase and will appear only if the pH in the crystallization system is below 7.

MG-S58m sample, with 2D-hexagonal mesoporous arrangement and high CaO content allows an intense Ca^{2+}–H_3O^+ exchange as a consequence of the open channel array, the high textural parameters, and the relatively high CaO content. This ionic exchange led to local acid pH values of 6.5 during the first stages, which favor the OCP formation (**Figure 9**). This phenomenon does not take place in the case of bioactive glasses, because the local pH is kept at pH 7.4 or even slightly higher from the beginning of the bioactive process, which would avoid the existence of OCP phase. This biomimetic behavior was monitored by TEM (**Figure 9**). After being soaked in the SBF for 1 h, MG-S58m sample developed a large amount of newly formed ACP layer with a Ca/P ratio of 1.2. This event has been widely observed in many bioactive compounds, and corresponds to the step 4 of the bioactive process as theorized by Hench.[160]

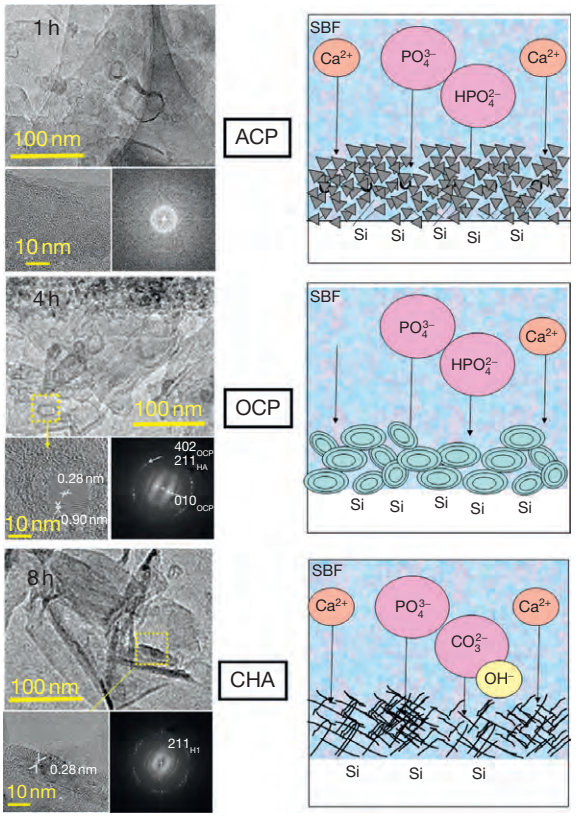

Figure 9 *In vitro* bioactive behavior of MG-S58m mesoporous glass with a 2D-hexagonal structure and $58SiO_2$–37%CaO–5%P_2O_5 composition. High-resolution TEM study of mesoporous glass surface after different soaking times in SBF together with the schematic depiction of the sequential transition from ACP to OCP to CHA observed by TEM are displayed.

To date, the mechanism of *in vitro* bioactivity involves the direct crystallization of CHA phase from the ACP. However, MBGs have shown a unique behavior allowing the growth of nanocrystalline oval biphasic nuclei composed of OCP with a small fraction of HA after 4 h in SBF, with a Ca/P ratio of 1.3. The transformation from oval OCP nuclei to needle-like nanocrystalline CHA was finally evident after being soaked in SBF for 8 h.

All these results bring up the possibility of controlling the reactive properties of MBGs by tailoring their compositional, textural, and structural properties. This new family of ordered

mesoporous materials widens the range of possibilities for the use SMMs as new generation bioceramics with outstanding bone-bonding capability.

4.429.6. Hierarchical Macroporous Scaffolds for Bone Tissue Engineering

The different research results reported so far confirm that ordered mesoporous materials are characterized by two valuable features: controlled delivery capability and *in vitro* bioactive behavior. It would be also feasible to combine both properties to design new bioceramics with an added value. Nevertheless, when dealing with ceramics aimed at bone tissue engineering applications, it is essential to keep in mind that the main role will be played by cells. Pore dimensions of mesoporous materials fall in the 2–50 nm range, whereas the dimensions of cells are in the 1–100 μm range. That is, mesopores are too small to allow cell uptake, which need dimensions in the order of microns. Bone porosity, which ranges between 1 and 3500 μm, is necessary for several physiological functions.[161,162] Bone tissue engineering requires the design of hierarchically 3D scaffolds with interconnected macroporosity, within the 20–1000 μm range.[163–165] Such macroporosity is essential to allow bone cell penetration, adherence, growth, and proliferation leading to bone tissue in-growth and eventually vascularization on implantation (see **Chapter 6.617, Bone Tissue Grafting and Tissue Engineering Concepts**).

SMMs, with ordered mesoporous channels and pore dimensions in the 2–50 nm range, are appropriate for applications in which drugs or biologically active molecules can be loaded and subsequently released where needed. On the other hand, macroporous materials, with pore dimensions in the microns scale, are adequate as scaffolds for bone tissue engineering. So, the challenge is to design and fabricate scaffolds that combine two scales of porosity; macroporosity to allow appropriate bone oxygenation and vascularization and mesoporosity for controlled delivery purposes (**Figure 10**). The aim is to fabricate biomaterials that help the human body to improve its regeneration role by recovering not only the structure of the damaged tissue, but also its function. So the current goal in biomaterials is to fabricate 3D scaffolds with hierarchical interconnected porosity that allows cells to proliferate and form new bone tissue following the natural processes of human tissue.

Several recent research works have been reported concerning the fabrication of 3D scaffolds using the highly bioactive MBGs as starting materials. Thus, Yun *et al.* reported the synthesis of ordered giant-, macro-, and mesoporous bioactive 3D glass scaffolds by using a combination of sol–gel, double polymers templating, and rapid prototyping (RP) techniques.[166] The resulting scaffolds presented three lengths of porosity: mesopores (~5 nm) obtained by using a triblock copolymer template ($EO_{100}PO_{65}EO_{100}$ (F127)), macropores (10–30 μm) produced by using methyl cellulose, and giant-sized pores (30–1000 μm) created by RP methods.[167,168] The *in vitro* tests in SBF revealed that the bioactive behavior of MBG was preserved because a CHA layer was formed onto the material surface after 24 h of assay.

Li *et al.* prepared hierarchically MBG-based scaffolds using P123 surfactant as mesostructure directing agent and polyurethane foam (PUF) as template for the macroporous structures.[169] The resulting materials presented hierarchical porosity with interconnected macropores of 200–400 μm or 500–700 μm and uniform mesopores of 3.7 nm. *In vitro* bioactivity tests showed that these MBG-based scaffolds induced the formation of a CHA layer on their surface after 4 h in SBF.

Other authors also have reported the employment of P123 and PUF to synthesize hierarchically structured 3D MBGs-based scaffolds with four different chemical compositions and their *in vitro* bioactivity and cell adherence evaluation.[170] These scaffolds exhibited similar mesostructural and textural features, showing interconnected macroporous networks with pore diameters in the 200–400 μm range and mesopores of

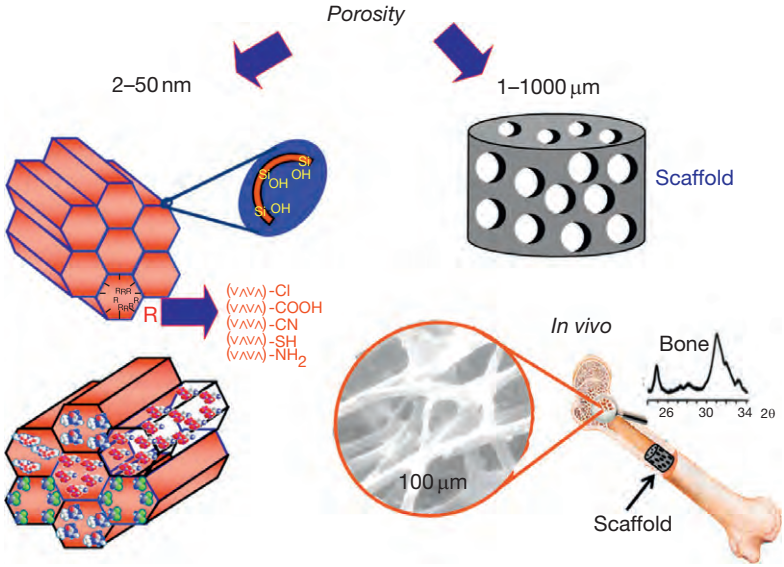

Figure 10 Schematic representation of the two scales of porosity present in an ideal 3D scaffold for bone tissue engineering. Macroporosity is similar to that of natural bone to allow new bone in-growth and mesoporosity to host drugs and biologically active species for controlled delivery functions.

4.9 nm in size. Cell cultures indicated that primary human bone-derived cells were able to attach and spread to different degrees on the different scaffolds. These authors also indicate that the differences observed in supporting cell growth and differentiation observed for different scaffolds could be related to the CHA formation on the surface of scaffold, which has been reported to affect cell activity.[171,172] Additionally, the release of calcium and silicon ions may be contributing to the modulation of cellular attachment.[173]

The design of 3D scaffolds capable to drive cell in-growth is an important challenge in tissue engineering (see **Chapter 6.617, Bone Tissue Grafting and Tissue Engineering Concepts**). The aim is to design and fabricate pieces that support and structure the newly formed tissue and such pieces must be made starting from the most appropriate materials for this purpose. Cells must be cultured onto this scaffold to subsequently give rise to the growth of new tissue. Wolf's law states that the bone remodels itself as a function of those forces acting on it, hence preserving its shape and density (**Figure 11**). The mechanical loads of stress, compression, flexion, and torsion in bones and the interstitial fluid contained in them originate stresses and deformations at the microscopical level, which stimulate the cells. The use of finite element calculation methods contributes to the study of interactions between materials, mechanical stimulations, and biological response. Such a method allows simulating the conditions that take place in bioreactors in the scaffolds. Moreover, the effect and deformation at each point of the scaffold can be quantified, for instance, at each node, and the relationship between mechanical loads and cell differentiation can be also quantified.[174]

One of the most employed approaches in bone tissue engineering involves the initialization of the regeneration process *in vitro* by soaking the scaffold in appropriate cell culture and in the presence of osteogenic agents (**Figure 11**). Then, the scaffold is implanted in the patient.[175,176] However, the current challenge in bone tissue engineering is to chemically graft such osteogenic agents into the 3D scaffold to be directly implanted in the patient, acting as osteoinductive signals for bone regeneration (**Figure 11**).

So, turning back to ordered mesoporous materials, the presence of silanol groups in the external surface of silica walls would allow the organic modification of the scaffold. The choosing of the appropriate functional groups could permit formation of strong chemical bonds between the material surface and different osteoinductive agents, such as certain peptides, proteins, or growth factors, as schematically displayed in **Figure 12**. This approach permits to 'decorate' the scaffold by chemically grafting different active agents, such as certain peptides, proteins, or growth factors, that act as potent osteoinductive signals able to promote the appropriate bone cellular functions in the place where needed.[177–179]

At is has been widely reported, SMMs allow the design of controlled delivery systems for drug loading and release. Among other applications, these systems could be very useful to locally treat several pathologies such as bone infection and inflammation, osteoporosis, cancer, etc. However, although such molecules could fit into the mesopore channels, the confinement of osteogenic agents into the mesopores would impede them in carrying out their function. The role of these molecules is to act as attracting signals for bone formation cells, but these cells are too large to fit inside the mesopores (**Figure 12**). However, it is possible to apply the acquired knowledge from these systems to the grafting of the mentioned peptides, proteins, or growth factors onto the external silica

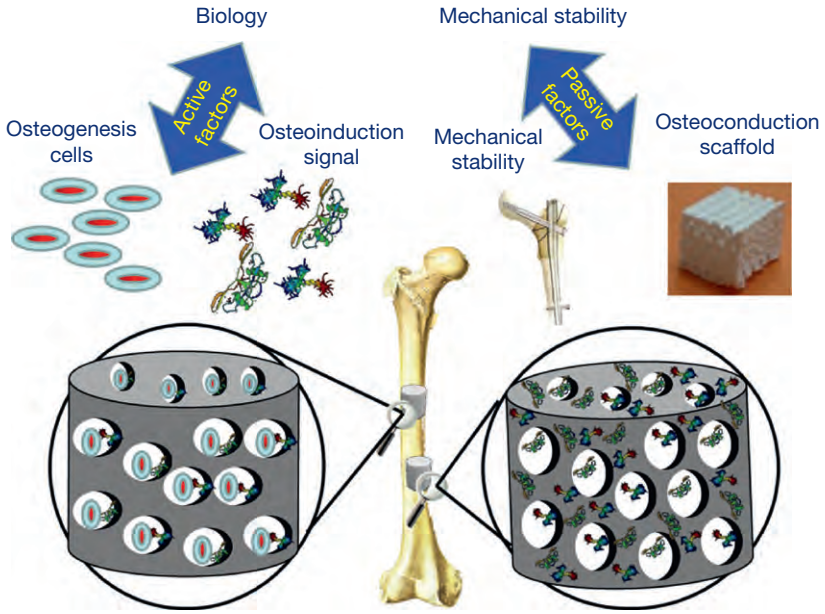

Figure 11 Scheme of the requirements for scaffolds aimed at bone tissue engineering. The biological point of view involves the presence of osteogenic cells. Osteogenesis process can be improved throughout by the presence of osteoinductive signals, which represents an added value. The mechanical aspect involves that bone remodels itself as a function of those forces acting on it. The two approaches used in bone tissue engineering are here displayed. Left down side: bone tissue regeneration starts *in vitro*. Right down side: osteogenic agents are grafted to the scaffold and implanted to allow the *in vivo* regeneration.

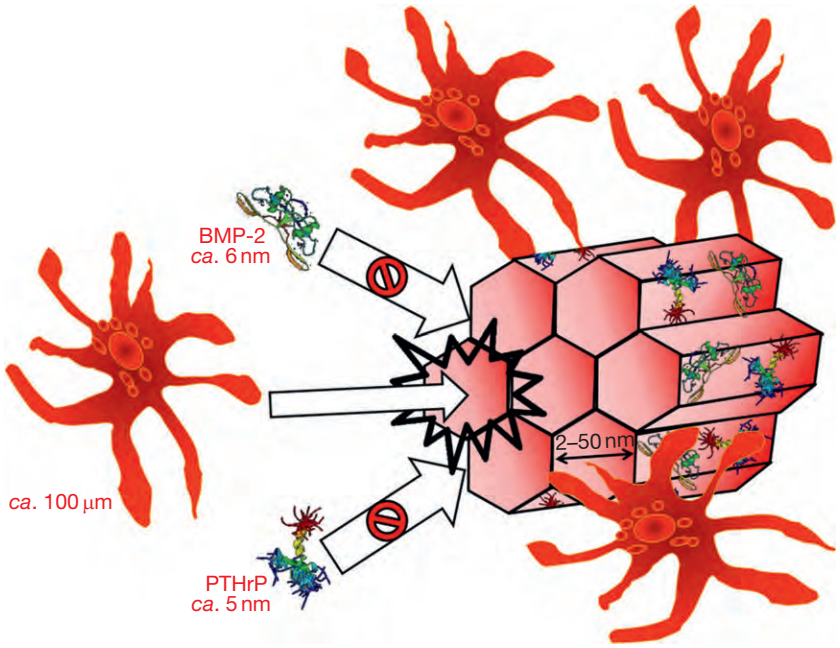

Figure 12 Schematic representation of a mesoporous silica material whose external surface has been organically modified to graft different osteogenic agents, such as growth factors or peptides. It is also schematically depicted that these osteogenic agents could fit inside the mesopores but that would obstruct them from playing their role. Such osteogenic agents act as signals for bone formation cells, and these cells (of ~100 μm) can never fit inside the mesopores (of 2–50 nm in size).

surface to induce bone tissue regeneration. Moreover, the possibility of using mesoporous matrices starting materials for the fabrication of 3D macroporous scaffolds provides these biomaterials an added value, their capability of hosting drugs to locally treat bone pathologies.

References

1. Scott, B. J.; Wirnsberger, G.; Stucky, G. D. *Chem. Mater.* **2001**, *13*, 3140–3150.
2. Taguchi, A.; Schuth, F. *Microporous Mesoporous Mater.* **2005**, *77*, 1–45.
3. Vallet-Regí, M.; Rámila, A.; del Real, R. P.; Pérez-Pariente, J. *Chem. Mater.* **2001**, *13*, 308–311.
4. Colilla, M.; Izquierdo-Barba, I.; Vallet-Regí, M. *Expert Opin. Ther. Pat.* **2008**, *18*, 639–656.
5. Colilla, M.; Manzano, M.; Vallet-Regí, M. *Int. J. Nanomed.* **2008**, *3*, 403–414.
6. Manzano, M.; Colilla, M.; Vallet-Regí, M. *Expert Opin. Drug Deliv.* **2009**, *6*, 1–18.
7. Manzano, M.; Vallet-Regí, M. *J. Mater. Chem.* **2010**, *20*, 5593–5604.
8. Vallet-Regí, M. *J. Chem. Soc. Dalton Trans.* **2006**, 5211–5220.
9. Vallet-Regí, M.; Balas, F.; Arcos, D. *Angew. Chem. Int. Ed.* **2007**, *46*, 7548–7558.
10. Vallet-Regí, M.; Balas, F.; Colilla, M.; Manzano, M. *Solid State Sci.* **2007**, *9*, 768–776.
11. Vallet-Regí, M. *J. Intern. Med.* **2010**, *267*, 22–43.
12. Vallet-Regí, M. *C. R. Chimie* **2010**, *13*, 174–185.
13. Wang, S. *Microporous Mesoporous Mater.* **2009**, *117*, 1–9.
14. Vallet-Regí, M. *Mat.-wiss. u. Werkstofftech.* **2006**, *37*, 478–484.
15. López-Noriega, A.; Arcos, D.; Izquierdo-Barba, I.; Sakamoto, Y.; Terasaki, O.; Vallet-Regí, M. *Chem. Mater.* **2006**, *18*, 3137–3144.
16. Yan, X. X.; Yu, C. Z.; Zhou, X. F.; Tang, J. W.; Zhao, D. Y. *Angew. Chem. Int. Ed.* **2004**, *43*, 5980–5984.
17. Izquierdo-Barba, I.; Arcos, D.; Sakamoto, Y.; Terasaki, O.; López-Noriega, A.; Vallet-Regí, *Chem. Mater.* **2008**, *20*, 3191–3198.
18. Izquierdo-Barba, I.; Manzano, M.; Colilla, M.; Vallet-Regí, M. *Key Eng. Mater.* **2008**, *377*, 133–150.
19. Izquierdo-Barba, I.; Colilla, M.; Vallet-Regí, M. *J. Nanomater.* **2008**, *2008*, 14 p.; Article ID 106970.
20. Vallet-Regí, M.; Colilla, M.; Izquierdo-Barba, I. *J. Biomed. Nanotechnol.* **2008**, *4*, 1–15.
21. Inagaki, S.; Fukushima, Y.; Kuroda, K. *Chem. Comm.* **1993**, *8*, 680–682.
22. Yanagisawa, T.; Shimizu, T.; Kuroda, K.; Kato, C. *Bull. Chem. Soc. Jpn* **1990**, *63*, 988–992.
23. Kresge, C. T.; Leonowicz, M. E.; Roth, W. J.; Vartuli, J. C.; Beck, J. S. *Nature* **1992**, *359*, 710–712.
24. Soler-Illia, G. J. A. A.; Sanchez, C.; Lebeau, B.; Patarin, J. *Chem. Rev.* **2002**, *102*, 4093–4138.
25. Ying, J. Y.; Mehnert, C. P.; Wong, M. S. *Angew. Chem. Int. Ed.* **1999**, *38*, 56–77.
26. Beck, J. S.; Vartuli, J. C.; Roth, W. J.; *et al. J. Am. Chem. Soc.* **1992**, *114*, 10834–10843.
27. Firouzi, A.; Atef, F.; Oertli, A. G.; Stucky, G. D.; Chmelka, B. F. *J. Am. Chem. Soc.* **1997**, *119*, 3596–3610.
28. Kaneda, M.; Tsubakiyama, T.; Carlsson, A.; *et al. J. Phys. Chem. B* **2002**, *106*, 1256–1266.
29. Kruk, M.; Jaroniec, M.; Sakamoto, Y.; Terasaki, O.; Ryoo, R.; Ko, C. H. *J. Phys. Chem. B* **2001**, *104*, 292–301.
30. Zhang, J.; Luz, Z.; Goldfarb, D. *J. Phys. Chem. B* **1997**, *101*, 7087–7094.
31. Ravikovitch, P. I.; Neimark, A. V. *Langmuir* **2002**, *18*, 9830–9837.
32. Ravikovitch, P. I.; Neimark, A. V. *Langmuir* **2002**, *18*, 1550–1560.
33. Zhao, D. Y.; Feng, J. L.; Huo, Q. S.; *et al. Science* **1998**, *279*, 548–552.
34. Bagshaw, S. A.; Prouzet, E.; Pinnavaia, T. J. *Science* **1995**, *269*, 1242–1244.
35. Ryoo, R.; Kim, J. M.; Ko, C. H.; Shin, C. H. *J. Phys. Chem. B* **1996**, *100*, 17718–17721.
36. Inagaki, S.; Koiwai, A.; Suzuki, N.; Fukushima, Y.; Kuroda, K. *Bull. Chem. Soc. Jpn* **1996**, *69*, 1449–1457.
37. Fan, J.; Yu, C.; Gao, F.; *et al. Angew. Chem. Int. Ed.* **2003**, *42*, 3146–3150.
38. Meng, Y.; Gu, D.; Zhang, F.; *et al. Angew. Chem. Int. Ed.* **2005**, *44*, 7053–7059.
39. Yu, C.; Yu, Y.; Zhao, D. Y. *Chem. Commun.* **2000**, 575–576.
40. Che, S.; García-Bennett, A. E.; Yokoi, T.; *et al. Nat. Mater.* **2003**, *2*, 801–805.
41. Chenite, A.; Lepage, Y.; Sayari, A. *Chem. Mater.* **1995**, *7*, 1015–1019.
42. Impéror-Clerc, M.; Davidson, P.; Davidson, A. *J. Am. Chem. Soc.* **2000**, *122*, 11925–11933.
43. Liu, Z.; Terasaki, O.; Ohsuna, T.; Hiraga, K.; Shin, H. J.; Ryoo, R. *Chemphyschem* **2001**, *2*, 229–231.
44. Che, S.; Lund, K.; Tatsumi, T.; *et al. Angew. Chem. Int. Ed.* **2003**, *49*, 2182.
45. Hartmann, M.; Vinu, A. *Langmuir* **2002**, *18*, 8010–8016.
46. Colilla, M.; Balas, F.; Manzano, M.; Vallet-Regí, M. *Chem. Mater.* **2007**, *19*, 3099–3101.
47. Martin, K. R. *J. Nutr. Health Aging* **2007**, *11*, 94–98.

48. Radin, S.; El-Bassyouni, G.; Vresilovic, E. J.; Schepers, E.; Ducheyne, P. In *Bioceramics 11*; LeGeros, R. Z., LeGeros, J. P., Eds.; World Scientific Publishing Co: Singapore, 1998; pp 529–532.
49. Radin, S.; El-Bassyouni, G.; Vresilovic, E. J.; Schepers, E.; Ducheyne, P. *Biomaterials* **2005**, *26*, 1043–1052.
50. Chia, S.; Urano, J.; Tamanoi, F.; Dunn, B.; Zink, J. I. *J. Am. Chem. Soc.* **2000**, *122*, 6488–6489.
51. Izquierdo-Barba, I.; Colilla, M.; Manzano, M.; Vallet-Regí, M. *Microporous Mesoporous Mater.* **2010**, *132*, 442–452.
52. Kortesuo, P.; Ahola, M.; Karlsson, S.; Kangasniemi, I.; Yli-Urpo, A.; Kiesvaara, J. *Biomaterials* **2000**, *21*, 193–198.
53. Blumen, S. R.; Cheng, K.; Ramos-Nino, M. E.; *et al*. *Am. J. Respir. Cell Mol. Biol.* **2007**, *36*, 333–342.
54. Chung, T. H.; Wu, S. H.; Yao, M.; *et al*. *Biomaterials* **2008**, *28*, 2959–2966.
55. Lu, J.; Liong, M.; Zink, J. I.; Tamanoi, F. *Small* **2007**, *3*, 1341–1346.
56. Radu, D. R.; Lai, C. Y.; Jeftinija, K.; Rowe, E. W.; Jeftinija, S.; Lin, V. S.-Y. *J. Am. Chem. Soc.* **2004**, *126*, 13216–13217.
57. Roy, I.; Ohulchanskyy, T. Y.; Pudavar, H. E.; *et al*. *J. Am. Chem. Soc.* **2003**, *125*, 7860–7865.
58. Son, Y. H.; Park, M.; Bin Choy, Y.; *et al*. *Chem. Commun.* **2007**, 2799–2801.
59. Trewyn, B. G.; Nieweg, J. A.; Zhao, Y.; Lin, V. S.-Y. *Chem. Eng. J.* **2008**, *137*, 23–29.
60. Vallhov, H.; Gabrielsson, S.; Stromme, M.; Scheynius, A.; Garcia-Bennett, A. E. *Nano Lett.* **2007**, *7*, 3576–3582.
61. Lin, Y. S.; Tsai, C. P.; Huang, H. Y.; *et al*. *Chem. Mater.* **2005**, *17*, 4570–4573.
62. Di Pasqua, A. J.; Sharma, K. K.; Shi, Y. L.; *et al*. *J. Inorg. Biochem.* **2008**, *102*, 1416–1423.
63. Lopez, T.; Basaldella, E. I.; Ojeda, M. L.; Manjarrez, J.; Alexander-Katz, R. *Opt. Mater.* **2006**, *9*, 75–81.
64. Wu, S. H.; Lin, Y. S.; Hung, Y.; *et al*. *Chembiochem* **2008**, *9*, 53–57.
65. Hudson, S. P.; Padera, R. F.; Langer, R.; Kohane, D. S. *Biomaterials* **2008**, *29*, 4045–4055.
66. García, A.; Colilla, M.; Izquierdo-Barba, I.; Vallet-Regí, M. *Chem. Mater.* **2009**, *21*, 4135–4145.
67. Lozano, D.; Manzano, M.; Doadrio, J. C.; *et al*. *Acta Biomater.* **2010**, *6*, 797–803.
68. Gómez-Gil, V.; Trejo, C.; García-Honduvilla, N.; *et al*. Mimetic biomaterials in compromised bone repair: PTHrP peptide (107–111) releasing silica mesoporous biomaterial improves bone neoformation in an experimental model of osteoporosis. In *22nd European Conference on Biomaterials*, Lausanne, Switzerland, Sept 7–11, 2009.
69. Trejo, C. G.; Lozano, D.; Manzano, M.; *et al*. *Biomaterials* **2010**, *31*, 8564–8573.
70. Langer, R. *Science* **2001**, *293*, 58–59.
71. Falaize, S.; Radin, S.; Ducheyne, P. *J. Am. Ceram. Soc.* **1999**, *82*, 969–976.
72. Nicoll, S. B.; Radin, S.; Santos, E. M.; Tuan, R. S.; Ducheyne, P. *Biomaterials* **1997**, *18*, 853–859.
73. Santos, E. M.; Radin, S.; Shenker, B.; Shapiro, I.; Ducheyne, P. *J. Biomed. Mater. Res.* **1998**, *41*, 87–94.
74. Santos, E. M.; Radin, S.; Ducheyne, P. *Biomaterials* **1999**, *20*, 1695–1700.
75. Cauda, V.; Fiorilli, S.; Onida, B.; *et al*. *J. Mater. Sci. Mater. Med.* **2008**, *19*, 3303–3310.
76. González, B.; Colilla, M.; López de Laorden, C.; Vallet-Regí, M. *J. Mater. Chem.* **2009**, *19*, 9012–9024.
77. Izquierdo-Barba, I.; Martínez, A.; Doadrio, A. L.; Pérez-Pariente, J.; Vallet-Regí, M. *Eur. J. Pharm. Sci.* **2005**, *26*, 365–373.
78. Izquierdo-Barba, I.; Sousa, E.; Doadrio, J. C.; *et al*. *J. Sol Gel Sci. Technol.* **2009**, *50*, 421–429.
79. Manzano, M.; Aina, V.; Areán, C. O.; *et al*. *Chem. Eng. J.* **2008**, *137*, 31–37.
80. Muñoz, B.; Rámila, A.; Pérez-Pariente, J.; Díaz, I.; Vallet-Regí, M. *Chem. Mater.* **2003**, *15*, 500–503.
81. Tang, Q. L.; Xu, Y.; Wu, D.; Sun, Y. H. *Chem. Lett.* **2006**, *35*, 474–475.
82. Tang, Q. L.; Xu, Y.; Wu, D.; *et al*. *J. Control. Release* **2006**, *114*, 41–46.
83. Cavallaro, G.; Pierro, P.; Palumbo, F. S.; Testa, F.; Pasqua, L.; Aiello, R. *Drug Deliv.* **2004**, *11*, 41–46.
84. Zeng, W.; Qian, X. F.; Zhang, Y. B.; Yin, J.; Zhu, Z. K. *Mater. Res. Bull.* **2005**, *40*, 766–772.
85. Ambrogi, V.; Perioli, L.; Marmottini, F.; Giovagnoli, S.; Esposito, M.; Rossi, C. *Eur. J. Pharm. Sci.* **2007**, *32*, 216–222.
86. Doadrio, A. L.; Sousa, E. M. B.; Doadrio, J. C.; Pérez-Pariente, J.; Izquierdo-Barba, I.; Vallet-Regí, M. *J. Control. Release* **2004**, *97*, 125–132.
87. Xue, J. M.; Shi, M. *J. Control. Release* **2004**, *98*, 209–217.
88. Vallet-Regí, M.; Doadrio, J. C.; Doadrio, A. L.; Izquierdo-Barba, I.; Pérez-Pariente, J. *Solid State Ionics* **2004**, *172*, 435–439.
89. Doadrio, J. C.; Sousa, E. M. B.; Izquierdo-Barba, I.; Doadrio, A. L.; Pérez-Pariente, J.; Vallet-Regí, M. *J. Mater. Chem.* **2006**, *16*, 462–466.
90. Yang, Q.; Wang, S. H.; Fan, P. W.; *et al*. *Chem. Mater.* **2005**, *17*, 5999–6003.
91. Qu, F. Y.; Zhu, G. S.; Huang, S. Y.; *et al*. *Microporous Mesoporous Mater.* **2006**, *92*, 1–9.
92. Yu, H.; Zhai, Q.-Z. *Microporous Mesoporous Mater.* **2009**, *123*, 298–305.
93. Mellaerts, R.; Mols, R.; Jammaer, J. A. G.; *et al*. *Eur. J. Pharm. Biopharm.* **2008**, *69*, 223–230.
94. Balas, F.; Manzano, M.; Horcajada, P.; Vallet-Regí, M. *J. Am. Chem. Soc.* **2006**, *128*, 8116–8117.
95. Colilla, M.; Izquierdo-Barba, I.; Vallet-Regí, M. *Microporous Mesoporous Mater.* **2010**, *135*, 51–59.
96. Nieto, A.; Balas, F.; Colilla, M.; Manzano, M.; Vallet-Regí, M. *Microporous Mesoporous Mater.* **2008**, *116*, 4–13.
97. Colilla, M.; Manzano, M.; Izquierdo-Barba, I.; Vallet-Regí, M.; Boissiere, C.; Sanchez, C. *Chem. Mater.* **2010**, *22*, 1821–1830.
98. Nieto, A.; Colilla, M.; Balas, F.; Vallet-Regí, M. *Langmuir* **2010**, *26*, 5038–5049.
99. López-Noriega, A.; Arcos, D.; Vallet-Regí, M. *Chem. A. Eur. J.* **2010**, *16*, 10879–10886.
100. Carino, I. S.; Pasqua, L.; Testa, F.; *et al*. *Drug Deliv.* **2007**, *14*, 491–495.
101. Pasqua, L.; Testa, F.; Aiello, R.; Cundari, S.; Nagy, J. B. *Microporous Mesoporous Mater.* **2007**, *103*, 166–173.
102. Song, S.-W.; Hidajat, K.; Kawi, S. *Langmuir* **2005**, *21*, 9568–9575.
103. Vallet-Regí, M.; Balas, F.; Colilla, M.; Manzano, M. *Prog. Solid State Chem.* **2008**, *36*, 163–191.
104. Gao, C. B.; Izquierdo-Barba, I.; Nakase, I.; *et al*. *Microporous Mesoporous Mater.* **2009**, *122*, 201–207.
105. Tourne-Peteilh, C.; Lerner, D. A.; Charnay, C.; Nicole, L.; Begu, S.; Devoisselle, J. M. *Chemphyschem* **2003**, *4*, 281–286.
106. Balas, F.; Manzano, M.; Colilla, M.; Vallet-Regí, M. *Acta Biomater.* **2008**, *4*, 514–522.
107. Vallet-Regí, M.; Balas, F.; Colilla, M.; Manzano, M. *Drug Metab. Lett.* **2007**, *1*, 37–40.
108. Kokubo, T.; Kushitani, H.; Sakka, S.; Kitsugi, T.; Yamamuro, T. *J. Biomed. Mater. Res.* **1990**, *24*, 721–734.
109. Deere, J.; Magner, E.; Wall, J. G.; Hodnett, B. K. *J. Phys. Chem. B* **2002**, *106*, 7340–7347.
110. Yiu, H. H. P.; Wright, P. A. *J. Mater. Chem.* **2005**, *15*, 3690–3700.
111. Peters, T. *All About Albumin: Biochemistry, Genetics and Medical Applications*; Academic Press: San Diego, 1996.
112. Sugio, S.; Kashima, A.; Mochizuki, S.; Noda, M.; Kobayashi, K. *Protein Eng.* **1999**, *12*, 439–446.
113. El-Safty, S. A.; Hanaoka, T.; Mizukami, F. *Chem. Mater.* **2005**, *17*, 3137–3145.
114. Kruk, M.; Jaroniec, M.; Sayari, A. *J. Phys. Chem. B* **1999**, *103*, 4590–4598.
115. Horcajada, P.; Rámila, A.; Pérez-Pariente, J.; Vallet-Regí, M. *Microporous Mesoporous Mater.* **2004**, *68*, 105–109.
116. Charnay, C.; Begu, S.; Tourné-Péteilh, C.; Nicole, L.; Lerner, D.; Devoisselle, J. M. *Eur. J. Pharm. Biopharm.* **2004**, *57*, 533–540.
117. Azaïs, T.; Tourné-Péteilh, C.; Aussenac, F.; *et al*. *Chem. Mater.* **2006**, *18*, 6382–6390.
118. Han, Y. J.; Stucky, G. D.; Butler, A. *J. Am. Chem. Soc.* **1999**, *121*, 9897–9898.
119. Zhang, X.; Guan, R. F.; Wu, D. Q.; Chan, K. Y. *J. Mater. Sci. Mater. Med.* **2007**, *18*, 877–882.
120. Schmidt-Winkel, P.; Lukens, W. W.; Zhao, D. Y.; Yang, P.; Chmelka, B. F.; Stucky, G. D. *J. Am. Chem. Soc.* **1999**, *121*, 254–255.
121. Schmidt-Winkel, P.; Lukens, W. W.; Yang, P.; *et al*. *Chem. Mater.* **2000**, *12*, 686–696.
122. Arcos, D.; López-Noriega, A.; Ruíz-Hernandez, E.; Terasaki, O.; Vallet-Regí, M. *Chem. Mater.* **2009**, *21*, 1000–1009.
123. Zhu, Y. F.; Shi, J. L.; Chen, H. R.; Shen, W. H.; Dong, X. P. *Microporous Mesoporous Mater.* **2005**, *84*, 218–222.
124. Zhu, Y. F.; Shi, J. L.; Shen, W. H.; Dong, X. P.; Ruan, M. L. *Nanotechnology* **2005**, *16*, 2633–2638.
125. Lin, V. S.-Y.; Lay, C.-Y.; Huang, J.; Song, S.-A.; Xu, S. *J. Am. Chem. Soc.* **2001**, *123*, 11510–11511.
126. Mal, N. K.; Fujiwara, M.; Tanaka, Y. *Nature* **2003**, *421*, 350–353.
127. Vallet-Regí, M.; Ruiz-González, L.; Izquierdo-Barba, I.; González-Calbet, J. M. *J. Mater. Chem.* **2006**, *16*, 26–31.
128. Hoffmann, F.; Cornelius, M.; Morell, J.; Froba, M. *Angew. Chem. Int. Ed.* **2006**, *45*, 3216–3251.
129. Kruk, M.; Asefa, T.; Jaroniec, M.; Ozin, G. A. *J. Am. Chem. Soc.* **2002**, *124*, 6383–6392.
130. Mori, Y.; Pinnavaia, T. J. *Chem. Mater.* **2001**, *13*, 2173–2178.

131. Tsay, C. T.; Pan, Y. C.; Ting, C. C.; *et al*. *Chem. Commun*. **2009**, 5018–5020.
132. Babonneau, F.; Camus, L.; Steunou, N.; Rámila, A.; Vallet-Regí, M. *Mater. Res. Soc*. **2003**, *775*, 3261–3266.
133. Horcajada, P.; Rámila, A.; Férey, G.; Vallet-Regí, M. *Solid State Sci*. **2006**, *8*, 1243–1249.
134. Suva, L. J.; Winslow, G. A.; Wettenhall, R.; Hammonds, R. G.; Moseley, J. M.; Diefenbachjagger, H. A. *Science* **1987**, *237*, 893–896.
135. Valin, A.; García-Ocaña, A.; DeMiguel, F.; Sarasa, J. L.; Esbrit, P. *J. Cell. Physiol*. **1997**, *160*, 209–215.
136. Arcos, D.; Vallet-Regí, M. *Acta Biomater*. **2010**, *6*, 2874–2888.
137. Balas, F.; Arcos, D.; Pérez-Pariente, J.; Vallet-Regí, M. *J. Mater. Res*. **2001**, *16*, 1345–1348.
138. Li, P.; Ohtsuki, C.; Kokubo, T.; *et al*. *J. Am. Ceram. Soc*. **1992**, *75*, 2094–2097.
139. Pereira, M. M.; Clark, A. E.; Hench, L. L. *J. Am. Ceram. Soc*. **1995**, *78*, 2463–2468.
140. Pereira, M. M.; Clark, A. E.; Hench, L. L. *J. Sol–Gel Sci. Technol*. **1996**, *7*, 59–68.
141. Vallet-Regí, M.; Arcos, D.; Pérez-Pariente, J. *J. Biomed. Mater. Res*. **2000**, *51*, 23–28.
142. Horcajada, P.; Rámila, A.; Boulahya, K.; González-Calbet, J.; Vallet-Regí, M. *Solid State Sci*. **2004**, *6*, 1295–1300.
143. Izquierdo-Barba, I.; Ruiz-González, L.; Doadrio, J. C.; González-Calbet, J. M.; Vallet-Regí, M. *Solid State Sci*. **2005**, *7*, 983–989.
144. Kokubo, T.; Takadama, H. *Biomaterials* **2006**, *27*, 2907–2915.
145. González-Calbet, J. M.; Ruiz-González, M. L.; Vallet-Regí, M. In *Turning Points in Solid-State, Materials and Surface Chemistry*; Harris, K. D. M., Edwards, P. P., Eds.; The Royal Society of Chemistry: Cambridge, UK, 2007; pp 727–744.
146. Vallet-Regí, M.; Izquierdo-Barba, I.; Salinas, A. J. *J. Biomed. Mater. Res*. **1999**, *46*, 560–565.
147. Vallet-Regí, M.; Izquierdo-Barba, I.; Rámila, A.; Pérez-Pariente, J.; Babonneau, F.; González-Calbet, J. M. *Solid State Sci*. **2005**, *7*, 233–237.
148. Daculsi, G.; legeros, R. Z.; Nery, E.; Lynch, K.; Kerebel, B. *J. Biomed. Mater. Res*. **1989**, *23*, 883–894.
149. Daculsi, G. *Biomaterials* **1998**, *19*(19), 1473–1478.
150. Vallet-Regí, M.; Rámila, A.; Padilla, S.; Muñoz, B. *J. Biomed. Mater. Res*. **2003**, *66*, 580–585.
151. Brinker, C. J.; Lu, Y. F.; Sellinger, A.; Fan, H. Y. *Adv. Mater*. **1999**, *11*, 579–585.
152. Yan, X. X.; Deng, H. X.; Huang, X. H.; *et al*. *J. Non-Cryst. Solids* **2005**, *351*, 3209–3217.
153. Yan, X. X.; Huang, X. H.; Yu, C. Z.; *et al*. *Biomaterials* **2006**, *27*, 3396–3403.
154. Yun, H. S.; Kim, S. E.; Hyeon, Y. T. *Mater. Lett*. **2007**, *61*, 4569–4572.
155. Leonova, E.; Izquierdo-Barba, I.; Arcos, D.; *et al*. *J. Phys. Chem. C* **2008**, *112*, 5552–5562.
156. Hench, L. L.; Wilson, J. *Science* **1984**, *226*, 630–636.
157. Bodier-Houlle, P.; Steuer, P.; Voegel, J. C.; Cuisinier, F. J. G. *Acta Crystallogr*. **1998**, *54*, 1377–1381.
158. Brown, W. E.; Eidelman, N.; Tomazic, B. *Adv. Dent. Res*. **1987**, *1*, 306–313.
159. Nancollas, G. H.; Tomazic, B. *J. Phys. Chem*. **1974**, *78*, 2218–2225.
160. Hench, L. L.; Andersson, O. In *An Introduction to Bioceramics*; Hench, L. L., Wilson, J., Eds.; World Scientific: Singapore, 1993; pp 41–62.
161. Frieb, W.; Werner, J. In *Handbook of Porous Solids*; Shüth, F., Klenneth, S., Sing, W., Kamps, W., Eds.; Wiley-VCH: Weinheim, Germany, 2000; pp 2923–2970.
162. Sánchez-Salcedo, S.; Werner, J.; Vallet-Regí, M. *Acta Biomater*. **2008**, *4*, 913–922.
163. Hollister, S. J. *Nat. Mater*. **2005**, *4*, 518–524.
164. Karageorgiou, V.; Kaplan, D. *Biomaterials* **2005**, *26*, 5474–5491.
165. Rho, J. Y.; Kuhn-Spearing, L.; Zioupos, P. *Med. Eng. Phys*. **1998**, *20*, 92–102.
166. Yun, H. S.; Kim, S. E.; Hyeon, Y. T. *Chem. Commun*. **2007**, 2139–2141.
167. Xie, B.; Parkhill, R. L.; Warren, W. L.; Smay, J. E. *Adv. Funct. Mater*. **2006**, *16*, 1685–1693.
168. Yeong, W. Y.; Chua, C. K. *Trends Biotechnol*. **2004**, *22*, 643–652.
169. Li, X.; Wang, X.; Chen, H.; Jiang, P.; Dong, X.; Shi, J. *Chem. Mater*. **2007**, *19*, 4322–4326.
170. Zhu, Y.; Wu, C.; Ramaswamy, Y.; *et al*. *Microporous Mesoporous Mater*. **2008**, *112*, 494–503.
171. Olmo, N.; Martín, A. I.; Salinas, A. J.; Turnay, J.; Vallet-Regí, M.; Lizarbe, M. A. *Biomaterials* **2003**, *24*, 3383–3393.
172. Wu, C. T.; Chang, J.; Zhai, W. Y.; Ni, S. Y. *J. Mater. Sci. Mater. Med*. **2007**, *18*, 857–864.
173. Valerio, P.; Pereira, M. M.; Goes, A. M.; Leite, M. F. *Biomaterials* **2004**, *25*, 2941–2948.
174. Tuan, H. S.; Hutmacher, D. W. *Comput. Aided Des*. **2005**, *37*, 1151–1161.
175. Jones, J. R.; Hench, L. L. *Curr. Opin. Solid St. M*. **2003**, *7*, 301–307.
176. Langer, R.; Vacanti, J. *Science* **1993**, *260*, 920–926.
177. Baeza, A.; Izquierdo-Barba, I.; Vallet-Regí, M. *Acta Biomater*. **2009**, *6*, 743–749.
178. Hench, L. L.; Polak, J. M. *Science* **2002**, *295*, 1014–1017.
179. Vallet-Regí, M. *Chem. Eng. J*. **2007**, *137*, 1–3.

4.430. Silica-Based Mesoporous Nanospheres

S Bhattacharyya and P Ducheyne, University of Pennsylvania, Philadelphia, PA, USA

© 2011 Elsevier Ltd. All rights reserved.

4.430.1.	**Introduction**	515
4.430.1.1.	History	516
4.430.2.	**Synthesis of Nonporous Silica Nanospheres**	516
4.430.2.1.	The Stöber Technique	516
4.430.3.	**Synthesis of MSNs**	517
4.430.3.1.	General Principles of Synthesis of Mesoporous Silica	517
4.430.3.2.	Formation Mechanisms of Mesoporous Silica	517
4.430.3.2.1.	Liquid crystal templating mechanism	517
4.430.3.2.2.	Transformation mechanism from lamellar to hexagonal phase	518
4.430.3.3.	Synthesis and Growth of MSNs	518
4.430.3.3.1.	Alternative methods	518
4.430.3.3.2.	Growth mechanism	518
4.430.3.4.	Morphology Control	519
4.430.3.4.1.	Particle size	519
4.430.4.	**Physicochemical Properties and Characterization**	520
4.430.4.1.	Properties	520
4.430.4.1.1.	Product crystallinity	520
4.430.4.1.2.	Thermal and hydrothermal stability	521
4.430.4.2.	Characterization	522
4.430.4.2.1.	Gas adsorption methods	522
4.430.4.2.2.	Surface area	523
4.430.4.2.3.	Pore volume	523
4.430.4.2.4.	Pore size	523
4.430.5.	**Unique Biomaterial Considerations**	523
4.430.5.1.	Host–Guest Encapsulation	524
4.430.5.2.	Surface Functionalization	525
4.430.5.3.	Biocompatibility	525
4.430.6.	**Conclusion**	526
References		526

Abbreviations

C_{16}TMABr	Hexadecyltrimethylammonium bromide
CMC	Critical micelle concentration
CTAB	Cetyltrimethylammonium bromide
EHTES	Epoxyhexyltriethoxysilane
FSM	Folded-sheet mesoporous material
MCM-X	(X = 41, 48, 50) Mobil Composition of Matter
MSN	Mesoporous silica nanosphere
MTT	3-(4,5-dimethylthiazol-2-yl)-2,5-diphenyltetrazolium bromide
NMR	Nuclear magnetic resonance
PSD	Pore size distribution
SAXS	Small angle X-ray scattering
SEM	Scanning electron microscopy
TBHP	Tert-butylhydroperoxide
TBOS	Tetrabutyl orthosilicate
TEA	Triethanolamine
TEOS	Tetraethyl orthosilicate
THMP	Trihydroxysilylpropyl methylphosphonate
TMOS	Tetramethyl orthosilicate
XRD	X-ray diffraction

4.430.1. Introduction

Over the last two decades, there has been a dramatic development in the synthesis of open-framework inorganic materials with well-defined pore geometry. The development of such materials consisting of, for example, silica and carbon with controlled pore shapes and sizes of high precision is of great importance in diverse fields of modern science and technology.[1–4] These materials have already been used successfully in several fields, such as heterogeneous catalysis, separation processing, and host–guest chemistry. Recent exploration of these materials in bioadsorption, controlled release of biomolecules,

and drug delivery reveals their enormous application potential in biomaterials science.

The development of microporous molecular sieves has been reviewed before.[5–9] In addition, the recently discovered macroporous solids have also been described.[10–17] Under the influence of the discovery of ordered mesophases, newer concepts in periodic porous materials have emerged in recent years.[18–21] These findings have been summarized by Zhao *et al.*,[22] Selvam *et al.*,[23] and Bhattacharyya *et al.*[24] Here, we focus on ordered spherical, mesoporous, silica nanoparticles, giving particular attention to MCM-41 (Mobil Composition of Matter)-based materials. We will adopt the IUPAC definition[25] of mesoporous materials: materials with pore diameters between 2 and 500 nm.

Subsequent to summarizing the history of its discovery, we discuss the general synthesis procedure of mesoporous silica materials. This is followed by a discussion of ways to adopt these synthesis procedures in order to obtain the mesoporous silica-based microspheres and nanospheres. Next, we discuss the physical and chemical properties of these materials along with the general characterization techniques used to characterize them. In the last section, we elaborate on their applications in the field of biomaterials.

4.430.1.1. History

In the early 1990s, Kuroda's group in Japan developed new alkylammonium–clay intercalation complexes by hydrothermal treatment and calcination.[19,21] These complexes had a highly ordered honeycomb mesoporous structure, referred to as folded-sheet mesoporous material (FSM 16). At the same time, research work at Mobil Oil Corporation revealed a series of new porous materials grouped under the name of the M41S family, with striking resemblances to the Japanese materials.[18,20] The process was patented in 1991 and 1992.[26–28] It is of interest to note that Chiola *et al.*[29] had reported the synthesis of low-density silica based on the hydrolysis and condensation of a silica precursor in the presence of a cationic surfactant. This had already been patented in 1971. The unique mesoporous properties of that silica remained unrecognized until 1997 when Di Renzo *et al.*[30] reproduced the experiments described in the patent[29] and showed that the resulting product presented all the characteristics and properties of the MCM-41. Nevertheless, the numerous Mobil discoveries and applications have provided an impetus to the field, as witnessed by the development of many new synthesis methods.[31–34]

In 1992, Mobil researchers disclosed the first family of highly ordered mesoporous molecular sieves, M41S (pore size in the range 2–10 nm), in which long chain cationic surfactants were used as the template or pore forming agents during the hydrothermal sol–gel synthesis.[35] Depending on starting materials and synthesis conditions, different mesoporous silica oxides with ordered structures in the form of hexagonal (denoted as MCM-41),[18,20,35–42] cubic (denoted as MCM-48),[36–42] and lamella (denoted as MCM-50),[20,43,44] were formed (see **Figure 1**). Since then, many synthetic routes and strategies have been developed to yield a wide variety of materials of various frameworks with different chemical compositions and pore structures.

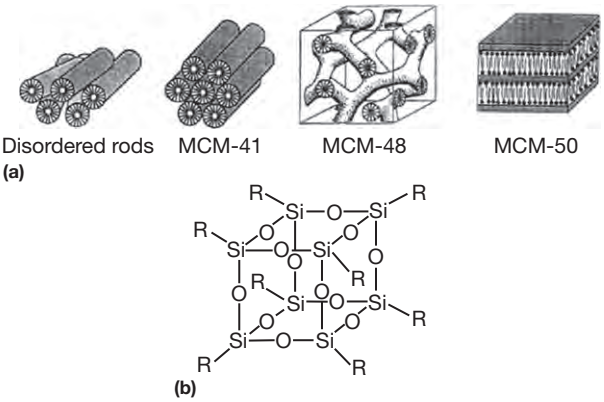

Figure 1 (a) Four main phases formed from $C_{16}TMA/SiO_2/H_2O$. (b) Surfactant–silica composite unit formed from $C_{16}TMA/SiO_2/H_2O$. Reproduced from Selvam, P.; Bhatia, S. K.; Sonwane, C. G. *Ind. Eng. Chem. Res.* **2001**, *40*, 3237–3261, with permission from American Chemical Society.

4.430.2. Synthesis of Nonporous Silica Nanospheres

4.430.2.1. The Stöber Technique

The Stöber process is the most common method for synthesizing colloidal silica-based nanoparticles that are <100 nm in size.[45] The process comprises hydrolysis of a silica alkoxide precursor (such as tetraethyl orthosilicate, TEOS) in a mixture of ethanol and aqueous ammonium hydroxide. During the hydrolysis, silicic acid is produced, which nucleates homogeneously and forms silica particles of submicron size when its concentration is above its solubility in ethanol. This method is intended for the preparation of pure silica nanoparticles.

In general, the process involves two steps: first, the hydrolysis reaction with singly hydrolyzed TEOS monomer $[(OR)_3Si(OH)]$ as a reaction product

$$Si(OR)_4 + H_2O \rightarrow (OR)_3Si(OH) + ROH$$

second, condensation of this intermediate reaction product to form silica according to

$$(OR)_3Si(OH) + H_2O \rightarrow SiO_2 \downarrow + 3ROH$$

We have to keep in mind that this is a simplified version of the very complex condensation processes that lead to the formation of the silica particles. Initial research on Stöber particles was mostly concentrated on the empirical prediction of the final particle size for a range of the initial reactant concentrations (0.1–0.5 M TEOS, 0.5–17.0 M H_2O, and 0.1–3.0 M NH_3) that lead to monodisperse colloids, the smallest achievable size being 10 nm and largest being 800 nm.[45,46] Later research was aimed at elucidating the mechanisms behind the formation and growth of the particles.[47–53] A consensus on the processes responsible for the particle formation and growth, and the eventual monodispersity, particle size, and particle shape has not yet emerged. Two models, monomer addition[47–49] and controlled aggregation,[52,53] have been proposed to describe the chemical and/or physical growth mechanisms of silica. The model proposed by Matsoukas and Gulari[47–49] contemplates that the particle formation and growth are solely governed by the kinetic equations that describe chemical reactions.

In their model, particle nucleation is the result of the reaction between two hydrolyzed monomers. Subsequently, the 'particle' grows only by monomer addition. The balance between monomer addition and nucleation determines the polydispersity and final particle size. Particle growth is rate-limited by the slowest step, the hydrolysis of the monomers. On the other hand, Zukoski and coworkers[50–53] described the nucleation and growth by a controlled aggregation of subparticles a few nanometers in size. Zukoski and coworkers assume that it is not hydrolysis that is the rate-determining step in the particle growth but that some step in the condensation pathway is rate-determining. Particle formation results from the aggregation during the entire reaction period. This aggregation process is controlled, in the sense that once the aggregates or 'particles' have reached a certain size (and thereby a certain colloidal stability because of their surface charge), the growth continues only by aggregation with the small subparticles and not by collisions with other (larger) particles. Growth, final particle size, and polydispersity are influenced in this model by parameters such as the surface charge and the size of the subparticles.

More recently, many other investigations have been devoted to the understanding of the particle growth mechanism,[54–56] and such studies have included microgravity experiments.[57]

4.430.3. Synthesis of MSNs

4.430.3.1. General Principles of Synthesis of Mesoporous Silica

A typical synthesis of MCM-41 requires a minimum of four reagents: a solvent (water and/or ethanol), a silica precursor (TEOS, tetramethyl orthosilicate (TMOS), tetrabutyl orthosilicate (TBOS)), an ionic (anionic or cationic) or noncharged surfactant, and a catalyst. Depending on the protocol, the reaction could occur in either an acidic or a basic medium, with different silica/surfactant ratios. The mixture is stirred, aged at room temperature or around 100 °C, and placed in a static autoclave for several hours. The surfactant template is removed by calcination. Novel routes have been proposed based either on a nonsurfactant templated method[58,59] or on a polyelectrolyte/hexadecyltrimethylammonium bromide method.[60]

Another alternative route[61,62] involves microwave treatment of a precursor gel first heated by microwave radiation around 100–150 °C followed by conventional heating. The advantages of the microwave-assisted preparation over the conventional hydrothermal method are a significant decrease in reaction time, and a more homogeneous heating, which leads to a better control of the texture and morphology. However, it has been superseded by faster methods that produce within a few hours materials of the same, if not better, quality.

4.430.3.2. Formation Mechanisms of Mesoporous Silica

Due to the important role of surfactant molecules in the synthesis of mesoporous silica materials, the formation mechanisms of its precursors have attracted much attention. Two typical mechanisms have been proposed so far: liquid crystal templating (LCT) mechanism[20] and mechanism of transformation from lamellar to hexagonal phase.[65]

4.430.3.2.1. Liquid crystal templating mechanism

A key feature of the LCT mechanism is that the liquid-crystalline mesophases, or micelles, act as templates rather than individual single molecules or ions. Accordingly, the final product is a silicate skeleton that contains voids with shapes similar to those of the mesophases. The silicate condensation is not the dominant factor in the formation of the mesoporous structure.[36,63,64] As illustrated in Figure 2, surfactant micelle molecules, assisted by a micelle self-assembly arrange themselves to form liquid-crystalline phases. Silicate species deposit between surfactant 'rods' and then condense to form an inorganic network, with a hexagonal ordering dictated by the interaction between the surfactant and the silicate species. After removal of the surfactant templates, a mesoporosity is obtained with pore size of 2–10 nm.

In general, the overall LCT mechanism is governed by two factors: (i) the dynamics of surfactant molecules to form assemblies, micelles, and ultimately, crystalline structures that function as templates and (ii) the ability of the inorganic oxide to undergo hydrolysis and polycondensation reactions, leading to a network surrounding the organic template. A wide variety of ionic surfactant molecules of different sizes, shapes, functionalities, and charges have been shown to be able to effectively function as pore structure-directing agents. These surfactant molecules can be classified on the basis of their head group chemistry and charge as follows:

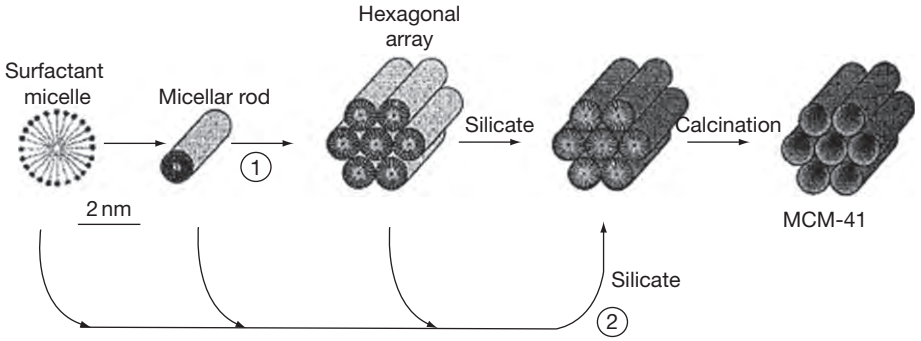

Figure 2 Schematic representation of two possible formation mechanisms of mesoporous silica: (1) liquid crystal templating mechanism and (2) transformation from lamellar to hexagonal phase. Reproduced from Selvam, P.; Bhatia, S. K.; Sonwane, C. G. *Ind. Eng. Chem. Res.* **2001**, *40*, 3237–3261, with permission from American Chemical Society.

Cationic surfactants: the hydrophilic group carries a positive charge, for example, tetraalkylammonium salts (C_nH_{2n+1})(CH_3)$_3$NX, $n = 6, 8, 9, 10, 12, 14, 16, 18, 20, 22$; X = OH, Cl, Br, HSO_4; (C_nH_{2n+1})(C_2H_5)$_3$N, $n = 12, 14, 16, 18$.

Anionic surfactants: the hydrophilic group carries a negative charge, for example, sulfates ($C_nH_{2n+1}OSO_3$ with $n = 12, 14, 16, 18$), sulfonates ($C_{16}H_{33}SO_3H$ and $C_{12}H_{25}C_6H_4SO_3Na$), and phosphates ($C_{12}H_{25}OPO_3H_2$, $C_{14}H_{29}OPO_3K$).

4.430.3.2.2. Transformation mechanism from lamellar to hexagonal phase

This is yet another formation mechanism proposed by Stucky and coworkers[65–67] who focused on the transformation mechanism from lamellar to hexagonal phase.

The mechanism postulates self-assembly of the liquid-crystal-like structures as a result of the mutual interactions between the silicate anion and the surfactant cations in the solution, that is, the silicate species generated in the reaction mixture influence the ordering of the surfactant micelles to the desired liquid–crystal phase. This was suggested by the identification of silica aggregates in the synthesis mixture using ^{14}N nuclear magnetic resonance (NMR) spectroscopy.[68] In addition, the formation of hexagonal, cubic, and lamellar structures through variations in the silica concentration at constant surfactant concentration represented strong support for this putative mechanism.[69] Huo *et al.*[70,71] and Inagaki *et al.*[72] carried out a more detailed analysis of the formation of these mesophases. They observed the formation of a layered silica–surfactant phase upon mixing the reactants that, with time, produced an MCM-41 structure (pathway 3 in **Figure 3**). Davis and Burkett[73] proposed a somewhat similar mechanism (pathway 2 in **Figure 3**) in which, depending on the reaction temperature, the formation of MCM-41 occurs via a disordered or lamellar structure.[74]

4.430.3.3. Synthesis and Growth of MSNs

Following the initial description of mesoporous materials, the synthesis of hierarchically ordered structures on different length scales, such as beads of controlled sizes, generated a great deal of interest, from both a fundamental and practical point of view. Holding centerstage in these studies was the control of the internal pore structure, as it is a challenging aspect of the synthesis of mesoporous M41S-based nanospheres.[75–83]

Grun *et al.*[84] first demonstrated the suitability of adapting the Stöber synthesis[45] of silica spheres for the production of spherical MCM-41 particles under basic conditions. Freshly distilled TEOS is combined with a dilute surfactant solution and ammonia as catalyst in a rapid room temperature preparation. The resultant silica solids are calcined at 550 °C in air to produce mesoporous solids that exhibit the characteristic low-angle X-ray diffraction (XRD) pattern associated with MCM-41 and the familiar reversible type IV nitrogen isotherm typical of these materials.[85] Scanning electron microscopy (SEM) reveals the spherical morphology of these solids. Since their advent, various assembly pathways have been used to produce mesoporous silica spheres[86–92] based on a procedure where TEOS is used as silica source, hexadecyltrimethylammonium bromide (C_{16}TMABr) as surfactant, alcohol as solvent, and aqueous ammonia as catalyst. It is to be noted that spheres can also be obtained in acidic medium by substituting HCl for ammonia.[93]

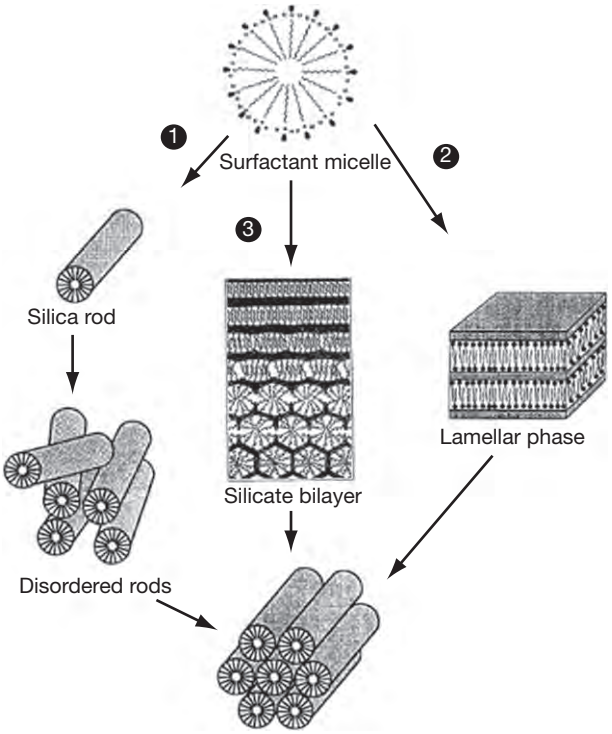

Figure 3 Proposed formation mechanistic pathways by (1) stacking of silicate surfactant rods via the formation of an initial (2) lamellar intermediate and (3) silicate bilayer. Reproduced from Kresge, C. T.; Vartuli, J. C.; Roth, W. J.; Leonowicz, M. E. *Stud. Surf. Sci. Catal.* **2004**, *148*, 53–72, with permission from Elsevier.

4.430.3.3.1. Alternative methods

Another route needs to be mentioned: the synthesis of silica spheres with a spray-drying process. Since the demonstration of the feasibility of this synthesis route by Lu *et al.*,[94] results of the preparation of high-quality mesoporous silica spheres by the evaporation-induced self-assembly (EISA) process[95,96] have been reported.[93,97–99] A sol, composed generally of a precursor of silica (TEOS), a cationic surfactant (C_{16}TMABr) and/or block copolymer (PEO–PPO–PEO), a solvent (isopropyl alcohol, ethanol), and water in an acidic medium, is atomized inside a drying chamber at a constant inlet temperature. Parameters such as C_{16}TMABr/Si molar ratio, pH, solvent quantity, and drying temperature influence the texture and the morphology of the final product. Very recently, Alonso *et al.*[99] have proposed a scheme for the formation of spheres by spray-drying alcoholic sols. Using ^{29}Si and ^{1}H solid-state NMR experiments, the formation mechanism consists of a droplet fragmentation due to the fast solvent evaporation, followed by aggregation and self-assembly of the surfactant molecules with the oxo-oligomers. The resulting mesophase extends inside the particles and forms ordered textures.

4.430.3.3.2. Growth mechanism

Although various morphologies have been achieved, the formation of MCM-41 nanospheres and the control of their morphologies have not been well mastered yet. Different morphologies and textures can be obtained by varying the amount of surfactant and solvents. Huo *et al.*[100] produced

marble-like spheres about 1 mm in diameter using TBOS based on emulsion biphase chemistry, which usually produces hollow mesoporous silica microspheres. Under basic conditions, TBOS undergoes hydrolysis to give butyl alcohol (BuOH), which is immiscible with water. The oil-in-water emulsion formed during the early reaction stage thus contains BuOH and partially hydrolyzed TBOS as the oil phase. The quaternary ammonium surfactants play an important role in the stabilization of this emulsion. Hydrogen bonding between the BuOH and water molecules provides a diffusion pathway for the surfactant and water to penetrate the TBOS/BuOH oil droplets and promotes the hydrolysis of TBOS. The resulting silicate polymerizes under the influence of the structure-directing surfactant and transforms into solid spheres via a soft silicate gel.

Very recently, the formation processes of spherical mesoporous silica were studied[101] in the case of a biphasic system containing a hydrophobic siloxane (TBOS) and an alkali solution with a surfactant. The water pools in the TBOS phase were shown to be connected to each other, and a regularly arranged nanostructure was formed by the self-assembly of the surfactant. Thus, the nanostructure of spherical mesoporous silica was determined to be the reverse of MCM-41, in which continuous mesopores were developed.

The effect of alcohol on the morphology of the spheres was investigated.[102–104] Increasing the ethanol concentration in the TEOS–C_{16}TMABr–ammonia–water system at room temperature led to the formation of a succession of mesophases in the order, MCM-41 (hexagonal phase), MCM-48 (cubic phase), and MCM-50 (lamellar phase). Such phase succession is the result of the cosurfactant behavior of the ethanol. At a lower alcohol concentration, SEM shows only undefined or barely spherical structures; when the alcohol concentration is increased, it mainly acts as a cosolvent, producing spherical particles. It was suggested that increasing the alcohol amount changes the surfactant packing parameter, g,[105,106] given by

$$g = \frac{V}{a_0 l}$$

where V is the total volume of the surfactant chain plus any cosolvent molecules between the chains, a_0 is the effective head group area at the organic–inorganic interface, and l is the surfactant chain length.

The parameter g directs the phase configuration in the synthesis of mesoporous materials. Small values of g stabilize more curved surfaces, such as MCM-41 ($1/3 < g < 1/2$), while larger values stabilize structures with less curvature, such as MCM-48 ($1/2 < g < 2/3$). The proposed mechanism of pore formation is shown in Figure 4.

The MCM-48 crystal core exhibits a truncated octahedron shape, in which each facet plays the role of a substrate for the growth of cylindrical pores in an epitaxial manner (Figure 4(a)). The epitaxial pores are forced to adopt the pore packing of the MCM-48 crystal facet surface. The pores growing on the {111} facets adopt a packing close to the hexagonal MCM-41, and those on the {001} facets, an intermediate packing between MCM-48 and MCM-41. The MCM-48 crystal core exhibits a truncated octahedron shape, in which each facet plays the role of a substrate for the growth of cylindrical pores in an epitaxial manner (Figure 4(a)). The epitaxial pores are forced to adopt the pore packing of the MCM-48

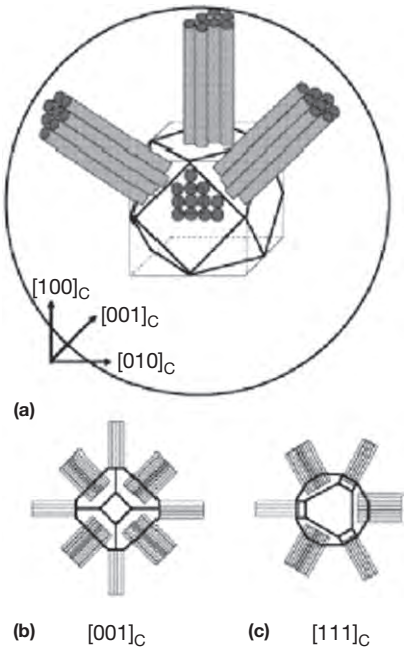

Figure 4 (a) Schematic representation of a spherical particle consisting of a nucleus of cubic MCM-48 and bundles of cylindrical pores grown epitaxially on the $\{111\}_C$ and $\{001\}_C$ facets. (b) and (c) Two projections of the particle, viewed along $[001]_C$ and $[111]_C$, are also presented. Reproduced from Lebedev, O. I.; Van Tendeloo, G.; Collart, O.; Cool, P.; Vansant, E. F. *Solid State Sci*. **2004**, *6*, 489–498, with permission from Elsevier.

crystal facet surface. The pores growing on the {111} facets adopt a packing close to the hexagonal MCM-41, and those on the {001} facets, an intermediate packing between MCM-48 and MCM-41.

4.430.3.4. Morphology Control

After the discovery of surfactant-templated synthesis of mesoporous silica materials in 1992,[18] significant advances were made in the functionalization and utilization of these materials for various applications, such as catalysis,[107] separation,[89] and sensing.[89] In spite of these exciting advancements, there were very few reports, if any, on the utilization of these materials for controlled release and delivery application until the early 2000s. One of the possible reasons is the lack of knowledge regarding the synthesis of MCM-41 with controlled morphology. The conventional synthetic methods for preparing mesoporous silica materials yielded amorphous chunks and particles of different shapes and sizes. In addition, the polydispersity and the amorphous nature of the mesoporous silicas presented a major challenge to the understanding and control of the adsorption and release properties at the nano level, which is of fundamental importance for drug delivery and controlled release in biological systems.

4.430.3.4.1. Particle size

4.430.3.4.1.1. Mesoporous silica microsphere

The synthesis of micrometer-sized mesoporous silica spheres of a narrow size distribution was achieved in the late 1990s.[100,107,108] The various groups focused on the synthesis

of monodisperse mesoporous silica spheres of controlled particle size for chromatographical applications,[89] and the method relies on the well-established Stöber reaction for the synthesis of monodisperse nonporous silica spheres. The reaction involved the cohydrolysis and subsequent condensation of tetraethoxysilane (TEOS) and an alkyltrialkoxysilane in a mixture of ethanol, water, and aqueous ammonia. Ethanol acted as a cosolvent to form a homogeneous solution, ammonia served as a morphological catalyst, and *n*-alkyltrialkoxysilane generated the porosity.[107] Other groups followed later and described a synthesis of mesoporous silica microspheres using surfactant-stabilized emulsion chemistry,[109] static acidic conditions,[108] or cosurfactant methods.[110] The synthesis of spheres of diameters in the submicrometer to micrometer range was successfully achieved by fine-tuning the reaction conditions such as the relative amounts of reagents (alkoxysilane, water, and ammonia) and the reaction temperature. The surface area and pore size of the mesoporous silica microspheres were regulated by using either *n*-alkyltrialkoxysilanes of various kinds or surfactants at different concentrations.[109]

4.430.3.4.1.2. Mesoporous silica nanospheres

The mesoporous silica microspheres are potentially useful for many nonbiological applications, but these particles are too big for many important biotechnological and biomedical applications. For example, these materials cannot serve as efficient agents for gene transfection or as carriers for intracellular drug delivery because mammalian cells cannot efficiently engulf large particles via endocytosis. Also, mesoporous silica microspheres are within the size window of bacteria and could potentially trigger acute inflammatory response *in vivo*.

Ying and coworkers[110] recently reported a fluorocarbon-surfactant-mediated synthesis for MSN. The particle size of the material was tuned from 50 to 300 nm, and different types of mesostructures, including 3D cubic, 2D hexagonal, foam like, and disordered (named IBN series), were successfully produced. The Bein and coworkers[111] recently reported the synthesis of colloidal mesoporous silica (CMS) material by introducing triethanolamine (TEA) to the condensation reaction of TEOS. By tuning the ratio of TEOS to TEA, they demonstrated that the particle size of CMS could be varied from 50 to 100 nm with a high surface area ($>1000\,m^2\,g^{-1}$) and a large pore volume ($\sim 1\,cm^3\,g^{-1}$). The pore geometry in CMS is unique: the pores grow radially from the center of the particle to the periphery.[111] Okubo and coworkers[112] used ethylene glycol (EG) in their synthesis to improve structural order and control particle size and morphology. The pore size of their MSN is around 2 nm when using cetyltrimethylammonium bromide (CTAB) as the structure-directing agent.

Lin and coworkers[113] recently demonstrated that MSN with adjustable pore sizes ranging from 3 to 6 nm could be synthesized by including mesitylene as a pore-expander. Their method took advantage of the well-known synthesis of MCM-41 mesoporous silica, in which TEOS was used as a silica source, a cationic surfactant, CTAB, was used as a structure-directing agent, water was used as a solvent, and sodium hydroxide was used as a morphological catalyst.[81] The template surfactant (CTAB) was then removed from the as-synthesized material either by solvent extraction (HCl in methanol solution) or by calcination to generate pores. Using this method, particles with the following characteristics can be made: an average particle diameter of 100 nm, an average surface area of $900\,m^2\,g^{-1}$, average pore size of 2 nm, an average pore volume of $0.9\,cm^3\,g^{-1}$, abundant surface silanol groups (about 30 mol%), and a hexagonal porous channel structure. Recently, Lelong *et al.*[115] conducted an extensive study on the effect of surfactant (CTAB) concentrations on the morphology of MSN and demonstrated the key role that the Si:CTAB ratio plays on both the texture and the morphology. They proposed that for the smallest surfactant concentration (0.1%), the internal hexagonal arrangements of pores are quite pronounced and in the region of the critical micelle concentration (CMC), and the surfactant molecules remain free or poorly organized into dynamic nanometer-sized spheres or cylinders. In this two-phase system, the positively charged free surfactant molecules present in the water phase become electrostatically adsorbed by the negatively charged silicate oligomers present in the TEOS phase, and a water-in-oil type microemulsion occurs. The nucleation and growth of the particles then obtains fully, following an order–disorder phase transition. The small amount of ethyl alcohol generated by the hydrolysis of TEOS acts as cosurfactant, leading to the formation of spherical objects in order to minimize the surface energy. The excess silicic acid in the medium then condenses around the mesoporous core, leading to the formation of an amorphous silica shell. When the Si:CTMABr ratio is lowered, the mean length of the cylindrical pores and the size of the bundle increase correspondingly. While the amount of TEOS is fixed for all the samples, the ethanol, which is the product of its hydrolysis by water, becomes progressively less efficient as a cosurfactant. Consequently, the mesoporous particles become larger with less rounded shapes, which is consistent with their microscopic observations (**Figure 5**).

4.430.4. Physicochemical Properties and Characterization

4.430.4.1. Properties

4.430.4.1.1. Product crystallinity

Although the pore walls of mesoporous silica materials are amorphous, the particles themselves have a long-range order. They are classified as semicrystalline solids. In general, the surfactants with 12, 14, and 16 carbon atoms, that is, C_{12}, C_{14}, and C_{16}, give good MCM-41 samples. Surfactants that have more than 18 carbon atoms ($\geq C_{18}$) are difficult to dissolve; on the other hand, the lower-molecular-weight surfactants ($\leq C_{10}$) seem to find it difficult to self-organize and, as a result, materials with broader pore size distributions (PSD) are produced. However, the use of a mixture of Gemini $[C_{20}H_{41}N(CH_3)_2(CH_2)_3N(CH_3)_2C_{20}H_{41}]$ and *n*-alkyltrimethylammonium ($n = 20$) surfactants results in the formation of good-quality MCM-41 with five or more well-indexed XRD reflections **Figure 6**.[116] A suitable mixture of *n*-alkyltrimethylammonium and *n*-alkyltriethylammonium surfactant cations ($n = 12 - 22$) gives highly ordered MCM-41 with various pore diameters as a result of the controlled packing of micelles.[71] The crystallinity and quality of MCM-41 materials can be altered by changing the pH of the synthesis gel and by the nature of the pH adjustment process. It has been

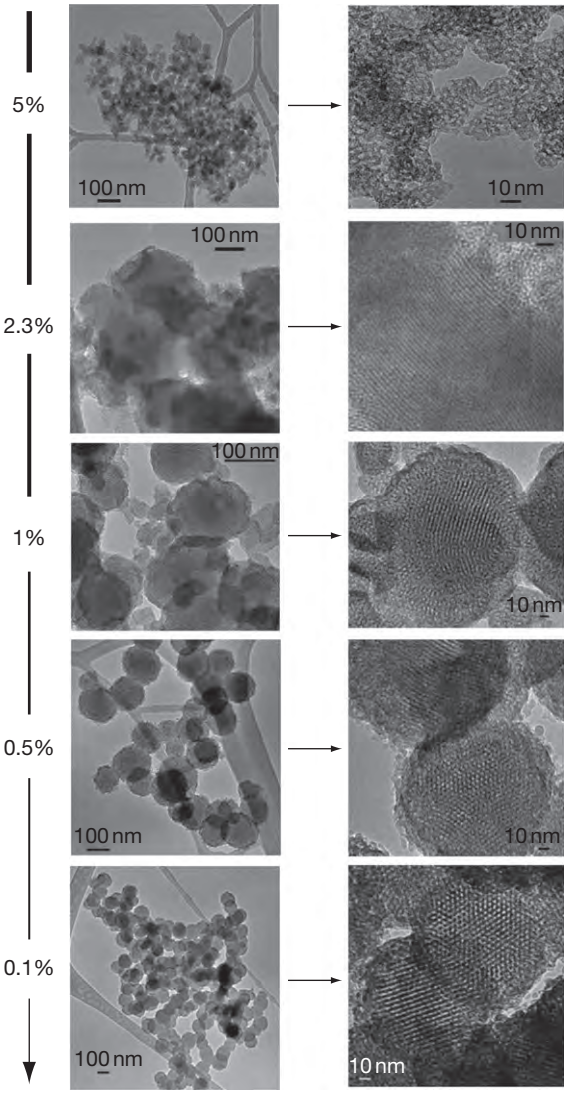

Figure 5 Transmission electron micrographs showing the evolution of the morphology and texture of the mesoporous silica with decreasing CTMABr concentration. Reproduced from Lelong, G.; Bhattacharyya, S.; Kline, S.; Cacciaguerra, T.; Gonzalez, M. A.; Saboungi, M. L. *J. Phys. Chem. C*. **2008**, *112*, 10674–10680.

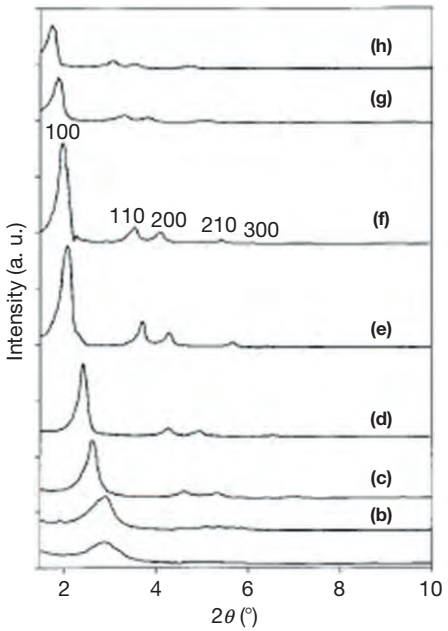

Figure 6 X-ray powder diffraction patterns of calcined MCM-41 prepared using surfactants of different carbon chain length. (a) C_8TMAB, (b) C_{10}TMAB, (c) C_{12}TMAB, (d) C_{14}TMAB, (e) C_{16}TMAB, (f) C_{18}TMAB, (g) C_{20}TMAB, and (h) C_{22}TMAB. Reproduced from Lin, H. P.; Mou, C. Y. *J. Cluster Sci*. **1999**, *10*, 271–293, with permission from Springer.

shown that the rapid adjustment of pH results in poorly crystallized/less ordered MCM-41, whereas a gradual or delayed adjustment of pH provides more time for the micelles and silica polyionic species to assemble into a more ordered structure.[116] Ryoo and Kim[117] reported that the repeated adjustment of pH can produce highly crystallized MCM-41. Their method include an initial heating of synthesis gel to 100 °C for 1 day. The resulting mixture was cooled to room temperature, and the pH was adjusted to 10 by the dropwise addition of 30 wt% acetic acid and vigorous stirring, followed by heating as before. The latter procedure was repeated twice before the solid product was removed from the reactor. Edler and White[118] reported a further development of the aforementioned method by the optimization of the various acids for maintaining the pH. The best result, with sharp diffraction peaks, was achieved with sulfuric acid and a pH of 9–10. Long-range structural ordering, as well as pore size uniformity, can be achieved by the appropriate choice and control of synthesis conditions, such as the pH of the synthesis gel, such that the polymerization equilibrium is shifted toward the mesophase region of MCM-41 (Figure 6).[117,118]

4.430.4.1.2. Thermal and hydrothermal stability

A material should have good thermal and hydrothermal stabilities in order to be utilized in different practical applications. MCM-41 exhibits a high thermal stability of up to 900 °C in dry air or in air having a low water vapor pressure.[118–122] Furthermore, it is also stable under acidic conditions, but it degrades readily in basic environments because of the known fact that (amorphous) silica dissolves partially in water, especially at high pH.[122,123] On the other hand, MCM-41 has a low hydrothermal stability in water, in aqueous solutions, and even in air saturated with water vapor.[124–126] In addition, the mechanical compressive force builds up because of the hydrolysis of siloxane bonds in the presence of adsorbed water, which results in a structural collapse, as is evident from the XRD patterns shown in Figure 7.[124]

It has been shown that MCM-41 structures can be stabilized by synthesizing in the presence of various salts[125,126] or ion exchange after synthesis.[127] Furthermore, chemical and mechanical stabilities of MCM-41 can be enhanced by post-synthesis treatment with acid,[128–130] modification by silylation,[63,131] or removal of silanol groups by alumina.[132] Igarashi *et al.*[133] have recently reported an increased stability of organically modified MCM-41 by a single-step synthesis procedure.

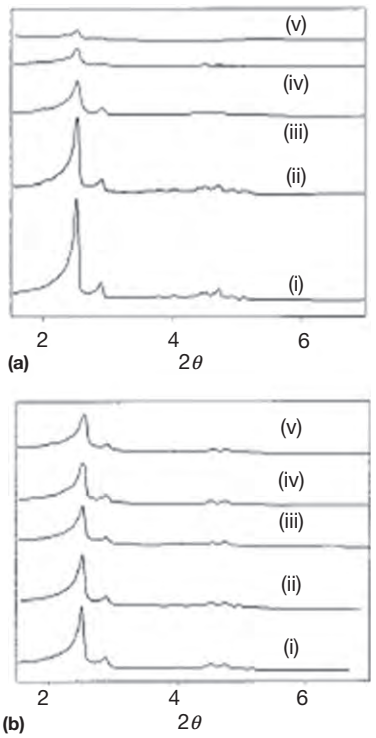

Figure 7 Change in X-ray diffraction pattern of MCM-48 by compression: (a) under air and (b) under dry nitrogen. (i) 0, (ii) 441, (iii) 882, (iv) 1323, and (v) 1764 kg cm^{-2}. Reproduced from Tatsumi, T.; Koyano, K. A.; Tanaka, Y.; Nakata, S. *Chem. Lett.* **1997**, *26*, 469–470, with permission from The Chemical Society of Japan.

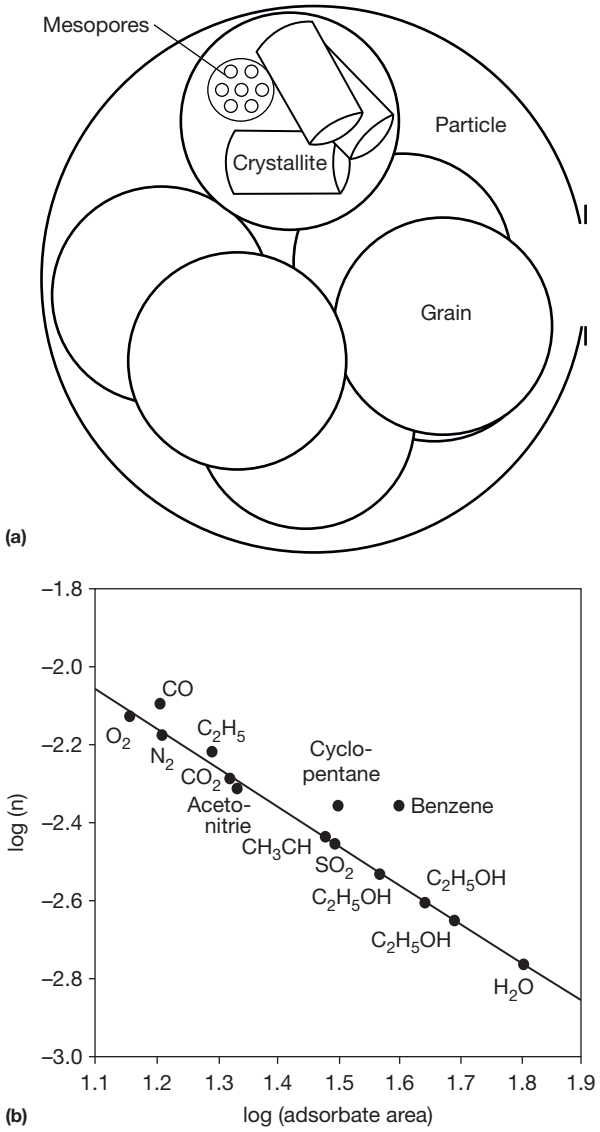

Figure 8 (a) Meso- and macro-structure of MCM-41. (b) Fractal characterization of MCM-41 by the molecular tiling method. Reproduced from Gregg, S. J.; Sing, K. S. W. *Adsorption Surface Area and Porosity*; Academic Press: New York, 1982.

4.430.4.2. Characterization

Various techniques have been successfully employed to elucidate structure and wall thickness, such as XRD, small angle X-ray scattering (SAXS), and transmission electron microscopy combined with electron diffraction. On the other hand, gas adsorption measurements[134] are the most widely used techniques to determine surface area, pore size, and PSD. A combination of these methods has demonstrated[135] that MCM-41 has a multilevel structure comprising mesopores, crystallites, and grains within the parent particles, as depicted in Figure 8(a). Typically, the crystallites have sizes of 30–50 nm, while the grain diameter is around 0.3–0.8 μm. The fractal interpretation of adsorption data for various compounds has revealed that the mesopore surface is smooth on molecular scales. This is evident from the correlation between monolayer capacity and molecular area,[136] as shown in Figure 8(b), yielding a slope of − 1 on the logarithmic coordinates.

Several techniques are available for estimating the pore sizes of MCM-41. Although each method has a limited length-scale of applicability for probing the structure, N_2 adsorption at its normal boiling point is the most popular because of its utility for both micropores and mesopores, and because of its convenience and low cost.

4.430.4.2.1. Gas adsorption methods

For the design and actual use of porous materials in the field of absorption and catalysis, evaluation of the pore structure is absolutely essential. The pore morphology, that is, PSD and connectivity of the pore network, dictate the transport and reaction properties of porous solids, for example, adsorbents and catalyst supports. The most widely used method, nitrogen sorption isotherms provide the input data for the analysis models to determine pore structure information.[134] For MCM-41, typical sorption measurements follow the type IV isotherm consisting of two steps, as illustrated in Figure 9, with a high porosity ($0.7–1.2\ cm^3\ g^{-1}$) and a large surface area exceeding $900\ m^2\ g^{-1}$. The prevailing adsorption process at low relative pressures ($P/P_0 < 0.25$) is the formation of a monolayer of adsorbed molecules. At higher pressures ($P/P_0 > 0.25$), the adsorption in mesopores leads to multilayer formation until condensation takes place, providing a sharp increase in adsorption volume. As the mesopores are filled, the

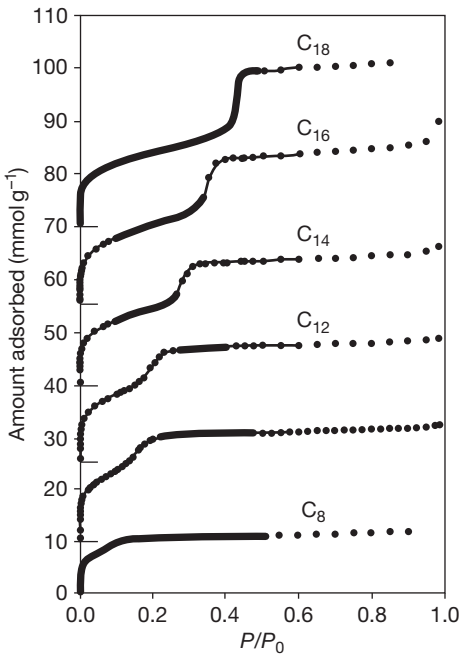

Figure 9 Nitrogen adsorption isotherms at 77.4 K on various MCM-41 samples prepared using surfactants of different carbon chain length (C_x, $x = 8$, 10, 12, 14, 16, 18). Reproduced from Gregg, S. J.; Sing, K. S. W. *Adsorption Surface Area and Porosity*; Academic Press: New York, 1982.

adsorption continues on the external surface. The isotherms are usually reversible for pores smaller than a critical size and exhibit a sharp inflection at $P/P_0 = 0.25 - 0.5$, depending on the pore size of the material. Qualitatively, the step in the isotherms reflects a narrow and uniform distribution of the pore size, while its height indicates the pore volume. The desorption via evaporation of the adsorbate from the mesopores occurs at a pressure lower than that of capillary condensation and results in hysteresis. In the case of disordered samples, the step of the isotherm becomes less sharp for the samples with the largest pores, suggesting a widening of the PSD. In general, the hysteresis originates as a result of the differences in the pore mouth sizes and pore bodies or because of the different adsorption and desorption behaviors in near-cylindrical pores. Materials with uniform pore sizes and shapes exhibit type H1 hysteresis (i.e., parallel adsorption and desorption branches), whereas those with nonuniform pore sizes and shapes show type H_2 hysteresis (i.e., nonparallel adsorption and desorption branches). In the latter case, condensation takes place in each section at the relative pressure provided by the Kelvin equation, but evaporation from the pore body cannot occur while the pore mouth remains filled. On the other hand, in the former case, the meniscus is cylindrical during condensation and hemispherical during evaporation.

Gas adsorption isotherms for a wide variety of gases, including nitrogen, oxygen, argon, water, etc., have been measured for MCM-41. It is interesting to note that MCM-41 adsorbs much greater amounts of organic species than water. For example, the amount adsorbed exceeds 0.4 g g^{-1} for cyclohexane, but is < 0.05 g g^{-1} for water at $P/P_0 = 0.4$,[68] which reveals that the internal surface is quite hydrophobic, albeit with the presence of silanol groups. On the other hand, trimethylsilation renders the materials repellent even to liquid water.[18,26]

4.430.4.2.2. Surface area

The commonly used BET surface area (S_{BET}) represents the total surface area rather than the mesopore area. Recent studies[137] have indicated that the BET method overestimates the surface area of MCM-41, possibly as a result of the considerable overlap of monolayer and multilayer adsorption in the recommended range of relative pressures ($P/P_0 = 0.05 - 0.35$).

4.430.4.2.3. Pore volume

The BET model still remains one of the most widely used methods for estimating the pore volume from adsorption measurements. The density of adsorbed N_2 has been assumed to be equal to the density of liquid N_2 at the same temperature.[134] However, the *t*-plot method is often used to obtain accurate and reliable pore volume data. The method is based on the observation that a plot of the adsorbed volume per unit surface area, that is, the statistical thickness (t) of the adsorbed layer versus pressure follows a single curve, independent of the solid.

4.430.4.2.4. Pore size

Several geometrical and classical methods have been applied for the determination of the mesopore diameter (D) of MCM-41. The Kelvin equation provides a useful model to transform the adsorption data into a PSD.[138,139] This model is widely used but cannot be applied for pore diameters below 2 nm. Below this pore size, the forces exerted by the pore wall become crucial, and the liquid cannot be considered a fluid with bulk properties. Theoretical calculations suggest that the properties of fluids in microporous structures are highly sensitive to the size of the pores. The established methods for the determination of the pore size are based on the Kelvin model or its variants, such as the Barrett–Joyner–Halenda (BJH)[140] and Broekhoff–de Boer (BdB)[141] methods, or other approaches such as the Horváth–Kawazoe (HK)[142] and Saito–Foley (SF)[143] methods and the density function theory (DFT) of Tarazona *et al.*[144] that consider the fluid–solid interaction.

4.430.5. Unique Biomaterial Considerations

As indicated earlier, the marked characteristics of MSNs are as follows:

(i) *Tunable particle size*: the particle size of MSNs can be controlled in the range between 50 and 300 nm. (ii) *Stable and rigid framework*: these MSNs are more resistant to heat, pH, mechanical stress, and hydrolysis-induced degradations than polymeric nanospheres. (iii) *Uniform and tunable pore size*: the controlled synthesis can provide very narrow PSD, and the pore diameter can be tuned between 2 and 15 nm. (iv) *High surface area and large pore volume*. As mentioned earlier, the total surface area (~ 900 m^2 g^{-1}) and pore volume (~ 0.9 cm^3 g^{-1}) are very large.

These unique properties render MSN very attractive for application as molecular hosts and delivery vehicles for drugs

and biological molecules. Here, we discuss some of the important considerations in the use of MSNs as biomaterials, including encapsulation strategies, surface functionalization, and biocompatibility.

4.430.5.1. Host–Guest Encapsulation

Materials that can be utilized in the area of controlled release of biomolecules or drug delivery could have high affinity for absorbing certain drug molecules, yet they would willingly release the same cargo upon reaching the designated sites.

The aforementioned versatility of silica nanospheres makes them ideal for the adsorption and release of a variety of compounds by organically modifying them with the desired functional group that is attached to and within the walls of the pores. Furthermore, the pore size and pore volume can be tuned to protect the encapsulated drug from unwanted leakage and to optimize the drug loading capacity.

Enzymes, proteins, and biocatalysts with high selectivities have been widely used in the food industry. Encapsulated enzymes and other proteins within inorganic host materials (**Figure 10**)[145] and especially in controlled porous glasses (CPG) represent one of the most rapidly growing fields over the past few years. It has already been established that biomolecules immobilized in inorganic matrices retain their functional characteristics to a large extent. However, the main disadvantages of CPG materials in adsorption studies are their high cost and the rapid decrease of the surface area with increasing pore size (30–200 nm). A comprehensive review by Hartmann[146] outlined the advantages of mesoporous MCM-41-based materials in bioadsorption. For the immobilization of biomolecules, the general procedures can be broadly categorized into two types, depending on the interaction between the biomolecules and host: covalent binding and adsorption, or encapsulation. For the applications in the aforementioned area, adsorption or encapsulation is highly preferred as it will not chemically affect the encapsulated molecules and their easy release when needed.

One of the earliest reports on immobilization by adsorption of globular enzymes, cytochrome c (bovine heart), papain (papaya latex), and trypsin (bovine pancreas), in the mesoporous molecular sieve MCM-41 was made by Diaz and Balkus[147] The efficiency of papain and trypsin immobilization was found to be pH dependent and favorable at pH values <7, while immobilization of cytochrome c was more efficient at pH >7 and less susceptible to pH changes. The adsorption of vitamin B2 (riboflavin) onto MCM-41 and MCM-48 was studied by Kisler *et al.*[148] The observation that MCM-41 shows significantly higher adsorption of vitamin B2 than MCM-48 (0.015 vs. 0.005 mmol g^{-1}) was suggested to result from the difference in pore sizes. Adsorbed vitamin B2 has a maximum size of ~60% of the MCM-48 pore size, and thus steric hindrance is believed to play an important role. Desorption experiments have revealed that some vitamin B2 remains adsorbed, showing that the adsorption is not completely reversible. Recently, Farzaneh *et al.*[149] found that Vit-B12/MCM-41 successfully catalyzes the oxygen transfer of tert-butylhydroperoxide (TBHP) to norbornene and trans-2-hexene-1-ol and formation of the corresponding epoxides with 90% reactivity and 100% selectivity.

For controlled-release applications, it has already been established that silica is able to store and gradually release therapeutically relevant drugs such as antibiotics[150,151] and others.[152] Furthermore, silica is used to enhance the biocompatibility of several other drug delivery systems such as magnetic nanoparticles,[153–155] biopolymers,[156] and micelles.[157]

Recently, Lin and coworkers[158–162] showed the ease and efficacy of the MSN materials for controlled release of different drug and biomolecules within the cells. They also showed the

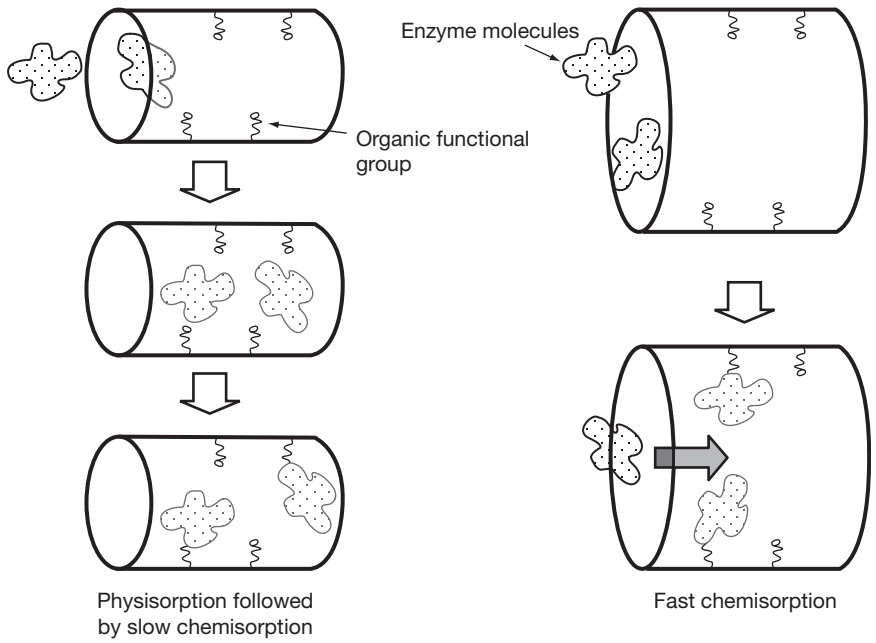

Figure 10 Illustrations showing two possible mechanisms of protein binding onto the functionalized surface of mesoporous silica. Reproduced from Yiu, H. H. P.; Wright, P. A. *J. Mater. Chem.* **2005**, *15*, 3690–3700, with permission from The Royal Society of Chemistry.

biocompatibility of this material. In particular, they successfully demonstrated that phenylboronic acid-functionalized MSN can serve as an efficient codelivery system for saccharide-responsive controlled release of insulin and cell membrane impermeable cyclic adenosine monophosphate (cAMP). The good biocompatibility, cellular uptake properties, and efficient intracellular release of cAMP are encouraging results for future *in vivo* controlled-release biomedical applications.

4.430.5.2. Surface Functionalization

Surface functionalization is a key step for the materials to be used in biological applications. For example, if one needs to formulate a targeted drug carrier, it is absolutely necessary to functionalize the surface of the carrier with cell-specific receptor molecules. At the same time, the availability of functionalization chemistry without the use of harsh chemicals would be an added advantage for biological applications.

In general, three strategies are pursued to tailor the microenvironment of mesoporous silica materials: cocondensation (one-pot synthesis), grafting (postsynthesis modification), and imprint coating method.[163,164] The cocondensation (precipitation) method utilizes various (organo)siloxane precursors in a one-pot (hydrothermal) sol–gel process.[81,165–174] This method is particularly viable for the incorporation of organic moieties into the pore walls as shown in the case of bifunctional periodic mesoporous organosilicas.[175–179] The advantages of this method are (a) it is applicable to a wide variety of organoalkoxysilanes; (b) it is suitable for a wide range of reaction conditions; (c) the coverage of functional groups is homogeneous; and (d) the loading amount of functional groups is high, and there is no dramatic effect on the structural ordering of the pores. Phase separation of the precursors and the cleavage of Si–C bonds during the sol–gel reaction and during surfactant removal have to be avoided in the cocondensation reactions. Lin and coworkers[180] investigated the different electrostatic matching effects of various anionic organoalkoxysilanes, such as thiolate-, carboxylate-, and sulfonate-containing organoalkoxysilane, on the degree of organic functionalization of the MSN. By cocondensation of two organoalkoxysilanes, they were able to introduce both acidic and basic functional groups into MSN.[181] This bifunctionalized MSN possesses interesting chemical properties that suggest a variety of novel applications.

Although the aforementioned approach is proposed to afford a more uniform distribution of functional groups protruding into the channel space, the *postsynthesis* approach allows, in a unique way, the grafting of chemically more precious organic functionalities, prone to hydrolysis and elimination reactions, onto calcined and dehydrated mesoporous silica materials.[182–184]

Grafting is commonly carried out by silylation on free ($\equiv$Si–OH) and geminal silanol ($=$Si(OH)$_2$) groups. If a high surface coverage with functional groups is desired, it is important to maintain a large amount of surface silanol groups after removal of the surfactant. Surfactant removal is usually carried out either by calcination or by appropriate extraction methods. Calcination promotes condensation of unreacted silanol groups, and many surface functional groups are lost at typical calcination temperatures (400–550 °C). Extraction processes (e.g., with acid/alcohol mixtures for cationic surfactants or with alcohols for neutral surfactants) minimize loss of surface silanols.

The most remarkable feature of the grafting method is the ability to selectively functionalize the external or the internal (pore) surfaces of the MSN. For example, we have demonstrated that 1,5,6-epoxyhexyltriethoxysilane (EHTES) can be successfully grafted on the external surface of MSNs before the removal of surfactant CTAB. The externally grafted groups can be further reacted; for example, in the case of EHTES, we were able to polymerize lactic acid on the external surface of MSN.[185] Recently, Tamanoi and coworkers[186] also modified the external surface of MSNs with trihydroxysilylpropyl methylphosphonate (THMP) after particle formation in order to reduce the aggregation and to increase the stability of the particles in aqueous solution.

In the grafting processes described earlier, the silylation reagents were typically added under dry conditions to avoid hydrolysis and self-condensation of the reagents away from the surface of MSN. When silylating under anhydrous conditions, the hydrophilic portion of the silica surface is preserved and the resulting functional groups are relatively isolated. By employing just enough water in the process to form a monolayer on the pore surface, more homogeneous coverage of organoalkoxysilanes can be obtained, leading to a higher concentration of functional groups in the final product.[187]

Recently, Burleigh and coworkers[164] reported a new imprint coating method. They coated the mesoporous surface of MCM-41 with ligands that were already bound to metal ions, not just to the free ligands. When the metal ions were removed, the ligands were already positioned for complexation with metal ions of the same type. The selectivity to binding the original metal ions in competitive binding experiments was greater than in randomly functionalized mesoporous materials.

4.430.5.3. Biocompatibility

Biocompatibility is the key factor for the materials to be used in biological applications. The biocompatibility of sol–gel-derived silica materials is well documented (**Chapter 4.428, Sol–Gel Processed Oxide Controlled Release Materials**).[188–192] Recently, Radin *et al.* extensively studied the *in vitro* and *in vivo* biocompatibility of sol–gel-derived silica micro granules, in our laboratory. They found excellent biocompatibility of silica macro granules both *in vitro* and *in vivo*; furthermore, they showed the potential use of these materials as controlled-release materials for the treatment of bone infections and as carriers for controlled delivery of drugs and larger biologically active molecules.[191,192] Given the particle size of MSN in the nanometer range and the difference in the sol–gel processing methodology, the biological response to these materials has recently come under investigation. Several reviews suggest that silica nanoparticles (solgels, xerogels, etc.) are biocompatible and degrade over time in the body.[193–196] Recently, Fisichella *et al.* studied the cytotoxicity of MSN in Henrietta Lacks (HeLa) and astrocytes cells and found that these materials are nontoxic up to a significant dose level of 100 μg ml^{-1}. More interestingly, they found that the most widely used 3-(4,5-dimethylthiazol-2-yl)-2,5-diphenyltetrazolium bromide (MTT) assay for evaluation of

cytotoxicity gives false positive results for toxicity as it is also found for other nanomaterials.[197,198] They suggested that at least three different assay techniques be performed for evaluation of the cytotoxicity of these materials. The biocompatibility of MSN with and without surface functionalization has also been tested by different methods. The viability and proliferation of various mammalian cells indicates that these properties are not affected by the internalization of MSN at concentrations below $100\,\mu g\,ml^{-1}$ per 105 cells even after seven cell cycles. Cell membrane integrity is also conserved after uptake of MSN as determined by selective DNA staining followed by flow cytometry.[199] Microscopic analysis shows normal cell morphology upon uptake of MSN. Mitochondrial activity remains at normal levels as determined by colorimetric assay with MTT.[200,201] Growth rates for cells exposed to MSN are similar to those of cells grown in the absence of MSN.[199,202] The long-term biocompatibility and the biodegradation of MSN have not yet been determined and understood, given the fact that this area of research is in its infancy.

4.430.6. Conclusion

In this chapter, we have conveyed the enormous potential of mesoporous silica nanoparticles for applications in the production of new materials and their use as biomaterials.

The increasing number of synthesis routes under development will greatly facilitate the preparation of materials with properties tailored to a specific application. It is remarkable that this explosion in the range of synthetic routes and targeted applications has taken place in little over a decade since the original discovery of the material.[18–21]

As for the utilization of these materials in biology, considerable progress has been made toward their application in the fields of drug delivery, gene delivery, and controlled release. While these results are encouraging and show great potential for future applications, new breakthroughs are still needed for this type of delivery system. Specifically, this system has not yet been extensively studied *in vivo*, so the necessary information regarding the blood circulation time, specificity toward the organs, long-term immunogenicity, and accumulation in different organs has yet to be determined. Such studies include the identification of the most appropriate animal models. In view of the targeted delivery of pharmaceuticals, surface functionalization is very important and needs to be explored with different ligands and receptor molecules.

Given that so much progress was achieved over a relatively short period of time, it can be anticipated that the major potential of mesoporous silica nanoparticles for biological use will soon be realized in the burgeoning field of nano-biomaterials.

References

1. Barton, T. J.; Bull, L. M.; Klemperer, W. G.; *et al*. *Chem. Mater*. **1999**, *11*, 2633–2656.
2. Ma, Y.; Tong, W.; Zhou, H.; Suib, L. *Microporous Mesoporous Mater*. **2000**, *37*, 243–252.
3. Cheetham, A. K.; Ferey, G.; Loiseau, T. *Chem. Int. Ed. Engl*. **1999**, *38*, 3269–3292.
4. Behrens, P. *Adv. Mater*. **1993**, *5*, 127–132.
5. Casci, J. L. *Stud. Surf. Sci. Catal*. **1994**, *85*, 329–356.
6. Corma, A. *Chem. Rev*. **1997**, *97*, 2373–2420.
7. Davis, M. E. *Ind. Eng. Chem*. **1991**, *30*, 1675–1683.
8. Smith, J. V. *Chem. Rev*. **1988**, *88*, 149–182.
9. Corma, A. *Chem. Rev*. **1995**, *95*, 559–614.
10. Imhof, A.; Pine, D. J. *Nature* **1997**, *389*, 948–951.
11. Yan, H.; Blanford, C. F.; Holland, B. T.; Smyrl, W. H.; Stein, A. *Chem. Mater*. **2000**, *12*, 1134–1141.
12. Ozin, G. A. *Accounts Chem. Res*. **1997**, *30*, 17–27.
13. Caruso, R. A.; Giersig, M.; Willig, F.; Antonietti, M. *Langmuir* **1998**, *27*, 6333–6336.
14. Zhao, D.; Huo, Q.; Feng, J.; Kim, J.; Han, Y.; Stucky, G. D. *Chem. Mater*. **1999**, *11*, 2668.
15. Antonelli, D. M. *Microporous Mesoporous Mater*. **1999**, *33*, 209.
16. Davis, M. E. *Nature* **2002**, *417*, 813.
17. Schuth, F., Sing, K. S. W., Weitkamp, J., Eds.; In *Handbook of Porous Solids*; Wiley-VCH: Weinheim, 2002; p 1311.
18. Kresge, C. T.; Leonowicz, M. E.; Roth, W. J.; Vartuli, J. C.; Beck, J. S. *Nature* **1992**, *359*, 710.
19. Yanagisawa, T.; Shimizu, T.; Kuroda, K.; Kato, C. *Bull. Chem. Soc. Jpn*. **1990**, *63*, 988.
20. Beck, J. S.; Vartuli, J. C.; Roth, W. J.; *et al*. *J. Am. Chem. Soc*. **1992**, *114*, 10835.
21. Inagaki, S.; Fukushima, Y.; Kuroda, K. *J. Chem. Soc. Chem. Commun*. **1993**, *1993*, 680.
22. Zhao, X. S.; Lu, G. Q.; Millar, G. J. *Ind. Eng. Chem. Res*. **1996**, *35*, 2075–2090.
23. Selvam, P.; Bhatia, S. K.; Sonwane, C. G. *Ind. Eng. Chem. Res*. **2001**, *40*, 3237–3261.
24. Bhattacharyya, S.; Lelong, G.; Saboungi, M. L. *J. Exp. Nanosci*. **2006**, *1*, 375–395.
25. Rouquerol, J.; Avnir, D.; Fairbridge, C. W.; *et al*. *Pure Appl. Chem*. **1994**, *66*, 1739–1758.
26. Beck, J. S. *Method for synthesizing mesoporous crystalline materials*. U.S. Patent 5,057,296, 1991.
27. Kresge, C. T.; Leonowicz, M. E.; Roth, W. J.; Vartuli, J. C. *Composition of synthetic porous crystalline material; its synthesis*. U.S. Patent 5,102,643, 1992.
28. Kresge, C. T.; Leonowicz, M. E.; Roth, W. J.; Vartuli, J. C. *Synthesis of mesoporous crystalline material*. U.S. Patent 5,102,643, 1992.
29. Chiola, V.; Ritsko, J. E.; Vanderpool, C. D. *Process for producing low-bulk density silica*. U.S. Patent 3,556,725, 1971.
30. Di Renzo, F.; Cambon, H.; Dutartre, R. *Microporous Mater*. **1997**, *10*, 283–286.
31. Zhao, D.; Feng, J.; Huo, Q.; *et al*. *Science* **1998**, *279*, 548–552.
32. Huo, Q.; Margolese, D. I.; Ciesla, U.; *et al*. *Nature* **1994**, *368*, 317–321.
33. Feng, P.; Bu, X.; Stucky, G. D.; Pine, D. J. *J. Am. Chem. Soc*. **2000**, *122*, 994–995.
34. Chen, C. Y.; Xiao, S. Q.; Davis, M. E. *Microporous Mater*. **1995**, *4*, 1–20.
35. Tanev, P. T.; Pinnavaia, T. J. *Science* **1995**, *267*, 865–867.
36. Raman, N. K.; Anderson, M. T.; Brinker, C. J. *Chem. Mater*. **1996**, *8*, 1682–1701.
37. Yan, Y.; Hoshino, Y.; Duan, Z.; Chaudhuri, S. R.; Sarkar, A. *Chem. Mater*. **1997**, *9*, 2583–2587.
38. Schubert, U.; Hüsing, N.; Lorenz, A. *Chem. Mater*. **1995**, *7*, 2010–2027.
39. Wen, J.; Wilkes, G. L. *Chem. Mater*. **1996**, *8*, 1667–1681.
40. Liu, C. L.; Chen, H. X.; Komarneni, S.; Pantano, C. G. *J. Porous Mater*. **1995**, *2*, 245–252.
41. Smaihi, M.; Jermoumi, T.; Marignan, J.; Noble, R. D. *J. Membrane Sci*. **1996**, *116*, 211–220.
42. Lim, M. H.; Blanford, C. F.; Stein, A. *Chem. Mater*. **1998**, *10*, 467–470.
43. Kresge, C. T.; Leonowicz, M. E.; Roth, W. J.; Vartuli, J. C.; Beck, J. S. *Nature* **1992**, *359*, 710–712.
44. Corma, A.; Fomes, V.; Garcia, H.; Miranda, M. A.; Sabatier, M. J. *J. Am. Chem. Soc*. **1994**, *116*, 9767–9768.
45. Stöber, W.; Fink, A.; Bohn, E. *J. Colloid Interface Sci*. **1968**, *26*, 62–69.
46. Bogush, G. H.; Tracy, M. A.; Zukoski, C. F. *J. Non-Cryst. Solids* **1988**, *104*, 95–106.
47. Matsoukas, T.; Gulari, E. *J. Colloid Interface Sci*. **1988**, *124*, 252–261.
48. Matsoukas, T.; Gulari, E. J. *J. Colloid Interface Sci*. **1989**, *132*, 13–21.
49. Matsoukas, T.; Gulari, E. J. *J. Colloid Interface Sci*. **1991**, *145*, 557–562.
50. Bogush, G.; Zukoski, C. *The Colloid Chemistry of Graving Silica Spheres (Ceramic Microstructures '86)*; Plenum: New York, 1987; Some of these results are also presented in Brinker, C. J., Scherer, G. W., Eds.; 1st ed.; *Sol–Gel Science* Academic Press: Boston, 1990 pp 199–203.
51. Kim, S.; Zukoski, C. F. *J. Colloid Interface Sci*. **1990**, *139*, 198–212.
52. Bogush, G. H.; Zukoski, C. F. *J. Colloid Interface Sci*. **1991**, *142*, 1–18.
53. Bogush, G. H.; Zukoski, C. F. *J. Colloid Interface Sci*. **1991**, *142*, 19–34.

54. (a) Van Blaaderen, A.; Kentgens, A. P. M. *J. Non-Cryst. Solids* **1992**, *149*, 161–178; (b) Burneau, A.; *et al*. *Colloid. Surface. A* **1993**, *75*, 111–121; (c) Chen, S. L.; Dong, P.; Yang, G. H.; Yang, J. J. *J. Colloid Interface Sci*. **1996**, *180*, 237–241.
55. Walcarius, A.; Despas, C.; Bessière, J. *Microporous Mesoporous Mater*. **1998**, *23*, 309–313; (b) Brinker, C. J.; Scherer, G. W. *Sol–Gel Science*; Academic Press: San Diego, 1990.
56. Green, D. L.; Lin, J. S.; Lam, Y. F.; *et al*. *J. Colloid Interface Sci*. **2003**, *266*, 346–358; (b) Vogelsberger, W.; Seidel, A.; Breyer, T. *Langmuir* **2002**, *18*, 3027–3033; (c) Pontoni, D.; Narayanan, T.; Rennie, A. R. *Langmuir* **2002**, *18*, 56–59; (d) Boukari, H.; Lin, J. S.; Harris, M. T. *J. Colloid Interface Sci*. **1997**, *194*, 311–318; (e) Boukari, H.; Long, G. G.; Harris, M. T. *J. Colloid Interface Sci*. **2000**, *229*, 129–139; (f) Boukari, H.; Lin, J. S.; Harris, M. T. *Chem. Mater*. **1997**, *9*, 2376–2384.
57. Smith, D. D.; Sibille, L.; Cronise, R. J.; *et al*. *Langmuir* **2000**, *16*, 10055–10060.
58. Pang, B. J.; Qiu, K. Y.; Wei, Y.; Lei, X. J.; Liu, Z. F. *Chem. Commun*. **2000**, *6*, 477–478.
59. Pang, B. J.; Qiu, K. Y.; Wei, Y. *Chem. Mater*. **2001**, *14*, 2361–2365.
60. Pantazis, C. C.; Trikalitis, P. N.; Pomonis, P. J.; Hudson, M. J. *Microporous Mesoporous Mater*. **2003**, *66*, 37–51.
61. Park, S. E.; Kim, D. S.; Chang, J. S.; Kim, W. Y. *Catalysis Today* **1998**, *44*, 301–308.
62. Wu, C. G.; Bein, T. *Chem. Commun*. **1996**, *8*, 925–926.
63. Ying, J. Y.; Mehnert, C. P.; Wong, M. S. *Angew. Chem. Int. Ed*. **1999**, *38*, 56–77.
64. Soten, I.; Ozin, G. A. In *Supramolecular Organization and Materials Design*; Jones, W., Rao, C. N. R., Eds.;; Cambridge University Press: Cambridge, 2002; p 34.
65. Monnier, A.; Schüth, F.; Huo, Q.; *et al*. *Science* **1993**, *261*, 1299–1303.
66. Huo, Q.; Margolese, D. I.; Ciesla, U.; *et al*. *Chem. Mater*. **1994**, *6*, 1176–1191.
67. Firouzi, A.; Kumar, D.; Bull, L. M.; *et al*. *Science* **1995**, *267*, 1138–1143.
68. Chen, C. Y.; Burkett, S.; Li, H. X.; Davis, M. E. *Microporous Mater*. **1993**, *2*, 27–34.
69. Kresge, C. T.; Vartuli, J. C.; Roth, W. J.; Leonowicz, M. E. *Stud. Surf. Sci. Catal*. **2004**, *148*, 53–72.
70. Huo, Q.; Margolese, D. I.; Ciesla, U.; *et al*. *Nature* **1994**, *368*, 317–321.
71. Ryoo, R.; Ko, C. H.; Park, I. S. *Chem. Commun*. **1999**, 1413–1414.
72. Inagaki, S.; Sakamoto, Y.; Fukushima, Y.; Terasaki, O. *Chem. Mater*. **1996**, *8*, 2089–2095.
73. Davis, M. E.; Burkett, S. L. *Zeolites (Jpn.)* **1995**, *12*, 33.
74. Luan, Z.; He, H.; Zhou, W.; Klinowski, J. *J. Chem. Soc. Faraday Trans*. **1998**, *94*, 979–983.
75. Run, M.; Wu, S.; Wu, G. *Microporous Mesoporous Mater*. **2004**, *74*, 37–47.
76. Han, S.; Hou, W.; Xu, J.; Li, Z. *Colloid Polymer Sci*. **2004**, *282*, 1286–1291.
77. Zhu, Y.; Shi, J.; Chen, H.; Shen, W.; Dong, X. *Microporous Mesoporous Mater*. **2005**, *84*, 218–222.
78. Van Bavel, E.; Cool, P.; Aerts, K.; Vansant, E. F. *J. Porous. Mater*. **2005**, *12*, 65–69.
79. Li, Y.; Shi, J.; Hua, Z.; Chen, H.; Ruan, M.; Yan, D. *Nano Lett*. **2003**, *3*, 609–612.
80. Zhao, D.; Sun, J.; Li, Q.; Stucky, G. D. *Chem. Mater*. **2000**, *12*, 275–279.
81. Huh, S.; Wiench, J. W.; Yoo, J. C.; Pruski, M.; Lin, V. S. Y. *Chem. Mater*. **2003**, *15*, 4247–4256.
82. Zhao, W.; Li, Q. *Chem. Mater*. **2003**, *15*, 4160–4162.
83. Sayari, A.; Han, B. H.; Yang, Y. *J. Am. Chem. Soc*. **2004**, *126*, 14348–14349.
84. Grun, M.; Lauer, I.; Unger, K. K. *Adv. Mater*. **1997**, *9*, 254–257.
85. Kruk, M.; Jaroniec, M. *Chem. Mater*. **2000**, *12*, 222–230.
86. Mou, C. Y.; Lin, H. P. *Pure Appl. Chem*. **2000**, *72*, 137–146.
87. Yang, H.; Vovk, G.; Coombs, N.; Sokolov, I.; Ozin, G. A. *J. Mater. Chem*. **1998**, *8*, 743–750.
88. Gallis, K. W.; Araujo, J. T.; Duff, K. J.; Moore, J. G.; Landry, C. C. *Adv. Mater*. **1999**, *11*, 1452–1455.
89. Unger, K. K.; Kumar, D.; Grun, M.; *et al*. *J. Chromat. A* **2000**, *892*, 47–55.
90. Nooney, R. I.; Thirunavukkarasu, D.; Chen, Y.; Josephs, R.; Ostafin, A. E. *Chem. Mater*. **2002**, *14*, 4721–4728.
91. Ma, Y.; Qi, L.; Ma, J.; Wu, Y.; Liu, O.; Cheng, H. *Colloid. Surface. A* **2003**, *229*, 1–8.
92. Yano, K.; Fukushima, Y. J. *J. Mater. Chem*. **2003**, *13*, 2577–2581.
93. Alonso, B.; Clinard, C.; Durand, D.; Verona, E.; Massiot, D. *Chem. Commun*. **2005**, *13*, 1746–1748.
94. Lu, Y.; Fan, H.; Stump, A.; Ward, T. L.; Rieker, T.; Brinker, C. J. *Nature* **1999**, *398*, 223–226.
95. Lu, Y.; Ganguli, R.; Drewien, C. A.; *et al*. *Nature* **1997**, *389*, 364–368.
96. Brinker, C. J.; Lu, Y.; Sellinger, A.; Fan, H. *Adv. Mater*. **1999**, *11*, 579–576.
97. Baccile, N.; Grosso, D.; Sanchez, C. *J. Mater. Chem*. **2003**, *13*, 3011–3016.
98. Bore, M. T.; Rathod, S. B.; Ward, T. L.; Datye, A. K. *Langmuir* **2003**, *19*, 256–264.
99. Alonso, B.; Douy, A.; Véon, E.; Perez, J.; Rager, M. N.; Massiot, D. *J. Mater. Chem*. **2004**, *14*, 1–16.
100. Huo, Q.; Feng, J.; Schüth, F.; Stucky, G. D. *Chem. Mater*. **1997**, *9*, 14–17.
101. Miyake, Y.; Kato, T. *J. Chem. Eng. Jpn*. **2005**, *38*, 60–66.
102. Liu, S.; Cool, P.; Collart, O.; *et al*. *J. Phys. Chem. B* **2003**, *107*, 10405–10411.
103. Van Tendeloo, G.; Lebedev, O. I.; Collart, O.; Cool, P.; Vansant, E. F. *J. Phys. Condens. Matter*. **2003**, *15*, S3037.
104. Lebedev, O. I.; Van Tendeloo, G.; Collart, O.; Cool, P.; Vansant, E. F. *Solid State Sci*. **2004**, *6*, 489–498.
105. Israelachivi, N.; Mitchell, D. J.; Niham, B. W. *J. Chem. Soc. Faraday Trans*. **1976**, *72*, 1525–1568.
106. Huo, Q.; Margolese, D. I.; Stucky, G. D. *Chem. Mater*. **1996**, *8*, 1147–1160.
107. Gruen, M.; Lauer, I.; Unger, K. K. *Adv. Mater*. **1997**, *9*, 254–257.
108. Qi, L.; Ma, J.; Cheng, H.; Zhao, Z. *Chem. Mater*. **1998**, *10*, 1623–1626.
109. Kosuge, K.; Singh, P. S. *Microporous Mesoporous Mater*. **2001**, *44–45*, 139–145.
110. Han, Y.; Ying, J. Y. *Angew. Chem. Int. Ed*. **2005**, *44*, 288–292.
111. Moeller, K.; Kobler, J.; Bein, T. *Adv. Funct. Mater*. **2007**, *17*, 605–612.
112. Gu, J.; Fan, W.; Shimojima, A.; Okubo, T. *Small* **2007**, *3*, 1740–1744.
113. Slowing, I. I.; Trewyn, B. G.; Lin, V. S. Y. *J. Am. Chem. Soc*. **2007**, *129*, 8845–8849.
114. Huh, S.; Wiench, J. W.; Yoo, J. C.; Pruski, M.; Lin, V. S. Y. *Chem. Mater*. **2003**, *15*, 4247–4256.
115. Lelong, G.; Bhattacharyya, S.; Kline, S.; Cacciaguerra, T.; Gonzalez, M. A.; Saboungi, M. L. *J. Phys. Chem. C*. **2008**, *112*, 10674–10680.
116. Lin, H. P.; Mou, C. Y. *J. Cluster Sci*. **1999**, *10*, 271–293.
117. Ryoo, R.; Kim, J. M. *J. Chem. Soc. Chem. Commun*. **1995**, 711–712.
118. Edler, K. J.; White, J. W. *Chem. Mater*. **1997**, *9*, 1226–1233.
119. Chen, C. Y.; Burkett, S.; Li, H. X.; Davis, M. E. *Microporous Mater*. **1993**, *2*, 27.
120. Cu, G.; Ong, P. P. *J. Phys. Chem. Solids* **1999**, *60*, 943–947.
121. Chen, C. Y.; Xiao, S. Q.; Davis, M. E. *Microporous Mater*. **1993**, *2*, 17–26.
122. Chen, L. Y.; Jaenicke, S.; Chuah, G. K. *Microporous Mater*. **1997**, *12*, 323–330.
123. Iler, R. K. *The Chemistry of Silica*; Wiley: New York, 1979.
124. Tatsumi, T.; Koyano, K. A.; Tanaka, Y.; Nakata, S. *Chem. Lett*. **1997**, *26*, 469–470.
125. Kim, J. M.; Jun, S.; Ryoo, R. *J. Phys. Chem. B* **1999**, *103*, 6200–6205.
126. Ryoo, R.; Jun, S. *J. Phys. Chem*. **1997**, *101*, 317–320.
127. Kim, J. M.; Kwak, J. H.; Jun, S.; Ryoo, R. *J. Phys. Chem. B* **1995**, *99*, 16742–16747.
128. Hitz, S.; Prins, R. *J. Catal*. **1997**, *168*, 194.
129. On, D. T.; Zaidi, S. M. J.; Kaliaguine, S. *Microporous Mesoporous Mater*. **1998**, *22*, 211–224.
130. Edler, K. J.; White, J. W. *J. Mater. Chem* **1999**, *9*, 2611.
131. Koyano, K. A.; Tatsumi, T.; Tanaka, Y.; Nakata, S. *J. Phys. Chem. B* **1997**, *101*, 9436–9440.
132. Mokaya, R.; Jones, W. *Chem. Commun*. **1996**, 981–982.
133. Igarashi, N.; Tanaka, Y.; Nakata, S.; Tatsumi, T. *Chem. Lett*. **1999**, *1*, 1–2.
134. Gregg, S. J.; Sing, K. S. W. *Adsorption Surface Area and Porosity*; Academic Press: New York, 1982.
135. Sonwane, C. G.; Bhatia, S. K. *Langmuir* **1999**, *15*, 2809–2816.
136. Sonwane, C. G.; Bhatia, S. K.; Calos, N. *Langmuir* **1999**, *15*, 4603.
137. Kruk, M.; Jaroniec, M.; Sayari, A. *Langmuir* **1997**, *13*, 6267–6273.
138. Brunauer, S.; Mikhail, R. S.; Bodor, E. E. *J. Colloid Sci*. **1967**, *24*, 451–463.
139. Defay, R.; Prigogine, I.; Bellemans, A.; Everett, D. H. *Surface Tension and Adsorption*; Longmans: London, 1989.
140. Barrett, E. P.; Joyner, L. G.; Halenda, P. P. *J. Am. Chem. Soc*. **1951**, *73*, 373–380.
141. Broekhoff, J. C. P.; De Boer, J. H. *J. Catal*. **1967**, *9*, 8–14.
142. Horváth, G.; Kawazoe, K. *J. Chem. Eng. Jpn*. **1983**, *16*, 470–475.
143. Saito, A.; Foley, H. C. *AlChE J*. **1991**, *37*, 429–436.
144. Tarazona, P.; Marconi, M. B.; Evans, R. *Mol. Phys*. **1987**, *60*, 573–595.
145. Yiu, H. H. P.; Wright, P. A. *J. Mater. Chem*. **2005**, *15*, 3690–3700.
146. Hartmann, M. *Chem. Mater*. **2005**, *17*, 4577–4593.
147. Diaz, J. F.; Balkus, K. F. *J. Mol. Catal. B* **1996**, *2*, 115–126.
148. Kisler, J. M.; Dähler, A.; Stevens, G. W.; O'Connor, A. J. *Microporous Mesoporous Mater*. **2001**, *44–45*, 769–774.
149. Farzaneh, F.; Taghavi, J.; Malakooti, R.; Ghandi, M. *J. Mol. Catal. A Chem*. **2006**, *244*, 252–257.
150. Meseguer-Olmo, L.; Ros-Nicolas, M. J.; Vicente-Ortega, V.; *et al*. *J. Orthop. Res*. **2006**, *24*, 454–460.
151. Radin, S.; El-Bassyouni, G.; Vresilovic, E. J.; Schepers, E.; Ducheyne, P. *Biomaterials* **2004**, *26*, 1043–1052.

152. Kortesuo, P.; Ahola, M.; Karlsson, S.; Kangasniemi, I.; Yli-Urpo, A.; Kiesvaara, J. *Biomaterials* **1999**, *21*, 193–198.
153. Dormer, K.; Seeney, C.; Lewelling, K.; Lian, G.; Gibson, D.; Johnson, M. *Biomaterials* **2005**, *26*, 2061–2072.
154. Arruebo, M.; Galan, M.; Navascues, N.; *et al*. *Chem. Mater.* **2006**, *18*, 1911–1919.
155. Zhao, W.; Gu, J.; Zhang, L.; Chen, H.; Shi, J. *J. Am. Chem. Soc.* **2005**, *127*, 8916–8917.
156. Allouche, J.; Boissiere, M.; Helary, C.; Livage, J.; Coradin, T. *J. Mater. Chem.* **2006**, *16*, 3120–3125.
157. Huo, Q.; Liu, J.; Wang, L. Q.; Jiang, Y.; Lambert, T. N.; Fang, E. *J. Am. Chem. Soc.* **2006**, *128*, 6447–6453.
158. Trewyn, B. G.; Nieweg, J. A.; Zhao, Y.; Lin, V. S. Y. *J. Chem. Eng.* **2008**, *137*, 23–29.
159. Sun, W.; Fang, N.; Trewyn, B. G.; Lin, V. S. Y. *Anal. Bioanal. Chem.* **2008**, *391*, 2119–2125.
160. Slowing, I. I.; Vivero-Escoto, J. L.; Wu, C. W.; Lin, V. S. Y. *Adv. Drug Deliv. Rev.* **2008**, *60*, 1278–1288.
161. Kim, T. W.; Chung, P. W.; Slowing, I. I.; Lin, V. S. Y. *Nano Lett.* **2008**, *8*, 3724–3727.
162. Zhao, Y. N.; Trewyn, B. G.; Slowing, I. I.; Lin, V. S. Y. *J. Am. Chem. Soc.* **2009**, *131*, 8398–8400.
163. Chen, H. T.; Huh, S.; Lin, V. S. Y. *Catal. Prep.* **2007**, 45–73.
164. Burleigh, M. C.; Dai, S.; Hagaman, E. W.; Barnes, C. E.; Xue, Z. L. *ACS Symp. Series* **2001**, *778*, 146–158.
165. Sutra, P.; Brunel, D. *Chem. Commun.* **1996**, 2485–2486.
166. Burkett, S. L.; Sims, S. D. *Mann, S. Chem. Commun.* **1996**, 1367–1368.
167. Macquarrie, D. J. *Chem. Commun.* **1996**, 1961–1962.
168. Lim, M. H.; Blanford, C. F.; Stein, A. *J. Am. Chem. Soc.* **1997**, *119*, 4090–4091.
169. Hall, S. R.; Fowler, C. E.; Lebeau, B.; Mann, S. *Chem. Commun.* **1999**, 201–202.
170. Richer, R.; Mercier, L. *Chem. Commun.* **1998**, 1775–1776.
171. Mercier, L.; Pinnavaia, T. J. *Adv. Mater.* **1997**, *9*, 500–503.
172. Richer, R.; Mercier, L. *Chem. Mater.* **2001**, *13*, 2999–3008.
173. Yang, Q.; Kapoor, M. P.; Inagaki, S. *J. Am. Chem. Soc.* **2002**, *124*, 9694–9695.
174. Fan, H.; Lu, Y.; Stump, A.; *et al*. *Nature* **2000**, *405*, 56–60.
175. Asefa, T.; Kruk, M.; MacLachlan, M. J.; *et al*. *J. Am. Chem. Soc* **2001**, *123*, 8520–8530.
176. Burleigh, M. C.; Markowitz, M. A.; Spector, M. S.; Gaber, B. P. *Chem. Mater.* **2001**, *13*, 4760–4766.
177. Burleigh, M. C.; Jayasundera, S.; Spector, M. S.; Thomas, C. W.; Markowitz, M. A.; Gaber, B. P. *Chem. Mater.* **2004**, *16*, 3–5.
178. Xi, Y.; Wan, W.; Mokay, R. *J. Am. Chem. Soc.* **2005**, *12*, 790–798.
179. Alauzun, J.; Mehdi, A.; Reye, C.; Corriu, R. J. P. *J. Am. Chem. Soc.* **2006**, *128*, 8718–8719.
180. Radu, D. R.; Lai, C. Y.; Huang, J.; Shu, X.; Lin, V. S. Y. *Chem. Commun.* **2005**, 1264–1266.
181. Huh, S.; Chen, H. T.; Wiench, J. W.; Pruski, M.; Lin, V. S. Y. *Angew. Chem. Int. Ed.* **2005**, *44*, 1836–1840.
182. Elings, J. A.; Ait-Medour, R.; Clark, J. H.; Macquarrie, D. J. *Chem. Commun.* **1998**, 2707–2708.
183. Anwander, R.; Nagl, I.; Widenmeyer, M.; *et al*. *J. Phys. Chem. B* **2000**, *104*, 3532–3544.
184. Kidder, M. K.; Britt, P. F.; Zhang, Z.; *et al*. *J. Am. Chem. Soc.* **2005**, *127*, 6353–6360.
185. Radu, D. R.; Lai, C. Y.; Wiench, J. W.; Pruski, M.; Lin, V. S. Y. *J. Am. Chem. Soc.* **2004**, *126*, 1640–1641.
186. Lu, J.; Liong, M.; Zink, J. I.; Tammanoi, F. *Small* **2007**, *3*, 1341–1346.
187. Feng, X.; Fryxell, G. E.; Wang, L. Q.; Kim, A. Y.; Liu, J.; Kemner, K. M. *Science* **1997**, *276*, 923–926.
188. Turyna, B.; Milt, J.; Lgczka, A.; Cholewa, K.; Lgczka, M. *Biomaterials* **1996**, *17,* 1379–1366.
189. Koskinen, M.; Toriseva, M.; Jokinen, M.; Jalonen, H.; Salonen, J.; Kähäri, V.-M. *Mol. Ther.* **2005**, *11*, S422–S427.
190. Kortesuo, P.; Ahola, M.; Karlsson, S.; Kangasniemi, I.; Yli-Urpo, A.; Kiesvaara, J. *Biomaterials* **2000**, *21*, 193–198.
191. Radin, S.; El-Bassyouni, G.; Vresilovic, E. J.; Schepers, E.; Ducheyne, P. In *Bioceramics*; LeGeros, R. Z., LeGeros, J. P., Eds.; World Scientific: New York, 1998; Vol. 11; pp 529–532.
192. Radin, S.; El-Bassyouni, G.; Vresilovic, E. J.; Schepersc, E.; Ducheyne, P. *Biomaterials* **2005**, *26*, 1043–1052.
193. Li, X.; Zhang, L. X.; Dong, X. P.; Liang, J.; Shi, J. L. *Microporous Mesoporous Mater.* **2007**, *102*, 151–158.
194. Barbe, C.; Bartlett, J.; Kong, L. G.; *et al*. *Adv. Mat.* **2004**, *16*, 1959–1966.
195. Roy, I.; Ohulchanskyy, T. Y.; Pudavar, H. E.; *et al*. *J. Am. Chem. Soc.* **2003**, *125*, 7860–7865.
196. Slowing, I. I.; Vivero-Escoto, J. L.; Wu, C. W.; Lin, V. S. Y. *Adv. Drug Deliv. Rev.* **2008**, *60*, 1278–1288.
197. Fisichella, M.; Dabboue, H.; Bhattacharyya, S.; *et al*. *Toxicol. Vitro* **2009**, *23*, 697–703.
198. Wörle-Knirsch, J. M.; Pulskamp, K.; Krug, H. F. *Nano Lett.* **2006**, *6*, 1261–1268.
199. Slowing, I. I.; Trewyn, B. G.; Lin, V. S. Y. *J. Am. Chem. Soc.* **2006**, *128*, 14792–14793.
200. Chung, T. H.; Wu, S. H.; Yao, M.; *et al*. *Biomaterials* **2007**, *28*, 2959–2966.
201. Kim, J. S.; Yoon, T. J.; Yu, K. N.; *et al*. *J. Vet. Sci.* **2006**, *7*, 321–326.
202. Lai, C. Y.; Trewyn, B. G.; Jeftinija, D. M.; *et al*. *J. Am. Chem. Soc.* **2003**, *125*, 4451–4459.

4.431. Encapsulation of Cells (Cellular Delivery) Using Sol–Gel Systems

S Braun, Hebrew University of Jerusalem, Jerusalem, Israel

© 2011 Elsevier Ltd. All rights reserved.

4.431.1.	**Introduction**	530
4.431.1.1.	Declaration of Intents	530
4.431.1.2.	Sol–Gel Materials	530
4.431.2.	**Sol–Gel Silicates**	531
4.431.2.1.	Silicon and Life	531
4.431.2.2.	Biocompatible Preparation of Sol–Gel Silica	531
4.431.2.3.	Additives: The Design of Silicate Composites	532
4.431.2.4.	Self-Organizing Systems	533
4.431.2.5.	Design of Prosthetic Organs: A Case Study	534
4.431.2.5.1.	Silica precursors in the gas phase: the BioSil method	534
4.431.2.5.2.	Aminopropyl-silicate membrane electrically bonded by external anionic polymers	535
4.431.2.5.3.	Rational engineering of tissues and organs	536
4.431.3.	**Cell Delivery in Temperature-Sensitive Sol–Gel Systems**	537
4.431.3.1.	Mechanisms of Sol–Gel Transition in Temperature-Sensitive Materials	537
4.431.3.2.	Composition of Temperature-Sensitive Gels	537
4.431.3.2.1.	Natural and semisynthetic polysaccharides	537
4.431.3.2.2.	Chitosan-based cell-assisted cartilage repair vehicles	538
4.431.3.2.3.	Copolymers of *N*-isopropyl-acrylamide	539
4.431.3.2.4.	PNIPAA composites	539
4.431.3.2.5.	Polyoxyethylene–polyoxypropylene (poloxamer or Pluronic®) aqueous gels	539
4.431.3.2.6.	Graft copolymers with poloxamer blocks	540
4.431.3.2.7.	Triblock copolymers containing poly-hydroxylic acids	540
4.431.3.3.	Availability of Injectable Cell Carriers for Practical Medicine	540
4.431.4.	**Conclusion and Future Directions**	541
References		541

Glossary

Autologous chondrocyte implantation (ACI) A medical procedure for the repair of damage to cartilage. It consists of expanding in culture the population of the patient's own chondrocytes followed by their implantation at the site of the damage.

BioSil method The method of coating cells, tissues, or other materials with a thin layer of silicate, where the alkoxysilane derivatives are delivered to a wet surface in a gas face; proposed by Giovanna Carturan.

CP hydrogels Materials formed by grafting poloxamer 407 onto chitosan.

Edmonton protocol A medically accepted procedure for the treatment of type 1 diabetes mellitus. It consists of implantation of isolated human pancreatic islets by infusion into the portal vein.

Extracellular matrix (ECM) ECM is the noncellular part of animal tissues. ECM of connective tissues is made of three major components: (i) fibrous elements such as proteins collagen, elastin, or reticulin, (ii) link proteins such as fibronectin or laminin, and (iii) space filling glycosaminoglycans.

Lower critical solution temperature (LCST) The lowest temperature, at which a temperature-sensitive sol–gel system forms a gel.

Poloxamers (Pluronic®) Poloxamers or, otherwise, Pluronic® are nonionic triblock copolymers composed of a central hydrophobic chain of polyoxypropylene flanked by two hydrophilic chains of polyoxyethylene; invented in 1973 by Irving Schmolka.

RGD The adhesive peptide, Arg–Gly–Asp, which is a part of active-site sequence of cell-adhesive proteins. Surface integration of this peptide promotes cells adhesion.

Sol–gel transition The transition of a suspension of discreet colloidal particles in a liquid (sol) to an apparently solid material (gel) containing a continuous liquid and a continuous solid phase.

Temperature-sensitive sol–gel systems Materials that undergo reversible sol–gel transition with the change of temperature. In this context, the term is used exclusively for the systems that transit from sol at ambient temperature to gel at body temperature.

Abbreviations

CS	Chondroitin sulfate
HA	Hyaluronic acid
PEG	Polyethyleneglycol
PLGA	Copolymer of L-lactic and glycolic acids
PNIPAA	Poly-*N*-isopropyl-acrylamide

4.431.1. Introduction

4.431.1.1. Declaration of Intents

Since its inception in the early 1990s, the biological application of sol–gel materials became the pursuit of many ambitious scientific teams and individual scientists. The sol-to-gel transition offers many opportunities to the design of encapsulation media for biological materials, including biocatalysts, cells, and even organs. The liquid sol allows for mixing components and producing a homogeneous or microheterogeneous environment for biological material without subjecting it to damaging shear. The mixture could then be delivered to a site of application, cast into any geometry, and integrated into architecture by enveloping the mechanical, stress-bearing 'skeleton.' After gelation, the sol–gel material becomes apparently solid, retaining the form into which it was cast, resisting mechanical stress, providing for the sites of attachment and forming a stable environment for the sensitive biological systems.

With a little exaggeration, one may say that the pioneers of sol–gel biomaterials must have felt akin to our ancestors on the verge of the 'Bronze Age.' The stone could be chiseled into a variety of useful forms, but at an enormous expense of brute force and materials. Suddenly, for the first time, it was replaced with metal. The flow of molten metal eased into smooth symmetrical forms ideal for weapons and utensils. Then and now, this feeling of innovation has motivated a wealth of creativity. The number of publications devoted to sol–gel materials and their biological uses expanded almost overnight. Today, it numbers in thousands. Research was immediately followed by patent applications, as useful products, and, especially, medical products seemed within sure and certain reach. One of the reasons that Life Sciences are amply financed, that the Life Science faculty dominates almost every university, is the fact that these Sciences are the theoretical basis of modern medicine. Of course, medicine has immediately become the major theme of sol–gel materials' research. One can safely say that medicine-related publications constitute their majority.

The field of biological and medical applications of sol–gel materials abounds with excellent recent reviews.[1–7]

The life span of research articles and, especially, of reviews appearing in journals is usually limited to a few years. 'Comprehensive Biomaterials,' an ambitious enterprise, cannot afford to be so ephemeral; it has to keep its value for an extended period. Therefore, following a short historical overview, I shall direct the discussion toward applications that are directly relevant to cell immobilization and cell delivery in xenografts, artificial organs, and implants. I will limit myself to a few thoroughly chosen topics as formulated by the editors. I will attempt (i) to formulate the demands which medicine makes on a designer of new materials, (ii) to analyze the current 'state of art' in light of this demands, and (iii) to make an educated guess of future trends in practical medical application of sol–gel materials.

4.431.1.2. Sol–Gel Materials

This review will concern itself with two types of materials: (1) materials based on sol–gel silica and (2) thermosensitive sol–gel systems. The use of the term sol–gel indicates that these materials are colloids. A sol is a colloidal suspension of solid particles (1–0.5 nm) in a liquid. Condensation and precipitation of sol particles (sol–gel transition) lead to the formation of apparently solid gels (Figure 1). Sol–gel transition provides the primary essentials of cell encapsulation and delivery. Cells are dispersed and delivered at low shear in the sol, while the subsequent formation of the gel ensures cell anchorage and sequestration. Gels may be cast filling up cavities deposited on the surfaces in thin layers by dipping or spin coating, and, sometimes, made into fibers and spun.

Unlike free-living unicellular eukaryotes and prokaryotes, the cells of multicellular organisms lack the thick and sturdy cell wall and, thus, are extremely sensitive to conditions in their environment such as shear stress, changes in the pH or temperature, and presence of solvents and detergents. Animal cells need constant delivery of oxygen, complex nutrients, various growth factors, and signal chemicals. Frequently, they require the presence of other types of cells (organ architecture) and of the extracellular matrix with its general and specific interactions, signaling pathways, etc.

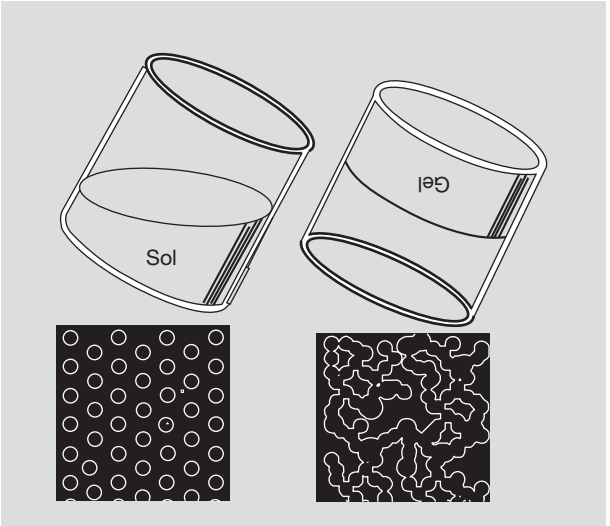

Figure 1 Sol–gel transition. The transition from the sol of discreet colloidal particles suspended in liquid to gel, a continuous solid phase distributed in the continuous liquid phase.

Medical application of encapsulated cells brings them into contact and, every now and then, into a conflict with the host organism. Short- and long-term interactions of the body with the immobilization matrix as well as with the embedded cells have to be considered to be of any practical use. Sometimes, the material should resist degradation, and sometimes, it needs to be degraded within a given period. Biocompatibility is always a problem in need of investigation in all its aspects: inflammation, macrophages' overgrowth, and immune responses, just to mention the most obvious. Not only chemistry but also the surface properties of sol–gel materials influence the interaction of mammalian cells with their substrate.[8]

These complex limitations make the practical application of cell and organ implants a formidable task. Enough to say that despite initial promise and years of highly sophisticated innovative research, there currently are no medically approved procedures using encapsulated cells.

4.431.2. Sol–Gel Silicates

Sol–gel process is a low-temperature method of obtaining porous inorganic materials, mostly silica gels (Figure 2), but also alumina,[9] titania, magnetic ferrihydrite gels,[10] etc. Sol–gel silica has early found its way into a variety of biological and biotechnological applications[11,12] for its presumed biological safety. Nonfibrous forms of silicate are generally accepted as safe and, perhaps, even beneficial to human health.[13] Silica has been approved for use as an ingredient of food or animal feed; it is increasingly used in diagnostic and biomedical research.

Silica-derived ceramic matrices are perceived to possess significant advantages over traditional polymer matrices.[14,15] These inorganic matrices are biologically inert.[16] They can be processed into a variety of shapes, and are not in themselves a source of nutrients for contaminating microorganisms. The sol–gel process is sufficiently tolerant to allow for the use of derivatized alkoxysilanes,[17] co-incorporation of cells with a variety of nutrients, polymers, and environmental protectors thereby reducing various stresses.[18] The large surface area and tunable porosity of sol–gel silica allow for unimpeded mass transport of small molecules, yet prevent contamination by external factors. Wet gels possess a developed system of hydrophilic hydrogen bond-forming silanol groups that may help preserve cell membrane and ternary protein structures, although these interactions may also seriously damage cell integrity and limit survival.[19] The degradation of sol–gel silica is amenable to chemical manipulation,[20,21] thus making it suitable for long- and short-term applications alike. In the last couple of decades, sol–gel immobilization of cells in silica[3,4,12,22] has been developed for a variety of uses ranging from biosensors to artificial organs.

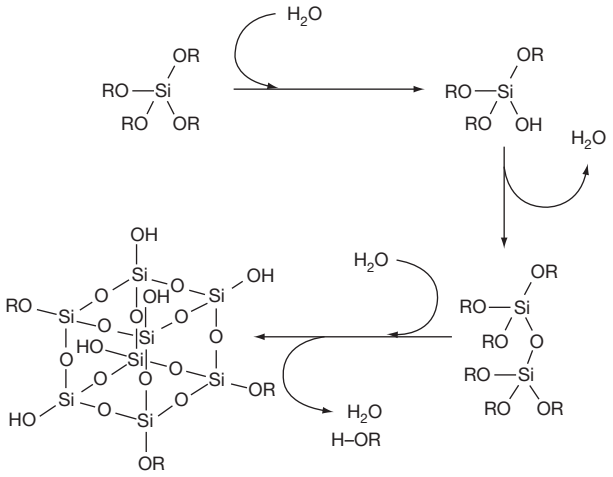

Figure 2 Formation of silica from tetraalkoxysilanes by hydrolysis and condensation. *R* = alkyl, usually, methyl, ethyl, or isopropyl group.

4.431.2.1. Silicon and Life

Silica is a ubiquitous material, and evolution has adapted organisms to tolerate relatively high levels of exposure to soluble silicates as well as to amorphous silica particles. Some sponges, radiolaria and, notably, diatoms (Figure 3)[23] use silica in building exoskeleton. Plants process water-borne silicates by depositing silica in various tissues as small uniform particles of opal. In animals, orthosilicic acid is present in small amounts in all body fluids.[24] Silica concentration in some tissues such as bone, cartilage, and skin are higher than in others, for example, brain or muscle. It seems that no other tissue compartment but mucopolysaccharides contain tightly bound silicate. Carlisle argued for a possible beneficial role of silicate in bone formation and repair.[25] Animals cope well with constant intake of silicate in drinking water by an efficient renal clearance. In normal renal function, silicon intake and clearance rates are well balanced.[26]

The silica xerogel implants produced by the sol–gel methods are slowly degraded.[27] Histological analysis did not show any tissue irritation at the site of the implantation, though fibrotic capsule was formed around the implant. No histological changes were observed in liver, kidney, lymph nodes, and uterus.[28] Nevertheless, high doses of amorphous silica nanoparticles were suspected to be cytotoxic.[29]

The biodegradation of sol–gel silicates may compromise some of their medical applications. Although the versatility of sol–gel silica seems advantageous for the engineering of artificial organs and xenografts, these materials cannot be relied upon as mechanical support or immunological barrier without a considerable chemical manipulation aimed at reducing their solubility in body fluids.

4.431.2.2. Biocompatible Preparation of Sol–Gel Silica

While amorphous silica seems to be quite safe, the sol–gel route to its generation is not gentle enough for the cells of higher organisms, affecting their viability negatively.[30]

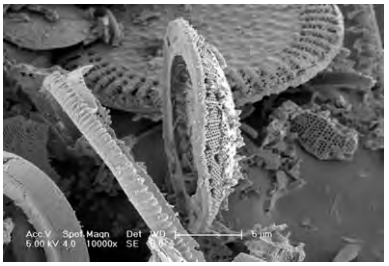

Figure 3 Diatomic earth. Silica-made exoskeleton of fossil diatoms.

The early bulk methods of adding biologicals, such as enzymes[11] in a buffer to tetramethoxy- (TMOS) or tetraethoxysilicate (TEOS), were poorly suitable for immobilization of animal cells due to, among other things, formation of alcohol following the initial hydrolysis of precursors and the high shear forces generated during gelation and shrinking of the maturing gel. The first successful immobilization of a eukaryote, the Baker's yeast in thin layers of sol–gel silica,[31] benefited from the unique sturdiness of these cells. Several techniques involving alcohol removal before entrapment in colloidal silica as well as doping of silica with polymers or other additives have been adapted to preserve cell viability.[32,33] These adaptations of the sol–gel method will be treated under a separated heading below.

A curious 'biological' enzymatic route for cell immobilization in silica was designed using either a recombinant enzyme, silicatein[34] or lysozyme.[35] The enzymes castalized colloid shell formation from a silicate monomer. The viscous silica shell as well as the silicate in the medium did not affect the growth kinetics of *Escherichia coli* and *Pichia pastoris* engineered with silicate-processing enzyme genes.

Elimination of cell contact with acid and alcohol has been achieved in a variety of ways. In two-step sol–gel processing, the acid hydrolysis of the precursors has been carried out to result in a colloidal sol. Alcohol has then been removed prior to the pH-neutral encapsulation–gelation step.[16,33,36,37] Alternatively, tetraalkoxysilanes precursors have been replaced altogether by commercial colloidal silica such as Du Pont's Ludox, which was neutralized prior to the introduction of the cells.[18,38–42]

In a typical sol–gel process, gelation occurs by the aggregation and growth of silica particles without significant volume changes. Loss of water causes shrinking of the gels subjecting immobilized cells to stress exceeding 100 mPa bringing about cell lysis.[18,22] Aging of silicate gels at the neutral pH is accompanied by the contraction of the gel, which may cause damage to shear-sensitive animal cells with their large size and the lack of cell wall. Even sturdy *E. coli* may be sensitive to shear caused by reshaping of the cavities in the aging gel. Thus, Nassif *et al.*[40] observed a 40% loss of cell viability within 1 h after gelation under conditions, where alcohol was avoided and the environmental conditions were favorable. Aged silica gels exhibit poor mechanical stability; they are brittle and easily crack on manipulation. Drying improves the stability of gels, yet very few organisms can survive it undamaged. The use of cryoprotectors such as glycerol[40,42] or D-glucose (21 wt%) may mediate to some extent the damage by preserving cell surface and maintaining the pore size during drying.[27]

Giovanna Carturan and his coworkers pioneered and worked out many variations of an elegant technique that minimizes the contact of immobilized biological materials with harmful chemicals and adverse environment. The central idea of this technique is that the sol–gel precursors are transported to the site of immobilization in the gaseous phase. They are hydrolyzed in the residual surface water layer, and coat the target with a robust silicate membrane, while the gas flow removes the resulting alcohol. Boninsegna *et al.*[43] used this method to coat isolated Langerhans islets.

4.431.2.3. Additives: The Design of Silicate Composites

A variety of additives, polymeric and otherwise has been used to mediate the harmful environmental impact of sol–gel process on the cells as well as to reduce shear during maturation of gels, rigidity, and brittleness of sol–gel matrices.

The material of choice for the preparation of hybrid sol–gel materials is alginate. Alginate is an acidic polysaccharide component of brown algae. It is a copolymer of β-D-mannuronic and α-L-guluronic acids linked by 1,4-bonds (**Figure 4**). Sodium alginate is water-soluble. Divalent ions interact with the neighboring polysaccharide chains. They form salt bridges and increase the apparent molecular size of the polymer, thus reducing its solubility and causing gelation. Ca^{2+} is the ion of choice for biological applications.

Commercial preparations of sodium alginate vary in their molecular weight and in the ratio of guluronic and mannuronic acid monomer units. At the same concentration of Ca^{2+} alginates of a higher molecular weight or with a higher guluronic acid content form harder gels, while low molecular size and higher content of mannuronic acid produce more elastic gels.[44] The preferred method for cell entrapment is the preparation of alginate beads by dropping sodium alginate solution into a receptacle containing a $CaCl_2$ solution. Ca^{2+} ion penetrates the alginate drop by diffusion, and therefore relatively high concentrations of both alginate and $CaCl_2$ are necessary to prevent coalescence of drops or a formation of distorted beads. Depending on the size of the drops, and time in contact with the $CaCl_2$ solution, beads may have a highly cross-linked firm outer skin and relatively elastic inner core. Poly-L-lysine (**Figure 4**) may replace Ca^{2+} ion as a skin-former partially or completely, if high concentration of alginate and $CaCl_2$ should be avoided or a more fluid inner core is required. Poly-L-lysine-alginate skin provides a barrier to immune system components,[45] yet one should be aware of possible toxic effects of poly-L-lysine.[46]

More uniform distribution of Ca^{2+} ions throughout the gel is achieved by mixing the sodium alginate solution containing, for example, D-glucono-δ-lactone with poorly soluble $CaCO_3$ particles. Spontaneous hydrolysis of gluconolactone acidifies the mixture releasing Ca^{2+}. This method results in uniform gels that may be made in casts.

A comparative study of cell stress and viability with yeast as a model has been performed by Perullini *et al.*[47] The ability

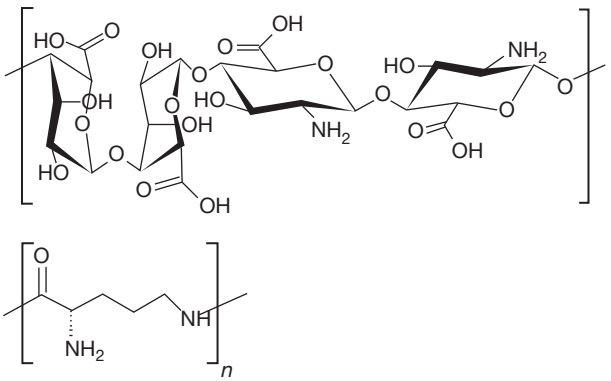

Figure 4 Alginate: the basic unit.

of the recombinant yeast to produce green fluorescent protein (GFP) in an exponentially growing culture has been employed as the reporter of stress. The authors used several well-established sol–gel cell immobilization procedures deemed biocompatible. Thus, they produced gels *via* (1) the Ludox colloidal silica route.[18] They also (2) performed the alcohol-free procedure of[33] with either tetraethoxysilane (TEOS) alone or (3) a mixture TEOS and glycidoxypropyl-trimethoxy-silane (GPTMS). Hydrolysis of precursors resulted in the formation of acid silica sol to which Perullini and his coworkers added cells suspended in 0.5 M phosphate buffer, pH 6.5. Finally, (4) yeast was immobilized in calcium alginate beads. The beads, in turn, were incorporated into silica gels using the same range of precursors as shown above. High concentrations of sodium alginate needed to obtain sturdy beads were damaging to yeast cells due to ionic stress, while lax beads with low alginate content did not protect cells during the stress generated by immobilization in silica. The results indicated that the mixture of TEOS and GPTMS in the alcohol-free procedure offers the best protection against stress.

In the system of trade-offs, offered by various methods of immobilization, the damage to cells caused by high concentrations of Na^+ ion during the preparation of silicate–alginate gels is considered a minor evil compared with advantages such as their unique sturdiness leading to successful applications.[48,49] There are several variations of these techniques. A mixture of colloidal silica with alginate[49] leads to the formation of homogenous silicate–alginate slabs. Silicate–alginate beads prepared by the immersion of alginate beads in the organic solvent (**Figure 5**) containing sol–gel precursors[50] cause extensive silica formation in the whole alginate network, although the outer shell is denser than the core.

Formation of thin silica membrane coating the outer surface of an alginate bead was achieved by multilayering techniques such as cross-linking alginate with positively charged poly-L-lysine, which could (i) activate silica condensation from diluted solutions of sodium silicate,[51] or (ii) catalyze hydrolysis of tetraalkoxysilane, thus driving deposition of a thin silica layer on the bead surface. A major consideration in favor of producing alginate core within the silicate membrane coat is the opportunity of liquefying alginate by removing Ca^{2+}. This becomes critical in applications where high cell density is required. The initial cell load that may be insufficient for the required purpose or may deteriorate in time, while cells confined in a hard alginate hydrogel cannot divide.[22] Liquefaction replaces Ca^{2+} ion with Na^+, thus limiting the concentration of alginate for the fear of ionic stress, therefore the use of cross-linkers to contain a semiliquid core of the bead is a necessity. The technique has been initially developed for yeast, *Sacharomyces cerevisiae*, and bacteria, *E. coli* and *Bacillus subtilis*,[52] but is now in use for plant[53] and animal cells[54] as well. Multilayer alginate–polylysine–silicate capsules[51,55] have shown improved mechanical stability and diffusion properties after liquefaction, when compared to an alginate–polylysine–alginate shells.

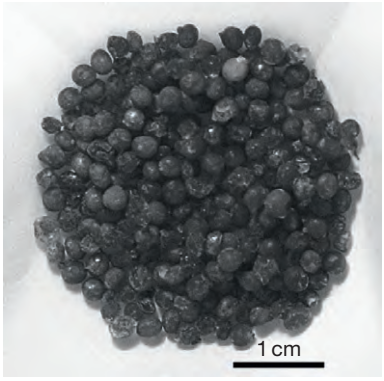

Figure 5 *Aspergillus terreus* mycelia immobilized in silicate–alginate beads according to Bressler *et al.*[48]

In a typical procedure,[53] a plant cell culture is mixed with Na alginate ($15\,g\,l^{-1}$) in a ratio 1:100. It is added dropwise under stirring to 0.1 M $CaCl_2$ solution. Following hardening for 10 min, the beads are separated and cast into suitable forms filled with a mixture of 1.25 M sodium silicate, commercial colloidal silica (LUDOX HS40, Aldrich) and succinic acid (5 wt%) at a ratio 2:1:1. Once gelation of silica occurs, the gels are immersed in potassium citrate ($5\,g\,l^{-1}$) to solubilize the Ca–alginate matrix creating liquid-filled cavities in the blocks of silicate. The citrate is then replaced with the suitable medium for the growth of cells.

In another approach to generation of macrocavities in TEOS and poly-dimethyl-siloxane (PDMS) scaffold formed by a sol–-gel method, sieved sucrose particles have been used as a pore-former. In these scaffolds, human hepatocellular carcinoma cells (HepG2) proliferated actively and formed cell clusters.[56]

Polymers other than alginate such as chitosan[57] and polyacrylamide–TMOS–TEOS[58] have also been widely applied. Some of these applications will be reviewed below in the 'case' studies.

4.431.2.4. Self-Organizing Systems

The common drop generation method to produce alginate beads is cumbersome and difficult to conduct aseptically. It may be considerably rationalized by a procedure involving stabilization of alginate in oil emulsions by porous microparticles of $CaCO_3$.

According to Liu *et al.*,[59] when one mixes a suspension of $CaCO_3$ particles in sunflower oil with a solution of sodium alginate in water, a stable water in oil emulsion is produced, which is stabilized solely by $CaCO_3$ particles residing at the oil–water interface (**Figure 6**). Addition of D-glucono-δ-lactone promotes the gelation of alginate. This results in a 'colloidosome' with an average diameter of 04 ± 01 nm. It is an important technical achievement, which considerably improves the control of the gel particle size thereby allowing for a better sterility of the preparation and, thus, reducing the stress due to high Ca^{2+} concentration.

However, alginate is not a perfect medium for medical applications. A recent thorough investigation[60] compared the stability of alginate implants at conditions imitating neuronal interfaces. Although some preferences have been formulated, all the implants exhibited fragmentation due, probably, to the leaching of Ca^{2+}, loss of polylysine coating and a general deterioration of the mechanical properties. The lability of

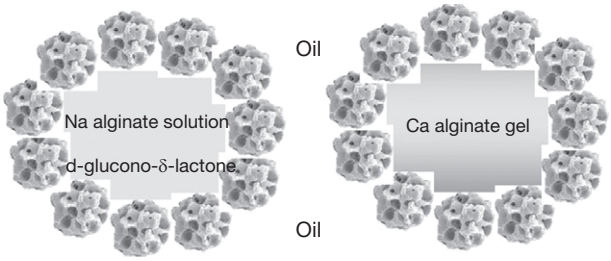

Figure 6 Preparation of colloidosomes. Porous microparticles of $CaCO_3$ self-assemble (left) at the alginate–oil interface. Hydrolysis of D-glucono-δ-lactone generates protons, which release Ca^{2+} ions and cause gelation (right) of the alginate. Reproduced from Liu, H. X.; Wang, C. Y.; Gao, Q. X.; Liu, X. X.; Tong, Z. *Int. J. Pharm.* **2008**, *351*, 104–112.

alginate membranes makes a strong argument in favor of composite encapsulation media.

Such a medium could be designed by coating or impregnating alginate colloidosomes with sol–gel silica, for example, using one of the three alternative procedures described by Callone *et al.*[61] In a wet coating method (i), alginate beads were immersed in a silica sol containing SiO_2 at the concentration of 100 g dm^{-3}, obtained by acid hydrolysis of $Si(OEt)_4$ in which ethanol was removed under reduced pressure. A better control of sterility may be achieved using another procedure (ii), whereby nitrogen saturated by passage through $Si(OEt)_4$ at 80 °C is bubbled through an emulsion of ethylene chloride in water (at a ratio 1:1, wt/wt). Alternatively (iii), air dried alginate beads may be taken through a gas coating method, in which air saturated with $CH_3Si(OEt)_3$ flows across the microspheres. In the last two procedures, the thickness of the coat is controlled by the amount of silica precursors available, while in the first procedure it is adjusted by the time of immersion.

An exciting possibility to engineer the structure, geometry, porosity, and the size of sol–gel silicate materials in self-organizing systems was provided by the discovery of mesoporous materials by Kresge *et al.* and Beck and Vartuli.[62,63] These authors observed that silicon alkoxides spontaneously form ordered micellar systems of varied morphology such as rods or spheres, when mixed with surfactants. Hydrolysis of silicon alkoxides results in sol–gel transition at the micellar interface. As a consequence, ordered structures are formed, whish retain their geometry even after the removal of the surfactants. This work was seminal in designing a wealth of self-organizing systems using a variety of templates (see Brinker *et al.*,[64] Davis,[65] and Soler-Illia *et al.*[66] for excellent reviews). Thus, large pore, 0.15–0.20 nm, wormlike and highly oriented cubic and hexagonal mesostructured xerogels were synthesized by what the authors termed evaporation-induced self assembly (EISA). Structure control was attained by changing the ratio of template (nonionic block copolymer) and water.[67]

Application of EISA to cell immobilization was developed by Baca *et al.*[68] This group observed that, when lipid-directed assembly of silica precursors was conducted in the presence of wet yeast biomass, the yeast cells seemed to mobilize lipids, which form around the yeast multilayered lipid vesicle, thus, modifying the forming ordered silica mesophase. This procedure called cell-directed assembly (CDA) provides for the biointerface, which maintains cells' functionality.[69]

4.431.2.5. Design of Prosthetic Organs: A Case Study

The ultimate goal of cell and tissue encapsulation, in their medical applications, is the design of organ prostheses. Scarcity of immunologically compatible tissue sources drives the investigator to the use of poorly compatible cells and tissues and eventually to xenographts. Thus, the primary function of encapsulation material is, while being biocompatible, to provide the barrier between the immune system of the body and the implant. The same or another material needs to function as the substrate compatible with cell maintenance or proliferation: respiration and supply of nutrients, removal of waste, transduction of signals. Yet another function of the material is to serve for engineering purposes, giving the construction the necessary mechanical stability. The variety of functions presupposes the use of several materials in an engineered environment.

The simplest construction of an implant is a small vesicle of functioning tissue. An example of this approach to implant engineering is the Edmonton protocol. The Edmonton protocol is a medically accepted method of implantation of isolated pancreatic islets for the treatment of type 1 diabetes mellitus.[70] The implant containing 11 000–12 000 human islets per kilogram of recipient body weight is infused into the portal vein. Use of immunosuppressant drugs prevents implant rejection. In the follow-up international trial,[71] 72% of subjects had full or partial control of diabetes following transplantation, 28% had complete loss of function within 1 year, 44% required insulin again at 2 years, and 14% retained the functional implant at 3 years. It seems that the size of isolated islets and their site of implantation satisfy the demand of the transplanted tissue for the functional maintenance of the cells in terms of blood supply, requirement for extracellular matrix and other factors. Thus, the Edmonton protocol, with its simplicity of operational procedure, sets the minimal criteria for a medically accepted implant. Encapsulation should provide for durable and biologically compatible xenograft without lowering the performance level.

The priority in the design of organ implants based on the sol–gel silica belongs to the group lead by Pope *et al.*[12] Pope and his coworkers encapsulated isolated murine islets by overlaying them with silica prepared by neutralization of acidic sol. The islet capsules collected from three donors per single recipient have been implanted intraperitoneally into mice rendered diabetic with streptozotocin injections. At least one mouse maintained full control of blood glucose for 10 weeks, after which the implant function was lost. The work has a very preliminary character, the statistic is lacking; it is primarily important as a pioneering application of sol–gel silicate chemistry for organ transplant research.

4.431.2.5.1. Silica precursors in the gas phase: the BioSil method

One of the most promising and widely published technologies in preparing silica gel encapsulated cells is the BioSil method developed by Giovanna Carturan.[3,72] According to BioSil technology, sol–gel precursors, usually a defined mixture of $(CH_3O)_4Si$ and $(CH_3O)_4SiCH_3$ are transported to the site of encapsulation in the gas phase. This allows for the precise control of the thickness, porosity, pore size, and composition

of the forming siliceous membrane. The hydrolysis of precursors occurs at the surface water layer covering cells or cell clusters. The gas flow removes the harmful products of hydrolysis leaving a smooth rather flexible silicate membrane.

It was shown[43] that isolated rat pancreatic islands may be safely coated with a silicate membrane in batches of 200–300 without loosing their viability and function, although some damage to the cells in the peripheral areas of the islet was observed and permeability of the membrane limited the insulin output by about a factor of 2 in comparison with an uncoated tissue. Surgical transplantation of silica-encapsulated islands (~800 islets per recipient) under left kidney capsule in incompatible rats provided the diabetic recipient with an adequate control of glycaemia for at least 8 weeks, when the experiment was terminated. Unencapsulated islets failed within the first week.

A prototype of membrane bioreactor for an artificial liver is described in Muraca *et al.*[73] A 0.5-mm-thick collagen layer was spread over rat hepatocytes, which was cultured to confluence on another 0.25-mm-thick collagen gel layer. This 'sandwich' was then exposed to silica precursors in the gas phase resulting in a 0.05–0.15 μm-thick silicate membrane. The construct showed unaffected viability and metabolic function typical of liver cells; some activities were even enhanced. There were indications that the membrane posed no transport limitations on the albumin-bound substrates.

For an easier handling of large amounts of cells and tissues necessary for grafting, a more elaborated procedure has been designed. Silicon precursors in the air flow were put in contact with microdroplets of Na alginate solution containing the tissues.[74] The droplets were hardened by falling into a $CaCl_2$ solution. The 0.2 μm-thick membrane formed on the droplet prior to the contact with $CaCl_2$ solution eliminated coalescence of droplets resulting in very uniform beads.[72] More important, this membrane prevented the activation of peripheral blood polymorphonucleate cells and deposition of connective tissue on the surface of the implant. When placed in the peritoneal cavity of a mouse, BioSil microcapsules were not colonized by peritoneal resident cells.

An attempt to implant BioSil microcapsules containing encapsulated pig islets ($1.0–1.2 \times 10^4$ islets per kilogram) in diabetic dogs using a close analog of the Edmonton protocol resulted in functional xenograft. However, its function deteriorated within 5 weeks.[72] Ten weeks past implant, there were no signs of inflammation or any immune reaction in the liver tissue at the site of implantation. Thus, it seems that the deterioration of the function should be attributed to the dedifferentiation of the islet cells. *In vitro*, the encapsulated islets lose their function within a few days.

It appears that the BioSil project has, currently, come to a standstill. The 2008 publication[72] reproduces in the same detail data presented in Carturan *et al.*[3]; there were no additional publications since. The Internet site of IRB srl, the Italian biotech company involved in the animal trials, contains no mention of further activity.

4.431.2.5.2. Aminopropyl-silicate membrane electrically bonded by external anionic polymers

The rigidity of sol–gel silicate matrix may present a problem for an implanted tissue or a growing mass of immobilized cells. Shinji Sakai and his group overcame this problem by constructing a liquid alginate reservoir surrounded by 3-aminopropyl-silicate membrane fortified and elastified by an external layer of alginate.[54,75,76]

Freshly isolated rat pancreatic islets were suspended in the 1.5 wt solution of sodium alginate in Ca^{2+}-free Krebs–Ringer–HEPES buffer. The suspension was extruded into 0.1 M $CaCl_2$ solution through an air-jet droplet generator set at preparing beads with a diameter of 0.6 ± 0.2 mm. The beads were put in *n*-hexane at the volume ratio of 10:14 followed by 3-aminopropyl-trimetoxysilane at 8% of the hexane phase, and finally by TMOS at 3%. After a short exposure at 4 °C, the positively charged silica precursor was absorbed at the negatively charged bead surface, whereby it underwent hydrolysis and condensation. The beads now coated in silicate membrane were transferred in 0.05% sodium alginate solution. Then, the free amino groups in the outer layer of the bead reacted with alginate coating the beads with an external alginate layer. Finally, Ca^{2+}-ions in the inner Ca alginate gel were exchanged with Na^+ (by incubation in 1 mM EGTA) causing the dissolution of the gel and formation of a microcapsule surrounded by a silicate–alginate membrane stabilized by salt bridges and containing the suspension of viable pancreatic islets (**Figure 7**).

When implanted in rat peritoneum, the empty beads coated with a silicate membrane prepared from the combination of 3-aminopropyl-trimetoxysilane and TMOS were superior to TMOS-derived coatings in the lack of fouling with proteins and fibrotic overgrowth[77] due to their anionic outer layer. However, the alginate–silicate–alginate beads containing the encapsulated islets were more prone to clumping and overgrowth, probably due to the release of attractants following necrosis.[78] The membrane, which had minimal resistance to the diffusion of glucose and insulin, hindered the diffusion of ovalbumin ($M_r = 45$ kDa) and completely excluded Bovine serum albumin ($M_r = 67$ kDa). The permeability of the alginate–silicate–alginate membrane depends upon the ratio of silicate precursors,[78] the sequence of their addition, and the time of contact of the precursors with the beads.[79] Molecular weight of alginate as well as the ratio of mannuronic to guluronic acid are also of importance.[76,80]

Peritoneal implantation of encapsulated rat pancreatic islets in mice (~10^3 islets per recipient) made diabetic by streptozotocin injection, resulted in normoglycemia for at least 100 days in the majority of implants.[78] It is postulated that the limitation has not been dictated by the stability or biocompatibility of microcapsules, but rather by the functional life span of the isolated islets.

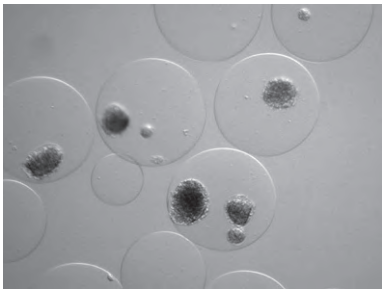

Figure 7 Rat pancreatic islets in microcapsules bounded by a flexible alginate–silicate membrane. Courtesy of Dr. Shinji Sakai.

In this respect, insulinoma cells with their ability to proliferate may be considered a viable alternative. Silicate–alginate–silicate membrane vesicles (~0.5 mm in diameter) have been applied for encapsulation of pancreatic β-cell line (MIN6) at the initial density of 4×10^7 cells ml^{-1}.[54,76] The cells happily proliferated in the inner compartment, forming, within 5 weeks, a spheroid roughly half of the bead diameter. Then, the cell population stabilized, probably, due to the constrains of mass transfer. The MIN6 cells, which were enclosed in the microcapsule, secreted insulin in a glucose-simulated manner. When inserted in the peritoneum of a diabetic mouse, they successfully maintained its blood glucose level for a month. The guluronic acid content of the alginate pool at the core of the vesicle influenced the quality of the preparation. The intermediate guluronic content was optimal for the MIN6 cells proliferation and for the long-term viability as measured by maintaining the blood glucose level maintained by the experimental animals.

Despite the undisputed elegance of vesicle construction, the project has not had practical implications yet. Mouse insulinoma cells are looked upon with suspicion for practical purposes. Long-term stability and biodegradation of alginate and silicate may counter-indicate the use of direct implantation of proliferating cell lines. Dr. Sakai informed me that there have not been follow up medical research and development of his vehicles, and that the work with his membranes has been abandoned.

4.431.2.5.3. Rational engineering of tissues and organs

If one agrees that organ implants are the major drive supporting the design of media for cell encapsulation, one should necessarily arrive to the conclusion that, so far, this drive produced no medical success. There are several gaps inherent in the use of encapsulated xenografts, which cannot be breached by a single research group or even a consortium of specialized laboratories and, perhaps, not ever within the limitations of current science. The difficulties may be divided in several categories, which will be reviewed subsequently. For the simplicity of illustration, the most common example of xenograft is used, almost exclusively investigated in the designs presented in this chapter – that of the pancreas.

Insulin replacement therapy is the main treatment for both type 1 and type 2 diabetes. However, periodical subcutaneous insulin delivery is blamed on many complications due to its nonphysiological periodicity and site of delivery.[81–83] It seems that currently artificial pancreas, rather than xenograft, has priority. In 2006, the FDA defined the continuous glucose monitoring-based artificial pancreas as a priority within its Critical Path Initiative. Successful clinical trials of closed loop systems have been reported.[84] The advantage of an implant over the system that automatically dispenses insulin, a hormone whose overdose could kill a patient, is its potential of safety.

Since it is quite impossible for all practical purposes, that a xenograft may deliver an overdose of insulin, what has to be done to make a functional implant? There are a number of physiological hurdles, which severely limit the useful life span of a transplant.

1. Pancreas consists of various types of tissues organized in a well adapted architecture. Since it is impossible to transplant the whole organ from an immunologically incompatible donor, one has to use only isolated Langerhans islets. Isolation, in itself, is a procedure, which reduces the viability of the tissues by depriving them of oxygen supply as well as causing chemical and mechanical damage. Further, it deprives the islets of the interactions and signals coming from the extracellular matrix and other surrounding tissues. The frequent result of such deprivation is dedifferentiation. The isolated islets in culture lose the ability to respond to glucose within days. The Edmonton protocol teaches us that, at best, one could expect a transplant to function for no more than a year.
2. This poses an additional constraint on the implant. One would not leave large amounts of useless foreign tissue, however, well protected against immune response, within the patient's body. Thus, the implant should be easily retrievable. This demand rules out the delivery of unbound microcapsules containing isolated islets delivered into a portal vein or into peritoneum, where their weight to surface ratio guarantees them adequate oxygen supply. Large retrievable macrocapsules have to be engineered in proper geometry and from materials (membranes) with large enough surface and permeability for oxygen.
3. The membranes should obey an additional large number of demands: they have to be biocompatible, but not biodegradable, should not elicit any immune response, should not bound any biopolymers abundant in body fluids for the fear of fouling the membrane, and should not anchor resident cells. Finally, all these properties should be stable within the life time of the device.
4. It is difficult to imagine a thin flat membrane with all the properties listed above that is also mechanically sturdy. Therefore, one should design a rough sturdy support membrane of suitable geometry.

As one sees from the above, a thorough engineering of the implant is the key priority in the practical application of a bioartificial pancreas using either hydrogels or any other biomaterials for foreign tissue encapsulation. The design of implants is a multiprofessional enterprise involving specialists of various sciences: material science, biology, physiology, as well as engineers and members of medical professions including clinicians. Organization of such a team and location of suitable funds should require a good promise of success and a change of priorities by regulatory agencies such as the FDA.

Two recent publications,[85,86] although not strictly within the reviewed field, mark the beginning of a multidisciplinary effort to devise a bioartificial pancreas. The group includes polymer scientists and engineers from the University of Akron, Ohio, medical professionals and clinicians from the Northeastern Ohio Universities College of Medicine and from the Cleveland Clinic Foundation. Their device has a complex design: it contains a thoroughly designed membrane, which is assembled from hydrophilic poly-(*N*,*N*-dimethyl acrylamide) and hydrophobic/oxyphilic PDMS chains cross-linked with hydrophobic/oxyphilic polymethylhydrosiloxane chains. This membrane, with an extraordinarily high oxygen permeability and small hydrophilic channel dimensions (3–4 nm), contains porcine islet cells. The key components are (i) a 5–10 μm-thick semipermeable amphiphilic conetwork

membrane reinforced for mechanical stability by (ii) the electrospun nano-mat of PDMS-containing polyurethane and (iii) a laser-perforated nitinol scaffold. The implant was tested on pancreatectomized dogs. The bioartificial pancreas protected pig islets from toxic environments *in vitro* and *in vivo*. Islets remained viable for up to 3 weeks without signs of rejection. Unfortunately for the concept, hyperglycemia was not reversed, possibly, because of insufficient islet mass.

4.431.3. Cell Delivery in Temperature-Sensitive Sol–Gel Systems

Answering the increasing demand for sophisticated delivery vehicles, pharmaceutical and biotechnological industry developed a variety of biocompatible nonimmunogenic polymers, primarily, for localized or extended drug delivery, but increasingly also for recombinant human hormones, genes, RNA, and other modern therapeutic vectors. Within the last 10 years, this technology has produced a multibillion industry. The vision of stem cells as the frontline of medical research has gradually shifted the attention more and more into the design and development of polymeric cell delivery systems. Not just future, but also current and proximal therapies create demand for cell delivery vehicles. Repair of cartilage, filling up cavities caused by large wounds, restoration of damaged retinas, restorative treatment of Parkinson disease, etc., could benefit from minimally invasive bio-supportive cell delivery technologies.

One may envision an ideal cell delivery procedure as being done by injection into the target cavity or space using a small gauge needle. This is precisely what the temperature-sensitive sol–gel systems can provide. The cells to deliver are mixed at ambient temperature with a low viscosity sol, which may also contain various soluble factors. At the injection site, the sol undergoes the transition into a mechanically stable gel induced by the higher temperature of the body. Although the sol–gel transition may be brought on by a variety of physical and chemical changes such as pH, change of a solvent or a chemical reaction, the *in situ* temperature shift is the least damaging to the sensitive animal cells and ensures homogeneity of the transition. Injectable hydrogels as a solid support either by themselves or by admixing other components can be designed to mimic extracellular matrix for cellular attachment and proliferation.

4.431.3.1. Mechanisms of Sol–Gel Transition in Temperature-Sensitive Materials

As in the case of silicates, the sol–gel transition in other systems is the function of solubility. In polymers, the solubility, among other factors, depends upon the aggregation state of the polymer. Polymeric sols are stabilized by polymer–solvent interactions favoring large surface area of contact between the polymer and the solvent. Thus, growth of large particles on the account of mass transfer from small ones or agglomeration of sol is energetically unfavorable. When the solvent is water, polymer–solvent interactions are governed by hydrogen bonding with water molecules and by hydration of charged residues. Interactions within and between the polymer molecules such as hydrophobic interactions, internal H-bonding, and formation of internal salt bridges favor phase separation with the preference of water–water and polymer–polymer interactions and, consequently, shrinking of the polymer–water contact surface area by growth of the particles until they form a continuous gel. In physical terms, the free energy of association in a given polymer–water system is given by: $\Delta G = \Delta H - T\Delta S$. Increase in temperature should eventually make the entropic component $T\Delta S$ larger than ΔH making the ΔG term negative, that is, favoring association of sol particles. The lowest temperature, at which sol–gel transition occurs, is termed the lower critical solution temperature (LCST). At LCST, the polymer system dehydrates. Alternatively, in some amphiphilic polymers, the previously stable micelles transit at the LCST to a continuous hydrophobic phase, this is so-called micellar mechanism of sol–gel transition.

4.431.3.2. Composition of Temperature-Sensitive Gels

Guided by the decision to limit the discussion by the principle of relevance to medicine, we shall review only these systems, which are biocompatible, and gel *in situ*, that is, possess LCST between the ambient and body temperature (for review see Ruel-Gariepy and Leroux[6]).

4.431.3.2.1. Natural and semisynthetic polysaccharides

Alkyl-substituted celluloses (Figure 8) such as methylcellulose (MC) and hydroxypropyl MC (HPMC) in diluted aqueous solutions exhibit thermosensitive gelation. Tate *et al.*[87] explored the use of MC solutions as cell carriers and scaffolds for the repair of brain trauma. MC solutions in concentrations below 8 wt% were free flowing at 23 °C and formed soft gels at

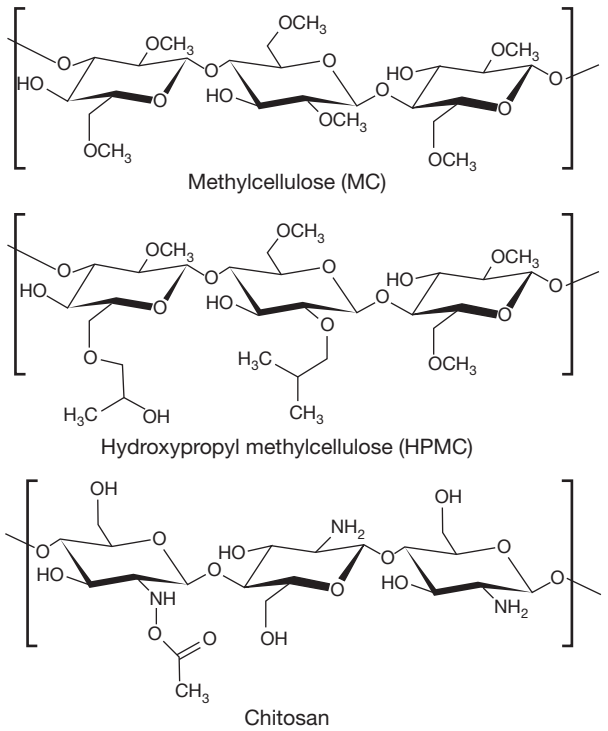

Figure 8 Natural and semi-synthetic polysaccharides.

37 °C. When microinjected into rat brain, they did not elicit neuron or astrocyte death and even promoted the formation of the glial scar.

Another biocompatible polysaccharide that attracted considerable attention due to its low cytoxicity is chitosan. Chitosan (**Figure 8**) is a linear polysaccharide containing β-(1→4)-linked chains of D-glusosamine. It is produced commercially by alkaline *N*-deacetylation of chitin and, therefore, contains various amounts of randomly distributed residues of *N*-acetyl-D-glusosamine. Chitosan is soluble in acids but forms gel-like precipitates at neutral pH. Ruel-Gariepy *et al.*[88] and Chenite *et al.*[89] proposed a composition of chitosan (~2 wt% solution) with β-glycerophosphate (~0.25 mol l^{-1}[90]), which forms stable neutral sols in cold. At ambient temperature, the viscosity of the solution increases after 3 months in storage indicating a slow process of gel formation. At 37 °C, a solid gel forms within 5 min for a mixture (1:1) of 84% and 94% deacetylated chitosan.

Solubility of chitosan in water is increased by β-glycerophosphate forming ionic pairs with its amino groups and by additional hydration of the complex by hydrogen bonding of the polyol residues to water. Dehydration of the polymer chains and increased polymer–polymer interactions govern the gelation at elevated temperatures. The LCST of chitosan complexes decreases with the degree of deacylation; for 91% deacylated chitosan, the LCST is 37 °C.[89] Subcutaneous injection of the sol in rats demonstrated that low deacylation of chitosan promoted both the rate of degradation of the implant and the inflammatory reaction. The 91% deacylated chitosan implant had a residence time of several weeks and produced no noticeable inflammation. Chitosan implants formulated with chondrocytes promoted the formation within the implant of proteoglycan-rich areas typical of normal cartilage.

Interested in understanding the ability of chitosan to promote the healing of cartilage microfractures, Simard *et al.*[91] investigated the recruitment of neutrophils by chitosan implants as the function of the degree of deacylation. While 80% deacylated chitosan attracted neutrophils in dose-dependent manner, 90% decylated chitosan was not an attractant. Nevertheless both chitosan preparations failed to elicit the release of granule enzymes or the generation of superoxide anions. Both chitosan preparations were internalized by polymorphonuclear neutrophils.

4.431.3.2.2. Chitosan-based cell-assisted cartilage repair vehicles

In the recent review of musculoskeletal tissue engineering in clinical applications, Roberts *et al.*[92] wrote: "Current gold standard for the repair of bone, cartilage and skeletal muscle entail intense surgical processes for reparative or replacement therapy … Therapies, which are utilized today for cartilage defects, include autologous chondrocyte implantation,[93] osteochondrial autografts[94] and in extreme case total joint replacement." Out of these, the autologous chondrocyte implantation (ACI) is the least damaging. In approximately 80% of patients, the current techniques of repairing cartilage defects by implantation result in function restored within 2 years. The cells are implanted with minimal surgical damage by injection. However, to speed up and improve recovery, proliferation of the chondrocytes in the cavity requires protection from shear stress and the facilitation of assembly in the tridimensional tissue. All of this may be provided for by a biodegradable artificial scaffold, on condition that the scaffold is injected with the cells and either self-assembles from solution or gels within the cavity after filling the defect.

Injectable cell delivery vehicles must not only meet such general demands for tissue engineering materials as biocompatibility, they also need to be biodegradable without producing debris and allow for complete integration with the repair tissue without forming discontinuities. They must form a perfect attachment interface with the damaged tissues including cartilage and the subchondral bone. In this sense, chitosan-β-glycerophosphate compositions, mentioned above, seem to be an attractive alternative, especially after the observation[95] that gels made with the admixture of whole blood form solid implants within cartilage microfractures, adhere well to the surrounding tissues and elicite improved cartilage healing compared to untreated microfractures. Chitosan clots stimulated cell recruitment, chondrogenic proliferation, hyaline matrix production, and subchondral angiogenesis.[96] The chitosan–glycerophosphate–blood scaffold was further commercially developed by BioSynTech under the trade name of BST-CarGel® (see Relevant Websites). This product now undergoes extensive human studies. It was reported that the nitial results completed by 2009 have been successful.

So far, BST-CarGel® has only been used as a scaffold for tissue regeneration. The same group reported an injectable adhesive vehicle for autologous cell transplantation.[97] This self-gelling system contains chitosan, glycerophosphate, glucosamine, and hydroxyethyl-cellulose. The addition of hydroxyethyl-cellulose allowed for gels with LCST within physiological limits and improved osmolarity due to lower glycerol phosphate content. Later, it was found that the effective agent in the mixture was not one of the components used purposefully, but rather the glyoxal additive present in the hydroxyethyl-cellulose. Glyoxal formed a covalent modification with chitosan. Chitosan–glycerol phosphate–glyoxal gels performed optimally, when the cross-linker was below the cytotoxic level of 1 mM.[98] Although primary chondrocytes were proliferating in the gel *in vitro*, the results of *in vivo* models were disappointing. In implants subjected to mechanical shear, the gel strength was insufficient. Inflammation and formation of fibrous or granulation tissue[97] bodes badly for tissue regeneration.

Recently, Cheng *et al.*[99] attempted to improve biocompatibility of thermosensitive chitosan/glycerol phosphate disodium salt hydrogels by adding gelatin (C/G/GP hydrogel) for its application as a cell carrier for nucleus pulposus (NP) regeneration. The sol–gel transition temperature of the C/G/GP hydrogel containing 1% gelatin was in the range of 31–34 °C at neutral pH. At the body temperature, the C/G/GP solution gelled in less than a minute. The gel strength was improved compared to the C/GP hydrogel. The gel supported the function of nucleus pulposa cells *in vitro* producing more extracellular matrix per DNA than surface culture of these cells. Undoubtedly, this research, which used only GRAS materials of acknowledged biocompatibility, is a good candidate for future use in minimally invasive intervertebral disk surgery.[99]

4.431.3.2.3. Copolymers of N-isopropyl-acrylamide

Water solutions of poly-*N*-isopropyl-acrylamide (PNIPAA) undergo sol–gel transition at the LCST of 32 °C.[100] The mechanism of this transition lies in the balance between the relatively hydrophilic linear poly-acrylamide chain and the hydrophobic isopropyl side chains. At LCST, hydrophobic interactions between the side chains govern the transition from sol to insoluble gel form. This 'main chain–side chain' balance may be modified either in the side chains or in the main chain by adding copolymers, thereby rendering the polymer more or less hydrophobic and thus tailoring both the LCST and the biocompatibility of the matrix for the desired use.

PNIPAA and its copolymers are nonbiodgradable and generally are not accepted as safe; therefore, if at all, they only may be suitable as implants for very long-term functioning artificial organs. Classical xenografts rarely perform for years due to dedifferentiation or necrosis. Thus, an acrylate (~2%) – acrylamide copolymer with the gelation temperature of 35 °C was investigated as a temporary cell carrier in a refillable hollow fiber pouch or in a diffusion chamber-type macrocapsule. The advantage of this copolymer over PNIPAA stems from the perfectly reversible sol–gel transition with no hysteresis and no swelling with change of temperature. Langerhans islets in the solution of this copolymer were injected into an immunoprotecting pouch installed in the patient.[101–103] Formation of the gel protected the islets, which resulted in their prolonged function compared to the free islets. Replacement of the islets required just lowering the pouch temperature below LCST rendering the content liquid and removing the liquid through a port. Further improvement of the system was achieved by using hemoglobin-PEO conjugate of the acrylate acrylamide copolymer.[104–107] The beneficial influence of the hemoglobin conjugate was, supposedly, due to improved supply of oxygen to the islets. A similar approach was used to build an artificial liver.[108]

4.431.3.2.4. PNIPAA composites

The thermosetting properties of PNIPAA attracted several attempts of tissue engineering, in which the polymer has been used in combination with the natural elements of the extracellular matrix or with materials mimicking ECM. Thus, injectable compositions were designed with PNIPAA chains grafted on denatured gelatin backbone.[109,110] About 30 graft chains of PNIPAA (MW ~10^5) were grafted on the gelatin molecule through the ε-amino group of lysine derivatized with dithiocarbamoyl residue. The graft copolymer has LCST of 34 °C; at 37 °C, a 5% solution forms an opaque gel.[111] During the period of the experiment (12 weeks), chondrocytes from rabbit articular cartilage, seeded in the hydrogel, accumulated *de novo*-produced extracellular matrix. The mechanical properties and the appearance of the 12-week old artificial cartilage were similar to that of normal rabbit hyaline cartilage. Similar results were obtained with a composite (of an unclear structure) obtained by the polymerization of *N*-isopropylamide in the presence of chitosan[112] (**Figure 9**).

A more complex graft was developed based on a copolymer of *N*-isopropylacrylamide, acrylic acid, *N*-acrylosuccinimide, and a macromer poly-trimethylene carbonate-hydroxyethyl methacrylate linked with collagen and chondroitin sulfate (CS).[113] Collagen and CS (mimicking the ECM) slightly

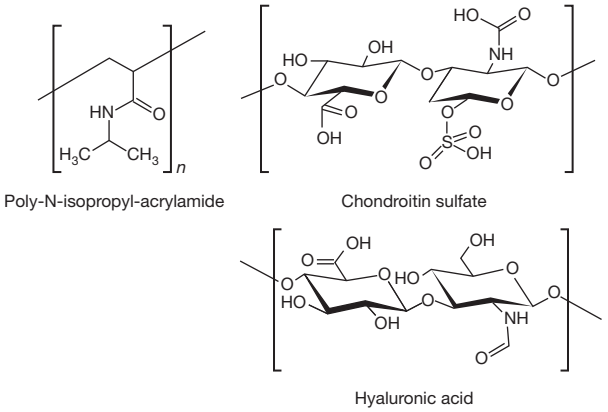

Figure 9 PNIPAA composites' components.

increased the LCST of the polymer in a concentration-dependent manner from about 24 to 27 °C. The 20% solution of the polymer gelled at 37 °C. The gel degraded slowly in the PBS *in vitro* losing about 10% of weight in 2 weeks. Without the ECM-mimicking components, mesenchymal stromal cells adhered to the surface of the gel about half as well as to the tissue culture plate. Cell adhesion has been dramatically improved in the graft containing collagen and CS. The cells encapsulated in the gel proliferated only in the presence of the growth factor IGF-1. Collagen alone graft performed better than one made with both collagen and CS.

Chen and Cheng[114] experimented with chitosan and hyaluronic acid (HA) grafted on PNIPAA. The material forms sturdy gels at 37 °C. Although inclusion of HA residues in the graft seemed to assist the surface chondrocyte proliferation on the polymer films, the results were not clear, since there was no report of experiments performed with encapsulated cells.

4.431.3.2.5. Polyoxyethylene–polyoxypropylene (poloxamer or Pluronic®) aqueous gels

"Poloxamers are nonionic triblock copolymers composed of a central hydrophobic chain of polyoxypropylene flanked by two hydrophilic chains of polyoxyethylene. The word 'poloxamer' was coined by the inventor, Irving Schmolka, who received the patent for these materials in 1973. Poloxamers are also known by their trade name Pluronics" (see Relevent Websites).

Concentrated poloxamer solutions in water undergo thermoreversible sol–gel transition by the micellar mechanism.[115] Thermosensitive sol–gels of the commercial poloxamer 407 (Pluronic® F127) have been suggested for use in short-term treatments such as pain management, infection treatment, fertility control, and in topical drug delivery.[6] Pluronic® F127 is generally accepted as safe, although in animal studies injection of doses exceeding 27.5 mg kg^{-1}[1116,117] caused serious increases in blood cholesterol and triglycerides (**Figure 10**).

Solutions of poloxamer 407 (~25%) are viscous liquids below 25 °C; at body temperature they form a semisolid gel. Weak mechanic strength, relatively high solubility in body fluids, and nonbiodegradability are the main hurdles for the use of poloxamer 407 in cell delivery systems. Introduction of the carbonate linkage between poloxamer 'blocks' and linking of poloxamers into structures of a higher molecular mass[118] were attempted to overcome these disadvantages. However,

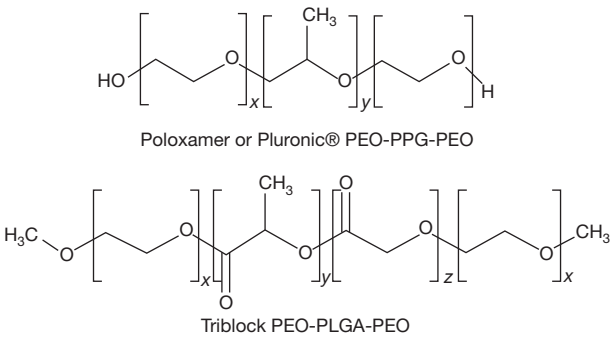

Figure 10 Poloxamers and their composites.

only more sophisticated synthetic procedures offering graft copolymers hold promise for the application as injectable cell carriers.

4.431.3.2.6. Graft copolymers with poloxamer blocks

One of the possible strategies to improve the stability, biocompatibility, and adhesion of poloxamer gels to extracellular matrix was explored by Chung *et al.*[119] in grafting poloxamer 407 onto chitosan using soluble carbo-di-imide and *N*-hydroxysuccinimide as coupling agents. The resulting graft materials (CP hydrogels) were water-soluble at neutral pH and displayed sol–gel transition at 30–35 °C at lower concentrations of the polymer than Pluronic® F127 alone (depending upon the grafting percentage of chitosan). It was proposed that the transition is governed by hydrophobic interactions between poloxamer chains in the same manner as in ungrafted poloxamer gels, while larger complexes are formed owing to the participation of chitosan chains. Similar hydrophobic–hydrophilic sol–gel transition mechanisms were demonstrated in aqueous solutions of acrylate/thiol-modified poloxamer 407 mixture[118] and poly (ethylene glycol)-polycaprolactone triblock and multiblock copolymers.[120] CP hydrogels are also considerably sturdier than poloxamer hydrogels, show less concentration-dependent swelling, and have a slower degradation rate. The swelling rate of CP hydrogels increases *in vitro* for up to 3 days reaching the ratio of 1.1–1.3. After 10 days, the swelling ratio decreases due to degradation of the esteric bonds in the hydrogel. The gels lose mechanical integrity within 30 days.[121] In contrast to alginate gels used as the control in this research, the chondrocytes proliferated, albeit slowly, in CP hydrogel matrix, accumulated glucosamineglucan (GAG) and expressed extracellular matrix proteins.

Besides CS, another analog of extracellular matrix, HA, grafted with Pluronic® F127 copolymer was investigated as a biomimetic hydrogel for cell delivery.[57] The graft copolymer was synthesized by conjugating amine end-capped Pluronic F127 to carboxylic groups of HA. Copolymers with vinyl groups were introduced to prepare more robust hydrogels by photo-cross-linking. For improved cellular adhesion and proliferation, cell-adhesive peptide (Arg–Gly–Asp (RGD)) was additionally conjugated to the HA backbone. The synthesized graft material exhibited thermosensitive sol–gel transition behaviors over the temperature range of 20–40 °C. The gels supported proliferation of bovine chondrocytes *in vitro*. The copolymer containing RGD supported linear growth kinetics of chondrocytes for 4 weeks. A tissue containing cartilage-like components such as GAG and type II collagen was successfully produced within the hydrogels. Although some of these materials seem promising, the complexity of chemical procedures for their synthesis, probably precludes their routine use.

4.431.3.2.7. Triblock copolymers containing poly-hydroxylic acids

Standard triblock copolymers (poloxamers) do not readily biodegrade but dissolve at physiological conditions from the surface resulting in the delivery of a soluble material with uncertain GRAS status into body fluids, thus rendering them rather impractical. Usefulness of the poloxamer compositions is also limited by their rheology: they are relatively viscous at 20 °C and have a low transition temperature. Recently, Jeong *et al.*,[122] Jeong *et al.*,[123] and Chung *et al.*[124] proposed biodegradable hydrogels with thermosensitive sol–gel transition based on triblock copolymers of polylactic-*co*-glycolic acid (PLGA) and polyethyleneglycol (PEG). PLGA has a long history of use in biodegradable surgical sutures and is considered safe. PEG–PLGA–PEG triblock copolymers have no surface erosion and have a lower content of nonbiodegradable polymer than poloxamers. The PEG–PLGA–PEG copolymers were synthesized using chemistry that allows for mass production. It consisted of obtaining diblock PEG–PLGA by ring-opening polymerization of lactide and glycolide onto PEG, followed by coupling of the diblocks with hexamethylene-diisocianate to obtain the desired triblock copolymers. The sol–gel transition of these copolymers from a free-flowing sol to gel depended moderately on the concentration; within the range of 17–14%, the LCST decreased from 36 to 30 °C at lower concentration. The gelation mechanism of the PEG–PLGA–PEG copolymers is similar to that of poloxamer gels. However, the aggregation number of micelles in the gel state is much higher, counting in thousands and resulting in much stronger gels. When implanted in rats, these gels remained mechanically intact even after a month.[123] The weight reduction on account of implant hydrolysis is accounted for by the loss of PEG-rich segment. The PEG-rich segment's loss results in a decrease of molecular size of the copolymer to a half and approximately 30% drop in weight over a month. It seems that following subcutaneous implantation, there was neither an inflammatory response nor formation of fibrous tissue on the surface of the implant.

4.431.3.3. Availability of Injectable Cell Carriers for Practical Medicine

Injectable cell delivery vehicles hold a considerable promise for the repair of lesions and cavities resulting from pathology or injury. Many efforts have been invested into the development of materials that would combine all the desired properties: biocompatibility with complete biodegradability, convenient rheology of the sol with mechanical stability of the gel, and cell adhesion with cell proliferation. However, these ideal cell carriers are not currently available. As concluded in the most recent review,[125] "current biomaterials are unable to meet all the design parameters simultaneously."

Evidently, the injectable cell delivery is still in its infancy. Yet, the clinical trials for the second generation ACI of such

gel-based, even though not sol–gel-based, seeded scaffolds as the bioresorbable fibrin–polymer matrix BioSeed-C® of BioTissue Technologies GmbH, Freiburg, FRG,[126] and hyaluronan-based Hyalograft C® of Fidia Advanced Biopolymers (FAB), Italy,[127,128] were highly successful. This success indicates that tissue engineering may, in the future, deliver on its high promises.

4.431.4. Conclusion and Future Directions

Alexander Pope once made an observation which perfectly describes the difficulty of discovery in Life Sciences:

> "... Following life through creatures you dissect.
> You lose it at the moment you detect".

Intervention in the function of the living organism, whether for the sole sake of investigation or for repairing a malfunction, is never simple, usually dangerous to the organism and always imperfect.

Achievement in Life Sciences necessitates the use of novel technologies. Life Sciences and their main practical application, the modern medicine, are, primarily, instrumental disciplines. Each new gadget, every new means of dissecting an organism, is producing a wave of innovation. Scientists are easily becoming enchanted with their new gadgets. They create a wealth of imaginative, novel work, frequently quite removed from practicality. Paraphrasing the famous dictum of Sir Isaac Newton: "I do not know what I may appear to the world, but to myself I seem to have been only like a boy playing on the seashore ...," I term this playful aspect of scientific innovation: Playing-on-the-Sea-Shore Syndrome or PSSS. The combination of advanced materials with medicine, which is the topic of this review, is fraught with PSSS.

This is not to accuse either Sir Isaac Newton or my learned colleagues of futile activity. No one can predict which research will start the chain of events, leading to a useful medical application. Nevertheless, it is clear that the majority of publications dealing with medical applications of sol–gel materials do not take into account the maxim of Alexander Pope and the complexity of the human body. Many teams lack specialists able to appreciate medical aspects of the work. Overt enthusiasm of some publications, the playful exhilaration over a new material constitutes precisely what I termed PSSS. In the body of this review, I have tried, with the benefit of hindsight, to discriminate between the practical and impractical.

After reading the rich collection of publications devoted to the medical use of sol–gel silica, I arrived to the conclusion that the promise of this material has not materialized yet in anything approaching medical practicality. The solubility in body fluids and complicatedness of stable incorporation of physiological elements such as ECM components, signals, etc., impair the usefulness of sol–gel silicate-based chemistry. The answer to both problems may be found in the increase of molecular mass of, and association of, sol–gel silica precursors. Oligomers of a high molecular mass, especially self-assembling into structures stabilized by noncovalent bonds could produce stable and biologically 'friendly' media. It seems that synthesis of trialkoxysilane compounds bearing silicon–carbon bonded linkers may open the road to derivatized silica membranes containing such ECM motives as gelatin, fibrinogen, or GAG-derived polysaccharides.

In Section 4.431.2.5.3, I discussed the desirability of engineering xenografts encapsulated in sol–gel silica-based macrocapsules, which ensure a convenient removal of the graft in case of failure. The life of a graft is usually quite short and rarely measures in years. The main reasons for this short life span are the lack of supportive tissues and difficulties in supplying macrocapsules with nutrients. Both could be overcome by engineering the tissues of the xenograft. An example of such engineering is shown in Hasson *et al.*[129] The authors took a cell therapy approach to induce angiogenesis. They implanted small skin or lung fragments (microorgans) in a microcapsule, which induce an angiogenic response causing capillary outgrowth on the surface of a synthetic membrane. One could use these microorgans and other tissue types to support the prolonged useful life of isolated Langerhans islets.

The research in thermosensitive sol–gel materials fared somewhat better in practicality than sol–gel silicates. Injectable cell delivery materials benefitted from the lesser complexity of the task they were expected to perform, which is to fill up a cavity caused by injury or pathology, providing protection of the wound and supplying cells able to regenerate the damaged tissue. However, even here the expected advantages of sol–gel materials did not manifest themselves in well-advanced practical solutions. In fact, the main argument for the use of sol–gel materials is that it makes major surgery during implantation redundant. Ideally, one would just use a small gauge needle to inject the implant into a cavity. Unfortunately, all reported injectable delivery vehicles are not completely bioresorbable and the majority does not have a clear GRAS status. In many cases, the defective tissue requires *a priori* surgical intervention for the debriefing of the wound, preparation of the surfaces, etc. No wonder, that all medically approved or nearly approved seeded gels are based on surgical delivery.

Of course, one should not underestimate the other advantage of sol–gel transition – the ability of the liquid sol to snuggly adhere, to form a well fitted contact with the surface of the wound. This advantage might be decisive in, for example, neurosurgical application. However, to be able to realize this advantage, one needs to develop entirely bioresorbable and biocompatible sol–gel products.

I hope that the effort and resourcefulness invested in the development of sol–gel materials will pay off, and that the future will substantiate the high hopes of the pioneers in this field.

Acknowledgments

The author is indebted to Drs. Ovadia Lev and Eduardo Mitrani of the Hebrew University for their valuable insights and helpful discussion, and to Ms. Deworah de Vries for the critical reading of the manuscript.

References

1. Avnir, D.; Coradin, T.; Lev, O.; Livage, J. *J. Mater. Chem.* **2006**, *16*, 1013–1030.
2. Bottcher, H.; Soltmann, U.; Mertig, M.; Pompe, W. *J. Mater. Chem.* **2004**, *14*, 2176–2188.

3. Carturan, G.; Dal Toso, R.; Boninsegna, S.; Dal Monte, R. *J. Mater. Chem.* **2004**, *14*, 2087–2098.
4. Coradin, T.; Boissiere, M.; Livage, J. *Curr. Med. Chem.* **2006**, *13*, 99–108.
5. Klouda, L.; Mikos, A. G. *Eur. J. Pharm. Biopharm.* **2008**, *68*, 34–45.
6. Ruel-Gariepy, E.; Leroux, J. C. *Eur. J. Pharm. Biopharm.* **2004**, *58*, 409–426.
7. Vallet-Regi, M.; Ragel, C. V.; Salinas, A. J. *Eur. J. Inorg. Chem.* **2003**, *2003*, 1029–1042.
8. Jedlicka, S. S.; McKenzie, J. L.; Leavesley, S. J.; *et al. J. Mater. Chem.* **2006**, *16*, 3221–3230.
9. Amoura, M.; Nassif, N.; Roux, C.; Livage, J.; Coradin, T. *Chem. Commun.* **2007**, *2007*, 4015–4017.
10. Amoura, M.; Brayner, R.; Perullini, M.; *et al. J. Mater. Chem.* **2009**, *19*, 1241–1244.
11. Braun, S.; Rappoport, S.; Zusman, R.; Avnir, D.; Ottolenghi, M. *Mater. Lett.* **1990**, *10*, 1–5.
12. Pope, E. J. A.; Braun, K.; Peterson, C. M. *J. Sol-Gel Sci. Technol.* **1997**, *8*, 635–639.
13. Martin, K. R. *J. Nutr. Health Aging* **2007**, *11*, 94–98.
14. Gill, I.; Ballesteros, A. *J. Am. Chem. Soc.* **1998**, *120*, 8587–8598.
15. Gill, I.; Ballesteros, A. *Trends Biotechnol.* **2000**, *18*, 469–479.
16. Conroy, J. F. T.; Power, M. E.; Martin, J.; *et al. J. Sol-Gel Sci. Technol.* **2000**, *18*, 269–283.
17. Gill, I.; Ballesteros, A. *Enzyme Eng. XIII* **1996**, *799*, 697–700.
18. Coiffier, A.; Coradin, T.; Roux, C.; Bouvet, O. M. M.; Livage, J. *J. Mater. Chem.* **2001**, *11*, 2039–2044.
19. Ferrer, M. L.; Garcia-Carvajal, Z. Y.; Yuste, L.; Rojo, F.; del Monte, F. *Chem. Mater.* **2006**, *18*, 1458–1463.
20. Viitala, R.; Jokinen, M.; Maunu, S. L.; Jalonen, H.; Rosenholm, J. B. *J. Non-Cryst. Solids* **2005**, *351*, 3225–3234.
21. Viitala, R.; Jokinen, M.; Tuusa, S.; Rosenholm, J. B.; Jalonen, H. *J. Sol-Gel Sci. Technol.* **2005**, *36*, 147–156.
22. Nassif, N.; Bouvet, O.; Noelle Rager, M.; Roux, C.; Coradin, T.; Livage, J. *Nat. Mater.* **2002**, *1*, 42–44.
23. Gautier, C.; Ponton, A.; Livage, J.; Lopez, P. J.; Coradin, T. *J. Sol-Gel Sci. Technol.* **2009**, *50*, 164–169.
24. Dobbie, J. W.; Smith, M. J. B. *Scott. Med. J.* **1982**, *27*, 17–19.
25. Carlisle, E. M. *Science* **1972**, *178*, 619–621.
26. Dobbie, J. W.; Smith, M. J. B. *Ciba Found. Symp.* **1986**, *121*, 194–213.
27. Nieto, A.; Areva, S.; Wilson, T.; Viitala, R.; Vallet-Regi, M. *Acta Biomater.* **2009**, *5*, 3478–3487.
28. Kortesuo, P.; Ahola, M.; Karlsson, S.; Kangasniemi, I.; Yli-Urpo, A.; Kiesvaara, J. *Biomaterials* **2000**, *21*, 193–198.
29. Chang, J. S.; Chang, K. L. B.; Hwang, D. F.; Kong, Z. L. *Environ. Sci. Technol.* **2007**, *41*, 2064–2068.
30. Kuncova, G.; Podrazky, O.; Ripp, S.; *et al. J. Sol-Gel Sci. Technol.* **2004**, *31*, 335–342.
31. Inama, L.; Dire, S.; Carturan, G.; Cavazza, A. *J. Biotechnol.* **1993**, *30*, 197–210.
32. Coradin, T.; Allouche, J.; Boissiere, M.; Livage, J. *Curr. Nanosci.* **2006**, *2*, 219–230.
33. Ferrer, M. L.; Yuste, L.; Rojo, F.; del Monte, F. *Chem. Mater.* **2003**, *15*, 3614–3618.
34. Muller, W. E. G.; Engel, S.; Wang, X. H.; *et al. Biomaterials* **2008**, *29*, l771–l779.
35. Guan, C. F.; Wang, G.; Ji, J.; Wang, J. H.; Wang, H. Y.; Tan, M. *J. Sol-Gel Sci. Technol.* **2008**, *48*, 369–377.
36. Branyik, T.; Kuncova, G.; Paca, J. *Appl. Microbiol. Biotechnol.* **2000**, *54*, 168–172.
37. Ellerby, L. M.; Nishida, C. R.; Nishida, F.; *et al. Science* **1992**, *255*, 1113–1115.
38. Bhatia, R. B.; Brinker, C. J.; Gupta, A. K.; Singh, A. K. *Chem. Mater.* **2000**, *12*, 2434–2441.
39. Chen, J. B.; Xu, Y.; Xin, J. Y.; Li, S. B.; Xia, C. G.; Cui, J. R. *J. Mol. Catal. B Enzym.* **2004**, *30*, 167–172.
40. Nassif, N.; Roux, C.; Coradin, T.; Rager, M. N.; Bouvet, O. M. M.; Livage, J. *J. Mater. Chem.* **2003**, *13*, 203–208.
41. Nguyen-Ngoc, H.; Tran-Minh, C. *Anal. Chim. Acta* **2007**, *583*, 161–165.
42. Pena-Vazquez, E.; Maneiro, E.; Perez-Conde, C.; Moreno-Bondi, M. C.; Costas, E. *Biosens. Bioelectron* **2009**, *24*, 3538–3543.
43. Boninsegna, S.; Bosetti, P.; Carturan, G.; Dellagiacoma, G.; Dal Monte, R.; Rossi, M. *J. Biotechnol.* **2003**, *100*, 277–286.
44. Amsden, B.; Turner, N. *Biotechnol. Bioeng.* **1999**, *65*, 605–610.
45. Gugerli, R.; Cantana, E.; Heinzen, C.; Von Stockar, U.; Marison, I. W. *J. Microencapsul.* **2002**, *19*, 571–590.
46. Strand, B. L.; Ryan, L.; Veld, P. I.; *et al. Cell Transplant.* **2001**, *10*, 263–275.
47. Perullini, M.; Jobbagy, M.; Moretti, M. B.; Garcia, S. C.; Bilmes, S. A. *Chem. Mater.* **2008**, *20*, 3015–3021.
48. Bressler, E.; Pines, O.; Goldberg, I.; Braun, S. *Biotechnol. Prog.* **2002**, *18*, 445–450.
49. Fukushima, Y.; Okamura, K.; Imai, K.; Motai, H. *Biotechnol. Bioeng.* **1988**, *32*, 584–594.
50. Heichal-Segal, O.; Rappoport, S.; Braun, S. *Bio/Technology* **1995**, *13*, 798–800.
51. Coradin, T.; Mercey, E.; Lisnard, L.; Livage, J. *Chem. Commun.* **2001**, *2001*, 2496–2497.
52. Perullini, M.; Jobbagy, M.; Soler-Illia, G. J. A. A.; Bilmes, S. A. *Chem. Mater.* **2005**, *17*, 3806–3808.
53. Perullini, M.; Rivero, M. M.; Jobbagy, M.; Mentaberry, A.; Blimes, S. A. *J. Biotechnol.* **2007**, *127*, 542–548.
54. Sakai, S.; Ono, T.; Ijima, H.; Kawakami, K. *J. Sol-Gel Sci. Technol.* **2003**, *28*, 267–272.
55. Coradin, T.; Nassif, N.; Livage, J. *Appl. Microbiol. Biotechnol.* **2003**, *61*, 429–434.
56. Kataoka, K.; Nagao, Y.; Nukui, T.; *et al. Biomaterials* **2005**, *26*, 2509–2516.
57. Lee, H.; Park, T. G. *J. Biomed. Mater. Res.* **2009**, *88A*, 797–806.
58. Kaibanova, L.; Dobreva, E.; Emanuilova, E.; Chernev, G.; Samuneva, B.; Salvado, I. *Minerva Biotechnol.* **2006**, *18*, 23–29.
59. Liu, H. X.; Wang, C. Y.; Gao, Q. X.; Liu, X. X.; Tong, Z. *Int. J. Pharm.* **2008**, *351*, 104–112.
60. Nunamaker, E. A.; Purcell, E. K.; Kipke, D. R. *J. Biomed. Mater. Res.* **2007**, *83A*, 1128–1137.
61. Callone, E.; Campostrini, R.; Carturan, G.; Cavazza, A.; Guzzon, R. *J. Mater. Chem.* **2008**, *18*, 4839–4848.
62. Kresge, C. T.; Vartuli, J. C.; Roth, W. J.; *et al. Sci. Technol. Catal.* **1995**, *92*, 11–19.
63. Beck, J. S.; Vartuli, J. C. *Curr. Opin. Solid State Mater. Sci.* **1996**, *1*, 76–87.
64. Brinker, C. J.; Lu, Y. F.; Sellinger, A.; Fan, H. Y. *Adv. Mater.* **1999**, *11*, 579–585.
65. Davis, M. E. *Nature* **2002**, *417*, 813–821.
66. Soler-Illia, G. J. A. A.; Crepaldi, E. L.; Grosso, D.; Durand, D.; Sanchez, C. *Chem. Commun.* **2002**, *2002*, 2298–2299.
67. Soler-illia, G. J. D.; Sanchez, C.; Lebeau, B.; Patarin, J. *Chem. Rev.* **2002**, *102*, 4093–4138.
68. Baca, H. K.; Ashley, C.; Carnes, E.; *et al. Science* **2006**, *313*, 337–341.
69. Baca, H. K.; Carnes, E.; Singh, S.; Ashley, C.; Lopez, D.; Brinker, C. J. *Acc. Chem. Res.* **2007**, *40*, 836–845.
70. Shapiro, A. M. J.; Lakey, J. R. T.; Ryan, E. A.; *et al. N. Engl. J. Med.* **2000**, *343*, 230–238.
71. Shapiro, A. M. J.; Ricordi, C.; Hering, B. J.; *et al. N. Engl. J. Med.* **2006**, *355*, 1318–1330.
72. Dal Toso, R.; Boninsegna, S. In *The Cell Cycle in the Central Nervous System*; Janigro, D., Ed.; Humana Press Inc: Totowa, NJ, 2008; pp 465–475.
73. Muraca, M.; Vilei, M. T.; Zanusso, G. E.; *et al. Artif. Organs* **2002**, *26*, 664–669.
74. Boninsegna, S.; Dal Toso, R.; Dal Monte, R. *J. Sol-Gel Sci. Technol.* **2003**, *26*, 1151–1157.
75. Sakai, S.; Ono, T.; Ijima, H.; Kawakami, K. *J. Biomater. Sci. Polym. Ed.* **2003**, *14*, 643–652.
76. Sakai, S.; Ono, T.; Ijima, H.; Kawakami, K. *Int. J. Pharm.* **2004**, *270*, 65–73.
77. Sakai, S.; Ono, T.; Ijima, H.; Kawakami, K. *Biomaterials* **2001**, *22*, 2827–2834.
78. Sakai, S.; Ono, T.; Ijima, H.; Kawakami, K. *Biomaterials* **2002**, *23*, 4177–4183.
79. Sakai, S.; Ono, T.; Ijima, H.; Kawakami, K. *J. Membr. Sci.* **2002**, *202*, 73–80.
80. Sakai, S.; Ono, T.; Ijima, H.; Kawakami, K. *J. Membr. Sci.* **2002**, *205*, 183–189.
81. Nathan, D. M. *N. Engl. J. Med.* **1993**, *328*, 1676–1685.
82. Nathan, D. M. *Lancet* **1998**, *352*, 832–833.
83. Tamborlane, W. V.; Beck, R. W.; Bode, B. W.; *et al. N. Engl. J. Med.* **2008**, *359*, 1464–1476.
84. Steil, G. M.; Rebrin, K.; Darwin, C.; Hariri, F.; Saad, M. F. *Diabetes* **2006**, *55*, 3344–3350.
85. Erdodi, G.; Kang, J. M.; Yalcin, B.; *et al. Biomed. Microdevices* **2009**, *11*, 297–312.
86. Grundfest-Broniatowski, S. F.; Tellioglu, G.; Rosenthal, K. S.; *et al. ASAIO J.* **2009**, *55*, 400–405.
87. Tate, M. C.; Shear, D. A.; Hoffman, S. W.; Stein, D. G.; LaPlaca, M. C. *Biomaterials* **2001**, *22*, 1113–1123.
88. Ruel-Gariepy, E.; Chenite, A.; Chaput, C.; Guirguis, S.; Leroux, J. C. *Int. J. Pharm.* **2000**, *203*, 89–98.
89. Chenite, A.; Chaput, C.; Wang, D.; *et al. Biomaterials* **2000**, *21*, 2155–2161.

90. Chenite, A.; Buschmann, M.; Wang, D.; Chaput, C.; Kandani, N. *Carbohydr. Polym.* **2001**, *46*, 39–47.
91. Simard, P.; Galarneau, H.; Marois, S.; *et al*. *Arthritis Res. Ther.* **2009**, *11*, R74–R83.
92. Roberts, S. J.; Howard, D.; Buttery, L. D.; Shakesheff, K. M. *Br. Med. Bull.* **2008**, *86*, 7–22.
93. Peterson, L.; Minas, T.; Brittberg, M.; Lindahl, A. *J. Bone Joint Surg. Am.* **2003**, *85A*, 17–24.
94. Paccola, C. A. J.; Xavier, C. A. M.; Goncalves, R. P. *Arch. Orthop. Trauma Surg.* **1979**, *93*, 253–259.
95. Hoemann, C. D.; Hurtig, M.; Rossomacha, E.; *et al*. *J. Bone Joint Surg. Am.* **2005**, *87A*, 2671–2686.
96. Hoemann, C. D.; Sun, J.; McKee, M. D.; *et al*. *Osteoarthr. Cartil.* **2007**, *15*, 78–89.
97. Hoemann, C. D.; Sun, J.; Legare, A.; McKee, M. D.; Buschmann, M. D. *Osteoarthr. Cartil.* **2005**, *13*, 318–329.
98. Hoemann, C. D.; Chenite, A.; Sun, J.; *et al*. *J. Biomed. Mater. Res.* **2007**, *83A*, 521–529.
99. Cheng, Y. H.; Lin, F. H.; Yang, K. C. *Tissue Eng. A* **2010**, *2010*, 695–703.
100. Stile, R. A.; Burghardt, W. R.; Healy, K. E. *Macromolecules* **1999**, *32*, 7370–7379.
101. Vernon, B.; Gutowska, A.; Kim, S. W.; Bae, Y. H. *Macromol. Symp.* **1996**, *109*, 155–167.
102. Vernon, B. L.; Kim, S. W.; Bae, Y. H. *Abstr. Pap. Am. Chem. Soc.* **1997**, *213*, 392-COLL.
103. Vernon, B.; Kim, S. W.; Bae, Y. H. *J. Biomater. Sci. Polym. Ed.* **1999**, *10*, 183–198.
104. Chae, S. Y.; Kim, S. W.; Bae, Y. H. *J. Drug Target.* **2001**, *9*, 473–484.
105. Chae, S. Y.; Kim, S. W.; Bae, Y. H. *Tissue Eng.* **2002**, *8*, 379–394.
106. Chae, S. Y.; Kim, Y. Y.; Kim, S. W.; Bae, Y. H. *Transplantation* **2004**, *78*, 392–397.
107. Kim, Y. Y.; Chae, S. Y.; Kim, S.; Byun, Y.; Bae, Y. H. *J. Biomater. Sci. Polym. Ed.* **2005**, *16*, 1521–1535.
108. Park, K. H.; Bae, Y. H. *Biosci. Biotechnol. Biochem.* **2002**, *66*, 1473–1478.
109. Morikawa, N.; Matsuda, T. *J. Biomater. Sci. Polym. Ed.* **2002**, *13*, 167–183.
110. Ohya, S.; Nakayama, Y.; Matsuda, T. *Biomacromolecules* **2001**, *2*, 856–863.
111. Ibusuki, S.; Fujii, Y.; Iwamoto, Y.; Matsuda, T. *Tissue Eng.* **2003**, *9*, 371–384.
112. Cho, J. H.; Kim, S. H.; Park, K. D.; *et al*. *Biomaterials* **2004**, *25*, 5743–5751.
113. Wang, F.; Li, Z.; Khan, M.; *et al*. *Acta Biomater.* **2010**, *6*, 1978–1991.
114. Chen, J.-P.; Cheng, T.-H. *Colloids Surfaces A Physicochem. Eng. Aspects* **2008**, *313–314*, 254–259.
115. Wanka, G.; Hoffmann, H.; Ulbricht, W. *Macromolecules* **1994**, *27*, 4145–4159.
116. Blonder, J. M.; Baird, L.; Fulfs, J. C.; Rosenthal, G. J. *Gel. Life Sci.* **1999**, *65*, PL261–PL266.
117. Wout, Z. G.; Pec, E. A.; Maggiore, J. A.; Williams, R. H.; Palicharla, P.; Johnston, T. P. *J. Parenter. Sci. Technol.* **1992**, *46*, 192–200.
118. Niu, G. G.; Du, F. Y.; Song, L.; *et al*. *J. Control. Release* **2009**, *138*, 49–56.
119. Chung, H. J.; Go, D. H.; Bae, J. W.; Jung, I. K.; Lee, J. W.; Park, K. D. *Curr. Appl. Phys.* **2005**, *5*, 485–488.
120. Bae, S. J.; Joo, M. K.; Jeong, Y.; *et al*. *Macromolecules* **2006**, *39*, 4873–4879.
121. Park, K. M.; Lee, S. Y.; Joung, Y. K.; Na, J. S.; Lee, M. C.; Park, K. D. *Acta Biomater.* **2009**, *5*, 1956–1965.
122. Jeong, B.; Bae, Y. H.; Kim, S. W. *Macromolecules* **1999**, *32*, 7064–7069.
123. Jeong, B.; Bae, Y. H.; Kim, S. W. *J. Biomed. Mater. Res.* **2000**, *50*, 171–177.
124. Chung, Y. M.; Simmons, K. L.; Gutowska, A.; Jeong, B. *Biomacromolecules* **2002**, *3*, 511–516.
125. Tan, H.; Marra, K. G. *Materials* **2010**, *3*, 1746–1767.
126. Kreuz, P. C.; Muller, S.; Ossendorf, C.; Kaps, C.; Erggelet, C. *Arthritis Res. Ther.* **2009**, *11*, R33.
127. Nehrer, S.; Dorotka, R.; Domayer, S.; Stelzeneder, D.; Kotz, R. *Am. J. Sports Med.* **2009**, *37*(Suppl 1), 81S–87S.
128. Podskubka, A.; Povysil, C.; Kubes, R.; Sprindrich, J.; Sedlacek, R. *Acta Chir. Orthop. Traumatol. Cech.* **2006**, *73*, 251–263.
129. Hasson, E.; Gallula, J.; Shimoni, Y.; Grad-Itach, E.; Marikovsky, M.; Mitrani, E. *J. Vasc. Res.* **2006**, *43*, 139–148.

Relevant Websites

http://www.Biosyntech.com – BioSynTech, the developer of BST-CarGel®.
http://en.wikipedia.org/wiki/Pluronic – Definition of Poloxamers or Pluronic®.
http://www.fda.gov/oc/initatives/criticalpath – FDA Critical Path Initiative.
http://www.irbtech.com/ – IRB srl, the company involved in the R&D of BioSil.

4.432. Layered Double Hydroxides as Controlled Release Materials

J H Choy, Ewha Womans University, Seoul, Korea
J M Oh, Yonsei University, Wonju, Gangwon-Do, Korea
S J Choi, Seoul Women's University, Seoul, Korea

© 2011 Elsevier Ltd. All rights reserved.

4.432.1.	**Introduction**	545
4.432.2.	**LDHs and Intercalation**	546
4.432.2.1.	Structure	546
4.432.2.2.	Preparation and Intercalation	546
4.432.3.	**Stabilization of Biomolecules via Intercalation**	546
4.432.4.	**Controlled Release of Intercalated Biomolecules**	551
4.432.5.	**Enhanced Cellular Uptake**	554
4.432.6.	**Conclusion and Perspectives**	555
References		556

Abbreviations

AMP	Adenosine-5′-monophosphate
CD	Circular dichroism
CLA	Conjugated linoleic acid
CMP	Cytidine-5′-monophosphate
DAPI	4′,6-DiAmidino-2-Phenyllndole
DNA	Deoxyribo nucleic acids
EE	Early endosome
FITC	Fluoroscein isothiocyanate
GLA	γ-linolenic acid
GMP	Guanosine-5′-monophosphate
HBSS	Hank's balanced salt solution
HEPES	4-(2-Hydroxyethyl)-1-piperazineethanesulfonic acid
IAA	Indole-3-acetic acid
LDH	Layered double hydroxide
LE	Late endosome
LMWH	Low molecular weight heparin
MTX	Methotrexate
PBS	Phosphate buffered saline
TR	Texas red
VA	Vanillic acid
VC	Vitamin C
VE	Vitamin E
ZBS	Zinc basic salt

4.432.1. Introduction

The efficient delivery of biomolecules to a specific target at an intended time has attracted great interest in recent years because targeted delivery maximizes the value and utility of the biomolecules.[1–3] A targeted delivery system not only diminishes the adverse effects caused by excessive dosage, but it can also increase the activity of drugs or other therapeutic molecules.[2,4] Generally, biomolecules are physically, chemically, and biologically vulnerable to the harsh external conditions, and therefore, protection by durable inorganic nanoparticles can stabilize these biomolecules. In this sense, inorganic nanoparticles such as aluminosilicates,[5–11] layered double hydroxides (LDHs),[12–19] silicas,[20–25] and calcium phosphate[26–30] have been widely studied as reservoirs or delivery carriers of biomolecules (see **Chapter 3.319, Characterization of Nanoparticles in Biological Environments**).

Among these nanoparticles, layered materials are attractive candidates for such applications as it is relatively simple to prepare heterostructured nanohybrids through an intercalation route which involves the reversible insertion of a guest species into a two-dimensional host lattice. By rearranging the orientation of molecules in the interlayer nanospace, it is possible to maximize the advantages of the introduced molecules and even expect synergistic effects from the interaction between the host (inorganic layers) and the guest (molecules). Various intercalative systems, such as inorganic/inorganic, organic/inorganic, and bio/inorganic nanohybrids, have been reported which can be used to develop new materials with unusual physicochemical properties.[13,14,31–37]

LDHs, also known as anionic clay, are potential candidate materials that can act as a reservoir or a delivery carrier for biomolecules. Similar to other layered inorganic materials, LDH lattices can tolerate severe conditions compared to the biomolecules themselves. Furthermore, LDHs exhibit characteristic merits that are suitable for storage of biomolecules such as high anion exchangeability, pH-dependent solubility, and comparatively low toxicity.

Various biomolecules and biofunctionalized molecules including deoxyribonucleotides, therapeutic antisense genes, peptides, proteins, drugs, organic acids, food ingredients, and vitamins have been successfully intercalated into LDHs in order to enhance their stability and for safe preservation.[12–15,38–45] In addition, they can be retrieved whenever necessary without any structural deformation, and their release profile can be controlled by manipulating the size, morphology, chemical

composition, charge density, and surface properties of LDHs, as well as by using various release conditions such as salt concentration, pH, etc. LDHs can easily permeate the plasma membrane and can therefore transport intercalated biofunctionalized molecules efficiently into intracellular organs. As the controlled release properties of LDHs depend on pH or salt concentration, the biofunctionalized molecules are expected to be liberated in lysosomes, which are slightly acidic and full of electrolytes.

In this chapter, we summarize techniques used for the stabilization and controlled release of biofunctionalized molecules into and out of LDHs, and also discuss how the enhanced cellular uptake and intracellular release of biofunctionalized molecules from LDHs can be applied as a drug delivery system.

4.432.2. LDHs and Intercalation

4.432.2.1. Structure

Layered metal hydroxides can be categorized into two classes. The most prevalent type, LDHs are known to have a hydrotalcite-like structure, in which positively charged layers of the general formula $\left[M^{2+}_{1-x}M^{3+}_{x}(OH)_2\right]^{x+}$ (M^{n+} stands for metal cations of M^{2+} = Mg^{2+}, Zn^{2+}, Ni^{2+}, Cu^{2+}, ...; M^{3+} = Al^{3+}, Fe^{3+}, ...) are stacked and their interlayer spaces filled with anions (A^{m-} = CO_3^{2-}, NO_3^-, SO_4^{2-}, and other anionic species) and H_2O molecules.[37] One layer of LDH consists of $M(OH)_6$ octahedrons which share their edges to form two-dimensional sheets; and the isomorphic substitution of M^{2+} with M^{3+}, in a brucite-like layer ($M^{II}(OH)_2$), results in a permanent positive charge. There is another type of layered metal hydroxides, the structure of which is often referred to as hydroxy double salts (HDSs). They have the general formula $\left[\left(M^{2+}_{1+x}Me^{2+}_{1+x}\right)(OH)_{3(1-\gamma)}\right]X^{n-}_{(1+3\gamma)/n}zH_2O$, where M^{2+} and Me^{2+} indicate divalent metal cations such as Zn^{2+}, Cu^{2+}, or Ni^{2+}, and X^{n-} is the interlayer anion.[46] Similar to LDHs, divalent metal ions in the HDS form two-dimensional sheets of edge-sharing $M(OH)_6$ octahedrons; however, HDSs periodically contain vacant sites, which are filled by $M(OH)_4$ tetrahedrons that are positioned above and below the hydroxide layers. An example of an HDS is a zinc basic salt (ZBS), which has the formula of $Zn_5(OH)_8(NO_3)_2{\cdot}nH_2O$, where a quarter of the O_h sites are vacant, thus forming tetrahedra (T_d).

4.432.2.2. Preparation and Intercalation

LDHs can typically be synthesized by coprecipitation of mixed metal cations by base titration, either with or without hydrothermal treatment, which can enhance crystallinity. Various sizes of LDH particles can be prepared by adjusting the synthetic parameters during coprecipitation or during postprecipitation treatment. LDHs with large particle sizes can be prepared by titrating the metal solution with a weak Brønsted base, like urea ($pK_b = 13.8$). The urea is slowly hydrolyzed to release ammonium and carbonate.[47] As the hydrolysis occurs uniformly and in a temperature-dependent manner, it is possible to maintain a low degree of supersaturation during precipitation, and as a consequence, large particle sizes can be achieved.[48]

$$CO(NH_2)_2 \rightarrow NH_4CNO : \text{slow}$$

$$NH_4CNO + 2H_2O \rightarrow (NH_4)_2CO_3 : \text{fast}$$

In addition, postprecipitation processes, such as hydrothermal treatment, can enhance the crystallinity and particle size of the LDHs. According to the equation $dL/dt = C\ \exp(-1/RT)$ (C: constant), where L is particle size and T is the reaction temperature,[49] both aging time and reaction temperature appear to be key factors controlling size. LDH particles, with homogeneous particle sizes from 80 to 4000 nm, can be successfully prepared based on the synthetic parameters above.[50] **Figure 1** shows a few selected scanning electron microscopic images for LDH particles synthesized by the urea hydrolysis method (**Figure 1(d)–(f)**) and hydrothermal treatment (**Figure 1(a)–(c)**).

In order to intercalate biomolecules into LDHs, any one of three synthetic routes, coprecipitation, anion exchange, and reconstruction, can be utilized[51] (**Scheme 1**). The coprecipitation route is the most frequently employed as it enables a one-step synthesis of both the LDH layer and its intercalation. Furthermore, it is possible to easily fine-tune the charge density of the layer and control its framework composition, anion properties, treatment conditions, etc., in the coprecipitation route. During typical syntheses, the metal solution is blended with the solution containing biomolecules and then titrated with an alkaline solution to the pH at which metal hydroxides will precipitate. In LDH synthesis, it is important to prevent contamination by airborne carbonate. In the anion exchange route, LDHs with readily exchangeable ions (NO_3^- or Cl^-) that have been prepared by the conventional coprecipitation can be utilized. In this method LDHs are dispersed in decarbonated water, and the solution containing excess biomolecules is added. The biomolecules are incorporated into the LDH layers according to their concentration gradient. Biomolecules can also be intercalated into LDHs via the reconstruction method. First, LDHs having carbonate anions are heat-treated to remove the H_2O and CO_2 moieties, and the resulting layered oxides are mixed with the biomolecule solution to provide H_2O and anionic species that facilitate reconstruction of the LDH lattices. Bio-LDH nanohybrids prepared using these methods are known to exhibit (i) stabilization, (ii) controllable release of biomolecules, and (iii) enhanced cellular uptake, all of which are essential for drug delivery (see **Chapter 4.425, Delivery of Nucleic Acids and Gene Delivery**).

4.432.3. Stabilization of Biomolecules via Intercalation

The sandwich structure made by the two-dimensional LDHs can be considered as pocket nanocapsules for biomolecules that are either thermodynamically unstable or kinetically labile.

Nucleotide monophosphates such as adenosine-5′-monophosphate (AMP), guanosine-5′-monophosphate (GMP), and cytidine-5′-monophosphate (CMP) and also deoxyribonucleotides (Herring testis DNA 100–2000 base pairs in length) have been successfully intercalated into MgAl-LDHs via ion-exchange reactions.[15,17,41] **Figure 2** shows schematic illustration of the interlayer orientation of DNA strands that have been intercalated into LDH and their circular dichroism (CD) spectra,

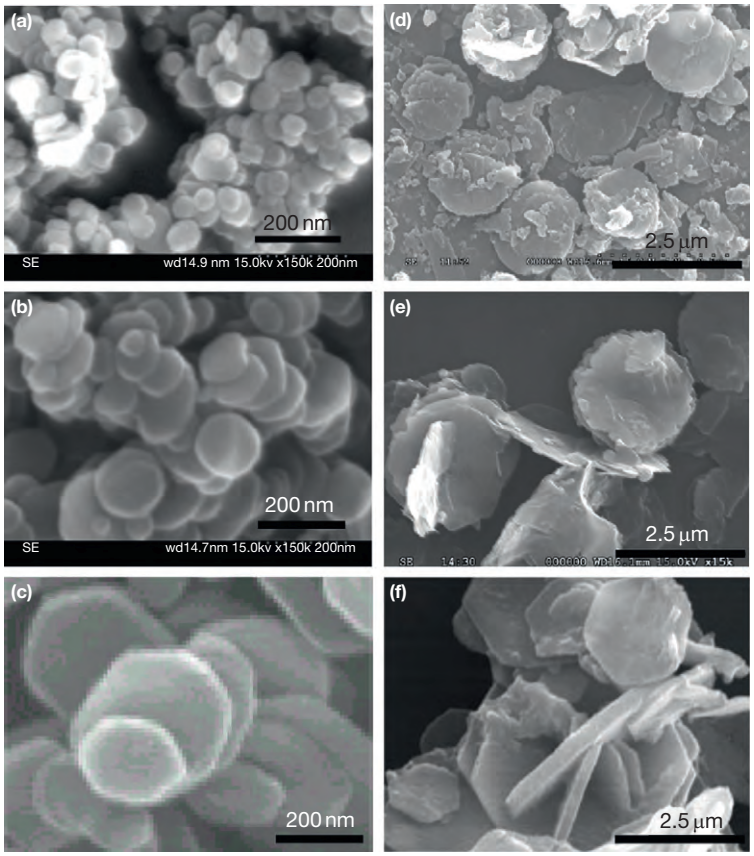

Figure 1 Scanning electron microscopic images for size controlled LDH particles (a) 80 nm, (b) 120 nm, (c) 350 nm, (d) 850 nm, (e) 2100 nm, and (f) 2800 nm. The particles sizes were controlled according to synthetic conditions such as total metal concentration, basicity of alkaline solution, aging time and reaction temperature. Reproduced from Oh, J. M.; Hwang, S. H.; Choy, J. H. *Solid State Ionics* **2002**, *151*(1–4), 285–291, with permission from Elsevier.

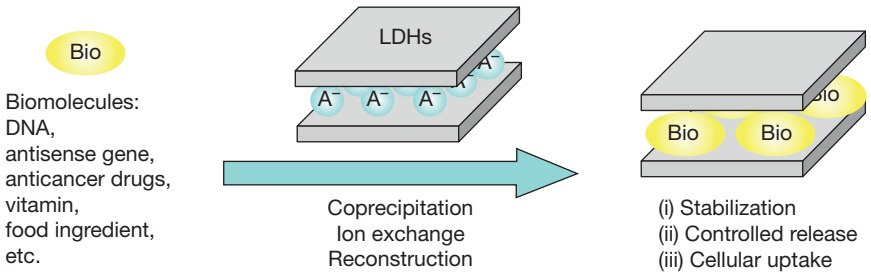

Scheme 1 Schematic illustration of biomolecule intercalation into layered double hydroxides. A^- stands for the exchangeable interlayer anion and Bio for biomolecules.

which indicate that the anionic DNA strands are tightly bound to the positively charged LDH layers, thus forming stable structures.

Generally, the phosphate group ($-PO_4^{2-}$) of the B-type DNA occurs every 3.4 Å, and the diameter of the double helix is ~20 Å. Thus, the DNA strands require 34 $Å^2$ of area per single negative charge. However, from X-ray diffraction patterns, it was determined that the positive charge of LDHs generated from trivalent cations can only provide 24.9 $Å^2$ of area per unit charge. Therefore, it can be concluded that the intercalated DNA becomes more twisted than free DNA in order to fit into the available area in the LDH lattice (Figure 2(a)).

i) Area demand per unit charge of DNA molecule:

$1\ bp = 2e^-$

therefore area per unit charge = 3.4 Å/1 bp × 20 Å/$2e^-$ = ~34 $Å^2/e^-$

ii) Area provided per unit charge by LDH lattice:

$a = 3.1\ Å/[Mg_{0.66}Al_{0.33}(OH)_2]^{0.33+}$

unit cell area = $a^2 \times \sin 60^\circ = 8.3\ Å^2$

therefore area unit charge = ~8.3 $Å^2 \times 3$ = ~24.9 $Å^2/e^-$

The CD spectra, shown in Figure 2(b), also support the concerted orientation of DNA in LDHs.[17] CD analysis is an effective method to examine conformational changes in the helical structure of DNA because CD sensitively reflects the change in polarization caused by any change in the helicity of

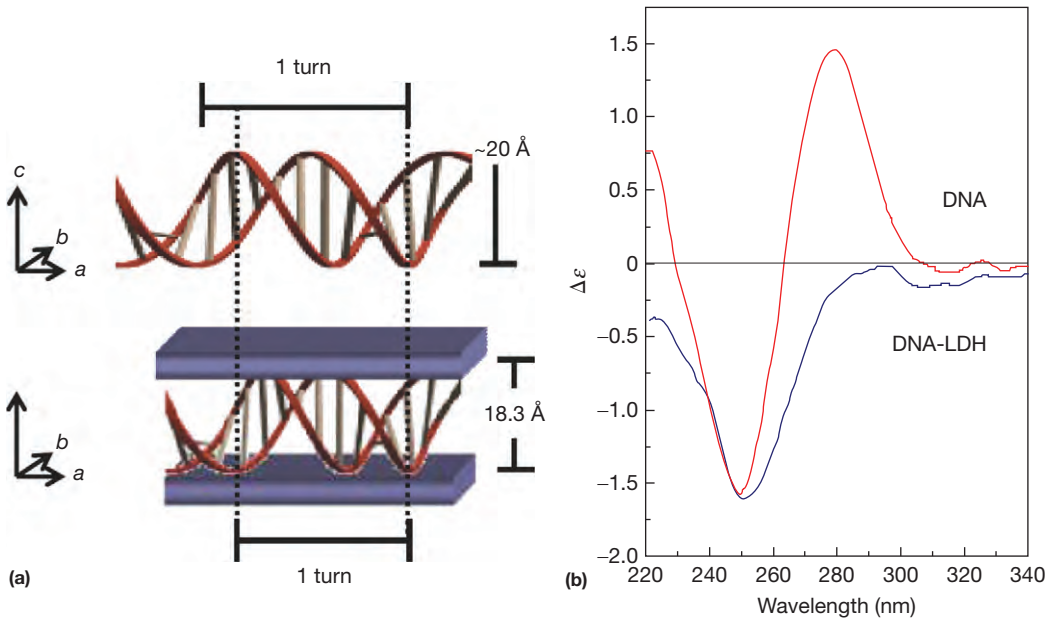

Figure 2 (a) Schematic illustration of the interlayer orientation of DNA strands and (b) circular dichroism spectra for free DNA in solution and DNA-LDH. Reproduced from Oh, J. M.; Kwak, S. Y.; Choy, J. H. *J. Phys. Chem. Solids* **2006**, *67*(5–6), 1028–1031, with permission from Elsevier.

nucleic acids or proteins. Compared to free DNA, the spectrum of DNA-LDH shows a collapsed CD band at around a wavelength of ~275 nm. A similar kind of band collapse can also be observed for DNA strands in high salt concentrations in which cation–anion interactions are better facilitated.

As trivalent ions such as aluminum readily form stable complexes with the phosphates on the DNA backbone, it has been difficult to prepare DNA-LDH intercalates by direct coprecipitation. Recently, however, Desigaux *et al.*[52] succeeded at intercalating DNA fragments of various sizes (100–500 and 6000–8000 bp) into an MgGa-LDH through coprecipitation. The intercalation of therapeutic genes, such as antisense oligonucleotides, into LDHs has also been reported.[13] Thyveetil *et al.*[53] computed the stability of DNA-LDH intercalates utilizing molecular dynamics simulations and showed that the phosphate backbone exactly aligns with the lattice of the trivalent ions. This result also suggests that the intercalated DNA molecules are stabilized by strong electrostatic interactions with the LDH layers.

The biological stability of DNA in a DNA-LDH intercalate can be quantitatively evaluated using a DNase I resistance test. DNA-LDH or DNA alone, with the same initial optical density of 0.4 at 260 nm, were identically treated with 192 units of DNase I and DNA degradation by DNase I was estimated by the change in optical density at 260 nm recorded as a function of time (Figure 3). By comparing the slopes of the degradation curves, which indicate the velocity of degradation, it was found that degradation of the DNA-LDH complex was negligible, while degradation of the naked DNA could be observed within a few minutes. This high resistance of the LDH against nuclease attack is highly advantageous and makes it a delivery material for DNA under

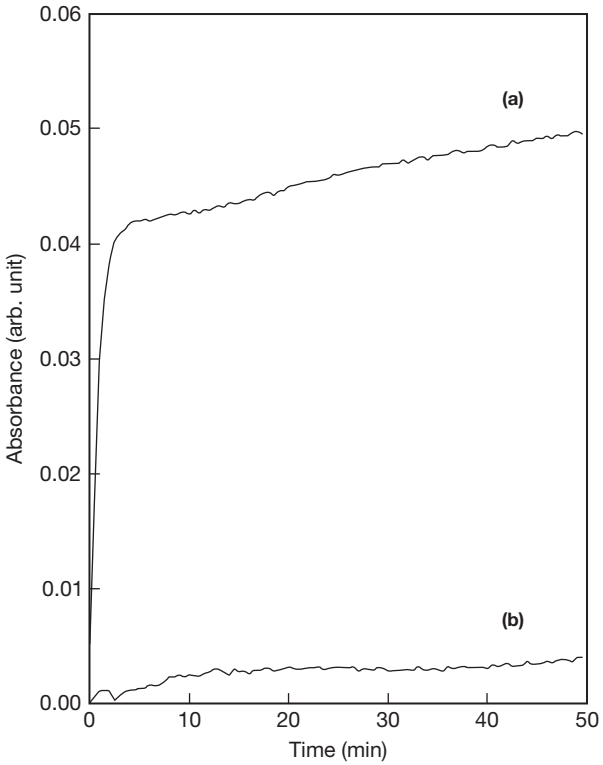

Figure 3 Profiles of UV absorbance for (a) DNA and (b) DNA-LDH hybrid treated with DNase I as a function of time. 500 μl of DNA-LDH hybrid (OD 0.4) was treated with 2 μl of DNase I (96 unit μl^{-1}) in 7.5 mM HEPES (pH 7.3) containing 75 mM NaCl at room temperature. The change in absorbance at 260 nm was recorded to estimate DNA degradation.

physiological conditions where DNA degradation through nuclease attack can take place.

Besides DNA, large biopolymers such as polysaccharides and proteins can be intercalated into LDHs. Darder *et al.*[54] prepared composites of LDHs with natural biopolymers such as alginic acids, pectin, carrageenan, and others by both the coprecipitation and the coorganized assembly routes. Shi *et al.*[55] intercalated the large protein bromelain, a mixture of proteolytic enzymes derived from pineapples, into LDHs by utilizing a reconstruction method in which calcined MgAl-LDH was mixed with bromelain/phosphate buffered saline (PBS). Another example of protein intercalation into LDHs was provided by Rahman *et al.*[18] They successfully incorporated lipase molecules onto LDH surfaces through physical and chemical adsorption which included electrostatic interactions. The incorporated enzymes were shown to have improved thermal stability, with more than 50% of their activity preserved.

Drug molecules and other biofunctional molecules require stabilization because they can easily be destroyed or expelled by various drug-resistant mechanisms in biological systems. We have recently reported the intercalation of folic acid and its derivatives into LDHs for use as a drug stabilization and delivery system.[31] Folic acid (*N*-(4-{[(2-amino-4-oxo-1,4-dihydropteridin-6-yl)methyl]amino}benzoyl)-L-glutamic acid) and its derivative, folinic acid ((*S*)-2-[4-[(2-amino-5-formyl-4-oxo-5,6,7,8-tetrahydro-1H-pteridin-6-yl)methylamino] benzoyl] aminopentanedioic acid) are used in cancer therapy and in the treatment of vitamin deficiencies. Another folate derivative, methotrexate (MTX: (2 *S*)-2-[(4-{[(2,4-diamino-7,8-dihydropteridin-6-yl)methyl] (methyl)amino}phenyl)formamido] pentanedioic acid), is known to act as a folic acid antagonist and inhibits the proliferation of certain cancers by regulating the biosynthesis of thymidylate.[56,57] Unfortunately, these are quite unstable in biosystems, with short plasma half lives of 6.2 h and 3–15 h (depending on dose) for folinic acid and MTX, respectively. The intercalation of these molecules into LDHs is thought to stabilize them physically, chemically, and biologically, and consequently we could expect longer half lives and lower dosage requirements (see **Chapter 1.115, Calcium Phosphates for Cell Transfection**).

As shown in X-ray diffraction patterns (**Figure 4(a)**), the intercalation of folic acid and its derivatives resulted in a significant increase in interlayer space. Given that the thickness of a brucite-like LDH sheet is 4.8 Å, the gallery heights are estimated to be 17.1, 14.3, and 15.1 Å for folic acid-, folinic acid- and MTX-LDH intercalates, respectively. These values are smaller than the longitudinal molecular dimensions of folic acid (≈19.7 Å), folinic acid (≈21.5 Å), and MTX (≈21.2 Å). These results suggest that the intercalated molecules are oriented in a tilted monolayer with tilt angles of ∼60°, 42°, and 45° between the LDH layer and folic acid, folinic acid, and MTX, respectively (**Figure 4(b)**).[31] Assuming that these molecules are packed in a zig-zag, the electrostatic interactions between the anionic terminal carboxylates and the cationic hydroxide layers can be maximized. The strong electrostatic interaction between folic acid species and the LDHs was also verified by infrared and UV–vis spectroscopy as well as thermogravimetric analyses.

LDHs can be utilized to encapsulate labile but bioactive substances like vitamins to protect them against rapid degradation by light, temperature, oxygen, alkali metals, etc.[42,58,59] In fact, their fast degradation greatly limits their application as active ingredients in cosmetics and foods. In particular, vitamin C oxidation is facilitated in the presence of oxygen and a small amount of metal ions. For effective protection and controlled delivery, vitamin C (VC) or E (VE) molecules were intercalated into ZnAl-LDH[42] or ZBSs.[59] The X-ray diffraction patterns (**Figure 5(a)**) for the pristine LDHs (host LDHs before intercalation) and LDH intercalates exhibit well developed (00 *l*) reflections showing *d*-spacing of 8.7, 10.5, and 53.8 Å for pristine, VC-LDH and VE-LDH, respectively. Based on the longitudinal dimensions of the vitamin molecules and the observed gallery space, a schematic illustration of the vitamin-LDH structures are shown in **Figure 5(b)**. The VE molecules are arranged as J-like aggregates with a tilting angle of 62°. It was also verified, using UV–vis spectroscopy, that α-(+)-tocopherol acid succinate molecules stack diagonally with respect to the basal plane, suggesting that the stabilization of vitamin molecules occurs via electrostatic interactions.

Recently, the intercalation procedure has been employed in food science to increase the stability and applicability of additives. For instance, essential fatty acids, such as conjugated linoleic acid (CLA) and γ-linolenic acid (GLA), and flavor molecules such as vanillic acid (VA) have been successfully introduced into layered materials. Won *et al.*[60] have reported that the intercalation of CLA and GLA into zinc hydroxide through coprecipitation greatly enhanced their thermal stability during storage. CLA alone, stored in a 50 °C chamber, completely decomposed in 7 days, while intercalated CLA exhibited long term thermal stability, for 49 days at 50 °C. Similar thermal stability was observed with GLA intercalates; the intercalated GLA preserved 50% of its fatty acid moieties after 28 days at 50 °C, whereas all unprotected GLA molecules were oxidized after 14 days in the same chamber. The X-ray diffraction pattern of these LDHs suggests that the interlayer orientation of fatty acids forms a close zig-zag packing of linear molecules. Both the electrostatic stabilization and the intermolecular hydrophobic interactions of fatty acid packing are considered to play important roles in the observed enhancement in thermal stability.

Vanillic acid (VA: 4-hydroxy-3-methoxybenzoic acid), which is frequently used as a flavoring or food additive, has been successfully intercalated into ZnAl-LDH with various metal ratios.[61] Data from X-ray diffractometry and infrared spectroscopy show that LDHs can well preserve VA molecules via electrostatic interactions, regardless of the metal ratio used. Similar to fatty acid intercalates, interlayer VA molecules appear to be arranged in a zig-zag orientation that maximizes their intermolecular π–π interactions. It has also been reported that the extra chemical stabilization energy from electrostatic interactions and intermolecular packing could strongly enhance thermal stability of the VA. VA molecules intercalated in a ZBS maintained most VA moieties for 1 h at 200 °C, but naked VA molecules readily melted within 20 min and were expected to decompose within 30 min.[62]

Yang *et al.*[63] have recently demonstrated the intercalation of indole-3-acetic acid (IAA) into ZnAl-LDH and ZBS for safe preservation and controlled release. IAA is a type of plant auxin

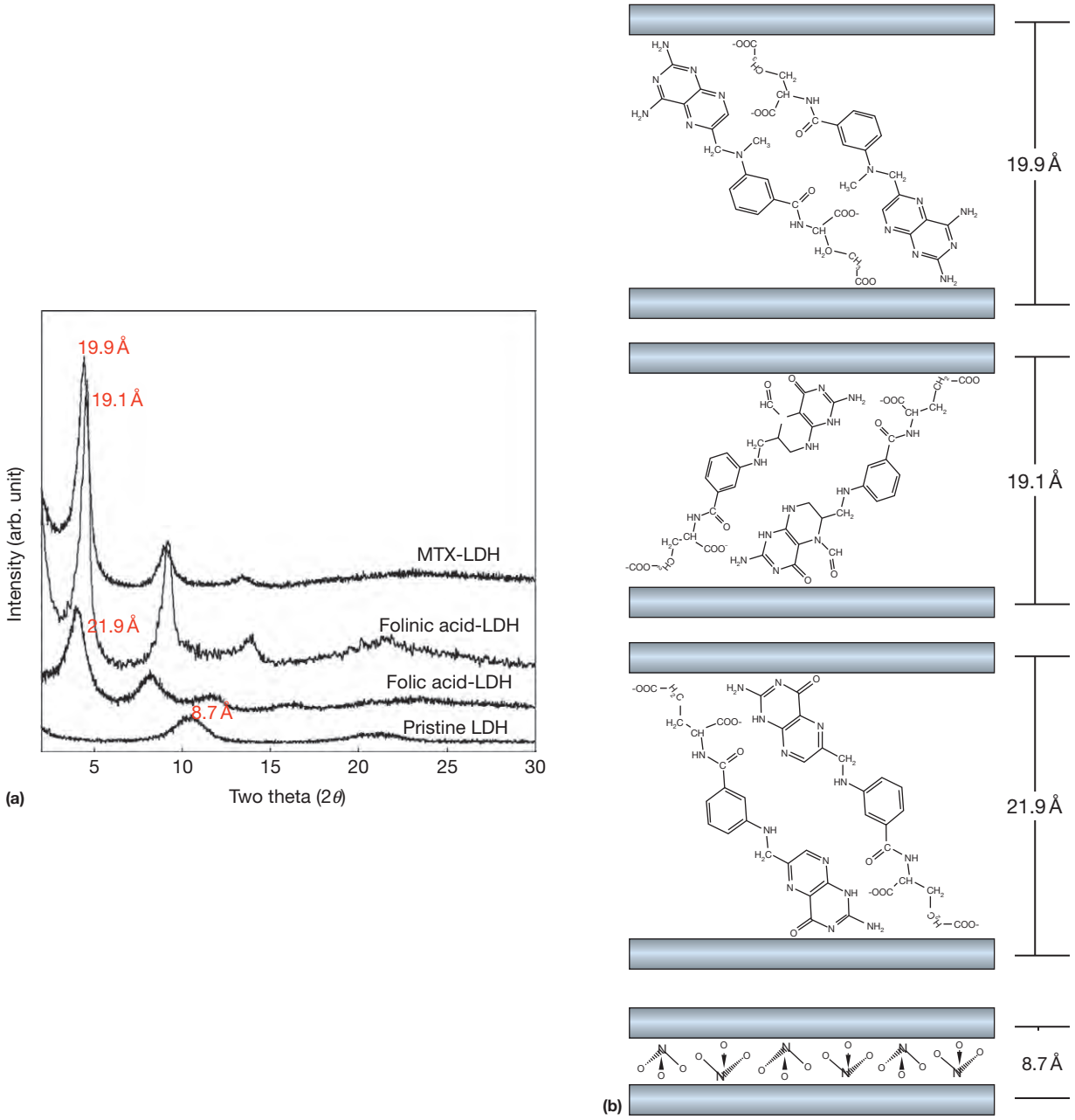

Figure 4 (a) X-ray diffraction patterns for various folate derivatives intercalated in LDH and (b) corresponding structures. Reproduced from Choy, J. H.; Jung, J. S.; Oh, J. M.; *et al*. *Biomaterials* **2004**, *25*(15), 3059–3064, with permission from Elsevier.

and has great potential as a prodrug or as a cosmetic or dermatological ingredient. However, it is very unstable in the presence of UV–vis irradiation and oxygen. In order to measure the enhancement in stability due to LDH interaction, IAA, IAA-LDH, and IAA-ZBS were dispersed in water and their concentrations were monitored for 10 days. As shown in Figure 6(a), over 10 days, the active concentration of the free IAA molecules decreased gradually to 40% of the initial concentration. However, IAA molecules stabilized with either LDH or ZBS retained most of their active moieties over the same time period. It was notable that, in this chapter, molecular orientation and stabilization could be determined by the type of lattice (Figure 6B (a) and (b)). Structural differences in the interlayer orientation result from the different charge densities of the ZBS and ZnAl-LDH ($5.8e^{-}/100\ Å^2$ and $5.0e^{-}/100\ Å^2$ for ZBS and LDH, respectively).[63] Consequently, ZBS can contain more IAA molecules per unit charge than LDH, resulting in a more compact molecular packing with a smaller tilting angle.

Infrared spectroscopy revealed that the IAA molecules are more tightly bound to a ZBS layer than to an LDH. For quantitative analysis, infrared spectra for IAA itself, Na^{+}-IAA salt, IAA-LDH, and IAA-ZBS were obtained, and the stretching modes of the IAA carboxylates were investigated. It was shown that the wave number difference between two stretching modes of carboxylate, $\Delta\nu_{as\text{-}s} = \nu_{as}(COO^{-}) - \nu_{s}(COO^{-})$, became larger when it was coordinated to a metal.[64–66] As described by

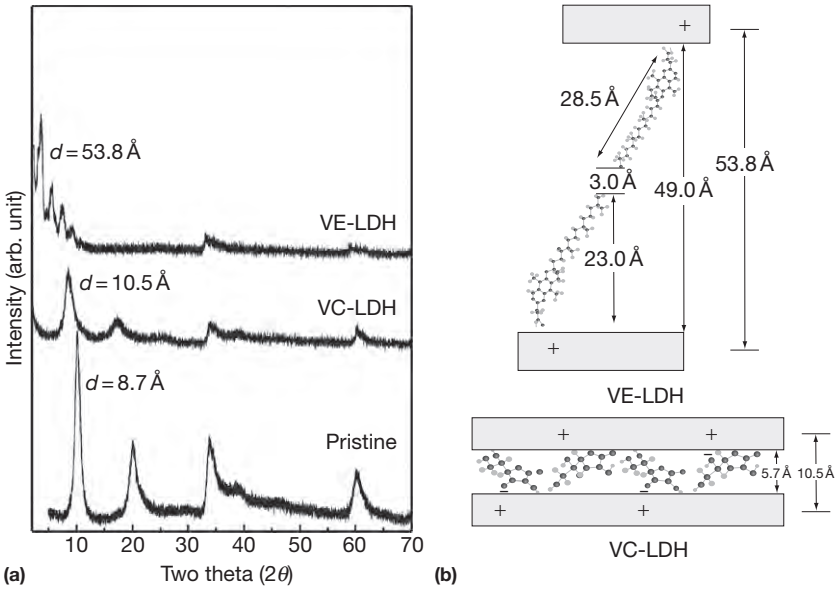

Figure 5 (a) X-ray diffraction patterns for various vitamins intercalated in LDH and (b) corresponding structures. Reproduced from Choy, J. H.; Son, Y. H. *Bull. Kor. Chem. Soc.* **2004**, *25*(1), 122–126, with permission from KCS.

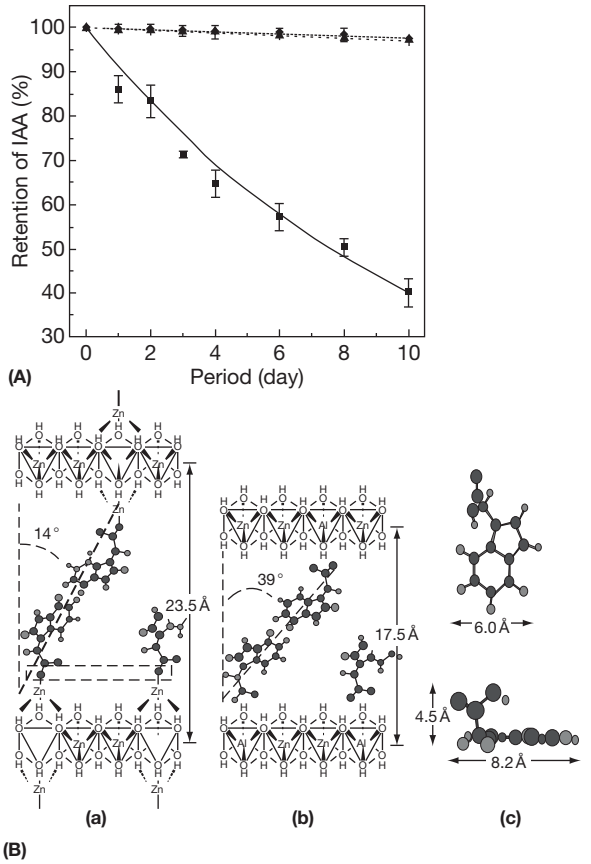

Figure 6 (A) Retention of IAA in aqueous solution of IAA (squares) and in IAA-ZBS (circles) and IAA-ZnAl-LDH (triangles) nanohybrids at 42 °C in aqueous solution. (B) Interlayer arrangement models of IAA in (a) IAA-ZBS and (b) IAA-ZnAl-LDH hybrids, and (c) molecular structure of IAA The dashed rectangle highlights coordination bonds between carbonyl groups of IAA and coordinatively unsaturated $Zn(OH)_3$ units of the ZBS lattice. Reproduced from Yang, J. H.; Han, Y. S.; Park, M.; Park, T.; Hwang, S. J.; Choy, J. H. *Chem. Mater.* **2007**, *19*(10), 2679–2685, with permission from ACS.

Yang *et al.*, the Δν value for Na^+-IAA, IAA-LDH, and IAA-ZBS were determined to be 161, 162, and 179 cm^{-1}, respectively. IAA-ZBS has a greater Δν value than Na^+-IAA, which is good evidence for coordination between COO^- of the IAA molecules and the exposed Zn^{2+} ions of the host ZBS.[63] In contrast, the Δν values for Na^+-IAA and IAA-LDH were almost the same, showing that electrostatic interactions occurred between IAA and the LDH lattice.

4.432.4. Controlled Release of Intercalated Biomolecules

As demonstrated in the above sections, intercalation into LDHs is a powerful method to stabilize biomolecules or biofunctional molecules. In addition, the intercalated molecules can be released intentionally, and their release properties can be controlled by various factors: particle size and charge density of layers, chemical interactions between host layer and guest molecules, pH and electrolyte conditions of release media, etc.

As LDHs can accommodate biomolecules via anion exchange reactions, the intercalated molecules can be reversibly released by an ion-exchange pathway. We have investigated the influence of anionic concentrations on the rate of release. For effective concentration monitoring, we intercalated the fluorescent molecule 5′-fluorescein-isothiocyanate (FITC) into MgAl-LDHs. FITC-LDH, thus obtained, was added to solutions with various concentrations of NaCl (1, 1×10^{-1}, 1×10^{-2}, 1×100^{-3}, 1×10^{-4}, 1×10^{-5}, and 1×10^{-6} M). After incubation at 37 °C for 8 h, the supernatant was collected and subjected to fluorophotometry for concentration check. The amount of released FITC as a function of NaCl concentration is displayed in Figure 7. As the concentration of NaCl solution increased, the amount of FITC released also increased significantly. Considering that the concentration-axis is displayed on a logarithm scale, the amount of released FITC increases

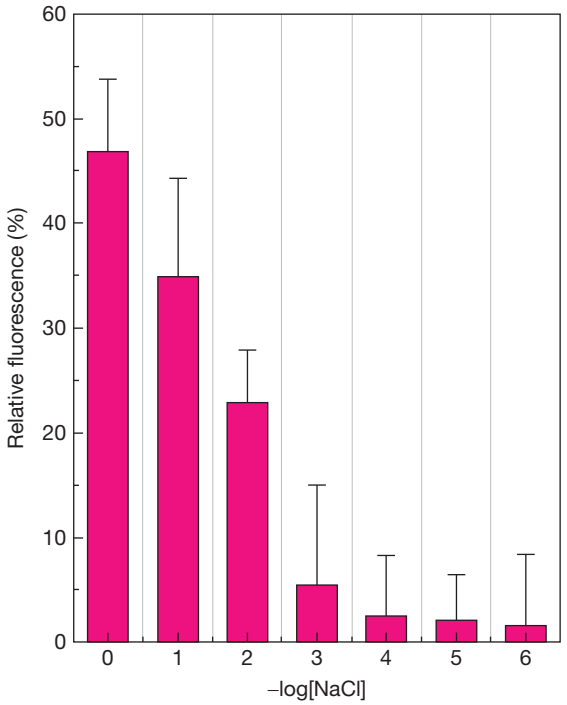

Figure 7 Histogram for the amount of disintercalated FITC at various NaCl concentrations. A fixed amount of FITC-LDH was added to 1, 1×10^{-1}, 1×10^{-2}, 1×10^{-3}, 1×10^{-4}, 1×10^{-5}, and 1×10^{-6} M NaCl solutions and incubated at 37 °C for 8 h.

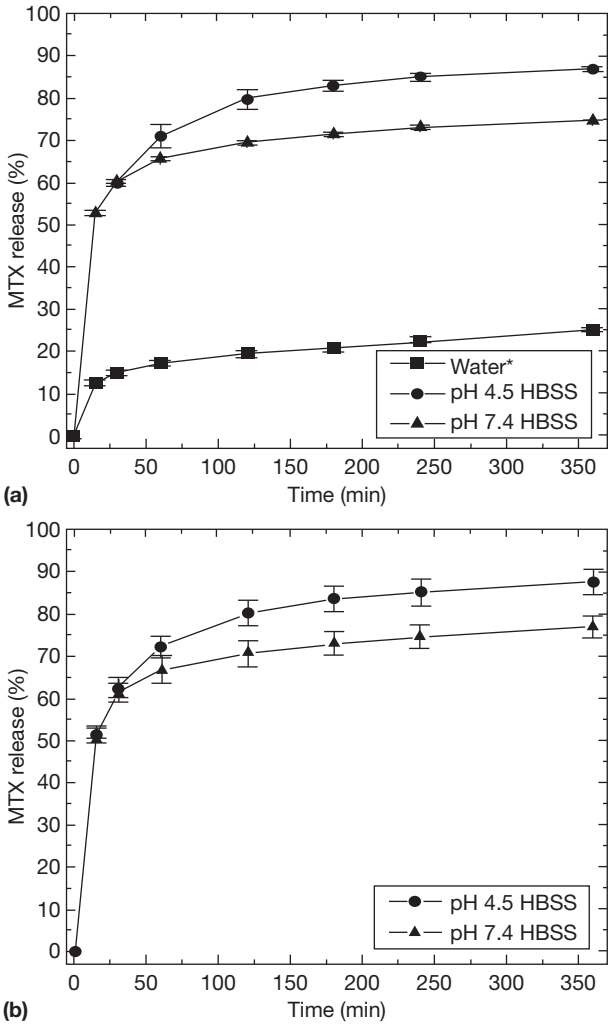

Figure 8 (a) Release profile of MTX from MTX-LDH in deionized water (rectangle) and in Hank's balanced salt solution (HBSS) (circles and triangles). (b) Release profile under the same conditions in the presence of protease. Reproduced from Kim, J. Y.; Choi, S. J.; Oh, J. M.; Park, T.; Choy, J. H. *J. Nanosci. Nanotech.* **2007**, *7*(11), 3700–3705, with permission from ASP.

exponentially with increasing NaCl concentration, before reaching a plateau. It is noteworthy that 23–35% of intercalated molecules can be released within 8 h at Cl^- concentrations of 1×10^{-2} or 1×10^{-3}M, which is similar to the electrolyte concentration in body fluids.

As biosystems have various subcellular organs with a variety of pH and enzymes, it is important for drug delivery studies to evaluate the dependence of release patterns of intercalates on pH and enzyme conditions. We prepared hybrid nanomaterials in which anticancer MTX drugs were intercalated into MgAl-LDH and examined the release patterns of MTX under a variety of conditions.[67] Figure 8 illustrates the release profile of MTX from MTX-LDH intercalates in a simulated body fluid, Hank's balanced salt solution (HBSS). In order to mimic endosomal and lysosomal conditions, the pH of the release media was adjusted to 7.4 (endosome) and 4.5 (lysosome), and the experiments were carried out with and without a lysosomal enzyme, protease. All the release patterns showed two distinct steps, an initial burst followed by a sustained release. This kind of two-step release is characteristic of a diffusion-controlled release process. Gu *et al.*[68] have also investigated this two-step release with low molecular weight heparin (LMWH) intercalated to LDHs. The cumulative release amount at 6 h was determined to be 75 and 90% for pH = 7.4 and 4.5, showing facilitated release in acidic media. The MgAl-LDH lattice is slightly soluble in acidic conditions, and this partial dissolution of LDH is thought to accelerate the release rate. It is interesting to note that the release patterns were not influenced by the presence of a protease (Figure 8(b)). This result indicates that the release of intercalated drug molecules is mainly dependent on ion exchange and the pH-dependent solubility of LDHs.

Several biomolecules such as VC and VE have been intercalated into LDHs for cosmetic applications. As cosmetics are applied on the skin, it should be investigated if the release pattern of intercalated vitamins can be controlled by atmospheric conditions like CO_2 concentration rather than body fluid conditions. We examined the release kinetics of VC-LDH and VE-LDH in a CO_2 saturated aqueous and a 50% ethanol solution, respectively.[42] As VC is spontaneously oxidized, we had to calibrate the release profile to account for the decomposition of released VC. The solid line in the inset of Figure 9 shows that the content of free VC in aqueous solution decreases exponentially, and the original release profile of VC-LDH before calibration (dotted line in the inset of Figure 9) showed a decrease after 8 h.

While biomolecule-LDH intercalates in simulated body fluid solution showed a rapid release profile during the early stages, vitamin release was observed to be relatively sustained under these conditions (Figure 9). The Henry's constant k_H of CO_2 is 29.41 l atm mol^{-1} ($\approx H_2CO_3$ concentration of 3.4×10^{-2} mol l^{-1}), and the pK_{a1} and pK_{a2} of carbonic acid are 2.5×10^{-4} and 5.6×10^{-11}, respectively. From these values, the saturated HCO_3^- and CO_3^{2-} concentrations were calculated to be lower than 10^{-5} mol l^{-1}, which is much lower than the electrolyte concentration in simulated body fluid solutions. Although the release rates were slow, both VC-LDH and VE-LDH showed an L-type release pattern that is typically observed in diffusion-controlled ion-exchange reactions. It is notable that the intercalated vitamins can be liberated in a controlled manner even in ambient conditions.

The release patterns of intercalated molecules can be controlled by the charge density of LDH layers. For the VA-LDH intercalates, three different LDHs with various M^{2+}/M^{3+} ratios were prepared.[61] The equivalent volume per unit charge ($Å^3/e^-$) of the three LDHs, Zn_2Al-, Zn_3Al-, and Zn_4Al-LDHs were determined to be 248.85, 338.31, and 418.01 $Å^3/e^-$, respectively. The release pattern of VA molecules from each of these intercalates was evaluated in a 0.9% NaCl solution, the simplest simulation of body fluid. Similar to the release patterns of other biomolecules in body fluid solutions, these profiles showed two steps, an initial burst followed by sustained release (Figure 10). It was also clearly demonstrated that VA release was fastest in the LDH with the highest layer charge, Zn_2Al-LDH, and the rate was slower in the LDHs with a lower layer charge, Zn_3Al-LDH and Zn_4Al-LDH. These results can be explained by the affinity of LDH host lattices to electrolytes in the release media; the highly positive LDH layer of Zn_2Al-LDH could accelerate anion exchange reactions with Cl^-, resulting in fast VA release.

Structure and interlayer interactions are also important factors in controlling release. In the previous section, we noted that IAA molecules, intercalated into LDH and ZBS, showed different interlayer conformations and interactions with the host lattice. As a result, it would be expected that the release profiles of IAA-LDH and IAA-ZBS would also be different. Yang *et al.* investigated the release profile of IAA from both intercalates in a 0.08% (w/w) NaCl solution. As shown in Figure 11, the release profile consists of two steps: a rapid release of IAA in the early stage, followed by slow disintercalation. In the first step, till 0.25 h, the fraction of the released IAA molecules was determined to be ~14% and ~45% for IAA-ZBS and IAA-LDH, respectively. It is notable

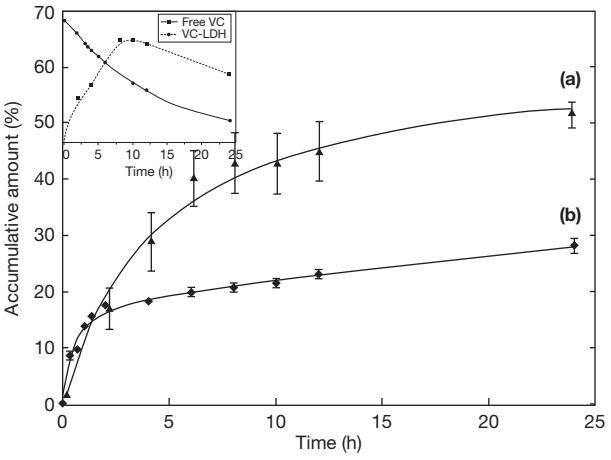

Figure 9 Release patterns of intercalated (a) vitamin C and (b) vitamin E from VC-LDH and VE-LDH, respectively. Inset shows that free vitamin C (solid lines) and disintercalated vitamin C (dotted lines). Reproduced from Choy, J. H.; Son, Y. H. *Bull. Kor. Chem. Soc.* **2004**, *25*(1), 122–126, with permission from KCS.

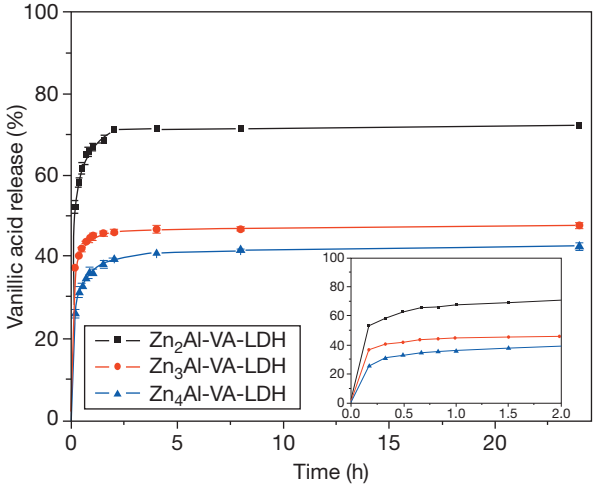

Figure 10 Release pattern of vanillic acid from LDHs with various layer charges (Zn_2Al-, Zn_3Al-, and Zn_4Al-LDHs) Reproduced from Hong, M. M.; Oh, J. M.; Choy, J. H. *J. Nanosci. Nanotech.* **2008**, *8*, 5018–5021, with permission from ASP.

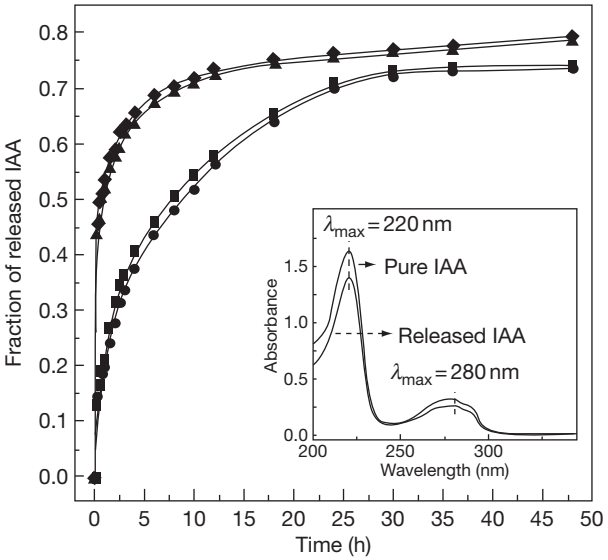

Figure 11 Time-controlled release profiles of IAA from IAA-ZBS prepared by ion exchange (squares), IAA-ZBS by coprecipitation (circles), IAA-LDH by ion exchange (triangles), and IAA-LDH by coprecipitation (diamonds). The inset represents the UV–vis spectra of pure IAA and the guest IAA released from IAA-ZBS or IAA-LDH. Reproduced from Yang, J. H.; Han, Y. S.; Park, M.; Park, T.; Hwang, S. J.; Choy, J. H. *Chem. Mater.* **2007**, *19*(10), 2679–2685, with permission from ACS.

that more than half of the intercalated IAA molecules were released from the LDH lattice within 1 h, while the IAA-ZBS preserves half of the intercalated molecules for longer than 7 h. Such a difference in release pattern originates from the differences in the chemical bonds between IAA and the layers. The strong coordinative interaction between the Zn^{2+} ions and the carboxyl groups of IAA contribute to the slower release rate in the ZBS intercalates. Thus the ZBS-type metal hydroxide can be developed as a powerful mode of sustained release for molecules like IAA.

4.432.5. Enhanced Cellular Uptake

As discussed above, intercalated molecules have good stability in LDHs, and their release can be controlled by the properties of the LDHs and the release conditions. In addition to safe protection and controlled release of biomolecules, developing a biomolecule delivery system also requires targeted delivery with enhanced cellular permeability.

We have investigated the enhanced cellular uptake of FITC intercalated into MgAl-LDHs. In order to evaluate concentration dependent cellular uptake, various concentrations of FITC-LDH (0, 5, 10, 20, 30, and 40 μM) were added to fibroblast NIH3T3 (8×10^4) cell culture lines and incubated for 2 h. Also, 10 μM of FITC-LDH was added to another cell culture line and incubated for 1, 2, 4, 6, and 8 h to study time-dependent cellular uptake.[13]

As shown in Figure 12(a), cellular uptake becomes increasingly more significant with increase in concentration and time. This implies that the FITC-LDH intercalates can effectively enter cells in both time- and dose-dependent manners. Further evidence of cellular uptake of the FITC-LDH hybrid was obtained from laser scanning confocal microscopy. NIH3T3 cell culture lines were treated with 1 μM of FITC-LDH or 5 μM of FITC alone, followed by incubation for 1, 4, and 8 h. Figure 12(b) shows that FITC-LDH is detected in cells within 1 h of incubation, and the fluorescence intensity increased continuously up to 8 h. In contrast, the cells treated with 5 μM FITC alone remained dark regardless of the incubation time. It can therefore be concluded that LDH plays an important role in mediating the cellular uptake of intercalated biomolecules. It is interesting to note that the punctuated fluorophores are distributed primarily around the cellular periphery during the early stages, suggesting the possibility of cellular uptake of LDHs through endocytosis.

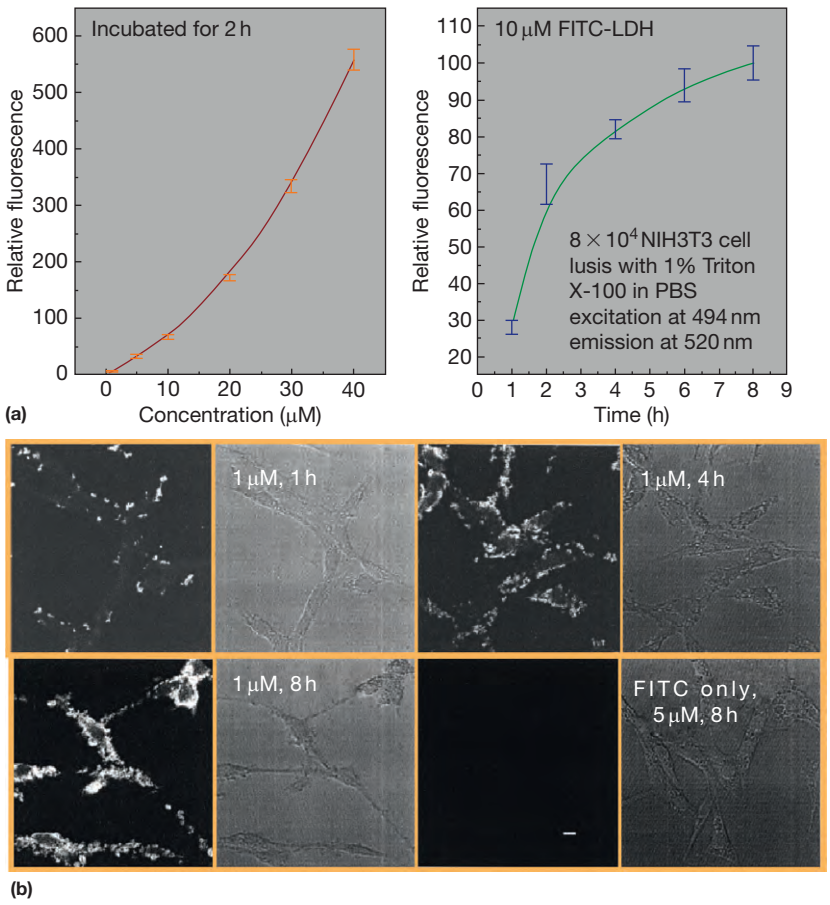

Figure 12 (a) Cellular-uptake kinetic profile of FITC-LDH into cells at various concentrations (left) and different incubation times (right). (b) Laser confocal fluorescence microscopy of the fluorophore in NIH3T3 cells. 6×10^4 cells per well were incubated with 1 μM FITC-LDH for 1, 4, and 8 h. The last fluorescence microphotograph was obtained with 5 μM FITC only. The bar is 10 μm. Reproduced from Choy, J. H.; Kwak, S. Y.; Jeong, Y. J.; Park, J. S. *Angew. Chem. Int. Ed.* **2000**, *39*(22), 4042–4045, with permission from Wiley.

In subsequent research, the cellular uptake mechanism of LDH was clarified.[35] As demonstrated above, the biomolecule-LDH intercalates possibly entered the cells through endocytosis; and there are several reports that describe cellular uptake pathways of inorganic nanoparticles as being mediated by endocytosis. Depending on the type of vesicle involved and its related proteins, endocytosis is divided into four subgroups: clathrin-mediated endocytosis, caveolae-mediated endocytosis, macropinocytosis, and phagocytosis.[69] In clathrin- or caveolae-mediated endocytosis, the most well known of all the processes, small vesicles (~100 and ~50 nm, respectively) develop at the plasma membrane which engulf foreign substances. On the other hand, macropinocytosis and phagocytosis typically show large pocket-shaped vesicles (0.5–5 μm in diameter) which are used to swallow the extracellular fluid or to devour microorganisms. Considering the size of the punctuations in **Figure 12(b)**, the endocytosis process involved in LDH uptake would either be clathrin- or caveolae-mediated. As shown in **Figure 13**, LDHs are likely to be internalized into cells via clathrin-mediated endocytosis. Two typical endocytic proteins, clathrin and caveolin-1, were stained with the red fluorophore Texas Red in human osteosarcoma MNNG/HOS cell culture lines and visualized by immunofluorescence and confocal microscopy. The nuclei were stained with blue DAPI dye. **Figure 13(a)** shows both clathrin (red fluorescence, TR) and LDH (green fluorescence, FITC) to be well colocalized, whereas no red fluorescent caveolin-1 staining was observed. The confocal microscope images also revealed that FITC-LDHs are highly colocalized with clathrin. These data show that LDHs efficiently enter cells through clathrin-mediated endocytosis.

It is well known that foreign substances internalized into cells by clathrin-mediated endocytosis are sequentially transported to early endosomes (EE), late endosomes (LE), and lysosomes. Endocytic compartments such as LEs and lysosomes are acidic with a pH ~4.5 and have abundant electrolytes. As the release of biomolecules intercalated into LDHs is facilitated by both electrolyte concentration and acidic pH, internalized drug-LDHs are likely to release their drug moiety in the LEs or lysosomes.

4.432.6. Conclusion and Perspectives

Hitherto, we have briefly reviewed the stabilization and controlled release of biomolecules after their intercalation into

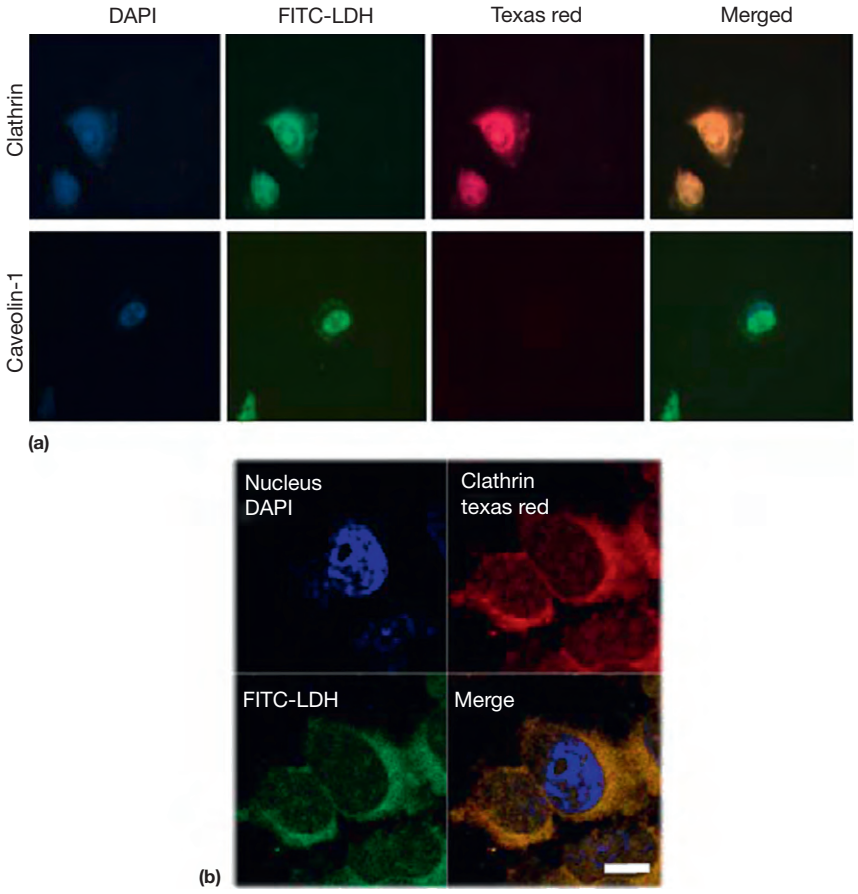

Figure 13 (a) Immunofluorescence microscope images showing the colocalization of clathrin and LDH in MNNG/HOS cells. (b) Confocal microscopy: colocalization of FITC-LDH and clathrin in MNNG/HOS cells. Cells were incubated with FITC-LDH for 2 h, treated with clathrin antibodies, and stained by TR and DAPI. Scale bar represents 10 μm. Copyright ACS, Reproduced from Oh, J. M.; Choi, S. J.; Kim, S. T.; Choy, J. H. *Bioconjug. Chem.* **2006**, *17*(6), 1411–1417, with permission from ACS.

LDHs, discussed the enhanced cellular uptake of LDHs, and described the intracellular release of biofunctionalized molecules as the end point of a drug delivery system. Intercalating unstable biomolecules into LDHs enhanced their physical, chemical, and biological stability. The stabilized biomolecules can be disintercalated intentionally, and the release pattern is mainly mediated by a diffusion-controlled ion-exchange process. The rate of release and the amount released could be controlled by the properties of the carrier LDH, such as charge density, host–guest interaction, and release media conditions such as electrolyte concentration, pH, CO_2 solubility, etc. Furthermore, the LDH intercalates showed enhanced cellular uptake through clathrin-mediated endocytosis. Finally, the molecules were released in lysosomal conditions of low pH and abundant electrolytes. Therefore, it can be concluded that three definite properties of biomolecules intercalated into LDHs (stabiliztion, controlled release and enhanced cellular uptake) would be favorable for the development of a cellular drug delivery system. Further intense studies to control the release rate of LDHs will be required to allow extensive applications in bio-related fields.

References

1. Aouadi, M.; Tesz, G. J.; Nicoloro, S. M.; *et al*. *Nature* **2009**, *458*(7242), 1180–1184.
2. Oh, J. M.; Choi, S. J.; Lee, G. E.; Han, S. H.; Choy, J. H. *Adv. Funct. Mater.* **2009**, *19*(10), 1617–1624.
3. Sengupta, S.; Eavarone, D.; Capila, I.; *et al*. *Nature* **2005**, *436*(7050), 568–572.
4. Peer, D.; Karp, J. M.; Hong, S.; FaroKhzad, O. C.; Margalit, R.; Langer, R. *Nat. Nanotechnol*. **2007**, *2*(12), 751–760.
5. Joshi, G. V.; Patel, H. A.; Bajaj, H. C.; Jasra, R. V. *Colloid Polymer Sci*. **2009**, *287*(9), 1071–1076.
6. Jung, H.; Kim, H. M.; Bin Choy, Y.; Hwang, S. J.; Choy, J. H. *Int. J. Pharm.* **2008**, *349*(1–2), 283–290.
7. Jung, H.; Kim, H. M.; Choy, Y. B.; Hwang, S. J.; Choy, J. H. *Appl. Clay Sci*. **2008**, *40*(1–4), 99–107.
8. Meng, N.; Zhou, N. L.; Zhang, S. Q.; Shen, J. *Int. J. Pharm.* **2009**, *382*(1–2), 45–49.
9. Park, J. K.; Bin Choy, Y.; Oh, J. M.; Kim, J. Y.; Hwang, S. J.; Choy, J. H. *Int. J. Pharm*. **2008**, *359*(1–2), 198–204.
10. Park, M.; Kim, C. Y.; Lee, D. H.; *et al*. *J. Phys. Chem. Solids* **2004**, *65*(2–3), 409–412.
11. Rojtanatanya, S.; Pongjanyakul, T. *Int. J. Pharm.* **2010**, *383*(1–2), 106–115.
12. Choy, J. H. *Sci. Technol. Hybrid Mater*. **2006**, *111*, 1–6.
13. Choy, J. H.; Kwak, S. Y.; Jeong, Y. J.; Park, J. S. *Angew. Chem. Int. Ed*. **2000**, *39*(22), 4042–4045.
14. Choy, J. H.; Kwak, S. Y.; Park, J. S.; Jeong, Y. J. *J. Mater. Chem.* **2001**, *11*(6), 1671–1674.
15. Choy, J. H.; Kwak, S. Y.; Park, J. S.; Jeong, Y. J.; Portier, J. *J. Am. Chem. Soc.* **1999**, *121*(6), 1399–1400.
16. Jin, S.; Fallgren, P. H.; Morris, J. M.; Chen, Q. *Sci. Technol. Adv. Mater*. **2007**, *8*(1–2), 67–70.
17. Oh, J. M.; Kwak, S. Y.; Choy, J. H. *J. Phys. Chem. Solids* **2006**, *67*(5–6), 1028–1031.
18. Rahman, M. B. A.; Yunus, N. M. M.; Hussein, M. Z.; Rahman, R.; Salleh, A. B.; Basri, M. *Biocatal. Biotransform.* **2005**, *23*(3–4), 233–239.
19. Ren, L. L.; He, J.; Evans, D. G.; Duan, X. *Chem. Res. Chin. Univ*. **2003**, *19*(3), 324–329.
20. Finnie, K. S.; Waller, D. J.; Perret, F. L.; *et al*. *J. Sol Gel Sci. Technol*. **2009**, *49*(1), 12–18.
21. Quintanar-Guerrero, D.; Ganem-Quintanar, A.; Nava-Arzaluz, M. G.; Pinon-Segundo, E. *Expert. Opin. Drug Deliv*. **2009**, *6*(5), 485–498.
22. Izquierdo-Barba, I.; Vallet-Regi, M.; Kupferschmidt, N.; Terasaki, O.; Schmidtchen, A.; Malmsten, M. *Biomaterials* **2009**, *30*(29), 5729–5736.
23. Yu, J.; Bai, X.; Suh, J.; Lee, S. B.; Son, S. J. *J. Am. Chem. Soc*. **2009**, *131*(43), 15574–15575.
24. Czarnobaj, K. *Drug Deliv*. **2008**, *15*(8), 485–492.
25. Kim, C. W.; Kim, Y. H.; Cha, H. G.; Han, Y. C.; Kang, Y. S. *J. Nano Res*. **2008**, *3*, 89–96.
26. Chevalier, E.; Viana, M.; Cazalbou, S.; Makein, L.; Dubois, J.; Chulia, D. *Acta Biomater*. **2010**, *6*(1), 266–274.
27. Dasgupta, S.; Bandyopadhyay, A.; Bose, S. *Acta Biomater*. **2009**, *5*(8), 3112–3121.
28. Epple, M.; Ganesan, K.; Heumann, R.; *et al*. *J. Mater. Chem*. **2010**, *20*(1), 18–23.
29. Morgan, T. T.; Muddana, H. S.; Altinoglu, E. I.; *et al*. *Nano Lett*. **2008**, *8*(12), 4108–4115.
30. Muddana, H. S.; Morgan, T. T.; Adair, J. H.; Butler, P. J. *Nano Lett*. **2009**, *9*(4), 1559–1566.
31. Choy, J. H.; Jung, J. S.; Oh, J. M.; *et al*. *Biomaterials* **2004**, *25*(15), 3059–3064.
32. Choy, J. H.; Kwon, S. J.; Park, G. S. *Science* **1998**, *280*(5369), 1589–1592.
33. Choy, J. H.; Lee, H. C.; Jung, H.; Kim, H.; Boo, H. *Chem. Mater*. **2002**, *14*(6), 2486–2491.
34. Chung, I. W.; Kwon, S. J.; Kim, S. J.; Jang, E. S.; Hwang, S. J.; Choy, J. H. *J. Phys. Chem. B* **2006**, *110*(33), 16197–16200.
35. Oh, J. M.; Choi, S. J.; Kim, S. T.; Choy, J. H. *Bioconjug. Chem*. **2006**, *17*(6), 1411–1417.
36. Paek, S. M.; Jung, H.; Park, M.; Lee, J. K.; Choy, J. H. *Chem. Mater*. **2005**, *17*(13), 3492–3498.
37. Vaccari, A. *Catal. Today* **1998**, *41*(1–3), 53–71.
38. Aisawa, S.; Higashiyama, N.; Takahashi, S.; *et al*. *Appl. Clay Sci*. **2007**, *35*(3–4), 146–154.
39. Aisawa, S.; Kudo, H.; Hoshi, T.; *et al*. *J. Solid State Chem*. **2004**, *177*(11), 3987–3994.
40. Aisawa, S.; Yasutake, A.; Takahashi, S.; Hirahara, H.; Narita, E. *J. Nanosci. Nanotech*. **2008**, *8*, 428–431.
41. Choy, J. H.; Oh, J. M.; Park, M.; Sohn, K. M.; Kim, J. W. *Adv. Mater*. **2004**, *16*(14), 1181–1184.
42. Choy, J. H.; Son, Y. H. *Bull. Kor. Chem. Soc*. **2004**, *25*(1), 122–126.
43. Costantino, U.; Ambrogi, V.; Nocchetti, M.; Perioli, L. *Microporous Mesoporous Mater*. **2008**, *107*(1–2), 149–160.
44. Oh, J. M.; Choi, C. L.; Yang, J. H.; Park, T.; Choy, J. H. *Kor. J. Cos. Dermatol*. **2007**, *4*, 18–29.
45. Ruiz-Hitzky, E. R.; Darder, M.; Aranda, P. *J. Mater. Chem*. **2005**, *15*(35–36), 3650–3662.
46. Choy, J. H.; Oh, J. M.; Choi, S. J. In *Bio-Inorganic Hybrid Nanomaterials; Strategies, Syntheses, Characterization and Applications*, 1st ed.; Wiley-VCH: Weinheim, 2008; Chapter 4, pp 401–418.
47. Shaw, W. H. R.; Bordeaux, J. J. *J. Am. Chem. Soc*. **1955**, *77*(18), 4729–4733.
48. Costantino, U.; Marmottini, F.; Nocchetti, M.; Vivani, R. *Eur. J. Inorg. Chem*. **1998**, *10*, 1439–1446.
49. Nyvlt, J. *The Kinetics of Industrial Crystallization*; Elsevier: Amsterdam, 1985.
50. Oh, J. M.; Hwang, S. H.; Choy, J. H. *Solid State Ionics* **2002**, *151*(1–4), 285–291.
51. de Roy, A.; Forano, C.; Besse, J. P. In *Layered Double Hydroxides: Present and Future*; Rives, V.; Ed. Nova scientific publisher Inc.: New York, 2001; pp 1–37.
52. Desigaux, L.; Ben Belkacem, M.; Richard, P.; *et al*. *Nano Lett*. **2006**, *6*(2), 199–204.
53. Thyveetil, M. A.; Coveney, P. V.; Greenwell, H. C.; Suter, J. L. *J. Am. Chem. Soc*. **2008**, *130*(14), 4742–4756.
54. Darder, M.; Lopez-Blanco, M.; Aranda, P.; Leroux, F.; Ruiz-Hitzky, E. *Chem. Mater*. **2005**, *17*(8), 1969–1977.
55. Shi, W. Y.; Wei, M.; Jin, L.; Li, C. J. *J. Mol. Cata. B Enzym*. **2007**, *47*(1–2), 58–65.
56. Bertino, J. R. *Am. J. Clin. Oncol*. **1993**, *11*(1), 5–14.
57. Hitchkings, G. H.; Smith, S. L. *Adv. Enzym. Regul*. **1980**, *18*, 367–371.
58. Hwang, S. H.; Han, Y. S.; Choy, J. H. *Bull. Kor. Chem. Soc*. **2001**, *22*(9), 1019–1022.
59. Yang, J. H.; Lee, S. Y.; Han, Y. S.; Park, K. C.; Choy, J. H. *Bull. Kor. Chem. Soc*. **2003**, *24*(4), 499–503.
60. Won, J.; Oh, M. H.; Oh, J. M.; Kang, M. S.; Choy, J. H.; Oh, S. *J. Food Sci*. **2008**, *73*, N39–N43.
61. Hong, M. M.; Oh, J. M.; Choy, J. H. *J. Nanosci. Nanotech*. **2008**, *8*, 5018–5021.
62. Oh, J. M.; Biswick, T. T.; Choy, J. H. *J. Mater. Chem*. **2009**, *19*(17), 2553–2563.

63. Yang, J. H.; Han, Y. S.; Park, M.; Park, T.; Hwang, S. J.; Choy, J. H. *Chem. Mater.* **2007**, *19*(10), 2679–2685.
64. Choy, J. H.; Kwon, Y. M.; Han, K. S.; Song, S. W.; Chang, S. H. *Mater. Lett.* **1998**, *34*(3–6), 356–363.
65. Nakamoto, K. *Infrared and Raman Spectra of Inorganic and Coordination Compounds*, 5th ed.; Wiely-Interscience: New York, 1997.
66. Poul, L.; Jouini, N.; Fievet, F. *Chem. Mater.* **2000**, *12*(10), 3123–3132.
67. Kim, J. Y.; Choi, S. J.; Oh, J. M.; Park, T.; Choy, J. H. *J. Nanosci. Nanotech.* **2007**, *7*(11), 3700–3705.
68. Gu, Z.; Thomas, A. C.; Xu, Z. P.; Campbell, J. H.; Lu, G. Q. *Chem. Mater.* **2008**, *20*(11), 3715–3722.
69. Marsh, M.; Pelchen-Matthews, A. *Traffic* **2000**, *1*(7), 525–532.

4.433. Porous Metal–Organic Frameworks as New Drug Carriers

P Horcajada and C Serre, Université de Versailles St-Quentin en Yvelines, Versailles, France
R Gref and P Couvreur, Université Paris-Sud, Châtenay-Malabry, France

© 2011 Elsevier Ltd. All rights reserved.

4.433.1.	**Introduction**	559
4.433.2.	**Adsorption and Delivery of Therapeutic Molecules**	560
4.433.2.1.	Model Drugs	561
4.433.2.2.	The Role of Flexibility	562
4.433.2.3.	Nanoplatforms	563
4.433.2.3.1.	Synthesis of nanoparticles	563
4.433.2.3.2.	Surface engineering	564
4.433.2.3.3.	Adsorption of challenging drugs	565
4.433.2.4.	*In Vitro* Activity Tests	566
4.433.2.5.	BioMOFs	567
4.433.2.5.1.	The use of active linkers	567
4.433.2.5.2.	The use of biologically active metals	567
4.433.3.	**Adsorption and Delivery of Biological Gases**	568
4.433.4.	**Toxicity and Stability Issues**	569
4.433.4.1.	*In Vitro* Biodegradability	569
4.433.4.2.	*In Vitro* Toxicity Tests	570
4.433.4.3.	*In Vivo* Toxicity Assays	570
4.433.5.	**Formulation**	571
4.433.6.	**Conclusion and Perspectives**	571
References		572

Abbreviations

AZT	Azidothimidine
AZT-Tp	Azidothimidine triphosphate
Bu	Busulfan
CDV	Cidofovir
Doxo	Doxorubicin
Ibu	Ibuprofen
i.v.	Intravenous administration
MOF	Metal–organic framework
NanoMOF	Nanoparticles of MOF
PEG	Poly(ethylene glycol)
RES	Reticuloendothelial system

4.433.1. Introduction

Porous solids are of an economic importance as they are related to industrial applications typically in catalysis, separation or fine chemistry. It concerns mostly the crystalline (inorganic) silica-based zeolites and organic activated carbons. Recently, within the last two decades, hybrid inorganic–organic porous solids, denoted MOFs (metal–organic frameworks) or PCPs (porous coordination polymers) have emerged.[1–4] These are built up from the association of an inorganic part, either metal clusters, chains, layers or 3D networks, and various types of organic linkers possessing complexing groups, typically carboxylates. The linkage between the inorganic subunit, comprised of almost all elements from the periodic table including alkaline earths (Ca, Mg), transition metals (Fe, Zn), or lanthanides (Gd, ...), is typically made of strong ionocovalent or dative bonds (Figure 1). This leads to the formation of hybrid porous frameworks. The key advantage of MOFs in comparison to their purely inorganic (zeolites, mesoporous silica) or organic (carbons) counterparts, concerns the huge number of available linkers leading to thousands of possible structures including aliphatics or aromatics organic spacers, associated with one or several complexing functions chosen among carboxylates, phosphonates, sulfonates, imidazolates, amines, pyridyls, ... or a combination of them. As a result, a huge number of MOFs with various pore sizes, typically within the 3–60 Å range, shapes (tunnels, cages, ...) and organic functionalities (polar, apolar) have been reported. Their synthesis is achieved under hydro or solvothermal conditions and pores are filled with solvent molecules or residual molecules of linker that are usually removed by solvent exchange followed by a heating and/or vacuum treatment. Finally, the resulting porous MOFs are light materials with density, typically between 0.2 and 1.5 $g\,cm^{-3}$, large pore volume (up to $3\,cm^3\,g^{-1}$) and high specific surface areas, up to $5000\,m^2\,g^{-1}$.

Most topical MOFs are those built up from metal clusters such as dimers, trimers, tetramers, or hexamers of metal polyhedra. For instance, the copper trimesate denoted HKUST-1 (dimers),[5] the iron or chromium trimesate MIL-100 (trimers),[6] the zinc terephthalate MOF-5 (tetramers)[2] and the zirconium

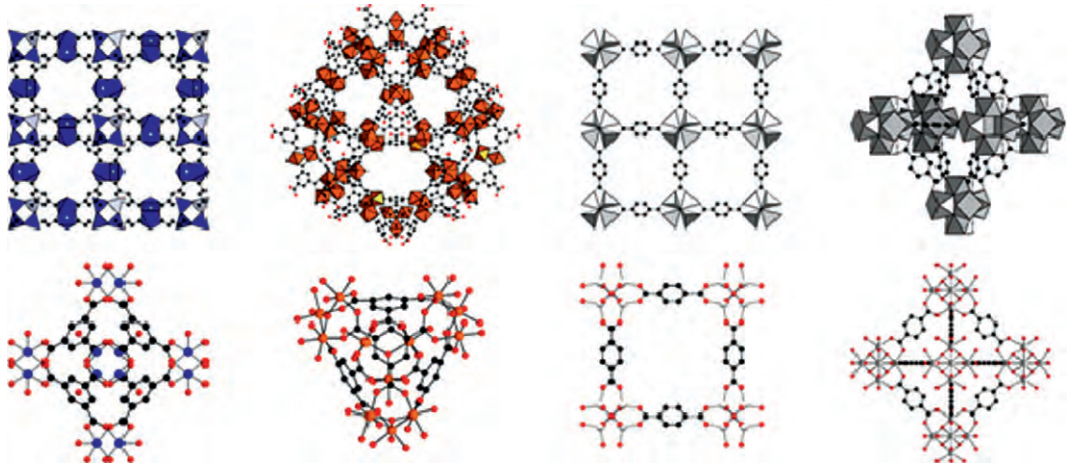

Figure 1 Top view of the structures of a few topical metal–organic frameworks. Bottom view of the corresponding hybrid building units. Copper, iron, zinc, and zirconium are in blue, orange, gray, and gray, respectively while oxygen and carbon atoms are in red and black, respectively.

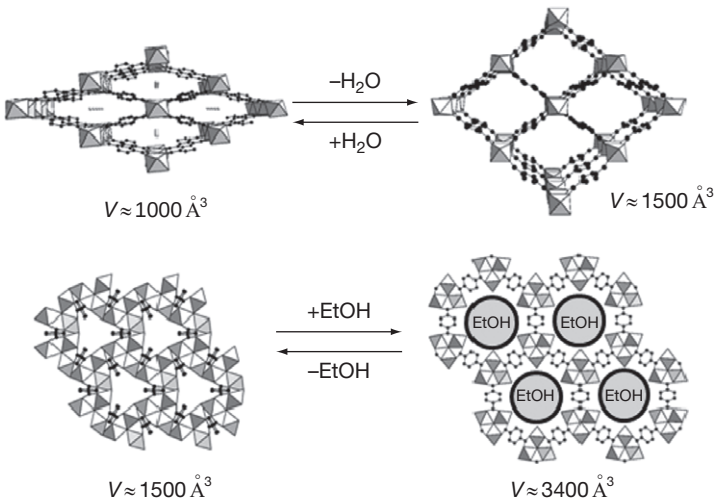

Figure 2 The breathing behavior of the iron terephthalates MIL-53 (top) and MIL-88B (bottom). Metal octahedra and carbon atoms are in white and gray, respectively.

terephthalate UiO-66 (hexamers),[7] result in all cases in large pore sizes (6–29 Å) and Brunauer–Emmett–Teller (BET) surface areas between 1200 and 3800 $m^2 g^{-1}$, respectively (Figure 2).[8,9]

Another interesting aspect of MOFs is the possibility of keeping the same structure type while increasing the size of the organic spacer thus enlarging the pore size.[5,10] For a given structure, pores can also be functionalized through grafting of a functional group either by substituting a proton of the linker by a functional group (apolar, polar, basic, acidic, ...) or through postsynthetic modification whilst keeping the same structure type, in order to tune its properties.[11]

MOFs possess usually a rigid framework like traditional porous solids but some of them swell or breathe in the presence of change in pressure, temperature, or during the adsorption of a gas or a solvent.[4d,12] Most topical examples are the metal terephthalates denoted MIL-53 (Al, Cr, Fe...),[13] or MIL-88 (Fe, Cr) (Figure 2),[10b,14] which exhibit a reversible and selective breathing amplitude between the solvated forms and the dried ones from 40 to 230% (in cell volume).

Such large and selective variations in volume might lead in a near future to new applications in terms of adsorption, storage and facile delivery of gases or biological molecules.[15,16]

Finally, it is interesting to point out that the stability of MOFs is on the whole lower than that of the pure inorganic (zeolites) or organic (carbons) porous solids. The thermal stability of MOFs is usually comprised between 150 and 400 °C under air while most MOFs degrade upon a long time exposure to water which restrict their domains of applications, even if a recent study has shown that some of them exhibit a reasonable hydrothermal stability.[17]

4.433.2. Adsorption and Delivery of Therapeutic Molecules

Controlled delivery systems present many advantages in comparison with conventional drug administration, which often involve toxicity issues and low efficiency values due to lack of

tissue/cell selectivity. Moreover, the discovery of macromolecules arising from biotechnologies (peptides, proteins, nucleic acids, etc.) makes necessary the development of new carriers for their use since they are either unstable in biological media with poor intracellular diffusion or poorly soluble. Thus, many drug candidates fail to reach clinical applications because of short blood half lives and inability to bypass natural barriers. Despite the increasing success of drug delivery systems (abraxane, doxil, ambisome, ...), there are still a large number of drug molecules of high therapeutic interest not with no adequate controlled release system. Consequently, the development of new carrier systems is needed to ensure the right drug plasmatic levels in the active sites, increasing the efficiency, decreasing the toxicity as well as increasing their half life, by protecting sometimes the drug from rapid metabolization.[18] Liposomes and polymeric nanodevices are actually the most common carriers for the controlled release of drugs.[19,20] An inorganic alternative based on amorphous porous silica solids[21–25] led, more recently, to a new approach based on ordered porous solids such as ordered mesoporous silicas[26–29] or zeolites.[30–33] However, both organic or inorganic routes can suffer from important drawbacks such as either a low drug loading and/or a rapid delivery,[34,35] as well as sometimes toxicity restrictions.[36–38]

Recently, a hybrid alternative was proposed using porous MOFs,[39] which combine a highly regular porosity with a crystalline hybrid inorganic–organic framework easily tunable. Some of these solids exhibit many interesting features suitable for their successful use as drug carriers: (1) low toxicity of numerous available porous MOFs structures, built up from low toxic metals (Fe, Ca, Mg, ...) and ligands (carboxylic or phosphonic acids); (2) biodegradability, tunable according with composition and structure; (3) a hydrophilic–hydrophobic internal microenvironment adapted to a large variety of active molecules; (4) drug encapsulation and delivery easily modulated by a controlled diffusion, through the control of the porous structure (interconnectivity, pore size, flexibility) and by an optimization of the host–guest interactions (functionalization of the organic linker).

4.433.2.1. Model Drugs

Our group has initiated recently the use of porous MOFs as new drug carriers,[39] starting from a model system with (1) ibuprofen (2-(4-(2-methylpropyl)phenyl)propanoic acid), an antiinflammatory and analgesic model drug, bearing a simple chemical structure with a carboxylic group, involved in 80% of the active drug molecules; and (2) two rigid mesoporous chromium carboxylates, MIL-100 (Cr) and MIL-101 (Cr) (MIL for Material of Institut Lavoisier). These Cr compounds were selected, despite the well-known toxicity of chromium, due to their excellent thermal and water stability allowing a better structural control of the drug insertion and release, MIL-101 (Cr)[40] and MIL-100 (Cr)[41] are indeed based on octahedral oxo-centered chromium trimers coordinated by benzene di or tricarboxylate linkers, respectively, resulting in giant hybrid structures with a cubic zeotype architecture delimiting two types of spherical cages (25 and 29 Å in MIL-100; 29 and 34 Å in MIL-101 (Cr)) accessible through microporous pentagonal or hexagonal windows.

In both cases, that is, MIL-100 and MIL-101, Ibuprofen was adsorbed by simple impregnation, suspending the previously dehydrated powder MOFs into a concentrated hexane drug solution. MIL-101 (Cr) showed an unprecedented amount of adsorbed drug, up to 1.4 g of Ibuprofen per gram of dehydrated MOF, which represents for each 'small' cage hosts ~56 Ibuprofen molecules and for the 'large' cage ~92 molecules. This exceptionally high loading capacity can be considered as a major result since one would require only very small amounts of transporter material even for a high dosage. Despite its important pore volume, MIL-100 (Cr) retains only 0.35 g of drug per gram of dried solid whatever the different parameters studied. This is due to the selective adsorption of the drug in the larger cages only considering the small free aperture of the accessible pentagonal windows of the smaller cages (0.5 nm), which are very close to the one of Ibuprofen (1.0×0.5 nm).

The integrity of the Cr-MOFs after the drug adsorption was checked by X-ray powder diffraction, N_2 adsorption performed at 77 K after the incorporation indicates almost no residual porosity, in agreement with the presence of large amounts of Ibuprofen located inside the cages. Monte Carlo computing simulation of Babarao *et al.*[42] have further confirmed the extraordinary drug loading capacity of MIL-101 (Cr).

Concerning the nature of the drug-guest interactions, it is interesting to note that the Ibuprofen molecules as shown by ^{1}H solid state nuclear magnetic resonance (NMR), are partially deprotonated, and it is likely that some of these molecules might be coordinated to the Lewis acid metal sites of the MOF through its carboxylate group. Dynamic fault tree (DFT) calculations have estimated the corresponding heat of adsorption being of $-73.17\,\mathrm{kJ\,mol^{-1}}$ (estimated by DFT calculations).[42] Thus, considering the number of metallic centers per unit formula (two Lewis acid sites per trimer), one can estimate that ~40% of the drug is coordinated to the Lewis acid metal sites. The remaining Ibuprofen moieties are probably interacting either with the framework through π–π interactions between the aromatic rings of Ibuprofen or simply interacting at the centre of the pores with other drug molecules.

Likewise, all adsorbed Ibuprofen can be delivered under simulated physiological conditions (simulated body fluid (SBF) at 37 °C under continuous stirring to avoid external diffusion processes) after 3 or 6 days, from the compacted Ibuprofen-containing MIL-100 (Cr) and MIL-101 (Cr) solids, respectively.[39] If one looks deeply into the Ibuprofen release profiles, three different stages can be distinguished according to the drug location/interaction in the cages: (1) Ibuprofen not in direct contact with the pore walls and thus quickly delivered in the first hours through a diffusion process; (2) a slower release of the Ibuprofen fraction located close to the pore wall into the larger cages; (3) and finally, with the slowest rate, the drug fraction in direct contact with the smaller cage walls. Therefore, the last two stages would be governed by a combination of diffusion and interactions phenomena. Thus, the slower release in MIL-101 (6 days) compared with MIL-100 (3 days), could be due to: (1) the higher proportion of aromatic rings (Ar/Cr = 1.0 [MIL-101]; Ar/Cr = 0.66 [MIL-100]) and (2) the larger proportion of accessible Lewis acid sites in MIL-101 since both small and large cages are available against the large cages only for MIL-100.

Table 1 Pore characteristics and encapsulation/release results of Ibuprofen of various porous solids

	Pore diameter (Å)	*Pore volume ($cm^3\,g^{-1}$)*	*S_{BET} ($m^2\,g^{-1}$)*	*Ibuprofen loading (g ibu/g dehyd. solid)*	*Time release (days)*
MIL-101 (Cr)	29–34	1.9–2.3	3500–4500	1.38	6
MIL-100 (Cr)	25–29	1.2	2200	0.35	3
MIL-100 (Fe)	25–29	1.1	1900	0.35	3
MIL-53 (Cr)	8.5	0.5	1400	0.22	21
MIL-53 (Fe)	8.5	0.5[a]	–	0.21	21
Faujasite	11.2	0.3	650	0.16	7
MCM-41	36	1.0	1150	0.34	2
MCM-41_NH_2	28	0.4	780	0.22	5

The release was achieved in PBS at 37 °C.

[a]MIL-53 (Fe), while nonporous in its dehydrated form, possesses in its open form, that is, in the presence of gases, vapours, or liquids, an equivalent pore volume of ~0.5 g cm^{-3}.

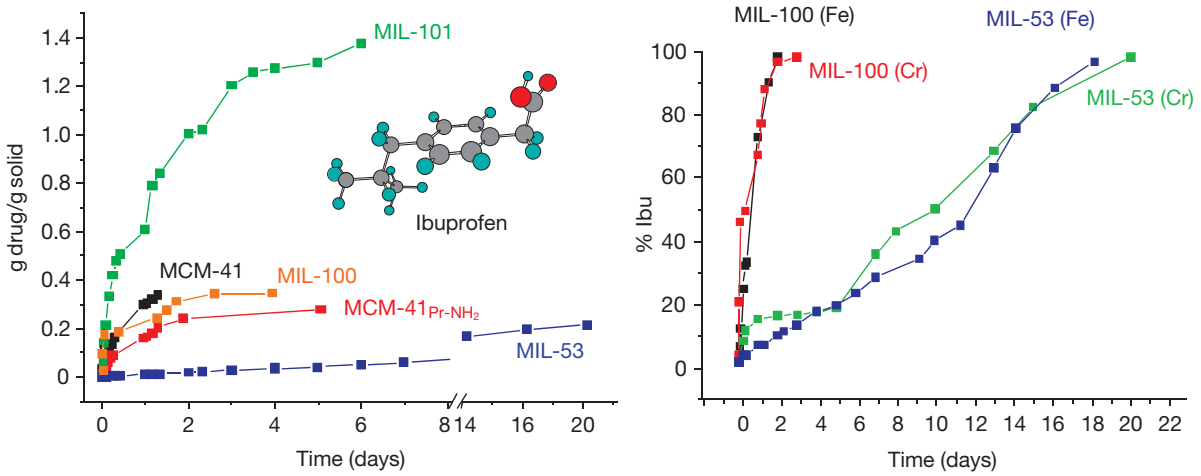

Figure 3 Left: delivery profiles of Ibuprofen from several porous carriers (PBS, 37 °C); right: delivery profiles from the flexible MIL-53 (Cr) and MIL-53 (Fe) solids compared to the one of MIL-100 (Fe) and MIL-101 (Cr).

From these results, the proof of principle of the use of MOFs for controlled drug encapsulation and release has been successfully evidenced, but what about their performances in comparison to other porous materials? MOFs offer higher drug loadings (up to 1.4 g g^{-1}) and longer delivery times (6 days) than other inorganic porous solids, such as the ordered mesoporous silica MCM-41 (pore diameter of 36 Å),[43] which releases its cargo (0.34 g g^{-1}) within 2 days (Table 1, Figure 3).

Furthermore, several nontoxic iron analogues MOFs are now available,[6,44] (rat oral dose: DL_{50}(Fe) = 30 g kg^{-1},[45] DL_{50}(trimesic acid) = 8.4 g kg^{-1},[46] DL_{50}(terephthalic acid) = 5 g kg^{-1}[47]) and have shown similar loadings and delivery rates as the toxic-chromium MOFs. This indicates that changing the nature of the metal does not drastically modify the release properties. Finally, one can establish that a new route in the drug delivery field has been initiated.

4.433.2.2. The Role of Flexibility

As afore-mentioned, some MOFs possess a flexible framework,[48] leading to a modulation of their pore size. This reversible 'breathing' effect induces a variation in cell volume from 40 to 235%, depending on the structure, the metal, and the organic spacer.[49,50] For instance, the microporous metal carboxylate MIL-53 (Cr, Fe) solids, exhibit a highly flexible framework built up from chains of corner-sharing metal(III) octahedra and terephthalate anions delimiting a one-dimensional pore channel system (ϕ~8 Å). These solids possess a different pore opening according to the size of the molecule located within of the cages, as evidenced by the reversible contraction/opening of the pores along *b* axis. This is in agreement with the breathing of the MIL-53 solids in the presence of gases,[51,52] liquids,[53] or vapors.[54] Our aim was thus to determine the effect of the breathing on the drug encapsulation and delivery properties.

Once more, Ibuprofen was chosen as model drug and both chromium- and iron-based MIL-53 were selected as flexible porous hybrid solids. Please note that in the presence of gas or vapors, the Cr and Fe compounds exhibit a different breathing behavior. The dried Cr solid denoted MIL-53 (Cr) ht (high temperature) has a fully open structure,[49,55] while the iron analogue has a closed structure.[44] However, upon adsorption of Ibuprofen by impregnation in the liquid phase, the Cr or Fe Ibuprofen-containing-MIL-53 solids exhibit a very close drug loading (20 wt%). In addition, the pore opening of the Ibuprofen loaded form is similar for both solids and can be considered as being intermediate between the one of the closed and opened forms of MIL-53 (Figure 4). The Ibuprofen-MIL-53 (Fe) X-ray powder pattern was indexed in a monoclinic

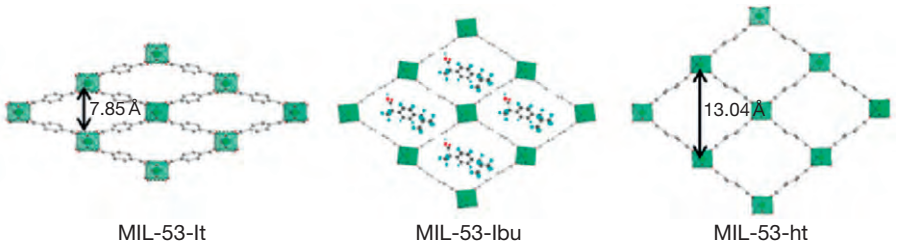

Figure 4 Comparison of the different pore opening of the MIL-53: left: water, center: Ibuprofen, right: open form. Metal octahedra, oxygen and carbon atoms are in green, red, and black, respectively.

cell (space group C2/c).[56] These results did not only show that the flexible MIL-53 solids are breathing while hosting drugs, but also indicate that one can follow the drug insertion by X-ray diffraction powder diffraction (XRPD) characterization.

The behavior of the MIL-53 flexible solids as drug carriers is also very different from those observed previously with the rigid large pores MIL-100 and MIL-101 materials. First, the time required for reaching the maximum loading of Ibuprofen is equal to 3 days for MIL-53 against 1 day for both MIL-100 and MIL-101. This is probably due to the smaller pore size ($\phi \sim 8$ Å) and the presence of a one-dimensional porosity, which leads to a slower diffusion rate of the drug into the channels of MIL-53. It is possible also that MIL-53 exhibit a stronger relative affinity for the solvent used through the impregnation process (hexane). Second, the amount of Ibuprofen adsorbed in the MIL-53 solids is much lower compared with the mesoporous solids, that is, only 20 wt%, which is in agreement with the smaller pore volume of MIL-53. Please note also that the drug content does not depend here on the nature of the metal.

Concerning the drug delivery profile, performed using the same conditions as the one described above, a very slow and progressive release of Ibuprofen from MIL-53 Cr or Fe up to 3 weeks was achieved with an unexpected zero-order kinetics, thus fully predictable and independent from the drug concentration within the solid. In order to gain understanding, one has to consider three different aspects: nature of host–guest interaction, flexibility and diffusion. First, a slow delivery rate is easily explained by the presence of strong interactions between the drug and the hybrid network. This is consistent with solid state NMR results that show a stronger confinement effect in MIL-53. This results from its smaller pore size and the presence of specific hydrogen bonds between the OH groups of the inorganic subunit and the carboxylic group of Ibuprofen, present in its protonated form contrary to the case of MIL-100 and MIL-101 whereas the molecule was in its anionic form. This was confirmed by infrared spectroscopy while computer modeling has estimated a heat of adsorption of Ibuprofen in MIL-53 by DFT calculation of $\sim -57\,\mathrm{kJ\,mol^{-1}}$. Of course, additional weaker interactions between the aromatic rings of MIL-53 and the organic part of Ibuprofen (phenyl, propyl) are also contributing to the total interaction with the framework.

Second, the zero order kinetics cannot be explained only through the presence of specific interactions but also through the maintenance of constant local environment throughout the whole delivery process. XRPD indeed shows that the structure, and thus the degree of pore opening, before and after drug delivery are very similar. Thus, the breathing phenomenon is an interesting advantage for drug delivery since it allows a better optimization of the interactions between the drug and the framework through the adaptation of the pore size to the one of the molecule of interest.

These exceptional features could be of great importance for drug delivery with a unique administration for very long therapies.

The study of Ibuprofen as a model drug has been done with several other porous carriers, which allows a direct comparison of their drug loading capacity and delivery profiles, with our porous hybrid solids (**Table 1**, **Figure 3**). For instance, microporous zeolites ($\phi \sim 7.4$ Å) possess drug capacities close to the one of MIL-53, but with much faster release rates.[57] Ordered mesoporous silica MCM-41 solids exhibit a drug loading higher than MIL-53, close to MIL-100, but much lower than MIL-101.[38] However, Ibuprofen is released much slower from the hybrid MILs solids (from 3 to 21 days, against 1 day for MCM-41). This is related to an increase in the interaction between the drug and the hybrid framework due to the presence of organic groups within the MOF, and maybe also to the presence of Lewis acid sites. Nevertheless, the presence of aminopropyl groups at the surface of functionalized MCM-41 solids slows down the delivery rate to reach a delivery up to 5 days, but with an unfortunate decrease in the drug capacity.[58] Thus, the combination of a regular porosity and the presence of organic group within the framework allow direct and efficient interactions between the drug and the hybrid skeleton without decreasing the drug loading capacity.

In conclusion, flexible MOFs represent excellent candidates for drug delivery with their easily tunable porosity, which leads to an optimization both of diffusion process and drug–matrix interactions for a controlled-manner drug release.

4.433.2.3. Nanoplatforms

4.433.2.3.1. Synthesis of nanoparticles

Control of particle size is essential for the administration of the drug carrier system by different routes such as intravenous (i.v.), intraperitoneal (i.p.), subcutaneous (s.c.), intranasal (i.n.), intraocular (i.o.), etc., in order to avoid tissular damages caused by embolism.

Intravenous administration of MOFs requires thus the elaboration of highly water stable homogeneous nanoparticles smaller than 200 nm to avoid unwanted phenomena such as aggregation, reactivity or precipitation. Up to now, the synthesis of MOFs has typically been performed using hydro/solvothermal conditions in polar solvents by adjustment of several parameters such as the temperature, pressure, the nature of the solvent, pH, stochiometry, and so on.

For structure determination purpose, the objective was also to produce as large as possible single crystals of a sufficient quality. However, recent studies have shown that synthetic methods such as (1) reverse emulsions[59–61] and (2) microwave assisted hydro/solvothermal routes[62–64] are suitable for the formation of narrow distributed nanoparticles of MOFs (nanoMOFs) (Figure 5).

1. Reverse-phase emulsions consist in performing a microemulsion of the metal source and linker in the presence of the cationic cetyltrimethylammonium bromide (CTAB)/isooctane/1-hexanol/water system. This simple and easily generalized method has been applied to different nonporous MOFs with imaging properties (based on lanthanides and Mn). For instance, nanorods of a gadolinium terephthalate (40×100 nm) or nanoplates of a gadolinium trimellitate (35×100 nm) could be obtained,[56] as well as block-like particles of a gadolium benzene hexacarboxylates ($25 \times 25 \times 100$ nm)[57] and nanorods of manganese trimesate (50×1000 nm) and terephthalate (50×750 nm).[58] Interestingly, the morphology of the manganese trimesate ($Mn_3(BTC)_2(H_2O)_6$) can be tuned by modifying some synthesis parameters, that is, from spiral nanorods of 50×1000 nm using a conventional microemulsion method to block-like nanoparticles of 50–300 nm range by combining reverse-phase microemulsion and microwave synthesis.[58] The main drawback of such inverse emulsion method is its low yield since very important volumes of emulsion are needed to obtain low amounts of nanoparticles. In addition, the toxicity of the components used to produce the emulsion is of concern for a practical *in vivo* use (CTAB LD_{50} (intravenous (i.v.) rats) = 44 mg kg^{-1},[65,66] isooctane LD_{50} (oral rats) = 3310 mg kg^{-1},[67] LD_{50} (oral rats) = 720 mg kg^{-1}).[68]
2. Microwave assisted hydro/solvothermal synthesis is a faster method which leads to high yields of nanoMOFs with a good control of the particle size and a narrow size distribution. Several examples have been recently reported, such as the mesoporous chromium terephthalate MIL-101 (22 nm, but highly toxic),[60] the microporous zinc imidazolate ZIF-8 (40 nm),[69] the flexible microporous iron terephthalate MIL-53 (350×1000 nm) and the mesoporous iron trimesate MIL-100 (200 nm) or the iron aminoterephthalate MIL-101_NH_2 (120 nm).[61]

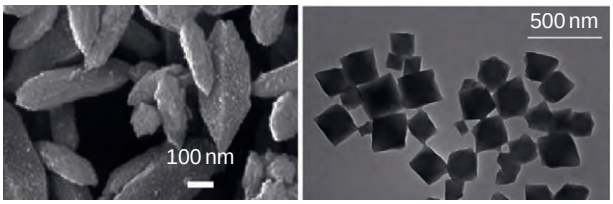

Figure 5 Scanning electron microscopy (SEM) and transmission electron microscopy (TEM) images of nanoparticles of MIL-88A (on the left) and MIL-101_NH_2 (on the right) made from solvothermal and microwave synthesis, respectively.

Additionally, it is nevertheless possible to obtain nanoMOFs using traditional hydro/solvothermal routes by playing on different parameters such as decreasing the synthesis time and/or the temperature, changing the concentration, modifying the pH or by the addition of moieties that slow down the reactivity (acetic acid, hydroxybenzoic acid, ...). For instance, nanoMOFs of the porous zinc terephthalate MOF-5,[70] and the flexible porous iron muconate MIL-89 (30 nm)[71] or iron fumarate MIL-88A (150 nm)[61] have been obtained as nanoparticles. However, this route usually leads to lower yields and a higher degree of polydispersity of the particle size compared with the microwave hydro/solvothermal method.

4.433.2.3.2. Surface engineering

Particle surface engineering, especially concerning nanoparticles, is another fascinating issue. Firstly, surface modification is helpful to increase the stability of nanoparticles, preventing from aggregation in solution to avoid embolism after i.v. injection. Indeed, grafting some molecules directly on the surface of the nanoparticles leads to a modification of the surface charge of the particles (Z-potential) required to avoid aggregation by electrostatic or by hindrance repulsion. However, the external functionalizing of the surface of MOFs with an appropriate organic molecule results also in the introduction of other biologically attractive properties such as furtivity (or stealth properties), targeting (or addressing to active sites) and/or bioadhesion (Figure 6).[72–74]

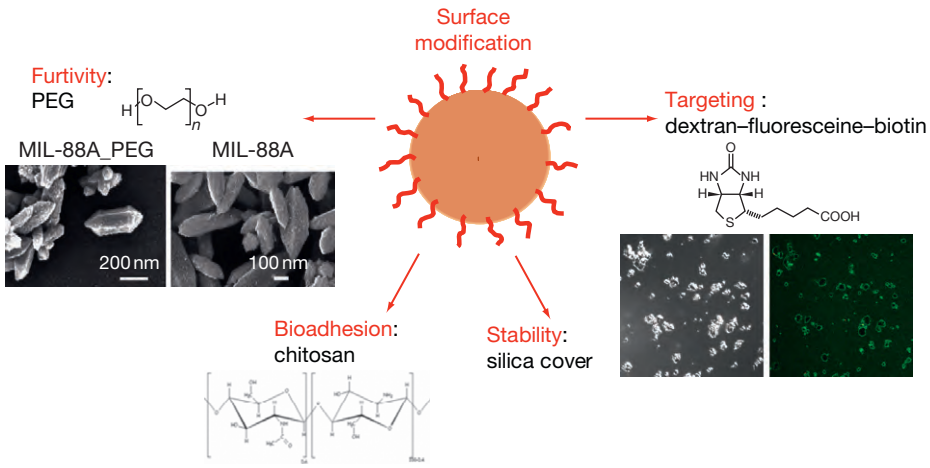

Figure 6 Examples of organic surface modification of metal–organic frameworks nanoparticles.

Engineered surface porous iron carboxylate nanoMOFs have been recently reported.[61] The surface of the nanoMOFs can be coated with organic modifiers using preformed nanoparticles either through postsynthetic functionalization or directly during the synthesis of the nanoMOFs.

Several examples of MOF surface engineering can be given. The most obvious one, commonly used for other carriers such as polymers, concerns the surface coatings using the hydrophilic polymer poly(ethylene glycol) (PEG) in order both to prevent normal interaction between the carrier and cells and avoid other destabilizing factors. The objective is to avoid the sequestration of the nanoMOFs by the reticuloendothelial system (RES) and thus increase after intravenous administration the longevity of the carrier in the bloodstream from minutes up to several hours.[75,76] Therefore, the mesoporous iron trimesate (MIL-100) and the flexible microporous iron fumarate (MIL-88A) or muconate (MIL-89) were superficially PEGylated, either through postsynthetic methods or during the synthesis, achieving PEG contents up to 17 wt%,[61] which is higher than those required to ensure 'stealth' properties.[77] Chitosan, a naturally occurring polysaccharide with bioadhesive properties (mucoadhesion and permeation enhancement),[78] has been also grafted on the external surface of MIL-88A nanoparticles (~20 wt%).[61] The surface of MIL-100 nanoparticles was also modified by amphiphilic polysaccharides dextran–fluorescein–biotin for addressing[79] and *in vitro* imaging.[61] Similarly, Lin and coworkers have modified different silica-covered nanoMOFs to ensure addressing or stealth properties. First, manganese terephthalate or trimesate MOFs were functionalized with a fluorescence moiety (rhodamine) and a c(RGDfK) ($\alpha_V\beta_3$ integrin; overexpressed in many angiogenic cancers) for *in vitro* imaging and targeting, respectively.[59] Second, nanoparticles of several lanthanide terephthalates MOFs were grafted with a Tb-complex and dipicolinic acid for imaging[80] and finally, nanoparticles of the iron aminoterephthalate MIL-101 were modified with an *in vitro* imaging agent (1,3,5,7-tetramethyl-4,4-difluoro-8-bromomethyl-4-bora-3*a*,4*a*-diaza-*s*-indacene) and a cisplatin prodrug (ethoxysuccinato-cisplatin).[81]

The possibilities of surface engineering of MOFs are almost infinite given the presence of diverse superficial reactive groups (metals, counter-anions, non-coordinated complexing functions, functional groups of the linker (amino)) that might interact with the organic polymer. For instance, in order to obtain specific stronger interactions for a given organic polymer, the surface of the nanoparticle can be functionalized with an appropriate organic moiety prior to the introduction of the organic polymer.

4.433.2.3.3. Adsorption of challenging drugs

So far, extensive research has been carried on to develop injectable nanocarriers such as liposomes, nanoemulsions, nanoparticles, or micelles, to enable the delivery of drugs that suffer from many administration drawbacks such as a low solubility in aqueous media, strong tendency to crystallize, short blood half lives and/or inability to bypass natural barriers.[18,19,82] Thus, there are still several clearly identified drugs that require new nanocarriers, especially in the field of cancer and AIDS treatment. Among the drug of interest are busulfan (Bu), tamoxifen, azidothimidine (AZT), or cidofovir (CDV). These anticancer or antiviral compounds are, indeed, encapsulated in currently available nanotechnologies with great difficulties and they are too rapidly released after administration ('burst effect').[83]

Busulfan (1,4-bis(methylsulfonyloxy)butane or Bu) is an amphiphilic alkylating agent widely used in combination with high-dose chemotherapy regimes in leukemias, especially in pediatry since it represents a good alternative to the total body irradiation.[84,85] However, Bu suffers from important drawbacks such as its poor aqueous stability and an important toxicity due to its possible crystallization in blood leading to hepatic veno-occlusive diseases.[86] Bu has been entrapped so far in several known nanocarriers such as liposomes or polymers resulting, however, in poor loadings, never exceeding of 5–6 wt%,[87] as well as inducing fast 'burst' releases'.[88] To overcome these problems, Bu was thus loaded in nanoparticles of several porous iron carboxylates using impregnation of the title solids in Bu concentrated solutions.[61] Note the relevance of the choice of the solvent for the drug encapsulation, not only considering the solubility of the drug but also considering the competitive adsorption of the solvent and the drug within the pores of the MOF. Solvent has also a major effect on the breathing behavior in flexible porous MOFs that might create diffusion problems when considering the adsorption of the drug.

Bu capacities were always higher than in existing nanocarriers whatever the MOF considered; from 8.0 to 25.5 wt%, depending mainly on the pore volume (**Table 2**). Indeed, Bu loading in the rigid mesoporous iron trimesate MIL-100 is 5 times higher than the previously highest reported loadings obtained using polymer nanoparticles (5–6 wt%)[84] and 60 times higher than with liposomes (0.4 wt%).[83,89] According to these results, the administration of the actual therapy of Bu would require a very low amount of MIL-100, around 20 mg kg^{-1} day^{-1}, during 4 consecutive days. Furthermore, such formulation would avoid the administration of toxic solvents such as the *N*,*N*-dimethylacetamide, present in the actual commercially available i.v. dosage of Bu (Busilvex®).[90]

In the treatment of cancer and viral infections, the mononucleosides exhibit a remarkable activity. However, the clinical use of phosphorylated nucleotide analogues is limited either by their poor stability in biological medium, resulting in short half-lives and low bioavailabilities,[91] or their highly hydrophilic character, which strongly limits their intracellular penetration.[92,93] For instance, anti-HIV AZT is a water stable drug but suffers from a poor intracellular activation by cellular kinases, while the corresponding active triphosphate azidothimidine triphosphate (AZT-Tp) molecule is highly water unstable. Additionally, both AZT and AZT-Tp exhibit a low membrane permeability. Nanocarriers could help to overcome such resistances but due to the very high hydrophilic character of these drugs, existing drug delivery systems are unable to achieve high drug loadings while, in addition, showing in all cases a 'burst' release profile.[94] In this context, we have shown that nanoMOFs could entrap very large amounts of AZT-Tp and also other active drugs such as CDV, the monophosphorylated form of the anticytomegalovirus phosphonate CDV, and doxorubicin, an antitumoral molecule (**Table 2**).[61] In this case, although drug aqueous solutions used for encapsulation were diluted, active ingredients could be nevertheless easily adsorbed with very high efficiencies

Table 2 Drug capacities of different drugs on several iron carboxylates nanoparticles

	MIL-89	*MIL-88A*	*MIL-100*	*MIL-101_NH$_2$*	*MIL-53*
Flexible solid	Yes	Yes	No	No	Yes
Pore size (Å)	11	6	25 (5.6) 29 (8.6)	29 (12) 34 (16)	8.6
Particle size (nm)	50–100	150[a]	200	120	350[a]
Busulfan	9.8	8.0	25.5	–	14.3
Azidothimidine triphosphate	–	0.60	21.2	42.0	0.24
Cidofovir	14	2.6	16.1	41.9	–
Doxorubicin	–	–	9.1	–	–
Ibuprofen	–	–	33	–	22
Caffeine	–	–	24.2	–	23.1
Urea	–	–	69.2	–	63.5
Benzophenone 4	–	–	15.2	–	5
Benzophenone 3	–	–	1.5	–	–

[a]Bimodal distribution of sizes, with micrometric particles.

(in most cases, >80%). For instance, MIL-100 nanoparticles hosted up to 21 wt% of AZT-Tp, 16 wt% CDV, and 9 wt% doxo, while the MIL-101_NH$_2$ nanoparticles uploaded the unprecedented amount of 42 wt% of both, AZT-Tp and CDV. These results are exceptional, as loadings lower than 1 wt% were reported previously, using other carriers, with these drugs.[91]

In order to know if nanoMOFs could be considered as 'universal' drug nanocarriers, other cosmetic active molecules with different composition and polarities were encapsulated using these nanoMOFs (Table 2). In all cases, important loadings were also obtained with the amphiphilic caffeine (liporeductor), hydrophilic urea (hydrating agent), hydrophobic benzophenone 3 and hydrophilic benzophenone 4 (UVA and UVB filters).[61] These MOFs materials have also proved previously being efficient for the encapsulation and release of hydrophobic Ibuprofen.[39,56] In conclusion, the exceptional loadings of drugs in MOFs whatever the polarity and structure of the active molecule is mainly due to their adapted internal microenvironment (amphiphilic: polar metal, oxygens from the linker and nonpolar organic spacer) suitable for a large number of host molecules.[95]

AZT-Tp, CVD, and doxo were found to be progressively released from MIL-100 nanoparticles under simulated physiological conditions showing no 'burst effect.' A total drug delivery was achieved *in vitro* after 3–5 days for AZT-Tp and CDV, and up to 2 weeks for the hydrophobic doxo (Figure 7). Considering the degradation profile of MIL-100, one can suggest that drug delivery is a consequence of a combination of interactions (drug-framework) and diffusion processes. If one cannot exclude a partial degradation of the MOFs that could trigger the release, this is not here (MIL-100) the main parameter since after 3 days, most of the AZT-Tp has been released while only 10% degradation of the MOF was observed.

With the exception of our work, other examples of drug delivery from MOFs are still very scarce. An *et al.*[96] have recently reported the adsorption and delivery of a cationic drug, the antiarrythmic agent procainamide, within the cationic zinc adeninate MOF showing an interesting capacity of 22 wt% and a total released in 3 days under biological simulated conditions. A cisplatin prodrug (ethoxysuccinato-cisplatin) was also encapsulated in a silica covered iron terephthalate MIL-101

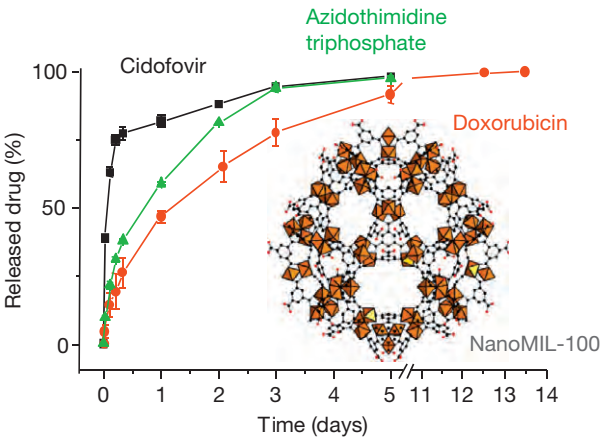

Figure 7 Drug delivery kinetics of cidofovir (black), azidothimidin triphosphate (green), and doxorubicin (red) from nanoparticles of iron trimesate MIL-100. Adapted from Horcajada, P.; Chalati, T.; Serre, C.; *et al*. *Nature Mater*. **2010**, *9*, 172–178.

(loading of 12.8 wt%) and delivered after 3 days under phosphate buffer solution (PBS) physiological conditions.[81]

4.433.2.4. *In Vitro* Activity Tests

Considering the promising data obtained with the challenging antiretroviral AZT-Tp and antitumoral Bu using the iron trimesate MIL-100, the *in vitro* activity of both drug-containing nanoparticles of MIL-100 was investigated.[61] Firstly, the cytotoxicity of the Bu-loaded MIL-100 in human leukemia (human T cell lymphoblast-like cell line, CCRF-CEM) and human multiple myeloma (RPMI-8226) cell lines were compared with those of empty nanoparticles of MIL-100 and free Bu. MIL-100 nanoparticles were able to deliver the intact form of Bu to the culture medium, showing no decrease in activity upon loading within the pores of the nanoparticles.

In addition, the *in vitro* activity of MIL-100 nanoparticles loaded with AZT-Tp was also evaluated in human peripherical blood mononuclear cells (PBMCs) using blood from healthy donors infected by HIV-1-LAI virus. Viral replication was measured by quantifying reverse transcriptase (RT) activity in cell

culture, confirming a significant anti-HIV effect only for AZT-Tp-containing MIL-100 nanoparticles (~90% of inhibition).

Remarkably, these results have evidenced the availability to these nanoMOFs carriers to entrap and deliver, in a controlled manner, in their active form, two challenging drugs such as Bu and AZT-Tp.

4.433.2.5. BioMOFs

4.433.2.5.1. The use of active linkers

MOFs are built up from the association of a linker and a metal. Encapsulation of drugs or biogases is the most obvious and easiest way to use MOFs for bioapplications. The degradation of the MOF carrier will however lead to a release, in contact with the body, not only from the biomolecule but also the metal and the linker issued from the MOF itself, introducing corresponding additional toxicity issues. To address this important problematic, the use of endogenous linkers is an acceptable solution. Several MOFs based on amino acids or exogenous linkers that exhibit a therapeutic activity, have been reported recently using zinc as the metal.[97]

Improving this approach consists in the development of biologically active MOFs. In fact, so far, the controlled release of drugs has been performed using a typical encapsulation/impregnation/release approach. The drug loading and the kinetics of release depend thus both on the pore volume of the carrier and the nature of the host–guest interactions between the drug and the framework. As a consequence, the presence of a MOF with a sufficient porosity is required while the release of the biomolecule is related to the nature of the interactions as well as the degradation of the MOF, raising additional toxicity concerns. A more convenient solution deals with the direct association of biomolecule, as the linker, and the metal to form the MOF (Figure 8). There is thus no need anymore of making a porous framework and the delivery of the drug is achieved directly through the degradation of the hybrid compound, ruling out the toxicity concerns from the use of traditionally nonbiologically active linkers. As a proof of principle, we have reported the use of iron and nicotinic acid (pyridine-3-carboxylic acid or niacin or vitamin B3).[2] This latter is an endogenous acid with pellagra-curative, vasodilating and antilipemic properties. A bioactive and degradable MOF denoted also Bio-MIL1 or $Fe_2^{III}Fe_{1-x}^{III}Fe_x^{II}O_{1-y}(OH)_y[O_2C\text{-}C_5H_4N]_5[O_2CCH_3]$ (x~0.15) (Bio-MIL for bioactive material from Institut Lavoisier) has been synthesized.

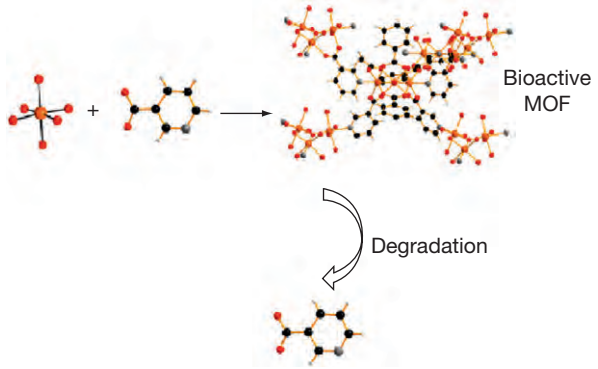

Figure 8 Schematic view of the formation of a BioMOF (Bio-MIL1) built up from bioactive linker and ist delivery. Here the bioactive linker is nicotinic acid. Iron, oxygen, nitrogen, and carbon atoms are in orange, red, gray, and black, respectively. Adapted from McKinlay, A. C.; Morris, R. E.; Horcajada, P.; *et al. Angew. Chem. Int. Ed.* **2010**, *49*, 6260–6266.

The delivery of nicotinic acid has been achieved in SBF at 37 °C, within 1 h.[98] This results from a rapid degradation of the bioactive MOF. This is in agreement with the poor stability observed previously with the iron aminoterephthalate MIL-101(Fe).[97] However, a much slower degradation rate was reported for other porous iron carboxylates such as the iron fumarate MIL-88A and the iron trimesate MIL-100 solids with a degradation time over 1 week in PBS. This shows that depending on the MOFs, that is, its structure, composition (metal, spacer, complexing group, ...), and the nature of the bioactive linker, one expects that different bioactive MOFs will exhibit different stabilities. Depending on the requirements for a given application, the choice of the metal and structure will thus be of a great importance to produce a bioactive MOFs with a suitable stability.

As most drugs are made from one or several complexing groups such as carboxylates, phosphates, phosphates, amines, and/or heterocycles, ..., our method can be considered as an alternative for the controlled released of biomolecules using biomaterials with a known toxicity and activity.

4.433.2.5.2. The use of biologically active metals

Another possibility of making a bioactive MOFs is to use an active metal. For instance, the activity of paramagnetic gadolinium complexes as magnetic resonance imaging (MRI) contrast agents is well known. This idea was reported by Lin *et al.* with the synthesis of nanoparticles of a Gd^{III}-based carboxylate MOF.[60,80,99] Large relaxivity values, several orders of magnitude higher than those of typical Gd^{III} complexes used as MRI contrast agents were obtained (Figure 9). However, the toxicity of the Gd^{III} combined with the degradation of MOFs in body fluid might rule out their clinical use. An alternative was the synthesis of nanoparticles of Mn^{II} carboxylates since Mn is much less toxic than rare earths.[61] The particles were however coated with silica to prevent from rapid degradation. The resulting relaxivities were lower than for the Gd carboxylates nanoparticles but probably for imaging.

A final use of active-metal-based MOFs for bioapplications would be theranostics. This would consist in following the drug release within the body using the imaging properties of the bioactive MOF. For instance, nanoparticles of the iron terephthalate MIL-101 have been surface-modified using the amino groups of the aminoterephthalate linkers. An anticancer drug (loading of 12.8 wt%) and a fluorophore (loading up to 11.6%) were introduced within the MOFs in order to associate *in vitro* optical imaging (fluorophore) and anticancer activity (drug). Once again, nanoparticles were covered with silica to prevent from the rapid degradation of the MOF and decrease the kinetics of release of the drug/fluorophore.

More recently, we have proposed a more suitable approach for theranostics. Nanoparticles of several nontoxic porous iron (III) carboxylates were shown to exhibit interesting relaxivity times (Figure 10), with R_2 relaxivities up to $50\,s^{-1}\,mM^{-1}$ (at 9.4 T), considered sufficient for an *in vivo* use.[100] Some of them also proved their ability to encapsulate very high

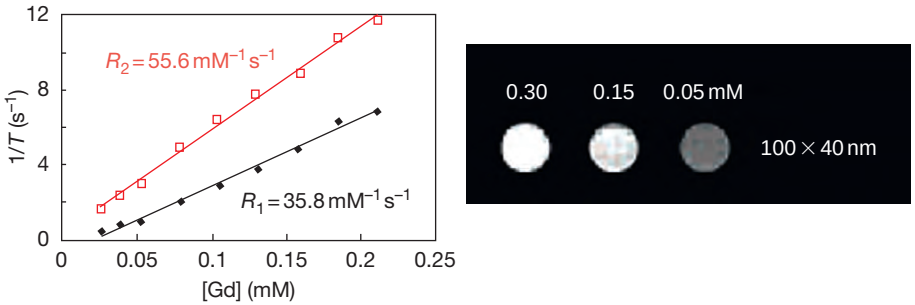

Figure 9 Left: R_1 and R_2 relaxivity curves of the Gd carboxylate nanoparticles of 100 × 40 nm dimensions; right: T1-weighted MR images of suspensions of 1 in water containing 0.1% xanthan gum. Adapted from Xie, Y.; Yu, Z.; Huang, X.; *et al. Chem. Eur. J.* **2007**, *13*, 9399–9405.

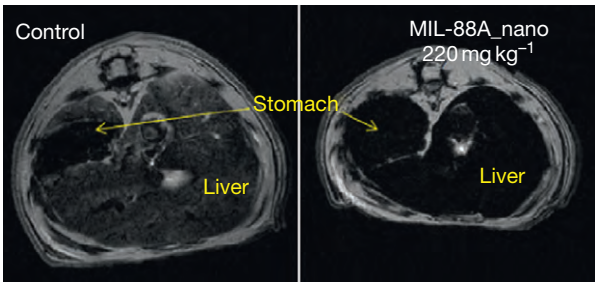

Figure 10 Magnetic resonance images collected at 9.4 T with gradient echo sequence of (left) control rats and (right) rats injected with 220 mg kg^{-1} of nanoparticles of MIL-88A in liver regions (results from C .Sebrie and B .Gillet from CNRS-Gif/Yvette, France). Reproduced from Horcajada, P.; Chalati, T.; Serre, C.; *et al. Nature Mater.* **2010**, *9*, 172–178.

loadings as well as controlled delivery of several challenging cyto-toxic drugs. If the high loading capacities are due to the presence of large pore volumes, the imaging properties are due to the paramagnetic iron trimers associated with a 3D pores system whereas free or bound water molecules bound to the acidic Lewis metal centers that can easily exchange their protons.

4.433.3. Adsorption and Delivery of Biological Gases

MOFs with their large pore volumes and their great structural and chemical diversity, are attractive candidates for the storage, capture and separation of strategic gases (H_2, CO_2, CH_4).[101] This concept can be further extended to bioactive gases such as NO, CO and even H_2S, which are highly toxic gases but are also, at very low concentration levels, part of several important mammalian biological processes. Nitric oxide (NO) has been recently studied with, for instance, first reports of cardiovascular system activity while the role of carbon monoxide (CO), still under investigation, plays an important role in several biological processes such as injury repairs involving heme oxygenase.[102] These results paved the way for the development of intense biomedical research involving these biogases. We will focus here our attention to the biological properties of NO, which is of an utmost importance in several biological processes such as signaling molecules, antibacterial, antithrombotic and wound healing applications.[103] The problem of NO or CO, besides its high toxicity above a certain concentration level, consists in its short life duration within the body fluid (<1 h for CO but less than a few minutes for NO)[2b] as well as the difficulty of delivering it at the right biological level (>10 ppm) on a controlled manner. Thus, controlling the release of NO using materials that store NO is an attractive alternative for many related applications.[104,105] Several types of carriers have been tried so far such as polymers,[106,107] porous inorganic silicas,[108] and zeolites.[109,110] For different reasons, these carriers suffer from serious drawbacks (toxicity, pro-inflammatory by products, fast release…) that restrict their use for certain applications.[111]

A nice feature of some porous MOFs is the presence of coordinatively unsaturated metal sites within their framework (Figure 11). At room temperature, under air atmosphere, these metal sites are nevertheless 'poisoned' by water molecules and only a careful thermal and/or vacuum treatment allows in most cases the full removal of the coordination water molecules.[112] The metal which has decreased its coordination number down to four- or fivefold, offers an accessible Lewis acid metal site, whose strength depends both on the oxidation state, usually +II or +III, and the environment of the metal (linker, structure). Thus, NO can easily be chemisorbed in large amounts, directly on the metal sites. Desorption of NO occurs then, more or less on a controlled manner, when one exposes back the solid to water moisture. So far, only a few selected MOFs have been tested for NO adsorption and release tests, such as the copper trimesate, denoted HKUST-1, and the metal(II) dihydroxoterephthalates series denoted CPO-27 (M = Co, Ni, Mg, …).[113]

In both cases, very large amounts of NO could be chemisorbed at room temperature and 1 bar, up to 7 mmol g^{-1}.[13] NO can be released upon exposure to water vapor for both solids (11% H_2O in nitrogen atmosphere). However, the profile of release strongly differs from HKUST-1 to CPO-27. The copper MOFs exhibit a rapid NO burst release over a few minutes followed by a residual desorption of NO over a few hours.

In the case, of CPO-27, a regular flux of pure NO is delivered on a controlled manner over a few hours (Figure 12), at a level ~7000 times higher than one of the copper MOFs, over the same duration and conditions. The initial 'antibacterial NO burst' that some MOFs exhibit upon

water triggered NO release, could however be useful for some cosmetic applications. One could imagine making composite creams based on NO-loaded MOFs in order to deliver gases onto human skin, such as those previously reported using zeolites. Depending on the nature of the cream, the delivery rate of NO can be tuned, in accordance with the composition of the formulation.[110] However, a controlled NO release is required to avoid unwanted side effects for most biomedical applications. Morris *et al.* have shown that CPO-27 materials loaded with NO could be used to control the vasodilation of porcine arteries.

The controlled release of NO at biological levels prevents platelet aggregations and thus such NO-loaded MOFs could be used as antithrombosis materials.

Another approach of using MOFs to deliver NO, reported by Rosseinsky and coworkers,[114] consists in coordinating an amine through one of the basic amino groups, directly on the Lewis acid site, that will further chemically react with NO to form diazonium moieties. The release of NO is then achieved through hydrolysis when exposed back to water moisture. However, the use of a toxic cobalt-based MOF rules out its use for any clinical use. More recently, a small pores and flexible copper sulfonate–carboxylate was shown to adsorb selectively only NO.[115]

In between these different methods or desorption behaviors, considering the large number of other existing MOFs with accessible metal sites, it is expected that other NO-delivering MOFs with various delivery capacity or release character will be available soon. Thus, tunable NO delivery systems might be designed by selecting the right material with the right NO capacity, kinetics of release as well as a suitable biodegradability and toxicity.

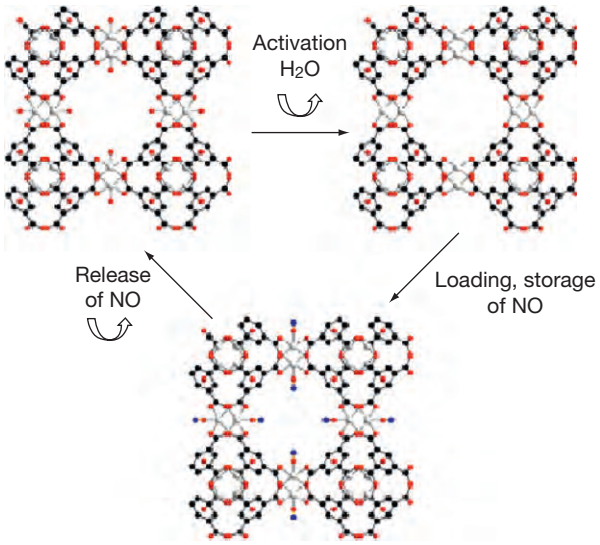

Figure 11 Schematic view of the activation/loading and release of NO in metal–organic frameworks with accessible metal sites (here, HKUST-1) with copper, carbon, nitrogen, and oxygen atoms in white, black, blue, oxygen. Adapted from McKinlay, A. C.; Morris, R. E.; Horcajada, P.; *et al. Angew. Chem. Int. Ed.* **2010**, *49*, 6260–6266.

4.433.4. Toxicity and Stability Issues

Developing bioapplications of MOFs requires the study of their toxicity. This issue can be studied sequentially in three steps: (1) the stability of the MOF in the biological medium; in the absence of biodegradation toxicity effects would arise caused by to the accumulation of MOF particles within the body; (2) the cytotoxicity of the nanoparticles; preliminary tests might help to gain understanding of the toxic effects at a cellular level; and finally, (3) *in vivo* toxicity.

4.433.4.1. *In Vitro* Biodegradability

Depending on the application, the carrier has to be stable enough to complete its function but degradation with time is necessary in order to allow body removing/recycling of the MOFs's components to prevent endogenous accumulation, and potentially toxicity effects. The stability of MOFs in general has been widely questioned due to first evidences of the low water stability of the well-known MOF-5.[17] However, the chemical and structural versatility of MOFs allows to tune the matrix biodegradation by changing either the composition (coordination number and oxidation state of the metal, solubility of the linker, complexing group (phosphonate, carboxylate, ...) and so on) and the structure type (pore size and

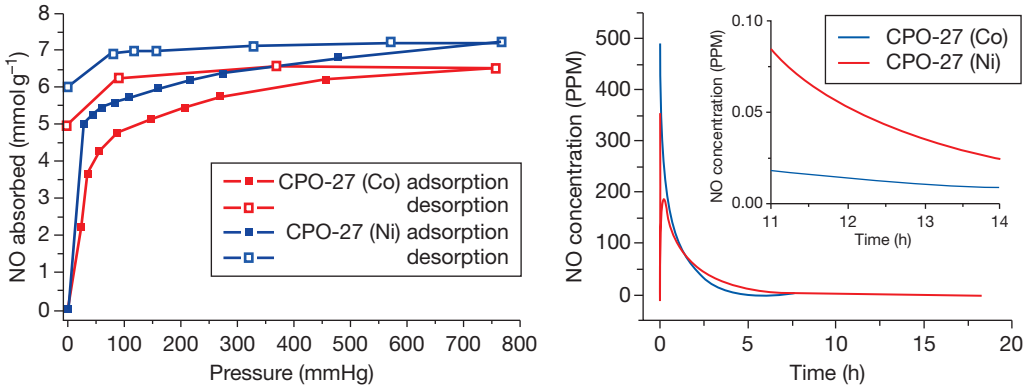

Figure 12 Left: adsorption, desorption isotherms of NO at 1 bar and 298 K; right: delivery profiles of NO from CPO-27 solids under a flux of wet nitrogen (11% humidity rate) at 298 K (results of Prof. R. Morris from St Andrews University). Adapted from McKinlay, A. C.; Xiaou, B.; Wragg, D. S.; Wheatley, P. S.; Megson, I. L.; Morris, R. E. *J. Am. Chem. Soc.* **2008**, *130*(31), 10440–10444.

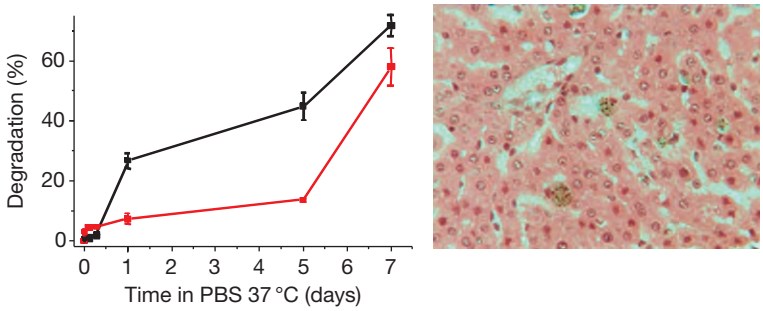

Figure 13 Left: *in vitro* degradation tests of MIL-100 (red) and MIL-88A (black) nanoparticles under simulated physiological conditions (PBS pH 7.4, 37 °C). Right: hepatic histology after the intravenous administration of 220 mg kg^{-1} of MIL-100 nanoparticles to rats (hematoxylin-eosin staining).

volume, pore connectivity, ...), the size of the nanoparticles and the type of formulation, in agreement with the desired application.

Hinks *et al.* have reported that the series M-CPO-27 (porous metal (II) hydroxoterephthalate (Ni, Co, ...)) are stable under physiological simulated conditions (PBS and bovine serum) for days, weeks and even longer.[116] Similarly, a tablet formulation of the flexible microporous iron terephthalate (MIL-53 (Fe)) has shown a stability over 3 weeks in a (SBF; same inorganic composition as human plasma).

NanoMOFs have also shown an acceptable stability. Recent studies, concerning the degradation of the iron carboxylates nanoparticles MIL-88A and MIL-100, have evidenced a partial degradation of 44% and 14%, respectively, after 5 days of incubation under physiological simulated conditions (PBS, pH 7.4, 37 °C; **Figure 13**). Other types of iron carboxylates such as amino-modified MIL-101(Fe) or the iron nicotinate Bio-MIL-1, showed a very rapid and total degradation, within a few hours, under similar conditions. This points out the diversity of biodegradability of MOFs as a result of their various structures and compositions. As an alternative, when degradation is too fast, it is possible to apply an external covering of the MOFs nanoparticles with silica to prevent fast degradation and thus achieved a better and targeted drug release.[95]

4.433.4.2. *In Vitro* Toxicity Tests

Cytotoxicity of two iron carboxylates nanoMOFs has been studied through 3-(4,5-dimethylthiazol-2-yl)-2,5-diphenyl tetrazolium bromide (MTT) assay.[62] The IC50 (half maximal inhibitory concentration) of the iron fumarate MIL 88A nanoparticles on mouse macrophages (J774.A1) was 57 ± 11 μg ml^{-1}. This value is comparable with those of currently available nanocarrier systems, thus confirming the lack of cytotoxicity of our nanoMOFs carriers.[117]

The same method has been used for the iron trimesate MIL-100 nanoparticles on human leukemia (CCRF-CEM) and human multiple myeloma (RPMI-8226) cells. Similarly, studies performed using human PBMCs have shown no cytotoxic effects even at the high doses.

4.433.4.3. *In Vivo* Toxicity Assays

In order both to determine what are the toxicity levels (doses) and the nature of the risks (toxicity effects), *in vivo* toxicity assays of nanoMOFs have been carried out. Therefore, three iron carboxylates have been selected: (1) flexible MIL-88A based on the hydrophilic aliphatic linker, fumaric acid, an endogenous molecule involved in the Krebs cycle, (2) rigid mesoporous MIL-100 based on the hydrophilic and exogenous aromatic trimesic acid, and (3) flexible MIL-88_4CH_3 with the hydrophobic exogenous aromatic tetramethylterephthalic acid. Different amounts of the nanosolids were intravenously administered to rats Wistar females over 4 weeks to determine the lethal dose 50 (LD_{50}). Surprisingly, the maximal dose was limited only by the stability of the suspension of nanoparticles in the glucose solution, used for the injection, and not due to their toxicity. After 7 days of administration of the maximal dose, 220 mg kg^{-1}, any sign of toxicity was observed. Note that the administered doses, up to 220 mg kg^{-1}, are considerably high compared to those of usual carriers.

For a more thorough evaluation of the toxicity of nanoMOFs, the first *in vivo* toxicity assay was performed through a unique intravenous administration of the maximum dose. Throughout three consecutive months, several parameters were followed such as weight, serum parameters to evaluate the hepatic function, the inflammatory and immunitary reaction and organs histology, as well as the hepatic enzymatic activity. Remarkably, no severe toxicity of iron carboxylate nanoMOFs was evidenced, even after the administration of very high doses. Nanoparticles were rapidly sequestered by the reticuloendothelial organs, spleen and liver, since in our case, no-stealth PEG coating of their surface was applied. Thus, as a consequence, an important iron accumulation can be detected in these target organs. However, after 1–3 months of injection, spleen and liver came back to normality (**Figure 13**), in agreement with the mobilization of the iron deposits that occurred the first moments after injection. The absence of any immune or inflammatory reactions, as well as the preservation of liver function, after the administration, support the lack of toxicity of the nanoMOFs. Moreover, the activity of Cytochrome P450 was not significantly modified in comparison with the control group, indicating that the nanoMOFs are probably not metabolized by the liver. The absence of the metabolization of the linker together with the high polarity of the polyacids, suggest a direct excretion of the ligand. Additionally, endogen acids as the fumaric acid might be reused by the body. Note that some currently approved iron oral prescribed drugs have the same chemical composition as the MIL-88A solid (i.e., iron fumarate or 'Ferrets®').

From the above results, one can clearly claim that iron carboxylate nanoMOFs exhibit no severe toxicity, even after the administration of important doses.

4.433.5. Formulation

One of the major concerns for developing real applications of MOFs, not only in biomedicine but also in other fields of interest such as separation, catalysis, and others, is their physical form. Some applications need very specific forms (tablets, pellets, extrudates, packed columns, ...). In the case of bioapplications, where one can think of various administration routes (topical, enteral, or parenteral), specific formulations are required. For most formulations, a control of the particle size is of interest. As described previously (see Section 4.433.2.3.1), this will limit the scope of the various administration route, but also influences other parameters (rheology, packing, external surface, ...) decisive for the processing of stable and reproducible formulations.

MOFs nanoparticles can be also used to make thin films other useful or types of formulations such as patches or coatings. Homogeneous thin films of MOFs can be prepared from stable colloidal solutions by a simple dip or spin coating method. This route allows the control of the film thickness by multilayer deposition or by controlling particle size and deposition conditions.[61,69]

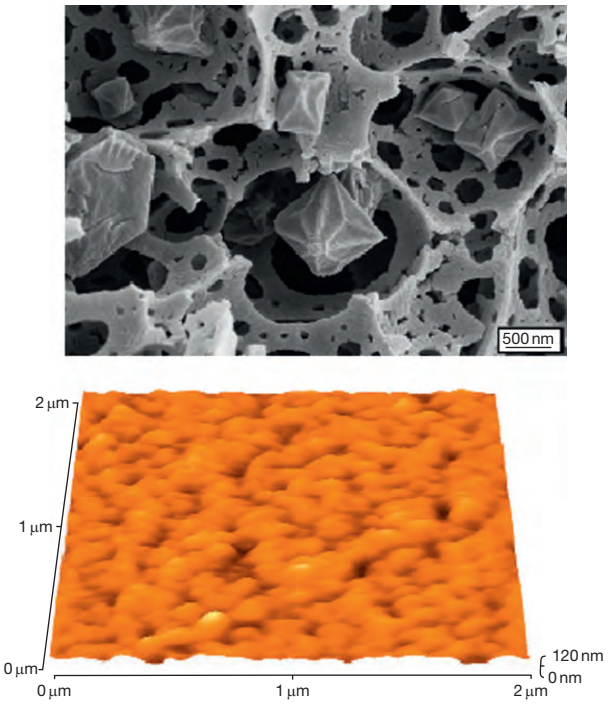

Figure 14 Top: SEM image of HKUST-1 particles entrapped into a macroporous polyHIPE. Adapted from Schwab, M. G.; Senkovska, I.; Rose, M.; *et al. Adv. Eng. Mater.* **2008**, *10*, 1151–1155. Bottom: Atomic force microscopy (AFM) of the surface of a MIL-101 thin film. Adapted from Demessence, A.; Horcajada, P.; Serre, C.; *et al. Chem. Commun.* **2009**, *46*, 7149–7151.

Finally, one could make composite materials from MOFs by mixing two nonmiscible materials, either integrating the MOF into a matrix or by a coating procedure (core–shell). Organic (i.e., polymers) or inorganic materials (i.e., silica) combine their properties to those of the MOFs within the final composite. A first example of MOFs composites has been recently reported by entrapping the copper trimesate HKUST-1 into a monolithic macroporous hydrophilic polymer (polyHIPEs) (Figure 14).[118]

Cream/ointment formulations of MOFs, very useful for biological gas release onto human skin, might also be produced in a near future. This concept has been already prepared using zeolites.[21]

Finally, the core–shell approach has been extended recently using several MOF nanoparticles, a polyvinilpyrrolidone polymer and a silica shell in order to avoid fast degradation and release of toxic metals.[59,78,79]

4.433.6. Conclusion and Perspectives

MOFs are a unique class of crystallized porous hybrid solids. Their composition, structure, pore size and volume can easily be tuned by changing either the metal (transition metal, lanthanide, or calcium/magnesium, ...), the linker (carboxylate, phosphonates, or imidazolates, ...) or through postsynthesis functionalization. This represents an advantage for optimizing their properties for a given application, compared with other porous solids (zeolites, carbons) with various structures but a unique composition. Some iron carboxylates based MOFs have been proven, at the preclinical level, to be nontoxic with injection doses in rats as high as 220 mg kg^{-1}. In addition, their *in vitro* degradability has been evidenced while modifying the composition and structure of MOFs strongly affects their kinetics of degradation from a few hours to weeks. Another advantage of MOFs is their loading capacity of drug molecules or gases over those of other carriers (polymers, zeolites, ...), with the possibility of encapsulating challenging anticancer or antiretroviral drugs with record loading capacity, followed in some cases by their controlled release into the environment. One can also introduce bioactivity in MOFs by directly selecting a bioactive molecule (drug, ...) as the linker and/or an active metal (Gd, Fe, ...) as the inorganic subnetwork, leading in some cases (Gd, Mn, Fe) to imaging properties useful for theranostics. The synthesis of MOFs nanoparticles suffers from no specific technical issue and can be achieved using either emulsion techniques or microwave assisted hydro or solvothermal conditions, even if in some cases their rapid degradation or the presence of reactive groups at their surfaces, leads to particle aggregation. Stealth, addressing or imaging properties of MOFs nanoparticles can be ensured through surface modifications with various organic biomolecules (PEG, chitosan, ...), either during or after the synthesis. The presence of both organic and inorganic moieties in MOFs renders also easier to produce composites of MOFs based either on polymers or inorganic matrixes suitable for patches, creams or any related applications.

Despite these promising results, the use of MOFs for biomedical applications is still in its infancy and several critical issues have still to be sorted out. First, from a fundamental point of view, if it is possible that MOFs drug loading capacity

can exceed that of other existing carriers, controlling the kinetics of delivery of biomolecules often times is major challenge. To determine the key parameters for controlled release, this might require to perform systematic encapsulation/release studies of model drugs with a full set of characterizations as well as state-of-the-art modeling techniques, in order to predict which is the best MOF materials for a given drug molecule and the related delivery time. Other important concerns are related to the origin of the difference in degradability from one MOF to another, in order to be able to design a specific MOF with a suitable stability for a given application. Finally, the synthesis of MOF nanoparticles and the corresponding surface modification, are time consuming processes that have been tested only for a few selected MOFs and extending these methods to other MOFs of interest will require in a near future a strong research investment.

Finally, the use of MOFs for biomedical applications is of a great interest with several breakthrough results, indicating that these hybrid crystallized porous carriers possess many advantages over existing systems. Considering the huge number of remaining existing encapsulation challenges such as the controlled release of the drug molecules that have not been commercialized due to their poor bioavailability (solubility, stability, ...), this confirms the high interest in further developing new bioapplications from MOFs.

Acknowledgements

EU for the funding via the ERC-2007-209241-BioMOFs. Prof. Gérard Férey, coworkers and students, related to bioapplications of MOFs, from Institut Lavoisier and Université Paris Sud are also thanked.

References

1. (a). Clearfield, A. *Prog. Inorg. Chem.* **1998**, *47*, 371–510; (b). Férey, G. *Chem. Soc. Rev.* **2008**, *37*, 191.
2. See the special issues: *Acc. Chem. Res.* **2005**, *38*, 215–378; *J. Solid State Chem.* **2005**, *178*, 2409–2574; Themed issue: Metal-organic frameworks. *Chem. Soc. Rev.* **2009**, 1201.
3. Eddaoudi, M.; Moler, D. B.; Li, H.; *et al. Acc. Chem. Res.* **2001**, *34*, 319–330.
4. Some major references in the field: (a) Yaghi, O. M.; O'Keeffe, M.; Ockwig, N. W.; Chae, H. K.; Eddaouddi, M.; Kim, J. *Nature* **2003**, *423*, 705–714; (b) Rowsell, J. L. C.; Yaghi, O. M. *Angew. Chem. Int. Ed.* **2005**, *44*, 4670–4679; (c) Rao, C. N. R.; Natarajan, S.; Vaidhyanathan, R. *Angew. Chem. Int. Ed.* **2004**, *43*, 1466–1496; (d) Kitagawa, S.; Kitaura, R.; Noro, S.-H. *Angew. Chem. Int. Ed.* **2004**, *43*, 2334–2375; (e) James, S. L. *Chem. Soc. Rev.* **2003**, *32*, 276–288; (f) Maspoch, D.; Ruiz-Molina, D.; Veciana, J. *Chem. Soc. Rev.* **2007**, *36*, 770–818; (g) Cheetham, A. K.; Rao, C. N. R. *Chem. Commun.* **2006**, 4780–4795; (h) Kepert, C. J. *Chem. Commun.* **2006**, 695–700.
5. MOFs are given a code such as HKUST-1, MIL-100, etc. This corresponds to the place of the first synthesis – for example MIL stands for Material from Institut Lavoisier – and generally define the structure of the materials. A different labelling corresponds to different shapes of pores and often a different chemical composition.
6. Horcajada, P.; Surblé, S.; Serre, C.; *et al. Chem. Commun.* **2007**, 2820.
7. Hafizovic Cavka, J.; Jakobsen, S.; Olsbye, U.; *et al. J. Am. Chem. Soc.* **2008**, *130*, 13850.
8. Chui, S. S. Y.; Lo, S. M. F.; Charmant, J. P. H.; Orpen, A. G.; Williams, I. D. *Science* **1999**, *283*, 1148–1150.
9. Li, H.; Eddaoudi, M.; O'Keeffe, M.; Yaghi, O. M. *Nature* **1999**, *402*, 276–279.
10. (a) Serre, C.; Millange, F.; Surblé, S.; Férey, G. *Angew. Chem. Int. Ed.* **2004**, *43*, 6285–6289; (b) Surblé, S.; Serre, C.; Mellot-Draznieks, C.; Millange, F.; Férey, G. *Chem. Commun.* **2006**, 84–286.
11. (a) Hwang, Y. K.; Hong, D.-Y.; Chang, J. S.; *et al. Angew. Chem. Int. Ed.* **2008**, *47*, 4144; (b) Wang, Z.; Cohen, S. M. *Angew. Chem. Int. Ed.* **2008**, *120*, 4777; *Angew. Chem. Int. Ed.* **2008**, *47*, 4699; (c) Devic, T.; Horcajada, P.; Serre, C.; *et al. J. Am. Chem. Soc.* **2010**, *132*, 1127–1136.
12. (a) Kitagawa, S.; Uemura, K. *Chem. Soc. Rev.* **2005**, *34*, 109–119; (b) Uemura, K.; Matsuda, R.; Kitagawa, S. *J. Solid State Chem.* **2005**, *178*, 2420–2429; (c) Férey, G.; Serre, C. *Chem. Soc. Rev.* **2009**, *38*(5), 1380–1399.
13. (a) Serre, C.; Millange, F.; Thouvenot, C.; *et al. J. Am. Chem. Soc.* **2002**, *124*, 13519–13526; (b) Loiseau, T.; Serre, C.; Huguenard, C.; *et al. Chem. Eur. J.* **2004**, *10*, 1373–1382; (c) Millange, F.; Guillou, N.; Walton, R. I.; Grenèche, J.-M.; Margiolaki, I.; Ferey, G. *Chem. Commun.* **2008**, 4732–4734.
14. (a) Mellot-Draznieks, C.; Serre, C.; Surblé, S.; Audebrand, N.; Férey, G. *J. Am. Chem. Soc.* **2005**, *127*, 16273–16378; (b) Serre, C.; Mellot-Draznieks, C.; Surblé, S.; Audebrand, N.; Fillinchuk, Y.; Férey, G. *Science* **2007**, *315*, 1828–1831.
15. (a) Fletcher, A. J.; Thomas, K. M.; Rosseinsky, M. J. *J. Solid State Chem.* **2005**, *178*, 2491–2510; (b) Maji, T. K.; Matsuda, R.; Kitagawa, S. *Nat. Mater.* **2007**, *6*, 142–148; (c) Bourrelly, S.; Llewellyn, P. L.; Serre, C.; Millange, F.; Loiseau, T.; Férey, G. *J. Am. Chem. Soc.* **2005**, *127*, 13519–13521; (d) Serre, C.; Bourrelly, S.; Vimont, A.; *et al. Adv. Mater.* **2007**, *19*, 2246–2251; (e) Millange, F.; Serre, C.; Guillou, N.; Férey, G.; Walton, R. I. *Angew Chem. Int. Ed.* **2008**, *47*, 4100; (f) Trung, T. K.; Trens, P.; Tanchoux, N.; *et al. J. Am. Chem. Soc.* **2008**, *130*(50), 16926–16932; (g) Hamon, L.; Llewellyn, P.; Devic, T.; *et al. J. Am. Chem. Soc.* **2009**, *131*(47), 17490–17499.
16. Horcajada, P.; Serre, C.; Maurin, G.; *et al. J. Am. Chem. Soc.* **2008**, *130*, 6774.
17. Low, J. J.; Benin, A. I.; Jakubczak, P.; Abrahamian, J. F.; Faheem, S. A.; Willis, R. R. *J. Am. Chem. Soc.* **2009**, *131*, 15834–15842.
18. Mainardes, R. M.; Silva, L. P. *Curr. Drug Targets* **2004**, *5*, 449–455.
19. See special issue and references related. *Adv. Drug Deliv. Rev.* **2008**, 60.
20. Peer, D.; *et al. Nat. Nanotechnol.* **2007**, *2*, 751–760.
21. Ellerby, L. M.; Nishida, C. R. *Science* **1992**, *225*, 1113–1115.
22. Böttcher, H.; Slowik, P.; Suss, W. *J. Sol–Gel Sci. Technol.* **1998**, *13*, 277–281.
23. Kortesuo, P.; Ahola, M.; Kangas, M.; *et al. Biomaterials* **2000**, *21*, 193–198.
24. Nicoll, S. B.; Radin, S.; Santos, E. M.; Tuan, R. S.; Ducheyne, P. *Biomaterials* **1997**, *18*, 853–859.
25. Radin, S.; Falaize, S.; Lee, M. H.; Ducheyne, P. *Biomaterials* **2002**, *23*, 3113–3122.
26. Vallet-Regi, M.; Ramila, A.; del Real, R. P.; Perez-Pariente, J. *Chem. Mater.* **2001**, *13*, 308–311.
27. Huo, Q.; Liu, J.; Wang, L. Q.; Jiang, Y.; Lambert, T. N.; Fang, E. *J. Am. Chem. Soc.* **2006**, *128*, 6447–6453.
28. Slowing, I. I.; Trewyn, B. G.; Giri, S.; Lin, V. S.-Y. *Adv. Funct. Mater.* **2007**, *17*, 1225–1236.
29. Manzano, M.; Colilla, M.; Vallet-Regí, M. *Expert Opin. Drug Deliv.* **2009**, *6*(12), 1383–1400.
30. Dyer, A.; Morgan, S.; Wells, P.; Williams, C. *J. Helminthol.* **2000**, *74*(2), 137–141.
31. Horcajada, P.; Márquez-Alvarez, C.; Rámila, A.; Pérez-Pariente, J.; Vallet-Regi, M. *Solid State Sci.* **2006**, *8*(12), 1459–1465.
32. Arruebo, M.; Fernández-Pacheco, R.; Irusta, S.; Arbiol, J.; Ibarra, M. R.; Santamaría, J. *Nanotechnology* **2006**, *17*, 4057–4064.
33. Rimoli, M. G.; Rabaioli, M. R.; Melisi, D.; *et al. J. Biomed. Mater. Res. A* **2008**, *87*(1), 156–164.
34. Freiberg, S.; Zhu, X. X. *Int. J. Pharm.* **2004**, *282*, 1–18.
35. Soppimath, K. S.; Aminabhavi, T. M.; Kulkarni, A. R.; Rudzinski, W. E. *J. Control. Release* **2001**, *70*, 1–20.
36. Levy, M. H.; Wheelock, E. F. *J. Immunol.* **1975**, *115*, 41–48.
37. Xie, G.; Sun, J.; Zhong, G.; Shi, L.; Zhang, D. *Arch. Toxicol.* **2009**; doi: 10.1007/s00204-009-0488-x.
38. Di Pasqua, A. J.; Sharma, K. K.; Shi, Y.-L.; *et al. J. Inorg. Biochem.* **2008**, *102*, 1416–1423.
39. Horcajada, P.; Serre, C.; Vallet-Regi, M.; Sebban, M.; Taullele, F.; Férey, G. *Angew. Chem. Int. Ed.* **2006**, *45*, 5974–5978.
40. Férey, G.; Mellot-Draznieks, C.; Serre, C.; *et al. Science* **2005**, *309*, 2040–2042.
41. Férey, G.; Serre, C.; Mellot-Draznieks, C.; Millange, F.; Surblé, S. *Angew. Chem. Int. Ed.* **2004**, *116*, 6456–6461.
42. Babarao, R.; Jiang, J. *J. Phys. Chem. C* **2009**, *113*(42), 18287–18291.
43. Vallet-Regi, M.; Rámila, A.; del Real, R. P.; Pérez-Pariente, J. *Chem. Mater.* **2001**, *13*, 308–311.
44. Whitfield, T. R.; Wang, X.; Liu, L.; Jacobson, A. J. *Solid State Sci.* **2005**, *7*, 1096–1103.
45. Sheftel, V. O. *Indirect Food Additives and Polymers: Migration and Toxicology*; Lewis Publishers: Boca Raton, FL, 2000; pp 148–154.

46. http://www.chemicalland21.com/specialtychem/perchem/TRIMESIC%20ACID.htm; 2008.
47. http://www.chem.unep.ch/irptc/sids/OECDSIDS/100-21-0.pdf; 2008.
48. Uemura, K.; Kitagawa, S.; Kondo, M.; *et al*. *Chem. Eur. J*. **2002**, *8*, 3586.
49. Serre, C.; Millange, F.; Thouvenot, C. *J. Am. Chem. Soc*. **2002**, *124*, 13519.
50. Serre, C.; Mellot-Draznieks, C.; Surblé, S.; Audebrand, N.; Filinchuk, Y.; Férey, G. *Science* **2007**, *315*, 1828.
51. Bourrelly, S.; Llewellyn, P. L.; Serre, C.; Millange, F.; Loiseau, T.; Férey, G. *J. Am. Chem. Soc*. **2005**, *127*, 13519.
52. Llewellyn, P. L.; Horcajada, P.; Maurin, G.; *et al*. *J. Am. Chem. Soc*. **2009**, *131*, 13002–13008.
53. Millange, F.; Serre, C.; Guillou, N.; Férey, G.; Walton, R. I. *Angew. Chem. Int. Ed*. **2008**, *47*, 4100–4105.
54. Trung, T. K.; Trens, P.; Tanchoux, N.; *et al*. *J. Am. Chem. Soc*. **2008**, *130*(50), 16926–16932.
55. Mellot-Draznieks, C.; Serre, C.; Surblé, S.; Audebrand, N.; Férey, G. *J. Am. Chem. Soc*. **2005**, *127*, 16273.
56. Horcajada, P.; Serre, C.; Maurin, G.; *et al*. *J. Am. Chem. Soc*. **2008**, *130*, 6774–6780.
57. Horcajada, P.; Marquez-Alvarez, C.; Ramila, A.; Perez-Pariente, J.; Vallet-Regi, M. *Solid State Sci*. **2006**, *8*(12), 1459–1465.
58. Munoz, B.; Ramila, A.; Perez-Pariente, J.; Diaz, I.; Vallet-Regi, M. *Chem. Mater*. **2003**, *15*(2), 500–503.
59. Rieter, W. J.; Taylor, K. M. L.; An, H.; Lin, W. *J. Am. Chem. Soc*. **2006**, *128*, 9024–9025.
60. Taylor, K. M. L.; Jin, A.; Lin, W. *Angew. Chem. Int. Ed*. **2008**, *47*, 7722–7725.
61. Taylor, K. M. L.; Rieter, W. J.; Lin, W. *J. Am. Chem. Soc*. **2008**, *130*, 14358–14359.
62. Jhung, S. H.; Lee, J.-H.; Yoon, J. W.; Serre, C.; Férey, G.; Chang, J.-S. *Adv. Mater*. **2006**, *19*(1), 121–124.
63. Demessence, A.; Horcajada, P.; Serre, C.; *et al*. *Chem. Commun*. **2009**, 7149–7151.
64. Horcajada, P.; Chalati, T.; Serre, C.; *et al*. *Nat. Mater*. **2010**, *9*, 172–178.
65. Isomaa, B.; Reuter, J.; Djupsund, B. M. *Arch. Toxikol*. **1976**, *35*(2), 91–96.
66. http://msds.chem.ox.ac.uk/HE/hexadecyltrimethylammonium_bromide.html; 2010.
67. https://irmm.jrc.ec.europa.eu/html/reference_materials_catalogue/catalogue/attachements/IRMM-442_msds.pdf; 2010.
68. http://msds.chem.ox.ac.uk/HE/1-hexanol.html; 2010.
69. Cravillon, J.; Munzer, S.; Lohmeier, S.-J.; Feldhoff, A.; Huber, K.; Wiebcke, M. *Chem. Mater*. **2009**, *21*(8), 1410–1412.
70. Hermes, S.; Witte, T.; Hikov, T.; *et al*. *J. Am. Chem. Soc*. **2007**, *129*, 5324.
71. Horcajada, P.; Serre, C.; Grosso, D.; *et al*. *Adv. Mater*. **2009**, *21*, 1931–1935.
72. Gupta, P. K. *J. Pharm. Sci*. **1990**, *79*(11), 949–962.
73. Gref, R.; Minamitake, Y.; Peracchia, M. T.; Trubetskoy, V.; Torchilin, V.; Langer, R. *Science* **1994**, *263*, 1600–1603.
74. Gabizon, A. *Cancer Res*. **2001**, *7*, 223–225.
75. Simard, P.; Hoarau, D.; Khalid, M. N.; Roux, E.; Leroux, J. C. *Biochim. Biophys. Acta* **2005**, *1715*, 37–48.
76. Vonarbourg, A.; Passirani, C.; Saulnier, P.; Benoit, J. *Biomaterials* **2006**, *27*, 4356–4373.
77. Gref, R.; Domb, A.; Quellec, P.; *et al*. *Adv. Drug Deliv. Rev*. **1995**, *16*, 215–233.
78. Lehr, C. M.; Bouwstra, J. A.; Schacht, E. H.; Junginger, H. E. *Int. J. Pharm*. **1992**, *78*, 43–48.
79. Chen, L.; Schechter, B.; Arnon, R.; Wilchek, M. *Drug Dev. Res*. **2000**, *50*(3–4), 258–271.
80. Rieter, W. J.; Taylor, K. M. L.; Lin, W. *J. Am. Chem. Soc*. **2007**, *129*, 9852–9853.
81. Taylor-Pashow, K. M. L.; Rocca, J. D.; Xie, Z.; Tran, S.; Lin, W. *J. Am. Chem. Soc*. **2009**, *131*(40), 14261–14263.
82. Couvreur, P.; Gref, R.; Andrieux, K.; Malvy, C. *Prog. Solid State Chem*. **2006**, *34*, 231–235.
83. Hasan, A. S.; Socha, M.; Lamprecht, A.; *et al*. *Int. J. Pharm*. **2007**, *344*, 53–61.
84. Vassal, G.; Gouyette, A.; Hartmann, O.; Pico, J. L.; Lemerle, J. *Cancer Chemother. Pharmacol*. **1989**, *24*, 386–390.
85. Vassal, G.; Deroussent, A.; Challine, D.; *et al*. *Blood* **1992**, *79*, 2475–2479.
86. Slattery, J. T.; Sanders, J. E.; Buckner, C. D.; *et al*. *Bone Marrow Transplant*. **1995**, *16*, 31–42.
87. Layre, A.; Gref, R.; Richard, J.; Requier, D.; Couvreur, P. *Nanoparticules polimériques composites* FR 04 07569, 7 July 2004.
88. Layre, A.; Couvreur, P.; Chacun, H.; *et al*. *J. Control. Release* **2006**, *111*, 271–280.
89. Hassan, Z.; Nilsson, C.; Hassan, M. *Bone Marrow Transplant*. **1998**, *22*, 913–918.
90. Madden, T.; de Lima, M.; Thapar, N.; *et al*. *Biol. Blood Marrow Transplant*. **2007**, *13*(1), 56–64.
91. Xiaoling, L.; Chan, W. K. *Adv. Drug Deliv. Rev*. **1999**, *39*, 81–103.
92. Loke, S. L.; *et al*. *Proc. Natl. Acad. Sci. USA* **1989**, *86*, 3474–3478.
93. Kukhanova, M.; Krayevsky, A.; Prusoff, W.; Cheng, Y. C. *Curr. Pharm. Des*. **2000**, *6*, 585–598.
94. Hillaireau, H.; Le Doan, T.; Besnard, M.; Chacun, H.; Janin, J.; Couvreur, P. *Int. J. Pharm*. **2006**, *324*(1), 37–42.
95. Alaerts, L.; Kirschhock, C. E. A.; Maes, M.; *et al*. *Angew. Chem. Int. Ed*. **2007**, *46*, 4293.
96. An, J.; Geib, S. J.; Rosi, N. L. *J. Am. Chem. Soc*. **2009**, *131*(24), 8376–8377.
97. Xie, Y.; Yu, Z.; Huang, X.; *et al*. *Chem. Eur. J*. **2007**, *13*, 9399–9405.
98. Miller, S. R.; Heurtaux, D.; Baati, T.; Horcajada, P.; Grenèche, J.-M.; Serre, C. *Chem. Commun*. **2010**, *46*, 4526.
99. Rieter, W. J.; Taylor, K. M. L.; An, H.; Lin, W.; Lin, W. *J. Am. Chem. Soc*. **2006**, *128*, 9024–9025.
100. Horcajada, P.; Chalati, T.; Serre, C.; *et al*. *Nat. Mater*. **2010**, *9*, 172–178.
101. (a) Panella, B.; Hönes, K.; Müller, U.; *et al*. *Angew. Chem. Int. Ed*. **2008**, *47*, 2138; (b) Latroche, M.; Surblé, S.; Serre, C.; *et al*. *Angew. Chem. Int. Ed*. **2006**, *45*, 8227–8231; (c) Lin, X.; Jia, J.; Zhao, X.; *et al*. *Angew. Chem. Int. Ed*. **2006**, *45*, 1–7; (d) Kaye, S. S.; Long, J. R. *J. Am. Chem. Soc*. **2006**, *127*, 6506; (e) Millward, A. R.; Yaghi, O. M. *J. Am. Chem. Soc*. **2005**, *127*, 17998–17999; (f) Llewellyn, P. L.; Bourrelly, S.; Serre, C.; *et al*. *Langmuir* **2008**, *24*, 7245–7250; (g) Finsy, V.; Kirschhock, C. E. A.; Vedts, G.; *et al*. *Chem. Eur. J*. **2009**, *15*, 7724–7731.
102. (a) Moncada, S.; Palmer, R. M. J.; Higgs, E. A. *Pharmacol. Rev*. **1991**, *43*, 109; (b) Mann, B. E.; Motterlini, R. *Chem. Commun*. **2007**, 4197–4208.
103. Butler, A. R.; Nicholson, R. *Life, Death and Nitric Oxide*; The Royal Society of Chemistry: Cambridge, 2003.
104. Zhu, H. F.; Ka, B.; Murad, F. *World J. Surg*. **2007**, *31*, 624.
105. Miller, M. R.; Megson, I. L. *Br. J. Pharmacol*. **2007**, *151*, 305.
106. Parzuchowski, P. G.; Frost, M. C.; Meyerhoff, M. E. *J. Am. Chem. Soc*. **2002**, *124*, 12182.
107. DeRosa, F.; Kibbe, M. R.; Najjar, S. F.; Citro, M. L.; Keefer, L. K.; Hrabie, J. A. *J. Am. Chem. Soc*. **2007**, *129*, 3786.
108. Shin, J. H.; Schoenfisch, M. H. *Chem. Mater*. **2008**, *20*, 239.
109. Wheatley, P. S.; Butler, A. R.; Crane, M. S.; *et al*. *J. Am. Chem. Soc*. **2006**, *128*, 502.
110. Mowbray, M.; Tan, X. J.; Wheatley, P. S.; Morris, R. E.; Weller, R. B. *J. Invest. Dermatol*. **2008**, *128*, 352.
111. Kroncke, K. D.; Suschek, C. V. *J. Invest. Dermatol*. **2008**, *128*, 258.
112. (a) Vimont, A.; Goupil, J.-M.; Lavalley, J.-C.; *et al*. *J. Am. Chem. Soc*. **2006**, *128*, 3218–3227; (b) Bordiga, S.; Regli, L.; Bonino, F.; *et al*. *PCCP* **2007**, *9*, 2676–2685; (c) Xiao, B.; Wheatley, P. S.; Zhao, X. B.; *et al*. *J. Am. Chem. Soc*. **2007**, *129*, 1203–1209.
113. (a) Xiao, B.; Wheatley, P. S.; Zhao, X. B.; *et al*. *J. Am. Chem. Soc*. **2007**, *129*, 1203–1209; (b) McKinlay, A. C.; Xiao, B.; Wragg, D. S.; Wheatley, P. S.; Megson, I. L.; Morris, R. E. *J. Am. Chem. Soc*. **2008**, *130*, 10440–10444.
114. Ingleson, M. J.; Heck, R.; Gould, J. A.; Rosseinsky, M. J. *Inorg. Chem*. **2009**, *48*, 9986–9988.
115. Xiao, B.; Byrne, P. J.; Wheatley, P. S.; *et al*. *Nat. Chem*. **2009**, *1*, 289–294.
116. Hinks, N. J.; McKinlay, A. C.; Xiao, B.; Wheatley, P. S.; Morris, R. E. *Micropor. Mesopor. Mater*. **2010**; doi: 10.1016/j.micromeso.2009.04.031.
117. Soma, C. E.; Dubernet, C.; Barratt, G.; Benita, S. *J. Control. Release* **2000**, *68*, 283–289.
118. Schwab, M. G.; Senkovska, I.; Rose, M.; *et al*. *Adv. Eng. Mater*. **2008**, *10*, 1151–1155.

4.434. Hybrid Magnetic Nanoparticles for Targeted Delivery

R Epherre, G Goglio, S Mornet, and E Duguet, CNRS, Université de Bordeaux, Pessac, France

© 2011 Elsevier Ltd. All rights reserved.

4.434.1.	**Introduction**	576
4.434.2.	**Magnetism of MNPs**	577
4.434.2.1.	Behavior in Static Magnetic Fields and Gradients	577
4.434.2.1.1.	Materials magnetism background	577
4.434.2.1.2.	Magnetism of nanoparticles	578
4.434.2.1.3.	Surface effects	580
4.434.2.1.4.	Forces exerted in magnetic field gradients	580
4.434.2.2.	Behavior in AC Magnetic Fields	580
4.434.2.2.1.	Specific absorption rate	581
4.434.2.2.2.	Loss mechanisms	581
4.434.3.	**MF Design and Preparation**	582
4.434.3.1.	Synthesis of MNPs	582
4.434.3.2.	Colloidal Stabilization in Physiological Medium	582
4.434.4.	**Size/Surface Requirements with Regard to i.v. Administration**	582
4.434.4.1.	Biocompatibility	582
4.434.4.2.	Biodistribution and Passive Targeting Strategies	583
4.434.4.3.	Active Targeting Strategies	584
4.434.4.4.	Surface Activation and Bioconjugation	584
4.434.5.	**MNPs as Contrast Agents for MRI**	584
4.434.5.1.	MRI Background	584
4.434.5.2.	MR Contrast Agents	585
4.434.5.3.	Liver MR Imaging	586
4.434.5.4.	Metastatic Lymph Node MR Imaging (MR Lymphography)	586
4.434.5.5.	Blood Pool Imaging	586
4.434.5.6.	Macrophage MR Imaging	586
4.434.5.7.	Molecular MR Imaging	587
4.434.5.8.	Stem Cell Tracking	587
4.434.5.9.	Next Developments	587
4.434.6.	**MNPs as Mediators for Magnetic Hyperthermia**	588
4.434.6.1.	Hyperthermia Modalities	588
4.434.6.2.	Magnetic Fluid Hyperthermia	589
4.434.6.2.1.	Nanocomposite magnetic microparticles administered by arterial embolization	589
4.434.6.2.2.	Superparamagnetic nanoparticles injected directly into the tumor	589
4.434.6.3.	Next Developments	590
4.434.6.3.1.	Mediators improvement	590
4.434.6.3.2.	Physics of magnetic loss phenomena	591
4.434.6.3.3.	Targeting strategies and limits	591
4.434.7.	**MNPs Within Carriers for Drug Delivery**	591
4.434.7.1.	Magnetic Guidance for Carriers	592
4.434.7.2.	Enhanced Drug Release Under the Mechanical Stress of an Oscillating Magnetic Field	592
4.434.7.3.	Heat-Triggered Drug Release Under AC Magnetic Field Control	592
4.434.8.	**Conclusion**	592
References		593

Abbreviations

AC	Alternating current
DC	Direct current
DNA	Deoxyribonucleic acid
FC	Field cooling
fcc	Face-centered cubic
ILP	Intrinsic loss power
i.v.	Intravenous
LD_{50}	Median lethal dose
MF	Magnetic fluid
MFH	Magnetic fluid hyperthermia
MNP	Magnetic nanoparticle
MPI	Magnetic particle imaging
MPS	Mononuclear phagocyte system

MRI	Magnetic resonance imaging
MTC	Magnetic targeted carrier
MTT	3-(4,5-Dimethylthiazol-2-yl)-2,5-diphenyltetrazolium bromide
NMR	Nuclear magnetic resonance
PEG	Poly(ethylene glycol)
rf	Radiofrequency
RNA	Ribonucleic acid
SAR	Specific absorption rate
Si-RNA	Small interfering ribonucleic acid
SPIO	Superparamagnetic iron oxide
TE	Delay time
TR	Repetition time
USPIO	Ultrasmall superparamagnetic iron oxide
ZFC	Zero-field cooling

Symbols

χ	Volumetric magnetic susceptibility
χ_w	Water magnetic susceptibility
η	Viscosity
μ_0	Vacuum permeability
ν	Velocity
ν_w	Water velocity
ρ	Density
τ	Relaxation time
τ_0	Time constant
τ_B	Brown relaxation time
τ_{eff}	Effective relaxation time
τ_N	Néel relaxation time
ω	Angular frequency
ξ	Magnetophoretic mobility
A	Exchange constant
B	Magnetic induction
D_C	Critical diameter
f	Frequency
F_d	Hydrodynamic drag force
F_m	Magnetic force
H	Magnetic field strength
H_C	Coercivity
k_B	Boltzmann constant
K_{eff}	Effective anisotropy constant
m	Magnetic moment
M	Magnetization
m_F	Mass of magnetic fluid
m_M	Mass of magnetic element
M_R	Residual magnetization
M_S	Saturation magnetization
r	Relaxivity
R_H	Hydrodynamic radius
t	Time
T	Absolute temperature
T_1	Longitudinal relaxation time
T_2	Transverse relaxation time
T_B	Blocking temperature
T_C	Curie temperature
V	Volume
V_H	Hydrodynamic volume

4.434.1. Introduction

Magnetism and medicine are sharing a fascinating common history for several tenths of centuries.[1] Some of the earlier applications of magnetic materials include removal of metallic objects from the bodies of animals and humans and the use of magnetite grains as antidote for the accidental swallowing of rust. In ayurvedic therapies, various kinds of iron oxides are still used as iron supplements for humans, especially children and pregnant women. More recently, miniaturization of electromagnets, development of superconducting electromagnets, and introduction of strong permanent magnets (Sm–Co and Nd–Fe–B) have stimulated the medical use of magnets in fields as diverse as radiology, dentistry, cardiology, neurosurgery, oncology, and immunoassays.

Moreover, well-calibrated magnetic nanoparticles (MNPs) in the size range 1–100 nm are currently produced in large quantities thanks to reproducible synthetic protocols. Several chemical routes allow modification of their surface for ensuring their colloidal stability in physiological media, protecting them from corrosion/dissolution, and making them less cytotoxic and derivatizable with biorelated molecules.

MNPs are of particular interest in medicine. First, they are smaller than cells (10–100 μm) and comparable to viruses (20–450 nm), proteins (5–50 nm), or genes (2-nm wide and 20–450-nm long). Therefore, they are able to circulate in the bloodstream (even in the thin lung capillaries), to cross biological membranes and to interact closely with biomolecules. Second, when their diameter is lower than about 10 nm, MNPs display unusual magnetic properties, that is, superparamagnetism, making them tractable in magnetic field gradients, capable of creating local magnetic fields, but not concerned with remanence magnetization. Because living tissues are transparent to magnetic fields, MNPs may be remotely manipulated *in vitro* or *in vivo*. Moreover, they may disturb the relaxation times of surrounding protons. Lastly, they may generate heat when they are subjected to AC magnetic fields, thanks to hysteresis, Brownian and/or Néel loss phenomena. So, formulated in aqueous liquids called magnetic fluids (MFs), MNPs became recently inescapable tools for biologists, pharmacologists, and physicians. They are now routinely used as contrast agents in magnetic resonance imaging (MRI) and very next applications are expected in the field of cancer thermal treatment, magnetic targeting, and heat-triggered drug release.

Even if some publications deal with oral MRI contrast agents for the gastrointestinal tract,[2] the majority of published studies concern the intravenous (i.v.) administration route. The use of MNPs in the blood compartment depends on

specific requirements with respect to their plasma half-life and their final biodistribution. The problem of the nonnatural stealthiness of the nanoparticles toward the immune system, and the possibilities for resolving it, have been widely studied in the field of drug delivery from liposomes and polymeric nanoparticles.[3] Indeed, retention of drugs in circulation is a key step in the design of drug delivery carriers. Even the most active compound *in vitro* is useless if it does not reside *in vivo* in the blood long enough to reach its target, while managing to avoid, to some extent, premature metabolism, immunological reactions, toxicity, rapid excretion and captation by undesired tissues.[4] Presently, many pieces of information are available concerning the immune system mechanisms, the factors affecting the biodistribution of nanoparticles, such as their size and shape, the hydrophobic/hydrophilic balance of their surface, their surface charge, and the solutions envisaged for targeting specific organs, tissues, or cells.

The aim of this review is to present simultaneously the basic knowledge and an updated survey of the potential of MNPs for *in vivo* applications through an understanding of the problems involved from the viewpoint of their overall requirements, their synthesis and their bulk and surface properties. One main intention of this contribution is to impart information about both the state of the art as well as the need for further progress and clinical development. Only typical examples among the most promising ones will be reported and discussed and a special emphasis will be made on cancer diagnosis and therapy. Only general references are provided for the reader to turn to for more information. It may be noted that, even if they are not within the scope of this chapter, MNP technology concerns also non-*in vivo* bioapplications, for example, cell sorting,[5,6] detoxification of biological fluids,[7] radionucleide and gene delivery (magnetofection),[5,7,8] retinal detachment,[6] cell membrane manipulation,[7,9] and magnetorelaxometry.[6]

4.434.2. Magnetism of MNPs

4.434.2.1. Behavior in Static Magnetic Fields and Gradients

4.434.2.1.1. Materials magnetism background

The magnetism of a solid is originated from the contributions of the electrons constituting a solid, thanks to their quantum properties, that is, their spin angular moment and their orbital angular moment, which contribute to their magnetic moment. These electrons also determine the strength of the interaction between atoms in a solid, making the basis of the different macroscopic behaviors observed in nature. Massive materials can thus be classified into diamagnetic, paramagnetic, ferromagnetic, ferrimagnetic, and antiferromagnetic according to the arrangement of their magnetic dipoles in the absence and presence of an external magnetic field.[10,11]

If a magnetic material is placed in a magnetic field of strength H, the individual atomic moments in the material contribute to its overall response, the magnetic induction B:

$$B = \mu_0(H + M) \quad [1]$$

where μ_0 is the vacuum permeability, and the magnetization $M = m/V$ is the magnetic moment per unit volume, where m is the magnetic moment on a volume V of the material.[8] All materials are magnetic to some extent, with their response depending on their atomic structure and temperature. They may be conveniently classified in terms of their volumetric magnetic susceptibility χ, where

$$M = \chi H \quad [2]$$

describes the magnetization induced in a material by H.

Figure 1 shows schematic diagrams of these five different situations. If a material does not have magnetic dipoles in the absence of an external field and has weak induced dipoles in the presence of a field, the material is referred to as diamagnetic. The magnetization of a diamagnet responds in the

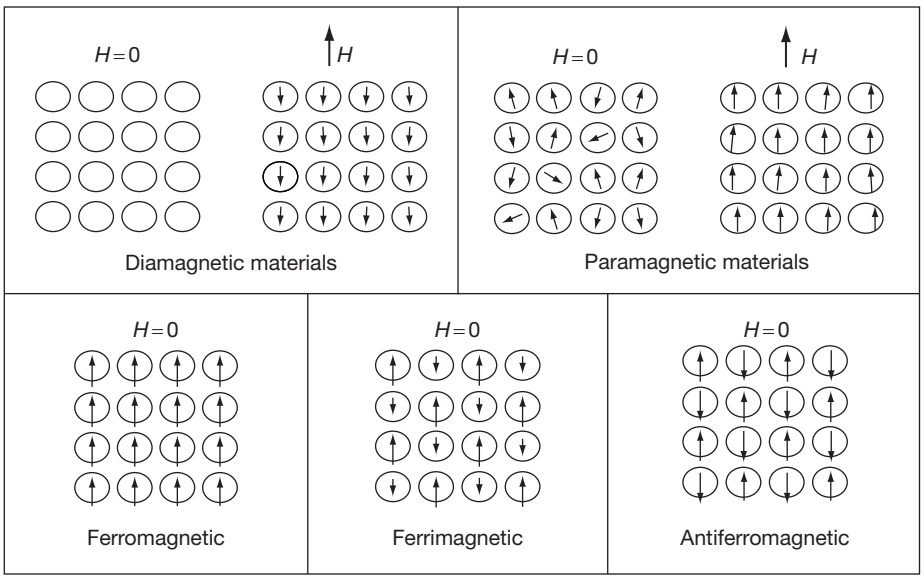

Figure 1 Scheme illustrating the arrangements of magnetic dipoles for five different types of materials in the absence or presence of an external magnetic field (H). Redrawn from Jeong, U.; Teng, X.; Wang, Y.; Yang, H.; Xia, Y. *Adv. Mater.* **2007**, *19*, 33–60.

opposite direction to the external field, with χ in the range -10^{-6} to -10^{-3}. If a material has randomly oriented dipoles that can be aligned in an external field, it is paramagnetic. The magnetization of a paramagnet responds in the same direction as the external field ($10^{-6} < \chi < 10^{-1}$). The magnetic interactions derived from the above two types of materials are very weak because the thermal agitation at room temperature can make the magnetic moments to flip over continuously.

However, some materials exhibit ordered magnetic states and are magnetic even without a field applied. For a ferromagnetic material, the magnetic dipoles always exist in the absence and presence of an external field and exhibit long-range order (Figure 1). Macroscopically, such a material displays a permanent magnetic moment and M is typically 10^4 times larger than would appear otherwise. The difference in the source of the net magnetic moment can also be used to distinguish ferromagnetism from both ferrimagnetism and antiferromagnetism. In a ferrimagnetic material there are always weaker magnetic dipoles aligned antiparallel to the adjacent, stronger dipoles in the absence of an external magnetic field. For an antiferromagnetic material, the adjacent dipoles are antiparallel in the absence of an external field and cancel each other.

That is why magnetic materials are referred to those characterized by either ferro- or ferrimagnetic features. Both ferro- or ferrimagnetic materials can be described using a number of basic parameters derived from the magnetization curve, where the magnetization M or flux density B is plotted against the magnetic field strength H (Figure 2). Although a ferromagnetic material should have all its magnetic moments pointing in the same direction, a macroscopic piece of material cannot have this configuration because the amount of magnetostatic energy stored should be huge.[12] The way in which a solid can reduce this otherwise huge magnetostatic energy is to break itself up into regions called magnetic domains, or Weiss domains. Within a single domain, all magnetic moments remain parallel, but each domain is randomly oriented so that the net magnetic moment of the sample is nearly cancelled (Figure 3(a)). This situation generates interfaces between domains called domain walls or Bloch walls, where adjacent magnetic moments are in a nonfavorable configuration, so that these domain walls are highly energetic. Even though some energy is stored inside domain walls, the overall decrease in the total magnetic energy favors the multidomain configuration. Being formed by a competition between magnetostatic and exchange energies, domain walls have a finite width, determined by the ratio between these energies.

The susceptibility in ferro- and ferrimagnetic materials depends not only on temperature, but also on H, which gives rise to the characteristic sigmoidal shape of the magnetization curve (M–H curve), with M approaching a saturation value at large values of H (Figure 2). Furthermore, one often sees hysteresis: it characterizes the irreversibility in the magnetization and demagnetization processes that are related to the pinning of magnetic domain walls at defects, dislocations, or vacancies within the material, as well as to intrinsic effects such as the magnetic anisotropy of the crystalline lattice. This gives rise to open M–H curves, called hysteresis loops. Actually, domain walls can move in response to an applied field: creation, growth, and extinction of domains can be induced by an external magnetic field because the external field imposes a preferred direction for the magnetic moments. For the spins in a given domain to change their orientation, it is required that the walls of that domain displace. However, the magnetic field required to eliminate all domain walls (i.e., to align all magnetic moments in the same direction) has a definite value for a given sample, and is very reproducible.

The saturation magnetization M_S (the maximum value of M), the remanence magnetization M_R (the residual magnetization at zero applied field strength), and the coercivity H_C (the external field required to reduce the magnetization back to zero) are deduced from the magnetization curve (Table 1). A material is called a soft magnet if it can be magnetized readily in a weak field of $\sim$10 Oe ($1\,\text{Oe} = 1000/4\pi\,\text{A m}^{-1}$). On the other hand, hard magnets have very strong H_C and require large external fields applied to the opposite direction in order to be demagnetized.

Lastly, as the temperature increases, thermal motion, or entropy, competes with the ferromagnetic tendency for the spins to align. When the temperature rises beyond a certain point, called the Curie temperature T_C, there is a second-order phase transition and the system can no longer maintain a spontaneous magnetization, although it still responds paramagnetically to an external field (Table 1).

4.434.2.1.2. Magnetism of nanoparticles

Magnetism is highly volume and temperature dependent because this property arises from the collective interaction of atomic magnetic dipoles.[13] When the size of a ferro- or ferrimagnet decreases to a certain critical value D_C, MNPs change from a state with multiple magnetic domains to one with a single domain (Figure 3(b)). In that transition situation, H_C is maximal and the hysteresis loop is broader (Figure 2). This critical

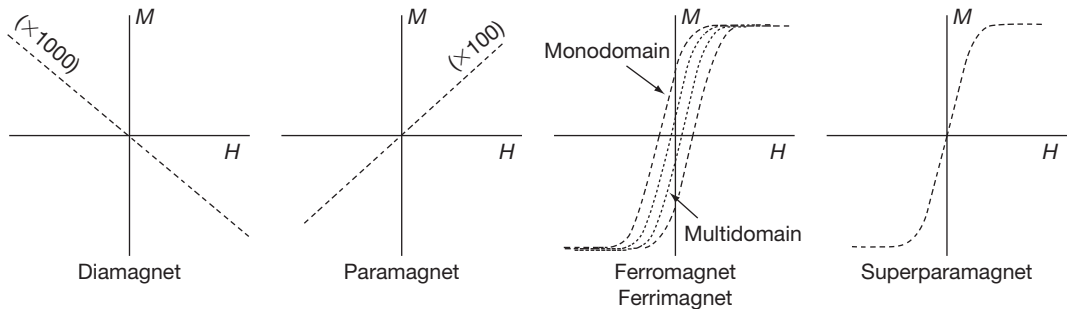

Figure 2 Typical M–H magnetization curves for the different types of magnetic materials.

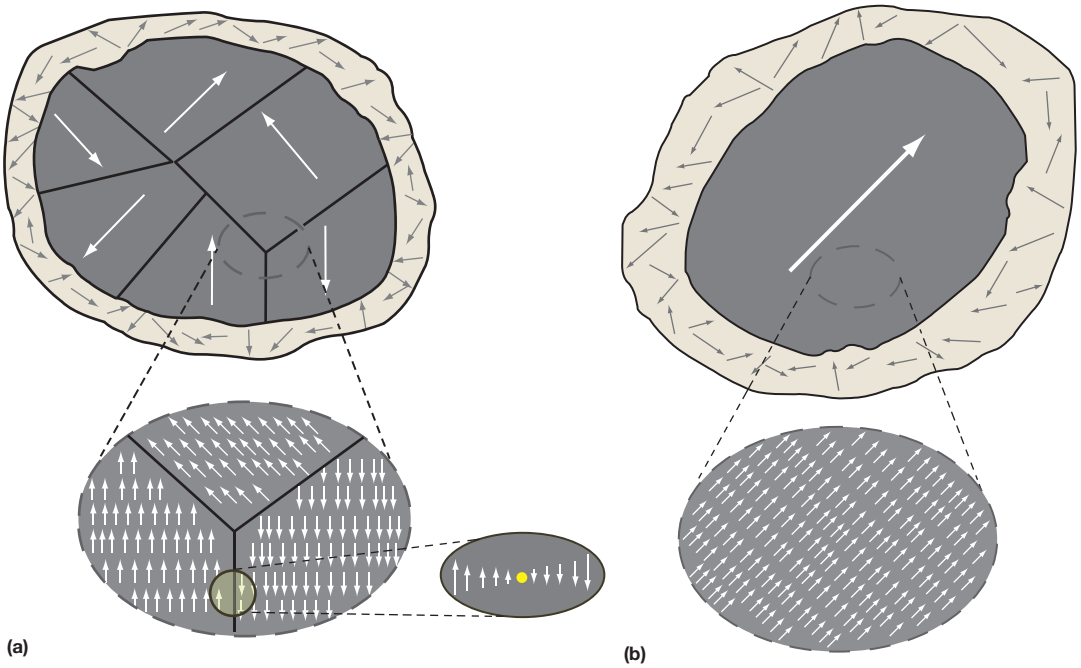

Figure 3 (a) Schematic view of magnetic domains in a multidomain ferromagnetic particle having size larger than the critical diameter ($D > D_C$). For this particle, the whole material breaks down into randomly oriented magnetic regions. At the interface between domains, magnetic moments are twisted to fit the orientation at both sides of the domain walls. (b) Schematic view of magnetic domains in a monodomain ferromagnetic particle having size smaller than the critical diameter ($D < D_C$). The spin disorder at the particle surface is represented by an annular region in both cases. Redrawn from Goya, G. F.; Grazú, V.; Ibarra, M. R. *Curr. Nanosci*. **2008**, *4*, 1–16.

Table 1 Typical values characterizing magnetic materials commonly used in biomedical applications

Magnetic material	M_S (*emu g*$^{-1}$)[a]	T_C (*K*)
α-Fe	218	1043
Ni	57	627
Co	163	1388
Fe_3O_4	92	858
$CoFe_2O_4$	81	796
α-Fe_2O_3	1	948
γ-Fe_2O_3	78	848
NdFeB	171	573
$SmCo_5$	164	998
$BaFe_{12}O_{19}$	72	703
FePt	68	750

[a]At room temperature.

size is achieved when the magnetostatic energy, which increases in proportion to the volume of the materials, becomes equal to the domain wall energy, which varies proportionally with the interfacial area between domains. For spherical and noninteracting MNPs, the critical size can be given as

$$D_C \approx \frac{18\sqrt{AK_{eff}}}{\mu_0 M_S^2} \quad [3]$$

where A is the exchange constant and K_{eff} is the effective anisotropy constant. This critical size, which is generally of a few nanometers to a few tens nanometers, varies from material to material.

Below the critical size D_C, the coercivity decreases to zero with the size. MNPs with zero coercivity simultaneously have zero remanence and are known as superparamagnets, in the sense that they behave as paramagnetic materials, but display much higher susceptibilities (there is a giant moment inside each particle). This leads to anhysteretic but still sigmoidal, M–H curves (**Figure 2**). In that situation, thermal fluctuations overcome anisotropy forces, and hence, magnetization of particle gets reversed easily from one easy direction to another one even in the absence of a magnetic field. It means that the energy barrier, which separates the two energetically equivalent easy directions of magnetization, is

$$K_{eff} V \leq k_B T \quad [4]$$

where K_{eff} is a function of magnetocrystalline, shape and surface anisotropies, V is the particle volume, k_B is the Boltzman's constant, and T is the absolute temperature.

The reversal of magnetization for superparamagnetic MNPs occurs as soon as the applied external magnetic field is removed according to two relaxation mechanisms: spin rotation (rotation of magnetic spin within the particles) or particle rotation (the actual physical rotation of the particle). Néel relaxation time (τ_N), which occurs due to the spin rotation, is related to the magnetic anisotropy of the material and can be expressed as follows:

$$\tau_N = \tau_0 \exp\left(\frac{K_{eff} V}{k_B T}\right) \quad [5]$$

where τ_0 is the time constant ($\sim 10^{-9}$ s).

The characteristic time for the randomization of the magnetization due to the physical rotation of the particle is known as Brown relaxation time (τ_B) and can be expressed as

$$\tau_B = \frac{3\eta V_H}{k_B T} = \frac{4\pi\eta R_H^3}{k_B T} \quad [6]$$

where η is the viscosity of the carrier liquid, V_H is the hydrodynamic volume of the particle, and R_H is the hydrodynamic radius of the particle.

The characteristic fluctuation time for the moment of a particle varies exponentially with temperature and the magnetization reappears to switch sharply to a stable state as the temperature is reduced. Hence, if a superparamagnetic nanoparticle is cooled below a critical temperature (blocking temperature T_B), it regains its ferro- or ferrimagnetic behavior. T_B is determined experimentally from the magnetization–temperature curve using a magnetometer. In a standard procedure, the sample is cooled from room temperature to 5 K or lower using helium with no applied magnetic field (the zero-field cooling (ZFC)) and then magnetization is measured when the sample is warmed up under a weak external field (~100 Oe). On the contrary, with the field cooling (FC) protocol, the sample is first cooled down under a magnetic field. During the ZFC protocol, the magnetization increases and then decreases as the temperature increases. The temperature corresponding to the maximum point is defined as the blocking temperature T_B (Figure 4). It depends on the effective anisotropy constant, the size of MNPs, the applied magnetic field, and the experimental measuring time.

At temperatures well below T_B (or for relaxation times much longer than the characteristic measurement time), the net moments of superparamagnetic MNPs are quasistatic. Whereas, at temperatures well above T_B (or for relaxation times much shorter than characteristic measurement time), the moment reversals are so rapid that in zero external field the time-averaged net moment on the particles is zero.

4.434.2.1.3. Surface effects

As the particles size decreases, a large percentage of all the atoms in a nanoparticle are surface atoms, which implies that surface and interface effects become more important. For example, for face-centered cubic (fcc) cobalt with a diameter of around 1.6 nm, about 60% of the total number of spins are surface spins.[14] Owing to this large surface atoms/bulk atoms ratio, the surface spins make an important contribution to the magnetization. As shown in Figure 3, MNPs have large number of spins over their surfaces. Owing to the high surface activity of spins, the magnetization value of MNPs is reduced compared to the bulk value. The decrease of magnetization is also attributed to the presence of a magnetic dead layer on the MNP surface, spin-glass-like behavior of the surface spins, or the presence of canted spins. Another surface-driven effect is the enhancement of the magnetic anisotropy (K_{eff}) with decreasing particle size. Lastly, a magnetically inert surface coating, for example, silica or organic polymer, may modify the extent of the dipolar coupling between MNPs because its thickness controls the minimum distance between them. Overall, it must be concluded that the magnetic response of a system to an inert coating is rather complex and system-specific, so that no firm correlations can be established at present.

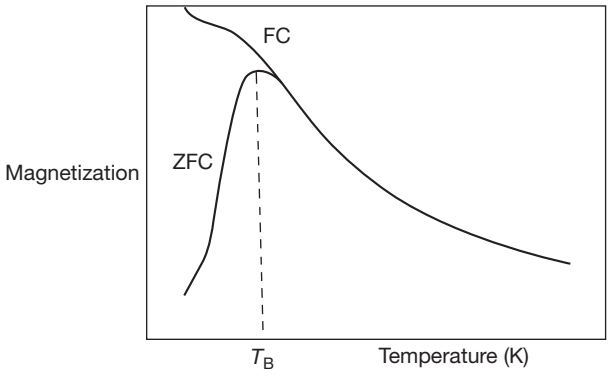

Figure 4 Typical magnetization versus temperature curves measured under zero-field cooling and field cooling conditions, respectively.

4.434.2.1.4. Forces exerted in magnetic field gradients

Magnetic field gradients are used to manipulate MNPs, because they are capable of exerting a force at a distance, whereas a uniform field gives rise to a torque, but no translational action.[8,15] For the case of a dilute suspension of MNPs in pure water (<5 vol%), it may be demonstrated that the magnetic force is

$$F_m = V(\chi - \chi_w)\nabla\left(\frac{B^2}{2\mu_0}\right) = V(\chi - \chi_w)\nabla\left(\frac{1}{2}BH\right) \quad [7]$$

where χ_w is the magnetic susceptibility of water. Therefore, the magnetic force is related to the differential of the magnetostatic field energy density $\frac{1}{2}BH$. Thus if $\chi > \chi_w$, the magnetic force acts in the direction of the steepest ascent of the energy density scalar field.

If the magnetic field gradient must immobilize MNPs by capturing them from a flowing liquid, this force needs to overcome the hydrodynamic drag force acting on the magnetic particle:

$$F_d = 6\pi\eta R_H(\upsilon - \upsilon_w) \quad [8]$$

where η is the viscosity of the liquid, and υ and υ_w are the velocities of MNPs and water, respectively. Equating the hydrodynamic drag and magnetic forces and writing:

$$V_H = 4/3\pi R_H^3 \quad [9]$$

gives the velocity of the MNPs relative to the fluid carrier as:

$$\Delta\upsilon = \frac{R_H^2\Delta\chi}{9\mu_0\eta}\nabla(B^2) = \frac{\xi}{\mu_0}\nabla(B^2) \quad [10]$$

where ξ is the magnetophoretic mobility of the particle, which indicates how 'manipulable' the MNPs are. The magnetophoretic mobility of magnetic microparticles can be much greater than that of nanoparticles, due to their larger size.

4.434.2.2. Behavior in AC Magnetic Fields

Returning to the hysteresis which gives rise to the open M–H curves seen for ferro- or ferrimagnets, it is clear that energy is needed to overcome the barrier to domain wall motion imposed by the intrinsic anisotropy and the pinning of

magnetic domain walls in the material. This energy is delivered by the applied field and can be characterized by the area enclosed by the hysteresis loop. This leads to the concept that if one applies a time-varying magnetic field to a ferro- or ferrimagnetic material, one can establish a situation in which there is a constant flow of energy into that material, which is perforce transferred into thermal energy. A similar argument regarding energy transfer can be made for superparamagnets, where the energy is needed to coherently align the particle moments to achieve the saturated state.[16]

4.434.2.2.1. Specific absorption rate

The heating ability of MFs in the presence of AC magnetic fields can be estimated by calorimetric method and it is termed as specific absorption rate (SAR). SAR is estimated on the basis of direct observation of temperature rise and can be defined as the amount of heat generated in a second by one gram of magnetic element:

$$\mathrm{SAR_T} = C\frac{m_\mathrm{S}}{m_\mathrm{M}}\frac{\mathrm{d}T}{\mathrm{d}t} \qquad [11]$$

where C is the specific heat capacity of the MF (or water in the case of diluted dispersions), $\mathrm{d}T/\mathrm{d}t$ is the slope of temperature versus time graph at the considered temperature T, m_S is the mass of MF and m_M is the mass of the magnetic element in the fluid.

Concerning the electromagnetic devices used for calorimetry experiments, the technology of an AC magnetic field is still under development. Most experiments were done with laboratory-made generators in the frequency range of 50 kHz to 1 MHz, with magnetic field amplitudes up to a few tens of kiloampere per meter. These parameters depended more on the technical availability of the generators used rather than on theoretical predictions for optimized SAR. Indeed, a frequency scan is technically tricky in this broad frequency range because of frequency-dependent skin effects and resistance of magnetic applicators. The majority of hyperthermia experiments were performed in an induction coil or in the air-gap of a magnetic inductor, cooled by water or air (Figure 5).

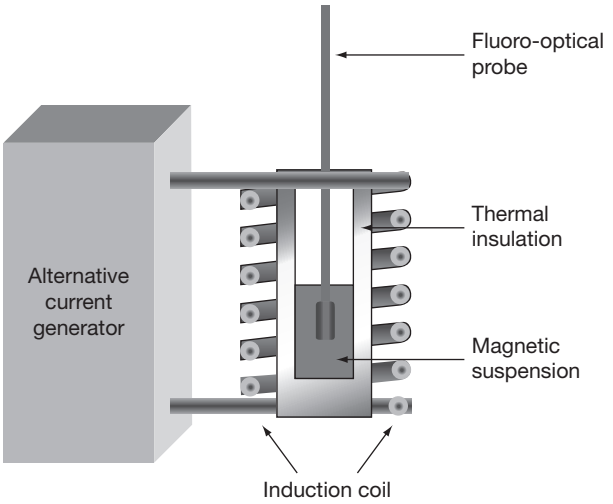

Figure 5 Typical laboratory inductor for the specific absorption rate measurement.

For clinical purposes, the heat generation, and hence, the SAR value, is very crucial. The higher the value, the lower is the injected dose. However, the SAR values measured by various scientists differed because of their strong dependence on factors such as the physical and chemical properties of the carrier fluid, the frequency and amplitude of the applied field, and the size, shape, surface coating, and chemical composition of the MNPs.[17] It is very difficult to give a general theoretical expression of SAR because of the large number of parameters.

4.434.2.2.2. Loss mechanisms

For ferro- or ferrimagnetic particles, their heating capability mainly results from hysteresis losses, and therefore, SAR is proportional to the field frequency and the area of the hysteresis loop.

The power loss of MFs based on superparamagnets in the presence of AC magnetic fields can also be determined on the basis of Néel and/or Brownian relaxation by:

$$P = \frac{(mH\omega\tau)^2}{2\tau kT\rho V(1+\omega^2\tau^2)} \qquad [12]$$

where ω is the angular frequency, ρ is the MNP density, T is the working temperature, and τ is the relaxation time (τ_N or τ_B).[17] It is worth mentioning that the Néel relaxation time depends exponentially on the core volume (V), while the Brown mechanism involves the hydrodynamic volume of the particles (V_H) that may differ from that of the crystalline cores due to the presence of a stabilizing shell or due to agglomeration.[18] The resulting diameter dependency of the corresponsive relaxation times is presented in Figure 6. In realistic systems, the faster process will dominate the overall remagnetization process, and for similar time scales, both mechanisms will contribute:

$$\tau_\mathrm{eff} = \frac{\tau_\mathrm{N}\tau_\mathrm{B}}{\tau_\mathrm{N}+\tau_\mathrm{B}} \qquad [13]$$

The power loss is expected to be maximum when $\omega\tau = 1$.

It is then observed that below a critical size of the particles, the Néel loss mechanism is more effective while above this the Brownian loss mechanism plays a major role. Near to the critical size, both types of losses act equivalently.

The Brownian losses generally depend upon hydrodynamic size of the particles, but not on the size of the magnetic cores. Therefore, the type and thickness of coating over the magnetic

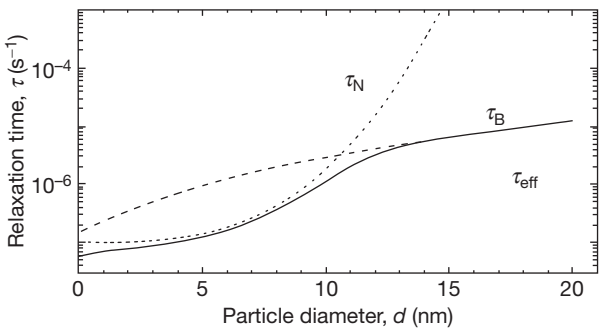

Figure 6 Theoretical Néel (τ_N) and Brown (τ_B) relaxation times and effective relaxation time (τ_eff) for Fe_3O_4 magnetic nanoparticles versus particle diameter. Reprinted with permission from Schmidt, A. M. *Colloid Polym. Sci.* **2007**, *285*, 953–966. Copyright © 2007 Springer Science.

materials can greatly influence heating. Lastly, in some situations, MFs based on ferro- and ferrimagnetic particles may also be concerned by Brownian losses.

4.434.3. MF Design and Preparation

4.434.3.1. Synthesis of MNPs

MNPs can be synthesized by a wide variety of techniques ranging from mechanical (top-down approach) to chemical processes (bottom-up approach). For *in vivo* applications, chemical processes are generally preferred, because they allow a better control of the purity, crystallinity, and size distribution. These processes include aqueous coprecipitation, thermal decomposition, sonochemistry, microemulsion, sol–gel, self-combustion, microwave refluxing, etc., for the synthesis of maghemite, magnetite, substituted iron oxides (γ–$M_xFe_{2-x}O_3$ or $M_xFe_{3-x}O_4$, where M = Al, Mn, Mg, Zn, Ni, Co, and Cu), metallic iron or cobalt and alloys such as FePt. For a detailed description of these synthetic routes, the reader will report on general review papers[13,14,19,20] or review papers more specifically dedicated to iron oxide MNPs for biomedical applications.[21–24]

These synthesis processes have their own benefits, but the achieved features of the MNPs depend strongly on the control of the experimental conditions. For instance, coprecipitation is a simple technique, but the type of salts (e.g., chlorides, sulfates, and nitrates), the cation oxidation states, the reaction temperature, the pH value and ionic strength of the media greatly influence the size, shape, and composition of the final particles. Moreover, the morphology and size of the nanoparticles synthesized by thermal decomposition process greatly depend upon the ratios of the organometallic precursor, solvent, and surfactant, the temperature, and the reaction duration.

4.434.3.2. Colloidal Stabilization in Physiological Medium

Like other dispersions, aqueous MNPs dispersions are subjected to a number of destabilizing forces that can lead to phase separation due to flocculation and sedimentation.[18] One of the main causes of phase separation is the Van der Waals interactions between the high-surface particles that result in the formation of agglomerated material. In contrast to this, the sedimentation of single particles by gravitational force is prevented by thermal motion in the size range up to 20 nm. However, by the formation of small agglomerates due to the Van der Waals interactions, thermal motion is greatly reduced, and sedimentation may play an important role in the destabilization of a magnetic colloid.

As an additional challenge, the magnetic dipolar particles also possess magnetic interactions in relation to their relative distance that may be further enhanced by alignment of the dipoles in outer magnetic field gradients.[25] Consequently, the colloids have to be stabilized against agglomeration by creating a protecting shell for each particle that prevents the particles from coming too close in contact with each other. This is possible using classical concepts from colloid chemistry, including electrostatic stabilization and steric stabilization.

As an example of electrostatically stabilized MFs, maghemite-based cationic fluids are easily prepared according to the method described by Massart.[26] In this process, magnetite nanoparticles are initially prepared by alkaline coprecipitation of iron (II) and iron (III) precursors in aqueous solution with an excess of concentrated ammonium hydroxide. Magnetite is oxidized into maghemite by heating in the presence of HNO_3 and iron (III) nitrate. Maghemite particles are peptized in dilute HNO_3 solution to create positive surface charges on the particles. Washing and decantation with acetone using a magnet can remove the acidic precipitates. Simply by dispersing these particles into water produces aqueous MFs. For *in vivo* applications, surface-charged nanoparticles are not advised and steric stabilization is generally preferred to electrostatic stabilization for physiological reasons (*cf.* **Section 4.434.4.2**). That is why the MFs are often prepared into aqueous solution of hydrophilic macromolecules or such macromolecules are grafted onto MNPs in a second step.

4.434.4. Size/Surface Requirements with Regard to i.v. Administration

4.434.4.1. Biocompatibility

Similar to other biomaterials, the biocompatibility of MNPs is assessed successively *in vitro* with animal or human cells, followed by *in vivo* tests with animals, before human clinical trials[27,28] (see **Chapter 1.109, Bioactive Ceramics**).

For *in vitro* cytotoxic assays, the animal or human cells are generally grown on the culture plates. Well-grown cells are then treated with bare or surface-modified MNPs or MFs for several hours (up to 96 h). The effect of the nanoparticles on the cells is then estimated by the comparative study of treated and untreated cells (control) by visual counting of the viable cells. More sophisticated cell viability assays are generally performed. MTT assay is based on the reduction of the tetrazolium salt MTT (3-(4,5-dimethylthiazol-2-yl)-2,5-diphenytetrazolium bromide) to formazan by succinate dehydrogenase. The formazan product is then quantified spectrofluorometrically, and hence, directly correlated to the activity of mitochondrial reductase enzymes. In sulforhodamine-B (SRB) assay, SRB binds to the basic amino acids of the cellular proteins. Thus, colorimetric measurement of the bound dye provides an estimate of the total protein mass that is related to the cell number.

The distribution of MNPs on the cells can also be estimated by staining the treated or untreated cells with Pearl's Prussian blue (which stains mainly Fe^{3+}) or with Turnbull's reagent (which stains Fe^{2+} ions).

Animals such as mice, rabbits, dogs, and sheep are often chosen for experimental *in vivo* studies. The animals are grown under the prescribed guidelines of the animal ethics committee. The required dose of MF is then injected into the body of the animal and all the clinical changes are observed very carefully. For different time periods, blood samples are collected for hematological and serum biochemical analysis. During hematological analysis, the amount of hemoglobin, platelets, erythrocytes, leukocytes, neutrophiles, lymphocytes, monocytes, basophiles, eosinophiles, and hematocrit are generally compared with that of the untreated animal. In serum biochemical analysis, serum level of total protein, bilirubin,

albumin, glucose, cholesterol, alanine transaminase, aspartate transaminase, triglyceride, blood urea nitrogen, phosphorus, creatinine, calcium, and lactic acid dehydrogenase are compared with those of normal untreated animals.

It seems difficult to assert today which nanoparticles are toxic and which ones are not. MNPs absorption, distribution, metabolism, excretion, and toxicity depend on multiple factors derived from inherent physicochemical properties such as concentration, size, surface charge, nature of the surface chemical groups, and redox activity. First, the toxicity of particles that may dissolve in physiological conditions even at a very low rate has to be considered also from the viewpoint of the toxicity of the released metal cations. In such situations, endogenous elements such as iron cations are preferred because the soluble iron becomes part of the normal iron pool (e.g., ferritin, hemosiderin, transferritin, hemoglobin).[29] The lethal dose LD_{50} of pristine iron oxide nanoparticles is 300–600 mg_{Fe} per kilogram of body mass. A barrier coating may be engineered around each nanoparticle in the case of toxic metal elements. Second, in the case of insoluble particles, surfaces matter more than chemical composition, and efforts are in progress for embedding MNPs in biocompatible coating, often made of hydrophilic macromolecules and/or silica.

It is obvious that the MNPs toxicity is directly related to the concentration required for the diagnostic or therapeutic effect. Once the active targeting strategies (*cf.* **Section 4.434.4.3**) become efficient, and hence, allow concentrating MNPs essentially in the targeted organs, MNPs nontoxicity will become a less-acute requirement.

4.434.4.2. Biodistribution and Passive Targeting Strategies

As soon as bare particles are, intentionally or otherwise, injected in the blood compartment, they are subjected to the action of the mononuclear phagocyte system (MPS).[30,31] It is defined as the cell family comprising bone marrow progenitors, blood monocytes, and tissue macrophages (such as Kupffer cells in liver). These macrophages are widely distributed and strategically placed in many tissues of the body to recognize and clear senescent cells, invading microorganisms or particles. The first step of the clearance mechanism is the opsonization process. Opsonins are circulating plasma proteins (various subclasses of immunoglobulins, complement proteins, fibronectin, etc.), that adsorb themselves spontaneously onto the surface of any invading entity. They are capable of interacting with the specialized plasma membrane receptors on monocytes and macrophages, thus promoting particle recognition by these cells. The second step consists in the endocytosis/phagocytosis of the particles by the circulating monocytes or the fixed macrophages, leading to their elimination from circulation and their simultaneous concentration in organs with high phagocytic activity. Therefore after i.v. administration, particles are cleared up within minutes from the bloodstream; their typical final biodistribution is 80–90% in the liver, 5–8% in the spleen and 1–2% in the bone marrow.[4] Consequently, the remarkable organization of the immune system is not compatible with long circulation times of any invading nanoparticle and MPS-mediated clearance is a major factor in determining their biodistribution. Nevertheless, it has provided an opportunity for the efficient delivery of therapeutic agents to these phagocytic cells, and therefore, to the related organs and more generally to any area where the macrophage activity is high, for example, infection/inflammation regions. Such an MPS-mediated targeting is called passive targeting.

If monocytes and macrophages are not the desired target, minimizing or delaying the nanoparticle uptake by the MPS is mandatory. The most satisfactory strategy consists of designing macrophage-evading nanoparticles (stealth nanoparticles) with plasma half-life as long as possible in order to increase the probability to attain the desired target. The more efficient route is to prevent the opsonin adsorption and therefore to avoid the macrophage recognition. Among the physicochemical factors which are known to affect the opsonization process, the size, the surface charge density, and the hydrophilicity/hydrophobicity balance have been widely studied.[30] Therefore, the smaller, the more neutral, and the more hydrophilic the carrier surface is, the longer is its plasma half-life.

In particular for hydrophobic particles, many studies concerned the development of core-corona structures where the corona is made of hydrophilic macromolecules for creating polymer brushes, acting as a steric surface barrier and reducing opsonin adsorption. Among the natural or artificial macromolecules, linear dextrans and derivatives are widely used. Other biological macromolecules have been investigated, for example, poly(sialic acid), heparin, and heparin-like polysaccharides complement regulatory proteins, etc., but because of their high cost and/or the possible immunological consequences associated with bacterial-made macromolecules, efforts have been directed to design synthetic hydrophilic macromolecules. Among these synthetic macromolecules, great efforts have dealt with the covalent anchorage of poly(ethylene glycol) (PEG) macromolecules onto the particle surface. Such a route is well known in galenical pharmacology where drugs (small molecules, but also peptides, proteins, antibodies, and oligonucleotides) are conjugated to PEG macromolecules to improve their circulation lifetime and bioavailability, and to decrease their immunogenicity, renal clearance rate, and dosing frequency.[4] This process is so widely used that it is called 'PEGylation.' In fact, PEG is a flexible polyether, hydrophilic (but also soluble in some organic media), not biodegradable, but easily excreted from living organisms. Its functional endgroups are available for derivatization leading to numerous routes for covalent attachment onto preformed functional surfaces or anchoring during the synthesis of particles. PEG has been shown to be the most effective polymer for suppressing protein adsorption, the optimal molecular weight varying between 2000 and 5000 g mol^{-1}.[30] These values are still in debate, and in particular, the surface density appears to be as important as the molecular weight.[31]

The escape of macrophage-evading particles from the circulation is normally restricted to sites where the capillaries have opened fenestrations as in the sinus endothelium of the liver or when the integrity of the endothelial barrier is perturbed by inflammatory processes (e.g., rheumatoid arthritis, infarction, infections) or by some types of tumors. Therefore the idea of exploiting such vascular abnormalities for extravasating and accumulating nanoparticles in these inflammatory sites or tumors is also particularly attractive. Such a strategy is also considered as a passive targeting one, but independently of the MPS mediation.

4.434.4.3. Active Targeting Strategies

For increasing the probability of redirecting long-circulating particles to the desired target, their surface has to be labeled with ligands that specifically bind to surface epitopes or receptors on the target sites (molecular recognition processes such as antibody–antigen interactions). Such a strategy should open the possibility of targeting specific cell types or subsets of cells within the vasculature and even elements of vascular emboli and thrombi.[31–34] In the case of cancer therapy, active targeting could allow the selective destruction of cancer cells, even if they have escaped the tumor mass and disseminated as metastatic cells.

These ligands must be coupled to the surface of stealth carriers. They include oligosaccharides, oligopeptides, folic acid, antibodies, and their fragments. The antibody coupling has at least two drawbacks: the overall dimensions of the antibodies (~20 nm), which cause particles to diffuse poorly through biological barriers, and their immunogenicity, that is, the property of being able to evoke an immune response within an organism. For this reason, the coupling of small nonimmunogenic ligands has been also investigated. Therefore, as an example of tumor targeting, folic acid (vitamin B essential for cell-division processes) may be used to take advantage of the frequent overexpression of folate receptors onto the surface of human cancer cells.[35] Interestingly, nanoparticles conjugated with folic acid appeared to interact more efficiently with folate receptors than free folic acid. This amazing result was interpreted as the consequence of the multivalent (and hence stronger) interaction of conjugated nanoparticles with the folate receptors, which are often arranged as clusters.

4.434.4.4. Surface Activation and Bioconjugation

In particular for active targeting purpose, the surface of MNPs shall be derivatized. The process of proper linkage of biomolecules with nanoparticles under mild conditions is commonly called bioconjugation. Two main approaches to attach biomolecules on the surface of MNPs are physisorption and chemisorption. In physisorption, biomolecules directly attach to the surface of particles owing to weak interaction (electrostatic or Van der Waals forces), whereas, in chemisorption, biomolecules attach by the formation of covalent chemical bonds.

Oxide or metal nanoparticles, by themselves, may not be capable of covalent attachment to biomolecules owing to their poor surface chemical properties. Hence, surface activation is required to create the chemical functions needed for coupling biomolecules to MNPs. The direct surface modification of metal oxides generally uses carboxylic acids, alkyltrialkoxysilanes, or alkyl phosphonates. A reactive function such as amino, thiol, aldehyde, carboxylic group is generally present on the alkyl fragment and becomes the main surface group. A coupling agent is generally required for linking this surface function with biomolecules (Table 2).

In numerous situations, the direct coupling with the inorganic surface is not preferred and one alternative strategy consists in taking advantage of the intrinsic reactivity of the hydrophilic macromolecules used for embedding and sterically stabilizing MNPs. In this way, the creation of nanoparticle libraries was recently reported on the basis of MNPs of iron oxide entrapped in a cross-linked corona of dextran bearing amino functions (Figure 7).

Table 2 Nonexhaustive list of coupling strategies of biomolecules on the activated surface of MNPs

Surface reactive function available on MNPs	*Reactive function available on biomolecules*	*Possible coupling agent*
Surface reactive function available on MNPs	Reactive function available on biomolecules	Possible coupling agent
$-COOH$	$-NH_2$	Sulfo-*N*-hydroxysuccimide
$-NH_2$	$-COOH$	Sulfo-*N*-hydroxysuccimide
$-NH_2$	$-NH_2$	Glutaraldéhyde
$-NH_2$	$-SH$	Sulfo-SMCC[a]
$-SH$	$-NH_2$	Sulfo-SMCC[a]
$-OH$	$-NH_2$	Carbonyl diimidazole

[a]SMCC: succinimidyl 4-(*N*-maleimidomethyl)cyclohexane-1-carboxylate.

4.434.5. MNPs as Contrast Agents for MRI

4.434.5.1. MRI Background

Medical applications of MRI have steadily widened over the past decade and MRI is now one of the preferred cross-sectional imaging modalities.[8,36] It is based on nuclear magnetic resonance (NMR) signal of protons from water in tissues, membrane lipids, proteins, etc., through the combined effect of a static magnetic field B_0 up to 3 T in current clinical apparatus and a transverse rf-field (5–100 MHz). After the rf-sequence, the net magnetization vector is once again influenced by B_0 and tries to realign with it along the longitudinal axis as protons attempt to return to a state of equilibrium: this phenomenon is called relaxation. This relaxation can be divided into two different, independent processes: (i) longitudinal relaxation, which is the return of longitudinal magnetization in alignment with B_0 and is termed T_1-recovery; and (ii) transverse relaxation, which is the vanishing of transverse magnetization and is termed T_2-decay. As the hydrogen atoms release the previously absorbed energy to the surrounding tissue (lattice) in their attempt to realign with B_0, T_1 recovery is also referred to as 'spin–lattice' relaxation. As a time constant, T_1 is the time it takes for 63% of the longitudinal magnetization to recover in the tissue. On the contrary, T_2 decay is not a process of dissipation or absorption of energy into tissue. During the rf-pulse, hydrogen nuclei are spinning in phase with each other. After the rf-pulse, the magnetic fields of all the nuclei interact with each other; energy is exchanged between those nuclei. The nuclei lose their phase coherence and spin in a random fashion. Because T_2 decay is the result of the exchange of energy between spinning protons, it is referred to as 'spin–spin' relaxation. Therefore T_2 is the time it takes for the transverse magnetization to decrease to 37% of its initial value. Owing to their different T_1 and T_2 relaxation, tissues may be differentiated.

In order to correlate the signal to its spatial origin, at least one of the two fields (i.e., B_0 or the rf-field) has to vary over space. Relaxation data are collected by a computer which applies a two-dimensional (2D) Fourier transform to give the amplitudes of NMR signals and permits reconstruction of the 3D images. Thanks to sequence parameters such as the repetition time TR (elapsed time between successive rf excitation

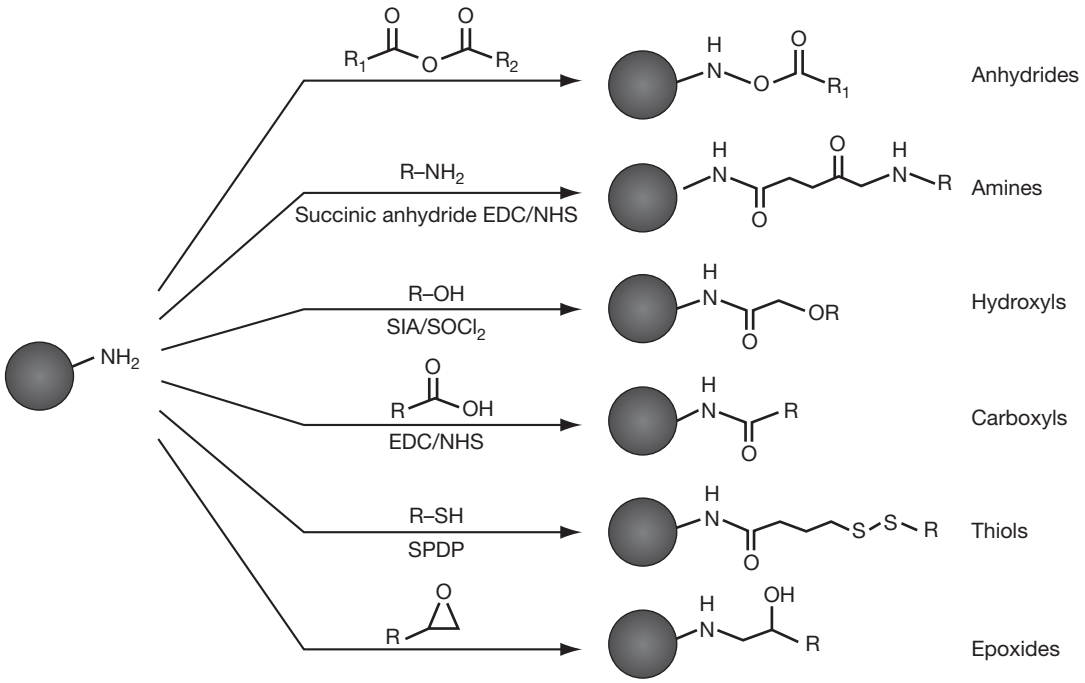

Figure 7 Conjugation strategies from iron oxide magnetic nanoparticles entrapped in a cross-linked corona of dextran bearing amino functions. Redrawn from Sun, E. Y.; Josephson, L.; Kelly, K. A.; Weissleder, R. *Bioconjugate Chem.* **2006**, *17*, 109–113.

pulses) and the delay time TE (time interval between the rf-pulse and the measurement of the first signal), the operator obtains the desired type of image contrast. Basically, short TRs increase T_1 effects, whereas long TRs allow tissues to reach complete longitudinal magnetization, reducing T_1 effects. Short TEs minimize T_2 effects of tissues whereas long TEs allow the loss of transverse signal, enhancing T_2 effects.

Therefore T_1-weighted imaging is obtained by utilizing a short TR and a short TE, allowing full recovery of tissues with a short T_1 (e.g., fat) while allowing only partial recovery of tissues with long T_1 (e.g., cerebrospinal fluid). On the other hand, for T_2-weighted imaging, long TRs and long TEs are used. Fluids have a very long T_2 and they are frequently associated with pathologies (e.g., internal injuries, cancer lesions), so T_2-weighted images are generally preferred for such diagnostics.

4.434.5.2. MR Contrast Agents

In actual practice, tissues may be differentiated on MR images because T_1 and T_2 depend on proton environment. However, in many clinical situations, these intrinsic differences are small and exogenous contrast media are sometimes required for a better delineation of tissues. These media are paramagnetic substances that allow altering the proton relaxation times. This ability to increase the relaxation rates of surrounding proton spins is called relaxivity $r_{1,2}$ and defined as:

$$(1/T_{1,2})_{\text{in presence of contrast agent}} = (1/T_{1,2})_{\text{without contrast agent}} + r_{1,2}[\text{contrast agent}]$$

where [contrast agent] is the contrast agent concentration in millimolars.

The first generation of these contrast agents consisted of high spin paramagnetic ions, usually Gd^{3+} in very stable nontoxic chelate form obtained through complexation by low molecular weight chelating molecules, such as diethylenetriaminepentaacetic acid.[37] Gd-chelates have an extracellular distribution before their excretion by the kidneys. Hydrogen atoms of water in proximity to such chelates experience a faster T_1-relaxation ($r_1 = 3.7\,\text{mM}^{-1}\,\text{s}^{-1}$). Consequently, differences in agent concentration result in contrast enhancement on T_1-weighted images ('positive' contrast). They have to be administered in concentrations of about $0.1\,\text{mmol}\,\text{kg}^{-1}$ of body mass to produce visible effects on the images. Gd-chelates are routinely used for distribution into the intravascular and interstitial space to enhance signal of fluid compartments or lesions (renal function, status of the blood–brain barrier, etc.). Their main disadvantages are their short plasma half-life and their relatively low relaxivity.

Superparamagnetic MNPs have also been developed as MR contrast agents because of their larger magnetic moment in the presence of B_0 (susceptibility agents).[2,38] Therefore, their relaxivity is much higher ($r_1 = 10$–$15\,\text{mM}^{-1}\,\text{s}^{-1}$ and $r_2 = 40$–$190\,\text{mM}^{-1}\,\text{s}^{-1}$) than that of Gd-chelates. In most situations, they are used for their significant capacity to produce predominantly T_2 relaxation effects, which result in signal reduction on T_2-weighted images ('negative' contrast). Basically, the phenomenon may be described from the large magnetic field heterogeneity around the nanoparticle through which water molecules diffuse. This predominant effect on the T_2 relaxation time does not prevent their use on the T_1 relaxation time on the condition of low concentrations and appropriate imaging sequences.

This new generation of contrast agents is often called (U)SPIO for (Ultrasmall) SuperParamagnetic Iron Oxide. They consist of nonstoechiometric iron oxide cores (3–10 nm in diameter), whose chemical composition varies continuously

from Fe_3O_4 to γ-Fe_2O_3. For i.v. administration, they are generally synthesized in a one-step process by alkaline coprecipitation or iron (II) and iron (III) precursors in aqueous solutions of hydrophilic macromolecules, essentially dextran or carboxydextran (see **Chapter 1.109, Bioactive Ceramics**). The role of this macromolecular corona is the limitation of the magnetic core growth during the synthesis, their steric stabilization in water (and later in physiological medium) and *in vivo* the reduction of the opsonization process. Interactions between magnetic cores and macromolecules are weak (essentially Van der Waals and hydrogen interactions) and generally prevent any efficient derivatization of dextran corona without macromolecule depletion.

(U)SPIO pharmacokinetics, biodistribution, and toxicity properties were studied and allowed to define the potential uses of these contrast agents. The lethal dose LD_{50} of a dextran–iron oxide complex was found to be 2000–6000 mg_{Fe} per kilogram of body mass, whereas it is 300–600 mg_{Fe} per kilogram for pristine iron oxide. (U)SPIO have in common their specific uptake by the MPS, explaining why, if they are not entirely captured by the liver and the spleen, they are currently widely evaluated as MRI contrast agents for the diagnosis of inflammatory and degenerative disorders associated with a high macrophage phagocytic activity. The nanoparticles are metabolized in lysosomes and it may be noticed that the iron load resulting from administration of the clinical dose ($\sim$1 mg_{Fe} per kilogram of body) is low compared with the total store in the human body (about 3500 mg).

4.434.5.3. Liver MR Imaging

SPIO, with a hydrodynamic diameter over 50 nm (up to 150 nm), are efficiently accumulated in MPS-organs ($\sim$80% of the injected dose in liver and 5–10% in the spleen with plasma half-life lower than 10 min). So, SPIO decrease liver and spleen signal within several minutes after i.v. administration. Malignant tumors or metastases as small as 2–3 mm, which are typically devoid of a substantial number of phagocytic Kupffer cells, appear as hyperintense (bright) lesions contrasted against the hypointense (black) liver on T_2-weighted sequences (**Figure 8**). The first SPIO, Endorem® (Guerbet, France), was marketed in Europe more than 15 years ago.

4.434.5.4. Metastatic Lymph Node MR Imaging (MR Lymphography)

Nodal disease is an independent adverse prognostic factor in many types of cancer. Thanks to their smaller size (lower than 40 nm) and the hydrophilicity of their dextran corona, USPIO may act as stealth particles; their plasma half-life is higher than 20 h and some particles leak to the interstitium, where they are cleared by the macrophages of the lymphatic system or drained via the lymphatic system and subsequently accumulated in the lymph nodes. So, they allow diagnosing hyperplastic and tumorous lymph node by MR lymphography. A decrease in signal intensity indicates active uptake of particles into macrophages in normally functioning nodes, whereas metastatic nodes remain isointense with the precontrast image (**Figure 9**). Clinical trials have reached phase III using Sinerem® (Guerbet, France) for the detection of lymph node metastases (head and neck and pelvis regions).[2]

4.434.5.5. Blood Pool Imaging

Because USPIO are more slowly up taken by the liver and spleen than SPIO, they remain in the blood circulation for a longer time. On the other hand, USPIO have a much more favorable T_1/T_2 ratio that facilitates T_1-weighted MR techniques at low B_0 (lower than 0.5 T). So, USPIO significantly shorten the T_1 of blood during the first hours after i.v. injection and may be used as T_1-agent. Thanks to these combined features, Sinerem® has been evaluated as MR blood pool agents for indications such as evaluation of cerebral perfusion, myocardial or renal perfusion, angiography or detection of hepatic vascular lesions.[2]

4.434.5.6. Macrophage MR Imaging

Animal experiments and clinical studies are currently dedicated to USPIO-tagged macrophage imaging in several inflammatory and degenerative diseases. This modality could be used not only primarily for disease detection, but also for prediction and follow-up of the therapeutic efficacy.[2] Encouraging results were obtained in the case of cerebral ischemic lesions

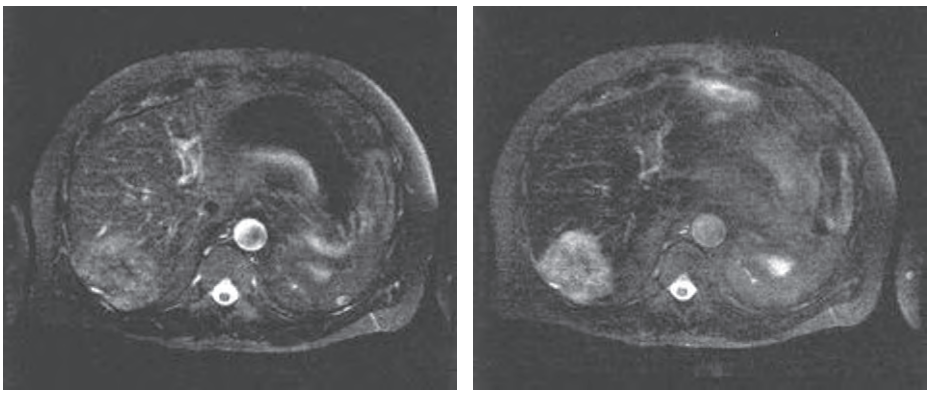

Figure 8 Axial T_2-weighted sequence of human liver with signal metastasis in segment 6: (a) before and (b) following infusion of Endorem®. Reprinted from Wallis, F.; Gilbert, F. J. *J. R. Coll. Surg. Edinb.* **1999**, *44*, 117–125, with permission from Elsevier.

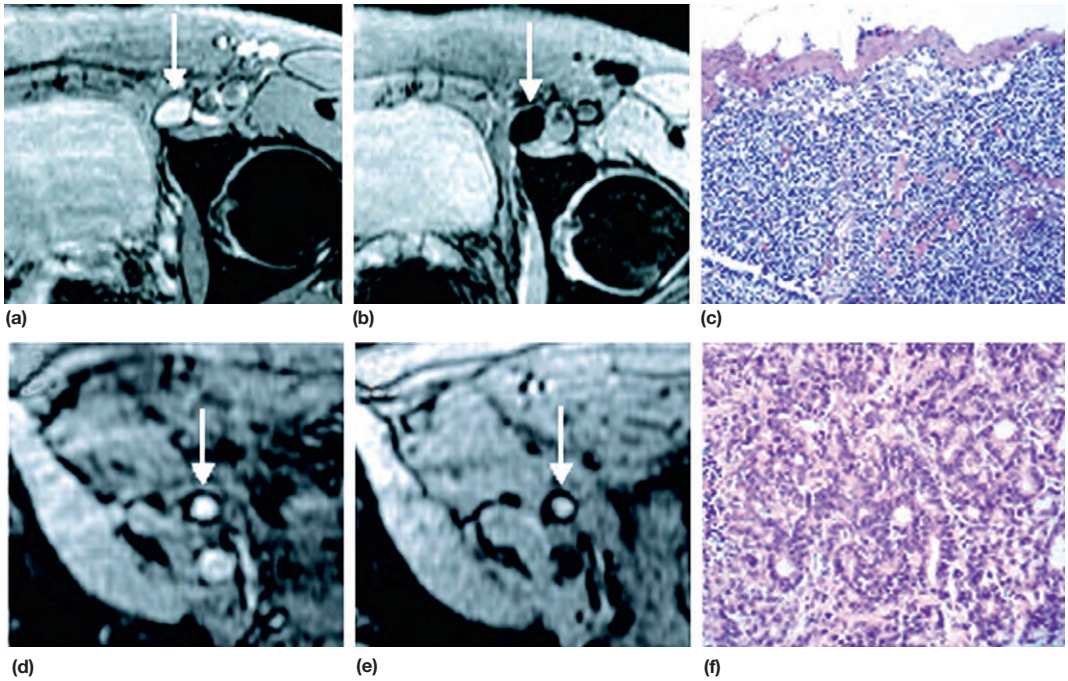

Figure 9 Magnetic resonance imaging nodal abnormalities in two patients with prostate cancer. As compared with conventional MRI (Panel A), MRI obtained 24 h after the administration of lymphotropic USPIO (Panel B) shows a homogeneous decrease in signal intensity due to the accumulation of lymphotropic superparamagnetic nanoparticles in a normal lymph node in the left iliac region (arrow). Panel C shows the corresponding histologic findings (hematoxylin and eosin, ×125). Conventional MRI shows a high signal intensity in an unenlarged iliac lymph node completely replaced by tumor (arrow in Panel D). Nodal signal intensity remains high (arrow in Panel E). Panel F shows the corresponding histologic findings (hematoxylin and eosin, ×200). Reprinted with permission from Harisinghani, M. G.; Barentsz, J.; Hahn, P. F.; *et al. New Engl. J. Med.* **2003**, *348*, 2491–2499. Copyright © 2003 Massachusetts Medical Society.

and brain inflammations, atheromatous plaques prone to rupture, multiple sclerosis, kidney disease, arthritis, infection caused by Staphylococcus aureus, and kidney and cardiac graft rejection. Moreover, USPIO are now reputed to be useful to evaluate (i) areas of blood–brain barrier dysfunction related to tumors and other neuroinflammatory pathologies, (ii) the cerebrovasculature using perfusion-weighted MRI sequences, and (iii) *in vivo* cellular tracking in central nervous system disease or injury.[39]

4.434.5.7. Molecular MR Imaging

Molecular MR imaging is one of the main MRI developments in progress, because clinicians dream about a contrast agent that would accumulate highly and specifically in malignant tumors, allowing an accurate diagnosis at a stage when the disease would be still treatable (see **Chapter 1.109, Bioactive Ceramics**). Such tools would also be of a great interest for cardiovascular, inflammatory and degenerative diseases. It concerns tissue-specific MR contrast agents.[37,40,41] Ligand-labeled (U)SPIO were designed (e.g., human polyclonal IgG, anti-carcinoembryonic antigen, anti-glioma, L6 antibody, anti-epidermal growth factor receptor, etc.) and investigations in small animals revealed that it is possible to achieve a distinct concentration of the magnetic label at the target. However, the required dose of the labeled antibody is still too high to make a commercial development realistic. That is why the use of small ligands, in particular, folate-mediation, appears more realistic for tumor MRI diagnostic. Lastly, spatial resolution is the key parameter for the detection of low concentrations of ligand-labeled (U)SPIO and the development of high magnetic field (up to 7 T) would allow achieving a high spatial resolution while maintaining a satisfactory signal-to-noise ratio.

4.434.5.8. Stem Cell Tracking

The development of stem-cell-based therapies requires quantitative and qualitative assessment of stem cell distribution to target organs (in the case of systemic administration), differentiation outcome, and engraftment. If labeled with MR contrast agents, they could be visualized and tracked by MR imaging. In the reported experiments, stem cells are generally labeled *in vivo* by using eventually a transfection agent (e.g., protamine sulphate, polylysine, cationic liposome, or cationic dendrimers) for USPIO, which are less efficiently internalized than larger SPIO. Labeled cells showed a gradual decline of intracellular iron oxide particles with increasing time after incubation, which can be attributed to cell division and exocytosis or release of iron from nonviable cells. Several experiments on animal models were reported and recently reviewed.[2]

4.434.5.9. Next Developments

Even if (U)SPIO contrast agents are now routinely used in hospitals, no precise structure/activity relationship has been

described to predict entirely their stability, as well as their pharmacokinetics and safety.[22] An extended physicochemical characterization is required but remains difficult owing to their small dimensions, reaching the analytical resolution limits of many commercial instruments.

In addition to the clinical developments presented in the previous sections, current efforts are concerning the improvement of the (U)SPIO platforms. In particular, their chemical stability is insufficient, if dextran macromolecules must be derivatized for bioconjugation (*cf.* Sections 4.434.5.2 and 145.5.7). Improvement may be achieved when dextran macromolecules are cross-linked in a second step for enhancing the mechanical entrapment of magnetic cores[42] or when they are chemically bonded to the magnetic cores through the use of coupling agents.[43]

In order to improve the MR contrast and/or decrease the magnetic core size, metal MNPs are currently investigated. Indeed, because of their higher saturation magnetization, larger effects on proton relaxation are expected. Moreover, below ~8 nm, inorganic nanoparticles can be readily excreted from the body by renal clearance.[44] For instance, cobalt, iron or FePt MNPs were recently obtained and evaluated as T_1 or T_2 contrast agents. Preliminary results were promising, nevertheless, chemical stability against oxidation, surface chemistry for bioconjugation, and toxicity/pharmacokinetics concerns shall be reconsidered in comparison to the well-known (U)SPIO. Enhanced MRI sensitivity was also achieved with $MnFe_2O_4$ MNPs that displayed the highest magnetic susceptibility and the strongest r_2 relaxivity value of $358\,mM^{-1}\,s^{-1}$ (to compare to $40–190\,mM^{-1}\,s^{-1}$ for conventional (U)SPIO). They would enable the MR detection of tumors as small as 50 mg ($2 \times 5 \times 5\,mm^3$).

Lastly, a significant development for the future of magnetic imaging in the human body concerns a new imaging modality, magnetic particle imaging (MPI), initially developed by Philips Research.[44] The technique takes advantage of the nonlinear magnetization curve of small magnetic particles to generate harmonic responses to time-varying fields that can be detected using standard lock-in methods to a high degree of precision, and with very little background signal to contend with. The imaging capability is the result of the following concept: that in the presence of a large enough DC magnetic field, the magnetization curve is flat, and as such, the harmonic signals disappear. The corollary of this is that if one applies a DC field to all but a small 'field-free point' on the sample, the only harmonic signal received comes from that field-free point, and all other signals are damped out. MPI has great potential for medical applications such as vascular or small intestine imaging, where fast dynamic information is required, and the targets are located relatively deep below the skin, the latter because the MPI signal is virtually unattenuated by intervening tissue.

4.434.6. MNPs as Mediators for Magnetic Hyperthermia

4.434.6.1. Hyperthermia Modalities

The choice of therapies against cancer such as surgery, radiation therapy, chemotherapy, hormone therapy, or biological therapy depends to a great extent upon the type and location of the cancer, the stage of the disease, age, and general health of the patient. Each has its own limitations, as they cause severe side effects to the surrounding tissues in the case of localized therapy and to the whole body in the case of systemic therapy. Heat, due to its intrinsic nature, can be applied locally or to the whole body according to the requirements and found to cause comparatively less side effects. Further, both *in vitro* and *in vivo* studies and clinical experiments showed improved results when hyperthermia is applied in combination with other therapies such as chemo- or radiotherapy.[45]

As the name indicates, the hyperthermia treatment is generally carried out in the temperature range of 42–46 °C, which is above physiological growth temperature (for humans, it is above 37 °C). This is termed as mild hyperthermia. In the above temperature range, tumor hypoxic (poorly oxygenated) cells are more heat-sensitive compared to the normal euoxic (well oxygenated) cells. Hence, the normal cells survive, while the cancerous cells get killed; this creates an interesting way for the therapy of cancer with minimal side effects. In addition, the cancerous tissues have inadequate blood supply, and thus, are not able to dissipate heat energy at the same rate as that of normal ones. Hyperthermia is applied sometimes above 46 °C and it is termed as thermoablation. The effect of hyperthermia exclusively depends upon the treatment temperature and on the exposure time at that temperature. Interestingly, it has been observed that a temperature decline of 1 °C in the temperature range of 42.5–47 °C required doubling of the exposition time, whereas below 42.5 °C, the heat exposure time has to be prolonged by four times to get the same effect.

Hyperthermia during *in vitro* studies can cause several morphological changes in the cells and can detach them from the culture flask and finally kill them.[46] The mechanism of heat-induced cell death causes numerous cellular changes such as in the cell membrane, pH, nuclear and cytoskeleton structures, cellular metabolism, macromolecular synthesis, intracellular signal transduction in hormone–receptor interactions, expression of the heat shock proteins, chromatin organization, and synthesis of DNA and RNA. The degeneration of mitochondria, enzymes, and various kinds of proteins also get induced by hyperthermia.

The cell death due to hyperthermia could be classified either by apoptosis or necrosis. Apoptosis is an orderly process of programmed cell death and can be characterized by distinct morphological features such as nuclear condensation, membrane blebbing, blisters, and echinoid. On the other hand, thermoablation treatment induces necrotic cell death, which is a pathologic phenomenon; it usually occurs when the cells find it difficult to survive following a major external damage. Necrotic cells have swollen nuclei without chromatin condensation, and can be characterized by a gradual dissolution of cell structure and lysis of the plasma membrane.

The selection of hyperthermia modalities that can be applied locally or to the whole body generally depends upon the heating source and on the types of cancer. On the basis of types of heating source, it can be divided into three groups, namely, heat applied from external source (e.g., hot bath, air, wax, blanket), contactless sources (e.g., radiofrequency, ultrasound, microwave, and infrared devices), and heat source inserted into body (e.g., probes, antenna, laser fibers, and mediators).[43]

The advanced hyperthermia devices such as ultrasound or electromagnetic radiation have their own limitations as the heat energy generated by them cannot be delivered to deeply situated cancer tissues without destroying the surrounding normal one. However, this could be overcome by inserting the heating source mediators inside the body where the electromagnetic energy applied on these deep situated mediators by an external electrical or magnetic field gets transformed into heat.

The inserted mediators can be either of macro-, micro-, or nanometric size and they can be stimulated either by capacitive applicators using the electrical component of electromagnetic fields (E-field), or by inductive applicators using magnetic component (H-field). Macroscopic mediators must be inserted within the body by surgical intervention, whereas micro- or nanoscale mediators can be injected as particle dispersion. However, during capacitive heating, E-field may cause heating of the surrounding tissues due to their conducting nature. Further, the difference in the dielectric permeabilities of different tissues leads to inhomogeneous temperature rise. On the other hand, in inductive mediator heating, this problem could be overcome as body tissues do not produce any heat in the presence of AC magnetic field. However, to negate the effect of E-field completely, the optimized value of the product of Hf (where H is the amplitude and f the frequency of the AC magnetic field) is restricted to $4.85 \times 10^8\,\mathrm{A\,m^{-1}\,s^{-1}}$ for a patient treated for an hour.[17] Depending on the diameter of the exposed body region, on the duration of treatment, and on the seriousness of the illness, this critical product may be exceeded. Moreover, to avoid neuromuscular electrostimulation, the frequency should be higher than 50 kHz and it should be lower than 10 MHz for appropriate penetration of the rf-field.

4.434.6.2. Magnetic Fluid Hyperthermia

Even by stressful intervention, the macroscopic inductive heating mediators such as ferromagnetic rods or seeds (1-mm diameter and 1–7-cm of length) cannot be accessible to all tumors. Nevertheless, lack of uniform temperature may also cause potential thermal underdosage to some critical regions. Hence, the magnetic fluid hyperthermia (MFH), in which colloidal dispersion of inductive heating mediators of micro- or nanoscale is used, appears as the most promising therapy. In this case, the particles could be homogeneously distributed due to their ultramicron size, and hence, could produce uniform temperature all around the tissue. It has already been discussed that the cells uptake MNPs by endocytosis and the uptake by the cancerous tissue is even higher owing to their leaky vasculature, which is further helpful during cancer therapy. There is the benefit of stable deposits of MNPs surrounding the tumor tissues in the sense that once the particles are applied, then repeated thermotherapy can be performed without any further addition of particles. Even the daughter cells from a particle-containing parent cell should contain up to 50% of the particle amount of the parent cell, and thus, the descendants would still be cured by future MFH sessions.

The concept of using magnetic hyperthermia as cancer therapy was initiated by Gilchrist and coll. in the late fifties.[47] After a considerable gap, investigations were renewed *in vitro*, and now, *in vivo*. Today, in oncology, there are at least two complementary clinical strategies being developed by Australian and German research teams, using nanocomposite magnetic microparticles and surface-modified superparamagnetic nanoparticles, respectively.

4.434.6.2.1. Nanocomposite magnetic microparticles administered by arterial embolization

This administration route exploits the fact that liver tumors are irrigated mainly by the hepatic arterial system, while healthy liver cells are supplied by the portal vein system. Experiments have been carried out on rabbits and pigs, yielding iron concentrations in the tumor five times higher than in the healthy tissues. The first experiments used 150-nm maghemite particles suspended in lipiodol (a mixture of iodine and vegetable oil, known for its ability to trap anticancer molecules in the chaotic network of blood vessels in tumors). Under magnetic induction conditions of 53 kHz and $30\,\mathrm{kA\,m^{-1}}$, an intratumoral temperature of 48 °C was reached in 5 min. However, since lipiodol proved to be too vasoocclusive for hepatic use, leading to extended necrosis, the maghemite particles were then encapsulated in polymer beads of average diameter 32 μm, dispersed in a 1% aqueous solution of dispersant (Tween) (Thermo-spheres®, registered trademark of SIRTeX Medical Ltd, Sidney). These beads have been shown to be nontoxic and well tolerated and positive results were obtained on animals.[48]

4.434.6.2.2. Superparamagnetic nanoparticles injected directly into the tumor

The first studies used magnetite nanoparticles surrounded by a dextran corona similar to the (U)SPIO contrast agents developed for MRI. *In vitro* experiments showed that these nanoparticles were internalized by cancer cells. Applying an alternating magnetic field (520 kHz, $7–13\,\mathrm{kA\,m^{-1}}$) caused the tumor to diminish in the same way as it would in a bath of hot water. Subsequently, dextran was abandoned because it would appear to degrade too soon. It was then shown that direct injection of particles into the tumor has an advantage (still not fully understood) called the thermal bystander effect: even though the particles are concentrated at the deposition points before applying the alternating magnetic field, they distribute themselves much more uniformly after the first application of the alternating magnetic field.[49]

Jordan, Maier-Hauff and their collaborators at Clinique Charité in Berlin are now the most famous clinical research team, because they developed a full-sized human magnetic field applicator (MFH® 300 F, Hyperthermiesystem GmbH, Berlin at a frequency: 100 kHz, variable field strength: $2.5–18\,\mathrm{kA\,m^{-1}}$, **Figure 10**) and a biocompatible MF made now of surface-aminated magnetite nanoparticles (MagForce Applications GmBH, Berlin and MagForce Nanotechnologies AG, Berlin, Germany), and they performed the first-ever clinical studies based on MFH. The MNPs dispersion is injected within the tumor under general anesthesia. To solve the problem of the temperature distribution, numerical simulations based on tomographic images of the tumor allow optimizing the position of the MNPs deposits (**Figure 11**). The expected heat distribution within the tumor is estimated by the NanoPlan® software planning system (MagForce Nanotechnologies AG, Berlin, Germany).



Figure 10 Human-sized magnetic field applicator developed by Hyperthermiesystem GmbH, Berlin. Extracted from www.magforce.de.

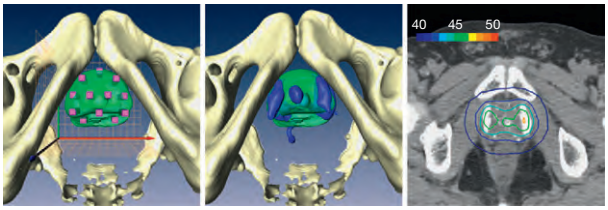

Figure 11 Left: Tomography of a prostate (green region), indicating the path of needles used to deposit 0.5–1 ml (per path) of the particle dispersion. Center: Tomography after injecting the nanoparticles (blue). Right: Image showing the nanoparticle deposits (white because denser than the prostate tissue) and calculated isotherms. Reprinted with permission from Johannsen, M.; Gneveckow, U.; Thiesen, B.; *et al*. *Eur. Urology*, **2007**, *52*, 1653–1662. Copyright © 2007 Elsevier.

Phase I clinical trials (feasibility studies) were performed to patients having prostrate carcinoma,[50] as well as glioblastoma multiforme.[51] This last study involved 14 patients receiving treatment via a combination of fractionated external beam radiotherapy and several sessions of thermotherapy. Aminated-MNPs were injected into multiple sites throughout each tumor. The choice of injection sites was based on data from a comprehensive series of MRI scans of the cranium coupled with the NanoPlan® software. The SPIO nanoparticles (core size 15 nm) were dispersed in water at a concentration of 112 $mg_{Fe}\,ml^{-1}$. Each tumor was injected with 0.1–0.7 ml of the MF per milliliter of tumor and then exposed to a magnetic field of 3.8–13.5 $kA\,m^{-1}$ alternating at 100 kHz. The study successfully demonstrated that this form of thermotherapy using MNPs could be safely applied to the treatment of brain tumors and that hyperthermic temperatures could be achieved. Follow-up computed tomography scans and reproducible temperature measurements confirmed that these deposits were stable over several weeks. Patient survival and local tumor control were not considered primary endpoints of this study; however, clinical outcomes were observed to be promising with the therapy being well tolerated by all patients. More complete evaluation of clinical outcomes is to be assessed in a phase II study (efficacy study) on 65 patients with recurrent glioblastoma multiforme. Phase I clinical trials concerning pancreatic and esophageal cancers and local recurrences of residual tumors (e.g., cervical and prostate cancers, sarcomas) are also in progress.

The rather long period of gestation from first *in vitro* studies to eventual clinical application reflects the considerable technological and regulatory difficulties to be overcome in any attempt to develop a clinically acceptable and useful therapy of this type.[44] It is not merely enough to develop MNPs that heat upon exposure to an AC magnetic field, although that is clearly an important prerequisite. It is also important to know how to appropriately administer enough of the particles to the intended target tissue and to be able to generate enough heat from them by exposure to a tolerable level of AC magnetic field that does not in itself cause any undesirable side effects. The methodology developed by the MagForce group successfully addresses each of these issues.

4.434.6.3. Next Developments

It is clear that if magnetically induced hyperthermia is to achieve the desired results, a certain number of aspects need to be improved. This includes not only the synthesis and properties of the MNPs-based mediators but also a better understanding of the physics involved in the loss phenomena, modeling of the *in vivo* temperature distribution, and development of a safe, efficient, and reasonably priced active targeting strategy.

4.434.6.3.1. Mediators improvement

Improving SAR values remains a challenging task, because the higher the SAR of the MNPs dispersion, the lower the dose to inject to the patient. Among the improvement routes, that which consists in the preparation of narrowed size-distribution MNPs is particularly pertinent for superparamagnetic mediators. Indeed, in conventional synthetic routes, the MNPs are far from being monodisperses in size, resulting in a distribution of relaxation times in the MNPs ensemble (eqn [5]). As a consequence, for a specific frequency of the AC magnetic field, only a small fraction of MNPs heat efficiently (those whose relaxation times are fitting). Therefore, narrowing the size distribution could greatly improve the SAR values, because all the MNPs will heat efficiently at the same frequency.

However, very efficient mediators should not forget that the temperature *in vivo* must be tuned very precisely (*cf.* Section 4.434.6.1) because, on the one hand, heat conduction and energy adsorption *in vivo* are widely unknown, and on the other hand, local overheating may damage safe tissue. An original route could exploit the temperature-dependence of magnetic properties of ferro-/ferrimagnets. So, it would consist in designing MNPs with a T_C adjusted to just above the temperature that should not be exceeded *in vivo*. In this way, should that temperature be reached, each nanoparticle mediator would function as its own fuse by losing its magnetic properties, and hence, also its heating capability. Such a strategy has already been developed for alloy seeds (macroscopic mediators) in order to prevent local tissue overheating and reduce the need for invasive thermometry. For MNPs, manganites ($La_{1-x}Sr_xMnO_3$) are promising materials whose T_C can be tuned in the range of 32–60 °C by varying the amount of Sr. The stabilization of temperature near T_C was observed for such MNPs when they were kept under AC magnetic fields.[52]

Their synthesis in the form of narrowed size-distribution MNPs, their biocompatibility, and surface chemistry are currently under investigation by several groups.

Some of these constraints pull in opposite directions, for example, under physiological conditions, maximal SAR values are attained for superparamagnetic compounds, while in principle, only ferromagnetic or ferrimagnetic compounds allow self-regulation. The aim here will thus be to find the best possible compromise. In addition, it does seem somewhat risky to depend only on Brownian relaxation to reach sufficiently high values of the SAR from the therapeutic point of view, because unfortunately, once in the target tissues, or target cells, it is not obvious that the particles will be able to turn round owing to a high local viscosity or strong interactions with the cell membranes.

4.434.6.3.2. Physics of magnetic loss phenomena

If the heating capacities of the mediators are to be improved, the models used up to now will need to be refined and extended, to increase their predictive power and to cover the whole range of sizes and magnetic behaviors. They must be systematically validated by experiment and the difficulties inherent in this approach will not be overcome without close collaboration between chemists and physicists, both in theory and practice. In particular, it is probably crucial to understand the influence of local clustering of MNPs in order to fully optimize the heating from real samples.[44] Moreover, SAR measurements by calorimetry must be performed in strict adiabatic conditions, that is, considering all the probable heat losses by convection, conduction, and radiation.[53]

As already discussed (*cf.* **Section 4.434.2.2.1**), SAR parameter is an extrinsic parameter which depends not only on the magnetic heating properties of the MNPs themselves, but also on external factors such as the AC magnetic field magnitude and frequency. In an attempt to allow better comparisons between measurements, the concept of intrinsic loss power (ILP) was recently introduced.[44] The ILP parameter is simply the SAR parameter normalized to H^2f. It may be easily derived from measured heat loss data, namely, the ILP measured in $\mathrm{nH\,m^2\,kg^{-1}}$ equals the SAR (in $\mathrm{W\,kg^{-1}}$) divided by the square of the field strength H (in $\mathrm{kA\,m^{-1}}$) and the frequency f (in kHz). The ILP concept may be a useful way to compare results from different groups who often obtain their results using different AC magnetic field conditions from one another. It would be also useful in making direct comparisons with theoretical models.

Lastly, modeling the temperature distribution *in vivo* remains a priority for determining the optimal ways of depositing energy, for example, continuously or in pulses.

4.434.6.3.3. Targeting strategies and limits

One of the last challenges will be to develop the intracellular hyperthermia route, which is based on i.v. administered stealth MNPs designed for selective uptake by tumor cells and which would be the optimal method allowing to selectively overheat tumor cells even in disseminated metastases in any region of the body. However, certain problems still exist as mentioned later.

The first one is the ligand-mediated targeting to improve the colloidal mediator uptake by cancer cells. Among several *in vitro* studies, a single group worked *in vivo*, with the use of ^{111}In-chimeric L6 monoclonal antibodies grafted onto dextran-coated iron oxide cores for human breast cancer in mice.[54] They reported a mean concentration of MNPs per gram of tumor of about 14% of the injected dose, equivalent to around 0.315 mg per gram of tumor (315 μg ml). This is an exceedingly small amount of MNPs being used to heat the tumor mass compared, for example, with the intratumoral concentrations obtained by the direct injection method of Jordan *et al.*, which were greater than $10\,\mathrm{mg\,ml^{-1}}$ of tumor.

The second one is the tissue distribution monitoring prior to the heating sequence. MRI appears to be the most suited method, and therefore, a great interest exists to investigate a unique and versatile magnetic device that will be able to reveal tumors and metastases and treat them by hyperthermia.

The last one concerns the debate about the expected higher efficacy of intracellular thermotherapy, that is, obtained with magnetic particles internalized within cells, with regard to extracellular thermotherapy. According to a theoretical model, it would seem that there is no thermotherapeutic effect on the nanoscale (the scale of the MNPs) or the microscale (the scale of the cells). In fact, thermotherapy operates on the millimeter scale (the scale of the tumor), since the thermal insulation behavior of the cell membrane is negligible.[55] Any difference that may be observed between intracellular and extracellular thermotherapy would thus appear to be due to a mechanical effect of rotation or vibration of the particles in the cell.

Extending this work to highlight the difficulties of using currently available MNPs to heat anything smaller than a 10-mm diameter tumor, an excellent analysis of the various opportunities and limitations was recently published.[56] The issue is essentially one of heat loss into the surrounding tissue. If one wishes to generate and sustain a large temperature imbalance within a tumor, the heat flow into that tumor has to be so large as to overcome the heat flow out. Roughly speaking, the bigger the tumor, the smaller the surface area to volume ratio, the less important the outward heat flow, and the easier it is to heat. Following this argument, the authors concluded that the MNPs SAR must be unrealistically high (certainly several orders of magnitude greater than the best currently reported) to heat a 3-mm cluster of cells, even with concentrations of iron in the cellular mass of $10–50\,\mathrm{mg\,ml^{-1}}$. These figures are relevant given that ~3 mm is the size of a subclinical metastasis that is undetectable by normal imaging techniques, and $10\,\mathrm{mg\,ml^{-1}}$ is substantially more than was used *in vivo* by DeNardo *et al.*, but in the realm of that used by Jordan *et al.* The situation becomes even worse if the aim is to heat individual cells.[44]

4.434.7. MNPs Within Carriers for Drug Delivery

The development of targeted delivery systems for drugs, proteins, genes, and Si-RNA has been one of the most sought after domain of research over the past decade in the broad area of nanotechnology. For the pharmaceutical industry, novel drug delivery technologies represent a strategic tool for expanding drug markets. Delivery systems offer many advantages over conventional dosage forms, including improved efficacy, reduced toxicity, improved patient compliance, and cost-effective therapeutic treatment. Drug delivery systems

capable of simultaneous targeting and controlled release can have an incredible impact on therapeutics.[57] Embedded in such systems, MNPs could become innovative tools for controlling the drug biodistribution in space (targeting) and time (controlled release kinetics).

4.434.7.1. Magnetic Guidance for Carriers

The principle of the magnetic guidance of drug delivery systems is based on submicronic particles containing simultaneously MNPs and drug molecules. When the carriers have entered the bloodstream, external high-gradient magnetic fields are used to concentrate them at a specific target site within the body (physical targeting).[8,13,58] Over the last few decades, a strategy has developed that uses nanocapsules, which are vesicular systems in which the drug is confined to a cavity along with MNPs surrounded by a unique polymer membrane, or nanospheres that are polymer matrix systems in which the drug and MNPs may be uniformly dispersed. The drug of interest may be also adsorbed or attached onto the surface.[21]

The main difficulties to overcome are the stealthiness toward the MPS, the *in vivo* aggregation of the particles and the inherent risk of embolization, the development of strong enough magnets for the targeting of deep tissues, and the disappointing results obtained in larger animal tests.[5] Indeed, preliminary investigations suggested that for most magnetite-based carriers, flux densities at the target site should be of the order of 0.2 T with field gradients of $\sim 8\,\mathrm{T\,m^{-1}}$ for femoral arteries and greater than $100\,\mathrm{T\,m^{-1}}$ for carotid arteries.[59]

A phase I clinical study was reported 10 years ago and concerned 14 patients with advanced unsuccessfully treated cancers or sarcomas.[60] The magnetic carriers were starch particles (50–150 nm) containing magnetic cores of iron oxyhydroxides and capable of adsorbing antitumoral drugs. Although rather a low response to the treatment was seen in the majority of the patients, the magnetic targeting was well tolerated. Evidences of the accumulation of carriers in the tumor mass were given and relatively light side effects were noticed.

Other clinical efforts were performed by FeRx, Inc., a privately held drug delivery company (currently out of business) pursuing the development and commercialization of its proprietary magnetic targeted carrier (MTC) drug delivery technology.[61] MTCs are microparticles composed of metallic iron and activated carbon, which serve as delivery vehicles for the site-specific targeting, retention, and release of pharmaceuticals. FeRx's completed phase I/II safety and dose escalation trial, conducted at seven sites throughout the United States, was designed to deliver MTC-doxorubicin to primary liver tumors. Thirty patients were treated, with no dose limiting toxicities observed, and with MTCs shown to successfully localize the drug in the tumor as demonstrated by MRI and tumor response. Unfortunately, the subsequent phase II/III clinical trials concerning 240 patients with primary liver cancer (hepatocellular carcinoma) were prematurely stopped because the endpoints appeared impossible to be met with statistical significance. The primary objective of this study was to detect a clinically and statistically significant increase in median survival time for MTC-Doxorubicin treated patients relative to patients treated with IV Doxorubicin. Other magnetic carriers are being in the pipeline of some companies.[62]

However, encouraging results emerged from a more recent clinical study concerning four patients and combining magnetic targeting and MRI, in which the authors were able to monitor the trans-catheter delivery of magnetically targeted doxorubicin to the hepatic artery using intra-procedural MRI.[63] The study demonstrated selective targeting to the tumor with a final fraction of treated tumor volume of 0.64–0.91 compared with only 0.07–0.30 in the normal liver tissue.

In order to create high-gradient magnetic fields, recent works demonstrated the interest to insert magnetic needles and meshes at the target site.[44] The potential advantages of planar, periodic magnetic bandages, and Halbach arrays for enhanced targeting were also modeled and evaluated.

The next challenges are a better knowledge of the hydrodynamics/field gradients correlation, the design of carriers of higher drug capacity, the combined use of specific ligands for increasing the targeting efficacy and retaining the particles in the vicinity of the target after removal of the external magnet, and an accurate control of the drug release.

4.434.7.2. Enhanced Drug Release Under the Mechanical Stress of an Oscillating Magnetic Field

The use of an oscillating magnetic field to modulate the rates of drug delivery from a polymer matrix was one of the first methodologies investigated to achieve an externally controlled drug delivery system. The field application leads the particles to oscillate and the drug to be released in these mechanical stress conditions. For instance, the release rate of insulin from poly (ethylene-*co*-(vinyl acetate)) loaded with 1-mm particles of $SmCo_5$ may be 50 times higher than in the absence of the magnetic field (0.5–60 Hz).[64] Today, as far as we know, this route seems to be abandoned since no recent paper deals with this strategy.

4.434.7.3. Heat-Triggered Drug Release Under AC Magnetic Field Control

A second strategy could take advantage of the ability of MNPs to heat in AC magnetic fields (see **Sections 4.434.2.2** and **145.6**). The temperature increase could greatly accelerate the drug diffusion across the carrier matrix. Some cross-linked hydrophilic polymers (hydrogels) are known to be thermosensitive (see **Chapter 1.109, Bioactive Ceramics**). It means that the homogenous solution of polymer starts undergoing phase transition from a soluble to insoluble state at a certain temperature, which is termed as cloud point or lowest critical solution temperature. So, even if its biocompatibility has not yet been demonstrated, copolymers based on N-isopropylacrylamide units suddenly collapse the structure causing a 'burst' release of the carried drug. A preliminary experiment was recently reported using ferromagnetic particles in an induction coil working at 10–50 $\mathrm{kA\,m^{-1}}$ and 300–500 kHz.[65]

4.434.8. Conclusion

In this chapter, recent advances in biomedical applications of MNPs are reviewed. Iron oxide MNPs are now routinely used as contrast agent in MRI and very next applications are expected

in the field of cancer thermal treatment, magnetic targeting, and remotely triggered drug release. These devices will be nanomaterials of higher and higher added value because they are expected to be multifunctional, smart, and versatile. Therefore their chemical composition shall be more and more hybrid combining inorganic, organic, and biologic components. Nevertheless, optimization efforts remain for improving the repeatability of surface functionalization, diagnostic or therapeutic efficacy, biodistribution, and *in vivo* stability and safety.

It is now expected that the next developments will also concern multifunctional platforms that will enable targeting specific organs, tissues, cells, or subcellular compartments, to be monitored by MRI, to carry drug and release it at the right place and time. Nevertheless, targeting remains the main challenge, for which concentrated efforts are required.

Such developments of medicine-directed nanotechnology are probably among the best examples where physicians, pharmacologists, biologists, chemists, and physicists are working together. In this day, when the public opinion worries rightly about the possible nanotechnology consequences on mankind and its environment, it is important to mention that the single aim of a large number of these research efforts on nanoparticles is the humanity survival and comfort.

References

1. Häfeli, U. In *Magnetism in Medicine: A Handbook*; Andrä, W., Nowak, H., Eds.; Wiley-VCH: Weinheim, 2007; pp 3–25.
2. Corot, C.; Robert, P.; Idée, J. M.; Port, M. *Adv. Drug Deliv. Rev.* **2006**, *58*, 1471–1504.
3. Moghimi, S. M.; Szebeni, J. *Prog. Lipid Res.* **2003**, *42*, 463–478.
4. Monfardini, C.; Veronese, F. M. *Bioconjug. Chem.* **1998**, *9*, 418–450.
5. Sonvico, F.; Dubernet, C.; Colombo, P.; Couvreur, P. *Curr. Pharm. Des.* **2005**, *11*, 2091–2105.
6. Tartaj, P.; Morales, M. P.; Veintemillas-Verdaguer, S.; González-Carreño, T.; Serna, C. *J. Phys. D Appl. Phys.* **2003**, *36*, R182–R197.
7. Gupta, A. K.; Gupta, M. P. *Biomaterials* **2005**, *26*, 3995–4021.
8. Pankhurst, Q. A.; Connolly, J.; Jones, S. K.; Dobson, J. *J. Phys. D Appl. Phys.* **2003**, *36*, R167–R181.
9. Berry, C. C.; Curtis, A. S. G. *J. Phys. D Appl. Phys.* **2003**, *36*, R198–R206.
10. O'Handley, R. C. *Modern Magnetic Materials: Principles and Applications*; Wiley: New York, 2000.
11. Spaldin, N. *Magnetic Materials: Fundamentals and Device Applications*; Cambridge University Press: Cambridge, UK, 2003.
12. Goya, G. F.; Grazú, V.; Ibarra, M. R. *Curr. Nanosci.* **2008**, *4*, 1–16.
13. Jeong, U.; Teng, X.; Wang, Y.; Yang, H.; Xia, Y. *Adv. Mater.* **2007**, *19*, 33–60.
14. Lu, A. H.; Salabas, E. L.; Schüth, F. *Angew. Chem. Int. Ed.* **2007**, *46*, 1224–1244.
15. Zborowski, M. In *Scientific and Clinical Applications of Magnetic Carriers*; Häfeli, U., Schütt, W., Teller, J., Zborowski, M., Eds.; Plenum Press: New York, 1997; pp 205–231.
16. Hergt, R.; Dutz, S.; Müller, R.; Zeisberger, M. *J. Phys. Condens. Matter* **2006**, *18*, S2919–S2934.
17. Hergt, R.; Andrä, W. In *Magnetism in Medicine: A Handbook*; Andrä, W., Nowak, H., Eds.; Wiley-VCH: Berlin, 2007; pp 550–570.
18. Schmidt, A. M. *Colloid Polym. Sci.* **2007**, *285*, 953–966.
19. Duran, J. D. G.; Arias, J. L.; Gallardo, V.; Delgado, A. V. *J. Pharm. Sci.* **2008**, *97*, 2948–2983.
20. Roca, A. G.; Costo, R.; Rebolledo, A. F.; *et al. J. Phys. D Appl. Phys.* **2009**, *42*, 224002–224011.
21. Dave, S. R.; Gao, X. *Wiley Interdiscip. Rev. Nanomed. Nanobiotechnol.* **2009**, *1*, 583–609.
22. Di Marco, M.; Sadun, C.; Port, M.; Guilbert, I.; Couvreur, P.; Dubernet, C. *Int. J. Nanomed.* **2007**, *2*, 609–622.
23. Lin, M. M.; Kim, D. K.; El Haj, A. J.; Dobson, J. *IEEE Trans. Nanobiosci.* **2008**, *7*, 298–305.
24. Majewski, P.; Thierry, B. *Crit. Rev. Solid State Mater. Sci.* **2007**, *32*, 203–215.
25. Jech, T. J.; Odenbach, S.; Odenbach, S. *Ferrofluids: Magnetically Controllable Fluids and Their Applications*; Springer-Verlag: New York, 2003.
26. Massart, R. *IEEE Trans. Magn.* **1981**, *17*, 1247–1248.
27. Neuberger, T.; Schöpf, B.; Hofmann, H.; Hofmann, M.; von Rechenberg, B. *J. Magn. Magn. Mater.* **2005**, *293*, 483–496.
28. Shubayev, V. I.; Pisanic, T. R.; Jin, S. *Adv. Drug Deliv. Rev.* **2009**, *61*, 467–477.
29. Okuhata, Y. *Adv. Drug Deliv. Rev.* **1999**, *37*, 121–137.
30. Moghimi, S. M.; Hunter, A. C.; Murray, J. C. *Pharmacol. Rev.* **2001**, *53*, 283–318.
31. Vonarbourg, A.; Passirani, C.; Saulnier, P.; Benoit, J. P. *Biomaterials* **2006**, *27*, 4356–4373.
32. Arruebo, M.; Valladares, M.; González-Fernández, A. *J. Nanomater.* **2009**, 24; article ID 439389.
33. Peng, X. H.; Qian, X.; Mao, H.; *et al. Int. J. Nanomed.* **2008**, *3*, 311–321.
34. Thierry, B. *Curr. Drug Deliv.* **2009**, *6*, 391–403.
35. Stella, B.; Arpicco, S.; Peracchia, M. T.; *et al. J. Pharm. Sci.* **2000**, *89*, 1452–1464.
36. Brown, M. A.; Semelka, R. C. *MRI: Basic Principles and Applications*, 3rd ed.; Wiley-LISS: New York, 2003.
37. Weinmann, H. J.; Ebert, W.; Misselwitz, B.; Schmitt-Willich, H. *Eur. J. Radiol.* **2003**, *46*, 33–44.
38. Bonnemain, B. *J. Drug Target.* **1998**, *6*, 167–174.
39. Weinstein, J. S.; Varallyay, C. G.; Dosa, E.; *et al. J. Cereb. Blood Flow Metab.* **2010**, *30*, 15–35.
40. Bulte, J. W. M.; Kraitchman, D. L. *NMR Biomed.* **2004**, *17*, 484–499.
41. McCarthy, J. R.; Weissleder, R. *Adv. Drug Deliv. Rev.* **2008**, *60*, 1241–1251.
42. Högemann, D.; Josephson, L.; Weissleder, R.; Basilion, J. P. *Bioconjug. Chem.* **2000**, *11*, 941–946.
43. Mornet, S.; Vasseur, S.; Grasset, F.; Duguet, E. *J. Mater. Chem.* **2004**, *14*, 2161–2175.
44. Pankhurst, Q. A.; Thanh, N. K. T.; Jones, S. K.; Dobson, J. *J. Phys. D Appl. Phys.* **2009**, *42*, 224001–224015.
45. Sneed, P. K.; Stea, B. In *Thermoradiotherapy and Thermochemotherapy*; Seegenschmiedt, M. H., Fessenden, P., Vernon, C. C., Eds.; Springer: Berlin, 1996; Vol. 2, pp 159–173.
46. Luchetti, F.; Mannello, F.; Canonico, B.; *et al. Apoptosis* **2004**, *9*, 635–648.
47. Gilchrist, R. K.; Medal, R.; Shorey, W. D.; *et al. Ann. Surg.* **1957**, *146*, 596–606.
48. Moroz, P.; Jones, S. K.; Metcalf, C.; Gray, B. N. *Int. J. Hyperther.* **2003**, *19*, 23–34.
49. Jordan, A.; Scholz, R.; Wust, P.; *et al. Int. J. Hyperther.* **1997**, *13*, 587–605.
50. Johannsen, M.; Gneveckow, U.; Eckelt, L.; *et al. Int. J. Hyperther.* **2005**, *21*, 637–647.
51. Maier-Hauff, K.; Rothe, R.; Scholz, R.; *et al. J. Neurooncol.* **2007**, *81*, 53–60.
52. Pollert, E.; Knížek, K.; Maryško, M.; Kašpar, P.; Vasseur, S.; Duguet, E. *J. Magn. Magn. Mater.* **2007**, *316*, 122–125.
53. Natividad, E.; Castro, M.; Mediano, A. *Appl. Phys. Lett.* **2008**, *92*, 093116.
54. DeNardo, S. J.; DeNardo, G. L.; Natarajan, A.; *et al. J. Nucl. Med.* **2007**, *48*, 437–444.
55. Rabin, Y. *Int. J. Hyperther.* **2002**, *18*, 194–202.
56. Hergt, R.; Dutz, S. *J. Magn. Magn. Mater.* **2007**, *311*, 187–192.
57. Duguet, E.; Mornet, S.; Vasseur, S.; Devoisselle, J. M. *Nanomedicine* **2006**, *1*, 157–168.
58. Douziech-Eyrolles, L.; Marchais, H.; Hervé, K.; *et al. Int. J. Nanomed.* **2007**, *2*, 541–550.
59. Voltairas, P. A.; Fotiadis, D. I.; Michalis, L. K. *J. Biomech.* **2002**, *35*, 813–821.
60. Lübbe, A. S.; Alexiou, C.; Bergemann, C. *J. Surg. Res.* **2001**, *95*, 200–206.
61. Johnson, J. Magnetics Business and Technology, http://www.magneticsmagazine.com/e-prints/ReRx.pdf
62. Arruebo, M.; Fernández-Pacheco, R.; Ricardo Ibarra, M.; Santamaria, J. *Nano Today* **2007**, *2*, 22–32.
63. Wilson, M. W.; Kerlan, R. K.; Fidelman, N. A.; *et al. Radiology* **2004**, *230*, 287–293.
64. Kost, J.; Wolfrum, J.; Langer, R. *J. Biomed. Mater. Res.* **1987**, *21*, 1367–1373.
65. Born, P. J. A.; Müller-Schulte, D. *Nanomedicine* **2006**, *1*, 235–249.

Relevant Websites

www.Magforce.de – MagForce Nanotechnologies AG.

5.501. Scaffolds: Flow Perfusion Bioreactor Design

E J Levorson, F K Kasper and A G Mikos, Rice University, Houston, TX, USA

© 2011 Elsevier Ltd. All rights reserved.

5.501.1.	**Introduction**	1
5.501.2.	**Mass Transport within Scaffolds**	1
5.501.3.	**Perfusion Bioreactors**	2
5.501.4.	**Design Parameters of Flow Perfusion Bioreactors**	4
5.501.4.1.	Direct Perfusion of Scaffolds	4
5.501.4.2.	Media Flow Pathway	4
5.501.4.3.	Maintenance of Sterility	5
5.501.4.4.	Environmental Control	5
5.501.4.4.1.	Nutrient supply and waste removal	5
5.501.4.4.2.	Gas exchange	6
5.501.5.	**Current Flow Perfusion Bioreactor Designs and Functions**	6
5.501.5.1.	Dynamic Cell Seeding	6
5.501.5.2.	Tissue Culture	6
5.501.5.2.1.	Cartilage	6
5.501.5.2.2.	Bone	7
5.501.5.2.3.	Cardiac tissue	7
5.501.6.	**Future Progress**	8
5.501.6.1.	Improving Efficiency	8
5.501.6.2.	Scaling Up	8
5.501.6.3.	Standardizing Bioreactor Systems	8
5.501.6.4.	Determining Shear Stresses within Constructs	9
5.501.7.	**Conclusions**	9
References		10

Abbreviations

ALP Alkaline phosphatase
ECM Extracellular matrix
GAGs Glycosaminoglycans
GMP Good manufacturing practices

5.501.1. Introduction

Tissue engineering has the ability to revolutionize the medical field and the treatment of patients. One methodology which is often used in tissue engineering combines cells, scaffolds, and signals to regenerate functional tissues (Figure 1). In this general model, scaffolds serve as the architecture that supports and directs cell growth in the presence of appropriate signals. While it is important to provide a three-dimensional structure to the cells for tissue development, the use of a scaffold introduces some obstacles that must be overcome in order to achieve a successfully engineered tissue. Some of the design challenges when using a scaffold include biocompatibility, mechanical stability, biodegradation, and mass transport. Likewise, a common design challenge is the introduction and sustenance of uniform cell distribution throughout the construct of isotropic tissues (for more information).[1]

5.501.2. Mass Transport within Scaffolds

The necessity for mass transfer within most tissues is evident from the fact that, in general, in native tissues, cells are not found further than 100 μm from blood capillaries.[2] Likewise, in tissue culture, the maximum cell layer thickness for which oxygen can be supplied by diffusion alone is 100–200 μm.[3] Simple diffusion through three-dimensional tissue-engineered scaffolds often does not provide sufficient amounts of oxygen and soluble nutrients needed for tissue regeneration *in vitro*.[1,4] Specifically, the boundary layer between the medium and the construct is resistant to mass transfer.[5] Therefore, specialized bioreactors have been designed to overcome this resistance to mass transfer through the boundary layer, including spinner flasks and rotating wall vessel bioreactors. In a study by Sikavitsas *et al.*,[6] differentiating osteoblasts cultured on scaffolds in spinner flasks and rotating wall vessel bioreactors exhibited high concentrations of cells and mineralization, in the form of calcium, around the exterior portion of the construct compared to statically cultured constructs. However, even if the boundary layer is overcome, mass transfer restrictions increase as we move further into the construct.[5]

Due to mass transfer limitations within scaffolds, many attempts to statically culture tissues *in vitro* led to constructs with viable cells and deposited extracellular matrix (ECM) on the exterior portion of the scaffold, leaving the interior devoid

of cells and ECM.[7] For example, poly(glycolic acid) scaffolds seeded with chondrocytes exhibited glycosaminoglycans (GAGs) on the outer surface of the scaffold with the interior relatively devoid of GAGs.[8,9] Likewise, osteoblasts cultured on biodegradable polymer scaffolds were only able to penetrate and develop mineralized tissue to a depth of ~200 μm.[10,11]

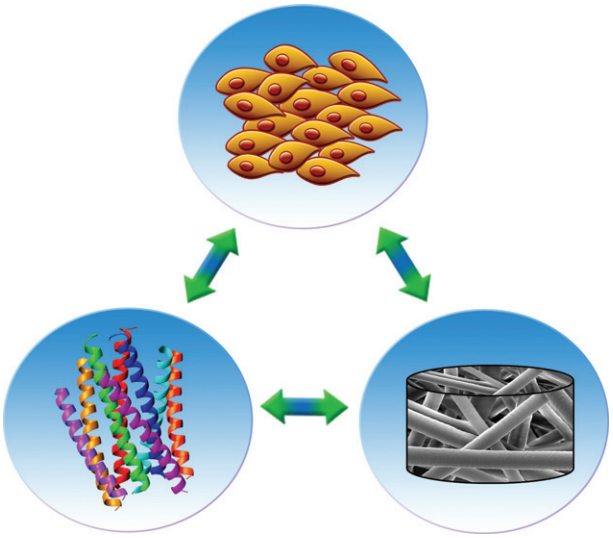

Figure 1 Tissue engineering paradigm. Cells, scaffolds, and signals are combined to regenerate functional tissues.

Beyond these cell penetration depths, necrosis occurs if adequate amounts of oxygen are not delivered to the cells throughout the entire scaffold.[12] For example, it has been shown that large cell spheroids will develop into a shell of thriving cells, ~200-μm thick, around a necrotic core due to limited oxygen availability at the center of the spheroid.[13]

As a result of deficiencies in oxygen transport, engineered tissues develop with inhomogeneous cellular distributions. The inability of cells to distribute uniformly throughout a tissue-engineered construct is extremely detrimental to the intended function of developing isotropic tissues. The issues of improving mass transport and maintaining a uniform cell distribution can be ameliorated by controlling culture conditions through the use of bioreactors.

5.501.3. Perfusion Bioreactors

In many cases, the term perfusion bioreactor refers to a system in which the culture medium is simply circulated into and out of the culture vessel. The simplest design incorporates a gas permeable bioreactor bag in which medium is pumped in using a syringe pump and flows out via hydrostatic pressure into a waste container (**Figure 2(a)**).[14] While this particular

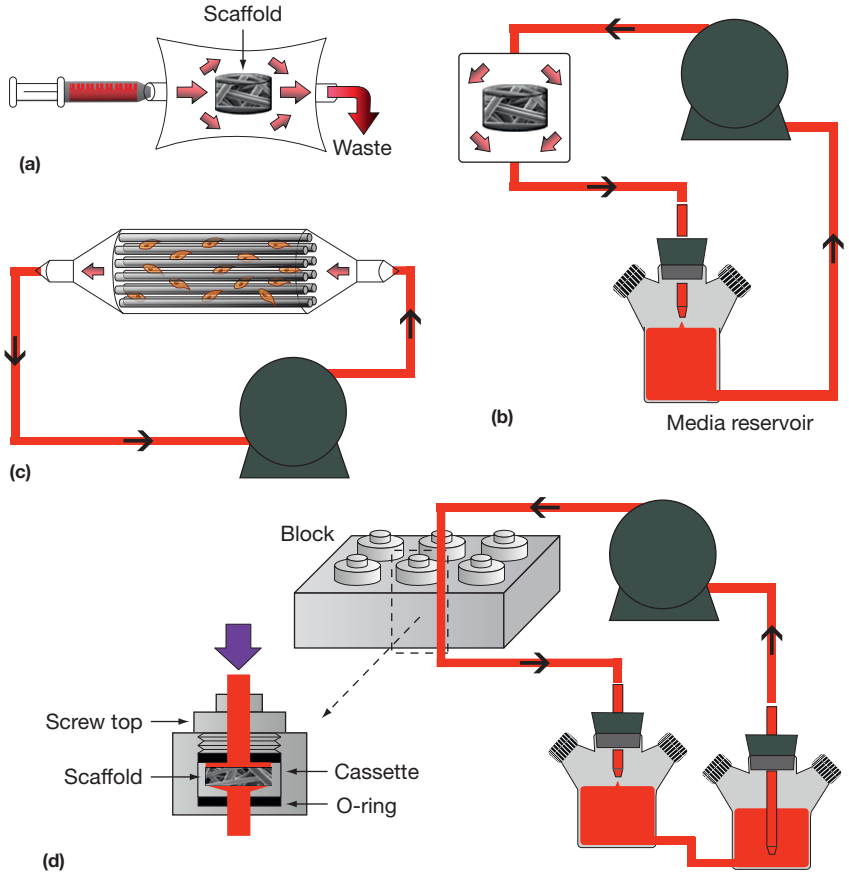

Figure 2 Diagram of different flow perfusion bioreactor designs. Bioreactor bag with syringe pump at the inlet and direct waste disposal at the outlet (a), bioreactor with perfused culture chamber and a closed media flow loop (b), hollow fiber bioreactor (c), direct perfusion bioreactor complete with two media reservoirs (d).

bioreactor design offers the benefit of automatically replenishing medium, it does not recycle any of the used media, thus depriving the culture system of the growth factors, cytokines, matrix proteins, and other signals secreted by the cells during tissue development which are beneficial to tissue generation.[15–17]

Slightly more sophisticated perfusion systems are composed of a culture chamber connected to a medium reservoir in a closed loop. In this case, scaffolds are suspended in a culture chamber into which medium is pumped (**Figure 2(b)**).[18,19] These systems allow circulation of the medium throughout the culture chamber and constant aeration of medium. However, simple perfusion bioreactors do not actively perfuse the interior of the scaffolds with medium. Patterns of medium flow that bypass the interior of the scaffold will not greatly improve the transfer of nutrients and oxygen to the interior of thicker constructs. As was discussed previously, sufficient mass transfer levels throughout a scaffold in its entirety are vital to the success of engineered tissues.

Hollow fiber bioreactors are another type of perfusion bioreactors that have been developed for the culture of various cell types. These systems use cells that have been immobilized within a culture chamber that has hollow capillary-like tubes through which the medium is perfused (**Figure 2(c)**).[20,21] The hollow fibers have pores that are impermeable to cells. However, nutrients and oxygen are able to freely diffuse through the fibers. The capillary-like function of the fibers in these hollow fiber bioreactors allow cells to be cocultured without coming into physical contact with each other. The absence of physical contact between different cell populations retains the benefits of coculturing that come from chemical signaling between different cell types while still maintaining separate cell populations that can be easily harvested.[21] Hollow fiber bioreactors do not have a traditional scaffold. Instead, in addition to being simply immobilized within the system, oftentimes, cells will adhere to the fibers of the bioreactor. In order to harvest cells from the bioreactor, traditional cell removal techniques such as trypsinization and mechanical agitation are used.[21] Also, cells cultured in the hollow fiber bioreactors are subject to flow-induced shear stresses, which have been shown to support cell differentiation in certain cell types.[21–25]

Perfusion is a natural process that takes place in all tissues and is required for the survival of cells. Body fluids permeate the interior of tissues to supply oxygen and nutrients while removing wastes.[26] For this reason, it is important that bioreactor designs account for perfusion through the interior of scaffolds. Flow perfusion bioreactors pump media through the pores and internal network of scaffolds allowing delivery of nutrients and removal of waste throughout the construct (**Figure 2(d)**).[27]

Direct perfusion of constructs will enable cells to thrive and evenly distribute throughout the interior of scaffolds, thus increasing the viability of engineered tissues. Pham *et al.*[28] showed that bilayered electrospun scaffolds, composed of micro and nanofiber layers, cultured in a flow perfusion bioreactor display greater cellular infiltration, compared to statically cultured constructs, by a factor of 5 (**Figure 3**). Likewise, as seen in **Figure 4**, complete cellular infiltration was seen only in scaffolds cultured in the flow perfusion bioreactor. Flow perfusion has an extremely positive effect on cellular distribution. Culturing tissues in a flow perfusion bioreactor enables cells to infiltrate nanofiber scaffolds, which under static conditions may hinder cellular migration due to decreased pore sizes.[28]

Medium flow throughout the construct is also incredibly beneficial, as it stimulates the cells by shear stresses. The application of shear stress on cells *in vivo* induces mechanotransduction signaling, which has been shown to be beneficial in the culturing of many tissues, including bone, cartilage, and cardiac tissue.[22–24]

It is thought that shear stress is a beneficial stimulus in tissue development because, as native tissues are loaded, interstitial fluid flows throughout the intercellular spaces in the tissue stimulating mechanotransduction pathways.[24,29] In the bone, fluid flow is responsible for inducing new bone formation and increasing the metabolic activity of osteoblasts.[30–32] Likewise, compressing cartilage subjects chondrocytes to shear stresses, among other mechanical stimuli.[33] Compression has been shown to induce tissue remodeling and increase the production of ECM elements in the cartilage.[34] Use of flow perfusion bioreactors mimics the conditions of interstitial fluid flow much better, thus harnessing the benefits of flow-induced shear stress to improve tissue development.[35]

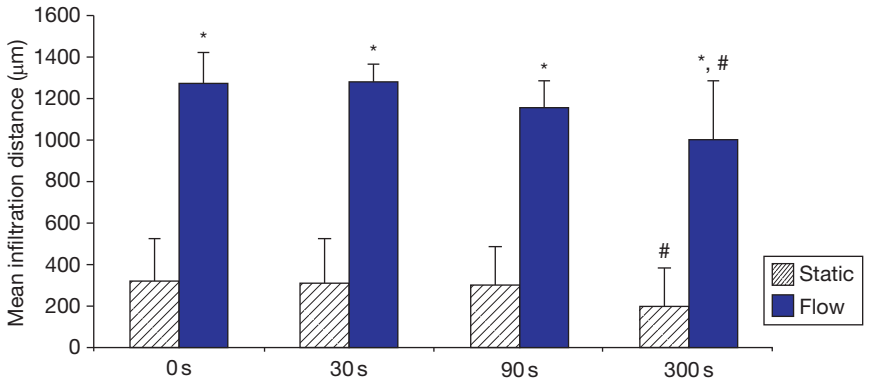

Figure 3 The mean infiltration distance achieved by mesenchymal stem cells cultured under static and flow conditions. The mesenchymal stem cells were cultured on scaffolds in which the top nanofiber layer was spun for 0, 30, 90, and 300 s. * indicates statistical significance between static and flow culture; # indicates statistical significance for that culture condition ($p < 0.01$). Reproduced with permission from Pham, Q. P.; Sharma, U.; Mikos, A. G. *Biomacromolecules* **2006**, *7*, 2796–2805.

5.501.4. Design Parameters of Flow Perfusion Bioreactors

There are a variety of parameters and design challenges that need to be considered when designing a flow perfusion system. In general, all of the design challenges arise from the central goal of having to provide proper culture conditions for a three-dimensional scaffold. These culture conditions include complete perfusion of the scaffold, media flow pathways, environmental control, and maintenance of sterility.

5.501.4.1. Direct Perfusion of Scaffolds

In order to achieve media flow directly through the scaffold, it may be necessary to restrict the media to unidirectional flow. If media flow is not restricted, the fluid will take the path of least resistance and one cannot guarantee perfusion of the entire scaffold (Figure 5). In the absence of true perfusion of the entire scaffold, uniform mechanical stimulation of the cells within the scaffold cannot be realized.[15]

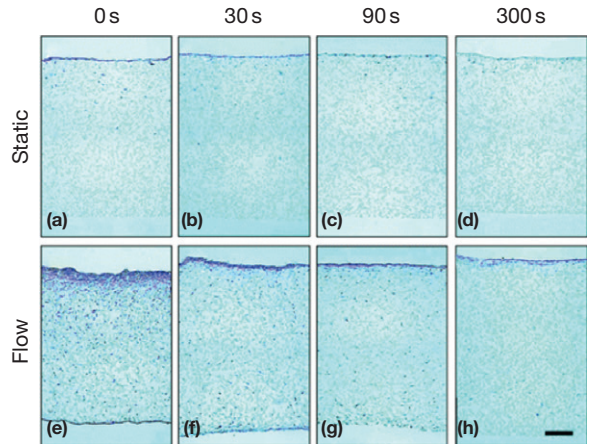

Figure 4 Images of histological sections stained with hematoxylin and eosin. (a–d) were cultured under static conditions. (e–h) were cultured under flow perfusion conditions. The scaffolds consisted of a bottom microfiber layer 5-μm thick, with a top nanofiber 600-nm thick spun for 0, 30, 90, and 300 s. Reproduced with permission from Pham, Q. P.; Sharma, U.; Mikos, A. G. *Biomacromolecules* **2006**, *7*, 2796–2805.

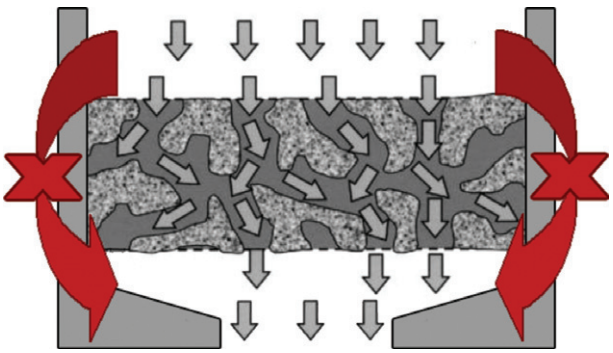

Figure 5 To ensure that media directly perfuses the scaffold, media flow around the scaffold perimeter must be prevented. Adapted and reproduced with permission from Bancroft, G. N.; Sikavitsas, V. I.; Mikos, A. G. *Tissue Eng.* **2003**, *9*, 549–554.

The bioreactor design must allow the media to flow in at one end of the scaffold and out the other end. To assure unidirectional flow, a bioreactor system must form a tight seal between the perimeter of the scaffold and the wall of the bioreactor.[15,27] A tight scaffold mount in the bioreactor is achieved in two primary ways: press-fitting scaffolds into bioreactor cassettes (Figure 2(d))[36–38] or applying low levels of compression to the scaffold by placing gaskets on either side of the scaffold.[39–41]

5.501.4.2. Media Flow Pathway

It is vital to provide a means of automatically forcing the medium through the scaffold and the rest of the system. Many bioreactor designs utilize a peristaltic pump to control media flow.[23,40–43] One concern with using a peristaltic pump is the degradation of the relatively low-durability gas permeable tubing.[27] For a bioreactor system design to be successful in the long term and prevent the tubing from degrading and mixing with the culture medium, more durable tubing should be used in media circuit that is in direct contact with the peristaltic pump. Wendt *et al.*[38] have completely avoided the issues involved with using a peristaltic pump by using a vacuum pump as an alternative. Vacuum pumps have the additional attribute of making medium flow easily reversible.

It is necessary to regulate the flow rate of media through the system so as to modulate the shear stress imposed on the constructs. The bioreactor design utilized by Carrier *et al.*[40] places four scaffold cartridges in series within the same media circulation loop. In a serological cartridge arrangement, it is difficult to ensure that identical flow conditions are achieved throughout all the four scaffolds in the series. When cultivating larger tissues, a serological arrangement may eventually lead to variation in the tissues that have developed due to the different levels of shear stresses throughout the flow pathway. It is for this reason that, in addition to the electrical controls for the pump, flow rate may be monitored using a flow meter in the media flow pathway.

It is also vital to tailor the flow rate of the bioreactor system to the specific tissue being cultured and the desired cellular response. Tailored flow rates are necessary because different native tissues possess varying levels of mechanical stimulation that are useful in promoting ECM production.[30,41,44–46] In order to achieve reproducible beneficial effects within constructs cultured in a bioreactor, fluid flow rate from the pump must be translated into shear stresses experienced by cells within the scaffold. Given that scaffold architectures are oftentimes random and complex, it is difficult to accurately estimate shear stresses within the constructs.[47,48] Due to the difficulty involved in estimating internal shear stresses, currently, most bioreactor systems utilize the trial and error method to elucidate the intended beneficial results within the tissue-engineered constructs.

Removing undissolved air from the bioreactor is imperative as trapped gas bubbles within the system disrupt the smooth distribution of media flow through the scaffolds.[27,49] In order to keep gas bubbles off the scaffolds and maintain an even distribution of fluid flow, Bancroft *et al.*[27] have described a system in which flow is directed in a top-down fashion. In this

design, any gas bubbles in the system will rise in the tubing, leaving the scaffold surfaces free of gas bubbles.

The bioreactor used by Grayson *et al.*[49] addresses the issue of trapped gas in a more direct manner. In this design, a syringe in a three-way connector is included in the media flow pathway just upstream of the inlet. Gas bubbles may be removed from the system by using the syringe, and when not in use, the syringe is blocked from fluid flow.

5.501.4.3. Maintenance of Sterility

Given that bioreactors are used to culture cells and developing tissues, it is necessary to ensure that the system is sterile at the beginning and remains so throughout the entire culture period. In order to guarantee system sterility in the beginning, it is important that the individual pieces of the bioreactor be able to withstand sterilization procedures, such as ethylene oxide and autoclave treatments. Materials that are commonly used for bioreactor assembly include: polycarbonate, poly (methyl methacrylate), poly(tetrafluoroethylene), silicone, glass, and stainless steel.[27,41,43,50]

A sterile culture environment with minimal exposure to the surroundings may be maintained by designing a system that can fit within an incubator.[51] Using an incubator confers size constraints on the system and the resulting throughput of the scaffold. In an effort to garner extra space within the incubator, it is possible to design a system so that the pumps may be placed outside the incubator.[43] Designs that use external pumps increase the amount of space available within the incubator and reduce any risk of contamination that may arise from the pump residing within the incubator during culture.

Contamination risks may be mitigated by limiting the number of scaffolds that are cultured within each flow circuit. Wang *et al.*[52] have used a system in which each scaffold is cultured individually in a single closed circuit with separate medium reservoirs. While the use of separate media reservoirs does greatly reduce the spread of contamination between scaffolds, it is also rather inefficient with regard to space constraints and the requirements of medium volume. Consequently, a successful bioreactor design must have a balance between efficiency and the number of scaffolds in each culture loop.

It is also important to enable quick and simple medium changes in order to reduce the risk of contamination within the system. One way to accomplish fast medium changes is to provide a method for exchanging medium without removing the entire bioreactor from the incubator. Du *et al.*[53] have connected silicone tubing from one of the medium reservoirs inside the incubator to fresh medium reserves in a culture hood outside the incubator.

The proper choice of medium reservoirs also plays a key role in ensuring fast medium changes. Reservoirs that are most amenable to quick medium changes possess easily removable caps such as side-armed flasks[27] and Schott bottles.[50]

5.501.4.4. Environmental Control

One of the primary purposes of any bioreactor is to provide a means of controlling the tissue culture environment. Maintaining a proper environment is fundamental to culturing viable tissues. The parameters that must be monitored and sustained include pH, oxygen tension, temperature, nutrient availability, and waste removal. It is relatively simple to regulate the temperature in a bioreactor by simply designing a system that is compact enough to operate from within an incubator (for more information, see **Chapter 5.502, Engineering Scaffold Mechanical and Mass Transport Properties**).

5.501.4.4.1. Nutrient supply and waste removal

As in any long-term method of culturing tissues, it is necessary to provide a method for delivery of fresh nutrient supplies and removal of waste from the culture system. Nutrient delivery and waste removal is accomplished by simply changing the medium at defined culture periods. As flow perfusion bioreactors are closed systems through which a medium is constantly pumping, medium changes are slightly more complicated. Also, while designing any tissue culture system, it is important to note that frequent medium changes increase the risk of contamination.[15,27] Therefore, it is necessary to design a bioreactor in which the medium can be exchanged quickly and without difficulty.

Most flow perfusion bioreactors enable quick and simple medium changes by including a medium reservoir in the medium flow loop. To exchange the medium, the researcher simply has to empty all of the medium into the reservoir, interrupt medium flow, remove the spent medium from the reservoir and replace it with fresh medium.[37,40] The primary issue with medium exchange in a bioreactor with only one reservoir is that medium flow must be interrupted, which allows air to enter into the system. As discussed previously, air bubbles trapped in the bioreactor obstruct the even distribution of medium flow through the constructs.[27,49]

In order to perform a complete medium change without interrupting the flow of medium through the construct, two medium reservoirs may be utilized as shown in the design outlined by Bancroft *et al.*[27] (**Figure 2(d)**). In a two reservoir system, there are two medium reservoirs connected by a small length of tubing. While the bioreactor is functioning normally, the medium is able to freely transfer from one reservoir to the next simply by the force of gravity. Medium changes are accomplished by simply clamping the tube connecting the two reservoirs. Then, after filling the first reservoir with new medium, the fresh medium flushes the used medium out of the system and into the second reservoir. Once the entire used medium has been pumped out of the system, the second reservoir is emptied and the clamp is removed, allowing the system to function normally.[27] As the flow of medium was never completely interrupted, a bioreactor which utilizes two medium reservoirs reduces the amount of air that gets into the system, thus reducing the amount of trapped gas within the system that could disrupt fluid flow through the constructs.

Sophisticated systems are used to monitor the medium throughout the culture period in order to analyze the biological components within the medium. In the bioreactor described by Zhao and Ma,[43] sampling ports are placed in the medium flow pathway on either side of the culture chamber. The inclusion and arrangement of medium sampling ports enables the measurement of glucose and lactate to determine the metabolic activity of the tissue.

Another improvement on common flow perfusion bioreactor designs would be the incorporation of an automatic method of pH monitoring. pH monitoring would allow the researcher to

gauge metabolic activity of the tissue and determine the optimal medium exchange periods. Automatic medium pH measurements may be accomplished by including a pH meter within the medium flow circuit[54,55] or an innovative noncontact optical measurement device.[56] An optical measurement device may be used to measure the pH in a culture environment through the change in the optical properties of the medium due to color changes with the pH indicator, phenol red.[56] Optical pH meters permit pH monitoring without coming in contact with the culture medium, thus reducing the risk of contamination.

5.501.4.4.2. Gas exchange

Due to the fact that flow perfusion bioreactors are designed as closed systems with one of the primary objectives being the increase of oxygen transport within the constructs, it is necessary to provide a method for gas exchange in the design of a bioreactor. Many flow perfusion bioreactor designs allow gas exchange through the use of gas permeable silicone in the form of tubing, membranes, and medium reservoir bags.[39,40,42,57] When using gas permeable materials for gas exchange, the oxygen tension within the medium will equilibrate with the gas concentration in the incubator inside which the bioreactor is housed. Another method of gas exchange in the medium utilizes mixing of the fluid flow with the headspace in the medium reservoir to incorporate oxygen in the medium.[50] In contrast, gas may be pumped directly into the system. Zhao and Ma[43] have accomplished direct gas exchange by pumping air into the medium reservoir through a sterile filter.

Monitoring oxygen tension within the bioreactor may be useful not only for ensuring that oxygen levels are satisfactory, but also for designing a bioreactor that enables tissue-engineered products to be produced under good manufacturing practices (GMP). Some bioreactors include oxygen sensors within the medium flow loop.[50,54] In the bioreactor design outlined by Janssen *et al.*,[37] oxygen sensors are placed in the medium pathway at both the inlet and the outlet. Oxygen sensors arranged on either side of the culture chamber allow the dynamic supervision of dissolved oxygen. They also provide information about the patterns of oxygen consumption within the constructs, thus enabling inferences to be made about cell proliferation. Zhao and coworkers[43,58] have monitored oxygen tension by taking a sample of the medium through specialized ports. The dissolved oxygen in the medium is then measured using a blood gas analyzer. While the testing of media samples using a blood gas analyzer is quite effective, it is more labor intensive than using an oxygen sensor that operates automatically in real time.

5.501.5. Current Flow Perfusion Bioreactor Designs and Functions

Flow perfusion bioreactors are utilized for two primary functions, namely, dynamic cell seeding and long-term tissue culture.

5.501.5.1. Dynamic Cell Seeding

Seeding techniques are responsible for initially establishing required cell numbers and distributions within the scaffolds. In turn, cell numbers and their distributions affect cellular processes such as proliferation and differentiation, which have a profound influence on the developing engineered tissue as they affect functions such as cell-to-cell interactions.[59,60] Similarly, in tissue engineering, it is extremely important to seed cells with the highest possible seeding efficiency as limited cell numbers are available owing to the restrictions in biopsy expansion.

The most prevalent seeding technique employed in tissue engineering is static seeding. Static seeding oftentimes leads to low seeding efficiencies (ratio of initial cell content in a scaffold to the total number of cells seeded) and nonuniform cell distributions.[61–63] In an effort to improve seeding efficiency and obtain a more uniform cell distribution, dynamic seeding techniques may be used. More specifically, cell seeding within flow perfusion bioreactors enables more efficient seeding and homogeneous cell distributions.[59]

Dynamic seeding of chondrocytes using perfusion for 3 days increased cell content by 80%, compared with statically seeded constructs.[64] Also, the flow rate utilized for dynamic seeding has a significant influence on the resultant cell content.[64] Therefore, it is imperative that the flow rate used for dynamic seeding be optimized for different scaffold types and architectures in order to achieve the most advantageous results.

It is also possible to dynamically seed cells on scaffolds by using oscillatory medium flow. Oscillatory flow is accomplished by simply reversing medium flow at a defined frequency. Like seeding with simple direct perfusion, seeding using oscillatory flow leads to significant increases in seeding efficiency over traditional static seeding techniques.[38,59] Likewise, dynamic seeding is successful in distributing cells throughout the entire scaffold while the cells remain localized at the top of statically seeded scaffolds.[38,59]

The bioreactor design used by Zhao and Ma[43] improves upon other bioreactors used for dynamic seeding in that it contains a dedicated inoculation loop in addition to the medium circulating loop. The inoculation loop allows direct injection of a cell suspension into the perfusing medium while bypassing the medium reservoirs. Bypassing the medium reservoirs reduces the dilution of the cell suspension, resulting in a more efficient application of the cells to the scaffolds.

5.501.5.2. Tissue Culture

Flow perfusion bioreactors are used for the long-term culture of a variety of different tissue types. The tissues that are being developed under a perfused medium flow are tissues that benefit not only from increased mass transport but also from the mechanical stimulation resulting from fluid flow through the constructs, tissues such as cartilage, bone, and cardiac tissue (for more information, see Chapter 5.506, Effects of Mechanical Stress on Cells).

5.501.5.2.1. Cartilage

Mechanical stimulation, such as fluid-induced shear stress, is extremely beneficial in cartilage development due to its ability to stimulate GAG and collagen synthesis in chondrocytes.[65] Flow perfusion bioreactors that perfuse media through the interstitial spaces of scaffolds cause internal shear stresses, and achieve larger amounts of ECM production and more homogeneous cell and ECM distributions compared to tissues

cultured statically or otherwise. In the study described by Pazzano *et al.*,[42] flow perfusion of chondrocytes over a period of 4 weeks led to dramatic increases in cell number, sulfated GAGs, and total collagen content compared to statically cultured chondrocytes.

Likewise, cells cultured in flow perfusion bioreactors tend to align in the direction of fluid flow within the scaffold.[42] The capability to induce cellular alignment, as a byproduct of perfusion, may be very favorable for the development of cartilage as it naturally exhibits regions of oriented cells and ECM.[66,67]

Also, it has been shown that chondrocytes cultured under dynamic conditions exhibit a flattened morphology with filopodia, while statically cultured chondrocytes are more likely to display rounded or less desirable morphologies.[41] Similarly, statically cultured chondrocytes display membrane vesicles, a sign of apoptosis in diseased cartilage, while chondrocytes cultured under perfusion exhibit smooth cell surfaces.[41] For the success of engineered tissues, it is imperative that culture conditions support the desired cell phenotype and morphology.

5.501.5.2.2. Bone

Bone-like tissue, when cultured under flow perfusion, displays a more homogeneous cell and mineral distribution throughout the entire scaffold, as opposed to being confined to the scaffold perimeter when statically cultured.[7,36,52,57] Similarly, cellularity in flow perfusion cultured constructs is significantly higher than in statically cultured bone-like tissue.[68,69] Furthermore, in a study performed by Bancroft *et al.*,[36] pore-like structures lined with cells, indicating *de novo* tissue modeling, were observed throughout constructs that were cultured under flow perfusion. These results show that the conditions provided by flow perfusion bioreactors increase the capacity of the constructs to develop into bone-like tissues.

Also, flow perfusion has a significant influence on osteogenic differentiation of mesenchymal stem cells (MSCs). When considering bone-like tissue development, increased mineralization is consistent with further osteo-differentiation. Holtorf *et al.*[69] indicated that MSCs in titanium meshes with different fiber diameters cultured under direct flow perfusion displayed significantly different amounts of mineralization, as indicated by the calcium content (**Figure 6**). Models also suggest that a decrease in the scaffold mesh size leads to an increase in fluid shear stress. Holtorf *et al.*[69] used 20 μm titanium mesh scaffolds and obtained an increase in shear stresses within the constructs, yielding an increase in mineralization at 16 days compared to 40 μm mesh constructs.[69]

Furthermore, flow perfusion may be used to induce osteogenic differentiation of MSCs even in the absence of the common induction agent, dexamethasone.[70] A similar study showed that the presence or absence of dexamethasone does not have a significant influence on the culture of osteoblasts under flow perfusion conditions.[71] Likewise, alkaline phosphatase (ALP), a marker of osteoblast differentiation, increases throughout the duration of perfused culture of MSCs on porous biphasic calcium phosphate ceramics. ALP levels in the perfused constructs were also significantly higher than in the static cultures.[57] These results indicate that the stimulation achieved through flow perfusion is sufficient to induce osteogenic differentiation without the traditional induction factors.

5.501.5.2.3. Cardiac tissue

As with the tissues mentioned above, culturing cardiomyocytes under perfusion greatly increase the spatial distribution of cells throughout the scaffold. Cardiomyocytes, cultured statically, develop a 100-μm thick external layer of cells with a relatively acellular scaffold interior.[40] In contrast, image processing supports the observation that perfused scaffolds maintain reasonably constant cell numbers per unit area.[40]

Likewise, cardiac tissue cultured under flow perfusion maintains a more favorable cell phenotype and function.

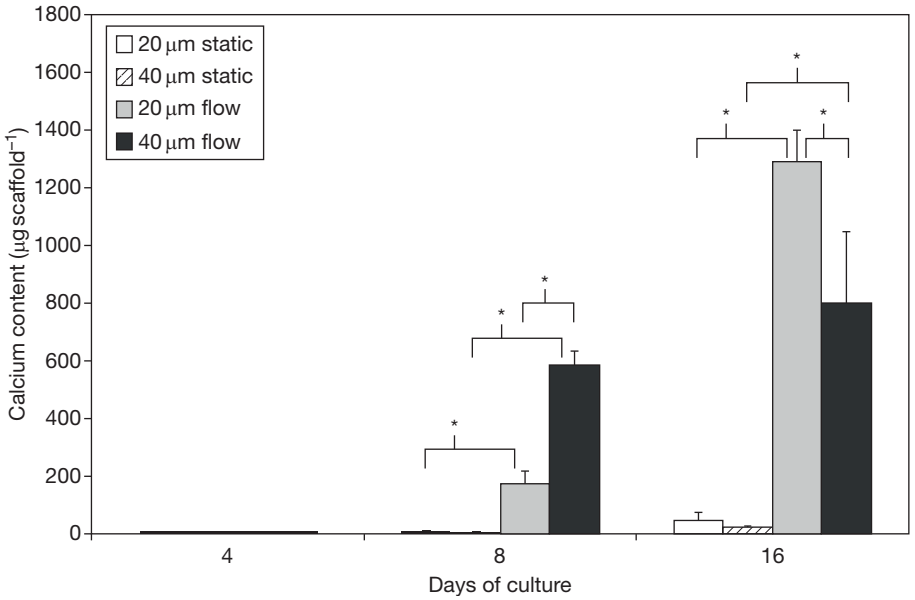

Figure 6 Calcium content in the extracellular matrix produced by mesenchymal stem cells cultured under static or flow perfusion conditions on titanium scaffolds with 20- or 40-μm fiber sizes for 4, 8, or 16 days. *indicates significant difference between groups ($p < 0.05$). Reproduced with permission from Holtorf, H. L.; Datta, N.; Jansen, J. A.; Mikos, A. G. *J. Biomed. Mater. Res.* **2005**, *74A*, 171–180.

Constructs cultured under perfusion display cardiac-specific markers and evidence of aerobic metabolism consistently throughout the entire scaffold.[40] In contrast, scaffolds cultured statically exhibit these traits only in the outer 100-μm thick section of the construct.[40] Similarly, cardiomyocytes cultured under pulsatile perfusion are more hypertrophic than cells grown in static culture.[39]

In addition to the differentiation markers, cardiac tissues cultured under perfusion retain more cardiac-like function than constructs cultured statically. For instance, cells cultivated under pulsatile flow are more contractile than statically cultured cells. A significantly lower excitation threshold and a higher contractile amplitude indicate an improvement in construct function upon pulsatile perfusion culture.[39]

5.501.6. Future Progress

Many studies have shown that flow perfusion bioreactors are valuable in successfully culturing tissues and obtaining clinically relevant amounts of ECM. Flow perfusion bioreactors also provide a means to overcome the problem of mass transport within scaffolds and allow better cellular infiltration and uniform distribution. Furthermore, the mechanical stimulation due to flow shear stress is quite useful in guiding cellular differentiation. While all of these characteristics have been demonstrated at the research level, there is still more progress that must be made in flow perfusion bioreactor design to make it more practical for widespread use.

5.501.6.1. Improving Efficiency

Most of the flow perfusion bioreactors described previously have been placed within the confines of an incubator. Incubators are used to maintain uniform and controllable temperature and atmospheric conditions to culture tissues. If incubators continue to be used in tissue culture with flow perfusion bioreactors, it is necessary to maximize the number of scaffolds per bioreactor on each shelf of the incubator. Current designs, which exhibit relatively low throughput with regards to space requirements, will be difficult to scale up in the future.

One approach to improve the efficiency of space utilization in flow perfusion bioreactors is to avoid using a traditional incubator altogether. To circumvent the use of a traditional incubator, the flow perfusion bioreactor system can be designed to manage environmental conditions autonomously. Stand alone, benchtop systems that are able to maintain the temperature, gas tension, and humidity necessary for tissue culture are more user-friendly and simple.[54,72] Bioreactor systems that are independent of traditional incubators also allow continuous 3D imaging of the developing tissue under flow conditions.[73]

Many tissue culture systems require the use of growth factors and other signaling chemicals to stimulate and maintain cellular differentiation.[74–76] Growth factors are rather expensive, costing hundreds of dollars for mere micrograms. Thus, to manufacture tissues that are economically viable, it is vital to design flow perfusion bioreactors that make efficient use of the culture medium. Using medium efficiently means reducing the ratio of medium volume to scaffold number within each bioreactor.

The bioreactor described by Flaibani *et al.*[77] is reasonably efficient in its use of culture medium, completely avoiding the use of a traditional medium reservoir. In the culture cassette, extra empty space is included to act as a medium reservoir (**Figure 2 (d)**). Eliminating a traditional medium reservoir greatly reduces the volume of medium needed for each scaffold. However, it is extremely important to consider the end effects and maintain fully developed fluid flow throughout the culture cassette. Therefore, for some systems, the utilization of a medium reservoir that is separate from the culture cassette may be necessary.

5.501.6.2. Scaling Up

A common challenge throughout tissue engineering is the issue of scaling up tissue development from the research scale to the industrial level. When scaling up a bioreactor, it is necessary to consider reproducibility and safety, and simultaneously furnish a design that is also fiscally competitive and clinically relevant.[78] Currently, bioreactor systems that have been scaled up focus on aseptically growing relevant tissue sizes within closed systems at high throughput.[79]

In order to take the research level bioreactors to the market, it may be important to make the transition from tissue culture to tissue implantation. Current bioreactor systems at the research level focus primarily on tissue development and culture. However, a more complete industrial level design would incorporate cell seeding, tissue formation, and product delivery in one system.[79,80] A more complete bioreactor design will enable the tissue (product) produced using the bioreactor to more easily meet GMP guidelines, such as protection against contamination and provision of quality assurance, by controlling components and processes. A full circle bioreactor more easily meets GMP guidelines because the number of processing and handling steps, and thus risk of contamination from production to delivery, will be reduced.[79,80]

5.501.6.3. Standardizing Bioreactor Systems

Engineering tissues is a difficult endeavor because different tissues of the body require different conditions and geometries for successful development.[5] Due to the differences in tissue requirements, it is necessary that both bioreactors and the various culture condition parameters be optimized and standardized to the specific tissue being cultured. A study by Bancroft *et al.*[36] determined that higher mineralization levels could be achieved using elevated bioreactor flow rates (**Figure 7**). While medium flow rate and the resulting mineralization were determined to be related, they were not linearly proportional. The absence of linearity indicates that there is a limit to the amount of mineralization that may be stimulated by fluid flow in a flow perfusion bioreactor. In order to achieve the best possible benefit, the parameters of flow perfusion bioreactors must undergo optimization.

The majority of bioreactor systems used in tissue engineering currently were developed individually, by separate laboratories, to suit specific research objectives. While the various systems presently employed bear many similarities, there is no standard system in use. In order to be able to generate reproducible results, it is necessary to produce a standardized bioreactor design that may be used by various members of

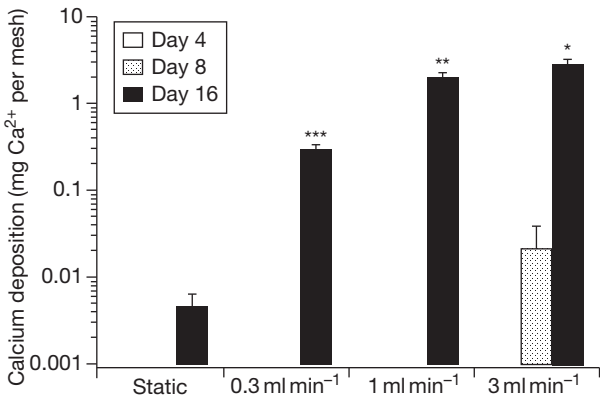

Figure 7 Calcium content of cultured scaffolds. Perfusion conditions from left to right: static, 0.3, 1, and 3 ml min^{-1}. Indicators: * highest, ** second highest, and *** third highest calcium content. All groups are statistically different ($p < 0.05$). Reproduced with permission from Bancroft, G. N.; Sikavitsas, V. I.; Van Den Dolder, J.; *et al*. *Proc*. *Natl*. *Acad*. *Sci*. *USA* **2002**, *99*, 12600–12605. Copyright 2002 National Academy of Sciences, USA.

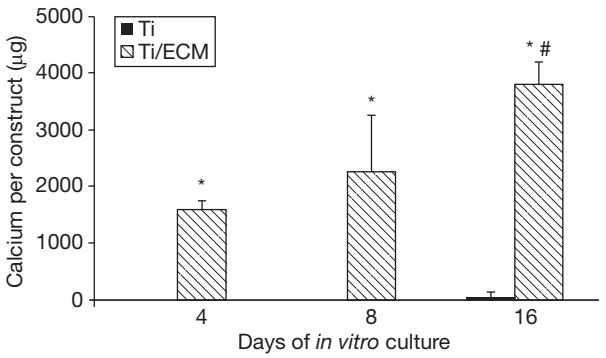

Figure 8 Calcium content in titanium and titanium/ECM composite scaffolds cultured in a flow perfusion bioreactor after 4, 8, and 16 days. * significantly different between Ti and Ti/ECM constructs, # significantly different from all other data points ($p < 0.05$). Reproduced with permission from Datta, N.; Pham, Q. P.; Sharma, U.; Sikavitsas, V. I.; Jansen, J. A.; Mikos, A. G. *Proc*. *Natl*. *Acad*. *Sci*. *USA* **2006**, *103*, 2488–2493. Copyright 2006 National Academy of Sciences, USA.

the tissue engineering community. In addition, a standard design would enable the comparison of results among different researchers. It would also facilitate the difficult transition that occurs while converting a specific technology from the research level to industrial scale production.

Future flow perfusion bioreactor studies should also move toward presenting medium flow as the resulting shear stresses within the construct, rather than simply as the flow rate through the bioreactor. Presenting medium flow as the resulting internal shear stress is very important because, currently, there is no standardized flow perfusion bioreactor system in use. Given that various researchers use slightly different systems, the same flow rate used in two different bioreactors may deliver dissimilar levels of mechanical stimulation inside the constructs, resulting in tissues with different properties.

5.501.6.4. Determining Shear Stresses within Constructs

Scaffolds with different microarchitectures cultured at the same flow rate in a perfusion bioreactor may exhibit very different results. Datta *et al.*,[81] reported significantly higher mineralization quantities with composite titanium/ECM constructs compared to bare titanium scaffolds (**Figure 8**). While the presence of *in vitro* generated ECM in a scaffold has been shown to have a positive influence on cellular differentiation,[82,83] smaller scaffold pore sizes have been shown to increase shear stress within constructs, thus eliciting different cellular responses.[69] Due to the effect of scaffold architecture on fluid flow-induced shear stress and thus on cellular responses, it is extremely important to report fluid flow within flow perfusion bioreactors as shear stress within the constructs.

In an effort to standardize the field of tissue engineering and enable the generation of reproducible culturing environments and the resultant tissues, it is important to model the shear stress that can occur within the interstitial spaces of the scaffolds. Elucidating the internal shear stress due to medium flow would also provide information about the shear stress experienced by the cells within the constructs, thus garnering more information about the cellular effects of mechanical stimulation, which will enable better design of scaffold architectures. Also, the internal shear stress may be used to optimize fluid flow conditions to match physiological conditions, rather than optimization through trial and error, which is the current norm.[5]

However, it is a difficult task to accurately estimate the shear stress due to flow within a tissue engineering scaffold, given the extremely irregular scaffold architectures that exist within constructs. At present, the more accurate method of estimating internal shear stress uses microcomputed tomography to determine the complex microarchitectures of the irregular scaffolds. Then, a computational fluid dynamics code is used to calculate the localized shear stress within the scaffolds.[47,48,84] In the future, improvements may be made to the 3D modeling of the shear stresses within irregular scaffolds by examining, more closely, the effects of boundary conditions and assumptions, on the accuracy of the models (for more information, see **Chapter 3.309, Fluid Mechanics: Transport and Diffusion Analyses as Applied in Biomaterials Studies**).

5.501.7. Conclusions

In tissue engineering, scaffolds are necessary for providing a three-dimensional architecture on which cells may proliferate and develop into a functioning tissue. However, mass transfer limitations within scaffolds are an extremely common issue in tissue engineering. Oftentimes, cells cultured statically on scaffolds develop a shell of viable cells and ECM, with the interior portion of the construct relatively devoid of cells. Flow perfusion bioreactors may be used to overcome the challenge of mass transfer within scaffolds.

To design a successful flow perfusion bioreactor, it is necessary to consider a variety of different design objectives. The primary objective of a flow perfusion bioreactor is to supply media directly through the scaffold so as to improve mass transport and impose beneficial shear stress on the cells within the scaffold. It is also important to consider methods for controlling environmental conditions within the bioreactor, including, the atmosphere, temperature, and sterility.

Currently, flow perfusion bioreactors are used for two primary purposes: dynamic cell seeding of scaffolds and long-term tissue culture. Dynamically seeding cells onto scaffolds using flow perfusion bioreactors has been shown to significantly improve seeding efficiencies and cell distributions within the scaffolds. Dynamic perfusion for long-term culture is currently being used for the development of cartilage, bone, and cardiac tissues. The shear stresses within the scaffolds, which result from media perfusion, have been shown to have a beneficial effect on cellular differentiation, ECM production, and cell distribution for these tissues.

The scaling up of flow perfusion bioreactors to achieve clinically relevant amounts of tissue will be a major challenge. For flow perfusion bioreactors to make a successful transition from the research level to an industrial scale, it will be necessary to standardize bioreactor systems. Also, it is extremely important to improve the efficiency of current systems with regards to space constraints, throughput, and media volumes. In the future, at both the research and industrial levels, it will be necessary to report media flow as the internal shear stress that occurs within the scaffolds.

Despite the advances that still need to be made in the design of bioreactors, flow perfusion bioreactors show immense promise for tissue engineering. Flow perfusion bioreactors provide the means to overcome many of the current issues that arise while attempting to develop tissues using three-dimensional scaffolds.

Acknowledgments

Work on fabrication of cell/scaffold constructs with flow perfusion bioreactors for tissue engineering applications has been funded by the National Institutes of Health (R01 AR57083). Erica Levorson gratefully acknowledges the support of Rice Institute of Biosciences and Bioengineering's Biotechnology Training Grant (NIH T32 GM08362).

References

1. Mikos, A. G.; Lu, L.; Temenoff, J. S.; Tessmar, J. K. In *Biomaterials Science*; Ratner, B. D., Hoffman, A. S., Schoen, F. J., Lemons, J. E., Eds.; Elsevier: San Diego, CA, 2004; pp 735–749.
2. Sherwood, L. In *Human Physiology: From Cells to Systems*; Brooks Cole: Belmont, CA, 2007; p 361.
3. Fassnacht, D.; Pörtner, R. *J. Biotechnol.* **1999**, *72*, 169.
4. Martin, I.; Wendt, D.; Heberer, M. *Trends Biotechnol.* **2004**, *22*, 80.
5. Pörtner, R.; Nagel-Heyer, S.; Goepfert, C.; Adamietz, P.; Meenen, N. M. *J. Biosci. Bioeng.* **2005**, *100*, 235.
6. Sikavitsas, V. I.; Bancroft, G. N.; Mikos, A. G. *J. Biomed. Mater. Res.* **2002**, *62*, 136–148.
7. Gomes, M. E.; Sikavitsas, V. I.; Behravesh, E.; Reis, R. L.; Mikos, A. G. *J. Biomed. Mater. Res.* **2003**, *67A*, 87–95.
8. Martin, I.; Obradovic, B.; Freed, L. E.; Vunjak-Novakovic, G. *Ann. Biomed. Eng.* **1999**, *27*, 656.
9. Vunjak-Novakovic, G.; Martin, I.; Obradovic, B.; *et al. J. Orthop. Res.* **1999**, *17*, 130–138.
10. Ishaug-Riley, S. L.; Crane-Kruger, G. M.; Yaszemski, M. J.; Mikos, A. G. *Biomaterials* **1998**, *19*, 1405.
11. Ishaug, S. L.; Crane, G. M.; Miller, M. J.; Yasko, A. W.; Yaszemski, M. J.; Mikos, A. G. *J. Biomed. Mater. Res.* **1997**, *36*, 17–28.
12. Harrison, B. S.; Eberli, D.; Lee, S. J.; Atala, A.; Yoo, J. J. *Biomaterials* **2007**, *28*, 4628.
13. Sutherland, R. M.; Sordat, B.; Bamat, J.; Gabbert, H.; Bourrat, B.; Mueller-Klieser, W. *Cancer Res.* **1986**, *46*, 5320–5329.
14. Solchaga, L. A.; Tognana, E.; Penick, K.; *et al. Tissue Eng.* **2006**, *12*, 1851–1863.
15. Darling, E. M.; Athanasiou, K. A. *Tissue Eng.* **2003**, *9*, 9–26.
16. Moos, V.; Sieper, J.; Herzog, V.; Müller, B. *Clin. Rheumatol.* **2001**, *20*, 353.
17. Mrugala, D.; Dossat, N.; Ringe, J.; *et al. Clon. Stem Cell.* **2009**, *11*, 61–76.
18. Fassnacht, D.; Rossing, S.; Stange, J.; Portner, R. *Biotechnol. Tech.* **1998**, *12*, 25.
19. Watanabe, S.; Inagaki, S.; Kinouchi, I.; Takai, H.; Masuda, Y.; Mizuno, S. *J. Biosci. Bioeng.* **2005**, *100*, 105.
20. Chromiak, J.; Shansky, J.; Perrone, C.; Vandenburgh, H. *In Vitro Cell. Dev. Biol. Anim.* **1998**, *34*, 694.
21. Redmond, E.; Cahill, P.; Sitzmann, J. *In Vitro Cell. Dev. Biol. Anim.* **1995**, *31*, 601.
22. Chen, H. C.; Hu, Y. C. *Biotechnol. Lett.* **2006**, *28*, 1415.
23. Dolder, J. V. D.; Bancroft, G. N.; Sikavitsas, V. I.; Spauwen, P. H. M.; Jansen, J. A.; Mikos, A. G. *J. Biomed. Mater. Res.* **2003**, *64A*, 235–241.
24. Sikavitsas, V. I.; Bancroft, G. N.; Holtorf, H. L.; Jansen, J. A.; Mikos, A. G. *Proc. Natl. Acad. Sci. USA* **2003**, *100*, 14683–14688.
25. Westmuckett, A. D.; Lupu, C.; Roquefeuil, S.; Krausz, T.; Kakkar, V. V.; Lupu, F. *Arterioscler. Thromb. Vasc. Biol.* **2000**, *20*, 2474–2482.
26. Schoen, F. J.; Mitchell, R. N. In *Biomaterials Science*; Ratner, B. D., Hoffman, A. S., Schoen, F. J., Lemons, J. E., Eds.; Elsevier: San Diego, CA, 2004; p 260.
27. Bancroft, G. N.; Sikavitsas, V. I.; Mikos, A. G. *Tissue Eng.* **2003**, *9*, 549–554.
28. Pham, Q. P.; Sharma, U.; Mikos, A. G. *Biomacromolecules* **2006**, *7*, 2796–2805.
29. Sikavitsas, V. I.; Temenoff, J. S.; Mikos, A. G. *Biomaterials* **2001**, *22*, 2581.
30. Hillsley, M. V.; Frangos, J. A. *Biotechnol. Bioeng.* **1994**, *43*, 573–581.
31. Pavalko, F. M.; Chen, N. X.; Turner, C. H.; *et al. Am. J. Physiol. Cell Physiol.* **1998**, *275*, C1591–C1601.
32. Kapur, S.; Baylink, D. J.; William Lau, K. H. *Bone* **2003**, *32*, 241.
33. Mow, V.; Wang, C. *Clin. Orthop.* **1999**, *367*, S204–S223.
34. Wong, M.; Siegrist, M.; Cao, X. *Matrix Biol.* **1999**, *18*, 391–399.
35. Hutmacher, D. W. *Biomaterials* **2000**, *21*, 2529.
36. Bancroft, G. N.; Sikavitsas, V. I.; Van Den Dolder, J.; *et al. Proc. Natl. Acad. Sci. USA* **2002**, *99*, 12600–12605.
37. Janssen, F. W.; Oostra, J.; Oorschot, A. V.; Van Blitterswijk, C. A. *Biomaterials* **2006**, *27*, 315.
38. Wendt, D.; Marsano, A.; Jakob, M.; Heberer, M.; Martin, I. *Biotechnol. Bioeng.* **2003**, *84*, 205–214.
39. Brown, M. A.; Iyer, R. K.; Radisic, M. *Biotechnol. Prog.* **2008**, *24*, 907–920.
40. Carrier, R. L.; Rupnick, M.; Langer, R.; Schoen, F. J.; Freed, L. E.; Vunjak-Novakovic, G. *Tissue Eng.* **2002**, *8*, 175–188.
41. Raimondi, M. T.; Boschetti, F.; Falcone, L.; *et al. Biomech. Model. Mechanobiol.* **2002**, *1*, 69.
42. Pazzano, D.; Mercier, K. A.; Moran, J. M.; *et al. Biotechnol. Prog.* **2000**, *16*, 893–896.
43. Zhao, F.; Ma, T. *Biotechnol. Bioeng.* **2005**, *91*, 482–493.
44. Klein-Nulend, J.; Bacabac, R. G.; Mullender, M. G. *Pathol. Biol.* **2005**, *53*, 576.
45. Malek, A. M.; Alper, S. L.; Izumo, S. *JAMA* **1999**, *282*, 2035–2042.
46. Smith, R. L.; Donlon, B. S.; Gupta, M. K.; *et al. J. Orthop. Res.* **1995**, *13*, 824–831.
47. Maes, F.; Ransbeeck, P. V.; Oosterwyck, H. V.; Verdonck, P. *Biotechnol. Bioeng.* **2009**, *103*, 621–630.
48. Porter, B.; Zauel, R.; Stockman, H.; Guldberg, R.; Fyhrie, D. *J. Biomech.* **2005**, *38*, 543.
49. Grayson, W. L.; Bhumiratana, S.; Cannizzaro, C.; *et al. Tissue Eng. A* **2008**, *14*, 1809.
50. Mahmoudifar, N.; Doran, P. M. *Biotechnol. Bioeng.* **2005**, *91*, 338–355.
51. Laganà, K.; Moretti, M.; Dubini, G.; Raimondi, M. T. *Proc. Inst. Mech. Eng. H* **2008**, *222*, 705.
52. Wang, L.; Hu, Y. Y.; Wang, Z.; *et al. J. Biomed. Mater. Res.* **2009**, *91A*, 102–113.
53. Du, D.; Furukawa, K. S.; Ushida, T. *Biotechnol. Bioeng.* **2009**, *102*, 1670–1678.
54. Khait, L.; Hecker, L.; Radnoti, D.; Birla, R. *Ann. Biomed. Eng.* **2008**, *36*, 713.
55. Li, A.; Barker, G.; Beck, D.; Colburn, S.; Monsell, R.; Pellegrin, C. *In Vitro Cell. Dev. Biol. Anim.* **1993**, *29*, 249.
56. Xu, X.; Smith, S.; Urban, J.; Cui, Z. *Med. Eng. Phys.* **2006**, *28*, 468.
57. Holtorf, H. L.; Sheffield, T. L.; Ambrose, C. G.; Jansen, J. A.; Mikos, A. G. *Ann. Biomed. Eng.* **2005**, *33*, 1238.
58. Zhao, F.; Pathi, P.; Grayson, W.; Xing, Q.; Locke, B. R.; Ma, T. *Biotechnol. Prog.* **2005**, *21*, 1269–1280.
59. Alvarez-Barreto, J.; Linehan, S.; Shambaugh, R.; Sikavitsas, V. *Ann. Biomed. Eng.* **2007**, *35*, 429.
60. Li, Y.; Ma, T.; Kniss, D. A.; Lasky, L. C.; Yang, S. T. *Biotechnol. Prog.* **2001**, *17*, 935–944.

61. Holy, C. E.; Shoichet, M. S.; Davies, J. E. *J. Biomed. Mater. Res.* **2000**, *51*, 376–382.
62. Kim, B. S.; Putnam, A. J.; Kulik, T. J.; Mooney, D. J. *Biotechnol. Bioeng.* **1998**, *57*, 46–54.
63. Van Den Dolder, J.; Spauwen, P. H. M.; Jansen, J. A. *Tissue Eng.* **2003**, *9*, 315–325.
64. Davisson, T.; Sah, R. L.; Ratcliffe, A. *Tissue Eng.* **2002**, *8*, 807–816.
65. Saini, S.; Wick, T. M. *Biotechnol. Prog.* **2003**, *19*, 510–521.
66. Kuettner, K. E. *Clin. Biochem.* **1992**, *25*, 155.
67. Roughley, P. J.; Lee, E. R. *Microsc. Res. Tech.* **1994**, *28*, 385–397.
68. Gomes, M. E.; Holtorf, H. L.; Reis, R. L.; Mikos, A. G. *Tissue Eng.* **2006**, *12*, 801–809.
69. Holtorf, H. L.; Datta, N.; Jansen, J. A.; Mikos, A. G. *J. Biomed. Mater. Res.* **2005**, *74A*, 171–180.
70. Holtorf, H. L.; Jansen, J. A.; Mikos, A. G. *J. Biomed. Mater. Res.* **2005**, *72A*, 326–334.
71. Du, D.; Furukawa, K.; Ushida, T. *Ann. Biomed. Eng.* **2009**, *37*, 146.
72. Wendt, D.; Riboldi, S. A.; Cioffi, M.; Martin, I. In *Bioreactor Systems for Tissue Engineering*; Advances in Biochemical Engineering/Biotechnology; Springer: Berlin/Heidelberg, 2009; Vol. 112, pp 1–27.
73. Stephens, J. S.; Cooper, J. A.; Phelan, F. R., Jr.; Dunkers, J. P. *Biotechnol. Bioeng.* **2007**, *97*, 952–961.
74. Elder, B. D.; Athanasiou, K. A. *Osteoarthr. Cartil.* **2009**, *17*, 114.
75. Jansen, J. A.; Vehof, J. W. M.; Ruhé, P. Q.; *et al. J. Control. Release* **2005**, *101*, 127.
76. Sundelacruz, S.; Kaplan, D. L. *Semin. Cell Dev. Biol.* **2009**, *20*, 646.
77. Flaibani, M.; Luni, C.; Sbalchiero, E.; Elvassore, N. *Biotechnol. Prog.* **2009**, *25*, 286–295.
78. Ratcliffe, A.; Niklason, L. E. *Ann. NY Acad. Sci.* **2002**, *961*, 210–215.
79. Naughton, G. K. *Ann. NY Acad. Sci.* **2002**, *961*, 372–385.
80. Mansbridge, J. *J. Anat.* **2006**, *209*, 527–532.
81. Datta, N.; Pham, Q. P.; Sharma, U.; Sikavitsas, V. I.; Jansen, J. A.; Mikos, A. G. *Proc. Natl. Acad. Sci. USA* **2006**, *103*, 2488–2493.
82. Datta, N.; Holtorf, H. L.; Sikavitsas, V. I.; Jansen, J. A.; Mikos, A. G. *Biomaterials* **2005**, *26*, 971.
83. Pham, Q. P.; Kurtis Kasper, F.; Scott Baggett, L.; Raphael, R. M.; Jansen, J. A.; Mikos, A. G. *Biomaterials* **2008**, *29*, 2729.
84. Cioffi, M.; Küffer, J.; Ströbel, S.; Dubini, G.; Martin, I.; Wendt, D. *J. Biomech.* **2008**, *41*, 2918.

5.502. Engineering Scaffold Mechanical and Mass Transport Properties

S J Hollister, University of Michigan, Ann Arbor, MI, USA

© 2011 Elsevier Ltd. All rights reserved.

5.502.1.	**Introduction**	14
5.502.1.1.	The Need for Engineering Scaffolds with Controlled Effective Properties	14
5.502.1.2.	Choosing Effective Properties as Design Targets	15
5.502.2.	**Hierarchical Computational Scaffold Design**	15
5.502.2.1.	Computational Representation of Hierarchical Scaffold Structure	16
5.502.2.2.	Computing Effective Scaffold Properties Using Homogenization	16
5.502.2.3.	Bounds on Effective Design Targets	17
5.502.2.4.	Designing Scaffold Architecture	19
5.502.2.5.	Integrating Hierarchical Design	22
5.502.2.6.	Hierarchical Scaffold Design: Summary	22
5.502.3.	**Fabricating Designed Scaffolds**	23
5.502.3.1.	Direct Solid-Free-Form Fabrication	23
5.502.3.2.	Indirect Solid-Free-Form Fabrication	25
5.502.3.3.	Postfabrication Surface Modification	26
5.502.3.4.	Scaffold Fabrication: Summary	27
5.502.4.	**Designed Scaffold Architecture Influences Tissue Regeneration**	28
5.502.4.1.	Cartilage	28
5.502.4.2.	Bone	29
5.502.4.3.	Neural Tissue	30
5.502.4.4.	Summary	31
5.502.5.	**Conclusion**	31
References		32

Glossary

Fixation Attachment of scaffold to surrounding host tissue.
Form Shape and volume required to fill a tissue defect.
Formation Ability of scaffold to enhance tissue regeneration through local micron environments, including mass transport, cell–material interaction and biofactor delivery.
Forward scaffold design method (FSDM) An approach in which the scaffold architecture is designed first, followed by calculation of effective properties.
Function Scaffold ability to perform mechanical, chemical and electrical functions in a tissue defect.
Homogenization Mathematical theory that allows solution of multiscale physics problems through the asymptotic expansion of the governing field variable.
Inverse scaffold design method (ISDM) An approach in which effective properties are defined and an optimization method is used to arrange material in 3D space to achieve the defined properties.
STL Standard file format representing objects through surface triangular facets.
Tuj1 Neuron-specific class III beta-tubulin.

Abbreviations

BMP2	Bone morphogenetic protein 2
BMP7	Bone morphogenetic protein 7
BMSC	Bone marrow stromal cells
CFD	Computational fluid dynamics
cGMP	Current good manufacturing practices
CT	Computed tomography
CVD	Chemical vapor deposition
DEF	Diethyl fumarate
FEA	Finite element analysis
GFAP	Glial fibrillary acidic protein
***H*(*)**	Heaviside function
HA	Hydroxyapatite
IKVAV	Ile-Lys-Val-Ala-Val sequence from laminin-1
ISE	Iterative Scaffold Engineering
MRI	Magnetic resonance imaging
PCL	Polycaprolactone
PEEK	Polyetheretherketone
PEGT/PBT	Poly(ethylene glycol)-terephthalate/poly (butylene terephthalate)
PGA	Polyglycolic acid
PGS	Poly(glycerolsebacate)
PLLA	Poly-L-lactic acid
POC	Poly(1,8-octanediol-*co*-citrate)
PPF	Poly(propylene fumarate)
PPX-NH_2	Poly[(4-amino-*p*-xylylene)-*co*-(*p*-xylylene)]
RGD	Arginine-glycine-aspartic acid
SBF	Simulated body fluid

SFF	Solid-free-form fabrication	**sulfo-SMCC**	Sulfosuccinimidyl-4-(*N*-maleimidomethyl) cyclohexane-1-carboxylate
sGAG	Sulfated glycosaminoglycans	**TCP**	Tricalcium phosphate
SLA	Stereolithography	**VEGF**	Vascular endothelial growth factor
SLS	Selective laser sintering		

5.502.1. Introduction

5.502.1.1. The Need for Engineering Scaffolds with Controlled Effective Properties

Biomaterial scaffolds fill critical roles in regenerative medicine. Scaffolds are needed to (1) provide anatomic fill and shape in tissue defects, (2) provide temporary function in anatomic defects while tissue regenerates, and (3) enhance tissue regeneration through material–cell interaction and delivery of biologics, including cells, proteins, and/or genes. In essence, we can summarize these requirements as the 4Fs: Form, Fixation, Function, and Formation. While there is agreement over these general 4F requirements, there is virtually no information on how these general scaffold requirements translate into specific scaffold design requirements. We must be able to quantitatively define these specific design requirements in order to have scaffold design targets. Obviously, both the type and magnitude of these design requirements is likely to vary between tissues and anatomic sites.

The need to fill anatomic defect shape (Form) is a readily defined requirement. Although typically not quantifiable using a mathematical equation, the anatomic shape is readily defined using an appropriate patient imaging modality such as computed tomography (CT) for bone and blood vessels with contrast agent and magnetic resonance imaging (MRI) for soft tissues. The mode of surgical fixation of the scaffold (Fixation) will be highly dependent on the shape of the surrounding tissue segments. Both the anatomic defect and the fixation segment shape can be defined using various imaging processing software such as MATLAB™ (www.mathworks.com), MIMICS™ (www.materialise.com), ANALYZE™ (www.analyzedirect.com), AMIRA™ (www.amira.com), or IDL™ (www.ittvis.com), to name a few. The resulting anatomic region is then defined by voxels within that region grouped in a set or mask, or a surface representation of triangular facets as in the .STL file format.

There is more uncertainty in defining temporary function (Function) than anatomic shape. Although function may be defined with regard to mechanical, electrical, or chemical, depending on tissue type, this chapter will focus on mechanical function. It is clear that the scaffold should not mechanically fail under physiologic forces within the anatomic site. Ideally, one would design the scaffold so that stresses under physiologic forces are below the scaffold material failure stresses. However, it is very difficult to determine boundary conditions on most tissues, thus introducing significant uncertainty into scaffold stress analysis. Alternatively, since native tissues adapt themselves to physiologic loads, scaffolds that match native tissue properties should be able to withstand physiologic loads. This design principle has been espoused in different forms by a variety of groups. Yaszemski *et al.*[1] stated the bone tissue engineering scaffolds should provide 'adequate strength' in bone defects, while Brekke and Toth[2] stated that scaffolds should be rigid enough to avoid tissue prolapse but otherwise possess 'certain minimum mechanical characteristics.' Hutmacher[3] suggested that scaffold mechanical properties should match those of the native tissue at implantation time. Engelmayr *et al.*[4] also reiterated the design target of matching native tissue properties when they sought to create polymer scaffolds that matched the tangent elastic modulus of rat myocardium.

Although native tissue properties are a plausible scaffold design target for function, the key question is "What properties should scaffolds match?" There are a wide range of constitutive models that have been used to characterize tissues including linear elasticity, nonlinear elasticity, viscoelasticity, and poroelasticity. Again, the choice of appropriate functional design target will depend on the tissue. Linear elasticity is appropriate for bone, but it is unclear whether linear elasticity (as utilized by Engelmayr *et al.*[4] for myocardium) is an appropriate design target for soft tissues exhibiting nonlinear stress strain relationships under large deformation and viscoelastic strain-dependent behavior. In addition to defining the appropriate constitutive model design target, there is also a need to define the appropriate magnitude of the constitutive model coefficients for use as design targets. Stating that scaffold effective mechanical properties should match those of native tissue is problematic on two fronts. First, what is the definition of native tissue? Is this tissue from a male or female, a 30-year old or a 60-year old? Second, although widely postulated, the hypothesis that scaffold mechanical properties matching native tissue mechanical properties produces better outcomes has never been rigorously tested, or really tested at all for that matter. Still, the postulate that scaffold mechanical properties should match native tissue properties remains the most plausible scaffold function design target (for more information on the native mechanical properties of bone see **Chapter 3.307, Finite Element Analysis in Bone Research: A Computational Method Relating Structure to Mechanical Function**; for more information on native cardiac tissue properties see **Chapter 3.308, The Mechanics of Native and Engineered Cardiac Soft Tissues** in this volume).

The third general scaffold requirement, that scaffolds should enhance tissue regeneration through cell–material interaction and biologic factor delivery (Formation), remains the most ambiguous of the four scaffold requirements. While the need to replicate anatomic shape can be addressed through patient image data, the need for fixation defined by the stiffness and strength that will avoid separation of scaffold and host tissue, and the need to provide temporary function addressed by matching tissue constitutive model parameters, the characteristics that are best related to enhanced tissue regeneration remain largely undefined. Although it is clear that biologics like growth factors and stem cells can enhance tissue regeneration, a question arises with regard to the choice of the scaffold material and porous architecture that can best

integrate and deliver these biologics. O'Brien *et al.*[5] and Van Cleynenbreugel *et al.*[6] have noted increased cell adhesion with increased scaffold surface area, suggesting the increased surface area will positively affect cell–material interaction. However, this may only be the case if the material itself is hydrophilic and provides the appropriate ligands for cell attachment.

Furthermore, mass transport issues, including the capacity for vascularization, will have a substantial influence on tissue regeneration. Vascularization remains a difficult objective to achieve, requiring either delivery of proangiogenic factors such as vascular endothelial growth factor (VEGF), or engineering of an arteriovenous loop within the scaffold. Beyond immediate perfusion and vascularization, mass transport within scaffolds can also be characterized by effective permeability and diffusivity. In fact, for *in vitro* bioreactor approaches, Lovett *et al.*[7] suggest that increased diffusivity is key to providing sufficient oxygen to seeded cells. Thus, with current capabilities lacking in the ability to produce an arterial–capillary–venous loop, effective permeability and diffusivity may be the best way to define scaffold mass transport characteristics (for more information on characterizing mass transport and diffusion, see **Chapter 3.309, Fluid Mechanics: Transport and Diffusion Analyses as Applied in Biomaterials Studies** in this volume).

Increasing efficacy of regenerative medicine scaffolds requires testing of specific hypotheses concerning how potential scaffold design targets affect tissue regeneration. By testing these design hypotheses, we can, theoretically, iterate until we hone in on the requirements for optimal regenerative medicine scaffolds. This iterative cycle, termed iterative scaffold engineering (ISE) would start with posing a set of scaffold design targets, proceed to designing scaffolds through material choice and hierarchical microstructure geometry, manufacturing the scaffolds according to design specifications, and finally evaluating the scaffolds using nondestructive imaging, bench tests, and *in vivo* testing (**Figure 1**).

ISE is a significant undertaking in itself, requiring multiscale computational design, biomaterial synthesis, multiscale manufacturing, biomaterial surface modification, nondestructive image-based evaluation, mechanical testing, *in vitro* cell testing, *in vivo* large functional animal testing, and ultimately, human clinical trials. It is beyond the scope of this chapter to discuss all aspects of ISE in detail. This chapter will largely focus on engineering the geometric/physical aspects of scaffolds (multiscale design, manufacturing, and evaluation) as opposed to the material aspects (biomaterial synthesis).

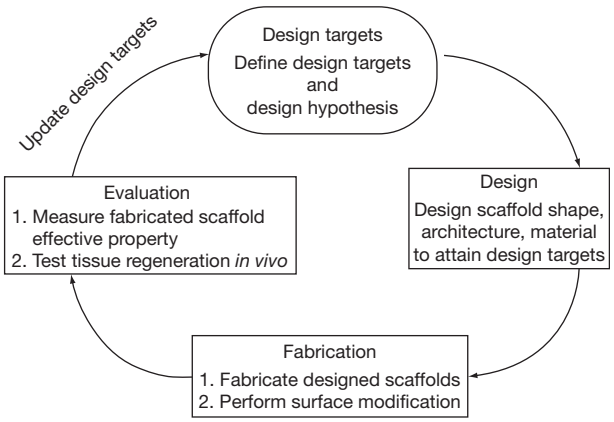

Figure 1 Iterative scaffold engineering cycle testing of scaffold parameters to determine optimal scaffold characteristics.

5.502.1.2. Choosing Effective Properties as Design Targets

Once effective properties are postulated as scaffold design targets, we need to specify what specific effective properties we should propose to govern the geometrical, functional, and tissue regeneration aspects of scaffold performance. Geometrically effective properties are the defect shape and volume determined by imaging data, as well as adjunct surgical fixation. Functional mechanical properties can be defined with appropriate constitutive models. Bone can be characterized as an anisotropic linear elastic material, while soft tissues are best characterized as isotropic or anisotropic nonlinear elastic or viscoelastic. Although a number of factors influence a scaffold's ability to enhance tissue regeneration, in this chapter, we will focus on physical characteristics and briefly touch upon biomaterial surface modification. The scaffold effective physical characteristics that most closely relate to tissue regeneration and biologic delivery are surface area/volume ratio, and mass transport. Surface area/volume ratio, also known as specific surface area, is related to cell–material interaction. Mass transport is not only related to the nutrient diffusion to and waste removal from cells within the scaffold, but can also define the ease or difficulty of cell migration and tissue ingrowth within the scaffold. Mass transport for both bone and soft tissues may be characterized using effective permeability and diffusion, although for soft tissues undergoing large deformation, both permeability and diffusion will be deformation-dependent. Thus, for the scaffold requirements of (1) maintaining/defining tissue defect volume, (2) providing temporary mechanical function, and (3) enhancing tissue regeneration, we can propose effective properties as design targets (**Table 1**).

Knowing if a proposed effective property design target is relevant, and more specifically, what magnitude is most appropriate, requires the iterative design testing proposed in ISE. Attaining design targets requires design variables or parameters that may be altered to reach the proposed targets. Most generally, design parameters for scaffolds are (1) the distribution of pores and material in three-dimensional (3D) space and (2) the choice of material(s) from which to fabricate the scaffold. The successful testing of design hypotheses for ISE then rests on developing computational schemes to manipulate these design parameters to achieve desired design targets, fabricating the resulting scaffold designs, and evaluating the results in both bench tests and *in vivo* models.

5.502.2. Hierarchical Computational Scaffold Design

The first step in ISE is actually designing the scaffold. Design includes both the external scaffold shape along with adjunct surgical fixation, and an internal porous architecture that can achieve the effective property design targets. Performing this design requires that the overall scaffold topology be represented computationally in a form for both analysis and manufacturing. Second, it requires that effective properties can

Table 1 Effective property design targets to fulfill scaffold requirements for shape filling, temporary mechanical function, and enhancement of tissue regeneration

Tissue	*Shape filling*	*Temporary mechanical function*	*Tissue regeneration and biologic delivery*
Bone	Segmented voxels within defect	Linear elasticity, E_{ijkl}	Diffusivity D_{ij} Permeability, K_{ij} Specific surface area, *SA*
Soft tissue	Segmented voxels within defect	Nonlinear elasticity, *W* Viscoelasticity, $G(t)$	Diffusivity, D_{ij} Permeability, K_{ij} Specific surface area, *SA*

E_{ijkl} denotes the fourth-order tensor of effective linear elastic constants, D_{ij} denotes a second-order tensor for effective diffusivity constants, K_{ij} denotes the tensor for effective permeability constants, SA denotes specific surface area (a scalar), *W* denotes nonlinear elasticity as an effective strain energy function, and $G(t)$ denotes a stress relaxation function for viscoelasticity.

be directly calculated from the porous architecture design to determine the relevant effective properties of a given architecture design.

5.502.2.1. Computational Representation of Hierarchical Scaffold Structure

Prior to performing any design operation, we must be able to represent complex 3D anatomy and hierarchical structure within a suitable data structure. Although parametric solids based on fundamental mathematical entities such as cylinders, spheres, etc., are widely used for engineering components, their use in anatomic biomaterial scaffold design is limited for two reasons. First, the tremendous complexity of anatomic structures frequently precludes representation by discrete mathematical formula. Second, the hierarchical nature of both tissues and porous biomaterial scaffolds makes it difficult to project solid geometry between different scales easily. A more natural computational representation of complex anatomy and hierarchical structure is voxel-based data structures, since they are generated directly from imaging modalities such as CT and MRI. Voxel data structures represent topology as a density distribution within a structured dataset, whose elements are isotropic or anisotropic cube structures. Each cube is identical; the only change is the density within the cube, with the aggregate density defining the topology. Although patient anatomy is represented by a single scalar value, it is straightforward to extend data representation in each cube to tensor fields such as the effective design targets in Table 1. Thus, anatomic defects of arbitrary 3D complexity can be represented using the same data structures.

Voxel datasets, in addition to being directly generated from patient imaging modalities, offer additional advantages for topology representation in hierarchical scaffold design. First and foremost, interpolation and boolean operations are straightforward using the image processing software noted in Section 5.502.1.1. Boolean operations are important for scaffold design, since we often design scaffold architecture separately from the anatomic scaffold design, and use boolean operation like intersection to place voxel datasets to different length scales. The length scales are matched using linear or cubic interpolation algorithms available in the image processing softwares noted in Section 5.502.1.1. Since boolean operations require features defined at the same length scales, it is necessary to interpolate anatomic voxel datasets to higher resolution equivalent to architecture datasets. Indeed, this equivalent feature requirement motivates the use of multiple image datasets to represent scaffold topology. Finally, voxel datasets are suitable and readily utilized as springboards to other data representations, including the direct calculation of surfaces for rapid manufacturing using marching cube algorithms and the direct conversion of voxel datasets into voxel finite element models for finite element analysis (FEA), topology optimization, and computational fluid dynamics (CFD).

5.502.2.2. Computing Effective Scaffold Properties Using Homogenization

Once we can represent scaffold architecture using voxel datasets, the next requirement is to compute the relationship of scaffold design parameters (basically, the distribution of material and pore in 3D space) to the resulting effective mechanical and mass transport design targets. Computing these scaffold structure–function relationships allows us to design for target effective properties by controlling scaffold architecture. To compute scaffold structure–function relationships, effective elasticity, permeability, and diffusivity properties must be calculated by solving the appropriate field equations at the architecture level and then averaging the results to determine the effective properties. These field equations include stress equilibrium for elasticity, creeping Stokes fluid flow for permeability, and local diffusivity for effective diffusivity.

Deriving structure–function relationships requires a mathematical theory that provides a consistent and rigorous derivation of the relationship between local and global scales. Homogenization is one such rigorously defined theory, that is specifically developed to analyze multiscale materials.[8,9] It has also been utilized to analyze multiscale tissue mechanics by our own group[10–12] and others.[13,14] Since 2000, our research group[15–21] has also applied homogenization theory as a means to analyze and design hierarchical tissue engineering scaffolds.

Homogenization theory assumes that a microstructured material is periodic, that is, the complete material volume can be made by repeating a basic unit mathematical cell in 3D space. The unit cell may be different at different locations in the material, allowing for heterogeneity. Homogenization theory addresses multiscale physics problems by first taking an asymptotic expansion of the relevant field variable as:

$$u_i^{\varepsilon} = u_i^0 + \varepsilon u_i^1 + \cdots \quad [1]$$

where u_i^ε is the total value of the field variable, u_i^0 is the average value at the global level, u_i^1 is the perturbation of the average value due to the presence of a microstructure, and ε is the ratio of the microstructure scale to the global scale, which is much less than 1. This field variable expansion is substituted with the associated gradient into the governing equations for elasticity, Stokes fluid flow, and diffusivity. By substituting the relevant field variable expansion and gradient into the governing equilibrium equation we obtain a microstructural equilibrium equation and a global equilibrium equation. These two scale equilibrium equations are linked by the effective physical property. For elasticity, we obtain the governing microstructural elasticity equation:

$$\frac{\partial}{\partial x_j^1} E_{ijkl} \frac{\partial \chi_k^{pq}}{\partial x_l^1} = \frac{\partial}{\partial x_j^1} E_{ijpq} \qquad [2]$$

For which χ_k^{pq} represent nine different microstructural displacements due to nine global unit strains and E_{ijkl} are the elastic properties of the base scaffold material. We can then directly calculate the effective elastic properties E_{ijkl}^{eff} as a function of base material elastic properties E_{ijkl} and the architectural arrangement of materials and voids in 3D represented by $\delta_{kp}\delta_{lq} - \frac{\partial \chi_p^{kl}}{\partial x_q^1}$ through the following integration over the microstructure:

$$E_{ijkl}^{\text{eff}} = \frac{1}{|V_{\text{micro}}|} \int_{V_{\text{micro}}} E_{ijpq} \left(\delta_{kp}\delta_{lq} - \frac{\partial \chi_p^{kl}}{\partial x_q^1} \right) \mathrm{d}V_{\text{micro}} \qquad [3]$$

Equation [3] thus gives us a direct mathematical way to compute the intuitive concept that effective scaffold elastic properties are determined by the base scaffold material elastic properties and the way these materials and pores are arranged in 3D space.

Similarly, for diffusion and electrical conductivity (which have the exact same form) we expand species concentration (for diffusion) or voltage (electrical conductivity) to obtain the following governing equation:

$$\frac{\partial}{\partial x_i^1} D_{ij} \frac{\partial \chi^p}{\partial x_j^1} = \frac{\partial}{\partial x_i^1} D_{ip} \qquad [4]$$

where χ^p represents local species concentration or voltage under three unit global concentration or voltage gradients. Again, we can directly calculate the effective diffusivity or electrical conductivity D_{ij}^{eff} by integrating the base scaffold diffusivity or conductivity D_{ij} times the quantity $\delta_{ip} - \frac{\partial \chi^p}{\partial x_j^1}$ that gives the architectural influence of material and pores arrangement in 3D space:

$$D_{ij}^{\text{eff}} = \frac{1}{|V_{\text{micro}}|} \int_{V_{\text{micro}}} D_{ip} \left(\delta_{jp} - \frac{\partial \chi^j}{\partial x_p^1} \right) \mathrm{d}V_{\text{micro}} \qquad [5]$$

Again, eqn [5] provides a mathematical computation for the concept that effective diffusivity (conductivity) depends on base scaffold material diffusivities (conductivities) and the way these materials and pores are arranged in 3D space.

A second effective mass transport property of interest is permeability. Permeability is defined by how easy or difficult it is for fluid to flow through a porous matrix. Thus, since we expect creeping flow, we solve Stokes flow at the microstructural level by expanding both the fluid pressure and velocity. This leads to the following equation that is solved to determine scaffold level pore fluid velocity under three unit pressure gradients:

$$\frac{\partial p^{1k}}{\partial x_i^1} - \frac{\partial}{\partial x_j^1} \left(\frac{\partial v_i^{0k}}{\partial x_j^1} \right) = e_i^k \qquad [6]$$

where p^{1k} is the internal pore pressure, v_i^{0k} is the average pore fluid velocity, and e_i^k represents three unit externally applied pressure gradients. The effective scaffold permeability K_{ik}^{eff} is then computed directly from the average pore fluid velocity as:

$$K_{ik}^{\text{eff}} = \frac{1}{\mu |V_{\text{micro}}^{\text{pore}}|} \int_{V_{\text{micro}}^{\text{pore}}} v_i^{0k} \mathrm{d}V_{\text{micro}}^{\text{pore}} \qquad [7]$$

where μ is the fluid viscosity and $V_{\text{micro}}^{\text{pore}}$ represents the pore volume occupied by fluid. It is interesting to note that permeability is only determined by the average pore fluid velocity and thus the 3D pore arrangement. Assuming the basic scaffold material is impermeable, effective scaffold permeability does not depend upon scaffold material.

The one effective design target that does not require the solution of a local field equation is specific surface area. This quantity is defined simply as the structural surface area divided by the total volume in which the structure exists. Surface area can most readily be calculated by generating an isosurface triangular facet from architecture voxel data, and then calculating the surface area from the resulting triangular mesh. Thus, we now have the capability to compute effective properties as design targets directly from voxel representations of scaffold architecture.

5.502.2.3. Bounds on Effective Design Targets

Although this section describes techniques by which we can calculate effective properties based on scaffold architecture, a number of questions remain regarding how effective properties are determined by scaffold architecture. A more important question is 'what are the possible range of effective properties that we can attain for a given amount of material?' The question relates to the absolute bounds that we can obtain on effective elasticity, permeability, diffusivity, and specific surface area for a given amount of material arranged in 3D space. If the bounds are rigorous, they define the range of effective properties attainable for a given amount of material, although realizing the actual design (discussed in **Section 5.502.2.4**) and actually fabricating the resulting design (discussed in **Sections 5.502.3.1** and **155.3.2**) remain significant hurdles.

The best known bounds regarding the relationship of volume fraction to attainable effective properties are the Voight and Reuss bounds, named after their respective developers. The Voight bound is known to be an absolute upper bound on attainable effective properties for a given volume fraction. This bound states that the effective property is equal to each individual material phase property; thus, for an effective tensor property, we have:

$$D_{ijkl}^{\text{eff}} = \sum_{n=1}^{N} v_f^n * D_{ijkl}^n \text{ for elasticity}$$

$$D_{ij}^{\text{eff}} = \sum_{n=1}^{N} \left(1 - v_f^n\right) * D_{ij}^n \text{ for mass transport} \qquad [8]$$

where D^{eff} with four indices denotes the effective elasticity tensor and with two indices, it denotes the effective diffusivity tensor, D^a with four indices v_f^a denotes the elasticity tensor of phase a and with two indices, it denotes the diffusivity tensor of phase a, and denotes the volume fraction (ranging between 0 and 1) of phase a. In the case of a two-phase material in which one phase is a solid and the other a pore, the effective elasticity is simply the volume fraction times solid phase elasticity and the effective diffusivity is simply one minus the volume fraction times the porous phase diffusivity (if one makes the assumption that diffusivity of the solid phase is zero). The Reuss bound is the complement of the Voight bound, with the inverse effective tensor properties weighted by volume fraction:

$$\left[D^{\text{eff}}_{ijkl}\right]^{-1} = \sum_{n=1}^{N} v_f^n * \left[D^n_{ijkl}\right]^{-1} \quad \text{for elasticity}$$

$$\left[D^{\text{eff}}_{ijkl}\right]^{-1} = \sum_{n=1}^{N} \left(1 - v_f^n\right) * \left[D^n_{ijkl}\right]^{-1} \quad \text{for mass transport} \qquad [9]$$

If any phase of a material or scaffold is zero, say, for example, zero elasticity for a pore or zero diffusivity for a solid, then the lower Reuss bound of any effective property is zero. This indeed holds for any bounds derived for porous materials. To illustrate, consider theoretically a collection of solid particles in a volume that are not connected. Even though the volume fraction is not zero, these particles could not carry any load and their effective elasticity would be zero. With regard to diffusion or permeability, we simply have to consider a closed cell (here cell is used in the sense of a cellular material as defined by Gibson and Ashby[22]; not a biological cell) structure where the pores are surrounded by solid walls, which will exhibit zero effective permeability and diffusivity.

Although the Voight bound is an absolute upper bound on effective properties, it is derived based on an idealized notion that the primary field variable (e.g., stress in elasticity) may be averaged in each phase solely based on the volume fraction in each phase, while the complementary field variable used to calculate energy (strain in elasticity) is constant across phases. Likewise, the Reuss bound is an absolute lower bound on effective properties because it assumes that the complementary field (strain in elasticity) variable may be averaged in each phase solely based on volume fraction, while the primary variable (stress in elasticity) is constant across phases. These conditions can only be approximated when the microstructure is as anisotropic as possible, which is when material is oriented as nonconnected fibers in one direction for elasticity or nonconnected pores in one direction for diffusivity and permeability (Figure 2). In other words, the red areas would be material fibers in Figure 2 for elasticity bounds while the red areas in Figure 2 would be pores for diffusivity/permeability bounds.

Indeed, if a homogenization calculation for elasticity is performed on Figure 2(b), assuming the red fibers are material, the effective elastic modulus is equal to the volume fraction times the elastic modulus of the base material, while the transverse effective elastic moduli are zero. Likewise, if we perform a homogenization diffusion analysis assuming the red fibers in Figure 2(b) are pores surrounded by material, the effective diffusion or permeability is equal to the volume fraction times the base diffusion, while the transverse diffusion

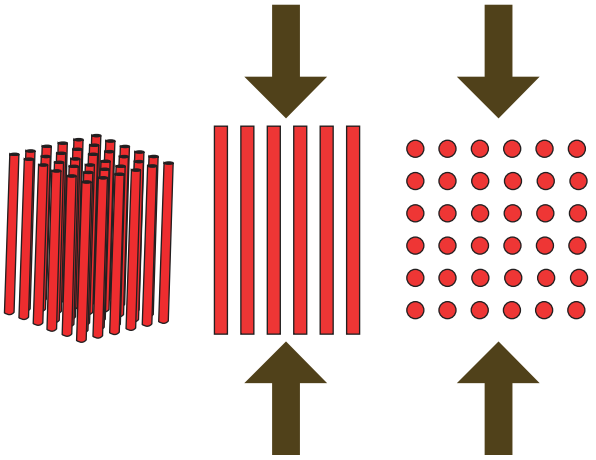

Figure 2 Example of anisotropic architectures that fulfill absolute Voight upper and Reuss lower bounds on effective properties. (a) Isometric view of a microstructure that satisfied Voight and Reuss bounds. (b) Fiber orientation parallel to axis of deformation/diffusion leads to Voight upper bound. (c) Fiber orientation perpendicular to axis of deformation/diffusion leads to Reuss lower bound. Note that fibers would be material for elasticity bounds while fibers would be pores for diffusivity/permeability bounds.

is zero. These structures represent the most anisotropic effective properties that are theoretically attainable.

Of course, structures such as that depicted in Figure 2 are not physically realistic for scaffold architectures. To withstand mechanical loading and provide shape deposition of tissue structures, scaffold architectures require material distributions along axes in 3D space. Once material is taken from the fiber direction and oriented across the fibers for elasticity (or conversely, pores are introduced perpendicular to the longitudinal axis, Figure 2(b)), we will obviously reduce the properties in the longitudinal direction along the fibers, and increase the properties in the transverse axes perpendicular to the fibers. Thus, any 'realistic' scaffold architecture will exhibit properties less than the upper bound completely anisotropic Voight prediction, and greater than the lower bound completely anisotropic Reuss prediction. Indeed, one can note that for many materials there is a wide spread between the Voight and Reuss bounds that can be realized by a wide variety of designed architectures.

At the opposite end of the spectrum from these maximally anisotropic structures are structures that demonstrate isotropic and cubically symmetric effective properties. For these structures, tighter bounds on effective elasticity and diffusivity have been obtained through the well known Hashin–Shtrikman bounds.[23] These bounds are derived using variational principles, and provide the most well-known bounds for effective isotropic elasticity and diffusivity. For a two-phase microstructure in which one of the phases is a void, the Hashin–Shtrikman bounds for isotropic (and cubic) effective diffusivity are:

$$D^{\text{eff}}_{ij} = \frac{2 - 2v_f D^{\text{pore}}}{2 + v_f} \qquad [10]$$

where D^{eff} is the effective diffusivity, v_f is the volume fraction of solid material, and D^{pore} is the intrinsic diffusivity of the

pore. The Hashin–Shtrikman bounds for elasticity (specifically bulk modulus) of a two-phase material consisting of a solid and void is:

$$K^{\text{eff}} = \frac{\left(\frac{3}{4}\right) v_f K^{\text{solid}} G^{\text{solid}}}{(1 - v_f) K^{\text{solid}} + \left(\frac{3}{4}\right) G^{\text{solid}}} \quad [11]$$

where K^{eff} is the effective bulk modulus, K^{solid} the bulk modulus of the solid material, G^{solid} the shear modulus of the solid material, and v_f is again the volume fraction of the solid material.

Deriving bounds on nonlinear elastic behavior is even more difficult than deriving bounds for linear elasticity. General Voight type bounds have been derived for general nonlinear elastic materials by Ogden[24] which state that the effective strain energy function for a porous nonlinear elastic material with one solid phase is bound by the volume fraction of material times the strain energy function of the base material:

$$W^{\text{eff}} = v_f W^{\text{solid}} \quad [12]$$

where W^{eff} is the effective strain energy function, v_f is the solid volume fraction, and W^{solid} is the strain energy function of the solid phase. The strain energy function depends on model constants and the right Cauchy deformation tensor that when differentiated with respect to the right Cauchy deformation tensor gives the second Piola–Kirchoff stress. Closer estimates for bounds on Neo-Hookean isotropic strain energy functions have been derived by Lopez-Pamies and Idiart,[25] but only for 2D porous elastomers.

No definitive analytical bounds are known for specific surface area as an effective property design target. The best guidelines come from work on bone-specific surface area in relationship to bone remodeling. Martin[26] first proposed a specific surface area curve versus volume fraction for bone tissue. Fyhrie *et al.*[27] later proposed a mathematical model fit for cancellous bone-specific surface area versus volume fraction in the form:

$$SA^{\text{eff}} = a_1 v_f (1 - v_f) \quad [13]$$

where SA^{eff} denotes the effective specific surface area, v_f is the material volume fraction, and a_1 is a model constant fit to experimental data. The expression in eqn [7] gives a bell shaped curve with a maximum specific surface area at a volume fraction of 0.5. Note that when there is no material ($v_f = 0$) or there is complete material ($v_f = 1.0$), the specific surface area by default becomes zero. In this chapter, a generalization of the Fyhrie model (eqn [7]) is proposed for general porous materials. This proposed model has the form:

$$SA^{\text{eff}} = a_1 v_f^{a_2} (1 - v_f)^{a_3} \quad [14]$$

where now a_2 and a_3 are additional model constants that dictate the shape of the curve relating specific surface area to volume fraction, and a_1 is a model constant that determines the maximum amount of surface area than can be contained within a given volume. This constant is scale dependent, as smaller the features in the structure, the greater is the surface area that we can generate within that volume. To ensure a physically realistic positive surface area, we restrict a_1, a_2, and a_3 to be strictly positive. If we further specify that a_1 be equal to the maximum of the specific surface over the volume fraction, then we can ensure that SA^{eff} will be normalized to a maximum of 1 as:

$$SA^{\text{eff}}_{\text{norm}} = \frac{1}{\max\left(v_f^{a_2}(1 - v_f)^{a_3}\right)} v_f^{a_2} (1 - v_f)^{a_3} \quad [15]$$

The maximum feasible upper bound is that all microstructures will produce a normalized surface area of 1, while the minimum lower bound consistent with results proposed by Fyhrie *et al.*[27] is that all microstructures will produce a surface area of 0, except at a volume fraction of 0.5. Based on the normalized specific surface area (eqn [9]), the absolute upper bound can be written using two Heaviside functions, denoted $H(x)$, as:

$$SA^{\text{upper}}_{\text{norm}} = H(1) - H(0) \quad [16]$$

which gives a step function that has value 1 between 0 and 1, and value 0 elsewhere. The absolute lower bound is given by a sequence of Gaussian functions, which in the limit as a goes to zero (a is much less than 1) and reaches to the Dirac Delta function:

$$SA^{\text{lower}}_{\text{norm}} = \frac{1}{M} \frac{1}{a\sqrt{\pi}} e^{-\frac{(v_f - 0.5)^2}{a^2}} \Rightarrow M = \text{Max}\left(\frac{1}{a\sqrt{\pi}} e^{-\frac{(v_f - 0.5)^2}{a^2}}\right) \quad [17]$$

Thus, based on previous mathematical bounds and physical reasoning, we can establish upper and lower bounds for all effective porous scaffold property design targets postulated in Table 1 for scaffold mechanical function and tissue regeneration performance, as summarized in Table 2.

Normalized lower and upper bounds for all effective mechanical and mass transport properties are plotted in Figure 3.

The absolute bounds for normalized specific surface area are plotted in Figure 4 along with the Fyhrie model of specific surface area for human cancellous bone.

The bounds given in Table 1, Figures 3 and 4 represent the absolute lower and upper bounds on effective properties that can be obtained for multiphase materials in which one phase is void. The scaffold base material elastic properties modulate the upper bound for effective elastic properties, but the lower bound will always be zero. Scaffold architecture design is the prime determinant of what effective properties can be obtained within the bounds. The bounds tell us, before the design and manufacturing process begins, what effective properties are theoretically attainable. As such, these bounds provide guidelines for designing scaffolds. What effective properties can be attained, and thus our ability to test how effective properties influence tissue regeneration, depends on computational methods for designing architecture and manufacturing methods that can actually make the designed architectures.

5.502.2.4. Designing Scaffold Architecture

Theoretically, any combination of effective properties will map into a specific architecture, just as the upper Voight bound and the lower Reuss bound can be mapped back into the parallel fiber architectures shown in Figure 2. However, there are no computational methods currently proven to map directly into a specific architecture for an arbitrary set of

Table 2 Proposed absolute lower and upper bounds for mechanical, mass transport, and surface area of porous microstructures

Effective property bounds	*Mechanical function: elasticity*	*Mass transport: diffusivity; permeability*	*Surface area (normalized)*
Bone: lower bound	0	0	$\frac{1}{M}\frac{1}{a\sqrt{\pi}}e^{\frac{-(v_f-0.5)^2}{a^2}}$, for $a \ll 1$
Bone: upper bound	$E^{\text{eff}}_{ijkl} = \sum_{n=1}^{N} v_f^n * E^n_{ijkl}$	$D^{\text{eff}}_{ij} = \sum_{n=1}^{N} (1-v_f^n) D^n_{ij}$ $K^{\text{eff}}_{ij} = \sum_{n=1}^{N} (1-v_f^n) K^n_{ij}$	$H(1)-H(0)$
Soft tissue: lower bound	0	0	$\frac{1}{M}\frac{1}{a\sqrt{\pi}}e^{\frac{-(v_f-0.5)^2}{a^2}}$, for $a \ll 1$
Soft tissue: upper bound	$W^{\text{eff}} = \sum_{n=1}^{N} v_f^n * W^n$	$D^{\text{eff}}_{ij} = \sum_{n=1}^{N} (1-v_f^n) D^n_{ij}$ $K^{\text{eff}}_{ij} = \sum_{n=1}^{N} (1-v_f^n) K^n_{ij}$	$H(1)-H(0)$

Note that v_f with superscript n refers to the volume fraction of phase n within a material, and that one phase of the material is a void (pore). $H(*)$ denotes the Heaviside function. M for the lower bound surface area denotes the maximum of the Gaussian sequence as specified in eqn [11].

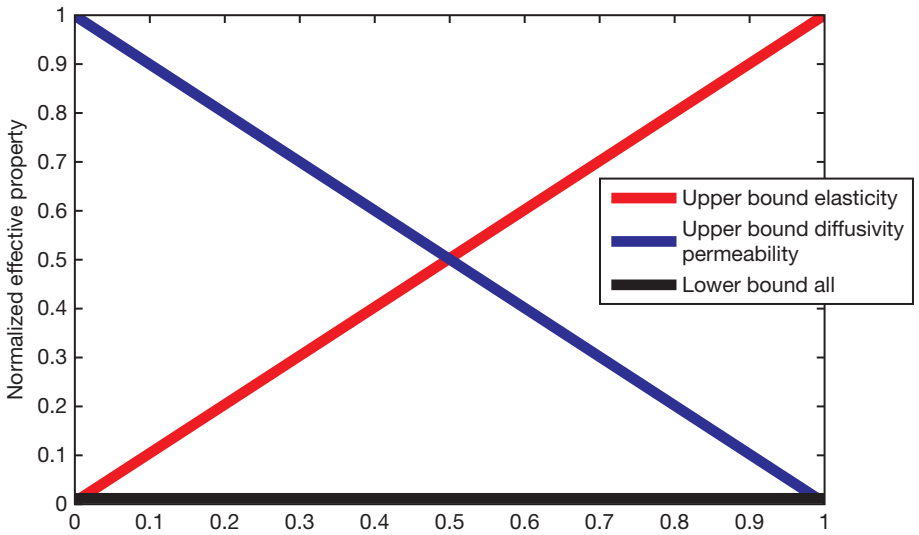

Figure 3 Normalized lower and upper bounds for effective elasticity and mass transport properties plotted versus volume fraction. Normalized upper bound elasticity (red solid) versus volume fraction in addition to lower and upper bound diffusivity and permeability (blue solid) versus volume fraction. Lower bounds for all effective properties are zero for porous materials denoted by the solid black line. (b) Normalized lower (dashed red) and upper (solid red) for specific surface area.

feasible (i.e., within defined bounds, **Section 5.502.2.3**) effective properties. Broadly, we can define computational methods for designing scaffold architecture as forward scaffold design methods (FSDM)[17] and inverse scaffold design methods (ISDM).[18,19,21,28–34] Both methods utilize the homogenization methods defined in **Section 5.502.2.2** to compute effective properties from a given voxel representation of architecture. In addition, both methods use a base unit mathematical cell that is periodically repeated in 3D space to create the final architecture. Note that this does not preclude heterogeneous or functionally graded architectures, as these are created by simply utilizing different unit cells.

In the forward method, we a priori design an architecture and then compute the effective properties from this designed architecture using eqns [3]–[7]. This is often done using a range of architectures from similar geometric families, for instance, interconnecting cylinders or interconnecting spheres. Hollister *et al.*[17] utilized this approach to design craniofacial scaffolds. In this approach, voxel-based data structures were generated based on geometric equations for cylinders, spheres or even wavy fiber structures. Such structures were created with a range of parameters, for instance, spherical diameter that could be modified to cover a range of volume fractions from 0 to 1. Effective properties computed for these structures using homogenization theory could then fit to polynomial functions. Thus, within this restricted topology, design parameters could be picked to fit a limited range of desired effective properties. The advantage of the FSDM is that architectures can be designed a priori to have manufacturable feature sizes (discussed in **Section 5.502.3**), as well as being targeted to

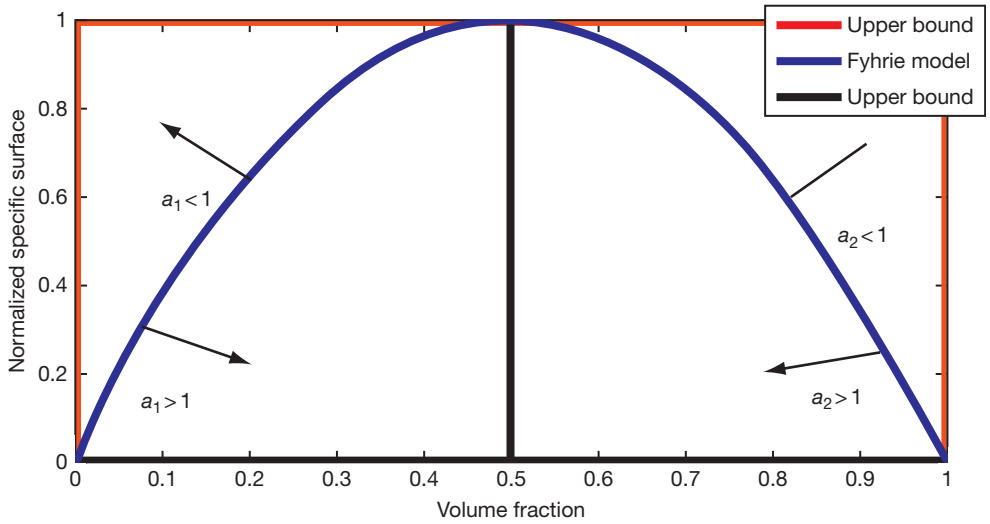

Figure 4 Normalized specific surface area bounds plotted versus volume fraction. Upper bound is plotted in red, lower bound in black, and the Fyhrie model is plotted in blue. The model coefficients a_1 and a_2 refer to the model of eqn [15]. As the coefficients increase from 1 the model in each half decreases towards the lower bound, while as the coefficients decrease from 1 the model increases toward the upper bound.

have more general changes for using heuristic design rules based on geometric models for cellular solids.[22] The limitations of the FSDM is that targeting specific effective properties becomes a trial and error approach.

The inverse method, as the name implies, starts from a set of desired properties and then attempts to calculate an architecture that fits these properties. This inverse homogenization problem was first formulated by Sigmund in 1994.[30] In this approach, an optimization problem is formulated in the general form of:

$$\begin{aligned}&\underset{v_f}{\text{Min}} \sum_{n=1}^{N}\left\{A^n_{ij(kl)} - \left[A^n_{ij(kl)}\right]^{\text{target}}\right\}^2\\ &\text{subject to :}\\ &B^n_{ij(kl)} \le \left[B^n_{ij(kl)}\right]^{\text{bound}}\\ &\int_{Vol} v_f \mathrm{d}Vol \le Vol^{\text{bound}}\\ &0 \le v_f \le 1\end{aligned} \qquad [18]$$

where $A_{ij(kl)}$ denotes the second (diffusion or permeability) or fourth rank (elasticity) tensor representation of effective property whose difference from a target value is minimized, $B_{ij(kl)}$ denotes a tensor whose value is constrained to be less than a bound value, Vol^{bound} is a bound on the total amount of material that may be used, and v_f is the volume fraction of material. Since optimization problems are inherently nonlinear (even if the effective target properties are linear) we must specify a starting material distribution. The chosen iteration algorithm (in many cases, the method of moving asymptotes, developed by Svanberg[35] is used) then sequentially updates the volume fraction in each voxel element of the mesh. At each step, the current material distribution, which defines the 3D scaffold architecture, is utilized in eqns [3]–[7] to solve the local homogenization equations in order to calculate effective properties. This process is repeated until a final optimized architecture is created.

Such inverse approaches could theoretically generate the full range of architectures to cover the range of effective property bounds. However, inverse approaches (in addition to forward approaches) are limited in general by the assumption of a single scale of architecture if a binary material/void solution is sought. In general, the unit cell volume typically covers a physical size scale of 0.5–3 mm. Within this volume, a typical voxel/element discretization may range up to 50 elements on a side, for a voxel resolution of 0.01 mm or 10 μm, due to computing limits for the nonlinear problem that may require up to 100 or more iterations. Thus, the minimum material feature that can be resolved is likely to be 2–3 voxel lengths or 20–30 μm. Beyond computing, most manufacturing techniques capable of creating controlled architectures (i.e., solid-free-form fabrication (SFF) techniques), are limited in resolution to features sizes above 100 μm. Because of both these computing and manufacturing limitations, inverse (and forward) design methods are realistically limited to one scale materials. Achieving structures that cover the complete range of possible effective properties requires architectures with multiple scale resolution, as nature itself shows in the construction of biologic tissues.

Examples of inverse scaffold design method (ISDM) for multiphysics problems (i.e., combined mass transport and mechanical property design targets) were presented by our group.[19] In this case, the architecture was designed to achieve the desired effective elastic and diffusivity properties simultaneously with a tight constraint on the range of volume fraction (typically $v_f \pm 2\%$):

$$\begin{aligned}&\text{Min } w_1\left(\frac{K^H}{K^*}-1\right)^2 + w_2\left(\frac{D^H}{D^*}-1\right)^2 + w_3 f_{\text{cubic}}\\ &\text{subject to } v_f^{\text{lower}} \le v_f \le v_f^{\text{lower}},\\ &0 < v_f(x_i) \le 1\end{aligned} \qquad [19]$$

where K^H denotes the homogenized (effective) bulk modulus, K^* denotes the target bulk modulus, D^H denotes homogenized (effective) bulk diffusivity, D^* denotes target diffusivity, w_i are

weighting functions, v_f denotes overall material volume fraction, $v_f(x_i)$ denotes the material volume fraction within a given voxel element, and the superscripts lower and upper denote the lower and upper bound on the overall volume fraction. The function $f3$ denotes a constraint that the effective elasticity has cubic symmetry and is defined as:

$$f_{\text{cubic}} = \left(\frac{E^{\text{H}}_{2222}}{E^{\text{H}}_{1111}} - 1\right)^2 + \left(\frac{E^{\text{H}}_{3333}}{E^{\text{H}}_{2222}} - 1\right)^2 + \left(\frac{E^{\text{H}}_{1111}}{E^{\text{H}}_{3333}} - 1\right)^2 + \left(\frac{E^{\text{H}}_{2233}}{E^{\text{H}}_{1122}} - 1\right)^2 + \left(\frac{E^{\text{H}}_{1133}}{E^{\text{H}}_{2233}} - 1\right)^2 + \left(\frac{E^{\text{H}}_{1122}}{E^{\text{H}}_{1133}} - 1\right)^2 + \left(\frac{E^{\text{H}}_{1313}}{E^{\text{H}}_{2323}} - 1\right)^2 + \left(\frac{E^{\text{H}}_{1212}}{E^{\text{H}}_{1313}} - 1\right)^2 + \left(\frac{E^{\text{H}}_{2323}}{E^{\text{H}}_{1212}} - 1\right)^2 \quad [20]$$

where E^{H} are the nine independent nonzero components of the effective elasticity tensor. Essentially, eqn [20] requires that the normal modulus related components are equal, the shear modulus related components are equal, and the Poisson's ratio/modulus components are equal to enforce cubic symmetry.

Kang *et al.*[19] demonstrated that the simultaneous elasticity/diffusion ISDM could produce architectures with different elasticity/diffusion coefficients that were near theoretical cross-property bounds (Figure 5).

An important point to note from Figure 5, which applies to ISDM approaches in general, is that predictions of distinct single scale architectures with binary material/void structures are generally predicted near the upper cross-property bounds. When ISDM is used to predict architectures within the cross-property bounds away from the boundaries, more grey material (in between solid material and void) is predicted. This indicates that the algorithm is predicting material of intermediate density that cannot be represented by single scale architectures, but require microstructures of multiple scales. Such multiple scale microstructures occur naturally in biological tissues, but are very difficult to realize in computational design, and especially in manufacturing.

5.502.2.5. Integrating Hierarchical Design

Once the scaffold anatomic design or scaffold envelope with fixation is defined using methods of Section 5.502.2.1 and the scaffold architecture has been defined using the methods of Sections 5.502.2.2 and 5.502.2.4, these two scales must be integrated to complete the final scaffold design. Using the image-based design techniques described by Hollister and colleagues,[15–18,21,36–38] integration of the two design scales is readily achieved by interpolating the envelope design represented in voxel format to the same resolution as the architecture design in voxel format. After interpolation, the voxel design datasets are combined using Boolean operations. Density values in the scaffold envelope design dataset serve as flags to locate density values from the appropriate architecture design database. In this way, the architecture topology represented by voxel density values is substituted into the appropriate location. Figure 6 illustrates this integrated design process for a mandibular reconstruction scaffold.

5.502.2.6. Hierarchical Scaffold Design: Summary

In summary, scaffold design techniques must account for the 4Fs of scaffold engineering: Form, Fixation, Function, and Formation. Form and Fixation are dictated by patient defect anatomy, and therefore, require the ability to process and design directly from CT or MRI image data at scales of multiple millimeters and larger. Function and mass transport aspects of Formation can be characterized by effective elastic, permeability, diffusivity, and specific surface properties. These effective properties are determined at the same scale as characteristics of the 'Form' level of

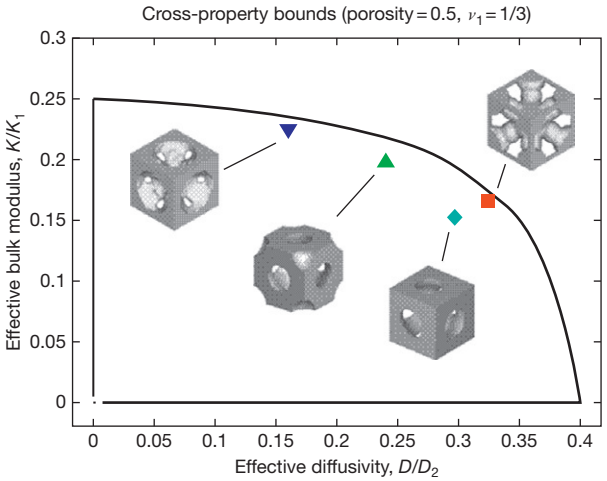

Figure 5 Representative architectures designed using the simultaneous elasticity/diffusion inverse scaffold design method approach by Kang *et al*. Note the wide variations in architecture that produce the different effective properties. Reproduced from Kang, H.; Lin, C. Y.; Hollister, S. J. *Struct. Multidisciplinary Optim.* (in press), with permission from Springer-Verlag.

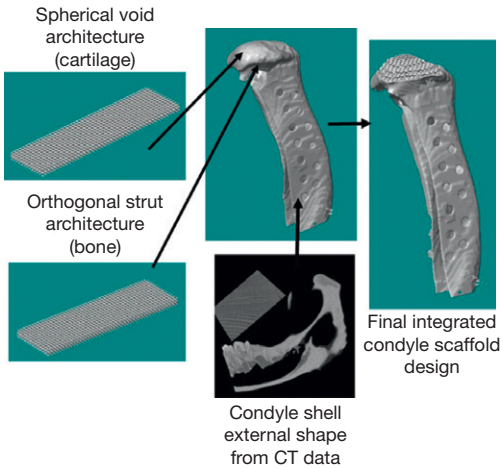

Figure 6 Schematic of hierarchical scale design integration process. (a) Voxel datasets representing heterogeneous designed architecture for different global regions. (b) Design of scaffold envelope including surgical fixation to surrounding host tissue from CT data. (c) Result of boolean intersection between architecture design datasets from (a) and scaffold envelope design from (b) to create the final scaffold.

design (multiple millimeters or larger), but by architectural features at the scale of 0.1–1 mm. In addition to effective mass transport and mechanical properties, formation is determined by growth factors and extracellular matrix proteins coupled to architecture features through surface modification, typical at scales of single microns or nanometers. Incorporating all these features requires both a data structure and a mathematical model that can represent multiple structural levels. Voxel-based methods are a natural method to represent hierarchical data. Homogenization theory provides a natural mathematical methodology to compute effective properties directly from architectural features. Voxel-based homogenization methods together provide a means to compute desired effective mechanical, mass transport, and specific surface properties for any anatomical defect. Both FSDM and ISDM can be used to directly design scaffold architecture to achieve desired effective properties. Finally, composite bounds give initial guidance as to the range of effective properties that can be expected even before computational design is performed.

5.502.3. Fabricating Designed Scaffolds

There are numerous techniques to fabricate scaffolds using both synthetic materials and natural extracellular matrix (for a review see Taboas *et al.*,[39] Hollister,[15,40] Hutmacher,[3,41] Hutmacher *et al.*,[42] Sachlos and Czernuszka[43]). These techniques include porogen leaching, electrospinning, gas foaming, emulsion, super critical fluid, and SFF. All these techniques offer advantages and disadvantages with regard to architecture feature size, control over architectural features, flexibility of use with different materials, and cost. In addition, these techniques can be combined to increase fabrication flexibility.[39,44] However, controlled architectures designed to achieve target effective properties (as in Figures 5 and 6), can only be fabricated using SFF techniques. SFF covers a broad range of technologies that build scaffolds (or any complex 3D structures) on a layer-by-layer basis using a variety of physical means including direct nozzle deposition, spraying chemical binders on material powders, sintering powders by laser, and photopolymerization. A schematic representation of different SFF processing methods is shown in Figure 7.

Sacrificial material or supports are used to hold hanging material in position. Furthermore, a design file, most commonly based on the STL file format that represents topology by triangular surface facets, directs material distribution in the layer. SFF scaffold building approaches can be categorized as direct or indirect.

5.502.3.1. Direct Solid-Free-Form Fabrication

Direct SFF means that the biomaterial of interest is built on the SFF system directly. Since each SFF method uses a different physical technique to process material, each biomaterial must be specifically adapted to each different machine. For example, stereolithography (SLA) techniques require materials in a form of polymerizable liquid resin that can be photo-cross-linked by ultraviolet (UV) light.[45] Selective laser sintering (SLS) techniques require materials that can be processed in powder form having particle sizes <125–150 μm[46,47] that have melting temperatures between 50 and 150 °C. 3D printing technologies also require particle sizes <150 μm that can be bound using specific chemical binders. Nozzle-based systems are more forgiving in their material requirements, mainly requiring materials that have low enough viscosity such that they can be dispensed under appropriate temperature and pressure, while having sufficient viscosity to maintain form after deposition. For ceramics and metals, this requires a slurry with appropriate viscosity. For polymers, this may require dissolution in a solvent. For some special nozzle-based systems such as fused deposition modeling, the material may have to be processed in a filament that can be fed into the system. These requirements for direct SFF manufacturing have two significant impacts on scaffold fabrication and attainable effective properties. First, it is obvious that the range of biomaterials that can be manufactured by direct SFF is limited, and that developing the means to process even one material, let alone a range of materials, for direct SFF requires significant effort. Second, and less obvious, is the fact that the physical processing method itself will determine the properties of the base material (both mechanical and mass transport), which in turn will affect the effective properties as defined in eqns [2]–[12].

SLA techniques have been primarily utilized with poly(propylene fumarate) (PPF) polymer, a degradable polyester made by synthesis of diethyl fumarate (DEF) with propylene glycol. PPF is created as a liquid resin by dissolving PPF in DEF, and adding bisacrylphosphrine oxide (BAPO) as a photoinitiator.[45] Different mixtures of PPF, DEF, and BAPO change the viscosity and molecular weight of the resulting liquid, thus affecting the scaffold base material properties and fabrication resolution, both again affecting the resultant effective properties. Using a commercial viper SLA system, Lee *et al.*[45] found that different ratios of PPF, DEF, and BAPO led to a base PPF compressive modulus ranging from ~20 to 140 MPa, with standard deviations ranging from 4 to 41% of the mean. Interconnected cubic and hexagonal pore scaffolds were fabricated using this technique, with a strut thickness of 300 μm and pore sizes ranging from 446 to 913 μm. This results in an effective compressive moduli 14–40 MPa, with standard deviation ranging from 6% to 17.5% of the mean. Thus, the physical material makeup created larger variability in properties than the fabrication process. Lee *et al.*[48] (a different group) introduced a customized microstereolithography with smaller laser beam spot size capable of building scaffolds with strut sizes of 120 μm and pore sizes of 250 μm. They reported base compressive modulus of 780 MPa, with a standard deviation of ~220 MPa, 28% of the mean. Effective compressive modulus ranged from 200 to 580 MPa, with standard deviations ranging from 6 to 45% of the mean.

SLS and selective laser melting have been used to manufacture materials and scaffolds from biomaterials that can be processed into the appropriate particle size range (<125–150 μm) with an appropriate melting temperature. For tissue engineering, this has mainly focused on polycaprolactone (PCL), polyetheretherketone (PEEK), PCL/hydroxyapatite (HA) composites, and titanium. Our group demonstrated the capability to fabricate designed PCL scaffolds with microstructures similar to those presented in Section 5.502.2 using laser sintering.[38,46,49] Pore sizes ranging from 1 to 2 mm and strut sizes ranging from 1 to 1.5 mm were achieved. Solid specimens had compressive moduli ranging from 120 to 317 MPa, with standard deviations

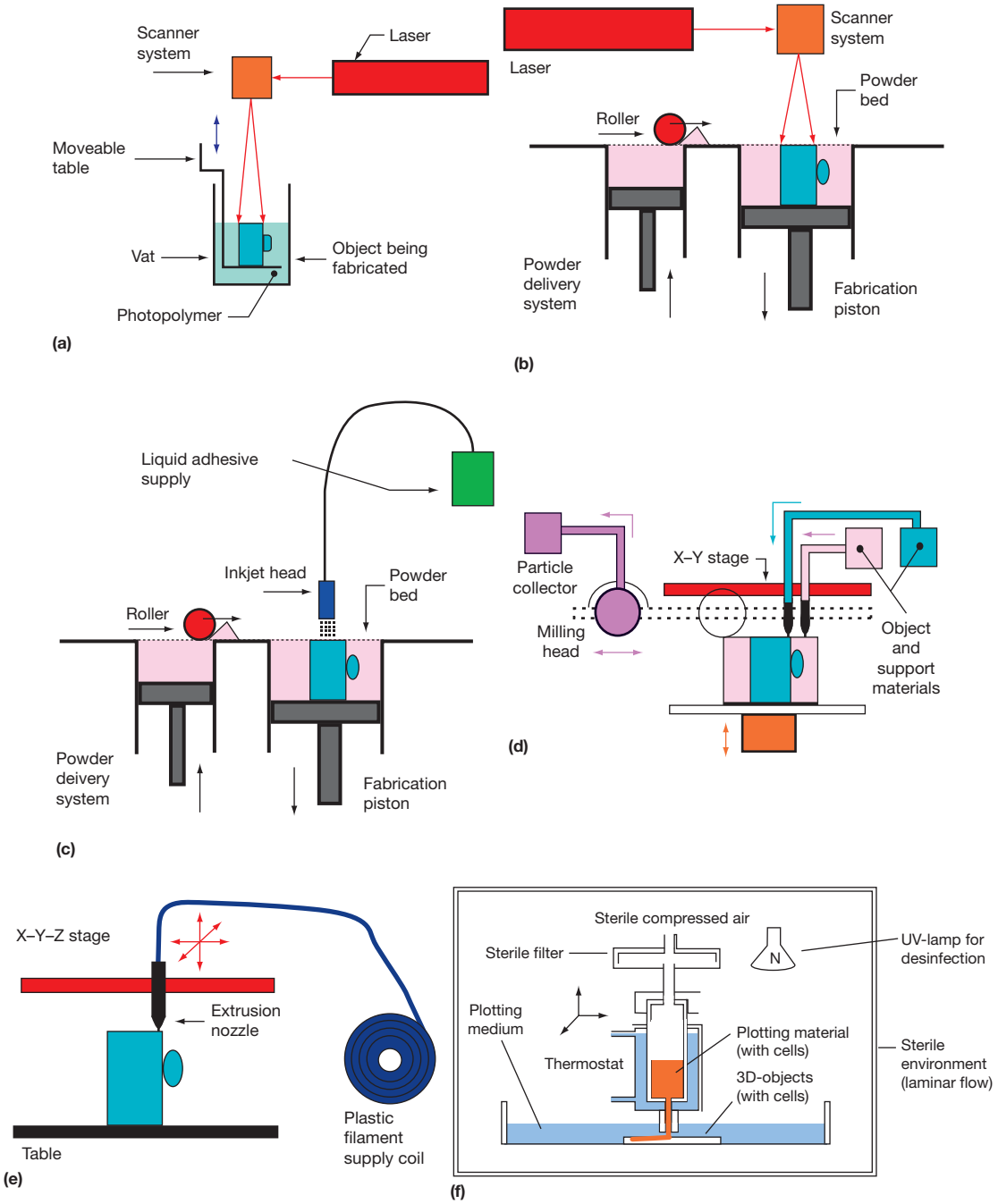

Figure 7 Schematic of solid-free-form fabrication technologies used to build biomaterial scaffolds. (a and b) Laser-based processing systems that either photopolymerize liquid (stereolithography) or directly sinter material particles together (laser sintering). (c and d) Printing-based systems that print by directly printing chemical binder onto powdered materials (3D printing) or by directly printing wax (Wax-based printer). (e and f) Nozzle-based systems that deposit material from a nozzle (fused deposition modeling) or deposit material in solvent through a syringe. Reproduced from Hollister, S. J. *Nat. Mater.* **2005**, *4*, 518–524, with permission from Nature Materials.

from 1 to 10% of the mean. For porous scaffolds with porosity ranging from 37 to 55%, effective compressive moduli ranged from 52 to 65 MPa with standard deviations ranging from 3 to 6% of the mean. Williams *et al.* also performed homogenization analysis for the scaffold designs, showing an R^2 correlation of 0.56 between computational and experimental results. This was one of the first instances of being able to accurately predict actual manufactured scaffold effective properties from computational designs. Cahill *et al.*[50] also performed a study comparing finite element predictions of PCL effective moduli to experimental measures. They were able to manufacture scaffolds, 659 μm pores and 431 μm struts. Solid PCL had a compressive modulus of 47 MPa, with a standard deviation that was 10.6% of the mean. PCL scaffolds had a

compressive modulus of 6 MPa, with a standard deviation that was 15% of the mean. Cahill *et al*. noted finite element predictions of modulus were 67% different than experimental measures, likely due to micropores and surface roughness artifacts from the manufacturing process. Chua, Leong, and colleagues also demonstrated fabrication of PCL solid discs from different materials[47,51,52] in addition to scaffolds.[53] Wiria *et al*.[47] reported compressive moduli for PCL/HA composites ranging from 33 to 102 MPa, dependent on the ratio of the composite phases. Standard deviations ranged from 8 to 18% of mean values. Yeong *et al*.[53] reported scaffolds with porosity ranging from 48 to 74%, with resulting compressive moduli ranging from 5 to 18 MPa.

Nozzle-based techniques have become widely adapted to directly build a range of scaffolds from ceramics to polymers. These systems include both commercial systems and custom-built systems. Wagoner-Johnson and colleagues[54–57] developed a micro-robotic ceramics slurry deposition techniques to produce 3D scaffolds by laying down rods of HA. By further incorporating 2–8 μm diameter polymethylmethacrylate (PMMA) beads that were burnt out after sintering, Wagoner-Johnson and colleagues were able to create ceramics scaffolds with two scale porosity. They determined effective compressive moduli ranging from 670 to 1240 MPa, with standard deviations ranging from 7 to 49% of the mean. Hutmacher, Teoh, and colleagues [3,58–60] developed a fused deposition modeling approach to fabricate PCL and PCL/TCP composite scaffolds to be used for craniofacial reconstruction and spine fusion. Zein *et al*.[60] fabricated PCL scaffolds with compressive moduli ranging from 42 to 77 MPa, with standard deviations ranging from ~7 to 11% of the mean. van Blitterswijk, Woodfield, Malda, Moroni, and colleagues[44,61–68] have done a substantial amount of work on fabricating copolymer polyethyleneoxide-terephtalate (PEOT) and polybutyleneterephtelate (PBT), as well as titanium scaffolds using a nozzle deposition system. Woodfield *et al*.[66] varied the spacing of deposited struts, creating different architectures for a narrow range of porosity between 60 and 87%. They measured equilibrium moduli ranging from 0.1 to 2.5 MPa, with standard deviations ranging form 15 to 40% of the mean. These equilibrium moduli covered the range of measured articular cartilage equilibrium moduli. Moroni *et al*.[63] performed an elastic FEA similar to a homogenization analysis to compute effective elastic properties for comparison to those measured from nozzle fabricated scaffolds. They found dynamic moduli ranging form 0.46 to 13.49 MPa, with standard deviations ranging form 17 to 81% of the mean. Effective elastic modulus calculations matched experimental data within 15% for most scaffold architectures.

5.502.3.2. Indirect Solid-Free-Form Fabrication

Although direct SFF provides significant advantages in terms of reproducibly building a large number of scaffolds, it presents challenges to implement as a platform for fabricating a range of biomaterials. SLA and SLS techniques have very specific material requirements to allow processing and often require significant quantities of material (in the 0.5–2 kg range) in order to build parts. Given the great expense of many polymeric biomaterials, it is often difficult to fund an experimental study using such techniques. Nozzle-based systems allow a broader range of materials, but there is still a significant effort required to adapt a given biomaterial to a nozzle-based system, whether it is fine tuning the material viscosity in slurries or solvents, or processing the material into a filament. In addition, nozzle-based systems have greater restrictions in terms of the final shapes of both pores and struts that can be manufactured for the resulting scaffolds.

Due to these limitations, many researchers desiring the architecture control provided by SFF but also desiring the capability to build from a wider range of biomaterials have turned to indirect SFF methods. Indirect SFF is so named because the biomaterial scaffold is not built directly on the SFF system. Instead, a mold is built on the SFF system into which a biomaterial is then cast, with the mold being removed using a lost wax technique (**Figure 8**).

Using the indirect SFF method, research groups have been able to fabricate scaffolds for a wide range of materials including HA, PCL, poly(lactic-*co*-glycolic acid) (PLGA), polyoctane diol citrate (POC), polyglycerol sebacate (poly(glycerolsebacate), PGS), and collagen, a much broader range of materials than have been built using direct SFF.

Chu *et al*.[69] presented one of the first reports of indirect SFF to create 40% porous HA scaffolds, which had a compressive modulus of 1400 MPa, and compressive strength of 30 MPa. Standard deviations for compressive modulus were 28.5% of the mean. Wilson *et al*.[70] used a similar inverse SFF technique in which a ceramic slurry was drawn into a mold fabricated using SFF, but did not present effective property data. Our group[39] generalized the inverse SFF technique to create polymer, ceramics, and polymer/ceramics composites. The inverse SFF was also combined with traditional porogen leaching and emulsion techniques to create hierarchical pore structures. We have further extended the inverse SFF techniques[71–74] to build a variety of degradable polymers including PCL, POC, and PGS. We then characterized the effective permeability, elastic, and nonlinear elastic properties of these scaffolds relative to the computationally designed properties. Kemppainen and Hollister[74] fabricated 3D PGS scaffolds under different curing times and molar ratios of glycerol to sebacic acid, measuring the nonlinear elastic properties and tangent moduli. We found that increased curing time and higher sebacic acid to glycerol ratios increased the nonlinear elastic response. We also found that effective elastic moduli calculated by homogenization matched closely with experimental tangent moduli (0.57 MPa experimental vs. 0.6 MPa computational), and that tangent moduli ranged from 0.03 to 1.13 MPa. The standard deviation was 42% of the mean. Jeong and Hollister[71] fabricated 3D designed porous POC scaffolds using image-based design methods and inverse SFF. We found that increasing the scaffold porosity not only decreased the tangent moduli, but also decreased the nonlinearity of the elastic response, as could be predicted by the nonlinear elastic bounds given in **Table 2**. Standard deviations in tangent compressive moduli ranged from 12 to 49% of the mean. We also measured effective scaffold permeability, which ranged 0.54×10^{-6} (32% porosity) to 5.24×10^{-6} $m^4\,Ns^{-1}$ (62% porosity) with standard deviations ranging from 7 to 22 of the mean. Jeong and Hollister[72] also fabricated PCL, PGS, and POC scaffolds of the same architecture using inverse SFF to compare the influence of scaffold material

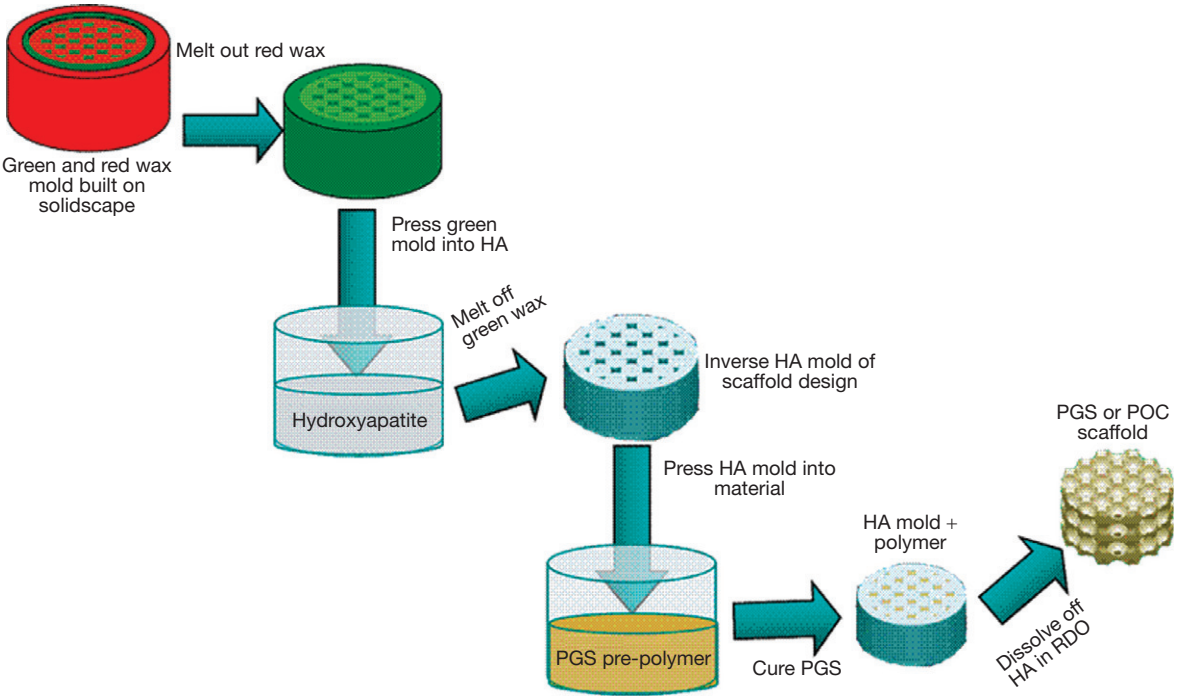

Figure 8 Schematic of indirect solid-free-form fabrication process for manufacturing 3D polymeric scaffolds. A wax mold is built on a 3D printing system. Hydroxyapatite is cast into the mold, and the wax is removed. The HA second mold is then pushed into the pre-polymer, which is then cured. The HA is removed by decalcification.

on effective properties and cartilage regeneration. As expected, PGS and POC as elastomers exhibited nonlinear elastic behavior with tangent moduli at 10% strain of 0.13 MPa for POC and 0.19 MPa for PGS. Standard deviations were 31% for POC and 30% for PGS. PCL exhibited linear elasticity with a tangent modulus of 21.8 MPa, and a standard deviation 20% of the mean. Effective permeability was also significantly dependent on material type, being $2.93 \times 10^{-7}\ m^4\ N\ s^{-1}$ for PCL, $3.51 \times 10^{-7}\ m^4\ N\ s^{-1}$ for POC and $8.31 \times 10^{-7}\ m^4\ N\ s^{-1}$ for PGS. Standard deviations ranged from 24 to 47% of the mean. Czernuszka, Sachlos, Liu and collegues[75–78] developed an inverse SFF technique to create collagen I scaffolds. A type I collagen dispersion was cast into wax molds, frozen at 20 °C with the wax and ice crystals removed using ethanol. All scaffolds were dehydrated under vacuum pressure with some scaffolds subsequently crosslinked using lysine. Storage moduli ranged from 0.1 to 1 MPa with higher moduli found for crosslinked collagen. Moduli decreased with increasing strain, indicating a nonlinear response (for more information on scaffold fabrication, see **Chapter 5.542, Organ Printing** in this volume).

5.502.3.3. Postfabrication Surface Modification

Controlled manufacture of scaffold architecture determines effective scaffold mechanical and mass transport properties, generally affecting large aggregates of cells. Effective properties, however, likely represent only average effects over local cell behavior. Cell behavior and differentiation are also significantly influenced by cell–material interactions, governed by cell–integrin interactions with local material chemistry and surface topography. The desire of course is then to directly affect cell attachment and differentiation on scaffolds by modifying cell–material interactions, essentially manufacturing features on the order of the cell or smaller, that is <10 μm. Viewed in the same hierarchy as design and manufacturing, these surface modification techniques can be thought of as 'manufacturing' materials at scales of 50 μm or less. It is obviously very difficult to build 3D structures that are cubic centimeters in volume by depositing material in 10–20 μm^3, or $1 \times 10^{-12}\ cm^3$, at a time. Therefore, to rapidly deposit 10 μm features or less within a 3D structure that is cubic centimeters in size, it is more feasible to first rapidly build the complex 3D structure at coarser 100–1000 μm^3 increments and then modify this base structure with either material features or extracellular matrix proteins that can influence cell attachment, and possibly, cell differentiation.

Of course, we can certainly contemplate doing micro or even nano solid fabrication. However, if the ultimate goal is a macroscopic scaffold aimed at reconstruction of a large defect, it is not realistic with the current state of the art to build such a structure directly only with micro- or nanofabrication. Therefore, the most realistic approach to distributing features <50 μm in size or biologic molecules in 3D space over large volumes is to first build a 3D substrate structure using one of the SFF techniques described in **Sections 5.502.3.1** and **155.3.2**, and then modifying the surfaces of this 3D substrate structure. The difficulty is that these manufactured 3D scaffold substrates will contain complex interconnected pore structures that cannot be modified using solid based manufacturing techniques.

A more feasible approach to modify 3D fabricated scaffold substrates is through the use of fluid or gas-based methods, which can enable perfusion through the interconnected pores. Such methods would include simulated body fluid (SBF) methods in which the scaffold is soaked in a circulating fluid (SBF),[79,80] conjugation methods in which a chemical cross-linker is perfused through the pore structure followed by a fluid containing the molecule of interest (e.g., RGD, IKVAV, BMP2, etc.), or chemical vapor deposition (CVD)[81,82] in which a substance is sublimated, carried at high temperature through a pyrolysis zone using an argon gas carrier, and then deposited on a substrate material. In this chapter, such methods will be denoted as postfabrication surface modification methods, or postfab surface modification, for short. Of note, the methods for design and manufacture for effective permeability and diffusivity will also affect the efficiency of these flow-based surface modification techniques.

Our own group has used fluid-based aminolysis techniques to modify 3D designed PCL scaffold subtrates for chemical conjugation.[83] In this technique, the scaffold is immersed in a solution of 1,6-hexanediamine and isoproposanol, which exposes NH_2 groups on the PCL surface. These groups allow the use of a chemical cross-linker, sulfosuccinimidyl-4-(*N*-maleimidomethyl)cyclohexane-1-carboxylate (sulfo-SMCC) to attach to the glycine portion of the arginine-glycine-aspartic acid (RGD) sequence. RGD is a peptide sequence known to improve cell adhesion through integrin binding. Zhang *et al.* demonstrated that there was a significant increase in both cell attachment and cell survival of rat bone marrow stromal cells (BMSC) on RGD-modified PCL scaffolds compared to unmodified PCL surfaces. Using this method, we obtained a relatively homogeneous distribution of RGD throughout the 3D scaffold. We found that RGD-modified PCL scaffolds demonstrated increased attachment and survival of BMSC. We also noted that the RGD-modified PCL scaffolds upregulated the integrin-mediated FAK-P13K-Akt pathway. Activation of Akt is associated with inhibition of proapoptotic factors, and thus may affect cell survival and growth.

A second approach to generate NH_2 groups on a PCL surface is through CVD. Hu *et al.*[84] used the CVD techniques developed by Lahann *et al.*[81,82] to deposit a reactive polymer poly[(4-amino-*p*-xylylene)-*co*-(*p*-xylylene)] (PPX-NH_2) on the surfaces of PCL scaffolds. The NH_2 groups created on the PCL surface were conjugated to amine–PEO_3–biotin. Adenovirus was also biotinylated and docked with the biotinlyated PCL surface. Hu *et al.* demonstrated that the adenovirus was conjugated to the PCL surface and was able to transduce fibroblasts in a spatially controlled manner on 3D PCL scaffolds. These results again demonstrate the usefulness of postfab surface modification to spatially distribute biologics (in this case viral vectors for gene delivery) in a controlled manner to enhance tissue regeneration.

A postfab fluid-based surface modification technique designed to create osteoconductive surfaces is biomineralization generated by mineral precipitation on material surfaces from SBF. This process has been applied to a variety of material surfaces[85–88] and was first described for application to porous degradable polymers by Murphy and colleagues.[79,89] In this method, the scaffold is bathed in a fluid solution containing many of the ionic constituents of blood plasma with the same pH and temperature. This solution leads to nucleation and growth of mineral on a template material negatively charged or polar oxygen functional groups.[90] Again, successful application of this fluid-based method to 3D interconnected porous scaffolds requires penetration of the fluid throughout the pores. Segvich *et al.*[91] addressed this issue by attaching a filtration system to a servohydraulic Instron system which forced the porogen-leached polymer scaffolds through a fluid bath. They noted that a uniform mineral coating could be obtained throughout the scaffold. Suarez-Gonzalez *et al.*[90] addressed the issue of fluid penetration by a rod system which forced SBF through alginate scaffolds with 200 μm pores fixed in a holder. Using micro-CT scanning, Suarez-Gonzalez *et al.* demonstrated that mineral was distributed throughout the scaffolds uniformly, while for scaffolds without forced fluid flow, mineral was only distributed on the scaffold periphery. They also demonstrated that the mineralized scaffolds supported increased proliferation of BMSC. Both of these studies show the need to incorporate forced fluid flow to increase efficiency and spatial distribution of biomineralization (for more information on scaffold and biomaterial surface modification, see **Chapter 1.113, Bioactive Layer Formation on Metals and Polymers**; **Chapter 2.201, Bio-inspired Silica Nanomaterials for Biomedical Applications**; **Chapter 4.411, Peptide- and Protein-Modified Surfaces**; and **Chapter 4.420, Drug Delivery via Heparin Conjugates** in this volume).

5.502.3.4. Scaffold Fabrication: Summary

In summary, significant progress has been made in scaffold fabrication using SFF technology since Giordano *et al.*[92] reported the first use of 3D printing for biomaterial fabrication. SFF in different forms, direct and indirect, can be used to fabricated 3D scaffolds with controlled architecture from almost any biomaterial utilized for tissue engineering. The first 10–15 years of SFF-based scaffold fabrication have been largely focused on the feasibility of the technology for actually making scaffolds from a range of biomaterials. In addition, recent work has demonstrated that SFF-manufactured scaffolds can be further modified post fabrication using fluid- and gas-based methods to enhance cell adhesion through the attachment of peptide sequences, and to localize, bind, and release proteins and genes that stimulate tissue growth. Thus, hierarchical manufacturing techniques are beginning to mature, with many more published studies existing than can be summarized in any review. Going forward, there are two significant, related issues for SFF scaffold technology that must be addressed: (1) benchmarking and quality control and (2) better integration of fabrication with computational design and evaluation. Benchmarks and quality control are needed to better understand the strengths and limitations of various fabrication technologies. It is clear that the physical process parameters for different machines and material formulation all can significantly alter resulting scaffold effective properties. Variations in scaffold effective properties ranged from lows of 1% to highs of over 80% of the mean values. It will be critical while going forward to have a better grasp of how material formulations and machine processing parameters affect the reproducibility of scaffold properties. This is

important not only for rigorous testing of scaffold design hypotheses, but also in moving toward clinical implementation to satisfy FDA quality control requirements for current good manufacturing processes (cGMP). Specifically, the influence of processing parameters on measured scaffold properties will have to be delineated, for example, using design of experiment (DOE) approaches as presented by Partee *et al.*[49] and Hoelzle *et al.*[54] Quality control can also be better studied across the research community by implementing benchmarks of standard scaffold designs that can be built and tested using different manufacturing methods for comparison. Quality control and evaluation measures will also be critical to assessing distribution of surface attached biologics (cells, genes, and proteins) in controlled 3D architectures. Better integration of fabrication with computational design and evaluation is critical to testing scaffold design hypotheses. Enhanced tissue regeneration via improved scaffold designs requires that we know if – and how – effective mechanical and mass transport properties influence tissue regeneration, and if so, what magnitudes of these effective properties are best. As stated in the introduction, although many researchers have postulated that optimal scaffolds should match tissue properties, these postulates remain untested.

5.502.4. Designed Scaffold Architecture Influences Tissue Regeneration

Given that controlling scaffold architecture and material through hierarchical design and manufacturing is a significant undertaking in itself, the blunt question is "Does it matter?" More diplomatically, does scaffold design actually influence tissue regeneration? If the answer is yes, then the ability to control scaffold architecture with different biomaterials should become a top priority in the tissue engineering and regenerative medicine community, in terms of testing scaffold design hypotheses, funding fabrication-centric research, and developing quality standards and benchmarks to support FDA regulation of scaffold-based therapies. Failure to fund research and development of controlled scaffold fabrication will significantly impede progression of these technologies to clinical application.

5.502.4.1. Cartilage

Articular cartilage is a singularly unique tissue in terms of its regenerative challenges and its effective properties. It is basically an avascular tissue that relies on mechanical compression and subsequent fluid movement to provide cell nutrition. Articular cartilage has the lowest effective permeability of any tissue, in the range of 10^{-14} to 10^{-15} $m^4\,N\,s^{-1}$. Although cartilage matrix is nonlinear elastic,[93] most researchers have reported effective aggregate or Young's modulus in the range of 0.03–1.13 MPa.[74] These effective mass transport and mechanical properties present a difficult challenge for articular cartilage scaffold design. Most commonly used degradable polyesters (poly-L-lactic acid (PLLA), polyglycolic acid (PGA), and PCL) have base material moduli ranging from 200 to 1500 MPa. Based on effective property bound estimates in Section 5.502.2.2, achieving effective moduli of 1 MPa or less would require a porosity ranging between 95% to over 99%. Of course, creating scaffolds with such large porosity would defeat the purpose of creating a scaffold with extremely low permeability, since 95% porous scaffolds with a non-woven mesh structure were shown by Li and Mak[94] to have permeability ranging from 2.5 to 4.5×10^{-6} $m^4\,N\,s^{-1}$, more than 8 orders of magnitude higher than the normal articular cartilage.

Of course, given that it is highly unlikely that the current most widely used scaffolding polymers can be designed to simultaneously match articular cartilage effective mass and mechanical properties, this leaves two paths to pursue. First, there are a number of biodegradable elastomers that can achieve properties in the range of articular cartilage, including POC and PGS. Second, given that the hypothesis that scaffold effective properties should match native tissues has not been proven, it is worthwhile to test tissue regeneration in scaffolds whose properties are much different than those of the native tissue to test the native tissue properties design hypothesis.

A first report of controlled 3D scaffold architecture effects versus porogen-leached architectures was presented by Malda *et al.*[67] Malda *et al.* compared biodegradable poly(ethylene glycol)-terephthalate/poly(butylene terephthalate) (PEGT/PBT) scaffolds made using 3D nozzle-based deposition (3DP) to those using compression molding and particle leaching (CM). CM scaffolds had 81% porosity with an average pore size of 182 μm and an effective modulus of 1.82 ± 0.33 MPa. 3DP scaffolds had 77% porosity with an average pore size of 525 μm and an effective modulus of 4.33 ± 0.52 MPa. Primary bovine chondrocytes were seeded into both the CM and 3DP scaffolds. A much greater penetration of cartilage matrix and increased sGAG content was seen in the 3DP scaffolds compared to the CM scaffolds. The interesting point to note is that the 3DP scaffold had a larger accessible pore volume than the CM scaffolds (680 vs. 120 μm), which suggests higher mass transport in the 3DP scaffolds, although effective permeability was not measured. These results would seem to go against the native tissue properties design hypothesis since the 3DP scaffold would presumably have much higher permeability than the CM scaffolds.

Our own group, Kemppainen and Hollister[73] specifically studied the relationship of designed scaffold effective permeability to chondrogenesis using PCL scaffolds with designed spherical pores. By changing the interconnectivity of spherical pores, we created scaffolds with effective permeability of $2.9\pm0.73\times10^{-7}$, $7.4\pm1.4\times10^{-7}$ ($2.5\times$ low), and 15.4 ± 2.8 10^{-7} $m^4\,N\,s^{-1}$ ($5.25\times$ low). The scaffolds of low-to-high permeability were 30, 47, and 60% porous. Each scaffold design was seeded separately with primary chondrocytes or chondrogenically pulsed BMSC. Scaffold permeability had a significant influence on chondrogensis by both chondrocytes and BMSC, although the effect was opposite on the two cell types. Low permeability scaffolds were associated with increased chondrogensis for primary chondrocytes, as measured by sGAG expression and type II/type I collagen gene expression ratio. For BMSC, high permeability scaffolds lead to increased type II/type I collagen gene expression, suggesting an increased tendency of the BMSC to become chondrogenic. Since BMSC are likely to be more highly metabolically active than chondrocytes, and since chondrogenic nutrition transport is key to chondogenic differentiation of BMSC, having higher permeability scaffolds is an advantage. The results for primary chondrocytes likely suggest

that chondrocytes may favor more hypoxic environments. However, the results of Malda *et al.* also suggest that there may be a lower bound or floor on the value of permeability that is beneficial to chondrogensis by primary chondocytes. Indeed, both results taken together suggest that there may be an optimal permeability zone for chondrogenesis by primary chondrocytes, and this zone, at least based on current *in vitro* and *in vivo* results, may be much higher than native articular cartilage as measured by permeability. It is definitive, however, that neither of these results and the resulting insight into cartilage tissue engineering could be obtained with the use of scaffold with designed and controlled 3D architecture (for more information on cartilage tissue engineering, see **Chapter 5.515, Cartilage Tissue Engineering** and **Chapter 5.514, Chondrocyte Transplantation and Selection** in this volume).

5.502.4.2. Bone

Bone is the tissue on which most studies have been performed relating scaffold architecture and effective properties to bone regeneration. Unfortunately, after over 30 years of research, there is no consensus regarding the effect of porous architecture on bone regeneration and ingrowth due to the confounding nature of the reported studies.[95] Early studies suggested that there was an optimal pore size of porous materials that favored bone ingrowth. Bobyn *et al.*[96] found that a pore size range between 50 and 400 μm was optimal for bone ingrowth in porous metal, as determined by the pushout strength measurements. The pore size, measured by 2D scanning electron microscopy (SEM) in porous metal represented a mean pore size, with a significant variation. Galois and Mainard[97] studied bone ingrowth into both HA and beta tricalcium phosphate (β-TCP) scaffolds with a range of pore sizes 45–80, 80–140, 140–200, and 200–250 μm. Scaffolds 6 mm in diameter and 10-mm long were implanted into rabbit femoral condyle defects. Results showed that bone ingrowth was significantly greater for pore sizes above 80 μm up to 120 days for both materials. After 120 days, bone ingrowth was not significantly different between pore sizes. Bone ingrowth occurred more rapidly in β-TCP implants, but again by 120 days there was no difference between materials. The pore size again represents a mean pore diameter with a range of pore sizes and pore interconnectivity.

The previous studies suggesting an optimal pore size were all performed using scaffolds in which that optimal pore size represented the mean of a range of pore sizes and interconnectivity. The conclusion that an optimal pore size exists was made using studies of scaffolds with a wide range of pore sizes. Other researchers have suggested that it is pore interconnectivity, which is significantly correlated with effective permeability, that is more strongly correlated with bone ingrowth than pore size. Li *et al.*[98] fabricated titanium cage scaffolds with controlled pore architecture that had pore sizes ranging from 160 μm in one design to a maximum of 680 μm in another design. Respective effective permeability ranged from $\sim 3.7 \times 10^{-7}$ to 8.2×10^{-7} $m^4\,Ns^{-1}$. When implanted in the transverse spinal processes of goats, they found that the total area of bone ingrowth and depth of bone penetration were only significantly different between the very lowest and very highest permeable scaffolds, although they stated that there was a trend toward greater bone ingrowth with greater permeability. Otsuki *et al.*[99] examined accessible pore space in titanium implants manufactured without controlled architecture. They found that implants with narrow pore throats (and likely lower effective permeability) were associated with less bone penetration and ingrowth. In a rigorous study looking at both controlled and uncontrolled scaffold architectures, Jones *et al.*[100] measured accessible pore volume for scaffolds manufactured by nozzle deposition with controlled pore architecture as well as scaffolds with uncontrolled architecture manufactured by compression molding of particles. Jones *et al.* also computed effective permeability and diffusivity using numerical methods similar to those outlined in **Section 5.502.2.2**. Their results showed that significantly less bone ingrowth was found in scaffolds with accessible pore radius of 100 μm or less. For accessible pore radii <100 μm, the computed effective permeability was $<1 \times 10^{-8}$ $m^4\,N\,s^1$ and the relative effective diffusivity was 0.05, in other words, the effective diffusivity was <5% of the base diffusivity of completely open space. For accessible pore radii >100 μm associated with significant bone ingrowth, the effective permeability was between 3×10^{-8} and 5×10^{-7} $m^4\,N\,s^{-1}$, with effective diffusivity ranging between 0.1 and 0.5. Jones noted that these results supported the concept of a threshold mass transport level supportive of bone ingrowth, as measured by effective permeability of 3×10^{-8} $m^4\,N\,s^{-1}$ and effective diffusivity of 0.1. They noted that this correlated well with the results of Hui *et al.*,[101] who found that obtaining effective permeability above a threshold value of 3×10^{-8} $m^4\,N\,s^{-1}$ was necessary with bone grafts to obtain significant integration with the host bone and bone formation.

Our own results with scaffolds having controlled architecture supports the notion of a threshold mass transport value necessary to obtain bone formation versus an optimal mass transport value. We implanted HA scaffolds with controlled architectures having designed pore sizes of 400, 900, and 1200 μm in 8 mm defects in Yucatan minipig mandibles.[36] The porosity values for all designs ranged from 42 to 50% and computed effective permeability ranged from 0.96×10^{-7} to 2.3×10^{-7} $m^4\,Ns^{-1}$, well above the 0.3×10^{-7} $m^4\,Ns^{-1}$ (equivalently, 3×10^{-8} $m^4\,Ns^{-1}$) given by Hui *et al.*[101] and Jones *et al.*[100] as a threshold value. At 16 weeks, there was no significant difference in bone ingrowth between designs, with all ingrowth values ranging from 70 to 78% of available scaffold pore volume. In studies of scaffolds delivering human gingival fibroblasts transduced with BMP7, we have also shown that there is no difference in bone ingrowth for pore sizes between 300 and 800 μm.[102,103] The study by Schek *et al.* also created exactly the same scaffold architecture from two different biomaterials, HA and a composite of PPF and TCP. For the same scaffold architecture design and delivered biologic, the HA scaffolds had twice the amount of bone as the PPF/TCP scaffolds. Thus, although the biomaterial results were intuitive, the ability to create scaffolds of different materials with exactly the same architecture eliminates architecture as a confounding variable.

The ability to create bone tissue engineering scaffolds has generated significant insight into the effect of both scaffold architecture and material on bone tissue ingrowth and regeneration, especially when viewed in contrast to scaffolds with

uncontrolled architecture. For one, by engineering scaffolds with regular interconnectivity but a wide range of pore sizes, it seems that the idea of an optimal pore size for a bone tissue engineering scaffold is largely debunked. Instead, the use of scaffolds with controlled pore sizes combined with tools for computationally and experimentally determining effective permeability and accessible pore space, suggests instead that there is a threshold value above which bone ingrowth is readily achieved but below which only fibrous tissue ingrowth is largely seen. It appears that there is at best a weak correlation and probably no correlation with bone growth increasing as effective permeability increases. It is interesting to note, however, that effective permeability and accessible pore size are a much better mass transport variable related to bone ingrowth than mean pore size or porosity. Indeed, there is a theoretical correlation between accessible pore size and permeability. Since permeability is determined by fluid flow and boundary layers, the smaller the accessible pore volume, the greater the boundary surface area and the more difficult it is to get flow through the material. Indeed, for the same porosity, we can achieve four orders of magnitude reduction in effective permeability by reducing the accessible pore size from 700 μm down to 70 μm. Using eqns [6] and [7], we reduce permeability from 10^{-7} to 3×10^{-11} m^4 Ns^{-1} just by reducing the accessible pore size from 700 to 70 μm no matter what the porosity, which correlates well with the findings of Jones *et al.*[100] In addition, Lu *et al.*[104] demonstrated the pore interconnections of at least 20 μm were necessary to allow osteoblast migration, and the 40 μm pore sizes or larger were preferable for osteoblast migration. This again correlates well with a minimum threshold of accessible pore volume for bone growth that can be characterized by effective permeability (for more information on bone tissue engineering, see **Chapter 6.617, Bone Tissue Grafting and Tissue Engineering Concepts**; **Chapter 5.521, Calcium Phosphates and Bone Induction** and **Chapter 5.518, Endocultivation: Computer Designed, Autologous, Vascularized Bone Grafts** in this volume).

5.502.4.3. Neural Tissue

Central nervous tissue is not often thought of with regard to scaffold design influences. However, investigations of scaffold architecture have become increasingly insightful in regeneration of neural tissue in both spinal cord and traumatic brain injury. Madigan *et al.*[105] noted that scaffold macroengineering (architecture engineering) was important to mimic the intrinsic spinal cord mechanical properties, allow vascularization of the construct, and provide 100–1000 μm tracts to support axonal outgrowth. In this sense, directed anisotropic permeability (given that permeability is a second-order tensor), may be associated with directed vascularization and axonal growth. Our own group fabricated PCL scaffolds with both controlled macro-architecture coupled with traditional porogen-leached architecture for application in a rat spinal cord transection model.[106] Five designs were created, three being the traditional channel design and two having an open core design (**Figure 9**).

Scaffolds were implanted empty without cells or neurotrophic factors. Axon growth was characterized using Tuj-1 staining and astrocyte activity was characterized using glial

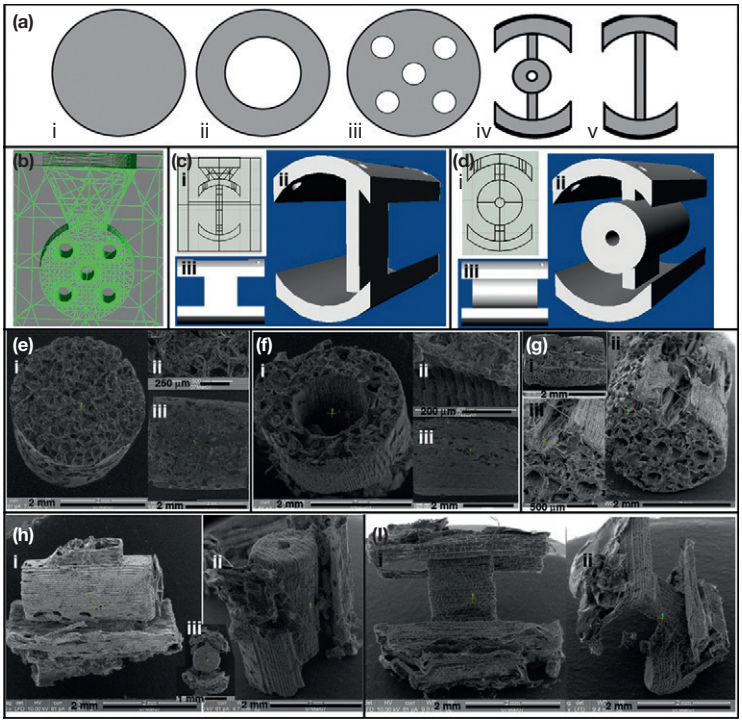

Figure 9 Example of spinal cord scaffolds with different designed macroarchitectures created by solid-free-form fabrication and microarchitectures created by porogen leaching. Scaffold designs iv and v demonstrated the best maintenance of neural tissue. Reproduced from Wong, D. Y.; Leveque, J. C.; Brumblay, H.; Krebsbach, P. H.; Hollister, S. J.; Lamarca, F. *J. Neurotrauma* **2008**, *25*, 1027–1037, with permission from Journal of Neurotrauma.

fibrillary acidic protein (GFAP). Scaffold architecture had a significant effect on axonal growth and death surrounding the initial 3 mm transection. Neuronal death resulting in an increased gap width was noted in traditional channel designs, while the open core scaffold architectures retained or even decreased the initial transected gap width, supporting axonal growth. Similarly, we also found that scaffolds with designed channels supported cell migration and showed significantly greater GFAP staining than porogen-leached channels without designed architecture. These results clearly demonstrate that scaffold architecture alone significantly influences neuronal growth and regeneration even without the delivery of cells or neurotrophic factors. Again, it is likely that success in scaffolds with designed architecture is due to mass transport factors that are related to cell migration and nutrition (for more information on neural tissue engineering, see **Chapter 5.531, Peripheral Nerve Regeneration**; **Chapter 5.532, Nerve Tissue Engineering**; **Chapter 5.533, Biomaterials for Central Nervous System Regeneration**; and **Chapter 6.630, Biomaterials for Spinal Cord Repair** in this volume).

5.502.4.4. Summary

Designed scaffold architecture and the resulting controlled effective properties significantly affect tissue regeneration. In most cases, controlled architecture and the resulting control of mass transport significantly increases tissue regeneration over scaffolds without designed architecture. Perhaps more importantly, controlled architecture allows us to test hypotheses concerning both scaffold design and material clearly without confounding experimental variables. This allows us to define basic scaffold design principles for tissue regeneration. For example, there is now strong evidence for the existence of a minimum effective permeability threshold that must be passed to effectively regenerate bone. This minimum threshold could not be established without experiments utilizing designed scaffolds. Furthermore, the existence of such design principles suggests that we may err on the side of more structurally dense scaffolds to support load bearing while still maintaining sufficient mass transport to allow bone ingrowth. For cartilage, the effect of mass transport on matrix regeneration is cell source-dependent. Chondrocytes benefit from low effective permeability, while BMSC benefit from high effective permeability. Whether a threshold of desirable mass transport exists for cartilage similar to bone is unknown. What is clear is that the ability to control scaffold architecture within different biomaterials is critical to testing design hypotheses and ultimately elucidating scaffold design principles that will lead to improved tissue engineering treatments.

5.502.5. Conclusion

Biomaterial scaffolds will play a critical role in potential regenerative medicine therapies. It is generally agreed that scaffolds must be engineered to satisfy the 4Fs: Form, Fixation, Function, and Formation. Form and fixation are readily defined as the scaffold filling specific anatomic defects and the attachment of the scaffold to surrounding host tissues, respectively. Specific requirements for function and formation are more difficult to pin down. Function in terms of load bearing is often defined in terms of mechanical properties (linear elasticity, nonlinear elasticity, and viscoelasticty) but the specific forms and magnitudes of the constitutive model and coefficients remains to be defined for most tissue applications. Formation remains even more ambiguous, given that several factors influence tissue formation, including mass transport, cell–material interaction factors such as specific surface area and hydrophobicity/hydrophilicity, and the ability to deliver biologics (cells/genes/proteins) in a local, controlled manner. Given that mass transport affects many aspects of tissue formation, including cell migration, nutrition, and biologic delivery, effective permeability and effective diffusivity as measures of mass transport are potential design targets for influencing formation. Specific surface area is another effective property design target, since it is one factor governing cell–material interaction.

Defining potential design targets (effective elasticity, permeability, diffusivity, specific surface area) is a critical first step since it allows us to develop specific scaffold design hypotheses. Tissue-specific mechanical and mass transport design targets fundamental to scaffold design hypotheses have been reviewed by Hollister *et al.*[107]. Testing these design hypotheses will then lead to the development of scaffold design principles, effectively design rules that can be followed to optimize scaffolds for a specific tissue application. The difficulty in testing scaffold design hypotheses concerning effective properties is that these properties must be first designed and controlled in scaffolds. If we seek to determine not only if effective properties are correlated with tissue formation, but perhaps whether thresholds for effective property influences on tissue regeneration exist (as likely exists for effective permeability and bone formation), then we must first be able to determine what are the possible extreme ranges of effective properties that may be attained, then devise computational algorithms to realize these ranges, and finally, develop scaffold manufacturing techniques to build the designs.

Each step becomes more difficult as we proceed from effective property bounds to design for specific effective properties to manufacturing specific designs. Absolute bounds (Voight and Reuss bounds) already exist for all effective properties, including nonlinear elasticity. These bounds, however, are extremely broad for porous materials, being zero at the lower bound. As such, absolute bounds provide useful information on the upper end, but relatively little information on the lower end. Tighter bounds have been derived for isotropic materials, including classic Hashin–Shtrikman bounds,[23] have been derived for linear effective properties, and also, in restricted cases, for nonlinear elasticity. Limited bounds exist for anisotropic materials.

Bounds on effective properties outline what effective properties are theoretically achievable, but do not provide any information on how to arrange material and void in 3D space to generate these properties. Homogenization based FSDM and ISDM do provide a basis for designing scaffold architecture, and recent advances have been made in simultaneous mechanical and mass transport design using ISDM. However, although ISDM can generate designs de novo to obtain desired effective properties near isotropic cross-property bounds, generating designs away from cross-property bounds

remains a challenge. FSDM remains a trial and error proposition, although significant insights into scaffold design have been made using this technique. Thus, the current state of the art for computational design is that architectures can be designed to fit some portions, but not all regions of mechanical-mass transport cross-property bounds. Design for nonlinear effective properties remains the purviews of FSDM, which themselves are in their infancy.

Controlled scaffold manufacturing has seen significant strides in the past 10 years. A range of both direct and inverse SFF techniques have been developed to fabricate polymer, ceramics, and metallic biomaterial scaffolds. Direct SFF feasibility has been proven for a limited range of materials, namely, PCL, PEOT/PBT, PPF, hydrogels, and titanium. Direct nozzle methods are more adaptable to a wider range of materials, but provide more limited pore architecture geometry. SLS and SLA techniques provide a broader range of pore architectures, but are more challenging in terms of adapting different biomaterials. Inverse SFF methods provide a wider potential range of both materials and pore architecture, but are much less automated and more time consuming than direct SFF methods.

Going forward, it is clear that our ability to rigorously test scaffold design hypotheses and advance regenerative medicine therapies is intimately coupled to our prowess in scaffold design and manufacturing.[40] The significant insights already gained by testing the influence of scaffold architecture and material on tissue regeneration clearly motivate expansion of scaffold design and manufacturing technologies. However, these technologies must be rigorously tested within *in vivo* applications, further refining scaffold design principles. Finally, the integration of scaffold design and manufacturing with *in vivo* system testing will form the foundation satisfying FDA current good manufacturing processes (cGMP) and moving scaffolding technology into clinical application.

Acknowledgments

The author gratefully acknowledges the graduate students and alumni of the Scaffold Tissue Engineering group whose work is reviewed in this article including Dr. Huina Zhang, Dr. Jessica Kemppainen, Dr. Claire Jeong, Dr. Juan Taboas, Dr. Elly Liao, Mr. Heesuk Kang, Ms. Colleen Flanagan, Dr. Chia-Ying Lin, Dr. Rachel Schek, Ms. Erin Moffitt, and Dr. Cheng-Yu Lin. He is also grateful for the input and discussion with many colleagues including Dr. Bill Murphy, Dr. Paul Krebsbach, Dr. Joerg Lahann, Dr. Gabriel Chu, Dr. Matt Wheeler, Dr. Steve Feinberg, and Dr. Frank LaMarca. The authors work presented in the review was funded by grants from the NIH R01 DE13608, R01 DE016129, R01 DE13416, and R01 AR 053379, as well as from the Coulter Foundation.

References

1. Yaszemski, M. J.; Payne, R. G.; Hayes, W. C.; Langer, R.; Mikos, A. G. *Biomaterials* **1996**, *17*, 175–185.
2. Brekke, J. H.; Toth, J. M. *J. Biomed. Mater. Res.* **1998**, *43*, 380–398.
3. Hutmacher, D. W. *J. Biomater. Sci. Polymer Ed.* **2001**, *12*, 107–124.
4. Engelmayr, G. C., Jr.; Cheng, M.; Bettinger, C. J.; Borenstein, J. T.; Langer, R.; Freed, L. E. *Nat. Mater.* **2008**, *7*, 1003–1010.
5. O'Brien, F. J.; Harley, B. A.; Yannas, I. V.; Gibson, L. J. *Biomaterials* **2005**, *26*, 433–441.
6. Van Cleynenbreugel, T.; Schrooten, J.; Van Oosterwyck, H.; Vander Sloten, J. *J. Med. Biol. Eng. Comput.* **2006**, *44*, 517–525.
7. Lovett, M.; Lee, K.; Edwards, A.; Kaplan, D. L. *Tissue Eng. B Rev.* **2009**, *15*, 353–370.
8. Guedes, J. M.; Kikuchi, N. *Comput. Meth. Appl. Mech. Eng.* **1990**, *83*, 143–198.
9. Sanchez-Palencia, E. *Non-Homogeneous Media and Vibration Theory*; Springer-Verlag: Berlin, 1980.
10. Hollister, S. J.; Brennan, J. M.; Kikuchi, N. *J. Biomech.* **1994**, *27*, 433–444.
11. Hollister, S. J.; Fyhrie, D. P.; Jepsen, K. J.; Goldstein, S. A. *J. Biomech.* **1991**, *24*, 825–839.
12. Hollister, S. J.; Kikuchi, N. *Biotechnol. Bioeng.* **1994**, *43*, 586–596.
13. Aoubiza, B.; Crolet, J. M.; Meunier, A. *J. Biomech.* **1996**, *29*, 1539–1547.
14. Yin, L.; Elliott, D. M. *J. Biomech.* **2005**, *38*(8), 1674–1684.
15. Hollister, S. J. *Nat. Mater.* **2005**, *4*, 518–524.
16. Hollister, S. J.; Levy, R. A.; Chu, T. M.; Halloran, J. W.; Feinberg, S. E. *Int. J. Oral Maxillofac. Surg.* **2000**, *29*, 67–71.
17. Hollister, S. J.; Maddox, R. D.; Taboas, J. M. *Biomaterials* **2002**, *23*, 4095–4103.
18. Hollister, S. J.; Lin, C. Y. *Comput. Meth. Appl. Mech. Eng.* **2007**, *196*, 2991–2998.
19. Kang, H.; Lin, C. Y.; Hollister, S. J. *Struct. Multidisciplinary Optim.* (in press).
20. Lin, C. Y.; Hsiao, C. C.; Chen, P. Q.; Hollister, S. J. *Spine (Philadelphia)*, **2004**, *1976*(29), 1747–1754.
21. Lin, C. Y.; Kikuchi, N.; Hollister, S. J. *J. Biomech.* **2004**, *37*, 623–636.
22. Gibson, L.; Ashby, M. F. *Cellular Solids; Structure and Properties*; Cambridge University Press: Cambridge, 1999.
23. Hashin, Z.; Shtrikman, S. *J. Mech. Phys. Solid.* **1963**, *11*, 127–140.
24. Ogden, R. W. *Int. J. Solid. Struct.* **1978**, *4*, 265–282.
25. Lopez-Pamies, O.; Idart, M. I. *J. Elasticity* **2009**, *95*, 99–105.
26. Martin, R. B. *Crit. Rev. Biomed. Eng.* **1984**, *19*, 179–222.
27. Fyhrie, D. P.; Lang, S. M.; Hoshaw, S. J.; Schaffler, M. B.; Kuo, R. F. *Bone* **1995**, *17*, 287–291.
28. Coelho, P. G.; Fernandes, P. R.; Rodrigues, H. C.; Cardoso, J. B.; Guedes, J. M. *J. Biomech.* **2009**, *42*, 830–837.
29. Guest, J. K.; Prevost, J. H. *Comput. Meth. Appl. Mech Eng.* **2007**, *196*, 1006–1017.
30. Sigmund, O. *Int. J. Solid. Struc.* **1994**, *31*, 2313–2329.
31. Sigmund, O. *Mech. Mater.* **1995**, *20*, 351–368.
32. Zhou, S. W.; Li, Q. *Mater. Lett.* **2008**, *62*, 4022–4024.
33. Zhou, S. W.; Li, Q. *J. Mater. Sci.* **2008**, *43*, 5157–5167.
34. Guest, J. K.; Prevost, J. H. **2006**.
35. Svanberg, K. *Int. J. Numer. Meth. Eng.* **1987**, *24*, 359–373.
36. Hollister, S. J.; Lin, C. Y.; Saito, E.; *et al. Orthod. Craniofac. Res.* **2005**, *8*, 162–173.
37. Levy, R. A.; Chu, T. M.; Halloran, J. W.; Feinberg, S. E.; Hollister, S. *Am. J. Neuroradiol.* **1997**, *18*, 1522–1525.
38. Smith, M. H.; Flanagan, C. L.; Kemppainen, J. M.; *et al. Int. J. Med. Robot.* **2007**, *3*, 207–216.
39. Taboas, J. M.; Maddox, R. D.; Krebsbach, P. H.; Hollister, S. J. *Biomaterials* **2003**, *24*, 181–194.
40. Hollister, S. J. *Adv. Math.* **2009**, *21*, 3330–3342.
41. Hutmacher, D. W.; Cool, S. *J. Cell. Mol. Med.* **2007**, *11*, 654–669.
42. Hutmacher, D. W.; Schantz, J. T.; Lam, C. X.; Tan, K. C.; Lim, T. C. *J. Tissue Eng. Regen. Med.* **2007**, *1*, 245–260.
43. Sachlos, E.; Czernuszka, J. T. *Eur. Cell. Mater.* **2003**, *5*, 29–39, discussion 39–40.
44. Moroni, L.; Hamann, D.; Paoluzzi, L.; Pieper, J.; de Wijn, J. R.; van Blitterswijk, C. A. *PLos One* **2008**, *3*, *e3032*.
45. Lee, K. W.; Wang, S.; Fox, B. C.; Ritman, E. L.; Yaszemski, M. J.; Lu, L. *Biomacromolecules* **2007**, *8*(4), 1077–1084.
46. Williams, J. M.; Adewunmi, A.; Schek, R. M.; *et al. Biomaterials* **2005**, *26*, 4817–4827.
47. Wiria, F. E.; Leong, K. F.; Chua, C. K.; Liu, Y. *Acta Biomater.* **2007**, *3*, 1–12.
48. Lee, J. W.; Lan, P. X.; Kim, B.; Lim, G.; Cho, D. W. *J. Biomed. Mater. Res. B Appl. Biomater.* **2008**, *87*(1), 1–9.
49. Partee, B.; Hollister, S. J.; Das, S. *J. Manuf. Sci. Eng.* **2006**, *128*, 531–540.
50. Cahill, S.; Lohfeld, S.; McHugh, P. E. *J. Mater. Sci. Mater. Med.* **2009**, *20*, 1255–1262.
51. Chua, C. K.; Leong, K. F.; Tan, K. H.; Wiria, F. E.; Cheah, C. M. *J. Mater. Sci. Mater. Med.* **2004**, *15*, 1113–1121.

52. Wiria, F. E.; Chua, C. K.; Leong, K. F.; Quah, Z. Y.; Chandrasekaran, M.; Lee, M. W. *J. Mater. Sci. Mater. Med.* **2008**, *19*, 989–996.
53. Yeong, W. Y.; Sudarmadji, N.; Yu, H. Y.; *et al. Acta Biomater.* **2010**, *6*(6), 2028–2034.
54. Hoelzle, D. J.; Alleyne, A. G.; Wagoner Johnson, A. J. *Acta Biomater.* **2008**, *4*, 897–912.
55. Lan Levengood, S. K.; Polak, S. J.; Wheeler, M. B.; *et al. Biomaterials* **2010**.
56. McIntosh, L.; Cordell, J. M.; Wagoner Johnson, A. J. *Acta Biomater.* **2009**, *5*, 680–692.
57. Woodard, J. R.; Hilldore, A. J.; Lan, S. K.; *et al. Biomaterials* **2007**, *28*, 45–54.
58. Abbah, S. A.; Lam, C. X.; Hutmacher, D. W.; Goh, J. C.; Wong, H. K. *Biomaterials* **2009**, *30*, 5086–5093.
59. Lam, C. X.; Hutmacher, D. W.; Schantz, J. T.; Woodruff, M. A.; Teoh, S. H. *J. Biomed. Mater. Res. A* **2009**, *90*, 906–919.
60. Zein, I.; Hutmacher, D. W.; Tan, K. C.; Teoh, S. H. *Biomaterials* **2002**, *23*, 1169–1185.
61. Malda, J.; Woodfield, T. B.; van der Vloodt, F.; *et al. Biomaterials* **2004**, *25*, 5773–5780.
62. Miot, S.; Woodfield, T.; Daniels, A. U.; *et al. Biomaterials* **2005**, *26*, 2479–2489.
63. Moroni, L.; de Wijn, J. R.; van Blitterswijk, C. A. *Biomaterials* **2006**, *27*, 974–985.
64. Moroni, L.; de Wijn, J. R.; van Blitterswijk, C. A. *J. Biomed. Mater. Res. A* **2005**, *75*, 957–965.
65. Woodfield, T. B.; Bezemer, J. M.; Pieper, J. S.; van Blitterswijk, C. A.; Riesle, J. *Crit. Rev. Eukaryot. Gene Expr.* **2002**, *12*(3), 209–236.
66. Woodfield, T. B.; Malda, J.; de Wijn, J.; Peters, F.; Riesle, J.; van Blitterswijk, C. A. *Biomaterials* **2004**, *25*(18), 4149–4161.
67. Malda, J.; Woodfield, T. B.; van der Vloodt, F.; *et al. Biomaterials* **2005**, *26*(1), 63–72.
68. Li, J. P.; de Wijn, J. R.; van Blitterswijk, C. A.; de Groot, K. *J. Biomed. Mater. Res. A* **2010**, *92*(1), 33–42.
69. Chu, T. M.; Orton, D. G.; Hollister, S. J.; Feinberg, S. E.; Halloran, J. W. *Biomaterials* **2002**, *23*, 1283–1293.
70. Wilson, C. E.; de Bruijn, J. D.; van Blitterswijk, C. A.; Verbout, A. J.; Dhert, W. J. *J. Biomed. Mater. Res. A* **2004**, *68*(1), 123–132.
71. Jeong, C. G.; Hollister, S. J. *J. Biomed. Mater. Res. B Appl. Biomater.* **2010**, *93B*, 141–149.
72. Jeong, C. G.; Hollister, S. J. *Biomaterials* **2010**, *31*, 4304–4312.
73. Kemppainen, J. M.; Hollister, S. J. *Biomaterials* **2010**, *31*, 279–287.
74. Kemppainen, J. M.; Hollister, S. J. *J. Biomed. Mater. Res. A* **2010**.
75. Liu, C. Z.; Xia, Z. D.; Han, Z. W.; Hulley, P. A.; Triffitt, J. T.; Czernuszka, J. T. *J. Biomed. Mater. Res. B Appl. Biomater.* **2008**, *85*, 519–528.
76. Wahl, D. A.; Sachlos, E.; Liu, C.; Czernuszka, J. T. *J. Mater. Sci. Mater. Med.* **2007**, *18*, 201–209.
77. Liu, C. Z.; Xia, Z. D.; Han, Z. W.; Hulley, P. A.; Triffitt, J. T.; Czernuszka, J. T. *J. Biomed. Mater. Res. B Appl. Biomater.* **2008**, *85*(2), 519–528.
78. Sachlos, E.; Reis, N.; Ainsley, C.; Derby, B.; Czernuszka, J. T. *Biomaterials* **2003**, *24*(8), 1487–1497.
79. Murphy, W. L.; Kohn, D. H.; Mooney, D. J. *J. Biomed. Mater. Res.* **2000**, *50*, 50–58.
80. Kokubo, T.; Ito, S.; Huang, Z. T.; *et al. J. Biomed. Mater. Res.* **1990**, *24*(3), 331–343.
81. Lahann, J.; Klee, D.; Thelen, H.; Bienert, H.; Vorwerk, D.; Hocker, H. *J. Mater. Sci. Mater. Med.* **1999**, *10*, 443–448.
82. Lahann, J. *Polymer Int.* **2006**, *55*, 1361–1370.
83. Zhang, H.; Lin, C. Y.; Hollister, S. J. *Biomaterials* **2009**, *30*, 4063–4069.
84. Hu, W. W.; Elkasabi, Y.; Chen, H. Y.; *et al. Biomaterials* **2009**, *30*, 5785–5792.
85. de Groot, K.; Wolke, J. G.; Jansen, J. A. *Proc. Inst. Mech. Eng. H* **1998**, *212*, 137–147.
86. Kokubo, T.; Kim, H. M.; Kawashita, M. *Biomaterials* **2004**, *24*, 2161–2175.
87. Ogino, M.; Ohuchi, F.; Hench, L. L. *J. Biomed. Mater. Res.* **1980**, *14*, 55–64.
88. Habibovic *et al*., 2002.
89. Murphy, W. L.; Mooney, D. J. *J. Am. Chem. Soc.* **2002**, *124*, 1910–1917.
90. Suarez-Gonzalez, D.; Barnhart, K.; Saito, E.; Vanderby, R.; Hollister, S.; Murphy, W. *J. Biomed. Mater. Res A* (in press).
91. Segvich, S.; Smith, H. C.; Luong, L. N.; Kohn, D. H. *J. Biomed. Mater. Res. B Appl. Biomater.* **2008**, *84*, 340–349.
92. Giordano, R. A.; Wu, B. M.; Borland, S. W.; Cima, L. G.; Sachs, E. M.; Cima, M. J. *J. Biomater. Sci. Polymer Ed.* **1996**, *8*, 63–75.
93. Martinez-Diaz, S.; Garcia-Giralt, N.; Lebourg, M.; *et al. Am. J. Sports Med.* **2010**, *38*, 509–519.
94. Li, J.; Mak, A. F. *J. Biomater. Appl.* **2005**, *19*(3), 253–266.
95. Karageorgiou, V.; Kaplan, D. *Biomaterials* **2005**, *26*, 5474–5491.
96. Bobyn, J. D.; Pilliar, R. M.; Cameron, H. U.; Weatherly, G. C. *Clin. Orthop. Relat. Res.* **1980**, *150*, 263–270.
97. Galois, L.; Mainard, D. *Acta Orthon. Belg.* **2004**, *70*(6), 598–603.
98. Li, J. P.; Habibovic, P.; van den Doel, M.; *et al. Biomaterials* **2007**, *28*, 2810–2820.
99. Otsuki, B.; Takemoto, M.; Fujibayashi, S.; Neo, M.; Kokubo, T.; Nakamura, T. *Biomaterials* **2006**, *27*, 5892–5900.
100. Jones, A. C.; Arns, C. H.; Hutmacher, D. W.; Milthorpe, B. K.; Sheppard, A. P.; Knackstedt, M. A. *Biomaterials* **2009**, *30*, 1440–1451.
101. Hui, P. W.; Leung, P. C.; Sher, A. *J. Biomech.* **1996**, *29*, 123–132.
102. Lin, C. Y.; Schek, R. M.; Mistry, A. S.; *et al. Tissue Eng.* **2005**, *11*, 1589–1598.
103. Schek, R. M.; Wilke, E. N.; Hollister, S. J.; Krebsbach, P. H. *Biomaterials* **2006**, *27*(7), 1160–1166.
104. Lu, J. X.; Flautre, B.; Anselme, K.; *et al. J. Mater. Sci. Mater. Med.* **1999**, *10*, 111–120.
105. Madigan, N. N.; McMahon, S.; O'Brien, T.; Yaszemski, M. J.; Windebank, A. J. *Respir. Physiol. Neurobiol.* **2009**, *169*, 183–199.
106. Wong, D. Y.; Leveque, J. C.; Brumblay, H.; Krebsbach, P. H.; Hollister, S. J.; Lamarca, F. *J. Neurotrauma* **2008**, *25*, 1027–1037.
107. Hollister, S. J.; Liao, E. E.; Moffitt, E. N.; Jeong, C. G.; Kemppainen, J. M. In *Fundamental of Tissue Engineering*; Meyer, U.; Meyer, T.; Handschel, J.; Wiesmann, H. P., Eds.; Springer: Heidelberg, Germany, 2009.

5.503. Biomaterials and the Microvasculature

B Joddar, The Ohio State University, Columbus, OH, USA
A L Sieminski and C J Tennant, Franklin W. Olin College of Engineering, Needham, MA, USA
K J Gooch, The Ohio State University, Columbus, OH, USA

© 2011 Elsevier Ltd. All rights reserved.

5.503.1.	**Introduction**	35
5.503.2.	**Biomedical Engineering Applications Dependent on Neovascularization In or Around Biomaterials**	36
5.503.2.1.	Tissue Engineering	36
5.503.2.2.	Cell-Based Gene Therapy	36
5.503.2.3.	Isolation Devices and Biosensors	36
5.503.3.	**Survey of Neovascularization**	37
5.503.3.1.	Types of Neovascularization	37
5.503.3.2.	Neovascularization and the Foreign Body Response	37
5.503.3.3.	*In Vitro* Models of Neovascularization	37
5.503.4.	**Properties of Biomaterials Regulating Microvascular Network Formation In, On, and Around Biomaterials**	37
5.503.4.1.	Structural and Mechanical Features of Biomaterials	37
5.503.4.1.1.	Macrostructure	37
5.503.4.1.2.	Porosity of biomaterial	39
5.503.4.1.3.	Microstructure of biomaterial: pore size	39
5.503.4.1.4.	Microstructure of biomaterial: fibrous materials	42
5.503.4.1.5.	Biomaterial stiffness	44
5.503.4.2.	Chemical and Biochemical Features of Biomaterials	45
5.503.4.2.1.	Endothelial cell adhesion to biomaterials *in vitro*	45
5.503.4.2.2.	Endothelial network formation on and in functionalized biomaterials	46
5.503.4.2.3.	The role of chemistry in FBR *in vivo*	46
5.503.4.2.4.	Angiogenic factors	46
5.503.5.	**Case Studies**	47
5.503.5.1.	Implantation of Preformed Microvascular Networks	47
5.503.5.2.	Extravascular Wraps for Grafted Veins	47
5.503.5.3.	Glucose Sensors	48
References		48

Abbreviation

bFGF	Basic fibroblast growth factor
CAM	Chick chorioallantoic membrane
ECM	Extracellular matrix
ePTFE	Expanded PTFE
FBR	Foreign body response
hGH	Human growth hormone
hMSCs	Human bone marrow-derived mesenchymal stem cells
MMP	Matrix metalloproteinase
MVN	Microvascular networks
NO	Nitric oxide
PDGF	Platelet-derived growth factor
PEG	Poly(ethylene glycol)
PEO	Polyethylene oxide
PEO	Polyurethane with silicone and polyethylene oxide
PTFE	Polytetrafluoroethylene
PU	Polyurethane
PVA	Polyvinyl alcohol
SC	Subcutaneous
SCID	Severe combined immunodeficient
VEGF	Vascular endothelial growth factor

5.503.1. Introduction

Nearly a century ago Alexis Carrel, a pioneer in the fields of cell culture and tissue transplantation, published a series of papers describing sustained growth of animal cell and tissue cultures.[1–4] Carrel sought to create the conditions whereby cultures could achieve 'permanent life.' Recognizing that nutrient transport was essential to *ex vivo* tissue viability, he noted that cells on the periphery of tissue culture flourished whereas internal cells isolated from the nutrient broth struggled to survive. As an alternate approach, Carrel used a patch of silk as a primitive scaffold, prompting planar rather than spherical growth, and in doing so took the first step toward enhancing the viability and durability of cultured tissues.

The principles illustrated by this experiment were further clarified when Carrel and Charles Lindbergh developed a mechanical perfusion system capable of sustaining organs *ex vivo*.[5] Using this perfusion system, cat hearts continued to beat for 12 h and thyroid glands remained viable and functional for up to 30 days.[6] By enabling continuous nutrient transport, this system prolonged the *ex vivo* survival of complex organs and tissues for the first time, providing a glimpse of the expansive potential of organ transplant and tissue engineering applications.

Almost 100 years later, the challenge of adequate nutrient transport remains one of the primary issues limiting the utility of tissue engineering applications. Perfusion of implanted tissue is essential to nutrient and oxygen supply and waste removal, and also is critical to enabling the complex molecular cascades that underlie cellular communication. As the viability of most cell types is dependent on proximity to blood vessels, the successful introduction of engineered tissues and organs *in vivo* is limited by the extent to which a microvascular network can develop *in situ*. Neovascularization *in situ* can be achieved by a number of methods. Regardless of the method by which it is achieved, neovascularization is a critical factor in the viability not only of engineered tissues and organs, but also of implanted sensors, cell-based gene therapy, and other bioengineering applications. These applications will be briefly reviewed and provide motivation and framework for the subsequent discussion of the factors that appear to govern neovascularization in and around biomaterial implants. Factors to be examined include the structural and mechanical features of biomaterials such as macrostructure, microarchitecture, and stiffness. The impact of chemical features (e.g., surface energy, hydrophobicity, and protein adsorption) and biochemical features (e.g., integrin-binding sites, enzymatic degradation sites, and specific angiogenic factors) will be reviewed. Lastly, case studies will be described that illustrate how recent successes in the development of microvascular networks for various biomedical applications can be largely understood in the context of the structural, mechanical, chemical and biochemical factors reviewed in this chapter.

5.503.2. Biomedical Engineering Applications Dependent on Neovascularization In or Around Biomaterials

5.503.2.1. Tissue Engineering

The measure of success for most tissue engineering applications is survival and functionality *in vivo*. Unfortunately, loss of cell viability and function following implantation often occurs to an extent that limits the utility of the engineered tissue. The decrease in viability and function of cells within engineered tissues often can be attributed to the lack of a functional microvascular system and subsequent transport deficiencies in the engineered tissue.[7,8] Since it is unlikely that implanted tissues could survive for the days or weeks likely required for host vessels to vascularize a larger avascular engineered tissue, a critical challenge is how to decrease the time required to establish functional (i.e., perfused) neovascularization within implanted tissues. Various methods of facilitating the formation of microvasculature derived from the host or the implant have been investigated. When implanted intraperitoneally, porous polymeric implants were invaded by vascularized fibrous tissue.[9] Though the ingrowth substantially decreased the porosity of the implant,[9] these prevascularized implants improved the survival of hepatocytes introduced subsequently.[10] With the eventual goal of improving the viability of grafted tissue-engineered skin, Black *et al.* constructed, *in vitro*, a microvascular network within the tissue-engineered graft.[7] This engineered microvasculature would be expected to anastomose with existing vessels in the host, as seen with native skin grafts,[11] thus facilitating vascularization and improving viability. This assertion is supported by reports that tissue-engineered microvascular networks formed by seeding endothelial cells on fibrous polyglycolic meshes[12] or embedding endothelial cells in extracellular matrix (ECM) gels,[10,13–15] incorporate with host vasculature and/or increase vascularization within the implants. Implantation of intact vascularized islets or avascular aggregates of pancreatic cells yields functional islet-specific vasculature; the former obtained a perfused microvasculature more quickly,[16] further highlighting the impact of an established microvasculature within implanted tissue. An elaborate method intended to facilitate the establishment of microvasculature in engineered tissue was explored by Griffith *et al.*, who employed three-dimensional (3D) micropatterning to facilitate self-organization of endothelial cell– hepatocyte cocultures into liver-like architecture *in vitro*.[17] Subsequent efforts to create microfabricated microvascular networks have created *in vitro* systems with spatially well-defined vascular networks lined with endothelial cells.[18,19] By rationally designing such networks, mass transport properties can be optimized.[20,21]

5.503.2.2. Cell-Based Gene Therapy

Two major approaches to cell-based gene therapy are implantation of genetically modified cells within the engineered tissue or in an isolation device, which may be considered similar to the tissue engineering or isolation devices (see **157.2.3**) and the techniques they employ. An alternative approach to cell-based gene therapy is the use of the microvasculature not to facilitate transport, but rather as a location from which genetically modified endothelial cells can deliver gene products directly to the circulation.[22,23] Engineered microvascular networks formed by endothelial cell progenitors[23,24] or microvascular endothelial cells[25] embedded in extracellular matrix gels have been shown to provide long-term stable delivery of transgene products to the circulation.

5.503.2.3. Isolation Devices and Biosensors

The use of semipermeable membranes to isolate implanted cells, e.g., for treatment of chronic pain,[26] neurological disease[27] as well as local[28] and systemic cell-based gene therapy[29] and implanted tissues, e.g., allogeneic islets[30] has been investigated in a number of contexts, primarily to isolate the implanted material from the host immune system. The survival of cells within an implanted isolation device is dependent on adequate transport of oxygen, nutrients, and metabolites, a task normally facilitated by the microvasculature. Additionally, efficient transfer from an isolation device is necessary for delivered

therapeutics to reach their targets (see Chapter 4.431, Encapsulation of Cells (Cellular Delivery) Using Sol–Gel Systems and Chapter 5.509, Cell Encapsulation).

Implanted biosensors can provide near real-time measurements of analyte concentration, which can be used to control the delivery of insulin or other therapeutics.[31] Inefficient transport between the microcirculation and the biosensor may potentially confound real-time measurements and result in inaccurate measurement of steady concentrations of analytes such as glucose or oxygen that are consumed or reacted within the tissue.

5.503.3. Survey of Neovascularization

5.503.3.1. Types of Neovascularization

The two major forms of neovascularization are angiogenesis and vasculogenesis. Angiogenesis, the sprouting of vessel offshoots from existing vessels, is achieved following the migration of vascular endothelial cells and subsequent assembly into capillary buds (Figure 1(a)). In contrast, vasculogenesis involves the development of de novo blood vessels from the migration and differentiation of endothelial precursor cells in the absence of local vasculature (Figure 1(b)). The details of angiogenesis and vasculogenesis have been extensively described in the literature.[32,33] Native neovascularization can also be accomplished by intussusception (or intussceptive angiogenesis). The defining event in intussusception is the formation of transvascular tissue pillars that divide one vessel into two (Figure 1(c)).[34,35] A final method of neovascularization, vascular tunneling (Figure 1(d)), is less clearly defined but may have an important role in biomaterial applications. In one model of vascular tunneling, monocytes/macrophages burrowed through the basement membrane gel Matrigel, forming tunnels filled with columns of monocytes/macrophages and various forms of progenitor cells after ~1 week.[36,37] By 4 weeks, some of these tunnels appeared to have matured into capillaries featuring endothelial walls and containing erythrocytes, while others had not fully matured. In both stages of maturation, bundles of collagen fibers were observed along the length of the tubes.

5.503.3.2. Neovascularization and the Foreign Body Response

One form of neovascularization of particular importance in several biomaterial applications is angiogenesis associated with the foreign body response (FBR). Biomaterial implants interact closely with the *in vivo* environment in which they are placed.[38] The mechanisms of this response include inflammation, immunological reactions and fibrosis, all of which can hinder the development of a microvasculature critical to implant viability. Initially, healing inflammation is marked by the formation of granulation tissue, which involves invasion of fibrovascular tissue due to angiogenesis and fibroblast proliferation. Granulation tissue, which may be seen as early as 3–5 days following implant, can be remodeled into vascularized tissue. However, formation of this tissue is often followed by a FBR, in which foreign body giant cells and the components of granulation tissue form a relatively avascular capsule around an implant (Figure 2(a)). This foreign body capsule isolates the implant and impairs angiogenesis, limiting the transport of biomolecules and nutrients between the microvasculature and implanted biomaterials and ultimately affecting the functionality of the implant. This is particularly important with engineered tissue implants and glucose sensors, both of which depend on the development of microvasculature, derived from the host or within the implant itself, for survival and functionality *in vivo*. The degree of the FBR is influenced not only by the local host environment but also by the physical and chemical characteristics of the implant, which will be reviewed in the following sections.

5.503.3.3. *In Vitro* Models of Neovascularization

As reviewed in detail by others,[39] there are numerous *in vitro* models of neovascularization. Some *in vitro* models focus on the assembly of isolated cells into multicellular structures, which resembles vasculogenesis, while other models focus on the sprouting of endothelial cells from endothelial monolayers, clusters, or intact vessel segments. When attempting to compare results between *in vitro* models or to extrapolate *in vitro* results to *in vivo* neovascularization, it is important to consider the strengths and limitations of the experimental model. For example, is it a model of angiogenesis or vasculogenesis? Does the model include only endothelial cells, or are important nonendothelial supporting cells also present? While some of these issues are relatively apparent, others are more subtle. For example, the planar culture of endothelial cells on top of various biomaterials is the basis of several *in vitro* models of neovascularization. In one such model, endothelial cells are seeded at a subconfluent density on top of preformed Matrigel. Over the course of several hours to days, the cells assemble into interconnecting, multicellular structures resembling an *in vivo* capillary network. While it is tempting to assume that a model using this arrangement is a faithful 2D analog of a biologically relevant 3D environment, the difference between 2D and 3D can be of paramount importance to the cells involved, literally representing the difference between life and death. Endothelial cells embedded within a 3D gel of Matrigel remain spherical and die within several days. This is not due to an inherent inability of the endothelial cells to survive within Matrigel, as the presence of fibroblasts or glass fibers in the Matrigel enables the endothelial cells to survive and elongate. Though somewhat simplified, the 2D Matrigel model can capture some of the effects of angiogenic and antiangiogenic factors. The point of this discussion is not to criticize a particular model system or simplified models of neovascularization in general. In contrast, these models can be powerful tools to address specific questions, provided their limitations are acknowledged and the extrapolation of their outcomes to other systems is performed with care.

5.503.4. Properties of Biomaterials Regulating Microvascular Network Formation In, On, and Around Biomaterials

5.503.4.1. Structural and Mechanical Features of Biomaterials

5.503.4.1.1. Macrostructure

Several studies have suggested that a greater implant thickness will lead to a greater capsule thickness and an increased FBR.

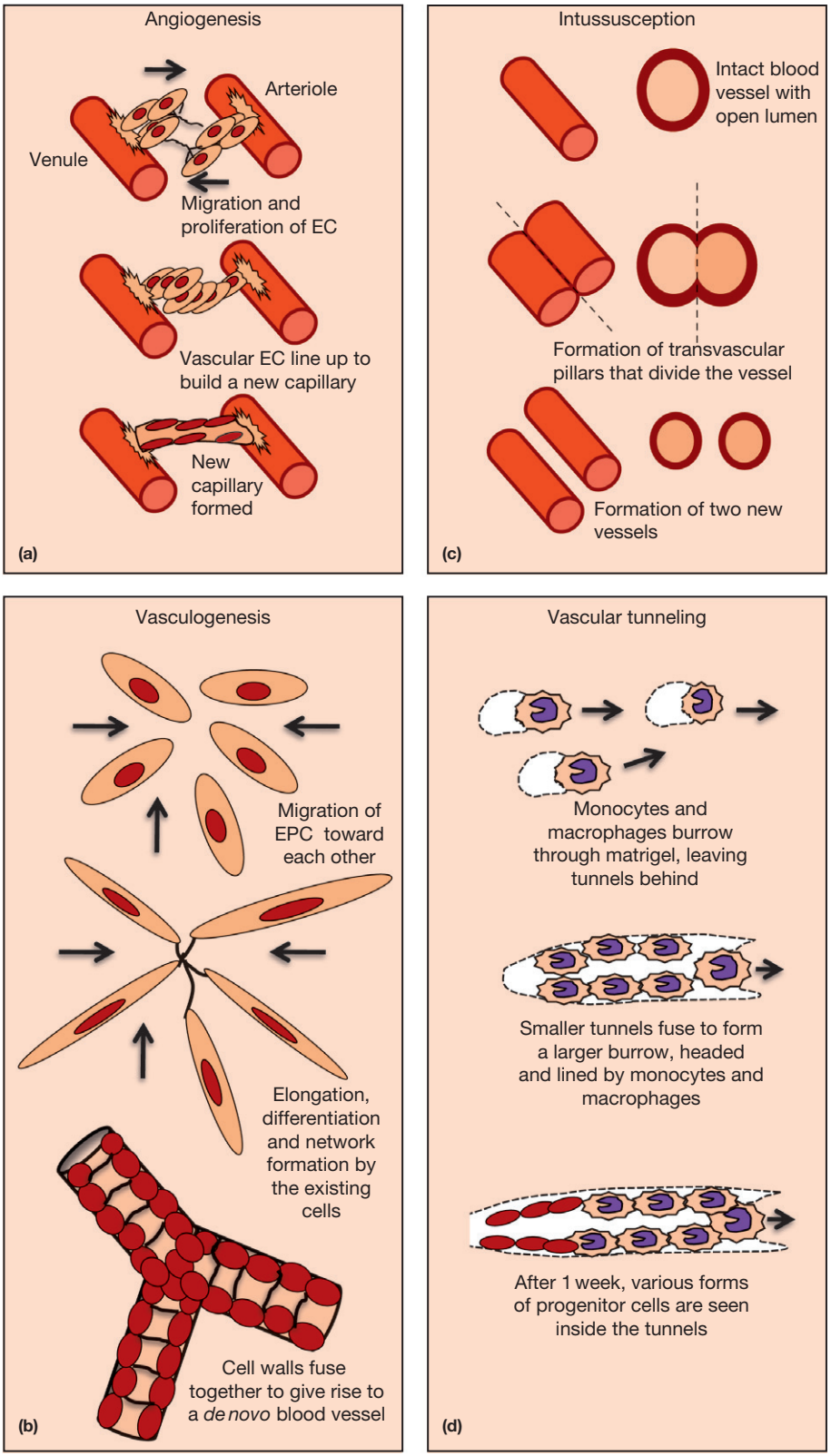

Figure 1 (a) Angiogenesis involves the sprouting of vessel offshoots from existing vessels, following the migration of vascular endothelial cells and subsequent assembly into capillary buds. (b) Vasculogenesis involves the development of *de novo* blood vessels from the migration and differentiation of endothelial precursor cells in the absence of local vasculature. (c) Intussusception is the formation of transvascular tissue pillars that divide one vessel into two. (d) In vascular tunneling, monocytes/macrophages burrow through Matrigel, forming tunnels filled with columns of monocytes/macrophages and various forms of progenitor cells after ~1 week.

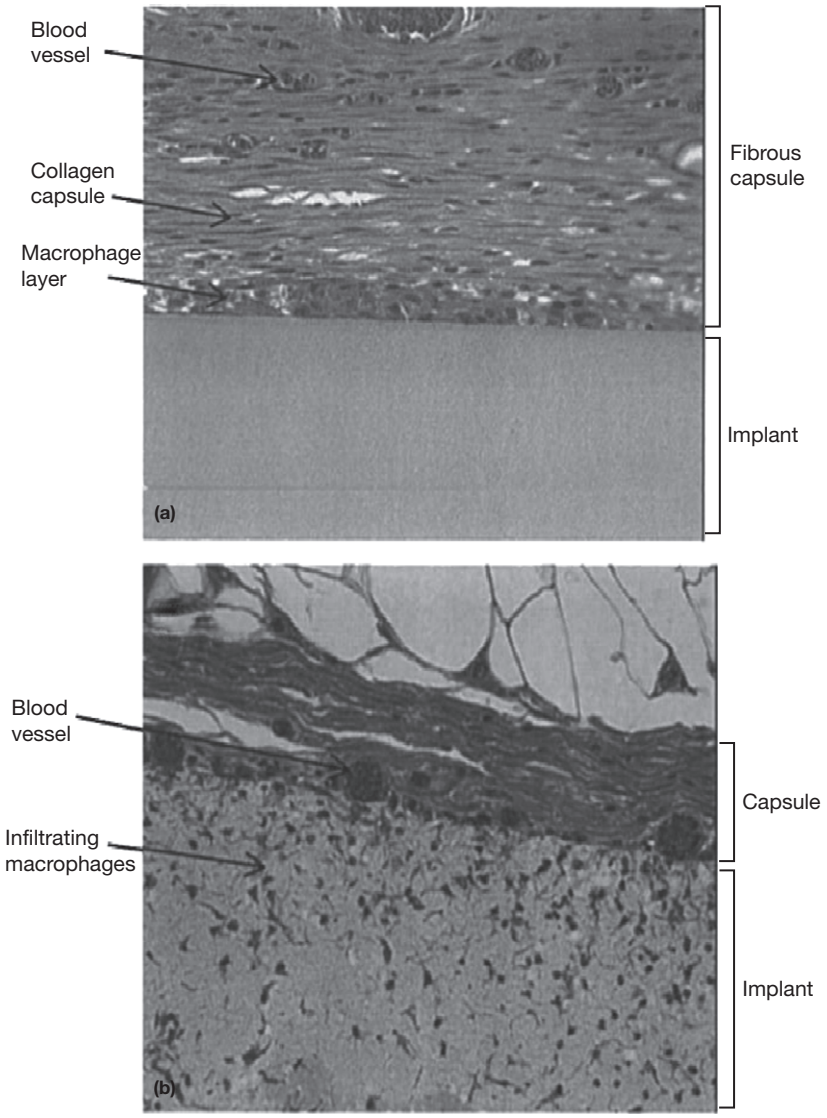

Figure 2 An example of a histological section stained with hematoxylin and eosin showing (a) a typical fibrous capsule surrounding a nonporous subcutaneous implant. Note the layer of macrophages at the implant surface, the dense, parallel arrangement of the collagen capsule, and the blood vessels in the granulation tissue. (b) A highly vascularized, thin capsule surrounding an implant with 8 μm pores. Note the blood vessels in contact with the implant and the macrophages within the pores. Original images kindly provided by Dr. Robert Padera. Reproduced from Sieminski, A. L.; Gooch, K. J. *Biomaterials* **2000**, *21*(22), 2232–2241, with permission from Elsevier.

Ward *et al.* observed a direct relationship between the thickness of implants composed of polyurethane with silicone and polyethylene oxide (PU–S–PEO) and the associated FBR response; the capsule that developed around a thin (300 μm) implant was significantly less than that which developed around a thick (2000 μm) implant (see **Chapter 4.413, Patterned Biointerfaces**).[40]

5.503.4.1.2. Porosity of biomaterial

Porous scaffolds allow for cellular penetration which in turn enables the integration of an implant within the host vasculature and leads to better implant function. Porous scaffolds allow for the ingrowth of fibrovascular tissue, which can improve the survival of implanted cells.[9] In another study, implantation of solid versus porous hydroxylapatite ceramics and their effects on healing bone defects into newly drilled beagle mandibular bone were compared. After 40 days, histological comparison indicated the presence of newly formed bone around both implants, but only the defects filled with porous hydroxylapatite showed bone incorporation and evidence of vascularization within the implant.[41] Thus, implantation of porous materials allows the ingrowth of tissue, enabling a more vascularized response in the surrounding tissue.

5.503.4.1.3. Microstructure of biomaterial: pore size

Given the benefit of using porous material for implants, one might assume that increasing the pore size would increase the degree of vascularization in and around the implants. However, there appears to be an optimum range of pore size that evokes the most vascularized FBR around implants regardless of the

implant material. Early studies by Campbell and von Recum[42] have shown that the thickness of foreign body capsules developing around samples of Versapor filter paper varied according to the paper's pore size, irrespective of the implant chemistry. Implants with pore diameters <0.5 μm showed nonadherent, contracting capsules and larger (≥3.3 μm) pore sizes became infiltrated with inflammatory tissue. However, an implant with pores sizes 1.4–1.9 μm evoked thin, tightly adherent fibrous capsules without inflammatory cells. After 12 weeks, there were a few small blood vessels around the outer edge of the capsule, and there were occasional capillaries or small vessels inside the capsule, lying directly against the implant.

The FBRs elicited by more than 150 membranes (including cellulose acetate, mixed-esters cellulose, polytetrafluoroethylene (PTFE), and acrylic copolymer) of various pore sizes (0.02–15 μm) were evaluated following subcutaneous implantation in rats.[43] Irrespective of composition, membranes with pore sizes of 5–15 μm resulted in vascularized capsules with blood vessels directly adjacent to the membrane surface (**Figure 2(b)**). In contrast, avascular capsules typical of a FBR surrounded membranes with smaller pore sizes (**Figure 2(a)**). Salzmann *et al.* showed that ePTFE implants with a pore size of 60 μm were associated with more rapid vascularization and thinner fibrous capsules than implants with pores of 30 or 100 μm.[44] Similar results were observed in studies investigating FBR around implants in which pore size was expressed in terms of fibril length or internodal distance. Implants with fibril lengths of 60 μm evoked the thinnest capsules and resulted in the largest degree of vascularization. Following implantation of porous PTFE vascular grafts into baboon iliac arteries,[45,46] grafts with an internodal distance of 60 μm (but not 30 μm) induced microvasculature to grow through the graft wall with capillaries ~100–500 μm apart.[45] Similarly, later studies of varying fibril lengths in porous ePTFE implants showed that neoendothelial healing on grafts with 60- and 90-μm-long fibrils was better than that observed on 20- and 40-μm-long fibril grafts.[47] These and additional studies suggesting that the size of pores in biomaterial affects the structure of neovascularization are summarized in **Table 1**.

An implanted biomaterial with an appropriate pore size allows formation of a vascularized capsule, which should facilitate transport of biomolecules and nutrients between the implant and host. Sharkawy *et al.* quantified the effects of biomaterial microarchitecture on parameters influencing transport from the host circulation to the implanted biomaterial, including vessel permeability, diffusivity, vessel density, and effective tissue response times.[51–53,57] The studies investigated porous (5–700 μm pore sizes) polyvinyl alcohol (PVA)

Table 1 Summary of vascularization in/around porous implanted biomaterials

Investigator	*Porous material*	*Optimal pore size (μm)*	*Application and test subject*	*Duration of investigation and outcome*
Brauker *et al.*[43]	PTFE	5	Membrane implanted in rat subcutis	3 weeks Vascularized membranes were maintained for up to 1 year.
Menger *et al.*[48]	PTFE	1–30	Membrane implanted in the skin flap of hamster	10 days Porous membranes with larger fibril lengths (30 μm) leading to stable vascularization at membrane surface. No vascular infiltration.
Clowes *et al.*[45,46]	PTFE	30–60	Membrane implanted in the artery of baboon	12 weeks and 3 months respectively Implanted porous vascular grafts allow microvessels to grow through. Effect is more pronounced with 60 μm intermodal distance.
Salzmann *et al.*[49] and Williams *et al.*[50]	PTFE	30–100	Membrane implanted subcutaneously or in fat of rats	Up to 5 weeks Implanted porous vascular grafts allow vascularization. Effect is most enhanced with 60 μm internodal distance.
Sharkawy *et al.*[51–53]	PVA	5–700	Membrane implanted in rat subcutis for 12–16 weeks	4 weeks, and 3–4 months Implanted porous membranes lead to increased vascularization of capsule. Intermediate size (60 μm) is most pronounced
Ward *et al.*[40]	ePTFE and PVA	ePTFE: 1 PVA: 47	Membrane implanted in rat subcutis	7 weeks Angiogenesis in both implants.
Updike *et al.*[54]	ePTFE	5–10	Glucose sensor implanted in dog subcutis	162 days[a] (best of six sensors)
Yu *et al.*[55]	Epoxy-enhanced polyurethane	Not specified	Glucose sensor implanted in rat subcutis	56 days[a] (best of nine sensors)
Gilligan *et al.*[56]	ePTFE	Not specified	Glucose sensor implanted in human subcutis	185 days[a] (best of five sensors)

ePTFE, expanded polytetrafluoroethylene; PVA, polyvinyl alcohol.
[a]Maximum time sensor remained functional *in vivo*.

grafts implanted subcutaneously in rats for 3–4 weeks; PTFE implants (0.5 or 5 μm pore sizes) were also evaluated.[52,53] The permeability of vessels around implants with 60 μm pores was comparable to normal tissue, whereas vessels within capsules around implants of other pore sizes had permeabilities 63–85% lower than normal tissue.[52,53] Typically, the capsule around an implant is relatively avascular, with the blood vessels nearest the implant concentrated in the tissue surrounding the capsule. Transport from the vasculature to the implant would be facilitated by decreasing this distance, either by increasing the vasculature within the capsule or by decreasing the capsule thickness. Capsules around implants with 60 μm pores contained 40% more blood vessels than found in normal tissue.[52,53] Additionally, vessels in these capsules, as well as those in the tissue that had grown into the pores, persisted for at least 12 weeks.[51–53]

Proposed mechanisms by which pore size influences neovascularization in and around implanted biomaterials focus on the prevention of undesirable cellular infiltration, improved tissue integration, and modulation of macrophage shape. Several researchers[44–47] who reported that pore sizes of ~60 μm evoked the maximum amount of vascularization in and around implants speculated that pore sizes >60 μm may allow undesired inflammatory cell infiltration, resulting in the formation of a capsule that ultimately hinders effective microvessel formation. Results from subcutaneous implantation of smooth or textured (surface irregularities of 10–50 μm) polyethylene disks in rats led Rosengren *et al.* to speculate that implant motion relative to host tissue shears adjacent cells, causing necrosis and inflammation. Textured or porous implants were associated with less necrosis and formation of smaller capsules, which the authors attributed to an ingrowth of tissue that minimized relative motion.[58] Similarly, enhanced tissue attachment to textured implant surfaces (but not to solid and smooth surfaces) has been suggested to ultimately reduce the foreign body capsule thickness *in vivo* (**Figure 3**). von Recum and van Kooten investigated whether a grooved surface presented to a connective tissue implantation bed could allow fibroblast attachment, potentially eliminating micro motion between cells and substrate and favorably influencing the overall tissue response to the implant; they found that macrophages and giant cells were absent whenever fibroblasts attached to the implant's surface.[59] Padera *et al.* hypothesized that the formation of a loosely packed, vascularized capsule rather than a well-organized avascular capsule may depend on the shape of the macrophages that interact with the implant.[60] They suggested that a larger pore size (8 μm in their study) allowed macrophages to remain round, which may have favored the secretion of angiogenic factors. In contrast, smaller pore sizes that did not permit cell infiltration led to macrophage spreading on the implant surface, which may have encouraged fibroblast proliferation and collagen secretion.[60] Although it is uncertain which of these hypotheses best explains the available data, the overall body of research illustrates the broad influence of biomaterial microstructure and especially pore size on the structure and function of the microvasculature.

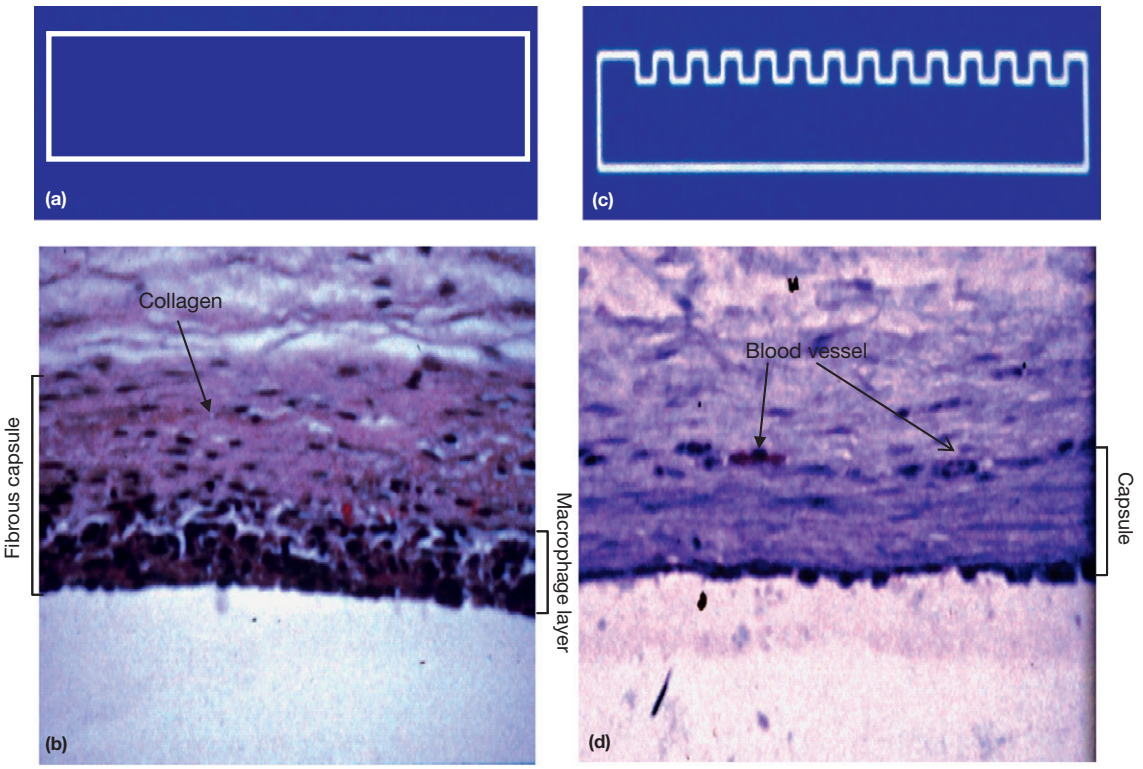

Figure 3 FBR around smooth and textured implants. Images kindly provided by Dr. Andreas Von Recum. Smooth surfaced solid bulk implants (a) show the development of a thick capsule (b), whereas the same implant when texturized to create grooves (c) shows the development of a less densely packed capsule with infiltrating cells in and around the implant (d).

5.503.4.1.4. Microstructure of biomaterial: fibrous materials

The studies reviewed in the previous section clearly demonstrate that biomaterial microstructure is an important, perhaps dominant, determinant of the microvascular structure in tissue surrounding implanted biomaterials. In these *in vivo* studies, the characteristic size of the microstructural elements stimulating neovascularization is on the order of 50 μm. Other studies, primarily conducted *in vitro*, suggest that microstructural elements on the submicron scale play important roles in the assembling of isolated endothelial cells into multicellular structures such as microvascular networks. The *in vitro* formation of microvascular networks from isolated endothelial cells on or within a scaffold or matrix resembles *in vivo* vasculogenesis. In both cases, isolated cells must come together to form an interconnected, branching, multicellular structure.

A recent study of endothelial cells cultured on polyacrylamide gels suggests that cells communicate mechanically through compliant substrates.[61] Adjacent cells on stiff gels (33 000 Pa) appeared relatively uninfluenced by nearby cells while those on gels of intermediate stiffness (2500–5500 Pa) repeatedly contacted and separated without moving far from one another. Endothelial cells on the most compliant gels studied (500 Pa) tended not to separate once contact had been made. By tracking fluorescent particles embedded in the gels, it was shown that endothelial cells were able to deform a larger area of softer gels relative to stiffer gels. The authors suggested that in compliant gels, separated cells could communicate with each other across ~50 μm by straining the intervening substrate. In stiffer gels, however, matrix deformation was of smaller magnitude and was limited to the regions closest to the cells, impairing intercellular communication. In another study[62] it was noted that relative to fibroblasts and mesenchymal stem cells cultured on modified polyacrylamide gels, cells on fibrin gels affected the orientation of other cells at much larger distances. These long-range effects with fibrin gels resulted in large-scale cellular patterning not seen with cells on polyacrylamide. Winer *et al.* attributed the longer-range signaling and organization in fibrin to either its fibrous nature or its strain-stiffening relative to polyacrylamide's linearly elastic behavior.[62]

The notion that cells exploit the effective transmission of forces by fibers to facilitate organization of multicellular structures is well supported in several 2D and 3D systems. In a series of elegant microscopy-based studies, Vernon, Sage and others showed that by exerting tension, endothelial cells on top of ECM gels remodeled the matrix to form bundles of ECM that connected nearby cells.[63,64] The cells then appeared to preferentially migrate along these fibers to form interconnected multicellular networks resembling a 2D or planar vascular plexus. Similarly, when small clusters or spheroids of endothelial cells were embedded within type-1 collagen gels, cells sprouted from individual clusters and moved toward one another. As in the 2D system, imaging revealed that aligned collagen fibers provided connections in which cells, initially separated, appeared to migrate toward one another. To confirm that collagen fiber alignment was the cause and not the result of directional fiber alignment, Korff and Augustin strained the collagen, thereby aligning the collagen fibers, before cell migration had begun.[65] Consistent with the notion that migration was in the direction of aligned fibers, the sprouting cells preferentially moved in the direction of the externally imposed collagen fiber alignment. Interestingly, Korff and Augustin noted that sprouting endothelial cells did not migrate toward other sprouts within fibrin, an observation that they attributed to the significantly shorter length of the fibrin fibers relative to the collagen fibers. To our knowledge, the only other gel material that supports robust 3D microvascular network formation *in vitro* resembling capillary networks *in vivo* is fibrin,[66] which has a fibrous structure, and self-assembling peptide gels, which possess a fibrous structure very similar to collagen gels.[67,68]

While the previous studies demonstrating the influence of fibrous materials on the migration and aggregation of isolated endothelial cells were all conducted *in vitro*, Vernon and Sage present arguments that similar tension- and fiber-mediated guidance of endothelial cells might account for the well-known ability of sprouting capillary tips to find one another and connect during angiogenesis, thereby forming a continuous route for blood flow. Additional evidence for the role of fiber guidance in endothelial cell migration *in vivo* includes intravital microscopy observations of newly forming capillaries. In three different forms of angiogenesis (normal tissue development, wound healing, and application of angiogenic factors), the large majority of new capillaries remained in contact with, and aligned with, preexisting elastin fibers, suggesting that the migration of endothelial cells and pericytes is guided by elastin fibers during capillary sprouting.[69] Based on the effect of endogenous ECM fibers on the directional sprouting of capillaries *in vivo*, Anderson *et al.* suggested that fibers in a tissue engineering construct could be rationally designed to control neovascularization of engineered tissues.

In both the *in vitro* and *in vivo* experiments described above, the fibrous matrices directing endothelial cell migration share similar properties. In each case, the diameter of the fibers are small relative to cells (on the order of 0.1–1 μm), have relatively long persistence lengths (e.g., the fibers are relatively straight on the length scale of the cell), and form interconnecting networks. Taken together, these experimental results suggest the following conceptual model of microvascular networks in a fibrous matrix summarized in **Figure 4**. Initially separated cells interact within a 3D ECM gel consisting of fibrous proteins (**Figure 4(a)**). The cells exert forces on the fibers, thereby remodeling the matrix by aligning fibers between cells (**Figure 4(c)**). These aligned fibers effectively transmit stresses over relatively large distances and the cells migrate along the aligned fibers to form multicellular structures (**Figure 4(d)**). As an initial step toward rigorously evaluating this conceptual model, Ma *et al.* used confocal reflectance microscopy images of endothelial cells and adjacent collagen fibers as a basis of finite element analysis of force transmission (**Figure 5(a)**).[70] This analysis revealed that collagen fibers can effectively transmit stresses over long distances (>100 μm) between separated cells in a cell-populated gel (**Figure 5(b)**). In contrast, their simulations revealed that in nonfibrous gels with the same bulk stiffness as the fibrous gels, stresses are not transmitted beyond ~10 μm from the cells (**Figure 5(c)**). These simulations provide quantitative support for the notion that the fibrous nature of stromal ECM and some synthetic biomaterials greatly increases the distance over which endothelial cells can transmit forces, thereby facilitating their assembly into multicellular microvascular networks.

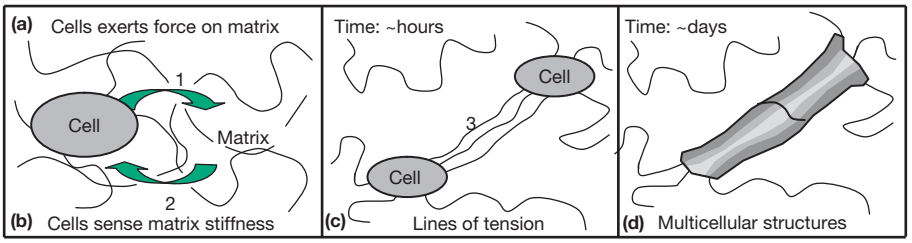

Figure 4 Dynamic reciprocal interactions between cells and matrix. (a) Cells exert forces on the matrix. (b) Mechanical properties of the matrix are sensed by cells and affect cellular function, including force generation. (c) Over a period of hours, cell-derived forces reorganize the matrix including aligned stress-bearing fibers connecting nearby cells. (d) Over a period of days, complex multicellular structures form. The architecture of these structures depends on the mechanical properties of the biomaterial.

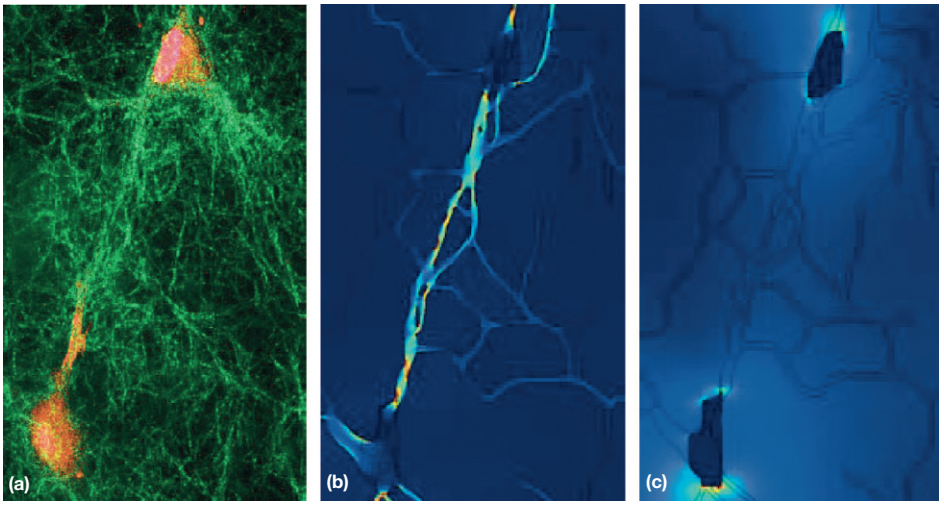

Figure 5 Confocal images (a) reveal the location of collagen fibers (green) and cells (red). Two cells realign the collagen fibers between them (a). Finite element analysis reveals that these fibers effectively carry forces over relatively large distances between the two cells (b). To ensure the concentration of stresses in the fibers is not a meshing or computational artifact, for the mesh used for (b), the modulus of the fiber and nonfiber regions were made the same, thus creating a homogenous material with a FE mesh the same as a fibrous material. In this homogeneous material (c), stress fields decayed rapidly, thereby diminishing the potential for effective, long-range mechanically mediated communication. Reproduced from Ma, X.; Gooch, K. J.; Sieminski, A. L.; Hart, R. T. Finite element modeling of the cellular mechanical environment. In *2008 BMES Annual Fall Meeting*, 2008.

The important role that the fibrous structure of the stromal ECM plays in *in vitro*, and potentially *in vivo*, neovascularization raises the question of whether a fibrous matrix is essential for neovascularization. Evidence suggests that although fibrous matrices are an important factor for neovascularization, they do not need to be directly provided. First, in porous scaffolds placed *in vivo*, cells invade pores and lay down new matrix, forming vascularized tissue which fills the porous volume, though the tissue does not enter the solid phase of the biomaterial.[9] Second, *in vitro* endothelial cells do not elongate or form microvascular networks within Matrigel, which lacks the fibrous structure of stromal ECM. However, if endothelial cells and fibroblasts are cocultured within Matrigel, the fibroblasts elongate, providing an alternative structural support upon which the endothelial cells can then elongate upon a rudimentary microvascular network form. In addition, upon implantation *in vivo*, Matrigel can become neovascularized as a result of vascular tunneling (described in **Section 5.503.3.1**). In this process, bundles of collagen fibers often run along the length of the resulting vascular tubes, suggesting that even in cases where stromal ECM fibers were not initially present, endogenous fibrous ECM are laid down and aligned before or during capillary formation.[37] Endothelial cells suspended within poly (ethylene glycol) (PEG) diacrylate hydrogels functionalized with the cell adhesive peptide RGDS, vascular endothelial growth factor (VEGF), and a collagenase-degradable motif formed tube structures and interconnecting networks, though the cells did not appear as elongated or interconnected as typically observed with endothelial cells in collagen gels or *in vivo*.[71] Interestingly, the endothelial cell seeding density used in modified PEG was 30-fold greater than typically used for collagen gels, suggesting that an impaired ability to transmit forces over long dimensions might be compensated by decreasing intercellular distances. Thus, the action of nonendothelial cells or perhaps very large concentrations of endothelial cells might enable at least rudimentary microvascular network formation in nonfibrous matrices. Another question is whether normal vascular structure and function can be achieved in biomaterials that do not have a fibrous structure. Though there are inadequate data to conclusively answer this question, results

thus far indicate that microvascular networks formed *in vitro* have more physiological structures (e.g., are more continuous, contain lumens) when created within natural or synthetic biomaterials with a fibrous structure resembling stromal ECM.

5.503.4.1.5. Biomaterial stiffness

While biochemical signals from soluble (e.g., growth factors) and insoluble ligands (e.g., integrin-binding sites) are known to affect numerous cell functions, only recently has biomaterial stiffness been recognized as an important factor regulating cellular proliferation, adhesion, migration, spreading, and differentiation. Though the focus of this chapter is primarily on the microvasculature, it is important to note that many studies have suggested that substrate stiffness affects the function of virtually all cell types, though the relevant absolute magnitude of stiffness varies with cell type. For example, the spreading of various cell types is dependent on both the density of binding ligands on a surface and the material's compliance, with spreading favored on stiffer surfaces.[72–74] Substrate stiffness also has been shown to affect the migration rate of numerous cell types including endothelial cells,[61] fibroblasts,[75] and smooth muscle cells[76] and to influence the differentiated activity of neurons,[77] myofibroblasts,[78] and mesenchymal stem cells (see **Chapter 5.504, Effect of Substrate Modulus on Cell Function and Differentiation**).[79]

A review of studies investigating the effect of biomaterial stiffness indicates that surface formation of endothelial cell networks is generally enhanced by seeding on softer substrates. Stiffening Matrigel[80] or collagen[81] by glycosylation decreased network formation by endothelial cells plated on the surface of the gels, although cells on stiffened Matrigel attached, spread, and proliferated as they had on unmodified Matrigel.[80] Trends towards decreased network formation by endothelial cells were also seen when cells were plated on collagen[82] or fibrin[83] gels stiffened by increasing the ECM concentration. Endothelial cells on ECM-coated polyacrylamide gels of decreasing stiffness were more rounded and began to form network-like structures.[84,85] In an early study highlighting the role of matrix mechanics and influence of boundary conditions, endothelial cells were seeded on Matrigel which had been gelled on a slant to provide a continuum of matrix thickness[82]; the cells increasingly formed networks as the Matrigel thickness increased, corresponding to a decrease in perceived stiffness.

As decreasing substrate stiffness has been associated with enhanced surface formation of microvascular networks on substrates, similar trends have been reported for cells within biomaterials. Recent studies extending 2D work into a 3D context have shown that cell spreading and migration depend upon matrix stiffness,[86,87] and numerous studies have shown that stiffness affects capillary morphogenesis in 3D biomaterials. One system designed to study capillary morphogenesis involves endothelial cells seeded on microcarrier beads which are embedded within, and subsequently sprout into, fibrin gels. Enhanced capillary morphogenesis within fibrin gels has been observed in more compliant gels when stiffness is modulated by changing the fibrin concentration,[13,88] or pH,[89] or by adding Factor VIII.[90] Similar results were observed in studies of endothelial cells suspended singly within collagen gels, where decreasing collagen concentration (and thus stiffness) was associated with more extensive capillary morphogenesis.[66,91] This trend was also observed in a study of endothelial cell network formation using self-assembling peptide gels, synthetic polypeptide-based biomaterials with microstructures similar to collagen.[68]

Because material properties of polymeric biomaterials are frequently altered by changing the monomer concentration, crosslink density or other aspects of the polymerization conditions (e.g., pH, cofactors), isolation of the key factors influencing network formation can be difficult. For example, changes in matrix structure (e.g., increased fiber density or decreased pore size) might impact both the ability of cells to penetrate the material and the diffusion of key growth factors,[92] while modifying the extracellular matrix concentration changes the density of integrin-binding sites. To more carefully decouple key parameters, many groups have developed synthetic polymeric systems, frequently based upon PEG with tethered cell adhesion sites (often RGD) in which binding site density and stiffness can be independently altered.[71,86,93] Alternately, materials such as self-assembling peptides show minimal changes in microarchitecture over broad changes in stiffness and concentration, minimizing the effect of changing pore size.[67] As adhesion to these materials is thought to be via adsorbed adhesion proteins,[67] their use may also minimize variation of adhesion sites while changing concentration. It is important to recognize that the stiffness perceived by cells is also a function of geometry and boundary conditions of the material due to cell-generated traction.[94] Though the difficulty in separating variables necessitate caution in generalizing results obtained in these different systems, the overall trend appears to be that biomaterial stiffness is an important determinant of endothelial cell function, with a tendency for capillary morphogenesis to be favored in relatively soft supports.

As described in **Section 5.503.4.1.5**, traction forces exerted by endothelial cells are an important aspect of capillary morphogenesis; network formation is dependent on functional contractile machinery and related signaling pathways.[95–97] Though not considered a primary function, endothelial cells clearly generate force, as demonstrated by their compaction of collagen gels,[82,94,98,100,101] with force generation increasing with 2D substrate stiffness.[101] In a comparison of endothelial cells from different sources cultured under different biochemical conditions, the extent of network formation correlated with the extent of force generation, as measured by gel compaction.[102] Further, a population of endothelial cells exerting higher forces showed enhanced network formation in relatively stiff collagen gels,[103,104] while cells exerting less force require more compliant gels to form extensive networks.[94] In comparison, the stiffness required to support robust network formation in self-assembling peptide gels is nearly an order of magnitude lower than that of collagen gels.[68] It has been hypothesized that this is due to a relative decrease in the strength of endothelial cell adhesion to peptide gels. This is consistent with the decrease in network formation seen when endothelial cell adhesion to collagen gels was blocked with blocking integrin antibodies.[102] Based on this body of work, capillary morphogenesis within a biomaterial appears to be modulated by a balance of the ability of a cell to apply force to the matrix (based on contractile or adhesion strength) with the ability of the biomaterial support to resist deformation. Endothelial cell traction force generation is a key aspect of the local remodeling

of fibrous biomaterials (also described in Section 5.503.4.1.5) important in capillary morphogenesis. Recent microscopic work investigating network formation in collagen gels demonstrates this sort of local remodeling.[105,106] This is consistent with the complex profile emerging for many cell types that the cell–matrix interaction is both reciprocal and dynamic.

A conceptual model that considers microvascular network formation as a balance between cell traction force and matrix stiffness[94] offers a framework to answer questions such as: Why do some endothelial cell lines appear to tolerate stiffer matrices while others require more compliant matrices for proper microvascular network formation? Why is the ideal stiffness for microvascular network formation by a particular endothelial cell line in one biomaterial several-fold greater than the ideal stiffness in another? Cell traction is a function of the cells' ability to generate force and to transmit force to the matrix, with the latter being dependent on cell–matrix adhesion. As illustrated in Figure 6, in this conceptual model, there is no ideal absolute value of matrix stiffness or endothelial traction for microvascular network formation. Instead, a proper ratio of cell traction and matrix adhesion is required. When cell traction is large relative to matrix stiffness, the cells compact the matrix excessively, leading to very high cell densities and a loss of cell viability. When cell traction is small relative to matrix stiffness, cells fail to form microvascular networks. Only when cell traction and matrix stiffness are balanced do microvascular networks form. The legend of Figure 6 discusses specific experimental results in the context of this conceptual model that illustrate the models to account for the effects of cell force generation, cell–matrix adhesion, and matrix stiffness on the formation of microvascular networks in natural and synthetic biomaterials. With a more complete understanding of the mechanical and molecular basis by which material stiffness regulates cellular function, we can provide answers to these questions and move toward the rational design of scaffolds to support the formation of microvascular networks for tissue engineering and regenerative medicine.

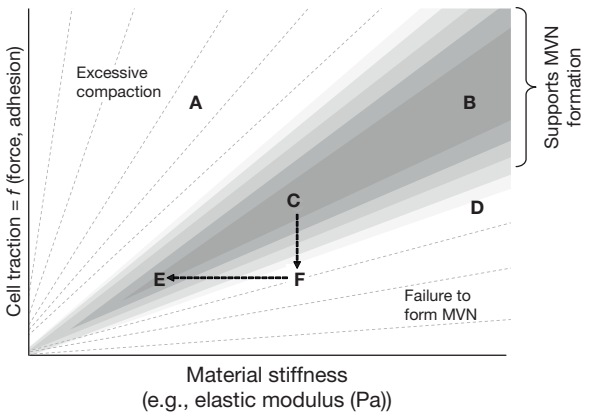

Figure 6 A schematic relating stiffness, traction and MVN formation on semiquantitative axes of cell traction and matrix stiffness. Material stiffness can be changed by changing concentration, polymerization conditions, cross-linking, and boundary conditions. Cell traction can be varied by using different cell sources with different force generation capability or by changing cell adhesion strength. For example, HBOEC in collagen gels exert more force (a, b) than HUVEC (c, d) as described in Sieminski, A. L.; Hebbel, R. P.; Gooch, K. J. *Exp. Cell Res.* **2004**, *297*(2), 574–584. Further, HUVEC in collagen gels (c) exert force more effectively than those in SAP gels (e, f), thus requiring a decrease in SAP stiffness to promote MVN formation (e) as described in Sieminski, A. L.; Was, A. S.; Kim, G.; Kamm, R. D. *Cell Biochem. Biophys.* **2005**, *49*(2), 73–83. The balance of these factors determines whether cells form MVN (gray region; b, c, and e) or do not (white regions) – with the region above the MVN-supporting area representing extreme compaction (a) and the region below representing failure to elongate and/or form multicellular structures (d, f). This framework allows us to understand why HUVEC form MVN in very soft SAP gels (e) and in moderately soft collagen gels (c) and HBOEC form MVN in considerably stiffer collagen gels (e.g. b). Schematic modified from Sieminski, A. L.; Hebbel, R. P.; Gooch, K. J. *Exp. Cell Res.* **2004**, *297*(2), 574–584.

While the previous examples come from *in vitro* studies, there is growing appreciation of the influence of tissue stiffness on cellular function *in vivo* as well. For example, there is evidence that the increased stiffness found in tumors is an important epigenetic factor regulating the expression of the transformed phenotype by oncogene expressing cells.[107] It is tempting to further speculate that the elevated stiffness in the tumor and surrounding tissue may contribute to atypical microvasculature morphology found in tumors such as the unusually large lumen areas, perhaps similar to the irregular capillary networks with excessively large lumens observed in an *in vitro* collagen-based assay performed with endothelial cells cultured in stiff matrices.[94] Along similar lines, tumor-derived endothelial cells show increased stiffness-dependent spreading and increased activity of Rho and ROCK, key players in contractility, and also form irregular structures with large lumens when cultured in Matrigel.[108] One could also speculate that the impaired angiogenesis observed in diabetics may be attributed to tissue stiffening mediated by cross-linking via advance glycosylation products,[81] or that the decreased angiogenesis and wound healing associated with aging could be linked to increasing collagen stiffness.[109]

5.503.4.2. Chemical and Biochemical Features of Biomaterials

5.503.4.2.1. Endothelial cell adhesion to biomaterials in vitro

The physiochemical properties of synthetic and naturally occurring biomaterials play a crucial role in biomaterial–microvasculature interactions. Investigations designed to clarify the nature of cell adhesion to biomaterials using endothelial cells and other adherent cell types have yielded generalizable trends. Some biomaterials contain cell adhesion sequences, either intrinsic (e.g., many ECMs) or by design (e.g., RGD-tethered materials). In the absence of these sequences, cellular adhesion must occur indirectly, typically via adsorbed adhesion proteins. The surface energy of the biomaterial has a great influence on the amount and structure of adsorbed proteins. Increasing hydrophobicity has been associated with increased adsorption of proteins[110] as well as increasing cell adhesion and spreading.[111,112] However, some functional groups on biomaterials have been noted to have an effect on cell adhesion independent of hydrophobicity.[49,113,114] Further, even materials with apparently similar surface properties may show drastic differences in protein adsorption and, thus,

behavior *in vivo*. The surface energy can also change the conformation of adsorbed proteins, which can affect the availability of cell adhesion motifs and influence the behavior of endothelial and other cell types.[115,116] In particular, proteins may become denatured on extremely hydrophobic surfaces,[116,117] limiting cell adhesion.[116]

5.503.4.2.2. Endothelial network formation on and in functionalized biomaterials

Endothelial network formation has been explored on 2D surfaces with adsorbed or covalently bound adhesion molecules. Early work investigating network formation as a function of collagen IV or fibronectin coating concentration on tissue culture plastic showed that network formation was promoted at an intermediate ECM concentration, with networks starting to form at high fibronectin concentrations if cell seeding density was increased.[73] More recent work in which collagen I density on polyacrylamide gels was precisely controlled showed an interplay between substrate stiffness and collagen density, with low collagen density promoting network formation on stiffer substrates.[84] PEG hydrogels functionalized with RGD-binding motifs have also been shown to promote formation of networks by endothelial cells seeded upon their surfaces.[118] Various PEG-RGD systems have been used to show that tethering the adhesion ligand, ephrin A1,[118] increases the length of network structures and that adding matrix metalloproteinase (MMP)-releasable thymosin β4, an actin-binding peptide, speeds up network formation.[119] Organization of endothelial cells into cord or tube-like structures has also been promoted by constraining their adhesion onto adhesive stripes micropatterned with ECM molecules or RGD-PEG.[119,120]

Only recently have several reports of *in vitro* angiogenesis assays within functionalized synthetic biomaterials been reported. The Chen group reported that PEG gels with RGD and MMP-sensitive sites support angiogenic sprouting from embedded chick aortic arch explants. They show that the longest sprouts occur in gels with the most highly degradable MMP sites.[121] In another study by the West group, endothelial cells cocultured with 10T1/2 cells in PEG gels functionalized with RGD and MMP-sensitive sites began to form tubular structures, with an intermediate concentration of PEG supporting cell structures for up to 6 days.[122] Functionalizing fibrin gels with a $\alpha_v\beta_3$ adhesion site, L1Ig6, enhanced sprouting of endothelial cells seeded on microcarrier beads and embedded in the gels.[123]

5.503.4.2.3. The role of chemistry in FBR in vivo

To some degree, development of a favorable FBR around an implant can be achieved through customization of an implant's chemical composition. An implant can have a chemical composition or surface tethered groups that will potentially inhibit FBR and capsule formation around the implant. For example, Ward *et al.*[40] showed that hydrophilic PEO implants developed much thinner capsules compared to PU implants. Another useful modification to implant chemistry may be designing implants that would release angiogenic factors such as nitric oxide (NO), potentially reducing FBR and capsule formation around the implant. Hetrick *et al.* implanted NO-releasing polymers in to Sprague-Dawley rats and showed that the FBR was decreased compared to controls. Additionally, more blood vessels in proximity to NO-releasing implants after 1 week were located compared to controls.[124]

5.503.4.2.4. Angiogenic factors

As described by Judah Folkman in his partially autobiographical account of the origin of controlled-release technology, many early attempts at prolonged, spatially controlled delivery of proteins focused on elucidating the role of specific proteins on the angiogenic response.[125] Using various *in vivo* systems, a variety of factors that stimulate angiogenesis have been identified. Controlled delivery of these factors to other vascular beds also promotes angiogenesis, with the effects of VEGF and basic fibroblast growth factor (bFGF) among the most widely studied.

In the first generation of controlled delivery systems, localized delivery of the angiogenic protein at a constant rate was often considered the ideal goal. Continuous delivery of angiogenic proteins has been achieved for more than a month,[126] and can lead to enhanced angiogenesis.[127–133] Depletion of the angiogenic factor in the controlled delivery system is often followed by regression of the new vessels, an effect similar to that observed following wound healing. More recently, efforts to improve the longevity of newly formed vessels have included localized delivery of cDNA or viral vectors coding for angiogenic proteins, with the rationale that genetically modified cells within the target area would represent a more permanent local source of angiogenic factors.[134] Animal studies as well as early stage clinical trials support the potential of gene delivery to stimulate and maintain new vessel formation as reviewed elsewhere.[135,136] Specific challenges associated with clinical implementation of this approach have recently been reviewed.[137] For example, early efforts to deliver VEGF via gene therapy resulted in overstimulation and the formation of hemangiomas.[136]

Rather than prolonging the delivery of angiogenic factors, an alternative approach to maintaining newly formed microvasculature is the introduction of biological factors that stabilize new vessels. One example of this approach employed a porous polymeric scaffold in which VEGF was associated with the surface and platelet-derived growth factor (PDGF) was embedded in the polymer. With this dual-delivery system, the majority of VEGF is delivered over the first ~10 days to promote the formation of new vessels, whereas the release of PDGF occurs over a longer period (~1 month) to facilitate the recruitment of mural cells to stabilize the newly formed vessels.[138] When implanted subcutaneously in rats for 4 weeks, the dual-delivery system increased the number and average size of vessels in the surrounding tissue relative to either factor alone and resulted in approximately fourfold increase in the number of mature vessels, as assessed by immunostaining for α-smooth muscle actin. An injectable version of a similar dual-delivery system also resulted in improved vessel maturity and tissue vascularization in a mouse model.[139]

The approaches described above represent attempts to achieve a predefined delivery rate of the desired factor(s). Others have explored methods in which the delivery rate of angiogenic factors from matrices is controlled by biological stimuli (so-called 'active-release' or 'cell-demanded release'). One example of this approach is the covalent modification of VEGF to a PEG gel via MMP-sensitive peptide linkers.[140] The release of biologically active VEGF from these gels would be triggered by exposure to MMP-2 or plasmin, the former likely

acting by cleaving peptide linkers and the latter by cleaving VEGF at a previously described plasmin-sensitive site. PEG gels containing covalently bound VEGF have been shown to induce angiogenesis when placed on a chick chorioallantoic membrane (CAM) and were invaded by vascular tissue when implanted subcutaneously in rats. Similarly, the use of factor XIIIa to covalently bind fibrin to a modified form of VEGF resulted in a fibrin gel exhibiting plasmin- and MMP-mediated VEGF release.[141] As with the PEG-based system, the covalently bound VEGF-fibrin gels induced angiogenesis in the CAM following subcutaneous implantation in the mouse. Interestingly, the very permeable or leaky vessels often associated with VEGF-induced angiogenesis were not present, suggesting that coupling the availability of VEGF to cellular activity (or perhaps by simply reducing local VEGF concentrations) enabled retention of the permeability barrier of the microcirculation.

5.503.5. Case Studies

In the final section, we will consider attempts at bioengineering neovascularization using biomaterials. The goal of this section is not to provide a complete review of these areas but to illustrate how the results of many of these studies can be understood in light of the principles discussed in this review.

5.503.5.1. Implantation of Preformed Microvascular Networks

Long-term function of 3D tissue constructs depends on adequate vascularization after implantation, which represents one of the major challenges in tissue engineering. Creation of microvascular networks within 3D tissue constructs *in vitro* prior to implantation may facilitate the introduction of engineered blood vessels that retain functional stability *in vivo*. Early work in this area was conducted in the context of cell-based gene therapy approaches in which preformed microvascular networks of genetically modified endothelial cells were implanted *in vivo* with the hopes of releasing the desired gene product directly into the circulation. Hemangioblasts implanted into 3D gels of Matrigel resulted in the formation of microvascular networks with a fraction of the cells expressing markers of endothelial cell differentiation.[22–24] If the hemangioblast cells were first stably transfected so that they secreted human growth hormone (hGH), implantation of hemangioblast/Matrigel constructs resulted in systemic delivery of hGH. In contrast, cultures of adult endothelial cells failed to form microvascular networks in Matrigel or to systemically deliver hGH *in vivo*.[25] To explore the potential role of nonendothelial cells in stabilizing microvascular network formation *in vitro* and *in vivo*, Sieminski *et al.* mixed hGH-expressing adult endothelial cells with non-hGH-expressing fibroblasts within a 3D gel of Matrigel.[25] Endothelial cell/fibroblast mixtures formed microvascular networks *in vitro* and delivered hGH systemically for at least 6 weeks.

Koike and Jain *et al.* showed that a stable, long-lasting network of blood vessels could be established in mice by implantation of 3D constructs made from human umbilical–vein endothelial cells and 10T1/2 mesenchymal precursor cells seeded and cocultured in a 3D fibronectin-type I collagen gel.[14,142] The formation of blood vessels *in vivo* was tracked by incorporation of enhanced green fluorescent protein into the endothelial cells. After 4 days, the endothelial and 10T1/2 mesenchymal precursor cell constructs formed long, interconnected tubes with branching, but no evidence of perfusion. However, at 4 weeks the tubes began to connect to the mouse's circulatory system and became perfused. After 4 months, the number of perfused vessels was increased and nonperfused vessels were not evident. The networks formed were stable and functional for 1 year *in vivo*.[14] Furthermore, the engineered vessels responded to vasoactive stimuli and demonstrated higher vascular permeability than normal blood vessels.[14] In contrast, the control 3D constructs that were made from endothelial cells alone showed evidence of minimal perfusion and disappeared after 1 month *in vivo*. More recent studies by Patrick and Jain *et al.*[142] suggested that human bone marrow-derived mesenchymal stem cells (hMSCs) may also serve as a source of cells for use in vascular tissue engineering. They showed that although hMSCs did not differentiate into endothelial tubes capable of carrying blood, they did function as perivascular cells when coimplanted with endothelial cells *in vivo*. These hMSC-derived perivascular cells constricted in response to stimulation by the endogenous vasoconstrictive peptide, endothelin-1, and were found to stabilize nascent blood vessels that remained functional for more than 130 days *in vivo*.

Studies from other groups have also shown that isolated and intact microvessel fragments retain their angiogenic potential and are capable of forming a microvascular bed when cultured in a 3D collagen I gel.[143] Further implantation of this microvascular construct into mice rapidly inosculated vessels from the construct into the host circulation after the first day of implantation. After 28 days, evaluation of these constructs revealed the presence of a mature functional microvascular bed.[144]

These studies, in conjunction with those in **Section 5.503.2.1**, demonstrate progress toward the creation of microvascular networks within engineered tissues and the ability of engineered microvascular networks to stably integrate with the host vasculature. The successful studies all shared a common element: the introduction of nonendothelial cells, either intentionally[14,25,102,142] or likely unintentionally as part of the microvascular fragments.[143] Furthermore, a comparison of the quality of microvascular networks across these studies indicates that those present in fibrous collagen were superior to those present in Matrigel.

5.503.5.2. Extravascular Wraps for Grafted Veins

Human saphenous veins are widely used for coronary artery bypass grafts despite the lower long-term success relative to arteries. Grafting a saphenous vein into the arterial circulation represents an abrupt transition from a mild mechanical environment (i.e., low pressure and shear stress with minimal pulsatility) to the more strenuous mechanical environment of the arterial circulation. It is often suggested that the elevated pressure (or pulsatility) in the arterial circulation subjects the vein to excessive circumferential stresses (or cyclic strains), which it is not designed to withstand, thereby mechanically injuring the vein and initiating a cascade of events that leads to intimal hyperplasia.[145–147] It has been suggested that introduction of a

supportive, tight-fitting extravascular wrap to reduce the mechanical stresses in the wall of grafted veins might improve their performance. Contrary to this hypothesis, supportive vascular wraps in a porcine model did not improve the performance of grafted veins; however, somewhat unexpectedly, performance of vein grafts was improved when sheathed in looser nonrestrictive wraps that did not mechanically support the veins. It was determined that the loose-fitting wraps were beneficial only when they were made of porous materials; loose-fitting wraps made from nonporous materials were not beneficial. Veins with the loose-fitting porous wraps developed a distinct 'neoadventitia' with abundant microvasculature in the perivascular space between the graft and the stent[148] which was not evident in unstented grafts or in grafts stented with a nonporous stent.[149] While not commented on by the authors of these studies, the vascularizing effects of the porous wraps are similar to that observed with biomaterials implanted subcutaneously (**Section 5.503.4.1.3**). Studies by Nugent and Edelman[150] have shown that gel foam sponges seeded with endothelial cells and wrapped around blood vessels prevent intimal hyperplasia, providing a potential link between the neovascularization of the extravascular space with porous loose-fitting vascular wraps and the observed inhibition of intimal hyperplasia.[148]

5.503.5.3. Glucose Sensors

Principles of enhancing vascularization have been utilized to prevent the formation of a fibrous capsule around implantable glucose sensors. Attempts to incorporate growth factors such as VEGF induced significant neovascularization surrounding the implanted sensor and greatly enhanced the glucose sensor function *in vivo* in an *ex ova* chicken embryo CAM-glucose sensor model.[151,152] Other groups have attempted to increase the diffusivity of the analyte glucose from the sensor to the host tissue by applying water soluble PVA hydrogel coatings.[153] This approach tends to reduce inflammation around the implant and therefore can increase vascularization. Combining these principles, Norton and Reichert have shown that glucose sensors coated with VEGF-releasing hydrogels increased vascularity and inflammation in the surrounding tissue after 2 weeks of implantation compared to hydrogel-coated sensors alone.[152] Finally, efforts to create porous coatings to improve vascularization around glucose sensor implants have been successful. In a study by Koswanez and Reichert[154] porous poly lactic acid coatings with pore sizes ranging from 36 to 84 μm applied to the sensor surface when implanted *in vivo* reduced fibrosis and promoted microvessel formation in adjacent tissues. Furthermore, the porous coatings did not interfere with sensor accuracy or its response rate *in vitro*.[154] All of these studies collectively demonstrate strategies to reduce FBR and enhance vascularization around implants as discussed previously.

Acknowledgment

This work was supported by NSF CMMI-0928739 to KJG.

References

1. Carrel, A. *J. Exp. Med.* **1912**, *15*(5), 516–528.
2. Carrel, A. *J. Exp. Med.* **1912**, *16*, 165–168.
3. Carrel, A. *J. Exp. Med.* **1913**, *18*(3), 287–298.
4. Carrel, A. *J. Exp. Med.* **1916**, *24*, 367–372.
5. Lindbergh, C. A. *J. Exp. Med.* **1935**, *62*(3), 409–431.
6. Dutkowski, P.; de Rougemont, O.; Clavien, P. A. *Am. J. Transplant.* **2008**, *8*(10), 1998–2003.
7. Black, A. F.; Berthod, F.; L'Heureux, N.; Germain, L.; Auger, F. A. *FASEB J.* **1998**, *12*(13), 1331–1340.
8. Cima, L. G. V. J.; Vacanti, C.; Ingber, D.; Mooney, D.; Langer, R. *J. Biomech. Eng.* **1991**, *113*(2), 143–151.
9. Mikos, A. G.; Sarakinos, G.; Lyman, M. D.; Ingber, D. E.; Vacanti, J. P.; Langer, R. *Biotechnol. Bioeng.* **1993**, *42*(6), 716–723.
10. Mooney, D. J.; Sano, K.; Kaufmann, P. M.; *et al. J. Biomed. Mater. Res.* **1997**, *37*(3), 413–420.
11. Cuono, C. B.; Langdon, R.; Birchall, N.; Barttelbort, S.; McGuire, J. *Plast. Reconstr. Surg.* **1987**, *80*(4), 626–637.
12. Holder, W. D. G.; Helen, E.; Roland, W. D.; *et al. Tissue Eng.* **1997**, *Summer*, 149–160.
13. Ghajar, C. M.; Chen, X.; Harris, J. W.; *et al. Biophys. J.* **2008**, *94*(5), 1930–1941.
14. Koike, N.; Fukumura, D.; Gralla, O.; Au, P.; Schechner, J. S.; Jain, R. K. *Nature* **2004**, *428*(6979), 138–139.
15. Messina, L. M.; Podrazik, R. M.; Whitehill, T. A.; *et al. Proc. Natl. Acad. Sci. USA* **1992**, *89*(24), 12018–12022.
16. Beger, C.; Cirulli, V.; Vajkoczy, P.; Halban, P. A.; Menger, M. D. *Diabetes* **1998**, *47*(4), 559–565.
17. Griffith, L. G.; Wu, B.; Cima, M. J.; Powers, M. J.; Chaignaud, B.; Vacanti, J. P. *Ann. N Y Acad. Sci.* **1997**, *831*, 382–397.
18. Chrobak, K. M.; Potter, D. R.; Tien, J. *Microvasc. Res.* **2006**, *71*(3), 185–196.
19. Golden, A. P.; Tien, J. *Lab Chip* **2007**, *7*(6), 720–725.
20. Janakiraman, V.; Mathur, K.; Baskaran, H. *Ann. Biomed. Eng.* **2007**, *35*(3), 337–347.
21. Janakiraman, V.; Sastry, S.; Kadambi, J. R.; Baskaran, H. *Biomed. Microdev.* **2008**, *10*(3), 355–365.
22. Squinto, S. P.; Madri, J. A.; Kennedy, S.; Springhorn, J. *In Vivo* **1994**, *8*(5), 771–780.
23. Wei, Y.; Quertermous, T.; Wagner, T. E. *Stem Cells* **1995**, *13*(5), 541–547.
24. Wei, Y.; Li, J.; Wagner, T. E. *Stem Cells* **1996**, *14*(2), 232–238.
25. Sieminski, A. L.; Padera, R. F.; Blunk, T.; Gooch, K. J. *Tissue Eng.* **2002**, *8*(6), 1057–1069.
26. Joseph, J. M.; Goddard, M. B.; Mills, J.; *et al. Cell Transplant.* **1994**, *3*(5), 355–364.
27. Tresco, P. A.; Winn, S. R.; Tan, S.; Jaeger, C. B.; Greene, L. A.; Aebischer, P. *Cell Transplant.* **1992**, *1*(2–3), 255–264.
28. Hoffman, D.; Breakefield, X. O.; Short, M. P.; Aebischer, P. *Exp. Neurol.* **1993**, *122*(1), 100–106.
29. al-Hendy, A.; Hortelano, G.; Tannenbaum, G. S.; Chang, P. L. *Hum. Gene Ther.* **1995**, *6*(2), 165–175.
30. Chick, W. L. P. J.; Lauris, V.; Low, D.; *et al. Science* **1977**, *197*(4305), 780–782.
31. Gough, D. A.; Armour, J. C. *Diabetes* **1995**, *44*(9), 1005–1009.
32. Folkman, J. *Ann. Rev. Med.* **2006**, *57*(1), 1–18.
33. Jin, S. W.; Patterson, C. *Arterioscler. Thromb. Vasc. Biol.* **2009**, *29*(5), 623–629.
34. Burri, P. H.; Hlushchuk, R.; Djonov, V. *Dev. Dyn.* **2004**, *231*(3), 474–488.
35. Djonov, V.; Baum, O.; Burri, P. H. *Cell Tissue Res.* **2003**, *314*(1), 107–117.
36. Anghelina, M.; Krishnan, P.; Moldovan, L.; Moldovan, N. I. *Stem Cells Dev.* **2004**, *13*(6), 665–676.
37. Anghelina, M.; Krishnan, P.; Moldovan, L.; Moldovan, N. I. *Am. J. Pathol.* **2006**, *168*(2), 529–541.
38. Ratner, B. D. *J. Control. Release* **2002**, *78*(1–3), 211–218.
39. Francis, M. E.; Uriel, S.; Brey, E. M. *Tissue Eng.* **2008**.
40. Ward, W. K.; Slobodzian, E. P.; Tiekotter, K. L.; Wood, M. D. *Biomaterials* **2002**, *23*(21), 4185–4192.
41. Gunhan, O.; Bal, E.; Celasun, B.; Sengun, O.; Finci, R. *Aust. Dent. J.* **1994**, *39*(1), 25–27.
42. Campbell, C. E.; von Recum, A. F. *J. Invest. Surg.* **1989**, *2*(1), 51–74.
43. Brauker, J. H.; Carr-Brendel, V. E.; Martinson, L. A.; Crudele, J.; Johnston, W. D.; Johnson, R. C. *J. Biomed. Mater. Res.* **1995**, *29*(12), 1517–1524.
44. Dennis, L. S.; Leigh, B. K.; Scott, S. B.; Stuart, K. W. *J. Biomed. Mater. Res.* **1997**, *34*(4), 463–476.
45. Clowes, A. W.; Kirkman, T. R.; Reidy, M. A. *Am. J. Pathol.* **1986**, *123*(2), 220–230.
46. Clowes, A. W.; Zacharias, R. K.; Kirkman, T. R. *Am. J. Surg.* **1987**, *153*(5), 501–504.
47. Hirabayashi, K.; Saitoh, E.; Ijima, H.; Takenawa, T.; Kodama, M.; Hori, M. *J. Biomed. Mater. Res.* **1992**, *26*(11), 1433–1447.

48. Menger, M. D.; Walter, P.; Hammersen, F.; Messmer, K. *Eur. J. Cardiothorac. Surg.* **1990**, *4*(4), 191–196.
49. Salzmann, D. L.; Kleinert, L. B.; Berman, S. S.; Williams, S. K. *J. Biomed. Mater. Res.* **1997**, *34*(4), 463–476.
50. Williams, S. K.; Berman, S. S.; Kleinert, L. B. *J. Biomed. Mater. Res.* **1997**, *35*(4), 473–481.
51. Sharkawy, A. A.; Klitzman, B.; Truskey, G. A.; Reichert, W. M. *J. Biomed. Mater. Res.* **1997**, *37*(3), 401–412.
52. Sharkawy, A. A.; Klitzman, B.; Truskey, G. A.; Reichert, W. M. *J. Biomed. Mater. Res.* **1998**, *40*(4), 586–597.
53. Sharkawy, A. A.; Klitzman, B.; Truskey, G. A.; Reichert, W. M. *J. Biomed. Mater. Res.* **1998**, *40*(4), 598–605.
54. Updike, S. J.; Shults, M. C.; Gilligan, B. J.; Rhodes, R. K. *Diabetes Care* **2000**, *23*(2), 208–214.
55. Yu, B.; Long, N.; Moussy, Y.; Moussy, F. *Biosens. and Bioelectron.* **2006**, *21*(2), 2275–2282.
56. Gilligan, B. C.; Shults, M.; Rhodes, R. K.; *et al. Diabetes Technol. Ther.* **2004**, *6*(3), 378–386.
57. Sieminski, A. L.; Gooch, K. J. *Biomaterials* **2000**, *21*(22), 2232–2241.
58. Agneta, R.; Nils, D.; Lars, M. B. *J. Biomed. Mater. Res.* **1999**, *46*(4), 458–464.
59. von Recum, A. F.; van Kooten, T. G. *J. Biomater. Sci. Polym. Ed.* **1995**, *7*(2), 181–198.
60. Padera, R. F.; Colton, C. K. *Biomaterials* **1996**, *17*(3), 277–284.
61. Reinhart-King, C. A.; Dembo, M.; Hammer, D. A. *Biophys. J.* **2008**, *95*(12), 6044–6051.
62. Winer, J. P.; Oake, S.; Janmey, P. A. *PLoS One* **2009**, *4*(7), e6382.
63. Vernon, R. B.; Lara, S. L.; Drake, C. J.; *et al. In Vitro Cell. Dev. Biol. Anim.* **1995**, *31*(2), 120–131.
64. Vernon, R. B.; Sage, E. H. *Am. J. Pathol.* **1995**, *147*(4), 873–883.
65. Korff, T.; Augustin, H. G. *J. Cell Sci.* **1999**, *112*(Pt 19), 3249–3258.
66. Sieminski, A. L.; Gooch, K. J. *J. Biomater. Sci. Polym. Ed.* **2004**, *15*, 237–242.
67. Sieminski, A. L.; Semino, C. E.; Gong, H.; Kamm, R. D. *J. Biomed. Mater. Res. A* **2008**, *87*(2), 494–504.
68. Sieminski, A. L.; Was, A. S.; Kim, G.; Gong, H.; Kamm, R. D. *Cell Biochem. Biophys.* **2007**, *49*(2), 73–83.
69. Anderson, C. R.; Ponce, A. M.; Price, R. J. *J. Histochem. Cytochem.* **2004**, *52*(8), 1063–1072.
70. Ma, X.; K. J. G.; Sieminski, A. L.; Hart, R. T. Finite element modeling of the cellular mechanical environment. In *2008 BMES Annual Fall Meeting,* 2008.
71. Leslie-Barbick, J. E.; Moon, J. J.; West, J. L. *J. Biomater. Sci. Polym. Ed.* **2009**, *20*(12), 1763–1779.
72. Engler, A.; Bacakova, L.; Newman, C.; Hategan, A.; Griffin, M.; Discher, D. *Biophys. J.* **2004**, *86*(1 Pt 1), 617–628.
73. Ingber, D. E.; Folkman, J. *J. Cell Biol.* **1989**, *109*(1), 317–330.
74. Yeung, T.; Georges, P. C.; Flanagan, L. A.; *et al. Cell Motil. Cytoskeleton* **2005**, *60*(1), 24–34.
75. Pelham, R. J., Jr.; Wang, Y. *Proc. Natl. Acad. Sci. USA* **1997**, *94*(25), 13661–13665.
76. Peyton, S. R.; Putnam, A. J. *J. Cell Physiol.* **2005**, *204*(1), 198–209.
77. Flanagan, L. A.; Ju, Y. E.; Marg, B.; Osterfield, M.; Janmey, P. A. *Neuroreport* **2002**, *13*(18), 2411–2415.
78. Grinnell, F.; Ho, C. H. *Exp. Cell Res.* **2002**, *273*(2), 248–255.
79. Engler, A. J.; Sen, S.; Sweeney, H. L.; Discher, D. E. *Cell* **2006**, *126*(4), 677–689.
80. Kuzuya, M.; Satake, S.; Miura, H.; Hayashi, T.; Iguchi, A. *Exp. Cell Res.* **1996**, *226*(2), 336–345.
81. Kuzuya, M.; Satake, S.; Ai, S.; *et al. Diabetologia* **1998**, *41*(5), 491–499.
82. Vernon, R. B.; Angello, J. C.; Iruela-Arispe, M. L.; Lane, T. F.; Sage, E. H. *Lab. Invest.* **1992**, *66*(5), 536–547.
83. Vailhe, B.; Ronot, X.; Tracqui, P.; Usson, Y.; Tranqui, L. *In Vitro Cell. Dev. Biol. Anim.* **1997**, *33*(10), 763–773.
84. Califano, J.; Reinhart-King, C. *Cell. Mol. Bioeng.* **2008**, *1*(2), 122–132.
85. Deroanne, C. F.; Lapiere, C. M.; Nusgens, B. V. *Cardiovasc. Res.* **2001**, *49*(3), 647–658.
86. Peyton, S. R.; Raub, C. B.; Keschrumrus, V. P.; Putnam, A. J. *Biomaterials* **2006**, *27*(28), 4881–4893.
87. Zaman, M. H.; Trapani, L. M.; Sieminski, A. L.; *et al. Proc. Natl. Acad. Sci. USA* **2006**, *103*(29), 10889–10894.
88. Kniazeva, E.; Putnam, A. J. *Am. J. Physiol. Cell Physiol.* **2009**, *297*(1), C179–C187.
89. Nehls, V.; Herrmann, R. *Microvasc. Res.* **1996**, *51*(3), 347–364.
90. Urech, L.; Bittermann, A. G.; Hubbell, J. A.; Hall, H. *Biomaterials* **2005**, *26*(12), 1369–1379.
91. Kanzawa S, E. H.; Shioya, N. *Ann. Plast. Surg.* **1993**, *30*(3), 244–251.
92. Ghajar, C. M.; Blevins, K. S.; Hughes, C. C.; George, S. C.; Putnam, A. J. *Tissue Eng.* **2006**, *12*(10), 2875–2888.
93. Kraehenbuehl, T. P.; Ferreira, L. S.; Zammaretti, P.; Hubbell, J. A.; Langer, R. *Biomaterials* **2009**, *30*(26), 4318–4324.
94. Sieminski, A. L.; Hebbel, R. P.; Gooch, K. J. *Exp. Cell Res.* **2004**, *297*(2), 574–584.
95. Cascone, I.; Giraudo, E.; Caccavari, F.; *et al. J. Biol. Chem.* **2003**, *278*(50), 50702–50713.
96. Connolly, J. O.; Simpson, N.; Hewlett, L.; Hall, A. *Mol. Biol. Cell* **2002**, *13*(7), 2474–2485.
97. Tan, W.; Palmby, T. R.; Gavard, J.; Amornphimoltham, P.; Zheng, Y.; Gutkind, J. S. *FASEB J.* **2008**, *22*(6), 1829–1838.
98. Davis, G. E.; Camarillo, C. W. *Exp. Cell Res.* **1995**, *216*(1), 113–123.
99. Kolodney, M. S.; Wysolmerski, R. B. *J. Cell Biol.* **1992**, *117*(1), 73–82.
100. Stevenson, M. D.; Sieminski, A. L.; McLeod, C. M.; Byfield, F. J.; Baracoas, V. H.; Gooch, K. J. *Biophys. J.* **2010**, *99*(1), 19–28.
101. Reinhart-King, C. A.; Dembo, M.; Hammer, D. A. *Biophys. J.* **2005**, *89*(1), 676–689.
102. Sieminski, A. L.; Hebbel, R. P.; Gooch, K. J. *Tissue Eng.* **2005**, *11*(9–10), 1332–1345.
103. Shentu, T. P.; Titushkin, I.; Singh, D.; *et al. Am. J. Physiol. Cell.* **2010**, *299*(2), C218–C229.
104. Byfield, F. J.; Tikku, S.; Rothblat, G. H.; Gooch, K. J.; Levitan, I. *J. Lipid Res.* **2006**, *47*(4), 715–723.
105. Kirkpatrick, N. D.; Andreou, S.; Hoying, J. B.; Utzinger, U. *Am. J. Physiol. Heart Circ. Physiol.* **2007**, *292*(6), H3198–H3206.
106. Lee, P. F.; Yeh, A. T.; Bayless, K. J. *Exp. Cell Res.* **2009**, *315*(3), 396–410.
107. Paszek, M. J.; Zahir, N.; Johnson, K. R.; *et al. Cancer Cell* **2005**, *8*(3), 241–254.
108. Ghosh, K.; Thodeti, C. K.; Dudley, A. C.; Mammoto, A.; Klagsbrun, M.; Ingber, D. E. *Proc. Natl. Acad. Sci. USA* **2008**, *105*(32), 11305–11310.
109. Wu, C. C.; Ding, S. J.; Wang, Y. H.; Tang, M. J.; Chang, H. C. *J. Biomater. Sci. Polym. Ed.* **2005**, *16*(10), 1261–1275.
110. Wilson, C. J.; Clegg, R. E.; Leavesley, D. I.; Pearcy, M. J. *Tissue Eng.* **2005**, *11*(1–2), 1–18.
111. Altankov, G.; Grinnell, F.; Groth, T. *J. Biomed. Mater. Res.* **1996**, *30*(3), 385–391.
112. Burmeister, J. S.; McKinney, V. Z.; Reichert, W. M.; Truskey, G. A. *J. Biomed. Mater. Res.* **1999**, *47*(4), 577–584.
113. Aoki, T.; Nagao, Y.; Sanui, K.; *et al. J. Biomater. Sci. Polym. Ed.* **1998**, *9*, 1–14.
114. McAuslan, B. R.; Johnson, G. *J. Biomed. Mater. Res.* **1987**, *21*(7), 921–935.
115. Baugh, L.; Vogel, V. *J. Biomed. Mater. Res. A* **2004**, *69*(3), 525–534.
116. Kim, J. H.; Kim, S. H.; Kim, H. K.; Akaike, T.; Kim, S. C. *J. Biomed. Mater. Res.* **2002**, *62*(4), 613–621.
117. Tanaka, M.; Motomura, T.; Kawada, M.; *et al. Biomaterials* **2000**, *21*(14), 1471–1481.
118. Moon, J. J.; Lee, S.-H.; West, J. L. *Biomacromolecules* **2006**, *8*(1), 42–49.
119. Dike, L.; Chen, C.; Mrksich, M.; Tien, J.; Whitesides, G.; Ingber, D. *In Vitro Cell. Dev. Biol. Anim.* **1999**, *35*(8), 441–448.
120. Moon, J. J.; Hahn, M. S.; Kim, I.; Nsiah, B. A.; West, J. L. *Tissue Eng. A* **2009**, *15*(3), 579–585.
121. Miller, J. S.; Shen, C. J.; Legant, W. R.; Baranski, J. D.; Blakely, B. L.; Chen, C. S. *Biomaterials* **2010**, *31*(13), 3736–3743.
122. Moon, J. J.; Saik, J. E.; Poche, R. A.; *et al. Biomaterials* **2010**, *31*(14), 3840–3847.
123. Hall, H.; Baechi, T.; Hubbell, J. A. *Microvasc. Res.* **2001**, *62*(3), 315–326.
124. Hetrick, E. M.; Prichard, H. L.; Klitzman, B.; Schoenfisch, M. H. *Biomaterials* **2007**, *28*(31), 4571–4580.
125. Folkman, J. *Biomaterials* **1990**, *11*(9), 615–618.
126. Ryu, W.; Huang, Z.; Prinz, F. B.; Goodman, S. B.; Fasching, R. *J. Control. Release* **2007**, *124*(1–2), 98–105.
127. Anat, P.; Yaacov, B.; Felix, W.; Gideon, S.; Gera, N.; Smadar, C. *J. Biomed. Mater. Res.* **2003**, *65A*(4), 489–497.
128. Elcin, A. E.; Elcin, Y. M. *Tissue Eng.* **2006**, *12*(4), 959–968.
129. Hosseinkhani, H.; Hosseinkhani, M.; Khademhosseini, A.; Kobayashi, H.; Tabata, Y. *Biomaterials* **2006**, *27*(34), 5836–5844.
130. Kwon, J. S.; Park, I. K.; Cho, A. S.; *et al. J. Control. Release* **2009**, *138*(2), 168–176.
131. Lee, J.; Lee, K. *Pharm. Res.* **2009**, *26*(7), 1739–1744.
132. Pike, D. B.; Cai, S.; Pomraning, K. R.; *et al. Biomaterials* **2006**, *27*(30), 5242–5251.
133. Shi, H.; Han, C.; Mao, Z.; Ma, L.; Gao, C. *Tissue Eng. A* **2008**, *14*(11), 1775–1785.
134. Trentin, D.; Hall, H.; Wechsler, S.; Hubbell, J. A. *Proc. Natl. Acad. Sci. USA* **2006**, *103*(8), 2506–2511.
135. Lokmic, Z.; Mitchell, G. M. *Tissue Eng. B Rev.* **2008**, *14*(1), 87–103.

136. von Degenfeld, G.; Banfi, A.; Springer, M. L.; Blau, H. M. *Br. J. Pharmacol*. **2003**, *140*(4), 620–626.
137. Giacca, M. *Int. J. Nanomed*. **2007**, *2*(4), 527–540.
138. Richardson, T. P.; Peters, M. C.; Ennett, A. B.; Mooney, D. J. *Nat. Biotechnol*. **2001**, *19*(11), 1029–1034.
139. Qinghua Sun, E. A. S.; Wang, A.; Fritton, J. C.; *et al*. *Pharm. Res*. **2010**, *27*(2), 264–271.
140. Ehrbar, M.; Zeisberger, S. M.; Raeber, G. P.; Hubbell, J. A.; Schnell, C.; Zisch, A. H. *Biomaterials* **2008**, *29*(11), 1720–1729.
141. Ehrbar, M.; Djonov, V. G.; Schnell, C.; *et al*. *Circ. Res*. **2004**, *94*(8), 1124–1132.
142. Au, P.; Tam, J.; Fukumura, D.; Jain, R. K. *Blood* **2008**, *111*(9), 4551–4558.
143. Hoying, J. B.; Boswell, C. A.; Williams, S. K. *In Vitro Cell. Dev. Biol. Anim*. **1996**, *32*(7), 409–419.
144. Shepherd, B. R.; Chen, H. Y. S.; Smith, C. M.; Gruionu, G.; Williams, S. K.; Hoying, J. B. *Arterioscler. Thromb. Vasc. Biol*. **2004**, *24*(5), 898–904.
145. Cornelissen, J.; Armstrong, J.; Holt, C. M. *Arterioscler. Thromb. Vasc. Biol*. **2004**, *24*(3), 451–456.
146. Motwani, J. G.; Topol, E. J. *Circulation* **1998**, *97*(9), 916–931.
147. Powell, J. T.; Gosling, M. *Curr. Opin. Cardiol*. **1998**, *13*(6), 453–458.
148. Angelini, G. D.; Izzat, M. B.; Bryan, A. J.; Newby, A. C. *J. Thorac. Cardiovasc. Surg*. **1996**, *112*(1), 79–84.
149. Jeremy, J. Y.; Gadsdon, P.; Shukla, N.; *et al*. *Biomaterials* **2007**, *28*(6), 895–908.
150. Nugent, H. M.; Rogers, C.; Edelman, E. R. *Circ. Res*. **1999**, *84*(4), 384–391.
151. Klueh, U.; Dorsky, D. I.; Kreutzer, D. L. *Biomaterials* **2005**, *26*(10), 1155–1163.
152. Norton, L. W.; Koschwanez, H. E.; Wisniewski, N. A.; Klitzman, B.; Reichert, W. M. *J. Biomed. Mater. Res. A* **2007**, *81*(4), 858–869.
153. Galeska, I.; Kim, T.-K.; Patil, S.; *et al*. *AAPS J*. **2005**, *7*(1), E231–E240.
154. Koschwanez, H. E.; Yap, F. Y.; Klitzman, B.; Reichert, W. M. *J. Biomed. Mater. Res. A* **2008**, *87*(3), 792–807.

5.504. Effect of Substrate Modulus on Cell Function and Differentiation

L Vincent and A J Engler, University of California, San Diego, La Jolla, CA, USA

© 2011 Elsevier Ltd. All rights reserved.

5.504.1.	**Introduction**	52
5.504.2.	**Young's Modulus**	52
5.504.2.1.	Definition and Measurement	52
5.504.2.1.1.	Microspheres under gravitational forces	52
5.504.2.1.2.	Microindenters	52
5.504.2.1.3.	Atomic force microscopy	53
5.504.2.1.4.	Additional considerations for measurement techniques	53
5.504.2.2.	Development, Maintenance, and Variation of Young's Modulus in Biology	53
5.504.2.2.1.	Development and maintenance of tissue stiffness	54
5.504.2.2.2.	Aging and disease	54
5.504.3.	**Fabrication of Substrates with Defined Material Modulus**	54
5.504.3.1.	Natural ECM Components	54
5.504.3.1.1.	Collagen	54
5.504.3.1.2.	Hyaluronic acid	55
5.504.3.1.3.	Alginate	55
5.504.3.1.4.	Matrigel	55
5.504.3.2.	Synthetic Hydrogels	55
5.504.3.2.1.	Polyacrylamide	55
5.504.3.2.2.	Polydimethylsiloxane	56
5.504.3.2.3.	Other systems	56
5.504.4.	**Cell Functions and Differentiation**	57
5.504.4.1.	Neutrophils	57
5.504.4.2.	Fibroblasts	58
5.504.4.3.	Neural Cells	59
5.504.4.4.	Myoblasts	59
5.504.4.5.	Stem Cells	60
5.504.4.6.	Cancer Cells	60
5.504.4.7.	Other Cell Types	61
5.504.5.	**Conclusion**	61
References		61

Glossary

Extracellular matrix The network of biological polymers assembled into a three-dimensional architecture that surrounds and provides anchorage sites for cells.

Young's modulus Ratio of the uniaxial stress over the uniaxial strain. Often this is measured in units of Pascal (Pa), which is a Newton per square meter.

Abbreviations

AFM	Atomic force microscopy
ECM	Extracellular matrix
ERK	Extracellular signal-regulated kinase
ESC	Embryonic stem cell
G	Guluronic acid
HA	Hyaluronic acid
M	Mannuronic acid
MSC	Mesenchymal stem cell
MSD	Mean squared displacement
PA	Polyacrylamide
PDMS	Polydimethylsiloxane
PEG	Polyethylene glycol
SMC	Smooth muscle cell
UV	Ultraviolet

5.504.1. Introduction

A cell's surrounding environment is composed of a variety of different components: adjacent cells to which they adhere via cadherin proteins, interstitial fluid containing soluble growth factors, and extracellular matrix (ECM), a three-dimensional (3D) protein scaffold to which cells adhere via heterodimers of α and β integrins. While ECM comes in many different forms and can be composed of many different proteins, cells can use the ECM to actively 'feel' their surroundings by pulling against it to transmit forces to adjacent cells. Neighboring cells can then use a series of mechanosensitive pathways to sense and respond to these forces via mechanical cross-talk. The nature of this communication between cells and their environment is regulated by several important properties of the ECM. One notable observation over the last decade has been that the ECM's Young's modulus, which is commonly referred to as 'stiffness' in biological literature, can direct cell response and drive specific functions. Studies examining how ECM properties affect cells have often employed synthetic hydrogels, which serve as an underlying substrate where one can decouple many of the chemical and physical properties that native ECM cannot. By studying each component independently, one can determine how a specific ECM property, for example, stiffness, topography (see **Chapter 4.409, Surfaces and Cell Behavior**), composition (see **Chapter 2.203, Protein-Engineered Biomaterials: Synthesis and Characterization**), etc., regulates cell behaviors, for example, spreading, migration, and differentiation, over a range of physiological conditions. Here, we first outline the techniques and materials used to modulate substrate modulus before describing how changes in modulus affect cell function and differentiation in widely studied 2D culture systems. In a concluding discussion, we contrast the behavioral differences of cells grown in 2D and 3D cultures.

5.504.2. Young's Modulus

5.504.2.1. Definition and Measurement

Young's modulus (abbreviated as E) is an intrinsic material parameter that describes the relationship between the unitless percent elongation of a material, that is, strain (ε), and the force applied per area, that is, stress (σ). Young's modulus can often be described by the linear relationship $E = \sigma/\varepsilon$, especially at low strain and is measured in units of Pascal (Pa) or Newton per square meter. Materials that are palpably stiffer will exhibit higher elastic moduli compared to softer materials. For biological tissues, most moduli range between the two extremes of bone and brain: the modulus of calcified bone is on the order of ~5 GPa,[1] though bone cells live within the nonmineralized 'osteoid,' while that of brain tissue is on the order of 1 kPa.[2] Such numbers are determined from small (< 20%) strain measurements, where many tissues and biomaterials exhibit a constant modulus.[3] At larger deformations, these materials tend to stiffen, in a process called strain stiffening, as materials begin to irreversibly deform, that is, fibrils within ECM permanently rearrange, causing a nonlinear modulus.[4,5] To account for this behavior, numerous nonlinear models have been developed,[6] but for cells in general, the strains generated do not exceed the 20% threshold.[7] Thus, our discussion here will be limited to techniques that determine Young's moduli at small strains.

The modulus of materials is most easily determined by applying a small force to a sample and measuring the resulting strain. As many biological tissues and cells experience smaller forces on the order of nano- or pico-Newtons, advanced methods have been developed to characterize the mechanics of cells and their surrounding tissue. Three of these techniques, microsphere indentation, microindenters, and atomic force microscopy (AFM), are summarized below. While we focus on micro- and nanoindentation methods here due to the length scale of cells and the magnitude of forces that they generate, it is important to note that there is a correlation between bulk mechanical properties and microscopic properties for many standard materials, for example, polyacrylamide (PA).[8] However, there are important deviations from this correlation, as in the case of poly(vinylpyrrolidone) hydrogels.[6,9] In subsequent sections, we will extend our description of these techniques to the materials of interest, for example, synthetic hydrogels and natural materials, where their mechanical properties depend on chemical composition and material structure.

5.504.2.1.1. Microspheres under gravitational forces

Microsphere indentation determines a material's Young's modulus by measuring the indentation depth of a metal microsphere on top of a substrate and comparing it to the gravitational force of the sphere[10] (**Figure 1(a)**). Beads typically a few hundred nanometers in diameter are confined in the substrate, and images of their positions before and after microspheres are placed on the substrate to enable one to compute indentation depth or displacement. The Young's modulus is then calculated from the sphere indentation model developed by Hertz[11]:

$$E = \frac{3(1-\nu^2)f^2}{4\delta^{3/2}r^{1/2}} \quad [1]$$

where ν is the Poisson's ratio, f is the buoyancy-corrected weight, δ is the depth of the indentation created by the ball, and r is the radius of the ball. This simple technique works with a high degree of reproducibility for E~2.2–33 kPa on both PA and gelatin substrates, where indentation is small but measurable.[12] However, determining Young's modulus of relatively thin (<100 μm) or exceedingly soft substrates, which are optimal for microscopy, requires a correction factor as the vertical displacement of the beads is affected by the underlying glass substrate. Moreover, this measurement technique requires confocal microscopy to accurately determine 3D bead positions, and, compared to more sensitive techniques, for example, AFM or microindenters, with moderately small displacements and beads, it can be prone to overestimate moduli. This technique also applies a single force determined by ball density and volume and thus cannot determine if the magnitude of indentation falls within the small strain linear range of the material or not. Despite such drawbacks, this measurement method is relatively straightforward and easy to perform.

5.504.2.1.2. Microindenters

Microindenters, originally developed to measure the Young's modulus of very stiff materials,[13] have recently been adapted to measure the Young's modulus of soft materials with

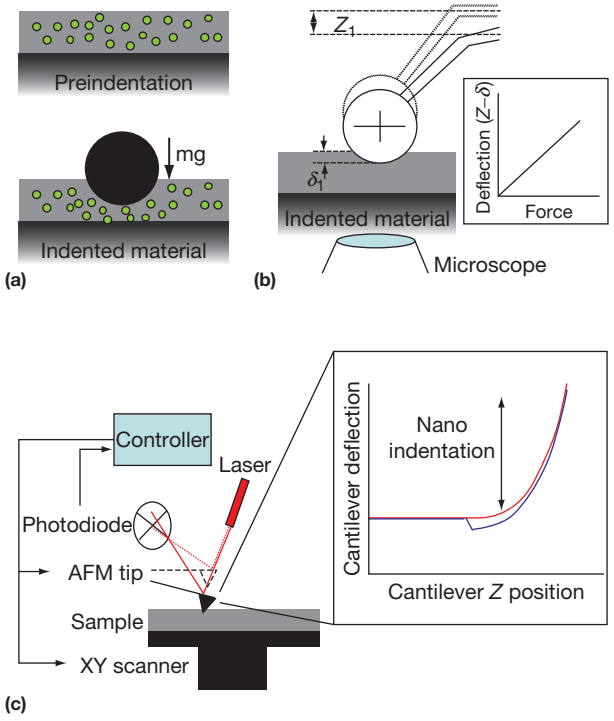

Figure 1 Techniques used to determine the Young's modulus of materials. Schematic representation of the experimental setup for microspheres (a), microindenters (b), and atomic force microscopy (c) to measure the Young's modulus of substrates.

biologically relevant stiffness in the range of kilo- and mega-Pascals (see **Chapter 3.306, Microindentation**).[14] Microindentation for soft materials typically uses a spherical tip with a radius of several microns, which is attached to the end of a flexible microneedle to probe the substrate (**Figure 1(b)**). Deformation of the tip is measured by optical microscopy and the resulting displacement compared to a standard curve to obtain the modulus as determined by the Hertz model (eqn [1]).[11] By tuning the stiffness of the indenter arm, varying ranges of substrate moduli can be measured. As such, microindentation measurements of soft hydrated materials such as PA substrates have been shown to correlate well with AFM measurements over the range ~2.5–40 kPa.[15] As with the microsphere technique, microindenters yield accurate moduli measurements when strains are kept small and when sample thickness is in the range of >100–150 μm. This technique relies on visual determination of tip position, and thus error from inaccurate vertical measurements can dramatically affect the modulus determined from the experiment. However, microindentation is performed on a microscope stage, and therefore offers an economical measuring technique for tissues over a wide range of sample geometries.

5.504.2.1.3. Atomic force microscopy

AFM was developed for imaging applications at microscale resolution (see **Chapter 3.302, Atomic Force Microscopy**) but has been extensively used to assess the mechanical properties of hydrated substrates.[16–19] This technique uses a precalibrated flexible cantilever with a pyramidal or spherical tip mounted on a piezoelectric device to indent the sample through a controlled amount of tip deflection (**Figure 1(c)**). A laser reflects off the backside of the tip, which is typically fabricated out of silicon nitride with a reflective gold coating on the top, onto a position-sensitive photodetector that measures the tip deflection during indentation. Since the tip behaves similarly to a Hookean spring, the indentation depth can be converted to force (f) using the tip spring constant, much like for microindenters. By separately comparing tip deflection when pressing on a hard material (where deflection scales perfectly to the piezomotor position), for example, glass, to the deflection when pressing into a soft material, it is possible to determine the actual indentation (δ) into the material. Using indentation models of a pyramid/cone developed by Sneddon (eqn [2])[20] or a sphere developed by Hertz (eqn [1]), it is possible to determine the Young's modulus, E:

$$f = \left[\frac{2\tan\alpha}{\pi}\right]\left[\frac{E}{1-\nu^2}\right]\delta^2 \qquad [2]$$

where α is the half opening angle of the pyramidal or conical tip. A thin film correction can be introduced to accurately determine the Young's modulus of substrates for sufficiently thin samples where the underlying support could dominate the mechanics absent this correction.[21] While the degree of correction is material-specific, for near linearly elastic materials, for example, PA gels, the correction enables one to measure Young's moduli of a sample independent of its thickness, provided that the sample thickness is a known quantity. For PA substrates, the correction has been shown to be necessary for gels below 20 μm thickness, independent of the material's actual bulk stiffness.[18] With these advantages, AFM is a preferred measurement technique over the other indentation methods to perform repeated measurements over small sample areas with high accuracy. However, instrument cost, limited longevity of cantilever tips, and adhesive interactions between the tip and the gel may make AFM difficult to implement for the average user.[22]

5.504.2.1.4. Additional considerations for measurement techniques

While many synthetic materials used in biological applications are hydrogels that are nearly linearly elastic, natural ECM is often not. Thus, it is important to note that materials are often anisotropic, meaning that their Young's modulus for the measured axis of indentation may not be identical to another axis of the material. In such instances, one must not rely solely on one indentation method but instead employ measurement techniques that probe different mechanical modes, for example, rheology. Though we will not go into great detail, rheology measures a shear modulus as it applies a force parallel to the top surface of a material rather than perpendicular as with the indentation techniques previously described. By converting shear to Young's moduli, direct comparison from multiple force modes is possible. So far, comparisons of AFM- and rheology-determined Young's moduli have shown good agreement for hydrogels.[23]

5.504.2.2. Development, Maintenance, and Variation of Young's Modulus in Biology

Cell and tissue modulus changes drastically during development and establishes the wide variation of elasticity in the body. Before producing materials on which to culture cells, it

is important to develop an understanding of the physiological context in which the cells of interest live, from development through aging, and ultimately disease.

5.504.2.2.1. Development and maintenance of tissue stiffness

In early development, the embryo is a conglomerate of cells with little architecture and is very compliant, that is, soft.[24,25] Further development into the three germ layers that comprise all tissues requires cell migration into the appropriate spatial configuration.[24,26] The ability of these cells to self-segregate into cells of similar type has been shown to depend on expression of particular markers such as E-cadherin and β-catenin involved in cell adhesion,[27] which has lead to the development of the idea of 'tissue affinity' or topobiology as coined by Edelman and colleagues.[28] However, cell sorting *in vivo* has also been attributed to the mechanics of the ECM.[26,29] For example, the stiffness of mesoderm dorsal tissue is orders of magnitude stiffer than endoderm in early amphibian embryos.[30] Additionally, amphibian embryos show a ~2-fold increase in stiffness during gastrulation,[24] which is specific to the germ layer in question as shown in zebrafish.[31] Young's modulus may therefore be a driving force in the development of tissues at the embryonic stage and not simply a consequence of development. Yet, once fully developed, biological tissues exhibit tremendous variation in stiffness. Appreciating this variation and designing materials to meet the needs of the cells of interest is critical for therapeutic applications, as discussed in **Section 5.504.4**. However, it is easy to appreciate this variation by considering the two extremes of bone and brain again: the bulk modulus of calcified bone is on the order of ~5 GPa[1] while that of brain tissue is on the order of 1 kPa or less.[2] While this variation is six orders of magnitude, it may represent a common misconception; the actual environment that osteoblasts inhabit is actually more representative of a highly cross-linked, collagenous environment with a modulus of 30–40 kPa.[32] Osteoblasts do not typically inhabit calcified regions of bone.[33] Nevertheless, it is absolutely critical to appropriately mimic one's *in vivo* surrounding *in vitro* (see **Figure 4**) to obtain meaningful cell behavior in culture.

5.504.2.2.2. Aging and disease

It should also be noted that the modulus of many tissues changes naturally with time and after the onset of certain diseases. For example, as we age our skin becomes less elastic,[34] and blood vessels[35] and articular cartilage[36] become progressively stiffer. At the root of these mechanical changes are protein level changes in ECM composition and cross-linking of adjacent matrix fibers. However, abnormal variations in modulus can also play a role in the development of many diseases.[35,37] Arthritis patients exhibit cartilage softening from progressive breakdown of the cartilage collagen meshwork[36] whereas patients with liver disease or myocardial infarction manifest enhanced stiffness due to the onset of fibrosis,[5,37] that is, the abnormal deposition of ECM. These changes impact the function and behavior of cells, owing to the constant cross-talk between cells and their microenvironment, and result in disease progression. With myocardial infarction, stiffening of the myocardial wall is accompanied by cell apoptosis, wall thinning, and a decrease in cardiac output as measured by ejection fraction.[5]

5.504.3. Fabrication of Substrates with Defined Material Modulus

To mimic the properties mentioned and measured above, we will profile a variety of natural and hydrogel-based supports that are often used in cell culture. For the former, close biomimicry provides a distinct advantage over all other materials. On the other hand, the latter provides materials with high water content that closely mimic physiological environments while at the same time allowing one to decouple variables, for example, ECM chemistry and mechanics, and observe how one matrix property in particular may influence cell behavior. Mechanical properties of both natural and synthetic matrices are based on (a) pore size, (b) polymer concentration, (c) polymer molecular weight, and (d) the degree of cross-linking among other parameters and can be varied by changing any one or a number of these factors. Below we offer material-specific discussions of how Young's modulus is changed using these parameters, starting with natural matrices and concluding with synthetic ones.

5.504.3.1. Natural ECM Components

With the complexity of the natural cellular environment, we focus on popular examples of several classes of biopolymers: collagen – representing the class of large network-forming matrix proteins, including fibronectin and laminin,[38] hyaluronic acid (HA) and alginate – representing the large carbohydrate polymers called glycosaminoglycans,[39] and Matrigel – a commercially available reconstituted basement membrane product. Though these matrices have shown particularly interesting results in how they regulate cell behavior, our discussion here will be limited to how these materials can be controlled to display a range of stiffness for cells.

5.504.3.1.1. Collagen

Fibrillar collagen is the most abundant ECM protein and constitutes a large portion of our connective tissue. There are a number of readily available sources, for example, rat tail, where collagen can be easily isolated.[38] By simply adjusting the pH of the solution[40] or collagen density,[38] polymerized matrices can be produced in the presence of cells (as a 3D matrix) or they can subsequently be added to the culture to provide a flat culture substrate (using collagen as a 2D coating). Given the relative ease with which one can produce these gels and the flexibility one has when using it, collagen has become a widely used cell scaffold. However, there are important mechanical considerations to be taken into account when using collagen. Altering collagen polymerization conditions or pretreating with pepsin can alter the pore size in the final product.[41] Changing the collagen concentration from ~0.1 to 3 mg ml^{-1} will also increase material modulus,[38,42] and these changes can also be presented in concentration gradients that also yield stiffness gradients.[43] Yet collagen gels have inherently coupled collagen density and stiffness: the more collagen ligand present, the stiffer the gel. Nonadhesive 'stiffening agents' can be introduced to try to decouple these components,[44] but as in the case of many 3D materials, smaller pores and ligand accessibility may alter cell adhesion and overall behavior in 3D,[45,46] making a link between stiffness and cell behavior more challenging.

That said, a number of applications of 2D and 3D collagen gels have actually been realized. Collagen has long been used as a surface coating and can dictate heart fibroblast behavior in 2D.[47] Collagen gels also have been engineered into sheet-based 3D models to study cell behavior[48] and compressed around cells to provide high-stiffness 3D environments similar to native tissue.[49] Overall, collagen gels exhibit good cytocompatibility, but given their mechanochemical coupling, they also possess drawbacks compared to more tunable synthetic systems, for example, PA, when examining *in vitro* cell characteristics.[50]

5.504.3.1.2. Hyaluronic acid

HA is a negatively charged linear polysaccharide made up of D-glucuronic and D-*N*-acetylglucosamine and commonly found in the ECM and connective tissue (see **Chapter 2.215, Collagen: Materials Analysis and Implant Uses**). Unique physical and chemical properties make HA an attractive biological substrate, but due to suboptimal mechanical properties and rapid degradation, chemical modification of the HA backbone is often performed to induce hydrogel formation and to build in specific functionality. For example, HA hydrogels can be formed by modifying the HA backbone and adding in cross-linkers, for example, thiolation to form disulfide bonds[51] or addition of polyethylene glycol (PEG)-diacrylate to the thiols,[52] or via direct conjugation of synthetic polymers, for example, PEG, poly(L-lysine) acid, poly(*N*-isopropylacrylamide), etc.[53] Copolymerization to form an interpenetrating network using collagen, alginate, or gelatin also yields stiffer hydrogels.[54,55] Most single-chemical modifications provide gels that are best suited to mimic the mechanics of soft tissues ~10–3500 Pa, such as brain.[55,56] HA can also readily undergo multiple, sequential modifications, such as being methacrylated for dithiol cross-linking via Michael-type addition and then undergoing radical polymerization via the free methacrylated sites (similar to photolithography techniques outlined in **Figure 3(b*ii*)**). This process enables multiple cross-linking steps to provide maximal flexibility and produce moduli ranging from 1 to 100 kPa.[58] As a natural polymer, HA is often used as an injectable material, and it has been shown to maintain left ventricle wall thickness during the normal remodeling process postmyocardial infarction.[59] While it is not certain if HA restores normal ventricle mechanical properties altered by the infarct,[5] it certainly implies that HA could be a promising natural material for regenerative use.

5.504.3.1.3. Alginate

Alginate is a derivative of sea algae that is often used for drug delivery, to encapsulate cells, or as a cell culture support.[60] Alginate gels are composed of interspersed elements of mannuronic (M) and guluronic acids (G) and divalent ions, for example, Ca^{+2}, which cross-link the alginate monomers into a reversible hydrogel. The M/G ratio has been shown to regulate how tightly cross-linked the hydrogel can become: gels with a low M/G ratio swell less than gels with a higher M/G ratio and thus yield stiffer hydrogels.[61] Alginate hydrogel stiffness can also be modulated by alginate concentration and chemical composition as well as the cationic species used. Increasing alginate and divalent ion concentration allows for higher cross-link density, yielding more rigid gels with moduli ranging from ~1 to 120 kPa.[62,63] Use of these gels in cell culture, however, reduces their stiffness up to 10-fold as the Na^{+} and Ca^{2+} present in culture media can interfere with cross-links,[64] but this can be overcome in part by using high-molecular-weight alginate and introducing covalent cross-links.[65] Gels composed of alginate derivatives such as poly(aldehyde guluronate) have been reported to achieve compressive modulus up to 1 MPa.[66]

5.504.3.1.4. Matrigel

Matrigel is a preparation of solubilized basement membrane proteins extracted from mouse sarcoma,[67] which typically contains varying amounts of laminin, collagen IV, heparan sulfate proteoglycans, entactin, and nidogen. To vary the mechanical properties of the material as with collagen, one must change the Matrigel concentration, and stiffness has been reported to range from 10 to 50 Pa, depending on concentration.[68] Copolymerization with type I collagen as an inner penetrating polymer network can further increase the composite's Young's modulus, but again over a limited range.[69,70] The lack of stiffness variation is an important consideration, but Matrigel is often used as a ligand coating or supporting matrix in conjunction with a synthetic material that independently varies stiffness, for example, mammary acinar cultures with Matrigel and PA hydrogels.[71] In this capacity, it is more often used in studies that want to ensure that the correct matrix composition is present, for example, during self-renewal of human embryonic stem cells (hESCs) in tissue culture.[72] Matrigel is not without its distinct advantages though; it is easily able to be cast into channels and shapes to pose questions about mechanics in pseudo-3D or 3D environments[73] without requiring functionalization.

5.504.3.2. Synthetic Hydrogels

5.504.3.2.1. Polyacrylamide

PA gels are inert, synthetic hydrogels most commonly used for protein separation in gel electrophoresis. As PA gels are easy to fabricate, have widely tunable mechanical properties, and are easily functionalized with adhesive ligands, these substrates are also well suited to study the effects of substrate modulus on a variety of cellular functions detailed in **Section 5.504.4**. Polymerization of PA hydrogels occurs through a free radical-driven reaction where acrylamide and bis-acrylamide solutions in varying concentrations are mixed with a free radical source, most commonly ammonium persulfate.[74] The mechanical properties of the synthesized gels vary from ~0.1 to 100 kPa (**Figure 2**),[18,75] where moduli values are based on common principles of condensed matter physics[76,77]; higher concentrations of acrylamide monomer yield stiffer gels (insets *iii and iv*) due to increased chain entanglement. Increasing cross-linker concentration, on the other hand, generates more physical tethers between the polymer backbone, thereby reducing individual chain flexibility and increasing the Young's modulus of the material (insets *ii* and *iv*). Uniform distribution of the free radical source or even mixing of the monomer and cross-linker generates static gels,[9] which are most commonly used for cell culture as they generate a roughly even cell response, making them suitable for many biochemical assays. However, PA gels can also be micropatterned with step or smooth gradients of Young's modulus made by polymerizing adjacent gels of different moduli (**Figure 3(a)**)[10,78] or by photoactivation of the

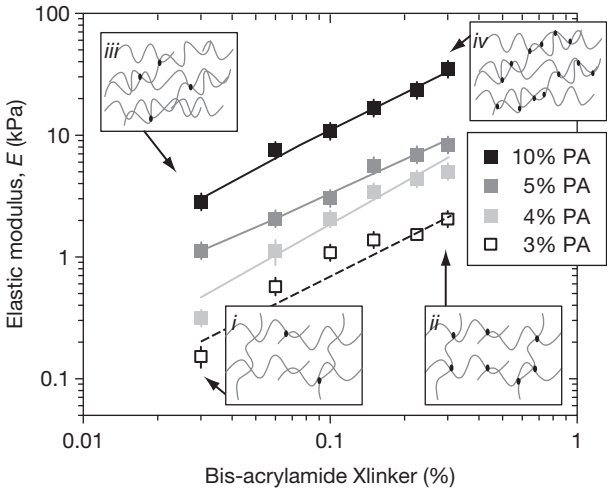

Figure 2 Elastic modulus of range of polyacrylamide gels. Elastic modulus of polyacrylamide substrates for gels with different concentrations of acrylamide monomer and bis-acrylamide cross-linker. Substrates polymerized in solutions with higher concentrations of acrylamide monomer yield stiffer gels (insets *iii* and *iv*) due to increased chain entanglement and nonspecific interactions between polymer chains. Adding increasing amounts of cross-linker in the polymerization mixture generates more physical tethers between the backbone of polymers and increases the Young's modulus of the material (insets *ii* and *iv*).

free radical initiator Irgacure 2959 via gradients of UV initiation (**Figure 3(b*i*)**)[79,80] or cross-linker concentration established in microchannels (**Figure 3(b*ii*)**),[57] respectively. Ultimately, these gradients study a cell's ability to undergo durotaxis ('duro' being latin for hard), that is, the characteristic movement of a cell along a stiffness gradient, and each of these techniques yields different gradient strengths, which has recently been shown to be important for cell behavior.[81] However, one of the main drawbacks to using PA substrates is acrylamide and initiator cytotoxicity. Gels must often be soaked in buffer before use to allow unreacted species to diffuse out of the substrates, thus limiting these polymers to 2D *in vitro* studies.

To facilitate cell attachment to the nonadhesive PA, proteins are usually covalently attached to the PA gel surface. Incubation with *N*-sulfosuccinimidyl-6-(4′-azido-2′-nitrophenylamino) hexanoate (sulfo-SANPAH), a UV-activatable cross-linker,[4] or hydrazine hydrate[82] allows for covalent tethering of ECM proteins such as fibronectin,[83] collagen,[84] or combinations of proteins[85] onto PA gels. In addition, spatial distribution of proteins has been achieved on PA gels using micropatterning[86,87] and microcontact printing.[85] Varying the concentration of solubilized protein added to these synthetic matrices allows for more or fewer cell attachment sites, allowing investigators to control the adhesion strength of cells on these matrices.[8]

5.504.3.2.2. Polydimethylsiloxane

Polydimethylsiloxane (PDMS) is a silicone elastomer most often used in microfluidic or lab-on-a-chip applications to form devices with defined microstructures. Many formulations of PDMS exist, with Sylgard 184 being the most commonly used in biological-based research.[88] Fabrication of polymer substrates involves mixing of a 10:1 ratio of elastomer to curing agent, degassing, and baking for a few hours at 90 °C. This polymerization process provides good strength, optical clarity, and ability to irreversibly bond glass, making PDMS an ideal substrate for studies that require both microscopy and defined physical gel features. As the elastomer maintains its shape after curing, PDMS is often poured over micropatterned substrates fabricated using soft photolithography to obtain gels with defined topographical features down to ~10 μm. By varying the ratio of the curing agent to the PDMS or baking time, substrates with a Young's modulus between ~12 and 2500 kPa can be achieved,[78,89] making it a suitable system for more contractile cells where the microenvironment is often >10 kPa.[7] Pouring the curing PDMS solution over micropatterned surfaces made by photolithography can also create useful surface topologies, such as with high-density pillar arrays, where posts can be engineered to have an effectively lower apparent substrate stiffness of ~2–130 kPa simply by changing the physical dimensions of the pillars on which the cells pull.[90] Deformable pillars are useful not only to generate compliant substrates but also to quantify substrate deformation and traction forces exerted by crawling cells. Photolithography has also been used to generate PDMS master molds capable of creating PA hydrogels with spatially varying mechanical properties, for example, step (**Figure 3(a)**)[78] or smooth 1D gradient (**Figure 3(b*i*)**).[57] Such micropaterning techniques can also create stiffness gradients to study durotaxis. PA hydrogels have been made via micropatterning using PDMS microchannels to study durotaxis. As with PA hydrogels, the surface of PDMS gels is easily modified to absorb proteins to facilitate cell attachment.[91] While this system can generate polymer substrates with considerably higher substrate moduli than the other systems discussed, it is not well suited to fabricate gels within a small range of moduli.

5.504.3.2.3. Other systems

A number of other synthetic systems have been used to investigate the role of stiffness on cellular function, each having a unique property not easily produced by the previously covered materials. Semi-interpenetrating polymer networks consisting of poly(*N*-isopropylacrylamide-*co*-acrylic acid) modified with synthetic peptides provide a different stiffness range and are more easily modified by cell adhesion ligand. In this context, they have been used to study the effects of matrix stiffness and ligand density of hESCs.[92] Interpenetrating polymer networks purposefully mix polymers to create domains on one polymer within the other and photolithography can segregate solutions to yield domains,[78] but incomplete free radical polymerization can also result in the formation of soft and stiff polymer domains within a material. For example, the nanodomains that form in bulk poly(vinyl pyrrolidone) hydrogels are due to nanoscale incomplete free radical polymerization,[9] though it is not clear if cells can sense those differences on such a small length scale. Biosynthetic hydrogels, particularly composed of PEG, are now more readily used due to their controlled chemical and mechanical properties, not to mention their lack of cytotoxicity, which enables them to be used to encapsulate cells in a 3D environment.[46] Purely synthetic PEG hydrogels also have the additional functionality of being able to undergo photoactivated degradation, effectively softening the

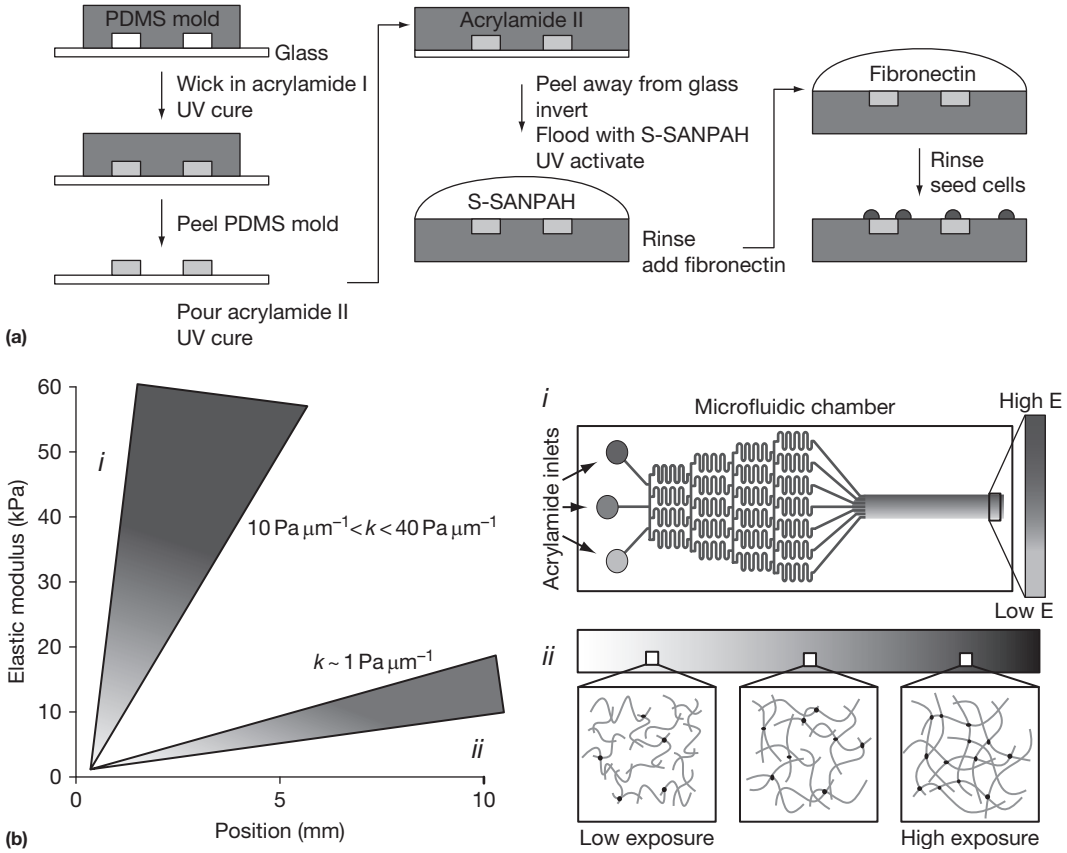

Figure 3 Methods to generate stiffness gradients. Several photolithographic methods have been used in synthetic systems to generate spatial gradients of stiffness, including (a) using sequential polymerization to generate step gradients and (b) photoactivatable methods where gradients are formed either by spatially controlling solution exposure to UV (*i*) or by employing microfluidic mixing to have cross-linker gradients with uniform activation (*ii*). Each of the latter cases can yield moduli of different ranges, which is critical for cell sensing.

hydrogel,[93] and the addition of diacrylate groups provide spatially tunable stiffening[94] as with HA hydrogels.[58] As with the biosynthetic hydrogels, PEG hydrogels can be polymerized into a 3D shape, enabling encapsulation. However, none of the systems highlighted above are without limitations. While some hydrogels provide better physical characteristics than others, careful consideration of each system and the specifics of the study should drive the choice of material.

5.504.4. Cell Functions and Differentiation

Though we have limited our discussion thus far to how matrix stiffness varies throughout the body (**Figure 4(a)**) and how one can generate environments of varying mechanical properties, treatment of the subject would be incomplete without discussing the impact of stiffness on various cell functions, for example, migration,[10] adhesion,[23] morphology,[75] differentiation,[32] and its interplay with ECM composition.[85,95] While the molecular mechanism(s) behind how substrate compliance drives cellular function are still debated, it should become apparent that the functions previously mentioned are optimal in environments that most closely match the *in vivo* environment and suggest that potential sensing mechanisms must be tuned to such an optimum. While we provide a description of several cell types and a table with addition cell types (**Table 1**), it is by no means an exhaustive list, and other reviews on this area should also be consulted for cell types not covered.[7,17,101–104]

5.504.4.1. Neutrophils

Neutrophils are short-lived phagocytic cells that circulate in the bloodstream before becoming active and migrating through the vascular endothelium and surrounding matrix to the site of infection. Given that neutrophils must move through tissues of varying stiffness, they have a variety of atypical behaviors not present in cells that are adherent throughout their lives. Upon activation, neutrophils adhere to substrates and spread, even on soft hydrogels.[23] Though the degree of spreading is uncertain, investigations all have reported that as with normally adherent cells, neutrophils noticeably spread more on stiffer substrates[105,106] and may even display optimal spreading.[106] Given the highly migratory state of these cells, cell migration is also a critical metric to follow. On soft substrates, neutrophils cannot generate sufficient traction forces, which hinders their ability to migrate while on stiff substrates, strong adhesion to the hydrogel prevents detachment and hence

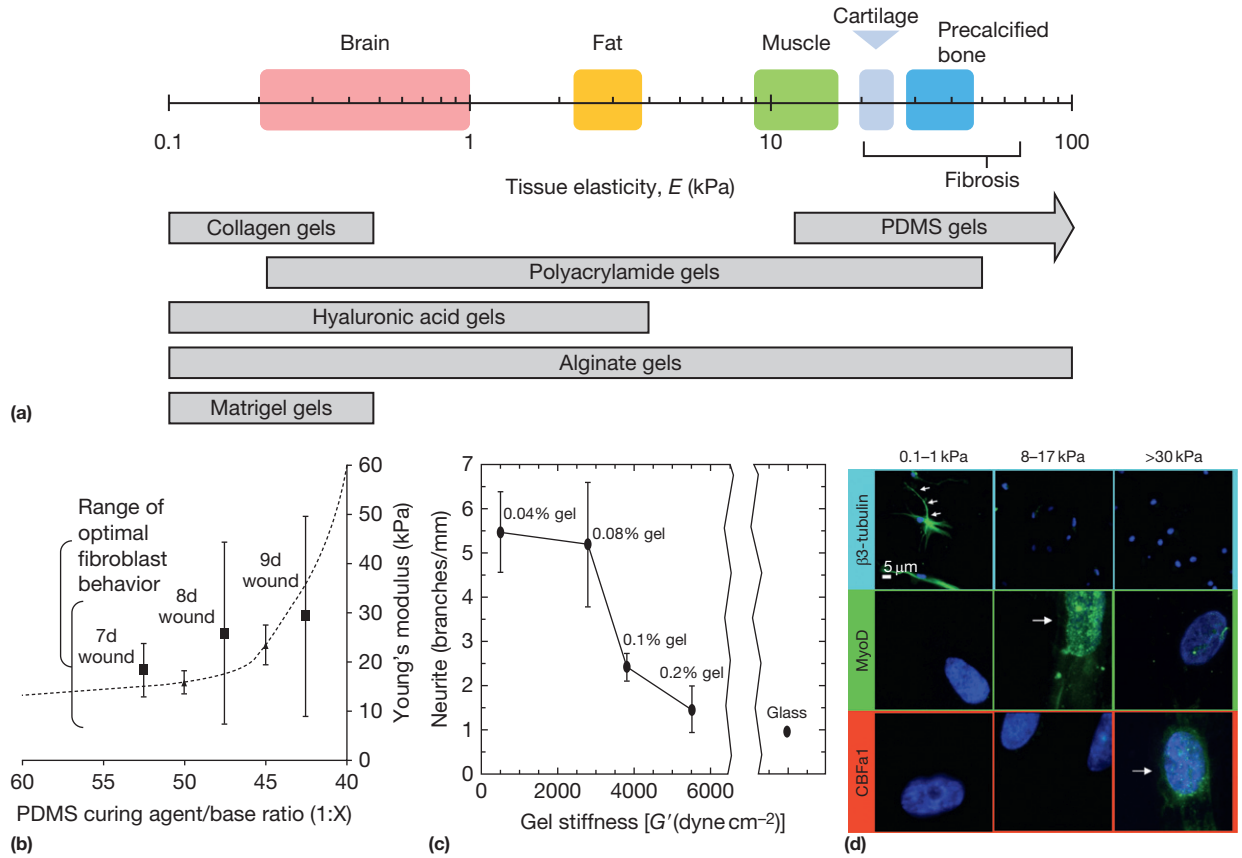

Figure 4 Natural variation in tissue elasticity and resulting cell behavior. (a) Schematic depicting the normal variation in elasticity of the indicated tissues and the hydrogel systems that span these ranges. (b) Stiffness of the wound environment of a fibroblast. Reproduced from Goffin, J. M.; Pittet, P.; Csucs, G.; Lussi, J. W.; Meister, J. J.; Hinz, B. *J. Cell Biol*. **2006**, *172*, 259 –268. (c) Neural cell behavior is optimal on matrices that have a stiffness that mimics brain. Reproduced from Flanagan, L. A.; Ju, Y. E.; Marg, B.; Osterfield, M.; Janmey, P. A. *Neuroreport* **2002**, *13*, 2411–2415. (d) Mesenchymal stem cell differentiation is specific to the stiffness of the original tissue. Engler, A. J.; Sen, S.; Sweeney, H. L; Discher, D. E. *Cell* **2006**, *126*, 677–689.

movement. Neutrophils thus exhibit a biphasic motility profile, with peak velocities occurring on 4–7 kPa hydrogels, depending on fibronectin coating density.[106] The shift in optimal stiffness may be explained by the ligand coating modulating adhesion strength, a trend also observed with smooth muscle cell (SMC) spreading.[8] Since traction stress scales with hydrogel stiffness,[105] it would appear that as with cardiomyocytes[107] there is an optimal amount of work done by adhesions to propel the neutrophil forward.[106] Though there is an optimal speed, the persistence time of migrating neutrophils is higher on substrates with increasing stiffness.[106] Thus regardless of net migration distance, the mean square displacement (MSD) of neutrophils is similar on substrates of varying moduli.[105] Given that these observations have been performed on static hydrogels and most tissue naturally varies within itself,[7,102] gradient hydrogels provide an interesting system to resolve these components in the future.

5.504.4.2. Fibroblasts

Fibroblasts play an important role in wound healing, synthesis, and deposition of ECM proteins such as collagen and fibronectin at the site of injury. To do so, they migrate through connective tissue to the site of injury in a mesenchymal mode by spreading and assembling highly adhesive focal interactions with the ECM[108]; fibroblasts durotax toward stiffer matrix[10] and assemble focal adhesions in a highly stiffness-dependent process that regulates the tension generated within these maturing adhesions.[109] While fibroblasts can form actin microfilaments on substrates as soft as ~3–4 kPa[23] and remain spindle-shaped,[75] they cannot maintain those behaviors on even softer hydrogels.[110] Fibroblasts exhibit drastically reduced proliferation on soft hydrogels, and the cell itself is less stiff, presumably from its inability to assemble a cytoskeleton.[110] What results is optimal behavior on substrates that most closely mimic the *in vivo* wound environment (**Figure 4(b)**),[109] where fibroblasts exhibit stronger traction forces than on softer hydrogels[111] and show an increase in fibroblast tyrosine phosphorylation.[75] These cells may therefore sense matrix rigidity through Src family kinases to activate downstream signaling effects[112] such as controlling the retrograde flux of actin filaments at focal adhesions in the lamella region.[113] As with other cell types, fibroblast traction forces are inversely correlated with cell migration speed[75,110] to the point where, on much stiffer >500 kPa substrates, migration favors not the typical protrusive model

Table 1 Studies on the effects of substrate compliance on cell behavior

Cell type	*Substrate*	*Modulus*	*Findings*
Vascular SMCs	Polyacrylamide/type I collagen	15, 28 kPa and ~1 Pa μm^{-1} gradient	Faster motility on intermediately stiff gels, preferential cell accumulation on stiff portion of gradient (durotaxis)[80]
		1–80 kPa, 10–40 Pa μm^{-1}	Cellular durotaxis increases on steeper stiffness gradients irrespective of absolute values of substrate elasticity[81]
SMCs	Poly(L-lysine) and hyaluronan with 20–60 layers	40–300 kPa	SMC spreading generally increases with increasing elastic modulus[96]
Aortic SMCs	Polyacrylamide/type I collagen, $(PLL/HA)_{20}$[96]/type I collagen	1–35 kPa (PA), 85 kPa $(PLL/HA)_{20}$	SMC spreading increases with increasing elastic modulus according to a hyperbolic fit, biphasic dependence of spreading on collagen density[18]
Bovine chondrocytes	RGD-functionalized alginate	12–127 kPa	Adhesion scales with matrix stiffness, rounded morphology on soft substrates compared to flat with stress fibers on stiffer gels[63]
	Poly(ethylene glycol) dimethacrylate	34–1370 kPa	Type II collagen synthesis in observed intermediate stiffness gels (360 kPa) and glycosaminoglycans diffuse through gels with large equilibrium swelling ratios[97]
MC3T3-E1 osteoblasts	Polyacrylamide/type I collagen	11–40 kPa	Maximum cells speeds on gels of intermediate stiffness, higher proliferation rates, and actin stress fiber formation on stiff substrates[84]
Bovine aortic endothelial cells	Polyacrylamide/RGD	0.5–33 kPa	Mean squared displacement (MSD) increases with gel stiffness for single cells, smaller increase for cell pairs. Cell pairs remain in contact on 5.5 kPa and dissociate on stiffer substrates[98]
Mouse aortic endothelial cells	Collagen/PA/glass 'sandwich gel'	0.45, 14 kPa	Spindle morphology with more pseudopodial branches on soft gels than on stiff substrates[99]
Human umbilical vein endothelial cells	Matrigel, copolymerization with collagen, polyacrylamide	–	Tube-like structures formed on soft substrata[69]
Human blood outgrowth endothelial cells, human umbilical vein endothelial cells	Type I collagen gels	6–10 kPa	Compliant substrates support capillary morphogenesis, but this effect is cell-type dependent within specific endothelial cell populations based on force generation capabilities[100]
MDCK epithelial cells	PDMS micropillars	1–100 kPa	Higher forces generated on stiffer gels, constant substrate deformation[90]

but rather a form of ameboid migration.[89] However, such measurements were made using PDMS, which also showed markedly less spreading on stiffer substrates[89] than did PA hydrogels,[10] further emphasizing the importance of material and ligand choice.

5.504.4.3. Neural Cells

Neural cells, including glia, sensory neurons, dorsal root ganglia, motor neurons, and interneurons, make up a large portion of the human nervous system. Neurons are known for sending out cell projections, or neurites, to form networks of processes that extend large distances to innervate muscles.[114] In light of the soft nature of brain tissue, that is, $\ll$1 kPa,[2,115,116] neurons had a significant threefold decrease in branch number, suggesting that neuronal morphology is acutely sensitive to substrate mechanical properties (**Figure 4(c)**).[117] Similar results were obtained with chick dorsal root ganglia cultured in 3D agarose hydrogels where the elongation rate of neurites was found to be decreased on hydrogels with increasing stiffness.[118] Astrocyte and glial cell behavior was also found to depend on substrate mechanics, but in a way that opposes the behavior of neurons: astrocytes on soft PA hydrogels display small, round morphologies that lack stress fibers in comparison with highly spread morphologies on harder hydrogels. While neurons grow well in mixed cultures on laminin-coated soft hydrogels, astrocytes do not proliferate and exhibit reduced adhesion.[115] Even glial cells failed to proliferate and did not survive on soft, deformable substrates.[117] In contrast, astrocytes and glial cells overgrow postmitotic neurons on stiffer hydrogels.[115,117] These findings suggest that various neuronal cell types respond differentially to matrix stiffness: neurons prefer to live in soft matrices of 0.1–1 kPa while astrocytes and glial cells, such as fibroblasts, appear to prefer stiffer matrices to spread and proliferate.

5.504.4.4. Myoblasts

Skeletal muscle formation involves the activation, proliferation, and differentiation of myoblasts into myocytes and subsequent fusion to form multinucleated myofibers.[119] While skeletal myoblast proliferation and differentiation have been shown to depend on surface ligand density,[120] matrix mechanical properties play an important role in the higher order functions of

muscle, for example, striation and contraction. For example, C2C12 skeletal myoblasts will fuse into myotubes after 48 h in culture, regardless of substrate stiffness, but myosin striations were maximal on hydrogels that exhibited muscle-like stiffness, for example, ~10 kPa.[121,122] Multinucleated myotubes on soft (<5 kPa) and stiff (>23 kPa) hydrogels showed little to no striations after 4 weeks of culture.[122] Similar reports have indicated that myoblast lines could spread and proliferate but not form myotubes on <1 kPa hydrogels,[62] and though subtle differences in behavior exist, they may be the result of different ligand type: fibronectin versus type I collagen. This again hints at the coupling of matrix chemistry and mechanics. Myoblasts seeded atop a layer of confluent myoblasts of the appropriate stiffness also differentiated into myotubes, forming myosin striations after 4 weeks in culture, but when plated on top of cells with suboptimal stiffness, striation was not apparent.[122] Together, these data support the claim that hydrogels that mimic the stiffness of native tissue are optimum for myotube differentiation. Freshly isolated primary myoblasts also exhibit a stiffness-dependent behavior, forming myotubes on 45 kPa hydrogels.[62] Given that these cells were allowed to form syncytially whereas normal muscle is aligned, studies using micropatterned collagen, where fusion and striation are tightly controlled by muscle-like stiffness, are perhaps more mimetic.[122] This implies that both mechanical and geometrical cues from the matrix are involved in myoblast function.

In addition to skeletal myocytes, cardiomyocytes have been studied significantly in terms of their stiffness sensitivity. Embryonic quail cardiomyocytes produce optimal work on their substrates and maintain rhythmic contraction[107] at matrix stiffness that mimics normal myocardium.[5] Neonatal rat ventricular myocytes were also found to generate the largest forces and beat most effectively as measured by large calcium transients present on muscle-like ~10 kPa PA substrates.[123] Rhythmic contraction of these cells seeded on a 3D PEG-containing fibrinogen matrix showed a dependence on substrate elasticity, but for hydrogels that were only 25–150 Pa. Increasing fibrinogen concentration, and thus Young's modulus, drastically reduced contractile activity,[124] but since ligand type and concentration significantly affects myoblast function,[120] this difference in behavior may be attributed to the large difference in ligand presentation in addition to the differences in dimensionality.

5.504.4.5. Stem Cells

Stem cells are a broad class of progenitor-type cells that have the ability to undergo self-renewal and can differentiate into many mature lineages when sufficiently stimulated to do so.[125] Adult bone-marrow-derived mesenchymal stem cells (MSCs) and embryonic stem cells (ESCs) are two commonly studied stem cell types whose differentiation is typically controlled by soluble factors. Having not yet committed to a lineage, stem cells have the ultimate ability to respond to local matrix cues such as stiffness.[126] True progenitor cells, those that are not fully committed to a lineage but that are not stem cells, also express some ability to mature in response to stiffness. For the latter case, MC3T3-E1 preosteoblast cells have increased growth rates on hydrogels of increasing stiffness, with moduli ranging from 20 to 110 kPa, but exhibit optimal differentiation on substrates mimicking osteoid stiffness.[32,127] This observation has been noted in other bone precursors[128] and in murine MSCs (D1). Similar behavior has been observed when cells are co-induced into an osteogenic lineage by growth factors.[129] MSCs plated on 34 kPa type I collagen- and fibronectin-coated PA hydrogels differentiated optimally down the osteogenic lineage as evident by the expression of a number of osteogenic markers (**Figure 4(d)**, bottom).[32,95]

MSCs have also been differentiated down myo-, neuro-, and adipogenic lineages by tuning substrate compliance. For instance, MSCs encapsulated in RGD-presenting alginate hydrogels differentiated down the adipogenic lineage best in 2.5–5 kPa hydrogels,[45] in agreement with the mechanical properties of adipose tissue *in vivo*.[130] On softer 0.1–1 kPa type I collagen-coated hydrogels that mimic the mechanical properties of brain tissue,[2,116] MSC morphologically resembles branched neuron-like structures, expressing neuron-specific markers such as nestin, β_3 tubulin, and neurofilament light chain, among others.[32] Similar neural induction has been obtained with rat adult neural stem cells, where cells preferentially differentiate into neurons on soft hydrogels (100–500 Pa) and into glial cells on hydrogels of intermediate stiffness (1–10 kPa).[131] When plated on hydrogels of intermediate stiffness, MSCs expressed myoD and desmin, indicating myogenic commitment.[32] It is interesting to note that MSC myogenic differentiation was maximal on type I collagen-coated PA hydrogels, where the stiffness was strikingly similar to the optimum stiffness for myoblast fusion and striation formation (**Section 5.504.4.4**), indicating that early and late differentiation toward mature myofibrils occurs on matrices with nearly identical mechanical properties as those reported for muscle tissue.[32,122] It is also important to note that all of these expression data are dependent on the ligand used for cell attachment; type I collagen and fibronectin permit stiffness-dependent differentiation but type IV collagen and laminin are not supportive, indicating again that the coupling of matrix-related cues many be more subtle than previously appreciated.[95]

In contrast to MSCs, little work has been done to determine to what extent ESC differentiation is stiffness dependent. Osteogenic differentiation of ESCs has been reported on PDMS substrates, but only with moduli >1 MPa.[132] While most of these moduli are supraphysiological, these data at least suggest that expression of pluripotency and early differentiation of genes may be modulated by substrate mechanics and certainly warrant further exploration.

5.504.4.6. Cancer Cells

The hallmarks of cancer include limitless replicative potential, sustained angiogenesis, loss of contact inhibition, and the ability to form new tumor foci in foreign tissues.[133] Cancer progression has previously been linked to differential integrin expression,[134] which in turn has been implicated in the maintenance of both the normal and transformed phenotype of mammary epithelial cells.[135] One factor that more recently has been proposed to contribute to the transformed phenotype is modification of the mechanical properties of the extracellular milieu, which can change how a cell 'feels' and reacts to this changing environment. Indeed, ECM stiffening has been implicated as a plausible prerequisite for carcinogenesis due

both to the onset of fibrosis[136] and the more tactile sensation one gets by feeling the stiff lump associated with a tumor mass, most notably in breast cancer.[71] Numerous examples now have immerged in the literature; neuroblastomas cultured on hydrogels >1 kPa grew longer neurites than on soft hydrogels,[137] in marked contrast to the previous section on neurons (**Section 5.504.4.3**). However, these cells still retain compliance sensitivity despite their transformed state[115] unlike other soft tumors,[71] illustrating the complexity of cancer.

In an effort to understand why cancers would prefer a stiffer environment, breast mammary epithelial cancers have been linked to increased tension and compressive forces as a result of ECM stiffening, implicating both mechanotransduction and tensional homeostasis as regulators of cancer development.[138] Accordingly, ECM stiffening disrupts mammary epithelial organization and acini formation in 3D Matrigel–PA hydrogels, forming gradients of stiffness in the affected stroma surrounding the tumor.[71] Since cancer cell motility is stiffness-sensitive[139] but often erratic,[111] cells may possibly see these gradients as durotactic cues for directed migration to new tumor sites. Again, migration is perhaps even more complex than these data may indicate as ligand density couples with this modulation; DU-145 human prostate carcinoma cells migrate fastest in 3D Matrigel gels with storage moduli $G' \sim 30$ Pa, but in hydrogels with lower concentrations of ligand, maximal migration speeds were observed on softer hydrogels.[68]

Increased cytoskeletal tension and extracellular signal-regulated kinase (ERK) activation due to the less compliant environment also influences cellular proliferation, and is a first step toward a cancerous phenotype. However, a partial normal phenotype can be restored in malignant mammary epithelial cells if the mechanosensing pathways, such as ERK activity and Rho signaling, are disrupted, which links cytoskeleton tension and focal adhesion assembly with mechanosignaling and repression of the malignant phenotype.[71] These studies suggest that there is perhaps an additional angle for cancer therapies: controlling the compliance of the environment or how cancer cells 'feel' their environment may be an avenue to prevent or delay cancer progression or even restore a normal phenotype.

5.504.4.7. Other Cell Types

Substrate compliance modulates behavior – adhesion, proliferation, migration, contraction, and ECM production – of many other cell types such as SMCs, chondrocytes, endothelial cells, and epithelial cells. While these are too numerous to describe in detail, we have summarized the findings of a number of studies involving matrix stiffness and these cell types in **Table 1**, and we refer the reader to the works cited for additional information.

5.504.5. Conclusion

From the discussion here, it is hopefully clear that there are various materials to test stiffness responses in cells, there are various means of measuring stiffness, and that cell types are affected by mechanical signals in different ways, ultimately changing behaviors, including migration, spreading, and differentiation. Thus, it is reasonable to conclude that substrate compliance may play an important role in embryonic development, angiogenesis, homeostasis, cancer, and disease progression. As a final consideration, it should be noted that our discussion was largely limited to 2D tissue culture results, and that while investigations performed in 2D are convenient to study cellular responses, they do not accurately mimic the 3D environment of tissues that surround cells *in vivo*. In fact, important differences exist between 2D and 3D studies; for instance, fibroblasts alignment is perpendicular to strain direction in 3D but parallel in 2D,[140,141] and human MSC morphology in 3D is independent of matrix stiffness unlike in 2D.[45] More striking is the observation that matrix stiffness has little effect on SMC proliferation in 3D, possibly due to the differential assembly of focal adhesions in 3D hydrogels compared to 2D hydrogels of comparable stiffness.[46,142] Taken together, these data in nascent 3D systems[44–46,126] strongly motivate the further refinement of mechanically tunable 3D models with similar flexibility to current 2D systems to gain a better perspective on the effect of substrate compliance on cellular functions. These new material models as well as a greater understanding of the molecular mechanics behind cellular mechanosensing will be instrumental in revolutionizing the current paradigms of cellular mechanobiology.

References

1. Choi, K.; Kuhn, J. L.; Ciarelli, M. J.; Goldstein, S. A. *J. Biomech.* **1990**, *23*, 1103–1113.
2. Gefen, A.; Margulies, S. S. *J. Biomech.* **2004**, *37*, 1339–1352.
3. Wang, N.; Tolic-Norrelykke, I. M.; Chen, J.; *et al. Am. J. Physiol. Cell Physiol.* **2002**, *282*, C606–C616.
4. Beningo, K. A.; Lo, C. M.; Wang, Y. L. *Methods Cell Biol.* **2002**, *69*, 325–339.
5. Berry, M. F.; Engler, A. J.; Woo, Y. J.; *et al. Am. J. Physiol. Heart Circ. Physiol.* **2006**, *290*, H2196–H2203.
6. Fung, Y.-C. *A First Course in Continuum Mechanics*. Prentice-Hall: Englewood Cliffs, NJ, 1994.
7. Discher, D. E.; Janmey, P.; Wang, Y. L. *Science* **2005**, *310*, 1139–1143.
8. Engler, A.; Bacakova, L.; Newman, C.; Hategan, A.; Griffin, M.; Discher, D. *Biophys. J.* **2004**, *86*, 617–628.
9. Flores-Merino, M. V.; Chirasatitsin, S.; Lopresti, C.; Reilly, G. C.; Battaglia, G.; Engler, A. J. *Soft Matter* **2010**, *6*(18), 4466–4470.
10. Lo, C. M.; Wang, H. B.; Dembo, M.; Wang, Y. L. *Biophys. J.* **2000**, *79*, 144–152.
11. Hertz, H. *J. Reine Angew. Mathematik* **1882**, *92*, 156–171.
12. Reinhart-King, C. A.; Dembo, M.; Hammer, D. A. *Langmuir* **2003**, *19*, 1573–1579.
13. Tai, K.; Qi, H. J.; Ortiz, C. *J. Mater. Sci. Mater. Med.* **2005**, *16*, 947–959.
14. Ebenstein, D. M.; Pruitt, L. A. *J. Biomed. Mater. Res. A* **2004**, *69*, 222–232.
15. Jacot, J. G.; Dianis, S.; Schnall, J.; Wong, J. Y. *J. Biomed. Mater. Res. A* **2006**, *79*, 485–494.
16. Binnig, G.; Quate, C. F.; Gerber, C. *Phys. Rev. Lett.* **1986**, *56*, 930–933.
17. Engler, A. J.; Rehfeldt, F.; Sen, S.; Discher, D. E. In *Methods in Cell Biology*; Discher, D. E., Wang, Y.-L., Eds.; Academic Press: New York, 2007.
18. Engler, A. J.; Richert, L.; Wong, J. Y.; Picart, C.; Discher, D. E. *Surf. Sci.* **2004**, *570*, 142–154.
19. Weisenhorn, A. L.; Hansma, P. K.; Albrecht, T. R.; Quate, C. F. *Appl. Phys. Lett.* **1989**, *54*, 2651–2653.
20. Sneddon, I. N. *Int. J. Eng. Sci.* **1965**, *3*, 47–57.
21. Dimitriadis, E. K.; Horkay, F.; Maresca, J.; Kachar, B.; Chadwick, R. S. *Biophys. J.* **2002**, *82*, 2798–2810.
22. Zhao, Y. P.; Shi, X.; Li, W. J. *Rev. Adv. Mater. Sci.* **2003**, *5*, 348–353.
23. Yeung, T.; Georges, P. C.; Flanagan, L. A.; *et al. Cell Motil. Cytoskeleton* **2005**, *60*, 24–34.
24. Dassow, M. V.; Davidson, L. A. *Dev. Dyn.* **2009**, *238*, 2–18.
25. Moore, S. W.; Keller, R. E.; Koehl, M. A. *Development* **1995**, *121*, 3131–3140.

26. Newman, S. A.; Comper, W. D. *Development* **1990**, *110*, 1–18.
27. Conti, M. A.; Even-Ram, S.; Liu, C.; Yamada, K. M.; Adelstein, R. S. *J. Biol. Chem.* **2004**, *279*, 41263–41266.
28. Edelman, G. M. *Topobiology: An Introduction to Molecular Embryology*; Basic Books: New York, 1988.
29. Davidson, L. A.; Keller, R. E. *Development* **1999**, *126*, 4547–4556.
30. Zhou, J.; Kim, H. Y.; Davidson, L. A. *Development* **2009**, *136*, 677–688.
31. Krieg, M.; Arboleda-Estudillo, Y.; Puech, P. H.; *et al. Nat. Cell Biol.* **2008**, *10*, 429–436.
32. Engler, A. J.; Sen, S.; Sweeney, H. L.; Discher, D. E. *Cell* **2006**, *126*, 677–689.
33. Sikavitsas, V. I.; Temenoff, J. S.; Mikos, A. G. *Biomaterials* **2001**, *22*, 2581–2593.
34. Daly, C. H.; Odland, G. F. *J. Investig. Dermatol.* **1979**, *73*, 84–87.
35. Wuyts, F. L.; Vanhuyse, V. J.; Langewouters, G. J.; Decraemer, W. F.; Raman, E. R.; Buyle, S. *Phys. Med. Biol.* **1995**, *40*, 1577–1597.
36. Stolz, M.; Gottardi, R.; Raiteri, R.; *et al. Nat. Nanotechnol.* **2009**, *4*, 186–192.
37. Georges, P. C.; Hui, J. J.; Gombos, Z.; *et al. Am. J. Physiol. Gastrointest. Liver Physiol.* **2007**, *293*, G1147–G1154.
38. Hay, E. D. *Cell biology of Extracellular Matrix*. Plenum Press: New York, 1991.
39. Burdick, J. A.; Vunjak-Novakovic, G. *Tissue Eng. A* **2009**, *15*, 205–219.
40. Elsdale, T.; Bard, J. *J. Cell Biol.* **1972**, *54*, 626–637.
41. Wolf, K.; Alexander, S.; Schacht, V.; *et al. Semin. Cell Dev. Biol.* **2009**, *20*, 931–941.
42. Battista, S.; Guarnieri, D.; Borselli, C.; *et al. Biomaterials* **2005**, *26*, 6194–6207.
43. Brown, R. A.; Wiseman, M.; Chuo, C.-B.; Cheema, U.; Nazhat, S. N. *Adv. Funct. Mater.* **2005**, *15*, 1762–1770.
44. Ulrich, T. A.; Jain, A.; Tanner, K.; Mackay, J. L.; Kumar, S. *Biomaterials 31*, 1875–1884.
45. Huebsch, N.; Arany, P. R.; Mao, A. S.; *et al. Nat. Mater.* **2010**, *9*, 518–526.
46. Peyton, S. R.; Kim, P. D.; Ghajar, C. M.; Seliktar, D.; Putnam, A. J. *Biomaterials* **2008**, *29*, 2597–2607.
47. Loftis, M. J.; Sexton, D.; Carver, W. *J. Cell. Physiol.* **2003**, *196*, 504–511.
48. Hadjipanayi, E.; Brown, R. A.; Mudera, V. *J. Tissue Eng. Regen. Med.* **2009**, *3*, 230–241.
49. Kim, A.; Lakshman, N.; Karamichos, D.; Petroll, W. M. *Invest. Ophthalmol. Vis. Sci.* **2009**, *51*(2), 864–875.
50. Wallace, D. G.; Rosenblatt, J. *Adv. Drug Deliv. Rev.* **2003**, *55*, 1631–1649.
51. Shu, X. Z.; Liu, Y. C.; Luo, Y.; Roberts, M. C.; Prestwich, G. D. *Biomacromolecules* **2002**, *3*, 1304–1311.
52. Cai, S.; Liu, Y.; Zheng Shu, X.; Prestwich, G. D. *Biomaterials* **2005**, *26*, 6054–6067.
53. Shu, X. Z.; Prestwich, G. D.; Hari, G. G.; Charles, A. H. & M. D. In *Chemistry and Biology of Hyaluronan*; Elsevier: Oxford, 2004.
54. Brigham, M. D.; Bick, A.; Lo, E.; Bendali, A.; Burdick, J. A.; Khademhosseini, A. *Tissue Eng. A* **2009**, *15*, 1645–1653.
55. Vanderhooft, J. L.; Alcoutlabi, M.; Magda, J. J.; Prestwich, G. D. *Macromol. Biosci.* **2009**, *9*, 20–28.
56. Hanjaya-Putra, D.; Yee, J.; Ceci, D.; Truitt, R.; Yee, D.; Gerecht, S. *J. Cell. Mol. Med.* **2009** [Epub ahead of print] DOI 10.1111/j.1582-4934.2009.00981.x.
57. Zaari, N.; Rajagopalan, P.; Kim, S. K.; Engler, A. J.; Wong, J. Y. *Adv. Mater.* **2004**, *16*, 2133–2137.
58. Marklein, R. A.; Burdick, J. A. *Soft Matter* **2010**, *6*, 136–143.
59. Ifkovits, J. L.; Tous, E.; Minakawa, M.; *et al. Proc. Natl Acad. Sci. USA* **2010**, 107, 11507–11512.
60. Smidsrod, O.; Skjakbraek, G. *Trends Biotechnol.* **1990**, *8*(3), 71–78.
61. Thu, B.; Bruheim, P.; Espevik, T.; Smidsrod, O.; Soon-Shiong, P.; Skjak-Braek, G. *Biomaterials* **1996**, *17*, 1031–1040.
62. Boontheekul, T.; Hill, E. E.; Kong, H. J.; Mooney, D. J. *Tissue Eng.* **2007**, *13*, 1431–1442.
63. Genes, N. G.; Rowley, J. A.; Mooney, D. J.; Bonassar, L. J. *Arch. Biochem. Biophys.* **2004**, *422*, 161–167.
64. Leroux, M. A.; Guilak, F.; Setton, L. A. *J. Biomed. Mater. Res.* **1999**, *47*, 46–53.
65. Kong, H. J.; Kaigler, D.; Kim, K.; Mooney, D. J. *Biomacromolecules* **2004**, *5*, 1720–1727.
66. Bouhadir, K. H.; Hausman, D. S.; Mooney, D. J. *Polymer* **1999**, *40*, 3575–3584.
67. Kleinman, H. K.; Mcgarvey, M. L.; Liotta, L. A.; Robey, P. G.; Tryggvason, K.; Martin, G. R. *Biochemistry* **1982**, *21*, 6188–6193.
68. Zaman, M. H.; Trapani, L. M.; Sieminski, A. L.; *et al. Proc. Natl Acad. Sci. USA* **2006**, *103*, 10889–10894.
69. Deroanne, C. F.; Lapiere, C. M.; Nusgens, B. V. *Cardiovasc. Res.* **2001**, *49*, 647–658.
70. Vernon, R. B.; Angello, J. C.; Iruela-Arispe, M. L.; Lane, T. F.; Sage, E. H. *Lab. Invest.* **1992**, *66*, 536–547.
71. Paszek, M. J.; Zahir, N.; Johnson, K. R.; *et al. Cancer Cell* **2005**, *8*, 241–254.
72. Mohr, J. C.; De Pablo, J. J.; Palecek, S. P. *Biomaterials* **2006**, *27*, 6032–6042.
73. Nelson, C. M.; Inman, J. L.; Bissell, M. J. *Nat. Protoc.* **2008**, *3*, 674–678.
74. Wang, Y.-L.; Pelham, R. J. *Meth. Enzymol.* **1998**, *298*, 489–496.
75. Pelham, R. J.; Wang, Y.-L. *Proc. Natl Acad. Sci. USA* **1997**, *94*, 13661–13665.
76. Flory, P. J. *Principles of Polymer Chemistry*; Cornell University Press: Ithaca, NY, 1953.
77. Landu, L. D.; Liftshiz, E. M. *Theory of Elasticity*. Butterworth-Heinemann: Oxford, UK, 1986.
78. Gray, D. S.; Tien, J.; Chen, C. S. *J. Biomed. Mater. Res. A* **2003**, *66*, 605–614.
79. Tse, J. R.; Engler, A. J. *Curr. Protoc. Cell Biol.* **2010**; Chapter 10, Unit 10.16.
80. Wong, J. Y.; Velasco, A.; Rajagopalan, P.; Pham, Q. *Langmuir* **2003**, *19*, 1908–1913.
81. Isenberg, B. C.; Dimilla, P. A.; Walker, M.; Kim, S.; Wong, J. Y. *Biophys. J.* **2009**, *97*, 1313–1322.
82. Damljanovic, V.; Lagerholm, B. C.; Jacobson, K. *Biotechniques* **2005**, *39*, 847–851.
83. Williams, C. M.; Engler, A. J.; Slone, R. D.; Galante, L. L.; Schwarzbauer, J. E. *Cancer Res.* **2008**, *68*, 3185–3192.
84. Khatiwala, C. B.; Peyton, S. R.; Putnam, A. J. *Am. J. Physiol. Cell Physiol.* **2006**, *290*, C1640–C1650.
85. Flaim, C. J.; Chien, S.; Bhatia, S. N. *Nat. Meth.* **2005**, *2*, 119–125.
86. Chen, C. S.; Mrksich, M.; Huang, S.; Whitesides, G. M.; Ingber, D. E. *Biotechnol. Prog.* **1998**, *14*, 356–363.
87. Chirasatitsin, S.; Engler, A. J. *J. Phys. Condens. Matter* **2010**, *22*, 194102.
88. Belanger, M. C.; Marois, Y. *J. Biomed. Mater. Res.* **2001**, *58*, 467–477.
89. Tzvetkova-Chevolleau, T.; Stephanou, A.; Fuard, D.; Ohayon, J.; Schiavone, P.; Tracqui, P. *Biomaterials* **2008**, *29*, 1541–1551.
90. Saez, A.; Buguin, A.; Silberzan, P.; Ladoux, B. *Biophys. J.* **2005**, *89*, L52–L54.
91. Tan, J. L.; Tien, J.; Chen, C. S. *Langmuir* **2001**, *18*, 519–523.
92. Li, Y. J.; Chung, E. H.; Rodriguez, R. T.; Firpo, M. T.; Healy, K. E. *J. Biomed. Mater. Res. A* **2006**, *79*, 1–5.
93. Kloxin, A. M.; Kasko, A. M.; Salinas, C. N.; Anseth, K. S. *Science* **2009**, *324*, 59–63.
94. Nemir, S.; Hayenga, H. N.; West, J. L. *Biotechnol. Bioeng.* **2010**, *105*, 636–644.
95. Rowlands, A. S.; George, P. A.; Cooper-White, J. J. *Am. J. Physiol. Cell Physiol.* **2008**, *295*, C1037–C1044.
96. Richert, L.; Engler, A. J.; Discher, D. E.; Picart, C. *Biomacromolecules* **2004**, *5*, 1908–1916.
97. Bryant, S. J.; Anseth, K. S. *J. Biomed. Mater. Res.* **2002**, *59*, 63–72.
98. Reinhart-King, C. A.; Dembo, M.; Hammer, D. A. *Biophys. J.* **2008**, *95*, 6044–6051.
99. Fischer, R. S.; Gardel, M.; Ma, X.; Adelstein, R. S.; Waterman, C. M. *Curr. Biol.* **2009**, *19*, 260–265.
100. Sieminski, A. L.; Hebbel, R. P.; Gooch, K. J. *Exp. Cell Res.* **2004**, *297*, 574–584.
101. Nelson, C. M.; Bissell, M. J. *Annu. Rev. Cell Dev. Biol.* **2006**, *22*, 287–309.
102. Reilly, G. C.; Engler, A. J. *J. Biomech.* **2010**, *43*, 55–62.
103. Vogel, V.; Sheetz, M. *Nat. Rev. Mol. Cell Biol.* **2006**, *7*, 265–275.
104. Wong, J. Y.; Leach, J. B.; Brown, X. Q. *Surf. Sci.* **2004**, *570*, 119–133.
105. Oakes, P. W.; Patel, D. C.; Morin, N. A.; *et al. Blood* **2009**, *114*, 1387–1395.
106. Stroka, K. M.; Aranda-Espinoza, H. *Cell Motil. Cytoskeleton* **2009**, *66*, 328–341.
107. Engler, A. J.; Carag-Krieger, C.; Johnson, C. P.; *et al. J. Cell Sci.* **2008**, *121*(22), 3794–3802.
108. Friedl, P.; Wolf, K. *J. Cell Biol.* **2010**, *181*, 11–19.
109. Goffin, J. M.; Pittet, P.; Csucs, G.; Lussi, J. W.; Meister, J. J.; Hinz, B. *J. Cell Biol.* **2006**, *172*, 259–268.
110. Ghosh, K.; Pan, Z.; Guan, E.; *et al. Biomaterials* **2007**, *28*, 671–679.
111. Munevar, S.; Wang, Y.; Dembo, M. *Biophys. J.* **2001**, *80*, 1744–1757.
112. Jiang, G.; Huang, A. H.; Cai, Y.; Tanase, M.; Sheetz, M. P. *Biophys. J.* **2006**, *90*, 1804–1809.
113. Guo, W. H.; Wang, Y. L. *Mol. Biol. Cell* **2007**, *18*, 4519–4527.
114. Peters, A.; Palay, S. L. J. A.; Webster, H. D. F. J. A. In *The Fine Structure of the Nervous System: The Neurons and Supporting Cells*; Peters, A., Palay, S. L., Webster, H.deF., Eds.; Saunders: Philadelphia, PA, 1976.
115. Georges, P. C.; Miller, W. J.; Meaney, D. F.; Sawyer, E. S.; Janmey, P. A. *Biophys. J.* **2006**, *90*, 3012–3018.
116. Miller, K.; Chinzei, K.; Orssengo, G.; Bednarz, P. *J. Biomech.* **2000**, *33*, 1369–1376.
117. Flanagan, L. A.; Ju, Y. E.; Marg, B.; Osterfield, M.; Janmey, P. A. *Neuroreport* **2002**, *13*, 2411–2415.
118. Balgude, A. P.; Yu, X.; Szymanski, A.; Bellamkonda, R. V. *Biomaterials* **2001**, *22*, 1077–1084.
119. Grounds, M. D.; White, J. D.; Rosenthal, N.; Bogoyevitch, M. A. *J. Histochem. Cytochem.* **2002**, *50*, 589–610.

120. Rowley, J. A.; Mooney, D. J. *J. Biomed. Mater. Res.* **2002**, *60*, 217–223.
121. Collinsworth, A. M.; Zhang, S.; Kraus, W. E.; Truskey, G. A. *Am. J. Physiol. Cell Physiol.* **2002**, *283*, C1219–C1227.
122. Engler, A. J.; Griffin, M. A.; Sen, S.; Bonnemann, C. G.; Sweeney, H. L.; Discher, D. E. *J. Cell Biol.* **2004**, *166*, 877–887.
123. Jacot, J. G.; Mcculloch, A. D.; Omens, J. H. *Biophys. J.* **2008**, *95*, 3479–3487.
124. Shapira-Schweitzer, K.; Seliktar, D. *Acta Biomater.* **2007**, *3*, 33–41.
125. Keller, G. *Genes Dev.* **2005**, *19*, 1129–1155.
126. Discher, D. E.; Mooney, D. J.; Zandstra, P. W. *Science* **2009**, *324*, 1673–1677.
127. Kong, H. J.; Polte, T. R.; Alsberg, E.; Mooney, D. J. *Proc. Natl Acad. Sci. USA* **2005**, *102*, 4300–4305.
128. Raisz, L. G. *Clin. Chem.* **1999**, *45*, 1353–1358.
129. Hsiong, S. X.; Carampin, P.; Kong, H. J.; Lee, K. Y.; Mooney, D. J. *J. Biomed. Mater. Res. A* **2008**, *85*, 145–156.
130. Patel, P. N.; Smith, C. K.; Patrick, C. W., Jr. *J. Biomed. Mater. Res.* **2005**, *73A*, 313–319.
131. Saha, K.; Keung, A. J.; Irwin, E. F.; *et al. Biophys. J.* **2008**, *95*, 4426–4438.
132. Evans, N. D.; Minelli, C.; Gentleman, E.; *et al. Eur. Cell Mater.* **2009**, *18*, 1–13; discussion 13–14.
133. Hanahan, D.; Weinberg, R. A. *Cell* **2000**, *100*, 57–70.
134. Guo, W.; Giancotti, F. G. *Nat. Rev. Mol. Cell Biol.* **2004**, *5*, 816–826.
135. Weaver, V. M.; Petersen, O. W.; Wang, F.; *et al. J. Cell Biol.* **1997**, *137*, 231–245.
136. Cutroneo, K. R.; White, S. L.; Chiu, J. F.; Ehrlich, H. P. *J. Cell. Biochem.* **2006**, *97*, 1161–1174.
137. Lam, W. A.; Cao, L.; Umesh, V.; Keung, A. J.; Sen, S.; Kumar, S. *Mol. Cancer* **2010**, *9*, 35.
138. Paszek, M. J.; Weaver, V. M. *J. Mammary Gland Biol. Neoplasia* **2004**, *9*, 325–342.
139. Thomas, T. W.; Dimilla, P. A. *Med. Biol. Eng. Comput.* **2000**, *38*, 360–370.
140. Eastwood, M.; Mudera, V. C.; Mcgrouther, D. A.; Brown, R. A. *Cell Motil. Cytoskeleton* **1998**, *40*, 13–21.
141. Girton, T. S.; Barocas, V. H.; Tranquillo, R. T. *J. Biomech. Eng.* **2002**, *124*, 568–575.
142. Cukierman, E.; Pankov, R.; Stevens, D. R.; Yamada, K. M. *Science* **2001**, *294*, 1708–1712.

5.505. Quantifying Integrin–Ligand Engagement and Cell Phenotype in 3D Scaffolds

R J DeVolder and H Kong, University of Illinois at Urbana-Champaign, Urbana, IL, USA

© 2011 Elsevier Ltd. All rights reserved.

5.505.1.	**Introduction**	65
5.505.2.	**Quantifying Integrin–Ligand Forces**	66
5.505.2.1.	Atomic Force Microscopy	66
5.505.2.2.	Magnetic Twisting Cytometry	66
5.505.2.3.	Traction Force Microscopy	67
5.505.2.4.	Fluorescence Resonance Energy Transfer	68
5.505.3.	**Quantifying Type and Number of Integrin–Ligand Binding**	69
5.505.3.1.	Immunochemical Techniques	69
5.505.3.2.	Fluorescence Resonance Energy Transfer	70
5.505.4.	**Conclusion**	70
References		71

Abbreviations

2P	Two-photon
ECM	Extracellular matrix
ELISA	Enzyme-linked serologic assay
ET-1	Endothelin-1 gene
FOC	Focal adhesion complex
FRET	Fluorescence resonance energy transfer
GFP	Green fluorescence protein
IF	Immunofluorescence
MATFM	Microarray traction force microscopy
MSC	Mesenchymal stem cells
MTC	Magnetic twisting cytometry
RGD	Arg-Gly-Asp
TFM	Traction force microscopy

5.505.1. Introduction

The use of cells in clinical therapies holds great promise for the treatment of a wide array of disorders and diseases. However, the control of the fate of transplanted cells remains a significant challenge, because cellular phenotypes are regulated by various signals from soluble factors (e.g., cytokine and growth factors), extracellular matrices (ECMs), and neighboring cells. It is well known that these signals are transmitted through specific bonds, such as those between cellular receptors and soluble factors, cellular integrins and adhesion ligands of ECMs, and cadherin bonds between adjacent cells.[1,2] Specifically, cells tend to probe and respond to the chemical and mechanical properties of their ECM environments, to which they adhere, using integrin–ligand bonds. For instance, the deposition of stiff fibrotic tissues in wounds causes fibroblasts to differentiate into a myofibroblast phenotype, and growth factor binding sites in the ECM can sequester the chemical cues necessary to promote or inhibit cellular differentiation.

Integrin ligation is a major component in maintaining cellular homeostasis and also stimulating cellular activities in response to external stimuli, including soluble factors and cyclic mechanical forces. The integrin family of cellular receptors are heterodimeric transmembrane glycoproteins that bind to epitopes and modulate cellular adhesion to the ECM. Cellular adhesion through integrin ligation is not only specific, but also requires divalent cations, Ca^{2+} or Mg^{2+}, for the binding process.[3] The type and quantity of integrin–ligand bonds and the forces exerted on these bonds have been shown to direct cellular fate and activity. Recently, numerous studies have demonstrated that several cellular ECM adhesion proteins (e.g., fibronectin, laminin, collagen, etc.) bind with specific cellular integrins (e.g., $\alpha 2\beta 1$, $\alpha 6\beta 1$, $\alpha V\beta 3$, etc.) and regulate cellular activities with densities and spatial organization of the cell adhesion molecules at varied length scales. In addition, these specific integrin–ligand bonds modulate the effects of soluble signals including various cytokine, growth factors, and antibodies, and insoluble signals such as the mechanical rigidity of the matrix and cyclic mechanical forces. Note that these aspects are discussed elsewhere.[4]

Therefore, extensive efforts have been made to develop methods to characterize the engagement of integrins with adhesion ligands and their effects on cell adhesion, signaling activation, and phenotypic activities, both *in vitro* and *in vivo*. These methods are largely categorized into two groups: quantifying the forces associated with integrin–ligand bonds and quantifying the number of these bonds formed between cells and their environment. This chapter therefore summarizes methods developed to quantitatively evaluate (1) cell adhesion forces and (2) the number of integrin–ligand bonds formed on two-dimensional (2D) and within 3D platforms, all of which can be examined with respect to cellular phenotypic properties and cellular fates.

5.505.2. Quantifying Integrin–Ligand Forces

Cells are continually exposed to various mechanical stimuli in their dynamic tissue environments. They exert forces on a matrix to which cells adhere and interpret mechanical forces from their surroundings through focal adhesion complexes (FOCs). FOCs are large macromolecular assemblies at sites of integrin binding through which mechanical forces and regulatory signals are transmitted to the cell, and have been shown to regulate cellular activities and phenotypic properties.[2] For instance, mesenchymal stem cells (MSCs) cultured within a stiff ECM tend to proliferate at higher rates than in softer environments, but were shown to have specific lineage and commit to phenotypes with extreme sensitivity to tissue-level elasticity.[1] To ultimately understand how mechanical forces translate into cellular phenotypic characteristics, it is important to understand the forces associated with integrin–ligand interactions.

There are several methods used to measure the binding forces between cellular integrins and ECM ligands. Some of these methods include atomic force microscopy (AFM), magnetic twisting cytometry (MTC), various forms of traction force microscopy (TFM), and fluorescence resonance energy transfer (FRET), all of which have their own unique advantages for quantifying the binding forces between integrin and ligands. Using these methods, the forces of these individual molecular bonds have been shown to range from 1 to 100 nN, depending on the types of ligands and integrins, cell types, and other external cellular variables.[5]

5.505.2.1. Atomic Force Microscopy

Since its introduction in 1986, AFM has been one of the most widely used biophysical tools used in cell biology. It is a high-resolution scanning probe microscopic technique developed to image various surface morphologies of biological and nonbiological materials on the nano- and microscale. AFM consists of a cantilever with a sharp tip that scans the surface of a specimen, and when the tip comes in contact with a surface, forces between the tip and the sample lead to a deflection of the cantilever. The deflection distances and forces are directly related to an image of the specimen and are measured, respectively. Depending on the specific situation, AFM can be used to measure mechanical contact forces, van der Waals forces, capillary forces, solvent forces, and chemical binding forces. In various biological studies, AFM has been widely used to study individual biomacromolecules, cell nuclei, and subcellular structures. Additionally, it has been used to examine the viscoelastic properties of cells and alterations in stiffness associated with cellular differentiation.[5]

Recently, AFM has emerged as a powerful tool for examining single-molecular conformational and binding properties. The forces associated with integrin ligation have been examined using AFM by measuring the unbinding force between integrins and ligands covalently immobilized on the tip and substrate, respectively (or vice versa). Lehenkari and Hortan used this technique to examine the adhesion forces between extracellular integrins and cell adhesion epitopes.[6] They immobilized various forms of oligopeptides containing the Arg-Gly-Asp (RGD) sequence, a cellular binding epitope, on AFM tips and measured the resulting unbinding forces from osteoclast bone cells. They determined that the specific adhesion force between RGD epitopes and osteoclast integrins ranges from 32 to 97 pN, depending on RGD amino acid sequence, pH, and divalent cation composition. Similarly, Wojcikiewicz *et al.* used the same AFM technique to study leukocyte migration and subsequent binding at injury sites.[7] They examined the inhibitory effects of external chemical cues on integrin binding. More specifically, they examined the role of soluble factors (e.g., phorbol myristate acetate) in mediating the binding affinity of the antigen LFA to the ligand ICAM-1.

AFM is a useful tool to examine the binding forces between ligands and integrins. It allows one to examine the specific ligand–integrin engagement and measure the subsequent cellular adhesion force. However, the cell adhesion forces measured by AFM often depend on the dynamic properties applied to the cells. For example, Merkel *et al.* demonstrated that increasing the rate at which forces were applied to cells alters the magnitude of the cell adhesion force up to 10-fold, which demonstrates the complexities involved with the deformation and relaxation of integrin–ligand bonds.[8] Additionally, AFM measurements are limited to examining integrin–ligand forces for cells adhered to a 2D substrate. Therefore, certain supplemental methods should be employed to fully understand how various soluble and insoluble factors of a 3D microenvironment affect cellular activities.

5.505.2.2. Magnetic Twisting Cytometry

MTC is a technique that examines controlled mechanical stresses applied to specific cell surface receptors using ligand-coated ferromagnetic beads under a magnetic field and was first employed for mechanotransduction studies by Wang *et al.*[9] Similar to AFM, MTC applies forces directly to cells, however, in the form of torque compared to tensile/compressive forces. MTC has been used to characterize multiple aspects of integrin–ligand bonds by applying mechanical stress to cells, for instance, (a) measurements of ligand–receptor adhesion strength, (b) mechanical linkages between a cell surface receptor and the cytoskeleton, (c) rheological properties of the cytoskeleton, and (d) intracellular biochemical changes.[5,10] Specifically, cells are incubated with ferromagnetic or superparamagnetic beads coated with ECM or cell adhesion proteins, typically with ~20 beads per cell. Upon the application of a magnetic field, the beads orientate according to their dipoles, which ultimately applies a torque to the cell surface (**Figure 1**). The shear stiffness of the specific binding is calculated by measuring the bead rotation and angular bead strain using a magnetometer.

Using this method, Wang *et al.* demonstrated a limited rotation of RGD-bound beads in comparison to beads coated with metabolic receptor antibodies.[9] This result addressed that ECM-bound integrins engage with the cellular cytoskeleton through FOC, subsequently demonstrating a mechanically coupled cytoskeleton–ECM interaction. They also demonstrated that specific integrin receptors, such as β1, αV, and α2, transfer forces across the cellular surface to the cytoskeleton, while other transmembrane proteins, such as scavenger receptors and endothelial cell adhesion molecules, do not.[11,12] This method can also be used to examine the rheological properties

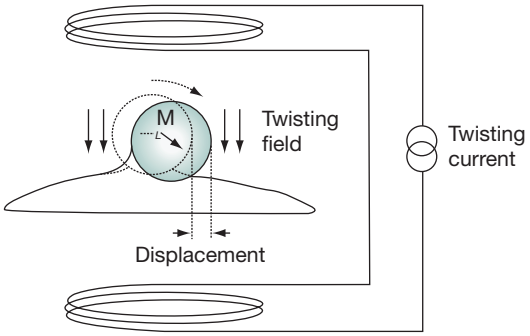

Figure 1 Magnet twisting cytometry (MTC). In MTC, a homogenous magnetic twisting field applied to cell surface-adhered beads causes the bead to rotate and to displace, thereby inducing shear stresses on the cell. Reproduced from Sen, S.; Kumar, S. *J. Biomech.* **2010**, *43*(1), 45–54.

of the cell membrane and cytoskeleton. For instance, using the β1 receptor–RGD complex, Wang and Ingber determined that cellular cytoskeleton stiffness was directly proportional to the level of stress applied to the cells and that the slope of the linear stiffening response differs depending on the shape of the cell.[12]

Additionally, MTC has been modified with an oscillating magnetic field to examine cellular responses under dynamic mechanical forces. For instance, Chen *et al.* examined endothelial cell expression of the endothelin-1 (ET-1) gene, which transcribes vascoconstricting peptides, using MTC with magnetic fields having varied amplitudes, durations, and frequencies.[13] Oscillating the magnetic field at controlled frequencies caused magnetic bead, oscillatory rotation, and resulted in a twofold increase of ET-1 expression compared to nonoscillatory conditions. Using this modified technique, mechanotransduction studies can be carried out to examine cellular responses to mechanically dynamic environments.

MTC is a useful technique that allows the examination of cellular activities and/or phenotypic changes in response to a controlled torque applied dynamically or statically to the cellular integrin–ligand adhesions. It also allows the rheological examination of cytoskeletons coupled with various environmental conditions. Although MTC is a useful tool for mechanotransduction studies, it is difficult to apply this technique in 3D environments, which are representative of native cellular environments. Also, these studies cannot account for potential alterations in cellular activities induced from the magnetic fields applied for MTC.

5.505.2.3. Traction Force Microscopy

Unlike AFM and MTC, where forces are applied directly to cells, TFM measures forces exerted by cells on their environments. During the early 1980s, cells were shown to visibly wrinkle silicon substrates as they migrated, demonstrating that they exert forces on their adhesion substrates.[14] This prompted the development of TFM, which quantitatively measures cellular traction forces exerted on a substrate to which cells adhere. TFM consists of embedding fluorescent beads in materials, such as silicon rubber, and observing the displacement of the beads due to the contractile activity of cells cultured on or in the material. The displacement of the fluorescent beads can be directly related to the force exerted by the cells, termed cell traction force, according to the mechanical properties of the substrate.[5]

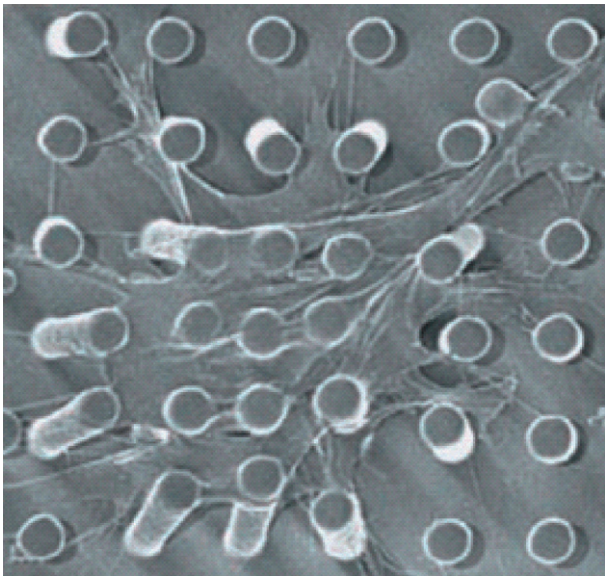

Figure 2 Smooth muscle cells cultured on arrays of posts coated with fibronectin applying traction forces, causing posts to bend. Reproduced from Tan, J. L.; Tien, J.; Pirone, D. M.; Gray, D. S.; Bhadriraju, K.; Chen, C. S. *Proc. Natl. Acad. Sci. USA* **2003**, *100*(4), 1484–1489.

Pelham *et al.* were some of the first to use this technique with polyacrylamide gel substrates, which are linearly elastic, optically transparent, and amenable to protein conjugations, allowing a simple platform for studying cell-generated forces.[15] The most widely used method for adding cell-binding ligands to a substrate for TFM is through the adsorption of natural ECM proteins. Even though this results in a random distribution of binding domains on substrate surfaces, it has been shown that cells tend to bind in 'island' patterns with nonuniform distributions due to the adsorption properties of the substrate (which is also extremely variant on substrate type and processing).[16]

With advances in polymer process technologies, TFM has been employed using a variety of different substrates, cell types, and ECM proteins. The stress–strain relationships have been further transformed into Fourier transform for improved analysis. Additionally, several micropatterning techniques have been used to examine cellular traction forces at FOC, independent of one another.[17] Tan *et al.* developed a new TFM technique to examine the forces cells apply to their adhesion substrates.[18] Using soft lithographic techniques, they developed a platform of microarray posts with varying geometries which can be displaced by cells cultured on top of them (**Figure 2**). This method allows the examination of contractile forces independent of neighboring forces, thus directly eliciting their subcellular distributions. They demonstrated that the magnitude of the tractile forces was modulated by the size of the posts, indicating a relationship between the subcellular force and the number of integrin–ligand adhesions.

As the uses of confocal and two-photon (2P) microscopic techniques have become increasingly popular, TFM has been

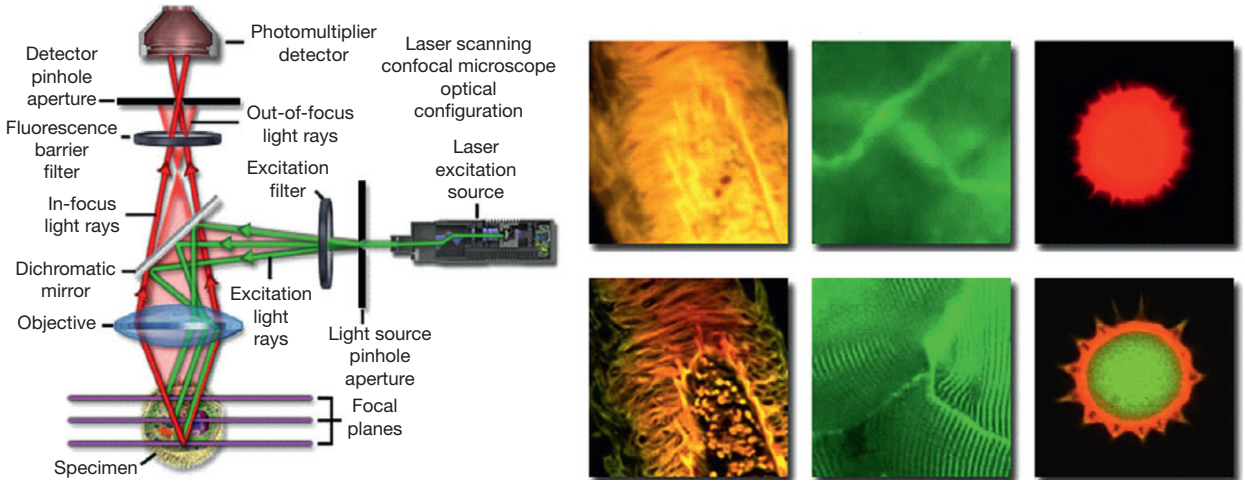

Figure 3 A diagram of confocal microscope that demonstrates the blocking of out-of-focus light (left). A comparison of images using normal fluorescence microscopy (right, top row) to the higher resolution of confocal microscopy (right, bottom row). Reproduced with permission from Fellers, T. J. and Davidson, M. W. – National High Magnetic Field Laboratory, The Florida State University, Tallahassee, Florida, USA.

adapted to examine cellular activities in 3D environments. Compared to normal fluorescence microscopy, confocal microscopy blocks background fluorescence, allowing a clear image of the excitation in a single focal plane; by stacking these plains in the *z*-axis, a 3D image is created (Figure 3). With these 3D images, the displacement of fluorescence beads encapsulated with cells in a biomaterial system can be monitored and related to cellular forces. These biomaterial systems can also be engineered to have specific types and concentrations of cellular binding domains (ligands) and other properties, which can be related to contractile forces and other cellular activities. Additionally, comparisons between 2D and 3D cellular environments can be made to develop a better understanding of cell–matrix interactions. Fraley *et al.* used TFM to examine the mechanism for cellular migration in 3D versus 2D environments, by embedding cells and marker beads in collagen matrices (3D environment) and adhering cells to collagen substrates with embedded marker beads (2D environment) (Figure 4).[19] They demonstrated distinct differences in migration mechanisms between 2D and 3D environments, in particular that focal adhesion proteins including vinculin, paxillin, and talin modulate migration speed in 3D, but had no distinct role in controlling 2D migration.

Various TFM techniques, including microarray TFM (MATFM), have also been combined with additional fluorescence techniques to examine the relationship between the forces exerted by cells and the formation of FOC. Balaban *et al.* used cells expressing green fluorescence protein (GFP)-tagged vinculin with MATFM to demonstrate that local forces exerted by cells are correlated to the orientation and fluorescence intensity and area.[17] By using additional fluorescence techniques, relationships between tactile forces and cellular activities, such as protein–protein interactions, can be developed.

Overall, TFM is a powerful technique for developing relationships between the forces exerted by cells on their adhesion matrices and cellular behavior and/or phenotypic activities. Advances in matrix design and microscopic imaging have allowed TFM measurements of cellular forces in both 2D and 3D microenvironments.

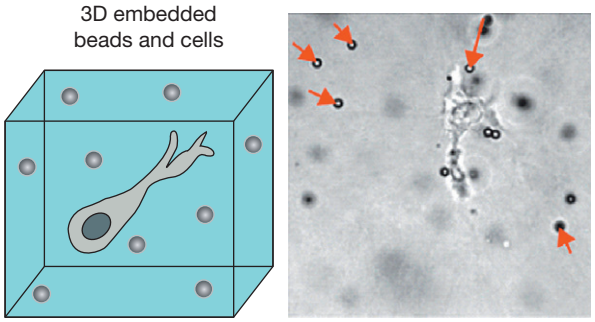

Figure 4 Schematic of cells embedded in three-dimensional environment with fiduciary beads that are monitored for traction force measurements (left). The movement of beads in the vicinity of cells and as indicated by the arrows (right). Reproduced from Fraley, S. I.; Feng, Y. F.; Krishnamurthy, R.; *et al. Nat. Cell Biol.* **2010**, *12*(6), 598–604.

5.505.2.4. Fluorescence Resonance Energy Transfer

FRET, which is a form of nonradiative energy transfer between two fluorescence molecules, has been extensively used to examine protein–protein interactions. When a donor fluorescence probe is in proximity (10 nM or less) to an acceptor fluorescence probe, energy is transferred through nonradiative dipole–dipole coupling, causing an excitation of the acceptor probe, which is then measured. FRET has two distinct advantages over typical immunofluoresence techniques. First, the distance required for energy transfer is so short that it allows the probing of molecular interactions, and second, the observable excitation range of the acceptor is very narrow and thus easily observed.[10] Since the distance required for energy transfer between fluorescence probes is so small, high-resolution images are produced to allow examination of molecular interactions on the nanoscale.

FRET is a useful technique that has been used to relate cellular activities and/or phenotypic characteristics with cellular traction forces. Kong *et al.* developed a method using FRET to quantify the forces exerted by preosteoblasts adhered on

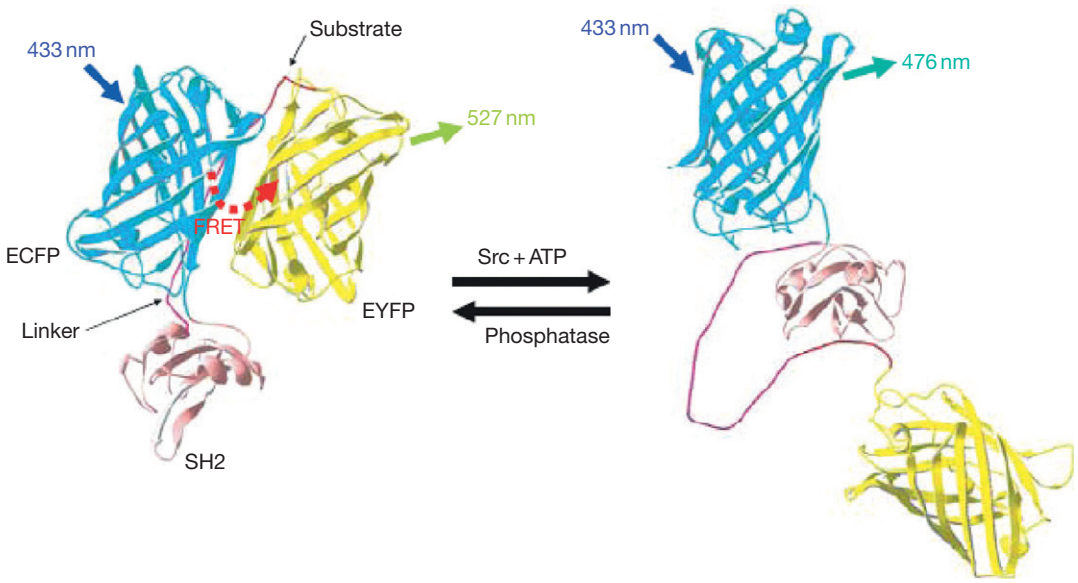

Figure 5 A schematic of an Src homo-FRET probe illustrating the effect of the Src reporter upon the activation of Src kinase or phosphatase. Reproduced from Wang, Y. X.; Botvinick, E. L.; Zhao, Y. H.; *et al*. *Nature* **2005**, *434*(7036), 1040–1045.

alginate gels through bonds between cellular integrins and RGD peptides linked to the gel.[20] They covalently attached two different fluorescence probes (a donor and an acceptor) to RGD peptides that were covalently attached to alginate polymers. As the cells exerted forces on gels through integrin–RGD binding, the emission of donor probes was decreased in the presence of the acceptor probe, and the quantified FRET efficiency was converted to the force exerted by cells. Recently, this FRET technique was extended to measure traction forces of cells encapsulated within hydrogel matrices. Huebsch *et al.* determined that specific elastic moduli of alginate hydrogels correlated to a maximal traction reorganization of integrin–ligand bonds for cells encapsulated within the gels.[3]

FRET can also be used in mechanotransduction studies to measure the dynamics of protein–protein interactions. Recently, FRET was used as a sensor to examine the phosphorylation of Src, a tyrosine-kinase, in endothelial cells subjected to external forces. In the study, a synthetic protein containing two fluorescent protein regions, a donor and an acceptor (CFP and YFP), were used to undergo homo-FRET.[21] More specifically, the conformational change, resulting from the phosphorylation of Src, causes proximity between the donor and acceptor probes, leading to fluorescence excitation (Figure 5). This real-time analysis allows measurements of cellular activity on the molecular level resulting from changes in a cell's mechanical environment.

5.505.3. Quantifying Type and Number of Integrin–Ligand Binding

There are numerous types of binding domains in natural ECM proteins, to which cells adhere. The role of the type of integrin–ligand bond in modulating cellular phenotypes is regulated by the density and spatial organization of cell adhesion ligands at nanometer and micrometer scales. Since these matrix variables affect the number of integrin–ligand bonds, various methods were developed to quantify the number of bonds. These methods include immunochemical techniques, genetic labeling, and FRET.

5.505.3.1. Immunochemical Techniques

Immunochemical techniques involve the use of antibodies that have a high affinity for specific peptides. These antibodies can be labeled with a variety of detectable probes, including fluorescence molecules, also known as immunofluorescence (IF), and bind to epitopes specific for particular integrins and ligands. Using IF techniques, the number and distribution of integrin–ligand bonds can easily be quantified by examining the excitation intensity and distribution of the labeled antibodies, respectively.[22] For instance, fluorescently labeled antibodies specific for the β_1 integrin–RGD ligand complex will bind to this specific cellular adhesion, and its subsequent excitation intensity and distribution will elicit the number and distribution of focal adhesions for a specific environment (Figure 6). Additionally, IF can be used to examine conformation and topography of adsorbed molecules and the bioavailability of antibody-binding epitopes.

IF is extensively used to characterize both the behavior of focal adhesion molecules (integrins) and downstream signaling (gene expression). It is a useful tool to examine emergent cellular behavior, but is limited to dynamic examination of cell–ECM interaction without noninvasive imaging techniques, including second-harmonic generation imaging and optical coherence tomography. An additional limitation to this method is the potential perturbations associated with the binding of fluorescent probes to FOC.[10] More specifically, the binding of antibodies with labeled probes can cause slight conformation changes to adhesion complexes, dissipating or attenuating their real physiological effects.

Additional methods used to examine the number and specificity of cell–ECM adhesions are immunoblotting

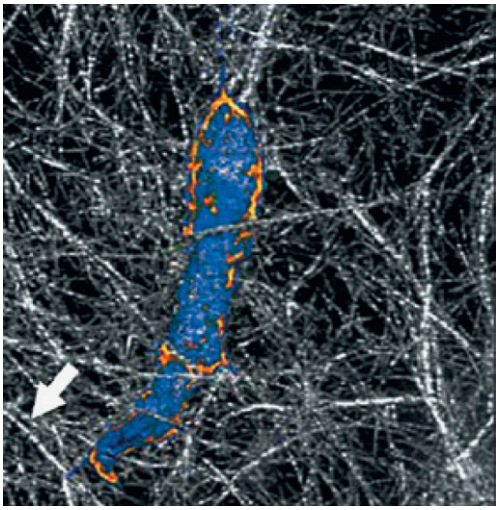

Figure 6 Image of a fibrosarcoma cell migrating within a three-dimensional collagen lattice, stained with nonblocking anti-β1 integrin antibody K20. Reproduced from Friedl, P. *Histochem. Cell Biol.* **2004**, *122*(3), 183–190.

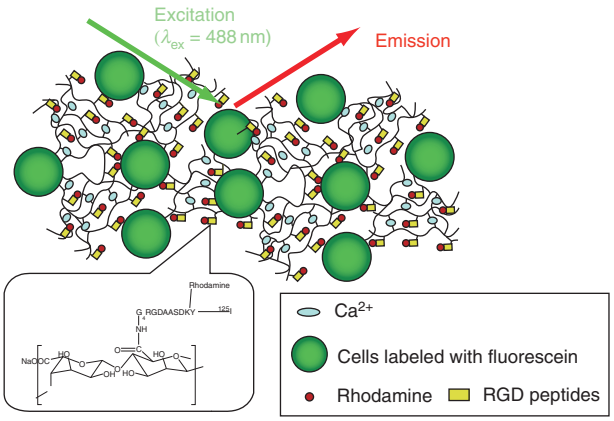

Figure 7 Schematic of the fluorescent cells that were mixed with various numbers of rhodamine–RGD–polymer molecules and the subsequent FRET emission. Gels were formed by cross-linking polymer chains with Ca^{2+} ions. Reproduced from Kong, H. J.; Boontheekul, T.; Mooney, D. J. *Proc. Natl. Acad. Sci. USA* **2006**, *103*(49), 18534–18539.

and enzyme-linked-immunosorbent serologic assays (ELISAs). Immunoblotting, more specifically known as Western blots, is a useful tool to examine the presence and quantity of integrins, ligands, or integrin–ligand complexes. This method consists of using gel electrophoresis, typically SDS-PAGE, which separates proteins according to their molecular weights in a polyacrylamide gel. The proteins, including the proteins of interest (integrin–ligands), are transferred from the polyacrylamide gel onto a membrane, normally nitrocellulose, where they are probed by antibodies specific for the desired protein. Western blots can be used to identify the presence of a variety of specific ligands and integrins by probing with a variety of antibodies. Additionally, running a naive gel electrophoresis alone can separate integrins and integrin–ligands due to the conformational change associated with binding, thus quantifying the amounts of bound and unbound integrins. ELISA is a method used to quantify the amount of a specific protein (integrin–ligand) in a solution. An ELISA consists of an antigen affixed to a surface, on which an antibody (integrin–ligand) is applied and binds to the antigen. The antigen is linked to enzymes that convert a specific substance into a detectable signal in accordance with the antigen–antibody binding. Western blots and ELISAs readily quantify the amount of specific integrin–ligands; however, they cannot be used in a dynamic cellular environment – cells have to be lysed to obtain protein solutions containing adhesion complexes.

5.505.3.2. Fluorescence Resonance Energy Transfer

Recently, FRET has been modified for quantifying the number of integrin–ligand bonds. Kong *et al.* labeled RGD peptides linked to hydrogel-forming polymers with acceptor fluorescent probes, and also labeled cells with donor fluorescent probes.[23] The fluorescently labeled cells were encapsulated into hydrogels with controlled quantities of RGD peptides. As cells formed adhesion complexes with the RGD peptides, the donor markers excited the acceptor markers, resulting in a measurable emission (Figure 7). This FRET technique enables the quantification of ligand–integrin bonds according to the degree of FRET, or in other words, the magnitude of the subsequent emissions. The number of adhesion bonds was further related to the proliferation and differentiation of the encapsulated cells and the subsequent relationships were dependent on the specific cell type encapsulated.

Quantifying the number of integrin–ligand bonds through FRET is a useful technique for examining their effects on cellular activities. Fischbach *et al.* examined the relationship between integrin engagement of cancer cells and their angiogenic capacity.[16] More specifically, they quantified the degree of integrin–ligand bonding for cells in 2D and 3D environments using FRET and determined that the cellular secretion of angiogenic factors was modulated by the number of integrin–ligand bonds formed. Huebsch *et al.* also used FRET for examining the effects of ECM mechanical properties on the fate of stem cells. They determined that the ECM stiffness regulated integrin–ligand binding and organization of adhesion ligands, which both correlated with osteogenic differentiation.[3] These examples demonstrate some of the numerous applications of FRET for quantifying integrin ligation in cellular studies.

5.505.4. Conclusion

The use of cells in clinical therapies has great promise for the treatment of a wide array of disorders and diseases; however, the control of the fate of transplanted cells is a significant challenge. Cellular phenotypic characteristics are strongly regulated by cell interactions with their physical and chemical environments. Studies quantifying the forces, type, and extent of ligand–integrin binding are extremely important to develop an understanding of how cell–environmental interactions contribute to cellular phenotypic characteristics. The microscopic and spectroscopic methods reviewed in this chapter, including AFM, MTC, TFM, IF, and FRET, are highly useful for examining the role of integrin–ligand engagement in cellular events at

varied length scales. As the understanding of biomechanical processes advances, new and improved techniques to elicit their functions on cellular activity will be developed. Taken together, characterization methods of integrin–ligand engagement will greatly advance matrix design and controllability of cellular activities, to further enhance the efficacy of cellular clinical treatments for biomedical applications.

References

1. Engler, A. J.; Sen, S.; Sweeney, H. L.; Discher, D. E. *Cell* **2006**, *126*(4), 677–689.
2. Griffith, L. G.; Swartz, M. A. *Nat. Rev. Mol. Cell Biol.* **2006**, *7*(3), 211–224.
3. Huebsch, N.; Arany, P. R.; Mao, A. S.; *et al. Nat. Mater.* **2010**, *9*(6), 518–526.
4. Kong, H. J.; Mooney, D. J. *Nat. Rev. Drug Discov.* **2007**, *6*(6), 455–463.
5. Sen, S.; Kumar, S. *J. Biomech.* **2010**, *43*(1), 45–54.
6. Lehenkari, P. P.; Horton, M. A. *Biochem. Biophys. Res. Commun.* **1999**, *259*(3), 645–650.
7. Wojcikiewicz, E. P.; Zhang, X. H.; Chen, A.; Moy, V. T. *J. Cell Sci.* **2003**, *116*(12), 2531–2539.
8. Merkel, R.; Nassoy, P.; Leung, A.; Ritchie, K.; Evans, E. *Nature* **1999**, *397*(6714), 50–53.
9. Wang, N.; Butler, J. P.; Ingber, D. E. *Science* **1993**, *260*(5111), 1124–1127.
10. Huebsch, N. D.; Mooney, D. J. *Biomaterials* **2007**, *28*(15), 2424–2437.
11. Potard, U. S. B.; Butler, J. P.; Wang, N. *Am. J. Physiol. Cell Physiol.* **1997**, *272*(5), C1654–C1663.
12. Wang, N.; Ingber, D. E. *Biochem. Cell Biol. Biochim. Et Biol. Cell.* **1995**, *73*(7–8), 327–335.
13. Chen, J. X.; Fabry, B.; Schiffrin, E. L.; Wang, N. *Am. J. Physiol. Cell Physiol.* **2001**, *280*(6), C1475–C1484.
14. Harris, A. K.; Wild, P.; Stopak, D. *Science* **1980**, *208*(4440), 177–179.
15. Pelham, R. J.; Wang, Y. L. *Proc. Natl. Acad. Sci. USA* **1997**, *94*(25), 13661–13665.
16. Fischbach, C.; Kong, H. J.; Hsiong, S. X.; Evangelista, M. B.; Yuen, W.; Mooney, D. J. *Proc. Natl. Acad. Sci. USA* **2009**, *106*(2), 399–404.
17. Balaban, N. Q.; Schwarz, U. S.; Riveline, D.; *et al. Nat. Cell Biol.* **2001**, *3*(5), 466–472.
18. Tan, J. L.; Tien, J.; Pirone, D. M.; Gray, D. S.; Bhadriraju, K.; Chen, C. S. *Proc. Natl. Acad. Sci. USA* **2003**, *100*(4), 1484–1489.
19. Fraley, S. I.; Feng, Y. F.; Krishnamurthy, R.; *et al. Nat. Cell Biol.* **2010**, *12*(6), 598–604.
20. Kong, H. J.; Polte, T. R.; Alsberg, E.; Mooney, D. J. *Proc. Natl. Acad. Sci. USA* **2005**, *102*(12), 4300–4305.
21. Wang, Y. X.; Botvinick, E. L.; Zhao, Y. H.; *et al. Nature* **2005**, *434*(7036), 1040–1045.
22. Friedl, P. *Histochem. Cell Biol.* **2004**, *122*(3), 183–190.
23. Kong, H. J.; Boontheekul, T.; Mooney, D. J. *Proc. Natl. Acad. Sci. USA* **2006**, *103*(49), 18534–18539.

5.506. Effects of Mechanical Stress on Cells

F A Herzog, Ecole Polytechnique Fédérale de Lausanne, Lausanne, Switzerland
C R Jacobs, Columbia University, New York, NY, USA

© 2011 Elsevier Ltd. All rights reserved.

5.506.1.	**Introduction**	73
5.506.2.	**Mechanical Environment of the Cell**	74
5.506.2.1.	Mechanical Properties of the Cell	74
5.506.2.1.1.	Cytoskeleton	74
5.506.2.1.2.	Cell membrane	75
5.506.2.1.3.	Glycocalyx	75
5.506.3.	**Subcellular Structures Involved in Mechanotransduction**	75
5.506.3.1.	Interactions with the ECM: FAs	75
5.506.3.2.	Interaction with Neighboring Cells: Adherens Junction	76
5.506.3.3.	Primary Cilia	76
5.506.3.4.	Caveolae	77
5.506.3.5.	Nucleus	77
5.506.4.	**Molecular Mechanotransduction**	77
5.506.4.1.	Mechanosensitive Ion Channels	77
5.506.4.2.	Exposure of Cryptic Sequences	78
5.506.4.3.	Receptor–Ligand Interactions that Strengthen if Strained	79
5.506.5.	**Response of Cells to Mechanical Stress and Implications for Tissue Engineering**	79
References		80

Abbreviations

AC	Adenylyl cyclase
COX	Cyclo-oxygenase
EC	Endothelial cell
ECM	Extracellular matrix
FA	Focal adhesion
FAK	Focal adhesion kinase
PC	polycystin
PGI2	Prostacyclin

5.506.1. Introduction

Mechanical stresses modulate and orchestrate cellular responses from the very beginning through the entire lifespan of an organism. Evidence for the fact that virtually every cell, not just highly specialized cells, such as cells for hearing and touch, is mechanoresponsive is growing. Cells have mechanical sensory capabilities and the ability to convert mechanical signals into a biochemical response. There are a variety of different mechanical signals acting on cells and a multitude of proteins involved in signal transduction, and the responses range from short-term changes in the cytoskeletal arrangement to long-term changes in gene expression. Often, multiple signaling pathways are activated by mechanical forces, and the orchestrated response enables the cell to adapt to changing mechanical conditions, which in turn modulates tissue morphology and remodeling.

One of the first tissues to be recognized as mechanoresponsive is bone. In the nineteenth century, the German anatomist and surgeon Julius Wolff described the relationship between bone architecture and function.[1] He stated that mechanical stress was responsible for the architecture of bone and that bone would adapt to mechanical changes. When loading on a bone increases, the structure of the bone will change to support the new loading and, conversely, when loading decreases, the bone becomes less strong. The decrease in bone density in astronauts during periods of weightlessness and the increase in it with exercise are some examples illustrating bone's adaption to changes in mechanical loading.

A living higher order organism is subject to and generates different type of stresses, through tension, compression, and shear. The mechanical stress is transmitted to the cellular level, and the magnitude and localization of the resulting force depend on both the mechanical environment and the mechanical properties of the cells. Cells can be shielded from stresses, or, in contrast, stress can be focused at specific locations. At these spots, the actual conversion of mechanical to biochemical signals takes place through specialized proteins or protein complexes.

The goal of this chapter is not to exhaustively review the broad literature on cellular mechanotransduction and its role in tissue homeostasis and remodeling but to show general schemes of how cells sense and respond to mechanical stimuli. Given the crucial role of mechanical stimuli for proper cell function, the importance of controlling stresses in tissue engineering constructs is discussed at the end of the chapter.

5.506.2. Mechanical Environment of the Cell

Cells are continuously exposed to different sources of mechanical stimulation, such as strain transmitted from contracting muscles, shear stress and pressure from blood or interstitial fluid flow, and forces generated from contracting neighboring cells. To what extent cells are exposed depends on their specific location in the body. Some cells are more susceptible to one stress than to another depending on their function. It seems that not just specialized cells, such as hair cells involved in hearing, or touch-sensitive neurons sense these stimuli but virtually every cell is competent to sense and respond to mechanical stresses.

Stresses are transmitted from the whole body system to the organs, tissues, and cells through the extracellular matrix (ECM). To what extent stresses are transmitted to the cell level is highly dependent on the pericellular mechanical behavior, the extracellular matrix (ECM), and the relative material properties of the cell itself.

The three basic mechanical stresses acting on cells are tension, compression, and shear (Figure 1). For example, tendon and ligaments sustain large tensile stresses, arteries are stretched and sheared from the pulsatile blood flow, and bones resist compressive and tensile stresses. But the predominant stress is not always the most important stimulus for cells. In bone, the strains induced by physiological compression are very small (on the order of 100 microstrains) and not sufficient to trigger a cellular response. Indeed, the current paradigm is that small strains squeeze interstitial fluid flow through a network of small channels, the canaliculi, much as a sponge does when a load is applied. The moving fluid leads to shear stress, and the magnitudes of shear stress estimated to occur physiologically in these channels have been shown to be potent stimuli for bone cells *in vitro*.[2,3] Additionally, flow through the canalicular network in the absence of strain has been shown to induce bone formation.[4] It is therefore crucial to understand the environment of the cell to know which type of stress is acting on the cell and which temporal patterns and magnitudes of stimulation elicit a cellular response.

Thus, in order to understand cellular mechanotransduction, it is critical to determine how stresses are transmitted from the organism level, down to the tissue and cellular levels by the ECM and pericelluar matrix, or directly from neighboring cells via cell–cell contact. The properties of the ECM differ from tissue to tissue, and a complete description is beyond the scope of this chapter. Furthermore, the micromechanical behavior of the pericellular matrix and its interaction with cellular mechanics is a topic that has received very little attention.

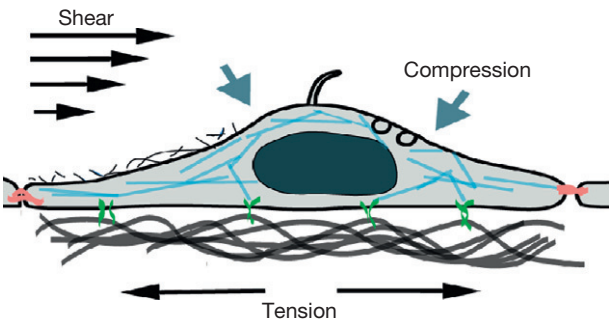

Figure 1 The basic mechanical stresses acting on a cell are shear, compression, and tension.

5.506.2.1. Mechanical Properties of the Cell

Understanding the mechanisms of mechanotransduction requires an understanding of the mechanics of the cell. Biophysical studies have revealed that the cell is far from a homogeneous material. The complex composition and architecture of the cell influence how stresses are transmitted, distributed, and focused. Here, we want to briefly describe the cytoskeleton, the cell membrane, and the glycocalyx in terms of composition and mechanical properties.

5.506.2.1.1. Cytoskeleton

Stresses are not equally distributed throughout the cells due to their complex architecture and the heterogeneous material properties of subcellular components. The shape and spatial organization of a cell are often mainly determined by the cytoskeleton, which is a highly dynamic and cross-linked mesh of microtubules, actin, and intermediate filaments. Microtubules are the most rigid cytoskeletal polymer and can support compressive forces. Actin filaments are less rigid than microtubules, but due to the high concentration of cross-linkers, they can also form stiff structures. The intermediate filaments are the least stiff cytoskeletal polymer and they resist tensile forces more than compressive forces.[5]

The cytoskeleton is linked to the ECM by focal adhesions (FAs) and to neighboring cells via adherens junctions. Both structures represent strategically important locations, and both are involved in mechanotransduction.

The architecture of the cytoskeletal network plays a crucial role in transmitting cellular stresses.[6] The network of cytoskeletal polymers has been described by the tensegrity model, a term invented in architecture for structures for which stability is based on compressive and tensional elements. Prestress is needed for the integrity of such a structure. In the case of a living cell, the prestress arises from the action of nonmuscle myosin that pulls on the actin filaments. These contractile forces are balanced by microtubules, which resist the compression, and by extracellular adhesions to the ECM and other cells.[7] Prestressed fibers allow immediate transmission of forces to distant sites. There is experimental evidence that physiological forces acting on FAs propagate over long distances into the interior of the cell.[8]

A passive property of such a network of polymers is the stiffening in response to shear as a result of filament entanglement and entropic elasticity of individual filaments, which resist further deformation.[9] Stress-induced deformations of the cytoskeleton are coupled to changes in plasma membrane tension and displacement of fluid in the cytoplasm.[5] It is important to recognize that the cytoskeleton is not a static structure but indeed highly dynamic. Actin filaments and microtubules are constantly polymerizing and depolymerizing, and the cytoskeleton can adapt and reorganize in response to external stresses.

5.506.2.1.2. Cell membrane

Cell membranes define the border between the extracellular and intracellular space. In many cells, they are a primary target of fluid shear stresses. Whether fluid shear acts directly on the lipid bilayer or if it is transmitted via the glycocalyx is discussed below. First, the direct effects of fluid shear, such as changes in bilayer tension and curvature, that potentially activate mechanosensitive proteins are considered.

The concept of membrane fluidity is based on the observation that proteins and lipids diffuse relatively freely in the plane of the lipid bilayer, with some restrictions by structural proteins and connections to the ECM or other cells. The rapidity of diffusion depends on membrane fluidity, which, in turn, depends on the bilayer composition. Unsaturated phospholipids or cholesterol decreases the fluidity of the membrane and influences the lateral diffusion rates of membrane molecules. Interestingly, it has been shown that fluid shear stress on the membrane leads to an increase of membrane fluidity.[10] This observed phenomenon can have an effect on diffusion-limited processes,[11] as long as a nonequilibrium condition is dominant. However, as soon as a new equilibrium is reached, the overall dynamics will be the same, even with altered membrane fluidity. One example of such a diffusion-limited process that could potentially be affected by shear stress is G-protein hydrolysis.[12,13] For example, it was shown that G-proteins isolated in lipid vesicles become activated by shear and that this activation is linked to membrane fluidity.[13]

Changes in shape and curvature of the cell membrane have the potential to alter the conformation of membrane proteins. Cell membranes become thinner when stretched, which means that the hydrophobic interior will decrease in width. Therefore, the thinning of the membrane might lead to a hydrophobic mismatch of membrane proteins forcing the protein to adapt a new conformation by compression, tilting or twisting their domains.[14] As a result, the functionality of a protein can be regulated by membrane stretch; the opening of ion channel is just one example. The same idea applies to changes in curvature, in which the three-dimensional (3D) arrangement of proteins can be altered. This effect is particularly important in caveolae that are highly sensitive to changes in membrane tension.

5.506.2.1.3. Glycocalyx

Eukaryotic cell membranes are covered with the glycocalyx – a layer of polysaccharides, which is covalently linked to glycoproteins and glycolipids residing in the membrane and attached to the cytoskeleton via membrane proteins. It is known from theoretical considerations that this porous collection of proteoglycans and glycoproteins has an important effect on fluid flow. The fluid velocity is vanishing small inside the matrix, and as a consequence, the effective shear stress on the cell membrane is highly attenuated.[15] But if shear stress on the membrane is almost absent, how can endothelial cells (ECs) respond to changes in blood flow?

One possibility is that the shear stresses acting on the glycocalyx are transmitted through the matrix to the cell body. An elastohydrodynamic model developed by Weinbaum[16] assumes that the brush-like structures of the glycocalyx have a flexural rigidity that withstands physiological ranges of fluid flow. In this case, the hydrodynamic forces acting on the tip of the core proteins lead to a deflection, which in turn acts as a bending moment on the underlying actin cortical cytoskeleton. Another model considers the glycocalyx to be a multicomponent material of interstitial fluid and a charged proteoglycan/glycoprotein/glycosaminoglycan solid matrix.[17] In this case, hydrodynamic drag will lead to tension in the glycocalyx, and, due to the connection to the cytoskeleton, the tension acts also on the underlying cortical cytoskeleton. In both cases, the glycocalyx serves as a transmitter of mechanical stresses and can explain the fact that cells can respond to changes in fluid flow even if the shear stress on the cell membrane is almost zero.

In vitro and *ex vivo* experiments with ECs showed that the fluid flow specific response is dependent on the intactness of the glycocalyx.[18–20] The shear-stress-induced increase of nitric oxide production in cultured ECs was inhibited when heparan sulfate, a major glycosaminoglycan of the glycocylyx, was dissolved with heparitinase.[19] In isolated canine femoral arteries, a similar effect was observed when hyaluronic acid glycosaminoglycans were degraded with hyaluronidase.[18] In addition, the thickness of the glycocalyx seems to correlate with the shear stress profile,[21] and the amount of hyaluronan increases in human umbilical vein ECs exposed to shear stress.[22] These studies suggest that specific components of the glycocalyx are necessary for the flow-induced increase in nitric oxide in ECs and that the composition and thickness of the glycocalyx can be modulated by fluid flow, which may be a positive feedback mechanism.[23] Interestingly, treatment with chondroitinase, which breaks down chondroitin sulphate, does not affect the characteristic nitric oxide production in response to flow,[24] and another key response of ECs to shear, the production of prostacyclin (PGI_2), is not affected by degradation of the glycocalyx with the above mentioned enzymes.[25] Therefore, no single mechanism can be responsible. Shear stress will also be transmitted to other attachment sites of the cell, such as the basal adhesions, which can lead to glycocalyx-independent activation of shear-stress-dependent signaling responses.[26]

5.506.3. Subcellular Structures Involved in Mechanotransduction

Cells are mechanically coupled to the ECM and neighboring cells through FAs and adherens junctions, respectively. Both structures have been implicated in mechanotransduction and their role is discussed in the following section, together with other mechanosensitive subcellular structures.

5.506.3.1. Interactions with the ECM: FAs

The actin cytoskeleton is mechanically coupled to the ECM via large and dynamic protein complexes called FAs. FAs anchor the cell to the ECM, and they have been shown to be involved in bidirectional signal transduction and mechanotransduction, by interacting with ligands in the ECM and responding to mechanical cues. Integrins, a family of dimeric transmembrane proteins, composed of α and β subunits complex to form the major connection between the actin cytoskeleton and the ECM. The extracellular domain has a high affinity for the RGD sequence, present on many ECM proteins such as fibronectin, collagen, laminin, and vitronectin. Intracellularly, the cytoplasmic

domain interacts with many signaling proteins, such as focal adhesion kinase (FAK), members of the Src family protein kinases, and Fyn and $p130^{CAS}$, and with cytoskeletal proteins, such as vinculin, paxilin, talin, tensin, and α-actinin.[27,28] Many of these FA-associated proteins bind to actin either directly or indirectly, thereby anchoring the cytoskeleton to the ECM.[29] Binding of integrins to ECM proteins results in a conformational change, which leads to a clustering of receptors and activation of kinases, such as FAK and src, and the small GTPase Rho, promoting the assembly of FAs and enhancing adhesion.[30]

Given the strategic position at the interface between the extracellular and the intracellular spaces, it is no surprise that FAs are involved in mechanosensation. Manipulation with magnetic beads coated with antibodies directed against integrins showed that force results in a local rearrangement of cytoskeletal filaments and force-dependent cell stiffening,[31] whereas application of similar forces to integrins via antibodies that do not bind to the RGD sequence does not.[32,33] This integrin-dependent cell stiffening response enables the cell to adapt to and sustain changes in the mechanical environment within seconds to minutes after application of external stresses.[32,34]

Activation of the GTPase Rho and its downstream effectors, Rho-associated kinase and mDIA, are required for the stress-dependent formation of FAs[34] and eventually leads to increased stability of the actin filaments. For instance, activated ROCK1, one of the downstream effectors, phosphorylates and activates LIM kinase, which in turn, phosphorylates cofilin, inhibiting its actin-depolymerizing activity. In ECs, shear stress is transmitted to the FAs and leads to the activation of integrin receptors,[35] which in turn activate FAK, paxilin, c-Src, Fyn, and $p130^{CAS}$, and finally the Ras-ERK pathway.[36,37] Another pathway involved is cAMP signaling, which was shown by micromanipulation of integrins with magnetic beads.[30] These examples show that stresses not only locally regulate the assembly of FAs but also will activate different signal pathways that modulate the cytoskeleton and gene expression, with effects on cell function at a longer timescale.

5.506.3.2. Interaction with Neighboring Cells: Adherens Junction

Cell–cell interactions seem to play another important role in mechanotransduction. Adherens junctions are a protein complex that mediate cell–cell contact. This dynamic structure is based on cadherins and shares many similarities with FAs[29]: Both link the actin cytoskeleton to the external environment and both structures consist of a large number of signaling and structural molecules that cluster and interact at the junction, some of which are present at both sites, including α-actinin, Arp2/3, zyxin, moesin, and vinculin.[38] The role of adherens junctions in mechanosensation is, however, less clear. Vascular endothelial cadherin, a specific type of cadherin present in ECs, is thought to associate with PECAM-1 and VEGFR2 to form a mechanosensory complex.[39] In this putative system, the vascular EC cadherin functions as an adaptor, PECAM-1 as a direct transmitter of mechanical force, and VEFGR2 as an activator of phosphatidylinositol-3-OH kinase. PECAM-1 and VE-cadherin knock-out mice show abnormal responses to shear stress, indicating that these proteins are required for mechanotransduction. But more investigation is required to elucidate the precise function of adherens junction in mechanotransduction and the question of whether other cell–cell junctions, such as desmosomes or tight junctions, are involved in sensing mechanical stimuli.

5.506.3.3. Primary Cilia

The primary cilium is one example of a specialized cellular substructure that has recently been implicated in mechanosensation. It is a hair-like protrusion from the apical cell membrane into the extracellular space present on the majority of mammalian cells. Its structure is based on nine doublet microtubules, which originate from the basal body and form a radially symmetric axoneme.

Although primary cilia have received little attention during most of the time since their discovery, it is becoming clear that they are a center of chemical and mechanical signal transduction during vertebrate development[40] in bone,[41,42] kidney, and liver.[43] Dysfunction is associated with many diseases[44] such as cancer,[45] polycystic kidney and liver disease,[43] adiposity,[46] and retinal degeneration.[47] A specialized protein transport system called intraflagellar transport mediates the assembly and dissociation of the primary cilium[48,49] and the trafficking of ciliary proteins. Among the variety of proteins present on the primary cilium, many signaling molecules localize to the ciliary membrane, including receptors for Sonic hedgehog, Wnt, platelet-derived growth factor, serotonin, and somatostatin.[42]

The mechanosensory role of the primary cilium was first demonstrated in renal epithelial cells. Fluid-shear- or micropipette-induced bending of the primary cilium in MDCK cells leads to an increase in intracellular calcium.[50] This mechanosensory response is mediated by polycystins 1 and 2 (PC1 and PC2) in kidney cells. Both transmembrane proteins localize to the base of the cilium, and functionality of both proteins is required for flow-induced increase in intracellular calcium.[51] PC1 has a large extracellular domain, which has been implicated as a sensor for mechanical forces,[52] but a nanometer scale structure may not experience enough force to directly sense shear and may be sensitive to thermal noise. Alternatively, one of the motifs present on the extracellular domain may bind to either an ECM protein or to another membrane protein. In this case, rather than direct sensing of shear, a displacement of the cilium could lead to a conformational change in PC1. This hypothesis is supported by the fact that the extracellular domain of PC1 exhibits remarkable mechanical strength.[53] A conformational change of PC1 could activate PC2 via the intracellular C-terminal of PC1 and thus lead to an opening of the PC2 channel. In any case, more investigation of the molecular mechanisms involved is clearly warranted.

In bone, primary cilia are required for the dynamic fluid flow-induced osteogenic and bone resorptive responses that are independent of Ca^{2+} flux and stretch-activated ion channels.[54] Further investigations showed that fluid flow leads to a decrease in intracellular cAMP, which depends on the primary cilium and, on a molecular level, on adenylyl cyclase isoform 6 (AC6) and Gd^{3+}-sensitive channels. Furthermore, this pathway was shown to mediate flow-induced cyclo-oxygenase-2 (COX-2) gene expression.[55] This suggests that the primary cilium mediates mechanosensitive signaling responses that

are tissue specific. In the bile duct, the primary cilia on cholangiocytes mediate a fluid-flow-induced change in both intracellular Ca^{2+} and cAMP through PC1, PC2, and AC6.[56]

In addition to the flow-sensing role of the primary cilium, it is also involved in direct transmission of strains in the ECM in cartilage. Chondrocytes reside in fibrillar-walled chondrons, which are embedded in the interchondronal matrix. Their primary cilia interdigitate among collagen fibers and condensed proteoglycans.[57] During compression, the fibrillar meshwork is strained and the chondron becomes flattened. As the chondrocyte cilium is attached to the fibrillar mesh via surface receptors such as integrins and NG2 at electron-opaque plaques, the strain will be transmitted and will lead to a bending of the cilium.[57,58] Which molecular mechanisms are ultimately responsible for the downstream signaling response remains unclear. Mechanosenory function of primary cilia has been suggested in other cell types as well, such as human airway smooth muscle cells[59] and ECs.[60]

5.506.3.4. Caveolae

Caveolae are another type of subcellular structure implicated in mechanotransduction. They are microdomains that are 50–100 nm invaginations of the plasma membrane present on many cell types. They contain a specialized proteome enriched with many receptors, ion channels, and protein kinases.[61] The link between caveolae and mechanotransduction was established initially in ECs.[62–64] Cultured ECs exposed to chronic shear stress alter the expression and distribution of caveolin, the scaffold protein of caveolae. The plasma membrane levels of caveolin as well as the surface density of caveolae increase with increasing shear stress. These shear-stress-induced changes result in increased mechanosensitivity in response to hemodynamic forces, increased phosphorylation of caveolin 1 (CAV1), and activation of signaling pathways such as endothelial nitric oxide synthase (eNOS) and mitogen-activated protein kinase (MAPK).[63] Cav1 knock-out mice showed an impaired blood-flow-dependent vasodilation and vascular remodeling. Reconstitution of Cav1 rescued both phenotypes, suggesting that CAV1 involved in mechanotransduction of shear stresses is critical to vascular function.[65] A redistribution of CAV1 to focal contacts in response to cyclic stretch was also observed in smooth muscle cells.[66]

Although evidence of the mechanosensory function of caveolae is growing, the underlying molecular mechanisms remain unclear. Due to their spherical structure, connected via a neck to the plasma membrane, it is plausible that caveolae are sensitive to changes in membrane tension. From a biophysical perspective, caveolae may act as equilibrated membrane reservoirs with tension regulated by their mechanical properties.[67] Which proteins would be affected by changes in membrane tension or which other mechanical stimuli are responsible for the observed mechanosensitivity of caveolar proteins needs further investigations.

5.506.3.5. Nucleus

Interestingly, there is evidence supporting a direct role of the nucleus in mechanotransduction (reviewed in Wang *et al.*[68] and Dahl *et al.*[69]). Stress on the cell can lead to deformation and rearrangement of the nucleus. This effect is not surprising, as the nucleus is directly integrated with the cytoskeleton. Some researchers speculate that the nuclear deformation might affect gene expression by changing the arrangement of chromatin. It is well known that gene expression is dependent on the accessibility of the promoter and the coding sequence in the highly condensed chromosomes; however, a mechanism by which specific genes can be regulated, and not others, remains elusive. If the nucleus is involved in mechanotransduction, mechanisms must be present to activate only specific genes. This could be possible by nuclear receptors activating transcription factors or other cell signaling pathways, but as of now, no such mechanosensors have been discovered.

5.506.4. Molecular Mechanotransduction

The transduction of a mechanical signal into a biochemical response is mediated by proteins. Their functionality depends primarily on their 3D structure. For example, catalytic sites often include amino acids that are distant in the protein sequence, but spatially close once the protein is correctly folded. The folding of the protein into a spatial conformation is driven by noncovalent interactions such as hydrophobic packing, Van der Waals forces, and hydrogen and ionic bonds. Application of forces on a protein can disrupt such interactions and deform or unfold domains or move one domain with respect to others by sliding or rotating around a flexible hinge.[70] Given that mechanical forces can change protein conformation, the function of any protein could potentially be altered by mechanical stress.[7] Indeed, many proteins undergo conformational changes during activity,[71] and by influencing the conformation, the kinetics of the reaction can be changed. For example, the rate of ATP hydrolysis decreases with increasing force in many motor proteins.[72,73]

However, not every protein is a potential mechanosensor. Candidate proteins are localized to strategic areas of the cell where they are more likely to experience mechanical loading, for example, the periphery[74] and specialized subcellular structures. Some general criteria can be advanced for a mechanosensitive protein. First, the function of the molecule should be titrated to the level of mechanical force applied to it, and second, the mechanosensor should participate in a response known to be mechanically regulated.[75,76] Extracellular forces act on the cellular membrane and are transmitted to the cytoskeleton. As a logical consequence, candidate mechanosensing proteins are either residing in the cell membrane or tethered to structural elements of the cell, or both. Examples of how mechanically induced conformational changes can lead to biochemical responses include opening of ion channels that can rapidly change intracellular ion concentrations, exposure of cryptic or apolar peptide sequences by unfolding or lid-opening, which might catalyze reactions or enhance binding affinities to biomolecules, and receptor–ligand interactions that act like a catch bond, which leads to more stable interactions with load.[74]

5.506.4.1. Mechanosensitive Ion Channels

Mechanosensitive ion channels are one example of a subset of proteins that translate mechanical signals into a biochemical

response. Three different concepts have been advanced for how the conductance of mechanosensitive ion channels can be changed in response to a mechanical stimulus. One concept is based on membrane tension, which directly acts on the channel and induces a conformational change; the second concept is based on the physical connection of the channel to the ECM and the cortical cytoskeleton and the third mechanism is indirect activation, where a primary mechanosensor sends a chemical signal that opens the ion channel (see **Figure 2**).

One example of a mechanosensitive ion channel that is specifically activated by membrane tension is the bacterial K^+ channel MscL. This channel serves as a security valve, which opens at high membrane tension, preventing lysis. The structure of the protein is known, and computational modeling as well as observations with electron paramagnetic resonance spectroscopy suggest that the increased tension in the membrane leads to tilting of the transmembrane helices similar to the iris of a camera, which opens and wets the pore interior.[77] Reconstituted MscL, MscS, and other prokaryotic mechanosensitive ion channels in liposomes are still mechanosensitive, demonstrating that lipid bilayer tension alone is sufficient for channel gating.[78] The required tension for channel opening is close to the lytic tension of the bilayer. However, typical physiologic membrane tensions in animal cells are a thousand-fold lower.[74,79] It is not clear if mechanosensitive ion channels in animal cells open by the same mechanism or if other out of plane forces are needed in addition to the in plane membrane tension.

The second concept requires connections between the channel and force bearing filaments. Opening of the channel needs a relative displacement of these structural proteins. In fact, many mechanosensitive ion channels in animal cells are tethered to the cytoskeleton or to the ECM,[78] but the simple fact of connectivity does not necessarily imply force transmission.[77] Inner ear hair cells provide a clear example in which a tether is responsible for gating mechanosensitive channel. However, even in this case, the molecular components have not totally elucidated,[80] and it is not clear if the tether directly pulls on a domain of the ion channel or if an indirect mechanism leads to the gating response. Thus, it appears likely that some eukaryotic mechanosensitive ion channels require connections to the cytoskeleton or respond to local deformation of the cell membrane while others respond to physiological changes in membrane tension.

Ion channels might also be indirectly mechanically regulated. In this model, a mechanosensitive protein is activated by mechanical stress and releases signaling molecules, which bind to and change the gating properties of an ion channel. No physical connections of the channel to other structures are necessary; the ion channel is just an intermediate of a mechanically induced signaling cascade.

5.506.4.2. Exposure of Cryptic Sequences

Many extracellular and FA-associated proteins consist of tandem repeats, forming multimodular domains. Talin, titin, fibronectin, cadherins, α-actinin, and dystrophin are only some of the many examples. Experimental and computational studies show that application of force on such proteins unfolds their domains, often in a stepwise manner, due to the breaking of hydrogen bonds.[81,82] Through this process of unraveling, peptide sequences that were buried inside the protein become exposed to the solvent and potentially become biochemically active. If different molecular recognition sites are present within these domains, different magnitudes of force could be converted into distinct molecular signals.

Fibronectin, a cell adhesive component of the ECM, consists of over 50 modular repeats. This protein binds via its RGD sequence to integrins and is therefore linked to the contractile cytoskeleton. Intracellular contraction forces are sufficient to, at least partially, unfold fibronectin.[83] Many cryptic sites that are buried in the folded state and are accessible only after extension of the protein and a change in conformation occurs.[84,85] These cryptic sequences have the potential to include phosphorylation sites or other enzymatic activity. For example, a partially cryptic disulphide isomerase[86] and a cryptic metalloprotease site[87] can be found in fibronectin, but it is unclear whether their activity is mechanically regulated.[74]

Talin and vinculin are important proteins involved in cell signaling, adhesion, and migration that localize to FAs. Talin links integrins to the actin cytoskeleton and recruits vinculin in response to tensile forces. In the unloaded configuration, the vinculin-binding sites are embedded. However, physiologically

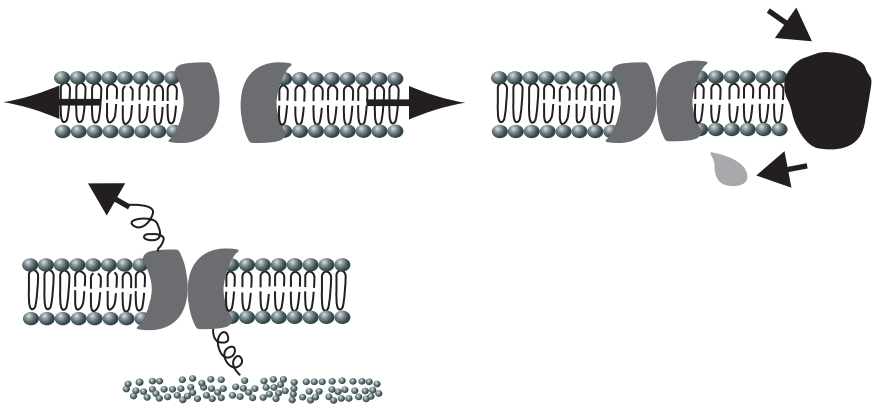

Figure 2 Activation of mechanosensitive ion channels. (top left) Membrane tension may directly induce a conformational change that opens the channel. (top right) An unknown primary mechanosensor releases a signaling molecule that activates the channel. (bottom) Physical coupling of the channel to the ECM and the cortical cytoskeleton transmit forces that open the ion channel.

relevant forces have been shown to cause stretching of single talin rods that expose these cryptic vinculin-binding sites.[88] Simulation studies predict that the binding site on talin rotates out of the hydrophobic core of a helix when the protein is stretched[89] or that the talin rod is fragmented into three helix subbundles that expose the binding site.[90]

Additionally, when the unraveling force on multimodular proteins is reduced, they generally refold properly. This refolding is necessary to return to the original conformation when the mechanical stimulus is removed or reduced. Whether ligand binding to cryptic sites inhibit or even prevent refolding is yet unknown.[84]

5.506.4.3. Receptor–Ligand Interactions that Strengthen if Strained

Normally, forces applied on noncovalent bonds diminish the bond lifetime, but there are certain bonds that strengthen with load. The dissociation lifetime of the so-called catch bonds increases with tensile forces, as long as the force does not exceed a certain limit. Evidence for catch bonds exists for the bacterial adhesion protein FimH[91] and P-selectins on leukocytes.[92] Recently, a study showed that $\alpha5\beta1$ integrin switches between a relaxed and tensioned state in response to myosin II-generated cytoskeletal force. Under normal conditions, integrin binds to the RGD sequence on fibronectin. In the tensioned state, a catch bond between integrin and fibronectin forms which requires the engaging of the synergy site in fibronectin in addition to the RGD-binding site.[93] This additional binding site increases the overall affinity and allows the complex to sustain larger tensional forces.

5.506.5. Response of Cells to Mechanical Stress and Implications for Tissue Engineering

Mechanical signals modulate almost all aspects of cell function, including cell growth, differentiation, migration, adhesion, and apoptosis.[94] Nonetheless, mechanical stimulation of cells has received little attention in tissue engineering. The process of cell differentiation and proliferation has to be robustly controlled for functional structural tissue engineering constructs that will be clinically successful. If undifferentiated cells remain pluripotent for example, they tend to form teratomas, which is a dramatic failure to regulate differentiation. The importance of chemical signals to direct these processes is well established. It has also become clear that cells respond differently to distinct types of materials and that the elasticity is one important property which is sensed by cells and is critical for lineage commitment. These two approaches are certainly very important in guiding cell proliferation and maturation, but mechanical stimuli have received relatively less attention. Studies in the field of bone and vascular biology show that mechanical stimulation of tissue engineering constructs yields promising results.

It is well-established that bone is regulated by mechanical loading *in vivo*. Some attempts have been made to mimic the mechanical environment of bone cells in 3D scaffolds. Different types of stimuli including compression, stretch, and fluid flow seem to be beneficial for *in vitro* tissue formation. For example, osteoblastic cells seeded in polyurethane open cell foam scaffolds loaded in compression at 1 Hz, 5% strain for 2 h every 5 days showed that mineralization compared to static controls and the mRNA expression of type I collagen, osteopontin, and osteocalcin was higher after one cycle of loading.[95] The effect of cyclic uniaxial strain on osteoblastic precursor cells cultured in 3D type I collagen matrices was examined by Ignatius *et al.*[96] They analyzed mRNA expression of different genes involved in cell proliferation, matrix production, and osteoblastic differentiation, such as histone H4, core-binding factor 1, alkaline phosphatase, osteopontin, osteocalcin, and collagen type I. Physiological stretching of the matrices increased cell proliferation and slightly elevated the expression of nearly all investigated genes. Previous 2D *in vitro* studies suggest that fluid flow is a more potent regulator of bone cell behavior than compression or substrate deformation. Bancroft *et al.* studied the effect of perfusion flow on differentiating marrow stromal osteoblasts in 3D constructs.[97] Different flow rates were applied, and all flow conditions increased mineral matrix production drastically and total calcium content increased proportionally to the flow rate. Perfusion flow *per se* has two effects, it increases the biochemical exchange and generates shear stresses on the cells. To date, it is not clear which, or if both together, are responsible for the observed increase in matrix mineral production.

The important role of mechanical stimulation of endothelial and smooth muscle cells has been recognized, and different types of bioreactors have been designed to mechanically stimulate engineered vascular grafts with physiological fluid shear stress and strain.[98] Hoerstrup *et al.* developed an *in vitro* pulse duplicator system for vascular graft engineering which provides a biomimetic environment and yields more mature, implantable grafts.[99] Ovine vascular myofibroblasts and ECs were seeded on a bioabsorbable polymer and grown for 4 days in static culture and then in the pulse duplicator bioreactor for up to 28 days. The pulsed graft showed a continuous increase in burst strength, whereas in static controls the burst strength decreased. The suture retention strength was more than fivefold higher in pulsed grafts compared to controls. In addition to the improved mechanical outcome of mechanically stimulated vascular grafts, it was shown by Jeong *et al.* that vascular smooth muscle cells aligned in the direction radial to the distention direction, similar to native tissue, when seeded on 3D PLCL scaffolds subjected to pulsatile strain and shear stress.[100] The expression of smooth muscle α-actin increased by 2.5-fold in the pulsed bioreactor compared to static control, which indicates a more differentiated phenotype of smooth muscle cells. Thus, a physiological mechanical environment can promote tissue maturation and enhance mechanical stability of vascular grafts.

In conclusion, the mechanical stimulation of tissue engineering constructs, in addition to biochemical stimulation, might overcome current challenges in tissue engineering, such as guiding cell differentiation, maintaining the cells in a differentiated state, and improving the mechanical properties of the engineered tissue. Future studies that simultaneously consider the mechanical, the material, and the biochemical environment of native and engineered tissues will hopefully provide new clinically successful therapies in the field of regenerative medicine.

References

1. Wolff, J. *The Law of Bone Remodelling*. Springer-Verlag: Berlin; New York, 1986; xii, 126 p.
2. Kim, C. H.; *et al*. *Bone* **2006**, *39*(5), 1043–1047.
3. Shivaram, G. M.; *et al*. *Philos. Transact. A Math. Phys. Eng. Sci.* **2010**, *368*(1912), 605–616.
4. Qin, Y. X.; *et al*. *J. Biomech.* **2003**, *36*(10), 1427–1437.
5. Fletcher, D. A.; Mullins, R. D. *Nature* **2010**, *463*(7280), 485–492.
6. Janmey, P. A.; McCulloch, C. A. *Annu. Rev. Biomed. Eng.* **2007**, *9*, 1–34.
7. Ingber, D. E. *FASEB J.* **2006**, *20*(7), 811–827.
8. Wang, N.; Suo, Z. *Biochem. Biophys. Res. Commun.* **2005**, *328*(4), 1133–1138.
9. Storm, C.; *et al*. *Nature* **2005**, *435*(7039), 191–194.
10. Haidekker, M. A.; L'Heureux, N.; Frangos, J. A. *Am. J. Physiol. Heart Circ. Physiol.* **2000**, *278*(4), H1401–H1406.
11. Axelrod, D. *J. Membr. Biol.* **1983**, *75*(1), 1–10.
12. Mitchell, D. C.; Lawrence, J. T.; Litman, B. J. *J. Biol. Chem.* **1996**, *271*(32), 19033–19036.
13. Gudi, S.; Nolan, J. P.; Frangos, J. A. *Proc. Natl Acad. Sci. USA* **1998**, *95*(5), 2515–2519.
14. Peter, J.; Butler, S. C. In *Cellular Mechanotransduction. Diverse Perspectives from Molecules to Tissues*; Mohammad, R. D. K., Mofrad, R. K., Eds.; Cambridge University Press: New York, 2010; p 61.
15. Secomb, T. W.; Hsu, R.; Pries, A. R. *Biorheology* **2001**, *38*(2–3), 143–150.
16. Weinbaum, S.; *et al*. *Proc. Natl Acad. Sci. USA* **2003**, *100*(13), 7988–7995.
17. Damiano, E. R.; Stace, T. M. *Biophys. J.* **2002**, *82*(3), 1153–1175.
18. Mochizuki, S.; *et al*. *Am. J. Physiol. Heart Circ. Physiol.* **2003**, *285*(2), H722–H726.
19. Florian, J. A.; *et al*. *Circ. Res.* **2003**, *93*(10), e136–e142.
20. Reilly, G. C.; *et al*. *Biorheology* **2003**, *40*(6), 591–603.
21. van den Berg, B. M.; *et al*. *Am. J. Physiol. Heart Circ. Physiol.* **2006**, *290*(2), H915–H920.
22. Gouverneur, M.; *et al*. *Am. J. Physiol. Heart Circ. Physiol.* **2006**, *290*(1), H458–H462.
23. Reitsma, S.; *et al*. *Pflugers Arch.* **2007**, *454*(3), 345–359.
24. Tarbell, J. M.; Pahakis, M. Y. *J. Intern. Med.* **2006**, *259*(4), 339–350.
25. Hecker, M.; *et al*. *Am. J. Physiol.* **1993**, *265*(3 Pt 2), H828–H833.
26. Weinbaum, S.; Tarbell, J. M.; Damiano, E. R. *Annu. Rev. Biomed. Eng.* **2007**, *9*, 121–167.
27. Burridge, K.; Chrzanowska-Wodnicka, M. *Annu. Rev. Cell Dev. Biol.* **1996**, *12*, 463–518.
28. Ruoslahti, E. *J. Clin. Invest.* **1991**, *87*(1), 1–5.
29. Chen, C. S.; Tan, J.; Tien, J. *Annu. Rev. Biomed. Eng.* **2004**, *6*, 275–302.
30. Parker, K. K.; Ingber, D. E. *Philos. Trans. R. Soc. Lond. B Biol. Sci.* **2007**, *362* (1484), 1267–1279.
31. Wang, N.; Butler, J. P.; Ingber, D. E. *Science* **1993**, *260*(5111), 1124–1127.
32. Choquet, D.; Felsenfeld, D. P.; Sheetz, M. P. *Cell* **1997**, *88*(1), 39–48.
33. Matthews, B. D.; *et al*. *Biochem. Biophys. Res. Commun.* **2004**, *313*(3), 758–764.
34. Riveline, D.; *et al*. *J. Cell Biol.* **2001**, *153*(6), 1175–1186.
35. Ando, J.; Yamamoto, K. *Circ. J.* **2009**, *73*(11), 1983–1992.
36. Li, S.; *et al*. *J. Biol. Chem.* **1997**, *272*(48), 30455–30462.
37. Ishida, T.; *et al*. *Circ. Res.* **1996**, *79*(2), 310–316.
38. Nagafuchi, A. *Curr. Opin. Cell Biol.* **2001**, *13*(5), 600–603.
39. Tzima, E.; Irani-Tehrani, M.; Kiosses, W. B.; *et al*. *Nature* **2005**, *437*(7057), 426–431.
40. Goetz, S. C.; Anderson, K. V. *Nat. Rev. Genet.* **2010**, *11*(5), 331–344.
41. Temiyasathit, S.; Jacobs, C. R. *Ann. NY Acad. Sci.* **2010**, *1192*(1), 422–428.
42. Anderson, C. T.; *et al*. *Anat. Rec. (Hoboken)* **2008**, *291*(9), 1074–1078.
43. Gunay-Aygun, M. *Am. J. Med. Genet. C Semin. Med. Genet.* **2009**, *151C*(4), 296–306.
44. Lancaster, M. A.; Gleeson, J. G. *Curr. Opin. Genet. Dev.* **2009**, *19*(3), 220–229.
45. Michaud, E. J.; Yoder, B. K. *Cancer Res.* **2006**, *66*(13), 6463–6467.
46. Sen Gupta, P.; Prodromou, N. V.; Chapple, J. P. *J. Endocrinol.* **2009**, *203*(3), 327–336.
47. Ramamurthy, V.; Cayouette, M. *Clin. Genet.* **2009**, *76*(2), 137–145.
48. Seeley, E. S.; Nachury, M. V. *J. Cell Sci.* **2010**, *123*(Pt 4), 511–518.
49. Pedersen, L. B.; *et al*. *Dev. Dyn.* **2008**, *237*(8), 1993–2006.
50. Praetorius, H. A.; Spring, K. R. *J. Membr. Biol.* **2001**, *184*(1), 71–79.
51. Nauli, S. M.; *et al*. *Nat. Genet.* **2003**, *33*(2), 129–137.
52. Zhou, J. *Annu. Rev. Physiol.* **2009**, *71*, 83–113.
53. Forman, J. R.; *et al*. *J. Mol. Biol.* **2005**, *349*(4), 861–871.
54. Malone, A. M.; *et al*. *Proc. Natl Acad. Sci. USA* **2007**, *104*(33), 13325–13330.
55. Kwon, R. Y.; *et al*. *FASEB J.* **2010**, *24*(8), 2859–2868.
56. Masyuk, A. I.; *et al*. *Gastroenterology* **2006**, *131*(3), 911–920.
57. Jensen, C. G.; *et al*. *Cell Biol. Int.* **2004**, *28*(2), 101–110.
58. McGlashan, S. R.; Jensen, C. G.; Poole, C. A. *J. Histochem. Cytochem.* **2006**, *54*(9), 1005–1014.
59. Wu, J.; *et al*. *Chest* **2009**, *136*(2), 561–570.
60. Hierck, B. P.; *et al*. *Dev. Dyn.* **2008**, *237*(3), 725–735.
61. Anderson, R. G. *Proc. Natl Acad. Sci. USA* **1993**, *90*(23), 10909–10913.
62. Rizzo, V.; *et al*. *J. Biol. Chem.* **1998**, *273*(52), 34724–34729.
63. Rizzo, V.; *et al*. *Am. J. Physiol. Heart Circ. Physiol.* **2003**, *285*(4), H1720–H1729.
64. Boyd, N. L.; *et al*. *Am. J. Physiol. Heart Circ. Physiol.* **2003**, *285*(3), H1113–H1122.
65. Yu, J.; *et al*. *J. Clin. Invest.* **2006**, *116*(5), 1284–1291.
66. Sedding, D. G.; *et al*. *Circ. Res.* **2005**, *96*(6), 635–642.
67. Sens, P.; Turner, M. S. *Phys. Rev. E Stat. Nonlin. Soft Matter Phys.* **2006**, *73*(3 Pt 1), 031918.
68. Wang, N.; Tytell, J. D.; Ingber, D. E. *Nat. Rev. Mol. Cell Biol.* **2009**, *10*(1), 75–82.
69. Dahl, K. N.; Ribeiro, A. J.; Lammerding, J. *Circ. Res.* **2008**, *102*(11), 1307–1318.
70. Bao, G. In *Cellular Mechanotransduction. Diverse Perspectives from Molecules to Tissues*; Mohammad, R. D. K., Mofrad, R. K., Eds.; Cambridge University Press: New York, 2010.
71. Min, W.; *et al*. *Acc. Chem. Res.* **2005**, *38*(12), 923–931.
72. Purcell, T. J.; Sweeney, H. L.; Spudich, J. A. *Proc. Natl Acad. Sci. USA* **2005**, *102*(39), 13873–13878.
73. Khan, S.; Sheetz, M. P. *Annu. Rev. Biochem.* **1997**, *66*, 785–805.
74. Vogel, V.; Sheetz, M. *Nat. Rev. Mol. Cell Biol.* **2006**, *7*(4), 265–275.
75. Stiber, J. A.; Seth, M.; Rosenberg, P. B. *J. Cardiovasc. Pharmacol.* **2009**, *54*(2), 116–122.
76. Christensen, A. P.; Corey, D. P. *Nat. Rev. Neurosci.* **2007**, *8*(7), 510–521.
77. Kung, C. *Nature* **2005**, *436*(7051), 647–654.
78. Martinac, B. *J. Cell Sci.* **2004**, *117*(Pt 12), 2449–2460.
79. Sheetz, M. P. *Nat. Rev. Mol. Cell Biol.* **2001**, *2*(5), 392–396.
80. Hudspeth, A. J. *C R Biol.* **2005**, *328*(2), 155–162.
81. Lu, H.; *et al*. *Biophys. J.* **1998**, *75*(2), 662–671.
82. Marszalek, P. E.; *et al*. *Nature* **1999**, *402*(6757), 100–103.
83. Baneyx, G.; Baugh, L.; Vogel, V. *Proc. Natl Acad. Sci. USA* **2002**, *99*(8), 5139–5143.
84. Vogel, V. *Annu. Rev. Biophys. Biomol. Struct.* **2006**, *35*, 459–488.
85. Pankov, R.; Yamada, K. M. *J. Cell Sci.* **2002**, *115*(Pt 20), 3861–3863.
86. Langenbach, K. J.; Sottile, J. *J. Biol. Chem.* **1999**, *274*(11), 7032–7038.
87. Schnepel, J.; Tschesche, H. *J. Protein Chem.* **2000**, *19*(8), 685–692.
88. del Rio, A.; *et al*. *Science* **2009**, *323*(5914), 638–641.
89. Lee, S. E.; Kamm, R. D.; Mofrad, M. R. *J. Biomech.* **2007**, *40*(9), 2096–2106.
90. Hytonen, V. P.; Vogel, V. *PLoS Comput. Biol.* **2008**, *4*(2), e24.
91. Thomas, W. E.; *et al*. *Cell* **2002**, *109*(7), 913–923.
92. Marshall, B. T.; *et al*. *Nature* **2003**, *423*(6936), 190–193.
93. Friedland, J. C.; Lee, M. H.; Boettiger, D. *Science* **2009**, *323*(5914), 642–644.
94. Orr, A. W.; *et al*. *Dev. Cell* **2006**, *10*(1), 11–20.
95. Sittichockechaiwut, A.; *et al*. *Bone* **2009**, *44*(5), 822–829.
96. Ignatius, A.; *et al*. *Biomaterials* **2005**, *26*(3), 311–318.
97. Bancroft, G. N.; *et al*. *Proc. Natl Acad. Sci. USA* **2002**, *99*(20), 12600–12605.
98. Riha, G. M.; *et al*. *Ann. Biomed. Eng.* **2005**, *33*(6), 772–779.
99. Hoerstrup, S. P.; *et al*. *Eur. J. Cardiothorac. Surg.* **2001**, *20*(1), 164–169.
100. Jeong, S. I.; *et al*. *Biomaterials* **2005**, *26*(12), 1405–1411.

5.507. Tissue Engineering and Selection of Cells

C E Petrie Aronin and N Z Kuhn, National Institutes of Health, Bethesda, MD, USA
R S Tuan, University of Pittsburgh School of Medicine, Pittsburgh, PA, USA

© 2011 Elsevier Ltd. All rights reserved.

5.507.1.	**Why Do Tissue Engineering Approaches Need a Cell Source?**	81
5.507.2.	**Cell Sources Used in Tissue Engineering Strategies**	82
5.507.2.1.	Overview of Autologous Versus Allogeneic Versus Xenogeneic Sources	82
5.507.2.2.	Tissue-Specific Cells from SELF	83
5.507.2.3.	Stem Cells: Defined as a Collective	83
5.507.2.4.	Mesenchymal Stem Cells	84
5.507.2.5.	Embryonic Stem Cells	85
5.507.2.6.	Induced Pluripotent Stem Cells	86
5.507.2.7.	Endogenous Host Populations	86
5.507.3.	**Patient Delivery Challenges: Controlling Cells in the Body**	87
5.507.3.1.	How Do We Control Cells to Survive *In Vivo* After Transplantation?	87
5.507.3.2.	How Do We Control Cells to Maintain Appropriate Phenotype *In Vivo*?	87
5.507.3.3.	How Do We Control Cells to Migrate . . . NOT to Migrate *In Vivo*?	88
5.507.4.	**Donor Versus Host Immune Issues**	88
5.507.4.1.	Immunomodulatory Role of MSC Populations	89
5.507.5.	**Donor Versus Host: Cell/Tissue Integration**	90
5.507.6.	**Safety and Stability**	91
5.507.7.	**Conclusion**	92
References		92

Abbreviations

APCs	Antigen presenting cells
DCs	Dendritic cells
EC	Embryonic carcinoma
ESCs	Embryonic stem cells
FDA	Food and Drug Administration
GVHD	Graft versus host disease
HSCs	Hematopoietic stem cells
iPSCs	Induced pluripotent stem cells
ISCT	International Society for Cellular Therapy
MHC	Major histocompatibility complex
MSC	Mesenchymal stem cell
SCID	Severe combined immunodeficiency
SCNT	Somatic cell nuclear transfer

5.507.1. Why Do Tissue Engineering Approaches Need a Cell Source?

Organ and tissue replacement is an increasingly unmet clinical need. According to the Organ Transplant Procurement Network, from 1988 to 2010, over 485 000 total organ transplants have been performed in the United States, including those of kidney, liver, heart, pancreas, intestine, and lung. In 2010, over 116 000 patients were registered on organ transplant lists (http://optn.transplant.hrsa.gov), and current statistics suggest that organ wait-list mortality hovers between 4% and 12%, depending on the organ type (http://www.ustransplant.org/). As the incidence of damaged, diseased, and missing tissues keeps growing, current clinical options such as self, donor, or cadaveric tissues are no longer able to meet the rapidly increasing demand. Furthermore, purely mechanical replacement devices, such as prosthetic limbs or heart valves, can only be used in limited applications and these devices do not fully restore complete organ function. Therefore, incorporating a cell source as part of the solution allows clinicians and bioengineers to capitalize on the unique biochemical features of the human cell, to aid in basic functions that no drug product or material can mimic (**Figure 1**).

Interestingly, cell-based strategies for improving human health are not new ideas. The first recorded human blood transfusion was performed in 1667 by Jean-Baptiste Denys, who successfully transfused sheep's blood into a 15-year-old boy.[1] Thereafter, subsequent patients of Denys died after receiving transfusions of animal blood, and the procedure was officially banned in France and Britain in 1670.[2] Close to 300 years later, Charles Lindbergh and his mentor, Alexis Carrel, described a new organ perfusion system, a technology that could cultivate organs and keep them sterile for extended periods of time outside the body. This new technology laid the foundation for modern day sterile cell culture.[3,4] Subsequently, Robert Good, a pioneer of modern immunology, established the first successful bone marrow transplant in 1968 to treat diseases other than cancer.[5] In 1994, Brittberg and Petersen developed a cartilage repair strategy based on autologous chondrocyte implantation, which has subsequently become a

In 2010, according to the Organ and Transplant Procurement Network, 116 949 patients are enrolled in organ waitlists across the United States.

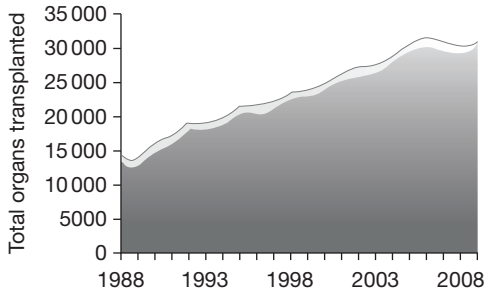

	Waiting list in 2010	Donated in 2009
Kidney	91 164	13 636
Liver	16 785	6958
Pancreas	1477	1741
Heart	3153	2281
Lung	1784	1569
Intestine	253	189

Data as of June 25, 2010.

Figure 1 These statistics highlight the need for alternative cell-based therapies, where the current number of donated organs is *4*× less than the clinical need. These data do not include statistics associated with nerve, bone, vessel, and other tissue grafts that *also* currently require human sources of donated tissue. Data collected from the National Organ Procurement Network.

clinically accepted procedure (Carticell®, Genzyme).[6] In 2000, clinical trials for entire organ replacement began with Anthony Atala and colleagues. Here, damaged bladders were replaced with an autologous cell source grown on an appropriate biomaterial structure shaped like the bladder.[7] More recently, in 2006, a 6-year-old patient received the first injections of neural stem cells directly into the brain, the goal being the production of critical enzymes important to healthy brain function.[8] In 2008, the first tissue-engineered trachea was successfully transplanted, using an approach that combined the patient's own stem cells and a biologically compatible material to successfully restore normal function to the patient's airway.[9] In 2009, cardiac stem cell transplantation was performed in a 39-year-old patient, with the donor cells being harvested from his heart tissue.[10] These examples highlight the therapeutic promise and rapidly expanding application of cell-based approaches across tissue types and clinical needs. Significant improvements in reproducibility and precision in cell isolation, cell expansion, and cell differentiation will allow many cell-based tissue engineering strategies to proceed to the clinic (Figure 2).

5.507.2. Cell Sources Used in Tissue Engineering Strategies

5.507.2.1. Overview of Autologous Versus Allogeneic Versus Xenogeneic Sources

Autologous materials are cells/tissues/organs harvested from the patient's own body and returned to SELF. Because autologous cells effectively come from SELF, they are perfectly matched immunologically with a none-to-low risk of antigenicity, and only reported when cells were genetically manipulated. Autologous sources have no risk of disease transmission but cannot be used in cases where the patient's own cells harbor the genetic defect or disease of interest. Common types of autologous sources include blood banking in preparation for a surgery or harvesting bone and vessel autografts from alternative sites in the patient's body. Autologous harvests always yield two sites of surgery with donor-site morbidity and increased risk of infection. Autologous sources are, by necessity, limited in supply and restricted in application, but remain the gold standard in many clinical practices.

Allograft materials are cells/tissues/organs harvested from human donors and transplanted into another human patient. Selected allograft materials can be donated by living donors, such as bone marrow transplants, liver, and kidney. Other allograft materials must be harvested from cadaveric tissue donors, including cornea, heart, and lung. Allograft materials have the possibility of graft rejection or of mounting an autoimmune response against the patient's own tissues because they are not from SELF. When the host mounts an immune attack against the allograft, it is called graft rejection. When transplanted allogeneic cells attack recipient tissue, it is called graft-versus-host disease (GVHD) response. Allografts thus carry the possibility of disease transmission and are also of limited supply.

Xenogeneic materials are cells/tissues/organs harvested from animal donors and transferred into human patients. Although several of the original sheep blood transfusions performed by Dr. Denys in 1667 resulted in patient mortality, novel strategies offer potential solutions for utilizing xenogeneic tissue in the clinic. Specifically, baboons and pigs are favored xenotransplant donors for humans. While baboons are the closest genetic match, pig anatomy is similar to humans in many respects. Typically, xenogeneic grafts result in hyperacute or delayed rejection due to significant major histocompatibility complex (MHC) mismatch. However, new strategies to eliminate mismatched immune recognition components could open possibilities for successful xenogeneic transplantation. For example, recent reports demonstrate elimination of the cell surface α-galactoside epitopes that are the major xenoantigens causing hyperacute rejection in pig-to-human transplantation.[11] These are the first steps to genetically modifying animal tissue by inserting human genes so that the transplanted organ will produce proteins and enzymes that the body recognizes as human and not animal. The first transplant of genetically modified pig liver was in 1995, which was

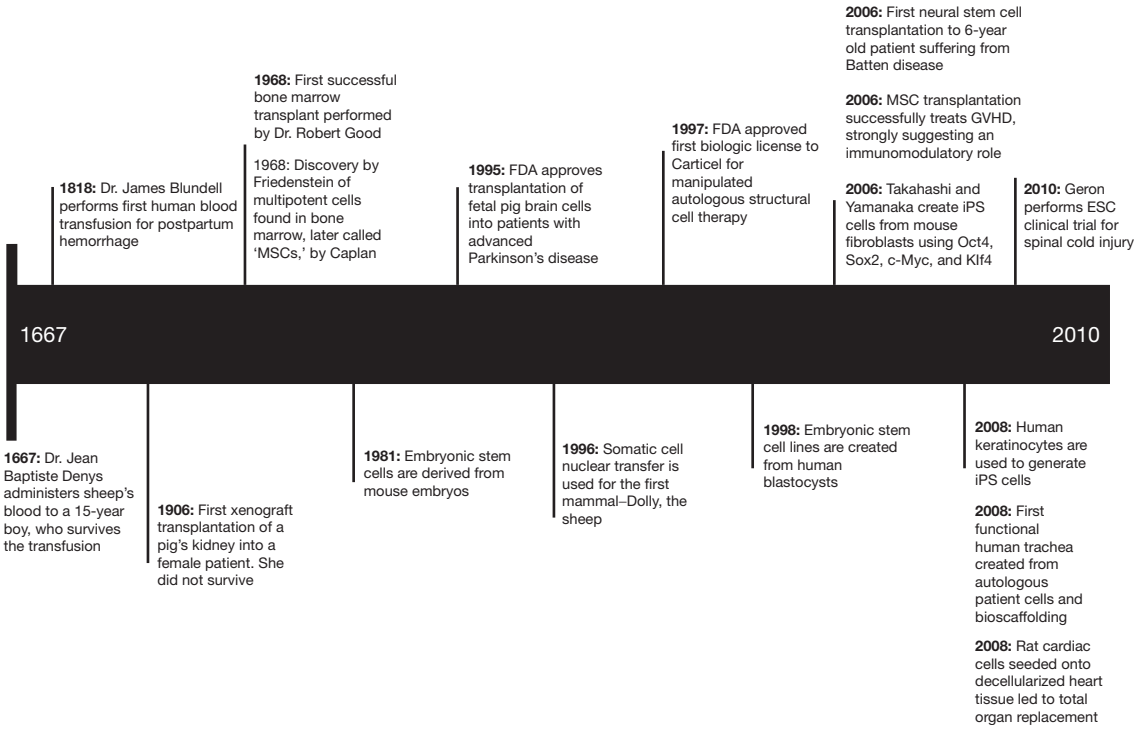

Figure 2 1667–2010: Chronological timeline highlighting significant advances in basic research, clinical application, and product development in the areas of cell-based therapies.

approved by the US Food and Drug Administration (FDA) for patients with end-stage liver disease.[12] The FDA has also approved transplantation of baboon bone marrow in AIDS patients to provide a source of immune cells that are resistant to HIV,[13] and transplantation of fetal pig brain cells into patients with advanced Parkinson's disease.[14] These early studies were conducted primarily to check for safety, not efficacy. Concerns about xenograft applications remain, including the risk of disease transmission and differences in tissue aging properties. Although gene therapies for xenograft transplantation are still in the early stages of development, such avenues could yield promising sources of cells and tissues for future medical applications.

5.507.2.2. Tissue-Specific Cells from SELF

Currently, the predominant cell source used for human application is autologous (SELF) differentiated tissue-specific cells: for example, taking a small biopsy of muscle tissue, isolating individual myoblasts via tissue digestion, expanding this population in culture, and returning this population to a repair site in the body. This choice is important for two reasons: (1) fully differentiated tissue-specific cells are thought to have reduced potential for forming teratomas (i.e., uncontrolled growth/differentiation) compared with less differentiated stem cells sources; and (2) fully differentiated tissue-specific cells are already equipped with tissue-specific function (i.e., osteoblasts secrete mineralized matrix), whereas undifferentiated stem cells require additional information from the surrounding host tissue or from the cotransplanted material to function appropriately as mature differentiated cells. From a clinical standpoint, tissue-specific cells are thought to be less risky and less complicated. However, there are exceptions and challenges to using fully differentiated cells. For example, neurons once fully differentiated do not proliferate. Therefore, generating large numbers of neurons in culture is not possible. Utilization of stem or progenitor cell sources where one could expand progenitors and subsequently induce neuronal maturation may be the best and only option when replacing damaged neurons. Alternatively, clinicians and bioengineers turn to stem cell sources that offer greater flexibility and choice in the tissue type formed.

5.507.2.3. Stem Cells: Defined as a Collective

The term 'stem cell' can be traced back to the late nineteenth century, when it was primarily used to describe what are today called the germline stem cells.[15,16] Later, the term was used to describe stem cells of the hematopoietic system.[17] Now, the identification of stem cells has progressed beyond early embryologic systems and, subsequently, resident niches of adult stem cell 'pools' have been discovered in almost every tissue in the adult body. The current definition according to the *Stem Cell Handbook* of the US National Institutes of Health (http://stemcells.nih.gov/info/basics/), is that stem cells are cells that can self-renew and have the potential to differentiate along more than one lineage. "Stem cells are defined as clonogenic, self-renewing progenitor cells that can generate one or more specialized cell types".[18,19] Originally, these key features were the factors that sparked interest within the biomedical community to develop therapeutic strategies using the various stem cell sources.

5.507.2.4. Mesenchymal Stem Cells

Mesenchymal stem cells (MSCs) are the nonhematopoietic fraction of bone marrow that display multipotent characteristics. MSCs were first described by Alexander Friedenstein, who described these 'osteogenic stem cells' as clonal and fibroblastic, and observed that these adherent colonies displayed robust osteogenic potential.[20–22] These cells were first termed 'mesenchymal stem cells' by Arnold Caplan,[23] and their classic multilineage differentiation potential into bone, cartilage, and fat tissue types was demonstrated by Pittenger *et al.*[24] Since the original discovery of MSCs in bone marrow, the reports identifying cells with similar characteristics have significantly expanded across many adult and fetal tissues. Moreover, the literature suggests that MSCs can differentiate into cells of endodermal, ectodermal, and mesodermal origin.[25]

The International Society for Cellular Therapy (ISCT) has established three minimal criteria for defining MSCs, on the basis of current knowledge.[26] MSCs isolated from human bone marrow and other mesenchymal tissues must demonstrate *in vitro* (a) adherence to plastic in standard culture conditions, (b) specific surface antigen expression, and (c) multipotent differentiation potential along the osteogenic, chondrogenic, and adipogenic lineages, as demonstrated by histological staining and other methods. Unlike specific markers or antigens that characterize embryonic[27] and hematopoietic stem cells (HSCs),[28] there have been differing reports on the identities of MSC surface markers. The consensus of the ISCT, which is subject to further modification, is that measurements by flow cytometry must show greater than 95% of the MSC population to express CD73 (ecto-5-nucleotidase), CD90 (Thy-1), and CD105 (endoglin), and no more than 2% of the cells may express CD34 (hematopoietic progenitor and endothelial cell marker), CD45 (pan-leukocyte marker), CD11b or CD14 (monocyte and macrophage markers), CD19 or CD79α (B-cell markers), and HLA-DR (marker of stimulated MSCs) (Figure 3).

Given the prevalence of MSC niches in a variety of adult tissues, these cells are a popular choice of stem cell for bone, cartilage, fat, and tissue-specific replacements strategies. These cells have extensive but finite expansion potential and limited differentiation potential, and thus reduce concerns of teratoma formation. Furthermore, emerging evidence suggests interesting immunomodulatory properties that may be advantageous in treating immune-related disorders or in allograft transplantation strategies, discussed later in this chapter. However, there remains ongoing controversy concerning the significant heterogeneity in this cell population and the lack of consensus in defining appropriate cell surface marker profiles. Complicating this issue is the fact that the expression of cell surface epitopes is highly dependent on the soluble and insoluble components of the extracellular milieu and on their physical properties and spatial orientation. In addition, interactions with supporting cells can functionally modify the cell surface epitope expression of MSCs. Moving forward, comparing information across different laboratories will be critical in the identification, isolation, and clinical application of MSCs for cellular therapies in the future.

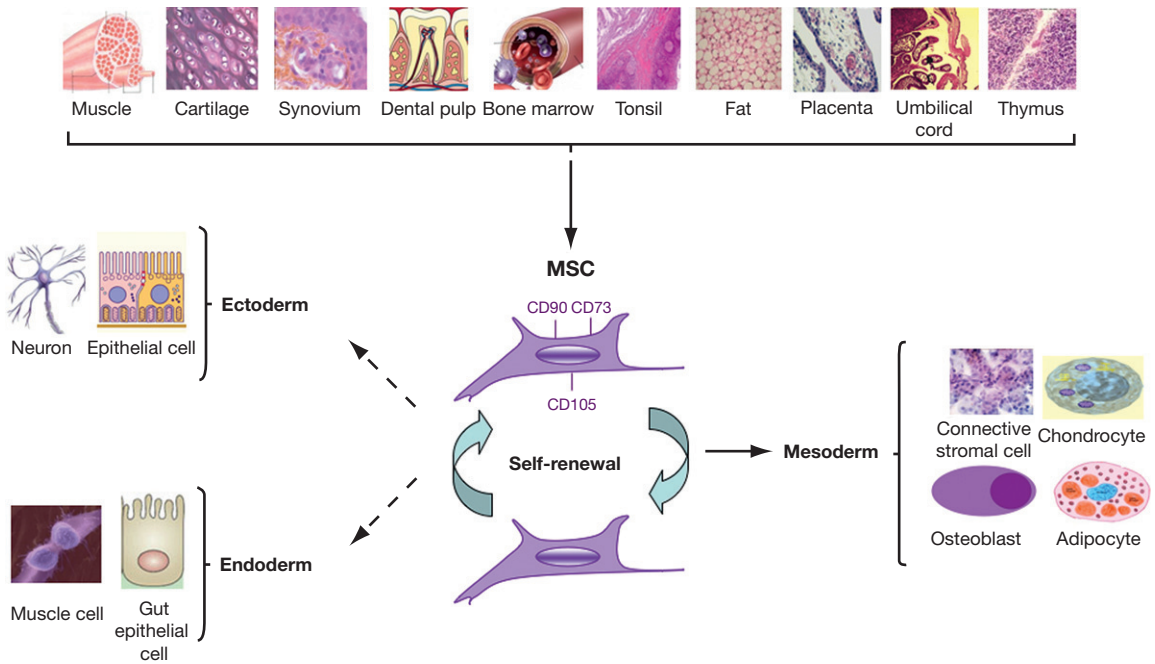

Figure 3 First discovered in bone marrow in 1968, mesenchymal stem cells (MSCs) are a resident multipotent stem cell source isolated from a wide range of adult tissues including muscle fat, and thymus. The most common phenotypic markers used to classify MSCs include CD90, CD73, and CD105. MSCs have the capability to self-renew and exhibit potential to differentiate predominantly along mesodermal lineages. Some studies suggest MSC differentiation along ectodermal and endodermal lineages as well. Reproduced from Kuhn, N. Z.; Tuan, R. S. *J. Cell Physiol.* **2010**, *222*(2), 268–277.

5.507.2.5. Embryonic Stem Cells

Embryonic stem cells (ESCs) are a pluripotent cell source, capable of giving rise to all cell types in the human body, including all three germ layers: mesoderm, endoderm, and ectoderm. ESCs are distinct from multipotent stem cells that have restricted differentiation potential along certain lineages. And, ESCs are not totipotent as they lack placenta and umbilical cord information, and thus cannot independently give rise to a human being. The discovery of ESCs began in 1964 when researchers successfully isolated a single cell type from a teratocarcinoma, a germline-derived tumor.[29] Researchers were able to isolate, culture, and expand these cell populations in culture. These cells, now called embryonic carcinoma (EC) cells, were largely used as an *in vitro* model to study early mouse development, but could never be applied clinically given their tendency for genetic mutation and karotypic instability. Less than 20 years later, in 1981, ESCs were generated from mouse embryos.[30] Seventeen years later, in 1998, the first report describing ESC lines derived from human blastocysts was published.[31] After undifferentiated proliferation over 4–5 months, this cell population still retained the ability to differentiate into multiple tissue types including gut, neuron, bone, cartilage, muscle, and kidney glomeruli (**Figure 4**).

The four fundamental characteristics that define an ESC include (a) pluripotency – potential to give rise to all cell types of all three germ layers (ectoderm, mesoderm, and endoderm); (b) immortality – ability to divide indefinitely under specific conditions; (c) ability to remain undifferentiated; and (d) karyotypic stability – unchanged number and appearance of chromosomes. The current molecular marker signatures used to characterize ESCs include (a) surface markers SSEA-1, SSEA-4, and TRA-1-60; (b) transcriptional factors Oct4, Nanog, and Sox2; and (c) high telomerase activity (http://www.stemgent.com). These cells can be subcultured and maintained in an undifferentiated state *in vitro* for several months by growing them on fibroblastic feeder layers with medium supplementation, including growth factors, leukemia inhibitory factor (LIF), and basic fibroblastic growth factor (bFGF). To initiate differentiation of ESC cultures, embryoid colonies are selectively removed from feeder layers and subcultured alone, thus stimulating embryoid body formation. Subsequently, directed differentiation can be achieved *in vitro* by the addition of growth factors for induction of specific lineage phenotypes, and committed and differentiated cells obtained by transfection with selectable, drug resistant, expression DNA constructs harboring lineage-specific promoters. Finally, terminal differentiation can be achieved by transplantation of progenitor cells into appropriate tissue sites *in vivo*.

Somatic cell nuclear transfer (SCNT) is a technology that has been developed to create a cloned embryo, whereby a nucleus from an adult somatic cell is introduced into an enucleated ovum.[32] This technique has been applied to achieve *reproductive* cloning in which the cloned embryo is subsequently implanted into a pseudopregnant surrogate mother

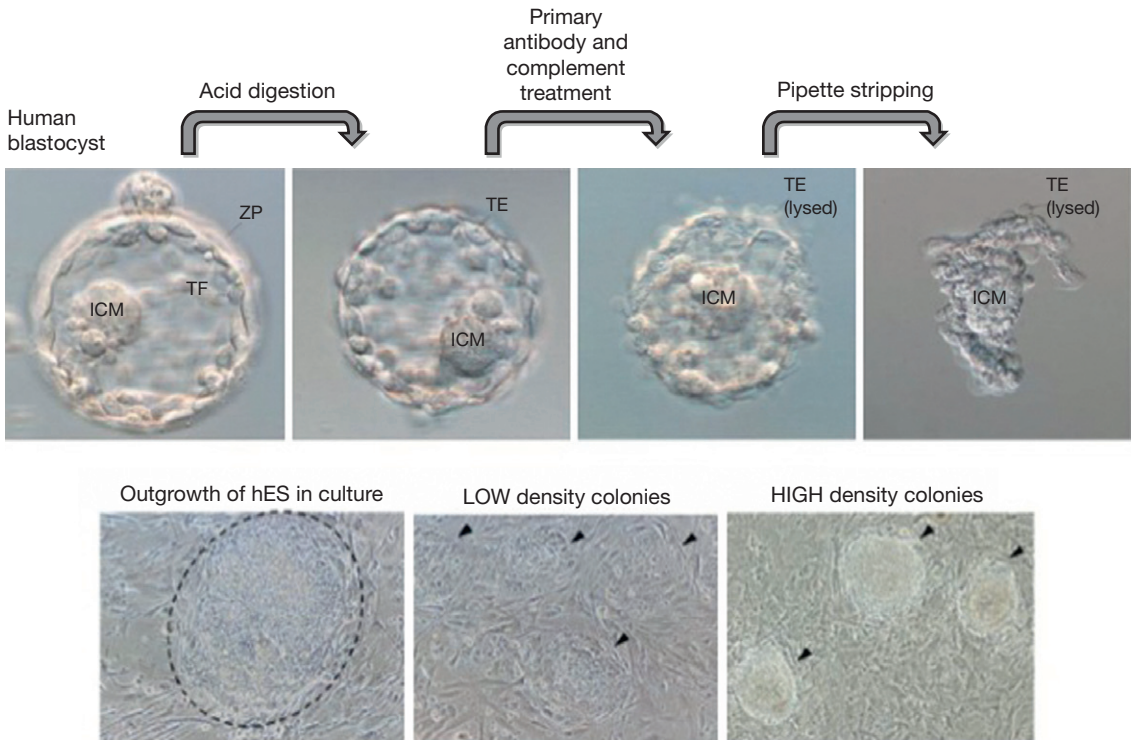

Figure 4 Technical steps to achieve embryonic stem cell isolation. First, acid digestion of zona pellucida (ZP). Second, utilization of a combination of primary antibody and complement-mediated lysis of trophectoderm (TE) cells, termed 'Immunosurgery.' Third, utilization of pipette to strip lysed TE layer away. Finally, collection of inner cell mast (ICM) cells to plate onto feeder layers of mouse embryo fibroblasts (MEFs). Colonies can be passaged to created ES lines. Reproduced from Chen, A. E.; Melton, D. A. *J. Vis. Exp.* **2007**, *10*, 574, with permission from JoVE.

and allowed to develop fully into a complete organism. One of the most famous animals cloned using SCNT technology was Dolly the sheep, by Ian Wilmut and his colleagues.[33] In a similar manner, the technology can also be applied for the purpose of *therapeutic* cloning to expand tissue-specific cell populations for therapeutic gain. Specifically, nuclei derived from patient cells taken from a biopsy are transferred to an enucleated donor oocyte. This exact patient clone is subcultured, expanded, and differentiated to the desired tissue type, and introduced into the patient as a completely immunologically compatible transplant. These SCNT technologies are beginning to enter the clinical arena. For example, Geron Corporation received FDA clearance in January 2009 to conduct the first human clinical trial of ESC-based therapies for acute spinal cord injury (http://www.geron.com/media). Despite the exciting potential of this technique for patient-compatible tissue replacement applications, therapeutic cloning efficiency remains extremely low; there are significant ethical concerns regarding the use of donor embryos, and fears remain of uncontrolled cell growth and differentiation with risk of teratoma formation.

5.507.2.6. Induced Pluripotent Stem Cells

Given the ethical concerns associated with applied ESC strategies, alternative approaches to generate pluripotent cells are currently being investigated. Questions such as "Can 'terminal' differentiation be reversed?" "Can mature adult cells be dedifferentiated?" and "Do committed cells possess plasticity?" and others are the driving force behind the discovery of induced pluripotent stem cells (iPSCs). In 2005, two separate groups reported on a new technique demonstrating cellular reprogramming by fusion with human ESCs.[34,35] These cells reprogrammed by fusion with ESCs had three key characteristics: expression of ESC markers Oct3/4, ESC-specific DNA methylation, and ESC-specific histone modifications. These discoveries, which represented a paradigm shift, opened up the possibility of reactivation of all genes required for normal development in terminally differentiated cells. Furthermore, these exciting findings also suggest that the key epigenetic factors necessary to effect reprogramming are contained within the cytoplasm of the oocyte and ESCs. Shortly after these studies, in 2006, Takahashi and Yamanaka presented the first paper describing the induction of pluripotent stem cells from mature mouse fibroblast cultures utilizing four defined transcription factors: Oct4, Sox2, c-Myc, and Klf4.[36] In 2008, efficient and rapid generation of iPSCs from human keratinocytes was achieved.[37] Here, a single hair bulb, placed in explant culture for 5 days after transduction of the four transcription factors resulted in iPSCs populations. Using this technique on a single hair follicle, researchers could derive cells to give rise to endoderm, mesoderm, and ectoderm tissues. The therapeutic potential behind these newly developed techniques suggested that cells derived from a single hair follicle could, for example, result in the entire replacement of dopaminergic neurons in a patient suffering from Parkinson's disease. Further advancements in iPSCs technology include feeder-free derivation of iPSCs from adult human adipose stem cells, opening up the possibility of liposuction waste being reutilized for cartilage replacement in rheumatoid arthritis damaged tissue.[38] Later in 2009, iPSCs derived from foreskin fibroblasts were differentiated to cardiomyocytes and functional studies measuring beat frequency were carried out following cardiac drug application. Results from such studies suggest that iPSC technology can be translated to toxicity and drug screening arrays (**Figure 5**).[39]

Cell therapy using iPSCs has significant potential. Most importantly, the use of iPSCs will circumvent the ethical issues surrounding ESCs because their creation does not involve destruction of human preimplanted embryos. Furthermore, the ease and reproducibility of generating patient-specific immune-compatible iPSCs in sufficient numbers for regenerative, therapeutic, and research (high-throughput screening) purposes is clearly advantageous. Dermal fibroblasts and bone marrow mesenchymal cells have proven to be reliable starting sources for human iPSC reprogramming.[40,41] However, concerns about continuous passage *in vitro* leading to karyotopic abnormalities remain. Risk of insertional mutagenesis is always associated with retroviral and lentiviral vector techniques. Given the heterogeneous nature of the resultant cell population, selection marker panels need to be developed to better characterize these populations. And again, the low efficiency of reprogramming, possibly due to endogenous anti-reprogramming mechanisms in differentiated cells, will require larger numbers of the starting cell population.

To overcome the poor efficiency of reprogramming and reduce the requirement of large initial populations, recent advances have incorporated the use of chemicals such as valproic acid, a histone deacetylase inhibitor,[42] and small molecule compound, Bix-01294, a TGF-β inhibitor.[43] Other strategies involve reducing the number of programming factors. Hester *et al.*[44] recently reported that the combination of Oct3/4 and either Klf4 or Myc are sufficient to generate iPSC cells from neuronal stem cells. Others have attempted to deliver all four factors in a single polycistronic viral vector, for a single integration site.[45] Still others have designed adenovirus, plasmids, or recombinase to excise reprogramming genes after iPSCs were generated, to increase reprogramming efficiency (http://stemcells.nih.gov). Finally, extensive screens of chemical libraries are currently under way to identify candidate small molecules that may be effective reprogramming agents.[43,46]

5.507.2.7. Endogenous Host Populations

Some tissue-engineered strategies do not involve the transplantation of cell-based therapies. Instead, biomaterials are designed in such a way that endogenous cells will appropriately respond via migration, proliferation, or differentiation. Endogenous cell populations can be recruited from local stem cell niches to proliferate and differentiate within a site of tissue damage. Local vascular beds can be recruited to form newly branched vessel networks within the material implant, and tissue-specific cells can be recruited to line the new material implant. For example, controlled release of small molecule, FTY720 (a target for various S1P receptors) from polymer-coated bone allografts improved bone ingrowth and increased total microvessel density within the defect space.[47] These studies highlight the ability of drug-eluting grafts to successfully recruit host cells to repopulate transplanted materials.

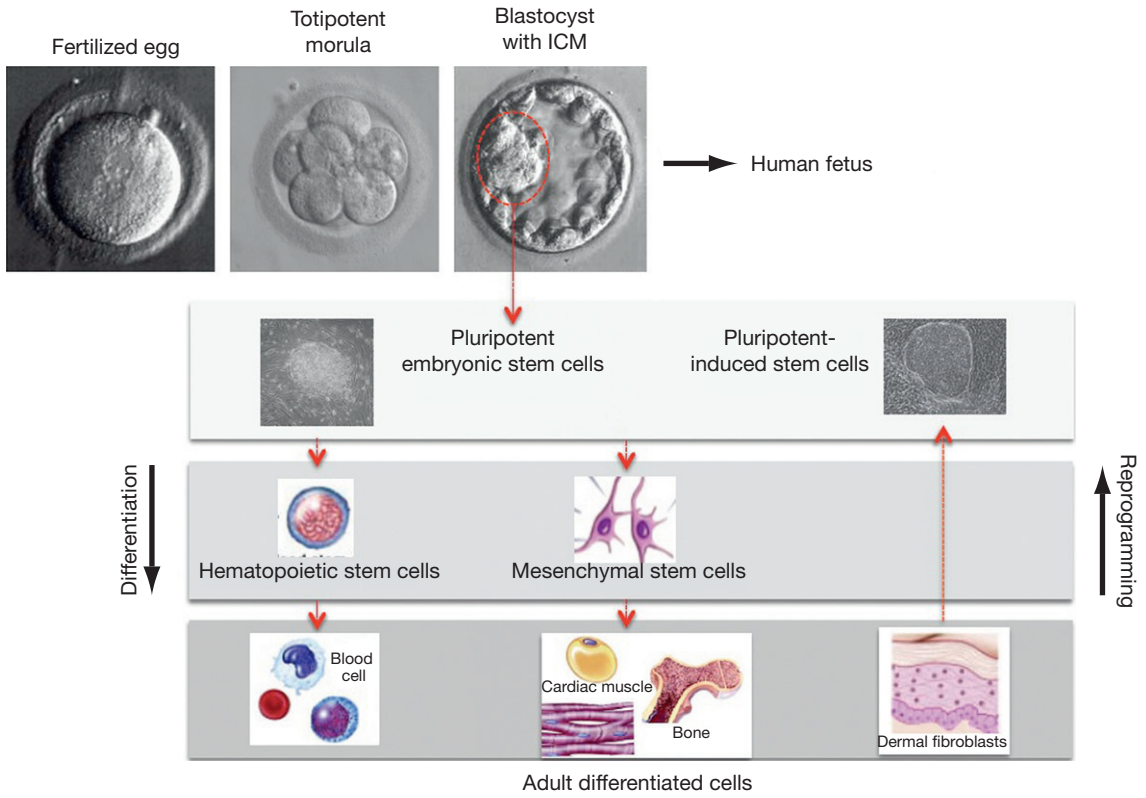

Figure 5 Conceptual flow diagram highlighting the differentiation pathway from fertilized egg to mature differentiated cell types of hematopoietic and mesenchymal lineages. Alternatively, reprogramming or dedifferentiation of mature committed cells can produce iPSCs that exhibit similar characteristics to pluripotent ESCs. These discoveries raise questions about terminal cell differentiation and the new role of plasticity in adult cells.

5.507.3. Patient Delivery Challenges: Controlling Cells in the Body

5.507.3.1. How Do We Control Cells to Survive *In Vivo* After Transplantation?

Delivery of cells *in vivo* exposes these populations to a host of survival challenges. Immune issues related to autoimmunity and inflammation are among the first pathways of assault and destruction of delivered cells. Degranulating neutrophil populations recruited to sites of tissue injury can release chemokines that can cause plasma leakage, recruitment/activation of phagocytic macrophage and mast cells that can lead to a hostile environment, and increased risk of cellular apoptosis and inflammation. Besides surviving the initial innate immune responses, transplanted colonies must also interact with the adaptive immune cascade or otherwise be targeted for elimination.

Apart from immunity, cells have basic metabolic requirements, including oxygen availability and waste exchange. It is now recognized that incorporation of functional mature vessel networks is required for all cell maintenance and tissue survival, save avascular sites such as cartilage. Proximity to existing vascular beds and the ability to establish and maintain new vascular networks are critical in maintaining this delicate balance of oxygen and nutrient requirements and waste removal. Material properties such as pore size and degradation can influence this balance.

5.507.3.2. How Do We Control Cells to Maintain Appropriate Phenotype *In Vivo*?

A significant challenge with all cell-based therapies is to ensure maintenance of appropriate phenotype *in vivo*, following transplantation. The challenge with transplanting tissue-specific cells is to *maintain* phenotype, following *ex vivo* expansion and reimplantation. The challenge with transplanting undifferentiated cells, including iPS cells, MSCs, and ESCs is to achieve appropriate *differentiation* and functional end-stage phenotype without leading to uncontrolled growth or inappropriate differentiation (Figure 6).

For undifferentiated cells, the intended end-stage phenotype may either be conferred before transplantation or posttransplantation. Thus soluble factors, mechanical or shear stimuli, can be applied in culture prior to implantation to establish appropriate differentiation. Alternatively, such factors or topographical surface features or chemistry can be applied to elicit similar differentiation pathways *in vivo* posttransplantation. Furthermore, interactions with the local milieu, including endogenous cells types, local matrix structures, and soluble chemokine gradients, can provide

Cell source	Donor type	*Ex vivo* expansion potential	Stemness	Tissue source	FDA approved for human use
Tissue-specific committed cells	Autologous or allogeneic	Low	Committed	Various	Yes, carticel for cartilage defects
Mesenchymal stem cells (MSCs)	Autologous or allogeneic	Mid	Multipotent	Bone marrow, fat, dental pulp, cord blood, placenta, muscle, cartilage, tonsil	Yes, Lou Gehrig's disease, heart disease, GVHD
Induced pluripotent stem cells (iPS)	Autologous	High	Pluripotent	Dermal fibroblasts, hair follicles	No
Embryonic stem cells (ESCs)	Allogeneic	High	Pluripotent	Fertilized egg	Yes, Geron for spinal cord injury
Endogenous host populations	Autologous	N/A	Committed	Various	Yes, i.e., devitalized bone grafts

Figure 6 The range of different cell sources utilized in cell-based therapies. Donor type, *ex vivo* expansion potential, tissue source, and examples of current FDA approval are highlighted for each cell source.

important instructional cues for appropriate differentiation and phenotypic maintenance.

5.507.3.3. How Do We Control Cells to Migrate . . . NOT to Migrate *In Vivo*?

Depending on the application, the desired motility of delivered cells could range from *stationary* (i.e., replace missing tissue) to *disseminating* (e.g., repopulate entire hematopoietic system). Sites of delivery can certainly influence these parameters. Subcutaneous injections provide initial point sources of cell entry, whereas intravenous injections immediately disseminate cells throughout the blood stream. Beyond this, biomaterials are expected to play an important role. For example, several cell-based vaccination approaches utilize alginate beads to physically encapsulate antigen-presenting cells (APCs) to act as a local hub for T-cell priming.[48] Coating delivery materials with extracellular matrix proteins or locally releasing growth factors can encourage host cell retention within the local regions. Other material properties such as stiffness,[49] pore size,[50] protease-control,[51] and integrin–ligand relationships[52] can all play a role in cell migration behaviors *in vivo*.

5.507.4. Donor Versus Host Immune Issues

The primary role of the immune system is to protect the individual against uncontrolled tissue damage and disease by appropriately identifying and destroying non-SELF pathogens and tumor cells. The ability of the immune system to effectively distinguish between SELF and non-SELF is critical in maintaining human health. Loss in this self-tolerance can lead to autoimmunity, a condition in which the immune system attacks healthy SELF cells misidentified as foreign. Autoimmune-mediated tissue destruction can result via two distinct pathways: (a) autoimmune disorders that arise from errors in self-regulating machinery and (b) immune responses triggered by delivering poorly matched allogeneic or xenogeneic materials into SELF. Cell-based transplantation therapies fall into the second category of autoimmune responses, where donor-derived T-cells can recognize recipient tissues as foreign, resulting in tissue attack and a 30–60% mortality rate.[53] Thus, all clinical therapies utilizing cell sources to replace damaged and diseased tissues must also address issues of immune surveillance.

Typically, autologous cells isolated from SELF, expanded, and reintroduced into SELF do not trigger foreign body responses because the cell source is identically matched to each patient. However, cell harvest from adult tissue is limited, associated with donor-site morbidity, and success rates in deriving multipotent cell lines from adult tissues are poor. Furthermore, there are various *ex vivo* treatments, including genetic modifications, that may significantly alter cellular properties so as to induce an immune response.[54] Thus, finding strategies to circumvent locally or alter immune surveillance systemically would enable wider applicability of allogeneic (cell sources from other human donors) and xenogeneic (cell sources from animal donors) cell-based therapies.

Cell transplantation from non-SELF sources triggers the immune system via mismatch in major histocompatibility molecules (MHC I and II). Professional APCs, including dendritic cells (DCs), macrophages, and B cells use these two classes of molecules as presentation platforms on the cell surface to display peptide fragments from both SELF and foreign

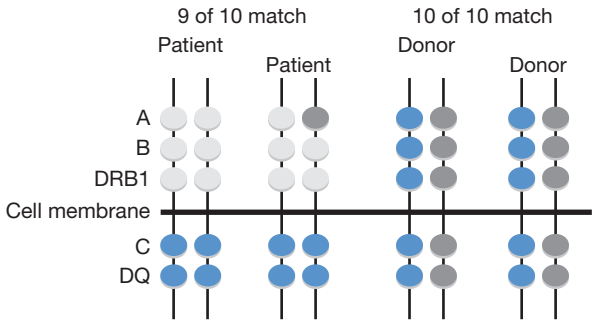

Figure 7 Major histocompatibility complex molecules come in two classes: I and II. These molecules are found on the surface of antigen-presenting cells (APCs), which include dendritic cells, macrophages, and B-cells. APCs use their MHC molecules as a platform to present antigen to local T-cells. Reorganization of an antigen signature by a T-cell initiates the adaptive immune cascade. In the case of cell transplantation, this can led to either graft rejection or autoimmunity. Half of one's HLA markers are inherited from one'smother. The other half are inherited from one's father. So identical donor matches from siblings is 25%. The National Marrow Donor Program sets a minimal requirement that five of six HLA markers must match to be used for transplant.

antigens to T-cells. One set of alleles (haplotype) is inherited from each parent, and thus haplotypes must be closely matched for successful allogeneic transplantation. Therefore, hyperacute (within hours) or delayed rejection (within days) of xenografts occurs primarily because of a severe mismatch in MHC and complement molecules (Figure 7).

Because haplotypes are inherited, immediate family members are typically the best match for a bone marrow transplant or a kidney donation. However, new strategies are emerging to combat this strict requirement for MHC matching. For example, the MHC locus may be targeted by homologous recombination (a type of genetic recombination to exchange nucleotide sequences between similar DNA molecules) to remove or replace donor-derived HLA molecules in donor ESCs.[55] Chromosomal-elimination cassettes can also be engineered to jettison the entire chromosome 6, which contains MHC haplotypes, during S phase and effectively replace donor chromosomes with recipient copies.[56] Conceptually, these strategies could eliminate mismatched MHC issues, but they are highly inefficient and potentially hazardous if karyotypic stability is affected. Alternatively, creation of a mixed chimera has also been attempted to induce donor-specific tolerance.[57] For example, a mixed chimera is created by irradiating SELF bone marrow and subsequently repopulating bone marrow with both SELF and donor bone marrow isolate. In this way, there is coexistence of SELF and donor HSCs, resulting in coengraftment of SELF and donor immune cells within the recipient thymus.

Fortuitously, allogeneic *cell* transplants have significantly reduced immunogenic issues compared with *whole-organ* transplants. For example, by selectively removing APCs (i.e., DCs, macrophages, and B cells) from the transplant pool, the potential of the newly transplanted cells to recognize SELF as foreign is reduced. Furthermore, immune surveillance can be minimized by delivering allogeneic cells to regions distal from vessel structures and/or encapsulated within delivery materials to prevent access from the host immune system via blood. Selecting allogeneic cell populations with reduced MHC expression will also help reduce host rejection of transplanted cells.

5.507.4.1. Immunomodulatory Role of MSC Populations

In 2002, emerging evidence began to suggest an interesting immunoregulatory role for adult MSCs. Specifically, this stem cell population has low antigenicity with no expression of MHC II and low expression of MHC I and costimulatory molecules. Furthermore, studies demonstrated that MSCs are capable of suppressing both T-cell proliferation and activation in response to allogeneic antigens. These immunomodulatory properties are not limited to bone marrow-derived MSCs alone, but have also been shown in MSCs derived from other tissues.[58] Also, T-cells are not the only cell type within the immune system upon which MSCs have been shown to exert their modulating effects. MSCs also play an influential role in DC differentiation, maturation, and phenotype maintenance. Specifically, coculture with both human and murine MSCs *in vitro* prohibits differentiation of monocytes and $CD34^+$ progenitor cells into antigen-presenting DCs.[59] Furthermore, MSCs can reduce expression of MHC II, CD40, and CD86 on DCs following maturation induction[60,61] and have also been shown to alter B-cell proliferation,[62,63] activation, IgG secretion,[64] differentiation, antibody production, and chemotactic behaviors (Figure 8).[65]

Perhaps the most exciting data supporting the immunomodulatory role of MSCs are from *in vivo* studies conducted in humans, which demonstrate successful treatment of GVHD, a condition where donor cells recognize SELF as foreign and attack recipient tissues. Specifically, treatment with *ex vivo* expanded allogeneic MSCs successfully resolved severe grade IV acute GVHD.[66] Thus, a growing body of *in vivo* evidence now supports the hypothesis that MSCs have immunosuppressive properties, including (*murine*) prevention of GVHD,[67] decreased graft rejection,[68] prevention of experimental acute encephalomyelitis,[69] (*baboon*) prolonged skin graft survival,[70] (*rat*) protection against renal ischemia/reperfusion injury,[71] (*human*) HSC engraftment with no GVHD,[72] platelet engraftment with low incidence of GVHD,[66] and resolution of severe acute GVHD.[73] Furthermore, new studies suggest that MSCs can retain these immunosuppressive properties even after manipulation, such as phenotypic differentiation and genetic engineering. Specifically, allogeneic MSCs that were differentiated toward a chondrogenic phenotype continued to suppress antigen-specific T-cell proliferation in rheumatoid arthritis[74] and locally transplanted MSCs genetically engineered to produce bone morphogenetic protein-2 (BMP-2) escaped immune rejection and induced ectopic bone formation *in vivo*.[75]

However, in 2005 Djouad *et al.* reported the first indication that immunomodulatory properties were not universal and unconditional. Specifically, allogeneic MSCs delivered to a murine collagen-induced arthritis model did not confer any benefit, and paw swelling worsened compared with control groups. Furthermore, coincubation with tumor necrosis factor-alpha (TNF-α) was sufficient to reverse the immunosuppressive effects of MSCs on T-cell proliferation.[76] Others reported similar

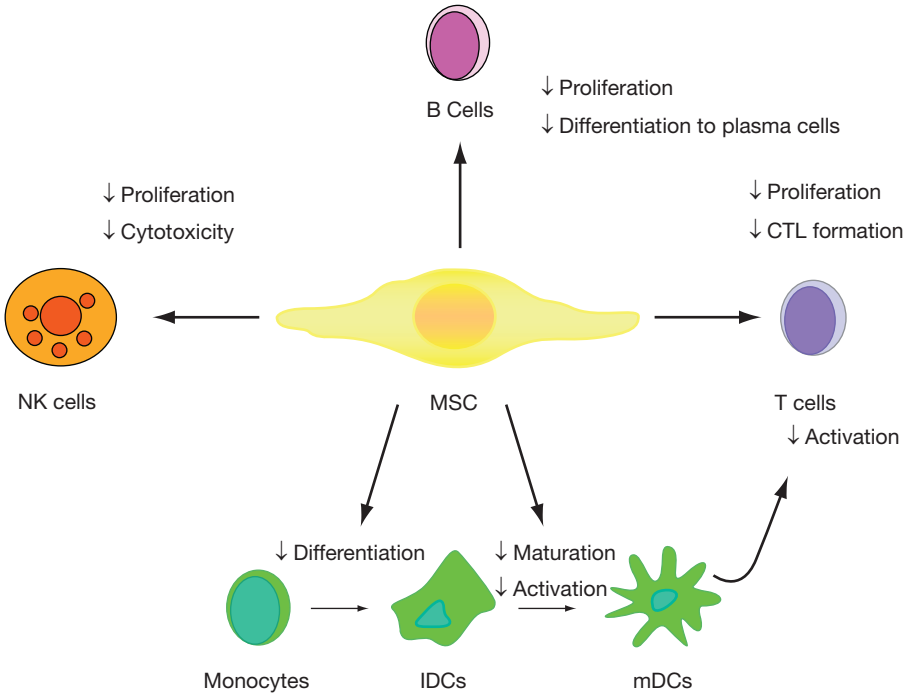

Figure 8 Signaling pathway map highlighting MSC immunomodulation properties on various cell types within the immune system. Overall, MSCs have been shown to decrease T-cell, B-cell, and NK cell proliferation and prevent maturation and differentiation along the monocyte/DC lineage. Reproduced from Nauta, A. J.; Fibbe, W. E. *Blood*, **2007**, *110*(10), 3499–3506.

results where MSC transplantation failed to alleviate GVHD in a murine model, even though *in vitro* assays confirmed suppression of T-lymphocyte proliferation.[77] More recently, repeated intravenous injections of MSCs failed to reduce GVHD-related recipient mortality. Most interestingly, local implantation of MSCs derived from bone marrow, placenta, or umbilical cord prompted ectopic bone formation in syngeneic recipients and ultimately led to transplant rejection by allogeneic mice.[78] Taken together, these results suggest that MSC phenotype is transient and context dependent.

That MSC phenotype and function may be particularly susceptible to the microenvironmental context suggests that, in terms of their trophic and phenotypic characteristics, MSCs may not have an entirely autonomous program, but instead may be influenced by the surrounding microenvironment. In this way, isolation from resident niches, subsequent expansion *ex vivo*, and redelivery to a remote inflamed or injured site where inflammatory chemokines and bioactive extracellular matrix fragments are abundantly present may heavily influence MSC behavior and function. Therefore, issues related to appropriate delivery mechanisms, timing of delivery, and manipulation of the injury site microenvironment are of utmost importance in the study and application of MSCs.

5.507.5. Donor Versus Host: Cell/Tissue Integration

To overcome the failure of organs and tissues is the goal of tissue engineering, and in this lies the expectation that the injected cells or the grafted cell-laden tissue construct will be well-integrated with the host tissue. Many levels of integration must occur, including physical, metabolic, and functional, which in turn determine the ultimate success of the cell-based therapy. For example, for musculoskeletal tissues, it has been well established that, unlike during musculoskeletal tissue development, postinjury regeneration between soft tissue and bone does not occur.[79] Interfaces that often challenge tissue engineers are cartilage-to-bone, ligament-to-bone, and tendon-to-bone integrations. Specific examples of advances in the cartilage-to-bone (osteochondral) integration are provided in this section to illustrate the importance of this issue.

Physical integration is particularly important when the interface is between such distinct tissue types. Specifically, it is desirable to engineer a functional gradient of mechanical properties that approximates that of the native interface. For example, at the osteochondral interface, which barriers articular cartilage and subchondral bone, there is a precisely controlled heterogeneity in the ultrastructure that is important for the load bearing and force distribution.[80] Directly interfacing the bone is the deep zone of articular cartilage that contains hypertrophic chondrocytes within a densely mineralized extracellular matrix.[81,82] Recently, scaffolds have been designed with multiple phases and seeded with phase-relevant cell populations to engineer the osteochondral interface.[83]

One early example of a biphasic scaffold approach was to take two separate scaffold—one a hyaluronan sponge seeded with MSCs stimulated with TGF-β1 for chondrogenic differentiation and the second a porous calcium phosphate scaffold seeded with MSCs stimulated with osteogenic media—and to join them by a fibrin sealant. In this study, Gao *et al.*[84] implanted the scaffold into rats and observed the presence of continuous collagen fibers between the two scaffolds at

6 weeks postimplantation. Continuous biphasic scaffolds have been developed, for example, by utilizing a sequential photopolymerization technique to form an osteochondral construct with a polyethylene glycol-diacrylate hydrogel. The top and bottom hydrogel layers contained MSC-derived chondrocytes and osteoblasts, respectively.[85] Histological examination 12 weeks postimplantation into a subcutaneous SCID mouse model revealed distinct cartilaginous and osseous regions with integration between the two scaffold layers. A number of other studies have confirmed these observations with MSCs cultured on biphasic scaffolds.[86–90]

With an increase in complexity, a triphasic scaffold was designed that had an agarose hydrogel-based cartilage region, a polymer–ceramic composite microsphere bone region, and an interfacial region consisting of a hybrid of the hydrogel and polymer–ceramic composite.[91,92] The hydrogel was seeded with chondrocytes and the composite with osteoblasts. Although *in vivo* validation has not yet occurred for triphasic scaffolds, they are intended to provide superior integration compared with other more simplified tissue-engineered constructs.

Important attributes to consider and evaluate for successful tissue integration *in vivo* are the host environment plus the precise effects of biochemical and physical stimulation on the interface. There is also the need for physiologically relevant *in vivo* models to determine the clinical potential of the designed scaffolds. It is also necessary to determine how existing tissues will attach to stratified scaffolds to direct tissue growth and reestablish the native interfacial organization. Additionally, the selection of multiple cell sources is typically necessary to ensure or enhance heterogeneous tissue formation. In addition to optimization of methods for sterilization and potentially long-term shelf storage of the scaffolds, the identification of an optimal cell source that is readily available (i.e., quickly isolated and expanded), such as an adult stem cell source, will be required for the clinical implementation of these scaffolds.

5.507.6. Safety and Stability

It is imperative to ensure the clinical safety and stability of stem cell-based products for their success in the clinic. The FDA is responsible for evaluating the safety profile of stem cell-based products that are intended for clinical studies. Because stem cells have an extensive ability to proliferate and differentiate, the FDA has put into place a gamut of safety concerns relating to each stem cell-based product.[93] With respect to the use of iPS and ESCs in particular, the FDA requires preclinical testing due to the characteristic ability of these pluripotent stem cells to form teratomas after injection into adult, immunodeficient mice. An example of a cell-based product approved by the FDA is Carticell, an autologous cartilage tissue replacement therapy (**Figure 9**).

Several additional safety concerns exist pertaining to the use of stem cell-based products, including the mobility of stem cells to a site other than where injected, spontaneous malignant transformation due to prolonged *ex vivo* expansion, the expression of cell/tissue donor human leukocyte antigen molecules that causes immunogenicity, and the possibility of cellular impurities in the differentiated cell product.

The *in vitro* culture of human ES and iPS cells has traditionally involved the use of irradiated mouse embryonic fibroblast feeder cells to maintain the cells in a stem state (i.e., proliferating and undifferentiated, yet maintaining pluripotency). The use of organs, tissues, and cells derived from animals to treat human disease, or xenotransplantation, raises concerns

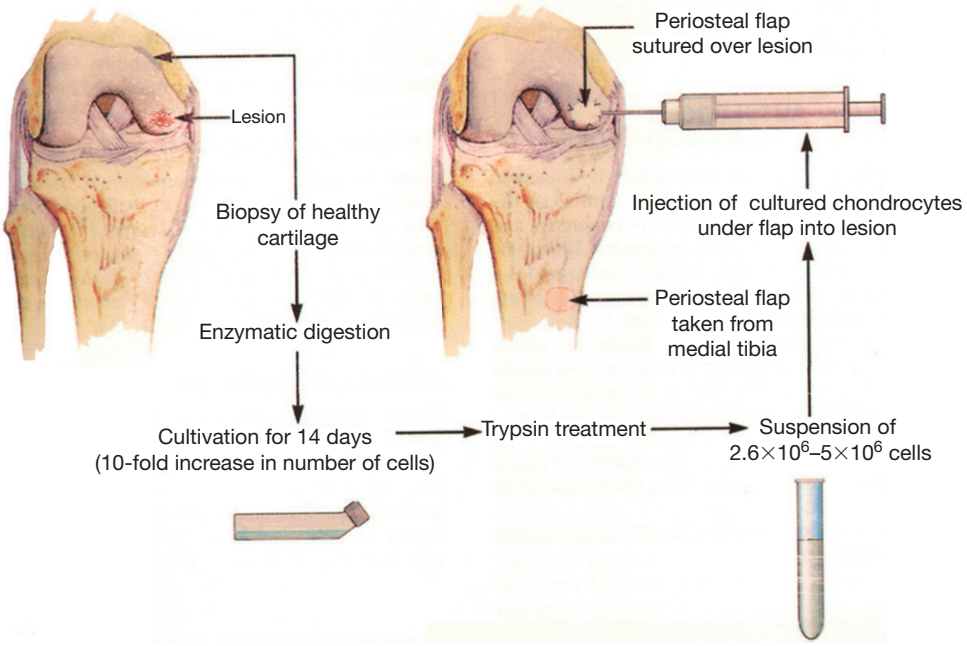

Figure 9 In 1997, FDA approves first biologic license to Carticel for manipulated autologous structural cell therapy. Here, biopsy of healthy cartilage is taken from the patient, expanded *ex vivo*, and reimplanted at the lesion site. Figure from http://www.drmendbone.com/swedish.htm

about the unintended transfer of animal viruses into humans. In turn, researchers have considered alternatives to the use of mouse feeder cells. For example, human foreskin fibroblasts have been shown to be comparable in their ability to maintain human ES and iPS cells in a stem state.[94,95] Furthermore, it has been shown that the stem state of these cells can be maintained by seeding them onto a commercially available basement membrane matrix and culturing them in medium conditioned by feeder cells.[96]

The FDA has suggested comprehensive characterization of stem cell-based products by using a multiparametric testing approach. The recommended tests that target cell types within a stem cell-based product include comprehensive examination of cellular morphology, phenotype-specific cell surface antigens, unique biochemical markers, and the genome and/or proteome profile. To test for safety against the possibility of spontaneous malignant transformation, the stem cells can be karyotyped and their *in vitro* growth kinetics can be routinely measured, along with their differentiation potential. Additionally, stem cell cultures should be tested to ensure that they are free of microbial (bacterial/fungal) and mycoplasma contamination.

Most stem cell cultures require the use of serum-containing medium for their growth and survival. The use of serum in clinical studies has long been under contention, especially due to the outbreak of bovine spongiform encephalopathy (BSE) in cattle herds (mostly those raised in the United Kingdom). The FDA has indicated that use of bovine serum is acceptable provided demonstration that the source of serum is from herds reared for the entirety of their lives in certified, BSE-free countries. Furthermore, the use of clinical-grade serum sourced from humans is also accepted. Alternatively, a serum-free, chemically defined medium can be developed that obviates risks associated with serum supplementation from either bovine or human sources.

In the design of preclinical animal studies, there are further toxicological assessments that need to be performed. Specifically, comprehensive histological examination should be performed to provide evidence for implant site reaction, inflammatory response in target and nontarget tissue, host immune response, cellular fate plasticity, morphologic alterations in target or nontarget tissues, cell survival posttransplantation, cell migration, tissue integration, and tumorigenicity (hyperplasia or uncontrolled growth). Moreover, the stem cells should be shown to have the desired biological activity. Relevant bioassays that measure the potency of stem cell preparations are important for showing that the cells are not inert.

In summary, the assessment of human stem cell safety requires a comprehensive multiparametric analysis. This analysis must begin from the initial isolation of the stem cells, and continue through the characterization and assessment of their safety and stability in culture and in preclinical animal studies. The strategies should be routine, systematic, and carefully scrutinized at every step of the process, for consideration by the FDA for approval of a cell-based therapy.

5.507.7. Conclusion

Cell-based therapies have expanded the possibilities in the clinic such that genetically faulty, dying, injured, or damaged cells can be effectively replaced. Adult tissue-derived MSCs, though limited in differentiation/expansion potential, are immune-privileged cells that are currently being used in a large number of clinical trials and applications. Better understanding of MSC immunomodulatory mechanisms may reduce rejection issues and expand applicability of allografts and xenografts and cells derived from these sources. ESCs represent an excellent platform for studying developmental and pathogenic processes, but their clinical application continues to encounter significant ethical complications. With the recently discovered cell reprogramming technology, iPSCs may be directly derived from adult somatic cells. However, their potential tumorigenicity and uncertain long-term functional stability must be overcome to realize the clinical therapeutic potential of this cell source. Xenogeneic cells offer new possibilities, provided immune rejection issues can be effectively overcome. Finally, the use of appropriate 'smart' biomaterials is critical for cell-based therapy to enhance cell delivery, host integration, range of function, and long-term recovery.

Acknowledgment

Supported in part by NIH Intramural Research program and the Commonwealth of Pennsylvania Department of Health.

References

1. Freitas, R. A., Jr. *Nanomedicine*; Landes Bioscience: Georgetown, 1999.
2. Roux, F. A.; Sai, P.; Deschamps, J. Y. *Xenotransplantation* **2007**, *14*, 208–216.
3. Carrel, A.; Lindbergh, C. A. *Science* **1935**, *81*, 621–623.
4. Lindbergh, C. A. *J. Exp. Med.* **1935**, *62*, 409–431.
5. Cooper, M. D. *J. Immunol.* **2003**, *171*, 6318–6319.
6. Brittberg, M.; Lindahl, A.; Nilsson, A.; Ohlsson, C.; Isaksson, O.; Peterson, L. *N. Engl. J. Med.* **1994**, *331*, 889–895.
7. Atala, A. *BJU Int.* **2000**, *85*(Suppl. 3), 24–34; discussion 36.
8. Mossman, K. *Scientific American*, 2006.
9. Sato, T.; Nakamura, T. *Lancet* **2008**, *372*, 2003–2004.
10. First human receives cardiac stem cells in clinical trial to heal damage caused by heart attacks. *Cedars-Sinai News*, 2009, June 30, 3009.
11. Phelps, C. J.; Koike, C.; Vaught, T. D.; *et al*. *Science* **2003**, *299*, 411–414.
12. Williams, R. D. *FDA Consumer*, 1996.
13. Baker, R. *BETA* **1995**, 7–8.
14. Hagell, P.; Schrag, A.; Piccini, P.; *et al*. *Brain* **1999**, *122*(Pt 6), 1121–1132.
15. Haeckel, E. *Anthropogenie*. Wilhelm Engelmann: Leipzig, 1877.
16. Ramalho-Santos, M.; Willenbring, H. *Cell Stem Cell* **2007**, *1*, 35–38.
17. Till, J. E.; Mc Culloch, E. *Radiat. Res.* **1961**, *14*, 213–222.
18. Anderson, D. J.; Gage, F. H.; Weissman, I. L. *Nat. Med.* **2001**, *7*, 393–395.
19. Potten, C. S.; Loeffler, M. *Development* **1990**, *110*, 1001–1020.
20. Friedenstein, A. J.; Chailakhjan, R. K.; Lalykina, K. S. *Cell Tissue Kinet.* **1970**, *3*, 393–403.
21. Friedenstein, A. J.; Chailakhyan, R. K.; Gerasimov, U. V. *Cell Tissue Kinet.* **1987**, *20*, 263–272.
22. Friedenstein, A. J.; Petrakova, K. V.; Kurolesova, A. I.; Frolova, G. P. *Transplantation* **1968**, *6*, 230–247.
23. Caplan, A. I. *J. Orthop. Res.* **1991**, *9*, 641–650.
24. Pittenger, M. F.; Mackay, A. M.; Beck, S. C.; *et al*. *Science* **1999**, *284*, 143–147.
25. Djouad, F.; Tuan, R. S. In *Regenerative Medicine*; Scott, E. W., Fisher, R. C., Eds.; Jones and Bartlett: Sudbury, 2010.
26. Dominici, M.; Le Blanc, K.; Mueller, I.; *et al*. *Cytotherapy* **2006**, *8*, 315–317.
27. Brivanlou, A. H.; Gage, F. H.; Jaenisch, R.; Jessell, T.; Melton, D.; Rossant, J. *Science* **2003**, *300*, 913–916.
28. Baum, C. M.; Weissman, I. L.; Tsukamoto, A. S.; Buckle, A. M.; Peault, B. *Proc. Natl. Acad. Sci. USA* **1992**, *89*, 2804–2808.
29. Andrews, P. W.; Matin, M. M.; Bahrami, A. R.; Damjanov, I.; Gokhale, P.; Draper, J. S. *Biochem. Soc. Trans.* **2005**, *33*, 1526–1530.

30. Martin, G. R. *Proc. Natl. Acad. Sci. USA* **1981**, *78*, 7634–7638.
31. Thomson, J. A.; Itskovitz-Eldor, J.; Shapiro, S. S.; *et al. Science* **1998**, *282*, 1145–1147.
32. Chen, A. E.; Melton, D. A. *J. Vis. Exp.* **2007**, *10*, 574.
33. Campbell, K. H.; Mcwhir, J.; Ritchie, W. A.; Wilmut, I. *Nature* **1996**, *380*, 64–66.
34. Cowan, C. A.; Atienza, J.; Melton, D. A.; Eggan, K. *Science* **2005**, *309*, 1369–1373.
35. Yu, J.; Vodyanik, M. A.; He, P.; Slukvin, I. I.; Thomson, J. A. *Stem Cells* **2006**, *24*, 168–176.
36. Takahashi, K.; Yamanaka, S. *Cell* **2006**, *126*, 663–676.
37. Aasen, T.; Raya, A.; Barrero, M. J.; *et al. Nat. Biotechnol.* **2008**, *26*, 1276–1284.
38. Sun, N.; Panetta, N. J.; Gupta, D. M.; *et al. Proc. Natl. Acad. Sci. USA* **2009**, *106*, 15720–15725.
39. Gai, H.; Leung, E. L.; Costantino, P. D.; *et al. Cell Biol. Int.* **2009**, *33*, 1184–1193.
40. Kunisato, A.; Wakatsuki, M.; Kodama, Y.; Shinba, H.; Ishida, I.; Nagao, K. *Stem Cells Dev.* **2010**, *19*, 229–238.
41. Lowry, W. E.; Richter, L.; Yachechko, R.; *et al. Proc. Natl. Acad. Sci. USA* **2008**, *105*, 2883–2888.
42. Teng, H. F.; Kuo, Y. L.; Loo, M. R.; *et al. J. Cell. Biochem.* **2010**, *110*, 995–1004.
43. Shi, Y.; Desponts, C.; Do, J. T.; Hahm, H. S.; Scholer, H. R.; Ding, S. *Cell Stem Cell* **2008**, *3*, 568–574.
44. Hester, M. E.; Song, S.; Miranda, C. J.; Eagle, A.; Schwartz, P. H.; Kaspar, B. K. *PLoS ONE* **2009**, *4*, e7044.
45. Gonzalez, F.; Barragan Monasterio, M.; Tiscornia, G.; *et al. Proc. Natl. Acad. Sci. USA* **2009**, *106*, 8918–8922.
46. Ichida, J. K.; Blanchard, J.; Lam, K.; *et al. Cell Stem Cell* **2009**, *5*, 491–503.
47. Petrie Aronin, C. E.; Sefcik, L. S.; Tholpady, S. S.; *et al. Tissue Eng. Part A* **2010**, *16*, 1801–1809.
48. Hori, Y.; Winans, A. M.; Huang, C. C.; Horrigan, E. M.; Irvine, D. J. *Biomaterials* **2008**, *29*, 3671–3682.
49. Oakes, P. W.; Patel, D. C.; Morin, N. A.; *et al. Blood* **2009**, *114*, 1387–1395.
50. Klenke, F. M.; Liu, Y.; Yuan, H.; Hunziker, E. B.; Siebenrock, K. A.; Hofstetter, W. *J. Biomed. Mater. Res. A* **2008**, *85*, 777–786.
51. Sarig-Nadir, O.; Seliktar, D. *Biomaterials* **2010**, *31*, 6411–6416.
52. Lammermann, T.; Bader, B. L.; Monkley, S. J.; *et al. Nature* **2008**, *453*, 51–55.
53. Barton-Burke, M.; Dwinell, D. M.; Kafkas, L.; *et al. Oncology (Williston Park)* **2008**, *22*, 31–45.
54. Babensee, J. E.; Anderson, J. M.; Mcintire, L. V.; Mikos, A. G. *Adv. Drug Deliv. Rev.* **1998**, *33*, 111–139.
55. Mannon, R. B.; Coffman, T. M. *Kidney Int.* **1999**, *56*, 18–27.
56. Matsumura, H.; Tada, M.; Otsuji, T.; *et al. Nat. Methods* **2007**, *4*, 23–25.
57. Gibbons, C.; Sykes, M. *Immunol. Rev.* **2008**, *223*, 334–360.
58. Weiss, M. L.; Anderson, C.; Medicetty, S.; *et al. Stem Cells* **2008**, *26*, 2865–2874.
59. Djouad, F.; Charbonnier, L. M.; Bouffi, C.; *et al. Stem Cells* **2007**, *25*, 2025–2032.
60. Jiang, X. X.; Zhang, Y.; Liu, B.; *et al. Blood* **2005**, *105*, 4120–4126.
61. Nauta, A. J.; Kruisselbrink, A. B.; Lurvink, E.; Willemze, R.; Fibbe, W. E. *J. Immunol.* **2006**, *177*, 2080–2087.
62. Augello, A.; Tasso, R.; Negrini, S. M.; *et al. Eur. J. Immunol.* **2005**, *35*, 1482–1490.
63. Glennie, S.; Soeiro, I.; Dyson, P. J.; Lam, E. W.; Dazzi, F. *Blood* **2005**, *105*, 2821–2827.
64. Deng, W.; Han, Q.; Liao, L.; You, S.; Deng, H.; Zhao, R. C. *DNA Cell Biol.* **2005**, *24*, 458–463.
65. Corcione, A.; Benvenuto, F.; Ferretti, E.; *et al. Blood* **2006**, *107*, 367–372.
66. Le Blanc, K.; Frassoni, F.; Ball, L.; *et al. Lancet* **2008**, *371*, 1579–1586.
67. Yanez, R.; Lamana, M. L.; Garcia-Castro, J.; Colmenero, I.; Ramirez, M.; Bueren, J. A. *Stem Cells* **2006**, *24*, 2582–2591.
68. Nauta, A. J.; Westerhuis, G.; Kruisselbrink, A. B.; Lurvink, E. G.; Willemze, R.; Fibbe, W. E. *Blood* **2006**, *108*, 2114–2120.
69. Zappia, E.; Casazza, S.; Pedemonte, E.; *et al. Blood* **2005**, *106*, 1755–1761.
70. Bartholomew, A.; Sturgeon, C.; Siatskas, M.; *et al. Exp. Hematol.* **2002**, *30*, 42–48.
71. Togel, F.; Hu, Z.; Weiss, K.; Isaac, J.; Lange, C.; Westenfelder, C. *Am. J. Physiol. Renal Physiol.* **2005**, *289*, F31–F42.
72. Lee, S. T.; Jang, J. H.; Cheong, J. W.; *et al. Br. J. Haematol.* **2002**, *118*, 1128–1131.
73. Lazarus, H. M.; Koc, O. N.; Devine, S. M.; *et al. Biol. Blood Marrow Transplant.* **2005**, *11*, 389–398.
74. Zheng, Z. H.; Li, X. Y.; Ding, J.; Jia, J. F.; Zhu, P. *Rheumatology (Oxford)* **2008**, *47*, 22–30.
75. Djouad, F.; Plence, P.; Bony, C.; *et al. Blood* **2003**, *102*, 3837–3844.
76. Djouad, F.; Fritz, V.; Apparailly, F.; *et al. Arthritis Rheum.* **2005**, *52*, 1595–1603.
77. Sudres, M.; Norol, F.; Trenado, A.; *et al. J. Immunol.* **2006**, *176*, 7761–7767.
78. Prigozhina, T. B.; Khitrin, S.; Elkin, G.; Eizik, O.; Morecki, S.; Slavin, S. *Exp. Hematol.* **2008**, *36*, 1370–1376.
79. Moffat, K. L.; Sun, W. H.; Pena, P. E.; *et al. Proc. Natl. Acad. Sci. USA* **2008**, *105*, 7947–7952.
80. Oegema, T. R.; Thompson, R. C. In *Articular Cartilage and Osteoarthritis*; Kuettner, K. E., Peyron, J. G., Schleyer, R., Hascall, V. C., Eds.; Raven Press: New York, 1992.
81. Bullough, P. G.; Jagannath, A. *J. Bone Joint Surg. Br.* **1983**, *65*, 72–78.
82. Oegema, T. R.; Thompson, R. C. In *Cartilage Changes in Osteoarthritis*; Brandt, K., Ed.; Indiana School of Medicine: Orlando, 1990.
83. Harley, B. A.; Lynn, A. K.; Wissner-Gross, Z.; Bonfield, W.; Yannas, I. V.; Gibson, L. J. *J. Biomed. Mater. Res. A* **2010**, *92*, 1078–1093.
84. Gao, J.; Dennis, J. E.; Solchaga, L. A.; Awadallah, A. S.; Goldberg, V. M.; Caplan, A. I. *Tissue Eng.* **2001**, *7*, 363–371.
85. Alhadlaq, A.; Mao, J. J. *J. Bone Joint Surg. Am.* **2005**, *87*, 936–944.
86. Chen, G.; Sato, T.; Tanaka, J.; Tateishi, T. *Mater. Sci. Eng. C* **2006**, *26*, 118–123.
87. Chiang, H.; Kuo, T. F.; Tsai, C. C.; *et al. J. Orthop. Res.* **2005**, *23*, 584–593.
88. Shao, X.; Goh, J. C.; Hutmacher, D. W.; Lee, E. H.; Zigang, G. *Tissue Eng.* **2006**, *12*, 1539–1551.
89. Swieszkowski, W.; Tuan, B. H.; Kurzydlowski, K. J.; Hutmacher, D. W. *Biomol. Eng.* **2007**, *24*, 489–495.
90. Tuli, R.; Nandi, S.; Li, W. J.; *et al. Tissue Eng.* **2004**, *10*, 1169–1179.
91. Jiang, J.; Tang, A.; Ateshian, G. A.; Guo, X. E.; Hung, C. T.; Lu, H. H. *Ann. Biomed. Eng.* **2010**, *38*, 2183–2196.
92. Lu, H. H.; Jiang, J. *Adv. Biochem. Eng. Biotechnol.* **2006**, *102*, 91–111.
93. Fink, D. W., Jr. *Science* **2009**, *324*, 1662–1663.
94. Hovatta, O.; Mikkola, M.; Gertow, K.; *et al. Hum. Reprod.* **2003**, *18*, 1404–1409.
95. Rodriguez-Piza, I.; Richaud-Patin, Y.; Vassena, R.; *et al. Stem Cells* **2010**, *28*, 36–44.
96. Xu, C.; Inokuma, M. S.; Denham, J.; *et al. Nat. Biotechnol.* **2001**, *19*, 971–974.

Relevant Websites

http://stemcells.nih.gov – Stem Cell Information, The National Institutes of Health resource for stem cell research.
http://optn.transplant.hrsa.gov – Organ Procurement and Transplantation Network, from the Health Resources and Services Administration.

5.508. Scaffold Materials for hES Cell Culture and Differentiation

S Willerth and D Schaffer, University of California, Berkeley, CA, USA

© 2011 Elsevier Ltd. All rights reserved.

5.508.1.	**Introduction**	96
5.508.1.1.	Defining Stem Cells and Potency	96
5.508.1.2.	Derivation of hESCs	96
5.508.1.3.	Standard Culture Methods for hESCs	97
5.508.1.4.	Techniques for Evaluating the Differentiation State of hESCs	98
5.508.1.4.1.	Markers for observing the differentiation state of hESCs	98
5.508.1.4.2.	Experimental techniques for observing the differentiation state of hESCs	98
5.508.1.5.	Using Biomaterials for the Culture and Differentiation of hESCs	99
5.508.1.6.	Comparison of Natural Versus Synthetic Biomaterials	100
5.508.2.	**Biomaterials for Undifferentiated hESC Culture**	100
5.508.2.1.	Natural Biomaterials for Undifferentiated hESC Culture	100
5.508.2.1.1.	Heterogeneous biomaterial scaffolds	100
5.508.2.1.2.	Homogeneous biomaterial scaffolds	102
5.508.2.2.	Synthetic Biomaterials for Undifferentiated hESC Culture	103
5.508.3.	**Biomaterials for hESC Differentiation**	104
5.508.3.1.	Natural Biomaterials for hESC Differentiation	104
5.508.3.1.1.	Alginate	104
5.508.3.1.2.	Dextran	105
5.508.3.1.3.	Collagen/laminin/matrigel	105
5.508.3.1.4.	Fibronectin	106
5.508.3.1.5.	Other naturally derived materials	106
5.508.3.2.	Synthetic Biomaterials for hESC Differentiation	107
5.508.3.2.1.	Poly(lactic-*co*-glycolic acid)	107
5.508.3.2.2.	Poly(ethylene glycol)	109
5.508.3.2.3.	Other synthetic materials	110
5.508.4.	**Conclusions and Future Work**	111
5.508.4.1.	Reflections on the Current State of Biomaterial Scaffolds for hESC Culture and Differentiation	111
5.508.4.2.	Future Directions	111
5.508.4.2.1.	Issues with hESC culture to be addressed	111
5.508.4.2.2.	Potential new materials for use in combination with hESCs	111
5.508.5.	**Summary**	112
References		112

Glossary

Biomaterial A material that can be either natural or synthetic and that comprises either the whole or a part of a living structure or biomedical device that performs, supplements, or replaces a natural function.

Conditioned media Media taken from cell culture that contains growth factors and other molecules that have been secreted by the cells.

Ectoderm One of the three germ layers formed during embryogenesis that gives rise to the nervous system and the epidermis.

Embryoid body Aggregates of embryonic stem cells usually grown in suspension culture.

Embryonic stem cell Pluripotent cells derived from embryos or fetal tissue with the capacity for self-renewal.

Endoderm One of the three germ layers formed during embryogenesis that gives rise to the gastrointestinal and respiratory tracts along with the organs of the endocrine system.

Extracellular matrix The matrix that surrounds cells and consists of a complex mixture of proteins, proteoglycans, and other molecules.

Feeder layer A layer of cells that secrete specific factors into the media to allow for the culture of the desired cell line in coculture.

Hydrogel A network of polymer chains that are water insoluble but possess a high water content.

Karotype Characterization of the chromosomal content of a eukaryotic cell that can be used to evaluate if a gross genomic aberrations or abnormalities are present in a cell line.

Matrigel A commercially available mixture of basement membrane proteins, including laminin and collagen, and proteoglycans that are secreted by Engelbreth–Holm–Swarm (EHS) mouse sarcoma cells as their extracellular matrix.
Mesoderm One of the three germ layers formed during embryogenesis that gives rise to muscle, bone, connective tissues, and the dermis layer of skin.
Niche Term used to describe the microenvironment that encompasses stem cells, composed of matrix, growth factors, small molecules, and adjacent cells.
Passage The process of maintaining a cell culture that has neared or reached confluence by diluting the number of cells present and replating to allow for continuous culture.
Self-assembled monolayer A monolayer that is formed by self-organizing amphipilic molecules that possess a polar head group and nonpolar tail where the polar head group shows a specific affinity for the substrate for monolayer formation.
Vasculature The network of blood vessels found in tissues.

Abbreviations

AT	Alkanethiols
bFGF	Basic fibroblast growth factor
Cbfa1	Core binding factor alpha1
EBs	Embryoid bodies
ECM	Extracellular matrix
EHS	Engelbreth-Holm-Swarm
ELISAs	Enzyme linked immunosorption assays
GABA	γ-aminobutyric acid
HA	Hyaluronic acid
hESC	Human embryonic stem cell
HGF	Hepatocyte growth factor
IKVAV	Isoleucine–lysine–valine–alanine–valine
IPSCs	Induced pluripotent stem cells
LIF	Leukemia inhibitory factor
MEF	Mouse embryonic fibroblast
NGF	Nerve growth factor
PCR	Polymerase chain reaction
PDL	Poly-(D-lysine)
PDMS	Polydimethylsiloxane
PEG	Poly-(ethylene glycol)
pHEMA	Poly-(hydroxyethyl methacrylate)
PLGA	Poly-(lactic-*co*-glycolic acid)
PLLA	Poly-(L-lactic acid)
PTFE	Poly-tetrafluroethylene
qPCR	Quantitative polymerase chain reaction
RGD	Arginine–glycine–aspartic acid
SAMs	Self-assembled monolayers
SCID	Severe combined immune deficiency
sIPNs	Semi-interpenetrating polymer networks
SSEA-3	Stage-specific antigen 3
SSEA-4	Stage-specific antigen 4
TGF-β	Transforming growth factor β
TRA-1-60	Tumor recognition antigen 1-60
TRA-1-81	Tumor recognition antigen 1-81
VEGF	Vascular endothelial growth factor
2D	Two dimensional
3D	Three dimensional

5.508.1. Introduction

This chapter will discuss the use of biomaterial scaffolds for the culture and differentiation of human embryonic stem cells (hESCs). The first section will provide definitions of stem cells and biomaterials and associated terminology, as well as describe the experimental techniques needed to study these cells. Section 5.508.2 will describe the research that has been conducted using biomaterials for culturing undifferentiated hESCs, while Section 5.508.3 will discuss the use of such materials for promoting hESC differentiation into specific phenotypes. Finally, Section 5.508.4 summarizes this field along with a discussion of future trends and directions.

5.508.1.1. Defining Stem Cells and Potency

Stem cells possess two defining characteristics: (1) the ability to self-renew, or proliferate and maintain themselves in an undifferentiated state, and (2) the ability to differentiate into one or more cell phenotypes. A variety of different stem cell types exist – including embryonic, fetal, and adult – and each has different properties such as varying degrees of potency, that is, the ability to differentiate into multiple cell types. Cells with the ability to differentiate into all of the cell types found in an organism along with the associated extraembryonic structures, such as the placenta, are referred to as totipotent. Pluripotent cells can differentiate into any cells in the different germ layers of an organism, and thereby give rise to all cell types in an adult organism, but lack the initial ability to generate the extraembryonic structures. Other classes of stem cells include unipotent (possessing the abilities to self-renew, but only to differentiate into one cell type) and multipotent (the ability to give rise to a subset of cell types). These final two typically include tissue-specific stem cells, such as muscle stem cells and neural stem cells, that typically differentiate into cells associated with that tissue.

5.508.1.2. Derivation of hESCs

hESCs are pluripotent cells derived from human embryos. The first hESC lines were generated in 1998 from the inner cell mass of human blastocysts (Figure 1),[1] which were obtained by culturing cleavage stage human embryos generated via *in vitro* fertilization. To confirm that viable and stable hESC lines are produced, the cells were continuously cultured for 4–5 months to demonstrate their ability to continuously proliferate,

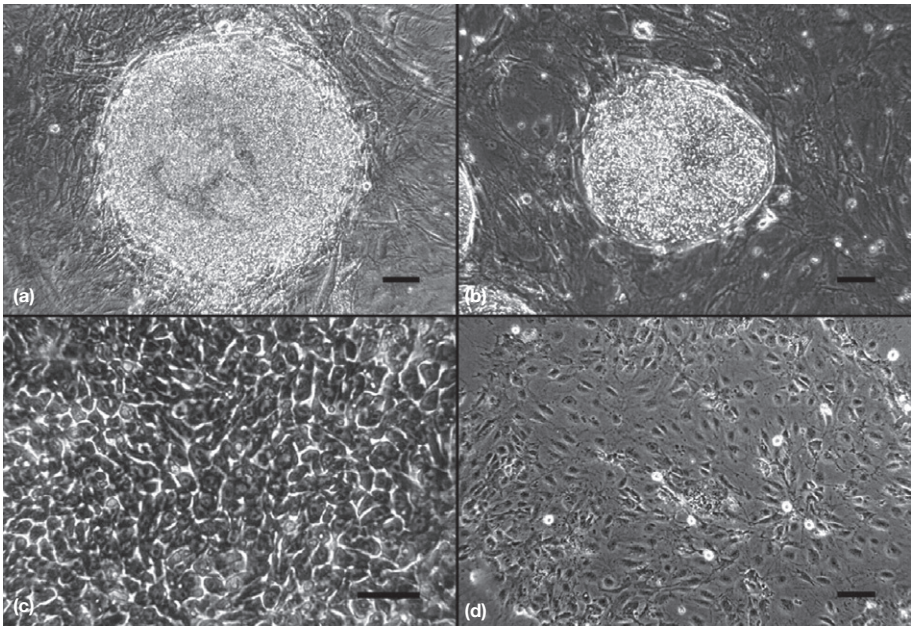

Figure 1 Derivation of the H9 cell line. (a) Inner cell mass-derived cells attached to a mouse embryonic fibroblast feeder layer after 8 days of culture, 24 h before their first dissociation. Scale bar, 100 μm. (b) H9 colony. Scale bar, 100 μm. (c) H9 cells at higher magnification. Scale bar, 50 μm. (d) Differentiated H9 cells, cultured for 5 days in the absence of mouse embryonic fibroblasts, but in the presence of human leukemia inhibitory factor (LIF) (20 ng ml^{-1}; Sigma). Scale bar, 100 μm. Reprinted from Thomson, J. A.; Itskovitz-Eldor, J.; Shapiro, S. S.; *et al*. *Science* **1998**, *282*, 1145–1147, with permission from The American Association for the Advancement of Science.

differentiate into cells from all three germ layers (endoderm, ectoderm, and mesoderm), and maintain a stable karyotype. Additionally, undifferentiated hESCs express a number of markers – including stage-specific antigens 3 and 4 (SSEA-3 and SSEA-4) and the transcription factors Oct4, Sox2, and Nanog – that can be used to confirm the successful generation of a new hESC line and confirm the maintenance of a hESC state for existing lines. Further studies have confirmed the ability of hESCs to differentiate into numerous cell types from various tissues, including neuronal, glial, endothelial, cardiomyocytes, beta cells, muscle cells, and osteogenic lineages.[2–5] Their pluripotency makes hESCs highly desirable for tissue engineering applications, as this single cell type provides the means to produce any cell present in the adult body, and their ability to self-renew yields a way to continually generate cells for these therapeutic purposes.

5.508.1.3. Standard Culture Methods for hESCs

The first hESC lines were isolated and cultured on feeder layers of irradiated mouse embryonic fibroblasts.[1,6] In general, feeder layers are a cellular monolayer that is cocultured with the desired cell type (in this case hESCs) and provides nutrients and growth factors necessary for the latter's survival and proliferation. A variety of cell types have since been used as feeder layers to support hESC culture, including human fetal, foreskin, and adult fibroblasts as well as adult human marrow cells.[7–9] In the interest of avoiding the use of feeder layers and thereby moving toward more defined and reproducible culture systems, hESC were then propagated on the substrate Matrigel in the presence of conditioned media derived from mouse embryonic fibroblast cultures.[10] Matrigel consists primarily of a mixture of basement membrane proteins, including laminin and collagen as well as proteoglycans that are secreted by the Engelbreth–Holm–Swarm (EHS) mouse sarcoma cell line as their extracellular matrix.[11] The highly complex and heterogeneous nature of Matrigel[12] means that its exact composition varies from batch to batch, making it less than ideal for hESC culture. Furthermore, the animal proteins present in Matrigel as well as from feeder layers could potentially transfer immunogens to hESCs, which could elicit a downstream immune response against transplanted stem cells.[13]

To generate hESC lines for clinical applications, the cells should ideally be cultured in fully defined conditions. To this end, many groups have worked toward developing defined hESC culture conditions, a challenging problem since the factors known to support mouse ESC culture did not directly translate to hESC culture. In 2006, Ludwig *et al*.[14] described the derivation of new hESC lines in defined media that did not require the use of a feeder layer. Their methodology involved using chemically defined media referred to as TeSR1 that contained basic fibroblast growth factor (bFGF), lithium chloride, γ-aminobutyric acid (GABA), pipecolic acid, and transforming growth factor-β (TGF-β), though the system still utilized Matrigel as a substrate for hESC adhesion. The Geron Corporation, a leading company advancing human stem cell therapies, has developed an alternative system composed of X-VIVO 10 medium (Cambrex Corporation) supplemented with bFGF and TGF-β1 for culturing their hESC lines on Matrigel.[15] More recent work has suggested that the use of Noggin in combination with the Matrigel culture system can help hESCs remain undifferentiated.[16] However, each of these

systems utilized Matrigel as a substrate, and there are considerable efforts underway to replace Matrigel with a defined substrate.

5.508.1.4. Techniques for Evaluating the Differentiation State of hESCs

Some of the most important considerations when working with hESCs are how to evaluate and characterize their differentiation potential and state. This section will discuss the different experimental techniques that are used for such purposes, including both analysis of marker expression and functional validation of pluripotency. It is important to have markers that can be used to identify hESCs to validate that such a line has been produced and confirm that the cells have remained undifferentiated after extended periods of culture. Similarly, it is necessary to identify specific markers of differentiation states when trying to generate specific cellular phenotypes from hESCs or confirm the pluripotency of a hESC line. Finally, these marker expression analyses should be combined with functional assays to confirm cell potency. See **Chapter 3.314, Materials to Control and Measure Cell Function** for further reading on analyzing cell behavior.

5.508.1.4.1. Markers for observing the differentiation state of hESCs

To take advantage of the potential of hESCs for therapeutic applications, it is important to analyze biological markers that can be used to assess their differentiation state. Previously identified markers that could be used for studying mouse ESCs do not always directly translate to hESCs, and this section will discuss the specific markers that can be used to study hESCs (summarized in **Table 1**).

Numerous markers are specifically or selectively expressed by undifferentiated hESCs,[25] including the glycolipids SSEA-3 and SSEA-4[17,26] that can be detected with antigen-specific antibodies. Another set of hESC markers includes the tumor rejection or tumor recognition antigens, TRA-1-60 and TRA-1-81, which are keratan sulfate derivatives.[1] Other very commonly used ones are transcription factors that are critical in maintaining hESCs pluripotency: Oct4, Sox2, and Nanog.[18–20]

In addition to analyzing self-renewal markers, the capacity for pluripotent differentiation, which can be characterized by the ability to differentiate into cells of the three germ layers found during human embryogenesis, must often be assessed. Markers used to identify the ectoderm lineage include nestin and β_{III}-tubulin.[21,22] Smooth muscle actin is often employed to detect cells from the mesoderm,[24] and α-fetoprotein is frequently utilized to identify the endodermal germ layer cells.[23] In addition to these commonly used markers, there are many alternatives used to detect cells from these germ layers. Finally, numerous downstream lineage- and cell-specific markers are utilized to monitor the process of hESC differentiation into a final desired differentiated phenotype.

Table 1 List of biological markers indicating differentiation state

Differentiation state	*Marker*	*References*
Undifferentiated hESCs	SSEA-3	[1]
	SSEA-4	[17]
	TRA-1-60	[1]
	TRA-1-81	[1]
	Nanog	[18]
	Oct4	[19]
	Sox2	[20]
Differentiated hESCs		
Ectoderm	Nestin	[21]
	β-tubulin	[22]
Endoderm	α-fetoprotein	[23]
Mesoderm	Smooth muscle actin	[24]

5.508.1.4.2. Experimental techniques for observing the differentiation state of hESCs

Numerous experimental methods exist to confirm the expression of the aforementioned markers, and this section will discuss the most frequently used techniques along with their relative advantages and disadvantages. Furthermore, in addition to marker expression, it is always important and often critical to utilize functional assays to confirm differentiation into specific cell phenotypes. While a variety of methods are employed to validate specific cellular phenotypes (such as electrophysiology for neuronal or cardiac differentiation, or enzyme and albumin synthesis for hepatocytes),[27,28] the commonly used functional assays for confirming hESC identity will be discussed in **Section 5.508.1.4.2.3**.

5.508.1.4.2.1. Immunostaining

Immunostaining is a standard technique that employs antibodies to detect and quantify antigen levels. This process involves using an antibody targeted against a specific molecule, referred to as the primary antibody, to detect its presence. A secondary antibody conjugated with either a fluorescent or enzymatic tag is used to bind to the primary antibody, and the presence of the marker can thereby be visualized and/or quantified through the use of a fluorescence microscope or by the addition of a colored substrate. While this process is extremely useful in allowing observation of proteins, it is important to perform proper controls to ensure that the desired antigen as opposed to background staining is being observed. Additionally, the quality of the staining is dependent on the specificity and quality of the primary antibody, and thus, different primary antibodies directed against the same target may yield different staining results. Nonspecific binding can often be reduced through enhancing blocking steps, often requiring the use of serum or other proteins, and through the use of wash steps that remove nonspecifically bound antibody.

Immunohistochemistry is a variant of immunostaining where the cells or tissue to be stained is preserved through fixation prior to the staining process. This method has the advantage of showing the various structures formed by cells in culture and in tissue. Other ways of performing immunostaining include the use of flow cytometry where the resulting mixture from the cells stained in solution is analyzed quantitatively using a flow cytometer instrument, allowing for the determination of the fraction of cells expressing a specific marker and at what levels. In addition to measuring fluorescence, the flow cytometer characterizes cells based on their size and granularity, which allows for the exclusion of dead cellular

matter as well as for the analysis of the composition of a specific cellular population based on size. Another commonly used immunostaining method is Western blotting. In this process, the cells to be analyzed are lysed, and the resulting protein mixture is electrophoresed on a gel to separate the proteins by size. The separated proteins are then transferred to a membrane that can be immunostained. The separation of proteins by size allows for a second confirmation of the antibody specificity by confirming that the protein being identified is the correct weight. Western blotting can also be used to compare the expression levels of target proteins in a semiquantitative manner. A more effective method for quantitatively comparing protein expression levels using immunostaining is enzyme-linked immunosorption assays (ELISAs). In this assay, the protein mixture to be analyzed is adsorped to a plate either through nonspecific binding or through the use of a capture antibody. A detection antibody conjugated with an enzyme is then used to detect the presence of the protein and the levels of protein are detected based on the enzymatic activity using either a colorimetric or chemiluminescence based substrate. One issue is the presence of background activity, which can be reduced through the use of blocking steps and washing. Overall, a variety of immunostaining techniques exist, and specific techniques should be chosen based on the desired information, such as protein location versus protein expression levels.

5.508.1.4.2.2. Polymerase chain reaction

Another means to assess the expression of the various differentiation markers is polymerase chain reaction (PCR). The process of PCR involves amplifying small quantities of DNA to generate detectable levels of DNA using a preset number of cycles that heat and cool the reaction containing the target DNA, gene-specific primers (short specific DNA sequences that bind to the target gene) and a thermostable polymerase, the enzyme that synthesizes new copies of the target gene. Thus, this method can be used to study the mRNA expression levels of target genes by first performing a reverse transcription reaction that converts mRNA isolated from hESCs into DNA. The PCR reaction can then be performed and the resulting products electrophoresed on an agarose gel to confirm that the target genes were expressed. While examining these products on a gel will allow for semiquantitative comparison of gene expression, numerous methods for quantifying DNA amplified in a PCR reaction, that is, quantitative PCR (qPCR), have been developed. One uses a fluorescently labeled dye that binds to double-stranded DNA, such that the amount of PCR product at each cycle can be quantified in real time using a qPCR cycler. Other methods involve the use of gene-specific DNA probes that fluoresce when they bind to a complimentary piece of DNA, or upon degradation of the probe by the polymerase during the amplification. These fluorescence-based detection methods require the use of a thermocycler (the instrument that cycles the temperatures during the PCR reactions) that is specially equipped to detect fluorescence. The additional use of a standard curve of known concentrations of the target gene can be used to calculate the number of copies of mRNA present in a sample. It is also possible to examine relative gene expression between two samples by normalizing the data for the samples obtained from a housekeeping gene such as β-actin that is constitutively expressed by the cells, though caution should be applied since the expression of housekeeping genes can sometimes vary with cell state. Additional caveats with using qPCR to analyze differentiation are that mRNA levels do not necessarily translate directly to protein expression, and that glycoproteins and polysaccharides cannot be detected by this method.

5.508.1.4.2.3. Functional assays for confirming hESC identity

In addition to these methods for analyzing the expression of characteristic markers by hESCs and their differentiated progeny, there are several standard assays conducted to confirm the integrity and functionality of hESC cells. These assays should also be performed periodically to confirm that an established hESC line is maintaining its properties. One of these methods is karotyping, a method used for characterizing the chromosomal content of a eukaryotic cell and evaluating whether aberrations or abnormalities such as chromosomal duplications or translocations are present in a cell line.[29] This process is important to ensure that cells with no gross genomic abnormalities are used for basic biological studies or downstream translational efforts, though modern methods such as next generation sequencing may aid in higher resolution analysis of genomic integrity. Another important assay for confirming hESC identity is to validate that the cells can undergo self-renewal – or be continuously cultured while maintaining pluripotency marker expression and normal karyotype – for an extended period of time, such as between 4 and 6 months. Another key assay is teratoma analysis, the injection of hESCs into immunodeficient mice to determine if they have the capacity to form teratomas, benign tumors that express tissues similar to those found in the three embryonic germ layers.[30] To confirm the presence of all three layers (ectoderm, endoderm, and mesoderm), histology followed by immunostaining for the aforementioned germ layer markers is performed.

5.508.1.5. Using Biomaterials for the Culture and Differentiation of hESCs

As described in Section 5.508.1.3, the use of chemically defined media in combination with Matrigel has been shown to support undifferentiated hESC culture. Matrigel is considered a biomaterial, and its success as a substrate for hESC culture suggests that other, more defined and controlled biomaterial surfaces could be used for this application. In general, a biomaterial can be defined as a material, either natural or synthetic, that comprises either the whole or a part of a living structure or biomedical device that performs, supplements, or replaces a natural function. In addition to coating two-dimensional (2D) surfaces for the culture and differentiation of hESCs, biomaterials can also be used as 3D scaffolds for these applications. This chapter will detail the various studies that have used biomaterials in combination with hESCs in both 2D and 3D culture, along with the relative advantages and disadvantages of such scaffolds. The first part of this chapter focuses on biomaterials used to culture and expand undifferentiated hESCs, and the latter discusses the use of scaffolds to direct hESC differentiation into specific phenotypes. These parts are further subdivided into natural materials, obtained from animals or plants, and synthetic biomaterials, of artificial origins.

5.508.1.6. Comparison of Natural Versus Synthetic Biomaterials

It is important to first consider the advantages and disadvantages of both natural and synthetic biomaterials. Natural materials have been developed from the different components that make up the extracellular matrix, such as proteins and polysaccharides, including, for example, Matrigel.[31] These components perform many roles *in vivo*, making the resulting materials attractive for tissue engineering applications since they typically contain sites for cellular adhesion and are biocompatible, meaning that the material does not typically induce an immune response upon implantation. However, some disadvantages include potentially large variability of the material depending on the source and the method of isolation, the need for robust purification of the protein or polysaccharide to both reduce variability and avoid triggering an immune response *in vivo*, potential challenges with supply in the case of human materials, and concerns with the transfer of pathogens from the animal or human materials into stem cells. Furthermore, as discussed below, scaffolds made from natural biomaterials tend to possess a limited range of mechanical properties compared to synthetic biomaterials, and it is very difficult to independently tune mechanics and the presentation of biochemical signals.

Synthetic biomaterials offer a number of advantages compared to natural biomaterials, including reproducibility due to their defined chemical composition and the ability to control the mechanical properties, degradation rate, and shape independently.[31] The mechanical properties of a scaffold have been shown to play an important role in influencing stem cell differentiation.[32,33] Synthetic scaffolds can also be shaped, allowing for production of scaffolds that conform to specifications of an injury site. Engineering synthetic scaffolds with specific degradation rates can regulate the lifespan of the scaffolds in an *in vivo* setting as well as offer the capacity for controlled release of drugs incorporated into such scaffolds. However, a disadvantage for synthetic biomaterials is their inherent lack of bioactivity, such as sites for cell adhesion. These scaffolds are thus often biofunctionalized to introduce adhesion ligands, growth factors, and other activities. Other challenges include the need to carefully tune the biocompatibility of the material and its potential for inducing an immune response. See **Chapter 4.410, Sterilization of Biomaterials of Synthetic and Biological Origin** for further reading on preparation of scaffolds for implantation.

5.508.2. Biomaterials for Undifferentiated hESC Culture

As mentioned in **Section 5.508.1.3**, the current methods for culturing and expanding undifferentiated hESCs suffer from numerous limitations. The current methods for passaging hESCs are laborious and time consuming. Additionally, the highly complex and undefined nature of Matrigel may result in considerable batch to batch variability in its constituent proteins and polysaccharides.[12] This variability could, for example, introduce challenges in consistently maintaining pluripotency over time. Thus, an increasing focus has been placed on identifying the specific cues necessary to culture undifferentiated hESCs and designing biomaterial surfaces with defined chemical compositions to eliminate the variability encountered when using Matrigel.[34,35] A summary of the studies discussed in this Section is given in **Table 2**.

Table 2 List of biomaterials used for hESC culture

Type of material	*Material*	*References*
Natural	Alginate	[36,37]
	Hyaluronic acid	[38]
	Matrigel	[10,16,39–41]
	Serum	[41,42]
Synthetic	Acrylates	[43]
	Self-assembling monolayers	[44]
	Semi-interpenetrating polymers	[34]

5.508.2.1. Natural Biomaterials for Undifferentiated hESC Culture

This Section will detail the use of natural biomaterials for hESC culture and expansion. Natural biomaterials have been developed from the various proteins and polysaccharides that compose the extracellular matrix. These materials can be classified as heterogeneous biomaterials scaffolds, such as Matrigel and adsorbed human serum, and homogenous scaffolds, which have undergone more rigorous purification processes. See **Chapter 2.207, Extracellular Matrix: Inspired Biomaterials**; **Chapter 2.220, Extracellular Matrix as Biomimetic Biomaterial: Biological Matrices for Tissue Regeneration**; and **Chapter 2.221, Decellularized Scaffolds** for further reading on this subject.

5.508.2.1.1. Heterogeneous biomaterial scaffolds

Despite the limitations discussed in **Section 5.508.1.3**, the combination of defined media and Matrigel coated onto a 2D surface remains the current standard for culturing hESCs.[14,15,45] However, even when hESCs are cultured under these specific conditions, some random differentiation occurs due to local variations in the microenvironment. Patterning of Matrigel onto surfaces has been used as a method to help dissect such microenvironmental factors and properties that regulate self-renewal and differentiation. As a key example, Zandstra and colleagues used Matrigel micropatterning on 2D substrates to show that hESC colony size and composition regulated hESC differentiation by controlling local cell–cell signaling.[46] As mentioned in **Section 5.508.1.3**, the signaling activity of TGF-β helps hESCs remain undifferentiated by inhibiting the activity of Smad1. The effect of colony size on both Oct4 (expressed by undifferentiated hESCs) and Smad1 activity (as indicated by phosphoSmad activity) are shown in **Figure 2**. As colony size increases, a corresponding increase in Oct4 staining and decrease in pSmad staining are observed. Additionally they used small interfering RNA to knock down Smad1, which prevented differentiation. This study suggests that a critical hESC colony size is needed to antagonize the effects of Smad1 and thereby prevent hESCs from differentiating when seeded on Matrigel, thereby illustrating the principle that controlling cell–cell interactions may be necessary for maintaining hESC self-renewal.

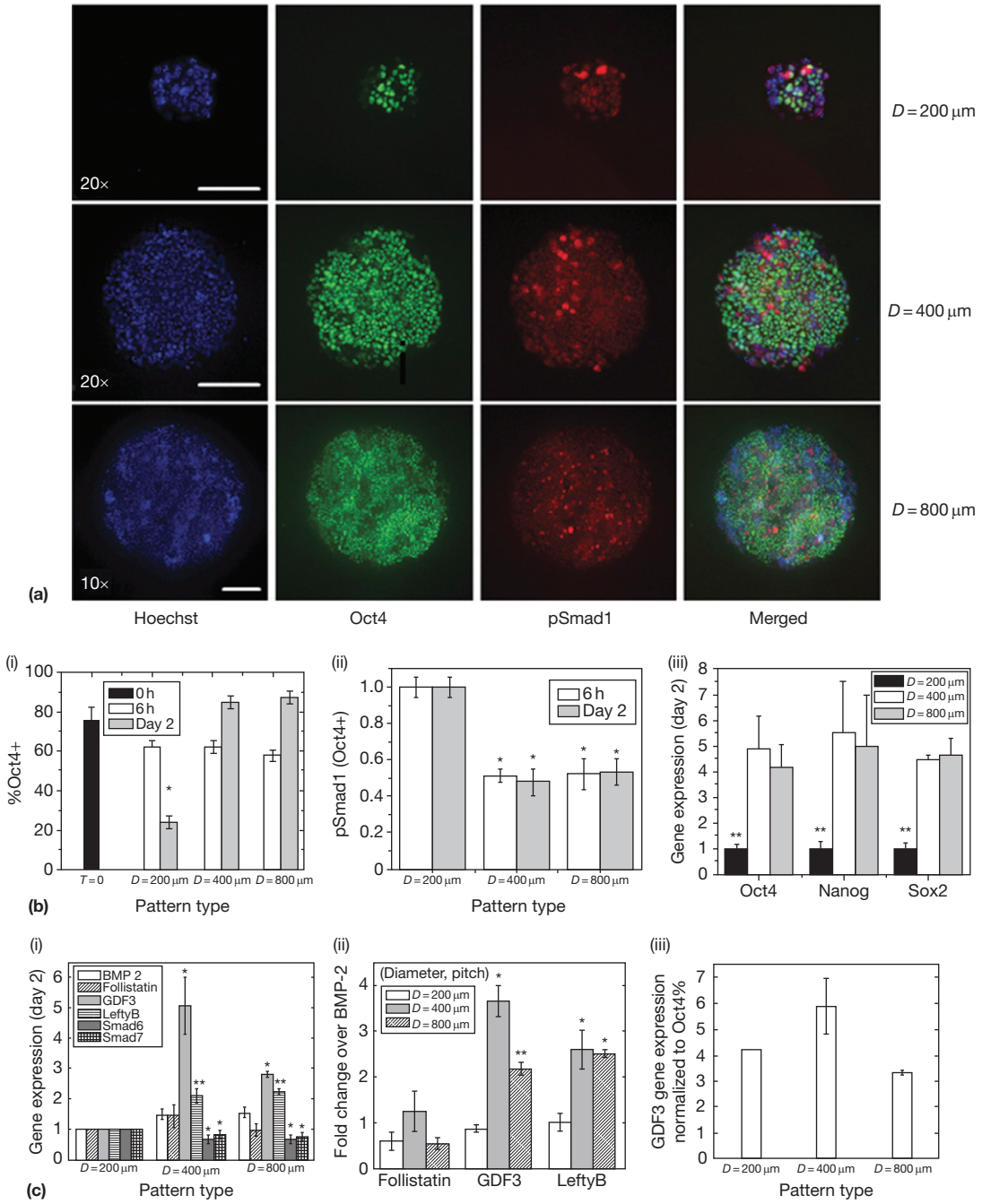

Figure 2 Micropatterning can be used to manipulate the human embryonic stem cell (hESC) microenvironment and control hESC fate. To demonstrate that the hESC microenvironment, and in particular local cell–cell interaction, directly controls hESC fate, H9 hESCs were plated on patterned tissue–culture substrates with Matrigel using microcontact printing. Colony diameters (*D*) ranged from 200 to 800 μm and distance between colonies, pitch (*P*), was fixed at 500 or 1000 μm. (a) Quantitative fluorescent microscopy of patterned H9 cultures in XV media after withdrawal of all growth factors for 48 h and stained for Hoechst, Oct4, and pSmad1. Scale bar is 200 μm. (b) Analysis of micropatterned colonies after 48 h. The percentage of Oct4 cells as a function of colony size (b-i). pSmad1 in the Oct4+ population as a function of colony size (b-ii). Gene expression for Oct4, Sox2, Nanog normalized to β-actin as a function of colony size (b-iii). (c) To elucidate the molecular mechanism for the changes in pSmad1 levels, gene expression was quantified as a function of colony size for Smad1 agonist, BMP2, and antagonists, Follistatin, GDF3 and LeftyB and I-Smads, Smad6, and Smad7. Gene expression after normalization to β-actin and relative to the 200 μm data set (c-i). Ratios of the transcripts of Smad1 antagonists, Follistatin, GDF3 and LeftyB, to the transcripts of Smad1 agonist, BMP2, as a function of colony size (c-ii). GDF3 gene expression as a function of colony size normalized to the percentage of Oct4+ cells present (c-iii). For (c-i), statistical comparisons were made between gene expression for each cytokine in 400 and 800 μm colonies against the expression at 200 μm colonies. For (c-ii), statistical comparisons were made between the ratio of the levels of transcripts of the antagonist to BMP2 between the 400 and 800 μm colonies against the ratio present in the 200 μm. Reprinted from Peerani, R.; Rao, B. M.; Bauwens, C.; *et al*. *Embo J*. **2007**, *26*, 4744–4755, with permission from the Nature Publishing Group.

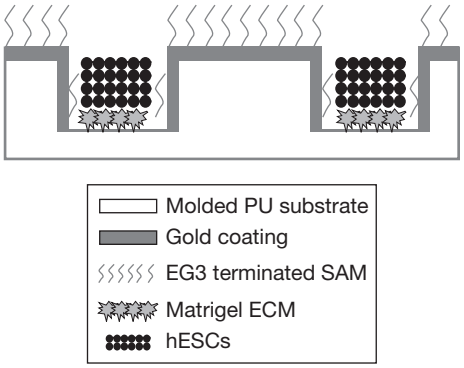

Figure 3 Schematic of microwell fabrication depicting spatial localization of physical and chemical constraints to human embryonic stem cell (hESC) attachment and propagation. Microwells are formed by cross-linking polyurethane (PU) prepolymer. Gold is evaporated on the surfaces surrounding the wells and the sides of the wells at an oblique angle, but the bottoms of the wells are shielded from gold. A triethylene glycol-terminated alkanethiol self-assembled monolayer (EG terminated SAM) is then assembled on the gold surface to repel extracellular matrix (ECM) proteins and cells. The wells are then treated with Matrigel, which adsorbs to the bare PU at the bottoms of the wells. Cells are then cultured in the Matrigel-coated wells. Structures are not to scale. Reprinted from Mohr, J. C.; De Pablo, J. J.; Palecek, S. P. *Biomaterials* **2006**, *27*, 6032–6042, with permission from Elsevier.

hESCs tend to aggregate, thereby forming 3D structures in 2D culture, and another group developed a 3D hESC culture that also involved Matrigel patterning (**Figure 3**).[39] To first generate the microwell structure, photolithography was used to pattern polydimethylsiloxane (PDMS) masters, which were used to mold polyurethane into the desired structures. The resulting microwells were stabilized by UV-induced cross-linking. The resulting microwells were then functionalized with self-assembled monolayers (SAMs) – a monolayer that is formed by self-organizing amphiphilic molecules that possess a polar head group and nonpolar tail, where the polar head group has a specific affinity for the substrate to yield monolayer coverage – which were then coated with Matrigel. The study showed that hESCs could be cultured as colonies inside of these 3D Matrigel-coated scaffolds while maintaining their expression of Oct4. The resulting hESCs maintained their ability to proliferate even when transferred back to traditional 2D Matrigel culture. This system demonstrated that there are beneficial effects to using 3D culture for maintaining the undifferentiated state of hESCs without passaging the cells, and as an additional benefit, it allows for generation of uniform hESC embryoid bodies.

Another group investigated human serum-coated substrates as a 2D biomaterial matrix for the culture of undifferentiated hESCs, as a potential alternative to Matrigel.[42] The use of human serum would avoid the xenogenic pathogens associated with the use of Matrigel, which is derived from a mouse tumor. Tissue culture plates were coated with human serum, and hESCs were then cultured on this biomaterial surface in the presence of conditioned media obtained from human fibroblast-like cells derived from hESCs. This combination of medium and surface maintained the undifferentiated, pluripotent state of the hESCs as well as a normal karotype after 21 passages, suggesting human serum could potentially be used as a Matrigel replacement. That said, although the use of human serum does avoid xenogenic components, it is even more heterogeneous and undefined than Matrigel. A subsequent study directly compared a variety of biomaterials and their suitability for culturing five different hESC lines.[41] Of the materials analyzed, interestingly only surfaces coated with human serum, fetal bovine serum, and Matrigel supported undifferentiated hESC culture for multiple passages. Of these options, Matrigel was the only surface that supported long term (>30 passages) culture of hESCs. On the whole, the materials that could support multiple passages all consisted of heterogeneous, undefined mixtures of extracellular matrix or serum, whereas a fully chemically defined biomaterial surface and medium that can support undifferentiated hESC culture would be ideal.

5.508.2.1.2. Homogeneous biomaterial scaffolds

This section will focus on scaffolds comprising a single natural biomaterial in contrast to the heterogeneous scaffold materials discussed previously in **Section 5.508.2.1.1**. One of the first studies to use a single 3D biomaterial scaffold for hESC culture involved using alginate scaffolds to promote the formation of embryoid bodies.[36] Alginate is a linear polysaccharide derived from algae that can be cross-linked with divalent cations such as calcium to form 3D scaffolds.[47] The alginate scaffolds were produced by cross-linking an alginate solution with calcium, followed by freezing the scaffold and a lyophilization process. The resulting porous scaffold was seeded with hESCs at a low or high density (**Figure 4(b)**). The microenvironments offered by these scaffolds promoted formation of round embryoid bodies and supported hESC proliferation, suggesting a potential method for hESC culture. Such scaffolds were later examined as a method of promoting the differentiation of hESCs after embryoid body formation. Another study also showed the use of alginate hydrogels for extended culture of undifferentiated hESCs.[37] Hydrogels consist of a network of polymer chains that are water insoluble but possess high water content.[48] Siti-Ismail *et al.* used alginate hydrogels to encapsulate the hESCs, which could then be cultured for up to 260 days in chemically defined media while maintaining their undifferentiated state provided the media was changed every 3–4 days. Although the number of hESCs produced was limited by the size of the alginate capsules, this process avoided the use of both animal products and a process of embryoid formation, suggesting the strong potential of hydrogels for hESC culture.

Another study investigated the use of hyaluronic acid (HA) hydrogels for the culture of hESCs.[38] HA is a linear glycosaminoglycan expressed in the extracellular matrix of hESCs as well as in the brain. In this work, the HA was chemically cross-linked to form stable hydrogels for hESC culture. When encapsulated inside of 3D HA scaffolds in the presence of conditioned media obtained from mouse embryonic fibroblasts, hESCs maintained their pluripotent state, whereas hESCs cultured on 2D HA surfaces did not. All of these studies indicate the potential for homogenous natural biomaterial scaffolds to be developed for maintenance of hESC culture. However, more work and rigorous testing will have to be performed before these systems can be coupled with chemically defined media and replace Matrigel as the standard for hESC culture.

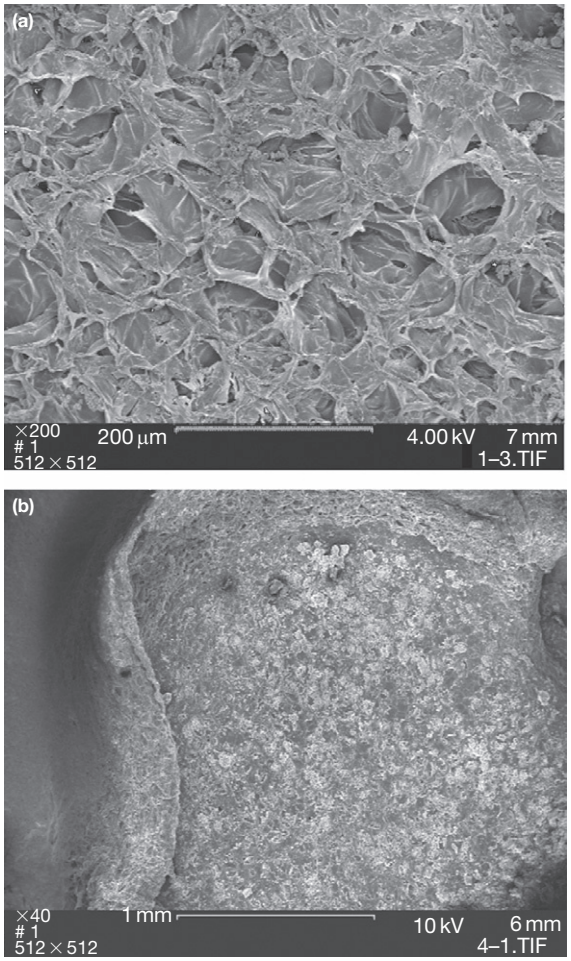

Figure 4 Scanning electron micrographs of human embryonic stem cell (hESC)-seeded LF120 alginate scaffolds after 1 month of cultivation. (a) A construct made with low hESC seeding concentration, demonstrating the porous structure of alginate scaffold. (b) Low-magnification image of a scaffold seeded with a high hESC concentration, demonstrating homogeneous cell distribution throughout the scaffold. Reprinted from Gerecht-Nir, S.; Cohen, S.; Ziskind, A.; Itskovitz-Eldor, J. *Biotechnol. Bioeng.* **2004**, *88*, 313–320, with permission of John Wiley & Sons, Inc.

5.508.2.2. Synthetic Biomaterials for Undifferentiated hESC Culture

While natural systems such as Matrigel supply the substrate signals needed to support hESC attachment and maintenance, synthetic materials offer the potential for a defined and reproducible system if they can be engineered with the necessary bioactivity. See **Chapter 2.209, Materials as Artificial Stem Cell Microenvironments** for further reading on this subject. To identify numerous synthetic biomaterials to support hESC culture, Anderson *et al*. developed combinatorial microarray to screen potential substrates.[43] Their microarray consisted of 576 combinations of acrylate, diacrylate, dimethacrylate, and triacrylate monomers presented on 2D surfaces consisting of poly (hydroxyethyl methacrylate) (pHEMA) using the mircroarray shown in **Figure 5**. For this study, they cultured the hESCs in knock-out replacement medium containing serum and other defined supplements. This high-throughput screening of potential biomaterials surfaces for hESC culture allowed them to identify several candidate materials, and additional characterization found that several could effectively support hESC differentiation induced by retinoic acid. Future work may analyze whether the materials themselves were bioactive or selectively adsorbed different factors from serum. Regardless, additional characterization may reveal valuable new signals that can regulate cell differentiation.

An analogous approach invovled a SAM array for screening potential peptide substrates for 2D hESC culture.[44] To generate the array, one layer of SAMs consisting of alkanethiols (ATs) was photopatterned onto the surface followed by the spot application of various peptide sequences conjugated to ATs to generate the desired array. These peptide sequences were derived from the sequence of laminin, a significant component of Matrigel. The authors hypothesized that peptide fragments based on laminin would be able to support hESC culture in a manner similar to Matrigel. hESCs were then cultured in mouse embryonic fibroblast (MEF)-conditioned media on the microarray for 6 days and evaluated for their ability to support hESC growth and maintain their undifferentiated state. Their results showed that hESCs prefer to be grown on peptides containing the arginine–glycine–asparatic acid (RGD) sequence when presented at high concentrations.

Earlier work from the Healy Lab investigated the use of semi-interpenetrating polymer networks (sIPNs, **Figure 6**) for the culture of undifferentiated hESCs.[34] For this study, the sIPN was designed to contain cross-links that could be degraded by proteases, to simulate 'natural' remodeling of tissues by cells, and functionalized with an RGD sequence derived from an integrin-binding site of bone sialoprotein to allow for hESC adhesion to the network. These networks were capable of supporting hESC culture for short time periods (~5 days) when used in combination with chemically defined media, representing for the first time a completely synthetic microenvironment used for short-term hESC maintenance. More recent work from the Healy and Schaffer Labs investigated the integrin 'fingerprint' necessary to support hESC attachment and to allow for culture and maintenance of undifferentiated hESC culture in the presence of chemically defined media.[35] They determined that the $\alpha_V\beta_3$, $\alpha_6\beta_1$, and $\alpha_2\beta_1$ integrins mediated hESC adhesion to Matrigel-coated surfaces. Based on these results, they synthesized peptides previously reported to bind these integrins and found that a combination of two integrin-engaging peptides along with an additional peptide designed to bind the heparan sulfate proteoglycan syndecan could support hESC adhesion and propagation for three passages, though the cells eventually lost expression of pluripotency markers. However, this study illustrates the concept that emulating the pattern of adhesion receptor engagement mediated by a natural biomaterial can extend the duration of hESC maintenance in a fully chemically defined culture system, a promising starting point for further work in developing synthetic scaffolds for hESC culture.

Overall, these studies highlight the promise and advantages of using synthetic scaffolds for hESCs. However, significant challenges remain in investigating the mechanisms of interaction between hESCs and natural substrates such as Matrigel, the downstream signaling mechanisms that support hESC

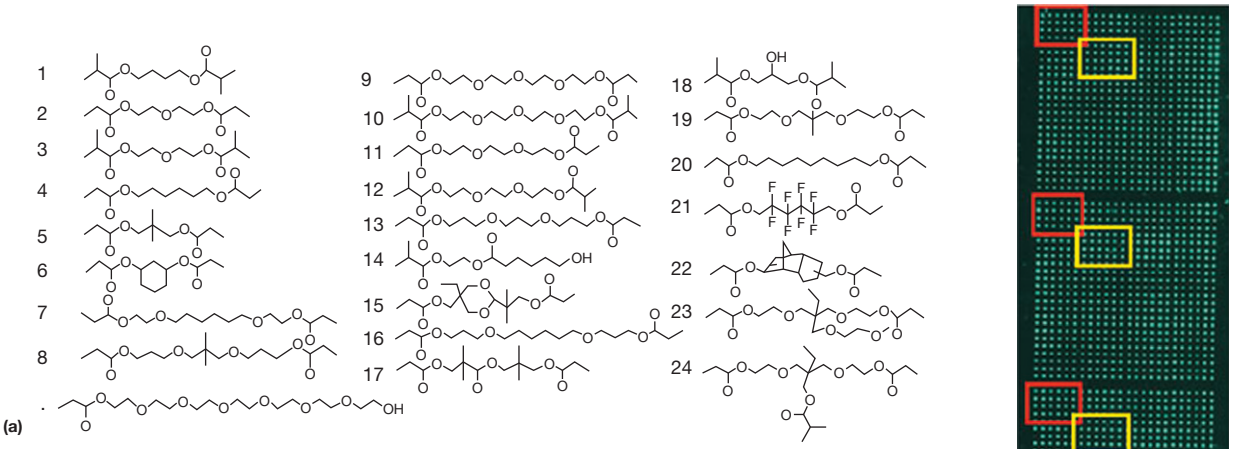

(b)

70% monomer 1 100% 1 30% 2 30% 3 30% 4 30% 5 30% 6 30% 7 30% 8 30% 9 30% 10 30% 11 30% 12 30% 13 30% 14 30% 15 30% 16 30% · 30% 18 30% 19 30% 20 30% 21 30% 22 30% 23 30% 24	70% 2 30% 1 100% 2... 30% 7... 30% 13... 30% 19...	70% 3 30% 1.... 30% 7... 30% 13... 30% 19...	70% 4 30% 1.... 30% 7... 30% 13... 30% 19...
70% monomer 5 30% 1 30% 2 30% 3 30% 4 100% 5 30% 6 30% 7...	70% 6 30% 1 30% 2... 30% 7...	70% 7 30% 1... 100% 7...	70% 8 30% 1... 30% 7...
70% monomer 9	70% 10	70% 11	70% 12
70% monomer 13	70% 14	70% 15	70% 16
70% monomer 17	70% 18	70% 19	70% 20
70% monomer 21	70% 22	70% 23	70% 24

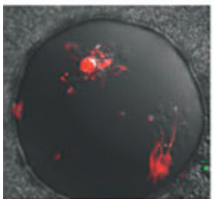

Figure 5 Biomaterial microarray design. (a) Monomers used for microarray synthesis. (b) Monomers were mixed at a 70:30 ratio pairwise in all possible combinations with the exception of monomer 17, which was substituted with * to increase polymer hydrophilicity. To facilitate analysis, all 24 polymers composed of 70% of a particular monomer were printed as a 6 × 4 group on the array, as highlighted by the red and yellow boxes. Three blocks of 576 polymers were printed on each slide, with a center to center spacing of 740 μm. (c) Printed polymer array imaged by an Arrayworx reader. Blocks composed of 70% monomer 1 and 70% monomer 6 are highlighted in red and yellow, respectively. (d) Differential interference contrast light microscopy of typical polymer spot overlaid with a few fluorescent cells (red). Reprinted from Anderson, D. G.; Levenberg, S.; Langer, R. *Nat. Biotechnol.* **2004**, *22*, 863–866, with permission from the Nature Publishing Group.

self-renewal, and synthetic ligands that can emulate these engagements. The first two studies described[43,44] demonstrate how such synthetic materials can be screened in a high-throughput manner, allowing for the identification of potential scaffold materials and ligands, and the final study initiates the process of dissecting Matrigel for key signals that activate particular adhesion receptors. As many of the signals that promote hESC survival and proliferation remain unidentified, additional searches aided by high-throughput approaches could potentially be used for identifying novel molecules and peptide sequences for these applications.

5.508.3. Biomaterials for hESC Differentiation

A considerable body of prior work has explored the use of biomaterial scaffolds for engineering various types of tissues (neural, dental, bone, vasculature),[47,49–51] and it is natural to use these biomaterial-based approaches as starting places when investigating methods to promote the differentiation of hESCs into specific lineages for therapeutic applications. As discussed in Section 5.508.2, maintaining hESCs in an undifferentiated state requires a complex combination of signals. Likewise, directing hESC differentiation requires specific cues, such as growth factors and morphogens, combined with biomaterial scaffolds. This section will discuss the current use of both natural and synthetic biomaterial scaffolds for promoting hESC differentiation into specific cell types.

When selecting a material for promoting hESC differentiation, scaffold materials should meet a number of criteria: to be biocompatible, to contain sites for cell adhesion, to promote the desired differentiation, and – if included as part of an implantable graft – to not induce an immune response upon implantation. Furthermore, the degradation rate of the scaffold should also be considered, especially in comparison to the time course required for the desired differentiation. If differentiation-promoting cues are incorporated into the scaffold, this degradation rate can also influence the release rate of these cues. Finally, as previously mentioned in Section 5.508.1.6, it is also important to consider the fact that the mechanical properties of the scaffolds can also influence the resulting differentiation.[32,33] Table 3 summarizes the efforts to engineer materials that investigate a number of these design criteria.

5.508.3.1. Natural Biomaterials for hESC Differentiation

5.508.3.1.1. Alginate

As mentioned in Section 5.508.2.1.1, the biomaterial alginate has been shown to support the hESC cell culture, and in the same study, Gerecht-Nir *et al.*[36] showed that embryoid bodies

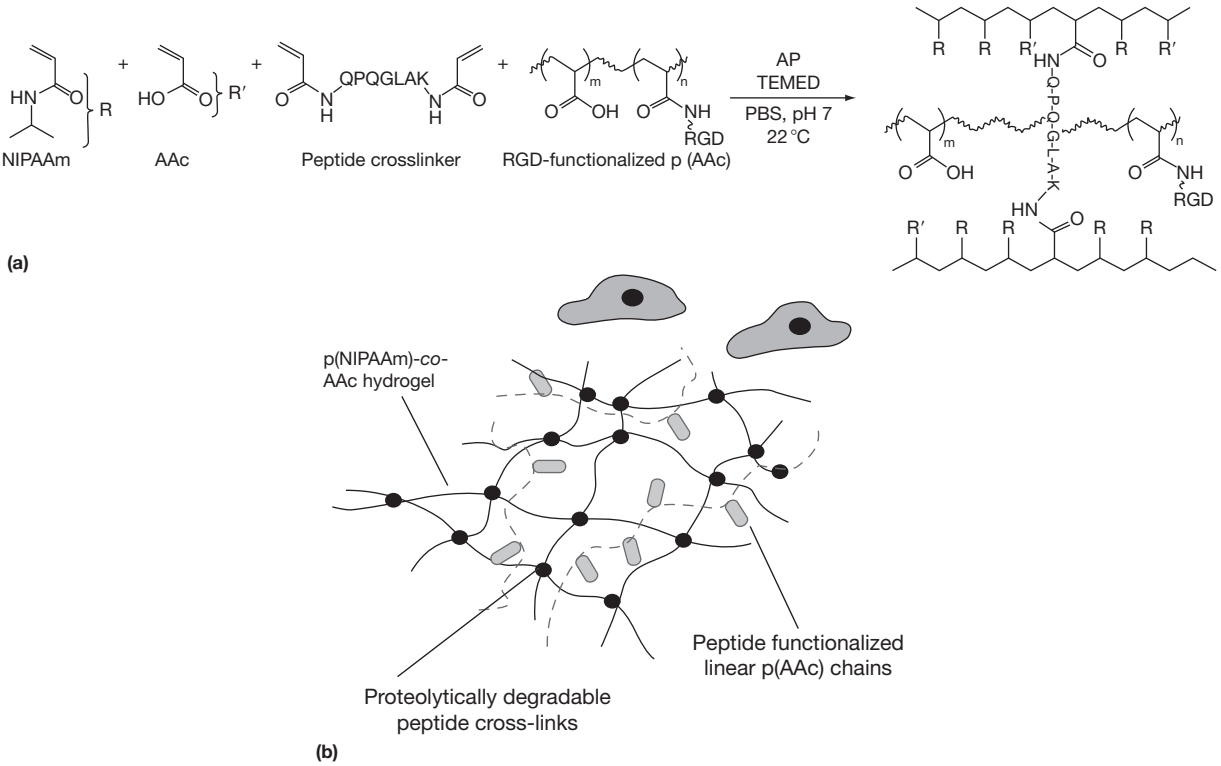

Figure 6 Semi-interpenetrating polymer networks (sIPN) synthesis: poly(*N*-isopropylacrylamide-*co*-acrylic acid) [p(NIPAAm-*co*-AAc)], interpenetrated by polyacrylic acid-graft-Arg-Gly-Asp [p(AAc)-*g*-RGD] linear polymer chains; (a) polymerization scheme and (b) schematic representation of the polymerized sIPN network. Reprinted from Li, Y. J.; Chung, E. H.; Rodriguez, R. T.; Firpo, M. T.; Healy, K. E. *J. Biomed. Mater. Res. A* **2006**, *79*, 1–5, with permission of John Wiley & Sons, Inc.

Table 3 List of biomaterials used for hESC differentiation

Type of material	*Material*	*References*
Natural	Alginate	[36,52]
	Dextran	[53]
	Fibronectin	[40,54]
	Laminin	[40]
	Matrigel	[40,55]
Synthetic	Carbon nanotubes	[56]
	Poly-D-lysine	[40]
	Poly(ethylene glycol)	[57]
	Poly(lactic-*co*-glycolic acid)	[58–62]
	Poly(tetrafluroethylene)	[63]

made from the hESCs could differentiate into vasculature. The authors hypothesized that the porous nature of their alginate scaffolds helped enhance the differentiation process compared to traditional 2D culture. Another group also investigated that use of alginate to encapsulate hESCs, followed by implantation into mice, and characterized the resulting phenotypes to determine the effects of encapsulation on differentiation.[52] They found that the encapsulated, transplanted cells differentiated primarily into an endoderm lineage. In addition, although it is unlikely that undifferentiated hESCs would be implanted for therapeutic application, this study found that the cells did not form teratomas, benign tumors that can be formed by immature transplanted hESCs, which could enhance the safety of a graft. They also hypothesized that the encapsulation process may help protect the hESCs from immune rejection.

5.508.3.1.2. Dextran

The use of a functionalized dextran scaffold for directing the differentiation of hESCs into vasculature was also investigated.[53] Derived from bacteria, dextran is a complex polysaccharide consisting of glucose subunits, and it resists both cell and protein adsorption.[47] To engineer the capacity for specific interactions with cells, the authors functionalized their dextran hydrogel scaffolds with RGD peptides. Additionally, they incorporated poly(lactic-*co*-glycolic acid) (PLGA, a synthetic polymer) microspheres (Figure 7(a)) that released vascular endothelial growth factor (VEGF) over a 10-day period (Figure 7(b)). Figure 7(c) shows the entire system including the dextran scaffold, the VEGF releasing PLGA microspheres, and hESCs. The hESCs cultured inside the hydrogels exhibited an increase in markers characteristic of differentiation into vasculature, including the VEGF receptor KDF/Flk-1. The authors emphasized that this biomaterial scaffold could potentially generate large numbers of endothelial cells for tissue engineering applications.

5.508.3.1.3. Collagen/laminin/matrigel

Another group explored a wide variety of 2D biomaterial surfaces for directing hESCs into neural phenotypes, that is, neurons, oligodendrocytes, and astrocytes – including Matrigel, type 1 collagen, laminin/poly-D-lysine (PDL) mixture,

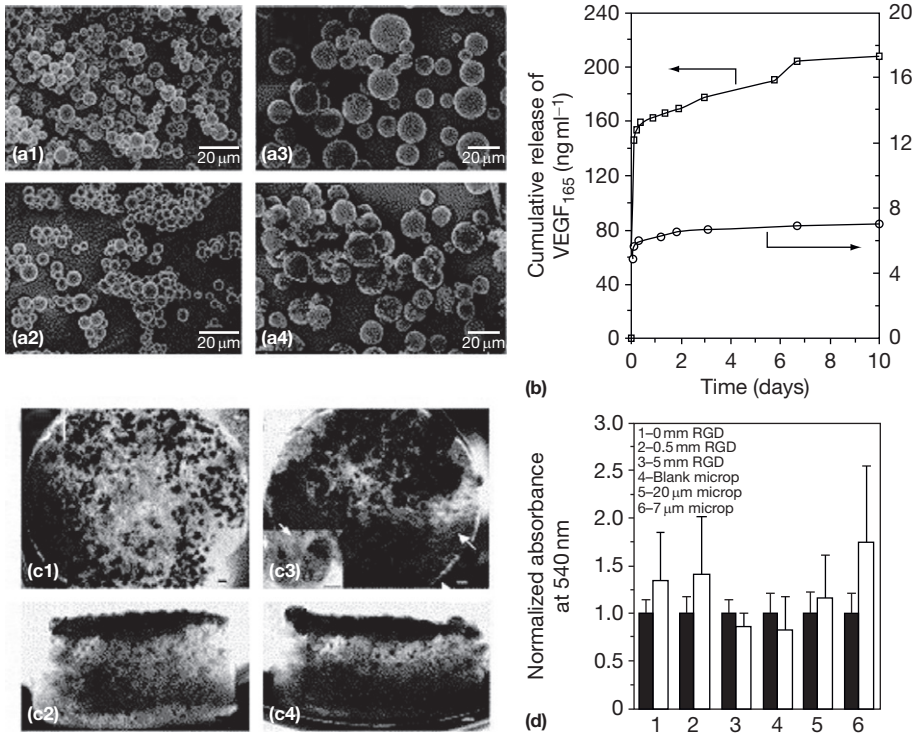

Figure 7 Distribution and viability of human embryonic stem cell (hESC) aggregates encapsulated within bioactive dextran-based hydrogels: (a) scanning electron micrographs of 7 μm (a1, a2) and 20 μm (a3, a4) poly(lactic-*co*-glycolic acid) (PLGA) microparticles at day 0 (a1, a3) and 10 (a2, a4), during the release of vascular endothelial growth factor $(VEGF)_{165}$. (b) Release profile of $VEGF_{165}$ from 7 μm (□) and 20 μm (○) microparticle formulations. (c) Distribution of hESC aggregates on dextran-based hydrogels with 0.5 mm Acr-PEG-RGD and 5 mg ml^{-1} VEGF-loaded 20-μm microparticles, at day 0 (c1, c2) and day 10 (c3, c4). Top (c1, c3) and side (c2, c4) views. Arrows in c3 and c4 indicate a clump of cells proliferating outside the hydrogel. Inset in c3 shows the incorporation of microparticles (arrow) within the hESC aggregates. Scale bar corresponds to 200 μm. (D) Mitochondrial metabolic activity (average ± SD, $n = 6$) of hESC aggregates encapsulated in dextran-based hydrogels with no Acr-PEG-RGD (1), 0.5 mm Acr-PEG-RGD (2), 5 mm Acr-PEG-RGD (3), 0.5 mm Acr-PEG-RGD with 5 mg ml^{-1} of blank microparticles (4), and 0.5 mm Acr-PEG-RGD with 5 mg ml^{-1} of $VEGF_{165}$ loaded 20 μm (5), or 7 μm (6) microparticles. The absorbance at 540 nm was measured after 1 day (black bars) and 10 days (white bars). Both absorbances were normalized to the day 1 absorbance. Reprinted from Ferreira, L. S.; Gerecht, S.; Fuller, J.; *et al*. *Biomaterials* **2007**, *28*, 2706–2717, with permission from Elsevier.

fibronectin/PDL mixture, and PDL alone (whose results will be discussed below in Section 5.508.3.2.[40] This study found that Matrigel and the laminin/PDL mixture promoted an increase in neural progenitor generation as well as subsequent neuronal generation compared to the other substrates (the neuronal subtypes were not analyzed). They also noted a laminin dose-dependency in these responses and thus concluded that laminin is a key molecule for promoting the generation of neural progenitors from hESCs.

Other researchers used a 2D micropatterning approach, with Matrigel in combination with growth factors, to direct hESC differentiation in mesoderm and endoderm lineages.[55] As discussed in Section 5.508.2, the local cellular microenvironment plays an important role in promoting hESC differentiation, and this study restricted the size of hESC colonies using patterns of adsorbed Matrigel. They showed that small, 200 μm colonies promoted hESC differentiation into endoderm, whereas larger, 1200 μm spots promoted mesodermal formation. This study thus illustrates how limiting the size of hESCs cultures can influence the resulting differentiation, which suggest the need to control the uniformity of embryoid body (EB) sizes to tune cell differentiation.

5.508.3.1.4. Fibronectin

Another interesting approach to promoting hESC differentiation involved coating gold nanoparticles with a layer-by-layer deposition of the extracellular matrix (ECM) protein fibronectin to enable cell attachment.[54] Gold is electrically conductive and enables an investigation of the effects of electrical stimulation on hESCs differentiation (Figure 8). They found that electrical stimulation promoted differentiation into osteogenic lineages, as indicated by the expression of collagen type 1 and the transcription factor core-binding factor alpha1 (Cbfa1), while a dramatic decrease in the expression of Oct4 was observed, suggesting that the majority of the hESCs had differentiated. The same effects were not observed in unstimulated cells.

5.508.3.1.5. Other naturally derived materials

Another potential application of hESCs involves periodontal tissue engineering.[64] Inanc *et al*. examined the capacity of tooth root slices, which consist of the soft tissue found in the root canal, as a natural 'microenvironment' to promote the differentiation of hESCs into tooth structures. They examined three different sets of culture conditions for hESCs, including

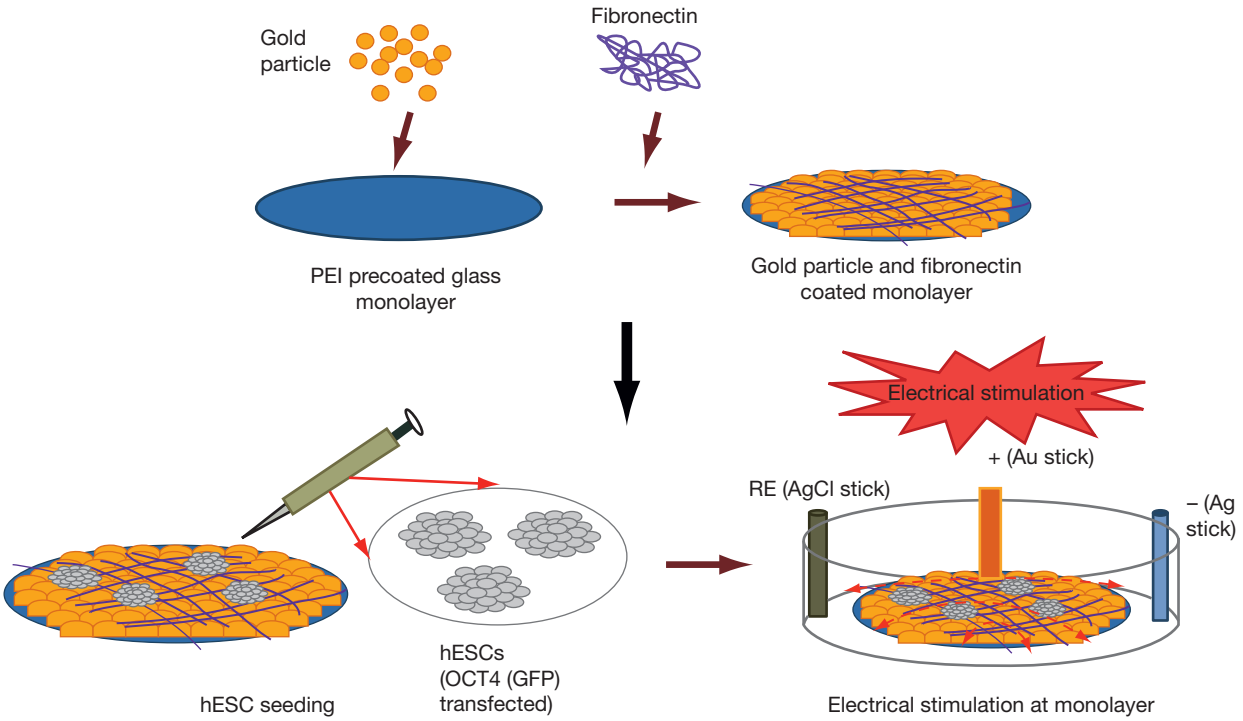

Figure 8 Schematic diagram of a fibronectin-coated gold nanoparticle surface for human embryonic stem cell (hESC) differentiation by alternating electrical stimulation. Reprinted from Woo, D. G.; Shim, M. S.; Park, J. S.; Yang, H. N.; Lee, D. R.; Park, K. H. *Biomaterials* **2009**, *30*, 5631–5638, with permission from Elsevier.

seeding them next to these root slices, seeding them on a feeder layer of periodontal fibroblastic cells with the root slices present in the presence of osteogenic media, and allowing the hESCs to spontaneously differentiate. They found that the presence of the tooth root slices and a feeder layer along with the osteogenic media promoted differentiation into bone tissue, suggesting a potential mechanism for engineering periodontal tissue.

These examples show the variety of natural biomaterials and approaches that can be used for directing hESC differentiation. The cell adhesion ligands naturally present in many of these materials, in conjunction with specific cues such as growth factors or small molecules, can aid in guiding cell differentiation; however, natural materials again suffer from some shortcomings, including reproducibility of composition and properties as well as potential transfer of immunogens or pathogens from the material to the cells.

5.508.3.2. Synthetic Biomaterials for hESC Differentiation

A number of synthetic biomaterial classes have been evaluated for directing hESC differentiation into numerous lineages, and this section will review the current state of the field.

5.508.3.2.1. Poly(lactic-co-glycolic acid)

A key early study examined how to control the differentiation of hESCs seeded inside a 3D scaffold consisting of a 50/50% blend of PLGA and poly(L-lactic acid) (PLLA).[58] hESCs were first mixed with Matrigel to aid survival upon seeding into the scaffolds. To direct hESCs into specific lineages, the following cues were used: retinoic acid (neural), TGF-β (osteogenic), and insulin-like growth factor (vasculature). They observed the ability of these factors to direct hESC differentiation into neural, cartilage, and liver tissue, respectively, through the use of immunohistochemistry, *in vitro*. Additionally, they observed the ability of hESCs to form blood vessels. Based on these promising results, they transplanted these scaffold-containing hESCs after 2 weeks of *in vitro* culture into severe combined immune deficiency (SCID) mice, such that implantation of such scaffolds containing hESCs would not trigger an immune response. Staining results indicate that the hESCs could survive and maintain these individual phenotypes in an *in vivo* setting (Figure 9). This key study demonstrated the potential of synthetic scaffold for promoting hESC differentiation by providing a 3D environment.

Many other studies have used PLGA as a scaffold to promote hESC differentiation. One group encapsulated hESCs in PLGA scaffolds that were coated with laminin, implanted these scaffolds into the livers of SCID mice, and characterized the resulting differentiation.[59] The cells differentiated into all three germ layers, and the scaffolds became highly vascularized. One issue encountered was the formation of teratomas inside these scaffolds due to the presence of undifferentiated hESCs. This issue would have to be addressed before such a strategy could be considered for clinical translation by ensuring that only differentiated hESCs are transplanted. Another group used scaffolds that consisted of PLGA-mixed hydroxyapatite to promote the differentiation of hESCs into bone tissue.[60] To achieve this goal, they first induced the hESCs to differentiate

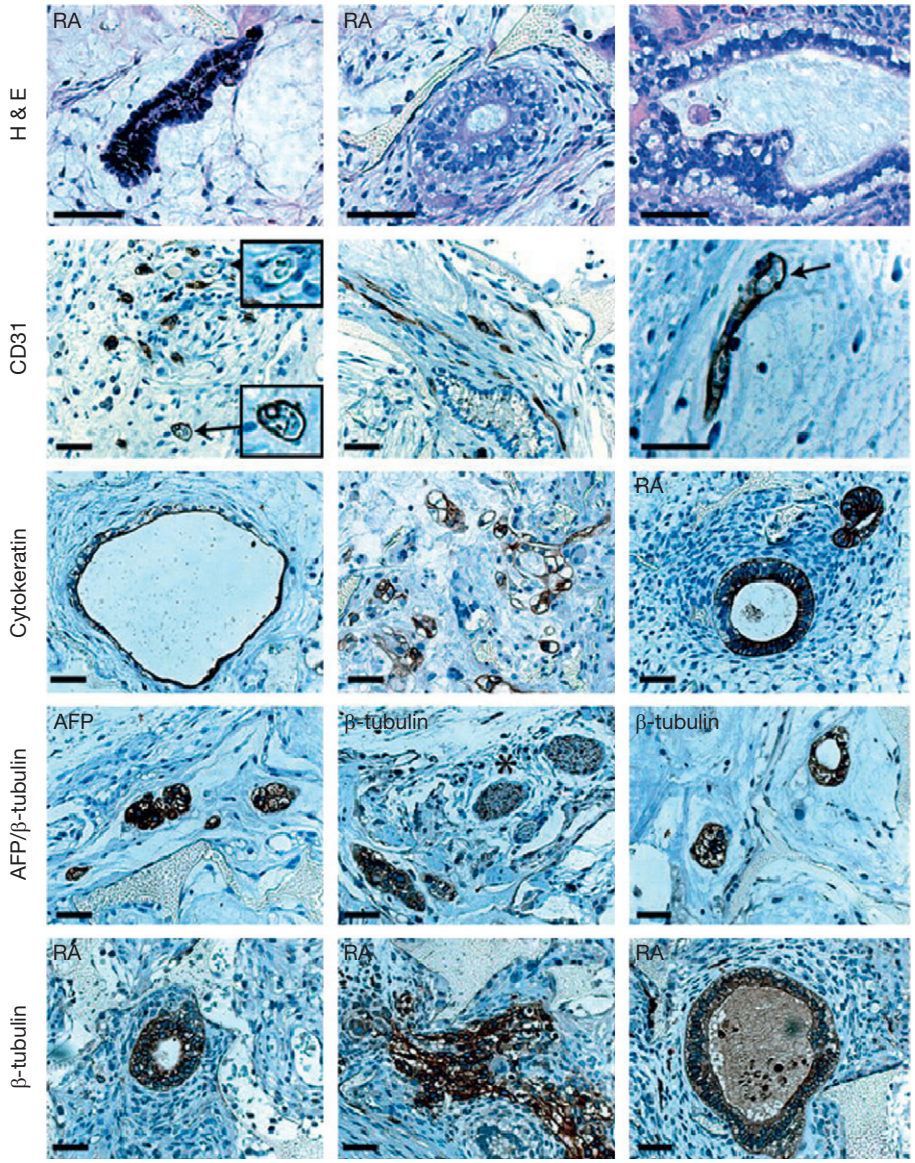

Figure 9 Transplantation of human embryonic stem cell (hESC)–scaffold constructs into severe combined immune deficiency (SCID) mice. Two-week-old constructs (treated with retinoic acid (RA) or control medium) were implanted subcutaneously in the dorsal region of SCID mice. Fourteen-day-old implants were stained with hematoxylin and eosin (H&E) or with antibodies against human CD31, cytokeratin, AFP, or β_{III}-tubulin. Human-specific CD31 staining demonstrated the presence of both immunoreactive (construct-origin, arrows) and nonimmunoreactive (host origin, arrowhead) vessels. In certain instances there appeared to be continued differentiation and organization of constructs postimplantation. After continued construct maturation *in vivo*, RA-conditioned constructs exhibited larger and better organized neural structures than those seen *in vitro* (or with control medium *in vitro* or *in vivo*) including ductular structures lined by tall columnar epithelium invested with long cilia resembling ependymal cells, and rosettes with abundant melanin granules (brown/black in H&E section; confirmed by bleaching with potassium permanganate, data not shown). β_{III}-tubulin antibodies stained neuroectodermal structures within the implant as well as murine peripheral nerve fibers in surrounding connective tissue (asterisk). Scale bar, 50 μm. Reprinted from Levenberg, S.; Huang, N. F.; Lavik, E.; Rogers, A. B.; Itskovitz-Eldor, J.; Langer, R. *Proc. Natl. Acad. Sci. USA* **2003**, *100*, 12741–12746, with permission from the National Academy of Sciences.

into osteogenic lineages through coculture with human bone-derived cells, since the latter secrete the factors necessary for promoting differentiation as previously reported.[65] They seeded the resulting hESC-derived osteogenic progenitor cells inside the aforementioned 3D scaffolds and implanted them subcutaneously in SCID mice. These cell–material scaffolds promoted the regeneration of bone (**Figure 10**), whereas control scaffolds seeded with dermal fibroblasts did not, suggesting that it was the hESC-derived cells that were responsible for the observed effects. This study illustrates the utility of hESC-derived cells for bone tissue engineering applications. To engineer neural tissue, 3D PLGA scaffolds combined with hESCs were treated with a combination of retinoic acid and nerve growth factor (NGF).[61] The researchers made the scaffold

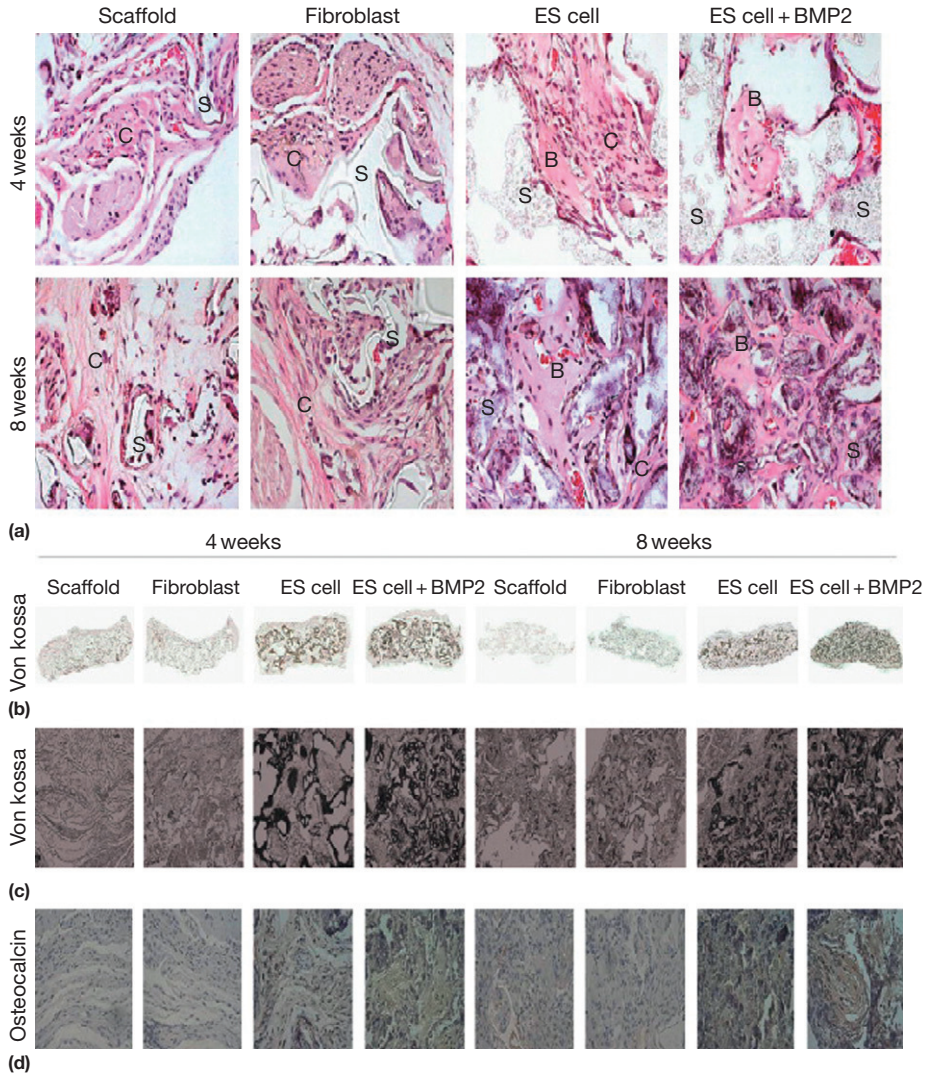

Figure 10 Histochemical evaluation of osteogenic induction 4 and 8 weeks after *in vivo* implantation. *In vivo* bone formations of osteogenic cells derived from human embryonic stem cells (OC-hESCs) were evaluated and compared in four treatment groups: scaffold only, fibroblasts in the scaffold, OC-hESCs in the scaffold, and OC-hESCs in the scaffold with BMP2: (a) H&E staining (B, C, and S represent bone tissue, connective tissue, and scaffold, respectively); (b) von Kossa staining; (c) an enlarged image of (b); and (d) osteocalcin immunostaining (×100). Reprinted from Kim, S.; Kim, S. S.; Lee, S. H.; *et al*. *Biomaterials* **2008**, *29*, 1043–1053, with permission from Elsevier.

porous to better enable cell proliferation and migration as well as the diffusion of the retinoic acid and NGF. They found that using 3D culture enhanced the expression of nestin and troponin (a skeletal muscle marker) compared to culturing the hESCs in 2D monolayer culture. The authors suggested that it may be beneficial to study hESCs in 3D to better emulate and understand behavior in an *in vivo* setting. A final study used hESCs and 3D PLGA scaffold to generate islet-like cells as a potential treatment for diabetes.[62] In this work, a five-step protocol for generating the islet-like cells *in vitro* that could secrete insulin was adapted. They then encapsulated these islet-like cells inside PLGA scaffolds and transplanted them into diabetic SCID mice. The mice receiving this treatment maintained the presence of the islet-like cells *in vivo* and exhibited a decrease in glucose levels compared to levels in control mice (Figure 11). These studies collectively illustrate the utility of PLGA scaffolds for promoting hESC differentiation for a variety of tissue engineering applications.

5.508.3.2.2. Poly(ethylene glycol)

An early study investigated the use of 3D poly(ethylene glycol) (PEG) hydrogels as a potential scaffold material for hESC differentiation into chondrocytes, resident cells of cartilage.[57] This important work by Elisseeff and colleagues used PEG diacrylate hydrogels chemically modified to present different sites that allow hESCs to bind to the scaffolds. Specifically, they compared the ability of PEG scaffolds conjugated with HA, type I collagen, and the RGD peptide to promote hESC adhesion and found that only RGD allowed hESCs to differentiate into neocartilage, as indicated by both cellular markers and the deposition of basophilic extracellular matrix indicated by glycosaminoglycan content.

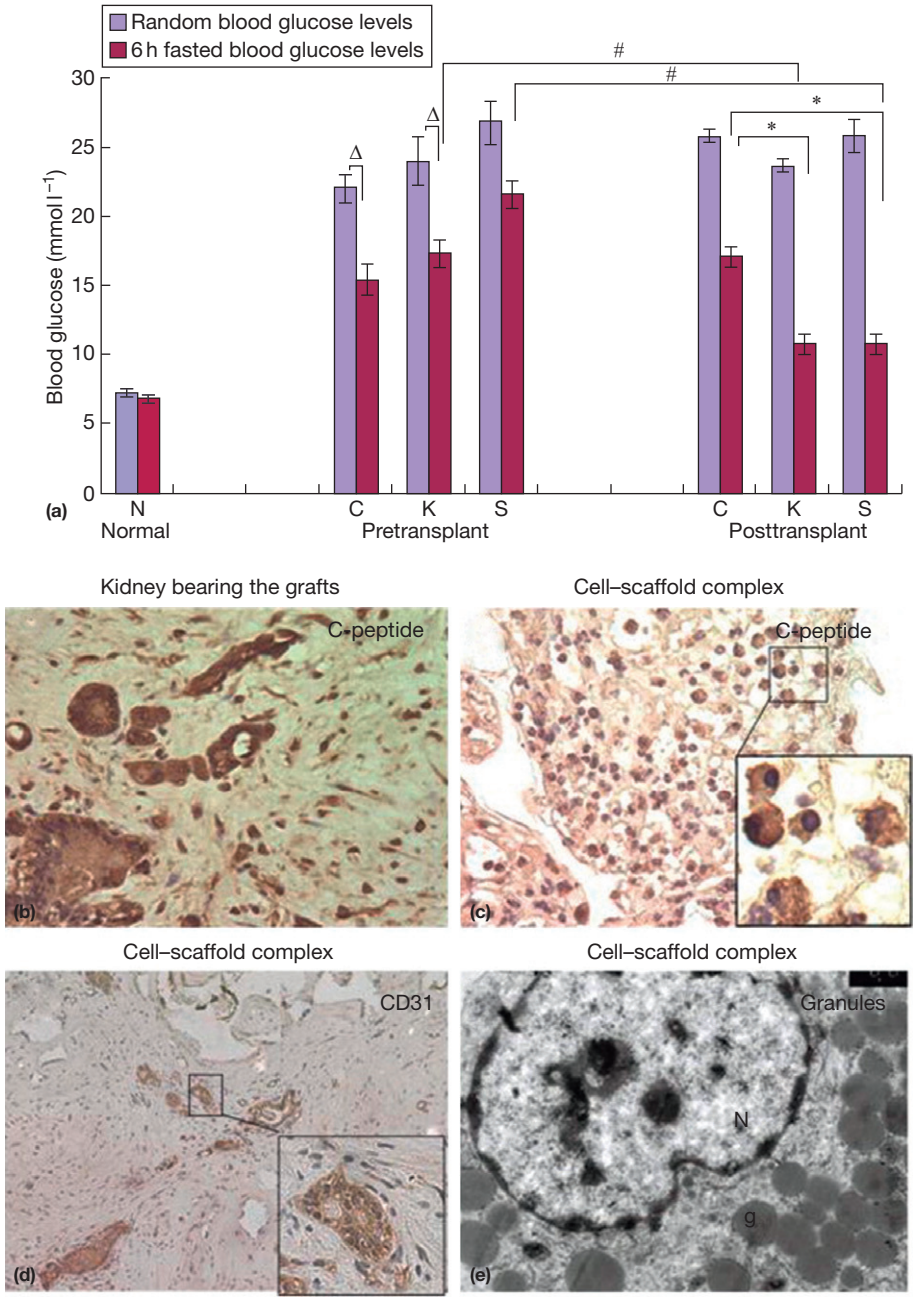

Figure 11 (a) Random-fed and 6 h fasted blood glucose levels in the mice transplanted under the kidney capsules and embedded subcutaneous cell–scaffold complexes. N, normal mice; C, sham-transplanted mice; K, cell transplanted under kidney capsule mice; S, cell–scaffold complex transplanted mice. * $p < 0.05$ versus sham-transplanted mice; Δ $p < 0.05$ versus random blood glucose levels; # $p < 0.05$ versus pretransplant 6 h fasted blood glucose. (b–e): identification of islet-like cells during cell transplantation process. (b) c-peptide$^+$ cells seeded in kidney capsule. c-peptide is a peptide derived from proinsulin. (c) c-peptide$^+$ cells seeded in scaffold graft. (d) Immunohistochemical staining of rabbit anti-mouse CD31 in blood vessels within scaffold. (e) Transmission electron microscopic examination of secretory granules (g) in islet-like cells seeded in scaffold. The cells show a round nucleus (N). Magnification (b and c) 400×, (d) 100×, (e) 40 000×. Reprinted from Mao, G. H.; Chen, G. A.; Bai, H. Y.; Song, T. R.; Wang, Y. X. *Biomaterials* **2009**, *30*, 1706–1714, with permission from Elsevier.

5.508.3.2.3. Other synthetic materials

Other synthetic polymers have been studied for their suitability as substrates for hESC differentiation. 2D polytetrafluroethylene (PTFE) surfaces coated with poly-amino-urethane were seeded with hESCs, and a variant of hepatocyte growth factor (HGF) as well as basic fibroblast growth factor (bFGF) were added to the media to induce differentiation into hepatocytes.[63] The resulting cells secreted both albumin and urea, indicating that the hESCs were becoming functional hepatocytes. A study discussed in Section 5.508.3.1,

investigated a number of natural and synthetic materials for the ability to support neural differentiation.[40] The study found that PDL – a synthetic polymer that is often used to enhance the ability of cells to attach to surfaces via ionic interactions between the amine groups and the negatively charged cellular glycocalyx[66] – could modestly support hESC differentiation into neural phenotypes, though the ECM proteins were more effective. A recent study investigated the use of thin films of carbon nanotubes as a 2D substrate for promoting the differentiation of hESCs into neurons,[56] and the nanotube-based surfaces allowed the cells to adhere and differentiate without cytotoxic effects. These are examples of other polymers that could potentially be used as substrates for hESC adhesion and differentiation.

5.508.4. Conclusions and Future Work

Overall, this chapter summarizes the current state of biomaterial scaffolds for the culture and differentiation of hESCs. The use of hESCs in conjunction with bioactive materials holds enormous therapeutic potential that these studies begin to highlight and help harness. This final section will discuss the challenges in current efforts and offer directions for the future of the field.

5.508.4.1. Reflections on the Current State of Biomaterial Scaffolds for hESC Culture and Differentiation

This chapter has discussed the current state of the field, and many valuable studies have shown that hESCs can differentiate into a wide variety of cells types for therapeutic applications, including neurons, bone, and islet-like cells. This work has also demonstrated that hESC behavior is heavily influenced by the culture system, and cues ranging from biochemical signals from matrix, small molecules, and growth factors can support and regulate hESC self-renewal and differentiation. Furthermore, 'geometric' cues such as local cell density and composition, as well as 2D versus 3D culture systems, can profoundly influence cell function. Collectively, this work has highlighted the promise and potential of hESC and biomaterial scaffolds for serving as a culture systems so as to aid cell expansion and differentiation *in vitro*, as well as for supporting the implantation of cells *in vivo*.

5.508.4.2. Future Directions

This section discusses challenges with current approaches, as well as suggests potential novel biomaterial scaffolds for the culture and differentiation of hESCs.

5.508.4.2.1. Issues with hESC culture to be addressed

As discussed in Section 5.508.1.3, progress must still be made in the development of *in vitro* culture systems for hESCs. A major limitation of current hESC culture methods is the use of Matrigel or other poorly defined components such as serum, conditioned medium, or other ECM proteins. The biomaterials described in this chapter have the potential to provide fully chemically defined conditions for cell expansion and differentiation, which would enhance safety, reproducibility, and scaleability. However, considerable progress must be made in identifying biochemical and mechanical cues in the stem cell microenvironment, including both substrate and matrix, to enable the development of defined biomimetic materials and liquid culture systems that can fully substitute for undefined components and support cell function. To address this issue, proteomic analysis of conditioned media was conducted to determine what components are necessary for maintaining undifferentiated hESCs. One hundred seventy-five proteins were found in the media, and a key subset of these factors must aid in maintaining undifferentiated hESCs.[67] Likewise, a recent proteomic study identified hundreds of proteins in Matrigel,[12] which renders the development of a synthetic matrix quite challenging. See **Chapter 4.409, Surfaces and Cell Behavior** and **Chapter 4.427, Cell-Demanded Release of Growth Factors** for further reading on presentation of cues that influence cell behavior.

Bioactive materials along with hESC-derived progeny may aid in overcoming challenges with engraftment, such as low cell viability. In addition, immune responses against the graft may be a challenge. hESCs cultured on Matrigel, in conditioned medium, in serum, or in the presence of animal proteins in general likely internalize and incorporate murine antigens,[13] which could trigger an immune reaction when implanted *in vivo*. This issue would be mitigated by the use of a defined culture system prior to implantation, and the coimplantation of nonimmunogenic biomaterials may to an extent shield cells from immune responses. Cells may well also face immune responses due to challenges in the histocompatibility of donor cells and patient recipients. However, patient-specific pluripotent stem cell lines are theoretically possible with the advent of induced pluripotent stem cells (iPSCs). iPSCs are generated from adult somatic cells, such as fibroblasts, by inducing the expression of specific genes that restore pluripotency.[68] Human iPS cells are similar to ESCs in their self-renewal, pluripotency, and teratoma formation,[69] and it is likely that biomaterials development studies will increasingly involve human iPSC lines.

An additional consideration when developing hESC-based therapies is avoiding teratoma formation *in vivo*. To achieve clinically relevant therapies, it is important to ensure that the cells are sufficiently and uniformly differentiated so as to avoid this hazardous possibility, and Section 5.508.3, details potential scaffold materials that can be used to control and potentially provide uniform hESC differentiation. Furthermore, cell encapsulation inside materials, in some cases, may physically contain cells and thereby inhibit tumor formation.

5.508.4.2.2. Potential new materials for use in combination with hESCs

A number of materials have been successfully investigated for hESC culture and differentiation, though a number of additional materials offer other key advantages that may be explored in future work.

5.508.4.2.2.1. Additional natural biomaterials

Many other natural biomaterials have been used in combination with mouse ESC culture, and these could also potentially be applied to hESCs. For example, fibrin and collagen are two potential protein-based materials that are found in the extracellular matrix, and these materials have been extensively

studied in biomaterial scaffolds.[70,71] Fibrin is a polymer that consists of fibrinogen monomers that are found in blood, which coagulate to form fibrin clots in response to vascular injury. Several groups have shown the feasibility of using fibrin scaffolds for both mouse and mesenchymal stem cell culture.[72–76] Another commonly used biomaterial for scaffolds is collagen, one of the major components in Matrigel, but little work has been conducted using pure collagen scaffolds for the culture and differentiation of hESCs. Previous work has shown that mouse neural stem cells seeded inside collagen scaffolds can form functional neuronal circuits.[77]

The other major group of natural biomaterials that could be investigated is polysaccharides. As mentioned in Section 5.508.3.1, dextran and alginate scaffolds have been successfully used for hESC culture and differentiation, suggesting that other polysaccharide-based biomaterial scaffolds could be used in a similar manner. Dextran is resistant to cell and protein adsorption, but it can be chemically modified to contain sites for cell adhesion, making it a potentially promising substrate for hESC culture. Agarose, a readily available polysaccharide isolated from seaweed, has been used as a scaffold material for differentiating primate ESC lines into cardiomyocytes.[78] The thermoresponsive properties of agarose can be used to regulate scaffold formation, suggesting that such scaffolds could be formulated to produce an injectable version. Another potential scaffold material is chitosan, which consists of glucosamine subunits. Chitosan scaffolds have been used to culture stem cells derived from human cord blood as well as mesenchymal stem cells.[79,80] It can fabricated using a variety of methods, such as encapsulation, spray drying, and gelation, to provide different methods of drug delivery.[81] It would be interesting to study hESC behavior inside scaffolds made from these polysaccharide, based on their suitability for the culture and differentiation of these other stem cell lines.

5.508.4.2.2.2. Additional synthetic biomaterials

Numerous synthetic polymers have been characterized for use as scaffolds in combination with stem cells other than hESCs, including pHEMA and polypyrrole. Scaffolds made from pHEMA do not degrade, and thus, maintain their initial shape after implantation. Such pHEMA scaffolds have been successfully fabricated into hydrogels that support mesenchymal stem culture.[82] Another attractive synthetic material for investigation is polypyrrole, a polymer consisting of connected pyrrole ring structures. It is highly conductive, a potentially interesting property as electrical stimulation has been shown to influence hESC behavior.[54] It has also been used to study mesenchymal stem cell behavior on 2D surfaces, where it was determined that the concentration of polypyrrole used influenced the resulting stem cell differentiation. These studies suggest that both of these synthetic polymers have the potential for use with hESCs.

Recently, several groups have developed novel self-assembling scaffolds based on short synthetic peptide sequences for stem cell culture and differentiation. Stupp and colleagues showed self-assembling scaffolds based on the peptide sequence IKVAV (isoleucine–lysine–valine–alanine–valine) derived from laminin promote the differentiation of fetal neural cells into neurons.[83] More recent studies have examined the use of similar peptide-based self-assembling scaffolds in combination with mesenchymal stem cells for osteogenic differentiation.[4,84,85] Likewise, Zhang and colleagues developed a novel self-assembling material based on a peptide, RADA-16-I, and used scaffolds derived from this peptide and related variants for promoting the differentiation of mesenchymal and neural stem cells.[86,87] These studies illustrate the utility of such novel peptide-based scaffolds, and such a strategy could be applied for hESC culture and differentiation, though precisely controlling the 3D assembly and mechanical properties of these short oligomers can be challenging. Furthermore, successfully implementing such a strategy may require the use of multiple peptide sequences due to the complex requirements of hESC culture.

5.508.5. Summary

This chapter has detailed the current state of the field, including the use of both natural and synthetic scaffolds for hESC culture and differentiation, along with discussing potential trends for future work to help maximize the therapeutic potential of hESCs. In general, hESCs have great therapeutic potential due to their ability to self-renew, which in principle can provide limitless quantities of cells, and their pluripotency, such that a single cell type can be harnessed to address numerous diseases. Many different biomaterial scaffolds have been investigated for hESC culture and differentiation due to their ability to provide the signals and cues, and thereby recreate cellular microenvironments, necessary to regulate and control self-renewal *in vitro* and differentiation *in vitro* and *in vivo*. Therefore, the integrated use of hESCs and engineered biomaterials hold great promise for greatly enhancing the therapeutic potential of tissue engineering and regenerative medicine.

References

1. Thomson, J. A.; Itskovitz-Eldor, J.; Shapiro, S. S.; *et al*. *Science* **1998**, *282*, 1145–1147.
2. Schuldiner, M.; Eiges, R.; Eden, A.; *et al*. *Brain Res*. **2001**, *913*, 201–205.
3. Levenberg, S.; Golub, J. S.; Amit, M.; Itskovitz-Eldor, J.; Langer, R. *Proc. Natl. Acad. Sci. USA* **2002**, *99*, 4391–4396.
4. Sottile, V.; Thomson, A.; Mcwhir, J. *Clon. Stem Cell*. **2003**, *5*, 149–155.
5. Mountford, J. C. *Transfus. Med*. **2008**, *18*, 1–12.
6. Reubinoff, B. E.; Pera, M. F.; Fong, C. Y.; Trounson, A.; Bongso, A. *Nat. Biotechnol*. **2000**, *18*, 399–404.
7. Hovatta, O.; Mikkola, M.; Gertow, K.; *et al*. *Hum. Reprod*. **2003**, *18*, 1404–1409.
8. Richards, M.; Fong, C. Y.; Chan, W. K.; Wong, P. C.; Bongso, A. *Nat. Biotechnol*. **2002**, *20*, 933–936.
9. Cheng, L.; Hammond, H.; Ye, Z.; Zhan, X.; Dravid, G. *Stem Cells* **2003**, *21*, 131–142.
10. Xu, C.; Inokuma, M. S.; Denham, J.; *et al*. *Nat. Biotechnol*. **2001**, *19*, 971–974.
11. Kleinman, H. K.; Martin, G. R. *Semin. Cancer Biol*. **2005**, *15*, 378–386.
12. Hansen, K. C.; Kiemele, L.; Maller, O.; *et al*. *Mol. Cell. Proteomics* **2009**, *8*, 1648–1657.
13. Martin, M. J.; Muotri, A.; Gage, F.; Varki, A. *Nat. Med*. **2005**, *11*, 228–232.
14. Ludwig, T. E.; Levenstein, M. E.; Jones, J. M.; *et al*. *Nat. Biotechnol*. **2006**, *24*, 185–187.
15. Zhang, Y. W.; Denham, J.; Thies, R. S. *Stem Cells Dev*. **2006**, *15*, 943–952.
16. Chaturvedi, G.; Simone, P. D.; Ain, R.; Soares, M. J.; Wolfe, M. W. *Cell Prolif*. **2009**, *42*, 425–433.
17. Thomson, J. A.; Kalishman, J.; Golos, T. G.; *et al*. *Proc. Natl. Acad. Sci. USA* **1995**, *92*, 7844–7848.
18. Mitsui, K.; Tokuzawa, Y.; Itoh, H.; *et al*. *Cell* **2003**, *113*, 631–642.
19. Nichols, J.; Zevnik, B.; Anastassiadis, K.; *et al*. *Cell* **1998**, *95*, 379–391.

20. Avilion, A. A.; Nicolis, S. K.; Pevny, L. H.; Perez, L.; Vivian, N.; Lovell-Badge, R. *Gene. Dev.* **2003**, *17*, 126–140.
21. Lobo, M. V.; Arenas, M. I.; Alonso, F. J.; *et al*. *Cell Tissue Res.* **2004**, *316*, 369–376.
22. Harlow, P.; Nemer, M. *Gene. Dev.* **1987**, *1*, 147–160.
23. Abelev, G. I. *Adv. Cancer Res.* **1971**, *14*, 295–358.
24. Jin, P.; Farmer, K.; Ringertz, N. R.; Sejersen, T. *Differentiation* **1993**, *54*, 47–54.
25. Adewumi, O.; Aflatoonian, B.; Ahrlund-Richter, L.; *et al*. *Nat. Biotechnol.* **2007**, *25*, 803–816.
26. Thomson, J. A.; Marshall, V. S. *Curr. Top. Dev. Biol.* **1998**, *38*, 133–165.
27. Dunlop, J.; Bowlby, M.; Peri, R.; Vasilyev, D.; Arias, R. *Nat. Rev. Drug Discov.* **2008**, *7*, 358–368.
28. Hengstler, J. G.; Brulport, M.; Schormann, W.; *et al*. *Expert Opin. Drug Metabol. Toxicol.* **2005**, *1*, 61–74.
29. Meisner, L. F.; Johnson, J. A. *Methods* **2008**, *45*, 133–141.
30. Aleckovic, M.; Simon, C. *Reprod. Biomed. Online* **2008**, *17*, 270–280.
31. Willerth, S. M.; Sakiyam-A-Elbert, S. E. *Combining Stem Cells and Biomaterial Scaffolds for Constructing Tissues and Cell Delivery*; Harvard Stem Cell Institute: Cambridge, MA, 2008.
32. Engler, A. J.; Sen, S.; Sweeney, H. L.; Discher, D. E. *Cell* **2006**, *126*, 677–869.
33. Engler, A. J.; Sweeney, H. L.; Discher, D. E.; Schwarzbauer, J. E. *J. Musculoskelet. Neuronal. Interact.* **2007**, *7*, 335.
34. Li, Y. J.; Chung, E. H.; Rodriguez, R. T.; Firpo, M. T.; Healy, K. E. *J. Biomed. Mater. Res. A* **2006**, *79*, 1–5.
35. Meng, Y.; Eshghi, S.; Li, Y.; Schimdt, R.; Schaffer, D. V.; Healy, K. E. *Faseb J.* **2009**, *24*, 1056–1065.
36. Gerecht-Nir, S.; Cohen, S.; Ziskind, A.; Itskovitz-Eldor, J. *Biotechnol. Bioeng.* **2004**, *88*, 313–320.
37. Siti-Ismail, N.; Bishop, A. E.; Polak, J. M.; Mantalaris, A. *Biomaterials* **2008**, *29*, 3946–3952.
38. Gerecht, S.; Burdick, J. A.; Ferreira, L. S.; Townsend, S. A.; Langer, R.; Vunjak-Novakovic, G. *Proc. Natl. Acad. Sci. USA* **2007**, *104*, 11298–11303.
39. Mohr, J. C.; De Pablo, J. J.; Palecek, S. P. *Biomaterials* **2006**, *27*, 6032–6042.
40. Ma, W.; Tavakoli, T.; Derby, E.; Serebryakova, Y.; Rao, M. S.; Mattson, M. P. *BMC Dev. Biol.* **2008**, *8*, 90.
41. Hakala, H.; Rajala, K.; Ojala, M.; *et al*. *Tissue Eng. A* **2009**, *15*, 1775–1785.
42. Stojkovic, P.; Lako, M.; Przyborski, S.; *et al*. *Stem Cells* **2005**, *23*, 895–902.
43. Anderson, D. G.; Levenberg, S.; Langer, R. *Nat. Biotechnol.* **2004**, *22*, 863–866.
44. Derda, R.; Li, L.; Orner, B. P.; Lewis, R. L.; Thomson, J. A.; Kiessling, L. L. *ACS Chem. Biol.* **2007**, *2*, 347–355.
45. Rao, B. M.; Zandstra, P. W. *Curr. Opin. Biotechnol.* **2005**, *16*, 568–576.
46. Peerani, R.; Rao, B. M.; Bauwens, C.; *et al*. *Embo J.* **2007**, *26*, 4744–4755.
47. Willerth, S. M.; Sakiyam-A-Elbert, S. E. *Adv. Drug Deliv. Rev.* **2007**, *59*, 325–338.
48. Tibbitt, M. W.; Anseth, K. S. *Biotechnol. Bioeng.* **2009**, *103*, 655–663.
49. Moioli, E. K.; Clark, P. A.; Xin, X.; Lal, S.; Mao, J. J. *Adv. Drug Deliv. Rev.* **2007**, *59*, 308–324.
50. Lee, S. H.; Shin, H. *Adv. Drug Deliv. Rev.* **2007**, *59*, 339–359.
51. Zhang, G.; Suggs, L. J. *Adv. Drug Deliv. Rev.* **2007**, *59*, 360–373.
52. Dean, S. K.; Yulyana, Y.; Williams, G.; Sidhu, K. S.; Tuch, B. E. *Transplantation* **2006**, *82*, 1175–1184.
53. Ferreira, L. S.; Gerecht, S.; Fuller, J.; *et al*. *Biomaterials* **2007**, *28*, 2706–2717.
54. Woo, D. G.; Shim, M. S.; Park, J. S.; Yang, H. N.; Lee, D. R.; Park, K. H. *Biomaterials* **2009**, *30*, 5631–5638.
55. Lee, L. H.; Peerani, R.; Ungrin, M.; Joshi, C.; Kumacheva, E.; Zandstra, P. *Stem Cell Res.* **2009**, *2*, 155–162.
56. Chao, T. I.; Xiang, S.; Chen, C. S.; *et al*. *Biochem. Biophys. Res. Commun.* **2009**, *384*, 426–430.
57. Hwang, N. S.; Varghese, S.; Zhang, Z.; Elisseeff, J. *Tissue Eng.* **2006**, *12*, 2695–2706.
58. Levenberg, S.; Huang, N. F.; Lavik, E.; Rogers, A. B.; Itskovitz-Eldor, J.; Langer, R. *Proc. Natl. Acad. Sci. USA* **2003**, *100*, 12741–12746.
59. Lees, J. G.; Lim, S. A.; Croll, T.; *et al*. *Regen. Med.* **2007**, *2*, 289–300.
60. Kim, S.; Kim, S. S.; Lee, S. H.; *et al*. *Biomaterials* **2008**, *29*, 1043–1053.
61. Inanc, B.; Elcin, A. E.; Elcin, Y. M. *Tissue Eng. A* **2008**, *14*, 955–964.
62. Mao, G. H.; Chen, G. A.; Bai, H. Y.; Song, T. R.; Wang, Y. X. *Biomaterials* **2009**, *30*, 1706–1714.
63. Soto-Gutierrez, A.; Navarro-Alvarez, N.; Rivas-Carrillo, J. D.; *et al*. *Cell Transplant.* **2006**, *15*, 335–341.
64. Inanc, B.; Elcin, A. E.; Elcin, Y. M. *Tissue Eng. A* **2009**, *15*, 3427–3435.
65. Ahn, S. E.; Kim, S.; Park, K. H.; *et al*. *Biochem. Biophys. Res. Commun.* **2006**, *340*, 403–408.
66. Varon, S. *Neurochem. Res.* **1979**, *4*, 155–173.
67. Prowse, A. B.; Mcquade, L. R.; Bryant, K. J.; Marcal, H.; Gray, P. P. *J. Proteome Res.* **2007**, *6*, 3796–3807.
68. Takahashi, K.; Yamanaka, S. *Cell* **2006**, *126*, 663–676.
69. Yu, J.; Vodyanik, M. A.; Smuga-Otto, K.; *et al*. *Science* **2007**, *318*, 1917–1920.
70. Ahmed, T. A.; Dare, E. V.; Hincke, M. *Tissue Eng. B Rev.* **2008**, *14*, 199–215.
71. Badylak, S. F.; Freytes, D. O.; Gilbert, T. W. *Acta Biomater.* **2009**, *5*, 1–13.
72. Willerth, S. M.; Arendas, K. J.; Gottlieb, D. I.; Sakiyama-Elbert, S. E. *Biomaterials* **2006**, *27*, 5990–6003.
73. Willerth, S. M.; Faxel, T. E.; Gottlieb, D. I.; Sakiyama-Elbert, S. E. *Stem Cells* **2007**, *25*, 2235–2244.
74. Willerth, S. M.; Rader, A.; Sakiyam-A-Elbert, S. E. *Stem Cell Res.* **2008**, *1*, 205–218.
75. Catelas, I.; Sese, N.; Wu, B. M.; Dunn, J. C.; Helgerson, S.; Tawil, B. *Tissue Eng.* **2006**, *12*, 2385–2396.
76. Juan-Pardo, E.; Hoang, M. B.; Conboy, I. M. *Int. J. Nanomed.* **2006**, *1*, 203–212.
77. Ma, W.; Fitzgerald, W.; Liu, Q. Y.; *et al*. *Exp. Neurol.* **2004**, *190*, 276–288.
78. Chen, S. S.; Fitzgerald, W.; Zimmerberg, J.; Kleinman, H. K.; Margolis, L. *Stem Cells* **2007**, *25*, 553–561.
79. Cho, C. H.; Eliason, J. F.; Matthew, H. W. *J. Biomed. Mater. Res. A* **2008**, *86*, 98–107.
80. Mrugala, D.; Bony, C.; Neves, N.; *et al*. *Ann. Rheum. Dis.* **2008**, *67*, 288–295.
81. Panos, I.; Acosta, N.; Heras, A. *Curr. Drug Discov. Technol.* **2008**, *5*, 333–341.
82. Kubinova, S.; Horak, D.; Sykova, E. *Biomaterials* **2009**, *30*, 4601–4609.
83. Silva, G. A.; Czeisler, C.; Niece, K. L.; *et al*. *Science* **2004**, *303*, 1352–1355.
84. Hosseinkhani, H.; Hosseinkhani, M.; Kobayashi, H. *Biomed. Mater.* **2006a**, *1*, 8–15.
85. Hosseinkhani, H.; Hosseinkhani, M.; Tian, F.; Kobayashi, H.; Tabata, Y. *Biomaterials* **2006b**, *27*, 4079–4086.
86. Garreta, E.; Genove, E.; Borros, S.; Semino, C. E. *Tissue Eng.* **2006**, *12*, 2215–2227.
87. Gelain, F.; Bottai, D.; Vescovi, A.; Zhang, S. *PLos One* **2006**, *1*, e119.

Relevant Websites

http://www.stembook.org/ – StemBook is a comprehensive, open-access collection of original, peer-reviewed chapters covering topics related to Stem Cell Biology.
http://www.cirm.ca.gov/ – The official website of the California Institute of Regenerative Medicine.
http://stemcells.nih.gov/research/nihresearch/scunit/ – The official website of the NIH Stem Cell Unit.
http://www.biomaterials.org/ – The official website of the Society of Biomaterials.
http://stemcells.wisc.edu/ – The official website of the University of Wisconsin–Madison Stem Cell and Regenerative Medicine Center.

5.509. Cell Encapsulation

H G Sundararaghavan and J A Burdick, University of Pennsylvania, Philadelphia, PA, USA

© 2011 Elsevier Ltd. All rights reserved.

5.509.1.	**Introduction**	116
5.509.2.	**Methods**	116
5.509.3.	**Process**	118
5.509.3.1.	Encapsulation Systems	118
5.509.3.2.	Natural Materials	119
5.509.3.2.1.	Collagen	119
5.509.3.2.2.	Fibrin	120
5.509.3.2.3.	Chitosan	120
5.509.3.2.4.	Hyaluronic acid	121
5.509.3.2.5.	Alginate	122
5.509.3.3.	Synthetic Polymer Materials	123
5.509.3.3.1.	Poly(ethylene) glycol	123
5.509.3.3.2.	Polyacrylates	124
5.509.3.3.3.	Polyfumarates	124
5.509.3.4.	Composites	125
5.509.4.	**Representative Applications**	125
5.509.4.1.	Diabetes Mellitus	125
5.509.4.2.	Liver	126
5.509.4.3.	Neurological Diseases	126
5.509.4.4.	Cancer	127
5.509.4.5.	Cartilage	127
5.509.5.	**Summary**	128
References		128

Glossary

Bioartifical liver device (BAL) An artificial device, usually used extracorporeally, consisting of functional hepatocytes for patients suffering from liver failure.

Bioartificial organ Synthetically fabricated tissue replacement consisting of functional cells encapsulated in natural or synthetic polymer materials.

Biocompatibility The ability of a material to integrate with cells and tissue and function as intended when implanted *in vivo*.

Cell encapsulation The confinement of cells within a natural or synthetic polymer network.

Cytocompatability The ability of a material to allow for the viable growth of cells and not to act as a toxic component.

Hydrogel A network of natural or synthetic polymer chains that can absorb a high volume of water.

Immune response The body's reaction to a foreign material including bacteria, viruses, and implanted tissue-engineered constructs.

Macroencapsulation Coating or confinement of larger (>2000 μm) particles or cells within a polymer network.

Membrane permeability The ease at which molecules pass through a specific membrane, which is usually a function of membrane porosity and molecule size.

Microencapsulation Coating of small particles or cells with a thin polymer network, generally <2000 μm in size.

Porosity The measure of void space in a material.

Abbreviations

BAL	Bioartificial liver
BDNF	Brain-derived neurotrophic factor
BMSCs	Bone marrow stromal cells
ECM	Extracellular matrix
ESCs	Embryonic stem cells
GAG	Glycosaminoglycan
HA	Hyaluronic acid
HEMA	Hydroxyethyl methacrylate
HUVECs	Human umbilical cord vein endothelial cells
MI	Myocardial infarction
MMP	Matrix metalloproteinase
MSCs	Mesenchymal stem cells
NIT-1	Mouse insulinoma cells
NPCs	Neural precursor cells
PEG	Poly(ethylene glycol)
PLL	Poly-L-lysine
PMMA	Poly(methyl methacrylate)

RDFs	Rat dermal fibroblasts
RGD	Arginine–glycine–aspartic acid
SCI	Spinal cord injury
Tβ4	Thymosin β4
TGF-β	Transforming growth factor beta
TNF-α	Tumor necrosis factor alpha
VEGF	Vascular endothelial growth factor

5.509.1. Introduction

Cell encapsulation generally involves fabricating three-dimensional (3D) scaffolds, either seeded with cells or with cells directly encapsulated, for use as healthy 'replacement' tissue after injury or for the delivery of cells that can release trophic or stimulatory factors to direct repair. A lack of donor organs and tissues and loss of function after tissue loss or injury motivate the need for cell-encapsulated 'bioartificial organ' therapies and replacement tissue. Important considerations when creating these cell delivery devices are cell source, biocompatibility, graft material, graft stability, and performance. Hydrogels are one group of materials that have promise in these strategies because they often have good membrane permeability, are bioactive, are easy to handle, are hydrated, and in some cases can be formed *in vivo*. Key diseases that are being targeted by cell encapsulation therapies include diabetes, liver failure, neurological disorders, bone and cartilage defects, and cancer.[1–3] In order to obtain the US Federal Drug Administration (FDA) approval for clinical use, it is also critical to use strict standardization protocols and consider practical aspects of design, such as scaling up for manufacturing, marketability, and ease of use for surgeons.

The first major factor for encapsulation systems is selecting the appropriate material. Important aspects to consider are material properties (i.e., mechanics, degradation characteristics, diffusion properties), cytocompatibility (especially if cells are present during gelation), the ability to support 3D cell growth and tissue development, and the ease of use for clinical application.[4] There are two major classifications for materials used in cell encapsulation systems, namely, natural and synthetic systems. Natural materials include collagen, fibrin, chitosan, hyaluronic acid (HA), and alginate. There are several advantages of using natural materials; most importantly, they are cytocompatible and cell tolerable. However, since they are naturally formed, it is more difficult to control the mechanics, degradation, cell adhesion, porosity, and gelation process and time. Synthetic materials offer better control over material properties but require additional modifications in order to allow for cell adhesion and promote cell function.

Without viable functional cells, these constructs will not perform, and therefore, a primary concern in encapsulation systems is cell viability. It is important to first consider the diffusion of nutrients, waste, and oxygen through the material, which are a direct function of material thickness and porosity. Depending on the nature of the material, porosity may be controlled by the chemical structure or cross-linking density. Additionally, several methods have been used to increase the porosity of polymer materials, including photopatterning,[5,6] particulate leaching,[7] and gas foaming[8]; however, these techniques are typically not adaptable for direct encapsulation since processing techniques are toxic to cells. Cell-tolerable techniques to control diffusion include chemical manipulations, such as varying the polymer concentration[9] or modulating the cross-link density.[10]

However, this physical control of diffusion may not be sufficient, and other techniques can be used to increase encapsulated cell survival. Examples of this have been shown with encapsulated islet cells, where nitric oxide scavenger cells were added to encapsulation devices to counteract the diffusion of NO_2 from the implant site,[11] and genetic engineering strategies that have been used to decrease the sensitivity of islet cells to NO_2.[12] Another recent strategy has been to use modifications of poly(ethylene glycol) (PEG) to fabricate a hydrogel conjugated to a peptide antagonist to tumor necrosis factor alpha (TNF-α), a proinflammatory cytokine. Using these TNF-α-antagonizing gels, decreased adhesion of TNF-α to cell surfaces and reduced TNF-α-mediated apoptosis was observed in PC-12 cells, mouse pancreatic islets, and human mesenchymal stem cells (MSCs).[13] A similar approach has been used to create a PEG-based hydrogel network that actively reduces reactive oxygen species damage[14] and can be used to target other inflammatory cytokines.

Control of the immune response may also be critical for effectiveness of cell encapsulation systems (see also **Chapter 4.403, The Innate Response to Biomaterials** and **Chapter 4.404, Adaptive Immune Responses to Biomaterials**).[3] A system with low biocompatibility will elicit a foreign body response, causing the formation of a thick fibrotic layer that encapsulates the scaffold and restricts diffusion and blood supply. An immune response is caused by nonspecific protein adsorption to the surface, which attracts macrophages and other immune cells and can trigger the inflammatory response cascade. Even in the best scenario, some inflammatory response may progress and lead to a thin layer of fibrosis; however, the density and size of the capsule needs to be controlled[15] to avoid immune rejection. Techniques to reduce protein adsorption and inflammatory cell adhesion include using a bioinert hydrogel or anchoring bioinert molecules to the material surface. Since natural materials are inherently biocompatible, they may be considered an ideal encapsulation material, yet they can have a stronger possibility of nonspecific protein absorption than many synthetic alternatives.[3] Materials such as alginate and PEG do not interact with many proteins and are therefore more likely to elicit a reduced immune response.[13] Combinations of these strategies may be important in cell encapsulation systems depending on the encapsulation site and properties of encapsulated cells. Other than material considerations, implant size and implantation methods also play a role in the intensity of host immune response.

5.509.2. Methods

Generally, to encapsulate cells into a polymer scaffold, cells and a liquid precursor (scaffold material) are first combined into a uniform suspension (see **Figure 1**). It is important to

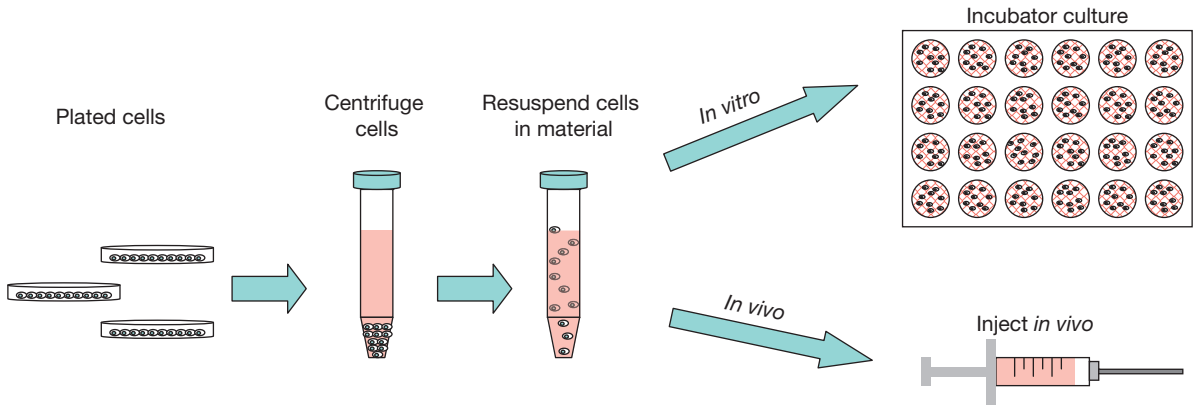

Figure 1 Schematic of cell encapsulation process. Cells are first grown using standard tissue culture procedures. Cells are then removed from the plate, centrifuged, and resuspended in the encapsulation material. After resuspension, cells and materials can be cultured *in vitro* in tissue culture plates or injected *in vivo*, depending on the application.

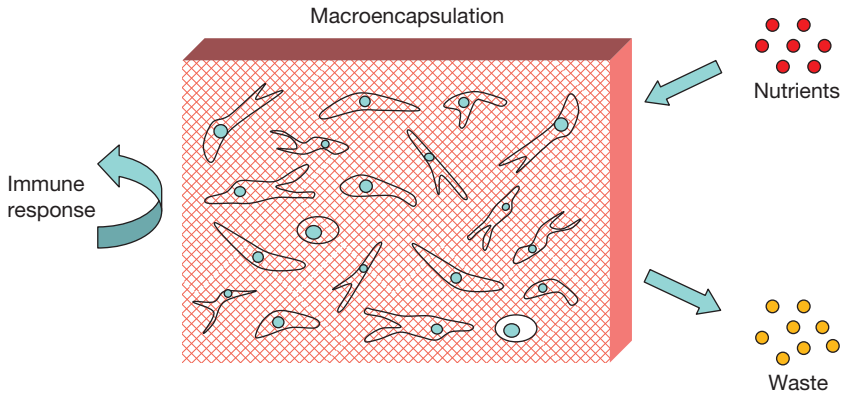

Figure 2 Macroencapsulation strategies involving encapsulation of cells into larger (> 2000 μm) scaffolds, generally used as 'replacement tissue' in various tissue engineering applications.

note the viscosity of the gel precursor solution because a material that is too viscous may produce a shear stress on the cell membrane that can cause cell death. After a uniform mixture of cells and polymer is prepared, the gelation process needs to be activated. Some natural materials, such as collagen, self-assemble with time or temperature. There are several other ways to cross-link materials including photo-cross-linking, redox reactions, thermal cross-linking, chemical cross-linking, and mixtures of the above. Photo-, redox- and thermal-cross-linking systems are controlled by radical-chain polymerization and have the benefit of reacting rapidly but may also produce radicals that can be toxic to cells. Mixed mode reactions take advantage of both methods of cross-linking. Regardless of the cross-linking method, the main considerations in gelation is cytocompatability and gelation time.[4] Depending on the application, cell-encapsulated scaffolds may be cultured *in vitro* prior to implantation or may be directly injected to the injury site *in vivo* as illustrated in Figure 1.

There are two types of common encapsulation systems: macroencapsulation (Figure 2) and microencapsulation (Figure 3). Macroencapsulation is ideal for a defect site where a void in healthy tissue needs to be replaced, such as with skin and neural tissue engineering. In these cases, cell-encapsulated

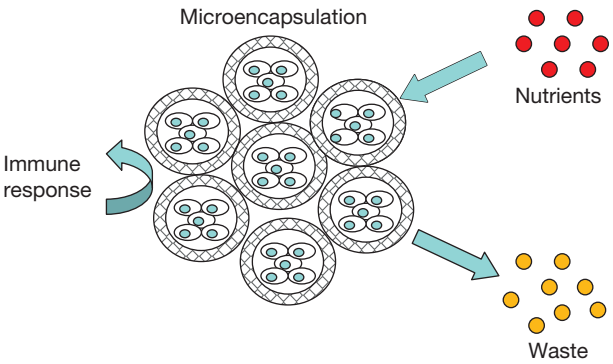

Figure 3 Microencapsulation strategies involving encapsulation of cells into smaller (< 2000 μm) microcapsules that can then be injected *in vivo* and are generally used for cell delivery applications.

devices are used to replace the injured tissue and must therefore be large enough to fill the injury site. For instance, in neural tissue engineering, tissue and encapsulated supporting cells are used to connect severed nerves and must have scaffold cues that span the entire defect. It is important to consider integration of macrocapsules with the surrounding tissue to prevent graft

rejection. Microencapsulation is defined as capsules that are <2000 μm, which generally involve a single cell suspension or a small aggregate of cells in each capsule.[3] This system is ideal for therapies where cell-released trophic factors are needed at a defect site that can be administered through encapsulated cells. In therapies for cancer, for example, cell encapsulation strategies are targeted at injecting genetically engineered encapsulated cells that release tumor reducing factors at the tumor site. Because they are not needed to replace tissue, microencapsulation may be more effective for trophic factor release due to the larger surface area for diffusion and the ability for injection.

Natural materials are commonly used for cell encapsulation processes because of their outstanding biocompatibility. The most commonly used systems are collagen, alginate, chitosan, fibrin, and HA. Collagen has been extensively used as a tissue engineering material and was the main component of an early FDA-approved tissue-engineered product (Apligraf®). It has been used as a base material for several tissue-engineered products including skin,[16] neural,[17] and haptotactic[18] applications. The main benefits of collagen is that it is very biocompatible, allows attachment of a variety of cell types, and self-assembles at 37 °C; however, the mechanics are hard to control and it degrades rapidly as it is replaced by new extracellular matrix (ECM) from interacting cells.

The most popular system for cell microencapsulation is alginate.[1,19] Alginate has been used commercially for years in the food and pharmaceutical industries; has been shown to have superior biocompatibility, long-term stability, and cell viability; and has been used in clinical trials with pancreatic islets as a therapy for diabetes.[20] Alginate encapsulation of islets improves islet cell viability and further improves islet utility by reducing fibrous capsule formation, yet needs rigorous purification steps for effectiveness.[21] Chemically modifying natural materials[22,23] or composites of natural and synthetic materials[24] may offer better control of material properties.

Synthetic materials have the advantage of potential control over gelation time, mechanics, and degradation. PEG,[13,25] polyacrylates (poly(HEMA)),[26] and polyfumarate-based[27] gels and composites[28] have been used for various cell encapsulation strategies. Since synthetic materials do not interact with cells, specific binding sites must be added to promote cell adhesion. This may be advantageous because there is more control over the type of cells that can attach to the material, avoiding problems caused by nonspecific cell adhesion and protein adsorption, which may lead to an increase in immune response. Even with control over mechanics and adhesion, the main disadvantage for synthetic materials is biocompatibility. Whereas natural materials are inherently biocompatible, synthetic materials have to be engineered for this and the biocompatibility of the cross-linker and degradation products must be considered. Commonly used natural and synthetic materials are shown in Table 1.

Beyond material considerations, the other main variable in cell encapsulation systems is the cell source. Cell encapsulation systems serve a function of either replacing damaged tissues at an injury site or providing chemokines released from encapsulated cells. Traditionally, autografts or allografts were used to obtain cells that can then be expanded *in vitro*, encapsulated, and implanted. This is possible in some cases where cells proliferate and expand *in vitro*, such as with skin. However, this is not possible in diseases where sufficient cell sources are not available, such as with liver failure (hepatocytes), diabetes (pancreatic islets), and neurological disorders. In some cases, xenografts are a possible cell source, but there is a concern of cross-species disease contamination. One example where xenografts have been used is with pancreatic islets from swine to treat diabetes.[29] Because of the fear of animal endogenous retrovirus contamination and implant rejection, xenografts have not been used routinely in implantation studies and focus in this field has been in using stem cells as a cell source for 'bioartificial organs' (see also **Chapter 2.209, Materials as Artificial Stem Cell Microenvironments**).

Table 1 Examples of natural, synthetic, and composite encapsulation materials

Natural materials	Collagen
	Fibrin
	Chitosan
	Hyaluronic acid
	Alginate
Synthetic materials	PEG
	Polyacrylates
	Polyfumarates
Composites	

Common stem cell sources are MSCs, bone marrow stromal cells (BMSCs), and embryonic stem cells (ESCs). The main advantage of ESCs is that they are pluripotent, meaning they can differentiate into any cell needed for a particular therapy and it is possible to get a large quantity of these cells. However, due to controversy in obtaining ESCs, and difficulty in controlling their fate, some researchers have refocused on more specialized adult stem cells, such as MSCs. MSCs and BMSCs are promising sources for stem cells, which can be obtained from the adult patient's bone marrow. Not only does this make the cell source noncontroversial but it also decreases the chance of immune rejection. However, they have limited pluripotency. MSCs were thought to only differentiate into mesoderm cells such as osteoblasts, adipocytes, and chondrocytes, though they have recently been shown to have more plasticity.[30] Other multipotent stem cells have also been discovered in various tissue sources such as hematopoietic stem cells and neural stem cells, which are capable of differentiating into cells of their respective organ type, though they may have more pluripotent capabilities.[31]

5.509.3. Process

5.509.3.1. Encapsulation Systems

For typical cell encapsulation processes, polymer and cells are mixed when the polymer solution is in a liquid state, and then the polymer is gelled to entrap cells within its structure (Figure 1). Cross-linking of the hydrogel is typically performed with self-assembly, ionic cross-linking, or chemical cross-linking. Self-assembling materials allow for little control over structural properties such as porosity, and gelation time. However, the main advantage is that it is not necessary to add exogenous components to the gel system that may be toxic to cells. Natural materials such as collagen often self-assemble at 37 °C and have physical cross-links, making it convenient

for cell encapsulation applications. Degradation of natural material is not readily controllable and can be too fast for many tissue engineering applications where new matrix has to be formed by cells to fill the defect site once the scaffold degrades. Also, with natural materials, it is difficult to control cell adhesion and the inflammatory response since this is usually inherent to the material.

Synthetic materials are modified to form gel systems and are generally cross-linked chemically,[32] through redox reactions,[33,34] through radical cross-linking, or by photo-cross-linking.[22,35,36] Through these modifications, polymer materials are able to form hydrogels and encapsulation systems. There are two important considerations to ensure cell viability; all materials and cross-linking solutions must be nontoxic to cells in the liquid phase and the material should gel at 37 °C. It is also important to consider how chemical cross-linking may affect the degradation and remodeling of the material. In some cases, it is possible to coordinate degradation rate with tissue formation rate by synthetically introducing degradation sites.[37] The main benefit of using polymer systems is the ability to control mechanics and pore structure as well as cell adhesion to the material, making it possible to have more control over cell adhesion and the inflammatory response.

Composite materials may offer a combination of both natural biocompatibility and synthetic control over material properties and degradation. Composites with biological materials such as collagen and fibrin allow for cell attachment, while the synthetic polymer offers more mechanical stability. For example, composites with PEG offer a possible reduction in immune response due to the bioinert quality of PEG. By using composite materials, scaffold properties can be tailored for each tissue engineering application. Advantages and disadvantages of natural and synthetic materials used in cell encapsulation systems are shown in **Table 2**.

5.509.3.2. Natural Materials

Natural materials have several advantages including support of cellular functions and endogenous factors that are present to promote cell adhesion, proliferation, and migration. However, since these materials are complex, it may be difficult to control any of these cellular functions. Several natural materials are commonly used for cell encapsulation strategies including collagen, fibrin, chitosan, HA, and alginate. These materials are often purified from tissue and therefore may have some batch-to-batch variation, which can cause problems for clinical applications. Also, they are often derived from animal tissue, which may lead to cross-species disease spreading and an immunogenic or allergic response. Although there are several problems with natural materials, to date, it has not been possible to imitate the complexity of natural tissues using synthetic counterparts, and therefore, these materials are still used for a variety of tissue engineering applications (see also **Chapter 2.220, Extracellular Matrix as Biomimetic Biomaterial: Biological Matrices for Tissue Regeneration**).

Table 2 Advantages and disadvantages of natural and synthetic materials

Natural materials	
Advantages	Cytocompatible
	Promotes cell adhesion, migration, proliferation
Disadvantages	Difficult to control material properties, that is, mechanics, degradation rate, adhesion, porosity
	Difficult to control immune response
	Batch-to-batch variations
Synthetic materials	
Advantages	Control over material properties, that is, mechanics, degradation rate, adhesion, porosity
	Better control over immune response
Disadvantages	Not inherently cytocompatible – may need chemical modification
	Difficult to mimic native structure synthetically
	Degradation products may not be cytocompatible

5.509.3.2.1. Collagen

Collagen is a major component of mammalian tissue and is used for a wide variety of tissue-engineered constructs due to its superior biocompatibility and gelation through self-assembly at 37 °C. The main advantage of collagen is that it contains several cell adhesion sites including RGD, which is a ubiquitous cell adhesion peptide shown to promote interactions with a variety of cells. Collagen gels have been used for several tissue engineering applications including skin, tendon, pancreas, and neural. They promote cell viability and function in 3D culture and cells are able to contract these gels and lay their own matrix to form 'tissue equivalents' for *in vitro* analysis and *in vivo* implantation, which is important for implant integration and vascularization (see also **Chapter 2.215, Collagen: Materials Analysis and Implant Uses** and **Chapter 2.216, Collagen–GAG Materials**).

Though collagen has many advantages, the main disadvantage is the difficulty to control cell adhesion and insufficient mechanics for many applications. One method that has been previously investigated to control the bioactivity of collagen is the conjugation of cell-specific peptides to promote adhesion of particular cell types,[38] which offers some control, but inherent adhesion sites in collagen can lead to adhesion of inflammatory cells, which can be problematic. The mechanics of collagen gels have also been previously controlled through chemical cross-linking using aldehydes, enzymes, and natural cross-linkers such as genipin; however, aldehydes cannot be used in cell encapsulation processes since they are toxic to cells.[39] Even with mechanical cross-linking, collagen stiffness may not be sufficient for some 'hard' tissue engineering applications.

Several approaches have been used in cell-encapsulated collagen gels directed at wound healing and skin repair. Enever *et al.* used rat dermal fibrobrasts (RDFs) encapsulated in collagen gels for skin development and wound healing.[16] Because skin is made up primarily of collagen and fibroblasts, collagen is a valuable material for skin tissue engineering. Chida *et al.* also used a collagen model for skin where collagen gels were contracted by kerotinocytes and fibroblasts to form a skin-like sheet,[40] showing the use of fibroblast-contracted collagen gels as a model for dermis. Schechner *et al.*[41] used collagen–fibronectin gels with human umbilical cord vein endothelial cells (HUVECs) *in vivo* and showed the formation of vasculature. This study shows the importance of using 3D constructs encapsulated with cells; these endothelial cells

increased the formation of vasculature in gels, which is important for graft integration and encapsulated cell survival. Subcutaneous implantation in mice showed that constructs were well vascularized after 31 days, which shows the ability to perfuse collagen gel tissue equivalents.

Cell-contracted collagen gels can be manipulated *in vitro* to increase strength and align fibers. MSCs have been encapsulated in collagen gels, contracted, and loaded in tension for 40 h[42] to form tendon-like structures. These constructs were implanted in a rabbit tendon defect model and significantly improved tendon repair when compared with suture alone, where biomaterial and cells were not used. Collagen encapsulation has also been used for protection and immunoisolation of islets from immune cells and enzymes *in vivo* to increase the viability and function of encapsulated islets.[43] Because of the porous structure of collagen, it allowed full diffusion of insulin, and it was shown that collagen constructs enhanced islet cell survival and function by decreasing immune-response-related cell death. Cell constructs also allowed better vascularization and therefore increased cell survival over 'free' implanted islets. Collagen has also been used for several neural applications including differentiation of ESCs to neural lineages, differentiation of neural precursor cells (NPCs),[44] directing neurons in collagen gels,[17] and promoting neuron growth *in vivo*.[45] Because of the inherent weakness of neural tissue, collagen mechanics may be ideal for this application.

5.509.3.2.2. Fibrin

Fibrin is a polymer that is blood-derived and has been shown to be very biocompatible, can be delivered with growth factors, and can form *in vivo* after injection. It consists of two components: fibrinogen and thrombin. When combined, fibrinogen converts to fibrin and polymerizes to a fibrin mesh similar to what is found during blood clotting *in vivo*. It has been used for a variety of tissue engineering applications including myocardium,[46] cartilage,[47] muscle,[48] liver,[49] skin,[50] neural,[51] and ocular[52] applications. The main advantages of fibrin are its biocompatibility, that it can be injected *in vivo*, and that it degrades into biocompatible products; however, it is often too weak and degrades too rapidly for many tissue engineering applications. It is easy to obtain from blood plasma and has been used alone or in combination with other materials with high potential in tissue engineering. Also, since it is derived from blood components, it can be purified from a patient's own blood to decrease the immune response (see also **Chapter 2.217, Fibrin**).

The mechanics of fibrin gels are traditionally controlled by the concentration of the two components of fibrin. Several studies have shown the effect of this control on angiogenesis, which is important to any cell-encapsulated system for graft cell survival.[53] Without the addition of any growth factors or adhesion sites, fibrin has been shown to promote activity of a variety of cell types, and compliance may be ideal for applications such as neural tissue engineering where soft tissue constructs are desired.[54] Cell-specific peptide adhesion domains have been conjugated to fibrin for further activity of specific cell types such as laminin-derived peptides and neurons. Fibrin has also been used as a glue or sealant for the integration of other engineering constructs.[55]

Because of the possibility of an injection delivery, fibrin has been used in applications where surgical implantation may risk increased infection. Martens *et al.*[46] used a fibrin gel system to improve retention of MSCs in the heart after injection. Previous work showed that use of MSCs is promising in heart repair after myocardial infarction, but they were only able to retain 11% of the cells in the heart after injection. Therefore, cell encapsulation in fibrin gels was used, where gel time and solution viscosity were tailored by varying the concentration of both the fibrinogen and thrombin components, and retention increased to 37%. A similar method was used by Bruns *et al.*[49] to study the injection of fibrin-gel-immobilized hepatocytes into the liver. Here, they found once again that fibrin gel was a suitable matrix for cell viability and support and a useful way to inject a healthy bolus of cells to the liver to improve diseased liver function.

Fibrin hydrogels have also been used as a material for directed stem cell differentiation. Willerth *et al.*[51] differentiated mouse ESCs into neural lineages using controlled differentiation in and on fibrin gels. They found that embryoid bodies encapsulated in fibrin gels (rather than 2D cultures) resulted in greater proliferation and differentiation. After 14 days, they were able to differentiate cells into neurons and astrocytes, which could then be used for neural tissue engineering therapies. Recent work with fibrin and MSCs shows the potential of fibrin structure manipulation in differentiation.[56] Here, they looked at variants in fibrin's binding domain to study MSC differentiation toward osteogenic lineages.

Advances in the use of fibrin include several applications where fibrin is combined with polymer materials to increase its effectiveness. By combining fibrin with controllable polymer materials, one can take advantage of fibrin's biocompatibility while improving its structural properties with a stronger material or one whose mechanics can be controlled. Examples of materials combined with fibrin include PEG,[24,57] polyurethane,[58] alginate,[59] HA,[60] and agarose.[61] These composites provide extra strength and controllability to fibrin gels. In one example, a PEG–fibrin hydrogel was fabricated that retained the biofunctionality of fibrin while having tunable permeability and mesh size, through manipulation of the PEG chain. They were able to correlate changes in structural properties with control of cellular morphology in smooth muscle cell-encapsulated gels.[24]

Although fibrin has many favorable properties for cellular interactions, the major disadvantages of using fibrin is that it degrades rapidly (within a few days), which can be improved through composites. In one study, fibrin was combined with HA to increase longevity in the body. These composite gels were encapsulated with chondrocytes and implanted *in vivo* using a rabbit patellar groove cartilage defect model. Results show that composite scaffolds had higher cell viability and implants lasted longer and better filled the defect site.[60] Composite fibrin materials show great promise in the future of tissue engineering as a cell-encapsulating material.

5.509.3.2.3. Chitosan

Chitosan is a material derived from chitin, which is found in the exoskeleton of crustaceans, and has been used in tissue engineering applications for its biocompatiblity[62] and because it can be degraded through enzymes.[63] Chitosan is a linear

polysaccharide of (1–4)-linked D-glucosamine and *N*-acetyl-D-glucosamine derived from chitin, where the degree of *N*-acetylation determines its crystallinity, which generally varies from 40 to 90%.[63,64] Chitosan has been previously used for encapsulation of hepatocytes and neural cells[65] through modifications with sugar residues and proteins. Because chitosan is a glycosaminoglycan (GAG) analog, and it is known that GAGs play an important role in chondrogenesis, chitosan is an ideal material for cartilage tissue engineering and has been used in many therapies.[64,66–68] Additionally, examination of chitosan implants for immune response show little evidence of foreign body reaction and almost no fibrosis. Several other studies show the use of chitosan-based scaffolds for wound healing,[69] orthopedics,[70] and epithelial cell applications (tracheal tissue)[71]; however, processing techniques make it difficult to encapsulate cells. In most cases, scaffolds are fabricated and used directly, eliciting a low immune response. Chitosan can be chemically modified through primary amino acid groups to increase its use in cell encapsulation. For example, chemically modified chitosan has been encapsulated with MSCs and shows promise as an injectable biomaterial (see also **Chapter 2.213, Chitosan**).[72]

Jin *et al.*[73] showed one application where chitosan was made into an injectable hydrogel through modifications that allow gelation at neutral pH and cross-linking with horseradish peroxidase and H_2O_2. Chondrocytes were encapsulated into these gels and were viable *in vitro* and retained a rounded morphology, which is critical for efficient chondrogenic matrix production. These scaffolds are a promising material for cartilage tissue engineering.

During xenotransplantation of insulin-producing cells as a therapy for diabetes, chitosan/gelatin scaffolds have been shown to have immunosuppressive properties and improved viability and function.[74] In this study, mouse insulinoma cells (NIT-1) were encapsulated in agarose microspheres, which were then encapsulated in a chitosan/gelatin solution and injected subcutaneously (toward the rear of each rat) into rats and the nonfasting blood glucose level was recorded from the tail vein puncturing postoperation. Chitosan/gelatin encapsulation was shown to be cytoprotective and prolonged normal blood sugar levels in rats when compared to unencapsulated constructs.

Chitosan has also been used in neural applications where bone marrow stromal-cell-derived Schwann cells were encapsulated in a chitosan sponge and implanted into a rat sciatic nerve defect model.[75] Schwann cells are supporting cells in the peripheral nervous system and have the ability to guide regenerating axons. In this study, Schwann-cell-encapsulated constructs showed significantly higher numbers and length of regenerating axons compared to non-cell-laden scaffolds. Four months postsurgery, chitosan gels were no longer present. The chitosan not only promoted axon growth but has also been shown to prevent fibrosis, which is important for reconnection of axons after nerve injury.[75,76]

5.509.3.2.4. Hyaluronic acid

HA is a naturally found, nonadhesive, biocompatible polysaccharide that comprises alternating D-glucuronic acid and *N*-acetyl-D-glucosamine and is found in most connective tissues. HA is enzymatically degradable and important in many cellular functions including attachment, proliferation, and migration, and has been previously used for cartilage tissue engineering,[77] neural tissue engineering,[78] and drug delivery. HA can be readily modified on its hydroxyl group with methacrylation[22] and photo-cross-linked to form a hydrogel for cell encapsulation. Varying methacrylation can be used to control the mechanical and degradation characteristics of the hydrogels.[22,79] Additionally, by adding hydrolytically degradable ester linkages, degradation characteristics can be further controlled.[23] **Figure 4** shows the chemical structure of HA with both methacryate and ester linkage conjugation as well as the degradation profiles of these gels. **Figure 4(c)** shows an example of MSCs encapsulated into these gels (see also **Chapter 2.214, Hyaluronic Acid**).

Naturally, HA is nonadhesive to cells; however, adhesive peptides, such as RGD, can be incorporated in the gels and concentrations of these peptides can be altered to control adhesivity. Because of the versatility of HA gels, they are a promising material for use in tissue engineering and, specifically, cell encapsulation strategies. HA has potential use in cardiac tissue engineering because it has recently been shown to have an anti-inflammatory effect and enhanced angiogenesis by the recruitment of endothelial cells, particularly in low molecular weight forms by promoting EC migration, proliferation, and sprouting.[80–82] Angiogenesis effects decrease with increasing molecular weight of HA[83] because it is thought to prevent cellular adhesion through interactions with the CD44 receptor.

HA is primarily utilized to encapsulate cells whose native ECM is rich in HA or GAGs. This allows the constructs to mimic the native cellular environment, which has been shown to positively affect cell fate and viability.[77,84–86] Cartilage and epithelial tissues tend to have a relatively high concentration of HA compared to other tissues, making them ideal for HA constructs. Since HA gelation can be controlled chemically, one approach is to develop an injectable hydrogel to fill defects, regardless of shape. In these systems, an HA solution preloaded with cells to be encapsulated can be injected *in situ* into defects and then polymerized into a gel construct. This way, a nonuniform defect can be filled homogenously without inducing further damage.

Chung *et al.*[36,77,87,88] used HA hydrogels to encapsulate chondrocytes from various sources, resulting in the *in vivo* production of ECM and neocartilage formation. They found that cell source directly affects the nature and composition of ECM produced. Specifically, constructs seeded with articular chondrocytes did not exhibit significant neocartilage formation or an increase in compressive modulus. Constructs composed of auricular chondrocytes, however, showed significant neocartilage formation and bulk growth as well as an increase in compressive modulus.[77] The same group found that seeding MSCs in HA matrices induce these cells to differentiate into chondrocytes.[36,88] By measuring gene expression for proteins upregulated in chondrocytes, such as type II collagen and aggrecan, they found that HA hydrogels seeded with MSCs showed significantly greater chondrogenesis than inert materials such as PEG.[36]

HA has also been investigated for use in repairing bone defects. However, Zou *et al.*[89] showed that HA downregulated bone-related gene expression and may have a moduli too weak

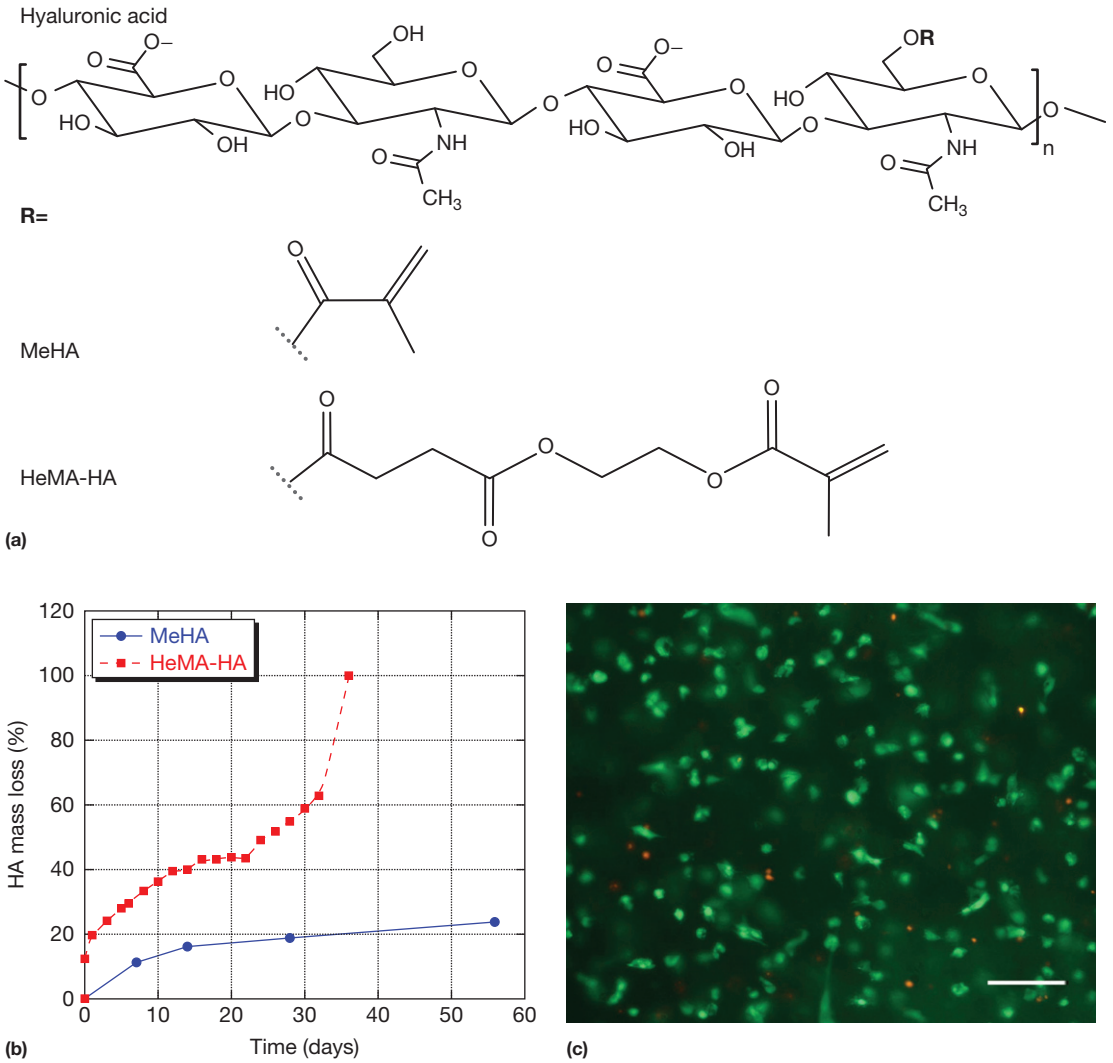

Figure 4 (a) Chemical structure of HA, MeHA, and HeMA-HA. (b) Degradation profile of MeHA and HeMA-HA. HeMA-HA has ester linkages incorporated into the structure allowing for hydrolytic degradation. (c) Live (calcein, green) and dead (ethidium homodimer, red) hMSCs at 1 h post-photo-encapsulation in hyaluronic acid (HA) based hydrogels conjugated with a RGD containing cell-adhesive peptide at a concentration of 1 mM. Scale bar = 100 μm.

for use in bone repair. Due to their compliant nature, HA hydrogels have been investigated for use in neurological disorders. As neurons do not divide or repair themselves, transplantation is an ideal approach. However, transplanted neural cells have low viability *in vivo*. HA has been investigated as a material for neural cell encapsulation constructs to increase viability. For instance, Pan *et al.*[90] found that HA hydrogels allowed NPCs to differentiate into neurons and glial cells for central nervous system repair. Other groups have also attached various differentiation factors to HA hydrogels to increase NPC differentiation and viability. Iwata *et al.* found that hydrogels with ionically attached brain-derived neurotrophic factor (BDNF) increased neuron survival *in vitro*.[91]

5.509.3.2.5. Alginate

Alginate is one of the oldest and most commonly used materials for cell encapsulation strategies due to its superior biocompatibility and bioinert qualities. Alginate is a naturally occurring polysaccharide found in the cell walls of bacteria and plants, most commonly seaweed,[92] and can form a gel in the presence of divalent cations (e.g., calcium or barium) via ionic cross-linking. Though some control of degradation and material mechanics is possible by variations in molecular weight and macromer concentration, as divalent cations are replaced with monovalent cations in the body, alginate will slowly dissolve. Recent chemical advances have afforded more control over mechanics, cross-linking, and degradation of alginate through alginate methacrylation.[4,93] Alginate is very biocompatible but not generally cell adhesive and must be conjugated with cell adhesion peptides[94] or combined with cell adhesive materials such as gelatin[95] to encourage cellular interactions.

Traditionally, alginate is used for immunoisolation of cells that release factors into the body, most commonly insulin-producing cells. This approach has been used as early as 30 years ago for encapsulating xenotransplants of islets[96,97]

to prevent destruction of islet cells by immune response. Though this strategy has had some success, the reverse of insulin dependence has not been able to sustain a long-term effect. Currently used alginate encapsulation systems generally use an alginate–poly-L-lysine (PLL) composite where a final coating of PLL helps control bead strength and diffusion characteristics. The main difficulty with using alginate materials is the need to produce consistent, well-purified, and reproducible gels.[98] Purification is particularly important for the survival of encapsulated cells in alginate microcapsules and current technology leads to a reoccurrence of insulin dependence of ~90% within 5 years of islet transplantation.

Other than for islet transplantation, alginate encapsulation systems have been used for several systems including stem cell differentiation, chondrocyte encapsulation for cartilage tissue engineering, cardiac tissue engineering, and nervous system disorders.[19,95,99–101] Most of the current focus is on decreasing the immunogenic response created by these systems. In a recent study, genetically modified MSCs were encapsulated in alginate–PLL microspheres and injected adjacent to glioblastoma tumors. Cells were genetically modified to release an angiogenesis inhibitor, and significant tumor volume reduction was observed.[102] Alginate–PLL microencapsulation provided immunoisolation for injected cells, increasing cell viability and allowing injection of cell containing microspheres to the site of the tumor.

Alginate has also been used for macroencapsulation studies specifically in cartilage tissue engineering applications. In a recent study with alginate–gelatin composite hydrogels, chondrocyte-laden hydrogels were implanted in a femoral defect sheep model where they showed that cell-laden scaffolds integrated well with surrounding tissue and showed improved cartilage regeneration at the defect site. Alginate–gelatin composites showed good biocompatibility and potential as an osteochondral regeneration matrix.[95]

Recent work has also shown the utility of alginate material for myocardial defects.[100,103] In one study, isolated fetal cardiac cells were grown in porous 3D alginate scaffolds and transplanted onto an infarcted heart, and echocardiography was performed 65 ± 5 days after implantation with cells or sham-operation control. Alginate scaffolds showed increased neovascularization and attenuated left ventricular (LV) dilatation with improved function compared to controls.[100] Other work with human ESCs injected into 3D implanted alginate scaffolds in a rat model of myocardial infarction (MI) showed attenuation of post-MI scar thinning and LV dysfunction.[103] These studies show the utility of cell-encapsulated alginate scaffolds for cardiac applications.

5.509.3.3. Synthetic Polymer Materials

Polymer materials offer advantages over natural materials such as better control over material properties including mechanics, degradation rate, and porosity, but may need to be engineered to introduce desired biological responses. Several synthetic materials are commonly used in cell encapsulation processes including PEG, polyacrylates, and polyfumarate-based gels. Through chemical modifications, the material properties of these scaffolds can be tailored for specific tissue engineering applications. However, since they may not be inherently biocompatible, cell adhesion needs to be controlled through modification with peptide adhesion sites or ECM proteins. In some cases, this can be advantageous by preventing adhesion of immune cells and thus reducing immune response. Additionally, materials can be customized for adhesion of specific cell types while inhibiting the adhesion of others. However, even with intricate chemistries, the goal of synthetic materials is to mimic the complexity of natural materials and this is difficult to accomplish while keeping materials, cross-linkers, and degradation products cell-tolerable (see also **Chapter 1.122, Structural Biomedical Polymers (Nondegradable)** and **Chapter 1.123, Degradable Polymers**).

5.509.3.3.1. Poly(ethylene) glycol

PEG-based gels are the most widely used synthetic polymer in tissue-engineered systems because they have a history of biocompatibility, are bioinert, and allow for chemical modifications to control material properties. Recently, PEG has been used in several composite systems, and a modified PEG has been used as a nontoxic cross-linker.[104] Additionally, several implant systems use PEG coatings to reduce the immune response. PEG has been used in cell encapsulation systems with various cell types including chondrocytes, vascular cells, neuronal cells, and fibroblasts for a wide range of

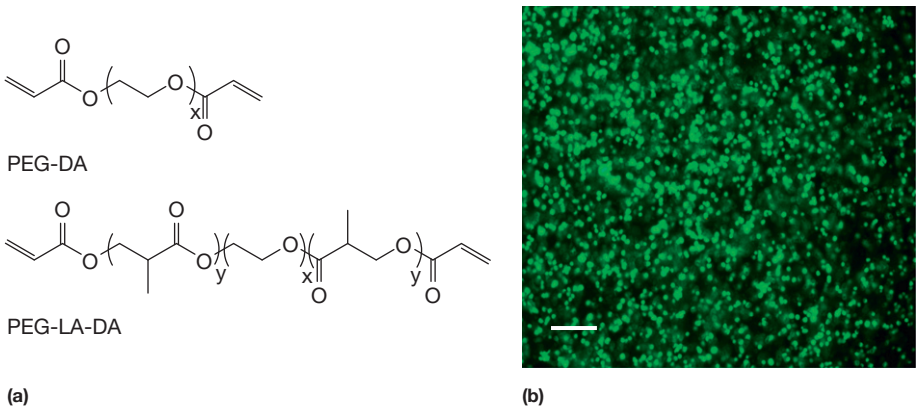

Figure 5 (a) Chemical structure of PEG-DA and PEG-LA-DA. (b) Live (calcein, green) and dead (ethidium homodimer, red) hMSCs at 24 h encapsulation in a PEG hydrogel. Scale bar = 200 μm.

applications.[105–110] Although PEG is naturally nonadhesive, it can be modified with cell-adhesive peptides or used in composite systems with natural bioadhesive materials to provide mechanical and degradation control. Examples of a degradable and a nondegradable PEG used in cell encapsulation systems are shown in Figure 5. Acrylated PEG (PEG-DA) can be conjugated with lactic acid units (PEG-LA-DA) to provide ester linkages for degradation control. MSCs are shown encapsulated in a PEG hydrogel 24 h postencapsulation (Figure 5(b)).

Due to the versatility and ability to modify PEG hydrogels, they are used in many specialized cell-encapsulated hydrogel systems. The simplest modification to increase cell adhesion is the addition of RGD peptide sequences, but various other synthetic peptide sequences have been added to promote specific function. For example, laminin-derived peptides (IKVAV, YIGSR, RGD, IKLLI, LRE, PDSGR) have been conjugated to PEG and were shown to increase viability and functionality of encapsulated β-cells, which are used for insulin production as a treatment for diabetes.[109] In another study, hydrolytically degradable lactide units are conjugated to PEG to allow the hydrogel mesh size to change with time.[105] NPCs were encapsulated in these gels and showed good viability and proliferation with control over degradation and mechanics, which is not possible in natural-based hydrogel systems such as collagen.

Traditionally, immunoisolation strategies rely on the mesh size to reduce the immune response, but proinflammatory cytokines may still diffuse through the barrier because of their small size. Further reduction of mesh size would prevent diffusion of nutrients and waste. A novel study with PEG shows that PEG hydrogels can be conjugated with a peptide sequence that contains a cytokine-antagonizing agent that sequesters TNF-α, a proinflammatory agent, and reduces its effect on encapsulated cells.[13] The diffusion of these cytokines has been shown to cause apoptosis or loss of function of encapsulated cells. Due to the ease of modification of PEG gels, this technique can successfully be adapted to other PEG-based cell encapsulation strategies and can potentially be used in PEG composites.

Another example of specialized hydrogels was recently demonstrated in PEG gels conjugated with matrix metalloproteinase (MMP) and co-encapsulated with HUVECs and a small bioactive peptide, thymosin β4 (Tβ4).[25] In this system, the gel acts as a controlled release device for Tβ4, which is important for HUVEC attachment, and induces vascular-like network formation. Tβ4 increased MMP-2 and MMP-9 secretion in HUVECs, which in turn triggered the release of Tβ4 and increased vascularization and further increased the function of HUVECs. This elegant system is an example of using PEG hydrogels for immunoisolation and cytokine release, which may be important for improved vascularization and can potentially be used with alternate bioactive peptide/cell systems.

Recent chemical advances show the versatility of PEG hydrogels for cell encapsulation and tissue engineering strategies. Additionally, much work has been done with PEG composites, where PEG–gelatin and PEG–fibrinogen composites have shown the utility of natural–synthetic composites which may offer both control and biocompatibility.[24,111] Combinations of these systems may hold the key to future tissue engineering strategies.

5.509.3.3.2. Polyacrylates

Polyacrylates are another form of synthetic polymers that have been used to encapsulate cells for tissue engineering systems and include poly (methyl methacrylate) (PMMA), polyacrylamide, and hydroxyethyl methacrylate (HEMA). Though polyacrylamide and PMMA are used for cell experiments, they are traditionally used in 2D systems, whereas HEMA has been used in several encapsulation studies. Acrylation or methacrylation of polymer materials allows for chemical control of gel formation and mechanics of hydrogels. Due to this increased control of gelation, they are often used in injectable systems to fill irregular-sized defects. One example is the use of goat MSCs encapsulated in an acrylated polymer, acrylated poly(6-aminohexyl propylene phosphate) (PPE-HA-Acrl). Goat MSCs were photoencapsulated and showed good viability and mineralization in the scaffold when grown in osteogenic media, demonstrating the potential for use in bone tissue engineering applications.[112]

HEMA has been used for several encapsulation studies.[26,113–116] In one example, HEMA-methyl methacrylate (HEMA-MMA) was used for immunoisolation of engineered vascular endothelial growth factor (VEGF) producing cells, and enhanced vascularization to improve cell survival *in vivo*.[116] Previous work has shown that HEMA-MMA microcapsules promote encapsulated cell survival only for at most 3 weeks with a significant decrease in cell survival at this time point. When engineered cells were encapsulated, VEGF secretion increased vascularization and therefore cell survival. Such strategies can be used in combination with other cell encapsulation systems to increase encapsulated cell survival through vascularization.

In another study, a collagen–HEMA composite material was used for hepatocyte encapsulation systems targeted for bioartificial liver (BAL) devices.[115] In this case, hepatocytes were encapsulated in microcapsules with a collagen core and HEMA outer shell that controlled mechanical strength and diffusion of nutrients, waste, and chemokines. Bilayer microcapsules were successfully fabricated and showed good viability and functionality of encapsulated hepatocytes. HEMA microcapsules have emerged as an alternative to alginate encapsulation, which traditionally have problems with mechanical strength and purity of alginate.

5.509.3.3.3. Polyfumarates

A more recently developed class of materials is fumarate based, which have the advantage of containing polymerizable vinyl groups and ester linkages that are susceptible to hydrolytic degradation. Since the degradation product is fumarate, which is natural and cytocompatible, this is an attractive material for cell encapsulation strategies.[4] Fumarate-based materials are formed with modifications for injectability, increased degradability, and thermal cross-linking strategies.[33,34,117–119]

In one study, oligo(poly(ethylene glycol) fumarate) (OPF) was used as an injectable, biodegradable cell encapsulation system using a thermal radical cross-linker for orthopedic tissue engineering applications.[33] This material showed good cell viability and differentiation of encapsulated MSCs, with mineralized matrix found throughout the scaffold after 28 days. Additionally, mechanics and degradability can be tailored for other tissue engineering applications through the selection

of cross-linking molecules. In this case, the goal was quick gelation at 37 °C, which was accomplished through a radical-initiation system.

Another example of a fumarate-based material used for cell encapsulation strategies is poly(lactide-*co*-ethylene oxide-*co*-fumarate) (PLEOF), which was used to encapsulate marrow stromal cells.[118] This material was made into an injectable hydrogel where gelation characteristics are controlled by the ratio of MMP-derived peptide cross-linker to methylene bisacrylimide. This material showed osteogenic differentiation of encapsulated cells with mineralized matrix production and has an advantage over natural materials due to the control of mechanics, degradation, and decreased immune response. It is also advantageous over some other synthetic material because it is injectable, which is attractive for irregularly shaped osteochondral defects.

Fumarate-based material composites have also been used for cell macroencapsulation strategies.[119] In one study, OPF hydrogels were combined with TGF-β loaded gelatin microspheres and rabbit marrow MSCs to evaluate the differentiation behavior of MSCs in OPF hydrogels with and without TGF-β and varying swelling ratios controlled by PEG cross-linking. In this study, the authors found that chondrogenic differentiation increased in gels with higher swelling ratios, or increased mesh size, and containing TGF-β microcapsules.

5.509.3.4. Composites

Composites can possess the advantages of several materials, making it possible to tailor tissue-engineered constructs for specific applications. In some cases, combinations of natural materials that are bioactive with polymer materials allow the use of polymer materials without the addition of peptide adhesion sites. In this way, natural materials offer biocompatibility, while synthetic materials can be used to control material properties. Additionally, composite materials may offer better control of mechanics, gelation time, cell adhesion, and porous structure than one material alone.

For example, Liao *et al.* used a composite material of HA and collagen for cartilage tissue engineering because they wanted to take advantage of HA's chondroprotective properties while being able to control gelation and residence time at the defect site through the use of collagen.[120] At optimal HA concentrations, they found an increase in cell proliferation and matrix synthesis compared to collagen alone. If HA is too high, this effect is reduced, which they believe was due to steric hindrance, self-association, and chain entanglement, preventing attachment of chondrocytes and nutrient and waste diffusion. A similar study with fibrin/HA gels showed a significant increase in cartilage-like matrix production and showed that HA was able to delay degradation compared to fibrin alone.[60] HA is a common composite material for cartilage tissue engineering due to its presence in native cartilage tissue.[36,87]

PEG is another material that is often used with composite structures because it reduces nonspecific protein absorption and therefore fibrosis.[121] PEG offers the advantage of being bioinert and having the ability to be chemically modified with various moieties for specific tissue engineering applications. An example of this is a hybrid scaffold of PEG and fibrin where the material retains its bioactivity due to its fibrin backbone, but structural properties such as mechanics and pore size can be chemically controlled. Additionally, a photoinitiated cross-linking mechanism can be incorporated, which is not native to fibrin gel systems.[24] By encapsulating smooth muscle cells, they showed good cell viability in these structures and a high level of physical control. A similar approach was used by Rizzi *et al.*[122] where a genetically engineered protein polymer was synthesized and combined with PEG to form a hybrid material with bioactive properties, as well as chemical control.

Collagen and fibrin are frequently used to make polymer materials bioactive and cell-adhesive.[120,123–127] In one example, fibrin was combined with polyurethane for cartilage tissue engineering. Fibrin (vs. no-fibrin) constructs had higher cell viability, more uniform cell distribution, a threefold increase in retained synthesized GAG, and a two- to sixfold increase in type II collagen and aggrecan gene expression, meaning that chondrocyte phenotype was maintained. However, there is still room for further optimization of fibrin properties in order to prolong chondrocyte phenotype and influence the formation of cartilage-like matrix throughout the constructs.

The future of cell encapsulation technology and the formation of bioartificial organs may be in composite materials that are tailored for each application. Control of adhesion, mechanics, degradation, porosity, and immune response will allow for the creation of materials and cell constructs tailored for each application.[128]

5.509.4. Representative Applications

5.509.4.1. Diabetes Mellitus

Patients suffering from diabetes have deficiencies in producing insulin and therefore cannot control blood glucose levels. Patients suffering from type I diabetes generally rely on exogenous insulin therapy either through injection or by a continuous flow pump. Tissue engineering therapies involve implanting insulin-producing cells to decrease exogenous insulin dependence, and therapies for diabetes are at the forefront of cell encapsulation technologies. The main difficulty in cell injection is rejection or fibrosis that prevents diffusion of insulin, and therefore encapsulation technologies are promising for immunoisolation and overcoming these problems. Several cell sources and materials have been explored. Cell sources include ESCs, tissue progenitor cells, islet cell lines, and xenografts. The most commonly used material for encapsulation is purified alginate, but alginate composites and polysulphones have also been investigated.[129] Initially, the most common cell source was xenografts, which showed a marked reduction in insulin dependence; however, the fear of retrovirus contamination quickly reduced the investigation of this therapy.

The progress of implantation of insulin-producing cells has been slower than initially expected due to the immune response created by implantation and the need for a reproducible immunoprotective barrier for implanted cells.[130] Major concerns for transplantation include hypoxia, biocompatibility of the material, and immunoprotective material properties. In diabetes, the problem is that the immune system destroys original β cells, so immunoprotection is particularly important. The polymer barrier is used to prevent diffusion of large

molecules of the immune system to the encapsulated cells but allow for small molecules such as nutrients and waste to diffuse through.[129] The main advantage of using encapsulated cells is that there is a shortage of donor islets, and using encapsulation methods to reduce immunosuppression will allow for the use of animal islets and engineered insulin-producing cells.[131]

Several materials have been used as a cell encapsulation system for insulin-producing cells, including PEG,[132] chitosan,[74] collagen,[133] and alginate.[134] Cell sources include engineered insulin-producing cells, stem cells, and xenografts, with xenografts being the best at regulating blood glucose levels. Alginate materials have been used in clinical trials, and composite materials of alginate–PEG and alginate–PLL have been investigated to decrease nonspecific protein absorption and increase islet cell survival.[20,135] Alginate provides an immune response suppression barrier that increases the survival rate of islet cells. Several studies have shown the use of alginate-encapsulated islets in various animal models.[98,136–138] The main delay to routine clinical use is the need for a source of highly purified, high-quality alginate. Because alginate is a natural biomaterial, changes in source may cause great variations in material quality. Additionally, specialized purification techniques will be required to decrease the immune response; the amount of purification has a direct effect on islet cell survival.[98] Furthermore, recent work shows the importance of the influence of a specific material on insulin secretion of islet cells, and this could be an important area of further investigation.[139] In a recent study of xenotransplantation of porcine islets into a diabetic dog model, it was found that dogs with implanted porcine islets showed a significant decrease in insulin need,[136] so if the possibility of retrovirus contamination can be reduced, this may be the most direct approach.

5.509.4.2. Liver

Currently, the only treatment for liver failure is a liver transplant, but the shortage of donor livers and risk of immune rejection create a need to find new therapies.[140] Two methods have been proposed for the use of tissue engineering to develop cell-based strategies to target liver failure: extracorporeal BAL devices and implantable tissue engineering constructs. Due to the lack of a proliferative ability of mature hepatocytes, and the anchorage dependency and material sensitivity of hepatocyte and hepatocyte-like cells, cell encapsulation techniques will be important for increased hepatocyte differentiation, to preserve functionality, and for increased cell viability.

For the development of a stable BAL device that can filter a patient's plasma extracorporeally, it is necessary to find a source for metabolically active liver cells. Therefore, the most important goal is to determine the optimal cell source and conditions that would keep these cells metabolically active. The 3D environment is very important for the culture of hepatocytes because they are very sensitive to material and are anchorage dependent.[141] In one example, human fetal hepatocytes were cultured in alginate microcapsules and showed mature hepatocyte properties after 4 weeks. In addition to differentiation and proliferation, cells showed the formation of bile ducts which are typical of the liver. By using alginate microcapsules, cells can easily be released after proliferation for use in therapies[142] or can be used in capsules *in vitro*. In this area of study, the main goal is to develop a large number of functional cells for use in BALs in order to filter plasma for patients with compromised liver function.

Another approach to liver failure is implantable cell therapies that involve cell encapsulation, where cells and materials are injected or implanted onto the compromised liver. Examples of implant material include PEG,[143] alginate,[144,145] collagen,[115] HA,[128] and fibrin.[55] The main advantage of cell encapsulation is that the material can help reduce immune rejection and increase cell survival to promote functionality. The most common material for hepatocyte encapsulation is alginate, which has been used with many cell sources including ESCs, progenitor cells, and mature hepatocytes. In order to maintain hepatocyte function or direct stem cell differentiation into hepatocyte-like cells, it has been shown that it is important for cells to be grown in a natural, liver-like, 3D environment. The first step in liver tissue engineering is developing a system to culture hepatocyte cells *in vitro* in order allow for proliferation to obtain enough cells for *in vivo* use. Since it is known that 3D culture is important, research has been focused on finding the appropriate material system to increase hepatocyte function. In addition to cell source and material, heterotypic implantation or heterotrophic stimulation may be important for hepatocyte function, and several approaches are being investigated.[146–149]

5.509.4.3. Neurological Diseases

The nervous system is one of the most complex systems in the body and requires a multifaceted collaboration between materials, cells, and growth factors for repair after injury or degeneration. The primary cells in the nervous system, neurons, do not proliferate but can grow after injury if provided the right environment. Therefore, tissue engineering strategies may be the key to providing this environment with the inclusion of appropriate materials and supporting cells to direct neurons. Cell encapsulation strategies may include neural precursors, stem cells, neural supportive cells, or genetically engineered cells. It is known that soft materials are important for nerve growth, and several tissue-engineered constructs have been used including collagen,[17] fibrin,[54] HA,[90] and PEG.[150] Cell therapies have been used to target several neurological diseases including multiple sclerosis,[151] Parkinson's disease,[152] Alzheimer's disease,[153] and spinal cord injury (SCI) (see also **Chapter 5.531, Peripheral Nerve Regeneration** and **Chapter 5.532, Nerve Tissue Engineering**).[154]

Though neurons can grow if provided the right environment, supporting cells are important to provide growth factors and myelination and, in some cases, additional neurons are needed for sufficient repair. Hence, cellular encapsulation therapies are a key component of nerve repair strategies including encapsulated Schwann cells, olfactory ensheathing cells, ESCs, and marrow stromal cells.[155] ESCs and NPCs have the potential to differentiate into neurons and glial cells, making them an ideal cell source; however, difficulties in controlling differentiation have limited their use. Encapsulated cells have the important role of providing growth factors and guidance channels for severed neurites and axons and myelinating new growth that was demyelinated due

to injury. Myelination is important for the transmission of electrical signals throughout the nervous system and is necessary for full recovery. Additionally, scaffold cell systems in the nervous system can influence cell alignment; scaffolds should provide a matrix where supporting cells (i.e., Schwann cells, olfactory ensheathing cells) will be aligned and provide guidance to growing axons through the scaffold toward nerve targets. Since an immune response often leads to fibrous tissue formation after nerve injury which blocks the regrowth of neurites, it is important for implant materials to limit this response and provide a matrix for nerve growth.

In encapsulated cell therapies for neurological disorders, it is particularly important to minimize host response because regrowing neurons are unable to cross fibrotic tissue and a decreased immune response increases encapsulated cell survival and function. One example of a cell-encapsulated strategy is for Parkinson's disease, which is characterized by dopamine deficiencies that can cause secondary brain deterioration, loss of motor function, and cognitive issues. In order to treat this, encapsulated dopamine-secreting cells have been implanted to provide a source of dopamine and have shown improved function in rat and primate models, and similar methods have gone into phase 1 clinical trials in Japan[152,153,156] with no immunosupression. Important factors to consider for these therapies are sufficient diffusion of neurotrophic factors through the membrane wall and addressing the lack of the ability of encapsulated cells to integrate with host tissue due to membrane properties.[152]

Several cell encapsulation strategies have been incorporated for central nervous system therapy, mostly targeted at creating cell-encapsulated growth factor-secreting glial cells or neural stem cells to the injury site to promote neurite growth.[150,157–160] In one example, neural progenitor cells were encapsulated in PEG/PLL photopolymerized hydrogels, which form a porous soft hydrogel environment for cell growth. Neural progenitor cells showed high viability and ~55% differentiation into mature neurons with the rest of the cells primarily in the undifferentiated state. These gels have potential in the central nervous system as an environment that supports neuron differentiation and growth potential in combination with other therapies,[150] possibly ones that will include directed differentiation of neural precursors to both neurons and glia. Another recent approach in cell encapsulation therapy for SCI is the implantation of alginate-encapsulated BDNF-producing fibroblasts. Encapsulated cells provided significantly greater functional recovery than unencapsulated cell implant controls. This study shows the functionality of alginate as an environment for neurite growth and the use of encapsulated engineered cells for release of therapeutic factors.[154] In researching cures for neurological disorders, it is expected that a combination of therapies will be necessary to reverse motor and cognitive loss. This therapy will most likely include the use of implanted materials, cells, and growth factors to promote growth of injured and degenerate neurons.

5.509.4.4. Cancer

In the last 10 years, genetically engineered cells that release chemotherapeutic factors targeted at the tumor site have shown promise for use in cancer therapies to avoid toxic effects of systemic administration. Initially, cells were injected into the injury site and this approach showed promise; however, graft rejection is often cited as the biggest concern. To overcome this problem, autologous cells have been used, but this process is time consuming and cannot be scaled up since each patient's cells must be custom-genetically-engineered. An alternative approach is cell-encapsulated constructs. By tailoring the encapsulation material, this strategy can reduce the immune response while implanting cells directly to the tumor site. Manipulating scaffold properties can control diffusion of chemotherapeutic factors. Several studies have shown the use of encapsulated cell technology for tumor suppression through cell release of different factors.[161–164] Novel technologies in cancer therapy involve genetically engineered cells that are programmed to secret molecules specific for tumor suppression.

One example of this is an approach by Cirone *et al.* to engineer nonautologous mouse myoblasts to secrete interleukin-2 while encapsulated in alginate–PLL–alginate microcapsules. Secreted interleukin-2 is targeted toward HER-2/*neu*-expressing tumors in a mouse model and this system has been shown to slow tumor progression and increase animal survival.[161] A similar approach was used in a phase I/II clinical trial where genetically modified allogenic cells that express the cytochrome P450 enzyme which locally activated systemically administered ifosfamide at a tumor site, leading to some success in targeted therapeutics.[163] Additionally, work has been done in encapsulating endostatin-secreting cells in alginate microcapsules and, when implanted proximal to glioblatomas, they were found to decrease tumor growth by >70%.[165–167] These studies illustrate the ability to use angiogenesis inhibitors for cancer treatment.

Hao *et al.*[162] recently investigated the use of genetically engineered alginate-encapsulated cells that release TNF-α. Systemic administration of TNF-α has been shown to regress tumors, but is only tolerated at low doses in human trials. In this approach, the encapsulated genetically engineered J558 cells that release TNF-α were implanted into the tumor and significant tumor cell necrosis and reduction of tumor size were observed.

5.509.4.5. Cartilage

In cartilage tissue engineering, there are important considerations of cell type and materials with the goal to deliver cells and growth factors to the defect site. Several cell types have been investigated, including chondrocytes, fibroblasts, and stem cells. Cartilage is composed of a sparse network of cells distributed in a dense matrix composed of type II collagen and proteoglycans important for specialized mechanics of cartilage tissue. As a result of an increased aging population, obesity, and a more active adult population, damage to cartilage due to osteoarthritis, degenerative joint disease, or injury is increasing, leading to the need for cartilage repair strategies. Due to the low numbers of natural chondrocytes available, other cell sources and materials that promote chondrogenesis and proliferation are being investigated. Various natural and synthetic materials have been used for cell encapsulation strategies in cartilage tissue engineering including collagen, chitosan,

fibrinogen, HA, alginate, PEG-based materials, and fumarate-based materials. Important considerations for cartilage materials are degradation control, cell viability, differentiation, proliferation, ECM production, diffusion of nutrients/waste, the ability to fill the defect site, interaction with surrounding native cartilage, and ability to provide mechanical support at the defect site.[168] Injectable scaffolds may be particularly useful in cartilage tissue engineering due to the irregular defect size (see also **Chapter 5.515, Cartilage Tissue Engineering**).

Natural materials most often used in cartilage tissue engineering strategies are chitosan and HA due to the high content of GAGs. In a recent study with injectable chitosan and sheep chondrocytes, injected chondrocytes encapsulated in temperature-responsive chitosan showed high matrix production *in vivo* and a potential to repair cartilage defects.[169] Though this approach was successful, the main issue is the lack of a sufficient source of chondrocytes for cartilage repair.

PEG is the most widely used synthetic material for cartilage tissue engineering. A recent approach with PEG-encapsulated chondrocytes used dynamic loading to promote cartilage development.[170,171] In this study, a hydrolytically degradable PEG was used and physiological loading conditions were used *in vitro* to evaluate the potential of PEG-based hydrogels for cartilage tissue engineering. Dynamic loading causes an increase in gel degradation behavior.[171] Chondrocyte function, specifically anabolic and catabolic activity, increased in PEG gels for scaffolds with early application of dynamic loading, which may be important for cartilage repair.[170] Due to the ease of tailoring PEG hydrogels, the possibility to control mechanics and degradation can influence chondrocyte function *in vivo*.

Another important approach is the use of HA and MSCs. MSCs have the potential to be a cell source for cartilage tissue engineering because they can proliferate and differentiate into chondrocytes. Mechanical properties of HA can be controlled by increases in methacrylate or acrylate modification, and *in vitro* and *in vivo* studies have shown the viability and functionally of MSCs encapsulated in HA hydrogels.[22,23,36,88,172] HA is naturally found in cartilage and contains cell surface receptors that may be important for chondrogenesis, including CD44, CD54, and CD168. When compared to differentiation in PEG, a bioinert scaffold, MSCs encapsulated in HA showed upregulation of cartilage-specific markers *in vivo*.[172] In a rabbit defect model, MSCs encapsulated in a composite of HA and gelatin were shown to increase defect repair when compared to material-only and cell-only controls. In the experimental group, defects were completely filled with firm, translucent cartilage at 12 weeks and showed superior integration with host tissue.[173]

5.509.5. Summary

It is becoming apparent that the encapsulation of cells in either natural or synthetic materials is a useful technology for a range of applications, including islet cell encapsulation for diabetes or for the delivery of cells for tissue regeneration. The material component is essential and must be designed appropriately from the gelation process to the final material properties that support the functionality of the approach, and considerations of cellular viability and immune response must be taken into account. The material component may be engineered for the appropriate physical properties, such as mechanics and cross-linking, as well as cellular interactions. The cell component may include allogenic transplants, xenogenic sources and may even involve genetic manipulation for enhanced results. Future directions will include advances in material design and processing, as well as in the engineering of cells for desired outcomes.

References

1. Lanza, R. P.; Hayes, J. L.; Chick, W. L. *Nat. Biotechnol.* **1996**, *14*, 1107–1111.
2. Orive, G.; Hernandez, R. M.; Gascon, A. R.; *et al. Nat. Med.* **2003**, *9*, 104–107.
3. Schmidt, J. J.; Rowley, J.; Kong, H. J. *J. Biomed. Mater. Res. A* **2008**, *87*, 1113–1122.
4. Nicodemus, G. D.; Bryant, S. J. *Tissue Eng. B Rev.* **2008**, *14*, 149–165.
5. Hahn, M. S.; Taite, L. J.; Moon, J. J.; Rowland, M. C.; Ruffino, K. A.; West, J. L. *Biomaterials* **2006**, *27*, 2519–2524.
6. Lee, S. H.; Moon, J. J.; West, J. L. *Biomaterials* **2008**, *29*, 2962–2968.
7. Studenovska, H.; Slouf, M.; Rypacek, F. *J. Mater. Sci. Mater. Med.* **2008**, *19*, 615–621.
8. Salerno, A.; Oliviero, M.; Di Maio, E.; Iannace, S.; Netti, P. A. *J. Mater. Sci. Mater. Med.* **2009**, *20*, 2043–2051.
9. Gunn, J. W.; Turner, S. D.; Mann, B. K. *J. Biomed. Mater. Res. A* **2005**, *72*, 91–97.
10. Khetan, S.; Katz, J. S.; Burdick, J. A. *Soft Matter* **2009**, *5*, 1601–1606.
11. Wiegand, F.; Kroncke, K. D.; Kolb-Bachofen, V. *Transplantation* **1993**, *56*, 1206–1212.
12. Rabinovitch, A.; Suarez-Pinzon, W.; Strynadka, K.; *et al. Diabetes* **1999**, *48*, 1223–1229.
13. Lin, C. C.; Metters, A. T.; Anseth, K. S. *Biomaterials* **2009**, *30*, 4907–4914.
14. Cheung, C. Y.; McCartney, S. J.; Anseth, K. S. *Adv. Funct. Mater.* **2008**, *18*, 3119–3126.
15. Uludag, H.; De Vos, P.; Tresco, P. A. *Adv. Drug Deliv. Rev.* **2000**, *42*, 29–64.
16. Enever, P. A.; Shreiber, D. I.; Tranquillo, R. T. *J. Surg. Res.* **2002**, *105*, 160–172.
17. Sundararaghavan, H. G.; Monteiro, G. A.; Firestein, B. L.; Shreiber, D. I. *Biotechnol. Bioeng.* **2009**, *102*, 632–643.
18. Ranucci, C. S.; Kumar, A.; Batra, S. P.; Moghe, P. V. *Biomaterials* **2000**, *21*, 783–793.
19. Maguire, T.; Novik, E.; Schloss, R.; Yarmush, M. *Biotechnol. Bioeng.* **2006**, *93*, 581–591.
20. Soon-Shiong, P.; Heintz, R. E.; Merideth, N.; *et al. Lancet* **1994**, *343*, 950–951.
21. Mallett, A. G.; Korbutt, G. S. *Tissue Eng. A* **2009**, *15*, 1301–1309.
22. Burdick, J. A.; Chung, C.; Jia, X.; Randolph, M. A.; Langer, R. *Biomacromolecules* **2005**, *6*, 386–391.
23. Sahoo, S.; Chung, C.; Khetan, S.; Burdick, J. A. *Biomacromolecules* **2008**, *9*, 1088–1092.
24. Dikovsky, D.; Bianco-Peled, H.; Seliktar, D. *Biomaterials* **2006**, *27*, 1496–1506.
25. Kraehenbuehl, T. P.; Ferreira, L. S.; Zammaretti, P.; Hubbell, J. A.; Langer, R. *Biomaterials* **2009**, *30*, 4318–4324.
26. Babensee, J. E.; Sefton, M. V. *Tissue Eng.* **2000**, *6*, 165–182.
27. Fisher, J. P.; Jo, S.; Mikos, A. G.; Reddi, A. H. *J. Biomed. Mater. Res. A* **2004**, *71*, 268–274.
28. Frisman, I.; Seliktar, D.; Bianco-Peled, H. *Acta Biomater.* **2009**, *6*, 2518–2524.
29. Hunter, P. *EMBO Rep.* **2009**, *10*, 554–557.
30. Uccelli, A.; Moretta, L.; Pistoia, V. *Nat. Rev. Immunol.* **2008**, *8*, 726–736.
31. Alison, M. R.; Poulsom, R.; Forbes, S.; Wright, N. A. *J. Pathol.* **2002**, *197*, 419–423.
32. Shu, X. Z.; Ahmad, S.; Liu, Y.; Prestwich, G. D. *J. Biomed. Mater. Res. A* **2006**, *79*, 902–912.
33. Temenoff, J. S.; Park, H.; Jabbari, E.; *et al. Biomacromolecules* **2004**, *5*, 5–10.
34. Zhang, M. W.; Park, H.; Guo, X.; *et al. Tissue Eng. C Meth.* **2009**.
35. Bryant, S. J.; Bender, R. J.; Durand, K. L.; Anseth, K. S. *Biotechnol. Bioeng.* **2004**, *86*, 747–755.
36. Chung, C.; Beecham, M.; Mauck, R. L.; Burdick, J. A. *Biomaterials* **2009**, *30*, 4287–4296.
37. Rice, M. A.; Homier, P. M.; Waters, K. R.; Anseth, K. S. *J. Tissue Eng. Regen. Med.* **2008**, *2*, 418–429.
38. Monteiro, G. A.; Fernandes, A. V.; Sundararaghavan, H. G.; Shreiber, D. I. *Tissue Eng. A* **2009**, *15*, 1–11.

39. Sundararaghavan, H. G.; Monteiro, G. A.; Lapin, N. A.; Chabal, Y. J.; Miksan, J. R.; Shreiber, D. I. *J. Biomed. Mater. Res. A* **2008**, *87*, 308–320.
40. Ikuta, S.; Sekino, N.; Hara, T.; Saito, Y.; Chida, K. *Biosci. Biotechnol. Biochem.* **2006**, *70*, 2669–2675.
41. Schechner, J. S.; Nath, A. K.; Zheng, L.; *et al. Proc. Natl. Acad. Sci. USA* **2000**, *97*, 9191–9196.
42. Young, R. G.; Butler, D. L.; Weber, W.; Caplan, A. I.; Gordon, S. L.; Fink, D. J. *J. Orthop. Res.* **1998**, *16*, 406–413.
43. Hiscox, A. M.; Stone, A. L.; Limesand, S.; Hoying, J. B.; Williams, S. K. *Tissue Eng. A* **2008**, *14*, 433–440.
44. Ma, W.; Fitzgerald, W.; Liu, Q. Y.; *et al. Exp. Neurol.* **2004**, *190*, 276–288.
45. Hatami, M.; Mehrjardi, N. Z.; Kiani, S.; *et al. Cytotherapy* **2009**, *11*, 1–13.
46. Martens, T. P.; Godier, A. F.; Parks, J. J.; *et al. Cell Transplant.* **2009**, *18*, 297–304.
47. Peretti, G. M.; Xu, J. W.; Bonassar, L. J.; Kirchhoff, C. H.; Yaremchuk, M. J.; Randolph, M. A. *Tissue Eng.* **2006**, *12*, 1151–1168.
48. Huang, Y. C.; Dennis, R. G.; Larkin, L.; Baar, K. *J. Appl. Physiol.* **2005**, *98*, 706–713.
49. Bruns, H.; Kneser, U.; Holzhuter, S.; *et al. Tissue Eng.* **2005**, *11*, 1718–1726.
50. Currie, L. J.; Sharpe, J. R.; Martin, R. *Plast Reconstr. Surg.* **2001**, *108*, 1713–1726.
51. Willerth, S. M.; Arendas, K. J.; Gottlieb, D. I.; Sakiyama-Elbert, S. E. *Biomaterials* **2006**, *27*, 5990–6003.
52. Rama, P.; Bonini, S.; Lambiase, A.; *et al. Transplantation* **2001**, *72*, 1478–1485.
53. Kniazeva, E.; Putnam, A. J. *Am. J. Physiol. Cell Physiol.* **2009**, *297*, C179–C187.
54. Uibo, R.; Laidmae, I.; Sawyer, E. S.; *et al. Biochim. Biophys. Acta* **2009**, *1793*, 924–930.
55. Ahmed, T. A.; Dare, E. V.; Hincke, M. *Tissue Eng. B Rev.* **2008**, *14*, 199–215.
56. Martino, M. M.; Mochizuki, M.; Rothenfluh, D. A.; Rempel, S. A.; Hubbell, J. A.; Barker, T. H. *Biomaterials* **2009**, *30*, 1089–1097.
57. Zhang, G.; Wang, X.; Wang, Z.; Zhang, J.; Suggs, L. *Tissue Eng.* **2006**, *12*, 9–19.
58. Eyrich, D.; Wiese, H.; Maier, G.; *et al. Tissue Eng* **2007**, *13*, 2207–2218.
59. Yoo, W. J.; Choi, I. H.; Chung, C. Y.; Cho, T. J.; Kim, I. O.; Kim, C. J. *Acta Orthop.* **2005**, *76*, 628–636.
60. Park, S. H.; Cui, J. H.; Park, S. R.; Min, B. H. *Artif. Organs* **2009**, *33*, 439–447.
61. Alaminos, M.; Del Carmen Sanchez-Quevedo, M.; Munoz-Avila, J. I.; *et al. Invest. Ophthalmol. Vis. Sci.* **2006**, *47*, 3311–3317.
62. VandeVord, P. J.; Matthew, H. W.; DeSilva, S. P.; Mayton, L.; Wu, B.; Wooley, P. H. *J. Biomed. Mater. Res.* **2002**, *59*, 585–590.
63. Drury, J. L.; Mooney, D. J. *Biomaterials* **2003**, *24*, 4337–4351.
64. Suh, J. K.; Matthew, H. W. *Biomaterials* **2000**, *21*, 2589–2598.
65. Lee, K. Y.; Mooney, D. J. *Chem. Rev.* **2001**, *101*, 1869–1879.
66. Bernstein, P.; Dong, M.; Corbeil, D.; Gelinsky, M.; Gunther, K. P.; Fickert, S. *Biotechnol. Prog.* **2009**, *25*, 1146–1152.
67. Breyner, N. M.; Hell, R. C.; Carvalho, L. R.; *et al. Cell Tissue Organs* **2009**, *191*, 119–128.
68. Tigli, R. S.; Gumusderelioglu, M. *Biotechnol. Bioeng.* **2009**, *104*, 601–610.
69. Boateng, J. S.; Matthews, K. H.; Stevens, H. N.; Eccleston, G. M. *J. Pharm. Sci.* **2008**, *97*, 2892–2923.
70. Hong, Y.; Mao, Z.; Wang, H.; Gao, C.; Shen, J. *J. Biomed. Mater. Res. A* **2006**, *79*, 913–922.
71. Risbud, M.; Endres, M.; Ringe, J.; Bhonde, R.; Sittinger, M. *J. Biomed. Mater. Res.* **2001**, *56*, 120–127.
72. Yan, J.; Yang, L.; Wang, G.; Xiao, Y.; Zhang, B.; Qi, N. *J. Biomater. Appl.* **2009**, *15*, 407–416.
73. Jin, R.; Moreira Teixeira, L. S.; Dijkstra, P. J.; *et al. Biomaterials* **2009**, *30*, 2544–2551.
74. Yang, K. C.; Wu, C. C.; Lin, F. H.; *et al. Xenotransplantation* **2008**, *15*, 407–416.
75. Ishikawa, N.; Suzuki, Y.; Dezawa, M.; *et al. J. Biomed. Mater. Res. A* **2009**, *89*, 1118–1124.
76. Ishikawa, N.; Suzuki, Y.; Ohta, M.; *et al. J. Biomed. Mater. Res. A* **2007**, *83*, 33–40.
77. Chung, C.; Erickson, I. E.; Mauck, R. L.; Burdick, J. A. *Tissue Eng. A* **2008**, *14*, 1121–1131.
78. Wei, Y. T.; Tian, W. M.; Yu, X.; *et al. Biomed. Mater.* **2007**, *2*, S142–S146.
79. Bencherif, S. A.; Srinivasan, A.; Horkay, F.; Hollinger, J. O.; Matyjaszewski, K.; Washburn, N. R. *Biomaterials* **2008**, *29*, 1739–1749.
80. Genasetti, A.; Vigetti, D.; Viola, M.; *et al. Connect. Tissue Res.* **2008**, *49*, 120–123.
81. Ibrahim, S.; Ramamurthi, A. *J. Tissue Eng. Regen. Med.* **2008**, *2*, 22–32.
82. Ji, Y.; Ghosh, K.; Shu, X. Z.; *et al. Biomaterials* **2006**, *27*, 3782–3792.
83. Borselli, C.; Oliviero, O.; Battista, S.; Ambrosio, L.; Netti, P. A. *J. Biomed. Mater. Res. A* **2007**, *80*, 297–305.
84. Almond, A. *Cell. Mol. Life Sci.* **2007**, *64*, 1591–1596.
85. Pan, L.; Ren, Y.; Cui, F.; Xu, Q. *J. Neurosci. Res.* **2009**, *87*, 3207–3220.
86. Pardue, E. L.; Ibrahim, S.; Ramamurthi, A. *Organogenesis* **2008**, *4*, 203–214.
87. Chung, C.; Mesa, J.; Randolph, M. A.; Yaremchuk, M.; Burdick, J. A. *J. Biomed. Mater. Res. A* **2006**, *77*, 518–525.
88. Erickson, I. E.; Huang, A. H.; Chung, C.; Li, R. T.; Burdick, J. A.; Mauck, R. L. *Tissue Eng. A* **2009**, *15*, 1041–1052.
89. Zou, L.; Zou, X.; Chen, L.; *et al. J. Orthop. Res.* **2008**, *26*, 713–720.
90. Pan, L.; Ren, Y.; Cui, F.; Xu, Q. *J. Neurosci. Res.* **2009**, *87*, 3207–3220.
91. Nakaji-Hirabayashi, T.; Kato, K.; Iwata, H. *Biomaterials* **2009**, *30*, 4581–4589.
92. Smidsrod, O.; Skjak-Braek, G. *Trends Biotechnol.* **1990**, *8*, 71–78.
93. Jeon, O.; Bouhadir, K. H.; Mansour, J. M.; Alsberg, E. *Biomaterials* **2009**, *30*, 2724–2734.
94. Orive, G.; De Castro, M.; Kong, H. J.; *et al. J. Control. Release* **2009**, *135*, 203–210.
95. Schagemann, J. C.; Erggelet, C.; Chung, H. W.; Lahm, A.; Kurz, H.; Mrosek, E. H. *Tissue Eng. A* **2009**, *15*, 75–82.
96. Gates, R. J.; Lazarus, N. R. *Lancet* **1977**, *2*, 1257–1259.
97. Lim, F.; Sun, A. M. *Science* **1980**, *210*, 908–910.
98. Langlois, G.; Dusseault, J.; Bilodeau, S.; Tam, S. K.; Magassouba, D.; Halle, J. P. *Acta Biomater.* **2009**, *5*, 3433–3440.
99. Karoubi, G.; Ormiston, M. L.; Stewart, D. J.; Courtman, D. W. *Biomaterials* **2009**, *30*, 5445–5455.
100. Leor, J.; Aboulafia-Etzion, S.; Dar, A.; *et al. Circulation* **2000**, *102*, III56–61.
101. Visted, T.; Bjerkvig, R.; Enger, P. O. *Neuro Oncol.* **2001**, *3*, 201–210.
102. Goren, A.; Dahan, N.; Goren, E.; Baruch, L.; Machluf, M. *FASEB J.* **2009**, *24*, 22–31.
103. Leor, J.; Gerecht, S.; Cohen, S.; *et al. Heart* **2007**, *93*, 1278–1284.
104. Park, H.; Temenoff, J. S.; Tabata, Y.; Caplan, A. I.; Mikos, A. G. *Biomaterials* **2007**, *28*, 3217–3227.
105. Mahoney, M. J.; Anseth, K. S. *Biomaterials* **2006**, *27*, 2265–2274.
106. Nuttelman, C. R.; Tripodi, M. C.; Anseth, K. S. *Matrix Biol.* **2005**, *24*, 208–218.
107. Nuttelman, C. R.; Tripodi, M. C.; Anseth, K. S. *J. Biomed. Mater. Res. A* **2006**, *76*, 183–195.
108. Salinas, C. N.; Cole, B. B.; Kasko, A. M.; Anseth, K. S. *Tissue Eng.* **2007**, *13*, 1025–1034.
109. Weber, L. M.; Hayda, K. N.; Haskins, K.; Anseth, K. S. *Biomaterials* **2007**, *28*, 3004–3011.
110. Weber, L. M.; He, J.; Bradley, B.; Haskins, K.; Anseth, K. S. *Acta Biomater.* **2006**, *2*, 1–8.
111. Zhang, J.; Skardal, A.; Prestwich, G. D. *Biomaterials* **2008**, *29*, 4521–4531.
112. Li, Q.; Wang, J.; Shahani, S.; *et al. Biomaterials* **2006**, *27*, 1027–1034.
113. Cheng, D.; Sefton, M. V. *Tissue Eng. A* **2009**, *15*, 1929–1939.
114. Gan, T.; Zhang, Y.; Guan, Y. *Biomacromolecules* **2009**, *10*, 1410–1415.
115. Quek, C. H.; Li, J.; Sun, T.; *et al. Biomaterials* **2004**, *25*, 3531–3540.
116. Vallbacka, J. J.; Sefton, M. V. *Tissue Eng.* **2007**, *13*, 2259–2269.
117. Guo, X.; Park, H.; Liu, G.; *et al. Biomaterials* **2009**, *30*, 2741–2752.
118. He, X.; Jabbari, E. *Biomacromolecules* **2007**, *8*, 780–792.
119. Park, H.; Guo, X.; Temenoff, J. S.; *et al. Biomacromolecules* **2009**, *10*, 541–546.
120. Liao, E.; Yaszemski, M.; Krebsbach, P.; Hollister, S. *Tissue Eng.* **2007**, *13*, 537–550.
121. Lee, D. Y.; Nam, J. H.; Byun, Y. *J. Biomater. Sci. Polym. Ed.* **2004**, *15*, 753–766.
122. Rizzi, S. C.; Ehrbar, M.; Halstenberg, S.; *et al. Biomacromolecules* **2006**, *7*, 3019–3029.
123. Hao, W.; Pang, L.; Jiang, M.; Lv, R.; Xiong, Z.; Hu, Y. Y. *J. Orthop. Res.* **2009**, *28*, 252–257.
124. Heymer, A.; Bradica, G.; Eulert, J.; Noth, U. *J. Tissue Eng. Regen. Med.* **2009**, *3*, 389–397.
125. Lee, C. R.; Grad, S.; Gorna, K.; Gogolewski, S.; Goessl, A.; Alini, M. *Tissue Eng.* **2005**, *11*, 1562–1573.
126. Li, Z.; Kupcsik, L.; Yao, S. J.; Alini, M.; Stoddart, M. J. *Tissue Eng. A* **2009**, *15*, 1729–1737.
127. Park, S. H.; Park, S. R.; Chung, S. I.; Pai, K. S.; Min, B. H. *Artif. Organs* **2005**, *29*, 838–845.
128. Serban, M. A.; Prestwich, G. D. *Methods* **2008**, *45*, 93–98.
129. Beck, J.; Angus, R.; Madsen, B.; Britt, D.; Vernon, B.; Nguyen, K. T. *Tissue Eng.* **2007**, *13*, 589–599.
130. van Schilfgaarde, R.; de Vos, P. *J. Mol. Med.* **1999**, *77*, 199–205.
131. de Vos, P.; Hamel, A. F.; Tatarkiewicz, K. *Diabetologia* **2002**, *45*, 159–173.

132. Xie, D.; Smyth, C. A.; Eckstein, C.; *et al*. *Biomaterials* **2005**, *26*, 403–412.
133. Manson, M. N.; Arnold, C. A.; Mahoney, M. J. *Tissue Eng. A* **2009**, *15*, 3799–3808.
134. Korbutt, G. S.; Mallett, A. G.; Ao, Z.; Flashner, M.; Rajotte, R. V. *Diabetologia* **2004**, *47*, 1810–1818.
135. Orive, G.; Hernandez, R. M.; Rodriguez Gascon, A.; *et al*. *Trends Biotechnol*. **2004**, *22*, 87–92.
136. Abalovich, A. G.; Bacque, M. C.; Grana, D.; Milei, J. *Transplant. Proc*. **2009**, *41*, 328–330.
137. Antosiak-Iwanska, M.; Sitarek, E.; Sabat, M.; Godlewska, E.; Kinasiewicz, J.; Werynski, A. *Pol. Arch. Med. Wewn*. **2009**, *119*, 311–317.
138. Teramura, Y.; Iwata, H. *Biomaterials* **2009**, *30*, 2270–2275.
139. Weber, L. M.; Anseth, K. S. *Matrix Biol*. **2008**, *27*, 667–673.
140. Dalgetty, D. M.; Medine, C. N.; Iredale, J. P.; Hay, D. C. *Am. J. Physiol. Gastrointest. Liver Physiol*. **2009**, *297*, G241–G248.
141. Kim, I. Y.; Seo, S. J.; Moon, H. S.; *et al*. *Biotechnol. Adv*. **2008**, *26*, 1–21.
142. Cheng, N.; Wauthier, E.; Reid, L. M. *Tissue Eng. A* **2008**, *14*, 1–7.
143. Underhill, G. H.; Chen, A. A.; Albrecht, D. R.; Bhatia, S. N. *Biomaterials* **2007**, *28*, 256–270.
144. Chandrasekaran, P.; Seagle, C.; Rice, L.; Macdonald, J.; Gerber, D. A. *Tissue Eng*. **2006**, *12*, 2001–2008.
145. Maguire, T.; Davidovich, A. E.; Wallenstein, E. J.; *et al*. *Biotechnol. Bioeng*. **2007**, *98*, 631–644.
146. Fiegel, H. C.; Kneser, U.; Kluth, D.; Metzger, R.; Till, H.; Rolle, U. *Pediatr. Surg. Int*. **2009**, *25*, 667–673.
147. Kneser, U.; Kaufmann, P. M.; Fiegel, H. C.; *et al*. *Pediatr. Surg. Int*. **1999**, *15*, 168–174.
148. Kneser, U.; Kaufmann, P. M.; Fiegel, H. C.; *et al*. *J. Biomed. Mater. Res*. **1999**, *47*, 494–503.
149. Uyama, S.; Kaufmann, P. M.; Kneser, U.; *et al*. *Transplantation* **2001**, *71*, 1226–1231.
150. Royce Hynes, S.; McGregor, L. M.; Ford Rauch, M.; Lavik, E. B. *J. Biomater. Sci. Polymer Ed*. **2007**, *18*, 1017–1030.
151. Pluchino, S.; Zanotti, L.; Brini, E.; Ferrari, S.; Martino, G. *Neurosci. Lett*. **2009**, *456*, 101–106.
152. Borlongan, C. V.; Sanberg, P. R. *Drug Discov. Today* **2002**, *7*, 674–682.
153. Emerich, D. F.; Salzberg, H. C. *Cell Transplant*. **2001**, *10*, 3–24.
154. Tobias, C. A.; Han, S. S.; Shumsky, J. S.; *et al*. *J. Neurotrauma* **2005**, *22*, 138–156.
155. Tabesh, H.; Amoabediny, G.; Nik, N. S.; *et al*. *Neurochem. Int*. **2009**, *54*, 73–83.
156. Date, I.; Shingo, T.; Yoshida, H.; Fujiwara, K.; Kobayashi, K.; Ohmoto, T. *Cell Transplant*. **2000**, *9*, 705–709.
157. de Guzman, R. C.; Ereifej, E. S.; Broadrick, K. M.; Rogers, R. A.; VandeVord, P. J. *J. Microencapsul*. **2008**, *25*, 487–498.
158. Kanter-Schlifke, I.; Fjord-Larsen, L.; Kusk, P.; Angehagen, M.; Wahlberg, L.; Kokaia, M. *Exp. Neurol*. **2009**, *216*, 413–419.
159. Namba, R. M.; Cole, A. A.; Bjugstad, K. B.; Mahoney, M. J. *Acta Biomater*. **2009**, *5*, 1884–1897.
160. Purcell, E. K.; Seymour, J. P.; Yandamuri, S.; Kipke, D. R. *J. Neural Eng*. **2009**, *6*, 026005.
161. Cirone, P.; Bourgeois, J. M.; Austin, R. C.; Chang, P. L. *Hum. Gene Ther*. **2002**, *13*, 1157–1166.
162. Hao, S.; Su, L.; Guo, X.; Moyana, T.; Xiang, J. *Exp. Oncol*. **2005**, *27*, 56–60.
163. Lohr, M.; Hoffmeyer, A.; Kroger, J.; *et al*. *Lancet* **2001**, *357*, 1591–1592.
164. Xu, W.; Liu, L.; Charles, I. G. *FASEB J*. **2002**, *16*, 213–215.
165. Joki, T.; Machluf, M.; Atala, A.; *et al*. *Nat. Biotechnol*. **2001**, *19*, 35–39.
166. Orive, G.; Gascon, A. R.; Hernandez, R. M.; Igartua, M.; Luis Pedraz, J. *Trends Pharmacol. Sci*. **2003**, *24*, 207–210.
167. Read, T. A.; Sorensen, D. R.; Mahesparan, R.; *et al*. *Nat. Biotechnol*. **2001**, *19*, 29–34.
168. Chung, C.; Burdick, J. A. *Adv. Drug Deliv. Rev*. **2008**, *60*, 243–262.
169. Hao, T.; Wen, N.; Cao, J. K.; *et al*. *Osteoarthr. Cartil*. **2009**, *18*, 257–265.
170. Nicodemus, G. D.; Bryant, S. J. *Osteoarthr. Cartil*. **2009**, *18*, 126–137.
171. Nicodemus, G. D.; Shiplet, K. A.; Kaltz, S. R.; Bryant, S. J. *Biotechnol. Bioeng*. **2009**, *102*, 948–959.
172. Chung, C.; Burdick, J. A. *Tissue Eng. A* **2009**, *15*, 243–254.
173. Liu, Y.; Shu, X. Z.; Prestwich, G. D. *Tissue Eng*. **2006**, *12*, 3405–3416.

5.510. Engineered Bioactive Molecules

C A Gersbach, Duke University, Durham, NC, USA

© 2011 Elsevier Ltd. All rights reserved.

5.510.1.	**Introduction**	132
5.510.2.	**Proteins**	132
5.510.2.1.	Extracellular Matrix Proteins	133
5.510.2.2.	Biomimetic Peptides	134
5.510.2.3.	Growth Factors	136
5.510.2.4.	Transcription Factors	137
5.510.2.5.	Methods for Synthesizing Engineered Proteins and Peptides	138
5.510.3.	**Nucleic Acids**	139
5.510.3.1.	Plasmid DNA	139
5.510.3.2.	Viruses	140
5.510.3.3.	RNA	142
5.510.3.4.	DNA as a Material	142
5.510.4.	**Lipids and Liposomes**	142
References		143

Glossary

Bioactive Capable of stimulating a biological response, in contrast to biologically inert.

Biomimetic Designed to mimic a naturally occurring biomolecule in structure and/or function.

Biomolecule A molecule consisting of biological components, typically proteins, nucleic acids, lipids, and/or carbohydrates.

Extracellular matrix The complex mixture of biomolecules present between cells in living tissues, largely consisting of secreted proteins, that is primarily responsible for mediating the interaction of a cell with its environment.

Growth factor A molecule, typically a protein produced and secreted by cells, capable of stimulating cell proliferation or differentiation.

Ligand A biomolecule that binds to a cellular receptor and activates cellular signaling. Ligands are typically produced and secreted by cells, after which they can diffuse and act in an autocrine, juxtacrine, or paracrine fashion.

Peptide Short polymers of amino acids, in contrast to proteins, which are generally longer.

Receptor A biomolecule that resides within a cell, typically a protein embedded in the cell membrane. Receptors change conformation after binding a ligand, leading to the transmission of biochemical signals to the cell.

Recombinant Comprised of material derived from multiple sources. For example, recombinant DNA may include a human gene incorporated into a bacterial plasmid for ease of propagation. When describing a protein, recombinant designates production from recombinant DNA.

Transcription factor A molecule, typically a protein, that regulates gene expression by binding directly to DNA sequences and modulating the recruitment of RNA polymerase and/or other cofactors.

Vector A carrier or delivery vehicle, such as a virus that delivers DNA to a cell.

Abbreviations

AAV	Adeno-associated virus
bFGF	Basic fibroblast growth factor
BMP	Bone morphogenetic protein
DNA	Deoxyribonucleic acid
ECM	Extracellular matrix
EGF	Epidermal growth factor
EGFR	Epidermal growth factor receptor
ELP	Elastin-like polypeptide
GAG	Glycosaminoglycan
GAM	Gene-activated matrix
HSV	Herpes simplex virus
mRNA	Messenger ribonucleic acid
NCA	N-carboxyanhydride
PCR	Polymerase chain reaction
PDGF	Platelet-derived growth factor
PEG	Poly(ethylene glycol)
PTH	Parathyroid hormone
RDL	Recursive directional ligation
RGD	Arginine-glycine-aspartic acid peptide
RNA	Ribonucleic acid
S1P	Sphingosine-1-phosphate
siRNA	Small interfering RNA
VEGF	Vascular endothelial growth factor

5.510.1. Introduction

The biomaterials field is undergoing a paradigm change. The early efforts in this area were limited to working with materials that were biocompatible and readily available, including metals, ceramics, and polymers. In this context, biocompatibility was characterized by a minimal biological response. This was largely due to insufficient understanding of the mechanisms that coordinate the cell–material interactions that lead to complex processes such as tissue regeneration, inflammation, and immune response against foreign objects. The work with these biologically inert materials provided the foundation for many of the modern advances in wound repair, implanted devices, and cell culture supports. However, it is now clear that this approach to biomaterial design neglects the tremendous opportunity of incorporating biological cues into the material to guide the biological response. Recent advances in biochemistry have provided important insights into the relationships of the structure and function of biomolecules, including proteins, nucleic acids, carbohydrates, and lipids. Furthermore, progress in cell and molecular biology has led to a more complete understanding of how these biomolecules coordinate the cellular processes that ultimately lead to tissue and organismal function. The biomaterials field is now capitalizing on this new information by building materials that incorporate bioactive molecules into implanted devices, scaffolds for tissue engineering, drug and gene delivery vehicles, and cell culture supports. Typically, the naturally occurring biomolecules are reengineered into forms that are more facile, economical, efficacious, or robust. In fact, the understanding of biological responses to materials has advanced to a level where bioactive molecules are often engineered *de novo*, on the basis of design principles developed from the study of natural molecules. Collectively, this work has established a novel conceptual approach to biomaterial design and created a new concentration in the area of applied molecular engineering. This chapter will review the classes of molecules that are being targeted for this purpose, the methods used for reengineering these molecules, and the applications in biomaterials and tissue engineering that have benefited from this approach (Table 1).

5.510.2. Proteins

Proteins, or polypeptides, are ubiquitous and essential components in a functional tissue environment and participate in nearly every cellular process. Therefore, several classes of proteins are targeted as promising candidates for the engineering of bioactive materials and tissue engineering scaffolds. Proteins are polymer structures composed of 20 distinct types of monomer units (amino acids) linked by amide bonds. The properties of complex protein-containing tissues and organs are exclusively determined by the physicochemical properties of these monomers and their sequence. Therefore, these natural biopolymers present unique opportunities for the engineering

Table 1 Examples of engineered bioactive molecules in various applications of tissue engineering

Tissue type	*Class of molecule(s)*	*Natural molecule*	*References*
Bone	Extracellular matrix	Fibronectin	47
	Biomimetic peptide	Type I collagen	15
	Biomimetic peptide	Fibronectin	39,40
	Biomimetic peptide	RGD	68
	Growth factor	Basic FGF	97
	Growth factor	EGF	105
	Transcription factor	Runx2	111
	DNA, growth factor, and peptide	BMP-4 and PTH1-34	137
	Retrovirus and transcription factor	Runx2	158
	AAV and growth factor	BMP-2	171
	AAV and growth factor	RANKL and VEGF	177
	Adenovirus and growth factor	BMP-7	180
	Lipid	Sphingosine-1-phosphate	207
Cartilage	Extracellular matrix	Type II collagen	16
	Biomimetic peptide	Elastin	24–26
Cardiovascular system	Biomimetic peptide	Fibronectin	35
	Growth factor	Basic FGF	92
	AAV and growth factor	VEGF	175,176
Nervous system	Biomimetic peptide	Elastin	28
	Biomimetic peptide	Laminin	36,84
	Growth factor	Neurotrophin-3	102
	DNA and growth factors	FGF2, BDGF, and NT3	139
	Adeno-associated virus	Capsid proteins	170
Wound healing and angiogenesis	Transcription factor	Hif-1α	113,114
	Transcription factor	Hif-1α/VP16	115
	Transcription factor	Artificial zinc fingers	122
	DNA and growth factor	PDGF	138
	AAV and growth factor	VEGF	173,174
	Lipid	Sphingosine-1-phosphate	204

of a rich complexity of structure and function by controlling sequence, hierarchical organization, and long-range interactions in much the same way as synthetic polymers.[1]

5.510.2.1. Extracellular Matrix Proteins

A large class of molecules relevant to this type of protein engineering is the extracellular matrix (ECM) proteins. The ECM is a tough, elastomeric network composed of various proteinaceous fibrils and fibers interconnected in a hydrated network of glycosaminoglycan (GAG) chains. These components of the ECM provide mechanical stability and structural integrity to tissues and organs by resisting tensile and compressive stresses. The ECM also contains biochemical cues that promote cellular adhesion, motility, and tissue production, and provides mechanical stimuli to cells through its intimate connections with the cellular cytoskeleton via cell surface receptors (**Figure 1**). A significant challenge in the fields of biomaterials and tissue engineering is the recreation of this exact microenvironment at the implantation site to promote favorable tissue anchorage and growth. The most promising approaches rely on engineering scaffold materials that mimic the native ECM proteins that contain functional information for promoting cell adhesion, proliferation, and differentiation.[2,3]

Natural ECM proteins perform a wide array of functions in their native context, including structural integrity, cellular adhesion and communication, storage, and catalysis. Their diverse set of functional properties makes them ideal templates for the engineering of bioactive molecules that closely mimic the native system. Collagen is one of the most promising biomaterials in regenerative medicine and tissue engineering as it is the predominant component of extracellular matrices in mammals, providing mechanical support to various connective tissues, such as skin, bone, tendon, ligament, cartilage, and blood vessels. Collagens, characterized by their unique triple-helical structures, not only provide significant structural integrity to tissues and organs, but also regulate a number of biological events, including cell attachment, migration, survival, proliferation, differentiation, and tissue regeneration. Many of these diverse functions are controlled through collagen-targeted cell surface receptors, such as integrins, discoidin domain receptors (DDR1 and DDR2), and annexin V, which promote cell adhesion and specific cellular functions.[4–6] The rational design of collagen-based biomaterials and tissue engineering scaffolds often incorporates the binding sequences from the native collagen molecule that are recognized by these various cell membrane receptors. In addition, it has been shown that cell adhesion-mediated signaling pathways are affected not only by the recognition sequence bound by the receptor, but also by the collagen molecule's triple-helical structure and assembly in the three-dimensional matrix.[7] For example, studies have demonstrated that fibrillar collagen regulates early integrin signaling differently from monomeric collagen, with the fibrils resulting in the inhibition of smooth muscle cell proliferation.[8] Therefore, the rational engineering of bioactive collagen-based materials often incorporates the specific receptor sequences from the native collagen molecule as well as particular forms, structures, and tertiary configurations of the collagen matrix that are most conducive to the design cell function and tissue performance.

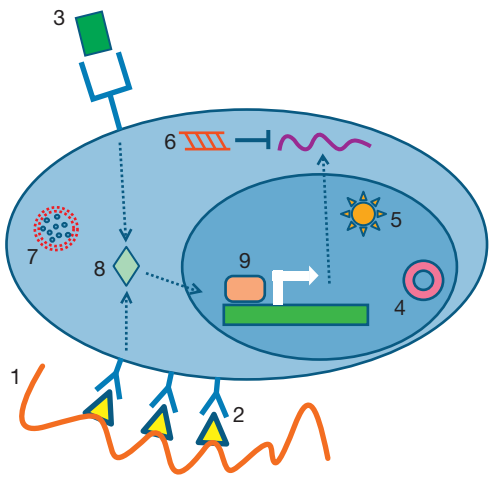

Figure 1 Classes of bioactive molecules that have been engineered for applications in biomaterials, tissue engineering, and regenerative medicine include (1) extracellular matrix proteins on the exterior of the cell, (2) small polypeptides that mimic the epitopes in the extracellular matrix that are involved in receptor binding, (3) soluble or matrix-bound growth factors, (4) plasmid DNA or (5) viral gene carriers that enter the cell and travel to the nucleus to deliver genetic material, (6) small RNAs delivered by polymeric drug carriers into the cytoplasm to disrupt mRNA stability and translation, (7) liposomes that act as drug delivery vehicles, and (8) second messengers that transmit signals from extracellular stimuli to the nucleus to modulate changes in gene expression that are regulated by (9) transcription factors.

Many of collagen's diverse functions are controlled by specific interactions of collagen-binding molecules (cell membrane receptors, soluble factors, and other matrix molecules) with certain structures and/or sequences displayed in the context of the collagen triple helices. Thus, synthetic triple-helical peptides that mimic the structure of native collagens and incorporate receptor-binding sequences have been used to design bioactive surfaces and scaffold substrates. For example, several studies indicate that the $\alpha_2\beta_1$ integrin interaction with type I collagen is a crucial signal for the induction of bone cell (osteoblast) differentiation and matrix mineralization.[9–12] The integrin $\alpha_2\beta_1$ recognizes the Gly–Phe–Hyp–Gly–Glu–Arg (GFOGER) motif in residues 502–507 of the α1[I] chain of type I collagen.[13] Reyes and colleagues demonstrated that an $\alpha_2\beta_1$ integrin-specific GFOGER-peptide triggers the activation of focal adhesion kinase (FAK) and alkaline phosphatase in osteoblast cells – two proteins that have been implicated in the osteoblastic differentiation pathway.[14] In this case, the functional activity of the peptide is entirely dependent on the engineering of the GFOGER recognition sequence in the context of a triple-helical peptide structure. These GFOGER-peptide surfaces also support the expression of multiple osteoblast-specific genes, including osteocalcin and bone sialoprotein, and induce calcification and matrix mineralization in a manner similar to type I collagen, demonstrating that this engineered bioactive peptide is a promising surface modification strategy for the design of collagen-mimetic surfaces that support bone formation. In fact, the GFOGER peptide has been used to dramatically enhance the osseointegration properties of titanium implants in animal models.[15]

Similarly, Ito and colleagues have rationally engineered collagen-like proteins with characteristics tailored specifically for cartilage engineering.[16] They identified the D4 region of human type II collagen as critical for the migration of chondrocytes and genetically engineered a collagen-like protein consisting of tandem repeats of the D4 domain assembled into a triple-helical structure. Scaffolds coated with this protein provided favorable culture conditions for chondrocytes, promoting migration, matrix formation, and maintenance of the chondrocyte phenotype.

Artificial self-polymerizing or self-assembling collagen-like materials have also been designed to mimic collagen suprastructures. Paramonov and colleagues designed collagenous peptide polymers of the form poly(Xaa–Yaa–Gly)$_n$.[17] These triple-helical polymers form nanofiber-like structures and can be engineered with various side-chain functional groups for binding. Cys residues on the polymers allow cross linking and additional functional modification. Koide *et al.* and Kotch and Rain also describe a system for obtaining collagen-like triple-helical supramolecules using a self-assembly process with self-complementary trimers of Pro–Hyp–Gly repeats.[18,19] Peptides are tethered by cysteine knots in a staggered arrangement to form elongated triple helices.

In addition to collagen, several other proteins are commonly found in the ECM and are promising templates for the design of bioactive molecules. The abundant ECM protein elastin, found in arteries, lung, and ligament, has unique elastomeric mechanical properties because of alternating hydrophilic and hydrophobic domains and multiple lysine cross-linking sites that allow for significant extensions and subsequent elastic recoil. Elastin-like polypeptides (ELP) have been derived by engineering repeat hydrophobic motifs from mammalian elastin, the most common being (VPGXG)$_n$, where X is any nonproline amino acid.[20,21] These polypeptides exhibit mechanical properties similar to those of native elastin, but are particularly suited for tissue engineering applications because they are thermally sensitive and undergo a reversible, inverse temperature phase transition. They have been used as thermally responsive injectable hydrogels that are water soluble below their transition temperature and self-aggregating above their transition temperature to form a gel-like, space-filling scaffold. Design principles from the field of polymer science can be applied to adjust the phase transition temperature to the desired *in vivo* application.[21] In addition, highly controlled genetic engineering strategies may be applied to design the precise amino acid sequence at the genetic level, allowing for the introduction of cross-linking sites that affect network modulus and reactive sites that allow the addition of functional ligands to control cell behavior or enzymatic recognition sites to control degradation.[22,23] The combination of polymer design principles and genetic engineering techniques in this system allows for the exquisite control of the physical properties of the scaffold network and the bioactivity and biocompatibility of the material in *in vivo* applications.

To address tissue engineering for cartilage repair, Betre and colleagues demonstrated that chondrocytes encapsulated in an ELP aggregate gel maintain morphology and phenotype *in vitro* for up to 15 days.[24] These cells grew and secreted the characteristic proteins of cartilage matrix, including type II collagen and sulfated GAG. They also demonstrated that ELP gels support the differentiation of human adult stem cells derived from adipose tissue into chondrocytes, as evidenced by the upregulation of genes that control the specific chondrocyte phenotype.[25] Subsequently, these ELP gels have also been used for the controlled release of drugs and other therapeutic agents in the intra-articular[26,27] and perineural[28] environment.

5.510.2.2. Biomimetic Peptides

In addition to bioactive materials that recapitulate the unique and specific structures of large ECM proteins, such as collagen and elastin, the identification of small oligopeptide adhesive and signaling sequences within such proteins has led to the design of ligand-functionalized materials. These materials capitalize on the mechanical properties of a bulk substrate and the specific receptor-binding activity of an attached peptide ligand that promotes cell adhesion and subsequent cellular activity (**Figure 1**). Cell adhesion to ECM proteins controls complex biological processes such as development, wound healing, immune response, and tissue function through specific and dynamic regulation of cell behavior.[29] Cell attachment to the ECM is primarily mediated by integrins, a widely expressed family of heterodimeric cell surface adhesion receptors consisting of noncovalently associated α- and β-subunits.[29] In addition to anchoring cells and providing tissue structure, integrins transmit intracellular signals that direct cell migration, proliferation, cell cycle progression, and differentiation.[30–32] Integrins thus function as the principal mediators of the molecular dialog between a cell and its ECM environment by specifically recognizing and binding to short amino acid motifs, or ligands, present in the ECM.

Engineering small bioactive peptides or ligands for immobilization onto a bulk substrate allows for specific tuning of integrin binding and activity by controlling ligand type, density, and spatial distribution (**Figure 2**). The use of the short peptide over the full-length native ECM protein also results in greater stability during the immobilization or modification process, as well as enhanced steric availability. The RGD (R: arginine; G: glycine; D: aspartic acid) sequence is one of the most effective and widely used peptide motifs for promoting cell adhesion on a synthetic surface. This tripeptide sequence was identified in 1984 by Pierschbacher and Ruoslahti as the minimal essential cell adhesion sequence in the ECM protein fibronectin.[33] Since then, RGD sites have been indentified in several other ECM proteins, such as vitronectin, fibrinogen, collagen, laminin, von Willebrand factor, tenascin, as well as in a variety of membrane proteins.[34] Nearly half of the 24 known integrins have been shown to bind to ECM proteins in some RGD dependent manner.[34] Other peptide sequences, such as Tyr–Ile–Gly–Ser–Arg (YIGSR) and Ile–Lys–Val–Ala–Val (IKVAV) from laminin or Arg–Glu–Asp–Val (REDV) from fibronectin, have also been immobilized onto the surfaces of various biomaterials.[35,36]

The recognition sequence itself is not the only factor in designing a bioactive peptide. Many ligand sequences require certain conformational states or neighboring amino acids for optimal activity. Therefore, the design of the bioactive peptide sequence beyond the simple recognition sequence may allow for greater activity or tunable cell behavior. It has long been recognized that the RGD sequence loses affinity and specificity

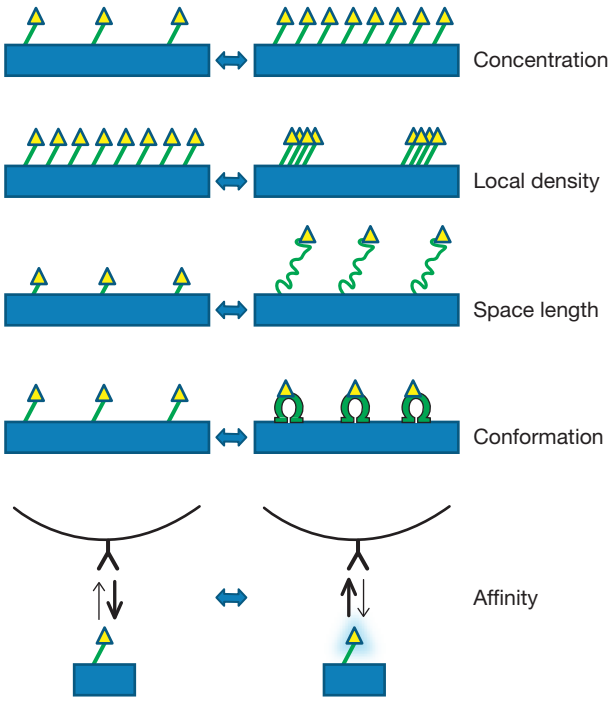

Figure 2 Various design criteria to consider when engineering bioactive molecules into biomaterials for presentation to cells. Each of these parameters can affect the cellular response to the material, including cell differentiation and tissue regeneration.

when presented outside the context of the native protein.[33,37] In fact, the RGD tripeptide alone shows little to no effect in blocking cell attachment.[38] Many efforts have been undertaken to rescue the activity of the RGD ligand by inserting flanking amino acids and adjusting the local conformation of the sequence (Figure 2). The activity of the sequence is improved by blocking the C-terminal carboxyl group on the tripeptide or by adding surrounding amino acids from the native sequence. For example, RGDS has higher activity than RGD and GRGDSP has higher activity that RGDS.[38] Furthermore, Petrie and colleagues have recently published a series of studies demonstrating enhanced bioactivity of a larger fragment of fibronectin encompassing RGD and neighboring epitopes also implicated in integrin binding.[37] This larger fragment has also been more effective in directing osseointegration of titanium implants.[39,40] The conformation and stereochemistry of the RGD sequence has been shown to affect both activity and specificity for particular integrins.[41–47] For example, a kinked RGD conformation favors $\alpha_v\beta_3$ integrin binding and a linear arrangement favors binding to the $\alpha_{IIb}\beta_3$ integrin.[44] The RGD cyclopeptide shows even greater affinity and cell attachment activity compared to linear peptides, which is most likely due to the fact that RGD exists in an exposed loop conformation in ECM proteins such as fibronectin.[48,49] Similarly, the Gly–Phe–Hyp–Gly–Glu–Arg (GFOGER) motif from type I collagen requires a triple-helical conformation to bind to the $\alpha_2\beta_1$ integrin.[50] Engineering the flanking environment and conformation of the recognition sequence in a bioactive peptide may allow precise control over a ligand's affinity and selectivity to various integrin subtypes, which in turn determines the cell types that preferentially interact with the implanted surface (Figure 2).

In the engineering of bioactive materials, there are a number of critical design factors that regulate the cellular interactions with the surface at a molecular level through receptor binding (Figure 2). Receptor binding subsequently determines the strength of cell adhesion,[51–53] the rates of cell migration and tissue infiltration,[54–56] and the extent of cytoskeletal formation and subsequent cell signaling.[57,58] These design parameters include immobilized peptide density and spacer length, receptor-ligand affinity, and spatial distribution or concentration of the bioactive peptide in the biomimetic material, all of which have been shown to affect biological responses. Using immobilized bioactive peptides on model substrates, several investigators have demonstrated a clear dependence of cell adhesion and cellular function on peptide density.[14,59–61] In fact, cell attachment as a function of ligand concentration shows a sigmoidal increase.[50,62,63] Differences in cell adhesion activity using fibroblasts seeded onto RGD-functionalized glass substrates and RGD-functional hydrogels also indicate that the hydrophobic/hydrophilic nature of the substrate affects peptide spacing results.[61,64]

In the engineering of peptide surfaces, cell adhesion is not the only aspect of cell behavior that should be considered. While high concentrations of bioactive peptide may result in greater cell attachment, they may impede cell migration and proliferation, which would adversely affect tissue growth and infiltration. Palacek *et al.* describe the biphasic trend of cell migration in response to ligand density, with cell migration increasing and then decreasing with increasing ligand density.[56] Similarly, Neff *et al.* demonstrate that fibroblast proliferation on RGD-modified polystyrene peaks at an intermediate concentration of RGD and then subsequently decreases with higher concentrations.[65] Hubbell and coworkers have shown that the amount of *in vitro* neurite extension in fibrin gels modified with RGD peptides shows biphasic behavior, with an intermediate concentration of peptide leading to maximal values of extension.[66,67] A similar biphasic response to adhesion peptides adsorbed onto biodegradable polymer scaffolds has also been observed for bone growth *in vivo*, with maximal values of growth at intermediate peptide densities.[68] These and other similar results showing migration, proliferation, and matrix production peaking at intermediate ligand densities suggest that the concentrations of bioactive peptide should be optimized for the particular cell function of interest rather than simply for cell adhesion.[67,69] Additionally, the incorporation of multiple, independent ligands that target unique receptors has been shown to result in synergistic biological activity.[70]

Integrin-mediated cell adhesion depends not only on receptor occupancy but also on receptor clustering (Figure 2). Therefore, peptide-modified surfaces may stimulate different cellular responses not only because of different peptide surface concentrations, as discussed above, but also because of the presentation of those peptides in a manner that allows or triggers integrin clustering or aggregation.[71–74] Maheshwari *et al.* designed surfaces with controlled RGD peptide density and nanoscale spatial distribution and demonstrated that fibroblasts exhibited greater shear resistance, and well-formed stress fibers and focal adhesions when the RGD peptide was presented in a clustered rather than random distribution.[75]

Therefore, designing the precise spatial distribution of a bioactive molecule may contribute to greater control over cell attachment and function.

In addition to peptide density and distribution, biological activity of the peptide recognition sequence must be considered while engineering functionalized surfaces (Figure 2). The immobilized peptide must be flexible enough to interact with the target receptor in the proper orientation and must protrude from the bulk surface sufficiently enough to minimize steric hindrance. To achieve these requirements, nonspecific, flexible peptide chains, such as repeating glycines,[50,76] or hydrophilic polymer chains, such as poly(ethylene glycol) (PEG),[59,77] have been engineered between the substrate or matrix polymer and the bioactive signaling sequence. Hern *et al.* demonstrated that cells adhere to a greater extent to RGD-functionalized surfaces with a PEG spacer than to those without the spacer, even at high surface densities. Similarly, Shin *et al.* showed that the length of PEG peptide spacers affected marrow stromal cells attached to modified hydrogels. Beer *et al.* explained this need for a spacer using an integrin model derived from electron microscopy.[78] The RGD peptide must be long enough to reach inside the globular binding pocket of the integrin. The length of the required RGD spacer varies in the literature, most likely because of differences in surface roughness or microconformations. However, cell attachment markedly decreases if that spacer length is too long because of the increased entropic energy of the long chain and the cell's preference for tight binding and rigid surfaces.[79,80]

Many of the aforementioned studies demonstrate several design principles that should be addressed while engineering bioactive molecules and materials (Figure 2). However, the optimal design parameters, such as peptide concentration and spacer length, vary depending on the cell type of interest, the desired cell function or phenotype, and the intrinsic material properties of the bulk matrix or substrate. The engineer must consider the interplay between all these criteria while designing a specific biomimetic system.

In addition to design factors that affect cell adhesion and functional activity, there are other considerations in the engineering of a bioactive peptide that may improve the ease of production or the long-term stability of the surfaces. In the case of covalent coupling of the ligand, including an accessible N-terminal lysine amino acid or other tethering moiety and avoiding bulky groups that may sterically hinder attachment will enhance coupling yields. Peptide solubility may also be tuned by adjusting the amino acids near the termini, for example, by adding charged side chains.[81] The proteolytic resistance of the peptide may be enhanced by using D-amino acids or cyclic conformations.[43,82]

Finally, the biodegradability of the matrix must be considered (Figure 3). For materials that degrade, surface tethering strategies may be insufficient as the surface can be rapidly removed *in vivo*. In these cases, it may be advantageous to develop polymers that display the bioactive peptide in the bulk material rather than on the surface. New peptide would be displayed continually as the material degraded. This issue has been investigated using the biodegradable material poly (lactic acid). Langer and coworkers synthesized the copolymer poly(lactic acid-*co*-lysine) in which the amino groups on the lysyl comonomer provide sites for peptide tethering.[83] Therefore, the bioactive peptide is presented on the transient surface through the degradation process. This type of bulk matrix incorporation is also relevant in the case of hydrogel scaffolds that undergo cellular infiltration. Migration-stimulating peptides, such as YIGSR and SIKVAV from laminin, have been impregnated in gels for nerve regeneration applications.[84] This allows the infiltrating neuronal cells to encounter the bioactive signal at all times during the infiltration process.

5.510.2.3. Growth Factors

In addition to the adhesion molecules discussed above, the ECM contains another class of morphogenetic molecules known as growth factors. These polypeptides are secreted

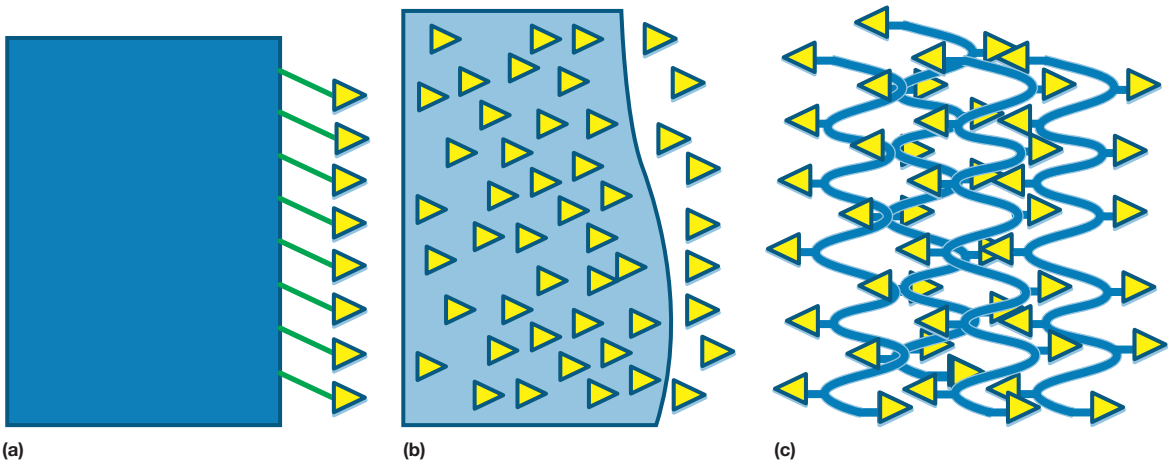

Figure 3 Strategies for incorporating bioactive molecules into biomaterials. (a) The bioactive molecule may be immobilized onto the surface of an implant or device to direct the activity of cells at that interface. This allows for control over the density and geometry of the presentation of the molecule to the cells. (b) The molecule may be incorporated into the bulk of a biodegradable material, such that the molecule is released slowly as the material breaks down and is replaced by host tissue. (c) The advantages of both (a) and (b) can be combined by constructing biodegradable materials that present the bioactive molecules from defined chemical structures.

from cells and subsequently bind to specific receptors on the surface of target cells and transmit signals that modulate cellular activities.[85] In the ECM, growth factors are often bound to proteoglycans, such as heparan sulfate and chondroitin sulfate, which protect them from proteolytic degradation and regulate their bioavailability.[86] These growth factors may be bound in the active state or may require enzymatic cleavage of the matrix or growth factor itself to reach maximal activity.[87]

Biomaterial and tissue engineers have begun to exploit this relationship between the matrix, growth factors, and cells to design systems for tissue repair and remodeling that promote cell growth, tissue production, and cellular invasion. While utilizing growth factors for these applications, it is critical that the functionality and activity of the immobilized growth factor are maintained during the matrix fabrication and release. The simplest approach has been to use an injectable hydrogel scheme in which the growth factor is incorporated into the matrix during the liquid-to-gel transition that occurs under physiological conditions.[88] The aqueous environment inside these hydrogels allows for the diffusion of the growth factor through and from the matrix. These injectable hydrogels may be delivered with minimal invasive surgery and can conform to a variety of complex tissue shapes.

Another approach has been to develop hydrogels or solid-phase biopolymeric materials to mimic the growth factor-binding characteristics of the native ECM. As many growth factors, such as vascular endothelial growth factor (VEGF) and basic fibroblast growth factor (bFGF), bind to heparan sulfate, several studies have sought to incorporate heparin, a molecule chemically similar to heparan sulfate, onto biomaterial surfaces in order to control the release of growth factors from implants.[89] In this case, the dissociation kinetics of the growth factor from the heparin controls the overall rate of release from the implanted matrix.

Alginate gels are one of the more widely used hydrogels in injury and wound management. Several investigators have sought to heparinize alginate gels to allow growth factor retention and controlled release by covalently conjugating heparin molecules[90] or encapsulating heparin-sepharose in the matrix.[91–93] In one example, sustained release of bFGF from heparinized-alginate pellets resulted in significant improvement of coronary blood flow in a porcine model of myocardial ischemia.[92]

As previously mentioned, collagen matrices are attractive candidates for tissue engineering scaffolds because of their mechanical properties, and cell adhesion and signaling characteristics. However, these scaffolds often display poor growth factor loading and retention. Several techniques have been employed to improve the incorporation and release kinetics of growth factors from collagen, including covalent attachment of heparin or modification of the network to couple growth factor release to the rate of bulk matrix degradation. For example, Tabata *et al.* demonstrated that varying the cross-linking density of collagen by using glutaraldehyde slowed matrix degradation rates and prolonged VEGF retention and release.[94] The same group showed that cross-linked gelatin (denatured collagen) hydrogels with bFGF incorporation by electrostatic interaction implanted into rabbit cranial defects enhanced bone regeneration.[95–97]

One of the more interesting engineered matrices for tissue engineering is fibrin, the provisional matrix formed during tissue repair. Because this matrix functions as a temporary scaffold for tissue repair and regeneration, its physiological role is to promote cellular ingrowth; it is gradually replaced by a more stable ECM upon healing. These are precisely the characteristics that are desired in an implantable tissue engineering scaffold. Sakiyama-Elbert and Hubbell have developed a system in which molecules can be linked onto a fibrin scaffold during the network cross-linking process.[98] They have used this technique to covalently incorporate a heparin-binding peptide into the fibrin matrix. This peptide binds heparin, which in turn immobilizes growth factors to the scaffold.[99,100] With this system, they demonstrated the controlled release of several nerve growth-stimulating growth factors from a fibrin matrix with a high excess of heparin-binding sites. Lee *et al.* and Taylor *et al.* subsequently showed that a fibrin matrix with bound neurotrophin-3 (NT3) enhanced regeneration of the sciatic nerve and the spinal cord.[101,102]

The same investigators also demonstrated that growth factors themselves can be engineered to bind fibrin directly without the heparin intermediate.[103,104] In this case, they developed a fusion protein consisting of factor XIIIa that binds fibrin at one terminus, a central domain containing proteolytic cleavage sites, and the bioactive growth factor at the other terminus. These fusion proteins exploit the proteolytic activity of plasmin and matrix metalloproteinases in the wound site to liberate the bioactive growth factor from the matrix by clipping the central linker.

In some cases, covalent tethering of the growth factors imparts a biological advantage compared to the incorporation of the soluble molecule. Griffith and coworkers demonstrated that surface-tethered epidermic growth factor (EGF) promotes both mesenchymal stem cell spreading and survival more strongly than saturating concentrations of soluble EGF. The same group showed that covalent tethering of EGF reduces epidermic growth factor receptor (EGFR) internalization and restricts signaling to the cell surface, enhancing osteogenic differentiation of bone marrow stromal cells.[105] This group also demonstrated that EGF conjugated to synthetic polymer surfaces is capable of directing hepatocytes to maintain their liver-specific morphology and function.[106]

These studies demonstrate that engineering principles may be applied to both the biomaterial matrix and the growth factor of interest to manipulate and optimize activity, concentration, and release kinetics.

5.510.2.4. Transcription Factors

Growth factors and ECM proteins function by inducing cellular signaling pathways that ultimately lead to changes in gene expression in the nucleus (**Figure 1**). These changes in gene expression are mediated by transcription factors that bind to specific gene sequences and regulate the activation of that locus. Several studies in the area of tissue engineering are now focusing on direct modification of gene regulation by the genetic engineering of cells with transcription factors, rather than by direction of cell activity with extracellular stimuli. For example, García and colleagues have genetically engineered cells to express the transcription factor Runx2 to enhance osteoblastic differentiation and bone formation.[107–110]

Incorporation of this strategy into an inducible gene expression system led to exogenous control of the magnitude and kinetics of cell differentiation and tissue formation *in vitro* and *in vivo*.[111] Furthermore, they have discovered novel mutations of Runx2 that mimic natural posttranslational modifications and lead to bone formation by otherwise recalcitrant cell types.[112]

Transcription factor-based strategies have also been prevalent in approaches for wound healing and therapeutic angiogenesis. In particular, Hif-1α is a transcription factor that regulates genes responsible for angiogenesis, including the growth factors VEGF and platelet-derived growth factor (PDGF). Trentin *et al.* delivered a stabilized form of Hif-1α, in which a natural degradation domain had been removed, to mouse dermal wounds, using a peptide-based gene delivery vector.[113] This led to enhanced angiogenesis relative to direct delivery of VEGF alone, as demonstrated by more stable and mature blood vessels. Similarly, stabilized Hif-1α showed enhanced angiogenesis relative to the VEGF in skeletal muscle.[114] Variants of Hif-1α have also been engineered to incorporate the strong transactivation domain from the herpes simplex virus (HSV) VP16 protein to enhance its transactivation properties. These Hif-1α/VP16 engineered molecules have been successful in treating animal models of limb ischemia[115] and have subsequently moved into clinical trials.[116]

In addition to naturally occurring transcription factors, it is now possible to engineer synthetic transcription factors that target-specific genes within mammalian genomes.[117] For example, artificial zinc finger proteins have been designed to regulate a variety of genes related to tumor development and sensitivity to cancer therapy.[118–121] One particularly successful application of this approach has been in the development of an artificial transcription factor that upregulates the endogenous VEGF gene.[122] This molecule was able to protect against experimental diabetic neuropathy and has now moved into clinical trials for a variety of indications.[123]

5.510.2.5. Methods for Synthesizing Engineered Proteins and Peptides

There are two general strategies for engineering bioactive peptide- and protein-based molecules – recombinant DNA expression and synthetic polymerization. The recombinant DNA approach uses genetically encoded sequences to generate the desired polypeptide. The engineer must first design a recombinant DNA segment that precisely encodes for the therapeutic protein of interest. This segment is then cloned into a suitable DNA plasmid to create a recombinant DNA molecule that can be delivered to cells with the appropriate machinery for expressing the desired protein. This plasmid is transformed into the host cells, which are then grown in culture for a prescribed length of time to allow for protein expression. The protein of interest is then purified from the cells or culture media. A critical step in this process is the generation of the gene of interest. For small polypeptides, short DNA sequences can be directly synthesized using standard solid-phase synthesis. For long proteins with repeating units, including many structural ECM proteins such as elastin, these shorter DNA sequences can be assembled into larger proteins that encode for repetitive structures of the desired molecular weight.[20] This can be accomplished by concatenation of oligonucleotides, recursive directional ligation (RDL), or amplification of gene segments by polymerase chain reaction (PCR).[20] Concatenation is a statistical method in which a distribution of genes encoding the monomer is ligated and the gene inserts are sorted on the basis of size. The desired insert is then ligated into the vector of choice. In RDL, the short DNA segments are linked using recombinant DNA techniques. The resulting larger genes can then be recursively combined until a gene of a desired length is obtained. This approach is modular and can be used to combine genes encoding different polypeptide sequences.[124,125] This method also provides a greater level of control over the size of the insert.

Recombinant protein expression has many advantages over chemical synthesis. It provides well-defined sequences, stereochemistry, and molecular weight based on the engineered genetic template.[20] The resultant transformed cells can be stored to provide an ongoing supply of the protein of interest. Finally, and most important for the generation of structurally complex bioactive peptides and proteins, the intrinsic protein folding machinery of the cell has the ability to form physiologically relevant secondary and tertiary structures. For example, integrin $\alpha_5\beta_1$-binding requires both the PHSRN sequence in the ninth type III repeat and the RGD motif in the tenth type III repeat of the ECM protein fibronectin.[126] Because of the acute sensitivity of $\alpha_5\beta_1$ to small perturbations in the orientation of these domains, the development of proper structural orientation using synthetic peptides remains a challenge. Recombinant molecular techniques have been successfully applied to recapitulate the native secondary and tertiary structure of this important fibronectin domain.[37] The disadvantages of these techniques include the time- and labor-intensive process of assembling the gene and cloning it into the desired vector and then optimizing expression conditions in the host cell line. In addition, these techniques are often limited to the standard 20 amino acids, and the incorporation of unnatural amino acids is a difficult and often inefficient venture. The addition of nonpeptide moieties, such as a synthetic polymer backbone or insert, is also not possible with this approach unless it is done after expression and purification. Finally, in many cases the desired polypeptide is not expressed well in the host cell line, making it difficult to obtain the requisite amounts of purified protein.

Part of the design process of a recombinantly expressed bioactive molecule includes the development of a strategy for protein expression and purification that will optimize the yield and quality of the final product. These conditions will vary according to the sequence, folding structure, and posttranslational modifications of the desired protein. Based on these criteria, different expression hosts are available, including bacteria, insect cells, and mammalian cells. Once a host is selected, the final bulk protein yield can be maximized by optimizing the expression conditions.

Alternatively, the synthetic polymerization approach uses standard techniques such as solid-phase peptide synthesis or α-amino acid *N*-carboxyanhydride (NCA) polymerization to produce the desired protein from individual amino acid monomers. In solid-phase synthesis, small porous beads are functionalized with linkers upon which peptide chains can be built, amino acid by amino acid. The peptide remains

covalently attached to the bead until it is clipped by a reagent such as trifluoroacetic acid. This allows the growing peptide to be retained during several filtration steps, wherein the liquid-phase reagents and reaction by-products are washed away. The general process of solid-phase synthesis includes repeated cycles of coupling and deprotection. The free N-terminal amine of the bead-attached peptide is coupled to a single N-protected amino acid moiety. This amino acid is then deprotected, revealing a new N-terminal amine to which the next amino acid can be linked. The disadvantages of this technique include low yields and an upper size tolerance of around 70–100 amino acids. Beyond this length, this approach is burdened by unavoidable deletions and truncations that result from incomplete deprotection and coupling steps.[127]

The most advantageous process for synthesizing high molecular weight peptide chains with significant yields in large quantities is the polymerization of NCAs.[127] In this technique, a nucleophile or base is used to initiate the polymerization of NCA amino acid monomers. The most common initiators used are primary amines and alkoxide anions.[127] The reagents required are simple and inexpensive; thus NCA polymerization is a very economical and expedient way to generate long polypeptides. The disadvantages of conventional NCA polymerizations include the fact that there is no control over the reactivity of the growing polymer chain end during the polymerization reaction.[127] After initiation, the resulting primary amine, carbamate, or NC anion end group can undergo a host of undesirable side reactions. New developments in the use of transition metal catalysis, however, can lead to products that, in many ways, rival biologically produced counterparts in terms of complexity and purity.[127] Studies have demonstrated the production of block copolypeptides of controlled molecular weight, sequence, composition, and molecular weight distribution with the use of this technique.

Although the recombinant genetic engineering approach may offer greater control over sequence, these synthetic methods allow for the incorporation of artificial or nonstandard amino acids, such as hydroxyproline, and for the creation of alternative stereochemistries, which can prevent protease-mediated degradation. Synthetic techniques also allow for the generation of hybrid molecules that consist of polypeptides fused or merged with other synthetic polymers.

5.510.3. Nucleic Acids

Although proteins are currently the most common biomolecule used in combination with biomaterials, the use of nucleic acids is becoming increasingly popular as a result of advances in genome technologies, genetic engineering, and nanotechnology, and in our understanding of the many varied roles that nucleic acids can play in controlling cell behavior.[128] Nucleic acids can be used to carry the genes that encode various proteins of interest, but this is only one example of their use in combination with biomaterials. For example, biomaterials may be used to deliver small RNAs that modulate cellular pathways. Alternatively, DNA has recently been exploited as a building material for the construction of complicated nanostructures. Nucleic acids are often more economical to produce than proteins, and are sometimes more resistant to decay or denaturation. Additionally, nucleic acids can provide sustained production of gene-encoded proteins over long periods of time, or be used to disrupt cellular pathways in ways that are currently not possible with proteins. Finally, there are a variety of ways by which bioactivity has been engineered into nucleic acids and/or their delivery vehicles. Therefore, nucleic acids are growing in importance in the fields of biomaterials, tissue engineering, and drug delivery.

5.510.3.1. Plasmid DNA

As described above, there are a number of challenges to the delivery of adhesion and growth factors in tissue engineering applications. In some cases, these delivery barriers could be overcome if those growth factors were delivered not as whole recombinant proteins but as DNA. DNA-based therapies for tissue regeneration merge the technologies of tissue engineering with those of gene therapy. In this genetic approach, DNA is delivered to the site of injury via a porous biomaterial scaffold to initiate tissue repair. The scaffold fills the wound and serves as the delivery vehicle for the DNA, allowing endogenous cells to migrate to the site. As these cells encounter the scaffold, they become transfected with the genetic material and function essentially as local *in situ* bioreactors that produce the therapeutic growth factor encoded by the exogenous DNA.[129] The main advantage of such a system is that delivery of genetic material provides sustained low-level expression by the repair cells. This pattern of expression would be more likely to avoid local toxicity associated with uncontrolled delivery of exogenous growth factors. In addition, this technique may result in low levels of system toxicity, given the high efficiency of DNA catabolism in the bloodstream[130] and the low transfection efficiencies observed in normal, non-wound-healing tissue environments.[131] Most of the work in this area focuses on the delivery of naked plasmid DNA. Plasmid DNA is inherently stable, and easy to manufacture and purify in large amounts, unlike the larger and more fragile growth factor proteins.

Bonadio and colleagues developed a local gene delivery system for tissue engineering applications, known as the gene activated matrix (GAM).[129,130] A GAM has two components: plasmid DNA encoding the growth factor of interest and a biodegradable matrix carrier. This system may be adapted as an implantable porous scaffold or sponge, an injectable gel or paste, or a biomedical device coating. Upon delivery of the matrix to the wound site, GAM-mediated plasmid transfer is inextricably linked with physiological events of wound healing. The GAM serves as a reservoir scaffold that holds the DNA in place until the endogenous wound-healing fibroblasts proliferate and migrate from the surrounding viable tissue. Once there, the fibroblasts take up and transiently express the plasmid DNA. This takes advantage of the natural propensity of fibroblast-mediated granulation tissue to grow into a wound-healing site, allowing for the physical targeting of the repair fibroblasts.[129] Therefore, the matrix serves two purposes: it contains the DNA in the wound site and acts as a scaffold to promote fibroblast migration and ingrowth. Once transfected, the fibroblasts express the plasmid-encoded proteins at near-physiological levels, stimulating wound repair.

Bonadio and others have observed substantial levels of transfection *in vivo* with these techniques.[133–135] In one study,

a collagen-sponge GAM resulted in 20–50% transfection of available canine wound-healing cells.[136] Plasmid gene retention and expression by fibroblasts were documented for at least 6 weeks. As the cascade of events associated with wound healing is near universal, this paradigm of matrix-mediated plasmid gene transfer can occur at repair sites in various tissues and organs across species. Investigators have demonstrated direct GAM plasmid gene transfer for wound repair in bone,[133,137] skin,[138] heart and skeletal muscle,[136] and cranial nerve[139] in rat and canine models. These and other studies have used GAM systems with natural biomaterials such as collagen sponges, pastes and gels, hyaluronan, and alginate, as well as synthetic materials such as carboxymethylcellulose, and poly(lactide-*co*-glycolide) (PLG), as the matrix carriers for plasmid DNA.[129] The matrix design must be optimized both for plasmid DNA loading and for the promotion of fibroblast migration and granulation tissue ingrowth.

The earliest GAM studies used the plasmid gene transfer techniques to repair bone in the adult rat. In these studies, GAMs with either bone morphogenetic protein-4 (BMP-4) plasmid or plasmid encoding a fragment of parathyroid hormone (PTH) induced bone filling in a defect.[137] This study also demonstrated the synergistic effects of a GAM encoding for both BMP-4 and the PTH peptide, resulting in faster bone formation than with either factor alone.

The design of the GAM delivery vehicle offers great flexibility in form and application. Mooney and colleagues demonstrated the efficacy of the plasmid gene delivery from a sustained release polymer matrix in rat dermis.[138] In this system, a high-pressure gas foaming process was used to efficiently incorporate supercoiled DNA into a three-dimensional porous matrix of PLG. The polymer was engineered to release the DNA over a period ranging from days to months *in vitro*, leading to the transfection of a large number of cells. *In vivo* delivery of the GAM matrix with plasmid DNA encoding PDGF enhanced granulation tissue deposition and blood vessel formation in the developing tissue of rat dermis. This was in contrast to the direct injection of PDGF plasmid, which showed no significant effect on local tissue formation. These results underscore the importance of the matrix carrier in delivering genetic material.

Berry *et al.* demonstrated that when collagen paste GAMs are placed between the proximal and distal stumps of severed rat optic nerves, DNA is retained within the GAM, promoting sustained transgene expression in the optic nerve, in the GAM itself, and, more importantly, in axotomized retinal ganglion cells (RGC).[139] They showed that plasmids encoding for basic fibroblast growth factor (FGF2), brain-derived neurotrophic factor (BDNF), and NT3 promoted sustained survival of RGC for over 3 months after the initial injury.

Taken together, these studies demonstrate the great potential of direct plasmid gene transfer in the context of tissue engineering. The GAM itself presents a number of opportunities for the application of engineering and design principles to optimize DNA loading and release, and scaffold material properties. Other issues that must be considered include the potential degradation or inactivation of the plasmid upon implantation or cellular uptake,[140–142] poor plasmid binding to cell membranes,[143] nonspecific plasmid internalization, and poor vector nuclear localization.[144–146] These potential barriers to efficient gene delivery and expression represent important areas of research in this growing field. For example, Ogris *et al.* demonstrated that PEGylation, the introduction of PEG chains, of DNA complexes strongly reduces plasma protein binding and erythocyte aggregation.[147] They observed prolonged circulation of these complexes in the blood as well as lower toxicity compared to non-PEGylated DNA complexes. Schaffer and Lauffenburger demonstrated that binding of the DNA complex to the cell surface is a major barrier to efficient gene transfer.[143] They showed that control of charge and optimization of other parameters that affect surface binding could improve efficiency and specificity of gene delivery. To efficiently target exogenous DNA to the nucleus of the cell, several investigators have engineered the construct to include nuclear localization signal peptides.[144–146] Synthetic DNA delivery vectors consisting of DNA and cationic polymers or peptides, or DNA and cationic lipids have also been explored as alternatives to overcome many of the challenges.[148,149] These systems may increase plasmid stability and transfection efficiency, and decrease degradation.[150] Similarly, DNA may be encapsulated in synthetic polymers to spatially and temporally control DNA release. Prior to encapsulation, DNA may be condensed with cationic polymers to decrease complex size and risk of degradation, enhance interaction with cell membranes, and encourage endosomal release.[151] Investigators have encapsulated DNA with either natural or synthetic polymers to form micro- and nanospheres, porous scaffolds, and hydrogels for sustained DNA release.[151] In this case, the physical and chemical properties of the polymer can be engineered to influence transfection efficiency.

In addition to these challenges to delivery and transfection, a potential drawback to the use of plasmid DNAs is their short half-life in the nuclei of the target cells. Many studies have sought to increase the expression of the plasmid-encoded therapeutic genes; however, concerns over oncogenesis from sustained growth factor expression or insertional mutagenesis remain.[152,153] Finally, a major concern with plasmid vectors is that they contain CpG motifs that can activate an immune response through Toll-like receptor action (similar to endotoxin). Studies have shown that plasmid DNA treatment in animals has resulted in pathogenic anti-DNA antibodies that lead to renal failure and premature death.[154] These complications may be addressed by the recent development of minicircle vectors devoid of bacterial DNA sequences.[155] Clearly, the potency, efficiency, and safety of plasmid DNA-based treatments must be addressed in the design process of the tissue engineered construct for human therapy.

5.510.3.2. Viruses

As alternatives to plasmid DNA delivery in GAMs, viral vectors derived from retrovirus, adenovirus, adeno-associated virus (AAV), and HSV may be engineered as part of a tissue engineered scaffold.[156] Viruses are biological agents that infect cells by inserting either DNA or RNA into the host, thereby utilizing the host's cellular machinery to replicate the viral genetic material. Viruses have naturally evolved to maximize their gene transfer efficiency and are, therefore, attractive candidates for the delivery of genetic information to target cells in a tissue engineering application. Each viral vector class has its own

advantages and disadvantages. Tissue engineers will have to address these issues while designing gene delivery vehicles for their particular application.

A retrovirus contains a single-stranded RNA molecule in its genome. Its replication process includes reverse transcription of the viral RNA into linear, double-stranded DNA, and subsequent integration of this DNA into the host cell's genome. Therefore, transcription and translation of the integrated viral DNA occur alongside that of the endogenous genes using the host's translational machinery. The RNA genome is encapsulated by a protein capsid shell and an external envelope of a lipid bilayer. The electrostatic properties of this lipid bilayer can be exploited to module virus interactions with biomaterials, leading to enhanced and controlled virus transduction of cells.[157,158] Retroviral vectors are delivery vehicles that are derived from natural retroviruses and engineered to carry the foreign gene of interest into the target cell. They are designed to be replication defective to avoid budding of new virions. Retroviral modification of target cells has been applied to several orthopaedic regeneration models as well as to wound healing and blood vessel formation.

In many applications, target cells are transduced *ex vivo* and then the cells, expressing the therapeutic of interest, are combined with a scaffold material and implanted into the defect site. Laurencin *et al.* used retroviral gene transfer techniques to develop bone morphogenetic protein-2 (BMP-2) producing murine bone marrow stromal cells.[159] These cells were seeded onto a polymer–ceramic scaffold and implanted into immunocompromised mice. The investigators observed that the scaffold successfully delivered bioactive BMP-2 to the implantation site and induced heterotopic bone formation. Huard and coworkers demonstrated that similar BMP-2 encoding retroviruses could be used to transduce muscle-derived cells, pushing them down an osteogenic lineage and enhancing bone formation.[160] Retroviruses have also been applied to articular cartilage repair. Studies have shown that retrovirally modified bone marrow-derived mesenchymal cells can produce enough transforming growth factor beta 1 (TGF-β1) to undergo chondrogenesis *in vitro*.[161] Analogous *in vivo* studies using fibroblasts have demonstrated the induction of cartilage repair and regeneration at the defect site.[162] Improvements in wound healing have also been observed using retrovirally transduced fibroblasts expressing PDGF alone or in combination with VEGF in poly(glycolic acid) (PGA) matrices.[163,164]

As retroviruses efficiently integrate their genetic material into the host genome, resulting in potentially permanent expression of the delivered therapeutic gene, these vectors are particularly attractive for applications that treat persistent conditions.[165] However, retroviral techniques may not be optimal for cases where transient gene expression is desirable in order to initiate a physiological cascade of events or treat an acute injury. A possible disadvantage of retroviral carriers is their inability to infect nondividing cells. Zang and Godbey note, however, that in tissue engineering applications that utilize *ex vivo* strategies, this may be considered an advantage as somatic cells would be protected from accidental transduction upon implantation of a construct containing transduced cells.[165] A number of safety concerns are also associated with retroviral systems, including the risk of generating replication competent viruses or the possibility of insertional mutations. The random insertions that result from retroviral infection have the potential to knock out an essential housekeeping or tumor-suppressing gene.[166]

AAVs are small DNA viruses with a linear, single-stranded genome. AAV is naturally replication deficient and replication is most often achieved in conjunction with a helper virus or through genotoxic stress, such as carcinogens or ultraviolet irradiation.[165] In addition to its apparent lack of pathogenicity, AAV is particularly attractive for gene therapy and tissue engineering because, unlike retroviruses, it can infect nondividing cells, remains as a stable episome inside the cell for long periods, and has the ability to stably integrate into the genome of the host cell at a specific site. This addresses the concerns regarding random insertional mutagenesis associated with retroviral systems.

The advantages of AAV systems include their ability to infect dividing and nondividing cells and the fact that they do not have the potential for insertional mutagenesis. They have the ability to mediate long-term transgene expression and are replication defective, nonpathogenic, and relatively nonimmunogenic.[165] The major disadvantages to AAV include limitations in transgene size and the requirement of helper viruses. Other challenges to AAV gene therapy include the potential of neutralizing antibodies and infection-resistant cell types. These challenges have recently been addressed in several elegant studies that have used directed molecular evolution to reengineer the properties of the AAV capsid proteins that are responsible for interacting with cellular receptors.[167,168] This has led to AAV vectors with enhanced infection efficiencies for both airway epithelium[169] and glia,[170] two tissues types relevant to regenerative medicine that have so far been resistant to conventional gene transfer technologies.

Unlike the *ex vivo* gene therapy techniques described above in which cells are transduced with virus prior to implantation, much of the AAV work in the tissue engineering field has focused on direct administration of AAV to the wound site. Studies have shown that myoblast cells exhibit osteogenic activity upon transduction with AAV to produce BMP-2 or BMP-4 in vitro.[171,172] These same AAV constructs were injected into rat skeletal muscle, resulting in the formation of new bone. In addition, treatments with AAV-VEGF have also been shown to stimulate angiogenesis and ECM formation through wound-healing mechanisms. This system has been applied to full thickness dermal excisions in rats[173] and partial thickness burn wounds in mice.[174] Similar AAV-VEGF constructs have also been successfully applied to ischemic myocardium.[175,176] AAV is also significantly more stable than retrovirus because it does not have a lipid envelope or RNA genome. As a result AAV can be freeze-dried onto implants and taken up by host cells postimplantation.[177]

Like AAV, adenovirus is a particularly stable viral gene delivery vehicle and can therefore be incorporated into biomaterials *ex vivo* to transduce host cells *in vivo* following implantation. For example, incorporation of adenovirus into hydrogels or protein matrices has led to control over the spatial and temporal delivery to surrounding tissue.[178] This method is also effective in protecting the adenovirus from loss of activity. Subsequently, the design parameters for these systems have been optimized.[179] This approach has been particularly

successful in promoting the healing and integration of dental implants in animal models, suggesting a promising application in oral defects and disease.[180]

Another interesting viral class is HSV. HSV-1 is a naturally neurotopic virus and is extremely efficient at infecting neurons. Therefore, HSV-1 vectors are particularly attractive for the treatment of central nervous system pathologies, such as Parkinson's disease. Restoration of brain function by neural transplants is largely dependent upon the survival of donor neurons. However, in both rodent models and human patients with Parkinson's disease, the survival rate of transplanted neurons has been low. HSV-1-VEGF constructs transduced *ex vivo* into neuronal aggregates have been shown to improve vascularization and implant survival *in vivo*.[181] HSV vectors also have the advantage that they have a large transgene capacity, and may therefore be able to encode for multiple genes of interest.[165]

Collectively, these studies are representative of the field of molecular engineering of virus-based gene delivery vehicles, including bioactive molecules that are delivered by the virus, constitute the virus, or act as a carrier for the virus to an *in vivo* site of tissue repair.

5.510.3.3. RNA

Until recently, incorporation of nucleic acids with biomaterials for tissue engineering and regenerative medicine was almost exclusively limited to delivery of gene-encoding DNA molecules. However, the recent discovery of mechanisms by which small RNAs can be used to inhibit the expression of certain genes through RNA interference has led to a new interest in delivering RNA to cells.[182,183] In particular, there are many applications of this new technology in tissue engineering for coordinating cellular functions that lead to tissue repair and regeneration.[184] Often, these approaches use the same cationic polymers as carriers to deliver RNA as have been previously utilized for DNA delivery.[185] This is a straightforward approach as these carriers are designed to exploit the chemical properties of nucleic acids that are shared between DNA and RNA. However, there are still several limitations to this approach, including significant cytotoxicity and inactivation of RNA/polymer complexes by anionic serum proteins.[186] Additionally, there are important differences in the characteristics and mechanistic action of DNA and small interfering RNAs that lead to different design criteria for RNA carriers. These include differences in molecular topography and size, duration of effect, cellular location of action, and resistance to degradation.[186] Consequently, a new class of drug delivery vehicles is being developed for the transfer of these molecules to cells *in vitro* and *in vivo*. Stayton and colleagues have pioneered the development of 'smart' delivery systems for biomolecular therapeutics that change their functional or structural properties on the basis of environmental stimuli, such as pH.[187] For example, Convertine *et al.* have recently described a novel diblock copolymer that combines siRNA condensing activity with pH sensitivity for enhanced endosomal escape, which is a primary barrier for effective siRNA delivery to the cell.[188] This work is representative of a growing field dedicated to the engineering of bioactive molecules in conjunction with RNA-based therapeutics for regenerative medicine.

5.510.3.4. DNA as a Material

The work described above focuses on the use of nucleic acids specifically for the *genetic* qualities of DNA and RNA. However, new fields are currently developing that use DNA as a building material, rather than as a carrier of genetic information. For example, DNA has been used as a 'smart glue' for programming the self-assembly of nanoparticles.[189,190] Francis and colleagues later functionalized cell surfaces with DNA oligonucleotides and used hybridization to complementary DNA sequences on material surfaces to program cell adhesion.[191] Gartner and Bertozzi then built on this method to program the assembly of cells into microtissues. By mixing different cell types that presented complementary sequences, they were able to direct the assembly of multicellular structures with controllable architecture.[192] This approach to cellular assembly based on the highly specific DNA base pairing may serve as a new approach to the engineering of complex tissues for regenerative medicine.

The field of structural DNA nanotechnology is another example of using DNA as a building material to generate complex structures.[193] This area is based on the use of Watson-Crick base pairing to guide the self-assembly of DNA into complex nanostructures. Initially, this work focused on the engineering of two-dimensional crystalline forms of DNA nanostructures.[194] Later, this idea was extended to 'DNA origami' that described methods for creating nanoscale shapes of any geometry.[195] More recently, Andersen *et al.* have demonstrated a method for assembling DNA into layers of helices arranged in a honeycomb lattice that allows for the construction of three-dimensional nanostructures.[196] In particular, they constructed a nanoscale box with a controllable lid that can be opened by specific 'DNA keys.' These innovative examples of bioactive molecule engineering are providing new ideas for reconstructing the nanoscale architectures within cells and tissues that are essential to the recreation or regeneration of this environment.

5.510.4. Lipids and Liposomes

In addition to proteins and nucleic acids, lipids are emerging as a class of biomolecules with unique chemical properties that may be used to direct cell behavior or serve as drug delivery vehicles. Lipids are a diverse group of organic compounds including fats, oils, hormones, and many components of the cellular membrane. In contrast to proteins, nucleic acids, and carbohydrates, lipids are hydrophobic because of the large hydrocarbon chains that form the majority of the molecule. Amphipathic lipids contain an additional hydrophilic chemical group at one end of the molecule. This structure facilitates the formation of vesicles, liposomes, and membranes in water in which the hydrophobic chains pack together, and the hydrophilic group is exposed to the aqueous environment. This is the basic structure of the cell membrane and many other structures within the cell responsible for trafficking cellular components.

The unique properties of lipids have led to their use in a variety of drug delivery schemes. For example, cationic lipids are routinely used to spontaneously package nucleic acids into nanoparticles, called lipoplexes.[197] The overall positive charge

of these lipoplexes enhances favorable interactions with the cell membrane and increases transfection efficiency over 1000-fold relative to naked nucleic acids.[198,199] Building on these simple systems, many advances have been made in lipid design to engineer liposomes and nanoparticles that enhance transfection efficiency, minimize toxicity, and confer additional functions such as cell-specific targeting and active endosomal escape.[200,201] Consequently, lipid-based gene and drug delivery has advanced to a level that rivals the efficiency of naturally occuring viral vectors.[202]

Lipid molecules also serve several important biological functions in cellular pathways in addition to forming structural membranes. For example, sphingosine-1-phosphate (S1P) is a lipid produced by the metabolism of sphingomyelin, an abundant membrane phospholipid. S1P may act as an intracellular messenger of chemical signals or be secreted to the extracellular compartment where it can access cell surface receptors. S1P is an important mediator of a variety of cellular signals relevant to tissue engineering and regenerative medicine, including immune response, angiogenesis, and vascular permeability.[203] Elbert and colleagues incorporated S1P into hydrogels for controlled release to surrounding cells.[204,205] This led to increased migration of endothelial cells and enhanced angiogenesis in the chorioallantoic membrane assay. The level of S1P released from the biomaterial was particularly important, as they later showed that only a narrow window of S1P concentration was effective in plasma.[206] Sustained release of S1P from a biomaterial scaffold was also shown to enhance microvascular remodeling and bone healing *in vivo*.[207] These studies have established lipids as a class of bioactive molecules that is complementary to proteins and nucleic acids for directing cell activity in applications of tissue engineering and regenerative medicine.

Acknowledgments

The author thanks Dr. Catherine D. Reyes for her critical review of this chapter and valuable discussions.

References

1. DeGrado, W. F.; Summa, C. M.; Pavone, V.; Nastri, F.; Lombardi, A. *Annu. Rev. Biochem.* **1999**, *68*, 779–819.
2. Hubbell, J. A. *Curr. Opin. Biotechnol.* **1999**, *10*(2), 123–129.
3. Lutolf, M. P.; Hubbell, J. A. *Nat. Biotechnol.* **2005**, *23*(1), 47–55.
4. McCarthy, J. B.; Vachhani, B.; Iida, J. *Biopolymers* **1996**, *40*(4), 371–381.
5. Vogel, W.; Gish, G. D.; Alves, F.; Pawson, T. *Mol. Cell* **1997**, *1*(1), 13–23.
6. von der Mark, K.; Mollenhauer, J. *Cell. Mol. Life Sci.* **1997**, *53*(6), 539–545.
7. Yang, C.; Hillas, P. J.; Baez, J. A.; *et al. BioDrugs* **2004**, *18*(2), 103–119.
8. Koyama, H.; Raines, E. W.; Bornfeldt, K. E.; Roberts, J. M.; Ross, R. *Cell* **1996**, *87*(6), 1069–1078.
9. Jikko, A.; Harris, S. E.; Chen, D.; Mendrick, D. L.; Damsky, C. H. *J. Bone Miner. Res.* **1999**, *14*(7), 1075–1083.
10. Mizuno, M.; Fujisawa, R.; Kuboki, Y. *J. Cell. Physiol.* **2000**, *184*(2), 207–213.
11. Mizuno, M.; Kuboki, Y. *J. Biochem.* **2001**, *129*(1), 133–138.
12. Suzawa, M.; Tamura, Y.; Fukumoto, S.; *et al. J. Bone Miner. Res.* **2002**, *17*(2), 240–248.
13. Knight, C. G.; Morton, L. F.; Peachey, A. R.; Tuckwell, D. S.; Farndale, R. W.; Barnes, M. J. *J. Biol. Chem.* **2000**, *275*(1), 35–40.
14. Reyes, C. D.; Garcia, A. J. *J. Biomed. Mater. Res. A* **2004**, *69*(4), 591–600.
15. Reyes, C. D.; Petrie, T. A.; Burns, K. L.; Schwartz, Z.; Garcia, A. J. *Biomaterials* **2007**, *28*(21), 3228–3235.
16. Ito, H.; Steplewski, A.; Alabyeva, T.; Fertala, A. *J. Biomed. Mater. Res. A* **2006**, *76*(3), 551–560.
17. Paramonov, S. E.; Gauba, V.; Hartgerink, J. D. *Macromolecules* **2005**, *38*, 7555–7561.
18. Koide, T.; Homma, D. L.; Asada, S.; Kitagawa, K. *Bioorg. Med. Chem. Lett.* **2005**, *15*(23), 5230–5233.
19. Kotch, F. W.; Raines, R. T. *Proc. Natl. Acad. Sci. USA* **2006**, *103*(9), 3028–3033.
20. Chow, D.; Nunalee, M. L.; Lim, D. W.; Simnick, A. J.; Chilkoti, A. *Mater. Sci. Eng. R Rep.* **2008**, *62*(4), 125–155.
21. Urry, D. W.; Pattanaik, A. *Ann. NY Acad. Sci.* **1997**, *831*, 32–46.
22. Lim, D. W.; Nettles, D. L.; Setton, L. A.; Chilkoti, A. *Biomacromolecules* **2007**, *8*(5), 1463–1470.
23. Lim, D. W.; Nettles, D. L.; Setton, L. A.; Chilkoti, A. *Biomacromolecules* **2008**, *9*(1), 222–230.
24. Betre, H.; Setton, L. A.; Meyer, D. E.; Chilkoti, A. *Biomacromolecules* **2002**, *3*(5), 910–916.
25. Betre, H.; Ong, S. R.; Guilak, F.; Chilkoti, A.; Fermor, B.; Setton, L. A. *Biomaterials* **2006**, *27*(1), 91–99.
26. Betre, H.; Liu, W.; Zalutsky, M. R.; Chilkoti, A.; Kraus, V. B.; Setton, L. A. *J. Control. Release* **2006**, *115*(2), 175–182.
27. Shamji, M. F.; Betre, H.; Kraus, V. B.; *et al. Arthritis Rheum.* **2007**, *56*(11), 3650–3661.
28. Shamji, M. F.; Whitlatch, L.; Friedman, A. H.; Richardson, W. J.; Chilkoti, A.; Setton, L. A. *Spine (Phila Pa)* **1976**, *33*(7), 748–754.
29. Hynes, R. O. *Cell* **2002**, *110*(6), 673–687.
30. Howe, A.; Aplin, A. E.; Alahari, S. K.; Juliano, R. L. *Curr. Opin. Cell Biol.* **1998**, *10*(2), 220–231.
31. Nobes, C. D.; Hall, A. *J. Cell Biol.* **1999**, *144*(6), 1235–1244.
32. Sechler, J. L.; Schwarzbauer, J. E. *J. Biol. Chem.* **1998**, *273*(40), 25533–25536.
33. Pierschbacher, M. D.; Ruoslahti, E. *Nature* **1984**, *309*(5963), 30–33.
34. Hersel, U.; Dahmen, C.; Kessler, H. *Biomaterials* **2003**, *24*(24), 4385–4415.
35. Hubbell, J. A.; Massia, S. P.; Desai, N. P.; Drumheller, P. D. *Biotechnology (NY)* **1991**, *9*(6), 568–572.
36. Ranieri, J. P.; Bellamkonda, R.; Bekos, E. J.; Vargo, T. G.; Gardella, J. A., Jr.; Aebischer, P. *J. Biomed. Mater. Res.* **1995**, *29*(6), 779–785.
37. Petrie, T. A.; Capadona, J. R.; Reyes, C. D.; Garcia, A. J. *Biomaterials* **2006**, *27*(31), 5459–5470.
38. Pierschbacher, M. D.; Ruoslahti, E. *J. Biol. Chem.* **1987**, *262*(36), 17294–17298.
39. Petrie, T. A.; Raynor, J. E.; Reyes, C. D.; Burns, K. L.; Collard, D. M.; Garcia, A. J. *Biomaterials* **2008**, *29*(19), 2849–2857.
40. Petrie, T. A.; Reyes, C. D.; Burns, K. L.; Garcia, A. J. *J. Cell. Mol. Med.* **2009**, *13*(8B), 2602–2612.
41. Aumailley, M.; Gurrath, M.; Muller, G.; Calvete, J.; Timpl, R.; Kessler, H. *FEBS Lett.* **1991**, *291*(1), 50–54.
42. Goodman, S. L.; Holzemann, G.; Sulyok, G. A.; Kessler, H. *J. Med. Chem.* **2002**, *45*(5), 1045–1051.
43. Gurrath, M.; Muller, G.; Kessler, H.; Aumailley, M.; Timpl, R. *Eur. J. Biochem.* **1992**, *210*(3), 911–921.
44. Haubner, R.; Gratias, R.; Diefenbach, B.; Goodman, S. L.; Jonczyk, A.; Kessler, H. *J. Am. Chem. Soc.* **1996**, *118*, 7461–7472.
45. Keselowsky, B. G.; Collard, D. M.; Garcia, A. J. *J. Biomed. Mater. Res. A* **2003**, *66*(2), 247–259.
46. Keselowsky, B. G.; Collard, D. M.; Garcia, A. J. *Biomaterials* **2004**, *25*(28), 5947–5954.
47. Keselowsky, B. G.; Collard, D. M.; Garcia, A. J. *Proc. Natl. Acad. Sci. USA* **2005**, *102*(17), 5953–5957.
48. Delforge, D.; Gillon, B.; Art, M.; Dewelle, J.; Raes, M.; Remacle, J. *Lett. Pept. Sci.* **1998**, *5*, 87–91.
49. van der Pluijm, G.; Vloedgraven, H. J.; Ivanov, B.; *et al. Cancer Res.* **1996**, *56*(8), 1948–1955.
50. Reyes, C. D.; Garcia, A. J. *J. Biomed. Mater. Res. A* **2003**, *65*(4), 511–523.
51. Gallant, N. D.; Michael, K. E.; Garcia, A. J. *Mol. Biol. Cell* **2005**, *16*(9), 4329–4340.
52. Garcia, A. J.; Takagi, J.; Boettiger, D. *J. Biol. Chem.* **1998**, *273*(52), 34710–34715.
53. Rezania, A.; Thomas, C. H.; Branger, A. B.; Waters, C. M.; Healy, K. E. *J. Biomed. Mater. Res.* **1997**, *37*(1), 9–19.
54. Dee, K. C.; Anderson, T. T.; Bizios, R. *Biomaterials* **1999**, *20*(3), 221–227.
55. Kouvroukoglou, S.; Dee, K. C.; Bizios, R.; McIntire, L. V.; Zygourakis, K. *Biomaterials* **2000**, *21*(17), 1725–1733.
56. Palecek, S. P.; Loftus, J. C.; Ginsberg, M. H.; Lauffenburger, D. A.; Horwitz, A. F. *Nature* **1997**, *385*(6616), 537–540.

57. Healy, K. E.; Rezania, A.; Stile, R. A. *Ann. NY Acad. Sci.* **1999**, *875*, 24–35.
58. Rezania, A.; Healy, K. E. *Biotechnol. Prog.* **1999**, *15*(1), 19–32.
59. Hern, D. L.; Hubbell, J. A. *J. Biomed. Mater. Res.* **1998**, *39*(2), 266–276.
60. Houseman, B. T.; Mrksich, M. *Biomaterials* **2001**, *22*(9), 943–955.
61. Massia, S. P.; Hubbell, J. A. *J. Cell Biol.* **1991**, *114*(5), 1089–1100.
62. Danilov, Y. N.; Juliano, R. L. *Exp. Cell Res.* **1989**, *182*(1), 186–196.
63. Kantlehner, M.; Schaffner, P.; Finsinger, D.; *et al. Chembiochem.* **2000**, *1*(2), 107–114.
64. Drumheller, P. D.; Elbert, D. L.; Hubbell, J. A. *Biotechnol. Bioeng.* **1994**, *43*(8), 772–780.
65. Neff, J. A.; Tresco, P. A.; Caldwell, K. D. *Biomaterials* **1999**, *20*(23–24), 2377–2393.
66. Schense, J. C.; Bloch, J.; Aebischer, P.; Hubbell, J. A. *Nat. Biotechnol.* **2000**, *18*(4), 415–419.
67. Schense, J. C.; Hubbell, J. A. *J. Biol. Chem.* **2000**, *275*(10), 6813–6818.
68. Eid, K.; Chen, E.; Griffith, L.; Glowacki, J. *J. Biomed. Mater. Res.* **2001**, *57*(2), 224–231.
69. Mann, B. K.; West, J. L. *J. Biomed. Mater. Res.* **2002**, *60*(1), 86–93.
70. Reyes, C. D.; Petrie, T. A.; Garcia, A. J. *J. Cell. Physiol.* **2008**, *217*(2), 450–458.
71. Banerjee, P.; Irvine, D. J.; Mayes, A. M.; Griffith, L. G. *J. Biomed.Mater. Res.* **2000**, *50*(3), 331–339.
72. Irvine, D. J.; Hue, K. A.; Mayes, A. M.; Griffith, L. G. *Biophys. J.* **2002**, *82*(1 Pt 1), 120–132.
73. Irvine, D. J.; Mayes, A. M.; Griffith, L. G. *Biomacromolecules* **2001**, *2*(1), 85–94.
74. Koo, L. Y.; Irvine, D. J.; Mayes, A. M.; Lauffenburger, D. A.; Griffith, L. G. *J. Cell Sci.* **2002**, *115*(Pt 7), 1423–1433.
75. Maheshwari, G.; Brown, G.; Lauffenburger, D. A.; Wells, A.; Griffith, L. G. *J. Cell Sci.* **2000**, *113*(Pt 10), 1677–1686.
76. Loebsack, A.; Greene, K.; Wyatt, S.; *et al. J. Biomed. Mater. Res.* **2001**, *57*(4), 575–581.
77. Shin, H.; Jo, S.; Mikos, A. G. *J. Biomed. Mater. Res.* **2002**, *61*(2), 169–179.
78. Beer, J. H.; Springer, K. T.; Coller, B. S. *Blood* **1992**, *79*(1), 117–128.
79. Pelham, R. J., Jr.; Wang, Y. L. *Biol. Bull.* **1998**, *194*(3), 348–349 discussion 349–350.
80. Wong, J. Y.; Kuhl, T. L.; Israelachvili, J. N.; Mullah, N.; Zalipsky, S. *Science* **1997**, *275*(5301), 820–822.
81. Craig, W. S.; Cheng, S.; Mullen, D. G.; Blevitt, J.; Pierschbacher, M. D. *Biopolymers* **1995**, *37*(2), 157–175.
82. Art, M.; Delforge, D.; Gillon, B.; Remacle, J.; Raes, M. *Polym. Preprints* **1995**, *36*, 115–116.
83. Cook, A. D.; Hrkach, J. S.; Gao, N. N.; *et al. J. Biomed. Mater. Res.* **1997**, *35*(4), 513–523.
84. Borkenhagen, M.; Clemence, J. F.; Sigrist, H.; Aebischer, P. *J. Biomed. Mater. Res.* **1998**, *40*(3), 392–400.
85. Babensee, J. E.; McIntire, L. V.; Mikos, A. G. *Pharm. Res.* **2000**, *17*(5), 497–504.
86. Ramirez, F.; Rifkin, D. B. *Matrix Biol.* **2003**, *22*(2), 101–107.
87. Hubbell, J. A. *Swiss Med Wkly* **2007**, *137*(Suppl. 155), 72S–76S.
88. Zisch, A. H.; Lutolf, M. P.; Hubbell, J. A. *Cardiovasc. Pathol.* **2003**, *12*(6), 295–310.
89. Edelman, E. R.; Nugent, M. A.; Smith, L. T.; Karnovsky, M. J. *J. Clin. Invest.* **1992**, *89*(2), 465–473.
90. Tanihara, M.; Suzuki, Y.; Yamamoto, E.; Noguchi, A.; Mizushima, Y. *J. Biomed. Mater. Res.* **2001**, *56*(2), 216–221.
91. Edelman, E. R.; Mathiowitz, E.; Langer, R.; Klagsbrun, M. *Biomaterials* **1991**, *12*(7), 619–626.
92. Harada, K.; Grossman, W.; Friedman, M.; *et al. J. Clin. Invest.* **1994**, *94*(2), 623–630.
93. Laham, R. J.; Sellke, F. W.; Edelman, E. R.; *et al. Circulation* **1999**, *100*(18), 1865–1871.
94. Tabata, Y.; Miyao, M.; Ozeki, M.; Ikada, Y. *J. Biomater. Sci. Polym. Ed.* **2000**, *11*(9), 915–930.
95. Muniruzzaman, M.; Tabata, Y.; Ikada, Y. *J. Biomater. Sci. Polym. Ed.* **1998**, *9*(5), 459–473.
96. Tabata, Y.; Nagano, A.; Muniruzzaman, M.; Ikada, Y. *Biomaterials* **1998**, *19*(19), 1781–1789.
97. Tabata, Y.; Yamada, K.; Miyamoto, S.; *et al. Biomaterials* **1998**, *19*(7–9), 807–815.
98. Schense, J. C.; Hubbell, J. A. *Bioconjug. Chem.* **1999**, *10*(1), 75–81.
99. Sakiyama-Elbert, S. E.; Hubbell, J. A. *J. Control. Release* **2000**, *69*(1), 149–158.
100. Sakiyama-Elbert, S. E.; Hubbell, J. A. *J. Control. Release* **2000**, *65*(3), 389–402.
101. Lee, A. C.; Yu, V. M.; Lowe, J. B., III; *et al. Exp. Neurol.* **2003**, *184*(1), 295–303.
102. Taylor, S. J.; McDonald, J. W., III; Sakiyama-Elbert, S. E. *J. Control. Release* **2004**, *98*(2), 281–294.
103. Sakiyama-Elbert, S. E.; Panitch, A.; Hubbell, J. A. *FASEB J.* **2001**, *15*(7), 1300–1302.
104. Zisch, A. H.; Schenk, U.; Schense, J. C.; Sakiyama-Elbert, S. E.; Hubbell, J. A. *J. Control. Release* **2001**, *72*(1–3), 101–113.
105. Platt, M. O.; Roman, A. J.; Wells, A.; Lauffenburger, D. A.; Griffith, L. G. *J. Cell. Physiol.* **2009**, *221*(2), 306–317.
106. Kuhl, P. R.; Griffith-Cima, L. G. *Nat. Med.* **1996**, *2*(9), 1022–1027.
107. Byers, B. A.; Pavlath, G. K.; Murphy, T. J.; Karsenty, G.; Garcia, A. J. *J. Bone Miner. Res.* **2002**, *17*(11), 1931–1944.
108. Garcia, A. J.; Guldberg, R. E.; Byers, B. A.; Gersbach, C. A.; Phillips, J. E. *IEEE Eng. Med. Biol. Mag.* **2003**, *22*(5), 65–70.
109. Gersbach, C. A.; Byers, B. A.; Pavlath, G. K.; Garcia, A. J. *Exp. Cell Res.* **2004**, *300*(2), 406–417.
110. Gersbach, C. A.; Byers, B. A.; Pavlath, G. K.; Guldberg, R. E.; Garcia, A. J. *Biotechnol. Bioeng.* **2004**, *88*(3), 369–378.
111. Gersbach, C. A.; Le Doux, J. M.; Guldberg, R. E.; Garcia, A. J. *Gene Ther.* **2006**, *13*(11), 873–882.
112. Phillips, J. E.; Gersbach, C. A.; Wojtowicz, A. M.; Garcia, A. J. *J. Cell Sci.* **2006**, *119*(Pt 3), 581–591.
113. Trentin, D.; Hall, H.; Wechsler, S.; Hubbell, J. A. *Proc. Natl. Acad. Sci. USA* **2006**, *103*(8), 2506–2511.
114. Pajusola, K.; Kunnapuu, J.; Vuorikoski, S.; *et al. FASEB J.* **2005**, *19*(10), 1365–1367.
115. Vincent, K. A.; Shyu, K. G.; Luo, Y.; *et al. Circulation* **2000**, *102*(18), 2255–2261.
116. Rajagopalan, S.; Olin, J.; Deitcher, S.; *et al. Circulation* **2007**, *115*(10), 1234–1243.
117. Segal, D. J.; Barbas, C. F., III *Curr. Opin. Biotechnol.* **2001**, *12*(6), 632–637.
118. Beerli, R. R.; Dreier, B.; Barbas, C. F., III *Proc. Natl. Acad. Sci. USA* **2000**, *97*(4), 1495–1500.
119. Blancafort, P.; Chen, E. I.; Gonzalez, B.; *et al. Proc. Natl. Acad. Sci. USA* **2005**, *102*(33), 11716–11721.
120. Blancafort, P.; Magnenat, L.; Barbas, C. F., III *Nat. Biotechnol.* **2003**, *21*(3), 269–274.
121. Snowden, A. W.; Zhang, L.; Urnov, F.; *et al. Cancer Res.* **2003**, *63*(24), 8968–8976.
122. Rebar, E. J.; Huang, Y.; Hickey, R.; *et al. Nat. Med.* **2002**, *8*(12), 1427–1432.
123. Price, S. A.; Dent, C.; Duran-Jimenez, B.; *et al. Diabetes* **2006**, *55*(6), 1847–1854.
124. Chilkoti, A.; Dreher, M. R.; Meyer, D. E. *Adv. Drug Deliv. Rev.* **2002**, *54*(8), 1093–1111.
125. Meyer, D. E.; Chilkoti, A. *Biomacromolecules* **2002**, *3*(2), 357–367.
126. Aota, S.; Nomizu, M.; Yamada, K. M. *J. Biol. Chem.* **1994**, *269*(40), 24756–24761.
127. Deming, T. J. *Adv. Drug Deliv. Rev.* **2002**, *54*(8), 1145–1155.
128. Gersbach, C. A.; Phillips, J. E.; Garcia, A. J. *Annu. Rev. Biomed. Eng.* **2007**, *9*, 87–119.
129. Bonadio, J. *Adv. Drug Deliv. Rev.* **2000**, *44*(2–3), 185–194.
130. Lew, D.; Parker, S. E.; Latimer, T.; *et al. Hum. Gene Ther.* **1995**, *6*(5), 553–564.
131. Schaffer, D. V.; Lauffenburger, D. A. *Curr. Opin. Mol. Ther.* **2000**, *2*(2), 155–161.
132. Bonadio, J. *J. Mol. Med.* **2000**, *78*(6), 303–311.
133. Bonadio, J.; Smiley, E.; Patil, P.; Goldstein, S. *Nat. Med.* **1999**, *5*(7), 753–759.
134. Leong, K. W.; Mao, H. Q.; Truong-Le, V. L.; Roy, K.; Walsh, S. M.; August, J. T. *J. Control. Release* **1998**, *53*(1–3), 183–193.
135. Ochiya, T.; Takahama, Y.; Nagahara, S.; *et al. Nat. Med.* **1999**, *5*(6), 707–710.
136. Labhasetwar, V.; Bonadio, J.; Goldstein, S.; Chen, W.; Levy, R. J. *J. Pharm. Sci.* **1998**, *87*(11), 1347–1350.
137. Fang, J.; Zhu, Y. Y.; Smiley, E.; *et al. Proc. Natl. Acad. Sci. USA* **1996**, *93*(12), 5753–5758.
138. Shea, L. D.; Smiley, E.; Bonadio, J.; Mooney, D. J. *Nat. Biotechnol.* **1999**, *17*(6), 551–554.
139. Berry, M.; Gonzalez, A. M.; Clarke, W.; *et al. Mol. Cell. Neurosci.* **2001**, *17*(4), 706–716.
140. Barron, L. G.; Meyer, K. B.; Szoka, F. C., Jr. *Hum. Gene Ther.* **1998**, *9*(3), 315–323.
141. Li, S.; Tseng, W. C.; Stolz, D. B.; Wu, S. P.; Watkins, S. C.; Huang, L. *Gene Ther.* **1999**, *6*(4), 585–594.
142. Zelphati, O.; Uyechi, L. S.; Barron, L. G.; Szoka, F. C., Jr. *Biochim. Biophys. Acta* **1998**, *1390*(2), 119–133.
143. Schaffer, D. V.; Lauffenburger, D. A. *J. Biol. Chem.* **1998**, *273*(43), 28004–28009.

144. Ludtke, J. J.; Zhang, G.; Sebestyen, M. G.; Wolff, J. A. *J. Cell Sci.* **1999**, *112*(Pt 12), 2033–2041.
145. Subramanian, A.; Ranganathan, P.; Diamond, S. L. *Nat. Biotechnol.* **1999**, *17*(9), 873–877.
146. Zanta, M. A.; Belguise-Valladier, P.; Behr, J. P. *Proc. Natl. Acad. Sci. USA* **1999**, *96*(1), 91–96.
147. Ogris, M.; Brunner, S.; Schuller, S.; Kircheis, R.; Wagner, E. *Gene Ther.* **1999**, *6*(4), 595–605.
148. Wagner, E. *Adv. Drug Deliv. Rev.* **1999**, *38*(3), 279–289.
149. Wolff, J. A.; Herweijer, H. *Adv. Drug Deliv. Rev.* **1997**, *27*(1), 5–16.
150. Adami, R. C.; Collard, W. T.; Gupta, S. A.; Kwok, K. Y.; Bonadio, J.; Rice, K. G. *J. Pharm. Sci.* **1998**, *87*(6), 678–683.
151. Storrie, H.; Mooney, D. J. *Adv. Drug Deliv. Rev.* **2006**, *58*(4), 500–514.
152. Baiker, A.; Maercker, C.; Piechaczek, C.; *et al. Nat. Cell Biol.* **2000**, *2*(3), 182–184.
153. Yant, S. R.; Meuse, L.; Chiu, W.; Ivics, Z.; Izsvak, Z.; Kay, M. A. *Nat. Genet.* **2000**, *25*(1), 35–41.
154. Deng, G. M.; Nilsson, I. M.; Verdrengh, M.; Collins, L. V.; Tarkowski, A. *Nat. Med.* **1999**, *5*(6), 702–705.
155. Chen, Z. Y.; He, C. Y.; Ehrhardt, A.; Kay, M. A. *Mol. Ther.* **2003**, *8*(3), 495–500.
156. Phillips, J. E.; Gersbach, C. A.; Garcia, A. J. *Biomaterials* **2007**, *28*(2), 211–229.
157. Gersbach, C. A.; Coyer, S. R.; Le Doux, J. M.; Garcia, A. J. *Biomaterials* **2007**, *28* (34), 5121–5127.
158. Phillips, J. E.; Burns, K. L.; Le Doux, J. M.; Guldberg, R. E.; Garcia, A. J. *Proc. Natl. Acad. Sci. USA* **2008**, *105*(34), 12170–12175.
159. Laurencin, C. T.; Attawia, M. A.; Lu, L. Q.; *et al. Biomaterials* **2001**, *22*(11), 1271–1277.
160. Lee, J. Y.; Peng, H.; Usas, A.; *et al. Hum. Gene Ther.* **2002**, *13*(10), 1201–1211.
161. Yoo, J. U.; Mandell, I.; Angele, P.; Johnstone, B. *Clin. Orthop. Relat. Res.* **2000**, (379 Suppl), S164–S170.
162. Lee, K. H.; Song, S. U.; Hwang, T. S.; *et al. Hum. Gene Ther.* **2001**, *12*(14), 1805–1813.
163. Breitbart, A. S.; Grande, D. A.; Laser, J.; *et al. Ann. Plast. Surg.* **2001**, *46*(5), 555–561; discussion 561–562.
164. Breitbart, A. S.; Mason, J. M.; Urmacher, C.; *et al. Ann. Plast. Surg.* **1999**, *43*(6), 632–639.
165. Zhang, X.; Godbey, W. T. *Adv. Drug Deliv. Rev.* **2006**, *58*(4), 515–534.
166. Baum, C.; Kustikova, O.; Modlich, U.; Li, Z.; Fehse, B. *Hum. Gene Ther.* **2006**, *17*(3), 253–263.
167. Li, W.; Asokan, A.; Wu, Z.; *et al. Mol. Ther.* **2008**, *16*(7), 1252–1260.
168. Maheshri, N.; Koerber, J. T.; Kaspar, B. K.; Schaffer, D. V. *Nat. Biotechnol.* **2006**, *24*(2), 198–204.
169. Li, W.; Zhang, L.; Johnson, J. S.; *et al. Mol. Ther.* **2009**, *17*(12), 2067–2077.
170. Koerber, J. T.; Klimczak, R.; Jang, J. H.; *et al. Mol. Ther.* **2009**, *17*(12), 2088–2095.
171. Chen, Y.; Luk, K. D.; Cheung, K. M.; *et al. Gene Ther.* **2003**, *10*(16), 1345–1353.
172. Luk, K. D.; Chen, Y.; Cheung, K. M.; Kung, H. F.; Lu, W. W.; Leong, J. C. *Biochem. Biophys. Res. Commun.* **2003**, *308*(3), 636–645.
173. Deodato, B.; Arsic, N.; Zentilin, L.; *et al. Gene Ther.* **2002**, *9*(12), 777–785.
174. Galeano, M.; Deodato, B.; Altavilla, D.; *et al. Crit. Care Med.* **2003**, *31*(4), 1017–1025.
175. Su, H.; Joho, S.; Huang, Y.; *et al. Proc. Natl. Acad. Sci. USA* **2004**, *101*(46), 16280–16285.
176. Su, H.; Lu, R.; Kan, Y. W. *Proc. Natl. Acad. Sci. USA* **2000**, *97*(25), 13801–13806.
177. Ito, H.; Koefoed, M.; Tiyapatanaputi, P.; *et al. Nat. Med.* **2005**, *11*(3), 291–297.
178. Schek, R. M.; Hollister, S. J.; Krebsbach, P. H. *Mol. Ther.* **2004**, *9*(1), 130–138.
179. Schek, R. M.; Wilke, E. N.; Hollister, S. J.; Krebsbach, P. H. *Biomaterials* **2006**, *27*(7), 1160–1166.
180. Dunn, C. A.; Jin, Q.; Taba, M., Jr.; Franceschi, R. T.; Bruce Rutherford, R.; Giannobile, W. V. *Mol. Ther.* **2005**, *11*(2), 294–299.
181. Casper, D.; Engstrom, S. J.; Mirchandani, G. R.; *et al. Cell Transplant.* **2002**, *11*(4), 331–349.
182. Rana, T. M. *Nat. Rev. Mol. Cell Biol.* **2007**, *8*(1), 23–36.
183. Siomi, H.; Siomi, M. C. *Nature* **2009**, *457*(7228), 396–404.
184. Yao, Y.; Wang, C.; Varshney, R. R.; Wang, D. A. *Pharm. Res.* **2009**, *26*(2), 263–275.
185. Pack, D. W.; Hoffman, A. S.; Pun, S.; Stayton, P. S. *Nat. Rev. Drug Discov.* **2005**, *4*(7), 581–593.
186. Gary, D. J.; Puri, N.; Won, Y. Y. *J. Control. Release* **2007**, *121*(1–2), 64–73.
187. Stayton, P. S.; El-Sayed, M. E.; Murthy, N.; *et al. Orthod. Craniofac. Res.* **2005**, *8*(3), 219–225.
188. Convertine, A. J.; Benoit, D. S.; Duvall, C. L.; Hoffman, A. S.; Stayton, P. S. *J. Control. Release* **2009**, *133*(3), 221–229.
189. Alivisatos, A. P.; Johnsson, K. P.; Peng, X.; *et al. Nature* **1996**, *382*(6592), 609–611.
190. Mirkin, C. A.; Letsinger, R. L.; Mucic, R. C.; Storhoff, J. J. *Nature* **1996**, *382* (6592), 607–609.
191. Chandra, R. A.; Douglas, E. S.; Mathies, R. A.; Bertozzi, C. R.; Francis, M. B. *Angew. Chem. Int. Ed. Engl.* **2006**, *45*(6), 896–901.
192. Gartner, Z. J.; Bertozzi, C. R. *Proc. Natl. Acad. Sci. USA* **2009**, *106*(12), 4606–4610.
193. Labean, T. H.; Li, H. *Nano Today* **2007**, *2*(2), 26–35.
194. Winfree, E.; Liu, F.; Wenzler, L. A.; Seeman, N. C. *Nature* **1998**, *394*(6693), 539–544.
195. Rothemund, P. W. *Nature* **2006**, *440*(7082), 297–302.
196. Andersen, E. S.; Dong, M.; Nielsen, M. M.; *et al. Nature* **2009**, *459*(7243), 73–76.
197. Martin, B.; Sainlos, M.; Aissaoui, A.; *et al. Curr. Pharm. Des.* **2005**, *11*(3), 375–394.
198. Dalby, B.; Cates, S.; Harris, A.; *et al. Methods* **2004**, *33*(2), 95–103.
199. Santel, A.; Aleku, M.; Keil, O.; *et al. Gene Ther.* **2006**, *13*(16), 1222–1234.
200. Montier, T.; Benvegnu, T.; Jaffres, P. A.; Yaouanc, J. J.; Lehn, P. *Curr. Gene Ther.* **2008**, *8*(5), 296–312.
201. Tseng, Y. C.; Mozumdar, S.; Huang, L. *Adv. Drug Deliv. Rev.* **2009**, *61*(9), 721–731.
202. Wagner, E. *Pharm. Res.* **2004**, *21*(1), 8–14.
203. Hla, T. *Semin. Cell Dev. Biol.* **2004**, *15*(5), 513–520.
204. Wacker, B. K.; Alford, S. K.; Scott, E. A.; Das Thakur, M.; Longmore, G. D.; Elbert, D. L. *Biophys. J.* **2008**, *94*(1), 273–285.
205. Wacker, B. K.; Scott, E. A.; Kaneda, M. M.; Alford, S. K.; Elbert, D. L. *Biomacromolecules* **2006**, *7*(4), 1335–1343.
206. Alford, S. K.; Kaneda, M. M.; Wacker, B. K.; Elbert, D. L. *J. Biomed. Mater. Res. A* **2009**, *88*(1), 205–212.
207. Sefcik, L. S.; Petrie Aronin, C. E.; Wieghaus, K. A.; Botchwey, E. A. *Biomaterials* **2008**, *29*(19), 2869–2877.

5.511. Rotating-Wall Vessels for Cell Culture

Q-Q Qiu, LifeCell Corporation, Branchburg, NJ, USA
P S Ayyaswamy and P Ducheyne, University of Pennsylvania, Philadelphia, PA, USA

© 2011 Elsevier Ltd. All rights reserved.

5.511.1.	**Introduction**	148
5.511.2.	**Operating Principles of RWV**	149
5.511.2.1.	Forces Acting on Microcarrier/Cell	150
5.511.2.2.	Modeling of Cell Culture Employing the HARV	150
5.511.2.2.1.	Determination of microcarrier trajectory and velocity	150
5.511.2.2.2.	Particle–particle and particle–wall collisions	151
5.511.2.2.3.	Microcarrier/cell spin	152
5.511.2.2.4.	Shear stress	153
5.511.2.2.5.	Mass transfer evaluation	156
5.511.2.3.	Optimal Conditions of RWV	157
5.511.3.	**Scaffolds and Microcarriers for Cell Culture in RWV**	157
5.511.3.1.	Criteria for Carriers	157
5.511.3.2.	Microcarriers and Scaffolds Used for Cell Culture in RWV	158
5.511.3.2.1.	Polymers	158
5.511.3.2.2.	Polymer–ceramic/glass composites	158
5.511.3.2.3.	Ceramics	158
5.511.4.	**Cell Culture in RWV**	159
5.511.4.1.	3D Cell Culture	160
5.511.4.1.1.	Bone cells	160
5.511.4.1.2.	Chondrocytes	162
5.511.4.1.3.	Stem cells	163
5.511.4.1.4.	Other	163
5.511.4.2.	Tissue Engineering	163
5.511.5.	**Other Applications of RWV**	164
156.5.1.	Space Biology	164
5.511.5.2.	Cancer Research	164
5.511.5.3.	Other	165
References		166

Glossary

Bioactive Having an effect on or causing a reaction in living tissue.

Fluid drag force Force that opposes the relative motion of an object through a fluid. It acts in a direction opposite to the oncoming flow velocity.

Gravitational buoyancy Upward force caused by fluid pressure that keeps things afloat.

Microcarrier A support matrix usually in spherical shape allowing for the growth of adherent cells in bioreactors. Carrier materials may be composed by degradable synthetic biopolymer, porous glass, collagen, or cellulose, with dimension of 100–500 μm.

Microsphere apparent density The weight per unit volume of microspheres, which takes count of air and pores in the microspheres. For a hollow or porous microsphere, apparent density is lower than the density of a solid microsphere.

Osteopenia A condition where bone mineral density is lower than normal. It commonly occurs among astronauts during space flight.

Rotating frame A special case of a noninertial reference frame that is rotating relative to an inertial reference frame.

Rotating-wall vessel NASA-designed vessels filled with culture medium and rotating about horizontal axis. The fluid media inside the vessels undergo solid body rotation and have very low shear stress. They can simulate microgravity and have been used to study cellular responses to microgravity and 3D cell cultures.

Shear stress A stress which is applied parallel or tangential to a face of a material, as opposed to a normal stress which is applied perpendicularly.

Simulated microgravity A microgravity condition simulated in rotating-wall vessels operated at ground level (unit gravity).

Stem cell Cells have ability to go through mitotic cell division and differentiating into a diverse range of specialized cell types. The two broad types of mammalian stem cells are embryonic stem cells that are isolated from an early stage of embryo, and adult stem cells that are found in adult tissues.

Abbreviations

ALPase	Alkaline phosphatase
BMP	Bone morphogenetic protein
hEBs	Human embryoid bodies
hMSC	Human mesenchymal stem cell
HARV	High aspect ratio vessel
HepG2	Human hepatoblastoma cells
MSCs	Mesenchymal stem cells
PGA	Polyglycolic acid
Pi	Phosphate ion
PLA	Polylactic acid
PLGA	Poly(D,L-lactic-*co*-glycolic acid)
Re_p	Reynolds number
STLV	Slow turning lateral vessel

Symbols

D_{ij}	Diffusion coefficient
F_b	Gravitational buoyancy
F_{cp}	Centripetal force
F_d	Fluid drag force
m_f	Mass of the displaced liquid
m_p	Particle mass
$m_p\omega r^2$	Centrifugal force
μ	Viscosity of the fluid medium
ν_f	Kinematic viscosity of the fluid

5.511.1. Introduction

Conventional bioreactors employed for three-dimensional (3D) cell culture and tissue engineering have many disadvantages that are primarily associated with gravity-induced sedimentation, large fluid shear stresses and turbulence, and inadequate oxygenation. In such bioreactors, sedimentation may be followed by the formation of attachment sites that bind cells to the walls of the bioreactors and distort morphology. To circumvent these disadvantages, NASA-designed rotating-wall vessels (RWVs), such as high aspect ratio vessel (HARV) and the slow turning lateral vessel (STLV), may be used. These vessels are completely filled with the culture medium and rotate about the horizontal axis. The fluid medium inside the RWV undergoes solid body rotation and it eliminates the occurrence of boundary layers, which is inherent to bioreactors in which the medium moves relative to the vessel wall. It is important to ensure that the vessels contain no air bubbles during their operation. Depending on the cell type (e.g., anchorage-dependent cells), microcarrier beads or scaffolds that offer structural support may be conveniently employed in the RWVs. The microcarriers/cells remain suspended during the entire duration of culture, and are provided with an environment that alleviates large shear while ensuring adequate mass transfer. Because the vessel has no agitator or mixing device, the bridges among cells and microcarriers are not easily destroyed. However, mixing and small shear forces do arise in the RWV as a result of the microcarrier's motion relative to the fluid. The relative velocity induces drag. Depending on the material properties (e.g., density) and assembly architectures, the microcarriers/scaffolds experience different levels of shear stresses.

In the RWV, suspension of the microcarrier/cell is maintained by balancing sedimentation induced by gravity with centrifugation caused by the vessel rotation and fluid drag.[1–6] The microcarrier/cell undergoes rotation about its own axis as it moves around in the vessel.[7–9] It results in the rotation of the gravity vector attached to the center of gravity of the carrier/cell. In view of these features, the RWV may be used to simulate some aspects of a microgravity environment in the laboratory. However, there are specific requirements to be satisfied in order to successfully simulate the aspects of microgravity.[10,11]

Tissue structures grown in RWVs often form 3D aggregates with many similarities to the native tissue. In comparison to 2D cell culture flasks, the RWVs not only can support high-density and large-scale 3D cell culture, but also provide adequate and controlled supplies of oxygen and nutrients.[12] In the last 20 years, extensive studies have been carried out to investigate 3D cell culture, tissue engineering, and microgravity effects on cells and tissues with use of the RWV.[13]

A typical RWV unit consists of a culture vessel fully filled with the culture medium, a base on which the vessel is mounted, and a controller that controls the rotational speed of the vessel. A RWV rotates about the horizontal axis. HARV and STLV configurations of RWVs are shown in Figure 1. HARV is a single cylinder vessel with a high diameter-to-thickness ratio, and a flat silicone rubber membrane is mounted on the back side of the cylindrical chamber for oxygenation transport (Figure 1(a) and 1(b)). The small thickness of the chamber enables efficient transport of oxygen throughout the vessel. HARV is commonly used to culture both suspension and anchorage-dependent cells. Different chamber volumes can be achieved by varying the diameter of the vessel. The STLV has concentric inner and outer cylinders which may co- or counter-rotate. It has a central core oxygenator covered by a silicone rubber membrane (Figure 1(c)). The distance between the central core and the wall of the vessel is kept small to ensure efficient gas transport throughout the vessel. STLVs are commonly used for microcarrier cell culture and explant tissue cultures. A variety of chamber volumes is achieved by varying the length of the vessel.

This chapter will explore the factors associated with the fluid mechanics and microcarrier dynamics that affect cell culture in an RWV. The focus will be on factors that affect shear stress, microcarrier trajectory and collisions, and mass transfer in the RWV. On the basis of the fluid flow analysis, the criteria for microcarrier and scaffolds selection will be described. It must be recognized, however, that the irregularity of scaffold shapes, variations in number densities of microcarriers, and the diversity in the material properties of various



Figure 1 Typical rotating-wall vessels. (a) high aspect ratio vessel, (b) high aspect ratio vessel features, and (c) slow turning lateral vessel. Images (a) and (c) from www.Synthecon.com.

supports render such criteria only to serve as a common guide. This chapter also provides a summary of the scaffolds and microcarriers that have been used for different cell cultures and tissue engineering employing RWVs. The advantages and disadvantages of using these carrier materials will be discussed. Because of a lack of detailed information on the microcarriers and scaffolds employed combined with the fact that many different types of cells are being studied, a systematic comparison of the carrier materials is in general difficult, and the performance of support systems in cell culture studies is difficult to evaluate.

Finally, a review on 3D cultures of different cell types, tissue engineering, and space biology research with the use of RWVs is included in the chapter. Although it is difficult to clearly separate 3D cell culture from tissue engineering, a distinction is offered on the basis of close correspondence between the tissues formed and actual functional tissue in man. The tissue engineering section primarily includes the 3D tissue-like assemblies that have many characteristics of the functional tissue, whereas the cell culture section contains 3D cell cultures that have not yet reached the stage of functional tissue formation.

5.511.2. Operating Principles of RWV

The cell cultures (particularly those employing microcarriers and scaffolds) in RWV experience hydrodynamic effects from motion relative to the fluid medium and are exposed to diffusion and flow-induced mass transfer of nutrients, metabolites, and oxygen.

A number of numerical and experimental studies and discussions for cell culture in the HARV have been published,[6,8,10,12,14–16] and will be summarized in the following sections. The numerical modeling has been evolved from considering the microcarrier as a point-mass particle assuming that the flow field is not affected by the presence of the microcarrier[6,12,14] to treating microcarriers as particles of finite size.[8,10]

Although the discussions here pertain to the HARV, similar considerations will apply for the use of STLV.

5.511.2.1. Forces Acting on Microcarrier/Cell

When the HARV or STLV rotates about the horizontal axis, suspension of a microcarrier or a cell in the fluid medium is maintained by balancing sedimentation induced by gravity with centrifugation caused by the vessel rotation and fluid drag.

In Figure 2(a), the various forces acting on a typical microcarrier particle suspended in a HARV are displayed. The forces are weight of the particle $F_W = m_p g$, gravitational buoyancy $F_b = m_f g$, centripetal force $F_{cp} = m_f \omega r^2$, centrifugal force $= m_p \omega r^2$, the fluid drag force F_d, and the lift force experienced by the particle F_l. While m_p is the particle mass and m_f is the mass of the displaced liquid, ω is the specified constant angular velocity of the vessel. The fluid drag force comes into effect when there is relative motion between the microcarrier and the suspending fluid. The forces acting on the particle govern the particle's trajectory. Similar considerations apply for a particle in the STLV. The coordinate system for numerical modeling of HARV culture is shown in Figure 2(b).

5.511.2.2. Modeling of Cell Culture Employing the HARV

5.511.2.2.1. Determination of microcarrier trajectory and velocity

Cell culture employing the HARV may be assisted by numerical modeling. In depth insights into the process may be obtained by a systematic model that accompanies or is carried out simultaneously in a complementary manner with the *in vitro* study. In this section, numerical modeling of solid microcarriers suspended in a HARV is described. Discussions relevant to porous microcarriers are also included.

An incompressible fluid occupying a bounded region $\Omega(t)$ with boundary $\Gamma(t)$ at a given time instant t is considered. There are N solid particles of spherical shape and arbitrary size freely moving in the fluid. The motion of both fluid and individual particles is determined as follows. In an inertial frame (stationary or fixed frame) of reference with its origin coinciding with the center of the cylinder, the fluid motion has to satisfy the conservation of mass,

$$\nabla \cdot \mathbf{u} = 0 \qquad [1]$$

and the conservation of momentum,

$$\rho_f \frac{D\mathbf{u}}{Dt} = \rho_f \boldsymbol{g} + \nabla \cdot \sigma \qquad [2]$$

where $\mathbf{u}$ is the fluid velocity vector observed in an inertial frame, ρ_f is the fluid density, $\boldsymbol{g}$ is the acceleration due to gravity vector, $\boldsymbol{\sigma}$ is the stress tensor, and the material derivative of the velocity $D\mathbf{u}/Dt$ is given by

$$\frac{D\mathbf{u}}{Dt} = \frac{\partial \mathbf{u}}{\partial t} + (\mathbf{u} \cdot \nabla)\mathbf{u} \qquad [3]$$

where the local time derivative $\partial/\partial t$ is with respect to a stationary observer. For a Newtonian fluid, the stress tensor is given by the constitutive relation,

$$\sigma = -P\mathbf{I} + \mu D[\mathbf{u}] \qquad [4]$$

$$D[\mathbf{u}] = \nabla \mathbf{u} + \nabla \mathbf{u}^T \qquad [5]$$

Here, P is the total pressure and μ is the viscosity of the fluid medium.

Next, consider the equations governing the motion of a typical particle (microcarrier).

The particle in the HARV rotates about its own axis while undergoing translation. Let there be a suspension of N particles.

The motion of a particle $(i = 1, 2, \ldots, N)$ in an inertial frame is governed by the following equations:

$$m_i \frac{d\mathbf{V}_i}{dt} = \mathbf{F}_i + \mathbf{G}_i \qquad [6a]$$

$$\frac{d}{dt}(\mathbf{I}_i \omega_i) = \mathbf{T}_i \qquad [6b]$$

$$\frac{d\mathbf{X}_i}{dt} = \mathbf{V}_i, \qquad [7a]$$

$$\frac{d\theta_i}{dt} = \omega_i \qquad [7b]$$

where the eqns [6a] and [7a] describe translation, while the eqns [6b] and [7b] describe the rotational parts of the motion of the ith particle. The rotational part is described in the inertial frame of reference fixed to the center of mass of the spherical particle (a body-fixed frame). Also, m_i is the particle mass, V_i is the translational velocity of the particle as observed in an inertial frame, F_i is the hydrodynamic force exerted by the fluid on the particle, G_i is the gravitational body force, X_i is the position of the centroid of the ith particle, I_i is the moment of inertia tensor (diagonal for a sphere), ω_i is the angular velocity of the ith particle as observed in an inertial frame, T_i is the hydrodynamic moment vector, and θ_i is the angular position of the particle in the body-fixed coordinate system. The forces and the moments imposed on the particle by the fluid are given by

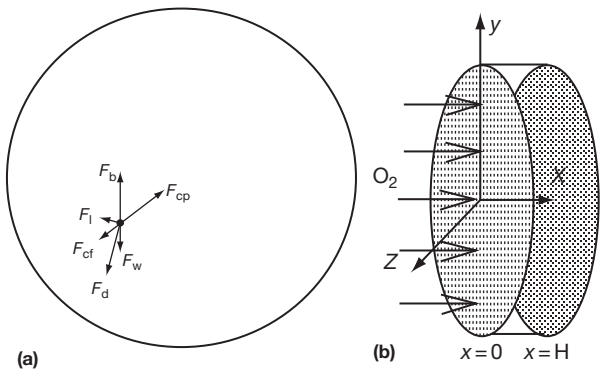

Figure 2 (a) The forces acting on a particle in a high aspect ratio vessel (HARV). (b) The coordinate system for numerical modeling of HARV culture.

$$\mathbf{F}_i = \int \sigma \cdot \hat{\mathbf{n}}\, d\Gamma \quad [8]$$

$$\mathbf{T}_i = \int \mathbf{r} \times (\sigma \cdot \hat{\mathbf{n}}) d\Gamma \quad [9]$$

where the integration is performed over the surface of the particle, $\hat{\mathbf{n}}$ is the unit normal vector on the surface of the particle pointing outward; and $\mathbf{r} = \mathbf{x} - \mathbf{X}_i$ is a vector from the center of the particle to its surface.

The initial conditions ($t = 0$) for the fluid and particle velocities are

$$\mathbf{u} = \boldsymbol{\omega} \times \mathbf{r}, \quad \mathbf{V}_i = \mathbf{u}(\mathbf{X}_i), \quad \boldsymbol{\omega}_i = 0 \quad [10]$$

where ω is the specified constant angular velocity of the vessel because of its rotation. The first condition states that the fluid is in rigid body rotation at $t = 0$. The transient spin-up is not considered here. The second condition states that the particles are released along the streamlines with the same velocity as the fluid; in other words, the initial velocity defect between the particle and the fluid is zero.

The boundary conditions for the rotating flow problem are

$$\mathbf{u} = \boldsymbol{\omega} \times \mathbf{R}_{\text{wall}}, \quad \text{on all boundary sections of the vessel} \quad \Gamma_0 \quad [11]$$

$$\mathbf{u} = \mathbf{V}_i + \boldsymbol{\omega}_i \times (\mathbf{x} - \mathbf{X}_i), \text{ on surface of particle } \Gamma_i, i = 1, 2, \ldots, N \quad [12]$$

Condition [12] represents the no-slip condition on the surface of the particle.

The governing equations together with the initial and boundary conditions are solved to describe the flow field, the trajectory of the particles, and the corresponding forces acting on the particles in an inertial frame of reference. In a rotating bioreactor problem, these results will be useful for evaluating the mass transfer and the net resultant force acting on any biological organism subjected to this type of flow.

The formulation of the problem in a rotating frame has been described in the previous studies.[8,9]

For the solution procedure, a generalized Galerkin finite element formulation, which incorporates both the fluid and particle equations of motion in a single variational equation, is preferable. In that formulation, the spatial domain occupied by the fluid is discretized using the finite element scheme. In the temporal direction, a finite difference method is used. Furthermore, as the spatial domain occupied by the fluid changes with time, a moving finite element mesh is adopted to discretize the fluid domain. To handle the movement of the finite element mesh, an arbitrary Lagrangian–Eulerian (ALE) technique is preferable. The nodes on the particle surface are assumed to move with the particle, and the grid is updated accordingly. The nodes in the interior of the fluid are computed using Laplace's equation. For a given finite element mesh, the ALE Galerkin finite element formulation can be discretized and be reduced to a nonlinear system of algebraic equations, which is solved through a modified Newton's scheme. The corresponding linearized system is solved with an iterative solver using a preconditioned generalized minimal residual (GMRES) algorithm. In this manner, the trajectories and the velocities of the particles are accurately determined.

Consider the situation where the fluid is flowing steadily around the particles beyond the very short duration spin-up stage. The motion of the combined fluid/particle system in that case may be simulated by the procedure developed by Hu *et al.*[17] In this procedure, the positions of the particles and the finite element mesh grid points in the fluid domain are updated explicitly, while the particle velocities and the fluid flow field are determined implicitly to avoid numerical instabilities. The details of the solution procedure are listed as follows:

1. Initialization $t_0 = 0, n = 0$ (index for time step), initialize particle information $\mathbf{X}_i(0)$, $\boldsymbol{\theta}_i(0)$, $\mathbf{V}_i(0)$, $\boldsymbol{\omega}_i(0)$, for $i = 1,2,\ldots,N$ generate an initial mesh $\mathbf{x}_0$
   initialize flow field $\mathbf{u}(\mathbf{x}_0, 0), p(\mathbf{x}_0, 0), \mathbf{u}_m(\mathbf{x}_0, 0)$
2. Explicit update
   select time step $\Delta t_{n+1} : t_{n+1} = t_n + \Delta t_{n+1}$
   update particle position

$$\begin{cases} \mathbf{X}_i(t_{n+1}) = \mathbf{X}_i(t_n) + \Delta t_{n+1}\mathbf{V}_i(t_n) \\ \theta_i(t_{n+1}) = \theta_i(t_n) + \Delta t_{n+1}\boldsymbol{\omega}_i(t_n) \end{cases}$$

$$\begin{cases} \mathbf{X}_i(t_{n+1}) = \mathbf{X}_i(t_n) + \Delta t_{n+1}\mathbf{V}_i(t_n) & \text{update mesh nodes} \\ \theta_i(t_{n+1}) = \theta_i(t_n) + \Delta t_{n+1}\boldsymbol{\omega}_i(t_n) & \hat{\mathbf{x}}(t_{n+1}) = \mathbf{x}(t_n) + \Delta t_{n+1}\mathbf{u}_m(t_n) \end{cases}$$

3. Remeshing and projection (if the updated mesh $\hat{\mathbf{x}}(t_{n+1})$ is too distorted):
   generate a new mesh $\mathbf{x}(t_{n+1})$
   project the flow field from $\hat{\mathbf{x}}(t_{n+1})$ onto $\mathbf{x}(t_{n+1})$
4. Flow solver: iteratively solve the new flow field

$$\mathbf{u}(\mathbf{x}(t_{n+1}), t_{n+1}), p(\mathbf{x}(t_{n+1}), t_{n+1}),$$
$$\mathbf{u}_m(\mathbf{x}(t_{n+1}), t_{n+1}), \mathbf{V}_i(t_{n+1}), \boldsymbol{\omega}_i(t_{n+1})$$

5. If the time t_{n+1} is less than a specified time, go to step (2), otherwise stop.

Using the above procedure, the velocities of the particles and their trajectories in the HARV may be calculated.

5.511.2.2.2. Particle–particle and particle–wall collisions

Particle–particle and particle–wall collisions change the trajectories, the instantaneous relative speed, and the shear stress on the surface of the particles. The collision may affect cell attachment and damage bridges in cell aggregates. Understanding of collision dynamics is needed to alleviate interparticle and particle–wall collisions. Numerical studies and stability analysis have revealed that the density difference between a microcarrier and fluid medium determines if the microcarrier can avoid collision with the wall of HARV.[6,8] Single-particle studies have shown that, if the microcarrier is lighter than the surrounding fluid medium, then it migrates from its initial position in a spiral fashion as viewed in an inertial frame to a final location in the central region of HARV. The trajectories in inertial and rotating frames for a lighter-than-fluid particle are shown in **Figure 3**. If the particle is heavier than the fluid medium, in the inertial frame, it moves spirally outward to reach or collide with the outer wall of the HARV after a period of time (**Figure 4**). These figures are based on the numerical solutions to the modified Maxey–Riley equations that approximately govern the motion of a point-mass particle. With these solutions, it may be shown that a lighter-than-fluid particle migrates to a stable equilibrium radial position in the fluid.

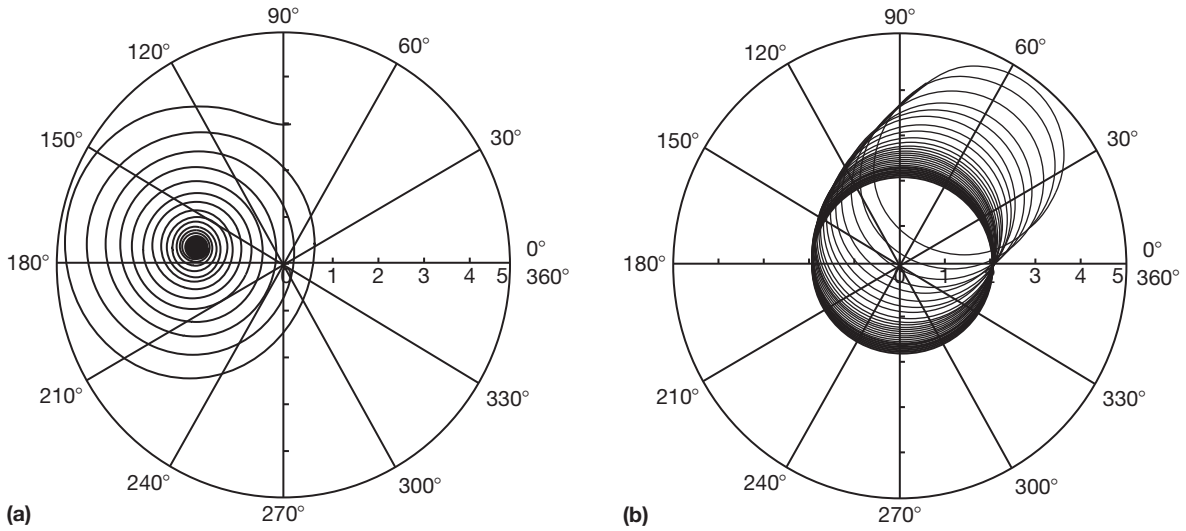

Figure 3 Trajectory of a microsphere particle in the rotating-wall vessel in the (a) inertial frame and (b) rotating frame of reference for ($\rho_p < \rho_l$). $\rho_p = 0.7\ g\ cm^{-3}$, $\rho_l = 1.0\ g\ cm^{-3}$, $\mu = 0.01\ g\ cm^{-1}\ s^{-1}$, $\omega = 35$ rpm, $a = 330\ \mu m$, initial position = 3 cm, HARV radius = 5 cm. Reproduced from Gao, H.; Ayyaswamy, P. S.; Ducheyne, P. *Microgravity Sci. Technol. X* **1997**, 154–165.

More detailed studies of single-particle dynamics also show similar behavior.[7,9] When the microcarrier particle density is equal to the density of fluid medium, the microcarrier will stay in any neutrally buoyant position moving along with the fluid, without relative motion. However, this situation is unstable, and with small perturbations, the particle will move away to different locations. For particles, scaffolds, or aggregates that do not have perfect spherical shape, the relative motion has to be carefully evaluated. With a denser microcarrier, it is important to know the migration time (t_w) to reach the outer wall of RWV as the collision with the wall may affect the cell growth and damage the cell/microcarrier aggregate (**Figure 4(c)**). The migration time increases with decrease in the density difference and microcarrier size, and it also increases with increase in fluid viscosity.[6] The migration time decreases as the rotational speed ω increases with other parameters held constant. However, at very low rotational speeds (e.g., <2 rpm with a full-sized HARV), the migration time begins to decrease and eventually it asymptotically approaches the Stokes sedimentation time as $\omega \to 0$ (**Figure 4(c)**).

To account for particle–particle and particle–wall collisions in a numerical study, the collision model described in previous studies[18,19] may be employed. In these models, it is assumed that there is always a very thin liquid film interspersed between the solid objects (particle–particle or particle–wall) even as they get near each other in very close proximity. In the numerical algorithm, a fictitious external short-range contact force on the colliding objects, normal to the contact area between the approaching objects, is introduced. The magnitudes of these contact forces are just large enough to keep objects away from actual touching or geometric overlapping. This contact force is activated when the minimum gap between the approaching objects is less than a prescribed critical distance. The introduction of the fictitious short-range force may itself modify the trajectories of the colliding particles. However, this modification may be minimized by choosing a very small critical gap size when this contact force is activated.[16]

The above analysis is based on a single-particle system. In an actual situation, cell culture is a multiparticle system. Thus, in addition to the factors considered in the single-particle system, the number of microcarriers and cells in the RWV is an important factor in terms of interparticle collisions. To reduce interparticle collisions, the reduction of solid volume fraction by diluting the suspension of particles is an effective approach.

5.511.2.2.3. Microcarrier/cell spin

In the HARV, a spherical particle/cell not only undergoes a circular translatory motion and a radial drift but also a spin about its own axis. A schematic of particle spin about its own axis is shown in **Figure 5(a)**. As a microcarrier rotates, so do the cells embedded within it or attached to its surface. As gravity vector is unidirectional in a laboratory reference frame, an observer sitting on a spinning microcarrier or the cell itself would experience time-varying gravity with a zero mean (vector-averaged gravity) whose frequency is essentially given by the rotation rate of the cell/microcarrier. The general assumption has been that the changes in gravity will appreciably alter the force balance within the cytoskeleton so as to mimic microgravity-like conditions. This assumption or equivalent assumptions have to be validated and the truly prevailing situation must be related to the speed of the microcarrier/cell spin in each study.[10] **Figure 5(b)** shows the numerically evaluated particle rotation rate (it spins about its own axis as a function of the rotation rate of the HARV) and the density of the particle for a 200-μm spherical microcarrier. The rotation speeds are representative of the biological culture conditions. It may be noted that the particle rotates with essentially the same speed as the HARV. It is therefore possible to optimize the rotation rate of the particle by controlling the rotation rate of the HARV in order to better simulate microgravity conditions.

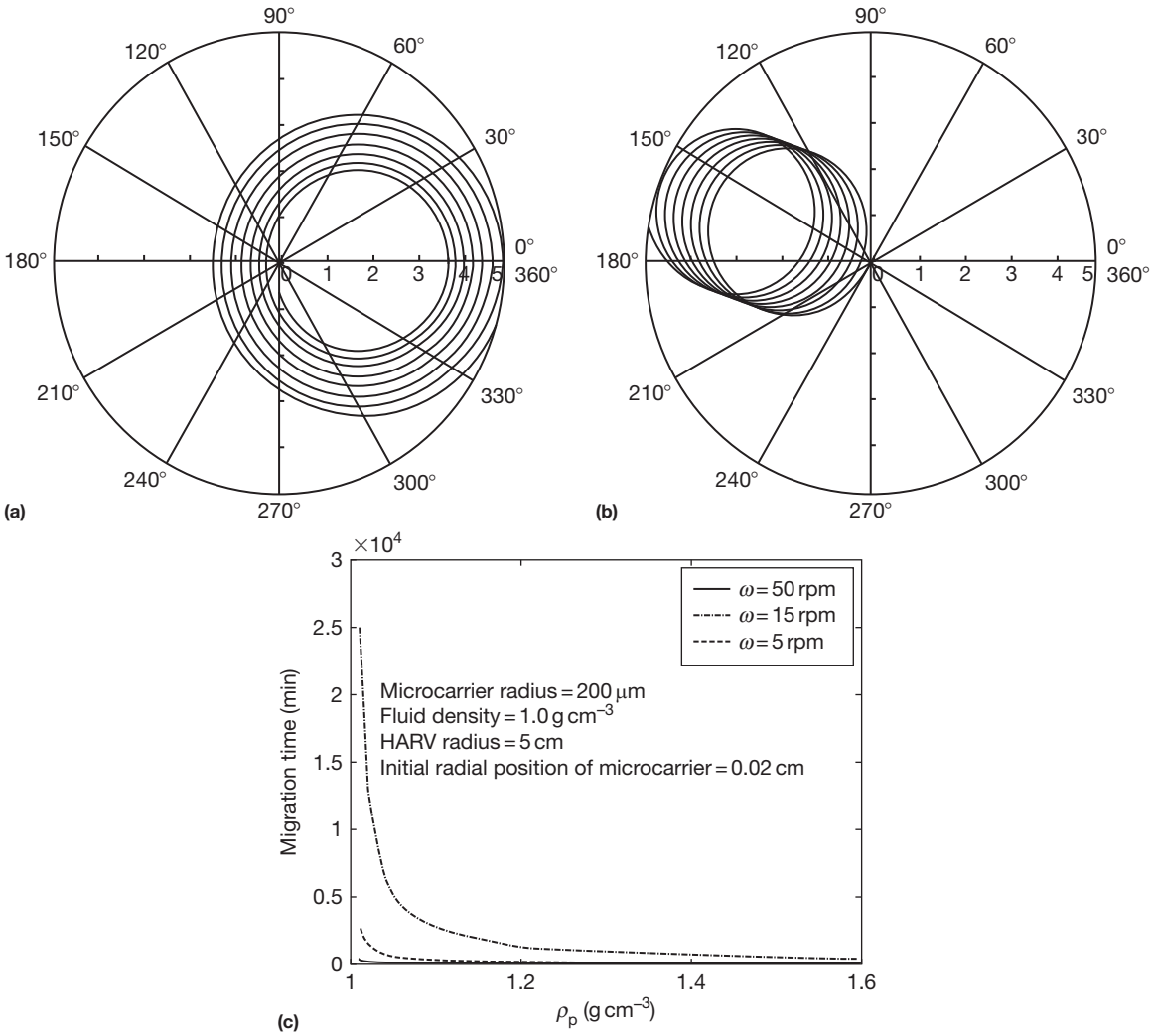

Figure 4 Trajectory of a microsphere particle in the rotating-wall vessel in the (a) inertial frame and (b) rotating frame of reference for ($\rho_p > \rho_l$). $\rho_p = 1.3\,g\,cm^{-3}$, $\rho_l = 1.0\,g\,cm^{-3}$, $\mu = 0.01\,g\,cm^{-1}\,s^{-1}$, $\omega = 25$ rpm, $a = 240\,\mu m$, initial position = 0.5 cm, HARV radius = 5 cm. Reproduced from Gao, H.; Ayyaswamy, P. S.; Ducheyne, P. *Microgravity Sci. Technol. X* **1997**, 154–165. (c) Particle migration time as a function of particle density. Reproduced from Ayyaswamy, P. S.; Mukundakrishnan, K. *Acta Astronaut*. **2007**, *60*(4–7), with permission from Elsevier.

5.511.2.2.4. Shear stress

The shear stresses that act on the microcarrier surfaces are caused by the minute motion of the microcarriers relative to the surrounding medium, and the maximum shear stress on a spherical particle surface, τ_{max}, may be evaluated from the numerical solution as all of the required quantities are available. The shear stress may also be deduced by employing a corotating camera with the HARV during experimentation.[20] For low Reynolds number, the steady-state drag for a single-particle case may be approximated by Stokes drag, and as a convenient estimate, the maximum shear may be calculated from the Stokes solution:

$$\tau_{max} = 3\mu V_{rel}/2a \qquad [13a]$$

where μ is viscosity, V_{rel} is the relative speed (slip velocity) between the particle and the fluid, and a is the radius of the particle. For higher Reynolds number simulations, a rectilinear empirical relation for the drag coefficient for a single-particle case, like the Schiller and Nauman correlation,[21] may be used, and this correlation is given by

$$F_D = C_D(\mathbf{U}_p - \mathbf{U}_f),\ C_D = 6\pi\mu a[1 + 0.15(Re_p)^{0.687}] \quad \text{for } Re_p \text{ up to } 800 \qquad [13b]$$

where $\mathbf{U}_p$ and $\mathbf{U}_f$ are the velocities of the particle and the fluid, respectively; Re_p is the particle Reynolds number given by $2aV_{rel}/\nu_f$; a is the radius of the particle; and ν_f is the kinematic viscosity of the fluid. In the above equation, the transverse lift forces acting on the particle (the transverse direction being perpendicular to the direction of instantaneous slip velocity), and history forces due to the unsteady nature of particle motion are neglected.

The maximum shear stress (τ_{max}) experienced by the surface of a particle is a function of the microcarrier velocity, density difference between microcarrier and fluid, and microcarrier size.[6,15] In Figure 6(a) and 6(b), the numerical results presented are based on the assumption that particles may be

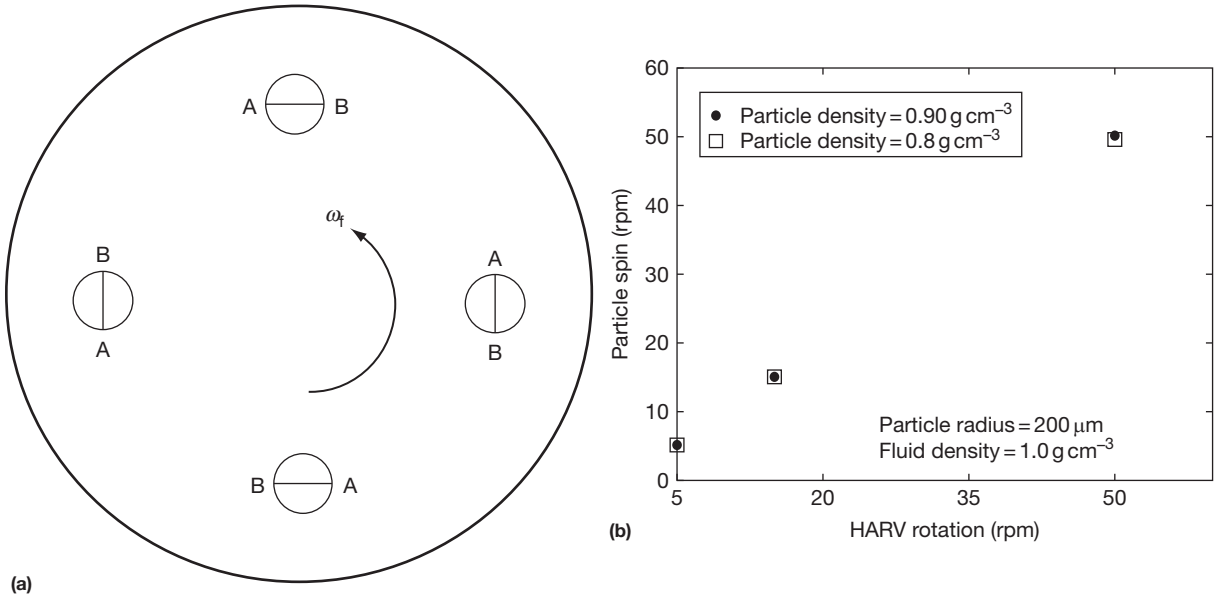

Figure 5 (a) Schematic of particle rotation in a high aspect ratio vessel (HARV). The line A–B is drawn to illustrate the sense of rotation of the particle as it goes around in a circular orbit. Reproduced from Mukundakrishnan, K. Ph.D. Thesis, University of Pennsylvania, 2005. (b) Angular velocity of the particle about its own axis as observed in an inertial frame of reference as a function of the rotation speed of the HARV. $a = 200\ \mu m$ and $\mu_f = 0.01\ g\ cm^{-1}\ s^{-1}$. Reproduced from Ayyaswamy, P. S.; Mukundakrishnan, K. *Acta Astronaut.* **2007**, *60*(4–7), with permission from Elsevier.

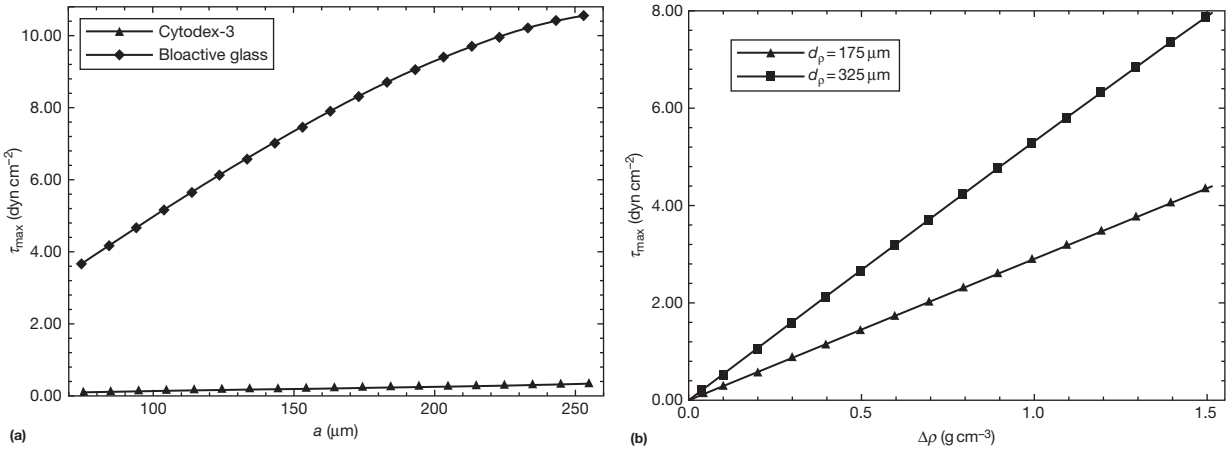

Figure 6 (a) Numerical results. The maximum shear stress on a Cytodex-3 microcarrier and a bioactive glass microcarrier as a function of the microcarrier radius. $\rho_{cy} = 1.04\ g\ cm^{-3}$, $\rho_{bio} = 2.00\ g\ cm^{-3}$, $\rho_f = 1.00\ g\ cm^{-3}$, $\mu = 0.01\ g\ cm^{-1}\ s^{-1}$, $\omega = 18$ rpm. (b) Numerical results. The maximum shear stress on a microcarrier as a function of the density difference between microcarrier and fluid, and of microcarrier size. $\mu = 0.01\ g\ cm^{-1}\ s^{-1}$, $\omega = 18$ rpm. Reproduced from Qiu, Q.; Ducheyne, P.; Gao, H.; Ayyaswamy, P. *Tissue Eng.* **1998**, *4*(1), 19–34.

regarded as mass points. The maximum shear stress increases linearly with the density difference between the microcarrier and fluid media (Figure 6(b)). When cell aggregates grow in size during suspension culture, the shear stress acting on the aggregate also increases, which may lead to cell damage and inhibit aggregate growth or cause its disruption. However, if the aggregates' density is equal or very close to that of culture medium, the shear stress is extremely low and increases only slightly with the increase in the size of the aggregate. If a microcarrier of high density is used, the maximum shear stress is much larger and increases faster as the size of the microcarrier increases (Figure 6(a) and 6(b)).

Figure 7 shows the variation in shear stress with particle radius for a solid microcarrier as calculated from a numerical computation where the finite size of the particle is taken into account. The density of the particle is less than that of the fluid. As expected, shear stress increases with increasing particle size and the very small values of the shear stress at smaller sizes are noteworthy.

The net acceleration experienced by a typical solid microcarrier as a function of its size is shown in Figure 8. It may be noted that a nearly neutrally buoyant microcarrier experiences some aspects of simulated microgravity while suspended in the HARV during culture.

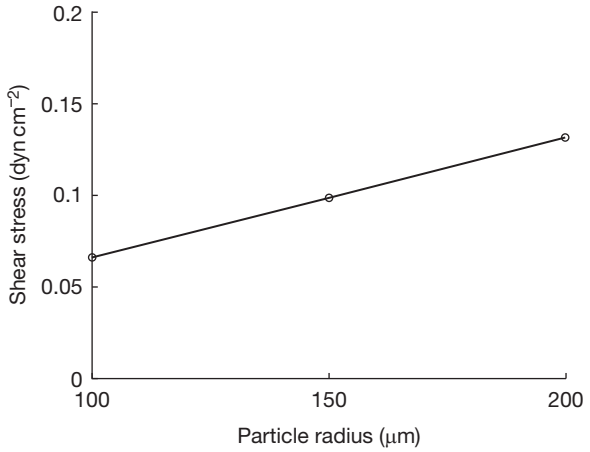

Figure 7 Shear stress variation for a solid microcarrier. $\rho_p = 0.98\ g\ cm^{-3}$, $\rho_l = 1.0\ g\ cm^{-3}$, $\mu = 0.01\ g\ cm^{-1}\ s^{-1}$, $\omega = 10$ rpm. Reproduced from Mukundakrishnan, K.; Ayyaswamy, P. S.; Risbud, M.; *et al. Ann. N. Y. Acad. Sci.* **2006**, *1027*(1), 85–98, with permission from Wiley.

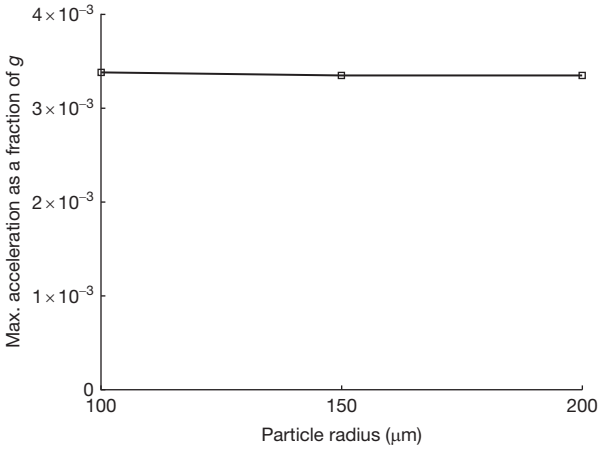

Figure 8 Maximum acceleration experienced by a solid microcarrier as a fraction of *g*. $\rho_p = 0.98\ g\ cm^{-3}$, $\rho_l = 1.0\ g\ cm^{-3}$, $\mu = 0.01\ g\ cm^{-1}\ s^{-1}$, $\omega = 10$ rpm. Reproduced from Mukundakrishnan, K.; Ayyaswamy, P. S.; Risbud, M.; *et al. Ann. N. Y. Acad. Sci.* **2006**, *1027*(1), 85–98, with permission from Wiley.

Figure 9 displays the variation in shear stress as a function of the HARV rotation rate for two different densities of a 200-μm spherical carrier. Shear stress significantly increases with increasing density while remaining constant for low to moderate rotation rates of the HARV. The shear stress remains constant for such rotation rates because the gravity-induced buoyancy force dominates over the centrifugal force and shear is largely generated as a result of gravity-induced slip velocity.

Thus a small, nearly neutrally buoyant microcarrier, coupled with moderate rotation rates (~50 rpm), is likely to simulate microgravity-like condition better than other combinations.

It is clear from the above discussions that the density difference plays a crucial role in the successful use of the HARV both for tissue culture and for simulating some aspects of microgravity. Because of the big difference between the densities of air and fluid, air bubbles, if present in a HARV, will experience

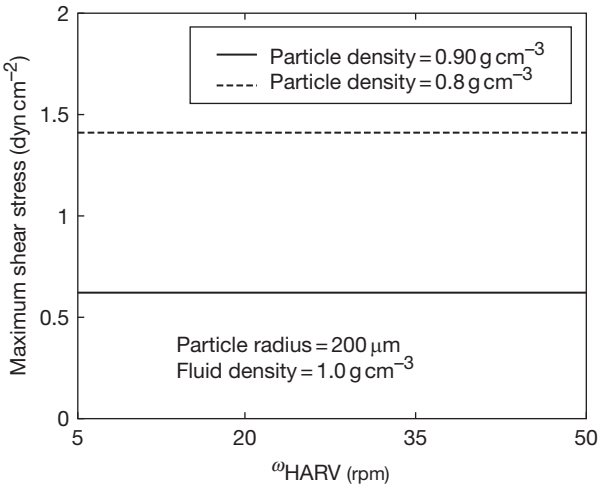

Figure 9 Significance of shear stress. Reproduced from Ayyaswamy, P. S.; Mukundakrishnan, K. *Acta Astronaut.* **2007**, *60*(4–7), with permission from Elsevier.

high shear stresses on their surfaces while in motion. When air bubbles collide with cell aggregates, they may damage the cells and destroy bridges in cell aggregates. Therefore, it is important to completely remove the air bubbles from the RWVs before the start of the study.

Cell cultures in HARV usually employ solid microcarriers with cells attached to their outer surface. One limitation of this system is that the ratio of the number of cells cultured per microcarrier is quite small as the cells are cultured only on the surface and not in the interior. A further disadvantage is that only a limited number of solid microcarriers can be used as a large number density will result in increased particle–particle collisions and damage the cells. To develop 3D tissue structures, porous microcarriers/scaffolds in which cells are immobilized in a 3D polymer network are very useful. In an attempt to quantify the shear stress and acceleration vector experienced by such a porous microcarrier, the modeling described above has to be modified.[8] The essential difference between this and the model for a rigid spherical microcarrier lies with the modification of the effective particle density and the drag coefficient. The effective particle density depends upon the degree of porosity. Also, the drag coefficient here depends on the degree of permeability of the microcarrier.[22] For identical parametric conditions in the HARV, the shear stress at the surface of a porous microcarrier is much smaller compared to the shear stress at the surface of a solid carrier. The time taken for particle migration toward the wall of the HARV is higher for a porous particle compared to that for a solid microcarrier. Furthermore, the net acceleration vector experienced by a porous microcarrier is much less in magnitude compared to that of a solid carrier. These three observations have implications for simulating aspects of microgravity conditions in the laboratory. In cultures without microcarriers, we note that the cell is usually denser than the culture medium. To minimize shear stress, these cells may have to be encapsulated in porous microcarriers made of suitable materials such as alginate hydrogels that do not interfere in any manner with the cell function. Figure 10 shows the variation in shear stress with particle radius for a porous microcarrier. As expected,

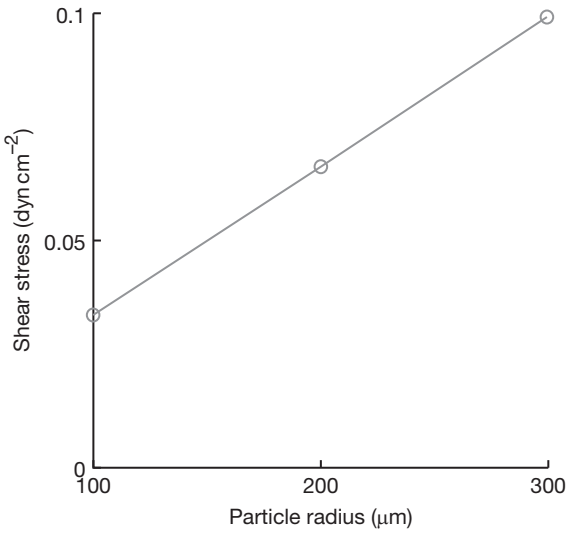

Figure 10 Shear stress variation for a porous microcarrier. $\rho_p = 1.01\ g\ cm^{-3}$, $\rho_l = 1.0\ g\ cm^{-3}$, $\mu = 0.01\ g\ cm^{-1}\ s^{-1}$, $\omega = 8$ rpm, $\kappa = 10^{-5}\ cm^2$. Porosity = 97%. Reproduced from Mukundakrishnan, K. Ph.D. Thesis, University of Pennsylvania, 2005.

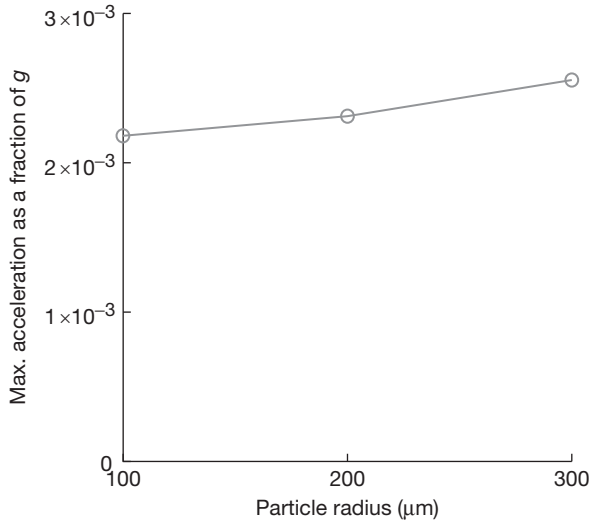

Figure 11 Maximum acceleration experienced by the porous microcarrier as a fraction of *g*. $\rho_p = 1.01\ g\ cm^{-3}$, $\rho_l = 1.0\ g\ cm^{-3}$, $\mu = 0.01\ g\ cm^{-1}\ s^{-1}$, $\omega = 8$ rpm, $\kappa = 10^{-5}\ cm^2$. Porosity = 97%. Reproduced from Mukundakrishnan, K. Ph.D. Thesis, University of Pennsylvania, 2005.

shear stress increases with increasing particle size and the very small value of shear stress is noteworthy. Figure 11 shows the net acceleration experienced by a typical porous particle as a function of its size. It is noted that porous microcarriers may be successfully employed in the HARV to simulate certain aspects of microgravity.

5.511.2.2.5. Mass transfer evaluation

With the fluid velocity evaluated as above, the mass transfer of any given species (glucose, oxygen, or other ions) to a typical

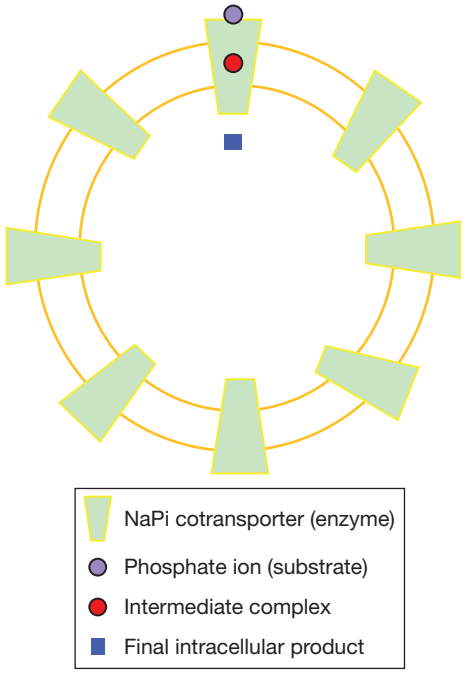

Figure 12 Illustration of extracellular Pi transporting into a cell. Reproduced from Mukundakrishnan, K. Ph.D. Thesis, University of Pennsylvania, 2005.

microcarrier in the HARV may be evaluated using a convection–diffusion–reaction mechanism.

As an example, the mass transfer of a representative ion, phosphate ion (Pi), will be discussed below to illustrate the modeling procedure.

The mass transfer of Pi in osteoblast culture, for example, may be evaluated using a convective–diffusive–reactive model. The consumption of Pi by osteoblasts may be assumed to follow Michaelis–Menten (MM) kinetics aided by NaPi cotransporter system (Figure 12). The MM mechanism approach views the NaPi cotransporter as a system for transporting extracellular Pi into the cell.

Let $C_i(\mathbf{x})$ denote the concentration of species i, which in our case is the Pi. Also let D_{ij} denote the diffusion coefficient of the ith species in the fluid medium. This coefficient is assumed to be a constant. Let $\mathbf{u}(\mathbf{x})$ denote the convective flow velocity (relative velocity obtained by solving the trajectory equations for the particle motion). The Pi consumption of osteoblasts is known to follow saturable kinetics,[23] which can be described by MM equations. Then the steady-state mass transfer equation becomes

$$D_{ij}\nabla\cdot(\nabla C_i(\mathbf{x})) = (\mathbf{u}(\mathbf{x})\cdot\nabla)C_i(\mathbf{x}) \qquad [14]$$

A steady state is assumed because with reference to the particle frame of reference, the fluid flow motion is approximately in the Stokes flow regime and the characteristic time scale of the cell culture is much larger than the convective time scale. In the above equation, it is assumed that there are no volumetric (point) sources or sinks present in the medium. The associated boundary conditions are as follows:

$$C_i = C_{\infty}, |\mathbf{x}| \to \infty \qquad [15]$$

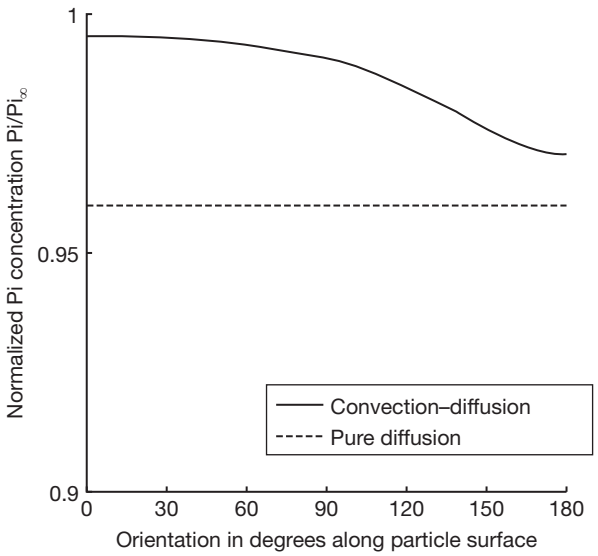

Figure 13 Distribution of Pi concentrations along particle surface in HARV. Reproduced from Ayyaswamy, P. S.; Mukundakrishnan, K. *Acta Astronaut*. **2007**, *60*(4–7), with permission from Elsevier.

$$\nabla C_i \cdot \hat{\mathbf{n}} = \frac{-\gamma V_{\max} C_i}{K_m + C_i} \quad |\mathbf{x}| = a \qquad [16]$$

where C_∞ is the physiological level of Pi concentration (also the serum level Pi concentration), $\hat{\mathbf{n}}$ is the unit normal vector on the surface of the particle, a is the radius of the microcarrier particle, γ is the cell-seeding density, V_{max} is the half-maximal rate of Pi consumption, and K_m is the MM constant. The details of the mass transfer calculations and numerical procedure employed for this purpose are reported by Mukundakrishnan.[8] Figure 13 shows that convection in the HARV enhances the Pi accumulation on the surface of the microcarrier (cell surface). A 4% increase in the accumulation of Pi (normalized concentration) under HARV culture conditions compared to Petri dish conditions is noted.

Similar calculations may be made for other species.

Nutrients and oxygen transport to the cells is critical for cell proliferation and function. Although an accurate prediction of the mass transfer requires detailed knowledge of the fluid field and metabolism reaction of cells, there are some general observations which may be made regarding mass transfer in RWVs. When a cell or a small cell aggregate has very low relative velocity – for example, close to zero – to the fluid medium, the nutrients and oxygen are primarily supplied via diffusion. When a cell aggregate is bigger, the relative velocity usually increases and the nutrients and oxygen are also supplied by convective flow. When the size of a microcarrier/cell aggregate increases, an increase of the rotational speed can help to keep the aggregates in suspension and also increase the mean oxygen concentration in the RWV.[24] In addition, introducing a gradient of fresh media through perfusion of the RWV will also help the transfer of nutrients to the cells.

5.511.2.3. Optimal Conditions of RWV

Optimal conditions for cell culture in RWV have been discussed in detail in a previous publication,[10] and the requirements are summarized as follows:

1. A very low value of shear at the microcarrier/cell surface.
2. An understanding of the role played by the microcarrier/cell spin about its own axis.
3. Adequate mass transport of nutrients and oxygen.
4. Where microcarriers are employed, interparticle and particle–vessel wall collisions must be minimized or eliminated.
5. Shape of the microcarrier or scaffold should be such as to minimize adverse flow effects.
6. Adequate and appropriate controls over cell culture period.
7. Microcarrier and scaffold should be biocompatible, ideally bioactive, and degradable where possible.

5.511.3. Scaffolds and Microcarriers for Cell Culture in RWV

For anchorage-dependent cells, scaffolds, or microcarriers are required for cell culture in RWVs. As discussed in the previous sections, the density and the architectures of the carriers play critical roles on shear stress imparted on carriers, and collisions and motions in RWVs, which may significantly affect cell attachment, proliferation, and differentiation. Therefore, the selection of carriers becomes critical for the success of 3D cell culture in RWVs. In this section, a review of the carriers used in RWVs and their advantages and disadvantages will be discussed. Because of the fact that very limited information on the shear stress and trajectories of carriers and scaffolds used in RWV is available, common knowledge derived from the previous sections will be applied in the discussion on possible shear stress on different types of carriers reviewed in this section.

5.511.3.1. Criteria for Carriers

In order to achieve very low shear stress on the carrier surface and to minimize collisions that can damage cells and cell aggregates, the carrier should meet the following requirements:

1. The apparent density of a microcarrier or the scaffold should be close to that of culture medium, ideally slightly lower than or equal to the density of the culture medium. As the shear stress increases with the increase of density difference between the carrier and culture medium, reducing the density difference will reduce the shear stress on the carrier. In addition, if the carrier is lighter or has the same density as the culture medium, it will avoid moving outward and eventually colliding with the outer wall of the RWV, which may cause cell damage and negatively affect cell attachment and proliferation.
2. The microcarrier size should be big enough for supporting cell attachment and proliferation but should be small enough to avoid inter-microcarrier collisions and allow formation of cell–microcarrier congregates.
3. The shape of the microcarrier should be such as to minimize adverse flow effects. Spherical microcarriers are preferred, although it is acknowledged that their shape will change with cell/aggregate growth and accommodations have to be made to correctly describe such variations.
4. Microcarriers must be biocompatible, ideally bioactive, and degradable where possible.

Table 1 Carriers used in cell cultures in RWVs

	Carrier	*Composition*	*Density (beads)/porosity (scaffolds)*	*Size*	*Surface layer*
Polymers	Cytodex-3 beads	Cross-linked dextran	1.04 g cm^{-3}	133–215 μm (dia.)	Gelatin (type I collagen)
	Biosilon beads	Polystyrene	1.05 g cm^{-3}	160–300 μm (dia.)	Nunclon
	PLGA microspheres	PLGA	0.65 g cm^{-3}	500–860 μm (dia.)	PLGA
	PLGA scaffolds	PLGA	90%	3 × 2 mm (dia. × thick)	PLGA
	PGA scaffolds	13 μm diameter PGA fibers	97%	10 × 2 mm (dia. × thick)	PGA
	HYAFF®	Benzilic ester of hyaluronic acid	–	4 × 4 cm	Hyaluronic acid
	Porous silk scaffold	Natural silk	95.5%	8 × 2 mm (dia. × thick)	Natural silk
	PEG hydrogel	PEG	92%	5 × 3 mm (dia. × thick)	PEG
	Alginate microspheres	Alginate	–	300 μm	Alginate
	Alginate–chitosan microspheres	Alginate–chitosan	–	5 mm (dia.)	Chitosan
Composites	Chitosan–HA microspheres	Chitosan–HA	–	350–450 μm (dia.)	Chitosan–HA
	PLA–BG microspheres	PLA/BG composite	–	100–200 μm (dia.)	Calcium hydroxyapatite
Ceramic	Bioceramic microspheres	Silica and calcium phosphate	0.8–1.0 g cm^{-3}	100–200 μm (dia.)	Calcium phosphate

dia.: diameter; BG: bioactive glass; PGA: polyglycolic acid; HA: hydroxyapatite; PLA: polylactic acid; PEG: poly(ethylene glycol); PLGA: poly(D,L-lactic-*co*-glycolic acid).

5.511.3.2. Microcarriers and Scaffolds Used for Cell Culture in RWV

A variety of scaffolds and microcarriers have been developed and used as carriers for anchorage-dependent cell cultures in RWVs. In general, the carriers can be classified into three categories based on their composition: polymer, polymer–ceramic/glass composite, and bioceramic. In the polymer category, the carriers are in microsphere or scaffold form. For the other two categories, they generally have a microsphere form. Some of the carriers are summarized in Table 1.

5.511.3.2.1. Polymers

5.511.3.2.1.1. Microcarriers

Cytodex-3 beads (133–215 μm diameter) are the most commonly used microspheres for 3D cell culture in RWVs. They are cross-linked dextran microspheres coated with collagen which is covalently linked to dextran. Because their density (1.04 g cm^{-3}) is very close to that of the culture medium, they experience a low shear stress in RWVs.

5.511.3.2.1.2. Scafffolds

Biodegradable polymer scaffolds have unique features: in addition to having defined shape and dimensions, they are biodegradable which allows their replacement by the cells and tissues being formed. As such, biodegradable scaffolds are commonly used for tissue engineering applications that require a specific shape and a high porosity, such as tissue engineering of cartilage tissue. The porous scaffolds made of fibrous polyglycolic acid (PGA) were first used for chondrocyte culture in RWV in the 1990s.[25] PGA scaffold is a nonwoven mesh composed of fine PGA fibers and has a high porosity (97%). Its mass decreases by ~40% or 63% of the initial mass during 4 or 8 weeks of cell culture, respectively.[26]

Because of the high porosity of the scaffold when it is in a RWV filled with culture medium, the apparent density of the scaffold is very close to that of the culture medium. Thus it experiences a low shear stress and can be suspended in the medium during the entire cell culture period without frequent collisions with the outer wall of the RWV.

5.511.3.2.2. Polymer–ceramic/glass composites

In orthopedic and dental applications, calcium phosphate (CaP)-based ceramics and bioactive glasses have been used by virtue of their ability to bond with bone tissues and to promote bone formation.[27] A composite microsphere with low density and a bioactive surface was developed by relying on the low density of polymers and coating polymeric spheres with a CaP film.[28] The composite microsphere has a core that is a mixture of polylactic acid (PLA) and modified bioactive glass powders, and an outer Ca–P-rich layer. As the densities of ceramic and glass are greater than that of culture medium, a composite microsphere needs to have high porosity in order to have an apparent density that is close to that of the culture medium in order to have low shear stress for cell culture in RWVs.

5.511.3.2.3. Ceramics

Because of the fact that ceramic has higher density than culture medium, a microsphere that is made of ceramic has to be hollow inside and/or has high porosity in order to have apparent density that is close to that of culture medium, which is one of the criteria for carriers used in RWVs.

Hollow bioceramic microspheres with a Ca–P surface were developed and used for bone cell cultures in RWVs.[20,29] When a hollow ceramic microsphere with an apparent density of 0.9 g cm^{-3} is placed in HARV at a rotational speed of 18 rpm, a microsphere moves spirally toward to the center and finally remains suspended in the central region of the vessel (Figure 14(a)). In a rotation frame, the microsphere moves in small circles while moving to the center (Figure 14(b)). On the basis of the recorded trajectory in a rotational frame (Figure 14), an empirical maximum shear stress imparted on the hollow

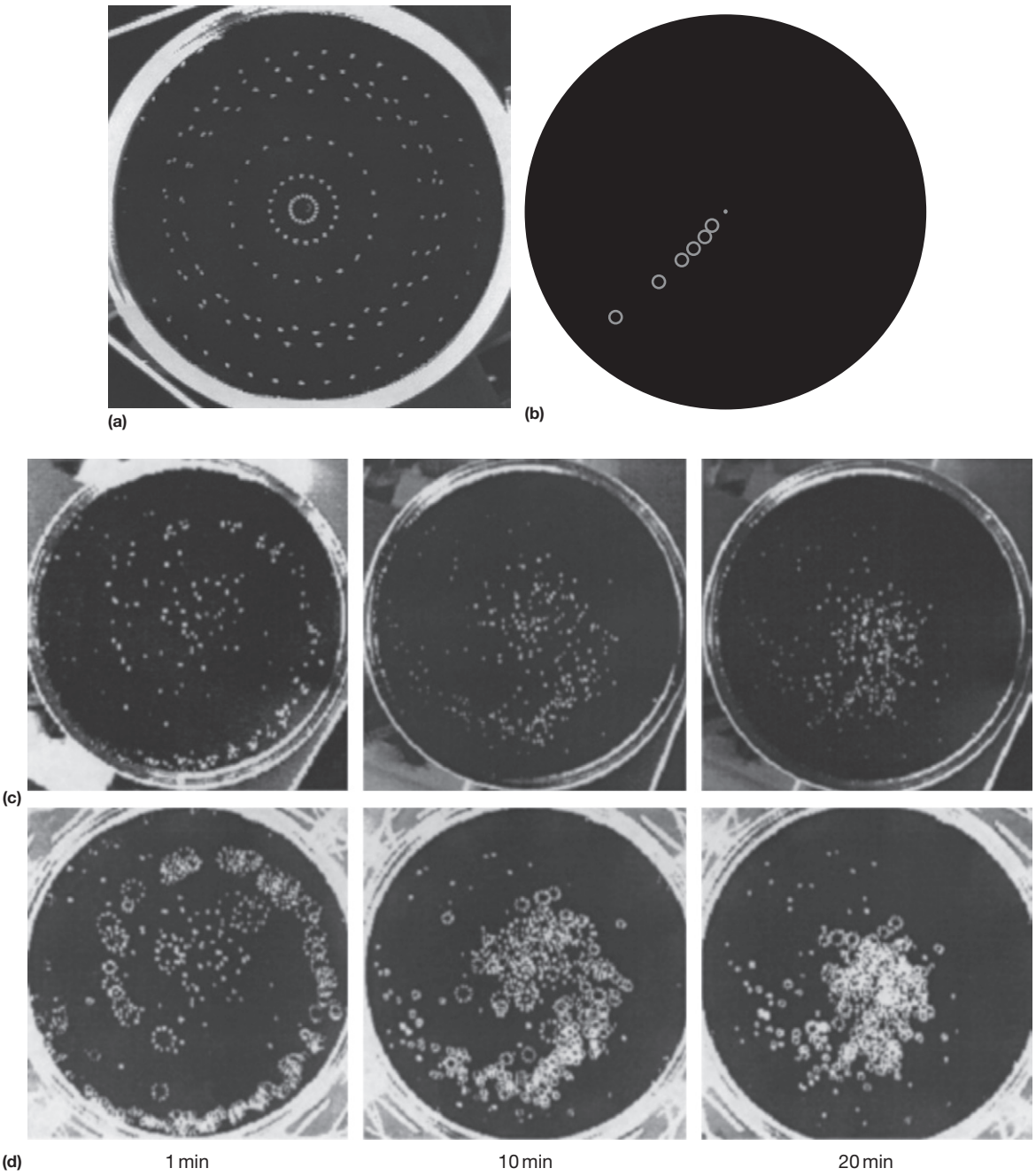

Figure 14 (a–b) Trajectory of a hollow microsphere (100 μm in diameter, density ~0.9 g cm^{-3}) in fluid medium (density 1.0 g cm^{-3}) a high aspect ratio vessel (HARV) from the start of rotation at 18 rpm in an inertial frame (a) and in a rotating frame (b). In the inertial frame, the camera records the locations of the particle while HARV rotates. In a rotating frame, the camera records the location of the particle while it rotates with the HARV at the same speed. The particle locations are displayed at every 1/6 s along the loops that the particle traversed. As the loops tended to overlap each other, a time lapse of 10 min was chosen between each loop displayed beyond the first few loops. (c–d) Trajectories of a large number of hollow microspheres (100–200 μm in diameter) in a RWV. (a) Snap shots of instantaneous locations of microcarriers at 1, 10, and 20 min from the start of rotation at 18 rpm. (b) Picture of closed loop motions of the same microcarriers in a rotating frame at 1-, 10-, and 20-min intervals. One full rotation has been photographed and composed. The particle locations are displayed at every 1/3 s along the loop the particle traversed. Reproduced from Qiu, Q.; Ducheyne, P.; Ayyaswamy, P. S. *Biomaterials* **1999**, *20*, 989–1001, with permission from Elsevier.

microsphere was found to be about 0.6 dyn cm^{-2},[20] which is smaller than the shear stress level that causes cell damage as reported previously, and is comparable to that experienced by polymer microcarriers, for example, Cytodex-3, in an RWV.[30]

5.511.4. Cell Culture in RWV

Cell cultivation in RWVs was pioneered at the NASA Johnson Space Center in the early 1990s.[1–3,31] As shown in the previous

sections, RWVs have advantages of low shear stress, controlled supplies of oxygen and nutrients, and support of 3D cell cultures,[1,3,6,12] and thus have gained great interest in applications of 3D cell culture and tissue engineering. This section will provide a brief review on cell cultures in RWVs.

5.511.4.1. 3D Cell Culture

As illustrated in the previous sections, the carrier materials play a critical role in shear stress and fluid mechanics that cells experience in RWVs. The general review in this section will group the cell culture studies on the basis of the carrier materials employed. A partial list of cell cultures carried out in RWVs is shown in Table 2.

As the model without the use of carrier as cell substrate can eliminate the complexity associated with the carriers, for example, high shear stress due to high density and shape of microcarriers or scaffolds, it is useful for investigating initial cell binding, proliferation, and differentiation processes in a simulated microgravity environment in RWVs and this has also been included in this section.

5.511.4.1.1. Bone cells

The bone loss that accompanies spaceflight is one of the most serious health problems associated with space travel.[88] After extended time in space, a marked reduction in bone mass, a condition known as spaceflight osteopenia, is commonly seen.[89,90] As RWVs can simulate some aspects of microgravity

Table 2 Cell cultures and microcarriers used in RWV

Cell culture type	*Scaffolds/microcarriers*	*Culture duration*	*References*
Bone cells			
Human osteoblast-like cells (SaOS-2)	Lighter-than-water PLGA microspheres	7 days	32
Human mesenchymal stem cells (hMSC)	Microcarrier beads	7 days	33
	No carrier		34
Human periodontal ligament fibroblasts (hPDLF)	PLGA scaffolds	3 weeks	35
	Chitosan–hydroxyapatite microspheres with cells encapsulated inside		36
Human bone marrow cells and chondrocytes	Alginate/chitosan with cells encapsulated inside	4 weeks	37,38
Human bone marrow stromal cells	Porous silk scaffold	5 weeks	39
Rabbit bone marrow cells	No carrier	7–21 days	40,41
Rat bone marrow stromal cells	Hollow bioceramic microspheres; bioactive composite microspheres	2 weeks	29
Rat marrow stromal cells	PLGA scaffolds	21 days	42
Rat calvarial osteoblast cells	PLGA scaffolds made with lighter-than-water and heavier-than-water microspheres	7 days	43
Rat calvarial cells	Gelated collagen	3 weeks	44
Rat osteoblast-like cell line (ROS.SMer#14)	No carrier	48 h	45
MC3T3-E1 osteoblast-like cells	Alginate beads with cells encapsulated inside	5, 14 days	46,47
Mouse osteoblast	No carrier	24 h	48
ROS17/2.8 osteoblast cells	Cytodex-3 and Biosilon	8–10 days	49
Chondrocytes			
Human articular chondrocytes	None used	12 weeks	50
Bovine calf articular chondrocytes	PGA scaffold	6 weeks	51,52
Bovine chondrocytes	PLLA nanofibrous scaffolds with cells embedded inside	6 weeks	53
Bovine chondrocytes	PGA scaffolds	8 weeks	54,55
Bovine chondrocytes	PEG hydrogels	5 days	56
Bovine chondrocytes	Cytodex-5 microcarriers	36 days	57
Rat chondrocytes	Cytodex-3 microspheres	41 days	58
Stem cells			
Human embryonic stem cells	None	30 days	59
Murine embryonic stem cells	Alginate beads with cells encapsulated inside	24 days	60
Embryonic limb cells	Cytodex-3 microspheres	65 days	61
Human mesenchymal stem cells (hMSCs)	Silk scaffolds	3 weeks	62
Human mesenchymal stem cells (hMSCs)	None	8 days	63
Murine embryonic stem cells	Alginate hydrogels	14 days	60
Cancer cells			
Human colon carcinoma cells, HT-29, MIP-101	Cytodex-3	17 days	1,64
Coculture of human prostate fibroblasts and human prostate cancer cells	Cytodex-3	10 days	65
Coculture of fibroblast spheroids with PC3 prostate cancer cells	None	4 weeks	66

(*Continued*)

Table 2 (Continued)

Cell culture type	*Scaffolds/microcarriers*	*Culture duration*	*References*
Coculture of human tumor epithelial and umbilical vein endothelial cells	Cytodex-3	10 days	67
LN1 ovarian tumor cell line	Cytodex-3	4.5 weeks	3,68
Coculture of human prostate cancer cell line, LNCaP, and prostate or bone stromal cells	Microcarrier beads	1 week	69
Human MIP-101 colorectal carcinoma cells	Cytodex-3	12 days	70
Human breast carcinoma cells	Cytodex-3	56 days	71
Human endothelial–tumor epithelial cells	Cytodex-3 microcarrier beads	10 days	67
Other			
Human promyelocytic cells	None	7 weeks	72
Human bone marrow CD34+ cells	None	4–6 days	73
Primary human liver cells	Cytodex-3, polystyrene beads, PGA scaffolds	60 days	74
Human hepatoblastoma cells (HepG2)	None	3 days	75
Dendritic cells differentiated from human CD34+ progenitors	None	12 days	76
Adrenal medullary PC12 pheochromocytoma cells	Cytodex-3	20 days	77
Bovine aortic endothelial cells	Cytodex-3	30 days	78
Bovine chondrocytes	Cytodex-3	5 weeks	79
Primary porcine aortic smooth muscle cells (SMC)	Nonwoven benzilic ester of hyaluronic acid	1 week	80
Rat satellite cells	Cytodex-3	5 days	81
Neonatal rat cardiac cells	Polystyrene beads	6 days	82
Neonatal rat heart ventricular cell	Bovine type I collagen matrix	3 weeks	83
Rat hepatocytes		30 days	84
Neonatal rat cardiomyocytes	PGA scaffolds	1 week	85
Mouse splenocytes	None	2 days	86
Mouse myoblasts C2C12	None	1 week	87

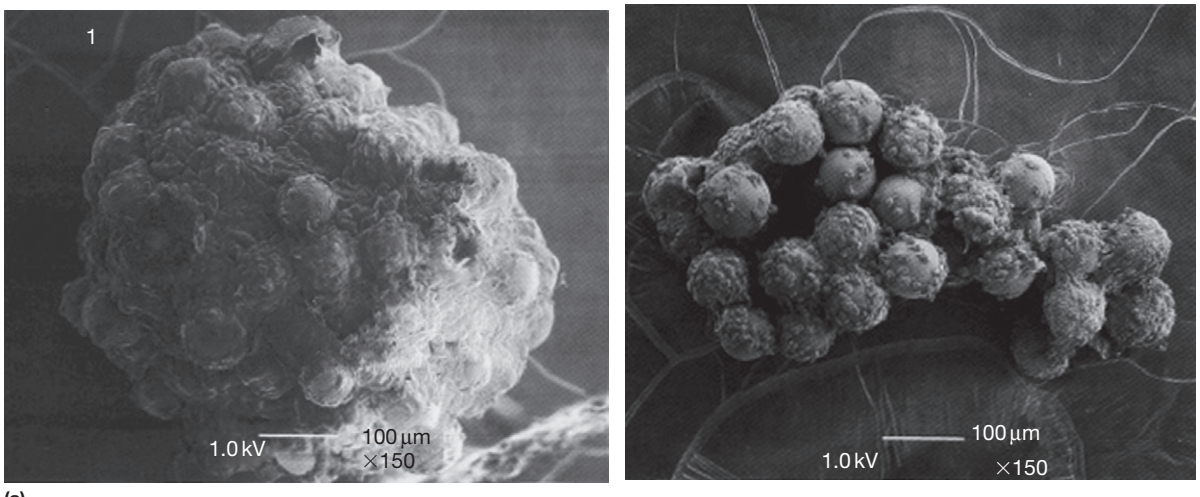

(a) (b)

Figure 15 Scanning electron micrographs of rat marrow stromal cells grown on Cytodex-3 microcarriers in a high aspect ratio vessel (a) and cell bag (b) for 14 days. Reproduced from Qiu, Q.; Ducheyne, P.; Gao, H.; Ayyaswamy, P. *Tissue Eng.* **1998**, *4*(1), 19–34.

in bone cell cultures, RWVs have been used to search for answers for loss of bone mass during space flight. Later on, studies were carried out with a goal for 3D bone tissue formation and engineering.[15,91] This section will only provide a brief review on 3D bone cell cultures in RWVs and will include the effect of simulated microgravity on cell cultures in a latter section.

5.511.4.1.1.1. Cells cultured on polymer microcarrier and scaffolds

Osteoblastic cells cultured on polymer microcarriers such as Cytodex-3 beads in RWV were found to be more differentiated than those cultured in 3D petri dish, and mineralization was observed in the 3D aggregates consisting of multiple cell-covered Cytodex-3 microcarriers bridged together[15,49] (**Figure 15**).

When osteoblastic cells were cultured on biopolymer scaffolds, they showed increased expression of ALPase activity, osteopontin, osteocalcin (OC), and cell proliferation in RWV compared with static cell culture.[35,92] It was believed that RWV provides a favorable environment for osteogenic differentiation.[36] However, some studies showed that osteoblastic cells cultured on 3D porous poly(D,L-lactic-*co*-glycolic acid) (PLGA) scaffolds in RWV did not show considerable ALPase activity and OC secretion, but showed reduced life span and increased osteoclast activity.[42,45]

The conflicting observations may be due to the complex fluid flow mechanics in RWVs which are associated with carrier properties (e.g., density and chemical composition) and configurations (e.g., shape and porosity) as well as cell types and culture conditions. For example, cells cultured on heavier-than-water microcarriers or scaffolds that have apparent density greatly different from the density of culture medium will experience higher shear stress and collisions with the outer wall of the vessel than cells cultured on microcarriers or scaffolds that have a density close to or equivalent to that of culture medium. The shear stress and collisions may significantly affect cell proliferation and differentiation.

5.511.4.1.1.2. Cells cultured on carriers lighter than culture medium

As bioceramic material has a density much greater than that of culture medium, it is not suitable to be used directly as a carrier for cell cultures in RWVs. In order to reduce its apparent density to reduce its shear stress and avoid microcarrier–wall collisions, hollow bioceramic microspheres with apparent density between 0.8 and 1.0 g cm^{-3} were developed and used for 3D bone-like tissue engineering in RWV.[20] The osteoblastic cells attached to and formed 3D aggregates with the hollow microspheres, and extracellular matrix and mineralization were observed in the aggregates formed in RWV after a 2-week culture period (**Figure 16**).

In the wake of this work with bioceramic and composite microspheres,[20] PLGA microspheres were also developed. The microspheres were formed into 3D scaffolds and used for osteoblastic cell culture in RWV.[32] Human SaOS-2 cells cultured on lighter-than-water PLGA scaffolds for 7 days retained their osteoblastic phenotype and showed significant increase in alkaline phosphatase expression compared with statically cultured controls.[32] Rat calvarial osteoblast cells were also cultured on 3D scaffolds made with lighter-than-water PLGA microspheres for 7 days in RWV.[43]

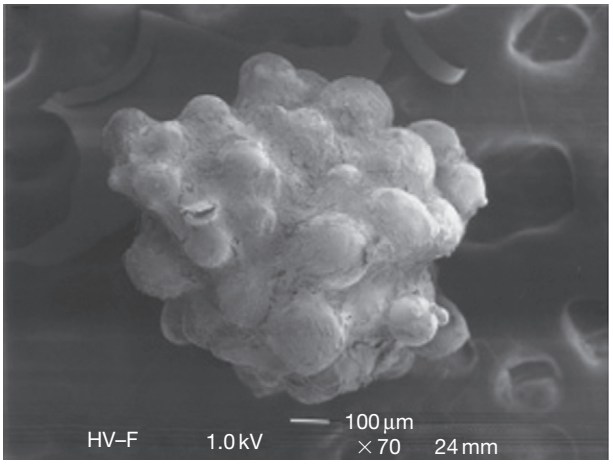

Figure 16 An aggregate of bone marrow stromal cells and hollow bioceramic microspheres in 14-day cell culture in a high aspect ratio vessel. Note the aggregate is in a nearly spherical shape. Reproduced from Qiu, Q.; Ducheyne, P.; Ayyaswamy, P. S. *Biomaterials* **1999**, *20*, 989–1001, with permission from Elsevier.

Previous studies have shown that the shear stress in the range of 3–10 dyn cm^{-2} is sufficient to inflict damage to cells.[93] A shear stress in this range has also been reported to downregulate alkaline phosphatase activity,[94] stimulate release of nitric oxide, and increase prostaglandin E_2 production in osteoblasts.[95,96] As the hollow bioceramic microspheres experience low shear stress ($\sim$0.6 dyn cm^{-2}),[20] they appear to alleviate the damage to cells/cell aggregates from shear stress and collisions.

5.511.4.1.1.3. Cells encapsulated in microcarriers or matrix

Use of microspheres or scaffolds with densities close to that of culture medium does not completely eliminate shear stress on cells in RWVs. For investigations that require no or negligible shear stress, such as studies on the effects of microgravity on cellular functions, further reduction of shear stress is desired. The approaches include encapsulation of cells in hydrogels or inside microcarriers to reduce the cell exposure to shear stress.

Various cell types including embryonic and bone marrow stem cells encapsulated in alginate and chitosan hydrogels, or gelated collagen have been cultured in HARV; 3D constructs formed have displayed morphological, phenotypical, and molecular attributes of the corresponding cell lineage.[38,44,60]

5.511.4.1.1.4. No carrier used

Although bone cells are anchorage-dependent cells, they can be cultured without any carrier in RWVs as they attach to each other to form cell aggregates and differentiate.

When rat or mouse osteoblast cells were cultured in RWV for short time periods, for example, 24–48 h, the cells appeared to be stimulated by regulating osteoblast secretion of crucial regulatory factors,[48] and they showed high levels of alkaline phosphatase activity and elevated expression of osteopontin, OC, and bone morphogenetic protein (BMP-3).[45] However, it was also reported that osteoblastogenesis of human mesenchymal stem cells (hMSC) was severely reduced after 7-day culture in RWV.[33] It was suggested that the cell culture environment in RWV may disrupt collagen I/integrin signaling during osteoblastic differentiation of hMSC.[34]

A regeneration of 3D large and homogenous cartilaginous tissue from rabbit bone marrow cells without a scaffold using RWV was also reported.[41] Bone marrow cells cultured for 4 weeks in the chondrogenic medium in the RWV formed cylindrical cartilaginous tissue with dimensions of 1.25 × 0.6 cm (height × diameter).

5.511.4.1.2. Chondrocytes

Biodegradable and highly porous 3D scaffolds made of PGA, PLGA, or silk fibers are the commonly used carriers for chondrocyte culture in RWVs. Common cell sources for chondrocytes include human and bovine calves.[97]

A high cell-seeding density, for example, 4–10 million cells per scaffold (10 mm diameter × 5 mm thick), plays a

crucial role in the initiation of chondrogenesis *in vitro*; thus it is one of the key parameters for cartilage cell culture and tissue engineering.[55,98] At the start of cell culture (chondrogenesis), cell density is the highest at the construct periphery, and chondrogenesis proceeds from the construct periphery toward its center during the cell culture period in RWVs.[97] It was found that the constructs cultured in RWVs were larger, contained continuous cartilage-like extracellular matrices with higher fractions of glycosaminoglycan and collagen, and better mechanical properties than those cultured in static culture and mixed flasks.[52]

In addition to scaffolds, PEG hydrogels and Cytodex-3 microcarriers have also been used for chondrocyte culture in RWV.[56,79] Chondrocytes can also be cultured without any scaffold in RWV, and form cartilage-specific extracellular matrix.[50]

It was found that major improvements for chondrocyte culture could be achieved using bioreactors that provide efficient mass transfer and controlled shear stress at the cell and implant surfaces over the static cell culture condition.[5]

5.511.4.1.3. Stem cells

Stem cells have the ability to proliferate and differentiate into a diverse range of specialized cell types and regenerate tissues. There are two main types of stem cells, embryonic and nonembryonic. Nonembryonic cells are also known as adult stem cells, usually from bone marrow, which has two types of stem cells: haemopoietic, which will differentiate into blood cells, and the less differentiated mesenchymal stem cells (MSCs). Only nonembryonic cells have been used in clinical therapies so far.[99]

Human stem cells cultured in RWVs showed greater cell proliferation than those in static cell culture,[100] and reduced osteogenic differentiation.[101] It was also found that the type of rotating vessel had a significant impact on the process of human embryoid body (hEB) formation and agglomeration.[59] In the STLV, hEBs were smaller in size and no large necrotic centers were seen, even after 1-month cultivation. In the HARV, hEB agglomeration was massive.

Human hematopoietic bone marrow cells cultured for 4–6 days in RWV exhibited reduced proliferation compared to static cell culture.[73]

5.511.4.1.4. Other

In addition to the cells described in the previous sections, various other cell types including C2C12 mouse myoblasts have also been studied with the use of RWVs.[73,77,81,82,87]

Because the fluid flow and environment experienced by cells in RWVs are influenced by many factors, such as carrier/aggregate density and shape, rotating speed, density of culture medium, cell-seeding density, etc., great caution should be taken when the observations in cell culture studies are interpreted. A better understanding of the fluid mechanics in each cell culture condition would be very helpful to improve cell culture design and studies. In general, major improvements can be achieved by providing efficient mass transfer and controlled shear stress at the surfaces of cells and aggregates.

5.511.4.2. Tissue Engineering

There is a great overlap between 3D cell culture and tissue engineering as cell attachment, proliferation, and differentiation occur at the early stage of tissue formation as well as throughout the entire cell culture and tissue formation period. To avoid extensive overlapping with 3D cell culture, this section will focus on the studies on cell cultures with a goal to form functional tissues and the culture period is at least 1-week long.

For anchorage-dependent cells, biodegradable and porous scaffolds are usually preferred. A biodegradable scaffold allows degradation of the same order of magnitude as the rate of extracellular matrix deposition. A highly porous scaffold could not only allow better mass and oxygen transfer, but also avoid high shear stress and frequent collisions associated with high density of microcarriers or scaffolds.

Among the different types of tissues in the human body, articular cartilage is an avascular tissue known to have a limited capacity for self-repair. Currently the only repair therapy approved by the US Food and Drug Administration is a cell-based method which involves obtaining autologous articular chondrocytes from the patient, expanding them in culture, and then reinjecting them under a periosteal flap at the defect site.[102] As RWVs were invented at NASA, extensive studies on cartilage engineering with the use of 3D biodegradable scaffolds and chondrocytes (or bone marrow stromal cells) have been carried out.[97,103] It was found that the constructs cultured in RWVs were superior to those grown in either static or mixed flasks with respect to GAG and collagen content, equilibrium moduli, and hydraulic permeabilities.[103] Studies on chondrogenesis in constructs of chondrocytes and PGA scaffolds showed that the constructs grown aerobically were superior to those grown anaerobically in wet weight, total cell number, GAG content and total collagen, and rates of cartilaginous matrix biosynthesis.[103,104] This observation indicates that oxygen plays an important role during the cultivation of engineered cartilage in RWVs.

Another source for cartilage tissue engineering is bone marrow stromal cells, which can differentiate into several mesenchymal lineages including osteoblasts, chondrocytes, adipocytes, and myocytes depending on local environments.[105] When human bone marrow stromal cells were cultured on porous silk scaffolds for 5 weeks in STLV, they formed large and homogenous bone-like tissue constructs with mineralization resembling those of the human trabecular bone.[39,62]

After porcine aortic smooth muscle cells (SMC) were cultured on tubular sheets made from benzilic ester of hyaluronic acid for 1 week in RWV, the cell proliferation was higher in RWV than in static control.[80] It was found that the constructs experienced higher maximum stress and lower elastic modulus than the control.

Hepatocyte cells isolated from human livers and cultured on biodegradable scaffolds in RWV formed aggregates which increased up to 3 cm long.[74] Hepatocyte spheroids cultured in a HARV could retain cellular and physiological properties of the intact liver.[84] Morphological evaluation revealed that hepatocyte spheroids cultured for 30 days in the HARV had a compact structure with tight cell–cell junctions, numerous smooth and rough endoplasmic reticulum, intact mitochondria, and bile canaliculi lined with microvilli.

Neonatal rat cardiomyocytes cultured on laminin-coated PGA mesh in RWV showed superior molecular and electrophysiological properties to those of the same cells cultured as

monolayers in terms of cell metabolism, contractile function, and intercellular communication.[85]

Small intestine epithelium and mesenchymal cells cocultivated on Cytodex-3 microcarriers in RWV for up to 40 days were differentiated to form tissue-like masses.[106] Bovine aortic endothelial cells cultured on Cytodex-3 in RWV for 30 days showed enhanced NO production and barrier properties.[78]

Rat and chick cardiac myocytes cultured on PGA scaffolds for 2 weeks showed spontaneously contractile cells. It was believed that high initial cell densities and utilization of RWVs improved structural and functional construct properties.[107]

Other cell types that have also been studied using RWVs include keratinocytes,[108] microvascular endothelial cells,[109] HepG2 cells,[110] hepatocytes,[111] epidermal keratinocytes,[112] and retinal and endothelial cells.[113]

It should emphasized here again that because of the complexity of the fluid mechanics in RWV, the interpretation of the effect on cellular and tissue responses in RWVs remains difficult. The factors include but are not limited to shear stress,[80] mass transfer, and carrier material properties.

5.511.5. Other Applications of RWV

156.5.1. Space Biology

Space flight is known to affect human biological systems including loss of bone mass, muscle strength, and cardiovascular fitness in astronauts.[113–115] It also has a significant negative impact on immune function. As RWVs can simulate some aspects of microgravity environment, they have been used to culture cells on 3D biodegradable scaffolds or microcarriers to investigate cellular responses to simulated microgravity.

It was reported that cartilaginous constructs cultured for 6 weeks in RWVs contained collagen matrix that resembled that of articular collagen with respect to overall organization, fiber diameter, and molecular structure.[51,97] However, the fraction of collagen and dynamic stiffness of constructs cultured in RWVs were significantly lower than those of cartilage explants.[117] In comparison to constructs grown in RWVs on earth, the constructs grown on Mir Space Station floated freely in the bioreactor and were more spherical, smaller, had less weight increase, and were mechanically inferior.[54] The videotapes showed that constructs floated freely in microgravity, but settled and collided with the rotating vessel wall at 1 g. The observation indicated that the collision and the difference in culture conditions might have contributed to the differences. In order to better simulate the microgravity environment on earth, it might be essential to avoid the collision with the vessel wall by choosing the right carriers, such as carriers with density close to and less than that of culture medium.

Embryonic mouse prebone tissues were placed in RWV at one of four different stages of chondrogenesis, ranging from undifferentiated mesenchyme cells to chondrocytes on the verge of undergoing terminal chondrocyte differentiation. The study has found that exposure to the RWV at early stages of chondrogenesis severely limits the ability for cartilage growth and yields abnormal downstream morphogenesis. However, at later stages of chondrogenesis, the RWV environment may be beneficial to enhance growth and development.[118]

A marked reduction in bone mass is common after extended time in space, a condition known as spaceflight osteopenia.[89,90] Osteoblasts cultured in microgravity are generally characterized by a contracted morphology, a decrease in cell number, a reduction in osteoblast-specific gene expression, and a lowered response to anabolic stimuli, relative to unit gravity conditions.[119] A significant problem in ground-based studies is that each system subjects cells to stimuli that could confound the effects of simulated microgravity, most importantly, fluid flow-induced shear stresses, vibration, and convective mixing. The divergent results reported highlight the need to control these extraneous factors. A system was developed that allows control osteoblasts to be cultured in normal (unit) gravity within the same HARV as cells experiencing simulated microgravity (vector-averaged gravity) (**Figure 17**). Two types of alginate bead were fabricated: polar and nonpolar carriers. As the HARV rotates, cells in nonpolar carriers are subjected to vector-averaged gravity while cells in polar carriers remain in normal gravity conditions. It was found that vector-averaged gravity did not reduce osteoblast viability (MC3T3-E1 cells). Furthermore, neither osteoblasts, nor progenitor-like cells were sensitized to apoptogens by exposure to vector-averaged gravity. Some differences in the phenotypic expression were observed in these cells; specifically, there was a decrease in alkaline phosphatase expression in simulated microgravity. These findings suggest that vector-averaged gravity alone is insufficient to induce or modulate the susceptibility of osteoblasts to agents that induce apoptosis.[47]

The studies on human hepatoblastoma cells (HepG2) showed that simulated microgravity in RWVs could modify the expression of several genes and that the RWV in combination with microarray technology might provide insight into the fundamental biological questions of how gravity affects the development and function of individual cells.[75]

Human nonadherent promyelocytic (HL-60) cells cultured in RWV for 7 weeks showed 3.8-fold fewer cells that were able to participate in respiratory burst activity than cells from 1-g cultures. The results demonstrated that simulated microgravity alters an innate cellular function (burst activity). If respiratory burst activity is impaired by true microgravity, then recovery from infections during spaceflight could be delayed.[72]

During spaceflight, astronauts also experience alterations of the immune response.[120,121] Existing evidence suggests that space travelers are immunosuppressed, presumably by microgravity environment stressors. Studies on dendritic cells showed that the cell generation and function were altered in RWV.[76] To prevent immunosuppression during and after space flight, use of dietary nucleotide (NT) supplementation was investigated. It was found that NT supplement could confer immune protection and enhance cytokine responses during space flight.[86]

5.511.5.2. Cancer Research

One of the challenges in cancer research using cell culture is to create conditions that closely simulate the *in vivo* conditions. One of the key features of *in vivo* conditions is 3D growth. As RWVs allow 3D cell cultures and efficient mass transfer, they have been used to culture various cancer cell types, including breast carcinoma cells,[71] ovary tumor cells,[3,68] prostate cancer

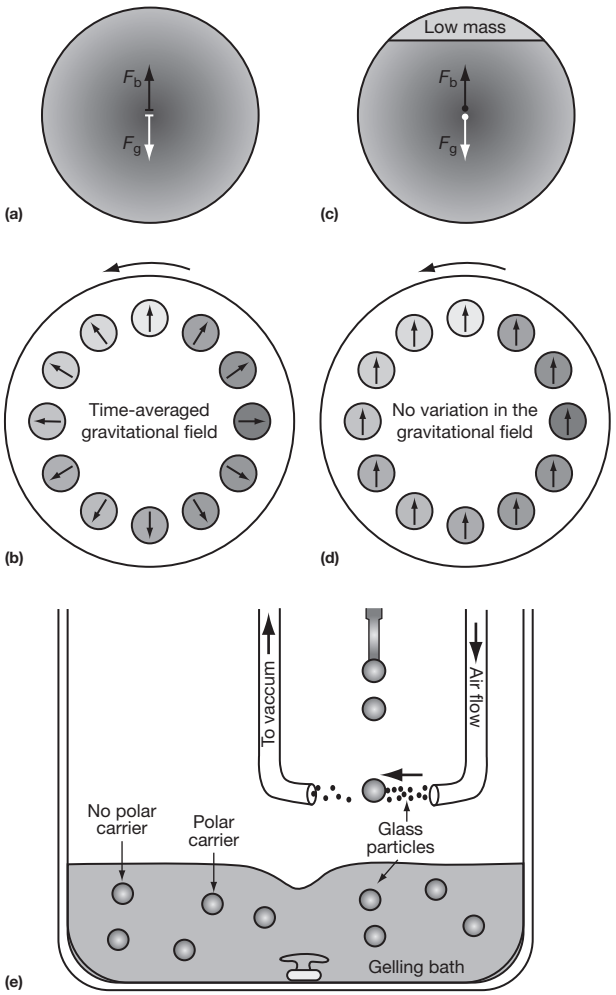

Figure 17 (a–d) Schematic of forces that control the spin of alginate carriers in the rotating high aspect ratio vessel (HARV). The carriers are designed so that the forces of gravity (F_g) and buoyance (F_b) are nearly balanced. As such, the carriers move in near solid body rotation with the fluid in the HARV. In a radially symmetric carrier, the center of buoyance coincides with the center of gravity (a). Such nonpolar carriers have no preferred orientation, and therefore, spin with the HARV rotation. The theoretical spin of a nonpolar carrier over one revolution of the HARV is shown in time lapse (b). The arrow on the carrier indicates its orientation at each phase of the rotation. In the polar carrier, they do not coincide, giving the carrier a preferred orientation (c). There polar carriers resist rotation and therefore resist spinning as the HARV turns. The theoretical stable orientation of a polar carrier over one revolution of the HARV is shown in (d). As the HARV rotates, nonpolar carriers are subjected to vector-averaged gravity while polar carriers remain in normal gravity conditions. (e) Cross-sectional diagram of the system used to encapsulate cells into nonpolar and polar alginate carriers. The alginate–cell suspension (1% alginate, 2×10^6 cells ml^{-1}) was extruded by a syringe pump (100 ml h^{-1}) through an 18-gauge needle. Droplets released from the needle tip polymerized in the $CaCl_2$/NaCl bath forming carriers seeded with cells. The gelling bath was stirred to prevent the carriers from deforming upon entry. The process was used to form nonpolar carriers of uniform size and sphericity. To form polarized carriers, aerosolized hollow glass particles were blown across the drop path. The glass particles were incorporated into the surface of the carriers upon polymerization. Reproduced from Bucaro, M. A.; Zahm, A. M.; Risbud, M.V.; *et al. J. Cell. Biochem.* **2007**, *102*(2), 483–495, with permission from Wiley.

cells,[65,69,121–123] colon adenocarcinoma cell lines,[1] epithelial tumor cells,[67] melanoma cells,[125] and leukemic cells.[126]

When human primary breast carcinoma cells were cultured in RWV for a prolonged time, they formed complex tissue-like constructs, exhibited significantly increased proliferative activity in conjunction with oncogene activation and developed into aggressive aneuploid populations.[71]

To study cellular interactions involved in the growth and differentiation of ovary tumors, a cell line established from ovary tumor was cultured on microcarrier beads in HARV. The tumor cell proliferated and exhibited 3D multicellular aggregates.[3] A cell line derived from a heterologous mixed mullerian tumor cell of the ovary was cultured on Cytodex-3 for 32 days in RWV. The data indicate that the RWV culture system is suitable for generating large quantities of ovarian tumor cells *in vitro* that are amenable to immunocytochemical, oncogenic, and morphologic characteristics demonstrated *in vivo*.[68]

DU 145 human prostate carcinoma cells cultured on Cytodex-3 beads for 2 weeks in RWV showed a lower proliferation rate, but were more differentiated than controls.[122] PC-3 human prostate cancer cells have also been cultured on Cytodex-3 bead in RWV in which glucose, lactate, and glutamine profiles were monitored noninvasively and in real time by near-infrared (NIR) spectroscopy.[123]

Human colon adenocarcinoma cell lines, HT-29 and HT-29kM, were cultivated on Cytodex-3 for up to 17 days.[1]

Human MIP-101 poorly differentiated colorectal carcinoma cells were cultured for 6 days in monolayers or in rotating 3D cultures either in microgravity in low-earth orbit (space shuttle, 3D, μg) or in unit gravity on the ground (3D, 1 g). Over the course of 6 days, static 3D cultures displayed the highest rates of proliferation and lowest apoptosis. Rotated 3D μg displayed significantly less apoptosis than rotated 3D 1 g cultures. Thus rotation appears to increase apoptosis and decrease proliferation.[70]

A novel *in vitro* human prostate cancer model was established by using a coculture technique in which isolated human prostate fibroblasts were observed to grow as a mixed culture with human prostate cancer cells on microcarriers in RWV.[65] Upon coculture of human prostate cancer cell line, LNCaP, with microcarrier beads either in presence or in the absence of prostate or bone stromal cells, 3D prostate organoids were formed after 7 days in RVW.[69]

The multicellular interaction between human tumor epithelial and human umbilical vein endothelial cells grown on Cytodex-3 for 10 days was investigated. It suggests that RWV provides a new model that allows us to investigate the regulatory factors that govern tumor angiogenesis.[67]

Growth patterns of a number of human tumor cell lines that form 3D structures of various architectures when cultured without carrier beads in RWS were also investigated.[66]

5.511.5.3. Other

RWVs have been used to expand human MSCs from isolated bone marrow mononuclear cells.[63] Upon induction, the bioreactor-expanded MSCs were able to differentiate into osteoblasts, chondrocytes, and adipocytes. The rotary bioreactor with the modified Myelocult medium reported in this study may be used to rapidly expand MSCs.

References

1. Goodwin, T. J.; Jessup, J. M.; Wolf, D. A. *J. Tissue Cult. Meth.* **1992**, *28A*, 47–60.
2. Schwarz, R. P.; Goodwin, T. J.; Wolf, D. A. *J. Tissue Cult. Meth.* **1992**, *14*, 51–58.
3. Becker, J. L.; Prewett, T. L.; Spaulding, G. F.; Goodwin, T. J. *J. Cell. Biochem.* **1993**, *51*(3), 283–289.
4. Jessup, J. M.; Goodwin, T. J.; Spaulding, G. *J. Cell. Biochem.* **1993**, *51*, 290–300.
5. Freed, L. E.; Vunjak-Novakovic, G.; Langer, R. *J. Cell. Biochem.* **1993**, *51*(3), 257–264; Review.
6. Gao, H.; Ayyaswamy, P. S.; Ducheyne, P. *Microgravity Sci. Technol.* **1997**, *10*, 154–165.
7. Coimbra, C. F. M.; Kobayashi, M. H. *J. Fluid Mech.* **2002**, *469*, 257–286.
8. Mukundakrishnan, K. Ph.D. Dissertation, University of Pennsylvania, Philadelphia, PA, 2005.
9. Mukundakrishnan, K.; Hu, H.; Ayyaswamy, P. S. *J. Fluid Mech.* **2008**, *599*, 169–204.
10. Ayyaswamy, P. S.; Mukundakrishnan, K. *Acta Astronaut.* **2007**, *60*, 397–405.
11. Lynch, S. V.; Mukundakrishnan, K.; Benoit, M. R.; Ayyaswamy, P. S.; Matin, A. *Appl. Environ. Microbiol.* **2006**, *72*, 7701–7710.
12. Gao, H.; Ayyaswamy, P. S.; Ducheyne, P. In *Advances in Heat and Mass Transfer in Biotechnology*; Clegg, S., Ed.; ASME International Mechanical Engineering Congress and Exposition: Dallas, TX, 1997; pp 59–68.
13. Navran, S. *Biotechnol. Annu. Rev.* **2008**, *14*, 275–296.
14. Gao, H.; Ayyaswamy, P. S.; Hu, H.; Zhu, M.; Ducheyne, P. In *Advances in Heat and Mass Transfer in Biotechnology*; Clegg, S., Ed.; ASME: New York, 1998; HTD-Vol. 362/BED-Vol. 40, pp 95–102.
15. Qiu, Q.; Ducheyne, P.; Gao, H.; Ayyaswamy, P. *Tissue Eng.* **1998**, *4*(1), 19–34.
16. Gao, H. Ph.D. Thesis, University of Pennsylvania, Philadelphia, PA, 2000.
17. Hu, H. H.; Patankar, N. A.; Zhu, M. Y. *J. Comp. Phys.* **2001**, *169*, 427–462.
18. Hu, H. H. *Int. J. Multiphase Flow* **1996**, *22*(2), 335–352.
19. Zhu, M.; Hu, H. H. Direct numerical simulation in the mixing of particulate flow. In *Proceedings of 1998 ASME Fluid Engineering Division Summer Meeting, ASME FEDSM* '98-4904, Washington, DC, 1998; pp 1–9.
20. Qiu, Q.; Ducheyne, P.; Ayyaswamy, P. S. *Biomaterials* **1999**, *20*, 989–1001.
21. Schiller, V. L.; Naumann, A. *Zeitschr. Ver. Deut. Ing.* **1933**, *77*(12), 318–320.
22. Padmavathi, B. S.; Amarnath, T. *Zamp* **1993**, *44*(1), 178–184.
23. Caverzasio, J.; Selz, T.; Bonjour, J. P. *Calcif. Tissue Int.* **1981**, *43*, 83–87.
24. Kwon, O.; Devarakonda, S. B.; Sankovic, J. M.; Banerjee, R. K. *Biotechnol Bioeng.* **2008**, *99*(1), 99–107.
25. Freed, L. E.; Vunjak-Novakovic, G. *Biotechnol. Bioeng.* **1995**, *46*, 306–313.
26. Freed, L. E.; Vunjak-Novakovic, G.; Biron, R. J.; *et al. Biotechnology* **1994**, *12*(7), 689–693.
27. Ducheyne, P.; Lemons, J. E. *Bioceramics: Materials Characteristics Versus In Vivo Behavior*; New York Academy of Sciences: New York, 1988; pp 54–71.
28. Qiu, Q.; Ducheyne, P.; Ayyaswamy, P. S. *J. Biomed. Mater. Res.* **2000**, *52*, 66–76.
29. Qiu, Q.; Ducheyne, P.; Ayyaswamy, P. S. *In Vitro Cell. Dev. Biol.* **2001**, *37*, 157–165.
30. Goodwin, T. J.; Prewett, T. L.; Wolf, D. A.; Spaulding, G. F. *J. Cell. Biochem.* **1993**, *51*, 301–311.
31. Prewett, T. L.; Goodwin, T. J.; Spaulding, G. F. *J. Tissue Cult. Meth.* **1993**, *15*, 29–36.
32. Botchwey, E. A.; Pollack, S. R.; Levine, E. M.; Laurencin, C. T. *J. Biomed. Mater. Res.* **2001**, *55*(2), 242–253.
33. Saxena, R.; Pan, G.; McDonald, J. M. *Ann. NY Acad. Sci.* **2007**, *1116*, 494–498.
34. Meyers, V. E.; Zayzafoon, M.; Gonda, S. R.; Gathings, W. E.; McDonald, J. M. *J. Cell. Biochem.* **2004**, *93*(4), 697–707.
35. Inanc, B.; Elcin, A. E.; Elcin, Y. M. *Tissue Eng.* **2006**, *12*(2), 257–266.
36. Inanç, B.; Elçin, A. E.; Koç, A.; Baloş, K.; Parlar, A.; Elçin, Y. M. *J. Biomed. Mater. Res. A* **2007**, *82*(4), 917–926.
37. Pound, J. C.; Green, D. W.; Chaudhuri, J. B.; Mann, S.; Roach, H. I.; Oreffo, R. O. *Tissue Eng.* **2006**, *12*(10), 2789–2799.
38. Pound, J. C.; Green, D. W.; Roach, H. I.; Mann, S.; Oreffo, R. O. *Biomaterials* **2007**, *28*(18), 2839–2849.
39. Marolt, D.; Augst, A.; Freed, L. E.; *et al. Biomaterials* **2006**, *27*(36), 6138–6149.
40. Yoshioka, T.; Mishima, H.; Ohyabu, Y.; *et al. J. Orthop. Res.* **2007**, *25*(10), 1291–1298.
41. Ohyabu, Y.; Kida, N.; Kojima, H.; Taguchi, T.; Tanaka, J.; Uemura, T. *Biotech Bioeng.* **2006**, *95*(5), 1003–1008.
42. Sikavitsas, V. I.; Bancroft, G. N.; Mikos, A. G. *J. Biomed Mater. Res.* **2002**, *62*(1), 136–148.
43. Yu, X.; Botchwey, E. A.; Levine, E. M.; Pollack, S. R.; Laurencin, C. T. *Proc. Natl. Acad. Sci. USA* **2004**, *101*(31), 11203–11208.
44. Su, G. N.; Hidaka, M.; Kimura, Y.; Yamamoto, G. *In Vitro Cell. Dev. Biol. Anim.* **2003**, *39*(8–9), 368–374.
45. Rucci, N.; Mifliaccio, S.; Zani, B. M.; Taranta, A.; Teti, A. *J. Cell. Biochem.* **2002**, *85*(1), 167–179.
46. Bucaro, M. A.; Fertala, J.; Adams, C. S.; *et al. Ann. N Y Acad. Sci.* **2004**, *1027*, 64–73.
47. Bucaro, M. A.; Zahm, A. M.; Risbud, M. V.; *et al. J. Cell. Biochem.* **2007**, *102*(2), 483–495.
48. Rucci, N.; Rufo, A.; Alamanou, M.; Teti, A. *J. Cell. Biochem.* **2007**, *100*(2), 464–473.
49. Granet, C.; Laroche, N.; Vico, L.; Alexandre, C.; Lafage-Proust, M. H. *Med. Biol. Eng. Comput.* **1998**, *36*(4), 513–519.
50. Marlovits, S.; Tichy, B.; Truppe, M.; Gruber, D.; Schlegel, W. *Int. J. Artif. Organs* **2003**, *26*(4), 319–330.
51. Riesle, J.; Hollander, A. P.; Langer, R.; Freed, L. E.; Vunjak-Novakovic, G. *J. Cell. Biochem.* **1998**, *71*(3), 313–327.
52. Vunjak-Novakovic, G.; Martin, I.; Obradovic, B.; *et al. J. Orthop. Res.* **1999**, *17*(1), 130–138.
53. Li, W. J.; Jiang, Y. J.; Tuan, R. S. *Tissue Eng. A* **2008**, *14*(5), 639–648.
54. Freed, L. E.; Langer, R.; Martin, I.; Pellis, N. R.; Vunjak-Novakovic, G. *Proc. Natl. Acad. Sci. USA* **1997**, *94*, 13885–13890.
55. Hu, J. C.; Athanasiou, K. A. *Biomaterials* **2005**, *26*(14), 2001–2012.
56. Villanueva, I.; Klement, B. J.; von Deutsch, D.; Bryant, S. J. *Biotechnol Bioeng.* **2009**, *102*(4), 1242–1250.
57. Baker, T. L.; Goodwin, T. J. *In Vitro Cell Dev. Biol. Anim.* **1997**, *33*(5), 358–365.
58. Kaeffer, B.; Trubuil, A.; Kervrann, C.; Pardini, L.; Cherbut, C. *In Vitro Cell. Dev. Biol. Anim.* **2002**, *38*(8), 436–439.
59. Gerecht-Nir, S.; Cohen, S.; Itskovitz-Eldor, J. *Biotech. Bioeng.* **2004**, *86*(5), 493–502.
60. Hwang, Y. S.; Cho, J.; Tay, F.; *et al. Biomaterials* **2009**, *30*(4), 499–507.
61. Duke, J.; Daane, E.; Arizpe, J.; *et al. Adv. Space Res.* **1995**, *17*(6–7), 289–293.
62. Augst, A.; Marolt, D.; Freed, L. E.; *et al. J. R. Soc. Interface* **2008**, *5*(25), 929–939.
63. Chen, X.; Xu, H.; Wan, C.; McCaigue, M.; Li, G. *Stem Cells* **2006**, *24*(9), 2052–2059.
64. Jessup, J. M.; Brown, D.; Fitzgerald, W.; *et al. In Vitro Cell. Dev. Biol. Anim.* **1997**, *33*(5), 352–357.
65. Zhau, H. E.; Goodwin, T. J.; Chang, S. M.; Baker, T. L.; Chung, L. W. *In Vitro Cell. Dev. Biol. Anim.* **1997**, *33*(5), 375–380.
66. Ingram, M.; Techy, G. B.; Saroufeem, R.; *et al. In Vitro Cell. Dev. Biol. Anim.* **1997**, *33*(6), 459–466.
67. Chopra, V.; Dinh, T. V.; Hannigan, E. V. *In Vitro Cell. Dev. Biol. Anim.* **1997**, *33*(6), 432–442.
68. Goodwin, T. J.; Prewett, T. L.; Spaulding, G. F.; Becker, J. L. *In Vitro Cell. Dev. Biol. Anim.* **1997**, *33*(5), 366–374.
69. Rhee, H. W.; Zhau, H. E.; Pathak, S.; *et al. In Vitro Cell. Dev. Biol. Anim.* **2001**, *37*(3), 127–140.
70. Jessup, J. M.; Frantz, M.; Sonmez-Alpan, E.; *et al. In Vitro Cell. Dev. Biol. Anim.* **2000**, *36*(6), 367–373.
71. Becker, J. L.; Blanchard, D. K. *J. Surg. Res.* **2007**, *142*(2), 256–262.
72. Hughes, J. H.; Long, J. P. *In Vitro Cell. Dev. Biol. Anim.* **2001**, *37*(4), 209–215.
73. Plett, P. A.; Frankovitz, S. M.; Abonour, R.; Orschell-Traycoff, C. M. *In Vitro Cell. Dev. Biol. Anim.* **2001**, *37*(2), 73–78.
74. Khaoustov, V. I.; Darlington, G. J.; Soriano, H. E.; *et al. In Vitro Cell. Dev. Biol. Anim.* **1999**, *35*(9), 501–509.
75. Khaoustov, V. I.; Risin, D.; Pellis, N. R.; Yoffe, B. *In Vitro Cell. Dev. Biol. Anim.* **2001**, *37*(2), 84–88.
76. Savary, C. A.; Grazziuti, M. L.; Przepiorka, D.; *et al. In Vitro Cell. Dev. Biol. Anim.* **2001**, *37*(4), 216–222.
77. Lelkes, P. I.; Galvan, D. L.; Hayman, G. T.; *et al. In Vitro Cell. Dev. Biol. Anim.* **1998**, *34*(4), 316–325.
78. Sanford, G. L.; Ellerson, D.; Melhado-Gardner, C.; Sroufe, A. E.; Harris-Hooker, S. *In Vitro Cell. Dev. Biol. Anim.* **2002**, *38*(9), 493–504.
79. Baker, T. L.; Goodwin, T. J. *In Vitro Cell. Dev. Biol. Anim.* **1997**, *33*(5), 358–365.
80. Arrigoni, C.; Chittò, A.; Mantero, S.; Remuzzi, A. *Biotechnol. Bioeng.* **2008**, *100*(5), 988–997.
81. Molnar, G.; Schroedl, N. A.; Gonda, S. R.; Hartzell, C. R. *In Vitro Cell. Dev. Biol. Anim.* **1997**, *33*(5), 386–391.

82. Akins, R. E.; Schroedl, N. A.; Gonda, S. R.; Hartzell, C. R. *In Vitro Cell Dev. Biol. Anim.* **1997**, *33*(5), 337–343.
83. van Luyn, M. J.; Tio, R. A.; Gallego, Y.; *et al*. *Biomaterials* **2002**, *23*(24), 4793–4801.
84. Brown, L. A.; Arterburn, L. M.; Miller, A. P.; *et al*. *In Vitro Cell. Dev. Biol. Anim.* **2003**, *39*(1–2), 13–20.
85. Bursac, N.; Papadaki, M.; White, J. A.; Eisenberg, S. R.; Vunjak-Novakovic, G.; Freed, L. E. *Tissue Eng.* **2003**, *9*(6), 1243–1253.
86. Hales, N. W.; Yamauchi, K.; Alicea, A.; Sundaresan, A.; Pellis, N. R.; Kulkarni, A. D. *In Vitro Cell. Dev. Biol. Anim.* **2002**, *38*(4), 213–217.
87. Marquette, M. L.; Byerly, D.; Sognier, M. *In Vitro Cell. Dev. Biol. Anim.* **2007**, *43*(7), 255–263.
88. Vose, G. P. *Am. J. Roentgenol. Radium Ther. Nucl. Med.* **1974**, *121*(1), 1–4.
89. Mack, P. B.; LaChance, P. A.; Vose, G. P.; Vogt, F. B. *Am. J. Roentgenol. Radium Ther. Nucl. Med.* **1967**, *100*, 503–511.
90. Collet, P.; Uebelhart, D.; Vico, L.; *et al*. *Bone* **1997**, *20*, 547–551.
91. Qiu, Q.; Ducheyne, P.; Ayyaswamy, P. S. *Ann. NY Acad. Sci.* **2002**, *974*, 556–564.
92. Song, K. D.; Yang, Z. M.; Liu, T. Q.; *et al*. *Biotech. Appl. Biochem.* **2006**, *45*, 65–74.
93. Cherry, R. S.; Papoutsakis, E. T. *Bioprocess Eng.* **1986**, *1*, 29–41.
94. Hillsley, M. V.; Frangos, J. A. *Calcif. Tissue Int.* **1997**, *60*, 48–53.
95. Reich, K. M.; McAllister, T. N.; Gudi, S.; Frangos, J. A. *Endocrinology* **1996**, *138*(3), 1014–1018.
96. Smalt, R.; Mitchell, F. T.; Howard, R. L.; Chambers, T. J. *Am. J. Physiol.* **1997**, *273*(4 Pt. 1), E751–E758.
97. Freed, L. E.; Hollander, A. P.; Martin, I.; Barry, J. R.; Langer, R.; Vunjak-Novakovic, G. *Exp. Cell Res.* **1998**, *240*, 58–65.
98. Freed, L. E.; Martin, I.; Vunjak-Novakovic, G. *Clin Orthop. Relat. Res.* **1999**, *367*(Suppl), S46–S58.
99. Tuch, B. E. *Aust. Fam. Physician* **2006**, *35*(9), 719–721.
100. Liu, Y.; Liu, T. Q.; Fan, X. B.; Ma, X. H.; Cui, Z. F. *J. Biotech.* **2006**, *124*(3), 592–601.
101. Zheng, Q.; Huang, G.; Yang, J.; *et al*. *Biol. Chem.* **2007**, *388*, 755–763.
102. Brittberg, M.; Lindahl, A.; Nilsson, A.; Ohlsson, C.; Isaksson, O.; Peterson, L. *N. Engl. J. Med.* **1994**, *331*(14), 889–895.
103. Freed, L. E.; Martin, I.; Vunjak-Novakovic, G. *Clin. Orthop. Relat. Res.* **1999**, *367*(Suppl.), S46–S58.
104. Obradovic, B.; Carrier, R. L.; Vunjak-Novakovic, G.; Freed, L. E. *Biotechnol. Bioeng.* **1999**, *63*(2), 197–205.
105. Prockop, D. J. *Science* **1997**, *276*, 71–74.
106. Goodwin, T. J.; Schroeder, W. F.; Wolf, D. A.; Moyer, M. P. *Proc. Soc. Exp. Biol. Med.* **1993**, *202*(2), 181–192.
107. Carrier, R. L.; Papadaki, M.; Rupnick, M.; *et al*. *Biotechnol. Bioeng.* **1999**, *64*(5), 580–589.
108. Chen, J.; Chen, R.; Gao, S. *Artif. Organs* **2007**, *31*(9), 722–731.
109. Cotrupi, S.; Ranzani, D.; Maier, J. A. M. *Biochim. Biophys. Acta* **2005**, *1746*, 163–168.
110. Coward, S. M.; Selden, C.; Mantalaris, A.; Hodgson, H. J. F. *Artif. Organs* **2005**, *29*(2), I52–I58.
111. Dabos, K. J.; Nelson, L. J.; Bradnock, T. J.; *et al*. *Biochim. Biophys. Acta* **2001**, *1526*, 119–130.
112. Doolin, E. J.; Geldziler, B.; Strande, L.; Kain, M.; Hewitt, C. *Tissue Eng.* **1999**, *5*(6), 573–581.
113. Dutt, K.; Sanford, G.; Harris-Hooker, S.; *et al*. *Tissue Eng.* **2003**, *9*(5), 893–908.
114. Holick, M. F. *Bone* **1998**, *22*(5), 105S–111S.
115. Churchill, S. E. *Fundamentals of Space Life Science*; Krieger Publishing: Malabar, 1997.
116. Hughes-Fulford, M.; Lewis, M. L. *Exp. Cell Res.* **1996**, *224*, 103–109.
117. Vunjak-Novakovic, G.; Searby, N.; De Luis, J.; Freed, L. E. *Ann. NY Acad. Sci.* **2002**, *974*, 504–517.
118. Klement, B. J.; Young, Q. M.; George, B. J.; Nokkaew, M. *Bone* **2004**, *34*(3), 487–498.
119. Hughes-Fulford, M. *Adv. Space Biol. Med.* **2002**, *8*, 129–157.
120. Borchers, A. T.; Keen, C. L.; Gershwin, M. E. *Nutrition* **2002**, *18*, 889–898.
121. Sonnenfeld, G.; Shearer, W. T. *Nutrition* **2002**, *18*, 899–903.
122. Clejan, S.; O'Connor, K. C.; Cowger, N. L.; Cheles, M. K.; Haque, S.; Primavera, A. C. *Biotechnol. Bioeng.* **1996**, *50*(5), 587–597.
123. Rhiel, M. H.; Cohen, M. B.; Arnold, M. A.; Murhammer, D. W. *Biotechnol. Bioeng.* **2004**, *86*(7), 852–861.
124. Winkenwerder, J. J.; Palechek, P. L.; Reecel, J. S.; *et al*. *Oncol. Rep.* **2003**, *10*, 783–789.
125. Taga, M.; Yamauchi, K.; Odle, J.; *et al*. *Aviat. Space Environ. Med.* **2006**, *77*, 1113–1116.
126. Vincent, L.; Avancena, P.; Cheng, J.; Rafii, S.; Rabbany, S. Y. *Ann. Biomed. Eng.* **2005**, *33*(10), 1405–1410.

Relevant Websites

www.synthecon.com – Synthecon Incorporated.
http://www.wikipedia.org – Wikipedia.

5.512. *In Vivo* Bioreactors

O Bleiziffer, R E Horch, and U Kneser, Friedrich Alexander University, Erlangen, Germany

© 2011 Elsevier Ltd. All rights reserved.

5.512.1.	**Introduction**	169
5.512.2.	**Elements of the *In Vivo* Bioreactor**	170
5.512.2.1.	Stem Cells or Progenitor Cells	170
5.512.3.	**Applications and Tissues**	171
5.512.3.1.	Skin	171
5.512.3.2.	Bone	171
5.512.3.3.	Small Intestine	172
5.512.3.3.1.	Transplant tolerance induction and restoration of metabolic and organ function by cotransplantation of thymus with solid organs	172
5.512.3.4.	Urinary Tract	173
5.512.3.4.1.	The arteriovenous loop model: an '*in vivo* bioreactor' to generate vascularized tissues and organs	173
References		174

Abbreviations

apoE	Apolipoprotein E
AV	Arteriovenous
bFGF	Basic fibroblast growth factor
BMP	Bone morphogenetic protein
CD	Cluster of differentiation
CSF	Colony-stimulating factor
CT	Computed tomography
CTA	Computed tomography angiography
ELISA	Enzyme-linked immunosorbent assay
EPC	Endothelial progenitor cells
FLC	Fetal liver cells
IE	Islet equivalents
IK	Islet kidneys
MGH	Massachusetts General Hospital
MHC	Major histocompatibility complex
MLR	Mixed lymphocyte reaction
MRA	Magnetic resonance angiography
SBS	Short bowel syndrome
SIS	Small intestinal mucosa
TESI	Tissue-engineered small intestine
TIK	Thymo-islet-kidneys
VEGF	Vascular endothelial growth factor

5.512.1. Introduction

The purpose of an *in vivo* bioreactor is to maximize the role of the patient's own body in the regeneration of tissues and organs. The elements traditionally contributing to tissue engineering applications include cells that may be modified to serve specific purposes or stem cells, signal molecules, that is, growth factors and cytokines that exert specific effects on these cells, bioactive scaffolds that may replace or support form or function of impaired tissues or organ systems, and the extracellular environment that maintains protection and nutrition (**Figure 1**).

Many different approaches to combine cells, scaffolds, and signal molecules have been employed in tissue engineering and regenerative medicine, emphasizing either the *in vitro* or the *in vivo* approach to a varying extent.

A bioreactor has thus far been defined as a device or system that supports a biologically active environment and has been extensively used in the past to optimize *in vitro* culture conditions, particularly in the field of liver[1] and bone[2] tissue engineering. On the contrary, the concept of an '*in vivo* bioreactor' is relatively new. To our knowledge, the term was first coined in 2005 by two independent research groups[3,4] in a successful attempt to induce formation of tissue-engineered bone *in vivo*. Even though the animal models and the study design were entirely different from each other, the advantages of an *in vivo* approach toward tissue engineering were similar and continue to be so: availability and chemotaxis of autologous pluripotent stem or progenitor cells, eliminating the need for *ex vivo* cell manipulation and transplantation; autologous supply of growth factors as well as other supportive stimuli; and potential for *in situ* creation of a vascular network supplying the tissue-engineered construct, including a main vessel axis, enabling a later transfer of the vascularized neo-tissue or organoid to the desired site.

Our overview will highlight attempts toward generating *in vivo bioreactors* in different compartments of the body with a broad range of applications which include not only tissue regeneration but also the investigation of tumor and metastasis formation,[5] tolerance induction in tissue and organ transplantation,[6] and substitution of metabolic function.[7,8]

As insufficient oxygen supply has been one of the major obstacles in the generation of bioartificial tissues and organs, we will particularly emphasize vascularization strategies and present the application possibilities of an axially vascularized separation chamber that could be employed not only to create

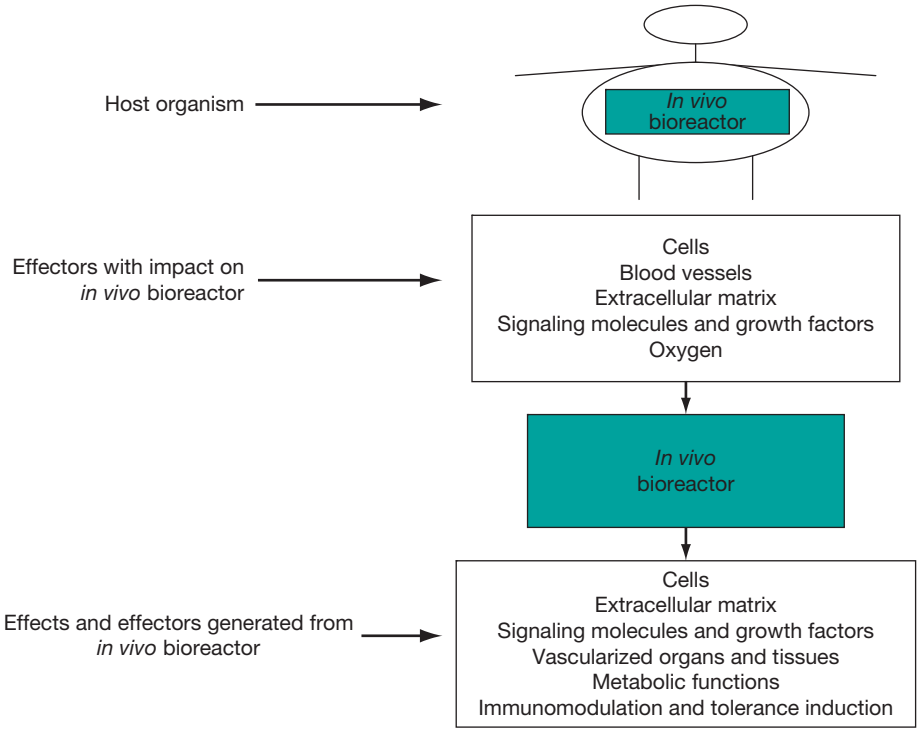

Figure 1 Principles and mechanisms involved in the *in vivo* bioreactor.

transplantable tissues or organoids with their own blood supply, based on a microsurgically created arteriovenous axis (reviewed in Polykandriotis *et al.*[9]) but may also be used as a platform for cancer research (reviewed in Hutmacher *et al.*[5]).

5.512.2. Elements of the *In Vivo* Bioreactor

5.512.2.1. Stem Cells or Progenitor Cells

Stem cells or progenitor cells are considered among the most promising tools today for regenerative medicine applications, but despite extensive research, control over trafficking, survival, proliferation, and differentiation remains extremely challenging and the underlying mechanisms largely unknown (review in Discher *et al.*[10]). The interplay of growth factors, cell–cell contacts, and cell–matrix adhesions taking place *in vivo*, determines the response of these cells to a certain stimulus determining their action and effect, but is very difficult to reproduce under *in vitro* conditions. Drawbacks of this *ex vivo* approach lie in the fact that stem and progenitor cell populations may be very heterogenous, making it difficult to obtain purity of the cell population, thereby limiting reproducibility. In addition, growth in two-dimensional (2D) culture systems may lead to changes in phenotype and differentiation and proliferation status, altering the cells' potential to exert their proper inherent function. Absence of physiological stimuli and factors such as the extracellular matrix, mechanical forces, and signaling molecules may all contribute to undesired changes in the cell's features and capacity for regeneration.

The *in vivo* bioreactor makes use of the fact that potentially useful cell populations already exist in the body and attraction of these cells to a desired anatomic site may provide new therapeutic options. At the same time, complexity of manipulation and cost associated with *in vitro* bioreactors can be reduced. Stevens *et al.* were the first to coin the term '*in vivo* bioreactor' and demonstrated the potential of *de novo* bone growth solely based on the creation of an artificial space between bone and periosteum, which was subsequently filled with a calcium alginate gel that cross-linked *in situ* and provided the scaffold for powerful generation of functional native bone.[3] Recently, an increasing number of studies have been aimed at the mobilization of endothelial progenitor cells (EPC) from bone marrow to ischemic tissues with chemotactic agents such as granulocyte colony-stimulating factor (CSF) or drugs such as statins.[11] *In vivo* vascularization of a given space containing a matrix or a scaffold is gaining increasing attention to prebuild a vascularized structure and deliver either pluripotent or specialized cells to it as the blood vessel tree continues to grow.[12] This approach avoids the typical inevitable problem of hypoxic periods encountered in the primarily *in vitro* approach where cells are combined with a matrix in a bioreactor followed by transplantation into an initially avascular recipient bed where the blood supply has yet to grow into the construct. As mentioned above, EPC have been under intense investigation in the past due to their angiogenic (either directly or via secondary cytokines such as VEGF[13]) and vasculogenic (via direct integration and subsequent *de novo* blood vessel formation).[14] In an attempt to increase homing of transplanted human EPC to a growing prevascularized tissue-engineered organoid in a separation chamber in a nude rat model, Simcock *et al.* administered the chemokine CXC chemokine ligand 12 (CXCL12) and achieved enhanced homing of xenogenic EPC to an angiogenic site developing around an arteriovenous loop inserted in a tissue engineering chamber.[12]

Similar approaches will undoubtedly be developed and optimized to attract vascular progenitor cells and other precursor or stem cells to the *in vivo* tissue engineering site.

5.512.3. Applications and Tissues

5.512.3.1. Skin

The skin is the largest organ in the body and primarily functions as a barrier between the organism and the environment. Major skin loss as a result of trauma and burns has been a major concern to physicians and lead to the development of a multitude of strategies to promote skin wound healing and restore surface integrity. Among them, skin tissue engineering has gained particular attention in recent years and has led to a wide variety of commercially available skin substitutes of different compositions. Significant drawbacks, however, include high costs or the need for extensive *ex vivo* manipulation.

The Eriksson group made the first attempt to use the skin's accessibility and inherent regenerative capacities for healing by creating a standardized and isolated *in vivo* liquid wound environment using a transparent flexible chamber for sealing. This system allowed the delivery of analgesics, antibiotics, growth factors via direct or cell-based gene transfer, growth media, and cells into the chamber, creating an *in vivo* incubator-like environment. The group demonstrated healing of clean wounds as fast as or faster than any other method, with less scarring.[15] The beneficial effects were also demonstrated in a clinical study.[16]

Easy access to the skin has induced interest beyond wound healing and skin regeneration. Keratinocytes secrete a wide variety of proteins that have a role in skin physiology, including proteins and proteinases for matrix remodeling, growth factors, and cytokines.[7] In addition, it has been demonstrated that skin cells, namely keratinocytes, secrete proteins that can reach the bloodstream and gain systemic impact. This effect was initially demonstrated by Teichman and coworkers who grafted human keratinocytes onto athymic mice and rats. Human apolipoprotein E (apoE) was thereafter detected in the systemic circulation of the animals as long as the graft remained on the animals.[17] Human apoE was reduced to undetectable levels within 24 h after graft removal.

The potential of using genetically altered skin cells such as keratinocytes and fibroblasts, given that a skin-derived protein attained systemic distribution, has been exploited in numerous studies since then.[7] Transgene products were not only detected in the serum, but also exhibited physiological effects. A study by Meng *et al.*,[18] in which an interleukin-10 expressing vector was injected into the dorsal skin of rats, demonstrated that the transgene was detected in the bloodstream and led to an inhibition of contact hypersensitivity at distant areas of the skin. A serious drawback of methods of transient gene transfer to exploit the skin's accessibility as a delivery route for systemically effective agents has been the fact that efficiency is low and the effect only transient, likely due to promoter silencing of the transgene and immunological responses.[7]

Therefore, transgenic mouse models have been used for experimental evaluation of the skin as a bioreactor, as gene expression was shown to be higher and more ubiquitous, and simultaneously eliminating a host immune response. Targeting of the therapeutic gene to specific layers of the dermis was achieved by stratum-specific promoters such as keratin 5 and keratin 14.

Gene delivery exploiting the skin's potential as an *in vivo* bioreactor may provide therapeutic options for metabolic diseases, such as growth hormone for dwarfism, coagulation factors for coagulopathies, and insulin for diabetes mellitus.[19]

5.512.3.2. Bone

Treatment of large bone defects still requires autologous transfer of vital bone. Due to the discrepancy between the need on the one hand and limited supply as well as significant donor site morbidity on the other hand, generation of bone by the principles of tissue engineering has become a subject of extensive research efforts.[20,21] Most experimental setups employ traditional principles of tissue engineering where harvested cells are cultured *in vitro*, combined with porous scaffolds, and stimulated with exogenous morphogens and mitogens *in vitro* and/or *in vivo*.

In contrast to this, the Langer group designed a rabbit model where an artificial space between the tibia and the adjacent periosteum was created, which was referred to as an '*in vivo* bioreactor'.[3] Owing to the exposition of this mesenchymal layer which is rich in pluripotent cells, the creation of significant volumes of bone was possible in a predictable manner, without the necessity for delivery of growth factors or cell transplantation. Biological functionality of the newly created bone was demonstrated by successful transplantation to contralateral tibia defects, resulting in complete integration without significant donor site morbidity. This study also showed that inhibition of angiogenesis in this setting and the creation of a more hypoxic environment promoted cartilage formation. A similar model has been described by Miller and coworkers who used a plastic chamber for periosteum-guided bone formation from the rib in a sheep model.[22]

The lack of a defined vascular axis, however, limits the size and potential to transplant ectopically grown neo-bone to the desired location. Therefore, the ideal bone graft would not only include osteoconductive scaffolds, osteoinductive proteins, and osteogenic cells, but also a vascular network based on a main vascular access constituted by an artery and a vein. Prefabrication is defined as 'the process of neovascularization by the implantation of a vascular pedicle into tissues to be transferred later to a distant site either on the pedicle or as a free graft by microvascular anastomosis'.[23] Many attempts focused on using the inferior epigastric pedicle as a vascular axis to supply the *in vivo* bone bioreactor created around a wide variety of scaffolds consisting of hydroxyapatite[24] and coralline,[4] among others, in a separation chamber. A certain degree of bone formation could be demonstrated after addition of BMP-2 and establishment of a vascular network. This *in vivo* bone bioreactor was also shown to be useful as a model of tumor–bone interaction.[25] A clinical application of *in situ*-generated vascularized engineered bone was reported by Terheyden's group to repair an extended mandibular defect. They created a custom-made construct based on a titanium mesh cage filled with bone mineral blocks and infiltrated with recombinant human bone morphogenetic protein-7 (BMP-7) and the patient's bone marrow. Thus prepared, the transplant was implanted into the

latissimus dorsi muscle and 7 weeks later, transplanted as a free bone–muscle flap to repair the mandibular defect. Follow-up by skeletal scintigraphy and CT showed bone remodeling and mineralization inside the mandibular transplant both before and after *in vivo* transplantation, thus providing radiological evidence of new bone formation.[26]

Our laboratory adopted and further developed an arteriovenous loop model based on the femoral vessels, including a venous graft from the contralateral side in a rat separation chamber, which also constitutes an *in vivo* bioreactor. Compared to the previously described model based on the epigastric vessels, it displays superior vascularization potential.[20,21]

5.512.3.3. Small Intestine

The management of patients with short bowel syndrome (SBS) has been unsatisfactory with conventional treatment strategies so far. Various studies from the Vacanti laboratory demonstrated improved recovery after massive small bowel resection (SBR) using tissue-engineered intestine.[27] The tissue-engineered small intestine (TESI) was constructed applying *in vivo bioreactor* principles. First, segments of intestine harvested from neonatal rats were minced and full-thickness plugs of intestine created. These so-called organoid units were then seeded onto a tubular biodegradable scaffold polymer and then wrapped into the omentum of adult rats which served as the *in vivo* bioreactor. These organoid units, arranged on the biodegradable scaffold, became vascularized by the omentum to form a cyst, which histologically resembled the small bowel.[28] Several biochemical features of digestive enterocyte function and polarity have been demonstrated in these cysts in later studies.[29] As a next step, the mature, vascularized TESI cyst was placed in continuity with the gastrointestinal tract at the time of an 85% enterectomy in rats. TESI animals returned to preoperative weight more rapidly when compared with the animals undergoing SBR alone. On histologic analysis, the TESI cysts appeared to resemble normal adjacent intestine. Furthermore, the neointestine had preserved expression of green fluorescent protein that had been introduced into the organoid units prior to implantation. These marker studies strongly suggested that the neointestine was derived primarily from the neonatal-derived intestine, as opposed to ingrowth of adjacent recipient intestine. Additional studies showed lymphangiogenesis as detected by expression of the lymphatic endothelial marker vascular endothelial growth factor receptor (VEGFR)-3 using immunohistochemistry, and the lymphangiogenic growth factor VEGF-C was quantified by ELISA. Moreover, tubular structures, which resembled lymphatics architecturally, developed, and were distinct from CD34-positive blood vessels, and lacked luminal erythrocytes. This was the first demonstration of lymphatic vessels in an engineered tissue.[30] Tissue-engineered intestine also had the capacity to develop a mucosal immune system with an immunocyte population similar to that of native small intestine depending on both exposure to luminal stimuli and the duration of this exposure.[31] These results demonstrate the possibility of ectopic formation of a biologically functional bioartificial organoid with access to blood and lymphatic circulation, which could even be transferred to an orthotopic site with subsequent proof of maintained biological function.

5.512.3.3.1. Transplant tolerance induction and restoration of metabolic and organ function by cotransplantation of thymus with solid organs

Organ transplantation to restore impaired or lost function is hampered by the short- and long-term complications of immunosuppression and the current worldwide shortage of donor organs.[32] The induction of donor-specific tolerance in allogeneic and xenogeneic transplantation offers a promising solution to these problems. The thymus has been identified as critical for systemic central tolerance to self-antigens in which potentially autoreactive T cells are deleted or anergized by exposure to the appropriate self-antigens presented either by bone marrow-derived cells or thymic stromal cells.[33,34] Based on these findings and their MGH miniature swine model, David Sachs and coworkers have developed composite allografts consisting of vascularized thymic tissue and the kidney as a solid organ to induce tolerance across major histocompatibility complex (MHC)-mismatched barriers.[35]

A new transplantable organ (thymokidney) was generated by autologous thymic grafts under the renal capsule. The thymic grafts exhibited normal macroscopic and microscopic structure, and normal thymocyte composition. To evaluate the thymic function of the graft, a composite thymokidney was transplanted into a recipient who had previously been thymectomized, had few circulating CD4-single positive cells, and had lost MLR reactivity. The number of CD4+/CD45RA+ cells in this animal increased steadily indicating functionality of the thymus within the composite thymokidney. In addition, MLR assays demonstrated that the recipient recovered immunocompetence.[36]

Additional work from the same laboratory demonstrated that transplantation of allogeneic thymic tissue as part of a composite vascularized graft was far more successful in terms of both engraftment and long-term survival than transplantation of thymic tissue or cells alone.[35] This concept of the vascularized composite neo-organ was subsequently extended to transplantation of allogeneic islets, comparing survival of islet cell suspensions to that of vascularized composite islet-kidneys (IK), prepared by injection of autologous islets underneath the renal capsule 2–3 months prior to allogeneic transplantation of the composite organ. Composite IK were transplanted successfully across minor and full MHC mismatch barriers, using treatment regimens previously demonstrated to induce long-term tolerance of kidney allografts across these barriers. IK allografts containing $\geq$5000 islet equivalents (IE) per kilogram recipient body weight were found capable of reversing surgically induced diabetes, while injection of comparable numbers of purified islets via the portal vein or under the renal capsule did not. An additional study was directed toward preparation of autologous 'thymo-islet-kidneys' (TIK), for potential use as xenografts, in which the thymic component was intended to induce tolerance and the islets to reverse diabetic hyperglycemia. To evaluate the function of the transplanted islets, three animals bearing TIK and IK underwent total pancreatectomy 3 months following islet transplantation. All three animals maintained normoglycemia thereafter. In two of these animals, the IKs were removed 2 months after the pancreatectomy, and in both cases normoglycemia was maintained thereafter by the TIK.

The combination of replacement of a lost metabolic function and vascular competence of the grafts, as well as the potential for immune tolerance induction, makes this model a particularly successful example of an unusual application of an *in vivo* bioreactor. Use of both types of composite organ transplants (IK and TIK) may eventually be applicable to the treatment of type I diabetic patients suffering from end-stage diabetic nephropathy.[37]

5.512.3.4. Urinary Tract

Congenital and acquired ureteric defects cause significant morbidity and have been notoriously difficult to regenerate by tissue engineering approaches to create a neoureter in the past. Such attempts to generate a neoureter in animal models failed because of major inflammatory response. Avoidance of such inflammation requires a well-differentiated urothelium. Baumert *et al.* investigated whether omental maturation of a small intestinal submucosa (SIS) matrix seeded with previously cultured urothelial and smooth muscle cells that had been derived from bladder biopsies in a pig model could achieve terminal differentiation of the urothelium to allow construction of a stricture-free neoureter. After 2 weeks of cell growth, the *in vitro* SIS-seeded construct was shaped around a silicone drain and wrapped by the omentum to obtain neoureters. These neoureters were left in the omentum without any contact with urine, and then harvested 3 weeks later for histologic and immunohistochemical studies. Before implantation, the *in vitro* constructs were composed of a mono- or bilayer of undifferentiated urothelium overlying a monolayer of smooth muscle cells. After 3 weeks of omental maturation, these constructs were vascularized and comprised a terminally differentiated multilayered urothelium with umbrella cells over connective tissue and smooth muscle cells, with no evidence of fibrosis or inflammation. This model of *in vivo* maturation using the omentum as an *in vivo* bioreactor enabled for the first time the generation of a mature neoureter composed of a well-differentiated multilayered urothelium.[38]

When looking at other parts of the genitourinary system, bladder regeneration is another challenging goal. One of the main problems is to limit the development of ischemic fibrosis during tissue maturation. Similar to their ureter tissue engineering, Baumert *et al.* described a model using the omentum as an *in vivo* bioreactor for a previously seeded scaffold. A highly vascularized tissue-engineered construct was generated that contracted in response to acetylcholine stimulation. The wall thickness was 4 mm, on average. Histologic and immunostaining analysis of the construct confirmed the presence of a multilayer urothelium on the luminal aspect and deeper fascicles of organized tissue composed of differentiated smooth muscle cells and mature fibroblasts without evidence of inflammation or necrosis. Large- and small-diameter vessels were clearly identified histologically in the tissue obtained. The omentum as an *in vivo* incubator permitted *in vivo* maturation of seeded scaffolds with the development of a dense vascularization that is anticipated to prevent fibrosis and loss of contractility. This *in vivo* maturation into the omentum could be the first step before *in situ* implantation of the construct.[39]

5.512.3.4.1. The arteriovenous loop model: an 'in vivo bioreactor' to generate vascularized tissues and organs

The development of a functional and adequate blood vessel network is a prerequisite for successful application of engineered tissues and organs. When *in vitro*-engineered constructs containing cells are transferred *in vivo*, they lack a defined axial blood supply consisting of a main arterial inflow and a venous outflow, respectively, and therefore rely on blood vessel ingrowth from their surroundings, that is, interstitial fluid diffusion and blood perfusion.[20,21] This limitation in blood supply constitutes the main drawback when transferring *in vitro* tissue engineering approaches to the *in vivo* environment. Cell support via diffusion occurs only up to 200 μm into the matrix,[40] resulting in insufficient nutrition and subsequent loss of cells located in the center of such *in vitro*-engineered constructs.[20,21] For these reasons, induction of vascularization is essential in virtually all successful tissue engineering applications, and a defined vascular axis is desirable whenever the bioengineered tissue or organ is yet to be transplanted to a different site within the host. In order to enable standardized transfer techniques of neo-tissues and organs to a different site, reconstructive surgeons have therefore aimed to generate axially vascularized tissues and organoids that are supplied by a defined arteriovenous axis and could hence be transferred to the desired site using microsurgical techniques of vascular anastomosis. As opposed to other techniques, these tissues are immediately connected to the systemic blood circulation upon implantation as free flaps are.[20,21]

Our laboratory adopted and further developed an arteriovenous loop model based on the femoral vessels, including a venous graft from the contralateral side in a rat separation chamber, which also constitutes an *in vivo* bioreactor. This work is based on the initial description by Erol and Spira[41] who successfully generated a prefabricated skin flap by creating an arteriovenous vessel loop using either arterial or venous grafts in a rat model. They observed the outgrowth of a dense 3D neovessel tree originating from the entire AV loop. This model was later further developed by isolation of the AV loop into isolation chambers and induction of vascularization in polymer matrices.[42–44] Based on these works, we successfully vascularized a custom-made processed bovine cancellous bone matrix by means of the AV loop.[20,21] We established a detailed analysis of the vascularization using invasive techniques such as corrosion casting as well as noninvasive methods such as micro-CT scanning. Using histology-based morphometric analysis, we meticulously quantified vascularization and demonstrated that more than 90% of the scaffold vascularized 8 weeks following implantation. Prevascularization of these matrices significantly improved survival of osteoblasts engrafted into the matrix, emphasizing the importance of an intrinsic blood supply for cell vitality within the construct.[45]

The AV loop model to vascularize tissue-engineered constructs is not limited to hard matrices and the attempt to create bone, but may be extended by using other matrices and cell populations. We have demonstrated that a fibrin gel approved for clinical use can be employed to generate a fibrin matrix, which was successfully vascularized and may be used as a platform to create soft tissues or organoids. The vascularization within this fibrin matrix was shown to respond to proangiogenic

stimuli by accelerating the vascular outgrowth when the recombinant growth factors VEGF and bFGF were suspended in the matrix.[46] We also demonstrated that transplantation of myoblasts into a previously vascularized fibrin matrix containing the AV loop enhanced cell survival and maintenance of the myogenic phenotype compared to fibrin matrices without AV loops, even though no formation of skeletal muscle-like tissue could be observed, possibly due to the lack of potent myogenic stimuli.[47]

The vascularized matrix embedded in the AV loop may also be employed to create organoids or replace organ functions. As a new approach to hepatic tissue engineering, fetal liver cells (FLC) were suspended in the fibrin matrix, resulting in neo-tissue formation containing viable fetal donor cells in the highly vascularized fibrin matrix after 14 days.[1] Previous work demonstrated that continuous hepatotrophic stimulation is necessary in tissue-engineered liver support systems, and it has been demonstrated that cocultivation with pancreatic islets may have stimulatory effects on hepatocytes and that they are mediated by soluble factors, and are dependent on insulin and glucagon.[48,49] Further investigations toward 3D transplantable hepatocyte-islet devices for continuous *in vivo* stimulation were conducted to provide hepatotrophic stimulation. Hepatocyte and pancreatic islets were coseeded into polyvinyl alcohol matrices and supported hepatotrophic stimulation of bioartificial liver equivalents equally well, compared to a protocaval shunt operation. The AV loop model may therefore well serve as a platform for the development of highly vascularized *in vivo* tissue engineering-based liver support systems using these cotransplantation strategies.

Successful engineering of cardiac muscles has been achieved by matrigel-suspended neonatal rat cardiomyocytes implanted inside the AV loop. The presence of gap junctions was shown between the cardiomyocytes at 4 and 10 weeks, and echocardiograms showed spontaneous contraction of the tissue *in vivo*. *In vitro*, positive chronotropy to norepinephrine and positive inotropy in response to calcium demonstrated biological function of the cardiac neo-organ.[50]

The AV loop separation chamber potential is not limited by the availability of local factors in its *in situ* tissue and organ engineering capacity. The regenerative potential of the established chamber construct may be even better exploited by chemotactic recruitment of supportive cells or signaling molecules. It was recently demonstrated that EPC that had been systemically injected before can be recruited from the circulation by CXCL12/stromal cell-derived factor 1,[12] potentially enabling further modulation of the vascularization process.

The isolation chamber setting with its potential to be monitored and manipulated may also be used as an investigation platform to investigate the phenomena and regulation of angiogenesis and antiangiogenesis in cancer research.[5]

Limitations to dimensions in small animal models have always been an argument against successful transfer of tissue engineering applications to clinical relevance. Therefore, our group recently established a large animal model (sheep) where *de novo* formation of axially vascularized tissue was demonstrated for the first time ever by sequential computed tomography angiography (CTA) and magnetic resonance angiography (MRA) *in vivo*, as well as by postexplantational micro-computed tomography (Figure 2) and histology. This constitutes further progress in approaching the first application of tissue engineering vascularized grafts with clinically relevant dimensions.[51,52]

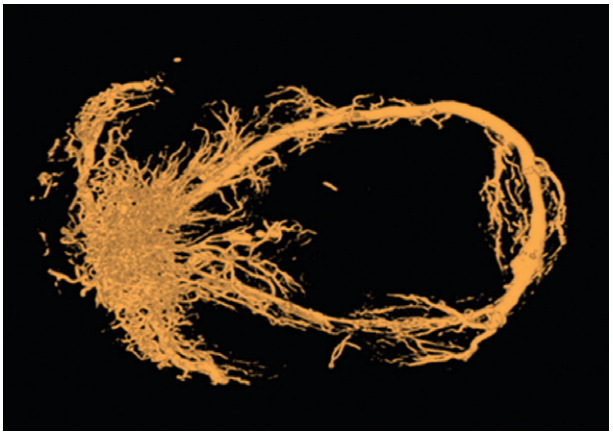

Figure 2 Micro-CT scan from a rat AV-loop following Microfil® – perfusion and explantation, demonstrating vascular sprouting originating from the AV-loop.

In conclusion, the arteriovenous loop model has been investigated mainly as a powerful tool to create bioartificial tissues and organoids, but may also be very useful as a platform to investigate angiogenetic and antiangiogenetic phenomena in general, with particular emphasis on cancer therapy.[5]

References

1. Fiegel, H. C.; Pryymachuk, G.; Rath, S.; *et al*. *J. Cell. Mol. Med*. **2010**, *14*(1–2), 267–274.
2. Fröhlich, M.; Grayson, W. L.; Wan, L. Q.; Marolt, D.; Drobnic, M.; Vunjak-Novakovic, G. *Curr. Stem Cell Res. Ther*. **2008**, *3*(4), 254–264.
3. Stevens, M. M.; Marini, R. P.; Schaefer, D.; Aronson, J.; Langer, R.; Shastri, V. P. *Proc. Natl. Acad. Sci. USA* **2005**, *102*(32), 11450–11455.
4. Holt, G. E.; Halpern, J. L.; Dovan, T. T.; Hamming, D.; Schwartz, H. S. *J. Orthop. Res*. **2005**, *23*(4), 916–923.
5. Hutmacher, D. W.; Horch, R. E.; Loessner, D.; *et al*. *J. Cell. Mol. Med*. **2009**, *13*(8A), 1417–1427.
6. LaMattina, J. C.; Kumagai, N.; Barth, R. N.; *et al*. *Transplantation* **2002**, *73*(5), 826–831.
7. Cao, T.; Wang, X. J.; Roop, D. R. *Hum. Gene Ther*. **2000**, *11*(16), 2297–2300.
8. Hussey, A. J.; Winardi, M.; Han, X.; *et al*. *Tissue Eng. A* **2009**, *15*(12), 3823–3833.
9. Polykandriotis, E.; Arkudas, A.; Euler, S.; Beier, J. P.; Horch, R. E.; Kneser, U. *Handchir. Mikrochir. Plast. Chir*. **2006**, *38*(4), 217–223; Article in German.
10. Discher, D. E.; Mooney, D. J.; Zandstra, P. W. *Science* **2009**, *324*(5935), 1673–1677.
11. Pittenger, M. F.; Martin, B. J. *Circ. Res*. **2004**, *95*(1), 9–20.
12. Simcock, J. W.; Penington, A. J.; Morrison, W. A.; Thompson, E. W.; Mitchell, G. M. *Tissue Eng. A* **2009**, *15*(3), 655–664.
13. Asahara, T.; Takahashi, T.; Masuda, H.; *et al*. *EMBO J*. **1999**, *18*(14), 3964–3972.
14. Tepper, O. M.; Capla, J. M.; Galiano, R. D.; *et al*. *Blood* **2005**, *105*(3), 1068–1077.
15. Eriksson, E.; Vranckx, J. *Am. J. Surg*. **2004**, *188*(1A Suppl.), 36–41.
16. Vranckx, J. J.; Slama, J.; Preuss, S.; *et al*. *Plast. Reconstr. Surg*. **2002**, *110*(7), 1680–1687.
17. Fenjves, E. S.; Gordon, D. A.; Pershing, L. K.; Williams, D. L.; Taichman, L. B. *Proc. Natl. Acad. Sci. USA* **1989**, *86*(22), 8803–8807.
18. Meng, X.; Sawamura, D.; Tamai, K.; Hanada, K.; Ishida, H.; Hashimoto, I. *J. Clin. Invest*. **1998**, *101*(6), 1462–1467.
19. Taichman, L. B. *Proc. Assoc. Am. Physicians* **1999**, *111*(3), 206–210.
20. Kneser, U.; Polykandriotis, E.; Ohnolz, J.; *et al*. *Tissue Eng*. **2006**, *12*(7), 1721–1731.
21. Kneser, U.; Schaefer, D. J.; Polykandriotis, E.; Horch, R. E. *J. Cell. Mol. Med*. **2006**, *10*(1), 7–19.
22. Cheng, M. H.; Brey, E. M.; Allori, A. C.; *et al*. *Plast. Reconstr. Surg*. **2009**, *124*(3), 787–795.
23. Gill, D. R.; Ireland, D. C.; Hurley, J. V.; Morrison, W. A. *J. Hand Surg. Am*. **1998**, *23*(2), 312–321.
24. Mizumoto, S.; Inada, Y.; Weiland, A. J. *J. Reconstr. Microsurg*. **1993**, *9*(6), 441–449.

25. Halpern, J.; Lynch, C. C.; Fleming, J.; *et al*. *Clin. Exp. Metastasis* **2006**, *23*(7–8), 345–356.
26. Warnke, P. H.; Springer, I. N.; Wiltfang, J.; *et al*. *Lancet* **2004**, *364*(9436), 766–770.
27. Grikscheit, T. C.; Siddique, A.; Ochoa, E. R.; *et al*. *Ann. Surg.* **2004**, *240*(5), 748–754.
28. Choi, R. S.; Vacanti, J. P. *Transplant. Proc.* **1997**, *29*(1–2), 848–851.
29. Choi, R. S.; Riegler, M.; Pothoulakis, C. *J. Pediatr. Surg.* **1998**, *33*(7), 991–996; discussion 996–997.
30. Duxbury, M. S.; Grikscheit, T. C.; Gardner-Thorpe, J.; *et al*. *Transplantation* **2004**, *77*(8), 1162–1166.
31. Perez, A.; Grikscheit, T. C.; Blumberg, R. S.; Ashley, S. W.; Vacanti, J. P.; Whang, E. E. *Transplantation* **2002**, *74*(5), 619–623.
32. Greenstein, J. L.; Sachs, D. H. *Nat. Biotechnol.* **1997**, *15*(3), 235–238.
33. Kappler, J. W.; Roehm, N.; Marrack, P. *Cell* **1987**, *49*(2), 273–280.
34. Sprent, J. In *Fundamental Immunology*; Paul, W. E., Ed.; Raven: New York, 1993; Vol. 3, pp 74–109.
35. Yamada, K.; Shimizu, A.; Utsugi, R.; *et al*. *J. Immunol.* **2000**, *164*(6), 3079–3086.
36. Yamada, K.; Shimizu, A.; Ierino, F. L.; *et al*. *Transplantation* **1999**, *68*(11), 1684–1692.
37. Vallabhajosyula, P.; Griesemer, A.; Yamada, K.; Sachs, D. H. *Cell Biochem. Biophys.* **2007**, *48*(2–3), 201–207.
38. Baumert, H.; Mansouri, D.; Fromont, G.; *et al*. *Eur. Urol.* **2007**, *52*(5), 1492–1498.
39. Baumert, H.; Simon, P.; Hekmati, M.; *et al*. *Eur. Urol.* **2007**, *52*(3), 884–890.
40. Folkman, J.; Hochberg, M. *J. Exp. Med.* **1973**, *138*(4), 745–753.
41. Erol, O. O.; Spira, M. *Surg. Forum* **1979**, *30*, 530–531.
42. Mian, R.; Morrison, W. A.; Hurley, J. V.; *et al*. *Tissue Eng.* **2000**, *6*(6), 595–603.
43. Hofer, S. O.; Knight, K. M.; Cooper-White, J. J.; *et al*. *Plast. Reconstr. Surg.* **2003**, *111*(3), 1186–1192; discussion 1193–1194.
44. Cassell, O. C.; Morrison, W. A.; Messina, A.; *et al*. *Ann. N. Y. Acad. Sci.* **2001**, *944*, 429–442.
45. Arkudas, A.; Beier, J. P.; Heidner, K.; *et al*. *Tissue Eng.* **2007**, *13*(7), 1549–1560.
46. Arkudas, A.; Pryymachuk, G.; Hoereth, T.; *et al*. *Tissue Eng. A* **2009**, *15*(9), 2501–2511.
47. Bach, A. D.; Arkudas, A.; Tjiawi, J.; *et al*. *J. Cell. Mol. Med.* **2006**, *10*(3), 716–726.
48. Kaufmann, P. M.; Fiegel, H. C.; Kneser, U.; Pollok, J. M.; Kluth, D.; Rogiers, X. *Tissue Eng.* **1999**, *5*(6), 583–596.
49. Kaufmann, P. M.; Kneser, U.; Fiegel, H. C.; *et al*. *Transplantation* **1999**, *68*(2), 272–279.
50. Morritt, A. N.; Bortolotto, S. K.; Dilley, R. J.; *et al*. *Circulation* **2007**, *115*(3), 353–360.
51. Beier, J. P.; Horch, R. E.; Arkudas, A.; *et al*. *Microsurgery* **2009**, *29*(1), 42–51.
52. Fiegel, H. C.; Kneser, U.; Kluth, D.; Metzger, R.; Till, H.; Rolle, U. *Pediatr. Surg. Int.* **2009**, *25*(8), 667–673.

5.513. Systems Biology in Biomaterials and Tissue Engineering

A Ananthanarayanan, NUS Graduate School for Integrative Sciences, Singapore; Institute of Bioengineering and Nanotechnology, Singapore
L Tucker-Kellogg, National University of Singapore, Singapore; Singapore-MIT Alliance, Computation and Systems Biology Program, Singapore
B C Narmada, NUS Graduate School for Integrative Sciences, Singapore
L Venkatraman, Singapore-MIT Alliance, Computation and Systems Biology Program, Singapore; School of Computer Engineering, Nanyang Technological University, Singapore
N A Abdul Rahim, National University of Singapore, Singapore
Y Wang and C H Kang, Institute of Bioengineering and Nanotechnology, Singapore
H Yu, NUS Graduate School for Integrative Sciences, Singapore; Institute of Bioengineering and Nanotechnology, Singapore; National University of Singapore, Singapore; Singapore-MIT Alliance, Computation and Systems Biology Program, Singapore; Singapore-MIT Alliance for Research and Technology, Singapore

© 2011 Elsevier Ltd. All rights reserved.

5.513.1. Introduction 178
5.513.2. Discrete Component-Centered Approach 179
5.513.3. High-Throughput Component-Centered Approach 180
5.513.3.1. Manufacturing Substrates 180
5.513.3.2. Measuring Substrate Properties 181
5.513.3.2.1. Surface chemistry and techniques 181
5.513.3.2.2. Mechanical characterization 181
5.513.3.3. Measuring Cellular Response 181
5.513.3.3.1. Genomics 181
5.513.3.3.2. Proteomics 182
5.513.3.3.3. Metabolomics 182
5.513.3.4. *In Vivo* Integration into Living Hosts 182
5.513.3.4.1. Image informatics: Transcending scales with improved speed and resolution 183
5.513.4. Process-Centered Systems Approach 184
5.513.4.1. Modeling of Systems in Tissue Constructs 184
5.513.4.2. Pathway Modeling for Process-Centered Approaches 185
5.513.4.3. Pathway Modeling for Activation of TGF-β1 in Liver Fibrosis 185
5.513.5. Future Outlook 186
References 187

Abbreviations

AFM	Atomic force microscopy
EB	Embryoid bodies
ECM	Extracellular matrix
ES cells	Embryonic stem cells
FT-IR	Fourier transform-infrared spectrometry
hMSC	Human mesenchymal stem cells
HSC	Hepatic stellate cells
iPS	Induced pluripotent stem cells
MALDI-TOF	Matrix-assisted laser desorption ionization time of flight spectrometry
MRI	Magnetic resonance imaging
mRNA	Messenger RNA
NMR	Nuclear magnetic resonance spectroscopy
PAI-1	Plasminogen activator inhibitor -1
PDMS	Polydimethylsiloxane
PEG	Polyethylene glycol
PET	Polyethylene terepthalate
PLGA	Poly(lactic-*co*-glycolic acid)
R&D	Research and development
Tg	Glass transition temperature
TGFβ1	Transforming growth factor beta -1
TSP-1	Thrombospondin -1
uPA	Urokinase-type plasminogen activator
VEGF	Vascular endothelial growth factor

5.513.1. Introduction

Biomaterials research for tissue engineering revolves around various permutations of four fundamental components: biomaterial scaffolds, cells, *in vitro* tissue constructs, and *in vivo* integration into living hosts. Some implantable biomaterials aim at recruiting the native mature or stem cells to the lesion for repair or regeneration; or simply serving as inert prosthesis to replace the functions of the injured or diseased tissues or organs. The choices of biomaterials, cell sources, or design parameters of the tissue constructs have been *ad hoc*, either due to component availability (for certain biomaterials or cell types) or due to the unique constraints of a specific application. This approach has worked well for simpler tissue constructs where the functions are not tightly coupled to the structure, such as extracorporeal devices, prostheses that are self-sufficient to replace the damaged tissues functionally, or cell transplantation that depend entirely on regeneration from the host *in vivo*. In such cases, simply taking available biomaterials and cells, and making a construct that roughly looks like the real tissue, can be reasonably successful. The first section of this chapter describes the discrete approach of working on one material at a time or one cell type at a time, and the discrete approach seems sufficient for these simpler applications. As the field progresses toward repairing and regenerating more complex tissues, the functional demands increase and the structure–function relationships become more tightly coupled. These challenges create a greater need to progress from the discrete approach to a higher throughput, systems-level approach, which typically involves large screens, combinatorial synthesis, or experiments on multiple components. The second section of the chapter summarizes several high-throughput or -omic level projects in tissue engineering, with particular focus on -omics technologies for characterizing cellular responses, and quantitative analytical tools for monitoring tissue integration *in vivo*. Researchers already adopting such systems-level approaches have successfully designed new biomaterials for optimization of complex tissue functions. The second section includes a summary of this progress, followed by a discussion of the limitations of the high-throughput approaches that are still primarily based on individual components (cells, biomaterials, constructs) rather than based on the functional process of interactions and relationships between the components. Quantitative relationships between *in vitro* constructs and *in vivo* responses must be established in order to guide rational biomaterials and tissue engineering efforts to achieve the desired results. High-throughput experiments on individual components may be capable of optimizing a set of parameters, but sometimes this success only highlights the gap of understanding between the optimized parameters and final biomedical goal with integration into a living host. Thus for improving function in tissue engineering, a process-centered approach, described in our third section, will become increasingly important (Figure 1). We have recently explored a process-centered approach to study and facilitate regeneration in a healing defect, liver fibrosis. Our approach, including innovative computational modeling, might be further adopted in the systematic development of biomaterials and tissue engineering applications of the future.

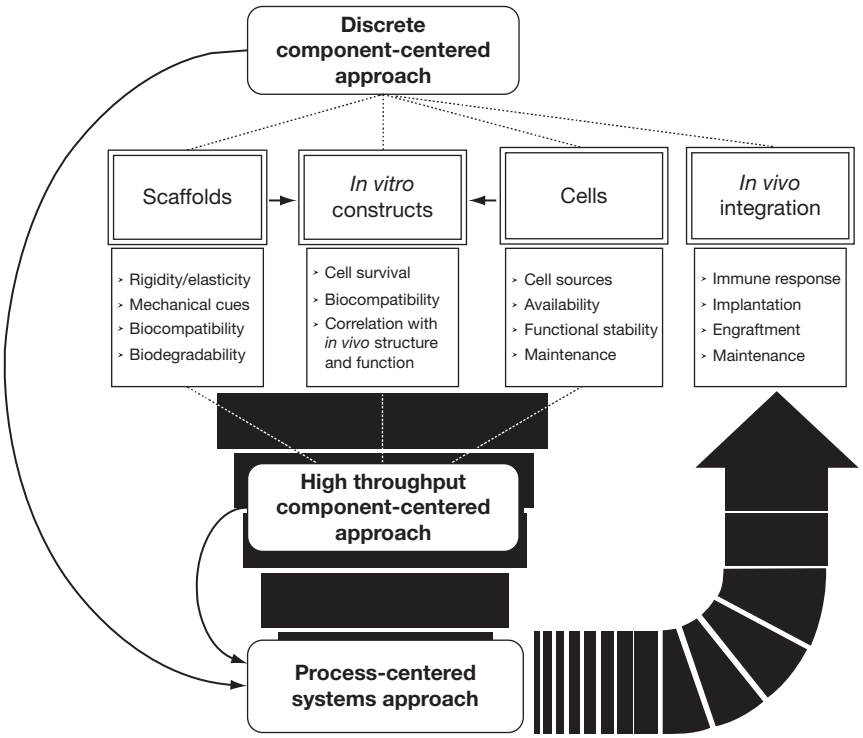

Figure 1 Diagram of the relationship of the four core components and the three tissue engineering approaches.

5.513.2. Discrete Component-Centered Approach

Tissue engineering is an integration of myriad fields, with the ultimate aim of reconstructing a functional tissue or organ for regenerative medicine. In the past decade, engineering tissues with *in vivo* fidelity has found applicability and broad impact in a wide array of additional fields. The chief hindrance to the progress of this field is the complexity of the human body, exemplified by the diversity of cell types; the interplay between the chemical, physical, and topographical factors that regulate cell function; the morphology of tissues; and the astoundingly precise development of organs.[1]

Various approaches have reconstructed living and functional tissue constructs *in vitro*, but over the past two decades, methods based on biomaterial scaffolds have occupied center stage.[2] These methods generally entail seeding cells on scaffolds that serve as centers of tissue regeneration. The scaffolds are tuned specifically for their chemical and biological parameters (e.g., solute diffusivity, porosity, elasticity, and biocompatibility) but are very rarely tuned for their ultimate biological effects or function. Working on one biomaterial or cell type at a time has yielded useful and satisfactory results for reconstructing certain tissues with straightforward structure–function linkage such as bone and ligament,[3] but has failed in areas where there is an intricate interplay between the structure and function such as liver and kidney.[1]

Another context where the focus on specific biomaterials has been successful is in regenerative medicine, where the primary role of the scaffold is simply to help nature take its course in mending lost or damaged tissues, and where control of the scaffold properties occurs on the scale of tens to hundredths of microns.[4,5] The remaining bottleneck in tissue engineering is to develop large *in vitro* models of complex tissues with *in vivo* fidelity, with the facilitation of angiogenesis.[6,7] This phase of research has been arduous, primarily due to poor understanding of the architectural and compositional requirements for creating a large functional tissue, and due to the disparate natures of the fields of biomaterials and biology. Early biomaterial scaffolds did not foster any form of tissue hierarchy and were not tailored for specific *in vitro* purposes, yet the success of these scaffolds *in vivo* fuelled the development of methods that hoped to induce complex tissue architectures.

Although the discrete component approach has been effective in so many different situations,[1–5] it still largely suffers from the narrow focus on either the development of improvised materials to render only a single function or using a construct with a single cell type to mimic multicellular complex tissue functions. A classic example would be the field of skin substitute development. All the commercially available replacements definitely serve the main purpose of rapid wound closure[8] amongst others.[9] But they invariably fall short in creating a complete functional skin (e.g., functions associated with wrinkle and hair follicle) despite the promising developments of new materials[8] and therapeutics for full-thickness skin injuries.[10]

In the perspective of cellular components used in constructs, there is again a growing concern that a single cell type would not be sufficient to emulate the multifaceted functions of any complex tissue. Though there are a few applications where only one type of cells would be deemed sufficient, like in cartilage reconstruction where a construct with chondrocytes and the right substrate[11] would facilitate cartilage repair, tissue engineering with multiple cells types is becoming more relevant with better functions. Interestingly, in urinary bladder replacements there has been a gradual shift from the orthotropic neobladder reconstruction techniques[12] (due to the imminent side effects) to the *ex vivo* engineered bladder constructs,[13,14] in which urothelial cells and smooth muscle cells were both successfully applied on the scaffold. There are other demanding scenarios that require the construct to orchestrate the formation of complex multifunctional structures like in blood vessel generation which can be done only with the appropriate recruitment and organization of different cells in the presence of the right proportions of growth factors.[15] Thus with a more thorough understanding of the inherent mechanisms involved with vascular growth,[16,17] the recent configurations with hydrogel matrices and PLGA scaffolds coupled with VEGF delivery[18,19] have been successful to a great extent in recapitulating various stages of this complex process.

A few methods are drawing attention for tissue engineering. (a) Microfabrication technology – with importance exemplified by its use for maintaining the differentiated phenotypes of primary cells (which had previously proven very difficult to maintain *in vitro*), and its use for probing homotypic and heterotypic cell interactions.[20,21] (b) Microscale flow – fluidic flows in microfluidic channels mimic the interstitial flow in vascularized tissues, and play important roles in mechanical and chemical signaling. The validity of microscale flow models has been demonstrated by microscale fluidic flow bioreactors.[1] (c) Synthetic microenvironments – this field has focused on mimicking the biochemical composition, fibrillar structure, and viscoelastic gel-like character of natural tissue matrices. A good early work has used PEG (polyethylene glycol) scaffolds, which are capable not only of remodeling, but can also be chemically customized to incorporate biological molecules that facilitate signaling, to and from the microenvironment.[22,23]

The explosion in the number of devices that can be implanted into the body includes tissue-engineered constructs, or biomedical implants such as glucose sensors and stents. The implantation of devices *in vivo* can lead to major complications in the body, or other detrimental effects reducing its functionality and longevity in the body. The fact that no single material is biocompatible under all conditions only creates further challenges in designing better biomaterials or tissue-engineered constructs.[24]

Although the diversity of factors governing inflammation and foreign body responses is well-documented,[25] the complexity of the response of the body to different biomaterials is poorly understood. The degree of the biological response is also governed by the (a) morphology and porosity, (b) shape, (c) size, (d) surface chemistry and roughness, (e) design, (f) composition, and (g) degradation.

One disease application where this plays a very important role is the cardiovascular system where stents have long been used with reasonable success, and where longevity has been improved via the use of drug eluting stents.[26,27] Even with technological advances, there has been limited understanding of device/host interactions, which hinders the development of better constructs for *in vivo* applications.[27] One source of the problem is the study and testing of particular constructs in isolation without considering the systemic effects of

biomaterial response and without considering regions beyond the immediate area of the implant.[26] Multiple dimensions of biological response governed by a large number of factors create a process of enormous complexity.[28,29]

5.513.3. High-Throughput Component-Centered Approach

To efficiently search a broad variety of possible cell culture conditions, scaffolds, or other tissue engineering parameters, new experimental platforms offer the possibility of massively parallel experiments, robotic execution of repetitive steps, high-content imaging with automated computational analysis, miniaturization and microfluidics, or lab-on-a-chip platforms that achieve dramatic improvements in experimental throughput. High-throughput measurements can give noisy results, often causing many type I (false positive) errors. Utilization of results from high-throughput experiments is inseparable from computational methods of statistical data analysis and data mining.[30] The availability of free[31,32] and economical general-purpose data analysis software allow data mining needs to be met without customized programming for the tissue engineering context. Meanwhile, a host of experimental tools specific to tissue engineering are necessary to create and assess large-scale multivariate quantitative systems.[33] Microarray and microfluidic technologies, including high-throughput live cell assays, have been developed for performing highly parallelized experimental perturbations, and measurements of the resulting cellular responses.

5.513.3.1. Manufacturing Substrates

In order to increase assay throughput and reduce reagent consumption, and reduce the number of cells required, the substrates being manufactured must be miniaturized. Emerging technologies may ultimately lead to array formats. Current tools include rapid prototyping, the setup of polymer gradients, and spotted microarrays, microwells, as well as microfluidics. Parameters of interest for control include porosity, volume fraction, mechanical properties, oxygen diffusion, degradation rate, tortuosity, permeability, homogeneity of composition, fiber orientation, surface chemistry, biomaterial composition, and protein adsorption.

Nanoliter volumes of different chemicals, biochemicals, and cells, as well as combinatorial combinations of these, can be dispensed in a spatially addressable pattern using automated robotic spotting technologies.[34,35] For example, a library of over 1700 photopolymerizable acrylate-based biomaterials was synthesized and the mechanical properties were measured with nanoindentation.[36] Other applications include toxicology assays,[37] compound screening,[38] gene function screening,[39] cell adhesion assays,[40] and probing embryonic stem cell[41] fate.[42,43] In the work of Flaim *et al.*[42,43], various extracellular matrix (ECM) compounds such as collagen-I, -III, -IV, laminin, and fibronectin were immobilized on hydrogel surfaces. A combination of ECM compounds was identified that most synergistically induced differentiation of ESCs to a hepatic fate. Also some interesting findings were made with regards to the crosstalk between various ECM proteins which culminated in the development of the right substrate for hepatocytes that lead to high levels of albumin synthesis *in vitro*. Combinatorial methods can also be used on the macroscale in well plates, but the miniaturization of such systems would aid in increasing throughput.[44]

For large-scale screening of cell–biomaterial interactions, a continuous polymer gradient can be generated, instead of discrete spots with varying compositions.[11,45] Both 2D and 3D gradients can be generated for exhibiting a gradient of some property along a biomaterial film, hydrogel, or other surfaces. The gradient as presented to cells and cellular response is observed in monolayer (2D)[46] or on cells seeded within porous scaffolds (3D).[47] This way, the optimal point of interaction along a gradually changing surface can be identified.[48,49] Besides being used as a screening tool, scaffolds with a gradation in properties could also serve as a template for the generation of a graded tissue.

Arrays of microwells with defined dimensions can be fabricated using soft lithography, which affords control over the substrate size and cellular aggregates.[34,50] Microwells are attractive because they allow control of parameters such as size, shape, and homogeneity of cellular aggregates, for instance in the expansion of human ES cells. As an example, 3D embryoid bodies (EBs) have been formed within poly(ethylene glycol)[17] microwells.[35,51] Microengineered hydrogel microwells have also been used to regulate ES cell fate in an aggregate size-dependent manner.[52] Similar template-based assembly of cells could also be used to form aggregated tissue sections that contain multiple cell types organized into specific geometries relative to each other.[50] Reproducibility of homogenous cultures has been identified as a potential problem in recreating exactly similar conditions across the board for valid experimental repeats, as in the current difficulty of controlling the homogeneity of EB formation within microwells.[53] Improved reproducibility may occur in the future with improvements in microwell material composition, cell seeding procedures, and handling of aggregates during retrieval.

Microfluidics also presents the opportunity for conducting high-throughput analysis of signals within an array system.[33,34] Microscale channels are formed by casting a polymer, polydimethylsiloxide (PDMS), on a prefabricated mold. Advantages include application and control of laminar flow, shear stress, spatial positioning of soluble factors including concentration gradient generation, and ease of imaging.[35] Systems that can be set up include platforms for drug toxicity studies and multiphenotype cell arrays.[50] By combining microwells and reversibly sealed microfluidic channels, Khademhosseini *et al.* were able to localize multiple cell phenotypes. This work gives an example of the ability to pattern tissues within microfluidics channels in a high-throughput way.[50]

For manufacturing of substrates on the larger scale, rapid prototyping technologies allow fast fabrication of porous biomaterial scaffolds with tunable micro- and macroscale structures.[54] This term generally refers to a computer-controlled manufacturing technique that allows layer-by-layer deposition and processing of materials, resulting in a totally controllable structure.[2,55] Some examples include fused deposition modeling, stereolithography, electron beam melting, and 2D printing.[56] Others include high-throughput laser printing,[57] electropatterning,[58] and solid free-form fabrication.[2]

5.513.3.2. Measuring Substrate Properties

Combinatorial chemistry has made it possible to develop vast assortments of polymers and biomaterials (see **Chapter 4.412, Rational and Combinatorial Methods to Create Designer Protein Interfaces**);[59] however this advance creates a pressing need for equally efficient methods to characterize the different polymers.[60] Because the surface chemistry, topology, and mechanical properties of biomaterials have profound effects on cell behaviors, these properties are crucially important to measure when evaluating their implications for tissue engineering.[61] The current trend in tissue engineering toward developing more customized and tailored biomaterials for specific applications, has amplified the need for fast and easy methods to characterize biomaterials.[62] The following sections describe methods for characterizing certain categories of material properties, with efficient methods highlighted.

5.513.3.2.1. Surface chemistry and techniques

An efficient and scalable method for characterizing the surface chemistry of biomaterials was developed by Kohn *et al.*, who established a correlation between glass transition temperature, hydrophobicity, mechanical properties, and polymer structure. To measure the underlying parameters for these correlation trends, they used differential scanning calorimetry (glass transition temperature, Tg), gel permeation chromatography (molecular weight), thermogravimetric analysis, goniometry, and the sessile drop method (water contact angle).[63] The results of these tests give insight into the structure–property relationship for large quantities of materials developed.

Another important development has been the use of MALDI-TOF (matrix-assisted laser desorption ionization time of flight) mass spectrometry for analysis of macromolecules. Inkjet printing of polymers has been shown to greatly improve the throughput of MALDI-based analysis.[64] Among the characterizations that have been most successfully implemented using high-throughput MALDI platforms are the measurement of molecular weights combined with high-speed columns, and parallelization combined with flow injection analysis.[33] These automation tools provide good predictive power and they vastly improve the speed of material detection, without much loss in resolution.

For high-throughput characterization with less technical complexity than MALDI-TOF methods, new optical methods have been developed, including measurements of absorbance and fluorescence, including the far and near infrared regions.[65] Light scattering and viscometry have also been shown to greatly improve the automated batch characterization of polymer solutions while continuous monitoring of the polymerization of the monomers is done using high-throughput optical techniques like FT-IR (Fourier transform infrared) spectroscopy.[66]

5.513.3.2.2. Mechanical characterization

The mechanical properties of biomaterials (such as tensile properties, modes of deformation and stress–strain behavior) are also of utmost importance for engineering functional constructs. Various studies have shown differential responses of cells when grown on substrates with differing mechanical properties.[67] For example, the mechanical stiffness of a substrate can direct stem cell differentiation into various cell lineages.[67] The mechanical properties are often measured by techniques like nanoindentation, which measures displacement at the nanometer scale. Strain-induced elastomer buckling can also be used for measuring mechanical properties of thin films. Measurement of the surface toughness and pattern formation is performed in a rapid manner using AFM (atomic force microscopy), with the field moving toward nanorobotics to characterize biomaterials with reduced human error (see **Chapter 3.302, Atomic Force Microscopy**).[41] The chemical and mechanical properties of biomaterials have a tremendous impact on cell–material interactions and on tissue engineering outcomes, thus emphasizing the need to characterize materials extensively before they are used for tissue engineering applications. The understanding of the interdependency between chemical and mechanical properties for cells and biomaterials will also play an important role in developing designer biomaterials for future tissue engineering applications.

5.513.3.3. Measuring Cellular Response

Systems-level approaches have afforded great advances at characterizing the responses of cells to different types of biomaterials. The -omics revolution has contributed tremendously to the understanding of biological responses to biomaterials, which aids in understanding which biomaterials and soluble factors achieve phenotypes closest to those observed *in vivo*. Contributions from genomics, proteomics, and metabolomics are helping to elucidate functional and structural aspects of subcellular systems, ultimately helping to engineer better tissues. This section describes how genomics, proteomics, and metabolomics have contributed to tissue engineering.

5.513.3.3.1. Genomics

Genomics, including functional genomics (gene expression analysis), has provided extensive evidence about the diversity of factors responsible for maintaining the function of highly specialized cells, and for determining the levels of mimicry of *in vitro* constructs to *in vivo* tissues.[68] The development of the microarray platform has provided broad insight into understanding the gene expression of *in vitro* constructs (see **Chapter 3.321, Microarrays in Biomaterials Research**). It has led to the large-scale (whole genome) screening of engineered tissue constructs and even to greater understanding of the responses of implants to hosts. Microarray technology has had tremendous impact on the fields of comparative and functional genomics and has improved the understanding of pathways that were perturbed or differentially regulated in culture versus *in vivo*. Gene expression analysis has been used for deriving how various culture configurations modulate pathways required for cell behavior to meet the requirements of bioartificial reactors and drug testing platforms.[69,70] Genomics has also provided insights and a mechanistic understanding on goals such as understanding the divergence of phenotypes in 3D and 2D cultured cardiac cells, and uncovering pathways that contribute to *in vitro* tissue genesis.[71] Culturing cells in a 3D environment has long been known to provide advantages for mimicking the *in vivo* phenotype, compared with 2D environments. 3D culture conditions are more conducive to the formation of multicellular organization, similar to that found *in vivo*.

Primary cells, such as cardiomyocytes for cardiovascular tissue engineering, and hepatocytes for liver tissue engineering,

are the cells of choice for studying tissue genesis, regeneration, and drug-induced toxicity.[72,73] For hepatocytes to maintain proper function, the flow of blood through the liver sinusoids has been hypothesized to induce necessary signals mediated by shear stress. The liver chip developed at MIT[69] demonstrated this by measuring gene expression levels for various important drug metabolism enzymes, comparing them with enzyme activity levels *in vitro*, and with gene expression levels *in vivo*, to confirm the relationship between the culture conditions and the *in vivo* mimicry.[69] This valuable information is obtained in a high-throughput manner, and the consistency of the data obtained makes it a powerful tool to study cell–biomaterial interactions and to determine the phenotypes of various tissue-engineered constructs.

5.513.3.3.2. Proteomics

Proteins are regulated by various mechanisms such as phosphorylation, glycosylation, and other posttranslational modifications (targeted cleavage and degradation) that occur downstream of mRNA that cannot be observed with functional genomics. The field of proteomics involves system-wide analyses at protein levels, sometimes including observations of posttranslational modifications, and often emphasizing differentially expressed proteins. Cellular responses traditionally have been characterized at the proteomic level using methods such as 2D gel electrophoresis and MALDI-TOF mass spectrometry.[74] Additional methods of high-throughput protein analysis such as protein microarrays and antibody microarray[75] are currently being developed. Traditional low-throughput methods of studying proteins have used, for example, antibody methods to detect the release of growth signals, cytokines, or proteins. For tissue engineering, techniques like 2D gel electrophoresis and MALDI-TOF are used to characterize the surface adsorption of proteins to biomaterials and to determine the relationship between the surface and the intracellular signaling pathways affecting cells.[76,77] Used synergistically, they have also helped identify proteins which are secreted into the medium and intracellular proteins which are present in cells cultured on polystyrene and titanium surfaces.[78,79] If similar methods can be pursued with a higher level of spatio-temporal resolution, they will be useful for characterizing cells in their environments *in vitro* or *in vivo*, since the complexity and the lack of reproducibility of this technique has made it difficult to apply it to study all cellular responses.[80,81]

There has been some progress made in utilizing this technology in studying *in vitro* constructs and in measuring protein expression during differentiation and in various cardiovascular diseases, but very little progress has been made in tissue engineering *per se*. Hepatocytes, when cultured *in vitro*, undergo a change in their proteome and many proteins are differentially regulated when compared to cells *in vivo*.[82] A coculture of hepatocytes with nonparenchymal cells like fibroblasts have been shown to increase hepatocyte differentiated functions.[83] In a quest to find out which of the factors is responsible for the improvement in hepatocyte function, we have carried out a proteomic analysis of the culture media of the cells cultured in the coculture configuration. We found that transforming growth factor-beta 1 (TGF-β1) was an important cytokine upregulated in the culture and the substitution of the TGF-β1 in the culture media replaced the need to coculture cells,[84] by maintaining higher order differentiated function of the cells.

Thus the understanding of how cells react when cultured with various cell types and identifying in detail the components responsible for the differential cellular responses could help us identify better biomaterials, supplements to improve and develop better cellular constructs.

5.513.3.3.3. Metabolomics

Another field of great interest today is metabolomics, which involves the measurement of metabolites, in order to create a metabolic map of different tissues or microorganisms. Understanding metabolite flux at a systems level helps provide a direct point of access for normal physiological systems. Metabolomic methods have recently helped identifying markers for cardiovascular diseases,[85] assessing drug toxicity,[86] and characterizing anti-inflammatory compounds.[87] Metabolomics has not been utilized extensively in the field of tissue engineering, but the combination of metabolomics and proteomics could provide a profoundly powerful characterization of *in vitro* constructs.[88]

For example, metabolomics are intricately informative about liver cell function, which meets the demand for robust methods to assess the functionality of liver cells for bioartificial liver devices.[89] Recent work has characterized metabolite profiles using nuclear magnetic resonance (NMR) spectroscopy, leading to the discovery that cells cultured in 2D and 3D bioreactors showed differential consumption of glutamine, lactate, and alanine.[90] The above examples illustrate how the integration of genomics, proteomics, and/or metabolomics can aid in defining culture conditions, media, supplements, or 3D configurations, thus furthering the goals of tissue engineering by allowing us to create constructs that better resemble natural tissues *in vivo*.

5.513.3.4. *In Vivo* Integration into Living Hosts

Over the years, technological advances have provided a wealth of information about how an introduction of foreign stimuli influences various individual molecular species.[91,92] These discoveries, although vitally important for biological progress, have not yet been successfully translated into clinical applications or other success stories *in vivo*.[93,94] For example, synthetic hip prostheses are one of the most widely used implants in the clinic. However, complications often emerge after implantation, which are mainly caused by mechanical failure of the implant material or by the coeffects of chronic inflammation. Revision surgery is often necessarily due to subsequent bone loosening and fracture.[95] Another example is the coronary artery stent, which is widely used in the established therapy of percutaneous coronary intervention for coronary heart diseases. The stent is placed inside the narrowed branch of a coronary artery to keep it open. However, the site with stent bracing up will inevitably become narrowed again gradually after the operation.[96] One of the major reasons is that the exogenous materials of the stent can trigger immune stimulation *in vivo* that creates chronic inflammation *in situ*. At the same time the stent damages the vascular wall by the force it creates inside the artery that will slowly recover by forming tightly

contracted scar. There are various kinds of adjuvant therapeutics to prevent clotting forming again, but still the patient needs another stent intervention when the renarrowing happens.

Observation of *in vivo* response is necessary for the R&D of implantable biomaterials. A typical biomaterials project with *in vivo* implantation might have the following pipeline: after design and fabrication of a construct, researchers will implant it into animal model; then systemic samples like blood are collected at different time points for toxicity analysis; function may be tested to check the phenotypic improvement; and finally the implanted construct is removed again for histological analysis. Interpretation of the above observations, directly or indirectly yields the conclusion about the *in vivo* responses. No single project can measure everything, but too often neglected are the detailed reactions *in situ*, the system-level effects in the body, and a breadth of observations that could identify the underlying mechanisms for positive or negative outcomes.

The *in vivo* integration challenges that remain will require a paradigm shift in the way we identify and associate molecules with specific phenotypes. The multifactorial nature of host/biomaterial interaction makes it crucially important to develop tools and detection methods for studying the entire system simultaneously.[94] This is a divergence from the traditional reductionist approach that is based on studying individual factors associated with complex interactions.[97] Along these lines, the identification of molecules or markers associated with the presence and response of host to biomaterials should rely on a better understanding of the biology at a systems level. To construct a holistic view of systems biology, multiple and different types of endpoints must therefore be combined, including the molecular scale (gene expression, proteomics, lipidomics, metabolomics,), cellular scale, and tissue/organ scale.[98–100] Clinical measurements (e.g., pathology) must also be incorporated when possible. *In vivo* imaging, particularly because of its scalability, is an ideal tool for deeper investigation and integrated pursuit of relationships across components and across scales, at a systems level in the living host.

5.513.3.4.1. Image informatics: Transcending scales with improved speed and resolution

Pursuing a project from molecular manipulations through to clinical endpoints creates difficult problems for integrating information across scales: from nanometers to centimeters, from microseconds to months, and from molecules to tissues. Changes at any scale can affect others, particularly the next higher level of scale.[101] There are no universal recipes for navigating such complexity, but computational modeling can be useful for integrating information derived from traditional bottom up data driven approaches, with top down knowledge, to achieve better predictions in areas of systems medicine and in prognosis of certain conditions (see **Chapter 3.313, Histological Analysis**; **Chapter 3.316, Immunohistochemistry**; **Chapter 3.317, Fluorescence Imaging of CellBiomaterial Interactions** and **Chapter 3.318, Molecular Imaging**).[102]

Imaging techniques, developed over the last century, have greatly advanced our understanding of biological systems and have played an important role in functional understanding of complex organs such as the brain. A great advantage of imaging is that many of the imaging tools are noninvasive and the information obtained is rich in the spatial and temporal dimensions.[103] The need for staining and the possibility of artifacts remain to be disadvantages of imaging techniques.[104] Current imaging systems also suffer from the inherent problems of low throughput of the techniques, which generate images at a high resolution. This has led to development of imaging tools, which can image at higher resolutions with higher throughput.

The working principle of high-throughput imaging-based screening systems is the automation in the imaging of microtiter plates, often in multiples of 96-wells, with images produced via detection of fluorescence.[66] Combined with robotic handling, high-throughput imaging methods result in a large amount of image data and statistically significant information,[105] that can be useful for systems biology analysis. One prominent application of automated microscopic techniques is the use of cell-based assays for screening small-molecule drugs from combinatorial synthesis.[4] Whole body imaging techniques have been developed using epiplanar illumination mechanism and have been useful in neurological detection of cathepsin activity in glioma tumors using MRI coregistered fluorescence tomography.[106] Imaging with infrared light has also improved penetrative power and has enabled the capture of images with higher resolution.[107] The development of new technologies like multifocal multiphoton microscopy hold great promise in imaging 3D tissues with high resolution and improved speed achieved by parallelized illumination.[108,109] Very often, the information obtained in a single measurement is the result of several different mechanisms acting simultaneously, which makes the interpretation challenging. Therefore, a major issue in cell-based imaging is to seek biological relevance from a large pool of collected data and subject them to rigorous statistical analysis.

Integrating, modeling, and understanding the data obtained from different techniques of image acquisition pose a challenge. Sartori *et al.*[110] have combined the use of multi-scale imaging by correlative light microscopy with cryo-electron tomography, to compare images obtained by both of these methods in 2D. Such comparison methods can also be used to correlate the structural information obtained using cryotomogram and the functional information obtained using fluorescent methods.[111] There have also been a few reports of imaging techniques that have been used to study response to a biomaterial. For example, Murata *et al.*[112] studied neointimal coverage after stent implantation, and they found a good correlation between optical coherence tomography and histology-based approaches, for the purposes of observing neointimal area, thickness and luminal area. Thus, by combining the various approaches available by transcending scales and linking data driven approaches with new technologies which provide information at a larger scale we will be able to get a better understanding of life processes and thus predict better integration of engineered constructs with *in vivo* systems.

High-throughput experimental platforms have provided valuable results for diverse applications, and tissue engineering has made significant strides at adapting high-throughput technologies for specific needs. As familiarity and facility with these methods improves, another phase of progress is beginning, where high-throughput or -omic experiments are starting to be used for discovering knowledge, constructing models, and inferring relationships that form the foundation of a system-level understanding and a process-centered approach.

5.513.4. Process-Centered Systems Approach

The transition toward high-throughput platforms may increase efficiency for screening and experimentation, but it does not change the fundamental orientation of most tissue engineering research toward optimizing particular components. In other words, the four core foci; biomaterials, cells, culture configurations *in vitro*, and integration *in vivo*; are most often considered individually and optimized, whether using low-throughput or high-throughput methods. Although we acknowledge that the components are interdependent, we often address them separately for lack of established quantitative relationships between the experimental variables *in vitro* and their ultimate effects *in vivo*. Even for *in vivo* tissue engineering, the choice of biomaterials, cells, and microenvironments must rely heavily on the unpredictable behaviors of cells to proliferate, migrate, and remodel their environments. Therefore, much of what we have accomplished has relied on an empirical, trial-and-error approach.

Future research in tissue engineering and biomaterials has the potential to achieve greater success particularly for functionally ambitious projects, by taking a process-centered approach. The study of components and processes can occur through the use of system-level computational models. With a better understanding of the way cells interact to form tissues in different contexts (e.g., embryonic development or tissue repair); we can identify subsets of parameters that should be covaried simultaneously in subsequent experiments. We can also choose to vary parameters that are mathematically predicted to have highest probability of having the desired impact on the outcome. Achieving fully functional tissues for regenerative medicine involves a huge number of variable dimensions, and performing an exhaustive screen of all simultaneous combinations of all variable parameters is not possible, even with high-throughput platforms. Instead we must understand the larger processes and system-level trends that determine the clinical outcome, and design focused screens that actively manage and quantitatively navigate the landscape of interdependent parameters. In this section on process-centered systems approaches, we discuss example projects that bridge the gap between component-centered approaches and a more holistic quantitative prediction of *in vivo* processes, often through the use of computational modeling and biophysics.

Classical biophysical models use measured parameters in construction of a model that better facilitates the understanding of how certain biomaterials affect or are affected by biological processes. Examples can be seen in the work of Shreiber *et al.*[113] who have modeled the effect of fibroblast cell migration on the compaction of ECM. Other examples of classical biophysical modeling include proliferation of liver cells as a function of the metabolic load on the cells[114] and bone regeneration on scaffolds as a function of substrate porosity.[115] These models are better known for their accuracy and complexity of construction, than for their ability to mimic broad physiological outcomes. These physical models are applicable to biological phenomena but their outlooks are oriented more toward understanding mechanistic issues in tissue engineering, rather than toward simulating clinical outcomes.

For predicting the interplay between complex and simultaneous effects, mathematical modeling has obvious usefulness, but knowledge of the effects is required before a network of multiple effects can be simulated. Initial models have most often been built for extremely well-studied systems, but in general filling this information gap will entail the creation of new knowledge. Better instrumentation is increasing the availability of information, and more biophysical parameters are becoming available for purposes like modeling.[116] A contrasting avenue for assembling information in the future may involve the reuse of high-throughput measurements, due to the following innovation: component-centered measurements become useful for process-centered work when assembled *en masse*, because automated data mining algorithms are increasingly capable of using observed correlations to infer relationships and to reconstruct networks of effects.[117–120] High-throughput studies are widely recognized for having a close interface with statistical data analysis methods, but in addition to data analysis is an opportunity for automated knowledge discovery, to elucidate system-level and process-oriented knowledge from experiments that may have been designed for narrower purposes.

A landmark study[121] reconstructed a genome-wide transcriptional network for mesenchymal transformation of gliomas. Network reconstruction was also used in a study of adipocyte differentiation[82] where correlations between gene expression patterns and transcription factor phosphorylation patterns from large-scale proteomics and phosphoproteomics experiments were sufficient to infer relationships between transcription factors and target genes. Complete biological pathways are too numerous to be fully elucidated by humans and they will increasingly often be pieced together by computational methods. As systems-level approaches become more common in fields such as molecular cell biology, the resulting accumulation of pathway knowledge, regulatory mechanisms, computational models, and other fruits of the research will become available to help advance process-centered system-level research in tissue engineering and regenerative medicine. Few examples of process-centered systems research have been published for biomaterials or regenerative medicine thus far, but among them are projects summarized below on *ex vivo* implants, pathways of cell regulation, and regulation of liver fibrosis.

5.513.4.1. Modeling of Systems in Tissue Constructs

Bridging the gap between more biophysical models and regenerative medicine is the still developing field of *ex vivo* implants.[122] In such implants, cells are seeded on biodegradable scaffolds and after culture for a period of time, are transferred to a region of defect inside the body. An exciting field of tissue engineering research emerges from the possibility of transplanting adult stem cells, such as induced pluripotent stem cells,[97] through engineered constructs. In such systems there is a fusion between basic bioengineering principles and the underlying biology of cells, to create a model that is useful if not exactly accurate for understanding the role of bioengineered substances in tissue engineering. Mathematical models using ordinary differential equations have been constructed by Lemon[123,124] to study the proliferation and adhesion of cells on *ex vivo* implants. The authors used human mesenchymal stem cells (hMSCs) cultured on fibrous PET

(polyethylene-terephthalate) scaffolds, and studied the effect of hypoxia on growth. There are also some detailed models of stem cell attachment on scaffolds which emphasize metabolite diffusion and cell growth kinetics.[125]

Successful survival of an *ex vivo* implant within the host tissue is facilitated by the development of vascular tissue, which can transfer essential nutrients to the stem cells via the capillaries. Lemon *et al.*[123] constructed a highly simplified model of angiogenesis on scaffolds for human embryonic stem cells, and used the chick chorioallantoic membrane[46] as an experimental assay for estimating parameters and validating predictions. Their model predicts that the rate of cell infiltration through the pores of the scaffold to form blood vessels is a limiting factor of angiogenesis. Angiogenesis is increased in VEGF pretreated scaffolds when compared to untreated ones, both in the model as well as the experiments, thereby increasing the success of *ex vivo* transplants. As angiogenesis is a determinant of the success of scaffold integration within tissue, there have been other studies of blood capillary formation in the presence of specific scaffolds.[126] The presence of implants stimulates an inflammatory response by the body. Chang *et al.*[127] have modeled the chain of events from substrate presence to inflammatory stimulation, including increased monocyte adhesion and conversion into foreign body giant cells. These modeling projects use very simplistic representations of how biomaterials affect system processes and might have poor accuracy because they neglect spatio-temporal knowledge. Also these models are coarse-grained and do not contain specific pathway knowledge. In some cases the effects of biomaterials on a system can be better understood when they are studied in relation to more specific pathways rather than the effect on general biological processes.

5.513.4.2. Pathway Modeling for Process-Centered Approaches

With recent advances in systems biology, well-defined and quantitatively calibrated pathway models are now available for apoptosis,[128] the cell cycle,[129] and various growth factor-induced signaling pathways.[130] Sorensen *et al.*[131] *built a* model of platelet activation incorporating the interactions between thrombin, prothrombin, and its inhibitor. Their model predicts the effects on platelet activation from the shear stress of blood flow, and adhesion to biomaterials, which are used as cardiovascular implants. In their subsequent publication[132] the model was validated using a collagen type-I substrate and a parallel-plate flow to show experimental results that agreed with the model predictions. Diverse types of information, about interaction pathways, cell-specific interactions, biophysical characteristics, and substrate–cell interactions, were integrated through modeling to provide guidance for the development of substrates with improved outcome in a physiological context.

5.513.4.3. Pathway Modeling for Activation of TGF-β1 in Liver Fibrosis

Our team undertook a process-centered approach aimed at regenerative therapy for liver fibrosis (Figure 2). Liver fibrosis is driven by high levels of the cytokine TGF-β1 and by the accumulation of fibrotic proteins secreted from activated hepatic stellate cells (HSCs). There are many causal influences in liver fibrosis, but we do not seek simply to perturb the most important cause driving the disease because the mechanisms important to fibrosis are also likely to be important for beneficial wound healing, repair and regeneration. Indeed, elevated TGF-β1 and HSC activation occur normally when the liver regenerates after an injury, and we do not want to impair the pathways of natural regeneration. Rather than considering alternative perturbations individually, we studied the system of TGF-β1 and closely related pathways, seeking to understand the differences in how a healthy system avoids excessive levels of TGF-β1 after a single injury repair event, versus how TGF-β1 activation remains pathologically elevated in the case of chronic injury and fibrosis.

TGF-β1 is secreted in latent form and its bioavailability is regulated by extracellular activation. We studied the regulation of TGF-β1 activation by measuring levels of TGF-β1 activating

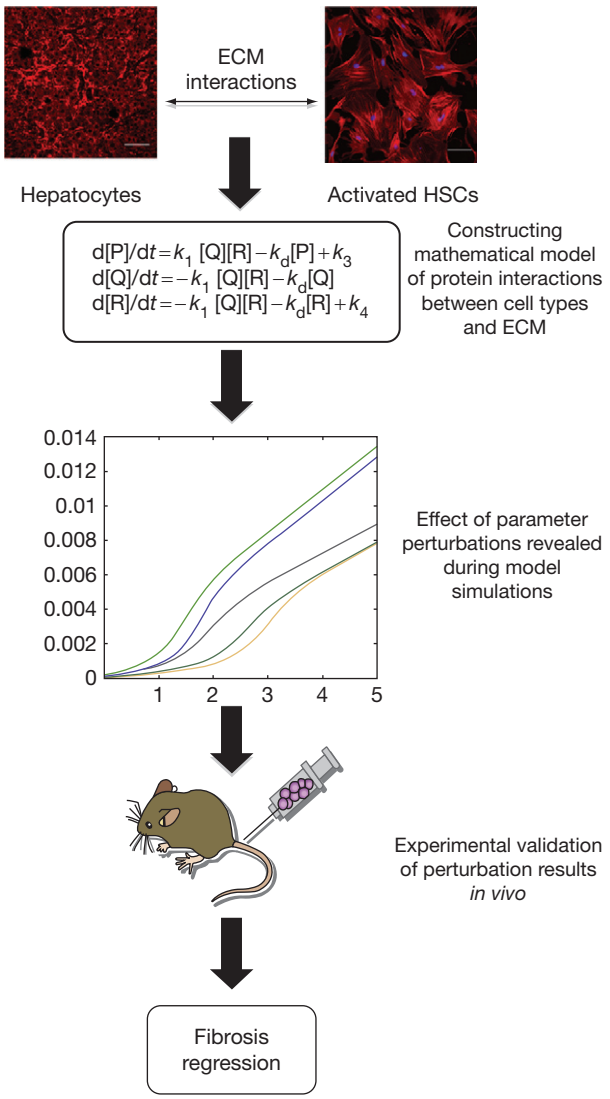

Figure 2 Workflow of systems biology-oriented therapy for liver fibrosis.

proteins in normal liver and at stages of fibrosis progression in rat models of liver fibrosis.[134] Thrombospondin-1, a known activator of TGF-β1, is strongly upregulated during liver fibrosis and has already been implicated as a driver of fibrosis.[133] Plasmin, another activator of TGF-β1, was found at significant levels normally and at dramatically lower levels during liver fibrosis progression.[133] This suggests that plasmin-mediated activation of TGF-β1 occurs in normal liver, and suggests that the thrombospondin-1 pathway becomes a more prominent mode of activation during fibrosis. Toward understanding why normal and fibrotic liver would utilize different pathways of TGF-β1 activation, one notes that TGF-β1 increases expression of plasminogen activator inhibitor-1 (PAI-1), an antagonist of plasmin activation.[135]

The decreased plasmin signaling during fibrosis thus has an explanatory mechanism, but why is the thrombospondin-1 pathway not more active in normal liver, except during injury response? A combination of results *in vitro*, *in silico*, and *in libris* (from data in the published literature) allowed us to establish a system-level model in which plasmin is acting both as a low-potency activator of TGF-β1, and a high-potency antagonist of the thrombspondin-1 pathway. Through its direct cleavage of thrombospondin-1, plasmin antagonizes the thrombospondin-1 pathway of TGF-β1 activation and reduces net TGF-β1 activation.[134] Therefore, plasmin has different downstream effects depending on the level at which it is studied. At a molecular level and in isolation, plasmin functions directly to activate TGF-β1. Meanwhile in a system of extracellular proteins, plasmin functions indirectly to decrease TGF-β1 activation. A process-centered mindset for approaching system-level issues facilitated our discovery of these dual roles of plasmin in the regulation of TGF-β 1 activation.

We next studied how this TGF-β1 activation machinery could be exploited for the therapeutic goal of triggering regeneration. A previous study of plasmin regulation and its upstream activation by uPA (urokinase-type plasminogen activator) revealed that plasmin activation occurs through a bistable switch-like feedback mechanism.[136] Combining this bistability with the previous model of TGF-β1 activation by plasmin and thrombospondin-1 yielded the hypothesis that, changes in the balance between plasmin and thrombospondin-1 might cause a distinct switch-like transition in the regulation of TGF-β1. Using rat models of liver fibrosis, sources of plasmin were added *in vitro* to the culture medium or *in vivo* by transplanting plasmin-secreting hepatocytes into the host.

The results in both experiments showed that TGF-β1 levels decreased and fibrotic disease markers returned to near-normal levels.[134,137] Elevating plasmin as a method to antagonize TGF-β1 is counterintuitive, but it proved to be remarkably effective. Moreover, it mimics the correlations found in the physiological system *in vivo*, and it may prove to be part of the physiological mechanism by which healthy liver tissue naturally switches away from fibrotic pathways during a normal injury response. From an engineering viewpoint, plasmin may also prove to be a relatively safe, robust way to downregulate TGF-β1 because its dual nature allows any overdose of its strong, indirect antagonistic function to be self-corrected via its mild but direct activating function.

Taking a process-centered approach helped us in multiple ways: to integrate knowledge about the various observed effects, to gain mechanistic insight into the switch-like regulation of the system, and to design an effective intervention for regenerative medicine in a rat model of liver fibrosis. However, the system-level nature of the project was only made possible by unusually extensive previous work that elucidated the detailed effects of the individual participants, at the molecular level and the cellular level. For general problems without such resources available, future research will be forced to establish the interactions and molecular relationships explicitly, perhaps one day simply from data mining and knowledge discovery in databases, or for the near term via additional biological experiments *ab initio*.

5.513.5. Future Outlook

Future goals for biomaterials and tissue engineering will require multiple interdependent components (biomaterials, cells, constructs), each with multifaceted optimization and variable parameters. Instead of the discrete or component based approaches studying particular biological outcomes of tissue engineering (**Table 1**) focus should be directed toward a systems-level perspective or process-centered approach.

Biochemical responses need to be assessed, possibly including functional genomics, proteomics, metabolomics, or other

Table 1 Broader perspectives of process-centered implications and approaches to study functional outcomes of tissue engineering

	Tissue engineering approaches	*Biological effects studied using tissue-engineered constructs*	*References*
Process-centered tissue engineering approaches	High-throughput approaches with process-centered implications	Mesenchymal stem cells gene expression	39
		Cell adhesion studies	40
		Embryonic stem cell fate	42
		Osteoblast adhesion, spreading and proliferation on biomaterial	49
	Classical biophysical models	Effect of cells on substrate/ECM compaction	113
		Bone regeneration on scaffolds	115
	Network reconstruction	Cancer gene prediction from B cell lymphoma interactome	118
		Mesenchymal transformation	121
	Systems modeling in tissue constructs	Stem cell attachment and spreading on *ex-vivo* implants	124
		Angiogenesis of human embryonic stem cell on scaffolds	123
	Pathway modeling for process-centered approach	Modeling the effect of vascular implants on the platelet aggregation	131
		Modeling activation of TGF-β1 in liver fibrosis	134

system-wide '-omic' responses. In addition, physical responses such as adhesion, migration, and morphological change need to be assessed. The chemical and physical properties of biomaterials would strongly influence cellular response and these parameters depend on both the underlying biomaterial as well as adsorbed proteins. On top of this are the biochemical and biophysical cues from the culture environment and the host microenvironment. Given this multilayered complexity, the most efficient and useful heuristics for correlating key experimental parameters with *in vivo* outcomes are to focus on biological processes and to define intermediate goals that have systematic and quantitative relationships with respect to the ultimate *in vivo* goal. Meanwhile, high-throughput methods will provide fast, parallel fabrication and measurement of cellular and tissue constructs,[33] and combinatorial synthesis approaches will be increasingly useful for biomaterials development.

References

1. Griffith, L. G.; Naughton, G. *Science* **2002**, *295*, 1009–1014.
2. Hutmacher, D. W. *J. Biomater. Sci. Polym. Ed.* **2001**, *12*, 107–124.
3. Kretlow, J. D.; Mikos, A. G. *Tissue Eng.* **2007**, *13*, 927–938.
4. Cooke, M. N.; Fisher, J. P.; Dean, D.; Rimnac, C.; Mikos, A. G. *J. Biomed. Mater. Res. B Appl. Biomater.* **2003**, *64*, 65–69.
5. Sun, W.; Lal, P. *Comput. Methods Programs Biomed.* **2002**, *67*, 85–103.
6. Kellar, R. S.; Landeen, L. K.; Shepherd, B. R.; Naughton, G. K.; Ratcliffe, A.; Williams, S. K. *Circulation* **2001**, *104*, 2063–2068.
7. Mansbridge, J.; Liu, K.; Patch, R.; Symons, K.; Pinney, E. *Tissue Eng.* **1998**, *4*, 403–414.
8. Shevchenko, R. V.; James, S. L.; James, S. E. *J. R. Soc. Interface* **2010**, *7*, 229–258.
9. Shakespeare, P. G. *Clin. Dermatol.* **2005**, *23*, 413–418.
10. Papini, R. *BMJ* **2004**, *329*, 158–160.
11. Yang, F.; Mei, Y.; Langer, R.; Anderson, D. G. *Comb. Chem. High Throughput Screen.* **2009**, *12*, 554–561.
12. Jon-Paul, M.; Derek, F.; David, G.; Rajendra, P. *BJU Int.* **2005**, *96*, 493–497.
13. Atala, A.; Bauer, S. B.; Soker, S.; Yoo, J. J.; Retik, A. B. *Lancet* **2006**, *367*, 1241–1246.
14. Soler, R.; Fullhase, C.; Atala, A. *Therapy* **2009**, *6*, 177–184.
15. George, E. D.; Kayla, J. B.; Anil, M. *Anat. Rec.* **2002**, *268*, 252–275.
16. Ehrbar, M.; Djonov, V. G.; Schnell, C.; *et al. Circ. Res.* **2004**, *94*, 1124–1132.
17. Ozawa, C. R.; Banfi, A.; Glazer, N. L.; *et al. J. Clin. Invest.* **2004**, *113*, 516–527.
18. Golub, J. S. G.; Kim, Y.-T.; Duvall, C. L.; *et al. Am. J. Physiol. Heart Circ. Physiol.* **2010**, *298*, H1959–H1965.
19. Zisch, A. H.; Lutolf, M. P.; Ehrbar, M.; *et al. FASEB J.* **2003**, *17*(15), 2260–2262. Epub 2003 Oct 16.
20. Albrecht, D. R.; Tsang, V. L.; Sah, R. L.; Bhatia, S. N. *Lab Chip* **2005**, *5*, 111–118.
21. Folch, A.; Toner, M. *Annu. Rev. Biomed. Eng.* **2000**, *2*, 227–256.
22. Lutolf, M. P.; Hubbell, J. A. *Nat. Biotechnol.* **2005**, *23*, 47–55.
23. Pratt, A. B.; Weber, F. E.; Schmoekel, H. G.; Muller, R.; Hubbell, J. A. *Biotechnol. Bioeng.* **2004**, *86*, 27–36.
24. Anderson, J. M.; Langone, J. J. *J. Control. Release* **1999**, *57*, 107–113.
25. Anderson, J. M. *Annu. Rev. Mater. Res.* **2001**, *31*, 81–110.
26. Ertefai, S.; Gough, D. A. *J. Biomed. Eng.* **1989**, *11*, 362–368.
27. Schoen, F. J.; Levy, R. J. *Ann. Thorac. Surg.* **2005**, *79*, 1072–1080.
28. Fournier, E.; Passirani, C.; Montero-Menei, C. N.; Benoit, J. P. *Biomaterials* **2003**, *24*, 3311–3331.
29. Sieminski, A. L.; Gooch, K. J. *Biomaterials* **2000**, *21*, 2232–2241.
30. Rose, S.; Stevens, A. *Curr. Opin. Chem. Biol.* **2003**, *7*, 331–339.
31. Gentleman, R. *Bioinformatics with R;* Chapman & Hall/CRC: Boca Raton, FL, 2008.
32. Holmes, G.; Donkin, A.; Witten, I. H. In *Second Australia and New Zealand Conference on Intelligent Information Systems*, Brisbane, Australia, 1994.
33. Peters, A.; Brey, D. M.; Burdick, J. A. *Tissue Eng. B Rev.* **2009**, *15*, 225–239.
34. Fernandes, T. G.; Diogo, M. M.; Clark, D. S.; Dordick, J. S.; Cabral, J. M. *Trends Biotechnol.* **2009**, *27*, 342–349.
35. Khademhosseini, A.; Langer, R.; Borenstein, J.; Vacanti, J. P. *Proc. Natl Acad. Sci. USA* **2006**, *103*, 2480–2487.
36. Tweedie, C. A.; Anderson, D. G.; Langer, R.; Vliet, K. J. V. *Adv. Mater.* **2005**, *17*, 2599–2604.
37. Lee, M. Y.; Kumar, R. A.; Sukumaran, S. M.; Hogg, M. G.; Clark, D. S.; Dordick, J. S. *Proc. Natl Acad. Sci. USA* **2008**, *105*, 59–63.
38. Fernandes, T. G.; Kwon, S. J.; Lee, M. Y.; Clark, D. S.; Cabral, J. M.; Dordick, J. S. *Anal. Chem.* **2008**, *80*, 6633–6639.
39. Yoshikawa, T.; Uchimura, E.; Kishi, M.; Funeriu, D. P.; Miyake, M.; Miyake, J. *J. Control. Release* **2004**, *96*, 227–232.
40. Falsey, J. R.; Renil, M.; Park, S.; Li, S.; Lam, K. S. *Bioconjug. Chem.* **2001**, *12*, 346–353.
41. Minne, S. C.; Yaralioglu, G.; Manalis, S. R.; *et al. Appl. Phys. Lett.* **1998**, *72*, 2340.
42. Flaim, C. J.; Chien, S.; Bhatia, S. N. *Nat. Methods* **2005**, *2*, 119–125.
43. Flaim, C. J.; Teng, D.; Chien, S.; Bhatia, S. N. *Stem Cells Dev.* **2008**, *17*, 29–39.
44. Yang, Y.; Bolikal, D.; Becker, M. L.; Kohn, J.; Zeiger, D. N.; Simon, C. G., Jr. *Adv. Mater.* **2008**, *20*, 2037–2043.
45. Simon, C. G., Jr.; Yang, Y.; Thomas, V.; Dorsey, S. M.; Morgan, A. W. *Comb. Chem. High Throughput Screen.* **2009**, *12*, 544–553.
46. Campbell, P. G.; Miller, E. D.; Fisher, G. W.; Walker, L. M.; Weiss, L. E. *Biomaterials* **2005**, *26*, 6762–6770.
47. Simon, C. G., Jr.; Stephens, J. S.; Dorsey, S. M.; Becker, M. L. *Rev. Sci. Instrum.* **2007**, *78*, 072207.
48. Mei, Y.; Elliott, J. T.; Smith, J. R.; *et al. J. Biomed. Mater. Res. A* **2006**, *79*, 974–988.
49. Zapata, P.; Su, J.; Garcia, A. J.; Meredith, J. C. *Biomacromolecules* **2007**, *8*, 1907–1917.
50. Khademhosseini, A.; Yeh, J.; Eng, G.; *et al. Lab Chip* **2005**, *5*, 1380–1386.
51. Mohr, J. C.; De Pablo, J. J.; Palecek, S. P. *Biomaterials* **2006**, *27*, 6032–6042.
52. Hwang, Y. S.; Chung, B. G.; Ortmann, D.; Hattori, N.; Moeller, H. C.; Khademhosseini, A. *Proc. Natl Acad. Sci. USA* **2009**, *106*, 16978–16983.
53. Moeller, H. C.; Mian, M. K.; Shrivastava, S.; Chung, B. G.; Khademhosseini, A. *Biomaterials* **2008**, *29*, 752–763.
54. Woodfield, T. B.; Moroni, L.; Malda, J. *Comb. Chem. High Throughput Screen.* **2009**, *12*, 562–579.
55. Lacroix, D.; Planell, J. A.; Prendergast, P. J. *Philos. Transact. A Math. Phys. Eng. Sci.* **2009**, *367*, 1993–2009.
56. Yeong, W. Y.; Chua, C. K.; Leong, K. F.; Chandrasekaran, M. *Trends Biotechnol.* **2004**, *22*, 643–652.
57. Guillemot, F.; Souquet, A.; Catros, S.; *et al. J. Acta Biomater.* **2010**, *6*(7), 2494–2500.
58. Albrecht, D. R.; Underhill, G. H.; Wassermann, T. B.; Sah, R. L.; Bhatia, S. N. *Nat. Methods* **2006**, *3*, 369–375.
59. Hoogenboom, R.; Meier, M. A. R.; Schubert, U. S. *Macromol. Rapid Commun.* **2003**, *24*, 13–14.
60. Peters, A.; Brey, D. M.; Burdick, J. A. *Tissue Eng. Part B Rev.* **2009**, *15*(3), 225–239.
61. Goldberg, M.; Mahon, K.; Anderson, D. *Adv. Drug Deliv. Rev.* **2008**, *60*, 971–978.
62. Pasch, H.; Kil, P. *Macromol. Rapid Commun.* **2003**, *24*(1), 104–108.
63. Brocchini, S.; James, K.; Tangpasuthadol, V.; Kohn, J. *J. Biomed. Mater. Res.* **1998**, *42*, 66–75.
64. Meier, M. A.; De Gans, B. J.; Van Den Berg, A. M.; Schubert, U. S. *Rapid Commun. Mass Spectrom.* **2003**, *17*, 2349–2353.
65. Zhang, D.; Dougal, S. M.; Yeganeh, M. S. *Langmuir* **2000**, *16*, 4528–4532.
66. Potyrailo, R. A.; Lemmon, J. P.; Leib, T. K. *Anal. Chem.* **2003**, *75*, 4676–4681.
67. Engler, A. J.; Sen, S.; Sweeney, H. L.; Discher, D. E. *Cell* **2006**, *126*, 677–689.
68. Harries, H. M.; Fletcher, S. T.; Duggan, C. M.; Baker, V. A. *Toxicol. In Vitro* **2001**, *15*, 399–405.
69. Sivaraman, A.; Leach, J. K.; Townsend, S.; *et al. Curr. Drug Metab.* **2005**, *6*, 569–591.
70. Tuschl, G.; Mueller, S. O. *Toxicology* **2006**, *218*, 205–215.
71. Akins, R. E.; Gratton, K.; Quezada, E.; Rutter, H.; Tsuda, T.; Soteropoulos, P. *DNA Cell Biol.* **2007**, *26*, 425–434.
72. Hewitt, N. J.; Lechon, M. J.; Houston, J. B.; *et al. Drug Metab. Rev.* **2007**, *39*, 159–234.
73. Remiao, F.; Carmo, H.; Carvalho, F.; Bastos, M. L. *In Vitro Cell. Dev. Biol. Anim.* **2001**, *37*, 1–4.
74. Lee, K. H. *Trends Biotechnol.* **2001**, *19*, 217–222.
75. Wilson, D. S.; Nock, S. *Curr. Opin. Chem. Biol.* **2002**, *6*, 81–85.

76. Ademovic, Z.; Klee, D.; Kingshott, P.; Kaufmann, R.; Hocker, H. *Biomol. Eng.* **2002**, *19*, 177–182.
77. Wagner, M. S.; Shen, M.; Horbett, T. A.; Castner, D. G. *J. Biomed. Mater. Res. A* **2003**, *64*, 1–11.
78. Boraldi, F.; Bini, L.; Liberatori, S.; *et al*. *Electrophoresis* **2003**, *24*, 1292–1310.
79. Granchi, D.; Ciapetti, G.; Stea, S.; *et al*. *Biomaterials* **1999**, *20*, 1079–1086.
80. Chaussabel, D. *Am. J. Pharmacogenomics* **2004**, *4*, 383–393.
81. Gorg, A.; Weiss, W.; Dunn, M. J. *Proteomics* **2004**, *4*, 3665–3685.
82. Beigel, J.; Fella, K.; Kramer, P. J.; Kroeger, M.; Hewitt, P. *Toxicol. In Vitro* **2008**, *22*, 171–181.
83. Bhatia, S. N.; Balis, U. J.; Yarmush, M. L.; Toner, M. *FASEB J.* **1999**, *13*, 1883–1900.
84. Chia, S. M.; Lin, P. C.; Yu, H. *Biotechnol. Bioeng.* **2005**, *89*, 565–573.
85. Dunn, W.; Broadhurst, D.; Deepak, S.; *et al*. *Metabolomics* **2007**, *3*, 413–426.
86. Nicholson, J. K.; Connelly, J.; Lindon, J. C.; Holmes, E. *Nat. Rev. Drug Discov.* **2002**, *1*, 153–161.
87. Verhoeckx, K. C.; Bijlsma, S.; Jespersen, S.; *et al*. *Int. Immunopharmacol.* **2004**, *4*, 1499–1514.
88. Reo, N. V. *Drug Chem. Toxicol.* **2002**, *25*, 375–382.
89. Southam, A. D.; Easton, J. M.; Stentiford, G. D.; Ludwig, C.; Arvanitis, T. N.; Viant, M. R. *J. Proteome Res.* **2008**, *7*(12), 5277–5285.
90. Seagle, C.; Christie, M. A.; Winnike, J. H.; *et al*. *Tissue Eng. Part C Methods* **2008**, *14*, 107–118.
91. Scharpe, J.; Maes, B.; Van Damme, B. *Acta Clin. Belg.* **2005**, *60*, 86–93.
92. Uhlenhaut, N. H.; Treier, M. *Trends Genet.* **2008**, *24*, 361–371.
93. Ein-Dor, L.; Zuk, O.; Domany, E. *Proc. Natl Acad. Sci. USA* **2006**, *103*, 5923–5928.
94. Rifai, N.; Gillette, M. A.; Carr, S. A. *Nat. Biotechnol.* **2006**, *24*, 971–983.
95. Callaghan, J. J.; Salvati, E. A.; Pellicci, P. M.; Wilson, P. D., Jr.; Ranawat, C. S. *J. Bone Joint Surg. Am.* **1985**, *67*, 1074–1085.
96. Topol, E. J. *N. Engl. J. Med.* **1998**, *339*, 1702–1704.
97. Ahn, A. C.; Tewari, M.; Poon, C. S.; Phillips, R. S. *PLoS Med.* **2006**, *3*, e208.
98. Kohl, P.; Noble, D. *Mol. Syst. Biol.* **2009**, *5*, 292.
99. Schadt, E. E.; Zhang, B.; Zhu, J. *Genetica* **2009**, *136*, 259–269.
100. Wheelock, C. E.; Wheelock, A. M.; Kawashima, S.; *et al*. *Mol. Biosyst.* **2009**, *5*, 588–602.
101. Kerckhoffs, R. C.; Narayan, S. M.; Omens, J. H.; Mulligan, L. J.; Mcculloch, A. D. *Heart Fail. Clin.* **2008**, *4*, 371–378.
102. Clermont, G.; Auffray, C.; Moreau, Y.; *et al*. *Genome Med.* **2009**, *1*, 88.
103. Li, N.; Jia, X.; Murari, K.; Parlapalli, R.; Rege, A.; Thakor, N. V. *J. Neurosci. Meth.* **2009**, *176*, 230–236.
104. Baumeister, W. *Curr. Opin. Struct. Biol.* **2002**, *12*, 679–684.
105. O'brien, P.; Irwin, W.; Diaz, D.; *et al*. *Arch. Toxicol.* **2006**, *80*, 580–604.
106. Mccann, C. M.; Waterman, P.; Figueiredo, J. L.; Aikawa, E.; Weissleder, R.; Chen, J. W. *Neuroimage* **2009**, *45*, 360–369.
107. Klohs, J.; Steinbrink, J.; Bourayou, R.; *et al*. *J. Neurosci. Methods* **2009**, *180*, 126–132.
108. Bahlmann, K.; So, P. T.; Kirber, M.; *et al*. *Opt. Express* **2007**, *15*, 10991–10998.
109. Kim, K. H.; Buehler, C.; So, P. T. *Appl. Opt.* **1999**, *38*, 6004–6009.
110. Sartori, A.; Gatz, R.; Beck, F.; Rigort, A.; Baumeister, W.; Plitzko, J. M. *J. Struct. Biol.* **2007**, *160*, 135–145.
111. Lucic, V.; Kossel, A. H.; Yang, T.; Bonhoeffer, T.; Baumeister, W.; Sartori, A. *J. Struct. Biol.* **2007**, *160*, 146–156.
112. Murata, A.; Wallace-Bradley, D.; Tellez, A.; *et al*. *JACC Cardiovasc. Imaging* **2010**, *3*, 76–84.
113. Shreiber, D. I.; Barocas, V. H.; Tranquillo, R. T. *Biophys. J.* **2003**, *84*, 4102–4114.
114. Furchtgott, L. A.; Chow, C. C.; Periwal, V. *Biophys. J.* **2009**, *96*, 3926–3935.
115. Byrne, D. P.; Lacroix, D.; Planell, J. A.; Kelly, D. J.; Prendergast, P. J. *Biomaterials* **2007**, *28*, 5544–5554.
116. Knapp, D. M.; Barocas, V. H.; Moon, A. G.; Yoo, A. K.; Petzold, A. L. R.; Tranquillo, A. R. T. *J. Rheol.* **1997**, *41*, 971–993.
117. Kimura, S.; Ide, K.; Kashihara, A.; *et al*. *Bioinformatics* **2005**, *21*, 1154–1163.
118. Mani, K. M.; Lefebvre, C.; Wang, K.; *et al*. *Mol. Syst. Biol.* **2008**, *4*, 169.
119. Nagasaki, M.; Yamaguchi, R.; Yoshida, R.; *et al*. *Genome Inform.* **2006**, *17*, 46–61.
120. Needham, C. J.; Bradford, J. R.; Bulpitt, A. J.; Westhead, D. R. *PLoS Comput. Biol.* **2007**, *3*, e129.
121. Carro, M. S.; Lim, W. K.; Alvarez, M. J.; *et al*. *Nature* **2010**, *463*, 318–325.
122. Levenberg, S.; Langer, R. *Curr. Top. Dev. Biol.* **2004**, *61*, 113–134.
123. Lemon, G.; Howard, D.; Tomlinson, M. J.; *et al*. *Math. Biosci.* **2009**, *221*, 101–120.
124. Lemon, G.; Waters, S. L.; Rose, F. R.; King, J. R. *J. Theor. Biol.* **2007**, *249*, 543–553.
125. Chung, C. A.; Yang, C. W.; Chen, C. W. *Biotechnol. Bioeng.* **2006**, *94*, 1138–1146.
126. Schugart, R. C.; Friedman, A.; Zhao, R.; Sen, C. K. *Proc. Natl Acad. Sci. USA* **2008**, *105*, 2628–2633.
127. Chang, D.; Saidel, G.; Anderson, J. *Cell. Mol. Eng.* **2009**, *2*, 573–590.
128. Bagci, E. Z.; Vodovotz, Y.; Billiar, T. R.; Ermentrout, G. B.; Bahar, I. *Biophys. J.* **2006**, *90*, 1546–1559.
129. Tyson, J. J.; Novak, B. *J. Theor. Biol.* **2001**, *210*, 249–263.
130. Bradshaw, J. M.; Kubota, Y.; Meyer, T.; Schulman, H. *Proc. Natl Acad. Sci. USA* **2003**, *100*, 10512–10517.
131. Sorensen, E. N.; Burgreen, G. W.; Wagner, W. R.; Antaki, J. F. *Ann. Biomed. Eng.* **1999**, *27*, 436–448.
132. Sorensen, E. N.; Burgreen, G. W.; Wagner, W. R.; Antaki, J. F. *Ann. Biomed. Eng.* **1999**, *27*, 449–458.
133. Gressner, A. M.; Weiskirchen, R.; Breitkopf, K.; Dooley, S. *Front. Biosci.* **2002**, *7*, d793–d807.
134. Venkatraman *et al*. Plasmin triggers a switch-like decrease in thrombospondin dependent activation of TGF-1. *PLoS Comput. Biol.* In review.
135. Zhang, L. P.; Takahara, T.; Yata, Y.; *et al*. *J. Hepatol.* **1999**, *31*, 703–711.
136. Venkatraman, L.; Yu, H.; Bhowmick, S. S.; Dewey, F.; Tucker-Kellogg, L. *Pac. Symp. Biocomput.* **2010**, 190–200.
137. Zhang, W.; Tucker-Kellogg, L.; Narmada, B. C.; *et al*. *Adv. Drug Deliv. Rev.* **2010**, *62*(7–8), 814–826. Epub 2010 Mar 1.

5.514. Chondrocyte Transplantation and Selection

A Lindahl, University of Gothenburg, Gothenburg, Sweden

© 2011 Elsevier Ltd. All rights reserved.

5.514.1.	**Introduction**	190
5.514.2.	**Cell Therapy and Cartilage Regeneration: State of the Art**	190
5.514.3.	**Cell Therapy Concepts in Cartilage Disease and Osteoarthritis**	190
5.514.4.	**Molecular Control Mechanisms in the Knee Joint – Implications for Cartilage Repair and OA**	191
5.514.5.	**The Uniqueness of Hyaline Cartilage Chondrocytes**	192
5.514.6.	**Adult Stem Cells and Stem Cell Niches**	193
5.514.7.	**Improvements in ACT Cell Technology – Alternative Cell Sources**	193
5.514.8.	**Autologous Use of Cells**	194
5.514.8.1.	Osteoarthritic Cells	194
5.514.8.2.	Bone Marrow Stromal Cells or Mesenchymal Stem Cells	194
5.514.8.3.	Fat Stromal Cells and Cartilage Regeneration	195
5.514.9.	**Universal Donor Cell Lines for Cartilage Repair**	195
5.514.9.1.	Derivation of Chondrocytes from Human Embryonic Stem Cells	195
5.514.9.2.	Derivation of Chondrocytes from Umbilical Cord Cells and Umbilical Cord Blood Cells	197
5.514.10.	**Conclusion**	197
References		198

Glossary

Articular cartilage A fibrous tissue comprising extracellular matrix proteins (mostly collagen and proteogylcans) produced by the cells (chondrocytes), and functioning to create a viscoelastic tissue with high biomechanical stability and low friction. It has a very limited ability for self-repair, mandating interventional approaches for repair.

Autologous chondrocyte transplantation (ACT) A regenerative medicine and multistep surgical procedure used to treat traumatic cartilage damage or osteochondrosis dissecans, but not degenerative arthritis in adults by harvest of cartilage from the patient, expansion of the chondrocyte progenitor cells, harvest, and transplant of these cells back into the patient's articulating cartilage site.

Chondrocyte Specialized musculoskeletal cell type producing type II collagens and specialized proteoglycans responsible for the structure and unique viscoelastic propeties of cartilage tissue. The only cell found in cartilage.

Chondroprogenitor donor cell-lines Cells representing chondrocyte precursors, capable of harvest and repeated culture to retain chondrocyte phenotypes, self-renewal, and tissue-regenerating properties of mature chondrocytes.

Hyaline cartilage Specialized articular cartilage found in synovial joint surfaces distinct in composition, structure and function from fibrillar cartilage

Osteoarthritis (OA) Cartilage degeneration characterized by cartilage degradation, the formation of osteophytes, and subchondral sclerosis, pain, and joint dysfunction.

Abbreviations

ACI	Autologous chondrocyte implantation
ACT	Autologous chondrocyte transplantation
ATSC	Adipose derived stromal cells
BMP	Bone morphogenetic protein
BMPr1a	Bone morphogenetic protein receptor 1a
BMSC	Bone marrow stromal cell
COMP	Cartilage oligomeric protein
DIO2	Iodothyronine deiodinase enzyme type 2
FGF	Fibroblast growth factor
FRZB	Frizzle related protein B
GDF5	Growth differentiation factor 5
GPR22	G protein coupled receptor protein 22
hES cells	Human embryonic stem cells
HLH	Helix loop helix
HMGB-1	High mobility chromosomal box protein-1
HSC	Hematopoetic stem cell
ID1	Inhibitor of differentiation 1
IL-1	Interleukin 1
MSC	Mesenchymal stem cell
OA	Osteoarthritis
SCN	Stem cell niche
WJCs	Wharton's jelly stem cells

5.514.1. Introduction

Over 250 years ago, the famous anatomist William Hunter stated "ulcerated cartilage is a troublesome thing and once destroyed, is not repaired," a statement that is still valid today.[1] Adult articular cartilage consists mainly of extracellular matrix proteins produced by the cells (chondrocytes), which have the function of creating a visco elastic tissue with high biomechanical stability and low friction (Figure 1). Even though the cartilage is exposed to continuous mechanical wear, the cellular and extracellular matrix turnover is low, which could be a reason for the inability of adult articular cartilage to respond to injuries and subsequently repair lesions.

The damage to cartilage could lead to the end-stage disease osteoarthritis (OA) that is characterized by cartilage degradation, the formation of osteophytes, and subchondral sclerosis. OA is one of the most common forms of musculoskeletal disease throughout the world with millions of affected individuals. The OA disease causes a burden to the society and health care system but despite the increase in knowledge in medical science no drug-based disease-modifying therapy exists basically due to the fact that (i) the disease process stretches over decades, (ii) no surrogate markers exist that can be used to monitor progression of OA, and (iii) no specific drug target and disease mechanism have been identified.[2] The limited repair capacity of articular cartilage defects after trauma is the major contributing factor to early OA with ~5% of the population between 35 and 54 years having radiographic signs of OA.[3,4]

5.514.2. Cell Therapy and Cartilage Regeneration: State of the Art

Articular cartilage has poor ability to self-repair[5] and attempts of replacing the articular joint surface with osteochondral grafts were tested by Eric Lexer in 1908. Following that sporadic attempts were tried (see review by Aichroth[6]) but the variable methodology and clinical outcome did not justify wider clinical applications. Failures have generally been attributed to insufficient bone fixation, and allografts have failed due to immunological rejections and autografts had a better success rate. Over the years treatment of smaller cartilage injuries have been mainly surgically based on the concept of recruiting bone marrow stromal cells (BMSCs) by drilling or microfracturing the subchondral bone, alternatively using osteochondral autografts.

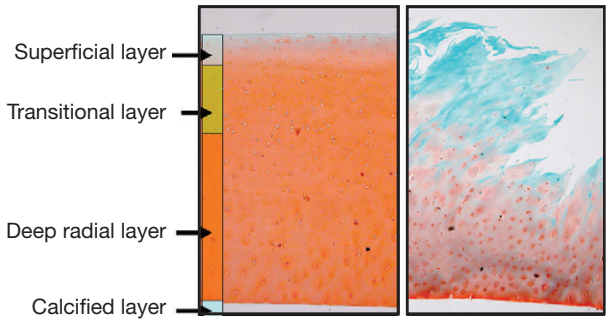

Figure 1 Normal healthy and osteoarthritic cartilage histology. Representive light micrographs of condylar cartilage obtained post mortem from joints with (a) normal healthy cartilage and (b) cartilage obtained at joint replacement surgery. Sections are stained with safranin-O fast green-iron haematoxylin. The different layers are an approximation and the calcified layer is indicated but not present in the sections. Figure modified from *Arthritis Res. Ther.* 2006, *8*(1), R2.

However, the resulting repair tissue is mostly fibrocartilaginous tissue lacking the biomechanical properties of the hyaline cartilage. Cellular attempts to regenerate cartilage were initiated in the 1960s when Green was able to isolate chondrocytes from cartilage and culture the cells.[7] The pioneering work of Bentley in 1971[8] demonstrated the possibility that transplanted and isolated articular chondrocytes as well as epiphyseal chondrocytes taken from very young rabbits (6-weeks old) that were injected into defects drilled in the upper tibial articular surfaces could induce repair. The articular chondrocytes were mostly rejected but the epiphyseal chondrocytes survived in small numbers and laid down normal staining hyaline matrix which filled the defects completely. In subsequent experiments, it was demonstrated that frozen chondrocytes also were able to regenerate an osteochondral defect.

The next step in cellular cartilage repair was taken with the autologous chondrocyte transplantation (ACT) technology developed by our group.[9] ACT or autologous chondrocyte implantation (ACI) has in the last decade emerged as the first disease-modifying treatment with long-term excellent clinical result in patients with isolated cartilage injuries[10,11] and osteochondral lesions in the knee and ankle.[12,13] The good clinical outcome of the ACT technique for the treatment of cartilage injuries has resulted in a worldwide spread of the technology with over 35 000 patients treated, among those, 1500 have been treated by our group over the last 15 years. Four randomized controlled clinical trials have demonstrated treatment superiority for ACT over conventional treatment[14–16] while one showed no difference, although ACT produced a better hyaline repair tissue.[17] However, the latter study does not take into account the fact that inclusion criteria for ACT treatment have repeatedly failed previous conventional treatments as one-third of patients with cartilage injuries diagnosed for the first time improve spontaneously after debridement.[18] Recent reports from our group with 15-year follow-up gives further support for the hypothesis that the ACT technology is a local disease-modifying treatment where the graft has contributed to local cartilage regeneration.[19] Furthermore, long-term follow-up with gadolinium enhancement demonstrated a hyaline repair tissue similar to surrounding cartilage.[20]

5.514.3. Cell Therapy Concepts in Cartilage Disease and Osteoarthritis

We have to accept the fact that OA is a chronic disease where the time between initiation of disease and fully developed OA stretches over decades. The challenge for the development of new OA treatments based on cellular or pharmacological technological base is hampered by the absence of early diagnostic tools. Classical biochemical assays are often based on the leakage of components from damaged cells (compare liver damage and released liver enzymes). The OA assays that are

available detect matrix components like cartilage oligomeric proteins (COMPs) inflammatory cytokines (interleukin-6 (IL-6) or high mobility chromosomal box protein-1 (HMGB-1). However, these markers are not sensitive enough for individual diagnostics at the early stage of the disease. The possibility of a regenerative approach to OA disease which could bridge the gap between the current stage of treatment (with the exception of traumatic defects which is not afflicted by OA disease) has changed given the recent advances in the knowledge of the regenerative capacity of different tissues (e.g., brain and heart) and the tissue ability to regenerate after injury.[21] The paradigm shift has changed the focus toward understanding the mechanisms of the regeneration system within each tissue, that is, identification of specific stem cell niches (SCNs) that harbor and maintain the stem cells through an intricate interaction and control (**Figure 2**). The homeostatic control involves a wide range of secreted soluble and matrix interactive signals. These signals represent a conserved 'developmental toolkit,' which is also important for embryonic development and includes, but is not limited to, bone morphogenetic proteins (BMPs), Fibroblast growth factors (FGFs), Notch, Hedgehog, and Wnt signaling pathways,[22,23] as well as the integrins and the cell surface proteoglycans. Particularly, the syndecans that represent a specific set of signaling molecules are able to modify intracellular events such as transcription. The signals are key players in disease mechanisms; for example, loss and gain of function studies in two Wnt coreceptors (Lrp5 and Lrp6) have drawn considerable attention to the importance of Wnt signaling pathways in skeletal biology.[24] Breakdown of the self-renewal system is a key event in the development of cancer and regeneration in aged muscles can be enhanced by restoration of normal signaling in the Notch pathway.[25] Continuous Wnt activation in the Klotho mice triggers accelerated cellular senescence of stem cells in several organs.[26] Furthermore, increased Wnt signaling during aging alters muscle stem cell fate and increases fibrosis, a process accelerated by Wnt3A while antagonists to the same pathway regain muscle lineage.[27] Future treatment of cartilage defects with cells and/or scaffolds have to adopt this new view of cartilage regeneration.

5.514.4. Molecular Control Mechanisms in the Knee Joint – Implications for Cartilage Repair and OA

In earlier studies, we found that the de- and redifferentiation process of human articular chondrocytes is similar to molecular programs found in fetal cartilage development.[28] Given the fact that there are stem cell markers in the knee joint and a SCN in the surroundings, the Notch signaling pathway has been studied as it is involved in the regulation of joint development and growth[29] and expressed in the surface layer of articular cartilage – *laminae splendance*.[30]

Since OA chondrocytes display an altered differentiation state compared to normal chondrocytes, it is expected that the expression of Notch markers in OA cartilage is altered. In healthy cartilage, Notch1, its ligand, Jagged1, and down stream effector gene *hes*5 (human version of the Drosophila gene, hairy and enhancer of split) are expressed in a few cells localized within the uppermost cell layers of the surface zone *lamina splendence*. This is in sharp contrast to the abundant expression of these markers detected in OA biopsies, where expression was extended to cells in deeper layers of the cartilage.[31] A recent population study added a new susceptible locus on chromosome 7q22 with a strong correlation related to the G protein coupled receptor protein 22 (GPR22).[32] Interestingly, the receptor could not be found in the articular cartilage but was localized to *lamina splendence*, thus colocalizing with the notch receptor in the superficial layer of articular cartilage.

Primary OA has an estimated heritability of 40% for the knee, 60% for the hip, and 65% for the hand.[2] To date, investigations of OA genetics have focused mainly on genome-wide linkage and candidate gene studies with controversial results due to lack of power and replication. Interestingly, two genes have been found to be consistently associated with OA in Caucasians: the growth differentiation factor 5 (GDF5)[33] and iodothyronine deiodinase enzyme type 2 (DIO2),[34] which are associated with SCN growth control.[34,35] Furthermore, hip OA is associated, in females, with the frizzle related protein B (FRZB), which is an inhibitor of the Wnt signaling pathway and is also involved in the stem cell signaling[36] (see **Chapter 5.524,**

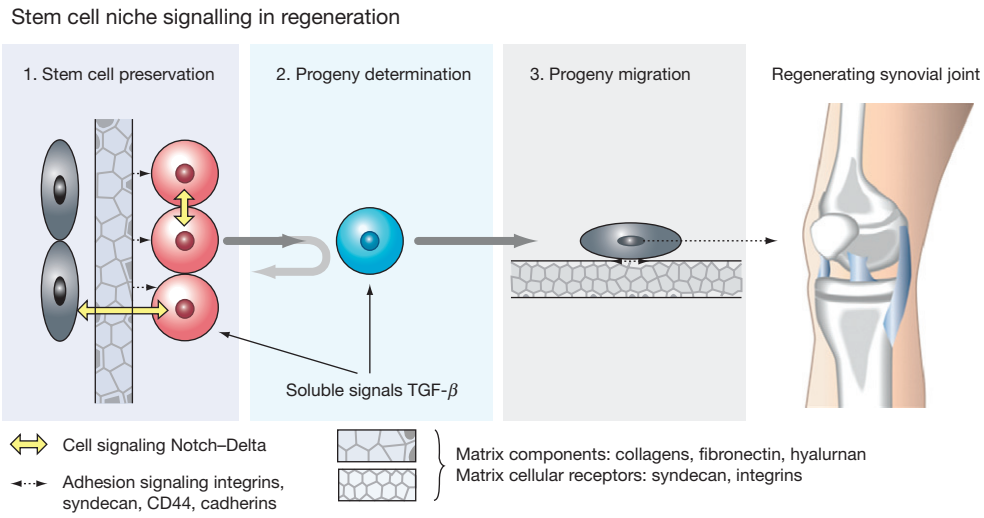

Figure 2 Schematic drawing of mechanisms in stem-cell-maintained tissue regeneration.

Biomaterials for Replacement and Repair of the Meniscus and Annulus Fibrosus).

5.514.5. The Uniqueness of Hyaline Cartilage Chondrocytes

When considering cartilage cell therapies it is necessary to recall the fundamental biology of cartilage and bone formation. Bone develops along two developmental pathways – either intramembraneous or by endochondral bone formation. Both processes are recognized by the process of cellular condensation where the endochondral bone formation has an intermediate cartilage step. Most of the skeletal bones are formed by endochondral formation and most of the skull bones are formed by intramebraneous formation.

The endochondral bone formation is characterized by deposition of matrix into a cartilaginous rod, which is the template for the long bones with cartilaginous tissue in the epiphysis as well as the long bone shaft. Subsequently, the chondrocytes hypertrophy in the long bone area and this process is followed by capillary ingrowth and the start of the process of mineralization. Initially the epiphysis remains cartilaginous but a second ossification zone develops in the central part of the epiphysis. Between the ossification center and the long bone the epiphyseal cartilage is formed that is responsible for the longitudinal bone growth. The proximal cartilage causes endochondral ossification in both distal and proximal directions. Subsequently, the ossification toward the epiphysis ceases and a laminar organization of chondrocytes develops in the distal direction.[37,38] Close to the bony epiphysis there is a uniformly distributed cell layer consisting of rarely dividing cells. This cell layer constitutes the stem cells of the growth plate and is usually called the germinal cell layer. This cartilaginous structure is connected with the articular cartilage and the perichondral ring responsible for the circumferential bone growth.

The articulating joint formation takes place in the cartilaginous rods where the formation of a small condensation zone named the digital ray is the first microscopic sign. This is followed by the formation of a three-layered interzone with two regions of high cell density with a region of lower density in between (Figure 3). The intermediate cell layer disappears through a process of apoptosis and thus forms the cavity of the joint while the surrounding high-density region forms the articulating surfaces.[39] The surrounding joint capsule and the tendons are formed from cellular condensations laterally to the digital ray thus creating the full articulating joint.

Little attention has been attributed to the cellular lineage of this structure since the concept has been that the joint is formed from the cartilage rod and thus similar to the hypertrophic cartilage, although the hypertrophic process is somewhat blocked. Several investigators have studied the factors responsible for cellular growth and structural patterning of the joint and in these studies the BMPs plays an important role. The first BMPs were isolated due to the remarkable capacity of ectopic bone formation. Subsequently many BMPs have been identified and studies of sequence homology have revealed that the BMPs form a subfamily within the TGF-β superfamily. GDF5 belongs to a new subgroup of the BMP family that includes GDFs 5, 6, and 7.

GDF5 has been hypothesized to having multiple functions in the skeletogenesis, since exogenously injected GDF5 protein stimulated cartilage development and inhibited surrounding GDF5 expression and joint formation.[40,41] Further evidence for a unique hyaline cartilage phenotype for articular cartilage was demonstrated in mice where cells expressing a member of the BMP family (GDF5) constitute a distinct cohort of progenitor

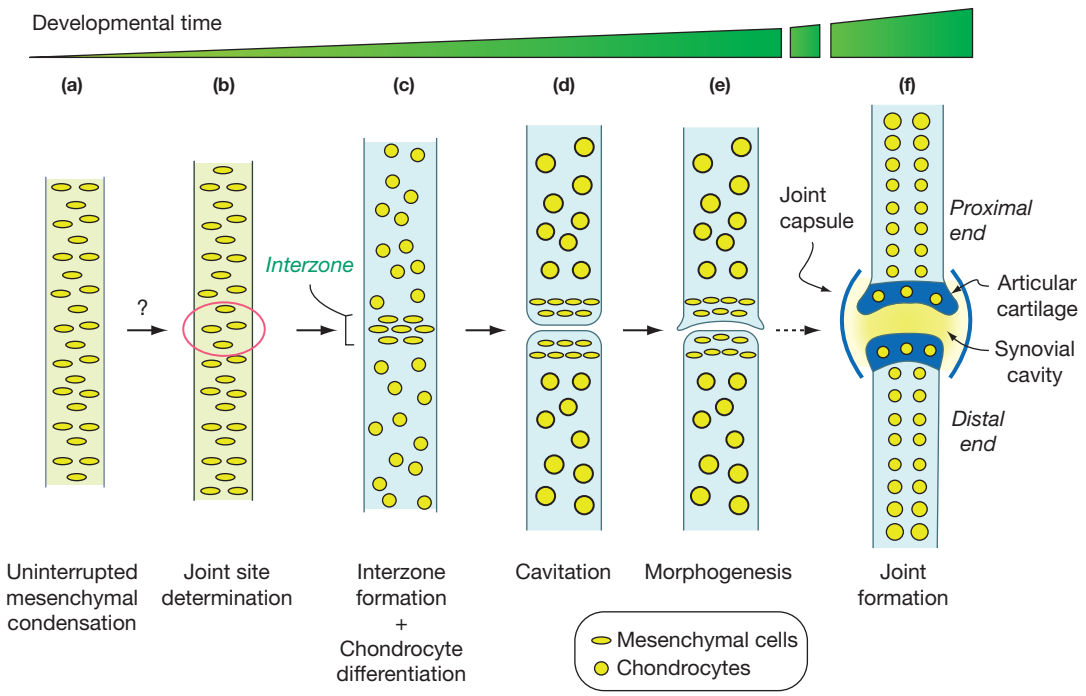

Figure 3 Schematic overview of the localization of the BrdU-positive cells in the knee. Reproduced from *J. Anat.* **2009**, *215*(3), 355–363.

cells responsible for limb joint formation including articular cartilage, ligaments, synovial lining, with limited contribution to the adjacent long bone cartilaginous shaft and growth plate formation.[42] Congenital mutations in the GDF5 gene cause defects in digits, wrist, and ankle[43] while deletion of antichondrogenic factors like *Wnt9a* causes limb and joint deformation.[44] This gives an additional support for a lineage specificity for articular cartilage that has to be taken into account when discussing cell therapy models in the joint (see **Chapter 5.538, Finger**).

5.514.6. Adult Stem Cells and Stem Cell Niches

The joint is a complex entity and it is still an important question if the joint and cartilage is a regenerating tissue with some repair capacity and in such case there has to exist a potential chondrogenic stem cell population within the joint. However, the poor capacity for self-repair of articular cartilage has been explained by cell senescence and the lack of chondroprogenitor cells. In contrast, human articular chondrocytes cultured *in vitro* display phenotypic plasticity with chondrogenic, adipogenic, and osteogenic potential[28,45,46] although whether this is due to dedifferentiation of the cells or selection of a progenitor cell population is debatable.

The anatomical location of the potential stem cells as well as the existence in a specific tissue *in vivo* is not well explored, particularly not in the joint. In recent years, it is becoming evident that stem cells are located in a special microenvironment termed stem cell niches (SCNs). The location and nature of these niches can vary depending on the tissue type but one common entity is that the signaling pathways are conserved.[23]

The bulge area of hair follicles where epithelial stem cells are resident and the intestinal SCN located near the crypt base has been extensively studied.[47,48] An area of potential interest with regard to progenitor cells in the joint is the circumferential anatomical structure first described by Ranvier in 1873 and formerly named the perichondrial groove of Ranvier. This area is located at the periphery of the epiphyseal growth plate and has been demonstrated to contain proliferating cells.[49] It has also been suggested that perichondrial cells from the ring of LaCroix, which is a fibrous band that surrounds the groove of Ranvier and is continuous with the periosteum of the metaphysis, serve as a reservoir for precartilaginous cells in the germinal layer of the epiphyseal growth plate.[50] The important role of an intact epiphyseal growth plate, and perichondrial zone, for longitudinal bone growth is well documented. Salter–Harris type VI fractures within the groove of Ranvier has demonstrated severe growth disturbances.[51]

An established method to identify stem cells within different tissues is the labeling of slow cycling cells corresponding to the stem cell population with bromodeoxyuridine (BrdU). Progenitor cells/stem cells can be identified and characterized due to expression of specific proteins, although no unique marker for these types of cells exists today. However, there are markers associated with stem cells in the literature, for example, Stro-1, bone morphogenetic protein receptor 1a (BMPr1a), Patched, Notch1, Integrin β1, and N-cadherin. Indeed a SCN in the zone of Ranvier close to the knee joint has been demonstrated with the technique of long-term labeling with BrdU. The SCN expressed similar immunohistochemical markers as other SCNs, that is, β-catenin, Notch1, Noggin, and c-kit[52] (**Figure 4**) and proliferating cells were present in the deeper areas of the articular cartilage. Although a significant decrease in the number of BrdU positive cells were detected at the later time points, some cells were still detected suggesting that progenitor cells might be present in the deeper layers of the cartilage. A similar SCN has also been identified in the intervertebral disk region[53] The interesting question is, if these niches could potentially be involved in human joint and disk regeneration and disease – a positive answer would mean a paradigm shift for the concept of cellular treatment for cartilage defects and the OA disease mechanism as well as disk degeneration.

5.514.7. Improvements in ACT Cell Technology – Alternative Cell Sources

OA patients and younger patients with small injuries are not subjected to ACT treatments due to the limited source of 'normal'

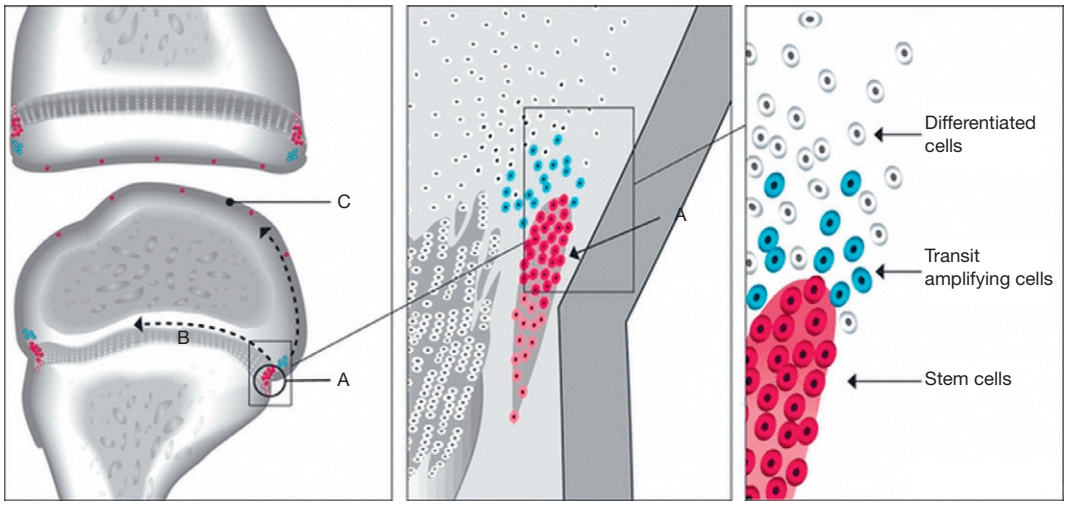

Figure 4 Development of bone and joint cartilage.

cartilage in an OA joint and the high costs of GMP-produced cells or grafts. This has raised the question if other cell types could replace the autologous chondrocytes (i.e., mesenchymal stem cells (MSCs), OA chondrocytes, human embryonic stem cells (hES cells), and umbilical cord or cord blood cells). When discussing different cell sources, there are requirements to be considered although some sources seem to be more easily accessible than others. Requirements for cells intended for hyaline cartilage repair is that they (i) are of the correct lineage and are able to differentiate toward hyaline cartilage. They should also be (ii) accessible and harvested with minimal (iii) morbidity for the patients. The requirement of multipotency and telomerase activity should be considered but more important is the (iv) capacity of cell expansion without loss of differentiation potential. Currently, the chondrocytes isolated from human articular cartilage are pluripotent with a unique differentiation capacity toward cartilage, bone and fat cells, and the cells are derived from the GDF5 lineage as earlier described. Alternative cell sources to consider would depend on the intended use. These could be divided into two distinct groups of treatments where one is *autologous* use and the second is *universal donor* use. The cell sources are discussed based upon these aspects as well as lineage specificity and expandability.

5.514.8. Autologous Use of Cells

5.514.8.1. Osteoarthritic Cells

The use of osteoarthritic cells could seem like a tempting source of cells which would mean that the doctor is able to harvest cells from a damaged knee for subsequent culture and expansion. Currently, autologous chondrocyte transplantation (ACT) is used to treat traumatic cartilage damage or osteochondrosis dissecans, but not degenerative arthritis.

The original ACT technology is based on culture-expanded chondrocytes transplanted under a cover of periosteum. The main indication was treatment of small isolated lesions but gradually over the last decade the indication has been expanded to include lesions up to 20 cm^2 in size. The implantation method has been followed by culture-expanded cells loaded on a membrane or into a biodegradable scaffold before implantation. Advantages of using scaffolds as cell carriers is that the cells can be positioned in the lesion arthroscopically and could potentially treat larger defects. This is especially interesting for young (under 60-years old) and active patients with developed OA, who at present lack an appropriate treatment alternative. Different scaffold materials have been used for this purpose, for example, different combinations of poly-L-lactic acid and poly(lactic-*co*-glycolic acid)[54] or materials obtained by esterification of hyaluronic acid.[55]

The etiology of OA has been suggested to contain a phenotypic alteration of the chondrocytes[56] due to systematic, mechanical, or unknown reasons. Chondrocytes isolated from OA cartilage have been shown to be more metabolically active than cells isolated from non-OA regions in the same joint[57] and proteoglycan synthesis in OA cells have been demonstrated in comparable amounts to normal cartilage from ACT donors although collagen synthesis is significantly lower.[58] Furthermore, chondrocytes isolated from less-severe grades of OA cartilage synthesize normal matrix components.[59]

When OA cells were cultured in a hyaluronan scaffold (Hyaff 11) only few genes were differentially expressed between OA and normal hyaline cartilage as determined by genome-wide oligonucleotide microarrays and the risk of differentiation into hypertrophic cartilage was not increased.[60] In such systems the OA cells could fulfill the requirements for matrix-associated cartilage implantation and OA patients could likely benefit from the treatment. In another study the gene expression patterns of osteoarthritic (OA) chondrocytes after primary culture and subculture were compared to these with healthy chondrocytes and with articular chondrocytes expanded for treatment of patients by ACT. In those studies OA chondrocytes showed highly elevated levels of interleukine 1β (IL-1β) mRNA, but type I and II collagen levels were comparable to those of healthy chondrocytes. After primary culture, IL-1 β levels decreased to baseline levels, while the type II and type I collagen mRNA levels matched those found in chondrocytes used for ACT. OA chondrocytes generated type II collagen and proteoglycan-rich cartilage when transplanted in a SCID mice model.[61] One conclusion from these studies could be that after expansion under suitable conditions, the cartilage of OA patients contains cells that are not significantly different from those from healthy donors prepared for ACT. OA chondrocytes supported by hyaluronan or collagen-based scaffolds could potentially be used for regenerating cartilage in humans although cells in single cell suspension are less suitable. Whether other types of scaffolds have similar capacity remains to be demonstrated.

5.514.8.2. Bone Marrow Stromal Cells or Mesenchymal Stem Cells

In the human bone marrow, a rare population of clonogenic nonhematopoietic stem cells (~1/100 000 of the bone marrow mononuclear cells) resides and the cells were earlier denoted as bone marrow stromal cells (BMSCs). The function of these cells is to support hematopoetic stem cell (HSC) function. Furthermore, these cells have the capacity to differentiate into cells of various connective tissue cells such as bone,[62,63] muscle,[64] adipose tissue,[65] cartilage,[66] and tendon.[67] Within the scientific literature, the acronym MSC has been used to represent (bone) marrow stromal cells,[68] MSC, and multipotent mesenchymal stromal cells, and this sometimes causes confusion since MSCs can be found in various tissues. It is more correct to give the MSCs a prefix depending on the source of harvest although the cells have similar capacity; for example, MSC derived from bone marrow aspiration would therefore be described and termed BMSC. Other MSCs that are candidate for replacing chondrocytes in cell-based repair of cartilage lesions could be derived from many other sources besides the bone marrow, that is, from adipose tissue, where the cells are termed adipose derived stromal cells (ATSCs), from Wharton's jelly in the umbilical cord (Wharton's jelly stem cells, WJCs), from umbilical cord blood (umbilical cord blood stem cells), or from synovial tissues, which also have the capacity to differentiate into specialized cells *in vitro* (see **Chapter 5.537, Adipose Tissue Engineering**).

However, it has not been clarified if MSCs can acquire the hyaline phenotype, and whether chondrocytes and MSCs show the same expression patterns of critical control genes in development. Several attempts have been made to achieve

regeneration of cartilage defects using MSC.[66,69] One major drawback of using these cells in cartilage or intervertebral disk tissue engineering is that human MSCs express type X collagen, a marker of chondrocyte hypertrophy associated with endochondral ossification.[70]

In high-density culture systems the gene expression patterns were compared between articular chondrocytes and iliac crest-derived MSCs. For articular cartilage, a significant decrease in expression of collagen type I was timed with increased expression of collagen types IIA and IIB during differentiation, thus indicating differentiation toward a hyaline phenotype. Chondrogenesis in MSCs on the other hand resulted in up-regulation of collagen types I, IIA, IIB, and X, demonstrating differentiation toward cartilage of a mixed phenotype. Expression of the helix loop helix (HLH) transcription factor 1 (HES1) increased significantly during chondrogenesis in chondrocytes while expression in MSCs was maintained at a low level. The HLH gene HES5 on the other hand was exclusively detected in chondrocytes. Expression of the HLH gene ID1 (inhibitor of differentiation 1) decreased significantly in chondrocytes while the opposite was seen in MSCs.[71] These findings suggest that chondrocytes and MSCs formed different subtypes of cartilage, the hyaline and a mixed cartilage phenotype, respectively. These results are important when considering the use of MSCs in cartilage repair.

The migration capacity of chondrocytes and mesenchymal stem cells (MSCs) is also important in cartilage regeneration and tissue engineering approach. A study analyzed growth factors and cytokines for their ability to induce migration of human articular chondrocytes and bone marrow-derived MSC in Boyden chamber assays. The platelet-derived growth factor was the most potent migrating agent but no differences between the two cell types could be detected.[72] When stimulated with GDF5 (formerly named cartilage-derived morphogenetic protein-1 (CDMP-1))[73] cartilaginous differentiation was demonstrated.

In conclusion, the MSC are easily accessible from the iliac crest but the harvest causes some morbidity to the patients; it is possible for the cells to expand in monolayer cultures and have multipotency but the default pathway demonstrated is not hyaline cartilage but hypertrophic cartilage and bone formation. This could be due to the fact that the cells are not in the GDF5 lineage although MSCs are able to differentiate into chondrocytes but the tissue represents an unmineralized hypertrophic cartilage.

5.514.8.3. Fat Stromal Cells and Cartilage Regeneration

Isolation procedure of adipose cells is well described and basically the liposuction material is thoroughly washed and digested by collagenase type I. The isolated cells are subsequently separated from adipose cells by centrifugation where superficial cells are the fat cells and the pellet contains the ATSCs. The differentiation capacities of these cells are similar to MSCs. The cell fraction has been evaluated in horses with cartilage defects and compared to treatment with MSC. Small differences were found although MSCs where more effective as treatment.[74] The human ATSCs were examined regarding phenotypes and gene expression profile in the undifferentiated states and compared with that of BMSC. Flow cytometric analysis showed that ATSCs have a marker expression that is similar to that of BMSC. ATSCs were superior to BMSC in respect to functionality in maintenance of proliferating ability, and microarray analysis of gene expression revealed differentially expressed genes between ATSCs and BMSCs. The proliferating ability and differentiation potential of ATSCs were variable according to the culture condition[75] including cartilage differentiation.[76] ATSCs are abundantly available as source for differentiation for cartilage repair but the differentiation pathway is similar to MSCs and thus end in mineralized bone. Furthermore, the harvest of cells is connected to an additional operative procedure with risk of patient morbidity.

5.514.9. Universal Donor Cell Lines for Cartilage Repair

Although widely used, there are some inherent problems with the use of autologous chondrocytes. They show restricted proliferative capacity in culture and rapidly lose their functional properties in culture. Harvesting these cells is itself an additional injury to the joint surface, and even if the harvest site is located some distance from the lesion, this cartilage might be affected by the injury as well. An alternative method is the use of adult MSC. One drawback with these cells is that they tend to differentiate toward hypertrophic cartilage instead of hyaline cartilage, resulting in a tissue that is not adapted to the pressure and shear force that the joint is subjected to.[66,69,70] Furthermore, the number of MSC, their proliferative capacity, as well as their synthetic abilities declines with age.[77] The ultimate goal for human cartilage cell-based repair would be an off-the-shelf arthroscopic product based on a universal donor cell line combined with a suitable scaffold. For such cells their ethical aspects have to be acceptable and the immunogenic properties low as well as chondrogenic properties high. For this purpose cells have to be cultured in an industrial scale or within a hospital setting. For this type of cells, ATCS, umbilical cord stromal cells, and cell derived from hES cells fulfill the requirements to various extents.

5.514.9.1. Derivation of Chondrocytes from Human Embryonic Stem Cells

Human embryonic stem (hES) cells, derived from the inner cell mass of the human blastocyst, may have significant potential to be used in cartilage tissue engineering. The most prominent advantage of using hES cells in cartilage regeneration is that they are immortal and could potentially provide unlimited numbers of chondrocytes or chondro-progenitors for transplantation.

The majority of the published research concerning *in vitro* differentiation of embryonic stem (ES) cells into chondrocytes has been conducted on murine cells, using medium supplementation with members of the transforming growth factor-beta family (TGF-β) or bone morphogenic protein-2 and -4 (BMP-2, -4),[78] or by coculturing with embryonic limb buds.[79] The microenvironment of the culture has the capacity to influence cellular differentiation, and the ability to drive differentiation toward specific lineages in various coculture systems of embryonic tissues with stem/progenitor cells has been evaluated.[80–82] These efforts have provided important knowledge and contribute to a better understanding of the mechanisms underlying chondrogenic differentiation, even though the use of differentiated cells for cartilage tissue engineering still remains a challenge.

Conditioned media from cartilage progenitor cells did not induce increased chondrogenesis instead it supported the growth of a hES cell line that could be cultured without feeders (MFG-hESCs).[83] When subjected to bone differentiation the cell line has high similarities with MSCs and has a higher expansion capacity and also retains its differentiation capacity at higher passages[83] although with limited chondrogenic potential.

In order to increase the chondrogenic differentiation of hES cell lines the cells have been cocultured with mitotically inactivated human articular chondrocytes *in vitro*. These cocultured progenitors demonstrated the best chondrogenic differentiation capacity so far from progenitors derived from hES cells.[84] The system allows intimate contact between different cell types, thus resulting in more efficient transduction of molecular signals that induce chondrogenesis. The surface receptors of cocultured cells come into direct physical contact, and the autocrine and paracrine factors secreted by one cell type readily interact with the other cell type. In contrast to hES cells prior to the coculture and likewise chondrocytes, the cocultured hES cells were able to form and grow as pellets when cultured in 3D pellet mass

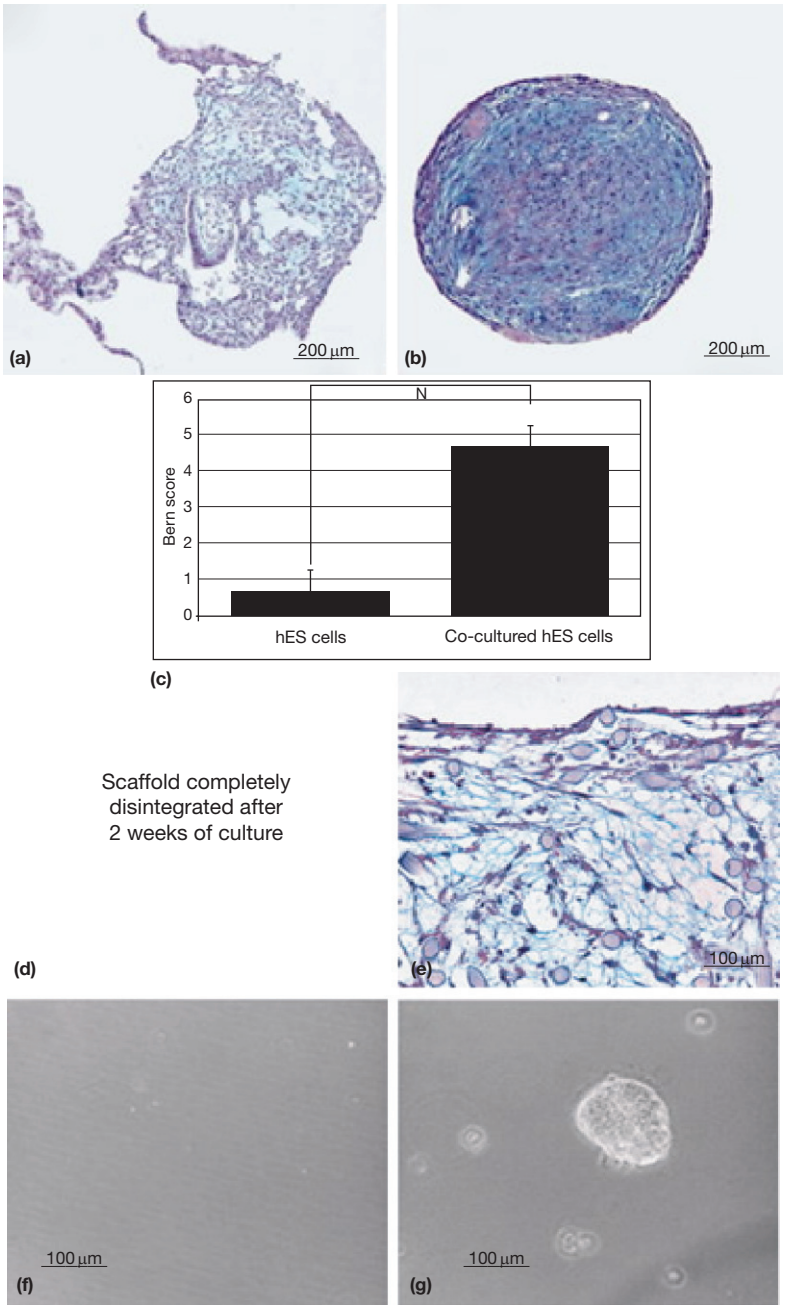

Figure 5 Chondrogenic differentiation. Pellet mass cultures stained with Alcian blue van Gieson of hES cells prior to (a) and after (b) coculture. Chondrogenesis of the pellets evaluated according to the Bern scale (c). Alcian blue van Gieson staining of hES cells prior to (d) and after (e) coculture in scaffold. Colony formation in agarose suspension culture of hES cells prior to (f) and after (g) coculture. hES cell, human embryonic stem cells. Reproduced from *Stem Cell*. **2009,** *27*(8), 1812–1821.

culture system. Interestingly, a number of studies have reported that coculture with chondrocytes has a positive effect on the osteogenic differentiation of MSC while coculture of chondrocytes and embryonic stem cells direct the cells into the chondrogenic lineage or significantly decreases the osteogenic potential of the cells.[81,85] MSC and hES cells thus respond differently to coculture with chondrocytes.

The cellular morphology of the cocultured cells in pellet cultures were similar to that of articular chondrocytes cultured in pellet mass cultures (Figure 5). Significantly improved differentiation toward the chondrogenic lineage of the cocultured cells was demonstrated both by their ability to form colonies in agarose-suspension culture with a morphology very similar to that of chondrocytes cultured under the same conditions as well as significantly increased accumulation of a cartilaginous matrix in pellet masses.[86] The only cell types with the ability to survive in agarose suspension culture are chondrocytes and tumor cells.[87,88] However, the cells had low expression of stem cell markers (CD117, CD133, SSEA-4), indicating a poor capacity of tumor formation of these cells.

Vats *et al*. recently demonstrated that coculture with chondrocytes from patients undergoing otorhinolaryngological–head and neck surgery and hES cells using well inserts for separating the cells displayed an increased accumulation of sulphated GAGs as well as expression of Sox9 and collagen type II.[89] In this study, differentiation was assessed after 28 days of coculture. Furthermore, mouse ES cells can be programmed to differentiate into chondrocyte-like cells by coculture with progenitor cells from the limb buds of the developing embryo.[79] In both of these studies, chondrocytes were present during the differentiation of the hES cells, either separated from the hES cells using a membrane or present in the micromass culture and eliminated after 4 days of culture.

In high-density pellet mass cultures it is difficult to direct the differentiation of the hES cells into only one specific lineage. Human ES cells cultured as pellets did not produce any cartilage-like matrix and the only hES pellet staining positive for Alcian blue van Gieson also resembled embryoid bodies with structures of cells differentiating into other tissues than cartilage. After coculture, a more homogenous, likely lineage restricted, population of cells have been formed with an increased potential for chondrogenic differentiation. In accordance, no teratoma formation could be detected in the cocultured cells after injection under the kidney capsule in SCID mice model confirming phenotypical alteration of the cells and lack of pluripotency. In conclusion, derivation of chondrocytes progenitors from human ES cells could be possible but a lot of work remains. Derivation of xeno-free culture systems has to be combined with better differentiation protocol since the cartilage formed has more similarities with fetal cartilage than with adult, a finding also demonstrated in keratinocytes derived from hES cells.[90]

5.514.9.2. Derivation of Chondrocytes from Umbilical Cord Cells and Umbilical Cord Blood Cells

The umbilical cord consists of umbilical veins and arteries and the supporting mesenchyme called Wharton's jelly (Figure 6) where MSC-like cells can be isolated. These cells are denoted WJCs and are derived from the surrounding matrix between the umbilical blood vessels.[91] The cells meet the criteria for stem cells as they have inherent self-renewal capacity and can be induced to differentiate into various cell types. The advantage of cells derived from the umbilical cord matrix is (i) the isolation of large numbers of cells without subsequent expansion in culture and (ii) that the cells are derived from fetal structures and could, like umbilical cord blood cells, thus have a better immunotolerance in the recipient patient.

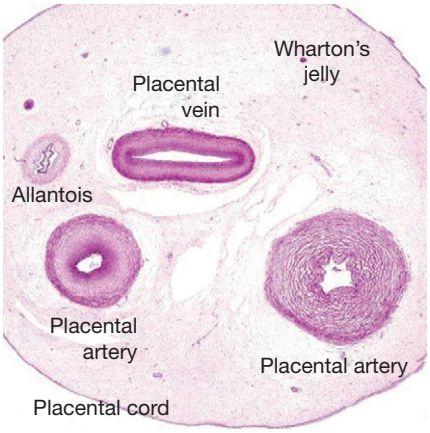

Figure 6 Wharton's jelly.

The question whether the different compartments of the umbilical cord have different MSCs has been addressed in experiments with cells isolated from umbilical cord blood, umbilical vein subendothelium, and the Wharton's jelly. Within Wharton's jelly, MSCs can been isolated from three indistinct regions: the perivascular zone, the intervascular zone, and the subamnion. It is not clear whether cells isolated from these different compartments of the umbilical cord represent distinctly different populations of MSCs. The WJCs express MSC surface markers, thus suggesting that they are of the MSC family; however, in experimental settings, WJCs differ from BMSCs because WJCs are slower in differentiating into adipocytes.[92] Since many features are shared with MSCs such as poor ability to differentiate to adipocytes, shorter doubling times than BMSCs, and greater numbers of passages to senescence, it not clear whether the MSCs derived from umbilical cord blood are different from those found in Wharton's jelly. For an extensive review, see Troyer and Weiss.[93]

However, the potential use of MSCs derived from umbilical cord or cord blood in the treatment of cartilage defects in humans remains to be established. Although the availability and immunogenicity could be of advantage, no scientific data today exist that support the notion that the cells are of lineage other than the bone default pathway.

5.514.10. Conclusion

The development of human cell therapy for cartilage repair over the last decades has both changed the stage and the view of cartilage as a nonregenerating tissue. We have only started to understand the cartilage tissue regeneration and repair and the potential use of cells for curing patients suffering from cartilage defects and OA. The autologous chondrocytes harvest is so far the best cell source for cartilage repair although other potential sources for a more universal treatment might be around the corner.

References

1. Hunter, W. *Philos. Trans.* **1744**, *42*, 514–521.
2. Wieland, H. A.; Michaelis, M.; Kirschbaum, B. J.; Rudolphi, K. A. *Nat. Rev. Drug Discov.* **2005**, *4*, 331–344.
3. Gelber, A. C.; Hochberg, M. C.; Mead, L. A.; Wang, N. Y.; Wigley, F. M.; Klag, M. J. *Ann. Intern. Med.* **2000**, *133*, 321–328.
4. Petersson, I. F.; Boegard, T.; Saxne, T.; Silman, A. J.; Svensson, B. *Ann. Rheum. Dis.* **1997**, *56*, 493–496.
5. Fuller, J. A.; Ghadially, F. N. *Clin. Orthop. Relat. Res.* **1972**, *86*, 193–205.
6. Aichroth, P. *J. Bone Joint Surg. Br* **1971**, *53*, 440–447.
7. Green, W. T., Jr. *Clin. Orthop. Relat. Res.* **1971**, *75*, 248–260.
8. Bentley, G.; Greer, R. B., III. *Nature* **1971**, *230*, 385–388.
9. Brittberg, M.; Lindahl, A.; Nilsson, A.; Ohlsson, C.; Isaksson, O.; Peterson, L. *N. Engl. J. Med.* **1994**, *331*, 889–895.
10. Peterson, L.; Brittberg, M.; Kiviranta, I.; Akerlund, E. L.; Lindahl, A. *Am J. Sports Med.* **2002**, *30*, 2–12.
11. Peterson, L.; Minas, T.; Brittberg, M.; Nilsson, A.; Sjogren-Jansson, E.; Lindahl, A. *Clin. Orthop.* **2000**, 212–234.
12. Petersen, L.; Brittberg, M.; Lindahl, A. *Foot Ankle Clin.* **2003**, *8*, 291–303.
13. Peterson, L.; Minas, T.; Brittberg, M.; Lindahl, A. *J. Bone Joint Surg. Am.* **2003**, *85-A*(Suppl. 2), 17–24.
14. Bentley, G.; Biant, L. C.; Carrington, R. W.; *et al. J. Bone Joint Surg. Br.* **2003**, *85*, 223–230.
15. Saris, D. B.; Vanlauwe, J.; Victor, J.; *et al. Am. J. Sports Med.* **2008**, *36*, 235–246.
16. Visna, P.; Pasa, L.; Cizmar, I.; Hart, R.; Hoch, J. *Acta Chir. Belg.* **2004**, *104*, 709–714.
17. Knutsen, G.; Engebretsen, L.; Ludvigsen, T. C.; *et al. J. Bone Joint Surg. Am* **2004**, *86-A*, 455–464.
18. Dozin, B.; Malpeli, M.; Cancedda, R.; *et al. Clin. J. Sport Med.* **2005**, *15*, 220–226.
19. Peterson, L.; Vasiliadis, H. S.; Brittberg, M.; Lindahl, A. *Am. J. Sports Med.* **2010**, *38*, 1117–1124.
20. Vasiliadis, H. S.; Danielson, B.; Ljungberg, M.; Mckeon, B.; Lindahl, A.; Peterson, L. *Am. J. Sports Med.* **2010**, *38*, 943–949.
21. Mimeault, M.; Hauke, R.; Batra, S. K. *Clin. Pharmacol. Ther.* **2007**, *82*, 252–264.
22. Canestro, C.; Yokoi, H.; Postlethwait, J. H. *Nat. Rev. Genet.* **2007**, *8*, 932–942.
23. Moore, K. A.; Lemischka, I. R. *Science* **2006**, *311*, 1880–1885.
24. Boyden, L. M.; Mao, J.; Belsky, J.; *et al. N. Engl. J. Med.* **2002**, *346*, 1513–1521.
25. Conboy, I. M.; Conboy, M. J.; Smythe, G. M.; Rando, T. A. *Science* **2003**, *302*, 1575–1577.
26. Liu, H.; Fergusson, M. M.; Castilho, R. M.; *et al. Science* **2007**, *317*, 803–806.
27. Brack, A. S.; Conboy, M. J.; Roy, S.; *et al. Science* **2007**, *317*, 807–810.
28. Tallheden, T.; Karlsson, C.; Brunner, A.; *et al. Osteoarthritis Cartilage* **2004**, *12*, 525–535.
29. Watanabe, N.; Tezuka, Y.; Matsuno, K.; *et al. J. Bone Miner. Metab.* **2003**, *21*, 344–352.
30. Archer, C. W.; Dowthwaite, G. P.; Francis-West, P. *Birth Defects Res. C Embryo Today* **2003**, *69*, 144–155.
31. Karlsson, C.; Brantsing, C.; Egell, S.; Lindahl, A. *Cells Tissues Organs* **2008**, *188*, 287–298.
32. Kerkhof, H. J.; Lories, R. J.; Meulenbelt, I.; *et al. Arthritis Rheum.* **2010**, *62*, 499–510.
33. Chapman, K.; Takahashi, A.; Meulenbelt, I.; *et al. Hum. Mol. Genet.* **2008**, *17*, 1497–1504.
34. Meulenbelt, I.; Min, J. L.; Bos, S.; *et al. Hum. Mol. Genet.* **2008**, *17*, 1867–1875.
35. Loughlin, J.; Dowling, B.; Chapman, K.; *et al. Proc. Natl Acad. Sci. USA* **2004**, *101*, 9757–9762.
36. Evangelou, E.; Chapman, K.; Meulenbelt, I.; *et al. Arthritis Rheum.* **2009**, *60*, 1710–1721.
37. Kember, N. F. *Clin. Orthop. Relat. Res.* **1973**, *95*, 288–294.
38. Shapiro, F. *Eur. Cell Mater.* **2008**, *15*, 53–76.
39. Pacifici, M.; Koyama, E.; Iwamoto, M. *Birth Defects Res. C Embryo Today* **2005**, *75*, 237–248.
40. Reddi, A. H. *Coll. Relat. Res.* **1981**, *1*, 209–226.
41. Storm, E. E.; Kingsley, D. M. *Dev. Biol.* **1999**, *209*, 11–27.
42. Koyama, E.; Shibukawa, Y.; Nagayama, M.; *et al. Dev. Biol.* **2008**, *316*, 62–73.
43. Thomas, J. T.; Kilpatrick, M. W.; Lin, K.; *et al. Nat. Genet.* **1997**, *17*, 58–64.
44. Spater, D.; Hill, T. P.; O'Sullivan, R. J.; Gruber, M.; Conner, D. A.; Hartmann, C. *Development* **2006**, *133*, 3039–3049.
45. Barbero, A.; Ploegert, S.; Heberer, M.; Martin, I. *Arthritis Rheum.* **2003**, *48*, 1315–1325.
46. Dell'Accio, F.; De Bari, C.; Luyten, F. P. *Exp. Cell. Res.* **2003**, *287*, 16–27.
47. Cotsarelis, G. *J. Clin. Invest.* **2006**, *116*, 19–22.
48. Watt, F. M. *Curr. Opin. Genet. Dev.* **2001**, *11*, 410–417.
49. Shapiro, F.; Holtrop, M. E.; Glimcher, M. J. *J. Bone Joint Surg. Am.* **1977**, *59*, 703–723.
50. Fenichel, I.; Evron, Z.; Nevo, Z. *Int. Orthop.* **2006**, *30*, 353–356.
51. Riseborough, E. J.; Barrett, I. R.; Shapiro, F. *J. Bone Joint Surg. Am.* **1983**, *65*, 885–893.
52. Karlsson, C.; Thornemo, M.; Henriksson, H. B.; Lindahl, A. *J. Anat.* **2009**, *215*, 355–363.
53. Henriksson, H.; Thornemo, M.; Karlsson, C.; Hagg, O.; Junevik, K.; Lindahl, A. *Spine* **2009**, *34*, 2278–2287.
54. Mooney, D. J.; Mazzoni, C. L.; Breuer, C.; *et al. Biomaterials* **1996**, *17*, 115–124.
55. Marcacci, M.; Berruto, M.; Brocchetta, D.; *et al. Clin. Orthop. Relat. Res.* **2005**, 96–105.
56. Sandell, L. J.; Aigner, T. *Arthritis Res.* **2001**, *3*, 107–113.
57. Teshima, R.; Treadwell, B. V.; Trahan, C. A.; Mankin, H. J. *Arthritis Rheum.* **1983**, *26*, 1225–1230.
58. Tallheden, T.; Bengtsson, C.; Brantsing, C.; *et al. Arthritis Res. Ther.* **2005**, *7*, R560–R568.
59. Bulstra, S. K.; Buurman, W. A.; Walenkamp, G. H.; Van Der Linden, A. J. *Clin. Orthop. Relat. Res.* **1989**, 294–302.
60. Dehne, T.; Karlsson, C.; Ringe, J.; Sittinger, M.; Lindahl, A. *Arthritis Res. Ther.* **2009**, *11*, R133.
61. Stoop, R.; Albrecht, D.; Gaissmaier, C.; *et al. Arthritis Res. Ther.* **2007**, *9*, R60.
62. Bruder, S. P.; Jaiswal, N.; Haynesworth, S. E. *J. Cell. Biochem.* **1997**, *64*, 278–294.
63. Friedenstein, A. J.; Chailakhyan, R. K.; Latsinik, N. V.; Panasyuk, A. F.; Keiliss-Borok, I. V. *Transplantation.* **1974**, *17*, 331–340.
64. Ferrari, G.; Cusella-De Angelis, G.; Coletta, M.; *et al. Science* **1998**, *279*, 1528–1530.
65. Dennis, J. E.; Merriam, A.; Awadallah, A.; Yoo, J. U.; Johnstone, B.; Caplan, A. I. *J. Bone Miner. Res.* **1999**, *14*, 700–709.
66. Kadiyala, S.; Young, R. G.; Thiede, M. A.; Bruder, S. P. *Cell Transplant.* **1997**, *6*, 125–134.
67. Young, R. G.; Butler, D. L.; Weber, W.; Caplan, A. I.; Gordon, S. L.; Fink, D. J. *J. Orthop. Res.* **1998**, *16*, 406–413.
68. Caplan, A. I. *J. Orthop. Res.* **1991**, *9*, 641–650.
69. Im, G. I.; Kim, D. Y.; Shin, J. H.; Hyun, C. W.; Cho, W. H. *J. Bone Joint Surg. Br.* **2001**, *83*, 289–294.
70. Ichinose, S.; Tagami, M.; Muneta, T.; Sekiya, I. *Cell Tissue Res.* **2005**, *322*, 217–226.
71. Karlsson, C.; Brantsing, C.; Svensson, T.; *et al. J. Orthop. Res.* **2007**, *25*, 152–163.
72. Mishima, Y.; Lotz, M. *J. Orthop. Res.* **2008**, *26*, 1407–1412.
73. Bai, X.; Xiao, Z.; Pan, Y.; *et al. Biochem. Biophys. Res. Commun.* **2004**, *325*, 453–460.
74. Frisbie, D. D.; Kisiday, J. D.; Kawcak, C. E.; Werpy, N. M.; Mcilwraith, C. W. *J. Orthop. Res.* **2009**, *27*, 1675–1680.
75. Lee, R. H.; Kim, B.; Choi, I.; *et al. Cell. Physiol. Biochem.* **2004**, *14*, 311–324.
76. Rada, T.; Reis, R. L.; Gomes, M. E. *Stem Cell Rev.* **2010**, *7*(1), 64–76.
77. Pittenger, M. F.; MacKay, A. M.; Beck, S. C.; *et al. Science* **1999**, *284*, 143–147.
78. Kramer, J.; Hegert, C.; Guan, K.; Wobus, A. M.; Muller, P. K.; Rohwedel, J. *Mech. Dev.* **2000**, *92*, 193–205.
79. Sui, Y.; Clarke, T.; Khillan, J. S. *Differentiation* **2003**, *71*, 578–585.
80. Fair, J. H.; Cairns, B. A.; Lapaglia, M.; *et al. Surgery* **2003**, *134*, 189–196.
81. Gerstenfeld, L. C.; Barnes, G. L.; Shea, C. M.; Einhorn, T. A. *Connect. Tissue Res.* **2003**, *44*(Suppl. 1), 85–91.
82. Song, H. J.; Stevens, C. F.; Gage, F. H. *Nat. Neurosci.* **2002**, *5*, 438–445.
83. Bigdeli, N.; Andersson, M.; Strehl, R.; *et al. J. Biotechnol.* **2008**, *133*, 146–153.
84. Bigdeli, N.; Karlsson, C.; Strehl, R.; Concaro, S.; Hyllner, J.; Lindahl, A. *Stem Cells* **2009**, *27*, 1812–1821.
85. Gerstenfeld, L. C.; Cruceta, J.; Shea, C. M.; Sampath, K.; Barnes, G. L.; Einhorn, T. A. *J. Bone Miner. Res.* **2002**, *17*, 221–230.
86. Thornemo, M.; Tallheden, T.; Sjogren Jansson, E.; *et al. Cells Tissues Organs* **2005**, *180*, 141–150.
87. Benya, P. D.; Shaffer, J. D. *Cell* **1982**, *30*, 215–224.
88. Wittelsberger, S. C.; Kleene, K.; Penman, S. *Cell* **1981**, *24*, 859–866.
89. Vats, A.; Bielby, R. C.; Tolley, N.; *et al. Tissue Eng.* **2006**, *12*, 1687–1697.
90. Iuchi, S.; Dabelsteen, S.; Easley, K.; Rheinwald, J. G.; Green, H. *Proc. Natl Acad. Sci. USA* **2006**, *103*, 1792–1797.
91. Mitchell, K. E.; Weiss, M. L.; Mitchell, B. M.; *et al. Stem Cells* **2003**, *21*, 50–60.
92. Lu, L. L.; Liu, Y. J.; Yang, S. G.; *et al. Haematologica* **2006**, *91*, 1017–1026.
93. Troyer, D. L.; Weiss, M. L. *Stem Cells* **2008**, *26*, 591–599.

5.515. Cartilage Tissue Engineering

W J McCarty, Q T Nguyen, A Y Hui, A C Chen, and R L Sah, University of California-San Diego, La Jolla, CA, USA

© 2011 Elsevier Ltd. All rights reserved.

5.515.1.	**Introduction**	200
5.515.2.	**Articular Cartilage Maturation and Synovial Fluid Formation**	201
5.515.2.1.	Articular Cartilage Structure and Maturation	201
5.515.2.1.1.	Overview	201
5.515.2.1.2.	Composition	201
5.515.2.1.3.	Structure	201
5.515.2.1.4.	Function	201
5.515.2.1.5.	Cartilage maturation	201
5.515.2.2.	Synovial Fluid Composition and Formation	202
5.515.2.2.1.	Overview	202
5.515.2.2.2.	Composition	202
5.515.2.2.3.	Formation, molecular transport, and mechanobiology	203
5.515.3.	**Mechanical Properties and Models of Articular Cartilage and Synovial Fluid**	203
5.515.3.1.	Biomechanics of Articular Cartilage	203
5.515.3.1.1.	Types of mechanical loading during joint articulation	203
5.515.3.1.2.	Physiological loading of articular cartilage during gait	203
5.515.3.2.	Rheology and Tribology of Synovial Fluid	203
5.515.3.2.1.	Rheological properties	203
5.515.3.2.2.	Tribological properties	204
5.515.3.3.	Modeling Joint Tissue Biology	204
5.515.3.3.1.	Models of individual joint tissues	204
5.515.3.3.2.	Multicomponent models of the synovial joint	204
5.515.3.3.3.	Extending current models of the synovial joint	204
5.515.4.	**Mechanical Effects on Cartilage Maturation and Synovial Fluid Pathology**	206
5.515.4.1.	Effect of Mechanical Stimuli on Cartilage Maturation	206
5.515.4.1.1.	Overview	206
5.515.4.1.2.	Effects of mechanical loads on cartilage metabolism	206
5.515.4.1.3.	Effects of mechanical loads on cartilage composition, structure, and function	207
5.515.4.2.	Synovial Fluid Pathology	207
5.515.4.2.1.	Overview	207
5.515.4.2.2.	Changes in composition	208
5.515.4.2.3.	Changes in formation and molecular transport	208
5.515.4.2.4.	Changes in rheology and tribology	208
5.515.5.	**Engineering Cartilaginous Tissue and Synovial Fluid**	208
5.515.5.1.	Engineered Cartilaginous Tissue	208
5.515.5.1.1.	General overview	208
5.515.5.1.2.	Bioreactors	208
5.515.5.1.3.	Effects of physical stimuli on cartilaginous tissue growth and maturation	209
5.515.5.2.	Tissue Engineering Synovial Fluid	210
5.515.5.2.1.	Overview	210
5.515.5.2.2.	Viscosupplementation	210
5.515.5.2.3.	Biomimetic approaches	210
References		210

Glossary

Articular cartilage The cartilage covering the articular surfaces of the bones participating in a synovial joint.
Compartmental model A mathematical model that simplifies the description of the behavior of spatially distributed physical systems into a topology consisting of discrete entities that approximate the behavior of the distributed system under certain assumptions.
Mechanobiology The study of how cells sense and respond to mechanical stimuli.
Modulus The physical measurement of stiffness in a material, equaling the ratio of applied load (stress) to the

resultant deformation of the material, such as compression, tension, or shear.

Osteoarthritis Arthritis characterized by erosion of articular cartilage, either primary or secondary to trauma or other conditions, which becomes soft, frayed, and thinned with eburnation of subchondral bone and outgrowths of marginal osteophytes; pain and loss of function result; mainly affects weight-bearing joints, is more common in old people and animals.

Rheology The study of the flow or deformation of materials.

Synovial fluid A clear thixotropic fluid, the main function of which is to serve as a lubricant in a joint, tendon sheath, or bursa; consists mainly of mucin with some albumin, fat, epithelium, and leukocytes; also helps to nourish the avascular articular cartilage.

Synovial joint A joint in which the opposing bony surfaces are covered with a layer of hyaline cartilage or fibrocartilage; there is a joint cavity containing synovial fluid, lined with synovial membrane and reinforced by a fibrous capsule and ligaments, and there is some degree of free movement possible.

Tribology The study of friction and its effects in biologic systems, especially in regard to articulated surfaces of the skeleton.

Viscosupplementation Intraarticular injection of a viscous agent, often hyaluronan-based compounds.

Abbreviations

ACL	Anterior cruciate ligament
BF	Bioengineered fluid
COL	Collagen
CPM	Continuous passive motion
ECM	Extracellular matrix
(s)GAG	(sulfated) Glycosaminoglycan
HA	Hyaluronic acid
IGF	Insulin growth factor
IL	Interleukin
LIF	Leukemia inhibitory factor
MMP	Matrix metalloproteinase
MW	Molecular weight
OA	Osteoarthritis
PG	Proteoglycan
PRG4	Proteoglycan 4
RA	Rheumatoid arthrtitis
SF	Synovial fluid
SZCs	Superficial zone chondrocytes
TGF	Transforming growth factor
TNF	Tumor necrosis factor

5.515.1. Introduction

Synovial joints are the most numerous type of joint in the body and allow for movement between long bones. Synovial joints, including the knees, hips, shoulders, elbows, and phalangeals, are characterized by articular cartilage, a connective tissue at the ends of the articulating bones, which is bathed in synovial fluid (SF), a viscous, lubricating fluid that is constrained within the joint by a fibrous joint capsule. Articular cartilage grows and matures through adulthood in response to physiological cues, including mechanical forces, while SF is an ultrafiltrate of blood plasma, filtered through the joint capsule with additional lubricant molecules secreted by local cell populations. The mechanical properties of these tissues allow for their physiological function. The extracellular matrix (ECM) of cartilage resists compression and tension, allowing for load-bearing during joint motion, while the viscous and lubricating properties of SF reduce cartilage wear due to articulation. The homeostasis of these tissues is dependent on mechanobiology – cell populations receiving mechanical cues to guide biosynthesis and thereby alter their microenvironment and tissue-scale mechanical properties.

Synovial joints are susceptible to damage from injury and disease, including osteoarthritis (OA). OA is an age-related degenerative joint disease characterized by erosion of articular cartilage, leading to joint pain and restricted motion. In addition to generalized cartilage erosion in OA, focal regions of degenerated or eroded cartilage are commonly seen during arthroscopy of non-OA joints. Treatment options for OA are limited, including injectible analgesics and total knee arthroplasty, while options for focal defects are more numerous, including auto- and allografts, and tissue-engineered cells and/or scaffolds, including autologous chondrocytes implantation and matrix-induced chondrocytes implantation, and a variety of other natural and synthetic, cellular and acellular scaffolds. Tissue engineering approaches to the treatment of cartilage degeneration are evolving toward more complex, biomimetic, and shaped constructs that can be used for even larger regions of cartilage damage and biological SF replacements.[1]

Advances in tissue engineering approaches to the *in vitro* development of articular cartilage and SF for the treatment and study of damaged synovial joints are covered in this chapter. Tissue engineering approaches are based on an understanding of human and animal joint physiology in health, injury, and disease, and data from and relating to those different states interpreted through analytical models (**Figure 1**). First, the composition, structure, and function of cartilage and SF, including the natural growth and development of cartilage and formation of SF, are discussed, followed by the mechanical properties of these tissues and the theoretical models that have been used to describe them, including a compartmental model for integrating different synovial joint tissue types. Next, the effects of mechanical stimuli on cartilage chondrocyte biosynthesis and pathological changes in SF composition and function are covered. Finally, advances in the tissue engineering of cartilaginous tissue and SF are reviewed, focusing on the mechanobiology of chondrocytes embedded in tissue-engineered constructs.

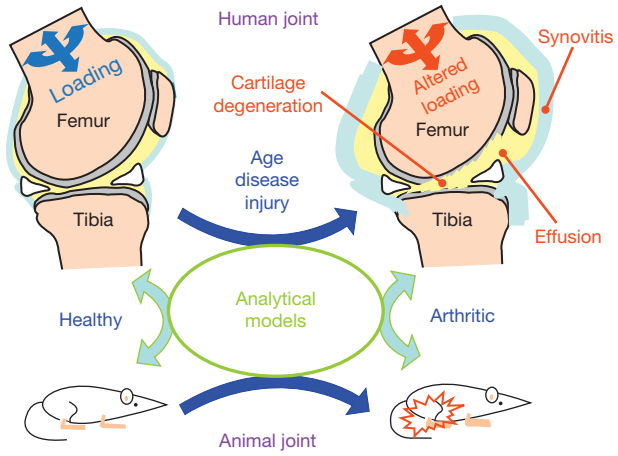

Figure 1 Schematic view of how data from the human system and animal models in normal and diseased states can be integrated and analyzed using models of the joint.

5.515.2. Articular Cartilage Maturation and Synovial Fluid Formation

5.515.2.1. Articular Cartilage Structure and Maturation

5.515.2.1.1. Overview

Articular cartilage is a connective tissue that covers the ends of long bones and functions as a load-bearing, low-friction, and wear-resistant surface to facilitate joint movement. Articular cartilage is composed of chondrocytes embedded in a hydrated and specialized ECM that consists mostly of collagen (COL) type II and proteoglycan (PG) (see **Chapter 2.215, Collagen: Materials Analysis and Implant Uses** and **Chapter 2.216, Collagen–GAG Materials**).[2] PG provides cartilage with compressive strength due to the fixed charge density of these molecules that create an osmotic swelling pressure. The COL network resists the swelling tendency of PG molecules and provides cartilage functional integrity, tensile and shear stiffness, and strength. Cell and matrix contents, as well as mechanical properties of cartilage, vary with depth from the superficial surface. During growth and maturation of articular cartilage, there are significant changes in cellular distribution, cartilage composition, structure, and mechanical function.

5.515.2.1.2. Composition

Chondrocytes, the main cell type of articular cartilage, contribute 1–10% of the total volume of cartilage and are responsible for maintenance of COL and PG by balancing synthesis and degradation. Cellular content and organization in articular cartilage vary with depth. Cell density is relatively high in the superficial zone (0–10% of total thickness)[3] and decreases by 59–67% in the deep zone (40–100% of total thickness).[4] The ECM of articular cartilage provides a suitable microenvironment to maintain chondrocytes' phenotype and biosynthetic homeostasis.[5] PG content ranges from 1 to 10% of total wet weight and increases with depth.[6,7] COL accounts for 10–20% of the wet weight of adult articular cartilage, is rich in the superficial layer, and is distributed evenly from middle to deep layer.[2,6–8]

5.515.2.1.3. Structure

Chondrocytes are arranged distinctly in the different zones of articular cartilage. In the superficial zone, cells are arranged in clusters parallel to the articular surface with a flattened morphology and smaller nuclei with similar shape. Cells in the middle region appear more rounded with some nuclei arranged in pairs. Cells in the deeper region of adult cartilage are organized into columns.[4,9]

The size and organization of collagen fibrils in articular cartilage varies with depth. Collagen in the superficial zone of adult cartilage consists of thin fibrils oriented parallel to the articular surface, while middle and deeper zones contain fibrils that are thicker and increasingly oriented in the vertical direction.[10] The depth-varying collagen structure contributes to the depth-dependent tensile and shear properties of cartilage.

5.515.2.1.4. Function

The PG content in cartilage, together with the COL network, is the major determinant of the tissue's compressive properties.[11,12] PG aggregates are large molecules formed as aggrecan monomers noncovalently associated with hyaluronan and stabilized by link protein. Each aggrecan monomer has a large number of sulfated glycosaminoglycan (sGAG) chains of chondroitin sulfate and keratan sulfate. The polyanionic sGAG moieties of aggrecan molecules, when restrained by the COL network, provide cartilage with a high osmotic pressure, a high tendency to retain water, and a high resistance to fluid flow. The swelling pressure exerted by the PG contributes to a high resistance to compression and the tensile stress of COL network.[13]

The COL network composition and organization, in part modulated by PG, appears to be the major determinant of cartilage tensile properties. The COL to PG ratio as well as COL network organization within the tissue correlates strongly with equilibrium tensile modulus of cartilage.[14,15] The balance of the swelling propensity of PG molecules and the restraining function of COL network influences tissue hydration, load-bearing, and tensile properties. *In vitro* inhibition of functional assembly of the COL network causes marked decrease in tensile strength of cartilage explants after 13 days in culture.[16,17] In immature cartilage, PG indirectly affects the tensile properties of cartilage. Depolymerization of chondroitin and dermatan sulfate glycosaminoglycan (GAG) chains of PG molecules by chondroitinase ABC[18] resulted in an increase in overall tensile modulus.[19–21] In addition, PG depletion in immature cartilage with guanidine markedly increases tissue tensile integrity.[16,17]

5.515.2.1.5. Cartilage maturation

Cellular density and organization in articular cartilage change markedly with growth and maturation. In bovine cartilage, cellular density undergoes minor changes from fetal to calf, but decreases significantly (~50%) from calf to adult. In the deep zone, chondrocytes of mature cartilage are arranged in columns, whereas those of immature cartilage do not exhibit zonal organization and appear similar to cells in the middle zone.[22]

The biochemical properties of articular cartilage change with growth and maturation. There are gradual alterations in COL network as well as COL and PG contents. At early developmental stages of cartilage, the COL network does not appear to organize in a zonal manner and orients parallel to the cartilage surface throughout the tissue.[23,24] As cartilage matures, its water content decreases markedly, COL and

pyridinoline crosslink densities increase, while PG density stays relatively constant.[12,15,25] At the young adult stage, the fibrils of the deep zone run predominantly perpendicular to the cartilage surface.[24] In adult tissue, COL fibers are arranged parallel to the articular surface in superficial zone, isotropic and random in the middle zone, and perpendicular in the deep zone.[10]

During growth and maturation of articular cartilage, the mechanical properties evolve toward that of the adult. In bovine articular cartilage, from the fetal stage, through the new born calf, and to the skeletally mature adult, cartilage becomes stiffer both in compression and tension as indicated by increases in equilibrium aggregate modulus (89 kPa in fetal, 197 kPa in newborn to 890 kPa in young adult bovine), equilibrium tensile modulus (2 MPa in calf to 5–6 MPa in young adult bovine), and tensile strength (4 MPa in calf to 15 MPa in young adult bovine).[5,16,17,26] The remarkable changes in biochemical and mechanical properties of cartilage with maturation may be due to regulation by mechanical and chemical factors. Once tissue reaches maturity, articular cartilage homeostasis in terms of composition and function is desirable.

5.515.2.2. Synovial Fluid Composition and Formation

5.515.2.2.1. Overview

SF is normally a clear, viscous liquid found inside synovial joints that functions as a biomechanical lubricant and as a medium for metabolites and soluble signaling factors. In the normal human knee joint, the volume of SF is on the order of 1 ml.[27] In their typical proportions and concentrations, the molecular constituents comprising normal SF give rise to its unique properties and functions in maintaining joint homeostasis. SF is composed of a blood plasma dialysate and molecules secreted by cells lining the synovial joint (**Figure 2**), including hyaluronic acid (HA) (see **Chapter 2.214, Hyaluronic Acid**) and proteoglycan 4 (PRG4, also known as lubricin and superficial zone protein). One main function of SF is to lubricate articulating joints, facilitating the low-friction and low-wear properties of cartilage. Additionally, it serves metabolic functions, facilitating the transport of nutrients, waste products, and other metabolites to and from synovial tissues. Finally, it mediates molecular communication by soluble factors between disparate cell populations in the joint.

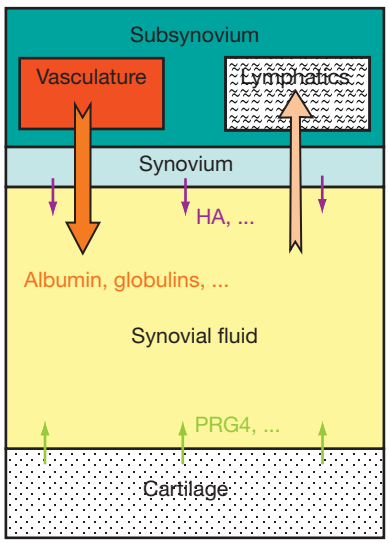

Figure 2 Schematic view of synovial fluid formation as an ultrafiltrate of blood plasma with additional lubricant molecules secreted by synoviocytes and chondrocytes.

5.515.2.2.2. Composition

5.515.2.2.2.1. Plasma proteins

The composition of SF reflects its origin as a plasma ultrafiltrate. The protein composition of SF is similar to that of plasma,[28,29] though synovium selectively retains most large plasma proteins in the vasculature and limits their entry into the synovial joint space. In normal human SF, the total protein content is 25–28 mg ml^{-1}, which is approximately one-third of the total protein concentration in plasma.[27,30] Large molecular weight (MW) plasma proteins, such as β_2 macroglobulin (1000 kDa), fibrinogen (340 kDa), β_1 lipoprotein (3200 kDa), α_2 macroglobulin (820 kDa), and α_2 glycoprotein (1000 kDa), are low or undetectable in normal SF as determined by immunoelectrophoresis, while small MW plasma proteins, such as albumin (69 kDa), α_1 glycoproteins, transferrin (90 kDa), and γ globulin (160 kDa), are found in high quantities in plasma and SF.[31,32] The most abundant macromolecule in SF is albumin (~10 mg ml^{-1}), which is found in SF at 40–45% of its plasma concentration, and is a major contributor to SF colloidal osmotic pressure and a minor contributor to SF viscosity.[33] Globulins are also present at ~0.5 mg ml^{-1}. SF does not contain fibrinogen.

5.515.2.2.2.2. Lubricant macromolecules

The main lubricating macromolecules present in SF are HA[34] and PRG4.[35,36] HA is a GAG consisting of repeating disaccharide units of D-glucuronic acid and D-*N*-acetylglucosamine. It exists in SF as a polydisperse population with 60–70% of the HA having a MW greater than 4 MDa and a weight average MW of 6–7 MDa.[37] The concentration of HA plays a major role in determining the viscosity of SF. In addition, HA provides outflow buffering, a phenomenon which decreases trans-SF loss under raised intraarticular pressures.[38] PRG4 is a mucinous glycoprotein with multiple O-linked β(1-3)Gal-GalNAc oligosaccharides, which mediate the molecule's function as a boundary lubricant,[39,40] and has a MW of ~300 kDa.[41] The PRG4 gene encodes a lubricating glycoprotein known as SZP, lubricin, or PRG4 found in SF, articular cartilage, synovium, and other synovial tissues.[42,43]

5.515.2.2.2.3. Cytokines and growth factors

Although a minor component of SF by mass, cytokines and growth factors, which include members of the transforming growth factor (TGF), interleukin (IL), and tumor necrosis factor (TNF) families, exert regulatory control over cell populations in the synovial joint (see **Chapter 5.522, Bone Tissue Engineering: Growth Factors and Cytokines**). These signaling factors may be derived from plasma through ultrafiltration or may be secreted by cells lining the synovial joint into SF. They can participate in intercell signaling, influencing cellular metabolism such as lubricant secretion rates. Proinflammatory cytokines, which have catabolic action in general, that are found in SF include IL-1α, IL-1β, TNF-α, leukemia inhibitory factor (LIF), IL-6, IL-8, IL-17, and IL-18.[44–46] Anti-inflammatory cytokines include IL-4, IL-10, and IL-13. Growth factors such as TGF-β1

and insulin growth factor 1 (IGF-1) have anabolic effects on tissues. Chondrocytes and synovial fibroblasts are the target of many of these biochemical signals.[47,48] By nature of its physical contact with all synovial joint tissues, SF serves as a medium through which these tissues, including cartilage, synovium, meniscus, and ligament, can interact.

5.515.2.2.2.4. Cells

Normal SF contains relatively few cells compared to whole blood. Monocytes and lymphocytes are the predominant nucleated cells present, with SF averaging ~63 nucleated cells per mm^3,[27] while erythrocytes are largely absent. Reference ranges for blood tests include $4.0–5.6 \times 10^6$ erythrocytes and $3.54–9.06 \times 10^3$ white blood cells per mm^3.[49]

5.515.2.2.3. Formation, molecular transport, and mechanobiology

5.515.2.2.3.1. Formation

SF is an ultrafiltrate of blood plasma with additional molecules secreted by cells lining synovial joints. The synovium functions as a semipermeable membrane that selectively retains and permits specific molecules based on size. The biosynthetic sources of SF lubricant molecules are the cell populations lining the synovial cavity, with synoviocytes mainly secreting HA and superficial zone chondrocytes (SZCs),[41] synoviocytes,[39,40,50,51] and meniscal cells[52] secreting PRG4. High MW species, such as the lubricant molecules HA and PRG4, are selectively retained within the synovial joint, while low MW species, such as most metabolic substrates and byproducts, cytokines, and growth factors, are not. Molecular sieving by the synovial membrane matrix is size dependent.[53] An active filtration process, together with secretory contributions from the cell populations lining the synovial joint, results in fluid with typical steady-state concentrations of 1–4 mg ml^{-1} HA[54] and 0.05–0.35 mg ml^{-1} PRG4.

5.515.2.2.3.2. Transport characteristics of synovium

Synovium, a highly cellular intimal tissue layer adjacent to the intraarticular space, is composed of ECM molecules, including HA, collagen, and PGs. It is the main barrier to the transport of molecules, such as lubricants, into and out of SF. Fluid flow through synovium occurs through the ~2 μm[55] wide intercellular regions of ECM, which has a hydraulic conductivity of $\sim 10^{-11}$ $cm^4(s^{-1}\,dyne^{-1})$ in rabbits.[33] Diffusive and convective passive transport of molecules occurs through pores in the ECM (~20–90 nm in diameter)[53,56] at these intercellular openings, making synovium permeability inversely related to molecule size. High MW lubricant molecules are retained in the joint, as the reflection coefficient of synovium to high MW HA has been reported as ~57–75%.[57]

5.515.2.2.3.3. Mechanobiology of lubricant-secreting cells

The secretion rates of the main lubricant molecules HA and PRG4 by synoviocytes and SZCs, respectively, are mechanosensitive. At the cellular level, HA secretion by isolated synoviocytes grown to confluence increased by 57% over 3 h when stretched by 10% for as little as 10 min.[58] At the joint scale, passive flexion of anesthetized rabbit knees resulted in a 100% increase in HA secretion over 5 h, decreasing the HA turnover time estimates from 17–30 to 8–15 h.[59] Dynamic mechanical shear of calf cartilage explants increased PRG4 expression to 300–400% of free-swelling and static compression controls.[60,61] In an experiment applying continuous passive motion (CPM) to *en bloc* calf knee joints, increased local cartilage superficial zone secretion rates of PRG4 correlated with areas in continuous or intermittent sliding contact with apposing surfaces.[62]

5.515.3. Mechanical Properties and Models of Articular Cartilage and Synovial Fluid

5.515.3.1. Biomechanics of Articular Cartilage

5.515.3.1.1. Types of mechanical loading during joint articulation

During normal joint articulation, cartilage is subjected to compression, shear, and sliding. When cartilage is compressed,[5] interstitial fluid pressurizes resulting in the load being mainly supported by hydrostatic pressure. As compression continues, fluid begins to exude out of the matrix, transferring load from interstitial fluid to the solid matrix and causing the cartilage to deform. Once equilibrium is reached, fluid flow out of the tissue ceases, and total load support is provided by the solid matrix.

5.515.3.1.2. Physiological loading of articular cartilage during gait

Articular cartilage deforms in response to joint loading. During normal activities such as walking or running, articular joint surfaces come into contact, roll, and slide past each other, subjecting cartilage tissue to both compression and shear. Knee cartilage is compressed by ~3–10% of its overall thickness following various physical activities, such as walking, cycling, running, and knee bending.[63,64] Under normal loading, talar cartilage appears to be compressed by 5–35%, with 42% of the contact area having compressive strain higher than 15%.[65] Cartilage also deforms in shear when subjected to combined compression and shear loads. For normal adult human femoral cartilage tested with normal SF, shear strain reached 5.6% near the articular surface and 2.8% overall, increasing markedly with degeneration to 28% and 4.1%, respectively.[66,67] After reaching a peak shear strain, with increasing lateral motion, cartilage surfaces slide relative to each other while peak shear is maintained.[66,67]

5.515.3.2. Rheology and Tribology of Synovial Fluid

5.515.3.2.1. Rheological properties

The rheological properties of SF have been characterized using measurements of viscosity and viscoelasticity. The viscosity of SF strongly correlates with the concentration of HA present.[68] SF exhibits non-Newtonian viscous behavior, acting as a shear-thinning fluid over a wide range of shear rates, with higher viscosities reported at higher HA concentrations.[69] Viscoelastic models of SF have demonstrated an elastic-like response from 'normal' SF at high frequencies of oscillation, with dynamic storage and loss moduli on the order of ~10 Pa, depending on shear rate.[70]

5.515.3.2.2. Tribological properties

Studies using a cartilage-on-cartilage friction test have identified HA and PRG4 as primary boundary lubricants in SF,[71,72] lowering friction in a dose-dependent manner, both alone and in combination.[73,74] Normal bovine SF values of boundary-mode kinetic friction coefficient in this setup were ~0.025. Cartilage on glass friction testing has shown that recombinant human lubricin lubricates cartilage in a dose-dependent manner and involves both lubricin bound to the surface and lubricin in solution.[75]

In addition to friction, the wear-reducing properties of SF have been measured in tissue- and joint-scale setups. Using a cartilage-on-cartilage system, the contributions of various SF lubricants to reducing wear have been determined.[6,7] Other counter surfaces have also been used to investigate cartilage wear, including stainless steel[76,77] and polymers.[78,79] At the joint scale, SF lubrication has been assessed using pendulum instruments on intact joints.[80]

5.515.3.3. Modeling Joint Tissue Biology

Tissue-level tissue engineering analyses rely on kinetic and physicochemical properties of the tissue components to develop models that are mechanistic, which are used to deduce the functional behavior of the system. Early models of the synovial joint focused on specific joint tissues. More recently, integrated models of the synovial joint have been developed and interactions between two or more joint tissues examined.

5.515.3.3.1. Models of individual joint tissues

Various models of SF have been constructed to explain its rheological properties and mechanical functions in synovial joints. The rheological properties of SF have been described as viscometric,[81] viscoelastic,[82,83] and as a Bingham plastic,[84] whose properties are primarily determined by the concentration and MW of HA, and recently as a micromorphic fluid containing deformable particles.[85] Several different mechanisms of SF lubrication of cartilage–cartilage contact have been suggested, including hydrodynamic and boundary modes as well as 'weeping' and 'boosted' lubrication. Hydrodynamic lubrication is generated by hydrostatic pressure in the SF because of cartilage loading and sliding.[86] Boundary mode lubrication occurs through direct cartilage–cartilage contact via monomolecular films that are chemically adherent to the cartilage surface.[87] 'Weeping' lubrication is a description of the flow of SF into and out of porous cartilage during compression and relaxation,[87] while 'boosted' lubrication describes pools of entrapped SF due to apposing cartilage surface irregularities where the lubricant concentrations are elevated as water is squeezed out.[88]

Cartilage has frequently been studied, with compartmental and continuous models at different scale levels detailing fluid and molecular transport in the tissue and mechanics under various conditions. Ion-exchange modeling revealed that the hydraulic permeability[89] and molecular transport[90] in cartilage are primarily determined by fixed charge density, which is proportional to the concentration of sGAG. Transport during cartilage loading has also been addressed using continuum-mixture theory[91,92] and, combined with solute-binding, porous media theory.[93] The transport and binding of molecules secreted by chondrocytes through the tissue have also been investigated in both compartmental[94] and continuous models.[95,96] The importance of cartilage interstitial fluid pressurization to support joint loading and reduce the effective friction coefficient was shown using a boundary friction model.[97] Poroviscoelastic models of cartilage have also been developed,[98] where the mechanical properties of the tissue are coupled to tissue composition, enabling study of the effects of changes in tissue composition, as might occur in certain disease states.

Fluid and mass transport through synovium play a major role in determining the composition of SF. Models of synovium compliance and hydraulic conductivity, based on pressure–volume measurements,[99,100] albumin[101] and macromolecular[102–104] transport through synovium, and the glucose transport through SF to cartilage,[102,104] have been described. In addition, the microvasculature physiology and exchange,[105] synovial perfusion measurement techniques,[106] and mass transport through synovium[102,104] have been reviewed previously.

5.515.3.3.2. Multicomponent models of the synovial joint

A few models have been developed to combine several joint tissues, allowing for computation and prediction of phenomena derived from multitissue interactions in the joint. Blewis *et al.*[107] constructed a compartmental model of the synovial joint to predict the dynamic recovery of steady-state SF lubricant concentrations. The model describes transport of lubricant molecules in four tissues: (i) SF surrounded by (ii) articular cartilage and (iii) synovium, which provides the outflow resistance and filtration of SF to the (iv) subsynovium. A mass balance is applied to the lubricant concentrations of HA and PRG4 resulting in a system of linear, first-order differential equations with three state variables that take into account rates of secretion, degradation, and flux across the synovial membrane. The behavior of the model can be analyzed under normal conditions and after specific perturbations, such as elevated cytokine levels, after joint lavage with saline, or after therapeutic injection of HA.

The Entelos PhysioLab® platform has been used to construct a mathematical model of rheumatoid arthritis (RA).[108] The model integrates inflammatory cells, endothelium, synovial fibroblasts, and chondrocytes within a synovial joint compartment, as well as cytokines and growth factors including IL-1β, TGF-β, IL-6, and TNF-α. Model predictions include synovial hyperplasia, cartilage degradation rate, bone erosion index, and soluble factor concentrations. The model can be used to predict different patient phenotypes in RA and determine the critical pathways that produce the observed phenotype *in silico*.

5.515.3.3.3. Extending current models of the synovial joint

5.515.3.3.3.1. Overview

An engineering framework for modeling of transport in the synovial joint is needed in order to utilize and interpret the wealth of molecular to tissue-scale information available (**Figure 3**). The transport of molecules within the synovial joint allows for the interactions between different joint tissues, making consideration of molecular transport an important

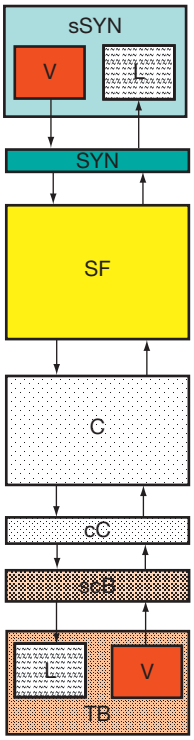

Figure 3 Generalized compartmental model schematic showing possible compartments, including the vasculature (V), lymphatics (L), subsynovium (sSYN), synovium (SYN), synovial fluid (SF), cartilage (C), calcified cartilage (cC), subchondral bone (scB), and trabecular bone (TB).

part of an integrated joint model (see **Chapter 3.309, Fluid Mechanics: Transport and Diffusion Analyses as Applied in Biomaterials Studies**). One possible approach is to generalize the molecular transport equations to allow for interactions between all molecules in the joint within a physiological framework, using experimental data to fill in the molecular concentration and secretion rates for different tissue states.

5.515.3.3.3.2. A generalized compartmental model of transport in the joint

Building upon the tissue-specific and partially integrated models discussed above, a generalized compartmental approach to modeling transport in the synovial joint[94,95,107] is described in this section. A schematic with possible compartments is shown in **Figure 3**, and the model variables and parameters are defined in **Table 1**. The equations can be grouped by purpose as the mass balance, transport, and physical coupling equations.

5.515.3.3.3.2.1. Mass balance equations For each compartment, the mass balance of each molecule considered is given by

$$\frac{\mathrm{d}}{\mathrm{d}t}\left[V^{\alpha}c_x^{\alpha}\right] = \left(\sum_{n=\beta}^{\varepsilon} J_x^{\alpha/n}\right) - \left(d_x^{\alpha}\right) - \left(b_x^{\alpha}\right) + \left(r_x^{\alpha}\right) \qquad [1]$$

where α represents the compartment under consideration, x each molecule, V the compartment volume, c the concentration of x in α, J the total mass flux directly to or from every other compartment, d the degeneration rate, b the binding of x in α, and r the secretion rate of x in α. Thus, to consider three compartments and 20 molecules, there would be 60 mass balance equations of this type to account for. The degradation, binding, and secretion rates are given as generic functions f of the relevant variables as their specific form will depend on which molecules and compartment are being considered. The degeneration rate of x in α

$$d_x^{\alpha} = c_x^{\alpha}V^{\alpha}f\left(\sum_{k=1}^{n_k} c_k^{\alpha}\right) \qquad [2]$$

is a function of the mass of x in α and the sum of the action by all catabolic mediators c_k, such as proteases, in the compartment. The binding rate of x in α

$$b_x^{\alpha} = f\left(c_x^{\alpha}, c_x^{*,\alpha}, c_l^{\alpha}\right) \qquad [3]$$

is a function of the concentration of x, the concentration of binding proteins c_l in the compartment, and c^* the concentration of x already bound

$$c_x^{*,\alpha} = f\left(b_x^{\alpha}t, c_x^{\alpha}\right) \qquad [4]$$

The secretion rate of x in α

$$r_x^{\alpha} = \chi^{\alpha}f\left(c_j^{\alpha}, F, \theta\right) \qquad [5]$$

is a function of the cell density, the concentration of cytokines c_j, and mechanobiology factors including loading F and articulation θ of the joint.

5.515.3.3.3.2.2. Diffusive and convective transport equations The diffusive and convective transport of mass J between each compartment is defined as

$$J_x^{\alpha/\beta} = p_x^{\alpha/\beta}\left[c_x^{\beta} - c_x^{\alpha}\right] + v_{\mathrm{H_2O}}^{\alpha/\beta}\left(1 - \sigma_x^{\alpha/\beta}\right)c_x^{\alpha} \qquad [6]$$

where v is the velocity of fluid from α to β, σ is the reflection coefficient of the boundary between α and β to x, and p is the permeability of x from α to β,

Table 1 List of variable units and descriptions for the generalized transport model

Variable	*Description*
c_i^{α} (mg cm^{-3})	Concentration of free i in α
$c_i^{*,\alpha}$ (mg cm^{-3})	Concentration of bound i in α
χ_i^{α} (cells cm^{-3})	Cell density of type i in α
$J_i^{\alpha/\beta}$ (mg s^{-1})	Mass of flux i from α' to β
d_i^{α} (mg s^{-1})	Degradation rate of i in α
b_i^{α} (mg s^{-1})	Binding rate of i in α
r_i^{α} (mg s^{-1})	Secretion rate of i in α
$v_{\mathrm{H_2O}}^{\alpha/\beta}$ (cm s^{-1})	Linear velocity of fluid from α to β
$p_i^{\alpha/\beta}$ (cm s^{-1})	Permeability of α to i
$k^{\alpha/\beta}$ (cm s^{-1} Pa^{-1})	Hydraulic conductance from α to β
$\sigma_i^{\alpha/\beta}$	Reflection coefficient of i from α to β
V^{α} (cm^3)	Volume of α
$A^{\alpha/\beta}$ (cm^2)	Surface area of α exposed to SF
P^{α} (Pa)	Hydrostatic pressure in α
Π^{α} (Pa)	Osmotic pressure in α
F (N)	Loading of joint
θ ($^{\circ}$ s^{-1})	Articulation of joint
t (s)	Time

$$p_x^{\alpha/\beta} = f\left(c_m^{\alpha}, c_m^{\beta}, \sigma_x^{\alpha/\beta}\right) \quad [7]$$

which depends on the concentration of structural molecules m in α and β and σ the reflection coefficient of the boundary between α and β to x.

$$\sigma_{x,\,H_2O}^{\alpha/\beta} = f\left(\sum c_x^{*,\,\alpha/\beta}, c_m^{\alpha,\beta}\right) \quad [8]$$

5.515.3.3.3.2.3. Physical coupling of the compartments

The compartments are coupled by the fluid flow and volume, which depend on the hydrostatic and osmotic pressures. The volume can be described by

$$V^{\alpha} = V_0^{\alpha} + \sum_{n=\beta}^{\gamma}\left(v_{H_2O}^{\alpha/n} A^{\alpha/n} t\right) + V_{Cells}^{\alpha}(t) \quad [9]$$

where V_0 is the initial volume, A is the area between compartments α and n, and V_{Cells} is the volume of additional cells in the compartment, such as red blood cells entering due to injury. The velocity of fluid moving between compartments can be described by

$$v_{H_2O}^{\alpha/\beta} = k^{\alpha/\beta}\left[\left(P^{\beta} - P^{\alpha}\right) - \sigma_{H_2O}^{\alpha/\beta}\left(\Pi^{\beta} - \Pi^{\alpha}\right)\right] \quad [10]$$

where the hydrostatic pressure P, osmotic pressure Π, and hydraulic conductance k are given as generic functions whose explicit form would depend on the compartment under consideration.

$$P^{\alpha} = f(V^{\alpha}, F, \theta) \quad [11]$$

$$\Pi^{\alpha} = RT\left(\sum c_x^{\alpha}\right) \quad [12]$$

$$k^{\alpha} = f\left(c_m^{\alpha}, V^{\alpha}, P^{\alpha}\right) \quad [13]$$

5.515.3.3.3.3. Example of model setup

There are a large number of interactions, concentrations, and secretion rates to define in order to implement a model based on this generic description. However, both protein- and genomic-level experimental data can suggest values for many of these variables from a single tissue source and tissue state, as well as how those values are altered during disease or injury (see **Chapter 5.513, Systems Biology in Biomaterials and Tissue Engineering**).

One example would be to focus on concentrations and secretion rates for lubricant molecules HA and PRG4 in SF. The most important compartments for this example are the synovium, SF, cartilage, and subchondral bone, especially if a disease state such as OA is to be considered. After defining initial values and rates, the system of equations would be solved numerically. Analysis of the system could include the effects of different perturbation stimuli relevant to the clinical situation: hemarthrosis by influx of blood and cells into the SF compartment, inflammation by increasing specific cytokine levels, OA by degeneration of cartilage structural molecules, and focal defects in cartilage by allowing fluid flow from the subchondral bone directly to SF.

Integration of the large amounts of experimental data with a model based on classical transport analysis will allow for the description of emergent system properties and molecular interactions with the goal of discovering novel clinical diagnostic, intervention, and treatment strategies.

5.515.4. Mechanical Effects on Cartilage Maturation and Synovial Fluid Pathology

5.515.4.1. Effect of Mechanical Stimuli on Cartilage Maturation

5.515.4.1.1. Overview

Mechanical cues resulting from joint loading and tissue deformation modulate chondrocyte and cartilage metabolism and cause coordinated changes in biochemical and mechanical properties of articular cartilage.[109–111] Hydrostatic pressure can modulate cartilage biosynthesis to various degrees depending on the magnitude, frequency, and duration of pressurization. Application of static compression inhibits collagen and PG biosynthesis in cartilage explants, whereas dynamic compression or dynamic shear superimposed on static compression offset at certain magnitudes and frequencies stimulates matrix metabolism (see **Chapter 5.502, Engineering Scaffold Mechanical and Mass Transport Properties**; **Chapter 5.504, Effect of Substrate Modulus on Cell Function and Differentiation**; and **Chapter 5.506, Effects of Mechanical Stress on Cells**).

5.515.4.1.2. Effects of mechanical loads on cartilage metabolism

5.515.4.1.2.1. Hydrostatic pressure

Hydrostatic pressure is a physiological factor that regulates cartilage biosynthesis independently of other factors such as cell/matrix deformation, fluid flow, or electrokinetic effects. Continuous or intermittent pressures of <3 MPa may[112–114] or may not[115] affect PG synthesis in normal articular cartilage. Higher pressures (5–50 MPa) modulate cartilage biosynthesis to various degrees depending on the magnitude, frequency, and duration of pressurization. Hydrostatic pressure in the presumably physiological range (~5–15 MPa) in the short term (up to 2 h) increased aggrecan and collagen biosynthesis, but higher pressures (20–50 MPa) had no effect.[113] Cartilage biosynthesis was inhibited with longer exposure (2 h) to pressures of 30–50 MPa. PG synthesis was upregulated in a subsequent 2 h following a single application of 5–15 MPa pressure for 20s or for 5 min, but was not altered with a single application of higher pressures (20–50 MPa).[113] The frequency of the applied pressure is also important as a 0.5 Hz cyclic 5 MPa pressure was shown to stimulate biosynthesis, while the application of the pressure with same magnitude at 0.0167–0.25 Hz did not have any effect on synthesis.[116]

5.515.4.1.2.2. Static compression

Static compression inhibits collagen and PG biosynthesis in cartilage explants. The inhibition of biosynthesis depends on the stress (or strain) magnitude as well as the duration of the applied load. At low level of compressive stress (<0.06 MPa), the protein synthesis rate was not significantly altered, whereas at higher levels of stress (0.06–3 MPa) or strain (10–50%), aggrecan synthesis was reduced 20–80% compared to that in unloaded cartilage explants.[117–121] Different zones of articular cartilage appear to respond similarly to static compressive

loading.[120] Inhibition of collagen and PG synthesis occurs within 1–2 h of load application and is increased under prolonged static compression (~24 h).[60,61,122,123] In contrast to the inhibition of protein synthesis, static compression causes a transient increase in transcripts of genes encoding for matrix proteins such as aggrecan and type II collagen within 1–8 h after loading,[124,125] followed by decreased expression to control levels while upregulating the expression of matrix proteases (MMP-3 and MMP-13), ADAMTS-5, and TGF-β.[125,126] The gene-expression patterns during 24 h of subsequent static compression are time-dependent and depend on intracellular calcium and activation of cyclic AMP.[125]

5.515.4.1.2.3. Dynamic compression

Dynamic compression superimposed on static compression offset at certain magnitudes and frequencies can regulate matrix metabolism.[60,61,111,119,127–130] In the radially unconfined compression configuration with a nonporous counter-surface, oscillatory strains of 1–5% at >0.01 Hz significantly stimulated collagen and aggrecan synthesis, whereas the same strain magnitude at lower frequencies <0.001 Hz had no effect on biosynthesis.[119,127,128] Other studies reported that unconfined dynamic compression in high frequency range (0.5 Hz) with a porous counter-surface had inhibitory effects on PG synthesis.[131] The inhibition was proportional to the applied stress, but not dependent on loading time. However, this loading protocol reversed the catabolic effect of IL-1 on mature bovine cartilage.[132] During 24 h of oscillatory compressive loading, the expressions of genes encoding for matrix proteins such as aggrecan and type II collagen, matrix metalloproteinases (MMP-3 and MMP-13), and ADAMTS-5 were upregulated,[133] indicating an increase in matrix metabolism. The gene-expression patterns depend on intracellular calcium and activation of cyclic AMP, as well as ERK1/2 and p38 activation,[134] suggesting that MAPK pathway is a central conduit for transducing mechanical forces into biological responses in cartilage.

5.515.4.1.2.4. Dynamic shear

Dynamic shear stimulation of cartilage explants markedly increased biosynthesis and expression of PG, collagen,[133–136] and PRG4.[137,138] Dynamic shear loading at 1–3% strain amplitude at frequencies between 0.01 and 1.0 Hz stimulated the synthesis of protein by approximately 50% and PGs by approximately 25%.[136] The stimulatory effect was relatively uniform in the radial and vertical directions, which was likely associated with uniform deformation of cells and pericellular matrix caused by simple shear loading. Levels of PRG4 expression and accumulation were increased by applying shear stress, depending on location within the knee, and decreased to control levels with the use of a specific inhibitor of TGF-β receptor type I kinase. CPM applied to whole joints in a way dependent on the duty cycle of cartilage sliding against opposing tissues also modulates PRG4 synthesis. In regions that were continuously or intermittently sliding against meniscus and tibial cartilage, PRG4 synthesis was higher with CPM than without.[62]

5.515.4.1.3. Effects of mechanical loads on cartilage composition, structure, and function

Both short- and long-term applications of compression and/or shear loads *in vitro* and *in vivo* modulate cartilage composition,[62,120,139] structure,[140,141] and function.[138,142] Cartilage regions that are continuously or intermittently sliding against meniscus and tibial cartilage expressed more PRG4 than noncontact regions.[62] In animal studies for extensive times (3–4 months), *in vivo* cyclical joint loading by repetitive flexion did not alter collagen content or cartilage thickness, but appeared to increase PG (normalized to collagen) content in mature articular cartilage by ~60%.[139] Mechanical loads have also been shown to induce age- and zone-dependent alteration in collagen structure of articular cartilage. The birefringence of collagen increased in the superficial zone cartilage, but decreased in the deep zone when cartilage was subjected to *in vitro* dynamic compression.[140] Running exercise increased cartilage collagen birefringence, indicating either a higher degree of fibril assembly and organization or increased amount of collagen, or both, in young pigs, but decreased birefringence in older pigs.[141] A short application of cyclic compressive load to cartilage explants *in vitro* induced a transient increase in denatured collagen and hydraulic permeability, and weakening of the collagen network compared to unloaded controls while it did not alter total collagen and sGAG contents.[120,142]

5.515.4.2. Synovial Fluid Pathology

5.515.4.2.1. Overview

The composition and function of SF are altered in injury and disease, because of inherent changes in both SF and other joint structures. SF is in direct contact with cartilage, synovium, meniscus, and ligament, which are themselves altered in injury and disease. Changes in cellular metabolism and structure in these tissues may be reflected by changes in SF composition and function. Such changes in SF, in particular reduced ability to lubricate joint articulation and an altered cytokine environment (**Figure 4**), are believed to contribute to joint pathologies including OA and RA. Thus, the disease-associated changes observed in SF likely contribute to and are exacerbated by the effects of pathology on other tissues.

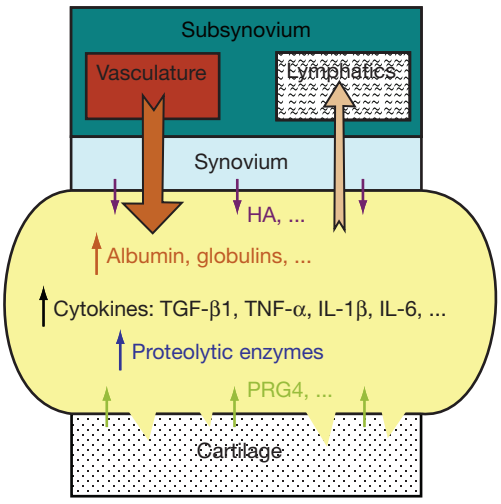

Figure 4 Schematic view of synovial fluid pathology including effusion, synovial hyperplasia, and altered protein, cytokine, and enzyme composition.

5.515.4.2.2. Changes in composition

5.515.4.2.2.1. Plasma proteins

Inflammation of the synovium, likely increasing synovium permeability, as occurs in RA, is associated with an increased protein content in SF. RA SF has an increased content of globulin and glycoproteins compared to normal SF, and the globulin content increases more than the increase in albumin such that the distribution of proteins in SF approaches that of proteins in serum. Similarly, a relative increase in α_2 glycoproteins in SF is observed in patients with RA, resulting in the distribution of glycoproteins in RA SF to approach that of serum.[31] Serum proteins can be detected in RA SF by immunoelectrophoresis, and in particular, large MW proteins such as β_2 macroglobulin, fibrinogen, β_1 lipoprotein, and α_2 macroglobulin which are low or absent in normal SF are significantly elevated in RA SF.[32]

5.515.4.2.2.2. Lubricant macromolecules

The concentration and quality of lubricant molecules are altered in different ways in OA, RA, and injury. Changes in SF HA in OA and RA have been reviewed elsewhere.[68] Briefly, the concentration of HA in SF is decreased in RA samples and, to a lesser extent, in OA samples. The MW of HA in OA is much lower than is found in normal SF, while the MW of HA in RA is only slightly smaller than that found in normal SF. In patients undergoing total knee arthroplasty, those requiring revision surgery for prosthetic failure have lower concentrations of HA.[54] Following acute injury, there is an increase in elastase activity and decrease in lubricin concentration and lubricating ability in SF, as well as an increase in cartilage degradation.[143] Sheep meniscectomy models of early OA show cartilage degeneration associated with a downregulation in PRG4 expression by SZCs.[144] In patients with the genetic disease camptodactyly-arthropathy-coxa vara-pericarditis syndrome (CACP), an autosomal recessive disease with loss-of-function mutations in the PRG4 gene, precocious cartilage degeneration and joint failure are observed.[145] PRG4 gene knockout mice develop fibrillation in the cartilage surface, loss of SZCs, and synovial hyperplasia, indicating the importance of PRG4 in maintaining joint homeostasis.[146]

5.515.4.2.2.3. Cytokines and growth factors

Alterations in cytokine levels in SF occur in joint disease and after injury.[45,46,147] In SF of ACL deficient knees, levels of IL-1β, IL-6, IL-8, and TNF-α are increased and level of IL-1RA is decreased compared to that in SF of uninjured knees.[148] Increased cartilage degeneration is also associated with higher levels of IL-1β and lower levels of IL-1RA.[149] Modulation of cytokine activity has been explored as a therapeutic approach. In a rat ACL injury model, inhibition of TNF-α with etanercept resulted in higher levels of lubricin in SF and on the cartilage surface, lower PG release from cartilage, and lower whole joint coefficient of friction values compared to untreated groups.[150]

5.515.4.2.2.4. Proteolytic enzyme activity

Proteolytic enzyme concentrations and activities are altered in the SF of joints in disease states that involve deranged cartilage matrix metabolism. Alterations in proteolytic activity are often inferred by measurements of degradation product levels. In a study of SF from patients with ACL rupture, measures of aggrecan fragments, stromelysin-1, and tissue inhibitor of metalloproteinases-1, all markers of cartilage matrix metabolism, first increased acutely and then decreased with time. In addition, symptomatic patients during the chronic phase had higher levels of degradation marker concentrations compared to asymptomatic patients.[151]

5.515.4.2.3. Changes in formation and molecular transport

Synovium in pathological joints displays altered transport characteristics and rheological properties, directly affecting the composition of SF. The permeability of synovium from joints with RA to proteins is increased,[152,153] with proportionately larger increases in permeability for larger proteins.[154] Increased Starling pressure due to the reduced oncotic gradient as protein accumulates in SF and increased permeability of capillaries during inflammation contribute to the buildup of fluid and protein in RA SF. The transport characteristics of synovium in OA are less affected than in RA, with significantly lower permeabilities to proteins measured over a range of MW.[155]

5.515.4.2.4. Changes in rheology and tribology

Pathological SF displays altered rheological properties. Lower viscosity and lower MW of HA have been reported in SF from OA joints, and much lower viscosity and low concentrations of HA in SF from joints with inflammatory disease, such as RA. In a rabbit knee injury model, SF boundary lubricating ability, determined by an artificial bearing system under load, and lubricin concentrations were decreased at weeks 2 and 3 after injury.[143]

5.515.5. Engineering Cartilaginous Tissue and Synovial Fluid

5.515.5.1. Engineered Cartilaginous Tissue

5.515.5.1.1. General overview

Engineered cartilaginous tissues can be formed by chondrocytes embedded in a hydrogel or seeded onto a scaffold (see **Chapter 2.220, Extracellular Matrix as Biomimetic Biomaterial: Biological Matrices for Tissue Regeneration**; **Chapter 5.501, Scaffolds: Flow Perfusion Bioreactor Design** and **Chapter 5.502, Engineering Scaffold Mechanical and Mass Transport Properties**). Hydrogels include polyethylene glycol (PEG),[156,157] agarose,[158,159] and others.[160] Scaffolds include polyglycolic acid.[129,130,161–163] Substrates include polyurethane[164,165] and calcium phosphate.[166] Alternatively, constructs can be formed scaffold-free.[167–169] Constructs may be subjected to different biological or mechanical stimuli to elicit particular responses that enhance composition (determined by ECM analysis or gene expression), structure (determined by histology or microscopy), and function (determined by biomechanical measurements).

5.515.5.1.2. Bioreactors

As mechanical forces play an important role during development and maturation, engineered tissues may be formed *in vitro* under controlled situations by application of

biophysical stimuli such as hydrostatic pressure, compression, tension, perfusion, and shear in a bioreactor. The combination of such mechanobiological stimuli with anabolic growth factors modulates the biosynthetic response (structure, composition, expression) and resulting tissue's functional biomechanical properties. The use of a bioreactor to deliver forces and flows to chondrocytes requires knowledge of how cells react to a particular stimulus, and the amount of stimuli needed to elicit a response. Such information may be gathered from *in vivo* kinematic studies and *in vitro* studies on whole joints or explants.

5.515.5.1.3. Effects of physical stimuli on cartilaginous tissue growth and maturation

5.515.5.1.3.1. Hydrostatic pressure

Static and dynamic hydrostatic pressures have been used as physical factors in cartilage tissue engineering. Continuous[169–173] or intermittent[168,169,174,175] pressures ranging from 3.4 to 10 MPa increased chondrocytes PG and collagen synthesis and construct compressive biomechanical properties.

PG biosynthesis by chondrocytes in 3D culture appears to respond differently on the basis of the magnitude of static hydrostatic pressure. In scaffold-free constructs, at low hydrostatic pressure (1 MPa), PG content did not appear to be elevated; however, at higher pressures (5 and 10 MPa), PG content increased.[169] At this same level, anabolic PG synthesis and mRNA expression for aggrecan and collagen II were markedly elevated.[171,172] Whether the effect of even higher hydrostatic pressure regimes on engineered cartilage has an anabolic or catabolic effect on chondrocyte biosynthesis remains to be determined.

The composition and functional response of chondrocytes in 3D culture to dynamic hydrostatic pressure is markedly different from that of static pressure. Dynamic pressure amplitude and frequency, and duty cycle play a role in affecting the mechanobiological response. At low dynamic hydrostatic pressure (3.4 MPa), and low frequency (0.25 Hz), little or no change in PG content was evident.[174,175] However, at higher pressure amplitudes and frequencies (5–10 MPa, 1 Hz), PG and collagen II content increased.[169,174,175] The exact duty cycle remains to be determined. The equilibrium Young's modulus of scaffold-free, chondrocytes-derived constructs increased when cultured under static or dynamic pressure compared to free-swelling conditions. Addition of growth factors, such as TGF-β1, during static culture also resulted in an increased modulus.[169]

5.515.5.1.3.2. Perfusion

Perfusion bioreactors are often used in cartilage tissue engineering.[161–163,176,177] One objective of such a bioreactor is to develop dynamic laminar flow conditions which may enhance cellular biosynthesis. Engineered constructs in perfusion bioreactors have been maintained for up to 7 months, with functional properties reaching similar values to that of native calf articular cartilage, and with matrix content, synthesis rates, and structural changes (COL, crosslink formation) increasing during the culture duration. Supplementation with IGF-1 during culture in the perfusion bioreactor can result in improved GAG, but not COL.[178] Constructs cultured in TGF-β1 during culture showed increases in type II collagen gene expression. Gene expression for type II collagen increased further when constructs were cultured in TGF-β1 and IGF-1.[177] Construct biomechanical properties are typically improved during dynamic perfusion culture, with increases in confined compression modulus (from ~0.2 to 0.4 MPa), and in Young's modulus (0.075–0.125 kPa).

5.515.5.1.3.3. Static compression

Static compression modulates the metabolism of chondrocytes in PGA and agarose-based cartilaginous constructs by inhibiting PG and COL biosynthesis.[129,130,158,179] *In vitro*, free-swelling cartilaginous constructs appear to be PG rich, but with reduced collagen content, and with biomechanical properties that are inferior to (~25% of) that of native articular cartilage.[180] Compressive loading (up to 50% for 24 h) suppresses PG and COL by 35 and 57%, respectively. Uniaxial static compression of up to 50% inhibits the expression of COL type I and II mRNA in chondrocyte-seeded COL I gels.[179] Static compression also reduces thymidine uptake by chondrocytes in agarose, suggesting decreased cell proliferation.[158]

5.515.5.1.3.4. Dynamic compression

Similar to its effect on native articular cartilage, dynamic compression modulates the composition, structure, and function of tissue-engineered cartilage. Dynamic compression at amplitudes of 3–5% has stimulatory effects on synthesis that are dependent on the static offset compression amplitude (10–50%) and dynamic compression frequency (0.001–3 Hz).[129,130,158,159,181–183] PG synthesis increases at 1 Hz compared to 0.3 Hz. However, collagen synthesis appears to be inverse of PG synthesis, being higher at 0.3 Hz compared to 3 Hz. The construct compressive modulus also increases for samples subjected to dynamic loading during culture when compared to free-swelling controls.[166,181,183,184] Nitrite production also appears to be suppressed when under dynamic loading compared to free-swelling controls. Cyclic loading can also increase catabolic MMP-3 and MMP-13 gene expression, in association with MAPkinase pathway signaling.[185]

The composition and function of engineered constructs can also be modulated by growth factors TGF-β1 and IGF-1 during dynamic loading.[159] PG and collagen content are stimulated by such cytokines and increase as culture duration increases, with even greater increases for samples subjected to dynamic loading. The construct compressive modulus in one study increased threefold over static cultures.[159]

The duty cycle of the dynamic compression protocol is likely important in determining the effects of the mechanical stimulation. Accounting for duty cycle, whether intermittent or continuous over experimental duration, is important for interpretation and comparisons of experimental data.

5.515.5.1.3.5. Dynamic shear

Dynamic shear generally increases chondrocytes matrix synthesis, leading to increased construct modulus. Application of 2% cyclic shear strain amplitude at 1 Hz to chondrocytes cultures stimulated PG and COL synthesis compared to free-swelling controls, with threefold increases in compressive modulus.[186] Such results demonstrate that intermittent application of dynamic shearing forces over a culture period improves the quality of cartilaginous tissue formed *in vitro*.

Fluid shear stress has also been shown to increase matrix composition and tensile biomechanical properties of engineered cartilaginous tissues.[129,130,187] In a stress-dependent manner, type II collagen was the highest in the high shear-stress group (0.1 Pa) when compared to lower shear-stress groups (0.001 Pa) and free-swelling controls. Type I and II collagen gene expression also increased after shear-stress stimulation. However, less PG was retained in the samples under high shear. Tensile Young's modulus (5 MPa) and failure strength (1.3 MPa) were also increased for samples under high shear.

5.515.5.1.3.6. Sliding

Engineered cartilaginous constructs may also be subjected to sliding to elicit a response in mRNA levels of anabolic or catabolic ECM genes, as well as PRG4.[164,165] A combination of static (10%) and dynamic compression (0–10%, 0.1 Hz) and shear ($\pm 25^{\circ}$) of chondrocytes seeded into a polyurethane scaffold stimulated PRG4 and cartilage oligomeric matrix, as well as increased collagen II mRNA expression. Aggrecan and TIMP-3 were also upregulated, suggesting that the mechanical effects applied by the surface motion can contribute to the maintenance of the chondrocyte phenotype of the seeded cells.

5.515.5.2. Tissue Engineering Synovial Fluid

5.515.5.2.1. Overview

The fabrication of synthetic or tissue-derived SF could be useful for a number of applications, including clinical treatment of OA joints and experimental use as a lubricant for cartilage friction, as well as wear testing at the tissue and joint scales. SF is altered in pathology, as described above, with changes to the protein content, lubricant composition, cytokine and growth factor environment, and proteolytic enzyme activity. Clinically replacing or supplementing such diseased SF with a lubricating and cartilage wear-reducing substitute fluid may provide pain relief and reduce the abnormal friction and wear that leads to further cartilage degeneration. Experimentally, SF is needed to replicate the *in vivo* environment during cartilage friction, wear, and biomechanical testing. Such testing has been done on cartilage explants and osteochondral cores at the tissue scale, as well at the joint-scale using pendulum testing and with a CPM device.

5.515.5.2.2. Viscosupplementation

Viscosupplementation of SF with exogenous preparations, typically HA-derived molecules, is used for intra-articular injection as an analgesic treatment for OA knees, though the mechanism of effect is not well defined. Several different preparations of HA-derived molecules are available clinically, including Euflexxa, Hyalgan, Synvisc, Supartz, and Orthovisc. Injection timing varies with preparation, ranging from one injection per 6 months to a program of weekly injections for several weeks. The clinical effects of such treatment typically show reduction in pain and modest improvement in function scores in the 5–13 week range postinjection. Several meta-analyses have been prepared summarizing the clinical data on such viscosupplements.[188,189]

5.515.5.2.3. Biomimetic approaches

Tissue engineering and tissue culture methods have also been used to generate a synoviocyte-derived lubricious fluid with viscosity and friction-reducing qualities approaching those of SF. On the basis of a model description of the biosynthesis, clearance, and degradation of lubricant molecules under specific cytokine conditions,[107,190,191] a bioreactor coculture system was designed and tested. The bioreactor contained two compartments separated by a semipermeable membrane. The first compartment contained synoviocytes in cell culture and cartilage explants, separated from the second compartment by the membrane, allowing for selective retention of high MW lubricant molecules on the basis of the pore size. The second compartment contained culture medium, providing nutrients to the cells and explants by diffusion through the membrane. The transport rates of HA and PRG4, as well as the biosynthesis rates of these molecules in the bioreactor were assessed in the bioreactor.[190,191] After 12 days in culture, the bioengineered fluid (BF) in the first compartment contained lubricant molecules HA and PRG4 in similar concentrations to normal SF, and the friction coefficient of the fluid in a cartilage-on-cartilage friction assay approached that of normal SF. The friction coefficients were negatively correlated with lubricant concentration. This biomimetic, tissue engineering approach created a BF biomaterial with similar lubricant composition and function as native SF. This type of bioreactor system may have application in generating BF for identifying molecules involved in lubricant regulations, experimental use in cartilage and joint friction and wear testing, and in developing viscosupplementation products.

References

1. Williams, G. M.; Chan, E. F.; Temple-Wong, M. M.; *et al*. *J. Biomech*. **2010**, *43*, 156–165.
2. Maroudas, A. In *Adult Articular Cartilage*; Freeman, M. A. R., Ed.; Pitman Medical: Tunbridge Wells, England, 1979; pp 215–290.
3. Stockwell, R. A.; Meachim, G. In *Adult Articular Cartilage*; Freeman, M. A. R., Ed.; Pitman Medical: Tunbridge Wells, England, 1979; pp 69–144.
4. Jadin, K. D.; Wong, B. L.; Bae, W. C.; *et al*. *J. Histochem. Cytochem*. **2005**, *53*(9), 1109–1119.
5. Mow, V. C.; Gu, W. Y.; Chen, F. H. In *Basic Orthopaedic Biomechanics and Mechano-Biology*; Mow, V. C., Huiskes, R., Eds.; Lippincott Williams & Wilkins: Philadelphia, PA, 2005; p 720.
6. Temple, M. M.; Bae, W. C.; Chen, M. Q.; *et al*. *Osteoarthr. Cartil*. **2007**, *15*, 1042–1052.
7. Temple, M. M.; Nguyen, Q.; Moy, T. M.; *et al*. *Trans. Orthop. Res. Soc*. **2007**, *32*, 611.
8. Muir, I. H. M. In *Adult Articular Cartilage*; Freeman, M. A. R., Ed.; Pitman Medical: Tunbridge Wells, England, 1979; pp 145–214.
9. Hunziker, E. B. In *Articular Cartilage and Osteoarthritis*; Kuettner, K. E., Schleyerbach, R., Peyron, J. G., Hascall, V. C., Eds.; Raven Press: New York, 1992; pp 183–199.
10. Weightman, B.; Kempson, G. E. In *Adult Articular Cartilage*; Freeman, M. A. R., Ed.; Pitman Medical: Tunbridge Wells, England, 1979; pp 291–332.
11. Mow, V.; Rosenwasser, M. In *Injury and Repair of the Musculoskeletal Soft Tissues*; Woo, S. L.-Y., Buckwalter, J. A., Eds.; American Academy of Orthopaedic Surgeons: Park Ridge, IL, 1988; pp 427–463.
12. Williamson, A. K.; Chen, A. C.; Sah, R. L. *J. Orthop. Res*. **2001**, *19*, 1113–1121.
13. Maroudas, A. *Nature* **1976**, *260*, 808–809.
14. Akizuki, S.; Mow, V. C.; Muller, F.; Pita, J. C.; Howell, D. S.; Manicourt, D. H. *J. Orthop. Res*. **1986**, *4*, 379–392.
15. Williamson, A. K.; Chen, A. C.; Masuda, K.; Thonar, E. J.-M. A.; Sah, R. L. *J. Orthop. Res*. **2003**, *21*, 872–880.
16. Asanbaeva, A.; Masuda, K.; Thonar, E. J.-M. A.; Klisch, S. M.; Sah, R. L. *Osteoarthr. Cartil*. **2008**, *16*, 1–11.

17. Asanbaeva, A.; Tam, J.; Schumacher, B. L.; Klisch, S. M.; Masuda, K.; Sah, R. L. *Arch. Biochem. Biophys.* **2008**, *474*, 175–182.
18. Yamagata, T.; Saito, H.; Habuchi, O.; Suzuki, S. *J. Biol. Chem.* **1968**, *243*, 1523–1535.
19. Li, J. T.; Mow, V. C.; Koob, T. J.; Eyre, D. R. *Trans. Orthop. Res. Soc.* **1984**, *9*, 35.
20. Schmidt, M. B.; Mow, V. C.; Chun, L. E.; Eyre, D. R. *J. Orthop. Res.* **1990**, *8*, 353–363.
21. Asanbaeva, A.; Masuda, K.; Thonar, E. J.; Klisch, S. M.; Sah, R. L. *Arthritis Rheum.* **2007**, *56*, 188–198.
22. Jadin, K. D.; Bae, W. C.; Schumacher, B. L.; Sah, R. L. *Biomaterials* **2007**, *28*, 230–239.
23. Brama, P. A.; TeKoppele, J. M.; Bank, R. A.; Barneveld, A.; van Weeren, P. R. *Equine Vet. J.* **2002**, *34*(3), 265–269.
24. Rieppo, J.; Hyttinen, M. M.; Halmesmaki, E.; *et al. Osteoarthr. Cartil.* **2009**, *17*(4), 448–455.
25. Pal, S.; Tang, L.-H.; Choi, H.; *et al. Coll. Relat. Res.* **1981**, *1*, 151–176.
26. Klein, T. J.; Chaudhry, M.; Bae, W. C.; Sah, R. L. *Trans. Orthop. Res. Soc.* **2004**, *29*, 170.
27. Ropes, M. W.; Rossmeisl, E. C.; Bauer, W. *J. Clin. Invest.* **1940**, *19*(6), 795–799.
28. Schmid, K.; Macnair, M. B. *J. Clin. Invest.* **1956**, *35*(7), 814–824.
29. Schmid, K.; Macnair, M. B. *J. Clin. Invest.* **1958**, *37*(5), 708–718.
30. Holley, H. L.; Patton, F. M.; Pigman, W.; Platt, D. *Arch. Biochem. Biophys.* **1956**, *64*(1), 152–163.
31. Decker, B.; Mc, K. B.; Mc, G. W.; Slocumb, C. H. *Arthritis Rheum.* **1959**, *2*(2), 162–177.
32. Schur, P. H.; Sandson, J. *Arthritis Rheum.* **1963**, *6*, 115–129.
33. Levick, J. R.; McDonald, J. N. *Ann. Rheum. Dis.* **1995**, *54*(5), 417–423.
34. Ogston, A. G.; Stanier, J. E. *J. Physiol.* **1953**, *119*(2–3), 244–252.
35. Swann, D. A.; Sotman, S.; Dixon, M.; Brooks, C. *Biochem. J.* **1977**, *161*(3), 473–485.
36. Swann, D. A.; Slayter, H. S.; Silver, F. H. *J. Biol. Chem.* **1981**, *256*(11), 5921–5925.
37. Lee, H. G.; Cowman, M. K. *Anal. Biochem.* **1994**, *219*(2), 278–287.
38. McDonald, J. N.; Levick, J. R. *J. Physiol.* **1995**, *485*(Pt 1), 179–193.
39. Jay, G. D.; Harris, D. A.; Cha, C. J. *Glycoconj. J.* **2001**, *18*(10), 807–815.
40. Jay, G. D.; Tantravahi, U.; Britt, D. E.; Barrach, H. J.; Cha, C. J. *J. Orthop. Res.* **2001**, *19*(4), 677–687.
41. Schumacher, B. L.; Block, J. A.; Schmid, T. M.; Aydelotte, M. B.; Kuettner, K. E. *Arch. Biochem. Biophys.* **1994**, *311*(1), 144–152.
42. Lee, S. Y.; Niikura, T.; Reddi, A. H. *Tissue Eng. A* **2008**, *14*(11), 1799–1808.
43. Bao, J. P.; Chen, W. P.; Wu, L. D. *Mol. Biol. Rep.* **2010**, Epub PMID: 20099082.
44. Goldring, M. B. *Curr. Rheumatol. Rep.* **2000**, *2*(6), 459–465.
45. Futani, H.; Okayama, A.; Matsui, K.; *et al. J. Immunother.* **2002**, *25*(Suppl. 1), S61–S64.
46. Doss, F.; Menard, J.; Hauschild, M.; *et al. Scand. J. Rheumatol.* **2007**, *36*(2), 136–139.
47. Blewis, M. E.; Lao, B. J.; Schumacher, B. L.; Bugbee, W. D.; Sah, R. L.; Firestein, G. S. *Tissue Eng. A* **2010**, *16*, 1329–1337.
48. Hyc, A.; Osiecka-Iwan, A.; Niderla-Bielinska, J.; Jankowska-Steifer, E.; Moskalewski, S. *Int. J. Mol. Med.* **2009**, *24*(4), 579–585.
49. Kratz, A.; Pesce, M. A.; Fink, D. J. In *Harrison's Principles of Internal Medicine*, 17th ed.; Fauci, A. S., Braunwald, E., Kasper, D. L., Hauser, S. L., Longo, D. L., Jameson, J. L., Loscalzo, J., eds. New York: McGraw-Hill Medical.
50. Schumacher, B. L.; Hughes, C. E.; Kuettner, K. E.; Caterson, B.; Aydelotte, M. B. *J. Orthop. Res.* **1999**, *17*(1), 110–120.
51. Jay, G. D.; Britt, D. E.; Cha, C. J. *J. Rheumatol.* **2000**, *27*(3), 594–600.
52. Schumacher, B. L.; Schmidt, T. A.; Voegtline, M. S.; Chen, A. C.; Sah, R. L. *J. Orthop. Res.* **2005**, *23*(3), 562–568.
53. Sabaratnam, S.; Arunan, V.; Coleman, P. J.; Mason, R. M.; Levick, J. R. *J. Physiol.* **2005**, *567*(Pt 2), 569–581.
54. Mazzucco, D.; Scott, R.; Spector, M. *Biomaterials* **2004**, *25*(18), 4433–4445.
55. Levick, J. R.; McDonald, J. N. *J. Physiol.* **1989**, *419*, 493–508.
56. Granger, H. J.; Taylor, A. E. *Circ. Res.* **1975**, *36*(1), 222–228.
57. Sabaratnam, S.; Coleman, P. J.; Mason, R. M.; Levick, J. R. *J. Physiol.* **2007**, *578*(Pt 1), 291–299.
58. Momberger, T. S.; Levick, J. R.; Mason, R. M. *Matrix Biol.* **2005**, *24*, 510–519.
59. Ingram, K. R.; Wann, A. K.; Angel, C. K.; Coleman, P. J.; Levick, J. R. *J. Physiol.* **2008**, *586*(6), 1715–1729.
60. Nugent, G. E.; Aneloski, N. M.; Schmidt, T. A.; Schumacher, B. L.; Voegtline, M. S.; Sah, R. L. *Arthritis Rheum.* **2006**, *54*, 1888–1896.
61. Nugent, G. E.; Schmidt, T. A.; Schumacher, B. L.; *et al. Biorheology* **2006**, *43*, 191–200.
62. Nugent-Derfus, G. E.; Takara, T.; O'Neill, J. K.; *et al. Osteoarthr. Cartil.* **2007**, *15*(5), 566–574.
63. Eckstein, F.; Lemberger, B.; Stammberger, T.; Englmeier, K. H.; Reiser, M. *J. Biomech.* **2000**, *33*(7), 819–825.
64. Kersting, U. G.; Stubendorff, J. J.; Schmidt, M. C.; Bruggemann, G. P. *Osteoarthr. Cartil.* **2005**, *13*(10), 925–934.
65. Wan, L.; de Asla, R. J.; Rubash, H. E.; Li, G. *J. Orthop. Res.* **2008**, *26*(8), 1081–1089.
66. Wong, B. L.; Bae, W. C.; Chun, J.; Gratz, K. R.; Lotz, M.; Sah, R. L. *Arthritis Rheum.* **2008**, *58*, 2065–2074.
67. Wong, B. L.; Bae, W. C.; Gratz, K. R.; Sah, R. L. *Mol. Cell. Biomech.* **2008**, *5*, 197–206.
68. Fam, H.; Bryant, J. T.; Kontopoulou, M. *Biorheology* **2007**, *44*, 59–74.
69. Schurz, J.; Ribitsch, V. *Biorheology* **1987**, *24*(4), 385–399.
70. Safari, M.; Bjelle, A.; Gudmundsson, M.; Hogfors, C.; Granhed, H. *Biorheology* **1990**, *27*(5), 659–674.
71. Davis, W. H.; Lee, S. L.; Sokoloff, L. *J. Biomech. Eng. Trans. ASME* **1979**, *101*(3), 185–192.
72. Forster, H.; Fisher, J. *Proc. Inst. Mech. Eng. H* **1996**, *210*, 109–119.
73. Schmidt, T. A.; Gastelum, N. S.; Nguyen, Q. T.; Schumacher, B. L.; Sah, R. L. *Arthritis Rheum.* **2007**, *56*, 882–891.
74. Schmidt, T. A.; Sah, R. L. *Osteoarthr. Cartil.* **2007**, *15*, 35–47.
75. Gleghorn, J. P.; Jones, A. R.; Flannery, C. R.; Bonassar, L. J. *J. Orthop. Res.* **2009**, *27*(6), 771–777.
76. Lipshitz, H.; Glimcher, M. J. *Wear* **1979**, *52*, 297–339.
77. Berrien, L. S.; Furey, M. J.; Veit, H. P. *Crit. Rev. Biomed. Eng.* **2000**, *28*(1–2), 103–108.
78. Kobayashi, M.; Oka, M. *J. Biomater. Sci. Polym. Ed.* **2004**, *15*(6), 741–751.
79. Katta, J. K.; Marcolongo, M.; Lowman, A.; Mansmann, K. A. *J. Biomed. Mater. Res. A* **2007**, *83*(2), 471–479.
80. Linn, F. C. *J. Bone Joint Surg. Am.* **1967**, *49A*, 1079–1098.
81. Rainer, F.; Ribitsch, V.; Ulreich, A. *Acta Med. Austriaca* **1980**, *7*(3), 92–95.
82. Ogston, A. G.; Stanier, J. E.; Toms, B. A.; Strawbridge, D. J. *Nature* **1950**, *165*, 571.
83. Nigam, K. M.; Manohar, K.; Chaudhry, K. K. *Wear* **1981**, *70*(1), 63–75.
84. Tandon, P. N.; Bong, N. H.; Kushwaha, K. *Int. J. Biomed. Comput.* **1994**, *35*(2), 125–140.
85. Chiroiu, V.; Mosnegutu, V.; Munteanu, L.; Ioan, R. *Mech. Res. Commun.* **2010**, *37*, 246–255.
86. MacConaill, M. A. *J. Anat.* **1932**, *66*, 210–227.
87. Charnley, J. *Ann. Rheum. Dis.* **1960**, *19*, 10–19.
88. Walker, P. S.; Dowson, D.; Longfield, M. D.; Wright, V. *Ann. Rheum. Dis.* **1968**, *27*(6), 512–520.
89. Maroudas, A. *Biophys. J.* **1968**, *8*(5), 575–595.
90. Maroudas, A. *Biophys. J.* **1970**, *10*(5), 365–379.
91. Torzilli, P. A.; Mow, V. C. *J. Biomech.* **1976**, *9*(8), 541–552.
92. Torzilli, P. A.; Mow, V. C. *J. Biomech.* **1976**, *9*(9), 587–606.
93. Zhang, L.; Gardiner, B. S.; Smith, D. W.; Pivonka, P.; Grodzinsky, A. *Arch. Biochem. Biophys.* **2007**, *457*(1), 47–56.
94. Hascall, V. C.; Luyten, F. P.; Plaas, A. H. K.; Sandy, J. D. In *Methods in Cartilage Research*; Maroudas, A., Kuettner, K., Eds.; Academic Press: San Diego, CA, 1990; pp 108–112.
95. DiMicco, M. A.; Sah, R. L. *Transp. Porous Media* **2003**, *50*, 57–73.
96. Klein, T. J.; Sah, R. L. *Biomech. Model. Mechanobiol.* **2007**, *6*, 21–32.
97. Ateshian, G. A. *J. Biomech. Eng.* **1997**, *119*(1), 81–86.
98. Wilson, W.; Huyghe, J. M.; van Donkelaar, C. C. *Osteoarthr. Cartil.* **2006**, *14*(6), 554–560.
99. Knight, A. D.; Levick, J. R. *J. Physiol.* **1982**, *328*, 403–420.
100. Knight, A. D.; Levick, J. R. *J. Physiol.* **1982**, *331*, 1–15.
101. Levick, J. R. *Microvasc. Res.* **1994**, *47*(1), 90–125.
102. Levick, J. R. *Q. J. Exp. Physiol.* **1984**, *69*(2), 289–300.
103. Levick, J. R. *Ann. Rheum. Dis.* **1998**, *57*, 339–344.
104. Levick, J. R. In *The Microcirculation*; Renkin, M., Michel, C., Eds.; Handbook of Physiology, Section 2. The Cardiovascular System; The American Physiological Society, 1984; Vol. IV, pp 917–947.
105. Levick, J. R. *Microcirculation* **1995**, *2*(3), 217–233.
106. Simkin, P. A. *Ann. Rheum. Dis.* **1995**, *54*(5), 424–428.
107. Blewis, M. E.; Nugent-Derfus, G. E.; Schmidt, T. A.; Schumacher, B. L.; Sah, R. L. *Eur. Cell Mater.* **2007**, *13*, 26–39.
108. Rullmann, J. A.; Struemper, H.; Defranoux, N. A.; Ramanujan, S.; Meeuwisse, C. M.; van Elsas, A. *Syst. Biol. (Stevenage)* **2005**, *152*(4), 256–262.
109. Jortikka, M. O.; Inkinen, R. I.; Tammi, M. I.; *et al. Ann. Rheum. Dis.* **1997**, *56*(4), 255–261.

110. Arokoski, J. P.; Jurvelin, J. S.; Vaatainen, U.; Helminen, H. J. *Scand. J. Med. Sci. Sports* **2000**, *10*(4), 186–198.
111. Grodzinsky, A. J.; Levenston, M. E.; Jin, M.; Frank, E. H. *Annu. Rev. Biomed. Eng.* **2000**, *2*, 691–713.
112. Kimura, J. H.; Schipplein, O. D.; Kuettner, K. E.; Andriacchi, T. P. *Trans. Orthop. Res. Soc.* **1985**, *9*, 365.
113. Hall, A. C.; Urban, J. P. G.; Gehl, K. A. *J. Orthop. Res.* **1991**, *9*, 1–10.
114. Lafeber, F.; Veldhuijzen, J. P.; Vanroy, J. L.; Huber-Bruning, O.; Bijlsma, J. W. *Br. J. Rheum.* **1992**, *31*, 437–442.
115. Lippiello, L.; Kaye, C.; Neumata, T.; Mankin, H. J. *Connect. Tissue Res.* **1985**, *13*, 99–107.
116. Parkkinen, J. J.; Ikonen, J.; Lammi, M. J.; Laakkonen, J.; Tammi, M.; Helminen, H. J. *Arch. Biochem. Biophys.* **1993**, *300*, 458–465.
117. Jones, I. L.; Klamfeldt, D. D. S.; Sandstrom, T. *Clin. Orthop. Relat. Res.* **1982**, *165*, 283–289.
118. Gray, M. L.; Pizzanelli, A. M.; Grodzinsky, A. J.; Lee, R. C. *J. Orthop. Res.* **1988**, *6*, 777–792.
119. Sah, R. L.; Kim, Y. J.; Doong, J. H.; Grodzinsky, A. J.; Plaas, A. H. K.; Sandy, J. D. *J. Orthop. Res.* **1989**, *7*, 619–636.
120. Guilak, F.; Meyer, B. C.; Ratcliffe, A.; Mow, V. C. *Osteoarthr. Cartil.* **1994**, *2*, 91–101.
121. Bonassar, L. J.; Grodzinsky, A. J.; Srinivasan, A.; Davila, S. G.; Trippel, S. B. *Arch. Biochem. Biophys.* **2000**, *379*(1), 57–63.
122. Gray, M. L.; Pizzanelli, A. M.; Lee, R. C.; Grodzinsky, A. J.; Swann, D. A. *Biochim. Biophys. Acta* **1989**, *991*, 415–425.
123. Li, K. W.; Williamson, A. K.; Wang, A. S.; Sah, R. L. *Clin. Orthop. Relat. Res.* **2001**, *391S*, 34–48.
124. Valhmu, W. B.; Stazzone, E. J.; Bachrach, N. M.; *et al. Arch. Biochem. Biophys.* **1998**, *353*, 29–36.
125. Fitzgerald, J. B.; Jin, M.; Dean, D.; Wood, D. J.; Zheng, M. H.; Grodzinsky, A. J. *J. Biol. Chem.* **2004**, *279*(19), 19502–19511.
126. Wheeler, C. A.; Jafarzadeh, S. R.; Rocke, D. M.; Grodzinsky, A. J. *Osteoarthr. Cartil.* **2009**, *17*(7), 944–952.
127. Palmoski, M. J.; Brandt, K. D. *Arthritis Rheum.* **1984**, *27*, 675–681.
128. Bonassar, L. J.; Grodzinsky, A. J.; Frank, E. H.; Davila, S. G.; Bhakta, N. R.; Trippel, S. B. *J. Orthop. Res.* **2001**, *19*(1), 11–17.
129. Davisson, T. H.; Kunig, S.; Chen, A. C.; Sah, R. L.; Ratcliffe, A. *J. Orthop. Res.* **2002**, *20*, 842–848.
130. Davisson, T. H.; Sah, R. L.; Ratcliffe, A. R. *Tissue Eng.* **2002**, *8*, 807–816.
131. Torzilli, P. A.; Grigiene, R.; Huang, C.; *et al. J. Biomech.* **1997**, *30*, 1–9.
132. Torzilli, P. A.; Bhargava, M.; Park, S.; Chen, C. T. *Osteoarthr. Cartil.* **2010**, *18*(1), 97–105.
133. Fitzgerald, J. B.; Jin, M.; Grodzinsky, A. J. *J. Biol. Chem.* **2006**, *281*(34), 24095–24103.
134. Fitzgerald, J. B.; Jin, M.; Chai, D. H.; Siparsky, P.; Fanning, P.; Grodzinsky, A. J. *J. Biol. Chem.* **2008**, *283*(11), 6735–6743.
135. Frank, E. H.; Jin, M.; Loening, A. M.; Levenston, M. E.; Grodzinsky, A. J. *J. Biomech.* **2000**, *33*(11), 1523–1527.
136. Jin, M.; Frank, E. H.; Quinn, T. M.; Hunziker, E. B.; Grodzinsky, A. J. *Arch. Biochem. Biophys.* **2001**, *395*(1), 41–48.
137. Nugent, G. E. Ph.D. Thesis, University of California, San Diego, 2006.
138. Neu, C. P.; Khalafi, A.; Komvopoulos, K.; Schmid, T. M.; Reddi, A. H. *Arthritis Rheum.* **2007**, *56*(11), 3706–3714.
139. Saadat, E.; Lan, H.; Majumdar, S.; Rempel, D. M.; King, K. B. *Arthritis Res. Ther.* **2006**, *8*(5), R147.
140. Kiraly, K.; Hyttinen, M. M.; Parkkinen, J. J.; *et al. Anat. Rec.* **1998**, *251*(1), 28–36.
141. Hyttinen, M. M.; Arokoski, J. P.; Parkkinen, J. J.; *et al. Osteoarthr. Cartil.* **2001**, *9*(8), 694–701.
142. Thibault, M.; Poole, A. R.; Buschmann, M. D. *J. Orthop. Res.* **2002**, *20*(6), 1265–1273.
143. Elsaid, K. A.; Jay, G. D.; Warman, M. L.; Rhee, D. K.; Chichester, C. O. *Arthritis Rheum.* **2005**, *52*(6), 1746–1755.
144. Young, A. A.; McLennan, S.; Smith, M. M.; *et al. Arthritis Res. Ther.* **2006**, *8*(2), R41.
145. Marcelino, J.; Carpten, J. D.; Suwairi, W. M.; *et al. Nat. Genet.* **1999**, *23*(3), 319–322.
146. Rhee, D. K.; Marcelino, J.; Baker, M.; *et al. J. Clin. Invest.* **2005**, *115*(3), 622–631.
147. Malemud, C. J. *Drugs Aging* **2010**, *27*(2), 95–115.
148. Cameron, M.; Buchgraber, A.; Passler, H.; *et al. Am. J. Sports Med.* **1997**, *25*(6), 751–754.
149. Marks, P. H.; Donaldson, M. L. *Arthroscopy* **2005**, *21*(11), 1342–1347.
150. Elsaid, K. A.; Machan, J. T.; Waller, K.; Fleming, B. C.; Jay, G. D. *Arthritis Rheum.* **2009**, *60*(10), 2997–3006.
151. Dahlberg, L.; Friden, T.; Roos, H.; Lark, M. W.; Lohmander, L. S. *Br. J. Rheumatol.* **1994**, *33*(12), 1107–1111.
152. Simkin, P. A. *Arthritis Rheum.* **1979**, *22*(7), 689–696.
153. Levick, J. R. *Arthritis Rheum.* **1981**, *24*, 1550–1560.
154. Kushner, I.; Somerville, J. A. *Arthritis Rheum.* **1971**, *14*(5), 560–570.
155. Pejovic, M.; Stankovic, A.; Mitrovic, D. R. *Br. J. Rheumatol.* **1995**, *34*(6), 520–524.
156. Bryant, S. J.; Anseth, K. S. *J. Biomed. Mater. Res.* **2002**, *59*(1), 63–72.
157. Schmidt, O.; Mizrahi, J.; Elisseeff, J.; Seliktar, D. *Biotechnol. Bioeng.* **2006**, *95*(6), 1061–1069.
158. Lee, D. A.; Bader, D. L. *J. Orthop. Res.* **1997**, *15*, 181–188.
159. Mauck, R. L.; Nicoll, S. B.; Seyhan, S. L.; Ateshian, G. A.; Hung, C. T. *Tissue Eng.* **2003**, *9*(4), 597–611.
160. Elisseeff, J.; McIntosh, W.; Anseth, K.; Riley, S.; Ragan, P.; Langer, R. *J. Biomed. Mater. Res.* **2000**, *51*(2), 164–171.
161. Freed, L. E.; Vunjak-Novakovic, G.; Biron, R. J.; *et al. Biotechnology* **1994**, *12*, 689–693.
162. Freed, L. E.; Langer, R.; Martin, I.; Pellis, N. R.; Vunjak-Novakovic, G. *Proc. Natl Acad. Sci. USA* **1997**, *94*, 13885–13890.
163. Vunjak-Novakovic, G.; Martin, I.; Obradovic, B.; *et al. J. Orthop. Res.* **1999**, *17*, 130–139.
164. Grad, S.; Lee, C. R.; Gorna, K.; Gogolewski, S.; Wimmer, M. A.; Alini, M. *Tissue Eng.* **2005**, *11*(1–2), 249–256.
165. Grad, S.; Gogolewski, S.; Alini, M.; Wimmer, M. A. *Tissue Eng.* **2006**, *12*, 3171–3179.
166. Waldman, S. D.; Spiteri, C. G.; Grynpas, M. D.; Pilliar, R. M.; Kandel, R. A. *Tissue Eng.* **2004**, *10*(9–10), 1323–1331.
167. Masuda, K.; Sah, R. L.; Hejna, M. J.; Thonar, E. J. *J. Orthop. Res.* **2003**, *21*(1), 139–148.
168. Hu, J. C.; Athanasiou, K. A. *Tissue Eng.* **2006**, *12*(4), 969–979.
169. Elder, B. D.; Athanasiou, K. A. *PLoS ONE* **2008**, *3*(6), e2341.
170. Mizuno, S.; Tateishi, T.; Ushida, T.; Glowacki, J. *J. Cell. Physiol.* **2002**, *193*(3), 319–327.
171. Toyoda, T.; Seedhom, B. B.; Kirkham, J.; Bonass, W. A. *Biorheology* **2003**, *40*(1–3), 79–85.
172. Toyoda, T.; Seedhom, B. B.; Yao, J. Q.; Kirkham, J.; Brookes, S.; Bonass, W. A. *Arthritis Rheum.* **2003**, *48*(10), 2865–2872.
173. Elder, B. D.; Athanasiou, K. A. *Tissue Eng. B Rev.* **2009**, *15*(1), 43–53.
174. Carver, S. E.; Heath, C. A. *Tissue Eng.* **1999**, *5*, 1–11.
175. Carver, S. E.; Heath, C. A. *Biotechnol. Bioeng.* **1999**, *62*(2), 166–174.
176. Riesle, J.; Hollander, A. P.; Langer, R.; Freed, L. E.; Vunjak-Novakovic, G. *J. Cell. Biochem.* **1998**, *71*, 313–327.
177. Li, W. J.; Tuan, R. S. *Tissue Eng. A* **2008**, *14*, 639–648.
178. Gooch, K. J.; Blunk, T.; Courter, D. L.; *et al. Biochem. Biophys. Res. Commun.* **2001**, *286*(5), 909–915.
179. Hunter, C. J.; Imler, S. M.; Malaviya, P.; Nerem, R. M.; Levenston, M. E. *Biomaterials* **2002**, *23*(4), 1249–1259.
180. Buschmann, M. D.; Gluzband, Y. A.; Grodzinsky, A. J.; Kimura, J. H.; Hunziker, E. B. *J. Orthop. Res.* **1992**, *10*, 745–758.
181. Buschmann, M. D.; Gluzband, Y. A.; Grodzinsky, A. J.; Hunziker, E. B. *J. Cell Sci.* **1995**, *108*(Pt 4), 1497–1508.
182. Mauck, R. L.; Seyhan, S. L.; Ateshian, G. A.; Hung, C. T. *Ann. Biomed. Eng.* **2002**, *30*(8), 1046–1056.
183. Buschmann, M. D.; Gluzband, Y. A.; Grodzinsky, A. J. *J. Cell Sci.* **1995**, *108*, 1497–1508.
184. Mauck, R. L.; Soltz, M. A.; Wang, C. C.; *et al. J. Biomech. Eng.* **2000**, *122*(3), 252–260.
185. De Croos, J. N.; Dhaliwal, S. S.; Grynpas, M. D.; Pilliar, R. M.; Kandel, R. A. *Matrix Biol.* **2006**, *25*(6), 323–331.
186. Waldman, S. D.; Spiteri, C. G.; Grynpas, M. D.; Pilliar, R. M.; Kandel, R. A. *J. Orthop. Res.* **2003**, *21*, 590–596.
187. Gemmiti, C. V.; Guldberg, R. E. *Biotechnol. Bioeng.* **2009**, *104*(4), 809–820.
188. Bellamy, N.; Campbell, J.; Welch, V.; Gee, T.; Bourne, R. B.; Wells, G. A. *Cochrane Database Syst. Rev.* **2006**, Issue 2. Art. No.: CD005321. DOI: 10.1002/14651858.CD005321.pub2.
189. Strauss, E. J.; Hart, J. A.; Miller, M. D.; Altman, R. D.; Rosen, J. E. *Am. J. Sports Med.* **2009**, *37*(8), 1636–1644.
190. Blewis, M. E.; Lao, B. J.; Schumacher, B. L.; Bugbee, W. D.; Sah, R. L.; Firestein, G. S. *Tissue Eng. A* **2010**, *16*, 1329–1337.
191. Blewis, M. E.; Lao, B. J.; Jadin, K. D.; *et al. Biotechnol. Bioeng.* **2010**, *106*(1), 149–160.

5.516. Biomaterials in Cartilage Tissue Engineering

B Reid and J Elisseeff, Johns Hopkins University, Baltimore, MD, USA

© 2011 Elsevier Ltd. All rights reserved.

5.516.1.	Introduction	213
5.516.2.	Cell Sources	214
5.516.3.	Scaffolds	214
5.516.3.1.	Hydrogels	214
5.516.3.2.	Sponges	215
5.516.3.3.	Fibers	216
5.516.4.	Growth Factors	216
5.516.5.	Clinical Repair Techniques	217
5.516.6.	Conclusion	219
References		219

Abbreviations

ACI	Autologous chondrocyte implantation
AMIC	Autologous matrix-induced chondrogenesis
CMP	Collagen mimetic peptide
CS	Chondroitin sulfate
ECM	Extracellular matrix
GAG	Glycosaminoglycan
HyA	Hyaluronic acid
PEG	Poly(ethylene glycol)
ROS	Reactive oxygen species
SZP	Superficial zonal protein

5.516.1. Introduction

Articular cartilage is an avascular, aneural tissue lining the surface of diarthrodial joints. This anisotropic tissue is composed of a superficial, middle, and deep zone. The articular cartilage zonal structure is generally consistent between species; however, considerable differences exist in thickness, cell distribution, and matrix properties.[1,2] The zonal architecture consists of variance in the organization of the collagen network which plays a significant role in the tensile and compressive properties of the tissue.[3] Specifically, the collagen fibrils are responsible for the anisotropic nature of the articular cartilage tissue. For instance, in the superficial zone, collagen fibrils are aligned parallel to the articular surface, thereby providing high tensile strength to endure the joint loading stresses. The middle zone consists of randomly oriented collagen fibers which allow the progression to the deep zone in which the fibers are aligned perpendicularly to the subchondral bone.[4]

While collagen is the most abundant component of cartilage, large aggregating proteoglycans are a large constituent as well. In fact, the proteglycan aggregates increase from the articular surface to the deep zone, even in fetal cartilage.[5] The aggregates comprise a hyaluronic acid backbone that has aggrecan monomers attached. The monomers consist of a core protein that is extensively glycosylated with negatively charged chondroitin sulfate (CS) and keratan sulfate glycosaminoglycans (GAGs). One contribution to the zonal variation in GAG content is the significant differences in the metabolic properties of the chondrocytes from different zones.[6,7] Chondrocytes from each zone have unique growth rates, gene expression, and levels of biosynthesis.[8] For example, chondrocytes from the superficial layer show enhanced superficial zonal protein (SZP) expression, while chondrocytes from middle and deep zones exhibit increased type II collagen expression.[9] The increase in collagen and GAG provides the mechanical properties for efficient distribution and transmission of loads across the joint surface to the subchondral bone.[10] This subject matter is treated at much greater length in the previous chapter.

Because of its avascularity, articular cartilage is considered hypoxic in comparison to other tissue types.[11] Levels of oxygen (O_2) are estimated between 5% and 7%, which is perhaps the reason as to why articular chondrocytes have few mitochondria.[12] Consequently, metabolism is largely anaerobic with little capacity for oxidative phosphorylation.[11,13,14] Recent evidence shows that O_2 tension is a critical parameter affecting chondrocyte phenotype, gene expression, and morphology.[15] For example, studies have shown a shift in energy metabolism, following chondrocyte introduction to a monolayer culture environment, from a characteristically glycolytic to an oxidative metabolism.[16] As a result, there is an increase in reactive oxygen species (ROS), and therefore 5% of oxygen consumption in the electron transport chain is diverted into superoxide production.[17] In turn, the enhanced ROS generation presents detrimental implications for long-term cell expansion especially in the case of articular chondrocyte transplantation, a technique expanding chondrocytes in monolayer under atmospheric oxygen tension.[18]

Tissue engineering has emerged as a promising potential for treating tissue damage and tissue loss to millions of people each year.[19] The fundamental approach is the use of cells, scaffolds, and signaling molecules, separately or in combination. Cartilage's limited ability to self-repair makes it an ideal

candidate for tissue engineering. This chapter will discuss approaches in articular cartilage repair with an emphasis on cell sources, biomaterials, and growth factors.

5.516.2. Cell Sources

First-generation autologous chondrocyte implantation (ACI) introduced autologous chondrocytes into the clinical setting after *in vitro* culture expansion.[20] As mentioned previously, monolayer expansion of chondrocytes alters phenotype, gene expression, and morphology. As a result, this early technique led to spindle-shaped fibroblast-like cells that secreted fibrous tissue or fibrocartilage when implanted *in vivo*. Later generation ACI techniques are in development and are an attempt to preserve the chondrogenic phenotype through the use of three-dimensional implants. Understanding the importance of the cell population has embarked efforts into selecting a chondrocyte subpopulation that possesses a specific marker profile predictive of the capability to form stable hyaline cartilage.[21]

Mesenchymal stem cells have also been investigated because of the limited proliferative capacity of the chondrocytes as well as their propensity to dedifferentiate *in vitro*. Numerous studies comparing the chondrogenic ability of various MSC sources show exceptional results with bone marrow-derived mesenchymal stem cells (BM-MSCs).[22,23] BM-MSCs are available in large quantities, and are able to differentiate into chondrocytes in response to chondrogenic signals.[24] These attractive characteristics lead to the introduction of culture-expanded BM-MSC implantation in the clinical setting to treat cartilage defects.[25] Thereafter, autologous matrix-induced chondrogenesis (AMIC) became a technique using local, unprocessed BM-MSCs recruited from the microfracture site onto a scaffold implanted *in situ*.[26] More recently, minimally processed BM-MSCs have been introduced in the clinical setting via the bone marrow aspirate concentrate (BMAC) technique. BMAC uses laboratory procedures within the operating room to isolate and concentrate the MSCs resident in the nucleated cell portion of the bone marrow for reimplantation.[27]

5.516.3. Scaffolds

A wide range of natural and synthetic materials are currently under investigation for cartilage tissue engineering. An ideal scaffold provides a three-dimensional environment that will enable the production of cartilaginous tissue. The scaffold should be biocompatible, resorbable, and mechanically stable to supply temporal support for the implanted cells, and allow diffusion of nutrients and waste products. Scaffolds are designed to degrade overtime while permitting sufficient time for extracellular matrix (ECM) tissue production, usually through hydrolytic or enzymatic degradation. Determining the balance of degradation is a pertinent factor as investigations have shown that slow degradation may impede new cartilaginous ECM production, while fast degradation may compromise structural support and shape retention.[28] Another important parameter when designing a scaffold is cell seeding density and seeding method. Many approaches show high seeding densities to facilitate greater ECM synthesis, most likely because of cell–cell interactions.[29,30]

Natural polymers explored frequently in tissue engineering include agarose, alginate, cellulose, chitosan, CS, collagen, fibrin, gelatin, and hyaluronic acid (HyA). Natural polymers exhibit bioactivity with cells via cell surface receptors thereby allowing regulation of cell function. As a result, this interaction may stimulate an immune response limiting the control of the materials degradation kinetics. In contrast, synthetic polymers do not exhibit cellular interaction unless it is a hydrophobic material or specific chemical functional groups are incorporated. Current synthetic polymers investigated for cartilage engineering include poly(α-hydroxy esters), poly(ethylene glycol/oxide), poly(NiPAAm), poly(propylene fumarate), poly(urethane), poly(vinyl alcohol), and self-assembling peptides. Unlike the case of natural polymers, *in vivo* synthetic polymer degradation and diffusion kinetics can be readily modified; but there are disadvantages with synthetic polymers such as toxic degradation by products causing inflammation and cell death.[31] Thus, each specific application will dictate scaffold of choice. One pertinent factor is the scaffold architecture, as it has been observed to play a significant role in determining cellular behavior. Scaffold architecture can be divided into hydrogels, sponges, and fibers. The following sections will describe scaffolds investigated for cartilage engineering.

5.516.3.1. Hydrogels

Hydrogels are three-dimensional hydrophilic polymer networks. Recently, injectable hydrogels have become appealing scaffolds because of the structural resemblance to extracellular matrix of many tissues and their minimally invasive delivery manner. Hydrogels support cell viability within a three-dimensional environment where encapsulated cells retain a rounded morphology, an essential parameter for chondrogenesis. In addition, the injectable nature of hydrogels provides a facile method to fill defects of any size and shape.

Hydrogels are formed through either physical or chemical cross-linking. Physical cross-linked gels are prepared through molecular entanglements and/or ionic or hydrogen bonding, or hydrophobic interactions, while chemically cross-linked gels are covalently bonded. Photopolymerization is one of the most common chemical cross-linking methods using ultraviolet or visible light.[32] Several factors including cross-linking method and density, macromer concentration, and molecular weight determine the physical and chemical properties of hydrogels.

Poly(ethylene glycol) (PEG) is currently FDA-approved for several medical applications.[33,34] PEG's relatively inert nature and resistance to protein adsorption make it an attractive candidate for cartilage engineering. An extensively studied PEG hydrogel system employs ultraviolet irradiation to generate radicals from appropriate photoinitiators.[35,36] The free radicals will react with modified PEG functionalized with acrylate groups to form a covalently cross-linked bond. Further modifications to PEG include copolymerization with degradable polymers such as poly(lactic acid), poly(glycolic acid), and poly(propylene fumarate) for improved cartilage tissue growth.[37] In addition, bioactive peptides such as collagen mimetic peptide (CMP) have been incorporated into PEG hydrogels. Lee and colleagues showed that PEG hydrogels conjugated with CMP increased ECM production of encapsulated chondrocytes by providing cell-manipulated

cross-links and collagen binding sites that simulate natural extracellular matrix.[38]

Another polymer commonly used in cartilage engineering is hyaluronic acid (HyA), a nonsulfated GAG found natively in cartilage. HyA plays an integral role in cell proliferation, morphogenesis, inflammation, and wound repair.[39] As a natural polymer, it can also interact with cell surface receptors for HyA enabling cell–scaffold interactions. HyA hydrogels can be formed by covalent cross-linking with hyrazide derivatives, esterification, and annealing and by functionalizing HyA with methacrylate groups for photopolymerization.[40–42] Varying HyA scaffold properties have shown to affect neocartilage formation by auricular chondrocytes *in vivo*.[43]

CS, another natural polymer and component of cartilage, can be photopolymerized with similar modifications as HyA and even more commonly can be incorporated with a synthetic polymer such as PEG. Varghese and colleagues showed that bone marrow-derived MSCs encapsulated in a PEG/CS hydrogel had enhancement of both chondrogenic gene expressions and cartilage-specific matrix production as compared to control PEG hydrogels containing no CS-moieties.[44]

Fibrin glue has also been used as a scaffold for chondrocytes in numerous clinical studies.[45] Fibrin is an appealing candidate because it can be made from autologous blood, and a gel can be polymerized with the presence of thrombin. Furthermore, the excellent adhesive properties, ease of application via injection, biocompatibility, and biodegradability make it an attractive candidate for ACI techniques. However, some drawbacks are its poor mechanical properties as well as its potential immunogenicity.[46,47]

Collagen is another attractive material as it is the main component of natural ECM. The basic structure of collagen composes of a tri-helical protein that contains ligands which enable cell adhesion, migration, and differentiation.[48] Chondrocytes encapsulated within a type I collagen gel regenerated cartilage tissue in rabbit defects.[49] Gelatin, a partial derivative of collagen, is formed by breaking the natural triple-helix structure of collagen into single-stranded molecules via hydrolysis.[50] Gelatin is less immunogenic compared to collagen and when incorporated with alginate encapsulated chondrocytes, expression of type II collagen increased in addition to having a rounded morphology.[51]

Alginate is a hydrophilic, linear polysaccharide, commonly used in biomedical applications because of its biocompatibility, low toxicity, and relatively low cost.[52] Alginate is a block copolymer with a linear structure composed of homopolymeric blocks of β-D-mannuronate (M) and α-L-guluronate (G) monomers. The G-blocks of alginate chains can be cross-linked with divalent cations through ionic interactions with carboxylic groups in alginate, which induces gelation. Alginate can also form hydrogels via cell-cross-linking, instead of ionic cross-linking.[52] Park and colleagues found that gels cross-linked by combining both cross-linking methods were effective to engineer cartilage tissues *in vivo*.[52]

Agarose is another linear polysaccharide derived from seaweed that solidifies when cooled. Ng and colleagues investigated agarose gels of various concentrations seeded with chondrocytes as a model for depth-dependent mechanical properties of articular cartilage.[53] Their results showed potential tissue engineering of inhomogeneous articular cartilage constructs.

Chitosan is composed of polyglucosamine, is liquid at room temperature, and gels at physiological temperatures. Its high positive charge allows water-insoluble complexes to be formed with a variety of negatively charged substances. Therefore, negatively charged growth factors can be loaded and released from this scaffold making it a promising potential to treat cartilage defects.[54] Degradation products of chitosan include CS, dermatan sulfate, HyA, keratin sulfate, and glycosylated type II collagen, all of which are nontoxic molecules involved in articular cartilage synthesis.[27]

Hydrogel composites such as p(NiPAAm-*co*-AAc) and HyA have been investigated for potential use as an injectable cell and growth factor carrier for cartilage tissue engineering applications.[55] The blended hydrogel loaded with transforming growth factorβ-3 (TGFβ-3) seeded with chondrocytes were injected subcutaneously into the nude mice. An increase in expression and synthesis of cartilage-specific ECM proteoglycans was found at the end of the study.[55]

Another group of synthetic polymers hydrogels are self-assembling peptides. They are formed by amino acid sequences of alternating ionic hydrophobic and uncharged hydrophilic side groups. Exposure to electrolyte solution enables self-assembling peptide hydrogels to form stable β-sheets of interwoven nanofibers. Kisiday and colleagues showed that articular chondrocytes maintain their phenotype and produce cartilage-like ECM when encapsulated in self-assembling peptide KLD-12 hydrogels *in vitro*.[56]

5.516.3.2. Sponges

Scaffold porosity affects cell infiltration and migration, matrix deposition and distribution, and nutrient and waste exchange. Many scaffold applications require a sponge-like architecture where tissue formation is dependent upon pore size and interconnectivity. Several methods have been employed to prepare three-dimensional biodegradable scaffolds including phase separation, emulsion freeze-drying, gas foaming, fiber bonding, and porogen leaching.[57] Phase separation methods cannot obtain large pores nor can the pore structure be easily controlled and fiber bonding techniques will often construct scaffolds lacking structural stability. The most established method providing simple control of pore structure is porogen leaching. This technique involves casting a mixture of polymer solution and porogen in a mold and drying the mixture, followed by leaching out the porogen with water to generate the pores. As porogen materials can be salts and carbohydrates, the pore structures can easily be manipulated by controlling the property and fraction of the porogen material. Chitosan can be formed into sponges via freeze-drying and lyophilization.[58] Kuo and colleagues investigated ECM production of chondrocytes in chitosan and chitin hybrid scaffolds.[59] They found that increase in weight percentage of chitin resulted in smaller pore diameters, increased surface area, a higher Young's modulus, and lower extensibility, all of which lead to an increase in cell number and ECM production.

Sponges can also be formed from silk fibroin through a solvent casting/salt leaching method. Silk fibroin is made up of a filament core protein, fibroin, along with a glue-like coat of sericin proteins. Wang and colleagues evaluated this method's support of both chondrocytes and stem cells.[60]

Type II collagen–GAG scaffolds have also been shown to mediate cell behavior. Vickers and colleagues seeded chondrocytes on type II collagen–GAG scaffolds with varying cross-linking densities and found that scaffolds with low cross-link densities experienced cell-mediated contraction, increased cell number densities, a greater degree of chondrogenesis, and an apparent increase in the rate of degradation of the scaffold compared to more highly cross-linked scaffolds that resisted cellular contraction.[61]

5.516.3.3. Fibers

Fiber networks can be woven or nonwoven. Variations in void volume, fiber diameter, and direction can dictate cell behavior. Nonwoven fiber networks tend to have higher void volumes and surface area, while, woven fiber networks are mechanically stronger and can be designed with a wide range of porosities. Fiber networks can be fabricated *in vitro* with cells and then later implanted *in vivo* for tissue repair. Moroni and colleagues developed a fiber scaffold using poly(ethylene oxide) terephthalate/poly(butylene) terephthalate (PEOT/PBT) having mechanical properties comparable to bovine articular cartilage.[62] Recently, electrospinning has become a popular technique for fabricating polymers that mimic structural similarity to natural ECM.[63] In this technique, polymer solution is drawn from a capillary forming a suspended droplet at the tip of the capillary by force of gravity or mechanical pumping combined with electrostatic charge. Nanofibers are formed by the narrowing of the ejected jet stream as it is subject to increasing surface charge density due to evaporation of the solvent. The nanofibrous structure produced by the electrospinning process has a high surface area-to-volume ratio, providing more substrate for cell attachment compared to other structures. Li and colleagues demonstrated that chondrocytes seeded on poly(ε-caprolactone) (PCL) nanofibrous scaffolds efficiently maintained their differentiated phenotype supporting nanofibrous structures as a suitable scaffold biomaterial for cartilage tissue engineering applications.[63]

Several natural materials such as cellulose and HyA have also been fabricated into fibrous scaffolds.[64,65] For instance, nonwoven HyA esters (HYAFF® derivatives) semisynthetic, resorbable fibrous networks have been shown to support cell adhesion, proliferation, and ECM production *in vitro* and *in vivo*.[66,67] Radice and colleagues conducted a pilot study with HYAFF®11 and even after complete degradation after 4 months of implantation, there was no inflammatory response.[67] Later clinical studies using Hyalograft® C (a graft of autologous chondrocytes cultured on HYAFF®11 scaffolds) to treat human articular cartilage defects showed considerable improvements even in joints with progressed osteoarthritis.[68]

5.516.4. Growth Factors

A number of different growth factors have an impact on articular cartilage repair, but the key for tissue engineering is combining these factors with cells and scaffolds. Members of the transforming growth factor (TGF) superfamily play a significant role in cartilage development. TGF-β is secreted in an inactive form, bound to a latency-associated peptide from which it dissociates before becoming active and binding to its target receptor.[69] Of the three isoforms, TGF-β1 is responsible for initial cell–cell interactions between condensing progenitor cells and as a result is the most widely investigated.[70] *In vitro* studies show TGF-β1 to induce chondrogenesis of MSCs, promote cell proliferation and proteoglycan synthesis, and inhibit the actions of matrix metalloproteinases.[71–74] However, there are negative effects observed with high doses leading to fibrosis and osteophytosis.[74,75]

A number of *in vitro* studies using rabbits have produced positive results with locally applied TGF-β1. Fan and colleagues demonstrated enhanced cartilage repair in a study applying a porous gelatin-chondroitin-hyaluronate tri-copolymer scaffold containing microspheres loaded with TGF-β1 to an osteochondral defect.[76] Similarly to *in vitro* studies, some *in vivo* studies have shown that higher doses of TGF-β1 lead toward osteophytosis.[77]

Bone morphogenetic proteins (BMPs) are also members of the TGF superfamily of growth factors and are of particular interest because of the clinical availability of both BMP-2 (Infuse, Medtronic, Minneapolis, Minnesota) and BMP-7 (Osteogenic Protein-1 (OP-1) Stryker Biotech, Hopkinton, Massachusetts).[31] BMPs enhance chondrogenesis and osteogenesis, and in particular can assist in osteochondral integration at implant site. BMP-2 and -7 improve ECM production in chondrocytes and progenitor cells. Specifically, BMP-2 upregulates TIMP-1, Sox 9, type II collagen, and aggrecan expression levels.[78,79] BMP-7 increases production of GAGs and suppresses fibroblast migration in the scaffold.[80] Mason and colleagues transfected BMP-7 into periosteal-derived MSCs and observed complete or near-complete bone and cartilage regeneration in an osteochondral rabbit defect model with a PGA scaffold after 8 weeks.[81]

Insulin-like growth factor-1 (IGF-1), the main anabolic growth factor of articular cartilage, is used to increase production of proteoglycans and type II collagen.[82,83] IGF-1's activity is likely regulated via the interaction between itself and binding proteins. As a result, the increase in catabolic activity causes proteolysis of these proteins, thereby modulating its release. Nixon *et al.*[84] coupled IFG-1 with fibrin composites in an equine osteochondral model. They found that the growth factor-treated defects showed improved histologic appearance over controls along with a significant increase in type II collagen. Elisseeff *et al.*[85] used a PEG hydrogel scaffold along with PLA microspheres containing both TGF-β1 and IGF-1 to culture bovine chondrocytes. Their results indicated an increase in ECM synthesis and cell content. While Worster *et al.*[86] found similar results *in vitro*, later *in vivo* studies showed contradicting results. Holland *et al.*[87] used a PEG hydrogel scaffold containing gelatin microparticles of TGF-β1 and IGF-1 and found no improvement in the cartilage defects of adult rabbits, but instead found that IGF-1 alone was better than TGF-β1, either alone or in combination, in terms of improving tissue composition.

Currently, there are a total of 22 different members of the FGF family identified, of which FGF-2 is the most widely investigated in articular cartilage repair.[88] FGF-2 is an important mitogen for cells of mesodermal origin and is a chemo-attractant for endothelial cells.[89] Kato and Iwamato[90] showed that FGF-2 inhibits terminal differentiation of chondrocytes. Their results provided future promise for inhibiting terminal differentiation

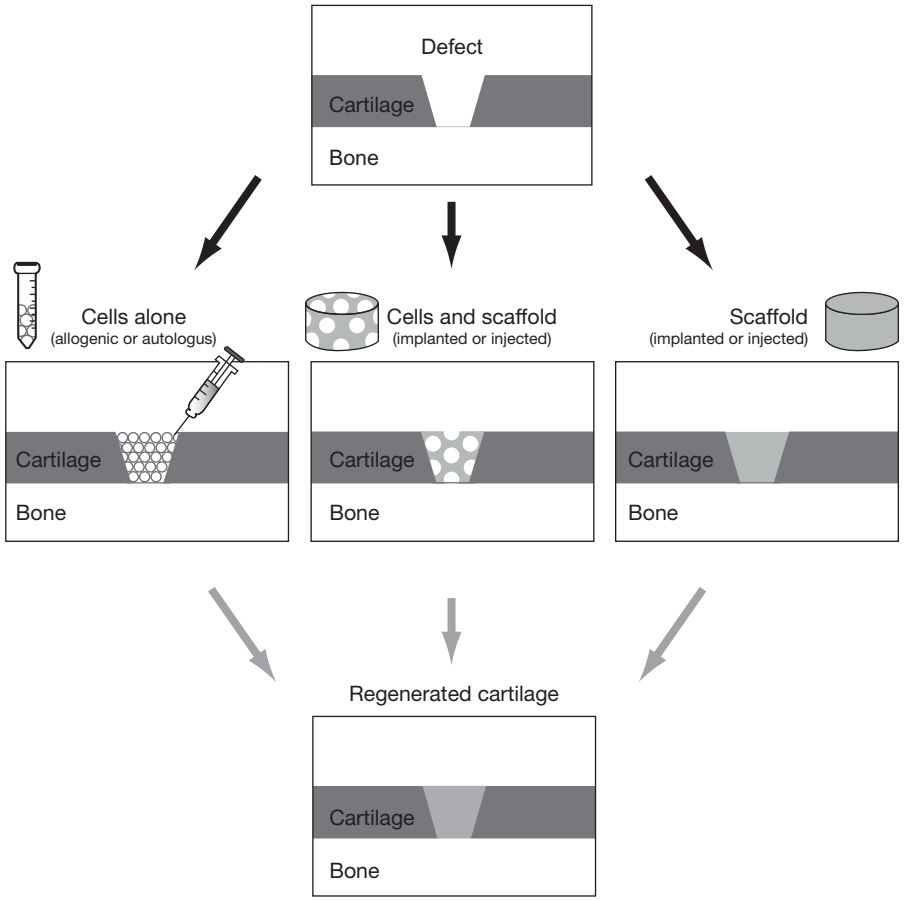

Figure 1 General schematic of approaches used in cartilage regeneration strategies, ranging from cell-only repair, cell–scaffold repair, and scaffold-only repair.

of MSCs undergoing chondrogenesis. Stewart *et al.*[91] demonstrated enhanced chondrogenic differentiation and stabilized phenotypic expression of bone marrow-derived mesenchymal stem cells cultured in a 3D pellet in the presence of FGF-2. Weisser *et al.*[92] found that FGF-2 cultured with chondrocytes in an agarose gel stabilize the chondrocyte-differentiated state while implanted into rabbit osteochondral defects. Weisser *et al.*[92] implanted FGF-2 incorporated within a triaxial 3D woven structure of ultra-high molecular weight polyethylene into a rabbit osteochondral defect. They found improved biomechanical properties nearly matching native tissue at 26 weeks post implantation. While FGF-2 is the most commonly investigated mitogen in its family, FGF-18 also has great potential in articular cartilage tissue engineering, with a number of recent studies showing its potential to stimulate cell proliferation and differentiation, and matrix production both *in vitro* and *in vivo*.[93,94]

Platelet-derived growth factors (PDGFs) are a chemoattractant stimulating macrophages and fibroblasts during healing.[89] As a result, it has become recognized as the key growth factor in microfracture techniques.[95] Several *in vitro* studies indicate PDGFs to contribute in roles other than as chemo-attractants, but also influencing mesenchymal stem cell differentiation, enhancing matrix production, as well as preventing the progression of chondrocytes down the endochondral maturation pathway.[71,96]

5.516.5. Clinical Repair Techniques

In any cartilage repair system, preparation of the defect site is necessary prior to receiving the implant. First, the defect area is debrided with a ring curette or a low-profile drill removing abnormal cartilage and fibrous tissue. Then the defect can be measured using an arthroscopic-graded probe and templated using sterile paper or aluminum for preparation of the implant if it is not in an injectable form.[27]

First-generation ACI injected a cell-suspension of chondrocytes under a sutured periosteal flap or collagen membrane sealed with fibrin glue. Drawbacks of this procedure were morbidity to donor cartilage, long recovery, graft failure, and periosteal flap hypertrophy.[97] In order to circumvent some of these complications, second-generation ACI emerged. This technique cultured chondrocytes on various membranes (matrices) that could be fixed with fibrin glue without sutures. Collagen became the most common matrix used and the technique was named matrix-induced autologous chondrocyte implantation (MACI). Autologous cartilage is harvested arthroscopically using a gauge or ring curette from healthy, nonweight-bearing areas of the knee. *In vitro* expansion usually achieves nearly 2 million cells per cm^2 of defect.[98] Once, the defect is prepared and measured and the knee is drained, the collagen matrix encapsulated with cells 3–4 days prior

implantation is cut to fit the defect size. Mini anchors with absorbable sutures are placed on opposite sides of the defect site. The suture is passed through the MACI matrix and the matrix is guided down the sutures to the defect by an inserter. Fibrin glue is applied within the defect, giving the matrix further support.

Another second-generation ACI scaffold is Hyalograft C. The hyaluronic acid patch is seeded with chondrocytes 3 weeks prior to implantation. The patch is then attached to a delivery device with a sharp edge which is introduced through the arthroscopic portal to overlie the defect. Then the graft is pushed out of the delivery device and adhered to the subchondral bone within the defect. If necessary, fibrin glue is applied to the defect to improve implant stability.

Bioseed C, another second-generation ACI scaffold is composed of poly(glycolic) acid, poly(lactic acid), and a polydioxanone fleece with fibrin gel to evenly distribute cells 3 weeks prior to implantation. Arthroscopic implantation of this technique requires the defect to be debrided to a rectangular shape. The four corners of the defects are drilled with guide wires through the cannula in an inside-out technique. Then the scaffold is placed within the corners with resorbable sutures and mounted on the corresponding guide wires. Finally the threads are pulled into the joint by the guide wires acting as a pulley leading the implant into the joint.

Eventually, several studies indicated the possibility of *in vitro* expanded chondrocytes cultured on three-dimensional matrices regaining their chondrogenic phenotype after *in vivo* implantation.[99,100] It was also found that mechanical stimulation of chondrocytes in three-dimensional culture can promote maintenance of the chondrogenic phenotype and produce stable mature hyaline matrix.[101,102] Therefore, to preserve chondrocyte phenotype, third-generation ACI evolved with new three-dimensional cartilage constructs. Techniques were developed to improve cell and/or scaffold implant by mechanically conditioning the three-dimensional constructs *in vitro* prior to implantation. In addition, third-generation ACI techniques utilized phenotypically stable characterized chondrocytes selected on the basis of quantitative gene expression markers predicting ability to form hyaline cartilage *in vivo*.[21]

For example, NeoCart, a third-generation ACI technique, is comprised of a three-dimensional bovine collagen type I matrix encapsulated with autologous chondrocytes and treated in a hydrostatic bioreactor for at least 7 days. After designing the construct to match the defect, it is then sandwiched with a collagen–poly(ethylene glycol) adhesive and fixed within the defect.[103]

Another third-generation ACI technique, alginate-cultured three-dimensional grafts (Cartipatch), is an agarose/alginate hydrogel scaffold seeded with autologous chondrocytes. This polysaccharide material can be manipulated at 37°C into complex shapes that solidify at about room temperature, thereby providing manageable handling properties. Once the defect is debrided, the cell-loaded agarose–alginate gel can be delivered to the site and simply press fitted with forceps.[104]

Alginate beads are also used for ACI techniques. Allogeneic chondrocytes harvested from donors' knees within 24 h of death are expanded and then mixed with alginate to form beads over a 2-week period. A mini-arthrotomy is performed to allow access to the defect. After the chondrocyte-cultured alginate beads are packed under the periosteal flap, fibrin glue is injected into the defect to fill empty spaces.[105] Even after cryopreservation and long-term storage, alginate-cultured allogeneic chondrocytes retained viability, thereby potentially providing 'chondrocyte banks' in the future.[106]

A current modification to third-generation ACI is minced articular cartilage. After harvest, articular cartilage is 'minced' into small fragments and encapsulated into a scaffold without any culture expansion. Chondrocytes from the fragments are capable of migrating into the surrounding scaffold or fibrin glue to produce ECM. A minimal amount of tissue (one-tenth the size of the original defect) is needed to produce enough chondrocytes for treatment of a relatively large defect.[107]

The cartilage autograft implantation system (CAIS) consists of minced cartilage and a resorbable copolymer foam scaffold of polycaprolactone (PCL) and PGA reinforced with a polydioxanone (PDS) mesh. The system utilizes a harvester made of a stainless steel tube with a controlled cutting tip and a disperser that directs the minced cartilage into the PCL/PGA scaffold. Fibrin glue is used to stabilize the fragments in the scaffold. After a mini-arthrotomy and designing of the scaffold, the implant is placed into the defect and fixed with resorbable PDS staples.[108]

Another similar application for cartilage regeneration and repair is DeNovo Natural Tissue (NT) graft. The implant consists of allogeneic minced juvenile cartilage treated under specific biological conditions. The graft is implanted in a single-stage arthroscopic procedure where the chondral defect is measured and the NT graft is trimmed accordingly, and then implanted in the defect. Fibrin glue adhesive is again used to fill areas between implant and subchondral bone.[108]

Wakitani *et al*.[25] introduced a method similar to ACI using BM-MSCs because of their abundance and chondrogenic potential as well as their potential to decrease donor site morbidity from chondrocyte harvest. First-generation techniques embedded culture-expanded BM-MSCs in acid-soluble bovine or porcine type-1 collagen 1–2 days prior to implantation and then placed the cell-laden collagen gel on a collagen sheet for additional support. After mini-arthrotomy, the implant was inserted into the defect and the periosteal patch was sutured without the need of fibrin glue. A later second-generation BM-MSC implantation method mixed BM-MSCs with platelet-rich fibrin glue and allowed them to gel. The addition of platelet-rich plasma decreased the adhesive properties of fibrin glue and as a result the implant had to be covered with a sutured periosteal flap.[27]

A modification to microfracture surgery is autologous matrix-induced chondrogenesis (AMIC). It is a relatively simple single-stage procedure that uses a collagen membrane to cover the microfracture defect for 5 min. Following bone marrow saturation, the matrix is measured and trimmed to fit defect along with fibrin glue for stability.[26]

Finally, BST-CarGel, a chitosan/glycerol hydrogel, provides another modification method to microfracture surgery. The gel is dispersed throughout uncoagulated whole blood, and then delivered to a surgically prepared lesion. BST-CarGel allows normal clot formation, reinforces the clot, impedes retraction, increases adhesiveness, and ensures prolonged residency of both the clot and critical tissue repair factors from

blood. Animal studies have shown BST-CarGel to increase the volume and hyaline character of repair tissue along with GAG and collagen content compared with microfracture controls.[109]

5.516.6. Conclusion

All current approaches to engineering articular cartilage have their advantages and limitations. The major concern facing these technologies is finding a method having vast superiority over general surgery technologies. Thus far, results of various studies have been both similar and controversial and do not show any method with clear superiority.[110] One of the biggest challenges is cell source. Current work on alternatives to chondrocytes is expanding, and the potential and limitations of stem cells are being explored. Novel biomaterials are continuously being developed and are progressing toward unique cell–scaffold interactions. Ultimately, the ideal tissue engineering solution for cartilage repair must be simple and cost-efficient if a successful product is to proceed from bench to bedside.

References

1. Hunziker, E. B. M. D. *Clin. Orthop. Relat. Res.* **1999**, *367*, S135–S146.
2. Reinholz, G. G.; Lu, L.; Saris, D. B. F.; Yaszemski, M. J.; O'Driscoll, S. W. *Biomaterials* **2004**, *25*, 1511–1521.
3. Basser, P. J.; Schneiderman, R.; Bank, R. A.; Wachtel, E.; Maroudas, A. *Arch. Biochem. Biophys.* **1998**, *351*, 207–219.
4. Eyre, D. *Arthritis Res.* **2002**, *4*, 30–35.
5. Klein, T. J.; Chaudhry, M.; Bae, W. C.; Sah, R. L. *J. Biomech.* **2007**, *40*, 182–190.
6. Aydelotte, M. B.; Greenhill, R. R.; Kuettner, K. E. *Connect. Tissue Res.* **1988**, *18*, 223–234.
7. Darling, E. M.; Hu, J. C. Y.; Athanasiou, K. A. *J. Orthop. Res.* **2004**, *22*, 1182–1187.
8. Klein, T. J.; Schumacher, B. L.; Schmidt, T. A.; *et al. Osteoarthritis Cartilage* **2003**, *11*, 595–602.
9. Hidaka, C.; Cheng, C.; Alexandre, D.; Bhargava, M.; Torzilli, P. *Cell Tissue Res.* **2006**, *323*, 127–135.
10. Schinagl, R. M.; Gurskis, D.; Chen, A. C.; Sah, R. L. *J. Orthop. Res.* **1997**, *15*, 499–506.
11. White, R.; Gibson, J. *J. Orthop. Surg. Res.* **2010**, *5*, 27.
12. Stockwell, R. A. *J. Anat.* **1991**, *175*, 251–261.
13. Otte, P. *Z. Rheumatol.* **1991**, *50*, 304–312.
14. Zhou, S.; Chiu, Z.; Urban, J. *Arthritis Rheum.* **2004**, *50*, 3915–3924.
15. Gibson, J.; Milner, P.; White, R.; Fairfax, T.; Wilkins, R. *Pflügers Arch. Eur. J. Physiol.* **2008**, *455*, 563–573.
16. Heywood, H. K.; Lee, D. A. *Biochem. Biophys. Res. Commun.* **2008**, *373*, 224–229.
17. Boveris, A.; Oshino, N.; Chance, B. *Biochem. J.* **1972**, *128*, 617–630.
18. Boubriak, O. A.; Brooks, J. T. S.; Urban, J. P. G. *Osteoarthritis Cartilage* **2009**, *17*, 1084–1092.
19. Langer, R. S.; Vacanti, J. P. *Sci. Am.* **1999**, *280*, 86–89.
20. Brittberg, M.; Lindahl, A.; Nilsson, A.; Ohlsson, C.; Isaksson, O.; Peterson, L. *N. Engl. J. Med.* **1994**, *331*, 889–895.
21. Saris, D. B. F.; Vanlauwe, J.; Victor, J.; *et al. Am. J. Sports Med.* **2008**, *36*, 235–246.
22. Kisiday, J. D.; Kopesky, P. W.; Evans, C. H.; Grodzinsky, A. J.; McIlwraith, C. W.; Frisbie, D. D. *J. Orthop. Res.* **2008**, *26*, 322–331.
23. Vidal, M. A.; Robinson, S. O.; Lopez, M. J.; *et al. Vet. Surg.* **2008**, *37*, 713–724.
24. Miljkovic, N. D.; Cooper, G. M.; Marra, K. G. *Osteoarthritis Cartilage* **2008**, *16*, 1121–1130.
25. Wakitani, S.; Imoto, K.; Yamamoto, T.; Saito, M.; Murata, N.; Yoneda, M. *Osteoarthritis Cartilage* **2002**, *10*, 199–206.
26. Kramer, J.; Böhrnsen, F.; Lindner, U.; Behrens, P.; Schlenke, P.; Rohwedel, J. *Cell. Mol. Life Sci.* **2006**, *63*, 616–626.
27. Haleem, A. M.; Chu, C. R. *Oper. Tech. Orthop.* **2010**, *20*, 76–89.
28. Solchaga, L. A.; Temenoff, J. S.; Gao, J.; Mikos, A. G.; Caplan, A. I.; Goldberg, V. M. *Osteoarthritis Cartilage* **2005**, *13*, 297–309.
29. Freed, L. E.; Marquis, J. C.; Langer, R.; Vunjak-Novakovic, G.; Emmanual, J. *Biotechnol. Bioeng.* **1994**, *43*, 605–614.
30. Iwasa, J.; Ochi, M.; Uchio, Y.; Katsube, K.; Adachi, N.; Kawasaki, K. *Artif. Organs* **2003**, *27*, 249–255.
31. Getgood, A.; Brooks, R.; Fortier, L.; Rushton, N. *J. Bone Joint Surg. Br.* **2009**, *91-B*, 565–576.
32. Bryant, S. J.; Anseth, K. S. *Biomaterials* **2001**, *22*, 619–626.
33. Harris, J. M.; Chess, R. B. *Nat. Rev. Drug Discov.* **2003**, *2*, 214–221.
34. Veronese, F. M.; Pasut, G. *Drug Discov. Today* **2005**, *10*, 1451–1458.
35. Bryant, S. J.; Nuttelman, C. R.; Anseth, K. S. *J. Biomater. Sci. Polym. Ed.* **2000**, *11*, 439–457.
36. Williams, C. G.; Malik, A. N.; Kim, T. K.; Manson, P. N.; Elisseeff, J. H. *Biomaterials* **2005**, *26*, 1211–1218.
37. Bryant, S. J.; Anseth, K. S. *J. Biomed. Mater. Res.* **2003**, *64A*, 70–79.
38. Lee, H. J.; Lee, J.-S.; Chansakul, T.; Yu, C.; Elisseeff, J. H.; Yu, S. M. *Biomaterials* **2006**, *27*, 5268–5276.
39. Chen, W. Y. J.; Abatangelo, G. *Wound Repair Regen.* **1999**, *7*, 79–89.
40. Campoccia, D.; Doherty, P.; Radice, M.; Brun, P.; Abatangelo, G.; Williams, D. F. *Biomaterials* **1998**, *19*, 2101–2127.
41. Liu, L.-S.; Thompson, A. Y.; Heidaran, M. A.; Poser, J. W.; Spiro, R. C. *Biomaterials* **1999**, *20*, 1097–1108.
42. Nettles, D. L.; Vail, T. P.; Morgan, M. T.; Grinstaff, M. W.; Setton, L. A. *Ann. Biomed. Eng.* **2004**, *32*, 391–397.
43. Chung, C.; Mesa, J.; Randolph, M. A.; Yaremchuk, M.; Burdick, J. A. *J. Biomed. Mater. Res.* **2006**, *77A*, 518–525.
44. Varghese, S.; Hwang, N. S.; Canver, A. C.; Theprungsirikul, P.; Lin, D. W.; Elisseeff, J. *Matrix Biol.* **2008**, *27*, 12–21.
45. Visna, P.; Pasa, L.; Cizmar, I.; Hart, R.; Hoch, J. *Acta Chir. Belg.* **2004**, *104*, 709–714.
46. Kawabe, N.; Yoshinao, M. *Clin. Orthop. Relat. Res.* **1991**, 279–293.
47. Van Susante, J. L. C.; Buma, P.; Schuman, L.; Homminga, G. N.; Van Den Berg, W. B.; Veth, R. P. H. *Biomaterials* **1999**, *20*, 1167–1175.
48. Kleinman, H. K.; Klebe, R. J.; Martin, G. R. *J. Cell Biol.* **1981**, *88*, 473–485.
49. Franceschi, L. D.; Grigolo, B.; Roseti, L.; *et al. J. Biomed. Mater. Res.* **2005**, *75A*, 612–622.
50. Tan, H.; Huang, D.; Lao, L.; Gao, C. *J. Biomed. Mater. Res. B Appl. Biomater.* **2009**, *91B*, 228–238.
51. Schagemann, J. C.; Mrosek, E. H.; Landers, R.; Kurz, H.; Erggelet, C. *Cells Tissues Organs* **2006**, *182*, 89–97.
52. Park, H.; Kang, S.-W.; Kim, B.-S.; Mooney, D. J.; Lee, K. Y. *Macromol. Biosci.* **2009**, *9*, 895–901.
53. Ng, K. W.; Wang, C. C.-B.; Mauck, R. L.; *et al. J. Orthop. Res.* **2005**, *23*, 134–141.
54. Kim, S. E.; Park, J. H.; Cho, Y. W.; *et al. J. Control. Release* **2003**, *91*, 365–374.
55. Na, K.; Kim, S.; Woo, D.-G.; *et al. J. Biotechnol.* **2007**, *128*, 412–422.
56. Kisiday, J.; Jin, M.; Kurz, B.; *et al. Proc. Natl. Acad. Sci. USA* **2002**, *99*, 9996–10001.
57. Tateishi, T.; Chen, G.; Ushida, T. *J. Artif. Organs* **2002**, *5*, 77–83.
58. Nettles, D. L.; Elder, S. H.; Gilbert, J. A. *Tissue Eng.* **2002**, *8*, 1009–1016.
59. Kuo, Y.-C.; Lin, C.-Y. *Biotechnol. Bioeng.* **2006**, *95*, 132–144.
60. Wang, Y.; Blasioli, D. J.; Kim, H.-J.; Kim, H. S.; Kaplan, D. L. *Biomaterials* **2006**, *27*, 4434–4442.
61. Vickers, S. M.; Squitieri, L. S.; Spector, M. *Tissue Eng.* **2006**, *12*, 1345–1355.
62. Moroni, L.; De Wijn, J. R.; Van Blitterswijk, C. A. *Biomaterials* **2006**, *27*, 974–985.
63. Li, W.-J.; Danielson, K. G.; Alexander, P. G.; Tuan, R. S. *J. Biomed. Mater. Res.* **2003**, *67A*, 1105–1114.
64. Girotto, D.; Urbani, S.; Brun, P.; Renier, D.; Barbucci, R.; Abatangelo, G. *Biomaterials* **2003**, *24*, 3265–3275.
65. Müller, F. A.; Müller, L.; Hofmann, I.; Greil, P.; Wenzel, M. M.; Staudenmaier, R. *Biomaterials* **2006**, *27*, 3955–3963.
66. Grigolo, B.; Lisignoli, G.; Piacentini, A.; *et al. Biomaterials* **2002**, *23*, 1187–1195.
67. Radice, M.; Brun, P.; Cortivo, R.; Scapinelli, R.; Battaliard, C.; Abatangelo, G. *J. Biomed. Mater. Res.* **2000**, *50*, 101–109.
68. Hollander, A. P.; Dickinson, S. C.; Sims, T. J.; *et al. Tissue Eng.* **2006**, *12*, 1787–1798.
69. Flaumenhaft, R.; Abe, M.; Sato, Y.; *et al. J. Cell Biol.* **1993**, *120*, 995–1002.
70. Tuli, R.; Tuli, S.; Nandi, S.; *et al. J. Biol. Chem.* **2003**, *278*, 41227–41236.

71. Cassiede, P.; Dennis, J. E.; Ma, F.; Caplan, A. I. *J. Bone Miner. Res.* **1996**, *11*, 1264–1273.
72. Lum, Z. P.; Hakala, B. E.; Mort, J. S.; Recklies, A. D. *J. Cell. Physiol.* **1996**, *166*, 351–359.
73. Rosier, R. N.; Okeefe, R. J.; Crabb, I. D.; Puzas, J. E. *Connect. Tissue Res.* **1989**, *20*, 295–301.
74. Vanbeuningen, H. M.; Vanderkraan, P. M.; Arntz, O. J.; Vandenberg, W. B. *Lab. Investig.* **1994**, *71*, 279–290.
75. van Beuningen, H. M.; Glansbeek, H. L.; van der Kraan, P. M.; van den Berg, W. B. *Osteoarthritis Cartilage* **1998**, *6*, 306–317.
76. Fan, H. B.; Hu, Y. Y.; Qin, L.; Li, X. S.; Wu, H.; Lv, R. *J. Biomed. Mater. Res.* **2006**, *77A*, 785–794.
77. Mierisch, C. M.; Cohen, S. B.; Jordan, L. C.; Robertson, P. G.; Balian, G.; Diduch, D. R. *Arthrosc. J. Arthroscopic Relat. Surg.* **2002**, *18*, 892–900.
78. Frenkel, S. R. P. D.; Saadeh, P. B. M. D.; Mehrara, B. J. M. D.; *et al. Plast. Reconstr. Surg.* **2000**, *105*, 980–990.
79. Park, Y.; Sugimoto, M.; Watrin, A.; Chiquet, M.; Hunziker, E. B. *Osteoarthritis Cartilage* **2005**, *13*, 527–536.
80. Kaps, C.; Bramlage, C.; Smolian, H.; *et al. Arthritis Rheum.* **2002**, *46*, 149–162.
81. Mason, J. M. P.; Breitbart, A. S. M. D.; Barcia, M. M. A.; Porti, D. B. A.; Pergolizzi, R. G. P.; Grande, D. A. P. *Clin. Orthop. Relat. Res.* **2000**, *379*, S171–S178.
82. Fukumoto, T.; Sperling, J. W.; Sanyal, A.; *et al. Osteoarthritis Cartilage* **2003**, *11*, 55–64.
83. Gooch, K. J.; Blunk, T.; Courter, D. L.; *et al. Biochem. Biophys. Res. Commun.* **2001**, *286*, 909–915.
84. Nixon, A. J.; Fortier, L. A.; Williams, J.; Mohammed, H. *J. Orthop. Res.* **1999**, *17*, 475–487.
85. Elisseeff, J.; McIntosh, W.; Fu, K.; Blunk, T.; Langer, R. *J. Orthop. Res.* **2001**, *19*, 1098–1104.
86. Worster, A. A.; Brower-Toland, B. D.; Fortier, L. A.; Bent, S. J.; Williams, J.; Nixon, A. J. *J. Orthop. Res.* **2001**, *19*, 738–749.
87. Holland, T. A.; Bodde, E. W. H.; Cuijpers, V.; *et al. Osteoarthritis Cartilage* **2007**, *15*, 187–197.
88. Lee, S.-H.; Shin, H. *Adv. Drug Deliv. Rev.* **2007**, *59*, 339–359.
89. Holland, T. A.; Mikos, A. G. *J. Control. Release* **2003**, *86*, 1–14.
90. Kato, Y.; Iwamoto, M. *J. Biol. Chem.* **1990**, *265*, 5903–5909.
91. Stewart, A. A.; Byron, C. R.; Pondenis, H.; Stewart, M. C. *Am. J. Vet. Res.* **2007**, *68*, 941–945.
92. Weisser, J.; Rahfoth, B.; Timmermann, A.; Aigner, T.; Bräuer, R.; Von der Mark, K. *Osteoarthritis Cartilage* **2001**, *9*, S48–S54.
93. Davidson, D.; Blanc, A.; Filion, D.; *et al. J. Biol. Chem.* **2005**, *280*, 20509–20515.
94. Moore, E. E.; Bendele, A. M.; Thompson, D. L.; *et al. Osteoarthritis Cartilage* **2005**, *13*, 623–631.
95. Steadman, J. R. M. D.; Rodkey, W. G. D. V.M.; Rodrigo, J. J. M. D. *Clin. Orthop. Relat. Res.* **2001**, *391*, S362–S369.
96. Kieswetter, K.; Schwartz, Z.; Alderete, M.; Dean, D. D.; Boyan, B. D. *Endocr.* **1997**, *6*, 257–264.
97. Wood, J. J.; Malek, M. A.; Frassica, F. J.; *et al. J. Bone Joint Surg. Am.* **2006**, *88*, 503–507.
98. Brittberg, M. *Injury* **2008**, *39*, 40–49.
99. Bonaventure, J.; Kadhom, N.; Cohen-Solal, L.; *et al. Exp. Cell Res.* **1994**, *212*, 97–104.
100. Freed, L. E.; Marquis, J. C.; Nohria, A.; Emmanual, J.; Mikos, A. G.; Langer, R. *J. Biomed. Mater. Res.* **1993**, *27*, 11–23.
101. Waldman, S. D.; Spiteri, C. G.; Grynpas, M. D.; Pilliar, R. M.; Hong, J.; Kandel, R. A. *J. Bone Joint Surg. A* **2003**, *85*, 101–105.
102. Waldman, S. D.; Spiteri, C. G.; Grynpas, M. D.; Pilliar, R. M.; Kandel, R. A. *J. Orthop. Res.* **2003**, *21*, 590–596.
103. Crawford, D. C.; Heveran, C. M.; Cannon, W. D.; Foo, L. F.; Potter, H. G. *Am. J. Sports Med.* **2009**, *37*, 1334–1343.
104. Selmi, T. A. S.; Verdonk, P.; Chambat, P.; *et al. J. Bone Joint Surg. Br.* **2008**, *90B*, 597–604.
105. Almqvist, K. F.; Dhollander, A. A. M.; Verdonk, P. C. M.; Forsyth, R.; Verdonk, R.; Verbruggen, G. *Am. J. Sports Med.* **2009**, *37*, 1920–1929.
106. Almqvist, K. F.; Wang, L.; Broddelez, C.; Veys, E. M.; Verbruggen, G. *Osteoarthritis Cartilage* **2001**, *9*, 341–350.
107. Lu, Y.; Dhanaraj, S.; Wang, Z.; *et al. J. Orthop. Res.* **2006**, *24*, 1261–1270.
108. McCormick, F. M. D.; Yanke, A. B. S.; Provencher, M. T. M. D. L. M. C. U. S. N.; Cole, B. J. M. D. *Sports Med. Arthrosc. Rev.* **2008**, *16*, 217–220.
109. Shive, M. S.; Hoemann, C. D.; Restrepo, A.; *et al. Oper. Tech. Orthop.* **2006**, *16*, 271–278.
110. Jakobsen, R. B.; Engebretsen, L.; Slauterbeck, J. R. *J. Bone Joint Surg. Am.* **2005**, *87*, 2232–2239.

5.517. Tissue Engineering of the Temporomandibular Joint

V P Willard, Rice University, Houston, TX, USA
L Zhang and K A Athanasiou, University of California at Davis, Davis, CA, USA

© 2011 Elsevier Ltd. All rights reserved.

5.517.1.	**Introduction**	222
5.517.2.	**Gross Anatomy and Physiology of the TMJ**	222
5.517.3.	**Characterization of TMJ Tissues**	223
5.517.3.1.	TMJ Disc	223
5.517.3.1.1.	Cells	223
5.517.3.1.2.	Collagen	224
5.517.3.1.3.	Glycosaminoglycans and proteoglycans	224
5.517.3.1.4.	Tissue mechanics	225
5.517.3.2.	Condylar and Fossa Cartilages	225
5.517.3.2.1.	Cells	225
5.517.3.2.2.	Extracellular matrix	226
5.517.3.2.3.	Tissue mechanics	226
5.517.3.3.	Mandibular Condyle and Temporal Fossa	226
5.517.4.	**Pathology of the TMJ**	227
5.517.5.	**Current Therapies**	227
5.517.6.	**Tissue Engineering**	228
5.517.6.1.	TMJ Disc	228
5.517.6.1.1.	Cell sources	229
5.517.6.1.2.	Scaffolds	229
5.517.6.1.3.	Bioactive agents	230
5.517.6.1.4.	Mechanical stimulation	230
5.517.6.2.	Condylar Cartilage	231
5.517.6.2.1.	Cell sources	231
5.517.6.2.2.	Scaffolds	231
5.517.6.2.3.	Bioactive agents	231
5.517.6.3.	Mandibular Condyle	231
5.517.6.3.1.	Cell sources	232
5.517.6.3.2.	Scaffolds	232
5.517.6.3.3.	Bioactive agents	232
5.517.7.	**Future Directions for TMJ Tissue Engineering**	232
5.517.7.1.	Progenitor Cells	233
5.517.7.2.	Mechanical Stimuli	233
5.517.7.3.	Other TMJ Tissues	233
5.517.7.3.1.	Disc attachments	233
5.517.7.3.2.	Joint capsule	233
5.517.8.	**Conclusions**	233
References		234

Glossary

Ankylosis Hypertrophic bone growth from the mandible and/or the fossa resulting in fusion of the joint.

Arthrocentesis A minimally invasive procedure where a needle and syringe are used to flush and drain fluid from the joint.

Arthroplasty A surgical procedure that involves reshaping of the articular surfaces of the joint.

Etiology The study of disease causation.

Fibrocartilage A tissue that contains properties of both hyaline cartilage and fibrous tissue such as tendon. This is typically characterized by the presence of both collagens I and II.

Glycosaminoglycan Long chains of repeating disaccharides, which typically contain a negative charge.

Internal derangement An abnormal position of the TMJ disc relative to the mandibular condyle and glenoid fossa.

Occlusal splint Removable acrylic molds that cover the upper and lower teeth. Typically used to protect the teeth from grinding or clenching.

Orthognathic surgery A surgical procedure involving the cutting and repositioning of bones in the mandible or maxilla.

Proteoglycan A molecule composed of protein core with at least one, but often many glycosaminoglycan side chains.

Stress relaxation Testing modality to measure the viscoelastic properties of a material. A constant strain is applied to the tissue and the decaying stress is measured over time.

Abbreviations

bFGF	Basic fibroblast growth factor
BMP-2	Bone morphogenic protein-2
C-ABC	Chondroitinase-ABC
CS	Chondroitin sulfate
DS	Dermatan sulfate
ECM	Extracellular matrix
ePTFE	Expanded polytetrafluoroethlyene
FDA	Food and Drug Administration
GAG	Glycosaminoglycan
HA	Hydroxyapatite
IGF-I	Insulin-like growth factor-I
IL-1	Interleukin-1
MMP	Matrix metalloproteinase
PCL	Polycaprolactone
PDGF	Platelet-derived growth factor
PEG	Poly(ethylene glycol)
PGA	Polyglycolic acid
PLA	Polylactic acid
PLLA	Poly-L-lactic acid
TGF-β1	Transforming growth factor-β1
TMD	Temporomandibular joint disorder
TMJ	Temporomandibular joint
UHMWPE	Ultra-high-molecular-weight polyethylene
VEGF	Vascular endothelial growth factor

5.517.1. Introduction

Tissue engineering of the temporomandibular joint (TMJ), or jaw joint, is still in its early development. While a large body of knowledge exists for the characterization and tissue engineering of other synovial joints, only recently has the TMJ received significant attention. Tissue engineering of the functional TMJ tissues is a promising technology for the treatment of TMJ disorders (TMDs), potentially improving the lives of millions of people. Because of the complex loading patterns that engineered tissues will experience in the TMJ, complete design parameters from native tissue are critical. Unfortunately, neither the normal nor the diseased states of the TMJ are fully understood at present, hindering tissue engineering efforts. Within the TMJ, the fibrocartilaginous disc has received the most attention thus far, but efforts are underway to engineer the mandibular condyle cartilage and bone as well. Implantation of engineered tissues may help alleviate pain, restore range of motion, and return the patient to normal jaw function. The potential impact of a biological TMJ replacement is even greater considering the significant lack of long-term treatment options for TMD patients. This chapter provides a survey of the literature related to the rapidly expanding field of TMJ tissue engineering.

5.517.2. Gross Anatomy and Physiology of the TMJ

The anatomy and physiology of the TMJ have been reviewed in detail in the literature.[1–4] This section provides a summary of the pertinent anatomy and physiology for engineers. The TMJ is composed of the condyle of the mandible articulating against the glenoid fossa and articular eminence of the temporal bone with an interposed disc (Figure 1). The mandibular condyle is the moving component of the articulation, while the fossa-eminence remains stationary relative to the cranium. Both of the articulating surfaces of the TMJ are covered by fibrocartilage, unlike the knee, where the articulating surfaces are covered by hyaline cartilage. Positioned between the condyle and fossa-eminence is a fibrocartilaginous disc that is attached to the periphery of the joint and is free to move over both the superior and inferior articulating surfaces. The TMJ disc serves to increase congruity between these surfaces, distribute load, and aid in joint lubrication.[5] The TMJ is surrounded by a capsule, which encloses the intra-articular environment and attaches to the disc near the condylar head.

Movement of the TMJ is unique because it includes both rotation relative to the transcranial axis and translation forward relative to the skull base. During normal mastication, the joint movement is mainly rotational, allowing vertical opening and closing of the mouth. It is only during wide mouth opening (to around 40 mm) that translation becomes a major component of the movement.[4] Under normal rotational movements, a complex pattern of compression and shear loading occurs between the anterior side of the condyle and posterior slope of the eminence.[6] A healthy TMJ disc and synovial fluid act to dissipate these loads across the joint. If the disc becomes displaced, the lack of force dissipation results in abnormal loading patterns and can cause degradation of the joint.

The attachments of the TMJ disc with the surrounding tissues are extremely important for the coordinated movements of the TMJ. Anteriorly, the disc attaches inferiorly to the anterior condyle and superiorly to the eminence by bending with the joint capsule. Posteriorly, it attaches to the bilaminar zone, which is in turn attached superiorly to the temporal bone and inferiorly to the posterior condyle. Laterally and medially, the disc attachments blend into the joint capsule near its attachment to the condylar head. This complex attachment pattern allows the condyle to rotate relative to the disc but still allows the disc and condyle to translate as a single unit during wide mouth opening.[1] Additionally, the disc and

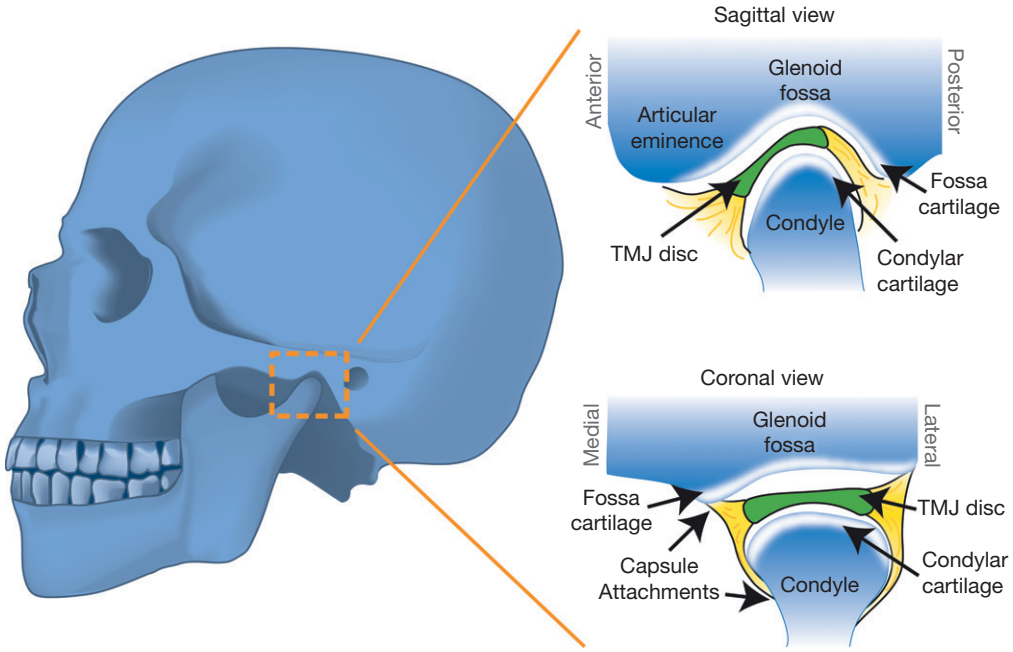

Figure 1 Location and anatomy of the temporomandibular joint (TMJ) in the sagittal and coronal planes. The TMJ is capable of both rotational and translational movement and is composed of three articulating structures: the mandibular condyle, TMJ disc, and the glenoid fossa. The mandibular condyle and glenoid fossa are both covered by fibrocartilage and the TMJ disc is positioned between these two structures.

its attachments separate the joint space into distinct inferior and superior regions. It has been proposed that the TMJ is mainly a translatory joint in the superior space and primarily a rotational joint in the inferior space.[7] This means that the loading patterns experienced by the two surfaces of the disc during normal motion are considerably different.

Like other diarthrodial joints, the TMJ is surrounded by a capsule, the inner surface of which is lined by synovium, a layer of cells that specialize in the production of synovial fluid. Synovial fluid serves two main functions within the TMJ. First, it acts as a lubricating fluid with a coefficient of friction of approximately 0.001.[8] Second, synovial fluid acts as a transmission medium for nutrients to the fibrocartilages within the joint and also serves to remove waste products. The volumes of synovial fluid in the inferior and superior joint spaces of the TMJ are about 0.5 and 1.0 ml, respectively.[2] As it nourishes all the tissues of the joint, the importance of a healthy synovium should not be overlooked by tissue engineers.

5.517.3. Characterization of TMJ Tissues

TMJ tissue engineering requires finely tuned design criteria in order for constructs to effectively handle the complex loading environment of the TMJ. These design criteria are determined through the characterization of the tissue in three major categories: cells contained in the tissue, its biochemical makeup, and its biomechanical properties. An understanding these components of TMJ tissues is critical for the development of mechanically functional engineered constructs, though the number of characterization studies of TMJ tissues remains relatively small in comparison to that of other synovial joints, such as the knee. Fortunately, recent characterization studies, particularly for the TMJ disc, have significantly increased our understanding of these complex tissues. Reviewing this information can greatly improve tissue engineering efforts by illuminating the TMJs structure–function relationships and providing gold standard specifications.

5.517.3.1. TMJ Disc

The TMJ disc is a biconcave fibrocartilaginous tissue that sits atop the mandibular condyle and articulates against the glenoid fossa of the temporal bone. It allows for smooth jaw movement during normal daily activities such as eating and talking. Because of its unique shape, the disc is commonly thought of consisting of three regions in the anteroposterior direction: the anterior band, intermediate zone, and posterior band (Figure 2). The intermediate zone also exhibits mediolateral variation and it is thus divided into the medial, central, and lateral regions. Finally, the two surfaces of the TMJ disc have varying properties, so the disc can also be classified into inferior and superior regions. The cellular, biochemical, and biomechanical properties that accompany this unique architecture provide the appropriate lubricating and cushioning functions for the joint. This section provides a summary of the salient TMJ disc properties for tissue engineers. Further information about the cellular, biochemical, and biomechanical properties of the disc has been reviewed in the literature.[7,9–12]

5.517.3.1.1. Cells

Similar to other fibrocartilages such as the knee meniscus, the TMJ disc contains a heterogeneous population of cells.

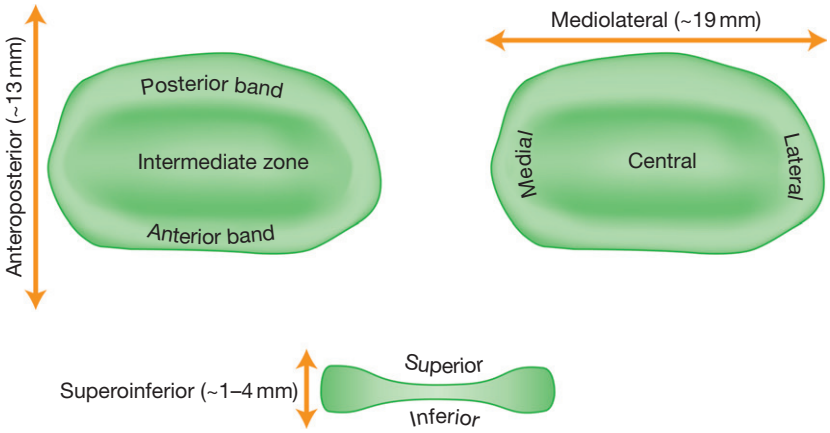

Figure 2 Regional variations and approximate dimensions of the temporomandibular joint (TMJ) disc. The TMJ disc is commonly classified into the posterior band, intermediate zone, and anterior band in the anteroposterior direction. In the mediolateral direction, the disc can be separated into the medial, central, and lateral regions. The disc exhibits a biconcave shape in the superoinferior direction, with each surface having distinct properties.

These cells possess characteristics of both fibroblasts and chondrocytes and are therefore termed fibrochondrocytes.[13] The overall cellularity of the disc is reported to be between 20 and 50 million cells per gram of tissue.[13,14] Although the TMJ disc contains multiple cell types, the overall population appears to be more fibroblastic than chondrocytic. Histological investigations have shown that approximately 70% of the disc cells are fibroblast-like, with the remaining 30% being chondrocyte-like.[15] The chondrocyte-like cells lack a pericellular matrix found around hyaline chondrocytes, and are mostly located in the intermediate zone.[15–17] Regional variations in cell number appear to vary with species. The anterior band was seen to contain the smallest number of cells in the porcine disc,[14,15] while the intermediate zone was found to have the fewest cells in primate discs.[17] Regardless of distribution, the heterogeneous fibrochondrocyte cell population has been seen in all species, and the difficulty involved in recreating this cellular environment should be appreciated by tissue engineers.

5.517.3.1.2. Collagen

The main extracellular matrix (ECM) component of the TMJ disc is collagen, which largely controls the functional properties of the tissue. Collagen makes up about 37% of the wet weight,[18] 50% of the wet volume,[19] or 69–85% of the dry weight.[14,20] Regional distribution of total collagen has been seen to vary depending on the animal model tested. The anterior and posterior bands were seen to contain most of the collagen in the rat disc,[17] while the intermediate zone was reported to contain more collagen in the porcine disc.[14] Although there are several types of collagen in the TMJ disc, collagen type I is by far the most prevalent.[13,17] Collagen type II, the primary component in hyaline cartilage, can be found in small amounts in the intermediate zone, surrounding chondrocyte-like cells.[13,17,21] Trace amounts of other fibrillar (type III) and nonfibrillar (types VI, IX, XII) collagens have also been found in the TMJ disc.[22–24] Collagen type I is by far the most prevalent component of the TMJ disc's ECM and will need to be recreated in a tissue replacement.

The orientation of collagen fibers in the TMJ disc is anisotropic, but there is a basic symmetry. Collagen fibers near the periphery of the disc align in a ring-like structure, while the collagen fibers in the intermediate zone run predominately in an anteroposterior direction.[21,25,26] In the center of the disc, transition regions are observed where the anteroposterior directed fibers of the intermediate zone meet the mediolateral directed fibers of the anterior and posterior bands.[26] It has been speculated that the outer ring of fibers serves to maintain the disc shape under both tensile and compressive loads.[27] The average collagen fiber diameter in the disc is $18 \pm 9\,\mu m$.[21] Finally, collagen fibers in the disc exhibit a wavy or crimped appearance throughout the full thickness of the tissue.[28] The unique ring-like collagen fiber orientation of the TMJ disc has important ramifications for the mechanical properties of the tissue, as described subsequently.

5.517.3.1.3. Glycosaminoglycans and proteoglycans

Together glycosaminoglycans (GAGs) and proteoglycans can contribute to the compressive and tensile properties of a tissue. GAGs are long repeating disaccharide chains with or without branching that possess at least one negatively charged side group. Proteoglycans are composed of a central protein core with one or many GAG side chains. There is little agreement in the literature about the total quantity and regional variation of GAGs in the TMJ disc. The total sulfated GAG content has been reported to be between 1 and 10% of the dry weight.[29,30] This is a large range, but most studies indicate that disc GAG content is below 5%.[14,20,21,29,31] Regionally, studies of the porcine TMJ disc have indicated that the posterior band has the least sulfated GAG.[14,21] Similar results have been seen in the bovine disc, where the bands were shown to have less GAG content than the intermediate zone.[31] The exact opposite distribution of GAGs has been seen in the primate disc, with the anterior and posterior bands having the highest content.[17] Regardless of conflicting results, it is clear that the GAG content of the disc is much lower than hyaline cartilage.[10]

The main proteoglycans in the TMJ disc are chondroitin sulfate (CS) and dermatan sulfate (DS). The GAG chains associated with these two proteoglycans make up 75–93% of the total GAG content of the disc.[20,21,31] Other proteoglycans including keratan sulfate and heparin sulfate have been found

in trace amounts.[20,21,29,31] As in the case of GAGs, there are conflicting reports about the regional proteoglycan distribution in the TMJ disc. In the rat disc, the highest concentrations of CS proteoglycans were found in the bands and the greatest concentration of DS proteoglycans was found in the intermediate zone.[32] The exact opposite trends in CS and DS proteoglycan distributions were seen in the porcine disc.[21] Unfortunately, the studies that have investigated regional distribution of proteoglycans and GAGs have all used different assays. As a result, it is difficult to determine whether the regional disparities seen are a result of interspecies variations or a byproduct of the different assays used.

5.517.3.1.4. Tissue mechanics

It is important to understand the mechanical properties of the TMJ, as engineered constructs will need to support the same loads imparted on the native tissue. The compressive properties of the disc have been studied fairly extensively, but the measured mechanical properties have varied widely between studies. Under unconfined compression, the porcine disc displays an instantaneous and a relaxed moduli of 500 and 30 kPa, respectively.[33,34] These results match well with those of other porcine and human disc studies.[35,36] The canine and bovine discs demonstrate a much larger compressive resistance, with instantaneous moduli of 31 and 15 MPa under unconfined compression and stress relaxation, respectively.[37,38] It is unclear whether these drastic differences are due to interspecies variations or the different testing modalities used. Regionally, the greatest instantaneous moduli have been seen in the anterior and medial portions of the disc from porcine and bovine samples.[33,34,38] Additionally, a large instantaneous modulus has been observed in the posterior band of the porcine disc, but this was not observed in bovine samples. The central portion of the disc is reported to have a modulus equal to or less than that of the anterior and posterior bands.[33,34,36,38] This is an interesting finding, as the center of the disc is generally reported to have more sulfated GAGs, which often correlates to compressive stiffness.[11] From these data, it appears that compressive properties are more closely related to total collagen content than GAG content, probably because of the exceedingly low GAG content in the TMJ disc.

Tensile testing of the TMJ disc has also resulted in large variations in reported mechanical properties. Reported tensile moduli for the TMJ disc range from 0.5 to 100 MPa.[37,39–41] This large range of recorded properties is related to dramatic variations in regional tensile properties, which are fairly consistent across studies. The tensile modulus of the porcine disc is higher in the anteroposterior direction than in the mediolateral direction.[40,41] Regionally in the mediolateral direction, the relaxation moduli of the posterior band, anterior band, and intermediate zone in the porcine disc are 23.4, 9.5, and 0.58 MPa, respectively.[41] Similar results have been seen in the canine disc.[39] The dramatic twofold decrease in tensile modulus between the posterior band and intermediate zone is interesting because it does not correspond to a dramatic difference in biochemical content. Instead, it is due to the fact that the collagen fibers in the intermediate zone are aligned in the anteroposterior direction, perpendicular to loading.[41] Tensile variation in the anteroposterior direction is not as substantial, but the central region is the stiffest followed by the medial, and then lateral sections.[37,41] It is clear that collagen alignment is important for the tensile properties of the tissue and should be considered in all engineering efforts.

5.517.3.2. Condylar and Fossa Cartilages

While characterization of the TMJ disc is not fully complete, it is far more comprehensive than the current characterization of condylar cartilage. This cartilage lines the articulating surface of the mandibular condyle and moves against the inferior surface of the TMJ disc. Like the disc, condylar cartilage is a fibrocartilaginous tissue with noted amounts of collagen types I and II. This tissue exhibits a zonal architecture and is commonly divided into four zones in a superior to inferior fashion: fibrous, proliferative, mature, and hypertrophic (**Figure 3**). The articulating fibrous zone is a fibrocartilaginous region that sits on top of a highly cellular proliferative zone. The mature and hypertrophic zones, which border the subchondral bone, are considered to be like hyaline cartilage. This section provides an overview of the salient properties of condylar and fossa cartilages. It should be noted, however, that scant information exists on fossa cartilage. More detailed reviews of structure and composition can be found in the literature.[12,42,43]

5.517.3.2.1. Cells

Similar to other fibrocartilages, the cells of condylar cartilage are a heterogeneous fibrochondrocyte population, but unlike the TMJ disc, true chondrocytes can be found in some regions.

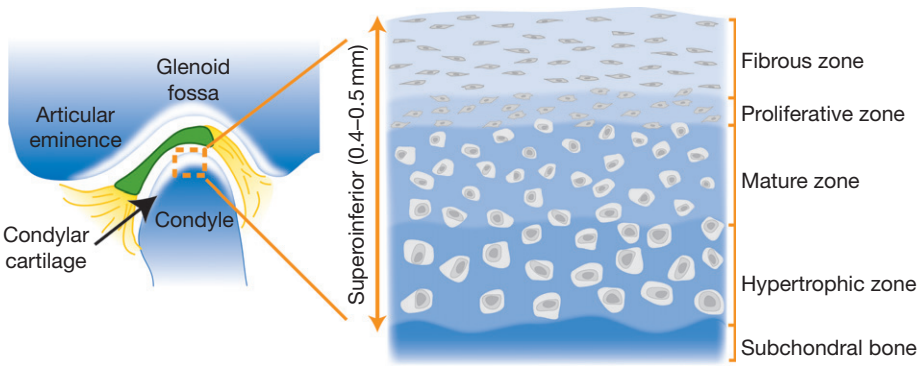

Figure 3 Zonal architecture and approximate dimensions of condylar cartilage. Condylar cartilage is commonly divided into four zones in the superoinferior direction: fibrous, proliferative, mature, and hypertrophic.

The articulating surface of mandibular cartilage contains flat fibroblast-like cells, which is indicative of this region being called the fibrous zone.[44,45] The proliferative zone is a highly cellular region that appears to play a role as a cell reservoir for the other zones. It produces cells for the overlying fibrous zone,[46,47] as well as chondrocyte precursors for the underlying mature zone.[48–50] Terminally differentiated chondrocytes are the main cell type in the mature and hypertrophic zones, although hypertrophic chondrocytes can be found near the junction with the subchondral bone.[51] The fact that the proliferative zone produces cells for all other zones should be noted by tissue engineers. If this layer can be purified, the cells it contains may be a potent cell source for engineering condylar cartilage.

5.517.3.2.2. Extracellular matrix

Although collagen appears to be the main constituent in condylar cartilage, there is little known about the exact quantity of collagen present. A value of 165 nmol of hydroxyproline/mg of dry weight has been reported,[52] as well as 2.2 $\mu g\,mg^{-1}$ of wet weight.[12] In contrast, the types of collagen present in condylar cartilage have been studied quite thoroughly using immunohistochemistry. Collagen type I can be found throughout the cartilage but is primarily located in the fibrous and proliferative zones.[16,53,54] Collagen type II is the primary collagen of the mature and hypertrophic zones,[16,53] although type X can also be found in these regions.[55] The fibrous zone contains collagen type III in addition to type I, which is representative of its fibrous nature.[54] More studies need to be completed on the quantitative distribution of collagens in condylar cartilage.

Collagen orientation in condylar cartilage has also been seen to have zonal heterogeneity. Microscopic investigations on the fibrous zone have indicated a transversely isotropic collagen fiber alignment, with sheets of fibers stacked on top of each other.[51,56,57] More recently, a macroscopic study of the fibrous zone showed anisotropic fiber orientation.[58] The proliferative zone is mostly cellular and contains few collagen fibrils.[59] The mature and hypertrophic zones exhibit randomly oriented collagen fiber bundles, indicating that there is an isotropic arrangement of collagen in these zones.[56,59] Overall, collagen organization results indicate the presence of a bilayered fiber structure with an anisotropic layer near the articular surface and an isotropic layer near the underlying bone.[43]

The total GAG content in mandibular cartilage is reported to be 6.4 $\mu g\,mg^{-1}$ wet weight in the rat,[54] or about 0.19 mg in the rabbit.[52] Keratin and chondroitin sulfates are the only GAGs that have been studied in mandibular cartilage, and there is contradictory evidence about their distribution. A primate study found these GAGs only in the mature and hypertrophic regions,[16] while they were found in the fibrous and proliferative zones of porcine and rat cartilage.[60,61] Regionally, cartilages from the anterior and posterosuperior portions of the condyle have been found to contain more CS than the superior region.[62] There is a zonal distribution of proteoglycans as well, with aggrecan located primarily on the mature and hypertrophic zones.[60,61] Decorin, on the other hand, is distributed fairly evenly throughout the cartilage.[63] Even though condylar cartilage contains chondrocytes, its GAG and proteoglycan content are significantly different from that of articular cartilage.

5.517.3.2.3. Tissue mechanics

Tensile testing of condylar cartilage has revealed a dramatic anisotropy in tensile stiffness, which matches the collagen fiber organization discussed earlier. The Young's moduli of condylar cartilage in the anteroposterior and mediolateral directions have been reported to be 9.0 and 6.6 MPa, respectively, when the cartilage is connected to subchondral bone.[64] When the cartilage is tested independent of bone, the moduli range from 8.0 to 11.0 MPa in the mediolateral direction, and 22 to 29 MPa in the anteroposterior direction.[58] This anisotropy has also been seen under dynamic shear testing, where the storage moduli of condylar cartilage were found to range from 1.50 to 2.03 MPa in the anteroposterior direction and 0.33 to 0.55 MPa in the mediolateral direction.[65,66] Overall, condylar cartilage is stiffer under tension and shear in the anteroposterior direction, which is also true for the TMJ disc.

Compressive testing of condylar cartilage has been conducted using numerous methodologies, but unfortunately there is no consensus about the anteroposterior variation in compressive properties. Studies using nanoindentation and dynamic compression have found that cartilage from the anterior region of the condyle was stiffer than that from the posterior region.[67,68] In contrast, studies using creep indentation and unconfined compression reported that the posterior cartilage was the stiffest.[69,70] With regard to mediolateral variation, multiple studies have agreed that cartilage from the medial region of the condyle is the stiffest.[67,70] In general, the aggregate modulus of condylar cartilage has been reported to be in the range of 45–75 kPa.[70] Unfortunately, there is no consensus about the regional variation in compressive properties of condylar cartilage, and more data are required to provide exact design requirements for tissue engineering.

Although little characterization of the fossa cartilage has occurred, the compressive properties have been tested using creep indentation. The average aggregate modulus of fossa cartilage was reported to be around 36 kPa, with cartilage from the posterior fossa being the stiffest and anterior fossa cartilage being the most compliant.[36] Overall, the fossa cartilage was found to be 57% thinner and 50% stiffer than the TMJ disc. Although this study provides a start for fossa characterization, a significant amount of further research is needed.

5.517.3.3. Mandibular Condyle and Temporal Fossa

The mandibular condyle, covered by a thin layer of fibrocartilage, is the major moving structure in the TMJ. It articulates against the glenoid fossa, also called mandibular fossa, which is a part of the upper temporal bone.[12] Looking at the structural organization of bones, they are typically composed of two microarchitectures: woven and lamellar bones, which are organized into dense cortical bone (compact bone) and porous cancellous bone (spongy or trabecular bone), as reviewed.[71] For example, underneath the condylar cartilage, a compact bone plate covers cancellous bone in the mandibular condyle.[42] From the viewpoint of chemical composition, bone is a well-organized composite matrix that is composed of a protein-based soft hydrogel template (e.g., collagens, noncollagenous proteins, and water) and hard inorganic components (such as hydroxyapatite, HA), as reviewed.[72] Specifically, a large amount of nanocrystalline HA, typically 20–80 nm long

and 2–5-nm thick, is found in the bone matrix.[71] Additionally, 90% of the organic phase in bone is made of type I collagen, which contributes to the elastic properties of bone. Other noncollagenous proteins, including various adhesive proteins (such as laminin, fibronectin, and vitronectin), bone-inductive proteins (such as osteopontin, osteonectin, and osteocalcin), growth factors, and cytokines, are found in the bone matrix to mediate cell–bone functions.[71,73] Unlike cartilage, bone has strong self-repairing potential. Various bone cells, including osteoblasts (bone-forming cells), osteoclasts (bone resorbing cells), and osteocytes (mature osteoblasts), are actively involved in normal bone functions, including ECM mineralization and new bone synthesis.

Clearly, the mandibular condyle's unique structure and composition must support a variety of mechanical loads during daily activities. To date, there have been several studies investigating the mechanical properties (such as stiffness and strength) of the cortical or cancellous bones in the TMJ.[74–78] For instance, it was reported that the cancellous bone of human mandibular condyle has anisotropic mechanical properties: the compressive elastic modulus and ultimate stress of axial specimens in mandibular condylar bones were 431 and 4.5 MPa when compared to 127 and 1.6 MPa of respective transverse specimens.[74] Cortical bone throughout the human mandibular condyle has been shown to posses significantly more stiffness than cancellous bone, exhibiting elastic moduli of roughly 12.2–26.6 GPa varying with different axes and locations.[76] It was also observed that the cortical plate on the lateral side was much thicker than the medial side. These anisotropic properties should be kept in mind when trying to engineer condylar bone. Unlike mandibular bone, little information exists about the bone of the glenoid fossa, and therefore, further characterization is needed.

5.517.4. Pathology of the TMJ

TMDs include a wide variety of conditions for which the etiology is not fully understood. Signs and symptoms of TMDs include limited mouth opening, deviation of the jaw during opening, dislocation, clicking, locking, and muscle pain during jaw movements.[79] Epidemiological studies report that about a quarter of the population has symptoms of TMD,[80] but after reviewing patient records, it appears that only 3–4% of the population seek treatment.[81] Three common pathologies of the TMJ which end up requiring clinical treatment are internal derangement, degenerative joint disease, and ankylosis. The first two mainly affect the soft tissues of the joint and the third affects the bony structures.

Internal derangement of the TMJ is defined as an abnormal relationship of the articular disc to the mandibular condyle and articular eminence.[2] It is believed to be the result of multiple pathological processes, including softening of the tissues, perforation of the disc, alterations in synovial fluid lubrication, and overactive musculature.[4] Disc displacement typically occurs on the anterior medial side of the condyle. The result of TMJ disc derangement depends largely on the extent and duration of the displacement. Long-term internal derangement typically results in altered loading patterns in the joint, reduced mobility, and increasing degradation of the soft tissues.[4] These long-term degenerative effects are thought to be caused by a direct mechanical injury and/or a hypoxia–reperfusion injury.[82] A progression of five stages of internal derangement has been described involving increasing joint degradation over time.[83] Most TMD patients with intermediate stage internal derangement progress into the later stages. An understanding of the internal derangement is particularly important, because a prior study has indicated that 70% of patients with TMD have disc displacement.[84]

Degenerative joint disease involves a catabolic loss of articular tissue and is a common form of degeneration in synovial joints. The main form of degenerative joint disease in the TMJ is osteoarthritis caused by excessive loading, but rheumatoid arthritis caused by autoimmune responses can also occur. Osteoarthritis of the TMJ is characterized by degradation and abrasion of the articular cartilage surfaces, which are accompanied by secondary inflammation.[85] The exact etiology of osteoarthritis in the TMJ is unknown, but it likely involves trauma to the joint, excessive loading, immobility, and increasing age.[86] During TMJ osteoarthritis, expression of matrix metalloproteinases (MMPs) and vascular endothelial growth factor (VEGF) in the joint is elevated, resulting in increased inflammation and degradation of the soft tissues.[87] The result is abnormal remodeling and breakdown of the TMJ cartilages. TMJ degenerative joint disease can result from internal defragment, or it can develop independently.

The next TMJ pathology differs from the preceding conditions, because it involves a disorder of bone metabolism, rather than of soft tissue. TMJ ankylosis involves hypertrophic bone formation in the condyle or temporal bones. This excessive bone growth reshapes the articulating surfaces, and if given time to grow, can completely bridge the joint space. This results in immobilization of the mandible and a complete lack of joint function. Trauma to the joint cavity in young children, or repetitive trauma from surgeries is connected to the development of ankylosis.[88] Removal of the hypertrophic bone is typically not a long-term solution for ankylosis, as the bone will commonly regenerate.

Engineers must appreciate the complex pathologies of the TMJ. Without understanding the factors responsible for destruction of the native joint, it will not be possible to produce a permanent biological replacement. For example, if the joint degradation is initially caused by a displaced disc, not only must the disc be repositioned or replaced, but the catabolic and inflammatory environment of the joint must also be addressed. Because of the joint disease, the synovial fluid will be saturated with inflammatory factors that, if left unchecked, will likely lead to destruction of the newly implanted disc. An understanding of TMJ pathology will significantly increase the likelihood of success for future tissue-engineered TMJ replacements.

5.517.5. Current Therapies

As TMJ pathology progresses, an increase in symptoms often causes patients to seek clinical care. The most common reason for TMD patients to request medical care is pain.[5] Current clinical treatment options can be divided into four categories: noninvasive, minimally invasive, invasive, and alloplastic

replacement. As detailed elsewhere,[89] the goals for treatment of TMD patients should include (1) decreased joint pain, swelling, and reflex masticatory pain; (2) increased joint function; (3) prevention of further damage; and (4) prevention of disability and disease-related morbidity. This section provides an overview of the common clinical treatments for TMD. More detailed information can be found in the literature.[4,89]

The first stage of clinical treatments for TMD is noninvasive and generally includes occlusal splints and physical, myofunctional, and behavioral therapy as well as medications. Occlusal splints provide physical separation of the teeth. The goal of occlusal splints is to eliminate occlusal factors which trigger parafunctional habits and masticatory muscle hyperactivity, thereby reducing the involuntary overloading of the joint. Mandibular repositioning splints are used in order to achieve a repositioning of a dislocated TMJ disc. Because of the multifactorial nature of TMDs and the numerous types and concepts for occlusal splints, there are mixed reports on the effectiveness of this treatment.[90] Physical therapy, including active and passive joint movement and myofunctional therapy, is another important component of noninvasive therapy which has been seen to reduce pain in TMD patients.[91] Occlusal splints and physical therapy are commonly combined with behavioral therapy such as biofeedback and techniques for stress management, which has emerged as an extremely important component of TMD therapy. Nonsteroidal anti-inflammatory agents, such as ibuprofen, are the most common medications given for TMJ pain.

Following or in conjunction with noninvasive treatments, minimally invasive therapies include injections, arthrocentesis, and arthroscopy. Corticosteroid injections are used occasionally for severe inflammation, but repeated injections can lead to cartilage destruction.[92] Intra-articular injections of hyaluronic acid to increase lubricity of the joint have been suggested,[93] but have not yet been approved for clinical practice. During arthrocentesis, a needle is used to flush and drain the joint space, with the goal of removing inflammatory mediators and enhancing lubrication. Arthroscopy of the TMJ is mainly used for the diagnosis of early stage arthritis,[94] although some manipulation can be done such as removing fibrotic tissue.

Even though a majority of TMD patients can be managed with minimally invasive treatment, there is a subset of patients (~20%) who will require surgical intervention.[95] TMJ arthroplasty is a relatively common surgical procedure that requires the replacement of the disc with, for example, an autogenic material. Typically, the local temporalis muscle flap is used for disc replacement,[96] although a tissue-engineered disc would be of great utility in this situation. Hemiarthroplasty, reshaping the fossa or replacing it with an alloplastic implant, became popular in the 1960s, but is rarely used today because of concerns about degradation of the remaining joint tissues.[4] Although orthognathic surgery is an option for TMD patients, it is not frequently used, as the outcomes are poor for patients with preexisting TMJ degradation.[97] Instead, orthognathic surgery is now used in conjunction with total joint replacement to enhance facial symmetry.

When advanced degenerative disease is present in the TMJ, currently, the only clinical option is an alloplastic total joint replacement. Replacing all or part of the TMJ with an alloplastic material will always come under intense scrutiny on the basis of the poor history of these procedures. In the late 1980s, a Teflon–Proplast implant was approved for TMJ disc replacement by the Food and Drug Administration (FDA). These implants ended up fragmenting under normal loading conditions, leading to a large foreign body giant cell inflammatory response and causing immense resorption of the condyle and fossa.[98] In spite of this failure, alloplastic total joint replacements for the TMJ have been researched intensely for the last 20 years (**Chapter 6.621, Biomaterials and Their Application in Craniomaxillofacial Surgery**). Currently, there are three total joint replacement systems approved by the FDA, manufactured by Christensen, Biomet, and TMJ Concepts. TMJ total joint replacements generally consist of a chromium–cobalt–molybdenum condylar head articulating against an ultra-high-molecular-weight polyethylene (UHMWPE) fossa. The total alloplastic TMJ reconstruction is considered an appropriate treatment of advanced-stage degenerative TMJ disease, although the lifetime of the device and the long-term implications for the surrounding tissues have not been known yet.[89] Tissue engineering may provide a functional and permanent biological replacement for the TMJ, eliminating the need for alloplastic regeneration.

5.517.6. Tissue Engineering

While many tissues in the body when injured have an innate capacity to self-repair, there are some tissues that have little to no self-repairing capacity. The tissues of the TMJ fall into the latter category. Additionally, because of the complex interplay of tissues within the joint, a deficiency in one area can detrimentally affect the surrounding tissues, causing pathology of the joint as a whole. Widespread injury of the TMJ, combined with its limited reparative capacity, necessitates some form of clinical intervention in order to maintain normal function and eliminate pain for the patient. Presently, clinical therapies fall short of addressing the full spectrum of issues and are only semipermanent. Tissue engineering may address these deficits by providing permanent, biomimetic, replacement tissue systems for the TMJ. To achieve this, scientists use the tissue engineering paradigm (**Figure 4**). In this paradigm, native tissue is first characterized to create design parameters for tissue engineering (**Chapter 5.519, Biomaterials Selection for Dental Pulp Regeneration**; **Chapter 5.524, Biomaterials for Replacement and Repair of the Meniscus and Annulus Fibrosus**; and **Chapter 5.535, Cartilage Regeneration in Reconstructive Surgery**). These design parameters are then used to inform the selection of an appropriate cell source, bioactive factors, biomechanical stimulation, and/or scaffold for the creation of an implantable biomimetic tissue. In this section, current tissue engineering efforts for the disc, condylar cartilage, and condyle will be reviewed.

5.517.6.1. TMJ Disc

Characterization data for the TMJ disc have determined certain specifications that should be considered when tissue engineering a suitable replacement. It is known that this tissue houses a distinct cell population and has unique geometry and mechanical properties, brought on by the anisotropic behavior of its biochemical components. Tissue engineering of the disc,

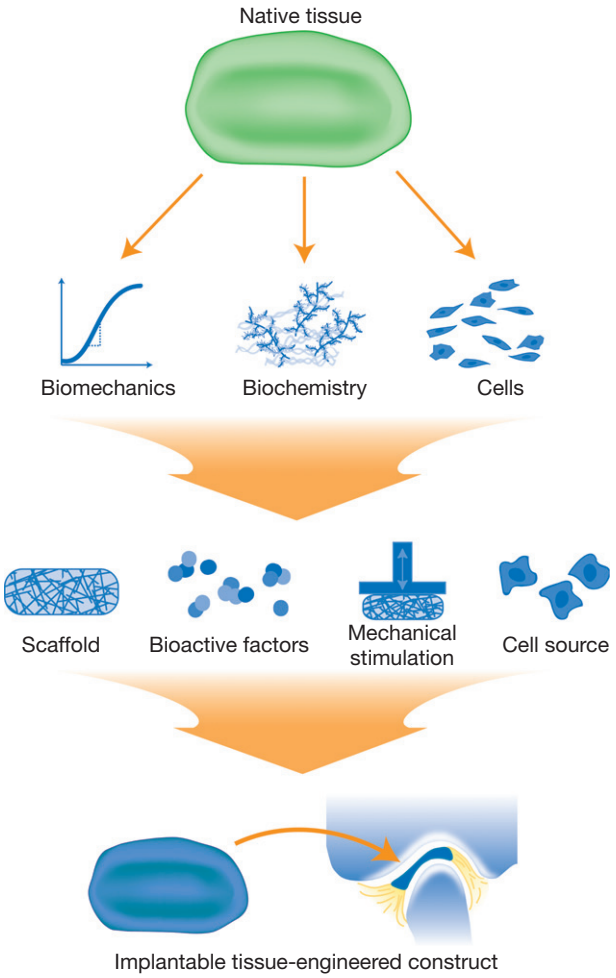

Figure 4 Tissue engineering paradigm for engineering temporomandibular joint (TMJ) tissues. The tissue engineering process is initiated by characterizing the biomechanical, biochemical, and cellular properties of the native tissue to create design parameters for tissue engineering. Next, cells are combined with scaffolds, bioactive agents, and mechanical stimuli to produce a tissue-engineered TMJ tissue that can be implanted *in vivo*.

therefore, must recapitulate these characteristics of the disc in order to preserve its function within the joint. Unlike other tissues of the TMJ, a considerable number of studies have investigated engineering of the disc. Although the first report of TMJ disc tissue engineering appeared in 1994, a majority of the tissue engineering efforts have been conducted recently. This section reviews important advances in cell and scaffold selection, as well as the role of bioactive factors and mechanical stimulation used in the field of TMJ disc tissue engineering.

5.517.6.1.1. Cell sources

Selection of a cell source is likely the most important aspect of any tissue engineering strategy (**Chapter 5.507, Tissue Engineering and Selection of Cells**). These cells are responsible for ECM production and maintenance, resulting in a functional replacement tissue. The most commonly used cells for engineering the TMJ disc have been primary disc cells.[99–109] Although primary TMJ disc cells have been studied extensively, there are two main problems with this cell source: (1) lack of donor cells and (2) donor site morbidity. It is possible to passage cells in monolayer to increase cell numbers, but unfortunately, TMJ disc cells dedifferentiate rapidly in culture and their phenotype is difficult to recover.[110–112] Because of concerns about donor site morbidity, costal chondrocytes have recently been investigated as an alternative cell source for TMJ disc engineering.[113–116] This research was prompted by the fact that oral surgeons already use costal rib grafts for the replacement of the mandibular condyle, and donor site morbidity is minimal.

To completely eliminate concerns about primary cell sources, progenitor cells will likely need to be used for future TMJ tissue engineering efforts. Recently, a series of self-renewing and highly potent human stem cells, such as multipotent mesenchymal stem cells (MSCs), umbilical cord matrix stem cells, and pluripotent embryonic stem cells (ESCs), have emerged and have shown promise for TMJ tissue regeneration. These stem cells, as shown in **Figure 5**, have a large proliferation capacity enabling them to expand without losing their phenotype. Even after expansion, they are able to differentiate into cartilage, bone, and tendon/ligament. Both adult and embryonic stem cells have been shown to be capable of differentiating into fibrochondrocytes that can be used for TMJ disc engineering.[117–120] Additionally, progenitor cells from the skin have been shown capable of differentiating down a chondrogenic lineage in response to ECM molecules.[121,122] Future studies will need to further investigate the differentiation of progenitor cells and their application in TMJ tissue engineering.

5.517.6.1.2. Scaffolds

Scaffolds are an important consideration in tissue engineering as they provide the constructs' initial mechanical integrity and allow for cell attachment. The first TMJ disc tissue engineering study used a porous collagen scaffold and produced constructs with appreciable size and ECM.[99] Similar success was seen with porous polyglycolic acid (PGA) and polylactic acid (PLA) scaffolds. Both materials were shown to support cell attachment and matrix production for up to 12 weeks.[123] Another early study compared PGA, polyamide filaments, expanded polytetrafluoroethylene (ePTFE), and bone blocks for disc engineering.[100] While all scaffolding materials supported cell attachment, there was poor ECM production in all groups. The majority of more recent TMJ disc engineering efforts have used PGA nonwoven mesh scaffolds.[101–103,105–107] While PGA scaffolds do support cell attachment and biosynthesis, PGA fibers degrade too rapidly, producing constructs of very small size. As a result, Allen and Athanasiou[109] compared the use of PGA to that of poly-L-lactic acid (PLLA) nonwoven meshes. PLLA scaffolds produced constructs with enhanced dimensions and mechanical integrity compared to PGA.[109] Additionally, encapsulation of TMJ disc cells in alginate hydrogels has been investigated, but cell viability and ECM production were quite low after 4 weeks.[101] Overall, significantly better results have been observed when culturing TMJ disc cells on natural and synthetic mesh scaffolds than encapsulating the cells in hydrogels.

Although scaffolds are typically an integral part of tissue engineering, it is also possible to produce scaffold-less constructs. Recent efforts to engineer the TMJ disc using costal chondrocytes have produced large functional constructs using a scaffold-less 'self-assembly' technique.[113–116] In this

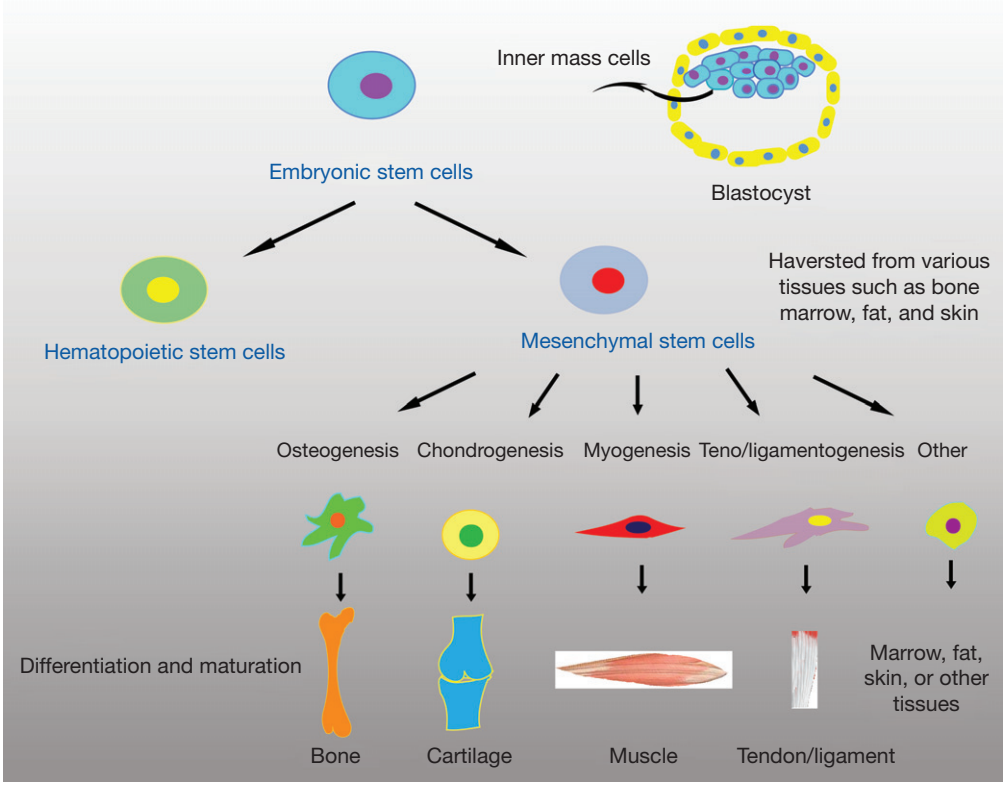

Figure 5 The hierarchal structure of human embryonic and mesenchymal stem cells. Embryonic stem cells are derived from the inner cell mass of the blastocyst and can differentiate down any of the three germ lineages. Mesenchymal stem cells are multipotent and can differentiate into any mesenchymal tissue, including cartilage and bone.

procedure, cells are seeded at very high density into a nonadherent well, which forces the cells to bind to one another.[124] The cells then secrete their own ECM scaffolding over time. Ultimately, both scaffold-less and scaffold-based approaches have seen beneficial results for tissue engineering the TMJ disc, and both techniques should be further investigated.

5.517.6.1.3. Bioactive agents

Growth factors are commonly used in tissue engineering because of their ability to enhance cellular proliferation and/or biosynthesis (**Chapter 5.522, Bone Tissue Engineering: Growth Factors and Cytokines**). So far, five different growth factors have been investigated for TMJ disc tissue engineering: platelet-derived growth factor (PDGF); basic fibroblast growth factor (bFGF); transforming growth factor-β1 (TGF-β1); transforming growth factor-β3 (TGF-β3); and insulin-like growth factor-I (IGF-I). In monolayer culture, TGF-β1, IGF-I, and bFGF have all been shown to increase TMJ disc cell proliferation and biosynthesis.[13,125] It was noted that high concentration of growth factors favored cell proliferation, while low concentrations of growth factors favored biosynthesis.[125] In three-dimensional culture, the effects of growth factors in TMJ disc tissue engineering have been investigated with both PGA and PLLA mesh scaffolds. On PGA scaffolds, both IGF-I and TGF-β1 were shown an increase in the collagen synthesis of porcine TMJ disc cells.[103] In contrast, with PLLA constructs, only TGF-β1 showed a significant increase in biochemical and biomechanical properties.[109] This differential effect may be related to the fact that PGA degrades much faster than PLLA. Growth factors have also been used to enhance TMJ disc tissue engineering using costal chondrocytes. IGF-I enhanced the cellular and biochemical properties of scaffold-less costal chondrocyte constructs.[114]

Although growth factors have received the most attention, other bioactive agents can have a significant impact on TMJ disc tissue engineering as well. TMJ disc cells cultured in media with 25 $\mu g\,ml^{-1}$ of ascorbic acid produced constructs with higher collagen content than cells cultured under concentrations of 0 or 50 $\mu g\,ml^{-1}$.[107] Molecules such as ascorbic acid are important to ECM protein synthesis and should be considered when choosing a media for tissue engineering. Recent evidence from articular cartilage engineering suggests that using catabolic agents can improve construct properties. Natoli *et al.*[126] recently demonstrated that applying chondroitinase-ABC (C-ABC, a GAG removing enzyme) during the midpoint of culture can improve the tensile properties of engineered cartilage. The GAGs that were depleted by C-ABC return by the end of culture and there is no loss in compressive properties.[126] Nontraditional bioactive agents such as this deserve future investigation for TMJ disc tissue engineering.

5.517.6.1.4. Mechanical stimulation

The native TMJ disc experiences significant loading which encompasses compression, tension, and shear components (**Chapter 5.506, Effects of Mechanical Stress on Cells**).[127] As the disc is such a mechanically important tissue, it makes

sense that mechanical stimuli may be required to produce an optimal tissue engineering construct. The first study to investigate mechanical cues on TMJ tissue engineering used a rotating wall bioreactor to create a low-shear fluid environment. Constructs grown in the rotating wall bioreactor ended up being statistically the same as culture controls, and no benefit of the low-shear environment was observed.[104] Continuous hydrostatic pressure of 10 MPa has been shown to increase ECM synthesis of TMJ disc cells both in monolayer and in PGA scaffolds.[105] In contrast, intermittent hydrostatic pressure of 10 MPa applied at 1 Hz was seen to be detrimental to TMJ disc cell biosynthesis. In two-dimensional culture, TMJ disc cells exposed to dynamic tensile strain significantly reduced production of MMPs in response to the proinflammatory cytokine interleukin-1β (IL-1β).[128] While it is clear that mechanical cues have an impact on TMJ disc tissue engineering, more research is needed to determine whether other stimuli used in articular cartilage engineering, such as compression and shear, are beneficial.

5.517.6.2. Condylar Cartilage

Of the three TMJ tissues for which tissue engineering has been attempted, condylar cartilage has received the least amount of attention. The first report of three-dimensional condylar cartilage engineering did not appear in the literature until 2007. Similar to the disc, condylar cartilage has limited repair capabilities and is an excellent candidate for tissue engineering. To this point, disc and condylar cartilage engineering have been conducted independent of each other, although tissue engineering results from one tissue will likely benefit the other. As engineering of condylar cartilage is a new field, efforts thus far have focused on the issues of cell source and application of bioactive agents.

5.517.6.2.1. Cell sources

The majority of condylar cartilage tissue engineering efforts thus far have used primary cells from the tissue.[129–134] Currently, two methods have been used for harvesting primary condylar chondrocytes. The first uses collagenase to digest the cartilage,[129] and the second allows the cells to migrate out of tissue explants.[130] The collagenase method isolates cells from all four cartilage zones, whereas the tissue explant method isolates only cells from the fibrous zone. While condylar chondrocytes do grow in culture and respond to growth factors, they show relatively low ECM production *in vitro*.[42] Because of the low matrix production, chondrocytes from other parts of the body have been used for condylar cartilage engineering. Articular chondrocytes from the ankle have been compared to condylar chondrocytes during both monolayer and three-dimensional culture. In monolayer, condylar chondrocytes showed greater proliferation but ankle chondrocytes produced tremendously more matrix.[135] On PGA scaffolds, ankle chondrocytes again produced an order of magnitude more ECM than condylar chondrocytes.[136] Future studies using primary cells will likely use a chondrocyte source from somewhere other than the condyle.

Because of the standard concerns about primary cell sources (insufficient cell number and donor site morbidity), progenitor cells have begun to be investigated for condylar cartilage engineering. Recently, human umbilical cord mesenchymal stromal cells (hUCMSCs) have been identified as an attractive cell source for condylar engineering. hUCMSCs are multipotent stem cells that develop from the extraembryonic mesoderm of the umbilical cord. When hUCMSCs were compared to condylar chondrocytes for tissue engineering, hUCMSCs were seen to proliferate more rapidly and produce significantly more matrix.[134] External stimuli have been shown to increase the matrix production of hUCMSCs even further.[119,120] Capitalizing on the deficiencies of primary cells, multipotent stem cells appear to have a bright future in condylar cartilage engineering.

5.517.6.2.2. Scaffolds

While there are many potential scaffolds for condylar cartilage engineering, at this point, only two scaffolding materials have been used. The most common scaffold choice has been a PGA mesh.[119,120,134,136] The choice of PGA has likely been influenced by TMJ disc engineering where it had previously been used. As mentioned earlier, PGA supports good cell attachment and matrix production, but degrades too rapidly in culture. Other than PGA, one study has investigated encapsulation of condylar chondrocytes in alginate gel beads.[137] After 4 weeks, the cells maintained a chondrogenic phenotype based on immunostaining. As the field of condylar cartilage expands, it is clear that attention will need to be paid to scaffold choice.

5.517.6.2.3. Bioactive agents

To date, the use of bioactive agents in condylar cartilage engineering has focused on the application of growth factors to condylar chondrocytes and hUCMSCs. The growth factors investigated are similar to those used for TMJ disc engineering, including bFGF, IGF-I, TGF-β1, and epidermal growth factor (EGF). A high concentration of bFGF appears to have the greatest effect on condylar chondrocyte proliferation, although it may inhibit ECM biosynthesis of the cells.[131–133] IGF-I has been shown to be a potent promoter of both cell proliferation and matrix synthesis, particularly GAG production.[133,138,139] Condylar chondrocyte biosynthesis has also been shown to increase with TGF-β1 application, but it is unclear whether it exhibits positive effects on cell proliferation.[133] Cells from the fibrous zone of condylar cartilage have been show to be stimulated by EGF, but the remaining zones have not been investigated.[130] Finally, IGF-I has also been shown to enhance the fibrochondrogenesis and matrix synthesis of hUCMSCs.[119,135] These results provide the basis for further investigations into using external stimuli to enhance condylar cartilage engineering.

5.517.6.3. Mandibular Condyle

Unlike tissue engineering the TMJ disc which began in the early 1990s, condylar engineering did not appear in the literature until 2000. Fortunately, bone tissue engineering in general has been studied extensively. Although still lagging behind the TMJ disc, there has been more effort to engineer the mandibular condyle than the condylar cartilage. The current field of mandibular condylar tissue engineering combines a variety of cell types (i.e., osteoblasts, chondrocytes), mandibular-condyle-shaped scaffolds (i.e., polymers, ceramics), and bioactive factors (i.e., TGF-β, IGF-I, bFGF), to

restore the functionality of damaged tissues. A majority of the efforts thus far have been focused on creating a condyle-shaped scaffold as this is a nontrivial shape.

5.517.6.3.1. Cell sources

Mature osteoblasts and chondrocytes are the most commonly used cell types to regenerate new bone and cartilage tissues. Specifically, osteoblasts have been investigated as one of the main cell sources for subchondral bone repair.[140] They can actively interact with proteins and minerals to adhere, proliferate, and develop a mineralized ECM and differentiate into mature bone. Weng *et al.*[141] created a tissue-engineered mandibular condylar construct via a combination of osteoblasts, chondrocytes, and scaffolds. They seeded osteoblasts into a PGA/PLA scaffold and then painted chondrocytes onto the surface of the scaffold.[141] This study showed that the formation of a bone/cartilage composite *in vivo* is promising for future mandibular condylar reconstructions.

The lack of clinical translatability for primary cells has also been recognized in mandibular condyle engineering. A recent push has been made to investigate the use of stem cells in condylar engineering. Many studies have revealed promising results of bone marrow-derived MSCs for repairing condylar defects.[142–145] Alhadlaq and colleagues[146] once encapsulated the chondrogenically and osteogenically differentiated bone marrow MSCs into biphasic poly(ethylene glycol) (PEG)-based hydrogels in order to create a human-shaped mandibular condyle. After 8 weeks of *in vivo* implantation, it was demonstrated histologically that cartilaginous and osseous phenotypes were present in two stratified layers.[143] In summary, stem cells are emerging as a promising cell source for mandibular condyle tissue regeneration, although they require more investigations to fully explore their medical potentials.

5.517.6.3.2. Scaffolds

Scaffolds play an important role in mandibular condylar tissue engineering through providing structural and mechanical supports for cell growth and tissue formation. Because of the ease of fabrication, good biocompatibility, suitable mechanical properties, and controllable biodegradability, natural or synthetic polymers have been extensively used as bone, and osteochondral tissue engineering scaffolds. Popular polymers for tissue engineering the mandibular condyle have been PEG, polycaprolactone (PCL), PLA, PGA, and poly-lactic-*co*-glycolic acid (PLGA). Ueki *et al.*[147] implanted PLA/PGA/gelatin sponges (PGS) with or without recombinant human bone morphogenic protein-2 (BMP-2) into condylar defects of rabbit TMJs. After 4 weeks, it was observed that the PGS scaffolds with or without BMP-2 induced new bone and cartilage-like tissues in the TMJ.[147] In another study, a tissue-engineered bone construct with a mandibular condyle shape was obtained by combining osteogenically differentiated MSCs and PLGA scaffolds.[148]

Calcium phosphate ceramics such as HA and tricalcium phosphate (α- or β-crystalline TCP) share a similar crystal structure and chemical composition with natural bone. As a result, they have good osteoconductive and osteoinductive properties and have been considered as popular bone substitutes, filler materials, and bone tissue engineering scaffolds.[72] For mandibular condylar tissue engineering, calcium phosphates are usually fabricated with polymers into a composite. The Hollister group has generated various load bearing tissue-engineered scaffolds with appropriate bulk geometry and microarchitecture through image-based design and solid free-form fabrication methods from polymers (PLA, PGA, PLGA, PPF, etc.), ceramics (HA or TCP), or their composites (PLA/HA, PPF/TCP, and HA/TCP).[149–153] For instance, a biphasic PLA/HA composite scaffold was made and fibroblasts with BMP-7 and chondrocytes were separately seeded into the HA and PLA phases.[150] The results showed simultaneous growth of bone, cartilage, and a mineralized interface tissue in the tissue-engineered scaffold. Thus, this technology holds the potential for repairing osteochondral defects in the TMJ.

Natural tissues or organs have numerous nano features and cells directly interacting with nanostructured ECM. Therefore, biomimetic nanomaterials, which have basic structural units, grains, particles fibers, or other constituent components smaller than 100 nm in at least one dimension, have been investigated for TMJ implants, bone, and cartilage regenerations.[72,154] For example, by using chemical vapor deposition technology, a nanostructured diamond film with high hardness and enhanced toughness was deposited on articulating surfaces of TMJ implants and exhibited excellent biocompatibility and mechanical properties.[155] In addition, some *in vitro* studies showed that nanophase HA significantly enhanced osteoblast adhesion and inhibited undesirable fibroblast adhesion compared to conventional HA.[71] Venugopal and colleagues[156] demonstrated that osteoblast proliferation, alkaline phosphatase activity, and mineralization were significantly improved on the electrospun fibrous PCL/HA/gelatin nanocomposite when compared to PCL alone. It was also reported that the electrospun PCL nanofibrous scaffolds effectively induced chondrogenic differentiation of MSCs *in vitro*,[157] and bone formation *in vivo*.[158] Even though few results of nanostructured scaffolds for mandibular condylar tissue engineering are available, it is a promising research field because of its use of biomimetic surface topography, increased wettability, and better mechanical properties.

5.517.6.3.3. Bioactive agents

Even though condylar engineering is a new field, one recent study has investigated the effects of growth factors on tissue development. Srouji *et al.*[159] evaluated *in vivo* mandibular defect repair by hydrogel scaffolds with IGF-I and TGF-β1. After 6 weeks, significant bone formation was observed in the mandibular defects implanted with TGF-β1, IGF-I, and TGF-β1 + IGF-I incorporated hydrogels.[159] Although this study provides a preliminary insight, more research needs to be performed to determine the full potential of bioactive agents for condylar engineering.

5.517.7. Future Directions for TMJ Tissue Engineering

TMJ tissue engineering has progressed quite dramatically over the last 10 years. Now, there are investigators actively working on biological replacements for the disc as well as

the cartilage and bone of the condyle. The current literature provides a reference point for tissue engineering challenges such as cell source and scaffold selection, although the amount of prior work varies between tissues. There is still a significant amount of work that needs to be completed to produce functional replacements for TMJ tissues. Clear directions for the future of TMJ tissue engineering include progenitor cells, enhanced external stimulation, and engineering of the remaining TMJ tissues.

5.517.7.1. Progenitor Cells

Previous work using primary TMJ cells has allowed the characterization of these cells *in vitro*, but a clinically relevant tissue-engineered construct will likely not contain these cells. Problems with primary cells have been discussed earlier and include a lack of donor tissue and high donor site morbidity. A practical cell source for TMJ engineering should originate from healthy tissues which, when removed, should not result in significant morbidity.[12] The likely choice is progenitor cells, whether adult or embryonic. Direct comparison has shown that multipotent progenitor cells outperform TMJ cells.[134] Both MSCs and embryonic stem cells have shown the ability to differentiate down fibrocartilaginous and osteogenic lineages.[118,120,143,160] Although stem cells have been used for TMJ tissue engineering, different cell types have been used for each tissue in an investigator dependent manner. Additionally, the differentiation of these progenitor cells into TMJ-like cells is not fully understood. In the future, there should be coordinated efforts to determine the appropriate progenitor cells for all TMJ tissues, as a total biological joint replacement must be the ultimate goal.

5.517.7.2. Mechanical Stimuli

Even though a significant number of TMJ tissue engineering studies have been completed, only three have investigated the effects of external mechanical stimuli. As TMJ is a frequently loaded joint, it makes sense that mechanical stimulation would enhance TMJ engineering. Biomechanical stimuli have been used extensively in articular cartilage engineering with great success.[161] Stimuli that may be beneficial for TMJ tissue engineering include compression, tension, shear, and hydrostatic pressure. All of these mechanical loads are present in the TMJ.[12] Hydrostatic pressure[105] and tensile loading[128] have both shown promise for disc engineering and should now be carried forward toward tissue engineering of other TMJ tissues. Compression and shear have not yet been evaluated for TMJ engineering, but should certainly be incorporated into future studies.

5.517.7.3. Other TMJ Tissues

While current tissue engineering efforts have focused on engineering the disc and condyle, other tissues of the joint, including the fossa cartilage, disc attachments, and capsule, should also be considered. Each of these tissues plays an important role in the joint, and needs to be considered toward engineering a total biological TMJ replacement. Although the fossa-eminence is not well characterized, fossa cartilage and bone engineering are likely to benefit directly from condylar cartilage and bone engineering studies. The disc attachments and joint capsule on the other hand are distinct tissues that will require independent characterization and tissue engineering efforts.

5.517.7.3.1. Disc attachments

Although significant attention has been paid to characterization and engineering of the disc, very little focus has been placed on the disc attachments. These attachments connect the disc to the capsule and bony structures of the joint. The discal attachments are important for keeping the position of the disc in the joint relative to the condyle and fossa.[1] Maintaining disc position is critical for preserving normal loading patterns, and a breakdown in the discal attachments will result in joint degradation. Characterization of the native disc attachments will provide important information about how a tissue-engineered disc should be implanted in the joint. It is possible to anchor an engineered disc directly to the condylar head, but this will prevent movement of the disc relative to the condyle and alter the loading pattern in the joint. A more likely solution would be to engineer a disc with its attachments so that the attachments could be anchored to the condyle and sutured to the capsule. This would allow a natural movement of the disc within the joint. Future studies will need to investigate the properties and the tissue engineering potential of the disc attachments.

5.517.7.3.2. Joint capsule

Like the discal attachments, the capsule is a critically important but poorly understood component of the TMJ. Globally, the capsule provides a barrier which isolates the intra-articular joint spaces. Unlike the fibrocartilages of the joint, the TMJ capsule is innervated with various groups of nerve endings, including Pacinian corpuscles.[4] Inclusion of these nerve endings may be necessary for a physiologically normal joint replacement. Additionally, the capsule is lined with synovium, which produces the lubricating and nourishing synovial fluid for the joint. Lubrication is critically important for maintaining normal TMJ loading and must be incorporated into an engineered replacement. The exact difficulties involved in recreating the TMJ capsule will need to be investigated in the future. Ultimately, all of the TMJ tissues, including the fossa, disc attachments, and capsule, will need to be tissue engineered to produce a total biological replacement for the TMJ.

5.517.8. Conclusions

Although it has only recently received attention, the field of TMJ tissue engineering is growing rapidly. The pathology of the TMJ is complex, but it is important to address these diseases for the millions of people suffering from TMD. Even though characterization of native TMJ tissues has not been completed yet, the available literature has provided a rough set of design and validation criteria on which tissue engineering efforts can be based. Current tissue engineering efforts provide a basis for selecting a cell source, scaffold, and external stimuli, although technological advancements provide new options regularly. The rapid increase in TMJ disc characterization and engineering studies over the last 10 years provides

optimism for the remaining TMJ tissues that are not as well studied. It is clear that significant effort must be put forth before the ultimate goal of creating a functional biological replacement for the TMJ can be reached, but the future looks bright for this technology.

References

1. Rees, L. A. *Br. Dent. J.* **1954**, *96*(6), 125–133.
2. Dolwick, M. F. In *Internal Derangements of the Temporomandibular Joint*; Helms, C. A., Katzberg, R. W., Dolwick, M. F., Eds.; Radiology Research and Education Foundation: San Francisco; CA, 1983; pp 1–14.
3. Werner, J. A.; Tillmann, B.; Schleicher, A. *Anat. Embryol.* **1991**, *183*(1), 89–95.
4. Wong, M. E.; Allen, K. D.; Athanasiou, K. A. In *Tissue Engineering and Artificial Organs*; Bronzino, J. D., Ed.; CRC Press: Boca Raton, FL, 2006.
5. Jagger, R. G.; Bates, J. F.; Kopp, S. *Temporomandibular Joint Dysfunction: Essentials*; Butterworth-Heinemann Ltd: Oxford, 1994.
6. Gallo, L. M.; Nickel, J. C.; Iwasaki, L. R.; Palla, S. *J. Dent. Res.* **2000**, *79*(10), 1740–1746.
7. Detamore, M. S.; Athanasiou, K. A. *Tissue Eng.* **2003**, *9*(6), 1065–1087.
8. Mabuchi, K.; Tsukamoto, Y.; Obara, T.; Yamaguchi, T. *J. Biomed. Mater. Res.* **1994**, *28*(8), 865–870.
9. Detamore, M. S.; Athanasiou, K. A. *J. Oral Maxillofac. Surg.* **2003**, *61*(4), 494–506.
10. Almarza, A. J.; Athanasiou, K. A. *Ann. Biomed. Eng.* **2004**, *32*(1), 2–17.
11. Allen, K. D.; Athanasiou, K. A. *Tissue Eng.* **2006**, *12*(5), 1183–1196.
12. Athanasiou, K. A.; Almarza, A. A.; Detamore, M. S.; Kalpakci, K. N. *Tissue Engineering of Temporomandibular Joint Cartilage*; Morgan & Claypool: Williston, VT, 2009.
13. Landesberg, R.; Takeuchi, E.; Puzas, J. E. *Arch. Oral Biol.* **1996**, *41*(8–9), 761–767.
14. Almarza, A. J.; Bean, A. C.; Baggett, L. S.; Athanasiou, K. A. *Br. J. Oral Maxillofac. Surg.* **2006**, *44*(2), 124–128.
15. Detamore, M. S.; Hegde, J. N.; Wagle, R. R.; *et al. J. Oral Maxillofac. Surg.* **2006**, *64*(2), 243–248.
16. Milam, S. B.; Klebe, R. J.; Triplett, R. G.; Herbert, D. *J. Oral Maxillofac. Surg.* **1991**, *49*(4), 381–391.
17. Mills, D. K.; Fiandaca, D. J.; Scapino, R. P. *J. Orofac. Pain* **1994**, *8*(2), 136–154.
18. Gage, J. P.; Shaw, R. M.; Moloney, F. B. *J. Prosthet. Dent.* **1995**, *74*(5), 517–520.
19. Berkovitz, B. K.; Robertshaw, H. *Arch. Oral Biol.* **1993**, *38*(1), 91–95.
20. Nakano, T.; Scott, P. G. *Arch. Oral Biol.* **1989**, *34*(9), 749–757.
21. Detamore, M. S.; Orfanos, J. G.; Almarza, A. J.; French, M. M.; Wong, M. E.; Athanasiou, K. A. *Matrix Biol.* **2005**, *24*(1), 45–57.
22. Carvalho, R. S.; Yen, E. H.; Suga, D. M. *Arch. Oral Biol.* **1993**, *38*(6), 457–466.
23. Ali, A. M.; Sharawy, M. M. *J. Oral Pathol. Med.* **1996**, *25*(2), 78–85.
24. Minarelli, A. M.; Liberti, E. A. *J. Oral Rehabil.* **1997**, *24*(11), 835–840.
25. Scapino, R. P.; Canham, P. B.; Finlay, H. M.; Mills, D. K. *Arch. Oral Biol.* **1996**, *41*(11), 1039–1052.
26. Minarelli, A. M.; Del Santo, M., Jr.; Liberti, E. A. *J. Orofac. Pain* **1997**, *11*(2), 95–100.
27. Taguchi, N.; Nakata, S.; Oka, T. *J. Oral Surg.* **1980**, *38*(1), 11–15.
28. Berkovitz, B. K. *J. Oral Rehabil.* **2000**, *27*(7), 608–613.
29. Axelsson, S.; Holmlund, A.; Hjerpe, A. *Acta Odontol. Scand.* **1992**, *50*(2), 113–119.
30. Sindelar, B. J.; Evanko, S. P.; Alonzo, T.; Herring, S. W.; Wight, T. *Arch. Biochem. Biophys.* **2000**, *379*(1), 64–70.
31. Nakano, T.; Scott, P. G. *Arch. Oral Biol.* **1996**, *41*(8–9), 845–853.
32. Mizoguchi, I.; Scott, P. G.; Dodd, C. M.; *et al. Arch. Oral Biol.* **1998**, *43*(11), 889–898.
33. Allen, K. D.; Athanasiou, K. A. *Ann. Biomed. Eng.* **2005**, *33*(7), 951–962.
34. Allen, K. D.; Athanasiou, K. A. *J. Biomech.* **2006**, *39*(2), 312–322.
35. Chin, L. P.; Aker, F. D.; Zarrinnia, K. *J. Oral Maxillofac. Surg.* **1996**, *54*(3), 315–318.
36. Kim, K. W.; Wong, M. E.; Helfrick, J. F.; Thomas, J. B.; Athanasiou, K. A. *Ann. Biomed. Eng.* **2003**, *31*(8), 924–930.
37. Tanne, K.; Tanaka, E.; Sakuda, M. *J. Dent. Res.* **1991**, *70*(12), 1545–1548.
38. del Pozo, R.; Tanaka, E.; Tanaka, M.; Okazaki, M.; Tanne, K. *Med. Eng. Phys.* **2002**, *24*(3), 165–171.
39. Shengyi, T.; Xu, Y. *J. Craniomandib. Disord.* **1991**, *5*(1), 28–34.
40. Beatty, M. W.; Bruno, M. J.; Iwasaki, L. R.; Nickel, J. C. *J. Biomed. Mater. Res.* **2001**, *57*(1), 25–34.
41. Detamore, M. S.; Athanasiou, K. A. *J. Biomech. Eng.* **2003**, *125*(4), 558–565.
42. Wang, L.; Detamore, M. S. *Tissue Eng.* **2007**, *13*(8), 1955–1971.
43. Singh, M.; Detamore, M. S. *J. Biomech.* **2009**, *42*(4), 405–417.
44. Appleton, J. *Arch. Oral Biol.* **1975**, *20*(12), 823–826.
45. Mizuno, I.; Saburi, N.; Taguchi, N.; Kaneda, T.; Hoshino, T. *Shika Kiso Igakkai Zasshi* **1990**, *32*(1), 69–79.
46. Silva, D. G.; Hart, J. A. *J. Ultrastruct. Res.* **1967**, *20*(3), 227–243.
47. Copray, J. C.; Liem, R. S. *Acta Anat. (Basel)* **1989**, *134*(1), 35–47.
48. Blackwood, H. J. *Arch. Oral Biol.* **1966**, *11*(5), 493–500.
49. Bibb, C. A.; Pullinger, A. G.; Baldioceda, F. *J. Dent. Res.* **1992**, *71*(11), 1816–1821.
50. Bibb, C. A.; Pullinger, A. G.; Baldioceda, F. *Arch. Oral Biol.* **1993**, *38*(4), 343–352.
51. Klinge, R. F. *Micron* **1996**, *27*(5), 381–387.
52. Pietila, K.; Kantomaa, T.; Pirttiniemi, P.; Poikela, A. *Cells Tissues Organs* **1999**, *164*(1), 30–36.
53. Mizoguchi, I.; Takahashi, I.; Nakamura, M.; *et al. Arch. Oral Biol.* **1996**, *41*(8–9), 863–869.
54. Delatte, M.; Von den Hoff, J. W.; van Rheden, R. E.; Kuijpers-Jagtman, A. M. *Eur. J. Oral Sci.* **2004**, *112*(2), 156–162.
55. Teramoto, M.; Kaneko, S.; Shibata, S.; Yanagishita, M.; Soma, K. *J. Bone Miner. Metab.* **2003**, *21*(5), 276–286.
56. de Bont, L. G.; Boering, G.; Havinga, P.; Liem, R. S. *J. Oral Maxillofac. Surg.* **1984**, *42*(5), 306–313.
57. Luder, H. U.; Schroeder, H. E. *Anat. Embryol. (Berl)* **1990**, *181*(5), 499–511.
58. Singh, M.; Detamore, M. S. *J. Biomech. Eng.* **2008**, *130*(1), 011009.
59. Shibata, S.; Baba, O.; Ohsako, M.; Suzuki, S.; Yamashita, Y.; Ichijo, T. *Bull. Tokyo Med. Dent. Univ.* **1991**, *38*(4), 53–61.
60. Roth, S.; Muller, K.; Fischer, D. C.; Dannhauer, K. H. *Arch. Oral Biol.* **1997**, *42*(1), 63–76.
61. Mao, J. J.; Rahemtulla, F.; Scott, P. G. *J. Dent. Res.* **1998**, *77*(7), 1520–1528.
62. Kantomaa, T.; Pirttiniemi, P. *Eur. J. Orthod.* **1998**, *20*(4), 435–441.
63. Del Santo, M., Jr.; Marches, F.; Ng, M.; Hinton, R. J. *Arch. Oral Biol.* **2000**, *45*(6), 485–493.
64. Kang, H.; Bao, G.; Dong, Y.; Yi, X.; Chao, Y.; Chen, M. *Hua Xi Kou Qiang Yi Xue Za Zhi* **2000**, *18*(2), 85–87.
65. Tanaka, E.; Iwabuchi, Y.; Rego, E. B.; *et al. J. Biomech.* **2008**, *41*(5), 1119–1123.
66. Tanaka, E.; Rego, E. B.; Iwabuchi, Y.; *et al. J. Biomed. Mater. Res. A* **2008**, *85*(1), 127–132.
67. Hu, K.; Radhakrishnan, P.; Patel, R. V.; Mao, J. J. *J. Struct. Biol.* **2001**, *136*(1), 46–52.
68. Tanaka, E.; Yamano, E.; Dalla-Bona, D. A.; *et al. J. Dent. Res.* **2006**, *85*(6), 571–575.
69. Kuboki, T.; Shinoda, M.; Orsini, M. G.; Yamashita, A. *J. Dent. Res.* **1997**, *76*(11), 1760–1769.
70. Singh, M.; Detamore, M. S. *J. Biomech. Eng.* **2009**, *131*(6), 061008.
71. Webster, T. J. In *Advances in Chemical Engineering*; Ying, J. Y., Ed.; Academic Press: San Diego, CA, 2001; pp 125–166.
72. Zhang, L.; Webster, T. J. *Nanotoday* **2009**, *4*(1), 66–80.
73. Kaplan, F. S.; Hayes, W. C.; Keaveny, T. M.; Boskey, A.; Einhorn, T. A.; Iannotti, J. P. In *Orthopaedic Basic Science*; Simon, S. P., Ed.; American Academy of Orthopaedic Surgeons: Rosemont, IL, 1994; pp 127–185.
74. Giesen, E. B.; Ding, M.; Dalstra, M.; van Eijden, T. M. *J. Biomech.* **2001**, *34*(6), 799–803.
75. Nomura, T.; Gold, E.; Powers, M. P.; Shingaki, S.; Katz, J. L. *Dent. Mater.* **2003**, *19*(3), 167–173.
76. Schwartz-Dabney, C. L.; Dechow, P. C. *Am. J. Phys. Anthropol.* **2003**, *120*(3), 252–277.
77. van Ruijven, L. J.; Giesen, E. B.; Farella, M.; van Eijden, T. M. *J. Dent. Res.* **2003**, *82*(10), 819–823.
78. Giesen, E. B.; Ding, M.; Dalstra, M.; van Eijden, T. M. *J. Dent. Res.* **2004**, *83*(3), 255–259.
79. Solberg, W. K.; *et al.* In *Diagnosis and Management of Temporomandibular Disorders*; Laskin, D., Greenfield, W., Gale, E., Eds.; *et al.* American Dental Association: Chicago, IL, 1983; pp 30–39.
80. Solberg, W. K.; Woo, M. W.; Houston, J. B. *J. Am. Dent. Assoc.* **1979**, *98*(1), 25–34.
81. Gray, R. J. M.; Davies, S. J.; Quayle, A. A. *Temporomandibular Disorders: A Clinical Approach*; British Dental Association: London, 1995.
82. Milam, S. B.; Schmitz, J. P. *J. Oral Maxillofac. Surg.* **1995**, *53*(12), 1448–1454.
83. Wilkes, C. H. *Arch. Otolaryngol. Head Neck Surg.* **1989**, *115*(4), 469–477.
84. Farrar, W. B.; McCarty, W. L., Jr. *J. Ala. Dent. Assoc.* **1979**, *63*(1), 19–26.
85. Zarb, G. A.; Carlsson, G. E. *Orofac. Pain* **1999**, *13*(4), 295–306.

86. Hinton, R.; Moody, R. L.; Davis, A. W.; Thomas, S. F. *Am. Fam. Physician* **2002**, *65*(5), 841–848.
87. Tanaka, E.; Aoyama, J.; Miyauchi, M.; *et al*. *Histochem. Cell Biol*. **2005**, *123*(3), 275–281.
88. Vasconcelos, B. C.; Porto, G. G.; Bessa-Nogueira, R. V.; Nascimento, M. M. *Med. Oral Patol. Oral Cir. Bucal*. **2009**, *14*(1), E34–E38.
89. Tanaka, E.; Detamore, M. S.; Mercuri, L. G. *J. Dent. Res*. **2008**, *87*(4), 296–307.
90. Forssell, H.; Kalso, E. *J. Orofac. Pain* **2004**, *18*(1), 9–22; discussion 23–32.
91. Nicolakis, P.; Burak, E. C.; Kollmitzer, J.; *et al*. *Cranio* **2001**, *19*(1), 26–32.
92. Toller, P. A. *Proc. R Soc. Med*. **1977**, *70*(7), 461–463.
93. Shi, Z. D.; Yang, F.; He, Z. X.; Shi, B.; Yang, M. Z. *Zhongguo Xiu Fu Chong Jian Wai Ke Za Zhi* **2002**, *16*(1), 5–10.
94. Holmlund, A.; Hellsing, G.; Wredmark, T. *Int. J. Oral Maxillofac. Surg*. **1986**, *15*(6), 715–721.
95. Mercuri, L. G. In *TMDs, an Evidence-Based Approach to Diagnosis and Treatment*; Greene, C. S., Laskin, D. M., Hylander, W. L., Eds.; Quintessence: Chicago, 2006; pp 455–468.
96. Feinberg, S. E.; Larsen, P. E. *J. Oral Maxillofac. Surg*. **1989**, *47*(2), 142–146.
97. Wolford, L. M.; Reiche-Fischel, O.; Mehra, P. *J. Oral Maxillofac. Surg*. **2003**, *61*(6), 655–660; discussion 661.
98. Trumpy, I. G.; Lyberg, T. *J. Oral Maxillofac. Surg*. **1993**, *51*(6), 624–629.
99. Thomas, M.; Grande, D.; Haug, R. H. *J. Oral Maxillofac. Surg*. **1991**, *49*(8), 854–856; discussion 857.
100. Springer, I. N.; Fleiner, B.; Jepsen, S.; Acil, Y. *Biomaterials* **2001**, *22*(18), 2569–2577.
101. Almarza, A. J.; Athanasiou, K. A. *Tissue Eng*. **2004**, *10*(11–12), 1787–1795.
102. Almarza, A. J.; Athanasiou, K. A. *Ann. Biomed. Eng*. **2005**, *33*(7), 943–950.
103. Detamore, M. S.; Athanasiou, K. A. *Ann. Biomed. Eng*. **2005**, *33*(3), 383–390.
104. Detamore, M. S.; Athanasiou, K. A. *Tissue Eng*. **2005**, *11*(7–8), 1188–1197.
105. Almarza, A. J.; Athanasiou, K. A. *Tissue Eng*. **2006**, *12*(5), 1285–1294.
106. Almarza, A. J.; Athanasiou, K. A. *Arch. Oral Biol*. **2006**, *51*(3), 215–221.
107. Bean, A. C.; Almarza, A. J.; Athanasiou, K. A. *Proc. Inst. Mech. Eng. [H]* **2006**, *220*(3), 439–447.
108. Johns, D. E.; Athanasiou, K. A. *Cells Tissues Organs* **2007**, *185*(4), 246–257.
109. Allen, K. D.; Athanasiou, K. A. *J. Dent. Res*. **2008**, *87*(2), 180–185.
110. Allen, K. D.; Athanasiou, K. A. *Orthod. Craniofac. Res*. **2006**, *9*(3), 143–152.
111. Allen, K. D.; Athanasiou, K. A. *Tissue Eng*. **2007**, *13*(1), 101–110.
112. Allen, K. D.; Erickson, K.; Athanasiou, K. A. *Arch. Oral Biol*. **2008**, *53*(1), 53–59.
113. Anderson, D. E.; Athanasiou, K. A. *Ann. Biomed. Eng*. **2008**, *36*(12), 1992–2001.
114. Johns, D. E.; Athanasiou, K. A. *Cell Tissue Res*. **2008**, *333*(3), 439–447.
115. Johns, D. E.; Wong, M. E.; Athanasiou, K. A. *J. Dent. Res*. **2008**, *87*(6), 548–552.
116. Anderson, D. E.; Athanasiou, K. A. *Arch. Oral Biol*. **2009**, *54*(2), 138–145.
117. Hoben, G. M.; Koay, E. J.; Athanasiou, K. A. *Stem Cells* **2008**, *26*(2), 422–430.
118. Hoben, G. M.; Willard, V. P.; Athanasiou, K. A. *Stem Cells Dev*. **2009**, *18*(2), 283–292.
119. Wang, L.; Detamore, M. S. *J. Orthop. Res*. **2009**, *27*(8), 1109–1115.
120. Wang, L.; Seshareddy, K.; Weiss, M. L.; Detamore, M. S. *Tissue Eng. A* **2009**, *15*(5), 1009–1017.
121. French, M. M.; Rose, S.; Canseco, J.; Athanasiou, K. A. *Ann. Biomed. Eng*. **2004**, *32*(1), 50–56.
122. Deng, Y.; Hu, J. C.; Athanasiou, K. A. *Arthritis Rheum*. **2007**, *56*(1), 168–176.
123. Puelacher, W. C.; Wisser, J.; Vacanti, C. A.; Ferraro, N. F.; Jaramillo, D.; Vacanti, J. P. *J. Oral Maxillofac. Surg*. **1994**, *52*(11), 1172–1177.
124. Hu, J. C.; Athanasiou, K. A. *Tissue Eng*. **2006**, *12*(4), 969–979.
125. Detamore, M. S.; Athanasiou, K. A. *Arch. Oral Biol*. **2004**, *49*(7), 577–583.
126. Natoli, R. M.; Responte, D. J.; Lu, B. Y.; Athanasiou, K. A. *J. Orthop. Res*. **2009**, *27*(7), 949–956.
127. Tanaka, E.; Hanaoka, K.; van Eijden, T.; *et al*. *J. Dent. Res*. **2003**, *82*(3), 228–231.
128. Deschner, J.; Rath-Deschner, B.; Agarwal, S. *Osteoarthr. Cartil*. **2006**, *14*(3), 264–272.
129. Takigawa, M.; Okada, M.; Takano, T.; Ohmae, H.; Sakuda, M.; Suzuki, F. *J. Dent. Res*. **1984**, *63*(1), 19–22.
130. Tsubai, T.; Higashi, Y.; Scott, J. E. *Arch. Oral Biol*. **2000**, *45*(6), 507–515.
131. Fuentes, M. A.; Opperman, L. A.; Bellinger, L. L.; Carlson, D. S.; Hinton, R. J. *Arch. Oral Biol*. **2002**, *47*(9), 643–654.
132. Ogawa, T.; Shimokawa, H.; Fukada, K.; *et al*. *J. Bone Miner. Metab*. **2003**, *21*(3), 145–153.
133. Delatte, M. L.; Von den Hoff, J. W.; Nottet, S. J.; De Clerck, H. J.; Kuijpers-Jagtman, A. M. *Eur. J. Orthod*. **2005**, *27*(1), 17–26.
134. Bailey, M. M.; Wang, L.; Bode, C. J.; Mitchell, K. E.; Detamore, M. S. *Tissue Eng*. **2007**, *13*(8), 2003–2010.
135. Wang, L.; Detamore, M. S. *Arch. Oral Biol*. **2009**, *54*(1), 1–5.
136. Wang, L.; Lazebnik, M.; Detamore, M. S. *Osteoarthr. Cartil*. **2009**, *17*(3), 346–353.
137. Chang, J.; Ma, X.; Wei, M.; Wang, J.; Jiao, Y. *Zhonghua Kou Qiang Yi Xue Za Zhi* **2002**, *37*(4), 246–248.
138. Delatte, M.; Von den Hoff, J. W.; Maltha, J. C.; Kuijpers-Jagtman, A. M. *Arch. Oral Biol*. **2004**, *49*(3), 165–175.
139. Suzuki, S.; Itoh, K.; Ohyama, K. *J. Orthod*. **2004**, *31*(2), 138–143.
140. Zhang, L.; Sirivisoot, S.; Balasundaram, G.; Webster, T. J. In *Advanced Biomaterials: Fundamentals, Processing and Applications*; Basu, B., Katti, D., Kumar, A., Eds.; Wiley: Hoboken, NJ, 2009; pp 205–241.
141. Weng, Y.; Cao, Y.; Silva, C. A.; Vacanti, M. P.; Vacanti, C. A. *J. Oral Maxillofac. Surg*. **2001**, *59*(2), 185–190.
142. Chen, F.; Mao, T.; Tao, K.; Chen, S.; Ding, G.; Gu, X. *J. Oral Maxillofac. Surg*. **2002**, *60*(10), 1155–1159.
143. Alhadlaq, A.; Mao, J. J. *J. Dent. Res*. **2003**, *82*(12), 951–956.
144. Alhadlaq, A.; Elisseeff, J. H.; Hong, L.; *et al*. *Ann. Biomed. Eng*. **2004**, *32*(7), 911–923.
145. Alhadlaq, A.; Mao, J. J. *J. Bone Joint Surg. Am*. **2005**, *87*(5), 936–944.
146. Alhadlaq, A.; Mao, J. J. *J. Den. Res*. **2003**, *82*(12), 951–995.
147. Ueki, K.; Takazakura, D.; Marukawa, K.; *et al*. *J. Craniomaxillofac. Surg*. **2003**, *31*(2), 107–114.
148. Abukawa, H.; Terai, H.; Hannouche, D.; Vacanti, J. P.; Kaban, L. B.; Troulis, M. J. *J. Oral. Maxillofac. Surg*. **2003**, *61*(1), 94–100.
149. Hollister, S. J.; Levy, R. A.; Chu, T. M.; Halloran, J. W.; Feinberg, S. E. *Int. J. Oral Maxillofac. Surg*. **2000**, *29*(1), 67–71.
150. Schek, R. M.; Taboas, J. M.; Segvich, S. J.; Hollister, S. J.; Krebsbach, P. H. *Tissue Eng*. **2004**, *10*(9–10), 1376–1385.
151. Hollister, S. J.; Lin, C. Y.; Saito, E.; *et al*. *Orthod. Craniofac. Res*. **2005**, *8*(3), 162–173.
152. Schek, R. M.; Taboas, J. M.; Hollister, S. J.; Krebsbach, P. H. *Orthod. Craniofac. Res*. **2005**, *8*(4), 313–319.
153. Smith, M. H.; Flanagan, C. L.; Kemppainen, J. M.; *et al*. *Int. J. Med. Robot*. **2007**, *3*(3), 207–216.
154. Adamopoulos, O.; Papadopoulos, T. *J. Mater. Sci. Mater. Med*. **2007**, *18*(8), 1587–1597.
155. Catledge, S. A.; Fries, M. D.; Vohra, Y. K.; *et al*. *J. Nanosci. Nanotechnol*. **2002**, *2*(3–4), 293–312.
156. Venugopal, J. R.; Low, S.; Choon, A. T.; Kumar, A. B.; Ramakrishna, S. *Artif. Organs* **2008**, *32*(5), 388–397.
157. Li, W. J.; Tuli, R.; Okafor, C.; *et al*. *Biomaterials* **2005**, *26*(6), 599–609.
158. Shin, M.; Yoshimoto, H.; Vacanti, J. P. *Tissue Eng*. **2004**, *10*(1–2), 33–41.
159. Srouji, S.; Rachmiel, A.; Blumenfeld, I.; Livne, E. *J. Craniomaxillofac. Surg*. **2005**, *33*(2), 79–84.
160. Gothard, D.; Roberts, S. J.; Shakesheff, K.; Buttery, L. D. *Tissue Eng. C Meth*. **2010**, *16*(4), 583–595.
161. Darling, E. M.; Athanasiou, K. A. *Tissue Eng*. **2003**, *9*(1), 9–26.

Relevant Websites

http://www.astmjs.org/ – American Society of Temporomandibular Joint Surgeons.
http://www.aaoms.org/ – American Association of Oral and Maxillofacial Surgeons.
http://www.arthritis.org/ – Arthritis Foundation.
http://www.tmjoints.org/ – Jaw Joints and Allied Musculo-Skeletal Disorders Foundation.
http://www.nidcr.nih.gov/ – National Institute of Dental and Craniofacial Research.
http://www.tmj.org/ – The TMJ Association.
http://www.tmjconference.org/ – TMJ Bioengineering Conference.
http://www.usbjd.org/ – United States Bone and Joint Decade.

5.518. Endocultivation: Computer Designed, Autologous, Vascularized Bone Grafts

P H Warnke, Bond University, Robina, QLD, Australia; University of Kiel, Kiel, Germany

© 2011 Elsevier Ltd. All rights reserved.

5.518.1.	**Introduction**	237
5.518.2.	**Endocultivation of Autologous Vascularized Bone Grafts**	239
5.518.2.1.	The Living Bioreactor (Musculus Latissimus Dorsi)	239
5.518.3.	**Clinical Applications of Endocultivation: Tissue Engineering of Autologous Customized Vascularized Bone Replacements *In Vivo***	240
5.518.3.1.	Operative Technique	240
5.518.3.1.1.	Step 1: Preoperative planning and CAD design	240
5.518.3.1.2.	Step 2: Scaffold preparation and implantation	241
5.518.3.1.3.	Step 3: Transplantation	242
5.518.3.1.4.	Step 4: Mechanical loading and functional integration	242
5.518.4.	**Clinical Results**	242
5.518.5.	**Future Improvements**	243
5.518.6.	**Summary**	244
References		244

Glossary

Computer-aided design (CAD) In this context to duplicate both bone form and function for molded in situ cultivated autologous bone grafts.

Critical sized defect A bone defect incapable of healing or regenerating sufficient new bone to close the defect without surgical intervention and grafting.

Endocultivation Use of autologous mesenchymal stem cells loaded within a preformed titanium mesh cage and implanted into a surgically created pouch within the right or left latissimus dorsi muscle. The pouch serves as *in vivo* bioreactor to produce vascularized bone for autologous transplant to a critical defect.

Latissimus dorsi A flat, fan-like muscle that arises directly from the spinal processes of the lower six thoracic vertebrae, the lumbar and sacral vertebrae and the dorsal iliac crest via the thoracolumbar fascia. The muscle inserts between the teres and pectoralis muscles at the humerus and together with the teres major, forms the posterior axillary fold.

5.518.1. Introduction

The repair of critical size skeletal defects from trauma, congenital malformations, infection or tumor resection remains a challenge in modern Orthopedic, Maxillofacial and Plastic-Reconstructive surgery.[1] Besides function and mechanical integrity the reconstruction of the skeleton must also meet high aesthetic demands of the prevailing patient especially when recreating the skull and mandible. For example: the mandible has a complex function and shape. It is involved in mastication with high mechanical loading which imposes requirements of high compressive and torsional stability. The ability to speak and articulate properly requires a comprehensive interaction of adjacent muscles and two evenly balanced temporomandibular joints. The size and shape of the mandible is important for the proper occlusion of teeth (or dental implants) with those of the opposite maxilla. And at least the aesthetic appearance of the individual is highly dependent on the position of the chin and the mandibular angles. However, many patients require to be 'made up' as they had been prior to their impairing disease. Thus, the perfect reconstruction of the mandible or the facial bones is an ambitious goal.

Today, major bone defects that create a discontinuity in the bone extending over more than 5 cm are usually repaired with an autologous vascularized graft such as a fibula, scapula, iliac crest, or rib transplant. However, a major disadvantage of these techniques is that harvesting the required bone grafts creates another skeletal defect which is associated with significant morbidity (Figure 1).[2]

Recent advances in the emerging field of regenerative medicine may offer new solutions for Orthopedic and Plastic-Reconstructive surgeons. 'Regeneration' implies repairing the damaged tissue by growing it anew by means of tissue engineering.[3] This circumvents the issue of immunological rejection, as the patient's own cells are used to cultivate the required tissue.

In vitro tissue engineering has been a focus of many research groups; however, *in vivo* techniques such as endocultivation may offer even greater potential today.[3,4] *In vitro* techniques often focus on an optimized combination of three factors: cells, signaling molecules, and scaffolds. This is known as the classical 'Triangle or Tissue Engineering' (Figure 2). These three factors are already part of endocultivation, as shown in Figure 2. However, there is also an ongoing discussion about

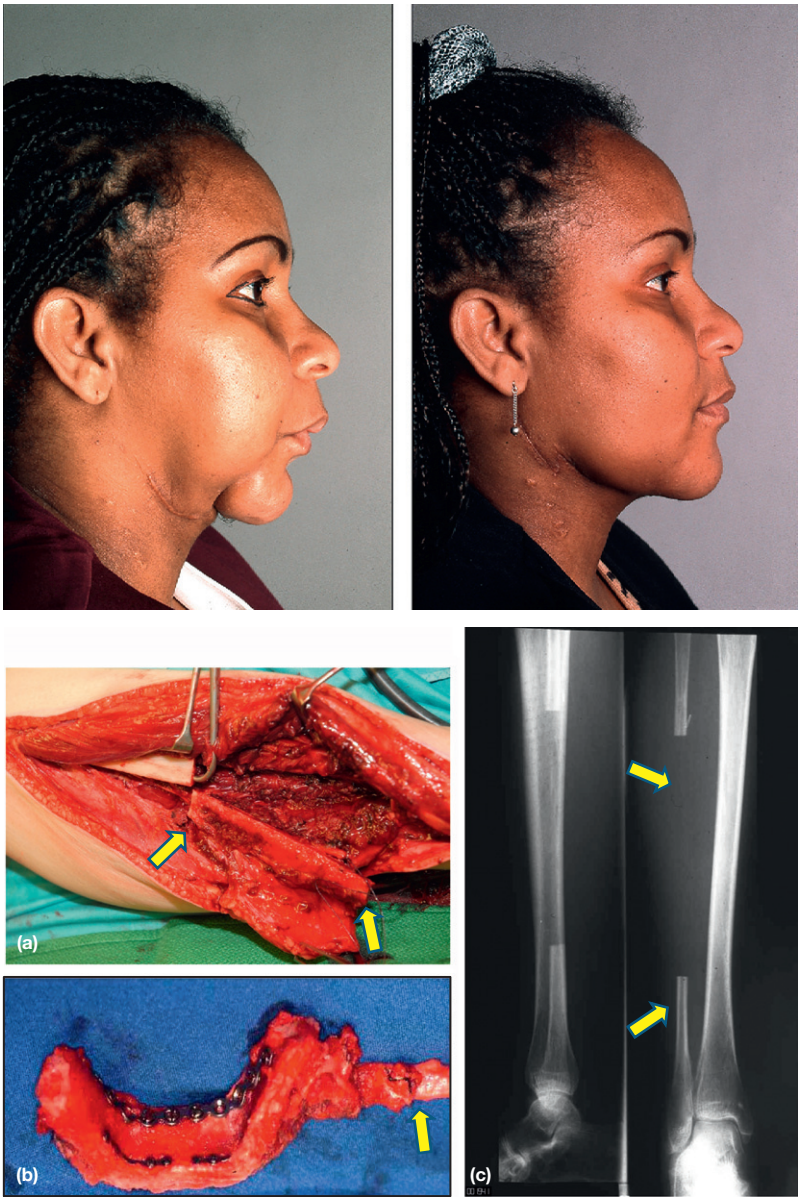

Figure 1 Autologous vascularized fibula grafts. Top left: Female with loss of mandible due to osteomyelitis. Impaired function and unsatisfactory aesthetic appearance (drop chin). Top right: After reconstruction with autologous vascularized fibula graft. Bottom: (a) When harvesting a fibula graft (between arrows) another reasonable skeletal and muscular defect is created. (b) The previously straight fibula being contoured into a mandibular shape and fixed with osteosynthesis plates. The arrow shows the vessel pedicle. (c) X-ray: The critical size defect along the fibula after harvest (arrows). Further complications such as instable ankle joint may occur at this site (Surgeons: Terheyden, Wiltfang, Springer, Warnke; Kiel, Germany).

the way as to how to best apply *in vitro* synthesized tissue and how to insert a vessel pedicle. Thereby, a hexagonal shaped model as shown in Figure 2 may be more appropriate for the future of tissue engineering.

There are additional factors that are especially important when focusing on the cultivation of entire organs with multiple different cell types. For example, a multifaceted organ such as the kidney cannot be engineered without the ability to synthesize and coordinate the orchestra of different cell pathways at the same time, same place and in the same milieu. In short, an organ is a coexistence of different cell types with different desires at the same place. So, how do we grow this? At least understanding how to grow and to control the minimum of two tissue types simultaneously together will be one key step forward. But many *in vitro* cultivation recipes for different cell types such as osteoblasts or chondrocytes for example require different competing environmental or bioreactor conditions to be cultivated. The hypothesis that is pursued here is that a more elegant solution can be found in endocultivation, where living bioreactors are applied.

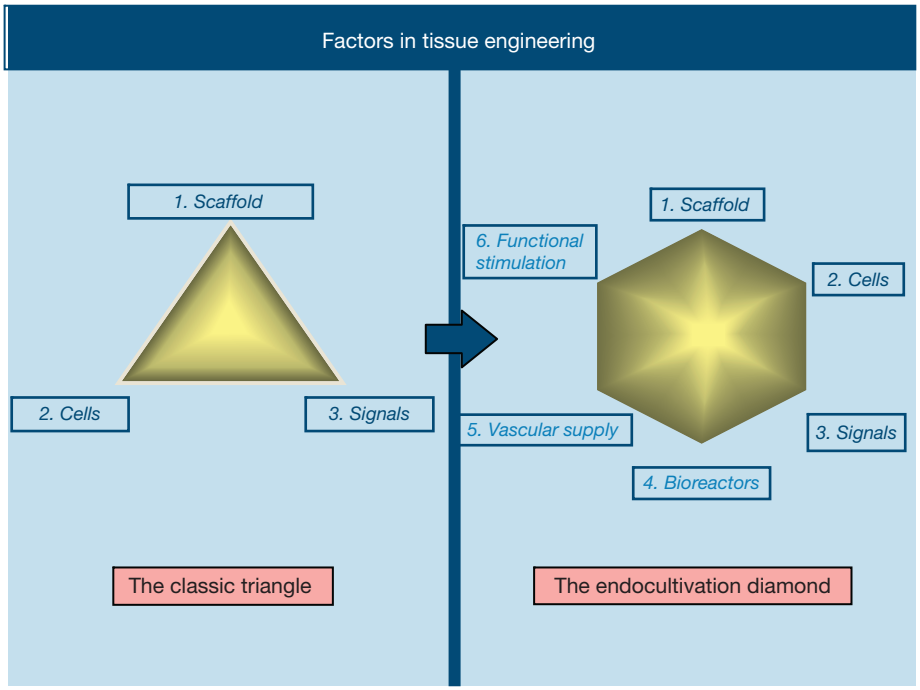

Figure 2 The classic triangle of three factors influencing tissue engineering changes into a diamond of six factors, when applying endocultivation. Many more factors may be identified in the future.

5.518.2. Endocultivation of Autologous Vascularized Bone Grafts

Endocultivation is a pioneering technique used to grow individually shaped bone replacements within the latissimus dorsi muscle of patients with severe skeletal defects. The goal is to use the patients as their own living bioreactors to avoid the common problems associated with engineering tissue *in vitro* (in the laboratory). The replacement scaffolds are individually designed prior to surgery using computer-assisted design (CAD) to enable for an excellent fit. The major advantages of the endocultivation technique are related to achieving an optimal three-dimensional esthetic outcome, and to preventing the creation of a secondary skeletal defect. In addition, good vascularization can be achieved using endocultivation, which remains a major challenge in the engineering of thick tissues *in vitro*.[13] However, as only autologous cells are applied, immune reactions problems caused by foreign tissue, as is known to occur in other disciplines of organ transplant surgery will not occur.[6]

5.518.2.1. The Living Bioreactor (Musculus Latissimus Dorsi)

The latissimus dorsi is a flat, fanlike muscle that arises directly from the spinal processes of the lower six thoracic vertebrae, the lumbar and sacral vertebrae and the dorsal iliac crest via the thoracolumbar fascia. The muscle inserts between the teres and pectoralis muscles at the humerus and, together with the teres major, it forms the posterior axillary fold.[7,16]

Parts of the latissimus dorsi muscle also sometimes serve as an autologous vascularized flap used in Plastic and Reconstructive surgery. Thus, the latissimus dorsi flap has accrued a broad spectrum of clinical applications. This is due to the large area of tissue available, thereby allowing flexibility in flap design. For example, the muscular flap can be combined with a skin pedicle or bone segment of the scapula, thus being one of the favorite autologous vascularized osteomyocutaneous flaps in Plastic and Reconstructive surgery.[16]

The main nutrient vessel of the muscle is the thoracodorsal artery, which regularly gives off a strong branch to the serratus anterior muscle. The length of the extramuscular part of the vessel course varies from 6 to 16 cm and is about 9 cm on average.[8] The extramuscular part gives off several minor branches.[7] At the point of origin from the subscapularis vessels, the thoracodorsal vessels have diameters of 1.5–4 mm (artery) and 3–5 mm (vein after unification of the two concomitant veins).[7,8]

This long and high-capacity vascular pedicle permits a relatively easy surgical procedure to achieve tissue transfer and microvascular anastamoses at the recipient site.[7,8]

Animal studies and initial clinical data demonstrate that the choice of a prepared muscle pouch inside the latissimus dorsi can be a highly successful site to function as a bioreactor. In fact, there is substantial evidence of heterotopic bone growth and remodeling within the graft.[5,9,12] The muscular bioreactor allows for neovascularisation of the bone replacement thanks to the thoracodorsal artery and vein, thereby allowing subsequent transfer of perfused and living cultivated tissue into the desired recipient region (**Figure 3**). The dimensions of the replacement determine the size of the pouch. It should be located near the lateral rim of the muscle due to the anatomical location of the thoracodorsal artery. Thus the

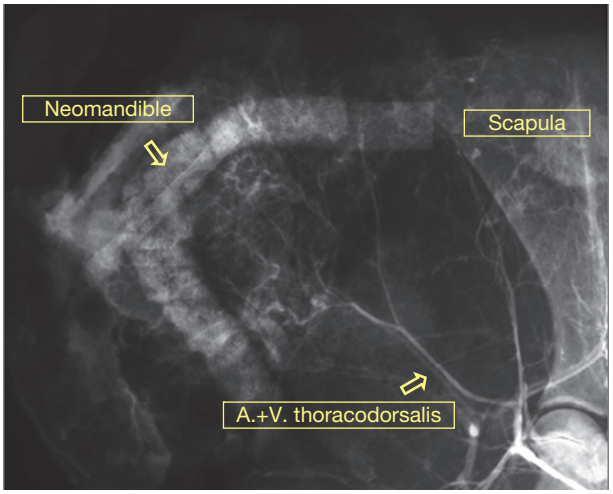

Figure 3 Angiography of an endocultivated new mandible inside the latissimus dorsi muscle of a pig 6 weeks after implantation of hydroxyapatite scaffolds and bone morphogenetic protein-7. The thoracodorsal artery and vein perfuse the neomandible entirely. Thus, transplantation and subsequent microsurgical anastomosis is possible. Note: The horseshoe-shaped neomandible was cultivated with a resorbable external scaffold and not titanium mesh in this case.

cultivated bone replacement will have sufficient blood supply after both transplantation and microsurgical anastomosis of the vessel pedicle.

This independent vascular supply makes it possible to grow constructs of the size of a mandible or in the future, possibly of a joint or even a complex organ.

5.518.3. Clinical Applications of Endocultivation: Tissue Engineering of Autologous Customized Vascularized Bone Replacements *In Vivo*

In 2004, we started using endocultivation techniques to grow customized computer-designed vascularized jaw replacements in the latissimus dorsi muscles of patients for subsequent transplantation to reconstruct their previously resected jaws[4,5] (Figure 4). These types of jaw replacements allowed for immediate masticatory function after transplantation into the recipient region. Besides this, patients are provided with a significantly superior quality of life given their improved esthetic appearance and enhanced ability to speak.

5.518.3.1. Operative Technique

The endocultivation procedure has one presurgical step (Step 1) for custom scaffold design and two different surgical steps (Steps 2 and 3).[16] There is also a subsequent phase for remodeling and integration of the graft into the recipient region (Step 4). These will be described for the cultivation of a mandible replacement in the following sections.

5.518.3.1.1. Step 1: Preoperative planning and CAD design

The aim is to grow a subtotal replacement mandible inside the latissimus dorsi muscle with an adequate vascular pedicle to allow for subsequent transplantation of a viable graft into the defect. Furthermore, the replacement should be individually shaped to fit the defect perfectly, thus improving the chances of adequate postoperative function and a satisfactory esthetic result.

Initially a three-dimensional computed tomography (CT) scan of the head must be performed to identify the mandibular defect and to design an ideal virtual replacement of the missing part(s) using computer-aided design (CAD)-planning techniques (Figure 4). The data describing the mandible replacement is then directed to a CAD-operated 3-axes-milling machine and a Teflon mandible model is created exactly matching the virtual dimensions of the replacement mandible.

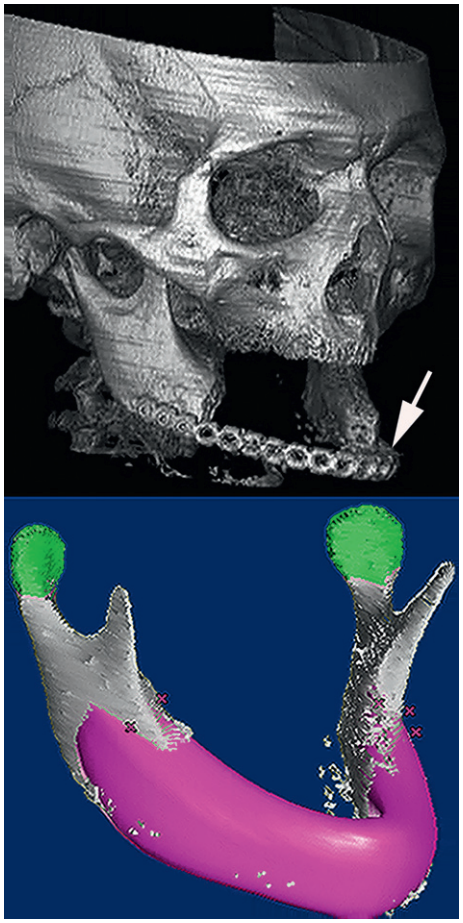

Figure 4 Top: Three-dimensional CT-scan of a 56-year-old male patient after ablative surgery for squamous cell cancer 8 years ago. The mandible was resected from paramedian left region to the retromolar right region. This critical size defect of over 7 cm had been bridged with a titanium reconstruction plate since the initial surgery. Lower image: The CT data of the mandible with defect region is separated. Using computer-aided design (CAD)-planning techniques, an ideal virtual mandibular transplant (pink) is designed that would fit exactly into the defect. The data of this virtual transplant is forwarded to a CAD operated 3-axes-milling-machine to form an identical Teflon model (compare with **Figure 2**). Reproduced from Warnke, P. H.; Springer, I. N.; Wiltfang, J.; *et al. Lancet* **2004**, *364*(9436), 766–770.

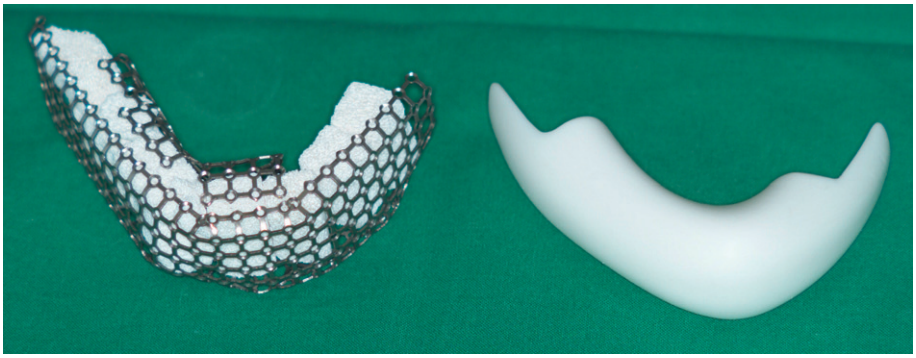

Figure 5 A Teflon mandible model (right) was prepared with a CAD-operated a 3-axes-milling machine. The model has identical dimensions as the virtually designed transplant (compare with **Figure 4**). A titanium mesh scaffold was then formed onto the Teflon model. After removing the Teflon model the remaining titanium mesh cage (left) has similar dimensions as the ideal virtual transplant. The cage is loaded with hydroxyapatite blocks serving as internal scaffold. The blocks will be later coated with bone morphogenetic protein-7 and autologous bone marrow. Reproduced from Warnke, P. H.; Springer, I. N.; Wiltfang, J.; *et al*. *Lancet* **2004**, *364*(9436), 766–770.

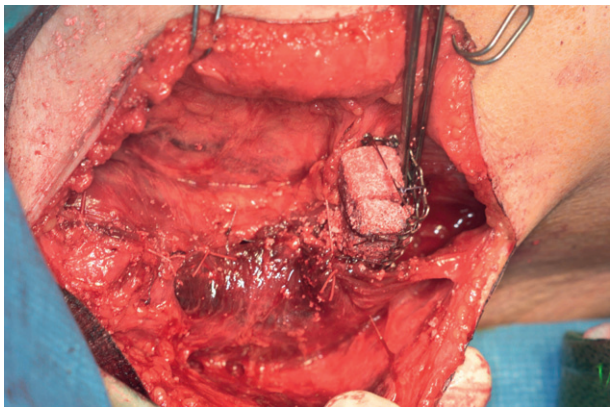

Figure 6 The loaded titanium mesh cage is implanted into a pouch of the right latissimus dorsi muscle of the patient. The surrounding muscle tissue is fixed on the cage with resorbable sutures to allow for maximum soft tissue contact for neovascularisation inside the graft. Reproduced from Warnke, P. H.; Springer, I. N.; Wiltfang, J.; *et al*. *Lancet* **2004**, *364*(9436), 766–770.

5.518.3.1.2. Step 2: Scaffold preparation and implantation

The Teflon mandible is then used as a mold from which a titanium mesh scaffold is created (**Figure 5**). The Teflon mandible is subsequently set aside and the titanium mesh cage (now serving as an external scaffold) is filled with an internal scaffold–bovine hydroxyapatite matrix. This internal scaffold is then coated with recombinant human bone morphogenetic protein-7 (BMP-7). Subsequently, 10–20 ml bone marrow are aspirated from the iliac crest and added to the hydroxyapatite matrix with the intention of providing undifferentiated precursor cells as a target for BMP-7. However, future developments with sterile GMP facilities available may allow for application of high numbers of autologous mesenchymal stem cells in patients at this stage.

The loaded titanium mesh cage (**Figure 6**) is then implanted into a surgically created pouch of the right or left latissimus dorsi muscle. The pouch serves as *in vivo* bioreactor. A 7–10 week cultivation phase is required to allow for both the growth of heterotopic bone and for ingrowth of new vessels from the thoracodorsal artery (**Figure 7**). The use of external titanium meshes is required as long as there are no shapable stable biodegradable scaffolds of the size of a mandible available.

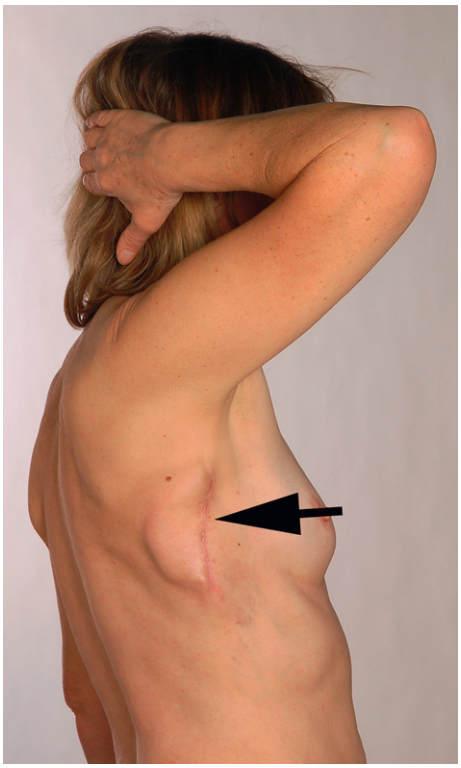

Figure 7 View on the lateral side of another female patient, where a mandibular replacement (arrow) is growing inside her lateral right latissimus dorsi muscle. The shoulder range of motion is not significantly reduced. Reproduced from Warnke, P. H. In *Grabbs Encyclopaedia of Flaps: Head and Neck*, 3rd ed.; Wolters Kluwer/Lippincott Williams & Wilkins: Philadelphia, 2007; Vol. 1.

CT after implantation and prior to transplantation is helpful to detect heterotopic bone growth or any increase in mineralization (**Figure 8**). In addition, bone scintigraphy (600 MBq technetium-99m-oxydronate-tracer) may be used to demonstrate extraskeletal osteoblast activity inside the

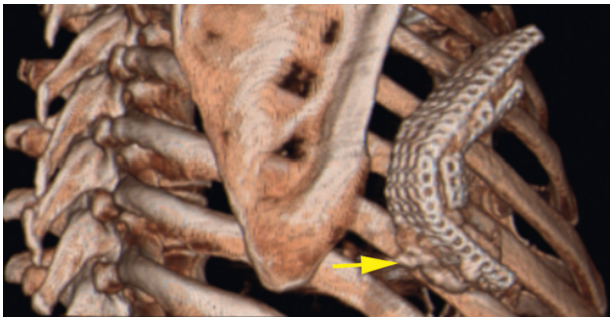

Figure 8 Three-dimensional (3D) CT scanning of the thorax. The mandible replacement is cultivated without contact to the skeleton laterally anterior of the tip of the scapula. New bone formation is even seen to be occurring through the titanium scaffold around the mandibular replacement. Reproduced from Warnke, P. H.; Springer, I. N.; Wiltfang, J.; *et al*. *Lancet* **2004**, *364*(9436), 766–770.

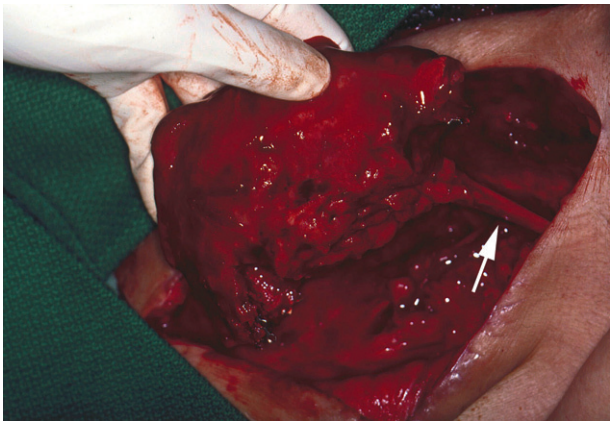

Figure 9 The mandible replacement is harvested with the surrounding muscle tissue and the adjacent thoracodorsal vessel pedicle (arrow). Reproduced from Warnke, P. H.; Springer, I. N.; Wiltfang, J.; *et al*. *Lancet* **2004**, *364*(9436), 766–770; Warnke, P. H. In *Grabbs Encyclopaedia of Flaps: Head and Neck*, 3rd ed.; Wolters Kluwer/Lippincott Williams & Wilkins: Philadelphia, 2007; Vol. 1.

replacement. This is useful to demonstrate the successful induction of new bone formation.

5.518.3.1.3. Step 3: Transplantation

After a cultivation period of a minimum of 7 weeks the mandible replacement is transplanted to repair a significant mandibular defect. The replacement is harvested with the surrounding muscular tissue and the adjacent vessel pedicle from the A. and V. thoracodorsalis (Figure 9). Transplantation into the defect region is performed via an extraoral approach. Minor bone overgrowth on the ends of the replacement can be curetted in order that the transplant fits easily into the defect. As the replacement has been customized using CAD design no further correction of the shape or form of the graft should be required. When a titanium mesh cage is being used as the external scaffold it is helpful to have overlapping edges at the docking points to the original mandible stumps. Thus, the replacement can be easily fixed onto the stumps with miniscrews (Figure 10). The transplant's vascular pedicle is then anastomosed onto the neck vessels utilizing standard microsurgical techniques.



Figure 10 3D CT scan of the male patient after transplantation of the endocultivated mandible replacement. The overlapping titanium-mesh wings of the replacement are fixed in the correct position thus returning the contour of the patient's jaw-line to approximately that present pre-morbidly. Reproduced from Warnke, P. H.; Springer, I. N.; Wiltfang, J.; *et al*. *Lancet* **2004**, *364*(9436), 766–770; Warnke, P. H. In *Grabbs Encyclopaedia of Flaps: Head and Neck*, 3rd ed.; Wolters Kluwer/Lippincott Williams & Wilkins: Philadelphia, 2007; Vol. 1.

5.518.3.1.4. Step 4: Mechanical loading and functional integration

After transplantation the bone graft will receive immediate mechanical loading. This will allow for integration of the graft into the recipient region. Thus, the cultivation of the graft is not over at this point. From now on the patient's body again will allow for remodeling and the graft will undergo an adaption process according to the requirements of the recipient site. This is especially the case after the external titanium scaffolds are removed. However, current studies focus on the prevention of such nonresorbable titanium scaffolds for providing shape.

5.518.4. Clinical Results

Experience in humans with this computer-assisted endocultivation technique is currently limited. The method is still experimental and at the time of publication of this chapter, still requires ethics approval as the use of BMPs at this anatomical site is an off-label use. As such, mandibular reconstructions using vascularized fibula, scapula, or iliac crest grafts remain the gold standard. The preoperative planning requires experience in CAD planning and rapid prototype development to allow for the exact fit of the replacement.

To date, patients who underwent this procedure have not complained of pain or sleep disturbance and relayed only minor concerns regarding the range of motion of their affected shoulder.

Wound closure can be a problem after transplantation of a massive replacement, particularly if the skin is nonelastic in the defect region given previous irradiation therapy and fibrosis. Although not ideal, a split-skin graft covering the adjacent muscle tissue of the graft may be employed if this proves to be particularly problematic.[4]

This type of mandible replacement allows for masticatory function when the external scaffold is properly fixed onto the mandible stumps. Patients are provided with a significantly superior quality of life given their improved esthetic appearance and enhanced ability to speak. To date, there has been no experience in the insertion of dental implants into such neomandibles.

The amount of bone that can be induced with BMP is limited. Follow-up computed tomographies have shown that bone density inside the replacements subsequently enhanced, probably as a result of masticatory functional loading.[5] We see this as a strong foundation for our hypothesis that the grafts undergo a process of functional integration into the recipient, as we describe here as Step 4. This phase might be underestimated in contemporary tissue engineering approaches. The human body seems to be capable to change the tissue engineered grafts according to its needs. Thus, it is an attractive idea to grow premature grafts inside the muscular bioreactor and then to transplant these for subsequent maturization. This could be important for *in vitro* tissue engineers as there seems not to be the absolute need for a 100% ready-to-go graft, when being applied in humans later. The human body may add the missing parts by itself.

A detailed 5 year follow-up for the first patients is currently in preparation.

5.518.5. Future Improvements

It is likely that with the endocultivation technique described above, it may not exceed the density of regular cancellous bone until transplantation at this current stage.[5,12] A firm cortical layer is expected to form only after functional loading of the graft. Thus a mechanically stable and formable external scaffold with sufficient size such as titanium mesh is still necessary to allow for mechanical loading after transplantation.

We are currently in the phase of designing CAD designable and individually formable resorbable hydroxyapatite matrices. A print and sintering processing has been proven to manufacture porous hydroxyapatite matrices. These can already be shape in the size of a simple joint-like-structure. Mechanical tests and *in vitro* plus *in vivo* biocompatibility tests are promising.[14,15] These matrices can also be combined with additional features such as vessel and nerve canals.

Future studies are also focusing on improvement of bone induction inside these matrices. Integrated canals inside the scaffolds may allow for further vascular ingrowth and may also serve as spaces for growth factor delivery to enhance bone formation. These spaces would offer the possibility to administer cell preparations such as autologous stem cells directly into the center of the scaffold. Also a periosteal cover is in preparation to direct cortical bone growth and outer shape of the graft. Thus, mechanically stable grafts might be produced inside the muscular bioreactor without the need for nonresorbable titanium.

The endocultivation method could be advantageous to couple the growth of different tissue types such as bone and cartilage as the cultivation potentials of the human organism are employed. Growth of bone and cartilage *in vitro* requires different culture environments. Whereas the living organism is able to grow even multifaceted organs and also to contol growth in one homogenous environment at the same time. Before we can grow an entire organ we should focus on only two different tissues such as bone and cartilage. Thus, the growth of a biological joint replacement using the endocultivation technique is the next major milestone. The European Union funded tissue engineering network is working toward achieving this goal (see www.myjoint.org) (**Figure 11**).



Figure 11 The concept of intramuscular endocultivation is addressed in growing a biological joint replacement by the research network 'MyJoint'.

5.518.6. Summary

Endocultivation is a pioneering technique used to grow individually shaped bone replacements within the latissimus dorsi muscle of patients with severe skeletal defects. The goal is to use the patient as his own bioreactor to prevent the common problems of engineering tissue *in vitro*.

Replacement scaffolds are designed prior to surgery using CAD to enable a perfect fit. The site of cultivation is a surgically created pouch in the lateral latissimus dorsi which allows for neovascularization, courtesy of the thoracodorsal artery and vein, thereby allowing subsequent free-flap transfer into the desired recipient region. This independent vascular supply makes it possible to grow constructs of the size of a mandible, or in the future, possibly even a complex organ.[10,11]

References

1. MacArthur, B. D.; Oreffo, R. O. C. *Nature* **2005**, *433*, 19.
2. Takushima, A.; Harii, K.; Asato, H.; Nakatsuka, T.; Kimata, Y. *Plast. Reconstr. Surg.* **2001**, *108*(6), 1555–1563.
3. Spector, M. *Basic Principles of Tissue Engineering: Tissue Engineering*. Quintessence: Chicago, USA, 1999.
4. Warnke, P. H.; Springer, I. N.; Wiltfang, J.; *et al*. *Lancet* **2004**, *364*(9436), 766–770.
5. Warnke, P. H.; Wiltfang, J.; Springer, I. N.; *et al*. *Biomaterials* **2006**, *27*, 3163–3167.
6. Warnke, P. H. *Lancet* **2006**, *368*(9531), 181–183.
7. Wolff, K. D.; Hölzle, F. *Raising of Microvascular Flaps: A Systematic Approach*. Springer: Berlin, 2005.
8. Bartlett, S. P.; May, J. W., Jr.; Yaremchuk, M. J. *Plast. Reconstr. Surg.* **1981**, *67*(5), 631–636.
9. Terheyden, H.; Warnke, P.; Dunsche, A.; *et al*. *Int. J. Oral Maxillofacial. Surg.* **2001**, *30*(6), 469–478.
10. Heliotis, M.; Lavery, K. M.; Ripamonti, U.; Tsiridis, E.; di Silvio, L. *Int. J. Oral Maxillofac. Surg.* **2006**, *35*(3), 265–269.
11. Arnander, C.; Westermark, A.; Veltheim, R.; Docherty-Skogh, A. C.; Hilborn, J.; Engstrand, T. *J. Craniofac. Surg.* **2006**, *17*(2), 275–279.
12. Warnke, P. H.; Springer, I. N.; Acil, Y.; *et al*. *Biomaterials* **2006**, *27*(7), 1081–1087.
13. Ko, H. C. H.; Milthorpe, B. K.; McFarland, C. D. *Eur. Cell Mater.* **2007**, *14*, 1–19.
14. Seitz, H.; Rieder, W.; Irsen, S.; Leukers, B.; Tille, C. *J. Biomed. Mater. Res. B Appl. Biomater.* **2005**, *74*, 782–788.
15. Becker, S. T.; Bolte, H.; Krapf, O.; *et al*. *Oral Oncol.* **2009**, *45*(11), e181–e188. Epub 2009 Aug 31.
16. Warnke, P. H. In *Grabbs Encyclopaedia of Flaps: Head and Neck*, 3rd ed.; Wolters Kluwer/Lippincott Williams & Wilkins: Philadelphia, 2007; Vol. 1.

5.519. Biomaterials Selection for Dental Pulp Regeneration

H Nie and J Kim, Columbia University Medical Center, New York, NY, USA
S Y Fu, Innovative Elements, LLC, New York, NY, USA
J J Mao, Columbia University Medical Center, New York, NY, USA

© 2011 Elsevier Ltd. All rights reserved.

5.519.1.	**Introduction**	245
5.519.2.	**Biomaterial Selections**	246
5.519.2.1.	Polymer Choices	246
5.519.2.2.	Scaffolding	248
5.519.3.	***In Vivo* Dental Pulp Regeneration: State of the Art**	250
5.519.4.	**Conclusions**	253
References		253

Glossary

Dental pulp The only vascularized connective tissue comprising collagen and elastic fibers in the tooth; maintains tooth homeostasis as a viable organ, and is embedded in highly mineralized structures including dentin, enamel, and cementum.

Pulpectomy The most common endodontic treatment involving extirpation of dental pulp, leaving no dental pulp stem cells in the same tooth for pulp regeneration following the surgical procedure. Due to pulp devitalization from surgical procedures, endodontically treated teeth become devitalized and brittle, susceptible to postoperative fracture and other complications including reinfections due to coronal leakage or microleakage.

Tissue engineering A biomedical engineering strategy that aims to achieve functional restoration of tissue structure and physiology to repair and regenerate impaired or damaged tissues due to congenital anomalies, cancers, infectious diseases or trauma, conventionally believed to require three key elements: cells, scaffolds, and signals.

Abbreviations

ALP	Alkaline phosphatase
β-TCP	β-tricalcium phosphate
bFGF	Basic fibroblast growth factor
BMP-2	Bone morphogenetic protein-2
BMP-7	Bone morphogenetic protein-7
BSP	Bone sialoprotein
DSPP	Dentin sialophosphoprotein
ECM	Extracellular matrix
HA	Hyaluronic acid
HAp	Hydroxyapatite
hMSCs	Human mesenchymal stem cells
NGF	Nerve growth factor
PCL	Poly(ε-caprolactone)
PDGF	Platelet-derived growth factor
PEG	Poly(ethylene glycol)
PGA	Polyglycolic acid
PLGA	Poly(D,L-lactide-*co*-glycode)
POC	Poly(1,8-octanediol-*co*-citrate)
SCID mouse	Mouse with severe combined immunodeficiency
VEGF	Vascular endothelial growth factor

5.519.1. Introduction

Dental pulp is the only vascularized tissue in the tooth and is embedded in highly mineralized structures, including dentin, enamel, and cementum. Dental pulp maintains the homeostasis of the tooth as a viable organ. The overall health of the tooth is compromised upon dental pulp trauma or infections, frequently manifested as dental pulp infections named pulpitis.[1] A typical endodontic treatment or root canal therapy for irreversible pulpitis is pulpectomy, involving pulp extirpation followed by root canal enlargement and obturation of root canal with gutta percha, a bioinert thermoplastic material.[1] Despite reported clinical success, endodontically treated teeth become devitalized and brittle, susceptible to postoperative fracture and other complications including reinfections due to coronal leakage or microleakage.[1,2] A substantial amount of tooth structures including enamel and dentin is removed during endodontic treatment, potentially leading to posttreatment tooth fracture and trauma.[1–3] Moreover, endodontically treated teeth have lost pulpal sensation, and are deprived of the ability to detect secondary infections.[1,2,4] As a result, the complications of current endodontic treatment are inevitable because of pulp devitalization or the loss of the tooth's innate homeostasis and defense mechanisms once dental pulp is replaced with bioinert materials.

Tissue engineering aims to achieve functional restoration of tissue structure and physiology to repair and regenerate impaired or damaged tissues due to congenital anomalies,

cancers, infectious diseases, or trauma.[5,6] Tissue engineering is conventionally believed to require three key elements as shown in Figure 1[7]: cells, scaffolds, and signals.

Existing effort in dental pulp regeneration has focused primarily on cell transplantation.[8–10] Several reports have documented regeneration of dental-pulp-like tissue *in vitro* or ectopically by transplantation of dental pulp stem cells.[11–13] Deciduous and adult dental pulp stem cells seeded in a self-assembling peptide-amphiphile (PA) hydrogel showed distinctive behavior: greater proliferative rate for deciduous cells but greater osteogenic differentiation potential for adult cells.[9,10] Delivery of collagen scaffolds with dental pulp stem cells and dentin matrix protein-1 in dentin slices in mice led to ectopic formation of pulp-like tissue.[14] Deciduous dental pulp stem/progenitor cells seeded in Matrigel in 1.5-mm cross-sectional tooth slices regenerated vascular pulp-like tissue following ectopic implantation in severe combined immunodeficiency (SCID) mice.[15] Similarly, stem/progenitor cells from apical papilla and dental pulp in root fragments yielded vascularized pulp-like tissue following ectopic implantation also in SCID mice.[14] Despite its scientific validity, dental pulp regeneration by stem cells encounters clinical and commercialization hurdles. Pulpectomy, the most common endodontic treatment, involves extirpation of dental pulp, and therefore leaves no dental pulp stem cells in the same tooth for pulp regeneration. For a patient who requires endodontic treatment in a given tooth but has intact dentition otherwise, no healthy tooth is to be sacrificed for isolation of dental pulp stem cells. Even in patients whose autologous dental pulp stem cells can be harvested, for example, from extracted wisdom teeth, clinical therapy of dental pulp regeneration is difficult to develop due to excessive costs including cell isolation, handling, storage, and shipping, *ex vivo* manipulation, immune rejection (for allogeneic cells), not to mention liabilities of potential contamination, pathogen transmission and tumorigenesis that may be associated with *ex vivo* cell manipulation.[16,17]

Therefore, the key challenges to dental pulp regeneration include the following:

1. Cells of dental pulp that are widely believed to be the regenerative cells for dental pulp regeneration are no longer available after pulpectomy in the same tooth.
2. Alternative cell sources for dental pulp regeneration, including dental pulp stem/progenitor cells, can rarely be harvested without sacrifice of healthy teeth.
3. Even when dental pulp stem/progenitor cells can be harvested without undue surgical trauma, the cost and hurdle for commercialization appear to be insurmountable.
4. Biological signals that may be important or critical for dental pulp regeneration have not been investigated until a recent report.[56]

This review focuses on biomaterial needs for dental pulp regeneration, with reference to both cell delivery and cell-homing approaches. Given that biological signals are rarely investigated in dental pulp regeneration, this review specifically explores delivery of bioactive cues in biomaterials for dental pulp regeneration.

5.519.2. Biomaterial Selections

The native extracellular matrix of dental pulp provides a scaffold for adhesion, proliferation, and differentiation of resident cells including odontoblasts, fibroblasts, vascular cells, and neural endings. In principle, ideal biomaterial scaffolds for dental pulp regeneration should allow the key functions of the native dental pulp. At a minimum, biomaterial scaffolds for dental pulp regeneration should be biocompatible, nontoxic, and promote regeneration of vascularized soft tissue that is analogous to the native dental pulp.

5.519.2.1. Polymer Choices

Biomaterial choices can be natural or synthetic polymers or a hybrid. The natural polymers, such as collagen and fibronectin, have advantages of good cytocompatibility and bioactivity,

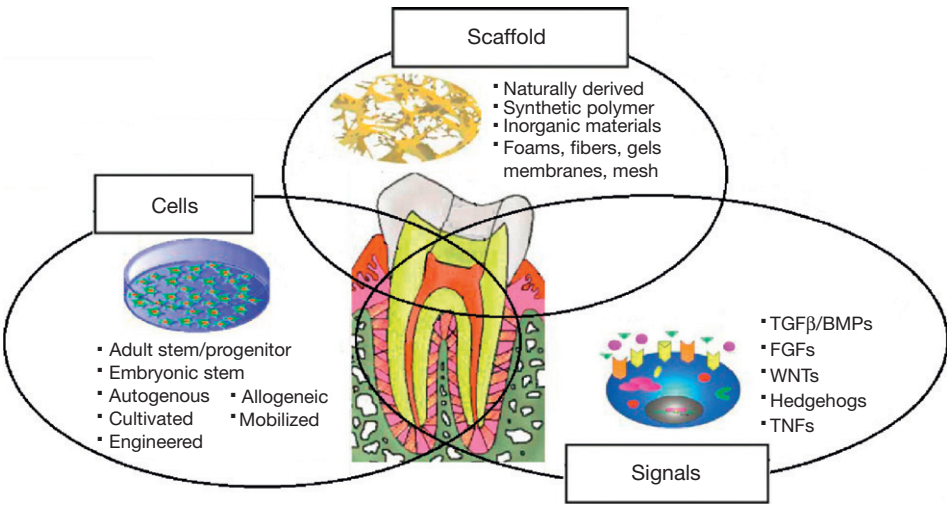

Figure 1 The key elements of tissue engineering and dental regenerations. The triad consists of stem cells, a scaffold of extracellular matrix, and bioactive cues. The figure is adapted from Nakashima, M. *Cytokine Growth Factor Rev.* **2005**, *16*, 369–376 with permission. Modified with permission from Dr. Nakashima, with permission from Elsevier.

while synthetic polymers allow precise control of the physicochemical properties such as mechanical properties, degradation rate, porosity, and microstructures.[18] For instance, dental pulp cells grown in collagenous, ceramic, or metal (titanium) matrices may develop differential expression of dental matrix markers such as dentin sialophosphoprotein (DSPP).[19] These cells initially express STRO-1, a marker for multipotent cells such as bone marrow-derived mesenchymal stem cells.

Extracellular matrix components such as fibronectin have been shown to mediate the binding of signaling molecules and regulate cell attachment, which aids in regulating the interactions between cells and extracellular matrix resulting in the reorganization of cytoskeleton in preodontoblasts during pulp wound healing.[20,21] Particularly, collagens regulate preodontoblast rearrangement and aid in the attachment of new odontoblasts to pulp tissue.[22] Bone sialoprotein (BSP) is a component of mineralized tissues such as bone, dentin, cementum, and calcified cartilage. As a noncollagenous protein, BSP used for the restoration of pulp defects appears to stimulate the differentiation of cells which secrete an organized extracellular matrix more efficiently than other capping materials such as calcium hydroxide.[23] Thus, the choice of composite materials for pulp regeneration must take into account the individual contribution of the biomaterials themselves during the regeneration process.

A number of synthetic materials have been fabricated into nanometer-scale structures in attempts to simulate the matrix environment for proliferation and differentiation of seeded cells toward desirable lineages.[24–27] Nanofibers formed by electrospinning have been shown to mimic the extracellular matrix environment to various degrees when cultured with several cell types.[28–32] Specifically, poly(D,L-lactide-*co*-glycolide) (PLGA) is widely used as scaffolding material in tissue engineering and has been approved for several biomedical applications in humans.[33–35] The porosity and tensile properties of electrospun PLGA nanofibers are favorable for medical applications,[36] and osteoblast adhesion were shown to occur when seeded in PLGA nanofibers.[36] Nanofibers made of another widely investigated polymer, namely poly(ε-caprolactone) (PCL), accommodated the differentiation of human mesenchymal stem cells (hMSCs) into adipogenic, osteogenic, and chondrogenic cells.[37] We have previously shown that hMSCs proliferate and maintain differentiation characteristics toward osteoblasts and chondrocytes when seeded in PLGA nanofibers.[38] In the study, PLGA of 85:15 ratio was electrospun into nonwoven fibers and cells attached them well (**Figure 2**).[38] After a 2-week culture on PLGA nanofiber scaffold, hMSCs remained as precursors upon

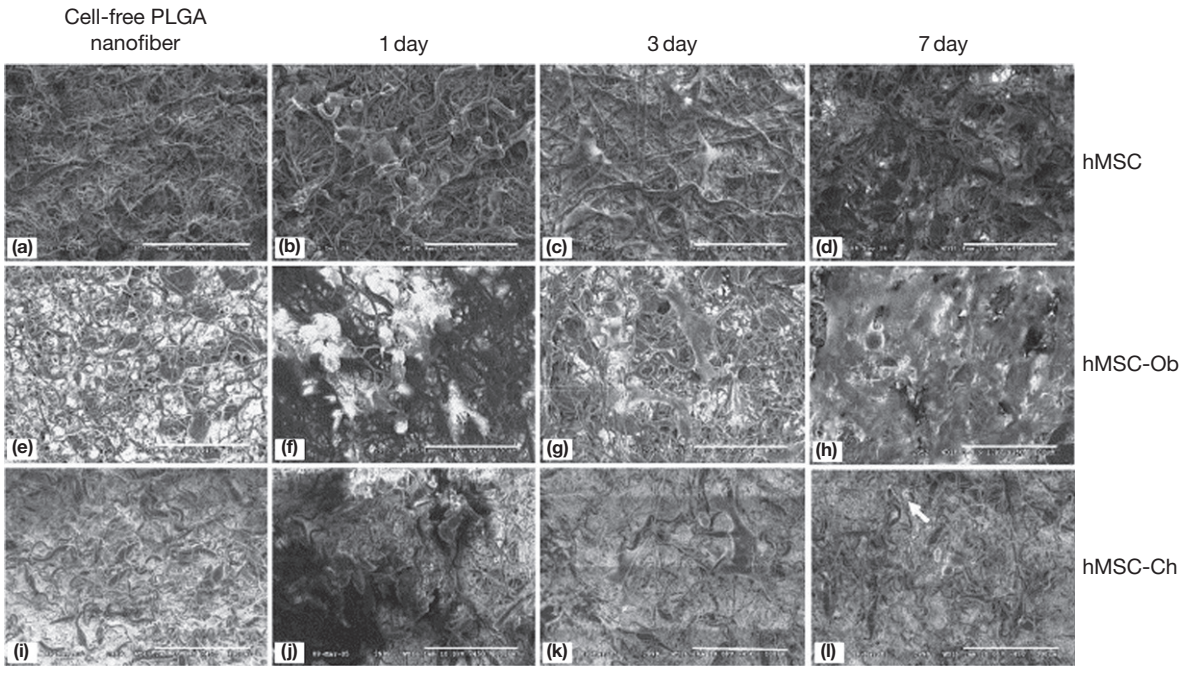

Figure 2 Electrospun poly(D,L-lactide-*co*-glycolide) (PLGA) nanofibers and the seeding of human mesenchymal stem cells (hMSCs), as well as hMSC-derived osteoblasts and hMSC-derived chondrocytes. (a), (e), (i) Prior to cell seeding, three randomly selected PLGA nanofiber scaffolds showed similar characteristics. Upon seeding of hMSCs (b, c, d), various extracellular matrices were apparently synthesized among PLGA nanofibers over time. By 7 days following hMSC seeding, the seeded cells apparently have attached to nanofiber surface and penetrated into the pores of PLGA nanofiber scaffolds (d), in comparison with 1 and 3 days after cell seeding (b and c, respectively). The morphology of hMSC-derived osteoblasts seeded in PLGA nanofibers also varied between 1, 3, and 7 days following cell seeding (f, g, and h, respectively). By 7 days following cell seeding, hMSC-Ob apparently synthesized a substantial amount of extracellular matrices (h), in comparison with 1 and 3 days after cell seeding (f and g, respectively). Human MSC-derived osteoblasts apparently attached to nanofiber substrates. Human MSC-derived chondrocytes revealed characteristic features after seeding in PLGA nanofibers (j, k, and l). Most PLGA nanofibers were still visible at 7 days following the seeding of hMSC-Ch (l), in comparison with the characteristics of hMSC-Ob seeded in PLGA nanofiber scaffolds after 7 days (h). A number of seeded hMSC-Ch apparently were located in lacunae-like structures, seen arrow (l) (scale bar = 100 mm). Reproduced from Xin, X.; Hussain, M.; Mao, J. J. *Biomaterials* **2007**, *28*, 316–325, with permission from Elsevier.

immunoblotting with hKL12 antibody. The overwhelming majority of hMSCs was viable and proliferated in PLGA nanofiber scaffolds up to the 14 days tested. In a separate experiment, hMSCs seeded in PLGA nanofiber scaffolds were differentiated into chondrogenic (hMSC-Ch) and osteogenic (hMSC-Ob) cells. Scanning electron micrograph (SEM) taken up to 7 days after cell seeding revealed that hMSCs, hMSC-Ob, and hMSC-Ch apparently attached to PLGA nanofibers. Moreover, histological assays revealed that hMSCs continuously differentiated into chondrogenic cells and osteogenic cells after a 2-week incubation on PLGA nanofibers.[38]

Dental pulp is a loose connective tissue with collagen and elastic fibers.[39] In the fibrous matrix, collagen fibers, type I and III, are present in an unbundled and randomly dispersed fashion, higher in density around blood vessels and nerves, and provide sufficient toughness and tensile strength to the matrix. Elastic fibers with high elasticity are interconnected with collagen fibers.[40] A collagen I-collagen III-elastic polymer composite scaffold may promote dental pulp regeneration. For example, poly(1,8-octanediol-*co*-citrate) (POC) is a soft scaffold and yet can recover from deformation. *In vitro* and *in vivo* evaluation using cell culture and subcutaneous implantation, respectively, confirmed cell and tissue compatibility.[39,41] POC has been used in regeneration of blood vessels, tendons, and ligaments, and may find its application in dental pulp regeneration.

The degree of polymerization is relevant to dental pulp regeneration. Chitosan is a naturally occurring substance that is chemically similar to cellulose and is derived from chitin. Chitosan increases the cross-linking efficiency of glutaraldehyde due to the longer chain of amino groups.[42–45] Chitomonosaccharide (chitosan monomer) has been attempted in dental pulp regeneration[46] with both *in vitro* and *in vivo* experiments to study cell metabolism and wound healing. After 3 days of osteoblast culture, alkaline phosphatase (ALP) activity significantly increased in the chitosan monomer group. Reverse-transcription polymerase chain reaction analysis revealed that chitosan monomer induced an increase in the expression of ALP mRNA after 3 days and bone morphogenetic protein-2 mRNA after 7 days of osteoblast incubation. Inflammatory cytokine, interleukin (IL)-8, synthesis in fibroblasts was strongly suppressed in the medium supplemented with chitosan monomer. After 1 day, inflammatory cell infiltration was weak when compared with chitosan polymer. After 3 days, remarkable proliferation of fibroblasts occurred near chitosan monomer, and the inflammatory cell infiltration virtually disappeared. After 5 days, fibroblastic proliferation progressed, and some odontoblastic cells appeared at the periphery of the proliferated fibroblasts.[46] These findings indicate that chitosan monomer may function as a scaffold at the initial stage of wound healing in comparison with chitosan polymer in view of its advantageous biocompatibility.

5.519.2.2. Scaffolding

Selection of a polymer for dental pulp regeneration is only half of the battle. Polymers must be fabricated and delivered as a scaffold for clinical utility. For dental pulp regeneration, the ideal scaffold should support the functions of multiple cell types, as well as vascularization and innervation. The successful utilization of fibrous scaffolds as synthetic matrices for pulp regeneration can be traced back to 1996, when dental pulp fibroblasts were found to adhere and proliferate in fibrous matrices fabricated from polyglycolic acid (PGA).[47] New tissues resembling dental pulp can be engineered by culturing human pulp-derived fibroblasts on these biodegradable scaffolds.[47] The cells proliferated on the scaffolds over time, and ultimately occupied the spaces between the polymer fibers (**Figure 3**). During the same time, the cells contracted the polymer matrix as it degraded, leading to decreased matrix volume over 60 days. A self-assembling PA hydrogel encapsulated with dental pulp stem cells in adult teeth, cultured *in vitro* in osteogenic medium, expressed osteoblast markers, and deposit mineral, while deciduous dental pulp stem cells showed little hard tissue formation.[11]

Porous hydroxyapatite/β-tricalcium phosphate (HAp/β-TCP), powdered HAp/β-TCP, and PGA fiber mesh were used as scaffolds and transplanted with cultured porcine dental-pulp-derived cells into the dorsum of nude mice.[48] Samples were harvested after 6 weeks, and newly formed hard tissue was observed in all transplants. When porous HAp/β-TCP was used, dentin-like hard tissue was observed on the inner wall with minimum cell inclusions and odontoblast-like cells were aligned adjacent to the hard tissue. When HAp/β-TCP powders or PGA were used, bone-like hard tissues showed cell inclusions and cell alignment was not observed. Hard tissue from the HAp/β-TCP block group was positive for type I collagen, osteonectin, BSP, and dentin sialoprotein (DSP). This result was confirmed by *in situ* hybridization with a DSP probe. Only the aligned cells were positive with an antisense probe. On the other hand, hard tissue from other scaffolds showed incomplete expression of both bone and dentin markers and they were negative for osteonectin and DSP. These results suggest that not only materials themselves, but also scaffold shapes affect the type of tissue regenerated by dental-pulp-derived cells.[48]

Another study investigated the *in vitro* and *in vivo* behavior of human dental pulp stem cells isolated from impacted third molars, when seeded onto different three-dimensional

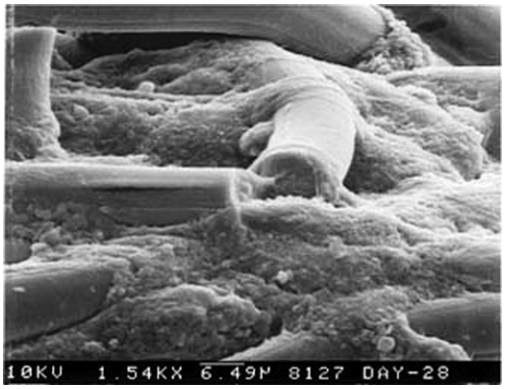

Figure 3 Photomicrograph of pulp-derived fibroblast filling the interstices between polymer fibers after 28 days in culture. Cell–polymer constructs were visualized using a scanning electron microscope. Reproduced from Mooney, D. J.; Powell, C.; Piana, J.; Rutherford, B. *Biotechnol. Prog.* **1996**, *12*, 865–868, with permission from Wiley.

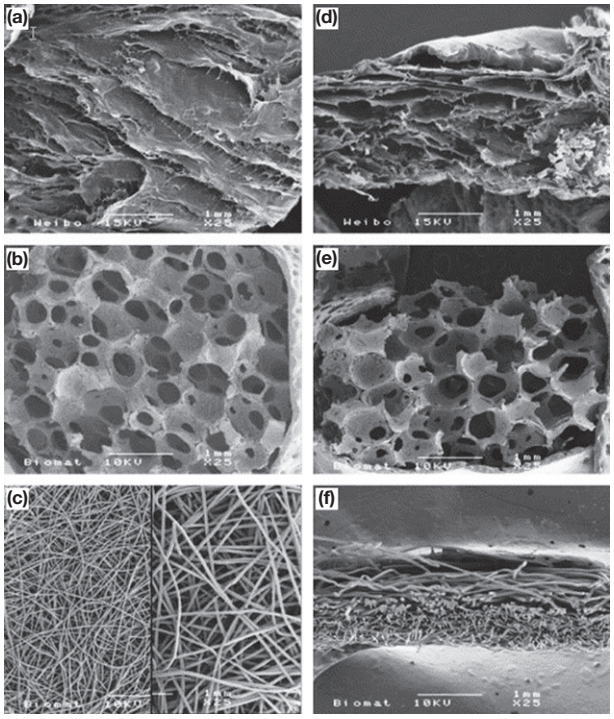

Figure 4 Scanning electron micrographs of different scaffolds (magnification 25×). (a) Collagen scaffold surface structure; (b) collagen scaffold cross-section; (c) hyaluronic acid (HA)/tricalcium phosphate (TCP) ceramic surface structure; (d) HA/TCP ceramic cross-section; (e) titanium scaffold surface structure (Left: bottom; Right: top); (f) titanium scaffold cross-section. Reproduced from Zhang, W.; Walboomers, X. F.; van Kuppevelt, T. H.; Daamen, W. F.; Bian, Z.; Jansen, J. A. *Biomaterials* **2006**, *27*, 5658–5668, with permission from Elsevier.

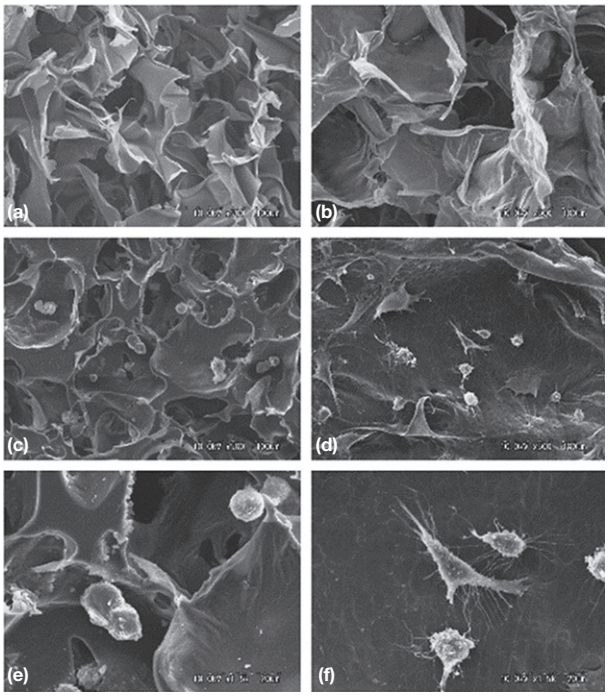

Figure 5 Scanning electron microphotographs of hyaluronic acid (a, c, e) and collagen (b, d, f) sponges with and without KN-3 cells. (a, b) Dry sponges showing porous structures. Original magnification, ×500; (c, d) sponges seeded with KN-3 cells. Original magnification, ×500; (e, f) higher magnification (×1500) of (c and d), respectively. Reproduced from Bohl, K. S.; Shon, J.; Rutherford, B.; Mooney, D. J. *J. Biomater. Sci. Polym. Ed.* **1998**, *9*, 749–764, with permission from Brill.

scaffolds: that is, a spongeous collagen, a porous ceramic, and a fibrous titanium mesh (Figure 4).[19] Scaffolds were loaded with dental pulp stem cells and divided into two groups. The first group was cultured in osteogenic differentiation medium *in vitro* for 4 weeks. The second group was implanted subcutaneously in nude mice for 6 or 12 weeks. *In vitro*, cells developed abundant deposition of mineralized extracellular matrix with expression of DSPP in all 3D scaffolds. *In vivo* implantation led to formation of DSPP positive tissue in all three scaffolds materials immediately. However, tissues in all *in vivo* implanted scaffolds resembled soft connective tissue rather than a dentin-like tissue. There was somewhat limited calcification only in ceramic scaffold.

Hydrogels are also widely investigated scaffolding materials for tissue regeneration, but its application in dental pulp regeneration is quite limited.[49] An injectable hydrogel is likely to be clinically preferable because pulp chamber and root canal have irregular shape. The effects of hyaluronic acid (HA) sponge on responses of the odontoblastic cell line (KN-3 cells) *in vitro*, as well as responses of amputated dental pulp of rat molar *in vivo* was investigated by Inuyama *et al.* *In vitro*, KN-3 cells adhered to the stable structure of HA sponge and that of collagen sponge (Figure 5). Expression of IL-6 and TNF-α in KN-3 cells seeded in HA sponge were nearly the same with those in the cells seeded in collagen sponge, while the numbers of granulated leukocytes invaded into HA sponge from amputated dental pulp was significantly lower than in collagen sponge, leading to a conclusion that HA sponge has an appropriate structure, biocompatibility, and biodegradation for use as a scaffold for dental pulp regeneration.[49]

The performance of different scaffold characteristics on dental pulp regeneration was further compared.[50] Human dental pulp fibroblasts were seeded onto three different synthetic matrices: PGA fibers, type I collagen hydrogel, and alginate. Culturing cells on PGA resulted in high cell density, whereas collagen underwent significant degradation. Alginate allowed little cell proliferation, whereas collagen gel only allowed moderate cellular growth after 45 days.[50]

Scaffold fabrication is critical not only for soft tissue regeneration, but also vascularization. In an *in vivo* investigation, biophysical and/or biochemical approaches were employed to induce neovascularization in soft tissue.[51] Hydrogel cylinders were fabricated from poly(ethylene glycol) diacrylate (PEG) in four configurations: PEG alone, PEG with basic fibroblast growth factor (bFGF), microchanneled PEG alone, or both bFGF-adsorbed and microchanneled PEG (Figure 6). *In vivo* implantation revealed no neovascularization in PEG, but substantial angiogenesis in bFGF-adsorbed and/or microchanneled PEG. It was unexpected that substantial angiogenesis was detected in microchanneled PEG without bFGF incorporation. The dramatic

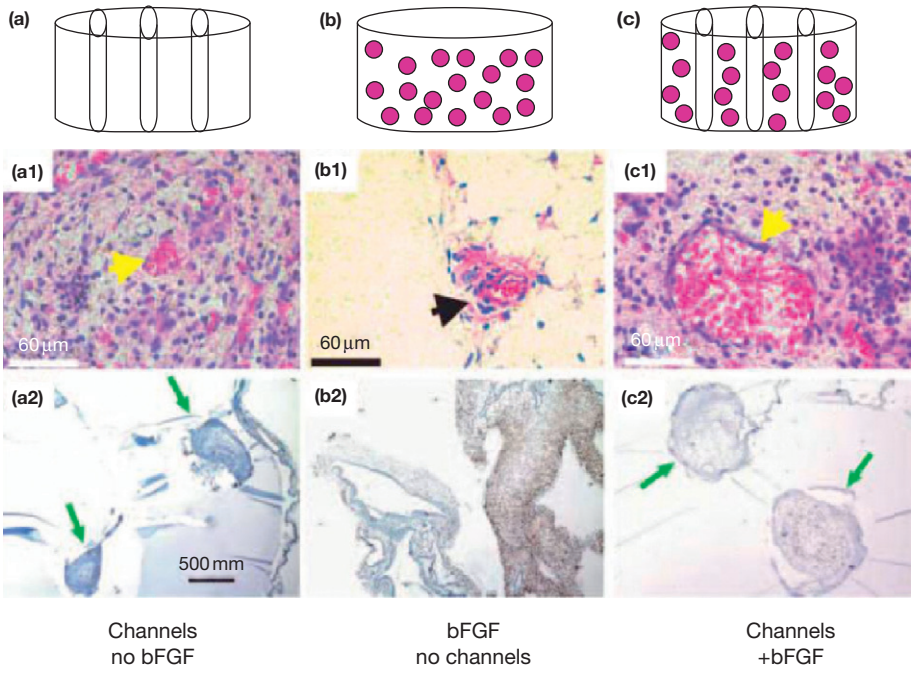

Figure 6 *In vivo* implantation of poly(ethylene glycol) (PEG) hydrogel. PEG hydrogel was fabricated in four configurations: PEG alone, PEG with basic fibroblast growth factor (bFGF), microchanneled PEG, or both bFGF-adsorbed and microchanneled PEG. (a) PEG hydrogel molded into 6 × 4 mm (diameter × height) cylinder (without either bFGF or microchannels). (b) PEG hydrogel with three microchannels. (c) PEG hydrogel cylinder with microchannels and adsorbed with both 0.5 μg μl^{-1} bFGF and three microchannels. Following *in vivo* implantation subcutaneously in the dorsum of immunodeficient mice, the harvested PEG hydrogel samples showed distinct histological features. (a1) PEG hydrogel with microchannels but without bFGF showed host tissue infiltration primarily in the lumen of microchannels, and scarcely in the rest of PEG hydrogel. The infiltrating host tissue includes erythrocyte-filled blood vessels that are lined by endothelial cells (arrow). (a2) Vascular endothelial growth factor (VEGF) was immunolocalized only to host-derived tissue within the lumen of microchannels, indicating the vascular nature of the infiltrating host tissue. Arrows point to microchannels and the infiltrating host tissue. (b1) PEG hydrogel with bFGF but without microchannels showed apparently random and isolated islands of infiltrating host tissue (arrow). There is random infiltration of host tissue into bFGF-adsorbed PEG hydrogel. The infiltrating host tissue includes vascular structures with erythrocyte-filled blood vessels that are lined by endothelial cells (arrow). (b2) VEGF was immunolocalized to host-derived tissue within PEG hydrogel (without microchannels). (c1) PEG hydrogel with both microchannels and bFGF showed host tissue infiltration only in the lumen of microchannels, but scarcely in the rest of the PEG hydrogel. The infiltrating host tissue includes vascular structures with erythrocyte-filled blood vessels that are lined by endothelial cells (arrow). (c2) VEGF was immunolocalized only to host-derived tissue within the lumen of microchannels. Since no cells were delivered in any of the PEG hydrogel samples in this experiment, tissue infiltration following *in vivo* implantation must be derived from the host. Arrows point to microchannels. Reproduced from Stosich, M. S.; Bastian, B.; Marion, N. W.; Clark, P. A.; Reilly, G.; Mao, J. J. *Tissue Eng.* **2007**, *13*, 2881–2890.

difference of neovascularization between PEG and microchanneled PEG suggests that microchannels promote the genesis of vascularized tissue phenotypes, and thus channeled or porous structures may be preferred for vascularized tissues. Especially, engineered microchannels may provide a generic approach for modifying existing scaffolds by providing conduits for vascularization and/or diffusion.

Controlled release approaches affect scaffold fabrication and the efficacy of tissue regeneration. Bioactive cues are usually expensive and when delivered without protection, lead to premature denature and diffusion. In order to achieve controlled and sustained release of BMP-2, Nie and colleagues[35,52] developed a PLGA-based fibrous scaffold releasing BMP-2 in a linear mode over a period of ~4 weeks and the scaffold performed well in repairing bone defects. In consideration of the lower cost of BMP-2 plasmid, the research group further developed a series of BMP-2 plasmid-delivery scaffolds, with shapes of fiber sheet (Figure 7)[53] and foam,[43,54] which presented different release patterns for different applications. Subsequent *in vivo* experiment demonstrated that DNA nanoparticles-loaded fibrous scaffold are advantageous over the traditional scaffolds prepared by protein adsorption or DNA adsorption.[24]

5.519.3. *In Vivo* Dental Pulp Regeneration: State of the Art

In vivo dental pulp regeneration represents translational approaches for ultimate applications of dental pulp regeneration in patients. All *in vitro* biomaterials and scaffolding experiments should eventually lead to *in vivo* dental pulp regeneration (Table 1).

A tooth slice model has been developed by cutting ~1 mm coronal slices for testing dentin–pulp regeneration.[57,58] This model has recently been modified to study dental pulp regeneration.[13,15] The basic approach for this model is to fill the center void of the 1-mm tooth slice with a biomaterial scaffold, followed by subsequent seeding with dental stem cells. When

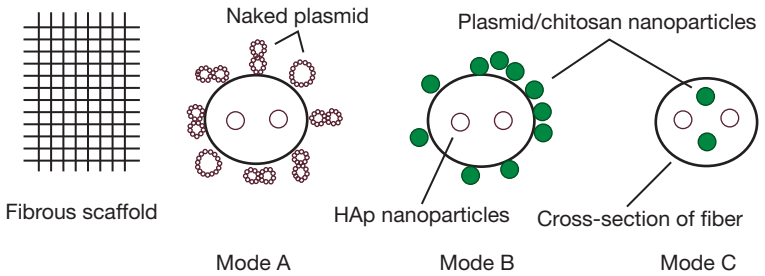

Figure 7 Schematic illustration of three loading modes of plasmid in fibrous scaffolds. Mode A: coating of naked plasmid on scaffolds after fiber fabrication by dripping; Mode B: coating of plasmid/chitosan nanoparticles on scaffolds after fiber fabrication by dripping; Mode C: encapsulation of plasmid/chitosan nanoparticles into scaffold by mixing them with poly(D,L-lactide-*co*-glycolide)/Hydroxyapatite (HAp) solution before fiber fabrication. HAp nanoparticles, as a biocompatible material, was employed in the study in order to enhance the release of plasmid or plasmid/chitosan nanoparticles from scaffolds. Reproduced from Nie, H.; Ho, M. L.; Wang, C. K.; Wang, C. H.; Fu, Y. C. *Biomaterials* **2009**, *30*, 892–901, with permission from Elsevier.

Table 1 Representative examples of *in vivo* dental pulp regeneration

Authors	*Cell sources*	*Biomaterials*	*Delivered bioactive factors*	In vivo *model*
Prescott *et al*.[13]	Dental pulp stem cells	Collagen scaffolds	Dentin matrix protein-1	Subcutaneous implantation of 2.5-mm dentin slices in mice
Iohara *et al*.[55]	$CD31^-$ and $CD146^-$ side population cells from a canine tooth		None	Partial pulpectomy model of pulp injury in the dog
Cordeiro *et al*.[15]	Dental pulp stem cells from exfoliated deciduous teeth	PLLA porous scaffold (by salt leaching)	None	1-mm tooth slices
Huang *et al*.[14]	Stem/progenitor cell-mediated *de novo* regeneration of dental pulp	A prefabricated PLGA scaffold (by gas foaming and particulate leaching)	None	
Kim *et al*.[56]	None	Collagen sponges and collagen gel	bFGF, VEGF, PDGF, BMP-7, NGF	An endodontically treated, real-size native human tooth

implanted *in vivo*, the seeded dental stem cells were able to differentiate into odontoblast-like cells and endothelial-like cells. However, it is not clear whether this thin tooth slice model can be successfully adapted to regenerate real-size, fully vascularized dental pulp tissue for clinical applications. Limited blood supply is a major concern for de novo pulp regeneration. Along the same direction, a human tooth root fragment (6–7 mm) was developed with an enlarged root canal (1–1.25 mm wide), with one end sealed to mimic a natural tooth root.[14] Dental pulp stem cells were seeded onto a PLGA scaffold fabricated using a gas foaming/particulate leaching process, and inserted into the fragmented tooth root. The cell-seeded tooth fragments were transplanted subcutaneously for 3–4 months. The results showed that the root canal space was filled with soft tissue. The cells in regenerated soft tissue reacted positively to antihuman mitochondria antibodies, indicating their human origin; however, host cell ingrowth was not ascertained. It is further unclear what kind of cells have infiltrated the fragmented root canal.

Dental pulp regeneration by transplantation of cells, including stem/progenitor cells, suffers from a number of shortcomings including a lack of clinically available cell source, excessive cost, and difficult and lengthy regulatory approval. Cell transplantation may well be justified for life-threatening diseases such as Parkinson's disease, cardiac infarcts, or spinal cord injuries. However, cell transplantation for dental pulp regeneration appears to lack clinical justification and commercial viability.

We recently attempted to regenerate dental-pulp-like tissue without cell transplantation, but rather by cell homing.[56] Clinically extracted, real-size human teeth were treated endodontically as in patients, with the exception of filling with gutta percha. Collagen scaffolds loaded with a series of growth factors were implanted in endodontically treated root canals. Upon *in vivo* implantation of endodontically treated real-size human teeth in mouse dorsum for the 3 weeks tested, delivery of bFGF and/or vascular endothelial growth factor (bFGF and/or VEGF) yielded recellularized and revascularized connective tissue that integrated to native dentinal wall in root canals. Furthermore, combined delivery of bFGF, VEGF, or platelet derived growth factor (PDGF) with a basal set of nerve growth factor (NGF) and bone morphogenetic protein-7 (BMP-7) generated cellularized and vascularized tissues positive of VEGF antibody staining and neo-dentin formation over the surface of native dentinal wall in some, although not all, endodontically treated teeth. Newly formed dental-pulp-like tissue appeared dense with disconnected cells surrounded by extracellular matrix. Erythrocyte-filled blood vessels were present with endothelial-like cell lining. Reconstructed, multiple microscopic images showed complete fill of dental-pulp-like tissue in the entire root canal from root apex to pulp chamber with tissue integration to dentinal wall upon delivery of bFGF, VEGF, or PDGF with a basal set of NGF and BMP-7. These findings demonstrate for the first time regeneration of

dental-pulp-like tissue in real, endodontically treated human teeth without the need for cell transplantation. Dental-pulp-like tissues were regenerated entirely by host endogenous cells that were recruited chemotactically by signaling molecules and migrated into the collagenous scaffold enclosed by endodontically treated tooth. Regeneration of dental pulp by cell homing, rather than cell delivery, may accelerate clinical translation.

Given the initial positive data with delivery of bFGF and/or VEGF, two potent angiogenic cytokines, Kim and colleagues followed up with an exploration of the efficacy of additional cytokines, with or without bFGF or VEGF, in pulp regeneration. A basal combination consisted of NGF and BMP-7 due to its potency on induction of odontoblast/osteoblast differentiation. Combined delivery of bFGF with basal cytokines (NGF and BMP-7) also yielded recellularization in the entire endodontically treated root canal of real-size human tooth as shown by reconstructed, multiple microscopic images (Figure 8(a1)). A representative close-up image shows abundant cells in the endodontically treated root canal and apparent integration of regenerated tissues with dentinal wall in root canal (Figure 8(a2)). A representative higher magnification image further shows the presence of erythrocyte-filled, blood vessel-like structures (arrows in Figure 8(a3)). Scattered islands of positive VEGF antibody staining were found in association with combined bFGF + basal cytokine delivery (Figure 8(a4)). Furthermore, combined delivery of VEGF with basal cytokines (NGF and BMP-7) induced recellularization in endodontically treated root canal as shown by reconstructed, multiple microscopic images (Figure 8(b1)). Abundant cells were present in the endodontically treated root canal and showed apparent integration with dentinal wall (Figure 8(b2)). Remarkably, a layer of amorphous dentin-like tissue was present on the surface of native dentinal wall (arrows in Figure 2(b2)), resembling newly formed secondary dentin. Multiple blood vessel-like structures were present in regenerated soft tissue in root canal (arrows in Figure 8(b3)). Areas of positive VEGF antibody staining were readily identified in association with VEGF + basal cytokine

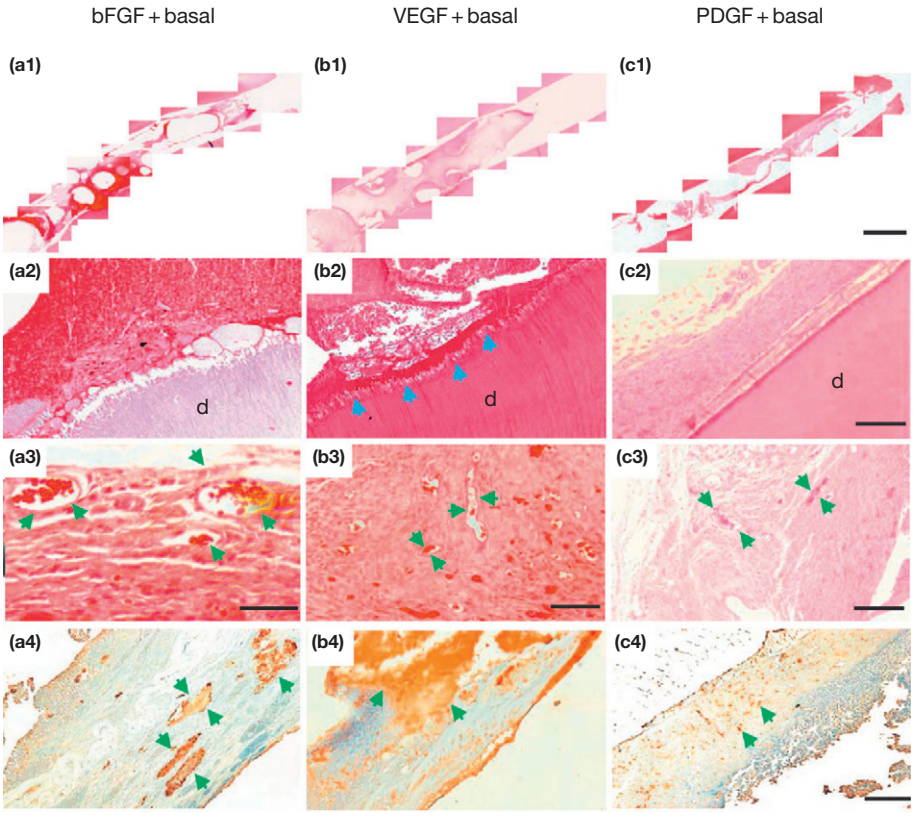

Figure 8 Combinatory cytokine delivery and chemotactic effects on pulp regeneration from host endogenous cells. (a1) Combined delivery of basic fibroblast growth factor with basal cytokines of nerve growth factor (NGF) and bone morphogenetic protein-7 (BMP-7) yielded recellularization in the entire endodontically treated root canal as shown by reconstructed, multiple microscopic images from root apex to pulp chamber. (a2) Close-up image showing abundant cells and integration with native dentin (d) in endodontically treated root canal. (a3) Higher magnification showing erythrocyte-filled blood vessels (arrows) in connective tissue. (a4) Scattered islands of positive vascular endothelial growth factor (VEGF) antibody staining (arrows). (b1) Combined delivery of VEGF with basal cytokines of NGF and BMP-7 induced recellularization in the entire endodontically treated root canal. (b2) Connective tissue with abundant cells integrated with native dentin (d), including a layer of dentin-like tissue between abundant cells and dentinal wall (arrows). (b3) Multiple blood vessel-like structures in regenerated connective tissue (arrows). (b4) Positive VEGF antibody staining. (c1) Combined delivery of platelet derived growth factor with basal cytokines of NGF and BMP-7 yielded fully regenerated tissues in the entire endodontically treated root canal. (c2) Abundant cells in connective tissue that integrated to native dentin (d). (c3) Blood vessel-like structures (arrows) in connective tissue. (c4) VEGF antibody staining. Scale bars = a1, b1, c1: 1 mm; a2, b2, c2: 100 μm; a3: 100 μm; b3, c3: 300 μm; a4, b4, c4: 300 μm. Reproduced from Kim, J. Y.; Xin, X.; Moioli, E. K.; *et al*. *Tissue Eng. A* **2010**.

delivery (Figure 8(b4)). Combined delivery of PDGF with basal cytokines (NGF and BMP-7) in an endodontically treated root canal resulted in recellularization along the entire root canal as shown by reconstructed, multiple microscopic images (Figure 8(c1)). A representative close-up image shows abundant cells and integration of regenerated tissue with dentinal wall in root canal (Figure 8(c2)). A representative higher magnification image further shows the presence of blood vessel-like structures (arrows in Figure 8(c3)) with abundant cells and some extracellular matrix. VEGF antibody staining revealed scattered positive locations in association with PDGF + basal delivery (Figure 8(c4)). Given that all human teeth utilized in the present work were endodontically treated and autoclaved to remove any biological tissue, all regenerated tissues, including vasculature, in the root canal are derived from host endogenous cells.

5.519.4. Conclusions

The doctrine of cells, biomaterial scaffolds, and biological signals has been the guiding principle for tissue engineering. Given the vast diversity of tissues that are being regenerated, it is difficult to conceive that one doctrine would govern all. In dental pulp regeneration, the triad of the doctrine is considered below:

Cells

- Fewer cells are needed for dental pulp regeneration due to its small scale than for regeneration of most other tissues such as skin, oral mucosa, or liver.
- Clinical treatment of pulpectomy removes all dental pulp cells in the very tooth that needs regeneration. Transplantation of dental or other stem cells may not be economically viable, given root canal treatment is far from a life-threatening disease.
- Cells are indeed required for dental pulp regeneration; however, cells do not necessarily need to be transplanted.

Scaffolds

- Biomaterial scaffolds are likely to be indispensable for dental pulp regeneration.
- Ideal scaffolds for dental pulp regeneration should allow functionality of multiple cell types including odontoblasts, pulp fibroblasts, vascular cells, and/or neural endings.
- Ideal scaffolds for dental pulp regeneration must be clinically viable, that is, easy to handle up to the point of a turn-key approach, must be possible to be readily sterilized, and with shelf life.
- Ideal scaffolds for dental pulp regeneration should be biocompatible, nontoxic, and may need to undergo biologically safe degradation.
- Either native or synthetic polymers, or a hybrid, are valid choices as scaffolding materials for dental pulp regeneration.

Bioactive cues

- Several angiogenic growth factors, including VEGF, bFGF, and PDGF, are effective in inducing revascularization and recellularization for dental pulp regeneration.
- Growth factors including BMP-2 and BMP-7 are capable of elaborating mineralization and probably odontoblast-like cells for dental pulp regeneration.
- Neuronal sprouting cues such as NGF are likely to be effective in elaborating neuronal sprouts for dental pulp regeneration.

In summary, the goal for dental pulp regeneration is clear: to regenerate revascularized and recellularized tissues in dental pulp that support the vitality and homeostasis of the teeth. Progress has been made to regenerate dental-pulp-like tissues with both cell delivery and cell-homing approaches. Biomaterials are critical if not indispensible for either cell delivery or cell-homing approach. Due to its small scale, dental pulp regeneration represents one of the lower hanging fruits in the regeneration of all tissues and organs.

References

1. Ingle, J. I.; Bakland, L. K. In *Endodontics*; Ingle, J. I., Bakland, L. K., Eds.; BC Decker: Hamilton, ON, 2002; pp 121–143.
2. Dammaschke, T.; Steven, D.; Kaup, M.; Ott, K. H. *J. Endod.* **2003**, *29*, 638–643.
3. Andreasen, J. O.; Farik, B.; Munksgaard, E. C. *Dent. Traumatol.* **2002**, *18*, 134–137.
4. Caplan, D. J.; Cai, J.; Yin, G.; White, B. A. *J. Public Health Dent.* **2005**, *65*, 90–96.
5. Nakashima, M.; Reddi, A. H. *Nat. Biotechnol.* **2003**, *21*, 1025–1032.
6. Reddi, A. H. *Nat. Biotechnol.* **1998**, *16*, 247–252.
7. Nakashima, M. *Cytokine Growth Factor Rev.* **2005**, *16*, 369–376.
8. Hargreaves, K. M.; Giesler, T.; Henry, M.; Wang, Y. *J. Endod.* **2008**, *34*, S51–S56.
9. Murray, P. E.; Garcia-Godoy, F.; Hargreaves, K. M. *J. Endod.* **2007**, *33*, 377–390.
10. Sloan, A. J.; Smith, A. J. *Oral Dis.* **2007**, *13*, 151–157.
11. Galler, K. M.; Cavender, A.; Yuwono, V.; *et al. Tissue Eng. A* **2008**, *14*, 2051–2058.
12. Gotlieb, E. L.; Murray, P. E.; Namerow, K. N.; Kuttler, S.; Garcia-Godoy, F. *J. Am. Dent. Assoc.* **2008**, *139*, 457–465.
13. Prescott, R. S.; Alsanea, R.; Fayad, M. I.; *et al. J. Endod.* **2008**, *34*, 421–426.
14. Huang, G. T.; Yamaza, T.; Shea, L. D.; *et al. Tissue Eng. A* **2010**, *16*, 605–615.
15. Cordeiro, M. M.; Dong, Z.; Kaneko, T.; *et al. J. Endod.* **2008**, *34*, 962–969.
16. Ahsan, T.; Bellamkonda, R.; Nerem, R. M. In *Translational Approaches in Tissue Engineering and Regenerative Medicine*; Mao, J. J., Vunjak-Novakovic, G., Mikos, A. M., Atala, A., Eds.; Artech House: Boston, MA, 2007; pp 3–16.
17. Mao, J. J. *NY State Dent. J.* **2008**, *74*, 20–24.
18. Sharma, B.; Elisseeff, J. H. *Ann. Biomed. Eng.* **2004**, *32*, 148–159.
19. Zhang, W.; Walboomers, X. F.; van Kuppevelt, T. H.; Daamen, W. F.; Bian, Z.; Jansen, J. A. *Biomaterials* **2006**, *27*, 5658–5668.
20. Nakashima, M.; Akamine, A. *J. Endod.* **2005**, *31*, 711–718.
21. Tziafas, D.; Smith, A. J.; Lesot, H. *J. Dent.* **2000**, *28*, 77–92.
22. Kitasako, Y.; Shibata, S.; Cox, C. F.; Tagami, J. *Int. Endod. J.* **2002**, *35*, 996–1004.
23. Decup, F.; Six, N.; Palmier, B.; *et al. Clin. Oral Investig.* **2000**, *4*, 110–119.
24. Nie, H.; Ho, M. L.; Wang, C. K.; Wang, C. H.; Fu, Y. C. *Biomaterials* **2009**, *30*, 892–901.
25. Noh, H. K.; Lee, S. W.; Kim, J. M.; *et al. Biomaterials* **2006**, *27*, 3934–3944.
26. Rahaman, M. N.; Mao, J. J. *Biotechnol. Bioeng.* **2005**, *91*, 261–284.
27. Zhang, Y. Z.; Venugopal, J.; Huang, Z. M.; Lim, C. T.; Ramakrishna, S. *Biomacromolecules* **2005**, *6*, 2583–2589.
28. Badami, A. S.; Kreke, M. R.; Thompson, M. S.; Riffle, J. S.; Goldstein, A. S. *Biomaterials* **2006**, *27*, 596–606.
29. Ma, Z.; Kotaki, M.; Inai, R.; Ramakrishna, S. *Tissue Eng.* **2005**, *11*, 101–109.
30. Mo, X. M.; Xu, C. Y.; Kotaki, M.; Ramakrishna, S. *Biomaterials* **2004**, *25*, 1883–1890.
31. Schindler, M.; Ahmed, I.; Kamal, J.; *et al. Biomaterials* **2005**, *26*, 5624–5631.
32. Xu, C.; Inai, R.; Kotaki, M.; Ramakrishna, S. *Tissue Eng.* **2004**, *10*, 1160–1168.
33. Agrawal, C. M.; Ray, R. B. *J. Biomed. Mater. Res.* **2001**, *55*, 141–150.
34. Athanasiou, K. A.; Niederauer, G. G.; Agrawal, C. M. *Biomaterials* **1996**, *17*, 93–102.
35. Fu, Y. C.; Nie, H.; Ho, M. L.; Wang, C. K.; Wang, C. H. *Biotechnol. Bioeng.* **2008**, *99*, 996–1006.
36. Li, W. J.; Laurencin, C. T.; Caterson, E. J.; Tuan, R. S.; Ko, F. K. *J. Biomed. Mater. Res.* **2002**, *60*, 613–621.
37. Li, W. J.; Tuli, R.; Huang, X.; Laquerriere, P.; Tuan, R. S. *Biomaterials* **2005**, *26*, 5158–5166.
38. Xin, X.; Hussain, M.; Mao, J. J. *Biomaterials* **2007**, *28*, 316–325.

39. Yang, J.; Webb, A. R.; Pickerill, S. J.; Hageman, G.; Ameer, G. A. *Biomaterials* **2006**, *27*, 1889–1898.
40. Linde, A. *J. Dent. Res.* **1985**, *64*(Spec No), 523–529.
41. Kibbe, M. R.; Martinez, J.; Popowich, D. A.; *et al*. *J. Biomed. Mater. Res. A* **2010**, *93*, 314–324.
42. Da Sacco, L.; Masotti, A. *Mar. Drugs* **2010**, *8*, 1518–1525.
43. Nie, H.; Lee, L. Y.; Tong, H.; Wang, C. H. *J. Control. Release* **2008**, *129*, 207–214.
44. Oktay, E.; Demiralp, B.; Senel, S.; Cevdet Akman, A.; Eratalay, K.; Akincibay, H. *J. Oral Implantol.* **2010**, *36*, 175–184.
45. Wen, P.; Gao, J.; Zhang, Y.; *et al*. *J. Biomater. Sci. Polym. Ed.* **2010**, *22*(1), 19–40.
46. Matsunaga, T.; Yanagiguchi, K.; Yamada, S.; Ohara, N.; Ikeda, T.; Hayashi, Y. *J. Biomed. Mater. Res. A* **2006**, *76*, 711–720.
47. Mooney, D. J.; Powell, C.; Piana, J.; Rutherford, B. *Biotechnol. Prog.* **1996**, *12*, 865–868.
48. Tonomura, A.; Mizuno, D.; Hisada, A.; *et al*. *Ann. Biomed. Eng.* **2010**, *38*, 1664–1671.
49. Inuyama, Y.; Kitamura, C.; Nishihara, T.; *et al*. *J. Biomed. Mater. Res. B Appl. Biomater.* **2010**, *92*, 120–128.
50. Bohl, K. S.; Shon, J.; Rutherford, B.; Mooney, D. J. *J. Biomater. Sci. Polym. Ed.* **1998**, *9*, 749–764.
51. Stosich, M. S.; Bastian, B.; Marion, N. W.; Clark, P. A.; Reilly, G.; Mao, J. J. *Tissue Eng.* **2007**, *13*, 2881–2890.
52. Nie, H.; Soh, B. W.; Fu, Y. C.; Wang, C. H. *Biotechnol. Bioeng.* **2008**, *99*, 223–234.
53. Nie, H.; Wang, C. H. *J. Control. Release* **2007**, *120*, 111–121.
54. Nie, H.; Khew, S. T.; Lee, L. Y.; Poh, K. L.; Tong, Y. W.; Wang, C. H. *J. Control. Release* **2009**, *138*, 64–70.
55. Iohara, K.; Zheng, L.; Ito, M.; *et al*. *Regen. Med.* **2009**, *4*, 377–385.
56. Kim, J. Y.; Xin, X.; Moioli, E. K.; *et al*. *Tissue Eng. A* **2010**, *16*(10), 3023–3031.
57. Dobie, K.; Smith, G.; Sloan, A. J.; Smith, A. J. *Connect. Tissue Res.* **2002**, *43*, 387–390.
58. Sloan, A. J.; Rutherford, R. B.; Smith, A. J. *Arch. Oral Biol.* **2000**, *45*, 173–177.

5.520. Bioactive Ceramics and Bioactive Ceramic Composite-Based Scaffolds

J Kim, S Bhattacharyya, and P Ducheyne, University of Pennsylvania, Philadelphia, PA, USA

© 2011 Elsevier Ltd. All rights reserved.

5.520.1.	**Introduction**	256
5.520.1.1.	Limitations of Natural Bone Grafts	256
5.520.1.2.	Synthetic Bone Grafts and Materials Used	256
5.520.2.	**Scaffold Requirements**	257
5.520.2.1.	Load-Bearing Properties	257
5.520.2.2.	Degradation and Resorption Kinetics	257
5.520.2.3.	Scaffold Architecture for Bone Ingrowth and Permeability of Nutrients and Neovascularization	257
5.520.3.	**Fundamentals of Ceramic Bioactivity**	257
5.520.3.1.	Surface Transformation	257
5.520.3.2.	Protein Adsorption onto the Biomineralized Surface and Selective Binding of Integrins	258
5.520.4.	**Characteristics of Bioactive Ceramics and Bioactive Ceramic Composite-Based Scaffolds for Bone Tissue-Engineering Scaffold**	258
5.520.4.1.	Bioceramics and Bioactive Glasses	258
5.520.4.1.1.	Bioactive glasses and glass ceramics	258
5.520.4.1.2.	Calcium phosphates	259
5.520.4.2.	Ceramic/Polymer Composite Materials	260
5.520.4.2.1.	Composite materials strategy	260
5.520.4.2.2.	PLA/PGA-based polymer/ceramic composites	260
5.520.4.2.3.	Protein-based polymer/ceramic composites	262
5.520.5.	**Modifications of Bioactive Ceramics and Bioactive Ceramic Composite-Based Scaffolds**	263
5.520.5.1.	Localized Delivery of Biomolecules and Cells	263
5.520.6.	**Conclusion and Future Directions**	264
References		265

Glossary

Bioceramics Ceramic materials that are specifically developed for use as medical and dental implants.

Biodegradable Capable of being broken down especially into innocuous products by the action of living things (as microorganisms).

Biomineralization Process by which living organisms produce minerals, often to harden or stiffen existing tissues.

Bone resorption Process by which osteoclasts break down bone and release the minerals, resulting in a transfer of calcium from bone fluid to the blood.

Composite materials Often shortened to composites, are engineered or naturally occurring materials made from two or more constituent materials with significantly different physical or chemical properties which remain separate and distinct at the macroscopic or microscopic scale within the finished structure.

Osteoconduction Process by which fibrovascular tissue and osteoprogenitor cells invade a porous structure, often acting as a temporary scaffold, and replace it with newly formed bone.

Osteoinduction Process that promotes mitogenesis of undifferentiated mesenchymalcells, leading to formation of osteoprogenitor cells that have osteogenic capacity.

Stress-shielding Reduction in bone density (osteopenia) as a result of removal of normal stress from the bone by an implant.

Abbreviations

ACP	Amorphous calcium phosphate	**ECM**	Extracellularmatrix
ALP	Alkaline phosphatase	**FDA**	Food and Drug Administration
bFGF	Basic fibroblast growth factor	**FN**	Fibronectin
BCP	Biphasic calcium phosphate	**HA**	Hydroxyapatite
BGs	Bioactive glasses	**HCA**	Hydroxylcarbonate apatite
BMP-2	Bone morphogenetic protein-2	**PCL**	Poly-ε-caprolactone
CA	Carbonated apatite	**PDLLA**	Poly-DL-lactic acid
CaP	Calcium phosphates	**PEG**	Polyethylene glycol
CDHA	Calcium-deficient hydroxyapatite	**PGA**	Polyglycolic acid
		PLA	Polylactic acid

PLGA	Polylactic-*co*-glycolic acid	**SCPC**	Silica–calcium phosphate nanocomposite
PLLA	Poly-L-lactic acid	**TCP**	Tetracalcium phosphate
poly(3HB)	Poly(3-hydroxybutyrate)	**TGF-β**	Transforming growth factor-β
poly(3HB-*co*-3HV)	Poly(3-hydroxybutyrate-*co*-hydroxyhexaoate)	**VEGF**	Vascular endothelial growth factor
PPF	Polypropylene fumarate	**β-TCP**	β-Tricalcium phosphate

5.520.1. Introduction

The holy grail in bone tissue engineering is the pursuit of scaffolds that act as a temporary support for cells to facilitate the regeneration of bone, as the requirements of scaffold materials are extremely challenging. Scaffolds provide cell anchorage sites, mechanical stability, and structural guidance, and *in vivo*, provide the interface to respond to physiologic and biologic changes as well. In addition, they serve to facilitate the remodeling of the extracellular matrix (ECM) in order to achieve the integration with the surrounding native tissue. As such, ideal scaffold materials need to be biocompatible, osteoinductive, osteoconductive, integrative, porous, and mechanically compatible with native tissue. To fulfill such a desired role, many biomaterials have been tested.[1]

Bioactive ceramics, such as calcium phosphates and bioactive glasses (BG), have been used for many years in dentistry, oral and maxillofacial surgery, and orthopedic trauma and joint replacement surgery. These materials bond to bone and enhance bone tissue formation (osteoconduction). They typically have chemical and physical characteristics mimicking the composition and structure of the mineral phase of the bone, or as a result of reacting with physiologic fluids, develop such a surface.

Ceramics are relatively stiff, brittle, and difficult to form into complex shapes. Conversely, polymers are more easily fabricated into complex structures, but they are typically too weak to meet the demands of surgery and the *in vivo* physiologic environment. Thus, composite scaffold comprising bioceramics and polymers are studied because the limited fracture toughness of the ceramic can be mitigated by a polymer matrix, all while the composite displays the osteoconductivity and delayed/sustained release characteristics typical for the ceramic component.

This chapter reviews recent development of bioactive ceramic and bioactive ceramic composite scaffolds in terms of material constituents, structural and bioactive properties, as well as *in vitro* and *in vivo* characteristics especially for applications in bone tissue engineering and tissue regeneration. In our analysis, we include only a short description of some critical aspects of composition and mechanism of biological activity, as these topics are discussed at much greater length elsewhere in this comprehensive (see **Chapter 1.109, Bioactive Ceramics** and **Chapter 1.114, Bioactivity: Mechanisms**).

5.520.1.1. Limitations of Natural Bone Grafts

The current gold standard for bone grafting is autografting using cancellous bone or vascularized grafts of the fibula or iliac crest.[2] This is because autografts provide osteogenic cells as well as essential osteoinductive factors needed for bone healing and regeneration. Unfortunately, however, harvesting autografts, typically from the iliac crest, adds cost to the surgery, is constrained by anatomic limitations, and is associated with significant donor-site morbidity.[1,3–5] Furthermore, the amount of graft needed clinically often makes autografting impossible. The conventional alternative to autograft has been allogenic bone obtained from cadaveric donors. Although it provides a natural bony scaffold, there is the potential risk of inducing an immunologic response due to genetic differences and the risk of both bacterial and viral transmission from the donor material to the host.[3,4,6,7] Moreover, the current supply of cadaveric bone is tight.[7]

5.520.1.2. Synthetic Bone Grafts and Materials Used

The limitations of biologic grafts have prompted the use of synthetic biomaterials as bone grafts. There is evidence suggesting that synthetic scaffolds merit consideration as the grafting material of the fracture for many indications. Presently, the application in which synthetic scaffolds show the most immediate promise is in treating large-defect fractures.[7] In this area, existing bone graft substitutes such as calcium phosphates[8–10] and BGs[11] have been found to yield results equal to those attained with autograft. The excellent results with these bioactive ceramics are primarily due to their bioactive property, which is a surface layer that is the equivalent of the bone mineral phase. When implanted in bone, bioactive materials enhance bone cell growth and direct bone deposition on their surfaces. Therefore, bioactive ceramics have been used as a bone-filling material to provide a scaffold for cell migration and rapid bone formation.

Polymeric materials, including naturally occurring[12,13] and synthetic polymers,[14] are widely considered materials for bone tissue-engineering applications. In particular, polyesters such as polylactic acid (PLA), polyglycolic acid (PGA) and their copolymers polylactic-*co*-glycolic acid (PLGA),[15–17] polydioxane and their copolymers are synthetic and biodegradable polymers with an extensive history of use in products that have been cleared by the US Food and Drug Administration (FDA).[18]

Ceramic/polymer composites have been considered for use as bone tissue-engineering scaffolds due to their combined advantages of improved physicochemical, biological, and mechanical properties, and in particular, the capacity they offer in tailoring their structure and degradation rate to the specific need at the implant site.[19–22] Typical examples of these composites are described by various authors.[23–25] Overall, as the engineering technology continues to evolve, future synthetic scaffolds can only be expected to perform better.

5.520.2. Scaffold Requirements

For successful treatment of bone defects, scaffolds for bone tissue engineering must fulfill three primary functions. First, the scaffold must be mechanically competent to withstand *in vivo* stresses and loading during tissue ingrowth. Second, the scaffold must degrade in a predictable rate without interfering into the tissue ingrowth and regeneration process. Third, the internal micostructure and surface properties of the scaffold must be able to guide cells to grow into the desired physical form, and it must be permeable to nutrients and neovascularization. The requirement of fulfilling the above-mentioned primary functions often poses conflicting design requirements. For example, in order to achieve the equivalent mechanical strength of bone, one needs minimally porous scaffolds. However, a high degree of porosity is essential to ensure cell migration, vascularization, and well-connected tissue formation within the scaffold. The issue of optimal design and fabrication of a scaffold which can fulfill the primary functions is still under extensive research.[26]

5.520.2.1. Load-Bearing Properties

In critical size bone defects, the goal of using bone scaffolds is primarily to implant these in bone defects that will not heal spontaneously. As sustained mechanical loading is needed in most cases, an ideal load-bearing scaffold must provide sufficient initial mechanical support to substitute for the mechanical function until the tissue-engineered transplant is fully remodeled by the host tissue.[27] It must also match as closely as possible bone mechanical behavior as issues arose with most materials by virtue of their higher stiffness than that of either trabecular or cortical bone. This inability to match stiffness results in the phenomenon called 'stress-shielding,' in that bone is insufficiently loaded compared to the scaffold, leading to the interruption of desired bone remodeling. While maximum mechanical properties can be obtained with a control of microarchitecture of the scaffolds, the materials choice is still one of the most important aspects in designing scaffolds. This is because, depending on the material properties, some biomaterials are either too weak or too stiff to be arranged into the desired architecture. Both the tissue and architectural levels must be designed to achieve both spatial distribution and a material that provide sufficient strength to sustain loading.[28]

5.520.2.2. Degradation and Resorption Kinetics

Biodegradation of ceramic implants used for bone regeneration is governed not only by material characteristics, but also by conditions of the biological environment. Either physicochemical dissolution or degradation by cellular, that is, osteoclastic activity, or by a combination of both are the major mechanisms for biodegradation. Tricalcium phosphate[29,30] and BG[31] degrade mainly by physicochemical dissolution; their degradation by osteoclasts was shown to be minor. Other ceramics, such as a dense hydroxyapatite (HA), however, appear to degrade mainly by osteoclastic activity.[11]

Biodegradable scaffolds are the best alternative for the temporary fixation for many different types of bone defects for various reasons. During the early stages of tissue healing, the biodegradable scaffold holds the healing tissue in place.[32] It is crucial that the rate of degradation of the scaffold parallels the rate of bone growth in order to maintain the required mechanical properties of the construct. If resorption occurs too quickly, pseudoarthrosis might occur. Conversely, if resorption occurs too slowly, this will interfere with bone ingrowth, also leading to pseudoarthrosis or, alternatively, to weakening of the newly formed bone.[1] At the optimal rate, resorption leads to the gradual transfer of stresses to the healing tissue, avoiding the stress-shielding effects. At the same time, such resorption does not require a removal operation of the surgical devices, which is a substantial benefit both economically and to the patient being treated.[32] Finally, it also would be advantageous to utilize this degradation property for any growth factor delivery intended to enhance bone formation and integration.

5.520.2.3. Scaffold Architecture for Bone Ingrowth and Permeability of Nutrients and Neovascularization

In the case of scaffold-based tissue-engineering approaches, it is important to focus on both the architecture and the material of the scaffold as they influence bone regeneration in combination. In particular, it is related to the effect of pore size and porosity. The scaffold microstructure must ensure cell migration as well as attachment and differentiation at the pore surfaces. Moreover, for easy migration of cells within the scaffolds, the pores must be large enough.[33] The optimal porosities higher than 80% and pore sizes in the range 100–500 μm are suitable for applications in bone tissue engineering, as a larger pore size results in fibrous tissue growth.[34] The precise pore dimension depends on the specific application.[35–40] In order to allow bone growth and functions, once cells are attached to the material surface, there must be enough space and channels to allow the key metabolic functions such as transportation of nutrients to cells that migrate through the scaffolds, waste evacuation,[27,40] protein transport, and vascularization upon implantation, which are obtainable with an interconnected network of pores. The degree of pore interconnectivity determines the permeability of scaffolds; this is thus another key factor influencing the scaffolds' ability to enhance tissue regeneration. Studies have found a direct correlation between the cell growth and permeation of nutrients through the porous structure during the cell culture process in a scaffold.[33,41–43]

5.520.3. Fundamentals of Ceramic Bioactivity

5.520.3.1. Surface Transformation

The nature of the biomaterial and its surface characteristics play important roles in determining bone adaptation to the implant material. Surface reactivity is one of the common characteristics of bone bioactive ceramics, and this attributes to biomineralization of a thin layer of calcium phosphate at the interface between the ceramics and host bony tissue that provides the bonding interface with tissues. Time-dependent assessments in animal models imply that after implantation the biologically equivalent carbonate apatite layer is formed on the bioactive surface at an early period, and thereafter mediates

integration of bone matrix to metabolize as a part of tissue.[44–46] BG with its surface turned into a calcium phosphate was the first material for which this property was described.[47]

The calcium phosphate formed on the bioactive ceramics is nanocrystalline calcium-deficient HA ($Ca_{10}(PO_4)_6(OH)_2$) (CDHA), containing sodium, magnesium, chlorine, and carbonate, and hybridized with biomacromolecules.[48] This hydroxyl carbonated apatite (HCA) phase that forms on bioactive implants is akin to the mineral phase in bone and is different from synthetic HA. The calcium phosphate, with its bone mineral-like characteristics recruits bone cells and leads them to proliferate in preference to fibroblasts, differentiating and producing an ECM composed of biological calcium phosphate and collagen.[46,49]

The interstitial body fluid is the very first medium that a bioactive ceramic interfaces with after being inserted in a bony defect. The development of a biologically equivalent CA layer is initiated through solution-mediated surface reactions that take place after immersion of bioactive ceramics in biological fluids.[46] The sequence of reactions leading to such layer includes dissolution, precipitation, and ion-exchange phenomena, concurrent adsorption of Ca-P in combination with protein adsorption events occurring at the bioactive ceramic surface.[49–54] In previous review papers, we summarized these events that were reported to occur at the bioactive ceramic–tissue interface.[49,50,55] The following list does not imply a ranking in terms of time sequence or importance: (1) dissolution from the ceramic[50,52,56–59]; (2) precipitation from solution onto the ceramic[50,52,58–60]; (3) ion exchange and structural rearrangement at the ceramic–tissue interface[50,52,58,59]; (4) interdiffusion from the surface boundary layer into the ceramic[61]; (5) solution-mediated effects on cellular activity[62,63]; (6) deposition of either the mineral phase (a) or the organic phase (b) without integration into the ceramic surface[56,64]; (7) deposition with integration into the ceramic[56]; and (8) chemotaxis to the ceramic surface.[11]

5.520.3.2. Protein Adsorption onto the Biomineralized Surface and Selective Binding of Integrins

It is also an important aspect that the transformed bioceramic surface composition and structure influences FN adsorption. There is support for the view that the enhanced cellular and tissue responses to bioactive ceramics are related to enhanced FN adsorption at their surfaces.[49,65]

FN is one of the major components of ECM and it is also secreted by osteoblasts. When adsorbed onto biomaterials, FN plays a crucial role in bone cell attachment, proliferation, and differentiation. It has been documented by Garcia *et al.*[66] that the formation on bioactive ceramics of a calcium phosphate surface layer with characteristics similar to those of the calcium phosphate mineral phase in bone resulted in enhanced FN-mediated cell adhesion in comparison to what transpires on control materials and an unreactive form of HA. This effect was not due to differences in adsorbed fibronectin (FN) concentration, but arose from differences in FN conformation. In fact, surface chemistry of the biomaterial surface was reported to modulate the structure and activity of adsorbed FN.[67] These differences in FN structure, in turn, influence integrin binding, membrane-associated adhesion receptors that mediate the cellular interactions between osteoblasts and the biomaterial surface,[68–71] and thus can result in selective binding of the different types and/or combinations of integrins (e.g., $\alpha_5\beta_1$ or $\alpha_v\beta_3$).[67] Recent findings suggest that selective binding of the $\alpha_5\beta_1$ integrin leads to upregulation of osteoblastic differentiation and matrix mineralization.[72] In addition to their role as adhesion receptors, integrins are also involved in transducing signals from the ECM to the interior of the cell,[73,74] resulting in the activation of signaling molecules and regulation of gene expression, thus modulating cellular migration, proliferation, differentiation, and apoptosis.[75–80] However, little is known about the intracellular events that follow osteoblast attachment to these bioactive ceramics, leading to differences in osteoblast activity. To obtain a fundamental understanding of the mechanisms by which bone tissue formation is stimulated, the atomic and molecular phenomena induced by osteoblast–implant materials interactions and their effects on signaling pathways of cells and tissues should be further investigated.[55]

5.520.4. Characteristics of Bioactive Ceramics and Bioactive Ceramic Composite-Based Scaffolds for Bone Tissue-Engineering Scaffold

5.520.4.1. Bioceramics and Bioactive Glasses

5.520.4.1.1. Bioactive glasses and glass ceramics

Bioactive glasses (BG) are a group of surface-reactive glass-ceramic biomaterials and include the original bioactive glass, Bioglass. It has excellent biocompatibility as well as the ability to bind to bone and other tissues, as was first described by Hench in the early 1970s.[47] It can be synthesized like conventional glass but with components SiO_2, Na_2O, CaO, and P_2O_5. BG possesses an excellent stimulatory effect on bone cell function.[11,49,66,81,82,83] It has been demonstrated that BG accelerates bone growth significantly more than a low reactivity HA when implanted in bone.[84,85] Excellent bioactivity of these materials resulted in their successful application as bone-substitute material for non-load-bearing applications in orthopedic and dental surgery.[7,82,86–88]

The reason behind the bonding ability of BG is the chemical reactivity of the BG through interfacial and cell-mediated reactions in which silicon bonds are broken and a CaP-rich layer is formed on top of the glass which crystallizes to HCA. BGs also support many other bioactivity such as enzyme activity[89,90]; vascularization[91,92]; foster osteoblast adhesion, growth, differentiation; and induce the differentiation of mesenchymal cells into osteoblasts.[11,93–96] Bioactivity, however, is not an exclusive property of BGs. Various forms of HA and related CaP also show an excellent osteoconductivity, which is critical in elimination of scaffold loosening.[96]

In order to have application in tissue engineering, along with the bioactivity, the BG should be degradable and porous. The porous BG can be prepared in a method similar to porous CaP ceramics. Yuan *et al.*[97] used a H_2O_2-foaming method to obtain a macroporous BG with pore sizes ranging from 100 to 600 μm. Chen *et al.*[85] were able to prepare a 86–93% porous BG by use of a polyurethane template which was immersed in a glass slurry, and the polymer was burned out after which the scaffold was sintered. Kaufmann *et al.*[98] used polyethylene

glycol (PEG)–glycol particles of different sizes and amounts to retrieve a porous BG substrate after sintering.[81]

It has been found that reactions on BG surfaces can release soluble Si, Ca, P, and Na ions, depending on the processing route and particle size, inducing intracellular and extracellular responses.[99,100] In recent investigations, 45S5 BG has also been shown to increase secretion of vascular endothelial growth factor (VEGF) *in vitro* and to enhance vascularization *in vivo*, which is critical to large tissue-engineered constructs.[30]

5.520.4.1.1.1. Compositions and bioactivity

The basic constituents of most BGs are SiO_2, Na_2O, CaO, and P_2O_5. 45S5 BG contains 45% SiO_2, 24.5% Na_2O, 24.4% CaO, and 6% P_2O_5, in weight percent. In spite of using a somewhat unsophisticated rat model and testing methodology, Hench and coworkers were able to describe the effect of compositional variation in the four-component glass systems with a constant 6 wt% P_2O_5 content. They summarized these data in review papers.[101,102] They divided the compositions into three regions according to their bioactivity. BGs (e.g., 45S5 Bioglass®) with compositions in the system SiO_2–Na_2O–CaO–P_2O_5, having <55% SiO_2, exhibit a high bioactivity index (in region A) and bond to both soft and hard connective tissues. Glasses of compositions in region B exhibit only osteoconductivity. Compositions in region C are resorbed within 10–30 days in tissue (**Figure 1**).[103]

Ease of control over the range of chemical properties and thus the rate of bioresorption makes BGs a very attractive scaffold material. Moreover, by varying either composition, or thermal or environmental processing history, the structure and chemistry of glasses can be controlled at a molecular level. This flexibility in synthesis process makes it possible to design glasses with degradation properties specific to a particular application of bone tissue engineering.[104,105]

However, it was also reported that the level of bioactivity decreases with the increase in crystallinity of BGs[105] and even turned into an inert material.[106] This is the main drawback that limits the application of BGs as scaffold materials, as full crystallization happens prior to densification by sintering[107] and extensive sintering is necessary to densify the struts of a scaffold to achieve the required mechanical stability.

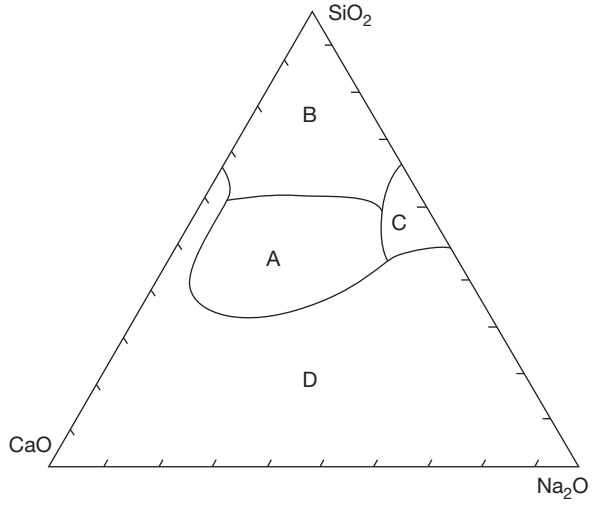

Figure 1 Behavior of BG of different compositions. Region (A), bone bonding, (B) fibrous tissue encapsulation, (C) dissolution, and (D) nonglass forming. All compositions have a constant 6% P_2O_5 by weight. Reproduced from Hench, L. L.; Wilson, J. *Science* **1984**, *226*(4675), 630–636, with permission.

5.520.4.1.1.2. Mechanical properties

Two key properties of the BG, ion release into physiologic solutions and the subsequent bioactivity reactions, are facilitated by its amorphous structure.[108] On the other hand, the amorphous structure of BG impairs the mechanical strength of the material and lowers its fracture toughness, especially in a porous form. Tensile strength of most of the BG compositions is in the range of 40–60 MPa and cannot be used alone in load-bearing situations. **Table 1** elaborates the compressive strength, elastic modulus, and some fracture toughness values for dense and porous bioactive ceramics.[103–117] It can be seen that particularly porous scaffolds which are essential for tissue engineering exhibit very low mechanical properties compared to cortical and cancellous bone. However, for some applications, low strength is offset by the glass's low modulus of elasticity of 30–35 GPa which is close to that of cortical bone (7–25 GPa).

Recently, it has been demonstrated that 45S5 BG can partially crystallize when heated to high temperatures (>950 °C) during scaffold fabrication and the mechanically strong crystalline phase can transform to a biodegradable, amorphous calcium phosphate (ACP) at body temperature in a biological environment.[85,118] This transformation enables the preparation of biodegradable mechanically competent BG scaffold. This discovery promises to go some way toward the scaffold optimization and its clinical application. In addition, bioactive glass-ceramic materials exhibit better mechanical properties than amorphous do glass and calcium phosphate ceramics (**Table 1**). For this reason, other ceramic components are sometimes added to the BG for reinforcement, referred to as glass-ceramic composites.[119,120]

5.520.4.1.2. Calcium phosphates

5.520.4.1.2.1. Calcium phosphates composition and bioactivity

Owing to the high abundance of $Ca_{10}(PO_4)_6(OH)_2$ and HA in bone, both HA and related calcium phosphates (CaP) have been looked at as the major component of scaffold materials for bone tissue engineering. Among different types of CaP-ceramics materials are mainly HA, β-TCP, biphasic calcium phosphate (BCP), ACP, or CDHA, and they are classified as useful for bone tissue growth.

On account of their close chemical and crystal structure resemblance to the mineral phase of bone, calcium phosphate exhibits excellent biocompatibility.[121] Calcium phosphates possess osteoconductive properties; however, they have not shown osteoinductivity.[122–124] Many *in vivo* and *in vitro* studies demonstrated that calcium phosphates, regardless of the form (bulk, coating, powder, or porous) and phase (crystalline or amorphous), always support the attachment, proliferation, and differentiation. However, the poor mechanical strength of this material limits their application in tissue engineering, especially at load-bearing sites.

Table 1 Mechanical properties of dense and highly porous HA, 45S5 BG, A/W glass-ceramic, and human cortical bone

Ceramics	*Compressive strength (MPa)*	*Tensile strength (MPa)*	*Elastic modulus (GPa)*	*Fracture toughness (MPa √m)*	*References*
HA	>400	~40	~100	~0.1	107,112
45S5 BG	~500	42	35	0.5–1	107,108,200
Glass-ceramic A/W	1080	215	118	2.0	111
Porous BG 70S30C (82%)	2.25	–	–	–	109
Porous HA (82–86%)	0.21–0.41	–	$0.83–1.6 \times 10^{-3}$	–	110
Cortical bone	130–180	50–151	12–18	6–8	114,201,202
Cancellous bone	4–12	–	0.1–0.5	–	106,113

Reproduced from Rezwan, K.; Chen, Q. Z.; Blaker, J. J.; Boccaccini, A. R. *Biomaterials* **2006**, *27*(18), 3413–3431, with permission.

5.520.4.1.2.2. Mechanical properties

Mechanical properties of synthetic calcium phosphates are highly dependent on their crystallinity, grain size, porosity, and composition. In general, the mechanical properties of synthetic calcium phosphates decrease with increasing amorphous phase, microporosity, and grain size. High crystallinity, low porosity, and small grain size result in high stiffness, compressive and tensile strengths, and greater fracture toughness.

In comparison, cortical bone has better compressive strength than HA and related calcium phosphates, although it is less dense than most HAs. Also, bone has higher fracture toughness than most dense HA. The mechanical properties are lower for porous HA structures. The unique composite structures, high tensile strength, and fracture toughness of bone come from the presence of tough and flexible collagen fibers reinforced by HA. Hence, calcium phosphates alone cannot be used for load-bearing scaffolds despite their excellent biocompatibility and osteoconductivity.[96]

5.520.4.2. Ceramic/Polymer Composite Materials

Today, composite materials composed of organic and inorganic phase are studied extensively because the combination of the tailored degradability and controlled release of the polymer with the osteoconductivity and delayed/sustained release characteristics of the ceramic material can fulfill the necessary requirements of an ideal scaffold (Table 2).[81] In addition, mechanical properties of ceramic materials can be enhanced with the presence of polymer. Ceramics and ceramic/organic composites are summarized in the following paragraphs. The use of this material for bone tissue engineering with conjoint biomolecules release is discussed in view of the previously formulated ideal scaffold characteristics.

5.520.4.2.1. Composite materials strategy

Inclusion of bioceramics and glasses in polymers provides the mechanical stability to constructs, prior to synthesis of new bone matrix by cells, as these materials have greater mechanical strength than polymer. However, ceramics and glasses are characterized by flaw sensitivity and inherent brittleness.[81] This puts ceramics at a disadvantage as scaffold materials. Conversely, polymers are easily fabricated to form complex shapes and structures yet, in general, they lack bioactivity (as defined above) and are too flexible and weak to meet the mechanical demands in surgery and in the physiologic environment. Thus, the formation of composites capitalizes on the advantages of both material types and minimizes their shortcomings. The combination of polymers and inorganic phases leads to composite materials with improved mechanical properties, exploiting the well-known composites approach by incorporation of stiffer particles into the softer matrix.[125] Moreover, as previously mentioned, addition of bioactive phases to bioresorbable polymers can alter the polymer degradation behavior, by allowing rapid exchange of protons in the aqueous phase for alkali in the glass or ceramic.[18] While release of acidic degradation from polymers can cause inflammatory reactions,[126,127] this mechanism provides the basic degradation of calcium phosphate or BGs that could buffer the acidic by-products of polymers, thus contributing to avoid the formation of an unfavorable environment for cells due to low pH values.[20] Development of composite materials is also attractive since their properties can be engineered to suit the mechanical and physiologic demands of the host tissue by controlling the structure of the polymer and volume fraction, and arrangement of the reinforcing phase.[94] Recently, inclusion of BGs has been shown to modify surface and bulk properties of composite scaffolds by increasing the hydrophilicity and water absorption of the hydrophobic polymer matrix,[128] thus altering the scaffold degradation kinetics.[129] In addition, composites are able to absorb water due to the internal interfaces formed between the polymer and more hydrophilic bioactive phases. It has been reported that polymer composites filled with HA particles hydrolyzed homogeneously due to water penetrating the interfacial regions.[130] In general, the degradation and resorption kinetics of composite scaffolds are designed to allow cells to proliferate and secrete their own ECM while the scaffolds gradually vanish, leaving space for new cell and tissue growth. The physical support provided by the 3D scaffold should therefore be maintained until the engineered tissue has sufficient mechanical integrity to support itself.[18]

5.520.4.2.2. PLA/PGA-based polymer/ceramic composites

The most often utilized biodegradable synthetic polymers for 3D scaffolds in tissue engineering is the family of poly (α-hydroxy ester)s and copolyesters of the lactic acid and glycolic acid. Members of this ester-backbone polymer group are poly(lactic acid) (PLA, PLLA) and PGA, as well as PLGA copolymers and poly(caprolactone) (PCL). The PLA/PGA group is interesting because a wide range of physical properties and degradation times can be achieved by varying the monomer ratios in lactide/glycolide copolymers. The basic chemical structure of all aliphatic polyester materials is the same and

Table 2 Selection of scaffold composites designed for bone tissue engineering and their properties

Scaffold composite		*Percentage of ceramic*	*Porosity (%)*	*Pore size (μm)*	*Compressive (C), tensile (T), flexural (F) strength (MPa)*	*Modulus (MPa)*	*Reference*
Ceramic	Polymer						203
1. Dense composites							204
HA fiber	PDLLA	2–10.5 (vol.)	–	–	45 (F)	$1.75–2.47 \times 10^3$	205,206
	PLLA	10–70 (wt.)	–	–	50–60 (F)	$6.4–12.8 \times 10^3$	207
	PLGA	40–85 (vol.)	–	–	22 (F)	1.1×10^3	
	PLLA-*co*-PEH	75 (wt.)	–	–	51 (F)	5.18×10^3	208
	PPF	25 (wt.)	–	–	7.5–7.7 (C)	191–134	114,201,202
A/W	PE	10–50 (vol.)	–	–	18–28 (B)	$0.9–5.7 \times 10^3$	
Cortical bone					50–150 (T) 130–180 (C)	$12–18 \times 10^3$	
2. Porous composites							
Amorphous CaP	PLGA	28–75 (wt.)	75	>100		65	133,209
HA	PLLA	50 (wt.)	85–96	100×300	0.39 (C)	10–14	25
	PLGA	60–75 (wt.)	81–91	800–1800	0.07–0.22 (C)	2–7.5	210
	PLGA		30–40	110–150		337–1459	211
BG	PLGA	75 (wt.)	43	89	0.42 (C)	51	212,213
	PLLA	20–50 (wt.)	77–80	~100 (macro) ~10 (micro)	1.5–3.9 (T)	137–260	22
	PLGA	0.1–1 (wt.)		50–300			212,214
	PDLLA	5–29 (wt.)	94	~100 (macro) 10–50 (micro)	0.07–0.08	0.65–1.2	215–217
Phosphate glass A/W	PLA–PDLLA	40 (wt.)	93–97				
	PDLLA	20–40 (wt.)	85.5–95.2	98–154	0.017–0.020 (C)	0.075–0.12	128,218
Cancellous bone					4–12 (C)	100–500	113

Reproduced from Rezwan, K.; Chen, Q. Z.; Blaker, J. J.; Boccaccini, A. R. *Biomaterials* **2006**, *27*(18), 3413–3431, with permission.

the only difference is the pendent groups. The degradation mechanism is a hydrolysis reaction in which the glycolic acid residue degrades faster than the PLA while the cleavage site of PLA is sterically hindered.

A combination of calcium-based ceramics and biodegradable polymers yields composites with desirable properties such as controlled degradation, improved osteoblast integration, and tailored mechanical properties. This is considered as a viable approach to make tissue scaffold for bone growth. These scaffolds can be either a porous or dense structure using BG, HA, ACP, and BCP as a ceramic component in a PLLA, PLGA, or PCL matrix. Navarro *et al.*[131] synthesized a glass-ceramic particle/PLA scaffold by homogeneous mixing of the glass-ceramic into a PLA solution and they used H_2O-solvable NaCl particles to create macroporosity in the scaffold. It is demonstrated that the mechanical properties of the PLA increased after adding up to 40% of glass-ceramic particles, but compressive strength was very low. On the contrary, Niemela *et al.*[132] observed that when BG was added to a poly-L,DL-lactide (70/30) bending strength/modulus as well as shear, compression, and torsion strength significantly decreased. BG renders the polymer carrier bioactive, as was observed by Yao *et al.*[63,133,134] These authors reported that the addition of BG particles promoted osteoblastic differentiation of marrow stromal cells.

In the case of PCL, a porous composite produced by a 3D printing method containing 10/20% CaP particles, the compressive strength increased dramatically compared to pure PCL.[135] *In vivo* studies of these composites with human embryonic palatal mesenchymal cells showed an increased proliferation in the 20% CaP composites. Along with the usual ceramic particles/polymer matrix, other ceramic/polylactic composites have also been formulated.[136,137]

On the other hand, porous composites of slow degrading PCL or PLLA with ceramic particles pose no difficulties to the addition of cells, but faster degrading polymers, such as low molecular weight PLGA or PLA, can elicit cytotoxic reaction due to the production of acidic degradation products. This is clearly evident when cells are implanted as well as in the *in vivo* studies with these polymer/ceramic composites without the addition of cells. Strong inflammatory response was observed by Ignatius *et al.*[138] after 24 months in sheep when

composites of PLA and α-TCP or a glass ceramic were implanted. This inflammatory response was accompanied by a strong reduction of the PLA and mechanical strength.

The possibility of incorporating drugs in PLA/PGA–ceramic implants and using them as scaffolds is intriguing. The drug is either incorporated into the polymer[139] or is absorbed onto the composite.[140] Gentamycin was incorporated in calcium phosphate/PLA blends and release kinetics showed a burst release followed by a slower sustained release, which is typical for PLA.[139] However after coating the implants with these composites, the burst release was reduced and a sustained release over a period of 10 weeks was observed. The aspects of incorporating growth factors within these composites[140] are discussed in detail in ceramics paragraph.

PLA/PGA microspheres can be utilized to synthesize PLA/PGA–CaP cement. In such a case, CaP-cements are processed at room temperature, while polymer microspheres are added as a porogen forming pores after *in vivo*/*in vitro* degradation as well as a possible carrier of growth factors.[96]

These composites showed a small sustained *in vitro* release (5–10%) of rhBMP-2 after 4 weeks[141] in medium. However, in the case of composites with low and high molecular weight, PLGA microspheres showed higher release efficiencies (25–50%) *in vivo*.[142] The highest release was observed for the low molecular weight PLGA microsphere composites, indicating that the drug in this formulation exhibited less interaction with the surrounding cement. The discrepancy between *in vitro* and *in vivo* results could be due to a more dynamic flow and the occurrence of high amounts of salts and proteins like albumin *in vivo* that positively influenced the release properties (**Figure 2**).[96]

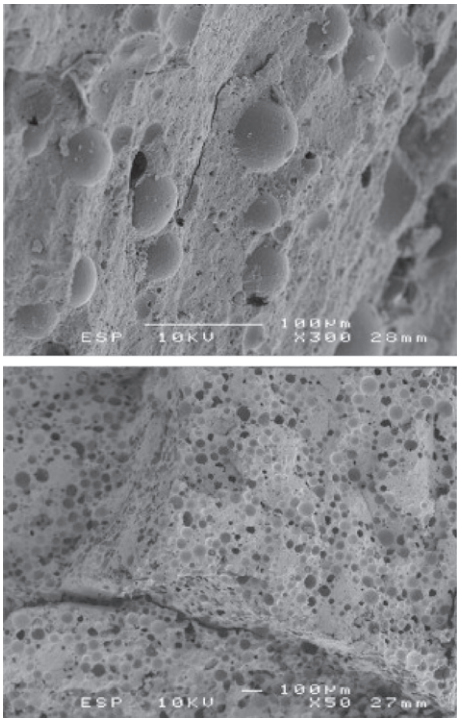

Figure 2 PLGA microsphere/CaP cement composites; close-up PLGA microspheres inside cement scaffold (above, original magnification 300×), 20% PLGA microsphere/CaP cement scaffold after 12 weeks *in vitro* degradation (below, original magnification 50×). Reproduced from Rezwan, K.; Chen, Q. Z.; Blaker, J. J.; Boccaccini, A. R. *Biomaterials* **2006**, *27*(18), 3413–3431, with permission.

5.520.4.2.3. Protein-based polymer/ceramic composites

Because of excellent biocompatibility and biological characteristics that are similar to the human bone, protein-based polymers and CaP-ceramics composites are investigated extensively. Well-known examples of this group of biopolymers are collagen and gelatin.

Collagen has been widely used for the regeneration of tissues, mostly for the repair of soft tissues. Collagen favors the cell adhesion and provides cellular recognition for regulating cell attachment and function. There are many collagen types and forms that are usually obtained by processing different animal tissues. Gelatin is a natural material derived from collagen by hydrolysis and has almost identical composition as that of collagen. Gelatin is a processed form of collagen that is usually derived from pig skin using an acidic process (type A) or from bovine origin with a basic (lime cured) process (type B). Both gelatin and collagen undergo enzymatic degradation which occurs in the body via enzymes, such as collagenases, gelatinase, and metalloproteinases, to yield the corresponding amino acids. The degradation rates can be altered by chemical cross-linking of the proteins. A combination of these biopolymers and ceramics can produce a composite scaffold with tailored degradation rates, and have the biological and mechanical/physical properties of both materials.

Porous gelatin/collagen scaffolds with ceramic particles have already synthesized,[143–145] especially the so-called gelatin sponges that are prepared by freeze-drying a gelatin/calcium phosphate mixture. Often times, the gelatin/collagen is highly cross-linked for a better mechanical stability, though this can also decrease biocompatibility, since cross-linking agents like glutaraldehyde can produce a cytotoxic reaction.[146] To avoid this drawback, Shibata *et al.*[144] prepared a colloidal β-TCP/collagen composite that does not need any extra treatment. Collagen type I was also used as a matrix for CaP mineralization to obtain a collagen/CaP composite.[147] In this study, the biomimetic properties of the collagen were exploited and 60–70% CaP composites were produced with a high tensile strength. In another study, a 10% gelatin composite was formed by soaking a macroporous HA ceramic in which the gelatin penetrated the bulk of the ceramic.[148] To ensure the biocompatibility, a low concentration of cross-linker was used to slow down diffusion of gelatin out of the scaffold.

CaP particle/biopolymer composites have not been widely investigated for the release of growth factors; even the release properties of gelatin, especially, is well investigated and relies on an electrostatic interaction between a positively/negatively charged gelatin and a drug of the opposite charge.[149] Takahashi *et al.*[145] synthesized the gelatin sponges by chemical cross-linking of the gelatin in the presence of different amounts of β-TCP granules. Bone morphogenetic protein-2 (BMP-2) was loaded by simply dropping a solution of the growth factor to freeze-dried sponges. *In vivo* release study of BMP-2 labeled with ^{125}I from these composites revealed a high initial release followed by a more sustained release. For all types of composites, the evidence of bone formation was observed, though high amounts of β-TCP granules made the sponge collapse during degradation, leading to denser structures and less bone

formation. Kim *et al.*[143] synthesized the gentamycin-loaded HA-particle/gelatin composite sponge and investigated the *in vitro* drug entrapment and release as a function of cross-linking density of the gelatin, amount of HA in the sponge, and drug loading. They have found that increasing the cross-linking density leads to a higher drug entrapment, a decreasing initial drug release, and a more sustained release pattern. An increase in the percentage of HA particles decreased the percentage drug entrapment, though release here is also more sustained. Because in this study no gelatin degrading enzyme was added, the degradation and release is due to the degradation of the cross-linker used (1-ethyl-(3,3-dimethyl-aminopropyl carbodiimide hydrochloride), EDC).

A collagen scaffold with HA nanoparticles and rhBMP-2 was studied *in vivo* and a positive influence of the added drug was observed in a loaded implant model in dogs.[150,151]

Composites of gelatin/collagen with calcium phosphate cements are formulated to obtain better handling properties and to improve biological response. A handful of studies have been done on the biological response as well as on the properties of the gelatin and calcium phosphate cement (α-TCP) composites.[152–154] An acceleration of the cement setting reaction as well as an increase in compression strength due to the high density of the gelatin was observed. Furthermore, an excellent biological response was observed with an improvement of osteoblast activity and differentiation. Fujishiro *et al.*[155] prepared a porous composite of a 5% and 20% gelatin-containing α-TCP-based cement. Pores of 20–100 μm were prepared by mixing a gelatin gel with α-TCP powder. Results showed an increase in mechanical properties over time with the 5% composites when compared to the original cement, though with 20% gelatin, the compressive strength was lower. The biomimetic abilities of gelatin that acts as a nucleation point of CaP-crystal growth are behind the good biological response and increase in mechanical strength of these composites.[156] Rammelt *et al.*[157] investigated the properties of collagen/CaP-cement composites. They have added 3% of collagen I to nanocrystalline HA cement which led to an increased bone remodeling in rat tibia defects. Another research group[158] added 1.0–2.5% collagen I to a commercial apatite cement and also observed mechanical and physical changes of the cement especially when osteocalcin was added. The behavior of osteoblasts cultured on the same 2.5% collagen-containing cement was investigated.[159] They observed that changes in the local microenvironment like the pH greatly influenced cell differentiation and proliferation on these composites.

Lode *et al.* investigated the release of VEGF from a collagen-containing apatite cement and compared it to the release pattern and VEGF activity of the normal cement.[160] Both the cumulative release (25%) and burst release were higher from the collagen cement composites, indicating a looser binding of the VEGF to the collagen. Furthermore, they analyzed the proliferation of endothelial cells after exposing them to the diluted release medium. They found that the introduction of phospherine and sodium citrate to the collagen-containing cement has a positive impact on VEGF activity.

Besides the gelatin and collagen, other protein-based polymers were explored to make composite material with CaP-ceramics and cements. Fibrin and especially fibrin glue was applied for the introduction of ceramic particles[161,162] or mixed together with calcium phosphate cement.[163]

Studies have been performed introducing alumina and TCP-particles in a casein and soybean protein scaffold,[164] and polypeptides into CaP-cement.[165] Again, main reasons for the use of these proteins were biodegradability, biomimetic properties, and mechanical reinforcement.

5.520.5. Modifications of Bioactive Ceramics and Bioactive Ceramic Composite-Based Scaffolds

5.520.5.1. Localized Delivery of Biomolecules and Cells

The additional function of scaffolds is to enable a controlled release of molecules as a carrier at the treatment site for a sufficient duration to aid therapeutic efficacy of those molecules released. The scaffold as a carrier material in bone tissue engineering should be biocompatible and should not physically interfere with the normal processes of osteogenesis or elicit any inflammatory or immunogenic response in the body. An ideal biomaterial carrier must maintain the activity of molecules and also allow initial cellular infiltration and subsequent integration with native tissue.

BMP-2, transforming growth factor-β (TGF-β), basic fibroblast growth factor (bFGF), and VEGF are common but vital growth factors that are introduced into the scaffolds due to their osteoinductive properties and vascularization.[166–168]

BMP delivery to localized sites has been explored for repair of bone defects and nonunions in several different experimental models.[169–182] Many delivery systems have been explored, such as demineralized bone matrix, collagen composites, fibrin, calcium phosphate, polylactide, poly(lactide-*co*-glycolide), polylactide–PEG, HA, dental plaster, and titanium.[183–188] It is worth mentioning here that none of these materials meet all of the demands for an ideal delivery system.

Ceramics like HA are known for their positive interaction with BMPs due to strong binding affinity to the growth factors/proteins. Owing to this phenomenon, high amounts of these growth factors are added in *in vivo* studies to guarantee a positive tissue response, which results in an increased level of BMPs compared to the clinical relevant values inside the human body and increases the cost of a single implant substantially, therefore decreasing a possible use of the material.

It has been observed by many researchers that incorporation of BMP in HA,[178,187] HA/collagen,[169] and HA/TCP composites[189,190] greatly accelerates bone formation. However, these systems suffer from a high degree of bioresorption and poor mechanical strength, which limits the effective application of these synthetic bone substitutes. Moreover, acute inflammatory and immunologic reactions are observed with the collagen composite, when calcium phosphate ceramics were used as carriers for osteoinductive factors.[191,192] Alam and colleagues impregnated different doses of recombinant human (rh)BMP-2 into BCP ceramic with varying ratios of HA to a TCP(HA/TCP ratios: 100/0 (pure HA, 75/25, 50/50, 25/75, and 0/100 (pure TCP)).[193] The samples were implanted under the pericranium in adult wistar male rats and were harvested 8 weeks after implantation. The extent of bone and bone marrow formation and the degree of resorption of the ceramic particles were significantly higher in the samples composed of 25% HA and 75% TCP.[193] The enhancement in the bioactivity of the composite 25HA/75TCP corresponds very well

with the high quantity of preadsorbed rhBMP-2 on the material surface. There is a possibility that the high rate of dissolution of the TCP-rich composite provides empty space to grow new bone. From this study, it is not possible to conclude whether the enhanced-rhBMP-2 adsorption was due to the variations in the chemical composition or the variations in the surface area of the substrate, as there is no quantification of the surface area and porosity of the material. Collagen type IV was also explored to effectively adsorb BMP to the ceramic.[173] They grafted TCP cylinders loaded with partially purified sheep BMP and Type IV collagen in the diaphyseal segmented defects in the tibia of sheep.[173] It is demonstrated that the TCP loaded with a high dosage (100 mg) of partially purified BMP has superior healing capacity for the segmental bone defects.

Silica-based porous glass xerogel was also explored for the delivery of growth factor such as TGF-β1 *in vitro*.[194] It is shown that the release of TGF-β1 can be facilitated by modifying the scaffold properties such as the degree of drying and surface area.[194] The same research group evaluated the silica xerogel composites for the release of BMP-2 *in vitro*.[192] They found that when rat stromal marrow cells were seeded onto the surface of xerogel discs with rhBMP-2, incorporated in the glass, adsorbed onto the surface of the glass, or added to the culture media,[195] cell differentiation was increased most when the BMP-2 was incorporated or adsorbed onto the xerogel glass.[195] Recent studies reported on a novel resorbable bioactive cyclo silicate (silica–calcium phosphate nanocomposite, SCPC) nanocomposite as a potential tissue-engineering scaffold for cells and biologic molecule delivery.[196,197] When the SCPC material was loaded with rhBMP-2, it provided an excellent release profile of biologically active rhBMP-2 compared with porous HA ceramic (HA-200). In addition, bone marrow cells attached to the SCPC-rhBMP-2 hybrid produced mineralized ECM and bone-like tissue that covered the material surface and filled the pores over the entire thickness of the template after 3 weeks in culture. Conversely, cells attached to the HA-rhBMP-2 produced a limited amount of unmineralized ECM after the same time period. From the results of these studies, it can be concluded that the silica-based materials have very high potential to be used as a scaffold for BMP delivery.

Certain bioceramics, such as BG, which have specific bone affinity, may affect cell behavior by regulating the expression of BMPs.[173] Northern hybridizations demonstrated similar trends in the mRNA levels of collagen Type I, alkaline phosphatase (ALP), and BMP-2 in Saos-2cells grown on the dishes and plates. However, the relative levels of mRNAs, BMP-2, collagen I, and ALP in cells cultured on BG plates were 9-, 6-, and 1.2-times higher than that on BG dishes, respectively. However, in this study, the prepared BGs were not characterized, and it is difficult to understand why there were differences on the cellular activity of cells cultured on the plates versus dishes when both are made of BG.[198]

5.520.6. Conclusion and Future Directions

The treatment to reconstruct and repair major bone loss due to injury or disease is one of the major problems in orthopedic and maxillofacial surgery. The development of new scaffolds to deliver cells and molecules has made remarkable progress to addressing these clinical issues. There are numerous composite systems comprising synthetic biodegradable polymers and bioactive phases, such as HA and BGs.

Outstanding mechanical properties and osteoconductivity of highly porous polymer/ceramic composite scaffold make them a promising substrate for bone tissue engineering. Biodegradable polymer scaffold may provide a number of benefits for bone tissue engineering; enhanced environment for cell seeding; survival, growth, and differentiate function because of the osteoconductive function imparted by HA, which increases mechanical properties that are essential for load bearing. High porosity also increases the resorption rates; however, it can decrease mechanical properties. A challenge is the brittleness of the ceramic, which makes implantation for load-bearing applications complex.

CaP cements/ceramics can be applied as promising carrier materials for drugs in which release patterns and efficiencies strongly depend on the type of ceramic/cement used. In general, ceramics suffer from initial burst release compared to cements that have a more sustained release pattern. Also, BG prepared by sol–gel can be used as a carrier for drugs.

The totally synthetic biodegradable polymer/inorganic bioactive phase composites reviewed here are particularly attractive as tissue-engineering scaffolds due to the flexibility in tailoring structural properties, bioactive behavior, and biodegradation kinetics. From the materials science perspective, the present challenge in tissue engineering is to design and fabricate reproducible bioactive and bioresorbable 3D scaffolds of tailored porosity and pore structure, which are able to maintain their structure and integrity for predictable times, even under load-bearing conditions. Poor compression strength and biological activity of the added polymers often undermine the advantages of the polymer/ceramic composites.

To enhance the *in vivo* cohesion and injection properties of the cement, biopolymers like chitosan, gelatin, and collagen are frequently added to calcium phosphate cement. Occasionally, the goal is to reinforce the cement, which is a result of the compact microstructure that is formed after mixing both inorganic and organic materials. The porosity and degradation rate of cement can also be altered with the addition of polymer microspheres/particles that degrade *in vivo*, as it was observed with PLGA microspheres. Furthermore, PLGA microsphere and collagen-containing cements have shown to be promising materials for drug release/entrapment.

Ceramic particles can also be added to a polymeric carrier to improve the mechanical properties and incorporate the nanotopographic features that mimic the nanostructure of natural bone. In general, scaffolds comprised of a ceramic in a polylactic, protein, or carbohydrate carrier show higher degradation rates than do pure ceramics. Furthermore, by changing the synthesis parameters such as molecular weight or cross-linking density of the polymer, degradation rates can be controlled. A compression strength of 100% ceramic composites is much higher than these scaffolds, but the addition of the polymer reduces the brittleness of the ceramic and makes it applicable for the purposes of tissue engineering. In general, release patterns from drug-loaded protein-based polymer/ceramic scaffolds show an initial burst release. This problem can be reduced by adding higher amounts of

ceramic particles to the composites or by increasing the cross-linking of polymer, which can provide a more sustained release of drugs/growth factors.

The possibility of incorporating growth factors into composites formed with the aim to accelerate local bone healing and vascularization is promising and has started to be explored. Inducing rapid vascular ingrowth during tissue development will continue to be of major importance in tissue engineering. The incorporation of biomolecules during scaffold processing, however, is not simple because it does not allow extreme temperature ranges (470 °C) or extremely aggressive chemical conditions during processing, this being a challenge to the scaffold fabrication process. Immobilization of proteins and growth factors via the surface functionalization of the scaffold can be a promising strategy.

With methods like protein adsorption or plasma treatment, there is ample scope in the application of surface modification to provide more cues to cell attachment and response, thus making the scaffold more biocompatible. Adsorption of proteins such as FN and collagen should cause improvements in wettability of highly hydrophobic polymers such as poly-DL-lactic acid (PDLLA). Further research should focus on understanding cell–material interactions at a molecular biology level, coupled with the design of a new generation of bioactive materials that activate proliferation and differentiation of cells to enhance rapid formation of ECM and tissue growth *in situ*. Successful tissue development may be achieved by chemical modifications including the incorporation of functional groups, chemotactic factors, matrix protein, or peptides.

The unique properties of nanomaterials can be exploited to enhance the properties of the scaffold for tissue engineering. For example, use of ceramic nanoparticles and carbon nanotubes (CNTs) may also improve the environment to enhance cell attachment and proliferation as well as adding extra functionalities to the base scaffold; however, critical issues like toxicity associated with nanoparticles and CNTs must be well addressed beforehand. Nanotechnology can provide an alternative way of processing bioceramics with high mechanical strength and enhanced bioactivity and resorbability. The nanometer grain sizes and high surface fraction of grain boundaries in nanoceramics increase osteoblast functions (such as adhesion, proliferation, and differentiation). The decrease in the grain size results in a significant increase in the grain boundaries, which modifies the overall physicochemical characteristics and, in particular, those related to the surface. Moreover, key properties like dissolution and protein adsorption, which are dependent on surface chemistry, energy, and roughness, can be optimized to enhance cell adhesion, proliferation, and differentiation. Other composite systems of interest are those combining nanostructured inorganic phases (e.g., nanoparticles and nanofibers) and biodegradable polymers, recently discussed in this series,[109] in order to influence cell response in contact with scaffold by mimicking the surface nanotopography of living tissues.

There is a lack of current understanding in the literature regarding the long-term *in vitro* characterization of the composites discussed here, specifically regarding the long-term effect of the incorporation of inorganic bioactive phases on the degradation and ion release kinetics of these highly porous systems. In this regard, the development of appropriate characterization techniques coupled with predictive analytical models is an important avenue of research in order to comprehensively assess the degradation of these systems with respect to pore structure, scaffolds geometry, fluid flow, and the influence of the bioactive additions. Here, the use of X-ray microtomography as a reliable tool for quantifying 3D pore structure parameters is likely to gain increased importance.[110]

Additionally, the properties of interfaces between the polymer matrix and inorganic inclusions need to be further investigated and characterized, since interfacial properties have a huge influence on degradation kinetics, ion concentration, and release profiles, as well as the effective composite mechanical properties. The use of improved cell seeding mechanisms and perfusion bioreactors should enable improved optimization of the scaffolds, especially with respect to the influence of ion concentration and release kinetics on cellular response. Moreover, improved cell biology assessment models are related to better understand the influence of media composition and volume, which can significantly influence the ion release kinetics and cell response.

In conclusion, it can be said that ceramics have been widely used in the biomedical engineering and bone substitution/regeneration field, whether it comprises a 100% ceramic composite, a composite of polymer with ceramic particles, or addition of polymeric additives/porogens to calcium phosphate. But still, significant improvements in the design and structure of porous bioactive ceramics are needed to overcome major drawbacks, such as their unpredictable osteoclastic activity and degradation/dissolution rates, as well as to facilitate controlled graft material resorption and tissue regeneration.[99]

References

1. El-Ghannam, A. *Expert Rev. Med. Devices* **2005**, *2*(1), 87–101.
2. Perry, C. R. *Clin. Orthop.* **1999**, *360*, 71–86.
3. Burg, K. J.; Porter, S.; Kellam, J. F. *Biomaterials* **2000**, *21*(23), 2347–2359.
4. Vacanti, C. A.; Bonassar, L. J.; Vacanti, J. P. In *Principles of Tissue Engineering*; Lanza, R. P., Langer, R., Vacanti, J., Eds.; Academic Press: San Diego, CA, 2000.
5. Younger, E. M.; Chapman, M. W. *J. Orthop. Trauma* **1989**, *3*(3), 192–195.
6. Asselmeier, M. A.; Caspari, R. B.; Bottenfield, S. *Am. J. Sports Med.* **1993**, *21*(2), 170–175.
7. Carson, J. S.; Bostrom, M. P. *Injury* **2007**, *38*(Suppl. 1), S33–S37.
8. Horstmann, W. G.; Verheyen, C. C.; Leemans, R. *Injury* **2003**, *34*(2), 141–144.
9. Trenholm, A.; Landry, S.; McLaughlin, K.; *et al. J. Orthop. Trauma* **2005**, *19*(10), 698–702.
10. Welch, R. D.; Zhang, H.; Bronson, D. G. *J Bone Joint Surg Am* **2003**, *85A*(2), 222–231.
11. Schepers, E.; de Clercq, M.; Ducheyne, P.; Kempeneers, R. *J. Oral Rehabil.* **1991**, *18*(5), 439–452.
12. Coombes, A. G.; Verderio, E.; Shaw, B.; *et al. Biomaterials* **2002**, *23*(10), 2113–2118.
13. Piskin, E. *Mater. Sci. Forum* **1997**, *250*, 14–42.
14. Griffith, L. G. *Acta Mater.* **2000**, *48*(1), 263–277.
15. Agrawal, C. M.; Ray, R. B. *J. Biomed. Mater. Res.* **2001**, *55*(2), 141–150.
16. Ma, P. X.; Zhang, R. *J. Biomed. Mater. Res.* **2001**, *56*(4), 469–477.
17. Wu, L.; Ding, J. *Biomaterials* **2004**, *25*(27), 5821–5830.
18. Boccaccini, A. R.; Blaker, J. J. *Expert Rev. Med. Devices* **2005**, *2*(3), 303–317.
19. Maquet, V.; Boccaccini, A. R.; Pravata, L.; *et al. J. Biomed. Mater. Res. A* **2003**, *66*(2), 335–346.
20. Maquet, V.; Boccaccini, A. R.; Pravata, L.; *et al. Biomaterials* **2004**, *25*(18), 4185–4194.
21. Thomson, R. C.; Yaszemski, M. J.; Powers, J. M.; Mikos, A. G. *Biomaterials* **1998**, *19*(21), 1935–1943.
22. Zhang, K.; Wang, Y.; Hillmyer, M. A.; Francis, L. F. *Biomaterials* **2004**, *25*(13), 2489–2500.

23. Rizzi, S. C.; Heath, D. J.; Coombes, A. G.; *et al*. *J. Biomed. Mater. Res.* **2001**, *55*(4), 475–486.
24. Verheyen, C. C.; de Wijn, J. R.; van Blitterswijk, C. A.; *et al*. *J. Biomed. Mater. Res.* **1993**, *27*(4), 433–444.
25. Zhang, R.; Ma, P. X. *J. Biomed. Mater. Res.* **1999**, *44*(4), 446–455.
26. Hollister, S. J.; Taboas, J. M.; Schek, R. M.; *et al*. In *Bone Tissue Engineering*; Hollinger, J. O., *et al*. Eds.; CRC Press: New York, 2005; pp 167–192.
27. Hutmacher, D. W. *Biomaterials* **2000**, *21*(24), 2529–2543.
28. Liebschner, M. A. K.; Wettergreen, M. A. In *Topics in Tissue Engineering*; Ferretti, P., Ashammakhi, N., Eds.; T. Waris & Ashammakhi, 2003; e-book on tissue engineering.
29. Suba, Z.; Takacs, D.; Matusovits, D.; *et al*. *Clin. Oral Impl. Res.* **2006**, *17*(1), 102–108.
30. Zerbo, I. R.; Bronckers, A. L.; de Lange, G.; Burger, E. H. *Biomaterials* **2005**, *26*(12), 1445–1451.
31. Tadjoedin, E. S.; de Lange, G. L.; Lyaruu, D. M.; *et al*. *Clin. Oral Impl. Res.* **2002**, *13*(4), 428–436.
32. Leonor, I. B.; Sousa, R. A.; Reis, R. L. In *Biodegradable Systems in Tissue Engineering and Regenerative Medicine*; Reis, R. L., Roman, J. S., Eds.; CRC Press: New York, 2005; pp 115–126.
33. Ochoa, I.; Sanz-Herrera, J. A.; Garcia-Aznar, J. M.; *et al*. *J. Biomech.* **2009**, *42*(3), 257–260.
34. Uebersax, L.; Hagenmuller, H.; Hofmann, S.; *et al*. *Tissue Eng.* **2006**, *12*(12), 3417–3429.
35. Bobyn, J. D.; Pilliar, R. M.; Cameron, H. U.; Weatherly, G. C. *Clin. Orthop. Relat. Res.* **1980**, *150*, 263–270.
36. Cheung, H. Y.; Lau, K. T.; Lu, T. P.; Hui, D. *Composites B* **2007**, *38*, 291–300.
37. Eggli, P. S.; Muller, W.; Schenk, R. K. *Clin. Orthop. Relat. Res.* **1988**, *232*, 127–138.
38. Galois, L.; Mainard, D. *Acta Orthop. Belg.* **2004**, *70*(6), 598–603.
39. Hing, K. A.; Best, S. M.; Tanner, K. E.; *et al*. *J. Biomed. Mater. Res. A* **2004**, *68*(1), 187–200.
40. Karageorgiou, V.; Kaplan, D. *Biomaterials* **2005**, *26*(27), 5474–5491.
41. Botchwey, E. A.; Dupree, M. A.; Pollack, S. R.; *et al*. *J. Biomed. Mater. Res. A* **2003**, *67*(1), 357–367.
42. Grimm, M. J.; Williams, J. L. *J. Biomech.* **1997**, *30*(7), 743–745.
43. Li, S.; De Wijn, J. R.; Li, J.; *et al*. *Tissue Eng.* **2003**, *9*(3), 535–548.
44. Neo, M.; Nakamura, T.; Ohtsuki, C.; *et al*. *J. Biomed. Mater. Res.* **1993**, *27*(8), 999–1006.
45. Ohtsuki, C.; Kushitani, H.; Kokubo, T.; *et al*. *J. Biomed. Mater. Res.* **1991**, *25*(11), 1363–1370.
46. Lee, K. Y.; *et al*. *Biomed. Mater.* **2006**, *1*(2), R31–R37.
47. Hench, L. L.; *et al*. *J. Biomed. Mater. Res. Symp.* **1972**, *2*, 117–141.
48. Kitsugi, T.; Yamamuro, T.; Kokubo, T. *J. Biomed. Mater. Res.* **1990**, *24*(2), 259–273.
49. El-Ghannam, A.; Ducheyne, P.; Shapiro, I. M. *J. Orthop. Res.* **1999**, *17*(3), 340–345.
50. Ducheyne, P.; Bianco, P.; Radin, S.; Schepers, E. In *Bone–Bioactive Materials*; Ducheyne, P., Kokubo, T., Van Blitterswijk, C. A., Eds.; Reed Healthcare Communications: Leiderdorp, Netherlands, 1993; pp 1–12.
51. Kaufmann, E. A.; Ducheyne, P.; Radin, S.; *et al*. *J. Biomed. Mater. Res.* **2000**, *52*(4), 825–830.
52. Kokubo, T. In *Bone–Bioactive Biomaterials*; Ducheyne, P., Kokubo, T., van Blitterswijk, C. A., Eds.; Reed Healthcare Communications: Leiderdorp, Netherlands, 1993; pp 31–46.
53. Radin, S.; Ducheyne, P. *J. Biomed. Mater. Res.* **1996**, *30*(3), 273–279.
54. Radin, S.; Ducheyne, P.; Berthold, P.; Decker, S. *J. Biomed. Mater. Res.* **1998**, *39*(2), 234–243.
55. Ducheyne, P.; Qiu, Q. *Biomaterials* **1999**, *20*(23–24), 2287–2303.
56. Daculsi, G.; LeGeros, R. Z.; Nery, E.; *et al*. *J. Biomed. Mater. Res.* **1989**, *23*(8), 883–894.
57. Ducheyne, P.; Radin, S.; King, L. *J. Biomed. Mater. Res.* **1993**, *27*(1), 25–34.
58. Radin, S.; Ducheyne, P.; Rothman, B.; Conti, A. *J. Biomed. Mater. Res.* **1997**, *37*(3), 363–375.
59. Radin, S. R.; Ducheyne, P. *J. Biomed. Mater. Res.* **1993**, *27*(1), 35–45.
60. Neo, M.; Nakamura, T.; Yamamuro, T.; *et al*. In *Bone–Bonding Biomaterials*; Ducheyne, P., Kokubo, T., van Blitterswijk, C. A., Eds.; Reed Healthcare Communications: Leiderdorp, Netherlands, 1993; pp 111–120.
61. Ducheyne, P.; Kim, C. S.; Pollack, S. R. *J. Biomed. Mater. Res.* **1992**, *26*(2), 147–168.
62. El-Ghannam, A.; Ducheyne, P.; Shapiro, I. M. *J. Biomed. Mater. Res.* **1997**, *36*(2), 167–180.
63. Yao, J.; Radin, S.; Reilly, G.; *et al*. *J. Biomed. Mater. Res. A* **2005**, *75*(4), 794–801.
64. de Bruijn, J. D.; Bovell, Y. P.; van Blitterswijk, C. A. *Biomaterials* **1994**, *15*(7), 543–550.
65. Davies, J. E. *Int. J. Prosthodont.* **1998**, *11*(5), 391–401.
66. Garcia, A. J.; Ducheyne, P.; Boettiger, D. *J. Biomed. Mater. Res.* **1998**, *40*(1), 48–56.
67. Keselowsky, B. G.; Collard, D. M.; Garcia, A. J. *J. Biomed. Mater. Res. A* **2003**, *66*(2), 247–259.
68. Cowles, E. A.; Brailey, L. L.; Gronowicz, G. A. *J. Biomed. Mater. Res.* **2000**, *52*(4), 725–737.
69. Gronowicz, G.; McCarthy, M. B. *J. Orthop. Res.* **1996**, *14*(6), 878–887.
70. Krause, A.; Cowles, E. A.; Gronowicz, G. *J. Biomed. Mater. Res.* **2000**, *52*(4), 738–747.
71. Rezania, A.; Healy, K. E. *J. Orthop. Res.* **1999**, *17*(4), 615–623.
72. Keselowsky, B. G.; Collard, D. M.; Garcia, A. J. *Proc. Natl. Acad. Sci. USA* **2005**, *102*(17), 5953–5957.
73. Juliano, R. L.; Haskill, S. *J. Cell Biol.* **1993**, *120*(3), 577–585.
74. Rosales, C. *Biochim. Biophys. Acta* **1995**, *1242*(1), 77–98.
75. Bates, R. C.; Lincz, L. F.; Burns, G. F. *Cancer Metastasis Rev.* **1995**, *14*(3), 191–203.
76. Faull, R. J.; Ginsberg, M. H. *Stem Cells* **1995**, *13*(1), 38–46.
77. Hildebrand, J. D.; Schaller, M. D.; Parsons, J. T. *Mol. Biol. Cell* **1995**, *6*(6), 637–647.
78. Hynes, R. O. *Cell* **1992**, *69*(1), 11–25.
79. Wary, K. K.; *et al*. *Cell* **1996**, *87*(4), 733–743.
80. Yamada, K. M.; Miyamoto, S. *Curr. Opin. Cell Biol.* **1995**, *7*(5), 681–689.
81. Habraken, W. J.; Wolke, J. G.; Jansen, J. A. *Adv. Drug Deliv. Rev.* **2007**, *59*(4–5), 234–248.
82. Ogino, M.; Ohuchi, F.; Hench, L. L. *J. Biomed. Mater. Res.* **1980**, *14*(1), 55–64.
83. Oonishi, H.; Kushitani, S.; Yasukawa, E.; *et al*. *Clin. Orthop. Relat. Res.* **1997**, *334*, 316–325.
84. Fujishiro, Y.; Hench, L. L.; Oonishi, H. *J. Mater. Sci. Mater. Med.* **1997**, *8*(11), 649–652.
85. Chen, Q. Z.; Thompson, I. D.; Boccaccini, A. R. *Biomaterials* **2006**, *27*(11), 2414–2425.
86. Schepers, E. J.; Ducheyne, P. *J. Oral Rehabil.* **1997**, *24*(3), 171–181.
87. Shapoff, C. A.; Alexander, D. C.; Clark, A. E. *Compend. Contin. Educ. Dent.* **1997**, *18*(4), 352–354; 356, 358 passim.
88. Wilson, J. In *An Introduction to Bioceramics*; Hench, L. L., Wilson, J., Eds.; World Scientific: River Ridge, NJ, 1993; pp 63–73.
89. Lobel, K. D.; Hench, L. L. *J. Biomed. Mater. Res.* **1998**, *39*(4), 575–579.
90. Ohgushi, H.; Dohi, Y.; Yoshikawa, T.; *et al*. *J. Biomed. Mater. Res.* **1996**, *32*(3), 341–348.
91. Day, R. M.; Boccaccini, A. R.; Shurey, S.; *et al*. *Biomaterials* **2004**, *25*(27), 5857–5866.
92. Keshaw, H.; Forbes, A.; Day, R. M. *Biomaterials* **2005**, *26*(19), 4171–4179.
93. Gatti, A. M.; Valdre, G.; Andersson, O. H. *Biomaterials* **1994**, *15*(3), 208–212.
94. Roether, J. A.; Gough, J. E.; Boccaccini, A. R.; *et al*. *J. Mater. Sci. Mater. Med.* **2002**, *13*(12), 1207–1214.
95. Lu, H. H.; Tang, A.; Oh, S. C.; *et al*. *Biomaterials* **2005**, *26*(32), 6323–6334.
96. Rezwan, K.; Chen, Q. Z.; Blaker, J. J.; Boccaccini, A. R. *Biomaterials* **2006**, *27*(18), 3413–3431.
97. Yuan, H.; de Bruijn, J. D.; Zhang, X.; *et al*. *J. Biomed. Mater. Res.* **2001**, *58*(3), 270–276.
98. Kaufmann, E. A.; Ducheyne, P.; Shapiro, I. M. *J. Biomed. Mater. Res.* **2000**, *52*(4), 783–796.
99. Xynos, I. D.; Edgar, A. J.; Buttery, L. D.; *et al*. *Biochem. Biophys. Res. Commun.* **2000**, *276*(2), 461–465.
100. Xynos, I. D.; Edgar, A. J.; Buttery, L. D.; *et al*. *J. Biomed. Mater. Res.* **2001**, *55*(2), 151–157.
101. Hench, L. L. *J. Am. Ceram. Soc.* **1991**, *74*, 1487–1510.
102. Hench, L. L.; Wilson, J. *Science* **1984**, *226*(4675), 630–636.
103. Hench, L. L. *J. Am. Ceram. Soc.* **1998**, *81*(7), 1705–1728.
104. Hench, L. L. *Curr Opin Solid State Mater Sci* **1997**, *2*, 604–610.
105. Pereira, M. M.; Clark, A. E.; Hench, L. L. *J. Biomed. Mater. Res.* **1994**, *28*(6), 693–698.
106. Li, P.; Zhang, F.; Kokubo, T. *J. Mater. Sci. Mater. Med.* **1992**, *3*, 452–456.
107. Clupper, D. C.; Hench, L. L. *J Non-Cryst Solids* **2003**, *318*, 42–48.

108. Anderson, O. H.; Kangasniemi, L. *J. Biomed. Mater. Res.* **1991**, *25*, 1019–1030.
109. Giesen, E. B.; Ding, M.; Dalstra, M.; *et al. J. Biomech.* **2001**, *34*(6), 799–803.
110. Hench, L. L. In *Bioceramics – Applications of Ceramic and Glass Materials in Medicine*; Shackelford, J. F., Ed.; Trans Tech Publications: Switzerland, 1999; pp 37–64.
111. Hench, L. L.; Kokubo, T. In *Handbook of Biomaterial Properties*; Black, J., Hastings, G., Eds.; Chapman & Hall: London, 1998; pp 355–363.
112. Jones, J. R.; Ehrenfried, L. M.; Hench, L. L. *Biomaterials* **2006**, *27*(7), 964–973.
113. Kim, H. W.; Knowles, J. C.; Kim, H. E. *J. Mater. Sci. Mater. Med.* **2005**, *16*(3), 189–195.
114. Kokubo, T. In *An Introduction to Bioceramics*; Hench, L. L., Wilson, J., Eds.; Word Scientific: London, 1999; pp 75–88.
115. LeGeros, R. Z.; LeGeros, J. P. In *An Introduction to Bioceramics*; Hench, L. L., Wilson, J., Eds.; Word Scientific: London, 1999; pp 139–180.
116. Yeni, Y. N.; Fyhrie, D. P. *J. Biomech.* **2001**, *34*(12), 1649–1654.
117. Zioupos, P.; Currey, J. D. *Bone* **1998**, *22*(1), 57–66.
118. Boccaccini, A. R.; Chen, Q.; Lefebvre, L.; *et al. Faraday Discuss* **2007**, *136*, 27–44; discussion 107–23.
119. Ebisawa, Y.; Miyaji, F.; Kokubo, T.; *et al. Biomaterials* **1997**, *18*(19), 1277–1284.
120. Kokubo, T.; Kim, H. M.; Kawashita, M. *Biomaterials* **2003**, *24*(13), 2161–2175.
121. Jarcho, M.; Kay, J. F.; Gumaer, K. I.; *et al. J. Bioeng.* **1977**, *1*(2), 79–92.
122. Denissen, H. W.; de Groot, K.; Makkes, P. C.; *et al. J. Biomed. Mater. Res.* **1980**, *14*(6), 713–721.
123. Hammerle, C. H.; Olah, A. J.; Schmid, J.; *et al. Clin. Oral Implants Res.* **1997**, *8*(3), 198–207.
124. Hollinger, J. O.; Battistone, G. C. *Clin. Orthop. Relat. Res.* **1986**, *207*, 290–305.
125. Matthews, F. L.; Rawlings, R. D. *Compostie Materials: Engineering and Science*; Chapman and Hall: London, 1994.
126. Bergsma, E. J.; Rozema, F. R.; Bos, R. R.; de Bruijn, W. C. *J. Oral Maxillofac. Surg.* **1993**, *51*(6), 666–670.
127. Bergsma, J. E.; de Bruijn, W. C.; Rozema, F. R.; *et al. Biomaterials* **1995**, *16*(1), 25–31.
128. Rhee, S. H. *Biomaterials* **2004**, *25*(7–8), 1167–1175.
129. Ladron de Guevara-Fernandez, S.; Ragel, C. V.; Vallet-Regi, M. *Biomaterials* **2003**, *24*(22), 4037–4043.
130. Shikinami, Y.; Okuno, M. *Biomaterials* **2001**, *22*(23), 3197–3211.
131. Navarro, M.; Ginebra, M. P.; Planell, J. A.; *et al. J. Mater. Sci. Mater. Med.* **2004**, *15*(4), 419–422.
132. Niemela, T.; Niiranen, H.; Kellomaki, M.; Tormala, P. *Acta Biomater.* **2005**, *1*(2), 235–242.
133. Qiu, Q. Q.; Ducheyne, P.; Ayyaswamy, P. S. *J. Biomed. Mater. Res.* **2000**, *52*(1), 66–76.
134. Yao, J.; Radin, S.; Leboy, P. S.; Ducheyne, P. *Biomaterials* **2005**, *26*(14), 1935–1943.
135. Mondrinos, M. J.; Dembzynski, R.; Lu, L.; *et al. Biomaterials* **2006**, *27*(25), 4399–4408.
136. Ambrosio, A. M.; Sahota, J. S.; Khan, Y.; Laurencin, C. T. *J. Biomed. Mater. Res.* **2001**, *58*(3), 295–301.
137. Ignjatovic, N.; *et al. Microsc. Res. Tech.* **2006**, *69*(12), 976–982.
138. Ignjatovic, N.; Ninkov, P.; Kojic, V.; *et al. J. Biomed. Mater. Res.* **2001**, *58*(6), 701–709.
139. Soriano, I.; Evora, C. *J. Control. Release* **2000**, *68*(1), 121–134.
140. Ziegler, J.; Mayr-Wohlfart, U.; Kessler, S.; *et al. J. Biomed. Mater. Res.* **2002**, *59*(3), 422–428.
141. Ruhe, P. Q.; Hedberg, E. L.; Padron, N. T.; *et al. J. Bone Joint Surg. Am.* **2003**, *85A*(Suppl. 3), 75–81.
142. Ruhe, P. Q.; Boerman, O. C.; Russel, F. G.; *et al. J. Control. Release* **2005**, *106*(1–2), 162–171.
143. Kim, H. W.; Knowles, J. C.; Kim, H. E. *J. Biomed. Mater. Res. A* **2005**, *72*(2), 136–145.
144. Shibata, Y.; Yamamoto, H.; Miyazaki, T. *J. Dent. Res.* **2005**, *84*(9), 827–831.
145. Takahashi, Y.; Yamamoto, M.; Tabata, Y. *Biomaterials* **2005**, *26*(23), 4856–4865.
146. Lin, F. H.; Yao, C. H.; Sun, J. S.; *et al. Biomaterials* **1998**, *19*(10), 905–917.
147. Du, C.; Cui, F. Z.; Zhang, W.; *et al. J. Biomed. Mater. Res.* **2000**, *50*(4), 518–527.
148. Tampieri, A.; Celotti, G.; Landi, E.; *et al. J. Mater. Sci. Mater. Med.* **2003**, *14*(7), 623–627.
149. Yamamoto, M.; Ikada, Y.; Tabata, Y. *J. Biomater. Sci. Polym. Ed.* **2001**, *12*(1), 77–88.
150. Itoh, S.; Kikuchi, M.; Koyama, Y.; *et al. Cell Transplant.* **2004**, *13*(4), 451–461.
151. Itoh, S.; Kikuchi, M.; Takakuda, K.; *et al. J. Biomed. Mater. Res.* **2001**, *54*(3), 445–453.
152. Bigi, A.; Bracci, B.; Panzavolta, S. *Biomaterials* **2004**, *25*(14), 2893–2899.
153. Bigi, A.; Panzavolta, S.; Sturba, L.; *et al. J. Biomed. Mater. Res. A* **2006**, *78*(4), 739–745.
154. Bigi, A.; Torricelli, P.; Fini, M.; *et al. Int. J. Artif. Organs* **2004**, *27*(8), 664–673.
155. Fujishiro, Y.; Takahashi, K.; Sato, T. *J. Biomed. Mater. Res.* **2001**, *54*(4), 525–530.
156. Bigi, A.; Boanini, E.; Panzavolta, S.; Roveri, N. *Biomacromolecules* **2000**, *1*(4), 752–756.
157. Rammelt, S.; Schulze, E.; Witt, M.; *et al. Cells Tissues Organs* **2004**, *178*(3), 146–157.
158. Knepper-Nicolai, B.; Reinstorf, A.; Hofinger, I.; *et al. Biomol. Eng.* **2002**, *19*(2–6), 227–231.
159. Hempel, U.; Reinstorf, A.; Poppe, M.; *et al. J. Biomed. Mater. Res. B Appl. Biomater.* **2004**, *71*(1), 130–143.
160. Lode, A.; Wolf-Brandstetter, C.; Reinstorf, A.; *et al. J. Biomed. Mater. Res. A* **2007**, *81*(2), 474–483.
161. Jegoux, F.; Goyenvalle, E.; Bagot-D'arc, M.; *et al. Arch. Orthop. Trauma Surg.* **2005**, *125*(3), 153–159.
162. Le Nihouannen, D.; Guehennec, L. L.; Rouillon, T.; *et al. Biomaterials* **2006**, *27*(13), 2716–2722.
163. Kneser, U.; Voogd, A.; Ohnolz, J.; *et al. Cells Tissues Organs* **2005**, *179*(4), 158–169.
164. Vaz, C. M.; Fossen, M.; van Tuil, R. F.; *et al. J. Biomed. Mater. Res. A* **2003**, *65*(1), 60–70.
165. Lin, J.; Zhang, S.; Chen, T.; *et al. J. Biomed. Mater. Res. B Appl. Biomater.* **2006**, *76*(2), 432–439.
166. Ginebra, M. P.; Traykova, T.; Planell, J. A. *J. Control. Release* **2006**, *113*(2), 102–110.
167. Jansen, J. A.; Vehof, J. W.; Ruhe, P. Q.; *et al. J. Control. Release* **2005**, *101*(1–3), 127–136.
168. Seeherman, H.; Wozney, J. M. *Cytokine Growth Factor Rev.* **2005**, *16*(3), 329–345.
169. Asahina, I.; Watanabe, M.; Sakurai, N.; *et al. J. Med. Dent. Sci.* **1997**, *44*(3), 63–70.
170. Cunningham, B. W.; Kanayama, M.; Parker, L. M.; *et al. Spine (Phila Pa 1976)* **1999**, *24*(6), 509–518.
171. Ferguson, D.; Davis, W. L.; Urist, M. R.; Hurt, W. C. *Clin. Orthop. Relat. Res.* **1987**, *219*, 251–259.
172. Gao, T.; Lindholm, T. S.; Marttinen, A.; Urist, M. R. *Int. Orthop.* **1996**, *20*(5), 321–325.
173. Gao, T. J.; Lindholm, T. S.; Kommonen, B.; *et al. J. Biomed. Mater. Res.* **1996**, *32*(4), 505–512.
174. Gerhart, T. N.; Kirker-Head, C. A.; Kriz, M. J.; *et al. Clin. Orthop. Relat. Res.* **1993**, *293*, 317–326.
175. Johnson, E. E.; Urist, M. R.; Finerman, G. A. *Clin. Orthop. Relat. Res.* **1988**, *236*, 249–257.
176. Koempel, J. A.; Patt, B. S.; O'Grady, K.; *et al. J. Biomed. Mater. Res.* **1998**, *41*(3), 359–363.
177. Levine, J. P.; Bradley, J.; Turk, A. E.; *et al. Ann. Plast. Surg.* **1997**, *39*(2), 158–168.
178. Linde, A.; Hedner, E. *Calcif. Tissue Int.* **1995**, *56*(6), 549–553.
179. Miyamoto, S.; Takaoka, K.; Ono, K. *J. Bone Joint Surg. Br.* **1993**, *75*(1), 107–110.
180. Sandhu, H. S.; Kanim, L. E.; Toth, J. M.; *et al. Spine (Phila Pa 1976)* **1997**, *22*(11), 1171–1180.
181. Suzawa, M.; Takeuchi, Y.; Fukumoto, S.; *et al. Endocrinology* **1999**, *140*(5), 2125–2133.
182. Yasko, A. W.; Lane, J. M.; Fellinger, E. J.; *et al. J. Bone Joint Surg. Am.* **1992**, *74*(5), 659–670.
183. Bostrom, M. P.; Camacho, N. P. *Clin Orthop Relat Res* **1998**, *355*(Suppl.), S274–S282.
184. Croteau, S.; Rauch, F.; Silvestri, A.; Hamdy, R. C. *Orthopedics* **1999**, *22*(7), 686–695; quiz 696–7.
185. Miyamoto, S.; Takaoka, K.; Okada, T.; *et al. Clin. Orthop. Relat. Res.* **1993**, *294*, 333–343.
186. Sakou, T. *Bone* **1998**, *22*(6), 591–603.
187. Tsuruga, E.; Takita, H.; Itoh, H.; *et al. J. Biochem.* **1997**, *121*(2), 317–324.
188. Whang, K.; Tsai, D. C.; Nam, E. K.; *et al. J. Biomed. Mater. Res.* **1998**, *42*(4), 491–499.

189. Ono, I.; Gunji, H.; Kaneko, F.; *et al*. *J. Craniofac. Surg.* **1995**, *6*(3), 238–244.
190. Ripamonti, U.; Ma, S. S.; van den Heever, B.; Reddi, A. H. *Plast. Reconstr. Surg.* **1992**, *90*(3), 382–393.
191. Doll, B. A.; Towle, H. J.; Hollinger, J. O.; *et al*. *J. Periodontol*. **1990**, *61*(12), 745–750.
192. Horisaka, Y.; Okamoto, Y.; Matsumoto, N.; *et al*. *Clin. Orthop. Relat. Res.* **1991**, *268*, 303–312.
193. Alam, I.; Asahina, I.; Ohmamiuda, K.; Enomoto, S. *J. Biomed. Mater. Res.* **2001**, *54*(1), 129–138.
194. Nicoll, S. B.; Radin, S.; Santos, E. M.; *et al*. *Biomaterials* **1997**, *18*(12), 853–859.
195. Santos, E. M.; Radin, S.; Shenker, B. J.; *et al*. *J. Biomed. Mater. Res.* **1998**, *41*(1), 87–94.
196. El-Ghannam, A.; Ning, C. Q.; Mehta, J. *J. Biomed. Mater. Res. A* **2004**, *71*(3), 377–390.
197. El-Ghannam, A. R. *J. Biomed. Mater. Res. A* **2004**, *69*(3), 490–501.
198. Gao, T.; Aro, H. T.; Ylanen, H.; Vuorio, E. *Biomaterials* **2001**, *22*(12), 1475–1483.
199. Abe, Y.; Hosono, H.; Ohta, Y.; Hench, L. L. *Phys. Rev. B Condens. Matter.* **1988**, *38*(14), 10166–10169.
200. Hench, L. L.; Wilson, J. *An Introduction to Bioceramics*, 2nd ed.; Word Scientific: London, 1999.
201. Keaveny, T. M.; Hayes, W. C. In *Bone Growth*; Hall, B. K., Ed.; CRC Press: Boca Raton, FL, 1993.
202. Seal, B. L.; Otero, T. C.; Panitch, A. *Materials Science & Engineering R-Reports* **2001**, *34*(4–5), 147–230.
203. Deng, X.; Hao, J.; Wang, C. *Biomaterials* **2001**, *22*(21), 2867–2873.
204. Kasuga, T.; Ota, Y.; Nogami, M.; Abe, Y. *Biomaterials* **2001**, *22*(1), 19–23.
205. Xu, H. H.; Quinn, J. B.; Takagi, S.; Chow, L. C. *Biomaterials* **2004**, *25*(6), 1029–1037.
206. Xu, H. H.; Simon, C. G., Jr. *J. Orthop. Res.* **2004**, *22*(3), 535–543.
207. Peter, S. J.; Miller, S. T.; Zhu, G.; Yasko, A. W.; *et al*. *J. Biomed. Mater. Res.* **1998**, *41*(1), 1–7.
208. Juhasz, J. A.; Best, S. M.; Brooks, R.; Kawashita, M.; *et al*. *Biomaterials* **2004**, *25*(6), 949–955.
209. Khan, Y. M.; Katti, D. S.; Laurencin, C. T. *J. Biomed. Mater. Res. A* **2004**, *69*(4), 728–737.
210. Guan, L.; Davies, J. E. *J. Biomed. Mater. Res. A* **2004**, *71*(3), 480–487.
211. Devin, J. E.; Attawia, M. A.; Laurencin, C. T. *J. Biomater. Sci. Polymer. Ed.* **1996**, *7*(8), 661–669.
212. Lu, H. H.; El-Amin, S. F.; Scott, K. D.; Laurencin, C. T.; *et al*. *J. Biomed. Mater. Res. A* **2003**, *64*(3), 465–474.
213. Stamboulis, A. G.; Boccaccini, A. R.; Hench, L. L. *Adv. Eng. Mater.* **2002**, *4*(3), 105–109.
214. Boccaccini, A. R.; Blaker, J. J.; Maquet, V.; Day, R. M.; *et al*. *Materials Science & Engineering C-Biomimetic and Supramolecular Systems* **2005**, *25*(1), 23–31.
215. Blaker, J. J.; Gough, J. E.; Maquet, V.; Notingher, I.; *et al*. *J. Biomed. Mater. Res. A* **2003**, *67*(4), 1401–1411.
216. Blaker, J. J.; Maquet, V.; Jerome, R.; Boccaccini, A. R.; *et al*. *Acta Biomater.* **2005**, *1*(6), 643–652.
217. Verrier, S.; Blaker, J. J.; Maquet, V.; Hench, L. L.; *et al*. *Biomaterials* **2004**, *25*(15), 3013–3021.
218. Li, H.; Chang, J. *J. Mater. Sci. Mater. Med.* **2004**, *15*(10), 1089–1095.

5.521. Calcium Phosphates and Bone Induction

H Yuan, University of Twente, Enschede, The Netherlands; Progentix Orthobiology BV, Bilthoven, The Netherlands
D Barbieri, Progentix Orthobiology BV, Bilthoven, The Netherlands
C A Van Blitterswijk, University of Twente, Enschede, The Netherlands
J D De Bruijn, Progentix Orthobiology BV, Bilthoven, The Netherlands; Queen Mary University of London, London, UK

© 2011 Elsevier Ltd. All rights reserved.

5.521.1. Bone and Its Biology 270
5.521.2. Bone Grafting and the Strategies 270
5.521.2.1. Bone Grafts 270
5.521.2.2. Synthetic Bone 270
5.521.2.2.1. Biomaterials 270
5.521.2.2.2. Growth factors 271
5.521.2.2.3. Bone tissue engineering 271
5.521.3. Biomaterials for Bone Substitution 271
5.521.3.1. From Bioinert Materials to Bioactive (Osteoconductive) Materials 271
5.521.3.2. From Bioactive (Osteoconductive) Materials to Materials Associated with Osteoinduction 271
5.521.4. Bone Induction Associated with Materials 271
5.521.4.1. Bone Induction Study Models 271
5.521.4.2. Bone Induction in the Presence of Calcium Phosphate-Based Ceramic Materials 272
5.521.4.2.1. Phenomenon 272
5.521.4.2.2. Animal dependence 272
5.521.4.2.3. Bone formation and osteoinduction in the presence of materials 272
5.521.4.3. Bone Induction by Non-CaP Materials 274
5.521.5. Role of Calcium Phosphate in Bone Induction 274
5.521.6. Material Factors 274
5.521.6.1. Chemistry 274
5.521.6.2. Microstructures 275
5.521.6.3. Macrostructures 275
5.521.7. Mechanism of Bone Induction 276
5.521.7.1. Protein Adsorption 276
5.521.7.2. Topography 276
5.521.7.3. Surface Calcification 276
5.521.7.4. Inflammation 276
5.521.8. Clinical Significance of Osteoinductive Materials 277
5.521.8.1. Repairing Small Bone Defects 278
5.521.8.2. Critical-Sized Defects 278
5.521.8.3. Spinal Fusion 278
5.521.9. Future Directions 279
References 279

Glossary

Osteoinductive material A synthetic material that gives rise to bone formation in nonosseous sites (i.e., in muscle or subcutis) without additional growth factors (such as bone morphogenetic proteins) or osteogenic cells.

Abbreviations

ACS	Absorbable collagen sponge
AIO	Alumina ceramic
ALP	Alkaline phosphatase
BCP	Biphasic calcium phosphate
BMPs	Bone morphogenetic proteins
BMP-2	Recombinant bone morphogenetic protein 2
BMP-7	Recombinant bone morphogenetic protein 7
BSEM	Backscattered electron microscope
β-TCP	Beta tri-calcium phosphate
CaP	Calcium phosphate materials
DBM	Demineralized bone matrix
HA	Hydroxyapatite
mRNA	Messenger ribonucleic acid
OCP	Octacalcium phosphate
OP-1	Recombinant bone morphogenetic protein 7

PGE2	Prostaglandin E2
PRP	Platelet-rich plasma
rhBMPs	Recombinant bone morphogenetic proteins
SEM	Scanning electron microscope
TCP	Tri-calcium phosphate
TCP-a	Pure tri-calcium phosphate ceramic particles
TCP-b	Pure tri-calcium phosphate ceramic particles
TCP-c	Tri-calcium phosphate ceramic containing traces of hydroxyapatite
TCP-B	Tri-calcium phosphate ceramic with large grains and large micropores
TCP-S	Tri-calcium phosphate ceramic with small grains and small micropores
TRAP	Tartrate resistant acid phosphatase

5.521.1. Bone and Its Biology

Bone is as vital to life as any other organ system. It provides the internal support of the body and is the framework for the attachment of the muscles and tendons essential for locomotion. It not only protects the vital organs of the heart, lungs, brain, and spinal cord but also encloses the blood-forming elements of the bone marrow. In addition, it contains 99% of the body's calcium, 85% of the body's phosphorous, and 65% of the body's sodium and magnesium. It plays important roles in the homeostatic regulation of the concentration of calcium and phosphorous in the blood and in other body fluids.[1,2]

The shape of bone in different parts of the body varies with their specific functions, but the structure of bones of different shape is basically similar. It is one of the unique connective tissues that are normally mineralized. Biochemically, bone is defined by its special blend of organic matrix (35%) and inorganic elements (65%).[1,2]

The inorganic matter of bone consists mainly of calcium and phosphate, a significant amount of citrate and carbonate ions, and traces of fluoride, magnesium, and sodium. Through a process of biomineralization, calcium phosphate in bone deposits vary similarly, but not identically, to mineral hydroxyapatite (HA) on collagen matrix. The mixture of calcium phosphate and collagen matrix gives bone strength and toughness.[1,2]

Despite its strength and hardness, bone is a dynamic living tissue with its own biology. In development, bone occurs by direct replacement of primitive connective tissues (intramembranous ossification) or by replacement of preexisting cartilage (endochondral ossification). In addition to embryonic bone development, bone is also renewed throughout the lifetime of the individual through a process of bone remodeling: existing bone is resorbed and new bone is formed in the resorbed bone bed (this bone formation is called secondary bone formation).[1–3]

Bone is also one of the few tissues that can fully repair itself. For instance, the fracture of bone activates osteogenesis and, eventually, the fracture heals without any scar formation.[1]

Sometimes, but not frequently, normal bone is formed in nonosseous sites.[1]

5.521.2. Bone Grafting and the Strategies

Although bone has the ability to repair itself, the ability decreases with the age, is affected by diseases (e.g., osteoporosis) and other factors, and is limited to small bone defects. When bone loss is too large (e.g., in case of excision of bone tumors or other bone diseases, in case of bone loss due to accidents, and in fractured bones that cannot repair themselves), surgery is necessary to repair the bone defects.

Several strategies are taken into consideration for cases of difficult bone repair. New surgical techniques and novel tools could allow mini-invasive or noninvasive surgery,[4,5] and novel instruments could improve the bone healing.[6] In any case, bone grafts are necessary and bone grafting materials with high bone regeneration ability are an important strategy for the achievement of the clinical outcome of bone repair.[7,8]

5.521.2.1. Bone Grafts

Several bone grafts are chosen for bone repair: autografts, allografts (including demineralized bone matrix, DBM), and synthetic materials.[9–12] Autogenous bone graft typically taken from the iliac crest has long been the gold standard, although it is associated with donor site morbidity. Although the non- or mini-invasive surgical techniques to harvest iliac crest autograft can minimize the donor site morbidity and pain, the amount of autograft that can be harvested is limited for bone defects where a large volume of grafting material is needed. Owing to the growth factors, osteogenic cells (i.e., osteoblasts and osteogenic progenitor cells), scaffolding substances and to the fact that it is obtained from the patient itself, autograft is biocompatible, osteoconductive, and osteoinductive. Biologically active substances intended to extend, enhance, or even replace autologous graft include allograft and DBM. However, these biologically active substances do not have the potency of autografts and promote less bone formation. Moreover, they can be associated with disease transmission. Various synthetic materials exist that are available in large quantities, and are biocompatible and bioactive (osteoconductive). Additionally, they do not carry the risk of disease transmission. Their effect on bone tissue formation varies widely as is described at length in other chapters of this publication.

5.521.2.2. Synthetic Bone

Synthetic bone that mimics one or more components of bone is under consideration, with the goal of achieving the degree of repair typically resulting from the use of autograft.

5.521.2.2.1. Biomaterials

Although the goal has been to make biomaterials that mimic bone chemically, physically, and mechanically, this is not simple to accomplish. Biomaterials can vary with chemistry, forms, and shapes for different applications. They can be

biocompatible and osteoconductive. Some metals are strong enough for bone augmentation in load-bearing sites. Calcium phosphate materials chemically mimic bone. The combination of polymeric materials and calcium phosphate could mimic bone both chemically and mechanically. Applying porous structures similar to cancellous bone to biomaterials enables them to mimic bone physically and thus, the resulting materials can become scaffolding substances for bone regeneration.

5.521.2.2.2. Growth factors

Loading growth factors to materials is a way to mimic autograft for bone repair. Among the growth factors, bone morphogenetic proteins (BMPs) and platelet-rich plasma (PRP) are of interest. BMPs are proteins having the potency to differentiate inducible cells to osteogenic cells that can form bone. Once BMPs are introduced to materials, the hybrid scaffold becomes osteoinductive and makes it possible to repair large bone defects.[13] BMPs have been introduced to patient care first with highly purified BMPs[14] and later on with recombinant BMPs (rhBMPs). Among the rhBMPs, BMP-2 and BMP-7 (also called OP-1) are currently used. However, the high dose of rhBMPs currently administered has led not only to high costs, but also to clinical issues.[15,16] PRP is a concentrated source of autologous platelets, which contains and releases (through degranulation) different growth factors (cytokines) that stimulate bone and soft tissue healing.[17,18] PRP may enhance bone formation but does not induce bone formation as BMPs do. Applying PRP to materials may therefore not be a good choice in mimicking autologous bone, and the variation of the quality with the processes of preparation is another shortcoming of PRP that makes it unsuitable for clinical uses.

5.521.2.2.3. Bone tissue engineering

Bone tissue engineering, an approach in which osteogenic cells are loaded onto materials, is another way to achieve repair similar to that achieved with autologous bone. This principle has been studied extensively, as is described elsewhere in this publication. Two studies, for example, are studies in rodents with relatively small defects.[19,20] The osteogenic cells can be obtained from *in vitro* expanded bone marrow stromal cells and from bone marrow aspiration. Mesenchymal stem cells from other tissues like adipose tissue can also be used. It is possible to fabricate tissue-engineered bone for large bone defects by using large-size scaffold materials. For large tissue-engineered bone, perfusion represents a limitation.

5.521.3. Biomaterials for Bone Substitution

5.521.3.1. From Bioinert Materials to Bioactive (Osteoconductive) Materials

Many materials have been used in bone repair procedures. First, select non-bone–bioactive materials (mainly metals and polymers), which do not give rise to any adverse tissue responses, were used to physically and/or mechanically repair bone. Later on, it was found that better bone repair could be achieved with bioactive calcium phosphate (CaP) materials (calcium phosphate ceramics and glasses in bulk, cement, composite, and coating form). These materials are not only biocompatible but also guide bone formation on their surface and bond to the newly formed bone.[21–26]

5.521.3.2. From Bioactive (Osteoconductive) Materials to Materials Associated with Osteoinduction

Bioactive materials support osteogenic cells to form bone on their surface and integrate with the newly formed bone. As bone formation on bioactive materials needs osteogenic cells and the migration of such cells from the surrounding tissues is limited with respect to distance, bioactive materials are not sufficient to repair large bone defects (e.g., critical-sized defects). To repair critical-sized defects, materials that are associated with events of osteoinduction are valuable to get full bone formation throughout large defects.

5.521.4. Bone Induction Associated with Materials

5.521.4.1. Bone Induction Study Models

When bone is observed in a nonosseous site, such bone formation is described by the terms heterotopic bone formation, heterotopic ossification, or ectopic bone formation.

Pathophysiological heterotopic bone formation is an uncommon but well-recognized complication of spinal injury, closed head injury, total hip arthroplasty, burns, and other trauma.[27] Controllable and reproducible bone induction was postulated to be very useful in musculoskeletal repair,[28] and efforts have been made to obtain osteoinductive bone substitutes. Introduction of growth factors (e.g., BMPs) to carriers[13] is one approach to the synthesis of osteoinductive bone substitutes, while induction of osteogenic progenitor cells to scaffolding materials is another (bone tissue engineering).[19,20]

Soft tissue implantation is the model to evaluate osteoinduction of bone substitutes. For example, subcutaneous implantation or intramuscular implantation in mouse or rat is quite often used to evaluate osteoinduction of bone substitutes bearing growth factors or osteogenic progenitor cells.[28,29]

The calcium phosphate literature of the 1980s and before described the properties of these materials as osteoconductive.[30]

Starting with the studies by Ripamonti,[31,32] and later by Schepers *et al.*,[33] data were published that showed an induction effect associated with various calcium phosphate ceramics, that is, bone formation in soft tissue sites, or bone formation by upregulation of precursor cells without osteoconduction taking place. Animals other than rodents were used to evaluate osteoinduction associated with materials and since then events of induction associated with specific materials have been shown in different animal species. The quite often used models to evaluate bone induction of materials are the intramuscular implantation and the subcutaneous implantation. It has been shown that, following intramuscular implantation, materials could give rise to better bone formation than following subcutaneous implantation, possibly because of the better vascularization of the implants in muscle.[34,35]

Bone induction with materials is identified by bone morphogenesis. Osteoinduction of growth factors can be evaluated *in vitro* with special cell types and the osteoinductive property of tissue-engineered bone (with osteogenic cells or osteogenic progenitor cells) can be partially tested *in vitro* as well, while there

is no *in vitro* evaluation system available so far for evaluating the osteoinductivity of materials alone. Although some materials enhance bone marker expression of osteogenic cells or osteogenic progenitor cells cultured on them,[36] the materials may fail to give rise to bone formation when implanted in soft tissue. Thus, it is then imprudent to use *in vitro* cell cultures to predict the osteoinduction associated with a material. For example, microstructures have shown to have an important role in bone induction associated with calcium phosphate materials,[37,38] while an *in vitro* study has reported an adverse role of microporosity in the behavior of human osteoprogenitor cells.[39] However, it would be useful to find *in vitro* markers for cells cultured on materials that are associated with the osteoinduction *in vivo*.

5.521.4.2. Bone Induction in the Presence of Calcium Phosphate-Based Ceramic Materials

5.521.4.2.1. Phenomenon

As the main inorganic component of bone, calcium phosphate has been developed as a material in different forms for bone regeneration. It has been demonstrated that calcium phosphate materials in their various forms are biocompatible, osteoconductive (i.e., they form a chemical bond with the newly formed bone), and resorbable.[21–26] Osteoconductive calcium phosphate materials are considered as alternatives to autograft for bone repair.

Osteoinduction associated with calcium phosphate materials was ruled out based on the results from rodents,[30] but ectopic bone formation associated with calcium phosphates was first found in specific HA ceramics following subcutaneous or intramuscular implantation in dogs and baboons by Yamasaki,[40] Zhang.[41] Since then, ectopic bone formation by other calcium phosphate materials has been found in different animal species (**Table 1**).

So far, bone formation of calcium phosphate materials has been observed in HA ceramics, biphasic calcium phosphate (BCP) ceramics, tricalcium phosphate (TCP) ceramics, calcium phosphate cements, and glass ceramic in nonosseous sites.

5.521.4.2.2. Animal dependence

Animal dependence of bone induction associated with materials has been shown by evaluating ectopic bone formation of calcium phosphate materials in different animal species.[35,48,68] The ectopic bone formation with calcium phosphate materials has been tested directly in various animal models (i.e., mouse, rat, rabbit, goat, sheep, pig, dog, monkey, and baboon) and indirectly in humans (**Table 1**). Although the ability of calcium phosphate materials to give rise to ectopic bone formation varies with the animal species, bone induction with calcium phosphate materials has been seen in all the aforementioned animal models except in rats till date.

Among the animal species, bone induction with calcium phosphate materials appears to occur in various models using baboons, dogs, and sheep. This is not the case among models that use rabbits, goat, and mice. In fact, variations occur in terms of the bone incidence, if any, the amount of bone formed, and the time for bone formation to occur intramuscularly or subcutaneously. In goats, the amount of the formed bone in calcium phosphate materials following intramuscular implantation is limited (±1% in the available space)[61,64] and variations between individual animals are often observed.[74] In some studies, no bone induction was seen.[35,80]

Although bone induction with calcium phosphate materials does not occur in all the animal species tested, it takes place in nonhuman primates (monkey and baboon) and also in nonosseous sites of humans. This prompts the concept of clinical significance for bone repair if such materials were capable of enhancing bone regeneration in large bone defects.

5.521.4.2.3. Bone formation and osteoinduction in the presence of materials

The process of bone induction associated with calcium phosphate materials was evaluated in animals for periods from 7 days up to 2.5 years.

Four patterns of structural tissue organization were found in HA ceramic following intramuscular implantation in baboons at 3, 6, and 9 months: first, fibrous connective tissue with pronounced cellular and vascular components was formed in the implants, then collagen fibers condensed in fibrous connective tissue at the interface of the HA, followed by morphogenesis of bone, remodeling of bone, formation of lamellar bone, and differentiation of bone marrow.[32]

A complex process, involving clot formation, vascular invasion, granulation-like tissue formation, polymorphic cell aggregation, osteoblast differentiation, and bone formation, was observed in BCP ceramic implanted in muscle of dogs at an early period of 7–45 days. Before bone formation started, alkaline phosphatase (ALP)-positive polymorphic cells aggregated on the inner surface of the implants and near the invading capillaries or small venules, followed by osteoblast differentiation of the polymorphic cells and bone formation on the pore surface.[50]

The chronological bone formation in the specific forms of BCP and HA (with their unique chemical and physical properties) was observed from 7 to 360 days following intramuscular implantation in dogs. Although bone formation started earlier and more bone formed inside BCP than in HA, the process of bone formation was the same, including cell attachment, proliferation and differentiation, formation of bone matrix by osteoblast-like cells, and mineralization of bone matrix on the material surface, followed by bone remodeling, bone marrow formation, and formation of mature bone. However, each step took place earlier in the BCP used than in the HA used. For instance, bone matrix formation, which is the indicator of early bone formation, was found in the BCP at day 30 and in the HA at day 45.[70]

Similar bone formation was observed chronologically with a specific form of β-TCP with unique chemical and physical properties implanted in dog dorsal muscles from 14 to 112 days. New bone was observed after 56 days, and α1 chain of type I procollagen mRNA-positive osteoblasts lined the newly formed bone.[67]

The time needed for bone induction varied with materials, while bone always started to form on the inner surface of the materials and was observed inside the implants, which were surrounded by a layer of connective tissue. The amount of the formed bone increased with time and stayed stable at longer time (up to 2.5 years).[32,56,57]

Bone formed in the presence of calcium phosphate materials is biologically and biochemically similar to normal bone: in fact, the cellular events observed in normal bone formation

Table 1 Evidences of bone induction by calcium phosphate-based materials

Calendar year	*References*	*Materials*	*Animal species*	*Implantation sites*
1990	40	HA	Dog	Subcutaneous
1991	31	HA	Baboon	Intramuscular
	32	HA	Baboon	Intramuscular
	41	HA	Dog	Intramuscular
1992	37	HA	Dog	Subcutaneous
	42	HA	Monkey	Subcutaneous
1993	43	BCP, TCP, and pyrocalcium phosphate	Dog	Subcutaneous
	44	HA	Baboon	Intramuscular
1994	45	HA	Dog	Intramuscular
	46	HA	Baboon	Intramuscular
1995	47	HA	Human patient	Orbital implants
1996	48	HA	Baboon, dog	Intramuscular
	35	BCP	Dog, pig	Intramuscular/subcutaneous
	49	HA	Baboon	Intramuscular
1997	50	BCP	Dog	Intramuscular
	51	HA	Rabbit	Orbital implants
1998	52	HA, BCP, TCP, and CaP cement	Dog	Intramuscular
1999	53	HA	Baboon	Intramuscular
	38	HA	Dog	Intramuscular
2000	54	OCP-coated tantalum	Dog	Intramuscular
	55	CaP cement	Dog	Intramuscular
2001	56	HA, BCP, and TCP	Dog	Intramuscular
	57	TCP	Dog	Intramuscular
	58	Glass ceramic	Dog	Intramuscular
2002	59	BCP	Rabbits	Intramuscular
	60	HA, BCP, and CaP cement	Sheep	Intramuscular/subcutaneous
	61	BCP	Goat	Intramuscular
2003	62	OCP-coated titanium	Goat	Intramuscular
2004	63	BCP and OCP-coated titanium	Goat	Intramuscular
	64	BCP	Goat	Intramuscular
2005	65	HA, BCP	Goat	Intramuscular
	66	BCP	Sheep	Intramuscular
2006	67	TCP	Dog	Intramuscular
	34	BCP	Goat	Intramuscular/subcutaneous
	68	BCP and HA	Dog, rabbit, and mouse	Intramuscular/subcutaneous
	69	BCP and HA	Goat	Intramuscular
	70	BCP and HA	Dog	Intramuscular
2007	71	BCP/titanium hybrid	Goat	Intramuscular
	72	HA, BCP, and carbon-impregnated HA	Baboon	Intramuscular
	73	BCP	Sheep	Intramuscular
2008	74	BCP	Goat	Intramuscular
	75	HA	Dog	Subcutaneous
	76	BCP	Baboon	Intramuscular
	77	BCP and TCP	Dog	Intramuscular
2009	78	TCP	Dog	Intramuscular
	79	HA and HA/carbonate	Baboon	Intramuscular

and bone remodeling occurred in inductive bone formation as well. The matrix fibers of the induced bone were mainly composed of type I collagen.[75] The pattern of crystal deposition in bone tissue induced in the presence of calcium phosphate materials and the structure of osteoblasts, osteocytes, bone lining cells, and osteoclast-like cells were similar to those of normal bone tissue.[75] The bone-forming cells are ALP-positive[50] and produce OP-1 and collagen IV.[72,79]

Unlike bone formation induced by BMPs, bone formation induced in the presence of calcium phosphate materials started directly with bone and no cartilage was observed along the induced bone formation. It appeared that bone formation induced in the presence of calcium phosphate materials follows intramembranous ossification.[32,50] However, it was noticed that multinucleated cells were present on the surface of the materials before bone formation started.[50,67] Meanwhile, the multinucleated cells yielded a positive result to osteoclast markers (TRAP and cathepsin K).[67] Moreover, EP4 agonist, which stimulated osteoclastogenesis, enhanced bone formation in TCP implanted in muscle of dogs.[78] The data indicate that bone formation induced in the presence of calcium phosphate materials likely resembles the pattern of bone formation during bone remodeling rather than during intramembranous formation.

5.521.4.3. Bone Induction by Non-CaP Materials

In addition to bone induction associated with calcium phosphate materials, ectopic bone formation was also found in materials other than calcium phosphates. As early as 1969, Winter and Simpson found that heterotopic bone formed in a synthetic sponge of polyhydroxyethylmethacrylate under the skin of young pigs.[81] Okumura *et al.*[82] observed bone tissue formation in titanium fiber mats implanted with osteogenic cells, albeit in a different pattern than in the HA implanted by Ohgushi *et al.*[83] in prior studies with the same model. Fujiibayashi and Takemoto found bone formation in physicochemically treated titanium metal following intramuscular implantation in dogs.[84,85]

Moreover, it was found that an alumina ceramic, which is normally considered as a bioinert material, was associated with osteoinduction when its surface was microstructured (Figure 1(a)). When cylindrical alumina ceramics (ø5 × 6 mm^3) made from Al_2O_3 powder with diluted H_2O_2, sintered at 1300 °C for 10 h, were implanted in back muscle of dogs for 3 months, bone was observed inside all the harvested implants. Bone formation started from the inner pore surface of alumina ceramic near plenty of blood vessels (Figure 1(c)), while mineralization of the bone matrix did not start directly on the alumina surface, leaving an unmineralized zone between the alumina surface and the mineralized bone (Figure 1(b)).

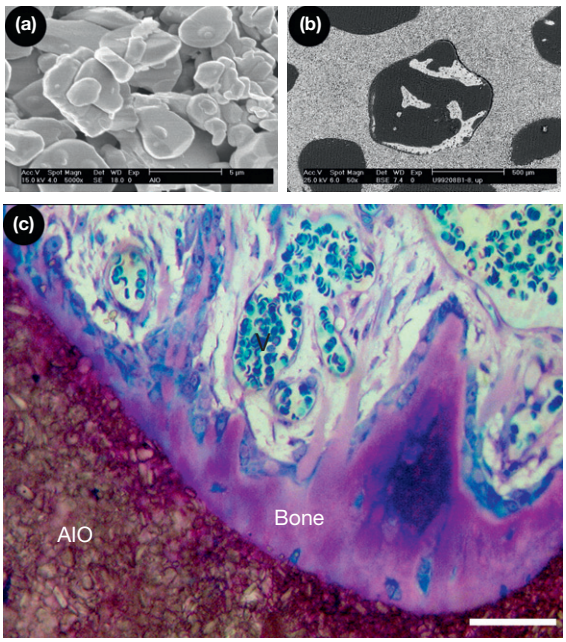

Figure 1 Bone induction in porous alumina ceramic following intramuscular implantation in dogs for 3 months. (a) SEM image showing the microstructured surface of the porous alumina ceramic. (b) BSEM image showing bone (white color) in pores of alumina ceramic (dark grey color). (c) Histology of porous alumina ceramic harvested from muscle of dog showing bone matrix (BONE) on inner pore surface of alumina ceramic (AlO), blood vessels can be seen near the bone (V) (undecalcified section, methylene blue and basic fuchsin staining, scale bar = 50 μm).

5.521.5. Role of Calcium Phosphate in Bone Induction

Bone induction is quite often observed in calcium phosphate materials. It appears that bone induction is a unique property associated with calcium phosphate materials at first sight. However, bone induction is also associated with non-CaP materials, suggesting that calcium phosphate may not be necessary for bone induction to take place.

However, the presence of calcium phosphates is a contributing factor to bone induction. Porous tantalum is not associated with bone induction, while it has been observed that after octacalcium phosphate (OCP) coating was applied on its porous surface, osteoinduction occurred.[54] The same findings were obtained with titanium alloy implants.[62] Non-CaP materials may form a CaP layer on their surface through *in vivo* calcification. This phenomenon was seen during bone induction in a synthetic sponge[81] and in physicochemically modified titanium implants.[84,85] As observed by Winter and Simpson, the surface of the materials was calcified before bone formation started in the synthetic sponge. It is noticeable that only the physicochemically treated titanium implants, whose surface allowed biological calcium phosphate layer to form, were associated with bone induction, while the untreated ones, where no calcium phosphate layer could form, were not.[84,85]

Calcium phosphates present in the materials may cause bone induction through their high ability to bind proteins (including growth factors), or through their specific architectures, or through an *in vivo* surface calcification. The same may happen to some non-CaP materials with microstructured surfaces, which can incorporate growth factors and thus attract osteogenic precursor cells to induce bone formation.

5.521.6. Material Factors

It has been observed that the osteoinductive potential in the presence of materials can vary with the type of material. Some materials induce bone formation as early as 30 days,[70] others after 3 months, and some do not induce bone formation even after 12 months.[79,84] In addition to the various times for the occurrence of bone formation in soft tissue implantation, it was found that the amount of the bone induced by a certain time varied with the materials.[70,85] Moreover, only the materials having a higher osteoinductive potential could induce bone formation in rodents.[68]

The chemistry, the microstructure, and the macrostructure have shown their influence on the osteoinductive potential associated with materials.

5.521.6.1. Chemistry

Calcium phosphate materials varying with chemistry have different dissolution rates and degradation rates. Generally speaking, dense HA is nondegradable or slowly degradable, TCP is fast degradable or degradable, and BCPs containing both HA and TCP are in between.[26] A study proved that too high a content of TCP is not good for bone induction. When compared in muscle of rabbits, BCPs having 70%HA/30%TCP induced bone formation, while BCPs having 20%HA/80%TCP

and pure TCP (0%HA/100%TCP) did not induce bone formation.[59] It was also noted that, in rabbits, the implants of BCP having 20%HA/80%TCP and pure TCP collapsed and lost their macroporous structures. The reason for the absence of bone induction may be the fact that the materials degraded too fast and a stable surface to support bone induction was not available anymore.[34,59]

5.521.6.2. Microstructures

The microstructure plays an important role in bone induction. HA with micropores on its macroporous surface induced bone formation, while HA without micropores on its surface did not induce any bone formation in dogs following soft tissue implantation, either under skin[37] or in muscle.[38] The influence of micropores on bone induction was also seen in BCP. BCP having higher microporosity (17%) induced bone formation in muscle of goats, while BCP having lower microporosity (4%) did not.[34]

Not only the presence of micropores, but also the dimension of the micropores has recently shown to influence bone induction as well. Two kinds of β-TCP ceramics (TCP-B and TCP-S, where TCP-B was TCP ceramic having large grains and large micropores, while TCP-S was TCP ceramic with small grains and small micropores) were prepared in particle form (1–2 mm) and implanted in muscle of dogs for 12 weeks. Large grains (±2 μm) and large micropores were present on the macroporous surface of TCP-B (**Figure 2(a)**) while small grains (±1 μm) and small micropores were present on the surface of TCP-S (**Figure 2(b)**). Mercury intrusion test showed that TCP-B had large micropores (the majority of the micropores were 2–5 μm), while TCP-S had small micropores (most of the micropores were 0.5–1.0 μm) (**Figure 2(c)**). Histology of the implants showed that only TCP-S gave rise to inductive bone formation in muscle of dogs in 3 months (**Figure 2(d)**, TCP-S), while no bone induction occurred in TCP-B (**Figure 4(d)**, TCP-B).

Small micropores was shown to favor bone induction; however, the ideal size of the small micropores for bone induction is not yet clear. How the microstructures affect bone induction is not clear either. The micropores may, in one hand, increase the surface area of the implants allowing the adsorption of higher amounts of growth factors, which have osteogenic potency, and then induce bone formation as secondary response or, on the other hand, if with the proper dimensions, the microstructures may directly initiate osteogenic differentiation of inducible cells able to form bone. There is no evidence either way at this time.

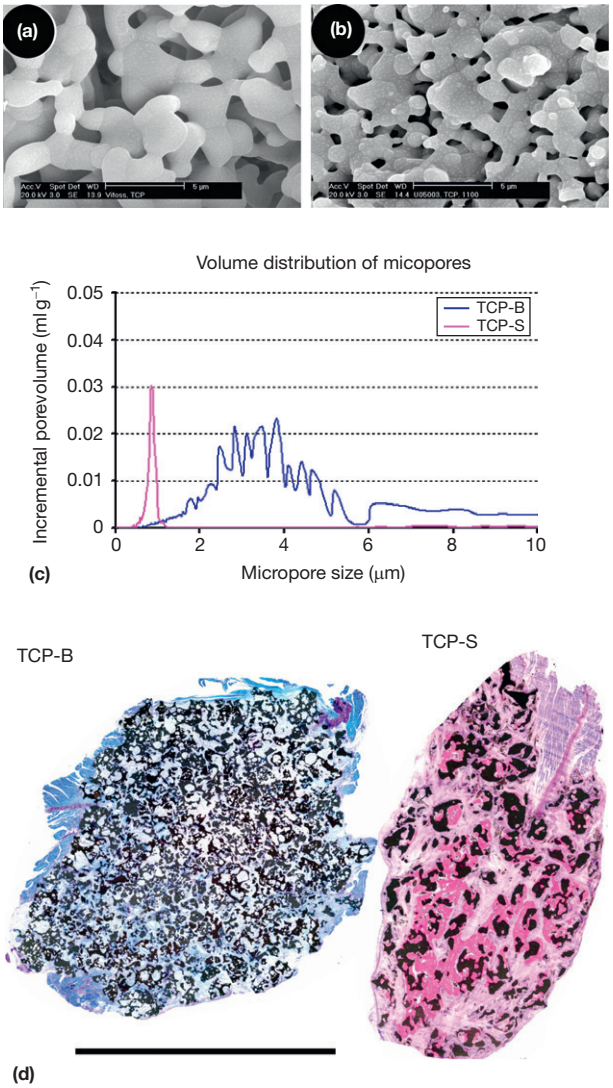

Figure 2 Influence of the microstructure dimension on bone induction of calcium phosphate ceramics. (a) SEM image of TCP-B showing large grains and large micropores. (b) SEM image of TCP-S showing small grains and small micropores. (c) Mercury intrusion data showing the micropores size distribution in the two considered tricalcium phosphates. (d) Histological overview of implants showing bone formation in TCP-S, while no bone formed in TCP-B 12 weeks after intramuscular implantation in dogs (red color; bone, black color: tricalcium phosphate ceramics, undecalcified section, methylene blue, and basic fuchsin staining, scale bar = 10 mm).

5.521.6.3. Macrostructures

Bone induction occurring inside the implants also indicated the importance of the macroporous structure of materials. A tridimensional environment[52,53] was suggested as necessary for the phenomenon of bone induction, as was also the case in transformed excavated bioactive glass granules reported by Schepers *et al.*[33] Cylinders (blocks) and particles of materials have been evaluated regarding their association with bone induction. It turned out that cylinders or blocks lead to more osteoinduction than particles.[46] In addition to the form of the implants, the size of the implants has shown its influence on bone induction: bone induction may not occur in small implants.[34]

With respect to the particles, the particle size of calcium phosphate materials plays a role. BCP particles with two different particle sizes (1–2 mm vs. 212–300 μm) were compared in dogs. One milliliter of each particle size was implanted in back muscle of eight dogs for 6 weeks. Histological analysis showed limited bone formation (2 ± 2%) in seven out of eight implants for the bigger particle size (**Figure 3(a)**), while more extensive bone formation (21 ± 15%) occurred in eight out of eight implants when smaller particles were used (**Figure 3(b)**).

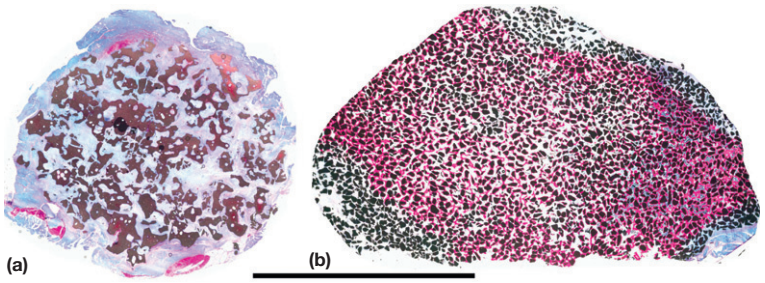

Figure 3 Influence of particle size on bone induction in biphasic calcium phosphate particles following intramuscular implantation in dogs for 6 weeks (undecalcified sections, methylene blue and basic fuchsin staining, black color: biphasic calcium phosphate ceramic, red color: bone, scale bar = 10 mm). (a) 1–2 mm particles and (b) 212–300 μm particles.

It is not yet known how macrostructures affect bone induction, although it has been mentioned that it is related to angiogenesis. The formation of blood vessels inside the implants may bring pericytes into the implants, and thereafter, the pericytes may differentiate into osteogenic cells able to form bone.[86] This hypothesis is supported by the fact that bone formation typically occurs nearby blood vessels.

5.521.7. Mechanism of Bone Induction

The sporadic bone formation observed in nonosseous sites indicates the presence of inducible cells in nonbony sites.[87] Once osteogenic signals are available, the inducible cells are differentiated into osteogenic cells to form bone. The inducible cells are present in many nonosseous tissues, including bone marrow, muscle, skin, adipose tissue, synovium, intestine, deciduous teeth, and nerve tissue.[88] It was found that the inducible cells isolated from the muscle have the ability to form bone.[89]

It is therefore possible to achieve bone induction in any of the nonosseous tissues having inducible cells if the osteogenic signals are present. What the osteogenic signals within materials in which osteoinduction has been observed are, is not known, but some hypotheses have been proposed.

5.521.7.1. Protein Adsorption

The first hypothesized cause of bone induction from materials is the protein adsorption. Calcium phosphate materials showed to have high affinity to BMPs.[90] It was thus suggested that calcium phosphate materials can concentrate growth factors, including osteogenic proteins (i.e., BMPs), and bone induction happens as a secondary response. Credence for this hypothesis also derives from the work on bioactive glasses, which develop a calcium phosphate surface layer. Protein absorption is one of the key steps leading to their extensive effect on bone tissue formation.[91–94] In addition to calcium phosphate materials, alumina is a strong absorbent for proteins.[95,96] As described earlier, with increased surface area thanks to the surface microstructure, microstructured alumina ceramic may concentrate growth factors as well and thereafter give rise to bone induction. Furthermore, protein adsorption is one of the explanations for bone induction by materials having high microporosity: by increasing the microporosity, the surface area of the implants increases; thus, more proteins can be concentrated, and consequently, bone induction happens. However, no direct evidence is available so far to support the role of protein adsorption in osteogenesis associated with materials, except with bioactive glasses.[91–93]

5.521.7.2. Topography

Microstructures play an important role. Although the protein adsorption effect is putative, they offer higher surface area available for protein adsorption. The effect may also be related to topography. As recently shown, highly controlled microstructures or nanoscaled disorders can differentiate mesenchymal stem cells into osteogenic cells. Rat bone marrow stromal cells not only proliferate, but also differentiate into mature osteoblasts on microstructured poly(methyl methacrylate) substrates.[97] Nanoscaled disorders stimulate human mesenchymal stem cells to produce bone mineral *in vitro* in the absence of osteogenic supplements.[98] It could then well be that the materials' microstructures, when in the range of proper dimensions (in the means of shapes and sizes) act as direct signals to differentiate inducible cells to osteogenic cells to form bone.

5.521.7.3. Surface Calcification

The role of surface calcification was seen in the case of bone induction occurring in synthetic polymeric sponges[81] and in treated titanium implants.[84,85] It is observed, or assumed, that before the onset of bone formation, the surface of the implants is a calcium phosphate surface. It has been proposed that *in vivo* surface calcification prepares a suitable environment for inducible cells to form bone, while osteogenic growth factors are trapped during calcification.[77] It is generally accepted that calcium phosphate materials have calcified surfaces,[25,26] a finding that actually underlays their osteoconduction. This is discussed at length in other chapters of this publication.

5.521.7.4. Inflammation

Inflammatory reactions occur upon the implantation of materials. It has been hypothesized that the initial inflammatory responses bring in and provide factors that attract and differentiate inducible cells.[99] One such factor is

prostaglandin E2 (PGE2), which is produced by macrophages during the inflammatory phase.[100,101] It was found that macrophages produce higher quantities of PGE2 in response to microstructured calcium phosphate ceramic as compared to calcium phosphate ceramic having smooth surfaces.[77] It is also an interesting observation that macrophages were present in the implants at early implantation times,[50,67] although this is not a proof for an association in and by itself.

5.521.8. Clinical Significance of Osteoinductive Materials

Although the causation and specific events associated with bone induction in materials have not yet been elucidated, and the current materials that show the effect may not be the best ones, materials associated with the event of osteoinduction do show their significance in bone repair not only in small or critical-sized bone defects, but also in spinal fusion procedures.

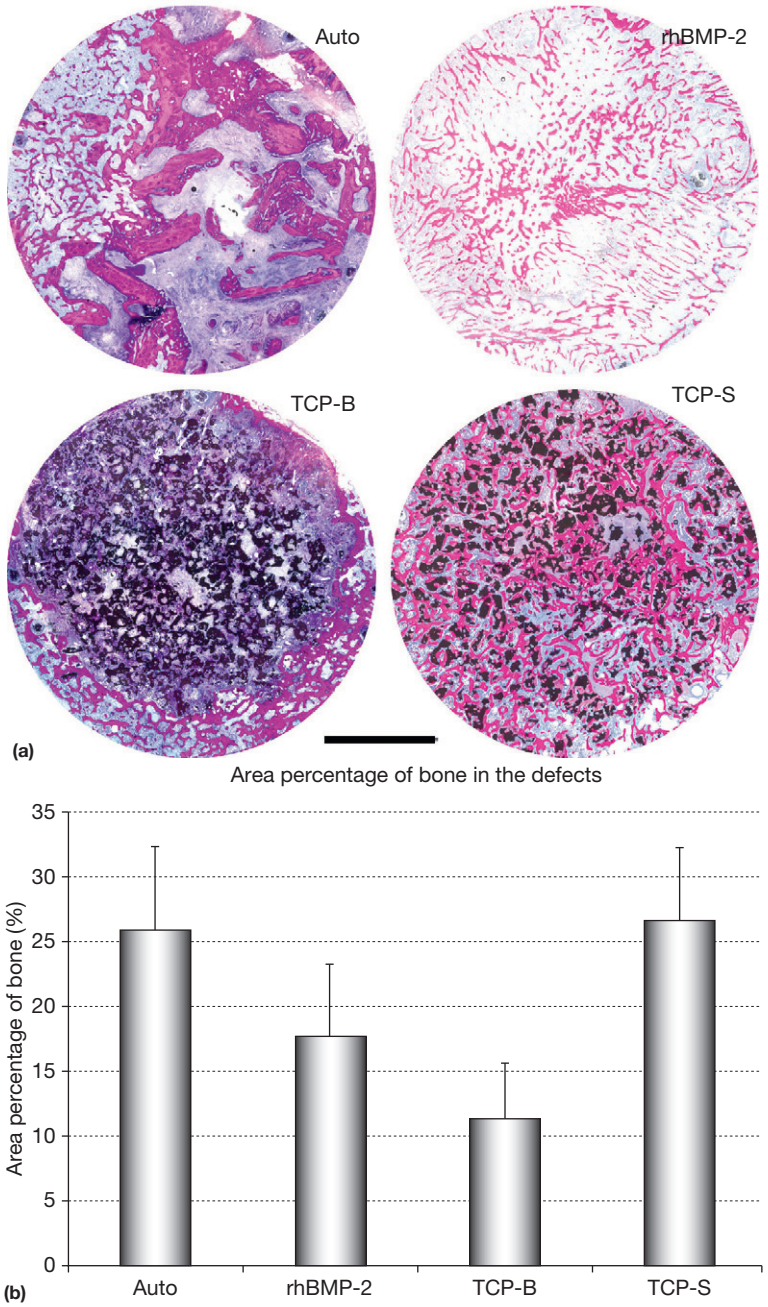

Figure 4 Comparison of autologous bone, rhBMP-2, and two forms of tricalcium phosphate. The sites were critical-sized defects in iliac crest of dogs for 12 weeks (auto: defect filled with autologous bone, rhBMP-2: defect filled with Infuse, TCP-B and TCP-S: defects filled with two forms of tricalcium phosphate). (a) Histological overviews of the defects (undecalcified sections, methylene blue and basic fuchsin staining, red color: bone, black color: tricalcium phosphate ceramic, scale bar = 5.0 mm). (b) Area percentage of bone in the defects.

5.521.8.1. Repairing Small Bone Defects

The usefulness of materials associated with osteoinduction for bone repair was first evaluated in small bone defects in femoral bone of dogs.[70] Two calcium phosphate ceramics (BCP and HA) were compared at different time periods from 7 to 360 days and it was found that the BCP used repaired bone defects faster than the HA.

5.521.8.2. Critical-Sized Defects

The possibility to repair critical-sized defects was evaluated in critical-sized defects in the iliac crest of goats using various forms of BCP.[69] Depending on the physicochemical characteristics of the BCP, 17-mm diameter (ø17 mm) bone defects were repaired or not at 12 weeks.

A subsequent study demonstrated that specific calcium phosphate materials could not only repair critical-sized bone defects, but also be better than rhBMP-2 and be comparable to autologous bone (Figure 4). TCP with small microstructures (TCP-S, 1–2 mm) and TCP with large microstructures (TCP-B, 1–2 mm), rhBMP-2 (Infuse, 400 µg rhBMP-2 on 1 ml ACS), and autologous bone chips (auto, 1–2 mm) were compared in critical-sized bone defects (ø17 mm) in iliac crest of dogs for 12 weeks. Bone was observed throughout the defects with autologous bone (Figure 4(a), auto), Infuse (Figure 4(a), rhBMP-2), and TCP-S (Figure 4(a), TCP-S), while no bone was observed in the center of the defects filled with TCP-B (Figure 4(a), TCP-B). Although bone formed in the center of the defects with Infuse, areas without bone tissue were noticed and the bone was thinner as compared to the bone in the defects containing the other implants (Figure 4(a), rhBMP-2). As a result, bone in the defects with rhBMP-2 was higher in terms of percentage area than the bone in the defects with TCP-B but it was not comparable to the bone formed in the defects with autologous bone (Figure 4(b)), while the bone formed in the defects with TCP-S was more than the bone in the defects with rhBMP-2 and comparable to the bone in the defects with autologous bone (Figure 4(b)).

5.521.8.3. Spinal Fusion

To study the potential of spinal fusion with calcium phosphate materials, three TCP ceramics (TCP-a: pure TCP, particle size 0.5–2.0 mm; TCP-b: pure TCP, particle size 0.5–2.0 mm and TCP-c: TCP with traces of HA, particle size 1–2 mm) and one HA ceramic (HA: pure HA, particle size 1–2 mm) were compared in muscle and in a noninstrumented spinal fusion model (L3–L4) in 16 dogs for 12 weeks. Histological analysis showed no bone formation in TCP-a and TCP-b, limited bone formation in HA, and extensive bone formation in TCP-c following intramuscular implantation. Extensive bone was formed between the two spinous processes with TCP-c (Figure 5(a), TCP-c), but bone was hardly formed with HA (Figure 5(a), HA), TCP-a (Figure 5(a), TCP-a), and TCP-b (Figure 5(a), TCP-b). In the region of interest (the region between the two spinous processes), a high percentage of bone was formed with TCP-c, while bone was limited in

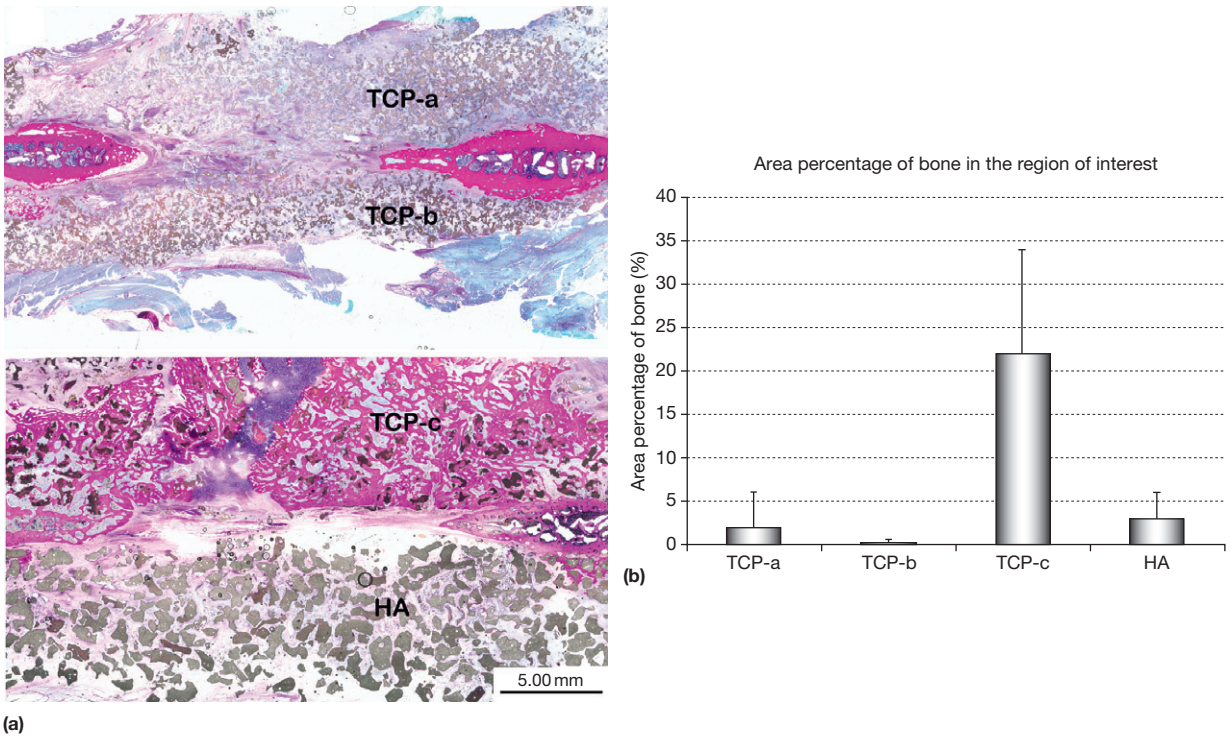

Figure 5 Spinal fusion in dogs with various calcium phosphate materials in a noninstrumented spinal fusion model in dogs for 12 weeks (HA: HA ceramic, 1–2 mm; TCP-a: tricalcium phosphate, 0.5–2.0 mm; TCP-b: tricalcium phosphate, 0.5–2.0 mm; TCP-c: 1–2 mm). (a) Histological overview of spinal fusion with calcium phosphate ceramics (undecalcified sections, methylene blue and basic fuchsin staining, scale bar = 5.0 mm). (b) Histomorphometry showing area percentage of bone in the region of the interest.

amount with HA, TCP-a, and TCP-b (Figure 5(b)). The results clearly indicated that spinal fusion could be obtained with calcium phosphate materials.

5.521.9. Future Directions

The progress made in the last two decades has paved the way for the development of materials that are associated with osteoinduction in various animal models for use in bone regeneration. This notwithstanding, the critical parameters associated with bone induction in calcium phosphates need to be further addressed.

Besides the mechanism of bone induction and developing more osteoinductive materials, other properties may be taken into account in order to improve bone regeneration with more powerful bone grafting materials. These properties include handling in surgery and improved mechanical properties.

References

1. Bloom, W.; Fawcett, D. W. In *A Textbook of Histology*; Bloom, W., Fawcett, D. W., Eds.; W.B. Saunders: Philadelphia, PA, 1986; p 199.
2. Rosenberg, A. In *Robins Pathological Basis of Disease*; Cortran, R. S., Kumar, V., Collins, T., Eds.; Saunders: Philadelphia, PA, 1999; p 199.
3. De Vernejoul, M. C. *Eur. J. Chem. Clin. Biochem.* **1996**, *34*, 729–734.
4. Kasis, A. G.; Marshman, L. A.; Krishna, M.; Bhatia, C. K. *Spine* **2009**, *34*, 572–577.
5. Lu, D. C.; Dhall, S. S.; Mummaneni, P. V. *J. Neurosurg. Spine* **2009**, *10*, 46–50.
6. Rose, P. S.; Lenke, L. G.; Bridwell, K. H.; *et al. Spine* **2009**, *34*, 852–857.
7. Boden, S. D. *Spine* **2002**, *27*, S26–S31.
8. Marchesi, D. G. *Eur. Spine J.* **2000**, *9*, 372–378.
9. Brandoof, J. F.; Silber, J. S.; Vaccaro, A. R. *Am. J. Orthop.* **2008**, *37*, 410–414.
10. Kwon, B.; Jeneis, L. G. *Spine J.* **2005**, *5*, S224–S230.
11. Parikh, S. N. *Orthopedics* **2002**, *25*, 1301–1309.
12. Vaccaro, A. R.; Chiba, K.; Heller, J. G.; *et al. Spine J.* **2002**, *2*, 206–215.
13. Seeherman, H.; Wozney, J. M. *Cytokine Growth Factor Rev.* **2005**, *16*, 329–345.
14. Sailer, H. F.; Kolb, E. *J. Craniomaxillofac. Surg.* **1994**, *22*, 2–11.
15. Glassman, S. D.; Carreon, L. Y.; Campell, M. J.; *et al. Spine J.* **2008**, *8*, 443–448.
16. Shields, L. B.; Rague, G. H.; Glassman, S. D.; *et al. Spine* **2006**, *31*, 2029–2030.
17. Nagata, M.; Messora, M.; Okamoto, R.; *et al. Bone* **2009**, *45*, 339–345.
18. Roukis, T. S.; Zgonis, T.; Tiernan, B. *Adv. Ther.* **2006**, *23*, 218–237.
19. Buma, P.; Schreurs, W.; Verdonschot, N. *Biomaterials* **2004**, *25*, 1487–1495.
20. Kanczler, J. M.; Oreffo, R. O. *Eur. Cell Mater.* **2008**, *15*, 100–114.
21. de Groot, K. *Biomaterials* **1980**, *1*, 47–50.
22. Ducheyne, P. *J. Biomed. Mater. Res.* **1985**, *19*, 273–291.
23. Ducheyne, P.; Cuckler, J. *Clin. Orthop.* **1992**, *276*, 102–114.
24. Hench, L. L. *Science* **1980**, *208*, 826–831.
25. Kokubo, T.; Kim, H. M.; Kawashita, M. *Biomaterials* **2003**, *24*, 2161–2175.
26. LeGeros, R. Z. *Clin. Orthop. Relat. Res.* **2002**, *395*, 81–98.
27. Boynton, M. D.; Enders, T. J. *J. Shoulder Elbow Surg.* **1999**, *8*, 495–497.
28. Urist, M. R. *Science* **1965**, *150*, 893–899.
29. Holtorf, H. L.; Jansen, J. A.; Mikos, A. G. *Biomaterials* **2005**, *26*, 6208–6216.
30. Osborn, J. F. In *Biomaterials Degradation*; Barbosa, M. A., Ed.; Elsevier: Amsterdam, 1991; p 185.
31. Ripamonti, U. *J. Oral Maxillofac. Surg.* **1991**, *49*, 817–830.
32. Ripamonti, U. *J. Bone Joint Surg.* **1991**, *73A*, 692–703.
33. Schepers, E.; DeClercq, M.; Ducheyne, P.; Kempeneers, R. *Oral Rehabil.* **1991**, *18*, 439–452.
34. Habibovic, P.; Sees, T. M.; van den Doel, M. A.; van Blitterswijk, C. A.; de Groot, K. *J. Biomed. Mater. Res.* **2006**, *77A*, 747–762.
35. Yang, Z.; Yuan, H.; Tong, W.; Zou, P.; Chen, W.; Zhang, X. *Biomaterials* **1996**, *17*, 2131–2137.
36. dos Santos, E. A.; Farina, M.; Soares, G. A.; Anselme, K. *J. Biomed. Mater. Res.* **2009**, *89A*, 510–520.
37. Yamasaki, H.; Saki, H. *Biomaterials* **1992**, *13*, 308–312.
38. Yuan, H.; Kurashina, K.; de Bruijn, J. D.; Li, Y.; de Groot, K.; Zhang, X. *Biomaterials* **1999**, *20*, 1799–1806.
39. Isaac, J.; Hornez, J. C.; Jian, D.; Descamps, M.; Hardouin, P.; Magne, D. *J. Biomed. Mater. Res.* **2008**, *86A*, 386–393.
40. Yamasaki, H. *Jpn. J. Oral. Biol.* **1990**, *32*, 190–192.
41. Zhang, X. In *Bioceramics and the Human Body*; Ravaglioli, A., Krajewski, A., Eds.; Elsevier Science: Amsterdam, 1991; p 408.
42. Vargervik, K. In *Bone Grafts & Bone Substitutes*; Habal, M. B., Reddi, A. H., Eds.; W.B. Saunders: Philadelphia, PA, 1992; p 112.
43. Toth, J. M.; Lynch, K. L.; Hackbarth, D. A. *Bioceramics* **1993**, *6*, 9–13.
44. Ripamonti, U.; Van den Heever, B.; Van Wyk, J. *Matrix* **1993**, *13*, 491–502.
45. Klein, C. P. A. T.; de Groot, K.; Chen, W.; Li, Y.; Zhang, X. *Biomaterials* **1994**, *15*, 31–34.
46. van Eeden, S. P.; Ripamonti, U. *Plast. Reconstr. Surg.* **1994**, *93*, 959–966.
47. Green, J. P.; Wojno, T. H.; Wilson, M. W.; Grossniklaus, H. E. *Am. J. Ophthalmol.* **1995**, *120*, 681–682.
48. Ripamonti, U. *Biomaterials* **1996**, *17*, 31–35.
49. Magan, A.; Ripamonti, U. *J. Craniofac. Surg.* **1996**, *7*, 71–78.
50. Yang, Z.; Yuan, H.; Zou, P.; Tong, W.; Qu, S.; Zhang, X. *J. Mater. Sci. Mater. Med.* **1997**, *8*, 697–701.
51. Sires, B. S.; Holds, J. B.; Kincaid, M. C.; Reddi, A. H. *Ophthal. Plast. Reconstr. Surg.* **1997**, *13*, 244–251.
52. Yuan, H.; Yang, Z.; Li, Y.; Zhang, X.; de Bruijn, J. D.; de Groot, K. *J. Mater. Sci. Mater. Med.* **1998**, *9*, 723–726.
53. Ripamonti, U.; Crooks, J.; Kirkbride, A. N. *S. Afr. J. Sci.* **1999**, *95*, 335–343.
54. de Bruijn, J. D.; Yuan, H.; Dekker, R.; van Blitterswijk, C. A. In *Bone Engineering*; Davies, J. E., Ed.; em squared incorporated: Toronto, 2000; p 421.
55. Yuan, H.; Li, Y.; de Bruijn, J. D.; de Groot, K.; Zhang, X. *Biomaterials* **2000**, *21*, 1283–1290.
56. Yuan, H.; Yang, Z.; de Bruijn, J. D.; de Groot, K.; Zhang, X. *Biomaterials* **2001**, *22*, 2617–2623.
57. Yuan, H.; de Bruijn, J. D.; Li, Y.; *et al. J. Mater. Sci. Mater. Med.* **2001**, *12*, 7–13.
58. Yuan, H.; de Bruijn, J. D.; Zhang, X.; van Blitterswijk, C. A.; de Groot, K. *J. Biomed. Mater. Res.* **2001**, *58*, 270–276.
59. Kurashina, K.; Kurita, H.; Wu, Q.; Ohtsuka, A.; Kobayashi, H. *Biomaterials* **2002**, *23*, 407–412.
60. Gosain, A. K.; Song, L.; Riordan, P.; *et al. Plast. Reconstr. Surg.* **2002**, *109*, 619–630.
61. Yuan, H.; van den Doel, M.; van Blitterswijk, C. A.; de Groot, K.; de Bruijn, J. D. *J. Mater. Sci. Mater. Med.* **2002**, *13*, 1271–1274.
62. Barrère, F.; van der Valk, C. M.; Dalmeijer, R. A.; *et al. J. Biomed. Mater. Res.* **2003**, *66A*, 779–788.
63. Habibovic, P.; van der Valk, C. M.; van Blitterswijk, C. A.; de Groot, K.; Meijer, G. *J. Mater. Sci. Mater. Med.* **2004**, *15*, 373–380.
64. Kruyt, M. C.; Dhert, W. J.; Yuan, H.; *et al. J. Orthop. Res.* **2004**, *22*, 544–551.
65. Habibovic, P.; Yuan, H.; van der Valk, C. M.; Meijerc, G.; van Blitterswijk, C. A.; de Groot, K. *Biomaterials* **2005**, *26*, 3565–3575.
66. Le Nihouannen, D.; Daculsi, G.; Saffarzadeh, A.; *et al. Bone* **2005**, *36*, 1086–1093.
67. Kondo, N.; Ogose, A.; Tokunaga, K.; *et al. Biomaterials* **2006**, *25*, 4419–4427.
68. Yuan, H.; van Blitterswijk, C. A.; de Groot, K.; de Bruijn, J. D. *Tissue Eng.* **2006**, *12*, 1607–1615.
69. Habibovic, P.; Yuan, H.; van den Doel, M.; Sees, T. M.; van Blitterswijk, C. A.; de Groot, K. *J. Orthop. Res.* **2006**, *24*, 867–876.
70. Yuan, H.; van Blitterswijk, C. A.; de Groot, K.; de Bruijn, J. D. *J. Biomed. Mater. Res.* **2006**, *78A*, 139–147.
71. Li, J.; Habibovic, P.; Yuan, H.; *et al. Biomaterials* **2007**, *28*, 4209–4218.
72. Ripamonti, U.; Richter, P. W.; Thomas, M. E. *Plast. Reconstr. Surg.* **2007**, *120*, 1796–1807.
73. Le Nihouannen, D.; Saffarzadeh, A.; Gauthier, O.; *et al. J. Mater. Sci. Mater. Med.* **2007**, *19*, 667–675.
74. Habibovic, P.; Kruyt, M. C.; Juhl, M. V.; *et al. J. Orthop. Res.* **2008**, *26*, 1363–1370.
75. Hattori, S. *Kokubyo Gakkai Zasshi* **2008**, *75*, 120–137.
76. Ripamonti, U.; Richter, P. W.; Nilen, R. W.; Renton, L. *J. Cell. Mol. Med.* **2008**, *12*, 2609–2621.
77. de Bruijn, J. D.; Shankar, K.; Yuan, H.; Habibovic, P. In *Bioceramics and their clinical applications*; Hokubo, T., Ed.; CRC Press: Boca Raton, FL, 2008; p 199.
78. Nasu, T.; Takemoto, M.; Akiyama, N.; Fujibayashi, S.; Neo, M.; Nakamura, T. *J. Biomed. Mater. Res.* **2009**, *89A*, 601–608.
79. Ripamonti, U.; Crooks, J.; Khoali, L.; Roden, L. *Biomaterials* **2009**, *30*, 1428–1439.

80. Fellah, B. H.; Gauthier, O.; Weiss, P.; Chappard, D.; Layrolle, P. *Biomaterials* **2008**, *29*, 1177–1188.
81. Winter, G. D.; Simpson, B. J. *Nature* **1969**, *223*, 88–90.
82. Okumura, M.; Ohgushi, H.; Ducheyne, P. In *Bioceramics 6*; Ducheyne, P., Christiansen, D., Eds.; Butterworths: Oxford, England, 1993.
83. Ohgushi, H.; Okumura, M.; Yoshikawa, T.; *et al*. *J*. *Biomed*. *Mater*. *Res*. **1992**, *26*, 885–896.
84. Fujiibayashi, S.; Neo, M.; Kim, H. M.; Kokubo, T.; Nakamura, T. *Biomaterials* **2004**, *25*, 443–450.
85. Takemoto, M.; Fujibayashi, S.; Neo, M.; *et al*. *Biomaterials* **2006**, *27*, 2682–2691.
86. Collett, G. D.; Canfield, A. E. *Circ*. *Res*. **2005**, *96*, 930–938.
87. Włodarski, K. H. *Clin*. *Orthop*. *Relat*. *Res*. **1990**, *252*, 276–293.
88. Fortier, L. A. *Vet*. *Surg*. **2005**, *34*, 415–423.
89. Mastrogiacomo, M.; Derubeis, A. R.; Cancedda, R. *J*. *Cell*. *Physiol*. **2005**, *204*, 594–603.
90. Urist, M. R.; Huo, Y. K.; Brownell, A. G.; *et al*. *Proc*. *Natl*. *Acad*. *Sci*. USA **1984**, *81*, 371–375.
91. Ducheyne, P.; Qiu, Q.-Q. *Biomaterials* **1999**, *20*, 2287–2303.
92. El-Ghannam, A. E.; Ducheyne, P.; Shapiro, I. *J*. *Orthop*. *Res*. **1999**, *17*, 340–345.
93. Garcia, A. J.; Ducheyne, P.; Boettiger, D. *J*. *Biomed*. *Mater*. *Res*. **1998**, *40*, 48–56.
94. Radin, S.; Ducheyne, P.; Rothman, B.; Conti, A. *J*. *Biomed*. *Mater*. *Res*. **1997**, *37*, 363–375.
95. Rosengren, A.; Pavlovic, E.; Oscarsson, S.; Krajewski, A.; Ravaglioli, A.; Piancastelli, A. *Biomaterials* **2002**, *23*, 1237–1247.
96. Sun, D. H.; Trindade, M. C.; Nakashima, Y.; *et al*. *J*. *Biomed*. *Mater*. *Res*. **2003**, *65A*, 290–298.
97. Engel, E.; Martínez, E.; Mills, C. A.; Funes, M.; Planell, J. A.; Samitier, J. *Ann*. *Anat*. **2009**, *191*, 136–144.
98. Dalby, M. J.; Gadegaard, N.; Tare, R.; *et al*. *Nat*. *Mater*. **2007**, *6*, 997–1003.
99. Caplan, A. I.; Boyan, B. D. In *Mechanisms of Bone Development and Growth*; Hall, B., Ed.; CRC Press: Boca Raton, FL, 1994; p 6.
100. Refai, A. K.; Textor, M.; Brunette, D. M.; Waterfield, J. D. *J*. *Biomed*. *Mater*. *Res*. **2004**, *70A*, 194–205.
101. Thomsen, P.; Gretzer, C. *Curr*. *Opin*. *Solid State Mater*. *Sci*. **2001**, *5*, 163–176.

5.522. Bone Tissue Engineering: Growth Factors and Cytokines

J O Hollinger, A Srinivasan, P Alvarez, E Hsu, and S McBride, Carnegie Mellon University, Pittsburgh, PA, USA
S Eppell and J Baskin, Case Western Reserve University, Cleveland, OH, USA
H Waters, Cleveland Clinic Foundation, Cleveland, OH, USA
R Gruber, Medical University of Vienna, Vienna, Austria

© 2011 Elsevier Ltd. All rights reserved.

5.522.1. Bone Biology 282
5.522.1.1. Introduction 282
5.522.1.2. Fundamental Process 282
5.522.1.3. Bone Morphogenesis 282
5.522.1.4. Bone 283
5.522.1.5. Modeling and Remodeling 284
5.522.1.6. Angiogenesis 284
5.522.1.7. Osteoblasts 284
5.522.1.8. Osteocytes 285
5.522.1.9. Osteoclasts 285
5.522.2. Growth Factors, Cytokines, Nomenclature, Mechanism of Action 285
5.522.3. Bone Tissue Engineering: Growth Factors and Cytokines 286
5.522.3.1. Transforming Growth Factor β 286
5.522.3.2. Bone Morphogenetic Proteins 286
5.522.3.3. Insulin-Like Growth Factors 286
5.522.3.4. Platelet-Derived Growth Factor 287
5.522.3.5. Vascular Endothelial Growth Factor 287
5.522.3.6. Fibroblast Growth Factors 288
5.522.3.7. Sclerostin 288
5.522.4. Cytokines and Bone 289
5.522.4.1. Receptor Activator of Nuclear Factor κβ Ligand 290
5.522.4.2. IL1β and TNF (Superfamily Member 2, TNF Alias TNF-α) 290
5.522.4.3. Bone Resorption 291
5.522.4.3.1. Osteoclast precursor signaling 291
5.522.4.3.2. Osteoclastogenesis 291
5.522.4.4. Bone Formation 292
5.522.5. Translational Applications of Growth Factors and Cytokines in Bone Tissue Engineering 292
5.522.5.1. Dental 292
5.522.5.1.1. Therapeutic bone regeneration in dentistry 292
5.522.5.2. Orthopedic and Craniomaxillofacial 292
5.522.5.2.1. Contextualizing the discussion 292
5.522.5.2.2. Interpreting preclinical data 292
5.522.5.2.3. Host factors 297
5.522.5.2.4. Growth factors and cytokines in clinical use 298
5.522.5.3. Future Clinical Directions 300
5.522.5.3.1. Defining the clinical performance criteria 300
References 300

Abbreviations

1,25D3	1,25-Dihydroxy-vitamin D3
ACS	Absorbable collagen sponge
ALP	Alkaline phosphatase
BMPR	Bone morphogenetic protein receptor
BMPs	Bone morphogenetic proteins
BMSCs	Bone marrow stromal cells
BMU	Basic multicellular unit
CD	Cluster of differentiation molecule
c-fos	Finkel-Biskis-Jinkins murine osteogenic sarcoma virus
CXCR1	Chemokine receptors
DAN	Deadenylating nuclease
DBM	Demineralized bone matrix
DKK1	Dickkopf-1
DO	Distraction osteogenesis
ECM	Extracellular matrix
EGF	Epidermal growth factor

FDA	Food and Drug Administration
FGF	Fibroblast growth factor
FLK	Fetal liver kinase
FLT4	Fms-related tyrosine kinase 4
FZD	Frizzled
GDF	Growth differentiation factor
GM-CSF	Granulocyte–macrophage colony-stimulating factor
GP130	Glycoprotein 130
HDE	Humanitarian Device Exemption
HIFs	Hypoxia inducing factors
HUGO	Human Genome Organization
IFN-γ	Interferon gamma
IFNGR	Interferon gamma receptor
IGF	Insulin-like growth factor
IGFBP	Insulin-like growth factor binding protein
IGFR	Insulin-like growth factor receptor
IL	Interleukin
ILR	Interleukin receptor
IRAK	IL-1 receptor-associated kinase
JAK/STAT	Janus kinase/signal transducer and activator of transcription
JNK	c-jun N-terminal kinase
KDR	Kinase insert domain receptor
LIF	Leukocyte inhibition factor
LRP	Lipoprotein receptor-related family
MAPK	Mitogen-activated protein kinase
M-CSF	Macrophage colony-stimulating factor
mRNA	Messenger ribonucleic acid
NF-κB	Nuclear factor kappa-light-chain-enhancer of activated B cells
NFATc1	Nuclear factor of activated T cells, cytoplasmic 1
NIK	Nuclear factor kappa beta inducing kinase
OCL	Osteoclast
OCPs	Osteoclast precursors
OP-1	Osteogenic protein 1
OPG	Osteoprotegerin
Osx	Osterix
P52	Phosphoprotein 52
PDGF	Platelet-derived growth factor
PI3K	Phosphoinositide 3-kinase
PKD	Protein kinase D
PPAR	Peroxisome proliferator-activated receptor
PTH	Parathyroid hormone
RANKL	Receptor activator of nuclear factor κβ ligand
RAP	Regional acceleratory phenomenon
RNA	Ribonucleic acid
Runx2	Runt-related transcription factor 2
SMAD	Mothers against decapentaplegic homolog
SOST	Sclerostin
TAB1	TAK1-binding protein 1
TAK1	TGF-β-activated kinases 1
TGF	Transforming growth factor
TH	T helper cell
TNF	Tumor necrosis factor
TNFRSF	Tumor necrosis factor receptor superfamily
TRAF	Tumor necrosis factor receptor-associated factor
TRANCE	Tumor necrosis factor (TNF)-related activation-induced cytokine
TRAP	Tartrate-resistant acid phosphatase
VEGFR	Vascular endothelial growth factor receptor
VEGFs	Vascular endothelial growth factors
Wnt	Wingless-type MMTV integration site

5.522.1. Bone Biology

5.522.1.1. Introduction

The focus of this chapter is the translational application of growth factors and cytokines for bone tissue engineering with the goal of regeneration. The outcome of regeneration is the restoration of form and function to tissues and organs to make them indistinguishable from their original state. The process of regeneration is highly complex, and involves spatially and temporally dynamic interactions among biological signaling molecules, cells, extracellular matrix (ECM) products, and mechanobiology. Assembling and harnessing in time, space, and dose the elements that drive the process of achieving a regenerative outcome is the quest for bone tissue engineers.

Many aspects of the regenerative process are unclear. However, there are some aspects that have been elucidated and may be exploited through tissue engineering. The authors emphasize what is currently known about the process of bone regeneration and the potential of tissue engineering to exploit this knowledge for clinical applications.

5.522.1.2. Fundamental Process

Growth factors and cytokines either directly or indirectly influence bone embryogenesis, homeostasis, modeling and remodeling, pathology and disease, as well as bone regeneration. Therefore, antecedent to the discussion of the bone regenerative process, fundamentals are described and the implications of regeneration are underscored.

The assembly and dynamic integration of component parts, the highly complex architecture of the resulting physiological structure, and the maintenance and enduring features of the vital tissue product (e.g., bone) are fundamental to tissue engineering. It is therefore reasonable to begin with morphogenesis: a road map that yields a three-dimensional structure.

5.522.1.3. Bone Morphogenesis

A consummate series of instructional cues bring mesenchymal cells together into a patterned, three-dimensional array as the vertebrate embryo forms.[1] The outcome of cell–matrix aggregate interactions in limb bud locales, spine and ribs, is the formation of a chondrogenic anlage that calcifies and is resorbed while being populated by osteogenic cell phenotypes (osteoclasts, osteoblasts, osteocytes); the product is a unique blend of collagenous and carbonated-hydroxyapatite matrices. The process is called endochondral ossification. In distinction to endochondral ossification is intramembranous ossification, which occurs in the cranium, mid-face and mandible where collections of mesenchymal cells divert directly to the

osteogenic phenotype without an intervening cartilaginous precursor. The outcome of both processes is bone formation.

Morphogenesis involves a highly complex dynamic process among cells, matrices and soluble signaling factors. The signaling factors are proteins encoded by conserved multigene families, including the bone morphogenetic proteins (BMPs), epidermal growth factors (EGFs), fibroblast growth factors (FGFs), hedgehogs, homeobox gene products, and Wingless-type MMTV integration sites (Wnts).[2] Though they are as yet partially described mechanisms, an assembly of biological parts exist that produce endochondrally and intramembranously derived bones. The assembly process is a marvelous consortium of movements honed by a molecular tool kit that determines the locations of occurrence of congregations of cells, the interactions among the cells, and the shape, size and positions of structures derived from that congregation, as well as the death of cells. During osteogenesis, controlling gates either stop or redirect events. The extracellular stopping mechanism may include cell contact and extracellular inhibitory signals. For example, BMPs are powerful inducers, and, left unbalanced, they will induce an aberrant outcome; consequently, BMPs are modulated by anti-BMPs, for example, noggin, fetuin, chordin, cerebrus, and deadenylating nuclease (DAN).[3]

5.522.1.4. Bone

Bone is an organ system.[4] We must appreciate the clever organization and function of this organ system if we are to be stewards of its engineering and regeneration. An organ is a part of the body that is arranged according to a characteristic structural plan and performs a special function or functions; it is composed of various tissues, one of which is primary in function.[5] Bone consists of two specialized tissues: vascular and calcified.

The vascular tissue of bone is positioned in the marrow as well as in the periosteal–diaphyseal–metaphyseal and epiphyseal–physeal vascular tapestries for metabolic exchange and trafficking of molecular signals to sustain osseous physiological dynamics and homeostasis. A lush web of vascular highways populate Haversian systems and Volkmann's canals in bone, thus underscoring a profound vascular dependency that begins during embryogenesis, continues through mineral homeostasis, modeling and remodeling and is pivotal to the regenerative osseous wound healing cascade. The vascular architecture of bone ensures that bone cells will neither perish nor be without a tributary for cell renewal. A partnership between osteoblasts and vascularity ensures that a vascular tributary enriches each cubic millimeter of bone volume. Consequently, engineering vascular tissue is a requisite for engineering bone.

The calcified tissue component of bone includes several cell phenotypes (e.g., hematopoietic and osteogenic), biological factors (e.g., proteins such as the transforming growth factors (TGFs) and platelet-derived growth factors (PDGFs), and many others that are discussed in subsequent sections of this chapter), and the inorganic (predominantly calcium-phosphate ions organized as carbonated hydroxyapatite) and organic (mostly type I collagen) matrices. The organizational hierarchy produces a macrostructural form that directly correlates with the functional properties of bone: protection, locomotion, and homeostasis. The macrostructural format consists of cortical and trabecular bone.

Cortical bone looks dense and compact; it constitutes 80% of the skeleton, forming the outer and inner layers of appendicular bone, inner and outer tables of the flat bones, and the inner and outer surfaces of vertebral bodies and pelvic structures.[4] On microscopic inspection, cortical bone is built from a series of melded plates, lamellae, that are crafted through resorption and formation drifts into transverse tubular structures in the appendicular skeleton: the Haversian systems (osteons) (Figure 1). The Haversian system consists of 4–20 circumferential rings with a central Haversian canal ~22–110 μm in diameter that houses blood vessels, lymphatics and, sometimes, nerves.[6] The average Haversian system in man is about 200 μm in diameter, a targeted dimensional parameter advocated for optimizing osteoconductive tissue-engineered scaffolds. Osteoconduction may be defined as follows: A tissue renewal process integrating angiogenesis and osteoprogenitor cells from the recipient site into a three-dimensional implanted material and graft. However, the budding tissue engineer must be mindful that defining osteoconductive properties according to pore-size dimension, range and distribution remains nonstandardized; the parameters have not been awarded universal concurrence, and therefore controversy may arise when we dogmatically insist upon strict

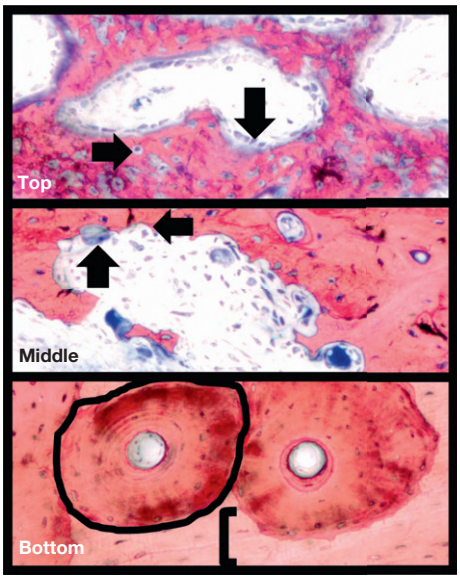

Figure 1 (Top) Osteoblasts (down arrow) produce osteoid (subjacent to the osteoblasts) that mineralizes and these elements comprise the woven bone depicted in the top panel. Rounded osteocytes (side arrow) reside in the woven bone. (Middle) Osteoclasts (up arrow) are bone-resorbing cells that form scalloped bays in the woven bone; these areas are called Howship's lacunae (side arrow). Osteoclasts are necessary for bone remodeling and structural adaptation of bone. (Bottom) Woven bone is remodeled into lamellar bone (black bracket). Osteonal (Haversian) systems form as the lamellar bone matures. An osteon is identified by the circumscribing black line. Each osteon consists of a central canal containing a vein, artery, and lymphatic with radially arranged concentric layers of bone populated by osteocytes that interconnect through a cytoplasmic network. Kindly provided by Stefan Tangl.

adherence to pore-size parameters. Features to underscore that temper the decisions on pore-size dimension, range and distribution (and interconnectivity) are the anatomical location to be implanted, patient physiology, biomechanical dynamics, and physicochemical properties of the implanted materials.[7] The important point to note is that by examining the structure and function of bone, we receive key instructional engineering guidance. Despite the assiduous study of form and function in bone for many decades, it is still unclear why Haversian systems are consistently in the ~200-μm-diameter size range.

The architectural design of the Haversian systems is built on concentrically layered lamellae, with each lamella populated by a variable number of osteocytes (**Figure 1**) and each osteocyte linked to siblings in the same and contiguous lamellae through a gossamery meshwork of cell-cytoplasmic process traversing 8-μm-diameter caverns: canaliculi. In addition to this integrated network are the Volkmann canals, which penetrate cortical bone obliquely, anastomosing with the Haversian systems to provide transit for metabolic exchange and trafficking of soluble signals. Highly noteworthy is the vascular dependency of bone that ensures that neither osteocyte nor osteoblast (see below) is more than 300 μm from a blood vessel.[8]

Sandwiched between cortical bone is spongy-looking trabecular or cancellous bone. Unlike cortical bone, which is designed for load bearing, cancellous bone is designed to respond to physiologic requirements. Roughly 20 times greater surface area and concomitant cell density per unit volume is associated with cancellous bone as compared to cortical bone.[9]

5.522.1.5. Modeling and Remodeling

Bone is a vascularized, dynamic organ that is constantly in motion, biomechanically stressed and continuously sculpted to address homeostasis, microfracture repairs and mechanical loading. Consequently, twenty-first century tissue engineers must address the dynamic nature of bone as an organ, and recognize and anticipate modeling and remodeling. Modeling may be viewed as the cellular, functional and biochemical events that shape maturing bone until epiphyseal plate closure.[2] Remodeling consists of similar events responsible for bone repair following epiphyseal closure, and results in the restoration of form and function.[10,11] Cortical bone remodels at a rate of about 2–10% per year; this metric is site-dependent and remodeling rates of up to 20% may occur around loaded endosseous implants.[12] Packets of bone-forming osteoblasts, bone-resorbing osteoclasts, and mechanosensory osteocytes function as a basic multicellular unit (BMU) during the remodeling process. The dynamics of bone resorption and formation are especial elements for tissue engineers who aim at regeneration of deficient bone through the implantation of a scaffold that will localize, protect and release biological cues; this scaffold will synchronously resorb to be replaced by a functional quantum of new bone. Bone forms at the rate of about 1–2 $\mu m\,day^{-1}$, but during the osseous wound healing cascade, the acceleration of the regenerative process accentuates bone deposition to a rate approaching 15–20 $\mu m\,day^{-1}$, an outcome referred to as the regional acceleratory phenomenon (RAP).[2] Therefore, bone tissue engineered scaffolds must be tuned synchronously to the dynamics of the bone architecture that is to be regenerated. If the scaffold is not resorbed in register with bone formation, but resorbs too slowly, formation is hindered. Moreover, if the scaffold resorbs too rapidly, fibrous tissue invades the void space, scar formation occurs, or soft tissue subsidence and prolapse of the soft tissue envelopes around the bone preclude osseous regeneration.

Bone regeneration is the culmination of multiple, interactive, complex cellular, matrix, and molecular events that will not occur without angiogenesis. Consequently, as we develop the discussion and subsequent appreciation for the process of regeneration, we highlight angiogenesis following it up with an overview of the recruitment and morphodifferentiation of the cellular craftsmen that enable bone regeneration and ensure its maintenance.

5.522.1.6. Angiogenesis

Angiogenesis is a physiological process involving the growth of new blood vessels from preexisting vessels. Angiogenesis is a normal and vital process in growth and development. It is additionally a necessary component of wound healing and of the transition of tumors from a dormant state to a malignant one. Though terminology related to it differs, angiogenesis occurs in two forms; sprouting angiogenesis and splitting angiogenesis, otherwise known as intussusceptive angiogenesis. *Angiogenesis* is the term used for spontaneous blood vessel formation, and *intussusception* is the term for new blood vessel formation by the splitting off of existing vessels.[13]

Angiogenesis occurs in several stages. Initially, angiogenic growth factors (e.g., vascular endothelial growth factor, VEGF) activate receptors present on endothelial cells in existing blood vessels. Activated endothelial cells release proteases that degrade the basement membrane to allow the endothelial cells to escape from the vessel walls (i.e., move through the vessel walls: *margination*) and proliferate into the surrounding matrix, forming a vessel lumen for the new blood vessels. The vasculature can result in several millimeters of new growth per day. In distinction to the process of intussusception just described, is the process of angiogenesis, where new vessels form independently of existing ones.[14]

With intussusception, the capillary wall extends into the lumen to split a single vessel into two. This occurs as two opposing capillary walls come into contact. The endothelial cell junctions reorganize and the vessel is perforated to allow growth factors and cells to penetrate into the lumen. At the zone of contact, a core is formed that is filled with pericytes and myofibroblasts. These cells begin laying collagen fibers into the core, providing an ECM for the growth of the vessel lumen. Intussusception is a reorganization of existing cells.[15]

Angiogenesis may be a target for treatment of diseases characterized by either poor or abnormal vasculature. Application of specific compounds that may inhibit or induce vasculature may control vascular-dependent pathologies, such as solid state tumors.

5.522.1.7. Osteoblasts

Osteoblasts are mononucleate cells that are responsible for bone formation and are derived from osteoprogenitor cells in the periosteum and the bone marrow. However, contemporary data have validated that several cell phenotypes, including

adipogenic and myogenic lineages, can be cued into an osteogenic lineage, and, thus, osteoprogenitor pathways are possible outside the classical pathway associated with bone.

Osteoprogenitors may be induced to differentiate under the influence of growth factors, such as BMPs, FGF, PDGF, and TGF-β. These growth factors promote the division (mitogenesis) of osteoprogenitors and may increase osteoblast populations, thereby boosting osteogenesis.[16] Once osteoprogenitors start to differentiate into osteoblasts, they begin to express a range of genetic markers including osterix (Osx), monocyte-colony-stimulating factor (M-CSF), osteocalcin, osteopontin, and osteonectin.

Osteoblasts are located on the surface of bone and are responsible for synthesizing the organic components of the bone matrix. The organic components include primarily type I collagen (90% of bone protein), proteoglycans and glycoproteins; however, other proteins may be identified. Osteoblasts synthesize the enzyme alkaline phosphatase, which is needed locally for the mineralization of osteoid, as well as zinc, copper, and sodium.[17]

5.522.1.8. Osteocytes

As the bone matrix calcifies under the influence of alkaline phosphatase, osteoblasts become trapped in the bone matrix and eventually change into osteocytes. The osteocytes cease to generate osteoid and mineralized matrix and, instead, act in a paracrine manner on active osteoblasts. Osteocyctes purportedly act in a mechanosensory manner, sensing mechanical forces on bone, and send signals to regulate bone turnover at the bone surface.[18–20]

Osteocytes reside in lacunae in the mineralized bone and are interconnected by their cytoplasmic processes within canaliculi. The processes of adjacent cells make contact at gap junctions and are responsible for the maintenance of osteocyte vitality by passing nutrients and metabolites between blood vessels and osteocytes, regulating ion homeostasis and transmitting electrical signals in bone.[21]

5.522.1.9. Osteoclasts

Osteoclasts are multinucleated giant cells that are derived from the monocytic-macrophage system and are responsible for bone resorption. Osteoclasts have fine, fingerlike cytoplasmic processes and are rich in lysosomes that are characterized by expression of tartrate-resistant acid phosphatase (TRAP) and cathepsin K.[22] Osteoclast formation requires the presence of the RANKL (receptor activator of nuclear factor κβ ligand) and M-CSF (macrophage colony-stimulating factor). These membrane-bound proteins are produced by neighboring osteoblasts and stromal cells, thus requiring direct contact between osteoblasts and osteoclast precursors.[23] There is a complex, highly interactive and exciting relationship between cytokines and osteoclasts that will be established later in this chapter.

Osteoclasts inhabit cavities in bone called Howship's lacunae. Mature osteoclasts are restricted to the resorbing surfaces of bone. However, upon activation, osteoclasts migrate to bone microfractures, attach via adhesion structures called podosomes and release hydrogen ions through the action of carbonic anhydrase, thus forming a resorptive cavity, acidifying and dissolving the mineralized bone matrix. In addition, hydrolytic enzymes such as cathepsin are secreted into the resorptive pit by lysosomes to digest the organic components of the matrix.[24]

Osteoclasts have a significantly shorter life span than osteoblasts and are seen infrequently in routine histological sections of normal bone. An increased number of osteoclasts on histological sections is characteristic of diseases with increased bone turnover.[25]

In conclusion, the didactic argument to emphasize bone biology is that it provides an instructional biological road map that must be navigated. A fundamental knowledge, appreciation and understanding of basic bone biology are epochal. Bone embryogenesis, homeostasis, modeling and remodeling are pillars upon which regenerative engineering therapeutics is constructed; the organizational synchrony must be masterfully integrated and the constitutive elements recognized. Spatial, temporal and mechanobiological directors are maestros, mysteriously assembling elements in a hierarchal cascade that is unclear and that contemporary tissue engineering science has not duplicated. Nevertheless, attention to the details of the biological road map that define bone as a dynamic organ capable of regeneration can be exploited for the rational development of regenerative therapeutics.

5.522.2. Growth Factors, Cytokines, Nomenclature, Mechanism of Action

Growth factors and cytokines are a group of endogenously produced mediators that characteristically act as signaling molecules between cells. The mode of action can be autocrine, paracrine, juxtacrine, and endocrine – meaning that local and systemic effects are possible.

Growth factors and cytokines bind to the respective receptors on the surface of target cells, causing activation of the intracellular signaling cascade. This ultimately changes the cellular function, which can be suppression or enhancement. Cellular function involves, but is not restricted to, proliferation, motility, synthesis of ECM, differentiation and even cell death. Activation of the intracellular signaling cascades further causes the expression of growth factors and cytokines that amplify or reduce the overall cellular response by positive or negative feedback loops, respectively. Growth factors and cytokines, however, also drive local and systemic pathological processes of inflammation, tumor-induced bone loss and osteoporosis.

An international nomenclature of growth factors and cytokines could provide a basis for communication. However, there is no consensus on the nomenclature. Growth factors and cytokines may be classified on the basis of the cell(s) of origin or target cell(s), genetic homologies and major activities. Moreover, there is no consensus recognition of the distinction between growth factors and cytokines and, therefore, both terms are often used interchangeably, leading to confusion.

The term *signaling molecules* was considered an umbrella term for growth factors and cytokines; however, this tactic also caused confusion. Intracellular signaling molecules are neither growth

factors nor cytokines. Consequently, in this chapter, we stay with the definition of the Human Genome Organization (HUGO) Gene Nomenclature Committee (www.genenames.org).

5.522.3. Bone Tissue Engineering: Growth Factors and Cytokines

5.522.3.1. Transforming Growth Factor β

The TGF-β family of proteins regulates cell proliferation and differentiation. TGF-β proteins, along with activins, growth differentiation factors (GDFs) and BMPs, are members of the TGF-β superfamily.[26] There are three isoforms of TGF-β in mammals: TGF-β_1, TGF-β_2, and TGF-β_3.

The TGF-βs are homodimeric proteins that are ~25 kDa[27] and are synthesized as inactive latent precursors, which are cleaved outside of the cell that expressed them and thus, extracellularly, form an active protein. There are three TGF-β receptors; the TGF-β ligand binds to the TGF-β receptor II and dimerizes with TGF-β receptor I. After phosphorylation, TGF-β activates a group of mothers against decapentaplegic homolog (SMAD) proteins via serine–threonine kinase and tyrosine kinase activity.[28] TGF-β further promotes the production of Runt-related transcription factor 2 (Runx2), which forms a complex with SMAD proteins, leading to osteoblast differentiation.

TGF-βs are present in cartilage, bone, and skin, and are produced by platelets, osteoblasts, and chondrocytes.[29] TGF-β s regulate bone cell metabolism and are important regulatory molecules in wound healing cascades.[30] The use of TGF-β in bone fracture repair and reconstructive surgery has been evaluated in numerous experimental models and the outcome is ambiguous: sometimes the protein may work, and bone may be formed; at other times, it does not work; and dosing issues are highly problematic.

5.522.3.2. Bone Morphogenetic Proteins

BMPs belong to the TGF-β superfamily. There are over 40 known BMP-like molecules.[31,32] BMP-2–BMP-17 and GDF2–GDF10 also belong to the BMP family.

BMPs are dimeric proteins of ~30 kDa with the two identical strands linked by a cysteine-binding group. Signaling begins with the binding of the BMP to its transmembrane receptor, type II (serine–threonine kinase: bone morphogenetic protein receptor 2 (BMPR2)). (Noggin and chordin are extracellular binding proteins that alter the binding of BMP molecules with their receptors.) Binding of BMPs causes the recruitment of a bone morphogenetic protein receptor 1, type A (BMPR1A) or type B (BMPR1B). The type I receptor phosphorylates receptor-regulated SMADs (I-SMADs; SMAD1, SMAD2, SMAD3, SMAD5, and SMAD8/9). Common-mediator SMAD (SMAD4) interacts with the R-SMADs during signaling, while inhibitory SMADs (SMAD6 and SMAD7) block this process. Phosphorylated I-SMADs, together with SMAD4, enter the nucleus and target BMP-response genes (e.g., alkaline phosphatase and osteocalcin). Thus, BMPs stimulate differentiation of mesenchymal progenitors into the osteo-chondrogenic lineage. This process of differentiation partially explains the unique capacity of BMPs to induce *de novo* bone formation by recapitulating the embryonic ossification. The Food and Drug Administration (FDA) has approved two recombinant BMP-containing products for clinical applications: Infuse BMP-2 and BMP-7 (the latter also termed osteogenic protein 1: OP-1; Figure 2).

5.522.3.3. Insulin-Like Growth Factors

Insulin-like growth factors (IGFs) are polypeptides that have a sequence similarity to insulin, and as such, have similar molecular structures. The IGFs exist in two isoforms (IGF-1

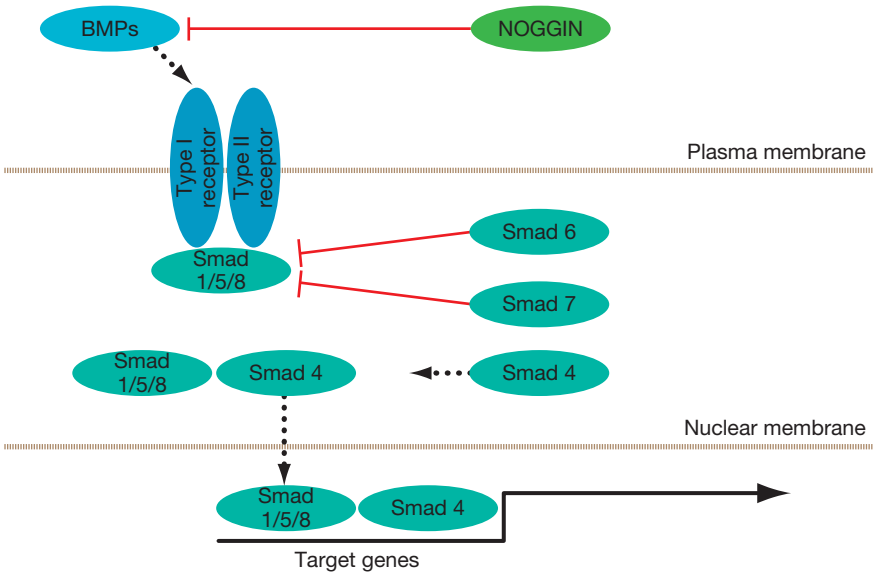

Figure 2 Bone morphogenetic proteins (BMPs) signal by binding to BMP receptor, type II (BMPR2). BMPR1A or BMPR1B are recruited and phosphorylate intracellular receptor-regulated mothers against decapentaplegic homologs (SMADs). SMAD4 supports signaling and activates responsive genes, while inhibitory SMADs (SMAD6 and SMAD7) block this process. Noggin and chordin are extracellular binding proteins that also inhibit this process at the extracellular level.

and IGF-2), and both bind to six different binding proteins. The IGF binding proteins (IGFBP1–6) regulate IGF concentration and modulate bioactivity by enhancing IGF activity and prolonging half-life.

The liver secretes IGF-1, the main IGF involved in muscle, cartilage and bone cells. IGF-1 binds primarily to IGF-1 receptor (IGF1R), which is a tyrosine kinase receptor. Binding initiates intracellular signaling and stimulates cell proliferation and differentiation.[33] Moreover, IGF-1 upregulates protein kinase D (PKD) and c-jun N-terminal kinase (JNK), which in turn have a significant impact on Osx expression.[34] Furthermore, Runx2 expression may be increased by IGF-1.[34] In addition, IGF-1 upregulates type I collagen and alkaline phosphatase gene expression in mesenchymal stem cells, all of which are key markers for osteoblast differentiation.[35]

5.522.3.4. Platelet-Derived Growth Factor

PDGF has four isoforms that cause cellular responses through two different receptors. The isoforms are PDGF α- and β-polypeptides (PDGFA; PDGFB), and PDGF C and D (PDGFC, PDGFD). PDGFA and PDGFB can form homo- and heterodimers, while PDGFC and PDGFD form homodynes only. Optimal concentrations of PDGF-AB (1 ng ml^{-1}) was shown to upregulate BMPR-1B messenger ribonucleic acid (mRNA) by 2.4-fold.[36] Two types of PDGF receptors (R) have been identified: PDGF receptor, α-polypeptide PDGFRA and PDGF receptor, β-polypeptide PDGFRB. The receptors form homo- and heterodimers.

PDGF-BB homodimer can activate all three combinations of receptors and is thus the most potent ligand. Ligand binding causes the receptors to dimerize and activate tyrosine kinase. Phosphorylated cytosolic domains provide binding sites for signaling proteins that initiate signal cascades, such as the phosphoinositide 3-kinase (PI3K) and mitogen-activated protein kinase (MAPK) family pathways.

Mesenchymal cells respond to PDGF-signaling by proliferation, motility and synthesis of ECM. The osteogenic differentiation of the cells is transiently suppressed.

The FDA has approved recombinant human PDGF-BB in a carboxy methyl cellulose delivery system (Regranex, Ortho-McNeil) in clinical applications for the treatment of diabetic patients and in combination with tricalcium phosphate (GEM-OS, OsteoHealth) for periodontal regeneration in dentistry (Figure 3).

5.522.3.5. Vascular Endothelial Growth Factor

VEGFs are a subfamily related to the PDGF family. VEGFA was first described and originally termed VEGF before related members were discovered, such as VEGFB, VEGFC, and V-fos FBJ murine osteosarcoma viral oncogene homolog (c-fos) induced growth factors (FIGF; VEGFD). VEGFA has characteristic splice variants ($VEGF_{121}$, $VEGF_{121}b$, $VEGF_{145}$, $VEGF_{165}$, $VEGF_{165}b$, $VEGF_{189}$, $VEGF_{206}$).

VEGF ligands bind to receptors that dimerize and activate tyrosine kinase. The phosphorylated signaling proteins, in turn, activate the downstream signaling cascades. VEGFA binds to Fms-related tyrosine kinase 1 (vascular endothelial growth factor/vascular permeability factor receptor; FLT1, VEGFR1), and kinase insert domain receptor (KDR, fetal liver kinase 1 (FLK1), VEGFR2). VEGFC and FIGF bind to a third

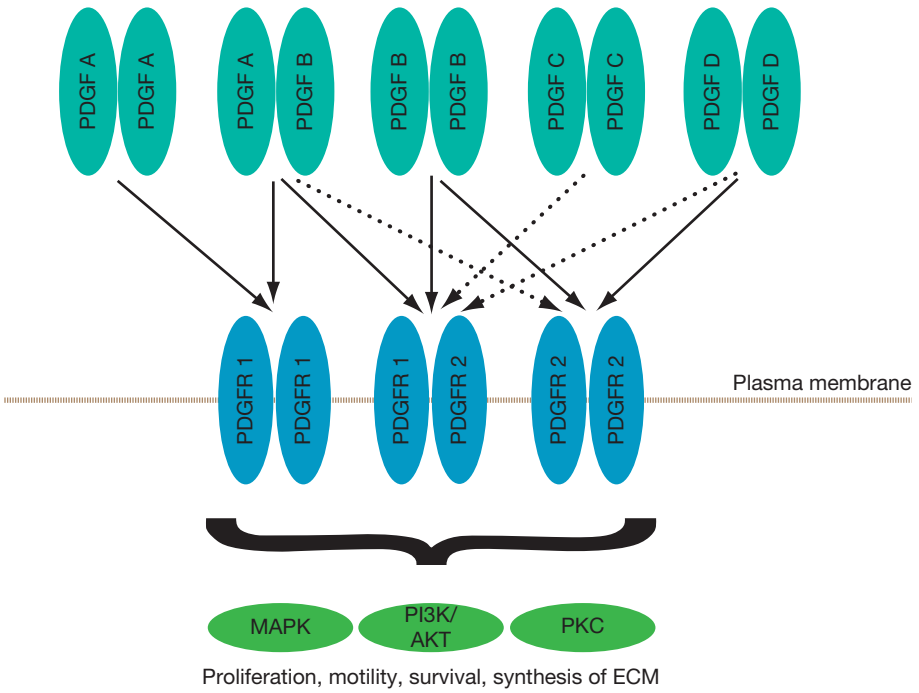

Figure 3 Platelet-derived growth factor (PDGF) isoforms signal via two different receptors. PDGFA and PDGFB can form homo- and heterodimers, while PDGFC and PDGFD form homodynes only. The receptors also form homo- and heterodimers. PDGF-BB can activate all three combinations of receptors and is thus the most potent ligand. Intracellular tyrosine kinases phosphorylation activates signaling proteins such as phosphoinositide 3-kinase and members of the mitogen-activated protein kinase family.

receptor (FLT4, VEGFR3). While FLT1 and KDR mediate vascular angiogenesis, FLT4 mediates lymphangiogenesis.

VEGF has been shown to promote angiogenic differentiation and enhance bone formation.[37] During endochondral ossification, VEGFA is produced by chondrocytes and osteoblasts, and it has a profound impact on the vascular invasion of cartilaginous tissue.[38] Further, VEGF increases endothelial progenitor cell mitogenesis and chemotaxis, which can lead to the formation of new blood vessels.[39,40] By inducing angiogenesis, VEGF increases the amount of oxygen and other nutrients required for osteogenesis.[38] Moreover, osteoblasts secrete VEGF, and osteoblasts and osteoclasts have been shown to secrete VEGF receptors.[41,42]

While VEGF may not have a direct osteogenic differentiation effect, it may promote bone formation by complementing and potentiating the osteogenic effect of other growth factors.[43] In addition, the homodimeric glycoprotein VEGFA has an affinity to VEGFR2, which is secreted by chondrocytes, and induces angiogenesis from the perichondrium, thereby leading to the recruitment of bone cells, osteoclasts and osteoblasts, and hematopoietic stem cells.[44] The therapeutic application of recombinant VEGFA to enhance bone regeneration is restricted to preclinical studies. However, in tumor therapy and macular degeneration, monoclonal antibodies that neutralize VEGFA (e.g., bevacizumab) and tyrosine kinase inhibitors (e.g., lapatinib) are undergoing clinical evaluation (Figure 4).

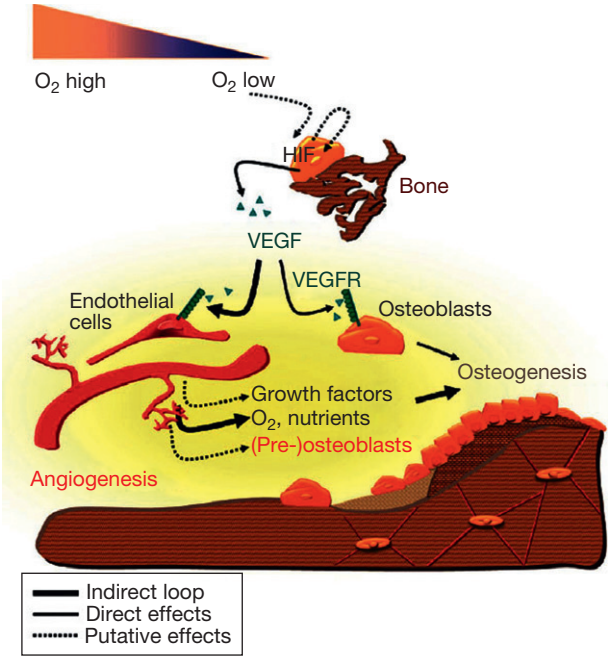

Figure 4 Regulation of osteogenic–angiogenic coupling by hypoxia inducing factor (HIF) and vascular endothelial growth factor (VEGF). Mature osteoblasts located on the bone surface express HIFs and respond to HIF activation, which may be induced in response to low oxygen tensions in the bone and marrow environment. Cell-autonomous effects of HIF may affect bone formation (osteogenesis), but a critical effect of HIF stabilization in mature osteoblasts is the increased accumulation of VEGF. VEGF can act through its receptors (VEGFR) on endothelial cells to induce angiogenesis and thereby indirectly increase the supply of oxygen and nutrients required for osteogenesis. Increased vascularization may also lead to a higher input of putative skeletal stem cells and/or (pre-)osteoblasts and to elevated levels of endothelium-derived osteogenic growth factors or anabolic signals. In addition, VEGF can affect osteogenesis through direct interactions with osteoblasts that also express VEGF receptors. Altogether, the HIF–VEGF pathway is likely to be critically important in coupling the processes of angiogenesis and osteogenesis.

5.522.3.6. Fibroblast Growth Factors

FGFs are a family of proteins, with 23 identified members, some of which promote bone formation through an anabolic effect.[45,46] FGF-1 and FGF-2 (the most abundant ligands) promote osteoblastic and angiogenic activity in addition to inducing VEGF.[45]

FGF-2 is an important mitogen in bone for precursor cells, such as mesenchymal stromal cells as well as for calvarial and mature osteoblasts.[47–49] However, the effects of FGF-2 in bone formation are controversial. While FGF-2 contributes to the proliferation of osteoblast cells, it also inhibits late stages of osteoblast differentiation and bone formation.[50,51]

FGF-2 and FGF-9 stimulate proliferation of mature osteoblasts, but can inhibit osteoblast marker genes and mineralization.[48] FGF-2 expression levels are elevated during fracture healing and this has been shown to accelerate wound healing in critical-sized bone defects.[52,53] Recent publications have shown that FGF-8 may cue bone marrow cells to differentiate into osteoblasts.[54] In addition, FGF-8 and FGF-18 stimulate the proliferation of osteoblasts *in vitro*.[55] FGF-8b and FGF-8e have been reported to induce osteoclastic differentiation, which is possibly dependent on the RANKL/osteoprotegerin (OPG) pathway.[54,56] A complex relationship exists between bone and the FGF family of growth factors, the precise biological details of which have not been suitably elucidated.

5.522.3.7. Sclerostin

Sclerostin (SOST) is a 22.5 kDa secreted glycoprotein almost exclusively expressed by osteocytes. It is released to the bone surface via the osteocyte canalicului system and binds to low density lipoprotein receptor-related protein 4 (LRP4) LRP5 and LRP6, which are coreceptors for frizzled homolog 1 (Drosophila; FZD1), alias Wnt receptor. SOST prevents Wnt-signaling, which requires FZD1 and the LRP-coreceptors to be activated by soluble Wnt-ligands. When activated, intracellular β-catenin is protected from degradation and can function as a transcription factor. In the presence of SOST or other inhibitors of Wnt-signaling such as dickkopf homolog 1 (*Xenopus laevis*; DKK1), β-catenin is targeted for proteosomal degradation. SOST has gained attention as a potential therapeutic target because mutations of the gene are associated with a high bone mass phenotype. Preclinical studies and clinical trials provided first evidence that blocking SOST by neutralizing antibodies stimulates an anabolic activity.

There are numerous additional biological molecules, for example, growth factors that have an impact on bone formation and resorption. The chapter focuses on the factors commonly recognized as being most significant and whose functional relationships are least controversial (Figure 5, Table 1).

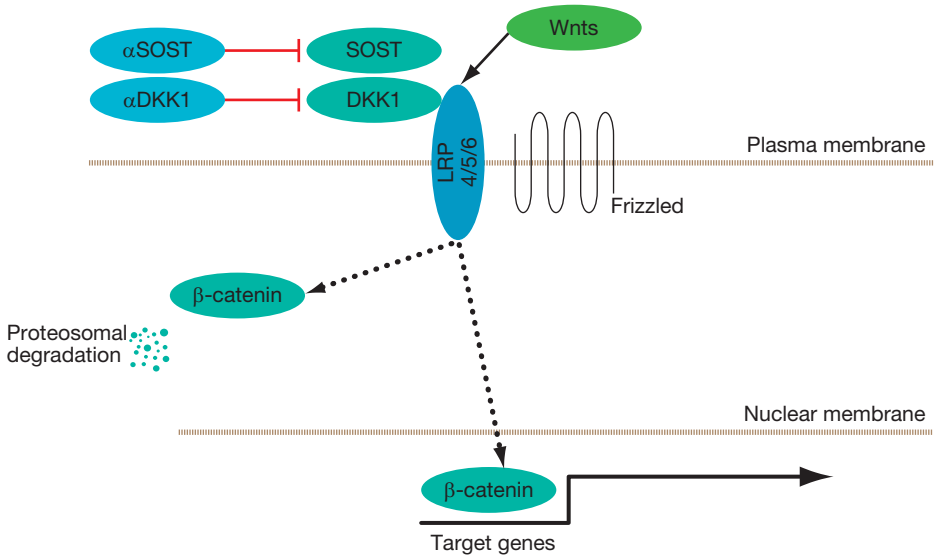

Figure 5 Wingless-type MMTV integration site signaling requires the receptor frizzled homolog 1 (Drosophila; FZD1) and the low density lipoprotein receptor-related protein (LRP)-coreceptors to be activated. Intracellular β-catenin is protected from degradation and can function as a transcription factor. Sclerostin (SOST), alias SOST binds to low density LRP4, LRP5, and LRP6, which are coreceptors for FZD1. SOST thus prevents canonical signaling and β-catenin is targeted for proteosomal degradation.

Table 1 Selected bone growth factors

Growth factors	*Source*	*Biological response*	*Action on bone*
BMP-2, -4, -7	Mesenchymal Osteoblast Endothelial Chondrocyte	Chondrogenic Osteogenic Osteoinductive	Chemotactic Maturation Differentiation
FGF-1 and -2	Mesenchymal Osteoblast Chondrocyte Inflammatory cells Endothelial	Angiogenesis Connective tissue cell proliferation	Chemotactic Proliferation
IGF-I and -II	Osteoblast Chondrocyte Hepatocyte Endothelial	Anabolic and catabolic effect on osteogenesis	Chemotactic Proliferation Maturation Differentiation Resorption
PDGF-BB	Platelet Osteoblast Inflammatory cells Endothelial	Angiogenesis Connective tissue cell proliferation	Chemotalic Proliferation
TGF-β	Platelet Osteoblast Chondrocyte Endothelial Inflammatory cells Fibroblast	Immunosuppression Angiogenesis Cell growth and differentiation	Proliferation Osteogenic ECM production
VEGF	Platelet Osteoblast Chondrocyte	Chemotactic Angiogenesis	Conversion of cartilage to bone, Chemotactic Proliferation

5.522.4. Cytokines and Bone

Cytokines are primarily involved in the inflammatory response and provide integration between immune and endocrine systems. The interconnected network between the skeletal and immune systems has led to the emergence of a new discipline referred to as osteoimmunology.[57] Cytokines comprise a group of regulatory factors with the following attributes: having a molecular weight of <80 kDa and biological activity in the 10^{-10}–10^{-13} M range, generally occurring as glycosylated

peptides, produced transiently by most nucleated cells, having pleiotropic properties, being autocrine or paracrine, and possessing overlapping biological activities.

In general, cytokines exert regulatory control over bone remodeling by serving as intermediaries for the indirect effects of hormones while also mediating the complex cell–cell communications between osteoblasts and osteoclasts. The principal cytokines involved in physiologic bone remodeling are RANKL, RANK, OPG, M-CSF, IGF-I, IGF-II, TGF-β, interleukin 1 (IL1), IL6, tumor necrosis factor α (TNF-α).[57] We emphasize a select few of the many cytokines associated with bone. There are, in fact, many cytokines; however, we want to focus on those cytokines that have been the most documented relative to bone formation and resorption.

5.522.4.1. Receptor Activator of Nuclear Factor κβ Ligand

RANKL is a transmembrane molecule expressed by mesenchymal cell and lymphocytes. The soluble form of RANKL is a consequence of proteolytic cleavage. RANKL binds to RANK on hematopoietic cells and activates cytoplasmic adaptor proteins (e.g., tumor necrosis factor receptor-associated factor 6, TRAF6). These events activate downstream signaling pathways involving nuclear factor kappa-light-chain-enhancer of activated B cells (NF-κB), MAPK family and nuclear factor of activated T cells, cytoplasmic 1 (NFATc1). However, RANKL is neutralized by its soluble decoy receptor OPG. It is consequently the ratio between RANKL and OPG that regulates the process of bone resorption. Based on this physiological principle, the monoclonal antibody that neutralizes RANKL (denosumab) may have efficacy in preventing fractures in osteoporotic patients. As a consequence of the importance of RANK/RANKL, this topic is discussed further under bone resorption (Figure 6).

5.522.4.2. IL1β and TNF (Superfamily Member 2, TNF Alias TNF-α)

IL1β and TNF-α are central mediators of inflammation and are produced by lymphocytes and mesenchymal cells. Interleukin 1 receptor, type I (IL1R1) is responsible for mediating the signaling response; IL1R2 has inhibitory action. The tumor necrosis factor receptor superfamily member 1A (TNFRSF1A alias TNFR1) is widely expressed, whereas, TNFRSF1B alias TNFR2 is expressed mainly by hematopoietic and immune cells. Both receptors activate adaptor proteins and downstream signaling molecules such as NF-κB and the MAPK family.

It is not surprising, given the hematopoietic lineage of osteoclasts, that many of the cytokines typically associated with the immune system influence bone modeling and remodeling. What is surprising is the complexity of this system given that there are only two primary cell types, the osteoblasts and osteoclasts, involved in the processes. At least 19 cytokines play some role in the regulation of these processes: IL-1, 3, 7, 10, 13, TNF-α and interferon-γ in the regulation of osteoblasts, and IL-1, 3, 4, 6–8, 10–13, 15, 17, 18, 23, TNF-α, OPG, leukocyte inhibition factor (LIF), M-CSF, and interferon-γ in the regulation of osteoclasts.

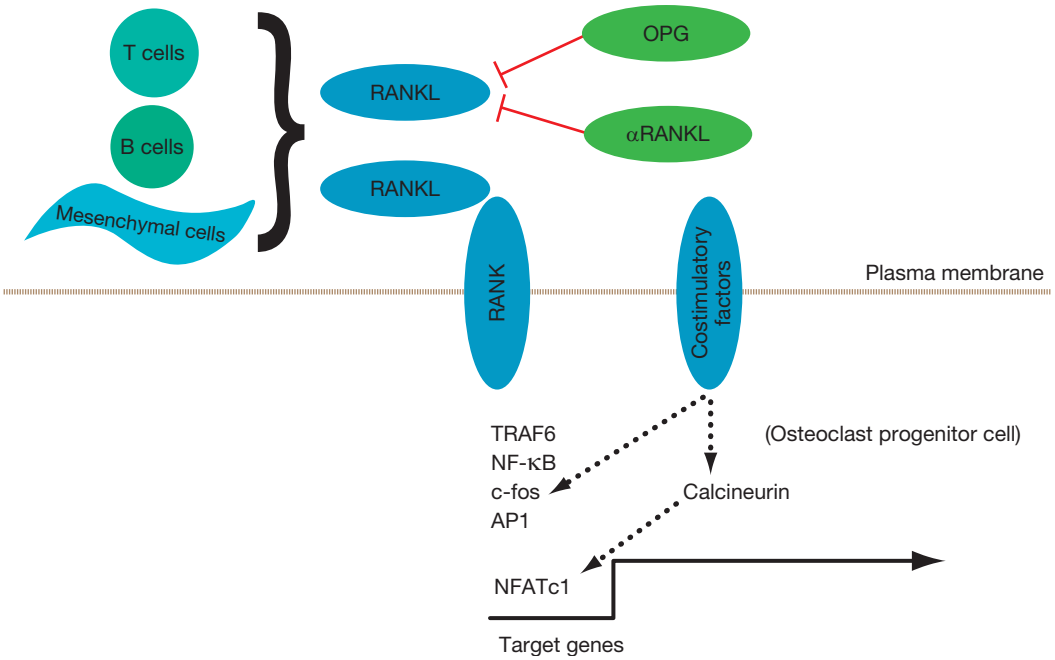

Figure 6 Receptor activator of nuclear factor kappa-light-chain-enhancer of activated B cells (NF-κB) ligand (RANKL), RANK and osteoprotegerin (OPG) build a triumvirate of molecules that control the formation, activity and the survival of osteoclasts. RANKL binds to RANK and activates cytoplasmic adaptor proteins (e.g., tumor necrosis factor receptor-associated factor 6). Downstream signaling pathways include NF-κB, mitogen-activated protein kinase family, and nuclear factor of activated T cells, cytoplasmic 1. RANKL is neutralized by its soluble decoy receptor OPG. Thus, the ratio between RANKL and OPG regulates the process of bone resorption.

5.522.4.3. Bone Resorption

After the implantation of a biomaterial in bone, events including hemorrhage, hemostasis, complement activation, inflammation, and bone resorption ensue. For the focus of this chapter, we underscore *resorption of bone*, where osteoclasts are the hallmark cells recruited to the implant site with macrophages as a requisite antecedent event prior to bone apposition and formation.

5.522.4.3.1. Osteoclast precursor signaling

IL-3 and -7 participate in osteoclast precursor signaling. IL-3, produced by mesenchymal stem cells, promotes osteoclast precursor formation.[58] IL-7 is produced by T cells. Systemically, IL-7 increases osteoclast precursor formation while local administration of IL-7 to hematopoietic stem cells decreases formation.[59]

5.522.4.3.2. Osteoclastogenesis

Osteoclastogenesis involves differentiation of osteoclast precursors to mononuclear osteoclasts via RANK/RANKL interaction. RANK is a membrane-bound receptor found on osteoclast precursors. RANKL is a membrane-bound molecule found on osteoblasts. (RANKL belongs to the TNF family of cytokines and is also called TRANCE, OPGL, and ODF.) The interaction is optimized[57] when three RANKs contact three RANKLs, usually when the RANKL-associated osteoblast is attached to the surface of bone.[60] While there have been reports of RANKL on T cells being able to induce osteoclastogenesis,[61] a more recent study concluded that this source of RANKL was insufficient to induce osteoclastogenesis.[60]

It has been shown that M-CSF and RANKL are necessary to achieve the differentiation of osteoclast precursors to mononuclear osteoclasts.[62] A number of cytokines are involved in the regulation of RANK and RANKL expression. These mechanisms are discussed one at a time.

5.522.4.3.2.1. RANKL upregulation

Upregulation of RANKL on osteoblasts is controlled by IL-1, 6, 7, 8, 17, LIF, TNF-α, and interferon gamma (IFN-γ). IL-1 influences RANKL expression indirectly by upregulating the production of IL-7.[63] When administered systemically, IL-7 promotes RANKL expression.[59] IL-6, produced by osteoblasts and bone marrow stromal cells (BMSCs), stimulates RANKL mRNA expression.[64] Likewise, IL-8, produced by macrophages, neutrophils, and endothelial cells, upregulates RANKL mRNA expression.[65] Cytokines are also produced by osteoclasts themselves, resulting in a paracrine feed-forward mechanism to promote osteoclastogenesis. IL-17 is a six member family of cytokines (IL-18A–F)[58] produced by the T helper cell 17 (TH17) subset of the CD4+ T cells.[66] It upregulates RANKL in osteoblasts[66] and T cells.[63] However, knockout mice deficient in IL-17 show normal bone formation, so this cytokine participates in, but is not essential to, healthy bone formation.[66] In T cells, it also stimulates production of IL-1 and TNF-α, acting as a feed-forward mechanism to promote osteoclastogenesis. LIF (part of the IL-6 or gp130 cytokine family)[67] stimulates both RANKL and Osteoprotegrin (OPG) expression.[58] OPG is secreted by marrow stromal cells and osteoblasts,[68] as well as B cells, after CD-40 binding T cells, and dendritic cells.[66] OPG plays a minor role in osteoclastogenesis by upregulating RANKL mRNA expression in T cells.[63] The main role of OPG is to act as a decoy protein by competitively binding to RANKL, thus frustrating osteoclastogenesis.[57,66]

5.522.4.3.2.2. RANKL downregulation

Downregulation of RANKL on osteoblasts is controlled by IL-4 and IL-13. IL-4, produced by activated T cells, decreases RANKL expression in osteoblast precursors.[69] IL-13, produced by TH2 cells[60] also decreases RANKL expression.[58] Both IL-4 and IL-13 are locally acting cytokines.

5.522.4.3.2.3. RANK expression

There are far fewer known controlling cytokines for RANK compared to RANKL. Takahashi *et al.*[70] reported that macrophage colony-stimulating factor (M-CSF) may cause monocyte/macrophage lineage cells to express RANK. Balancing this, Palmqvist *et al.*[69] reported that IL-4 decreases RANK mRNA expression in cultured rat calvaria.

5.522.4.3.2.4. Upregulation of osteoclastogenesis

The cytokines IL-1, 6, 7, 8, TNF-α, and M-CSF promote the formation of osteoclasts. IL-1 upregulates osteoclastogenesis by stimulating the production of IL-7. IL-6 participates in the Janus kinase/signal transducer and activator of transcription (JAK/STAT) pathway, and turns on osteoclast genes after RANK/RANKL binding.[71,72] IL-7, when administered systemically, increases the number of osteoclast precursor cells.[59] IL-8 is involved in G-receptor coupled signaling, which causes mononuclear cells to differentiate into osteoclasts.[19] TNF-α augments the response of osteoclasts to RANKL[66]; this mechanism is M-CSF dependent.[58] TNF-α may induce osteoclastic genes via the canonical (involving translocation to the nucleus of P50 and P65 dimers) and noncanonical (involving translocation of P52 and Re1B dimers to the nucleus) pathways.[68] Finally, M-CSF produced by osteoblasts works with RANKL to initiate and maintain osteoclast differentiation.[57]

5.522.4.3.2.5. Downregulation of osteoclastogenesis

The cytokines IL-3, 4, 7, 10, 12, 18, and interferon-γ decrease the formation of osteoclasts after the RANK/RANKL production. IL-3, produced by mesenchymal stem cells, inhibits RANKL-mediated osteoclastogenesis.[73] IL-4 suppresses RANKL-mediated osteoclastogenesis by upregulating OPG expression.[69] When administered locally to hematopoietic stem cells, IL-7 influences the stem cell commitment toward the B cell pathway, thus decreasing the population of osteoclast precursors. This is not a strictly post-RANK/RANKL binding mechanism. IL-10 disrupts Ca^{2+} mobilization, which interferes with NFATc1 activity, needed to upregulate osteoclast genes downstream of the RANK/RANKL binding event.[74] In addition, IL-10 upregulates M-CSF which may promote more macrophages rather than more osteoclasts to differentiate from hematopoietic precursors.[75] IL-12, produced by dendritic cells, macrophages and B cells also disrupts NFATc1 activity. IL-18 increases expression of OPG, thus blocking RANK/RANKL binding.[76] Further, IL-12 increases expression of IFN-γ, which

results in the downregulation of osteoclastogenesis.[77] IFN-γ also decreases osteoclast formation by inhibiting vitamin D (25D3), parathyroid hormone (PTH), and IL-1 activity.[78]

5.522.4.4. Bone Formation

Following localized osteoclastic action in the bone repair cascade, bone-forming units arrive. Cytokine control over this process may be coupled with growth factors such as the BMPs to regulate differentiation, proliferation, motility, attachment, and anabolic ECM activities.

During bone formation and repair, *osteoblastogenesis* is upregulated by TNF-α, which induces the TAK1/TAB1/NIK signaling cascade in mesenchymal stem cells.[79] TNF-α aids in osteoblast differentiation as well as in downregulation of osteoblast proliferation. IL-3, on the other end, inhibits osteoblast differentiation.[73] IL-13 stimulates osteoblast migration.[58] In general, bone formation is suppressed by IL-7,[80] and IL-10 inhibits type I collagen, osteocalcin and the onset of mineralization (Table 2).[82]

5.522.5. Translational Applications of Growth Factors and Cytokines in Bone Tissue Engineering

This chapter has reviewed the growth factors and cytokines involved either indirectly or directly with the dynamics of bone embryology, homeostasis, modeling–remodeling and regeneration. Moreover, as the authors of this chapter have underscored, there is an astonishingly lush symphony of activities choreographed for each contributing element involved in the process of bone regeneration. It is, consequently, remarkably counter-intuitive to presume that, through tissue engineering, a scientist could engineer a single biological element that will produce a complex outcome: regeneration. Yet, single growth factors such as BMP-2 and PDGF discussed earlier in this chapter, have been used therapeutically in patients to regenerate bone. How can this outcome occur? Why does this outcome occur? Can we do better? (Figure 7)

The focus of the last section of the chapter showcases the growth factors and cytokines that have demonstrated a clear clinical benefit and produced a regenerative outcome. Especial emphasis is given to the factors that have achieved FDA approval.

5.522.5.1. Dental

Dentistry offers a large spectrum of possible applications of growth factors in bone tissue engineering. One therapeutic target is the periodontium, a complex structure that anchors the tooth in the alveolar bone of the mandible and the maxilla.[83] As a consequence of a multifactorial etiology, periodontal disease destroys the periodontium. Moreover, it is noteworthy that periodontal disease is the most prevalent disease in the United States and Western Europe, with more than two-thirds of the elderly population being afflicted.[84] Consequently, regeneration of the periodontium has become a serious clinical challenge (Figures 8 and 9).

The combination of recombinant human (rh) PDGF-BB and β-tricalcium phosphate (Growth-factor Enhanced Matrix®; OsteoHealth Company: GEM 21S) has been approved by the FDA for periodontal regeneration. Recently, gene therapeutic approaches based on PDGF-BB were successful in preclinical models of periodontal defects.[85] These observations may be a consequence of the mitogenic and chemotactic activity of PDGF-BB for mesenchymal cells. Moreover, PDGF-BB is a pro-angiogenic molecule, which stimulates angiogenesis.[86]

Recombinant BMP-2 is an osteoinductive growth factor that, in combination with type I bovine collagen (known as INFUSE® Bone Graft: Medtronic Sofamor Danek), has been approved by the FDA as an alternative to an autogenous bone graft for maxillary sinus augmentation. Moreover, approval was obtained for localized alveolar ridge augmentations for defects associated with extraction sockets.

Other growth factors and cytokines have been linked with dentistry but remain mostly at the preclinical level. For example, recombinant VEGFA and gene therapeutic approaches combined with BMP have been suggested for bone regeneration procedures.[87,88] Local and systemic application of PTH has been mentioned for osseointegration of dental implants.[89,90] Neutralizing antibodies against SOST might promote osseointegration.[91] Blocking bone resorption either directly by neutralizing RANKL[92] or by an anti-inflammatory strategy that blocks IL-1 or TNF[93] might reverse periodontal disease.[94]

5.522.5.1.1. Therapeutic bone regeneration in dentistry

Therapeutic bone regeneration may be required when there is impaired angiogenesis. Other limiting factors are insufficient mesenchymal cells that can become chondrocytes or osteoblasts during endochondral or intramembranous ossification, respectively. Thus, a compelling indication for a growth factor-based therapy is a situation of compromised bone healing, typically observed with the elderly patient.[95] Additional patients at risk for poor bone healing are diabetics and those with osteoporosis.

5.522.5.2. Orthopedic and Craniomaxillofacial

5.522.5.2.1. Contextualizing the discussion

The gold standard for bone regenerative purposes is a vascularized bone-like tissue. Unfortunately, the attendant morbidity and mortality with autografting procedures inspires the profoundly compelling need for alternatives that will not involve multiple invasive procedures. Consequently, recombinant genetically engineered molecules that induce bone regeneration and supportive angiogenesis have been assiduously studied and are being brought into the clinic.[96,97]

5.522.5.2.2. Interpreting preclinical data

Studies have shown that growth factors in combination with any number of carriers or vehicles can stimulate robust new bone growth in just about every aspect of the skeleton.[96,98–101] This is promising in itself but data has also suggested that there are significant differences in bone biology between humans and animal models. Consequently, clinicians have to be mindful about extrapolating results from animal data to the clinical setting. This might be because the timing of bone healing in humans is different than in animals and the duration of growth factor expression during healing processes across species also differs. In this context, it has become apparent that the strategy for growth factor delivery and the release kinetics are critical to clinical success. This is made more complex by the fact that different skeletal sites have unique characteristics,

Table 2 Cytokines in bone cell metabolism

Cytokine	*Produced by*	*Cell it signals to*	*Mechanism of action*	*Additional information*
IL-1	Osteoclasts and osteoclast precursors (OCP's) can secrete TNF leading to feed forward for resorption. This happens when OCP's contact bone matrix[68]	Promotes MSC to blast by inhibiting MSC to adipocyte[79]	IL-1-induced TAK1/TAB1/NIK signaling cascade attenuates PPAR-gamma-mediated adipogenesis by inhibiting the binding of PPAR-gamma to the DNA response element[79]	
			First cytokine (along with IL-6) involved in bone loss due to estrogen deficiency[80]	
		T cells[63]	Increases RANKL mRNA expression[63]	
		Stromal marrow cells and osteoblasts[63]	Enhance osteoclastogenesis via RANK/RANKL mechanisms by upregulating IL-7 production[63]	
	Osteoblast			
		Osteoclast precursor	Enhances RANKL expression[62]	
		Osteoclasts[58]		
IL-3	Mesenchymal stems	T-lymphocytes	Inhibits osteoblast formation[73]	
		Osteoclast precursors[58]	Inhibits RANKL-mediated osteoclastogenesis but otherwise promote osteoclast precursor formation (along with GM-CSF)[58]	
IL-4/IL-13	Activated T-cells	Osteoblast precursors	Suppress RANKL-induced osteoclast differentiation (IL-4)[69]	IL-4 and IL-13 bind to IL-4Rα and IL-13α1 activating JAK/STAT6 pathway of tyrosine kinase phosphorylation. This in turn effects NF-κB, peroxisome proliferator-activated receptor-γ1, MAPK and Ca^{2+} signaling, NFATc1 and c-Fos[129]
		Osteoclasts	Increase OPG and decrease RANKL and RANK expression, thereby inhibiting osteoclast differentiation (IL-4 and IL-13)[69]	
IL-5	Eosinophil in asthma and rhinitis and nothing directly on bone			
IL-6	Osteoblasts, BMSC	Osteoclast progenitor cells	Induce osteoclastogenesis and bone resorption	Differentiate into mature osteoclasts[72] Stimulates RANKL and OPG mRNA production in bone[64] Enhances production of prostaglandins[130] Specific IL-6 binding protein binds IL-6, this then activates cells that contain the gp 130 signal peptide, signal transduction occurs through JAK/STAT pathway of tyrosine kinase phosphorylation[71]
IL-7	T cells[59]		Suppresses bone formation[80] (no mechanism given). Promotes RANKL expression and upregulates osteoclastogenesis when administered systemically. Upregulates the number of osteoclast precursor cells.[59] When administered locally to HSCs, decreases OCP population by influencing lineage commitment toward B cell development pathway	
IL-8	Macrophages, neutrophils, endothelial cells, osteoclasts	Osteoblasts	Induce osteoclastogenesis[65]	Stimulate RANKL mRNA expression[65]
		Human bone marrow-derived osteoclast-like cells[131] (osteoclast progenitor cells)		Directly stimulates differentiation of mononuclear cells into osteoclasts

(*Continued*)

Table 2 (Continued)

Cytokine	*Produced by*	*Cell it signals to*	*Mechanism of action*	*Additional information*
				IL-8 binds to CXCR1 receptor which, is a G-protein-coupled receptor, triggers a flux of intracellular Ca^{2+} ions for cell response[19]
IL-10	Activated T and B lymphocytes	Mononuclear cells (osteoclast progenitor cells)[132]	Inhibits osteoclastogenesis	Increases M-CSF gene expression in bone marrow (thereby increasing macrophage production disproportionately)[75]
		Mesenchymal osteoblastic precursors		Increased tyrosine phosphorylation of a variety of proteins in osteoclast precursor cells[133]
				Suppreses RANKL-induced NFATc1 activity via disruption of Ca^{2+} mobilization[74]
				Inhibit ALP, collagen type 1 and osteocalcin (bone proteins) and inhibit onset of mineralization at early osteogenic differentiation stages[82]
IL-11 (part of the IL-6 or gp130 cytokine family)[67]		T cells[63]	Enhances bone resorption[63]	
			Increases RANKL mRNA expression[63]	
		Osteoblasts	Downregulates type II glucocorticoid receptors	
			Has no effect on isolated osteoclasts *in vitro*[58]	
IL-12	Dendritic cells, macrophages, B cells	Osteoclast precursors	Inhibits osteoclastogenesis	Inhibits RANKL-induced NFATc1 expression for osteoclast differentiation[134]
				IL-12 binds to IL-12R-beta2 receptor, IL-12R-beta2 becomes tyrosine phosphorylated and signal transduction occurs through JAK/STAT pathway[135]
IL-13 (a locally acting cytokine along with IL-4)[58]	TH2[60]		Inhibits IL-1 stimulated bone resorption by decreasing prostaglandin levels and cyclooxygenase-2 activity[58]	
		Osteoblast	Stimulates osteoblast migration and regulates osteoclast formation and activity by increasing OPG and decreasing RANKL production	
IL-15 (a member of the IL-2 superfamily)[58]	T-lymphocytes[58]	Osteoclast precursors	Involved in maintenance of stromal cell population but no direct link to blasts or clasts.[66] Leads to increased osteoclastogenesis in RA patients[58]	
			Increases osteoclast precursor cell numbers in culture[58]	
IL-17 (a 6 member family IL-17A-F)[58]	TH17 subset of the CD4+ T-cells	Osteoblasts	Stimulates bone resorption by upregulation of RANKL[66]	
	IL-17A[58]			
			However, mice deficient in IL-17 showed normal bone so it doesn't seem essential to bone formation[66]	
		Osteoclast precursors	Stimulate osteoclastogenesis in mixed hematopoietic cell/osteoblasts cultures via prostaglandin synthesis and RANKL expression[58]	
		T cells[63]		
			Increases RANKL mRNA expression[63]	
			Stimulates production of IL-1, IL-6, and TNF[60]	

IL-18	Osteoblasts, macrophages	Osteoclasts	Inhibits osteoclastogenesis	1. T cell production of GM-CSF[136] 2. Increased expression of IFN-γ[77] 3. Synergistically increases IFN-γ production with IL-12[137] 4. Increased expression of OPG[76] IL-18 signals through the IRAK receptor to induce translocation of NF-κB complex[136]
TNF	Osteoclasts and osteoclast precursors can secrete TNF leading to feedforward for resorption[68]	Osteoclast precursor	Regulates expression of SDF-1 by marrow stromal cells which promotes osteoclast precursor egression from marrow to blood.[68] Also causes expression of osteoclastic genes via two pathways (1) Canonical: phosphorylation and degradation of in inhibitory kappa kinase b $\rightarrow$ free NF-κB P65 and P50 dimers which translocates to the nucleus, inducing expression of osteoclastogenic genes (2) Noncanonical: Phosphorylation and degradation of p100 (p100 normally attached to Re1B, an inhibitory NF-κB protein), a P52 fragment of P100 binds to Re1B and the dimmer translocates to the nucleus to turn on osteoclastogenic genes[68] TNF upregulates expression of NF-κB p100 in OCP's[68]	
TNF-α		Osteoclast	Directly stimulates them and augments their response to RANKL.[66] Ability to do this is M-CSF dependent[58]	
		T-cells[63]	Increases RANKL mRNA expression[63]	
		Stromal marrow cells and osteoblasts[63]	Enhance osteoclastogenesis via RANK/RANKL mechanisms by upregulating IL-7 production.[63] Ability to do this is IL-1 dependent and can be accomplished in the absence of RANK although the effect is substantially weakened in this case[58]	
		Mesenchymal stem cells[79]	Promotes osteoblastogenesis by inducing TAK1/TAB1/NIK signaling cascade that attenuates PPAR-gamma-mediated adipogenesis by inhibiting the binding of PPAR-gamma to the DNA response element.[79] In contrast to the summary of Takada, Lee summarizes that TNF-α inhibits osteoblast differentiation and Type 1 collagen production and is even proapoptotic for osteoblasts. However, mice without TNF receptors produce normal bone suggesting that the cytokine's effects are only seen during inflammation and not during normal bone formation[58]	
OPG (osteoprotegrin)	Osteoblast produce in response to other cytokines, hormones, and mechanical stress.[68] Also secreted by osteoblastic stromal cells.[68] Produced by B cells after CD-40 binding with T cell.[66] Also produced by T cells and dendritic cells	Osteoclast precursor	Inhibits RANK thus inhibiting osteoclastogenesis.[57] Inhibition is by binding to RANKL to act as a decoy receptor[66] Decreases production of IL-6, IL-11 in response to dendritic cell stimulation by RANKL, also decreases IL-12 and IL-15 from T cells[63]	
	On surface of dendritic cells[63]	T cells[63]	Increases RANKL mRNA expression[63]	

(*Continued*)

Table 2 (Continued)

Cytokine	*Produced by*	*Cell it signals to*	*Mechanism of action*	*Additional information*
RANKL receptor activator of NF-κB ligand (a TNF family protein also called TRANCE, OPGL, ODF)	Osteoblast produce in response to other cytokines, hormones, and mechanical stress[68] and activated CD4 and CD8 T cells[66] also produced by Th17 cells and B cells.[138] Also found on TH1 and TH2 cells[60]	Osteoclast precursor	Principal mediator between blasts and clasts. With M-CSF initiates osteoclastogenesis.[57] Sequentially activates NF-κB, c-Fos, and NFATc1 to result in osteoclastogenesis but does not upregulate NF-κB p100 as TNF does.[68] Requires 3:3 dimers of RANK/RANKL to be formed for optimal stimulation.[139] Only a few papers prove a direct contribution of RANKL on T cells to osteoclastogenesis as even tH17 cells could not induce osteoclastogenesis in the absence of osteoclastogenesis-supporting cells, it was tentatively concluded that the expression of RANKL on T cells was not sufficient for the induction of osteoclastogenesis[60]	
M-CSF (macrophage colony-stimulating factor)	Osteoblast	Osteoclast precursor	Works with RANKL to initiate and maintain osteoclasts[57]	
Interferon-γ	TH1[60]	It is a species specific cytokine[60]	Inhibits bone formation.[66] Enhances RANKL and TNF-α production[58] Inhibits osteoclastogenesis by interfering with the RANK-RANK system[80] by interfering with TNF receptor-associated factor 6 (TRAF-6) expression there by inhibiting transcription pathways stimulated by RANKL[63] but does not directly affect resorption by mature osteoclasts[58] Inhibits the abilities of 1,25-dihydroxyvitamin D3, PTH, and IL-1 to stimulate OCL formation in bone marrow cultures[58] Inhibits osteoblast proliferation[58] All above effects are *in vitro*. *In vivo* the results are different. Intraperitoneal injections in rats induced osteopenia and partially reversed the effects of osteopetrosis in humans[58]	
IFN-γ	Th1 cells, Tc cells, dendritic cells, NK cells	Osteoclast progenitor cells	Inhibits osteoclasts	Inhibits formation multinucleated cells by inhibiting 1, 25D3, PTH, and IL-1 thereby inhibiting osteoclast formation[78] Production of IFN-γ by T cells suppresses osteoclastogenesis by interfering with RANKL signaling by inducing rapid degradation of the RANK adapter protein TRAF6 that in turn inhibits NF-kB[81] IFN-γ binds to IFNGR1 and IFNGR2 activating JAK/STAT pathway
T helper cytokines				
Th1	IFN-γ		Inhibit osteoclastogenesis	
Th2	IL-4, IL-6, IL-10[82]		Inhibit/induce osteoclastogenesis	
Th17	IL-17[19]		Induce osteoclastogenesis	

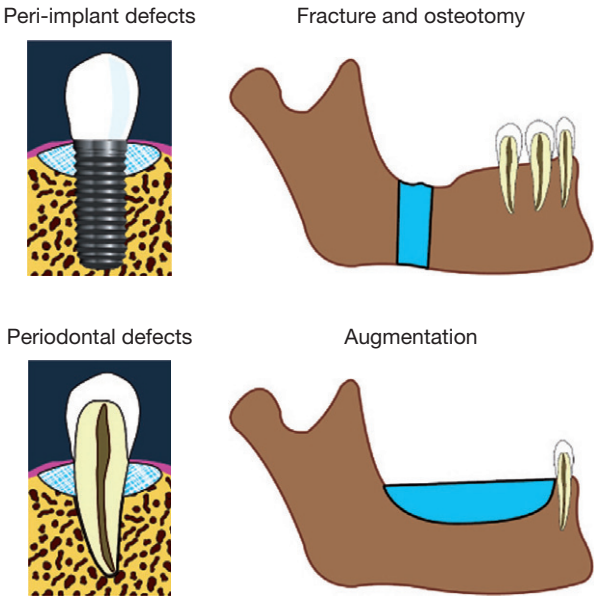

Figure 7 Dentistry offers a large spectrum of possible applications related to tissue engineering. Therapeutic targets for local treatment include, but are not restricted to, peri-implant and periodontal defects, as well as segmental defects and augmentation sites. Even though all sites are in the same anatomical region, they have their unique requirements to a therapeutic concept. For example, a therapeutic concept that solely causes bone formation might not be suitable to support the regeneration of the complex structure of the periodontal ligament.

making some growth factors (and carriers) appropriate for some sites but not for others. Consideration of these host and site specific factors has regulatory implications as well.

5.522.5.2.3. Host factors

The characteristics that are specific to defect type and host factors in general can have a profound impact on the clinical response to growth factor administration, for example, when reconstructing a bone defect in a field previously exposed to radiation or in massive orthopedic trauma where blood supply has been compromised.

5.522.5.2.3.1. Strategies for growth factor delivery

Many strategies have been described for delivering growth factors. The primary objective of growth factor delivery is provision of sustained biologically relevant concentrations at the site of administration. The simplest technique would be direct injection. The problem with this approach is that growth factors are rapidly metabolized in the body, resulting in short half lives.

A sustained local concentration can be achieved by one of two methods:

1. Gene therapy that will be sequestered locally and thus result in local expression or
2. Packaging the growth factor protein in a carrier with release kinetics matched to the localized wound healing cascade.

Gene therapy (whether by transduction or transfection) has potential, but there are issues of safety that have to be resolved before full clinical implementation. Consequently, the method currently being used clinically involves growth factors plus a

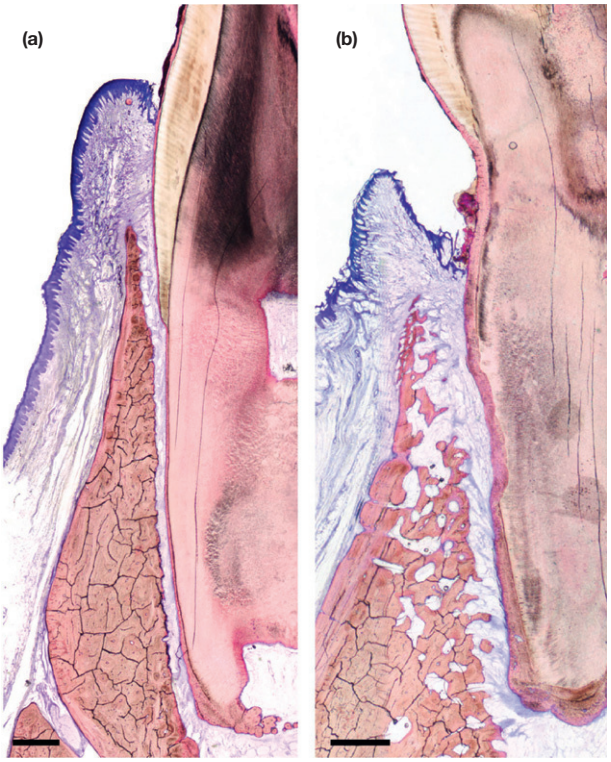

Figure 8 Histologic section through a premolar showing the alveolar bone crest, periodontal ligament and the dentogingival region in a healthy sheep (a) compared to a diseased sheep from the test group (b). In the elderly osteoporotic animals, there is alveolar bone resorption and the concomitant attachment loss. Undecalcified ground sections, Levai–Laczko stain, bars equal 1 min. Adapted from Dvorak, G.; Reich, K.; Tangl, S.; *et al*. *Arch. Oral Biol*. **2009**, *54*, 857–863 and kindly provided by Karoline Reich.

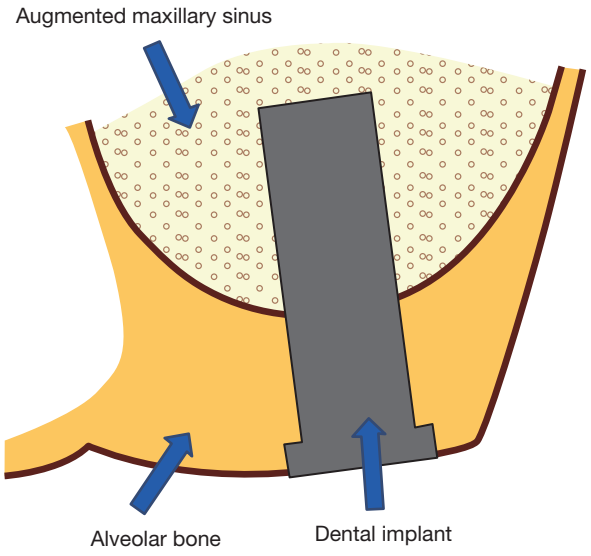

Figure 9 This surgical procedure creates an artificial space beneath the sinus mucosa and the atrophic local bone that is filled with grafting material. Implants can be inserted into the augmented area in a one-stage or two-stage approach.

delivery system. The delivery system, as mentioned previously in this chapter, must be biocompatible, the pharmacokinetics of the factor released must match the local healing cascade, and the delivery system must be calibrated to biodegrade in register with new bone formation.

From a practical, clinical standpoint, surgeons administering therapeutics to patients often emphasize the need to have something that is simple to use. Therefore, a delivery system for a complex biological that is complicated to use, will likely not be used by the surgeon. From a surgical perspective, the surgeon wants a biomaterial that is easy to handle, is fully resorbable and has robust mechanical properties.

In addition, the three-dimensional architecture of a carrier (i.e., biological delivery system) can dramatically affect the release kinetics and, therefore, the biological activity. The carrier must allow vascular ingrowth throughout its structure. This means finding ways of improving surface area to volume ratios in the scaffold. When constructing a material intended for load-bearing applications out of a resorbable material (whether the substrate is biologically derived or not), a balance must be struck between the biological activity of the scaffold itself and the biomechanical properties of the material.

5.522.5.2.4. Growth factors and cytokines in clinical use

5.522.5.2.4.1. Nonrecombinant sources of growth factor and cytokines

A discussion of growth factors and cytokines in clinical use should include platelet gel and demineralized bone matrix (DBM); both are used clinically in many of the same applications. Platelet gel is prepared by isolating a patient's platelet concentrate from blood and activating the release mechanism of α-granules by adding calcium and thrombin. Platelet gel is attractive to clinicians for several key reasons: it is autogenous, inexpensive and fairly easy to process. However, it has variable concentrations of relevant growth factors and consequently, is subject to high variability among individuals. Platelet gel by itself has not been shown to add significant benefit when used for spinal fusion[102] though it has shown some positive effects in some dental applications.[103] Dallari *et al.*[104] showed in a prospective, randomized and controlled study that platelet gel, alone or combined with BMSCs, on lyophilized bone chips causes increased bony healing in high tibial osteotomies.

DBM is processed allogeneic bone and contains multiple growth factors and cytokines. DBM is regulated by the FDA as a reprocessed human tissue and as an off-the-shelf product. DBM has, in the past, been widely used either alone or in combination with autogenous bone as a bone substitute in non-load-bearing sites. However, there are studies that indicate its ineffectiveness in many applications.[105,106] Issues with allograft material include limited supply, erratic performance, perhaps due to varying processing techniques and donor age,[106–109] and the risk, albeit small, of disease transmission. The clinical use of DBM has declined as recombinant human growth factors have become available to surgeons and dentists.

5.522.5.2.4.2. Recombinant sources of growth factor and cytokines

The most commonly used growth factors for bone regeneration in the clinical setting are rhBMP-2 and -7 OP-1. PDGF has also

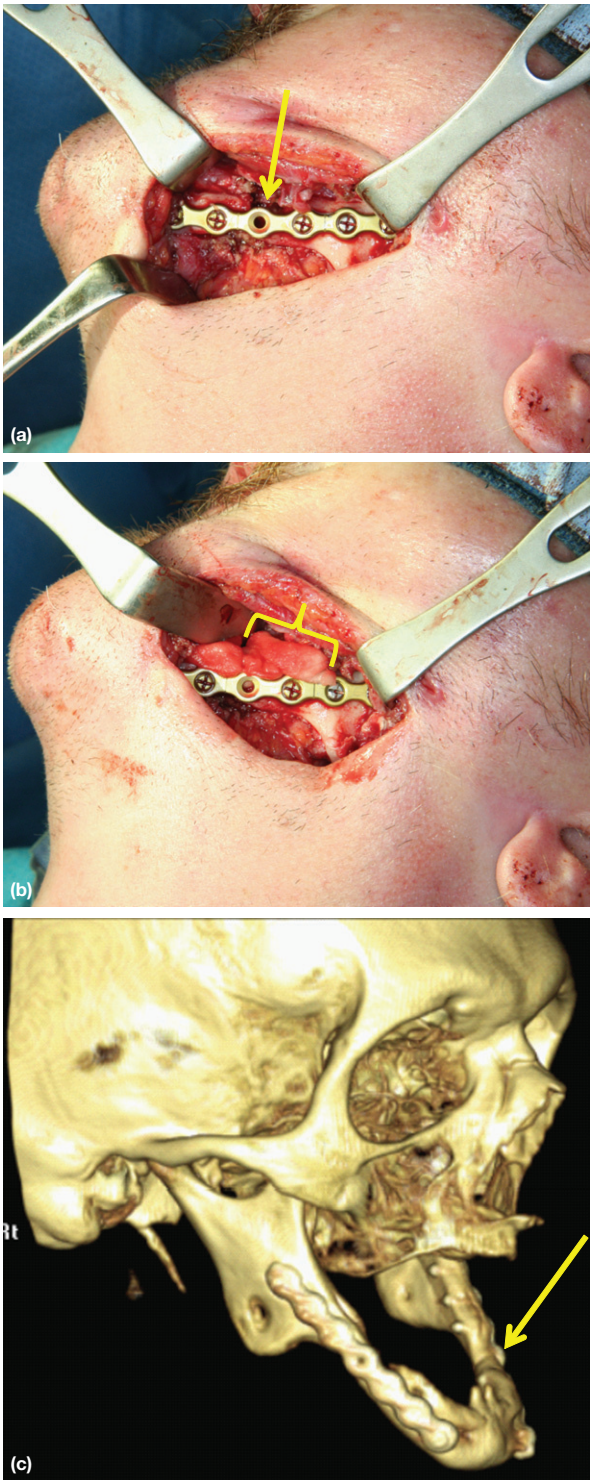

Figure 10 This patient suffered from traumatic bone loss in the left body of the mandible, with a 3 cm defect in an atrophic mandible. (a) A titanium reconstruction plate was used to stabilize the fracture (the arrow points to the missing bone). (b) Following stabilization, the defect was packed with BMP-2/ACS (bracket). (c) After 10 weeks, there has been complete spanning of the defect with bone that radiographically appears normal (arrow in (c)). The patient has regained function. Note: patient had a right side body fracture as well.

been gaining clinical attention. The BMP-2 in the INFUSE® Bone Graft product comes in a kit containing 12 mg dibotermin-α (1.5 mg BMP-2/ml after reconstitution), which is applied to an absorbable collagen sponge (ACS). BMP-7 comes in 1-g lyophilized powder form with 3.5 mg eptotermin-α that is combined with type I bovine collagen for a maximum dosage of 2 g. The BMP dosages that have been found to be effective in humans are quite high. For instance, the amount of BMP-7 in a package intended for one human application is roughly equivalent to the total BMP-7 quantity in two full grown people.[110] A large quantity of the exogenous rhBMP is released after implantation, resulting in supraphysiologic dosages. The supraphysiologic dose is needed to produce a therapeutic effect: bone regeneration. Complications from this approach have included inflammation, hematomas, and ectopic bone formation in the spinal canal.[111–116] These complications could be related to the release kinetics associated with the ACS (collagen) carrier for rhBMP-2 and -7.

5.522.5.2.4.2.1. Clinical applications: Recombinant human BMP-2 The FDA approval for rhBMP-2-containing INFUSE® Bone Graft product was for anterior lumbar interbody fusion. This approval was based on a prospective, randomized, multicenter clinical trial that compared rhBMP-2/ACS to autogenous iliac bone (**Figure 10**).[100,117] Surgeons have also evaluated rhBMP-2 in posterior lumbar and transforaminal lumbar interbody fusion and found the fusion rates comparable to those of autogenous grafting.[118,119] Outcome from a randomized controlled study that evaluated rhBMP-2 in an ACS in open tibial fractures suggested reduced healing time, with a decrease in the number of revisional procedures for delayed fracture healing and infection.[120] However, there are concerns reported with the clinical use of rhBMP-2; specifically, rhBMP-2 used in the cervical spine has caused sequelae of edema and dysphagia (inability to swallow), causing airway compromise.[115,121] Purportedly, these complications are attributable to an initial bolus release of unbound rhBMP-2 from the collagen delivery sponge that is a component of the INFUSE® Bone Graft. The outcome of a rapid bolus release produces inflammation. Moreover, rhBMP-2-containing InFuse® Bone Graft has been reported to produce ectopic bone formation (foraminal), which leads to neurologic impairment.[116,122] Consequently, complications from rhBMP-2 for cervical fusions contraindicate its use in the cervical spine.[115]

Clinical applications of rhBMP-2-containing INFUSE® Bone Graft have been reported throughout the craniofacial skeleton despite the fact that the FDA approval is only for localized alveolar ridge defects and maxillary sinus augmentation (**Figure 11**).

In a review conducted on 14 patients for mandibular defect reconstruction with INFUSE® Bone Graft, the results were positive.[123] The clinical outcome suggested successful restoration of bony continuity and at least some dental function in all patients. However, in another series of five patients, the same degree of success was not reported.[124]

5.522.5.2.4.2.2. Recombinant human BMP-7 In the United States, rhBMP-7 received FDA approval under a Humanitarian Device Exemption (HDE) in 2001 for recalcitrant nonunions in the long bones. In 2004, the FDA extended approval under an HDE for revision of posterolateral (intertransverse) lumbar spinal fusions. The significance of the HDE is that rhBMP-7 cannot be used in more than 4000 applications a year. However, rhBMP-7 has received full regulatory approval in several other countries. In several UK medical centers, reports of BMP-7 in 653 patients was associated with successful bony union in over 80% of cases.[99] In a prospective,

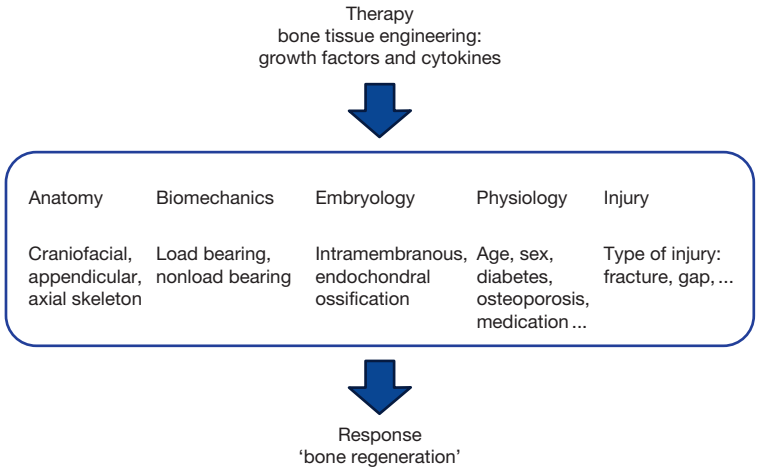

Figure 11 The sequential process of bone regeneration runs with the robustness of clockwork. However, while 'clockworks' are based on mechanical movement, subtle changes may influence the regenerative capacity of bone. Moreover, systemic diseases and their pharmacologic therapy can influence the regenerative capacity of bone. Compromised bone regeneration therefore has an impact on the clinical success of a therapy. Thus, the response of a patient to a therapy, and thus to a bone tissue engineering concept, is complex and involves various aspects, for example, the defect site, the biomechanical conditions, the embryologic origin of the bones, the numerous physiological and pharmacological variables, and the type of injury. These variables should be considered in the planning phase of bone tissue engineering strategies. Modified with permission from Hollinger, J. O.; Hart, C. E.; Gruber, R.; Doll, B. A. In *Tissue Engineering: Applications in Oral and Maxillofacial Surgery Periodontics*, 2nd ed.; Lynch, S., Marx, R. E., Nevins, M., Wisner-Lynch, L. A., Eds.; Quintessence Publishing Co, Inc.: 2008; pp 3–25.

randomized, double blinded clinical study, it was reported that rhBMP-7 promoted osteogenic activity in critical size fibular defects.[125] Other studies have underscored efficacy of rhBMP-7 compared to autogenous bone in posterolateral spine fusion[101,126,127] and anterior cervical fusion procedures.[128]

5.522.5.3. Future Clinical Directions

5.522.5.3.1. Defining the clinical performance criteria

The future for clinical applications of growth factors and cytokines is highly promising, provided researchers and clinicians pay attention to fundamental bone biology, modeling and remodeling, and bone healing cascades.

Moreover, as release kinetics and clinical performance properties are improved for delivery systems so that they are more tightly matched to biology, the therapeutic effectiveness of growth factors and cytokines will also be profoundly improved and the adverse effects significantly diminished. Furthermore, multiple factors dynamically interact in a rigorously defined temporal, spatial and dose-dependent cascade during wound healing. Those complex and complicated interrelationships have not been sufficiently defined; nor have performance properties of materials been satisfactorily matched to the biological and biomechanical needs.

All these aspects must be blended to produce a therapeutic package that will predictably and safely promote a regenerative tissue outcome.

References

1. Hogan, B. *Cell* **1999**, *96*, 225–233.
2. Hollinger, J. O. In *Bone Regeneration and Repair*; Lieberman, J., Freidlaender, G., Eds.; Humana Press: Ottawa, ON, 2005; pp 1–20.
3. Schmitt, J. M.; Hwang, K.; Winn, S. R.; Hollinger, J. O. *J. Orthop. Res.* **1999**, *17*, 269–278.
4. Burgess, E. A.; Hollinger, J. O. In *Frontiers in Tissue Engineering*; Patrick, C. W., Mikos, A. G., Mcintire, L. V., Eds.; Elsevier: New York, 1998; pp 383–399.
5. Dorland, W. A. N. *Dorland's Illustrated Medical Dictionary*; W. B. Saunders: Philadelphia, PA, 1988.
6. Hollinger, J.; McAllister, B. In *Bioceramics*, Proceedings of the International Symposium on Ceramics in Medicine; Wilson, J., Hench, L., Greenspan, D., Eds.; Elsevier: Ponte Vedra, 1995; pp 3–10.
7. Chang, B. S.; Lee, C. K.; Hong, K. S.; *et al*. *Biomaterials* **2000**, *21*, 1291–1298.
8. Kelly, P. J. *J. Bone Joint Surg.* **1968**, *50-A*, 766–783.
9. Buckwalter, J. A.; Glimcher, M. J.; Cooper, R. R.; Recker, R. *J. Bone Joint Surg.* **1995**, *77-A*, 1256–1275.
10. Parfitt, A. M. *J. Cell. Biochem.* **1994**, *55*, 273–286.
11. Parfitt, M. A. *Calcif. Tissue Int.* **1984**, *36*, 37–45.
12. Roberts, W. E.; Helm, F. R.; Marshall, K. J.; Gongloff, R. K. *Angle Orthod.* **1990**, *59*, 247–256.
13. Folkman, J.; Klagsbrun, M. *Science* **1987**, *235*, 442–447.
14. Gavin, T. P.; Robinson, C. B.; Yeager, R. C.; England, J. A.; Nifong, L. W.; Hickner, R. C. *J. Appl. Physiol.* **2004**, *96*, 19–24.
15. Burri, P. H.; Hlushchuk, R.; Djonov, V. *Dev. Dyn.* **2004**, *231*, 474–488.
16. Aubin, J. E. *Rev. Endocr. Metab. Disord.* **2001**, *2*, 81–94.
17. Unger, N. J.; Odorfer, K. I.; Weber, K.; Sandgren, E. P.; Erben, R. G. *Histochem. Cell Biol.* **2007**, *127*, 669–674.
18. Ehrlich, P. J.; Lanyon, L. E. *Osteoporos. Int.* **2002**, *13*, 688–700.
19. Lorenzo, J.; Horowitz, M.; Choi, Y. *Endocr. Rev.* **2008**, *29*, 403–440.
20. You, J.; Yellowley, C. E.; Donahue, H. J.; Zhang, Y.; Chen, Q.; Jacobs, C. R. *J. Biomech. Eng.* **2000**, *122*, 387–393.
21. Jiang, J. X.; Siller-Jackson, A. J.; Burra, S. *Front. Biosci.* **2007**, *12*, 1450–1462.
22. Nijweide, P. J.; Burger, E. H.; Feyen, J. H. *Physiol. Rev.* **1986**, *66*, 855–886.
23. Kollet, O.; Dar, A.; Lapidot, T. *Annu. Rev. Immunol.* **2007**, *25*, 51–69.
24. Athanasou, N. A. *J. Bone Joint Surg. Am.* **1996**, *78*, 1096–1112.
25. Mundy, G. R. *Bone* **1987**, *8*(Suppl. 1), S9–S16.
26. Kingsley, D. M. *Genes Dev.* **1994**, *8*, 133–146.
27. Massague, J. *Prog. Med. Virol.* **1985**, *32*, 142–158.
28. Centrella, M. *J. Biol. Chem.* **1987**, *262*, 2869–2874.
29. Seyedin, S. M.; Thompson, A. Y.; Bentz, H.; *et al*. *J. Biol. Chem.* **1986**, *261*, 5693–5695.
30. Barnes, G. L.; Kostenuik, P. J.; Gerstenfeld, L. C.; Einhorn, T. A. *J. Bone Miner. Res.* **1999**, *14*, 1805–1815.
31. Miyazono, K. *J. Cell Sci.* **2000**, *113*(Pt 7), 1101–1109.
32. Scheufler, C.; Sebald, W.; Hulsmeyer, M. *J. Mol. Biol.* **1999**, *287*, 103–115.
33. Cohen, P.; Peehl, D. M.; Lamson, G.; Rosenfeld, R. G. *J. Clin. Endocrinol. Metab.* **1991**, *73*, 401–407.
34. Celil, A. B.; Campbell, P. G. *J. Biol. Chem.* **2005**, *280*, 31353–31359.
35. Pie, Y.; Xw, M. E. N. G.; Zhou, X. Y.; Xing, X. P.; Xia, W. B. *Acta Pharmacol. Sin.* **2003**, *24*, 975–984.
36. Singhatanadgit, W.; Salih, V.; Olsen, I. *J. Cell Physiol.* **2006**, *209*, 912–922.
37. Wernike, E.; Montjovent, M. O.; Liu, Y.; *et al*. *Eur. Cell. Mater.* **2010**, *19*, 30–40.
38. Schipani, E.; Maes, C.; Carmeliet, G.; Semenza, G. L. *J. Bone Miner. Res.* **2009**, *24*, 1347–1353.
39. Becker, P. M.; Verin, A. D.; Booth, M. A.; Liu, F.; Birukova, A.; Garcia, J. G. *Am. J. Physiol. Lung Cell. Mol. Physiol.* **2001**, *281*, L1500–L1511.
40. Carpini, J. D.; Karam, A. K.; Montgomery, L. *Angiogenesis* **2010**, *13*, 43–58.
41. Deckers, M. M.; Karperien, M.; Van der Bent, C.; Yamashita, T.; Papapoulos, S. E.; Lowik, C. W. *Endocrinology* **2000**, *141*, 1667–1674.
42. Tombran-Tink, J.; Barnstable, C. J. *Biochem. Biophys. Res. Commun.* **2004**, *316*, 573–579.
43. Eckardt, H.; Ding, M.; Lind, M.; Hansen, E. S.; Christensen, K. S.; Hvid, I. *J. Bone Joint Surg. Br.* **2005**, *87*, 1434–1438.
44. Kanczler, J. M.; Oreffo, R. O. *Eur. Cell. Mater.* **2008**, *15*, 100–114.
45. Carano, R. A.; Filvaroff, E. H. *Drug Discov. Today* **2003**, *8*, 980–989.
46. Ornitz, D. M.; Marie, P. J. *Genes Dev.* **2002**, *16*, 1446–1465.
47. Berrada, S.; Lefebvre, F.; Harmand, M. F. *In Vitro Cell. Dev. Biol. Anim.* **1995**, *31*, 698–702.
48. Fakhry, A.; Ratisoontorn, C.; Vedhachalam, C.; *et al*. *Bone* **2005**, *36*, 254–266.
49. Ling, L.; Murali, S.; Dombrowski, C.; *et al*. *J. Cell. Physiol.* **2006**, *209*, 811–825.
50. Rodan, S. B.; Wesolowski, G.; Thomas, K. A.; Yoon, K.; Rodan, G. A. *Connect. Tissue Res.* **1989**, *20*, 283–288.
51. Vora, S. R.; Palamakumbura, A. H.; Mitsi, M.; *et al*. *J. Biol. Chem.* **2010**, *285*, 7384–7393.
52. Bolander, M. E. *Proc. Soc. Exp. Biol. Med.* **1992**, *200*, 165–170.
53. Kawaguchi, H.; Kurokawa, T.; Hanada, K.; *et al*. *Endocrinology* **1994**, *135*, 774–781.
54. Lin, J. M.; Callon, K. E.; Lin, J. S.; *et al*. *Am. J. Physiol. Endocrinol. Metab.* **2009**, *297*, E142–E150.
55. Shimoaka, T.; Ogasawara, T.; Yonamine, A.; *et al*. *J. Biol. Chem.* **2002**, *277*, 7493–7500.
56. Valta, M. P.; Tuomela, J.; Bjartell, A.; Valve, E.; Vaananen, H. K.; Harkonen, P. *Int. J. Cancer* **2008**, *123*, 22–31.
57. Fini, M.; Carpi, A.; Borsari, V.; *et al*. *Front. Biosci. (Schol. Ed.)* **2010**, *2*, 468–482.
58. Lee, S. H.; Kim, T. S.; Choi, Y.; Lorenzo, J. *BMB Rep.* **2008**, *41*, 495–510.
59. Lee, S. K.; Surh, C. D. *Immunol. Rev.* **2005**, *208*, 169–180.
60. Takayanagi, H. *Nat. Rev. Rheumatol.* **2009**, *5*, 667–676.
61. D'Amelio, P.; Grimaldi, A.; D I Bella, S.; *et al*. *Bone* **2008**, *43*, 92–100.
62. Kwan Tat, S.; Padrines, M.; Theoleyre, S.; Heymann, D.; Fortun, Y. *Cytokine Growth Factor Rev.* **2004**, *15*, 49–60.
63. Bezerra, M. C.; Carvalho, J. F.; Prokopowitsch, A. S.; Pereira, R. M. *Braz. J. Med. Biol. Res.* **2005**, *38*, 161–170.
64. Palmqvist, P.; Persson, E.; Conaway, H. H.; Lerner, U. H. *J. Immunol.* **2002**, *169*, 3353–3362.
65. Bendre, M. S.; Montague, D. C.; Peery, T.; Akel, N. S.; Gaddy, D.; Suva, L. J. *Bone* **2003**, *33*, 28–37.
66. Di Rosa, F. *Immunol. Cell Biol.* **2009**, *87*, 20–29.
67. Angeli, A.; Dovio, A.; Sartori, M. L.; *et al*. *Ann. N. Y. Acad. Sci.* **2002**, *966*, 97–107.
68. Boyce, B. F.; Yao, Z.; Zhang, Q.; *et al*. *Ann. N. Y. Acad. Sci.* **2007**, *1116*, 245–254.
69. Palmqvist, P.; Lundberg, P.; Persson, E.; *et al*. *J. Biol. Chem.* **2006**, *281*, 2414–2429.
70. Takahashi, N.; Udagawa, N.; Kobayashi, Y.; Suda, T. *Methods Mol. Med.* **2007**, *135*, 285–301.
71. Kishimoto, T.; Taga, T.; Akira, S. *Cell* **1994**, *76*, 253–262.
72. Manolagas, S. C.; Jilka, R. L. *N. Engl. J. Med.* **1995**, *332*, 305–311.

73. Giuliani, N.; Mangoni, M.; Rizzoli, V. *Exp. Hematol.* **2009**, *37*, 879–886.
74. Evans, K. E.; Fox, S. W. *BMC Cell Biol.* **2007**, *8*, 4.
75. Owens, J. M.; Gallagher, A. C.; Chambers, T. J. *J. Immunol.* **1996**, *157*, 936–940.
76. Makiishi-Shimobayashi, C.; Tsujimura, T.; Iwasaki, T.; *et al. Biochem. Biophys. Res. Commun.* **2001**, *281*, 361–366.
77. Kawase, Y.; Hoshino, T.; Yokota, K.; *et al. J. Bone Miner. Res.* **2003**, *18*, 975–983.
78. Takahashi, N.; Mundy, G. R.; Roodman, G. D. *J. Immunol.* **1986**, *137*, 3544–3549.
79. Takada, I.; Kouzmenko, A. P.; Kato, S. *Expert Opin. Ther. Targets* **2009**, *13*, 593–603.
80. Zallone, A. *Ann. N. Y. Acad. Sci.* **2006**, *1068*, 173–179.
81. Takayanagi, H.; Ogasawara, K.; Hida, S.; *et al. Nature* **2000**, *408*, 600–605.
82. Van Vlasselaer, P.; Borremans, B.; Van Den Heuvel, R.; Van Gorp, U.; De Waal Malefyt, R. *Blood* **1993**, *82*, 2361–2370.
83. Bosshardt, D. D.; Sculean, A. *Periodontol. 2000* **2009**, *51*, 208–219.
84. Hugoson, A.; Norderyd, O. *J. Clin. Periodontol.* **2008**, *35*, 338–345.
85. Chang, P. C.; Cirelli, J. A.; Jin, Q.; *et al. Hum. Gene Ther.* **2009**, *20*, 486–496.
86. Hellberg, C.; Ostman, A.; Heldin, C. H. *Recent Results Cancer Res.* **2010**, *180*, 103–114.
87. Casap, N.; Venezia, N. B.; Wilensky, A.; Samuni, Y. *Tissue Eng. A* **2008**, *14*, 247–253.
88. Peng, H.; Wright, V.; Usas, A.; *et al. J. Clin. Invest.* **2002**, *110*, 751–759.
89. Jung, R. E.; Cochran, D. L.; Domken, O.; *et al. Clin. Oral Implants Res.* **2007**, *18*, 319–325.
90. Mair, B.; Tangl, S.; Feierfeil, J.; Skiba, D.; Watzek, G.; Gruber, R. *Clin. Oral Implants Res.* **2009**, *20*, 400–405.
91. McDonald, M. M.; Peacock, L.; Mikulec, K.; *et al. Bone* **2010**, *46*, S27.
92. Burkiewicz, J. S.; Scarpace, S. L.; Bruce, S. P. *Ann. Pharmacother.* **2009**, *43*, 1445–1455.
93. Taylor, P. C.; Feldmann, M. *Nat. Rev. Rheumatol.* **2009**, *5*, 578–582.
94. Mayer, Y.; Balbir-Gurman, A.; Machtei, E. E. *J. Periodontol.* **2009**, *80*, 1414–1420.
95. Gruber, R.; Koch, H.; Doll, B. A.; Tegtmeier, F.; Einhorn, T. A.; Hollinger, J. O. *Exp. Gerontol.* **2006**, *41*, 1080–1093.
96. Calori, G. M.; Donati, D.; Di Bella, C.; Tagliabue, L. *Injury* **2009**, *40*(Suppl. 3), S67–S76.
97. Li, R. H.; Bouxsein, M. L.; Blake, C. A.; *et al. J. Orthop. Res.* **2003**, *21*, 997–1004.
98. Devescovi, V.; Leonardi, E.; Ciapetti, G.; Cenni, E. *Chir. Organi Mov.* **2008**, *92*, 161–168.
99. Giannoudis, P. V.; Tzioupis, C. *Injury* **2005**, *36*(Suppl. 3), S47–S50.
100. McKay, W. F.; Peckham, S. M.; Badura, J. M. *Int. Orthop.* **2007**, *31*, 729–734.
101. White, A. P.; Vaccaro, A. R.; Hall, J. A.; Whang, P. G.; Friel, B. C.; McKee, M. D. *Int. Orthop.* **2007**, *31*, 735–741.
102. Weiner, B. K.; Walker, M. *Spine (Phila Pa 1976)* **2003**, *28*, 1968–1970; discussion 1971.
103. Sammartino, G.; Tia, M.; Marenzi, G.; DI Lauro, A. E.; D'Agostino, E.; Claudio, P. P. *J. Oral Maxillofac. Surg.* **2005**, *63*, 766–770.
104. Dallari, D.; Savarino, L.; Stagni, C.; *et al. J. Bone Joint Surg. Am.* **2007**, *89*, 2413–2420.
105. Liljenqvist, U.; O'Brien, J. P.; Renton, P. *Eur. Spine J.* **1998**, *7*, 125–131.
106. Russell, J. L. *Tissue Eng.* **2000**, *6*, 435–440.
107. Chakkalakal, D. A.; Strates, B. S.; Garvin, K. L.; *et al. Tissue Eng.* **2001**, *7*, 161–177.
108. Takikawa, S.; Bauer, W.; Kambic, H.; Togawa, D. *J. Biomed. Mater. Res.* **2003**, *65*, 37–42.
109. Zhang, M.; Powers, R. M., Jr.; Wolfinbarger, L., Jr. *J. Periodontol.* **1997**, *68*, 1085–1092.
110. Bishop, G. B.; Einhorn, T. A. *Int. Orthop.* **2007**, *31*, 721–727.
111. Gautschi, O. P.; Frey, S. P.; Zellweger, R. *ANZ J. Surg.* **2007**, *77*, 626–631.
112. Giannoudis, P. V.; Kanakaris, N. K.; Einhorn, T. A. *Osteoporos. Int.* **2007**, *18*, 1565–1581.
113. Shields, L. B.; Raque, G. H.; Glassman, S. D.; *et al. Spine (Phila Pa 1976)* **2006**, *31*, 542–547.
114. Uludag, H.; Gao, T.; Porter, T. J.; Friess, W.; Wozney, J. M. *J. Bone Joint Surg. Am.* **2001**, *83-A*(Suppl. 1), S128–S135.
115. Vaidya, R.; Carp, J.; Sethi, A.; Bartol, S.; Craig, J.; Les, C. M. *Eur. Spine J.* **2007**, *16*, 1257–1265.
116. Wong, D. A.; Kumar, A.; Jatana, S.; Ghiselli, G.; Wong, K. *Spine J.* **2008**, *8*, 1011–1018.
117. Burkus, J. K.; Gornet, M. F.; Dickman, C. A.; Zdeblick, T. A. *J. Spinal Disord. Tech.* **2002**, *15*, 337–349.
118. Haid, R. W., Jr.; Branch, C. L., Jr.; Alexander, J. T.; Burkus, J. K. *Spine J.* **2004**, *4*, 527–538; discussion 538-9.
119. Mummaneni, P. V.; Pan, J.; Haid, R. W.; Rodts, G. E. *J. Neurosurg. Spine* **2004**, *1*, 19–23.
120. Govender, S.; Csimma, C.; Genant, H.; *et al. J. Bone Joint Surg.* **2002**, *84-A*, 2123–2134.
121. Buttermann, G. R. *Spine J.* **2008**, *8*, 426–435.
122. Zou, X.; Zou, L.; Foldager, C.; Bendtsen, M.; Feng, W.; Bunger, C. E. *Biomaterials* **2009**, *30*, 991–1004.
123. Herford, A. S.; Boyne, P. J. *J. Oral Maxillofac. Surg.* **2008**, *66*, 616–624.
124. Carter, T. G.; Brar, P. S.; Tolas, A.; Beirne, O. R. *J. Oral Maxillofac. Surg.* **2008**, *66*, 1417–1425.
125. Geesink, R. G.; Hoefnagels, N. H.; Bulstra, S. K. *J. Bone Joint Surg. Br.* **1999**, *81*, 710–718.
126. Vaccaro, A. R.; Patel, T.; Fischgrund, J.; *et al. Eur. Spine J.* **2003**, *12*, 495–500.
127. Vaccaro, A. R.; Patel, T.; Fischgrund, J.; *et al. Spine (Phila Pa 1976)* **2004**, *29*, 1885–1892.
128. Leach, J.; Bittar, R. G. *J. Clin. Neurosci.* **2009**, *16*, 1417–1420.
129. Wei, S.; Wang, M. W.; Teitelbaum, S. L.; Ross, F. P. *J. Biol. Chem.* **2002**, *277*, 6622–6630.
130. Liu, X. H.; Kirschenbaum, A.; Yao, S.; Levine, A. C. *Endocrinology* **2005**, *146*(4), 1991–1998.
131. Rothe, L.; Collin-Osdoby, P.; Chen, Y.; Sunyer, T.; Chaudharv, L.; Tsay, A.; *et al. Endocrinology* **1998**, *139*, 4353–4363.
132. Moore, K. W.; de Waal, M. R.; Coffman, R. L.; O'Garra, A. *Annu. Rev. Immunol.* **2001**, *19*, 683–765.
133. Hong, M. H.; Williams, H.; Jin, C. H.; Pike, J. W. *J. Bone Miner. Res.* **2000**, *15*(5), 911–918.
134. Amcheslavsky, A.; Bar-Shavit, Z. *J. Cell Physiol.* **2006**, *207*(1), 244–250.
135. Hsieh, C. S.; Macatonia, S. E.; Tripp, C. S.; Wolf, S. F.; O'Garra, A.; Murphy, K. M. *Science* **1993**, *260*(5107), 547–549.
136. Horwood, N. J.; Udagawa, N.; Elliott, J.; Grail, D.; Okamura, H.; Kurimoto, M.; Dunn, A. R.; Martin, T.; Gillespie, M. T. *J. Clin. Invest.* **1998**, *101*(3), 595–603.
137. Yamada, N.; Niwa, S.; Tsujimura, T.; Iwasaki, T.; Sugihara, A.; Futani, H.; Hayashi, S.; Okamura, H.; Akedo, H.; Terada, N. *Bone* **2002**, *30*(6), 901–908.
138. Quinn, J. M.; Saleh, H. *Mol. Cell Endocrinol.* **2009**, *310*(1–2), 40–51.
139. Sipos, W.; Pietschmann, P.; Rauner, M. *Curr. Med. Chem.* **2008**, *15*, 127–136.

5.523. Carbon Nanotubes: Applications for *In Situ* Implant Sensors

S Sirivisoot, Wake Forest University, Winston-Salem, NC, USA
T J Webster, Brown University, Providence, RI, USA

© 2011 Elsevier Ltd. All rights reserved.

5.523.1.	**Introduction**	303
5.523.2.	**Making Orthopedic Implant Sensors**	304
5.523.2.1.	Step 1: Preparation of Nanotubular Anodized Titanium	304
5.523.2.2.	Step 2: Cobalt-Catalyzed CVD for Growing MWCNTs	305
5.523.3.	**Biological Responses to Orthopedic Implant Sensors**	305
5.523.4.	**Sensing Ability of Orthopedic Implant Sensors**	306
5.523.5.	**Discussion**	309
5.523.6.	**Conclusions**	314
References		314

Glossary

Biosensing The use of devices to determine or sense a biological event.
Carbon nanotubes A helical arrangement of carbon creating a tube diameter with nanodimensions.
Cyclic voltammetry (CV) A type of potentiodynamic electrochemical measurement that can be used to determine events surrounding an implant.
Dexamethasone An anti-inflammatory steriod.
Multiwalled carbon nanotubes Carbon nanotubes which have greater than two walls, or layers of helical carbon.
Nanomaterials Traditionally defined as a material with at least one dimension (like a grain, fiber, or particle) <100 nm in at least one direction.
Nanomedicine The use of nanotechnology in medicine.
Nanotechnology The use of nanomaterials to improve a particular property of a material.
Osteoblasts Bone-forming cells.
Penicillin An antibiotic.
Poly-lactic-*co*-glycolic acid An FDA-approved polymer commonly used in tissue engineering.
Polypyrrole An electrically conductive polymer.
Single-walled carbon nanotubes Carbon nanotubes with only one layer of helical carbons.
Titanium A commonly used orthopedic implant material.

Abbreviations

CNTs	Carbon nanotubes
CV	Cyclic voltametry
CVD	Chemical vapor deposition
EDS	Energy dispersive spectroscopy
HA	Hydroxyapatite
MWCNTs	Multi-walled carbon nanotubes
PECVD	Plasma-enhanced chemical vapor deposition
SWCNTs	Single-walled carbon nanotubes
XRD	X-ray diffraction

5.523.1. Introduction

Osteoblasts and osteoclasts are located in bone, a natural nanostructured-mineralized organic matrix. While osteoblasts make bone, osteoclasts decompose bone by releasing acid that degrades calcium phosphate-based apatite minerals into an aqueous environment. The synthesis, deposition, and mineralization of this organic matrix, in which osteoblasts proliferate and mineralize (i.e., deposit calcium), require the ordered expression of a number of osteoblast genes. Bone has the ability to self-repair or remodel routinely (for more on bone see **Chapter 6.617, Bone Tissue Grafting and Tissue Engineering Concepts**). However, osteoporosis (unbalanced bone remodeling) and other joint diseases (such as osteoarthritis, rheumatoid arthritis, or traumatic arthritis) can lead to bone fractures. These disabilities associated with bone lead to difficulties in performing common activities and may require an orthopedic implant. However, the average functional lifetime of, for example, a hip implant (usually composed of titanium) is only 10–15 years. A lack of fixation into surrounding bone eventually loosens the implant and is the most common cause of hip replacement failure (for more on orthopedic implants see **Chapter 6.605, Porous Coatings in Orthopedics** and **Chapter 6.606, Biological Effects of Wear Debris from Joint Arthroplasties**).

Approximately 200 000 total and 100 000 partial hip replacements as well as 36 000 revision hip replacement surgeries were performed in the United States in 2003.[1] Unfortunately, only limited techniques, such as insensitive imaging (through X-rays or bone scans), exist to determine if sufficient bone

growth is occurring next to a titanium implant after surgery. Thus, techniques used in orthopedic diagnostics need to more accurately identify musculoskeletal injuries and conditions after implantation. Although there have been improvements in implants to increase bone formation, the clinical diagnosis of new bone growth surrounding implants remains problematic, sometimes significantly increasing hospital stay and decreasing the ability of doctors to quickly prescribe a change in action if new bone growth is insufficient.

Currently, a physical examination (e.g., palpation or laboratory testing) might be completed before imaging techniques are used to inform a clinician about a patient's health. Although advanced imaging techniques, such as bone scans, computer tomography scans, and radiographs (X-rays), are important in medical diagnosis, each has its own limitations and difficulties. A bone scan is used to identify areas of abnormal active bone formation, such as in arthritis, infection, or bone cancer. However, bone scans require an injection of a radioactive substance (e.g., technetium) and a prolonged delay for absorbance before performing the scan. Computer tomography combines X-rays with computer technology to produce a two-dimensional cross-sectional image of a body on the computer screen. Although this technique produces more detail than an X-ray, in some cases (e.g., severe trauma to the chest, abdomen, pelvis, or spinal cord), a dye (e.g., barium sulfate) must be injected in order to improve the clarity of the image. This often causes pain to the patient. Another technique, called electromyography, has been used to analyze/diagnose nerve functions inside body conditions. Thin electrodes are placed in soft tissues to help analyze and record electrical activity in the muscles. However, this electrode technique leads to pain and discomfort for the patient. When the needles are removed, soreness and bruising can occur.

Electrochemical biosensors on the implant itself shows promise for medical diagnostics *in situ* to possibly determine new bone growth surrounding the implant (for more on sensors see **Chapter 3.330, Carbon Nanotube-Based Sensors: Overview**). Yet, this technology has not been fully explored. Incorporation of such electrochemical biosensors into current bone implants may be possible through nanotechnology; different types of nanoscale biomaterials have varying abilities to enhance *in vitro*/*in vivo* bone formation. Carbon nanotubes (CNTs) are macromolecules of carbon, classified either as single-walled carbon nanotubes (SWCNTs) with diameters of 0.4–2 nm or multiwalled carbon nanotubes (MWCNTs) with diameters of 2–100 nm.[2,3] Because of their unique electrical, mechanical, chemical, and biological properties,[4–11] CNTs have shown promise for bone implantation. For example, nanocomposites of polylactic acid and MWCNTs increased osteoblast proliferation by 46% and calcium production by >300% when an alternating current was applied *in vitro*.[12,13] In addition, combining MWCNTs with precursor powders improves the mechanical properties of as-aligned hydroxyapatite (HA) composite coatings.[9] MWCNTs, reinforced with HA coatings, promoted human osteoblast proliferation *in vitro*, as observed in the appearance of cells near MWCNT regions.[8] Osteoblasts extended in all directions within the CNT scaffold that formed on polycarbonate membranes.[14] Osteoblasts significantly enhanced their adhesion on vertically aligned MWCNT arrays, according to Giannona *et al.*[15] by recognizing nanoscaled features. In addition, Zanello *et al.*[7] showed that CNTs are suitable for the proliferation of osteosarcoma ROS 17/2.8 cells on single and MWCNT scaffolds. Human osteoblast-like (Saos2) cells grown on the MWCNT scaffold showed a higher cell density and transforming growth factor-β1 concentration compared with those grown on polystyrene and polycarbonate scaffolds.[16]

Our previous studies have shown greater osteoblast differentiation on MWCNT-Ti than on Ti alone.[17] Moreover, MWCNTs are a promising material for electrochemical biosensors because they also possess relatively well-characterized behavior in terms of electron transport.[18–21] Coating CNTs on Ti electrodes also increases the active surface area and enhances direct electron transfer.[22,23] These studies encourage the use of MWCNTs to modify currently used Ti for orthopedic implants. CNTs can be produced by the laser furnace arc and chemical vapor deposition (CVD) methods. Unlike the laser furnace arc, CVD is a scalable and controllable method of obtaining a high purity of CNTs.[24] A strong mechanical connection between CNTs and the metal is needed for nanosensor applications,[25] and the reduced resistance between the Ti and CNTs[26] leads to increased current passage. For example, Sato *et al.* showed potential for using CNTs in electrochemical biosensors by using CVD to grow MWCNTs with Ti biometallic particles and cobalt (Co) as a catalyst. They revealed that Co has the ability to combine with Ti[27] and as CNTs were grown by using a Co catalyst in that study, a strong electrical contact between metallic Ti and MWCNTs was possible.

As mentioned, in order to form a more robust interconnection, CNTs have been anchored in the pores of anodized nanotubular Ti. MWCNTs have then been grown (using CVD techniques) out of the anodized Ti nanotubes (with diameters of 50–60 nm and depths of 200 nm) as a template. *In vivo*, many cell processes important during new bone growth rely on the redox reactions of various biomolecules and ions. The mechanisms of electron transfer reaction and the role of proteins in aiding the electron transfer of redox processes can be examined by electrochemical analysis. In electronic theory, when two different materials come in contact with each other, electron transfer will occur in an attempt to balance Fermi levels, causing the formation of a double layer of electrical charge at the interface. Because the formation of electric contact between the redox proteins and the electrode surface is the fundamental challenge of electrochemical biosensor devices, in one study, the redox reactions of iron(II/III) and the osteoblast extracellular components at the surface of Ti, anodized Ti, and MWCNT-Ti have been investigated. How to create such novel orthopedic sensors along with the latest data concerning their use is presented below.

5.523.2. Making Orthopedic Implant Sensors

5.523.2.1. Step 1: Preparation of Nanotubular Anodized Titanium

In order to create orthopedic sensors, currently implanted titanium (Ti) has been modified to have a nanotube-structured thin layer of titanium dioxide (TiO_2) by anodization.[17] Briefly, 99.2% commercially pure Ti sheets (Alfa Aesar) can be cut into squares (1 cm^2) and cleaned with acetone and 70% ethanol under sonication for 10 min each.

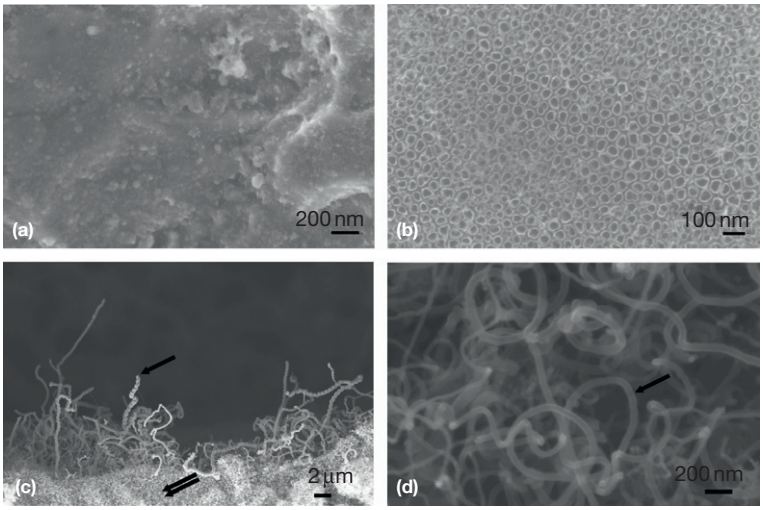

Figure 1 Scanning electron microscopy (SEM) micrographs of the electrode surfaces: (a) conventional Ti and (b) anodized Ti; (c) side view and (d) top view of multiwalled carbon nanotube Ti (MWCNT-Ti). Single arrow shows MWCNTs, whereas the double arrows show the anodized Ti template.

After rinsing with deionized water, Ti can be etched for 10 s in a solution of 1.5% by weight of nitric acid and 0.5% by weight of hydrofluoric acid to remove the existing oxidized layer on Ti. Immediately after etching, Ti can be placed as an anode and a high purity platinum (Pt) mesh (Alfa Aesar) can be used as a cathode. In a Teflon beaker, both electrodes can be immersed in an electrolyte solution of 1.5% by weight of hydrofluoric acid in deionized water. The distance between Ti and the platinum mesh should be around 1 cm. A direct current power supply (3645A; Circuit Specialists) can then be used at 20 V between the anode and cathode for 10 min to create uniform nanotubes of TiO_2 on commercially pure Ti. It is from these uniform titanium nanotubes that electrically active sensing MWCNTs can be grown, as described next.

5.523.2.2. Step 2: Cobalt-Catalyzed CVD for Growing MWCNTs

Afterward, MWCNTs can be grown out of the nanoporous TiO_2 by CVD. A plasma-enhanced chemical vapor deposition (PECVD) system (Applied Science & Technology, Inc.) can be used to grow MWCNTs from the nanotubular anodized Ti. To do this, the anodized Ti samples can be soaked in a solution of 5% by weight of cobaltous nitrate (Allied Chemical) in methanol for 5 min prior to CVD process. Then, cobalt-catalyzed anodized Ti should be rinsed with distilled water and dried with compressed air. The samples can then be placed in the CVD chamber and the air pumped out to a base pressure below 10 mTorr. The samples can be heated at 700 °C in a flow of 100 sccm (standard cubic centimeters per minute) hydrogen gas (H_2) for 20 min. The gas composition can be changed to 40 sccm H_2 and 160 sccm acetylene gas (C_2H_2) for 30 min to grow MWCNTs. The MWCNT-Ti should be cooled in a 100 sccm Argon flow. The dense and entangled MWCNTs can form a three-dimensional structure on the Ti surface with exceptional electrical conductivity and surface area. In particular, conventional Ti, shown in Figure 1(a), exhibits a smooth Ti oxide surface. After anodization, nanopores of Ti oxide formed on the Ti surface uniformly with diameters of 50–60 nm and depths of 200 nm, as shown in Figure 1(b). After the CVD process described here, MWCNTs covered the anodized Ti as shown in Figure 1(c) side view and 1(d) top view.

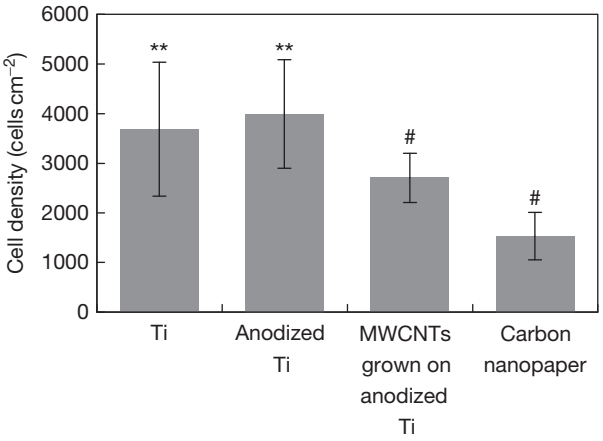

Figure 2 Osteoblast adhesion for 4 h on Ti, anodized Ti, multiwalled carbon nanotubes (MWCNTs) grown on anodized Ti, and carbon nanopaper. Values are mean ±S.E.M; $n = 3$; $^{**}p < 0.05$ compared to carbon nanopaper; # $p < 0.05$ compared to MWCNTs grown on anodized Ti.

5.523.3. Biological Responses to Orthopedic Implant Sensors

Importantly, results have shown that similar numbers of osteoblasts adhered after 4 h on unanodized Ti, anodized nanotubular Ti without MWCNTs, and anodized nanotubular Ti with MWCNTs (Figure 2); the numbers of osteoblasts adhering on all were greater than the number adhering on the carbon nanopaper (used as a chemical control). This initial data was important as it indicated that the MWCNT sensor was not detrimental to osteoblast functions. Moreover, osteoblasts were observed with cytoplasmatic prolongation on the

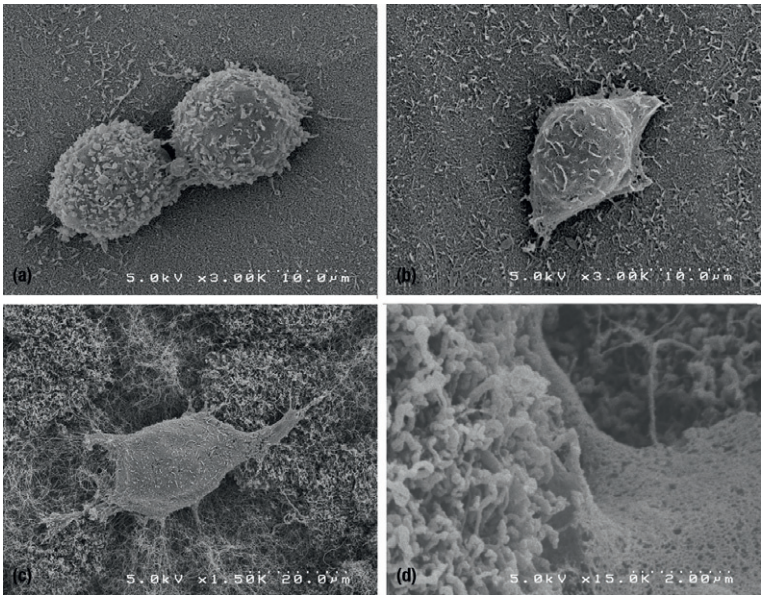

Figure 3 Osteoblast morphology after 4 h adhesion on (a, b) anodized Ti (Scale bars = 10 μm). Round-shaped osteoblasts are on the anodized Ti substrate without multiwalled carbon nanotubes (MWCNTs); and (c, d) MWCNTs grown on anodized Ti (Scale bars = 20 μm left and 2 μm right). Single arrow shows the cytoplamatic prolongations of osteoblasts to MWCNTs. Double arrows show MWCNTs, while triple arrows show the osteoblast membrane.

surfaces of MWCNTs grown out of anodized nanotubular Ti (**Figure 3(c)** and **3(d)**), resulting in stronger adhesion (more density of the points of contact) and some might say resembling osteoblast interactions with extracellular matrix proteins.[17] In contrast, osteoblasts on anodized Ti without MWCNTs were not observed to have cytoplasmic prolongation (**Figure 3(a)** and **3(b)**). Zanello *et al.* also observed a thin neurite-like cytoplasmic prolongation of osteoblasts that reached the nanotube bundles after cell culture for 5 days. More impressively, results have demonstrated that alkaline phosphatase activity and calcium deposition by osteoblasts increased on the MWCNTs grown from anodized nanotubular Ti sensors compared to that on anodized nanotubular Ti without MWCNTs, unanodized Ti, and carbon nanopaper after 21 days (**Figure 4**). This result suggested even better osteoblast responses on MWCNT sensors than currently used Ti.

5.523.4. Sensing Ability of Orthopedic Implant Sensors

Of course, the next question is how well do these MWCNTs sense new bone growth? As a starting point, experiments were conducted with the $Fe(CN)_6^{4-/3-}$ redox system. The $Fe(CN)_6^{4-/3-}$ redox system with an exhibition of heterogeneous one-electron transfer ($n = 1$) is one of the most extensively studied redox couples in electrochemistry.[28] The study has been performed in the cyclic voltammetry (CV) experiments of the $Fe^{2+/3+}$ redox couple by placing MWCNT-Ti in an electrolyte solution of 10 mM $K_3Fe(CN)_6$ and 1 M KNO_3. In potassium ferricyanide ($K_3Fe(CN)_6$), the reduction process is $Fe^{3+}(Fe(CN)_6^{3-} + e^- \rightarrow Fe(CN)_6^{4-})$ followed by the oxidation of Fe^{2+} $(Fe(CN)_6^{4-} \rightarrow Fe(CN)_6^{3-} + e^-)$ under a sweeping voltage. In such studies, the iron(II/III) redox couple did not exhibit any observable peaks for bare Ti or anodized Ti electrodes, as shown in **Figure 7(a)** and **7(b)**. This implies that the electrochemical reaction is slow on both these electrodes. However, the highly direct electron transfer at the MWCNT-Ti sensor electrode were observed as redox peaks, shown in **Figure 10(c)**. At a scan rate of 100 mV s^{-1} in **Figure 10(c)**, a well-defined redox peak appears with the anodic (E_{pa}) and cathodic (E_{pc}) potentials at 175 and 345 mV, respectively. Moreover, on the inner set of **Figure 7(c)**, the relationship is linear between the anodic and cathodic peak currents versus the square root of the scan rate, while the ratio of I_{pa}/I_{pc} is about 1, corresponding to the Randles–Sevcik eqn [1]. Because the root scan rate has this linear relationship with the peak currents, the mass transport in this process must be by diffusion. Zhang *et al.* found that the heterogeneous charge-transfer rate constant (k) of the $Fe(CN)_6^{4-/3-}$ complex with H_2O as a solvent is 0.05 cm s^{-1}.[29] As the k value is in the range of 10^{-4}–10^{-1} cm s^{-1} and $\Delta E_p > 59/n$ mV (in this case $n = 1$ and $\Delta E_p \sim 170$ mV), this process is quasireversible.

To analyze the electrochemical behavior at the surface of the MWCNT-Ti sensor electrodes, researchers have used the Randles–Sevcik equation for quasireversible processes, eqn [1]. Hence, the peak current (I_p) is given by

$$I_p = 2.99 \times 10^5 A D^{1/2} n (n_a \gamma)^{1/2} C \qquad [1]$$

where n is the number of electrons participating in the redox process, n_a is the number of electrons participating in the charge-transfer step, A is the area of the working electrode (cm^2), D is the diffusion coefficient of the molecules in the electrolyte solution ($cm^2\ s^{-1}$), C is the concentration of the probe molecule in the bulk solution (molar), and γ is the scan rate of the sweep potential ($V\ s^{-1}$). When the $Fe(CN)_6^{4-/3-}$ redox system exhibits heterogeneous one-electron transfer ($n = n_a = 1$) and the concentration C is equal to 10 mM, the diffusion coefficient

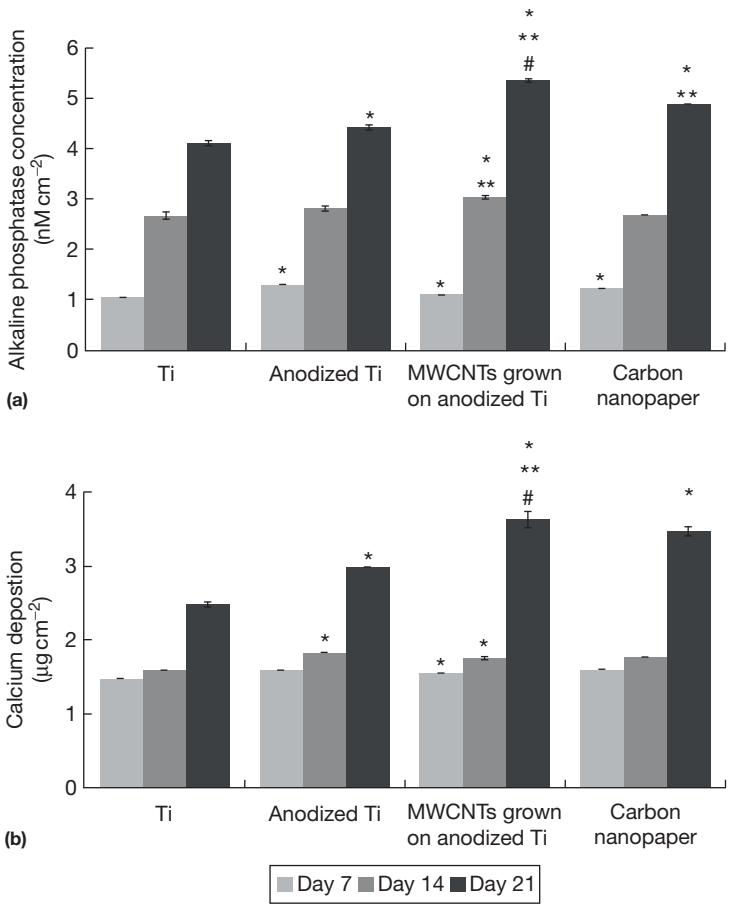

Figure 4 Osteoblast long-term functions: (a) alkaline phosphatase activity; values are mean ± S.E.M; $n = 3$; * $p < 0.05$ compared to Ti; ** $p < 0.1$ compared to anodized Ti; and # $p < 0.1$ compared to carbon nanopaper and (b) calcium deposition; values are mean ±S.E.M; $n = 3$; * $p < 0.1$ compared to Ti; ** $p < 0.1$ compared to anodized Ti; and # $p < 0.05$ compared to carbon nanopaper.

D is equal to $6.7 \pm 0.02 \times 10^{-6}$ cm^2 s^{-1}.[30,31] Hence, the quasi-reversible redox of iron(II/III) is truly enhanced by the novel MWCNT sensors.

To estimate how such sensors would work for bone growth, osteoblasts were cultured for 21 days and energy dispersive spectroscopy (EDS) was performed to verify the presence of the various minerals in newly formed bone. Figure 5 shows the results of one such study doing this in which the peaks of many inorganic substances, consisting of magnesium (Mg), phosphorus (P), sulphur (S), potassium (K), and calcium (Ca), were detected. The Ca/P weight ratio of minerals deposited by osteoblasts in that study on Ti (1.34) was less than that on a MWCNT-Ti sensor (1.52). However, the Ca/P ratio of HA, the main calcium phosphate crystallite in bone, is typically about 1.67.[32,33] This study demonstrated that the minerals deposited by osteoblasts on MWCNT-Ti were more similar to natural bone than the minerals deposited on Ti. X-ray diffraction (XRD) analysis also showed that more HA was deposited on MWCNT-Ti sensors than on both conventional and anodized Ti after 21 days of culture, as shown in Figure 6. In addition, the amount of calcium deposited by osteoblasts as determined by a calcium quantification assay kit was 1.481 μg cm^{-2} for 7 days, 1.597 μg cm^{-2} for 14 days, and 2.483 μg cm^{-2} for 21 days on conventional Ti, as shown in Figure 10(b). These results imply a greater deposition of calcium by osteoblasts on MWCNT-Ti sensors than on currently implanted Ti.

Bone resorption and remodeling involve the secretion of hydrochloric acid (HCl) by osteoclasts.[34] Osteoclasts dissolve bone mineral by isolating a region of the matrix and then secreting HCl and proteinases at the bone surface, resulting in the bone acting as a reservoir of Ca^{2+}, PO_4^{3-}, and OH^- minerals.[35] This can be the reason that HCl is so prevalent in laboratories to dissolve calcium minerals deposited on osteoblast-seeded scaffolds *in vitro* and the supernatant solution is used in a calcium deposition assay. Thus, after dissolving with 0.6 N HCl, it is likely that Ca^{2+}, PO_4^{3-}, and OH^- are contained in the solution of the osteoblast extracellular components.

The formation of bone matrix minerals first depends on achieving a critical concentration of calcium and phosphorus. Then phospholipids, anionic proteins, as well as calcium and phosphorus aggregate in nucleation pores that are in the 35 nm 'hole-zone' between collagen molecules.[36] The addition of calcium, phosphate, and hydroxyl ions contributes to the growth of crystalline HA. However, the crystals are not pure as they also contain carbonate, sodium, potassium, citrate, and traces of other elements, such as strontium and lead. The imperfection of HA contributes to its minerals' solubility, which plays a role in the ability of osteoclasts to resorb the

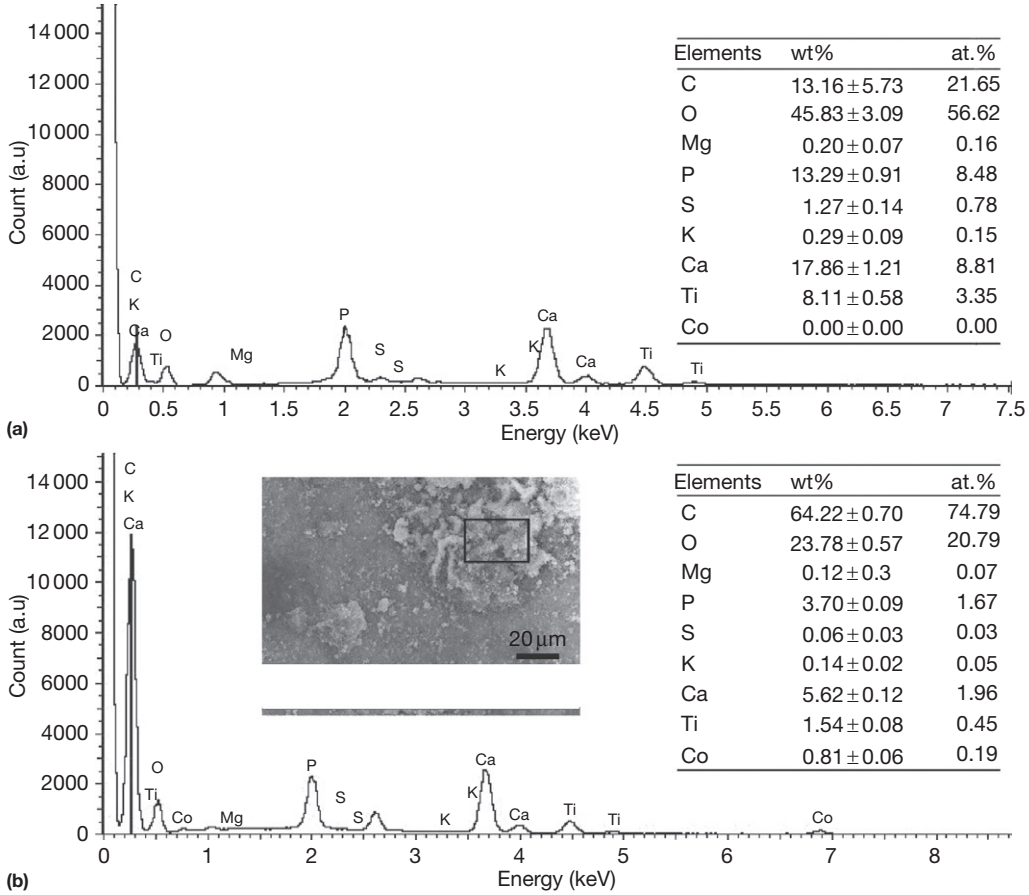

Figure 5 Energy dispersive spectroscopy analysis of osteoblasts cultured for 21 days on (a) Ti and (b) multiwalled carbon nanotube Ti (MWCNT-Ti). Scanning electron microscopy micrograph of inset (b) shows the analyzed area. For the MWCNT-Ti, more Ca and P deposited by osteoblasts were observed. Tables in (a) and (b) show the composition of the mineral deposits after osteoblasts were cultured for 21 days. The Ca/P weight ratio on bare Ti was 1.32 and on MWCNT-Ti was 1.52.

mineral phases. Although osteoblasts synthesize type I collagen, which is the predominant organic component of bone, type III/V/VI collagens also exist in bone. Moreover, noncollagen proteins in bone (such as growth factors, osteocalcin, osteopontin, and osteonectin) and proteins in serum and other tissues (such as fibronectin, vitronectin, and laminin) are absorbed into the mineral component during bone growth. These components are directly involved in the genesis and maintenance of bone. Thus, not only minerals, but also other noncollagen proteins are broken down after dissolution with HCl. As such, nonspecific proteins may exist in the supernatant of bone formation when CV is performed with MWCNT-Ti sensors and may contribute to the observed redox process presented in this chapter. On an electrode surface, the native conformation of a protein may be retained (reversible or diffusion-controlled) or distorted (irreversible or adsorption-controlled), depending on the extent of the interactions (such as the electrostatic or covalent bonds) between them.

The type of electrolyte is important to the redox reaction because the gained capacitance and scan rate window are dependent on it.[37] Studies to date have not degassed with nitrogen or argon when performing the CV with MWCNT sensors; therefore, the redox reactions in CV are related to the H_2O decomposition, which includes H^+ reduction and OH^- oxidation. The pH of the electrolyte also affects the H_2O decomposition. In the case of acidic 1 N HCl solution (without other electroactive molecules), the H^+ ions induced the formation of H_2 gas at -0.2 V as a result of the increased reduction current.[37] In the alkaline 1 M KOH solution, OH^- ions resulted in the formation of O_2 gas at 0.7 V by the oxidation process. This fact should be noted because *in vivo*, these decompositions may occur at the interface of the Ti implant because of pH changes and the presence of H_2O and O_2 around the implant.

Other studies have shown promising results when using CNT-modified electrodes in biosensing. As MWCNTs have good electrochemical characteristics as electron mediators and adsorption matrices,[38] they may further enhance applications in biosensor systems. For example, Harrison and Atala[11] showed that CNTs offer a promising method to enhance detection sensitivity because they have high signal-to-noise ratios. The structure-dependent metallic character of CNTs should allow them to promote electron-transfer reactions for redox processes, which can provide the foundation for unique biochemical sensing systems at low overpotentials.[19] The electrolyte–electrode interface barriers are reduced by CNTs because they facilitate double-layer effects.[39] Typically, when the supporting electrolyte is at least a 100-fold stronger than the active electrolyte,[40] the charge in the electrolyte solution causes the Debye layer

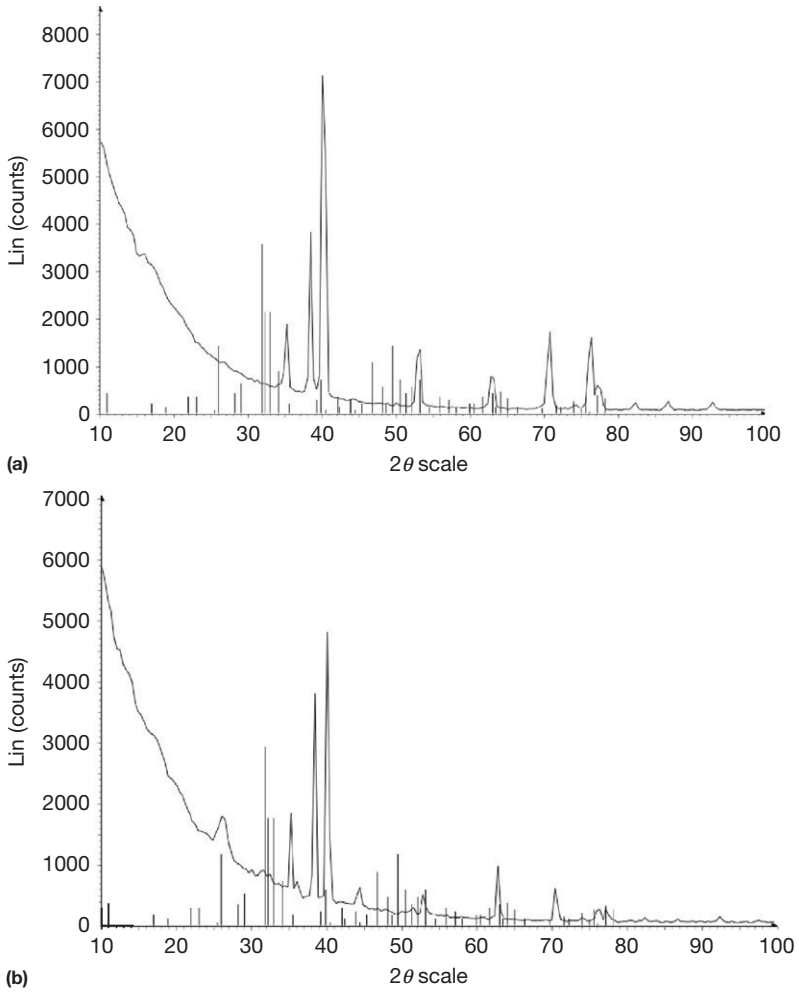

Figure 6 X-ray diffraction analysis of hydroxyapatite-like (HA; $Ca_5(PO_4)_3OH$) deposited minerals after osteoblasts were cultured for 21 days on (a) Ti and (b) multiwalled carbon nanotube Ti (MWCNT-Ti). The micrographs show that the peak pattern of HA more closely matches that of the mineral deposited by osteoblasts when cultured on MWCNT-Ti than on Ti.

to be more compact. Therefore, this compact layer can rapidly exchange electrons between electroactive proteins and the surface of an MWCNT-Ti electrode. This is likely the reason why sharpened cathodic and anodic peaks have been observed in CV, as shown in Figures 7(c), 8(c), 9(b), and 7(a).

Although the area of the working electrode is constant in the presence of MWCNTs, the overall surface area and the electroactivity of the surface are increased. The MWCNTs act as a nanobarrier between the titanium oxide layer, which was their growth template, and the electrolyte solution. The surface atoms or molecules of MWCNTs play an important role in determining their bulk properties because of their nanosize effects.[41] A large surface, corresponding to the greater electrocatalytic activity, confers a catalytic role on the MWCNTs in the chemical reaction. Well-defined and persistent redox peaks are shown in Figure 7(c), confirming the increases of electron transfers and higher electrochemical activities at the MWCNT-Ti surface. CV was also performed with a glassy carbon electrode (GCE; bioanalytical) and a platinum electrode (PTE; bioanalytical), and it also showed $\Delta E_p > 59/n$ mV (data not shown). Importantly, for the same scan rate, CV of GCE and PTE showed the redox reactions with similar but more widely separated anodic and cathodic peaks, confirming the performance of the MWCNT-Ti electrode.

However, in Figure 7(a) and 7(b), the Ti and anodized Ti did not show any redox peaks. This is likely due to the inert inhibiting property of the titanium oxide on electron transfer through them. Figure 7(a) and 7(b) show that bare Ti has less capacitance than MWCNT-Ti. The capacitance relation is derived from $i = C\left(\frac{dv}{dt}\right)$, where $\frac{dv}{dt}$ is a scan rate.[28] Hence, the capacitance between the working and reference electrodes during CV was calculated by dividing the current in CV by the specific scan rate, as shown in Figures 7(d) and 9(d). In summary, the electrochemical response of the MWCNT-Ti electrode promoted a higher charge transfer than the Ti and anodized Ti electrodes.

5.523.5. Discussion

The result from the previous section and studies showed the utility of MWCNT-Ti as an electrode for detecting $Fe^{2+/3+}$ redox couples. For biological applications, it is also necessary

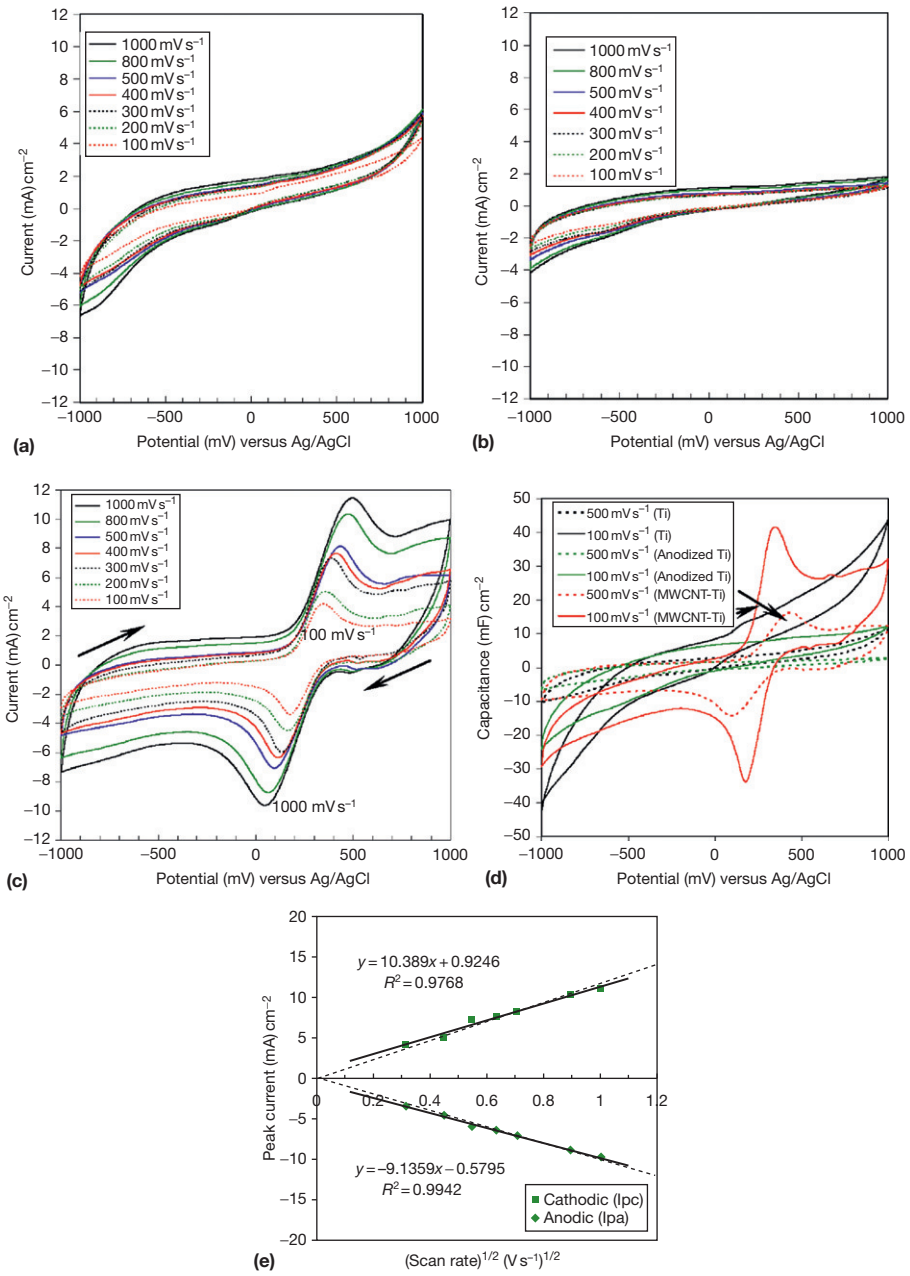

Figure 7 Cyclic voltammograms with an electrolyte solution of 10 mM $K_3Fe(CN)_6$ in 1 M KNO_3 for: (a) conventional Ti; (b) anodized Ti; and (c) multiwalled carbon nanotube Ti. (d) The capacitance of all the electrodes in comparison. (e) The plot of the square root of scan rates with anodic peak currents (I_{pa}) and cathodic peak currents (I_{pc}).

to show that MWCNT-Ti can detect redox reactions associated with osteoblast differentiation. The extracellular components from osteoblasts in an HCl solution have been used to mimic the biological environment around an orthopedic implant. Figure 8(a) and 8(b) show that the bare Ti and anodized Ti electrodes cannot detect any redox process. The results in Figure 8(c) confirmed that MWCNTs enhance the direct electron transfer through Ti by means of the highly conductive surface of the MWCNTs.

After decreasing the surface area of the MWCNT-Ti electrode from 1 cm^2 to 1 mm^2, the redox potentials were also decreased as shown in Figures 8(c) and 9(b). The faradic current of the oxidation process dropped ~10 times with respect to a decrease in surface area A, corresponding to eqn [1]. Corresponding with the Randles–Sevcik equation, the peak current was linearly proportional to the area. When plotting the anodic (I_{pa}) and cathodic peak (I_{pc}) currents of MWCNT-Ti, a linear relationship to the square root of the scan rates was observed, as shown in Figure 9(c).

The CV showed well-defined redox peaks in the osteoblast supernatants at all concentrations. The peaks detected in the solution at the calcium concentrations of 1.481 $\mu g\,cm^{-2}$ (after 7 days), and 1.597 $\mu g\,cm^{-2}$ (after 14 days) have less faradic current and I–V graph area than the concentration

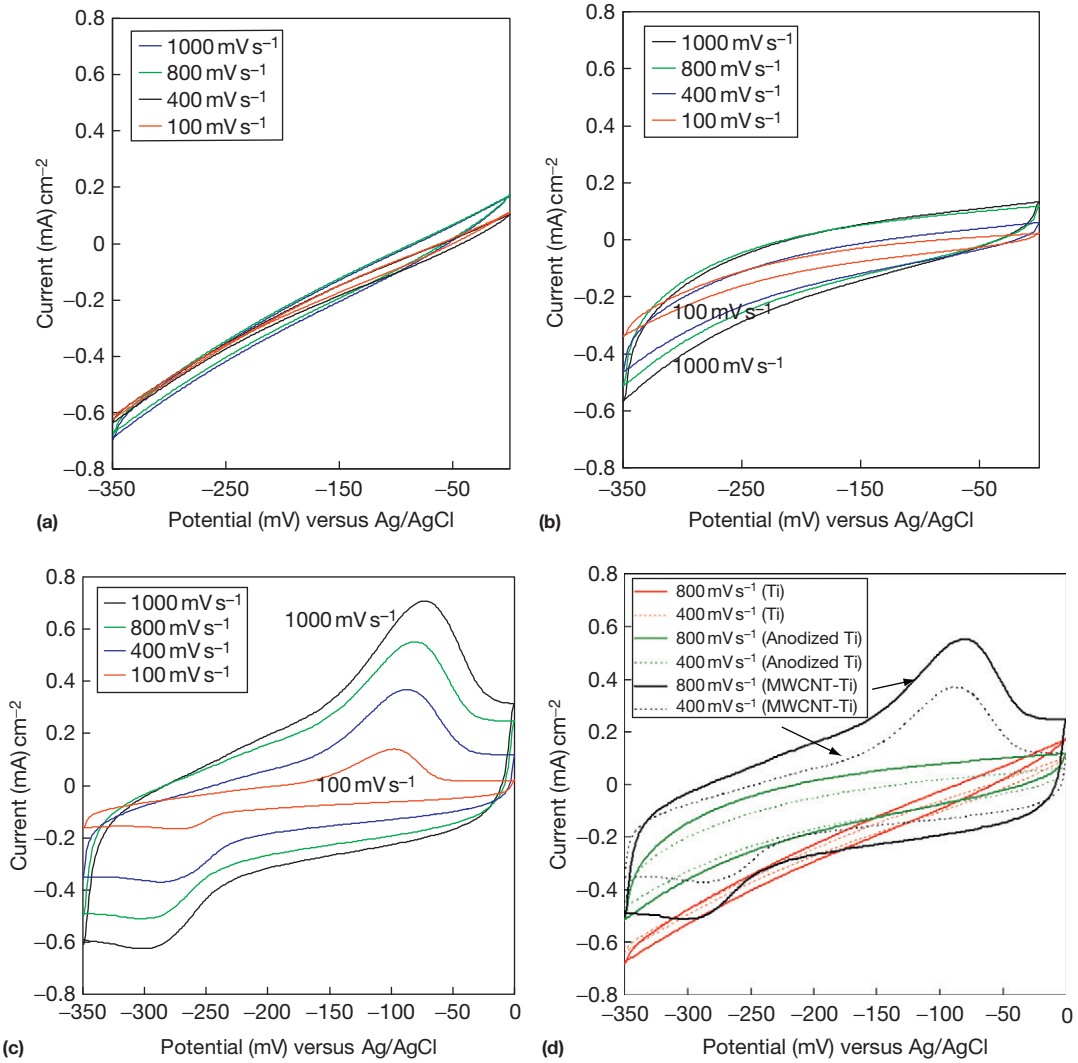

Figure 8 Cyclic voltammograms (CVs) with an electrolyte solution of the extracellular matrix secreted by osteoblasts after 21 days of culture for (a) conventional Ti; (b) anodized Ti; and (c) multiwalled carbon nanotube Ti (MWCNT-Ti) with a working area of 1 cm^2. (d) CV of all three electrodes in comparison. Only MWCNT-Ti possessed the quasireversible redox potential, while conventional Ti and anodized Ti did not.

of 2.48 $\mu g\,cm^{-2}$ (after 21 days), as shown in Figure 10(a) and 10(b). Typically, the more HA deposited and synthesized by osteoblasts, the higher the calcium and protein concentrations are. Therefore, it is likely that the supernatant of 21 days had higher protein concentrations than the solutions of 7 and 14 days, leading to the stronger redox reactions and higher capacitance between the electrode surfaces.

In addition, interpretation of CV results must consider other factors. In particular, a measurement of the redox reactions when oxygen was dissolved in the electrolyte solution showed that the peak currents were shifted toward negative values. Furthermore, a change in the pH of the electrolyte solution and the presence of water may also shift the current and affect the potential of the redox peaks. Thus, CV with the potential range between − 1 and 1 V of MWCNT-Ti was performed in a pure solution of 0.6 N HCl without other proteins or ions. An H^+ reduction peak at a potential between − 0.5 and − 0.8 V was found (data not shown). Moreover, the H^+ reduction peak still appeared when window ranges from − 5 to 5 V and from − 0.35 to 0 V were used, confirming that H_2O decomposition occurred in our CV experiments.

It is clear the MWCNT-Ti electrodes showed the potential for better performance than commercially available electrodes, such as GCE and PTE. When using the sweep voltage from − 1 to 1 V, a set of mixed redox peaks with two oxidations and two reductions appeared (data not shown). These two redox peaks in the CV indicated that the process likely involved more than one-electron transfer. For each couple, the amplitude and position of the oxidation peak in CV were unequal to those of the reduction peak. The second oxidation peak (omitted from Figures 8(c) or 6(b)) was observed at 236 mV for the MWCNT-Ti electrode, 405 mV for the GCE, and − 33 mV for the PTE, all with a scan rate of 100 $mV\,s^{-1}$. However, for the GCE and the PTE electrodes, a second reduction did not appear, while the MWCNT-Ti showed two complete and well-defined redox reactions. These two peaks reflected that more than one-electron transfer was involved; one occurred at a positive and the other at a negative potential

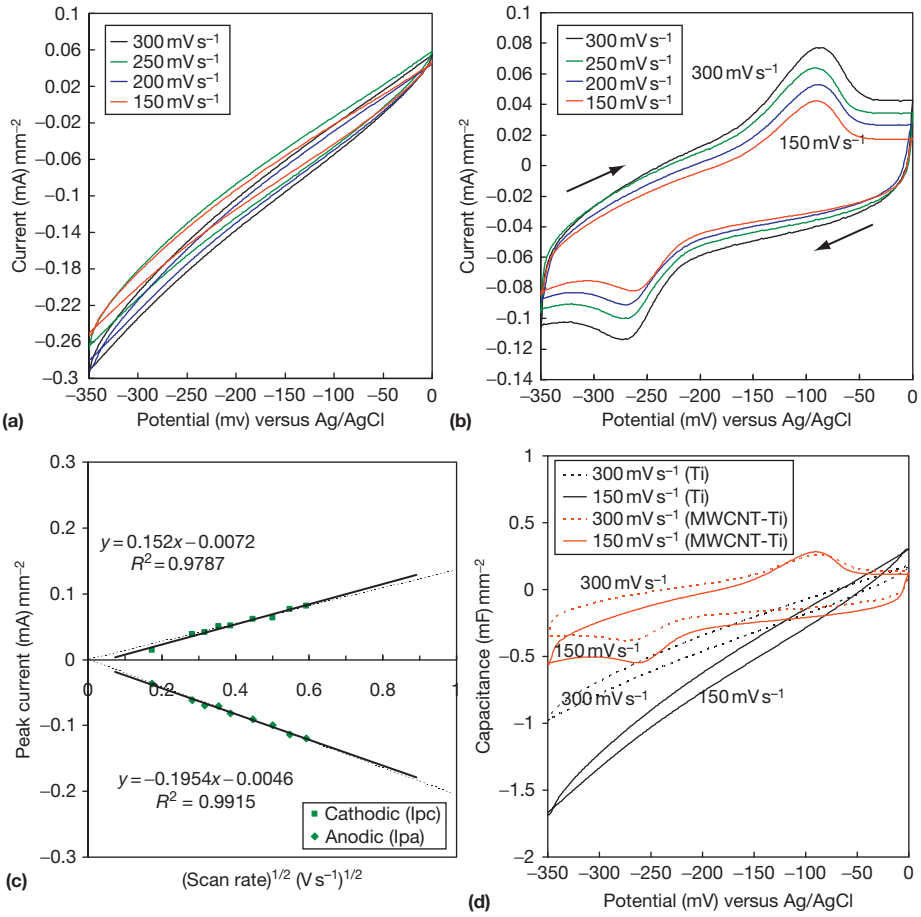

Figure 9 Cyclic voltammograms with an electrolyte solution of the extracellular matrix secreted by osteoblasts after 21 days of culture for (a) conventional Ti and (b) multiwalled carbon nanotube Ti (MWCNT-Ti) with a working area of 1 mm^2. (c) Plot of the experimental cathodic and anodic peak currents, obtained from (b), versus the square root of the scan rates, and (d) the compared capacitance of MWCNT-Ti and Ti.

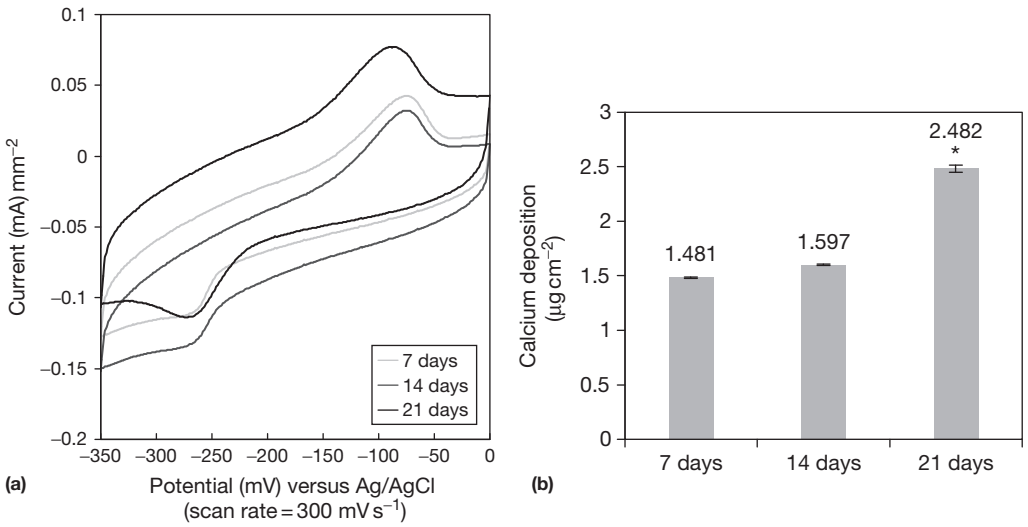

Figure 10 (a) Cyclic voltammograms of multiwalled carbon nanotube Ti electrodes in an electrolyte solution of the extracellular matrix secreted by osteoblasts cultured on conventional Ti after 21 days. (b) Results from the calcium deposition assay determined calcium concentrations in an electrolyte solution of the extracellular matrix secreted by osteoblasts on conventional Ti after 7, 14, and 21 days of culture. Data = mean ±S.E.M; $n = 3$; $^*p < 0.01$ (compared to 7 and 14 days).

in the CV. Further, the current amplitude for the MWCNT-Ti peaks was noticeably larger than that for GCE and PTE. Thus, it can be concluded that the MWCNT-Ti electrode had higher electron transfer as well.

At first, it can be hypothesized that these redox reactions happened because of redox of inorganics such as Ca or P. In the case of Ca, the reduction of Ca^{2+} to Ca crystal (nucleation) typically is expected with the reduction current for a highly negative potential. A positive feedback on IR compensation (IRC) needs to be applied to the CV in order to drive the oxidation current to dissolve the Ca crystal into Ca^{2+}. For example, an overpotential of more than − 1 V, IRC of 0.771 Ω, melting temperature of 900 °C, and scan rate of 50 mV s^{-1} were required.[42] Without applying IRC in this study, diffusion-controlled behavior, which electrochemically depletes calcium cations near the electrode surface, has been impossible to achieve. In addition, the reduction and oxidation of titanium oxides, which are the reaction counterparts of calcium redox, appeared at a positive potential between 0 and 0.25 V, respectively, which did not appear in our CV studies. In the case of P, the CV experiments have been performed further in phosphate buffered saline (PBS). A final concentration of 1 M PBS, which was prepared in-house, had 137 mM NaCl, 10 mM phosphate, 2.7 mM KCl, and a pH of 7.4. The metal orthophosphate ions exhibit a high stability to reduce from P(V) (such as PO_4^{3-}, PO_4^{-}) to P(III), or further to P(I). However, no redox peaks appeared in the potential range of − 1 to 1 V (data not shown). It is therefore likely that neither the redox reactions of calcium ions nor of phosphate occurred because of the absence of the peaks. Instead, it has been hypothesized that the appearance of the redox peaks when using an MWCNT-Ti electrode is likely because of the reduction and oxidation of proteins from the osteoblast supernatant.

The observed quasireversible redox reaction reflected the fact that MWCNT-Ti sensors promote electrochemical reactions. However, an irreversible process can occur at the interface of an electrode because of the denaturation of proteins, or ion reduction. Typically, when the carbon bonds of proteins are changed, irreversible organic reduction or oxidation only happens.[43] The configurations of ions (Ca^{2+}, PO_4^{3-}, OH^{-}) which remain unchanged can also lead to the irreversible process, only because of their reduction or oxidation. Importantly, without MWCNTs on the Ti surface, nonspecific protein adsorption may readily occur, leading to an electrochemically insulating surface layer. Nevertheless, the redox at MWCNT-Ti did not decrease its oxidation and reduction current after applying the sweep voltage for some time, so protein adsorption did not occur apparently in significant amounts at the MWCNT-Ti electrode. Indeed, in the osteoblast supernatant, the MWCNT-Ti electrode provides a relatively specific surface to which the proteins can bind reversibly by diffusion while retaining their function. The protein redox is also dependent on the pH of the electrolyte solution (acidic or basic).[44] This shift appears because of the influence of 0.6 N HCl with H_2O as a solvent which influences proteins, leading the peak shift into the negative potential, as shown in **Figures 8(b)**, **9(c)**, and **10(a)**.

It has been hypothesized that proteins were involved in these redox reactions at the surface of MWCNT-Ti in the solution of osteoblast extracellular components. If those proteins maintain their function and are detected by the MWCNT-Ti electrode, the excellent electrochemical behavior explained here may show that MWCNT-Ti sensors are superior candidates for biosensor applications. However, investigating the type and size of acidic resistant proteins is still in progress.

As shown here, the electrodic performance of MWCNT-Ti sensors, but not of the bare Ti, provides excellent redox reactions. As mentioned, the electrochemical experiments were performed so far without degassing with bubble nitrogen gas. This omission may have resulted in an apparent background signal, which was mixed and appeared in current–voltage curves (*CV*). Moreover, the redox reaction at the MWCNT-Ti sensor mentioned here may depend on various ion sources, including reversible protein adsorption, dissolved oxygen, and acidic nature of HCl. However, the redox reactions of iron(II/III) and the osteoblast extracellular components still occurred only when using MWCNT-Ti sensors, and not when using Ti or anodized Ti. Importantly, it was shown that MWCNT sensors performed as the electrocatalysts for the oxidation and reduction of iron(II/III) and of extracellular components, which included various proteins and inorganic substances synthesized and deposited by osteoblasts.

The electrolyte solution of osteoblast extracellular components was composed of inorganic and organic substances. This solution was not classified in terms of the types of molecules in solution, but rather, all components were dissolved together in the acidic solution and used in all CV experiments in this study. Future work needs to classify the type of proteins in such osteoblast supernatants.

However, it is likely that *in vivo* the capacitance and the electroactive surface of Ti will be enhanced after bone tissue is formed without the presence of MWCNTs. After hip implant insertion, blood and body fluids surround the Ti implant, creating a specific capacitance for the Ti electrode in the beginning. Within 1 month, as osteoblasts deposit calcium around the implant, the capacitance of the implant and bone tissue increases. Cell membranes also have electric potentials and perform redox processes,[45,46] and it has been found that after 14 days *in vitro* these redox processes at the surface of bare Ti increased.

In vitro, nevertheless, MWCNTs have been used to modify the electrodes to detect other biomolecules, such as nicotinamide adenine dinucleotide (NADH),[47] hydrogen peroxide,[21,47] glucose,[22] putrescine,[48] and DNA,[49] Specifically, the growth of MWCNTs from nanoporous metals electrodes can enhance many diverse sensor applications. For example, MWCNTs functionalized with thiol groups have been used for sensing aliphatic hydrocarbons (such as methanol and ethanol), forming unique electrical identifiers.[18] Moreover, MWCNTs grown on silicon substrates enhanced ionic conductivity and have been integrated with unmodified plant cellulose as a film, and used as a cathode electrode in a lithium ion battery, or as a supercapacitor with bioelectrolytes (such as biological fluid and blood).[50] Interestingly, both supercapacitors and batteries derived from a MWCNTs-nanocomposite film, can be integrated to build a hybrid, or dual-storage battery-in-supercapacitor device. The cytocompatible MWCNT device may be useful to integrate with an orthopedic implant biosensor as passive energy storage.

Not only can an implanted electronics circuit be powered by an implant battery (fabricated or self-integrated) within the

implant material, but it also can be induced by an external power supply. For orthopedic applications, telemetric devices started in 1966 and became imperative as telemetric orthopedic implants in order to transmit a signal to an external device.[51–56] For example, Graichen *et al.*[57] developed a new 9-channel telemetry transmitter used for *in vivo* load measurements in three patients with shoulder Ti endoprostheses. The low radio frequency (RF) of an external inductive power source generates power transmission through the implanted metal. At the end of the Ti implant, the pacemaker feedthrough rounds a single loop antenna to transmit the pulse interval signal, which is modulated at a higher RF by the microcontroller, to an external device. Then, the RF receiver of the external device synchronizes with the modulated pulse interval to recover the data stream and report to a clinician. Thus, either an implanted battery or a telemetry system can supply the electrical power to a calcium-detectable chip inside the orthopedic implant for clinical use.

The automatically sensing concept for bone growth juxtaposed to orthopedic implants can also apply for determining infection and scar tissue formation (for more on bacteria and the immune response to implants see **Chapter 4.404, Adaptive Immune Responses to Biomaterials**; **Chapter 4.406, Protein Interactions with Biomaterials**; and **Chapter 4.407, Bacterial Adhesion and Biomaterial Surfaces**). An energy source energizes a telemetric-implanted circuit, and allows it to transmit data to an external receiver to determine bone growth. Indeed, the electrochemical biosensor may reduce the complexity of imaging techniques and patient difficulties.

5.523.6. Conclusions

The capabilities of using titanium (Ti) as an electrochemical electrode have been increased remarkably by growing MWCNTs out of anodized Ti nanopores (MWCNT-Ti). MWCNTs improved the sensitivity of the bare Ti electrode displaying redox peaks in CVs and interestingly high capacitance. Such results provide evidence that MWCNT-Ti can serve as a novel electrochemical electrode with great electrocatalytic properties due to increased surface area and conductivity. Moreover, MWCNTs were shown to be more highly electroactive in chemical transformation than the metallic (Ti) surface, which typically undergoes electrochemical oxidation or dissolution of metal oxides, but is chemically susceptible to corrosion. MWCNTs promoted a redox reaction by enhancing the direct electron transfer through their electrically conductive surface surrounded by ionic solutions, which contained the electroactive species, herein ferri/ferricyanide and the extracellular components from osteoblasts. Moreover, MWCNTs are cytocompatible, promoted osteoblast differentiation after 21 days, and can be integrated into a supercapacitor or battery to enhance the functionalities of biosensing systems *in vivo*. Therefore, MWCNT-Ti sensors are exceptional candidates as electrochemical electrodes to determine *in situ* new bone growth surrounding an orthopedic implant. Further, the ability of MWCNT-Ti to sense osteoblast extracellular components by detecting their redox reaction profiles in specific concentrations may improve the diagnosis of orthopedic implant success or failure, and thus improve clinical efficacy.

Acknowledgments

The authors would like to thank the Coulter Foundation for funding some of the results in this chapter.

References

1. Zhan, C.; Kaczmarek, R.; Loyo-Berrios, N.; Sangl, J.; Bright, R. A. *J. Bone Joint Surg. Am.* **2007**, *89*(3), 526–533.
2. Iijima, S. *Nature* **1991**, *354*(6348), 56–58.
3. Lin, Y.; Taylor, S.; Li, H.; *et al*. *J. Mater. Chem.* **2004**, *14*(4), 527–541.
4. Webster, T. J.; Waid, M. C.; McKenzie, J. L.; Price, R. L.; Ejiofor, J. U. *Nanotechnology* **2004**, *15*(1), 48–54.
5. Smart, S. K.; Cassady, A. I.; Lu, G. Q.; Martin, D. J. *Toxicol. Carbon Nanomater.* **2006**, *44*(6), 1034–1047.
6. Zanello, L. P. *Micro Nano Lett.* **2006**, *1*(1), 19–22.
7. Zanello, L. P.; Zhao, B.; Hu, H.; Haddon, R. C. *Nano Lett.* **2006**, *6*(3), 562–567.
8. Balani, K.; Anderson, R.; Laha, T.; *et al*. *Biomaterials* **2007**, *28*(4), 618–624.
9. Chen, Y.; Zhang, T. H.; Gan, C. H.; Yu, G. *Carbon* **2007**, *45*(5), 998–1004.
10. Wei, W.; Sethuraman, A.; Jin, C.; Monteiro-Riviere, N. A.; Narayan, R. J. *J. Nanosci. Nanotechnol.* **2007**, *7*, 1284–1297.
11. Harrison, B. S.; Atala, A. *Cell. Mol. Biol. Tech. Biomater. Eval.* **2007**, *28*(2), 344–353.
12. Supronowicz, P. R.; Ajayan, P. M.; Ullmann, K. R.; Arulanandam, B. P.; Metzger, D. W.; Bizios, R. *J. Biomed. Mater. Res.* **2002**, *59*(3), 499–506.
13. Ciombor, D. M.; Aaron, R. K. *Orthobiologics* **2005**, *10*(4), 579–593.
14. Aoki, N.; Yokoyama, A.; Nodasaka, Y.; *et al*. *J. Biomed. Nanotechnol.* **2005**, *1*, 402–405.
15. Giannona, S.; Firkowska, I.; Rojas-Chapana, J.; Giersig, M. *J. Nanosci. Nanotechnol.* **2007**, *7*, 1679–1683.
16. Tsuchiya, N.; Sato, Y.; Aoki, N.; *et al*. In *4th International Workshop on Water Dynamics, Evaluation of Multi-Walled Carbon Nanotube Scaffolds for Osteoblast Growth*; Tohji, K., Tsuchiya, N., Jeyadevan, B., Eds.; AIP: New York, 2007; pp 166–169.
17. Sirivisoot, S.; Yao, C.; Xiao, X.; Sheldon, B. W.; Webster, T. J. *Nanotechnology* **2007**, *18*(36), 365102.
18. Padigi, S. K.; Reddy, R. K. K.; Prasad, S. *Biosens. Bioelectron.* **2007**, *22*(6), 829–837.
19. Roy, S.; Vedala, H.; Choi, W. *Nanotechnology* **2006**, *17*(4), S14–S18.
20. Tang, H.; Chen, J. H.; Huang, Z. P.; *et al*. *Carbon* **2004**, *42*(1), 191–197.
21. Kurusu, F.; Koide, S.; Karube, I.; Gotoh, M. *Anal. Lett.* **2006**, *39*, 903–911.
22. Liu, Y.; Wang, M.; Zhao, F.; Xu, Z.; Dong, S. *Biosens. Bioelectron.* **2005**, *21*(6), 984–988.
23. Liu, S.; Lin, B.; Yang, X.; Zhang, Q. *J. Phys. Chem. B* **2007**, *111*(5), 1182–1188.
24. Robertson, J. *Mater. Today* **2004**, *7*(10), 46–52.
25. Talapatra, S.; Kar, S.; Pal, S. K.; *et al*. *Nat. Nanotechnol.* **2006**, *1*, 112–116.
26. Ngo, Q.; Petranovic, D.; Krishnan, S.; *et al*. *IEEE Trans. Nanotechnol.* **2004**, *3*, 311–317.
27. Sato, S.; Kawabata, A.; Kondo, D.; Nihei, M.; Awano, Y. *Chem. Phys. Lett.* **2005**, *402*(1–3), 149–154.
28. Tamir, G.; Moti, B.-D.; Itshak, K.; *et al*. *Nanotechnology* **2007**, *3*, 035201.
29. Zhang, Y.; Baer, C. D.; Camaioni-Neto, C.; O'Brien, P.; Sweigart, D. A. *Inorg. Chem.* **1991**, *30*(8), 1682–1685.
30. Hrapovic, S.; Liu, Y.; Male, K. B.; Luong, J. H. T. *Anal. Chem.* **2004**, *76*(4), 1083–1088.
31. Hrapovic, S.; Luong, J. H. T. *Anal. Chem.* **2003**, *75*(14), 3308–3315.
32. Calafiori, A.; Di Marco, G.; Martino, G.; Marotta, M. *J. Mater. Sci. Mater. Med.* **2007**, *18*, 2331–2338.
33. Wang, H.; Lee, J.-K.; Moursi, A.; Lannutti, J. J. *J. Biomed. Mater. Res. A* **2003**, *67A*(2), 599–608.
34. Zaidi, M.; Moonga, B. S.; Huang, C. L.-H. *Biol. Rev.* **2004**, *79*(1), 79–100.
35. Blair, H. C.; Zaidi, M.; Schlesinger, P. H. *Biochem. J.* **2002**, *364*(2), 329–341.
36. Bronner, F.; Farach-Carson, M. C. *Bone Formation*. Springer: New York, 2003.
37. Hong, M. S.; Lee, S. H.; Kim, S. W. *Electrochem. Solid State Lett.* **2002**, *5*(10), A227–A230.
38. Sotiropoulou, S.; Gavalas, V.; Vamvakaki, V.; Chaniotakis, N. A. *Biosens. Bioelectron.* **2003**, *18*(2–3), 211–215.

39. Fang, W. C.; Sun, C. L.; Huang, J. H.; *et al*. *Electrochem. Solid State Lett.* **2006**, *9*(3), A175–A178.
40. Christian, G. D. *Analytical Chemistry*. Wiley: New York, 1980; pp 172–173.
41. Cao, G. *Nanostructures & Nanomaterials: Synthesis, Properties & Applications*. Imperial College Press: London, 2004; pp 4–11.
42. Chen, G. Z.; Fray, D. J. *J. Electrochem. Soc.* **2002**, *149*(11), E455–E467.
43. Schuring, J. *Redox Fundamentals, Processes, and Application*. Springer: New York, 2000.
44. Battistuzzi, G.; Loschi, L.; Borsari, M.; Sola, M. *J. Biol. Inorg. Chem.* **1999**, *4*(5), 601–607.
45. Jeansonne, B. G.; Feagin, F. F.; McMinn, R. W.; Shoemaker, R. L.; Rehm, W. S. *J. Dent. Res.* **1979**, *58*(4), 1415–1423.
46. Jeansonne, B. G.; Feagin, F. F.; Shoemaker, R. L.; Rehm, W. S. *J. Dent. Res.* **1978**, *57*(2), 361–364.
47. Lin, Y.; Yantasee, W.; Wang, J. *Front. Biosci. A J. Virtual Library* **2005**, *10*, 492–505.
48. Luong, J. H. T.; Hrapovic, S.; Wang, D. *Electroanalysis* **2005**, *17*(1), 47–53.
49. He, P.; Xu, Y.; Fang, Y. *Microchim. Acta* **2006**, *152*(3), 175–186.
50. Pushparaj, V.; Shaijumon, M.; Kumar, A.; *et al*. *Proc. Natl. Acad. Sci*. **2007**, *104*(34), 13574–13577.
51. Kaufman, K.; Kovacevic, N.; Irby, S.; Colwell, C. *J. Biomech.* **1996**, *29*(5), 667–671.
52. Bergmann, G.; Deuretzbacher, G.; Heller, M.; *et al*. *J. Biomech.* **2001**, *34*(7), 859–871.
53. Bergmann, G.; Graichen, F.; Rohlmann, A.; Verdonschot, N.; van Lenthe, G. H. *J. Biomech.* **2001**, *34*(4), 421–428.
54. D'Lima, D. D.; Townsend, C. P.; Arms, S. W.; Morris, B. A.; Colwell, C. W. *J. Biomech.* **2005**, *38*(2), 299–304.
55. Graichen, F.; Bergmann, G. *J. Biomed. Eng.* **1991**, *13*(5), 370–374.
56. Graichen, F.; Bergmann, G.; Rohlmann, A. *J. Biomech.* **1999**, *32*(10), 1113–1117.
57. Graichen, F.; Arnold, R.; Rohlmann, A.; Bergmann, G. *IEEE Trans. Biomed. Eng.* **2007**, *54*(2), 253–261.

5.524. Biomaterials for Replacement and Repair of the Meniscus and Annulus Fibrosus

D M Elliott, R L Mauck, R P Shah, and T P Schaer, University of Pennsylvania, Philadelphia, PA, USA
S A Maher, Hospital for Special Surgery, New York, NY, USA

© 2011 Elsevier Ltd. All rights reserved.

5.524.1.	**Overview**	318
5.524.2.	**Introduction**	318
5.524.3.	**Structure and Function of the Knee Meniscus**	319
5.524.4.	**Structure and Function of the AF**	319
5.524.5.	**Current Clinical Treatments for Damage to or Degeneration of the Meniscus and AF**	320
5.524.5.1.	Current Meniscus Repair Methods	320
5.524.5.2.	Current AF Repair Methods	320
5.524.6.	**Current Products for Meniscus and AF Repair and Replacement**	321
5.524.6.1.	Current Products for Meniscus Repair	321
5.524.6.2.	Current Products for AF Repair	321
5.524.7.	**Emerging Products for Meniscus and AF Repair and Replacement: Tissue Engineering**	324
5.524.7.1.	Recent Developments in Meniscus Tissue Engineering	325
5.524.7.2.	Recent Developments in Disc Tissue Engineering	326
5.524.8.	**Engineering Fiber-Reinforced Tissues with Nanofibrous Scaffolds**	327
5.524.8.1.	Electrospinning: The Base Technology	327
5.524.8.2.	Engineering the Meniscus with Nanofibrous Scaffolds	327
5.524.8.3.	Engineering the AF with Nanofibrous Scaffolds	328
5.524.9.	**Preclinical Models and Evaluation Tools for Engineered AF and Meniscus Products**	329
5.524.10.	**Conclusions and Future Directions**	329
References		330

Glossary

Annulus fibrosus (AF) A highly organized fiber-reinforced, layered fibrocartilage and critical component of the intervertebral disc in the spine. The AF is a highly organized fiber-reinforced, layered fibrocartilage. Within each lamella, collagen fibers are oriented at 28°–44° with respect to the transverse axis and fiber angles in adjacent lamella alternate. AF mechanical properties are anisotropic (i.e., directionally dependent) and intrinsically nonlinear.

Fibrocartilage A tissue whose composition is reflective of fibrous tissues (such as tendons and ligaments) that are collagen-rich and designed to withstand tensile loading, and cartilaginous tissues (such as the articular cartilage lining the ends of long bones) that are both collagen- and proteoglycan-rich and designed to withstand a more complex compressive loading environment.

Intervertebral disc A mechanical fibrous tissue-bearing surface between vertebrae that supports loads, permits motion, and dissipates spinal loading energy with daily activities. Incorporated into the motion segment, this semi-flexible symphysis joint (i.e., the bone–disc–bone unit) is subjected to compression, tension, bending, and torsion with normal activities. The intervertebral disc comprises four distinct subcomponents: the vertebral body attachments, the cartilaginous endplate, the gelatinous nucleus pulposus (NP), and the fiber-reinforced annulus fibrosus (AF).

Knee meniscus A cartiligous tissue in the knee joint positioned such as to add congruity to the joint and act as a bushing to complete the curvature of the femoral condyle as it impinges on the tibial plateau. Its chief functions are to transmit and distribute load over the tibial plateau, increase joint congruency, stabilize the joint, and improve articular cartilage nutrition and lubrication.

Abbreviations

ACL	Anterior cruciate ligament
AF	Annulus fibrosus
BMP2	Bone morphogenetic protein 2
CAIS	Cartilage autograft implantation system
DART	Disc annular repair technology
ECM	Extracellular matrix
FDA	US Food and Drug Administration
IDE	Investigational Device Exemption
IVD	Intervertebral disc
IVD	In vitro diagnostic
MFC	Microfibrillar collagen
MRI	Magnetic resonance imaging
MSC	Mesenchymal stem cell

NP	Nucleus pulposus	**PLLA**	Poly(L-lactic acid)
OA	Osteoarthritis	**SEM**	Scanning electron microscope
PCL	Poly(e-caprolactone)	**SIS**	Small intestine submucosa
PDN	Prosthetic disc nucleus	**TE**	Tissue engineering
PDS	Poly(dioxanone)	**TFAS**	Total facet arthroplasty system
PEEK	Poly(ether ether ketone)	**TFCC**	Triangular fibrocartilage complex
PG	Proteoglycan	**TMJ**	Temporomandibular joint
PGA	Poly(glycolic acid)	**UHMWPE**	Ultrahigh molecular weight polyethelene
PLA	Poly(lactic acid)	**USC**	Unseeded scaffolds

5.524.1. Overview

Dense fibrous connective tissues play critical load-bearing roles in the musculoskeletal system and represent a significant medical problem when their function is interrupted by progressive degeneration or acute injury. In this chapter, we outline the functional aspects of two such tissues, the fibrocartilaginous knee meniscus and the annulus fibrosus (AF) of the intervertebral disc of the spine. We discuss the hallmark mechanical and biochemical features of each tissue, the incidence and most common avenues through which the tissues are damaged or degenerate, and the current clinical practices for their repair and/or replacement. Given the prevalence of damage to these tissues, numerous commercial products are, or will soon be, available in the marketplace. These products are discussed in the context of the structure and function of the native tissue they are intended to replace. The biomaterials chosen for the implants, the engineering principles applied to the design of the products, and their current regulatory status are explored. Finally, functional benchmarks, preclinical models, and future directions in this burgeoning field are reviewed.

5.524.2. Introduction

As the name implies, a fibrocartilage is a tissue whose composition is reflective of fibrous tissues (such as tendons and ligaments) that are collagen rich and designed to withstand tensile loading, and cartilaginous tissues (such as the articular cartilage lining the ends of long bones) that are collagen and proteoglycan rich and designed to withstand a more complex compressive loading environment. Specific examples of fibrocartilaginous tissues are the knee meniscus, the temporomandibular disc, and the intervertebral disc. However, other structures, such as the regions of tendons that wrap around a boney prominence, exhibit a local transition toward the fibrocartilaginous phenotype, indicating that fibrocartilage can arise inhomogeneously through otherwise homogeneous tissues, based on the local mechanical environment. These and other fibrocartilages are distributed throughout the body (see Table 1).

In the adult, fibrocartilage is typified by a dense collagenous structure, most of which is type I collagen (see Table 2). These molecules are generally assembled into large bundles oriented in the direction of primary tensile loading. Proteoglycans (PGs) are present within the tissue, but at a considerably reduced level compared to articular cartilage. Indeed, rather than being distributed throughout the tissue substance, in the meniscus, for example, most PG is located between fiber bundles. These tissues are also relatively acellular in the adult, though all progress through a cell-rich phase during development. They likewise generally lack a robust vascular supply. This, coupled with the low cellularity, severely retards endogenous repair when such tissues are damaged acutely after skeletal maturity.

In this chapter, we focus on two prominent examples of fibrocartilage, the knee meniscus and the AF of the intervertebral disc of the spine (see Figure 1). This focus is mandated by the unique features that define these tissues, the incidence with which their function is interrupted, and the negative sequelae that result from their dysfunction in terms of health and quality of life.

Table 1 List of fibrocartilaginous tissues throughout the human body

Intraarticular
Knee meniscus
Wrist triangular fibrocartilage complex (TFCC)
Sternoclavicular intraarticular fibrocartilage
Acromioclavicular intraarticular fibrocartilage
Temporomandibular joint (TMJ) articular disc
Connecting
Annulus fibrosus
Pubic symphysis
Circumferential
Glenoid labrum
Acetabular labrum
Fracture callous

Source: Gray, H.; Pick, T. P.; Howden, R. *Anatomy, Descriptive and Surgical*; Lea Brothers & Co: Philadelphia/New York, 1901

Table 2 Biochemical composition of fibrocartilages (meniscus, annulus fibrosus) compared to articular cartilage, tendon, ligament, and skin

	Water (% wet weight)	*Collagen (% wet weight)*	*Proteoglycan (% wet weight)*
Articular cartilage[1]	65–80	10–11	4–7
Meniscus[2]	72–77	8–13	1
Annulus fibrosus (AF)	72.5[3]	19[1]	1[4]
Tendon	70	25	2
Ligament[1]	70	25	<1
Skin	60	32	1

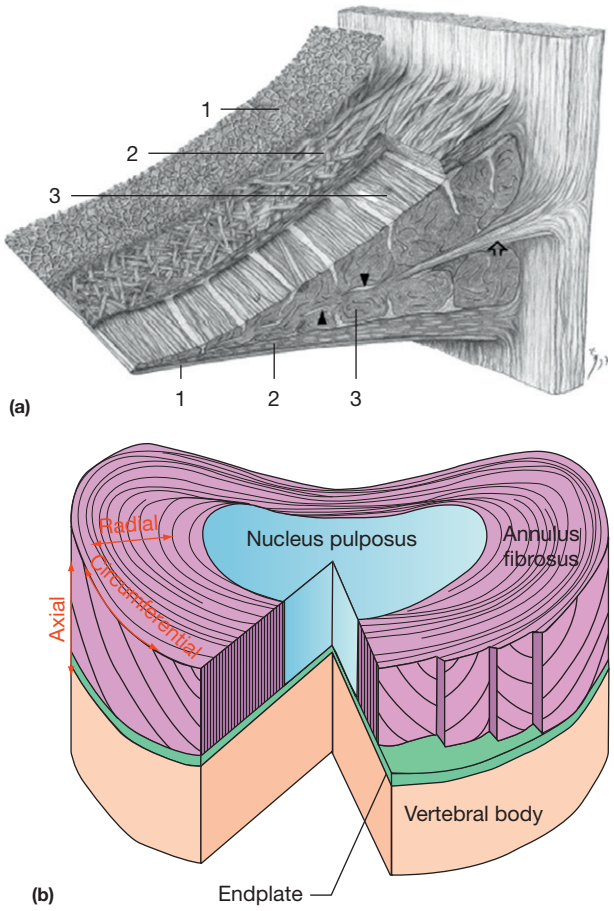

Figure 1 Meniscus and intervertebral disc (IVD) anatomy and structure. Schematics of the (a) meniscus (reproduced from Petersen, W.; Tillmann, B. *Anat. Embryol.* **1998**, *197*, 317–324) and (b) intervertebral disc (reproduced from Guerin, H. A. L.; Elliott, D. M. In *Spine Technology Handbook*; Kurtz, S. M., Edidin, A. A., Eds.; Elsevier Academic Press: Oxford, 2006b) showing tissue microstructure and organization.

5.524.3. Structure and Function of the Knee Meniscus

The tibiofemoral joint represents a significant engineering challenge, where stability and the need for significant range of motion countermand one another. Unlike hinge joints (e.g., in the digits), multiple degrees of freedom are required to allow mobility. Anatomically, the knee consists of the interaction between the rounded femoral condyles and the relatively flat tibial plateau. The two boney portions are held together via the intraarticular (i.e., anterior cruciate and posterior cruciate) and extra-articular (i.e., medial and lateral collateral) ligaments, with contributions via the patellar tendon and the flexors and extensors of the thigh. The knee menisci, of which there is a medial and a lateral in each knee, are positioned such as to add congruity to the joint and act as a bushing to complete the curvature of the femoral condyle as it impinges on the tibial plateau.

In the adult meniscus, the inner avascular region is more like hyaline or articular cartilage, with a higher concentration of PGs, while the outer vascular region is more fibrous, with a higher collagen content. This is particularly the case in the body of the meniscus as compared to the horns.[5] The meniscus extracellular matrix (ECM) contains 85–95% dry weight collagen, of which greater than 90% is type I,[6] with the remaining collagen consisting mostly of types II, III, V, and VI[7] (see **Table 2**). These collagens of the meniscus are of the most highly cross-linked in the body, providing the tissue with a tough fibrous character.[8] PGs makes up less than 2–3% of the dry weight, eight times less than is seen in articular cartilage.[7–9] The meniscus, like articular cartilage, is highly hydrated, with 72–77% of the wet weight comprised of water.[9]

In terms of vascularity, the peripheral 10–25% of the meniscus is supplied by a perimeniscal capillary plexus, while the inner stroma is largely avascular.[10,11] During development, the meniscus is vascular throughout, though these vessels regress with time.[11–13] Similarly, the cell type of the meniscus (i.e., the meniscus fibrochondrocyte) is a heterogeneous population – in the inner avascular region these cells have a chondrocyte-like phenotype, while in the outer rim these cells are fibroblast-like in appearance and matrix deposition.[14,15] In both regions, a significant decrease in cell density is observed with skeletal maturation.

As may be expected for such a fiber-reinforced matrix, the mechanical properties of this tissue are highly anisotropic and strongly dependent on the prevailing fiber direction[16,17] (see **Figure 1**). The tensile properties of the meniscus range from 48–259 MPa in the circumferential direction and 3–70 MPa in the radial direction.[2,8,16–21] The compressive properties of the meniscus varies between the species and with location (e.g., it is highest anteriorly)[8,12,22] but it is approximately one-half that of articular cartilage (100–400 kPa, aggregate modulus). The meniscus, while having a lower modulus, is also much less permeable than articular cartilage,[8] suggesting that the tissue is optimized to enhance congruency, load distribution, and shock absorption across the joint.[17]

The main functions of the meniscus are to transmit and distribute load over the tibial plateau, increase joint congruency, stabilize the joint, and improve articular cartilage nutrition and lubrication.[23] These functions are achieved by the unique load shifting that occurs between the more hyaline inner region and the more fibrous outer region of the meniscus. When the joint is loaded, axial loads impinging on the wedge-shaped portion of the meniscus are redirected laterally, causing lateral extrusion. This extrusion is resisted by the osseous anchors originating from the anterior and posterior horns,[17] generating hoop stresses within the dense network of circumferentially oriented collagen fibers. Lateral extrusion is thereby resisted and the joint stabilized.[2,12,23,24] The secondary stability offered by the meniscus is particularly important in the anterior cruciate ligament (ACL) deficient knee.[25] With normal knee kinematics, forces that are many times the body weight may be generated within the joint.[26–30] The menisci transmit 50–100% of joint load in a healthy knee,[24,27,31] which results in deformations within the tissue on the order of 2–6% with normal activity.[32,33]

5.524.4. Structure and Function of the AF

The spine is comprised of repeating soft and hard segments; the hard segments are the boney vertebral bodies, and the soft

segments are the intervertebral disc (IVD) that is interposed between them. The function of the IVD is mechanical – it supports loads, permits motion, and dissipates energy with daily activities. This semiflexible symphysis joint (i.e., the bone–disc–bone unit) is sometimes referred to as the motion segment. Motion about this joint subjects the intervening disc to compression, tension, bending, and torsion with normal activities. Loads acting across this joint can reach many times the body weight, given the relatively short lever arms (e.g., the spinous processes and the inferior and superior articular processes that interact through synovial facet joints) over which the muscles of the back operate. This translates to stresses acting on the IVD reaching ~1 MPa applied at frequencies of 1 Hz, with superimposed rotations ranging up to ±6°.[34] These considerable and varied mechanical forces necessitate the complex and durable organization and mechanical properties of the IVD and its substructures.

The IVD itself is typically considered as having four distinct subcomponents: the vertebral body attachments, the cartilaginous endplate, the gelatinous nucleus pulposus (NP), and the fiber-reinforced AF (see **Figure 1**). The AF is a highly organized fiber-reinforced, layered fibrocartilage. Within each lamella, collagen fibers are oriented at 28–44° with respect to the transverse axis,[35,36] and fiber angles in adjacent lamella alternate. The mechanical properties of AF are anisotropic (i.e., direction dependent) and nonlinear, and are compromised in degeneration.[37–41] The major constituents of the IVD are collagens (50–70% dw) and PGs (10–50% dw).[42,43] The collagens provide high tensile properties to the AF, while PGs in the NP allow it to resist large compressive loads. AF and NP cells are distinct in phenotype, with NP cells more chondrocyte-like, producing type II collagen and PG, while AF cells are fibrous, producing less PG and a mix of collagen I and II.[44–48]

5.524.5. Current Clinical Treatments for Damage to or Degeneration of the Meniscus and AF

Given the central location of the meniscus in terms of knee function, and the AF in terms of spine function, it is not surprising that these two tissues are prone to injury, and that failure leads to significant health issues. This section describes current treatment modalities that do not rely heavily on the use of implanted biomaterials.

5.524.5.1. Current Meniscus Repair Methods

While the meniscus can function well over a lifetime of use, 60–70 meniscus tears per 100 000 persons occur each year.[49–51] Given this prevalence, arthroscopic treatment of meniscal injuries has become one of the most common orthopedic procedures performed in the United States.[52] Tears that occur longitudinally (i.e., splitting between fibers) are amenable to repair when located in the peripheral or vascular zone. The most common and successful repair strategy for these tears is to suture torn structures back into apposition, either via open repair or arthroscopic surgery.[53] Arthroscopic methods include the inside-out technique (i.e., inside the joint capsule to outside the meniscus periphery) and the outside-in technique (i.e., from the periphery to the internal space).[54,55] Symptomatic radial tears located in the avascular region that interrupt collagenous architecture present a more difficult problem, and current treatment strategies involve partial meniscectomy without an effective alternative. Partial meniscectomy changes load transmission in the knee, and can lead to radiographic narrowing of the joint space.[56] In animal models, partial meniscectomy leads to erosion of the underlying cartilage over the long term. If repair is attempted in the avascular region, rasping of the synovium or the intercondylar notch is employed to increase the vascular response.[57,58] Indeed, it has been suggested that whenever repair of the avascular zone is attempted, some form of healing enhancement technique should be considered.[54]

When damage to the meniscus is considerable, such that all the meniscus is compromised, allograft transplantation of a whole fresh-frozen or cryopreserved meniscus from a human donor can be attempted. Allografts restore some aspects of load transmission after total meniscectomy. However, several studies have reported cartilage degeneration following implantation, most likely attributable to improper sizing of the implants.[59–62] This finding may be related to the fact that isolated tears and partial meniscectomy have very similar results,[63] suggesting that even a minor structural abnormality can lead to a change in meniscus function and can translate into significant damage to the articular surface. Moreover, allografts raise concerns regarding the methods of cryopreservation, graft sterility, and the proper method of fixation.[61] Clinical results suggest that function is only partially restored and that poor integration makes the grafts susceptible to premature failure.[64] These findings highlight the need for a functional repair strategy short of total replacement for the clinical treatment of meniscal tears.

5.524.5.2. Current AF Repair Methods

As with the meniscus, back pain arising from damage or degeneration of the soft tissues of the spine is a significant health problem in society; it is the most common reason that adults under the age of 45 limit their daily activities.[65] While genetics and other factors play a role, patterns of activity also have an impact on spine health and back pain. Disc pain is particularly prevalent in active populations, such as those in active duty military service. In one study, as many as 44% of US Gulf War veterans reported low back pain within 2–5 years following service, an incidence rate that is 14% higher than nonactive duty veterans and nearly twice that of the general US population.[66] Degeneration of the disc involves progressive failure of each of the substructures. In the NP, a loss of PG results in depressurization and increasing tissue fibrosus. In the AF, tensile mechanical properties decrease and internal collapse is observed.[37]

When the source of back pain is typically from tears of the AF, patients typically present with pain and radicular neurological complaints (e.g., weakness and parasthesias) resulting from the extruded NP impinging on a nerve root or nerve. Imaging and a thorough physical exam can help identify the level of involvement of the spine. In many patients, nonsurgical methods of treatment can alleviate symptoms; these treatments include activity modification, traction, soft collars, nonsteroidal anti-inflammatory drugs, selective nerve root injections, and physical therapy. Failing those treatments,

surgical intervention may offer relief in indicated patients. The mainstay of surgical treatment is a decompression of the affected nerve root, usually involving a foraminotomy or laminoforaminotomy, and possibly fusion.[67] A foraminotomy is the surgical opening (or deroofing) of the interverbral foramina, while laminoforaminotomy refers to surgically opening the lamina as well. Decompression can be achieved by annulotomy followed by discectomy or microdiscectomy. Newer experimental methods utilize low-energy radiofrequency waves to create an ionic plasma field from sodium atoms within the nucleus. The tissue is converted into gas by molecular disassociation, thereby achieving intradiscal decompression.[68]

When decompression is not enough, the next level of surgical intervention is rigid stabilization or fusion of adjacent vertebral bodies. Rigid stabilization involves fixing the distance between two adjacent vertebral bodies via metal implants that run along the spinal column and are fixed to the bone stock of the vertebral body. Fusion describes the process by which the disc is removed and replaced with materials, usually bone graft, to encourage boney connections between adjacent vertebral bodies. Fusion is a terminal procedure that completely eliminates motion at that segment. Products on the market, based on BMP-2 delivery from collagenous sponges within a titanium cage, seek to achieve fusion in a faster and more predictable way and reduce the need for allograft or autograft bone materials (e.g., INFUSE Bone Graft, Medtronic Sofamore Danek). While both traditional and BMP-2 enhanced fusions do reduce pain at the affected spinal segment, adjacent disc disease has been reported due to the reduced mobility at the fused segment.[69–71]

While not in widespread use, several reports of allogeneic disc transfer from cadaveric sources exist. In the mid-1990s, disc allograft transplants were performed in canine and nonhuman primate studies.[72–74] In the rhesus monkey, disc autografts and allografts were anchored from the outer AF to the adjacent transverse processes via sutures; no other fixation was applied.[72,73] Complete bony union was achieved, some cell metabolism was reported, and biomechanics were similar to control. However by 24 months, disc height loss, decreased water and PG content, and gross morphological evidence of degeneration were observed.[73] This team recently reported human cervical disc allograft transplant in five patients with mixed results.[75] Good bony union was achieved by 3 months, neurological symptoms improved, no immunoreaction occurred, and only mild degenerative changes were seen. However, disc height loss, reduced sagittal motion in one disc, and significant hydration loss, as measured on MRI at 5 years, were reported in three discs. Overall, the evidence for disc implantation is promising, but quite limited, and is subject to the same general limitations as for meniscus allograft procedures, namely the potential for disease transmission, limited availability of donor materials, and limited sizing options.

5.524.6. Current Products for Meniscus and AF Repair and Replacement

To address the limited and often unsatisfactory performance of current repair strategies, private sector research and development programs have focused innovation toward devices for the treatment of meniscus and disc degeneration. These devices, comprised of a variety of biomaterials depending on the specific application, are in varying stages of development, from basic science *in vitro* research to implants with full US Food and Drug Administration (FDA) approval. Early regulatory successes have come largely from mechanical arthroplasty solutions, while tissue engineered devices are new to the marketplace. This section and the corresponding tables (see **Tables 3** and **4**) overview several such devices for the knee meniscus and the AF.

5.524.6.1. Current Products for Meniscus Repair

Pathology in the knee meniscus can frequently lead to knee arthropathy and eventually arthritis. Approaches to treat end-stage arthritis of the knee have historically focused on arthrodesis and arthroplasty, with newer innovations centered on early prevention of progressive later stage disease. These devices are of three types: arthroplasty, meniscal repair, and tissue engineered cartilage and meniscal replacement. Our focus is on the latter two categories, though some common athroplasty tools are shown in **Table 3**.

As discussed above, there is a strong association between damage to the meniscus and the precipitous onset of osteoarthritis (OA). Focus in this field is thus on maintenance of meniscus anatomy (e.g., minimizing the size of the meniscectomy performed) and restoring stability to the damaged segment. Meniscus tears in the outer portion of meniscus, and some of those in younger patients, can be repaired primarily using suture, screw, barbed anchor, or hybrid repair systems.[104] MaxFire (Biomet, Inc.) uses a braided polyethylene/polypropylene suture applied with a harpoon style deployment system. The RapidLoc Meniscal Repair System (DePuy Mitek, Inc.) is another hybrid system that consists of an absorbable poly(lactic acid) (PLA) or poly(dioxanone) (PDS) anchor, a Panacryl or Ethibond suture, and an absorbable PLA or PDS 'top hat' that compresses the tear against the anchor. Biostinger (ConMed Linvatec) is a poly(L-lactic acid) (PLLA) absorbable barbed cannulated anchor. A similar concept device that begins to harness biological means of healing is seen in the BioDuct device (Stryker Orthopaedics). This is a cylindrical, biodegradable PLLA device with a suture that is intended to repair peripheral meniscus tears in less vascular regions. The device purports to allow a central axis channel for fibrin clot formation and a conduit for later migration of cells and blood vessels.[79] Many of these devices can be employed using arthroscopic all-inside techniques that shorten surgical times, allow easier approaches for implantation, and reduce surgical risk. While promising and generally easier to use, the fixation strengths resulting from these devices are no better than vertical mattress sutures.[105–109] These fixation devices also degrade with time, depending on their polymer composition, and exhibit different failure modes depending on implantation duration and mechanical testing modality.[105,110,111]

5.524.6.2. Current Products for AF Repair

Treatments for axial spine symptoms have trended away from fusion, with new surgical solutions that attempt to be more anatomic and functional. Medical devices that address spinal

Table 3 Characteristics of knee and meniscus products

Name	*Composition*	*Function*	*Status*	*Manufacturer*
Arthroplasty, generally	Typically a metal (e.g., cobalt chrome alloy) femur and tibia and an ultra-high-molecular-weight polyethelene (UHMWPE) spacer	Total knee arthroplasty	FDA approved	Varies
Marketed devices				
Small intestinal submucosa (restore)[76]	Ten layers of processed porcine small intestine submucosa	Used to reinforce a meniscus repair or bridge gaps in the meniscus	FDA approved for reinforcement of the soft tissues, which are repaired by suture or suture anchors, during rotator cuff repair surgery	DePuy Orthopaedics/ Johnson and Johnson
Menaflex/collagen meniscus implant[77]	Molded type 1 collagen scaffold (derived from bovine Achilles tendon)	Indicated for reinforcement and repair of the medial meniscus; the patient must have an intact meniscal rim and anterior and posterior horns for attachment of the mesh. In addition, the surgically prepared site for the collagen scaffold must extend at least into the red/white zone of the meniscus to provide sufficient vascularity	FDA approved for use in the medial meniscus (CE Mark approval for both medial and lateral meniscus), Undergoing post-FDA approval review	Regen Biologics, Inc.
Actifit[78]	Porous scaffold made of aliphatic polyurethane with both soft segments and stiff segments. About 80% of the material is soft, made of poly(ε-caprolactone) (PCL). The other 20% is stiff, made of urethanes derived from 1,4-butanediisocyanate and 1,4-butanediol moieties. Reportedly has a pore size of 150–355 μm and 80% porosity	Indicated as an implant to fill partial lateral or medial meniscectomy defects	CE Mark (July 2008)	Orteq Ltd.
Bioduct[79]	Bioabsorbable cannulated poly(lactic acid) (PLA) device secured with suture	Intended for arthroscopic fixation of longitudinal vertical meniscus (bucket handle) lesions located in the vascularized (red-white) zone of the meniscus when used with suture	510(k) (April 2007)	Stryker Orthopaedics
Preclinical				
Engineered hydrogel meniscus[80]	A hydrogel meniscal replacement made from Salubria, a nondehydrated poly(vinyl alcohol) cyrogel	Formed hydrogels intended for full or partial meniscal replacement	Preclinical results showed failure at 1 year in an ovine model	Salumedica, Inc.
Engineered hydrogel meniscus[81]	Anatomic constructs formed from image guided injection molding techniques. Bovine microfibrillar collagens (MFCs) are seeded into an alginate gel, which is cross-linked after injected into the mold	Anatomically shaped meniscal constructs for replacement of meniscal defects	Preclinical	n/a
Engineered porous polymer meniscus [82]	Synthetic porous polymer meniscal scaffold composed of Estane polymers and formed using a sucrose porogen	Meniscal scaffold for replacement of meniscal defects	Preclinical	n/a
Engineered nanofibrous meniscus[83]	Aligned PCL nanofiber scaffold implanted into defects in the posterior horn of the ovine medial meniscus	Meniscal scaffold for the replacement of meniscal defects	Preclinical	n/a
Tarexx[84]	Injectable collagen cross-linking reagent (e.g., genepin)	Nonsurgical prevention of knee meniscus degradation	Preclinical	Orthopeutics, L.P.
Frog glue[85]	Protein-based adhesive elastomer secreted by the Australian frog *Notaden bennetti*	Biological adhesive for meniscal tears	Preclinical	n/a

Table 4 Characteristics of spine and IVD devices

Name	*Composition*	*Function*	*Stage of development*	*Manufacturer*
Discal arthroplasty				
Arthoplasty, generally	Typically metal (e.g., cobalt chrome alloy) endplates and a UHMWPE spacer	Total disc replacement	Several FDA approved	Varied
Facet arthroplasty				
TFAS (total facet arthroplasty system)[86]	Titanium alloy, cobalt, chromium, molybdenum, barium sulfate, and poly(methyl methacrylate) bone cement	Total facet arthroplasty	FDA IDE	Archus Orthopedics, Inc. (currently dissolved)
Dynamic stabilization				
X-Stop[87]	Titanium alloy device	Dynamic stabilization: interspinous distraction devices	FDA approved (November 2005)	St. Francis Medical Technologies, Inc./ Medtronic Sofamor Danek
Dynesys[88]	Titanium alloy (Protasul-100) pedicle screws, poly(ethyleneterephthalate) (Sulene-PET) cords, and poly(carbonateurethane) (Sulene-PCU) spacers	Dynamic stabilization: ligaments across pedicle screws	FDA approval as an adjunct to fusion (March 2004)	Zimmer Holdings, Inc.
Nucleus pulposus arthroplasty				
Nubac[89]	PEEK on PEEK mechanical articulation, tantalum markers	NP intradiscal arthroplasty	FDA IDE	Pioneer Surgical Technology
EBI Regain[89]	One piece: graphite substrate with pyrolytic carbon coating	NP intradiscal arthroplasty	Preclinical	Biomet, Inc.
Nucleus pulposus replacement, without mechanical articulation				
Knitted titanium,[90]	Knitted titanium filaments formed into a mesh	NP replacement	Preclinical	BUCK Enterprises
Prosthetic disc nucleus (PDN-SOLO)/ hydraflex (2nd gen)[91]	Hydrolyzed poly(acrylonitrile) and poly (acrylamide) copolymer preformed within a jacket	NP replacement	FDA IDE	Raymedica, Inc.
Newcleus[91]	Poly(carbonate urethane) coiled into a spiral	NP replacement	Preclinical, ceased development	Zimmer Spine
Aquarelle[89]	Semihydrated poly(vinyl alcohol) hydrogel, without a jacket	NP replacement	Preclinical, ceased development	Stryker Orthopaedics
Neudisc[89]	Radially anisotropic implant, modified hydrolyzed poly(acrylonitrile) polymer (aquacryl) reinforced with a Dacron mesh	NP replacement	Preclinical	Replication Medical, Inc.
DASCOR[92]	Polyurethane polymer in polyurethane balloon	Injectable NP replacement	CE Mark (2005), FDA IDE	Disc Dynamics, Inc.
Gelifex	Thermoresponsive polymer hydrogel injected into an NP void	Injectable NP replacement	Preclinical	Synthes, Inc.
NuCore[89]	Silk elastin polymer with a chemical crosslinking agent	Injectable NP replacement	FDA IDE	Spine Wave, Inc.
SINUX ANR[93]	Liquid poly(methylsiloxane) polymer, curing in 15 min	Injectable NP replacement	CE mark	Sinitec AG/DePuy Spine
BioDisc NPR[94]	Injectable NP void filler made of 45% purified bovine albumin, and 10% gluteraldehyde	Injectable NP replacement	Clinical	CryoLife, Inc.
Partial disc replacement device	Silicone composites forming an injectable viscous liquid that cures *in situ*; injected into an expandable silicone shell	Injectable NP replacement	Australia, clinical trial (on hold)	Columna Ltd.
Annulus fibrosus repair				
Barricade	Woven polyethylene mesh backstop that is anchored to the bone through a titanium insert	Mechanical annular defect buttress	CE Mark (April 2009)	Intrinsic Therapeutics, Inc.
Disc annular repair technology (DART)	PEEK cone-shaped device inserted into an annular defect	Mechanical annular defect buttress	CE Mark (April 2009)	Magellan Spine Technologies, Inc.
Inclose	Polyethylene mesh	Mechanical annular defect buttress; opens as an umbrella within a defect	FDA approved (August 2005)	Anulex Technologies, Inc.

(*Continued*)

Table 4 (Continued)

Name	*Composition*	*Function*	*Stage of development*	*Manufacturer*
Xclose	Suture device system	Intended to suture closed an annulotomy	FDA approved (September 2006)	Anulex Technologies, Inc.
Atelocolalgen AF sponge[95]	Purified type 1 atelocollagen, molded into honeycomb structures with freeze-drying and UV irradiation. Cultured with AF cells	Tissue engineered scaffold for AF regeneration	Preclinical	n/a
Hybrid alginate/ chitosan fibers[96]	Alginate fiber scaffolds wet-spun into loops and coated with chitosan	Tissue engineered scaffold for AF regeneration	Preclinical	n/a
Engineered collagen AF[97]	Collagen gels seeded with ovine annulus fibrosus cells. Alignment induced by contracting annular gels around a cylindrical post	Tissue engineered aligned AF	Preclinical	n/a
Intralink[84]	Injectable collagen cross-linking reagent (e.g., genepin)	Nonsurgical modification of spinal discs	Preclinical	Orthopaeutics, L.P.
Composite discs				
Composite engineered disc[98,99]	IVD composite composed of PGA and PLA mesh (AF) seeded with ovine AF cells, surrounding an alginate gel (NP) seeded with ovine NP cells	Tissue engineered composite disc scaffold	Preclinical	n/a
Engineered collagen disc[100]	Condensed type 1 collagen matrix	Tissue engineered disc scaffold	Preclinical	n/a
NP/AF amalgam (HANFS)[101]	IVD composite composed of electrospun PLLA (AF) surrounding a seeded hyaluronic acid hydrogel center (NP)	Tissue engineered composite disc scaffold	Preclinical	n/a
Composite nanofibrous/ hydrogel disc[102]	IVD Composite composed of electrospun aligned PCL, spot welded with angle-ply orientation to form the AF, surrounding an agarose NP, both seeded with bovine mesenchymal stem cells	Tissue engineered composite disc scaffold	Preclinical	n/a
Composite nanofibrous/ hydrogel disc[103]	IVD composite composed of electrospun PCL (AF) surrounding a chondrocyte seeded agarose gel	Tissue engineered composite disc scaffold	Preclinical	n/a

disc degeneration fall into three broad categories: arthroplasty, NP replacement, and AF repair. Examples of several such devices are shown in **Figure 2** and **Table 4**. Our focus in this chapter, however, is on the final category, namely, AF repair.

Annulus repair technologies have been sought after, in part, to solve the problem of NP device extrusion. Some repairs have sought to further traditional suture designs (Xclose, Anulex Technologies, Inc.), while others are developing novel constructions. These include Barricade (Intrinsic Therapeutics, Inc.), which combines a titanium bone anchor to a woven mesh backstop, Disc Annular Repair Technology (DART, Magellen Spine Technologies, Inc.), which is a bullet-shaped device made of poly(ether ether ketone) (PEEK) that resembles a wine stopper, and Inclose (Anulex Technologies, Inc.), which is specially designed for cannulated defects in the AF. It is a polyethylene mesh barrier that expands like an umbrella once inserted through the AF. Nonsurgical exogenous cross-linking therapy (NEXT and Intralink, Orthopeutics, L.P.) is a novel strategy of directly injecting a collagen cross-linking reagent into the AF. Genepin is one such candidate reagent. As may be appreciated from the description of NP devices above, there exist many newer devices specifically focused on AF repair. This may be partly attributed to the primary focus on restoring and maintaining disc height, and partly in recognition that repair of fiber-reinforced tissues is a more intractable problem.

5.524.7. Emerging Products for Meniscus and AF Repair and Replacement: Tissue Engineering

Considerable advances have already been made, centered on new material-based devices, for furthering the repair of the meniscus and AF. Indeed, the last decade has witnessed an explosion in the development of such devices, providing the surgeon with numerous options for restoration of function without compromising anatomic integrity or motion about the damaged area. Notwithstanding this progress in device design, additional steps are being undertaken to minimize the biomaterial footprint, that is, how much artificial materials are implanted and for how long they persist, and to maximize the biologic underpinnings of these repair techniques. Into this research space falls tissue engineering (TE). The goal of TE is the creation of fully biologic substitutes for tissue repair that may serve as an alternative or functional bridge to prosthetic replacement. Since first coined, the original TE paradigm has changed little from the concept of combining cells, scaffolds, and inducers of neotissue formation.[112] A TE construct typically consists of a natural or synthetic polymer scaffold seeded with autologous cells possessing functionality similar to that of the native cell type. Alternatively, these tissues may be generated from adult mesenchymal stem cells (MSCs), a progenitor population

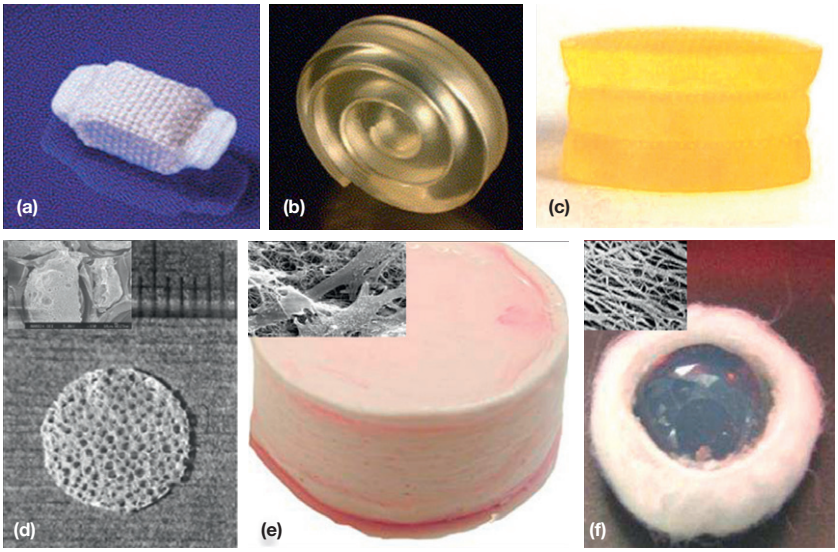

Figure 2 Examples of intervertebral disc tissue engineering products on the market and in development. (a) PDN-Solo is a preformed copolymer hydrogel with jacket used for NP replacement. Reproduced from Lau, S.; Lam, K. S. *Curr. Orthop.* **2007**, *21*, 25–39. (b) Newcleus is a poly(carbonate urethane) coiled into a spiral. Reproduced from Lau, S.; Lam, K. S. *Curr. Orthop.* **2007**, *21*, 25–39. (c) Neudisc is a poly(acrylonitrile) polymer reinforced with Dacron mesh. Courtesy of Dr. James J. Yue. (d) Type 1 atelocollagen honeycomb scaffold for AF regeneration (inset: SEM of honeycomb pockets with cultured AF cells). Reproduced from Sato, M.; Kikuchi, M.; Ishihara, M.; *et al. Med. Biol. Eng. Comput.* **2003**, *41*, 365–371. (e) Condensed type I collagen matrix scaffold for NP replacement (inset: SEM of seeded scaffold). Reproduced from Wilke, H. J.; Heuer, F.; Neidlinger-Wilke, C.; Claes, L. *Eur. Spine J.* **2006**, *15*(Suppl. 3), S433–S438. (f) Composite disc fabricated from electrospun PCL surrounding a seeded agarose gel (inset: SEM of PCL scaffold). Courtesy of Michael Detamore, Presented at the 55th Annual Meeting of the Orthopaedic Research Society, March 2009, Paper 310. Reproduced from Lazebnik, M.; Glatt, P.; Singh, M.; Zhao, L.; Berkland, C.; Detamore, M. S. *A Biomimetic Approach to the Intervertebral Disc Regeneration*. 55th Annual ORS 2009, Paper no. 310.

found within bone marrow that can be induced to differentiate along a number of relevant musculoskeletal lineages. In many of these TE formulations, chemical or mechanical stimuli are provided as part of the *in vitro* culture environment via the delivery of growth factors or the action of bioreactors that duplicate some portion of the normal *in vivo* mechanical environment. These various parameters (i.e., cells, scaffolds, and culture environment) have been extensively explored for the creation of tissue equivalents for most tissues of the musculoskeletal system, including the meniscus and the AF. For fiber-reinforced tissues in particular, challenges include recapitulating the dense ordered collagenous structure, as well as biologic union of these neotissues within the wound site. This section describes recent advances in meniscus and AF tissue engineering.

5.524.7.1. Recent Developments in Meniscus Tissue Engineering

Arthroplasty solutions still dominate the treatment of knee disorders; however, TE approaches are beginning to gain ground. Early focus in the knee was on the articular cartilage itself, with Carticel (Genzyme Corp.) emerging as the first cell-based solution to cartilage damage. This technique consists of harvesting autologous cartilage cells, expanding them in culture, and reimplanting the cells under a flap at the defect site. Types of flaps include autologous periosteum and processed porcine small intestine submucosa (SIS) (Restore, DePuy Orthopaedics, Inc.). More recent approaches have simplified this approach toward a single procedure where cartilage cells are harvested and placed on a bioabsorbable scaffold before being reimplanted into the patient. An example of this is the Cartilage Autograft Implantation System (CAIS), also from DePuy Orthopaedics, Inc. Similarly, NeoCart (Histogenics Corp.) involves harvesting cartilage cells, seeding them onto a collagen scaffold, and then culturing the cells in a bioreactor that emulates the biomechanical milieu of native cartilage. An early area of focus for tissue engineers, cartilage engineering has taught investigators valuable lessons that are applicable to meniscus and disc TE.

With therapies such as Carticel, CAIS, and Neocart addressing focal cartilage damage, attention is turning toward meniscus TE, given its important role in forestalling OA progression. While meniscus TE is an active area of development and innovation (see **Figure 3**), only one device has received FDA approval for marketing in the United States. Menaflex (ReGen Biologics, Inc.) is a molded collagen scaffold derived type 1 collagen purified from bovine Achilles tendon. Following purification, the collagen is swollen in the presence of hyaluronic acid and chondroitin sulfate.[113] One-year follow-up biopsy specimens have suggested that the porous implant appears to encourage meniscus-like fibrochondrocytic matrix production.[77]

Porcine SIS, already discussed with autologous cartilage implantation, is another tissue engineered device for treating meniscus defects. SIS is a naturally occurring ECM containing collagens, PGs, and growth factors. It is believed to provide a three-dimensional scaffold for clot formation and cell conduction, allowing for new meniscal tissue production.[76,114] One-year outcomes in dogs were reported to be good when the

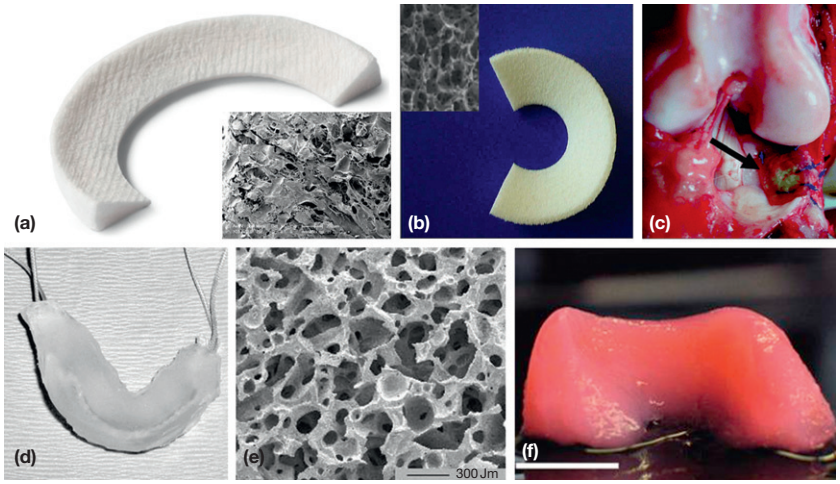

Figure 3 Examples of meniscus tissue engineering products on the market and in development. (a) The Menaflex device (courtesy of ReGen Biologics, Inc.) (inset: SEM of the surface). (b) The Actifit device (reproduced from van Tienen, T. G.; Hannink, G.; Buma, P. *Clin. Sports Med.* **2009**, *28*, 143–156) (inset: SEM of the core; reproduced from Brophy, R. H.; Cottrell, J.; Rodeo, S. A.; Wright, T. M.; Warren, R. F.; Maher, S. A. *J. Biomed. Mater. Res. A* **2009**, *92*, 1154–1161). (c) Canine intraoperative image of the Restore patch (arrow) (reproduced from Cook, J. L.; Fox, D. B.; Malaviya, P.; *et al. Am. J. Sports Med.* **2006**, *34*, 32–42). (d) A poly(vinyl alcohol) hydrogel meniscal implant with embedded sutures (reproduced from Kelly, B. T.; Robertson, W.; Potter, H. G.; *et al. Am. J. Sports Med.* **2007**, *35*, 43–52). (e) SEM of an Estane polymer scaffold (reproduced from Tienen, T. G.; Heijkants, R. G.; de Groot, J. H.; *et al. Biomed. Mater. Res. B Appl. Biomater.* **2006**, *76*, 389–396). (f) Anatomic constructs fabricated by injection molding techniques using bovine meniscus cells in an alginate gel (reproduced from Ballyns, J. J.; Gleghorn, J. P.; Niebrzydowski, V. *et al. Tissue Eng. A* **2008**, *14*, 1195–1202).

meniscal defect extended to the vascular zone, a source for initial clot was ensured, the implant was stabilized, and the implant was protected for an initial period.[76,114] As yet, this product has not been approved by the FDA for use in treating meniscus defects in humans.

As an alternative to these biologic materials, a synthetic meniscus replacement device has received CE Mark approval in Europe. Actifit (Orteq Ltd.) is a porous scaffold comprised of 80% soft segments and 20% stiff segments. The soft segments are made of poly(ε-caprolactone) (PCL) and the stiff segments consists of urethanes made from 1,4-butanediisocyanate and 1,4-butanediol moieties.[115] After the soft segments degrade, about 4% of the implant volume will remain as stiff segments, slowly degrading over 4–6 years. This biphasic degradation pattern allows prolonged structural strength during the period of cellular ingrowth.

In addition to these products at or near market, preclinical candidate tissue engineered substrates for meniscus regeneration abound. Chiari *et al.* reported the *in vivo* results of one such scaffold in replacing a total meniscus in sheep.[116] They produced a porous composite of PCL and a class of benzyl esters of hyaluronic acid (HYAFF, Fidia Advanced Biopolymers). Meniscus-like structures were molded with pore sizes of 200–300 μm and augmented with circumferential PLA to enable fixation through bone tunnels. After 6 weeks, the authors reported compression of the porous structure and partial extrusion. However, the partial replacement arm of the study showed thorough tissue ingrowth and some vascular invasion deep into the implant.

Tienen *et al.* reported on two other synthetic porous scaffold materials created for meniscal replacement; one was based on Estane polymers and another on an aliphatic 1,4-butanediisocyanate-based poly(esterurethane) (PCLPU).[82] The Estane material consisted of a hard component to provide for the compressive modulus, 4,4-methylenediphenyldiisocyanate, and a soft component poly(tetramethyl adipate). Its production used sucrose as a porogen. The PCLPU material consisted of a hard segment of 1,4-butanediisocyanate and butanediol and a soft segment of poly(caprolactone) initiated on 1,4-butanediol. The porogen used was sodium chloride crystals. Estane implant outcomes at 6 months in dogs showed fast tissue ingrowth and collagen deposition, but poor cartilage preservation properties.[82,117] The group ultimately preferred the PCLPU material over the Estane material due to less toxicity and synovial reaction.[82]

Hydrogels have also been investigated as suitable meniscus replacements. Kelly *et al.* reported *in vivo* results using Salubria (SaluMedica), a poly(vinyl alcohol) cyrogel, in sheep.[80] The hydrogels were formed to match sheep meniscus anatomy and were secured with suture running through the peripheral circumference. While results were promising at 2 months following surgery, graft failure and cartilage degeneration harbingered a worse performance at 4 and 12 months compared to allograft transplantation. More recently, Ballyns *et al.* demonstrated the feasibility of image-guided production of anatomically shaped mensical implants using injection molding of meniscal cells in alginate gel.[81] These alginate gels provide for cell delivery and maturation upon implantation, and can be formed by advanced three-dimensional techniques to perfectly mirror the native meniscus anatomy.

5.524.7.2. Recent Developments in Disc Tissue Engineering

Though significant development is still occurring with traditional spinal devices, innovation for treating spinal disc pathology is moving toward tissue engineered devices. In the

simplest formation, work has begun on the delivery of scaffold-only (i.e., cell-free) biomaterials to the defect site. In a slightly more complicated formulation, cell-based TE is also an emerging area of device innovation in NP and AF replacement. These methods involve seeding cells – frequently stem cells – onto structural scaffolds to fabricate functional tissues to match the native tissue properties. Several efforts are underway in preclinical stages to design spinal devices with biomechanical properties resembling native tissue, and clinical testing is expected in the next decade.

In one early example of disc TE, Sato *et al*. designed an atelocollagen honeycomb-shaped scaffold with a membrane seal[118] (see **Figure 2**). The scaffold is derived from a gel created from type 1 atelocollagen from bovine dermis.[119] The scaffold may be delivered on its own or preseeded with native tissue cells. In this study, AF cell seeded constructs were implanted into the disc space of Japanese white rabbits; these constructs showed 90% viability at 12 weeks and improved preservation of disc height compared to controls. Another approach is elastomeric materials augmented with cells, vis-à-vis hydrogels, which can reproduce some of the functional properties of native NP tissue[120] and are amenable to cell delivery. Reza and Nicoll encapsulated bovine NP cells in a photopolymerizable gel of carboxymethylcellulose, a water soluble derivative of the same cellulose in plant cell walls.[121] Other naturally derived materials have also been studied as potential NP hydrogel candidates, including chitosan hydrogels, hyaluronic acid hydrogels, and alginate hydrogels.[122] The scaffold portion of these constructs provides early mechanical stability, while cultured cells are expected to provide long-term biological integration and native tissue mechanical properties. Naked type I collagen that has been condensed into a three-dimensional matrix has also been shown to restore disc height and stability.[100] Alini *et al*. cultured both AF and NP cells in a 9:1 collagen:hyaluronan cross-linked scaffold.[123] Séguin *et al*. created scaffolds by sintering calcium polyphosphate powder into porous cylindrical substrates that were then seeded with bovine NP cells.[124] Chang and colleagues showed that AF cells attach to and produce AF-like ECM on porous silk-based biomaterials, and that dynamic culture improved this outcome.[125,126] More recently, alginate microfibers have been produced and seeded with AF cells; these fibers provide some directionality in the engineered AF construct, and begin to approximate native tissue architecture.[96] Along a similar line, Bowles and Bonassar recently reported on the formation of collagen-based AF constructs. In their work, collagen gels seeded with cells were allowed to contract around a cylindrical post, allowing for cell alignment in a lamellar pattern.[97]

As progress is made in engineering of the NP or the AF alone, these two goals are merging into the TE of composite devices that contain both regions. In one of the earliest examples, Mizuno *et al*. created a composite disc using a nonwoven mesh of 15 μm poly(glycolic acid) (PGA) fibers coated with PLA and seeded with AF cells. This AF segment was filled with an alginate gel containing NP cells.[98] Similarly, Wan and colleagues produced a laminate structure containing bone matrix gelatin and poly(polycaprolactone triol malate).[127] Nesti *et al*. also recently described a disc-like amalgam with a hyaluronic acid NP and a PLLA nanofibrous scaffold annulus, both seeded with human MSCs and induced into IVD cell-like phenotype with a chemically defined medium containing TGF-β1.[101]

With each increasing step of complexity, it is the intent that these TE efforts more completely reproduce the complexity of the native tissue structure. Though less studied, it is a requisite, for clinical translation, that the mechanical properties of these materials and cell-formed constructs, both at the time of implantation and after a period of maturation *in vivo*, approach that of the native tissue. The benchmarks for these requisite mechanical properties have recently been reviewed in the context of disc TE.

5.524.8. Engineering Fiber-Reinforced Tissues with Nanofibrous Scaffolds

A challenge in the development of any tissue engineered construct is matching the complex mechanical properties of the native tissue, which in the case of the meniscus and the NP are anisotropic and inhomogeneous. The use of fibers allows for unique control over the directional-dependent properties of a construct and this realization has led to the development of novel nanoscale fabrication methods specific to the manufacture of fiber-reinforced TE implants. In this section, we briefly review the technology behind electrospinning and illustrate several applications that may forward this technology toward clinical relevance for the repair of these two tissues.

5.524.8.1. Electrospinning: The Base Technology

Electrospinning is a relatively simple but elegant scaffold fabrication technique involving the electrostatic charging of a polymer solution until charge repulsion overcomes surface tension, resulting in the formation of a polymer jet.[128,129] As the jet is drawn through a high-voltage gradient, drawing and stretching occurs.[130] With time, these polymeric fibers accumulate to create a random mesh with fiber diameters ranging from 50 to 1000 nm, similar in scale to collagen fibers found in native tissues[130,131] (see **Figure 4(a)**). When formed as random meshes, nanofibrous scaffolds exhibit isotropic mechanical properties reflective of their polymer composition.[132,133] Production of nanofibrous meshes via electrospinning has been carried out with numerous polymers, including biodegradable polyesters and natural biopolymers, as reviewed in Refs.[134,135] Additionally, aligned nanofibrous scaffolds with controllable anisotropic mechanical properties can be formed by focusing deposition onto a rotating drum.[132,136,137] Given the importance of ordered matrix for both meniscus and AF tissue, this technology has proven useful for directing formation of these tissues *in vitro*.

5.524.8.2. Engineering the Meniscus with Nanofibrous Scaffolds

Given the ordered composition of the meniscus (i.e., the prevailing circumferential collagen bundles that define its tensile anisotropy), an ideal scaffold would be one that can direct new tissue formation to mimic this order. Over the past several years, considerable progress has been made in the formation of engineered meniscus constructs based on aligned nanofibrous scaffolds. In early work, it was demonstrated that the aligned

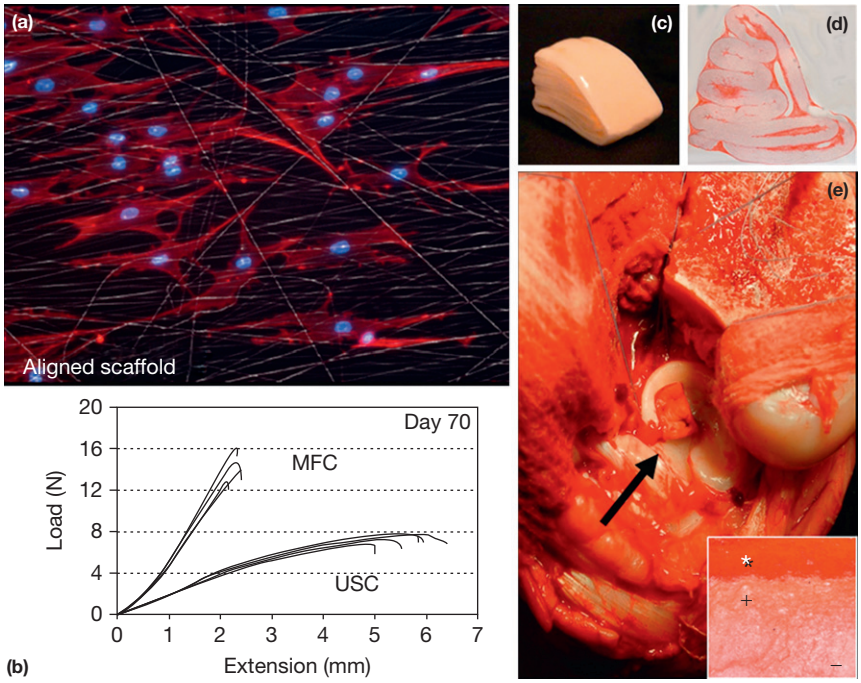

Figure 4 Anisotropic electrospun nanofibrous scaffolds for meniscus repair. (a) Immunofluorescence of aligned nanofiber scaffolds seeded with human meniscus cells. (b) Mechanical data showing an increase in modulus for meniscus cell-seeded scaffolds compared to unseeded scaffolds (USC). (c) Image of a cell-seeded scaffold fabricated into a meniscal wedge shape. (d) Picosirius red stain of the scaffold wedge following 2 weeks of culture. (e) Ovine intraoperative image of the scaffold wedge implanted into a defect created in the posterior horn of the medial meniscus (inset: 6 month Picrosirius Red stain of the junction between scaffold and native ovine meniscus (+, scaffold; *, native; scale bar: 200 μm). Reproduced from Decoons, R. M.; Shah, R. S.; Gee, A. O.; *et al. In vivo* meniscus repair with anatomic nanofibrous scaffolds: A preliminary report. 56th Annual ORS, 2010.

substrate dictates cell orientation and three-dimensional matrix deposition, and that this ECM provides enhanced functional properties in the fiber direction over long durations of *in vitro* culture[138,139] (see **Figure 4(b)**). These findings were apparent for both bovine and human meniscus fibrochondrocytes.[138,140] Improvements in scaffolding technology, for example, the inclusion of a sacrificial, pore-forming fiber population,[141] as well as combinations of different fiber populations in the same scaffold[142] have improved the ability of cells to populate these scaffolds, as well as provided for tuning of the tensile properties of the implant to match that of the native meniscus. More recently, these scaffolds have been further modified to provide the capacity to deliver growth factors and other biologic agents directly from the scaffold, further increasing their functionality upon implantation.[143] At present, one scaffold formulation, composed purely of PCL nanofibers, is undergoing evaluation in a sheep model of partial meniscus replacement. Early findings from this work show that the scaffold does not elicit any inflammatory responses, and is partially colonized by native tissue cells over a 6-month time course (see **Figure 4(e)**, inset). Ongoing work is exploring how scaffold modifications can improve cell and tissue deposition in this *in vivo* setting. In the long term, the goal of this work is to provide a fully formed, anatomically shaped scaffold that can guide meniscus regeneration through the topography of the aligned nanofibers (instructing cell and matrix organization) as well as growth factor delivery (instructing cell behavior and colonization).

5.524.8.3. Engineering the AF with Nanofibrous Scaffolds

Just as the meniscus has a defined collagenous order, so too does the AF. In the AF, this order may be considered even more complicated, in that there are lamellae of organized collagen that do not coincide with the circumferential direction, but rather alternate at ~30° with respect to this direction, and switch polarity in each layer. This hierarchical 'angle-ply' structure has important implications for the mechanical function of the disc, and is necessitated by the complex loads experienced about this joint (i.e., bending, compression, and torsion). To address this complexity, recent work from our group has used aligned nanofibrous scaffolds to produce AF constructs (see **Figure 5**). By excising the base scaffold unit at an angle from the primary fiber direction, a single ply of the AF can be formulated with a fiber direction that is not coincident with the long axis of the scaffold.[144] When these scaffolds are seeded with AF cells and MSCs, the tensile properties of the construct increase with time in culture.[145] Layering one cell-laden scaffold ply upon the other and culturing in this conjoined fashion produces mechanically viable laminates that begin to recapitulate the structural hierarchy of the native AF tissue. Indeed, such biologic laminates can match native tissue properties within 10 weeks of culture.[146] Finally, toward complete recapitulation of an entire disc, these layers can be formed concentrically to generate an angle-ply multilamellar AF region, which can then be combined with biocompatible stem cell-laden hydrogel NP-like regions. These disc-like angle-ply

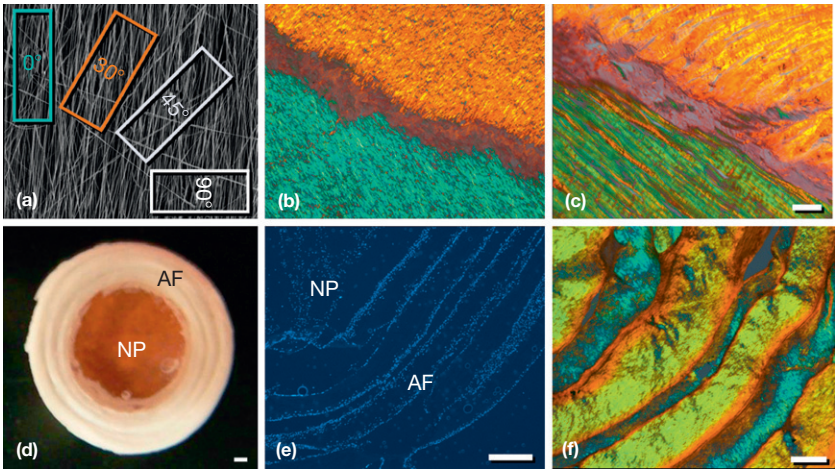

Figure 5 AF and disc tissue engineering with nanofibrous scaffolds. (a) Removal of rectangular scaffolds rotated from the prevailing fiber directions recapitulates the single lamellar fiber architecture of the AF. Reproduced from Nerurkar, N. L.; Elliott, D. M.; Mauck, R. L. *J. Orthop. Res.* **2007**, *25*, 1018–1028. (b) Formation of bilamellar constructs produces biologic laminates that direct ordered and opposing ECM deposition in adjacent layers, mimicking the angle-ply structure of the native AF (c, scale bar: 100 μm). Reproduced from Nerurkar, N. L.; Baker, B. M.; Sen, S.; Wible, E. E.; Elliott, D. M.; Mauck, R. L. *Nat. Mater.* **2009**, *8*, 986–992. Higher-order disc-like structures (d, scale bar: 1 mm) can be formed by concentric wrapping of alternating nanofibrous lamellae (AF) around a central gelatinous core (NP). Seeding with MSCs produces cell laden disc-like constructs with distributed cellular morphology representing the native disc (e, scale bar: 1 mm), with alternating angle-ply deposition of ECM. (f) Polarized light microscopy of a Picrosirius Red stained section from a disc-like construct (scale bar: 250 μm).

composites increase in mechanical properties with time in culture, and begin to approximate the full anatomy of the IVD.[102] Efforts are under way now to test these disk-like constructs *in vivo*.

5.524.9. Preclinical Models and Evaluation Tools for Engineered AF and Meniscus Products

Product development lines for tissue engineered replacements follow a similar pattern to that of traditional materials, namely a gradual evolution from cadaveric testing, through small and large animal trials, and eventually into clinical trials. As TE becomes more prominent, the outcome measures and their limitations need to be considered and optimized to reduce the iteration times during product development. For example, in meniscus applications, the most common outcome measure after meniscectomy is joint space narrowing. This is a gradual process, taking years in humans to become apparent after partial meniscectomy. Animal trials of the meniscus implants described above have outcomes related to the quality of the tissue formed within the implant, as well as the quality of the existing cartilage at up to 1 year of followup. Longer term followup is required to determine the true efficacy of these products, though this comes at a considerable expense. New methods that offer quantitative assessment of the healing meniscus may provide better guidance during this technology development phase, and shorten the time to market for these projects. For example, studies by Maher and colleagues have shown that force distribution under the meniscus can be dynamically measured using newly emerging measurement technologies (e.g., Tekscan sensors)[147,148] (see **Figure 6**). As shown, these measurements can provide important information regarding load transfer through meniscus replacement devices, both at the time of implantation as well as after a period of *in vivo* growth. Such outcomes will provide for ready optimization of the material itself, as well as the methods used to anchor it to native tissue. In addition, imaging techniques such as specialized MRI sequences adapted to visualize meniscus structure and the articular cartilage content[149,150] can be used as noninvasive tools for charting progress of implant integration and function *in vivo*. Similar concerns can be addressed for IVD replacement. Traditional measures of biomechanical function (i.e., motion segment testing[151]) are invaluable as final outcomes. Short of that, noninvasive imaging of disk height and NP and AF proteoglycan content (via MRI) can provide real-time insight into the function of the implant. In both meniscus and disc applications, however, pain is not typically measured, but is the primary concern of the patient. Most large animal models do not necessarily address this, as it is a difficult parameter to measure in a nonverbal population. Methods to address this, such as gait analysis coupled with force plate recordings, may provide additional insight into the ability of the implant to improve overall functionality, over and above simply reproducing anatomic form. Advances in these disciplines will lessen the time it takes for these tissue engineered materials to make their way to clinical application.

5.524.10. Conclusions and Future Directions

The last two decades have been characterized by an explosion in the development of biomaterial-based devices for musculoskeletal repair. In this process, the route is proceeding inexorably from metal and plastic implants toward a day when biologics will be the standard of care. This progress has been noted by the continual optimization of existing biomaterials for new applications in meniscus and AF repair, as well as by

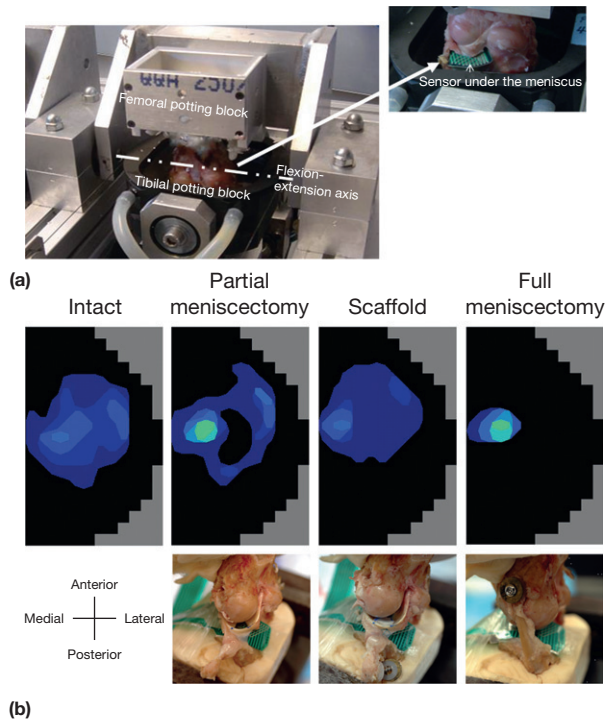

Figure 6 Quantitative preclinical assessment of engineered meniscus products. *In vitro* pressure-force mapping of ovine stifles with implanted tissue engineered meniscus scaffold candidates. (a) Modified knee joint simulator showing a potted stifle and Tekscan sensor in place (arrow). Reproduced from Cottrell, J. M.; Scholten, P.; Wanich, T.; Warren, R. F.; Wright, T. M.; Maher, S. A. *J. Biomech.* **2008**, *41*, 2324–2349. (b) From left to right, peak pressure map showing intact stifle, increased pressure concentration away from the meniscus with a partial meniscectomy, improved pressure distribution with implanted scaffold, and high concentration of pressure after full meniscectomy. Reproduced from Brophy, R. H.; Cottrell, J.; Rodeo, S. A.; Wright, T. M.; Warren, R. F.; Maher, S. A. *J. Biomed. Mater. Res. A* **2009**, *92*, 1154–1161.

considerable work in new materials and devices developed specifically for this purpose.

As history shines upon the groundbreaking work by Fernström, Nachemson, and Gluck, so too will it illuminate the biomaterial development described herein as the foundations of future biological devices. We have already started seeing traditional mechanical devices, such as total disc replacements, adopting anatomically influenced features (cf. the M6 device). As the complexities of tissue regeneration are unraveled, engineers will produce biomaterials that harness the ability of tissues to heal. One such biomaterial substrate is the electrospun nanofiber scaffold, which holds great promise in recapitulating the complex mechanical properties and function of fibrocartilaginous structures.

While some limitations have been encountered with TE based on the program of electrospinning synthetic materials, newer innovations are being developed to address these problems. Combinations of synthetic materials are being devised that will allow tuning of mechanical performance that will rival and perhaps exceed that of native tissue. Newer methods of electrospinning will enhance our ability to create materials that match the contour of meniscus anatomically. Concerns about the physiological toxicity of polymer metabolites *in vivo* may be met by the development of natural fiber scaffolds, such as collagen. Limitations in tissue colonization of these scaffolds are being addressed by presenting larger ingress routes in the scaffold and channels within the scaffolds, as well as by incorporating chemotactic moieties into both natural and synthetic fibers. Combined with the potential for geographic drug delivery, scaffolds will move closer to the reality of expeditious autocolonization and maturation.

These advances will not be limited to meniscus and AF treatments but can be generalized to all musculoskeletal tissues, as well as other organ systems. The intuition is that, as we move away from the mechanical age of orthopedics into a biological age, scientists and physicians will effectively harness the inherent healing capacity of the human body and so provide better, more durable, and more functional treatments for damage and degeneration of musculoskeletal tissues.

Acknowledgments

This work was supported with funding from the National Institutes of Health (R01 AR056624 and R01 EB02425), the Penn Center for Musculoskeletal Disorders, and the Penn Department of Orthopaedic Surgery. The authors would like to acknowledge Mr. Brendon Baker and Mr. Nandan Nerurkar for providing images of engineered meniscus and AF tissues, respectively.

References

1. Buckwalter, J. A.; Einhorn, T. A.; O'Keefe, R. J. American Academy of Orthopaedic Surgeons, *Orthopaedic Basic Science: Foundations of Clinical Practice*; American Academy of Orthopaedic Surgeons: Rosemont, IL, 2007.
2. Mow, V. C.; Ratcliffe, A.; Chern, K. Y.; Kelly, M. A. In *Knee Meniscus: Basic and Clinical Foundations*; Mow, V. C., Arnoczky, S. P., Jackson, D. W., Eds.; Raven Press, Ltd: New York, 1992.
3. Scott, J. E.; Bosworth, T. R.; Cribb, A. M.; Taylor, J. R. *J. Anat.* **1994**, *184*(Pt 1), 73–82.
4. Inerot, S.; Axelsson, I. *Connect. Tissue Res.* **1991**, *26*, 47–63.
5. O'Connor, B. L. *Am. J. Anat.* **1976**, *147*, 407–417.
6. Eyre, D. R.; Wu, J. J. *FEBS Lett.* **1983**, *158*, 265–270.
7. McDevitt, C. A.; Webber, R. J. *Clin. Orthop. Relat. Res.* **1990**, 8–18.
8. Fithian, D. C.; Kelly, M. A.; Mow, V. C. *Clin. Orthop.* **1990**, 19–31.
9. Adams, M. E.; Hukins, D. W. L. In *Knee Meniscus: Basic and Clinical Foundations*; Mow, V. C., Arnoczky, S. P., Jackson, D. W., Eds.; Raven Press, Ltd: New York, 1992.
10. Arnoczky, S. P. In *Knee Meniscus: Basic and Clinical Foundations*; Mow, V. C., Arnoczky, S. P., Jackson, D. W., Eds.; Raven Press, Ltd: New York, 1992.
11. Arnoczky, S. P.; Warren, R. F. *Am. J. Sports Med.* **1982**, *10*, 90–95.
12. Arnoczky, S. P.; Adams, M. E.; DeHaven, K. E.; Eyre, D. R.; Mow, V. C. In *Injury and Repair of the Musculoskeletal Soft Tissues*; Woo, S. L., Buckwalter, J. A., Eds.; American Academy of Orthopeadic Surgeons: Park Ridge, IL, 1988.
13. Rath, E.; Richmond, J. C. *Br. J. Sports Med.* **2000**, *34*, 252–257.
14. Hellio Le Graverand, M. P.; Ou, Y.; Schield-Yee, T.; *et al. J. Anat.* **2001**, *198*, 525–535.
15. Upton, M. L.; Chen, J.; Setton, L. A. *J. Orthop. Res.* **2006**, *24*, 1562–1570.
16. Bullough, P. G.; Munuera, L.; Murphy, J.; Weinstein, A. M. *J. Bone Joint Surg. Br.* **1970**, *52*, 564–567.
17. Setton, L. A.; Guilak, F.; Hsu, E. W.; Vail, T. P. *Clin. Orthop.* **1999**, S254–S272.
18. Bursac, P.; Arnoczky, S.; York, A. *Biorheology* **2009**, *46*, 227–237.
19. Bursac, P.; York, A.; Kuznia, P.; Brown, L. M.; Arnoczky, S. P. *Am. J. Sports Med.* **2009**, *37*, 884–889.
20. Proctor, C. S.; Schmidt, M. B.; Whipple, R. R.; Kelly, M. A.; Mow, V. C. *J. Orthop. Res.* **1989**, *7*, 771–782.
21. Tissakht, M.; Ahmed, A. M. *J. Biomech.* **1995**, *28*, 411–422.

22. Sweigart, M. A.; Zhu, C. F.; Burt, D. M.; *et al*. *Ann. Biomed. Eng.* **2004**, *32*, 1569–1579.
23. Ghosh, P.; Taylor, T. K. *Clin. Orthop. Relat. Res.* **1987**, 52–63.
24. Walker, P. S.; Erkman, M. J. *Clin. Orthop. Relat. Res.* **1975**, 184–192.
25. Levy, I. M.; Torzilli, P. A.; Gould, J. D.; Warren, R. F. *J. Bone Joint Surg. Am.* **1989**, *71*, 401–406.
26. Ahmed, A. M. In *Knee Meniscus: Basic and Clinical Foundations*; Mow, V. C., Arnoczky, S. P., Jackson, D. W., Eds.; Raven Press, Ltd: New York, 1992.
27. Ahmed, A. M.; Burke, D. L. *J. Biomech. Eng.* **1983**, *105*, 216–225.
28. Brown, T. D.; Shaw, D. T. *J. Orthop. Res.* **1984**, *2*, 190–199.
29. Huberti, H. H.; Hayes, W. C. *J. Bone Joint Surg. Am.* **1984**, *66*, 715–724.
30. Manouel, M.; Pearlman, H. S.; Belakhlef, A.; Brown, T. D. *J. Biomech.* **1992**, *25*, 627–635.
31. Seedhom, B. B. *Physiotherapy* **1976**, *62*, 223.
32. Richards, C. J.; Gatt, C. J.; Langrana, N.; Calderon, R. *Trans. Orthop. Res. Soc.* **2003**, *28*, 649.
33. Uezaki, N.; Kobayashi, A.; Matsushige, K. *J. Biomech.* **1979**, *12*, 65–73.
34. Nerurkar, N. L.; Elliott, D. M.; Mauck, R. L. *J. Biomech.* **2010**, *43*(6), 1017–1030.
35. Cassidy, J. J.; Hiltner, A.; Baer, E. *Connect. Tissue Res.* **1989**, *23*, 75–88.
36. Marchand, F.; Ahmed, A. M. *Spine* **1990**, *15*, 402–410.
37. Acaroglu, E. R.; Iatridis, J. C.; Setton, L. A.; Foster, R. J.; Mow, V. C.; Weidenbaum, M. *Spine* **1995**, *20*, 2690–2701.
38. Ebara, S.; Iatridis, J. C.; Setton, L. A.; Foster, R. J.; Mow, V. C.; Weidenbaum, M. *Spine* **1996**, *21*, 452–461.
39. Elliott, D. M.; Setton, L. A. *J. Biomech. Eng.* **2001**, *123*, 256–263.
40. Fujita, Y.; Duncan, N. A.; Lotz, J. *J. Orthop. Res.* **1997**, *15*, 814–819.
41. Guerin, H. A.; Elliott, D. M. *J. Biomech.* **2006**, *39*, 1410–1418.
42. Eyre, D. R. *Int. Rev. Connect. Tissue Res.* **1979**, *8*, 227–291.
43. Oegema, T. R., Jr. *Clin. Sports Med.* **1993**, *12*, 419–439.
44. Baer, A. E.; Setton, L. A. *J. Biomech. Eng.* **2000**, *122*, 245–251.
45. Chou, A. I.; Bansal, A.; Miller, G. J.; Nicoll, S. B. *Spine* **2006**, *31*, 1875–1881.
46. Horner, H. A.; Roberts, S.; Bielby, R. C.; Menage, J.; Evans, H.; Urban, J. P. G. *Spine* **2002**, *27*, 1018–1028.
47. Trout, J. J.; Buckwalter, J. A.; Moore, K. C. *Anat. Rec.* **1982**, *204*, 307–314.
48. Wang, J. Y.; Baer, A. E.; Kraus, V. B.; Setton, L. A. *Spine* **2001**, *26*, 1747–1751; discussion 1752.
49. Greis, P. E.; Bardana, D. D.; Holmstrom, M. C.; Burks, R. T. *J. Am. Acad. Orthop. Surg.* **2002**, *10*, 168–176.
50. Hede, A.; Hempel-Poulsen, S.; Jensen, J. S. *J. Bone Joint Surg. Am.* **1990**, *72*, 550–552.
51. Nielsen, A. B.; Yde, J. *J. Trauma* **1991**, *31*, 1644–1648.
52. Renstrom, P.; Johnson, R. J. *Clin. Sports Med.* **1990**, *9*, 523–538.
53. Venkatachalam, S.; Godsiff, S. P.; Harding, M. L. *Knee* **2001**, *8*, 129–133.
54. DeHaven, K. E. *Am. J. Sports Med.* **1999**, *27*, 242–250.
55. Rodeo, S. A. *Instr. Course Lect.* **2000**, *49*, 195–206.
56. Meredith, D. S.; Losina, E.; Mahomed, N. N.; Wright, J.; Katz, J. N. *Arthroscopy* **2005**, *21*, 211–223.
57. Freedman, K. B.; Nho, S. J.; Cole, B. J. *Arthroscopy* **2003**, *19*, 794–798.
58. Okuda, K.; Ochi, M.; Shu, N.; Uchio, Y. *Arthroscopy* **1999**, *15*, 281–286.
59. Elliott, D. M.; Jones, R., III; Setton, L. A.; Scully, S. P.; Vail, T. P.; Guilak, F. *Knee Surg. Sports Traumatol. Arthrosc.* **2002**, *10*, 109–118.
60. Garrett, J. C. In *Knee Surgery, Current Practice*; Aichroth, P. M., Canon, W. D., Eds.; Raven Press, Ltd: New York, 1992.
61. Jackson, D. W.; Simon, T. M. In *Knee Meniscus: Basic and Clinical Foundations*; Mow, V. C., Arnoczky, S. P., Jackson, D. W., Eds.; Raven Press, Ltd: New York, 1992.
62. Mora, G.; Alvarez, E.; Ripalda, P.; Forriol, F. *Arthroscopy* **2003**, *19*, 833–841.
63. Wyland, D. J.; Guilak, F.; Elliott, D. M.; Setton, L. A.; Vail, T. P. *J. Orthop. Res.* **2002**, *20*, 996–1002.
64. Rath, E.; Richmond, J. C.; Yassir, W.; Albright, J. D.; Gundogan, F. *Am. J. Sports Med.* **2001**, *29*, 410–414.
65. Andersson, G. B. *Lancet* **1999**, *354*, 581–585.
66. Kang, H. K.; Mahan, C. M.; Lee, K. Y.; Magee, C. A.; Murphy, F. M. *J. Occup. Environ. Med.* **2000**, *42*, 491–501.
67. Vaccaro, A. R. *Spine: Core Knowledge in Orthopaedics*; Mosby: St Louis, 2005.
68. Fabrizi, A. P.; Zucchelli, M. *Acta Neurochir. Suppl.* **2005**, *92*, 107–109.
69. Lee, C. K.; Langrana, N. A. *Spine (Phila Pa 1976)* **1984**, *9*, 574–581.
70. Matsumoto, M.; Okada, E.; Ichihara, D.; *et al*. *Spine (Phila Pa 1976)* **2010**, *35*, 36–43.
71. Weinhoffer, S. L.; Guyer, R. D.; Herbert, M.; Griffith, S. L. *Spine (Phila Pa 1976)* **1995**, *20*, 526–531.
72. Luk, K. D.; Ruan, D. K.; Chow, D. H.; Leong, J. C. *Clin. Orthop. Relat. Res.* **1997**, *337*, 13–26.
73. Luk, K. D.; Ruan, D. K.; Lu, D. S.; Fei, Z. Q. *Spine (Phila Pa 1976)* **2003**, *28*, 864–869; discussion 870.
74. Matsuzaki, H.; Wakabayashi, K.; Ishihara, K.; Ishikawa, H.; Ohkawa, A. *Spine (Phila Pa 1976)* **1996**, *21*, 178–183.
75. Ruan, D.; He, Q.; Ding, Y.; Hou, L.; Li, J.; Luk, K. D. *Lancet* **2007**, *369*, 993–999.
76. Cook, J. L.; Fox, D. B.; Malaviya, P.; *et al*. *Am. J. Sports Med.* **2006**, *34*, 32–42.
77. Rodkey, W. G.; DeHaven, K. E.; Montgomery, W. H., III; *et al*. *J. Bone Joint Surg. Am.* **2008**, *90*, 1413–1426.
78. van Tienen, T. G.; Hannink, G.; Buma, P. *Clin. Sports Med.* **2009**, *28*, 143–156.
79. Cook, J. L.; Fox, D. B. *Am. J. Sports Med.* **2007**, *35*, 1877–1887.
80. Kelly, B. T.; Robertson, W.; Potter, H. G.; *et al*. *Am. J. Sports Med.* **2007**, *35*, 43–52.
81. Ballyns, J. J.; Gleghorn, J. P.; Niebrzydowski, V.; *et al*. *Tissue Eng. A* **2008**, *14*, 1195–1202.
82. Tienen, T. G.; Heijkants, R. G.; de Groot, J. H.; *et al*. *J. Biomed. Mater. Res. Part B Appl. Biomater.* **2006**, *76*, 389–396.
83. Decoons, R. M.; Shah, R. S.; Gee, A. O.; *et al*. In vivo *Meniscus Repair with Anatomic Nanofibrous Scaffolds: A Preliminary Report*. 56th Annual ORS 2010.
84. Hedman, T. P.; Saito, H.; Vo, C.; Chuang, S. Y. *Spine (Phila Pa 1976)* **2006**, *31*, E480–E485.
85. Melrose, J.; Smith, S. M.; Little, C. B.; Moore, R. J.; Vernon-Roberts, B.; Fraser, R. D. *Eur. Spine J.* **2008**, *17*, 1131–1148.
86. Zhu, Q.; Larson, C. R.; Sjovold, S. G.; *et al*. *Spine (Phila Pa 1976)* **2007**, *32*, 55–62.
87. Sengupta, D. K. *Orthop. Clin. North Am.* **2004**, *35*, 43–56.
88. Schwarzenbach, O.; Berlemann, U.; Stoll, T. M.; Dubois, G. *Orthop. Clin. North Am.* **2005**, *36*, 363–372.
89. Coric, D.; Mummaneni, P. V. *J. Neurosurg. Spine* **2008**, *8*, 115–120.
90. Kettler, A.; Kaps, H. P.; Haegele, B.; Wilke, H. J. *SAS J.* **2007**, *1*, 125–130.
91. Lau, S.; Lam, K. S. *Curr. Orthop.* **2007**, *21*, 25–39.
92. Ahrens, M.; Tsantrizos, A.; Donkersloot, P.; *et al*. *Spine (Phila Pa 1976)* **2009**, *34*, 1376–1384.
93. Bertagnoli, R.; Karg, A.; Voigt, S. *Orthop. Clin. North Am.* **2005**, *36*, 341–347.
94. Carl, A.; Ledet, E.; Yuan, H.; Sharan, A. *Spine J.* **2004**, *4*, 325S–329S.
95. Sato, M.; Asazuma, T.; Ishihara, M.; *et al*. *J. Biomed. Mater. Res. A* **2003**, *64A*, 249–256.
96. Shao, X.; Hunter, C. J. *J. Biomed. Mater. Res. A* **2007**, *82*, 701–710.
97. Bowles, R. D.; Williams, R. M.; Zipfel, W. R.; Bonassar, L. J. *Tissue Eng. A* **2010**, *16*, 1339–1348.
98. Mizuno, H.; Roy, A. K.; Zaporojan, V.; Vacanti, C. A.; Ueda, M.; Bonassar, L. J. *Biomaterials* **2006**, *27*, 362–370.
99. Mizuno, H.; Roy, A. K.; Zaporojan, V.; Vacanti, C. A.; Ueda, M.; Bonassar, L. J. *Spine (Phila Pa 1976)* **2004**, *29*(12), 1290–1297.
100. Wilke, H. J.; Heuer, F.; Neidlinger-Wilke, C.; Claes, L. *Eur. Spine J.* **2006**, *15*(Suppl 3), S433–S438.
101. Nesti, L. J.; Li, W. J.; Shanti, R. M.; *et al*. *Tissue Eng. A* **2008**, *14*, 1527–1537.
102. Nerurkar, N. L.; Sen, S.; Huang, A. H.; Elliott, D. M.; Mauck, R. L. *Spine (Phila Pa 1976)* **2010**, *35*(8), 867–873.
103. Lazebnik, M.; Glatt, P.; Singh, M.; Zhao, L.; Berkland, C.; Detamore, M. S. *A Biomimetic Approach to the Intervertebral Disc Regeneration*. 55th Annual ORS 2009; Paper no. 310.
104. King, D. J.; Matava, M. J. *Oper. Tech. Sports Med.* **2004**, *12*, 161–169.
105. Arnoczky, S. P.; Lavagnino, M. *Am. J. Sports Med.* **2001**, *29*, 118–123.
106. Barber, F. A.; Herbert, M. A. *Arthroscopy* **2000**, *16*, 613–618.
107. Durselen, L.; Schneider, J.; Galler, M.; Claes, L. E.; Bauer, G. *Clin. Biomech. (Bristol, Avon)* **2003**, *18*, 44–49.
108. Farng, E.; Sherman, O. *Arthroscopy* **2004**, *20*, 273–286.
109. Post, W. R.; Akers, S. R.; Kish, V. *Arthroscopy* **1997**, *13*, 731–736.
110. Lavagnino, M.; Arnoczky, S. *Trans. Orthop. Res. Soc.* **2000**, *25*, 795.
111. Seil, R.; Rupp, S.; Kohn, D. M. *Arthroscopy* **2000**, *16*, 505–510.
112. Langer, R.; Vacanti, J. P. *Science* **1993**, *260*, 920–926.
113. Stone, K. R.; Steadman, J. R.; Rodkey, W. G.; Li, S. T. *J. Bone Joint Surg. Am.* **1997**, *79*, 1770–1777.
114. Cook, J. L.; Fox, D. B.; Malaviya, P.; *et al*. *J. Knee Surg.* **2006**, *19*, 159–167.
115. van Minnen, B.; van Leeuwen, M. B.; Kors, G.; Zuidema, J.; van Kooten, T. G.; Bos, R. R. *J. Biomed. Mater. Res. A* **2008**, *85*, 972–982.
116. Chiari, C.; Koller, U.; Dorotka, R.; *et al*. *Osteoarthr. Cartil.* **2006**, *14*, 1056–1065.
117. Tienen, T. G.; Heijkants, R. G.; de Groot, J. H.; *et al*. *Am. J. Sports Med.* **2006**, *34*, 64–71.
118. Sato, M.; Kikuchi, M.; Ishihara, M.; *et al*. *Med. Biol. Eng. Comput.* **2003**, *41*, 365–371.

119. Sato, M.; Asazuma, T.; Ishihara, M.; *et al*. *Spine* **2003**, *28*, 548–553.
120. Cloyd, J. M.; Malhotra, N. R.; Weng, L.; Chen, W.; Mauck, R. L.; Elliott, D. M. *Eur. Spine J*. **2007**, *16*, 1892–1898.
121. Reza, A. T.; Nicoll, S. B. *Acta Biomater*. **2010**, *6*, 179–186.
122. Chou, A. I.; Akintoye, S. O.; Nicoll, S. B. *Osteoarthr. Cartil*. **2009**, *17*, 1377–1384.
123. Alini, M.; Li, W.; Markovic, P.; Aebi, M.; Spiro, R. C.; Roughley, P. J. *Spine* **2003**, *28*, 446–453.
124. Seguin, C. A.; Grynpas, M. D.; Pilliar, R. M.; Waldman, S. D.; Kandel, R. A. *Spine (Phila Pa 1976)* **2004**, *29*, 1299–1306; discussion 1306–1307.
125. Chang, G.; Kim, H. J.; Kaplan, D.; Vunjak-Novakovic, G.; Kandel, R. A. *Eur. Spine J*. **2007**, *16*, 1848–1857.
126. Chang, G.; Kim, H. J.; Vunjak-Novakovic, G.; Kaplan, D. L.; Kandel, R. *J. Biomed. Mater. Res. A* **2010**, *92*, 43–51.
127. Wan, Y.; Feng, G.; Shen, F. H.; Laurencin, C. T.; Li, X. *Biomaterials* **2008**, *29*, 643–652.
128. Reneker, D. H.; Chun, I. *Nanotechnol*. **1996**, *7*, 216–223.
129. Shin, Y. M.; Hohman, M. M.; Brenner, M. P.; Rutledge, G. C. *Polymer* **2001**, *42*, 9955–9967.
130. Deitzel, J. M.; Kleinmeyer, J.; Harris, D.; Becktan, N. C. *Polymer* **2001**, *42*, 261–272.
131. Riesle, J.; Hollander, A. P.; Langer, R.; Freed, L. E.; Vunjak-Novakovic, G. *J. Cell. Biochem.* **1998**, *71*, 313–327.
132. Li, W. J.; Cooper, J. A., Jr.; Mauck, R. L.; Tuan, R. S. *Acta Biomater.* **2006**, *2*, 377–385.
133. Tan, E. P.; Ng, S. Y.; Lim, C. T. *Biomaterials* **2005**, *26*, 1453–1456.
134. Li, W. J.; Mauck, R. L.; Tuan, R. S. *J. Biomed. Nanotechnol*. **2005**, *1*, 259–275.
135. Mauck, R. L.; Baker, B. M.; Nerurkar, N. L.; *et al*. *Tissue Eng. Part B Rev*. **2009**, *15*(2), 171–193.
136. Li, D.; Xia, Y. N. *Adv. Mater*. **2004**, *16*, 1151–1170.
137. Mauck, R. L.; Li, W. J.; Yuan, X.; Tuan, R. S. In Proceedings of the 51st Annual Orthopaedic Research Society Meeting, Washington, DC, 2005; Vol. 30, p 1722.
138. Baker, B. M.; Mauck, R. L. *Biomaterials* **2007**, *28*, 1967–1977.
139. Li, W. J.; Mauck, R. L.; Cooper, J. A.; Yuan, X.; Tuan, R. S. *J. Biomech*. **2007**, *40*, 1686–1693.
140. Baker, B. M.; Nathan, A. S.; Huffman, G. R.; Mauck, R. L. *Osteoarthr. Cartil*. **2009**, *17*, 336–345.
141. Baker, B. M.; Gee, A. O.; Metter, R. B.; *et al*. *Biomaterials* **2008**, *29*, 2348–2358.
142. Baker, B. M.; Nerurkar, N. L.; Burdick, J. A.; Elliott, D. M.; Mauck, R. L. *J. Biomech. Eng*. **2009**, *131*, 101012.
143. Ionescu, L. C.; Lee, G. C.; Sennett, B. J.; Burdick, J. A.; Mauck, R. L. *Biomaterials* **2010**, *31*(4), 4113–4120.
144. Nerurkar, N. L.; Elliott, D. M.; Mauck, R. L. *J. Orthop. Res*. **2007**, *25*, 1018–1028.
145. Nerurkar, N. L.; Mauck, R. L.; Elliott, D. M. *Spine (Phila Pa 1976)* **2008**, *33*, 2691–2701.
146. Nerurkar, N. L.; Baker, B. M.; Sen, S.; Wible, E. E.; Elliott, D. M.; Mauck, R. L. *Nat. Mater*. **2009**, *8*, 986–992.
147. Brophy, R. H.; Cottrell, J.; Rodeo, S. A.; Wright, T. M.; Warren, R. F.; Maher, S. A. *J. Biomed. Mater. Res. A* **2009**, *92*, 1154–1161.
148. Cottrell, J. M.; Scholten, P.; Wanich, T.; Warren, R. F.; Wright, T. M.; Maher, S. A. *J. Biomech*. **2008**, *41*, 2324–2329.
149. Borthakur, A.; Mellon, E.; Niyogi, S.; Witschey, W.; Kneeland, J. B.; Reddy, R. *NMR Biomed*. **2006**, *19*, 781–821.
150. Koff, M. F.; Potter, H. G. *Radiol. Clin. North Am.* **2009**, *47*, 495–504.
151. Boxberger, J. I.; Orlansky, A. S.; Sen, S.; Elliott, D. M. *J. Biomech*. **2009**, *42*, 1941–1946.

5.525. Tissue Engineering Approaches to Regeneration of Anterior Cruciate Ligament

H Liu, Beihang University, Beijing, China
J C H Goh, National University of Singapore, Singapore

© 2011 Published by Elsevier Ltd.

5.525.1.	**Introduction**	333
5.525.1.1.	Structure and Function of the ACL	333
5.525.1.2.	Limitations in Traditional Implantable Solutions	334
5.525.1.3.	A New Option: Tissue Engineering	334
5.525.2.	**Biomaterials for Ligament Tissue Engineering**	334
5.525.2.1.	Synthetic Biomaterials	334
5.525.2.2.	Natural Biomaterials	335
5.525.2.3.	Silk Biomaterials	336
5.525.3.	**Scaffold Design**	336
5.525.3.1.	Scaffolds Design Criteria	336
5.525.3.2.	Braided Scaffolds	337
5.525.3.3.	Knitted Scaffolds	337
5.525.4.	**Cell Source**	338
5.525.5.	**Bioreactor System**	338
5.525.6.	**Local Delivery of Growth Factors**	340
5.525.7.	**Animal Models for ACL Regeneration**	340
5.525.8.	**Ligament–Bone Interface**	341
5.525.9.	**Summary**	342
References		342

Abbreviations

ACL	Anterior cruciate ligament
ACLFs	ACL fibroblasts
bFGF	Basic fibroblast growth factor
bMSCs	Bone marrow-derived mesenchymal stem cells
ECM	Extracellular matrix
EGF	Epidermal growth factor
IGF	Insulin-like growth factor
MCL	Medial collateral ligament
NDGA	Dicatechol nordihydroguaiaretic acid
PDGF	Platelet-derived growth factor
PLGA	Polylactide-*co*-glycolide
PLGA	Poly-L-lactic acid
PTFE	Polytetrafluoroethylene
RT-PCR	Real-time reverse transcriptase-polymerase chain reaction
SEM	Scanning electronic microscopy
SIS	Small intestinal submucosa
TCP	Tissue culture plate
TGF	Transforming growth factor
VEGF	Vascular endothelial cell growth factor
3D	Three dimensional

5.525.1. Introduction

The anterior cruciate ligament (ACL) plays an essential role in the knee joint, providing stability as well as guiding joint motion. It connects the femur to the tibia and is completely enveloped by the synovium. The primary function of the ACL is mechanical in nature. It is to limit excessive anterior translation and twisting of the tibia with respect to the femur. Its mechanical properties are well suited to its function. However, the ACL is the most frequently damaged ligament in the knee joint. Among the general population of the United States, the annual incidence of acute ACL disruptions has been estimated at 1 in 3000 and as many as 95 000 ACL reconstructions are carried out each year.[1,2] The seriousness of ACL injury is exacerbated by the fact that the ACL exhibits a very poor capacity for healing. Currently, the 'gold standard' treatment is autograft reconstruction; however, it cannot completely restore knee joint function. Furthermore, it may lead to donor site morbidity, causing pain and tendonitis as well as long recovery periods and muscle atrophy.[3–6]

5.525.1.1. Structure and Function of the ACL

In order to reconstruct a damaged ACL, it is necessary to understand the anatomy, orientation, and attachment sites of the normal ligament. The human ACL has a length of between 27 and 32 mm and a cross-sectional area of between 44.4 and 57.5 mm^2.[7] The ACL is part of the bone–ligament–bone

complex that includes bone, fibrocartilage, and a soft-tissue midsubstance, consisting largely of type I collagen, a sheath for protection, vascularity for nourishment, and nerves for proprioception. The ACL attaches the femur and tibia via collagen fibers that integrate to bone structures at both ends. The abrupt change from flexible ligament tissue to rigid bone is mediated by a transitional zone of fibrocartilage, which allows a gradual change in even distribution of stress.[8] The normal ACL comprises parallel collagen bundles, which are cross-linked to one another. The collagen fibers, cross-linked to one another, give high tensile strength. As they withstand cyclic loads of ~300 N for about 1.5 million times per year, it is important for fibroblasts to maintain collagen fibers in good condition dynamically.[9] It is interesting to note that cell densities in ligaments are generally low. The fibroblasts in the ACL are attached to individual collagen bundles and have elongated morphology along the longitudinal axis.[9] Fibroblasts not only synthesize fibrillar collagen but also enzymatically break down and remove old collagen as part of a renewal process. The collagen molecule is a glycine-rich triple helix. The molecules assemble sequentially into microfibrils, subfibrils, and fibrils (20–150 nm in diameter) before forming fibers (1–20 μm in diameter) with cross-links to one another and further make up a subfascicular unit (100–250 μm in diameter). These subfascicular units are surrounded by a loose band of connective tissue known as the endotenon. Three to twenty subfasciculi subsequently form a fasciculus (from 250 μm to several millimeters in diameter), which is surrounded by an epitenon. This interfascicular connective tissue also supports the neurovascular elements of the ligament.[8] These individual fascicles are either oriented in a spiral fashion around the long axis of the ligament or they pass directly from the femur to the tibial attachment. The entire continuum of fascicles is surrounded by the paratenon, a connective tissue cover similar to, but much thicker than, the epitenon.[10]

5.525.1.2. Limitations in Traditional Implantable Solutions

In the regeneration of the ACL, the graft must be positioned so as to minimize the change in length within the ligament, as the knee is flexed and extended.[11] Traditionally, ACL injuries have been treated with biological grafts, autografts, or allografts.[12] Autograft material for ACL repair is usually taken from the patellar tendon, hamstring tendon, or quadriceps tendon of the patient. The patella and hamstring tendons have been the autografts of choice for most surgeons. The patellar tendon graft material is usually removed with a piece of bone from the patella and from the insertion point at the tibia. The 'bone–patellar bone' graft is then fed through a tunnel drilled through the tibia, drawn across the knee, and anchored into a tunnel drilled through the femur. Allografts are tissues such as the patellar tendon, hamstring tendon, and Achilles tendon, obtained from cadavers.[12] The benefits of using allografts include the elimination of a second surgery for tissue harvest. There is also no limit to the supply of graft tissue as experienced with autografts. Both autografts and allografts possess good initial mechanical strength and promote cell proliferation and new tissue growth. However, both these options suffer from a number of disadvantages. For example, autografts have limited availability and require additional surgery for tissue harvest, which may cause donor site morbidity. Allografts could potentially transmit disease, cause bacterial infection, elicit an unfavorable immunogenic response from the host, and cannot be sterilized without altering the mechanical properties of the tissue.[13]

5.525.1.3. A New Option: Tissue Engineering

Despite significant progress in understanding ACL anatomy, structure, biomechanics, and healing, there is still no biological graft or prosthesis ideally suited for ACL regeneration. Clearly, such a complex structure is very difficult to replicate using traditional biomaterial approaches and/or biological grafts. Tissue engineering offers the possibility of creating functionally engineered tissues to treat ACL injuries without many of the undesirable side effects associated with current reconstructive options. The advantage of a tissue-engineered scaffold over other treatment methods lies in its interdisciplinary approach to tissue repair. Tissue engineering is the application of biological, chemical, and engineering principles toward the development of substitutes for the repair or restoration of tissue function.[14] The components to tissue engineering are as follows: three-dimensional (3D) porous scaffolds that promote tissue regeneration, isolated cells that have been expanded *in vitro*, and bioreactors and growth factors. A combination of all or any of these components may be used. The fundamental basis of ligament tissue engineering is the development of a biocompatible, resorbable, cell-seeded scaffold that can provide functional support while gradually transferring the mechanical loads borne by the scaffold to neoligament tissue.

5.525.2. Biomaterials for Ligament Tissue Engineering

5.525.2.1. Synthetic Biomaterials

Synthetic biodegradable polymers are biocompatible and commercially available. They are appealing for this application because their critical properties, such as strength, strength retention, and degradation rate, can be customized during processing.

It is well known that polylactide-*co*-glycolide (PLGA, 10:90) is commonly used as surgical suture material. In our previous studies, we studied the adhesion, proliferation, and morphology of rabbit ACL cells and bone marrow-derived mesenchymal stem cells (BMSCs) on several synthetic biodegradable polymeric films. From the results, high molecular weight PLGA (50:50, 75:25) was shown to be better in allowing BMSCs and ACL cell attachment and proliferation.[15] As for a 3D scaffold, knitted scaffolds of poly-L-lactic acid (PLLA) yarns and copolymeric yarns of PLLA and PLGA were fabricated and characterized.[16–18] The knitted scaffolds were immersed in a medium for 20 weeks, and changes in mechanical properties, as well as mass loss, molecular weight, and pH value change in the medium, were evaluated at different time points. Results showed that the knitted scaffolds had 44% porosity. There was no significant pH value change during degradation, while there was obvious mass loss during the initial 4 weeks, as well as smooth molecular weight drop of PLLA. PLGA degraded at a high rate, while PLLA kept its integrity for at least 20 weeks. Young's modulus increased while tensile

strength and strain at break decreased with degradation time; however, all of them could maintain the basic requirements for ACL regeneration. Moreover, knitted PLGA scaffolds seeded with BMSCs and wrapped with fascia have been used to reconstruct the ACL in a rabbit model.[16–18] However, the *in vivo* results of tissue engineering using these synthetic materials demonstrated rapid degradation rates and inferior mechanical properties compared with the normal tissues.

5.525.2.2. Natural Biomaterials

Collagen is the major structural component of connective tissues, especially the tendon and ligament; therefore, it is reasonable to reconstruct the ACL with it.[19,20] Collagen is widely used in cell culture studies, as fibroblasts attach, proliferate, and secrete matrix extremely well on collagen scaffolds. Collagen has numerous biological functions, serving as the natural scaffold supporting cell attachment, proliferation, and matrix synthesis within the body.[21–23] Highly purified type I collagen, which is commercially available, has been used either in gel form or bundles of parallel fibers.

Collagen has been the material of choice because of its ability to support the growth of ligament fibroblasts under static tension. Previous studies had used cross-linked collagen fibers seeded with human BMSCs and had shown that fibrous collagen supported cell attachment, spreading, and fiber coverage with extracellular matrix (ECM) deposition. After 1 day of culture, the cells formed focal contacts, adopted a spindle-like morphology, and aligned along the scaffold fibers. After 3 days of culture, a smooth cell sheet was formed, and the number of cells increased with time in culture. Unfortunately, the capacity of the engineered construct to support mechanical loading decreased with time in culture, and as a result, the scaffold fibers could not impart repeatable stresses to the attached BMSCs as previously observed.[24–26] The poor mechanical integrity of the fibers created further concerns regarding anchoring of the fibers both *in vitro* (in the bioreactor) and *in vivo* (in the knee). The mechanical deficiencies, the bioburden associated with the use of bovine collagen products, and leaching of chemical cross-linking agents, combined with the poor mechanical integrity of the collagen fibers, prompted the search for improved biomaterials.[27]

Methods for stabilizing collagen-based materials with catechol containing monomers were developed to produce fibers with mechanical properties in tension comparable to those of normal tissues.[28] Fibers produced from pepsin-solubilized, bovine tendon type I collagen were polymerized with the dicatechol nordihydroguaiaretic acid (NDGA). Polymerization was based on the chemical oxidation of the constituent *o*-catechols to reactive *o*-quinone functionalities. NDGA caused a dose-dependent increase in the tensile strength and stiffness of the type I collagen fibers. A second treatment with NDGA improved the tensile properties significantly. Comparison of the effects of NDGA with those of biologically relevant monocatechols indicated that the bicatechol functionality of NDGA was responsible for generation of the superior tensile properties. Elimination of unreacted intermediates from the treated fibers with ethanol increased the effectiveness of the cross-linking process while simultaneously sterilizing the material. Catalyzing oxidation by saturating the reaction buffer with oxygen increased the effectiveness of polymerization and the resulting tensile properties of the treated fibers. The ultimate tensile strength of the optimized NDGA-treated fibers averaged 90 MPa; the elastic modulus of these fibers averaged 580 MPa. Both values are comparable to native tendon and ligament. The material properties of the NDGA cross-linked fibers exceed the properties of collagen fibers treated with other cross-linking strategies such as glutaraldehyde and carbodiimide. These results indicate that NDGA cross-linking may provide a viable approach to stabilizing collagenous materials for use in repair of ruptured, lacerated, or surgically transected tendons and ligament, as well as other biomaterial constructs for surgical repair of musculoskeletal injuries and disease.

Sandusky *et al.*[29,30] have shown that acellular resorbable scaffold material derived from the small intestinal submucosa (SIS) can be rapidly resorbed. Furthermore, it is capable of supporting early and abundant new blood vessel growth, and several studies had concluded that it can serve as a template for the constructive remodeling of several body tissues, including musculoskeletal structures,[31–33] for example, skin[34] and blood vessels.[35] The SIS material consists of naturally occurring ECM, which has been shown to be rich in components that support angiogenesis, such as fibronectin, glycosaminoglycans, several kinds of collagens including types I, III, IV, V, and VI, and angiogenic growth factors, for example, basic fibroblast growth factor-2 (FGF-2) and vascular endothelial cell growth factor (VEGF).[36,37] Badylak *et al.* evaluated the tissue response to the SIS when this material was used to repair an experimentally induced Achilles tendon defect in a dog model.[32] A unilateral 1.5-cm segmental defect of the Achilles tendon was surgically created in 20 dogs, which was subsequently repaired with the acellular connective tissue derived from porcine SIS. Results showed that the SIS remodeled neotendons tend to be stronger than the musculotendinous origin or the bony insertion (>1000 N) by 12 weeks after surgery and consisted of organized collagen-rich connective tissue similar to the contralateral normal tendons. Immunohistochemical studies suggested that the SIS biomaterial degraded within the first 8 weeks and therefore could serve only as a temporary scaffold around which the body deposited appropriate and organized connective tissue.

Xenogeneic and allogeneic cellular antigens are, by definition, recognized as foreign body by the host and therefore will normally induce an inflammatory response or an immune-mediated rejection of the tissue. However, components of the ECM are generally conserved among species and are well tolerated even by xenogeneic recipients.[38,39] ECM from tendons[40] and ligaments[41] has been studied for ligament tissue engineering. The goal of decellularization is to efficiently remove all cellular and nucleus material while minimizing any adverse effect on the composition, biological activity, and mechanical integrity of the remaining ECM. Harrison and Gratzer[42] developed a decellularized bone–ACL–bone allograft for treatment of the ACL disruption in young or active patients. This study demonstrated the feasibility of seeding decellularized ACL tissue with primary ligament fibroblasts. Porcine ACLs were decellularized by one of the three protocols, each differing only by the detergent/solvent used during the second wash (SDS, Triton-X, or TnBP). Cell counting on histological sections verified that Triton-X and TnBP-treated ligaments were

more receptive to cellular ingrowth than SDS-treated samples. Both the Triton-X and TnBP decellularization treatments provide suitable, naturally derived scaffolds for the ingrowth of primary ACL fibroblasts.

5.525.2.3. Silk Biomaterials

Silk fibers offer a novel alternative to traditional native and synthetic nondegradable and degradable biomaterials by combining the optimal traits of both groups. Superior mechanical properties and environmental stability make silk fibroin (the core protein of silk) a more suitable biomaterial for ligament tissue engineering applications. Silk has already been investigated as a possible scaffold material for ligament tissue engineering, particularly by Kaplan's group at Tufts University.[43–45] The fundamental facts about silk are well known. The core silk fibers are encased in a sericin coat, a family of glue-like proteins that hold the fibroins together to form the composite fibers. Sericin is a globular protein and water-soluble glue, unlike silk fibroin which is an oriented fiber protein. When subjected to physical, chemical, or enzymatic processes, sericin can be degraded into sericin peptides or partially hydrolyzed. Sericin proteins are known to be the major cause of adverse biocompatibility and hypersensitivity reactions resulting from implanted native untreated silk.[46,47] Therefore, sericin must be removed if silk fibers are to be used as a biomaterial.

In the process of removing sericin from the raw silk scaffold, the fibroin's structural integrity is often challenged, leading to mechanical depreciation. Our recent study identified the factors and conditions contributing to fibroin degradation during alkaline degumming and the parameters involved in achieving the preservation of fibroin structure and properties. The methodology involves degumming knitted silk scaffolds for various durations (5–90 min) and temperatures (60, 75, and 100 °C). Mechanical agitation and the use of refreshed solution are included in the degumming process to study how the respective factors contribute to sericin removal, mechanical integrity, and structural aspect of degummed silk fibroin. Characterization of the silk fibroin morphology, mechanical properties, and protein components are determined by scanning electronic microscopy (SEM), single fiber tensile tests, and SDS-PAGE analysis, respectively. Sericin removal is ascertained via SEM imaging and a protein fractionation method involving SDS-PAGE. Knitted scaffolds degummed with mechanical agitation for 30 min at 100 °C have sericin effectively removed and experience negligible mechanical and structural degradation. This study thus presents an optimization process for sericin removal from silk scaffolds, where the mechanical and structural properties are to be preserved.

"The US Pharmacopia defines an absorbable material as one that loses most of its tensile strength within 60 days" *in vivo*. By this definition, it is correct to classify silk as a nondegradable material. However, in scientific literature, silk has been shown to degrade over a longer period of time as a function of proteolytic degradation that is usually mediated by an *in vivo* foreign body response.[46,48–50] Several studies have described silk degradation *in vivo* at variable rates, depending on the model and implantation site.[51–54] In general, silk fibers lose the majority of their tensile strength within 1 year *in vivo* and fail to be recognized in the implantation site within 2 years. Silk loses 55% of its tensile strength over a 6-week period when circumferentially implanted subcutaneously in rats.[43,45] Bucknall *et al.*[55] reported an 83% loss in silk fiber tensile strength after 10 weeks *in vivo* when implanted subcutaneously in rats. Lam *et al.* were unable to detect silk as well as a foreign body response 24 weeks following implantation in the abdominal muscle layer in rats.[50] Salthouse *et al.*[46] observed a reduction in the number of silk filaments and the overall diameter of silk sutures 42 days following implantation in the cornea, sclera, and ocular muscle of the rabbit and complete absorption within 90 days *in vivo*. Our *in vivo* studies in a rabbit model showed that, after 24 weeks, the strength retention of tissue-engineered ligament with BMSCs seeding on the silk scaffolds was 18.7% of native ACL's maximum load. Moreover, the strength retention of tissue-engineered ligament was comparable to the reported retention (15%) of autograft (patellar tendon) for ACL regeneration in a rabbit model.[56,57]

5.525.3. Scaffold Design

5.525.3.1. Scaffolds Design Criteria

Tissue engineering scaffolds provide a structural and logistic template for cell adherence and tissue development, and they biodegrade in parallel with the accumulation of neotissue components. Most studies suggest that a scaffold is essential for promoting orderly tissue repair.[58–62] Scaffold structure, mechanical properties, and the rate of degradation largely determine the mass transport and mechanotransduction at the cellular and tissue levels. Ideally, a scaffold should be made of biocompatible, biodegradable material and should degrade at a rate matching the rate of new tissue deposition.[63] An important requirement for scaffold design while engineering load-bearing tissues is the maintenance of the mechanical properties of the scaffold until the new tissue becomes mechanically competent.

The musculoskeletal tissues will have to bear significant mechanical loads *in vivo*; therefore, the mechanical properties of the scaffold must be considered for tissue engineering applications. In fact, some early attempts to develop tissue-engineered ligaments failed because the scaffold had inadequate strength and stiffness. Examples include the use of collagen gels seeded with cells *in vitro*.[24–26] Although these cell-seeded scaffolds appeared to be 'ligament-like' based on histology and biochemical markers, they lacked the key functional component required for a ligament, that is, mechanical strength. Recently, the concept of functional tissue engineering has emerged as a hot topic. The principles of functional tissue engineering defined by Butler *et al.*[64] stress the importance of the mechanical properties of skeletal tissues and recognize the need to define mechanical requirements for tissue-engineered grafts and utilize physical signals to direct cellular activity and phenotype toward functional tissue assembly, and thereby achieve mechanical-competent tissue repair.

Native ACL comprises bands of dense collagen fibers. A fiber is a simple element of anisotropic structure. As such, ACL scaffolds and synthetic ACL prostheses developed so far are practically made up of fibers in various textile-type

structures. However, the simplest form being parallel structure, the lack of interlinking between fibers restricts its application. Twisting fiber bundles is an elegant way to solve the problem.[44] Twisted fiber grafts are morphologically closer replicas of the normal ACL that may be able to accommodate the peak forces in extension.[65] Due to the complexity of the ACL mechanical environment, researchers have been keen to adopt more complex textile structures in ACL regeneration, and therefore, all four textile patterns, that is, woven, knitted, braided, and nonwoven, have been explored for ligament regeneration. However, the braided and knitted structures have inherent advantages and have been well studied.

5.525.3.2. Braided Scaffolds

The properties of textile grafts depend on the characteristics of the constituent yarns or fibers as well as the geometry of the formed structure. In general, braided grafts are dimensionally very stable but less extensible and porous than the other structures, for example, the Gore-Tex ligament prosthesis, which is a braided bundle of polytetrafluroethylene (PTFE).[66] This graft has high strength and fatigue life, but poor tissue ingrowth due to low porosity.[27] However, the pore size of the braided structures can be regulated by yarn bundle size and braiding angles.[67]

Laurencin and his colleagues have developed a tissue-engineered solution based on a cell-seeded, degradable, 3D braided PLLA scaffold.[67] This method produces a heterogeneous scaffold that is able to adapt to the intraarticular region of the ligament, withstand the rigors of surgical fixation within the bone tunnels, and promote guided healing. The study showed that the tissue-engineered ligament scaffold has the mechanical properties of the normal ACL and the porosity for tissue ingrowth. During cell culture, the attachment and proliferation of primary ACL cells and BALB/C mouse fibroblasts demonstrated the biocompatibility of the scaffold.

Altman *et al.*[44] reported on the development of a 6-cord silk wire-rope matrix as a scaffold for ACL tissue engineering. The matrix was successfully designed to match the complex and demanding mechanical requirements of a native human ACL, including satisfactory fatigue performance. The protein matrix supported the attachment, expansion, and differentiation of adult human progenitor bone marrow stromal cells, according to SEM examination, DNA quantitation, and the expression of collagen types I and III and tenascin-C markers. The results supported the conclusion that properly prepared silkworm fiber matrices, in addition to providing unique benefits in terms of mechanical properties as well as biocompatibility and slow degradability, can provide suitable biomaterial matrices for the support of adult stem cell differentiation toward ligament lineages. These results point toward this matrix as a new option for ACL repair to overcome current limitations in synthetic and other degradable materials.

Our group has developed a silk-cable-reinforced gelatin/silk fibroin hybrid scaffold for ligament tissue engineering.[56,57] The scaffold was fabricated by lyophilizing the cross-linked gelatin and silk fibroin mixture with braided silk cables. SEM observation showed that microporous gelatin/silk fibroin sponges formed around silk cables mimicked the microstructures of ligament ECM. The silk cables significantly increased the tensile strength of the scaffold to meet the mechanical requirements for ligament tissue engineering. The scaffold possessed good cell adhesion property, and when BMSCs were seeded on it, cells proliferated profusely. After 2 weeks of culture, seeded BMSCs were distributed uniformly throughout the scaffold and were highly viable. Occurrence of cell death during culture was not significant. Deposition of collagen on the scaffold was found to increase with time. Differentiation of BMSCs into ligament fibroblasts was verified by expressions of ligament ECM-specific markers in gene and protein levels. Immunohistochemistry stains also confirmed the production of key ligament ECM components on the scaffold.

5.525.3.3. Knitted Scaffolds

When compared with braided fabrics, knitted structures are highly porous and have the potential to support tissue ingrowth. Barrett *et al.*[68] reported that using a knitted velour layer over the Dacron artificial ligament promoted ingrowth of fibrous tissue, although the overall result of the artificial ligament was unfavorable. Textile materials for tissue engineering applications typically have specific performance requirements relating to porosity and mechanical properties.

Unlike braided fabric, knitted scaffolds have been shown to favor deposition of collagenous connective tissue matrix, which is crucial for ligament regeneration. Cell seeding on knitted scaffolds often requires a gel system, which was found to be practically unsuitable for ACL regeneration as the cell–gel composite often gets dislodged from the scaffold in the *in vivo* dynamic situations. A biodegradable nano-microfibrous polymer scaffold was developed by our group by electrospinning PLGA nanofibers onto a knitted PLGA scaffold to provide a large biomimetic surface for cell attachment.[69] Porcine BMSCs were seeded onto either the nano-microfibrous scaffolds by pipetting a cell suspension (Group I) or the knitted PLGA scaffolds by immobilizing in fibrin gel (Group II). Cell attachment was comparable and cell proliferation was faster in Group I. Moreover, cellular function was more active in Group I, as evident by the higher expression of collagen type I, decorin, and biglycan genes.

In order to improve cell attachment on the knitted silk scaffolds, we fabricated a combined silk scaffold with web-like microporous silk sponges formed in the openings of a knitted silk scaffold[70,71] (**Figure 1**). BMSCs adhered to and grew well on the combined silk scaffolds. Moreover, in comparison with the knitted silk scaffolds seeded with BMSCs in fibroin gel, the cellular function was more active on the combined silk scaffolds as evident from real-time reverse transcriptase-polymerase chain reaction (RT-PCR) analysis for ligament-related gene markers, as well as immunohistochemical and Western blot evaluations of ligament-related ECM components. While the knitted structure holds the microporous silk sponges together and provides the structural strength of the combined silk scaffold, the microporous structure of the silk sponges mimic the ECM which consequently promotes cell proliferation, function, and differentiation. This feature overcomes the limitation of knitted scaffold for ligament tissue engineering application.

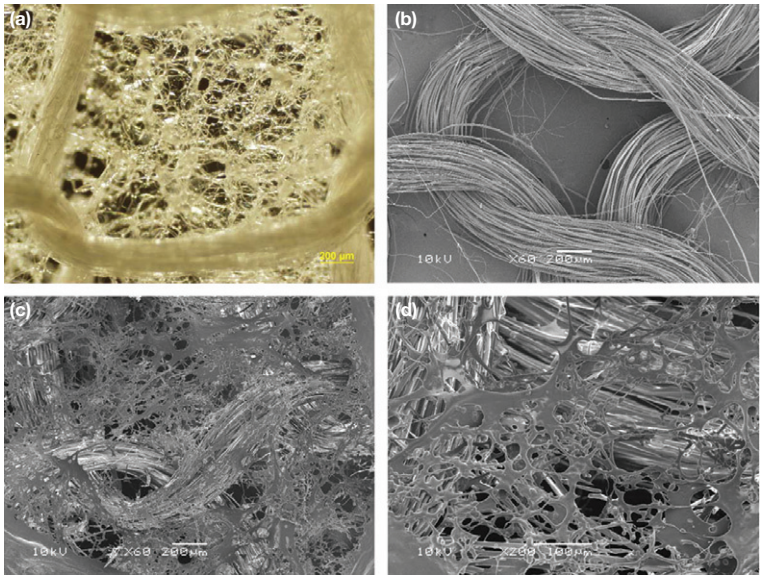

Figure 1 Phase contrast (a) and SEM (b–d) images of the knitted (b) and combined (a, c, d) silk scaffolds showing web-like microporous silk sponges formed in the openings of the knitted silk scaffold. (a–c) Scale bars = 200 μm; (d) scale bars = 100 μm.

5.525.4. Cell Source

Although scaffolds provide temporary mechanical support, the long-term success of tissue-engineered ligaments depends on the ability of cells to deposit and remodel a new matrix. Due to differences in phenotypes and functionalities of various cell types, seeding of different cells on scaffolds will greatly influence the outcome of tissue-engineered ligament grafts. A variety of cell types have been scrutinized in our laboratory in an attempt to enhance our understanding of ligament development and define a suitable cell line for ligament engineering. The appropriate cell type for ACL tissue engineering must show enhanced proliferation and production of an appropriate ECM and must be able to survive in an intraarticular environment in the patient's knee.[72] ACL fibroblasts (ACLFs) are cells specialized in producing all the ligament constituents and maintaining the ligament tissue in the appropriate conformation. In comparison with cells derived from the medial collateral ligament (MCL), Achilles tendon, and patellar tendon, ACLFs have the highest gene expression for the phenotypic markers.[73] Another possible candidate is BMSC, which has been shown to have the potential to differentiate into various types of mesenchymal cell phenotypes, including osteoblasts, chondroblasts, myoblasts, and fibroblasts.[74] They are present in large quantities in the human body and can also be easily obtained just by a simple aspiration of iliac crests and expanded *in vitro* to large amounts.[75,76] Moreover, BMSCs have been successfully used to promote repair of a number of connective tissues, such as bone,[77] cartilage,[78] tendon,[79] and ligament.[16–18]

In our previous study, fibroblasts isolated from rabbit ACL, MCL, and BMSC were cultured on a tissue culture plate (TCP) and compared using the following parameters: proliferation rate, collagen excretion, and expression of ligament-related ECM markers. It was found that BMSC, ACL, and MCL fibroblasts were all highly stained with antibodies for collagen types I and III and α-smooth muscle actin, while BMSCs had the best proliferation and collagen excretion rate among the three cell types.[16–18] However, the choice of cell may also be mediated by its affinity for the scaffold that is used and its susceptibility to molecular and mechanical influences. Therefore, our recent study has focused on rabbit ACLFs and BMSCs culturing on the combined silk scaffolds, to investigate their biological cellular responses *in vitro* and *in vivo*, which can be used to determine the cell source most appropriate for a tissue-engineered ligament.[70,71] The results of comparing cell proliferation indicated that BMSCs proliferated faster than ACLFs (**Figure 2**). Gene expression of the phenotypic markers measured using RT-PCR indicated the transcript levels of BMSCs were significantly increased after 2 weeks of culture, whereas those of ACLFs had no significant difference. The protein levels and localization were determined by Western blots and immunohistochemical staining, and the results showed more production of ligament-related ECM by BMSCs as compared to ACLFs. Moreover, at 4 weeks postoperatively, more fluorescent cells were present in BMSC-loaded constructs than in ACLFs-loaded constructs. Therefore, based on the cellular response *in vitro* and *in vivo*, BMSC was found to be a better cell source than ACLFs for ACL tissue engineering. In the future, other cell sources may also be available, including embryonic stem cells, synovium stem cells, and induced pluripotent stem cells.

5.525.5. Bioreactor System

The disadvantages of static culture are well documented; they include inefficient nutrient delivery by diffusion, reduced cell viability, minimal cell activity at the center of tissue constructs, inadequate distribution of nutrients, and removal of waste products within the constructs.[80–82] The rationale for using perfusion bioreactors is that it is capable of transporting nutrients and metabolites to the interior of the construct. The culture

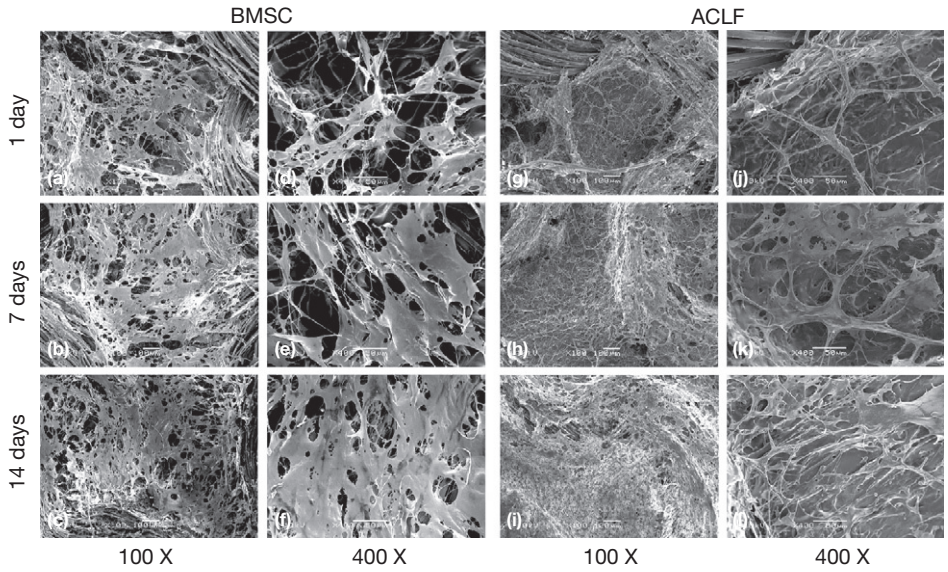

Figure 2 SEM photomicrographs showing adherence, proliferation, and cell sheet formation by BMSCs (a–f) and ACLFs (g–l) cultured on the novel knitted silk scaffolds for 1, 7, and 14 days. (a–c, g–i) Scale bars = 100 μm; (d–f, j–l) scale bars = 50 μm.

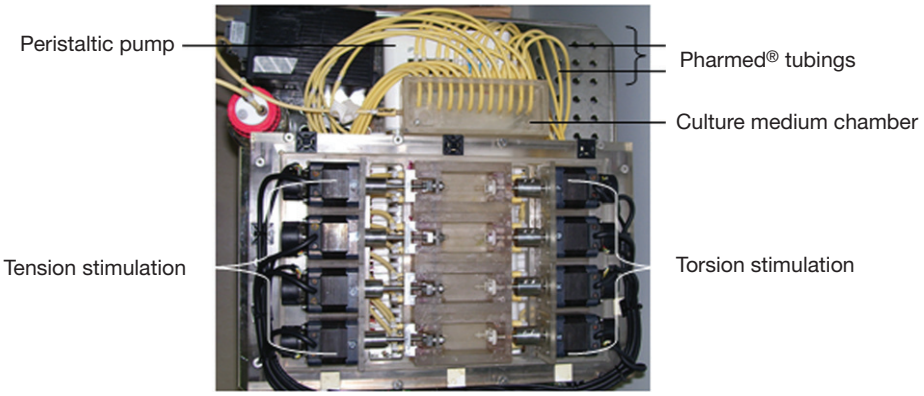

Figure 3 Four-chamber bioreactor system.

medium is continually renewed to supply gas and nutrients to cells, remove metabolites and catabolites (this will improve mass transport throughout the 3D tissue-engineered constructs cultured *in vitro*), and provide flow-mediated mechanical stimuli such as shear stress, compression, and hydrostatic pressure for cells to accurately grow, differentiate, and function. Mechanical loads can provide critical signals that influence cells[83–85] and help control musculoskeletal tissue development, growth, remodeling, and repair.[86,87] In addition, mechanical loads can increase collagen production by ligament fibroblast and interact synergistically with growth factors to influence fibroblast behavior.[84,85]

There are two approaches to tissue engineering: one is to implant a cell–scaffold composite directly into the injured site, so that the body acts like a 'bioreactor'; the other is to culture the cell–scaffold composite in a bioreactor *ex vivo* for a period of time before transplantation.[88] The *ex vivo* bioreactor allows controlled introduction of biochemical and physical regulatory cues to guide cell differentiation, proliferation, and tissue development. As such, engineering of tissue *ex vivo* in a bioreactor offers several exciting prospects, such as better understanding of tissue development and the mechanisms of disease, off-the-shelf provision of essential transplantable tissue, and possible scale-up for commercial production of engineered tissues.

As shown in Figure 3, a four-chamber perfusion cum mechanical stimulation system has been designed by our group to sustain cell viability and promote cell proliferation and tissue formation *in vitro*. The focus is on growing BMSCs on combined silk scaffolds for tissue engineering of ACL. Key functions of the bioreactor system include the following:

- enabling perfusion throughout the scaffold–cell construct;
- allowing environmental condition monitoring;
- providing cyclic translational and rotational mechanical loading;
- using software-controllable multidimensional tension and/or torsion effects on 3D cell growth;
- providing force monitoring and feedback system;

- providing independent but concurrent control over translational and rotational strains.

5.525.6. Local Delivery of Growth Factors

Growth factors are soluble peptides that influence normal tissue morphogenesis, repair, and regeneration. Numerous studies have tried to define the role of growth factors in ligament healing and determine appropriate strategies for the use of growth factors in ligament tissue engineering. Various growth factors, such as transforming growth factor (TGF), epidermal growth factor (EGF), platelet-derived growth factor (PDGF), and insulin-like growth factor (IGF), have been shown to have the ability to improve ligament cell proliferation or matrix formation *in vitro* or *in vivo*.[89–94]

A potential problem with these soluble growth factors is rapid diffusion away from the site where activity is required *in vivo*. The duration of growth factor activity may be prolonged by incorporating these soluble factors within a scaffold delivery vehicle. In our recent study, we have demonstrated that basic fibroblast growth factor (bFGF) could be successfully incorporated as well as randomly dispersed within blended-electrospun nanofibers and released in a bioactive form over 1 week[95] (**Figure 4**). The released bioactive bFGF activated tyrosine phosphorylation signaling of seeded BMSCs. The bFGF-releasing nanofibrous scaffolds facilitated BMSC proliferation, upregulated gene expression of ligament-specific ECM proteins, increased production and deposition of collagen and tenascin-C, reduced multipotency of the BMSCs, and induced ligament-like fibroblastic differentiation.

5.525.7. Animal Models for ACL Regeneration

In the investigation of *in vivo* ligament regeneration, it is prudent to choose animal models that have a similar type and degree of ligament injuries to those found in humans. It is also imperative to realize that the results from animal research may be species and ligament specific and may not necessarily simulate those of humans. Frequently used animal models in ligament research are dogs, rabbits, goats, and sheep. The reasons for using dogs are the ease in handling, receptiveness to various exercise regimens, and availability of well-published information.[96] Goats and sheep are widely used for ACL regeneration, particularly in studies related to biological grafts and ligament prostheses. This is because goats and sheep have large knee joints and a lesser degree of flexion.[97,98] Rabbits are commonly used in biomedical research because of their docile nature and relatively inexpensive cost of maintenance. Furthermore, there is extensive information on the biochemical and functional properties of rabbit knee ligaments.[99]

Our group had investigated ACL regeneration using BMSCs and silk scaffold in a rabbit model.[56,57] After 24 weeks, histological observation showed that BMSCs were distributed throughout the regenerated ligament and exhibited fibroblast morphology. The key ligament ECM components were produced in significant quantities. Furthermore, direct ligament–bone

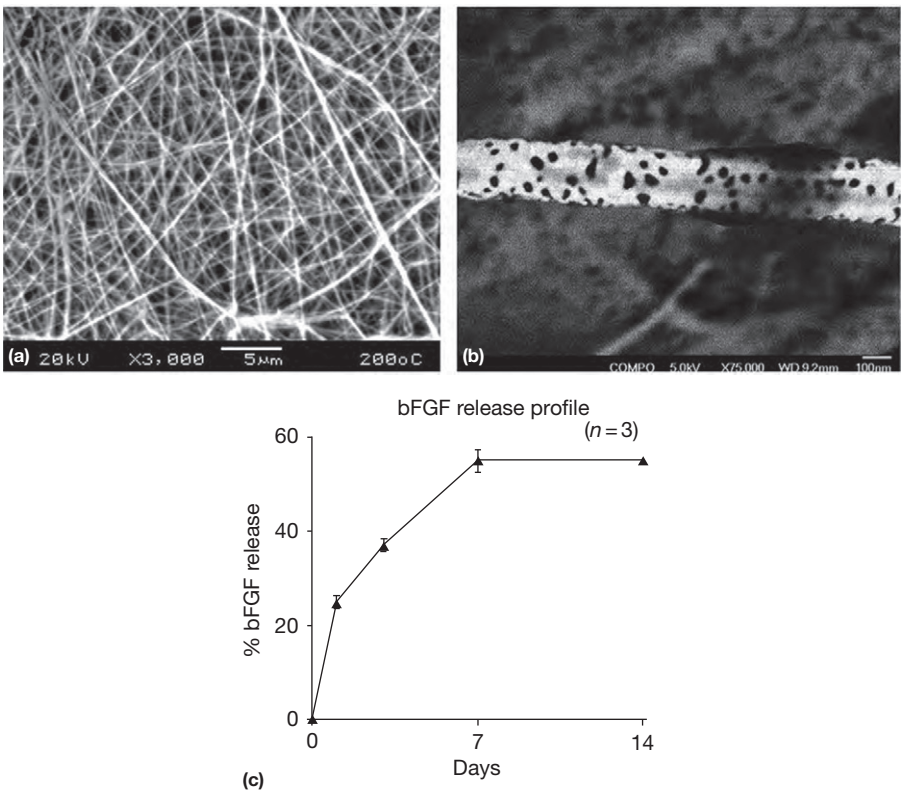

Figure 4 SEM images showing blended nanofibers of 200–700 nm diameter, with a random distribution of protein within. The bFGF was released over 1 week.

insertion (i.e., the typical four interfacial zones – bone, mineralized fibrocartilage, nonmineralized fibrocartilage, and ligament) was reconstituted. It resembled the native structure of ACL–bone insertion (Figure 5). The tensile strength of regenerated ligament also met the mechanical requirements. Moreover, its histological grading score was significantly higher than that of the control group (i.e., without cell seeding).

However, it should be noted that rabbits spend a larger part of their time in deeper knee flexion when compared with large animals (e.g., pig, goat, and sheep). Although the ACL has been regenerated in rabbits, studies on large animals are still needed to extrapolate the findings from animal data to humans.[56,57] The ACL is a two-bundle ligament consisting of anteromedial (AM) and posterolateral (PL) bundles. The differences between the ACLs of various species may be due to variations in AM bundles but not PL bundles. Studies indicate that pig knee differs from human knee only in the magnitude and direction of force in the PL bundle. In contrast, sheep and goat knees show different magnitude and direction of force in both bundles when compared with human knee. Therefore, goat and sheep knees may have limitations in modeling the human ACL, while pig knee may be the preferred model for experimental studies.[100,101] To further investigate the clinical potential of silk material, we were able to regenerate the ACL in a pig model using BMSCs and silk scaffold.[102] At 24 weeks postoperatively, the key ligament-specific ECM components were produced prominently and indirect ligament–bone insertion with three zones (bone, Sharpey's fibers, and ligament) was observed. The maximum tensile load of regenerated ligament did not decrease after 24 weeks of implantation. In conclusion, the results imply that the silk-based tissue-engineered ligament has great potential for clinical application in the future.

5.525.8. Ligament–Bone Interface

One of the keys to success in surgical reconstruction of damaged ligament is the healing of graft ligament to bone. Acceleration of the appropriate healing process at the insertion site would allow patients to undergo early rehabilitation. Normal ACL insertion is characterized as a direct ligament insertion

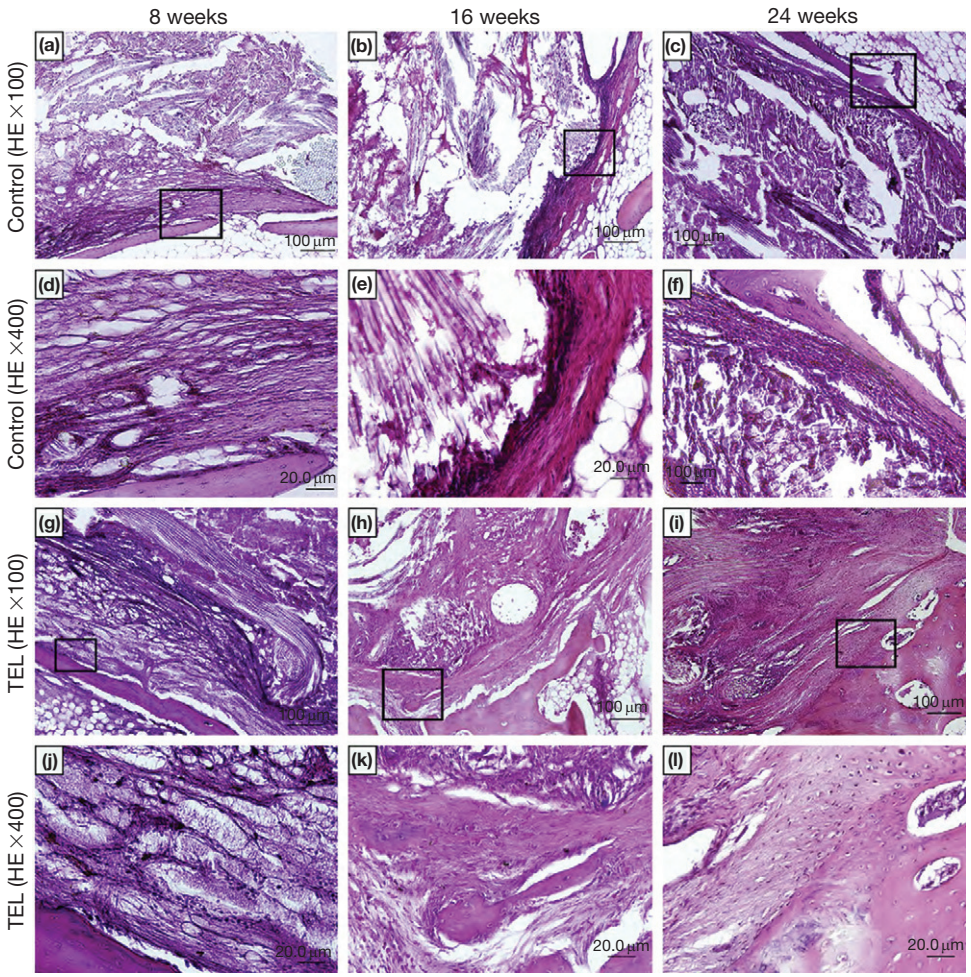

Figure 5 Histological observation of reconstructed ligament–bone insertion in control group without cell seeding (a–f) and tissue-engineered ligament group (g–l) by HE staining at 8, 16, and 24 weeks postoperatively. (Note: d–f and j–l are magnified views of black rectangles from a–c and g–i, respectively.)

consisting of four distinct zones: bone, mineralized cartilage, fibrocartilage, and ligament.[43–45] This specific insertion site structure is designed to distribute longitudinal and shear forces from the ligament proper into the subchondral bone plate, thus minimizing stresses on individual collagen bundles. There is a tidemark between the zones of calcified and uncalcified cartilage, which represents the mineralization front. The normal insertion site is a highly specialized zone of tissue that functions to transmit stress from hard tissue to soft tissue.[103] In contrast, indirect insertion comprises three zones including ligament, Sharpey's fibers, and bone. Sharpey's fibers extend from ligament tissue deep into bone.[104]

Helen Lu and her colleague developed a stratified scaffold predesigned to mimic the multitissue transition found at the ACL-to-bone interface.[105] The scaffold consists of three distinct yet continuous phases: Phase A for ligament formation, Phase B for the interface, and Phase C for the bone region. Interface-relevant cell types, specifically fibroblasts, chondrocytes, and osteoblasts, were tricultured on this scaffold, and the formation of cell-type- and phase-specific matrix heterogeneity as well as fibrocartilage formation was evaluated over 8 weeks in a subcutaneous athymic rat model. Acellular scaffolds as well as scaffolds cocultured with fibroblasts and osteoblasts served as controls. It was found that the triphasic scaffold supported multilineage cellular interactions as well as tissue infiltration and abundant matrix production *in vivo*. In addition, controlled phase-specific matrix heterogeneity was induced on the scaffold, with distinct mineral and fibrocartilage-like tissue regions formed in the tricultured group.

In the rabbit model we used, direct ligament–bone insertion with the four typical zones (bone, mineralized fibrocartilage, fibrocartilage, and ligament) was reconstructed, which resembled the native structure of ACL–bone insertion. In the pig model, the healing of regenerated ligament–bone junction began with proliferation of fibrovascular tissue in the interface. A mature direct insertion with the four typical zones was observed after 24 weeks, which was consistent with other studies.[106,107] However, the healing proceeded by means of fibrous tissue at the regenerated ligament–bone junction in the pig model. The collagen fibers resembling Sharpey's fibers projected from regenerated ligament into bone tissue. The indirect insertion was observed after 24 weeks. The disparities between these two animal models may be due to differences in the species and mechanical environment. This would require further investigations.

5.525.9. Summary

Ligament tissue engineering has achieved much progress in recent years and many potential tissue-engineered ligaments used for ligament regeneration have been reported. The success of ligament regeneration procedure depends on three major factors: implant characteristics (scaffolds, cells, and signals), surgical procedure, and postsurgery rehabilitation protocol. The main difficulties are complex mechanical stress faced by tissue-engineered ACLs, harsh environment, and poor blood supply after ACL ruptures. As tissue-engineered ligaments combine three dominant components, that is, scaffolds, cells, and signaling molecules, we have discussed ACL anatomy, current challenges in tissue repair, biomaterials and scaffold design, cell sources, bioreactors, delivery of growth factors, and animal models in ligament tissue engineering. With greater research intensity and better understanding, a suitable substitute for ligament regeneration can be developed for clinical application.

Acknowledgments

The authors' research on tissue-engineered ligaments was supported by grants from the Academic Research Fund, Biomedical Research Council, and National Medical Research Council, Singapore.

References

1. Miyasaka, K.; Daniel, D.; Stone, M.; Hirshman, P. *Am. J. Knee Surg.* **1991**, *4*, 3–8.
2. Gentleman, E.; Livesay, G.; Dee, K. C.; Nauman, E. A. *Ann. Biomed. Eng.* **2006**, *34*, 726–736.
3. Bach, B. R., Jr.; Levy, M. E.; Bojchuk, J.; Tradonsky, S.; Bush-Joseph, C. A.; Khan, N. H. *Am. J. Sports Med.* **1998**, *26*, 30–40.
4. Bach, B. R., Jr.; Tradonsky, S.; Bojchuk, J.; Levy, M. E.; Bush-Joseph, C. A.; Khan, N. H. *Am. J. Sports Med.* **1998**, *26*, 20–29.
5. Crawford, C.; Kainer, M.; Jernigan, D. *Clin. Infect. Dis.* **2005**, *41*, 195–200.
6. Harner, C. D.; Fu, F. H. *Am. J. Knee Surg.* **1993**, *6*, 45–46.
7. Noyes, F. R.; Grood, E. S. *J. Bone Joint Surg. Am.* **1976**, *58*, 1074–1082.
8. Akeson, W. H.; Woo, S. L. Y.; Amiel, D.; Frank, C. B. *Rehabilitation of the Injured Knee*; Mosby: St. Louis, MO, 2004.
9. Danylchuk, K. D.; Finlay, J. B.; Krcek, J. P. *Clin. Orthop.* **1978**, *131*, 294–298.
10. Arnoczky, S. P.; Warren, R. F. In *The Crucial Ligaments: Diagnosis and Treatment of Ligamentous Injuries about the Knee*; Feagin, J. A., Ed.; Churchill Livingstone: New York, 1994.
11. Ge, Z. G.; Yang, F.; Goh, J. C. H.; Ramakrishna, S.; Lee, E. H. *J. Biomed. Mater. Res.* **2006**, *77A*, 639–652.
12. Bell, E. *Tissue Eng.* **1995**, *1*, 163–179.
13. Snook, G. A. *Clin. Orthop.* **1983**, *172*, 11–13.
14. Lijensten, E.; Gisselfalt, K.; Edberg, B.; Bertilsson, H.; Flodin, P.; Peterson, L. *J. Mater. Sci. Mater. Med.* **2002**, *13*, 351–359.
15. Ouyang, H. W.; Goh, J. C. H.; Mo, X. M.; Teoh, S. H.; Chong, S. W.; Lee, E. H. *Mater. Sci. Eng. C Biol.* **2002**, *20*, 63–69.
16. Ge, Z. G.; Goh, J. C. H.; Wang, L.; Tan, E. P. S.; Lee, E. H. *J. Biomater. Sci. Polym. Ed.* **2005**, *16*, 1179–1192.
17. Ge, Z. G.; Goh, J. C. H.; Lee, E. H. *Cell Transplant.* **2005**, *14*, 763–773.
18. Ge, Z. G.; Goh, J. C. H.; Lee, E. H. *Cell Transplant.* **2005**, *14*, 573–583.
19. Haut, R. C. In *The Anterior Cruciate Ligament: Current and Future Concepts*; Jackson, D. W., Arnoczky, S. P., Frank, C. B., Woo, S. L. Y., Simon, T. M., Eds.; Raven: New York, 1993.
20. Hutmacher, D. W.; Goh, J. C. H.; Teoh, S. H. *Ann. Acad. Med. Singapore* **2001**, *30*, 183–191.
21. Weadock, K.; Olson, R. M.; Silver, F. H. *Biomater. Med. Devices Artif. Organs* **1983**, *11*, 293–318.
22. Weadock, K.; Miller, E. J.; Bellincampi, L. D.; Dunn, M. G. *J. Biomed. Mater. Res.* **1995**, *29*, 1373–1379.
23. Weadock, K.; Miller, E. J.; Keuffel, E. L.; Dunn, M. G. *J. Biomed. Mater. Res.* **1996**, *32*, 221–226.
24. Dunn, M. G.; Tria, A. J.; Kato, Y. P.; Ochner, R. S. *Am. J. Sports Med.* **1992**, *20*, 507–515.
25. Dunn, M. G.; Liesch, J. B.; Tiku, M. L.; Zawadsky, J. P. *J. Biomed. Mater. Res.* **1995**, *29*, 1363–1371.
26. Dunn, K. J.; Perez-Polo, J. R.; Wood, T. G. *Int. J. Dev. Neurosci.* **1996**, *14*, 61–68.
27. Vunjak-Novakovic, G.; Altman, G.; Horan, R.; Kaplan, D. *Ann. Rev. Biomed. Eng.* **2004**, *6*, 131–156.
28. Koob, T. J.; Hernandez, D. J. *Biomaterials* **2002**, *23*, 203–212.
29. Sandusky, G. E.; Lantz, G. C.; Badylak, S. F. *J. Surg. Res.* **1995**, *58*, 415–420.
30. Sandusky, G. E.; Badylak, S. F.; Morff, R. J.; Johnson, W. D.; Lantz, G. *Am. J. Pathol.* **1992**, *140*, 317–324.
31. Hodde, J. P.; Badylak, S. F.; Shelbourne, K. D. *Tissue Eng.* **1997**, *3*, 27–37.

32. Badylak, S. F.; Voytik, S. L.; Kokini, K.; *et al*. *J. Biomed. Mater. Res.* **1995**, *29*, 977–985.
33. Aiken, S. W.; Badylak, S. F.; Toombs, J. P.; *et al*. *Vet. Comp. Orthop. Traumatol.* **1994**, *7*, 124–128.
34. Prevel, C. D.; Eppley, B. L.; Summerlin, D. J.; Jackson, J. R.; McCarty, M.; Badylak, S. F. *J. Plast. Surg.* **1995**, *35*, 381–388.
35. Badylak, S. F.; Lantz, G. C.; Coffey, A.; Geddes, L. A. *J. Surg. Res.* **1989**, *47*, 74–80.
36. McPherson, T. B.; Badylak, S. F. *Tissue Eng.* **1998**, *4*, 75–83.
37. Voytik-Harbin, S. L.; Brightman, A. O.; Kraine, M.; Waisner, B.; Badylak, S. F. *J. Cell Biol.* **1997**, *67*, 478–491.
38. Constantinou, C. D.; Jimenez, S. A. *Matrix* **1991**, *11*, 1–9.
39. Exposito, J. Y.; D'Alessio, M.; Solursh, M.; Ramirez, F. *J. Biol. Chem.* **1992**, *267*, 15559–15562.
40. Cartmell, J. S.; Dunn, M. G. *J. Biomed. Mater. Res.* **2000**, *49*, 134–140.
41. Woods, T.; Gratzer, P. F. *Biomaterials* **2005**, *26*, 7339–7349.
42. Harrison, R. D.; Gratzer, P. F. *J. Biomed. Mater. Res.* **2005**, *75A*, 841–854.
43. Altman, G. H.; Diaz, F.; Jakuba, C.; Calabro, T.; Kaplan, D. L. *Biomaterials* **2003**, *24*, 401–416.
44. Altman, G. H.; Horan, R. L.; Lu, H. H.; Richmond, J.; Kaplan, D. L. *Biomaterials* **2002**, *23*, 4131–4141.
45. Altman, G. H.; Frank, D.; Caroline, J.; *et al*. *Biomaterials* **2003**, *24*, 401–416.
46. Salthouse, T. N.; Matlaga, B. F.; Wykoff, M. H. *Am. J. Ophthalmol.* **1977**, *84*, 224–233.
47. Salthouse, T. N. *Otolaryngol. Head Neck Surg.* **1980**, *88*, 658–664.
48. Rossitch, E., Jr.; Bullard, D. E.; Oakes, W. J. *Childs Nerv. Syst.* **1987**, *3*, 375–378.
49. Soong, H. K.; Kenyon, K. R. *Ophthalmology* **1984**, *91*, 479–483.
50. Lam, K. H.; Nijenhuis, A. J.; Bartels, H.; *et al*. *J. Appl. Biomater.* **1995**, *6*, 191–197.
51. Hayashi, C. Y.; Lewis, R. V. *J. Mol. Biol.* **1998**, *275*, 773–784.
52. Wen, C. M.; Ye, S. T.; Zhou, L. X.; Yu, Y. *Ann. Allergy* **1990**, *65*, 375–378.
53. Zaoming, W.; Codina, R.; Fernandez-Caldas, E.; Lockey, R. F. *J. Inv. Allergy Clin. Immunol.* **1996**, *6*, 237–241.
54. Dewair, M.; Baur, X.; Ziegler, K. *J. Allergy Clin. Immunol.* **1985**, *76*, 537–542.
55. Bucknall, T. E.; Teare, L.; Ellis, H. *Eur. Surg. Res.* **1983**, *15*, 59–66.
56. Fan, H. B.; Liu, H. F.; Wong, E. J. W.; Toh, S. L.; Goh, J. C. H. *Biomaterials* **2008**, *29*, 3324–3337.
57. Fan, H. B.; Liu, H. F.; Wang, Y.; Toh, S. L.; Goh, J. C. H. *Cell Transplant.* **2008**, *17*, 1389–1401.
58. Chu, C. R.; Coutts, R. D.; Yoshioka, M.; Harwood, F. L.; Monosov, A. Z.; Amiel, D. *J. Biomed. Mater. Res.* **1995**, *29*, 1147–1154.
59. Hunziker, E. B. *Clin. Orthop. Relat. Res.* **1999**, *367*(Suppl.), 135–146.
60. Schaefer, D.; Martin, I.; Jundt, G.; Seidel, J.; Heberer, M. *Arthritis Rheum.* **2002**, *46*, 2524–2534.
61. Caplan, A. I.; Elyaderani, M.; Mochizuki, Y.; Wakitani, S.; Goldberg, V. M. *Clin. Orthop. Relat. Res.* **1997**, *342*, 254–269.
62. Freed, L. E.; Vunjak-Novakovic, G.; Biron, R.; Eagles, D.; Lesnoy, D. *Biotechnology* **1994**, *12*, 689–693.
63. Yannas, I. V. *Tissue and Organ Regeneration in Adults*; Springer: New York, 2001.
64. Butler, D. L.; Goldstein, S. A.; Guilak, F. *J. Biomechan. Eng.* **2000**, *122*, 570–575.
65. Barber, F. A.; Click, J. N. *Arthroscopy* **1992**, *8*, 437–441.
66. Miller, R. H. In *Campbell's Operative Orthopaedics*; Canale, S. T., Ed.; Mosby: St. Louis, MO, 2003.
67. Cooper, J. A.; Lu, H. H.; Ko, F. K.; Freeman, J. W.; Laurencin, C. T. *Biomaterials* **2005**, *26*, 1523–1532.
68. Barrett, G. R.; Line, L. L. J.; Shelton, W. R.; Manning, J. O.; Phelps, R. *Am. J. Sports Med.* **1993**, *21*, 367–373.
69. Sahoo, S.; Ouyang, H. W.; Goh, J. C. H.; Tay, T. E.; Toh, S. L. *Tissue Eng.* **2006**, *12*, 91–99.
70. Liu, H. F.; Fan, H. B.; Wang, Y.; Toh, S. L.; Goh, J. C. H. *Biomaterials* **2008**, *29*, 662–674.
71. Liu, H. F.; Fan, H. B.; Toh, S. L.; Goh, J. C. H. *Biomaterials* **2008**, *29*, 1443–1453.
72. Van, E. F.; Saris, D. B.; Riesle, J.; Willems, W. J.; Van, B. C. A.; Verbout, A. J. *Tissue Eng.* **2004**, *10*, 893–903.
73. Cooper, J. A.; Bailey, L. O.; Carter, J. N.; *et al*. *Biomaterials* **2006**, *27*, 2747–2754.
74. Pittenger, M. F.; Mackay, A. M. *Science* **1999**, *284*, 143–147.
75. Colter, D. C.; Class, R.; DiGirolamo, C. M.; Prockop, D. *Proc. Natl. Acad. Sci. USA* **2000**, *97*, 3213–3218.
76. Jiang, Y.; Jahagirdar, B. N. *Nature* **2002**, *418*, 41–49.
77. Bruder, S. P.; Jaiswal, N.; Ricalton, N. S.; Mosca, J. D.; Kraus, K. H.; Kadiyala, S. *Clin. Orthop.* **1998**, *355*(Suppl.), 247–256.
78. Fan, H. B.; Hu, Y. Y.; Zhang, C. L.; Li, X. S.; Lv, R.; Zhu, R. *Biomaterials* **2006**, *27*(26), 4573–4580.
79. Ouyang, H. W.; Goh, J. C. H.; Thambyah, A.; Teoh, S. H.; Lee, E. H. *Tissue Eng.* **2003**, *9*(3), 431–439.
80. Hsieh, A. H.; Tsai, C. M.; Ma, Q. J.; Lin, T.; Akeson, W. H.; Sung, K. L. *J. Orthop. Res.* **2000**, *18*, 220–227.
81. Toyoda, T.; Matsumoto, H.; Fujikawa, K.; Saito, S.; Inoue, K. *Clin. Orthop.* **1998**, *353*, 247–255.
82. Banes, A. J.; Weinhold, P.; Yang, X.; *et al*. *Clin. Orthop.* **1999**, *367*(Suppl.), S356–S370.
83. Ruoslahti, E. *Science* **1997**, *276*, 1345–1346.
84. Banes, A. J. *Biochem. Cell Biol.* **1995**, *73*, 349–365.
85. Banes, A. J. *J. Biochem.* **1995**, *28*, 1505–1513.
86. Wren, T. A.; Beaupre, G. S.; Carter, D. R. *J. Biochem.* **1998**, *31*, 107–114.
87. Benjamin, M.; Hillen, B. *Eur. J. Morphol.* **2003**, *41*, 3–7.
88. Goh, J. C. H.; Ouyang, H. W.; Teoh, S. H.; Chan, C. K. C.; Lee, E. H. *Tissue Eng.* **2003**, *9*, S31–S44.
89. Spindler, K. P.; Imro, A. K.; Mayes, C. E.; Davidson, J. M. *J. Orthop. Res.* **1996**, *14*, 542–546.
90. Murphy, P. G.; Loitz, B. J.; Frank, C. B.; Hart, D. A. *Biochem. Cell Biol.* **1994**, *72*, 403–409.
91. Marui, T.; Niyibizi, C.; Georgescu, H. I.; *et al*. *J. Orthop. Res.* **1997**, *15*, 18–23.
92. Hildebrand, K. A.; Woo, S. L. Y.; Smith, D. W.; *et al*. *Am. J. Sports Med.* **1998**, *26*, 549–554.
93. Letson, A. K.; Dahners, L. E. *Clin. Orthop.* **1994**, *308*, 207–212.
94. Kobayashi, D.; Kurosaka, M.; Yoshiya, S.; Mizuno, K. *Knee Surg. Sports Traumatol. Arthrosc.* **1997**, *5*, 189–194.
95. Sahoo, S.; Ang, L. T.; Goh, J. C. H.; Toh, S. L. *Differentiation* **2010**, *79*, 102–110.
96. McDougall, J. J.; Bray, R. C. *Animal Models in Orthopaedic Research*; CRC: New York, 1999.
97. Jackson, D. W.; Grood, E. S.; Arnoczky, S. P.; Butler, D. L.; Simon, T. M. *Am. J. Sports Med.* **1987**, *15*, 528–538.
98. Jackson, D. W.; Grood, E. S.; Arnoczky, S. P.; Butler, D. L.; Simon, T. M. *Am. J. Sports Med.* **1987**, *15*, 295–303.
99. An, H. Y.; Friedman, R. J. *Animal Models in Orthopaedic Research*; CRC: New York, 1999.
100. Xerogeanes, J. W.; Fox, R. J.; Takeda, Y.; Kim, H. S.; Ishibashi, Y.; Carlin, G. J. *Ann. Biomed. Eng.* **1998**, *26*, 345–352.
101. Carpenter, J. E.; Hankenson, K. D. *Biomaterials* **2004**, *25*, 1715–1722.
102. Fan, H. B. *Biomaterials* **2009**, *30*, 4967–4977.
103. Cooper, R. R.; Misol, S. *J. Bone. Joint Surg. Am.* **1970**, *52*, 1–20.
104. Weiler, R. F.; Hoffmann, H. J.; Bail, O.; Südkamp, N. P. *Arthroscopy* **2002**, *18*, 124–135.
105. Spalazzi, J. P.; Dagher, E.; Doty, S. B.; Guo, X. E.; Rodeo, S. A.; Lu, H. H. *J. Biomed. Mater. Res.* **2008**, *86A*, 1–12.
106. Lim, J. K.; Hui, J.; Li, L.; Thambyah, A.; Goh, J. C. H.; Lee, E. H. *Arthroscopy* **2004**, *20*, 899–910.
107. Panni, A. S.; Milano, G.; Lucania, L.; Fabbriciani, C. *Clin. Orthop.* **1997**, *343*, 203–212.

5.526. Tissue Engineering of Muscle Tissue

I Conboy, J Freimer, and L Weisenstein, University of California, Berkeley, CA, USA

© 2011 Elsevier Ltd. All rights reserved.

5.526.1.	**Introduction**	345
5.526.2.	**Importance of Skeletal Muscle Tissue Engineering**	346
5.526.3.	**Muscle Development and Repair**	346
5.526.4.	**Scaffolding Materials**	347
5.526.4.1.	Hydrogels	347
5.526.4.2.	Synthetic Materials	347
5.526.4.3.	Natural Materials	349
5.526.4.4.	Collagen	349
5.526.4.5.	Fibrin	350
5.526.4.6.	Hyaluronic Acid	350
5.526.4.7.	Alginate	350
5.526.4.8.	Chitosan	350
5.526.4.9.	Matrigel	351
5.526.4.10.	Hydrogels for Vascularization	351
5.526.5.	**Additions to Current Matrices**	352
5.526.6.	**Vascularization**	352
5.526.7.	**Innervation**	353
5.526.8.	**Alternative Cell Types for Skeletal Muscle Engineering**	353
5.526.9.	**Electrical and Mechanical Stimulation of Skeletal Muscle**	354
5.526.10.	**Matrix Metalloproteinases**	354
5.526.11.	**Immune Response to Engineered Muscle**	355
5.526.12.	**The Aged Niche**	355
5.526.13.	**Pathological Environment**	356
5.526.14.	**Future Directions**	357
5.526.14.1.	Culturing Satellite Cells	357
5.526.14.2.	Genomics, Proteomics, and Metabolomics	358
References		358

Glossary

Angiogenesis The formation of new blood vessels.
Bolus A single, large dose of a drug.
Cross-link To covalently or ionically bond two polymer chains.
Electrospin A process in which an electric charge is used to draw up very fine fibers from a liquid polymer solution.
Innervation The distribution of nerve fibers to an organ or body region.
Micropattern To control the spatial arrangement at a microscopic level.
Photolithography The use of light energy to transfer a geometric pattern to a light-sensitive material.
Quiescent In a state of rest; a cell that is not dividing.
Sarcomere The contractile unit of a myofibril in striated muscle.
Striated muscle Contractile tissue under conscious control that consists of fibrils combined into a parallel fiber.
Topography The form and structure of a surface.
Vascularization The formation of blood vessels and capillaries in living tissue.
Xeno-free Solely of human origin (without animal contaminants).

5.526.1. Introduction

As specific cell types and their environments are becoming increasingly well characterized, it is becoming possible to manipulate and direct cells for precise functions. Scientists are studying how to grow and differentiate cells with the hope that any tissue in the body can be replaced. For instance, advances in tissue engineering could allow skeletal muscle fibers or muscle precursor cells to be grown in culture and then transplanted into a patient whose natural muscle regeneration has been impaired due to disease, age, or injury. However, much work remains to be done studying the complex signaling pathways and environmental cues that direct cell function and fate. In order to effectively grow tissue for therapeutic use, it is important to understand and perhaps, to mimic at least to some degree, the natural molecular composition of

such tissue. Currently, a major obstacle in tissue engineering using transplanted cells has been the efficient survival, proliferation, and differentiation of cells *in vivo*.

When designing a modern biomaterial for use in tissue engineering, various properties must be taken into account including the chemical composition of the material, the mechanical properties of the material, and any biological factors that will be incorporated. This chapter discusses several of the most common biomaterials including synthetic polymers and biomaterials based on natural nonmammalian and mammalian proteins. Additionally, since the natural environment is dynamic, this chapter discusses current work on the effect of stress, strain, and electrical current on biomaterials. Last, it discusses which biologically active molecules, such as peptides, growth factors, and other signaling molecules, can be incorporated in order to efficiently direct cell fate in tissue engineering.

Since cells inhabit a diverse range of environments, a universal biomaterial would not be suitable for all tissue types. To be most effective, a biomaterial should be designed for a specific type of tissue. This chapter focuses on defining the environment and important signaling molecules for skeletal tissue engineering by highlighting the importance of skeletal tissue engineering, discussing natural skeletal muscle development and repair, and discussing the current and future state of applicable biomaterials.

5.526.2. Importance of Skeletal Muscle Tissue Engineering

One of the major diseases affecting skeletal muscle is muscular dystrophy, a genetic hereditary disease, in which patient's muscles are weakened due to a loss of muscle-specific proteins, such as dystrophin. There are several types of muscular dystrophy ranging in severity: some cause little disability while others such as Duchenne muscular dystrophy (DMD) are often fatal. DMD mostly affects children from a young age and gets progressively worse. People with this form of muscular dystrophy are often unable to walk by the time they are a teenager and many die before their mid-twenties. There is currently no cure for muscular dystrophy, but skeletal muscle tissue engineering offers the prospect of regenerating a patient's muscles.

Additionally, tissue engineering can be used to help facilitate muscle regeneration in aged individuals whose ability to maintain or regrow muscle is greatly reduced, which causes the debilitating age-specific muscle wasting, lack of mobility, and independence.

Last, the development of biomaterials that emulate the natural tissue milieu can be used for *in vitro* studies. By studying cells in a more realistic, yet closely controlled environment, new models of young and aged, normal or pathological tissues can be studied with higher molecular precision.

5.526.3. Muscle Development and Repair

Skeletal muscle is composed of many individual fibers which are grouped into bundles and surrounded by connective tissue. Each muscle fiber is a long multinucleated cell composed primarily of actin and myosin myofibrils arranged into repeat units known as sarcomeres. In order for the muscle to function properly, it is critical that it is both highly vascularized and innervated.

During embryonic development, skeletal muscle arises from mesodermal precursor cells.[1] Upregulation of MyoD and Myf5 transcriptional activators directs these precursor cells to the myogenic linage.[2] MyoD/Myf5 positive cells become myoblasts then stop proliferating and terminally differentiate into cells that begin expressing myogenin, myosin heavy chain (MHC), and muscle creatine kinase (MCK), which are muscle-specific genes. The fusion-competent myoblasts fuse to form multinucleated myotubes which later on mature into muscle fibers. Additionally, quiescent satellite cells, a myoblast precursor that escaped terminal myogenic differentiation, populate the myofibers and are activated upon injury to regenerate damaged myofibers.[3–5]

Adult muscle regeneration can be broken into two phases, a degenerative phase in which damaged tissue is removed and a regenerative phase in which new tissue is grown. Injury often results in an increase of myofiber permeability, which results in increased serum levels of muscle proteins released by dying muscle fibers. At this time, molecular signals are sent for neutrophils to invade the muscle. Then, macrophages enter the injured site to phagocytose damaged cells and clear the way for muscle regeneration to begin.[6] It has been shown that the removal of damaged tissue and the secretion of growth factors by macrophages are required for normal muscle regeneration.[7] Furthermore, undergoing regeneration requires remodeling of the extracellular matrix (ECM). Where extensive damage occurs, or in the aged tissue, the ECM does not get completely remodeled, muscle injury site does not regenerate entirely, and fibroblasts form scar tissue which impairs muscle repair and muscle function.

The ECM serves as a structural support for tissue and is also vital for controlling cellular responses, for example, adhesion, migration, growth, and differentiation. Therefore, when designing biomaterials to be used in tissue engineering, it is important to accurately recreate the ECM effects on the key regenerative properties of muscle cells. *In vivo*, the basal lamina, which constitutes much of the skeletal muscle ECM, is composed of numerous components, including collagen, perlecan, laminin, entactin, fibronectin, as well as several glycoproteins and proteoglycans.[8] These proteins serve as a scaffold to provide support for cells to bind to and align in order to form parallel myofibers. Fibronectin in particular is important for the maintenance of skeletal muscle because it can bind to both integrin receptors on cells and other molecules in the ECM. Additionally, the ECM traps and regulates the diffusion of growth factors whose effect on cell fate will be discussed later in the chapter. Last, once the fibers have matured, movement generated from the contraction and relaxation of muscle fibers relies on cells binding to the ECM.

Adult skeletal muscles have a robust system of repair. It has been found that a large number of new myotubes arise within a couple days of acute muscle damage.[9] As mentioned earlier, skeletal muscle is made up of many muscle fibers which are long, multinucleated cells which arise from the fusion of myoblasts, a muscle progenitor cell. These myoblasts derive from satellite cells which are involved in postnatal regeneration of

skeletal muscle throughout adult life.[3,10] Satellite cells are mononucleated cells located on top of the plasma membrane of a muscle fiber and beneath the basal membrane, which surrounds the muscle fiber.[11,12] Satellite cells are believed to be the primary stem cells responsible for muscle regeneration and have been shown to be capable of self-renewal as well as differentiation into more specific muscle precursor cells (two key characteristics of stem cells).[13,14] The idea that they are self renewing is supported by the fact that in normal healthy individuals the number of satellite cells and their regenerative capacity remains fairly constant through multiple rounds of injury and repair.[9] Additionally, the theory that they are responsible for muscle regeneration is supported by experiments that show satellite cells alone are capable of regenerating damaged skeletal muscle.[9]

Satellite cells are quiescent, meaning that they remain in G0 phase of a cell cycle, until they receive certain stimuli at which point they activate, proliferate, and differentiate into muscle progenitor cells called myoblasts. Several common stimuli which trigger the activation of satellite cells include exercise, injury from myotoxins, disease, denervation, or other muscle damage. The satellite cells quickly become myoblast precursor cells, which differentiate into fusion-competent myoblasts. These myoblasts continue proliferating until there is a sufficient number for them to begin fusing with existing fibers or with other myoblasts to form new multinucleated myotubes.[5] Much work still needs to be done to characterize satellite cells and their niche (a specific microenvironment where muscle stem cells reside) in order to determine the exact combination of factors promote quiescence, self-renewal, and differentiation of satellite cells.

Currently, much of the research around muscle regeneration is focused on myoblasts since they are a muscle progenitor cell that can easily be expanded *in vitro*. However, myoblasts can only be cultured for a certain number of passages before the cells lose their regenerative capacity. Additionally, experiments using transplanted myoblasts have run into several issues.[15] First, majority of transplanted myoblasts die within the first few days after transplantation.[5] Second, myoblasts do not migrate more than ~200 μm from their initial injection site.[16] Last, transplantation requires immunosupressants, otherwise the cells are rejected by the host's immune system. Therefore, it would be ideal to develop a biomaterial that would allow satellite cells to be cultured.

Interestingly, it has been found that muscle stem cells maintain telomerase activity as opposed to their more differentiated progeny, myoblasts; and that aged mouse muscle fibers do not have shortened telomeres.[17] Therefore, it is advantageous to engineer muscle tissue from satellite cells which have telomerase activity, as opposed to expanded in culture myoblasts which would likely have shortened telomeres.

For functional muscle, innervations and vascularization are just as important as proper myofiber development. Functional muscle requires the transport of oxygen, carbon dioxide, and nutrients as well as waste, all of which is carried through the blood. Therefore, skeletal muscle requires an abundant blood supply, with blood vessels permeating throughout the muscle. A recent study emphasizing satellite cells' reliance on being close to blood vessels found that in humans 68% of satellite cells and in mice 82% of satellite cells are found within 5 μm of either capillaries or vascular endothelial cells.[18] Furthermore, in order for muscle to be functional, it must be able to receive and respond to nerve impulses. Therefore, any methods of engineering skeletal muscle must be capable of forming and promoting neuromuscular junctions. Summarily, for any engineered muscle tissue to be successful *in vivo*, it will have to promote and maintain the formation of vascularized and innervated myofibers.

5.526.4. Scaffolding Materials

5.526.4.1. Hydrogels

A hydrogel is classified as a highly hydrated polymeric material, usually with a water weight content of at least 30%. Due to this high water content, hydrogels have a high degree of flexibility that is often similar to that of natural tissue.[19] Hydrogels are composed of hydrophilic polymer chains and can be made from either natural or synthetic materials. These polymer chains exist as a liquid polymer solution in which cells of interest can be suspended. The polymer chains can be connected by a process called cross-linking: linking by an ionic or covalent bond. Cross-linking can be triggered by light, allowing for control over gelation based on light exposure. These scaffolds are advantageous in tissue engineering for many reasons: hydrogels are typically degradable, are highly variable in composition, can be produced under mild conditions, can be delivered in a minimally invasive manner, and share many mechanical and structural properties with natural tissues and the ECM.[20] Hydrogels provide a three-dimensional (3D) environment for which cells can adhere to and grow in. This environment can be varied based on the materials used or by the method of gel formation.[21]

5.526.4.2. Synthetic Materials

The use of synthetic materials in scaffolds allows for strict control of composition and chemical properties making the gel variable and reproducible. The degree of variation possible in synthetic hydrogels makes them an attractive choice as a scaffold for a wide variety of tissue engineering applications. Factors such as molecular weight, cross-linking sites, and degradable linkages can be varied in order to manipulate gel formation, density, and degradation properties.[20] These manipulations aid in the development of biomaterials that can have a specific, desired biological effect on cells.[22]

Of the synthetic materials currently being used in tissue engineering, poly-ethylene oxide (PEO), poly-ethylene glycol (PEG), and poly-vinyl alcohol (PVA) are polymers that are used most prevalently. These polymers are hydrophilic and can be modified by the addition of acrylates or methacrylates to each end.[20] These are salts and esters of acrylic and methacrylic acid, respectively, and they are used in polymer synthesis because they contain very reactive double bonds. This reactivity allows for the linking of polymer chains. The addition of these salts or esters is done by a process called photo-cross-linking in which light energy is used to make a covalent bond between two macromolecules. A hydrogel can then form when these modified polymers are exposed to UV light and cross-linked. The gel can be modified further to be degradable

by the creation of block copolymers, which incorporate hydrolytically degradable poly-lactic acid (PLA) and enzyme specific cleavage sequences of oligopeptides. The rate of degradation can then be controlled by the number of cleavage sites in the polymer and the amount of enzymes present in the scaffold environment.[20] This technique can be used to vary the degradation times of synthetic scaffolds for specific applications.

Although many of these synthetic materials have shown promise as scaffolds for artificial muscle growth, they suffer from a few drawbacks. Hydrogels, while largely nontoxic and nonimmunogenic, do not promote significant cell adhesion, which is critically required for myoblast migration and fusion. Therefore, for a functional scaffolding material, these hydrogels must be modified in order to create an adhesive surface. This modification involves covalent bonding of ECM proteins or peptide sequences to the polymer that are recognizable to myogenic cell receptors. Such technique has been, in fact, utilized in many recent studies, some of which are discussed below.

Another disadvantage to polymeric scaffolds in muscle tissue engineering is that they have a very high tensile modulus and a low yield elongation (3–4%), rendering them relatively inflexible and unable to undergo significant compaction. It is hypothesized that functional skeletal muscle tissue will fully develop *in vitro* only when subjected to strains that mimic those that occur during growth in the natural niche.[23] The inability of polymeric scaffolds to be compacted means that these scaffolds do not serve as an accurate representation of the natural environment in which muscle tissue develops functions and regenerates. During early phases of development of skeletal muscle, contractions of muscle fibers help stimulate the expression of proteins required for continued growth and development of muscle tissue. Without compaction of the scaffold, several key proteins involved in muscular development, namely actin and integrin, may not be properly induced for expression or become mislocalized within muscle cells. The lack of compaction and protein misexpression will likely hinder the synthesis and deposition of collagen and other key ECM proteins, ultimately perturbing the 3D structure of skeletal muscle.[24] Thus, correct compaction of the scaffold is required for the formation of artificial muscle tissue to be able to properly form and contract.

Many recent studies have attempted to alter polymeric scaffolds to overcome the drawbacks mentioned above. These alterations largely involve the specific geometric shaping of scaffolds in order to favor the growth of muscle tissue that is similar to natural muscle. By incorporating components into these scaffolds to which cells can bind, progress has been made in engineering muscle tissue that is structurally and functionally quite similar to natural tissue. Additionally, by using fabrication tools, such as photolithography (described below), etching, and molding, polymeric (and natural) scaffolds can be altered so as to provide a favorable topography for directional growth of tissue.[25,26] A few recent applications of polymeric scaffolds are discussed next.

Poly(L-lactic acid) (PLLA) has been used as a scaffolding substrate in both film and fiber forms. Strong, elastic fibers can be created by a process called wet-spinning, in which PLLA in a solvent (usually chloroform) is drawn up through a thin needle and extruded into a coagulating solution. In this solution, PLLA particles agglomerate and form fibers, which can then be removed from solution and integrated into scaffolds.[27] The fibers, when coated with ECM proteins such as laminin and fibronectin, allow for improved cell adhesion because the presence and moreover fibrillar topography of these proteins provide cells with numerous points for attachment. Additionally, the synthetic fibers provide a 3D scaffold favorable to elongated muscle fiber formation. In one study, these coated fibers were shown to promote myoblast differentiation into multinucleated myofibers, expressing muscle-specific markers such as myosin and α-actinin. The myoblasts were able to fuse to form linear, parallel myofibers along the individual PLLA fibers, mimicking natural skeletal muscle development.[28]

Similarly, polypropylene fibers (10–15 μm in diameter) coated with laminin have been used to create cell sheets. By stringing fibers together in close proximity, such as with a small comb, the individual coated fibers are allowed to interact with adjacent fibers. When placed 30–55 μm apart, the coated fibers encouraged the formation of a contractile skeletal muscle cell sheet with parallel-oriented myofibers.[29] The parallel alignment of these myofibers is directed by the geometry of the fibers; the small diameter allows for growth only along the axis of the fiber. When placed in close proximity, the layers of cells on single fibers can merge and form a cell sheet. However, as the study pointed out, upon sheet formation, the forced-parallel effect of single fibers disappears. As layers grow higher on the scaffold, they are no longer restricted by the fibers to a longitudinal alignment, so myotubes on the outermost layers will be less aligned than those in the center. This divergence in alignment could be limited by stacking thinner cell sheets together or by creating a 3D scaffold with horizontal and vertical planes so as to inhibit overly thick (and therefore misaligned) cell layers.[29] Once the techniques for functional cell sheets are perfected, these sheets could have important clinical use, such as use in grafts for abdominal hernias or muscle tears.

Polydimethylsiloxane (PDMS) is another material that has been used for scaffolding, especially in the field of microfabrication. PDMS is a silicon-based organic polymer with a repeat unit of $SiO(CH_3)_2$. It is generally nontoxic and inert and is FDA approved making it a good choice for use in scaffolding. Because of its dual elastic and viscous (viscoelastic) nature, PDMS can be used as a molding material. At high temperatures, PDMS will be viscous, while at lower temperatures and longer set times it will act as an elastic solid. Therefore, PDMS can be poured over a mold and left overnight (long set time) and it will take the shape of the mold and harden.[30]

In a recent study, PDMS scaffolds with microgrooves were shown to promote the growth of organized muscle tissue. In this approach, a photoresist was patterned by light in a process called photolithography, which uses light to transfer a geometric pattern to a light-sensitive material by selectively removing parts of the material. The microgrooves, which were 2 μm wide and 7 μm tall, were designed to be narrower in width than, but about the same height as, the size of the myoblasts that would be cultured on the scaffold. This was so the myoblasts in the bottom layer would be forced to sit either on the top of the ridge or to squeeze into a groove. Most myoblasts preferentially sunk into the grooves, allowing directional organization of the primary layer of cells. This was compared to shallower

microgrooves (2 μm in height) in which the myoblasts could lie across several layers and aligned poorly. When additional layers of myoblasts were seeded on top of this aligned primary layer, the myoblasts followed the parallel alignment of the first layer and formed mostly aligned myotubes. This muscle construct had multinucleate myotubes that also stained positive for myosin, showing its similarity to natural striated muscle. Furthermore, it was shown that the multilayered construct could be peeled off the PDMS scaffold, pointing to the utility of this approach.[30] Fabricated tissues could be grown on this scaffold and then detached for use in grafts and other clinical applications. It is important to note, however, that the myotubes in the secondary and higher layers differed morphologically from the primary layer of cells. Namely, the nuclei in the primary layer were elongated while those in the higher layers were rounded, and the expression levels of myosin differed between layers.[30] These differences show that surface topography has an important impact on myotube morphology and gene expression and, thus, should be considered in scaffold designs aimed at skeletal muscle engineering.

In another interesting study, PDMS scaffolds were created on molds patterned with abrasives. These molds were fabricated by grinding fine sandpaper (150 and 400 grit) linearly along an iron block. PDMS was poured over these molds to create micropatterned scaffolds. When coated with laminin, these scaffolds were also shown to promote proliferation of myoblasts and alignment of myotubes along the direction of grinding.[31] As opposed to other commonly used methods, this method is very easy, low cost, and does not require special equipment.

Patterned scaffolds have also been created out of other materials such as glass. Glass is a noncrystalline solid that can be micropatterned by several different methods. A recent work showed that borosilicate glass (composed of silica and boron oxide) patterned with aluminum allowed for myotube formation and alignment without any coating. This scaffold was created by layering aluminum on top of the glass where a photoresist and photolithography were used to create a micropattern on the aluminum. The aluminum was then patterned using a process called reactive ion etching followed by an etching of the glass. The final scaffold consisted of only a 1.5-μm thick aluminum layer and etched glass. The channels, which were optimally 6.7-μm deep and 20-μm wide, promoted neat, parallel arrangement of myoblasts, which fused to form myotubes. Visualization by staining showed long bundles of actin filaments, as well as elongated nuclei – properties evocative of natural muscle. The myotubes were also shown to be capable of spontaneous and electrically induced unidirectional contractions, demonstrating that this technique could be useful for studying the basis of contraction in muscle tissue. Also, due to the neat arrangement of myotubes, individual cells with their protein expression were able to be distinguished.[32]

In order to overcome the drawback of inflexibility of typical polymeric scaffolds, recent attempts have been made to create a synthetic material with more favorable mechanical properties. One such material is a degradable block copolymer of polyesterurethane called DegraPol. This scaffold is created by a process called electrospinning in which an electric charge is used to draw very fine fibers from a liquid.[33] DegraPol exhibits linear elastic behavior up to 10% deformation, meaning it can be stretched significantly without losing its shape. It also has an elastic modulus around 10 MPa, a 1000-fold reduction from other polymeric scaffolds.[23] This high elasticity of the scaffold owes to the reticulated structure of the membrane (from electrospinning) as well as the elasticity of the block copolymer itself. This elasticity is a suitable match to the elasticity of soft tissues such as skeletal muscle. Regarding cellular response on these scaffolds, myoblast adhesion and directional organization along the scaffold fibers were similar to the physiological muscle in which myoblasts develop into parallel-oriented myotubes. Additionally, DegraPol has been shown to be nontoxic and it is degradable by hydrolysis.[23] These findings point to the potential of DegraPol as an alternative promising scaffold for muscle tissue engineering.

5.526.4.3. Natural Materials

Naturally derived polymers have also been widely used in hydrogel and scaffold synthesis. These natural polymers either are part of, or contain components similar to the natural ECM. Collagen, fibrin, hyaluronic acid (HA), alginate, and chitosan are some of the most common natural polymers used. Collagen is the most abundant protein in mammalian tissues and therefore is a suitable choice for a hydrogel matrix. Similarly, HA, alginate, and chitosan are found in all tissues of adult mammals. These are linear polysaccharides that integrate well *in vivo* due to their natural niche. These purified or recombinantly produced ECM components can be combined with other natural components, for example, bioactive peptides, growth factors, etc., to create a well defined and potentially less immunogenic muscle engineering scaffold.

5.526.4.4. Collagen

Collagen is composed of three polypeptide chains wrapped around one another to form a rope-like structure. The strands are held together by both hydrogen and covalent bonds and can self assemble stably. Collagen fibers can be manipulated with the help of cross-linkers, so as to vary their mechanical properties. This manipulation includes cross-linking with chemicals such as glutaraldehyde or formaldehyde, physical cross-linking using UV radiation or freezing/heating treatments, and by the addition of other polymers such as HA, PLA, and PGA (poly-glycolic acid). Another advantage of collagen as a scaffold material is that it is naturally degraded by collagenase. This means that the degradation of collagen gels can be controlled locally by cells included in engineered tissue or adjacent to the transplant.[20]

Collagen has been a popular choice for use in muscle engineering scaffolds. Hydrogels composed largely of collagen have been shown to induce the formation of mature sarcomeres. However, one notable limitation is that collagen gels have been shown to exhibit poor nutrient diffusion, which leads to a lower oxygen consumption by the artificially created muscle.[34] Collagen matrices have also been combined with microfabricated scaffolds in order to promote 3D tissue formation. This is done with PDMS molds with staggered posts. These molds can be layered with a collagen/fibrin hydrogel in order to create porous tissue networks. These networks allow

for improved nutrient and oxygen transport through the gel as well as effective cell alignment.[24] Using this technique, pore size, thickness, and spatial cell distribution can be reproducibly varied, allowing for controlled manipulation of artificially engineered muscle tissue. For example, by creating a PDMS mold with tall and very thin posts, the size of the pores will be minimized, thereby maximizing the tensile strength of the engineered muscle while still allowing nutrients and oxygen to reach the growing cells.[24]

5.526.4.5. Fibrin

Fibrin is a naturally occurring fibrous, elastic protein that also has favorable properties for scaffold formation. Fibrin plays an important role in the body for blood clotting; when injury occurs, a soluble precursor to fibrin, called fibrinogen, is cleaved by a protease called thrombin. Fibrin fibers then are cross-linked to form an interlacing, insoluble mesh, known as a clot. This clotting process can be utilized in order to create self-assembling scaffolds of fibrin, which is a natural biocompatible and biodegradable protein. Unlike polymeric scaffolds, fibrin has a high affinity for biological surfaces and molecules making it a good candidate for muscle tissue engineering and transplantation vehicle.

Taking the advantage of the fibrin–thrombin system, a recent work demonstrates a dual compartment injection device that is a 3D injectable scaffold. In the device, one compartment was loaded with fibrinogen and the other was loaded with thrombin and cultured myoblasts. When these two compartments were combined in a lower chamber, fibrin polymerized in about 30 s creating a 3D fibrin–myoblast matrix. This liquid to gel transition allowed successful 'filling' of muscle defects in a rat model.[35] This study focused on the idea of culturing myoblasts *in vitro* but allowing differentiation to occur *in vitro*. This ensures that the artificial muscle will fit the muscle defect, as opposed to prefabricated constructs, which might not be of optimal shape. Upon implantation, the matrix allowed the localization of myoblasts at the site of injury and fusion of the transplanted male myoblasts with host female muscle fibers successfully occurred.[35] Introducing vascularization into the fibrin–myoblast matrix could further improve the therapeutic potential of this scaffold.

5.526.4.6. Hyaluronic Acid

HA is a simple glycosaminoglycan composed of a repeating disaccharide and is often seen *in vivo* during wound healing. Hydrogel formation with HA is done by esterification, by annealing, and by covalent cross-linking with hydrazide (a compound with a nitrogen–nitrogen covalent bond and an acyl group) derivatives. HA can also be combined with collagen and alginate to form compounded hydrogels. HA is naturally degraded by hyaluronidase, and like collagen, its degredation can be regulated by cells present in the engineered tissue.[20]

5.526.4.7. Alginate

Alginate is another commonly used natural material, though the purity of commercially available alginate has continually been a problem. Alginate is a linear polysaccharide that is derived from brown seaweed and bacteria. It is composed of alternating mannuronic acid and guluronic acid monomers. In order for gel formation to occur, divalent cations such as Ca^{2+} come into contact with the monomer blocks and interact with the guluronic acid to form ionic bridges between polymer chains. Variation of the amount of mannuronic acid compared to guluronic acid will change the cross-linking density of the gel, and therefore, properties such as pore size and stiffness can be tuned. Another technique of gel formation is cross-linking of alginate with adipic hydrazide (a dicarboxylic hydrazide) and PEG.[20] An important aspect of alginate scaffolds is the addition of cell adhesion ligands so that mammalian cell interaction can occur. RGD can be covalently attached to alginate scaffolds and, at specific densities, has been shown to promote efficient myoblast differentiation.[36]

The degradation of ionically cross-linked alginate hydrogels is not specific, but rather the gel degrades very slowly and without control. The rate of dissolution depends on the ionic environment that the scaffold is placed in. As ion exchange of calcium occurs, individual polymer chains dissociate leading to a loss in mechanical stiffness. As a result of dissolution, high molecular weight polymer chains are released, which may present a problem when using these gels for *in vivo* tissue engineering applications.[20] In order to counter this unfavorable degradation, work has been done to synthesize partially oxidized alginate that can undergo hydrolysis in aqueous solutions. It was shown that alginate that is oxidized to about 5% will degrade with a rate depending on the pH and temperature of the aqueous solution. This partially oxidized polymer retained all of the functionality of a traditional alginate hydrogel, but its degradation time was reduced to nine days.[37] Another study showed that myoblasts had a high proliferation rate on degradable alginate gels of controllable mechanical stiffness (13–45 kPa) compared to nondegradable gels.[38] Additionally, alginate has been used as part of a polymeric delivery vehicle for myoblasts. A system consisting of a macroporous alginate scaffold and growth factors (HGF and FGF2) greatly increased the viability and migration potential of seeded myoblasts over a period of 5 days.[39] This kind of delivery system, once perfected, would be of great utility to site-specifically deliver myoblasts and

5.526.4.8. Chitosan

Chitosan has been used in tissue engineering scaffolds due to its similarity to natural glycosaminoglycans. Chitosan is derived from chitin and is a linear polysaccharide composed of D-glucosamine derivatives. The free amino groups of chitosan can be protonated making chitosan soluble in acids. The dissolved chitosan can then form a gel with an increase in pH or by the extraction of the solution into a nonsolvent. Gel formation can also occur by cross-linking with glutaraldehydes, UV radiation, and temperature changes. Chitosan is degradable by lysozyme, a common enzyme present in humans. The speed of degradation can be controlled by the intrinsic properties of the chitosan: the degree of nitrogen deacetylation varies usually from about 50% to 90% and will determine the crystallinity of the chitosan gel. The rate of

degradation of these gels is inversely related to the degree of crystallinity: the less crystalline the material, the faster it degrades.[20]

An important potential application of hydrogels is their ability to be reversibly cross-linked based on changing conditions. This property can be used when tuning these gels for clinical applications. For example, many studies have shown development of hydrogels with specific gelling temperatures. These so-called thermoreversible gels will transform from solution to a gel above a certain temperature. This is especially applicable for the development of injectable hydrogels as an *in vivo* tissue engineering scaffold. In one study, a PEG–chitosan copolymer was shown to gel above 25 °C and in a pH range of 6.4–8.5, and thus gels readily in physiological conditions.[40] The mechanism behind thermoreversible behavior has to do with changes in intermolecular bonding with temperature variation. At low temperatures, hydrogen bonding between water and chitosan and PEG chains prevails, disrupting association between polymer chains, thus making the PEG–chitosan copolymer soluble in water. As the temperature is increased, water molecules begin to fall off the polymer chains, allowing an increased interaction between the polymer chains. Without competition from water, hydrogen bonding between chitosan chains as well as intermolecular interactions between PEG chains can occur, leading to gelation.[40] As opposed to other studies in which cross-linking was used to create copolymers, this study utilized a process called grafting. In this process, a PEG–aldehyde was reacted with chitosan to create an imine (a compound containing a carbon–nitrogen double bond) and then reduced to form the PEG-grafted chitosan. Using this technique, the amount of PEG grafted can be varied in order to tune the viscosity, gelling temperature, and solubility of the copolymer.[40] As a side note, it is also important to note that the use of chitosan, a natural polysaccharide, and PEG, an FDA-approved polymer, makes this gel biocompatible as well as biodegradable. With these properties, this gel has the potential to be used clinically as an injectable scaffold loaded with cells.

Chitosan has also been used as a biodegradable surface onto which cellular micropatterns have been added.[41] These micropatterns can contain growth factors or cells themselves, so as to facilitate spatial control over the adhesion and differentiation of cells. In this way, cells can be exposed to different signals on the same scaffold, allowing a more dynamic signaling network and therefore a more biologically relevant growth environment. One example of such micropatterning is the stamping of lanes of immobilized vascular endothelial growth factor (VEGF) (covalently attached to collagen IV) onto a non-cell adhesive layer of photo-cross-linkable chitosan. When embryonic stem cells (ESCs) were seeded onto this surface, they were shown to preferentially differentiate into endothelial cells when on the VEGF lanes, but differentiated into vascular smooth muscle-like cells on the collagen only lanes (without VEGF). By using this technique with further improvements, such as layering of sheets, it may be possible to grow vascularized tissue by using a common progenitor population. However, the study mentioned involves the growth of smooth muscle tissue, and work remains to be done with this technique and skeletal muscle tissue.[42]

5.526.4.9. Matrigel

Matrigel is a commercially available matrix that is often used for coculture with other natural matrix materials such as collagen. Matrigel is derived from a mouse tumor rich in laminin, collagen, and other ECM proteins.[43] Due to its murine origins and potential tumorigenicity, Matrigel cannot be used in humans. However, it is a useful component in scaffolds as a growth factor and adhesion factor combination and was extensively used to study approaches to engineering muscle and other tissues and to maintain ESCs in culture.[44]

5.526.4.10. Hydrogels for Vascularization

Skeletal muscle is a thick, highly vascularized tissue and in the engineering of skeletal muscle tissue, a critical hurdle to overcome is the difficulty in obtaining well-vascularized engineered tissue. Vascularization of artificial muscle tissue *in vitro* is an important factor in maintaining cell viability during tissue growth, inducing proper structural organization of the muscle, and promoting functional vascularization upon implantation.

Many studies have attempted to induce vascularization of muscle tissue *in vivo* by delivery of growth factors.[45–47] However, recent attempts have been focused on the induction of endothelial vessel networks in engineered muscle tissue *in vitro*. In this approach, a highly porous 3D matrix composed of 50% PLLA and 50% poly-lactic-glycolic acid (PLGA) was seeded with mouse myoblasts and human embryonic (or umbilical vein) endothelial cells. With this construct, it was shown that the myoblasts successfully differentiated to form partially aligned and elongated myotubes. Moreover, the endothelial cells organized into tubular structures in between these myotubes to form vessel networks. When implanted, the prevascularized construct showed functional integration with *in vivo* muscle tissue; host blood vessels permeated into the constructs and after 2 weeks, the construct-derived vessels had anastomosed with host vessels.[45] Consequently, blood perfusion to the implant was relatively effective, pointing to an improved survival probability of these prevascularized implants *in vivo*. The success of this multicell tissue engineering illuminates the potential to provide the appropriate signals for organization and vascularization of skeletal muscle tissue first *in vivo* and then successful transplantation into a patient.

As an alternative to using biomaterials as scaffolding materials for growth of functional tissue, the use of polymer-coated materials has been explored. By coating conventional surfaces with a temperature sensitive polymer (poly(*N*-isopropylacrylamide)) at nanoscale thickness, changes in the surface properties of the scaffold can be manipulated by simply changing the temperature. At high temperatures, that is, those above a certain critical temperature, the polymer-coated surface is slightly hydrophobic, allowing for cell adhesion and proliferation. However, at temperatures below the critical temperature, the surface becomes slightly hydrophilic, allowing for the formation of a hydration layer between the attached cells and the culture surface. This permits easy harvest of intact cell sheets so as to maintain the important cellular connections within the sheet. This technique facilitates not only the growth

of thick, vascularized tissue, but also the easy transfer of cell sheets to other cultures or host tissues.[48]

5.526.5. Additions to Current Matrices

As discussed, current polymers serve as an important first step when designing a scaffold for tissue regeneration.[49,50] However, in the body, cells are tightly regulated and directed by a myriad of signals. To construct a more useful matrix and to better mimic the *in vivo* environment, biologically active molecules such as proteins and growth factors can be incorporated into polymers. During natural regeneration, there are three types of factors that act on the cell: molecules that make up the ECM, both autocrine and paracrine signaling molecules, and physical forces (such as pressure, flow, and shear). When designing a matrix which is more complex than a simple polymer, there are several requirements that must be considered. These requirements include the ability to embed cells, degradability to allow natural tissue formation, incorporation of factors that promote the growth of specific cell types (myofibers, capillaries) while impeding the growth of other cell types (scar tissue), as well as the spatial and temporal release of these growth factors.

Currently, the transplantation of myoblasts has not been very successful. Studies have found that myoblasts injected systemically are unable to cross vasculature barriers and must, therefore, be transplanted at the site of injury.[51] However, a large number of injected myoblasts die within several days. A material's ability to elicit aspects of natural regeneration in conjunction with transplanted cells may improve cell survival and integration.

Before discussing more advanced biomaterials, it is important to note that the natural environment of an organ (especially pathological or injured and regenerating tissue) is incredibly complex, and it is likely that it will be impossible to recreate it perfectly. However, cells secrete their natural extra cellular matrix proteins.[52] Furthermore, it has been shown the molecules that make up the ECM are upregulated as myoblasts fuse and mature to form myotubes. If suitable matrices can be engineered that effectively promote the initial cell viability, migration into injury site and support the regenerative responses, then, as these cells expand and differentiate, they will secrete molecules and proteins that change the engineered ECM into the natural ECM of skeletal muscle. Signals are passed bidirectionally between cells and their environment and cells contained in the muscle transplant will dynamically change their responses based on environmental cues that are provided by engineered niche and those emanating from the site of the transplantation.[53]

One way to vastly improve engineered matrices is with the incorporation of growth factors. These growth factors are often absorbed in the ECM so that the signals are targeted to the surrounding cells rather than throughout the body. By introducing desired growth factors, it is possible to enhance the proliferation of myoblasts, formation myofibers and encourage vascularization.[6,52] Various growth factors that are important in adult muscle tissue formation have been identified. A few important ones include: hepatocyte growth factor (HGF) which activates satellite cells, fibroblast growth factor (FGF) which increases satellite cell proliferation and perturbs differentiation, and insulin-like growth factor (IGF) which increases proliferation and increases differentiation.[3,54] Furthermore, culturing muscle precursor cells *in vitro* in the presence of growth factors increases their survival upon implantation.[55] These molecules are of course tempting candidates to be added to scaffolds for skeletal muscle engineering.

Several studies have tried to improve muscle tissue engineering by supplementing transplantation of matrices and/or cells with injections of growth factors. However, bolus injects have proved ineffective due to their low specificity for the target cell population, the short half life of many growth factors, and the possible side effects of increased growth factor concentration in other parts of the body.[56,57] Growth factors can be incorporated into polymers and then released over time to a precise location. By embedding proteins within the polymer, they are protected from premature denaturation and loss of activity. Furthermore, the creation of high-pressure gas foaming technique allowed the growth factors to be incorporated into polymers without using harsh chemicals or high temperatures which often lead to denaturation and loss of function.[57] As discussed earlier, the degradation of a polymer or its permeability can precisely be controlled, which means that the release rate of embedded growth factors can be tightly regulated. One of the most studied uses of growth factors is to promote vascularization in regenerating tissue is VEGF.[52,56,58]

5.526.6. Vascularization

As discussed earlier, vascularization is critical for cell survival and thus neovasculizarization will be an important consideration when attempting to regenerate muscle. A variety of approaches are being explored ranging from using growth factors to recruit endothelial cells *in vivo* to attempting to induce vasculzarization *in vitro* and then form transplant capillaries. To emphasize again the importance of efficient vascularization, it has been found that if the distance between capillaries and cells is greater than a few hundred microns, cells will not receive adequate oxygen and hypoxia will occur.[58] Vascularization begins with the recruitment of endothelial progenitor cells that bind to signaling molecules, for example, specific peptide sequences and growth factors. For example, the amino acid sequence REDV, which is derived from fibronectin, specifically binds endothelial cells.[59] By incorporating REDV into a polymer, it might be possible to attract endothelial cells to desired location (e.g., at the site of transplantation or injury) and induce them to form capillaries there.

Polymers embedded with growth factors that regulate the formation of blood vessels' vascularization are also being developed. PDGF, VEGF, and basic fibroblast growth factor (bFGF), which are some of the most important and well characterized regulators in endothelial cell responses, have been successfully incorporated into hydrogels. VEGF has been found to be one of the most important growth factors in all stages of neovascularization. It facilitates the recruitment of endothelial progenitor cells and induces their proliferation. It also initiates the sprouting of new blood vessels and keeps immature vessels alive until they are stabilized by mural cells and

the surrounding ECM.[56,58] Platelet-derived growth factor (PDGF) regulates the maturation of blood vessels. bFGF participates in vascularization by promoting endothelial cell proliferation and physically organizing endothelial cells so that they can form vessels.[57] While these factors are important for vascularization, they must be delivered properly in order to coordinate the desired ogranogenic effect. As mentioned earlier, bolus inject can result in severe side effects. It has been found that excess VEGF can cause vascular leakage, hypertension, malformed vessels, abnormal vascular stress, and cardiovascular malformation in addition to neovascularization of nontarget tissue.[58] Additionally, over expression of bFGF has been found to increase the risk of tumor formation.[60] Furthermore, some studies have found that using increasing levels of VEGF through adenovirus or direct injection did not lead to a significant increase in vascularization.[58] These findings suggest that it might be necessary to mimic the release kinetics of natural neovascularization by embedding the growth factors in a polymer and controlling their release more precisely through the degradation rate.

Additionally, some research is being done vascularizing the tissue *in vitro* before transplantation.[61] For example, endothelial cells were positioned in between myoblasts and allowed to form vessel networks *in vitro*. This prevascularization resulted in increased blood perfusion and muscle tissue survival after transplantation.[62] This concept is being explored by microfabrication techniques that would allow endothelial cells and growth factors to be printed into networks on a polymer and induced to form vascular networks in predictable way and either prior to or during the transplantation of the engineered muscle.

In addition to introducing growth factors themselves, ways to genetically modify cells to secrete overxpressed exogenous growth factors are being explored. Human myoblasts which were genetically engineered to secrete VEGF promoted vascularization.[63] Additionally, engineered matrices allow one to use plasmid DNA that can be incorporated into synthetic polymers and transfect neighboring cells *in vivo* in order to produce specific growth factors in the desired location. It has been shown that the constant release of plasmid DNA coupled with the right mechanical cues greatly increases transfection levels *in vivo*.[64] All these methods might one day greatly improve the ability to engineer and transplant artificial muscle tissue. At the same time, the danger of hyperactive formation of blood vessels should be certainly considered in such approaches as it might lead to tissue neoplasty.

5.526.7. Innervation

Another consideration when dealing with large muscle injuries is denervation. After injury, lack of innervation is the main cause of poor restoration of muscle regeneration, resulting in the lack function and muscle atrophy. Denervated muscle can become reinnervated as axons grow across lesion sites eventually reaching denervated muscle and reestablishing neuromusclular junctions.[65,66] The bioengineering approaches to control muscle innervation are not yet well developed. However, there have been some studies in which synthetic conduits with growth factors have been used to successfully improve innervation. Neurotrophins are a type of growth factor that influence the survival and differentiation of neurons. During innervation and muscle regeneration, neurotrophins are secreted by the muscle to promote the regeneration of axons. In an interesting study, over expression of glial cell-derived neurotrophic factor (GDNF) resulted in enhanced reinnervation after muscle injury.[66] Additionally, brain-derived neurotrophic factor (BDNF) is expressed by skeletal muscle and is important for the survival, growth, and differentiation of neurons in that tissue.[66] Glial growth factor (GGF) embedded in PLGA increased the number of axons and blood vessels in living animals.[67] Additionally, nerve conduits based on natural ECM molecules or synthetic polymers are being developed. These scaffolds can be used to guide and aid the regeneration of axons. Natural ECM molecules such as fibronectin and collagen have been shown to influence axon outgrowth.[66] Fibronectin has also been shown to promote Schwann cell migration.[68,69] Furthermore, some ECM scaffolds appear to have interesting inherent properties that help innervating muscular tissue.One study has found that ECM scaffolds promote neuronal and Schwann cell survival and outgrowth in regenerating muscle. The study found that the topology of ECM scaffolds supported neuronal growth *in vitro*. The study also found that, during remodeling, the degradation of the ECM scaffold produced matricryptic peptides that caused the migration of Schwann cells into the regenerating area.[70] Additionally, other molecules such as poly-3-hydroxybutyrate (PHB) are being investigated as nerve conduits. An interesting work found that PHB can be used to aid nerve repair as well as allowing angiogenesis without evoking an inflammatory response. The study found that PHB could allow nerves to regrow across a 10 mm gap (reviewed in[66]). In addition to nerve conduits, the incorporation or activation of Schwann cells may help reinnervation. Schwann cells play an important role in nerve regeneration by supporting and guiding regenerating axons. They secrete and display many trophic factors that promote the survival, growth, and extension of motor neurons. While the role of growth factors and guiding scaffolds was extensively studied with respect to peripheral nerve regeneration, their application specifically to reinnervation of injured or pathological skeletal muscle remains unexplored.[71]

5.526.8. Alternative Cell Types for Skeletal Muscle Engineering

In addition to studying satellite cells and myoblasts for potential therapeutic uses, some researchers are also exploring myogenic potential of various stem cells. ESCs are both self renewing and pluripotent meaning that they can differentiate into any cell type in the body and maintain their pool virtually indefinitely.[72] ESCs are, therefore, very promising for regenerative medicine, since large quantities of the cells can be grown and then differentiated into the desired tissue. Currently, ESCs can be successfully cultured, but fully directing their differentiation toward skeletal muscle lineage remains elusive and the efficiency remains low, as most approaches start with embryoid body-based spontaneous differentiation. However, some studies have shown that it is possible to direct ESCs to a myogenic lineage. Specifically, by over-expressing Pax3, it was

possible to expand the numbers of paraxial mesoderm cells in embryoid bodies and then sort cells based on PDGF-αR^{+}/Flk-1^{-} profile to obtain myogenic progenitor cells.[73] It has been shown that Pax3 is an important regulator of myogenesis, which turns on several downstream myogenic factors and without Pax3 skeletal musclulature does not form during embryonic development.[5] ESCs that are induced to differentiate into myogenic lineage upregulate Pax3, Myf5, Myod1, Myogenin, and MHC in that order, demonstrating a progression from less differentiated muscle precursor to terminally differentiated myotube.[73] Additionally, these cells differentiate into skeletal muscle in cardiotoxin injured muscle and dystrophic muscle in mice, demonstrating their *in vivo* myogenic potential.[73]

However, there are several drawbacks of human ESCs (hESCs). There is a debate about whether it is ethical to use ESCs since they are derived from the inner cell mass of the blastocyst, a process which destroys a human embryo. Additionally, when hESCs are injected into an animal they form a teratoma, which is essentially a big tumor. Therefore, any hESC-derived cells must be fully differentiated and completely isolated before they can be transplanted into a patient. One alternative to ESCs is induced pluripotent stem cells (iPS). iPS cells are somatic cells which can be induced to an ESC-like state and then differentiated into a different cell type.[74–78] iPS cells have their own problems; currently, iPS cells are not identical to ESCs and the efficiency of reprogramming a somatic cell to an iPS cell is very low. Undifferentiated iPS cells also form teratomas. However, iPS cells also have several advantages. They avoid the ethical considerations of destroying a human embryo and since they can be derived from a patient's own tissue they will be a perfect match for that person and will not experience immune rejection. Another alternative cell type that people are exploring for muscle regeneration is multipotent adipose-derived stem cells (hMADS). One study found that injection to mdx mice (which serve as an animal model for human muscular dystrophy) of hMADS cells resulted in the formation of new myofibers expressing dystrophin. Furthermore, the study found that hMADS decreased necrosis in the muscle of these mice.[79]

5.526.9. Electrical and Mechanical Stimulation of Skeletal Muscle

One alternative to transplanting muscle precursor cells to an injury is to differentiate these cells *in vitro* and then transplant muscle grafts. Previous studies have shown poor delivery to the injury site as well as poor survival and integration of transplanted cells. Therefore, some researchers are exploring the possibility of developing mature muscle sections *in vitro* which can later be grafted to an injured site. In addition to the synthetic scaffolds already discussed, the use of mechanical and electrical stimulation *in vitro* is explored for mimicking some of the signals that forming muscle receives during repair after injury *in vivo*. It is believed that during early fetal development, muscle tension created by bone growth contributes to muscle development.[80] Similarly, during exercise, muscles number and the sine of muscle fibers increase if that organ is stressed.[81] Studies have shown that mechanical forces help recapitulate the natural cellular environment by providing mechanical cues to help direct cell orientation. When pulled with light tension, muscle fibers adapt and are conditioned to function correctly; studies have shown that mechanical stimulation affects metabolic activity, protein localization, gene regulation as well as increases myofiber organization and cell proliferation. Cyclic strain can activate quiescent satellite cells as well as increase the proliferation of myoblasts.[82] Additionally, an interesting work demonstrates that sustained tension regulated the alignment and fusion of myoblasts into myofibers.[82] Furthermore, strain and relaxation increased the elasticity, myofiber diameter, and myofiber area of muscle fibers engineered *in vitro*.[82]

In addition to mechanical stimulation, electrical stimulation has been shown to play an important role in skeletal muscle differentiation by increasing cell proliferation and inducing proper orientation of myoblast prior to their fusion into myotubes.[29] By incorporating an exogenous electric field across the polymer fibers, the signals of neurons *in vivo* can be mimicked: the timing of the exogenous electric signals can be matched to that of the action potentials down axons. Signals delivered as impulses, in about 3 ms intervals of 70 mV, very closely mimic those signals sent by neurons in natural development.[83] These signals help activate certain chemical cascading systems in the muscle tissue, aiding the muscle tissue's growth. In another study, it was shown that electrical stimulation did not affect cell viability and increased the release of NO which typically activates the regenerative myogenic responses of satellite cells.[84] Furthermore, it was found that electrical stimulation increased the expression of MyoD and Desmin, two myogenic markers. Overall, it has been found that electrical stimulus improves the activation of satellite cells, myoblast fusion, myotube growth, and myofiber density. Therefore, in addition to scaffolds previously mentioned, some research is being done on designing polymers with electrical conducting properties. Conducting polymers are being explored as a material for *in vitro* differentiation because they provide a scaffold for support, allow the transmission of mechanical and electrical stimuli and can be modified by biologically functional molecules such as ECM components mentioned earlier in this chapter.[85]

5.526.10. Matrix Metalloproteinases

As discussed earlier, the phagocytosis and break down of the existing ECM is essential for any new tissue, including new muscle to form. Much of this degradation is regulated by matrix metalloproteinases (MMPs) and tissue inhibitors of metalloproteinases (TIMPs). TIMPs regulate the activity of MMPs by binding them and inactivating them while membrane-type MMPs (MT-MMP) activate MMPs. In healthy tissue, MMPs are expressed in low levels, while TIMPs are expressed at a high level. During muscle regeneration and inflammation, cytokines, growth factors, and hormones are activated which in turn increases the production of MMPs and down regulates the expression of TIMPs.[86] Both MMP-2 and MMP-9 break down the major components of the ECM and the basal lamina to allow myoblasts to migrate into an injury site.[87] In several studies, it has been found that over expression of MMP-2 significantly increased myoblast migration *in vivo*.[88]

Additionally, MMPs work to prevent the accumulation of excess ECM molecules, for example, scarring and fibrosis. The formation of scar tissue impedes muscle regeneration by providing a physical barrier to vascularzation as well as myoblast migration and differentiation. Furthermore, fibrosis provides chemical signals that can disrupt the natural muscle regeneration. MMP-1 is able to digest scar tissue and thus improve muscle regeneration.[89–91] Additionally, it has been found that myogenic factors are upregulated by MMP-1 and that MMP-1 is also able to induce myoblast migration and differentiation.[91] MMPs serve a vital role in clearing an injury site so that the necessary steps for muscle regeneration, such as vascularization and formation of new peripheral nerves, can occur.[89–92] Therefore, incorporation of MMPs into biomaterials or factors which promote the production of MMPs by cells of the transplant or locally in the host's tissue may be useful to enhance muscle regeneration.

5.526.11. Immune Response to Engineered Muscle

Mediating the immune response will be vital to successful muscle regeneration. Studies have shown that an initial inflammation has a positive role in recovery; however, excessive inflammation can lead to scar formation and impede regeneration.[54,93,94] When the muscle is injured, inflammatory cells and cytokines accumulate at the site of injury. The first cells to respond are neutrophils which begin to phagocytose necrotic tissue as well as release proinflammatory cytokines to magnify the inflammatory process.[54] Next macrophages are recruited to the injury site. Macrophages are believed to be involved in many steps of regeneration including: participating in phagocytosis of cellular debris, mediating the immune response to switch from promoting inflammation to reducing inflammation when regeneration starts, releasing growth factors to promote muscle precursor cell activation, proliferation, and differentiation as well as vascularization of new muscle.[54] Studies have shown the importance of macrophages for muscle regeneration by demonstrating that a decreased number of macrophages results in reduced satellite cell differentiation and growth of myofibers. Furthermore, studies have shown that when taken for longer than several days nonsteroidal anti-inflammatory drugs (NSAID), which inhibit inflammation, lead to decreased muscle regeneration and increased fibrosis.[54] Additionally, either a coculture of myoblasts and macrophages or macrophage conditioned media increased myoblast proliferation and myotube formation.[95,96] These findings suggest that inflammatory cells play a vital role in muscle repair. First, they aid MMPs in clearing the injury site of damaged tissue so that healthy tissue can be formed, and then they secrete growth factors which promote the regeneration of muscle tissue. Using the cells and cytokines of native immune response as components in muscle tissue engineering might, thus, be a good strategy.

5.526.12. The Aged Niche

It is well known that during aging, skeletal muscle atrophies and declines in function. These effects are due to a number of age-imposed changes, including a reduced ability of muscle satellite cells to regenerate new tissue. In order to fully understand this decline in function, it is important to study the changes that occur with age in the satellite cell niche. The niche consists of many components and is a heavily dynamic environment that influences the quiescence or activation of satellite cells. During aging, several of these components are altered causing a reduced regenerative capacity of satellite cells residing in the old muscle stem cell niche.

With aging, it appears that the reduction in muscle regeneration comes not from a reduction in the satellite cell population, but rather, a reduced satellite cell functionality.[97,98] On one hand, this is influenced by changes in the satellite cells themselves; the nuclear to cytoplasmic ratio has been shown to be higher in satellite cells in an aged environment.[99] On the other hand, the activation of satellite cells is dependent on external factors, and during aging, satellite cells have shown a delayed and decreased response to activating stimuli, such as muscle injury.[97] It is now known that these changes are mostly due to the changing satellite cell niche and are evolutionarily conserved between mice and humans.[100–103]

Another important feature in the satellite cell niche is the myofiber, which serves as the main cellular contact point for the satellite cell.[7] In aged muscle, the size and number of myofibers decrease, causing a marked change in the satellite cell niche. While little is known about the molecular signals expressed by the myofibers, recent studies have illuminated the changes in the Notch pathway that occur during aging. In normal adult muscle, Delta (a transmembrane ligand) is upregulated by myofibers after injury and binds Notch, thereby activating the Notch signaling cascade in satellite cells. This induces the proliferation of satellite cells. However, in aged muscle, a failure in the induction of Delta in myofibers weakens Notch signaling and impairs muscle regeneration.[97] Additionally, it has been reported in mice that old muscle produces excessive amounts of transforming growth factor (TGF-β). This increase induces an unusually high activation of the transcription factor pSmad3, which is an antagonist to Notch in terms of satellite cell proliferation control. In young muscle, Notch blocks the TGF-β induced upregulation of cyclin-dependent kinase (CDK) inhibitors, allowing satellite cells to enter the cell cycle and begin the regenerative process. However, in aged muscle, increased TGF-β signaling along with a decrease in Notch signaling inhibits the cell cycle by the activation of CDK inhibitors. This leads to significant reduction in the regenerative capacity of aged muscle. In essence, with age, the balance of factors regulating muscle stem cell responses shifts from active Notch to active TGF-β/pSmad3, causing the aforementioned reduced regenerative capacity.[103] As stated above, these mechanisms of aging have been recently shown to be evolutionarily conserved between mice and humans.[101,102] This conservation is important, as it points to the ability to use mouse models to further the study of aging in humans.

Finally, the basal lamina, which separates myofibers and their respective satellite cells from adjacent myofibers and the interstitium, plays a key role in satellite cell activity. Fibronectin, laminin, glycoprotein, and proteoglycans and that support satellite cell proliferation and growth serve as a location for growth factors to be converted to active forms by proteolytic enzymes in response to muscle injury.[7] In aging muscle,

the by-products of these enzymatic cleavages begin to build up and become toxic. This process compromises the essential functions of a basal lamina as a scaffold for growth and has been shown to cause necrosis.[104]

In order to further understand the effects on aging on the satellite cell microniche, it is also necessary to study factors external to the niche. These factors, which include vascular, neural, interstitial, and systemic constituents, undergo age-related changes that likely influence declining satellite cell function during aging. In the vascular system, endothelial cells have been shown to positively influence skeletal muscle growth by the secretion of soluble growth factors from nearby blood vessels.[18] Secretion of these factors, such as VEGF and endothelial nitric oxide synthase (eNOS), is reduced with age.[7] This age-related reduction, no doubt, affects the satellite cell macro and microniche and contributes to the limited regenerative capacity of aged muscle. Age-related changes in the neural system include remodeling of the neuromuscular junction, partial denervation, and a decline in myotrophic (muscle strengthening) factor production.[7] All of these changes hinder neural communication in muscle tissue, causing myofibers atrophy and thereby altering the productive satellite cell–myofiber interaction. Age-specific changes in the immune system are also very significant for muscle maintenance and repair, as removal of necrotic tissue by macrophages is necessary for effective myogenesis. Aged immune cells such as neutrophils and monocytes have shown reduced phagocytic activity, which limits their ability to destroy damaged tissue.[105] Finally, some of the age-related changes in the systemic environment, such as a reduction in thyroid hormones that direct muscle metabolism and growth as well as an increase in TGF-β, levels have all been shown to negatively influence the repair of old muscle.[101,102,106]

Although several mechanisms of aging are relatively well understood in relation to muscle regeneration, as described above, this area of research is certainly in progress and much is to be defined. With a more complete understanding of the effects of aging on the satellite cell niche with all its complex elements, the success of an anti-aging therapy and muscle engineering for older individuals would become more realistic. By targeting specific processes responsible for reduced muscle regeneration, satellite cell activity could be enhanced and maintained in old muscle deliberately and independently of the aged prohibitive environments. The use of biomaterials for this type of research is a promising option. One avenue to be explored is the use of biomaterials in scaffolding to study the aged niche and suspended satellite cells *in vitro*. Both natural and synthetic biomaterials can be used to create scaffolds that support the growth of functional muscle tissue (as described earlier in this chapter). The environment of such artificial muscle tissue can then be altered so as to mimic the *in vivo* aged muscle niche. This would involve a selective deactivation of signaling molecules and other important factors, such as Delta, antagonists of TGF-β/pSmad VEGF, and immune cells, or the selective over expression of 'aging' factors such as TGF-β. Also, the rigidity of the scaffold could be increased to replicate the excessive fibrosis that occurs in aged muscle tissue with time. With a tightly controlled replica of the aged niche, the effects of aging can be studied more closely and understood better. Alternatively, old muscle stem cells could be exposed to artificial environments/scaffolds that mimic young niche in modulus and growth factors and the regenerative responses of these satellite cells could be enhanced.[97,100,103]

5.526.13. Pathological Environment

As mentioned earlier, one of the most common muscular disorders is muscular dystrophy. The most severe form is DMD which is caused by a mutation in the dystrophin gene. The lack of normal dystrophin leads to muscle degeneration and eventually death of differentiated muscle fibers.[107] The most common animal model to study DMD is the mdx mouse which has a mutation causing incorrect alternative splicing of dystrophin transcript. In mdx mice, muscle degeneration begins around 3 weeks of age with large areas of necrosis by 7 weeks.[107] The mdx mice can be used to study the mechanism by which the loss of dystrophin leads to muscle degeneration.[107] Furthermore, mdx can be used to study how satellite cell populations are eventually exhausted and muscle is unable to be regenerated.

The mdx mouse is widely used to test potential therapies for muscular dystrophy. One of the first suggested therapies was the transfer of healthy myoblasts into mdx mice. This strategy had initial success; however, early clinical trials in humans did not produce promising results. One of the main problems was the minimal proliferation of myoblasts, massive cell death, and other factors in humans that quickly diminished the population of injected myoblasts.[108] These results suggest that relying on mouse models to recreate a pathological environment in humans might not be ideal. One thing to consider is that human cells have short telomeres which limit the proliferative capacity of somatic cells, while most laboratory mice do not appear to have this limiting mechanism.[108] Additionally, the mdx model does not match the severity of DMD in humans.[107] This means that it is difficult to test the effectiveness of a therapy in mdx mice because their lifespan is only shortened by approximately 20%.[109] Many other mouse models that facilitate studies of DMD have been developed, including 5cv mice that are mildly affected, dystrophin and utropin double knockout animals which are severely ill, but none of the mouse strains emulate the human pathology or disease progression closely. One of the main reasons could be the differences in life span: in contrast to people, mice are short-lived species.

Therefore, it will be important to improve and develop alternative models to test new therapies for muscular dystrophy. Future biomaterials could alleviate some of the problems with testing current therapies in mice. For example, in order to study and understand the progression of this disease, it would be advantageous to create a human disease model in artificial scaffolds. Similar to the aged niche model, biomaterials can be used to create an environment that would mimic the *in vivo* conditions of muscle in patients with the congenital muscle wasting. Muscle cells from patients that harbor mutations in dystrophin can be grown on engineered scaffolds with specific geometries and molecular milieu to mimic the disease of interest. In this way, scientists can study the progression of the dystrophy on in order to better understand the pathology of the disease. Another benefit to

this disease model is the ability to alter the diseased environment in a controlled manner as a method to explore possible therapies.

5.526.14. Future Directions

As the previous sections have illustrated, regeneration of skeletal muscle is controlled by a tightly regulated cascade of many different signals. The preceding sections have discussed various growth factors, cytokines, peptides, and scaffolds that have been discovered and are currently being tested to improve muscle regeneration. However, as the sections have pointed out the perfect biomaterial for skeletal muscle replacement or repair does not yet exist. Currently, most research and scaffolds work on including one or a few types of growth factors or peptide mentioned above. As discussed FGF increase satellite cell proliferation, while IGF increases myoblast cell proliferation and differentiation.[3,54] Many experiments have also been carried out with scaffolds that include VEGF since it has been found to be one of the most important growth factors to promote vascularization.[52,56,58] Additionally, BDNF and GGF have been embedded in hydrogels to promote innervation.[66,67] The next step in muscle tissue engineering will be to produce a biomaterial that combines all of this previous research into a single smart scaffold. This material will have to promote the efficient vascularization and innervation of new muscle. Additionally, this material will have to modulate the immune response so that macrophages and MMPs can clear necrotic and scar tissue without preventing wound healing through excessive inflammation. Lastly, and most importantly, this material will have to promote the proliferation of muscle progenitor cells and the efficient formation of myotubes which are the functional units of healthy muscle tissue. An advanced biomaterial should support the survival of transplanted myoblasts or be able to activate sufficient number of satellite cells to produce myoblasts and ultimately, new muscle fibers. Furthermore, this material should be biodegradable and not negatively affect other parts of the body. In essence, the ideal biomaterial will orchestrate an induced regeneration without scarring and perfectly replenish any injured muscle. A schematic of what is necessary in a smart biomaterial can be seen in Figure 1.

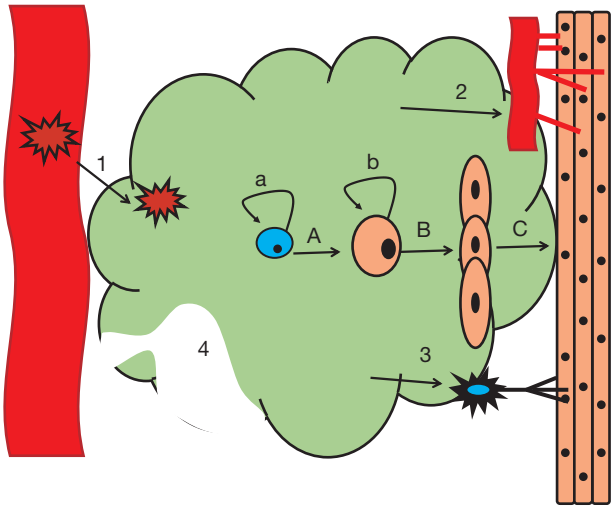

Figure 1 An optimal biomaterial will promote muscle regeneration, vascularization, innervation, and will modulate an immune response. (A–C): Artificial scaffold is embedded with muscle stem, satellite, cells which differentiate into myoblasts (A) and self-renew (a); myoblasts align and fuse into mytubes (B) and self-renew (b); myotubes mature into functional skeletal muscle fibers (C). The self-renewal and differentiation capacity of stem and progenitor cells enable their survival and integration into tissue *in vivo*. Engineered scaffold also tightly regulates cell proliferation and differentiation in order to replace all damaged muscle without neoplasty. (1–4): Regeneration of functional muscle cannot proceed without productive immune response, vascularization and innervation, which are all orchestrated by the engineered scaffold. (1) Biomaterial releases macrophage homing molecules; macrophages enter the wound site, remove necrotic tissue and secrete factors that promote myogensis. (2) Growth of new blood vessels and (3) reestablishment of neuromuscular junctions are promoted by specific growth factors released by this biomaterial. (4) Following tissue regeneration scaffold is biodegraded.

5.526.14.1. Culturing Satellite Cells

To date, most of the research exploring the muscle cell niche has been based on the culturing of primary myoblasts. Although the use of these myoblasts does allow the generation of muscle tissue, it limits the study of the satellite cell niche and yields the engineered tissue that is not regenerative and is terminally differentiated. Myoblast cultures are not similar to satellite cells in their properties, including the most important, self-renewal, as in contrast to satellite cell, which associate with myofibers and maintain muscle for life span, myoblasts exist only transiently *in vivo*.[8,9] It would be of great benefit to develop a method for robustly culturing satellite cells; currently this has not been accomplished, due to the difficulty in maintaining the 'stemness' of the satellite cells once they are removed from the *in vivo* niche. When taken out of their niche, satellite cells quickly lose their self-renewal capacity and differentiate into myoblasts.[8] In order to culture satellite cells, it is necessary to understand and recreate the complex regulatory machinery of the *in vivo* satellite cell niche.

In order to synthesize an accurate representation of the satellite cell niche, knowledge of the interplay between important signaling molecules such as Notch, TGF-β/pSmad, Wnt, and myogenic factors, such as Pax3, Pax7, MyoD, and Myf need to be used in conjunction with smart biomaterials. Strategies such as ligand patterning and release in hydrogels can be used to deliver important signaling molecules in spatial and temporal profiles that are similar to their release *in vivo*.[8,98] Further, the use of hydrogel materials that are resistant to nonspecific adhesion, experimentally determined surface modifications could be achieved and used in conjunction with particular ligands to facilitate cell adhesion through specific protein interactions. In this way, instead of encountering soluble growth factors in medium, cells interact with growth factors that are 'tethered' – a more physiologically relevant interaction.[8] Once again, a particular combination and concentration of each factor would need to be first determined and then, released by the biomaterial that is designed for the maintenance of muscle stem cells. The application of these

and other emerging biomaterial technologies brings closer the prospect of recreating the satellite cell niche. With a reliable *in vitro* representation of this niche, scientists can glean novel information about the molecular cues necessary for *in vitro* maintenance and growth of skeletal muscle stem cells.

5.526.14.2. Genomics, Proteomics, and Metabolomics

Currently, the most used methods in functional genomics and cell or tissue profiling involve gene manipulation and subsequent observation of the downstream effects. Technologies such as DNA microarrays can monitor the changes in gene transcripts (mRNAs) after a specific manipulation of the genome. This can help highlight the changes in protein synthesis that may occur due to specific genetic modifications. However, the drawback to this approach is that it does not take into account the changes in protein structure or concentration that occur downstream of transcription and/or translation. Changes in mRNA concentration will not necessarily reflect changes in protein expression and vice-versa. Protein concentration and expression can be affected by many posttranslational mechanisms such as phosphorylation, acetylation, ubiquitilation, allosteric modifications, and destruction rate.[110] The limitation of current genomic techniques to monitor these downstream changes calls for the use of newer technologies such as proteomics and metabolomics.

Both proteomics and metabolomics allow for the observation of concentrations, expression, and activity of important molecules in a certain system. More specifically, proteomics is defined as the study of the full set of proteins that are encoded by a genome, while metabolomics is the study of the range of metabolites present in the cell or other defined system. Proteomics studies are done using gel electrophoresis techniques to separate proteins of different sizes. More recently, fluorescent dying has been coupled to 2D electrophoresis in order to more accurately image the separated proteins. Metabolic profiles are developed using H NMR spectroscopy and can display concentration changes in important metabolites such as taurine, creatine, lactate, and phosphocholine.[111] An increase or decrease in the concentration of these and other metabolites can help illuminate the reason behind certain muscle behaviors and pathologies.

These techniques have been slow in development but are very important when considering the synergistic and complex environment of the cell or of stem cell niches. The number of protein interactions and metabolic pathways within these systems is vast, but the mechanisms involved are, for the most part, poorly understood. Moreover, no current biochemical technology has the ability to fully elucidate all of the proteins that are involved in skeletal muscle function; in proteomic profiling, low-concentration proteins are often masked by higher concentration proteins making them difficult to isolate.[110] To overcome this, it is necessary to perform individual studies on protein subsets so as to establish a more complete proteomic map, with both minimally and heavily expressed proteins. With this map, the exploration of protein activity in aged or diseased environments can be furthered. A deeper understanding of these complex environments affords the ability to pinpoint deleterious changes in protein expression, therefore providing opportunities for therapeutic intervention.

With regard to skeletal muscle engineering, the use of metabolomic or proteomics assays is an important avenue to consider. For example, by determining the metabolic profile of a certain state of muscle, say a pathological state, a specific biomaterial can be developed to improve the condition of the muscle. This biomaterial could contain essential metabolites that have been detrimentally downregulated or would have molecules that help inhibit inappropriately upregulated metabolites. This type of localized release to pathological tissue can potentially aid in the regeneration of functional muscle tissue.

References

1. Buckingham *et al*., 2009
2. Rudnicki, M. A.; *et al*. *Cold Spring Harb. Symp. Quant. Biol*. **2008**, *73*, 323–331.
3. Kuang, S.; *et al*. *Cell Stem Cell* **2008**, *2*, 22–31.
4. Otto, A.; *et al*. *J. Anat*. **2009**, *215*, 477–497.
5. Péault, B.; *et al*. *Mol. Ther*. **2007**, *15*, 867–877.
6. Chargé, S. B.; *et al*. *Physiol. Rev*. **2004**, *84*, 209–238.
7. Gopinath, S. D.; *et al*. *Aging Cell* **2008**, *7*, 590–608.
8. Cosgrove, B. D.; *et al*. *Differentiation* **2009**, *78*, 185–194.
9. Wagers, A. J.; Conboy, I. M. *Cell* **2005**, *122*, 659–667.
10. McKinnell, I. W.; *et al*. *Curr. Top. Dev. Biol*. **2005**, *71*, 113–130.
11. Morgan, J. E.; *et al*. *Int. J. Biochem. Cell Biol*. **2003**, *35*, 1151–1156.
12. Zammit, P. S.; *et al*. *J. Histochem. Cytochem*. **2006**, *54*, 1177–1191.
13. Goldring, K.; *et al*. *J. Pathol*. **2002**, *197*, 457–467.
14. Le Grand, F.; *et al*. *Curr. Opin. Cell Biol*. **2007**, *19*, 628–633.
15. Partridge, T. *Neuromuscul. Disord. Suppl*. **2002**, *1*, S3–S6.
16. Skuk, D.; *et al*. *Exp. Neurol*. **1999**, *155*, 22–30.
17. O'Connor, M. S.; *et al*. *Biotechnol. Prog*. **2009**, *25*, 1130–1137.
18. Christov, C.; *et al*. *Mol. Biol. Cell* **2007**, *18*, 1397–1409.
19. Kopecek, J.; Yang, J. *Polym. Int*. **2007**, *56*, 1078–1098.
20. Mooney, D. J.; Drury, J. L. *Biomaterials* **2003**, *24*, 4337–4351.
21. Khademhosseini, A.; Langer, R. *Biomaterials* **2007**, *28*, 5087–5092.
22. Kohane, D. S.; Langer, R. *Pediatr. Res*. **2008**, *63*, 487–491.
23. Riboldi, S. A.; *et al*. *Biomaterials* **2005**, *26*, 4606–4615.
24. Bian, W.; Bursac, N. *Biomaterials* **2009**, *30*, 1401–1412.
25. Borenstein, J. T.; *et al*. *Tissue Eng*. **2007**, *13*, 1837–1844.
26. Khademhosseini, A.; *et al*. *Proc. Natl. Acad. Sci. USA* **2006**, *103*, 2480–2487.
27. Nelson, K. D.; *et al*. *Tissue Eng*. **2003**, *9*, 1323–1330.
28. Cronin, E. M. *et al*. Protein-coated poly(L-lactic acid) fibers provide a substrate for differentiation of human skeletal muscle fibers. Wiley Periodicals, 2004; pp 373–381.
29. Neumann, T.; *et al*. *Tissue Eng*. **2003**, *9*, 995–1003.
30. Zhao, Y.; *et al*. *Biotechnol. Bioeng*. **2008**, *102*, 624–631.
31. Shimizu, K.; *et al*. *Biotechnol. Bioeng*. **2009**, *103*, 631–638.
32. Yamamoto, D. L.; *et al*. *J. Histochem. Cytochem*. **2008**, *56*, 881–892.
33. Doshi, J.; Reneker, D. H. *J. Electrostat*. **1995**, *35*, 151–160.
34. Rhim, C.; *et al*. *Muscle Nerve* **2007**, *36*, 71–80.
35. Beier, J. P.; *et al*. *Plast. Reconstr. Surg*. **2006**, *118*, 1113–1121.
36. Rowley, J. A.; Mooney, D. J. *J. Biomed. Mater. Res*. **2002**, *60*, 217–223.
37. Bouhadir, K. H.; *et al*. *Biotech. Prog*. **2001**, *17*, 945–950.
38. Boontheekul, T.; *et al*. *Tissue Eng*. **2007**, *13*, 1431–1442.
39. Hill, E.; *et al*. *Tissue Eng*. **2006**, *12*, 1295–1304.
40. Lee, W.; *et al*. *Biomaterials* **2009**, *30*, 5505–5513.
41. Karp, J. M.; *et al*. *Biomaterials* **2006**, *27*, 4755–4764.
42. Chiang, C. K.; *et al*. *Acta Biomater*. **2009**.
43. Ohashi, K.; *et al*. *Methods for implantation of BD Matrigel Matrix into mice and tissue fixation*. BD Biosciences, 2006.
44. Khvorostov, I.; *et al*. *J. Vis. Exp*. **2008**, *9*.
45. Levenberg, S.; *et al*. *Nat. Biotechnol*. **2005**, *23*, 879–884.
46. Lu, Y.; *et al*. *Circulation* **2001**, *104*, 594–599.
47. Zisch, A. H.; *et al*. *Cardiovasc. Pathol*. **2003**, *12*, 295–310.
48. Yang, J.; *et al*. *Biomaterials* **2007**, *28*, 5033–5043.
49. Karp, J. M.; *et al*. *Curr. Opin. Biotechnol*. **2007**, *18*, 454–459.
50. Lavike, E.; *et al*. *Appl. Microbiol. Biotechnol*. **2004**, *65*, 1–8.
51. Skuk, D.; *et al*. *Neuromuscul. Disord*. **2007**, *17*, 38–46.
52. Mikos, A. G.; *et al*. *Tissue Eng*. **2006**, *12*, 3307–3339.
53. Sands, R. W.; *et al*. *Curr. Opin. Biotechnol*. **2007**, *18*, 448–453.

54. Smith, C.; *et al*. *Sports Med*. **2008**, *38*, 947–969.
55. Brimah, K.; *et al*. *Hum. Gene Ther*. **2004**, *15*, 1109–1124.
56. Fischbach, C.; *et al*. *Biomaterials* **2007**, *28*, 2069–2076.
57. Silva, E. A.; *et al*. *Curr. Top. Dev. Biol*. **2004**, *64*, 181–205.
58. Cao, L.; *et al*. *Adv. Drug Deliv. Rev*. **2007**, *59*, 1340–1350.
59. Hubbell, J. A.; *et al*. *Biotechnology* **1991**, *9*, 568–572.
60. Sola, F.; *et al*. *Angiogenesis* **1997**, *1*, 102–116.
61. Rivron, N. C.; *et al*. *Eur. Cell. Mater*. **2008**, *15*, 27–40.
62. Liao, H.; *et al*. *Tissue Eng. B Rev*. **2009**, *15*, 319–331.
63. Thorrez, L.; *et al*. *Mol. Ther*. **2006**, *14*, 442–445.
64. Mooney, D. J.; *et al*. *Cell Stem Cell* **2008**, *2*, 205–213.
65. Kang, H.; *et al*. *J. Neurocytol*. **2003**, *32*, 975–985.
66. Kingham, P. J.; *et al*. *J. Anat*. **2006**, *209*, 511–526.
67. Bryan, D. J.; *et al*. *Tissue Eng.* **2000**, *6*, 129–138.
68. Ahmed, Z.; *et al*. *Cell Motil. Cytoskeleton* **1999**, *42*, 331–343.
69. Ahmez, Z.; *et al*. *Tissue Eng*. **2003**, *9*, 219–231.
70. Agrawal, V.; *et al*. *J. Tissue Eng. Regen. Med*. **2009**, *3*, 590–600.
71. Grothe, C.; *et al*. *Brain Res. Rev*. **2006**, *51*, 293–299.
72. Stojkovic, M.; *et al*. *Reproduction* **2004**, *128*, 259–267.
73. Darabi, R.; *et al*. *Nat. Med*. **2008**, *14*, 134–143.
74. Okita, K.; *et al*. *Science* **2008**, *322*, 949–953.
75. Park, I. H.; *et al*. *Cell* **2008**, *134*, 877–886.
76. Park, I. H.; *et al*. *Nature* **2008**, *451*, 141–146.
77. Takahashi, K.; *et al*. *Cell* **2006**, *126*, 663–676.
78. Takahashi, K.; *et al*. *Cell* **2007**, *131*, 861–872.
79. Quattrocelli, M.; *et al*. *Cell Death Differ*. 2009.
80. Stewart, D. M. In *Regulation of Organ and Tissue Growth*, Academic Press: New York, 1972; pp 77–100.
81. Powell, C. A.; *et al*. *Am. J. Physiol. Cell Physiol*. **2002**, *283*, C1557–C1565.
82. Bian, W.; *et al*. *IEEE Eng. Med. Biol. Mag*. **2008**, *27*, 109–113.
83. Flaibani, M.; *et al*. *Tissue Eng. A* **2009**, *15*, 2447–2457.
84. Serena, E.; *et al*. *Neurol. Res*. **2008**, *30*, 207–214.
85. Gilmore, K. J.; *et al*. *Biomaterials* **2009**, *30*, 5292–5304.
86. Kovanen, V. *Exerc. Sport Sci. Rev*. **2002**, *30*, 20–25.
87. Lewis, M. P.; *et al*. *Eur. J. Oral Sci*. **2001**, *109*, 209–221.
88. El Fahime, E.; *et al*. *Exp. Cell Res*. **2000**, *258*, 279–287.
89. Bedair, H.; *et al*. *J. Appl. Physiol*. **2007**, *102*, 2338–2345.
90. Kaar, J. L.; *et al*. *Acta Biomater*. **2008**, *4*, 1411–1420.
91. Wang, W.; *et al*. *Am. J. Pathol*. **2009**, *174*, 541–549.
92. Carmeli, E.; *et al*. *Muscle Nerve* **2004**, *29*, 191–197.
93. Brunelli, S.; *et al*. *Pharmacol. Res*. **2008**, *58*, 117–121.
94. Chazaud, B.; *et al*. *Exerc. Sport Sci. Rev*. **2009**, *37*, 18–22.
95. Cantini, M.; *et al*. *J. Neuropathol. Exp. Neurol*. **1995**, *54*, 121–128.
96. Massimino, M. L.; *et al*. *Biochem. Biophys. Res. Commun*. **1997**, *235*, 754–759.
97. Conboy, I. M.; *et al*. *Science* **2003**, *302*, 1575–1577.
98. Conboy, I. M.; Rando, T. A. *Dev. Cell* **2002**, *3*, 397–409.
99. Snow, M. H. *Cell Tissue Res*. **1977**, *185*, 399–408.
100. Carlson, M. E.; Conboy, I. M. *Aging Cell* **2007**, *6*, 371–382.
101. Carlson, M. E.; *et al*. *EMBO Mol. Med*. **2009**, *1*, 381–391.
102. Carlson, M. E.; *et al*. *Aging Cell* **2009**, *8*, 676–689.
103. Conboy, I. M.; *et al*. *Nature* **2008**, *454*, 528–532.
104. Robert, L.; Labat-Robert, J. *Biogerontology* **2000**, *1*, 123–131.
105. Ashcroft, G. S.; *et al*. *Biogerontology* **2002**, *3*, 337–345.
106. Larsson, L.; *et al*. *J. Physiol*. **1994**, *481*, 149–161.
107. Banks, G. B.; *et al*. *Curr. Top. Dev. Biol*. **2008**, *84*, 431–453.
108. Mouly, V.; *et al*. *Acta Myol*. **2005**, *24*, 128–133.
109. Chamberlain, J. S.; *et al*. *FASEB J*. **2007**, *21*, 2195–2204.
110. Griffin, J. L.; Des Rosiers, C. *Genome Med*. **2009**, *32*, 1–11.
111. Doran, P.; *et al*. *Proteomics* **2009**, *9*, 989–1003.
112. Brack, A. S.; Rando, T. A. *Stem Cell Rev*. **2007**, *3*, 226–237.
113. Brack, A. S.; *et al*. *Science* **2007**, *317*, 807–810.
114. Conboy, I. M.; *et al*. *Nature* **2005**, *433*, 760–764.
115. Huber, A.; *et al*. *Eur. Cell Mater*. **2007**, *14*, 56–63.

5.527. Cardiovascular Tissue Engineering

R S Kellar, Northern Arizona University, Flagstaff, AZ, USA
J J Lancaster and S Goldman, Southern Arizona VA Medical Center, Tucson, AZ, USA
T N McAllister and N L'Heureux, Cytograft Tissue Engineering, Inc., Novato, CA, USA

© 2011 Elsevier Ltd. All rights reserved.

5.527.1. Introduction 362
5.527.1.1. Bench Top to Bedside 362
5.527.1.2. Successful Tissue Engineering Translations 363
5.527.2. Cardiac Patches 363
5.527.2.1. Direct Injection Versus Tissues Constructs 363
5.527.2.2. Biomaterials for Cardiac Tissue Engineering 363
5.527.2.2.1. Scaffold-based systems 363
5.527.2.2.2. Hydrogels 364
5.527.2.2.3. Cellular sheet structures 364
5.527.2.2.4. Limitations of cardiac constructs 365
5.527.3. Cell Delivery Using Biomaterials 366
5.527.3.1. Hydrogels 366
5.527.3.2. Nanofibers 366
5.527.3.3. ECM Proteins 367
5.527.3.4. Synthetic Polymer Scaffolds 367
5.527.4. Tissue Engineering of Artificial Vesseles 367
5.527.4.1. The Evolution of Tissue-Engineered Blood Vessels 368
5.527.4.2. Biodegradable Scaffolds 368
5.527.4.3. A Cell-Synthesized Scaffold 369
5.527.4.4. Elastin as a Natural Scaffold 370
5.527.4.5. Mechanical Testing 371
5.527.4.6. Size and Scope of the Peripheral Market 372
5.527.4.6.1. Market size and growth 372
5.527.5. Tissue Engineering of Heart Valves 373
5.527.5.1. Classic Mechanical and Biological Heart Valves 373
5.527.5.2. Device Challenges 373
5.527.5.3. Tissue-Engineered Heart Valves 373
5.527.5.3.1. Regeneration versus repopulation 374
5.527.5.3.2. Biomaterials used for heart valves 374
References 375

Glossary

Alginate An insoluble anionic polysaccharide found in the cell walls of brown algae.
Allograft Tissue graft generated from the same species as the recipient.
Elastin An elastic, fibrous glycoprotein in connective tissue, important role in blood vessels function.
Extracellular matrix (ECM) Multifunctional component of the extracellular portion of tissue providing structural support, growth factor sequestering, intracellular communication, and a key component of wound healing.
Fibrin An insoluble, nonglobular protein made from fibrinogen.
Hydrogels Derived from either synthetically or natural polymers are water-insoluble, and display flexibilities similar to natural tissue.
Polyglycolides (PGAs) Biodegradable, synthetic polymer that degrades through hydrolysis.
Polyhydroxyalkanoates (PHAs) Bacterial derived polyesters from fermentation of sugar or lipids.
Tissue engineering The *in vitro* construction of working biological systems utilizing a combination of cells and biomaterials to replace or repair either whole organ or portions of compromised tissue.
Vicryl Absorbable, synthetic polyglactin which becomes absorbed by hydrolysis.
Xenograft Tissue graft generated from a different species than the recipient.

Abbreviations

BOOST trial	Bone-marrow-derived cell transfer after ST-elevation myocardial infarction trial
BPAECs	Bovine pulmonary artery endothelial cells
BPV	Bovine pericardial valves
CAD	Coronary artery disease
CaP	Calcium phosphate
ECM	Extracellular matrix
ECs	Endothelial cells
EHT	Engineered heart tissue
ePTFE	Expanded polytetrafluoroethylene
ESRD	End-stage kidney disease
GAGs	Glycosaminoglycans
H&E	Hematoxylin and eosin
hECM	Human extracellular matrix
IEL	Internal elastic lamina
IL-1	Interleukin-1
IL-6	Interleukin-6
IM	Internal membrane
MSCs	Mesenchymal stem cells
PAV	Porcine aortic valves
PCL	Poly-ε-caprolactone
PCU	Polycarbonate soft segment
PEG	Polyethylene glycol
PET	Polyethylene terephthalate
PEU	Polyether urethane
PGA	Polyglycolides
PHA	Polyhydroxyalkanoates
PIPAAm	Poly(*N*-isopropylacrylamide)
PLGA	Poly (D, L-lactic-*co*-glycolic acid)
POSS-PCU	Polyhedral ologomeric silsesquioxanes – polycarbonate soft segment
PTFE	Polytetrafluoroethylene
PUs	Polyurethane
PVA	Polyvinyl alcohol
PVD	Peripheral vascular disease
SBTE	Sheet-based tissue engineering
SIS	Small intestinal submucosa
SMCs	Smooth muscle cells
SPARC	Secreted protein acidic and rich in cysteine
TEBV	Tissue-engineered blood vessels
TEHVs	Tissue-engineered heart valves
TESA	Tissue engineering by self-assembly
TEVG	Tissue-engineered vessel grafts
TNF	Tumor necrosis factor

5.527.1. Introduction

The fields of cardiovascular tissue engineering and regenerative medicine have experienced tremendous expansion and progress over the past 20 years. Strategies have focused on the use of cells, tissues, scaffolds, and numerous combinations of these three components to address both scientific questions and clinical needs.

The most widely used definition of tissue engineering was proposed by Langer and Vacanti in a 1993 issue of *Science*, as "an interdisciplinary field that applies the principles of engineering and life sciences toward the development of biological substitutes that restore, maintain, or improve tissue function or a whole organ."[1] This working definition is still relevant to the application of tissue engineering toward solving cardiovascular diseases. The subsequent chapter will focus on the following applications of tissue engineering in the cardiovascular field:

1. Cardiac patches
2. Cell delivery using biomaterials
3. Artificial blood vessels
4. Heart valves

While not an exhaustive list of topics within the field of cardiovascular tissue engineering, this list covers major areas of research advancement over the past few decades. Whether cardiac or peripherally focused, progress in these areas of research has the potential to impact tissue and organ function throughout the body. Because the cardiovascular system is dispersed throughout the human body, cardiovascular tissue engineering advancements can be seen as a rate-limiting factor for the development of thick tissues to repair or replace every critical physiological system (circulatory, endocrine, urinary, respiratory, musculoskeletal, digestive, lymphatic, integumentary, etc.). Without a well established cardiovascular system or microvascular perfusion, tissues would be confined by the limitations of the diffusion distance of oxygen in various tissues. This limitation would ultimately confine and restrict future advancements in tissue engineering. Therefore, long-term advancements in tissue engineering will depend, in part, on the ability to stimulate or facilitate the development of an appropriate vascular supply.

5.527.1.1. Bench Top to Bedside

The successful translation of discovery – when cardiovascular tissue engineering advancements find clinical or commercial homes – will depend on choices made during the development pathway from science to product. For example, the success of the translation from basic research findings into preclinical models depends, in part, on the appropriateness of the *in vitro* model. Likewise, the subsequent transition into the clinic depends, in part, on the relevance of the preclinical model to the clinical disease targeted. Finally, a balance of risks versus benefits must be considered when exploring the clinical translation of new discoveries. For certain technologies, a peripheral cardiovascular route to first-in-man clinical trials may have lower hurdles to overcome than a route going directly to cardiac applications. Initial clinical success in a lower risk procedure can help set the stage for future trials in higher risk applications.

To create a successful tissue-engineered construct, device, or technology, manufacturing as well as economic issues must be taken into account.[2] For example, scale-up considerations for tissue engineering products can present serious challenges. Researchers and scientists often view the reproducible creation

of small series of tissue-engineered constructs for benchtop or preclinical testing as a significant problem. This problem is only amplified when the production must be scaled up to meet the demands of a US population suffering in record numbers from vascular diseases. These diseases include the following:

1. heart failure that affects close to 6 million Americans (American Heart Association),
2. coronary heart disease that led to 448 000 bypass procedures in 2006,[3]
3. peripheral vascular disease that affects ~5 million adults,[4]
4. aortic valve stenosis that affects ~2% of people over the age of 65 and 3% of people over age 75.

If these manufacturing challenges can be overcome, mass production can transform a very expensive *in vitro* model into a commercially viable product. Thanks to economies of scale, the average cost per unit to create a product decreases as the volume is increased. This, in fact, may influence the choice of first target markets for tissue engineering companies looking for a hugely successful product launch. While this 'economies of scale' strategy has proven very successful in the device world, it has not been a lucrative approach for most tissue engineering companies. An alternative approach is to aim at niche markets with high-value products where economies of scales play a lesser role but where even a limited percentage margin results in significant profits. This can lead to sustainability and long-term growth. This model may be particularly appropriate for more complex technologies that still face significant development steps, and thus, more costly processes.

5.527.1.2. Successful Tissue Engineering Translations

Despite all of these challenges, many new tissue-engineering technologies are finding their way to successful clinical translation. In fact, economic activity in the combined fields of tissue engineering, regenerative medicine, and stem cell therapies has grown a remarkable fivefold from 2002 to 2007.[5] As of mid 2007, ~50 businesses offered commercial tissue-regenerative products or services with collective annual sales > $1.3 billion.[5] For continued success in cardiovascular tissue-engineered technology, scientists will need to overlay the future regulatory, clinical, manufacturing, and economic hurdles. The ability to do so will help secure the translation of future benchtop findings into the clinic.

5.527.2. Cardiac Patches

As the use of cell-based therapies in regenerative medicines has developed over the last decade, enthusiasm remains high that such treatments will provide a therapeutic option for patients with life-threatening cardiomyopathies. Work to date in this field has evaluated numerous cell types in both basic science and clinical settings for their ability to provide a source of cardiomyocytes (or promote their growth) and for their ability to provide tangible tissue regeneration *in vivo* (see **Chapter 5.507, Tissue Engineering and Selection of Cells**). A great deal of this work has utilized direct injection methods (i.e., syringe or catheter based), in which the desired cells are injected directly into the troubled heart tissue. Newer approaches rely on techniques where biologically active scaffolds or tissues are engineered *in vitro* and then implanted (see **Chapter 6.624, Cardiac Patch with Cells: Biological or Synthetic**). Most of these constructs utilize a biomaterial scaffold to support tissue assembly; however, other methods favor completely biological approaches.

5.527.2.1. Direct Injection Versus Tissues Constructs

To date, a number of cell-based therapies for treating cardiac injuries have been evaluated. These studies, both in the laboratory and in patients have primarily utilized direct injection as a delivery technique. While results from these clinical trials have demonstrated that these delivery techniques are safe and the cells well tolerated,[6–12] their limited success in regenerating lost heart muscle or regaining cardiac function leaves room for improvements. Evidence suggests that the major problem with direct cell injection into the heart is that few of the injected cells survive.[13,14]

In order to improve cell retention, many newer cell delivery methods have focused on bioengineered constructs, in which the desired cells are cultured and grown into biologically active tissue-like constructs,[15–17] which are currently being evaluated. They include (1) scaffold-based systems where cells are grown onto a degradable[18–20] material, (2) cell-containing hydrogels,[21,22] or (3) cellular sheets, free of any scaffold support.[17,23] Investigators have proposed that constructs for cardiac repair should be (1) contractile, (2) electrophysiologically stable, (3) mechanically robust, (4) quickly vascularized, and (5) nonimmunogenic (see **Chapter 5.503, Biomaterials and the Microvasculature**).[16,21,22]

5.527.2.2. Biomaterials for Cardiac Tissue Engineering

5.527.2.2.1. Scaffold-based systems

Various biological and synthetic materials are currently being evaluated as the structural backbone for a number of *in vitro* engineered constructs. These include biological extracellular matrices such as collagens, elastin, fibrin, alginates, silk, etc., as well as biodegradable synthetic polymers such as polyglycolides (PGAs) (e.g., Vicryl™), polylactides, poly-ε-caprolactone (PCL), etc. Collagens, such as collagen type I sponge scaffolds, are flexible and porous allowing cellular integration. The placement of inert collagen type I scaffolds supplemented with adjunct cytokine administration has been shown to promote microvessel formation within injured rat myocardium.[24] Alginates have proven efficient in constructing tissue-engineered scaffolds. They can be efficiently seeded, retaining a high percentage of seeded cells within a brief time.[25,26] Alginate patches, however, appear to have poor integration into the myocardium because of limited microvessel formation. Integration may be improved through heterotopic transplantation, but questions about its clinical application exist.[15]

Extracellular matrices or various combinations of extracellular matrix (ECM) proteins have been explored as scaffold structures for tissue engineering purposes such as carriers for cell-based therapies. These materials can be readily casted, electrospun, or cultured using a variety of strategies to optimize surface area and void volume to create specifically designed scaffold carriers for cell therapies[27–29] (**Figure 1**).

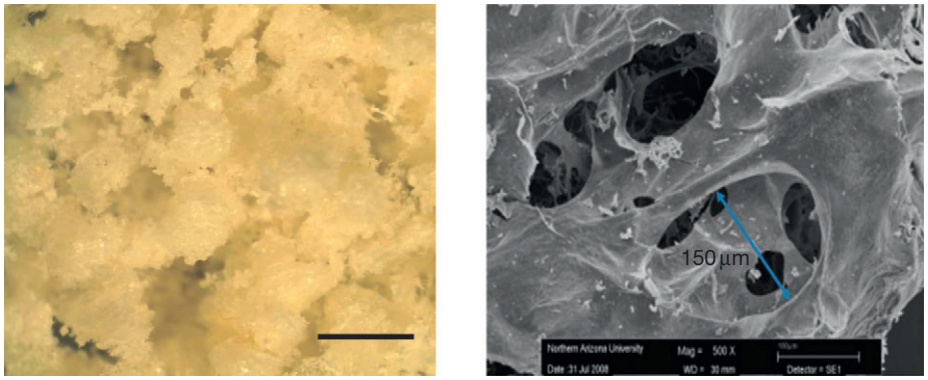

Figure 1 Left, lyophilized human extracellular matrix (ECM). Scale bar = 1 mm. Right, scanning electron micrograph of lyophilized human ECM. Arrow shown = 150 μm.

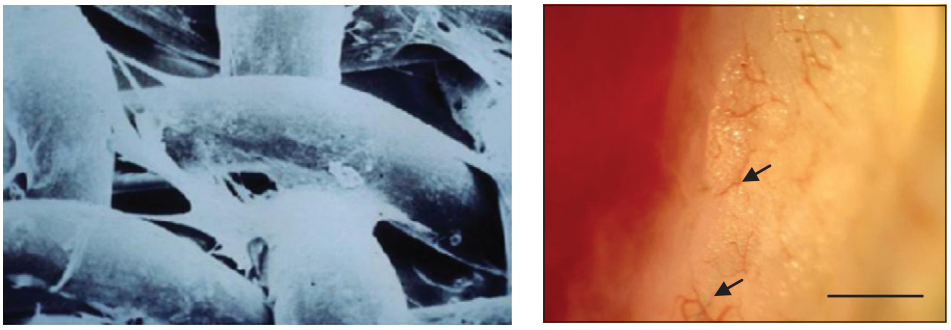

Figure 2 Left, scanning electron micrograph of a Vicryl™ scaffold seeded with human fibroblasts (cardiac patch). Scale bar = 50 μm. Right, cardiac patch placed onto the epicardial surface in a rodent infarct model. Arrows highlight new microvessels. Scale bar = 150 μm.

A number of laboratories have used Vicryl™ mesh or PGAs in construct formations. In addition, PGAs are employed in preseeded dermal repair constructs currently on the market (Theregen Inc.; Figure 2). PGAs are flexible and degradable and can be used to create woven or nonwoven scaffolds. Under standard culture conditions, PGAs degrade roughly 50% over 4 weeks. Such materials allow for spontaneous and synchronized contractions of seeded cardiomyocytes.[19,30,31]

5.527.2.2.2. Hydrogels

There has been work with liquid collagen I and Matrigel™ with additional growth supplements to create engineered heart tissue (EHT) *in vitro*.[21,22] These constructs were fabricated as circular bands and then fused together into 'multiloop' EHTs. These EHTs beat spontaneously and have been sutured onto the epicardial surface of the myocardium following acute myocardial infarction in rats. After 4 weeks, implanted EHTs remained on the epicardial surface of the myocardium with limited integration into the myocardium. Implanted EHTs contributed to improve cardiac function and even electrically coupled with the host myocardium.[21,22]

5.527.2.2.3. Cellular sheet structures

The creation of cells sheets that can be removed from their culture containers dates back to, at least, the mid-1970s and the work of Green and his associates. After painstakingly developing the appropriate culture media for the serial proliferation of human keratinocytes, a method was developed to produce, and enzymatically detach, cohesive sheets of human epithelium.[32,33] Soon after, this approach was used clinically and autologous sheets were produced and successfully implanted in seriously burned patients.[34] To our knowledge, this is the first cell-based therapy using cultured cells.

In the last decade, Okano and his group have popularized the use of poly(*N*-isopropylacrylamide)-coated cell culture plates to successfully create thin sheets of epithelial cells as well as cells of mesenchymal origin.[23,35,36] This coating is a temperature-sensitive polymer that allows for harvesting of fully intact cell sheets by lowering the ambient temperature, without the need for enzymatic digestion or mechanical manipulation (see **Chapter 5.530, Medical Applications of Cell Sheet Engineering**). Constructs grown and harvested in this manner can have multiple advantages. First, they do not include any foreign scaffolding that could create inflammatory responses and compromise the healing of a typically very fragile tissue, for example, cornea epithelium.[37] Second, the elimination of any enzymatic treatment preserves the integrity of the basement membrane of the cells sheets. As a result, these tissues can be directly applied to the desired tissue areas without the need for suture or other means of adhesion because of the preserved basal surface. Finally, the lack of enzymatic treatment also preserves the cellular organization of the sheet, and more particularly, relevant to cardiac applications, can help

maintain the cell–cell communication through gap junctions.[38] This is a critical advantage to create a contractile tissue as gap junctions are the structures that allow electrical transmission that results in the synchronous pulsation of the entire heart.[39] Culture containers coated with temperature responsive polymers are now commercially available under the brand name UpCell™ and are produced by Nunc™ (now part of ThermoFisher Scientific).

The creation of cardiac tissue using this approach is encumbered with two limitations. While cultured sheets of stratified epitheliums are notoriously fragile, which is part of the attraction of the thermally responsive culture surfaces, even sheets made out of cardiomyocytes or mesenchymal stem cells (MSCs) appear to also be mechanically weak (Biomaterials 2005).[40] As the weakness of epithelial sheets is likely due to the lack of ECM in these constructs, one would expect cells of mesenchymal origin to be able to produce a more robust tissue. However, in some studies, cells were cultured in the absence of ascorbate compounds that are known to be necessary to stimulate maximal collagen production. Recently, cell sheets were produced using this same approach from cultures of smooth muscle cell (SMC) and fibroblasts.[41] These cultured cell sheets were supplemented with ascorbate 2-phosphate and 18.8 pM of copper (II) sulfate (believed to increase collagen cross-linking by lysyl oxidase) but were only cultured for a total of 7 days, which may be insufficient to generate sufficient mechanical strength. No sheets produced using this approach have been formally tested for their mechanical strength, and this appears to be a significant challenge for the design of cardiac patches that would play a significant mechanical role. Using much longer culture periods could provide sufficient time for the cell to assemble complex and relatively mature ECM structures leading to the production of stronger sheets. Another option could be to introduce a synthetic scaffold to provide the requisite mechanical strength, but some preclinical results suggest that a biological patch can lead to better tissue regeneration and function even in not cell seeded.[42]

Another limitation of this approach, and of most other tissue engineering approaches, is the limited thickness of tissues that can be produced as a result of diffusion limitations. This is particularly important for a clinically relevant heart patch as the wall of the human heart is over 1 cm thick. While a heart patch product can aim at having a purely parachrine effect, particularly if applied to a recently injured heart (myocardial infarct), it would be clearly beneficial to also be providing mechanical support as such support has been shown to be beneficial.[43] In addition, a robust patch that could be used to repair full- or near full-thickness defects could be used for more aggressive surgical intervention that would be needed to address many degenerative heart diseases. To address this limitation, Okano's group has proposed a number of strategies. One general method is to include endothelial cells in a stack of cells of mesenchymal origin (Biomaterials 2010).

This can be achieved by creating sheets from co-cultures, including endothelial cells or sheets made exclusively from endothelial cells as intercalated in the stack. Initial results *in vitro* were promising as the endothelial cells appear to reassemble into a network of elongated channels mimicking the native microvasculature. However, it remains to be seen if this network can be assembled and connected to the host circulation before cells in the middle part of the construct suffer from hypoxia. While preliminary studies in rats are promising,[44] scaling-up to a human size construct could be challenging. Another strategy proposes to serially implant sheets to allow each layer to be vascularized by the host[45] before the implantation of the next layer. This method has produced contractile and well perfused myocardial tissues of up to 1 mm in a rat model. Furthermore, these tissues could be successfully ectopically transplanted with their newly formed vasculature. This strategy of using the body as an *in vivo* bioreactor has certainly gained momentum in recent years.[46,47] While the multiple surgeries required would be a significant risk to the patient, the upside would clearly justify the risk in the case of a cardiomyopathy (**Figure 3**).

5.527.2.2.4. Limitations of cardiac constructs

While biomaterials such as polymer scaffolds provide structural support for culture of tissue constructs, there are a number of potential limitations surrounding biomaterial-based scaffolds,[17,21,22] including (1) the potential for inflammatory response, (2) possible toxic degradation products,[23,48] (3) variance of compliance between polymers and heart tissue,[21,22] and (4) the lack of interconnectedness between cells because of interference from the scaffold material.[21,22,48] The use of

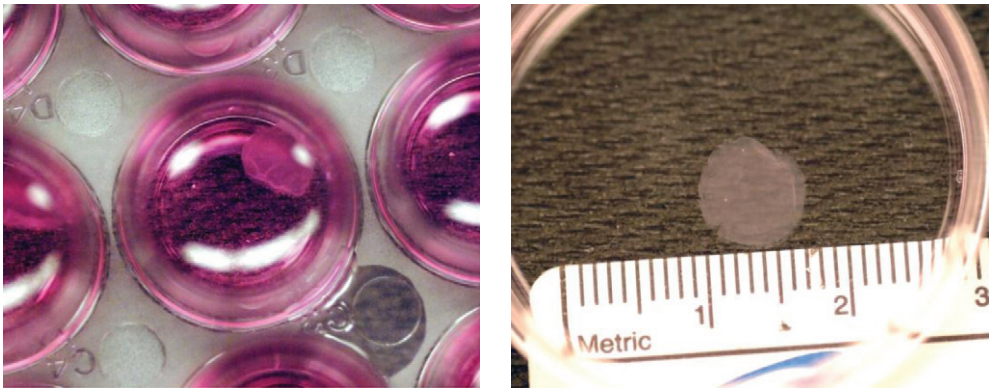

Figure 3 Bovine pulmonary artery endothelial cells (BPAEC) sheets harvested using 24-well PIPAAm temperature sensitive culture plates. Left, disassociated BPAEC cell sheet in culture well and media. Right, harvested BPAEC cell sheet harvested from original culture plate. Courtesy by J. Lancaster, 2009.

completely biological cell-sheets would likely avoid all the limitations mentioned above but may be restricted by their mechanical strength. Apart from the limitations described, a major obstacle of further developments, particularly enrollment into clinical applications, will be the procurement of suitable human stem or progenitor cells.

5.527.3. Cell Delivery Using Biomaterials

In recent years, many investigators have invested significant efforts into the use of living cells as a therapeutic agent (see **Chapter 5.507, Tissue Engineering and Selection of Cells**). These cells are intended to deliver certain products (e.g., growth factors) or to be a replacement cell type to replace lost tissues. These living cell therapies require that cells maintain their activity at the transplant location whether it is the bone marrow, skin, liver, or heart. This has presented a significant hurdle. Thus far, the best-published results of the beneficial effects of bone marrow cell transplantation after acute myocardial infarction come from the bone marrow transfer to enhance ST-elevation infarct regeneration (BOOST) trial.[49] In this study, significant improvements in left ventricular ejection fraction were seen at 6 months after treatment with bone marrow cells. However, these improvements were no longer significant at 18 months. A few investigators have reported cell retention as a major obstacle for these types of cell replacement therapies, indicating that only 1.3–2.6% of infused bone marrow cells are retained in the heart.[50] While these cell-based therapies continue to advance through the clinical trial gauntlet, many investigators are looking into a variety of delivery agents such as hydrogels, alginates, and polymer scaffolds to provide a hospitable environment for transplant cells that can subsequently be delivered into the target tissue.

Future cell therapy will depend on the delivery of a sufficient number of living functional cells, to the appropriate location for an ideal amount of time. While most therapies are initially combined with a traditional surgical intervention, these therapies can also take advantage of the wealth of minimally invasive strategies that have been developed to avoid traumatic procedures such as a thoracotomy. These minimally invasive techniques rely on injectable or collapsible biomaterials combined with a target cell population. The development of such interventional techniques has multiple advantages. For example, in cardiac applications, minimally invasive cell delivery can allow high-risk patient populations to be treated who may not be medically stable for large open surgical procedures. Additionally, recovery time for these patients can be minimized, which significantly benefits the patient's quality of life and decreases morbidity and mortality rates. A recent example of the clinical benefits of minimally invasive approaches for the treatment of cardiovascular disease is demonstrated by the rapid adoption of thoracic endografting instead of open surgical repair in patients with descending thoracic aortic aneurysms. The benefits of thoracic endografting are (1) less perioperative morbidity, (2) lower hospital costs, and (3) equal mid-term life expectancy when compared to open surgical repair.[51] Another clinical example where minimally invasive approaches have been leveraged in efforts to treat higher surgical risk patients is the use of minimally invasive robotic coronary bypass using the da Vinci S System. These procedures are performed under endoscopic vision with surgical assistance from the da Vinci S robotic system. These conditions allow for minimally invasive coronary artery bypass grafting with an enhanced ability to control precise and stable operative manipulations.[52]

Future cell-based therapies will likely focus significant efforts upon minimally invasive delivery. Additionally, the delivery vehicle or the avenue by which transplant cells are introduced into the target tissue will remain a key area of investigation. A variety of delivery formats are described below.

5.527.3.1. Hydrogels

Polymers that form hydrogels are potentially useful for both tissue engineering and drug delivery therapeutic approaches. Hydrogels offer multiple advantages such as a good safety profile, a simple and rapid assembly process, and a large range of achievable geometries. They can also be injectable, and are a cost effective and cell-friendly substrate. However, because of their very high water content, hydrogels lack sufficient mechanical strength to be used as the main scaffold in many applications. Another drawback of hydrogels is that cell activity will often alter their shape. One classic example of this phenomenon is the so-called 'contraction' of collagen gels seeded with cells.[53] This compaction process is typically anisometric and can reduce the dimensions of these constructs by a large percentage. This can limit the usefulness of these scaffolds for the production of an intricate structure. Hydrogels can be classified as either naturally occurring or synthetically derived. Natural hydrogels include collagen (see **Chapter 2.215, Collagen: Materials Analysis and Implant Uses**), gelatin, fibrin (see **Chapter 2.217, Fibrin**), alginate, agarose, and hyaluronate (see **Chapter 2.214, Hyaluronic Acid**). Some synthetically derived polymer hydrogels include poly(acrylic acid), poly (vinyl alcohol), polyphosphazene, and poly(ethylene oxide).[54] Compatibility with the patient is an important consideration when using hydrogels because potential for mild or severe inflammatory response exists.[55] For example, alginates rich in mannuronic acid have been shown to stimulate an inflammatory response through a monocyte-activation pathway. These stimulated monocytes produced a variety of proinflammatory cytokines including TNF, IL-1, and IL-6.[56] It is also important to consider the rate of degradation once administered, as each hydrogel has its own specific characteristics and degradation profiles.[57] Ideally, the degradation behavior of the hydrogel should match or be closely compatible to the rate of new tissue formation.[58] The rate of new tissue formation is greatly tissue-dependant and the mechanical properties of these hydrogels are critical to their ability to create and maintain a space for new tissue formation *in vivo*.

5.527.3.2. Nanofibers

Another biomaterial approach for cell delivery for cardiovascular repair utilizes self-assembling peptide[59–61] or alginate[62] nanofibers (see **Chapter 2.205, Self-Assembling Biomaterials**). Both peptide and alginate nanofibers provide the heart with structural and physical support by replacing the lost or

compromised ECM; meanwhile, alginate derived versions appear to gradually dissolve[62] and therefore lack a long-term contribution of mechanical support. As reported by Davis *et al.*[59] and Padin-Iruegas *et al.*,[61] peptide nanofibers appear to help significantly with cellular survival, whether in conjunction with the exogenously administered cells or the endogenous cell populations of the target tissue, possibly through the establishment of microenvironments. In addition, incorporation of growth factor or cell signaling elements could greatly contribute to the therapeutic potential of nanofiber-based therapies.

5.527.3.3. ECM Proteins

ECM proteins have been evaluated as a potential scaffold structure to support various cell-based therapies (see **Chapter 2.207, Extracellular Matrix: Inspired Biomaterials** and **Chapter 2.220, Extracellular Matrix as Biomimetic Biomaterial: Biological Matrices for Tissue Regeneration**). For example, stem cell therapies have evaluated the use of a complex tumor matrix, Matrigel™. This product is marketed by BD Biosciences and is composed of Engelbreth-Holm-Swarm (EHS) mouse sarcoma cells. Matrigel™ has demonstrated the ability to facilitate the growth of various stem cell populations and maintain an undifferentiated state for a period of time.[63] The main ECM proteins within Matrigel™ are laminin and collagen. However, some of the challenges of Matrigel are that its origin is from a tumor-based etiology and the matrix itself is poorly defined.

Other investigators have looked at harnessing the cell-based ECM produced by tissue culture. Here, human ECM (hECM) can be produced to have embryonic-like characteristics and therefore may serve as a hospitable environment for culturing transplant cells (**Figure 4**), especially adult or embryonic stem cells.[64] Utilizing a hECM material as a delivery vehicle for cell-based therapies may facilitate improvement in engraftment and long-term outcomes of the therapy. In these studies, bioreactors were developed to expose neonatal fibroblasts to early embryonic conditions during the production of their ECM and conditioned culture media. The resulting hECM contained a protein matrix that includes collagen I (see **Chapter 2.215, Collagen: Materials Analysis and Implant Uses** and **Chapter 2.216, Collagen–GAG Materials**), tenacin, hyaluronic acid, and fibronectin, as well as proteins that have been found to be prevalent in embryonic ECM such as collagens III, V, and SPARC.

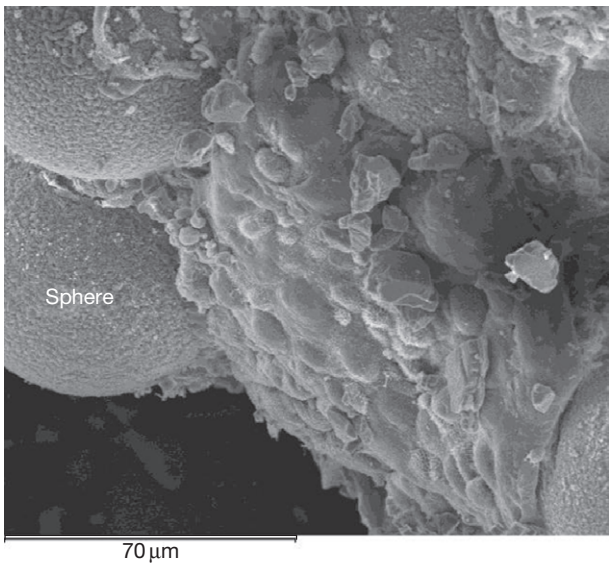

Figure 4 Embryonic stem cells were grown and expanded on the human extracellular matrix material.

5.527.3.4. Synthetic Polymer Scaffolds

Other cell delivery strategies have focused on the use of synthetically created polymer scaffolds. For orthopedic tissue engineering applications, biomimetic scaffolds provide a necessary framework for bone analogs. The osteogenic potential of PCL/calcium phosphate (CaP) matrices have been closely studied for their ability to facilitate growth and residence of a human MSC population for periods of up to 8 weeks. In these studies, MSCs were able to adhere, migrate, and differentiate along the osteogenic lineage within these scaffolds. The PCL/CaP scaffolds showed up to a 27-fold increased degradation compared to PCL scaffolds alone.[65]

Other synthetic polymer scaffolds that have been explored as cell delivery agents are resorbable or degradable poly(D,L-lactic-*co*-glycolic acid) (PLGA) microspheres. While these polymer scaffolds, to date, have not seen wide use within the cardiovascular research space, they are actively being studied for orthopedic applications.[66] In this application, initial cell viability studies have demonstrated the feasibility of using a PLGA/Polyethylene glycol (PEG) polymer matrix and a cell or drug technology.

Furthermore, a PLGA microsphere platform has been demonstrated to support bovine chondrocyte culture onto the PLGA microspheres. Positively charged PLGA microspheres showed the highest cell attachment, growth, and function compared to hydrophobic and negatively charged microspheres. It has been concluded that surface-modified PLGA microspheres can potentially be used as an injectable delivery system for cells into a tissue defect site.[67]

The resorbable PLGA microsphere platform has been widely evaluated as a drug delivery[68–71] platform but its use has been limited as a cell delivery vehicle, mostly into the orthopedic field.[67,72] This resorbable polymer technology may be limited by the relatively rapid degradation rate of PLGA *in vivo*, resulting in obliteration of its mechanical integrity prior to adequate tissue growth.

5.527.4. Tissue Engineering of Artificial Vesseles

Synthetic polymeric vascular grafts were developed to address three issues in vascular surgery: (1) the fact that there are no 'spare' large diameter vessels in the human body for autologous repair, (2) the unsatisfactory performance of nonautologous natural grafts (xeno- and homografts), and (3) the limited availability of small diameter autologous grafts (see **Chapter 6.628, Vascular Grafts**).[73] The development of synthetic vascular prosthesis is often credited to Voorhees, Jaretski, and Blakemore, who first published on synthetic

tubes.[74] In the following decades, two synthetic materials rapidly emerged as the most clinically successful; expanded polytetrafluoroethylene (ePTFE) and woven or knitted polyethylene terephthalate (PET) fibers (Dacron). While these materials performed well as large and even medium diameter conduits, synthetic vascular grafts have not proven successful in small diameter applications (<6 mm ID).[75,76]

Today, coronary artery disease (CAD) is the largest single cause of mortality in both men and women in the United States (American Heart Association). Despite the rapid adoption of percutaneous interventions for coronary procedures, there were still 448 000 bypass procedures performed in 2006. Peripheral vascular disease (PAD) is also a condition that can be treated by the use of a small diameter bypass graft. PAD affects ~8 million Americans and is associated with significant morbidity and mortality.[77] CAD and PAD have similar risk factors and, not surprisingly, are often found in the same patients.[78] In cardiac and peripheral bypass surgery, the best outcomes are achieved when diseased vessels are replaced with autologous veins or arteries. For example, the internal mammary artery has >90% patency over 7 years in cardiac applications, while the saphenous vein maintains ~50% patency after 7.5 years in peripheral sites.[79] However, many patients do not have adequate blood vessels for use as grafts because of either poor quality or insufficient quantity after a previous harvest. This is particularly true for PAD cases where good autologous vessels are often preferentially used to treat CAD. In these cases, the patients are restricted to modest treatment modalities often leading to myocardial infarction or limb amputation. Therefore, there is a substantial unmet clinical need for an alternative supply of vessels to replace small diameter diseased arteries.

5.527.4.1. The Evolution of Tissue-Engineered Blood Vessels

The clinical complications of small diameter synthetic prostheses commonly result from an inflammatory response to and pathologic remodeling of the prosthetic material. These failure modes have led to enhanced interest in new approaches for designing vascular grafts. A tissue engineering approach may overcome certain obstacles faced by synthetic grafts in small-diameter vascular applications.[80] For example, a tissue-engineered blood vessel (TEBV) would presumably be more responsive to physiological signals and avoid the pathological remodeling seen in synthetic grafts. To be successful, a tissue-engineered vessel grafts (TEVG) must have sufficient strength to withstand cyclic loading and changes in blood pressure. It should also have an antithrombotic luminal surface, and ideally, should match the compliance of the host vessels at the anastomotic sites.[80] While one would hope that tissue-engineered constructs would enhance their functionality over time via tissue remodeling *in vivo*, it should be noted that a TEVG must fulfill its mechanical role immediately upon implantation. Similarly, unlike tissue-engineered skin, cornea or other nonload bearing tissues, the remodeling of the blood vessel must not lower its mechanical strength below a certain threshold to avoid dilation and rupture. Consequently, inflammation, rejection, or other biodegradation processes are of particular importance for the successful outcome of a TEBV.

Often cited as the first TEBV, a construct produced by casting a tube of collagen gel containing bovine vascular cell lines (SMCs, fibroblasts, and endothelial cells) was reported by Weinberg *et al.*[81] in 1986. This first model did not have any synthetic material with the aim of avoiding the detrimental effect of introducing foreign materials into the body. This was in line with the developing concept, which would later be called 'tissue engineering,' of creating 'biological substitutes that restore, maintain, or improve tissue function.' However, without additional mechanical support, these vessels were highly distensible and failed during burst strength testing at low intraluminal pressures.[81] This approach was widely repeated in the following decade with collagen or other biological gels, and while valuable as *in vitro* models, these completely biological constructs still displayed limited burst strengths.[53,82–84] The next generation TEBVs were hybrids incorporating synthetic and biological materials.[85] In the ensuing years, the field of vascular tissue engineering became dominated by biomaterial design and the original vision of a biological construct was relegated to the realm of 'desirable but unachievable.' However, it eventually became evident that the presence of a permanent synthetic scaffold would negate the potential benefits of including biological or living components.

5.527.4.2. Biodegradable Scaffolds

In the late 1980s and early 1990s, numerous investigators used various resorbable synthetic polymers to produce fully biodegradable vascular grafts.[86–89] The hope was to produce an 'off-the-shelf' template that would guide the body's natural repair process toward vascular regeneration. However, to this day, finding the right balance between scaffold degradation and extracellular regeneration in order to maintain sufficient mechanical strength has proven to be very challenging. In 1999, Niklason *et al*. produced TEBVs by culturing bovine and porcine cells under pulsatile conditions on poly(glycolic acid) (PGA) felt for 8 weeks. These small diameter vessels had rupture strengths of up to 2150 mmHg.[90] However, it was found that PGA degradation may have led to dedifferentiation of the SMCs, which could possibly lead to hyperplasia and graft occlusion.[91] Over the last decade, this approach did not yield mid- or long-term results in an animal model and attempts to develop a construct with similar mechanical strength using human cells were unsuccessful.[92–94] Around the same period, Shum-Tim *et al.*[95] produced medium diameter graft using a PGA:polyhydroxyalkanoate (PHA) copolymer and ovine vascular cells. Short segments implanted in the abdominal aorta of lambs showed promising results up to 3 months with favorable patency. In parallel, Shin'oka *et al.*[96] developed a similar approach, using PCL and PGA, which led to the first implantation of a TEVG in a human. These TEBVs were implanted in the low-pressure pulmonary circulation of infants with severe congenital defects. This method has evolved toward the use of bone marrow cells and a PGA/ε-caprolactone/L-lactide copolymer.[97] While this tremendous success does not address the need for arterial bypass conduits, it finally established the feasibility and potential of vascular autologous cell-based therapy.

Other researchers have examined the use of various processed animal tissues as another type of biodegradable scaffold

for tissue engineering. While homografts and xenografts have been shown to be poor conduits, over a decade of efforts in developing decellularization technologies has brought the promise of natural scaffolds that would not trigger immune response. This approach is based on the idea that the removal of all cellular components could leave behind exclusively the ECM. One of the first and most widely used decellularized ECM is the porcine small intestinal submucosa (SIS), which has been used clinically for many years. As a vascular graft, SIS has been used in animal models since 1990 with relatively positive results[98,99] but has yet to be tested in humans for that application. Recently, a modified porcine SIS was used as a vascular prosthesis.[100] After implantation in a rabbit, these grafts required native endothelial cell infiltration and aggressive anticoagulation therapy in order to prevent thrombosis. These results underline the importance of endothelial cell coverage in TEBV for small diameter arterial bypass. This was also exemplified in studies using ePTFE grafts endothelialized with autologous EC isolated from vein, fat, or blood.[101–103] Using this technique, dramatic improvements have been seen in some clinical cases, particularly for below-the-knee procedures.[104,105] While decellularized tissues offer an attractive option for many regenerative approaches, these tissues appear to, at least partly, trigger some immune recognition.[106,107] This suggests that they may not be appropriate for vascular tissue engineering where even a minor inflammatory reaction could lead to a negative outcome.

5.527.4.3. A Cell-Synthesized Scaffold

In the mid-1990s, L'Heureux *et al*. came to the conclusion that reconstituted ECM proteins such as collagen were unlikely to provide the requisite mechanical strength needed for creating an implantable TEBV. Even if these reconstituted matrix proteins did provide the requisite mechanical strength after various physicochemical treatments, these scaffolds would be aggressively degraded by the immune system because of their unnatural chemical or tridimensional organization. Faced with this realization, L'Heureux turned to cultured cell as a source of unprocessed and naturally organized ECM. The general approach, which was later termed 'tissue engineering by self-assembly' (TESA), takes advantage of the ability of cells of mesenchymal lineage to assemble complex and abundant ECM when cultured for extended periods in the presence of ascorbate. While TESA can be used to direct cells to deposit natural ECM in various geometries, the initial developmental work was aimed at producing sheets of living cells and the ECM they produced. This particular version of TESA was labeled 'sheet-based tissue engineering' (SBTE).

For building blood vessels, L'Heureux *et al.*[108] created sheets from human adult dermal skin fibroblasts and from umbilical vein SMCs. After a month of culture, the sheets were detached from their culture substrate and were wrapped around a temporary tubular support. After an additional culture period, referred to as 'maturation,' of 8 weeks in a bioreactor providing active perfusion, all the individual layers fused together to form a cohesive living cylinder. In this initial model, three concentric layers were formed to mimic the native architecture of a human blood vessel. The outermost layer was formed by a rolled fibroblast sheet and played the role of the adventitia. The median layer was formed by a rolled sheet of SMCs and played the role of the tunica media. The innermost layer was called the 'internal membrane' (IM) and was made of a rolled fibroblast sheet that was matured and then devitalized by dehydration. The IM was included in the design to mimic the antimigratory role of the internal elastic lamina (IEL). The IEL is an effective physical barrier that separates the SMCs of the media from the plasma and the more fragile and less proliferative endothelial cells. Damage to the IEL has been identified as an important factor in the development of atherosclerosis but also of intimal hyperplasia observed after balloon angioplasty.[109,110] One would also expect it to be a key factor in the development of intimal hyperplasia at the anastomosis with a vascular graft. The IEL is largely made of elastin, which is known to be resistant to most enzymes produced by SMCs. However, the IM is largely made of collagen, which is sensitive to many matrix metalloproteinases. Accordingly, the IM was designed to be much thicker than the native IEL; the strategy being that cell migration toward the lumen would be significantly inhibited during the inflammatory phase following implantation. In fact, future long-term *in vivo* studies would confirm that the IM is not readily degraded and remains acellular for months.[111] These constructs could then be removed from around the mandrel and its lumen that is seeded with endothelial cells (**Figure 5**).

These TEBVs had supra-physiological burst pressures in excess of 2500 mmHg at 3 mm internal diameter. They were implanted in a canine arterial bypass model and, as such, were the first completely TEBVs with clinically relevant mechanical properties.

In the next decade, L'Heureux and his team focused on translating these promising early results into clinical reality. For that purpose, the assembly strategy was streamlined and SMCs were eliminated from the process without affecting the mechanical strength of the vessels. In addition, the TESA method was adapted to cells (fibroblasts and venous endothelial cells) isolated from age- and risk-matched individuals, that is, older individuals suffering from cardiovascular disease. Finally, the bioreactor system was simplified to be compatible with a high-throughput, reliable, and economically viable production process. The resulting vessels displayed an average burst pressure of 3468 ± 500 mmHg at a diameter of 4.2 mm.[111] This new human TEBV design was tested in immunosuppressed canines and primates as well as in nude rats for up to 9 months without signs of mechanical failure. On the basis of the promising preclinical results, vessels were built for a series of 10 patients (age 29–89) suffering from end-stage renal disease (ESRD) and in need of a vascular graft for hemodialysis access. These TEBVs displayed burst pressures as high as 5763 mmHg (average 3340 ± 849) at a diameter of 4.8 mm and were implanted as an arteriovenous shunt. The clinical protocol called for a 3-month observation period to demonstrate mechanical stability followed by the use of the graft for hemodialysis access, that is, the graft would be punctured with two 16-gauge needles 3 times per week. In the initial report, one graft had a primary patency (patency without intervention) of 11.5 months despite the very unfavorable hemodynamics and mechanical injuries associated with this clinical application.[112] In a later report, these TEBVs showed primary

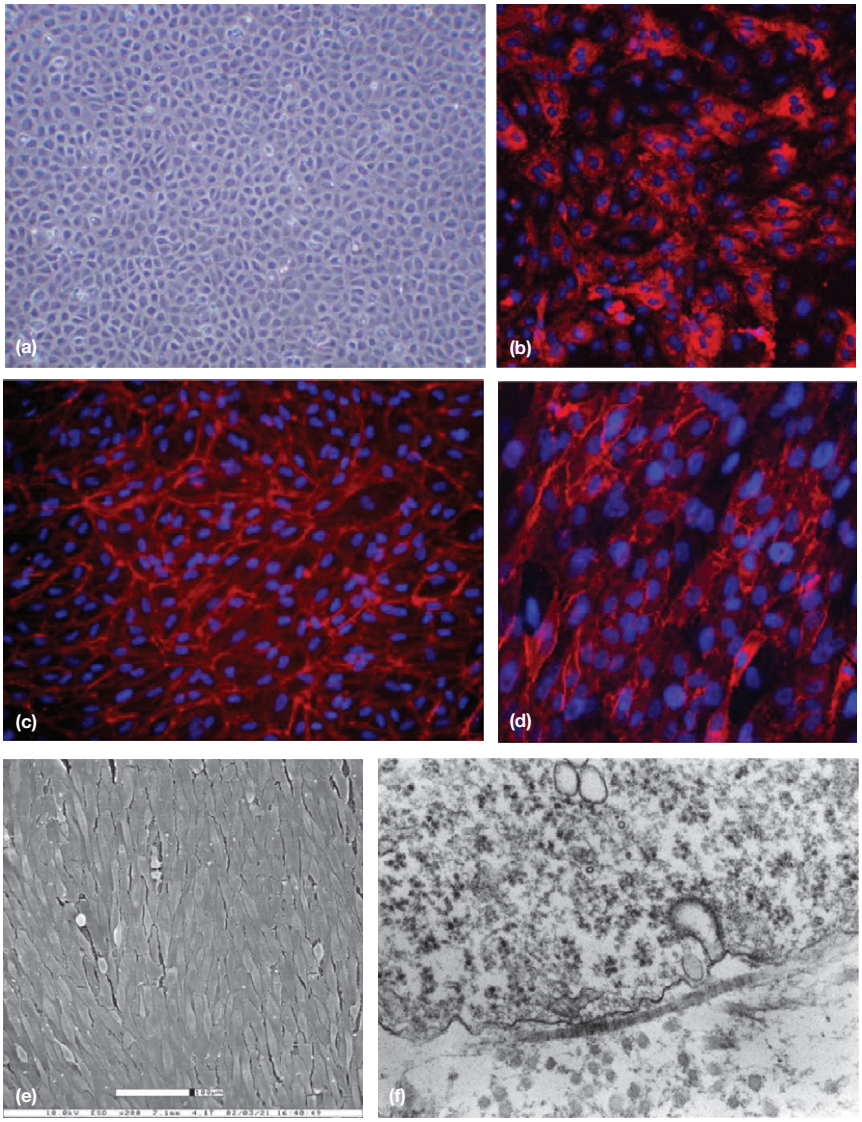

Figure 5 Endothelialization of tissue-engineered blood vessel produced by tissue engineering by self-assembly. (a) A phase contrast micrograph shows the typical 'cobble stone' appearance of a confluent culture of human venous endothelial cells on polystyrene tissue culture flask. (b) Von Willebrand factor (red) is a marker specific to endothelial cells and is commonly used to identify and characterize the purity of culture *in vitro* using immunolabeling techniques (nuclei are blue stained by Hoechst 33258). ECs can also be labeled on the surface of tissue-engineered blood vessel to determine the degree of confluence of the cells as well as their phenotype. (c) *En face* view of a confluent endothelium on the luminal surface. The actin microfilaments have been stained with phalloidin (red) to demonstrate a pericytoplasmic arrangement suggestive of a mature endothelium (nuclei in blue). The endothelium of the tissue-engineered blood vessel can also be stained for specific markers to confirm the nature of the monolayer. (d) PECAM/CD31 (red) specifically labels the cell–cell contacts between endothelial cells in confluent endothelium. (e) Scanning electron microscopy can also be used to ascertain the coverage of the luminal surface of a tissue-engineered blood vessel but this method can often cause cell losses due to the harsh treatment. (f) Transmission electronic microscopy can be used to study biomaterial/EC interaction. In this micrograph, the cytoplasmic membrane of an EC can be seen in close apposition with a collagen fiber of the luminal surface. The characteristic 67 nm periodicity of the striation of a native collagen fiber can be observed.

patency rates of 78% at 1 month, and 60% at 3 and 6 months after implantation.[113] These rates approached the objectives of the Dialysis Outcomes Quality Initiative (a program run by the National Kidney Foundation Disease) across all patient populations for native vein fistulas.[114] Considering that native veins perform practically twice as well as ePTFE grafts and that this study included only patients with a high-risk of graft failure, these results suggest that this new self-assembled 'biomaterial' could be particularly well-suited for vascular applications (**Figure 6**) (see **Chapter 2.205, Self-Assembling Biomaterials**).

5.527.4.4. Elastin as a Natural Scaffold

Natural polymers such as elastin are potential alternatives to synthetic materials. Unlike collagen, this ECM has the potential to be assembled in mechanically strong tissues that are capable of resisting the body's degradative responses.[115]

Elastin, derived from its water-soluble precursor tropoelastin, consists of repetitive glycine-rich hydrophobic domains of variable length interspaced with alanine-rich regions containing crosslinkable lysine residues. In its native form, elastin is a network of elastic fibers that are cross-linked between lysine residues. Cross-linking enhances elastin's biostability and controls its mechanical properties. Cross-linking occurs after cellular secretion of tropoelastin with local fiber deposition. Because elastin cannot be recovered from tissue in its native form, simpler proteins comprising repetitive polypeptide sequences have been assembled in an effort to duplicate the desirable properties of elastin.

McMillan and coworkers have produced large elastin-like proteins by assembling gene segments encoding the peptides VPGVG and VPGKG that represent the mobile domains in elastin. The genes isolated from this assembly process are up to 3000 base pairs long, contain 39 repeats of the sequence $(VPGVG)_4$ (VPVKG), and produce an 81 kDa protein after expression in *E. coli*.[116] This protein can be spun into fibers, filaments, and ribbons with a tensile strength of about 35 MPa and the material modulus 1.8 GPa.[117] Elastin-like polymers made by these methods have been used as carriers for antitumor drug delivery.[118]

Polymeric scaffolds of varying sizes based on the repeating elastin sequence VPGVG have also been constructed by sequential polymerization of the pentapeptide after solid-state chemical synthesis. These elastin-like proteins will self assemble to form fibers.[119] Materials with similar properties comprising the pentapeptides VPGKG and VPGIG have also been made using recombinant approaches,[120] and elastin-mimetic proteins can be crosslinked into flexible films and filaments by a variety of methods.[121–123] In addition, the solid polymer blocks that form from these proteins have also been used as a substrate to assemble functional biomotors.[124]

Further modifications to these polypeptides, providing additional complexity, are necessary for the attachment or adhesion of human endothelial cells, an important milestone for the *in vivo* use of these polymers as substrates.[29] A sequence derived from the cell binding domain of fibronectin[125] has been incorporated during assembly of polypeptides as an essential component of the polymer substrate[126–130] to support endothelial cell adhesion, function, and activity.

Elastin-like materials with as many as four different domains have been synthesized and assembled to provide additional functionality to the synthetic elastin-like molecules.[131,132] These structures may potentially be useful in tissue engineering applications such as vascular grafts, stem cell matrices, and organs such as bladders.[117] However, assemblies of repeating peptides cannot match the complexity or biological activity of native elastin. With the exception of some early work by Urry *et al.*,[133] no *in vivo* data on elastin-like proteins have been published, and their performance as engineered structures is unknown. In contrast, electrospun tropoelastin fibers support attachment, migration, and extensive proliferation of human mesenchymal cells.[134] What is already known about tropoelastin suggests that this material may serve as a novel biomaterial with complex structure and superior performance for vascular scaffolds.[27]

The challenge of engineering blood vessels that have the mechanical properties of native vessels has been and remains significant. The native human artery structure is ~30–50% elastin (Figure 7). In a variety of rat strains, the percent dry weight of elastin has been reported to be between 30 and 40%.[135] The aging process has been shown to produce a number of vascular changes including a progressive rise in arterial stiffness.[136,137] Studies show that elastin's characteristics are critical to vascular grafts and that 'to ensure appropriate mechanical function of the vessel and to prevent vessel stenosis, successful tissue-engineered vascular replacements must incorporate an elastic component.'[138] According to leading researchers, "successful tissue-engineered blood vessels incorporating elastin are, therefore, the Holy Grail of future vascular interventions."[139]

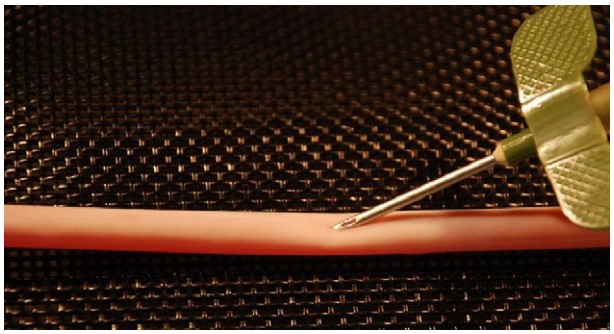

Figure 6 A completely biological human tissue-engineered blood vessel. This small diameter blood vessel (4.8 mm internal diameter) was produced with cells from a female patient suffering from end-stage renal disease and on dialysis. Vessels produced for this patient had an average burst pressure of 5204 ± 424 mmHg, which is higher than the burst pressure of the saphenous vein commonly used for bypass surgery, and higher than most human arteries of a similar diameter. The vessel is shown as it is being tested for its ability to resist a puncture from a 16 Ga hemodialysis needle. While burst pressure may be a good indicator for the suitability of a graft to perform as a typical bypass graft, resilience to injury is a key property for a good arteriovenous shunt. This *in vitro* test is performed under hydrostatic pressure to observe leaking during puncture, which will last up to 4 h in the clinical setting, and after removal of the needle. Synthetic grafts are notorious for their propensity to bleed once the needles are removed from the graft. This natural tissue, because it can be easily punctured at an angle, easily seals after removal of the needle even *in vitro* where only aqueous solutions are used.

5.527.4.5. Mechanical Testing

The mechanical properties of native vessels are well understood scientifically and held as the primary reason for their outstanding performance as bypass grafts. However, the field has not yet been able to produce a biomaterial that ideally matches the mechanical characteristics of native arteries and that has a low biological impact. Native arteries such as the canine carotid artery are not only composed of a variety of cell types (e.g., endothelial cell lining and SMC media layer), but also have an important basement membrane and ECM composed of elastin (Figure 8). These specific cell types have important biological and mechanical properties for a functioning blood vessel. Additionally, the biomechanical properties offered by elastin have not yet been replicated synthetically in the field by any of a variety of polymer scaffolds.

For example, Figure 9 shows the stress–strain curves of a canine carotid artery versus a polyurethane scaffold tube. The dramatic differences can be seen where the native carotid artery exhibits the typical viscoelastic behavior in contrast to the linear behavior of the polyurethane scaffold tube.

5.527.4.6. Size and Scope of the Peripheral Market

As many as 12 million Americans over the age of 50 are affected by peripheral artery disease (biotechnologyireland.com (a)). Approximately 600 000 grafts are implanted each year in the United States alone and this is growing annually because of an aging population (gore.com). The estimated $2.0 billion market for vascular grafts (biotechnologyireland.com (a)) is a subset of the worldwide interventional cardiology market, which was estimated at $11 billion in 2008 (biotechnologyireland.com (b)). The market for vascular grafts is global in reach, but the vast majority of vascular grafting procedures occur in the United States and other developed nations. Only the most remote third world medical providers do not have regular access to these grafts. In determining the ideal initial market, the regulatory environments are key factors. With recent changes in European regulatory practices, it is expected that the time required for obtaining approvals will become substantially similar to those in the United States.

5.527.4.6.1. Market size and growth

A clearly defined market size for vascular grafts is somewhat difficult to obtain as each existing player in this market defines it differently. A general study of this market tells us that today this market is in the $20–30 billion range.

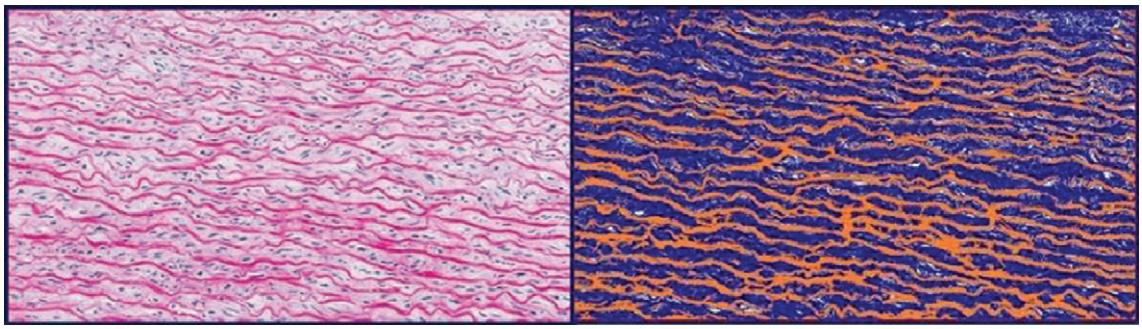

Figure 7 Left: H&E staining of a porcine aorta. Right: Area quantification of elastic fibers in a porcine aorta. Orange markup shows elastic fibers at 39.1% of total area.



Figure 8 Immunohistochemical staining of smooth muscle cell differentiation markers and basement membrane protein (elastin) in canine carotid arteries.

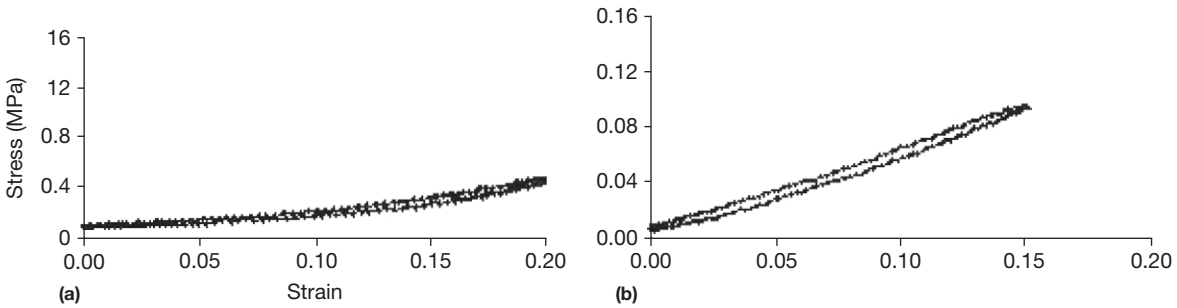

Figure 9 Stress-strain curves for (a) native carotid artery, (b) unseeded polyurethane vascular scaffold.

The vascular graft market has been consistently showing an average growth of 10–20% for last several decades (data from annual reports). As population grows and ages, the need for such devices increases. The market for these devices is directly dependent on aging population and is somewhat resilient to economic recessions and fluctuations.

An example of a peripheral target for first-in-man clinical application is a TEBV for vascular access in hemodialysis patients. Dialysis vascular access is the lifeline of the ESRD patient undergoing hemodialysis. A typical ESRD patient receives 1.5–2 interventions per year to maintain vascular access for hemodialysis. The grafts implanted to provide this access typically fail because of compromised patency. A tissue engineering solution to this problem has been the Holy Grail for many investigators who aim to improve patency rates and long-term survival of the vascular access graft. Once a TEBV technology demonstrates clinical success in the dialysis vascular access market, numerous additional clinical markets will likely follow (e.g., peripheral bypass).

In 2004, the total annual cost of vascular access complications was estimated to be nearly $8000 per patient risk year, with a total of $1–1.5 billion, or ~10% of the total ESRD budget. More than 20% of hospitalizations of ESRD patients are attributed to complications with vascular access. The growth of ESRD patients is expected to double by the year 2010. Thus, dialysis access care will grow into a multibillion dollar cost.

5.527.5. Tissue Engineering of Heart Valves

The first replacement heart valves were made from autologous or homologous sources of human tissue (Figure 10).[140] Since the 1960s, allograft replacement valves have been used to repair compromised or nonfunctioning heart valves in patients. These replacement valves are classified as either mechanical or biologically derived (see Chapter 6.626, Cardiac Valves: Biologic and Synthetic). To date, efforts to create tissue-engineered heart valves (TEHVs) have shown limited effectiveness. In this section, we will briefly discuss the field as a whole, how biomaterials will contribute to future developments, and the place tissue engineering may serve for this clinical application (see Chapter 5.528, Tissue Engineering of Heart Valves).

5.527.5.1. Classic Mechanical and Biological Heart Valves

Currently, a number of mechanically and biologically derived heart valves are available. Mechanical valves are derived mainly from nonbiological materials such as polymers or other biomaterials. Biological valves or bioprostheses are derived from human or animal tissues.[141] Bioprostheses are derived mainly from porcine aortic valves (PAV) or bovine pericardial valves (BPV) and are glutaraldehyde preserved.[142] These valves are defined by predictable rates of deterioration, with >50% of the replacement valves failing within 15 years.[143]

5.527.5.2. Device Challenges

Heart valve replacement surgery represents the only therapy for end-stage aortic valve disease. However, prosthetic valves have a number of limitations. Both the classic mechanical and biological heart valves are limited by deterioration that results from either calcification or noncalcification.[144] These problems ultimately affect the overall function and implant life of the valves. Calcification deterioration arises when calcium accumulates within the valve as a result of the inability of the glutaraldehyde treated tissue to maintain low calcium levels. Noncalcification degradation generally refers to the natural deterioration of replacement valves.

Additionally, mechanical valves are typically recognized by the body as a foreign substance and therefore facilitate concerns with thromboembolic complications, requiring lifelong anticoagulation therapy.[145] Because of the well described leaflet deterioration and calcification with biological or bioprosthetic valves, reoperation and replacement are common future clinical outcomes.[145,146]

Finally, both mechanical and biological valves lack the fundamental ability to grow, repair, or remodel in the patient.[147] This is especially important when considering the treatment of congenital heart valve disease in pediatric patient populations.[148]

5.527.5.3. Tissue-Engineered Heart Valves

Tissue engineering is currently being evaluated to determine if it can offer an alternative to mechanical or biological heart valves.

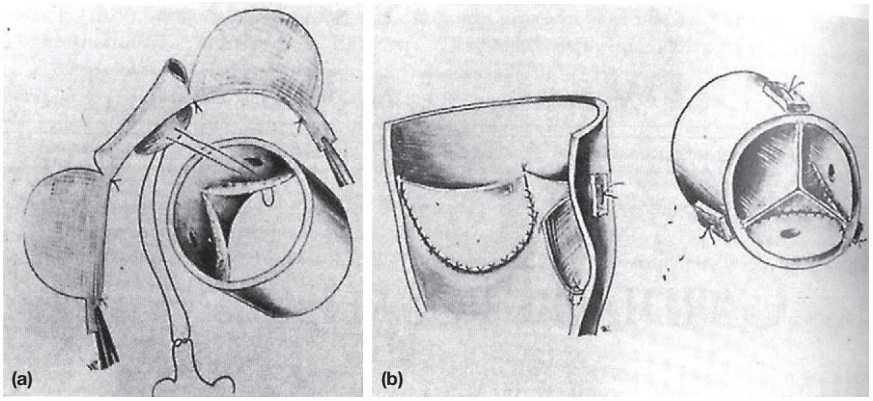

Figure 10 (a) Fascia lata strip cut to form three cusps. Then it is sutured to the aortic annulus. (b) The commissures are anchored with sutures placed through the aortic wall and tied over Ivalon sponge pledgets. Reproduced from Senning, Å. *J. Thorac. Cardiovasc. Surg.* **1967**, *54*, 465–470.

Tissue engineering may offer solutions to overcome current limitations of mechanical or biological heart valves while offering unique advantages. These advantages may include a living autologous structure, improved biocompatibility, and the ability to grow, repair, and remodel.[149–151] Classically the 'Holy Grail' of replacement valves would be neither obstructive nor thrombogenic, capable of lasting the lifetime of the patient, and would possess cellular regenerative and homeostatic properties.[144] In theory, TEHVs may allow for creation of such a replacement valve. Recent works for developing TEHVs have evaluated varying endothelial cell types cells for population of decellularized[152,153] or synthetic valves.[154]

Focus on decellularized scaffolds has presented promising opportunities for the development of a TEHV (see **Chapter 2.221, Decellularized Scaffolds**). Once the field has progressed to the point of wide-utility of a decellularized scaffold, the next major decision that needs to be addressed is whether it should be an allograft only (e.g., human origin), or if it could be a xenograft (see **Chapter 5.507, Tissue Engineering and Selection of Cells**). If decellularized xenograft scaffolds are to be explored, they present source and acquisition advantages while presenting certain key complications such as disinfection criteria and suspected antigenicity of xenograft (ECM) proteins.[155] This idea has previously been suggested by *in vitro* and *in vivo* studies.[156–158]

A significant concern exists with the concept that a decelluarized xenograft scaffold may actually be more inflammatory than current iterations of cryopreserved homografts. An unfortunate clinical example of a decelluarized xenograft heart valve (Synergraft) highlights the importance of truly understanding the ability of a decellularized ECM to provoke the immune system as well as the innate nonspecific inflammatory pathway.[159] In other studies, decellularized porcine leaflets were reported to be more attractive (stimulated macrophage response) than extracts of human native pulmonary cusps that had not been decellularized.[155] These studies suggest that future decisions on an appropriate decellularized ECM point to the human allograft over a xenograft source.

5.527.5.3.1. Regeneration versus repopulation

Attempts at producing TEHVs are classified as either regeneration or repopulation based. Regeneration methods involve an implantable biologically active matrix comprising both cellular and connective elements. Repopulation methods utilize harvested valves rinsed and voided of cellular elements and repopulated *in vivo* by the recipients own cells.[147]

5.527.5.3.2. Biomaterials used for heart valves

The use of biomaterial scaffolds for the development of replacement heart valves will continue to face the complex offering provided in the native biological ECM of heart values. Specifically, this ECM consists of collagen, elastin, and GAGs (see **Chapter 2.215, Collagen: Materials Analysis and Implant Uses** and **Chapter 2.216, Collagen–GAG Materials**). Collagen is primarily responsible for the structural integrity and biomechanical strength of native heart valves.[160] Elastin provides significant tissue resilience over time and over repetitive heart cycles. glycosa minoglycans (GAGs) play a pivotal

Table 1 Summary of biomaterials evaluated for use in the development of heart valves

Material	*Advantages*	*Disadvantages*	*Comments*	*References*
Silicone	Favorable flexibility and biocompatibility	Short durability; distorted and thickened leaflets; tearing; thrombosis formation	Structural failures and impaired hemodynamic performance and durability	[163,164]
Polytetrafluoroethylene (PTFE)	Favorable hemodynamic properties	Low resistance to thromboembolism and calcification; free edge inversion and stiffening of the leaflet	PTFE was found to be unsuitable because of major complications	[165–168]
PUs: Polyester	Good viscoelasticity	Susceptible to hydrolysis	Biodegradation and calcification have been reported as the main problems	[168,169,170]
PUs: Urethane	Good resistance to hydrolysis	Low resistance to oxidation (PEU) and prone to calcification (PCU)	Biodegradation and calcification have been reported as the main problems	[171–173]
PVA	Good mechanical properties	Not suitable for dipcasting	Mechanical properties were satisfactory but PVA needs to be further studied	[174]
SIBS	Enhanced resistance to hydrolysis, oxidation	Causes platelet activation and thrombogenicity	Resistance to oxidation and hydrolysis along with its biostability makes it a leading material for development of heart valves	[170,175]
POSS-PCU nanocomposite	Excellent resistance to oxidation, hydrolysis and calcification; excellent biocompatibility; antithrombogenicity	No reports yet	Positive material characteristics have led to the current evaluation of POSS-PCU as a heart valve	[162,176]

role in enabling valve tissue to withstand compressive forces.[148] In recent years, a number of biomaterials have been evaluated during the development of mechanical heart valves. These include polymers such as polylactic acid (PLA)/PGA and copolymers, which were used in the mid 1990s and more recently, PHAs. PHAs are naturally occurring bacteria derived polymers and a possible alternative to petroleum-based plastics with many potential uses.[147,161]

Efforts in the development of synthetic heart valves leaflets have included strategies that use nanocomposite polymers. For example, polycarbonate soft segment (PCU) and polyhedral oligomeric silsesquioxanes (POSS) nanoparticle (POSS-PCU) has been evaluated as a synthetic material for heart valve leaflets because of its favorable biocompatibility and biostability.[163] Tensile strength of POSS-PCU has been shown to be significantly higher than PCU alone materials, 55.9 ± 3.9 versus 28.8 ± 3.4 N mm^{-2} at 37 °C, respectively.[163]

Numerous other biomaterials have been explored for use in polymer heart value development. A summary in **Table 1** helps to describe some of the key biomaterials that have been evaluated to date.

References

1. Langer, R.; Vacanti, J. *Science* **1993**, *260*, 920–926.
2. Ahsan, T.; Nerem, R. M. *Orthod. Craniofac. Res.* **2005**, *8*, 134–140.
3. National Health Statistics Report 2008, 5, 1–2
4. Sharrett, A. R. *Peripheral Arterial Disease*; Armenian Health Network, 2007; Health.am. http://www.health.am/vein/more/peripheral-arterial-disease-prevalence/.
5. Lysaght, M. J.; Jaklenec, A.; Deweerd, E. *Tissue Eng. A* **2008**, *14*, 305–315.
6. Assmus, B.; Honold, J.; Schächinger, V.; *et al. N. Engl. J. Med.* **2006**, *355*, 1222.
7. Janssens, S.; Dubois, C.; Bogaert, J.; *et al. Lancet* **2006**, *367*, 113.
8. Lunde, K.; Solheim, S.; Aakhus, S.; *et al. N. Engl. J. Med.* **2006**, *355*, 1199.
9. Schächinger, V.; Assmus, B.; Britten, M.; *et al. J. Am. Coll. Cardiol.* **2004**, *44*, 1690.
10. Schächinger, V.; Erbs, S.; Elsässer, A.; *et al. N. Engl. J. Med.* **2006**, *355*, 1210.
11. Dow, J.; Simkhovich, B.; Kedes, L.; *et al. J. Am. Coll. Cardiol.* **2005**, *46*, 1651.
12. Wollert, K. C.; Meyer, G. P.; Lotz, J.; *et al. Lancet* **2004**, *364*, 141.
13. Dow, J.; Simkhovich, B.; Kedes, L.; *et al. Cardiovasc. Res.* **2005**, *67*, 301.
14. Müller-Ehmsen, J.; Whittaker, P.; Kloner, R.; *et al. J. Mol. Cell. Cardiol.* **2002**, *34*, 107.
15. Dvir, T.; Kedem, A.; Ruvinov, E.; *et al. Proc. Natl. Acad. Sci. USA* **2009**, *106*, 14990–14995.
16. Leor, J.; Amsalem, Y.; Cohen, S. *Pharmacol. Ther.* **2005**, *105*, 151–163.
17. Stevens, K.; Pabon, L.; Muskheli, V.; *et al. Tissue Eng. A* **2009**, *15*, 1211.
18. Kellar, R.; Landeed, L.; Shepherd, B.; *et al. Circulation* **2001**, *104*, 2063–2068.
19. Lancaster, J.; Johnson, N.; Juneman, E.; *et al. J. Card. Fail.* **2009**, *15*, S45.
20. Thai, H.; Juneman, E.; Lancaster, J.; *et al. Cell Transplant.* **2009**, *18*, 283–295.
21. Zimmermann, W.; Didié, M.; Döker, S.; *et al. Cardiovasc. Res.* **2006**, *71*, 419.
22. Zimmermann, W.; Melnychenko, I.; Wasmeier, G.; *et al. Nat. Med.* **2006**, *12*, 452–458.
23. Shimizu, T.; Yamato, M.; Kikuchi, A.; *et al. Biomaterials* **2003**, *24*, 2309.
24. Gaballa, M.; Sunkomat, J.; Thai, H.; *et al. J. Heart Lung Transplant.* **2006**, *25*, 946–954.
25. Dar, A.; Schacher, M.; Leor, J.; *et al. Biotechnol. Bioeng.* **2002**, *80*, 305–312.
26. Leor, J.; Aboulafia-Etzion, S.; Dar, A.; *et al. Circulation* **2000**, *102*, III-56–III-61.
27. Boland, E.; Mattews, J.; Pawlowski, K.; *et al. Front. Biosci.* **2004**, *9*, 1422–1432.
28. Smith, M.; McClure, M.; Sell, S.; *et al. Acta Biomater.* **2008**, *4*, 58–66.
29. Welsh, E.; Tirrell, D. *Biomacromolecules* **2000**, *1*, 23–30.
30. Carrier, R.; Papadaki, M.; Rupnick, M.; *et al. Biotechnol. Bioeng.* **1999**, *64*, 580–589.
31. Papadaki, M.; Bursac, N.; Langer, B.; *et al. Am. J. Physiol. Heart Circ. Physiol.* **2001**, *280*, 168–178.
32. Green, H.; Kehinde, O.; Thomas, J. *Proc. Natl. Acad. Sci. USA* **1979**, *76*, 5665–5668.
33. Rheinwald, J.; Green, H. *Cell* **1975**, *6*, 331–343.
34. O'Connor, N.; Mulliken, J.; Banks-Schlegel, S.; *et al. Lancet* **1981**, *1*, 75–78.
35. Elloumi-Hannachi, I.; Yamato, M.; Okano, T. *Intern. Med.* **2010**, *267*(1), 54–70.
36. Shimizu, T.; Sekine, H.; Okano, T. *Curr. Pharm. Des.* **2009**, *15*(24), 2807–2810.
37. Nishida, K.; Yamato, M.; Hayashida, Y.; *et al. N. Engl. J. Med.* **2004**, *351*, 1187–1196.
38. Shimizu, T.; Yamato, M.; Isoi, Y.; *et al. Circ. Res.* **2002**, *90*, e40–e48.
39. Shimizu, T.; Yamato, M.; Akutsu, T.; *et al. J. Biomed. Mater. Res.* **2002**, *60*, 110–117.
40. Miyahara, Y.; Nagaya, N.; Kataoka, M.; *et al. Nat. Med.* **2006**, *12*, 459–465.
41. Hobo, K.; Shimizu, T.; Sekine, H.; *et al. Arterioscler. Thromb. Vasc. Biol.* **2008**, *28*, 637–643.
42. Badylak, S.; Kochupura, P.; Cohen, I.; *et al. Cell Transplant.* **2006**, *15*(Suppl 1), S29–S40.
43. Kochupura, P.; Azeloglu, E.; Kelly, D.; *et al. Circulation* **2005**, *112*(Suppl 9), I144–I149.
44. Sasagawa, T.; Shimizu, T.; Sekiya, S.; *et al. Biomaterials* **2010**, *31*(7), 1646–1654.
45. Shimizu, T.; Sekine, H.; Yang, J.; *et al. FASEB J.* **2006**, *20*, 708–710.
46. Campbell, G.; Turnbull, G.; Xiang, L.; *et al. J. Tissue Eng. Regen. Med.* **2008**, *1*, 50–60.
47. Lokmic, Z.; Mitchell, G. *Tissue Eng. B Rev.* **2008**, *14*(1), 87–103.
48. Eschenhagen, T.; Zimmermann, W. *Circ. Res.* **2005**, *97*, 1220.
49. Meyer, G.; Wollert, K.; Lotz, J.; *et al. Circulation* **2006**, *113*(10), 1287–1294.
50. Hofman, M.; Wollert, K.; Meyer, G.; *et al. Circulation* **2005**, *111*, 2198–2202.
51. Glade, G.; Vahl, A.; Wisselink, W.; *et al. Eur. J. Vasc. Endovasc. Surg.* **2005**, *29*(1), 28–34.
52. Jones, B.; Desai, P.; Poston, R. *Heart Surg. Forum.* **2009**, *12*(3), E147–E149.
53. L'Heureux, N.; Germain, L.; Labbe, R. *J. Vasc. Surg.* **1993**, *17*, 499–509.
54. Lee, K. Y.; Mooney, D. J. *Chem. Rev.* **2001**, *101*, 1869–1879.
55. Rihova, B. *Adv. Drug Deliv. Rev.* **2000**, *42*, 65–80.
56. Otterlei, M.; Ostgaard, K.; Skjåk-Braek, G.; *et al. J. Immunother.* **1991**, *10*, 286–291.
57. Lee, K. Y.; Bouhadir, K.; Mooney, D. J. *Macromolecules* **2000**, *33*, 97–101.
58. Kim, B. S.; Mooney, D. *Trends Biotechnol.* **1998**, *16*, 224.
59. Davis, M.; Motion, M.; Narmoneva, D.; *et al. Circulation* **2005**, *111*, 442–450.
60. Del Re, D.; Sadoshima, J. *Circulation* **2009**, *120*, 831–834.
61. Padin-Iruegas, M.; Misao, Y.; Davis, M.; *et al. Circulation* **2009**, *120*, 876–887.
62. Landa, N.; Miller, L.; Feinberg, M.; *et al. Circulation* **2008**, *117*, 1388–1396.
63. Hughes, C.; Postovit, L.; Lajoie, G. *Proteomics* **2010**.
64. Naughton, G.; Kellar, R. *Med. Device Diagn. Ind.* **2008**, *30*(5), 102–109.
65. Schantz, J.; Brandwood, A.; Hutmacher, D.; *et al. J. Mater. Sci. Mater. Med.* **2005**, *16*(9), 807–809.
66. Fernández-Carballido, A.; Pastoriza, P.; Barcia, E.; *et al. Int. J. Pharm.* **2008**, *352* (1–2), 50–57.
67. Chun, K.; Yoo, H.; Yoon, J.; *et al. Biotechnol. Prog.* **2004**, *20*(6), 1797–1801.
68. Bertram, J.; Jay, S.; Hynes, S.; *et al. Acta Biomater.* **2009**, *8*, 2860–2871.
69. Kirby, D.; Rosenkrands, I.; Agger, E.; *et al. J. Drug Target.* **2008**, *16*(4), 282–293.
70. Lu, J.; Jackson, J.; Gleave, M.; *et al. Cancer Chemother. Pharmacol.* **2008**, *61*(6), 997–1005.
71. Zhu, X.; Wang, C.; Tong, Y. *J. Biomed. Mater. Res. A* **2009**, *89*(2), 411–423.
72. Kang, S.; Jeon, O.; Kim, B. *Tissue Eng.* **2005**, *11*(3–4), 438–447.
73. Didisheim, P.; Watson, J. In *Cardiovascular Applications in Biomaterials Science*, Academic Press: San Diego, CA, 1996; pp 283–297.
74. Voorhees, A.; Jaretzki, A.; Blakemore, A. *Ann. Surg.* **1952**, *135*, 332–338.
75. Canver, C. *Chest* **1995**, *108*, 1150.
76. Zdrahala, R. *Biomater. B Appl. Biomater.* **1996**, *10*, 309.
77. Hirsch, A.; Criqui, M.; Treat-Jacobson, D.; *et al. J. Am. Med. Assoc.* **2001**, *286*, 1317–1324.
78. Lloyd-Jones, D.; Adams, R.; Brown, T.; *et al. Circulation* **2009**, *17*, 17.
79. Fitzgibbon, G.; Kafka, H.; Leach, A.; *et al. J. Am. Coll. Cardiol.* **1996**, *28*, 616.
80. Ratcliffe, A. *Matrix Biol.* **2000**, *19*, 353.
81. Weinberg, C.; Bell, E. *Science* **1986**, *231*, 397.
82. Grassl, E.; Oegema, T.; Tranquillo, R. *J. Biomed. Mater. Res. A* **2003**, *66*, 550–561.
83. Seliktar, D.; Black, R.; Vito, R.; *et al. Ann. Biomed. Eng.* **2000**, *28*, 351.
84. Tranquillo, R.; Girton, T.; Bromberek, B.; *et al. Biomaterials* **1996**, *17*, 349.
85. Miwa, H.; Matsuda, T. *J. Vasc. Surg.* **1994**, *19*, 658–667.
86. Galletti, P.; Aebischer, P.; Sasken, H.; *et al. Surgery* **1988**, *103*, 231–241.
87. Galletti, P.; Gogolewski, S.; Ussia, G.; *et al. Ann. Vasc. Surg.* **1989**, *3*(3), 236–243.
88. Greisler, H.; Endean, E.; Klosak, I.; *et al. J. Vasc. Surg.* **1988**, *7*, 697–705.

89. Greisler, H.; Joyce, K.; Kim, D.; *et al*. *J. Biomed. Mater. Res.* **1992**, *26*, 1449–1461.
90. Niklason, L.; Gao, J.; Abbott, W.; *et al*. *Science* **1999**, *284*, 489.
91. Niklason, L.; Abbott, W.; Gao, J.; *et al*. *J. Vasc. Surg.* **2001**, *33*, 628.
92. Zhaodi, G.; Niklason, L. *FASEB J.* **2008**, *18*, 18.
93. McKee, J.; Banik, S.; Boyer, M.; *et al*. *EMBO Rep.* **2003**, *4*, 633–638.
94. Poh, M.; Boyer, A.; Solan, S.; *et al*. *Lancet* **2005**, *365*, 2122–2124.
95. Shum-Tim, D.; Stock, U.; Hrkach, J.; *et al*. *Ann. Thorac. Surg.* **1999**, *68*, 2298–2305.
96. Shin'oka, T.; *et al*. *N. Engl. J. Med.* **2001**, *344*, 532–533.
97. Hibino, N.; McGillicuddy, E.; Matsumura, G.; *et al*. *J. Thorac. Cardiovasc. Surg.* **2010**, *139*(2), 431–436.
98. Lantz, G.; Badylak, S.; Coffey, A.; *et al*. *J. Invest. Surg.* **1990**, *3*, 217–227.
99. Sandusky, G.; Lantz, G.; Badylak, S.; *et al*. *J. Surg. Res.* **1995**, *58*, 415–420.
100. Huynh, T.; Abraham, G.; Murray, J.; *et al*. *Nat. Biotechnol.* **1999**, *17*, 1083.
101. Zilla, P.; Fasol, R.; Grimm, M.; *et al*. *J. Thorac. Cardiovasc. Surg.* **1991**, *101*, 671.
102. Williams, S.; Rose, D.; Jarrell, B. *J. Biomed. Mater. Res.* **1994**, *28*, 203.
103. Boyer, M.; Townsend, L.; Vogel, L.; *et al*. *J. Vasc. Surg.* **2000**, *31*, 181.
104. Deutsch, M.; Meinhart, J.; Fischlein, T.; *et al*. *Surgery* **1999**, *126*, 847.
105. Deutsch, M.; Meinhart, J.; Zilla, P.; *et al*. *J. Vasc. Surg.* **2009**, *49*, 352–362.
106. Raeder, R.; Badylak, S.; Sheehan, C.; *et al*. *Transpl. Immunol.* **2002**, *10*, 15–24.
107. Badylak, S.; Gilbert, T. *Semin. Immunol.* **2008**, *20*, 109–116.
108. L'heureux, N.; Pâquet, S.; Labbé, R.; *et al*. *FASEB J.* **1998**, *12*, 47.
109. Chapman, S.; Sicot, X.; Davis, E.; *et al*. *Arterioscler. Thromb. Vasc. Biol.* **2010**, *1*, 68–74.
110. Hsiang, Y.; White, R.; Kopchok, G.; *et al*. *J. Invest. Surg.* **1990**, *3*(1), 11–21.
111. L'Heureux, N.; Dusserre, N.; Konig, G.; *et al*. *Nat. Med.* **2006**, *12*, 361–365.
112. L'Heureux, N.; Fuente, L.; McAllister, T. *N. Engl. J. Med.* **2007**, *357*, 1451–1453.
113. McAllister, T.; Maruszewski, M.; Garrido, S.; *et al*. *Lancet* **2009**, *373*, 1440–1446.
114. National Kidney Foundation. *Am. J. Kidney Dis.* **2002**, *39*(Suppl 1), S1–S266; A prospective, multicenter study. *Nephrol. News Issues* **2003**, *17*, 61–64, 66–68, 99.
115. Sallach, R.; Cui, W.; Balderrama, F.; *et al*. *Biomaterials* **2010**, *31*(4), 779–791.
116. McMillan, R.; Lee, T.; Conticello, V. *Macromolecules* **1999**, *32*, 3643–3648.
117. Huang, L.; McMillan, R.; Apkarian, R.; *et al*. *Macromolecules* **2000**, *33*, 2989–2997.
118. Chow, D.; Nunalee, M.; Lim, D.; *et al*. *Mater. Sci. Eng. R Rep.* **2008**, *62*, 125–155.
119. Sciortino, F.; Urry, D.; Palma, M.; *et al*. *Biopolymers* **1990**, *29*, 1401–1407.
120. Yamaoka, T.; Tamura, T.; Seto, Y.; *et al*. *Biomacromolecules* **2003**, *4*, 1680–1685.
121. Lim, D.; Nettles, D.; Setton, L.; *et al*. *Biomacromolecules* **2007**, *8*, 1463–1470.
122. Nagapudi, K.; Brinkman, W.; Leisen, J.; *et al*. *Macromolecules* **2002**, *35*, 1730–1737.
123. Nowatzki, P.; Tirrell, D. *Biomaterials* **2004**, *25*, 1261–1267.
124. Diehl, M.; Zhang, K.; Lee, H.; *et al*. *Science* **2006**, *311*, 1468–1471.
125. Wang, R.; Clark, R.; Mosher, D.; *et al*. *J. Biol. Chem.* **2005**, *280*, 28803–28810.
126. Di Zio, K.; Tirrell, D. *Macromolecules* **2003**, *36*, 1553–1558.
127. Heilshorn, S.; Di Zio, K.; Welsh, E.; *et al*. *Biomaterials* **2003**, *24*, 4245–4252.
128. Heilshorn, S.; Lui, J.; Di Zio, K.; *et al*. *Biomacromolecules* **2005**, *6*, 318–323.
129. Liu, J.; Heilshorn, S.; Tirrell, D. *Biomacromolecules* **2004**, *5*, 497–504.
130. Panitch, A.; Yamaoka, T.; Fournier, M.; *et al*. *Macromolecules* **1999**, *32*, 1701–1703.
131. Arias, F.; Reboto, V.; Martin, S.; *et al*. *Biotechnol. Lett.* **2006**, *28*, 687–695.
132. Girotti, A.; Reguera, J.; Rodríguez-Cabello, J.; *et al*. *J. Mater. Sci. Mater. Med.* **2004**, *15*, 478–484.
133. Urry, D.; Pattanaik, A.; Xu, J.; *et al*. *J. Biomater. Sci.* **1998**, *9*, 1015–1048.
134. Li, M.; Mondrinos, M.; Gandhi, M.; *et al*. *Biomaterials* **2005**, *26*, 5999–6008.
135. Behmoaras, J.; Osborne-Pellegrin, M.; Gauguier, D.; *et al*. *Am. J. Physiol. Heart Circ. Physiol.* **2005**, *288*, H769–H777.
136. Dobrin, P. B. In *Handbook of Physiology*; Shepherd, J. T. A. F., Ed.; American Physiological Society: Bethesda, MD, 1983; Vol. 3, pp 65–102.
137. Levy, B.; Michel, J.; Salzmann, J.; *et al*. *Circ. Res.* **1988**, *63*, 227–239.
138. Patel, A.; Fine, B.; Sandig, M.; *et al*. *Cardiovasc. Res.* **2006**, *71*, 40–49.
139. Kakisis, J.; Liapis, C.; Breuer, C.; *et al*. *J. Vasc. Surg.* **2005**, *41*, 349–354.
140. Senning, Å. *J. Thorac. Cardiovasc. Surg.* **1967**, *54*, 465–470.
141. Jamieson, W. *J. Cardiovasc. Surg.* **1993**, *8*, 89–98.
142. Jayakrishnan, A.; Jameela, S. *Biomaterials* **1996**, *17*, 471–484.
143. Rahimtoola, S. *J. Am. Coll. Cardiol.* **2003**, *41*, 893–904.
144. Schoen, F.; Levy, R. *J. Biomed. Mater. Res.* **1999**, *47*, 439–465.
145. Hammermeister, K.; Sethi, G.; Henderson, W.; *et al*. *J. Am. Coll. Cardiol.* **2000**, *35*, 1152.
146. Bloomfield, P.; Wheatley, D.; Prescott, R.; *et al*. *N. Engl. J. Med.* **1991**, *324*, 573.
147. Vesely, I. *Circ. Res.* **2005**, *97*, 743–755.
148. Hjortnaes, J.; Bouten, C.; Van Herwerden, L.; *et al*. *Tissue Eng. B Rev.* **2009**, *15*(3), 307–317.
149. Hopkins, R. A. *Circulation* **2005**, *111*, 2712.
150. Medelson, K.; Schoen, F. J. *Ann. Biomed. Eng.* **2006**, *34*, 1799.
151. Rabkin, E.; Schoen, F. I. *J. Cardiovasc. Tissue Eng. Cardiovasc. Pathol.* **2002**, *11*, 305.
152. Bader, A.; Schilling, T.; Teebken, O.; *et al*. *Eur. J. Cardiothorac. Surg.* **1998**, *14*, 279–284.
153. Fang, N.; Xie, S.; Wang, S.; *et al*. *Chin. Med. J.* **2007**, *120*, 696–702.
154. Sales, V. *Tissue Eng. A* **2010**, *16*, 257–267.
155. Rieder, E.; Seebacher, G.; Kasimir, M.; *et al*. *Circulation* **2005**, *111*, 2792–2797.
156. Hawkins, J.; Hillman, N.; Lambert, L.; *et al*. *J. Thorac. Cardiovasc. Surg.* **2003**, *126*, 247–252.
157. Hogan, P.; Duplock, L.; Green, M.; *et al*. *J. Thorac. Cardiovasc. Surg.* **1996**, *112*, 126–127.
158. Ketchedjian, A.; Kreuger, P.; Lukoff, H.; *et al*. *J. Thorac. Cardiovasc. Surg.* **2005**, *129*, 159–166.
159. Simon, P.; Kasimir, M.; Seebacher, G.; *et al*. *Eur. J. Cardiothorac. Surg.* **2003**, *23*, 1002–1006.
160. Balguid, A.; Rubbens, M.; Mol, A.; *et al*. *Tissue Eng.* **2007**, *13*, 1501.
161. Department of Energy. Biomass Program, Bioproducts, 2006.
162. Kidane, A.; Burriesci, G.; Edirisinghe, M.; *et al*. *Acta Biomater.* **2009**, *5*(7), 2409–2417.
163. Kiraly, R.; Yozu, D.; Hillegrass, D.; *et al*. *J. Artif. Organs* **1982**, *6*, 190–197.
164. Roe, B.; Kelly, P.; Myers, J.; *et al*. *Circulation* **1966**, *33*, I124–I130.
165. Nistal, F.; Garcia-Martinez, V.; Arbe, E.; *et al*. *J. Thorac. Cardiovasc. Surg.* **1990**, *99*, 1074–1081.
166. Bernacca, G.; Mackay, T.; Wilkinson, R.; *et al*. *Biomaterials* **1995**, *16*, 279–285.
167. Wheatley, D.; Raco, L.; Bernacca, G.; *et al*. *Eur. J. Cardiothorac. Surg.* **2000**, *17*, 440–448.
168. Imamura, E.; Kaye, M.; Davis, G. *Circulation* **1977**, *56*, 1053–1058.
169. Daebritz, S.; Fausten, B.; Hermanns, B.; *et al*. *Heart Surg.* **2004**, *7*, E525–E532.
170. Gallocher, S.; Aguirre, A.; Kasyanov, V.; *et al*. *J. Biomed. Mater. Res. B Appl. Biomater.* **2006**, *79*, 325–334.
171. Christenson, E.; Dadsetan, M.; Wiggins, M.; *et al*. *J. Biomed. Mater. Res. A* **2004**, *69*, 407–416.
172. Christenson, E.; Anderson, J.; Hiltner, A. *J. Biomed. Mater. Res. A* **2004**, *70*, 245–255.
173. Tang, Y.; Labow, R.; Santerre, J. *J. Biomed. Mater. Res.* **2001**, *57*, 597–611.
174. Jiang, H.; Campbell, G.; Boughner, D.; *et al*. *Med. Eng. Phys.* **2004**, *26*, 269–277.
175. Yin, W.; Gallocher, S.; Pinchuk, L.; *et al*. *Artif. Organs* **2005**, *29*, 826–831.
176. Kannan, R.; Salacinski, H.; Butler, P.; *et al*. *Acc. Chem. Res.* **2005**, *38*, 879–884.

Relevant Websites

http://www.gore.com/en_xx/news/propaten-expands-line-grafts.html – Gore Inc.
http://www.biotechnologyireland.com/pooled/articles/BF_DOCART/view.asp?Q=BF_DOCART_210850 – Biotechnology Ireland (a).
http://www.biotechnologyireland.com/pooled/articles/BF_DOCART/view.asp?Q=BF_DOCART_210853 – Biotechnology Ireland (b).

5.528. Tissue Engineering of Heart Valves

B Weber and S P Hoerstrup, University Hospital Zurich, Zurich, Switzerland

© 2011 Elsevier Ltd. All rights reserved.

5.528.1.	**The Ideal Valvular Substitute**	377
5.528.1.1.	Heart Valve Disease and State of the Art	377
5.528.1.2.	The 'Gold Standard': Architecture of Native Heart Valves	378
5.528.1.3.	Requirements for the Ideal Valvular Substitute	379
5.528.2.	**Strategies in Autologous Heart Valve Tissue Engineering**	379
5.528.3.	***In Vitro* Heart Valve Tissue Engineering**	379
5.528.3.1.	Principal Strategies	379
5.528.3.2.	Scaffold Materials	380
5.528.3.2.1.	Native, decellularized biological matrices	380
5.528.3.2.2.	Polymeric starter matrices	381
5.528.3.2.3.	Biological/polymeric hybrid starter matrices	382
5.528.3.2.4.	Collagen-based scaffolds	382
5.528.3.2.5.	Fibrin-based scaffolds	382
5.528.3.2.6.	From animal to human: *in vivo* performance of tissue-engineered heart valves	382
5.528.3.3.	*In Vitro* Heart Valve Tissue Formation	382
5.528.3.4.	Bioreactors for Heart Valve Tissue Engineering: Design and Function	383
5.528.4.	***In Vivo* Heart Valve Tissue Engineering**	384
5.528.4.1.	Principal Strategies	384
5.528.4.2.	Native, Decellularized Scaffold Materials	384
5.528.4.3.	Synthetic Scaffolds Materials	384
5.528.4.4.	The 'Biovalve' Concept: The Patient as a Perfect Bioreactor?	385
5.528.4.5.	The *In Vivo* Tissue Engineering Approach: Significance of a Novel Concept	385
5.528.5.	**Cell Sources for Heart Valve Tissue Engineering**	385
5.528.5.1.	Cardiovascular-Derived Cells	385
5.528.5.2.	Bone Marrow-Derived Cells	385
5.528.5.3.	Blood-Derived Cells	386
5.528.5.4.	Umbilical Cord-Derived Cells	387
5.528.5.5.	Prenatally Harvested Progenitor Cells	387
5.528.5.6.	Adipose Tissue-Derived Cells	387
5.528.6.	**Toward Clinical Application – Outlook for the Future**	388
References		388

Glossary

Alpha smooth-muscle actin (α-SMA) Cytoskeletal protein.
Ethylenediamine-tetraacetic acid (EDTA) Chelating agent with the ability to sequester di- and tricationic metal ions.
Glycosaminoglycans (GAGs) Unbranched polysaccharides consisting of a repeating disaccharide unit.
Low-density lipoprotein (LDL) Lipoprotein that transports cholesterol/triglycerides from the liver to peripheral tissues.
Vascular endothelial growth factor (VEGF) Platelet-derived growth factor involved in vasculogenesis and angiogenesis.

5.528.1. The Ideal Valvular Substitute

5.528.1.1. Heart Valve Disease and State of the Art

Heart valve disease represents a major part of the global disease load with high incidence in the developing world due to rheumatic disease, and in the developed world, in an increasing number of patients who are affected by degenerative valve disease.[1–3] Consequently, the advances in medical treatment of cardiovascular diseases have also been significant; particularly, treatment with tissue substitution has proved that functional replacements of tissue and organs could be lifesaving. In particular, the replacement of diseased and insufficient heart valves has markedly improved the life expectancy of patients with severe valvular heart disease and receiving optimum medical therapy.[4] Annually, more than 290 000 heart valve replacements are performed worldwide and the number of patients requiring heart valve replacement is estimated to triple by the year 2050.[5,6] In spite of this remarkable progress in treatment, valvular heart disease still remains a significant cause of morbidity and mortality worldwide.[7]

The most common treatment for end-stage heart valve disease is surgical replacement of the dysfunctional tissue with either a mechanical or bioprosthetic substitute. Today's valve replacement surgery is efficacious, and currently available valvular substitutes display excellent structural durability (reviewed by Ruel and Lachance[8]). However, the state-of-the-art heart valve prostheses in clinical use possess a series of substantial limitations. These include the lack of growth, repair, and remodeling capabilities once they are implanted into the patient. Additionally, mechanical valvular substitutes are inherently prone to thromboembolic events due to high shear stress, nonphysiological flow profiles and blood damage. Lifelong anticoagulation therapy seems indispensable in these patients, which results in a substantial risk of spontaneous hemorrhage and thromboembolic incidences (reviewed by Yoganathan *et al.*[9] and Dasi *et al.*[10]). Apart from this, further complications may occur due to the side effects of these drugs, for example, embryo toxicity in young females. Bioprosthetic valves, either of animal origin (xenografts) or from human donors (homografts), are more susceptible to structural valve degeneration, and the associated need for repeat reoperations makes them less suitable for middle-aged and younger patients.[11] This is also reflected by the current clinical guidelines that recommend the use of bioprostheses in patients aged 65 years and older.[12] Theoretically, cryopreserved donor heart valves represent the valvular replacements closest to natural valves with low thrombogenicity and infectious risk.[13] However, the lack of availability, reflecting worldwide organ scarcity, represents a seemingly unsolvable obstacle with regard to a widespread implementation of this cardiac valve replacement concept.[14] (see **Chapter 6.626, Cardiac Valves: Biologic and Synthetic**)

Overall, these considerable shortcomings indicate that current options for heart valve replacements are suboptimal for a substantial group of patients and that the ideal valvular replacement has yet to be developed.[6] The native heart valve is composed of living, dynamic tissue capable of continuous remodeling to adapt to its constantly alternating hemodynamic environment *in vivo*.[15] None of the currently available valve replacements is capable of fully restoring the native valvular function due to the lack of these adaptive capacities. Ultimately, this will also affect the integrity of the physiologic cardiac function. Tissue engineering of heart valves represents an emerging field of research with the potential to overcome these limitations by creating a viable living autologous valve replacement that prevents an immune response, clotting activation, and valvular degeneration on the one hand, and makes allowances for growth, remodeling, and repair throughout the patient's lifetime on the other hand (see also **Chapter 6.626, Cardiac Valves: Biologic and Synthetic**).

5.528.1.2. The 'Gold Standard': Architecture of Native Heart Valves

The ultimate rationale of tissue engineering is the creation of living neo-tissues identical, or at least very close to, native human valvular structures. Therefore, an accurate understanding of the fundamentals of normal heart valves – representing the 'gold standard' – constitutes an inalienable prerequisite to a successful development of native-analogous tissue-engineered valvular substitutes. Interestingly, it is the research on tissue engineering in recent years that has fundamentally stipulated a novel interest in native heart valve architecture and development, giving many important implications to the entire field of valvular heart disease.

In general, all four human heart valves share several microstructural similarities. However, the semilunar aortic valve best illustrates the essential features, and also serves as a paradigm for microstructural and cellular adaption to functional requirements. This trileaflet valve facilitates the blood flow from the left ventricle to the aorta and peripheral blood vessels through a complex opening and closing mechanism in an unrelenting, physiologically demanding environment over a wide range of hemodynamic conditions.[4,16] Its valvular leaflets are covered by a continuous layer of endothelial cells (ECs), enabling the smooth blood flow during opening and closing of the valve and regulating immune as well as inflammatory reactions (reviewed by Simmons[17]). The load-bearing part of adult semilunar valve leaflets reveals a layered architecture within the endothelial coverings, allowing for the remarkable changes in shape and dimension. The human heart valve leaflet tissue itself consists of three layers: the ventricularis, the fibrosa, and the spongiosa (**Figure 1**). These individual layers within the valvular leaflets show different mechanical characteristics, which are mainly due to their disparities in microstructural composition. In particular, the collagen and elastic fibers show a preferential arrangement and orientation within specific valvular connective tissue layers (reviewed by Misfeld and Sievers[18] and Hjortnaes *et al.*[19]).

The ventricularis, the layer at the inflow surface, predominantly consists of radially aligned elastin fibers. The inner layer, the spongiosa, is largely composed of loosely arranged collagen and abundant amounts of glycosaminoglycans (GAGs). The fibrosa or arterial layer, which is situated at the outflow surface, contains coarse bundles of circumferentially aligned collagen fibers that form the macroscopical folds parallel to the free edge of the leaflets. These collagen fibers represent the strongest part of the valve leaflets and are mainly responsible for bearing diastolic stress. All of these collagen bundles diverge into the aortic wall, thereby transferring the gross load of the leaflets to the wall of the aortic root. Thus, the fibrosa layer is considered the major load-bearing part of the valvular leaflet, enabling a stress increase while preventing a prolapse of the leaflets.[20–22] In contrast, the elastin in the ventricularis layer restores the contracted configuration of the leaflets in a systolic pressure environment. During opening of the valve, elastin extends at minimal load in the ventricularis to return the fibrosa in its original corrugated state, facilitated by the spongiosa that dissipates the arising shear stresses. When the valve is closing, the elastin fibers get unfolded and the main load shifts from elastin to collagen. In addition, the hydrophilic GAGs in the loose spongiosa layer may serve as a shock and shear absorber by readily absorbing water and decreasing the pressure difference across the valve.[23–25]

Between the extracellular components reside valvular interstitial cells that can be divided into two major cellular phenotypes: smooth muscle cells, arranged in bundles or just as single cells,[26,27] and fibroblasts, maintaining the extracellular matrix (ECM). Approximately 60% of the fibroblasts represent myofibroblasts,[28] cells that possess phenotypic features of both fibroblasts and smooth muscle cells, depending on their biological and mechanical microenvironment.[29,30]

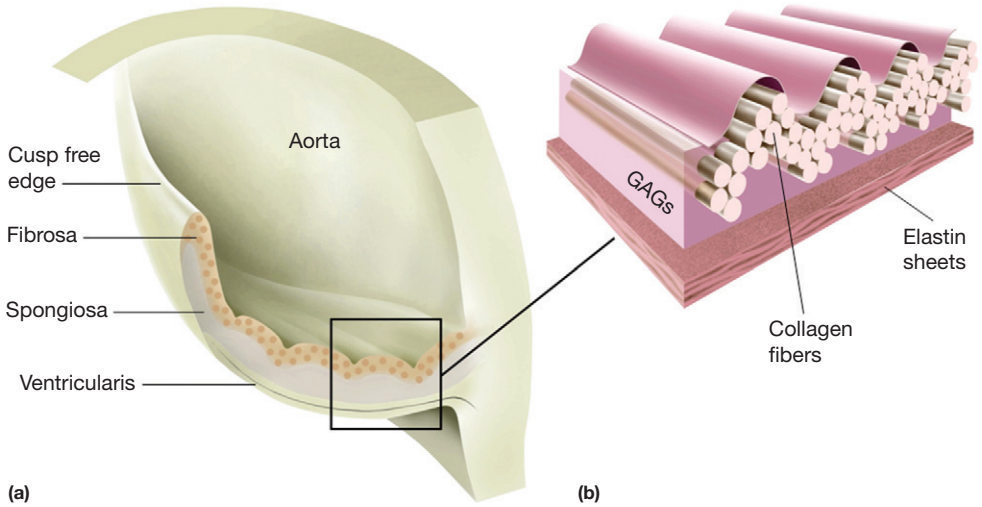

Figure 1 Native heart valve architecture. (a) Configuration of the fibrosa, spongiosa, and ventricularis within the aortic valvular leaflet. (b) Formation of the valvular extracellular matrix comprising glycosaminoglycans (GAGs), collagen fibers, and elastin sheets.

5.528.1.3. Requirements for the Ideal Valvular Substitute

The ideal valvular substitute would be a copy of its native counterpart comprising durability, resistance to infections, adequate hemodynamic performance, and potential to grow, as well as the absence of thrombogenic, immunogenic, and/or inflammatory reactions. Dwight E. Harken, a pioneer in heart valve surgery, first outlined these essential characteristics of the ideal valvular substitute and summarized them as the 'Ten Commandments'.[31] Unfortunately, these requirements – equaling the fundamental properties of natural, living, autologous tissues – are not met by today's cardiovascular replacements.

Apart from these characteristics, the ideal replacement would exhibit mechanical properties similar to its native counterpart comprising appropriate physiological compliance and tissue strength in order to withstand hemodynamic pressure changes without failure, and it would adequately respond to physiological changes within the cardiovascular system as well (see **Chapter 3.308, The Mechanics of Native and Engineered Cardiac Soft Tissues**).

5.528.2. Strategies in Autologous Heart Valve Tissue Engineering

Langer and Vacanti[32] defined the term 'tissue engineering' as an interdisciplinary field, applying the methods and principles of engineering to the development of biological substitutes that can restore, maintain, or improve tissue formation. According to this definition, two principle strategies have been developed to generate living autologous heart valve replacements. One requires an *in vitro* phase, generating the valvular substitute *ex vivo*.[32] This traditional tissue engineering paradigm comprises the isolation and expansion of cells from the patient, subsequent seeding onto an appropriate scaffold material, *in vitro* tissue formation, and finally, reimplantation into the patient from whom the cells were taken. This paradigm, further referred to as the *in vitro* tissue engineering approach, is being employed as the principal approach for heart valve tissue engineering and aims at full development of the tissue substitute *in vitro* (**Figure 2**). The second approach, *in vivo* heart valve tissue engineering, circumvents the *in vitro* tissue culture phase by straight implantation of natural tissue-derived heart valve matrices, aiming at potential cell ingrowth and remodeling *in situ*.[33]

5.528.3. *In Vitro* Heart Valve Tissue Engineering

5.528.3.1. Principal Strategies

According to the approach of *in vitro* tissue engineering, the successful fabrication of viable autologous heart valve replacements similar to the native prototype is supported by three main elements. First, autologous cells that resemble their native counterparts in phenotype and functionality are isolated and expanded using standard cell culture techniques. Second, these cells are then seeded onto a temporary biodegradable supporter matrix fabricated in the shape of a trileaflet heart valve, termed the scaffold, which promotes tissue strength until the produced ECM guarantees functionality on its own. Third, in order to promote adequate tissue formation and maturation, the seeded scaffolds are exposed to stimulation transmitted via a culture medium (biological stimuli) or via 'conditioning' of the tissue in a bioreactor (mechanical stimuli). This aims at optimal cellular differentiation, proliferation, and ECM production to form a living tissue model, called the construct. This construct is subsequently implanted orthotopically as a valvular replacement, and further *in vivo* remodeling is intended to recapitulate physiological valvular architecture and function.[15,34,35] (see **Chapter 5.507, Tissue Engineering and Selection of Cells**).

The attempt to develop a scaffold for heart valve tissue engineering has proceeded along two fronts: a fully synthetic scaffold and a biological matrix material.[36] Regardless of the matrix material used, the design of a scaffold capable of supporting cellular growth and of withstanding the unrelenting

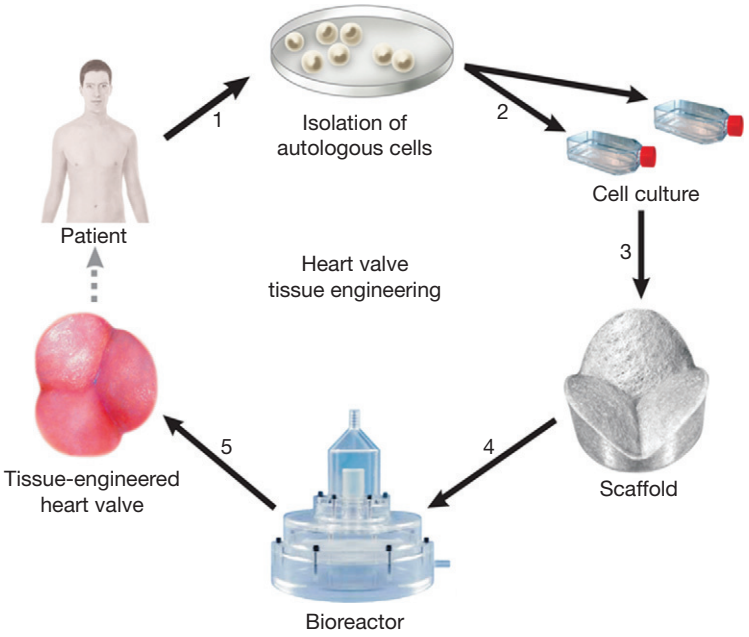

Figure 2 The concept of *in vitro* heart valve tissue engineering. Autologous cells are harvested from the patient (1) and expanded *in vitro* (2). When sufficient numbers are reached, cells are seeded onto a biodegradable scaffold (3). Constructs are positioned in a bioreactor (4) and conditioned. When *in vitro* tissue formation is sufficient, tissue-engineered heart valves (5) are ready for implantation into the patient.

cardiovascular environment, while forming a tight seal during closure, is critical to the success of the tissue-engineered construct. In addition to meeting all the standard design criteria of traditional tissue heart valves – in which durability and biocompatibility are effectively passive attributes of the underlying materials – and selecting the optimal scaffold material, it requires consideration of the active behavior of the cells in the regulation of tissue growth, remodeling, and homeostasis for fully laying the foundation for a future clinical implementation. Overall, the major goal is the *in vitro* creation of a living autologous tissue-engineered heart valve with structural differentiation, anatomically appropriate and high-quality ECM, viable valvular interstitial cells available to respond to varying physiological needs and to repair structural injury by remodeling ECM, and the capacity to grow with the patient (reviewed by Brody and Pandit[37] and Sacks *et al.*[38]). In this chapter, we provide a comprehensive overview of the two key bioengineering aspects of *in vitro* heart valve tissue engineering: the development of an optimal biodegradable and biomimetic scaffold material, and the use of bioreactors targeting at the guidance of valvular tissue formation *in vitro* (see **Chapter 5.507, Tissue Engineering and Selection of Cells**).

5.528.3.2. Scaffold Materials

As part of the *in vitro* heart valve tissue engineering concept, isolated and expanded cells are seeded onto appropriate scaffolds, serving as starter matrices of the heart valve fabrication process (**Figure 3**). The matrices must be capable of supporting cellular growth and cell-to-cell interaction, thus guiding tissue formation into a functional organ with organotypic ECM. The surfaces of these starter vehicles must be biodegradable, providing an optimized degradation rate for cellular expansion, and biocompatible, allowing for adequate cellular ingrowth and

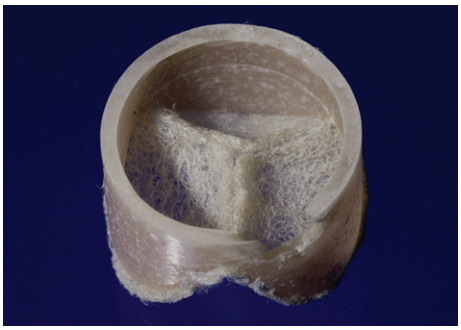

Figure 3 Stented heart valve design based on a nonwoven PGA coated with 1% poly-4-hydroxybutyrate. Reproduced from Mol, A.; Driessen, N. J.; Rutten, M. C.; *et al. Ann. Biomed. Eng.* **2005**, *33*(12), 1778–1788.

the formation of antithrombogenic cell linings (reviewed by Brody and Pandit[37]). These specific requirements entailed the development of various approaches in order to identify the optimal scaffold material, including the creation of biological[39] and synthetic scaffold materials.[35,40,41] These can be further subdivided into native tissue-derived ECM scaffolds,[42] polymeric scaffolds,[43–47] biological/polymeric hybrid scaffolds,[48–50] and fibrin gel or collagen scaffolds.[51–54] Although significant advances have been made in all these approaches, the polymeric scaffolds have, to date, received most attention with regard to *in vitro* heart valve tissue engineering (see **Chapter 1.122, Structural Biomedical Polymers (Nondegradable)**).

5.528.3.2.1. Native, decellularized biological matrices

Animal-derived heart valves (xenografts) or donor heart valves (homografts) are among the most obvious choices for scaffold materials. They are fixed and depleted of cellular antigens,

which makes them less immunogenic, and thus, eligible to be used as scaffold material in cardiovascular tissue engineering. The removal of cellular components results in a template composed of ECM proteins that serves as an intrinsic medium for subsequent cellular attachment. Nonetheless, they still possess a native-like geometry and architecture with biomechanical and hemodynamic properties comparable to their native counterpart (reviewed by Brody and Pandit,[37] Schmidt *et al.*,[35] and Mol *et al.*[55]).

Several different decellularization techniques have been extensively investigated in order to minimize the residual immunologic potential of biological matrices. Although it is crucial to remove all cellular components, the decellularization treatment should at the same time avoid any harm or alteration of the ECM properties. This efficiency of cellular removal, as well as preservation of the matrix integrity, is highly dependent on the method used for acellularization.[56] Various decellularization methodologies for heart valve scaffold fabrication have been reported, including trypsin/EDTA,[56–58] freeze drying,[59] osmotic gradients,[60] nonenzymatic detergent treatment,[56,61–64] and multistep enzymatic procedures.[65] The use of nonenzymatic detergent-based techniques has been shown to result in a much more efficient cellular removal while preserving the overall matrix integrity of the scaffold when compared to other more aggressive acellularization techniques such as trypsin/EDTA.[56,64,66,67] In order to avoid this impairment of function and matrix integrity due to tissue-derived protease activation, the use of suitable protease inhibitors has been recommended.[63] In addition, nuclease digestion steps should be included into the decellularization procedure to remove any remaining DNA or RNA within the scaffold matrix.[61–63]

After seeding of decellularized matrix scaffolds with ECs, and subsequent *in vitro* culturing, the constructs showed a confluent EC lining.[59,61,68–71] In 2003, Schenke-Layland *et al.* even proved that complete decellularization of porcine pulmonary heart valves with preservation of ECM structure and subsequent reseeding is feasible. Also, *in vivo* implantation of decellularized valves repopulated with autologous ECs and myofibroblasts in the pulmonary position in a sheep model revealed promising results.[58] In addition, Kim[72] demonstrated partial recellularization and endothelialization of decellularized scaffolds repopulated with bone marrow-derived cells 3 weeks after implantation as aortic valve replacements in dogs. Analysis of explanted valve substitutes also showed that originally seeded cells were still present on the engineered valve constructs, implying that seeded cells contribute to the regenerative process of implanted tissue.

Despite this proof of principle and great strides toward a clinically applicable xenogenic scaffold, decellularized biological matrices, as an obvious source of scaffold materials for heart valve replacement therapy, have mainly been used for the *in situ* tissue engineering approach. To some extent, this might also be due to their major shortcomings, in particular when compared to synthetic materials. When using xenografts, the risk of zoonoses, in terms of human diseases caused by animal-derived infectious agents, is a critical aspect that has to be considered.[73,74] In particular, the recent identification of porcine endogenous retroviruses (PERV[75–82]) and prionic diseases[83,84] has given rise to widespread concern. Even if deemed to be minimal,[85] the hypothetical risk of infection in the course of xenotransplantation constitutes a substantial shortcoming of a possible large-scale clinical application of the concept.[86] When the matrix material is from homogenic origin, the limited availability of donor valves and associated ethical concerns represent a considerable limitation. In addition, the lack of evidence of growth and remodeling capacities of valvular replacements when using biological scaffolds seems to be a further drawback as this represents an indispensable prerequisite for a future clinical implementation into the pediatric field.[87,88] These shortcomings and uncertainties raise a common concern associated with the use of decellularized starter matrices, also fuelling the search for synthetic scaffold alternatives.

5.528.3.2.2. Polymeric starter matrices

The use of polymeric scaffold matrices for heart valve tissue engineering has already been broadly demonstrated. The ideal scaffold material has to be at least 90% porous[89] and comprise an interconnected pore network, as this is essential for cell growth, nutrient supply, and removal of metabolic waste products. Besides being biocompatible, biodegradable, and reproducible, the scaffold material should also display a cell-favorable surface chemistry and match the biomechanical properties of the native heart valve tissue.[35] In addition, the matrix degradation rate should be controllable and commensurate with the rate of novel tissue formation in order to provide a sufficient mechanical stability of the construct over time.[15,90]

Several different synthetic biodegradable polymers have been investigated as potential starter matrices for heart valve tissue engineering. Polyglactin (PG), polyglycolic acid (PGA), polyhydroxyalcanoates (PHA), polylactic acid (PLA), polyvinyl alcohol (PVA), polycaprolactone (PCL), poly-L-lactic acid (PLLA), poly-4-hydroxybutyrate (P4HB), as well as a copolymer of PGA and PLA (PLGA/PGLA) were the materials of choice (reviewed by Brody and Pandit[37]). All of them represent biodegradable scaffold materials that vary in their manufacturing possibilities and degradation rates.

5.528.3.2.2.1. Aliphatic polyesters

PLA, PG, and PGA are all part of the aliphatic polyester family, and degrade by cleavage of the polymer chains due to hydrolysis of their ester bonds. The resulting monomer either enters the tricarboxylic acid cycle or is excreted via urinary secretion.[89] In order to fabricate single valvular leaflets, the creation of scaffolds was initially based on combinations of aliphatic polyesters, including PG nonwoven PGA meshes with layers of PGLA and nonwoven PGA meshes. The major shortcomings of aliphatic polyesters are their thickness, initial stiffness, and nonpliability, making the fabrication of trileaflet heart valves a difficult process.

5.528.3.2.2.2. Polyhydroxyalcanoates

The PHA family comprises polyesters built up from hydroxyacids that are produced as intracellular granules by various bacteria.[91] P4HB as well as polyhydroxyoctanoates have been used to fabricate trileaflet heart valve conduits.[92,93] These materials possess thermoplastic properties and can be molded into any desired shape with the use of stereolithography.[94,95] The major drawback of PHAs can be found in their slow degradation. Combinations of PHAs and aliphatic polyesters have also been employed as alternative composite materials.[96–98]

Particularly, the use of PGA coated with P4HB, combining the thermoplastic properties of P4HB and the high porosity of PGA, for the fabrication of complete trileaflet valvular structures revealed promising results in a rapidly growing sheep model.[35,96,97,99,100]

5.528.3.2.3. Biological/polymeric hybrid starter matrices

Recently, a further strategy for the fabrication of scaffold materials in tissue engineering emerged, using biological/polymeric composite materials as starter matrices.[101] These hybrid starter matrices can also constitute complex three-dimensional structures such as heart valves, for example, fabricated from decellularized porcine aortic valves and dip-coated with a bioresorbable polymer.[48–50] Furthermore, scaffolds equipped with molecular cues mimicking certain structural or functional aspects of extracellular microenvironments have been developed in recent years.[102,103] In particular, gene delivery from the scaffold represents a versatile approach to manipulate the local environment for directing cellular function and promoting tissue formation.[104]

5.528.3.2.4. Collagen-based scaffolds

In an attempt to provide heart valve replacements consisting solely of autologous tissue, biodegradability turned out to be an indispensable prerequisite for scaffold materials. Collagen is one of these biological materials that display bioresorbable properties and can theoretically be obtained directly from the patient. Thus, it has been investigated as a possible matrix material for heart valve tissue engineering by using collagen (type I) foams,[105,106] gels or sheets,[51,90,107–111] sponges,[112] and even as fiber-based scaffolds.[113,114] However, besides a low degradation rate, collagen has the major drawback of a very low availability in humans as it is difficult to obtain from the patient. Therefore, most collagen scaffolds are based on animal-derived collagens, which potentially involve common shortcomings associated with the use of animal-derived tissues such as the risk of transmission of zoonoses.

5.528.3.2.5. Fibrin-based scaffolds

Fibrin is a further biological material that also offers controllable bioresorbable properties. Besides its potential to serve as an autologous biodegradable scaffold material, fibrin gel has also been used as a cell carrier to seed cells into a fiber-based[115] or porous synthetic scaffold.[116] As the patients' blood could serve as a source for fibrin gel production, no toxic degradation or inflammatory response is expected upon reimplantation.[13] By using the technique of injection molding of the cell–gel mixture followed by enzymatic polymerization of fibrinogen, three-dimensional structures can be obtained. The rate of degradation is controlled by adding aprotinin, a proteinase inhibitor that slows down or even stops fibrinolysis.[117–119] Immobilization of growth factors in specific areas has also been shown as a feasible option to control degradation of fibrin scaffolds.[120]

Besides these seemingly favorable features, the use of fibrin as a scaffold material has several drawbacks, including its tendency to shrink, its poor initial mechanical properties, and importantly, its reduced diffusion and washout capacity into the surrounding medium compared to other porous matrices.[117,119] Although various measures have been developed to limit these shortcomings, such as poly-L-lysine chemical fixation that prevents shrinkage and improving mechanical properties, further investigations are needed to determine its effective value as a scaffold material for heart valve tissue engineering in the future.

5.528.3.2.6. From animal to human: in vivo performance of tissue-engineered heart valves

In 1995, the first successful replacement of a single pulmonary valvular leaflet with an *in vitro* tissue-engineered substitute, based on a synthetic scaffold, was demonstrated in a lamb model.[121,122] In the following years, complete trileaflet valve replacements based on synthetic scaffolds were introduced.[64,92,98,123] After the development of the mechanical conditioning approach as a substantial improvement of the *in vitro* culture phase, the fabricated valves showed adequate functionality and remodeling into native-like heart valves up to 5 months in animal studies (**Figure 4**[96]). A 2 year follow up study of pulmonary artery substitutes in a lamb model even showed clear evidence of growth of implanted tissue-engineered structures.[124] However, the actual proof of a growth capacity of valvular structures fabricated on the basis of synthetic scaffolds is still missing. In first clinical experiences, synthetic scaffold-based tissue-engineered patches were successfully used for the reconstruction of the pulmonary artery in humans.[125,126] Besides these promising *in vivo* results, biodegradable synthetic polymers offer a number of advantages over biological scaffold materials, including greater control over mechanical properties and fabrication, better reproducibility and degradation rates, advanced geometrical design specifications, and lower immunogenicity. Even if several challenges such as improvement of the elastic network formation and matrix degradation control remain to be addressed by further investigations prior to a clinical implementation of the concept, synthetic scaffold-based heart valve replacements hold great promise for the future.

5.528.3.3. *In Vitro* Heart Valve Tissue Formation

A major challenge in tissue engineering of functional heart valve substitutes is to mimic the biomechanical properties and dominant tissue structures of native heart valves in order to provide valvular replacements that hold promise for long-term graft functionality after implantation. According to native tissues, these biomechanical properties are predominantly based on the structural organization, composition, and quality of the ECM. In the effort to create adequate ECM production,

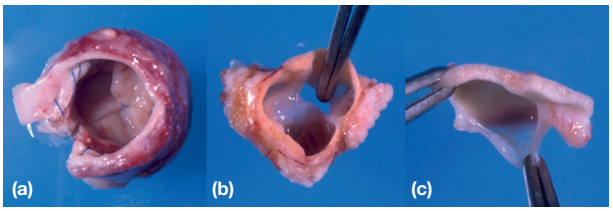

Figure 4 Tissue-engineered heart valves explanted after 6 weeks (a) and 20 weeks (b) from a lamb model. Note the thin and pliable leaflet structure at 20 weeks postimplantation (c). Reproduced from Hoerstrup, S. P.; Sodian, R.; Daebritz, S.; *et al*. *Circulation* **2000**, *102*(19 Suppl 3), III44–III49, with permission from Wolters Kluwer Health.

cellular differentiation, and proliferation, the seeded scaffolds are exposed to stimulation transmitted via a culture medium (biochemical stimuli) or via 'mechanical conditioning' of the tissue (mechanical stimuli) prior to *in vivo* implantation. This comes along with strict isolation of the *in vitro* system ensuring a long-term maintenance of sterile culture conditions.[96,127] Besides ECM production, the collagen cross-link concentration has also been shown to play a critical role for the biomechanical behavior of heart valves.[128]

The use of biochemical conditioning in terms of using biological stimuli, such as growth factors, to promote tissue growth and regeneration during *in vitro* development, represents a common conditioning approach in tissue engineering. In heart valve tissue engineering, different growth factors such as bFGF,[129] HGF,[130] TGF-β1,[52,131] EGF,[58] vascular endothelial growth factor (VEGF),[129] and PDGF,[131] have been investigated to render preferred cellular differentiation within the engineered constructs. However, precaution is recommended when considering a possible clinical implementation of the concept, as several pathways of the mentioned growth factors have not yet been fully elucidated.

For further improvement of tissue architecture and biomechanical properties, mechanical stimulation during the *in vitro* culture phase has also been widely used in heart valve tissue engineering.[132–135] Various mechanical conditioning approaches have been investigated in view of their influence on ECM development and biomechanical tissue properties using model systems of fast degrading scaffolds seeded with human adult vascular-derived cells. As a substantial amount of these vascular-derived cells exhibit a myofibroblast-like phenotype, they generate a long-lasting tensile activity in terms of continuous isometric tension on their environment.[136,137] Allowing these myofibroblasts to exert their tensile activity by application of static mechanical constraint has been shown to be an asset for tissue component alignment during tissue organization.[138] In particular, the beneficial effects of intermittent dynamic straining[139] and continuous long-term dynamic straining[140,141] have been shown to further optimize tissue formation in various ways. In return, large straining magnitudes revealed a negative effect on the mechanical properties of tissues.[140] In addition, stretch, flow, and cyclic flexure have been demonstrated to exhibit both independent and coupled stimulatory effects on cell and ECM development in tissue-engineered heart valves.[140,142–144] By using this system, Engelmayr *et al.*[145,146] demonstrated the profound role of the coupled effects of two physiological mechanical stimuli – cyclic flexure and laminar flow – that seem to be highly relevant to heart valve tissue formation *in vitro* using a novel flex–stretch–flow (FSF) bioreactor system (reviewed by Sacks *et al.*[38]). Recently, Balguid *et al.*[147] presented another highly promising conditioning approach using hypoxia. By culturing tissue-engineered valvular constructs under hypoxic culture conditions (7% O_2), they were able to generate valvular substitutes displaying near-native mechanical properties.[147]

5.528.3.4. Bioreactors for Heart Valve Tissue Engineering: Design and Function

A bioreactor is a biomimetic system that exposes the developing tissue to mechanical conditioning, primarily through pressure changes and cyclic flow (**Figure 5**; reviewed by Breuer *et al.*,[36] Mertsching and Hansmann,[148] Mol *et al.*,[55] Ruel and Lachance,[8] and Sacks *et al.*[38]). By mimicking the physiological environment of native heart valves *in vitro*, the bioreactor enhances neo-tissue development, changes cellular orientation, improves cell attachment, and increases production of ECM proteins, such as collagen and elastin.[149] Importantly, bioreactors can also be used to modulate the biomechanical properties of developing neo-tissues, which is of particular importance in the development of tissue-engineered heart valves.[127,133,134,142,144,150,151] Different bioreactors have been developed using strain,[152–154] flow,[95,127,151,155,156] and cyclic stretching[53,157] as their main mechanical cues to fabricate living blood vessels and heart valves *in vitro*. For the engineering of heart valves, a diastolic pulse duplicator (DPD) system has been developed in order to mimic only the diastolic phase of the cardiac cycle – the phase in which the leaflet tissue is primarily exposed to cyclical straining.[152] This pulsatile conditioning approach provides physiological pressure and flow to the developing heart valve structure and promotes both the development of mechanical strength and the modulation of cellular function.[127,150,151] In particular, the application of a pressure difference across the growing valvular leaflets, inducing local dynamic strains, is of critical importance. On the whole, this strategy of *in vitro* conditioning, which solely mimics the straining phase of the cardiac cycle, offers a highly innovative bioreactor design that has

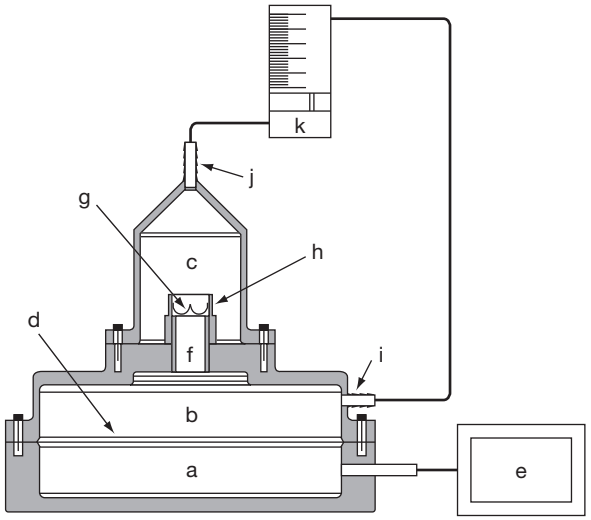

Figure 5 The two-chamber bioreactor design. The pulsatile flow chamber (bioreactor) consists of two principal chambers: the air chamber (a) at the bottom level and the cell media fluid chamber (b,c) at the upper level, separated by a thin silicone diaphragm (d; 0.5 mm). The air chamber is connected to a respirator pump (e; dual phase). The fluid chamber (total volume: 500 ml) is divided into two compartments: the lower compartment (b) is connected via a tube (f) to the smaller top compartment (c; valve perfusion chamber). The tissue-engineered heart valve (g) is fixed to a removable silicone tube (h) by suturing. The media flow is directed from the bottom compartment (b) via the connecting tube (f) to the mounted tissue-engineered heart valve in the perfusion chamber. The upper compartment is connected via a valved inlet (i) and outlet (j) tubing to a separate media reservoir (k; total volume: 500 ml).

been used by several groups up to now for heart valve conditioning.[35,40,99,127,158–160] By rendering human tissue-engineered valvular structures that may even sustain the systemic circulation, the DPD regime represents a major step toward a tissue-engineered aortic human heart valve replacement.[100] Recent investigations have also pursued the idea of monitoring and simultaneously controlling the applied deformations during tissue culture in terms of developing a feedback control loop design.[38,161] In consideration of this effort, Kortsmit *et al.*[162,163] demonstrated the value of volumetric deformation measurement and the inverse experimental-numerical estimation method as to the realization of a real-time quality control system next to a controllable culture environment. Overall, the optimal conditioning protocol depends on various parameters such as the sensitivity of the cell phenotype to mechanical cues, the scaffold design, the transfer of mechanical cues from the scaffold to the cells, as well as the type and degree of mechanical exposure.

5.528.4. *In Vivo* Heart Valve Tissue Engineering

5.528.4.1. Principal Strategies

The *in vivo* tissue engineering approach, also known as '*in situ* tissue engineering' or 'guided tissue regeneration,' relies on the natural regenerative potential of the body. Its principal strategy aims at the implantation of a nonhemolytic, nonthrombogenic, and nonimmunogenic, functional scaffold that is capable of autologous host cell reseeding and subsequent remodeling *in vivo*. It is sometimes deemed to offer a more clinically attractive alternative in comparison to the *in vitro* approach considering a possible off-the-shelf availability. By circumventing the extensive *ex vivo* processing of valvular substitutes of the *in vitro* approach, it would certainly represent a cheap, quick, and on-demand approach. In particular, the absence of the complex preseeding procedure could significantly minimize and simplify the fabrication process, and postimplantation, this approach might have the potential to reduce immunogenic reactions *in situ* (reviewed by Vesely,[164] Sievers,[165] and Schleicher *et al.*[166]).

5.528.4.2. Native, Decellularized Scaffold Materials

Several investigations have focused on decellularized homo- or xenografts as these suggest highly attractive scaffold materials, in particular, for guided tissue regeneration of heart valves. Several groups have demonstrated the overall feasibility of *in vivo* repopulation of decellularized scaffolds in animal models.[57,167–175] However, the success of these attempts was mainly linked to the actual mode of decellularization and whether homo- or xenografts were used.[66] When using SynerGraftTM as the acellularization technique, leaflet explants showed up to 80% cellular repopulation and a distribution of α-SMA positive cells comparable to that of natural valves.[168,169,171] Conversely, when trypsin/EDTA digestion was used for decellularization, allogenic ovine valve conduits did not show any interstitial valve tissue reconstitution due to severe calcification. Only xenogenic porcine valves implanted into the pulmonary position in sheep revealed histologic reconstitution of valvular tissue.[57,174] A comparative study of different decellularization approaches indicated that a novel detergent-based technology, using Triton X-100 combined with sodium deoxycholate, offers the most favorable scaffold for cellular repopulation.[66] Accordingly, several *in vivo* studies further indicated that besides cellular repopulation also adaptive matrix remodeling and even growth could be found in implanted acellularized valvular constructs.[167,170]

However, the transferability of these promising results from animal models to the human organism still has to be evaluated, even if several groups have reported promising results in adult heart valve recipients[171,176,177] – in particular, when considering the clinical results of Simon *et al.*[178] that showed early failure of porcine SynerGraftTM-treated heart valves in children. In the course of their clinical trial, implanted valvular substitutes caused a strong inflammatory response, followed by structural failure and rapid degeneration of the graft within a few weeks to months.[178] These results, clearly demonstrating the ineffectiveness of the 'SynerGraftTM technology,' also suggest that acellularization of xenogenic heart valves, according to this technology, holds significant risks for the patient and should be avoided. Subsequent investigations, focusing on the molecular mechanism of this residual immunogenicity of decellularized grafts, indicated that acellularization of porcine xenografts, even when fully depleted of cells and cellular components, did not fully eliminate thrombogenicity and inflammatory stimulation response. In spite of missing attraction of monocytes and lymphocytes in completely decellularized tissue, the recruitment of granulocytes was still evident.[179,180] Bastian *et al.*[181] suggested that this inflammatory response is predominantly caused by the loss of specific ECM proteins during the decellularization process, which normally prevents these excessive immunologic phenomena. Several investigations, aiming for a substantial decrease of the susceptibility of acellularized matrices to an immunologic response, that is, by using polymer impregnation, offered several improvements, also with regard to a possible future clinical establishment of the concept.[50,182–184] However, some of them may have yet exceeded the scope of the *in vivo* tissue engineering approach, that is, by using *ex vivo* endothelialization of matrices.

By contrast, the use of decellularized homografts seems to be beneficial over the use of xenogenic decellularized scaffold materials due to their reduced risk of infection and lower thrombogenicity.[185,186] Even the clinical use of SynerGraftTM-treated homografts as pulmonary valve replacements in adults showed surprisingly good results.[168,169,187,188] Yet, actual clinically manifest benefits of decellularized substitutes over conventional homografts, and thus, conclusive reasons for preferable clinical application, are still missing.[189,190] Altogether, the clinical applicability of acellularized homogenic as well as xenogenic heart valve replacements with spontaneous cellular repopulation *in vivo* remains a controversial field within tissue engineering.

5.528.4.3. Synthetic Scaffolds Materials

The use of synthetic scaffold materials constitutes another approach to *in vivo* heart valve tissue engineering, offering several advantages when compared to decellularized scaffolds. Besides their decreased immunogenic potential, they also

enable a better definition of expectant physical and chemical properties. While the implantation of a plain scaffold was unsuccessful, leading to thrombus formation and inappropriate cellular repopulation,[191] scaffolds compounded with a collagen microsponge matrix revealed promising results in several animal studies.[192–195]

Another concept, also utilizing synthetic matrix materials, is the seeding of freshly isolated autologous cells onto scaffold materials prior to implantation. Several different cell sources and surgical procedures have been investigated using this principle of same-day harvesting of desired cell types via a single biopsy and subsequent reimplantation of preseeded synthetic scaffolds.[125,196–200] However, it seems as if this is an approach that is again located at the interface between *in vivo* and *in vitro* heart valve tissue engineering, given the use of *ex vivo* cell seeding technologies.

5.528.4.4. The 'Biovalve' Concept: The Patient as a Perfect Bioreactor?

First implemented by De Visscher *et al.*,[201] a novel subtle way of repopulating scaffold materials for valvular replacement surgery is the use of the peritoneal cavity as a 'natural bioreactor.' By using this approach, scaffolds are preimplanted into the abdominal cavity, inducing an intraperitoneal foreign body reaction and an *in vivo* cellularization that is mainly driven by a host-mediated immune response.[201,202] Also, a subcutaneous implantation of scaffold prototypes in rabbits revealed fairly good results.[203,204]

At any rate, the concept of *in vivo* autologous heart valve tissue engineering with the patient as an autologous 'bioreactor' is doubtlessly appealing. However, it remains exceedingly questionable whether this concept renders correct cell types and if these obtained cells, which are primarily due to an encapsulation reaction, are capable of withstanding the unrelenting hemodynamic forces of a native valvular position.[165,205]

5.528.4.5. The *In Vivo* Tissue Engineering Approach: Significance of a Novel Concept

By using the patient as a 'natural bioreactor,' the guided tissue regeneration approach in heart valve tissue engineering seems to be highly attractive in view of avoiding the extensive *in vitro* conditioning phase. It may have also shown some success in animal studies[206]; however, up to now there is no striking scientific evidence that heart valve scaffolds will be sufficiently recellularized when implanted into humans.[164] In return, several authors described this approach as 'highly unlikely' or 'highly speculative'.[207] Even if some endothelial repopulation has been found to develop on vascular grafts implanted into animals, studies have also proven that vascular grafts implanted into humans do not spontaneously form an endothelial lining.[178] As an adequate endothelial lining of the construct seems indispensable for providing a thromboresistant surface, and also constitutes a precondition for the formation of a proper interstitial cell compartment, the *in vivo* approach remains highly questionable and its position will have to be justified as a feasible approach for heart valve tissue engineering in the future.

5.528.5. Cell Sources for Heart Valve Tissue Engineering

In tissue engineering of implantable cardiovascular structures such as heart valves, the *in vitro* formation of a durable, well structured, and viable tissue is known to be crucial for an adequate *in vivo* functionality of the construct. Therefore, several technologies have been introduced in order to meet these demands of designing heart valve replacements with optimum functional durability. However, the cell source used for engineering these cardiovascular structures remains the least controlled factor, yet being most important for the quality of the viable part of the replacement. The quality of these cells depends on the individual tissue characteristics of its origin, and thus, varies between individuals.[208,209] Therefore, the choice of the optimal cell source constitutes the key to the long-term success of heart valve regeneration (**Figure 6**[15]).

5.528.5.1. Cardiovascular-Derived Cells

In most heart valve tissue engineering approaches, cells were harvested from donor tissues, for example, from peripheral arteries, and mixed vascular cell populations were obtained for seeding.[34,210] Out of these, two cell lines can be isolated: ECs, forming a confluent EC lining with antithrombogenic features, and myofibroblast/fibroblast-like cells, responsible for the ECM development.[122,209,211] With regard to the clinical implementation of the concept, several human cell sources have been investigated throughout the last few years. Following extensive studies using ovine vascular-derived cells,[96,121,122,209,212] the suitability of human cells from different sources was evaluated. Experiments using human aortic myofibroblasts and ECs demonstrated easy isolation and *in vitro* culture.[92] These human aortic-derived cells were then seeded on biodegradable scaffolds where they revealed a layered tissue formation. Moreover, cells from saphenous veins also showed excellent growth properties and tissue formation after seeding on biodegradable scaffolds, comparable to aortic cells[208] and mammary artery cells.[213] Saphenous vein cells can be obtained by a minor surgical intervention under local anesthesia, and thus, represent an even more attractive cell source for cardiovascular tissue engineering.

5.528.5.2. Bone Marrow-Derived Cells

With regard to the future routine clinical realization of the cardiovascular tissue engineering concept, human bone marrow-derived stem cells (BMSCs) were identified as promising alternative candidates.[99,214,215] The overall capability of BMSCs of forming solid organ tissue cells, including hematopoietic stem cells, in particular, functional cardiomyocytes and vascular structures, has already been demonstrated by several groups.[216,217] Human BMSCs were also successfully used for the *in vitro* fabrication of living trileaflet heart valves (**Figure 7**[99,214]) and showed satisfactory *in vivo* function as pulmonary valve substitutes for at least 8 months.[123] The usage of BMSCs in cardiovascular tissue engineering may offer several advantages: (i) BMSCs can be obtained without major

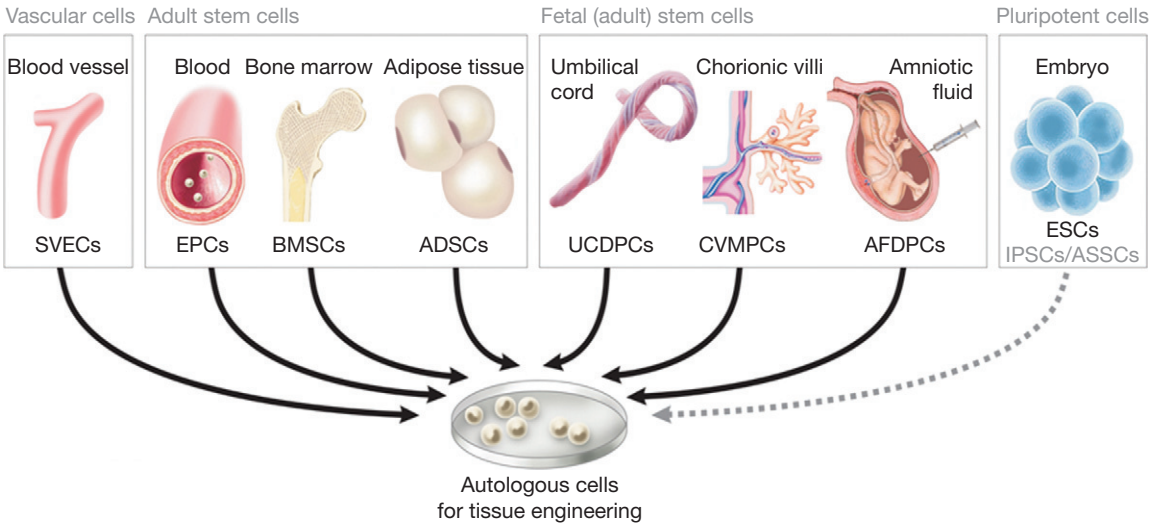

Figure 6 Available cell sources for heart valve tissue engineering: standard vascular endothelial cells (SVECs), endothelial progenitor cells (EPCs), bone marrow-derived mesenchymal stem cells (BMSCs), adipose-derived stem cells (ADSCs), umbilical cord-derived progenitor cells (UCDPCs), chorionic villi-derived mesenchymal progenitor cells (CVMPCs), amniotic fluid-derived progenitor cells (AFDPCs), embryonic stem cells (ESCs), adult spermatogonial stem cells (ASSCs), and induced pluripotent stem cells (IPSCs).

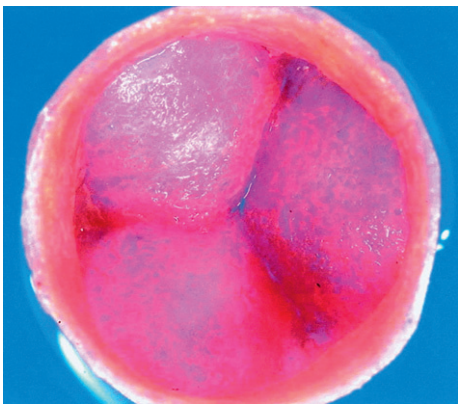

Figure 7 BMSC-based tissue-engineered heart valve leaflets after 14 days in the *in vitro* pulse duplicator system (bioreactor). Reproduced from Hoerstrup, S. P.; Kadner, A.; Melnitchouk, S.; *et al. Circulation* **2002**, *106*(12 Suppl 1), I143–I150, with permission from Wolters Kluwer Health.

surgical interventions by a simple bone marrow puncture, thus representing an easy-to-access cell source in a clinical scenario; (ii) they exhibit the potential to differentiate into multiple cell lineages under biochemical[218] and mechanical[219] stimulation, showing the potential to differentiate into multiple cell lineages; (iii) they demonstrate unique immunological characteristics, allowing the persistence in allogenic settings; and (iv) they also show an extensive *in vitro* proliferation capacity.

5.528.5.3. Blood-Derived Cells

It has been shown that the presence of endothelium on cardiovascular surfaces significantly reduces the risk for both inflammatory complications and coagulation (reviewed by Tanaka *et al.*[220]). Therefore, in order to improve the functional capacities, the tissue-engineered heart valve constructs are usually covered with a layer of autologous human ECs as an antithrombogenic lining.[221] Fully matured ECs have been isolated from several different vascular donor sources, demonstrating promising results in heart valve tissue engineering.[92,96,121,122] However, the expansion rate of these mature ECs is comparatively slow and the proliferation capabilities are limited, requiring a large number of ECs to be harvested for therapeutic use.[222] Endothelial progenitor cells (EPCs), first discovered in human peripheral blood by Asahara *et al.*,[223] have been established as possible sources of ECs. These blood-derived EPCs constitute a highly attractive alternative cell source of ECs, in particular, for pediatric patients, as they can be isolated from bone marrow, peripheral blood, as well as from umbilical cord blood (reviewed by Kim and Recum[224,225]). They have been successfully used for the repair of injured vessels, regeneration or neovascularization of ischemic tissue in both preclinical models,[226–228] and more recently, early-phase clinical trials (reviewed by Martin-Rendon *et al.*[229] and Pearson[230]). Importantly, further studies[231–234] also demonstrated the feasibility of using human umbilical cord blood-derived EPCs (HUCB-EPCs) for the generation of constant neo-endothelial phenotypes in tissue-engineered cardiovascular replacements. Lately, they also showed the fabrication of biologically active living heart valve leaflets by using peri- and prenatally available human umbilical cord-derived progenitor cells as the only cell source.[87]

Overall, EPCs constitute an auspicious cell source for endothelialization of engineered cardiovascular replacements, such as heart valves. In spite of these pioneering studies showing great promise, the application of EPCs in tissue engineering is still in its infancy.[224] Since EPCs are easily accessible, current research increasingly aims at their transdifferentiation into a mesenchymal, myofibroblast-like phenotype in an

attempt to provide new strategies to guide tissue formation in engineered cardiac valves[235] and to ultimately establish blood as a single cell source for heart valve tissue engineering.

5.528.5.4. Umbilical Cord-Derived Cells

In an attempt to provide tissue-engineered constructs for congenital heart defects, including heart valve disease, alternative cell sources have been investigated, paying particular attention to preserving the intact vascular donor structure of the newborn patients.[236] The human umbilical cord is readily available, easy to obtain, and by means of modern cell and tissue banking technologies, it could be used as an autologous cell pool during the patient's lifetime.[236,237] Overall, the umbilical cord contains several different cell sources that can be utilized for heart valve tissue engineering: (i) SVECs (standard vascular ECs) including HUVECs (human umbilical cord vein-derived ECs) and HUAECs (human umbilical cord artery-derived ECs), (ii) HUCMF (human umbilical cord-derived myofibroblasts), and (iii) HUCB-EPCs.

In culture, these human umbilical cord-derived cells demonstrated excellent growth properties and sufficient cell numbers for seeding of biodegradable scaffolds. After seeding and *in vitro* culture, good tissue formation was observed. Micro- and ultrastructural analysis revealed viable, layered tissues showing cell and matrix features known from native tissue.[236,238–240] Schmidt *et al.*[232] used differentiated HUCB-EPCs seeded on vascular scaffolds for the formation of vascular neo-tissue in both biomimetic and static *in vitro* environment. In 2005, Schmidt *et al.* demonstrated the successful *in vitro* generation of living autologous cardiovascular replacements (patches) based on myofibroblasts derived from Wharton's jelly and EPCs derived from umbilical cord blood. Recently, they were able to optimize the usage of umbilical cord-derived cells for cardiovascular tissue engineering by generating functional tissue-engineered blood vessels,[234] and by ultimately fabricating biologically active living heart valve leaflets *in vitro*.[87] Sodian *et al.*[160] demonstrated the use of cryopreserved human umbilical cord cells (CHUCCs) for the *in vitro* fabrication of tissue-engineered heart valves.

Taken as a whole, the major advantage of UCCs as an autologous cell source, is deemed to be the avoidance of invasive harvesting of intact vascular structures from pediatric patients and the easy perinatal availability of a large amount of juvenile, fast growing cells for scaffold seeding in a short period of time.[241] With regard to the approach in the pediatric population, the umbilical cord may serve as an optimal perinatal autologous cell source for tissue engineering of cardiovascular constructs in the future.

5.528.5.5. Prenatally Harvested Progenitor Cells

In most congenital heart defects, the early surgical correction of the malformations is deemed to be indispensable to prevent secondary damage to the immature neonatal cardiovascular system. Owing to the advances in imaging technology, these cardiac pathologies are often already detectable prior to delivery by routine ultrasound examination. Therefore, the ideal pediatric tissue engineering paradigm would comprise a prenatal cell harvest, providing time for the *in vitro* fabrication of an autologous living implant that is ready to use directly or shortly after birth to prevent any secondary damage. In a first attempt, human progenitor cells derived from umbilical cord tissue, as well as umbilical cord blood[87,160,232,234] have been established as a promising cell source for this concept as prenatal ultrasound-guided precutaneous umbilical cord blood sampling is already a routine and well-established procedure. Moreover, a new concept using human prenatal progenitor cells derived from chorionic villi and umbilical cord blood for the fabrication of living autologous heart valve leaflets, was introduced by Schmidt *et al.*[88] This was seen as a further milestone toward the clinical realization of the pediatric heart valve tissue engineering approach.

Besides the umbilical cord and the chorionic villi, the amniotic fluid represents an accessory attractive fetal cell source for this concept, as it also enables an easy prenatal access to fetal progenitor cells from all three germ layers in a low-risk procedure (reviewed by Miki and Strom,[242] Toda *et al.*,[243] and Parolini *et al.*[244]). This is of particular importance for the possible clinical realization of the concept in order to further reduce the risk associated with prenatal cell sampling, as both cell types should ideally be obtained in a single procedure from a single cell source. In a recent investigation, Schmidt *et al.*[40] demonstrated the use of prenatally harvested human amniotic fluid-derived progenitor cells (AFDPCs) as a sole cell source for the fabrication of living autologous heart valves prior to birth resulting in functional tissues *in vitro*. In order to expand the versatility of these cells, also for adult application, cryopreserved AFDCs were investigated as a potential lifelong available cell source, once again showing successful fabrication of viable heart valve leaflets *in vitro*.[159] Despite this futuristic strategy of prenatally harvested progenitors as a novel class of cardiovascular replacements potentially leading to innovative therapies for both pediatric and elderly patients in the future, several concerns associated with this cell source have to be addressed in further investigations.

5.528.5.6. Adipose Tissue-Derived Cells

Human adipose tissue has been shown to contain mesenchymal stem cells that have the potential to differentiate into various phenotypes *in vitro*, depending on the presence of lineage-specific induction factors.[245,246] Due to the high availability of adipose tissue – as it can be obtained in large quantities with minimal discomfort – adipose-derived stem cells (ADSCs) have been considered a potential alternative stem cell source to bone marrow-derived MSCs.[247] Several studies revealed that ADSCs hold characteristics of EPCs, express endothelial-specific markers *in vitro* when cultured with VEGF, and hold the potential to differentiate into ECs *in vivo*.[248–250] First investigations on ADSCs, focusing on their use as potential reservoirs of autologous stem cells for cell-based therapies, suggest that adipose tissue appears to be a viable cell source for cardiovascular tissue engineering.[251,252] When compared to vascular-derived cells, potential advantages of ADSCs seem to be the ease of harvest and their high availability, thus preventing sacrifice of donor vascular structures.

However, at present, the long time required for differentiation may offset this advantage of ADSCs for their use in the field of cardiovascular tissue engineering.

5.528.6. Toward Clinical Application – Outlook for the Future

Heart valve tissue engineering represents a highly promising approach for the creation of living functional autologous replacements that holds exciting potential for significantly improving treatment of heart valve disease in the future. Pediatric patients, in particular, would greatly benefit from growing replacement materials for the repair of congenital heart defects. Since its inception in the early nineties, major advances have been made, and for the first time, the ultimate goal of the transition from experimental models to clinical reality is within our grasp. However, before clinical application of this concept will be routine, several steps have to be surmounted in the laboratory. Primary among these is our limited knowledge about the immunological and biochemical characteristics of the cells and tissues undergoing *in vitro* growth. Even when having first indications as to the influence of age and *in vitro* conditions, the most favorable cell sources for *in vitro* seeding and ultimate survival *in vivo* still have to be defined. Furthermore, the disposition of implanted structures to typical biomaterial tissue interactions of medical devices, such as thrombosis, calcification, and excessive inflammatory response, have to be elucidated. A further important consideration concerns the definition of the ideal scaffold material for heart valve tissue engineering, providing a template for directing new tissue growth and organization, as well as for regulating cellular migration, adhesion, and differentiation. Importantly, while ECM is produced and organized, the ideal scaffold would degrade until the matrix material has been completely replaced by functionally integrated neo-tissue. In view of the inevitable concerns as to the potential transmission of microbiological hazards by tissues of xenogenic origin, it seems as if synthetic scaffold materials will make the grade as standard scaffolds for future clinical implementation. These biodegradable synthetic polymers may offer several advantages over biological materials, including greater control over degradation rates, fabrication, mechanical properties, and reproducibility.

A further key consideration is the fact that today's valvular replacements reveal predictable behavior in terms of durability and biocompatibility, whereas tissue-engineered substitutes, potentially relying on remodeling *in situ*, might show substantial variability among different individuals due to the heterogeneity of the physiological tissue remodeling potential. This implies that the implementation of tissue-engineered constructs, such as heart valves, into the clinical field has to be accompanied by the development of consistent clinical guidelines, specifying the inclusion criteria for certain patient populations according to quality, efficacy, and safety of the engineered products. Therefore, the demonstration of a long-term efficacy and benefit, as well as safety of implanted constructs in specific patient populations in preclinical studies will be of fundamental importance for a possible routine clinical translation of the concept. In the course of this attempt to understand, monitor, and potentially control individual differences of *in situ* tissue remodeling capacities, the identification of biomarkers as independent predictors of implant outcomes increasingly becomes a point of contention. This is closely associated with the major need for substantial advances of our understanding of valvular cell biology. A thorough understanding of molecular mechanisms as well as embryonic and fetal heart valve development may also permit control of heart valve morphogenesis both *in vitro* and *in vivo*.

Due to the demographic development the prevalence of heart valve disease shows an increasing trend with increasing age. More and more elderly patients will suffer from heart valve disease and will thus require valvular replacement therapy. Therefore, the development of tissue-engineered heart valves based on a stented design might represent an important step toward improving the expectancy and quality of life of these patients. Ideally, when tissue engineering technologies make it to the clinical scenario in the future, the schedule for this specific patient population, primarily diagnosed with degenerative valve disease, may be: (i) cell isolation from designated sources (i.e., by a bone marrow puncture under local anesthesia); (ii) differentiation and expansion of cells and engineering of an autologous valvular substitute *in vitro*; and (iii) following yet-to-be-defined quality criteria (histological, biological, biosafety, etc.,), reimplantation of the tissue-engineered construct into patients after a time period of, at the most, 6–8 weeks.

References

1. Iung, B.; Vahanian, A. *Lancet* **2006**, *368*(9540), 969–971.
2. Otto, C. M.; Lind, B. K.; Kitzman, D. W.; *et al*. *N. Engl. J. Med.* **1999**, *341*(3), 142–147.
3. Supino, P. G.; Borer, J. S.; Preibisz, J. *Heart Fail. Clin.* **2006**, *2*, 379–393.
4. Yacoub, M. H.; Cohn, L. H. *Circulation* **2004**, *109*, 942–950.
5. Mikos, A. G.; Herring, S. W.; Ochareon, P.; *et al*. *Tissue Eng.* **2006**, *12*(12), 3307–3339.
6. Yacoub, M. H.; Takkenberg, J. J. *Nat. Clin. Pract. Cardiovasc. Med.* **2005**, *2*, 60–61.
7. Nkomo, V. T.; Gardin, J. M.; Skelton, T. N.; *et al*. *Lancet* **2006**, *368*(9540), 1005–1011.
8. Ruel, J.; Lachance, G. *Ann. Biomed. Eng.* **2009**, *37*(4), 674–681.
9. Dasi, L. P.; Simon, H. A.; Sucosky, P.; *et al*. *Clin. Exp. Pharmacol. Physiol.* **2009**, *36*(2), 225–237.
10. Yoganathan, A. P.; He, Z.; *et al*. *Annu. Rev. Biomed. Eng.* **2004**, *6*, 331–362.
11. Zilla, P.; Brink, J.; Human, P.; *et al*. *Biomaterials* **2008**, *29*, 385–406.
12. Bonow, R. O.; Carabello, B. A.; Kanu, C.; *et al*. *Circulation* **2006**, *114*(5), e84–e231.
13. Lee, K. Y.; Mooney, D. J. *Chem. Rev.* **2001**, *101*(7), 1869–1879.
14. Senthilnathan, V.; Treasure, T.; Grunkemeier, G.; *et al*. *Cardiovasc. Surg.* **1999**, *7*(4), 393–397.
15. Schoen, F. J. *Circulation* **2008**, *118*, 1864–1880.
16. Yacoub, M. H.; Kilner, P. J.; Birks, E. J.; *et al*. *Ann. Thorac. Surg.* **1999**, *68*(3 Suppl), S37–S43.
17. Simmons, C. A. *J. Am. Coll. Cardiol.* **2009**, *53*, 1456–1458.
18. Misfeld, M.; Sievers, H. H. *Philos. Trans. R. Soc. Lond. B Biol. Sci.* **2007**, *362* (1484), 1421–1436.
19. Hjortnaes, J.; Bouten, C. V.; Van Herwerden, L. A.; *et al*. *Tissue Eng. B Rev.* **2009**, *15*(3), 307–317.
20. Butcher, J. T.; Simmons, C. A.; Warnock, J. N. *J. Heart Valve Dis.* **2008**, *17*(1), 62–73.
21. Peskin, C. S.; McQueen, D. M. *Am. J. Physiol.* **1994**, *266*(1 Pt 2), H319–H328.
22. Thubrikar, M. J.; Aouad, J.; Nolan, S. P. *J. Thorac. Cardiovasc. Surg.* **1986**, *92*, 29–36.
23. Schoen, F. J.; Levy, R. J. *Biomed. Mater. Res.* **1999**, *47*(4), 439–465.
24. Scott, M.; Vesely, I. *Ann. Thorac. Surg.* **1995**, *60*(2 Suppl), S391–S394.
25. Scott, M. J.; Vesely, I. *J. Heart Valve Dis.* **1996**, *5*(5), 464–471.

26. Bairati, A., Jr.; De Biasi, S.; Pilotto, F. *Experientia* **1978**, *34*(12), 1636–1638.
27. Bairati, A.; DeBiasi, S. *Anat. Embryol. (Berl.)* **1981**, *161*(3), 329–340.
28. Roy, A.; Brand, N. J.; Yacoub, M. H. *J. Heart Valve Dis.* **2000**, *9*(3), 459–464.
29. Della Rocca, F.; Sartore, S.; Guidolin, D.; *et al. Ann. Thorac. Surg.* **2000**, *70*(5), 1594–1600.
30. Messier, R. H., Jr.; Bass, B. L.; Aly, H. M.; *et al. J. Surg. Res.* **1994**, *57*(1), 1–21.
31. Harken, D. E. *Ann. Thorac. Surg.* **1989**, *48*(3 Suppl), 18–19.
32. Langer, R.; Vacanti, J. P. *Science* **1993**, *260*, 920–926.
33. Matheny, R. G.; Hutchison, M. L.; Dryden, P. E.; *et al. J. Heart Valve Dis.* **2000**, *9*, 769–775.
34. Mol, A.; Bouten, C. V.; Baaijens, F. P.; *et al. J. Heart Valve Dis.* **2004**, *13*(2), 272–280.
35. Schmidt, D.; Mol, A.; Kelm, J. M.; *et al. Methods Mol. Med.* **2007**, *140*, 319–330.
36. Breuer, C. K.; Mettler, B. A.; Anthony, T.; *et al. Tissue Eng.* **2004**, *10*(11–12), 1725–1736.
37. Brody, S.; Pandit, A. *J. Biomed. Mater. Res. B Appl. Biomater.* **2007**, *83*(1), 16–43.
38. Sacks, M. S.; Schoen, F. J.; Mayer, J. E. *Annu. Rev. Biomed. Eng.* **2009**, *11*, 289–313.
39. Lichtenberg, A.; Cebotari, S.; Tudorache, I.; *et al. Methods Mol. Med.* **2007**, *140*, 309–317.
40. Schmidt, D.; Stock, U. A.; Hoerstrup, S. P. *Philos. Trans. R. Soc. Lond. B Biol. Sci.* **2007**, *362*(1484), 1505–1512.
41. Schmidt, D.; Achermann, J.; Odermatt, B.; *et al. Circulation* **2007**, *116*, I64–I70.
42. Sales, V. L.; Engelmayr, G. C., Jr.; Johnson, J. A., Jr.; *et al. Circulation* **2007**, *116* (11 Suppl), I55–I63.
43. Affonso da Costa, F. D.; Dohmen, P. M.; Lopes, S. V.; *et al. Artif. Organs* **2004**, *28*, 366–370.
44. Allen, B. S.; El-Zein, C.; Cuneo, B.; *et al. Ann. Thorac. Surg.* **2002**, *74*, 771–777.
45. Bielefeld, M. R.; Bishop, D. A.; Campbell, D. N.; *et al. Ann. Thorac. Surg.* **2001**, *71*, 482–487.
46. Carr-White, G. S.; Glennan, S.; Edwards, S.; *et al. Circulation* **1999**, *100*(19 Suppl), II103–II106.
47. Grauss, R. W.; Hazekamp, M. G.; van Vliet, S.; *et al. J. Thorac. Cardiovasc. Surg.* **2003**, *126*, 2003–2010.
48. Hong, H.; Dong, G. N.; Shi, W. J.; *et al. ASAIO J.* **2008**, *54*(6), 627–632.
49. Hong, H.; Dong, N.; Shi, J.; *et al. Artif. Organs* **2009**, *33*(7), 554–558.
50. Stamm, C.; Khosravi, A.; Grabow, N.; *et al. Ann. Thorac. Surg.* **2004**, *78*, 2084–2092.
51. Neidert, M. R.; Tranquillo, R. T. *Tissue Eng.* **2006**, *12*(4), 891–903.
52. Robinson, P. S.; Johnson, S. L.; Evans, M. C.; *et al. Tissue Eng. A* **2008**, *14*, 83–95.
53. Syedain, Z. H.; Weinberg, J. S.; Tranquillo, R. T. *Proc. Natl. Acad. Sci.* **2008**, *105* (18), 6537–6542.
54. Williams, C.; Johnson, S. L.; Robinson, P. S.; *et al. Tissue Eng.* **2006**, *12*(1489).
55. Mol, A.; Smits, A. I.; Bouten, C. V.; *et al. Expert Rev. Med. Devices* **2009**, *6*(3), 259–275.
56. Kasimir, M. T.; Rieder, E.; Seebacher, G.; *et al. Int. J. Artif. Organs* **2003**, *26*(5), 421–427.
57. Leyh, R. G.; Wilhelmi, M.; Rebe, P.; *et al. Ann. Thorac. Surg.* **2003**, *75*(5), 1457–1463.
58. Steinhoff, G.; Stock, U.; Karim, N.; *et al. Circulation* **2000**, *102*, 50–55.
59. Curtil, A.; Pegg, D. E.; Wilson, A. *J. Heart Valve Dis.* **1997**, *6*(3), 296–306.
60. Wilson, G. J.; Courtman, D. W.; Klement, P.; *et al. Ann. Thorac. Surg.* **1995**, *1995* (60), 353–358.
61. Bader, A.; Schilling, T.; Teebken, O. E.; *et al. Eur. J. Cardiothorac. Surg.* **1998**, *14*(3), 279–284.
62. Bertiplaglia, B.; Ortolani, F.; Petrelli, L.; *et al. Ann. Thorac. Surg.* **2003**, *75*, 1274–1282.
63. Booth, C.; Korossis, S. A.; Wilcox, H. E.; *et al. J. Heart Valve Dis.* **2002**, *11*(4), 457–462.
64. Kim, W. G.; Cho, S. K.; Kang, M. C.; *et al. Int. J. Artif. Organs* **2001**, *24*(9), 642–648.
65. Zeltinger, J.; Landeen, L. K.; Alexander, H. G.; *et al. Tissue Eng.* **2001**, *7*, 9–22.
66. Rieder, E.; Kasimir, M. T.; Silberhumer, G.; *et al. J. Thorac. Cardiovasc. Surg.* **2004**, *127*(2), 399–405.
67. Tudorache, I.; Cebotari, S.; Sturz, G.; *et al. J. Heart Valve Dis.* **2007**, *16*, 567–573.
68. Cushing, M. C.; Jaeggli, M. P.; Masters, K. S.; *et al. J. Biomed. Mater. Res. A* **2005**, *75*(1), 232–241.
69. Kim, W. G.; Park, J. K.; Lee, W. Y. *Int. J. Artif. Organs* **2002**, *25*(8), 791–797.
70. Knight, R. L.; Booth, C.; Wilcox, H. E.; *et al. J. Heart Valve Dis.* **2005**, *14*(6), 806–813.
71. Schenke-Layland, K.; Opitz, F.; Gross, M. *Cardiovasc. Res.* **2003**, *60*, 497–509.
72. Kim, S. S.; Lim, S. H.; Hong, Y. S.; *et al. Artif. Organs* **2006**, *30*(7), 554–557.
73. Takeuchi, Y. *Transplant. Proc.* **2000**, *32*, 2698–2700.
74. Weiss, R. A.; Magre, S.; Takeuchi, Y. *J. Infect.* **2000**, *40*, 21–25.
75. Martin, U.; Kiessig, V.; Blusch, J. H.; *et al. Lancet* **1998**, *352*, 692–694.
76. Martin, U.; Winkler, M. E.; Id, M.; *et al. Xenotransplantation* **2000**, *7*(2), 138–142.
77. Moza, A. K.; Mertsching, H.; Herden, T.; *et al. J. Thorac. Cardiovasc. Surg.* **2001**, *121*, 697–701.
78. Patience, C.; Takeuchi, Y.; Weiss, R. A. *Nat. Med.* **1997**, *3*(3), 282–286.
79. Patience, C.; Switzer, W. M.; Takeuchi, Y.; *et al. J. Virol.* **2001**, *75*, 2771–2775.
80. Prabha, S.; Verghese, S. *Indian J. Med. Microbiol.* **2008**, *26*(3), 228–232.
81. Specke, V.; Rubant, S.; Denner, J. *Virology* **2001**, *285*, 177–180.
82. Wilson, C. A.; Wong, S.; Muller, J.; *et al. J. Virol.* **1998**, *72*, 3082–3087.
83. Knight, R.; Brazier, M.; Collins, S. J. *Contrib. Microbiol.* **2004**, *11*, 72–97.
84. Knight, R.; Collins, S. *Contrib. Microbiol.* **2001**, *7*, 68–92.
85. Kallenbach, K.; Leyh, R. G.; Lefik, E.; *et al. Biomaterials* **2004**, *25*(17), 3613–3620.
86. Walles, T.; Lichtenberg, A.; Puschmann, C. *Eur. J. Cardiothorac. Surg.* **2003**, *24*, 358–363.
87. Schmidt, D.; Mol, A.; Odermatt, B.; *et al. Tissue Eng.* **2006**, *12*(11), 3223–3232.
88. Schmidt, D.; Mol, A.; Breymann, C.; *et al. Circulation* **2006**, *114*(1 Suppl), I125–I131.
89. Agrawal, C. M.; Ray, R. B. *J. Biomed. Mater. Res.* **2001**, *55*(2), 141–150.
90. Hutmacher, D. W.; Goh, J. C.; Teoh, S. H. *Ann. Acad. Med. Singapore* **2001**, *30*(2), 183–191.
91. Kessler, B.; Witholt, B. *J. Biotechnol.* **2001**, *86*(2), 97–104.
92. Sodian, R.; Hoerstrup, S. P.; Sperling, J. S.; *et al. Circulation* **2000**, *102*, 22–29.
93. Sodian, R.; Hoerstrup, S. P.; Sperling, J. S.; *et al. ASAIO J.* **2000**, *46*, 107–110.
94. Schaefermeier, P. K.; Szymanski, D.; Weiss, F.; *et al. Eur. Surg. Res.* **2009**, *42*(1), 49–53.
95. Sodian, R.; Loebe, M.; Hein, A.; *et al. ASAIO J.* **2002**, *48*, 12–16.
96. Hoerstrup, S. P.; Sodian, R.; Daebritz, S.; *et al. Circulation* **2000**, *102*(19 Suppl 3), III44–III49.
97. Rabkin, E.; Hoerstrup, S. P.; Aikawa, M.; *et al. J. Heart Valve Dis.* **2002**, *11*(3), 308–314.
98. Stock, U. A.; Nagashima, M.; Khalil, P. N. *J. Thorac. Cardiovasc. Surg.* **2000**, *119*, 732–740.
99. Hoerstrup, S. P.; Kadner, A.; Melnitchouk, S.; *et al. Circulation* **2002**, *106*(12 Suppl 1), I143–I150.
100. Mol, A.; Rutten, M. C.; Driessen, N. J.; *et al. Circulation* **2006**, *114*(1 Suppl), I152–I158.
101. Grabow, N.; Schmohl, K.; Khosravi, A.; *et al. Artif. Organs* **2004**, *28*(11), 971–979.
102. Lutolf, M. P.; Hubbell, J. A. *Nat. Biotechnol.* **2005**, *23*(1), 47–55.
103. Tabata, Y. *J. R. Soc. Interface* **2009**, *6*, 311–324.
104. De Laporte, L.; Shea, L. D. *Adv. Drug Deliv. Rev.* **2007**, *59*(4–5), 292–307.
105. Rothenburger, M.; Volker, W.; Vischer, J. P.; *et al. ASAIO J.* **2002**, *48*(6), 586–591.
106. Rothenburger, M.; Völker, W.; Vischer, P.; *et al. Tissue Eng.* **2002**, *8*(6), 1049–1056.
107. Butcher, J. T.; Nerem, R. M. *J. Heart Valve Dis.* **2004**, *13*(3), 478–485; discussion 485–486.
108. Butcher, J. T.; Nerem, R. M. *Tissue Eng.* **2006**, *12*(4), 905–915.
109. Flanagan, T. C.; Wilkins, B.; Black, A.; *et al. Biomaterials* **2006**, *27*(10), 2233–2246.
110. Taylor, P. M.; Sachlos, E.; Dreger, S. A.; *et al. Biomaterials* **2006**, *27*, 2733–2737.
111. Tedder, M. E.; Liao, J.; Weed, B.; *et al. Tissue Eng. A* **2009**, *15*, 1257–1268.
112. Taylor, P. M.; Allen, S. P.; Dreger, S. A. *J. Heart Valve Dis.* **2002**, *11*, 298–306.
113. Rothenburger, M.; Vischer, P.; Volker, W.; *et al. Thorac. Cardiovasc. Surg.* **2001**, *49*(4), 204–209.
114. Shi, Y.; Ramamurthi, A.; Vesely, I. *Biomed. Sci. Instrum.* **2002**, *38*, 35–40.
115. Mol, A.; van Lieshout, M. I.; Dam-de Veen, C. G.; *et al. Biomaterials* **2005**, *26*(16), 3113–3121.
116. Ameer, G. A.; Mahmood, T. A.; Langer, R. *J. Orthop. Res.* **2002**, *20*(1), 16–19.
117. Jockenhoevel, S.; Chalabi, K.; Sachweh, J. S.; *et al. Thorac. Cardiovasc. Surg.* **2001**, *49*(5), 287–290.
118. Jockenhoevel, S.; Zund, G.; Hoerstrup, S. P.; *et al. Eur. J. Cardiothorac. Surg.* **2001**, *19*(4), 424–430.
119. Ye, Q.; Zünd, G.; Benedikt, P.; *et al. Eur. J. Cardiothorac. Surg.* **2000**, *17*, 587–591.
120. Schense, J. C.; Hubbell, J. A. *Bioconjug. Chem.* **1999**, *10*(1), 75–81.
121. Shin'oka, T.; Breuer, C. K.; Tanel, R. E. *Ann. Thorac. Surg.* **1995**, *60*(6), 513–516.
122. Shin'oka, T.; Ma, P. X.; Shum-Tim, D.; *et al. Circulation* **1996**, *94*, II164–II168.

123. Sutherland, F. W.; Perry, T. E.; Yu, Y.; *et al*. *Circulation* **2005**, *111*, 2783–2791.
124. Hoerstrup, S. P.; Cummings, M. I.; Lachat, M.; *et al*. *Circulation* **2006**, *114*(1 Suppl), I159–I166.
125. Matsumura, G.; Hibino, N.; Ikada, Y.; *et al*. *Biomaterials* **2003**, *24*(13), 2303–2308.
126. Shin'oka, T.; Imai, Y.; Ikada, Y. *N. Engl. J. Med.* **2001**, *344*, 532–533.
127. Hoerstrup, S. P.; Sodian, R.; Sperling, J. S.; *et al*. *Tissue Eng.* **2000**, *6*(1), 75–79.
128. Balguid, A.; Rubbens, M. P.; Mol, A.; *et al*. *Tissue Eng.* **2007**, *13*(7), 1501–1511.
129. Stock, U. A.; Vacanti, J. P.; Mayer, J. E., Jr. *Thorac. Cardiovasc. Surg.* **2002**, *50*, 184–193.
130. Huang, S. D.; Liu, X. H.; Bai, C. G.; *et al*. *Heart Vessels* **2007**, *22*(2), 116–122.
131. Rogers, K. A.; Boughner, D.; Appleton, C. T.; *et al*. *Tissue Eng. Part A* **2009**, *15*(2), 3889–3897.
132. Isenberg, B. C.; Tranquillo, R. T. *Ann. Biomed. Eng.* **2003**, *31*(8), 937–949.
133. Mendelson, K.; Schoen, F. J. *Ann. Biomed. Eng.* **2006**, *34*(12), 1799–1819.
134. Mol, A.; Bouten, C. V.; Zünd, G.; *et al*. *Thorac. Cardiovasc. Surg.* **2003**, *51*(2), 78–83.
135. Seliktar, D.; Nerem, R. M.; Galis, Z. S.; *et al*. *Tissue Eng.* **2003**, *9*(4), 657–666.
136. Hinz, B.; Gabbiani, G. *Curr. Opin. Biotechnol.* **2003**, *14*(5), 538–546.
137. Parizi, M.; Howard, E. W.; Tomasek, J. J. *Exp. Cell Res.* **2000**, *254*(2), 210–220.
138. Grenier, G.; Rémy-Zolghadri, M.; Larouche, D.; *et al*. *Tissue Eng.* **2005**, *11*(1–2), 90–100.
139. Rubbens, M. P.; Mol, A.; Boerboom, R. A.; *et al*. *Tissue Eng. A* **2009**, *15*(5), 999–1008.
140. Boerboom, R. A.; Rubbens, M. P.; Driessen, N. J.; *et al*. *Ann. Biomed. Eng.* **2008**, *36*(2), 244–253.
141. Rubbens, M. P.; Mol, A.; van Marion, M. H.; *et al*. *Tissue Eng. A* **2009**, *15*(4), 841–849.
142. Engelmayr, G. C., Jr.; Hildebrand, D. K.; Sutherland, F. W.; *et al*. *Biomaterials* **2003**, *24*(14), 2523–2532.
143. Engelmayr, G. C., Jr.; Rabkin, E.; Sutherland, F. W.; *et al*. *Biomaterials* **2005**, *26*(2), 175–187.
144. Jockenhoevel, S.; Zund, G.; Hoerstrup, S. P.; *et al*. *ASAIO J.* **2002**, *48*(1), 8–11.
145. Engelmayr, G. C., Jr.; Sales, V. L.; Mayer, J. E., Jr.; *et al*. *Biomaterials* **2006**, *27* (36), 6083–6095.
146. Engelmayr, G. C., Jr.; Soletti, L.; Vigmostad, S. C.; *et al*. *Ann. Biomed. Eng.* **2008**, *36*(5), 700–712.
147. Balguid, A.; Mol, A.; van Vlimmeren, M. A.; *et al*. *Circulation* **2009**, *119*(2), 290–297.
148. Mertsching, H.; Hansmann, J. *Adv. Biochem.* **2009**, *112*, 29–37.
149. Stock, U. S.; Wiederschain, D.; Kilroy, S. M.; *et al*. *J. Cell Biochem.* **2001**, *81*, 220–228.
150. Sodian, R.; Lemke, T.; Loebe, M.; *et al*. *J. Biomed. Mater. Res.* **2001**, *58*, 401–405.
151. Sodian, R.; Lemke, T.; Fritsche, C.; *et al*. *Tissue Eng.* **2002**, *8*, 863–870.
152. Mol, A.; Driessen, N. J.; Rutten, M. C.; *et al*. *Ann. Biomed. Eng.* **2005**, *33*(12), 1778–1788.
153. Niklason, L. E.; Gao, J.; Abbott, W. M.; *et al*. *Science* **1999**, *284*(5413), 489–493.
154. Stegemann, J. P.; Nerem, R. M. *Ann. Biomed. Eng.* **2003**, *31*, 391–402.
155. Narita, Y.; Hata, K.; Kagami, H.; *et al*. *Tissue Eng.* **2004**, *10*(7–8), 1224–1233.
156. Williams, C.; Wick, T. M. *Tissue Eng.* **2004**, *10*, 930–941.
157. Syedain, Z. H.; Tranquillo, R. T. *Biomaterials* **2009**, *30*(25), 4078–4084.
158. Lee, D. J.; Steen, J.; Jordan, J. E.; *et al*. *Tissue Eng. A* **2009**, *15*(4), 807–814.
159. Schmidt, D.; Achermann, J.; Odermatt, B. *J. Heart Valve Dis.* **2008**, *17*(4), 446–455.
160. Sodian, R.; Lueders, C.; Kraemer, L.; *et al*. *Ann. Thorac. Surg.* **2006**, *81*(6), 2207–2216.
161. Hildebrand, D. K.; Wu, Z. J.; Mayer, J. E., Jr.; *et al*. *Ann. Biomed. Eng.* **2004**, *32*(8), 1039–1049.
162. Kortsmit, J.; Driessen, N. J.; Rutten, M. C.; *et al*. *Tissue Eng. A* **2009**, *15*(4), 797–806.
163. Kortsmit, J.; Driessen, N. J.; Rutten, M. C.; *et al*. *Ann. Biomed. Eng.* **2009**, *37*(3), 532–541.
164. Vesely, I. *Circ. Res.* **2005**, *97*, 743–755.
165. Sievers, H. H. *J. Thorac. Cardiovasc. Surg.* **2007**, *134*, 20–22.
166. Schleicher, M.; Wendel, H. P.; Fritze, O.; *et al*. *Regen. Med.* **2009**, *4*(4), 613–619.
167. Dohmen, P. M.; da Costa, F.; Holinski, S.; *et al*. *Eur. Surg. Res.* **2006**, *38*(1), 54–61.
168. Elkins, R. C.; Dawson, P. E.; Goldstein, S.; *et al*. *Ann. Thorac. Surg.* **2001**, *71*(5 Suppl), S428–S432.
169. Elkins, R. C.; Goldstein, S.; Hewitt, C. W.; *et al*. *Semin. Thorac. Cardiovasc. Surg.* **2001**, *13*(4 Suppl 1), 87–92.
170. Erdbrügger, W.; Konertz, W.; Dohmen, P. M.; *et al*. *Tissue Eng.* **2006**, *12*(8), 2059–2068.
171. Goldstein, S.; Clarke, D. R.; Walsh, S. P.; *et al*. *Ann. Thorac. Surg.* **2000**, *70*(6), 1962–1969.
172. Iwai, S.; Torikai, K.; Coppin, C. M.; *et al*. *J. Artif. Organs* **2007**, *10*(1), 29–35.
173. Kim, W. G.; Huh, J. H. *ASAIO J.* **2004**, *50*(6), 601–605.
174. Leyh, R. G.; Wilhelmi, M.; Walles, T.; *et al*. *J. Thorac. Cardiovasc. Surg.* **2003**, *126*(4), 1000–1004.
175. Takagi, K.; Fukunaga, S.; Nishi, A.; *et al*. *Artif. Organs* **2006**, *30*, 233–241.
176. Dohmen, P. M.; Konertz, W. *Circ. Res.* **2006**, *97*(8), 743–755.
177. Dohmen, P. M.; Hauptmann, S.; Terytze, A.; *et al*. *J. Heart Valve Dis.* **2007**, *16*(4), 447–449.
178. Simon, P.; Kasimir, M. T.; Seebacher, G. *Eur. J. Cardiothorac. Surg.* **2003**, *23*, 1002–1006.
179. Kasimir, M. T.; Rieder, E.; Seebacher, G.; *et al*. *J. Heart Valve Dis.* **2006**, *15*(2), 278–286.
180. Rieder, E.; Nigisch, A.; Dekan, B.; *et al*. *Biomaterials* **2006**, *27*(33), 5634–5642.
181. Bastian, F.; Stelzmüller, M. E.; Kratochwill, K.; *et al*. *Biomaterials* **2008**, *29*(12), 1824–1832.
182. Lichtenberg, A.; Cebotari, S.; Tudorache, I.; *et al*. *J. Heart Valve Dis.* **2006**, *15*(2), 287–293 discussion 293–294.
183. Lichtenberg, A.; Tudorache, I.; Cebotari, S.; *et al*. *Biomaterials* **2006**, *27*(23), 4221–4229.
184. Stamm, C.; Steinhoff, G. *J. Thorac. Cardiovasc. Surg.* **2006**, *131*, 843–852.
185. Rieder, E.; Seebacher, G.; Kasimir, M. T.; *et al*. *Circulation* **2005**, *111*(21), 2712–2714.
186. Sayk, F.; Bos, I.; Schubert, U.; *et al*. *Ann. Thorac. Surg.* **2005**, *79*(5), 1755–1758.
187. Miller, D. V.; Edwards, W. D.; Zehr, K. J. *J. Thorac. Cardiovasc. Surg.* **2006**, *132*(1), 175–176.
188. Zehr, K. J.; Yagubyan, M.; Connolly, H. M.; *et al*. *J. Thorac. Cardiovasc. Surg.* **2005**, *130*(4), 1010–1015.
189. Bechtel, J. F.; Müller-Steinhardt, M.; Schmidtke, C.; *et al*. *J. Heart Valve Dis.* **2003**, *12*(6), 734–739.
190. Bechtel, J. F.; Stierle, U.; Sievers, H. H. *J. Heart Valve Dis.* **2008**, *17*(1), 98–104.
191. Shin'oka, T.; Shum-Tim, D.; Ma, P. X.; *et al*. *J. Thorac. Cardiovasc. Surg.* **1998**, *115*(3), 536–545.
192. Iwai, S.; Sawa, Y.; Ichikawa, H.; *et al*. *J. Thorac. Cardiovasc. Surg.* **2004**, *128*(3), 472–479.
193. Iwai, S.; Sawa, Y.; Taketani, S.; *et al*. *Ann. Thorac. Surg.* **2005**, *80*(5), 1828.
194. Torikai, K.; Ichikawa, H.; Hirakawa, K.; *et al*. *J. Thorac. Cardiovasc. Surg.* **2008**, *136*, 37–45.
195. Yokota, T.; Ichikawa, H.; Matsumiya, G.; *et al*. *J. Thorac. Cardiovasc. Surg.* **2008**, *136*, 900–907.
196. Brennan, M. P.; Dardik, A.; Hibino, N.; *et al*. *Ann. Surg.* **2008**, *248*(3), 370–377.
197. Hibino, N.; Shin'oka, T.; Matsumura, G.; *et al*. *J. Thorac. Cardiovasc. Surg.* **2005**, *129*(5), 1064–1070.
198. Matsumura, G.; Miyagawa-Tomita, S.; Shin'oka, T.; *et al*. *Circulation* **2003**, *108*(14), 1729–1734.
199. Matsumura, G.; Ishihara, Y.; Miyagawa-Tomita, S.; *et al*. *Tissue Eng.* **2006**, *12*(11), 3075–3083.
200. Shin'oka, T.; Matsumura, G.; Hibino, N.; *et al*. *J. Thorac. Cardiovasc. Surg.* **2005**, *129*(6), 1330–1338.
201. De Visscher, G.; Vranken, I.; Lebacq, A.; *et al*. *Eur. Heart J.* **2007**, *28*(11), 1389–1396.
202. De Visscher, G.; Blockx, H.; Meuris, B.; *et al*. *J. Thorac. Cardiovasc. Surg.* **2008**, *135*(2), 395–404.
203. Hayashida, K.; Kanda, K.; Yaku, H.; *et al*. *J. Thorac. Cardiovasc. Surg.* **2007**, *134*(1), 152–159.
204. Nakayama, Y.; Yamanami, M.; Yahata, Y.; *et al*. *J. Biomed. Mater. Res. B Appl. Biomater.* **2009**, *6*(1).
205. Vranken, I.; De Visscher, G.; Lebacq, A.; *et al*. *Biomaterials* **2008**, *29*, 797–808.
206. Ruiz, C. E.; Iemura, M.; Medie, S.; *et al*. *J. Thorac. Cardiovasc. Surg.* **2005**, *130*(2), 477–484.
207. Stock, U. A.; Schenke-Layland, K. *Biomaterials* **2006**, *27*, 1–2.
208. Schnell, A. M.; Hoerstrup, S. P.; Zund, G.; *et al*. *Thorac. Cardiovasc. Surg.* **2001**, *49*(4), 221–225.
209. Shin'oka, T.; Shum-Tim, D.; Ma, P. X. *Circulation* **1997**, *96*, II102–II107.
210. Mol, A.; Hoerstrup, S. P. *Int. J. Cardiol.* **2004**, *95*(Suppl 1), S57–S58.
211. Hoerstrup, S. P.; Zund, G.; Schoeberlein, A.; *et al*. *Ann. Thorac. Surg.* **1998**, *66*(5), 1653–1657.
212. Zund, G.; Hoerstrup, S. P.; Schoeberlein, A.; *et al*. *Eur. J. Cardiothorac. Surg.* **1998**, *13*, 160–164.
213. Schmidt, D.; Hoerstrup, S. P. *Swiss Med. Wkly* **2007**, *155*, 80–85.
214. Kadner, A.; Hoerstrup, S. P.; Zund, G.; *et al*. *Eur. J. Cardiothorac. Surg.* **2002**, *21*(6), 1055–1060.

215. Perry, T. E.; Kaushal, S.; Sutherland, F. W.; *et al*. *Ann. Thorac. Surg.* **2003**, *75*(3), 761–767.
216. Orlic, D.; Kajstura, J.; Chimenti, S.; *et al*. *Nature* **2001**, *410*(6829), 701–705.
217. Sata, M.; Saiura, A.; Kunisato, A.; *et al*. *Nat. Med.* **2002**, *8*(4), 403–409.
218. Oswald, J.; Boxberger, S.; Jorgensen, B.; *et al*. *Stem Cells* **2004**, *22*(3), 377–384.
219. Huang, C. Y.; Hagar, K. L.; Frost, L. E.; *et al*. *Stem Cells* **2004**, *22*(3), 313–323.
220. Tanaka, K. A.; Key, N. S.; Levy, J. H. *Anesth. Analg.* **2009**, *108*, 1433–1446.
221. Kasimir, M. T.; Weigel, G.; Sharma, J.; *et al*. *Thromb. Haemost.* **2005**, *94*(3), 469–470.
222. Alsberg, E.; von Recum, H. A.; Mahoney, M. J. *Expert Opin. Biol. Ther.* **2006**, *6*, 847–866.
223. Asahara, T.; Murohara, T.; Sullivan, A.; *et al*. *Science* **1997**, *275*(5302), 964–967.
224. Kim, S.; von Recum, H. A. *Tissue Eng. B Rev.* **2008**, *14*(1), 133–147.
225. Kim, S.; von Recum, H. A. *Tissue Eng. Part A* **2009**, *15*(2), 3709–3718.
226. Hofmann, M.; Wollert, K. C.; Meyer, G. P.; *et al*. *Circulation* **2005**, *111*, 2198–2202.
227. Iwasaki, H.; Kawamoto, A.; Ishikawa, M.; *et al*. *Circulation* **2006**, *113*, 1311–1325.
228. Kocher, A. A.; Schuster, M. D.; Szabolcs, M. J.; *et al*. *Nat. Med.* **2001**, *7*, 430–436.
229. Martin-Rendon, E.; Brunskill, S.; Dorée, C.; *et al*. *Cochrane Database Syst. Rev.* **2008**, *8*(4), CD006536.
230. Pearson, J. D. *J. Thromb. Haemost.* **2009**, *7*(2), 255–262.
231. Fang, N. T.; Xie, S. Z.; Wang, S. M.; *et al*. *Chin. Med. J. (Engl.)* **2007**, *120*(8), 696–702.
232. Schmidt, D.; Breymann, C.; Weber, A.; *et al*. *Ann. Thorac. Surg.* **2004**, *78*(6), 2094–2098.
233. Schmidt, D.; Mol, A.; Neuenschwander, S.; *et al*. *Eur. J. Cardiothorac. Surg.* **2005**, *27*(5), 795–800.
234. Schmidt, D.; Asmis, L. M.; Odermatt, B. *Ann. Thorac. Surg.* **2006**, *82*(4), 1465–1471.
235. Sales, V. L.; Engelmayr, G. C., Jr.; Mettler, B. A.; *et al*. *Circulation* **2006**, *114*(1 Suppl), I193–I199.
236. Hoerstrup, S. P.; Kadner, A.; Breymann, C. I.; *et al*. *Ann. Thorac. Surg.* **2002**, *74*, 46–52.
237. Armson, B. A. Maternal/Fetal Medicine Committee, Society of Obstetricians and Gynaecologists of Canada. *J. Obstet. Gynaecol. Can.* **2005**, *27*(3), 263–290.
238. Kadner, A.; Hoerstrup, S. P.; Tracy, J.; *et al*. *Ann. Thorac. Surg.* **2002**, *74*(4), S1422–S1428.
239. Kadner, A.; Zund, G.; Maurus, C.; *et al*. *Eur. J. Cardiothorac. Surg.* **2004**, *25*(4), 635–641.
240. Sipehia, R.; Martucci, G.; Lipscombe, J. *Artif. Cells Blood Substit. Immobil. Biotechnol.* **1996**, *24*, 51–63.
241. Breymann, C.; Schmidt, D.; Hoerstrup, S. P. *Stem Cell Rev.* **2006**, *2*(2), 87–92.
242. Miki, T.; Strom, S. C. *Stem Cell Rev.* **2006**, *2*(2), 133–142.
243. Toda, A.; Okabe, M.; Yoshida, T.; Nikaido, T. *J. Pharmacol. Sci.* **2007**, *105*(3), 215–228.
244. Parolini, O.; Soncini, M.; Evangelista, M.; *et al*. *Regen. Med.* **2009**, *4*(2), 275–291.
245. Pansky, A.; Roitzheim, B.; Tobiasch, E. *Clin. Lab.* **2007**, *53*(1–2), 81–84.
246. Tuan, R. S.; Boland, G.; Tuli, R. *Arthritis Res. Ther.* **2003**, *5*, 32–45.
247. Zuk, P. A.; Zhu, M.; Mizuno, H.; *et al*. *Tissue Eng.* **2001**, *7*, 211–228.
248. Cao, Y.; Sun, Z.; Liao, L.; *et al*. *Biochem. Biophys. Res. Commun.* **2005**, *332*(2), 370–379.
249. Miranville, A.; Heeschen, C.; Sengenès, C.; *et al*. *Circulation* **2004**, *110*(3), 349–355.
250. Planat-Benard, V.; Silvestre, J. S.; Cousin, B.; *et al*. *Circulation* **2004**, *109*(5), 656–663.
251. Colazzo, F.; Sarathchandra, P.; Chester, A. H.; *et al*. *An evaluation of adipose-derived stem cells for heart valve tissue engineering*. In Presented at the *5th Biennial Meeting of the Society of Heart Valve Disease*, Berlin, June 28–30, 2009.
252. DiMuzio, P.; Tulenko, T. *J. Vasc. Surg.* **2007**, *45*(Suppl A), A99–A103.

5.529. Biomaterials for Cardiac Cell Transplantation

K R Kam, University of California – Berkeley, Berkeley, CA, USA
F S Angeli, University of California – San Francisco, San Francisco, CA, USA
R Gupta, University of California – Berkeley, Berkeley, CA, USA
Y Yeghiazarians, University of California – San Francisco, San Francisco, CA, USA
K Mehtani, University of California – San Francisco, San Francisco, CA, USA
K E Healy, University of California – Berkeley, Berkeley, CA, USA

© 2011 Elsevier Ltd. All rights reserved.

5.529.1. Introduction 393
5.529.2. Biomaterial Design Requirements for Cardiac Cell Transplantation 395
5.529.2.1. Three-Dimensional Scaffold 395
5.529.2.2. Biological Cues: Cells Communicate with the ECM Through Cell–Surface Receptors 396
5.529.2.3. Mechanical Properties 396
5.529.2.4. Oxygen Transport 397
5.529.2.5. Electromechanical Coupling 397
5.529.3. Current Materials 397
5.529.3.1. Naturally Derived Materials as Scaffolds 397
5.529.3.1.1. Collagen 397
5.529.3.1.2. Alginate 398
5.529.3.1.3. Fibrin 398
5.529.3.1.4. Chitosan 399
5.529.3.1.5. Hyaluronic acid 399
5.529.3.2. Synthetic Biomaterials as Scaffolds 400
5.529.3.2.1. Poly(glycolide) and poly(lactide) 400
5.529.3.2.2. PEG-based hydrogels 401
5.529.3.2.3. Poly(*N*-isopropylacrylamide) 401
5.529.3.3. Hybrid Biosynthetic Materials 401
5.529.3.3.1. Smart biomaterials: growth factors and self-assembling peptides 402
5.529.4. Concluding Remarks 403
References 403

Abbreviations

bFGF	Basic fibroblast growth factor
BMCs	Unfractionated bone marrow cells that include hematopoietic stem cells (HSCs), endothelial progenitor cells (EPCs), and mesenchymal stem cells (MSCs)
BMMNC	Bone marrow mononuclear cell
CHF	Congestive heart failure
EF	Ejection fraction; also LVEF – left ventricular ejection fraction
EPC	Endothelial progenitor cell
FS	Fractional shortening
HSC	Hematopoietic stem cell
HyA	Hyaluronic acid
MSC	Mesenchymal stem cell
P(NIPAAm)	Poly(*N*-isopropylacrylamide)
PEG	Polyethylene glycol
PLG	Poly(lactide-*co*-glycolide) – a copolymer composed of poly(glycolide) (PG) and poly (lactide) (PL)
RGD	Arginine-glycine-aspartic acid
VEGF	Vascular endothelial growth factor

5.529.1. Introduction

Cardiovascular disease is the leading cause of death worldwide. Of the almost 17 million people who die each year from cardiovascular causes, over 11 million die as a result of cardiac disease. Myocardial infarction (MI) carries a short-term mortality rate of ~7% in patients under optimal treatment, while congestive heart failure (CHF) reaches a 20% one-year mortality rate. Despite major advances in therapy over the last few decades, the global burden remains substantial,[1] as the standard therapeutic strategies fail to reconstitute dead myocardium with new functional cardiomyocytes and vessels. Therefore, the need for new therapies for myocardial preservation and regeneration has led to intense research aiming at the identification of new therapeutic approaches.[2–4]

The discovery of stem cell populations with cardiogenic potential, followed by the development of techniques for the isolation and expansion of these cells, has made cell-based

therapies a potential novel treatment modality in cardiovascular disease (Figure 1).[5–10] For cardiac repair, many clinical investigators use unfractionated bone marrow cells (BMCs), which include hematopoietic stem cells (HSCs), endothelial progenitor cells (EPCs), and mesenchymal stem cells (MSCs). This strategy provides ease in cell accessibility and does not require extensive manipulation *in vitro*. After nearly two decades of research, the overall clinical evidence suggests that stem cell therapy is safe and has a modest degree of positive impact on cardiac function and cardiac remodeling after an infarct (see Table 1). However, these studies have had contradictory performance results, and it has become clear that many challenges need to be overcome before this therapy achieves its full potential.[11–18] For example, The HEBE and ASTAMI trials showed no benefit with infusion of BMC. The BOOST trial showed a short-term benefit from stem cell transplantation, and the REPAIR-AMI trial indicated a sustained improvement in left ventricular ejection fraction (LVEF) with infusion of BMC in patients with larger infarcts treated after 5 days. There may be many reasons for the differences in outcomes. Notably, there was no standardized protocol for the collection and infusion of stem cells in these studies. Even the types

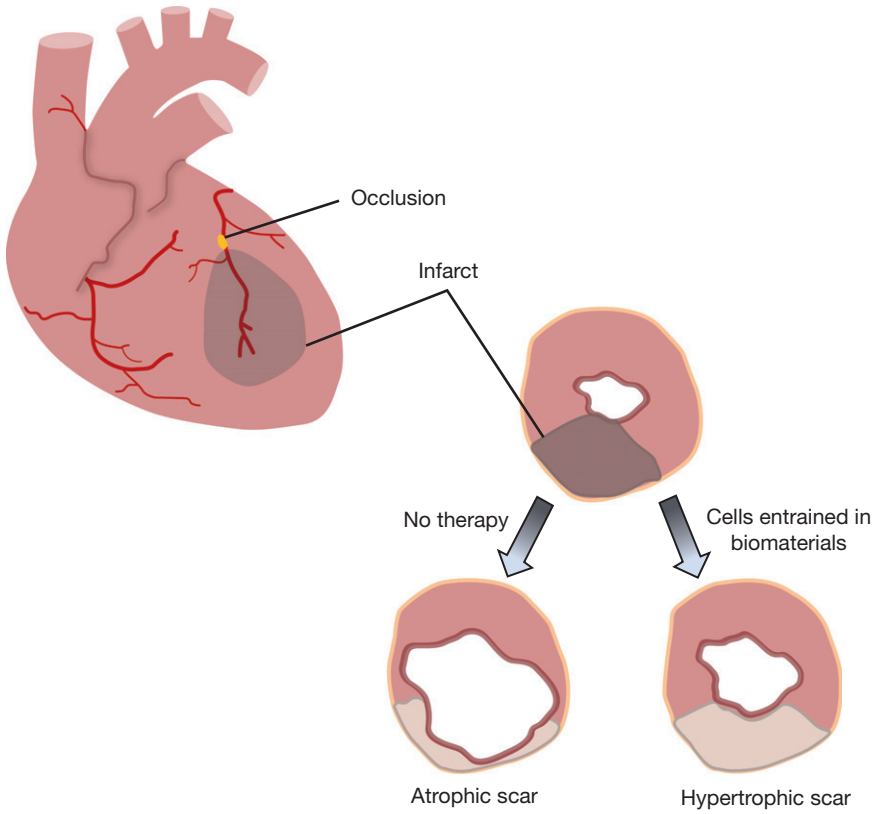

Figure 1 An occlusion in a coronary artery leads to a myocardial infarction downstream of the blockage. The scar region eventually extends and expands outward causing ventricular dilation and wall thinning. Laplace's law predicts that tension in the heart wall increases when wall thickness decreases. Therefore, by increasing the wall thickness with a cell–biomaterial therapy, the tension in the heart wall will decrease and lead to a hypertrophic scar instead of an atrophic scar. Figure adapted from Laflamme *et al*.

Table 1 Summary of randomized clinical trials evaluating cell therapy for acute myocardial infarction or ischemic heart failure

Trial name	*Type of cell*	*Number of patients*	*Results*
BOOST	BMC	60	Improvement in LVEF short term[20]
REPAIR-AMI	BMC	187	Improved LVEF for 12 months[21]
HEBE	BMC	200	No change in systolic function at 4 months[22]
ASTAMI	BMC	97	No difference after 6 or 12 months[23]
FINCELL	BMC	77	Improvement in LVEF[24]
REGENT	BMC	200	Improvement in LVEF only in severe patients[25]
Leuven-AMI	BMC	67	No change in LVEF, reduction in myocardial infarct size[26]
MAGIC	Skeletal muscle cells	97	No change in LVEF, reduction in LV end diastolic and systolic volume[27]
TOPCARE-CHD	BMC vs. blood derived CPC	58	Improvement in LVEF with BMC, not with CPC[28]

of stem cells used for transplantation were not consistent among the trials. The number of cells transplanted in each study varied greatly and thus could drastically change outcomes. Finally, the numbers of patients in these trials were small. Therefore, larger trials that use an established protocol for stem cell transplantation may provide more consistent and reproducible results. Currently, there are numerous ongoing trials to evaluate the safety and efficacy of cell infusion.[19]

One of the most significant barriers to cardiac cell transplantation is the limited cell retention and engraftment after cell delivery into the myocardium.[29–31] To improve outcomes after cell therapy, a sizeable percentage of the injected stem cells into the heart would presumably need to remain viable, differentiate into fully functional cardiomyocytes, and electromechanically couple with the existing cardiomyocytes. Alternatively, increased viability of BMCs that secrete paracrine factors, rather than differentiate into CMs, may also lead to significant improvements in cardiac function. In either case, biomaterial or matrix-assisted stem cell transplantation has emerged as a potential method to increase cell retention, survival, and engraftment.[32–36] The ability to entrain the stem cells in a biomaterial scaffold that mimics the natural myocardial extracellular matrix (ECM) and retains the cells at the location of interest, potentially acting as a substitute for malfunctioning myocardium, is a major focus of ongoing research. This chapter addresses the biomaterial design criteria for cell transplantation and the different synthetic and naturally derived biomaterials used in cardiac cell transplantation, and summarizes the various techniques used to characterize these biomaterials.

5.529.2. Biomaterial Design Requirements for Cardiac Cell Transplantation

5.529.2.1. Three-Dimensional Scaffold

The success and viability of the transplanted cells depends largely on the surrounding matrix having the appropriate molecular composition, biological cues, architecture, and mechanical behavior to stimulate robust proliferation of the transplanted cells and their coupling to the viable myocardium's blood supply (Figure 2). In addition, these cells must be able to dynamically infiltrate and remodel the diseased ECM, and deposit their own matrix over time. Therefore, the three-dimensional (3D) scaffold should serve as a structural and logistic template for tissue regeneration while degrading at a rate controlled by the transplanted cells.[37–40] This could be achieved using two disparate strategies: a classic tissue

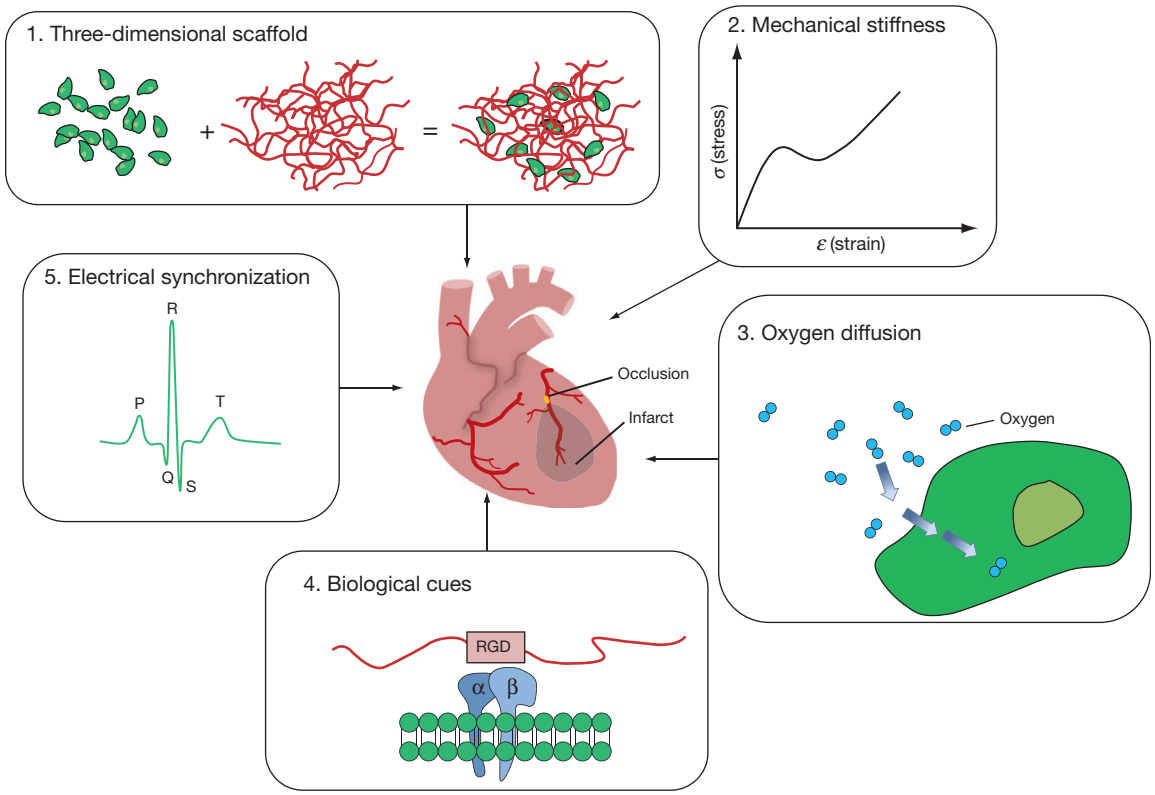

Figure 2 The five biomaterial design strategies for addressing the challenges of cardiac cell transplantation: (1) The transplanted cells are entrained in a 3D biomimetic scaffold to mimic the natural myocardium. (2) Cardiomyocytes are sensitive to the mechanical properties of the extracellular matrix, suggesting that biomaterial modulus is an important design criteria. (3) The infarcted region is a highly hypoxic environment and biomaterials should be designed for optimal oxygen diffusion. (4) Incorporating biological cues into the biomaterial such as specific ligands or growth factors will help with cell adhesion, regulation of cellular phenotype, cell survival, and remodeling. (5) Integrated cardiac beating can occur only when electromechanical coupling occurs between the transplanted cells and the host myocardium.

engineering approach by seeding cells on an engineered matrix, promoting cell expansion *in vitro*, and then surgically implanting the construct; or, alternatively, by simultaneous implantation of the biomaterial and the stem cells using minimally invasive techniques. The focus of this chapter is on the latter, as it has the potential for significant savings in cost, minimal intervention, and wider clinical adoption.

5.529.2.2. Biological Cues: Cells Communicate with the ECM Through Cell–Surface Receptors

The absence of cell adhesion to the ECM can lead to transplanted cell death.[41] Therefore, controlling cell–materials interactions is a promising approach for enhancing cell viability for transplantation strategies. Integrins are heterodimeric transmembrane receptors that are the fundamental components in ECM cell interactions. They play major roles in cell adhesion to the ECM, regulation of cellular phenotype, cell survival, remodeling, cell migration, and tissue development. Integrins are mechanotransducers that provide ligand–integrin engagement causing intracellular signaling events that lead to a cascade termed 'outside-in' signaling.[42,43] These receptors are important mediators between the cell and the ECM. Therefore, one promising design strategy is to incorporate specific ligands into cardiac biomaterial scaffolds in order to specifically guide the cells of interest.

Integrins are heterodimers composed of α- and β-subunits that are transmembrane glycoproteins. They interact with numerous ECM proteins such as fibronectin, laminin, collagen, and vitronectin. Each subunit is composed of a large extracellular domain (700–1100 amino acids long) and a short cytoplasmic segment (20–60 amino acids). Currently, there are 18 α-subunits and 8 β-subunits, and they preferentially associate with each other for a total of 24 pairs of integrin receptors.[44,45]

The integrins on a particular cell type are unique and can vary depending on the pathological state and developmental stage of the cell. Specific integrins and subunits have also been identified as key players during the remodeling process following an AMI. For example, Shewchuck *et al.* reported that impaired integrin activity can be linked to cardiac remodeling.[46] They investigated how oxidative stresses affect integrin upregulation. By using hydrogen peroxide to mimic the hypoxic conditions of the infarct area, they showed that the β_3-subunit increases at the site of infarction in a rat ligation model. This subunit plays an important role in preventing cardiomyocyte apoptosis under hypoxic conditions.[46] Additionally, Yang *et al.* reported the importance of the α_4-subunit in cardiac remodeling and development.[47] They reported that α_4 associates with β_1 and β_7 to bind to a non-arginine–glycine–aspartic acid (RGD) peptide motif in fibronectin as well as to vascular adhesion molecule 1. Therefore, by determining which integrins are present on the cell of interest through RT-PCR and fluorescence-activated cell sorting, complementary peptide ligands can be identified and then immobilized onto the surface of the biomaterial to engage with the cell.[48,49] Although it may be easy to identify the integrins present on a cell, it is challenging to identify peptide ligands, which has led to the use of both phage and bacteria display technologies to identify peptide ligands for a specific cell type.[50,51] This strategy could aid in cell retention and localization that has plagued the field of myocardial infarct therapy.

5.529.2.3. Mechanical Properties

The modulus of the material used as an artificial matrix in cardiac tissue engineering is critical for cardiomyocyte survival, proliferation, and differentiation. Mechanotransduction is the cellular mechanism whereby physical signals of the ECM are transduced, via cell surface receptors (e.g., integrin receptors) engaging with the ECM, into cytoskeletal organization and intracellular biochemical signals that consequently affect cell behavior and fate decisions. Engler *et al.* demonstrated that MSCs differentiated into various tissue-specific cells when the matrix stiffness was tuned to a stiffness range that matched the mechanical properties of native tissue.[52] This phenomenon of matrix modulus-induced differentiation was observed for MSCs, seeded on the surface of collagen-coated poly(acrylamide) hydrogels, that committed to muscle, osteogenic, and neural lineages. To date, no studies have demonstrated that cardiomyocyte differentiation is affected by matrix stiffness, but it is logical to assume that BMSs and MSCs transplanted into an infarcted myocardium could be influenced by the supporting matrix mechanics.

It is known that cardiomyocytes are highly sensitive to the mechanical properties of the ECM as well as to the tension imparted by surrounding myocytes in the dynamically beating environment of the heart. A 3D matrix based on fibrinogen was developed as an *in vitro* system to investigate the effects of matrix stiffness on the coordinated contraction of cardiomyocyte and overall tissue construct contraction.[53] An inverse relationship was observed between the stiffness and the amplitude of contraction for the neonatal cardiomyocytes seeded within the matrix, where stiffer hydrogels resulted in less-synchronized contraction of the constructs.

In vivo, the compliance of the infarct scar post-MI has been associated with the attenuation of negative LV remodeling.[54] Normal LV remodeling after MI involves the overproduction of collagen and consequently results in a highly stiff scar. By injecting human MSCs directly into the infarcted region of a rodent myocardium, cardiac function was improved, apoptosis reduced, and myocardial thickness increased, without regenerating contracting cardiomyocytes. Theoretically, the injected MSCs 'softened' the infarct environment and attenuated post-MI remodeling, thereby improving the compliance of the cardiac muscle. Mathematical models of noncontractile materials with a wide range of mechanical properties, either synthetic materials or dead cells, implanted in the border zone (BZ) of the infarct can reduce elevated wall stresses,[55] suggesting that injection of biomaterials in the left ventricle might attenuate postinfarct myofiber stresses and ameliorate both ventricular remodeling and infarct extension.

Collectively, these studies implicate the mechanical properties of matrices for cell transplantation as a critical design parameter in promoting the differentiation into specific cell lineages or the coordinated contraction of cardiomyocytes, or modifying the mechanical properties of the infarct. The exact modulus of the matrix may depend on whether

undifferentiated cells (i.e., BMS or MSC) or committed cardiac progenitors are used as the cell type, and on the engineering limitations imposed by minimally invasive placement.

5.529.2.4. Oxygen Transport

The infarct region post-MI is a hypoxic environment that contributes to massive cell death. One of the biggest challenges to the regeneration of the damaged myocardium is the transport of oxygen into the scar region, as it determines potential host stem cell remodeling, cell viability, and function. In order to meet this oxygen demand, cells throughout the body are typically found no more than 100–200 μm from the nearest capillary to ensure adequate diffusion of oxygen and nutrients, and clearance of waste products.[56] In the heart, however, the oxygen consumption is significantly higher and this demand is met with a dense vasculature with capillaries spaced only 20 μm apart.[57]

Various methods are used to address the problem of oxygen transport. One approach is to functionalize the scaffold with angiogenic growth factors, such as vascular endothelial growth factor (VEGF), basic fibroblast growth factor (bFGF), platelet-derived growth factor (PDGF), and sonic hedgehog (SHh) to promote neovascularization.[58–65] The growth factors of interest can be loaded into the biomaterials using a variety of methods including encapsulation, the release of which is dictated by diffusion or controlled by material degradability; tethering to natural or synthetic materials, which may release the factor by enzymatic degradation; or by affinity binding to heparin or heparin-binding components.[66] For example, to promote vascularization, VEGF has been incorporated into alginate scaffolds[67], loaded into poly(lactic-*co*-glycolic acid) (PLGA) scaffolds[68], and associated within fibrin networks for cell-mediated release by local cell-associated enzymatic activity.[69,70] The latter approach, being more sophisticated, avoids known issues with VEGF-induced angiogenesis (e.g., aberrant leaky vessels) and promotes formation of vessels with normal morphologies and ultrastructure. Alternatively, one can take a physical approach and decrease the volume fraction of the matrix by fabrication of channels to increase the perfusion of oxygen.[71–73] The latter approach has limitations for minimally invasive transplantation approaches, but is creditable for traditional tissue engineering *ex vivo* cell expansion.

5.529.2.5. Electromechanical Coupling

Understanding the interplay between electrophysiology and the mechanics of myocytes is a central challenge in designing a scaffold for myocardial therapy. One of the key challenges in stem cell transplantation is achieving electromechanical synchronization between the host myocardium and the engineered construct while not eliciting arrhythmias. This coupling allows for integrated beating, whereby electrical signals are transmitted across intracellular junctions in an organized manner to form the necessary mechanical contractions for pumping blood through the heart.

The structure of the heart muscle is a complex hierarchical assembly of oriented components: 75% of the solid heart consists of cardiomyocytes, which are cylindrically shaped with diameters of 10–25 μm and lengths of 100 μm.[74] These myocytes are arranged in bundles of myofibers that are oriented from outside in with a clockwise rotation and from inside out with a counterclockwise rotation (e.g., reciprocal spiral architecture).[75] Therefore, the heart is a highly reinforced structure with a heterogeneous architecture that requires 1D contraction of myocytes for mechanical pumping. Maintaining this architecture and alignment of the fibers when designing a scaffold implant may be an important requirement for electrical coupling with the host myocardium. It is unlikely that minimally invasive approaches for cell transplantation will achieve this level of tissue architecture. However, engineered grafts have been shown to develop electrical coupling host myocardium.[76] They observed a normalization of epicardial electrical propagation between the engineered heart graft and the host myocardium, which was attributed to the host heart overpacing the construct and electrically conditioning it with time.[76] It has also been shown that electrical stimulation as well as electrical gradient exposure can induce cell alignment and coupling. Thus, there are two possible mechanisms of electrical integration: stretch-induced depolarization and direct electrical stimulation.[77,78] These different strategies should be incorporated into the design of the biomaterial scaffold for cardiac repair.

5.529.3. Current Materials

5.529.3.1. Naturally Derived Materials as Scaffolds

Naturally derived materials have frequently been used as scaffolds for cardiac tissue engineering.[79] These materials have advantages over their synthetic counterparts because they are components of or have similar biological properties to the natural ECM. Natural materials engage cell surface receptors and also provide the physiological environment to regulate cell function.[39] The natural biomaterials used to date for stem cell transplantation are listed in **Table 2**. However, they also have disadvantages, such as lot-to-lot variability, immune rejection that may come from xenogeneic protein components, and high contamination potential.[79]

5.529.3.1.1. Collagen

Collagen is a major component of connective tissue and makes up ~30% of all proteins in the human body.[91] It is widespread and found in skin, bone, fascia, and in most areas requiring strength and flexibility. There are at least 29 different types of collagens, of which collagen type I is the most prevalent.[79] All types of collagen are composed of 3 peptide subunits that are each approximately 1050 amino acid residues long

Table 2 Natural biomaterials used for cardiac cell delivery and tissue engineering

Material	*Applications*
Collagen	Cell delivery into infarct region[80–83]
Alginate	Cell delivery into infarct region[34,84]
Fibrin	Cell delivery into infarct region[32,85,86]
Chitosan	Thermoreversible, cell delivery into infarct region[87]
Hyaluroinc acid	Improving neovascularization into ischemic tissues[61,88–90]

and show a strong sequence homology. These chains coil to form a triple helix that is cross-linked through covalent and hydrogen bonding. The resulting collagen fibrils offer opportunities for specific cell adhesion events, as collagen contains integrin-binding domains such as RGD and GFOGER[92–94] to assist in cell attachment. Additionally, the free ε-amines on the lysine residues can be used for chemical modification with bioactive molecules, such as peptides. Moreover, collagen is broken down by collagenases and serine proteases, which allows for localized biodegradation when cells are present.

Studies by Dai *et al.* have shown that injecting collagen with or without MSCs into the infarcted heart is beneficial.[95] Injecting collagen alone into 1-week-old myocardial infarcts of rats showed significant thickening of the LV wall, improved LV stroke volume, and increased EF after 6 weeks.[95] A later study in 2009 by the same group showed that a collagen matrix considerably improves the localization of transplanted MSCs in the infracted myocardium. Using radioactive-labeled bone marrow-derived rat MSCs labeled with isotopic colloidal nanoparticles containing europium measured the radioactivity in the myocardium as well as remote tissues, such as the lung, liver, spleen, and kidney. Four weeks after the injection, the tissues were sampled for radioactivity signals. It was concluded that the collagen matrix effectively retained the MSCs in the infarcted myocardium, preventing cell loss in the noninfarcted myocardium and the remote organs after 4 weeks. Moreover, Kutschka *et al.* reported that collagen matrices enhanced the survival of H9c2 cardiomyoblasts when injected into infarcted hearts. After 4 weeks, fractional shortening (FS) and EF of the scaffold injected with cells showed improvement compared with the saline control.[82]

5.529.3.1.2. Alginate

Alginate is a naturally derived polysaccharide harvested from brown algae that is composed of (1→4)-linked β-D-mannuronic acid and α-L-guluronic acid, as shown in **Figure 3**.[96] In the presence of divalent cations such as Ca^{2+}, adjacent alginate chains cooperatively bind to form ionic interchain bridges.[96] Alginate is an attractive material for injectable cell transplantation as it gels in the presence of Ca^{2+}. As alginate is derived from algae, it has no biological interaction with mammalian cells, and acts like a blank slate that can be chemically modified with specific peptides via the carboxylic acid functional groups to promote cell anchorage and cell–material interaction.[96] Therefore, this biopolymer is comparable to synthetic polymers in that it elicits minimal biological response and can be decorated with integrin-engaging peptides with a high signal-to-noise biological response.[96]

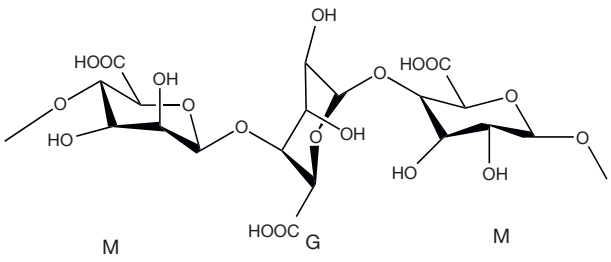

Figure 3 Chemical structure of the naturally occurring polymer alginate with the repeating subunits β-D-mannuronic acid (M) and α-L-guluronic acid (G).

Many groups have reported the benefits of injecting alginate without cells, both chemically modified and unmodified, to attenuate the negative remodeling process in myocardial infarcted hearts. For example, Yu *et al.* injected alginate conjugated with RGD peptides into the infarcted area of rats.[97] Both the modified and nonmodified alginate hydrogels significantly improved cardiac function and also increased arteriole density compared with the BSA in the PBS control group.[97] Landa *et al.* demonstrated that injecting biotin-labeled alginate into infarcted rat hearts 7 and 60 days post-MI resulted in thicker LV walls and attenuated LV systolic and diastolic dilatation. They also reported that the benefits of the alginate surpassed those of the neonatal cardiomyocyte group.[98] Moreover, alginate has been shown to be an effective injectable hydrogel system that also serves as a delivery vehicle for growth factors. Hao *et al.* reported improved cardiac function after injecting an alginate hydrogel that sequentially delivered VEGF-A_{165} and PDGF-BB.[99] The sequential delivery of these growth factors promoted a high density of α-actin positive vessels (i.e., vessels with a mature smooth muscle layer) compared to the single-dose administration.[99] Furthermore, Leor *et al.* reported the success of injecting alginate with fetal cardiac cells into the infarcted region of rat hearts. After 9 weeks, a large number of blood vessels were observed along with significant attenuation of LV dilation.[84] This study is one of the longest successful *in vivo* studies reported that predicts alginate as a promising biomaterial for myocardial infarct therapy.

5.529.3.1.3. Fibrin

Fibrin, also referred to as fibrin glue, is a plasma-derived biopolymer that is used as a biodegradable tissue sealant in a number of surgical applications.[100,101] During the last step of the coagulation cascade, thrombin enzymatically cleaves fibrinogen to polymerize a semirigid fibrin clot.[32] This biopolymer acts as a tissue sealant by binding to biological tissue via covalent, hydrogen, or electrostatic bonds. Mechanical interlocking also plays a large role in the anchoring of the fibrin clot to the tissue.[101] Furthermore, many studies have reported that fibrin has considerable angiogenic properties.[32,102,103] The degradation products stimulate the migration of monocytes and subsequent macrophages to the clot, where they remove the degraded fibrin by-products via phagocytosis. Fibroblasts bind and migrate into the clot network and secrete urinary plasminogen activators or tissue type plasminogen activators that lyse fibrin, favoring neovascularization.[101] Fibrin also serves as an attractive cardiac tissue scaffold material since it is biocompatible, approved in devices by the FDA, does not exhibit extensive fibrosis or tissue necrosis, is biodegradable, and promotes angiogenesis.[101]

Studies have reported that fibrin can improve cardiac function after MI. Ryu *et al.* reported that injecting bone marrow mononuclear cells (BMMNCs) into a cryoinjured rat myocardium using a fibrin matrix resulted in enhanced neovascularization and extensive tissue regeneration compared to the BMMNC implanted without the matrix.[85] Christman *et al.* injected skeletal myoblasts with fibrin glue into the LV of infarcted rat hearts. After 5 weeks, it was apparent that the fibrin scaffold increased cell transplant survival, improved

blood flow to the ischemic region, and decreased the infarct size.[102] It was noted that the fibrin glue did not significantly increase cell retention, but instead increased cell survival over the BSA control group. They attribute the cell survival to the fact that fibrin promotes angiogenesis, increasing blood flow to the cells in the ischemic environment of the infarct. Additionally, they attributed the low cell retention to the fact that the fibrin solution remains a liquid only for a few seconds before gelling, which would allow enough time for the cells to leak out of the injection site.[102] Therefore, optimizing the rate of cross-linking so that the cells remain at the desired site upon injection would be important for further investigatation.

5.529.3.1.4. Chitosan

Chitosan is a linear polysaccharide of β(1→4)-D-glucosamine units derived from the exoskeletons of animals such as crustaceans, mollusks, and insects.[104,105] It can also be extracted from the fungal fermentation processes.[91] In aqueous solutions, chitin is insoluble; however, partial deacetylation of chitin in an alkaline environment[104] forms chitosan (deacetylation <60%), which is soluble in aqueous acids, such as acetic acid.[106] An arbitrary molecular structure of chitosan is shown in Figure 4. It is a biodegradable cationic biopolymer that is known to cause slight inflammation in mammals. The biodegradation rate of chitosan is determined by the residual acetyl content, a parameter that can be easily tuned. The major pathway for the biodegradation *in vivo* is through lysozyme that depolymerizes the polysaccharide.[91] Due to its low toxicity and acceptable biocompatibility, it has been used in many medical applications.

In a study by Lu *et al.*, thermoresponsive chitosan with ESCs were injected into the infarcted regions of rat hearts. This 4-week-long study showed that the hydrogel and ESC injection preserved cardiac function and exhibited significantly higher microvessel densities than the PBS group. Additionally, the chitosan hydrogel facilitated ES cell retention.[35] Yeo *et al.* made a photo-cross-linkable hydrogel composed of chitosan and acryloyl-poly(ethylene glycol)-RGDS for encapsulating VEGF and C2C12 cells derived from murine myoblasts. They showed that the hydrogel supported attachment, proliferation, and differentiation of the myoblasts. Finally, the hydrogel was successfully localized at the surface of the rat heart and in the ventricle wall due to the photo-cross-linkable qualities of the hydrogel.[107]

5.529.3.1.5. Hyaluronic acid

Hyaluronic acid or hyaluronan (HyA) is an anionic, nonsulfated linear glycosaminoglycan that is found in the ECM of all mammalian connective tissues.[108] This biopolymer is composed of repeating units of β-D-glucuronic acid and *N*-acetyl-β-D-glucosamine, where the linkage is (1→3) from glucuronic acid to *N*-acetyl-β-D-glucosamine and (1→4) from *N*-acetyl-β-D-glucosamine to glucuronic acid, and has molecular weights ranging from 10^4 to 10^7 Da, as shown in Figure 5.[109] It is a desirable biomaterial since it does not elicit significant inflammatory or foreign body reactions *in vivo*. HyA also serves many biological functions in the body, but it is most commonly known for its inert lubricating functions in the synovial fluid of joints.[88] HyA is naturally degraded by the enzyme hyaluronidase, which causes the lowering of the molecular weight to decrease viscosity and increase tissue permeability. Furthermore, as a chief component of the ECM, HyA has the ability for specific binding through its main classes of cell surface receptors.[108] For example, CD44 is a type I single-pass transmembrane glycoprotein that is a receptor for HyA. It is responsible for mediating cell adhesion, migration, and proliferation. Additionally, RHAMM is a soluble protein that binds to HyA and is thought to play a role in the regulation of mitosis.

HyA has biological properties that are dependent on molecular weight. For example, low molecular weight HyA is an attractive biopolymer for tissue engineering scaffolds because of its angiogenic properties during wound-healing processes.[89] Encouraging blood vessel growth is especially important for cardiac tissue engineering because the post-MI myocardium is an ischemic environment for transplanted cells.[90] In a study by West *et al.*, electron microscopy showed a significantly larger number of small blood vessels in myocardial infarcts from animals treated with high levels of hyaluronidase to degrade the HyA than in hearts from untreated (no hyaluronidase) animals.[90] The size distribution of HyA for angiogenic activity was determined to be between 4 and 25 disaccharides in length. Therefore, incorporating low molecular weight HyA or high levels of hyaluronidase into tissue engineering scaffold may be a beneficial therapy for blood vessel growth in cardiac cell transplantation.

A challenge to this approach is that the low molecular weight fragments will have weaker biomechanical properties, but HyA can be chemically cross-linked to form infinite molecular weight hydrogel networks. One solution is to covalently

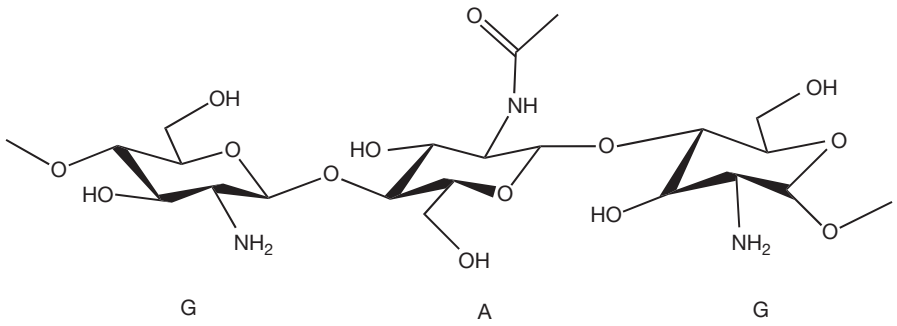

Figure 4 Chemical structure of the naturally occurring polymer chitosan. This linear polysaccharide is composed of randomly distributed β(1→4)-D-glucosamine units (G: deacetylated unit) and *N*-acetyl-D-glucosamine (A: acetylated unit).

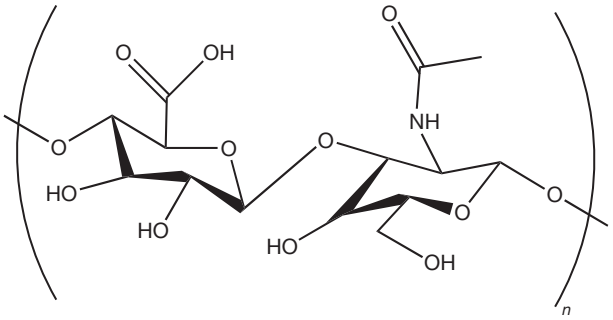

Figure 5 Chemical structure of the naturally occurring polymer hyaluronic acid. The repeating disaccharide is composed of D-glucuronic acid (left) linked β(1→3) to *N*-acetyl-D-glucosamine units (right), which is then β(1→4) linked to the D-glucuronic acid.

cross-link the low molecular weight HyA fragments to add mechanical integrity to the scaffold. Ghosh *et al*. have reported the feasibility of cross-linking thiol-functionalized HyA with polyethylene glycol diacrylate (PEGDA) through a controllable Michael-type addition reaction.[88] It is also possible to use a diacrylate cross-linker that is biodegradable such as an MMP-sensitive peptide sequence so that the low molecular weight HyA fragments are delivered overtime while simultaneously maintaining mechanical integrity. HyA may also be used as a carrier for angiogenic molecules. For example, Wall *et al*. have covalently conjugated SHh protein through the carboxyl group on the HyA using the heterobifunctional cross-linker, EMCH.[61] The polyvalency of the SHh–HyA conjugate leads to enhanced angiogenic activity.

5.529.3.2. Synthetic Biomaterials as Scaffolds

Synthetic biomaterials offer advantages over naturally derived materials as scaffolds in cardiac stem cell transplantation as they can be chemically, mechanically, and structurally well defined. These important features are advantageous for scaffolds because they can be easily tuned and systematically optimized with batch-to-batch reproducibility. They also offer a range of chemistries unavailable to natural materials, which have the potential for various applications such as time-controlled release of bioactive compounds from the matrix and tunability of mechanical properties. Furthermore, biomaterials can be redesigned and modified in an iterative manner for improved performance, which is a benefit over naturally occurring materials, which typically have little latitude in modification. Synthetic biomaterials do not have the problems associated with injecting naturally derived materials *in vivo* such as disease transmission and/or rejection. However, a downside to synthetic materials is that the biodegradation can often induce inflammatory responses such as small-particle disease. For example, the acidic degradation products from polylactic- and polyglycolic acid-based materials can lower the pH of the microenvironment, which may have serious physiological effects.

5.529.3.2.1. Poly(glycolide) and poly(lactide)

The polyesters belonging to the poly (α-hydroxy acid ester) family, such as poly(glycolide) (PG), poly(lactide) (PL), and poly(ε-caprolactone) (PCL), are the most widely used

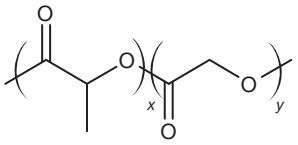

Figure 6 Chemical structure of the repeating unit of poly(lactide-*co*-glycolide).

synthetic biodegradable polymers in medicine. PL is typically synthesized by ring-opening polymerization of the lactide monomer, a chiral molecule with three forms (i.e., D, L, and *meso*), that can produce PDL, PLL, or PDL.[110](*Note*: PL is also referred to as poly(lactic acid) (PLA) and PG as poly(glycolic acid) (PGA) based on earlier synthesis methods exploiting condensation polymerization of lactic or glycolic acid.) While PL is a hydrophobic polymer because of its extra methyl group that retards hydrolytic degradation, PG is relatively more hydrophilic and therefore degrades more rapidly. To improve mechanics and vary degradation rates, lactide monomers are generally copolymerized with glycolide monomers to make a wide range of copolymers.[110,111] The chemical structure of poly(lactide-*co*-glycolide) (PLG) is shown in **Figure 6**. PLG copolymers exhibit a highly tunable degradation rate over the individual polymers and are commonly used as controlled-released carriers for various exogenous agents.[112] The ratio of PL to PG can be modulated to change the degradation rate to coincide with the amount of time necessary for cellular infiltration and matrix deposition.[112] PL, PG, and PLG are FDA approved in devices because of their proven biocompatibility. PCL is polymerized from a cyclic lactone monomer to produce a semicrystalline polymer that degrades more slowly *in vivo*. Copolymers of PCL with other polyesters such as PLL are commonly produced for tissue engineering applications.[113,114]

PLG is a common biomaterial used in tissue engineering scaffolds, vascular grafts, and cardiac tissue constructs. Wang *et al.* reported a tubular scaffold system composed of PLGA loaded with bFGF that was implanted into the infarcted area of the heart. The PLGA scaffolds with bFGF showed significant improvement in FS compared to the control group.[112] Additionally, there was increased neovascularization and perfusion in the scaffold groups.

One concern regarding the use of PLGA as a bulk implant material is the delayed inflammatory reaction that often occurs due to the release of the acidic degradation products.[115–118] Hydrolysis of PLG leads to lactic acid and glycolic acid as degradation products, resulting in a local pH decrease in the vicinity of the implant.[118] Agrawal *et al*. investigated the use of incorporating basic salts such as calcium carbonate, calcium hydroxyapatite, and sodium bicarbonate into PLG scaffolds to offset the acidic by-products.[118] The control media with the implant showed a significant drop in pH (3.0) after 9 weeks. In comparison, implants that contained calcium carbonate, calcium hydroxyapatite, or sodium bicarbonate controlled the pH values in the range of 7.4–6.3, 6.9–4.3, and 8.2–4.5, respectively. Although incorporating basic salts into the PL, PG, and PLPG implant helps to avoid the harmful acidic levels that arise from the degradation products, this approach may lead to ectopic calcification in the heart and is therefore a high risk approach.

5.529.3.2.2. PEG-based hydrogels

PEG has been used in numerous tissue engineering applications because of its low toxicity and nonfouling character. The chemical structure of PEG is shown in Figure 7. In a study by Dobner, *et al.*, a PEG hydrogel was chosen as an injectable therapy because of its biocompatibility and mechanical strength.[119] Studies by Wall *et al.* and Sabatine *et al.* have shown that the injection of stiffer materials maximizes the attenuation of remodeling by relieving the buildup of stress felt by cardiomyocytes[55,120]. Therefore, in this study, a stiff 5% PEG (20 kDa) hydrogel was injected into the infarcted region of Wister rats, and the resulting FS and infarct volume decreased significantly at 2 and 4 weeks. At these time points, there was also complete prevention of wall thinning and decreased heart dimensions. However, these benefits were lessened by week 13 when dilation occurred. Perhaps, this late negative remodeling in the PEG-treated group was due to a delayed buildup of cardiomyocyte stresses above a threshold level. The therapeutic benefits of the PEG hydrogel were only present in the immediate postinfarct healing phase, unlike the results from the poly(*N*-isopropylacrylamide-*co*-acrylic acid) semi-interpenetrating polymer network (sIPN) hydrogels study.[36] In addition, a study by Zhang *et al.* showed that a MPEG–PCL–MPEG triblock copolymer hydrogel injected into rabbit MIs prevented scar expansion and wall thinning compared to the PBS control. They also reported that the hydrogel injected group had a significantly higher EF (56%) compared to the control group (37%), with no difference in vessel density between the two groups.[121]

5.529.3.2.3. Poly(N-isopropylacrylamide)

Thermoresponsive materials are attractive candidates for noninvasive cardiac therapies because they preclude the need for invasive open heart surgeries. One strategy could be the employment of the principle of lower critical phase separation. Polymer mixtures that demonstrate this behavior phase-separate as the temperature is increased above the lower critical solution temperature (LCST).[122,123] One such polymer is poly(*N*-isopropylacrylamide) P(NIPAAm), which is an amphiphilic thermoresponsive polymer that swells significantly in water to form a hydrated 3D hydrogel network (Figure 8). When P(NIPAAm) is heated, it undergoes a coil to globule transformation at its LCST, which occurs at ~34 °C, conveniently situated between room and body temperature. The polymer exists as a free-flowing viscous liquid at room temperature and a rigid viscoelastic solid above the LCST. Lower critical phase separation is generally regarded as a phenomenon governed by the balance of hydrophilic and hydrophobic moieties on the polymer chain and driven by a negative entropy of mixing.[124–126] In addition, the temperature dependence of certain molecular interactions, such as hydrogen bonding and hydrophobic effects, contributes to this type of phase separation.[127] At the LCST, the hydrogen bonding between the polymer and water becomes unfavorable compared to polymer–polymer and water–water interactions,[126] and an abrupt transition occurs as the hydrated hydrophilic macromolecule quickly dehydrates and changes to a more hydrophobic structure.[126,127]

sIPNs composed of P(NIPAAm) have been used as biomimetic ECMs for cardiac stem cell transplantation and myocardial stabilization.[36] GFP-positive BMSCs were entrained in environmentally responsive poly(*N*-isopropylacrylamide-*co*-acrylic acid) hydrogels incorporated with matrix metalloproteinase labile cross-linkers (e.g., MMP-2, -9, and -13) and peptides containing integrin-binding domains (i.e., RGD), and were directly injected into infarcted murine left ventricles without inducing arrhythmias. Wall *et al.*[36] reported significant differences in comparisons of pooled data from treatment groups that received MSCs. At 2 weeks, the addition of MSCs resulted in a significantly higher FS and a numerically higher EF compared to controls; however, at 6 weeks, hearts that received stem cells had worse FS as well as EF. Interestingly, injection of the sIPNs without cells resulted in superior LV function at 6 weeks compared to groups with cells and saline controls. Donor GFP(+) cells were detected only 6 weeks after matrix-enhanced transplantation, but not without matrix support, and infarct thickness was increased in animal subgroups that had histologically confirmed matrix contained within the infarct border zone ($p < 0.05$). Thus, sIPN hydrogels succeeded in both mechanically supporting the injured myocardium and enhancing donor cell survival. These results are consistent with a theoretical mathematical model that reported that injection of biomaterials in the left ventricle might ameliorate both ventricular remodeling and infarct extension.[55]

Fujimoto *et al.* reported copolymerization of P(NIPAAm), acrylic acid, and hydroxyethyl methacrylate-poly(trimethylene carbonate) as a bulking agent for myocardial repair.[128] The goal was for the hydrogel to gel at 37 °C and then slowly solubilize at physiological temperature as the PTMC residues were hydrolytically cleaved. The authors reported an 8-week *in vivo* study showing that the LV cavity area and contractility were preserved in the hydrogel group. Additionally, tissue ingrowth and a higher capillary density were observed in the hydrogel injected versus the PBS control group.[128] Both of these studies indicate that biomaterials alone, without the inclusion of stem cells, may be a viable treatment for post-MI injuries.

5.529.3.3. Hybrid Biosynthetic Materials

To take advantage of the tunability of synthetic materials and the bioactivity of naturally occurring materials, many groups have coupled these two types of materials as a biosynthetic strategy for treating MIs. As described previously, PEG is one of

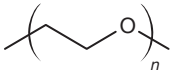

Figure 7 Chemical structure of the repeating unit of poly (ethylene glycol).

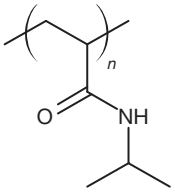

Figure 8 Chemical structure of the repeating unit of poly(*N*-isopropylacrylamide).

the most commonly used synthetic polymers in biomedical applications. Many groups have incorporated bioactive components through chemical conjugation to synthetic PEG-based backbones. For example, Kraehenbuehl *et al*. showed that synthetic MMP-sensitive 3D PEG hydrogels with matrix-bound RGDSP peptide could direct differentiation of pluripotent cardioprogenitors *in vitro*.[129] The passive and synthetic qualities of PEG allowed for the bioactive components to be modulated independently from the matrix stiffness.[129] This kind of study would not have been possible with a natural material where the bioactivity and the mechanical properties are coupled. Therefore, the use of a synthetic base material with added bioactivity allowed for a more comprehensive study to determine the important features involved in directed cardioprogenitor differentiation. This study showed that the softer PEG-based matrices that had comparable stiffnesses to cardiac tissue ($E = 322 \pm 64.2$ Pa) directed the cardiac commitment of pluripotent P19 EC cells (**Figure 9**).[129]

Other studies have demonstrated the use of synthetic conducting polymers blended with naturally occurring materials as a potentially successful MI therapy. A conducting material is attractive for this application because it is hypothesized that it helps restore electrical conduction in the infarct. Additionally, the attachment, proliferation, and migration of cells may be tuned by electrical stimulation of the conducting polymer. One of the most commonly used conducting polymers is polypyrrole, a polycationic polymer that is easily synthesized into thin films, thick films, and colloidal particles. *In vivo*, the material has been shown to be noncytotoxic and can support the proliferation and differentiation of many cell types such as neurons and endothelial cells. However, one limitation of polypyrrole is that it can be brittle and difficult to process. To overcome this limitation, Mihardja *et al*. blended polypyrrole with naturally occurring alginate, which is a more compliant material.[130] They chose to introduce polypyrrole because of its conductivity as well as its cationic charge to help with proliferation and differentiation of vascular cells. The group found that higher ratios of polypyrrole to alginate increased attachment of human umbilical vein endothelial cells *in vitro*. They also reported that injection of 0.025% polypyrrole blended with alginate into the infarcted zone of a rat model resulted in significantly greater arteriogenesis at 5 weeks compared to the alginate only and saline control groups.

Another biosynthetic strategy is to use synthetic hydrogels as a delivery vehicle for biological agents. Wang *et al*. used a hydrogel composed of α-cyclodextrin MPEG–PCL–MPEG triblock copolymer to deliver erythropoietin (EPO).[131] EPO is a hormone that protects the myocardium by stimulating endothelial cells to promote ischemia-induced neovascularization. However, it also plays a role in potential thromboembolic complications. If delivered in a locally sustained way, the systemic toxicity is reduced. In this study, they injected the triblock copolymer with recombined human EPO (rhEPO) into MI rats. The controls were PBS, hydrogel alone, and rhEPO in PBS. Overall, the hydrogel with rhEPO improved cardiac performance significantly by inhibiting cell apoptosis, increasing neovasculature, and decreasing the infarct size compared to either PBS alone, hydrogel alone, or rhEPO in PBS. Therefore, this study demonstrated greater cardioprotective effects when the synthetic hydrogel and hormone were delivered in combination.

5.529.3.3.1. Smart biomaterials: growth factors and self-assembling peptides

Cardiac tissue engineering is not limited to cell- and cell–material-based approaches. A promising strategy in this field is the delivery of growth factors for myocardial protection against apoptosis, enhancement of angiogenesis, and recruitment of cells. As described previously, many studies have reported poor retention of transplanted cells in the myocardium with little functional integration. This observation might suggest that the benefits from cell transplantation therapies are

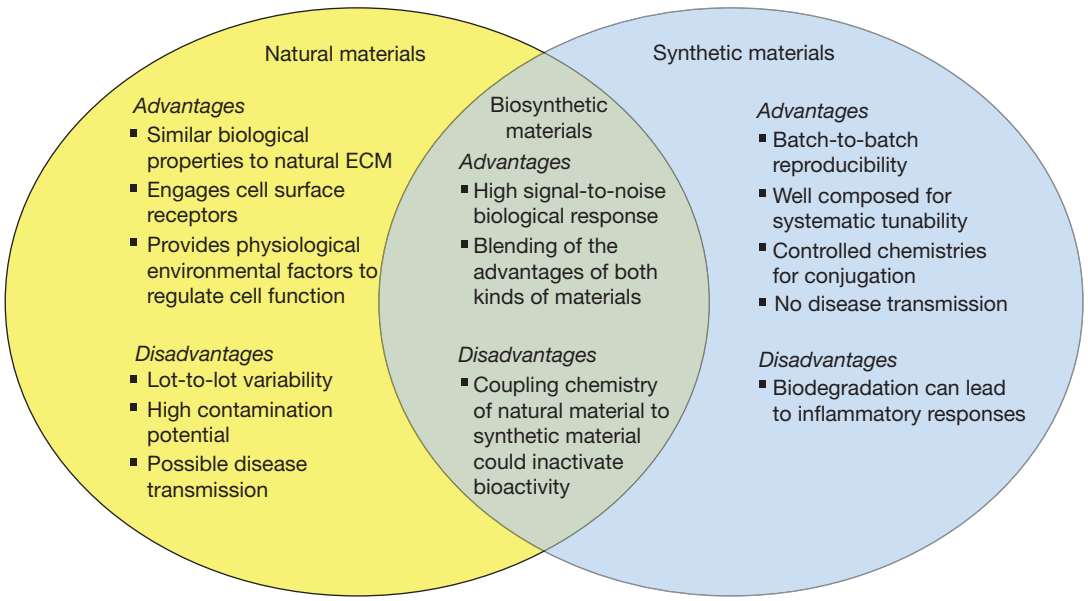

Figure 9 Comparison of synthetic, biosynthetic, and natural materials for cardiac cell transplantation.

paracrine-factor related and that growth factors may enhance this effect.[132] Growth factors are small in size and, consequently, they rapidly diffuse out of the injection site.[133] Many groups have tethered these growth factors onto self-assembled nanofibers through different chemistries for controlled release.[132–136] These nanofibers are composed of amphiphilic peptides that thermodynamically self-assemble upon exposure to physiological osmolarity and pH.[133] The resulting nanofibers are approximately 5–10 nm in length and mimic the filamentous structure of naturally occurring ECM fibers.[133]

Davis and Motion *et al*. used RAD16-II peptides, which are short sequences of 8–16 amino acids.[133,137] When injected into the myocardium of mice, the self-assembled nanofibers recruited progenitor cells that expressed endothelial markers and vascular smooth muscle cells, despite the fact that the peptides themselves have no known biological signaling sequence.[137] In another study by the same group, insulin-like growth factor 1 (IGF-1) was tethered to the same peptide (RAD16-11) nanofibers through a biotin sandwich strategy.[133] The complexation with IGFF-1 did not interfere with the self-assembly process. IGF-1 is a cardiomyocyte growth and survival factor and has been reported to protect against apoptosis after MI.[133] Neonatal cardiomyocytes that were injected into infarcted rat myocardium with the IGF-1-biotinylated nanofibers improved systolic function and reduced ventricular dilation. Finally, they showed that the IGF-1 complexed with the nanofibers decreased cell apoptosis and improved maturation of neonatal cardiomyocytes as evidenced by troponin expression.

Similarly, Dubois *et al*. investigated the use of RAD16-1 and RAD16-II self-assembling peptide nanofibers for delivering skeletal myoblasts to the infarcted left ventricle of rats[134] alone and tethered to PDGF-BB. PDGF-BB has been shown to be a crucial factor in endothelial cell-mediated cardiomyocyte protection.[133,134,138] All of the experimental groups were injected into rats 2 weeks after infarctions were induced. After 4 weeks, LV function was not improved in any of the experimental groups compared with the controls, but there was improved angiogenesis. This experimental study was similar to the study by Davis *et al*., but showed opposite results. The authors suggest that the benefits of the self-assembling nanofibers are highly dependent on (1) the time of injection and (2) the cell type.[134] Davis *et al*. injected neonatal cardiomyocytes with self-assembling peptides immediately after MIs, while Dubois *et al*. injected skeletal myoblasts 2 weeks after infarction.[134]

5.529.4. Concluding Remarks

In order to overcome the burden of MIs and related CHF in patients, novel treatment approaches are needed. Biomaterials alone or in combination with transplanted cells hold great promise as a therapy to treat CHF. Cell transplantation for cardiac tissue regeneration will hinge upon enhanced cell survival after injection, integration into the host tissue, and temporal expansion, which can be controlled by the material scaffold. To drive cardiac regeneration, the appropriate temporal, spatial, and signaling regulatory factors are necessary to incorporate into the biomaterial in order to stimulate the appropriate response. To do this, five major scaffold design goals have been proposed: (1) 3D support, (2) myocardial stiffness matching, (3) adequate oxygen and nutrient transport, (4) electromechanical integration with the host tissue, and (5) appropriate biological cues incorporated into the biomaterial. The field of biomaterials holds considerable promise at addressing these challenges to bring cardiac tissue engineering into clinical application.

References

1. Rosamond, Heart Disease and Stroke Statistics-2007, *Circulation* **2007**, *115*, e69.
2. Hartwell, D.; *et al*. *Health Technol. Assess*. **2005**, *9*, 1.
3. Kannel, W. B.; Feinleib, M. *Am. J. Cardiol*. **1972**, *29*, 154.
4. Lloyd-Jones, D.; *et al*. *Circulation* **2009**, *119*, 480.
5. Balsam, L. B.; *et al*. *Nature* **2004**, *428*, 668.
6. Beltrami, A. P.; *et al*. *Cell* **2003**, *114*, 763.
7. Asakura, A.; Komaki, M.; Rudnicki, M. *Differentiation* **2001**, *68*, 245.
8. Dawn, B.; Bolli, R. *Basic Res. Cardiol*. **2005**, *100*, 494.
9. Murry, C. E.; Wiseman, R. W.; Schwartz, S. M.; Hauschka, S. D. *J. Clin. Investig*. **1996**, *98*, 2512.
10. Anversa, P. *Circ. Res*. **2003**, *92*, 579.
11. Murry, C. E.; Keller, G. *Cell* **2008**, *132*, 661.
12. Rose, R. A.; Keating, A.; Backx, P. H. *Circ. Res*. **2008**, *103*, e120.
13. Seeger, F. H.; Zeiher, A. M.; Dimmeler, S. *Nat. Clin. Pract. Cardiovasc. Med*. **2007**, *4*(Suppl. 1), S110.
14. Shantsila, E.; Watson, T.; Lip, G. Y. *J. Am. Coll. Cardiol*. **2007**, *49*, 741.
15. Tendera, M.; Wojakowski, W. *Eur. Heart J*. **2009**, *30*, 640.
16. Abdel-Latif, A.; *et al*. *Arch. Intern. Med*. **2007**, *167*, 989.
17. Menasche, P. *Mol. Ther*. **2009**, *17*, 758.
18. Oettgen, P.; Boyle, A. J.; Schulman, S. P.; Hare, J. M. *Circulation* **2006**, *114*, 353.
19. Wollert, K. C.; Drexler, H. *Nat. Rev. Cardiol*. **2010**, *7*, 204.
20. Meyer, G. P.; *et al*. *Eur. Heart J*. **2009**, *30*, 2978.
21. Schachinger, V.; *et al*. *Eur. Heart J*. **2006**, *27*, 2775.
22. van der Laan, A.; *et al*. *Neth Heart J*. **2008**, *16*, 436.
23. Lunde, K.; Aakhus, S. *Eur. Heart J. Suppl*. **2008**, *10*, K35.
24. Miettinen, J. A.; *et al*. *Heart* **2010**, *96*, 362.
25. Tendera, M.; *et al*. *Eur. Heart J*. **2009**, *30*, 1313.
26. Janssens, S.; *et al*. *Lancet* **2006**, *367*, 113.
27. Menasche, P.; *et al*. *Circulation* **2008**, *117*, 1189.
28. Schachinger, V.; *et al*. *Clin. Res. Cardiol*. **2006**, *95*, 13.
29. Müller-Ehmsen, J.; *et al*. *J. Mol. Cell. Cardiol*. **2002**, *34*, 107.
30. Yeghiazarians, Y.; *et al*. *Mol. Ther. J. Am. Soc. Gene Ther*. **2009**, *17*, 1250.
31. Zhang, M.; *et al*. *J. Mol. Cell. Cardiol*. **2001**, *33*, 907.
32. Christman, K. L.; Fok, H. H.; Sievers, R. E.; Fang, Q. H.; Lee, R. J. *Tissue Eng*. **2004**, *10*, 403.
33. Eschenhagen, T.; *et al*. *FASEB J*. **1997**, *11*, 683.
34. Leor, J.; *et al*. *Heart* **2007**, *93*, 1278.
35. Lu, W. N.; *et al*. *Tissue Eng. A* **2009**, *15*, 1437.
36. Wall, S. T.; Yeh, C. C.; Tu, R. Y.; Mann, M. J.; Healy, K. E. *J. Biomed. Mater. Res. A* **2010**, *95*, 1055.
37. Hubbell, J. A. *Nat. Biotech*. **1995**, *13*, 565.
38. Kim, S.; Healy, K. E. *Biomacromolecules* **2003**, *4*, 1214.
39. Saha, K.; Pollock, J. F.; Schaffer, D. V.; Healy, K. E. *Curr. Opin. Chem. Biol*. **2007**, *11*, 381.
40. Vunjak-Novakovic, G.; Radisic, M.; Obradovic, B. *J. Chem. Technol. Biotechnol*. **2006**, *81*, 485.
41. Song, S.-W.; *et al*. *Stem Cells* **2009**, *27*, 1358.
42. Harbers, G.; Barber, T.; Stile, R.; Sumner, D.; Healy, K. CRC Press, 2010.
43. Massia, S. P.; Hubbell, J. A. *J. Cell Biol*. **1991**, *114*, 1089.
44. Hynes, R. O. *Science* **2009**, *326*, 1216.
45. Manso, A. M.; Kang, S.-M.; Ross, R. S. *J. Investig. Med*. **2009**, *57*, 856.
46. Shewchuk, L. J.; Bryan, S.; Ulanova, M.; Khaper, N. *Can. J. Physiol. Pharmacol*. **2010**, *88*, 324.
47. Yang, J. T.; Rayburn, H.; Hynes, R. O. *Development* **1995**, *121*, 549.
48. Massia, S. P.; Hubbell, J. A. *J. Biol. Chem*. **1992**, *267*, 14019.
49. Meng, Y.; *et al*. *FASEB J*. **2010**, *24*, 1056.
50. Murayama, O.; Nishida, H.; Sekiguchi, K. *J. Biochem. Tokyo* **1996**, *120*, 445.
51. Little, L. E.; Dane, K. Y.; Daugherty, P. S.; Healy, K. E.; Schaffer, D. V. *Biomaterials* **2011**, *32*, 1484.

52. Engler, A. J.; Sen, S.; Sweeney, H. L.; Discher, D. E. *Cell* **2006**, *126*, 677.
53. Shapira-Schweitzer, K.; Seliktar, D. *Acta Biomater.* **2007**, *3*, 33.
54. Berry, M. F.; *et al*. *Am. J. Physiol. Heart Circ. Physiol.* **2006**, *290*, H2196.
55. Wall, S. T.; Walker, J. C.; Healy, K. E.; Ratcliffe, M. B.; Guccione, J. M. *Circulation* **2006**, *114*, 2627.
56. Sherwood, L. M.; Parris, E. E.; Folkman, J. *N. Engl. J. Med.* **1971**, *285*, 1182.
57. Korecky, B.; Hai, C.; Rakusan, K. *Can. J. Physiol. Pharm.* **1982**, *60*, 23.
58. Andrae, J.; Gallini, R.; Betsholtz, C. *Genes Dev.* **2008**, *22*, 1276.
59. Lovett, M.; Lee, K.; Edwards, A.; Kaplan, D. L. *Tissue Eng. B Rev.* **2009**, *15*, 353.
60. Thurston, G.; *et al*. *Science NY* **1999**, *286*, 2511.
61. Wall, S. T.; *et al*. *Bioconjug. Chem.* **2008**, *19*, 806.
62. Zisch, A. H.; *et al*. *FASEB J.* **2003**, *17*, 2260.
63. Pola, R.; *et al*. *Eur. Heart J.* **2002**, *23*, 56.
64. Pola, R.; *et al*. *Circulation* **2003**, *108*, 479.
65. Pola, R.; *et al*. *Nat. Med.* **2001**, *7*, 706.
66. Pollock, J. F.; Healy, K. E. In *Strategies in Regenerative Medicine*; Santin, M., Ed.; Springer: New York, 2009.
67. Elçin, Y. M.; Dixit, V.; Gitnick, G. *Artif. Organs* **2001**, *25*, 558.
68. Kaigler, D.; Wang, Z.; Horger, K.; Mooney, D. J.; Krebsbach, P. H. *J. Bone Miner. Res.* **2006**, *21*, 735.
69. Ehrbar, M.; *et al*. *Circ. Res.* **2004**, *94*, 1124.
70. Ehrbar, M.; Metters, A.; Zammaretti, P.; Hubbell, J. A.; Zisch, A. H. *J. Control. Release* **2005**, *101*, 93.
71. Park, H.; Radisic, M.; Lim, J. O.; Chang, B. H.; Vunjak-Novakovic, G. *In Vitro Cell. Dev. Biol. Anim.* **2005**, *41*, 188.
72. Radisic, M.; *et al*. *Biotechnol. Bioeng.* **2006**, *93*, 332.
73. Mikos, A. G.; *et al*. *Polymer* **1994**, *35*, 1068.
74. Göktepe, S.; Kuhl, E. *Comput. Mech.* **2010**, *45*, 227.
75. Buckberg, G. D. *J. Thorac. Cardiovasc. Surg.* **2002**, *124*, 863.
76. Zimmermann, W.-H.; *et al*. *Nat. Med.* **2006**, *12*, 452.
77. Cherubini, C.; Filippi, S.; Nardinocchi, P.; Teresi, L. *Prog. Biophys. Mol. Biol.* **2008**, *97*, 562.
78. Grayson, W. L.; Martens, T. P.; Eng, G. M.; Radisic, M.; Vunjak-Novakovic, G. *Semin. Cell Dev. Biol.* **2009**, *20*, 665.
79. Drury, J. L.; Mooney, D. J. *Biomaterials* **2003**, *24*, 4337.
80. Kofidis, T.; *et al*. *J. Heart Lung Transplant.* **2005**, *24*, 737.
81. Kofidis, T.; *et al*. *Circulation* **2005**, *112*, I173.
82. Kutschka, I.; *et al*. *Circulation* **2006**, *114*, I167.
83. Xiang, Z.; Liao, R.; Kelly, M. S.; Spector, M. *Tissue Eng.* **2006**, *12*, 2467.
84. Leor, J.; *et al*. *Circulation* **2000**, *102*, 56.
85. Ryu, J. H.; *et al*. *Biomaterials* **2005**, *26*, 319.
86. Simpson, D.; Liu, H.; Fan, T. H.; Nerem, R.; Dudley, S. C., Jr. *Stem Cells* **2007**, *25*, 2350.
87. Curtis, M. W.; Russell, B. *J. Cardiovasc. Nurs.* **2009**, *24*, 87.
88. Ghosh, K.; *et al*. *Biomacromolecules* **2005**, *6*, 2857.
89. Brey, E. M.; Uriel, S.; Greisler, H. P.; Patrick, C. W.; McIntire, L. V. *Tissue Eng.* **2005**, *11*, 567.
90. West, D. C.; Hampson, I. N.; Arnold, F.; Kumar, S. *Science* **1985**, *228*, 1324.
91. Lanza, R. P.; Langer, R. S.; Vacanti, J. *Principles of Tissue Engineering*. Academic Press: New York, 2000.
92. Knight, C. G.; *et al*. *J. Biol. Chem.* **2000**, *275*, 35.
93. Xu, Y.; *et al*. *J. Biol. Chem.* **2000**, *275*, 38981.
94. Reyes, C. D.; Garcia, A. J. *J. Biomed. Mater. Res.* **2003**, *65A*, 511.
95. Dai, W.; Wold, L. E.; Dow, J. S.; Kloner, R. A. *J. Am. Coll. Cardiol.* **2005**, *46*, 714.
96. Rowley, J. A.; Madlambayan, G.; Mooney, D. J. *Biomaterials* **1999**, *20*, 45.
97. Yu, J.; *et al*. *Biomaterials* **2009**, *30*, 751.
98. Landa, N.; *et al*. *Circulation* **2008**, *117*, 1388.
99. Hao, X.; *et al*. *Cardiovasc. Res.* **2007**, *75*, 178.
100. Jakob, H.; Campbell, C. D.; Qiu, Z. K.; Pick, R.; Replogle, R. L. *J. Vasc. Surg.* **1984**, *1*, 171.
101. Radosevich, M.; Goubran, H. I.; Burnouf, T. *Vox Sang.* **1997**, *72*, 133.
102. Christman, K. L.; *et al*. *J. Am. Coll. Cardiol.* **2004**, *44*, 654.
103. Dvorak, H. F.; *et al*. *Lab. Investigation* **1987**, *57*, 673.
104. Alves, N. M.; Mano, J. F. *Int. J. Biol. Macromol.* **2008**, *43*, 401.
105. Lu, G.; Hallett, M.; Pollock, S.; Thomas, D. *Nucleic Acids Res.* **2003**, *31*, 3755.
106. Mazeau, K.; Perez, S.; Rinaudo, M. *J. Carbohydr. Chem.* **2000**, *19*, 1269.
107. Yeo, Y.; *et al*. *J. Biomed. Mater. Res. B Appl. Biomater.* **2007**, *81B*, 312.
108. Garg, H. G.; Hales, C. A. *Chemistry and Biology of Hyaluronan*. Elsevier: Amsterdam, 2004.
109. Hokputsa, S.; Jumel, K.; Alexander, C.; Harding, S. E. *Eur. Biophys. J.* **2003**, *32*, 450.
110. Amass, W.; Amass, A.; Tighe, B. *Polym. Int.* **1998**, *47*, 89.
111. Griffith, L. G. *Reparat. Med. Growing Tissues Organs* **2002**, *961*, 83.
112. Wang, Y.; *et al*. *Tex. Heart Inst. J.* **2009**, *36*, 89.
113. Ye, W. P.; Du, F. S.; Jin, J. Y.; Yang, J. Y.; Xu, Y. *React. Funct. Polym.* **1997**, *32*, 161.
114. Dong, Y. X.; Liao, S.; Ngiam, M.; Chan, C. K.; Ramakrishna, S. *Tissue Eng. B Rev.* **2009**, *15*, 333.
115. Ashammakhi, N.; *et al*. *J. Mater. Sci. Mater. Med.* **2006**, *17*, 1275.
116. Giordano, G. G.; Chevezbarrios, P.; Refojo, M. F.; Garcia, C. A. *Curr. Eye Res.* **1995**, *14*, 761.
117. Tiainen, J.; *et al*. *J. Mater. Sci. Mater. Med.* **2006**, *17*, 1315.
118. Agrawal, C. M.; Athanasiou, K. A. *J. Biomed. Mater. Res.* **1997**, *38*, 105.
119. Dobner, S.; Bezuidenhout, D.; Govender, P.; Zilla, P.; Davies, N. *J. Card. Fail.* **2009**, *15*, 629.
120. Shimpo, M.; *et al*. *Circulation* **2004**, *109*, 2186.
121. Jiang, X.-J.; *et al*. *J. Biomed. Mater. Res. A* **2009**, *90*, 472.
122. Casassa, E. F. In *Fractionation of Synthetic Polymers: Principles and Practices*; Tung, L. H., Ed.; Marcel Dekker: New York, 1977; pp 3–55.
123. Kamide, K. *Thermodynamics of Polymer Solutions: Phase Equilibria and Critical Phenomena*. Elsevier: New York, 1990.
124. Taylor, L. D.; Cerankowski, L. D. *J. Polym. Sci. Polym. Chem. Ed.* **1975**, *13*, 2551.
125. Heskins, M.; Guillet, J. E. *J. Macromol. Sci. Chem. Ed.* **1968**, *A2*, 1441.
126. Schild, H. G. *Prog. Polym. Sci.* **1992**, *17*, 163.
127. Bae, Y. H.; Okano, T.; Kim, S. W. *Pharm. Res.* **1991**, *8*, 531.
128. Fujimoto, K. L.; *et al*. *Biomaterials* **2009**, *30*, 4357.
129. Kraehenbuehl, T. P.; *et al*. *Biomaterials* **2008**, *29*, 2757.
130. Mihardja, S. S.; Sievers, R. E.; Lee, R. J. *Biomaterials* **2008**, *29*, 4205.
131. Wang, T.; *et al*. *Biomaterials* **2009**, *30*, 4161.
132. Webber, M. J.; *et al*. *J. Tissue Eng. Regen. Med.* **2010**, *4*(8), 600–610.
133. Davis, M. E.; *et al*. *Proc. Natl Acad. Sci. USA* **2006**, *103*, 8155.
134. Dubois, G.; *et al*. *J. Biomed. Mater. Res. B Appl. Biomater.* **2008**, *87*, 222.
135. Guddati, A. K.; *et al*. *Int. Heart J.* **2009**, *50*, 783.
136. Segers, V. F. M.; *et al*. *Circulation* **2007**, *116*, 1683.
137. Davis, M. E.; *et al*. *Circulation* **2005**, *111*, 442.
138. Hsieh, P. C. H.; Davis, M. E.; Gannon, J.; MacGillivray, C.; Lee, R. T. *J. Clin. Investig.* **2006**, *116*, 237.

5.530. Medical Applications of Cell Sheet Engineering

D Chang and T Okano, Tokyo Women's Medical University, Shinjuku-ku Tokyo, Japan

© 2011 Elsevier Ltd. All rights reserved.

5.530.1.	**Introduction**	405
5.530.1.1.	Cell Sheet Engineering	405
5.530.1.2.	Organized Combination of the Structure and Function of Cell Sheet	407
5.530.1.3.	Gap Junctions and Cell Sheet Engineering	409
5.530.2.	**Functional Tissue Engineering with Cell Sheets**	409
5.530.2.1.	Electrical Coupling Between Layered Cardiomyocyte Sheets	409
5.530.2.2.	3-D Manipulation of Cardiomyocyte Sheets	411
5.530.2.3.	Production of Multilayer Myoblast Sheet Constructs *In Vitro*	415
5.530.3.	**Clinical Application of Cell Sheet Tissue Engineering**	416
5.530.3.1.	Heart Failure Therapy by Using Cell Sheet Engineering	416
5.530.4.	**Conclusions**	418
References		418

Glossary

Cell sheet Cultured cells are connected through cell–cell junctional proteins and are harvested as an intact monolayer cell sheet containing native deposited extracellular matrices.
Cell sheet engineering Reconstructing tissue with cell sheets harvested from temperature-responsive culture dishes.
Extracellular matrix (ECM) Complex network that consists of proteins and polysaccharides, and it is secreted from cells.
Gap junctions Functional structures which bridge gaps between adjacent cells, creating direct passageways from the cytoplasm of one cell into the other.
Hydrophilic surfaces Proliferating and adhering cells spontaneously detach themselves from temperature-responsive culture dish surfaces at temperatures below 32 °C.
Hydrophobic surfaces Adhered cells can proliferate to confluence and flatten on the surface of temperature-responsive culture dish surfaces at temperatures above 32 °C.
Poly(*N*-isopropylacrylamide) Polymer material exhibits temperature-responsive soluble/insoluble changes in an aqueous solution and has a lower critical solution temperature (LCST) at 32 °C.
Polysurgery Cell sheets are repeatedly implanted into a living body for more than two times.
Prevascularizing method Multilayered cultures combining micropatterned endothelial cells with fibroblast monolayer sheets are used for fabricating prevascularized tissue equivalents.
Temperature-responsive culture dish Poly (*N*-isopropylacrylamide) is grafted on cell culture dishes, and the surfaces show a temperature-responsive characteristic (LCST: 32 °C).

Abbreviations

2-D	Single-layer sheet
3D	Three-dimensional
BNP	Brain natriuretic peptide
COE	Center of Excellence
DCM	Dilated cardiomyopathy
EB	Electron beam
ECM	Extracellular matrix
EGM-2	Endothelial growth medium
HRC	High-Tech Research
HUVECs	Human umbilical endothelial cells
LCST	Lower critical solution temperature
LV	Left ventricle
LVAD	Left ventricular assist device
MSCs	Mesenchymal stem cells
NEDO	The New Energy and Industrial Technique Development Organization
PIPAAm	Poly(*N*-isopropylacrylamide)
PIPAAm-TCPS	PIPAAm-coated TCPS
TCPS	Tissue culture polystyrene

5.530.1. Introduction

5.530.1.1. Cell Sheet Engineering

The basic principle of tissue engineering is the seeding of cells into a three-dimensional (3-D) biodegradable scaffold, to be used for the replacement of damaged or lost tissues of living organisms and for the reconstruction of living tissues.[1–3] The use of these scaffold-based designs in the recreation of some tissues such as bone,[4] cartilage,[5–7] skin,[8] blood vessels,[9,10] and heart valves has been reported by many

researchers.[11,12] However, the applications in cell-dense reconstruction have been limited by these conventional tissue engineering approaches because bone and cartilage are far less complex and cell-sparse tissues and require reduced internal vasculature. On the other hand, for thicker structures such as the heart, the liver, and the kidney, finding a way to integrate the requisite blood supply into a 3-D tissue without using a scaffold, which may cause pathological fibrosis, remains a challenge. Furthermore, if structures lack appropriate vasculature, cells will become necrotic in the center of the constructs, due to the limits of passive diffusion. The insufficient delivery of oxygen and nutrients, and the poor removal of metabolic waste results in reduced functionality and, ultimately, necrosis. Naturally, the high cell-density and the complex structure of heart tissue is more difficult to recreate with conventional tissue engineering strategies. Additionally, resorbable polymers can be associated with proinflammatory degradation byproducts, which can limit the functionality of the various organs that are being repaired.[13] Therefore, a new method that avoids the current limitations in clinical tissue reconstruction using biodegradable scaffolds is necessary for the further development of tissue engineering.

In 1990, cell sheet engineering using temperature-responsive culture dishes was developed by our group with an innovative approach.[14,15] Temperature-responsive polymer, poly(*N*-isopropylacrylamide), (PIPAAm) is polymerized and grafted onto various surfaces by electron beam radical polymerization. These intelligent temperature-responsive surfaces can control the attachment and detachment of living cells with temperature changes from 37 to 32 °C. The principal advantage of the cell sheet approach is that a monolayer cell sheet can be harvested without using proteolytic enzymes. By simply reducing the culture temperature to lower than 32 °C for less than 30 min, the sheet can be harvested. Eliminating the necessity for proteolytic enzymes preserves the basal surface extracellular matrix (ECM) proteins even after detachment and produces a basic building block that can be further manipulated to assemble more complex tissues and organs.[16–18] Using this technology, living cell sheets can be immediately transplanted into the various kinds of host tissues without using biodegradable scaffolds and sutures. We have also demonstrated thicker, multilaminate tissue constructs by layering cell sheets. More complex versions of this stacking approach can include cocultured or patterned cell sheets, using two or more different kinds of cell sources. We have succeeded in demonstrating the *in vivo* long-term survival of tissue-engineered pulsatile cardiac grafts in animal models.[19] We have also used cell sheet technology to repair various tissues and organs, including the cornea,[20–22] esophagus,[23,24] heart,[25–29] liver,[30,31] kidney,[32] lung,[33], periodontium[34,35], and many others (**Figure 1**). Other groups have similarly demonstrated clinical successes with the use of sheet-based approaches.[36–38] In this chapter, we review our achievements with the use of temperature-responsive cell culture dishes, temperature-dependent cell attachment, and the applications of this technique for regenerative medicine.

It is popularly known that PIPAAm is an 'intelligent' polymer, meaning that the material exhibits temperature-responsive soluble/insoluble changes in an aqueous solution and has a lower critical solution temperature (LCST) at 32 °C[39] (**Figure 2**). PIPAAm was introduced on the surfaces of commercially available tissue culture polystyrene (TCPS) dishes.[14,15,40] Using temperature-responsive culture dishes, IPAAm monomers are first dissolved in 2-propanol solutions, and then the solutions are uniformly spread over TCPS dish surfaces. IPAAm monomers are polymerized and simultaneously coated covalently onto the TCPS surface with a 0.3 MGy dose of electron beam (EB) irradiation. Owing to the hydration of the grafted PIPAAm chains, PIPAAm-coated TCPS (PIPAAm-TCPS) surfaces exhibit hydrophilic and cell-repellent surfaces at temperatures below 32 °C. In contrast, PIPAAm-TCPS surfaces alter from a hydrophilic to a hydrophobic state due to the dehydration of the grafted PIPAAm chains, as the temperature rises above 32 °C. Consequently, cells attach, adhere, and proliferate on PIPAAm-TCPS at temperatures above 32 °C.

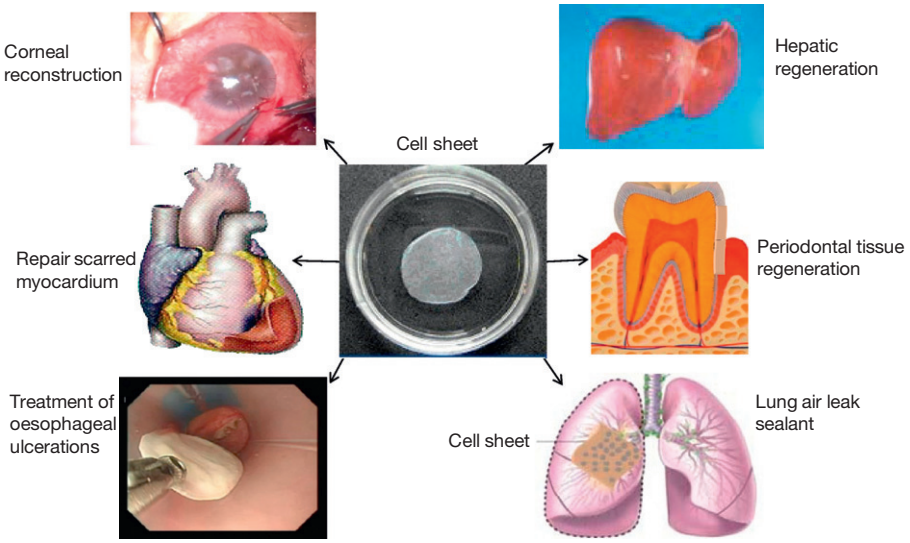

Figure 1 Tissue reconstruction from cell sheets. Many clinical trials in the field of regenerative medicine, such as corneal, heart, esophagus, liver, periodontal tissue, and lung have successfully applied cell sheet engineering.

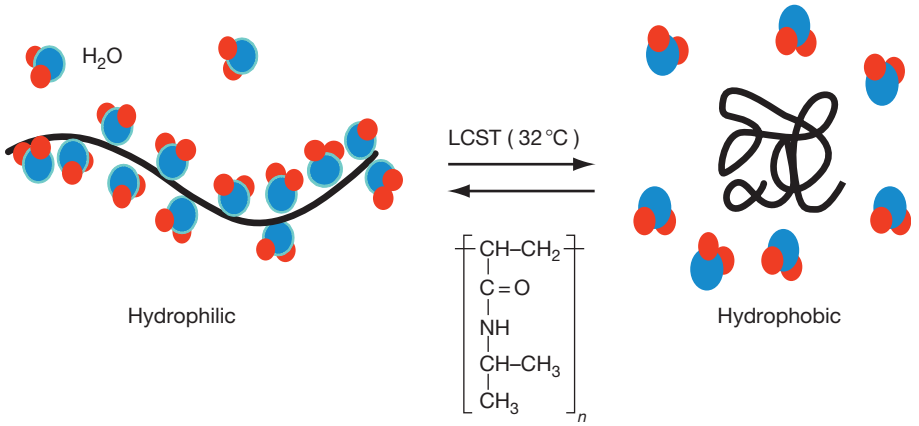

Figure 2 Coil–globule transition of poly(*N*-isopropylacrylamide) (PIPAAm). PIPAAm exhibits temperature-responsive soluble/insoluble changes in an aqueous solution and has a lower critical solution temperature (LCST) at 32 °C. At temperatures below 32 °C, PIPAAm molecules are highly hydrated, so the PIPAAm-grafted surfaces are hydrophilic. At temperatures above 32 °C, the surfaces suddenly change to hydrophobic due to extensive dehydration of PIPAAm molecules.

The adhered cells spontaneously detach themselves from PIPAAm-TCPS surfaces, when the temperature is reduced below 32 °C. This change is completely determined by wettability, which is measured by the captive bubble method in pure water and confirmed by the observation of the ability of endothelial cells to adhere to the surface.[41]

The temperature-dependent cell attachment and detachment is observed on 15–20 nm thick PIPAAm-grafted surfaces, between 20 and 37 °C. When the coated layer is more than 30 nm in thickness, cells are unable to attach. The contact angle of the layer is small at 37 °C and decreases the degree of thermal change of the angle. Because the dehydration of PIPAAm chains is incomplete, it provides a poor interaction between the PIPAAm layer and the cells. As the contact angle for the highest grafting density is much smaller than the others, the PIPAAm layer is still highly hydrated even at 37 °C and suppresses cell adhesion.

In contrast, when the coated layer is less than 15 nm in thickness and the temperature is reduced to below 32 °C, the surface is fully covered with PIPAAm molecules, and the effect of the uncoated polystyrene surfaces is insufficient to induce cell detachment; thus, the contact angle of the surface reduces with an increase in the polymer density and thickness.[42] Indeed, the coating thickness and density are dominant parameters for driving cell attachment and detachment.

It was reported in previous studies that the configuration of the polymer chain and its mobility affect the wettability of PIPAAm-grafted surfaces with changing temperatures. Single terminal coatings of PIPAAm with liberated mobile chains give more hydrophilic surfaces. In contrast, the looped-chain configuration followed by the multipoint coating of PIPAAm chains gives more restricted polymer chains, showing more hydrophobic surfaces. A comparison of the swelling ratio of single-side fixed / cross-linked PIPAAm hydrogel and nonfixed/cross-linked PIPAAm gel reveals a higher swelling ratio, which is significantly restricted with the single-side fixed gel. Further comparison of single-side fixed/cross-linked PIPAAm hydrogels with different thicknesses reveals that the swelling ratio of the thinner gels is less than half of that of the gels with double thickness.[40,41] These results suggest that the mobility of polymer chains in PIPAAm gel fixed on a covered glass surface is limited at the interface of the basal cover slips. The limited mobility produces extensive hydrophobic aggregate and also limits the hydration of the polymer chain. The limitations of polymer chain mobility progressively reduce the responses of the general polymer network, through cross-linked points inside the polymer gel. PIPAAm chains have more free mobility and a greater ability to respond to stimuli and hydration in the outer regions than in the inner regions. This consideration is extended to PIPAAm-TCPS systems, with an ultrathin PIPAAm layer.

For a thinner PIPAAm layer, the limited mobility of the polymer chains in the restricted layer promotes the dehydration of PIPAAm chains. The outermost surfaces are sufficiently hydrophobic to show adhesive properties for cells at 37 °C. The restricted layer region is considered to be between 15 and 20 nm (**Figure 3**). Such dehydration promotion and the limitations of the polymer chains result in the modulation of the cell attachment and detachment, in response to temperature changes. In contrast, for thicker PIPAAm layers, the dehydration of PIPAAm chains at the outermost surface (hydrated region) is discouraged even above the LCST, and the surface is free from the limitations of the polymer chains and dehydration generated at the basal PS surfaces. It is well known that cells are unable to adhere to thicker PIAAm hydrogels even at 37 °C. PIPAAm chains in the dehydrated layer are still hydrated without physical restriction like a free molecule.[42] As a result, cells are unable to adhere onto the surface of the PIPAAm-TCPS with a thick PIPAAm layer. Therefore, controlling PIPAAm surface graft density is a critical issue to reliably produce the temperature-responsive cell adhesion and detachment behavior of the surface.

5.530.1.2. Organized Combination of the Structure and Function of Cell Sheet

Conventionally, enzymatic treatment is required for recovering cultured cells from cell culture surfaces such as TCPS.[43] Cells physically adhere more strongly to hydrophobic surfaces than hydrophilic surfaces. When ATP is used after cells have come

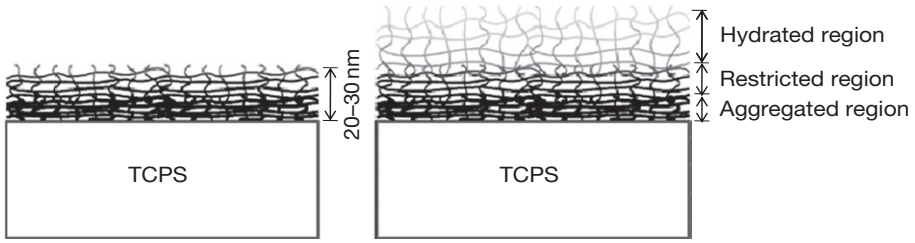

Figure 3 Schematic illustration of the influence of molecular mobility of grafted chains of PIPAAm layers on cell-adhesive characteristics at 37 °C. When grafted, PIPAAm layer thickness is between 20 and 30 nm, cell adhesion and detachment are observed (left side). No cell adhesion occurs when grafted PIPAAm layer is thicker than 30 nm (right side). Aggregated region: highly hydrophobic and aggregated PIPAAm chains do not let adhered cells detach by lowering temperature. Restricted region: restricted hydration and mobility of PIPAAm chains due to the strong hydrophobicity of the aggregated layer allow temperature-dependent cell adhesion-detachment behavior. Hydrated region: dehydrated but less restricted PIPAAm chains do not support cell adhesion.

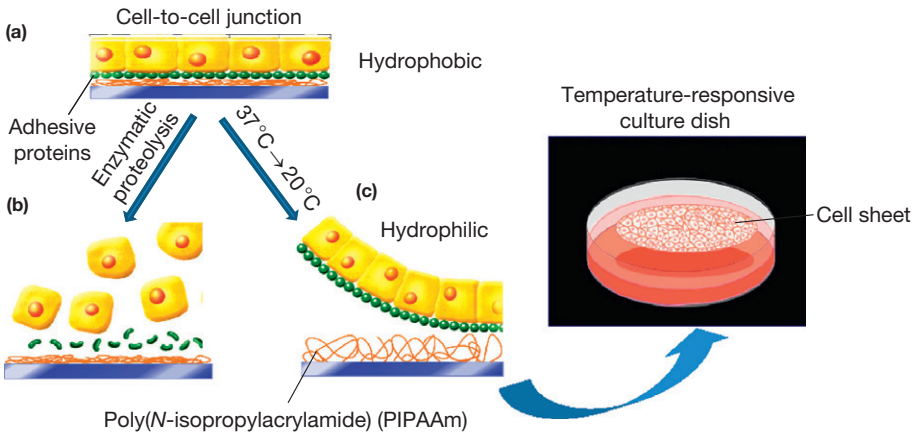

Figure 4 Confluent cells are subjected to two types of harvest methods. (a) Cells attach to hydrophobic culture surface via ECM and connect to each other through cell-to-cell junction proteins. (b) When enzymatic digestion is used, cell-to-cell connections and ECM are disrupted and cells are released separately. (c) When cells are cultured on temperature-responsive culture surfaces, the interconnection between ECM and hydrophilic culture surface is released only by low temperature. Cell-to-cell connections are completely preserved and the cells are detached as a contiguous cell sheet. ECM retained underneath the cell sheets works as an adhesive agent.

into physical contact with a surface, the metabolic process causes attached cells to undergo morphological changes. Adhered cells proliferate to confluence and flatten on the hydrophobic surface of the temperature-responsive culture dish as well as they would on a normal polystyrene culture dish. Spreading cells detach themselves from the hydrophobic surface, without the reversing events associated with morphology changes from spread to round cell shapes and the release of surface-engaged receptors. By simply reducing the temperature of the culture to below 32 °C, proliferating and adhering cells spontaneously detach themselves from the temperature-responsive culture dish surface. This is the result of the hydration of the PIPAAm surface. No enzyme such as trypsin or neutral protease (Dispase®) is required in this detachment process, just the physically mild condition of temperature change. Enzymes cut cell-to-cell junctions and free cells from their ECM, producing single cell suspensions. Using a temperature-responsive culture dish, confluent cells can be collected as a contiguous intact monolayer that retains cell-to-cell junctions[17,44] (Figure 4). Moreover, the ECM of the recovered cell sheets is preserved by this method. This is a novel concept that allows us to modulate the cell attachment and detachment on PIPAAm-coated surfaces. Various kinds of cells such as stem cells, oral mucosal epithelium cells, myoblast cells, cardiomyocyte cells, endothelial cells, and hepatocytes have been harvested from PIPAAm-coated culture dishes, under general incubation conditions.

Metabolic changes occur in the cell during detachment from hydrated PIPAAm-coated surfaces.[45] Optimum temperatures for maximizing cell recovery efficiency from PIPAAm-grafted surfaces vary with cell types. Temperature 20 and 10 °C are optimized culture temperatures for endothelial cells and hepatocytes, respectively. Even cells treated with sodium azide, an ATP synthesis inhibitor, or other chemicals, undergo no change in morphology and keep their adherent status on PIPAAm-coated surfaces at low temperatures. These findings suggest that cell detachment from hydrated PIPAAm-coated surface is governed by active energy-consuming metabolic processes, which contain intracellular signal transductions and the reorganization of the cytoskeleton.[46]

During the detachment process, morphological transitions in the cell sheet observed at 20 °C begin to detach from the periphery of the dish surfaces, while maintaining cell-to-cell connections and producing some sheet contractility. In order to collect and manipulate the cell sheet, supporting membranes such as poly(ethylene terephthalate), and poly(vinylidene-difluoride), and parchment paper sheets have been used

to prevent contraction.[17,47] The cell sheets can be manipulated with the supporting membranes by physicochemical interaction such as interfacial tension. They can then be directly transferred onto other cell sheets or native tissues, using the adhesive effects retained by the ECM on the basal surface of the recovered cell sheets.

This cell sheet engineering produces various tissues and organs such as myocardial cell sheet 3-D tissue,[26,27] microspherical heart-like pump,[19] and prevascularized 3-D cell-dense tissues. The cell sheet technique allows the reconstruction of functional, 3-D myocardial tissue, prepared by layering multiple cardiomyocyte sheets harvested from the temperature-responsive culture dishes. When the culture temperature is reduced from 37 to 20 °C, the cultured cells remain connected to each other through cell–cell junctional proteins and are harvested as a single sheet, with their deposited ECM intact. As this method allows the cell sheets to be harvested without disturbing the cell–cell connections and ECM proteins such as ion channels and growth factor receptors, cardiomyocyte sheets can beat synchronously after detachment. Single cell sheets can be directly transplanted onto host tissues with 2-D (single-layer sheet) manipulation and can improve cardiac function.

Using the homotypic layering of cell sheets, 3-D (multilayer sheet) functional cardiac tissues, such as cardiac muscle, can be constructed. Having no biodegradable scaffolds, the sheets interact directly with each other and can couple electrically, resulting in synchronous beating *in vitro* and long-term survival *in vivo*. Moreover, there is no adverse reaction due to the degradation of by-products, which results from the breakdown of a biodegradable scaffold. Therefore, cell sheet engineering is recognized to be the best approach to organize the structure and function of cell sheets without any adverse effects from unnecessary by-products.

5.530.1.3. Gap Junctions and Cell Sheet Engineering

It is known that gap junctions are functional structures that bridge gaps between adjacent cells, creating direct passageways from the cytoplasm of one cell into the other. The channels formed by the gap junctional proteins allow inorganic ions and other molecules smaller than 1200 Da to pass through a narrow path between the cells, thereby coupling the cells both electrically and metabolically.[48,49] Individual gap junction is found in transmission electron micrographs as a patch where the membranes of two adjacent cells are separated by a uniform narrow gap of ~2–4 nm.

Gap junction channels are formed by the members of the protein family called connexins, which share homologous extracellular and transmembrane regions but contain unique cytoplasmic domains that likely constitute physiological gating structures.[50] Different connexins form channels with varied biophysical properties.[51–53] Cell–cell communication through these channels is considered to play an important role in the control of cell embryonic development, proliferation, cell differentiation, and the regulation of differentiated function in postmitotic cells.[54–57] This communication is also an important mechanism for regulating events among cells during embryogenesis and during the functional development of organs such as the heart.

In heart tissue, gap junctions in mammalian cardiac function provide low-resistance channels between adjacent cells for the exchange of small molecules as the secondary messengers.[58,59] Several studies relating to the assembly of gap junctions in the heart have suggested that, during the postnatal development of ventricular myocardium and hypertrophic cardiomyopathy, the gap junctions may play an important role in the maturation of electromechanical function.[60,61] Furthermore, altered gap junction distribution occurs in ischemic heart disease.[62–67] The abnormal distribution of gap junctions in the epicardial border zone of infarcts may contribute to arrhythmogenesis. Thus, it is very important to establish these functional gap junctions among cells for synchronous beating and reconstruction of damaged heart tissues.

5.530.2. Functional Tissue Engineering with Cell Sheets

5.530.2.1. Electrical Coupling Between Layered Cardiomyocyte Sheets

Gap junctions are very important in normal and abnormal heart tissues. Electrical conduction in the heart tissue is dependent on current transfer through gap junctions. It has been reported that metabolic inhibitors or protein synthesis inhibitors fail to affect gap junction assembly in prostate epithelial cells. Therefore, it is proposed that gap junction formation proceeds through previously existing precursors within cell membranes.[68,69] Several reports that gap junction precursors exist on cell membranes show unveiled connexin hemichannels by electrophysiological measurements, dye transfer assay, or connexin-43–GFP chimera.[70–76] We identified that connexin-43 existed on the cell membrane as well as at cell-to-cell interfaces[77] (**Figure 5**). These gap junction precursors are preserved during the harvest of confluent cardiomyocytes from temperature-responsive culture dishes and can give a rapid electrical coupling between layered cell sheets. In addition, the cell sheets also maintain ECM on the basal surface and can adhere to other cell sheets or various surfaces. For this reason, the presence of ECM also promotes intimate attachment between layered cell sheets and may accelerate the docking of gap junction precursors.

Using cell sheet engineering, rat cardiomyocyte sheets were fabricated on temperature-responsive culture dishes to produce 3-D structures. We examined the electrical communication of two partially overlapped monolayer cardiomyocyte cell sheets by using microelectrodes (**Figure 6**). After one cardiomyocyte sheet was placed on a collagen-coated multielectrode dish probe for 1 h, the second sheet was partially overlapped on the first. Then, the electrical potentials of the cardiomyocyte sheets were recorded simultaneously, and the synchronization time and conduction velocities were analyzed.

We observed that once some gap junctions were established between the two cell sheets, electrical impulses reached the monitoring electrode through both direct conduction from the pacemaker cell sheet and detour conduction through the established gap junctions. Eventually, the conductions began to synchronize, with a slight delay after 30 min. These delays diminished in a time-dependent manner, and the electrical potentials became completely synchronized after 45 min. These findings suggest that additional gap junctions are randomly formed between the layered cell sheets and electrical communication is established throughout the interface within 45 min

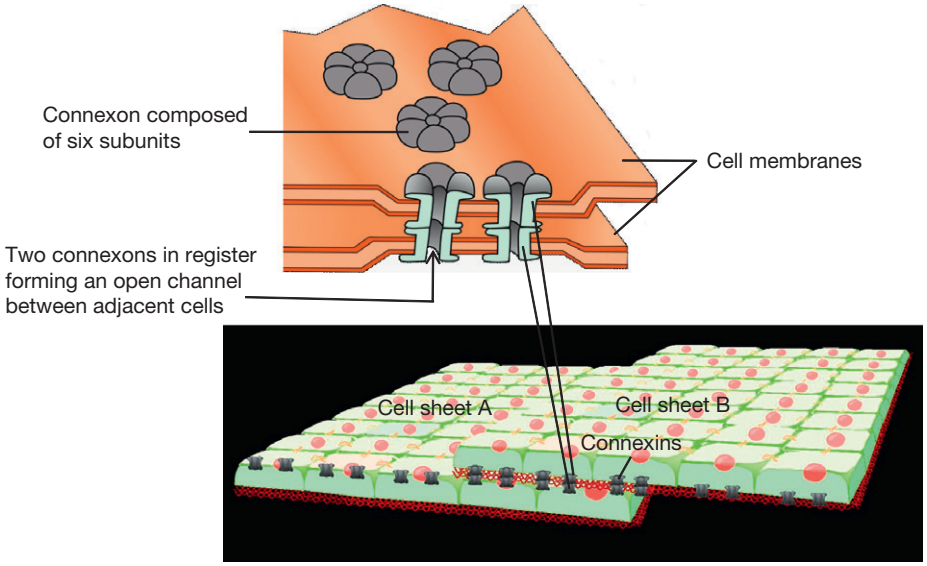

Figure 5 Connexon composed of six subunits. A gap junction consists of many connexon pairs in parallel, forming a sort of molecular sieve. Since the cell sheets contain intact gap junction precursors in addition to the deposited ECM when two pulsing cell sheets (a, b) are layered, they were found to synchronize their pulsations through their gap junction-related protein, connexin-43.

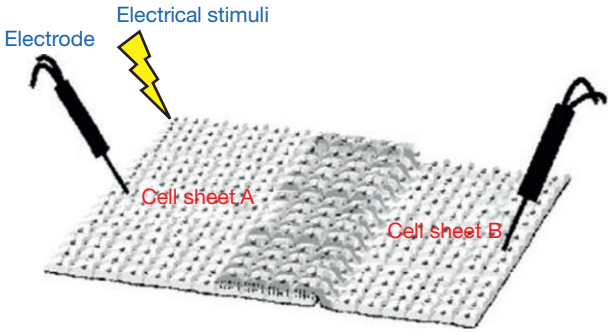

Figure 6 Electrical communication between layered sheets. Two cardiomyocyte sheets (a, b) detached from PIPAAm-coated culture dishes are overlaid partially for examining the electrical synchronization. Two electrodes are set over monolayer parts of both cell sheets to detect the electrical potentials separately. Reproduced with permission from Shimizu, T.; Yamato, M.; Kikuchi, A.; Okano, T. *Biomaterials* **2003**, *24*, 2309–2316.

(Figure 7). This agrees with the established fact that the ECM side of the bone marrow mesenchymal stem cell multilayered cell sheet significantly enhanced the adhesion of the multilayered cell sheets onto the surface of normal heart tissue for more than 30 min after the transplantation in large animal models (Figure 8). ECM proteins, which are one of the key factors in tissue regeneration, are distributed on the bottom of the cell sheet and directly contact the host heart tissue. The presence of ECM on cell sheets reduced the time required for creating stronger adhesion between cell sheets and heart tissue. Histological and scanning electron microscope analysis indicated that the transplanted cell sheets were almost totally separated from native heart tissue at 30 min posttransplantation. This study clearly indicated that the existence of ECM proteins facilitated the attachment process between cell sheets and native heart tissue in a shorter amount of time.[78]

Several reports show that three gap junction proteins, connexin-43, connexin-45, and connexin-40, have been found in mammalian cardiac myocytes. These proteins form channels with different electrophysiological properties and have different distributions in cardiac tissues with disparate conduction properties.[50] Precursors are detected on the free cell membrane as well as on the cell-to-cell interface. We found that connexin-43, a gap junction-related protein, existed not only at cell-to-cell interfaces but also on the free cell membrane in the cardiomyocyte sheet. Moreover, only connexin-43 was identified between bilayer cardiomyocyte sheets within 30 min of layering; neither connexin-40 nor connexin-45 was detected. We also confirmed that connexin-43 is preserved upon the harvest of cardiomyocytes from temperature-responsive culture dishes, and the protein may facilitate a rapid electrical coupling between layered cell sheets.[77]

In cardiac tissue engineering, electrical and structural cell-to-cell tight junctions are critical to synchronized, functional beating because they are very important in the electrical and morphological communication that is established between two cell sheets. In comparison to the general approach of the enzymatic seeding of dissociated cells into biodegradable scaffolds, cell sheet engineering is advantageous in that it enables rapid formation of gap junctions and functional communication between layered cardiomyocyte sheets.

Cells are less compact when biodegradable scaffolds are used, and the material used to fabricate the scaffold may itself be electrically obstructive. However, cell sheet engineering that layers cell sheets fabricated on temperature-responsive culture dishes to form 3-D structures results in rapid gap junction formation and functional communication between layered cardiomyocyte sheets.[26,27] The transplantation of cardiomyocyte sheets to reverse damage caused by myocardial infarction also promotes electrical communication and coupling between cell sheets and host tissue due to the presence of initial gap junction precursors for direct cell-to-cell communications.

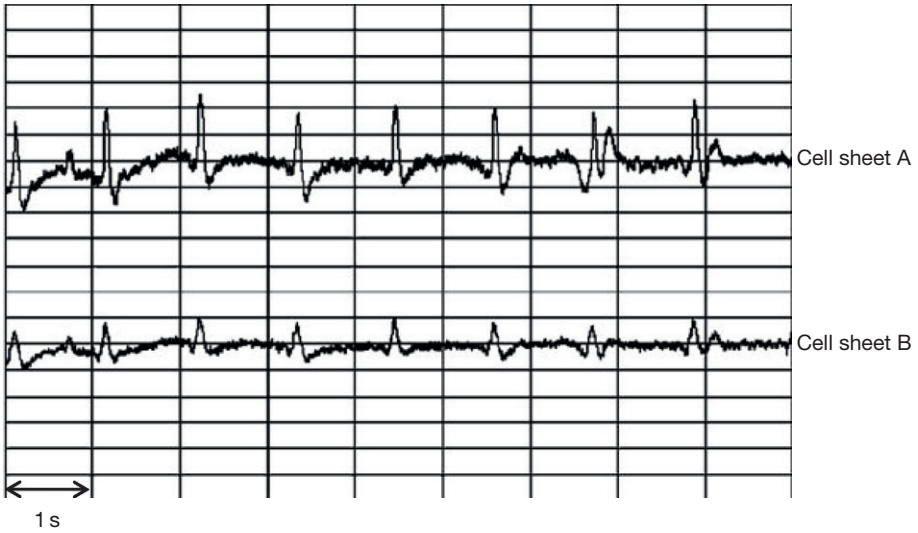

Figure 7 Schematic illustration of electrical analysis of layered cardiomyocyte sheets. Synchronization of layered cardiomyocyte sheets. Representative tracings of electrical potentials of cell sheet A and B show complete synchronization. Reproduced with permission from Shimizu, T.; Yamato, M.; Kikuchi, A.; Okano, T. *Biomaterials* **2003**, *24*, 2309–2316.

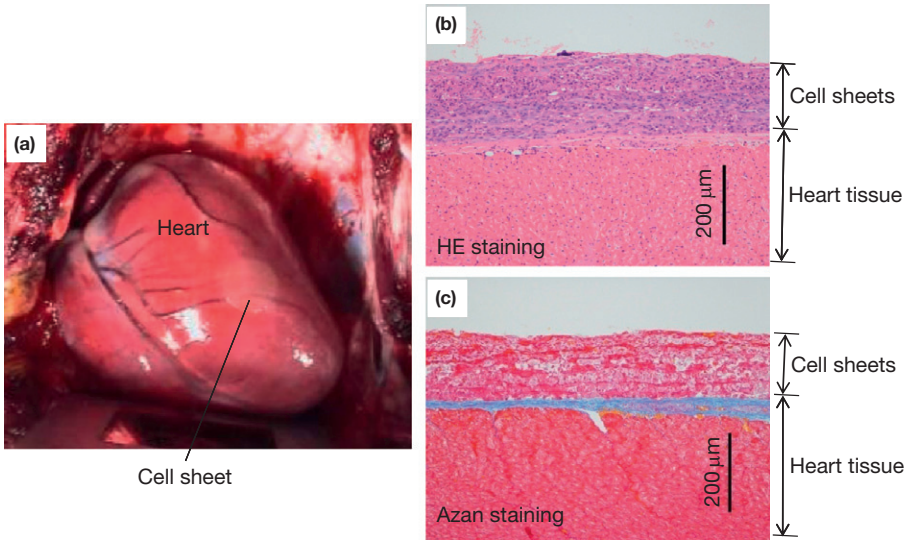

Figure 8 The multilayered sheets (three layers) from bone marrow-derived mesenchymal stem cells (MSCs) of a pig were transplanted onto the myocardium of the left ventricle with the ECM-side (a). Histological analysis of heart-sheet by hematoxylin-eosin staining (b) and azan staining. Collagen-rich epicardium was identified as a blue band by azan staining (c). At 30 min posttransplantation, the adhesion between the cell sheet and the native heart tissue has been significantly detected.

5.530.2.2. 3-D Manipulation of Cardiomyocyte Sheets

As previously discussed, when cardiomyocyte sheets are used alone or layered, they electrically couple and display impressive functional characteristics. However, the establishing of a method for growing functional multilayered 3-D structures continues to be a significant challenge. *In vitro*, triple cell layers (the thickness: ~100–130 μm) are recognized to be the maximal number of layers for cell sheets (Figure 9). In an effort to build a thicker construct, quadruple- and quintuple-layered cell sheets were assembled by stacking one- to three-layered constructs. We were attempting to simulate the presence of blood vessels to allow tissues to attain greater thickness.

In cardiac cell sheets, we observed cardiomyocyte clusters surrounding areas enriched with endothelial cells. This finding suggests that the endothelial networks are activated by both direct cell-to-cell interactions and secreted proteins from cardiomyocytes. On this ground, a mutually beneficial relationship between cardiomyocytes and endothelial cells is likely to contribute to the formation of endothelial cell networks *in vitro*. Neovascularizations within the grafts were observed to start promptly after the implantation, and the vascular networks were organized after a few days *in vivo*. The observed blood vessel reconstruction was completed by endothelial cell networks that originated from within the graft.[79] These newly

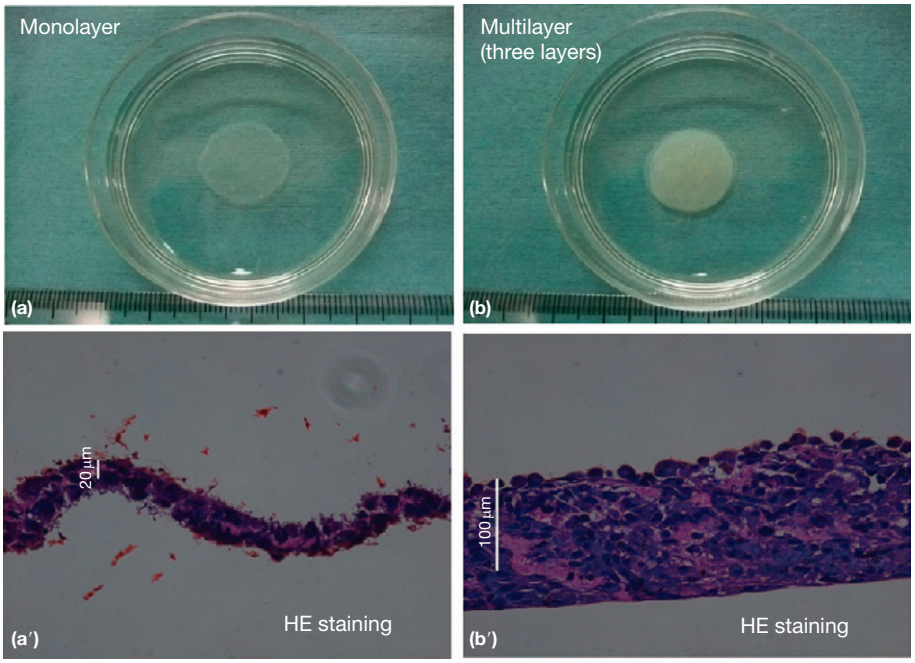

Figure 9 Multilayered construct made from bone marrow-derived mesenchymal stem cells. Photographs and histological cross-section of cell sheets from bone marrow-derived mesenchymal stem cells. (a) Cell sheet composed of a monolayer of MSCs and (b) cell sheet composed of three layers of MSCs. Each cell sheet is ~20 mm in diameter; (a′) the thickness is ~50 μm for monolayer and (b′) the thickness is ~20 μm for three layers of MSCs. Scale bars: 100 μm.

formed graft-derived arterioles also sprouted into the underlying host tissue to form functional connections with the host vasculature. Similarly, endothelial cell networks *in vitro* formed functional microvessels and sprouted into the host tissues after the transplantation.

In cardiac cell sheets harvested from temperature-responsive culture dishes, their deposited ECM is preserved, and the cell sheets are also able to retain intact and undisrupted endothelial networks as well as the expression of angiogenesis promoters such as VEGF and HGF. By controlling the endothelial cell population within the cardiac cell sheets, a potential for vascularization can also be regulated, which may resolve the limits of mass transport in the manufacture of thick and functional tissues. However, perfusion flow and shear stress are necessary to form mature vascular networks under *in vitro* conditions.[80,81] Most thick layers are simply unable to supply enough oxygen and nutrients for growing tissue. On the contrary, living human heart muscle is up to 2 cm thick. When three sheets are layered, the innermost cells are far from the supply of fresh growth medium and struggle to thrive.

One approach to sidestepping the problem is by growing single layers of cells that can then be implanted into an animal's body to create functional 3-D tissues.[26,27] Neonatal rat cardiomyocyte cell sheets, which consisted of monolayer to triple layers, were stacked, one on top of another, until they fused, and then multilayered cardiac cell sheets were implanted into the dorsal subcutaneous tissue of immunodeficient rats, using the animal body itself as a bioreactor for creating a 30-layered cell sheet with a final thickness of ~1 mm.

A critical obstacle facing cardiac tissue fabrication is the inability to constantly and rapidly supply sufficient vascularization to prevent necrosis. This obstacle prevents the unlimited stacking of additional cell sheets. Two days after the transplantation, the separation of two grafts by connective tissue was observed (Figure 10). Three days after the transplantation, two grafts were completely separated by thick connective tissues and were electrically dissociated. By contrast, when triple-layered cell sheets were transplanted ten consecutive times, with one-day intervals between implantations, spontaneous and synchronized pulsation was observed (Figure 11). The surface electrograms of the sheet were detected independently from the host electrocardiograms 3 weeks after the transplantations.

One month after the procedure, the constructs were retrieved and analyzed. We observed cell-dense, thick tissues with whole tissue survival and well-organized microvascular networks. Constructs with three or fewer layers survived without necrosis. Quadruple- and quintuple-layered constructs formed *in vitro* demonstrated disordered vasculature and connective tissue. Azan staining of the decupled triple-layered graft revealed that the construct had multilayered cell-dense myocardium and well-organized microvessels throughout the transplanted tissues. The engineered cardiac tissue demonstrated spontaneous beating and was vascularized by host blood vessels, which could be observed macroscopically when the skin was opened 6 months later. These engineered synchronously beating heat-like tissues survived for over 1 year. Thus, we conclude that the serial stacking 'polysurgery' with cell sheet technology can overcome the critical thickness-restricted limitation caused by passive diffusion limit and allows us to grow 3-D structures that contain more than a few layers of muscle cells and functional myocardial tissue.

We are also attempting to move toward reconstruction of organ-like structures, using tissue-engineered cell sheets.

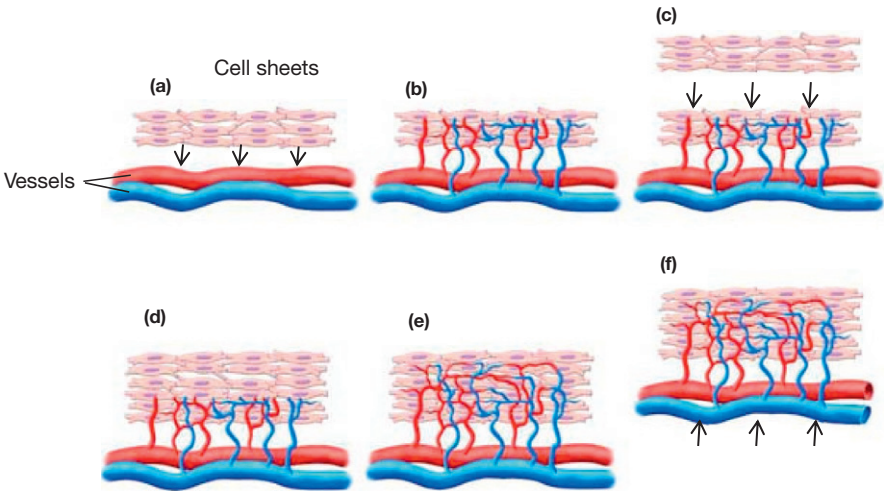

Figure 10 Schematic illustration of bioengineering multilayer grafts with surgically connectable vessels (a). Graft was transplanted over a surgically accessible artery and vein (b). The graft was supplied with both new vasculature and blood directly from the existing vessels in this case (c, d). After sufficient vascularization had occurred in the first graft, the second graft was then transplanted onto the first graft (e, f). Eventually, the microvascularized construct accompanied by graftable vessels harvested from the host is fully perfused by host vessels and surgically resected. Reproduced with permission from Shimizu, T.; Sekine, H.; Yang, J.; *et al*. *FASEB J*. **2006**, *20*.

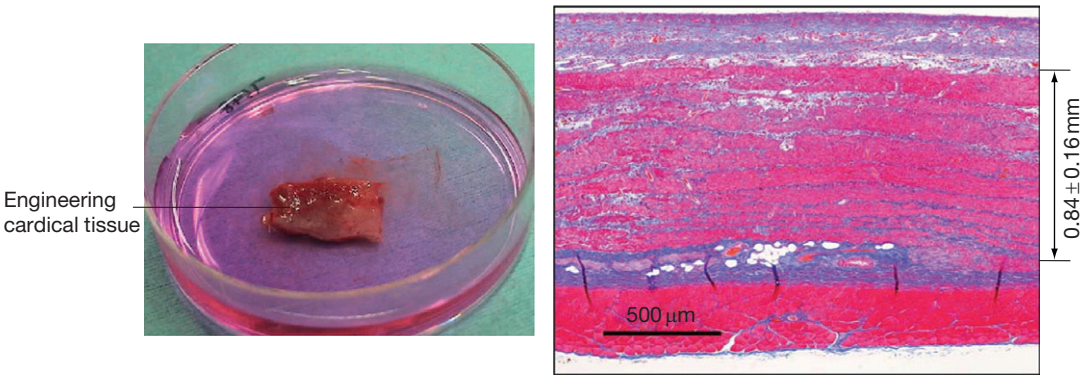

Figure 11 The engineered cardiac tissue by using 10-times polysurgery was beating and blood vessels had permeated it (left side). Azan staining shows that multilayer cell-dense myocardium with well-organized microvessels can be created by using 10-times polysurgery with a 1-day interval. Bidirectional arrow indicates viable myocardial cell sheet layers. The measured thickness of the grafts was 0.84 ± 0.16 mm. Data are mean $\pm$ SD ($n = 3$). Reproduced with permission from Shimizu, T.; Sekine, H.; Yang, J.; *et al*. *FASEB J*. **2006**, *20*.

In cardiac tissue engineering, the ultimate goal is the creation of a functional myocardial chamber that pumps blood around the body, with the ability of generating significant independent pressures from its spontaneous contractions.[82,83] In this regard, we have given the construction of pulsatile myocardial tubes a potential for circulatory support *in vivo*.[84] Three neonatal rat cardiomyocyte sheets were harvested and wrapped around fibrin tubes, using a novel cell sheet-wrapping device. The tubular constructs demonstrated spontaneous, synchronized pulsation within 3 h of cell sheet wrapping. The tissue-engineered myocardial tubes presented measurable inner pressure changes induced by tube contraction (~.15 mmHg). Histological analyses revealed both well-differentiated sarcomeres and diffuse gap junctions within the myocardial tissues that resembled native cardiac muscle. These data indicate that tissue-engineered myocardial tubes have native heart-like structure and function.

We have created myocardial tubes by wrapping six neonatal rat cardiomyocyte cell sheets around a resected rat aorta. These are potentially capable of providing independent cardiac support. We believe that the construction of pulsatile myocardial tubes will provide *in vivo* circulatory support. Sextuple-layered cardiomyocyte sheets were wrapped around the 1.5 cm portion of resected thoracic aorta from adult rats *in vitro*. The myocardial tubes were then transplanted into the abdomen of other nude rats to connect abdominal aorta by cuff method with sutures[19] (**Figure 12**). The implanted myocardial tubes provided a spontaneous and synchronized pulsation 4 weeks after the transplantation. The myocardial tubes produced a circulatory supportive blood pressure of 5.9 ± 1.7 mmHg, independent of the host hearts (**Figure 13**). Interestingly, 4 weeks after the transplantation, the thickness of the aortic replacement tubes was significantly higher than the myocardial grafts that had simply been inserted into the abdominal cavity; this was due to the pulsations created by blood flow within the lumen of the aortic replacement tubes and had an inductive effect on generating thicker, hypertrophic

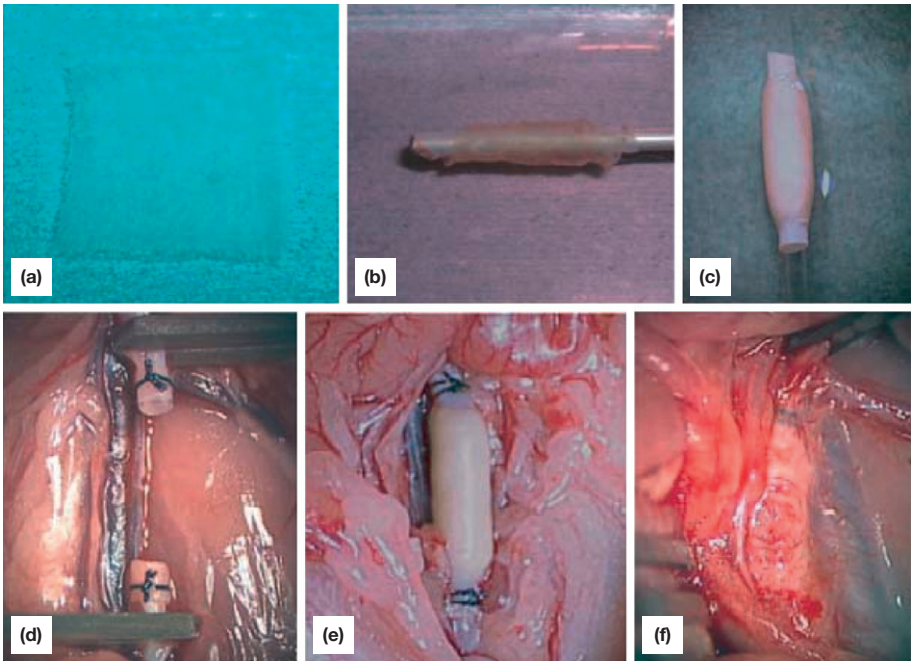

Figure 12 Fabrication and transplantation of myocardial tubes. Cardiomyocyte sheets detached from temperature-responsive culture dishes (a) were sequentially wrapped around a resected thoracic aorta (b) to manufacture six layers of myocardial tubes *in vitro* (c). After the clamping and resecting of the host abdominal aorta (d), the myocardial tube is anastomosed to host vasculature (e). Four weeks after the aortic replacement, the myocardial tubes integrated with the host tissues (f). Reproduced with permission from Sekine, H.; Shimizu, T.; Yang, J.; Kobayashi, J.; Okano, T. *Circulation* **2006**, *4*, 88–93.

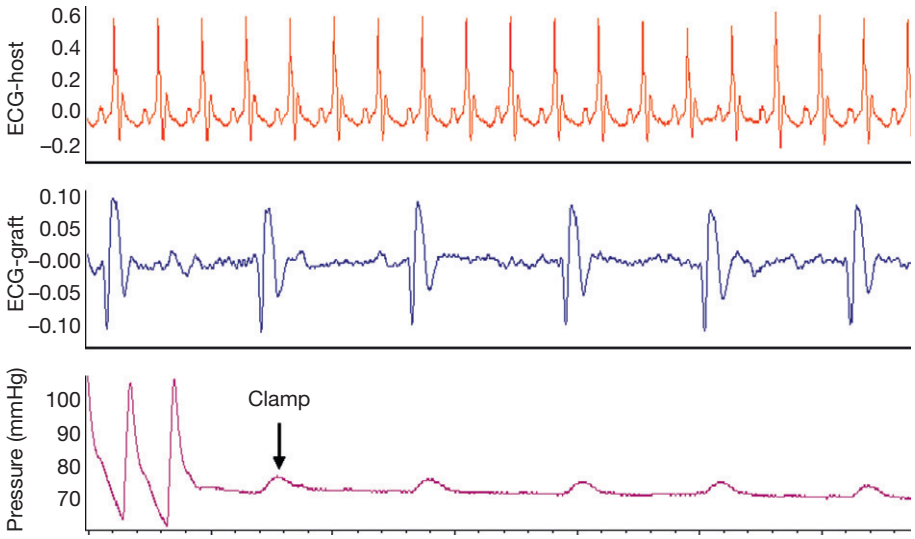

Figure 13 The implanted myocardial tubes provided a spontaneous and synchronized pulsation four weeks after the transplantation. The myocardial tubes produced a circulatory supportive blood pressures of 5.9 ± 1.7 mmHg, independent of the host hearts. Reproduced with permission from Sekine, H.; Shimizu, T.; Yang, J.; Kobayashi, J.; Okano, T. *Circulation* **2006**, *4*, 88–93.

myocardial tissues. These findings suggested that the hypertrophy of the functional myocardial tube is induced by mechanical stretching due to host blood flow pulsation within the lumen of the tube.

By growing tissues in the body cavity of artery and vein, it is conceivable to create an environment that duplicates the conditions for the development of a normal tissue. Using cardiomyocyte sheets wrapped around fibrin frameworks, we are continuing to develop tissue-engineered myocardial tubes for producing functional tubular structures that can act as potential cardiac assist devices. On the basis of these findings, we assert that layering of cardiomyocyte sheets has a significant edge over the use of biodegradable scaffolds in creating cell-dense, functional myocardial tissues.

5.530.2.3. Production of Multilayer Myoblast Sheet Constructs *In Vitro*

We were experimenting with the use of an animal's body itself as a bioreactor to create 3-D manipulations of cardiomyocyte sheets *in vivo*. This method faces challenges such as production of multilayer cell sheets *in vitro*, preservation of 3-D cell-dense thick tissues that can keep heart-like tissues beating during implantation until the patient's own vessels begin to colonize the implant, and furtherance of improvements in dealing with hypoxia, nutrient insufficiency, and the accumulation of waste products affecting the survival of 3-D cell-dense thick tissues after transplantation. Most researchers are working on ways of simulating the presence of blood vessels in or around the scaffold to allow tissues to achieve greater thicknesses. It has been reported that endothelial cells can be cocultured with other cell types to form capillary-like networks *in vitro*, using scaffold-based 3-D cell culture[85] or scaffold-free 3-D cell aggregate culture.[86] However, some common drawbacks of the use of scaffolds are insufficient cell migration into the scaffolds and host inflammatory reactions. In contrast to the conventional scaffold-based tissue engineering, we used cell sheet stacking manipulation technology and designed prevascularized 3-D cell-dense tissues.[87]

Human umbilical endothelial cells (HUVECs) were sandwiched between two myoblast sheets by a gelatin-coated plunger. Then, the sandwiched construct was transferred onto an FBS-coated dish. The double-layer myoblast sheet construct containing HUVECs was cultured with sterile endothelial growth medium (EGM-2) for 3 days. The inserted HUVECs formed network structures after 3 days of culture (**Figure 14**).

To further examine the organization of prevascularized tissues *in vitro*, we attempted to produce quintuple-layered myoblast sheet constructs containing HUVECs between the layers collected by the fibrin-coated plunger. The endothelial cells connected through the layers and partially formed capillary-like structures in the quintuple-layered myoblast sheet constructs after 4 days of culture. We also confirmed that the quintuple-layered myoblast sheet constructs with endothelial network have the ability of neovascularization *in vitro*.

Myoblast sheets with or without HUVECs were stacked up to five layers, and two types of five-layer myoblast sheet constructs combined with fibrin gel were engrafted on the dorsal subcutaneous tissue of immunodeficient rats after 4 days of culture. One week after the transplantation, capillary-like networks were connected to the host vessels and a number of microvessels containing red blood cells were observed in the HUVEC-positive transplanted grafts (**Figure 15**). These results suggest that prevascularized myoblast sheet constructs with HUVECs can induce functional anastomosis. A rapid and sufficient vascularization is important for the survival of 3-D cell-dense thick tissues after transplantation.

A practical approach to solving this problem is making endothelial cell networks in engineered tissues before transplantation. Moreover, the transplantation of engineered myocardial tissues containing capillary-like networks enhances neovascularization and improves the cardiac function of ischemic hearts.[79] Therefore, the preparation and setting up of prevascularization in engineering tissues before anastomosis to the surrounding host vessels is important. Using ell sheet stacking manipulation technology, we fabricated prevascularized cell dense tissue constructs *in vitro* and examined the contribution of these constructs *in vivo*. This cell sheet engineering-based 3-D sandwich coculture system can enhance the cellular density and orientation of inserted endothelial cells by the microfabrication techniques of culture surfaces such as patterning[88] and microtexture.

Multilayered cultures that combined micropatterned endothelial cells as vascular precursors, with fibroblast monolayer

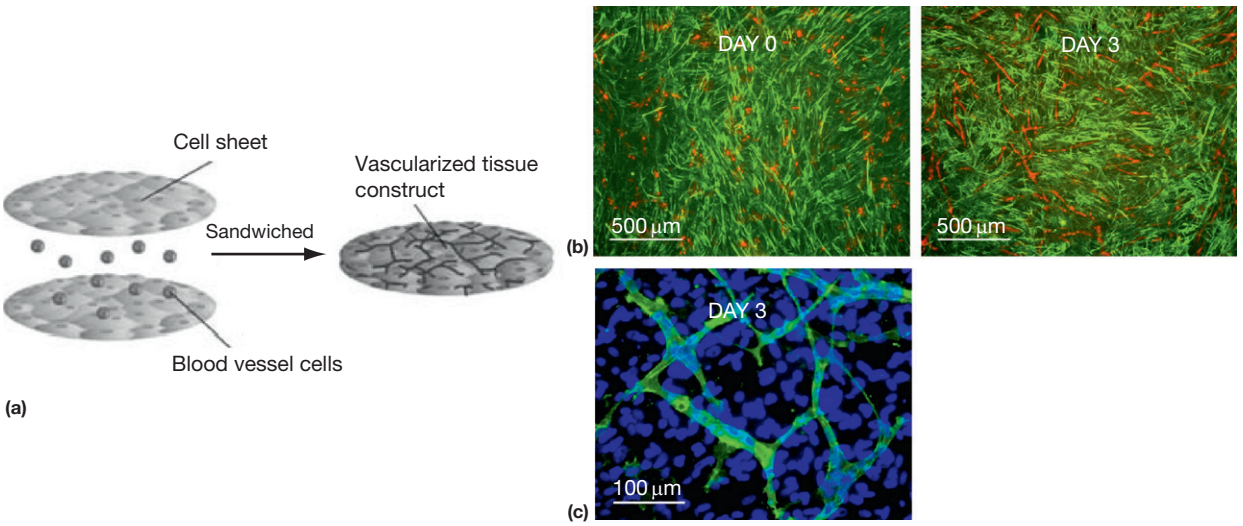

Figure 14 Formation of endothelial cell network in double-layered myoblast sheet construct. (a) Schematic illustration shows the vascularized tissue fabrication strategy by sandwiching blood vessel cells between two cell sheets. (b) The human umbilical vein endothelial cells (HUVECs) were sandwiched between two myoblast sheets by a gelatin-coated plunger. This sandwich construct was transferred onto another culture dish to culture. Sandwiched HUVECs and the cells formed on the myoblast sheet were strained with UEA-I (the red color) and antidesmin antibody (the green color), respectively. (c) The networked cells were stained with antihuman CD31 (the green color). Nuclei were counterstained with Hoechst 33342 (the blue color). Reproduced with permission from Sasagawa, T.; Shimizu, T.; Sekiya, S.; *et al*. Biomaterials **2010**, *3*, 1646–1654.

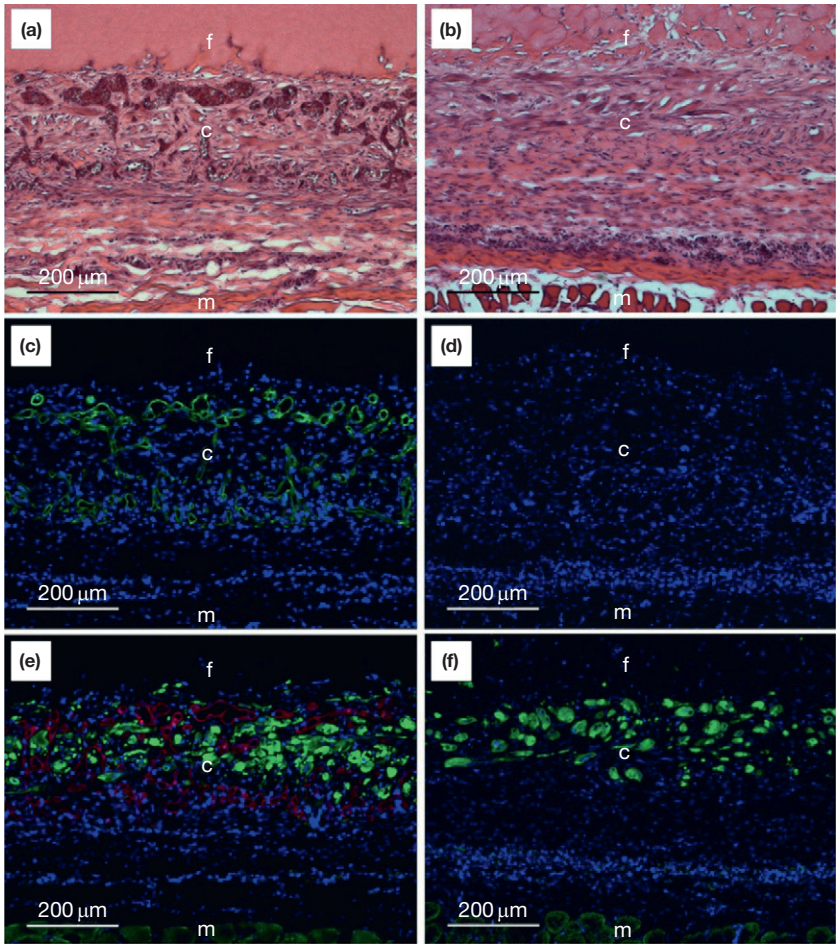

Figure 15 Induction of neovascularization by the transplantation of five-layer myoblast sheet constructs containing endothelial networks. The left and the right are the five-layer myoblast sheets with and without human umbilical vein endothelial cells (HUVECs), respectively. The specimens of the transplanted constructs in the first row (A and B) were stained with hematoxylin and eosin at one week after the transplantation. The specimens in the second row (C and D) were stained with antihuman CD31 antibody (the green color). The microvessels containing host blood cells were observed in HUVEC-positive specimen (C), but no stain was seen in HUVEC-negative specimen (D). The specimens in the third row (E and F) were stained with antidesmin antibody (the green color) and human endothelial cell-specific lectin (UEAI) (the red color). The nuclei of both the specimens were also counterstained with Hoechst 33342 (the blue color). The marked region with f, c, and m are the fibrin gel, the cell sheet construct, and the muscle tissue of the animal, respectively. Reproduced with permission from Sasagawa, T.; Shimizu, T.; Sekiya, S.; *et al.* Biomaterials **2010**, *3*, 1646–1654.

sheets as tissue matrix, were used to fabricate prevascularized tissue equivalents. Stratified tissue equivalents are constructed by alternately layering fibroblast monolayer sheets with patterned endothelial cell sheets harvested from temperature-responsive micropatterned surfaces, alternating 20-mm-wide cell-adhesive lanes with 60-mm nonadhesive zones. Cell culture substrates covalently coated with different thermoresponsive polymers permit the spatial switching of cell attachment and detachment, with the application of slight temperature changes. Endothelial cell patterning fidelity was maintained within the multilayer tissue constructs after assembly, leading to self-organization into microvascular-like networks after 5 days of tissue culture. This technique holds promise for the study of cell–cell communications and angiogenesis in reconstructed, 3-D environments as well as for the fabrication of tissues. Prevascularizing methods, using cell sheet stacking manipulation technology, provide substantial scope for the development of various types of 3-D tissues and for the furtherance of regenerative medicine. These can also shorten the time for connecting the cell sheet vascular system in secret to the host vascular system.

5.530.3. Clinical Application of Cell Sheet Tissue Engineering

5.530.3.1. Heart Failure Therapy by Using Cell Sheet Engineering

Many clinical trials in the field of regenerative medicine, such as corneal reconstruction,[20,21] esophageal transplantation, and blood vessel construction,[36–38] have successfully applied cell sheet engineering. Several tissue engineering applications have also utilized the cell sheet technique. Nearly all organs are complicated multilayer tissues composed of various types of cells. For this reason, multilayered cell sheets from multipotent mesenchymal stem cells (MSCs) or cardiomyocytes

may be a useful technology for organ repair[18] (Figure 16). In both acquired and congenital heart defects, a large number of myocardial cells are damaged and lose their functions. One of the clinical approaches to the treatment of myocardial injury is the repair and regeneration of the damaged tissue through the direct transplantation of stem or myocardial cells into the injured area.[89–92] Unfortunately, this approach has failed to live up to its potential in applications in clinical trials. Although direct injection of cells can successfully mend small damaged areas,[93,94] repairing the large areas of ischemic damage requires lab-grown patches of cell sheets. In addition, the direct injection of cells into the heart is hazardous because of possible blockage of circulatory pathways, which might result in more life-threatening complications. Also, injected or transplanted cells are unable to fuse stably with the host heart tissue following the transplantation. Therefore, it is important to improve adhesion between the host heart and the transplanted cells for localizing the cells directly onto the host heart wall.

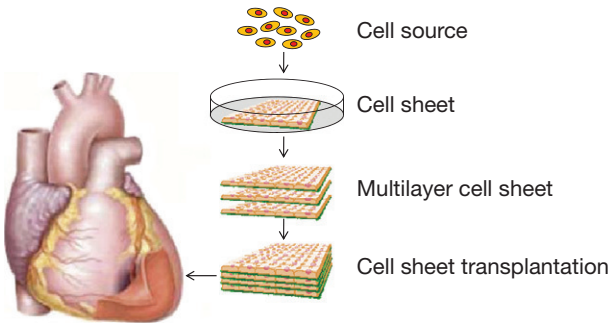

Figure 16 Cardiac patch cell sheet engineering. Cardiac myocyte sheets are harvested from temperature-responsive culture dishes when the temperature is reduced from 37 to 20 °C. Three or four cell sheets are stacked together to form a multilayered sheet that retained all cell–cell contacts. The multilayered sheets are then transplanted to ischemic hearts as cardiac patches. Reproduced with permission from Shimizu, T.; Yamato, M.; Kikuchi, A.; Okano, T. *Biomaterials* **2003**, *24*, 2309–2316.

Cell sheet transplantation may be a promising strategy for partial cardiac tissue reconstruction. Cell sheets assembled from autologous MSC were used to treat a patient suffering from dilated cardiomyopathy (DCM). DCM is one type of chronic heart failure whose pathology is characterized by global myocardial remodeling, which mainly consists of myocardial fibrosis associated with changes in the cytoskeletal and sarcolemmal proteins in cardiomyocytes, leading to a reduction in the number and function of these cells.[95,96] Today, medical therapy has improved the prognosis of heart failure, such as left ventricular remodeling operations, implantable defibrillators, and cardiac resynchronization.[97] However, mechanical support using left ventricular assist device (LVAD) and heart transplantation are the accepted ultimate lifesaving means for supporting these patients.[98,99] The patient had been fitted with an LVAD till the time that a donor heart became available. However, cardiac transplantation has limitations, such as donor shortages, rejection, and infection, and the usefulness of an LVAD is limited by its durability. Therefore, novel strategies are necessary for treatment of ischemic cardiomyopathy.

The skeletal myoblast sheets were transplanted onto the patient's heart.[100] Muscle tissue from the patient's thigh was collected because cells differentiate through a way similar to those found in the heart. Ten skeletal myoblast sheets ~4 cm in diameter were created by growing the cells on temperature-responsive culture dishes. After removal from the dish, the cell sheets were transplanted onto the patient's heart (Figure 17). As the cells in the sheets continued to produce growth factors, they were able to improve the damaged heart's function significantly. Three months after the transplantation of the cell sheets, the echocardiography demonstrated that the dilated left ventricle (LV) dimension was significantly reduced, the heart showed a progression of LV dilation, and the patient was able to get off the LVAD. The brain natriuretic peptide (BNP) was significantly reduced from ~1000 to 10 pg ml^{-1}. The transplanted sheets enhanced the left ventricular ejection fraction and allowed the patient's weakened heart to grow strong. After 6 months, the patient was able to walk out of

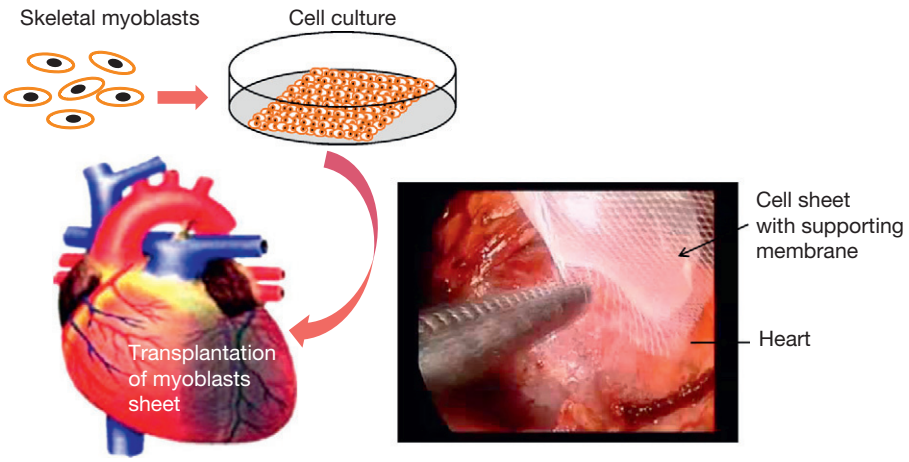

Figure 17 Skeletal myoblasts from patients were cultured on temperature-responsive culture dishes to form cell sheets to treat cardiomyopathy (left side). Ten skeletal myoblast sheets approximately four centimeters in diameter were transplanted onto the patient's heart by supporting membrane (right side).

hospital. The transplantation of cell sheets improves cardiac performance and prolongs life expectancy.

Additionally, the longer preservation of cardiac performance by sheet-shaped myoblast implantation in DCM in an animal model was investigated by using cell sheet technology.[101] Myoblasts isolated from hamsters were cultured on temperature-responsive culture dishes to produce the cell sheets. After the sheet-shaped myoblast grafts were implanted, the echocardiography demonstrated that the dilated LV dimension was significantly reduced, and the hearts were found to have a progression of LV dilation. Three months after the operation, the LV wall thickness was increased with viable myoblasts. These findings suggest that the implantation of myoblast grafts can preserve cardiac performance and decrease the extent of myocardical remodeling.

The adult heart lacks reserve cardiocytes and cannot regenerate on its own. Therefore, a large acute myocardial infarction often develops into congestive heart failure. Monolayered cell sheets prepared from adipose tissue-derived mesenchymal stem cells have multipotent and self-propagating properties after transplantation into infarcted rat heart.[25] Adipose tissue-derived mesenchymal stem cells characterized by flow cytometry were cultured on temperature-responsive culture dishes to prepare a monolayer cell sheet, which was then transplanted onto the scarred myocardium of rat. The engrafted sheet gradually grew to form a thick stratum that included newly formed vessels after transplantation. The mesenchymal stem cell sheet also acted through paracrine pathways to trigger angiogenesis, reversed wall thinning in the scar area, and improved the cardiac function in rats with myocardial infarction. Thus, the transplantation of monolayered mesenchymal stem cells may be a novel strategy for cardiac tissue regeneration. The cell sheet system made on temperature-responsive dishes provides a powerful advanced tissue engineering matrix that can be easily transplanted and applied in various tissue engineering indications. Cardiac tissue engineering based on cell sheet engineering is feasible for clinical cardiovascular tissue repair.

5.530.4. Conclusions

These cell sheet manipulation techniques can be applied to various cell types and tissue structures. As cardiomyocyte sheets containing intact gap junction precursors in addition to deposited ECM give rapid and complete electrical communications, 2-D or 3-D cell sheets can be manufactured. Cell sheet engineering is recognized to be a useful, fundamental, and generalized technology for next-generation tissue engineering and regenerative medicine.

Acknowledgments

We are deeply grateful to Prof. Masayuki Yamato, Prof. Tatsuya Shinmizu, Dr. Hidekazu Sekine, Dr. Yuji Haraguchi, Dr. Tadashi Sasagawa, and Dr. Sachiko Sekiya for their contributions to this study. We also appreciate Dr. Norio Ueno, Dr. Todd McAllister, Ms. Marissa Peck and Prof. Hossein Hosseinkhani for proofreading this manuscript. This work was supported in part by the Center of Excellence (COE) Program for the 21st Century, the High-Tech Research (HRC) Program from the Ministry of Culture, Sports, Science, and Technology and the New Energy and Industrial Technique Development Organization (NEDO) of Japan.

References

1. Nugent, H. M.; Edelman, E. R. *Circ. Res.* **2003**, *92*, 1068–1078.
2. Shin, H.; Jo, S.; Mikos, A. G. *Biomaterials* **2003**, *24*, 4353–4364.
3. Stock, U. A.; Vacanti, J. P. *Annu. Rev. Med.* **2001**, *52*, 443–451.
4. Puelacher, W. C.; Vacanti, J. P.; Ferraro, N. F.; Schloo, B.; Vacanti, C. A. *Int. J. Oral Maxillofac. Surg.* **1996**, *25*(3), 223–228.
5. Brittberg, M.; Lindahl, A.; Nilsson, A.; Ohlsson, C.; Isaksson, O.; Peterson, L. *N. Engl. J. Med.* **1994**, *331*, 889–895.
6. Cao, Y.; Vacanti, J. P.; Paige, K. T.; Upton, J.; Vacanti, C. A. *Plast. Reconstr. Surg.* **1997**, *100*(2), 297–302; discussion 303–294.
7. Vacanti, C. A.; Langer, R.; Schloo, B.; Vacanti, J. P. *Plast. Reconstr. Surg.* **1991**, *88*(5), 753–759.
8. Kirsner, R. S.; Falanga, V.; Eaglstein, W. H. *Trends Biotechnol.* **1998**, *16*, 246–249.
9. Shin'oka, T.; Imai, Y.; Ikada, Y. *N. Engl. J. Med.* **2001**, *344*, 532–533.
10. Shinoka, T.; Shum-Tim, D.; Ma, P. X.; *et al. J. Thorac. Cardiovasc. Surg.* **1998**, *115*, 536–545; discussion 545–536.
11. Shinoka, T.; Breuer, C. K.; Tanel, R. E.; *et al. Ann. Thorac. Surg.* **1995**, *60*, S513–S516.
12. Shinoka, T.; Ma, P. X.; Shum-Tim, D.; *et al. Circulation* **1996**, *94*, II-164–II-168.
13. Leor, J.; Aboulafia-Etzion, S.; Dar, A.; Shapiro, L.; Barbash, I. M.; Battler, A.; *et al. Circulation* **2000**, *102*, III56; [Abstract].
14. Okano, T.; Yamada, N.; Sakai, H.; Sakurai, Y. *J. Biomed. Mater. Res.* **1993**, *27* (10), 1243–1251.
15. Yamada, N.; Okano, T.; Sakai, H.; Karikusa, F.; Sawasaki, Y.; Sakurai, Y. *Makromol. Chem. Rapid Commun.* **1990**, *11*, 571–576.
16. Kushida, A.; Yamato, M.; Konno, C.; Kikuchi, A.; Sakurai, Y.; Okano, T. *J. Biomed. Mater. Res.* **2000**, *51*, 216–223.
17. Kushida, A.; Yamato, M.; Konno, C.; Kikuchi, A.; Sakurai, Y.; Okano, T. *J. Biomed. Mater. Res.* **1999**, *45*(4), 355–362.
18. Yamato, M.; Utsumi, M.; Kushida, A.; Konno, C.; Kikuchi, A.; Okano, T. *Tissue Eng.* **2001**, *7*, 473–480.
19. Sekine, H.; Shimizu, T.; Yang, J.; Kobayashi, J.; Okano, T. *Circulation* **2006**, *4*, 88–93.
20. Nishida, K.; Yamato, M.; Hayashida, Y.; Watanabe, K.; Yamamoto, K.; Adachi, E.; *et al. N. Engl. J. Med.* **2004**, *352*, 1187–1196.
21. Nishida, K.; Yamato, M.; Hayashida, Y.; Watanabe, K.; Maeda, N.; Watanabe, H.; *et al. Transplantation* **2004**, *77*, 379–385.
22. Watanabe, K.; Yamato, M.; Hayashida, Y.; *et al. Biomaterials* **2007**, *28*, 745–749.
23. Ohki, T.; Yamato, M.; Murakami, D.; Takagi, R.; Yang, J.; Namiki, H.; *et al. Gut* **2006**, *55*, 1704–1710.
24. Oyama, T.; Tomori, A.; Hotta, K.; Morita, S.; Kominato, K.; Watanabe, K.; *et al. Clin. Gastroenterol. Hepatol.* **2005**, *3*, S67–S70.
25. Miyahara, Y.; Nagaya, N.; Kataoka, M.; *et al. Nat. Med.* **2006**, *12*(4), 459–465.
26. Shimizu, T.; Yamato, M.; Akutsu, T.; Shibata, T.; Isoi, Y.; Kikuchi, A.; *et al. J. Biomed. Mater. Res.* **2002**, *60*, 110–117.
27. Shimizu, T.; Yamato, M.; Isoi, Y.; Akutsu, T.; Setomaru, T.; Abe, K.; *et al. Circ. Res.* **2002**, *90*, e40–e48.
28. Shimizu, T.; Yamato, M.; Kikuchi, A.; Okano, T. *Tissue Eng.* **2001**, *7*, 141–151.
29. Shimizu, T.; Yamato, M.; Kikuchi, A.; Okano, T. *Biomaterials* **2003**, *24*, 2309–2316.
30. Harimoto, M.; Yamato, M.; Kikuchi, A.; Okano, T. *Macromol. Symp.* **2003**, *195*, 231–236.
31. Ohashi, K.; Yokoyama, T.; Yamato, M.; *et al. Nat. Med.* **2007**, *13*, 880–885.
32. Kushida, A.; Yamato, M.; Kikuchi, A.; Okano, T. *J. Biomed. Mater. Res.* **2001**, *54*, 37–46.
33. Kanzakia, M.; Yamato, M.; Yang, J.; *et al. Biomaterials* **2007**, *28*, 4294–4302.
34. Hasegawa, M.; Yamato, M.; Kikuchi, A.; Okano, T.; Ishikawa, I. *Tissue Eng.* **2005**, *11*, 469–478.
35. Shiroyanagi, Y.; Yamato, M.; Yamazaki, Y.; Toma, H.; Okano, T. *Tissue Eng.* **2003**, *9*, 1005–1012.
36. L'Heureux, N.; Dusserre, N.; Konig, G.; *et al. Nat. Med.* **2006**, *12*(3), 361–365.

37. L'Heureux, N.; McAllister, T. N.; de la Fuente, L. M. *N. Engl. J. Med.* **2007**, *357*(14), 1451–1453.
38. McAllister, T. N.; Maruszewski, M.; Garrido, S. A.; *et al*. *Lancet* **2009**, *373*(9673), 1440–1446.
39. Heskins, M.; Gulillet, J. E. *Sci. Chem. A*. **1968**, *2*, 1441–1445.
40. Akiyama, Y.; Kikuchi, A.; Yamato, M.; Okano, T. *Langmuir* **2004**, *20*, 5506–5511.
41. Nagase, K.; Kobayashi, J.; Okano, T. *J. R. Soc. Interf.* **2009**, *6*, S293–S309.
42. Akiyama, Y.; Kushida, A.; Yamato, M.; Kikuchi, A.; Okano, T. *J. Nanosci. Nanotechnol*. **2007**, *7*, 796–802.
43. Waymouth, C. *In Vitro* **1974**, *10*, 97–111.
44. Kushida, A.; Yamato, M.; Isoi, Y.; Kikuchi, A.; Okano, T. *Eur. Cell Mater*. **2005**, *10*, 23–30; discussion 23–30.
45. Okano, T.; Yamada, N.; Okuhara, M.; Sakai, H.; Sakurai, Y. *Biomaterials* **1995**, *16*, 297–303.
46. Yamato, M.; Okuhara, M.; Karikusa, F.; Kikuchi, A.; Sakurai, Y.; Okano, T. *J. Biomed. Mater. Res*. **1999**, *44*, 44–52.
47. Kikuchi, A.; Okuhara, M.; Karikusa, F.; Sakurai, Y.; Okano, T. *J. Biomater. Sci. Polym. Ed*. **1998**, *9*, 1331–1348.
48. Beyer, E. C. *Int. Rev. Cytol*. **1993**, *137C*, 1–37.
49. Loewenstein, W. R. *Physiol. Rev*. **1981**, *61*, 829–913.
50. Beyer, E. C.; Paul, D. L.; Goodenough, D. A. *J. Membr. Biol*. **1990**, *116*, 187–194.
51. Ebihara, L.; Beyer, E. C.; Swenson, K. I.; Paul, D. L.; Goodenough, D. A. *Science* **1989**, *243*, 1194–1195.
52. Eghbali, B.; Kessler, J. A.; Spray, D. C. *Proc. Natl. Acad. Sci. USA* **1990**, *87*, 1328–1331.
53. Fishman, G. I.; Spray, D. C.; Leinwand, L. A. *J. Cell Biol*. **1990**, *111*, 589–598.
54. Bennett, M. V. L.; Barrio, L. C.; Bargiello, T. A.; Spray, D. C.; Hertzberg, E.; Saez, J. C. *Neuron* **1991**, *6*, 305–320.
55. Kumar, N. M.; Gilula, N. B. *Semin. Cell Biol*. **1992**, *3*, 3–16.
56. Lard, D. W. *J. Bioenerg. Biomembr*. **1996**, *28*, 311–318.
57. Warner, A. E.; Guthrie, S. C.; Gilula, N. B. *Nature* **1984**, *311*, 127–131.
58. Bruzzone, R.; White, T. W.; Paul, D. L. *Eur. J. Biochem*. **1996**, *238*, 1–27.
59. Luque, E. A.; Veenstra, R. D.; Beyer, E. C.; Lemanski, L. F. *J. Morphol*. **1994**, *222*, 203–213.
60. Kanter, H. L.; Laing, J. G.; Beyer, E. C.; Green, K. G.; Saffitz, J. E. *Circ. Res*. **1993**, *73*, 344–350.
61. Peters, N. S.; Severs, N. J.; Rothery, S. M.; Lincoln, C.; Yacoub, M. H.; Green, C. R. *Circulation* **1994**, *90*, 713–725.
62. Leor, J.; Patterson, M.; Quinones, M. J.; Kedes, L. H.; Kloner, R. A. *Circulation* **1996**, *94*(Suppl. II), II-332–II-336.
63. Matsushita, T.; Takamtsu, T. *Virchows Arch*. **1997**, *431*, 453–458.
64. Peters, N. S. *Microsc. Res. Tech*. **1995**, *31*, 375–386.
65. Sepp, R.; Severs, N. J.; Gourdie, R. G. *Heart* **1996**, *76*, 412–417.
66. Severs, N. J. *J. Cardiovasc. Electrophysiol*. **1994**, *5*, 462–475.
67. Smith, J. H.; Green, C. R.; Peters, N. S.; Rothery, S.; Severs, N. J. *Am. J. Pathol*. **1991**, *139*, 801–821.
68. Peters, N. S.; Coromilas, J.; Severs, N. J.; Wit, A. L. *Circulation* **1997**, *95*, 988–996.
69. Tadvalkar, G.; Silva, P. *J. Cell Biol*. **1983**, *96*, 1279–1287.
70. Contreras, J. E.; Saez, J. C.; Bukauskas, F. F.; Bennett, M. *Proc. Natl. Acad. Sci. USA* **2003**, *100*, 11388–11393.
71. Contreras, J. E.; Sanchez, H. A.; Eugenin, E. A.; Speidel, D.; Theis, M.; Willecke, K.; *et al*. *Proc. Natl. Acad. Sci. USA* **2002**, *99*, 495–500.
72. Ebihara, L.; Steiner, E. *J. Gen. Physiol*. **1993**, *102*, 59–74.
73. Gupta, I.; Berthoud, V. K.; Atal, V. M.; Jarillo, N.; Barrio, L. C.; Beyer, E. C. *Invest. Ophthalmol. Vis. Sci*. **1994**, *35*, 3747–3758.
74. John, S. A.; Kondo, R.; Wang, S. Y.; Goldhaber, J. I.; Weiss, J. N. *J. Biol. Chem*. **1999**, *274*, 236–240.
75. Jordan, K.; Solan, J. L.; Dominguez, M.; Sia, M.; Hand, A.; Lampe, P. D.; *et al*. *Mol. Biol. Cell* **1999**, *10*, 2033–2050.
76. Paul, D. L.; Ebihara, L.; Takemoto, L. J.; Swenson, K. I.; Goodenough, D. A. *J. Cell Biol*. **1991**, *115*, 1077–1089.
77. Haraguchi, Y.; Shimuzu, T.; Yamato, M.; Kikuchi, A.; Okano, T. *Biomaterials* **2006**, *27*, 4765–4774.
78. Chang, D. H.; Shimizu, T.; Haraguchi, Y.; Sakaguti, K.; Umezu, M.; Okano, T. Time course of cell sheet adhesion to porcine heart after transplantation. In TERMIS 2nd World Congress, 2009 p S94; [Abstract].
79. Sekiya, S.; Shimizu, T.; Yamato, M.; Kikuchi, A.; Okano, T. *Biochem. Biophys. Res. Commun*. **2006**, *341*, 573–582.
80. Chen, B. P.; Li, Y. S.; Zhao, Y.; *et al*. *Physiol. Genomics* **2001**, *7*, 55–63.
81. Cullen, J. P.; Sayeed, S.; Sawai, R. S.; Theodorakis, N. G.; Cahill, P. A.; Sitzmann, J. V. E. M. *Arterioscler. Thromb. Vasc. Biol*. **2002**, *22*, 1610–1616.
82. Tanaka, Y.; Morishima, K.; Shimizu, T.; Kikuchi, A.; Yamato, M.; Okano, T. *Lab Chip* **2006**, *6*, 362–368.
83. Tanaka, Y.; Morishima, K.; Shimizu, T.; *et al*. *Lab Chip* **2006**, *6*, 230–235.
84. Kubo, H.; Shimizu, T.; Yamato, M.; Fujimoto, T.; Okano, T. *Biomaterials* **2007**, *28*, 3508–3516.
85. Rouwkema, J.; de Boer, J.; Van Blitterswijk, C. A. *Tissue Eng*. **2006**, *12*, 2685–2693.
86. Levenberg, S.; Rouwkema, J.; Macdonald, M.; Garfein, E. S.; Kohane, D. S.; Darland, D. C.; *et al*. *Nat. Biotechnol*. **2005**, *23*, 879–884.
87. Sasagawa, T.; Shimizu, T.; Sekiya, S.; *et al*. *Biomaterials* **2010**, *3*, 1646–1654.
88. Tsuda, Y.; Shimizu, T.; Yamato, M.; Kikuchi, A.; Sasagawa, T.; Sekiya, S.; *et al*. *Biomaterials* **2007**, *28*(33), 4939–4946.
89. Bel, A.; *et al*. *Circulation* **2003**, *108*, II247–II252.
90. Kocher, A. A.; *et al*. *Nat. Med*. **2001**, *7*, 430–436.
91. Reinlib, L.; Field, L. *Circulation* **2000**, *101*, E182–E187.
92. Schuster, M. D.; *et al*. *Am. J. Physiol. Heart Circ. Physiol*. **2004**, *287*, H525–H532.
93. Menasché, P.; Hagège, A. A.; Vilquin, J.-T.; *et al*. *J. Am. Coll. Cardiol*. **2003**, *41*(7), 1078–1083.
94. Pouzet, B.; Vilquin, J.-T.; Albert, A.; Hagège, A. A.; Marcio Scorsin, M.; Emmanuel Messas, E.; Marc Fiszman, M.; Schwartz, K.; Menasché, P. *Circulation* **2000**, *102*(Suppl. III), III-210–III-215.
95. Abelmann, W. H.; Lorell, B. H. *J. Am. Coll. Cardiol*. **1989**, *13*, 1219–1239.
96. Bowles, N. E.; Bowles, K. R.; Towbin, J. A. *Herz* **2000**, *25*, 168–175.
97. Towbin, J. A.; Bowles, N. E. *Nature* **2002**, *415*, 227–233.
98. Hosenpud, J. D.; Bennett, L. E.; Keck, B. M.; Fiol, B.; Boucek, M. M.; Novick, R. J. *J. Heart Lung Transplant*. **1998**, *17*, 656–668.
99. Packer, M.; Bristow, M. R.; Cohn, J. N.; Colucci, W. S.; Fowler, M. B.; Gilbert, E. M.; *et al*. *N. Engl. J. Med*. **1996**, *334*, 1349–1355.
100. Okano, T.; Sawa, Y. A new hope in regenerative medicine. Cell sheet therapy. Highlighting Japan through articles. *Cell sheets* **2009** August 28–29. [An interview].
101. Kondoh, H.; Sawa, Y.; Miyagawa, S.; *et al*. *Cardiovasc. Res*. **2006**, *69*, 466–475.

Relevant Websites

http://www.mtlf.org/docs/26598/Teruo%20Okano%20Presentation.pdf – Cell sheet.
http://joe.endocrinology-journals.org/cgi/reprint/173/1/13.pdf – Cell–cell junctional proteins.
http://circres.ahajournals.org/cgi/content/abstract/90/3/e40 – Cardiac grafts.
http://www.carimmaastricht.org/index.php/research-program/ii-cardiac-function-and-failure – Cardiac function.
http://en.wikipedia.org/wiki/Poly(N-isopropylacrylamide – Poly(N-isopropylacrylamide).
http://en.wikipedia.org/wiki/Regenerative_medicine – Regenerative medicine.
http://sciencelinks.jp/j-east/article/199918/000019991899A0451447.php – Temperature-responsive culture surface.
http://circres.ahajournals.org/cgi/content/abstract/circresaha;90/3/e40 – Three-dimensional functional cardiac tissues.
http://en.wikipedia.org/wiki/Tissue_engineering – Tissue engineering.
http://en.wikipedia.org/wiki/Blood_vessel – Vessels.

5.531. Peripheral Nerve Regeneration

A Jain, C M Valmikinathan, and R V Bellamkonda, Georgia Institute of Technology/Emory University School of Medicine, Atlanta, GA, USA

© 2011 Elsevier Ltd. All rights reserved.

5.531.1.	**Introduction**	421
5.531.1.1.	Anatomy and Physiology of the Nervous System	421
5.531.1.2.	Peripheral Nerve Injury: Degeneration and Regeneration	422
5.531.2.	**Current Approaches to Bridging Nerve Gaps**	422
5.531.2.1.	Physical Versus Biological Contributors to Peripheral Nerve Repair	422
5.531.2.2.	Biological Grafts and Synthetic Nerve Guidance Conduits	422
5.531.2.2.1.	Biological-based grafts	422
5.531.2.2.2.	Biomaterials and tissue engineered nerve guidance conduits	423
5.531.2.2.3.	Filler materials for nerve guidance conduits	424
5.531.2.3.	Scaffold Fabrication Strategies	425
5.531.2.4.	The Use of Bioactive Biomolecules	426
5.531.2.5.	Role of Schwann cells in the Peripheral Nerve Regeneration Process	429
5.531.2.6.	Stem Cells for Peripheral Nerve Regeneration	431
5.531.3.	**Concluding Statements**	431
References		431

Abbreviations

3D	Three dimensional
BDNF	Brain-derived neurotrophic factor
CDI	1,1′-Carbonyldiimidazole
CNS	Central nervous system
DRG	Dorsal root ganglia
ECM	Extracellular matrix
FGF	Fibroblast growth factor
GDNF	Glial-derived growth factor
NGC	Nerve guidance conduit
NGF	Nerve growth factor
NSC	Neural crest-derived stem cells
NT-3	Neurotrophin-3
PCL	Polycaprolactone
PGA	Polyglycolic acid
PHEMA-*co*-MMA	Poly (2-hydroxyethyl methacrylate-*co*-methyl methacrylate)
PLA	Polylactic acid
PLGA	Poly(lactide-*co*-glycolic) acid
PLLA	Poly(L-lactide)
PNI	Peripheral nerve injury
PNS	Peripheral nervous system
PPE	Poly(phosphoester)
PTFE	Polytetrafluoroethylene

5.531.1. Introduction

In the United States, 200 000 peripheral nerve injuries (PNIs) occur each year.[1] In cases where the gap is small (~<10–12 mm), spontaneous regeneration occurs, where the blood clot/fibrin bridge enables Schwann cells to play a significant role by their proliferating and migrating into the nerve gap, successfully physically bridging the gap between the proximal and distal nerve ends, and promoting axonal regeneration. However, in cases of more severe injuries, causing a more significant gap (>10 mm), the migration of Schwann cells into the gap is limited and regeneration is compromised. In such cases, surgical intervention by means of implantation of an autograft, allograft, or a tissue engineered nerve guidance conduit (NGC) is necessary to serve as a bridge to physically reconnect the severed nerve ends together.[2,3] The focus of this chapter is to review engineered biomaterials and how their interplay with extracellular matrix (ECM) proteins, trophic factors, and cells may be used to aid in peripheral nerve regeneration.

5.531.1.1. Anatomy and Physiology of the Nervous System

Anatomically, the nervous system is complex with a physical and biochemical architecture that allows it to control and modulate the function of other organs. The nervous system is composed of two main components, the peripheral (PNS) and the central (CNS) nervous systems. The CNS is located inside the cranial and spinal cavities and the PNS is subdivided into the sensory-somatic and the autonomic nervous systems. The sensory-somatic nervous system consists of the cranial and spinal nerves and the autonomic nervous system consists of sensory and motor neurons between the CNS and the internal organs. The nervous system consists of the neurons and the supporting glia, which have synergetic roles to play in the proper functioning of the nervous system. In the PNS, the neurons play a significant role in the transfer of information and are composed of a soma (cell body), an arbor (dendritic tree), which does not extend beyond a few millimeters, and the axon, which carries the impulses over long distances, from a few centimeters to meters. The dendrites play a major role in

receiving and processing chemically rich synaptic inputs and then transmitting electrical signals to and from the neural soma. An axon, on the other hand, typically extends from the soma to target organs and tissues and transports information through electrochemical signals to and from the CNS.[4]

On the other hand, the glial cells usually account for 90% of total cell numbers in the nervous system and play very diverse roles, depending on their location, usually ranging from insulation to production of a growth and regenerative milieu. In the PNS, the major glial cell type are the Schwann cells, and they myelinate axons, enabling fast electrical propagation, and also produce key proteins that are vital for the survival, regeneration, and maintenance of the nervous system.

On the basis of functional classification, the peripheral nerve axons are subdivided into those with motor functions and those with sensory functions. The motor neurons connect the muscles to the CNS; meanwhile, the sensory neurons play roles where senses of touch, vision, and taste are involved. However different their roles might be, structurally motor and sensory axons are composed of a bundle of connective tissue forming an anatomically defined trunk.

5.531.1.2. Peripheral Nerve Injury: Degeneration and Regeneration

Common causes of PNI are trauma, tissue resection due to plastic surgery, or tumor removal and congenital defects. Based on the type of injury, the axon is usually damaged, leading to a disruption of neuronal contiguity with or without a physical gap, leading to loss of motor or sensory functions. In such cases, the distal part of the axon is separated from the cell body, and the axons begin to degenerate; the degeneration is termed as anterograde or Wallerian degeneration. Waller described these changes using a frog injury model in the PNS.[5] The degeneration mechanism involves dissociation of the distal stump from the nutrient rich cell body and an upregulation of calcium-dependent protease activity.[6] On the other hand, due to the lack of contact with an innervating muscle or organ, slight degeneration of the proximal portion of the axon occurs over a short distance, which is termed retrograde degeneration.

Retrograde degeneration however does not affect the survival of the axon as specific proteins and cell markers begin to infiltrate into the site, playing a major role in the survival of the axon. Postinjury, the cytoskeleton of the supporting glial cells degrades and the Schwann cells surrounding the distal end of the axon shed their myelin lipids. This event causes the Schwann cells in the proximal and distal nerve portions to proliferate. Also, an increased influx of macrophages occurs, and along with the Schwann cells, begins to clear up debris from the degenerated axon fragments present in the nerve segments.[7] This is usually followed by a remodeling at the site of injury and the formation of a fibrin cable. This further enhances the influx of glial cells and blood vessels, which provide nutrients for the regenerative process and the survival and targeting of the ensuing axon along this cable.

Schwann cells and macrophages, apart from playing major roles in the signaling and repair of an injury site, produce critical cytokines, growth factors, and ECM proteins, which help in regeneration across the nerve gap, either with or without surgical intervention.[8–11] Also, mast cells proliferate at the injury site and produce copious amounts of histamine and heparin, which affect the vascular permeability and facilitate proliferation of yet more macrophages into the wound site. In cases with small nerve gaps or successful surgical intervention, regeneration starts at the proximal end and extends toward the distal end, being rich in nutrients as a result of connection to the cell soma. Here, the Schwann cells play a significant role in the regenerating process by flooding the microenvironment with growth-promoting factors and biological compounds as well as creating a conducive basal lamina, composed of aligned matrix proteins known as the Bands of Büngner, which form the path for axonal migration and reconnection with the distal end.[12] Some of the most common factors that the Schwann cells produce for matrix modification are collagen, fibrin, and laminin, and they also produce diffusive cues or neurotrophic factors that are essential for the survival of axons and axonal migration.[13,14] An understanding of the process described above is important as it is the basis for some of the regeneration promoting strategies described below.

5.531.2. Current Approaches to Bridging Nerve Gaps

5.531.2.1. Physical Versus Biological Contributors to Peripheral Nerve Repair

Injury to the nerve in the PNS can result in spontaneous regeneration if the gap is within 4 mm. For this phenomenon, various cellular and molecular events occur that provide both a physical and biological support for regeneration. Nerve gaps that are between 4 and 10 mm can be sutured together. The severing of the nerve requires surgical treatment, referred to as direct repair, where the two ends of the nerve are sutured together. There are three types of direct repair: (1) end-to-end, (2) end-to-side, and (3) epineural sleeve. If the tension within the nerve is too great, then direct repair no longer remains an option and the alternative is the use of nerve or synthetic grafting. Therefore, current strategies to regenerate the PNS incorporate both the physical and biological attributes.

5.531.2.2. Biological Grafts and Synthetic Nerve Guidance Conduits

Throughout the progression of peripheral nerve regeneration, various forms of grafts and conduits have been developed and investigated. Autografts, allografts, and synthetic NGCs have been studied to determine which one regenerates the peripheral nerve allowing full functional recovery; this involves looking at the electrophysiology, behavioral analysis, histology, and weight conservation of the innervating muscle.

5.531.2.2.1. Biological-based grafts

Autografts and allografts provide a similar microenvironment to that of the distal segment of a damaged nerve. The use of autografts emerged in the late nineteenth century and soon after was implemented clinically. After further refinement of the required surgical skills, autografts have now proven to be the 'gold standard.' Although autografts are the preferred therapeutic treatment for PNI, if the deficit in the nerve is large, or if donor nerves are limited as a result of disease or other factors, the availability of an autograft is limited and an alternative

becomes necessary. Allografts can also be used to promote full functional recovery in the PNS. However, the main disadvantages in using a nerve allograft are the host rejection, possible risk of disease transmission, and complications due to immunosuppression. The development of acellular nerve grafts involves eliminating the immunogenic host response to nerve allografts. This was done by decellularizing the graft and leaving the ECM components intact. It has been demonstrated that the length of axonal growth in acellular grafts was similar to that in cellular grafts up to a 20 mm distance, and clinically restoring motor function and sensation[15]; however, axons failed to extend through the entire 40 mm gap.[16] It has been shown that when ECM, trophic factors, and various cell types are utilized in the grafts, there are increased number of axons, the migration of endogenous Schwann cells that aid in the axonal growth through the graft, and improved vascularization. In more recent studies, further treatments have been applied to make the acellular grafts more conducive for axonal growth and promote endogenous Schwann cell migration. Pretreatment of the acellular autograft or allograft with vascular endothelial growth factor improved the migration of endogenous Schwann cells and neovascularization, where as the treatment with nerve growth factor (NGF) increased the number of axons that grew into the graft.[17] In the same study, laminin was also used in the pretreatment of the acellular graft, but no beneficial effect was observed.[17] In another study, the acellular nerves were treated with promoting biomolecules; however, in another short duration study, the acellular allografts were pretreated with chondroitinase ABC, an enzyme that cleaves the glycosaminoglycan side chains of chondroitin sulfate proteoglycans, which are inhibitory to axonal growth, and it was demonstrated that there was a significantly higher number of axons entering into the graft compared to controls.[18] Studies also investigated the beneficial effect of cells cultured within acellular grafts. When isogenic Schwann cells were cultured within the acellular grafts, the grafts did not display improved number of axons compared to the control grafts.[19] However, in another study, in a primate long nerve gap injury, autologous Schwann cells in the cold-preserved allografts displayed enhanced nerve density and fiber counts compared to that in the controls.[20] In a study using Rhesus monkeys, autologous nonhematopoietic mesenchymal stem cells were implanted into acellular allogenic grafts that bridged a 40 mm nerve gap, and it was demonstrated that after 6 months, the ulnar nerves were structurally and functionally repaired to an extent similar to that of autologous nerve grafts.[21]

Other biological alternatives to using cellular and acellular nerve autografts and allografts have been veins, muscles, and arteries as biological nerve conduits to bridge nerve gaps. The vein wall is made up of three layers, the laminin-rich basal lamina, the muscle layer in the middle, and the adventitia, which is collagen rich. In a study, the vein was turned inside out so that the adventitia is the inner lumen.[22] This change presented the growth promoting collagen to the regenerating axons, thus demonstrating a greater number of axons entering into the graft.[22] Vein grafts injected with Schwann cells demonstrated axons regenerated across the entire nerve gap,[23] as well as evoking muscle action potentials and new myelinated nerve fascicles similar to autografts.[24] A study compared the use of only a nerve graft with that of a nerve graft within a vein conduit graft to determine whether the number of axons, nerve conduction, and gait function were enhanced; however, there was no significant difference.[25] Besides veins, arteries were also used as potential grafts to bridge the nerve lesion. In a study that compared the axonal regeneration through nerve, muscle, and arterial grafts, the artery-based graft did not exhibit promising properties and it was concluded that arteries should not be utilized.[26] Although the failure of the use of the artery graft was published, Rodrigues and Silva later published a study that compared the arterial graft to an inside-out artery graft, similar to the inside-out vein graft conducted by Wang *et al.* Axons were present in the inside-out artery graft, where as the standard artery graft had axons that were surrounded by connective tissue.[27] For muscle grafts, the appealing feature of using this biological graft is the thick basal lamina that surrounds the muscle, which is similar to the vein and artery basal lamina, providing growth promoting proteins. Acellular muscle grafts in a 6 mm nerve gap in a mouse model demonstrated that the remaining basal lamina tubes allowed axons to regenerate through the graft, forming thick myelinated fibers.[28] Fawcett and Keynes demonstrated that the muscle basal lamina bridging a 40 mm nerve gap had an increased number of axons into the distal stump and improved functional limbs recovery compared to nerve autografts.[29] Although vein and muscle grafts have shown to have regenerating myelinated axons, problems such as collapsing of the vein grafts and axons growing outside of the muscle grafts have led to studies that combined both the muscle and vein grafts. The muscle was used to fill the vein graft to prevent collapsing. When comparing nerve, vein, and muscle grafts with the combination of vein and muscle, it was found that only the vein and muscle grafts were inferior in performance compared to the combination, which provided a functional recovery similar to that of the nerve grafts, and greater number of axons.[30] Similar results were also seen in other studies.[31,32] In a study to understand the microenvironment that makes the combined vein–muscle graft successful, it was determined that within 5 days of the graft implantation, endogenous Schwann cells were present within the graft, as well as the neurotrophins, NGF, and brain-derived neurotrophic factor (BDNF).[33]

Because of disadvantages with the nerve auto- and allografts, other biological grafts were investigated. However, compared to the autograft, axonal regeneration and functional recovery remain unsatisfactory in the other grafts and do not match autograft performance. Therefore, the development and use of synthetic NGCs and other biological alternatives have been appealing and further investigated.

5.531.2.2.2. Biomaterials and tissue engineered nerve guidance conduits

Although autografts are successful in facilitating regeneration across large nerve gaps (>10 mm), they have drawbacks such as limited availability, size mismatch, and importantly loss of function at the donor site. With the advent of several microtechnologies, nanotechnological tools and biomaterials tissue engineered grafts have been developed and applied as conduits to evaluate their ability to regenerate nerve gaps. Several classes of materials ranging from natural to synthetic and nonbiodegradable to biodegradable have been fabricated for repair and regeneration of peripheral nerve conduits typically with a

tubular conduit design to physically bridge the two nerve endings. The tubular architecture provides a closed physical environment to allow for concentration and accumulation of cells, growth factors, and other ECM components. It also provides a barrier that limits the migration of undesired macrophagic cell types into the site of injury. Nerve conduits also serve as a platform to include exogenous surface bound and topographical guidance cues, 3D gels, and nano/microcarriers for controlled release of critical growth factors such as NGF, glial-derived growth factor (GDNF), neurotrophin-3 (NT-3), and BDNF.

Among the first polymeric materials to be used as a nerve conduits were silicone grafts.[34] Grafts made of silicone were considered as a gold standard among artificial nerve conduits, and studies with other materials and fillings, such as collagen, were compared against those with silicone-based materials.[35,36] However, impediments in the application of silicone to human subjects for regeneration of large nerve conduits, such as the nonbiodegradable nature and inherent rigidity of the graft, lack of allowance for swelling of the regenerating nerve, as well as causing compressive stresses and scarring on the nerve, caused failure of the implant to regenerate large gaps.[37] Also, as suggested earlier, in order to enhance the rate and the quality of regeneration, several 'filler' materials have been included into the lumen of the tubular silicone-based nerve conduits. Some of the common biological materials to be tested as fillers and conduits include collagen, laminin, a cocktail of growth factors in saline, fibrin, and even tissues such as gut, muscle, vein, and subintestinal mucosa. Also, several nondegradable materials such as PTFE-,[38,39] polycarbonates-,[40] and nylon-based[41] constructs have been used for repair of PNIs, albeit only limited repair was observed (**Figure 1**).

5.531.2.2.3. Filler materials for nerve guidance conduits

Natural biomaterials, such as collagen, have been used as fillers in the nonbiodegradable materials and have enhanced their performance when compared to unfilled or saline filled tubular constructs.[36] This can be attributed to the fact that autografts, the current gold standard, are composed of a matrix essentially made of collagen and other basement membrane proteins such as laminin and fibronectin, and allografts are typically decellularized collagen grafts. Collagen-based nerve conduits perform similar to autografts over short lengths.[42] A collagen-based microstructured three-dimensional (3D) NGC containing numerous longitudinal guidance channels with dimensions resembling natural tubes has been produced.[43] Bozkurt *et al.* showed that the grafts enhanced Schwann cell migration, axonal regeneration, and even formation of significant bands of Büngner. Also, several blends of collagen with other materials such as collagen with polycaprolactone (PCL) and collagen with chitosan have been developed and have shown improved performance as compared to the single components in its entirety. Patel *et al.* have shown enhanced sensory and motor neural functions using blends of collagen and chitosan, 12 weeks postimplantation in a rat model.[44,45]

However, collagen may be associated with an immune response, and isolating collagen from the patient or a different species remains challenging. In order to minimize the immune activity of collagen, gelatin, a thermally denatured collagen, has been applied as a nerve conduit. Several studies have shown enhanced regeneration in gelatin containing scaffolds, with gelatin either in entirety or as a blend with common materials, such as PCL[46–53] or poly (lactide-*co*-glycolic) acid (PLGA).[54–61] Several gellation techniques have been employed to fabricate gels based on gelatin.[62–70] Commonly, photocurable gelatin, genipin cross-linked,[63,67,70–72] and glutaraldehyde cross-linked gelatin[62,65,67,73] have been employed as grafts for regeneration across nerve gaps.

Another natural biomaterial, fibrin, has demonstrated positive outcomes in the peripheral nerve regeneration. The use and favorable results of fibrin as a material may be due to its critical role as a fibrin clot in the wound healing process, and it forming an oriented matrix that guides cell migration across the length of injury.[74,75] Also, fibrin binds to neurotrophic factors that are critical in the regeneration process, and fabrication of fibrin-based hydrogel scaffolds has the advantage of not requiring any cytotoxic chemicals or reagents unlike collagen- or gelatin-based scaffolds.[76,77]

Several studies have also shown that hydroxyethylated agarose has appropriate mechanical, charge, and stiffness characteristics to support 3D neurite extension and regeneration across nerve gaps.[78–86] Functionalized agarose-based scaffolds have

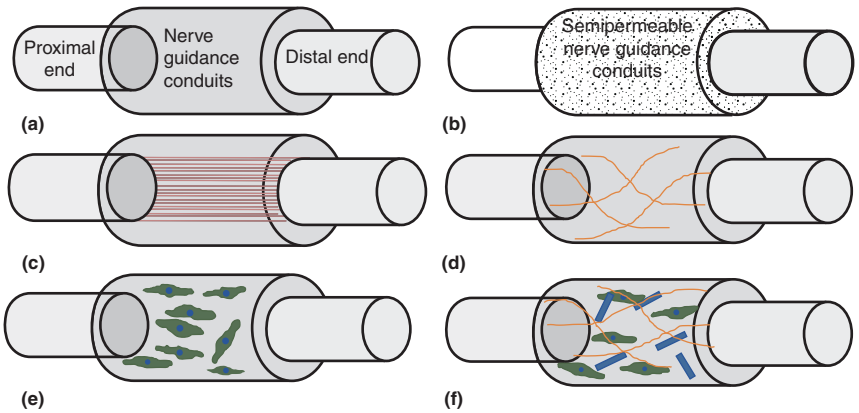

Figure 1 Therapeutic strategies for peripheral nerve regeneration. (a) Nerve gap bridged with nerve guide conduits (NGCs). (b) Semipermeable NGCs. (c) Aligned nanofiber-filled NGCs. (d) Hydrogel matrix containing NGCs. (e) Cellular transplantation within NGCs. (f) Example of a combinational strategy containing hydrogel matrix, slow releasing delivery vehicles and transplanted cells within NGCs.

demonstrated regeneration comparable to autografts across 10 mm nerve gap. Agarose, being thermally phase reversible does not require any secondary cross-linking agent and also allows for functionalization with suitable growth factors and ECM proteins such as laminin.[2,82,86,87] It has been demonstrated that several blends of agarose, usually collagen[88] or chitosan,[80,81] have shown promising regeneration in the PNS and CNS.

Additionally, chitosan has been promising as a scaffolding material for nerve repair.[46,89–98] It provides several surface active moieties that allow for functionalization, is not water soluble and therefore does not necessarily need an external cross-linking mechanism, and more importantly has shown to possess electron conductive properties, which are essential in the regeneration process, especially in the nervous system. Also, chitosan can be fabricated into films, blends, nanofibrous mesh-like scaffolds, and hydrogels. However, there have been studies that have shown some macrophage responses to chitosan implantation, leading to inflammation and ultimately rejection of the implant in longer study durations.

Other natural biomaterials, such as alginate,[99–106] hyaluronic acid,[107–113] cellulose,[107,114] and dextran[115–117] have been used to promote regeneration in the PNS. Unfortunately across these many systems, axonal regeneration has typically not been comparable to that of the autografts when the gaps are larger than 10 mm.

In order to overcome these drawbacks, several studies have shown the application of synthetic biodegradable materials for peripheral nerve regeneration NGCs. Some of the most common materials used for such applications are polyglycolic acid (PGA), poly lactic acid (PLA), and its copolymers PLGA. Also, PCL, poly anhydrides, and poly hydroxyl butyrates have been developed for such applications. One advantage of synthetic polymers is their capability to be fabricated to several architectures with micro and nanoscale control. Also, most of these polymers do not need any external cross-linking mechanism as they are soluble in organic compounds and only slowly degrade when exposed to water, usually via ester bond cleavage mechanisms. Some of the most common biomaterials and their associated studies with outcomes are delineated in **Table 1**.

Another interesting outcome of using a biodegradable matrix is the fact that it can act as a reservoir to include critical growth factors for peripheral nerve regeneration and the agents are usually released over long durations as needed by the regeneration process, as the material slowly degrades over time.

5.531.2.3. Scaffold Fabrication Strategies

Several fabrication techniques have been developed to fabricate scaffolds for peripheral nerve regeneration from synthetic and natural polymers. In the choice of the biomaterial and the fabrication process, it is essential to note that several factors might affect the response of neural cells on the scaffolds, which include material composition, end groups, and concentration, as well as macro-, micro-, and nanoarchitecture, porosity, and mechanical properties. Chemical composition has shown to affect the response of sensory neurons in several studies.[2,85,93,144,150] Some of critical considerations for materials choice, design, and fabrication of grafts for peripheral nerve include, but are not limited to, biodegradability at the rate of regeneration; optimal mechanical properties for ease of implantation, prevention of collapse, ability to suture easily, and allowing for diffusion of nutrients through the wall of the scaffold; and resistance to deterioration in chemical, mechanical, and biological properties upon sterilization.[2,46,47,59,90,131,151,152] Upon consideration of the above required properties, there are several principles by which scaffolds could be manufactured from biomedical polymers. Some of the procedures that are used include phase separation, solvent casting, electrospinning, extrusion based either from melts or solvents, photo-cross-linking, and gellation systems for hydrogels.

For the phase separation and solvent casting techniques, use of a suitable solvent–polymer combination is essential. Upon solvent evaporation the polymer usually exhibits a microfiber like architecture with appropriate mechanical properties and pore geometries.[153–157] Also, in order to enhance the porosity of the matrix, salt crystals of similar dimensions are usually included in the matrix prior to solvent casting. Upon scaffold fabrication, the scaffolds are leached in water to extract the salt from the scaffolds and leave behind a porous architecture. Furthermore, in order to obtain tubular constructs that mimic native nerves, molds of different shapes and materials have been shown to be suitable for tube preparation.[57,59,60,116,118,129,140,147,148,158,159] In order to create oriented architectures that mimic native nerves, combined techniques have been developed to construct grafts. Typically scaffolds with microchannel architectures that allow for guidance of axons across the grafts and also enhance nutrient diffusion into the scaffolds have been developed.[2,116,138,160]

Recently, melt-processing-based approaches have been used to fabricate nerve guidance channels. The inherent

Table 1 Biodegradable polymers for peripheral nerve regeneration

Polymeric biomaterials	*Fabrication method*	*References*
Poly (L-lactic acid) (PLLA)	Phase separation and solvent evaporation	48,49,118–124
	Electrospun nanofibers and filaments	91,125–128
Poly (lactide-*co*-glycotide) (PLGA)	Phase separation and solvent evaporation	55–57,60,90,94,124,127
	Microsphere sintering	129–132
	Electrospinning and microfilaments	54,132,133
Polycaprolactone	Phase separation and solvent evaporation	46,48,134–136
	Electrospun nanofibers and microfilaments	52,133,136–139
Polyhydroxy butyrate	Phase separation and solvent evaporation	140–143
Polyethylene glycol	Hydrogels	144–146
Polyurethanes	Phase separation and solvent evaporation	147–149

advantage of this technique is that it does not need a solvent to fabricate the required shape. However, as the temperatures are higher for fabrication of such systems, incorporation of temperature labile growth factors and cells becomes challenging. Several new polymer systems are currently being developed, where in the fabrication temperatures are in the physiological range, thereby allowing for incorporation of growth factors and cells.[46,134]

Anatomically, peripheral nerves are composed of an aligned matrix, which plays very critical roles in the contact guidance process, thereby orienting the regrowing or developing axons across the gap. Therefore, during the fabrication of grafts for PNS repair, consideration should be given to fabricate a matrix that mimics native ECM. Several studies have shown a favorable response in the regeneration process for aligned nanofibrous scaffolds as compared to scaffolds without a specific architecture (**Figure 2**).[2,3,50,125,126,137,161–166]

One other approach to create scaffolds with microarchitectures mimicking native ECM is via freeze drying. The advantage of this technique is that aqueous as well as organic solvents have been used to create scaffolds of required geometry. Also, this technique allows for fabrication of scaffolds from natural biomaterials such as collagen and chitosan. Furthermore, as this technique allows the use of aqueous solvents, incorporation of growth factors during scaffold fabrication can be achieved (**Figure 3**).[59,89,94,160,167–169]

5.531.2.4. The Use of Bioactive Biomolecules

During development, there are various families of molecules that allow for the growth of axons to make the connections to their targets; these include neurotrophic factors, ECM proteins, and intracellular signaling pathway molecules. In the previous section, we reviewed the use of synthetic grafts as replacement nerves. This section discusses the combination of the synthetic grafts with the use of biomolecules to promote axonal regeneration. Predominantly, neurotrophic factors, such as NGF, BDNF, and NT-3, are used in the PNS. The ECM molecules that are used are laminin, collagen, and fibronectin. These proteins act as a chemoattractant to Schwann cells and also are secreted by the cells to attract axons to extend. Oligopeptides from these proteins, such as RGD, YIGSR, and IKVAV, are also used instead of the whole protein to promote cell adhesion and migration. Typically these bioactive moieties are presented to the nerve gap using the conduits, filler materials, or nano/microparticles.

As mentioned earlier, growth factors, neurotrophic factors specifically, have an important role in neural development and in adult life for axonal regeneration. After injury, NGF is upregulated because of Schwann cells and other cells migrating to the injured area and releasing the neurotrophin. Another growth factor, fibroblast growth factor (FGF) has also shown to enhance axonal growth,[170] as well as angiogenesis.[171] When using biomaterials in conjunction with biomolecules, it is important to construct a scaffold that allows axons to extend through; has the mechanical integrity to support cell migration, such as that of Schwann cells, into the scaffold; allows the delivery of growth factors, such as neurotrophins, that encourage axonal growth; and integrates the scaffold and ECM.

In order to covalently couple proteins and oligopeptides to modify scaffolds, carriers, fibers, and conduits, different types of cross-linkers have been used. There are thermochemical bifunctional cross-linkers, such as 1,1′-carbonyldiimidazole (CDI), which can couple the protein to a surface. Another class of cross-linkers that have been used for PNS repair is photo-cross-linkers, which are activated by shining UV light.[82,87,172,173] Using UV light to photo-cross-link proteins to scaffolds allows the laser beam to create protein-based patterns in the hydrogel. In the study, UV laser beam was used to create protein channels through the agarose gel, providing directional cues for the neuritis.

As mentioned in an earlier section, agarose is a hydrogel that is used as a scaffold for PNS regeneration. Besides its favorable mechanical properties, the hydrogel is also beneficial for covalently coupling growth promoting molecules to the agarose hydrogel, which would mimic the microenvironment allowing for axonal outgrowth through the nerve gap into the distal nerve. *In vitro* studies have shown that tethering a growth promoting ECM molecule, such as laminin, to the agarose gel encouraged neurite outgrowth compared to a scaffold that did not have any modifications.[174,175] Oligopeptides have been cross-linked to the hydrogels as well. The oligopeptides that influence cell–matrix interactions include RGD, which is involved in the interaction between fibronectin and an integrin receptor, and YIGSR, a peptide on the β1 chain of laminin aiding in cell attachment.[176] In an *in vivo* study, laminin was covalently coupled to the agarose scaffold contained within a polysulfone tube and a slow release system of NGF within the agarose was implanted within a nerve gap, demonstrating that regenerated myelinated axons were comparable to the regeneration found in autografts across 10 mm gaps.[86]

There are other hydrogels that are made from ECM proteins. Matrigel, NeuroGel™, and Biomatrix are three of those hydrogels. Matrigel is a mixture of laminin and collagen, which when embedded with Schwann cells has shown to promote axonal regeneration.[177,178] NeuroGel™, made of *N*-2-(hydroxypropyl) methacrylamide, used for regeneration in the CNS, has shown beneficial properties.[179,180] Lastly, Biomatrix is another hydrogel composed of ECM proteins; however, other hydrogels have shown to be more beneficial.[181]

Polymeric fibers have also been used to direct axonal growth through the nerve gap. For regeneration, the fibers are contained within an NGC and the ends are sutured to the proximal and distal nerve ends. Poly (L-lactide) (PLLA) is a common polymer used to make the fibers. In an *in vitro* study, laminin was coated around the PLLA fibers, which demonstrated significantly greater neurite outgrowth compared to uncoated PLLA and poly-L-lysine coated fibers.[182] Besides using the full laminin protein, oligopeptides, YIGSR, and IKVAV were tethered to various polymeric biomaterials to improve neurite extension.[174,183,184]

The third polymeric surface that presents ECM and trophic factors is NGCs. NGCs have been extensively reviewed elsewhere;[185–188] therefore, only NGCs that have been used to present trophic factors and ECM molecules to promote axonal regeneration are discussed here. In one study, NGF was encapsulated into poly(phosphoester) (PPE) microspheres and were then loaded into the NGCs. It was demonstrated that the density, diameter, and population of the fibers at the distal

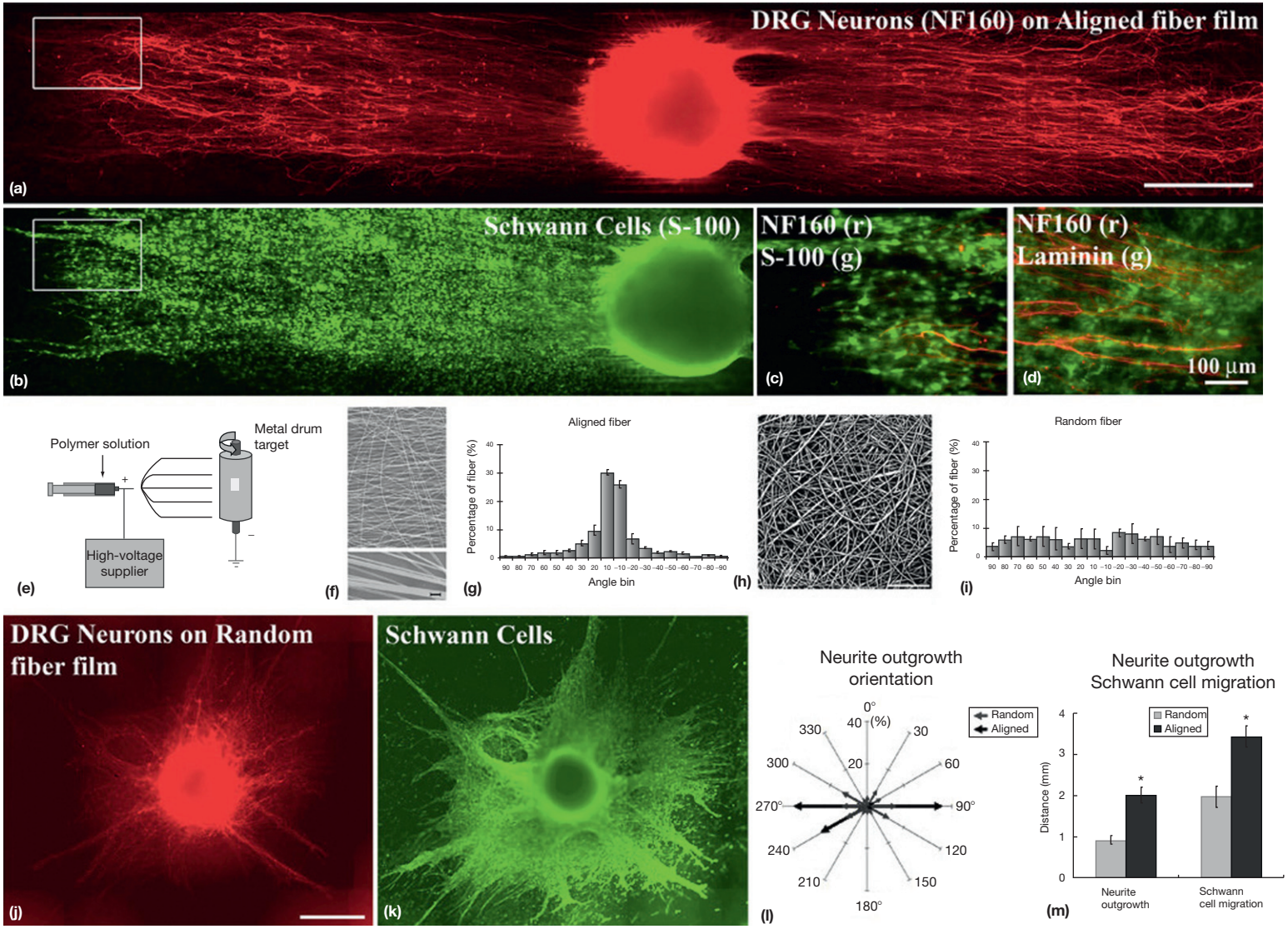

Figure 2 Dorsal root ganglia (DRGs) on aligned and random fiber film *in vitro*. (a–d) Double immunostained DRG on the aligned fiber film: (a) representative montage of NF160 (a marker for axons) immunostained DRG neurons on the film and (b) montage of S-100 (a marker for Schwann cells) immunostained Schwann cells on the film. (c) Magnified NF160 (red, from box in (a) and S-100 (green, from box in (b) overlapped image. (d) Double immunostained aligned axons (NF160, red) and endogenously deposited laminin protein (laminin, green). (e–i) Fabrication of the fiber films and distribution of alignment of the films. (e) Schematic of aligned fiber film fabrication by electrospinning process. Random fiber film was deposited on a flat metal target instead of on a high-speed rotating metal drum. (f and h) Representative SEM image of the aligned fibers (f, magnified fibers below) and the random fibers (h). Scale bar = 1 and 30 μm, respectively. Distribution of fiber alignment in aligned (g) and random fiber (i). (j and k) Double immunostained DRG on the random fiber film: (j) representative montage of $NF160^+$ neurons and (k) $S\text{-}100^+$ Schwann cells. Scale bar = 500 μm. (l) shows the quantitative comparison of orientation of neurite outgrowth on the aligned and random fiber film. Direction of arrows indicates the orientation of neurite outgrowth, and length of arrows indicates the rate of occurrence (percentage) ($n = 25$ per DRG). (m) shows the quantitative comparison of the extent of neurite outgrowth and Schwann cells migration on the films. The distance between the longest neurite outgrowth ($n = 25$ per DRG)/the furthest migrated Schwann cells ($n = 10$ per DRG) and DRG was measured and averaged. $^*P < 0.05$. Error bar = SEM. Reproduced from Kim, Y. T.; Haftel, V. K.; Kumar, S.; Bellamkonda, R. V. *Biomaterials* **2008**, *29*, 3117–3127, with permission from Elsevier.

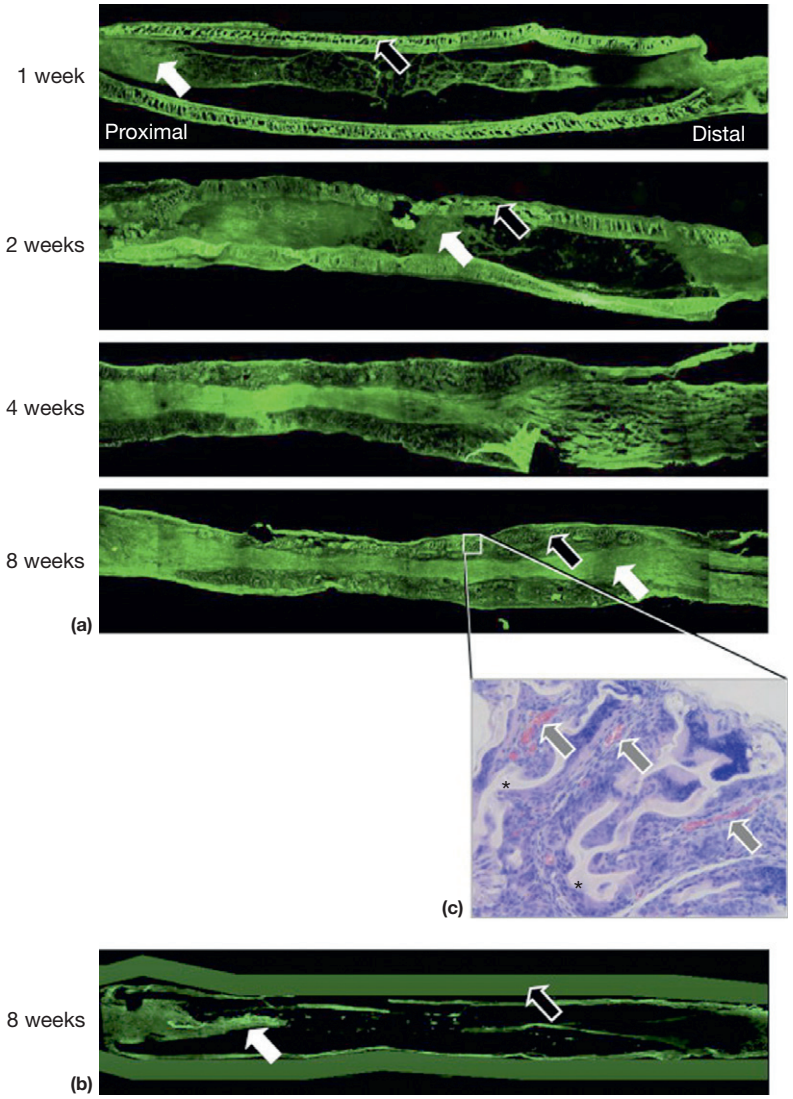

Figure 3 Longitudinal sections of the regenerated nerve through (a) PLGA/F127 (3 wt%) and (b) silicone tubes (anti-neurofilament staining, ×4; white arrow, regenerated nerve; black arrow, tube wall), and (c) cross-sectional view of PLGA/F127 (3 wt%) tube wall showing the existence of blood vessels infiltrated inside the wall (H&E staining, ×400; gray arrow, blood vessel; asterisk, PLGA/F127). Reproduced from Oh, S. H.; Kim, J. H.; Song, K. S.; *et al*. *Biomaterials* **2008**, *29*, 1601–1609, with permission from Elsevier.

nerve end were significantly greater than that of the axons found in empty conduits.[189] In a similar study, NGF was encapsulated into the PLGA microspheres and then mixed into the polymeric NGC solution to fabricate either single or multiple lumen NGCs. It was shown in conditions with the multiple versus single lumen, as well as NGF mixed into the polymer solution without microspheres, that there was no significant difference in neurite length for *in vitro* cultures. In a subsequent study, NGF was used to coat the inner lumen of poly(2-hydroxyethyl methacrylate-*co*-methyl methacrylate) (PHEMA-*co*-MMA)-based conduits using three different methods for encapsulating NGF into the NGCs: (1) NGF encapsulated in a PLGA microsphere, which was then added to the polymer solution prior to fabricating the NGCs, similar to the Xu *et al.* study; (2) NGCs were fabricated and then soaked in a NGF solution; and (3) studies were performed by Shoichet's laboratory where NGCs were fabricated with chitosan or PHEMA-*co*-MMA and then the inner lumen was coated with microspheres encapsulating NGF.[130,131] Of the three different NGF embedded conduits, the NGF mixed in the polymeric solution and then used to coat the inner lumen presented the greatest amount of NGF release over a 30-day period; however, *in vitro* or *in vivo* biological data were not published.[131] Another study investigated the release of NGF, but instead of using microspheres as the controlled release vehicle, two layers of PLGA were coated on the inner lumen of polyelectrolyte alginate/chitosan conduits, where the NGF was loaded between the two PLGA layers. This release system allowed for NGF to be released on the order of nanograms per day for 15 days.[190]

Lastly, the micro- and nanocarriers utilize various polymers to release trophic factors to promote axonal growth. The first of the carriers is microspheres. Studies have used microspheres

that are 12–16 μm in size to promote axonal regeneration. The polymeric materials that have mostly been used are PLGA, PLA, and PPEs. The use of copolymers and altering the ratio of polymers can affect the biodegradation profiles because of the polymeric characteristics, such as glass transition temperature and hydrophilicities.[191] In the previous section regarding NGCs, it was mentioned that microspheres encapsulating NGF were used. This has been the predominant utilization of the microspheres for PNS regeneration. In another study, NGF was encapsulated into PLGA microspheres, which were mixed into fibrin glue that surrounded the acellular nerve conduit in the microenvironment. Although the acellular graft surrounded by fibrin glue containing NGF microspheres had improved conserved muscle mass and improved axonal diameter, number, and myelination, the graft performance was inferior to that of the autograft.[192] It has been noted however that microspheres may elicit severe immunological response, thus leading to the engulfment of the microspheres by macrophages prior to any therapeutic benefit, and creating an obstruction to axonal regeneration.

Another delivery method to release protein for axonal regeneration in the nervous system is lipid microtubes or lipid-based 'hollow straws.' Lipid microtubes are hollow cylinders with an inner diameter of 0.5 μm (**Figure 4**).[193–196] The length of the microtubes can be altered during fabrication on the basis of the desired release profile of the biomolecule of interest. The microtube releases the molecule from the ends of the hollow tube through passive diffusion into the surrounding environment. To aid in axonal regeneration in the PNS, a two-step release system was developed. The first release step incorporated the diffusion of NGF from the microtubes to agarose, which filled an NGC. The second release entailed diffusion of the NGF from the agarose to the surrounding microenvironment.[86] This two-step release system allows the NGF to last longer in the nerve gap and prevents degradation or dilution by macrophages and other fluids. Two months postimplantation, the number of myelinated axons was comparable to that of autografts. A study was conducted that contained a fibrin matrix that had heparin tethered to the backbone, which interacted with neurotrophins. It was shown *in vitro* that the neurite outgrowth was enhanced by the neurotrophins released from the matrix rather than by soluble neurotrophins added to the matrix.[74] When the heparin immobilized fibrin matrix was implanted between the nerve gaps, fiber sprouting was observed at the distal end of the conduit.[76]

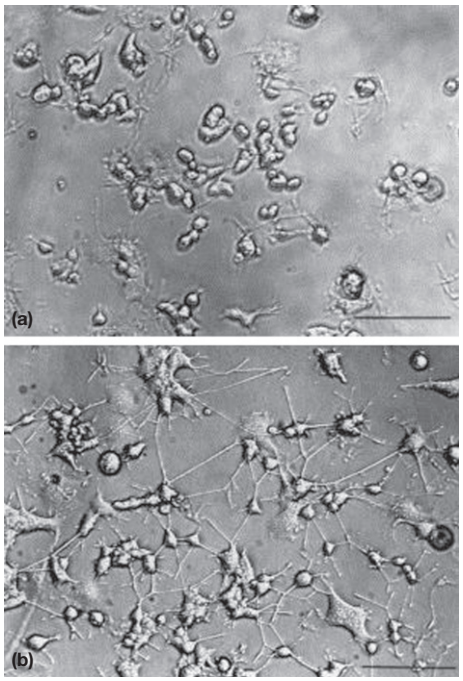

Figure 4 PC12 cells incubated with lipid microtubules loaded with (a) PBS and (b) NGF. PBS-loaded microtubules produced very little (<5%) neurite outgrowth (see (a)). Microtubules loaded with NGF were able to deliver sufficient NGF on their seventh day of release at 37 °C to induce PC12 cells to extend neurites (see (b)). Scale bar 100 μm. Reproduced from Meilander, N. J.; Yu, X.; Ziats, N. P.; Bellamkonda, R. V. *J. Control. Release* **2001**, *71*, 141–152, with permission from Elsevier.

Most of the delivery systems and scaffolds that have been mentioned thus far have uniformly distributed protein and trophic factors. However, during the developmental stages in the nervous system, proteins, trophic factors, and other molecules are presented in a spatially and temporally controlled fashion to regulate neuronal migration.[197] However, *in vitro* studies have shown that gradients of ECM proteins would promote axonal growth more than isotropic environments.[198] Recently, in an *in vivo* peripheral nerve regeneration study, anisotropic scaffolds were made of laminin and NGF. Laminin was covalently coupled to agarose and the NGF was delivered using microtubes. It was demonstrated that the anisotropic scaffolds had axonal diameter distribution, as well as conserved muscle weight, similar to that of the autografts, and both factors were significantly greater compared to those of the isotropic scaffolds (**Figure 5**).[82]

5.531.2.5. Role of Schwann cells in the Peripheral Nerve Regeneration Process

As described earlier, Schwann cells are the most abundant cells in the PNS. Their major roles include the process of myelination of axons,[199] provision of guidance cues to the regenerating axons (**Figure 6**),[132,161,200] secretion of critical growth factors for survival, and maintenance and regeneration of the PNS postinjury.[13] Also, several studies have indicated the enhanced potential of Schwann cells to produce growth factors when genetically altered to contain the gene of interest.[201] Considering these factors, Schwann cells are considered a major candidate for transplantation and application in the regeneration process.

Employing such hypothesis, several studies have shown the successful transplantation of Schwann cells within a synthetic nerve conduit.[60,101] However, the success of the regeneration process varies owing to several factors, mostly related to the source of the cells, cell number, and age of the patient. Mosahebi *et al.* demonstrated that the presence of Schwann cells in the graft enhanced the regeneration rate in a PNI model.[142,202,203]

However, this approach is hindered by the availability of Schwann cells for transplantation. Autologous source of Schwann cells is the most ideal source of cells; however, this approach is deemed unfeasible because the time required in

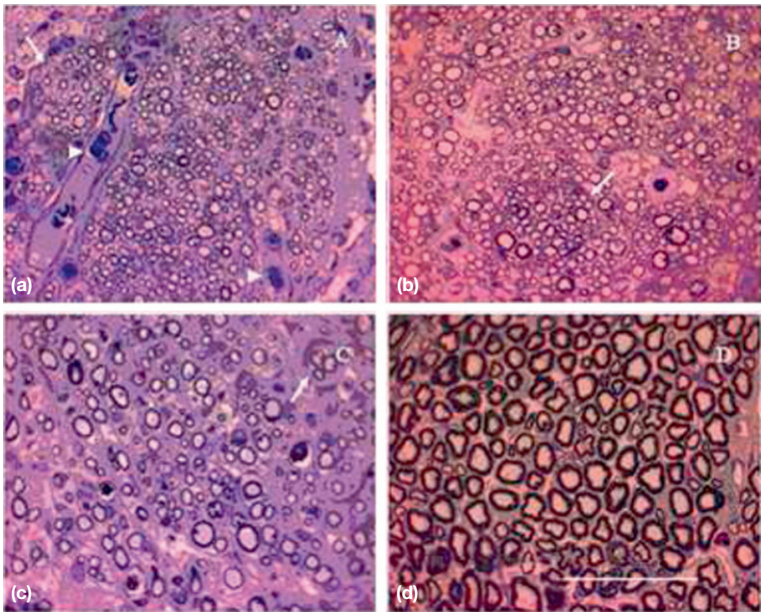

Figure 5 Light micrographs of nerve sections from groups with successful axonal regeneration. Toluidine-blue stained cross-sections at mid-length (10 mm) are shown here. Anisotropic scaffolds with step-gradient (a) and continuous-gradient (b) of LN-1, have higher density of axons and smaller-diameter axons than nerve grafts (c) and normal nerve (d). Note the fiber grouping in small fascicles (indicated by arrow) and presence of red blood cells (arrowhead). Scale bar 50 μm. Reproduced from Dodla, M. C.; Bellamkonda, R. V. *Biomaterials* **2008**, *29*, 33–46, with permission from Elsevier.

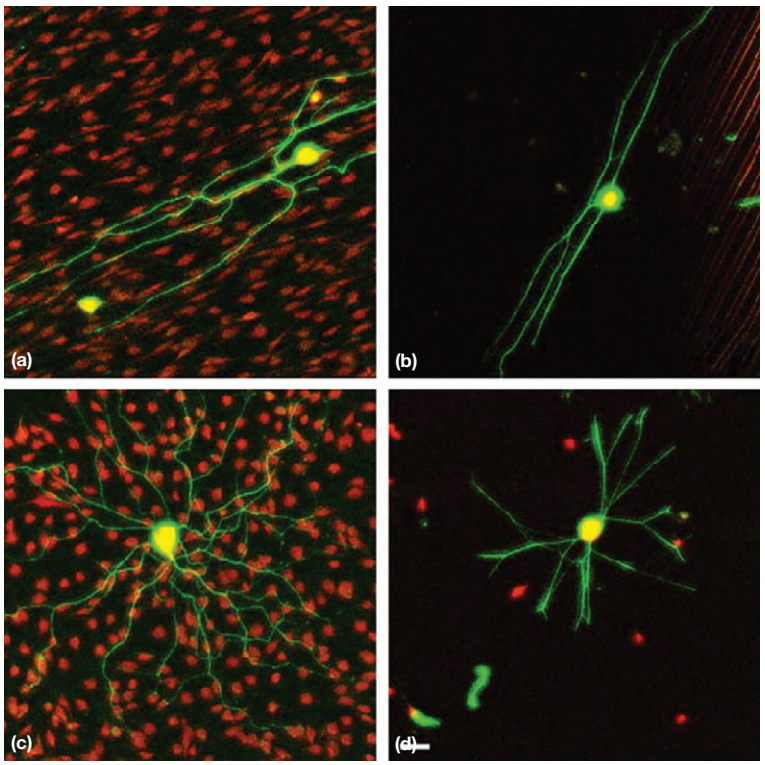

Figure 6 Neurite outgrowth on (a) aligned Schwann cell monolayer, (b) micropatterned laminin, (c) unaligned Schwann cell monolayer, and (d) uniform laminin. Scale bar = 50 μm. Reproduced from Thompson, D. M.; Buettner, H. M. *Ann. Biomed. Eng.* **2006**, *34*, 161–168, with permission from Springer.

harvesting and expanding cells to sufficient quantities is very long, usually long enough that it causes retrograde axonal death and scar formation, thereby decreasing the chances of a complete functional recovery.[202,204] Several other approaches have been studied to mitigate retrograde degeneration of the axons, primarily by the application of neuroprotective agents or growth factors such as NGF that enhance the survival of the severed axon.[205]

On the other hand, allogenic source of Schwann cells allows for banking, postharvest, and expansion and the cells are available for transplantation in large quantities. However, this technique elicits immune responses and needs administration of immunosuppressive agents, which have other side effects. Mosahebi *et al.*, showed the application of allogenic Schwann cells, without the support of immune suppression.[142] They observed no significant enhancement in the regeneration, and on detailed analysis, it was observed that the immune related clearance of the allogenic Schwann cells implanted was much faster than the migration and beneficial effect of the Schwann cells that could be observed.

Meanwhile, several other studies have shown successful transplantation and outcome of Schwann cell containing grafts with immunosuppression.[206,207] Minimal rejection and enhanced regeneration have been observed in both these studies. However, the quality of functional recovery was minimal and had been attributed to the migration of Schwann cells in the graft and the uniformity of cell loading in the grafts. In order to overcome this, several studies have shown the application of ideal matrices with appropriate ECM chemistry,[208–211] contact guidance cues,[137,140,212] and nanotopographies to promote Schwann cells migration uniformly and completely into the scaffolds.[2,163] Also, several studies have employed a bioreactor-based approach to uniformly and completely seed grafts with Schwann cells in the inner lumen. Even though the studies did not include any *in vivo* studies, positive results in terms of increased Schwann cell attachment and proliferation were observed.[60,114]

Despite observing positive responses from the inclusion of Schwann cells in the grafts, more detailed studies are required to elucidate the interface between the role of Schwann cells and the regeneration process. Also, grafts that support uniform and complete cellularization with either allogenic or autologous source need to be developed if any significant improvement in the regeneration process is to be observed.

5.531.2.6. Stem Cells for Peripheral Nerve Regeneration

Recently, there has been a lot of interest in the application of stem cells for the regeneration of PNIs. The reason for this increased interest is the ability of the stem cells to differentiate into glial cells and neuronal cell lineages along with other cells that help in the regeneration process.[213–217] Bone marrow-derived mesenchymal stem cells have shown potential for transplantation in models of PNI and increased expression of markers for glial cell lineages, typically Schwann cell like, on exposure to suitable differentiation factors composed of a cocktail of growth factors and agents.[215,218–221] Several other studies have shown that undifferentiated mesenchymal stem cells implanted into nerve conduits in the PNI model stimulate axonal growth and motor function recovery.[215,222–225] Several different biomaterials-based nerve conduits have been employed for *in vivo* delivery of the differentiated or undifferentiated mesenchymal stem cells. The outcomes in a rat model for similar studies have been very promising and have resulted in enhanced nerve regeneration.[222,226–229] The reason for the success of such an approach in the peripheral nerve regeneration milieu has been attributed to the ability of the differentiated mesenchymal stem cells to secrete critical neurotrophins[220,221] that have shown ability to upregulate myelin associated genes and proteins when cocultured with neuronal cells in an *in vitro* model.[230]

Similarly, there have also been studies showing the application of adipose-derived stem cells in the peripheral nerve regeneration process.[51,231–233] The advantages of the adipose-derived stem cells are that a large amount of cells can be obtained from lipoaspirates and the isolation of the cells does not require a painful procedure involving cell retrieval from the bone marrow and also that the amount of stem cells found in the adipose tissue is several fold higher than in the bone marrow.[234–236]

Neural crest-derived stem cells (NSCs) can be isolated and differentiated from several neural crest target structures, in addition to the migratory neural crest.[237–244] Of particular interest in the peripheral nerve regeneration arena are the NSCs that are found at the site of gliogenesis, including the sciatic nerve and dorsal root ganglia (DRG).[245] On observation and expansion, these cells displayed multipotency and self-renewal capacity and have clearly expressed glial markers such as P0, S-100, and PMP22.[245] There have also been several studies delineating the interaction of the glial cells derived from the NSCs with the axons of the PNS. Also, upon maintenance in an optimal cocktail over longer durations, the NSCs did not dedifferentiate into other cell types and maintained their phenotypes over such studies. All these results point towards a very successful application of differentiated neural stem cells in the regeneration of the PNS.

5.531.3. Concluding Statements

Nerve bridges are needed for injuries greater than 10 mm to promote peripheral nerve regeneration. The nerve autograft remains the gold standard to treat such nerve injuries. This chapter reviewed natural and synthetic grafts that have been used as potential alternative to autografts to promote axonal regeneration. Future nerve conduits/grafts should exploit our increasing understanding of the critical limitations in nerve regeneration across gaps to design novel scaffolds that embody unique combinations of physical and biochemical cues so that endogenous repair mechanisms are optimized, and regeneration across long nerve gaps is successful.

References

1. Noble, J.; Munro, C. A.; Prasad, V. S.; Midha, R. *J. Trauma* **1998**, *45*, 116–122.
2. Bellamkonda, R. V. *Biomaterials* **2006**, *27*, 3515–3518.
3. Ngo, T. T.; Waggoner, P. J.; Romero, A. A.; Nelson, K. D.; Eberhart, R. C.; Smith, G. M. *J. Neurosci. Res.* **2003**, *72*, 227–238.
4. Gray, H. *Anatomy of the Human Body*; Lea & Febiger: Philadelphia, 1918.
5. Waller, A. *Philos. Trans. R. Soc. Lond.* **1850**, *140*, 7.

6. George, E. B.; Glass, J. D.; Griffin, J. W. *J. Neurosci.* **1995**, *15*, 6445–6452.
7. Stoll, G.; Griffin, J. W.; Li, C. Y.; Trapp, B. D. *J. Neurocytol.* **1989**, *18*, 13.
8. Chaudhry, V.; Glass, J. D.; Griffin, J. W. *Neurol. Clin.* **1992**, *10*, 613–627.
9. Norrby, K. *APMIS* **2002**, *110*, 355–371.
10. Rosenstein, J. M.; Krum, J. M. *Exp. Neurol.* **2004**, *187*, 246–253.
11. Zochodne, D. W.; Cheng, C. *J. Anat.* **2000**, *196*(Pt 2), 279–283.
12. Bunge, R. P. *Curr. Opin. Neurobiol.* **1993**, *3*, 805–809.
13. Heumann, R.; Korsching, S.; Bandtlow, C.; Thoenen, H. *J. Cell Biol.* **1987**, *104*, 1623–1631.
14. Martini, R. *J. Neurocytol.* **1994**, *23*, 1–28.
15. Mackinnon, S. E.; Doolabh, V. B.; Novak, C. B.; Trulock, E. P. *Plast. Reconstr. Surg.* **2001**, *107*, 1419–1429.
16. Gulati, A. K. *J. Neurosurg.* **1988**, *68*, 117–123.
17. Sondell, M.; Lundborg, G.; Kanje, M. *Brain Res.* **1999**, *846*, 219–228.
18. Krekoski, C. A.; Neubauer, D.; Zuo, J.; Muir, D. *J. Neurosci.* **2001**, *21*, 6206–6213.
19. Frerichs, O.; Fansa, H.; Schicht, C.; Wolf, G.; Schneider, W.; Keilhoff, G. *Microsurgery* **2002**, *22*, 311–315.
20. Hess, J. R.; Brenner, M. J.; Fox, I. K.; *et al. Plast. Reconstr. Surg.* **2007**, *119*, 246–259.
21. Hu, J.; Zhu, Q. T.; Liu, X. L.; Xu, Y. B.; Zhu, J. K. *Exp. Neurol.* **2007**, *204*, 658–666.
22. Wang, K. K.; Costas, P. D.; Bryan, D. J.; Eby, P. L.; Seckel, B. R. *Microsurgery* **1995**, *16*, 65–70.
23. Foidart-Dessalle, M.; Dubuisson, A.; Lejeune, A.; *et al. Exp. Neurol.* **1997**, *148*, 236–246.
24. Zhang, F.; Blain, B.; Beck, J.; *et al. J. Reconstr. Microsurg.* **2002**, *18*, 295–300.
25. Keskin, M.; Akbas, H.; Uysal, O. A.; *et al. Plast. Reconstr. Surg.* **2004**, *113*, 1372–1379.
26. Itoh, S.; Shinomiya, K.; Samejima, H.; Ohta, T.; Ishizuki, M.; Ichinose, S. *Microsurgery* **1996**, *17*, 525–534.
27. Rodrigues Ade, C.; Silva, M. D. *Microsurgery* **2001**, *21*, 102–107.
28. Ide, C. *Neurosci. Res.* **1984**, *1*, 379–391.
29. Fawcett, J. W.; Keynes, R. J. *J. Neurosurg.* **1986**, *65*, 354–363.
30. Brunelli, G. A.; Battiston, B.; Vigasio, A.; Brunelli, G.; Marocolo, D. *Microsurgery* **1993**, *14*, 247–251.
31. Di Benedetto, G.; Zura, G.; Mazzucchelli, R.; Santinelli, A.; Scarpelli, M.; Bertani, A. *Biomaterials* **1998**, *19*, 173–181.
32. Geuna, S.; Tos, P.; Battiston, B.; Guglielmone, R.; Giacobini-Robecchi, M. G. *Anat. Embryol.* **2000**, *201*, 475–482.
33. Pagnotta, A.; Tos, P.; Fornaro, M.; Gigante, A.; Geuna, S.; Battiston, B. *Microsurgery* **2002**, *22*, 300–303.
34. Lundborg, G.; Gelberman, R. H.; Longo, F. M.; Powell, H. C.; Varon, S. *J. Neuropathol. Exp. Neurol.* **1982**, *41*, 412–422.
35. Chamberlain, L. J.; Yannas, I. V.; Arrizabalaga, A.; Hsu, H. P.; Norregaard, T. V.; Spector, M. *Biomaterials* **1998**, *19*, 1393–1403.
36. Chamberlain, L. J.; Yannas, I. V.; Hsu, H. P.; Strichartz, G. R.; Spector, M. *J. Neurosci. Res.* **2000**, *60*, 666–677.
37. Shen, Z. L.; Lassner, F.; Becker, M.; Walter, G. F.; Bader, A.; Berger, A. *Microsurgery* **1999**, *19*, 356–363.
38. Miloro, M.; Macy, J. M. *Oral Surg. Oral Med. Oral Pathol. Oral Radiol. Endod.* **2000**, *89*, 292–298.
39. Stanec, S.; Stanec, Z. *J. Reconstr. Microsurg.* **1998**, *14*, 227–232.
40. Plant, G. W.; Harvey, A. R. *Cell Transplant.* **2000**, *9*, 759–772.
41. Brown, M. C.; Perry, V. H.; Lunn, E. R.; Gordon, S.; Heumann, R. *Neuron* **1991**, *6*, 359–370.
42. Li, S. T.; Archibald, S. J.; Krarup, C.; Madison, R. D. *Clin. Mater.* **1992**, *9*, 195–200.
43. Bozkurt, A.; Deumens, R.; Beckmann, C.; *et al. Biomaterials* **2009**, *30*, 169–179.
44. Patel, M.; Vandevord, P. J.; Matthew, H. W.; De-Silva, S.; Wu, B.; Wooley, P. H. *J. Biomater. Appl.* **2008**, *23*, 101–121.
45. Patel, M.; Vandevord, P. J.; Matthew, H. W.; Desilva, S.; Wu, B.; Wooley, P. H. *Tissue Eng Part C Methods* **2008**, *14*, 365–370.
46. Ciardelli, G.; Chiono, V. *Macromol. Biosci.* **2006**, *6*, 13–26.
47. Clavijo-Alvarez, J. A.; Nguyen, V. T.; Santiago, L. Y.; Doctor, J. S.; Lee, W. P.; Marra, K. G. *Plast. Reconstr. Surg.* **2007**, *119*, 1839–1851.
48. Pierucci, A.; De Duek, E. A.; De Oliveira, A. L. *Tissue Eng. A* **2008**, *14*, 595–606.
49. Pierucci, A.; Duek, E. A.; De Oliveira, A. L. *J. Mater. Sci. Mater. Med.* **2009**, *20*, 489–495.
50. Prabhakaran, M. P.; Venugopal, J. R.; Chyan, T. T.; *et al. Tissue Eng. A* **2008**, *14*, 1787–1797.
51. Santiago, L. Y.; Clavijo-Alvarez, J.; Brayfield, C.; Rubin, J. P.; Marra, K. G. *Cell Transplant.* **2009**, *18*, 145–158.
52. Valmikinathan, C. M.; Defroda, S.; Yu, X. *Biomacromolecules* **2009**, *10*, 1084–1089.
53. Valmikinathan, C. M.; Wang, J.; Smiriglio, S.; Golwala, N. G.; Yu, X. *Comb. Chem. High Throughput Screen.* **2009**, *12*, 656–663.
54. Bini, T. B.; Gao, S.; Xu, X.; Wang, S.; Ramakrishna, S.; Leong, K. W. *J. Biomed. Mater. Res. A* **2004**, *68*, 286–295.
55. Bryan, D. J.; Tang, J. B.; Doherty, S. A.; *et al. J. Neural Eng.* **2004**, *1*, 91–98.
56. Chang, C. J.; Hsu, S. H. *Ultrasound Med. Biol.* **2004**, *30*, 1079–1084.
57. Chang, C. J.; Hsu, S. H. *Biomaterials* **2006**, *27*, 1035–1042.
58. Francel, P. C.; Smith, K. S.; Stevens, F. A.; *et al. J. Neurosurg.* **2003**, *99*, 549–554.
59. Hadlock, T.; Elisseeff, J.; Langer, R.; Vacanti, J.; Cheney, M. *Arch. Otolaryngol. Head Neck Surg.* **1998**, *124*, 1081–1086.
60. Hadlock, T.; Sundback, C.; Hunter, D.; Cheney, M.; Vacanti, J. P. *Tissue Eng.* **2000**, *6*, 119–127.
61. Yang, Y.; De Laporte, L.; Rives, C. B.; *et al. J. Control. Release* **2005**, *104*, 433–446.
62. Braun, R. M. *Surg. Forum* **1964**, *15*, 452–454.
63. Chang, J. Y.; Ho, T. Y.; Lee, H. C.; *et al. Artif. Organs* **2009**, *33*, 1075–1085.
64. Chang, J. Y.; Lin, J. H.; Yao, C. H.; Chen, J. H.; Lai, T. Y.; Chen, Y. S. *Macromol. Biosci.* **2007**, *7*, 500–507.
65. Chen, M. H.; Chen, P. R.; Hsieh, S. T.; Lin, F. H. *J. Biomed. Mater. Res. A* **2006**, *79*, 846–857.
66. Chen, P. R.; Chen, M. H.; Sun, J. S.; Tsai, C. C.; Lin, F. H. *Biomaterials* **2004**, *25*, 5667–5673.
67. Chen, Y. S.; Chang, J. Y.; Cheng, C. Y.; Tsai, F. J.; Yao, C. H.; Liu, B. S. *Biomaterials* **2005**, *26*, 3911–3918.
68. Liu, B. S. *J. Biomed. Mater. Res. A* **2008**, *87*, 1092–1102.
69. Liu, B. S.; Yao, C. H.; Hsu, S. H.; Yeh, T. S.; Chen, Y. S.; Kao, S. T. *J. Biomater. Appl.* **2004**, *19*, 21–34.
70. Lu, M. C.; Hsiang, S. W.; Lai, T. Y.; Yao, C. H.; Lin, L. Y.; Chen, Y. S. *J. Biomater. Sci. Polym. Ed.* **2007**, *18*, 843–863.
71. Chang, C. J. *Tissue Eng. A* **2009**, *15*, 547–557.
72. Chang, C. J. *J. Biomed. Mater. Res. A* **2009**, *91*, 586–596.
73. Mligiliche, N.; Endo, K.; Okamoto, K.; Fujimoto, E.; Ide, C. *J. Biomed. Mater. Res.* **2002**, *63*, 591–600.
74. Sakiyama-Elbert, S. E.; Hubbell, J. A. *J. Control. Release* **2000**, *69*, 149–158.
75. Sakiyama-Elbert, S. E.; Hubbell, J. A. *J. Control. Release* **2000**, *65*, 389–402.
76. Lee, A. C.; Yu, V. M.; Lowe, J. B., 3rd; *et al. Exp. Neurol.* **2003**, *184*, 295–303.
77. Wood, M. D.; Moore, A. M.; Hunter, D. A.; *et al. Acta Biomater.* **2009**, *5*, 959–968.
78. Balgude, A. P.; Yu, X.; Szymanski, A.; Bellamkonda, R. V. *Biomaterials* **2001**, *22*, 1077–1084.
79. Chernousov, M. A.; Kaufman, S. J.; Stahl, R. C.; Rothblum, K.; Carey, D. J. *Glia* **2007**, *55*, 1134–1144.
80. Dillon, G. P.; Yu, X.; Bellamkonda, R. V. *J. Biomed. Mater. Res.* **2000**, *51*, 510–519.
81. Dillon, G. P.; Yu, X.; Sridharan, A.; Ranieri, J. P.; Bellamkonda, R. V. *J. Biomater. Sci. Polym. Ed.* **1998**, *9*, 1049–1069.
82. Dodla, M. C.; Bellamkonda, R. V. *Biomaterials* **2008**, *29*, 33–46.
83. Labrador, R. O.; Buti, M.; Navarro, X. *NeuroReport* **1995**, *6*, 2022–2026.
84. Stokols, S.; Sakamoto, J.; Breckon, C.; Holt, T.; Weiss, J.; Tuszynski, M. H. *Tissue Eng.* **2006**, *12*, 2777–2787.
85. Yu, X.; Bellamkonda, R. V. *J. Neurosci. Res.* **2001**, *66*, 303–310.
86. Yu, X.; Bellamkonda, R. V. *Tissue Eng.* **2003**, *9*, 421–430.
87. Dodla, M. C.; Bellamkonda, R. V. *J. Biomed. Mater. Res. A* **2006**, *78*, 213–221.
88. Chen, H. H.; Liu, H. M. *Proc. Natl. Sci. Counc. Repub. China B* **1994**, *18*, 58–63.
89. Amado, S.; Simoes, M. J.; Armada Da Silva, P. A.; *et al. Biomaterials* **2008**, *29*, 4409–4419.
90. Cao, W.; Cheng, M.; Ao, Q.; Gong, Y.; Zhao, N.; Zhang, X. *J. Biomater. Sci. Polym. Ed.* **2005**, *16*, 791–807.
91. Chavez-Delgado, M. E.; Mora-Galindo, J.; Gomez-Pinedo, U.; *et al. J. Biomed. Mater. Res. B Appl. Biomater.* **2003**, *67*, 702–711.
92. Chiono, V.; Pulieri, E.; Vozzi, G.; Ciardelli, G.; Ahluwalia, A.; Giusti, P. *J. Mater. Sci. Mater. Med.* **2008**, *19*, 889–898.
93. Crompton, K. E.; Goud, J. D.; Bellamkonda, R. V.; *et al. Biomaterials* **2007**, *28*, 441–449.
94. Huang, Y. C.; Huang, Y. Y.; Huang, C. C.; Liu, H. C. *J. Biomed. Mater. Res. B Appl. Biomater.* **2005**, *74*, 659–664.
95. Ishikawa, N.; Suzuki, Y.; Ohta, M.; *et al. J. Biomed. Mater. Res. A* **2007**, *83*, 33–40.

96. Patel, M.; Mao, L.; Wu, B.; Vandevord, P. *J. Biomed. Mater. Res. A* **2009**, *90*, 154–165.
97. Patel, M.; Vandevord, P. J.; Matthew, H.; Wu, B.; Desilva, S.; Wooley, P. H. *Tissue Eng.* **2006**, *12*, 3189–3199.
98. Pfister, L. A.; Papaloizos, M.; Merkle, H. P.; Gander, B. *J. Biomed. Mater. Res. A* **2007**, *80*, 932–937.
99. Kataoka, K.; Suzuki, Y.; Kitada, M.; *et al. Tissue Eng.* **2004**, *10*, 493–504.
100. Kataoka, K.; Suzuki, Y.; Kitada, M.; *et al. J. Biomed. Mater. Res.* **2001**, *54*, 373–384.
101. Mosahebi, A.; Simon, M.; Wiberg, M.; Terenghi, G. *Tissue Eng.* **2001**, *7*, 525–534.
102. Mosahebi, A.; Wiberg, M.; Terenghi, G. *Tissue Eng.* **2003**, *9*, 209–218.
103. Novikova, L. N.; Mosahebi, A.; Wiberg, M.; Terenghi, G.; Kellerth, J. O.; Novikov, L. N. *J. Biomed. Mater. Res. A* **2006**, *77*, 242–252.
104. Sufan, W.; Suzuki, Y.; Tanihara, M.; *et al. J. Neurotrauma* **2001**, *18*, 329–338.
105. Suzuki, K.; Suzuki, Y.; Ohnishi, K.; Endo, K.; Tanihara, M.; Nishimura, Y. *NeuroReport* **1999**, *10*, 2891–2894.
106. Suzuki, Y.; Tanihara, M.; Ohnishi, K.; Suzuki, K.; Endo, K.; Nishimura, Y. *Neurosci. Lett.* **1999**, *259*, 75–78.
107. Adanali, G.; Verdi, M.; Tuncel, A.; Erdogan, B.; Kargi, E. *J. Reconstr. Microsurg.* **2003**, *19*, 29–36.
108. Favaro, G.; Bortolami, M. C.; Cereser, S.; *et al. ASAIO Trans.* **1990**, *36*, M291–M294.
109. Ikeda, K.; Yamauchi, D.; Osamura, N.; Hagiwara, N.; Tomita, K. *Br. J. Plast. Surg.* **2003**, *56*, 342–347.
110. Jansen, K.; Van Der Werff, J. F.; Van Wachem, P. B.; Nicolai, J. P.; De Leij, L. F.; Van Luyn, M. J. *Biomaterials* **2004**, *25*, 483–489.
111. Sakai, Y.; Matsuyama, Y.; Takahashi, K.; *et al. Biomed. Mater. Eng.* **2007**, *17*, 191–197.
112. Seckel, B. R.; Jones, D.; Hekimian, K. J.; Wang, K. K.; Chakalis, D. P.; Costas, P. D. *J. Neurosci. Res.* **1995**, *40*, 318–324.
113. Wang, K. K.; Nemeth, I. R.; Seckel, B. R.; *et al. Microsurgery* **1998**, *18*, 270–275.
114. Sun, T.; Norton, D.; Vickers, N.; *et al. Biotechnol. Bioeng.* **2008**, *99*, 1250–1260.
115. Blits, B.; Dijkhuizen, P. A.; Boer, G. J.; Verhaagen, J. *Exp. Neurol.* **2000**, *164*, 25–37.
116. De Ruiter, G. C.; Onyeneho, I. A.; Liang, E. T.; *et al. J. Biomed. Mater. Res. A* **2008**, *84*, 643–651.
117. Gordon, T.; Sulaiman, O.; Boyd, J. G. *J. Peripher. Nerv. Syst.* **2003**, *8*, 236–250.
118. Evans, G. R.; Brandt, K.; Katz, S.; *et al. Biomaterials* **2002**, *23*, 841–848.
119. Evans, G. R.; Brandt, K.; Niederbichler, A. D.; *et al. J. Biomater. Sci. Polym. Ed.* **2000**, *11*, 869–878.
120. Evans, G. R.; Brandt, K.; Widmer, M. S.; *et al. Biomaterials* **1999**, *20*, 1109–1115.
121. Koh, H. S.; Yong, T.; Chan, C. K.; Ramakrishna, S. *Biomaterials* **2008**, *29*, 3574–3582.
122. Li, J.; Mcnally, H.; Shi, R. *J. Biomed. Mater. Res. A* **2008**, *87*, 392–404.
123. Li, J.; Shi, R. *J Neurosci. Methods* **2007**, *165*, 257–264.
124. Widmer, M. S.; Gupta, P. K.; Lu, L.; *et al. Biomaterials* **1998**, *19*, 1945–1955.
125. Cai, J.; Peng, X.; Nelson, K. D.; Eberhart, R.; Smith, G. M. *J. Biomed. Mater. Res. A* **2004**, *69*, 247–258.
126. Cai, J.; Peng, X.; Nelson, K. D.; Eberhart, R.; Smith, G. M. *J. Biomed. Mater. Res. A* **2005**, *75*, 374–386.
127. Yang, F.; Murugan, R.; Wang, S.; Ramakrishna, S. *Biomaterials* **2005**, *26*, 2603–2610.
128. Yang, F.; Xu, C. Y.; Kotaki, M.; Wang, S.; Ramakrishna, S. *J. Biomater. Sci. Polym. Ed.* **2004**, *15*, 1483–1497.
129. Camarata, P. J.; Suryanarayanan, R.; Turner, D. A.; Parker, R. G.; Ebner, T. J. *Neurosurgery* **1992**, *30*, 313–319.
130. Goraltchouk, A.; Scanga, V.; Morshead, C. M.; Shoichet, M. S. *J. Control. Release* **2006**, *110*, 400–407.
131. Piotrowicz, A.; Shoichet, M. S. *Biomaterials* **2006**, *27*, 2018–2027.
132. Valmikinathan, C. M.; Tian, J.; Wang, J.; Yu, X. *J. Neural Eng.* **2008**, *5*, 422–432.
133. Panseri, S.; Cunha, C.; Lowery, J.; *et al. BMC Biotechnol.* **2008**, *8*, 39.
134. Chiono, V.; Tonda-Turo, C.; Ciardelli, G. *Int. Rev. Neurobiol.* **2009**, *87*, 173–198.
135. Galla, T. J.; Vedecnik, S. V.; Halbgewachs, J.; Steinmann, S.; Friedrich, C.; Stark, G. B. *Int. J. Artif. Organs* **2004**, *27*, 127–136.
136. Schnell, E.; Klinkhammer, K.; Balzer, S.; *et al. Biomaterials* **2007**, *28*, 3012–3025.
137. Chew, S. Y.; Mi, R.; Hoke, A.; Leong, K. W. *Biomaterials* **2008**, *29*, 653–661.
138. Flynn, L.; Dalton, P. D.; Shoichet, M. S. *Biomaterials* **2003**, *24*, 4265–4272.
139. Ghasemi-Mobarakeh, L.; Prabhakaran, M. P.; Morshed, M.; Nasr-Esfahani, M. H.; Ramakrishna, S. *Tissue Eng. A* **2009**, *15*, 3605–3619.
140. Bian, Y. Z.; Wang, Y.; Aibaidoula, G.; Chen, G. Q.; Wu, Q. *Biomaterials* **2009**, *30*, 217–225.
141. Mohanna, P. N.; Young, R. C.; Wiberg, M.; Terenghi, G. *J. Anat.* **2003**, *203*, 553–565.
142. Mosahebi, A.; Fuller, P.; Wiberg, M.; Terenghi, G. *Exp. Neurol.* **2002**, *173*, 213–223.
143. Young, R. C.; Wiberg, M.; Terenghi, G. *Br. J. Plast. Surg.* **2002**, *55*, 235–240.
144. Dadsetan, M.; Knight, A. M.; Lu, L.; Windebank, A. J.; Yaszemski, M. J. *Biomaterials* **2009**, *30*, 3874–3881.
145. Donaldson, J.; Shi, R.; Borgens, R. *Neurosurgery* **2002**, *50*, 147–156; discussion 156-7.
146. Gunn, J. W.; Turner, S. D.; Mann, B. K. *J. Biomed. Mater. Res. A* **2005**, *72*, 91–97.
147. Cui, T.; Yan, Y.; Zhang, R.; Liu, L.; Xu, W.; Wang, X. *Tissue Eng Part C Methods* **2009**, *15*, 1–9.
148. Hausner, T.; Schmidhammer, R.; Zandieh, S.; *et al. Acta Neurochir. Suppl.* **2007**, *100*, 69–72.
149. Pfister, L. A.; Papaloizos, M.; Merkle, H. P.; Gander, B. *J. Peripher. Nerv. Syst.* **2007**, *12*, 65–82.
150. Ren, Y. J.; Zhang, H.; Huang, H.; *et al. Biomaterials* **2009**, *30*, 1036–1044.
151. Rosner, B. I.; Siegel, R. A.; Grosberg, A.; Tranquillo, R. T. *Ann. Biomed. Eng.* **2003**, *31*, 1383–1401.
152. Shi, W.; Yao, J.; Chen, X.; Lin, W.; Gu, X.; Wang, X. *Artif. Cells Blood Substit. Immobil. Biotechnol.* **2010**, *38*, 29–37.
153. Liu, X.; Ma, P. X. *Biomaterials* **2009**, *30*, 4094–4103.
154. Liu, X.; Ma, P. X. *Biomaterials* **2010**, *31*, 259–269.
155. Mikos, A. G.; Lyman, M. D.; Freed, L. E.; Langer, R. *Biomaterials* **1994**, *15*, 55–58.
156. Mikos, A. G.; Thorsen, A. J.; Czerwonka, L. A.; *et al. Polymers* **1994**, *35*, 1068–1077.
157. Wei, G.; Ma, P. X. *Biomaterials* **2009**, *30*, 6426–6434.
158. Bryan, D. J.; Tang, J. B.; Holway, A. H.; *et al. J. Reconstr. Microsurg.* **2003**, *19*, 125–134.
159. Freier, T.; Montenegro, R.; Shan Koh, H.; Shoichet, M. S. *Biomaterials* **2005**, *26*, 4624–4632.
160. Hu, X.; Huang, J.; Ye, Z.; *et al. Tissue Eng. A* **2009**, *15*, 3297–3308.
161. Clements, I. P.; Kim, Y. T.; English, A. W.; Lu, X.; Chung, A.; Bellamkonda, R. V. *Biomaterials* **2009**, *30*, 3834–3846.
162. Gupta, D.; Venugopal, J.; Prabhakaran, M. P.; *et al. Acta Biomater.* **2009**, *5*, 2560–2569.
163. Kim, Y. T.; Haftel, V. K.; Kumar, S.; Bellamkonda, R. V. *Biomaterials* **2008**, *29*, 3117–3127.
164. Murugan, R.; Ramakrishna, S. *Tissue Eng.* **2006**, *12*, 435–447.
165. Murugan, R.; Ramakrishna, S. *Tissue Eng.* **2007**, *13*, 1845–1866.
166. Nicoli Aldini, N.; Fini, M.; Rocca, M.; Giavaresi, G.; Giardino, R. *Int. Orthop.* **2000**, *24*, 121–125.
167. Chang, C. J.; Hsu, S. H.; Yen, H. J.; Chang, H.; Hsu, S. K. *J. Biomed. Mater. Res. B Appl. Biomater.* **2007**, *83*, 206–215.
168. Ishikawa, N.; Suzuki, Y.; Dezawa, M.; *et al. J. Biomed. Mater. Res. A* **2009**, *89*, 1118–1124.
169. Oh, S. H.; Kim, J. H.; Song, K. S.; *et al. Biomaterials* **2008**, *29*, 1601–1609.
170. Aebischer, P.; Salessiotis, A. N.; Winn, S. R. *J. Neurosci. Res.* **1989**, *23*, 282–289.
171. Baird, A.; Walicke, P. A. *Br. Med. Bull.* **1989**, *45*, 438–452.
172. Luo, Y.; Shoichet, M. S. *Biomacromolecules* **2004**, *5*, 2315–2323.
173. Luo, Y.; Shoichet, M. S. *Nat. Mater.* **2004**, *3*, 249–253.
174. Bellamkonda, R.; Ranieri, J. P.; Aebischer, P. *J. Neurosci. Res.* **1995**, *41*, 501–509.
175. Yu, X.; Dillon, G. P.; Bellamkonda, R. B. *Tissue Eng.* **1999**, *5*, 291–304.
176. Borkenhagen, M.; Clemence, J. F.; Sigrist, H.; Aebischer, P. *J. Biomed. Mater. Res.* **1998**, *40*, 392–400.
177. Guenard, V.; Kleitman, N.; Morrissey, T. K.; Bunge, R. P.; Aebischer, P. *J. Neurosci.* **1992**, *12*, 3310–3320.
178. Valentini, R. F.; Aebischer, P.; Winn, S. R.; Galletti, P. M. *Exp. Neurol.* **1987**, *98*, 350–356.
179. Woerly, S.; Doan, V. D.; Evans-Martin, F.; Paramore, C. G.; Peduzzi, J. D. *J. Neurosci. Res.* **2001**, *66*, 1187–1197.
180. Woerly, S.; Doan, V. D.; Sosa, N.; De Vellis, J.; Espinosa-Jeffrey, A. *J. Neurosci. Res.* **2004**, *75*, 262–272.
181. Wells, M. R.; Kraus, K.; Batter, D. K.; *et al. Exp. Neurol.* **1997**, *146*, 395–402.
182. Rangappa, N.; Romero, A.; Nelson, K. D.; Eberhart, R. C.; Smith, G. M. *J. Biomed. Mater. Res.* **2000**, *51*, 625–634.

183. Ranieri, J. P.; Bellamkonda, R.; Bekos, E. J.; *et al*. *Int. J. Dev. Neurosci*. **1994**, *12*, 725–735.
184. Shaw, D.; Shoichet, M. S. *J. Craniofac. Surg*. **2003**, *14*, 308–316.
185. Bellamkonda, R.; Aebischer, P. *Biotechnol. Bioeng*. **1994**, *43*, 543–554.
186. Dahlin, L. B.; Lundborg, G. *Neurosurg. Clin. N. Am*. **2001**, *12*, 341–352.
187. Hudson, T. W.; Evans, G. R.; Schmidt, C. E. *Orthop. Clin. North Am*. **2000**, *31*, 485–498.
188. Schmidt, C. E.; Leach, J. B. *Annu. Rev. Biomed. Eng*. **2003**, *5*, 293–347.
189. Xu, X.; Yee, W. C.; Hwang, P. Y.; *et al*. *Biomaterials* **2003**, *24*, 2405–2412.
190. Pfister, L. A.; Alther, E.; Papaloizos, M.; Merkle, H. P.; Gander, B. *Eur. J. Pharm. Biopharm*. **2008**, *69*, 563–572.
191. Sinha, V. R.; Trehan, A. *J. Control. Release* **2003**, *90*, 261–280.
192. Yu, H.; Peng, J.; Guo, Q.; *et al*. *Microsurgery* **2009**, *29*, 330–336.
193. Meilander, N. J.; Yu, X.; Ziats, N. P.; Bellamkonda, R. V. *J. Control. Release* **2001**, *71*, 141–152.
194. Schnur, J. M. *Science* **1993**, *262*, 1669–1676.
195. Spargo, B. J.; Cliff, R. O.; Rollwagen, F. M.; Rudolph, A. S. *J. Microencapsul*. **1995**, *12*, 247–254.
196. Yager, P.; Schoen, P. E. *Mol. Cryst. Liq. Cryst*. **1984**, *106*, 371–381.
197. Baier, H.; Bonhoeffer, F. *Science* **1992**, *255*, 472–475.
198. Adams, D. N.; Kao, E. Y.; Hypolite, C. L.; Distefano, M. D.; Hu, W. S.; Letourneau, P. C. *J. Neurobiol*. **2005**, *62*, 134–147.
199. Hall, S. *J. Hand Surg. Br*. **2001**, *26*, 129–136.
200. Thompson, D. M.; Buettner, H. M. *Ann. Biomed. Eng*. **2006**, *34*, 161–168.
201. Li, Q.; Ping, P.; Jiang, H.; Liu, K. *Microsurgery* **2006**, *26*, 116–121.
202. Mosahebi, A.; Woodward, B.; Wiberg, M.; Martin, R.; Terenghi, G. *Glia* **2001**, *34*, 8–17.
203. Tohill, M. P.; Mann, D. J.; Mantovani, C. M.; Wiberg, M.; Terenghi, G. *Tissue Eng*. **2004**, *10*, 1359–1367.
204. Mckay Hart, A.; Brannstrom, T.; Wiberg, M.; Terenghi, G. *Exp. Brain Res*. **2002**, *142*, 308–318.
205. Hart, A. M.; Terenghi, G.; Wiberg, M. *Neurol. Res*. **2008**, *30*, 999–1011.
206. Kvist, M.; Danielsen, N.; Dahlin, L. B. *J. Peripher. Nerv. Syst*. **2003**, *8*, 251–259.
207. Sulaiman, O. A.; Voda, J.; Gold, B. G.; Gordon, T. *Exp. Neurol*. **2002**, *175*, 127–137.
208. Kalbermatten, D. F.; Kingham, P. J.; Mahay, D.; *et al*. *J. Plast. Reconstr. Aesthet. Surg*. **2008**, *61*, 669–675.
209. Labrador, R. O.; Buti, M.; Navarro, X. *Exp. Neurol*. **1998**, *149*, 243–252.
210. Matsumoto, K.; Ohnishi, K.; Kiyotani, T.; *et al*. *Brain Res*. **2000**, *868*, 315–328.
211. Tong, X. J.; Hirai, K.; Shimada, H.; *et al*. *Brain Res*. **1994**, *663*, 155–162.
212. Thompson, D. M.; Buettner, H. M. *Ann. Biomed. Eng*. **2004**, *32*, 1120–1130.
213. Cuevas, P.; Carceller, F.; Dujovny, M.; *et al*. *Neurol. Res*. **2002**, *24*, 634–638.
214. Dezawa, M.; Hoshino, M.; Nabeshima, Y.; Ide, C. *Curr. Mol. Med*. **2005**, *5*, 723–732.
215. Dezawa, M.; Takahashi, I.; Esaki, M.; Takano, M.; Sawada, H. *Eur. J. Neurosci*. **2001**, *14*, 1771–1776.
216. Shimizu, S.; Kitada, M.; Ishikawa, H.; Itokazu, Y.; Wakao, S.; Dezawa, M. *Biochem. Biophys. Res. Commun*. **2007**, *359*, 915–920.
217. Woodbury, D.; Schwarz, E. J.; Prockop, D. J.; Black, I. B. *J. Neurosci. Res*. **2000**, *61*, 364–370.
218. Dezawa, M. *Anat. Sci. Int*. **2002**, *77*, 12–25.
219. Hidayah, H. N.; Mazzre, M.; Ng, A. M.; Ruszymah, B. H.; Shalimar, A. *Med. J. Malaysia* **2008**, *63*(Suppl. A), 39–40.
220. Mahay, D.; Terenghi, G.; Shawcross, S. G. *Biotechnol. Appl. Biochem*. **2008**, *51*, 167–176.
221. Mahay, D.; Terenghi, G.; Shawcross, S. G. *Exp. Cell Res*. **2008**, *314*, 2692–2701.
222. Hou, S. Y.; Zhang, H. Y.; Quan, D. P.; Liu, X. L.; Zhu, J. K. *Neuroscience* **2006**, *140*, 101–110.
223. Pereira Lopes, F. R.; Camargo De Moura Campos, L.; Dias Correa, J., Jr.; *et al*. *Exp. Neurol*. **2006**, *198*, 457–468.
224. Wang, D.; Liu, X. L.; Zhu, J. K.; *et al*. *Brain Res*. **2008**, *1188*, 44–53.
225. Zheng, L.; Cui, H. F. *J. Mater. Sci. Mater. Med*. 2010.
226. Choi, B. H.; Zhu, S. J.; Kim, B. Y.; Huh, J. Y.; Lee, S. H.; Jung, J. H. *Int. J. Oral Maxillofac. Surg*. **2005**, *34*, 537–542.
227. Yamakawa, T.; Kakinoki, R.; Ikeguchi, R.; Nakayama, K.; Morimoto, Y.; Nakamura, T. *Cell Transplant*. **2007**, *16*, 811–822.
228. Zhang, P.; He, X.; Zhao, F.; Zhang, D.; Fu, Z.; Jiang, B. *J. Reconstr. Microsurg*. **2005**, *21*, 565–571.
229. Zhao, F. Q.; Zhang, P. X.; He, X. J.; *et al*. *Biomed. Environ. Sci*. **2005**, *18*, 326–333.
230. Tohill, M.; Mantovani, C.; Wiberg, M.; Terenghi, G. *Neurosci. Lett*. **2004**, *362*, 200–203.
231. Kingham, P. J.; Mantovani, C.; Terenghi, G. *Neurosci. Lett*. **2009**, *467*, 164–168.
232. Radtke, C.; Schmitz, B.; Spies, M.; Kocsis, J. D.; Vogt, P. M. *Int. J. Dev. Neurosci*. **2009**, *27*, 817–823.
233. Saunders, F. W. *Can. J. Neurol. Sci*. **1980**, *7*, 221–222.
234. Lin, G.; Garcia, M.; Ning, H.; *et al*. *Stem Cells Dev*. **2008**, *17*, 1053–1063.
235. Lin, T. M.; Tsai, J. L.; Lin, S. D.; Lai, C. S.; Chang, C. C. *Stem Cells Dev*. **2005**, *14*, 92–102.
236. Strem, B. M.; Hicok, K. C.; Zhu, M.; *et al*. *Keio J. Med*. **2005**, *54*, 132–141.
237. Alessandri, G.; Emanueli, C.; Madeddu, P. *Ann. N. Y. Acad. Sci*. **2004**, *1015*, 271–284.
238. Bixby, S.; Kruger, G. M.; Mosher, J. T.; Joseph, N. M.; Morrison, S. J. *Neuron* **2002**, *35*, 643–656.
239. Chen, J.; Kwon, C. H.; Lin, L.; Li, Y.; Parada, L. F. *Genesis* **2009**, *47*, 122–131.
240. Gao, J.; Coggeshall, R. E.; Chung, J. M.; Wang, J.; Wu, P. *NeuroReport* **2007**, *18*, 565–569.
241. Guo, B. F.; Dong, M. M. *Otolaryngol. Head Neck Surg*. **2009**, *140*, 159–164.
242. Heine, W.; Conant, K.; Griffin, J. W.; Hoke, A. *Exp. Neurol*. **2004**, *189*, 231–240.
243. Kruger, G. M.; Mosher, J. T.; Bixby, S.; Joseph, N.; Iwashita, T.; Morrison, S. J. *Neuron* **2002**, *35*, 657–669.
244. Neville, C. M.; Huang, A. Y.; Shyu, J. Y.; Snyder, E. Y.; Hadlock, T. A.; Sundback, C. A. *Int. J. Neurosci*. **2009**, *119*, 15–39.
245. Hagedorn, L.; Suter, U.; Sommer, L. *Development* **1999**, *126*, 3781–3794.

5.532. Nerve Tissue Engineering

A Sannino, M Madaghiele, M Carrozzo, and L Salvatore, University of Salento, Lecce, Italy
L Ambrosio, National Research Council, Naples, Italy

© 2011 Elsevier Ltd. All rights reserved.

5.532.1.	**Introduction**	436
5.532.1.1.	Why Nerve Tissue Engineering?	436
5.532.1.2.	Social Impact of Nerve Injuries	436
5.532.1.3.	PNS and CNS: Structures and Physiological Responses to Injury	437
5.532.1.3.1.	Peripheral nervous system	437
5.532.1.3.2.	Central nervous system	438
5.532.2.	**State of the Art of PNS Tissue Engineering**	439
5.532.2.1.	Entubulation Technique and Nerve Conduit Design	439
5.532.2.2.	Overview of Ongoing Research and Potential for Therapeutic Use	442
5.532.2.3.	Case Study: Collagen-Based Tubes with Oriented Porous Patterns	445
5.532.3.	**State of the Art of CNS Tissue Engineering**	447
5.532.3.1.	Cellular Strategies	447
5.532.3.2.	Molecular Strategies	448
5.532.3.3.	Biomaterial-Based Strategies	449
5.532.3.4.	From Biomaterials to Tissue-Engineered Devices: Combinatorial Strategies	450
5.532.4.	**Concluding Remarks**	451
References		451

Glossary

Apoptosis Active process of programmed cell death (PCD), including chromosomal DNA cutting, chromatin condensation, and nuclear and cell fragmentation, that may occur in multicellular organisms.

Astrocytes The most important glial cells in the central nervous system (CNS), having nutritive functions and forming, in CNS peripheral zones, a continuous cellular coating around blood vessels, creating the blood–brain barrier.

Autograft Tissue transplantation from one part of the body to another in the same individual.

Blood–brain barrier Anatomofunctional barrier, consisting of astrocytes in contact with the wall of cerebral vessels, which selectively restricts the entry of substances within the central nervous system.

Cerebrospinal fluid Liquid composed of 90% water, rich in sodium, potassium, and chlorine. It is located in the intrathecal space, the brain ventricles, and the central canal of the spinal cord. It is important for metabolic activities and protection of the CNS.

Chromatolytic reaction Series of cellular modifications in the nerve cell body, including the soma swelling, the fragmentation of the endoplasmic network, the eccentric position of the nucleus, a global increase of protein and RNA synthesis, and a variation of neuron-expressed genes.

Corticosteroids Hormones produced in the adrenal cortex. Corticosteroids are involved in a wide range of physiological processes such as immune response and inflammation regulation.

Frequency of reinnervation Percent of defects that were bridged by myelinated axons.

Gene therapy Inclusion of genetic material (DNA) inside cells. This inclusion process is called transfection.

Intrathecal space Space located between the arachnoid and the pia mater of the brain and the spinal cord.

Macrophages Phagocytic white blood cells performing an important role during inflammatory and immune response.

Neural parenchyma Nervous tissue functionally active in genesis and transmission of electrochemical impulses.

Neurotrophic factors Nutritive (trophic) factors necessary for the growth of nerve endings, playing an important role in their postinjury survival.

Plasticity Changing of the structure, function, and organization of neurons in response to particular stimuli.

Abbreviations

AcNHGlc	N-Acetylglucosamine
aFGF	Acidic fibroblast growth factor
bFGF	Basic fibroblast growth factor
BMPs	Bone morphogenetic proteins
BDNF	Brain-derived neurotrophic factor
CNS	Central nervous system
CNTF	Ciliary neurotrophic factor
DG	Dentate gyrus
DNA	Deoxyribonucleic acid
ECM	Extracellular matrix
ES	Embryonic stem cells

EtO	Ethylene oxide
GDNF	Glial cell line-derived neurotrophic factor
GMP	Good manufacturing practice
HPMA	*N*-2-Hydroxypropyl methacrylamide
MAG	Myelin associated glycoprotein
MSCs	Mesenchymal stem cells
NGF	Nerve growth factor
NHGlc	Glucosamine
NPCs	Neural progenitor cells
NT-3	Neurotrophin-3
OECs	Olfactory ensheathing cells
OMgp	Oligodendrocyte myelin glycoprotein
OPCs	Oligodendrocyte precursor cells
PAN/PVC	Polyacrylonitrile/polyvinylchloride
PCL	Poly-ε-caprolactone
PGA	Poly(glycolic acid)
PHB	Poly-β-hydroxybutyrate
PHEMA–MMA	Poly(2-hydroxyethyl methacrylate-*co*-methyl methacrylate)
PHPMA	Poly[*N*-(2-hydroxypropyl) methacrylamide]
PLA	Poly(lactic acid)
PLGA	Poly(lactic-*co*-glycolic) acid
PNS	Peripheral nervous system
RGD	arginine (R)-glycine (G)-aspartic acid (D), peptide sequence
RNA	Ribonucleic acid
SCI	Spinal cord injury
SCID	Severe combined immune deficiency
Sema4D/CD100	Semaphorin-4D, also known as cluster of differentiation 100
SGZ	Subgranular zone
SVZ	Subventricular zone
TGF-β	Transforming growth factor beta

5.532.1. Introduction

5.532.1.1. Why Nerve Tissue Engineering?

Permanent cells are defined as cells that are unable to replicate in postnatal life. Nervous cells, also termed neurons, together with skeletal muscle and cardiac cells, are included in this group, which traditionally identifies the human tissues that are incapable of spontaneous regeneration.

It is well known, however, that the ability of cells to proliferate does not ensure regeneration of an injured adult tissue. Tissues that can regenerate spontaneously may not do so when severely injured (e.g., bone); also, cell replacement (i.e., cell transplantation) and/or recruitment of endogenous stem cells in nonregenerative tissues may not suffice to induce regeneration. Indeed, adult tissues tend to repair themselves by replacing the injury site with connective tissue (i.e., scar tissue), which closes the wound and limits a further extension of the damage. Tissue engineering aims at inducing tissue regeneration by (a) identifying the endogenous factors that prevent spontaneous regeneration and (b) modifying the postinjury cellular microenvironment, by suppressing or limiting the action of the inhibitory factors, to direct cells toward regeneration rather than repair.

The intrinsic ability of axons to regrow under specific environmental stimuli makes nerve regeneration a possible, realistic goal, together with the possibility of inducing or regulating the plasticity of intact axons for some functional recovery. However, the sophisticated wiring of peripheral and central nervous systems (PNS and CNS, respectively) makes nerve tissue engineering particularly challenging. Even in cases where a certain degree of axonal regeneration has been induced, the full recovery of motor or sensory functions, which depends on the establishment of proper nerve reconnections, is far from being a reality. As yet, the clinical treatment of PNS neurotmesis (i.e., the most severe PNS injury, the complete transection of the nerve) mostly relies on the use of autograft tissues, when these are available, while the current therapies for CNS injury are directed toward minimizing inflammation in the acute setting and stimulating the little endogenous plasticity of the adult CNS. Unfortunately, the efforts made so far by tissue engineers to develop novel molecular, cellular, and/or scaffold-based therapies for functional recovery after nerve injury have often led to clinical trials that yielded equivocal results with regard to the safety and effectiveness of a given therapy.

The aim of this chapter is to discuss the state of the art of nerve tissue engineering, with a critical view of the tremendous gap existing between the laboratory/experimental setting and clinical practice. The development of a tissue-engineered medical product is a highly complex process, and this is especially true in nerve tissue engineering, where the supply of exogenous cells and molecules is likely to be necessary (at least for CNS repair), making the regulatory requirements harder to meet compared to those for cell-free products. In the following introductory sections, a brief description of PNS and CNS pathophysiology is provided, with some insights into the socioeconomic impact of nerve injuries, in an attempt to explain why nerve tissue engineering is likely the most promising way to go for functional nerve recovery.

5.532.1.2. Social Impact of Nerve Injuries

There are several factors that can give rise to PNS injuries or damage: systemic diseases (e.g., diabetes), infections (e.g., Lyme disease), and direct trauma or pressure on the nerve, which may result from motor vehicle accidents, falls, sports injuries, surgical interventions, etc. Although relatively little data are available on the incidence of PNS injuries, it is estimated that in the United States alone, approximately 200 000 surgical procedures are performed annually, while in Europe up to 300 000 cases of nerve injury are reported each year.[1] The consequences of PNS injury depend on the extent of the damage and may range from pain or impaired sensitivity to muscle weakness or paralysis, which could dramatically restrict the patient's daily activities. The PNS's capability of functional recovery is also affected by the extent of the damage, and lifelong disabilities, unfortunately, are common.

The incidence of CNS injuries is lower than that of PNS injuries, but their impact on the patient's life, as well as their socioeconomic costs, is definitely more devastating. As an example of CNS injury, in this and in the following paragraphs, we refer to spinal cord injury (SCI), which, if complete, leads to permanent loss of sensorimotor function at all body parts below the lesion site. SCI is highly complex and no cure currently exists. It is estimated that 253 000 people are affected by SCI in the United States, 45.7% of whom have permanent paraplegia or tetraplegia, with 11 000 new cases of SCI each year.[2] As for PNS injuries, the etiology of SCI accounts for multiple factors. Motor vehicle crashes represent approximately 40% of injuries, followed by falls and acts of violence (about 20% each) and sporting activities.[3] The human cost is incredibly high, also considering that SCI patients are mostly young adults (the median age is 26), who have to cope with their SCI disability for the rest of their lives.

5.532.1.3. PNS and CNS: Structures and Physiological Responses to Injury

The nervous system represents a complex network of coordination and control that receives, elaborates, and responds to all information coming from the external and internal environments. In vertebrates, it is organized in two main units: the CNS and the PNS. The former includes the brain and the spinal cord, while the latter is formed by the nerves branching out from the CNS and going to the periphery, called the cranial and spinal nerves, respectively. Although it corresponds to the definition of cranial nerve, the optic nerve is derived from the diencephalon during embryonic development and thus is structurally similar to CNS nervous tissues. Therefore, it is considered part of the CNS and is often used as a model in studies regarding the capability of the CNS for recovery following an injury.

The nervous system includes several kinds of cells, which can be grouped into two classes: nervous cells, or neurons, and glial cells, or simply glia. The neuron represents the functional unit of the nervous system and, from a morphological point of view, it shows four different zones (Figure 1). The cell body, or soma, is the cell metabolic center. Dendrites of short length develop from it and represent the main apparatus for receiving messages from neighboring neurons. The axon, a cytoplasmic extension of the cell body, represents the conductive element through which messages or signals, in the form of electric impulses, are delivered. The presynaptic endings are the units devoted to transferring the messages to their proper target, that is, other neurons, muscle cells, or glands. Glial cells, typically 10 times more numerous than nervous cells, are not directly involved in the processing of information, but provide supporting tissues. Some glial cells (i.e., oligodendrocytes in the CNS and Schwann cells in the PNS) are responsible for the ensheathing of axons with insulating myelin, which improves the conduction and the speed of the electric impulse. Microglia cells may play an important role in inflammation processes, working as phagocytes.

5.532.1.3.1. Peripheral nervous system

Peripheral nerves making up the PNS are complex organs whose structure presents a cylindrical arrangement (Figure 2).

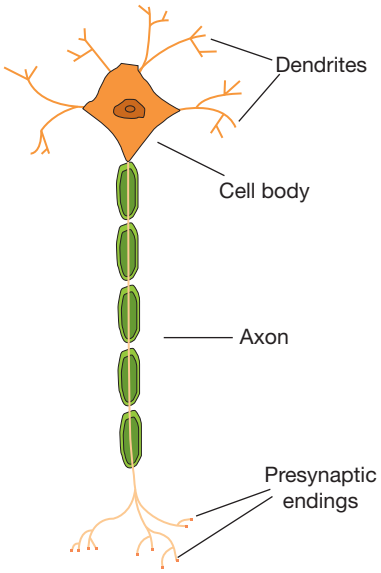

Figure 1 Schematic view of a neuronal cell. The axon is surrounded by myelin sheaths generated by Schwann cells. The gaps between the myelin sheaths are the nodes of Ranvier, which give rise to a saltatory conduction.

A nerve trunk can comprise one or more fascicles, each consisting of many nerve fibers. Each nerve fiber comprises an axon, wrapped in a sheath of myelin that is synthesized by Schwann cells, and a tubular basement membrane lining the external surface of the Schwann cells and myelin. Nerve fibers, which are also referred to as neuronal tissues, are surrounded and supported by nonneuronal tissues, that is, the endoneurium, the perineurium, and the epineurium. The endoneurial stroma surrounds each nerve fiber and provides support to it by means of vascularization. The perineurium is a tight, multilayered tissue that surrounds each nerve fascicle and acts as a permeability barrier. The epineurium is a strong sheath that surrounds the entire multifascicular assembly or nerve trunk.

Most injuries to the PNS and CNS affect the axons. Injured peripheral nerves are capable of spontaneous regeneration only when the nerve trunk is not transected and the Schwann cell basal lamina is undamaged, that is, in mild crushing injuries. Seddon's classification[4] divides PNS injuries into three classes: neuropraxia, axonotmesis, and neurotmesis. Neuropraxia is the mildest injury, which may result from mechanical compression or ischemia, but it does not cause any structural damage or loss of nerve continuity. Recovery is rapid and complete.

Regeneration is still obtained in case of axonotmesis, where the axon is interrupted but the basement membrane and the stromal tissues attached to it are preserved. Following axonotmesis, the proximal segment, which is directly linked to the cell body, is able to survive, although the cell body may undergo a series of morphological and metabolic reorganizational changes, comprehensively called chromatolytic reaction, that are reversible in case of regeneration. Some retrograde degeneration, in the form of demyelination of the proximal end, also occurs but is usually limited to only a few myelin segments. Conversely, the distal segment is subjected to anterograde or Wallerian degeneration. The primary histological

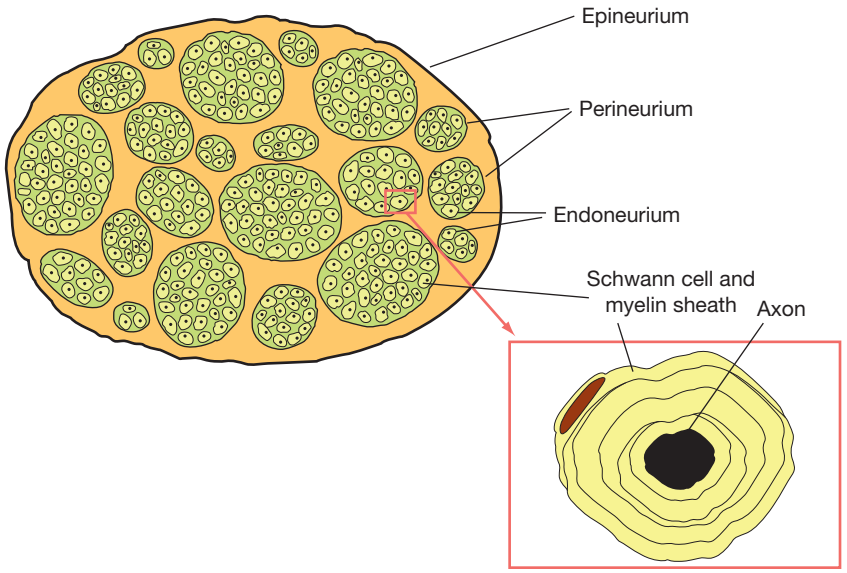

Figure 2 Schematic cross-sectional view of a peripheral nerve. For the sake of simplicity, the epineurial, perineurial, and endoneurial blood vessels are not reported in the scheme.

change in Wallerian degeneration involves physical fragmentation of both axons and myelin, a process that begins within hours after the injury. In the degeneration of the distal stump, the axoplasm (composed of neurofilaments and microtubules) disintegrates and is converted into granular and amorphous debris. The main event that triggers this process appears to be an increase in the axoplasmic calcium level due to the transection of the nerve fibers. The debris resulting from the degeneration is efficiently cleared by macrophages and Schwann cells, and the final outcome is the formation of an endoneurial tube (i.e., a cylindrical basement membrane free of axons and myelin). While Wallerian degeneration is taking place, an intense proliferation of Schwann cells, which is not observed in undamaged nerves, occurs both in the proximal and distal segments. Once the degeneration is complete, regeneration can finally occur. Schwann cells form linear structures (bands of Büngner) along the empty basement membrane, while the proximal end sends out sprouts, which are attracted by the growth factors secreted by the Schwann tube. When a sprout reaches the tube, it can penetrate the distal segment and finally reinnervate the target tissue.

In the case of neurotmesis, in which the complete interruption of the entire nerve bundle occurs, there is a local vascular trauma that leads to hemorrhage and edema, resulting in a vigorous inflammatory response. Fibroblasts proliferate and a dense fibrous scar is formed at both nerve stumps (neuroma formation). Both the scar and the long gap between the stumps interfere with the spontaneous axonal regeneration discussed above (i.e., the proximal sprouts cannot reach the endoneurial tubes formed in the distal stump), permanently compromising the nerve structure and functionality. In such cases, nerve regeneration can be stimulated by means of surgical techniques involving the implantation of autograft tissues or synthetic grafts between the nerve stumps, as discussed later. The quality of the nerve regeneration induced by the graft compared to that of the normal nerve can be evaluated quantitatively in terms of histological and/or electrophysiological data.[5] However, if the surgery is delayed or the nerve gap is too long, the endoneurial tubes formed in the distal stumps may undergo degeneration before the proximal axons can reach them. In such cases, the disruption of the Schwann cell basement membrane does not support further reinnervation, and chronic denervation of the distal stump is established.[6]

5.532.1.3.2. Central nervous system

Unlike what happens in the PNS, the proximal ends of injured CNS axons are mostly unable to elongate and form new synapses, preventing the *de facto* restoration of pretrauma conditions. Several hypotheses have been formulated in an attempt to explain this striking difference between the CNS and the PNS with regard to regenerative capacity. A line of research focuses on the inherent differences in the maturation of the two nervous systems, characterized by the loss of growth capacity in central neurons with increasing age. However, the main hypotheses are related to the intrinsic structural differences and the different microenvironments established after an injury in the CNS and the PNS.

SCI provides a CNS injury model that encompasses all the environmental changes to which CNS axons are exposed following the initial mechanical insult. The spinal cord, located in the vertebral column, extends from the brain stem to the first lumbar vertebra, beyond which the spinal nerves form the so-called cauda equina, which extends to the coccyx. When viewed in cross section, the spinal cord reveals a butterfly-shaped core of gray matter, consisting mostly of cell bodies and glial cells, and an exterior region of white matter, consisting mostly of axons and oligodendrocytes that wrap axons in white insulating myelin. The ventral half of the gray matter, divided into two ventral lobes or horns, contains the cell bodies of motor neurons, which send out axons to muscles; on the other side, the two dorsal horns contain the cell bodies of sensory neurons, which receive information from the

periphery through the dorsal roots. Thirty-one pairs of spinal nerves enter and exit the spinal cord throughout its length: 8 pairs of cervical nerves, 12 pairs of thoracic nerves, 5 pairs of lumbar nerves, 5 pairs of sacral nerves, and 1 pair of coccygeal nerves (**Figure 3**). Damage to the spinal cord usually occurs where the spine is more flexible, which is at regions C5–C7 in the neck and T10–L2 in the lower back.[7] While damage to the segmental gray matter affects function only at that segment, damage to the long tracts of white matter has devastating consequences as it eliminates function at all levels below the injury site.

The initial mechanical insult to the spinal cord triggers a cascade of secondary events that lead to neuronal death and to a highly inhibitory microenvironment for axonal growth.[8,9] A brief description of such a complex cascade is provided in the following section. With regard to neuronal death, several events have to be considered. First, as a direct result of the injury, blood flow is disrupted, causing oxygen deprivation in some parts of the spinal cord and eventually cell death, as these cells become oxygen-starved. Internal bleeding can occur at the site of injury, resulting in a further compression of the spinal cord through increased swelling of the surrounding tissues. The disruption of the blood–brain barrier that regulates the delivery of substances between the CNS and the blood supply exposes the spinal neurons to toxic molecules such as free radicals.[10] This harsh environment can cause a further loss of neurons and glial cells, triggering the immune system's response to the injury. Retrograde degeneration of the proximal end of a transected axon is another mechanism that can lead to neuronal death.

Multiple events are thought to lead to the establishment of a cellular microenvironment opposing axonal regeneration. Following axotomy, distal segments of CNS axons are subjected to Wallerian degeneration. However, oligodendrocytes do not intervene in the clearance of the myelin debris, as

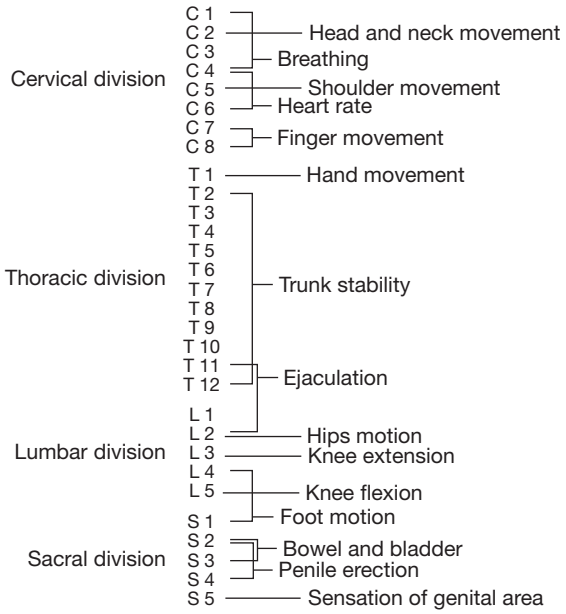

Figure 3 Functional levels along the spinal cord. Damage to the white matter at a specific level compromises function at all levels below the site of injury.

performed by Schwann cells in the PNS; they rather undergo apoptosis or enter a state of rest.[11] Myelin debris, which is cleared by microglia cells and macrophages in a much slower fashion than in the PNS, is known to contain several molecules inhibitory to axonal regeneration. It is thus postulated that the persistence of myelin at the injury site might be one of the causes of the failure of the CNS to regenerate. Furthermore, astrocytes are recruited at the damaged site following the injury, and they begin to form the glial scar, a dense connective tissue representing both a physical and chemical barrier to axonal regeneration and remyelination.[12]

However, the adult CNS shows some plasticity.[3,13] Axonal sprouting by surviving neurons can occur, but the reconnection with the appropriate targets is, of course, limited, leading to very little functional recovery or improvement following SCI. Besides surgical stabilization and decompression to limit further damage to the spinal cord, a high-dose administration of corticosteroids to minimize inflammation is the only treatment clinically available for SCI. Several strategies to stimulate the endogenous CNS plasticity and/or axonal regeneration are currently under investigation, which are mainly based on either increasing the permissive cues or decreasing the nonpermissive cues of the existing microenvironment. A combination of strategies is likely required to improve the extent of functional recovery.

5.532.2. State of the Art of PNS Tissue Engineering

5.532.2.1. Entubulation Technique and Nerve Conduit Design (see Chapter 00183)

As discussed earlier, while regeneration and functional recovery occur spontaneously in neuropraxia and axonotmesis, neurotmesis requires surgical intervention. In cases of small gap lengths (<5 mm), direct end-to-end suturing is still feasible without causing tension of the nerve, which would be detrimental to regeneration.[14] For longer gaps, the most widely used treatment consists in bridging with autograft tissue, which represents the gold standard for PNS regeneration. Donor nerves are usually small-diameter sensory nerves harvested from either the arm or the leg (e.g., the sural nerve). However, the morbidity caused to the donor site, the possible lack of a sufficient amount of donor tissue, and the wide variation in functional recovery (which may range from poor to good, depending on age, injury site, and time of surgery) make the alternative use of synthetic grafts attractive. Indeed, although some studies have reported complete restoration of sensation by means of autogenous nerve grafts, the recovery of motor function is usually less than 40%.[15] Since the first examples of entubulation, that is, the use of tubular conduits to bridge peripheral nerve defects, in the late nineteenth century,[16] a number of synthetic tubes, including nonresorbable ones (e.g., silicone tubes), have been investigated and demonstrated to facilitate PNS regeneration. The time needed for surgery has also been reduced compared to autografting procedures.

However, the regenerative mechanisms induced by the entubulation of the nerve stumps began to be understood only in the early 1980s. At the time, an impermeable silicone tube was implanted in a 10-mm rat sciatic nerve gap and the content of the implanted tube analyzed at various time points along the nerve regeneration process.[17] In particular, a clear fluid secreted

by the damaged nerve ends and containing neurotrophic factors was found to fill the tube lumen within hours. After 7 days, a fibrin cable connecting the two stumps was detectable within the exudate fluid. Notably, the cable tended to taper slightly toward the center of the gap. Fibrin fibers were longitudinally oriented and served as a matrix for the immigration of cells from both nerve stumps, including Schwann cells, fibroblasts, endothelial cells, and perineurial cells. After a few weeks, the cable was remodeled into a nerve trunk. In particular, the prior presence of Schwann cells within the cable appeared to be necessary for the elongation of axons from the proximal stump. Additionally, this and later independent investigations revealed that the regenerated nerve trunk was ensheathed by a thick connective tissue comprising myofibroblasts.[18–22] This contractile cell type[23] is likely responsible for the closure of the transected stumps by contraction, in the event of neuroma formation.

The tubular device is thus expected to provide a chamber environment, which is likely to play multiple key functions required for axonal elongation, such as allowing the formation of a fibrin matrix to direct axons from the proximal to the distal stump, concentrating the growth factors secreted by the injured nerve cells at the site of injury, preventing the infiltration of surrounding tissues, and minimizing the formation of scar tissue. Even though a silicone tube suffices to induce axonal elongation,[24,25] nonresorbable conduits give rise to a chronic foreign body reaction in the long term, causing nerve compression and requiring surgical removal.[26,27] Therefore, their use is not recommended for clinical applications, although a great deal of research has been focused on nonresorbable nerve guides other than silicone chambers.[28–31] Among nonresorbable conduits, it is worth citing those based on piezoelectric polymers,[32] which may promote axonal growth by electrical stimulation,[33] and those made of synthetic hydrogels, such as poly(2-hydroxyethyl methacrylate-*co*-methyl methacrylate) (PHEMA–MMA) hydrogels.[34] Although some successful results have been reported in animal studies in the short term, PHEMA–MMA hydrogel conduits have failed in the long term compared to autografts, likely due to their biodurability and, in some cases, to mechanical deformation.[35,36]

When approaching the design of a nerve conduit, a few basic requirements should be kept in mind. An ideal conduit should be resorbable, with a degradation rate preferably matching the rate of nerve trunk formation; flexible, but also able to retain its shape during the implantation and along the regeneration process; easily processable and sterilizable; and easy to handle and suture. Clearly, the design variables affecting the regenerative performance of the conduit are dictated by the biomaterial used and by the processing variables that can affect the functional properties of the conduit in terms of diameter, wall thickness, permeability, porosity, surface roughness, degradation rate, and mechanical strength (**Table 1**).

Synthetic polymers are usually preferred for tube fabrication, as their degradation and mechanical properties are more easily tunable compared to those of naturally derived biomaterials. Among the most widely employed synthetic polymers, several polyesters have been reported to have gained successful results, including poly(lactic acid) (PLA), poly(glycolic acid) (PGA), poly(ε-caprolactone) (PCL), and their copolymers.[37–40] Polyphosphoesters and polyurethanes have also been investigated, although their fast degradation rate and degradation-induced fracture limit their potential for the fabrication of therapeutic devices (see **Chapter 1.122, Structural Biomedical Polymers (Nondegradable)**).[41,42]

Polymers of natural origin used to produce tubular nerve chambers mainly include macromolecules derived from the extracellular matrix (ECM), such as collagen and laminin, and, more recently, chitosan, although the latter is usually combined with synthetic polymers, such as PLA, because of its brittleness (see **Chapter 2.213, Chitosan**; **Chapter 2.215, Collagen: Materials Analysis and Implant Uses**; and **Chapter 2.216, Collagen–GAG Materials**).[43–46] Other natural biomaterials, such as alginate and decellularized matrices, have been reported in studies related to PNS regeneration, but they have been employed in the form of full cylindrical matrices rather than empty conduits. Although the chemical composition of natural polymers cannot be regarded as a design variable, it is possible to adjust both the degradation rate and the mechanical strength of such polymers by means of cross-linking methods. When increasing the degree of cross-linking of a given polymer network, the stiffness increases while the degradation rate is lowered, as demonstrated for collagen-based scaffolds.[47,48] Clearly, cross-linking treatments that avoid the incorporation of any toxic molecules are strongly recommended, such as those based on ultraviolet irradiation, dehydrothermal treatment, and carbodiimide-mediated cross-linking reaction.[49,50]

It is worth stressing that, although the degradability of the nerve chamber is well known to improve the quality of nerve regeneration, the quantification of the degradation rate for

Table 1 Main design properties and design variables for the development of biomaterial-based devices for peripheral nerve regeneration

Properties of conduit and/or filling matrix	*Optimization of the desired property for specific devices*		*Design variables*			
	Tube	*Filling matrix or fibers*	*Biomaterial*	*Degree of cross-linking*	*Pore size*	*Pore orientation*
Degradation rate	49	45,73	✓	✓	✓	
Mechanical stiffness and strength	35,36	73	✓	✓		✓
Surface area	57–60	45,52,72,73,79	✓		✓	
Contact guidance	57,80,81	73,78,79	✓		✓	✓
Protein/cell permeability	44,45,54–56	45,52,72	✓	✓	✓	✓

The symbol ✓ highlights the variables that tune the device properties known to affect the quality of induced nerve regeneration. Where the symbol ✓ is not present, the design variable is supposed to have either no effect at all or, at least, no significant known effect on the selected device property.

different tubular devices, expressed as mass half-life, is rarely reported in the literature.[51] It is reasonable to postulate that the degradability of a conduit can significantly affect the nerve regenerative process if the timescales of the two processes are approximately coincident. Evidence from several independent investigations seems to suggest that the initial regeneration of a rat sciatic nerve in a 10-mm gap, with innervation of the distal stump for some functional recovery, requires about 10–12 weeks to occur,[17,52,53] although the completion of the regenerative process can take as long as 2 years.[43] Resorbable conduits requiring a much longer time than 12 weeks to degrade in a rat model would likely have no significant effect on the quality of nerve regeneration, at least in the short term.[41] Conversely, a comparative study related to the application of collagen tubes with different degrees of cross-linking (corresponding to half-lives in the range of 1–10 weeks) into a 15-mm rat sciatic nerve gap confirmed that an optimal degradation rate of the conduit does exist for improved nerve regeneration.[49] For the collagen tubes tested, a chamber half-life of approximately 2–3 weeks provided the best histomorphometric results at the gap midpoint, after a 9-week period (see **Chapter 2.216, Collagen–GAG Materials**).

The permeability of the tube wall appears to play a key role in the regenerative processes induced by the tube. In particular, cell-permeable tube walls (i.e., with pores approximately equal to or larger than 20 μm) have been reported to perform better than protein-permeable or nonpermeable ones, at least when considering porous collagen conduits.[5] The documented presence of myofibroblasts in the inner wall of the collagen-based tubes[19,44,45] has led to the reasonable hypothesis that the device's capability to host myofibroblasts might limit or prevent the myofibroblast-exerted contraction on the nerve stumps, thus facilitating nerve regeneration. However, the effect of this speculative mechanism on the favorable action of pores in the inner tube wall needs further investigation. What is generally considered when designing a conduit is that the tube wall should be porous enough to allow an efficient transport of nutrients and oxygen from the surrounding environment, and at the same time prevent infiltration into, or formation of fibrous tissue in, the wound site. These requirements translate into a porous tube wall that is at least protein-permeable. The limitation of fibrous tissue formation within the defect would be addressed by cell-impermeable pores, but, in principle, these could be present either at the outer tube wall or at the inner tube wall. While the role of conduit cell permeability has not been widely explored, recent studies have highlighted the development of fabrication techniques that lead to a gradient in pore size along the tube wall.[54–56] Two of these studies, in particular, have focused on the control of pore orientation, in addition to pore size. Collagen-based tubes with radially aligned porosity, cell-permeable pores at the inner wall, and cell-impermeable pores at the outer wall show the potential to regulate myofibroblast attachment and migration.[55] Conversely, PLGA–pluronic composite tubes, possessing radial pores with a cell-impermeable inner wall and a cell-permeable outer wall, have been developed to allow a good nutrient transport while isolating the defect from external fibrous tissues.[56] Regardless of the different biomaterials used, the application of these devices in animal models could help in understanding the effect of tube wall porosity (in terms of both pore size and orientation) on the quality of nerve regeneration, which is still unclear. Nonetheless, findings from a number of independent investigations suggest that the surface area of the inner wall of the tubular device is a key variable to be considered when designing a nerve conduit, better nerve regeneration being achieved with increased surface area.[57–60] For PCL tubes with a macroporous outer wall, a microporous inner wall (pore size 1–10 μm) is found to be more advantageous for nerve regeneration, compared to nonporous and macroporous inner walls.[58]

However, it is worth noting that, for some devices, the presence of pores on the tube wall might be detrimental. This has been recently confirmed by a study on polyester-based conduits, which evidenced that the tubes possessing porous walls, with a pore size of 10–20 μm, hampered nerve regeneration compared to nonporous tubes, likely due to the porosity-induced change in the mechanical properties and degradation rate of the conduit.[61]

The tube macro- and microstructures depend on the processing method used to produce the conduit. Some pioneering techniques for the fabrication of conduits with porous tube walls included the rolling and sealing of foam sheets,[62] fiber deposition onto a rotating mandrel and subsequent freeze-drying,[63] and immersion precipitation methods.[64] The current approach is to combine multiple manufacturing methods to increase the level to which the scaffold microstructure can be manipulated. Microfabrication by means of soft lithography is also largely exploited for the production of microgrooved conduits, which increase the available surface area for cell interaction and may provide contact guidance to Schwann cells and axons.[65] As more technologically developed alternatives, rapid prototyping techniques are emerging as excellent methods to produce customized tissue engineering scaffolds, including nerve conduits. However, only a limited number of materials can be processed by means of such techniques. Some recent progress has nevertheless been reported regarding the applicability of rapid prototyping techniques to collagen-based composites for nerve regeneration.[66]

The overall experimental evidence collected so far suggests that the regenerative capability of a tubular device depends strongly on its size. Traditionally, the gap length has been considered the limiting factor for induced nerve regeneration. For a given conduit or tubular configuration, there seems to be a critical length size related to the animal species, above which the capability of the device to allow axonal regeneration drops below 50%, in terms of frequency of reinnervation.[5] For example, in the case of an empty silicone tube, the critical gap length for the rat sciatic nerve is about 10 mm.[67] Assuming the silicone tube as a negative control, it makes sense to compare the regenerative performance of any novel device with that of the silicone tube only for gaps equal or longer than the critical size. Unfortunately, investigators often choose the main variables of their experiments arbitrarily (i.e., animal species, gap length, and time and location of observation along the regenerating nerve trunk), which makes a comparison among the different devices tested hard to perform. Importantly, the lack of experimental standardization also hinders the comprehension of the regenerative mechanisms induced by the specific device configuration.

In addition to the gap length, another important and often underestimated factor that determines the defect size and

affects the performance of a conduit is the nerve diameter. The inner diameter of the conduit is, of course, directly related to that of the nerve, being slightly larger than the latter for a smooth accommodation of the nerve stumps. Even when encouraging animal data have been provided for a given tubular device, clinical studies on relatively large human nerves, such as the ulnar and median nerves (which have a diameter of ~3–4 mm), have mostly led to unsuccessful results with very rare positive outcomes.[31,68,69] It is important to underscore the fact that animal models, including nonhuman primates, are not able to reproduce the large caliber of human nerves (with the exception of porcine sciatic nerve), which is a factor to be considered in view of clinically bridgeable gap lengths in humans. The nerve diameters treated in rodent models, which are the most widely employed, are in the range of 1–2 mm. It has been recently hypothesized that the overall volume of the nerve chamber, determined by both length and diameter, is the true limiting factor in nerve regeneration.[70] This would imply that, for a given chamber and a fixed animal species, the critical gap length is dramatically reduced as the nerve diameter is increased (i.e., the gap length is reduced by 4 when the nerve diameter is doubled). A possible explanation for a critical chamber volume lies in the inability of the chamber to provide a sufficient concentration of neurotrophic factors as well as a crossing fibrin cable, in larger volumes.

Due to the wide range of animal species and gap models employed in independent investigations, it is difficult to estimate the largest nerve defect volume bridged experimentally by an empty conduit. Currently, only a small number of nerve conduits have reached the field of clinical practice (Table 2), and their use is limited to the treatment of small defects (not longer than 30 mm) in small-diameter nerves (e.g., digital and radial sensory nerves). Moreover, in spite of the advances in the tube manufacturing techniques and the optimization of the surgical procedures, no tubular device has proved superior to the nerve autograft as yet, even in small animal models.

An important aspect to evaluate is the morphology of the regenerated nerve trunk, compared to that of the normal nerve. In particular, the evidence collected so far shows that the ability of nerves to remyelinate after regeneration is not optimal, leading to thinner myelinated axons and impaired functional recovery. G-ratio measurements (axon diameter vs. fiber diameter) are far below the normal value of uninjured axons.[71] A long-term study regarding the use of collagen tubes to bridge a 10-mm gap in the rat sciatic nerve showed that myelinated axons undergo significant remodeling and increase their diameter between 30 and 60 weeks of the tube implant.[44,45] However, in spite of this late remodeling, the number and the diameter of myelinated axons remain below the normal values. Very little is currently known about the mechanisms because of which Schwann cells do not remyelinate completely after injury. Another important difference between a regenerated nerve and a normal nerve lies in their stromal tissues. Clear evidence of the *in vivo* regeneration of physiological endoneurium and epineurium has not been reported.[5] The evolution from tubular conduits to more complex tissue-engineered devices to improve both the quality and the extent of nerve regeneration is the subject of extensive research and is concisely discussed in the following section.

5.532.2.2. Overview of Ongoing Research and Potential for Therapeutic Use

The ongoing investigations on PNS tissue engineering are mostly directed toward increasing the bridgeable gap length and diameter as well as improving the quality of the regenerated nerve trunk to enhance functional outcome.

Table 2 Commercial nerve guidance conduits for the regeneration of peripheral nerves

Commercial products	*Biomaterial/description*	*Available sizes (mm) (L = length; ID = inner diameter)*	*Manufacturer/Web site*
Axoguard™ Nerve Connector (formerly Surgisis® Nerve Cuff)	Surgisis® (porcine acellular small intestinal submucosa)	$L = 10$ ID up to 5	Cook Biotech, Inc., IN, USA, www.cookbiotech.com
Neuragen®	Bovine type I collagen	$L = 20; 30$[a] ID = 1.5; 2; 3; 4; 5; 6; 7	Integra Lifesciences Corp., NJ, USA, www.integra-ls.com
Neuroflex™ Neuromatrix™	Bovine type I collagen; Neuroflex™ is more flexible compared to Neuromatrix™	$L = 25$ ID = 2; 2.5; 3; 4; 5; 6	Collagen Matrix, Inc., NJ, USA www.collagenmatrix.com
GEM Neurotube®	Polyglycolic acid (PGA) mesh tube	$L = 20; 40$[a] ID = 2.3; 4; 8	Synovis Micro Companies Alliance, Inc., AL, USA, www.synovismicro.com
Hydrosheat™ (formerly SaluBridge™)	Tubular implant, made up of Salubria (PVA-based hydrogel); nondegradable	N/A	SaluMedica, LLC, GA, USA, www.salumedica.com
Neurolac®	Tubular implant, made up of poly (D,L-lactide-ε-caprolactone); transparent	$L = 30$ ID = 1.5; 2; 2.5; 3; 4; 5; 6; 7; 8; 10	Polyganics BV, Netherlands, www.polyganics.com
RevolNerv®	Porcine type I/III collagen; transparent	$L = 10; 15$ ID = 2; 4; 6	Orthomed, SA, France, www.orthomed.fr

N/A, not available.

[a] The longest size is available only for the smallest inner diameter.

The presence of a filling in the tube lumen is considered fundamental to improve the regenerative response of a conduit, by providing adequate neurotrophic support and directional guidance in cases where endogenous supply is limited (i.e., in large defects). Many tube fillings have been investigated in recent years (**Figure 4**), including porous- or fibrous-oriented matrices, hydrogels, cell suspensions, molecular regulators (e.g., growth factors), and their various combinations. The regenerative activity of several filled nerve chambers has proved significantly higher than that of empty ones in terms of increased critical gap length.[5]

Several devices that possess axially oriented pores of various sizes can be included among the porous matrices explored so far as luminal fillers (for different kinds of conduits) in an attempt to mimic the structure of the fibrin cable formed between the nerve stumps and originating from the nerve exudate. Such scaffolds, which can become coated with endogenous fibrin *in vivo*, are meant to provide an immediate support for the migration of Schwann cells within the chamber and for the elongation of axons. The pore size is expected to play an important role in determining the matrix bioactivity as it affects the specific surface area available for cell attachment. Oriented collagen matrices with a pore size of 20 μm have proved optimal for PNS regeneration in the rat sciatic nerve model and provided results comparable to the nerve autograft when coupled with a collagen tube in a 10-mm gap.[45,52,72] As collagen is a component of the ECM, it is reasonable to question whether, and to what extent, this ECM nature may contribute to the regenerative activity of the tube filling. Recent evidence suggests that the aligned microstructure of the collagen matrix is likely the key element for a successful nerve regeneration.[73] Indeed, porous collagen fillings without any appreciable orientation have been found to hamper regeneration when inserted into collagen conduits.[74] The same negative effect on nerve regeneration has also been reported when using collagen gels to deliver exogenous Schwann cells within the nerve chamber.[75]

In addition to matrices with longitudinally oriented pores, fibrous matrices, obtained by assembling filaments or fibers of several biomaterials, such as collagen,[76] polyesters,[77,78] and silk,[60] have also been investigated. However, the existence of an optimal fiber configuration, in terms of number and diameter of fibers, has not been widely addressed. With regard to collagen filaments used to bridge a rat sciatic nerve defect, a higher number of filaments was found to enhance the number of regenerated axons,[79] likely due to increased surface area and contact guidance. A recent study related to the application of electrospun fibers on the inner surface of a nerve conduit confirmed that the surface area of the nerve chamber may play a key role in nerve regeneration and also affect the diameter of the regenerated nerve trunk.[57] In this study, a 15-mm gap in the rat sciatic nerve was bridged by conduits possessing electrospun fibers, oriented either longitudinally or circumferentially, on the inner surface. Surprisingly, there was no significant histomorphometric difference in the nerve trunk regenerated by means of these two types of conduits, suggesting that the increased surface area of the conduit may affect its regenerative capacity more significantly than the contact guidance. However, functional recovery was not appreciable for those conduits, unless the fibers were used to deliver exogenous glial cell line-derived neurotrophic factor (GDNF). Moreover, evidence from another independent study highlighted that contact guidance of the tube wall affects the quality of induced nerve regeneration[80,81] significantly. In spite of the different results reported for different conduits, it is possible to argue that a luminal filler possessing proper surface area and directional guidance cues, rather than a surface modification of the conduit, is more likely to elicit a functional nerve recovery.

The use of a nerve conduit filled with either fibers or an aligned matrix, in the absence of any other exogenous

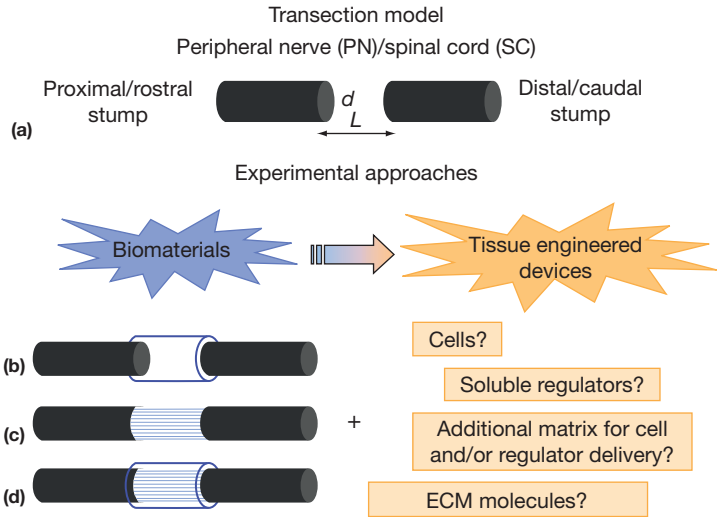

Figure 4 Transection model (a) and experimental approaches to bridge the gap (b–c–d) for either peripheral nerves or spinal cord. (a) The volume to be bridged is determined by the nerve diameter *d* and the length *L* of the induced gap; (b) entubulation; (c) gap bridged by a porous matrix with pores that are preferentially axially oriented; (d) combined use of a tube and a porous matrix. Cells, soluble regulators, any additional matrix for cell and/or regulator delivery (e.g., hydrogels, microspheres) and/or any ECM molecules can be added to the basic configurations (b–c–d) to develop complex tissue-engineered devices.

factor (cells and soluble molecular regulators), has dramatically increased the bridgeable gap length in animal models. For example, a gap of 30 mm in the dog sciatic nerve has been bridged by using PGA filaments within a chitosan conduit, leading to a degree of functional recovery comparable to that of the autograft control.[78] A limitation of this study, however, was that it lacked an evaluation of the regenerative activity of the chitosan empty tube, to reliably evaluate the effective contribution of the tube filling to regeneration.

The use of an axially oriented matrix within a tube is particularly attractive for the development of combinatorial approaches, as the matrix may also serve as a delivery vehicle for exogenous cells (e.g., Schwann cells) and/or molecular regulators. Indeed, although injections of cell suspensions into the tube lumen may improve nerve regeneration, a structural support is recommended to ensure the survival of transplanted cells. It is worth recalling that the regenerative process of a nerve fiber, described previously, does not require an exogenous supply of cells. The rationale for delivering exogenous cells to the injury site thus lies in the fact that such cells may work as an invaluable source of neurotrophic factors, which help nerve regeneration and early functional outcome. As reported above, nerve conduits may indeed be unable to bridge large defects also due to a lower local concentration of soluble growth factors released by the nerve stumps.

Hydrogels, especially those based on ECM macromolecules, can also be used to embed exogenous cells and/or provide a sustained release of selected growth factors. However, as reported above for collagen gels, hydrogels may not provide a permissive environment for axonal regeneration, likely due to the absence of oriented fibers and/or sufficient surface area for cell migration. As an alternative method of cell delivery, the micropatterning of the conduit surface may be exploited to increase the specific surface area for improved cell seeding.[65]

Schwann cells appear the most promising autologous cell type for transplantation, compared to mesenchymal stem cells (MSCs)[82] and olfactory ensheathing cells (OECs).[83,84] Heterologous cells have also been investigated for PNS regeneration, but they are definitely less likely to find their way to clinical application, due to ethical issues and the requirement of an immunosuppression therapy. Even when delivered as a cell suspension or in a hydrogel matrix, Schwann cells can dramatically increase the regenerative activity of a nerve conduit.[85] While hydrogels are the most common devices used to deliver Schwann cells, a number of recent investigations have focused on the seeding of exogenous cells on the conduit inner wall, proving that such a method for cell delivery is successful in terms of improved regenerative outcome.[86,87] Very recently, a collagen gel sheet seeded with Schwann cells has also been proposed as a nerve conduit.[88] Although the use of aligned porous or fibrous matrices to deliver Schwann cells *in vivo* appears promising, the seeding of cells within such matrices gives rise to some practical problems that limit the application of this combinatorial approach for nerve regeneration.

The regenerative performance of a nerve conduit can also be enhanced by coupling exogenous growth factors to it, instead of cells. Neurotrophic factors can enhance nerve regeneration by controlling the survival, migration, proliferation, and differentiation of various neural cell types. A number of factors have been investigated and proved effective for PNS regeneration, including nerve growth factor (NGF),[89] neurotrophin-3 (NT-3),[90] brain-derived neurotrophic factor (BDNF),[91] GDNF,[57] fibroblast growth factors (acidic (aFGF) and basic (bFGF)),[90] and many others.[92] Due to the short half-life of many growth factors *in vivo*, these can be delivered efficiently by means of polymeric devices that allow their sustained release for a relatively long period. Hydrogel matrices and polymeric microspheres are the most widely employed delivery devices in experimental settings. However, for most growth factors, with very few exceptions, the dosage range to be used for a therapeutic effect is yet to be determined.[91] It is also important to highlight the recent approach of combining multiple growth factors in a nerve chamber. Although the underlying molecular and cellular mechanisms are unclear, these studies evidence a synergistic effect of growth factors, which may lead to improved nerve regeneration by using lower doses of each single growth factor. The most recent advances in PNS regeneration experiments have favored the exploitation of gene therapy to instruct the desired cell type to overexpress a given neurotrophic factor. The cell transfection can be achieved either *in vivo*[93] or *ex vivo*,[94] showing some promising results in both cases. However, some concerns exist regarding the ideal gene vector, and the benefit/cost ratio of this approach is likely to be more convenient in studies concerning CNS rather than PNS regeneration, due to the more hostile environment of CNS following an injury.

Several detailed and up-to-date reviews of the current experimental approaches for PNS regeneration, as well as of the clinical outcome of commercially available conduits, have been published very recently and are suggested to the reader for further information.[68,92,95–97] In this brief overview, we would like to provide some basic considerations related to the development of tissue-engineered medical products for PNS regeneration, that is, on the actual therapeutic potential of experimental devices.

The development of a tissue-engineered device comprising two or more of the four aforementioned elements (i.e., conduit, matrix, cells, and molecular regulators) is obviously complex. First of all, the choice of the biomaterial(s) to be used for the conduit and the matrix is fundamental in view of a possible clinical application. This is related not only to the safety of the biomaterial itself (and of any degradation product), but also to the processing technique(s) adopted for manufacturing the device and to the possible methods of sterilization. Every processing step should be easily controlled and permit scale-up to develop production protocols that are respectful of good manufacturing practice (GMP) guidelines. Biomaterial-based, cell-free products currently dominate the overall market of tissue engineering,[98] mainly because the regulatory requirements are less strict and the associated costs more affordable for biomedical companies. With specific regard to PNS tissue engineering, the absence of cell-based therapies in the clinical setting is also attributable to several practical reasons. For example, autologous Schwann cells need a long time to expand *in vitro*, during which period the untreated, injured nerve is likely to degenerate, thus compromising subsequent recovery.[99] Moreover, the most suitable means to deliver cells *in vivo* and the optimal cell density are still subjects of debate. Similarly, the supply of exogenous growth factors in the clinical setting is hindered by the necessity to keep the

concentration of the given growth factor in a therapeutic range for a given time window. This gives rise to yet more open questions regarding the right dosage of growth factor as well as the identification of a suitable delivery vehicle for its sustained release.

Some successful attempts to bridge long nerve gaps by using multicomponent nerve chambers have been reported in the literature. Matsumoto and colleagues reported that an 8-cm-long gap could be bridged in a dog model, with functional recovery, by using a PGA conduit filled with laminin-coated collagen fibers.[100] This seems to be the longest gap bridged to date in an animal model, and it is important to note that no exogenous cells or growth factors were employed. However, despite such encouraging results, true evidence of the efficacy of a given device in the clinical setting seems to be difficult to obtain.

It has been postulated that the discrepancy between the experimental and the clinical levels might be due to the choice of inappropriate experimental configurations. As reported above, in addition to the fact that animal models are intrinsically limited as they cannot reproduce large human nerves, a standardization of animal models and experimental design among independent investigations is still lacking. Moreover, many studies are performed without the necessary presence of both a negative (i.e., silicone tube) and a positive (i.e., autograft) control being considered, which may lead to erroneous or limited evaluations of the actual regenerative capability of a device. More importantly, the use of small animal models (e.g., rat, mouse) for PNS injury is particularly debatable, as rodents show a superior neuroregeneration activity compared to higher mammals, and the nerve distances involved are much shorter than those found in humans. Even assuming that the speed of axonal growth in humans is comparable to that found in rodents, that is, 1–4 mm day^{-1},[6,17] such a speed would be unable to cover the entire gap length before chronic denervation occurred in the distal stump of the human nerve.[6] It has been recently suggested that rodent models would likely provide more reliable data for the development of novel therapies for humans, if the evaluation of nerve regeneration was performed at relatively early time points, when differences among positive and negative control groups are still significant. Alternatively, the animal model could account for denervation of the distal segment before repair, that is, a delayed repair.[101] The timing of outcome measurement is thus an experimental variable that greatly affects the evaluation of PNS regeneration. Further studies are also directed toward overcoming the limitations in functional recovery after PNS injury by accelerating the axonal growth across the injury site, for example, by means of electrical stimulation.[102]

With regard to clinical trials currently testing scaffolds or biomaterials for PNS regeneration, the reader is directed to some accredited, free databases available online. At the time of writing this chapter, only three trials seem to be ongoing: two of them are postmarketing, comparative studies (phase IV) on the Avance™ nerve graft (acellular graft from a donor tissue), while a third trial, using a chitin conduit for bridging small nerve gaps, is reported from China. To the best of our knowledge, no trial is in progress for tubular configurations or matrices exploring the use of exogenous cells and growth factors, in spite of the plethora of studies published in the literature on the subject.

5.532.2.3. Case Study: Collagen-Based Tubes with Oriented Porous Patterns

As discussed above, the regenerative performance of a nerve conduit may be increased either by using a tube filling or by designing the conduit wall porosity and/or surface topography. In this section, we focus on the improvement of the tube wall design for a specific class of devices, that is, collagen-based tubes, with the view of developing novel nerve guides for clinical use. Such a work has been undertaken in the last few years by some of the authors of this chapter, and is discussed here as a case study, to highlight the basic issues related to the development of a medical device.

In the last two decades, collagen-based tubes have been extensively used as nerve guidance conduits in a number of independent investigations.[43,103–107] Some of these devices have been approved for clinical use and are currently being marketed (**Table 2**), although most of the literature available on them favors their application on animal models rather than humans.[43,103,104] It is worth noting that the manufacturers of the collagen devices currently adopted do not show evidence of any specific microporous structure in their devices. Either type I collagen of bovine origin or type I/III collagen from porcine skin is employed for these commercial devices.

As reported above, it has been demonstrated that a layer of myofibroblasts can attach to the inner surface of collagen tubes,[19,44,45] which thus might inhibit or limit the contraction exerted by those cells on the nerve stumps, facilitating nerve regeneration. The question arises as to whether the limited performance of currently available collagen conduits is attributable to the microstructure and cell permeability of their tube walls. To answer such a question, collagen-based tubes with controlled and oriented porous patterns within the tube wall have been recently developed.[55] The tubular structure is obtained by spinning a collagen suspension, as occurs in a centrifugal casting process. After a proper spinning time at high speed, the collagen suspension is frozen in liquid nitrogen and finally subjected to a freeze-drying process to get a porous collagen tube. A radially aligned porosity in the tube wall, as well as a radial gradient in pore size, is the direct result of the spinning process, which causes the establishment of a collagen concentration gradient within the spun suspension, due to centrifugal effects. In particular, a compact structure, with a pore size of approximately 5 μm, is achieved at the outer wall of the collagen tube, while cell-permeable pores, with a diameter of about 50 μm, are obtained at the inner wall (**Figure 5**). More recent data have also produced evidence that the centrifugation of the collagen suspension can be modeled by means of the Lamm equation.[108] With a few assumptions, the modeling provides reliable estimations of the conduit inner diameters, wall thicknesses, and collagen concentration gradients resulting from different spinning procedures. This is important for designing fabrication protocols for the production of nerve guides with different inner diameters for therapeutic use.

In view of a clinical assessment of the novel collagen-based tubes, an important factor to be considered is the industrial source of collagen. The specific collagen chosen should be already employed in the clinical setting for approval of the final device for human use or at least for acceleration of

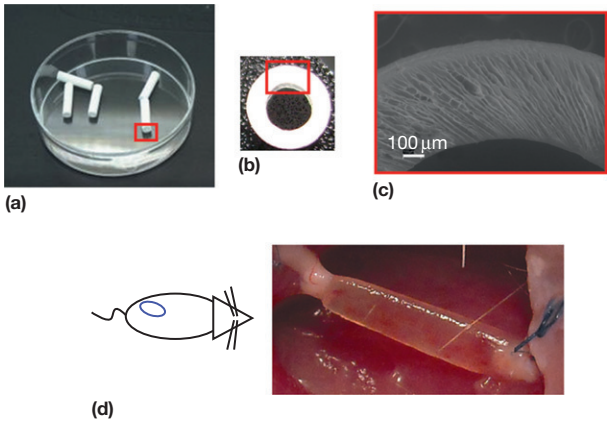

Figure 5 Morphology of micropatterned collagen-based tubes. Longitudinal (a) and cross-sectional (b) macroscopic views of the collagen tubes; the devices show an aligned microporous pattern along the tube wall (c); gross morphology of a tube implanted in a 10-mm rat sciatic nerve gap, 8 days after the implant (d).

the process of regulatory approval. Based on our own experience, the choice of the biomaterial should be made early in the design process of the medical device, before the planning of any preclinical studies. This is particularly relevant for devices based on collagen (or on any other naturally derived biomaterial), as the properties of the final device and its processing conditions are strongly affected by the specific collagen employed. Indeed, collagens of the same type can differ significantly in terms of fibrillar or microfibrillar structure, purity, solubility, cross-link density, etc., depending on the extraction process, the animal species, the animal age, the harvested tissue, and so on.

An initial design study performed in our laboratory involved, for the fabrication of micropatterned collagen tubes, the use of three different industrial sources of type I collagens derived from bovine skin, all used for clinical purposes. This study confirmed that the collagen source dramatically affects the tube processing conditions and the final properties of the tube, in terms of mechanical strength, flexibility, porosity, and degradation rate (unreported data). Such a study has thus been fundamental for the choice of the most suitable collagen source and for setting up a fabrication process tailored to the specific biomaterial.

Yet another issue to be addressed in view of a clinical application is the sterilization of the product (see **Chapter 4.410, Sterilization of Biomaterials of Synthetic and Biological Origin**), which should ensure the absence of microorganisms while preserving the structural and biological properties of the device.[109,110] First of all, in the case of the collagen tubes, the choice of the sterilization treatment should take into account the sensitivity of collagen to the combined effect of heat and water, which induce collagen denaturation.[111] Even more importantly, the treatment should not collapse the peculiar microporous structure of the collagen devices, which is the variable hypothesized to have a significant effect on nerve regeneration. At the same time, the sterilization process should not accelerate the process of *in vivo* degradation or induce any cytotoxic effects. Irradiation-based treatments, compared to ethylene oxide (EtO) ones, have been reported to induce adverse structural and biological changes in collagen sponges,[109] although some studies report that sterilization by low-dose γ or β irradiation can be performed on collagen devices.[110] Some concerns exist about the cytotoxicity of EtO-sterilized devices, which are addressed by means of an accurate monitoring of EtO residues within the sterile, final products. It is worth noting that EtO sterilization is widely employed for collagen-based devices and is the method adopted for the collagen-based nerve conduits currently available. Dry-heat sterilization (160–190 °C) on collagen has the advantages of being safe and effective, despite inducing some cross-linking of the collagen structure. As the fabrication of the novel collagen tubes encompasses a mild cross-linking by means of dehydrothermal treatment (120 °C for 48 h), we first investigated the feasibility of dry-heat sterilization to increase their mechanical strength and biostability. In particular, an additional dehydrothermal and sterilizing step at 160 °C for 2 h proved to have no detrimental effect on the pore structure of the collagen tubes or on their mechanical stability. However, dry-heat sterilization is very difficult to be implemented in an industrial production. An EtO sterilization treatment is currently under development and analysis, and preliminary results are encouraging, in terms of preservation of the microstructure and mechanical stability of the tubes.

Recent preclinical studies in a 10-mm rat sciatic nerve defect have highlighted that the novel collagen conduits (sterilized by means of dry heat) facilitate and accelerate more efficiently the processes of Schwann cell migration, axonal contact, formation of basal lamina, and remyelination, compared to the collagen devices available on the market. In particular, the conduits not only perform much better than commercial tubes, but also, more importantly, allow the formation of a normal nerve, with a normal number of fibers and a normal *G*-ratio (data to be published yet), which is an outstanding result when looking at those reported so far in the literature. Normal endoneurium and perineurium were also appreciable. Further preclinical studies on the performance of the same micropatterned tubes, sterilized by means of EtO, are currently in progress.

Although the molecular mechanisms by which the micropatterned conduits act on nerve regeneration need to be understood further, we postulate that these devices have the potential to improve PNS regeneration and functional recovery in humans. To perform a clinical trial, the fabrication of the devices has been shifted from the laboratory to a GMP facility, as required for clinical devices. The ethical committee of the San Raffaele Hospital (Milan, Italy), where the animal studies have been performed, has approved the use of the novel collagen tubes in 10 patients undergoing biopsy of the sural nerve, for diagnostic purposes. While keeping in mind the differences between animal models and humans discussed earlier, we expect that micropatterned collagen tubes will be able to create a nerve chamber environment that is more favorable to regeneration than that achieved with the currently available nerve conduits. Should the clinical trial(s) prove this, it would be conceivable to critically question whether the use of exogenous cells and growth factors is truly necessary to enhance PNS regeneration. The stimulation of endogenous regenerative mechanisms by means of artificial conduits and/or porous matrices is likely to be the most promising way to improve nerve regeneration in the clinical setting, at least in the near future.

5.532.3. State of the Art of CNS Tissue Engineering (see Chapter 00185 and Chapter 00238))

As described earlier, CNS axonal regeneration appears to be partly impeded by myelin-associated inhibitors,[112–114] loss in adult neurons of an intrinsic ability to overcome inhibitory cues,[112] and formation of a postlesion scar barrier.[115] Currently, no therapy exists for the restoration of function after CNS injury. While the traditional experimental approaches, directed toward creating a permissive environment for axonal regeneration and stimulating endogenous plasticity, involved the transplantation of exogenous cells and/or the supply of environmental regulators, the recent advances in tissue engineering have prompted the use of biomaterial-based smart devices, which can be used not only as vehicles for the controlled delivery of cells and soluble regulators, but also as collaborators with the host tissue, providing supporting guidance to axons. Some of these devices have found application, at least in animal models, in the management of both PNS and CNS injuries. The experimental evidence suggests that combinatorial strategies, involving the *in vivo* delivery of at least two exogenous factors out of cells, regulators, and biomaterials, are the most promising ones for a successful CNS repair. Both *in vivo* and *ex vivo* gene therapies are also emerging as powerful means to boost the regenerative capability of tissue-engineered devices.

The research focusing on CNS repair is still in its developmental stage because of the extreme complexity of the CNS environment; thus, the field is open to all possible therapeutic options. Due to the potentially infinite number of tissue-engineered devices that can be developed for the CNS, a detailed review of the existing literature is quite a cumbersome challenge. Some reviews have been published recently, each focusing on particular design aspects and/or applications of the devices, and the reader is directed to them for further information.[2,116–119]

In this section, the cellular, molecular, and biomaterial-based approaches attempted to date are briefly illustrated, with particular regard to the treatment of SCI, and with the aim of emphasizing the regenerative role played by the biomaterials themselves, used alone or in combinatorial strategies. The reader is also cautioned about the fact that standardization of animal models for SCI is lacking, even when considering the same animal species: site of injury (e.g., cervical vs. thoracic), type of injury (e.g., contusion, total transection, hemisection), volume of damaged area, and therapeutic time window (subacute vs. chronic SCI) are only some of the variables that researchers can choose arbitrarily. Transection models are, of course, not representative of most of the SCIs that can be found in humans. However, they are widely employed as the most severe type of injury. In this regard, some concerns exist about the actual therapeutic potential of preformed scaffolds to bridge spinal cord defects: they are widely used in animal models, but do not seem to be truly applicable in the clinical setting. The only exception seems to be provided by the use of injectable hydrogels, which can be delivered to the injured spinal cord without causing further damage and thus appear more promising as therapeutic devices. In this short overview, selected tissue-engineered devices will be illustrated, not attempting a comparative analysis of their regenerative performance but simply discussing their design. Though their potential as future therapeutic products does not seem evident, as for noninjectable devices, their accurate design might allow a deeper comprehension of the regenerative mechanisms of the CNS, for the further development of feasible therapies.

The basic concepts discussed earlier for the design of a PNS guidance device hold for the development of tissue-engineered products for CNS repair as well. The higher the complexity of the device, the more challenging and time consuming the proof of safety and efficacy required for any clinical use. However, sophisticated tissue-engineered products appear as the only therapeutic means for functional CNS recovery.

5.532.3.1. Cellular Strategies

As discussed above, SCI causes the irreversible loss of neurons. Acute SCI also results in severe loss of oligodendrocytes, leading to demyelination of surviving axons and severe functional impairment.[120] The transplantation of exogenous cells thus seems necessary to replace some of the lost cells and/or to facilitate remyelination.[121] Cellular therapy is also potentially useful for filling up any cavities or cysts that can form after SCI, and for creating a favorable environment for axonal regeneration (e.g., by means of neurotrophic factors secreted by cells).

While designing a cellular therapy for clinical application, several issues need to be addressed: (a) the optimal cell source; (b) the optimal route of cell administration; and (c) the microenvironmental mechanisms that regulate the survival, differentiation, and integration of transplanted cells within the host tissue. With regard to the cell source, different nonstem versus stem cell types have been investigated so far, at least at a preclinical level, to approach SCI, including macrophages, Schwann cells, and OECs in the former, and adult neural progenitor cells (NPCs), embryonic stem (ES) cells, and oligodendrocyte precursor cells (OPCs) in the latter. Both ES cells and NPCs are particularly promising, as they are intrinsically able to adapt their specification fate to different environmental needs.[122] The potential of ES cells in animal models of SCI, as well as the use of OPCs that have been predifferentiated from ES cells before transplantation, is currently being investigated, and results with regard to functional recovery appear encouraging.[123–125] However, apart from ethical considerations, the therapeutic use of ES cells is still constrained by some key issues, such as feeder-independent growth (expansion) and *in vivo* teratocarcinoma formation,[126] which need to be solved before proposing any ES cell-based therapy for human applications.

On the other hand, NPCs might represent a ready-to-use cell source for cell-based therapies, as they can be obtained from different tissues (e.g., embryonic, fetal, and adult) and have been widely used *in vivo* without causing tumor formation and overt toxic/side effects.[127] Adult NPCs isolated from the subgranular zone (SGZ) of the dentate gyrus (DG) of the hippocampus, from the subventricular zone (SVZ) of the lateral ventricles, or from the spinal cord, have been shown to self-renew and to be multipotent *in vitro* and after transplantation into the CNS.[128,129] The population of NPCs residing in the forebrain and spinal cord is maintained for life and can be considered a potential source of transplantable cells for individuals with SCI or other myelin disorders.[130,131] Transplantation of adult human NPCs into the intact and acutely injured spinal cord of severe combined

immunodeficient (SCID) mice, is associated with the differentiation of transplanted cells preferentially into oligodendrocytes (only few astrocytes)[132] and recovery of locomotor function.[133] Moreover, NPCs transplanted in the subacute phase of SCI with a combination of growth factors and anti-inflammatory molecules (e.g., minocycline and cyclosporin A) to optimize the survival of grafted adult NPCs improved functional recovery. However, chronic (8 weeks postinjury) transplantation of NPCs failed to exert any detectable ameliorative effect.[134]

This last finding suggests that the timing of cell transplantation is critical to the success of a given therapy and generates interest in the identification of the optimal route of cell administration. The anatomopathological features of focal CNS disorders, such as SCI, suggest that direct local (intralesional) cell transplantation might facilitate tissue regeneration. However, it has been recently shown that in multifocal CNS disorders, systemic (e.g., intravenous, intrathecal) transplantation of NPCs can be therapeutically efficacious, owing to the ability of transplanted cells to follow, via the blood stream or cerebrospinal fluid circulation, a gradient of chemoattractants (e.g., proinflammatory cytokines and chemokines) occurring at the site of inflammatory lesions.[135–138] While promoting interaction between transplanted NPCs and activated endothelial and ependymal cells surrounding inflamed CNS tissues, this chemoattractive gradient leads to selective and specific homing of transplanted cells in multifocal inflammatory CNS areas. In experimental models of CNS inflammation, there is solid evidence showing that NPCs survive transplantation procedures within the host (although most of the transplanted cells are lost), specifically migrate within the damaged tissue, and maintain their multipotency. However, there are limited data supporting the concept that these cells give rise to terminally differentiated neural cells that are, in turn, capable of sustaining a program of CNS repair via massive cell replacement.[139] Embryonic, fetal, and neonatal cerebellar NPCs injected into models of SCI do not differentiate at all into terminally differentiated neuronal cells.[132,140–142] The scarce and inappropriate terminal differentiation and the propensity of maintaining an undifferentiated phenotype within the host tissue suggest that transplanted NPCs might be therapeutically efficacious via mechanisms alternative to cell replacement, that is, neuroprotection and regulation of the immune response. Transplanted cells may significantly reduce the scar formation and/or increase the survival and function(s) of endogenous glial and neuronal progenitors that have survived the initial insult. This neuroprotective effect – which is usually accompanied by increased *in vivo* bioavailability of major neurotrophins (e.g., NGF, BDNF, CNTF, GDNF) – has been shown in rodents suffering from primary inflammatory CNS disorders, for example, SCI[141,142] and stroke,[143,144] as well as in rodents affected by neurodegenerative disorders accompanied by reactive inflammation, for example, Parkinson's disease[145] and epilepsy.[143,144]

A deeper understanding of the mechanisms underlying the interaction of transplanted cells with the host tissue would definitely help in developing an appropriate cellular therapy. The possible use of biomaterials as an alternative means to deliver exogenous cells is being explored and will be discussed in a subsequent section.

5.532.3.2. Molecular Strategies

Molecular therapies for the treatment of SCI might be developed with the multiple purposes of protecting neurons from secondary cell death, promoting axonal growth, preventing the action of inhibitory molecules, and/or impeding glial scar formation.

Many studies have demonstrated the neuronal survival and growth-promoting effect of neurotrophic molecules or neurotrophins, a family of polypeptides that are believed to be at least partially responsible for keeping developing neurons viable until their projecting axons reach their target tissue.[8,9] Exogenous administration of neurotrophic growth factors has thus been proposed as one potential therapeutic treatment for SCI. Different types of growth factors have been tested and BDNF,[146,147] NGF,[148] NT-3, NT-4, and NT-5,[147,149] as well as bFGF[150] have been proved to be protective when locally administered to rodents with acute spinal cord injuries.

In the injured CNS, a number of inhibitory molecules exist. While permissive molecules provide directional cues for routing axons to their correct target, inhibitory molecules either deflect growing axons from their optimal route or completely block the route.[7] Some of the inhibitory factors expressed during CNS development, such as proteoglycan NG2, keratin, and chondroitin sulfate, may be reexpressed after injury to the mature brain and spinal cord.[9] Considerable effort has been made on identifying, localizing, and reversing the effects of these growth inhibiting molecules. Several recent studies have led to the identification of certain myelin-associated components that can inhibit axon outgrowth *in vitro*, including myelin-associated glycoprotein (MAG),[151–153] oligodendrocyte myelin glycoprotein (OMgp),[152] the transmembrane semaphorin 4D (Sema4D/CD100)[154] and 3A,[155] and ephrin B3.[156]

Another target of molecular therapies for CNS repair is the undesired massive gliosis, that is, formation of the glial scar. After SCI, astrocytes proliferate reactively, resulting in the formation of the glial scar. Such a scar tissue at the lesion site has long been considered a possible detrimental factor impeding regeneration in the CNS, which in the injured spinal cord is aggravated by the formation of cystic cavities. Indeed, the glial scar tissue may act not only as a physical barrier to axonal growth, but also as a chemical inhibitor, being particularly rich in chondroitin sulfate. The massive gliosis after SCI is likely to be mediated by the local release of major glial regulators, such as transforming growth factors (TGF)-β, bFGF, and bone morphogenetic proteins (BMPs).[13] Significant upregulation of BMP-7, BMP-2,[157,158] and TGF-β has been observed in the acutely injured spinal cord.[159] Multiple types of evidence show that synthetic anti-TGF-β antibodies represent a potentially applicable tool to prevent/limit the extent of deposition of ECM components and to maintain and/or restore the functional integrity of the injured CNS.[160] An alternative and effective molecular treatment to inhibit the formation of the glial scar, recently proposed, consists of the supply of exogenous chondroitinase ABC to digest chondroitin sulfate proteoglycans.[161]

As discussed above for cellular therapies, several questions, relating to the identification of the molecule(s) to be administered, the quantification of the optimal dosage, the choice of a convenient administration route, and the identification/

selection of the time window in which the molecules are expected to be effective, need to be answered before a molecular strategy can be envisaged in the clinic. Another important aspect is the evaluation of possible synergic effects among different therapeutic strategies. So far, molecular therapies have been tested either with or without cellular therapies,[162] and the selected molecules have been usually applied to site(s) of injury by local injection,[150] continuous infusion,[148] or insertion of an artificial saturated polymeric carrier.[146] Viral vector-mediated transfer of molecules to the injured spinal cord is emerging as a new and effective strategy. *In vivo* gene therapy has been tested in models of SCI using several viruses, including herpes simplex virus, adenovirus, lentivirus, and Moloney leukemia virus (see **Chapter 2.202, Engineering Viruses For Gene Therapy**).[163] Molecular therapies on SCI have also involved *ex vivo* gene therapy approached with cells – usually fibroblasts – that have been transduced with genes encoding for neurotrophins.[149,164] The recent use of polymeric devices (e.g., scaffolds, hydrogels, microspheres) (see **Chapter 4.424, Nanoparticles for Nucleic Acid Delivery** and **Chapter 4.425, Delivery of Nucleic Acids and Gene Delivery**) to ensure a sustained release of bioactive molecules to the injured spinal cord is discussed in the following section along with combinatorial strategies.

5.532.3.3. Biomaterial-Based Strategies (see Chapter 00185 and Chapter 00238)

The basic tissue-engineering concept underlying this approach is that a biomaterial-based device, with controlled molecular, mechanical, and microstructural properties, can provide a physical system to support and guide axons to their correct targets during regeneration, as occurs with nerve guidance channels and oriented substrates in the PNS.

Several proof of principle studies have demonstrated that physically guiding the linear growth of CNS axons through the lesion site helps the axons to regenerate, even though the artificial implant, either a tubular device or a porous matrix, does not contain any exogenous molecules and/or cellular components. In such experiments, correct design of the artificial substrate is fundamental to achieving the desired regenerative response of the host tissue. In the following section, a few examples of plain biomaterial implants are reported to underscore the fact that the choice of the base material, the design of the mechanical properties, and the design of the scaffold porosity are key factors that significantly affect the cellular response to the implant. For example, an alginate sponge with random porosity, implanted in a transected infant rat spinal cord, has been found to support the elongation of both corticospinal and dorsal column axons and to guide them up to the distal stump of the transected spinal cord.[165] Although the mechanisms leading to enhanced axonal elongation remain unclear, it has been hypothesized that alginate itself may localize neurotrophic factors released from both stumps of the transected spinal cord, and the following degradation of the gel may provide a space and a supportive environment to promote the growth of CNS axons. Moreover, the alginate substrate may reduce the formation of the glial scar.

Several investigations have dealt with the role played by the mechanical properties of the implanted biomaterial. The use of an empty hydrogel channel, obtained by PHEMA–MMA, has been reported to bridge a 4-mm gap in a complete transection model in the adult rat spinal cord.[166] In this study, it was suggested that the regenerative performance of the hydrogel channel, even in the absence of exogenous cells, was likely determined by the mechanical properties of the substrate, designed to be similar to those of the spinal cord, which are between 230 and 600 kPa, depending on the species, the measuring system, and the time after death.[34] In fact, a mismatch in mechanical properties between the implant and the surrounding tissue can result in implant failure or cause the scaffold to compress or lacerate the relatively soft neural tissue. It is worth stressing that studies involving the use of nondegradable implants, such as the conduits cited above, should be considered as proofs of concept rather than as feasible therapeutic options, because of the constriction of the spinal cord and foreign body reaction that may develop in the long term.

Due to their high equilibrium water content, hydrogels provide a high permeability to trophic molecules and a viscoelastic behavior similar to that of soft tissues.[167] Moreover, injectable hydrogel formulations can be developed to deliver the biomaterial as well as any added cells or soluble regulators to the lesion site, in a minimally invasive manner. Hydrogels also exhibit a particular potential for peptide or protein addition, that is, they are ideal platforms for the design of biomaterials with specific bioactivity. Indeed, with the aim of recreating a cellular microenvironment similar to that found *in vivo*, recent efforts have been made in the field of tissue engineering to incorporate specific peptide sequences in the scaffold architecture, not only to encourage biospecific cell adhesion but also to induce and control other cellular functions such as migration, proliferation, ECM synthesis, and tissue remodeling. In an attempt to overcome the limited regenerative growth of CNS, different hydrogels of *N*-(2-hydroxypropyl)methacrylamide (HPMA) containing peptide or amino sugar sequences that exist in the natural ECM have been synthesized in a pioneering study, and implanted in either the lesioned optic tract or the cerebral cortex of rat.[168] Glucosamine (NHGlc), *N*-acetylglucosamine (AcNHGlc), and the short peptide sequence of arginine-glycine-aspartic acid (RGD) were incorporated in the hydrogel network, and the resulting scaffold was proved to increase the cellular response significantly, in terms of cellular migration and axonal ingrowth. RGD-linked polymers, in particular, contained large numbers of astrocytes and macrophages and supported the ingrowth of large numbers of axons, for the greatest distance. A similar poly(*N*-(2-hydroxypropyl)methacrylamide) (PHPMA) hydrogel containing RGD peptides was later shown to enhance tissue regeneration in the injured rat spinal cord.[167] In this study, the complex modulus of the PHPMA hydrogel was comparable with that of the rat brain tissue (~100 Pa), and it was proved that the introduction of the short peptides allowed the best match between the mechanical and viscoelastic properties of the hydrogel and those of the neural parenchyma.

With regard to the effect of the biomaterial microstructure on the growth of CNS axons, several devices with longitudinally aligned porosity have been implanted in the injured spinal cord and proved to support axonal regeneration. Agarose-based scaffolds with aligned pores promoted axonal regeneration in a transected adult rat spinal cord, either with

or without exogenous BDNF.[169] Alginate-based anisotropic hydrogels, with capillary channels, induced aligned axonal growth in an acute SCI model in adult rats.[170] Very recently, nanofiber hydrogels based on self-assembling peptides have been reported to promote locomotor functional recovery following SCI and to reduce glial reaction and inflammation in the acutely injured brain.[171,172] Laminin-coated, porous chitosan conduits have also enhanced functional recovery in adult rats following SCI.[173] Collagen filaments grafted parallel to the axis of the spinal cord have been shown to reduce scar tissue formation, to support the expression of neurotrophic factors, and to serve as a scaffold for the growth of spinal axons.[174] Functional restoration by means of collagen filaments in a rabbit SCI model has been recently reported.[175] However, the effect of the diameter and number of the collagen fibers on the regenerative response of the device has not been investigated. As observed for the PNS, the balance between contact guidance and surface area provided by the scaffold plays a key role. In our opinion, tuning those variables might lead to a deeper understanding of the interactions between the host tissue and the scaffold and to an optimal scaffold design for maximized performance.

Based on the encouraging results reported for PNS regeneration, tubular collagen implants, as well as collagen porous matrices with axially oriented pores,[176,177] have also been proposed as scaffolding materials for the treatment of SCI. It is worth noting that plain collagen-based tubes have been investigated, with positive results, in studies involving the bridging of the spinal cord to the PNS, in both rats and monkeys.[105–107]

5.532.3.4. From Biomaterials to Tissue-Engineered Devices: Combinatorial Strategies

The regenerative potential of a biomaterial-based device can be definitely improved by coupling it with exogenous cells or regulators, as proved for the regeneration of the PNS. The rationale for delivering cells by means of biomaterials is that such scaffolding can provide the necessary physical environment in which transplanted cells may survive and begin to consider integration with a very hostile domain, ultimately contributing to CNS repair.[178] Hydrogel scaffolds are particularly promising, both for cell delivery and for controlled release of any incorporated bioactive molecules.

The first approaches to combinatorial strategies involved the application of several tubular implants in combination with Schwann cells. Among the devices tested, tubes based on polyacrylonitrile/polyvinylchloride (PAN/PVC), poly(D,L-lactic acid) (PLA), and poly-β-hydroxybutyrate (PHB) coated with fibronectin-containing alginate hydrogel were all found to promote regeneration and myelination of damaged axons in the injured adult rat spinal cord.[166,179,180] More recently, advances in biomaterial processing techniques have led to the development of more complex devices, which need to be coupled with Schwann cells or other cell types. PHB conduits with predominantly unidirectional fiber orientation have been recently developed and seeded with Schwann cells, and these have been demonstrated to support cell survival as well as axonal regeneration in the adult rat injured spinal cord.[181] PLGA scaffolds with parallel channels have been seeded with Schwann cells and implanted in the transected rat spinal cord, showing promising results.[182–184] Remarkably, one of these investigations has proved that the diameter of the scaffold channels has a direct effect on the regenerative performance, with smaller diameter channels promoting greater regeneration.[183] This finding seems to suggest that, as observed for the PNS, the surface area of the implanted device should be fine-tuned for optimal nerve regeneration.

The transplantation of stem cells in combination with polymer scaffolds, rather than differentiated cells, might show a greater therapeutic potential. One of the first examples of accurate scaffold design and further seeding with NPCs for spinal cord repair was reported in 2002.[142] The scaffold was designed to mimic the architecture of the healthy spinal cord: the inner portion emulated the gray matter via a porous polymer layer designed to be seeded with neural stem cells for cellular replacement as well as for trophic support; the outer portion emulated the white matter with axially oriented pores for axonal guidance. Both the inner and outer scaffolds were fabricated from a blend of poly(lactic-*co*-glycolic acid) and a block copolymer of poly(lactic-*co*-glycolic acid)–polylysine, thus making them completely biodegradable. The experimental results suggested that the combination of NPCs with the polymer scaffold promoted long-term functional recovery in adult rats with hemisection of the spinal cord. Histology and immunocytochemical analysis suggested that this functional recovery might be attributable to a reduction in tissue loss from secondary injury processes, as well as diminished glial scarring. While the scaffold alone appeared to play an important role in functional recovery by reducing glial scar formation, NPCs remained largely undifferentiated, suggesting that their role was trophic support rather than cellular replacement. A PGA scaffold seeded with neural stem cells has also been employed to repair massive lesions in rat brain.[185] The results are quite exciting, documenting vascular infiltration of the cell-seeded scaffold, the dissolution of the PGA, and the differentiation of stem cells into neuronal and glial phenotypes, with the neurons both receiving and giving rise to axonal connections. However, the connections between the donor and the host cells have not been proved to be functional. A recent study has demonstrated that the use of multichannel PLGA scaffolds seeded with neural stem cells facilitated the bridging of a spinal cord defect.[186]

Another stem cell type explored for spinal cord repair is provided by MSCs, which can be easily obtained from bone marrow aspirates. Hydrogels based on HPMA, modified with the peptide sequence RGD, have been seeded with MSCs and used to repair a chronic contusive SCI, with some functional improvement recorded in adult rats.[187] MSCs have also been investigated in combination with a fibrin matrix.[188] However, the beneficial effect provided by MSCs, at least in models of PNS injury, seems to be comparable to that provided by Schwann cells.[189]

Among the novel technologies that enable the design of complex cell-seeded scaffolds for the treatment of SCI, it is worth citing some rapid prototyping techniques, including 3D printing[190] and biological laser printing. The latter is an emerging technology for the creation of specific patterns of living cells in biomaterials, and has been recently applied in the production of hydrogels with aligned microchannels of OECs, which hold promise for the treatment of SCI.[191]

However, the most recent investigations on the treatment of SCI are concerned with the production of tissue-engineered devices more sophisticated than cell-seeded scaffolds, that is, devices comprising cells, scaffolds, and environmental regulators, which can be either added to the scaffold, or supplied by genetically modified cells, or delivered as genes to transfect host cells *in vivo*. The direct addition of the regulators to the scaffold is usually performed in cases of a hydrogel-based scaffold, as the hydrogel can easily incorporate the selected molecules and supply them to the injury site on demand.[192–195] As mentioned above, a hydrogel scaffold may exhibit several advantages in SCI settings. It can be directly injected into the injury site for conformal repair; it can be designed for optimal cell response and degradation rate; and the hydrogel network can be finely controlled to tune the release kinetics of the embedded molecule(s). A composite hydrogel matrix has recently been shown to allow the sustained release of multiple bioactive neurotrophic factors suitable for SCI treatment, over 28 days.[196] Polymeric microspheres can also be used for a sustained delivery of exogenous molecules. Recent studies have focused on the coupling of microspheres and hydrogel matrices for the fine-tuning of the release kinetics in SCI models.[80,81,196,197] Gene therapy appears to be a versatile, alternative technique that allows the *in vivo* delivery of selected molecules by using either porous scaffolds seeded with transfected cells[169,198] or scaffolds incorporating genes encoding for them. As an example of the latter technique, multichannel PLGA scaffolds have recently been used to deliver *in vivo* DNA lipoplexes, and the experimental evidence has shown higher levels of transgene expression compared to naked plasmid.[199] This result might generate renewed interest in nonviral gene delivery, whose efficacy is usually much lower than that of viral vector-mediated gene transfer.

Despite the wide range of promising combinatorial devices found in the literature, the production of biomaterial-based, tissue-engineered devices for CNS repair is not conceivable in the near future. The short- and medium-term way to clinical application is likely easier to be achieved with cellular and/or molecular strategies, based on more traditional administration routes (e.g., bolus delivery), which might provide some, albeit modest, functional improvement following SCI.

5.532.4. Concluding Remarks

In this overview, we have attempted to provide a critical analysis of the current state of the art of nerve tissue engineering, highlighting the limitations of the field in terms of the development of feasible therapies. Apart from the choice of appropriate animal models and standardized experimental conditions, a proper design of biomaterial-based devices (e.g., nerve guidance conduits) is fundamental to the comprehension of the cellular and molecular mechanisms underlying the regeneration of both the PNS and the CNS, as well as to the development of a tissue-engineered product for clinical use. In particular, PNS tissue engineering is likely to achieve satisfactory clinical results, in terms of bridgeable nerve defects and quality of the regenerated nerve trunk, with the use of plain biomaterial devices, devoid of exogenous cells, and/or soluble regulators. On the other hand, combinatorial strategies, involving the use of scaffolds, cells, regulators, or genes encoding for them, seem the only conceivable way to a functional restoration following CNS injury. The complexity of these tissue-engineered devices leads us to presume that their application in the clinical setting cannot be envisaged in the near future. However, the promising results obtained so far in animal models should make us strive for the long-term achievement of true landmarks in restorative neurology.

References

1. Ichiara, A.; Inada, Y.; Nakamura, T. *Injury* **2008**, *39*(Suppl. 4), S29–S39.
2. Madigan, N. N.; McMahon, S.; O'Brien, T.; Yaszemski, M. J.; Windebank, A. J. *Respir. Physiol. Neurobiol.* **2009**, *169*, 183–199.
3. Ding, Y.; Kastin, A. J.; Pan, W. *Curr. Pharm. Des.* **2005**, *11*, 1441–1450.
4. Seddon, H. J. *Brain* **1943**, *66*, 237–288.
5. Yannas, I. V. *Tissue and Organ Regeneration in Adults*. Springer: New York, 2001.
6. Höke, A. *Nat. Clin. Pract. Neurol.* **2006**, *2*, 448–454.
7. Myckatyn, T. M.; Mackinnon, S. E.; McDonald, J. W. *Transpl. Immunol.* **2004**, *12*, 343–358.
8. Gurgo, R. D.; Bedi, K. S.; Nurcombe, V. *J. Clin. Neurosci.* **2002**, *9*, 613–617.
9. Horner, P. J.; Gage, F. H. *Nature* **2000**, *407*, 963–970.
10. McDonald, J. W.; Sadowsky, C. *Lancet* **2002**, *359*, 417–425.
11. Schaal, S. M.; Marcillo, A. E.; Stagg, M.; Pearse, D. D. *J. Immunol.* **2007**, *178*, 96.11.
12. Horner, P. J.; Gage, F. H. *Arch. Neurol.* **2002**, *59*, 1717–1720.
13. Yiu, G.; He, Z. *Nat. Rev. Neurosci.* **2006**, *7*, 617–627.
14. Schmidt, C. E.; Leach, J. B. *Annu. Rev. Biomed. Eng.* **2003**, *5*, 293–347.
15. Moneim, M.; Omer, G. In *Management of Peripheral Nerve Problems*; Omeg, G., Spinner, M., Van Beek, A., Eds.; Saunders: Philadelphia, PA, 1998; pp 414–419.
16. Huber, G. C. *J. Morphol.* **1895**, *11*, 629–735.
17. Williams, L. R.; Longo, F. M.; Powell, H. C.; Lundborg, G.; Varon, S. *J. Comp. Neurol.* **1983**, *218*, 460–470.
18. Azzam, N. A.; Zalewski, A. A.; Williams, L. R.; Azzam, R. N. *J. Comp. Neurol.* **1991**, *314*, 807–819.
19. Chamberlain, L. J.; Yannas, I. V.; Hsu, H.-P.; Spector, M. *J. Comp. Neurol.* **2000**, *417*, 415–430.
20. Hurtado, H.; Knoops, B.; Van den Bousch de Aguilar, P. *Exp. Neurol.* **1987**, *97*, 751–757.
21. Williams, L. R.; Varon, S. *J. Comp. Neurol.* **1985**, *231*, 209–220.
22. Yannas, I. V.; Orgill, D. P.; Silver, J.; Norregaard, T.; Zervas, N. T.; Schoene, W. C. In *Advances in Biomedical Materials*; Gebelein, C. G., Ed.; American Chemical Society: Washington, DC, 1987.
23. Gabbiani, G. *Cardiovasc. Res.* **1998**, *38*, 545–548.
24. Lundborg, G.; Dahlin, L. B.; Danielsen, N. *Scand. J. Plast. Reconstr. Hand Surg.* **1991**, *25*, 79–82.
25. Lundborg, G.; Rosén, B.; Abrahamson, S. O.; Dahlin, L.; Danielsen, N. *J. Hand Surg. B (Br. Eur.)* **1994**, *19*, 273–276.
26. Mackinnon, S. E.; Dellon, A. N.; Hudson, A. R.; Hunter, D. A. *Ann. Plast. Surg.* **1984**, *13*, 112–120.
27. Merle, M.; Dellon, A. N.; Campbell, J. N.; Chang, P. S. *Microsurgery* **1989**, *10*, 130–133.
28. DaSilva, C. F.; Langone, F. *Braz. J. Med. Biol. Res.* **1989**, *22*, 691–694.
29. Kljavin, I. J.; Madison, R. D. *Cells Mater.* **1991**, *1*, 17–28.
30. Stanec, S.; Stanec, Z. *J. Reconstr. Microsurg.* **1998**, *14*, 227–232.
31. Stanec, S.; Stanec, Z. *Br. J. Plast. Surg.* **1998**, *51*, 637–639.
32. Fine, E. G.; Valentini, R. F.; Bellamkonda, R.; Aebischer, P. *Biomaterials* **1991**, *12*, 775–780.
33. Huang, J.; Hu, X.; Lu, L.; Ye, Z.; Zhang, Q.; Luo, Z. *J. Biomed. Mater. Res. A* **2010**, *93*, 164–174.
34. Dalton, P. D.; Flynn, L.; Soichet, M. S. *Biomaterials* **2002**, *23*, 3843–3851.
35. Belkas, J. S.; Munro, C. A.; Soichet, M. S.; Johnston, M.; Midha, R. *Biomaterials* **2005**, *26*, 1741–1749.
36. Katayama, Y.; Montenegro, R.; Freier, T.; Midha, R.; Belkas, J. S.; Soichet, M. S. *Biomaterials* **2006**, *27*, 505–518.
37. Aldini, N. N.; Perego, G.; Cella, G. D.; *et al. Biomaterials* **1996**, *17*, 959–962.
38. Bryan, D. J.; Holway, A. H.; Wang, K. K.; *et al. Tissue Eng.* **2000**, *6*, 129–138.
39. Dellon, A. L.; Mackinnon, S. E. *Surg. Annu.* **1988**, *20*, 59–100.
40. den Dunnen, W. F. A.; van der Lei, B.; Schakenraad, J. M.; *et al. Microsurgery* **1993**, *14*, 508–515.

41. Borkenhagen, M.; Stoll, R. C.; Neuenschwander, P.; Suter, U. W.; Aebischer, P. *Biomaterials* **1998**, *19*, 2155–2165.
42. Wang, S.; Wan, A. C.; Xu, X.; *et al*. *Biomaterials* **2001**, *22*, 1157–1169.
43. Archibald, S. J.; Sheffner, J.; Krarup, C.; Madison, R. D. *J. Neurosci*. **1995**, *15*, 4109–4123.
44. Chamberlain, L. J.; Yannas, I. V.; Arrizabalaga, A.; Hsu, H.-P.; Norregaard, T. V.; Spector, M. *Biomaterials* **1998**, *19*, 1393–1403.
45. Chamberlain, L. J.; Yannas, I. V.; Hsu, H.-P.; Strichartz, G.; Spector, M. *Exp. Neurol*. **1998**, *154*, 315–329.
46. Xie, F.; Li, Q. F.; Gu, B.; Liu, K.; Shen, G. X. *Microsurgery* **2008**, *28*, 471–479.
47. Lee, C. R.; Grodzinsky, A. J.; Spector, M. *Biomaterials* **2001**, *22*, 3145–3154.
48. Pek, Y. S.; Spector, M.; Yannas, I. V.; Gibson, L. J. *Biomaterials* **2004**, *25*, 473–482.
49. Harley, B. A.; Spilker, M. H.; Wu, J. W.; *et al*. *Cells Tissues Organs* **2004**, *176*, 153–165.
50. Itoh, S.; Takakuda, K.; Kawabata, S.; *et al*. *Biomaterials* **2002**, *23*, 4475–4481.
51. Schlosshauer, B.; Dreesmann, L.; Schaller, H. E.; Sinis, N. *Neurosurgery* **2006**, *59*, 740–748.
52. Chang, A. S.; Yannas, I. V.; Perutz, S.; *et al*. In *Progress in Biomedical Polymers*; Gebelein, C. G., Ed.; Plenum: New York, 1990.
53. Fields, R. D.; Ellisman, M. H. *Exp. Neurol*. **1986**, *92*, 48–60.
54. Chang, C. J.; Hsu, S. H. *Biomaterials* **2006**, *27*, 1035–1042.
55. Harley, B. A.; Hastings, A. Z.; Yannas, I. V.; Sannino, A. *Biomaterials* **2006**, *27*, 866–874.
56. Oh, S. H.; Lee, J. H. *J. Biomed. Mater. Res. A* **2006**, *80*, 530–538.
57. Chew, S. Y.; Mi, R.; Hoke, A.; Leong, K. W. *Adv. Funct. Mater*. **2007**, *17*, 1288–1296.
58. Vleggeert-Lankamp, C. L. A. M.; Ruiter, G. C. W.; Wolfs, J. F. C.; *et al*. *J. Biomed. Mater. Res. A* **2007**, *80*, 965–982.
59. Wang, W.; Itoh, S.; Matsuda, A.; *et al*. *J. Biomed. Mater. Res. A* **2007**, *84*, 557–566.
60. Yang, Y.; Ding, F.; Wu, J.; *et al*. *Biomaterials* **2007**, *28*, 5526–5535.
61. Meek, M. F.; den Dunnen, W. F. *Microsurgery* **2009**, *29*, 473–478.
62. Mooney, D. J.; Mazzoni, C. L.; Breuer, C.; *et al*. *Biomaterials* **1996**, *17*, 115–124.
63. Li, S.-T.; Archibald, S. J.; Krarup, C.; Madison, R. D. *Clin. Mater*. **1992**, *9*, 195–200.
64. Wan, A. C. A.; Mao, H.-Q.; Wang, S.; Leong, K. W.; Ong, L. K. L. L.; Yu, H. *Biomaterials* **2001**, *22*, 1147–1156.
65. Hsu, S. H.; Su, C. H.; Chiu, I. M. *Artif. Organs* **2009**, *33*, 26–35.
66. Cui, T.; Yan, Y.; Zhang, R.; Liu, L.; Xu, W.; Wang, X. *Tissue Eng. C Methods* **2009**, *15*, 1–9.
67. Lundborg, G.; Dahlin, L. B.; Danielsen, N.; *et al*. *Exp. Neurol*. **1982**, *76*, 361–375.
68. Meek, M. F.; Coert, J. H. *Ann. Plast. Surg*. **2008**, *60*, 466–472.
69. Weber, R. A.; Breidenbach, W. C.; Brown, R. E.; Jabaley, M. E.; Mass, D. P. *Plast. Reconstr. Surg*. **2000**, *106*, 1036–1045.
70. Moore, A. M.; Kasukurthi, R.; Magill, C. K.; Farhadi, F.; Borschel, G. H.; Mackinnon, S. E. *Hand* **2009**, *4*, 180–186.
71. Dyck, P. J.; Dyck, P. J. B.; Engelstad, J. N. In *Peripheral Neuropathy*; Dick, P. J., Thomas, P. K., Eds.; W.B. Saunders: Philadelphia, PA, 2005; pp 733–829.
72. Chang, A. S.; Yannas, I. V.; Krarup, C.; Sethi, R. R.; Norregaard, T. V.; Zervas, N. T. *Proc. ACS Div. Polym. Mater. Sci. Eng*. **1988**, *59*, 906–910.
73. Yao, L.; Billiar, K.; Windebank, A. J.; Pandit, A. *Tissue Eng. C Methods* **2010**, *16*(6), 1585–1596.
74. Stang, F.; Fansa, H.; Wolf, G.; Reppin, M.; Keilhoff, G. *Biomaterials* **2005**, *26*, 3083–3091.
75. Evans, G. R. D.; Brandt, K.; Katz, S.; *et al*. *Biomaterials* **2002**, *23*, 841–848.
76. Okamoto, H.; Hata, K.; Kagami, H.; *et al*. *J. Biomed. Mater. Res. A* **2010**, *92*, 859–868.
77. Hu, W.; Gu, J.; Deng, A.; Gu, X. *Biotechnol. Lett*. **2008**, *30*, 1937–1942.
78. Wang, X.; Hu, W.; Cao, Y.; Yao, J.; Wu, J.; Gu, X. *Brain* **2005**, *128*, 1897–1910.
79. Yoshii, S.; Oka, M.; Shima, M.; Taniguchi, A.; Akagi, M. *J. Biomed. Mater. Res. A* **2003**, *67*, 467–474.
80. Kim, H.; Tator, C. H.; Soichet, M. S. *Biotechnol. Prog*. **2008**, *24*, 932–937.
81. Kim, Y. T.; Haftel, V. K.; Kumar, S.; Bellamkonda, R. V. *Biomaterials* **2008**, *29*, 3117–3127.
82. Zheng, L.; Cui, H. F. *J. Mater. Sci. Mater. Med*. **2010**, *21*, 1713–1720.
83. Li, B. C.; Jiao, S. S.; Xu, C.; You, H.; Chen, J. M. *J. Biomed. Mater. Res. A* **2010**, *94*(3), 769–780.
84. Verdu, E.; Navarro, X.; Gudino-Cabrera, G.; *et al*. *NeuroReport* **1999**, *10*, 1097–1101.
85. Ansselin, A. D.; Fink, T.; Davey, D. F. *Neuropathol. Appl. Neurobiol*. **1997**, *23*, 387–398.
86. Cheng, B.; Chen, Z. R. *Microsurgery* **2002**, *22*, 133–137.
87. Rutkowski, G. E.; Miller, C. A.; Jeftinija, F.; Mallapragada, S. K. *J. Neural Eng*. **2004**, *1*, 151–157.
88. Goto, E.; Mukozawa, M.; Mori, H.; Hara, M. *J. Biosci. Bioeng*. **2010**, *109*, 512–518.
89. Boyd, J. G.; Gordon, T. *Mol. Neurobiol*. **2003**, *27*, 277–323.
90. Midha, R.; Munro, C. A.; Dalton, P. D.; Tator, C. H.; Soichet, M. S. *J. Neurosurg*. **2003**, *99*, 555–565.
91. Boyd, J. G.; Gordon, T. *Eur. J. Neurosci*. **2002**, *15*, 613–626.
92. Jiang, X.; Lim, S. H.; Mao, H. Q.; Chew, S. Y. *Exp. Neurol*. **2010**, *223*, 86–101.
93. Sakamoto, T.; Kawazoe, Y.; Shen, J. S.; *et al*. *J. Neurosci. Res*. **2003**, *72*, 54–64.
94. Shi, Y.; Zhou, L.; Tian, J.; Wang, Y. *Acta Otolaryngol*. **2008**, *129*(8), 1–9.
95. Chang, W. C.; Kliot, M.; Sretavan, D. W. *Neurol. Res*. **2008**, *30*, 1053–1062.
96. de Ruiter, G. C.; Malessy, M. J.; Yaszemski, M. J.; Windebank, A. J.; Spinner, R. J. *Neurosurg. Focus* **2009**, *26*, E5.
97. Walsh, S.; Midha, R. *Neurosurg. Focus* **2009**, *26*, E2.
98. Lysaght, M. J.; Jaklenec, A.; Deweerd, E. *Tissue Eng. A* **2008**, *14*, 305–319.
99. Casella, C. T. B.; Bunge, R. P.; Wood, P. M. *Glia* **1996**, *17*, 327–338.
100. Matsumoto, K.; Ohnishi, K.; Kiyotani, T.; *et al*. *Brain Res*. **2000**, *868*, 315–328.
101. Shi, W.; Yao, J.; Chen, X.; Lin, W.; Gu, X.; Wang, X. *Artif. Cells Blood Substit. Immobil. Biotechnol*. **2010**, *38*, 29–37.
102. Gordon, T.; Chan, K. M.; Sulaiman, O. A.; Udina, E.; Amirjani, N.; Brushart, T. M. *Neurosurgery* **2009**, *65*, A132–A144.
103. Alluin, O.; Wittmann, C.; Marqueste, T.; *et al*. *Biomaterials* **2009**, *30*, 363–373.
104. Archibald, S. J.; Krarup, C.; Sheffner, J.; Li, S.-T.; Madison, R. D. *J. Comp. Neurol*. **1991**, *306*, 685–696.
105. Kassar-Duchossoy, L.; Duchossoy, Y.; Rhrich-Haddout, F.; Horvat, J. C. *Brain Res*. **2001**, *908*, 25–34.
106. Liu, S.; Bodjarian, N.; Langlois, O.; *et al*. *J. Neurosci. Res*. **1998**, *51*, 723–734.
107. Liu, S.; Peulve, P.; Jin, O.; *et al*. *J. Neurosci. Res*. **1997**, *49*, 425–432.
108. Sannino, A.; Silvestri, L.; Madaghiele, M.; Harley, B.; Yannas, I. V. *J. Appl. Polym. Sci*. **2010**, *116*, 1879–1888.
109. Noah, E. M.; Chen, J.; Jiao, X.; Heschel, I.; Pallua, N. *Biomaterials* **2002**, *23*, 2855–2861.
110. Weigand, C.; Abel, M.; Ruth, P.; *et al*. *J. Biomed. Mater. Res. B* **2009**, *90*, 710–719.
111. Miles, C. A.; Avery, N. C.; Rodin, V. V.; Baley, A. J. *J. Mol. Biol*. **2005**, *346*, 551–556.
112. Cai, D.; Qiu, J.; Cao, Z.; McAtee, M.; Bregman, B. S.; Filbin, M. T. *J. Neurosci*. **2001**, *21*, 4731–4739.
113. Chen, M. S.; Huber, A. B.; van der Haar, M. E.; *et al*. *Nature* **2000**, *403*, 434–439.
114. Martino, G. *Lancet Neurol*. **2004**, *3*, 372–378.
115. Fitch, M. T.; Doller, C.; Combs, C. K.; Landreth, G. E.; Silver, J. *J. Neurosci*. **1999**, *19*, 8182–8198.
116. Lu, P.; Tuszinsky, M. H. *Exp. Neurol*. **2008**, *209*, 313–320.
117. Orive, G.; Anitua, E.; Pedraz, J. L.; Emerich, D. F. *Nat. Rev. Neurosci*. **2009**, *10*, 682–692.
118. Straley, K. S.; Foo, C. W.; Heilshorn, S. C. *J. Neurotrauma* **2010**, *27*, 1–19.
119. Tabesh, H.; Amoabediny, G.; Nik, N. S.; *et al*. *Neurochem. Int*. **2009**, *54*, 73–83.
120. Blight, A. R. *Nat. Neurosci*. **2002**, *5S*, 1051–1054.
121. Kocsis, J. D.; Akiyama, Y.; Lankford, K. L.; Radtke, C. *J. Rehabil. Res. Dev*. **2002**, *39*, 287–298.
122. Emsley, J. G.; Mitchell, B. D.; Kempermann, G.; Macklis, J. D. *Prog. Neurobiol*. **2005**, *75*, 321–341.
123. Liu, S.; Qu, Y.; Stewart, T. J.; *et al*. *Proc. Natl. Acad. Sci. USA* **2000**, *97*, 6126–6131.
124. McDonald, J. W.; Liu, X.-Z.; Qu, Y.; *et al*. *Nat. Med*. **1999**, *5*, 1410–1412.
125. Keirstead, H. S.; Nistor, G.; Bernal, G.; *et al*. *J. Neurosci*. **2005**, *25*, 4694–4705.
126. Vogel, G. *Science* **2005**, *310*(5751), 1100.
127. Galli, R.; Gritti, A.; Bonfanti, L.; Vescovi, A. L. *Circ. Res*. **2003**, *92*, 598–608.
128. Kuhn, H. G.; Dickinson-Anson, H.; Gage, F. H. *J. Neurosci*. **1996**, *16*, 2027–2033.
129. Weiss, S.; Reynolds, B. A.; Vescovi, A. L.; Morshead, C.; Craig, C. G.; van der Kooy, D. *Trends Neurosci*. **1996**, *19*, 387–393.
130. Ming, G. L.; Song, H. *Annu. Rev. Neurosci*. **2005**, *28*, 223–250.
131. Horner, P. J.; Power, A. E.; Kempermann, G.; *et al*. *J. Neurosci*. **2000**, *20*, 2218–2228.
132. Cummings, B. J.; Uchida, N.; Tamaki, S. J.; *et al*. *Proc. Natl. Acad. Sci. USA* **2005**, *102*, 14069–14074.
133. Cummings, B. J.; Uchida, N.; Tamaki, S. J.; Anderson, A. J. *Neurol. Res*. **2006**, *28*, 474–481.

134. Karimi-Abdolrezaee, S.; Eftekharpour, E.; Wang, J.; Morshead, C. M.; Fehlings, M. G. *J. Neurosci.* **2006**, *26*, 3377–3389.
135. Ben-Hur, T.; Einstein, O.; Mizrachi-Kol, R.; *et al. Glia* **2003**, *41*, 73–80.
136. Pluchino, S.; Quattrini, A.; Brambilla, E.; *et al. Nature* **2003**, *422*, 688–694.
137. Pluchino, S.; Zanotti, L.; Rossi, B.; *et al. Nature* **2005**, *436*, 266–271.
138. Ransohoff, R. M. *J. Infect. Dis.* **2002**, *186*, S152–S156.
139. Pluchino, S.; Furlan, R.; Martino, G. *Curr. Opin. Neurol.* **2004**, *17*, 247–255.
140. Fujiwara, Y.; Tanaka, N.; Ishida, O.; *et al. Neurosci. Lett.* **2004**, *366*, 287–291.
141. Lu, P.; Jones, L. L.; Snyder, E. Y.; Tuszinsky, M. H. *Exp. Neurol.* **2003**, *181*, 115–129.
142. Teng, Y. D.; Lavik, E. B.; Qu, X.; *et al. Proc. Natl. Acad. Sci. USA* **2002**, *99*, 3024–3029.
143. Chu, K.; Kim, M.; Park, K.; *et al. Brain Res.* **2004**, *1016*, 145–153.
144. Chu, K.; Kim, M.; Jung, K. H.; *et al. Brain Res.* **2004**, *1023*, 213–221.
145. Richardson, R. M.; Broaddus, W. C.; Holloway, K. L.; Fillmore, H. L. *Brain Res.* **2005**, *1032*, 11–22.
146. Houweling, D. A.; van Asseldonk, J. T.; Lankhorst, A. J.; *et al. Neurosci. Lett.* **1998**, *251*, 193–196.
147. McTigue, D. M.; Horner, P. J.; Stokes, B. T.; Gage, F. H. *J. Neurosci.* **1998**, *18*, 5354–5365.
148. Namiki, J.; Kojima, A.; Tator, C. H. *J. Neurotrauma* **2000**, *17*, 1219–1231.
149. Shumsky, J. S.; Tobias, C. A.; Tumolo, M.; Long, W. D.; Giszter, S. F.; Murray, M. *Exp. Neurol.* **2003**, *184*, 114–130.
150. Lee, T. T.; Green, B. A.; Dietrich, W. D.; Yezierski, R. P. *J. Neurotrauma* **1999**, *16*, 347–356.
151. McKerracher, L.; David, S.; Jackson, D. L.; Kottis, V.; Dunn, R. J.; Braun, P. E. *Neuron* **1994**, *13*, 805–811.
152. Wang, K. C.; Koprivica, V.; Kim, J. A.; *et al. Nature* **2002**, *417*, 941–944.
153. Wang, K. C.; Kim, J. A.; Sivasankaran, R.; Segal, R.; He, Z. *Nature* **2002**, *420*, 74–78.
154. Moreau-Fauvarque, C.; Kumanogoh, A.; Camand, E.; *et al. J. Neurosci.* **2003**, *23*, 9229–9239.
155. Behar, O.; Mizuno, K.; Badminton, M.; Woolf, C. J. *Proc. Natl. Acad. Sci. USA* **1999**, *96*, 13501–13505.
156. Benson, M. D.; Romero, M. I.; Lush, M. E.; Lu, Q. R.; Henkemeyer, M.; Parada, L. F. *Proc. Natl. Acad. Sci. USA* **2005**, *102*, 10694–10699.
157. Setoguchi, T.; Yone, K.; Matsuoka, E.; *et al. Brain Res.* **2001**, *921*, 219–225.
158. Setoguchi, T.; Nakashima, K.; Takizawa, T.; *et al. Exp. Neurol.* **2004**, *189*, 33–44.
159. Lagord, C.; Berry, M.; Logan, A. *Mol. Cell. Neurosci.* **2002**, *20*, 69–92.
160. Logan, A.; Green, J.; Hunter, A.; Jackson, R.; Berry, M. *Eur. J. Neurosci.* **1999**, *11*, 2367–2374.
161. Bradbury, E. J.; Moon, L. D. F.; Popat, R. J.; *et al. Nature* **2002**, *416*, 636–640.
162. Thuret, S.; Moon, L. D.; Gage, F. H. *Nat. Rev. Neurosci.* **2006**, *7*, 628–643.
163. Hendriks, W. T.; Ruitenberg, M. J.; Blits, B.; Boer, G. J.; Verhaagen, J. *Prog. Brain Res.* **2004**, *146*, 451–476.
164. Tobias, C. A.; Shumsky, J. S.; Shibata, M.; *et al. Exp. Neurol.* **2003**, *184*, 97–113.
165. Kataoka, K.; Suzuki, Y.; Kitada, M.; *et al. J. Biomed. Mater. Res.* **2001**, *54*, 373–384.
166. Tsai, E. C.; Dalton, P. D.; Shoichet, M. S.; Tator, C. H. *J. Neurotrauma* **2004**, *21*, 789–804.
167. Woerly, S.; Pinet, E.; de Robertis, L.; Van Diep, D.; Bousmina, M. *Biomaterials* **2001**, *22*, 1095–1111.
168. Plant, G. W.; Woerly, S.; Harvey, A. R. *Exp. Neurol.* **1997**, *143*, 287–299.
169. Stokols, S.; Tuszinsky, M. H. *Biomaterials* **2006**, *27*, 443–451.
170. Prang, P.; Muller, R.; Eljaouhari, A.; *et al. Biomaterials* **2006**, *27*, 3560–3569.
171. Guo, J.; Leung, K. K.; Su, H.; *et al. Nanomedicine* **2009**, *5*, 345–351.
172. Guo, J.; Su, H.; Zeng, Y.; *et al. Nanomedicine* **2007**, *3*, 311–321.
173. Cheng, H.; Huang, Y. C.; Chang, P. T.; Huang, Y. Y. *Biochem. Biophys. Res. Commun.* **2007**, *357*, 938–944.
174. Yara, T.; Kato, Y.; Kataoka, H.; *et al. Med. Mol. Morphol.* **2009**, *42*, 150–154.
175. Yoshii, S.; Ito, S.; Shima, M.; Taniguchi, A.; Akagi, M. *J. Tissue Eng. Regen. Med.* **2009**, *3*, 19–25.
176. Madaghiele, M.; Sannino, A.; Yannas, I. V.; Spector, M. *J. Biomed. Mater. Res. A* **2008**, *85*, 757–767.
177. Spilker, M. H.; Yannas, I. V.; Kostyk, S. K.; Norregaard, T. V.; Hsu, H.-P.; Spector, M. *Restor. Neurol. Neurosci.* **2001**, *18*, 23–38.
178. Steindler, D. A. *Nat. Biotechnol.* **2002**, *20*, 1091–1093.
179. Novikov, L. N.; Novikova, L. N.; Mosahebi, A.; Wiberg, M.; Terenghi, G.; Kellerth, J. O. *Biomaterials* **2002**, *23*, 3369–3376.
180. Patist, C. M.; Mulder, M. B.; Gautier, S. E.; Maquet, V.; Jerome, R.; Oudega, M. *Biomaterials* **2004**, *25*, 1569–1582.
181. Novikova, L. N.; Pettersson, J.; Brohlin, M.; Wiberg, M.; Novikov, L. N. *Biomaterials* **2008**, *29*, 1198–1206.
182. Chen, B. K.; Knight, A. M.; de Ruiter, G. C.; *et al. J. Neurotrauma* **2009**, *26*, 1759–1771.
183. Krych, A. J.; Rooney, G. E.; Chen, B.; *et al. Acta Biomater.* **2009**, *5*, 2551–2559.
184. Moore, M. J.; Friedman, J. A.; Lewellyn, E. B.; *et al. Biomaterials* **2006**, *27*, 419–429.
185. Park, K. I.; Teng, Y. D.; Snyder, E. Y. *Nat. Biotechnol.* **2002**, *20*, 1111–1117.
186. Olson, H. E.; Rooney, G. E.; Gross, L.; *et al. Tissue Eng. A* **2009**, *15*, 1797–1805.
187. Hejcl, A.; Sedy, J.; Kapcalova, M.; *et al. Stem Cell Dev.* **2010**, *19*(10), 1535–1546.
188. Itosaka, H.; Kuroda, S.; Shichinohe, H.; *et al. Neuropathology* **2009**, *29*, 248–257.
189. Keilhoff, G.; Goihl, A.; Stang, F.; Wolf, G.; Fansa, H. *Tissue Eng.* **2006**, *12*, 1451–1465.
190. Silva, N. A.; Salgado, A. J.; Sousa, R. A.; *et al. Tissue Eng. A* **2010**, *16*, 45–54.
191. Othon, C. M.; Wu, X.; Anders, J. J.; Ringeisen, B. R. *Biomed. Mater.* **2008**, *3*, 034101.
192. Jain, A.; Kim, Y. T.; McKeon, R. J.; Bellamkonda, R. V. *Biomaterials* **2006**, *27*, 497–504.
193. Johnson, P. J.; Tatara, A.; Shiu, A.; Sakiyama-Elbert, S. E. *Cell Transplant.* **2010**, *19*, 89–101.
194. Mehrotra, S.; Lynam, D.; Maloney, R.; *et al. Adv. Funct. Mater.* **2010**, *20*, 247–258.
195. Park, J.; Lim, E.; Back, S.; Na, H.; Park, Y.; Sun, K. *J. Biomed. Mater. Res. A* **2010**, *93*, 1091–1099.
196. Baumann, M. D.; Kang, C. E.; Stanwick, J. C.; *et al. J. Control. Release* **2009**, *138*, 205–213.
197. Goraltchouk, A.; Scanga, V.; Morshead, C. M.; Soichet, M. S. *J. Control. Release* **2006**, *110*, 400–407.
198. Hurtado, A.; Moon, L. D.; Maquet, V.; Blits, B.; Jerome, R.; Oudega, M. *Biomaterials* **2006**, *27*, 430–442.
199. De Laporte, L.; Yang, Y.; Zelivyanskaya, M. L.; Cumming, B. J.; Anderson, A. J.; Shea, L. D. *Mol. Ther.* **2009**, *17*, 318–326.

Relevant Websites

http://clinicaltrials.gov/ – ClinicalTrials.gov – A service of the US National Institute of Health.
http://apps.who.int/trialsearch/ – World Health Organization – International Clinical Trial Registry Platform Search Portal.
http://www.controlled-trials.com/ – Current Controlled Trials.

5.533. Biomaterials for Central Nervous System Regeneration

V M Tysseling, Northwestern University, Chicago, IL, USA
J A Kessler, The Frances Evelyn Feinberg Clinical Neuroscience Research Institute, Chicago, IL, USA

© 2011 Elsevier Ltd. All rights reserved.

5.533.1.	**Introduction**	456
5.533.2.	**Biomaterial Therapy Options**	456
5.533.2.1.	Drug Delivery	456
5.533.2.1.1.	Introduction	456
5.533.2.1.2.	Systemic delivery systems	456
5.533.2.1.3.	Local delivery systems	457
5.533.2.2.	Scaffolds for CNS Repair	457
5.533.2.2.1.	Introduction	457
5.533.2.2.2.	Characteristics of scaffolds in CNS	457
5.533.2.3.	Nerve Channels	458
5.533.2.3.1.	Introduction	458
5.533.2.3.2.	Characteristics of nerve channels	458
5.533.3.	**Spinal Cord Injury**	459
5.533.3.1.	Introduction	459
5.533.3.2.	Scaffolds in SCI	460
5.533.3.3.	Drug Delivery and Nerve Channels in SCI	460
5.533.4.	**Alzheimer's Disease**	461
5.533.4.1.	Introduction	461
5.533.4.2.	Biomaterial Therapies for Alzheimer's	462
5.533.5.	**Parkinson's**	462
5.533.5.1.	Overview of Parkinson's	462
5.533.5.2.	Biomaterials in Treatment for Parkinson's Disease	463
5.533.6.	**Biomaterials Used with Stem Cell Therapy**	463
5.533.6.1.	Stem Cell Use in CNS Injury	463
5.533.6.2.	Biomaterials and Stem Cells	463
5.533.7.	**Summary of Biomaterial Therapies in CNS Injury/Disease**	464
References		465

Glossary

Alzheimer's disease Progressive mental deterioration that can occur in middle or old age, due to generalized degeneration of the brain. It is the most common cause of premature senility.

Amyotrophic lateral sclerosis (Lou Gehrig's disease) A progressive degeneration of the motor neurons of the central nervous system, leading to wasting of the muscles and paralysis.

Astrocyte Characteristic star-shaped glial cells in the brain and spinal cord. They perform many functions, including biochemical support of endothelial cells, which form the blood–brain barrier, provision of nutrients to the nervous tissue, maintenance of extracellular ion balance, and play a principal role in the repair and scarring process of the brain and spinal cord following traumatic injuries.

Astrogliosis Abnormal increase in the number of astrocytes due to the destruction of nearby neurons, typically because of hypoglycemia or oxygen deprivation (hypoxia).

Blood–brain barrier Separation of circulating blood and cerebrospinal fluid (CSF) in the central nervous system (CNS).

Differentiation Process by which a less specialized cell becomes a more specialized cell type.

Embryonic stem cells Pluripotent stem cells derived from the inner cell mass of the blastocyst, an early-stage embryo.

Extracellular matrix Protein-based connective tissue that usually provides structural support and instruction to the surrounding animal cells.

Growth factor Naturally occurring substance capable of stimulating cellular growth, proliferation, and cellular differentiation.

Inflammation Biological response of vascular tissues to harmful stimuli, such as pathogens, damaged cells, or irritants. Inflammation is a protective attempt by the organism to remove the injurious stimuli as well as initiate the healing process for the tissue.

Neural progenitor cells Progenitor cells have a capacity to differentiate into a specific type of cell. In contrast to stem cells, however, they are already far more specific: they are pushed to differentiate into their 'target' cell.

Neuron Electrically excitable cell that processes and transmits information by electrical and chemical signaling, the latter via synapses, specialized connections with other cells.

Neurotrophic factor Family of proteins that induce the survival, development, and function of neurons.
Oligodendrocyte A glial cell concerned with the production of myelin for insulation of the neurons in the central nervous system.
Parkinson's disease Degenerative disorder of the central nervous system that often impairs the sufferer's motor skills, speech, and other functions.

5.533.1. Introduction

Central nervous system (CNS) dysfunctions are caused by disease or trauma; they are diverse, frequently severe, and nondiscriminatory in affecting the whole world's population. Traumatic injuries such as brain injury and spinal cord injury severely and immediately affect the person's physical and/or cognitive abilities. Neurodegenerative disorders such as Alzheimer's disease, Parkinson's disease, or amyotrophic lateral sclerosis (Lou Gehrig's disease) slowly or rapidly degenerate CNS neurons, again resulting in deficits in movement and cognition. The causes of many neurodegenerative disorders are complex, mostly unknown, and may be associated with genetic abnormalities, but advancing age, environmental influences, and dysfunctional immunity are likely even more influential.[1] Even when potential treatments are discovered, the difficulties involved in accessing the CNS may make surgical intervention to implement such treatment more debilitating, and the presence of the blood–brain barrier (BBB), which normally is protective of the CNS, inhibits therapeutic molecules and proteins from passing into the CNS (**Figure 1**). Regeneration is difficult in the CNS due to the presence of many molecules inhibitory to regeneration as well as a huge heterogeneity in intricate and individualized circuitry. Additionally, diverse tissue response cascades following disease/injury in the CNS add more challenges to regeneration, such as increased inflammation, invading cells, and glial scarring.

Biomaterials, especially nanotechnology derived, have begun to be utilized as tools in combating tissue response, drug delivery issues, and changes in the environmental milieu. Examples include nanofibers, liposomes, nanoparticles, nerve channels, and scaffolds. These materials can be custom-designed to provide a facilitory environment for regeneration and/or a blocker of inhibitory environmental cues and tissue processes. In this chapter, we review different categories of biomaterials that can be modified for specific CNS needs. We also present an overview of traumatic CNS injuries and neurodegenerative diseases and discuss ways in which biomaterials can assist in regeneration.

5.533.2. Biomaterial Therapy Options

5.533.2.1. Drug Delivery

5.533.2.1.1. Introduction

Generally, many substrates, including neurotrophic factors or other growth factors, mitotic drugs, anti-inflammatory medications, or antiapoptotic drugs, can not only prevent some of the secondary and tertiary expansions of CNS damage, but also encourage axonal regeneration, cell survival, and/or differentiation. One of the difficulties in the delivery of such agents to the injured CNS is the presence of the BBB, which blocks the access of many cells and proteins from the bloodstream into the CNS.[2–4] Biomaterials have begun to enter the arena to help systemic, targeted, or local delivery of drugs.[5]

5.533.2.1.2. Systemic delivery systems

Systemic delivery systems are noninvasive as they are generally administered either intravenously or through other peripheral injection, such as intraperitoneal or subcutaneous. The delivery can be continuous or repeated, and allows for dose changes throughout the treatment. However, despite attempts at targeted delivery, the systemic delivery of a drug poses challenges in terms of unexpected target finds, biodegradability, and recognition by phagocytic immune cells prior to delivery to the lesioned area. Two biomaterials in this category include liposomes and polymeric nanoparticles.

5.533.2.1.2.1. Liposomes

Liposomes are small vesicles whose outer membrane is made out of the same material composing cell membranes, a phospholipid bilayer. The vesicles can be small and simple (25–50 nm in diameter) to large and multilamellar (200–5000 nm).[6–9] The inner core of the liposome can house drugs or proteins of interest and release them once the liposome binds to another phospholipid bilayer. Because of their similarity to cell membranes, liposomes are very biocompatible and biodegradable. Unfortunately, they are also readily targeted by blood immune cells that phagocytize small foreign particles while being transported through the vascular system.[10] One approach to this problem is to add polyethylene glycol to the surface of the liposome, which inhibits the liposomal aggregation and recognition by the immune system.[2,7,8]

Also, liposomes do not cross the intact BBB well. In some cases, such as after trauma, certain disease processes, and tumors, lesioned areas of the CNS can still be accessible as they have a compromised BBB where the liposomes can pass through more easily. More targeted methods that may facilitate BBB passage may be required by a process known as active targeting. In this approach, the liposome surface can be modified with an antibody or a ligand that will specifically attach to the targeted cells.[2,8] In this case, the targeted cells would be ones that actively transport cells across the BBB. Additionally, active targeting can then assist the liposomes in finding their direct CNS cell targets.

5.533.2.1.2.2. Polymeric nanoparticles

Polymeric nanoparticles, made from synthetic (poly-lactic or -glycolic acid) or natural (alginate or gelatin) polymers, form nanospheres or nanocapsules, are similarly sized as liposomes (10–1000 nm), and are a very diverse group in which the drug can be located throughout the particle or localized to

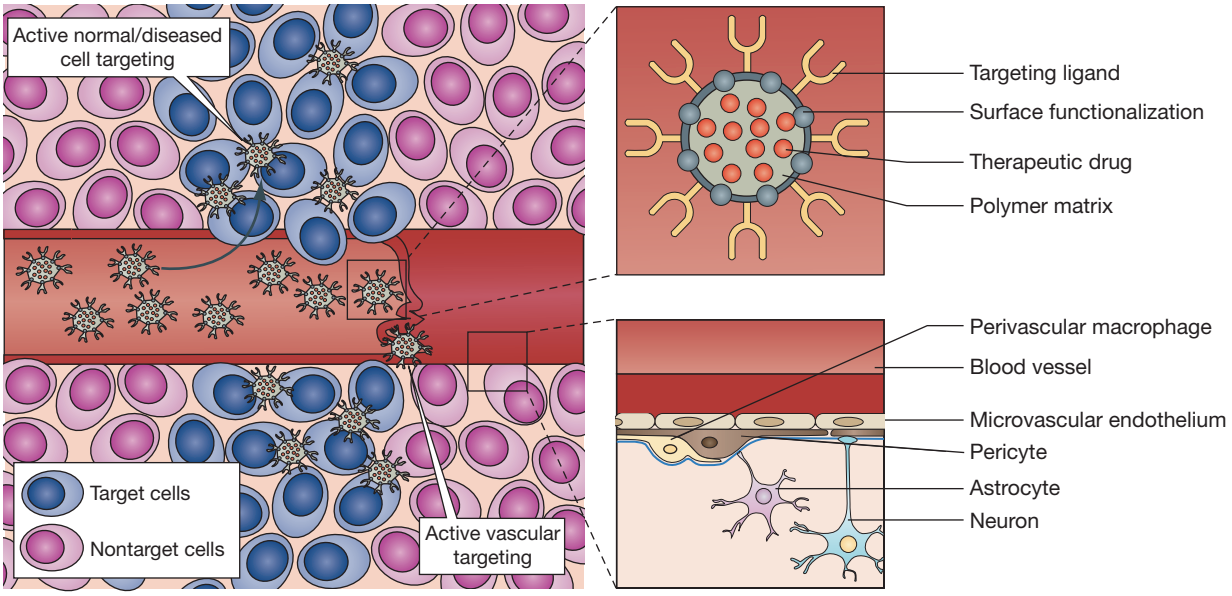

Figure 1 Blood–brain barrier and active targeting for drug delivery. The blood–brain barrier is regulated by the neurovascular unit, which comprises perivascular macrophages, astrocytes, and neurons (bottom right panel). This regulation determines the amount of communication between the central nervous system and the periphery, restricting the passage of proteins and cells through tight junctions between endothelial cells in the blood vessels. Biomaterials such as liposomes or other nanoparticles can be created to house surface ligands that will specifically bind to target cells. They will also house other proteins such as polyethylene glycol that will increase the biomaterial's longevity within the peripheral blood system. Additional targeting ligands or antibodies can further direct the biomaterial toward receptors on its end target for drug delivery. Adapted from Orive, G.; Anitua, E.; Pedraz, J. L.; Emerich, D. F. *Nat. Rev. Neurosci.* **2009**, *10*, 682–692, with permission from Nature Publishing Group; Neuwelt, E.; Abbott, N. J.; Abrey, L.; *et al. Lancet Neurol.* **2008**, *7*, 84–96, with permission from Lancet Publishing Group; Farokhzad, O. C.; Langer, R. *ACS Nano* **2009**, *3*, 16–20, with permission from American Chemical Society.

Table 1 Summary of important biomaterial characteristics

Cell adhesion/encapsulation/transplantation	Biomolecule delivery	Injectability
Topography/mechanical strength	Biodegradation	Internal matrix
Electrical activity	Porosity	Channels/fibers

Used and modified with permission from Nature Publishing Group (2009). Orive, G.; Anitua, E.; Pedraz, J. L.; Emerich, D. F. *Nat. Rev. Neurosci.* **2009**, *10*, 682–692.

its core or surface.[7,10–12] They are more stable in the body than liposomes, but still require similar surface modifications to increase longevity within the body and can deliver the drug in a more controlled, time-release manner.[13] For example, nanoparticles coated with polysorbate 80 have been shown to be successfully transported through the BBB.[13]

5.533.2.1.3. Local delivery systems

As stated earlier, despite attempts at targeted delivery, the systemic delivery of a drug poses challenges in terms of unintended target finds, biodegradability and systemic side effects, and detection and removal by cells from the immune system before the drug finds the appropriate target. An alternative to systemic delivery would be a direct transplantation of the biomaterial, ideally with a timed-release delivery system and biodegradability of the nondrug material. The transplantation itself, however, may cause further trauma, and a nonbiodegradable biomaterial may cause continued inflammatory responses.

5.533.2.2. Scaffolds for CNS Repair

5.533.2.2.1. Introduction

Often, post-CNS injury or disease, the new abnormal environment plays a key role in advancing the disease process. Scaffolds can support and direct cells in the environment by creating a new extracellular matrix important for healthy and normal cell–cell interactions and signaling (Table 1).

5.533.2.2.2. Characteristics of scaffolds in CNS

Scaffolds have been created with many different biomaterials such as hydrogels, collagen, methylcellulose, and agarose in the CNS.[14–17] These scaffolds are diverse in their configuration, material strength, biodegradability, cell adhesion, and signaling.

The proper configuration of scaffolds depends on the end use. Biomaterials produced to facilitate nerve or axonal regeneration may require long channels directing the regeneration in a particular direction.[3] This scaffold may also contain certain amino acid sequences that promote regeneration in general

and also toward/away from a topographical and/or chemical gradient. Other more generally supportive materials may be used for extracellular matrix or cellular support such as nanogels or sponges.[3] These also may be at least partially constructed with specific protein sequences that promote cell differentiation, survival, or differentiation. All scaffolds for CNS regeneration, regardless of model, require general characteristics.[17,18] As in local drug delivery, the potential for additional damage when inserting the scaffold may outweigh its benefits. To this end, scaffolds must be flexible and easily inserted into the tissue. The scaffold should be biocompatible and biodegradable so as to not elicit additional chronic inflammatory responses. Also, if the permissive scaffold does not biodegrade, the regenerating cells would grow into the scaffold, but never reenter the CNS, creating a sinkhole for regeneration. The scaffold must allow for diffusion of nutrients to maintain the health of the incorporated tissue and also enough room for cells or for axons to grow through it. Examples of scaffold materials include synthetic versions such as poly-2-hydroxyethyl methacrylate and poly-*N*-2-hydroxypropyl methacrylamide as well as natural forms, such as collagen, chitosan, fibrin, and dextran.

Scaffolds also differ in their mechanical strength and biodegradability. Covalent cross-linking produces a stiffer material, which is more difficult to elegantly transplant into the CNS and usually harder to degrade. Physical cross-linking produces a more compliant, softer product, which biodegrades more easily. The closer a material is to matching the mechanical strength of the environment, the more likely it is for cells and axons to cross barriers between the natural environment and the scaffold.[19,20] As stated earlier, the biodegradability of the tissue, related to stiffness, is of importance to decrease prolonged inflammatory processes. The scaffold can degrade from hydrolysis or from proteolytic degradation of more natural materials.[21,22]

Cell or axonal adhesion and signaling are other important characteristics of a successful scaffold. If the material itself is not naturally cell-adhesive, the material can be laced with amino acid sequences presented in high-density promoting growth or bonding to CNS cells.[23] This is also quite important when considering cell transplantation along with the scaffold to provide a facilitatory niche for the cells. Most scaffolds are designed to not only physically support, but also direct cells, through scaffold–cell interaction. This does not occur without cell attachment to the scaffold. The scaffold must promote a certain function of the cells and, therefore, adhesion and signaling are key. For example, neural progenitor cells may be transplanted for neuronal differentiation to assist with local circuitry or for increased oligodendrocyte differentiation for increased myelination.

Signaling of the scaffold can be static or time release. Signaling may also be directed at endogenous adult cells for regeneration of compromised axons or differentiation of endogenous progenitor cells. Signaling can also be directed at quenching inhibitory environmental cues or attenuating scar formation postinjury. For example, brain-derived neurotrophic factor (BDNF) can facilitate regeneration and plasticity.[16,24] Alternatively, the IKVAV sequence of laminin has been shown to not only promote neurite extension and axonal regeneration, but also inhibit astrogliosis (**Figure 2**).[23,25] However, it may be beneficial at times to provide the environment with more than one signal for multiple tissue responses or for more direct topographical cues on regeneration of axons.[26] The scaffold would have to be designed in such a way that it has appropriate three-dimensional patterning.[27,28] Patterning of different peptide sequences, cell-adhesive versus cell nonadhesive areas, and texture of the surface may all have a role to play in differential events within the scaffold. Because the nature of the CNS is highly heterogeneous and that of CNS injury even more so, the most successful scaffold will need to combine techniques.

5.533.2.3. Nerve Channels

5.533.2.3.1. Introduction

Promotion of specific neurite and axonal growth and/or conductivity may require a scaffold channel consisting of nanotubes or nanofibers (**Table 1**). The length, volume, and diameter of the channel can be manipulated to promote conductivity or guide axonal growth. The shape itself can allow for a different molecular makeup within the tube than outside of the tube, thereby sending the axon or neurite an elongation cue and the surrounding environment a different cue. The nanofiber structure would also offer a high exposure of the neurite and its environment to the instructional molecules, potentially overwhelming the system toward a more permissive, less destructive niche. Alternatively, the inside of the fibers or tubes could house drugs or other proteins to be time- or gradient-released while the outside of the fiber would serve as a conduit for axonal regeneration or neurite growth or affect the extracellular matrix.

5.533.2.3.2. Characteristics of nerve channels

Nerve channels can be made out of biodegradable or nonbiodegradable material. As stated earlier, nonbiodegradable material presents increasing challenges due to not only its increased incidence of chronic inflammation, but also its mostly noncell adhesive nature. Examples of these materials are silicone, polyacrylonitrile, polytetrafluoroethylene, and poly-2-hydroxyethyl methacrylate.[29] Biodegradable material is usually superior as it does not cause these long-term inflammatory changes and degrades as the nerve and the environment regenerate. This also allows the nerve to pass from the permissive environment of the material back into the CNS. If the material is permissive enough for the axon to grow but does not degrade, the axon may grow into, and stay within, the material instead of passing through and forming the necessary connections for function. The biomaterial can be natural or synthetic, but the by-products of degradation must also be tested for toxicity. Common biodegradable compounds are the polymer family of poly-α-hydroxyacids, collagen, chitosan, and poly-β-hydroxybutyrate.[29]

An additional consideration for nerve channel composition is whether to create the channel to have electrical properties. Neurons are very electrically active cells and having an electrically charged extracellular environment may help regeneration.[30,31] The three main types that currently exist are all nonbiodegradable and include polymers with a quasipermanent charge, an electric charge generated with mechanical stress, or electrically conducting polymers. Examples of these

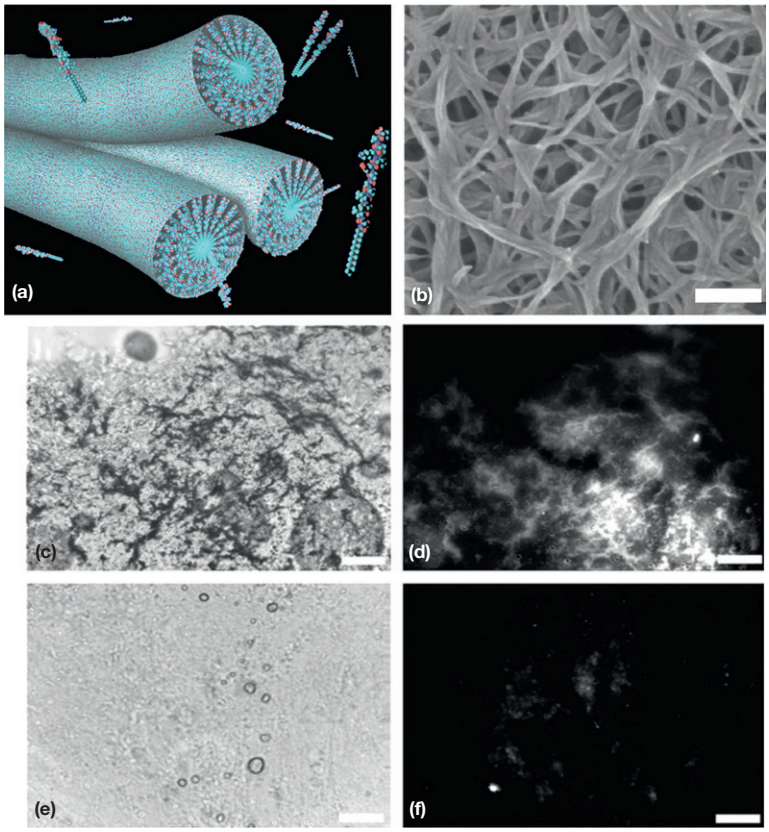

Figure 2 IKVAV PA structure, self-assembly, and biodegradability. (a) Schematic representation showing the makeup of individual PA molecules assembled into a bundle of nanofibers interwoven to produce the IKVAV PA scaffold. (b) Scanning electron micrograph image shows the network of nanofibers *in vitro*. Scale bar = 200 nm. (c–f) Phase (left) and fluorescent (right) images showing biodegradability of the PA through a fluorescent derivative in the injured spinal cord quite visible at 2 weeks (c, d) but then quite diminished at 4 weeks (e, f) postinjection. Scale bars: (b) 200 nm, (c–f) 50 μm.

materials are poly-tetrafluoroethylene, polyvinylidene fluoride, and polypyrrole.[29]

Mechanical strength can provide structure to a dysfunctional environment and prevent channel collapse and resultant nerve or axon compression, but can also inhibit biodegradability and create a sharp contrast in tissue properties between the implant and the natural CNS tissue. Many factors, including biodegradation, activity, and inflammatory cells, can cause collapse of the biomaterial channel, which in turn can cause damage to the axons or neurites that are regenerating.[32] The damage due to this collapse must be balanced against the decrease in biodegradability and the stress of a strong, firm material against the soft CNS tissue. Cross-linking of the biomaterial and/or adding coils to the walls of the channels can both provide structural permanence to the channel.

Adhesion of the axons or neurites to the channel is necessary for regeneration attempts. The key is to either mimic a permissive environment or even revert to a developmental environment to provide chemotaxis. This can be accomplished by either nonspecific binding through surface charge, roughness, or topography or specific adhesion to molecules in the environment.[33,34] Nonspecific binding can be seen using chitosan and polylysine, which assist binding via charge.[21,34] Specific adhesion, however, can more intimately guide the desired effects of the neurites by choosing whole or portions of proteins proven to promote regeneration, such as the whole protein of laminin or the five amino acid sequence of laminin, IKVAV.[35,36]

Nerve guidance channels can also have an internal medium, which increases available functions, such as internal cell adhesion, drug delivery, and neurite extension through increased surface area.[37–44] The internal environment of the nerve channels can also consist of a scaffold, such as collagen, matrigel, or laminin.[43,45–47]

5.533.3. Spinal Cord Injury

5.533.3.1. Introduction

Spinal cord injury progresses in three stages: acute, subacute, and chronic. The acute phase of spinal cord injury begins with petechial hemorrhages at the original mechanical trauma (primary injury) and lasts for 8–24 h. During this time, the injury site undergoes hemorrhagic necrosis.[48–50] Total calcium levels increase within an hour, peak at 8 h, and remain elevated for 1 week postinjury.[51–53] This excess calcium has toxic effects on many cellular functions and may serve as a common signal for cell death.[54,55] Other such signals include free radicals from

phospholipid hydrolysis, infiltrating neutrophils undergoing oxidative bursts, and the autoxidation of catecholamines.[56,57] Excitotoxicity occurs from the release of the excitatory amino acids, glutamate and aspartate, with peak levels noted shortly posttrauma.[58,59] All these events result in waves of apoptosis in the cells surrounding the primary injury. The first occurs 24–48 h postinjury in the neurons surrounding the primary site. All these toxic events cause a very rapid and intense gene response. In addition to gene upregulation, proinflammatory cytokines activate microglia and recruit lymphocytes, neutrophils, and monocytes, which kill and phagocytose cells.

The subacute phase begins at 12–24 h postinjury and is marked by the influx of polymorphonuclear granulocytes and monocytes/macrophages to the injury site to clean up the dead cells and by the reactive gliosis of microglia and astrocytes, which fill in the cavity.[60] Adult CNS neurons continue to upregulate immediate early genes, such as nuclear proteins, cytoskeletal proteins, and growth-associated protein (GAP-43), which is a major phosphoprotein of neuronal growth cones. At this time, the axons sprout, but do not elongate. After ~2 weeks, the upregulation is followed by a downregulation of these genes and a halt in the regenerative process.[61] The second wave of apoptosis occurs at 1–2 weeks affecting all neural cells but mostly oligodendroglia in the degenerating white matter tracts, resulting in a significant loss of conductance.[62–68] Also at this stage, the injury site fills with blood vessels, Schwann cells, meningeal cells, fibroblasts, and activated astrocytes.[69] Toward the end of the subacute stage, the damaged spinal tracts begin to retract and are surrounded by macrophages and apoptotic oligodendrocytes. Reactive astrocytes as well as microglia and macrophages start to form a scar at the junction between the spinal cord and the lesion consisting of a dense network of processes.[60,70] This scar formation progresses into the chronic phase of injury.

The chronic phase does not begin until several weeks postinjury. The cavity in the injured cord is filled with a matrix of the glial scar, macrophages, astrocytes, fibroblasts, and Schwann cells from spinal roots, with a thin wall of white matter tracts along the outside. The cord is thinner due to the loss of cells and myelination at the injury site. The lesion in mice fills with a dense connective tissue filled with macrophages, fibroblasts, and capillary epithelium.[71–73] The connective tissue becomes revascularized and the fibroblasts convert to myofibroblasts that actually pull together the ends of the lesion, which reduces the distance in which regenerating axons need to travel.[74,75] Some sensory axons have been shown inside the connective tissue matrix, but most sensory axons and all corticospinal, rubrospinal, reticulospinal, and sertonergic fibers retract from the injury site and form retraction bulbs.[76] By 1 month and thereafter, most axons remain myelinated, but with a very thin sheath as compared to their uninjured counterparts.[77,78]

Three main strategies have been used to promote function following SCI. First, neuroprotection strategies aim to decrease the effects of secondary inflammation and apoptosis that greatly accentuate the injury. Second, axonal regeneration or sprouting approaches attempt to restore the damaged supraspinal and intersegmental inputs. Third, modulation of the endogenous sublesional spinal cord circuitry can promote locomotor patterns without descending input.

5.533.3.2. Scaffolds in SCI

As noted earlier, damage to the spinal cord can produce cell necrosis and waves of additional cell death, leaving an environment of empty cavitations and a thick inhibitory scar. Many of these changes are reactions of the cells to the caustic lesion environment. Acutely and subacutely, changing this environment with a scaffold promoting regeneration, inhibiting astrogliosis, and/or supporting cell proliferation and survival could drastically change the tissue response.

A molecularly designed biomatrix composed of peptide amphiphile molecules that self-assemble from aqueous solution into cylindrical nanofibers displaying bioactive epitopes on their surface was used in a model of spinal cord injury and highlights the characteristics listed earlier.[23,25,79,80] The nanoscale peptide amphiphiles have a hydrophobic tail end and a charged middle that allows the separation of individual fibers under noncationic conditions.[23,25,79,80] Once the gel is injected into the spinal cord or the retina, the physiologic cationic conditions neutralize the charged peptides and the fibers undergo hydrophobic collapse, forming long nanofibers.[23,25] Thus, this is a biomaterial that is a liquid in aqueous solution as it is being delivered, but turns into a gel or more solid form after being introduced to the spinal cord. The nanofibers are biocompatible as they are entirely composed of amino acids naturally found in the body and are biodegraded in the spinal cord after a period of weeks postinjection.[23] The formed nanogel product was found not only to allow sufficient nutrient diffusion to support cell life both *in vitro* and *in vivo*, but also to support neurite outgrowth from encapsulated neural stem cells and axonal regeneration in the injured spinal cord.[23,25] *In vivo*, the nanoscale peptide amphiphile also acted as a more positive extracellular matrix by signaling via its concentrated head group to inhibit astrogliosis, attenuate cell death, and once again promote regeneration of different types of axons.[23] Most importantly, the injection of the nanofibers resulted in a behavioral improvement in the spinal cord-injured mice.[23]

5.533.3.3. Drug Delivery and Nerve Channels in SCI

Spinal cord damage following injury could greatly benefit from the delivery of neuroprotective or regenerative drugs. Acutely and subacutely, less cell death would occur if a therapy were delivered acutely that quench the excitotoxicity drenching the damaged area. Specific and temporally appropriate pro- or anti-inflammatory medications may decrease the invasion of immune cells and/or swelling that could cause further damage to cells and axons traversing the spinal cord. Neurotrophic factors or growth factors could be delivered to increase cell and axon survival or promote axonal regeneration prior to the formation of a thick, impermeable glial scar.[38,39,43] Alternatively, blockers of astrocyte hypertrophy could allow the astrocytes to cordon off the invading cells, but not to hypertrophy to a point where it blocks the regeneration of axons. Chronically, drugs that can infiltrate and break up thick scarring could promote regeneration if combined with other axonal regenerative agents. Bridges or grafts could also promote regeneration of axons around or through the lesioned spinal cord (**Figure 3**). Importantly, combined therapy reaching out to many of the processes occurring post-SCI, such as cell

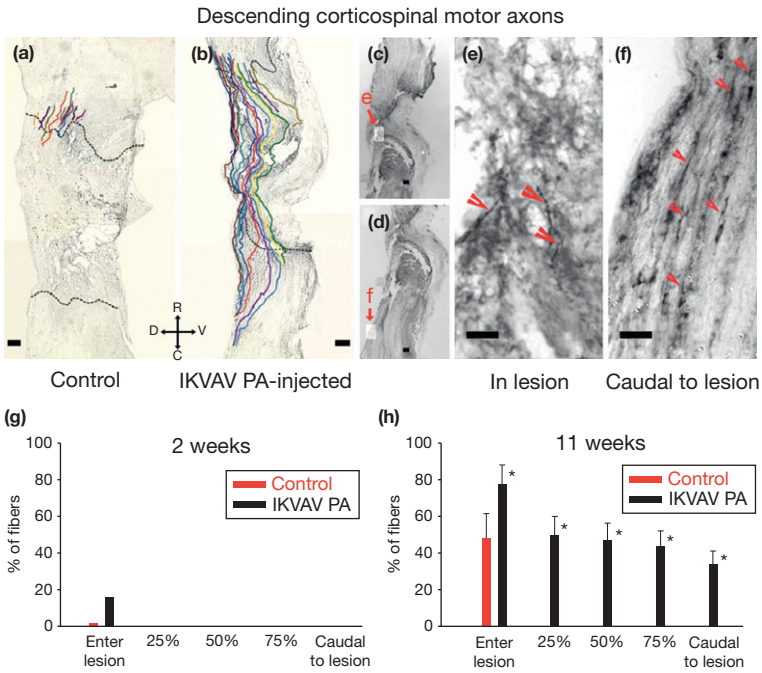

Figure 3 IKVAV PA promotes regeneration of axons after SCI. (a, b) Representative neurolucida tracings of labeled descending motor fibers within a distance of 500 μm rostral of the lesion in control vehicle-injected (a) and IKVAV PA-injected (b) animals. The dotted lines demarcate the borders of the lesion. (c–f) Bright-field images of BDA-labeled tracts in lesion (c, e) and caudal to lesion (d, f) used for neurolucida tracings in an IKVAV PA-injected spinal cord (a, b). (g, h) Bar graphs show the extent to which labeled corticospinal axons penetrated the lesion. *The groups representing three control and three IKVAV PA mice and the tracing of 130 individual axons differ from each other at $p < 0.03$ by the Wilcoxon rank test. R, Rostral; C, caudal; D, dorsal; V, ventral. Scale bars: (a–d) 100 μm, (e–f) 25 μm.

proliferation or glial scar attenuation along with axonal regeneration, will eventually have the best functional outcome.

The study of delivery of growth factors has offered new methods of releasing growth factors into the environment. Stimuli-responsive hydrogels have been developed in which external stimuli, such as temperature, light, or pH stimulate the release of growth factors. For example, Das *et al.*[81] engineered gold nanoshells into scaffolds that absorb light at a fixed wavelength, heat up, and release growth factors. Alternatively, other scaffolds release growth factors in response to pH such as to the low pH in the endosome.[82,83]

In order to combat disorganized axon growth, nerve channels have been used to promote growth unidirectionally in the injured spinal cord. Stokols and Tuszynski[84] utilized this technology along with drug delivery. They produced linearly oriented channels made of agarose by forming ice crystals from an agarose solution and freeze-drying (**Figure 4**). When crystallizing the nerve channels, the protein BDNF, was added to further promote axon regeneration. After 1 month, the nerve channels were well incorporated within the spinal cord tissue, and the combination of nerve channel and growth factor increased the amount of axon entry into the channel by 2–3 times.

5.533.4. Alzheimer's Disease

5.533.4.1. Introduction

Alzheimer's disease, the most common form of dementia, is characterized by a decline in memory and other cognitive functions that eventually leads to death within 10 years of diagnosis. Many molecular lesions have been identified in Alzheimers, although the accumulation of misfolded proteins remains the central cause. This misfolding leads to oxidative and inflammatory damage, which leads to loss of neurons and synapses and, therefore, to gross atrophy of the affected areas: temporal, parietal, and frontal lobes.[85]

The most recognizable pathological features of Alzheimer's are the β-amyloid peptide and tau plaques and neurofibrillary tangles, which are clearly visible by microscopy in brains of those afflicted by Alzheimer's disease.[86,87] The accumulation of both β-amyloid and tau is linked to the deficiency of cholinergic projections in Alzheimer's disease.

β-Amyloid is a 36–43 amino acid metabolic by-product of the proteolysis of the amyloid precursor protein consisting that is more commonly found as a monomer than in an aggregate. When there is an accumulation of β-amyloid through increased metabolism of the amyloid precursor protein and imbalance of enzymes regulating the levels of β-amyloid, the protein begins to aggregate into fibrils and can form insoluble fibers, termed amyloid plaques. Although plaques and tangles are a natural result of aging, Alzheimer's patients have a much higher percentage of them in the brain areas listed earlier.[87] In the Alzheimer's brain, β-amyloid selectively builds up in the mitochondria in the neurons, and inhibits certain enzyme functions and the utilization of glucose by neurons.[88]

Tangles (neurofibrillary tangles), another hallmark of Alzheimer's disease, are thought to follow β-amyloid accumulation. Tangles involve irregular folding of a microtubule-associated protein, tau, which normally helps stabilize microtubules for normal cell transport. In Alzheimer's disease, tau

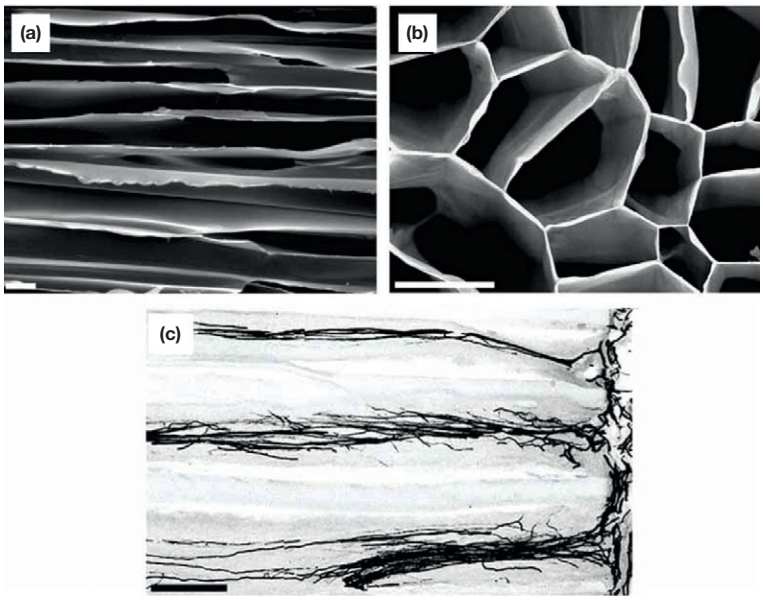

Figure 4 Aligned agarose nerve tubes synthesized by ice crystallization. (a, b) Scanning electron microscopy images of freeze-dried tubes longitudinally (a) and cross-sectionally (b). (c) Dye showing axonal penetration *in vivo* through the agarose tubes. Scale bars = 100 μm.

becomes hyperphosphorylated and, therefore, insoluble, creating neurofibrillary tangles and destroying the transport system within the neuron.[89]

As in most, if not all, other diseases and trauma processes, inflammatory processes and cytokines contribute to the pathology of Alzheimer's disease.[90]

Neurotrophic factor levels, which normally promote proliferation, differentiation, and survival of CNS cells, have also been correlated with the decline of Alzheimer's disease. Both nerve growth factor (NGF) and BDNF have shown improvements in animal studies.[91,92]

As in most, if not all, diseases and trauma processes, inflammation contributes to Alzheimer's disease. Both activated microglia and reactive astrogliosis occur around the plaques as well as throughout the brain. Again, similar to other tissue responses, it is not entirely clear whether the actions of the increased inflammatory response are positive or negative.[93–95]

5.533.4.2. Biomaterial Therapies for Alzheimer's

The amount of metal ions that accumulate in the brain increases over time and has additional deleterious effects on Alzheimer's. Metals, such as copper and zinc, can initiate oxidative stress in cells forming radicals disrupting DNA and protein cascades.[96] The hallmark plaques of Alzheimer's disease contain increased levels of both copper and zinc compared to the normal brain. Therefore, a new approach to slowdown the progression of Alzheimer's disease came with the introduction of iron-chelating compounds, which have little effect on normal brain tissue.[96,97] One study designed a nanoparticle encapsulating the chelating compounds in a design that would facilitate crossing of the BBB.[97] *In vitro*, these nanoparticles had the potential to resolubilize the plaques under reducing conditions.[97]

Another approach, also involving metals and Alzheimer's, attempts to destroy the plaques altogether. Nanoparticles that will cross the BBB are designed to carry gold particles specifically to accumulations of the β-amyloid protein. Once the gold particles have stably bound to the β-amyloid accumulation, weak and normally safe microwave fields heat up the gold-infused β-amyloid and not only break up the fibrils, but also lower the incidence of reaggregation.[98,99] A similar approach may also be effective in the treatment of many types of disorders, such as cancer, HIV, and diabetes.[100]

The introduction of subfragments of β-amyloid may also protect neurons from Alzheimer's, but permeability of the BBB remains a challenge. Early research in this area determined that chitosan nanoparticles loaded with β-amyloid crossed the BBB, were taken up in the brain, and had a favorable immunogenicity.[101] Further work will explore its efficacy in treating Alzheimer's disease.

Targeting therapeutic interventions remains challenging as well. One group examined the use of magnetic chitosan microparticles for treatment of Alzheimer's disease.[102] Tacrine, a reversible cholinesterase inhibitor used in the treatment of Alzheimer's disease, was loaded into the microparticles, and the particles were injected intravenously, while a magnet was held at the target region. This delivery system significantly increased the amount of tacrine in the brain. Another method is the use of smart nanovehicles consisting of a chitosan polymeric core with a modified antiamyloid antibody on the surface as a biosensor.[103] In this method also, the modified vehicle did cross the BBB, but the uptake of the vehicle in the brain was 8–11 times higher than in controls.

5.533.5. Parkinson's

5.533.5.1. Overview of Parkinson's

The three major symptoms of Parkinson's disease are tremor at rest, rigidity, and bradykinesia. Other nonmotor symptoms,

such as autonomic changes, cognitive changes, and sleep disturbances, are also usually seen. The underlying cause of Parkinson's disease is injury to the dopaminergic projections from the substantia nigra pars compacta to the striatum and death of the striatal dopamine and nigral neurons. Pathologically, intraneuronal Lewy bodies and Lewy neurites are readily found not only in the diseased brain areas, but also throughout out the brain.[104,105] Genetic predisposition and environmental exposure are both linked to the onset of Parkinson's.[106,107]

The neurodegeneration seen in Parkinson's could be related to mitochondrial dysfunction, oxidative stress, excitotoxicity, apoptosis, and inflammation.[108] Genes such as α-synuclein, parkin, and ubiquitin hydrolase that are linked with Parkinson's suggest the possibility that dysfunction of the ubiquitin-proteasome system in the dopaminergic cells may underlie Parkinson's disease.[109] Normally, ubiquitin proteins bind to damaged proteins and signal their need for degradation by the 26S proteasome. Mutations of all three genes will hinder the normal protein degradation process and result in damaged protein accumulation within the cell.[110] This theory is supported in that Lewy bodies include proteins that would normally be degraded, but were not and that the substantia nigra pas compacts of patients with Parkinson's have high levels of proteins resistant to degradation.[109,111] However, the definitive cause of the protein accumulation that culminates in cell death is still unknown.

5.533.5.2. Biomaterials in Treatment for Parkinson's Disease

Gene therapy has been discussed as a treatment for nearly all CNS injuries/disorders, but it may have a role in Parkinson's disease as well.[112] If the cause is genetic, the correct version of the gene may be delivered to neurons to avoid protein accumulation and dysfunction. Cell survival genes may also be delivered to ailing dopaminergic neurons. For example, a combined macrophage-nanotechnology system was designed to deliver antioxidants to the substantia nigra pars compacta. In this model, the macrophages delivered engineered enzymes, which reduce oxidative stress in models of Parkinson's disease.[113] Alternatively, an approach is being explored where DNA plasmids are condensed into nanoparticles and delivered to stop neurodegeneration.[114]

Liposomes are another vehicle for gene therapy in Parkinson's disease. PEGylated liposomes modified to cross the BBB have been used to carry gene replacement therapy in Parkinson's models. Using various reporter systems, these liposomes have been shown to transiently infect the brain with the gene of interest through the expression of a ligand to a commonly represented receptor in the brain (such as transferrin).[115,116]

Glial cell line-derived neurotrophic factor (GDNF) has also been a target for the treatment of Parkinson's due to its survival effect on dopaminergic neurons. Microspheres loaded with recombinant GDNF and injected into a rat model of Parkinson's disease, improved the function of the rats, showed an increase in dopaminergic fibers, and were determined safe as no rat developed antibodies against GDNF.[117]

5.533.6. Biomaterials Used with Stem Cell Therapy

5.533.6.1. Stem Cell Use in CNS Injury

Stem cells, which exist in all organ systems from conception through adulthood, can divide and give rise to other stem cells, as well as to a more lineage-committed cell. Different types of stem cells have been used in transplantation studies, including olfactory nervous system cells, hematopoietic stem cells, embryonic stem cells (ESCs), and many different types of neural stem cells.[118] The most success seen so far has been with utilizing neural stem cells and oligodendrocyte precursors.[119–121]

Another great use for stem cells as a therapeutic agent in the CNS is gene delivery. Genes can be delivered to the CNS through many vehicles; engineered cells, viruses, or direct injection. Continued direct injection for months into the CNS may cause unremitting damage and increased scarring and unreliable gene placement. Virus injections carrying the gene of interest have been successful, but the random site of integration may produce further complications to the endogenous tissue. Cells not endogenous to the CNS such as fibroblasts can be engineered to secrete the protein of interest and have shown success, but fibroblasts are not native to the spinal cord, and the effects of the fibroblasts on the CNS and scar formation have not been studied. Stem cells are a great option not only because they can differentiate into native neural cells, but also because ESCs are capable of homologous and nonhomologous recombination and can use environmental cues to migrate.[122–124]

The use of stem cells as a therapeutic intervention has been well studied in spinal cord injury. Transplanting neural stem cells into spinal cord injury can address the loss of local neurons and oligodendrocytes following spinal cord injury. The loss of neurons can cause both local and circuit defects, although possibly more injurious to function is the loss of oligodendrocytes. ESCs following neural or oligodendroglial differentiation have been injected into a lesioned spinal cord and shown to differentiate into tissue endogenous to the CNS, improving behavioral scores of the lesioned animals.[119,120] In mild to moderate SCI models, spared axons are present and require remyelination to function properly. Myelination supports normal axonal conduction and may help preserve spared axons.[125,126] As adult human neural progenitors syngeneic to individual patients would be difficult to obtain and culture, several groups have focused on generating neural and/or oligodendroglial progenitors from ESCs.[119,120] In these studies, oligodendrocyte precursors from ESCs have been shown to remyelinate and promote recovery.

5.533.6.2. Biomaterials and Stem Cells

In vivo, stem cells require a special niche to develop, proliferate, and differentiate. Transplanted stem cells also need such an environment to attach, survive, develop, proliferate, and differentiate. Biomaterials constructed to support stem cells utilize already established beneficial peptide sequences of integrins, growth factors, or specific differentiation cue proteins to help direct the specific needs of the injury/disease model. *In vitro*,

biomaterial scaffolds have been used to provide these cues for embryonic and neural stem cells.[25,127–129] Some success with biomaterials *in vivo* has been demonstrated in models of brain hypoxia.[130–133] The scaffolds altered the way transplanted cells survived, were distributed, and sprouted neurites.

An example of stem cell transplantation enhanced by the use of biomaterials is shown in Parkinson's research. GDNF therapies have also been used to improve the outcome of fetal dopaminergic cell transplantation studies.[134] Pharmacologically active microcarriers (PAM) are able to convey cells and release a growth factor to affect the cells. In one study, the PAM released GDNF while conveying fetal ventral mesencephalic cells. This allowed improvement of the grafted cell survival and of fiber outgrowth compared to cell transplantation alone.

5.533.7. Summary of Biomaterial Therapies in CNS Injury/Disease

As reviewed, CNS dysfunctions are heterogeneous and complex, vary widely in their symptomology, and severely affect the lives of the involved persons. The causes of many neurodegenerative disorders are complex and mostly unknown, and may be associated with genetic abnormalities, but advancing age, environmental influences, and dysfunctional immunity are likely even more influential.[1] Even when potential treatments are discovered, they are difficult to implement because access to the CNS is limited and therefore, surgical intervention to implement such treatment may prove to be more debilitating. The presence of the BBB, which normally is protective of the CNS, inhibits potentially helpful therapeutics, molecules

Table 2 Examples of preclinical and clinical biomaterial therapies in CNS disease

Preclinical studies CNS disease/ model	*Material description*	*Outcome*
Alzheimer's disease	NGF-loaded microspheres implanted into the rat basal forebrain to provide local sustained delivery	Significant protection of cholinergic neurons in the medial septum and diagonal band associated with recovery of spatial learning[135,136]
	NGF-producing fibroblasts encapsulated into polymers and implanted into the lateral ventricle of rats with fimbria-fornix lesions	Significant protection of cholinergic neurons[137]
Parkinson's disease	GDNF-loaded microspheres implanted into the 6-OHDA lesioned rat striatum	Behavioral recovery, regrowth of tyrosine hydroxylase-positive fibers in the striatum, and recovery of dopamine transporters[117]
Huntington's disease	CNTF-producing fibroblasts encapsulated into polymers and implanted into the lateral ventricle of quinolinic acid lesioned monkeys	Significant prevention of the loss of multiple populations of striatal neurons[138]
Lesioned optic tract	Positively and negatively charged amino acids that self-assembled into a nanofiber scaffold were implanted into the lesioned hamster optic tract	Axonal regeneration occurred along the scaffold between the two ends of the lesion to produce visual recovery[139]
Cortical trauma	Cylindrical porous scaffolds implanted into cortical cavities in rats	Scaffolds reduced secondary cell loss and promoted ingrowth of host neurons into the scaffold[140,141]
Hypoxia-ischemia	Polymer scaffold containing neural stem cells implanted into the infarction cavity produced by hypoxia-ischemia in mice	New brain tissue regenerated around the degenerating scaffold and a network of arborized host and donor neurites emerged with apparent axonal regeneration[131]

Clinical studies CNS disease/ model	*Material description*	*Outcome*
Amyotrophic lateral sclerosis	CNTF-producing fibroblasts encapsulated into polymers with a vitrogen matrix and implanted intrathecally	Sustained delivery of CNTF, no toxicity[142,143]
Chronic pain	Chromaffin cells encapsulated into polymers with an alginate matrix and implanted into the subarachnoid space	Prolonged cell survival, no reduction in pain[144]
Huntington's disease	CNTF-producing fibroblasts encapsulated into polymers with a vitrogen matrix and implanted into the lateral ventricles	Sustained delivery of CNTF, no toxicity[145]
Macular degeneration	CNTF-producing retinal epithelial cells encapsulated into polymers with coaxially situated poly(ethylene terephthalate) strands of yarn as a matrix	Ongoing phase II[a]
Retinitis pigmentosa	CNTF-producing retinal epithelial cells encapsulated into polymers with coaxially situated poly(ethylene terephthalate) strands of yarn as a matrix implanted into the vitreous humor	Phase I safety, sustained CNTF delivery, phase II/III ongoing[146]
Canavan disease	Nonviral plasmid-polymer-cationic liposome delivery of aspartoacyclase gene	Two children reportedly safely treated[147]

[a]Neurotech USA press release (see Further Information). CNTF, ciliary neurotrophic factor; GDNF, glial-cell-derived neurotrophic factor; NGF, nerve growth factor; 6-OHDA, 6-hydroxydopamine.

and proteins, from passing into the CNS. Regeneration itself in the CNS is difficult due to the huge heterogeneity in the CNS, presence of many ligands inhibitory to regeneration, as well as the intricate and individualized circuitry. Additionally, many tissue response cascades in the CNS add more challenges to regeneration, such as increased inflammation, invading cells, and glial scarring.

Biomaterials, especially nanotechnology derived, have begun to be used as a tool in combating tissue response, drug delivery issues, and changes in the environmental milieu. These materials can be custom-designed to promote certain activities by expressing only the relevant parts of drugs or proteins, while excluding those that may cause side effects.

Biomaterials appropriate for CNS regeneration need to be designed with general characteristics in mind. When first forming a biomaterial system, the system should be very adaptable to control many varied environments. The backbone must be ready for the discovery of different, more effective peptide sequences or different signaling cues for topographic distribution. In addition, time-release intervention may facilitate the needed processes. The material must be biocompatible with and not toxic to the host tissue. Most tissue responses post-injury or diseases already include an inflammatory component. An additional or exaggerated inflammatory response to the biomaterial may prove to be further detrimental as well or may create a barrier from use by the CNS. By-products of biomaterial breakdown may also be toxic and this should therefore be carefully considered. In most cases, however, longer-term inflammation can be limited by the biodegradability of the material. Biodegradability can also avoid a limited regenerative process. If the biomaterial itself promotes regeneration, a continued presence of the material may block reentry of the regenerating axon into its host tissue and produce a sinkhole effect. The biomaterial does have to be stable in the environment to provide its intended function.

Although a relatively new therapeutic approach, biomaterials for regeneration in CNS injury/disease have become, fairly popular, as seen in Table 2. The amazing modifications to existing technology have sped this transition. Biomaterials can address three-dimension issues in a three-dimensional way and provide a permissive and positive niche for endogenous as well as transplanted cells.

References

1. Mayeux, R. *Annu. Rev. Neurosci.* **2003**, *26*, 81–104.
2. Garcia-Garcia, E.; Andrieux, K.; Gil, S.; Couvreur, P. *Int. J. Pharm.* **2005**, *298*, 274–292.
3. Misra, A.; Ganesh, S.; Shahiwala, A.; Shah, S. P. *J. Pharm. Pharm. Sci.* **2003**, *6*, 252–273.
4. Wang, P. P.; Frazier, J.; Brem, H. *Adv. Drug Deliv. Rev.* **2002**, *54*, 987–1013.
5. Neuwelt, E.; Abbott, N. J.; Abrey, L.; *et al. Lancet Neurol.* **2008**, *7*, 84–96.
6. Ishida, T.; Takanashi, Y.; Kiwada, H. *Biol. Pharm. Bull.* **2006**, *29*, 397–402.
7. Sahoo, S. K.; Labhasetwar, V. *Drug Discov. Today* **2003**, *8*, 1112–1120.
8. Schnyder, A.; Huwyler, J. *NeuroRx* **2005**, *2*, 99–107.
9. Yoshida, J.; Mizuno, M. *J. Neurooncol.* **2003**, *65*, 261–267.
10. Lockman, P. R.; Mumper, R. J.; Khan, M. A.; Allen, D. D. *Drug Dev. Ind. Pharm.* **2002**, *28*, 1–13.
11. Brigger, I.; Dubernet, C.; Couvreur, P. *Adv. Drug Deliv. Rev.* **2002**, *54*, 631–651.
12. Roney, C.; Kulkarni, P.; Arora, V.; *et al. J. Control. Release* **2005**, *108*, 193–214.
13. Kreuter, J.; Ramge, P.; Petrov, V.; *et al. Pharm. Res.* **2003**, *20*, 409–416.
14. Gupta, D.; Tator, C. H.; Shoichet, M. S. *Biomaterials* **2006**, *27*, 2370–2379.
15. Gutowska, A.; Jeong, B.; Jasionowski, M. *Anat. Rec.* **2001**, *263*, 342–349.
16. Jain, A.; Kim, Y. T.; Mckeon, R. J.; Bellamkonda, R. V. *Biomaterials* **2006**, *27*, 497–504.
17. Zhong, Y.; Bellamkonda, R. V. *J. R. Soc. Interface* **2008**, *5*, 957–975.
18. Orive, G.; Anitua, E.; Pedraz, J. L.; Emerich, D. F. *Nat. Rev. Neurosci.* **2009**, *10*, 682–692.
19. Woerly, S.; Doan, V. D.; Sosa, N.; De Vellis, J.; Espinosa-Jeffrey, A. *J. Neurosci. Res.* **2004**, *75*, 262–272.
20. Yu, X.; Bellamkonda, R. V. *J. Neurosci. Res.* **2001**, *66*, 303–310.
21. Freier, T.; Koh, H. S.; Kazazian, K.; Shoichet, M. S. *Biomaterials* **2005**, *26*, 5872–5878.
22. Pittier, R.; Sauthier, F.; Hubbell, J. A.; Hall, H. *J. Neurobiol.* **2005**, *63*, 1–14.
23. Tysseling-Mattiace, V. M.; Sahni, V.; Niece, K. L.; *et al. J. Neurosci.* **2008**, *28*, 3814–3823.
24. Cowansage, K. K.; Ledoux, J. E.; Monfils, M. H. *Curr. Mol. Pharmacol.* **2009**.
25. Silva, G. A.; Czeisler, C.; Niece, K. L.; *et al. Science* **2004**, *303*, 1352–1355.
26. Yu, L. M.; Wosnick, J. H.; Shoichet, M. S. *J. Neurosci. Methods* **2008**, *171*, 253–263.
27. Wosnick, J. H.; Shoichet, B. K. *Chem. Mater.* **2008**, *20*, 55–60.
28. Wylie, R. G.; Shoichet, M. S. *J. Mater. Chem.* **2008**, *18*, 2716–2721.
29. Straley, K. S.; Foo, C. W.; Heilshorn, S. C. *J. Neurotrauma* **2010**, *27*, 1–19.
30. Fine, E. G.; Valentini, R. F.; Bellamkonda, R.; Aebischer, P. *Biomaterials* **1991**, *12*, 775–780.
31. Kotwal, A.; Schmidt, C. E. *Biomaterials* **2001**, *22*, 1055–1064.
32. Belkas, J. S.; Munro, C. A.; Shoichet, M. S.; Johnston, M.; Midha, R. *Biomaterials* **2005**, *26*, 1741–1749.
33. Curtis, A.; Wilkinson, C. *Biomaterials* **1997**, *18*, 1573–1583.
34. Haipeng, G.; Yinghui, Z.; Jianchun, L.; Yandao, G.; Nanming, Z.; Xiufang, Z. *J. Biomed. Mater. Res.* **2000**, *52*, 285–295.
35. Meiners, S.; Mercado, M. L. *Mol. Neurobiol.* **2003**, *27*, 177–196.
36. Suzuki, M.; Itoh, S.; Yamaguchi, I.; *et al. J. Neurosci. Res.* **2003**, *72*, 646–659.
37. Ao, Q.; Wang, A.; Cao, W.; *et al. J. Biomed. Mater. Res. A* **2006**, *77*, 11–18.
38. Bloch, J.; Fine, E. G.; Bouche, N.; Zurn, A. D.; Aebischer, P. *Exp. Neurol.* **2001**, *172*, 425–432.
39. Dodla, M. C.; Bellamkonda, R. V. *Biomaterials* **2008**, *29*, 33–46.
40. Fouad, K.; Schnell, L.; Bunge, M. B.; Schwab, M. E.; Liebscher, T.; Pearse, D. D. *J. Neurosci.* **2005**, *25*, 1169–1178.
41. Nomura, H.; Zahir, T.; Kim, H.; *et al. Tissue Eng. A* **2008**, *14*, 649–665.
42. Novikova, L. N.; Pettersson, J.; Brohlin, M.; Wiberg, M.; Novikov, L. N. *Biomaterials* **2008**, *29*, 1198–1206.
43. Tsai, E. C.; Dalton, P. D.; Shoichet, M. S.; Tator, C. H. *Biomaterials* **2006**, *27*, 519–533.
44. Venugopal, J.; Low, S.; Choon, A. T.; Ramakrishna, S. *J. Biomed. Mater. Res. B Appl. Biomater.* **2008**, *84*, 34–48.
45. Chen, Y. S.; Hsieh, C. L.; Tsai, C. C.; *et al. Biomaterials* **2000**, *21*, 1541–1547.
46. Verdu, E.; Labrador, R. O.; Rodriguez, F. J.; Ceballos, D.; Fores, J.; Navarro, X. *Restor. Neurol. Neurosci.* **2002**, *20*, 169–179.
47. Wells, M. R.; Kraus, K.; Batter, D. K.; *et al. Exp. Neurol.* **1997**, *146*, 395–402.
48. Ducker, T. B.; Salcman, M.; Perot, P. L., Jr.; Ballantine, D. *Surg. Neurol.* **1978**, *10*, 60–63.
49. Hayashi, N.; De La Torre, J.; Green, B. *Surg. Forum* **1980**, *31*, 461–463.
50. Stokes, B. T.; Garwood, M.; Walters, P. *Am. J. Physiol.* **1981**, *240*, H761–H766.
51. Happel, R. D.; Smith, K. P.; Banik, N. L.; Powers, J. M.; Hogan, E. L.; Balentine, J. D. *Brain Res.* **1981**, *211*, 476–479.
52. Moriya, T.; Hassan, A. Z.; Young, W.; Chesler, M. *J. Neurotrauma* **1994**, *11*, 255–263.
53. Stokes, B. T.; Fox, P.; Hollinden, G. *Exp. Neurol.* **1983**, *80*, 561–572.
54. Farber, J. L. *Lab. Invest.* **1982**, *47*, 114–123.
55. Siesjo, B. K. *Ann. NY Acad. Sci.* **1988**, *522*, 638–661.
56. Mccord, J. M. *Fed. Proc.* **1987**, *46*, 2402–2406.
57. Mitsuhashi, T.; Ikata, T.; Morimoto, K.; Tonai, T.; Katoh, S. *Paraplegia* **1994**, *32*, 524–530.
58. Liu, D.; Thangnipon, W.; Mcadoo, D. J. *Brain Res.* **1991**, *547*, 344–348.
59. Panter, S. S.; Yum, S. W.; Faden, A. I. *Ann. Neurol.* **1990**, *27*, 96–99.
60. Lindsay, R. *Astrocytes: Cell Biology and Pathology of Astrocytes*. Academic: Orlando, FL, 1986.
61. Tetzlaff, W.; Alexander, S. W.; Miller, F. D.; Bisby, M. A. *J. Neurosci.* **1991**, *11*, 2528–2544.
62. Abe, Y.; Yamamoto, T.; Sugiyama, Y.; *et al. J. Neurotrauma* **1999**, *16*, 945–952.
63. Crowe, M. J.; Bresnahan, J. C.; Shuman, S. L.; Masters, J. N.; Beattie, M. S. *Nat. Med.* **1997**, *3*, 73–76.
64. Dong, H.; Fazzaro, A.; Xiang, C.; Korsmeyer, S. J.; Jacquin, M. F.; Mcdonald, J. W. *J. Neurosci.* **2003**, *23*, 8682–8691.

65. Li, G. L.; Farooque, M.; Holtz, A.; Olsson, Y. *Acta Neuropathol. (Berl)* **1999**, *98*, 473–480.
66. Liu, X. Z.; Xu, X. M.; Hu, R.; *et al*. *J. Neurosci*. **1997**, *17*, 5395–5406.
67. Shuman, S. L.; Bresnahan, J. C.; Beattie, M. S. *J. Neurosci. Res*. **1997**, *50*, 798–808.
68. Springer, J. E.; Azbill, R. D.; Knapp, P. E. *Nat. Med*. **1999**, *5*, 943–946.
69. Blakemore, W. F. *J. Neurocytol*. **1975**, *4*, 745–757.
70. Reier, P. J.; Houle, J. *Functional Recovery in Neurological Disease*. Raven: New York, NY, 1988.
71. Fujiki, M.; Zhang, Z.; Guth, L.; Steward, O. *J. Comp. Neurol*. **1996**, *371*, 469–484.
72. Ma, M.; Wei, P.; Wei, T.; Ransohoff, R. M.; Jakeman, L. B. *J. Comp. Neurol*. **2004**, *474*, 469–486.
73. Zhang, Z.; Fujiki, M.; Guth, L.; Steward, O. *J. Comp. Neurol*. **1996**, *371*, 485–495.
74. Martin, P. *Science* **1997**, *276*, 75–81.
75. Stadelmann, W. K.; Digenis, A. G.; Tobin, G. R. *Am. J. Surg*. **1998**, *176*, 26S–38S.
76. Schwab, M. E.; Bartholdi, D. *Physiol. Rev*. **1996**, *76*, 319–370.
77. Bunge, M. B. *J. Neurol*. **1994**, *242*, S36–S39.
78. Harrison, B. M.; Mcdonald, W. I. *Ann. Neurol*. **1977**, *1*, 542–551.
79. Hartgerink, J. D.; Beniash, E.; Stupp, S. I. *Science* **2001**, *294*, 1684–1688.
80. Hartgerink, J. D.; Beniash, E.; Stupp, S. I. *Proc. Natl. Acad. Sci. USA* **2002**, *99*, 5133–5138.
81. Das, M.; Sanson, N.; Fava, D.; Kumacheva, E. *Langmuir* **2007**, *23*, 196–201.
82. Henry, S. M.; El-Sayed, M. E.; Pirie, C. M.; Hoffman, A. S.; Stayton, P. S. *Biomacromolecules* **2006**, *7*, 2407–2414.
83. Yin, X.; Hoffman, A. S.; Stayton, P. S. *Biomacromolecules* **2006**, *7*, 1381–1385.
84. Stokols, S.; Tuszynski, M. H. *Biomaterials* **2006**, *27*, 443–451.
85. Wenk, G. L. *J. Clin. Psychiatry* **2003**, *64*(Suppl. 9), 7–10.
86. Hashimoto, M.; Rockenstein, E.; Crews, L.; Masliah, E. *Neuromolecular Med*. **2003**, *4*, 21–36.
87. Tiraboschi, P.; Hansen, L. A.; Thal, L. J.; Corey-Bloom, J. *Neurology* **2004**, *62*, 1984–1989.
88. Chen, X.; Yan, S. D. *IUBMB Life* **2006**, *58*, 686–694.
89. Hernandez, F.; Avila, J. *Cell. Mol. Life Sci*. **2007**, *64*, 2219–2233.
90. Greig, N. H.; Mattson, M. P.; Perry, T.; *et al*. *Ann. NY Acad. Sci*. **2004**, *1035*, 290–315.
91. Cooper, J. D.; Salehi, A.; Delcroix, J. D.; *et al*. *Proc. Natl. Acad. Sci. USA* **2001**, *98*, 10439–10444.
92. Nagahara, A. H.; Merrill, D. A.; Coppola, G.; *et al*. *Nat. Med*. **2009**, *15*, 331–337.
93. Fiala, M.; Lin, J.; Ringman, J.; *et al*. *J. Alzheimers Dis*. **2005**, *7*, 221–232; discussion 255–262.
94. Mcgeer, P. L.; Mcgeer, E. G. *Neurobiol. Aging* **2007**, *28*, 639–647.
95. Vlad, S. C.; Miller, D. R.; Kowall, N. W.; Felson, D. T. *Neurology* **2008**, *70*, 1672–1677.
96. Lovell, M. A.; Robertson, J. D.; Teesdale, W. J.; Campbell, J. L.; Markesbery, W. R. *J. Neurol. Sci*. **1998**, *158*, 47–52.
97. Cui, Z.; Lockman, P. R.; Atwood, C. S.; *et al*. *Eur. J. Pharm. Biopharm*. **2005**, *59*, 263–272.
98. Kogan, M. J.; Bastus, N. G.; Amigo, R.; *et al*. *Nano Lett*. **2006**, *6*, 110–115.
99. Olmedo, I.; Araya, E.; Sanz, F.; *et al*. *Bioconjug. Chem*. **2008**, *19*, 1154–1163.
100. Boisselier, E.; Astruc, D. *Chem. Soc. Rev*. **2009**, *38*, 1759–1782.
101. Songjiang, Z.; Lixiang, W. *AAPS PharmSciTech* **2009**, *10*, 900–905.
102. Wilson, B.; Samanta, M. K.; Santhi, K.; Sampath Kumar, K. P.; Ramasamy, M.; Suresh, B. *J. Neurosci. Methods* **2009**, *177*, 427–433.
103. Agyare, E. K.; Curran, G. L.; Ramakrishnan, M.; Yu, C. C.; Poduslo, J. F.; Kandimalla, K. K. *Pharm. Res*. **2008**, *25*, 2674–2684.
104. Braak, H.; Del Tredici, K.; Rub, U.; De Vos, R. A.; Jansen Steur, E. N.; Braak, E. *Neurobiol. Aging* **2003**, *24*, 197–211.
105. Wakabayashi, K.; Takahashi, H. *Eur. Neurol*. **1997**, *38*(Suppl. 2), 2–7.
106. Payami, H.; Larsen, K.; Bernard, S.; Nutt, J. *Ann. Neurol*. **1994**, *36*, 659–661.
107. Priyadarshi, A.; Khuder, S. A.; Schaub, E. A.; Priyadarshi, S. S. *Environ. Res*. **2001**, *86*, 122–127.
108. Samii, A.; Nutt, J. G.; Ransom, B. R. *Lancet* **2004**, *363*, 1783–1793.
109. Mcnaught, K. S.; Olanow, C. W.; Halliwell, B.; Isacson, O.; Jenner, P. *Nat. Rev. Neurosci*. **2001**, *2*, 589–594.
110. Goedert, M. *Nat. Rev. Neurosci*. **2001**, *2*, 492–501.
111. Halliwell, B.; Jenner, P. *Lancet* **1998**, *351*, 1510.
112. Dass, B.; Kordower, J. H. *Handb. Clin. Neurol*. **2007**, *84*, 291–304.
113. Batrakova, E. V.; Li, S.; Reynolds, A. D.; *et al*. *Bioconjug. Chem*. **2007**, *18*, 1498–1506.
114. Suk, J. S.; Suh, J.; Choy, K.; Lai, S. K.; Fu, J.; Hanes, J. *Biomaterials* **2006**, *27*, 5143–5150.
115. Pardridge, W. M. *Neuron* **2002**, *36*, 555–558.
116. Shi, N.; Zhang, Y.; Zhu, C.; Boado, R. J.; Pardridge, W. M. *Proc. Natl. Acad. Sci. USA* **2001**, *98*, 12754–12759.
117. Garbayo, E.; Montero-Menei, C. N.; Ansorena, E.; Lanciego, J. L.; Aymerich, M. S.; Blanco-Prieto, M. J. *J. Control. Release* **2009**, *135*, 119–126.
118. Thuret, S.; Moon, L. D.; Gage, F. H. *Nat. Rev. Neurosci*. **2006**, *7*, 628–643.
119. Keirstead, H. S.; Nistor, G.; Bernal, G.; *et al*. *J. Neurosci*. **2005**, *25*, 4694–4705.
120. Mcdonald, J. W.; Liu, X. Z.; Qu, Y.; *et al*. *Nat. Med*. **1999**, *5*, 1410–1412.
121. Mitsui, T.; Shumsky, J. S.; Lepore, A. C.; Murray, M.; Fischer, I. *J. Neurosci*. **2005**, *25*, 9624–9636.
122. Hall, P. A.; Watt, F. M. *Development* **1989**, *106*, 619–633.
123. Potten, C. S.; Loeffler, M. *Development* **1990**, *110*, 1001–1020.
124. Weissman, I. L. *Cell* **2000**, *100*, 157–168.
125. Lasiene, J.; Shupe, L.; Perlmutter, S.; Horner, P. *J. Neurosci*. **2008**, *28*, 3887–3896.
126. Mcdonald, J. W.; Belegu, V. *J. Neurotrauma* **2006**, *23*, 345–359.
127. Bhang, S. H.; Lim, J. S.; Choi, C. Y.; Kwon, Y. K.; Kim, B. S. *J. Biomater. Sci. Polym. Ed*. **2007**, *18*, 223–239.
128. Brannvall, K.; Bergman, K.; Wallenquist, U.; *et al*. *J. Neurosci. Res*. **2007**, *85*, 2138–2146.
129. Willerth, S. M.; Arendas, K. J.; Gottlieb, D. I.; Sakiyama-Elbert, S. E. *Biomaterials* **2006**, *27*, 5990–6003.
130. Bible, E.; Chau, D. Y.; Alexander, M. R.; Price, J.; Shakesheff, K. M.; Modo, M. *Biomaterials* **2009**, *30*, 2985–2994.
131. Park, K. I.; Teng, Y. D.; Snyder, E. Y. *Nat. Biotechnol*. **2002**, *20*, 1111–1117.
132. Tate, C. C.; Shear, D. A.; Tate, M. C.; Archer, D. R.; Stein, D. G.; Laplaca, M. C. *J. Tissue Eng. Regen. Med*. **2009**, *3*, 208–217.
133. Tate, M. C.; Shear, D. A.; Hoffman, S. W.; Stein, D. G.; Archer, D. R.; Laplaca, M. C. *Cell Transplant*. **2002**, *11*, 283–295.
134. Tatard, V. M.; Sindji, L.; Branton, J. G.; *et al*. *Biomaterials* **2007**, *28*, 1978–1988.
135. Gu, H.; Long, D.; Song, C.; Li, X. *Neurosci. Lett*. **2009**, *453*, 204–209.
136. Pean, J. M.; Menei, P.; Morel, O.; Montero-Menei, C. N.; Benoit, J. P. *Biomaterials* **2000**, *21*, 2097–2101.
137. Winn, S. R.; Hammang, J. P.; Emerich, D. F.; Lee, A.; Palmiter, R. D.; Baetge, E. E. *Proc. Natl. Acad. Sci. USA* **1994**, *91*, 2324–2328.
138. Emerich, D. F.; Winn, S. R.; Hantraye, P. M.; *et al*. *Nature* **1997**, *386*, 395–399.
139. Ellis-Behnke, R. G.; Liang, Y. X.; You, S. W.; *et al*. *Proc. Natl. Acad. Sci. USA* **2006**, *103*, 5054–5059.
140. Wong, D. Y.; Hollister, S. J.; Krebsbach, P. H.; Nosrat, C. *Tissue Eng*. **2007**, *13*, 2515–2523.
141. Wong, D. Y.; Krebsbach, P. H.; Hollister, S. J. *J. Neurosurg*. **2008**, *109*, 715–722.
142. Aebischer, P.; Schluep, M.; Deglon, N.; *et al*. *Nat. Med*. **1996**, *2*, 696–699.
143. Zurn, A. D.; Henry, H.; Schluep, M.; *et al*. *Cell Transplant*. **2000**, *9*, 471–484.
144. Buchser, E.; Goddard, M.; Heyd, B.; *et al*. *Anesthesiology* **1996**, *85*, 1005–1012 discussion 29A–30A.
145. Bachoud-Levi, A. C.; Deglon, N.; Nguyen, J. P.; *et al*. *Hum. Gene Ther*. **2000**, *11*, 1723–1729.
146. Sieving, P. A.; Caruso, R. C.; Tao, W.; *et al*. *Proc. Natl. Acad. Sci. USA* **2006**, *103*, 3896–3901.
147. Leone, P.; Janson, C. G.; Bilaniuk, L.; *et al*. *Ann. Neurol*. **2000**, *48*, 27–38.
148. Wilson, B.; Samanta, M. K.; Santhi, K.; Kumar, K. P.; Ramasamy, M.; Suresh, B. *Nanomedicine* **2010**, *6*, 144–152.

5.534. Skin Tissue Engineering

Q Zeng, L K Macri, A Prasad, and R A F Clark, State University of New York-Stony Brook, Stony Brook, NY, USA
D I Zeugolis, C Hanley, Y Garcia, and A Pandit, National University of Ireland, Galway, Ireland

© 2011 Published by Elsevier Ltd.

5.534.1. Skin Anatomy and Function 468
5.534.1.1. Basic Anatomy and Function of the Skin 468
5.534.1.2. Epidermis 469
5.534.1.2.1. Structure and cell constituents of epidermis 469
5.534.1.2.2. Functions of epidermis 469
5.534.1.3. Dermal–Epidermal Junction 469
5.534.1.4. Dermis 469
5.534.1.4.1. Structure and cell constituents of dermis 469
5.534.1.4.2. Functions of the dermis 470
5.534.1.5. Hypodermis (Subcutaneous Fat Layer) 471
5.534.2. Biology of Cutaneous Wound Healing 471
5.534.2.1. Inflammatory Phase 471
5.534.2.2. Tissue Formation Phase 471
5.534.2.3. Remodeling Phase 472
5.534.2.4. Interruption of Wound Healing 472
5.534.3. Wound Classifications and Prognosis 472
5.534.4. The Significance of Tissue-Engineered Skin Application 472
5.534.5. Design Principles of Tissue-Engineered Skin Substitute 474
5.534.6. Materials for Skin Tissue Engineering 475
5.534.6.1. Development of Nonbiodegradable Synthetic Materials 475
5.534.6.2. Development of Biodegradable Natural-Based Materials 475
5.534.6.2.1. Collagen 476
5.534.6.2.2. Fibronectin 476
5.534.6.2.3. Fibrin 476
5.534.6.2.4. Hyaluronic acid 477
5.534.6.3. Development of Smart Matrix: New Concept for Biodegradable Synthetic Biomaterials 477
5.534.7. The Development of Tissue-Engineered Skin Constructs: The Past and the Present Status 477
5.534.7.1. Overview 477
5.534.7.2. Epidermal Skin Substitutes 478
5.534.7.2.1. Epicel and EpiDex 478
5.534.7.2.2. Laserskin 478
5.534.7.2.3. Bioseed-S 478
5.534.7.2.4. MySkin 478
5.534.7.2.5. ReCell/CellSpray 478
5.534.7.3. Dermal Skin Substitutes 480
5.534.7.3.1. Collagen-based dermal analogs: AlloDerm, GraftJacket, Karoderm, SureDerm, Permacol Surgical Implant, and Matriderm 480
5.534.7.3.2. Collagen-based sponge: Pelnac, Terudermis 484
5.534.7.3.3. Collagen-based composites: Integra, Biobrane, TransCyte 484
5.534.7.3.4. Dermagraft 485
5.534.7.3.5. OASIS Wound Matrix 485
5.534.7.3.6. EZ Derm 485
5.534.7.3.7. Hyalomatrix PA, Hyalograft 3D 486
5.534.7.4. Dermo–epidermal (composite) Skin Substitutes 487
5.534.7.4.1. Karoskin 487
5.534.7.4.2. Apligraf 488
5.534.7.4.3. OrCel 488
5.534.7.4.4. TISSUETech Autograft system 488
5.534.8. Problems and Challenges of Available Skin Substitutes 488
5.534.8.1. Biocompatbility 488
5.534.8.2. Physical Properties 489
5.534.8.3. Limited Vascularization and Poor Engraftment into Wound Site 489
5.534.8.4. Scarring 490

5.534.8.5. Others 490
5.534.9. Divine Garments Without Seams (Ancient Chinese Proverb): The Inspiration for Tissue-Engineered Skin Substitute from Lessons of Nature 490
5.534.9.1. Mammalian External Ear: Examples of Regeneration in Adult Animal 490
5.534.9.1.1. Rabbit ear 490
5.534.9.1.2. MRL/MpJ mouse ear 490
5.534.9.2. Mammalian Skin Hair Follicle: Examples of Regeneration in Adult Animal 491
5.534.9.3. Embryonic Skin: Examples of Scarfree Regeneration in Fetal Animal 491
5.534.9.4. Inspiration from Mammalian External Ear and Fetal Skin Regeneration 491
5.534.9.4.1. Stem cells: cell-based regeneration strategy 491
5.534.9.4.2. Vascularization: sustaining pipelines to construct the skin substitutes 492
5.534.9.4.3. Incorporation of bioactive molecules in the design of an intelligent skin substitute 493
5.534.9.4.4. Smart scaffold/matrix: structural determinant biological activity 494
5.534.10. Conclusions 494
References 495

Abbreviations

ACMs	Atelopeptide collagen/silicon membrane
AMPs	Anti-microbial proteins
ASCs	Adipose-derived stem cells
ATSCs	Adipose tissue-derived stromal cells
BM-MSCs	Bone marrow-derived MSCs
CD	Cluster of differentiation
CEAs	Cultured epithelial autografts
Da	Dalton
DEJ	Dermal–epidermal junction
DNA	Deoxyribonucleic acid
EB	Epidermolysis bullosa
ECM	Extracellular matrix
EPC-ECs	EPC-derived endothelial cells
EPCs	Endothelial progenitor cells
FDA	Food and Drug Administration
FGFs	Fibroblast growth factors
FN	Fibronectin
GAGs	Glycosaminoglycans
GM-CSF	Granulocyte–Macrophage Colony Stimulating Factor
GT	Granulation tissue
HA	Hyaluronic acid
hESC-ECs	hESC-derived endothelial cells
hESCs	Human embryonic stem cells
HGF	Hepatocyte growth factor
IGF	Insulin-like growth factor
IL	Interleukin
iPS cells	Induced pluripotent stem cells
KGF-1	Keratinocyte growth factor
M-CSF	Macrophage colony-stimulating factor
MSCs	Mesenchymal stem cells
NGF	Nerve growth factor
NPs	Nanoparticles
PDGF	Platelet-derived growth factor
PHSRN	Proline-histidine-serine-arginine-asparagine
RGD	Arginine–glycine–aspartic acid
SCID	Severe combined immune deficient
TGF	Transforming growth factor
VEGF	Vascular endothelial growth factor

5.534.1. Skin Anatomy and Function

5.534.1.1. Basic Anatomy and Function of the Skin

Skin is the largest organ of the body in vertebrates and is composed of the epidermis and dermis with a complex nerve and blood supply (Figure 1). Average thickness of skin is 1–2 mm, being considerably thinner in infants and the elderly. Mammalian skin is typically described in the context of three major layers: the epidermis, dermis, and hypodermis. The epidermis is the outermost protective region of the skin providing barrier, immune, and photoprotective functions. It is a highly organized and stratified cellular layer that is capable of self-renewal by a continuous process of proliferation and differentiation, referred to as keratinization.[1] The dermis comprises connective tissue that provides mechanical integrity to the skin. It is primarily composed of extracellular matrix (ECM) molecules and contains skin appendages and receptors for sensory stimuli. The hypodermis predominantly consists of a subcutaneous reservoir of fat that provides insulation against heat loss, but it also contains the hair follicular roots. In addition, the hypodermis is also a source for mesenchymal stem cells.

The most important and well-recognized function of the skin is its role as a permeability barrier, preventing entry of pathogens and particulates and the loss of water from the body by evaporation. The second line of antimicrobial resistance in skin is antimicrobial proteins (AMPs), a broad class of gene-encoded antibiotics that fall into two types: defensins and cathelicidins. In the event of a successful invasion by pathogens, the immune cells of the epidermis and dermis induce an immune response. An immune response is elicited by antigen-presenting cells, which present antigen–major histocompatibility complexes to T-lymphocytes. Another major function of skin is temperature regulation. The skin also possesses pain receptors, touch receptors, and other mechanoreceptors.

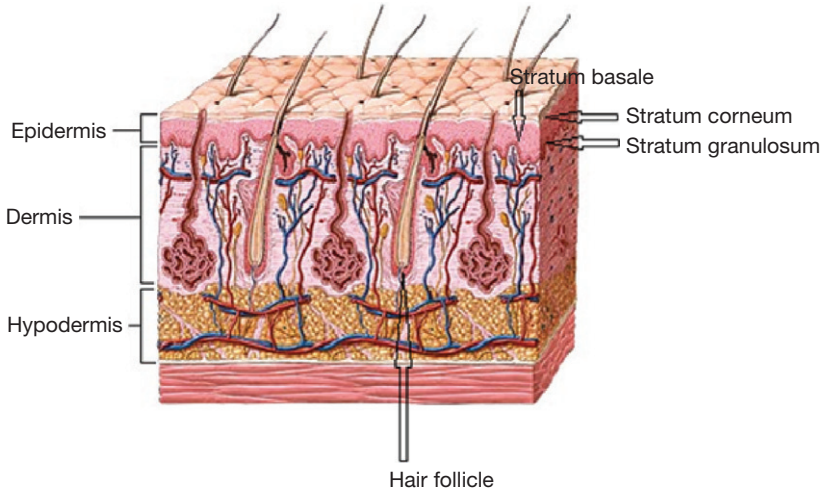

Figure 1 Layers of skin. Reprinted from http://www.clarian.org/ADAM/doc/In-DepthReports/10/000032.htm

5.534.1.2. Epidermis

5.534.1.2.1. Structure and cell constituents of epidermis

The key cell constituents of the epidermis are keratinocytes, melanocytes, Langerhans cells, and Merkel cells.

Keratinocytes make up 95% of the cells found in the epidermis and undergo differentiation and keratinization as they migrate through four regions that have distinct morphologies: the *stratum basale*, the *stratum spinosum*, the *stratum granulosum*, and the *stratum corneum* (**Figure 1**).

The basal layer is the deepest layer of the epidermis and contains the most mitotically active cell population, of which 10% are stem cells. The thickness of this layer depends on its anatomical location. Overall, keratinocyte morphology varies with distance from the basement membrane: cuboidal (basal layer) to polyhedral (suprabasal) to flattened appearance (upper layers). Corneocytes of the stratum corneum are almost exclusively made of cross-linked keratin fiber, which, together with intracellular lipids, forms the permeability barrier.

Melanocytes are the cells in the basal layer that produce pigment melanin which gives skin its characteristic color. Melanin production is varied as a function of genetic predisposition, photostimulus, and secretion of melanocyte stimulating hormone by keratinocytes.

Merkel cells are found clustered beneath epidermal rete ridges and are associated with sensory nerve endings. They act as neuroendocrine cells in the developing epidermis by producing nerve growth factor to aid innervation of the epidermis.[2]

Langerhan's cells are bone-marrow-derived immune cells that are located in the suprabasal layer and migrate to regional lymph nodes when an immune response is elicited.

In addition to the aforementioned differentiated cell populations, stem cells also reside in the basal layer. This population is essential for the renewal of keratinocytes in the epidermis.[3] The main class of stem cells found is the interfollicular epidermal stem cell. The other class of stem cells in the skin is the hair follicular stem cell in the dermis. Cues for cell proliferation or renewal of cell population by the stem cells are provided by the matrix proteins (glycosaminoglycans (GAGs) and proteoglycans) of the basement membrane (dermal–epidermal junction, DEJ). The DEJ serves to anchor the epidermis tightly to the dermis.

5.534.1.2.2. Functions of epidermis

The following are the functions of the epidermis:

- It acts as a permeability barrier;
- It provides sensory function;
- It carries out the social-interactive function;
- It renews skin cells every 2–3 weeks.

5.534.1.3. Dermal–Epidermal Junction

The basement membrane or DEJ is the membrane that anchors the upper epidermis to the lower dermis. Highly proliferative keratinocytes reside in the DEJ and serve to constantly renew the pool of keratinocytes in the epidermis. These are supplied by the rich vascular network of the papillary dermis. The fibrous matrix is made up largely of Type IV and VII collagen. Electron microscopic analyses[4] reveal four distinct regions within the DEJ:

- Hemidesmosomes of the basal keratinocyte layer
- Lamina lucida zone
- Lamina densa or basal lamina, made up of Type IV Collagen
- Sublamina densa fibrillar zone with microfibers and anchoring elements (Type VII collagen fibrils)
- Matrix molecules in these layers such as Laminin-1 and -5 influence key decisions in the keratinocyte life cycle: migration vs. terminal differentiation.

5.534.1.4. Dermis

In contrast to the epidermis, the dermis contains few cells and predominantly comprises extracellular fibrous matrix, which provides mechanical stability to the skin. In addition, the dermis contains nerve endings, vascular networks, and dermal cells. The dermis is highly innervated and vascularized.

5.534.1.4.1. Structure and cell constituents of dermis

The two major layers of the dermis are the upper papillary dermis and the lower reticular dermis, which are separated by a subpapillary plexus.

Papillary dermis: The papillary dermis consists of bundles of collagen fibrils and oxytalan elastic fibers. Metabolically active fibroblasts populate the dermis, with greater activity seen in the papillary than the reticular dermis. Capillaries extend leading in from the subpapillary plexus and between the rete pegs (that project from the epidermis into the dermis).

Reticular dermis: This is the thicker and deeper portion responsible for durability and anchoring of skin appendages. The reticular dermis is characterized by interwoven bundles of large-diameter collagen fibrils. Diameter of collagen fibrils in the normal mature dermis decreases from the papillary (53 ± 3.0 nm) to the reticular (82 ± 4.9 nm) dermis[5] (Figure 2). The same trend is seen in normal scars but there is a uniform decrease in fibril diameter in hypertrophic scars.[5] The collagen fibrils and surrounding elastic fibers provide the dermis with a strong mechanically stable structure because of collagen fibrils and surrounding elastic fibers. Collagen is the major fiber present in the dermis, and several types of collagen fibers have been identified in the skin; specifically, Types I and III form the interstitial fibrils.

Matrix proteins: The elastic fibers reside within a gel-like ECM composed of GAGs, proteoglycans, and glycoproteins. GAGs are linear polymers of repeating units of disaccharides. The major GAG in the dermis is hyaluronic acid (HA), made of repeating units of glucuronic acid and *N*-acetyl glucosamine.

HA is usually covalently linked to a core protein to form a proteoglycan; however, it is unique in that it exists in the body unbound. The species of GAG present determines the stability of the matrix and the relative ease of cell movement. From the fetal stage through maturation, the dermis is increasingly composed of sulfated GAGs, leading to greater stability. Dermal fibroblasts secrete a slew of proteoglycans and glycoproteins into the extracellular space, specifically, chondroitin sulfates/dermatan sulfate (biglycan, decorin, and versican), heparan/heparan sulfate proteoglycans (syndecan and perlecan), and chondroitin-6 sulfate proteoglycans. Cationic dyes must be used to view proteoglycans in the dermis.

Fibroblasts (major cell type): Fibroblasts are the cells of mesenchymal origin which are normally present in the dermis and produce normal dermal replacement components. After injury, these cells migrate into the wound and proliferate in order to produce increased quantities of these dermal proteins and matrix.

Fibroblast products: These can be collagen (type one in skin), matrix proteins (fibronectin, tenascin, others), proteoglycans, GAG, HA, other matrix components, cytokines, and other growth stimulants.

Dermal dendritic cells: These cells of mesenchymal origin are normally present in tissue but increase in number after injury, attracted by chemical messages released by the activation of inflammation. The long-lived cells release the protein chemical messages, growth factors, and growth stimulants which orchestrate healing in an organized fashion.

Dermal dendritic cell products: These are growth factors, growth stimulants, and opsonins.

Endothelial cells: These cells make up the lining of micro and macro vessels and also make up the lining of new capillaries produced after injury. These cells, like fibroblasts, do differentiate from local mesenchymal cells and are also attracted into the wound by local signals.

Dermal appendages: The dermal appendages include hair follicles, sebaceous glands, and the eccrine glands. Hair follicles sprout hair, and the length of each follicle depends on the anatomical location. Associated with the hair follicle are the sebaceous gland and the bulge region of stem cells. The sebaceous gland produces the oily sebum layer covering the skin, while the bulge region supplies stem cells to renew dermal cell populations. More sebum is produced at certain locations (face, nose) than others. In contrast are the stand-alone eccrine glands that are the sweat glands and act to control body temperature by sweating. They are controlled by postganglionic sympathetic nerve fibers. Density of eccrine glands depends on anatomical location (highest on palms and soles).

5.534.1.4.2. Functions of the dermis

The collagen composition of skin is responsible for its mechanical strength. Elastin fibers provide the elastic nature of the skin, which can extend 10–50%. This characteristic is especially important in instances where the skin is forced to stretch, such as during pregnancy. The dermis exerts control over temperature, nutrient delivery, and fluid balance by controlling blood flow. The dermis is involved in thermoregulation through special thermoreceptors.

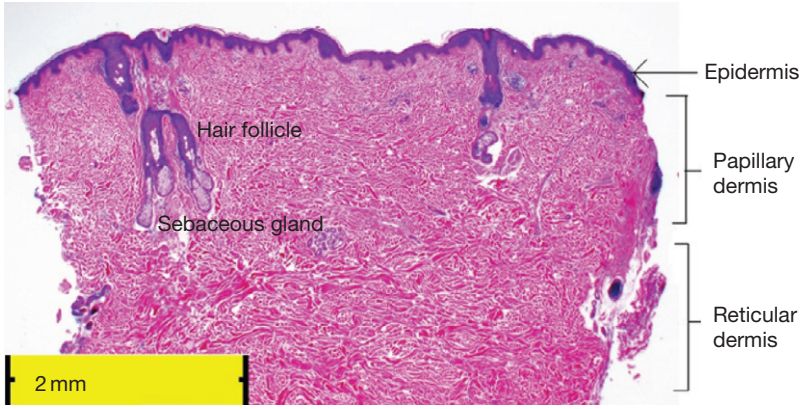

Figure 2 Dermal structure. Masson's trichrome-stained histology image of normal human dermis. Fine structure of papillary dermal collagen fibers are discerned from coarse structure of collagen fibrils in the reticular dermis. Sebaceous glands are also seen in association with hair follicles.

Thermoreceptors sense changes in body temperature and initiate sweating through the eccrine glands of the dermis.

5.534.1.5. Hypodermis (Subcutaneous Fat Layer)

Below the reticular dermis resides the hypodermis, a subcutaneous layer of fat that is highly vascularized and innervated. This layer cushions the upper epidermal and dermal layers and has cosmetic significance in shaping the body. There is a striking contrast in structure between the dermis (made of matrix proteins) and the fat-rich hypodermis. While the fat acts as a reservoir of energy, it is also the origin of fat-derived mesenchymal stem cells (MSCs) which can regenerate the cellular constituents of the upper layers. While heat loss occurs by convection, conduction, radiation, and evaporation, heat insulation is provided by the fat layer of the hypodermis.

5.534.2. Biology of Cutaneous Wound Healing

Wound healing is a complex process that involves cells, the ECM, plasma-derived proteins, and programmed angiogenesis. It is a well-orchestrated process that it is divided into three overlapping phases of inflammation, tissue formation, and tissue remodeling.

5.534.2.1. Inflammatory Phase

Inflammation is the body's highly effective, innate, initial response to injury. The inflammatory phase involves two different reactions: vascular responses including blood coagulation and hemostasis, and cellular responses including infiltration of neutrophils and macrophages.

Immediately after injury, homeostasis is achieved and a fibrin clot is developed. Platelets are the first cell type to respond to vascular injury and play a central role in normal hemostasis. Activated platelets release many mediators including adenosine diphosphate, serotonin, thromboxane A2; adhesive proteins such as fibronectin, fibrinogen, and thrombospondin; and growth factors such as platelet-derived growth factor-AB (PDGF-AB) and transforming growth factor-β1 (TGF-β1). The coagulation factors induce platelets to aggregate and form a platelet plug that facilitates fibrin clot formation. The fibrin clot acts both as a scaffold for the migration of neutrophils, endothelial cells, fibroblasts, and keratinocytes and as a reservoir of growth factors. The cells present within the clot release many vasodilators and chemoattractants, which activate the complement cascade and trigger an inflammatory response.[6]

In the early inflammatory phase, neutrophils and monocytes are the predominant cells recruited to the wound by chemotactic factors. Activated integrin receptors located at the cell surface of neutrophils interact with endothelials cells, promote diapediasis through the blood vessel wall, and facilitate cell migration through the connective tissue to the site of injury. Neutrophils are responsible for removing bacteria, damaged matrix proteins, and other foreign material from the wound via enzymatic degradation and phagocytosis. Monocytes typically transform into macrophages in the late inflammatory phase. Macrophages are the most important regulatory cells in this phase and perform multiple functions, such as release biologically active oxygen species and enzymatic proteins as well as phagocytose pathogenic organisms, destroy remaining neutrophils, and scavenge tissue debris. Macrophages produce a series of chemotactic factors, growth factors, and angiogenic factors that recruit fibroblasts and promote cell migration, proliferation, matrix production, and new blood vessel growth. Thus, macrophages play a primary role in angiogenesis, the formation of granulation tissue, and the transition from inflammation to the proliferation phase.

5.534.2.2. Tissue Formation Phase

Tissue formation, the second stage of cutaneous wound healing, overlaps with the first stage as re-epithelialization begins within hours of injury. Re-epithelialization is characterized by the migration of epidermal cells from the surrounding epidermis and skin appendages such as hair follicles, the proliferation of keratinocytes, the differentiation of the neoepidermis, and the restoration of the highly ordered basement membrane that connects the epidermis and the underlying dermis[7] (**Figure 3**). During the process of tissue repair, keratinocytes located at the wound edge secrete a plethora of matrix molecules, such as fibronectin (FN) and laminin, and express FN receptors (integrin α5β1), laminin receptors (integrin α3β1), and collagen receptors (integrin α2β1). Together, they provide 'start' signals that promote keratinocyte migration to achieve re-epithelialization.[7–9]

In contrast to the almost immediate response of re-epithelialization, dermal reconstitution begins 4 days after injury in response to the abundance of growth factors and cytokines present in the wound bed. The neodermis is characterized clinically by granulation tissue formation consisting of angiogenesis and fibroplasia. In response to the injury, angiogenesis proceeds as follows: (1) activation of endothelial cells, (2) local degradation of the vessel basement membrane, (3) new blood vessel sprouts 'punching' into the wound bed, (4) proliferation of endothelial cells, (5) new tubule structure

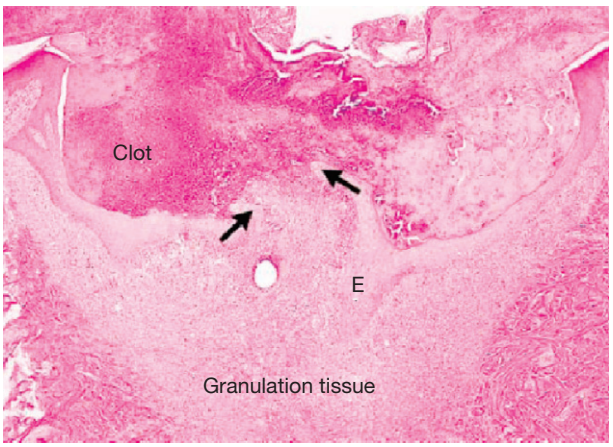

Figure 3 Re-epithelialization of a cutaneous wound in porcine (hematoxylin and eosin, × 40). Epidermal cells (E) are seen under the fibrin clot and across the wound. The advancing edge of the epidermal cells is shown with arrows. The white oval is an artifact of preparation. Reproduced from Singer, A. J.; Clark, R. A. *N. Engl. J Med*. **1999**, *341*(10), 738–746.

formation, (6) reconstitution of vessel basement membrane, and (7) regression and involution of vasculature that provides nutrition and oxygen to the newly formed dermis.

Fibroplasia is defined as the formation of fibrous tissue and characterized by fibroblast proliferation at the wound edge and migration into the fibrin clot. After fibroblasts have migrated into the wound, they transform their phenotype into a profibrotic type that functions to synthesize proteins and form new matrix. Fibroblasts are also responsible for converting the provisional fibrin/FN matrix into a collagen matrix via enzymatic degradation and massive collagen production.[10]

5.534.2.3. Remodeling Phase

The final phase of wound healing is characterized by newly synthesized ECM of mainly type I collagen, reorganization of the neomatrix, and wound contraction. ECM reorganization/remodeling goes on throughout the entire wound healing process but accelerates during the remodeling phase. Dermal remodeling is dependent on a balance between new collagen synthesis and old collagen lysis, which are tightly controlled by biomechanical stress and strain placed across the wound as well as chemical clues.

Wound contraction occurs within the second and third week post injury and involves the well-orchestrated interaction of cells, ECM, and cytokines. Wound contraction is primarily mediated by myofibroblasts and requires cell–cell and cell–matrix interaction. Myofibroblasts possess large bundles of actin-containing microfilaments that bind extracellular FN, which in turn links collagen fibers across the wound. Then, myofibroblasts gather in the collagen fibers and thereby induce wound contraction.

Once the closure of the wound has been completed, the process of remodeling can continue for months to years. Ultimately, the preinjury dermis is gradually replaced by a stable postinjury phenotype (scar) consisting predominantly of type I collagen. The tensile strength of scars reaches a maximum of about 70% of preinjury dermis.[11]

5.534.2.4. Interruption of Wound Healing

Cutaneous tissue injury results in a fairly rapid and acute wound healing response under normal physiologic conditions. However, when the underlying pathology interrupts the normal wound healing process, a failure to heal occurs, leading to a chronic wound (ulcer).[12] Many pathological factors can impair healing. Systemic factors include advanced age, malnutrition, diabetes, ischemia secondary to vascular disease, and renal disease.[13,14] Local factors include ischemia, infection, prolonged inflammation, presence of foreign bodies, and tissue maceration.[15] In addition, abnormal wound microenvironments such as the imbalance of proteolytic enzymes and their inhibitors,[16] the presence of senescent cells and/or local cellular response, abnormal time/spatial distribution of bioactive molecules such as growth factors, can also cause difficulties in healing.[17,18] Overall, cutaneous wound healing is a complex biological process that can be positively and negatively manipulated by various factors[19] (**Figure 4**). It is important to address, correct, or ameliorate the diseased state before applying engineered cutaneous therapy.

5.534.3. Wound Classifications and Prognosis

Burns resulting from thermal, electrical, or chemical contact as well as trauma are two of the most common reasons for acute skin wounds and significant cutaneous tissue loss.[20] Based on the damaged depth of skin, wounds are categorized into four groups: superficial (epidermal), superficial partial thickness, deep partial thickness, and full thickness (**Figures 5** and **6**). As a result, the standard of care and prognosis of wounds of varying severity differ to a great extent.

Superficial injuries affect the epidermis and are characterized by erythema and minor pain. These injuries can occur from sunburns or light scalds. These injuries typically re-epithelialize and heal within 21 days without a scar.

Injuries that penetrate through the epidermis and into the dermis are classified as partial-thickness wounds. These wounds are subdivided into superficial or deep partial-thickness wounds. Superficial partial-thickness wounds affect the upper layers of the dermis (papillary dermis) and are associated with burning sensation and acute pain. Such wounds heal by re-epithelialization from the wound edge and the remaining skin appendages, such as hair follicles or sweat glands. Deep partial-thickness injuries involve the deeper layers of dermis (both papillary and reticular), where most, if not all, skin appendages are destroyed. These wounds generally take longer than 21 days to close and heal with aesthetically displeasing scars and loss of function.

Full-thickness wounds affect both the epidermis and dermis and extend into the hypodermis. In this case, the skin has lost all skin appendages as well as regenerative cells and tissues. Full-thickness wounds simultaneously close via re-epithelialization from the wound edge and by contraction. The wounds repair with extensive scarring, which can result in limited joint motion and severe cosmetic deformities. Full-thickness skin wounds with a diameter exceeding 4 cm cannot heal without autologous split-thickness skin grafting,[21] which is the clinical 'gold standard' treatment.[22,23]

Another common type of skin injury is chronic wounds resulting from different diseases states, such as diabetes, genetic disorders such as bullous condition, and even surgical interventions.[24] As discussed in **Section 5.534.2**, wound healing is a complex biologic process and many systemic and local factors can potentially impair healing and cause chronic wounds.[25] Typical chronic wound management includes pressure relief, debridement of callous, pressure offloading footwear, and employing compressive bandages; however, these means are often insufficient to promote healing. As a result, several advanced healing treatments such as bioactive dressings, growth-factor-based therapies, acellular matrices, autologous skin grafts, and bioengineered skin substitutes have become available as additional therapies.[17]

5.534.4. The Significance of Tissue-Engineered Skin Application

Serious injury to the skin requires restoring barrier function and coverage to prompt healing immediately. Wound healing with large surface area and/or deep wounds are a clinical challenge. The standard of care for severe extensive skin wounds first requires excision of necrotic tissue to reduce

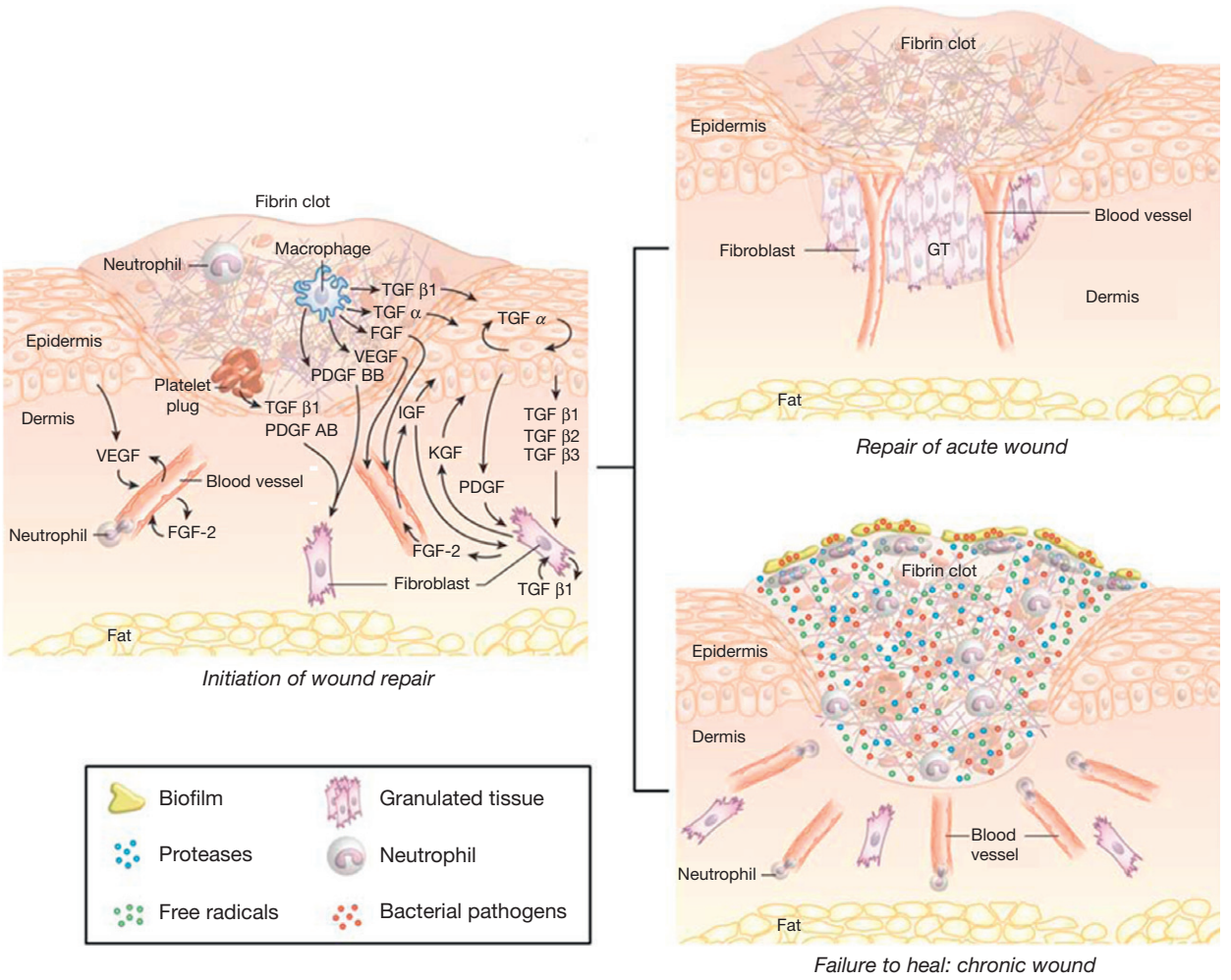

Figure 4 Different wound repair process in an acute wound healing response under normal physiologic conditions or in a chronic wound underlying pathology or microbial invasion interruption. (Left panel) Inflammatory phase: Tissue injury precipitates blood clotting, platelet aggregation, and migration of leukocytes, including neutrophils and macrophages, to the site of injury; (Upper right panel) Repair of acute wound: Under normal physiologic conditions the wound continues to heal at 5 days with an ingrowth of granulation tissue composed of fibroblasts, additional macrophages, and neovasculature; (Lower right panel) Interruption of wound healing-chronic wound/ulcer: When underlying pathobiology or microorganism invasion interferes with the wound healing process, a failure to heal occurs often leading to a chronic wound (ulcer). Reproduced from Clark, R. A.; Ghosh, K.; Tonnesen, M. G. *J. Invest. Dermatol.* **2007**, *127*(5):1018–1029.

infection, minimize hypertrophic scar formation, and avoid multiple organ failure. Autologous split-thickness skin grafting is the gold standard of treatment for deep partial-thickness and full-thickness wounds that cannot heal on their own. This treatment requires secondary surgery to harvest a sheet of autologous skin (epidermis and varying thickness of dermis). Generally, the thickness of the skin graft is inversely proportional to wound contracture. The site of the harvest, known as the donor site, heals by re-epithelialization usually within 7–14 days, similar to superficial partial-thickness wounds. However, there are two major drawbacks to this procedure: limited autograft availability and donor site management. The donor sites become increasingly limited in patients with greater than 50% burned skin area. Likewise, in chronic wounds, such as diabetic foot ulcers, the skin graft success rate is limited. In this case, naturally occurring grafts such as allografts (from a nongenetically identical individual of the same species), xenografts (from different species), and amniotic membranes have been used as an alternative to autografts for many years; however, these are only suitable as temporary wound coverings. Graft rejection is a major issue of both allografts and xenografts, which typically occurs within several days to weeks after graft implantation. Furthermore, the precarious supply source and the possibility of disease transmission limit their application.

To overcome the limitations associated with skin grafts, tissue-engineered skin substitutes are being developed to meet the need for a cost-effective and user-friendly synthetic or engineered skin graft that can be used to treat both acute and chronic wounds. During the last 40 years, a large number of biological and synthetic skin substitutes and products have been commercialized. Skin substitutes are typically categorized according to function as temporary skin substitutes used to protect the wound bed, optimize the healing environment,

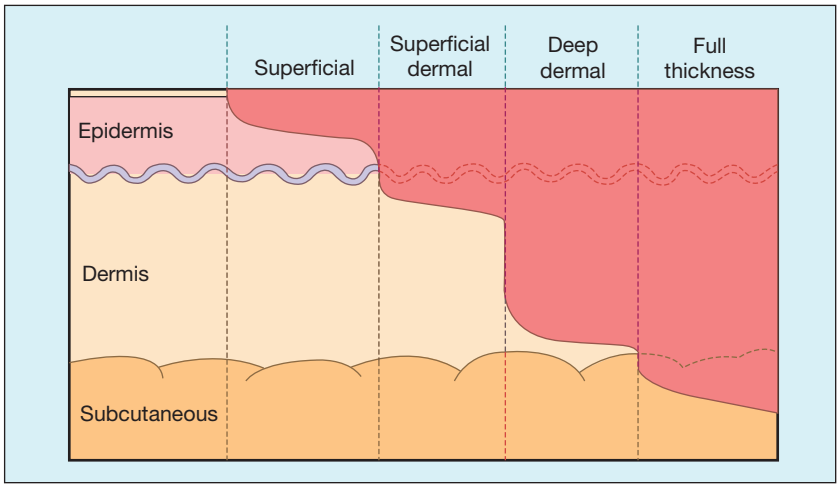

Figure 5 Diagram of different burn depths of skin tissue and the relationship of different degree of burn trauma. Reproduced from Hettiaratchy, S.; Papini, R. *Br. Med. J.* **2004**, *329*(7457), 101–103.

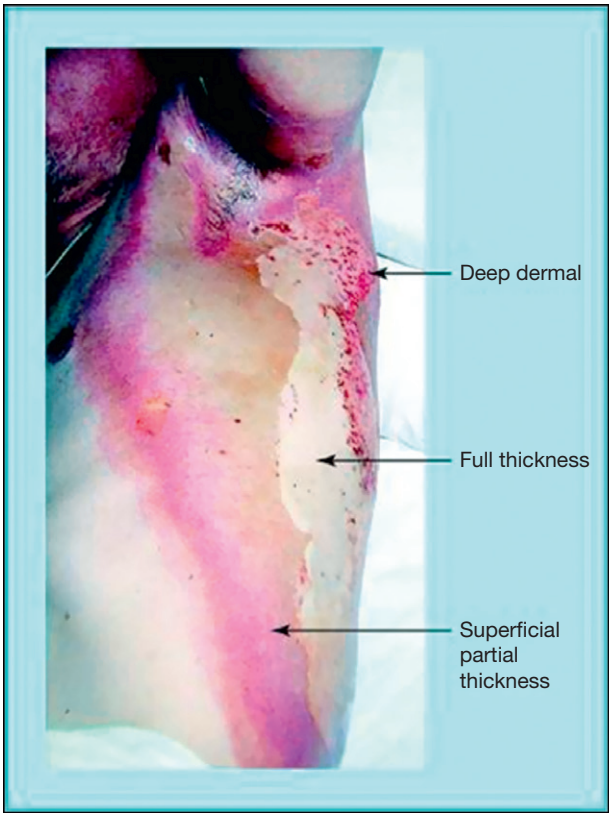

Figure 6 Flame injury showing all burn depths in human skin. Reproduced from Papini, R. *Br. Med. J.* **2004**, *329*(7458), 158–160.

relieve pain, promote healing, and serve as a bridge to autografting; or permanent skin substitutes used to replace one or both skin layer components and/or complement autografts, thus restoring skin function and aesthetics. Researchers and clinicians are collaborating to design, fabricate, and test tissue-engineered skin substitute that will offer the following benefits to the patient:

decrease the need of autografts and/or facilitate donor site healing,
decrease wound scarring and contracture,
decrease treatment costs and hospital stay,
accelerate wound closure, and
improve skin functionality.

5.534.5. Design Principles of Tissue-Engineered Skin Substitute

The design and development of the ideal tissue-engineered skin substitute must be safe to the patient, clinically efficacious, and user friendly. In addition, the skin substitute must be biocompatible, that is, nontoxic, noninflammatory, and nonimmune reactive, and have no risk of transmissible infection. It is important that the skin substitute induce rapid wound closure and mimic properties and functions of normal skin, such as biomechanical properties and barrier function. Ideally, the skin substitute should promote new tissue formation and degrade as it is replaced by the regenerating skin. Finally, the skin substitute should be convenient to handle and apply to the wound, and 'off-the-shelf' availability favors rapid treatment in the clinic. In addition, a relatively long shelf life and matched cost-effectiveness ratio are also ideal.[23,26]

Shakespeare[27] outlined '4P' principles of general functions which a different bioengineered skin substitute should offer.

Protection – This is achieved by establishing a mechanical barrier to restrict fluid loss, wound colonization, and a calculable rate of vapor transit. Early studies on skin substitutes[28] indicated that the pore size of the scaffold (outer layer) must serve as a barrier to microorganisms while allowing water vapor to escape to avoid subgraft fluid accumulation.

Procrastination – Following early wound debridement, temporary wound covering is necessary to provide a stable environment in the wound bed until permanent wound closure can be achieved, especially for extensive wounds that require serial skin substitutes or cultured autologous graft applications.

Promotion – The delivery of matrix molecules, cells, and growth factors to the wound bed may create the optimal microenvironment to promote and enhance the host wound healing process. Opposite of 'protection,' the pore size of the scaffold (inner layer) should permit the ingrowth of neo-fibrovascular tissue from the wound bed, which requires a pore size diameter of greater than 80 μm.[28] Therefore, the optimum skin substitute requires at least two layers with different pore sizes, or a monolayer with different pore sizes in the inner and outer face.

Provision – The cultured cells or dermal collagen acts as an organized and persisting new cell and matrix element, which can incorporate and accelerate the wound healing process and persist in the healed wound as infill.

The effective use of the skin substitute is essential to ensure the optimal management of wound repair. One possible design is to engineer the skin substitute *in vitro* and allow it to integrate into the wound site after implantation. Another approach is to fabricate a biocompatible and bioresorbable matrix that can act as a three-dimensional scaffold and attract host cells to stimulate nonscar wound healing. The ideal temporary or permanent skin substitute should have the following characteristics, adapted from Pruitt and Levine[29]:

Absence of antigenicity
Tissue compatibility
Absence of local or systemic toxicity
Provision of mechanical protection
Water vapor transmission similar to normal skin
Impermeability to exogenous microorganisms
Pain relieving property
Rapid and firm adherence to wound and easily removable without pain or trauma (important for 'temporary' skin substitute)
Rapid and sustained adherence to wound (important for 'permanently' skin substitute)
Stimulation of wound healing
Flexibility and pliability to permit conformation to irregular wound surface
Elasticity to permit motion of underlying body tissue
Resistance to linear and shear stresses
Prevention of proliferation of wound surface flora and reduction of bacterial density of wound
Tensile strength to resist fragmentation and retention of membrane fragments when removed
Biodegradability (important for 'permanent' skin substitute)
Low cost
Long shelf life
Minimal storage requirements.

5.534.6. Materials for Skin Tissue Engineering

5.534.6.1. Development of Nonbiodegradable Synthetic Materials

Over five decades ago (1954–1960s), the earliest materials used as temporary skin substitutes/wound coverings were synthetic nonbiodegradable materials including spray-on plastics (a copolymer of hydroxyvinylchloride acetate and sebacic acid),[30] polyox (a polymer of ethylene oxide),[29] and Ivalon sponge.[31] Subsequent reports included the use of laminated nylon velour,[32] polyurethane foam laminated to polypropylene film,[33] poly amino acid films,[34] films of Goretex (polytetrafluoroethylene), and ultrathin silicone polymer membranes laminated to a meshed inner layer.[35] These incipient nonbiodegradable synthetic materials encountered many issues such as submembrane suppuration, foreign-body inflammatory reaction, and infection. Three decades ago, several unilaminate membranes were developed as wound coverings and applied to preclinical animal experiments and clinical trials. Warren and Snelling[36] reported on the application of Hydron (polyhydroxyethylmethacrylate) to burn wounds and concluded that it has limited value in the clinic. Wokalek[37] developed a transparent liquid gel that was composed of agar and copolymerized with acrylamide. Its efficacy was evaluated in fresh operative wounds; however, its low tensile strength and adherence to the wound bed limited its use solely as a temporary wound covering. In the 1980s, a series of bilaminate membrane bioconstructs (Integra, Biobrane) were developed using a thin silicone film outer layer and an irregular nylon filament weave-bonded with a type I collagen inner layer.[38–40] The silicone membrane served to mimic the natural epidermis and was semipermeable to allow the release of water vapor to the environment but prohibit bacterial contamination into the wound bed. The composite of nylon and collagen layer served to mimic the dermis having high elasticity and permit full range of motion to the grafted body part. A decade later, the inner layer of the bilaminate membrane (TransCyte) was improved by seeding with fibroblasts that secrete natural matrix molecules.[41,42]

5.534.6.2. Development of Biodegradable Natural-Based Materials

In the recent three decades, the development of biodegradable biomaterials for skin substitutes has rapidly expanded. Different materials have been used as scaffolds to support cells and promote their adhesion, proliferation, differentiation, and deposition of new ECM. The exploration of biomaterials has been based on the comprehensive understanding of the biology of wound healing and inflammation and attempts to control interactions between biomaterials and cells. Materials used as engineered ECM in skin substitutes include those derived from natural-based systems and those manufactured synthetically.[43]

Compared to natural ECM, biomaterials of natural origin, that is, biopolymers, have similar biological macromolecular structure and performance. Theoretically, natural-based biomaterials have no hazards related to immunological reactions and chronic inflammation, including foreign body reaction, which may occur with synthetic polymers. There are many different naturally derived biomaterials that are suitable for skin tissue engineering. The major classes of naturally derived materials used as main constituents of engineered constructs with or without modification include (1) protein-based biopolymers isolated from blood and soft tissue, such as fibrin, collagen, FN; and (2) polysaccharide-based materials isolated from animals, such as alginates, chitosan, and GAGs including hyaluronan.

5.534.6.2.1. Collagen

Collagen is one of the most abundant proteins in the body. It is responsible for maintaining ECM structural integrity. Collagen has a triple-helical structure and the presence of 4-hydroxyproline provides a distinctive marker of these molecules.[44] Collagens located in the skin tissue are predominantly synthesized by fibroblasts and arranged in fibrils. To date, 28 collagen types have been identified and collagen I, II, III, and V are found in the skin.[45] The dermis mainly comprises collagen with some elastin and GAGs, which provide elasticity and plasticity to the skin and buffer mechanical injury.[46] Type I collagen is the major component of the dermis, contributing 70–80% of its dry weight and providing the skin with tensile strength.[47] Collagen types III and V are also located in the dermis of skin, especially around blood vessels and appendages.[45]

Collagen has been evaluated as a biologic dressing in various forms for several decades.[48,49] Also, it is a desirable skin substitute component because it can be isolated from allogeneic and xenogeneic tissues (such as rat tail tendon, bovine hides, and porcine or bovine Achilles tendon) by acidic/enzymatic solutions to produce high yields.[50] The collagen obtained after extraction contains variable levels of telopeptide content and is mainly present in the form of monomers with different amounts of cross-linked components (dimers, trimers, and some higher components).[51] This protein has a highly conserved amino acid composition in its helical regions, resulting in minimal immunogenic and allergenic properties; however, the telopeptide regions are not as highly conserved and can elicit reactions.[52,53] Collagen can provide hemostatic activity,[52] excellent tensile strength when in the form of large fiber bundles, and cell adhesive sites mediated by its helical domains or by arginine-glycine-aspartic acid (RGD) peptide sequences.[54]

Type I collagen has been isolated, studied, manipulated, and utilized as the main component of skin substitutes for many years.[23] Scaffolds fabricated from collagen act as a temporal structural support for intrinsic dermal regeneration. In addition, collagen can be seeded with fibroblasts and used as a scaffold on which to grow stratified epidermal sheets. For example, both Apligraf (Organogenesis, Inc.) and OrCel (Forticell Biosciences) are examples of FDA-approved and commercialized bilayered skin substitutes in which allogeneic keratinocytes are cultured on xenogeneic-derived collagen sponges containing fibroblasts. Apligraf is indicated to treat diabetic foot ulcers and venous leg ulcers, and OrCel for acute surgical excisions and graft donor sites.

Collagen-based matrices have also been used to construct a vascularized dermal skin substitute. In this model, collagen was shown to promote the spontaneous formation of a capillary-like network.[55,56] In addition, composites consisting of type I collagen and GAGs have been shown to regenerate both the dermis and epidermis in a porcine model.[57] Thus, the feasibility of utilizing engineered collagen scaffolds as cell-seeded systems for skin tissue engineering has been validated *in vitro* and *in vivo*. However, there are several associated drawbacks relevant to its use, such as mechanical weakness when in the form of small randomly oriented fibers, possible immune reaction when telopeptides are present, and pathogen transmission when derived from xenogeneic sources.[58]

For skin tissue engineering applications, the most common designs employing collagen are hydrogels, sponges, and lattice matrices. They have different physical and biochemical characters. Hydrated collagen hydrogels, which are composed of small randomly oriented fibers, have lower mechanical properties as compared to the sponge or lattice design. Dehydrated collagen sponges that are produced via freeze drying have stronger mechanical properties and have been shown to promote wound healing.[59] In the past 10 years, several skin substitutes have utilized the collagen sponge technology, such as Pelnac Standard/Fortified (Gunze Ltd.) and Terudermis (Olympus Terumo Biomaterials Corp.).[60–62] Furthermore, collagen can be blended with some synthetic materials, such as polycaprolactone, and then electrospun into nanofibers to more closely mimic the fibrous morphology of the natural ECM.[63,64]

5.534.6.2.2. Fibronectin

FN is a high molecular weight ECM glycoprotein that exists as a dimer composed of 220–250 kDa monomers which are linked by a pair of disulfide bonds.[65] FN can be found in humans in both soluble and insoluble forms as major components of blood and ECM, respectively. As the concentration of soluble FN increases in the pericellular matrix, short fibrils of FN form. As the process of matrix assembly continues, the short fibrils become more robust and eventually become the insoluble fibers found in the ECM.[66]

FN serves as a substrate for cell attachment, adhesion, and spreading through RGD, found in the tenth type III repeat, and the so-called synergy site, proline-histidine-serine-arginine-asparagine (PHSRN), located in the ninth type III repeat.[67,68] Cells bind FN at these sites via the integrins $\alpha5\beta1$ (RGD + synergy site) and $\alpha v\beta3$ (RGD alone) and then form adhesion complexes that influence their ability to activate associated downstream signaling. Biomaterials have been enhanced with RGD cell-attachment peptides to promote adhesion and spreading.[69,70] However, RGD alone tethered to scaffolds may not be sufficient to promote vascularization, as the synergy site is required for the binding and activation of $\alpha5\beta1$ integrins, which are the key regulators of angiogenesis.[71,72] However, mechanical stretching is known to affect FN function,[73] and using computational simulations it has been proposed that excessive tension generated by cells in contact with biomaterials may render FN fibrils nonangiogenic and potentially inhibit vascularization.[74]

Thus, cell migration, differentiation, and wound healing are modulated by FN. Fibroblast migration is the rate-limiting step in granulation tissue formation[75] and FN is required for fibroblast transmigration from a collagen matrix that surrounds wounds into a fibrin and FN gel that comprises the wound site.[76] Furthermore, a combination of FN domains and hyaluronan optimally supported granulation tissue formation during wound repair.[20] However, FN is rapidly degraded and absent[77] in chronic wounds as a result of high protease activity.[78,79] This, in fact, may be a substantial pathobiological event in the chronic nonhealing nature of these wounds.

5.534.6.2.3. Fibrin

Fibrin is a complex network naturally formed during blood coagulation by polymerization of fibrinogen and provides the primary scaffold for the provisional matrix of the nascent wound.[80,81] It is gradually replaced by the regular constituents

of the ECM, such as collagen. Fibrin in combination with FN has been shown to support keratinocyte and fibroblast proliferation and spreading both *in vitro* and *in vivo*, and may enhance cellular migration into cutaneous wounds.[82] Fibrin has been a useful cell delivery matrix in the regeneration of the skin and is currently approved by the U.S. Food and Drug Administration (FDA) and commercialized as fibrin glue in clinical applications.[82] Also, fibrin-based matrices have been shown to be robust delivery vehicles for growth factors that may be used to accelerate wound healing and skin regeneration (see Hubbell[70] and Gwak *et al.*[83] for more detail).

5.534.6.2.4. Hyaluronic acid

Hyaluronic acid, also known as hyaluronan or hyaluronate, is an anionic, nonsulfated linear disaccharide consisting of D-glucuronic acid and D-*N*-acetylglucosamine. It is composed of disaccharide repeats and ranges from 5000 to 20 000 000 Da in molecular weight. HA was first isolated in 1934 from the vitreous humor of the eye[84] and subsequently synthesized *in vitro* in 1964.[85] Also, it has been collected from other sources such as rooster combs, soft connective tissues, synovial fluids, and umbilical cords. In addition, HA can be produced on a large scale through recombinant microbial fermentation, which is a process that avoids the risk of animal-derived pathogens and disease transmission. HA comprises a small part of the ECM but is nonallergenic among the different species secondary to its conserved structure.[86] Like FN, HA is involved in the process of wound repair by modulating the release of cytokines and other bioactive molecules and regulating cell responses to these agents.[87–89]

The degradation products of HA are variable in length, described as short or long chains, and appear to modulate wound healing. Longaker *et al*. have shown that there are elevated levels of HA present during fetal wound healing that may contribute to the limited fibrosis observed in these wounds.[90] After degradation, HA fragments appeared to stimulate fibroblast proliferation[91,92] but decrease their total collagen production, which may contribute to nonscar healing.[93] The application of exogenous HA has been shown to enhance keratinocyte proliferation[94,95] and suggests that HA may benefit the re-epithelialization aspect of wound healing. An HA hydrogel which is intermolecularly cross-linked to protect the HA from hyaluronidase digestion and tethered with bioactive FN domains beneficially enhanced cutaneous wound healing *in vivo* in a swine model.[96,97] Importantly, HA hydrogels with viscoelastic properties between that of a fibrin clot and the normal dermis promoted healing best.

5.534.6.3. Development of Smart Matrix: New Concept for Biodegradable Synthetic Biomaterials

The incorporation of bioactive signals into scaffold materials may create a series of novel 'smart' matrices[98] including scaffold materials linked to synthetic peptides, semisynthetic scaffolds incorporating protein domains, engineered mutant variants of existing proteins, and engineered peptides capable of self-assembly into nanofibers. Engineered peptide products may enhance natural-based protein or peptide application in skin tissue engineering. Numerous studies have verified that the incorporation of the integrin-binding motif RGD promoted cell attachment and spreading in tissue-engineered bioconstructs of wound healing.[99] Shu *et al.* developed a hydrogel construct comprising thiol-modified hyaluronan capable of tethering cysteine-tagged functional domains or bioactive peptides. This construct tethered with cysteine-tagged RGDS peptides was shown to induce and support NIH 3T3 fibroblast proliferation *in vitro*[100]; however, it did not support fibroblast migration into the wound area *in vivo*.[96] Since the ideal tissue-engineered construct should be both inductive and conductive, the hydrogel was redesigned to include three fibronectin functional domains, FNIII(8–11), FNIII(12–15), and FNIII(12–V–15), which did support optimal fibroblast migration in both two- and three-dimensional systems *in vitro*.[101] In addition, Ghosh *et al.* demonstrated that the HA construct modified with the aforementioned three FN functional domains stimulated primary human dermal fibroblast spreading and proliferation *in vitro* and, furthermore, promoted dermal fibroblast recruitment in a cutaneous wound porcine model *in vivo*.[96]

The major challenge for current and future research is to optimize existing and novel matrices through modifications with bioactive peptides, such as recombinant protein domains or less expensive smaller synthetic peptides. Such smart matrices may improve the biological activities of synthetic materials beyond the physical properties of its polymer composition by promoting cell adhesion and enhancing the performance of cell activity.[102]

5.534.7. The Development of Tissue-Engineered Skin Constructs: The Past and the Present Status

5.534.7.1. Overview

Fabricius Hildanus (1560–1634) was the 'Father of German Surgery.' In his book *On burns De combustionibus* (1607), one of the earliest books that addresses the treatment of thermal injuries, he categorized burns in a practical, systematic way. The acute partial-thickness wound was described as *redness and blistering of the skin or withering without charring*, and the full-thickness wound as *eschar formation and charring*.

It has been recognized for many centuries that using a 'skin-like' dressing could improve wound healing. Xenografts derived from reptiles and animals were first used in fifteenth-century Europe, and frog skin is still in use today in Brazil. Swine skin became popular in the 1960s and continues to be the most common xenograft material. The first reported use of human-derived skin substitutes were in the mid-nineteenth century. Since 1950, cadaver skin and human amnion are routinely used for wound management.

With the advancement in technology, alternative skin substitutes have been developed and commercialized to replace xenografts and allografts.[19,103] Early studies carried out by Rheinwald and Green,[104] Bell *et al.*,[105] and Yannas's laboratory[106–108] established a basis for dermal, epidermal, and composite skin replacements. Thereafter, the focus of research has been on engineered skin substitutes comprising living cells and natural or synthetic cellular matrix components.[109] From our perspective, skin substitutes can be classified as follows:

(i) Type of biomaterial
biological: autologous, allogeneic, xenogeneic;
synthetic: biodegradable, nonbiodegradable

(ii) Skin substitute composition regarding cellular component
acellular
cellular
(iii) Duration of use
temporary
semipermanent
permanent
(iv) Anatomical structure
epidermal
dermal
dermo–epidermal (composite)

In this chapter, most of the tissue-engineered skin substitutes that are currently commercialized or have been in the past are summarized and organized according to anatomical structure.

5.534.7.2. Epidermal Skin Substitutes

Human keratinocytes were first reliably cultured by Rheinwald and Green about 35 years ago,[104,110] and later developed into cultured epithelial autografts (CEAs, a sheet of cells with two or three layers thick, see **Figure 7**)[111] for the treatment of burns.[112,113] This technique has been successfully translated into the clinic and has contributed to the dramatic increase in the survival rates of burn patients (Epicel and EpiDex). Over the last two decades, confluent sheets of CEAs have successfully been used to treat extensive full-thickness burn wounds worldwide. However, CEAs are susceptible to infection, require a dermal support layer, have a graft uptake success rate that varies from 15% to 85%, and are associated with high costs and a short shelf life (24 h).[114]

The aforementioned product drawbacks have stimulated research on alternative delivery systems for preconfluent keratinocyte monolayers, such as fibrin glue or membrane (Bioseed-S). Fibrin glue has been shown to help control bleeding and improve cell attachment to the wound bed, but unfortunately did not improve the CEA uptake rate. Delivery membranes are made of synthetic materials such as silicone with a specially formulated surface coating (MySkin), polyurethane, decellularized dermis, or biological degradable/natural biomaterial such as collagen, hyaluronan (Laserskin), and fibrin.[115] Another approach to deliver keratinocytes is via an aerosol cell suspension (ReCell/CellSpray).[116] The current commercially available epidermal skin substitutes are shown in **Table 1**.

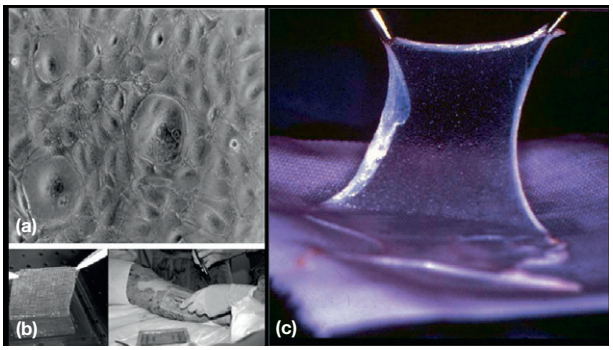

Figure 7 (a) Confluent keratinocyte sheet. (b) Keratinocyte sheet on a carrier grafted on the wound bed. Reproduced from Atiyeh, B. S.; Costagliola, M. *Burns* **2007**, *33*(4), 405–413. (c) A sheet of cultured keratinocytes. Reproduced from Anthony, E. T.; Syed, M.; Myers, S.; Moir, G.; Navsaria, H. *Drug Discov. Today: Therapeut. Strat.* **2006**, *3*, 81–86.

5.534.7.2.1. Epicel and EpiDex

Epicel (Genzyme Corp., Cambridge, MA) is an integrated CEA sheet developed from the methodology originally pioneered in 1981.[117] The patient is biopsied, and the autologous keratinocytes are isolated *in vitro* and cultured into a sheet that is applied to the wound. Similarly, Epidex (Modex Therapeutics Ltd., Lausanne, Switzerland) is an alternative CEA product derived from autologous hair follicles.

5.534.7.2.2. Laserskin

Laserskin (Fidia Advanced Biopolymers, Turin, Italy) is an example of a composite biocompatible skin graft. It comprises autologous keratinocytes cultured on a thin HA membrane that is laser-microperforated to facilitate ingrowth and proliferation of cells (**Figure 8**). Laserskin requires a lower seed density and reduced culture time, when compared to conventional CEAs. In addition, it is more easily transferred from the culture dish because the cells are grown on a transferable membrane, which avoids enzymatic digestion and contraction in the transplant site.[118] The micropores promote keratinocyte migration into the wound bed.[119]

5.534.7.2.3. Bioseed-S

Bioseed-S (BioTissue Technologies AG, Freiberg, Germany) consists of cultured subconfluent autologous keratinocytes resuspended in a fibrin encapsulant. In preclinical studies, Bioseed-S has shown re-epithelialization of full-thickness wounds[120] and the graft uptake rate was comparable to spraying keratinocytes directly without fibrin. Bioseed-S has primarily been used to treat chronic venous leg ulcers[121] and data suggest a 50% increase in wound healing when compared with standard treatment.[122]

5.534.7.2.4. MySkin

MySkin (Altrika Ltd., Sheffield, UK) is a product comprising subconfluent autologous keratinocytes cultured on a chemically defined silicone layer and applied to the patient.[123] It is indicated to treat superficial burns, skin graft donor sites, and full-thickness wounds in combination with meshed dermal grafts. It has also been applied to diabetic, neuropathic, and pressure foot ulcers with positive clinical outcomes.[124] This product has several advantages, such as ease of handling and relatively short-term cell culture, and can be applied to the wound in a flexible time frame when compared to conventional CEAs.[125]

5.534.7.2.5. ReCell/CellSpray

ReCell is a stand-alone, rapid, autologous cell harvesting, processing, and delivery technology/device as CellSpray is a cultured epithelial autograft suspension (Avita Medical, Australia). Through the spray device it delivers cultured or noncultured subconfluent autologous keratinocytes in a suspension to the wound site. First, a biopsy of skin is obtained from the patient. Then, the cells are cultured *in vitro* and the most actively

Table 1 Commercially available epidermal skin substitutes

Trade name and manufacturer information	*Cell component*	*Cell source*	*Primary cellular growth site*	*Scaffold source and material type*	*Duration of the cover*	*Advantages*	*Disadvantages*
Epicel Genzyme Corp., Cambridge, MA, US	Cultured keratinocytes (confluent cell sheet)	Autologous	*In vitro*	N/A	Permanent	• Earliest approaches in keratinocyte delivery system • Large area of permanent wound coverage with little risk of rejection and high proliferation rate • A valuable life-saving treatment in extensive injuries	• Long cell culture period (3 weeks) • Difficulties in handling and application • Fragile, risk of blistering due to incomplete anchoring • Variable uptake rate • Poor long-term results • Necessity for dermal support • High cost • Short shelf life (24 h)
EpiDex Modex Therapeutiques, Lausanne, Switzerland	Cultured keratinocytes from outer root sheath of scalp hair follicles (confluent cell sheet)						
Laserskin (Vivoderm) Fidia Advanced Biopolymers, Turin, Italy	Cultured keratinocytes (confluent cell sheet)	Autologous	*In vitro*	Recombinant Hyaluronic Acid membrane (microperforated)	Permanent	• Good graft uptake rate • High biocompatibility • Low infection rate • Easy handling properties	• Three weeks cell culture period • Short shelf life (several days)
Bioseed-S BioTissue Technologies AG, Freiberg, Germany	Cultured keratinocytes (subconfluent cell suspension)	Autologous	*In vitro*	Allogeneic Fibrin sealant	Permanent	• Outpatient procedure • Improved handling and cell attachment	• Several weeks cell culture period • Short shelf life (2 days)
Myskin Altrika Ltd., Sheffield, UK	Cultured keratinocytes (subconfluent cell sheet)	Autologous	*In vitro*	Synthetic Silicone coated with a plasma-polymerized surface	Permanent	• Easy handling and application • Decreased time for cell culture • Flexible delivery time	• Reapplication required for satisfactory clinical outcome
ReCell/CellSpray Avita Medical, Australia	Non/cultured keratinocytes (subconfluent cell suspension)	Autologous	*In vitro*	N/A	Permanent	• High proliferation rate • Easy to apply • Provides wound coverage • Reduced cell culture time	• Limited to partial-thickness and graft donor site wounds

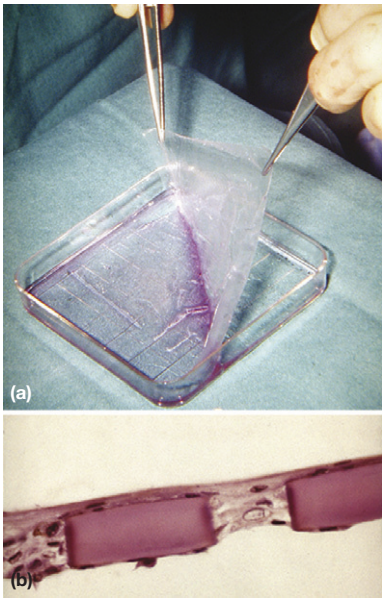

Figure 8 Laserskin: (a) raw material and (b) photomicrograph of populated material demonstrating cells migrating through pores. Reproduced from Price, R. D.; Berry, M. G.; Navsaria, H. A. *J. Plast. Reconstr. Aesthet. Surg.* **2007**, *60*(10), 1110–1119.

proliferating cells are harvested and applied to the wound site to improve wound closure and epithelialization.[115] This cell delivery system utilizes a reduced cell culture period and is an extremely convenient way to treat partial thickness and graft donor site; however, CellSpray must be used in combination with a dermal layer to function as a permanent skin replacement in full-thickness wound treatment.

5.534.7.3. Dermal Skin Substitutes

The dermis is an extremely important component of a skin substitute which may drastically improve the epidermal graft uptake success rate. *In vivo* studies have shown that keratinocyte spraying requires a dermal bed to achieve complete re-epithelialization.[126] Clinical practice has emphasized that therapies consisting of cultured keratinocytes are of limited value in treating full-thickness wounds without a well-vascularized recipient dermal wound bed.[127] The dermal construct should mimic the three-dimensional morphology of the natural ECM. The tissue-engineered construct may or may not incorporate cells, such as fibroblasts. The dermal construct may be commercialized alone or as a bilayered construct that includes epidermal cells. Many commercialized dermal constructs are acellular and avoid immunogenic response and rejection.[128] A list of commercialized dermal constructs has been compiled in **Table 2**.

5.534.7.3.1. Collagen-based dermal analogs: AlloDerm, GraftJacket, Karoderm, SureDerm, Permacol Surgical Implant, and Matriderm

Currently, there are several commercially available acellular products that serve as dermal replacements, such as allogeneic grafts (AlloDerm, GraftJacket, Karoderm, SureDerm) and xenogeneic grafts (Permacol Surgical Implant and Matriderm). Many dermal substitutes only partially engraft into the wound bed; however, they successfully serve as a dermal matrix for further autologous skin graft application. Nevertheless, both allogeneic- and xenogeneic-derived dermal grafts require rigorous screening to reduce the transmission of disease and virus infection and address safety and ethical issues.

AlloDerm (LifeCell Corporation, Branchburg, NJ) is a freeze-dried human acellular dermal matrix containing basement membrane.[129] It has a porous and fibrillar structure prepared from naturally derived human dermis by decellularization and lyophilization techniques. As a dermal replacement bioconstruct, Alloderm failed to support dermal fibroblast ingrowth due to the dense structure of the collagen fibrils[130] and has an unpredictable rate of vascularization.[27] However, Alloderm combined with extra-thin split-thickness skin grafts has performed fairly well in terms of function and aesthetics.[131] Alloderm is indicated for use in hernia repair and breast reconstruction; however, it has been used off-label on burn wounds.[132]

GraftJacket (Wright Medical Technology, Inc., Arlington, TN) is manufactured by both LifeCell Corporation and Wright Medical Group, Inc., as a premeshed human, acellular, extra-thin dermal replacement indicated for low-extremity ulcer repair.[133] It is first packaged aseptically in a peel-pouch, freeze-dried, and then sealed within a foil bag under inert atmospheric conditions. Kim *et al.*[134] reported that GraftJacket successfully treated superficial and deep wounds. In addition, a recent prospective, randomized, controlled clinical study demonstrated that diabetic foot ulcers treated with GraftJacket regenerative tissue matrix have a 2–3 times higher probability of healing compared to standard wound management.[135]

Karoderm (Karocell Tissue Engineering AB, Karolinska University Hospital, Stockholm, Sweden) is an acellular, human-derived dermis used to grow keratinocytes on full-thickness wounds. These donated dermal grafts replace the injured or debrided dermis and have been shown to accelerate wound closure and reduce scarring and contracture. Karoderm is particularly useful in treating injuries on growing children and is used to fill soft tissue defects that may result from skin cancer or trauma.

SureDerm (Surederm, Hans Biomed Corp., Korea) is similar to Karoderm in that it is an acellular, human-derived dermal replacement.[136] It has been indicated to repair soft tissue, such as nasal septal perforation,[137] abdominal wall defects,[138] and wounds due to burns. The product requires a 10-min rehydration procedure before use and can be stored for up to 2 years.

Permacol Surgical Implant (Tissue Science Laboratory, Inc., Covington, GA) is a sterile, off-white, moist, tough, and flexible fibrous flat sheet of acellular porcine dermal collagen and its constituent elastin fibers. Permacol is a patented product that is processed to remove noncollagenous and cellular components and is cross-linked to enhance biocompatibility and durability. It is used mainly for abdominal wall hernia reconstruction[139]; however, its clinical use is limited due to the slow ingrowth of cells and angiogenesis.[140]

Matriderm (Dr. Suwelack Skin & Health Care AG, Billerbeck, Germany) is a dermal replacement comprising structurally intact native bovine collagen coated with α-elastin hydrolysate. The collagen fibers are less densely packed as compared to Integra dermal regeneration template, which

Table 2 Commercially available dermal skin substitutes

Trade name and manufacturer	*Cell component*	*Cell source*	*Primary cellular growth site*	*Scaffold source and material type*	*Form*	*Duration of the cover*	*Advantages*	*Disadvantages*
AlloDerm Life Cell Corporation, Branchburg, NJ, US	N/A	N/A	*In vivo*	Allogeneic Human donor acellular lyophilized dermis	Collagen-based dermal analogs	Permanent	• Reduce antigenic components and immune response • Extra-thin for rapid host tissue incorporation (take) • Premeshed for easy passage of wound exudate • Immediately available • Small and large surface	• Risk of graft rejection and viral disease transmission • Deep surgical excision required • Secondary grafting necessary • Donor screening difficulties • Multiple donors
GraftJacket Wright Medical Technology, Inc., Arlington, TN, US								
Karoderm Karocell Tissue Engineering AB, Karolinska University Hospital, Stockholm, Sweden								
SureDerm HANS BIOMED Corporation, Seoul, Korea							• Nonimmunogenic • Easy manipulation	
Matriderm Dr Suwelack Skin & HealthCare AG, Billerbeck, Germany				Xenogeneic Bovine non-cross-linked lyophilized dermis, coated with α-elastin hydrolysate			• Comparable biological properties such as take rate, revascularization with Integra	• Combined with autologous skin grafts necessary for full-thickness skin defects
Permacol Surgical Implant Tissue Science Laboratories InC, Covington, UK				Xenogeneic porcine acellular diisocyanite cross-linked dermis			• Nonimmunogenic • Supports host fibroblast infiltration and revascularization	• Revascularization inefficient to support epidermal graft
Pelnac Standard/Pelnac Fortified Gunze Ltd., Kyoto, Japan	N/A	N/A	*In vivo*	Xenogeneic+synthetic Out layer-silicone/ silicone fortified with silicone gauze TREX; Inner layer-atelocollagen derived from porcine tendon	Collagen-based sponge	Semi-permanent	• Long shelf life • Easy to handle • Excellent long-term results	• Two-stage operative procedure • Combined with autologous skin grafts necessary for full-thickness skin defects

(*Continued*)

Table 2 (Continued)

Trade name and manufacturer	*Cell component*	*Cell source*	*Primary cellular growth site*	*Scaffold source and material type*	*Form*	*Duration of the cover*	*Advantages*	*Disadvantages*
Terudermis Olympus Terumo Biomaterial Corp., Tokyo, Japan				Xenogeneic + synthetic Out layer-silicone; Inner layer- lyophilized cross-linked bovine collagen sponge				
Integra (Dermal Regeneration Template) Integra LifeSciences Corporation, Plainsboro, NJ, US	N/A	N/A	*In vivo*	Xenogeneic+synthetic Epidermal-synthetic polysiloxane polymer; Dermal-bovine cross-linked tendon collagen (type I collagen) and GAGs	Collagen-based composites Bilayered template	Semipermanent	• Control fluid loss • Immediate wound cover • Encourages ingrowth of fibroblasts and epithelial cells	• Antigenicity and risk of disease transmission • Risk of infection • Three weeks *in vitro* lag period required to expand cells
Biobrane/Biobrane-L Smith & Nephew UK Limited, London, UK	N/A	N/A	*In vivo*	Xenogeneic + synthetic Epidermal-silicon film; Dermal – tri or monofilament nylon fabric mesh coated with porcine collagen	Collagen-based composites Wound dressing	Temporary	• Long shelf life • Dressing changes is unnecessary	• Difficult to remove if left more than 2 weeks
TransCyte Advanced BioHealing, Inc., Westport, CT and La Jolla, CA, USA.	Cultured neonatal fibroblasts	Allogeneic	*In vitro*	Xenogeneic + synthetic Epidermal-silicon film; Dermal – porcine dermal collagen-coated nylon mesh	Collagen-based composites Cassette with two sheets (frozen)	Temporary	• Cells provide a source of cytokines and growth factors to aid wound healing • No deep surgical excision needed	• Need for subsequent autograft or reapplication • Potential risk of rejection and disease transmission

Dermagraft Advanced BioHealing, Inc., Westport, CT and La Jolla, CA, USA.	Cultured neonatal fibroblasts	Allogeneic	*In vitro*	Allogeneic + synthetic ECM, PGA/PLA	Frozen film	Temporary	• Cells provide a source of cytokines and growth factors to aid wound healing • Long shelf life (6 months)	• Potential risk of rejection and disease transmission
EZ Derm AM Scientifics Limited, Geneva, Switzerland	N/A	N/A	*In vivo*	Xenogeneic Porcine aldehyde cross-linked reconstituted dermal collagen	Perforated or nonperforated dressing rolls	Temporary	• Long shelf life • Reduced pain	• Increased wound exudate • Does not vascularize and sloughs off • Mesh-like final appearance
Hyalomatrix PA Fidia Advanced Biopolymers, Turin, Italy	N/A	N/A	*In vivo*	Allogeneic + synthetic Out layer-silicone Inner layer-HYAFF (an ester of hyaluronic acid)		Temporary	• Biocompatible due to allogeneic or xenogeneic components • Good barrier function	• Temporary wound coverage • Use requires dermabrasion
Hyalomatrix 3D Fidia Advanced Biopolymers, Turin, Italy	Cultured fibroblasts	Autogeneic	*In vitro*	Allogeneic HYAFF membrane (microperforated)		Permanent	• Living cellular 3D layer • Enhance epidermal construct take when combined use • Reduce hypertrophy and wound contracture rates	• Complicated surgical intervention
OASIS Wound Matrix Healthpoint, Ltd., US	N/A	N/A	*In vivo*	Xenogeneic Porcine acellular lyophilized small intestine submucosa		Permanent	• Long shelf life	• Several reapplications may be required

is an irreversibly cross-linked collagen/glycosaminoglycan matrix (Figure 9). Recently, Schneider *et al.* compared the use of Matriderm to Integra in a rat study.[141] They demonstrated that Matriderm was not significantly different from Integra regarding their biological properties or performance, such as engraftment rate, granulation tissue accumulation, and neovascularization. Matriderm has also shown promising effects on healing when used in conjunction with split-thickness skin grafts on various wound types including full-thickness skin defects,[142] burns,[143–145] and electrical injuries,[144,145] as well as for covering exposed tendons.[146]

5.534.7.3.2. Collagen-based sponge: Pelnac, Terudermis

Pelnac (Gunze Limited, Kyoto, Japan) is an artificial bilayered dermis composed of an inner porcine collagen sponge layer about 3 mm thick with pore sizes ranging from 70 to 110 μm, a pore volume fraction of 80–95%, and an outer silicone layer of 150 μm thickness.[147] This dermis is freeze-dried and can be stored in dry conditions under ambient temperature for 3 years. Prior to use, it must be immersed in physiologic saline solution for 1 h to remove residual air. Suzuki *et al.* reported successful long-term results in 90% of cases when used in conjunction with extra-thin split-thickness skin grafts to treat full-thickness skin defects and deep burns.[148] In a clinical study of 55 patients, Pelnac was shown to induce rapid granulation tissue formation superior to that of Integra and Terudermis.[149]

Terudermis (Olympus Terumo Biomaterials Corp., Tokyo, Japan) has been available in Japan since 1993. It comprises a lyophilized collagen sponge cross-linked by dehydrothermal treatment. The collagen is reconstituted from fibrillar and heat-denatured low-antigenic bovine atelocollagen (a water-soluble form of collagen used in cosmetics and for culturing cells), where fibrillar atelocollagen provides scaffolding for surrounding cells and heat-denatured atelocollagen stimulates infiltration of host cells. Terudermis can be applied to mucosal and dermal defects resulting from burns, palatoplasty, trauma, and excisions.[150–152] It is useful in reconstructive surgery, and four versions of the product are available: silicone membrane type, mesh-enforced type, collagen monolayer type, and drainage slits type. The silicone membrane prevents infection and controls moisture flux,[153,154] similar to Integra.

5.534.7.3.3. Collagen-based composites: Integra, Biobrane, TransCyte

Integra Dermal Regeneration Template (Integra LifeSciences Corporation, Plainsboro, NJ) (Figure 10) was first designed by Yannas and Burke in 1980.[108] It is a bilayered dermal replacement that comprises an inner layer of lyophilized bovine type I collagen and shark chondroitin-6-sulfate glycosaminoglycan (8 wt%) and an outer layer of silicone which serves as a temporary epidermal barrier. It is necessary to remove the nondegradable silicone layer 2–3 weeks after granulation tissue formation and neovascularization is complete.[38] Integra has been successfully used in the clinic in burn wound management since 1981[38,155] and was shown to improve full-thickness wound closure with aesthetically pleasing results. Thus, Integra has become the clinical 'gold standard' dermal substitute. In addition, it is biocompatible, easy to use, and associated with a limited risk of transmissible infection, and has a relatively long shelf life. Although it seems to meet the design principles of skin substitutes, there are still some major associated product drawbacks: it is not a stand-alone treatment, it requires a second operative procedure to approach permanent wound closure, it requires a 2-week period required for neovascularization, and it cannot be used on infected wounds.

Biobrane (Smith & Nephew UK Limited, London, UK) is an acellular biosynthetic temporary skin construct of a silicone film bonded to a porcine collagen cross-linked with trifilament nylon fabric. It has a long shelf life without special storage requirements, and has a high cost-effective ratio.[156] Biobrane

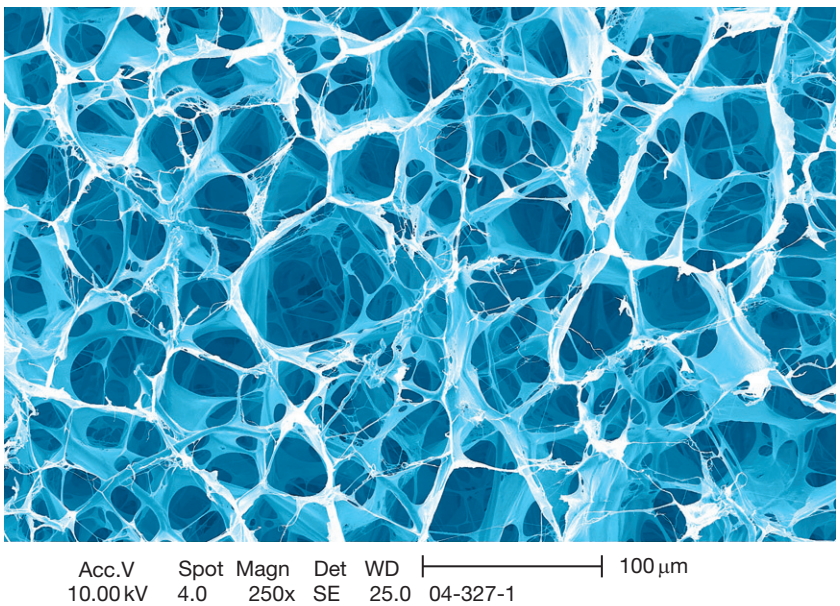

Figure 9 Matriderm: collagen–elastin matrix (250× magnification). Courtesy of Britta Feil, Clinical Affairs Manager of Dr. Suwelack Skin & Health Care AG, Billerbeck, Germany.

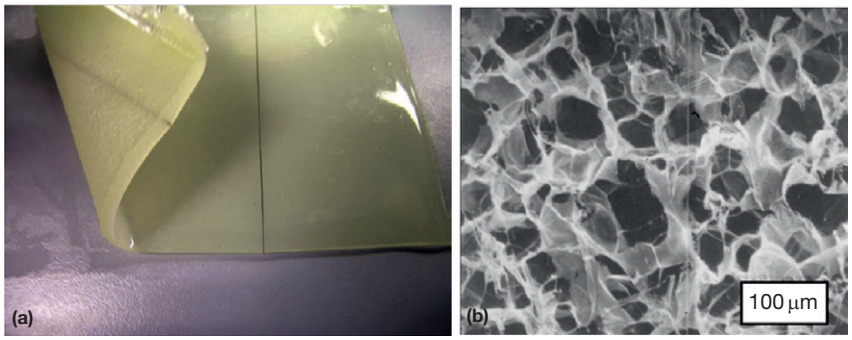

Figure 10 (a) Integra template: the upper silicon layer *in situ* and the lower dermal replacement matrix. Reproduced from Anthony, E. T.; Syed, M.; Myers, S.; Moir, G.; Navsaria, H. *Drug Discov. Today: Therapeut. Strat.* **2006**, *3*, 81–86. (b) SEM of a collagen-based scaffold (Intergra). Reproduced from Yannas, I. V. *J. R. Soc. Interface* **2005**, *2*(5), 403–417.

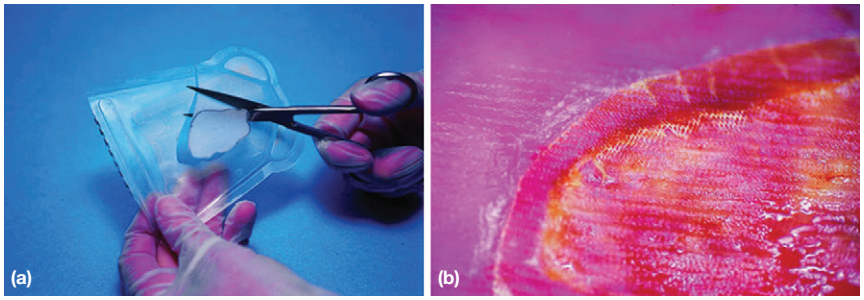

Figure 11 Dermagraft: nonimmunogenic neonatal fibroblasts cultured on a polyglactin mesh. (a) The dressing is stored frozen and the edges are trimmed after warming in a saline bath. (b) It is applied to the wound which lies within the ulcer boundary. Reproduced from Harding, K. G.; Morris, H. L.; Patel, G. K. *Br. Med. J.* **2002**, *324*(7330), 160–163.

has been commercially available since 1979 and is used to treat patients with partial-thickness burns and relatively fresh wounds (<24–48 h) with low bacterial counts.[157,158] In addition, Biobrane has been shown to decrease pain and reduce exudate when used on autograft donor sites[159]; however, no effects have been observed on deep partial-thickness and full-thickness burns. After healing, Biobrane can be intentionally removed or is naturally separated from the wound bed as healing progresses.

TransCyte is a cellular Biobrane product originally termed Dermagraft-TC, which was commercialized by Advanced Tissue Sciences, Inc., and received FDA approval in March 1997. In 2006, Advanced BioHealing, Inc. (ABH) purchase Dermagraft and TransCyte from Smith & Nephew. TransCyte is composed of a semipermeable silicone membrane and human neonatal fibroblasts cultured on a collagen-coated nylon mesh.[42] The fibroblasts are responsible for secreting various ECM components, such as FN and collagen, and growth factors onto the nylon mesh to provide an environment that stimulates wound healing.[160] TransCyte serves as a temporary wound covering for surgically excised full-thickness and deep partial-thickness burn wounds in patients who require autografts.[161] However, the price of TransCyte is 16 times more than that of Biobrane, 13 times more than that of an allograft, and 2.3 times more than that of Integra.[162] The product must be stored between −20 and −70 °C, and thawed at 37 °C prior to use. It has a shelf life of 18 months at the proper temperature and is difficult to handle, when compared to the above synthetic products.

5.534.7.3.4. Dermagraft

Dermagraft (ABH) is a cryopreserved skin construct with knitted polyglycolic acid/polylactic acid (PGA/PLA, namely polyglactin) mesh and living cultured human neonatal fibroblasts from foreskin within it. The typical polyglactin mesh is shown in Figure 11. The bioresorbable scaffold degrades via hydrolysis in 3–4 weeks while fibroblasts proliferate and produce ECM components to reconstitute a dermal layer (Figure 12).[134] The product does not have an epidermal equivalent layer. Dermagraft stimulates the ingrowth of fibrovascular tissue, but does not close the wound. It is primarily used to treat debrided, uninfected, and well-vascularized chronic wounds, such as diabetic foot ulcers and venous ulcers.[163,164]

5.534.7.3.5. OASIS Wound Matrix

OASIS Wound Matrix (Healthpoint, Ltd., USA) is an intact, freeze-dried, decellularized matrix naturally derived from porcine small intestine submucosa that serves as a temporary skin substitute/bioactive wound dressing.[165,166] It has been shown to support epidermal differentiation and basement membrane formation *in vitro*,[167] but has no effect on epithelialization *in vivo*.[168]

5.534.7.3.6. EZ Derm

EZ Derm (AM Scientifics Limited, Geneva, Switzerland) is a reconstituted porcine-derived collagen that has been chemically cross-linked with an aldehyde to improve its tensile strength and durability and allowing convenient storage at

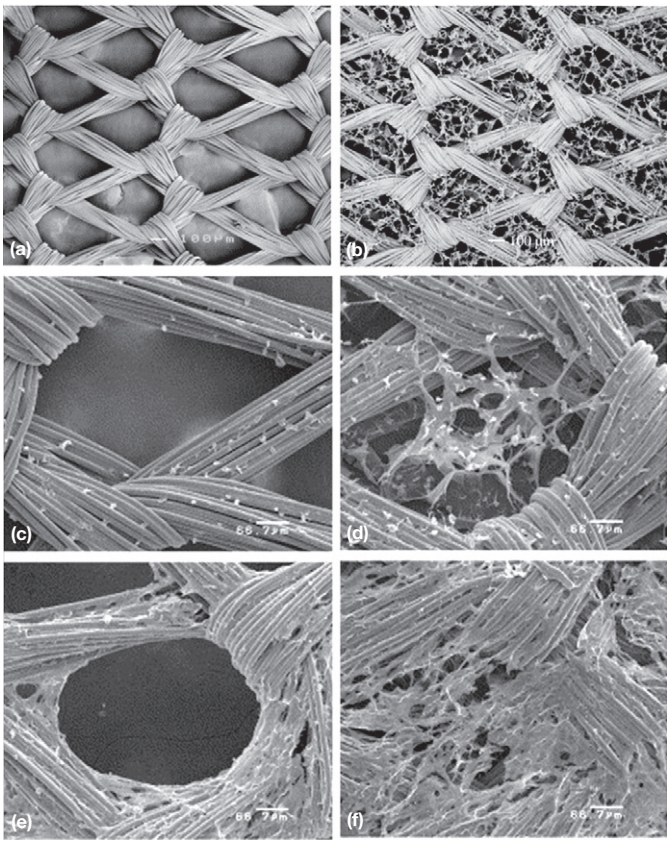

Figure 12 SEM photomicrographs of (a) PLGA (Polyglactin) knitted mesh. (b) Collagen-hybridized polyglactin mesh (Dermgraf) at original magnification × 90. (c) Fibroblasts cultured in polyglactin knitted mesh for 30 min and (e) for 5 days. (d) Fibroblasts cultured in collagen-hybridized polyglactin mesh (Dermgraf) for 30 min and (f) for 5 days at original magnification × 200. Modified from Chen, G.; Sato, T.; Ohgushi, H.; Ushida, T.; Tateishi, T.; Tanaka, J. *Biomaterials* **2005**, *26*(15), 2559–2566.

room temperature. The product acts as a temporary protective barrier/bioactive wound dressing that allows the natural healing process to continue undisturbed.[169] EZ Derm is available in both perforated and nonperforated versions for wounds requiring early exudate management and those requiring maximum fluid retention and optimum cosmetic results, respectively.

5.534.7.3.7. Hyalomatrix PA, Hyalograft 3D

Hyalomatrix PA and Hyalograft 3D (Fidia Advanced Biopolymers, Turin, Italy) were developed from HA derivatives (Figure 13). Hyalomatrix PA is an acellular dermal construct with a temporary silicone epidermal replacement, while Hyalograft 3D lacks the silicone layer but contains cultured autologous fibroblasts that secrete growth factors and cytokines. Hyalomatrix PA serves as a temporary dermal substitute to cover deep partial-thickness burns after dermabrasion. It acts as 'bridge' between necrotic debris and stimulates regeneration in a humid and protected environment (Hyalomatrix PA dressing). Recently, a national retrospective study was done to compare the treatment of deep partial-thickness and full-thickness burns with Hyalomatrix PA and autografting.[170] The Vancouver Scar Scale showed more promising results for those adults treated with Hyalomatrix PA; however, no difference was observed for burn depth. As a result, Hyalomatrix PA is indicated for use as a temporary covering before grafting or alone on deep partial-thickness and full-thickness burns in both children and adults.

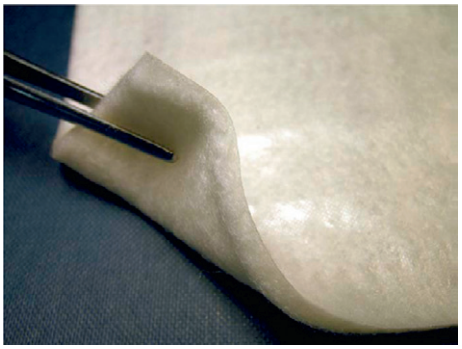

Figure 13 Hyalomatrix 3D with the addition of an upper silicon layer. Reproduced from Anthony, E. T.; Syed, M.; Myers, S.; Moir, G.; Navsaria, H. *Drug Discov. Today: Therapeut. Strat.* **2006**, *3*, 81–86.

In clinical practice, Hyalograft 3D is used for foot ulcer management in conjunction with Laserskin,[171] which is also known as the TissueTech Autograft System (see below). This product is reported to improve epidermal architecture with regular differentiation development *in vitro*, provide the basis

of epidermal homeostasis, and help DEJ maturation in the reconstructed skin constructs.[172,173]

5.534.7.4. Dermo–epidermal (composite) Skin Substitutes

Composite skin substitutes are bilayered skin constructs consisting of both epidermal and dermal layers aimed to mimic the anatomy of normal skin. There are three purposes that a composite skin substitute should have: (1) engraft into the wound site and serve as a replacement to an autograft; (2) act as a temporary covering until the autograft is applicable; and (3) stimulate the host's wound healing response by providing a scaffold and supply of bioactive molecules and/or ECM components.[174] Most composite skin grafts that have been developed incorporate allogeneic fibroblasts and keratinocytes into the dermal and epidermal compartments, respectively. Since these cellular constituents are derived from allogeneic sources, they only survive for a few weeks.[19] For example, clinical studies[175] and porcine studies[176] have shown that allogeneic fibroblasts can survive for 7 days post implantation, 3 weeks,[177] or even up to 2 months.[178,179] Although allogeneic cells act as a temporary solution, they supply bioactivity to wound dressings[23] by producing growth factors, cytokines, and ECM components, which deposit into the scaffold and modulate the recipient's wound healing process. The commercially available dermo–epidermal skin substitutes are summarized in Table 3.

5.534.7.4.1. Karoskin

Karoskin (Karocell Tissue Engineering AB, Karolinska University Hospital, Stockholm, Sweden) is human full-thickness skin obtained from donors, which is used as a temporary, durable covering for acute or chronic partial- and full-thickness wounds awaiting autologous split-thickness skin grafts. The allograft provides a reduction in pain and protection from infection for the first few weeks post injury. If the allograft is left in the wound for 3–4 weeks, the keratinocytes stimulate a host reaction, which results in graft tissue rejection and requires a replacement with an autograft.

Table 3 Commercially available dermo–epidermal (composite) skin substitutes. PEO, polyethylene oxide terephthalate; PBT, polybutylene terephthalate; HAM, hyaluronic acid membrane (microperforated)

Brand name and manufacturer	*Cell component*	*Cell source*	*Primary cellular growth site*	*Scaffold source and material type*	*Duration of the cover*	*Advantages*	*Disadvantages*
Karoskin Karocell Tissue Engineering AB, Karolinska University Hospital, Stockholm, Sweden	Native skin	Allogeneic	Native	Allogeneic Native human cadaver skin with dermal and epidermal cells	Temporary	• Provide pain relief and temporary durable cover	• Risk of graft rejection and disease transmission • Material availability uncertain
Apligraf Organogenesis Inc., Canton, MA, US	Cultured keratinocytes and fibroblasts	Allogeneic	*In vitro*	Xenogeneic Bovine collagen	Temporary	• Graft high take rate • No signs of keratinocyte rejection observed	• Risk of disease transmission
Orcel Forticell Bioscience, Englewood Cliffs, NJ, US	Epidermal-human allogeneic neonatal Keratinocytes Dermal-human allogeneic neonatal foreskin fibroblasts	Allogeneic	*In vitro*	Xenogeneic Bovine collagen sponge	Temporary	• Cells provide a source of cytokines and growth factors to aid wound healing • Nine months shelf life	
TISSUETech Autograft system (Laserskin and Hyalograft 3D) Fidia Advanced Biopolymers, Abano Terme, Italy	Cultured keratinocytes and fibroblasts	Autologous	*In vitro*	Recombinant Hyaluronic acid membrane (microperforated)	Permanent	• Successful treatment of diabetic foot ulcers with low reocurrence rates	• Requires two consecutive grafting procedures, associated with a complicated surgical intervention

5.534.7.4.2. Apligraf

Apligraf (Organogenesis, Inc, Canton, MA) (formerly known as Graftskin and Living Skin Equivalent) (Figure 14) is a composite skin substitute based on the pioneering work of Bell *et al.* on a collagen-based cellular construct.[105] It was the first FDA-approved medical device that incorporated living allogeneic cells. Apligraf contains two types of cells: fibroblasts and keratinocytes. In the dermal layer of the construct, human neonatal foreskin fibroblasts are suspended in a bovine type I collagen solution and converted into a contracted matrix within 6 days. In the epidermal layer, neonatal keratinocytes are seeded on the dermal layer and exposed to an air–liquid interface to promote maturation and cornification of a stratum corneum. Although Apligraf is reported to remain viable in the wound bed for 14 days and improve healing of acute and chronic wounds, such as chronic venous leg ulcers and diabetic foot ulcers,[179,180] it cannot support the regeneration of dermal appendages. Apligraf is supplied as a round disk that is 75 mm in diameter and 0.75 mm thickness. The product is packaged in a polyethylene bag containing a 10% CO_2/air ratio and agarose nutrient medium. Apligraf has a 5-day shelf life and must be stored at 20–23 °C.

5.534.7.4.3. OrCel

OrCel was first invented by Dr. Mark Eisenberg of Australia[181] and further developed by Forticell Bioscience Inc. (Englewood Cliffs, NJ) and licensed in 2001 to treat autograft donor sites required for the treatment of burns and dystrophic epidermolysis bullosa (EB). Like Apligraf, it contains both fibroblasts and keratinocytes that secrete many cytokines and growth factors, such as FGF-1 (bFGF), NGF, GM-CSF, IL-1α, IL-1β, IL-6, HGF, KGF-1 (FGF-7), M-CSF, PDGF-AB, TGF-α, TGF-β1, TGF-β2, and vascular endothelial growth factor (VEGF), that condition the wound bed for the application of an autogolous skin graft. In the dermal layer of the construct, human neonatal foreskin dermal fibroblasts are incorporated into a porous collagen matrix. In the epidermal layer, keratinocytes are incorporated into a nonporous collagen gel that is coated onto the dermal layer.[182] OrCel is as a resorbable, biocompatible matrix that provides a favorable environment for host cell migration and wound healing; however, it does not contain dermal appendages, such as Apligraf and Dermagraft.[53] Like all devices containing allogeneic cells, OrCel-treated donor sites retain no allogeneic cell deoxyribonucleic acid (DNA) after three weeks.

5.534.7.4.4. TISSUETech Autograft system

TISSUETech (Fidia Advanced Biopolymers, Turin, Italy) is an equipment that can fabricate autologous skin substitutes from tissue biopsies. From a small biopsy, fibroblasts and keratinocytes are isolated and separately cultured on HA to form an autologous epidermal and dermal replacement, known as Laserskin and Hyalograft 3D, respectively.[183] Reports from clinical trials have shown that TISSUETech has successfully been used to treat diabetic foot ulcers, many of which were full-thickness wounds with surface areas greater than 5 cm^2.[183] Recently, another prospective study showed that TISSUETech prevented depression or neck scars after parotid surgery.[184] Although this system may improve wound closure, it is not a 'true' composite skin substitute because it requires a two-layered grafting procedure.

5.534.8. Problems and Challenges of Available Skin Substitutes

The optimal skin substitute should mimic the performance and multifunctionality of the natural skin, such as permeability and infection barrier, color match, durability, compliance/stiffness and elasticity (physical properties), vascularization (take rate), regeneration of sweat and sebaceous glands, and hair follicles. However, all of the currently available skin substitutes are suboptimal, and in this section we will describe a few of their major limitations.

5.534.8.1. Biocompatbility

A challenge in the design of many currently available skin substitutes is the lack of biocompatibility. In general, autologous cells are biocompatible, whereas allogeneic and xenogeneic cells will eventually be rejected by the immune system of the host. In addition, specific allergies to animal-derived products can restrict their use in skin substitutes. For example, Orcel, Apligraf, and/or TransCyte cannot be applied to patients with known allergies to bovine products.[185] Although biocompatibility is a crucial criterion of the ideal skin substitute, autologous cells, which are typically derived from a small biopsy, require a 3-week *in vitro* culture period to expand cells to the needed population size. On the other hand, allogeneic and xenogeneic cells offer 'off-the-shelf' availability and these cells secrete a plethora of bioactive molecules and ECM components that play an invaluable role in wound healing.[186]

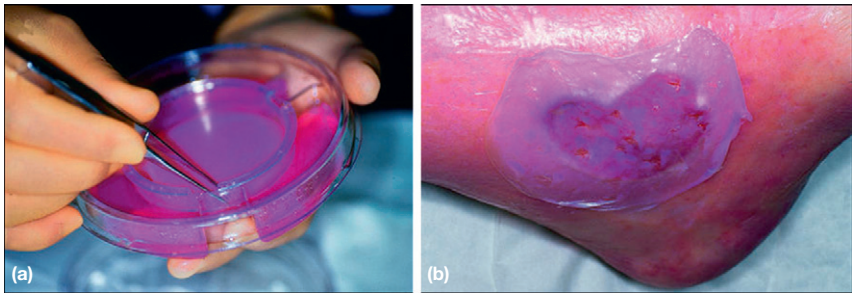

Figure 14 Apligraf: a bilayered skin equivalent containing newborn dermal fibroblasts cultured in a bovine collagen matrix with overlying epidermal cells. (a) It is stored frozen lying on a culture gel, and (b) small slits are trimmed after warming and is laid onto the wound surface whose the edges overlie the ulcer boundary. Reproduced from Harding, K. G.; Morris, H. L.; Patel, G. K. *Br. Med. J.* **2002**, *324*(7330), 160–163.

The body's defense mechanism can also vary according to the composition of the skin substitute. For example, Integra has been reported to cause greater foreign body reaction than the acellular dermal matrixes Alloderm and Dermagraft.[187]

There are three major sources of cells that may be considered when designing a skin substitute: local, systemic, and progenitor cell populations. Cells found locally include fibroblasts, keratinocytes, melanocytes, adipocytes, and follicular cells, and these systemically reside in the peripheral blood or bone marrow. Progenitor cells are found locally in the hair follicles and subcutaneous fat and systemically in adult bone marrow and in the embryo inner cell mass. Currently available skin substitutes are designed as a single-layer or bilayered structure and typically utilize two locally derived cell types, namely, keratinocytes and fibroblasts. The lack of melanocytes, Langerhans cells, and endothelial cells leaves the skin vulnerable to ultraviolet radiation and contamination and with inadequate vascular supply for oxygenation and nutrition, respectively. Commercially available devices also lack other skin structures, like sweat glands, sebaceous glands, nerves, and hair follicles, and as a result they do not provide thermoregulation or sensation to temperature, pressure, and touch.

Many investigators have studied improving skin substitutes through the addition of other cell types, including endothelial cells,[188,189] Langerhans cells,[190,191] melanocytes,[192–194] hair follicles, and sebaceous glands.[195] Among them, the incorporation of melanocytes in the correct concentration and from an appropriate donor for functional and cosmetic purposes seems to be most promising. For example, human skin substitutes containing cell slurries of keratinocytes and fibroblasts, with or without melanocytes, were grafted onto severe combined immunodeficient (SCID) mice.[192] At 16 weeks, Caucasian donor-derived skin substitutes with melanocytes were clearly darker than those without melanocytes, and a darker pigmentation was produced from donors of African descent.

Recently, bone-marrow-derived mesenchymal cells or adipose tissue-derived stromal cells (ATSCs) have gained widespread attention because of their unique proliferative and differentiation abilities.[196–198] Nambu *et al.* mixed freshly isolated ATSCs with an atelopeptide collagen/silicon membrane (ACMS) and demonstrated significantly advanced granulation tissue formation, capillary formation, and epithelialization in diabetic healing-impaired wounds compared to vehicle alone.[197] Although the aforementioned cell sources show promise for improving skin substitutes, their low host acceptance rate and the trend to tissue repair rather than tissue regeneration are major hurdles.[46]

Concerns regarding the potential of disease transmission via cadaveric human sources or even xenogenic sources (pig endogenous retrovirus) are still an issue.[162,185,186]

5.534.8.2. Physical Properties

Mechanical fragility and blistering of the epidermal component can occur during the maturation period of the basement membrane formation and constitute a limitation for the use of skin substitutes seeded with keratinocytes. Additional failures are likely if the skin originates from autologous sources isolated from older donors where the keratinocyte growth rate is slow, culture life span reduced, and colony forming ability diminished.[199] The absence of a dermal component in the skin substitute can often result in a reduced engraftment rate, as reported for Laserskin, EpiDex, and Epicel.[23,53,185,199–201] Keratinocytes in Epicel achieve stratification at 6 days but undulations at the epidermal–dermal interface known as 'rete ridges' that depend on basement membrane are lacking.[162] Only at 3 weeks can the basement membrane be distinguished and hemidesmosomes observed.[162] Anchoring fibrils such as collagen type VII are sparse and immature for the first 6–12 months, a fact that explains the fragility of this layer.[162] Additional destabilizing effects inflicted on the basement membrane could be attributed to the proteases used when harvesting keratinocytes cultured *in vitro*.[201]

Frequently, more than one surgical intervention is necessary to achieve satisfactory healing. Full-thickness wounds need time to develop a dermal component and skin substitutes such as BioBrane and TransCyte, which stimulate dermal repair, require the synthetic layers to be removed prior to autologous keratinocyte application.[185] For use of autologous cells, the lag period between skin biopsy and the requisite cell expansion can take 2–3 weeks. This time involves hospitalization and nursing care, which adds to the intrinsic high cost of these tissue-engineered products.[162,185] Furthermore, the short shelf life of not only autologous but also allogeneic skin substitutes is a practical disadvantage for the commercialization of some products. For example, Apligraf lasts for only 5–10 days at room temperature.

5.534.8.3. Limited Vascularization and Poor Engraftment into Wound Site

One of the most common limitations of bilayered cell-containing skin substitutes, or any scaffold for that matter, is the scaffold's limited vascularization rate.[202] The survival of the uppermost cell layer in the scaffold will be in jeopardy if adequate blood perfusion and nourishment are not provided, which would consequently threaten successful engraftment.[203] In clinical practice, skin substitutes applied to fat or to a poorly vascularized wound bed often fail and require replacement. However, the success of engraftment significantly increases when the wound bed is pretreated with a dermal substitute, such as Integra, which stimulates vascularization prior to grafting.[204,205]

Vascularization also affects the attachment of keratinocytes to the underlying dermis. In general, thicker grafts lead to better mechanical (resistance to pressure and shear forces, graft shrinkage), functional (sensibility), and aesthetic properties; however, they are more difficult to vascularize.[206] The maximum depth that new blood vessels can reach in a skin bioconstruct that stimulates angiogenesis is about 400 μm. When grafts are thicker than 400 μm, new blood vessels cannot grow quickly enough from wound bed into the whole layer to sustain viability, thereby resulting in graft loss.[207]

Prevascularization involves creating a microvasculature inside an engineered tissue prior to implantation. It is believed that the preexisting vascular network will lead to the generation of engineered skin substitutes of more physiologically functional complexity and improved regenerative potential.[208,209] One strategy has been to reconstruct a human capillary-like network *in vitro*. Black *et al.* cocultured dermal fibroblasts, keratinocytes,

and human umbilical vein endothelial cells on chitosan/collagen scaffolds, which stimulated the self-organization of endothelial cells into capillary-like structures.[210] Immunohistochemical analysis and transmission electron microscopy of the endothelialized skin substitute showed typical microvasculature characteristics: that is, von Willebrand factor, Weibel–Palade bodies, basement membrane material, and intercellular junctions. Tremblay *et al.* observed similar results when human keratinocytes, fibroblasts, and endothelial cells were cocultured on a collagen sponge *in vitro* and implanted at a wound site.[56] The study suggested that prevascularization of the skin substitute resulted in inosculation within the recipient's capillaries, rather than neo-vascularization.

5.534.8.4. Scarring

Poor cosmetic results, namely scarring, of most of the skin substitutes are still a problem and therefore constitute a limitation for their use. Scars are areas of fibrous tissue (fibrosis) that have replaced normal skin. Scars are assessed clinically by a scar scale such as the Manchester Scar Proforma[211] or Vancouver Scar Scale[212]: atrophic, hypertrophic, and keloidal. An atrophic scar takes the form of a sunken recess in the skin that has a pitted appearance. These are caused when underlying structures supporting the skin, such as fat or muscle, are lost. Hypertrophic scars occur when the body overproduces collagen, which causes the scar to be raised above the surrounding skin. Keloids are a more serious form of scarring, with elevated, expansive, and excessive growth beyond the margin of the original wound.[213]

Uncontrolled scarring results in loss of function and poor aesthetics. Some scar formations can result in tightness, pain, and itching, and may result in tissue contractures that restrict movement. In addition, most skin appendages, such as sweat glands, sebaceous glands, and hair follicles, do not regenerate with scar tissue, and, in general, scar tissue is less resistant to ultraviolet radiation due to the lack of melanocytes. Uneven pigmentation due to the absence of melanocytes and the lack of dermal appendages (hair follicles and glands) are the most frequently reported undesired cosmetic outcomes.[23,51] The use of autologous fibroblasts is still preferred over allogeneic fibroblasts, as scar formation and inflammatory reaction are substantially reduced in the former.[214] Therefore, it is important that any new generation of skin substitute target scarless healing.

5.534.8.5. Others

The application of any skin substitute requires that the recipient's physiologic state is optimized, any underlying condition is stabilized, and the wound bed is properly prepared[199] including debridement of all microbial contamination and necrotic tissue to increase the probability of engraftment.[215] Products such as Integra, Alloderm, BioBrane, TransCyte, Apligraf, Dermagraft, and OrCel have been reported to be prone to developing contamination, and extra care is needed on maintaining aseptic environment[185,200] via physical or chemotherapeutic methods. Poor patient compliance is another factor that cannot be underestimated in wound healing and is often the cause of the high incidence of ulcer recurrence.[216] Other factors, such as disturbance of normal daily activities, have been linked with the level of patient compliance. The patient's adherence to a recommended course of treatment could also be influenced by religious and ethical issues. Some biologically based products,[185] in particular the use of cadaveric skin, are factors in these latter matters. If the local and systemic pathobiological states of the patient as well as personal and societal issues are considered along with the inherent characteristics of the engineered skin biomaterial, improvement in success rates will be obtained. From the use of cultured autologous epidermal sheets to the development of complex bilayered skin substitutes, the evolution of tissue engineering constructs and their clinical application has truly been phenomenal.

5.534.9. Divine Garments Without Seams (Ancient Chinese Proverb): The Inspiration for Tissue-Engineered Skin Substitute from Lessons of Nature

Regenerative medicine is a new and expanding field in biomedical engineering research and is focused on the 3R principle: replace, restore, and regenerate damaged or diseased cells, tissues, and organs.[217,218] The key objective is to produce novel skin substitutes that mimic the structural and functional properties of normal skin and integrate them into the host tissue without scarring, like the famous Chinese proverb states, 'divine garments without seams.' In nature, there are few vertebrate species capable of perfect regeneration. For example, the xenopus and axolotl can regenerate entire limbs,[219,220] deer can replace lost antlers,[221,222] bats can fix wing membranes, rabbits,[223] pikas, cats, echo-locating bats,[224] and two experimental mice strain, namely, MRL/MpJ mouse[225] and athymic nude-nu mice,[226] can regenerate external ears, and fetal skin can regenerate with scarless healing.[227,228] A deeper understanding of these mechanisms may result in a breakthrough in skin substitute technology and lead to regeneration rather than healing with scars.

5.534.9.1. Mammalian External Ear: Examples of Regeneration in Adult Animal

5.534.9.1.1. Rabbit ear

Rabbit was one of the first mammals discovered to have the capacity to regenerate new skin tissue for through-and-through holes ear repair (observation originally described by Markelova (1953), translated by Vorontsova and Liosner (1960)).[229] Wound healing around the margins of rabbit ear holes is uniquely characterized by the development of prominent epidermal downgrowths adjacent to the severed sheets of dermis in the integument of the ear. These downgrowths act as epidermal blockades and play an important role in scarless regeneration by allowing blastema cell accumulation. Unlike rabbits, dogs and sheep were not able to regenerate ear tissue due to the absence of these epidermal downgrowths.[223,224]

5.534.9.1.2. MRL/MpJ mouse ear

A similar ear punch regeneration phenomenon was found on MRL/MpJ strain murine model where 2-mm punch wounds regenerated completely after 4–5 weeks.[225] In 2003, histological

analysis revealed that regenerating MRL/MpJ ear edges closely resembled the blastema of a regenerating limb.[230] Rajnoch *et al.* hypothesized that regeneration was the result of a thickened epithelium that provided growth and differentiation factors in the proper spatiotemporal pattern. Interestingly, the regenerative ability of MRL/MpJ strain mice is restricted to the ear.[229] A possible reason is that the small dimensions of the ear may promote the diffusion of growth factors and establish appropriate gradients similar to embryonic development, whereas in large thick tissues, for example, the skin, this may not be possible.[230] In addition, reduced inflammatory infiltrates,[231] decreased concentrations of TGF-β1 and PDGF,[232] and the absence of CD8+T-lymphocytes[226,232] have correlated with scarless healing and suggest that regeneration is highly modulated by the inflammatory system.

5.534.9.2. Mammalian Skin Hair Follicle: Examples of Regeneration in Adult Animal

The mammalian skin hair follicle is believed to develop only during embryogenesis and is lost as an adult. However, there were several profound reports of the development of adult hair follicles *de novo* following wounding in rabbits, mice, and humans nearly 60 years ago.[233–237] Recently, Ito *et al.*[238] discovered that the epidermis of wounded murine adult skin can regenerate new hair follicles during healing, which was shown to recapitulate embryogenesis at the molecular level. Wounding activated the Wnt-mediated signaling pathway, which is essential for normal hair development and cycling. Inhibition of Wnt signaling after re-epithelialization completely abolished wounding-induced folliculogenesis, whereas overexpression of Wnt ligand in the epidermis increased the number of regenerated hair follicles.[238] These results provide a potential therapeutic window for promoting the growth of hair follicles by manipulating the Wnt signaling pathway.

5.534.9.3. Embryonic Skin: Examples of Scarfree Regeneration in Fetal Animal

Early fetal wound healing is essentially a scarless regenerative process,[239,240] with minimal inflammation and complete restoration of normal skin structure, including ECM deposition of hyaluronan, various collagen types, and tenascin-C,[241–243] and regrowth of hair follicles, capillaries, and glands. Repair and regeneration of the skin is correlated with the degree of skin differentiation and the inflammatory response to wounding.[240] Fetal skin repair changes with gestation age and varies with wound size.[244] In large- and small-animal models, early gestation skin wounds heal without scarring.[245] In monkeys, sheep, and rats, the transition between scarless healing and wounds that heal with scarring occurs around 80 days of gestation (early second trimester),[246] middle of the third trimester,[247] and between 16–18 days of gestation (full term is 21.5 days),[248] respectively. In general, wounds of 2–4 mm in diameter are more likely to heal without scarring, whereas wounds of 6–10 mm in diameter were more likely to heal with a scar.[249]

It is has been shown that the differential expression of healing-related cytokines plays a key role in modulating early fetal scarless healing and late fetal or postnatal healing with scar formation.[239] The fetal wound environment has a diminished acute inflammatory response with a decreased number of differentiated inflammatory cells,[243] reduced fibrin clot formation and platelet degranulation, and increased levels of molecules relevant to skin morphogenesis and growth,[46,250] when compared to adult wounds. In addition, concentrations of growth factors in adult and fetal wounds are different.[251] For example, fetal wounds contain decreased levels of TGF-β1 and TGF-β2 and increased TGF-β3 (a skin morphogenetic molecule), as compared to adult wounds.[252] Similarly, PDGF, FGF-1, and FGF-2 expression in fetal wounds is lower than in the adult.[243,252] Therefore, the ideal skin substitute may require the modulation of the adult wound environment to mimic more closely that of the fetal wound. For example, some approaches to reduce scar formation have been to block TGF-β1 and TGF-β2 with neutralizing antibodies, and add exogenous TGF-β3 to the wound.[239,253,254]

The capacity for regeneration is probably inherent to the composition of fetal skin. Coolen *et al.* reported that the levels of dermal ECM molecules such as FN, chondroitin sulfate, and elastin in fetal skin were different from adult skin.[255] Similarly, fetal skin and wounds have a relatively high amount of collagen type III[245,248] and hyaluronan.[90] In the rat model, fetal wounds expressed greater amounts of matrix metalloproteinases in relation to tissue inhibitor of metalloproteinases.[256,257] These data suggest that dermal components are essential to fetal scarless wound healing.

5.534.9.4. Inspiration from Mammalian External Ear and Fetal Skin Regeneration

Understanding and characterizing the elements involved in scarfree embryonic wound healing and adult skin regeneration from a tissue engineering perspective may provide important clues for the ultimate goals of skin tissue engineering: (1) Create a skin construct that promotes complete regeneration of functional skin, including all its layers (epidermis and dermis) and appendages (hair follicles, sweat glands and sensory organs); (2) Promote the rapid uptake (vascularization) and establishment of a network of nerves; (3) Integrate with the surrounding host tissue without scarring. As reported in this section, the issues of cell source, structure, vascularization, and scarring are major limitations of the currently available skin substitutes. However, solutions may be inspired from the aforementioned examples of adult skin regeneration and fetal scarless wound healing.

5.534.9.4.1. Stem cells: cell-based regeneration strategy

Stem cells are central functional units of regeneration. These multipotent cells are capable of both self-renewal and differentiation. The use of stem cells in cell-based regenerative medicine for skin tissue engineering shows promise toward the improvement of therapeutic technologies.

Epidermal stem cells may be an important source of cells relevant to cutaneous wound healing.[258–260] There are two subpopulations of epidermal stem cells located in the skin: stem cells residing in the bulge region of the outer root sheath, and a basal keratinocyte population found in the interfollicular epithelium.[195,261,262] Epithelial keratinocytes have been successfully utilized in skin grafting for many years (see **Section 5.534.7** on CEAs).[104,204,263] Recently, several

studies have demonstrated that progenitor cells offer superior qualities to that of differentiated keratinocytes[264–266] because of their multipotency and easy accessibility.[267,268] Although *in vitro* and *in vivo* assays exist to label, culture, and analyze skin-derived stem cells, it is currently not possible to isolate a pure stem cell population. The identification of one or more specific epidermal stem cell markers is imperative to the successful use of this technology. Furthermore, there are a limited number of stem cells within the interfollicular epithelium and the outer root sheath of the hair follicle, and this mandates cell culture technology that maintains their viability post isolation and rapidly expands them to a useful concentration.

Mesenchymal stem cells (MSCs) derived from bone marrow or adipose tissue may also be suitable candidates for skin tissue engineering. Bone-marrow-derived MSCs (BM-MSCs) leave the bone marrow, circulate in the blood, home to injured tissues, then differentiate into cells of the residing tissue, which accelerates cutaneous wound regeneration in both animals and humans[269–272] and partially restores normal function.[198,273,274] Sasaki *et al.* demonstrated that BM-MSCs could differentiate into keratin-14-positive cells (basal epidermal cell phenotype), endothelial cells, and pericytes *in vivo*.[274] Several reports on the clinical application of BM-MSCs in wound therapies have revealed that grafted MSCs facilitate skin regeneration, both in acute and in chronic wounds.[198,275–277] In Badiavas' study, it was demonstrated that autologous BM-MSCs delivered in a fibrin spray could accelerate healing in human cutaneous wounds. Autologous BM-MSCs have also been shown to play an important role in promoting tissue regeneration after radiation injury.[273] In addition, the transplantation of autologous and allogeneic MSCs on the surface of deep burn wounds in rats has been shown to decrease inflammatory cell infiltration into the wound and accelerate the formation of new vessels and granulation tissue.[217] MSCs have been also shown to produce bioactive substances that accelerate regeneration after wounding.[278] Although current studies have reported that MSCs have the ability of improving wound re-epithelialization in a site-specific manner, the perfect regeneration of hair follicles or sweat glands was not observed; such stem cells have shown a stable self-renewal potential, but their plasticity was limited.[279,280] MSC engrafting and their immunosuppressive properties are also important unintentional side effects.[281–283] Further studies are required to elucidate the underlying mechanism associated with BM-MSCs and wound healing; however, a few hypotheses include cell differentiation, wound contraction, release of pro-angiogenic factors, and maintenance of the ECM.[272,284]

ASCs isolated from liposuction procedures are currently being explored as an alternative to MSCs. In experimental wound models, ASCs accelerated wound closure by improving re-epithelialization and angiogenesis. In this model, the delivery of ASCs via a human acellular dermal matrix or a matrix composed of atelopeptide collagen or silk fibroin-chitosan to improve local tissue regeneration is also being explored.[197,285–288]

Human embryonic stem cells (hESCs) are immature, pluripotent cells that can differentiate into all human cell types, and are another potential candidate in tissue regeneration.[289] However, ethical and moral objections restrict commercial development of hESCs. Recently, scientists have generated induced pluripotent stem cells (iPS cells) from adult human skin fibroblasts and keratinocytes by gene transduction involving cells reprogramming. Cells of this type are less controversial and may prove to be as efficacious as embryonic stem cells in regenerative medical applications.[290–292] In addition, the plasticity of stem cells, especially iPS cells, and their unstable cellular phenotypes might lead to the regenerative tissue structural and/or functional instabilities and ultimately give rise to malignant cells. In conclusion, stem cells offer multiple advantages to consider when creating the ideal skin substitute; however, it is important to study and overcome their associated drawbacks.

5.534.9.4.2. Vascularization: sustaining pipelines to construct the skin substitutes

Vascularization of the engineered skin construct has been a major obstacle associated with commercially available products. The distance of nutrients and oxygen delivery by diffusion is limited to 2 mm in a vascular tissue. The vascular system acts as an important role in mass transport; furthermore, evidences have accumulated to support an intrinsic role of the vascular system in the regulation of tissue formation and differentiation.[293–295] Thus, the penetration of new blood vessels into a skin graft allows the transport of molecules or cells (i.e., macrophages or endothelial progenitor cells (EPCs)), regulating wound healing and/or grafted tissue survival and integration. As mentioned above, stem cells are central functional units of regeneration; however, those cells are oxygen sensitive. Therefore, it is necessary to stimulate rapid vascularization of skin-substitute-sustaining pipelines for their survival and function.

In theory, there are three fundamental mechanisms that incorporate vascularization into a skin bioconstruct: (i) angiogenesis, to promote sprouting and ingrowth of vessels from the host; (ii) vasculogenesis, to form *de novo* vascular network by endothelial progenitors in the construct before implantation, that is, prevascularization; and (iii) artificial functionalized ECM matrices, to promote angiogenesis and vasculogenesis.[208,296,297]

Natural maturation of a vascular system is dependent on specific spatial and temporal orchestration of cells and bioactive molecules. This can be achieved by promoting invasion and sprouting of the host vasculature into the implant through angiogenesis. The delivery of growth factors that participate in angiogenesis is an attractive way to promote vascularization. For example, Murphy *et al.* encapsulated VEGF into a synthetic poly(lactide-*co*-glycolide) scaffold and demonstrated the sustained release of VEGF, which is a critical angiogeneic factor.[298] However, the ability to simultaneously deliver multiple mitotic and differentiating factors in the proper dose, rate, and presentation is a major current challenge of the skin engineering community.[299]

An alternative approach is to fabricate a skin substitute that contains vasculature prior to implantation, which is called prevascularization. After implantation, host blood vessels would presumably connect with the preformed vasculature within the engineered construct, leading to accelerated engraftment. Clearly, this sequence of events would depend on correct clues emanating from the graft.

Another approach is to develop an artificial, but functionalized ECM that promotes angiogenesis and vasculogenesis *in vivo* or *in vitro*. Through the use of peptides/molecules that have a natural affinity for relevant growth factors, a biomimetic scaffold may be the ideal approach to guide sprouting of the host's endothelial cells.[300] However, peptide-containing scaffolds may be subject to enzymatic degradation and instability *in vivo*, which may result in a suboptimal presentation of the clues for vascularization.

Another major challenge is the source of endothelial cells that should be used to create the vascular network. The cells should be clinically easy to obtain, purify, and expand *in vitro*, and therefore autologous cells are ideal for avoiding host immune responses. To date, the use of several mature endothelial cells, including human umbilical vein endothelial cells and human dermal microvascular endothelial cells, have been used to generate vascular networks *in vivo*.[210,301,302] The utilization of hESC-ECs in regenerative medicine has also been reported.[303,304] However, as previously mentioned, the use of hESCs is currently a subject of ethical debate.[305] Alternatively, there are many significant evidences to support the angiogenic potential of EPCs.[306–308] Autologous EPCs are present in human peripheral blood, which makes them available as an attractive cell type in regenerative vascularization.[309] EPCs have been shown to form robust vascular networks in engineered tissue constructs in the presence of stromal cells, and can function *in vivo* for up to 28 days.[306–308] Recently, a three-dimensional engineered vessel network derived from cord blood EPC-derived endothelial cells (EPC-ECs) and fibroblasts was developed in a fibrin gel *in vitro*. Results demonstrated that both EPC-ECs and a high density of fibroblasts accelerated the rate of functional anastomosis significantly. Such an *in vitro* prevascularization model might have potential application in tissue engineering.[310]

In 1998, Black *et al.* demonstrated the *in vitro* formation of microvessels within an engineered skin substitute.[210] A skin bioconstruct scaffold made of chitosan/collagen was cocultured with dermal fibroblasts, keratinocytes, and human umbilical vein endothelial cells. Self-organization of the endothelial cells into a tubular network that included lumen with typical intercellular junctions, Weibel–Palade bodies, and a basement membrane of laminin and collagen IV was observed.[210] In a similar engineered skin construct, the presence of prevascularization improved the skin bioconstruct's perfusion time *in vivo* (4 vs. 4–14 days), which was comparable to that observed for full-thickness human skin grafts. The number of vessels did not significantly decrease after 14 days, indicating that the prevascularization vessel network was stable over time.[56] A third study was performed using human progenitor cell-derived endothelial cells from umbilical cord blood. The vascularized skin substitutes were prepared by seeding those endothelial cells on the surface of decellularized human dermis following keratinocytes spreading the epidermal surface. These skin bioconstructs were then transplanted onto mice model and analyzed 21 days later. The results demonstrated that endothelial cells differentiated from circulating progenitor cells can be utilized to vascularize human skin bioconstructs. However, no *in vivo* experiments were further performed to assess the functionality of the construct.[311]

5.534.9.4.3. Incorporation of bioactive molecules in the design of an intelligent skin substitute

Regeneration involves several cell types and a complex pattern of molecular cues and signaling networks, including numerous growth factors, cytokines, and chemokines in a spatiotemporal manner.[312,313] Growth factors are important molecules because they instruct cellular development and function, such as proliferation, migration, differentiation, and tissue formation, in an organized, time-dependent manner. Cell signaling results in a cascade of events that regulate and control cell function. Therefore, it has been hypothesized that the incorporation of bioactive molecules into tissue-engineered skin constructs may improve the regeneration of skin. However, the challenge is how to incorporate those molecules and in what concentration into a bioengineered material.

The growth factors involved in skin regeneration include bFGF, EGF, GM-CSF, IGF, PDGF, TGF-β, and VEGF. PDGF-BB has already been approved by the FDA (Regranex, Johnson & Johnson) and is currently used in the treatment of chronic ulcers. It has also been suggested that reduced levels of PDGF may play a role in the mechanism of scarless cutaneous repair. TGF-β family is known to contain the most potent growth factors involved in the wound healing process throughout the body.[239] In particular, TGF-β1 and TGF-β2 have been implicated in the formation of scars, whereas TGF-β3 may have antiscarring effects.[239] The FGF family has also been implicated in scarless healing.[314] Dang *et al.* hypothesized that differential expression of FGF isoforms and receptors occur during fetal skin development and that this differential expression pattern may regulate the transition from scarless regeneration to repair with scar formation.[256] The results demonstrate an overall downregulation of FGF expression during scarless healing. As with many bioactive molecules, there is a critical concentration of FGF that may promote scarless healing and sufficient angiogenesis.

Currently, multiple novel delivery systems including vectors and slow-releasing polymers are being investigated.[315] The primary role of the skin is to serve as a protective barrier. Thus, membrane-like devices have been a common design of skin substitutes capable of the incorporation and delivery of growth factors for improving healing and/or regeneration. Another approach to the design of a delivery system is the use of particles loaded with bioactive molecules. The particulate systems used to deliver growth factors are typically on the 'micro' scale and have shown very interesting properties for application in skin tissue engineering. For example, gelatin-based microspheres have been used to deliver TGF-β1[316] and bFGF.[317] The skin substitute may also combine two technologies; for example, Park *et al.* embedded bFGF-loaded gelatin microparticles into chitosan scaffolds and demonstrated accelerated wound closure of pressure ulcers.[318] Furthermore, particulate systems on the 'nano' scale are capable of more precise spatial distribution of bioactive signals when compared to microparticles[319] and may offer an optimal delivery system to modulate cell function. Recently, nanoparticles fabricated from dextran sulfate and chitosan for FGF-10 delivery provided promise as systemic (intravenous) and local therapies.[320] The particle system may also be used to deliver multiple drugs in different spatiotemporal patterns to a single site. For example, both VEGF and PDGF were loaded into a single matrix, but

their sequential release was achieved by differences in their affinities to the system's components, which spatially restricted each growth factor to a different layer of the delivery system.[299,321] The codelivery of growth factors using nanoparticles may be allowed for tunable release kinetics, elevated targeting specificity, and enhanced regeneration (Figure 15).

An alternative approach is to use living-cell systems that secrete appropriate growth factors at appropriate times. For example, both healthy keratinocytes and fibroblasts produce at least 17 different growth factors[322] that modulate signaling cascades to determine cell fate, function, and healing. Thus, living cells in bioengineered skin constructs may be suitable for sustained, simultaneous multiple growth factor delivery. To this end, much recent interest has focused on different cell type of skin and stem cell delivery (for details please see Section 5.534.9.4.1). Apligraf (Organogenesis, Canton, MA) is a bilayered bioengineered skin substitute that was the first living-cell, therapeutic, engineered skin the FDA approved to promote the healing of ulcers. However, it failed in 1998 secondary to scale-up problems but later (2000) received approval for treatment of diabetic foot ulcers.[323,324] More recently, systems that mimic embryonic development through establishment of a niche cell–matrix and/or cell–cell microenvironment have been used for growth factor/cytokine delivery.[325]

5.534.9.4.4. Smart scaffold/matrix: structural determinant biological activity

The ultimate goal of biomaterial design for skin tissue engineering is to provide the necessary signals to induce and conduct cell processes to restore both structure and function to the skin. Smart matrices possess biomimetic characteristics that induce regeneration *in vivo* through the (i) presence of ligands for cell adhesion; (ii) mechanism of controlled and localized matrix dissolution, ideally in temporal and spatial synchrony with cell invasion and regeneration; and (iii) delivery of morphogenetic signals that attract endogenous progenitor cells and induce their differentiation into a tissue-specific pathway.

Nature has optimized its microenvironment to maintain homeostasis and direct tissue development and differentiation in a spatiotemporal manner. It has been hypothesized that the optimal skin substitute should mimic the natural ECM, specifically its physical and biochemical properties. The microstructure of the ideal scaffold should have a specific chemical composition, ECM-mimicking topology,[326] high degree of porosity, interconnected pores, controlled pore size and geometry control, appropriate polymer degradation rate, and high surface area to volume ratio.[327] Yannas *et al.* have demonstrated that the induction of adult skin regeneration requires a scaffold that serves as a topological template for new stromal synthesis and provides bioactive signals, such as those that block wound contraction.[106–108,227,328,329] In addition, new-generation skin substitutes should mimic the regulatory functions of the natural ECM and its ability to bind and present growth factors to cells.

There are many new materials that have been developed and studied for skin tissue engineering, including hyaluronan coupled with FN functional domains,[96] silk fibroin and alginate,[330] poly(lactic-*co*-glycolic acid)/chitosan hybrid nanofibrous membrane,[331] peptide-derived polymers,[332] ICX-SKN skin graft replacement,[333] collagen–glycosaminoglycan–chitosan dermal matrix seeded with fibroblasts,[334] porcine collagen paste,[335] bovine collagen cross-linked with microbial transglutaminase,[336] biodegradable polyurethane scaffolds,[337] asymmetric chitosan membrane containing collagen I nanospheres,[338] marine gelatin/oxidized alginate hydrogel,[339] and many others (reviewed by Shevchenko *et al.*[103]).

5.534.10. Conclusions

There are two major approaches to achieve regeneration of the skin (Figure 16). The first is a cell-based therapy, which utilizes a matrix or carrier system for cells and/or bioactive molecules to induce morphogenesis *ex vivo*, and eventually, is implanted

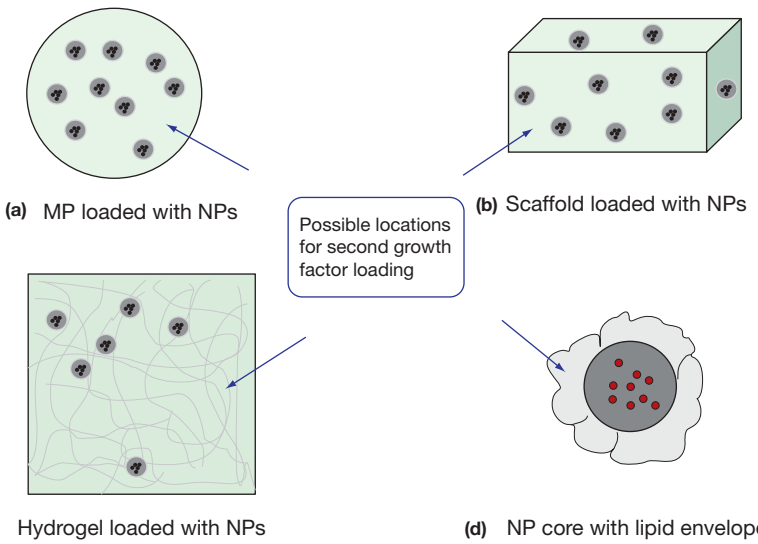

Figure 15 Different design of nanoparticles (NPs) with incorporation into (a) a microsphere, (b) a tissue engineering scaffold, (c) a hydrogel, and (d) NP core with lipid envelope for the sustained release of growth factors. Reproduced from Zhang, S.; Uludağ, H. *Pharm. Res.* **2009**, *26*(7), 1561–1580.

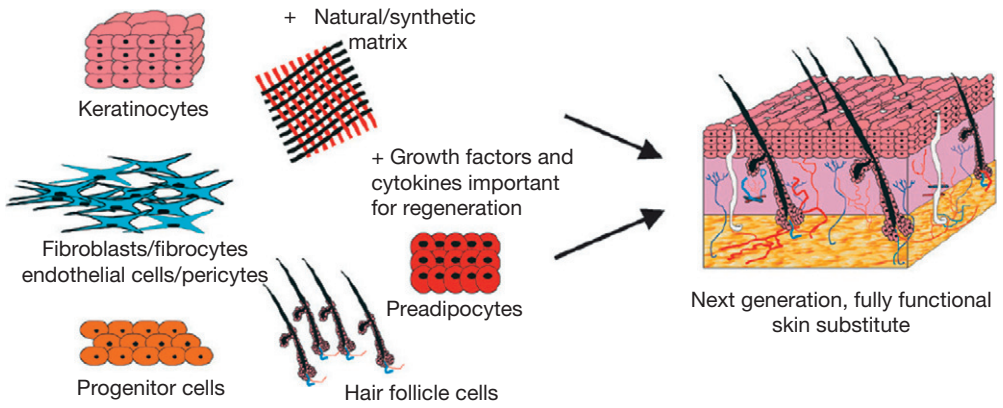

Figure 16 Next generation of skin tissue engineering. The different skin stem and progenitor cells are mixed with natural or synthetic matrix and bioactive molecules to induce regeneration of a fully functional skin. Modified from Metcalfe, A. D.; Ferguson, M. W. *Cell Mol. Life Sci.* **2008**, *65*(1), 24–32.

and ideally engrafted into to the wound site. The other approach is an acellular therapy that utilizes a biomaterial to induce and conduct host cell proliferation, migration, differentiation, and regeneration *in situ*. Regardless of the strategy employed, biomaterials play a central role in regenerative skin tissue engineering as an artificial biophysical and biochemical microenvironment that directs cellular behavior and function. The ideal biomaterials should provide a provisional three-dimensional infrastructure that mimics the natural ECM both physically and biochemically to ensure guidance in the proper spatiotemporal pattern. The rapid progress in tissue engineering in combination with stem cell therapy holds promise for the successful regeneration of acute and chronic skin defects.

Acknowledgment

Wound healing and skin tissue engineering research in the author's laboratory is funded by the RC2 stimulus award (AR059384) from NIAMS/NIH.

References

1. Haake, A.; Scott, G. A.; Holbrook, K. A. In *The Biology of the Skin*; Freinkel, R. K., Woodley, D. T., Eds.; Parethenon Publishing: New York, 2001; p 19.
2. Narisawa, Y.; Hashimoto, K.; Nihei, Y.; Pietruk, T. *J Histochem Cytochem* **1992**, *40*, 65–71.
3. Lavker, R. M.; Sun, T. T. *J Invest Dermatol* **1983**, *81*, 121s–127s.
4. Briggaman, R. A.; Wheeler, C. E., Jr. *J Invest Dermatol* **1975**, *65*, 71–84.
5. Stewart, K. J. *Clin Anat* **1995**, *8*, 334–338.
6. Yamada, K. M.; Clark, R. A. F. In *The Molecular and Cellular Biology of Wound Repair*, 2nd ed.; Clark, R. A. F., Ed.; Plenum Press: London, 1996; pp 51–94.
7. Singer, A. J.; Clark, R. A. *N. Engl. J. Med.* **1999**, *341*(10), 738–746.
8. Cavani, A.; Zambruno, G.; Marconi, A.; Manca, V.; Marchetti, M.; Giannetti, A. *J. Invest. Dermatol.* **1993**, *101*(4), 600–604.
9. Haapasalmi, K.; Zhang, K.; Tonnesen, M.; *et al. J. Invest. Dermatol.* **1996**, *106*(1), 42–48.
10. Clark, R. A. F. *Dermatol. Clin.* **1993**, *11*, 647–666.
11. Abercrombie, M.; Flint, M. H.; James, D. W. *J. Embryol. Exp. Morphol.* **1956**, *4*, 167–175.
12. Martin, P. *Science* **1997**, *276*(5309), 75–81.
13. Jaul, E. *Drugs Aging* **2010**, *27*(4), 311–325.
14. Stechmiller, J. K. *Nutr. Clin. Pract.* **2010**, *25*(1), 61–68.
15. Harding, K. G.; Morris, H. L.; Patel, G. K. *Br. Med. J.* **2002**, *324*(7330), 160–163.
16. Toy, L. W. *J. Wound Care* **2005**, *14*(1), 20–22.
17. Rizzi, S. C.; Upton, Z.; Bott, K.; Dargaville, T. R. *Expert Rev. Med. Devices* **2010**, *7*(1), 143–154.
18. Goldman, R. *Adv Skin Wound Care.* **2004**, *17*(1), 24–35.
19. Clark, R. A.; Ghosh, K.; Tonnesen, M. G. *J. Invest. Dermatol.* **2007**, *127*(5), 1018–1029.
20. Ghosh, K.; Clark, R. A. F. In *Principles of Tissue Engineering*; Lanza, R., Langer, R., Vacanti, J. P., Eds.; Elsevier/Academic Press: New York, 2007.
21. Herndon, D. N.; *et al. Ann. Surg.* **1989**, *209*, 547–552.
22. Andreassi, A.; Bilenchi, R.; Biagioli, M.; D'Aniello, C. *Clin. Dermatol.* **2005**, *23*, 332–337.
23. Supp, D. M.; Boyce, S. T. *Clin. Dermatol.* **2005**, *23*, 403–412.
24. Whitney, J. D. *Nurs. Clin. North Am.* **2005**, *40*(2), 191–205.
25. Medina, A.; Scott, P. G.; Ghahary, A.; Tredget, E. E. *J. Burn Care Rehabil.* **2005**, *26*(4), 306–319.
26. MacNeil, S. *Nature* **2007**, *445*, 874–880.
27. Shakespeare, P. G. *Clin. Dermatol.* **2005**, *23*, 413–418.
28. Oluwasanmi, J.; Chvapil, M. *J. Trauma* **1976**, *16*(5), 348–353.
29. Pruitt, B. A., Jr.; Levine, N. S. *Arch. Surg.* **1984**, *119*(3), 312–322.
30. Choy, D. S. J. *Arch. Surg.* **1954**, *68*, 33–43.
31. Chardack, W. M.; Brueske, D. A.; Santomauro, A. P.; Fazekas, G. *Ann. Surg.* **1962**, *155*, 127–139.
32. Hall, C. W.; Liotta, D.; De Bakey, M. E. *Trans. Am. Soc. Artif. Intern. Organs* **1966**, *12*, 340–345.
33. Alexander, J. W.; Wheeler, L. M.; Rooney, R. C.; McDonald, J. J.; MacMillan, B. G. *J. Trauma* **1973**, *13*(4), 374–383.
34. Walder, A. I.; May, P. D.; Bingham, C. P.; Wright, J. R. *Trans. Am. Soc. Artif. Intern. Organs* **1969**, *15*, 29–32.
35. Kornberg, J.; Burns, N. E.; Kafesjian, R.; Bartlett, R. H. *Trans. Am. Soc. Artif. Intern. Organs* **1972**, *18*, 39–44.
36. Warren, R. J.; Snelling, C. F. *Plast. Recosntr. Surg.* **1980**, *66*(3), 361–368.
37. Wokalek, H.; Schöpf, E.; Vaubel, E.; *et al. Aktuel. Dermal.* **1979**, *5*, 255–265.
38. Burke, J. F.; Yannas, I. V.; Quinby, W. C.; Bondoc, C. C.; Jung, W. K. *Ann. Surg.* **1981**, *194*, 413–428.
39. Nathan, P.; Robb, E. C.; Dressler, D.; MacMillan, B. G. *Burns Incl. Therm. Inj.* **1982**, *8*(5), 328–332.
40. Yang, J.; Tsai, Y. *Burns* **1989**, *15*, 197–203.
41. Demling, R. H.; DeSanti, L. *Burns* **1999**, *25*, 256–261.
42. Purdue, G. F.; Hunt, J. L.; Still, J. M., Jr.; *et al. J. Burn Care Rehabil.* **1997**, *18*, 52–57.
43. Ratner, B. D.; Bryant, S. J. *Annu. Rev. Biomed. Eng.* **2004**, *6*, 41–75.
44. Grant, M. E. *Int. J. Exp. Pathol.* **2007**, *88*(4), 203–214.
45. Smith, K.; Rennie, M. J. *Curr. Opin. Clin. Nutr. Metab. Care* **2007**, *10*(5), 582–590.
46. Metcalfe, A. D.; Ferguson, M. W. J. *J. R. Soc. Interface* **2007**, *4*(14), 413–437.
47. Waller, J. M.; Maibach, H. I. *Skin Res. Technol.* **2006**, *12*(3), 145–154.
48. Norton, L.; Chvapil, M. *J. Trauma* **1981**, *21*(6), 463–468.
49. Tavis, M. J.; Harney, J. H.; Thornton, J. W.; Bartlett, R. H. *J. Biomed. Mater. Res.* **1975**, *9*(3), 285–301.
50. Yost, M. J.; Terracio, L.; Price, R. L. In *Encylopedia of Biomaterials and Biomedical Engineering*; Wnek, G. E., Bowlin, G. L., Eds.; Informa Healthcare: Netherlands, 2004; pp 348–354.

51. Kadler, K. E.; Holmes, D. F.; Trotter, J. A.; Chapman, J. A. *Biochem. J.* **1996**, *316* (Pt 1), 1–11.
52. Lee, C. H.; Singla, A.; Lee, Y. *Int. J. Pharmacol.* **2001**, *221*, 1–22.
53. Ruszczak, Z. *Adv. Drug Deliv. Rev.* **2003**, *55*, 1595–1611.
54. Li, S. T. In *The Biomedical Engineering Handbook*, 2nd ed.; Bronzino, J. D., Ed.; CRC Press: Boca Raton, FL, 2000; Vol. 1.
55. Hudon, V.; Berthod, F.; Black, A. F.; Damour, O.; Germain, L.; Auger, F. A. *Br. J. Dermatol.* **2003**, *148*, 1094–1104.
56. Tremblay, P. L.; Hudon, V.; Berthod, F.; Germain, L.; Auger, F. A. *Am. J. Transplant.* **2005**, *5*, 1002–1010.
57. Butler, C. E.; Orgill, D. P. *Adv. Biochem. Eng. Biotechnol.* **2005**, *94*, 23–41.
58. Koide, T. *Philos. Trans. R. Soc. Lond. B Biol. Sci.* **2007**, *362*(1484), 1281–1291.
59. Still, J.; Glat, P.; Silverstein, P.; Griswold, J.; Mozingo, D. *Burns* **2003**, *29*(8), 837–841.
60. Kinneberg, K. R.; Nirmalanandhan, V. S.; Juncosa-Melvin, N.; *et al. J. Orthop. Res.* **2010**, *28*(8), 1092–1099.
61. Kubo, K.; Kuroyanagi, Y. *J. Artif. Organs* **2003**, *6*(2), 138–144.
62. Nakanishi, A.; Hakamada, A.; Isoda, K.; Mizutani, H. *J. Dermatol.* **2005**, *32*(5), 376–380.
63. Powell, H. M.; Boyce, S. T. *Tissue Eng. A* **2009**, *15*(8), 2177–2187.
64. Soliman, S.; Pagliari, S.; Rinaldi, A.; *et al. Acta Biomater.* **2010**, *6*(4), 1227–1237.
65. Clark, R. A. F. *The Molecular and Cellular Biology of Wound Repair*, 2nd ed.; Springer: New York, 2002.
66. Ruoslahti, E. *J. Clin. Invest.* **1991**, *87*(1), 1–5.
67. Ruoslahti, E.; Pierschbacher, M. D. *Science* **1987**, *238*, 491–497.
68. Sethi, K. K.; Yannas, I. V.; Mudera, V.; Eastwood, M.; McFarland, C.; Brown, R. A. *Wound Repair Regen.* **2002**, *10*(6), 397–408.
69. Calonder, C.; Matthew, H. W. T.; Van Tassel, P. R. *J. Biomed. Mater. Res. A* **2005**, *75*, 316–323.
70. Hubbell, J. A. *Curr. Opin. Biotechnol.* **2003**, *14*, 551–558.
71. Blystone, S. D.; Slater, S. E.; Williams, M. P.; Crow, M. T.; Brown, E. J. *J. Cell Biol.* **1999**, *145*, 889–897.
72. Siman, K. O.; Nutt, E. M.; Abraham, D. G.; Rodan, G. A.; Duong, L. T. *J. Biol. Chem.* **1997**, *272*, 29380–29389.
73. Rosso, F.; Marino, G.; Giordano, A.; Barbarisi, M.; Parmegiani, D.; Barbarisi, A. *J. Cell Physiol.* **2005**, *203*, 465–470.
74. Vogel, V.; Baneyx, G. *Annu. Rev. Biomed. Eng.* **2003**, *5*, 441–463.
75. McClain, S. A.; Simon, M.; Jones, E.; *et al. Am. J. Pathol.* **1996**, *149*, 1257–1270.
76. Greiling, D.; Clark, R. A. F. *J. Cell Sci.* **1997**, *110*(Pt 7), 861–870.
77. Herrick, S. E.; Sloan, P.; McGurk, M.; Freak, L.; McCollum, C. N.; Ferguson, M. W. J. *Am. J. Pathol.* **1992**, *141*, 1085–1095.
78. Grinnell, F.; Ho, C. H.; Wysocki, A. J. *J. Invest. Dermatol.* **1992**, *98*, 410–416.
79. Grinnell, F.; Zhu, M. *J. Invest. Dermatol.* **1996**, *106*, 335–341.
80. Clark, R. A. *J. Invest. Dermatol.* **2003**, *121*(5), xxi–xxii.
81. Clark, R. A. F. *Thromb. Haemost.* **2003**, *90*, 1003–1006.
82. Currie, L. J.; Sharpe, J. R.; Martin, R. *Plast. Reconstr. Surg.* **2001**, *108*, 1713–1726.
83. Gwak, S. J.; Kim, S. S.; Sung, K.; Han, J.; Choi, C. Y.; Kim, B. S. *Cell Transplant.* **2005**, *14*, 809–817.
84. Weigel, P. H.; Frost, S. J.; LeBoeuf, R. D.; *et al. Ciba Found. Symp.* **1989**, *143*, 248–264.
85. Schiller, S. *Biochem. Biophys. Res. Commun.* **1964**, *15*, 250–255.
86. Mummert, M. E. *Immunol. Res.* **2005**, *31*, 189–206.
87. Abatangelo, G.; Martelli, M.; Vecchia, P. *J. Surg. Res.* **1983**, *35*, 410–416.
88. Voinchet, V.; Vasseur, P.; Kern, J. *Am. J. Clin. Dermatol.* **2006**, *7*, 353.
89. Weigel, P. H.; Frost, S. J.; McGary, C. T.; LeBoeuf, R. D. *Int. J. Tissue React.* **1988**, *10*, 355–365.
90. Longaker, M. T.; Chiu, E. S.; Adzick, N. S.; Stern, M.; Harrison, M. R.; Stern, R. *Ann Surg.* **1991**, *213*, 292–296.
91. Greco, R. M.; Iocono, J. A.; Ehrlich, H. P. *J. Cell. Physiol.* **1998**, *177*, 465–473.
92. Mesa, F. L.; Aneiros, J.; Cabrera, A.; *et al. Histol. Histopathol* **2002**, *17*, 747–753.
93. Croce, M. A.; Dyne, K.; Boraldi, F.; *et al. Tissue Cell* **2001**, *33*, 326–331.
94. Fatini, G.; Gallenga, G.; Veltroni, A. *Osp. Ital. Chir.* **1968**, *19*, 283–287.
95. Nishida, T.; Nakamura, M.; Mishima, H.; Otori, T. *Exp. Eye Res.* **1991**, *53*, 753–758.
96. Ghosh, K.; Ren, X. D.; Shu, X. Z.; Prestwich, G. D.; Clark, R. A. *Tissue Eng.* **2006**, *12*, 601–613.
97. Ghosh, K.; Shu, X. Z.; Mou, R.; *et al. Biomacromolecules* **2005**, *6*, 2857–2865.
98. Anderson, D. G.; Burdick, J. A.; Langer, R. *Science* **2004**, *305*(5692), 1923–1924.
99. Pierschbacher, M. D.; Polarek, J. W.; Craig, W. S.; Tschopp, J. F.; Sipes, N. J.; Harper, J. R. *J. Cell Biochem.* **1994**, *56*, 150–154.
100. Shu, X. Z.; Ghosh, K.; Liu, Y.; *et al. J. Biomed. Mater. Res.* **2004**, *68A*, 365–375.
101. Clark, R. A.; An, J. Q.; Greiling, D.; Khan, A.; Schwarzbauer, J. E. *J. Invest. Dermatol.* **2003**, *121*(4), 695–705.
102. Boontheekul, T.; Mooney, D. J. *Curr. Opin. Biotechnol.* **2003**, *14*(5), 559–565.
103. Shevchenko, R. V.; James, S. L.; James, S. E. *J. R. Soc. Interface* **2010**, *7*(43), 229–258.
104. Rheinwald, J. G.; Green, H. *Cell* **1975**, *6*, 331–343.
105. Bell, E.; Ehrlich, H. P.; Buttle, D. J.; Nakatsuji, T. *Science* **1981**, *211*, 1052–1054.
106. Dagalakis, N.; Flink, J.; Stasikelis, P.; Burke, J. F.; Yannas, I. V. *J. Biomed. Mater. Res.* **1980**, *14*(4), 511–528.
107. Yannas, I. V.; Burke, J. F.; Gordon, P. L.; Huang, C.; Rubenstein, R. H. *J. Biomed. Mater. Res.* **1980**, *14*(2), 107–132.
108. Yannas, I. V.; Burke, J. F. *J. Biomed. Mater. Res.* **1980**, *14*(1), 65–81.
109. Auger, F. A.; Berthod, F.; Moulin, V.; Pouliot, R.; Germain, L. *Biotechnol. Appl. Biochem.* **2004**, *39*(Pt 3), 263–275.
110. Rheinwald, J. G.; Green, H. *Nature* **1977**, *265*, 421–424.
111. Green, H.; Kehinde, O.; Thomas, J. *Proc. Natl. Acad. Sci. USA* **1979**, *76*, 5665–5668.
112. Gallico, G. G.; O'Connor, N. E.; Compton, C. C.; Kehinde, O.; Green, H. *N. Engl. J. Med.* **1984**, *311*, 448–451.
113. O'Connor, N. E.; Mulliken, J. B.; Banks-Schlegel, S.; Kehinde, O.; Green, H. *Lancet* **1981**, 75–78.
114. Atiyeh, B. S.; Costagliola, M. *Burns* **2007**, *33*(4), 405–413.
115. Chester, D. L.; Balderson, D. S.; Papini, R. P. *J. Burn Care Rehab.* **2004**, *25*, 266–275.
116. Navarro, F. A.; Stoner, M. L.; Park, C. S.; *et al. J. Burn Care Rehab.* **2000**, *21*, 513–518.
117. Dai, N. T.; Williamson, M. R.; Khammo, N.; Adams, E. F.; Coombes, A. G. A. *Biomaterials* **2004**, *25*, 4263–4271.
118. Lam, P. K.; Chan, E. S.; Liew, C. T.; Lau, C.; Yen, S. C.; King, W. W. *ANZ J. Surg.* **2002**, *72*, 360.
119. Ramos-e-Silva, M.; Ribeiro de Castro, M. C. *Clin. Dermatol.* **2002**, *20*(6), 715–723.
120. Grant, I.; Warwick, K.; Marshall, J.; Green, C.; Martin, R. *Br. J. Plast. Surg.* **2002**, *55*, 219–227.
121. Johnsen, S.; Ermuth, T.; Tanczos, E.; *et al. Vasa* **2005**, *34*, 25–29.
122. Vanscheidt, W.; Ukat, A.; Horak, V.; *et al. Wound Repair Regen.* **2007**, *15*, 308–315.
123. Moustafa, M.; Simpson, C.; Glover, M.; *et al. Diabet. Med.* **2004**, *21*, 786–789.
124. Moustafa, M.; *et al. Regen. Med.* **2007**, *2*, 887–902.
125. Hernon, C. A.; Dawson, R. A.; Freedlander, E.; *et al. Regen. Med.* **2006**, *1*, 809–821.
126. Wood, F. M.; Stoner, M. L.; Fowler, B. V.; Fear, M. W. *Burns* **2007**, *33*, 693–700.
127. Travia, G.; Palmisano, P. A.; Cervelli, V.; Esposito, G.; Casciani, C. U. *Ann. Burns Fire Disast.* **2003**, *XVI*.
128. Anthony, E. T.; Syed, M.; Myers, S.; Moir, G.; Navsaria, H. *Drug Discov. Today Ther. Strateg.* **2006**, *3*, 81–86.
129. Wainwright, D.; Madden, M.; Luterman, A.; *et al. J Burn Care Rehabil.* **1996**, *17*(2), 124–136.
130. Ojeh, N. O.; Frame, J. D.; Navsaria, H. A. *Tissue Eng.* **2001**, *7*, 457–472.
131. Callcut, R. A.; Schurr, M. J.; Sloan, M.; Faucher, L. D. *Burns* **2006**, *32*, 583–588.
132. Kearney, J. N. *Burns* **2001**, *27*, 545–551.
133. Brigido, S. A. *Int. Wound J.* **2006**, *3*, 181–187.
134. Kim, P. J.; Dybowski, K. S.; Steinberg, J. S. *Podiatry Today* **2006**, *19*, 38–55.
135. Reyzelman, A.; Crews, R. T.; Moore, J. C.; *et al. Int. Wound J.* **2009**, *6*(3), 196–208.
136. Kim, H. T.; Ahn, S. T.; Park, J. G. *J. Korean Soc. Plast. Reconstr. Surg.* **2003**, *30*, 224–230.
137. Lee, K. C.; Lee, N. H.; Ban, J. H.; Jin, S. M. *Yonsei Med. J.* **2008**, *49*(2), 244–248.
138. Pirayesh, A.; Dur, A. H.; Paauw, N. J.; *et al. Eur. Surg. Res.* **2008**, *41*(4), 346–352.
139. Parker, D. M.; Armstrong, P. J.; Frizzi, J. D.; North, J. H., Jr. *Curr. Surg.* **2006**, *63*, 255–258.
140. MacLeod, T. M.; Williams, G.; Sanders, R.; Green, C. J. *Br. J. Plast. Surg.* **2005**, *58*, 518–532.
141. Schneider, J.; Biedermann, T.; Widmer, D.; *et al. Burns* **2009**, *35*(1), 51–57.
142. Haslik, W.; Kamolz, L. P.; Manna, F.; Hladik, M.; Rath, T.; Frey, M. *J. Plast. Reconstr. Aesthet. Surg.* **2010**, *63*(2), 360–364.
143. Atherton, D. D.; Tang, R.; Jones, I.; Jawad, M. *Plast Reconstr. Surg.* **2010**, *125*(2), 60e–61e.
144. Ryssel, H.; Germann, G.; Kloeters, O.; Gazyakan, E.; Radu, C. A. *Burns* **2010**, *36*(8), 1248–1253.

145. Ryssel, H.; Radu, C. A.; Germann, G.; Otte, M.; Gazyakan, E. *Int Wound J*. **2010**, *7*(5), 385–392.
146. Wetzig, T.; Gebhardt, C.; Simon, J. C. *Dermatology* **2009**, *219*(3), 272–273.
147. Suzuki, S.; Matsuda, Kazuya; Nishimura, Yoshihiko; *et al*. *Tissue Eng*. **1996**, *2*(4), 267–275.
148. Suzuki, S.; Kawai, K.; Ashoori, F.; Morimoto, N.; Nishimura, Y.; Ikada, Y. *Br. J. Plast. Surg*. **2000**, *53*, 659–666.
149. Nam, Y. O.; Lee, J. W.; Koh, J. H.; Seo, D. K.; Oh, S. J.; Jang, Y. C. *J. Korean Burn Soc*. **2006**, *9*, 115–120.
150. Choi, M. H.; Yi, S. B.; Hwang, J. W.; Yang, W. S.; Lee, K. K. *J. Korean Soc. Plast. Reconstr. Surg*. **1999**, *26*, 491–497.
151. Lee, J. W.; Jang, Y. C.; Oh, S. J. *Ann. Plast. Surg*. **2005**, *55*, 500–502.
152. Yurugi, S.; Hatoko, M.; Kuwahara, M.; Tanaka, A.; Iioka, H.; Niitsuma, K. *Aesthetic Plast. Surg*. **2002**, *26*, 360–364.
153. Matsui, R. *J. Jpn. Assoc. Regenerative Dent*. **2008**, *6*(1), 9–20.
154. Osaki, K.; Miura, A.; Koide, M.; Katakura, T.; Sugihara, T. *J. Dermatol*. **1996**, *23*(2), 83–88.
155. Heitland, A.; Piatkowski, A.; Noah, E. M.; Pallua, N. *Burns* **2004**, *30*, 471–475.
156. Hansbrough, J. F.; Mozingo, D. W.; Kealey, G. P.; Davis, M.; Gidner, A.; Gentzkow, G. D. *J. Burn Care Rehabil*. **1997**, *18*, 43–51.
157. Bauman, L. W.; Hawkins, M. L.; Howdieshell, T. R.; Till, A. H.; Treat, R. C. *Am. Surg*. **1991**, *57*, 131–133.
158. Demling, R. H. *J. Burn Care Rehabil*. **1995**, *16*, 329–330.
159. Housinger, T. A.; Wondrely, L.; Warden, G. D. *J. Burn Care Rehabil*. **1993**, *14*, 26–28.
160. Hansbrough, J. F. *Surgery* **1994**, *115*, 633–644.
161. Pape, S. A.; Byrne, P. O. *J. Burn Care Rehabil*. **2000**, *21*, 390.
162. Jones, I.; Currie, L.; Martin, R. *Br. J. Plast. Surg*. **2002**, *55*, 185–193.
163. Marston, W. A.; Hanft, J.; Norwood, P.; Pollak, R. *Diabetes Care* **2003**, *26*, 1701–1705.
164. Omar, A. A.; Mavor, A. I.; Jones, A. M.; Homer-Vanniasinkam, S. *Eur. J. Vasc. Endovasc. Surg*. **2004**, *27*, 666–672.
165. Brown-Etris, M.; Cutshall, W. D.; Hiles, M. C. *Wounds* **2002**, *14*, 150–166.
166. Mostow, E. N.; Haraway, G. D.; Dalsing, M.; Hodde, J. P.; King, D. *J. Vasc. Surg*. **2005**, *41*, 837–843.
167. Lindberg, K.; Badylak, S. F. *Burns* **2001**, *27*, 254–266.
168. Prevel, C. D.; Eppley, B. L.; Summerlin, D. J.; *et al*. *Ann. Plast. Surg*. **1995**, *35*, 381–388.
169. Healy, C. M.; Boorman, J. G. *Burns Incl. Therm. Inj*. **1989**, *15*, 52–54.
170. Gravante, G.; Sorge, R.; Merone, A.; *et al*. *Ann. Plast. Surg*. **2010**, *64*(1), 69–79.
171. Caravaggi, C. De.; Giglio, R.; Pritelli, C.; *et al*. *Diabetes Care* **2003**, *26*, 2853–2859.
172. Stark, H. J.; Boehnke, K.; Mirancea, N.; *et al*. *J. Invest. Dermatol. Symp. Proc*. **2006**, *11*(1), 93–105.
173. Stark, H. J.; Willhauck, M. J.; Mirancea, N.; *et al*. *Eur. J. Cell Biol*. **2004**, *83* (11–12), 631–645.
174. Sabolinski, M. L.; Alvarez, O.; Auletta, M.; Mulder, G.; Parenteau, N. L. *Biomaterials* **1996**, *17*, 311–320.
175. Kolokol'chikova, E. G.; Budkevich, L. I.; Bobrovnikov, A. E.; Badikova, A. K.; Tumanov, V. P. *Bull. Exp. Biol. Med*. **2001**, *131*(1), 89–93.
176. Price, R. D.; Das-Gupta, V.; Harris, P. A.; Leigh, I. M.; Navsaria, H. A. *Plast. Reconstr. Surg*. **2004**, *113*(6), 1719–1729.
177. Morimoto, N.; Saso, Y.; Tomihata, K.; *et al*. *J. Surg. Res*. **2005**, *125*(1), 56–67.
178. Eaglstein, W. H.; Alvarez, O. M.; Auletta, M.; *et al*. *Dermatol. Surg*. **1999**, *25*, 195.
179. Griffiths, M.; Ojeh, N.; Livingstone, R.; Price, R.; Navsaria, H. *Tissue Eng*. **2004**, *10*(7–8), 1180–1195.
180. Kirsner, R. S. *J. Dermatol*. **1998**, *25*(12), 805–811.
181. Martin, L. K.; Kirsner, R. S. *Adv. Skin Wound Care* **2002**, *15*, 260, 262, 264.
182. Eisenberg, M.; Llewelyn, D. *Br. J. Plastic Surg*. **1998**, *51*, 608–613.
183. Uccioli, L. TissueTech Autograph System Italian Study Group. *Int. J. Low Extrem. Wounds* **2003**, *2*(3), 140–151.
184. Bianchini, C.; Pelucchi, S.; Galassi, G.; Mandrioli, G.; Ciorba, A.; Pastore, A. *J. Otolaryngol. Head Neck Surg*. **2008**, *37*(2), 174–178.
185. Enoch, S.; Grey, J. E.; Harding, K. G. *Br. Med. J*. **2006**, *332*(7547), 962–965.
186. Stock, U. A.; Vacanti, J. P. *Ann. Rev. Med*. **2001**, *52*, 443–451.
187. Truong, A. T.; Kowal-Vern, A.; Latenser, B. A.; Wiley, D. E.; Walter, R. J. *J Burns Wounds*. **2005**, *4*, e4.
188. Ponec, M.; El Ghalbzouri, A.; Dijkman, R.; Kempenaar, J.; van der Pluijm, G.; Koolwijk, P. *Angiogenesis* **2004**, *7*, 295–305.
189. Tonello, C.; Vindigni, V.; Zavan, B.; *et al*. *FASEB J*. **2005**, *19*, 1546–1548.
190. Dezutter-Dambuyant, C.; Black, A.; Bechetoille, N.; *et al*. *Biomed. Mater. Eng*. **2006**, *16*, S85–S94.
191. Regnier, M.; Patwardhan, A.; Scheynius, A.; Schmidt, R. *Med. Biol. Eng. Comput*. **1998**, *36*, 821–824.
192. Hachiya, A.; Sriwiriyanont, P.; Kaiho, E.; Kitahara, T.; Takema, Y.; Tsuboi, R. *J. Invest. Dermatol*. **2005**, *125*(2), 364–372.
193. Hedley, S. J.; Layton, C.; Heaton, M.; *et al*. *Pigment Cell Res*. **2002**, *15*, 49–56.
194. Lee, J. H.; Kim, J. E.; Kim, B. J.; Cho, K. H. *Photodermatol. Photoimmunol. Photomed*. **2007**, *23*, 73–80.
195. Blanpain, C.; Lowry, W. E.; Geoghegan, A.; Polak, L.; Fuchs, E. *Cell* **2004**, *118*, 635–648.
196. Fioretti, F.; Lebreton-Decoster, C.; Gueniche, F.; *et al*. *Wound Repair Regen*. **2008**, *16*, 87–94.
197. Nambu, M.; Kishimoto, S.; Nakamura, S.; *et al*. *Ann. Plast. Surg*. **2009**, *62*(3), 317–321.
198. Yoshikawa, T.; Mitsuno, H.; Nonaka, I.; *et al*. *Plast. Recosntr. Surg*. **2008**, *121*, 860–877.
199. Balasubramani, M.; Kumar, T. R.; Babu, M. *Burns* **2001**, *27*(5), 534–544.
200. Chong, A. K.; Chang, J. *J. Hand Surg. Am*. **2006**, *31*(3), 349–358.
201. Ho, W. S.; Ying, S. Y.; Burd, A. *Lancet*. **2002**, *359*(9310), 925.
202. Kirkpatrick, C. J. *Eur. Cells Mater*. **2004**, *7*(Suppl. 2), 1.
203. Schechner, J. S.; Crane, S. K.; Wang, F.; *et al*. *FASEB J*. **2003**, *17*(15), 2250–2256.
204. Boyce, S. T.; Goretsky, M. J.; Greenhalgh, D. G.; Kagan, R. J.; Rieman, M. T.; Warden, G. D. *Ann. Surg*. **1995**, *222*, 743–752.
205. Stern, R.; McPherson, M.; Longaker, M. T. *J. Burn Care Rehabil*. **1990**, *11*(1), 7–13.
206. Hierner, R.; Degreef, H.; Vranckx, J. J.; Garmyn, M.; Massagé, P.; van Brussel, M. *Clin. Dermatol*. **2005**, *23*(4), 343–352.
207. Sahota, P. S.; Burn, J. L.; Heaton, M.; *et al*. *Wound Repair Regen*. **2003**, *11*, 275–284.
208. Rivron, N. C.; Liu, J. J.; Rouwkema, J.; de Boer, J.; van Blitterswijk, C. A. *Eur. Cell Mater*. **2008**, *15*, 27–40.
209. Laschke, M. W.; Vollmar, B.; Menger, M. D. *Tissue Eng Part B Rev*. **2009**, *15*(4), 455–465.
210. Black, A. F.; Berthod, F.; L'Heureux, N.; Germain, L.; Auger, F. A. *FASEB J*. **1998**, *12*, 1331–1340.
211. Beausang, E.; Floyd, H.; Dunn, K. W.; Orton, C. I.; Ferguson, M. W. J. *Plast. Reconstr. Surg*. **1998**, *102*, 1954–1961.
212. Powers, P. S.; Sarkar, S.; Goldgof, D. B.; Cruse, C. W.; Tsap, L. V. *J. Burn Care Rehabil*. **1999**, *20*, 54–60.
213. Roseborough, I. E.; Grevious, M. A.; Lee, R. C. *J. Natl. Med. Assoc*. **2004**, *96*(1), 108–116.
214. Lamme, E. N.; van Leeuwen, R. T.; Mekkes, J. R.; Middelkoop, E. *Wound Repair Regen*. **2002**, *10*(3), 152–160.
215. Enoch, S.; Harding, K. *Wounds* **2003**, *15*(7), 213–229.
216. Ehrenreich, M.; Ruszczak, Z. *Tissue Eng*. **2006**, *12*(9), 2407–2424.
217. Dieckmann, C.; Renner, R.; Milkova, L.; Simon, J. C. *Exp. Dermatol*. **2010**, *19*(8), 697–706.
218. Theoret, C. *Vet Surg*. **2009**, *38*(8), 905–913.
219. Gardiner, D. M.; Bryant, S. V. *Int. J. Dev. Biol*. **1996**, *40*(4), 797–805.
220. Goss, R. J.; Holt, R. *J. Exp. Zool*. **1992**, *261*(4), 451–457.
221. Allen, S. P.; Maden, M.; Price, J. S. *Dev. Biol*. **2002**, *251*(2), 409–423.
222. Goss, R. J. *Anat. Rec*. **1995**, *241*(3), 291–302.
223. Goss, R. J.; Grimes, L. N. *J. Morphol*. **1975**, *146*(4), 533–542.
224. Goss, R. J. *Clin. Orthop. Relat. Res*. **1980**, *151*, 270–282.
225. Clark, L. D.; Clark, R. K.; Heber-Katz, E. *Clin. Immunol. Immunopathol*. **1998**, *88*, 35–45.
226. Gawronska-Kozak, B. *Tissue Eng*. **2004**, *10*(7/8), 1251–1265.
227. Yannas, I. V. *Adv. Biochem. Eng. Biotechnol*. **2005**, *93*, 1–38.
228. Yannas, I. V. *J. R. Soc. Interface* **2005**, *2*(5), 403–417.
229. Metcalfe, A. D.; Willis, H.; Beare, A.; Ferguson, M. W. *J. Anat*. **2006**, *209*(4), 439–446.
230. Rajnoch, C.; Ferguson, S.; Metcalfe, A. D.; Herrick, S. E.; Willis, H. S.; Ferguson, M. W. *Dev Dyn*. **2003**, *226*(2), 388–397.
231. Ueno, M.; Lyons, B. L.; Burzenski, L. M.; *et al*. *Invest. Opthmalmol. Vis. Sci*. **2005**, *46*(11), 4097–4106.
232. Gawronska-Kozak, B.; Bogacki, M.; Rim, J. S.; Monroe, W. T.; Manuel, J. A. *Wound Repair Regen*. **2006**, *14*(3), 265–276.
233. Billingham, R. E.; Russell, P. S. *Nature* **1956**, *177*, 791–792.
234. Billingham, R. E.; Russell, P. S. *Nature* **1956**, *177*(4513), 791–792.
235. Breedis, C. *Cancer Res*. **1954**, *14*, 575–579.
236. Kligman, A. M.; Strauss, J. S. *J. Invest. Dermatol*. **1956**, *27*(1), 19–23.
237. Lacassagne, A.; Latarjet, R. *Cancer Res*. **1946**, *6*, 183–188.

238. Ito, M.; Yang, Z.; Andl, T.; *et al*. *Nature* **2007**, *447*, 316–320.
239. Ferguson, M. W.; O'Kane, S. *Philos. Trans. R. Soc. Lond. B Biol. Sci*. **2004**, *359* (1445), 839–850.
240. McCallion, R. L.; Ferguson, M. W. J. In *The Molecular and Cellular Biology of Wound Repair*, 2nd edn.; Clark, R. A. F., Ed.; Plenum: New York, 1996; pp 561–600.
241. Chin, G. S.; Stelnicki, E. J.; Gittes, G. K.; Longaker, M. T. In *Scarless Wound Healing*; Garg, H. G., Longaker, M. T., Eds.; Marcel Dekker: New York, 2000; pp 239–262.
242. Lindblad, W. J. *Wound Repair Regen*. **1998**, *6*(3), 186–193.
243. Whitby, D. J.; Ferguson, M. W. *Dev. Biol*. **1991**, *147*, 207–215.
244. Yannas, I. V.; Kwan, M. D.; Longaker, M. T. *Tissue Eng*. **2007**, *13*(8), 1789–1798.
245. Longaker, M. T.; Adzick, N. S. *Plast. Reconstr. Surg*. **1991**, *87*, 788–798.
246. Lorenz, H. P.; Whitby, D. J.; Longaker, M. T.; Adzick, N. S. *Ann Surg*. **1993**, *217*, 391–396.
247. Longaker, M. T.; Whitby, D. J.; Adzick, N. S.; *et al*. *J. Pediatr. Surg*. **1990**, *25*, 63–68; discussion 68–69.
248. Beanes, S. R.; Hu, F. Y.; Soo, C.; *et al*. *Plast. Reconstr. Surg*. **2002**, *109*, 160–170.
249. Cass, D. L.; Bullard, K. M.; Sylvester, K. G.; Yang, E. Y.; Longaker, M. T.; Adzick, N. S. *J. Pediatr. Surg*. **1997**, *32*, 411–415.
250. Martin, P.; Leibovich, S. J. *Trends Cell Biol*. **2005**, *15*(11), 599–607.
251. Bullard, K. M.; Longaker, M. T.; Lorenz, H. P. *World J. Surg*. **2003**, *27*(1), 54–61.
252. Olutoye, O. O.; Yager, D. R.; Cohen, I. K.; Diegelmann, R. F. *J. Pediatr. Surg*. **1996**, *31*, 91–95.
253. O'Kane, S.; Ferguson, M. W. *Int. J. Biochem. Cell Biol*. **1997**, *29*(1), 63–78.
254. Shah, M.; Foreman, D. M.; Ferguson, M. W. *J. Cell Sci*. **1995**, *108*(Pt 3), 985–1002.
255. Coolen, N. A.; Schouten, K. C.; Middelkoop, E.; Ulrich, M. M. *Arch. Dermatol. Res*. **2010**, *302*(1), 47–55.
256. Dang, C. M.; Beanes, S. R.; Soo, C.; *et al*. *Plast. Reconstr. Surg*. **2003**, *111*(6), 1969–1979.
257. Dang, C. M.; Beanes, S. R.; Lee, H.; Zhang, X.; Soo, C.; Ting, K. *Plast. Reconstr. Surg*. **2003**, *111*, 2273.
258. Lau, K.; Paus, R.; Tiede, S.; Day, P.; Bayat, A. *Exp. Dermatol*. **2009**, *18*, 921–933.
259. Limat, A.; Hunziker, T. *Cells Tissues Organs* **2002**, *172*, 79–85.
260. Pellegrini, G.; Ranno, R.; Stracuzzi, G.; *et al*. *Transplantation* **1999**, *68*, 868–879.
261. Kloepper, J. E.; Tiede, S.; Brinckmann, J.; *et al*. *Exp. Dermatol*. **2008**, *17*, 592–609.
262. Morris, R. J.; Liu, Y.; Marles, L.; *et al*. *Nat. Biotechnol*. **2004**, *22*, 411–417.
263. Boyce, S. T.; Kagan, R. J.; Greenhalgh, D. G.; *et al*. *J. Trauma* **2006**, *60*, 821–829.
264. Bianco, P.; Robey, P. G. *Nature* **2001**, *414*, 118–121.
265. Dunnwald, M.; Tomanek-Chalkley, A.; Alexandrunas, D.; Fishbaugh, J.; Bickenbach, J. R. *Exp. Dermatol*. **2001**, *10*, 45–54.
266. Pouliot, N.; Redvers, R. P.; Ellis, S.; Saunders, N. A.; Kaur, P. *Exp. Dermatol*. **2005**, *14*, 60–69.
267. Ito, M.; Liu, Y.; Yang, Z.; *et al*. *Nat. Med*. **2005**, *11*, 1351–1354.
268. Tiede, S.; Kloepper, J. E.; Bodo, E.; Tiwari, S.; Kruse, C.; Paus, R. *Eur. J. Cell Biol*. **2007**, *86*, 355–376.
269. Fathke, C.; Wilson, L.; Hutter, J.; *et al*. *Stem Cells* **2004**, *22*, 812–822.
270. Ishii, G.; Sangai, T.; Sugiyama, K.; *et al*. *Stem Cells* **2005**, *23*, 699–706.
271. Liu, P.; Deng, Z.; Han, S.; *et al*. *Artif. Organs* **2008**, *32*, 925–931.
272. McFarlin, K.; Gao, X.; Liu, Y. B.; *et al*. *Wound Repair Regen*. **2006**, *14*, 471–478.
273. Lataillade, J. J.; Doucet, C.; Bey, E.; *et al*. *Regen. Med*. **2007**, *2*, 785–794.
274. Sasaki, M.; Abe, R.; Fujita, Y.; Ando, S.; Inokuma, D.; Shimizu, H. *J. Immunol*. **2008**, *180*, 2581–2587.
275. Badiavas, E. V.; Falanga, V. *Arch. Dermatol*. **2003**, *139*, 510–516.
276. Falanga, V.; Iwamoto, S.; Chartier, M.; *et al*. *Tissue Eng*. **2007**, *13*, 1299–1312.
277. Rasulov, M. F.; Vasilchenkov, A. V.; Onishchenko, N. A.; *et al*. *Bull. Exp. Biol. Med*. **2005**, *139*, 141–144.
278. Shumakov, V. I.; Onishchenko, N. A.; Rasulov, M. F.; Krasheninnikov, M. E.; Zaidenov, V. A. *Bull. Exp. Biol. Med*. **2003**, *136*, 192–195.
279. Fu, X. B.; Fang, L. J.; Li, X. K.; Cheng, B.; Sheng, Z. Y. *Wound Repair Regen*. **2006**, *14*, 325–335.
280. Lemoli, R. M.; Bertolini, F.; Cancedda, R.; *et al*. *Haematologica* **2005**, *90*(3), 360–381.
281. Caplan, A. I.; Dennis, J. E. *J. Cell Biochem*. **2006**, *98*, 1076–1084.
282. Docheva, D.; Popov, C.; Mutschler, W.; Schieker, M. *J. Cell Mol. Med*. **2007**, *11*, 21–38.
283. Spees, J. L.; Olson, S. D.; Ylostalo, J. Lynch; *et al*. *Proc. Natl. Acad. Sci. USA* **2003**, *100*, 2397–2402.
284. Wu, Y.; Chen, L.; Scott, P. G.; Tredget, E. E. *Stem Cells* **2007**, *25*, 2648–2659.
285. Altman, A. M.; Matthias, N.; Yan, Y.; *et al*. *Biomaterials* **2008**, *29*, 1431–1442.
286. Altman, A. M.; Yan, Y.; Matthias, N.; *et al*. *Stem Cells* **2009**, *27*, 250–258.
287. Ebrahimian, T. G.; Pouzoulet, F.; Squiban, C.; *et al*. *Arterioscler. Thromb. Vasc. Biol*. **2009**, *29*, 503–510.
288. Trottier, V.; Marceau-Fortier, G.; Germain, L.; Vincent, C.; Fradette, J. *Stem Cells* **2008**, *26*, 2713–2723.
289. Thomson, J. A.; Itskovitz-Eldor, J.; Shapiro, S. S.; *et al*. *Science* **1998**, *282*, 1145–1147.
290. Aasen, T.; Raya, A.; Barrero, M. J.; *et al*. *Nat. Biotechnol*. **2008**, *26*, 1276–1284.
291. Lowry, W. E.; Richter, L.; Yachechko, R.; *et al*. *Proc. Natl. Acad. Sci. USA* **2008**, *105*, 2883–2888.
292. Yu, J.; Vodyanik, M. A.; Smuga-Otto, K.; *et al*. *Science* **2007**, *318*, 1917–1920.
293. Beaudry, P.; Hida, Y.; Udagawa, T.; *et al*. *J. Pediatr. Surg*. **2007**, *42*, 1190–1198.
294. Lammert, E.; Cleaver, O.; Melton, D. *Science* **2001**, *294*, 564–567.
295. Maes, C.; Stockmans, I.; Moermans, K.; *et al*. *J. Clin. Invest*. **2004**, *113*, 188–199.
296. Ennett, A. B.; Mooney, D. J. *Expert Opin. Biol. Ther*. **2002**, *2*, 805–818.
297. Lutolf, M. P.; Hubbell, J. A. *Nat. Biotechnol*. **2005**, *23*(1), 47–55.
298. Murphy, W. L.; Peters, M. C.; Kohn, D. H.; Mooney, D. J. *Biomaterials* **2000**, *21*(24), 2521–2527.
299. Richardson, T. P.; Peters, M. C.; Ennett, A. B.; Mooney, D. J. *Nat. Biotechnol*. **2001**, *19*, 1029–1034.
300. Lutolf, M. P.; Lauer-Fields, J. L.; Schmoekel, H. G.; *et al*. *Proc. Natl. Acad. Sci. USA* **2003**, *100*(9), 5413–5418.
301. Koike, N.; Fukumura, D.; Gralla, O.; Au, P.; Schechner, J. S.; Jain, R. K. *Nature* **2004**, *428*, 138–139.
302. Nor, J. E.; Peters, M. C.; Christensen, J. B.; *et al*. *Lab Invest*. **2001**, *81*, 453–463.
303. Ferreira, L. S.; Gerecht, S.; Shieh, H. F.; *et al*. *Circ. Res*. **2007**, *101*, 286.
304. McCloskey, K. E.; Gilroy, M. E.; Nerem, R. M. *Tissue Eng*. **2005**, *11*, 497.
305. Drukker, M.; Katchman, H.; Katz, G.; *et al*. *Stem Cells* **2006**, *24*, 221.
306. Au, P.; Daheron, L. M.; Duda, D. G.; *et al*. *Blood* **2008**, *111*, 1302–1305.
307. Melero-Martin, J. M.; De Obaldia, M. E.; Kang, S. Y.; *et al*. *Circ. Res*. **2008**, *103*, 194.
308. Traktuev, D. O.; Prater, D. N.; Merfeld-Clauss, S.; *et al*. *Circ. Res*. **2009**, *104*, 1410–1420.
309. Barber, C. L.; Iruela-Arispe, M. L. *Pediatric Res*. **2006**, *59*(4 Pt 2), 26R–32R; Erratum in: *Pediatric Res*. **2006**, *59*(5), 722.
310. Chen, X.; Aledia, A. S.; Popson, S. A.; Him, L.; Hughes, C. C.; George, S. C. *Tissue Eng. A*. **2010**, *16*(2), 585–594.
311. Shepherd, B. R.; Enis, D. R.; Wang, F.; Suarez, Y.; Pober, J. S.; Schechner, J. S. *FASEB J*. **2006**, *20*(10), 1739–1741.
312. Barrientos, S.; Stojadinovic, O.; Golinko, M. S.; Brem, H.; Tomic-Canic, M. *Wound Repair Regen*. **2008**, *16*(5), 585–601.
313. Buchanan, E. P.; Longaker, M. T.; Lorenz, H. P. *Adv. Clin. Chem*. **2009**, *48*, 137–161.
314. Yokoyama, H. *Dev. Growth Differ*. **2008**, *50*(1), 13–22.
315. Degim, Z. *J. Drug Target* **2008**, *16*, 437–448.
316. Holland, T. A.; Tessmar, J. K. V.; Tabata, Y.; Mikos, A. G. *J. Control. Release* **2004**, *94*, 101–114.
317. Kawai, K.; Suzuki, S.; Tabata, Y.; Nishimura, Y. *Br. J. Plast. Surg*. **2005**, *58*, 1115–1123.
318. Park, C. J.; Clark, S. G.; Lichtensteiger, C. A.; Jamison, R. D.; Johnson, A. J. *Acta Biomater*. **2009**, *5*, 1926–1936.
319. Panyam, J.; Labhasetwar, V. *Adv. Drug. Deliv. Rev*. **2003**, *55*, 329–347.
320. Huang, M.; Berkland, C. *J. Pharm. Sci*. **2009**, *98*, 268–280.
321. Chen, R. R.; Silva, E. A.; Yuen, W. W.; Mooney, D. J. *Pharm. Res*. **2007**, *24*, 258–264.
322. Brem, H.; Young, J.; Tomic-Canic, M.; Isaacs, C.; Ehrlich, H. P. *Surg. Technol. Int*. **2003**, *11*, 23–31.
323. Cavorsi, J.; Vicari, F.; Wirthlin, D. J.; *et al*. *Wound Repair Regen*. **2006**, *14*(2), 102–109.
324. Streit, M.; Braathen, L. R. *Int. J. Artif. Organs* **2000**, *23*(12), 831–833.
325. Zaulyanov, L.; Kirsner, R. S. *Clin. Interv. Aging* **2007**, *2*(1), 93–98.
326. Lawrence, B. J.; Madihally, S. V. *Cell Adh. Migr*. **2008**, *2*(1), 9–16.
327. Kim, B. S.; Baez, C. E.; Atala, A. *World J. Urol*. **2000**, *18*, 2–9.
328. Murphy, G. F.; Orgill, D. P.; Yannas, I. V. *Lab Invest*. **1990**, *62*(3), 305–313.
329. Yannas, I. V.; Tzeranis, D. S.; Harley, B. A.; So, P. T. *Philos. Trans. A Math. Phys. Eng. Sci*. **2010**, *368*(1917), 2123–2139.
330. Roh, D. H.; Kang, S. Y.; Kim, J. Y.; *et al*. *J. Mater. Sci. Mater. Med*. **2006**, *17*, 547–552.
331. Duan, B.; Wu, L.; Yuan, X.; *et al*. *J. Biomed. Mater. Res. A* **2007**, *83A*, 868–878.
332. Bourke, S. L.; Kohn, J. *Adv. Drug Deliv. Rev*. **2003**, *55*(4), 447–466.

333. Boyd, M.; Flasza, M.; Johnson, P. A.; Roberts, J. S.; Kemp, P. *Regen. Med.* **2007**, *2*(4), 363–370.
334. Kellouche, S.; Martin, C.; Korb, G.; *et al. Biochem. Biophys. Res. Commun.* **2007**, *363*, 472–478.
335. Shevchenko, R. V.; Sibbons, P. D.; Sharpe, J. R.; James, S. E. *Wound Repair Regen.* **2008**, *16*, 198–207.
336. Garcia, Y.; Wilkins, B.; Collighan, R. J.; Griffin, M.; Pandit, A. *Biomaterials* **2008**, *29*, 857–868.
337. Li, A.; Dearman, B. L.; Crompton, K. E.; Moore, T. G.; Greenwood, J. E. *J. Burn Care Res.* **2009**, *30*(4), 717–728.
338. Chen, K. Y.; Liao, W. J.; Kuo, S. M.; *et al. Biomacromolecules* **2009**, *10*(6), 1642–1649.
339. Zeng, Q.; Chen, W. *Biomaterials* **2010**, *31*(22), 5772–5781.
340. Burleson, R. L.; Ennulat, N. *J. Surg. Res.* **1978**, *25*(6), 523–529.
341. Capla, J. M.; Ceradini, D. J.; Tepper, O. M.; *et al. Plast. Reconstr. Surg.* **2006**, *117*(3), 836–844.
342. Chen, G.; Sato, T.; Ohgushi, H.; Ushida, T.; Tateishi, T.; Tanaka, J. *Biomaterials* **2005**, *26*(15), 2559–2566.
343. Colwell, A. S.; Beanes, S. R.; Soo, C.; *et al. Plast. Reconstr. Surg.* **2005**, *115*, 204–212.
344. Corin, K. A.; Gibson, L. J. *Biomaterials* **2010**, *31*(18), 4835–4845.
345. Curran, M. P.; Plosker, G. L. *Biodrugs* **2002**, *16*, 439–455.
346. Davis, G. E.; Koh, W.; Stratman, A. N. *Birth Defects Res. C Embryo Today* **2007**, *81*(4), 270–285.
347. Falanga, V.; Isaacs, C.; Paquette, D.; *et al. J. Invest. Dermatol.* **2002**, *119*, 653–660.
348. Falanga, V.; Margolis, D.; Alvarez, O.; *et al. Arch. Dermatol.* **1998**, *134*, 293–300.
349. Freyman, T. M.; Yannas, I. V.; Pek, Y. S.; Yokoo, R.; Gibson, L. J. *Exp. Cell Res.* **2001**, *269*(1), 140–153.
350. Freyman, T. M.; Yannas, I. V.; Yokoo, R.; Gibson, L. J. *Biomaterials* **2001**, *22*(21), 2883–2891.
351. Goldman, R. *Adv. Skin Wound Care* **1975**, *X17*(1), 24–35.
352. Gravante, G.; Delogu, D.; Giordan, N.; Morano, G.; Montone, A.; Esposito, G. *J. Burn Care Res.* **2007**, *28*(2), 269–274.
353. Han, K.; Lee, K. D.; Gao, Z. G.; Park, J. S. *J. Control. Release* **2001**, *75*, 259–269.
354. Hao, X. J.; Silva, E. A.; Mansson-Broberg, A.; *et al. Cardiovasc. Res.* **2007**, *75*, 178–185.
355. Herrick, S. E.; Ireland, G.; Simon, D.; McCollum, C.; Ferguson, M. W. J. *J. Invest. Dermatol.* **1996**, *106*, 187–193.
356. Hersel, U.; Dahmen, C.; Kessler, H. *Biomaterials* **2003**, *24*, 4385–4415.
357. Hettiaratchy, S.; Papini, R. *Br. Med. J.* **2004**, *329*(7457), 101–103.
358. Huang, S.; Fu, X. *J. Control. Release* **2010**, *142*(2), 149–159.
359. Kamolz, L. P.; Lumenta, D. B.; Kitzinger, H. B.; Frey, M. *Eur. Surg.* **2008**, *40*(1), 19–26.
360. Mackie, R. M. *Essential skin biology: Structure, function and immunology.*, *Clinical Dermatology*, 4th ed.; Oxford University Press: Oxford, 1997; p 9.
361. Metcalfe, A. D.; Ferguson, M. W. *Cell Mol. Life Sci.* **2008**, *65*(1), 24–32.
362. Nishi, S. *Med. Postgraduates* **1974**, *12*, 419–442.
363. Papini, R. *Br. Med. J.* **2004**, *329*, 158–160.
364. Patel, P. N.; Zhang, X.; Ting, K.; Chang, X.; Soo, C. *J. Am. Coll. Surg.* **2005**, *201*, S60.
365. Phillips, T. J.; Manzoor, J.; Rojas, A.; *et al. Arch. Dermatol.* **2002**, *138*, 1079–1081.
366. Pierschbacher, M. D.; Ruoslahti, E. *Nature* **1984**, *309*, 30–33.
367. Powell, H. M.; Boyce, S. T. *J. Biomed. Mater. Res. A* **2008**, *84*, 1078–1086.
368. Price, R. D.; Berry, M. G.; Navsaria, H. A. *J. Plast. Reconstr. Aesthet. Surg.* **2007**, *60*(10), 1110–1119.
369. Smith, D. J., Jr. *J. Burn Care Rehabil.* **1995**, *16*, 317–320.
370. Soo, C.; Hu, F. Y.; Zhang, X.; *et al. Am. J. Pathol.* **2000**, *157*, 423–433.
371. Stayton, P. S.; Shimoboji, T.; Long, C.; *et al. Nature* **1995**, *378*(6556), 472–474.
372. Stenn, K. S.; Cotsarelis, G. *Curr. Opin. Biotechnol.* **2005**, *16*(5), 493–497.
373. Sun, T.; Mai, S.; Norton, D.; Haycock, J. W.; Ryan, A. J.; MacNeil, S. *Tissue Eng.* **2005**, *11*, 1023–1033.
374. Tzeranis, D. S.; Roy, A.; So, P. T.; Yannas, I. V. *J. R. Soc. Interface* **2010**; Epub ahead of print.
375. Ueno, C.; Hunt, T. K.; Hopf, H. W. *Plast. Reconstr. Surg.* **2006**, *117*(7 Suppl), 59S–71S.
376. Veves, A.; Falanga, V.; Armstrong, D. G.; Sabolinski, M. L. *Diabetes Care* **2001**, *24*, 290–295.
377. Zhang, S.; Uludağ, H. *Pharm. Res.* **2009**, *26*(7), 1561–1580.

5.535. Cartilage Regeneration in Reconstructive Surgery

S Liao, C A Vacanti, and K Kojima, Harvard Medical School, Boston, MA, USA

© 2011 Elsevier Ltd. All rights reserved.

5.535.1.	**Introduction**	501
5.535.2.	**Role of Tissue Engineering**	502
5.535.3.	**Cell Sources and Materials**	502
5.535.3.1.	Cells	502
5.535.3.2.	Materials	503
5.535.4.	**Characterization of Scaffolds *In Vitro* and *In Vivo***	503
5.535.4.1.	*In Vitro* Model Using a Thermoreversible Polymer	503
5.535.4.2.	*In Vitro* Model Using a Biodegradable Polymer	504
5.535.4.3.	Autologous *In Vivo* Model Using a Thermoreversible Polymer	504
5.535.4.4.	Autologous *In Vivo* Model Using a Biodegradable Polymer	505
5.535.5.	**Conclusions**	506
References		506

Glossary

Allograft Tissue that is transplanted from a donor of the same species, but different genotype.
Autograft Transplanted tissue in which the donor and recipient are the same individual.
Autologous Derived from the same donor or a donor of an identical genotype.
Hydrogel A colloidal gel which uses water as the dispersion medium.
Mesenchymal stem cells Multipotent stem cells derived from adult bone marrow; also known as marrow stromal cells.
Microtia Aplasia or hypoplasia of the external ear.
Neocartilage Neotissue that displays the properties of cartilage.
Neotissue Living tissue created through tissue engineering techniques, often involving the combination of cells, scaffold materials, and adjuvant therapies.
Porosity The ratio of the volume of a material's interstitial airspace to the volume of its mass.
Sol–gel transition The transition of a suspension of solid particles in a liquid (sol) to a solid material of jelly-like consistency (gel).
Xenograft Tissue that is transplanted from a donor of one species to a recipient of a different species.

Abbreviations

3D	Three-dimensional
DMEM	Dulbecco's modified Eagle medium
FGF	Fibroblast growth factor
GAG	Glycosaminoglycan
IGF	Insulin-like growth factor
NIPAAm	*N*-Isopropylacrylamide
PGA	Polyglycolic acid
PLA	Polylactic acid
RNA	Ribonucleic acid
TET	Tissue-engineered trachea
TGF	Transforming growth factor
TGP	Thermoreversible gelation polymer

5.535.1. Introduction

As modern medicine has advanced its understanding of how cells grow, survive, and replicate, we have found ourselves able to perform increasingly challenging reconstructive surgical procedures, with the major limitation being the source of replacement tissue. Traditionally, these sources have included living donors, cadavers, and synthetic materials. However, the utilization of these sources has its own limitations. Regarding living donors, the ethical questions behind the provision of compensation preclude many from voluntarily providing tissue. Furthermore, the potential medical complications of donation make it such that most cases are only justified by use in life-saving procedures. Transplanted tissue, whether from living or cadaveric sources, also carries with it the risks of both infection and rejection by the recipient immune system.

Functional and esthetic procedures have created a large market for synthetic replacement materials because of the scarcity of living tissue. Successful reconstructive procedures using synthetic implants include that of the auricle, the tip of the nose, and the orbital floor, among other areas.[1–3] However, the currently available materials often have their own problems, including the inability to sufficiently approximate the properties of living tissue, as well as complications of extrusion,

incomplete fusion with host tissues, and provocation of an inflammatory response.[4,5] Thus, the ultimate goal of perfecting a procedure by which adequately functional living tissue can be used for defect repair still remains.

For reconstructive operations, many of the sites that may require surgical restoration are structurally composed of cartilage. The goals of cartilage-based reconstruction depend on the desired function and location of the replacement tissue. For plastic surgery procedures, the most important feature of an implant is its ability to take on and preserve the shape of the area to be reconstructed. In contrast to the types of reconstructive procedures found in orthopedics, which usually involve weight-bearing areas of the body, cartilage reconstruction for plastic surgery generally does not have the obligation for the implanted tissue to maintain its structural integrity under a mechanical load. As such, there may not be the same mechanical requirements for tensile strength or shear. However, the implant must still have the resilience to hold against general wear and tear, as well as maintain the desired visual appearance.

Other qualities such as elasticity and flexibility are important features for forms that serve esthetic purposes, such as the nose and the ears. Yet, those that maintain a more structural support function, such as the orbital floor or the trachea, may require a more-rigid, less-elastic composition. At present, reconstructive surgical procedures utilizing autogenous cartilage include that of the auricle, trachea, nasal tip, and cleft palate, among others.[5–8]

5.535.2. Role of Tissue Engineering

The modern field of tissue engineering has added an alternative method of obtaining replacement materials for cartilage-based structures to the traditional cadaveric and synthetic sources. In order to be viable for widespread application, however, the engineering process must be able to start with a relatively small initial cell source and expand the number of functional cells for tissue generation. After viable cells are harvested, they must be maintained in a cell culture medium that not only promotes growth and replication but also prevents dedifferentiation from the chondrocyte phenotype. Once the appropriate cell count is achieved, the next step is the selection of a scaffold on which to deliver the cells to the recipient site. Many different types of vehicles have been tested, from fibrous meshes to hydrogels, each with its own set of advantages and disadvantages. Finally, after implantation, the chondrocytes must continue to survive and express the genes appropriate for cartilage formation, even in the setting of an intact recipient immune system. Only then can the final neotissue be tested for the characteristics of strength, shape, and other mechanical attributes necessary for use in surgical procedures in human subjects.

Most of the earliest tissue engineering attempts focused on cartilage or skin replacement.[9] In the 1970s, W. T. Green conducted a series of experiments aimed at the formation of new cartilage from chondrocytes that were implanted into nude mice using sterile bone as a carrier.[10] For the subsequent two decades, researchers contributed additional knowledge to the field, including that of *in vitro* culture conditions, cell attachment to various scaffold materials, and the limited capacity for cartilage self-repair.[11–13] However, it was not until the 1990s that any experiment was able to successfully produce a large quantity of cartilage tissue in any particular morphologic shape, and which was not required to be formed in association with endogenous bone or cartilage. In 1991, Vacanti *et al.*[14] described a novel method of cartilage generation using synthetic polymer scaffolds implanted subcutaneously into nude mice. Three years later, Kim and Vacanti[15] demonstrated the possibility of forming cartilage in predetermined shapes using molded fiber scaffolds.

Since that time, there have been many potential target areas for which researchers have attempted to engineer tissue. In particular, much attention has been paid to efforts in regenerating cartilage for the reconstruction of the auricle in patients with microtia, and the trachea for patients with laryngotracheal defects.

In 1997, Cao and Vacanti created neocartilage in a nude mouse model that retained the original form of a scaffold made of a combination of polyglycolic–polylactic acid (PGA–PLA) fibrous mesh that had been pressed into an auricle-shaped mold.[16] However, subsequent experiments have shown that, while the use of fibrous mesh scaffolds has produced good quality cartilage in immunocompromised animal models, when analyzed for histological properties and RNA expression, the same has not been true in immune-competent animals. For PGA, in particular, studies have shown a distinct inflammatory reaction to a local acid release by the degradation of the scaffold over time.[17] Subsequent experiments have shown hydrogel carriers to generally avoid this inflammatory response; however, the hydrogels that have currently been tested lack the ability to sufficiently maintain a complex shape in the formed neocartilage. Nevertheless, a recent study in human subjects performed by Yanaga *et al.*[18] was successful in utilizing a chondrocyte-generated gelatinous matrix for delivery in a two-step auricle reconstruction, during which a sufficient block of neocartilage was generated to allow the surgical carving that is currently done with a rib graft.

Other areas of reconstruction for which tissue engineering of cartilage has been studied include the nose, nipples, and temporomandibular disk.[19–21]

5.535.3. Cell Sources and Materials

5.535.3.1. Cells

The acquisition of cells for the creation of human body structures is one of the major challenges in reconstructive operations. The ultimate goal in this regard would be to create a large number of cell banks composed of universal cells that would be immunologically nonreactive with any recipient. At present, tissue can be harvested from autograft, allograft, or xenograft sources. However, autologous grafts are the most reliable with which to fabricate structures, as using a patient's own cells obviates the need for immunosuppressant drugs to block tissue rejection. Nowadays, stem cell biology involving embryonic stem cells holds great promise for the fields of tissue engineering and regenerative medicine. However, we are still far from complete understanding of the principles of stem cell and progenitor cell biology, and it remains a significant challenge

to apply these concepts to tissue engineering. We must also continue to be aware of the potential ethical implications of using these types of cell sources. Once the cell donor is chosen, the harvested tissues should be ones that can be dissociated easily from their surrounding structures in a minimally invasive manner. Subsequent cell growth and development, as well as the ability for population expansion, are also important factors.

There is no consensus yet as to what cell type is the best for regenerative medicine, as present practice focuses primarily on individual disease states and patient-related factors and conditions. For cartilage tissue engineering in particular, the current focus is on the use of the patient's own autologous cartilaginous tissue or mesenchymal stem cells as the donor source.

At present, the source of cartilage, which is most effective for tissue engineering applications and requires the least invasive procedure for harvesting the cellular sample, is still undefined. We have observed that the nasal septum is a promising site for obtaining an adequate sample of tissue for further tissue engineering applications. The advantage of using hyaline cartilage from the nasal septum is that it not only has properties similar to those of tracheal cartilage but is also a source of epithelial cells and connective tissue. Thus, the obvious benefit is that one is able to obtain the three cell types necessary for *in vitro* three-dimensional (3D) tissue construction from the same biopsy site. However, cartilage harvested from nasal tissue should not be considered the universal or unique source for all cases of tracheal injury in which tissue engineering could be beneficial. For instance, the availability of nasal cartilage may be limited in children or victims of smoke inhalation, and its use in these instances could be counterproductive. On the other hand, regarding reconstruction of the auricle, while hyaline cartilage can certainly be used as a viable cell source for tissue engineering, one should consider whether an auricular source containing a more flexible elastic cartilage, if available, would provide better mechanical results in the final neotissue.

Other cellular sources that have the potential for use in tissue engineering studies need further investigation. Cao's group at the Shanghai Jiao Tong University School of Medicine has done interesting work on the induction of adult dermal fibroblasts into fibrocartilage using cartilage-derived morphogenetic proteins. They have been able to demonstrate chondrogenic differentiation by immunostaining and RNA expression of *in vitro* constructs both in monolayer and 3D scaffolding using PGA. Recently, adult stem cells have also been shown to be a possible source that could be exploited by tissue engineers. Our laboratory believes that mesenchymal stem cells hold the greatest therapeutic potential for engineering bone and cartilage. An additional advantage of using mesenchymal stem cells is that the harvesting procedure is less invasive than, for example, removing a sample of nasal cartilage.

5.535.3.2. Materials

Once the donor cells have been harvested, the number expanded, and the chondrocytic phenotype maintained, the next step is to deliver them to the recipient host. There are currently so many potential scaffolds for use in tissue engineering that the challenge of choosing the correct material is enormous. Large categories include biodegradable polymers (e.g., PGA), hydrogels (e.g., Pluronic F-127), ceramics (e.g., hydroxyapatite), metals (e.g., titanium), synthetics, and even composite hybrids between types. In terms of the desirable properties of these materials, of course, it is preferable for the material not to cause an inflammatory reaction either in its natural state or in the form of breakdown products, and it should not have toxic effects on the donor or recipient cells. Furthermore, it should be a good substrate for cell attachment, so that cells are not lost from the desired implantation site. Previous studies have shown that cells injected directly into the host without a scaffold will disperse away from the injection site, such that the concentration is insufficient for subsequent tissue formation.[22]

The material should also have a porosity that allows cells and nutrients to intercalate evenly throughout the material. Without sufficient pore size, distribution, or interconnection, one risks creating merely a scaffold-shaped shell of tissue, because of cell death due to malnutrition or lack of cell dispersion to the center of the material. Pore size has also been shown to affect the differentiation of the attached cells, with studies on osteogenesis showing that smaller pore sizes lead to osteochondral formation and larger pore sizes result in direct osteogenesis.[23] Finally, the scaffold should ideally degrade at a rate that is matched with neocartilage development.

5.535.4. Characterization of Scaffolds *In Vitro* and *In Vivo*

5.535.4.1. *In Vitro* Model Using a Thermoreversible Polymer

There are several commercially available thermoreversible gels, each with different characteristics. We examined the potential of a novel thermoreversible gelation polymer (TGP) to act as a 3D hydrogel scaffold in the delivery of both chondrocytes and growth factors.[24] This TGP is composed of poly-NIPAAm aggregates and precipitates in aqueous solution upon heating above 32 °C as a result of hydrophobic interactions. This temperature, called the lower critical solution temperature, can be adjusted by randomly copolymerizing NIPAAm with other monomers. The lower critical solution temperature increases or decreases when NIPAAm is copolymerized with a more hydrophobic monomer or a hydrophilic monomer, respectively. The sol–gel transition temperature for the TGPs can be set at any temperature from 5 to 70 °C, below which the polymer will liquefy and above which the polymer solidifies. Briefly, lyophilized TGP was dissolved in Ham's F-12 medium at 4 °C overnight, yielding a 10% (by weight) viscous transparent hydrogel. The sol–gel transition temperature of the gel used in this experiment was 7 °C, and it was observed to gel immediately when heated above 7 °C.

Chondrocytes from a calf shoulder source were suspended in chilled aqueous solutions of TGP with 200 ng ml^{-1} of insulin-like growth factor-1 (IGF-1) and 50 ng ml^{-1} of transforming growth factor-β2 (TGF-β2). The cell–polymer mixtures were kept below 7 °C to maintain the liquid state of the copolymers and placed in a syringe for injection into a silicone ring for molding. The contents were immediately warmed above 7 °C in order to solidify the biopolymer, yielding a short cylindrical structure. The cell–polymer structure was

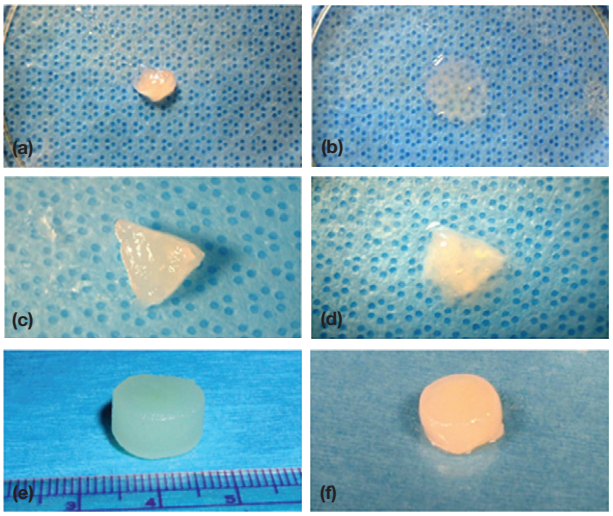

Figure 1 The sol–gel transition of the cell–polymer constructs after different *in vitro* culture periods (a, b – 2 weeks, c, d – 4 weeks, e, f – 8 weeks). The photos on the left are at room temperature (25 °C). Once the constructs were cooled below 7 °C, the cell–polymer constructs turned to liquid after 2 weeks of *in vitro* culture, but remained in a solid state after 8 weeks.

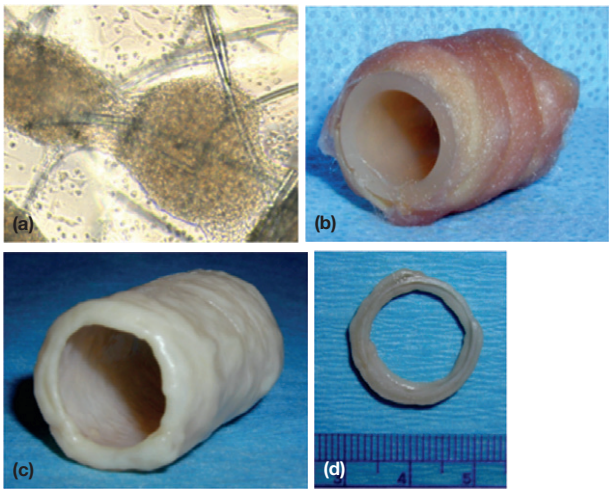

Figure 2 The cells attached to the PGA fibers during the *in vitro* culture period at 7 days (a). The cell-seeded PGA meshes were then wrapped around a silicone tube template (b). At 10 weeks after further *in vitro* culture, a solid, glistening white cartilaginous tube was formed (c, d).

subsequently cultured in Ham's F-12 medium supplemented with 10% fetal bovine serum (FBS) and 25 ng ml^{-1} L-ascorbic acid at 37 °C for up to 16 weeks. After 2 weeks in culture, the cell–polymer construct kept its 3D structure at room temperature; however, when cooled below 7 °C, the structure liquefied (Figure 1(a) and 1(b)). After a culture period of 4 weeks, much of the 3D shape was maintained, even upon cooling to 4 °C (Figure 1(c) and 1(d)). Longer *in vitro* culture periods, that is, 8 weeks, generated tissue-engineered neotissue, which did not change shape when cooled (Figure 1(e) and 1(f)).

This novel *in vitro* culture system for the generation of tissue-engineered cartilage has much potential for application in reconstructive plastic surgery, particularly in cases where defects may be filled via injection; thus, providing a relatively noninvasive technique.

5.535.4.2. *In Vitro* Model Using a Biodegradable Polymer

We evaluated the feasibility of using autologous bovine mesenchymal stem cells cultured on a PGA mesh to engineer a tube-shaped cartilage equivalent of a functional trachea. TGF-β2 has been shown to play a major role in cartilage development, and our data has demonstrated that TGF-β2 helps support chondrogenesis during the development of 3D tissue constructs. Bone marrow was obtained by iliac crest aspiration from a calf shoulder. The aspirates were cultured in Dulbecco's modified Eagle medium (DMEM) containing 10% FBS.

After 2 weeks, confluent cell suspensions were concentrated at 50×10^6 cells ml^{-1} and seeded on 100 × 10 × 2 mm nonwoven meshes of PGA fibers. The serum-containing medium was then replaced with DMEM containing ITS+Premix, L-ascorbic acid 2-phosphate, 100 nM dexamethasone, 10 ng ml^{-1} TGF-β2, and 25 ng ml^{-1} IGF-1. The cell-seeded mesh samples were cultured continuously for 1 week *in vitro* (Figure 2(a)). The structures were then wrapped around silicone templates, 20 mm in diameter × 50 mm in length (Figure 2(b)). The composite structures were cultured again in the same conditions and media for up to 10 weeks. The gross appearance of the tissue-engineered trachea (TET) was solid and glistening white, in the shape of a cartilaginous tube (Figure 2(c) and 2(d)).

The tissue surface was smooth and cartilage formation was evident. Type II collagen staining was strongly positive in the engineered cartilage.

5.535.4.3. Autologous *In Vivo* Model Using a Thermoreversible Polymer

As previously stated, one of the most complicated and challenging tasks in reconstructive surgery is to make tissue in a particular desired shape. We have had much experience with the use of Pluronic F-127, which has *in vitro* properties similar to the previously mentioned TGP. Pluronic F-127 is a solid that is soluble in water and becomes a gelatinous solid (hydrogel) at room temperature (25 °C) or above. One disadvantage of the Pluronic F-127 hydrogel, however, is its inability to maintain a stable, predetermined shape *in vitro*. Saim *et al.*[25] demonstrated the generation of mature autologous tissue-engineered elastic cartilage in the approximate size and shape of an adult human auricular helix *in vivo*. External ear cartilage was harvested from male Yorkshire swine. After the perichondrium was meticulously excised, the cartilage was minced into small fragments and digested. Under general anesthesia, folds were made in the skin of the ventral surface of the swine resembling the shape of a human auricular helix. The skin was then stitched using 2-0 Vicryl suture to create a hollow, curved channel. The autologous chondrocytes were suspended in Pluronic F-127 and injected into the skin fold channel. Ten weeks after implantation, the harvested construct demonstrated a helical shape with firm, yet flexible consistency, compatible with elastic cartilage. This injectable technique may be

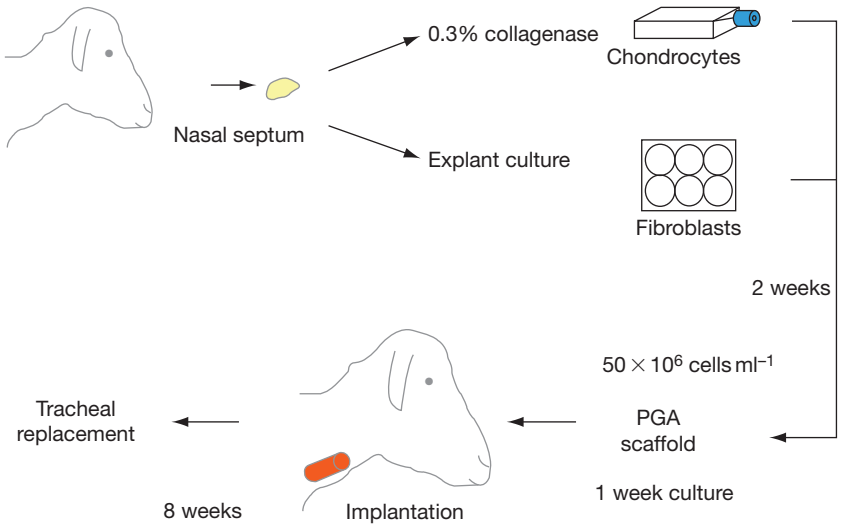

Figure 3 Diagram showing the steps of tissue harvest, cell isolation, *in vitro* culture, scaffold seeding, *in vivo* implantation, and tracheal replacement.

useful to form the shapes necessary to repair cosmetic problems such as microtia or other facial deformities.

From our unpublished data, fibroblast growth factor (FGF) can also be added to hydrogel carriers in which chondrocytes are suspended. We believe it takes fewer than 10 weeks to produce a firm, reliable cartilage using this technique.

5.535.4.4. Autologous *In Vivo* Model Using a Biodegradable Polymer

Extensive tracheal reconstruction is often required in patients with both benign and malignant diseases. Tracheal reconstruction can be safely carried out by direct anastomosis after resection of up to one-half of the trachea in adults and one-third of the trachea in children. For more extensive tracheal resection, however, there is no general agreement on the ideal reconstructive material. The use of prosthetic materials often causes complications because of their propensity for infection and extrusion, and the use of autologous tissue, thus far, has been limited by poor structural characteristics and technical complexity. As a result, laser treatment or stent placement is currently the only available temporizing therapy for patients with severe tracheal stenosis. We have been involved in the generation of an autologous TET for potential use in reconstructive surgery.[26] One of the main limitations in this approach is the need for the engineered tissue to meet the specific mechanical requirements of the native trachea. The trachea must maintain flexibility in the longitudinal direction to allow for free movement of the head, while maintaining the rigidity necessary to prevent luminal collapse during breathing.

We obtained two separate 5×5 mm samples of nasal septum from 2-month-old sheep to generate two identical templates per animal (Figure 3). Chondrocytes were harvested from the cartilage, and fibroblasts were harvested from the connective tissue in each sample. After 2 weeks of *in vitro* culture, the chondrocytes (50×10^6 cells ml^{-1}) and fibroblasts (25×10^6 cells ml^{-1}) were seeded separately onto PGA mesh and cultured for another week. A spiral helical template,

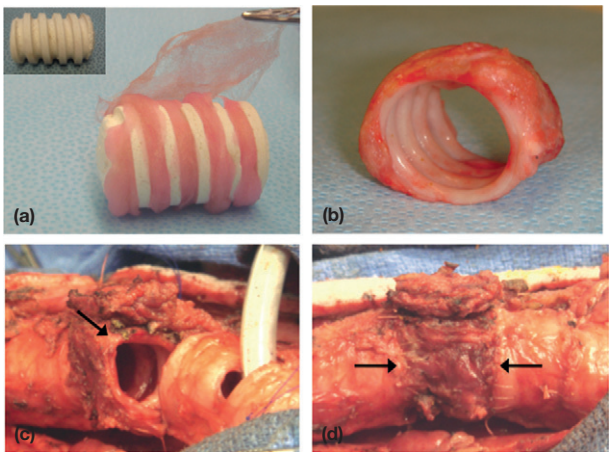

Figure 4 A spiral helical template created using a silicone mold and the chondrocyte-seeded PGA mesh wrapped around the inner groove of the template. Fibroblast-seeded mesh was subsequently wrapped around the entire structure (a). The entire structure was implanted into the neck of the autologous sheep donor, harvested after 8 weeks, and the helical template removed. The appearance of the tissue-engineered trachea (TET) was smooth and glistening white (b). A section of native trachea was resected and the TET placed into the resection site. The arrow indicates the distal end of the TET before anastamosis (c). The TET was then connected to the native trachea by end-to-end anastamoses. The arrows indicate the promixal and distal ends of the TET (d).

20 mm in diameter $\times$ 50 mm in length, was made with a Silastic ERTV mold-making kit and the chondrocyte-seeded mesh was placed into the grooves. This structure was then wrapped with the corresponding fibroblast-seeded mesh (Figure 4(a)). Each template was then implanted into its corresponding donor sheep through a longitudinal incision made in the neck, just above the sternocleidomastoid muscle. During the procedure, a pocket was created under the muscle, and the cell-seeded scaffold template was inserted into this space. After 8 weeks, the TET

was harvested from the neck (Figure 4(b)), the template removed, and a 10-cm-long resection was performed on the sheep's cervical trachea. The TET was connected to the native trachea by end-to-end anastomoses using a 3-0 absorbable running suture (Figure 4(c) and 4(d)). Postoperatively, the sheep breathed spontaneously with no subcutaneous emphysema and were voluntarily ambulatory. However, the sheep were required to be sacrificed by day 15 because of extensive tracheomalacia. The gross appearance of the TETs showed a distinct structure containing both cartilage and connective tissue, similar to native trachea. On histological examination, the engineered tracheal surfaces were smooth and cartilage formation was evident. Hematoxylin and eosin staining revealed the presence of mature cartilage surrounded by connective tissue, as observed in native trachea. These data indicate that the failure of the sheep TET is likely due to lower levels of collagen type II and glycosaminoglycan (GAG) in the tissue-engineered cartilage, resulting in deficient structural strength.

5.535.5. Conclusions

Given the immense need for replacement tissue in modern-day reconstructive and cosmetic plastic surgery, the field of tissue engineering holds great promise as a future source to fulfill this requirement. There are, however, numerous considerations that must be taken into account regarding our current state of knowledge in cartilage tissue replacement when bringing this approach to patient care.

The donor source for future chondrocytes must be considered carefully and tailored to the appropriate situation. Presently, there is a variety of choices between adult chondrocytes, adult mesenchymal cells, and embryonic stem cells. But, for example, a cancer patient with bone metastases may not have uncontaminated marrow available for autologous donation, thus reducing the available options. One must also consider which donor site in the body will provide the easiest, safest, and least invasive source to reduce donor morbidity. In a neonatal patient, the use of umbilical stem cells may be a viable option, but until cord blood banking becomes a more prevalent practice, most adults will need to endure more invasive procedures for cell extraction. Finally, the harvest source will need to provide enough cells for the initial *in vitro* expansion to generate a useful final amount of neocartilage. As we learn more about the final properties of the neotissue created from these various sources, we will need to begin devising standards for the harvesting procedure to bring this process safely and successfully to the clinical realm.

Once the cells are obtained, they must be delivered to the recipient. The material chosen for the cell scaffold preferably should not cause an adverse inflammatory reaction and should not have toxic effects. It should be a good substrate for cell attachment, have a porosity that allows cells and nutrients to intercalate evenly throughout, and degrade at a rate that is matched with neocartilage development. Although much work has been done to characterize different scaffolding materials, we still do not know which material is ideal for the production of tissue-engineered cartilage. Many of the fibrous meshes, such as PGA, are easily premolded into the desired shape and allow for even distribution of cells and nutrients, but, unfortunately, also cause an inflammatory reaction in the recipient. The hydrogels have been shown to be more biocompatible, but lack the advantage of preformed shaping, which translates clinically into the need for additional operations before attaining the desired structure.

One area that is yet to be well characterized is the choice of implantation site in the recipient. Implantation of the cells directly into the reconstruction site would reduce the number of necessary future procedures, but we have little information at present comparing the effects of different recipient sites on neocartilage formation. Some studies have been performed to examine the effect of vascularity of implantation sites on ectopic bone formation, but with conflicting conclusions as to any difference in final tissue formation.[27,28] It is also difficult to say whether the results seen with vascularized neotissues are applicable to avascular neocartilage formation. Unpublished data from our laboratory suggests that implantation subcutaneously at the back of an immunocompetent rat model provides a better environment for cartilage growth compared to the temporal-auricular region. Thus, despite the properties of cartilage as an avascular tissue, increased vascularity of the implantation site may well be important in neotissue formation. Yanaga *et al.*[18] also make an important point that, in human subjects, the thinness of the cutaneous layer and the reduced vascularity of the temporal region may lead to disastrous scaffold exposure.

Above all, perhaps the most important consideration in the application of cartilage tissue engineering techniques to plastic surgery is that, with the notable exception of tracheal reconstruction, most of the procedures utilizing cartilage perform mostly a cosmetic function. Therefore, in the transition from bench to clinic, one must be absolutely sure that the techniques and methods employed are near perfect and can be safely applied to human subjects. Nevertheless, tissue engineering is certainly an exciting and rapidly expanding field that holds great promise for the generation of new tissues for reconstructive repair.

References

1. Quatela, V. C.; Chow, J. *Facial Plast. Surg. Clin. North Am.* **2008**, *16*(1), 1–10, v.
2. Romo, T., III; Litner, J. A.; Sclafani, A. P. *Facial Plast. Surg.* **2003**, *19*(4), 341–348.
3. Romo, T., III; Reitzen, S. D. *Facial Plast. Surg.* **2008**, *24*(1), 120–128.
4. Caicedo, M. S.; Desai, R.; McAllister, K.; Reddy, A.; Jacobs, J. J.; Hallab, N. J. *J. Orthop. Res.* **2009**, *27*(7), 847–854.
5. Eavey, R. D.; Monroy, A.; Nicolau, Y.; Shabdiz, F. *J. Oral. Maxillofac. Surg.* **2006**, *64*(11), 1655–1663.
6. Jin, H. R.; Won, T. B. *Otolaryngol. Head Neck Surg.* **2009**, *140*(4), 526–530.
7. Koltai, P. J.; Ellis, B.; Chan, J.; Calabro, A. *Arch. Otolaryngol. Head Neck Surg.* **2006**, *132*(6), 631–634.
8. Vacanti, C. A.; Paige, K. T.; Kim, W. S.; Sakata, J.; Upton, J.; Vacanti, J. P. *J. Pediatr. Surg.* **1994**, *29*(2), 201–204; discussion 204–205.
9. Vacanti, C. A. *J. Cell Mol. Med.* **2006**, *10*(3), 569–576.
10. Green, W. T., Jr. *Clin. Orthop. Relat. Res.* **1977**, *124*, 237–250.
11. Grande, D. A.; Pitman, M. I.; Peterson, L.; Menche, D.; Klein, M. *J. Orthop. Res.* **1989**, *7*(2), 208–218.
12. Langer, R.; Vacanti, J. P. *Science* **1993**, *260*(5110), 920–926.
13. Webber, R. J. *Clin. Orthop. Relat. Res.* **1990**, *252*, 114–120.
14. Vacanti, C. A.; Langer, R.; Schloo, B.; Vacanti, J. P. *Plast. Reconstr. Surg.* **1991**, *88*(5), 753–759.
15. Kim, W. S.; Vacanti, J. P.; Cima, L.; *et al. Plast. Reconstr. Surg.* **1994**, *94*(2), 233–237; discussion 238–240.

16. Cao, Y.; Vacanti, J. P.; Paige, K. T.; Upton, J.; Vacanti, C. A. *Plast. Reconstr. Surg.* **1997**, *100*(2), 297–302; discussion 303–304.
17. Ceonzo, K.; Gaynor, A.; Shaffer, L.; Kojima, K.; Vacanti, C. A.; Stahl, G. L. *Tissue Eng.* **2006**, *12*(2), 301–308.
18. Yanaga, H.; Imai, K.; Fujimoto, T.; Yanaga, K. *Plast. Reconstr. Surg.* **2009**, *124*(3), 817–825.
19. Cao, Y. L.; Lach, E.; Kim, T. H.; Rodriguez, A.; Arevalo, C. A.; Vacanti, C. A. *Plast. Reconstr. Surg.* **1998**, *102*(7), 2293–2298.
20. Puelacher, W. C.; Wisser, J.; Vacanti, C. A.; Ferraro, N. F.; Jaramillo, D.; Vacanti, J. P. *J. Oral. Maxillofac. Surg.* **1994**, *52*(11), 1172–1177; discussion 1177–1178.
21. Zhang, J.; Liu, L.; Gao, Z.; *et al. J. Oral. Maxillofac. Surg.* **2009**, *67*(2), 257–264.
22. Cao, Y.; Rodriguez, A.; Vacanti, M.; Ibarra, C.; Arevalo, C.; Vacanti, C. A. *J. Biomater. Sci. Polym. Ed.* **1998**, *9*(5), 475–487.
23. Karageorgiou, V.; Kaplan, D. *Biomaterials* **2005**, *26*(27), 5474–5491.
24. Yasuda, A.; Kojima, K.; Tinsley, K. W.; Yoshioka, H.; Mori, Y.; Vacanti, C. A. *Tissue Eng.* **2006**, *12*(5), 1237–1245.
25. Saim, A. B.; Cao, Y.; Weng, Y.; *et al. Laryngoscope* **2000**, *110*(10 Pt 1), 1694–1697.
26. Kojima, K.; Bonassar, L. J.; Roy, A. K.; Vacanti, C. A.; Cortiella, J. *J. Thorac. Cardiovasc. Surg.* **2002**, *123*(6), 1177–1184.
27. Hartman, E. H.; Vehof, J. W.; de Ruijter, J. E.; Spauwen, P. H.; Jansen, J. A. *Biomaterials* **2004**, *25*(27), 5831–5837.
28. Kusumoto, K.; Bessho, K.; Fujimura, K.; *et al. Ann. Plast. Surg.* **2000**, *45*(4), 408–414.

5.536. Tissue-Engineering Hollow Noncardiac Intrathoracic Organs: State-of-the-Art 2010

J M Fishman and M A Birchall, The Royal National Throat, Nose and Ear Hospital, London, UK
P Macchiarini, University Hospital Careggi, Florence, Italy

© 2011 Elsevier Ltd. All rights reserved.

5.536.1.	**Introduction**	510
5.536.2.	**Historical Background**	511
5.536.2.1.	Alloplastic Tracheal Transplantation: Solid Prostheses	511
5.536.2.2.	Alloplastic Tracheal Transplantation: Porous Prostheses	511
5.536.2.3.	Tracheal Reconstruction with Autogenous Tissues	511
5.536.2.4.	Nonviable Cadaveric Human Tracheal Allograft Transplantation	511
5.536.2.5.	Viable Tracheal and Laryngeal Allograft Transplantation	512
5.536.3.	**Tissue-Engineered Trachea: Basic Sciences to Clinical Application and Transplantation**	513
5.536.3.1.	Suitable Scaffolds (Natural, Synthetic)	514
5.536.3.2.	Decellularized, Nonimmunogenic Matrices (Allogenic, Xenogenic)	514
5.536.3.3.	Seeding with Stem Cells	516
5.536.3.4.	Bioreactors	517
5.536.3.5.	Transplantation in Animal Models and Humans	518
5.536.4.	**Tissue-Engineered Larynx for Total Laryngeal Replacement and Transplantation: The Ultimate Goal**	521
5.536.4.1.	Generation of Muscle	521
5.536.4.2.	Reinnervation	521
5.536.4.3.	Revascularization	522
5.536.4.4.	Immunogenicity	523
5.536.5.	**Future Challenges and Goals**	524
5.536.5.1.	Tissue Engineering the Esophagus: A Preliminary Step Toward Generating a Tissue-Engineered Larynx	524
5.536.6.	**Conclusions**	525
References		525

Glossary

Allogeneic/allograft/allotransplantation Allogenic (also known as allogeneic) cells are obtained from the body of a nonself donor of the same species. Allotransplantation (or allograft) refers to a graft of tissue from a nonself donor; such grafts are invariably rejected unless the recipient is immunosuppressed.

Alloplastic An alloplast or alloplastic device (also known as an implant or prosthesis) is an inert inorganic (artificial, synthetic) material used for transplantation into living tissues.

Angiogenesis Angiogenesis is a process involving the growth of new blood vessels. It is a normal, physiological process in growth and development, as well as in wound healing. Vascularization is an essential factor for successful implants of bioengineered tissues, and a tissue of more than a few millimeters in volume cannot survive by diffusion and requires formation of new blood capillaries to supply essential oxygen and nutrients.

Autologous/autograft/autogenous Autologous cells are obtained from the same individual to which they will be reimplanted. Autologous transplantation (or autograft), also known as autogenous tissue transfer, refers to a transfer of tissue from one site to another in the same individual.

Bioreactor A bioreactor may refer to any device or system that supports a biologically active environment in order to grow cells or tissues in the context of cell culture.

Homograft A graft of tissue from a donor of the same species as the recipient.

Major histocompatibility complex The major histocompatibility complex (MHC) is a cluster of genes on human chromosome 6 or mouse chromosome 17. It encodes a set of membrane glycoproteins that play a role in antigen processing and host defense. HLA, the acronym for human leukocyte antigen, is the genetic designation for the human MHC.

Mesenchymal stem cell (MSC) A stem cell that is an isolated homogeneous population that can differentiate into cells of more than one connective tissue type (i.e., multipotent).

Primary cells Primary cells are from an organism, as opposed to secondary cells from a cell bank.

Satellite cell Elongated, spindle-shaped, quiescent myogenic cells located adjacent to the plasma membrane of myofibers beneath the basal lamina. Compelling evidence indicates that they are committed myogenic progenitors that mediate both postnatal growth and regeneration after injury of muscles. Once activated, satellite cells divide to produce

muscle precursor cells (MPCs) that proliferate before committing to differentiation and fusing into myotubes, which finally mature into myofibers.
Scaffold/matrix Tissue scaffolds (or matrices) are cell growth support structures composed of biocompatible materials that enable cell attachment (or seeding) and migration in tissue engineering.
Stem cells Cells that continuously renew themselves, while maintaining the ability to differentiate into various cell types. Adult stem cells are defined by two major functions: self-renewal and multilineage differentiation.
Syngeneic Syngeneic (also known as syngenic) or isogeneic (also known as isogenic) cells are isolated from genetically identical organisms such as twins, clones, or highly inbred research animal models.
Tissue engineering Tissue engineering is an interdisciplinary field that applies the principles andmethods of engineering and the life sciences toward the development of biological substitutes that can restore, maintain, or improve tissue function.
Xenogenic Xenogenic (also known as xenogeneic) cells are those isolated from individuals of another species (i.e., animal cells).

Abbreviations

AFS	Amniotic fluid stem cells
BDNF	Brain-derived neurotrophic factor
bFGF	Basic fibroblast growth factor
CT	Computed tomography
DMD	Duchenne muscular dystrophy
DNA	Deoxyribonucleic acid
ECM	Extracellular matrix
EDTA	Ethylenediaminetetraacetic acid
ES	Embryonic stem cells
GFP	Green fluorescent protein
HLA	Human leukocyte antigen
iPS	Induced pluripotent stem cells
MDSC	Muscle-derived stem cells
MEMS	Microelectromechanical systems
MHC	Major histocompatibility complex
MPC	Muscle precursor cell
MSC	Mesenchymal stem cells
NGF	Nerve growth factor
NT-3	Neurotrophin-3
NT-4	Neurotrophin-4
PCL	Polycaprolactone
PDGF	Platelet-derived growth factor
PGA	Polyglycolic acid
PLA	Polylactic acid
PLG	Poly(lactide-*co*-glycolide)
PLGA	Poly(lactic-*co*-glycolic acid)
VEGF	Vascular endothelial growth factor

5.536.1. Introduction

> All things are possible until they are proved impossible – and even the impossible may only be so, as of now.
> Pearl Buck, A Bridge for Passing (1962)

Airway reconstruction is necessary in patients with extensive tracheal stenosis caused by neoplasia, trauma, or congenital disease. Today, most tracheal lesions can be resected and primary reconstruction safely carried out by end-to-end anastomosis. Unfortunately, there are cases in which primary anastomosis is not possible, such as after extensive burns, trauma, tumor resection, or postintubation injuries. Additionally, the treatment of congenital tracheal atresia or stenosis can be hindered by the lack of sufficient tissue for surgical reconstruction, as the length of trachea involved may be extensive. Tracheal substitution is needed in the case of very severe stenosis that cannot be safely corrected by slide tracheoplasty, and of extended tumors in which invasion of the larynx or mediastinum does not prevent complete resection with reconstruction of the larynx. The general limits of safe resection are about half the tracheal length in adults (around 6 cm) and probably one-third in small children.[1,2] Tracheal resection longer than these limits requires replacement.

According to Belsey,[3] a tracheal substitute must fulfill the following requirements:

(i) be a laterally rigid, but longitudinally flexible tube and
(ii) possess a surface lining comprising ciliated respiratory epithelium.

Furthermore, the conduit must be initially airtight and become integrated into adjacent tissues, so that chronic inflammation, growth of the granulation tissue, infection, and erosion do not occur. In addition, materials for tracheal replacement must be biocompatible, nontoxic, nonimmunogenic, and noncarcinogenic; must not dislocate or erode over time; ideally should provide or facilitate epithelial resurfacing; should avoid stenosis or late buckling; should resist bacterial colonization; should avoid accumulation of secretions; and must be permanent constructions.

Immunosuppressive therapy is undesirable for many reasons, especially because the principal reason for tracheal replacement in many cases is extensive carcinoma (squamous cell and adenoid cystic). Finally, for a method to be practically considered, the technique of construction or insertion of the conduit must be surgically straightforward and the results predictably successful.

Given the above requirements, tracheal homograft represents the ideal substitute. However, the growth potential of the tracheal homograft is not known and long-term stenosis can often occur.[4]

5.536.2. Historical Background

5.536.2.1. Alloplastic Tracheal Transplantation: Solid Prostheses

Many types of material have been examined for use in tracheal prostheses since the first report by Daniel.[5] The apparent simplicity of tracheal replacement encouraged trials of alloplastic transplantation with tubular conduits, initially made of solid materials, such as polytetrafluoroethylene, polypropylene mesh, Dacron polyurethane mesh, and silicone rubber.[6]

However, these foreign materials could not become incorporated by local tissues, and there were problems of infection, dislodgement, migration, extrusion, and stenosis. Re-epithelialization, was, of course, impossible on the inner lumen and led to the formation of granulation tissue or dehiscence at the interface between the prosthesis and the native trachea, usually within several months. Furthermore, solid tubes can never be removed, because the connective tissue tract formed around them proceeds to obstruct with new connective tissue formation and by contraction in the absence of a stent. For the above reasons, the nonporous tracheal prosthesis is now seldom used clinically.

Despite all of these complications, a rigid prosthesis can maintain an open airway for some time, despite a lack of healing. Such a result is, however, episodic and unpredictable. This situation starkly contrasts with the use of vascular conduits, which have been safely applied in clinical settings for decades. One of the reasons that prosthetic tracheal reconstruction is more difficult than use of a vascular prosthesis may be that the trachea is in contact with the external environment (i.e., the airway represents an interface between internal and external environments), unlike an artificial vascular graft, which is placed in a sterile mesenchymal environment and has no external interface after implantation.

5.536.2.2. Alloplastic Tracheal Transplantation: Porous Prostheses

Attention then turned to porous materials – often meshes of various substances – which theoretically might encourage tissue ingrowth and possibly even epithelialization in time. It was found that a minimal porosity of 40–60 μm is necessary for capillary ingrowth.[7] It was hoped that this bed of autogenous new connective tissue would serve as a base for migration of adjacent tracheal epithelium. Regeneration of epithelium was described, with evolution from squamous to cuboidal to pseudostratified ciliated cells (respiratory epithelium). However, delayed epithelial regeneration remains a particular problem.[8,9]

Connective tissue ingrowth served to fix and incorporate some porous prostheses as noted. However, the continued proliferation of scar tissue most often led to obstruction and stenosis. Epithelium generally failed to migrate sufficiently to cover the entire neotracheal surface, allowing continued cicatrix formation and bacterial colonization, usually in the center of the replacement. Although very short interpositions might achieve full epithelialization, which seemed to prevent further cicatrization, the rate and completeness of epithelial migration was usually insufficient to prevent central granulations, cicatrization, and stenosis. Obviously, very short tracheal replacements offered no solutions to the problem addressed.

5.536.2.3. Tracheal Reconstruction with Autogenous Tissues

Autologous tissue reconstruction is always preferable to alloplastic materials. Previous attempts included free tissue autografts with and without foreign material support, vascularized autogenous tissue flaps, and autogenous tube construction.

Various autogenous tissue grafts as patches, or in tubular form, have been tried for tracheal reconstruction where primary end-to-end anastomosis cannot be performed, including fascia lata,[10,11] tracheal wall,[5] pericardium,[12–14] periosteum with omental wrap,[15,16] buccal mucosa and auricular cartilage,[17] omentum,[18] esophagus,[19–22] jejunal patches with microvascular reconstruction,[23] rib and ear perichondrium,[24] nasal cartilage with attached mucosa,[25] bronchial patches,[26] epidermis,[27] aortic grafts,[28–30] carotid artery patches,[31] auricular cartilage,[32] and costal cartilage.[33] The results indicate that small defects can be successfully treated with graft repairs. However, stenosis is a recurring problem.

Various attempts have been made to use autogenous grafts in conjunction with artificial materials, in order to maintain a rigid wall and prevent collapse of the lumen while various autogenous tissue grafts grow across the partial defects. Associated complications with foreign material were mostly related to lack of biocompatibility and included local infection, anastomotic dehiscence, vascular erosion, granulomatous lesions, and stenosis.

Although tissue grafts can successfully regenerate partial tracheal defects, circumferential or large defects require blood supply and mucosal lining for satisfactory reconstruction. The advantages of flap tissue over graft materials are the independence of its blood supply and its reliability in terms of wound healing. Flap surgery can be done to irradiated or heavily scarred areas, where grafting techniques have less chance of being successful.

Tissues from nearly every part of the body have been utilized in an attempt to find the best tissue for tracheal replacement. Local, regional, and distant free flaps, usually including a skeletal muscle component, have been reported for experimental tracheal reconstruction. Yu *et al.*[34] used a radial forearm free flap with polymex mesh and hemishield vascular graft, creating a nonstented airway with normal swallowing and voice. More recently, Maciejewski *et al.*[35] have reported success with the use of radial forearm flap combined with a biodegradative mesh suspension. Although vascularized autogenous tissue flaps have overall produced some successful results with patent, nonstenotic airways, they generally support only short segments of tracheal reconstruction. In addition, the limiting factor in nearly every procedure remains the complexity and multistage requirement, limiting the practicality of the procedure.

Clinically, autogenous tube construction has been successfully completed by several groups.[36,37] However, all procedures were multistage difficult procedures used as a last resort. Most attempts at autogenous tube construction have resulted in difficult or negative outcomes.

5.536.2.4. Nonviable Cadaveric Human Tracheal Allograft Transplantation

Cadaveric trachea and other tissues, fixed chemically, irradiated, frozen, or lyophilized, have been used both

experimentally and clinically as tracheal replacements.[38–41] They were initially developed as a more long-term tracheal preservation strategy to help overcome the anticipated shortfall in donor organs. Such implantations are often erroneously referred to as 'transplantation' or 'tracheal allografts' but both these terms are misnomers due to the graft's nonviable, denatured status. 'Bioprosthesis' or 'implant' may be a better term, because a fixed tissue is more akin to a silicone rubber tube than it is to transplanted tissue in the usual sense.

As these implants do not present viable cells and all major histocompatibility complex (MHC) markers, immunosuppression is not necessary.[42] Nevertheless, preserved or lyophilized tissues are usually replaced in time by host scar tissue,[43] the rate possibly dependent on the locus of implantation. Tracheal allografts therefore need long-term tracheal stenting where longer segments of trachea with a greater circumference have to be replaced. Despite the complete luminal epithelialization of the implanted grafts, there is no live cartilage in the donor trachea. It has been hypothesized that the lack of cell ingrowth could be responsible for the observed stenosis and tracheomalacia.[44] In addition, Liu *et al.*[45] showed that maintaining cartilage viability in a tracheal graft is necessary to maintain a patent airway.

Despite some limited successes, the exact mechanism of reduction of graft antigenicity after cryopreservation is still unclear, and the question of how long a tracheal graft can be preserved is unanswered. In addition, there are concerns regarding devitalization of cartilage and there is no standardized technique widely applicable. In short, dead tissue cannot be expected to function as a template for regeneration of the complex structure of the trachea in accord with any basic biological processes yet identified. An exception to the generally disappointing results obtained with nonviable cadaveric human tracheal allografts has occurred in the pediatric population, where pediatric tracheal homograft reconstruction has led to encouraging short- to medium-term results for children with long-segment congenital tracheal stenosis.[46,47]

5.536.2.5. Viable Tracheal and Laryngeal Allograft Transplantation

Tracheal transplantation has been studied for several decades. The reasons for the lack of success are mainly due to graft ischemia and rejection. Fresh tracheal allografts without aid of immunosuppressive therapy initiate rejection.[48] Fresh tracheal allografts were early demonstrated to necrose and liquefy,[49] or, if short, to result in fibrous stenosis.[50] In addition to the problem of immunological rejection, tissue loss also arises from devascularization, reperfusion injury, and/or surgical trauma.

Beigel *et al.*[51] found from experimentation in inbred rats that tracheal transplants carry antigens and have an immunogenic action from the donor, and that mucosa is rejected and replaced by recipient's cells. Hence, they concluded that tracheal transplants follow the same rules as other tissues, contrary to the earlier belief that the trachea had weak antigenicity.[52] Bujia *et al.*[53] also agreed that the mucosa from human trachea was most likely to be the major antigenic structure responsible for the immunogenic action of tracheal allografts.

Cryopreserved tracheal allografts seem to inhibit allogenicity while structural integrity appears to be maintained. Mukaida *et al.*[54] observed gradual replacement of graft epithelium by recipient epithelial cells after 50–60 days. Tojo *et al.*[55] in orthotopic cryopreserved tracheal allografts in rats without immune suppression also identified the late (2 months) graft epithelium to be of recipient origin while the chondrocytes were of donor origin. They concluded that the recipient origin of epithelium over the donor trachea accounted for the reduced antigenicity of the cryotransplanted trachea. These findings were confirmed by Genden *et al.*[56] MHC antigens (MHC II, MHC I) are expressed in epithelium and mixed glands of the trachea and not in cartilage.[53]

Based on the likelihood that the mucosa and mixed glands, but not the cartilage, are the major antigenic structure of the trachea, Liu *et al.*[57] removed tracheal graft epithelium and mixed glands with a detergent in dogs, in an attempt to eliminate the antigenicity of tracheal allografts completely while maintaining their viability. Omental revascularization was provided. Cartilage remained viable. Allografts (without immunosuppressive therapy) were incorporated without stenosis, compared with granulation tissue formation and stenosis in untreated controls. This concept later led to the idea of creating nonimmunogenic, decellularized matrices in tissue-engineering experiments.[58]

It would appear that viability of cartilage is also important in the preparation of low-antigenic tracheal allografts by detergent treatment in dogs. Liu *et al.*[45] showed that maintaining cartilage viability in a tracheal graft is necessary for successful immunosuppressant-free allotransplantation and consequently to maintain a patent airway. Damage to chondrocytes caused by the detergent regime resulted in serious stenosis. Early collapse of the graft was thought to be due mainly to lack of cartilage viability, rather than acute rejection, because most of the antigenic structure had been removed, and no lymphocyte or monocyte infiltration into the grafts was observed. When the viability of the cartilage was maintained, grafts were incorporated by the host trachea, without stenosis or granulation. Indeed, one dog survived for more than 26 months and no tracheomalacia was confirmed by bronchoscopic examination.

Clinical tracheal allotransplantation has been tried in humans, with success reported in one patient after 9 weeks.[52] The report was made 9 weeks after the actual allotransplantation, but unfortunately there were no follow-up reports. The donor trachea was first implanted heterotopically in the sternocleidomastoid muscle and pedicled orthotopically in 3 weeks. No immunosuppressive therapy was used. In another human, long-segment allograft with omental revascularization and immunosuppressive therapy, necrosis, and stenosis occurred, requiring a stent that could not be removed.[59] More recently, the Leuven Tracheal Transplant Group have reported successful tracheal allotransplantation after withdrawal of immunosuppressive therapy.[60] Indirect revascularization of the graft was achieved by first placing the graft in a heterotopic position (the recipient's forearm fascia). However, the membranous posterior wall of the allograft underwent avascular necrosis. Its 'success' must be questioned.

Kluyskens and Ringoir attempted the first human laryngeal transplantation (subtotal or partial laryngeal transplant) in

1969 in a patient who underwent incomplete laryngectomy for cancer.[61] The graft was unmatched and episodes of rejection were treated with azathioprine, prednisolone, actinomycin C, and antilymphocyte serum. Rapidly fatal recurrence of cancer secondary to the immunosuppression overshadowed graft survival, and further transplantation attempts in humans were abandoned for decades. In retrospect, the long-term viability of Kluyskens and Ringoir's graft would have been unlikely, as no vascular or neural anastomoses were performed.

Strome *et al.*[62] described fresh laryngeal nonvital organ transplantation with complete HLA matching, which included a five-ring segment of trachea, thyroid, and parathyroids, and a portion of attached pharyngeal wall, plus both superior laryngeal nerves and right recurrent nerve, to replace a totally scarred larynx secondary to previous trauma in a 40-year-old male. The donor was a 40-year-old male who had died from a ruptured cerebral aneurysm. Arterial, venous, and neural anastomoses were done, and perfusion was established early in the procedure. Over time, the patient regained vocal cord function and normal deglutition. Despite one episode of rejection, health and function were good at 40 months, with continued immunosuppressive therapy. To date, the patient continues to speak with a good voice and swallow without difficulty[63] (**Figure 1**).

This experience has been expanded substantially by Tintinago *et al.*, in Columbia, who have reported a series of 20 clinical laryngeal and tracheal transplants.[64] The Columbian group reports high-quality functional outcomes and peer-reviewed published reports of this series are awaited with great interest. However, it was reported at recent meetings in Washington and Rome that although the tracheal recipients are doing well, two of three laryngeal recipients, both with a primary laryngeal cancer operation, subsequently died.

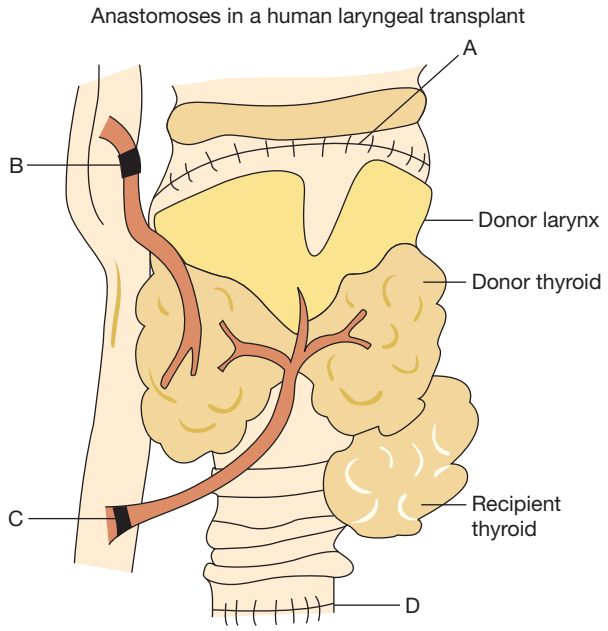

A = hypopharynx and tongue base, B = superior thyroid artery end-to-end, C = inferior thyroid vein end-to-side to internal jugular vein, D = trachea. In addition, the recurrent laryngeal nerves may be repaired directly or by use of ansa cervicalis.

Figure 1 Anastomoses in human laryngeal allotransplantation. Reproduced from Birchall, M. *Lancet* **1998**, *351*(9102), 539–540, with permission from Elsevier.

Although these cases have shown that human laryngeal transplantation is now technically possible, several issues need to be resolved before the operation can be introduced into routine clinical practice. For a start, success in making severed laryngeal nerves work again has proved elusive. In addition, loss of a larynx because of trauma is rare. Most people who would merit a laryngeal transplant would have a present or past history of laryngeal carcinoma, and such patients would have to be subjected to a lifelong immunosuppressive therapy to prevent rejection, with the increased risk of rapid tumor recurrence. This is not only what happened to the 1969 patient, but also to the world's first tongue transplant recipient, who also had advanced squamous cell cancer, in 2004.[61,65]

5.536.3. Tissue-Engineered Trachea: Basic Sciences to Clinical Application and Transplantation

Given that no predictable and dependable replacement had yet been found, attention turned to tissue engineering. Tissue engineering implies formation of tissue by cultivated cells introduced into a framework of biodegradable synthetic polymer, which guides the shape and size of a macrostructure, such as a tube. Although it is widely assumed to be a relatively new field, the first report of tissue engineering was published in 1933, when tumor cells were implanted into a pig, wrapped in a polymer membrane to protect them from immune attack.[66] However, the modern era of tissue engineering could be said to have begun at the start of the 1980s with the development and clinical use of skin replacements. The field continues to expand and tissue bioengineering has already provided functional human organ replacements elsewhere[67,68] (**Figure 2**).

Tissue engineering applies the principles of engineering, material science, and biology toward the development of biological substitutes that restore, maintain, or improve tissue function. The three major approaches to tissue engineering include guided tissue regeneration using engineered matrices alone, the injection of isolated cells alone, or the use of cells seeded on or within matrices (cell matrix construct). The latter two methods are the most common. Using isolated cells or cell substitutes avoids potential surgical complications and allows cell manipulation prior to injection/infusion (such as gene therapy), but has the drawbacks of possible rejection or loss of function.[69]

Tissue engineering requires cells, a matrix/scaffold on which to seed them, and a means of providing sustenance and blood supply. Scaffolds without cells take many months to repopulate,[8,9] and, without blood supply, all but the smallest, thinnest grafts will ultimately fail. A tissue-engineering technique that maximizes cell growth, adhesion, and structural integrity is required. A major advance in tissue engineering has been the recognition of the huge advantages offered by stem cells; these include primarily their ability to self-renew, providing a theoretically inexhaustible supply, and to differentiate to any cell type when grown under the appropriate conditions.

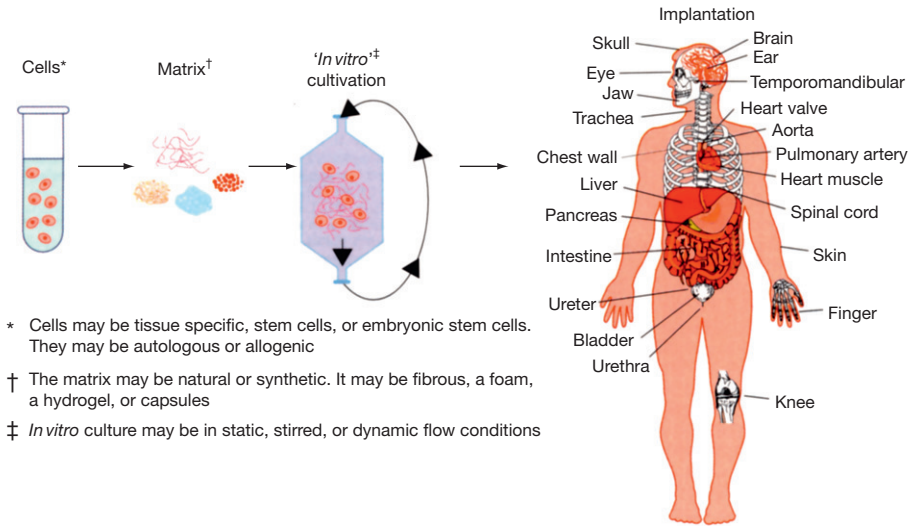

Figure 2 The tissue-engineering process. Reproduced from Vacanti, J. P.; Langer, R. *Lancet* **1999**, *354*(Suppl. 1), S32–S34, with permission from Elsevier.

5.536.3.1. Suitable Scaffolds (Natural, Synthetic)

The prime requirements for any scaffold in tissue engineering are biocompatibility, nonimmunogenicity, the capacity to sustain and/or promote the growth of the relevant cells/tissue, and provision of a template for tissue growth in three dimensions. Many different materials (natural and synthetic, biodegradable and permanent) have been investigated.

Scaffolds constructed from natural materials have been studied to evaluate their ability to support cell growth. They are usually composed of particular derivatives of the extracellular matrix (ECM) (and as such would possess natural interactive properties such as cell adhesiveness). Proteic materials, such as collagen, alginate or fibrin, and polysaccharidic materials, like glycosaminoglycans (e.g., hyaluronic acid derivatives), have all proved suitable in terms of cell compatibility, but some issues with potential immunogenicity still remains. In addition, there are obvious limitations associated with biological materials, including lack of consistency, biodegradability, and structure malleability.

The developments in materials science that have occurred in recent years, particularly in relation to the generation of bioactive materials, have provided a major advance in tissue engineering. The use of synthetic scaffolds, as used by the Wake Forest group,[67] has the advantage that structures can be tailored to the size and shape required for a particular patient. In addition, material properties such as strength, degradation time, porosity, and microstructure can be more easily controlled. Furthermore, there are no issues related to a limited donor pool. There are many potential materials under investigation for this application, including peptides, collagen, and ceramics. They lack the 'natural' macro- and microanatomic qualities of decellularized scaffolds. However, by studying the way cells and stem cells migrate and differentiate *in vitro* and within scaffolds, it should be possible to determine which combinations of molecules may be added to give optimal cell performance and angiogenesis.

The most commonly used polymers in synthetic matrices are biodegradable aliphatic polyesters. These polymers degrade through nonenzymatic hydrolysis of the ester bonds. The degradation products are nontoxic, natural metabolites and are eliminated from the body in the form of carbon dioxide and water. A synthetic material in common use is polylactic acid (PLA). This is a polyester that degrades within the human body to form lactic acid, a naturally occurring chemical that is easily removed from the body. Similar materials include polyglycolic acid (PGA) and polycaprolactone (PCL); their degradation mechanism is similar to that of PLA, but they exhibit a faster and a slower rate of degradation, respectively, compared to PLA. Polymers of PGA (first developed as Dexon, a synthetic biodegradable suture material) were first shown to be effective as matrices for new tissue formation,[70] and subsequently found to be adaptable in creating highly specific shapes such as that seen in structural cartilage.[71]

These polymers can be produced in a number of shapes and physical forms, including meshes, sponges, and films with a biodegradation rate that can be changed through copolymer proportions (e.g., altering chemical composition by varying the ratio of lactic to glycolic acid in the poly(lactic-*co*-glycolic acid), or PLGA, copolymers). Over the past decade, new synthetic materials and material-processing techniques have provided matrices, which, used in combination with chondrocytes, have produced high-quality tissue-engineered cartilage in a variety of different shapes, including the human ear,[72] nasoseptal implants,[73] a temporomandibular joint disk,[74] as well as joint resurfacing[75] and meniscal replacement[76] (**Figure 3**).

5.536.3.2. Decellularized, Nonimmunogenic Matrices (Allogenic, Xenogenic)

In the last decades, increasing evidence has enlightened that acellular, nonimmunogenic matrices, obtained with the detergent–enzymatic method, act as scaffolds and can stimulate

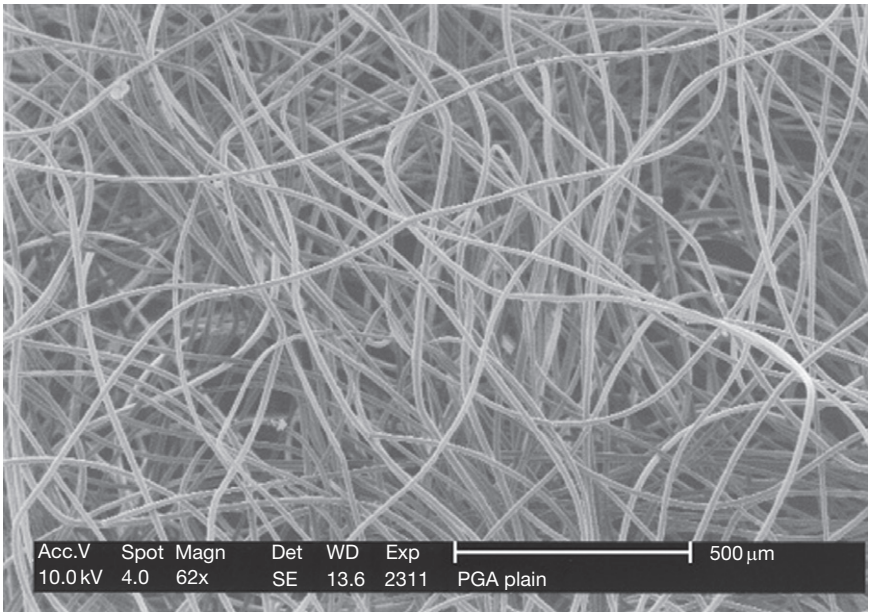

Figure 3 Scanning electron microscopy of a fiber-based polymer scaffold consisting of a nonwoven mesh of polyglycolic acid fibers.

in vivo the ingrowth of host cells, matrix formation, and the binding of new cells and matrix to host tissue.[58,77] Those characteristics would eventually prevent the formation of stenosis. Scaffolds derived from decellularized tissues have been used successfully in both preclinical animal studies and in human clinical applications.[78]

Behrend *et al.*[79] addressed the challenge of treating nonhuman tissue such that low immunogenicity on transplantation is achieved while preserving the tissue's structural integrity. Results showed that trypsin/EDTA tissue preparation caused a substantial reduction in the tensile strength of the trachea, making this an unsuitable method for preparing tracheal tissue intended for transplantation. In an *in vitro* study by Conconi *et al.*,[80] porcine tracheal matrices were treated with 18 cycles of a detergent–enzymatic method to reduce the antigenicity of matrices, thus better supporting adhesion of both chondrocytes and tracheal epithelial cells when compared with formalin, thimerosal, and acetone preparations.

In another experiment, autologous costal chondrocytes, smooth muscle cells, respiratory epithelium, and endothelial progenitor cells were cultured *in vitro* and then seeded on acellularized jejunal segments that served as a vascularized matrix.[81] Chondrocyte growth and extracellular cartilaginous matrix production were observed within 2 weeks, and thus, this experiment yielded the fundamental elements for a tissue-engineered trachea. This study also addressed the need for a three-dimensional (3D) scaffolding to mimic the native trachea.

Macchiarini *et al.*,[82] created a tissue-engineered tracheal patch using autologous muscle and fibroblasts seeded on a collagen matrix from a decellularized porcine proximal jejunum segment. After incubating for 3 weeks in a bioreactor, the bioartificial construct was used to close the tracheal defect in a 58-year-old man who had undergone a right completion carinal pneumonectomy. Postoperative endoscopies confirmed that the graft was airtight and covered with autologous ciliated respiratory epithelium. After 12 weeks, the bioartificial patch was functionally and morphologically integrated into the adjacent airway without signs of chronic inflammation, infection, or the growth of granulation tissue. This case report shows promise that tissue engineering may be the solution when therapeutic interventions are limited (**Figure 4**).

However, the bioengineering process in these previous experiences was labor intensive and required too many steps to gain wide clinical acceptance. Jungebluth *et al.*[83] demonstrated that the *in vitro* detergent–enzymatic method, described previously, used to generate short, but vital, tracheal matrices[80] is also a simple and effective method to bioengineer *in vivo* tracheal matrices of sufficient length to have potentially useful clinical application. Such matrices lack any MHC antigens and were shown to maintain structural and functional integrity, similar to that of native tracheas. Seventeen cycles, or around 35 days of detergent–enzymatic treatment, were necessary to bioengineer a tracheal tubular matrix that was structurally and mechanically similar to native trachea, but lacked sufficient immunogenicity to avoid rejection in animal models. A higher number of cycles led to worsening of the mechanical properties of the tracheal matrices to such an extent that implantation could be jeopardized. Interestingly, the immunologic and mechanical characteristics of the matrices remained unaffected by a 2-month storage in phosphate-buffered saline (containing 1% antibiotic and antimycotic, at 4 °C).

To confirm the nonimmunogenic properties of the decellularized matrices, the group went on to implant them in HLA-unmatched pigs and mice, mimicking allotransplantation and xenotransplantation settings, respectively. Implants were left over a period of 30 days without immunosuppression. They displayed no histological signs of local or graft rejection and significantly less inflammatory reaction and activation of

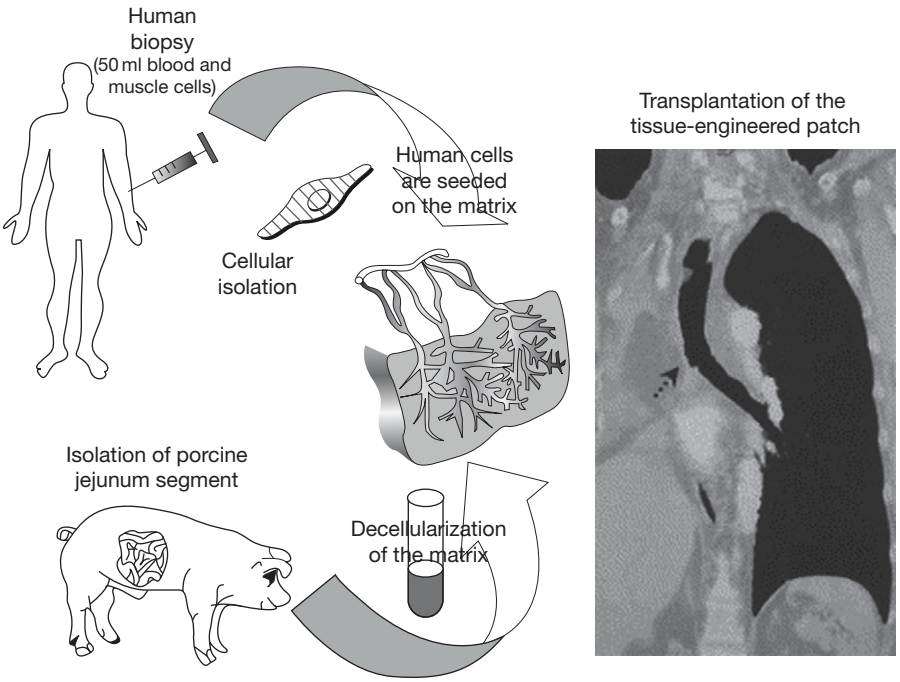

Figure 4 Process of engineering the bioartificial patch. Muscle cells and fibroblasts are isolated from a biopsy specimen obtained from the patient. These cells are seeded on a biologic matrix representing a collagen network generated from a decellularized porcine jejunal segment. During the incubation period, the cells start to remodel the xenogenic matrix and replace it with autologous connective tissue. Within 4 weeks, this autologous bioartificial implant can be clinically used. The computed tomographic scan of the chest 6 weeks after graft implantation shows the site (arrow) where the tissue-engineered patch was transplanted. Reproduced from Macchiarini, P.; Walles, T.; Biancosino, C.; Mertsching, H. *J. Thorac. Cardiovasc. Surg.* **2004**, *128*(4), 638–641, with permission from Elsevier.

adhesion molecules (e.g., P-selectin), or expression of swine leukocyte antigen antibodies, when compared with control or untreated tracheas during the study period.

A technique similar to the one described by Jungebluth *et al.*,[83] Go *et al.*,[84] and Conconi *et al.*[80] was employed by Macchiarini *et al.*[58] to decellularize a human trachea that was then seeded with autologous cells and used to replace a long-segment stenosed airway secondary to tuberculosis in a 30-year-old patient. The graft immediately provided the recipient with a functional airway, improved her quality of life, and had a normal appearance and mechanical properties at 4 months. The patient had no antidonor antibodies and was not on immunosuppressive drugs. At 1 year postimplantation, the graft is still functioning well and there are no signs of rejection.[85] The results show that we can produce a cellular, tissue-engineered airway with mechanical properties that allow normal functioning, and which is free from the risks of rejection.

The potential strengths of the decellularized scaffold approach lie in the similarity to normal anatomy and biomechanics that can be achieved. To this may be added observations of improved angiogenesis and cell migration, hypothetically via residual peptides left on the scaffold by the washing process, and by the presence of mesenchymal stem cells (MSCs). In other words, the decellularized scaffold seemed to fulfill the properties of an 'ideal matrix,' namely biocompatibility, bioabsorbability, nonimmunogenity, support of cell attachment and growth, and an ability to induce angiogenesis.

Compared with biodegradable synthetic scaffolds, natural decellularized xenogenic and allogenic scaffolds maintain the natural ECM composition, do not produce toxic biodegradation products, do not induce inflammation, and have already been successfully used for tissue engineering of heart valves, blood vessels, and urinary bladder.[86] A potential drawback, however, is the need for cadaveric donors. Still, tissue can be banked for later use and is nonallogenic, thereby increasing the potential donor pool compared to conventional transplanted organs.

5.536.3.3. Seeding with Stem Cells

Cells used in tissue engineering can be derived from numerous sources, including primary tissues and cell lines. Cells may be allogenic, xenogenic, syngeneic, or autologous. Ideally, the cells should be nonimmunogenic, highly proliferative, and easy to harvest and should have the ability to differentiate into a variety of cell types with specialized functions.

The single most important element to the success of tissue engineering is the ability to generate sufficient numbers of cells that maintain the appropriate phenotype and perform the required biological functions. For example, cells must produce ECM in the correct organization, secrete cytokines and other signaling molecules, and interact with neighboring cells/tissues. Immediately, this raises a number of potential problems, not least of which is obtaining appropriate cell numbers to promote repair.

To tissue engineer the trachea, the key components are reproducible cell lines with tracheal characteristics and a synthetic scaffolding to reproduce the structural requirements. Tissue preparations and culture media have been compared to find a combination that supports high levels of cell differentiation and maintains cellular structure and strength. Sachs *et al.*[87] found that primary human tracheal epithelial cells cultured in media with high concentration of retinoic acid produced better cell differentiation when compared with media with low or no retinoic acid. Primary human laryngeal epithelial cells from normal individuals have also been isolated and characterized, and it has been shown that they can be cultured *in vitro*.[88]

Although autologous cells are most desirable compared to allogenic and xenogenic cells, with regards to immunological compatibility and pathogen transmission, in general, they are differentiated and postmitotic. This can also be compounded by the tendency of some cell types to dedifferentiate during *ex vivo* cultivation and express an inappropriate phenotype. Although primary, especially autologous, cells are still used in tissue engineering,[89–91] yields and proliferation rates tend to be low and for some phenotypes, harvesting from a patient or donor is not an option. In particular, the standard approach of harvesting autologous cells (e.g., cartilage) for surgical reconstruction of the trachea has disadvantages such as donor site pain and limited tissue availability. These limitations have stimulated studies to find and develop alternative cell sources for tissue-engineering strategies and stem cells are already providing solutions to some of the problems encountered using primary cells released from explanted tissues.

Stem cells play a crucial role in the development and regeneration of human tissues. They are defined as cells that continuously renew themselves, while maintaining the ability to differentiate into various cell types.[92] The flexibility of stem cells, whether adult, embryonic, or induced embryonic, is an important component of this future. Embryonic stem cells, which have the capacity to develop into all three germ layers, have an immense regenerative capacity in animal models. However, use of embryonic stem cells comes with ethical dilemmas and concerns over immunological rejection of tissue, infection risks (including transmission of prions) and risks of tumor formation. Amniotic fluid is also a rich source of stem cells and these can be induced to differentiate into cell types representing each embryonic germ layer, including cells of adipogenic, osteogenic, myogenic, endothelial, neuronal, and hepatic lineages. In addition, they were found to be nontumorigenic.[93]

The recent discovery that adult cells can be persuaded to take on all the antigenic and behavioral characteristics of embryonic stem cells (inducible pluripotent stem cells) opens up a whole new vista for regenerative medicine,[94,95] although their clinical safety in terms of virus infection or tumorigenicity has not been established. Recently, however, it has been shown that the generation of inducible pluripotent stem cells is possible without any genetic alteration of the adult cell (so-called protein-induced pluripotent stem cells). A repeated treatment of the cells with certain proteins channeled into the cells via polyarginine anchors was sufficient to induce pluripotency.[96] Meanwhile, adult MSCs have already proven their versatility and safety in a number of phase I/II human clinical trials (e.g.,[97]).

The use of adult MSCs as a cell line is advantageous for several reasons. First, bone marrow aspirates can be done under local anesthesia, averting the risks associated with general anesthesia in critically injured patients. Second, in combination with *in vitro* tissue culturing, it is possible to obtain large numbers of each of the cell types from MSCs, sparing the patient from multiple procedures. In theory, therefore, these cells could be removed from a patient, incorporated into a tissue construct, and put back into the same individual when repair becomes necessary, thereby removing the need for immunosuppression (**Figure 5**).

Nakamura's group have designed acellular, biosynthesized prostheses with a porous polypropylene framework to mimic the cartilaginous mechanical properties of the native trachea, conjugated with a lyophilized collagen layer (collagenous sponge), which enables host cells to migrate and proliferate. This has been applied to canine models and human studies.[8,9,98] Their work in animal models and clinical studies with acellular scaffolds showed that epithelialization of the luminal surface is rather slow. They argue that cell-seeding approaches should be considered in terms of epithelialization speed, as both the study by Macchiarini *et al.*[58] and further animal experiences by the same group show.[99–101] However, recently Go *et al.*[84] have shown that both epithelial and mesenchymal stem-cell-derived chondrocytes are necessary for optimal survival of tissue-engineered airway transplants in pigs.

5.536.3.4. Bioreactors

Most of the early work in tissue engineering relied on the use of standard static cell-culture conditions for the *in vitro* fabrication of tissue before implantation. Producing a dynamic *in vitro*

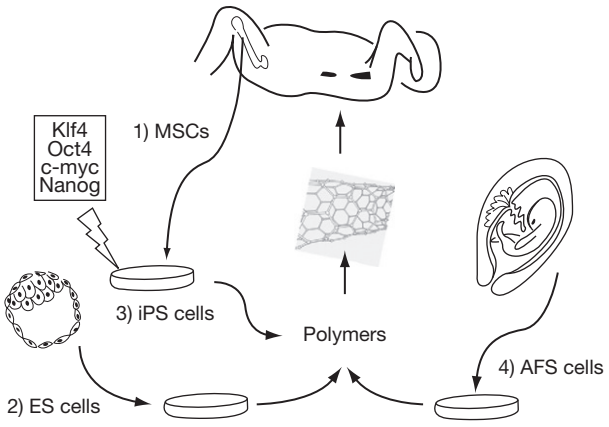

Figure 5 Sources of stem cells. Mesenchymal stem cells (MSCs) can be derived from the bone marrow of a patient and expanded *in vitro*. The same cells can be either directly seeded onto a polymer or transfected as to express stemness genes (Klf4, Oct4, c-myc, Nanog), hence becoming induced pluripotent stem (iPS) cells. iPS will then be expanded *in vitro* and seeded onto a polymer. Alternatively, embryonic stem (ES) cells can be derived from a donor blastocyst, expanded *in vitro*, and finally seeded onto a polymer. Amniotic fluid stem (AFS) cells can be collected from the amniotic fluid of a donor, or patient, prenatally, expanded *in vitro* and seeded onto a polymer. The polymer seeded with either cell type will finally be transplanted to replace the native organ. Adapted from Zani, A.; Pierro, A.; Elvassore, N.; De Coppi, P. *Semin. Pediatr. Surg.* **2009**, *18*(1), 57–62.

microenvironment culture system (bioreactor) for tissues may be an important aspect in guiding the formation of tissue with certain structural and functional characteristics. The use of bioreactors enables the *in vitro* culture of greater volumes of cells than could be obtained with conventional tissue-culture techniques. Furthermore, the use of bioreactors allows the investigator the opportunity to control flow and mixing, which can enhance mass transfer of nutrients, gases, metabolites, and regulatory molecules.

Bioreactors can also provide mechanical regulatory signals, such as directly applied compression, to stimulate the cells to produce specific biomolecules. Vunjak-Novakovic *et al.*,[102] for example, have shown that hydrodynamic conditions in convective-flow tissue-culture bioreactors can improve the quality of cartilage produced in comparison to standard static culture conditions and can modulate the composition (matrix components), morphology, mechanical properties, and electromechanical function of tissue-engineered cartilage. Hydrodynamic stimulation of the cartilage resulted in the production of greater amounts of ECM components such as glycosaminoglycans and collagen, leading to improved biomechanical properties. Mechanical stimulation is needed to favor cellular proliferation, maintenance of cellular differentiation, ECM production, and tissue organization with overall maturation of the cell construct.

Major challenges in functional airway bioengineering require uniform and highly efficient cell seeding on both the outer and inner surfaces of the 3D tubular matrix, coculturing different cell types, and optimum mass transport between the culture medium and the growing tissues. To address these issues, a novel double-chamber, rotating bioreactor has been developed, suitable for *in vitro* engineering of long airway grafts.[58] Early on, it was realized that the two different cell types (epithelial cells and chondrocytes) required different culture conditions. Therefore, the prototype bioreactor created for preclinical work was designed to provide two separate sterile compartments, each with a rotating air-medium interface. Viability of cells in both compartments was maintained and the dynamic culture environment in the bioreactor was controllable and reproducible; an essential requirement for the nutrient supply and waste removal needed to sustain large 3D constructs. The rotation provides the hydrodynamic shear stress necessary to promote metabolic activity and proper differentiation of the seeded cells.

Currently, the major limitation of the rotating bioreactor is the low level of automation of the system. An automatic medium conditioning and exchange system is desirable in order to minimize contamination risks and protect homeostasis. This would operate unattended over a period of days or weeks, while permitting intermittent, sterile evaluation of pH, nutrient, or waste concentration. A system controller would also be useful to manage the tissue-engineering process. Monitoring the data provided by sensors, allied to closed-loop feedback, will allow more control and, thereby, reproducibility of expansion, differentiation and migration of cells within the scaffold.[85]

The group has confirmed the persistence of viable chondrocytes, and a layer of viable epithelial cells at 2 months post-surgery.[85] However, the epithelial layer, whilst macroscopically intact and clearing mucus by this time, was microscopically discontinuous. Thus, further work to improve epithelial cell coverage of the internal surface of the graft preoperatively is necessary, and this is an important design consideration for further refinements of the bioreactor. In addition, the application of flow stimuli to the internal compartment of the bioreactor may encourage appropriate alignment, orientation, and function of cilia prior to implantation, thereby initiating appropriate clearance of mucus from the first postoperative day (**Figures 6** and **7**).

5.536.3.5. Transplantation in Animal Models and Humans

Langer and Vacanti's[69] review seemed to boost the trend of tissue-engineering approaches in this field. In 1994, epithelial tissue was first induced on a tissue-engineered trachea.[103] In that study, tracheal epithelial cells were isolated from newborn lambs in advance to induce an epithelial lining on the reconstructed site. These epithelial cells were injected into a previously manufactured cylindrical cartilage tube made from cells harvested from calves. These *in vitro* formed tubes were then implanted into subcutaneous pockets of ten nude mice, aged 6 weeks. Four of the ten implanted tubes were found to develop an epithelial lining on the inner surface, whereas the other six tubes became infected.

Development of tracheal cartilage has also been studied in rats by means of tissue engineering.[104] Kojima *et al.*[105] ambitiously tried to create cartilage with a biodegradable sheet of PGA and chondrocytes from the nasal septa of sheep. They prepared two bioabsorbable PGA mesh sheets, which were separately seeded *in vitro* with fibroblasts and chondrocytes. The two sheets were formed into a tube and implanted under the sternocleidomastoid muscle before tracheal replacement. Disappointingly, their attempt gave poor results; their animals survived only 2–7 days after surgery because of malacia and stenosis. The graft degenerated and was unable to maintain the mechanical properties required of a functional trachea.

Okamoto *et al.*[106] have made tracheal cartilage using bone morphogenetic protein 2 in dogs. In their canine model, a 1×5 cm slit defect of the tracheal cartilage was created in the trachea in advance, while carefully preserving the tracheal mucosa. Subsequently, regeneration of the cartilage was recognized around the stumps of the resected cartilages. Although these tissue-engineering trials have met with some limited success, achievement of a long-term durable tracheal cartilage with mechanical properties similar to those of native tracheal cartilage still seems a long way off.

Although there are previous reports of generation of small volumes of tracheal cartilage and clinical application,[81,82] progress with long-segment grafts up until recently has been limited by lack of an ideal scaffold, well-established epithelial and chondrocyte culture techniques, and an appropriate bioreactor environment. The approach of Macchiarini *et al.*[58] differed from that of Vacanti's group in that, instead of regenerating cartilage from chondrocytes, they used a cadaveric trachea with a cartilage backbone as a matrix. The group removed cells and MHC antigens from a human donor trachea using the detergent–enzymatic technique described previously in animal studies,[80,83] in order to create a nonimmunogenic, decellularized matrix.

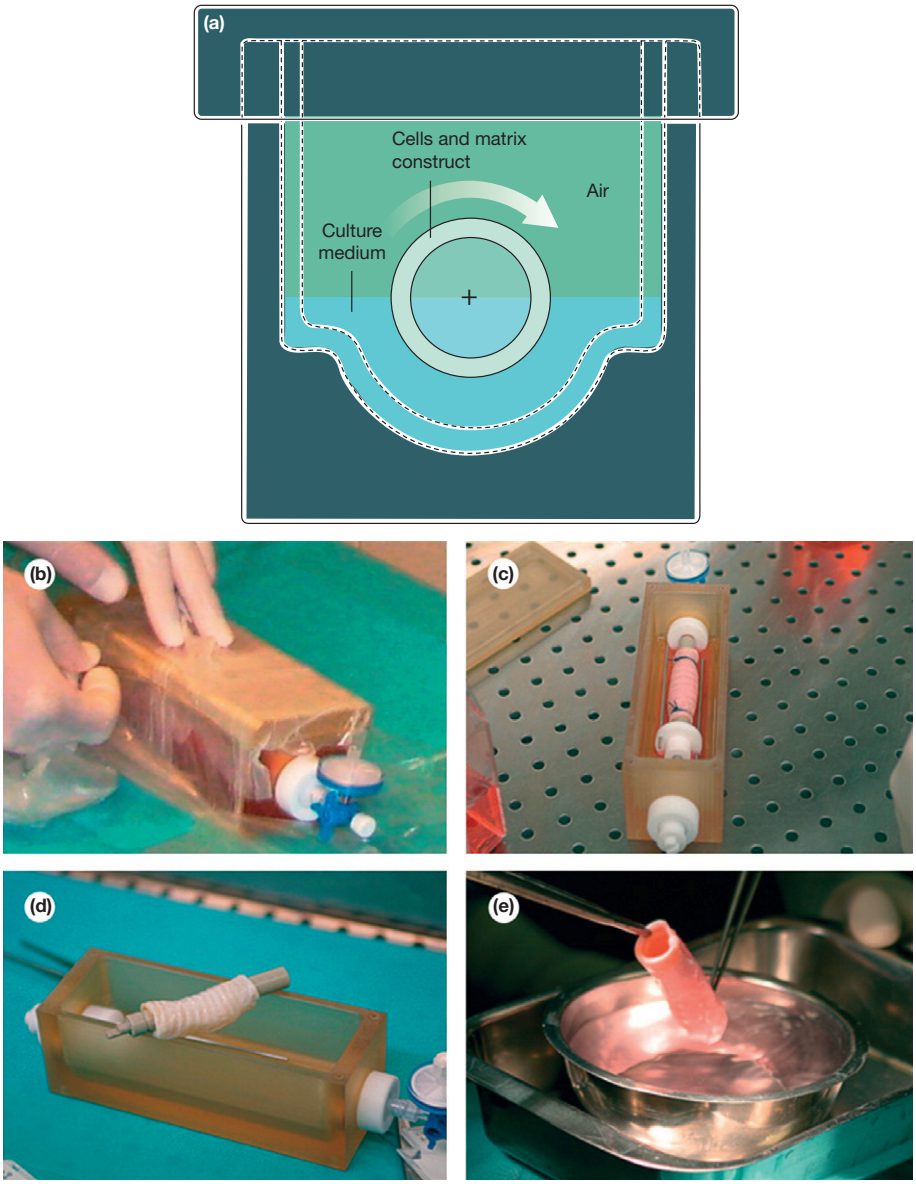

Figure 6 Bioreactor developed for airway tissue engineering. Reproduced from Macchiarini, P.; Jungebluth, P.; Go, T.; *et al*. *Lancet* **2008**, *372*(9655), 2023–2030, with permission from Elsevier.

Twenty-five cycles were required to remove nearly all HLA-positive cells from the tracheal matrices. This was then readily colonized by autologous epithelial cells and mesenchymal stem-cell-derived chondrocytes that had been cultured from cells taken from the recipient (a 30-year-old woman with end-stage bronchomalacia). This tissue-engineered graft was successfully implanted in order to replace the recipient's left main bronchus. The tissue-engineered airway remained patent 4 months after the operation and the patient had an improved quality of life. Importantly, the patient had no anti-donor antibodies and was not on any immunosuppressive drugs. The graft is still functioning well and there is no sign of rejection at 1 year postimplantation[85] (**Figure 8**).

Although the graft in the above study was completely covered with viable mucosa at 1 month, it is still not clear whether these epithelial cells originated from the seeded cells, or whether they grew in from an adjacent healthy airway. Previous studies have suggested that early on, it is the implanted cells that are important, and later on, they may grow in from the adjacent recipient site.[54,55,107]

A longer follow-up interval is required prior to a full-scale clinical trial, to fully assess the tissue-engineered airway's efficacy and safety. In particular, longer follow-up is necessary to assess the long-term retention of the graft's biomechanical properties, whether new chondrogenesis (or osteogenesis) occurs from the seeded chondrocytes, and to monitor for

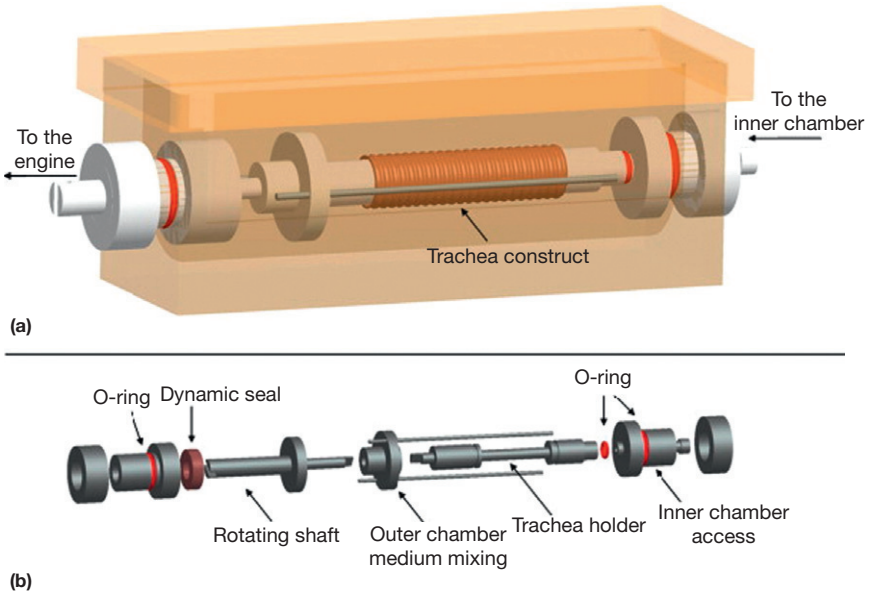

Figure 7 Three-dimensional view of the bioreactor assembly (a) and exploded view of its components (b). Adapted from Asnaghi, M. A.; Jungebluth, P.; Raimondi, M. T.; *et al. Biomaterials* **2009**, *30*(29), 5260–5269.

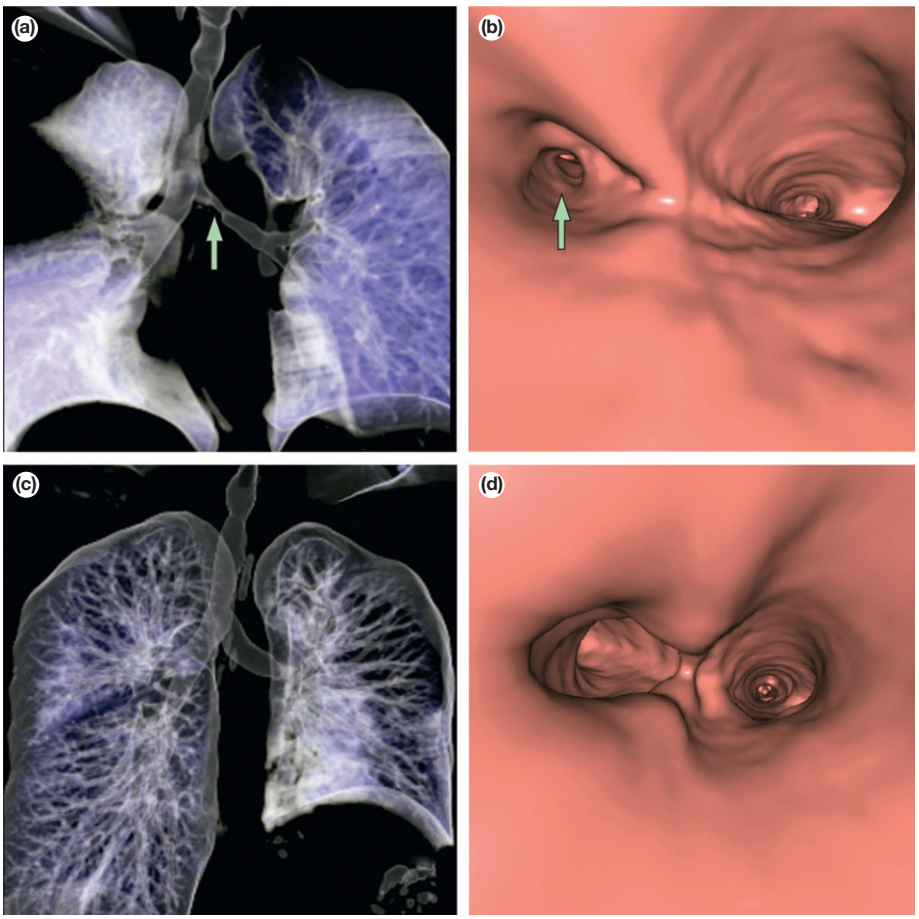

Figure 8 Volume-rendering CT (a and c), and virtual bronchoscopic (b and d) reconstructions before (a and b) and 1 month after (c and d) engraftment of tissue-engineered trachea to replace left main bronchus. Reproduced from Macchiarini, P.; Jungebluth, P.; Go, T.; *et al. Lancet* **2008**, *372*(9655), 2023–2030, with permission from Elsevier.

signs of restenosis, rejection, or the presence of antidonor antibodies.

5.536.4. Tissue-Engineered Larynx for Total Laryngeal Replacement and Transplantation: The Ultimate Goal

The replacement of movement, as would be necessary to replace larynx or esophagus, introduces another order of magnitude of complexity. Nevertheless, progress toward these goals is starting to bear fruit.

5.536.4.1. Generation of Muscle

One of the challenges in developing a fully functional tissue-engineered larynx suitable for total laryngeal replacement is being able to generate muscle as would be required to reproduce normal vocal cord movements to allow laryngeal speech and breathing and to protect the airway from aspiration. *In vitro* engineering of functional skeletal muscle tissue would also be a very important issue in reconstructive surgery, particularly for the repair of congenital defects, and when a large amount of muscle is lost following trauma, oncological resection, or prolonged denervation.

Adult mammalian muscle cells are terminally differentiated and cannot replace themselves. Muscle regeneration, through cell transplantation, has long been explored as a potential therapeutic approach for muscle disorders such as Duchenne muscular dystrophy (DMD). At present, in addition to the obvious need to modulate the immunological, inflammatory response, two major concerns need to be addressed: what are the best muscle progenitors and what is the most efficient way of delivering them?

Different cell sources have been tested to find the optimal cell type that would proliferate and integrate into the regenerating muscle. The most well-known muscle progenitor cells are satellite cells. Satellite cells, first described in 1961,[108] are dormant progenitors located at the periphery of skeletal myofibers that can be triggered to proliferate for both self-renewal and differentiation into myogenic cells. In adult skeletal muscle, satellite cells reside beneath the endomysium (basal lamina) of muscle, closely juxtaposed to muscle fibers, and make up 2–5% of the nuclei associated with a particular fiber. Satellite cells are normally mitotically quiescent, but are activated (i.e., enter the cell cycle) in response to stress induced by weight bearing, or by trauma such as injury.

Two general approaches are adopted to engineer artificial skeletal muscle tissue. One way is to regenerate autologous satellite cells by biopsy, expand and differentiate cells *in vitro* in a 3D-defined environment (such as an artificial bioreactor), and reimplant the neotissue after differentiation has taken place (*in vitro* tissue engineering). The second approach involves the generation of satellite cells, expansion of cells *in vitro*, and reimplantation of donor cells using a transport matrix, which allows differentiation into myotubes to occur *in vivo* (myoblast transfer therapy). In the latter scenario, implanted myoblasts might also serve as vehicles for the delivery of recombinant proteins and/or growth factors (*in vivo* tissue engineering).

Myoblast transplantation (also known as myoblast transfer therapy) is a possible treatment for congenital and acquired muscular disorders, including several muscular dystrophies, and has been piloted for the treatment of vocal fold paralysis.[109] The initial demonstration that myoblast transplantation could restore the expression of dystrophin in nude/mdx mouse muscle fibers (an animal model of DMD) came as early as 1989.[110] However, the clinical trials that followed produced either negative or very limited positive results. Allogeneic myoblasts transplanted into DMD patients have been largely inefficient owing to immune rejection, rapid death, and limited intramuscular migration.

An important and poorly understood limitation of the satellite cell is its *in vitro* proliferative capacity.[111] After isolation, satellite cells can only divide a small number of times, and *in vitro* expansion reduces *in vivo* differentiation potency.[112] On the other hand, a small amount of tissue-resident satellite cells, *in vivo*, is sufficient to regenerate large parts of muscle tissue.[112–114] Collins *et al.*,[113] for example, showed that transplantation of single, intact myofibers with their attached satellite cells led to high levels of cell integration and proliferation. The inability to recapitulate the proliferative capacity *in vitro* is probably due to loss of the highly specific niche that normally surrounds these cells. In addition, satellite cells lack the ability to cross the muscle endothelium when delivered systemically (i.e., intravenous or interarterial), and because of this limited migration, they must be injected intramuscularly.

In the past few years, attention has focused on the myogenic potential of other stem cells. In addition to muscle-committed satellite cells, multilineage stem cells encountered in embryonic, as well as adult, tissues exhibit myogenic potential in experimental conditions and have been able to form skeletal muscle myofibers. These multilineage stem cells include bone marrow-derived MSCs, skeletal muscle side population cells, muscle-derived stem cells (MDSCs), $CD133^+$ ($AC133^+$) stem cells, mesoangioblasts, and pericytes, in addition to embryonic stem cells, amniotic fluid stem cells, and umbilical cord stem cells.[93,115–123]

One of the main obstacles in the formation of new muscle tissue is the lack of an adequate support for expanded satellite cells. To overcome this obstacle, many groups are trying to develop adequate synthetic and biological matrices to act as delivery systems for implanted cells.[124–133] Current studies on the optimal biochemical and physical conditions of the scaffolds to support myoblast survival and differentiation are aimed at improving this therapeutic platform. The studies are based on the premise that the environment should resemble the natural recipient environment as much as possible to fully support differentiation and maturation of myoblasts into adult skeletal muscle. Growth factors could also be employed and absorbed in the polymer prior to cell seeding. This could be released *in vivo*, with time-promoting proliferation, integration, and differentiation of the transplanted myoblasts.

5.536.4.2. Reinnervation

The main barrier to successful laryngeal transplantation is restoration of normal laryngeal speech and breathing functions. The larynx has the most complex motor function of

any muscular-based system in the human body as may be appreciated by listening to high-performance singing. This complexity is reflected by the comparatively high density of motor fibers in the recurrent laryngeal nerve, as compared to the small size of the muscles it innervates. While sensation is certainly important in eliciting cough, restoration of near-normal mobility of the arytenoids, and hence of the vocal cords, is essential.

Peripheral branches of cranial nerves are thought to regenerate more easily than nerves of the central nervous system. Indeed, damaged peripheral axons usually extend even through the gap caused by the injury. Functionally, however, some peripheral branches of cranial nerves, such as the oculomotor, facial, and recurrent laryngeal nerves regenerate as poorly as those of the central nervous system. Indeed the recurrent laryngeal nerve is known to be one of the peripheral branches of cranial nerves least likely to regenerate functionally once it is cut. At present, however, it is not clear why this may be the case. Major reasons for failure are thought to be failure of the regenerating axons to reach the original target organs, degeneration of the vocal cord muscles, and aberrant simultaneous innervation of antagonistic muscles caused by misdirection of regenerating axons.[134]

Unfortunately, direct repair of the recurrent laryngeal nerve results in synkinesis (mass movement) of muscles as repair in adult animals fails to recapitulate the successful axonal pathfinding of embryogenesis.[135] Thus, although recent electromyography of the patient from the Strome *et al.*[62] study has confirmed some recurrent nerve reinnervation on the right side,[136] the significant abduction that would be required to allow closure of his tracheostomy is still lacking.

A second way of replacing recurrent nerve function is anatomical reinnervation. There is only one muscle that causes laryngeal abduction and posterior motion of the arytenoids, the posterior cricoarytenoid muscle. The unique position of this muscle in laryngeal function, particularly breathing, has given its reinnervation greater prominence than that of the other intrinsic muscles. Fex[137] was the first to show that the phrenic nerve could be rerouted in animals to drive the posterior cricoarytenoid, although reports also suggest that the technique (and related rerouting techniques using other motor nerves such as the ansa cervicalis) may still result in aberrant reinnervation of adjacent muscles, as well as the target abductors with functionally suboptimal results.

The use of laryngeal pacemakers that are triggered on inspiration to stimulate abductor (opening) muscles has been explored by Zealear *et al.*[138] Implantation of a device based on a cardiac pacemaker allowed the removal of a tracheostomy in three of six patients with bilateral recurrent nerve damage implanted, five of whom were reported to have good cord movement. Although the reported system was bulky, groups in the USA and Europe are presently obtaining encouraging results with refined models. These devices may ultimately either provide short-term function and retention of muscle bulk while nerve regeneration proceeds (the so-called 'baby-sitting' effect), or be used as a permanent solution. However, these systems are still far from ideal and do not affect the process of regeneration itself.

Another, complementary, possibility is to work in partnership with peripheral nerve biologists to achieve faster, more accurate reinnervation of a laryngeal graft. Nerve growth factor (NGF), brain-derived neurotrophic factor (BDNF), neurotrophin-3 (NT-3), and neurotrophin-4 (NT-4) have all shown promise in speeding up peripheral nerve repair and are presently being applied in models of laryngeal reinnervation.[139] The application of insulin-like growth factor-1 (a potent myotrophic stimulus) to laryngeal muscles, using a viral vector, is also being tried as a means of retaining end-organ function when reinnervation eventually occurs.[140] Important areas to be investigated are which growth factors to use when, and how to retain them at the repair site.[141]

A tissue-engineered approach to recurrent laryngeal nerve reinnervation has been tried by Kanemaru *et al.*[134] Using a biodegradable artificial nerve conduit constructed of PGA tube coated with collagen, they were able to functionally regenerate four out of six recurrent laryngeal nerves across a 10-mm gap in adult dogs. No functional regeneration was observed where the recurrent laryngeal nerves were reconstructed with an autologous nerve graft (greater auricular nerve). On the other hand, misdirection of regenerated axons to inappropriate muscles was still seen. Perfect recovery of vocal cord movements requires that regenerating axons find the appropriate path leading to their target muscles and reinnervate them accurately.

5.536.4.3. Revascularization

A major potential problem with bioengineered organs is the provision of a functional blood supply. Vascularization is an essential factor for successful implants of bioengineered tissues, and a tissue of more than a few millimeters in volume cannot survive by diffusion and requires formation of new blood capillaries to supply essential oxygen and nutrients. Without revascularization, tracheal grafts of substantial length will possibly undergo necrosis.

Several approaches have been used to induce angiogenesis to a target site, including wrapping a graft with a pedicled omental flap, incorporation of angiogenic factors into the bioengineered tissue, seeding endothelial cells with other cell types and prevascularization of matrices prior to cell seeding.[142]

The use of angiogenic factors is a popular approach to induce neovascularization in engineered tissues. However, bolus injection of recombinant angiogenic proteins such as vascular endothelial growth factor (VEGF) or basic fibroblast growth factor (bFGF) has limitations due to the inherent instability of these proteins *in vivo* and the possibility of uncontrolled effects at distant sites. In order to overcome these problems, investigators designed systems of biodegradable polymers that provided localized and sustained growth factor release.

The embedment of angiogenic proteins inside different material-based implant devices has been actively pursued and several polymeric systems, both natural (alginate, fibrin, hydroxyapatite and chitosan, agarose, collagen, and gelatin) and synthetic (polyethylene glycol, PLA/glycolic acid, silica gel) have been investigated in order to facilitate the development of vascular-inductive tissue-engineering matrices.[126]

An alternative method for angiogenic factor delivery uses naked (plasmid) DNA and viral vectors for recombinant expression of angiogenic factors to the engineered tissue.[143] Matrices of poly(lactide-*co*-glycolide) (PLG) were loaded with plasmid, which was subsequently released over a period ranging from days to a month *in vitro*. Sustained delivery of plasmid DNA encoding PDGF from the matrices led to transfection of large numbers of cells, resulting in enhanced matrix deposition and blood vessel formation in the developing tissue. In another study, De Coppi *et al.*[129] combined the isolation and genetic engineering of myoblasts, with tissue transplantation, in an attempt to create well-vascularized muscle tissue. Rat myoblasts were transfected with a bicistronic plasmid encoding VEGF and green fluorescent protein (GFP), or with a plasmid encoding a nonfunctional VEGF–alkaline phosphatase (AP) fusion protein. The transfected cells were suspended in collagen type I and injected subcutaneously into nude mice. Neovascularization and muscle tissue mass significantly increased with functional VEGF-transfected cells, compared with nonfunctional VEGF-transfected cells.

Microfabrication technology, having largely arisen out of biomedical microelectromechanical systems (MEMS), is a rapidly emerging science with many applications including biomedical engineering.[144–146] It was originally developed for the circuit industry, and allows complex branching patterns at the 1-μm level to be imprinted onto silicon or Pyrex wafers using photolithography and a series of subtractive etching techniques. These templates can be used as molds to replicate their branching patterns onto bioresorbable polymer films, which can then be seeded with endothelial cells to form endothelialized microvasculature networks. The technique allows for a resolution that is required to form templates at the microcirculation level (i.e., the capillaries), which are of the order of 10 μm in diameter. Additionally, micromagnetic resonance imaging and microcomputerized tomography may provide detailed 3D images of the microvasculature for mathematical modeling of flow, branching angles, and resistance to optimize template design (**Figure 9**).

Macchiarini *et al.*[58] did not use any specific measures to aid revascularization in their graft. Nevertheless, they observed rapid recovery of blood flow and luminal mucosal appearance. Indeed, laser-Doppler measurements showed a healthy, adjacent microvascular bed from postoperative day 4 and active mucosal bleeding at 30 days, indicating successful revascularization.

Jungebluth *et al.*[83] have shown that angiogenic cytokines (bFGF, transforming growth factor β) might be present within decellularized matrices, and postulated that similar expression might contribute to timely revascularization. In support of this view, when they implanted sections of detergent–enzymatic method-treated pig trachea into a Balb/c mouse dorsal skin pouch, graft neovascularisation was seen by 2 weeks.

Another possibility is that the seeded epithelial cells and chondrocytes in the biological prosthesis before the implantation may have induced early revascularization. However, it is still unclear whether the seeded cells regenerated any tissue, including the cartilage and mucosa. Until the functions of the seeded cells are more clearly elucidated, it remains unclear whether the results should be regarded as a fully tissue-engineered replacement, or an allotransplantation of the trachea.

5.536.4.4. Immunogenicity

By contrast with solid organ transplants, which take place in sterile mesenchymal environments (e.g., kidney, liver, heart), the airway represents an interface between the internal and external environment. Unsurprisingly, the airway mucosa has immunologically active cells playing a key part in airway transplantation,[53] and these contribute to acute allograft rejection, which requires high-dose immunosuppression. Unlike other transplants, airway replacement is rarely a life-saving procedure, so a completely nonimmunogenic allograft with preserved functional and mechanical characteristics is the minimum target for organ replacement.

Using multiple color immunofluorescence histology, Birchall's group has described a dense, organized network of immunologically active cells, including many dendritic cells in pig[147–150] and human[151] laryngeal mucosae. Human laryngeal epithelial cells also express MHC molecules.[88] Thus, all the indications are that at least the mucosal element of the larynx will represent a strong graft.

In support, Genden's studies of murine tracheal grafts have shown that replacement of the epithelium by host epithelial cells completely prevents rejection after withdrawal of immunosuppression.[56] As re-epithelialization therefore appeared as an attractive strategy for airway grafts, Genden's group went on to show that subsequently the process could be significantly speeded up with the application of VEGF carried by a fibrin matrix to the mucosa.[152]

These observations suggest that tissue (mucosa) specific interventions may be highly effective in preventing laryngeal (or other mucosal organ) allograft rejection and thus removing the need for conventional immunosuppression. Such strategies would also open the door to transplantation for the large pool of potential recipients with laryngeal cancer. This view is tempered somewhat, however, by the observation that rat and mouse laryngeal grafts appear to exhibit early rejection throughout all tissues, not just the laryngeal mucosa,[63,153] and other 'compartments' within the larynx also contain antigenic tissue.[154]

Conconi *et al.*,[80] Macchiarini *et al.*,[58] and Jungebluth *et al.*[83] have developed a technique to generate decellularized tracheal matrices by detergent–enzymatic methods (containing sodium deoxycholate/deoxyribonuclease lavations). They are able to generate decellularized tracheal matrices of sufficient length to be clinically useful, with functional and mechanical properties similar to native tracheas, but without the problems of immunogenicity. The immunologic ignorance resulting from this procedure avoids allorejection and xenorejection in animal models[83] and humans,[58] and therefore there is no need for immunosuppression. One possible contributory factor to avoidance of hyperacute and acute rejection is the lack of an immediate dedicated blood supply, although vessels were seen to grow into the implanted tissue with time. This protocol opens the door to the creation of clinically functional, fully tissue-engineered airway and organ replacements in the near future.

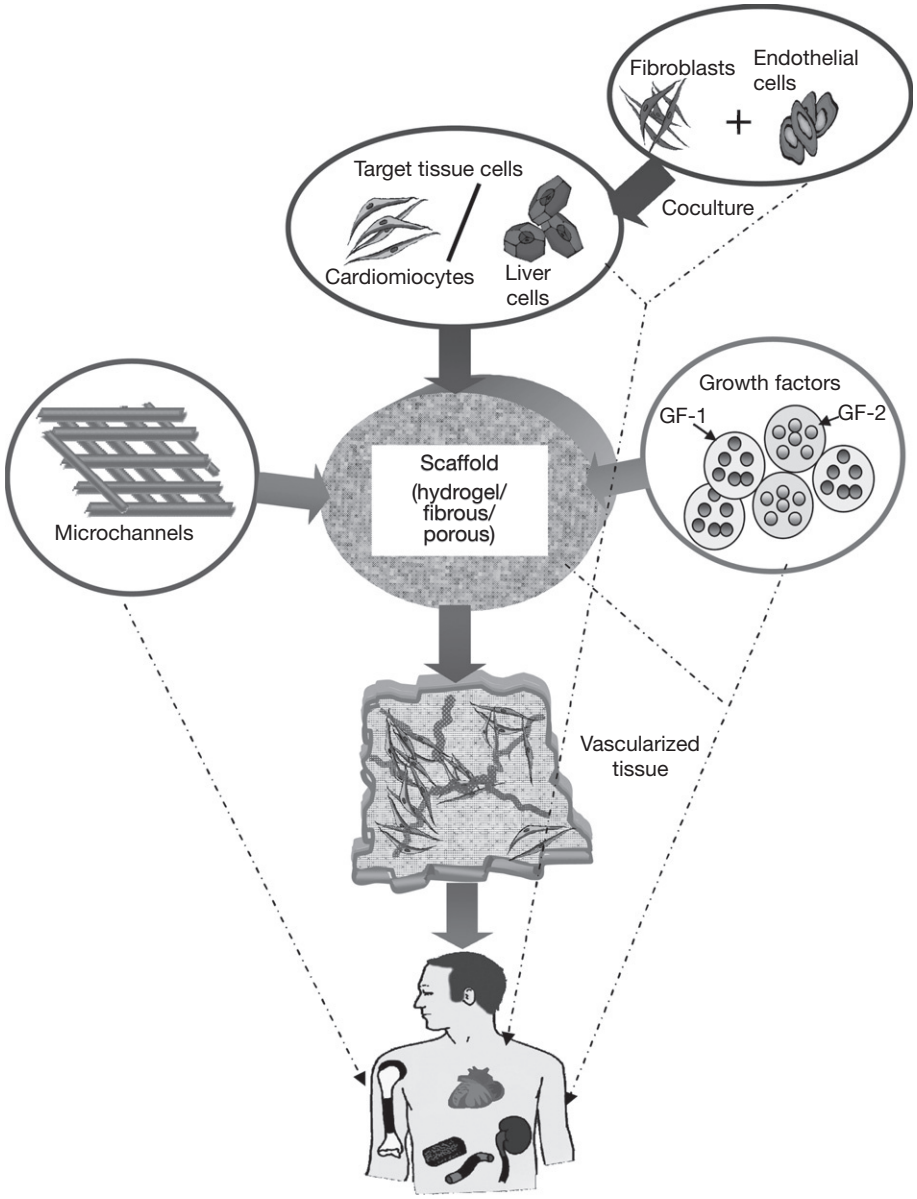

Figure 9 Vascularization strategies for tissue engineering. Independently, each approach can be directly applied *in vivo* for angiogenesis support and enhancement–schematic view. Solid arrows denote integration of the approaches *in vitro* and implantation of vascularized tissue construct. The dashed lines denote direct application *in vivo* of one or several of the approaches. Adapted from Kaully, T.; Kaufman-Francis, K.; Lesman, A.; Levenberg, S. *Tissue Eng. B Rev.* **2009**, *15*(2), 159–169.

5.536.5. Future Challenges and Goals

5.536.5.1. Tissue Engineering the Esophagus: A Preliminary Step Toward Generating a Tissue-Engineered Larynx

Esophageal cancer is a difficult gastrointestinal malignancy to treat, and esophagectomy is often a highly morbid procedure with significant postoperative complications. The stomach, jejunum, or colon are often used in reconstruction procedures, and the patient may suffer from malnutrition postoperatively secondary to poor functioning of the substitute or loss of length and function of the gastrointestinal tract that is being used. Additionally, the treatment of long-gap esophageal atresia often poses a challenge for pediatric surgeons. Current surgical therapies include stretching, circular myotomy, and colonic interposition. These procedures, although often successful, can be complicated by leakage, stricture, and elongation of the interposed colon.

The history of reconstructive surgery of the esophagus dates back to the beginning of the last century. As early as 1907, Bircher first reported the use of a tube of skin to substitute the esophagus.[155] Over the last 80 years, development of an artificial, and more recently a tissue-engineered, esophageal replacement has been investigated as a means to treat these esophageal diseases. Progress in this area may shed some light on the development of a tissue-engineered larynx, for total laryngeal replacement, when the larynx is diseased or dysfunctional.

The esophagus, like the trachea, is an epithelial-lined tubular structure, but tissue engineering of a myoepithelial tube presents additional challenges, namely generating functioning muscle, together with reinnervation and a supportive blood supply; the very same challenges that current investigators attempting to tissue engineer the larynx face. In addition, the esophagus is less rigid and therefore lacks the same support as the trachea.

Many attempts at creating a replacement for the esophagus using artificial materials including rubber, polyethylene, teflon, and polypropylene, among others have been investigated.[156] Most of these materials were eventually extruded, and complications of leakage and stenosis in the long term often developed, as in the case of trachea. Additionally, autologous tissues and homografts have been used as esophageal substitutes. The skin, trachea, and fascia have been used, but complications such as anastomotic leakage and stenosis again often ensued.[156]

Sato *et al.*[157] have been investigating methods to create a tissue-engineered esophageal replacement. Their goal is to harvest a small amount of normal esophageal tissue from a patient with esophageal cancer before operation, culture the cells, and create a natural esophageal replacement *in vitro*. Then they propose to graft the replacement into the same patient at the time of operation.

Toward these goals, Sato *et al.*[157] cultured esophageal epithelial cells on the surface of collagen gels in which biodegradable PGA mesh was embedded. They then sutured the mesh to create a tubular structure lined with cultured cells and wrapped these tubes in the latissimus dorsi muscle flaps of athymic mice. The tubular structure was maintained *in vivo*, and appeared histologically similar to normal esophageal epithelium. A basement membrane was also identified by antilaminin staining. The same group also then embedded fibroblasts into the collagen gels as a feeder layer and repeated the experiment. They noted that the fibroblasts accelerated the proliferation and differentiation of the epithelial cells both *in vitro* and *in vivo*.[158]

Beckstead *et al.*[159] looked at the interaction of esophageal epithelial cells with natural and synthetic scaffolds. Parameters such as calcium concentration, scaffold composition and pore size, and epithelial behavior on synthetic and natural scaffolds were analyzed. The authors concluded that both decellularized human skin (AlloDerm) and degradable polyesters (PLA, PLGA, PCL) supported esophageal epithelial cell adhesion and proliferation. However, natural scaffolds proved to lead to architecturally superior epithelial organization and stratification, compared to synthetic scaffolds, with no need for induced modifications. Modification of the synthetic scaffold's pore size and surface properties (including identification of the proteins or growth factors within the natural matrices responsible) may be necessary to mimic epithelial behavior on natural scaffolds.

More recently, Marzaro *et al.*[160] produced esophageal substitutes composed of homologous esophageal acellular matrix and autologous smooth muscle cells, both isolated from the esophagus of newborn pigs. Acellular matrices obtained by detergent–enzymatic methods did not present any MHC markers, expressed bFGF (demonstrating angiogenic activity), and supported cell adhesion. The authors implanted acellular matrices, with and without cultures of autologous smooth muscle cells, *in vivo* after creating a porcine esophageal wall defect. Constructs containing autologous smooth muscle cells proved to have less severe inflammation and showed an early organization into small fascicules.

To overcome the issue of absent peristaltic contractility in an artificial esophagus, Watanabe *et al.*[161] developed nickel–titanium shaped memory alloy coils, which were placed in an annular manner on a Gore-Tex vascular graft. Interestingly, low-voltage electrical current passing through the coils generated peristaltic movements in the artificial esophagus implanted in a goat model.

5.536.6. Conclusions

The prospect of being able to build customized, nonimmunogenic tissues and organs from scratch, via tissue engineering, is an attractive one. The potential strengths of the decellularized scaffold approach lie in the similarity to normal anatomy and biomechanics that can be achieved, with the opportunities for improved angiogenesis and cell migration.

However, there are many questions that urgently need to be addressed before the technology is accepted and made universally available. Future research should focus on the functions and determining fates of the stem cells *in vitro* and *in vivo*, angiogenesis regulation, optimal bioreactor design and conditions, immunogenicity, and long-term clinical follow-up.

The trachea is an excellent model for addressing these critical questions in the wider picture of cell- and tissue-engineered organ replacements. The trachea is a luminal structure with a relatively thin wall through which nutrients, cells, and new blood vessels pass with relative ease. The replacement of movement, as would be required to replace the larynx, or the replacement of organs that perform similarly complex functions (such as esophagus), introduces another order of magnitude of complexity. Nevertheless, we are one step closer to fulfilling these goals.

References

1. Grillo, H. C.; Dignan, E. F.; Miura, T. *J. Thorac. Cardiovasc. Surg.* **1964**, *48*, 741–749.
2. Mulliken, J. B.; Grillo, H. C. *J. Thorac. Cardiovasc. Surg.* **1968**, *55*(3), 418–421.
3. Belsey, R. *Br. J. Surg.* **1950**, *38*, 200–205.
4. Grillo, H. C. *Ann. Thorac. Surg.* **2002**, *73*(6), 1995–2004.
5. Daniel, R. A. *J. Thorac. Surg.* **1948**, *17*(3), 335–349.
6. Neville, W. E.; Bolanowski, J. P.; Kotia, G. G. *J. Thorac. Cardiovasc. Surg.* **1990**, *99*(4), 604–612.
7. Scherer, M. A.; Ascherl, R.; Geissdorfer, K.; *et al. Arch. Otorhinolarynol.* **1986**, *243*(4), 215–223.
8. Omori, K.; Nakamura, T.; Kanemaru, S.; *et al. Ann. Otol. Rhinol. Laryngol.* **2005**, *114*(6), 429–433.
9. Omori, K.; Tada, Y.; Suzuki, T.; *et al. Ann. Otol. Rhinol. Laryngol.* **2008**, *117*(9), 673–678.
10. Davis, J. S. *Ann. Surg.* **1911**, *54*(6), 734–748.
11. Swift, E. A.; Grindlay, J. H.; Clagett, O. T. *J. Thorac. Surg.* **1952**, *24*(5), 482–492.
12. Bryant, L. R. *J. Thorac. Cardiovasc. Surg.* **1964**, *48*, 733–740.
13. Cheng, A. T.; Backer, C. L.; Holinger, L. D.; Dunham, M. E.; Mavroudis, C.; Gonzalez-Crussi, F. *Arch. Otolaryngol. Head Neck Surg.* **1997**, *123*(10), 1069–1072.
14. Idriss, F. S.; DeLeon, S. Y.; Ilbawi, M. N.; Gerson, C. R.; Tucker, G. F.; Holinger, L. *J. Thorac. Cardiovasc. Surg.* **1984**, *88*(4), 527–536.
15. Cohen, R. C.; Filler, R. M.; Konuma, K.; Bahoric, A.; Kent, G.; Smith, C. *J. Thorac. Cardiovasc. Surg.* **1986**, *92*(2), 296–304.

16. Fonkalsrud, E. W.; Plested, W. G. *J. Thorac. Cardiovasc. Surg.* **1966**, *52*(5), 666–674.
17. Farkas, L. G.; Farmer, A. W.; McCain, W. G.; Wilson, W. D. *Plast. Reconstr. Surg.* **1972**, *50*(3), 238–241.
18. Kuwabara, Y.; Sato, A.; Mitani, M.; *et al*. *Ann. Thorac. Surg.* **2001**, *71*(2), 409–413.
19. Fonkalsrud, E. W.; Sumida, S. *Arch. Surg.* **1971**, *102*(2), 139–142.
20. Hodjati, H.; Kazemi, K.; Jalaeian, H.; Reza Sharifzad, H.; Roshan, N.; Tanideh, N. *J. Surg. Res.* **2008**, *150*(1), 74–77.
21. Kato, R.; Eguchi, K.; Izumi, Y.; *et al*. *Surg. Today* **1995**, *25*(9), 806–810.
22. Kato, R.; Onuki, A. S.; Watanabe, M.; *et al*. *Ann. Thorac. Surg.* **1990**, *49*(6), 951–954.
23. Jones, R. E.; Morgan, R. F.; Marcella, K. L.; Mills, S. E.; Kron, I. L. *Ann. Thorac. Surg.* **1986**, *41*(6), 636–638.
24. Ohlsen, L.; Nordin, U. *Scand. J. Plast. Reconstr. Surg.* **1976**, *10*(2), 135–145.
25. Drettner, B.; Lindholm, C. E. *Acta Otolaryngol.* **1970**, *70*(5), 401–407.
26. MacHale, S. J. *J. Thorac. Cardiovasc. Surg.* **1972**, *64*(1), 6–10.
27. Abbott, O. A.; Vanfleit, W. E.; Roberto, A. E. *J. Thorac. Surg.* **1955**, *29*(3), 217–237.
28. Azorin, J. F.; Bertin, F.; Martinod, E.; Laskar, M. *Eur. J. Cardiothorac. Surg.* **2006**, *29*(2), 261–263.
29. Martinod, E.; Seguin, A.; Holder-Espinasse, M.; *et al*. *Ann. Thorac. Surg.* **2005**, *79*(3), 942–948.
30. Martinod, E.; Seguin, A.; Pfeuty, K.; *et al*. *Ann. Thorac. Surg.* **2003**, *75*(5), 1572–1578.
31. Dodge-Khatami, A.; Nijdam, N. C.; Broekhuis, E.; Von Rosenstiel, I. A.; Dahlem, P. G.; Hazekamp, M. G. *J. Thorac. Cardiovasc. Surg.* **2002**, *123*(4), 826–828.
32. Caputo, V.; Consiglio, V. *J. Thorac. Cardiovasc. Surg.* **1961**, *41*, 594–596.
33. Kimura, K.; Mukohara, N.; Tsugawa, C.; *et al*. *J. Pediatr. Surg.* **1982**, *17*(6), 869–871.
34. Yu, P.; Clayman, G. L.; Walsh, G. L. *Ann. Thorac. Surg.* **2006**, *81*, 714–716.
35. Maciejewski, A.; Szymczyk, C.; Połtorak, S.; Grajek, M. *Ann. Thorac. Surg.* **2009**, *87*(2), 608–610.
36. Edgerton, M. T.; Zovickian, A. *Plast. Reconstr. Surg.* **1954**, *13*, 167–192.
37. Serrano, A.; Ortiz-Monasterio, F.; Andrade-Pradillo, J. *Plast. Reconstr. Surg.* **1959**, *24*, 333–340.
38. Mukaida, T.; Shimizu, N.; Aoe, M.; *et al*. *J. Thorac. Cardiovasc. Surg.* **1998**, *116*(2), 262–266.
39. Tojo, T.; Niwaya, K.; Sawabata, N.; *et al*. *Ann. Thorac. Surg.* **1998**, *66*(1), 209–213.
40. Yokomise, H.; Inui, K.; Wada, H.; *et al*. *J. Thorac. Cardiovasc. Surg.* **1994**, *107*(6), 1391–1397.
41. Yokomise, H.; Inui, K.; Wada, H.; Ueda, M.; Hitomi, S. *J. Thorac. Cardiovasc. Surg.* **1996**, *111*(5), 930–934.
42. Jacobs, J. P.; Quintessenza, J. A.; Andrews, T.; *et al*. *Ann. Thorac. Surg.* **1999**, *68*(3), 1043–1051.
43. Grillo, H. C.; McKhann, C. F. *Transplantation* **1964**, *2*, 48–59.
44. Tanaka, H.; Maeda, K.; Okita, Y. *J. Pediatr. Surg.* **2003**, *38*(12), 1707–1711.
45. Liu, Y.; Nakamura, T.; Sekine, T.; *et al*. *ASAIO J.* **2002**, *48*(1), 21–25.
46. Elliott, M. J.; Haw, M. P.; Jacobs, J. P.; Bailey, C. M.; Evans, J. N.; Herberhold, C. *Eur. J. Cardiothorac. Surg.* **1996**, *10*(9), 707–712.
47. Jacobs, J. P.; Elliott, M. J.; Haw, M. P.; Bailey, C. M.; Herberhold, C. *J. Thorac. Cardiovasc. Surg.* **1996**, *112*(6), 1549–1558.
48. Pacheco, C. R.; Rivero, O.; Porter, J. K. *J. Thorac. Surg.* **1954**, *27*(6), 554–564.
49. Jackson, T. L.; O'Brien, E. J.; Tuttle, W.; Meyer, J. *J. Thorac. Surg.* **1950**, *20*(4), 598–612.
50. Harrington, W. T.; Hung, W. C.; Binns, P. M. *J. Laryngol. Otol.* **1977**, *91*(2), 101–110.
51. Beigel, A.; Steffins-Knutzen, R.; Muller, B.; Schumacher, U.; Stein, H. *Arch. Otorhinolaryngol.* **1984**, *241*(1), 1–8.
52. Rose, K. G.; Sesterhenn, K.; Wustrow, F. *Lancet* **1979**, *1*(8113), 433.
53. Bujia, J.; Wilmas, E.; Hammer, C.; Kastenbauer, E. *Acta Otolaryngol.* **1990**, *110*(1–2), 149–154.
54. Mukaida, T.; Shimizu, N.; Aoe, M.; Andou, A.; Date, H.; Moriyama, S. *Ann. Thorac. Surg.* **1998**, *66*(1), 205–208.
55. Tojo, T.; Kitamura, S.; Gojo, S.; Kushibe, K.; Nezu, K.; Taniguchi, S. *J. Thorac. Surg. Cardiovasc. Surg.* **1998**, *116*(4), 624–627.
56. Genden, E. M.; Govindaraj, S.; Chaboki, H.; *et al*. *Ann. Otol. Rhinol. Laryngol.* **2005**, *114*(4), 279–288.
57. Liu, Y.; Nakamura, T.; Yamamoto, Y.; *et al*. *J. Thorac. Cardiovasc. Surg.* **2000**, *120*(1), 108–114.
58. Macchiarini, P.; Jungebluth, P.; Go, T.; *et al*. *Lancet* **2008**, *372*(9655), 2023–2030.
59. Levashov, Y. N.; Yablonsky, P. K.; Cherny, S. M.; Orlov, S. V.; Shafirovsky, B. B.; Kuznetzov, I. M. *Eur. J. Cardiothorac. Surg.* **1993**, *7*(7), 383–386.
60. Delaere, P.; Vranckx, J.; Verleden, G.; De Leyn, P.; Van Raemdonck, D.; Leuven Tracheal Transplant Group. *N. Engl. J. Med.* **2010**, *362*(2), 138–145.
61. Kluyskens, P.; Ringoir, S. *Laryngoscope* **1970**, *80*(8), 1244–1250.
62. Strome, M.; Stein, J.; Esclamado, R.; *et al*. *N. Engl. J. Med.* **2001**, *344*(22), 1676–1679.
63. Lott, D. G.; Shipchandler, T. Z.; Dan, O.; Lorenz, R. R.; Strome, M. *Laryngoscope* **2010**, *120*(1), 39–43.
64. Duque, E.; Duque, J.; Nieves, M.; Mejia, G.; Lopez, B.; Tintinago, L. *Transplant. Proc.* **2007**, *39*(7), 2076–2078.
65. Birchall, M. A. *Lancet* **2004**, *363*(9422), 1663.
66. Bisceglie, V. *Ztschr. Krebsforsch* **1933**, *40*, 122–140.
67. Atala, A.; Bauer, S. B.; Soker, S.; Yoo, J. J.; Retik, A. B. *Lancet* **2006**, *367*(9518), 1241–1246.
68. Pham, C.; Greenwood, J.; Cleland, H.; Woodruff, P.; Maddern, G. *Burns* **2007**, *33*(8), 946–957.
69. Langer, R.; Vacanti, J. P. *Science* **1993**, *260*(5110), 920–926.
70. Vacanti, J. P.; Morse, M. A.; Saltzman, W. M.; Domb, A. J.; Perez-Atayde, A.; Langer, R. *J. Pediatr. Surg.* **1988**, *23*(1 Pt 2), 3–9.
71. Vacanti, C. A.; Langer, R.; Schloo, B.; Vacanti, J. P. *Plast. Reconstr. Surg.* **1991**, *88*, 753–759.
72. Vacanti, C. A.; Cima, L. G.; Ratkowski, D.; Upton, J.; Vacanti, J. P. *Mater. Res. Soc. Symp. Proc.* **1992**, *252*, 367–373.
73. Puelacher, W. C.; Mooney, D.; Langer, R.; Upton, J.; Vacanti, J. P.; Vacanti, C. A. *Biomaterials* **1994**, *15*, 774–778.
74. Puelacher, W. C.; Wisser, J.; Vacanti, C. A.; Ferraro, N. F.; Jaramillo, D.; Vacanti, J. P. *J. Oral Maxillofac. Surg.* **1994**, *52*, 1172–1178.
75. Vacanti, C. A.; Kim, W.; Schloo, B.; Upton, J.; Vacanti, J. P. *Am. J. Sports Med.* **1994**, *22*(2), 485–488.
76. Ibarra, C.; Jannetta, C.; Vacanti, C. A.; *et al*. *Transplant. Proc.* **1997**, *29*, 986–988.
77. Sutherland, R. S.; Baskin, L. S.; Hayward, S. W.; Cunha, G. R. *J. Urol.* **1996**, *156*(2 Pt 2), 571–577.
78. Gilbert, T. W.; Sellaro, T. L.; Badylak, S. F. *Biomaterials* **2006**, *27*(19), 3675–3683.
79. Behrend, M.; Kluge, E.; Von Wasielewski, R.; Klempnauer, J. *J. Invest. Surg.* **2002**, *15*, 227–236.
80. Conconi, M. T.; De Coppi, P.; Di Liddo, R.; *et al*. *Transpl. Int.* **2005**, *18*, 727–734.
81. Walles, T.; Giere, B.; Hofmann, M.; *et al*. *J. Thorac. Cardiovasc. Surg.* **2004**, *128*(6), 900–906.
82. Macchiarini, P.; Walles, T.; Biancosino, C.; Mertsching, H. *J. Thorac. Cardiovasc. Surg.* **2004**, *128*(4), 638–641.
83. Jungebluth, P.; Go, T.; Asnaghi, A.; *et al*. *J. Thorac. Cardiovasc. Surg.* **2009**, *138*(3), 586–593.
84. Go, T.; Jungebluth, P.; Baiguero, S.; *et al*. *J. Thorac. Cardiovasc. Surg.* **2010**, *139*(2), 437–443.
85. Asnaghi, M. A.; Jungebluth, P.; Raimondi, M. T.; *et al*. *Biomaterials* **2009**, *30*(29), 5260–5269.
86. Kim, B. S.; Baez, C. E.; Atala, A. *World J. Urol.* **2000**, *18*(1), 2–9.
87. Sachs, L. A.; Finkbeiner, W. E.; Widdicombe, J. H. *In Vitro Cell. Dev. Biol. Anim.* **2003**, *39*, 56–62.
88. Rees, L. E.; Gunasekaran, S.; Sipaul, F.; Birchall, M. A.; Bailey, M. *Mol. Immunol.* **2006**, *43*(6), 725–730.
89. Komura, M.; Komura, H.; Kanamori, Y.; *et al*. *J. Pediatr. Surg.* **2008**, *43*(12), 2141–2146.
90. Komura, M.; Komura, H.; Tanaka, Y.; *et al*. *Pediatr. Surg. Int.* **2008**, *24*(10), 1117–1121.
91. Walles, T.; Giere, B.; Macchiarini, P.; Mertsching, H. *Ann. Thorac. Surg.* **2004**, *78*(2), 444–448.
92. Thomson, J. A.; Itskovitz-Eldor, J.; Shapiro, S. S.; *et al*. *Science* **1998**, *282*(5391), 1145–1147.
93. De Coppi, P.; Bartsch, G., Jr.; Siddiqui, M. M.; *et al*. *Nat. Biotechnol.* **2007**, *25*(1), 100–106.
94. Takahashi, K.; Yamanaka, S. *Cell* **2006**, *126*(4), 663–676.
95. Woltjen, K.; Michael, I. P.; Mohseni, P.; *et al*. *Nature* **2009**, *458*(7239), 766–770.
96. Zhou, H.; Wu, S.; Joo, J. Y.; *et al*. *Cell Stem Cell* **2009**, *4*(5), 381–384.
97. Lee, P. H.; Kim, J. W.; Bang, O. Y.; Ahn, Y. H.; Joo, I. S.; Huh, K. *Clin. Pharmacol. Ther.* **2008**, *83*(5), 723–730.
98. Nakamura, T.; Teramachi, M.; Sekine, T.; *et al*. *Int. J. Artif. Organs* **2000**, *23*(10), 718–724.

99. Nomoto, Y.; Kobayashi, K.; Tada, Y.; Wada, I.; Nakamura, T.; Omori, K. *Ann. Otol. Rhinol. Laryngol.* **2008**, *117*(1), 59–64.
100. Okano, W.; Nomoto, Y.; Wada, I.; *et al. Ann. Otol. Rhinol. Laryngol.* **2009**, *118*(11), 796–804.
101. Suzuki, T.; Kobayashi, K.; Tada, Y.; *et al. Ann. Otol. Rhinol. Laryngol.* **2008**, *117*(6), 453–463.
102. Vunjak-Novakovic, G.; Martin, I.; Obradovic, B.; *et al. J. Orthop. Res.* **1999**, *17*(1), 130–138.
103. Sakata, J.; Vacanti, C. A.; Schloo, B.; Healy, G. B.; Langer, R.; Vacanti, J. P. *Transplant. Proc.* **1994**, *26*(6), 3309–3310.
104. Vacanti, C. A.; Paige, K. T.; Kim, W. S.; Sakata, J.; Upton, J.; Vacanti, J. P. *J. Pediatr. Surg.* **1994**, *29*(2), 201–204.
105. Kojima, K.; Bonassar, L. J.; Roy, A. K.; Vacanti, C. A.; Cortiella, J. *J. Thorac. Cardiovasc. Surg.* **2002**, *123*(6), 1177–1184.
106. Okamoto, T.; Yamamoto, Y.; Gotoh, M.; *et al. J. Thorac. Cardiovasc. Surg.* **2004**, *127*(2), 329–334.
107. Genden, E. M.; Iskander, A. J.; Bromberg, J. S.; Mayer, L. *Arch. Otolaryngol. Head Neck Surg.* **2003**, *129*(1), 118–123.
108. Mauro, A. *J. Biophys. Biochem. Cytol.* **1961**, *9*, 493–495.
109. Halum, S. L.; Naidu, M.; Delo, D. M.; Atala, A.; Hingtgen, C. M. *Laryngoscope* **2007**, *117*(5), 917–922.
110. Partridge, T. A.; Morgan, J. E.; Coulton, G. R.; Hoffman, E. P.; Kunkel, L. M. *Nature* **1989**, *337*(6203), 176–179.
111. Rosenblatt, J. D.; Lunt, A. I.; Parry, D. J.; Partridge, T. A. *In Vitro Cell. Dev. Biol. Anim.* **1995**, *31*(10), 773–779.
112. Montarras, D.; Morgan, J.; Collins, C.; *et al. Science* **2005**, *309*(5743), 2064–2067.
113. Collins, C. A.; Olsen, I.; Zammit, P. S.; *et al. Cell* **2005**, *122*(2), 289–301.
114. Sacco, A.; Doyonnas, R.; Kraft, P.; Vitorovic, S.; Blau, H. M. *Nature* **2008**, *456*(7221), 502–506.
115. Barberi, T.; Bradbury, M.; Dincer, Z.; Panagiotakos, G.; Socci, N. D.; Studer, L. *Nat. Med.* **2007**, *13*(5), 642–648.
116. Dellavalle, A.; Sampaolesi, M.; Tonlorenzi, R.; *et al. Nat. Cell Biol.* **2007**, *9*(3), 255–267.
117. Ferrari, G.; Cusella-De Angelis, G.; Coletta, M.; *et al. Science* **1998**, *279*(5356), 1528–1530.
118. Gussoni, E.; Soneoka, Y.; Strickland, C. D.; *et al. Nature* **1999**, *401*(6751), 390–394.
119. Nunes, V. A.; Cavaçana, N.; Canovas, M.; Strauss, B. E.; Zatz, M. *Biol. Cell* **2007**, *99*(4), 185–196.
120. Peault, B.; Rudnicki, M.; Torrente, Y.; *et al. Mol. Ther.* **2007**, *15*(5), 867–877.
121. Pittenger, M. F.; Mackay, A. M.; Beck, S. C.; *et al. Science* **1999**, *284*(5411), 143–147.
122. Sampaolesi, M.; Blot, S.; D'Antona, G.; *et al. Nature* **2006**, *444*(7119), 574–579.
123. Torrente, Y.; Belicchi, M.; Marchesi, C.; *et al. Cell Transplant.* **2007**, *16*(6), 563–577.
124. Boldrin, L.; Elvassore, N.; Malerba, A.; *et al. Tissue Eng.* **2007**, *13*(2), 253–262.
125. Boldrin, L.; Malerba, A.; Vitiello, L.; *et al. Cell Transplant.* **2008**, *17*(5), 577–584.
126. Conconi, M. T.; Bellini, S.; Teoli, D.; *et al. J. Biomed. Mater. Res. A* **2009**, *89*(2), 304–316.
127. Conconi, M. T.; De Coppi, P.; Bellini, S.; *et al. Biomaterials* **2005**, *26*(15), 2567–2574.
128. De Coppi, P.; Bellini, S.; Conconi, M. T.; *et al. Tissue Eng.* **2006**, *12*(7), 1929–1936.
129. De Coppi, P.; Delo, D.; Farrugia, L.; *et al. Tissue Eng.* **2005**, *11*(7–8), 1034–1044.
130. Levenberg, S.; Rouwkema, J.; Macdonald, M.; *et al. Nat. Biotechnol.* **2005**, *23*(7), 879–884.
131. Marzaro, M.; Conconi, M. T.; Perin, L.; *et al. Int. J. Mol. Med.* **2002**, *10*(2), 177–182.
132. Saxena, A. K.; Marler, J.; Benvenuto, M.; Willital, G. H.; Vacanti, J. P. *Tissue Eng.* **1999**, *5*(6), 525–532.
133. Saxena, A. K.; Willital, G. H.; Vacanti, J. P. *Biomed. Mater. Eng.* **2001**, *11*(4), 275–281.
134. Kanemaru, S.; Nakamura, T.; Omori, K.; *et al. Ann. Otol. Rhinol. Laryngol.* **2003**, *112*(6), 492–498.
135. Crumley, R. L. *Ann. Otol. Rhinol. Laryngol.* **2000**, *109*, 365–371.
136. Lorenz, R. R.; Hicks, D. M.; Shields, R. W., Jr.; Fritz, M. A.; Strome, M. *Otolaryngol. Head Neck Surg.* **2004**, *131*, 1016–1018.
137. Fex, S. *Acta Otolaryngol.* **1970**, *69*, 294–301.
138. Zealear, D. L.; Billante, C. R.; Courey, M. S.; *et al. Laryngoscope* **2003**, *113*, 1149–1156.
139. Kingham, P. J.; Hughes, A.; Mitchard, L.; *et al. Eur. J. Neurosci.* **2007**, *25*(2), 331–340.
140. Flint, P. W.; Nakagawa, H.; Shiotani, A.; Coleman, M. E.; O'Malley, B. W., Jr. *Laryngoscope* **2004**, *114*, 368–371.
141. Kapur, T. A.; Shoichet, M. S. *J. Biomater. Sci. Polym. Ed.* **2003**, *14*, 383–394.
142. Nomi, M.; Atala, A.; Coppi, P. D.; Soker, S. *Mol. Aspects Med.* **2002**, *23*(6), 463–483.
143. Shea, L. D.; Smiley, E.; Bonadio, J.; Mooney, D. J. *Nat. Biotechnol.* **1999**, *17*(6), 551–554.
144. Borenstein, J. T.; Weinberg, E. J.; Orrick, B. K.; Sundback, C.; Kaazempur-Mofrad, M. R.; Vacanti, J. P. *Tissue Eng.* **2007**, *13*(8), 1837–1844.
145. Kaully, T.; Kaufman-Francis, K.; Lesman, A.; Levenberg, S. *Tissue Eng. B Rev.* **2009**, *15*(2), 159–169.
146. Lovett, M.; Lee, K.; Edwards, A.; Kaplan, D. L. *Tissue Eng. B Rev.* **2009**, *15*(3), 353–370.
147. Barker, E. V. *Ann. R. Coll. Surg. Engl.* **2007**, *89*(3), 197–202.
148. Barker, E.; Haverson, K.; Stokes, C. R.; Birchall, M.; Bailey, M. *Clin. Exp. Immunol.* **2006**, *143*(1), 6–14.
149. Barker, E.; Murison, P.; Macchiarini, P.; *et al. Clin. Exp. Immunol.* **2006**, *146*(3), 503–508.
150. Gorti, G. K.; Birchall, M. A.; Haverson, K.; Macchiarini, P.; Bailey, M. *Transplantation* **1999**, *68*(11), 1638–1642.
151. Rees, L. E.; Ayoub, O.; Haverson, K.; Birchall, M. A.; Bailey, M. *Clin. Exp. Immunol.* **2003**, *134*(3), 497–502.
152. Govindaraj, S.; Gordon, R.; Genden, E. M. *Ann. Otol. Rhinol. Laryngol.* **2004**, *113*(10), 797–804.
153. Strome, S.; Brodsky, G.; Darrell, J.; Wu, J.; Strome, M. *Ann. Otol. Rhinol. Laryngol.* **1992**, *101*(2 Pt 1), 156–160.
154. Shaari, C. M.; Farber, D.; Brandwein, M. S.; Gannon, P.; Urken, M. L. *Head Neck* **1998**, *20*(6), 522–527.
155. Bircher, E. *Zentralbl. Chir.* **1907**, *34*, 1479–1482.
156. Sato, M.; Ando, N.; Ozawa, S.; Miki, H.; Hayashi, K.; Kitajima, M. *Mater. Sci. Forum* **1997**, *250*, 105–114.
157. Sato, M.; Ando, N.; Ozawa, S.; Miki, H.; Kitajima, M. *ASAIO J.* **1994**, *40*, M389–M392.
158. Miki, H.; Ando, N.; Ozawa, S.; Sato, M.; Hayashi, K.; Kitajima, M. *ASAIO J.* **1999**, *45*, 502–508.
159. Beckstead, B. L.; Pan, S.; Bhrany, A. D.; Bratt-Leal, A. M.; Ratner, B. D.; Giachelli, C. M. *Biomaterials* **2005**, *26*(31), 6217–6228.
160. Marzaro, M.; Vigolo, S.; Oselladore, B.; *et al. J. Biomed. Mater. Res. A* **2006**, *77*(4), 795–801.
161. Watanabe, M.; Sekine, K.; Hori, Y.; *et al. ASAIO J.* **2005**, *51*(2), 158–161.

5.537. Adipose Tissue Engineering

C T Gomillion and K J L Burg, Institute for Biological Interfaces of Engineering, Clemson, SC, USA

© 2011 Elsevier Ltd. All rights reserved.

5.537.1.	**Introduction**	529
5.537.2.	**Adipose Tissue Engineering**	530
5.537.3.	**Adipose Tissue Structure and Function**	530
5.537.3.1.	Cellular Composition	530
5.537.3.2.	Adipogenesis	531
5.537.3.3.	Secretory Function of Adipose Tissue	531
5.537.3.4.	Adipose-Derived Stem Cells	531
5.537.4.	**Biomaterials for Adipose Tissue Engineering**	532
5.537.4.1.	Natural Biomaterials	532
5.537.4.1.1.	Alginate	532
5.537.4.1.2.	Chitosan	533
5.537.4.1.3.	Collagen and gelatin	534
5.537.4.1.4.	Fibrin	535
5.537.4.1.5.	Hyaluronic acid	535
5.537.4.1.6.	Matrigel™	536
5.537.4.1.7.	Other naturally derived materials	536
5.537.4.2.	Synthetic Biomaterials	536
5.537.4.2.1.	Biodegradable polymers	537
5.537.5.	**Future Outlook**	538
References		538

Glossary

Adipocyte A mature fat cell.
Adipogenesis The process by which preadipocytes differentiate to become mature fat cells.
Autologous Derived from a patient's own body.
Biocompatible Material or substance that does not cause negative reaction with surrounding tissue or host upon implantation.
Expansion Increase in cell number, proliferation.
Natural biomaterial A material derived from natural sources used for biological applications.
Preadipocyte A precursor fat cell that has not yet matured.
Scaffold A substrate derived from natural or synthetic material that is intended to mimic tissue in the body and support cell growth while building new, healthy tissue.
Synthetic biomaterial A material manufactured or produced from synthetic polymers and used for biological applications.

Abbreviations

bFGF	Basic fibroblast growth factor
HA	Hyaluronic acid
IL-6	Interleukin-6
PAI-1	Plasminogen activator inhibitor-1
PEG	Poly(ethylene glycol)
PL	Poly(lactide)
PLG	Poly(lactide-*co*-glycolide)
Pref-1	Preadipocyte factor-1
TGF-β	Transforming growth factor-β
TNF-α	Tumor necrosis factor-α

5.537.1. Introduction

Cases of traumatic injury, congenital defect, or tumor resection often result in soft tissue defects, where loss or removal of volumes of adipose tissue, within the subcutaneous layer of skin, results in alterations of the skin's normal contour.[1] Soft tissue defects are repaired clinically using plastic and reconstructive procedures to restore the missing volume of adipose tissue. Clinical procedures used to repair such defects include autologous fat tissue grafts and tissue flap transfers, implants, or injectable fillers that reconstruct and fill the void space. While many options for soft tissue reconstruction are used in clinical application, there is, however, not one strategy that is useful for the wide range of defects that may exist. Additionally, the methods currently used for soft tissue reconstruction are limited in their success due to complications, such as tissue resorption, resulting in loss of tissue volume over time.[1–6] Researchers are, therefore, working to develop methods for

engineering autologous adipose tissue that may be used to fill soft tissue defects. This chapter will provide an overview of adipose tissue structure and function along with a discussion of specific biomaterials used in adipose tissue engineering strategies and a current review of the success and limitations of these strategies in the field of adipose tissue engineering.

5.537.2. Adipose Tissue Engineering

Tissue engineering methods are being investigated to develop a wide range of tissues, including bone, skin, cartilage, vascular, and adipose tissue for patients in need.[7,8] The development of natural, autologous engineered tissue using a patient's own cells will eliminate the need for tissue or organ transplants where immunological rejection is often of concern for patients receiving donor tissue.[7,9] Most tissue engineering strategies are based on the premise of taking healthy cells from a patient and culturing them in a laboratory setting to attain a larger quantity of cells sufficient for seeding onto scaffolds. Scaffolds for tissue engineering are support structures designed to facilitate cellular growth and proliferation upon implantation into the patient. As cells covering the scaffold increase in number and differentiate, the scaffold will degrade or absorb, resulting in newly formed autologous tissue.[10,11]

The development of tissue-engineered adipose tissue would ideally provide replacement tissue that is similar in texture and structure as the native soft tissue in need of reconstruction. Engineered adipose tissue has the potential to provide reconstruction options that are natural and that use the patient's own healthy cells. Additionally, the advent of minimally invasive technologies, enhanced by tissue engineering strategies, could provide reconstruction options better suited for plastic and reconstructive surgical patients.[12] Minimally invasive, tissue-engineered strategies could effectively reduce postsurgical trauma that patients would endure from the typically used open procedures required for implantation of tissue expansion devices, implants, and tissue transfers.[13]

Many factors must be considered to design the optimal adipose tissue engineering system. Attention must be paid to all key aspects of the tissue engineering process, including the cell source, scaffold material, cellular environment, and means of device delivery.[14,15] Logistically, the ideal cell source should be readily available, simply obtained, and easily expanded in culture.[2] The ideal scaffold material should provide a surface that facilitates cell attachment and proliferation, be esthetically similar in texture to native soft tissue, and also be biocompatible with host tissue upon implantation.

5.537.3. Adipose Tissue Structure and Function

In order to successfully engineer any tissue, it is first necessary to understand the natural physical and functional characteristics of the tissue of interest. Two forms of adipose tissue exist – white and brown. As white adipose tissue is the type found within the subcutaneous layer of soft tissues, our discussion will focus only on white adipose tissue. Adipose tissue is characterized as a viscoelastic material, possessing the characteristics of both viscous and elastic materials that are capable of resisting flow and also returning to their original shapes after deformation is applied.[16,17] The stiffness for viscoelastic materials has been shown to depend on the rate of strain applied. The reported values for the elastic modulus of adipose tissue range from 0.5 to 25 kPa. This wide range may be attributed to the source or *in vivo* location of the evaluated samples, in addition to the lipid and water content of the evaluated samples.[18–22]

Adipose tissue has many functions within the body, serving as a thermal insulator within the body and providing protective cushioning to the body's internal organs. Additionally, adipose tissue serves as an energy storage locale and secretory organ that produces hormones and cytokines that function in metabolic processes.[23,24] The multifunctional role of adipose tissue within the body means that there are many characteristics of adipose tissue that must be further understood in order to successfully engineer new adipose tissue.

5.537.3.1. Cellular Composition

Adipose tissue is characterized as a loose connective tissue composed primarily of lipid-filled, mature cells called adipocytes. The adipocytes are bound together by collagen fibers, primarily collagen type IV, which form the structural network.[23] In addition to adipocytes, other cell types within adipose tissue include smooth muscle cells, endothelial cells, fibroblasts, blood cells, and preadipocytes, which account for one- to two-thirds of adipose tissue composition and are found within the stromal-vascular fraction of the tissue.[25–29]

The intracellular space in an adipocyte is filled to approximately 90% with a single, unilocular, lipid droplet. The lipid within mature adipocytes fills the cell such that the cell's nucleus is pushed to the periphery of the cell membrane, forming a thin ring within the cell.[30,31] Mature fat cells can range in diameter from 10 to 200 μm depending on the size of the lipid droplets within the cell.[24,32] The lipid-filled nature of mature adipocytes leaves them fragile and sensitive to mechanical deformation. Mature adipocytes are obtained either through excision or liposuction, which may cause damage to the vascular supply or to the cell body, respectively. This cellular damage results in a large cell population that will not retain the desired cell volume *in vivo*.[5] Mature adipocytes in culture are limited in their proliferative capabilities and are not readily expanded. This characteristic is attributed to their terminally differentiated state, which further discourages their use in tissue engineering.[4,31,33]

Preadipocytes, which are precursor cells committed to the adipocyte lineage, are contained within the stromal-vascular fraction of enzymatically digested tissue. These cells are fusiform or fibroblast-like in appearance before they are differentiated.[5,31] Differentiation of these cells results in morphological and biochemical changes, where the cells become rounded in shape, and begin to accumulate triacylglycerol and form lipid vacuoles.[4,33] Preadipocytes are deemed more advantageous as a cell source than mature adipocytes because they are easily cultured, easily expanded, and easily obtained. They are capable of both proliferating to obtain larger cell numbers and of differentiating to build the tissue of interest.[26,34–36]

5.537.3.2. Adipogenesis

The process of adipogenesis, or the formation of fat, is a multistep process involving the proliferation and differentiation of preadipocytes. The steps involved in adipogenesis have been widely evaluated through the use of preadipocyte cell lines such as 3T3-L1 and 3T3-F442A.[37] During the proliferation stages of cell growth where cell number increases, preadipocytes morphologically resemble fibroblasts, as shown in Figure 1. This shape is maintained throughout the proliferation stages. At confluence, proliferation of the cells is inhibited by cell–cell contact and growth arrest occurs. The preadipocytes then enter the differentiation stage.[26,37–40] Once differentiation is induced, morphological changes in the cell occur. The preadipocytes become more spherical in shape and lipid is accumulated within the cell such that the cell forms a unilocular mature adipocyte.[37,39–47]

For differentiation of preadipocyte cell lines to occur, differentiation inducers consisting of insulin, dexamethasone, and 3-isobutyl-1-myethylxanthine (IBMX) are added to the cultures to initiate and accelerate the differentiation process.[37,41,42,48–51] The ability to isolate and culture primary preadipocytes from several species has been demonstrated. When studying differentiation of these cells, the use of primary cells offers several advantages. Primary preadipocytes can be obtained from adipose deposits in different locations on a wide variety of animals, which can provide information on species and tissue microenvironment variations. Additionally, it has been shown that primary cultures may differentiate in the presence of low concentrations of insulin when cultured in serum or with high concentrations of insulin in a serum-free medium.[37]

As preadipocytes progress through the differentiation process to become mature adipocytes, they not only undergo morphological changes, but also change at the genetic level where genes are expressed at different stages of development. One gene expressed by preadipocytes is growth arrest and DNA damage-inducible protein (GADD) 153, which is also known as CCAAT/enhancer-binding protein ζ (C/EBPζ) and CHOP-10.[40,42,52] GADD is responsible for blocking the G1 to S transition between phases of the cell cycle, which initiates growth arrest, and subsequently differentiation.[52] Another gene characteristic of cells of the adipose lineage is peroxisome proliferator activator receptor (PPAR)-γ, which is expressed early in the differentiation process at low levels.[37,53–55] As differentiation progresses, the level of PPAR-γ expression has been shown to increase.[37,54,56] PPAR-γ belongs to the family of nuclear hormone receptors and is key in the induction and maintenance of differentiated adipocytes. The expression of PPAR-γ has also been shown to induce growth arrest and to initiate adipogenesis in fibroblast cell lines.[37,57] The expression of adipocyte-specific fatty-acid-binding protein-2 can be detected in mature adipocytes[58]; this lipid-binding protein is expressed when cells accumulate lipid.[39,41,53,56,59] The expression of these transcription factors may be evaluated with reverse transcriptase polymerase chain reaction (RT-PCR) to assess the stages of preadipocyte differentiation. Assessment of the developmental stage of cells is particularly crucial for the analysis of primary adipose-derived tissue cultures.[37]

5.537.3.3. Secretory Function of Adipose Tissue

Long thought to function solely to cushion the organs of the body and store the body's fuel supply, white adipose tissue has now become recognized as an endocrine or secretory organ within the body. Adipocytes are capable of secreting many proteins and cytokines (termed adipokines) that may influence the behavior of other cells within the body.[60–62] Factors secreted by adipocytes have been categorized by function, including extracellular matrix (ECM) development, cell metabolism, immunological function, or other processes within the body.[60] Table 1 highlights several of the factors secreted by adipose cells and their function within the body. These secreted factors not only function to influence the behavior of surrounding tissues, but factors such as transforming growth factor-β (TGF-β) and preadipocyte factor-1 (pref-1) function in an autocrine manner to inhibit adipogenesis.[28,60,61,73,97–100] The factors secreted by the cells found within the adipose tissue play an important role in adipogenesis and may play a role in the development of tissue engineering strategies.

5.537.3.4. Adipose-Derived Stem Cells

More recently, adipose tissue has been identified as a source of multipotent cells that have the capacity to differentiate to cells of adipogenic, myogenic, chondrogenic, and osteogenic lineages when cultured with a specific stimuli.[101–114] These adipose-derived stem cells (ADSCs) may be obtained from liposuction aspirates or through abdominoplasty procedures and have been deemed advantageous for tissue engineering applications because of their ability to differentiate to multiple cell types. Additionally, adipose tissue is often available in an abundant, expendable amount within the body, which yields a readily available tissue source that is easy to harvest in

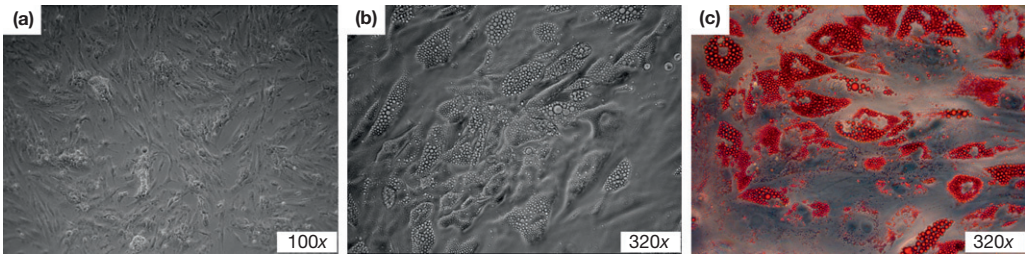

Figure 1 (a) Human preadipocytes isolated from fresh adipose tissue samples exhibit a fibroblast-like morphology. (b) Differentiation of human preadipocytes for 14 days results in the formation of intracellular lipid droplets and morphological changes characteristic of mature adipocytes. (c) Oil Red O staining of intracellular lipid shows the accumulation of lipid droplets within cells differentiated for 14 days.

Table 1 Common factors secreted from adipose tissue

Secreted factor	*Expressed by*	*References*
Role: Metabolic function		
Adiponectin	Adipocytes	63–65
Leptin	Adipocytes	66–71
Resistin	Adipocytes	72
Adipsin	Adipocytes	30,73
Visfatin	Adipocytes	74,75
Preadipocyte factor-1	Preadipocytes	76–80
Role: Immunological or inflammatory function		
Tumor necrosis factor-α	Adipocytes, macrophages	81–84
Interleukin-6	Adipocytes	73,85
Transforming growth factor-β	Adipocytes, macrophages	82,83,86–89
Plasminogen activator inhibitor-1	Adipocytes	82,86,90–96

comparison to bone marrow aspiration procedures that result in significant pain.[35,101,112,115]

5.537.4. Biomaterials for Adipose Tissue Engineering

When selecting a material for use as scaffolding in adipose tissue engineering, several aspects must be considered. Scaffold selection depends on the physical, mechanical, and chemical properties of the material.[116] Because the tissue that is being reconstructed is a 'soft' tissue, a scaffold material that imparts a natural feel is ideal, particularly for restoration of breast tissue in women.[33,117,118] Additionally, the cell type of interest will affect the material selected for use as a scaffold. Adipocytes and preadipocytes are anchorage-dependent cells, meaning that they require a surface, that is, substrate, of defined stiffness so that attachment, proliferation, and differentiation can occur.[1,4,34] The porosity of a scaffold surface can be selectively modified to both encourage cellular attachment and to allow the diffusion of nutrients and vascular ingrowth within a scaffold.[33,119] More specifically, it has been shown that dispersed, cultured fat is difficult to maintain on two-dimensional (2D) surfaces in static flow,[57] perhaps attributable to the fact that mature adipocytes are capable of a phenomenon known as dedifferentiation, where the cells lose accumulated lipid and revert to a previous fusiform state observed in preadipocytes.[58,120] Moreover, culturing anchorage-dependent cells on appropriate substrata will result in increased proliferation and ultimately the presence of a greater number of cells with the potential to differentiate in culture.[3]

Scaffolds used in tissue engineering may be implanted either by surgical incision or by injection. The materials used for constructing the scaffolds, whether intended for injection or implantation following incision, must possess several essential properties. These materials should be biocompatible, biodegradable, easily manufactured and sterilized, and easily managed during surgical procedures, and should guide the differentiation, migration, and proliferation of cells.[3,9,10,121–123] Additionally, the materials should possess mechanical properties in line with that of natural tissue and have nontoxic by-products. In order to allow adequate cellular growth, the scaffold design should be porous to allow the permeation, both inflow and outflow, of nutrients and waste products.[9] Thus, the size of the scaffold should also be taken into consideration, not only with respect to the method of implantation, but also with respect to cellular nourishment throughout the scaffold. Of the implantable materials that are available for use in tissue engineering, those most widely used have been porous biodegradable polymers, which include poly-L-lactide, poly(glycolide) (PG), and copolymers of the two.[9,124] Injectable hydrogels, such as alginate and chitosan, appear to have the ideal implantation characteristics for use specifically in breast tissue regeneration; however, their low moduli often do not provide sufficient support for anchorage-dependent cells. Studies have been conducted using calcium alginate gels, as well as hyaluronic acid (HA) gels, where the interactions of preadipocytes with the gel material have been investigated.[3,4,27]

Additionally, the surface topography of the pores within a scaffold may be altered to influence cellular behavior. Pore size and shape has been shown to affect cellular attachment, by providing formed sites into which cells may grow. Scaffolds designed for adipose tissue engineering must have pores large enough so as not to inhibit the proliferation and differentiation of preadipocytes. As preadipocytes mature, they significantly increase in size because of an increase in cell number and an increase in volume associated with lipid formation.[6,36,39–41,43–45,47,125–127] Adequate sizing of pores is essential in scaffold design for adipose tissue engineering.

Biomaterials may be derived from natural or synthetic sources. Many natural and synthetic biomaterials have been researched to evaluate their potential use for engineering adipose tissue. The selection of a specific biomaterial for adipose tissue engineering will depend on the desired characteristics of the implant. **Table 2** presents a summary of the advantages and disadvantages associated with natural and synthetic biomaterials. Further discussion of specific natural and synthetic materials and their use in adipose tissue engineering is provided in the following text.

5.537.4.1. Natural Biomaterials

Natural polymeric biomaterials include collagen, gelatin, alginate, HA, and chitosan.[10,27,119,128] Natural materials are advantageous for use in tissue engineering because they are readily available and may be degraded by enzymatic activity. Additionally, natural materials are recognized by cells and are known to have high cell affinity. However, disadvantages when using natural materials are apparent. These materials have source variability, that is, they are derived from natural sources that can only be controlled to a limited extent, and they remodel relatively quickly and unpredictably *in vivo*. Natural materials have also been shown to elicit immunogenic reactions *in vivo*, which may limit their successful implantation.

5.537.4.1.1. Alginate

Alginate is a natural polysaccharide that is derived from brown seaweed and algae, and is commercially available as sodium salt or sodium alginate.[129] It is a copolymer made up of two monomer units: β-D-mannuronic acid (M blocks) and α-L-guluronic acid (G blocks) that are linked by a (1→4) glycosidic bond. The M and G blocks are arranged sequentially with either repeating or alternating blocks.[122,133] The amount and

Table 2 Comparison of natural and synthetic biomaterials

Natural materials	10,27,119,128,129
Advantages	
Readily available	
Degraded by enzymatic activity	
Recognized by cells leading to high cell affinity	
Disadvantages	
Source variability	
Remodeled quickly and unpredictably *in vivo*	
Synthetic materials	119,122,129–132
Advantages	
Controlled production, leading to controlled batches	
Ability to alter chemically and structurally to suit application	
Predictable degradation	
Disadvantages	
Cell affinity may be affected	
Biocompatibility	

distribution of each M or G block is dependent on the properties of the seaweed from which the alginate is derived. This distribution of M and G blocks also contributes to the mechanical properties of the alginate when it is gelled. Gelation of alginate occurs when a divalent cation, such as Ca^{2+}, Mg^{2+}, or Ba^{2+}, binds with the G blocks to form ion bridges between the polymer chains.[134] The degree of cross-linking correlates with the number of G blocks found in the molecule; the higher the content of G blocks, the stiffer the resulting gel.[135] The ability to manipulate the cross-linking density provides a means of controlling the mechanical and swelling properties of the alginate. Alginate has many uses in drug delivery, cell encapsulation, and in tissue engineering because it is biocompatible, low in toxicity, and relatively low in cost.[136] However, degradation of the gel is not directly controlled by enzymes. Rather, cross-linked chains are broken down upon the loss of divalent ions to the surrounding environment, and the smaller chains are then gradually carried from the body through normal kidney function.[137] Longer alginate chains are not degraded and released from the human body, as they are degraded by alginase, an enzyme not found in humans.[138] Also, because of the hydrophilic nature of alginate, protein adsorption is inhibited, thereby limiting the number of cells that will attach to and proliferate on alginate surfaces. It is for this reason that in many tissue engineering applications some form of surface modification is applied to promote cellular attachment.[27,118,139,140]

Indeed, alginate is a natural hydrogel material that is hydrophilic in nature, thereby discouraging the adsorption of proteins to its surface.[141] The inhibition of protein adsorption results in a diminished ability of anchorage-dependent cells to attach to the surfaces of the material.[27,118,134] Typically, for alginate hydrogels to support cell–surface interactions, the material is covalently modified by the addition of peptides, such as arginine, glycine, and aspartic acid (RGD), that create cell adhesion ligands to help the material support cell attachment.[27,117,118,134,139]

Early *in vivo* studies were performed by Loebsack and coworkers to determine the efficacy of using porous alginate beads coupled with RGD to stimulate the formation of adipose tissue within the subcutaneous space of rats. Long-term evaluation following 6 months of implantation showed that the porous alginate-RGD beads were biocompatible and did facilitate tissue ingrowth while remaining stable over time.[142]

Halberstadt and coworkers injected alginate-RGD fragments into the subcutaneous space of sheep necks to contrast the effect of chemically modified alginate versus unmodified alginate for adipose tissue engineering. Alginate-RGD fragments, approximately 500 μm in diameter, were seeded with sheep preadipocytes isolated from sheep omentum tissue. Following implantation for up to 3 months, it was found that the modifications to the alginate fragments did support cell adhesion and proliferation, resulting in adipose tissue formation in the sheep.[117]

Alginate scaffolds containing poly(lactide-*co*-glycolide) (PLG) microspheres loaded with basic fibroblast growth factor (bFGF) were evaluated for their ability to facilitate vascularization of implants for tissue engineering applications. Perets and coworkers showed that implantation of bFGF-releasing alginate–PLG composite scaffolds resulted in vasculature formation after only 5 days of implantation. Further evaluation of samples after 21 days *in vivo* revealed an increase in vasculature density over the course of time. The implantation of the bFGF-loaded microspheres within the alginate scaffold resulted in a controlled release of the bFGF that facilitated new vasculature formation.[143]

Modified forms of alginate gels have, therefore, been shown to remain stable over long periods of time *in vivo*, indicating that they may be useful for support scaffolds for adipose tissue engineering. Additionally, the ability to produce various shapes and forms of alginate scaffolds, that is, beads, thick gels, etc., may be advantageous in filling defects of various shapes and sizes. The use of alginate for adipose tissue engineering, however, appears limited by the apparent need to chemically modify the alginate surface for sufficient cellular attachment.

5.537.4.1.2. Chitosan

Chitosan is a natural biomaterial derived from the deacetylation of chitin (a copolymer of *N*-acetyl-glucosamine and *N*-glucosamine units linked by β(1→4) glycosidic bonds).[144–146] Behind cellulose, chitin is the second most abundant polysaccharide on earth and is typically found in the exoskeleton of crustaceans such as crabs and shrimp.[134,136,147] As a natural material, the source of chitin and derivation process used to obtain chitosan will result in products of varied molecular weight and degree of deacetylation (DD). Chitosan may range in molecular weight from 300 to more than 1000 kDa with DD values from 30 to 95%.[144,146] The degradation of chitosan, therefore, is based on the molecular weight and DD, where chitosan degradation of chitosan will decrease as the DD increases.[147] Chitosan is typically insoluble in water or basic pH environments, but is soluble in acidic environments. Degradation of chitosan *in vivo* occurs via lysozyme enzymatic activity and hydrolysis.

Chitosan has been widely investigated for biomedical applications such as wound healing, antimicrobial treatment of bacteria, and drug delivery.[146,148,149] The use of chitosan for biomedical applications is so extensive because it is readily available, cost-effective, biocompatible, biodegradable, and easily processed to form structures of varied shape and porosity.[145,149,150] As a result of these desirable attributes, chitosan

has been investigated for engineering skin, bone, cartilage, liver, nerve, and vascular tissues.[151–153]

Because of its low strength, chitosan is often blended with other materials such as alginate or HA to form scaffolds optimal for cellular attachment.[147] Chitosan has been combined with synthetic materials such as PLG to form fibrous scaffolds used for tissue engineering.[154] Additionally, chitosan–gelatin blends have been used to form films useful for additional biomedical applications.[155]

Wu and coworkers evaluated glutaraldehyde-cross-linked collagen–chitosan hydrogel scaffolds seeded with preadipocytes for adipose tissue engineering applications. Preadipocytes isolated from the epididymal fat pats of rats were shown to successfully attach and proliferate on the porous scaffolds *in vitro*. Further evaluation of the scaffolds was performed *in vivo* by implanting the preadipocyte-seeded scaffolds within the back musculature of Lewis rats for 7 and 14 days. Histological evaluation at the completion of the *in vivo* studies showed that animal tests proved that the scaffolds were biocompatible, induced vascularization, and formed adipose tissue.[156]

The use of chitosan for adipose tissue engineering has not been widely investigated by many researchers; however, great potential for chitosan in adipose tissue engineering applications exists. Chitosan is easily processed into scaffolds of various shapes and sizes. Fabrication of injectable microspheres that would be well suited for minimally invasive applications, such as those where adipose tissue engineering would be useful, has been reported by several researchers.[153,157] Preliminary evaluation of chitosan–gelatin beads for adipose tissue engineering, Yang and coworkers (Clemson University, unpublished data), has shown that chitosan–gelatin beads not only support the attachment and proliferation of adipose cells, but also facilitate the differentiation of preadipocytes to mature adipocytes *in vitro*. As shown in **Figure 2**, intracellular lipid droplets, characteristic of mature adipocytes, were observed from Oil Red O staining of cells bovine cells grown on chitosan–gelatin beads, following 21 days of culture *in vitro*. The ease of combining growth factors and therapeutics within chitosan may potentially provide scaffolds that will facilitate adipose cell attachment and differentiation to mature fat cells to form new tissue *in vivo*.

5.537.4.1.3. Collagen and gelatin

Collagen, the most abundant protein in the human body, has been widely regarded and used in tissue engineering strategies. As the major protein component of ECM, it is a major component of many bodily tissues, including bone, tendons, skin, and cartilage. Additionally, it provides the structural framework of tissues such as blood vessels and adipose tissue.[129,140,145,152] Numerous forms of collagen exist; however, type I is the most abundant and therefore the most widely used. Properties of collagen, such as its biocompatibility, its ability to degrade enzymatically, its ability to be processed into a variety of shapes and forms (sheets, sponges, injectable microspheres, etc.), and its ability to have tailored degradation and mechanical properties (due to cross-linking), have contributed to its wide use in tissue engineering applications. However, because collagen is often derived from animal tissues, specifically, bovine and porcine bone, skin, or tendon, concerns regarding its use have been raised. Additionally, collagen is quickly remodeled and, as a stand-alone scaffold, does not have the long-term mechanical integrity necessary to guide the formation of new tissue.

Gelatin, another natural biomaterial used in tissue engineering, is derived from denatured collagen proteins; the denaturation occurs as a result of processing collagen with acid thermal modification. Like collagen, gelatin is widely used because of its biodegradability and biocompatibility. Its denatured state results in relatively low antigenicity as compared to collagen of animal origin.[152] Gelatin scaffolds of various shapes are widely used in tissue engineering applications, particularly because gelatin has been shown to support cell attachment and proliferation.

Collagen sponges and meshes seeded with human preadipocytes were evaluated, by von Heimburg and coworkers, *in vitro* and *in vivo* to evaluate their utility for adipose tissue engineering.[127,158] Evaluation of the collagen scaffolds within nude mice showed that these porous structures support cellular ingrowth and matrix synthesis; however, high numbers of cells seeded onto the scaffolds are required for significant adipose tissue growth.[116,127,158]

Composite collagen scaffolds made of collagen fibers embedded within collagen gels have also been evaluated for use in adipose tissue engineering. Gentleman and coworkers incorporated short collagen fibers within collagen gels to minimize contraction of the gels, once cultured *in vitro* with cells, and to maintain the ability of nutrients to be transported throughout the gels.[159] Evaluation of the composite collagen scaffolds seeded with preadipocytes for 21 days *in vitro* showed that incorporation of fibers within the gels aided in maintaining the structural integrity of the gel, which in turn facilitated growth of viable cells throughout the gel. The preadipocytes

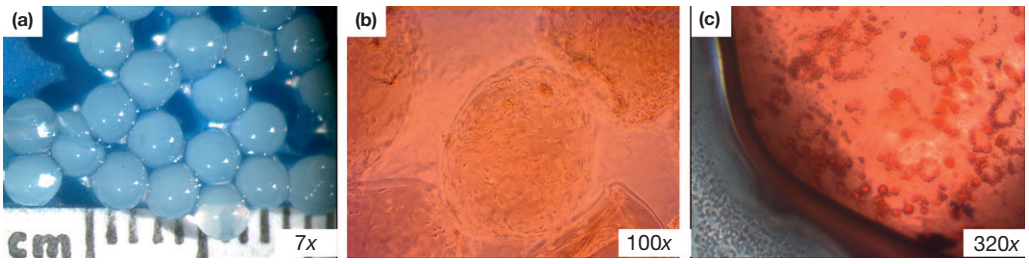

Figure 2 (a) Stereomicroscopic image of chitosan–gelatin beads. (b) Primary bovine preadipocytes seeded on chitosan–gelatin beads. (c) Oil Red O staining of primary bovine adipose cells, on the surface of chitosan–gelatin beads, showed the presence of intracellular lipid droplets characteristic of mature adipocytes following differentiation for 21 days. Images B and C courtesy of Dr. Chih-Chao Yang of the Institute for Biological Interfaces of Engineering at Clemson University.

were able to differentiate, as indicated by the lipid present within the gels. Composite collagen scaffolds, therefore, are potentially useful for maintaining implant shape while encouraging adipose tissue formation.[159]

Gelatin sponges have been used for culturing both preadipocytes and human mesenchymal stem cells (MSCs) for soft tissue engineering purposes.[127,158,160] Additionally, microspheres made of gelatin have been widely used for adipose tissue engineering. Masuda and coworkers evaluated photocured styrenated gelatin microspheres (SGMs) loaded with bFGF and insulin growth factor-1 (IGF-1) to stimulate angiogenesis and adipogenesis simultaneously. Implantation of the microspheres within Wistar rats resulted in new adipose tissue formation with associated vasculature; however, further evaluation of the system is needed to determine optimal concentrations of each growth factor to include in the system.[161–163]

Investigators have also studied collagen–gelatin combination scaffolds for adipose tissue engineering, including gelatin microspheres loaded with FGF and embedded within collagen gels or collagen sponges. Vashi and coworkers showed that collagen gels containing FGF-gelatin microspheres facilitated the formation of mature, vascularized adipose tissue after implantation in mice for 6 weeks.[164] Meanwhile, Hiraoka and coworkers and Kimura and coworkers demonstrated the ability to generate adipose tissue *in vivo* using scaffolds made of gelatin microspheres loaded with FGF, embedded within collagen sponges, and seeded with rat and human preadipocytes, respectively.[165–167]

Gelatin microcarriers have also been used for evaluating large animal models for adipose tissue engineering. Primary adipose cells isolated from fresh bovine tissue samples were seeded on gelatin microspheres by Gomillion and coworkers, as shown in **Figure 3**. Following implantation of the gelatin microspheres into Holstein heifers, histological evaluation showed that the gelatin microcarriers elicited a minimal inflammatory response while allowing tissue ingrowth. The formation of new adipose tissue deposits was not observed; however, the microcarriers were shown to be biocompatible within a bovine animal model.[168]

Like other natural biomaterials, chitosan and gelatin may be used to fabricate scaffolds of various shapes and sizes that may be useful for adipose tissue engineering applications. Studies to date evaluating collagen and gelatin scaffolds for adipose tissue engineering have yielded various methods that result in new adipose tissue formation. These methods, however, have not yet been successfully implemented to create larger volumes of adipose tissue.

5.537.4.1.4. Fibrin

Fibrin is the insoluble protein matrix formed by fibrinogen that plays a major role in blood clotting and wound repair. Fibrin glue is widely used clinically, and has proved useful as a cell delivery matrix for tissue engineering when combined with other biodegradable materials.[145] Additionally, fibrin gels have been used in tissue engineering applications, the structure of which is influenced by the concentration of fibrinogen along with pH and other factors.[152] Fibrin gel matrix alone has been shown to have poor mechanical properties and is unable to withstand forces produced during adipose tissue formation; however, the use of fibrin gel as a delivery medium for *in vivo* implantation of preadipocytes with related growth factors has proved sufficient for injectable delivery of adipose cells.[169,170]

5.537.4.1.5. Hyaluronic acid

HA, or hyaluronan, is a natural polysaccharide biomaterial commonly found in connective tissues such as articular cartilage, synovial fluid, and the umbilical cord.[152] This material can be derived from rooster combs and can be fabricated into a variety of shapes, including membranes, fibers, sponges, and microspheres.[129,140] The chemical structure of HA consists of disaccharide units of D-glucuronic acid and *N*-acetyl-D-glucosamine; it is water-soluble and forms viscous solutions.[171] As a biomaterial, HA is known to aid in tissue repair by promoting mesenchymal and epithelial cell migration, thus enhancing collagen deposition and angiogenesis.[116,129] Commercially available forms of HA, such as Restylane® and Juvederm®, are FDA-approved products used cosmetically as dermal fillers for wrinkle and other contour defects within soft tissue.[172–174] These injectable forms of HA-based materials are widely used because they provide similar structural and mechanical properties as natural soft tissue.[174]

For adipose tissue engineering applications, the angiogenesis-promoting characteristic of HA has proved very advantageous. Researchers, von Heimburg and coworkers, evaluated preadipocyte-seeded HA sponges or nonwoven carriers implanted in nude mice and found that pore size influenced the development of adipose tissue; increased vascularization was observed in larger-pore constructs, while greater adipose differentiation was observed with smaller pore constructs.[36,116,127] HA gels seeded with preadipocytes were also tested within pigs, resulting in the formation of mature adipocytes and blood vessels within the gel; however, only a minimal volume of tissue was produced that was not entirely stable following 6 weeks of implantation.[116]

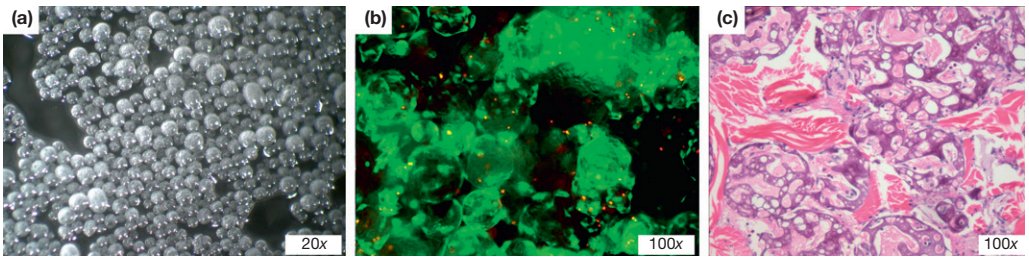

Figure 3 (a) Stereomicroscopic image of gelatin microspheres. (b) Results of LIVE/DEAD cell viability assay show viable primary bovine adipose cells (green) attached to the surface of the gelatin microspheres. (c) Following implantation within a bovine animal model to assess biocompatibility, histological analysis shows that the gelatin microcarriers elicit a minimal inflammatory response and allow ingrowth of collagen.

5.537.4.1.6. Matrigel™

Matrigel™ is a reconstituted basement membrane derived from extracts of Engelbreth-Holm-Swarm mouse tumors.[175] The basement membrane is structurally a thin layer of ECM sheets that consist primarily of collagen type IV, entactin, perlecan (heparan sulfate proteoglycan), and laminin. This laminin-rich mixture of Matrigel™ closely resembles the complex extracellular environment of the basement membrane and is used for cell-culturing model systems, particularly for evaluating angiogenesis and cellular differentiation.[175,176] Matrigel™ has been commercially available for licensing through the National Institutes of Health Technology Transfer Office since 1984 and has been used for cellular applications since that time.[175]

Matrigel™ has been evaluated for adipose tissue engineering applications. Early studies performed by Kawaguchi and coworkers evaluated injections of Matrigel™ with bFGF, both with and without preadipocyte cells, in a nude mouse model. Adipose tissue formation was observed not only within the cellular samples, but also within the samples containing only bFGF and Matrigel™. After comparison of all study samples, Kawaguchi and coworkers concluded that the combination of Matrigel™ with bFGF induced neovascularization, which in turn recruited adipose precursor cells to the implant site, which ultimately differentiated to form new adipose tissue.[177]

Additional studies to evaluate the ability of Matrigel™ to facilitate *de novo* adipogenesis were conducted by Tabata and coworkers. Gelatin microspheres loaded with bFGF were incorporated into Matrigel™ scaffolds to control the release of the bFGF *in vivo*. Evaluation within a nude mouse model showed that increased release of bFGF resulted in more adipose tissue formation; however, high levels of bFGF resulted in fibrous tissue formation caused by rapidly growing vasculature.[166,178] Characterization of cells that migrated into the Matrigel™ upon implantation showed that adipocyte precursors readily migrated into gels formed by Matrigel™, further suggesting that the ECM components, laminin and collagen type IV, found in Matrigel™, may play key roles in adipose tissue formation.[163]

Because it is derived from a tumor cell model, the exact components of Matrigel™ are not consistent or well defined. While neovascularization and adipose tissue formation are induced with Matrigel™ based implants,[29,179] use of Matrigel™ scaffolds within recovering cancer patients may not be recommended. Additionally, the use of Matrigel™ within humans will likely not be biocompatible due to its tumor cell origins. These facts should be taken into consideration before selection of Matrigel™ for adipose tissue engineering strategies. Perhaps, a more ideal solution would be to consider incorporation of the Matrigel™ components, laminin and collagen type IV, which have been hypothesized to play roles in adipogenesis, into scaffolding materials for engineering new adipose tissue,[180] or to derive new basement membrane gels from normal tissues such as tendon.[181]

5.537.4.1.7. Other naturally derived materials

Researchers have evaluated the potential of other naturally derived materials as scaffolds for adipose tissue engineering. In a study conducted by Masuda and coworkers, fragments of omentum tissue combined with rat preadipocytes were evaluated within a Wistar rat model. The omentum is a highly vascularized, fat-filled tissue extending from the stomach to below the colon and small intestine. Characterization of the omentum tissue shows that it possesses microvascular endothelial cells and produces significant amounts of vascular endothelial growth factor (VEGF). Implantation of the fragmented omentum with preadipocytes within rats for up to 3 months resulted in formation of adipose tissue masses with high triacylglycerol content. The outcome was thought to be attributed to the long-standing presence of VEGF from the omentum tissue that was instrumental in neovascularization and, ultimately, adipose tissue formation.[161,162]

An alternate method for adipose tissue engineering was investigated by Flynn and coworkers. Scaffolds made of placental decellular matrix (PDM) and cross-linked with hyaluronan were formed and evaluated for adipogenic potential. Human placental tissue was decellularized and primary ADSCs were either encapsulated within the PDM or seeded on the surface of the PDM that was then cross-linked with HA. *In vitro* evaluation of the scaffolds after 14 days of culture showed differentiating adipose cells within each scaffold; however, further analysis of these scaffolds is needed to more fully assess their potential in adipose tissue engineering.[182,183] Similarly, preliminary assessment of tendon-derived basement membrane material suggests potential use for this biomaterial in adipose tissue engineering.[181]

Additional adipose tissue engineering methods using scaffolds based on adipose tissue ECM have been investigated. Vermette and coworkers conducted a study to evaluate the potential of adipose-derived stromal cells to 'self-assemble' in the presence of ascorbic acid, forming their own ECM and ultimately forming sheets of all natural adipose tissue that produced lipid and expressed detectable quantities of leptin.[184]

Finally, more recent studies have evaluated the use of injectable ECM powders produced from fat tissue as scaffolding material for adipose tissue engineering. As shown in **Figure 4**, human adipose tissue obtained from liposuction patients was washed and processed until a gel-like suspension was formed. The suspension was then frozen, freeze-dried, and crushed to form ECM powders. *In vitro* evaluation of the adipose tissue ECM powders with human ADSCs showed that cells readily adhered to and proliferated on the ECM powder scaffolds. *In vivo* evaluation of the cellular ECM powders within a nude mouse model showed that the ECM powders supported adipogenesis when implanted with and without cells.[185]

5.537.4.2. Synthetic Biomaterials

Synthetic materials, such as poly(lactide) (PL), PG, and various copolymers, are also widely used in tissue engineering. For select applications, synthetic polymers can offer greater advantages than naturally occurring materials. Synthetic polymers can be produced under controlled conditions, which results in a uniform batch of material that may be altered chemically and structurally to suit a specific application. This reduction in variability also allows predictable degradation of synthetic materials, unlike their natural material counterparts.[10,119,130,132] Synthetic polymers may be modified to have high mechanical integrity, and they can also be produced in a variety of shapes, including meshes, sponges, films, and microparticles.[10]

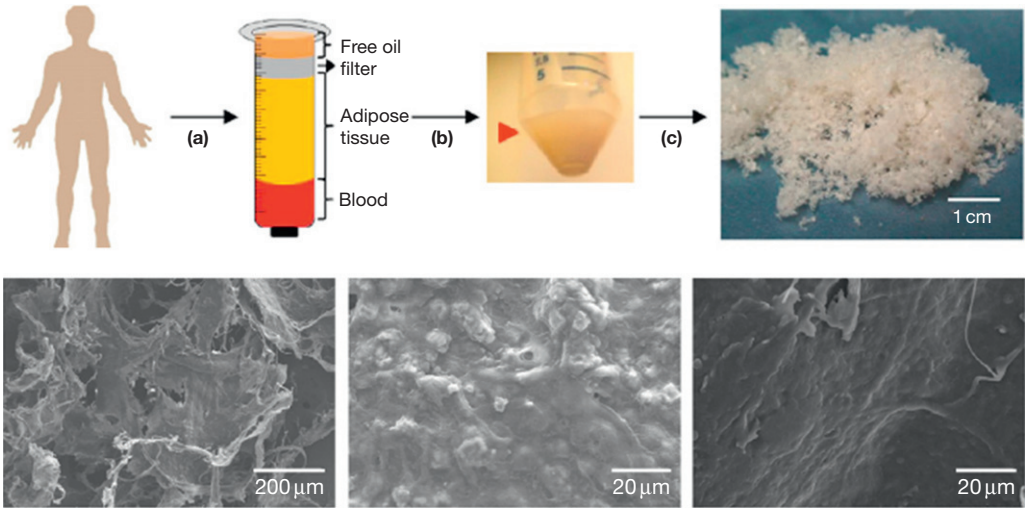

Figure 4 Injectable human ECM powders were prepared by Choi and coworkers from liposuction tissue (a) that was washed to separate blood and oil (b), then processed to form a gel-like suspension (c) that was freeze-dried to form the extracellular matrix powders. Scanning electron micrograph images show the resulting texture of the extracellular matrix powders. Reprinted from Choi, J. S.; Yang, H. J.; *et al. J. Control. Release* **2009**, *139*(1), 2–7, with permission from Elsevier.

5.537.4.2.1. Biodegradable polymers

Synthetic biodegradable polymers comprise a category of biomaterials that are widely used in tissue engineering applications. Uniform batches of materials that can be altered chemically and structurally may be produced under controlled conditions, specific to the application. Minimal batch variation allows predictable degradation of synthetic materials, unlike their natural material counterparts.[10,119,130,132] A variety of shapes, including meshes, sponges, films, disks, and microparticles, may be formed using these polymers.[10] The most commonly used polymers for adipose tissue engineering include PG and PLG, a copolymer of PG and PL.

PLG disks and foam scaffolds seeded with preadipocytes were used by Patrick and coworkers for *in vivo* implantation into rats. Mature fat cells with newly forming blood vessels were initially observed at early time points (2–5 weeks); however, longer implantation resulted in scaffold degradation with simultaneous tissue resorption.[1,186,187] In an effort to produce volume-stable adipose tissues, Cho and coworkers used a combination of PLG with fibrin matrix. Preadipocyte cells suspended in the fibrin matrix were injected into a dome-shaped PLG support placed within a subcutaneous pocket in nude mice. Over a 6-week period, adipose tissue of a stable volume was formed.[188] When PG meshes seeded with preadipocytes were used by Fischbach and coworkers, minimal cell spreading was observed and no adipose tissue was formed; however, the PG meshes, when used in 3D culture with preadipocytes, facilitated the production of viable adipose tissue.[48]

Injectable microspheres made of PLG were formed by Choi and coworkers and evaluated for adipose tissue engineering. Primary rabbit MSCs were seeded on PLG microspheres and implanted into nude mice. *In vivo* evaluation showed new adipose tissue formation when microspheres were seeded with rabbit MSCs that were differentiated with adipogenic medium before implantation.[189] Further analysis by Choi and coworkers evaluating the PLG microspheres seeded with human ADSCs, similarly showed new adipose tissue formation when implanted in nude mice.[190]

Another synthetic material that has been used for adipose tissue engineering strategies is poly(ethylene glycol) (PEG). Microspheres made of a PLG/PEG mixture were loaded with insulin and IGF-1, factors known to influence adipogenesis. The inclusion of PEG was shown to lead to the formation of microchannels on the surface of the microspheres. Following implantation for 4 weeks within a rat model, it was shown that deposits of adipose tissue formed within the samples of microspheres loaded with insulin, IGF-1, and the combination of insulin and IGF-1, but not within the plain microspheres. The release of the insulin and IGF-1 facilitated the recruitment of cells that formed new adipose tissue.[191]

Photopolymerizable PEG hydrogel systems were also evaluated by Patel and coworkers. Degradable and nondegradable forms of PEG hydrogels, with and without cell adhesion ligands, were produced and seeded with preadipocytes isolated from the epididymal fat pads of rats. *In vitro* analysis of cell adhesion and cell viability showed that preadipocytes readily attached to the PEG hydrogels with the cell adhesion ligand incorporated; cells, however, did not proliferate on the nondegradable hydrogels. Degradable PEG hydrogels with incorporated cell adhesion ligands proved most optimal for potential adipose tissue engineering applications.[192]

More recently, Stacey and coworkers evaluated diacrylated PEG (PEG-DA) and methacrylated HA (HA-MA) for potential use in providing an adipogenic culturing environment. Preadipocytes or freshly isolated adipocytes were encapsulated in PEG-DA and HA-MA scaffolds and cultured *in vitro* at specified conditions for up to 16 days. Adipogenesis was assessed by comparing levels of adipogenic-specific factors expressed by the cells in PEG-DA, HA-MA, and in 2D culture. Analysis at the completion of the study showed that the PEG-based scaffolds supported the greatest adipogenic differentiation. Further analysis of the system, however, is needed.[193]

5.537.5. Future Outlook

Efforts to engineer autologous adipose tissue have been widely researched for more than 10 years, and yet there still is not one method that has been implemented into clinical practice that yields volume-stable quantities of adipose tissue *in vivo*. While many strategies have been investigated, their success has been limited because of their inability to

- Maintain cell and tissue viability for long-term implantation
- Maintain implanted cell capacity to differentiate *in vivo*
- Facilitate neovascularization or angiogenesis for implants
- Treat large volume defects

With the current difficulties and limitations, the future for adipose tissue engineering is filled with great opportunity for novel ideas to address these problems. As several of the limitations surrounding adipose tissue engineering success stem from the cell basis used in these strategies, further investigation of the factors affecting adipogenesis and fat cell differentiation is required. Numerous factors have been shown to inhibit or enhance adipogenesis; therefore, fully understanding the key regulatory factors of adipogenesis and being able to use these factors to control adipogenesis could be significantly useful. The control of adipogenesis could potentially be accomplished using specific cell–cell interactions or culture medium additives specific for adipose development.[194] In developing successful adipose tissue engineering strategies, combination or composite devices may also be useful. Growth factors and fat differentiation inducing components could potentially be incorporated into scaffold materials and used to enhance the overall effectiveness of engineered adipose tissue implants. In conclusion, the relationship between cellular components and biomaterials plays a significant role in the efficacy of adipose tissue engineering strategies. Not until the appropriate combination of cellular and biomaterial components is found will a successful method for clinically engineering adipose tissue exist.

References

1. Patrick, C. W., Jr. *Anat. Rec.* **2001**, *263*(4), 361–366.
2. Gomillion, C. T.; Burg, K. J. *Biomaterials* **2006**, *27*(36), 6052–6063.
3. Katz, A. J.; Llull, R.; *et al. Clin. Plast. Surg.* **1999**, *26*(4), 587–603; viii.
4. Patrick, C. W., Jr. *Semin. Surg. Oncol.* **2000**, *19*(3), 302–311.
5. Patrick, C. W.; Mikos, A. G.; *et al. Frontiers in Tissue Engineering*; Pergamon: New York, 1998.
6. Von Heimburg, D.; Serov, T.; *et al. Fat tissue engineering*, University of Oulu, 2003.
7. Langer, R. *Pharm. Res.* **1997**, *14*(7), 840–841.
8. Stock, U. A.; Vacanti, J. P. *Annu. Rev. Med.* **2001**, *52*, 443–451.
9. Walgenbach, K. J.; Voigt, M.; *et al. Anat. Rec.* **2001**, *263*(4), 372–378.
10. Fuchs, J. R.; Nasseri, B. A.; *et al. Ann. Thorac. Surg.* **2001**, *72*(2), 577–591.
11. Griffith, L. G.; Naughton, G. *Science* **2002**, *295*(5557), 1009–1014.
12. Burg *et al.* (2000).
13. Gomillion, C. T.; Parzel, C. A.; *et al. Tissue engineering: Breast*. In *Encyclopedia of Biomaterials and Biomedical Engineering*, 2007; pp 1–8.
14. Bauer-Kreisel, P.; Goepferich, A.; *et al. Adv. Drug Deliv. Rev.* **2010**, *62*(7–8), 798–813.
15. Brey, E. M.; Patrick, C. W., Jr. *IEEE Eng. Med. Biol. Mag.* **2000**, *19*(5), 122–125.
16. Fung, Y. C. *Biomechanics: Mechanical Properties of Living Tissues*. Springer: New York, 1993.
17. Gefen, A.; Dilmoney, B. *Technol. Health Care* **2007**, *15*(4), 259–271.
18. Comley, K.; Fleck, N. A. *J. Biomech.* **2010**, *43*(9), 1823–1826.
19. McKnight, A. L.; Kugel, J. L.; *et al. AJR Am. J. Roentgenol.* **2002**, *178*(6), 1411–1417.
20. Samani, A.; Zubovits, J.; *et al. Phys. Med. Biol.* **2007**, *52*(6), 1565–1576.
21. Sinkus, R.; Lorenzen, J.; *et al. Phys. Med. Biol.* **2000**, *45*(6), 1649–1664.
22. Van Houten, E. E.; Doyley, M. M.; *et al. J. Magn. Reson. Imaging* **2003**, *17*(1), 72–85.
23. Mariman, E. C.; Wang, P. *Cell. Mol. Life Sci.* **2010**, *67*(8), 1277–1292.
24. Trujillo, M. E.; Scherer, P. E. *Endocr. Rev.* **2006**, *27*(7), 762–778.
25. Ailhaud, G. *Mol. Cell. Biochem.* **1982**, *49*(1), 17–31.
26. Ailhaud, G.; Grimaldi, P.; *et al. Annu. Rev. Nutr.* **1992**, *12*, 207–233.
27. Lanza, R. P.; Langer, R. S.; *et al. Principles of Tissue Engineering*. Academic Press: San Diego, CA, 2000.
28. Sorisky, A. *Crit. Rev. Clin. Lab. Sci.* **1999**, *36*(1), 1–34.
29. Stillaert, F.; Blondeel, P.; *et al. Adv. Exp. Med. Biol.* **2006**, *585*, 403–412.
30. Avram, A. S.; Avram, M. M.; *et al. J. Am. Acad. Dermatol.* **2005**, *53*(4), 671–683.
31. Patrick, C. W. *Annu. Rev. Biomed. Eng.* **2004**, *6*, 109–130.
32. Kawada, T.; Takahashi, N.; *et al. J. Nutr. Sci. Vitaminol. (Tokyo)* **2001**, *47*(1), 1–12.
33. Beahm, E. K.; Walton, R. L.; *et al. Clin. Plast. Surg.* **2003**, *30*(4), 547–558.
34. Atala, A.; Lanza, R. P. *Methods of Tissue Engineering*; Academic Press: San Diego, CA, 2002.
35. De Ugarte, D. A.; Ashjian, P. H.; *et al. Ann. Plast. Surg.* **2003**, *50*(2), 215–219.
36. Hemmrich, K.; von Heimburg, D.; *et al. Biomaterials* **2005**, *26*(34), 7025–7037.
37. Gregoire, F. M.; Smas, C. M.; *et al. Physiol. Rev.* **1998**, *78*(3), 783–809.
38. Ailhaud, G.; Dani, C.; *et al. Environ. Health Perspect.* **1989**, *80*, 17–23.
39. Butterwith, S. C. *Pharmacol. Ther.* **1994**, *61*(3), 399–411.
40. Cornelius, P.; MacDougald, O. A.; *et al. Annu. Rev. Nutr.* **1994**, *14*, 99–129.
41. MacDougald, O. A.; Mandrup, S. *Trends Endocrinol. Metab.* **2002**, *13*(1), 5–11.
42. Mandrup, S.; Lane, M. D. *J. Biol. Chem.* **1997**, *272*(9), 5367–5370.
43. Sugihara, H.; Funatsumaru, S.; *et al. J. Lipid Res.* **1989**, *30*(12), 1987–1995.
44. Sugihara, H.; Yonemitsu, N.; *et al. J. Lipid Res.* **1987**, *28*(9), 1038–1045.
45. Sugihara, H.; Yonemitsu, N.; *et al. J. Lipid Res.* **1988**, *29*(5), 691–697.
46. Sul, H. S. *Curr. Opin. Cell Biol.* **1989**, *1*(6), 1116–1121.
47. Warne, J. P. *J. Endocrinol.* **2003**, *177*(3), 351–355.
48. Fischbach, C.; Spruss, T.; *et al. Exp. Cell Res.* **2004**, *300*(1), 54–64.
49. Guo, X.; Liao, K. *Gene* **2000**, *251*(1), 45–53.
50. Rosen, E. D.; Spiegelman, B. M. *Annu. Rev. Cell Dev. Biol.* **2000**, *16*, 145–171.
51. Song, H.; O'Connor, K. C.; *et al. Tissue Eng.* **2002**, *8*(6), 1071–1081.
52. Burton, G. R.; Guan, Y.; *et al. Gene* **2002**, *293*(1–2), 21–31.
53. Boney, C. M.; Gruppuso, P. A.; *et al. Mol. Endocrinol.* **2000**, *14*(6), 805–813.
54. Tamori, Y.; Masugi, J.; *et al. Diabetes* **2002**, *51*(7), 2045–2055.
55. Wright, H. M.; Clish, C. B.; *et al. J. Biol. Chem.* **2000**, *275*(3), 1873–1877.
56. Gerhold, D. L.; Liu, F.; *et al. Endocrinology* **2002**, *143*(6), 2106–2118.
57. Tontonoz, P.; Hu, E.; *et al. Cell* **1994**, *79*(7), 1147–1156.
58. Lau, D. C.; Schillabeer, G.; *et al. Int. J. Obes. Relat. Metab. Disord.* **1996**, *20* (Suppl. 3), S16–S25.
59. Cowherd, R. M.; Lyle, R. E.; *et al. Semin. Cell Dev. Biol.* **1999**, *10*(1), 3–10.
60. Halberg, N.; Wernstedt-Asterholm, I.; *et al. Endocrinol. Metab. Clin. North Am.* **2008**, *37*, 753–768.
61. Hauner, H. *Proc. Nutr. Soc.* **2005**, *64*(2), 163–169.
62. Miner, J. L. *J. Anim. Sci.* **2004**, *82*, 935–941.
63. Dieudonne, M. N.; Bussiere, M.; *et al. Biochem. Biophys. Res. Commun.* **2006**, *345*(1), 271–279.
64. Fu, Y.; Luo, N.; *et al. J. Lipid Res.* **2005**, *46*(7), 1369–1379.
65. Yokota, T.; Meka, C. S.; *et al. J. Immunol.* **2003**, *171*(10), 5091–5099.
66. Considine, R. V. *Semin. Vasc. Med.* **2005**, *5*(1), 15–24.
67. Gottschling-Zeller, H.; Birgel, M.; *et al. Eur. J. Endocrinol.* **1999**, *141*(4), 436–442.
68. Gullicksen, P. S.; Della-Fera, M. A.; *et al. Apoptosis* **2003**, *8*(4), 327–335.
69. Laharrague, P.; Larrouy, D.; *et al. FASEB J.* **1998**, *12*(9), 747–752.
70. Machinal-Quelin, F.; Dieudonne, M. N.; *et al. Am. J. Physiol. Cell Physiol.* **2002**, *282*(4), C853–C863.
71. Tessitore, L.; Vizio, B.; *et al. Int. J. Oncol.* **2004**, *24*(6), 1529–1535.
72. Nagaev, I.; Bokarewa, M.; *et al. PLoS ONE* **2006**, *1*, e31.
73. Schaffler, A.; Scholmerich, J.; *et al. Nat. Clin. Pract. Gastroenterol. Hepatol.* **2005**, *2*(6), 273–280.
74. Hammarstedt, A.; Pihlajamaki, J.; *et al. J. Clin. Endocrinol. Metab.* **2006**, *91*(3), 1181–1184.
75. Hug, C.; Lodish, H. F. *Science* **2005**, *307*(5708), 366–367.
76. Lee, K.; Villena, J. A.; *et al. J. Clin. Invest.* **2003**, *111*(4), 453–461.
77. Smas, C. M.; Sul, H. S. *Cell* **1993**, *73*(4), 725–734.
78. Smas, C. M.; Sul, H. S. *Crit. Rev. Eukaryot. Gene Expr.* **1997**, *7*(4), 281–298.
79. Sul, H. S.; Smas, C.; *et al. Int. J. Obes. Relat. Metab. Disord.* **2000**, *24*(Suppl. 4), S15–S19.

80. Zhang, H.; Noohr, J.; *et al*. *J. Biol. Chem.* **2003**, *278*(23), 20906–20914.
81. Guilherme, A.; Virbasius, J. V.; *et al*. *Nat. Rev. Mol. Cell Biol.* **2008**, *9*(5), 367–377.
82. Samad, F.; Yamamoto, K.; *et al*. *Mol. Med.* **1997**, *3*(1), 37–48.
83. Torti, F. M.; Torti, S. V.; *et al*. *J. Cell Biol.* **1989**, *108*(3), 1105–1113.
84. Xu, H.; Barnes, G. T.; *et al*. *J. Clin. Invest.* **2003**, *112*(12), 1821–1830.
85. Lacasa, D.; Taleb, S.; *et al*. *Endocrinology* **2007**, *148*(2), 868–877.
86. Alessi, M. C.; Bastelica, D.; *et al*. *Diabetes* **2000**, *49*(8), 1374–1380.
87. Choy, L.; Derynck, R. *J. Biol. Chem.* **2003**, *278*(11), 9609–9619.
88. Choy, L.; Skillington, J.; *et al*. *J. Cell Biol.* **2000**, *149*(3), 667–682.
89. Grainger, D. J.; Mosedale, D. E.; *et al*. *J. Cell Sci.* **2000**, *113*(Pt 13), 2355–2361.
90. Alessi, M. C.; Poggi, M.; *et al*. *Curr. Opin. Lipidol.* **2007**, *18*(3), 240–245.
91. Birgel, M.; Gottschling-Zeller, H.; *et al*. *Arterioscler. Thromb. Vasc. Biol.* **2000**, *20*(6), 1682–1687.
92. Crandall, D. L.; Busler, D. E.; *et al*. *J. Clin. Endocrinol. Metab.* **2000**, *85*(7), 2609–2614.
93. Liang, X.; Kanjanabuch, T.; *et al*. *Am. J. Physiol. Endocrinol. Metab.* **2006**, *290*(1), E103–E113.
94. Mertens, I.; Van Gaal, L. F. *Obes. Rev.* **2002**, *3*(2), 85–101.
95. Shimomura, I.; Funahashi, T.; *et al*. *Nat. Med.* **1996**, *2*(7), 800–803.
96. Venugopal, J.; Hanashiro, K.; *et al*. *J. Cell. Biochem.* **2007**, *101*(2), 369–380.
97. Anghel, S. I.; Wahli, W. *Cell Res.* **2007**, *17*(6), 486–511.
98. Avram, M. M.; Avram, A. S.; *et al*. *J. Am. Acad. Dermatol.* **2007**, *56*(3), 472–492.
99. Fonseca-Alaniz, M. H.; Takada, J.; *et al*. *J. Pediatr.* **2007**, *83*(Suppl. 5), S192–S203.
100. Heilbronn, L.; Smith, S. R.; *et al*. *Int. J. Obes. Relat. Metab. Disord.* **2004**, *28*(Suppl. 4), S12–S21.
101. De Ugarte, D. A.; Alfonso, Z.; *et al*. *Immunol. Lett.* **2003**, *89*(2–3), 267–270.
102. Erickson, G. R.; Gimble, J. M.; *et al*. *Biochem. Biophys. Res. Commun.* **2002**, *290*(2), 763–769.
103. Gimble, J. M. *Expert Opin. Biol. Ther.* **2003**, *3*(5), 705–713.
104. Gronthos, S.; Zannettino, A. C.; *et al*. *J. Cell Sci.* **2003**, *116*(Pt 9), 1827–1835.
105. Guilak, F.; Lott, K. E.; *et al*. *J. Cell. Physiol.* **2006**, *206*(1), 229–237.
106. Huang, J. I.; Kazmi, N.; *et al*. *J. Orthop. Res.* **2005**, *23*(6), 1383–1389.
107. Knippenberg, M.; Helder, M. N.; *et al*. *Tissue Eng.* **2005**, *11*(11–12), 1780–1788.
108. Lin, T. M.; Tsai, J. L.; *et al*. *Stem Cells Dev.* **2005**, *14*(1), 92–102.
109. Lin, Y.; Luo, E.; *et al*. *J. Cell. Mol. Med.* **2005**, *9*(4), 929–939.
110. Peterson, B.; Zhang, J.; *et al*. *Tissue Eng.* **2005**, *11*(1–2), 120–129.
111. Strem, B. M.; Hicok, K. C.; *et al*. *Keio J. Med.* **2005**, *54*(3), 132–141.
112. Tholpady, S. S.; Llull, R.; *et al*. *Clin. Plast. Surg.* **2006**, *33*(1), 55–62; vi.
113. Zuk, P. A.; Zhu, M.; *et al*. *Mol. Biol. Cell* **2002**, *13*(12), 4279–4295.
114. Zuk, P. A.; Zhu, M.; *et al*. *Tissue Eng.* **2001**, *7*(2), 211–228.
115. Moseley, T. A.; Zhu, M.; *et al*. *Plast. Reconstr. Surg.* **2006**, *118*(Suppl. 3), 121S–128S.
116. Hemmrich, K.; von Heimburg, D. *Expert Rev. Med. Devices* **2006**, *3*(5), 635–645.
117. Halberstadt, C.; Austin, C.; *et al*. *Tissue Eng.* **2002**, *8*(2), 309–319.
118. Rowley, J. A.; Madlambayan, G.; *et al*. *Biomaterials* **1999**, *20*(1), 45–53.
119. Burg, K. J. L.; Shalaby, S. W. *Biodegradable Materials*; R.G. Landes Co: Austin, 1999.
120. Tholpady, S. S.; Aojanepong, C.; *et al*. *Ann. Plast. Surg.* **2005**, *54*(6), 651–656.
121. Alhadlaq, A.; Tang, M.; *et al*. *Tissue Eng.* **2005**, *11*(3–4), 556–566.
122. Chen, G.; Ushida, T.; *et al*. *Macromol. Biosci.* **2002**, *2*, 67–77.
123. Kohane, D. S.; Langer, R. *Pediatr. Res.* **2008**, *63*(5), 487–491.
124. Holder, W. D., Jr.; Gruber, H. E.; *et al*. *J. Biomed. Mater. Res.* **1998**, *41*(3), 412–421.
125. Hausman, D. B.; DiGirolamo, M.; *et al*. *Obes. Rev.* **2001**, *2*(4), 239–254.
126. Hausman, G. J. *Gen. Comp. Endocrinol.* **2003**, *133*(1), 61–70.
127. von Heimburg, D.; Zachariah, S.; *et al*. *Biomaterials* **2001**, *22*(5), 429–438.
128. Burg, K. J.; Boland, T. *IEEE Eng. Med. Biol. Mag.* **2003**, *22*(5), 84–91.
129. Nair, L. S.; Laurencin, C. T. *Adv. Biochem. Eng. Biotechnol.* **2006**, *102*, 47–90.
130. Burg, K. J.; Holder, W. D.; *et al*. *J. Biomater. Sci. Polym. Ed.* **1999**, *10*(2), 147–161.
131. Griffith, L. G. *Ann. N. Y. Acad. Sci.* **2002**, *961*, 83–95.
132. Sachlos, E.; Czernuszka, J. T. *Eur. Cell. Mater.* **2003**, *5*, 29–39; discussion 39-40.
133. Eiselt, P.; Yeh, J.; *et al*. *Biomaterials* **2000**, *21*(19), 1921–1927.
134. Lee, K. Y.; Mooney, D. J. *Chem. Rev.* **2001**, *101*(7), 1869–1879.
135. Simpson, N. E.; Grant, S. C.; *et al*. *Biomaterials* **2003**, *24*(27), 4941–4948.
136. Drury, J. L.; Mooney, D. J. *Biomaterials* **2003**, *24*(24), 4337–4351.
137. Kong, H. J.; Kaigler, D.; *et al*. *Biomacromolecules* **2004**, *5*(5), 1720–1727.
138. Alshamkhani and Duncan (1995).
139. Rowley, J. A.; Mooney, D. J. *J. Biomed. Mater. Res.* **2002**, *60*(2), 217–223.
140. Silva, G. A.; Ducheyne, P.; *et al*. *J. Tissue Eng. Regen. Med.* **2007**, *1*(1), 4–24.
141. Smetana, K., Jr. *Biomaterials* **1993**, *14*(14), 1046–1050.
142. Loebsack, A.; Greene, K.; *et al*. *J. Biomed. Mater. Res.* **2001**, *57*(4), 575–581.
143. Perets, A.; Baruch, Y.; *et al*. *J. Biomed. Mater. Res. A* **2003**, *65*(4), 489–497.
144. Kim, I. Y.; Seo, S. J.; *et al*. *Biotechnol. Adv.* **2008**, *26*(1), 1–21.
145. Mano, J. F.; Silva, G. A.; *et al*. *J. R. Soc. Interface* **2007**, *4*(17), 999–1030.
146. Shi, C.; Zhu, Y.; *et al*. *J. Surg. Res.* **2006**, *133*(2), 185–192.
147. Bumgardner, J. D.; Wiser, R.; *et al*. *J. Biomater. Sci. Polym. Ed.* **2003**, *14*(5), 423–438.
148. Boucard, N.; Viton, C.; *et al*. *Biomaterials* **2007**, *28*(24), 3478–3488.
149. Huang, Y.; Onyeri, S.; *et al*. *Biomaterials* **2005**, *26*(36), 7616–7627.
150. Alves, N. M.; Mano, J. F. *Int. J. Biol. Macromol.* **2008**, *43*(5), 401–414.
151. Di Martino, A.; Sittinger, M.; *et al*. *Biomaterials* **2005**, *26*(30), 5983–5990.
152. Malafaya, P. B.; Silva, G. A.; *et al*. *Adv. Drug Deliv. Rev.* **2007**, *59*(4–5), 207–233.
153. Munarin, F.; Petrini, P.; *et al*. *J. Mater. Sci. Mater. Med.* **2009**, *21*(1), 365–375.
154. Shim, I. K.; Lee, S. Y.; *et al*. *J. Biomed. Mater. Res. A* **2008**, *84*(1), 247–255.
155. Pulieri, E.; Chiono, V.; *et al*. *J. Biomed. Mater. Res. A* **2008**, *86*(2), 311–322.
156. Wu, X.; Black, L.; *et al*. *J. Biomed. Mater. Res. A* **2007**, *81*(1), 59–65.
157. Cruz, D. M.; Ivirico, J. L.; *et al*. *J. Tissue Eng. Regen. Med.* **2008**, *2*(6), 378–380.
158. von Heimburg, D.; Kuberka, M.; *et al*. *Int. J. Artif. Organs* **2003**, *26*(12), 1064–1076.
159. Gentleman, E.; Nauman, E. A.; *et al*. *Tissue Eng.* **2006**, *12*(6), 1639–1649.
160. Hong, L.; Peptan, I.; *et al*. *Ann. Biomed. Eng.* **2005**, *33*(4), 511–517.
161. Masuda, T.; Furue, M.; *et al*. *Tissue Eng.* **2004**, *10*(11–12), 1672–1683.
162. Masuda, T.; Furue, M.; *et al*. *Tissue Eng.* **2004**, *10*(3–4), 523–535.
163. Toriyama, K.; Kawaguchi, N.; *et al*. *Tissue Eng.* **2002**, *8*(1), 157–165.
164. Vashi, A. V.; Abberton, K. M.; *et al*. *Tissue Eng.* **2006**, *12*(11), 3035–3043.
165. Hiraoka, Y.; Yamashiro, H.; *et al*. *Tissue Eng.* **2006**, *12*(6), 1475–1487.
166. Kimura, Y.; Ozeki, M.; *et al*. *Tissue Eng.* **2002**, *8*(4), 603–613.
167. Kimura, Y.; Ozeki, M.; *et al*. *Biomaterials* **2003**, *24*(14), 2513–2521.
168. Gomillion, C.; Cavin, A. N.; *et al*. In *Transactions of the 30th Annual Meeting of the Society for Biomaterials, Memphis, TN*, 2005.
169. Cho, S. W.; Kim, I.; *et al*. *Biochem. Biophys. Res. Commun.* **2006**, *345*(2), 588–594.
170. Torio-Padron, N.; Baerlecken, N.; *et al*. *Aesthetic Plast. Surg.* **2007**, *31*(3), 285–293.
171. Duranti, F.; Salti, G.; *et al*. *Dermatol. Surg.* **1998**, *24*(12), 1317–1325.
172. Gutowska, A.; Jeong, B.; *et al*. *Anat. Rec.* **2001**, *263*(4), 342–349.
173. Kablik, J.; Monheit, G. D.; *et al*. *Dermatol. Surg.* **2009**, *35*(Suppl. 1), 302–312.
174. Newman, J. *Clin. Cosmet. Investig. Dermatol.* **2009**, *2*, 141–150.
175. Kleinman, H. K.; McGarvey, M. L.; *et al*. *Biochemistry* **1986**, *25*(2), 312–318.
176. Kleinman, H. K.; Graf, J.; *et al*. *Ann. N. Y. Acad. Sci.* **1987**, *513*, 134–145.
177. Kawaguchi, N.; Toriyama, K.; *et al*. *Proc. Natl. Acad. Sci. USA* **1998**, *95*(3), 1062–1066.
178. Tabata, Y. *Tissue Eng.* **2003**, *9*(Suppl. 1), S5–S15.
179. Findlay, M. W.; Messina, A.; *et al*. *Plast. Reconstr. Surg.* **2009**, *124*(4), 1077–1084.
180. Chaubey and Burg (2008).
181. Abberton, K. M.; Bortolotto, S. K.; *et al*. *Cells Tissues Organs* **2008**, *188*(4), 347–358.
182. Flynn, L.; Prestwich, G. D.; *et al*. *Biomaterials* **2007**, *28*(26), 3834–3842.
183. Flynn, L.; Woodhouse, K. A. *Organogenesis* **2008**, *4*(4), 228–235.
184. Vermette, M.; Trottier, V.; *et al*. *Biomaterials* **2007**, *28*(18), 2850–2860.
185. Choi, J. S.; Yang, H. J.; *et al*. *J. Control. Release* **2009**, *139*(1), 2–7.
186. Patrick, C. W., Jr.; Chauvin, P. B.; *et al*. *Tissue Eng.* **1999**, *5*(2), 139–151.
187. Patrick, C. W., Jr.; Zheng, B.; *et al*. *Tissue Eng.* **2002**, *8*(2), 283–293.
188. Cho, S. W.; Kim, S. S.; *et al*. *Biomaterials* **2005**, *26*(17), 3577–3585.
189. Choi, Y. S.; Park, S. N.; *et al*. *Biomaterials* **2005**, *26*(29), 5855–5863.
190. Choi, Y. S.; Cha, S. M.; *et al*. *Biochem. Biophys. Res. Commun.* **2006**, *345*(2), 631–637.
191. Yuksel, E.; Weinfeld, A. B.; *et al*. *Plast. Reconstr. Surg.* **2000**, *105*, 1721–1729.
192. Patel, P. N.; Gobin, A. S.; *et al*. *Tissue Eng.* **2005**, *11*(9–10), 1498–1505.
193. Stacey, D. H.; Hanson, S. E.; *et al*. *Tissue Eng. A* **2009**, *15*(11), 3389–3399.
194. Yang, C. C.; Ellis, S. E.; *et al*. *J. Tissue Eng. Regen. Med.* **2007**, *1*(2), 146–153.

Relevant Websites

http://3dcellculture.com/ – 3-D Cell Culture News and Articles.
http://www.clemson.edu/centers-institutes/ibioe/tiger.html – Clemson University Institute for Biological Interfaces of Engineering (IBIOE): Bioengineering Learning Module.
http://www.mirm.pitt.edu/ – McGowan Institute for Regenerative Medicine.
http://stemcells.nih.gov/info/basics/ – National Institutes of Health (NIH) Resource for Stem Cell Research.
http://www.regenerativemedicine.net – Regenerative Medicine.

5.538. Finger

N Isogai and T Tokui, Kinki University School of Medicine, Osaka-Sayama, Japan

© 2011 Elsevier Ltd. All rights reserved.

5.538.1.	**Introduction**	541
5.538.2.	**Periosteum for Human Phalanx Model**	542
5.538.3.	***In Vivo* Model for Phalanx**	542
5.538.3.1.	Biomaterials	542
5.538.3.2.	Techniques for Fabrication	542
5.538.3.2.1.	Preparation of the phalanx	542
5.538.3.2.2.	Preparation of the joint cartilage	542
5.538.3.2.3.	Preparation of the human phalanx model *in vitro*	542
5.538.3.2.4.	*In vivo* implantation of the human phalanx model	542
5.538.4.	**Development of the Human Phalanx Model**	543
5.538.4.1.	Gross Morphology	543
5.538.4.2.	X-Ray Findings	543
5.538.4.3.	Histology	544
5.538.5.	**Assessment of the Human Phalanx Model**	544
5.538.5.1.	Mechanism of Ossification	544
5.538.5.2.	Osteogenic Capability of the Copolymer	544
5.538.5.3.	Signal Pathway Between Periosteum and Joint Cartilage	545
5.538.6.	**Conclusion and Future Directions**	545
References		546

Abbreviations

3D	Three-dimensional
BMP-2	Bone morphogenetic protein-2
BSP	Bone sialoprotein
FBS	Fetal bovine serum
HA	Hydroxyapatite
IGF-1	Insulin-like growth factor-1
Ihh	Indian hedgehog
LCM	Laser capture microdissection
P(LA-CL)	Poly(L-lactide-ε-caprolactone)
PGA	Polyglycolic acid
PLLA	Polylactic acid
PTHrP	Parathyroid hormone-related protein
RGD	Arg-glu-asp
TGF-β	Transforming growth factor-β

5.538.1. Introduction

In 1999, we began to explore the feasibility of phalangeal regeneration. A copolymer of biodegradable polyglycolic acid (PGA) and polylactic acid (PLLA) was shaped into a human phalanx with a periosteum wrapped around it. PGA sheets seeded with chondrocytes were subsequently attached to both ends of the phalanx for the regeneration of a phalanx with joint cartilage *in vivo*.[1] In this human phalanx model, however, the three-dimensional (3D) morphological characteristics of the human phalanx were not maintained, indicating that a copolymer of PGA and PLLA was an inadequate material for our purposes.[2–5]

To overcome this drawback, attention was directed to Poly(L-lactide-ε-caprolactone) (P(LA-CL)), a copolymer of PLLA and polycaprolactone.[6,7] P(LA-CL) is known to be a readily moldable and biodegradable copolymer with characteristics adequate for tissue regeneration.[8,9] The 3D morphology has been reported to be maintained over a long period when P(LA-CL) is used for the induction of cartilage tissue.[10] Furthermore, we developed a new osteoinductive biodegradable copolymer with improved mechanical strength and bone conduction capacity by incorporating hydroxyapatite (HA) particles[11] into the internal structure of P(LA-CL).

In this chapter, we describe our renewed attempts at phalangeal regeneration by applying an osteoinductive biodegradable 3D copolymer of P(LA-CL) with HA particles, shaped into a human phalanx. By combining a high-performance biodegradable copolymer with periosteum, we sought to achieve a better induction of phalangeal regeneration. Maintenance of joint cartilage after cartilage formation is functionally important. Periosteum has been suggested to play an important role in the regulation of joint cartilage, although the mechanism is not precisely known. An analytical study of the interaction between the periosteum and the joint cartilage in our model was undertaken. Periosteum was attached circumferentially around one half of a phalanx-molded biodegradable copolymer and the regenerative ability of bone between the periosteal and nonperiosteal sides was compared with respect to tissue-forming properties and 3D-maintained shape. Thus, our study was designed from both functional (human phalanx shape) and analytical

viewpoints. A basic knowledge and understanding of the developmental processes that occur in phalangeal regeneration are clearly necessary for future clinical applications.

5.538.2. Periosteum for Human Phalanx Model

The periosteum is known to have three roles: (1) a source of osteocytes/chondrocytes that differentiate from pluripotent undifferentiated mesenchymal cells, (2) a scaffold for the proliferation of osteocytes/chondrocytes, and (3) a source of growth factors.[12]

Histologically, the periosteum consists of a superficial thick fibrous layer and a deep thin cambium layer. In the cambium layer, a large number of osteoblasts (pleuripotent undifferentiated mesenchymal cells), which stain eosinophilically with toluidine blue, are present, and they differentiate into osteocytes and chondrocytes. The periosteum is involved in bone growth (appositional growth) through the proliferation and differentiation of osteoblasts, and increases bone thickness and strength.[13] Also, the thickness of the cambium layer and the number of cells in it are known to markedly reduce with age, with decreases in the capacity for bone growth.[12,14]

Recently, more detailed research has been conducted on the periosteum, and the structure of the periosteum has been reported to differ as regards the diaphysis and the metaphysis. The metaphysial periosteum has a thick cambium layer with a large number of cells in it, and shows no structural changes associated with aging. The diaphysial periosteum, on the other hand, is thinner than the metaphysial periosteum, and both the thickness of the cambium layer and the number of cells in it have been reported to decrease markedly with age.[15]

5.538.3. *In Vivo* Model for Phalanx

5.538.3.1. Biomaterials

P(LA-CL) was prepared by infusing a polymer solution (5% (w/w); 1,4-diaxane and P(LA-CL) mixed at 75:25) into casts prepared in advance from a human phalangeal specimen (17 mm long, 7 mm wide, and 5 mm high) using a pipette to avoid foam formation, and then mixed with HA particles of about 30 μm diameter (70:30 wt%). The casts into which each polymer was infused were transferred to a refrigerator and allowed to stand for 2 h at −40 °C. The polymers were removed from the casts and freeze-dried at 40 Pa and −40 °C over 12 h (TF10-80ATA, Takara Seisakusho, Tokyo). Finally, the monomers and the vehicle were removed by vacuum drying (60 °C, 12 h), and osteoinductive biodegradable 3D copolymer with the shape of a human phalanx was obtained. The prepared P(LA-CL) had a molecular weight of 367 000, an interior with a spongy structure, a pore size of 50–100 μm, and a porosity of 95%. It was biodegraded in 4–6 months *in vivo*. HA particles were incorporated into the spongy structure of P(LA-CL).

5.538.3.2. Techniques for Fabrication

5.538.3.2.1. Preparation of the phalanx

Fresh periosteum was elevated from the radial diaphysis of a calf (within 1 month after birth) using a periosteum elevator and collected. The collected periosteum was wrapped circumferentially around one half of a biodegradable copolymer molded after the human phalanx and fixed by suturing with an absorbable thread (5-0 Vicryl®, Ethicon, Somerville, NJ, USA). In suturing, the cambium layer was brought into direct contact with the copolymer surface to allow osteoblasts and undifferentiated cells released from the cambium layer to migrate into the copolymer. To the prepared periosteum–copolymer complex, a modified M199 culture medium (Gibco, Grand Island, NY, USA) supplemented in advance with 10% fetal bovine serum (FBS, Sigma-Aldrich, St. Louis, MO, USA), 50 μg ml^{-1} ascorbic acid, 100 units ml^{-1} penicillin G, 100 μg ml^{-1} streptomycin, and 0.25 μg ml^{-1} amphotericin B was added, and the complex was incubated at 37 °C and in 5% CO_2 for 6 days (**Figure 1**).

5.538.3.2.2. Preparation of the joint cartilage

Cartilaginous tissue was collected from the shoulder joint of a calf using a #10 scalpel according to the method of Klagsbrun.[16] After the collected tissue was minced into 5 × 5-mm fragments, it was treated with 0.3% collagenase type II (Worthington Biochemical, Freehold, NJ, USA) at 37 °C for 14 h. The mixture was filtered through a nylon mesh (pore size: 300 μm), and the enzyme reaction was stopped by adding a modified F12 culture medium (Gibco, Grand Island, NY, USA) supplemented with 10% FBS, 50 μg ml^{-1} ascorbic acid, 100 units ml^{-1} penicillin G, 100 μg ml^{-1} streptomycin, and 0.25 μg ml^{-1} amphotericin B. The chondrocyte suspension obtained was washed three times with Ca^{2+}- and Mg^{2+}-free phosphate buffer (PBS, Mediatech INC, Herndon, VA, USA) and centrifuged (4 °C, 400 G, 10 min). To this chondrocyte suspension, the modified F12 culture medium was added, the cell concentration was adjusted to 100 × 10^6 cells ml^{-1}, and the cell suspension seeded on PGA (Gunze Co., Ltd., Kyoto; Size: 10 × 10 × 2 mm). The cell–polymer complex was placed in an incubator (37 °C, 5% CO_2) and allowed to stand for 4 h to have the seeded cells adhere to the polymer surface. Then, the modified F12 culture medium was gently added, and the suspension was placed again in the incubator (37 °C, 5% CO_2) for 5 days.

5.538.3.2.3. Preparation of the human phalanx model in vitro

The chondrocyte–polymer complexes were sutured to both ends of the periosteum–copolymer complex using an absorbable thread. The human phalanx model thus prepared was incubated in the modified M199 culture medium at 37 °C in 5% CO_2 for 24 h.

5.538.3.2.4. In vivo *implantation of the human phalanx model*

As preanesthetic medications, atropine sulfate (0.04 mg kg^{-1}, atropine sulfate; Phoenix Scientific Inc., MO, USA) and tolbutamide (3 mg kg^{-1}, trobugesic N; Dodge Animal Health, IW, USA) were administered to the nude mice by subcutaneous injection. Under general anesthesia with isoflurane (Pittman and Moores, Mundelein, IL, USA), the backs of the nude mice were disinfected with povidone iodine (The Purdue Frederick Company, Stamford, CT, USA), and a skin incision about 2 cm long was made. A human phalanx model was inserted into the subcutaneous pocket, which was closed by suturing with a 5-0 nylon suture (Sigma, Tokyo).

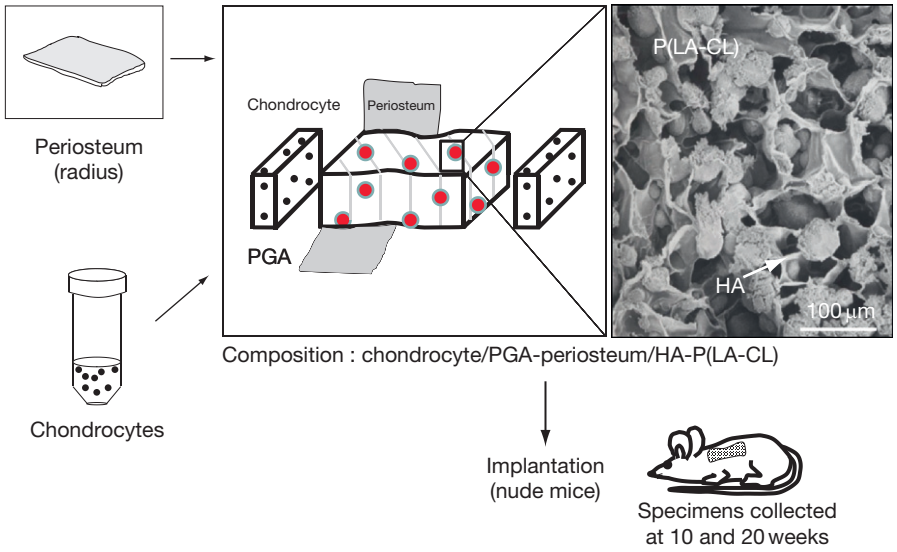

Figure 1 Experimental protocol.

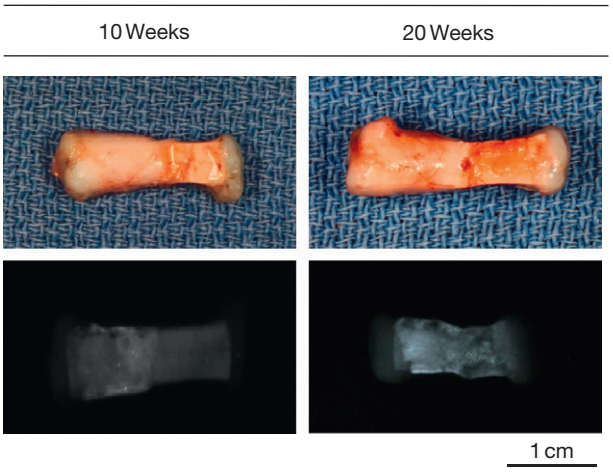

Figure 2 Gross morphology and X-ray. Calcification extending to the interior of the phalanx (10 weeks after implantation) and to the nonperiosteal side (20 weeks after implantation) was noted (bar = 1 cm).

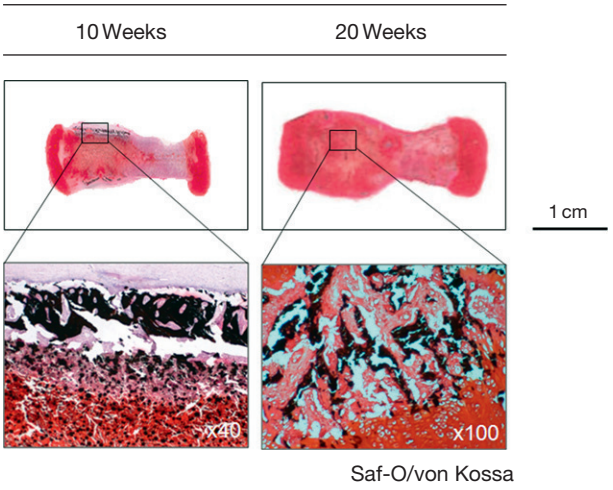

Figure 3 Histology of the human phalangeal models. Samples are from 10 to 20 weeks after implantation. Safranin-O and von Kossa staining (bar = 1 cm).

5.538.4. Development of the Human Phalanx Model

5.538.4.1. Gross Morphology

In the human phalanx models excised at 10 and 20 weeks after implantation, the phalangeal part to which the periosteum was attached (periosteal side) and the part to which it was not attached (nonperiosteal side) could be clearly distinguished by the presence or absence of white periosteum (Figure 2). On the periosteal side, the 3D structure of the phalanx was retained. On the nonperiosteal side, however, areas around the copolymer were slightly reddened and downsized. Significant elongation of the phalanx with time after implantation was noted, and it was more notable on the periosteal side. Joint cartilage was observed to be smooth, white, flexible, and markedly glossy at both ends of the periosteal and nonperiosteal sides of the samples removed 10 and 20 weeks after implantation. These findings suggest that satisfactory bone formation was induced by osteogenic cells that migrated from the periosteum into the interior of the copolymer on the periosteal side of HA-P(LA-CL), but adjacent blood vessels directly infiltrated into the interior of the copolymer and caused marked degradation and absorption of the copolymer on the nonperiosteal side.

5.538.4.2. X-Ray Findings

No clear calcification was noted on the nonperiosteal side after 10 weeks of implantation. On the periosteal side, an area of calcification extending to the interior of the phalanx could be noted after just 10 weeks, and radiopacity due to calcification decreased further and also extended to the nonperiosteal side after 20 weeks. These results suggest the high osteoinductive property of the copolymer with periosteum (Figure 2).

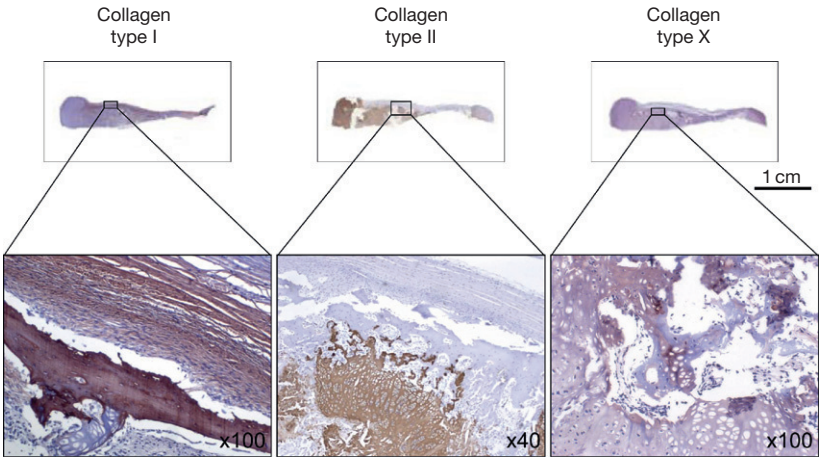

Figure 4 Immunohistochemistry to examine the mechanism of ossification. (Above) Cross-section (staining for type I, II, and X collagen, bar = 1 cm). (Below) Periosteal side (staining for type I collagen; × 100, staining for type II collagen; × 40, staining for type X collagen; × 100). Positive areas were observed below the periosteum for type I, and within the phalanx for type II. Areas stained for type X collagen were observed between the area stained for type I collagen and the area stained for type II collagen at 20 weeks after implantation.

5.538.4.3. Histology

In the groups of the human phalanx model excised 10 and 20 weeks after implantation, calcified areas that reacted positively with von Kossa staining were observed on the side to which the periosteum was attached (periosteal side). Positive areas were localized under the periosteum after 10 weeks, but extended to the interior of the phalanx after 20 weeks. On the nonperiosteal side, no area with positive reaction was noted. The periosteal sides showed intense positive responses to safranin-O over a wide area of the interior of the phalanx model at 20 weeks after implantation, indicative of proteoglycan in large amounts. These results suggest that calcified areas are initially localized under the periosteum but widen over the interior of the phalanx with time. Joint cartilages were positively stained for safranin-O staining at 10 and 20 weeks after implantation at both ends of the model (Figure 3).

5.538.5. Assessment of the Human Phalanx Model

5.538.5.1. Mechanism of Ossification

In order to examine the mechanism of ossification, immunostaining for type I, II, and X collagen was performed at 20 weeks after implantation. On the periosteal side, in particular, areas positive for immunostaining for type I collagen were localized under the periosteum, in which the trabeculae were formed. In the deeper areas of the trabeculae, large round chondrocytes were regularly arranged in a columnar pattern. This region corresponded to the area positive for type II collagen immunostaining. Areas positive for type X collagen were observed in the hypertrophic chondrocyte layer. This corresponded to the area between the type I collagen-positive and type II collagen-positive areas (Figure 4). These results suggest that bone formation occurs by endochondral ossification. On the nonperiosteal side, no area positive on immunostaining for type I, II, or X collagen was noted.

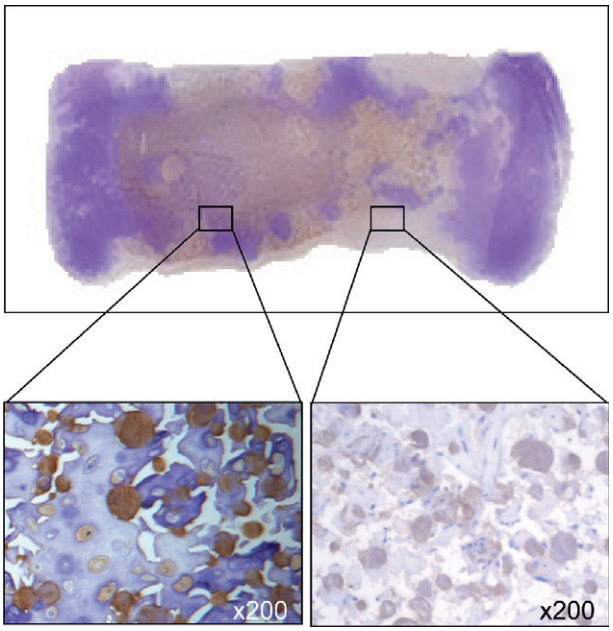

Figure 5 Immunohistochemistry to examine osteogenic capability of the copolymer. (Above) Cross-section (BSP staining). (Below) Periosteal and nonperiosteal parts (BSP staining, × 200). Bone sialoprotein (BSP) was performed to examine osteogenic capacity. An area positive for BSP that extended from the periosteal to the nonperiosteal side was markedly shifted to the nonperiosteal side at 20 weeks after implantation.

5.538.5.2. Osteogenic Capability of the Copolymer

Bone sialoprotein (BSP) has a molecular weight of 70 000–80 000 and is a protein almost specific to bone. It is synthesized by osteoblasts, promotes the adhesion of osteoblasts and osteoclasts to the matrix by the RGD (Arg-Glu-Asp) cell adhesion sequence, is adsorbed on the surface of HA by the continuous sequence of glutamic acid, and forms

plate-like HA.[17,18] According to recent reports,[19,20] BSP is considered to be distributed in newly formed osteoid, interact with collagen fibers of initial osteoid, and thus play an important role in the initial stage of bone formation. BSP also binds with calcium and HA and shows a marked bone-forming capability.[21]

On immunostaining for BSP, positive areas were observed over the entire side of the phalanx to which the periosteum was attached (periosteal side). On the side to which no periosteum was attached (nonperiosteal side), no area positive for BSP was noted. Moreover, BSP-positive areas extended from the periosteal to the nonperiosteal side, and the border between the positive and negative areas was markedly shifted to the nonperiosteal side (Figure 5). These results suggest that the expression of BSP is markedly promoted by the combination of the osteoinductive biodegradable 3D copolymer with periosteum.

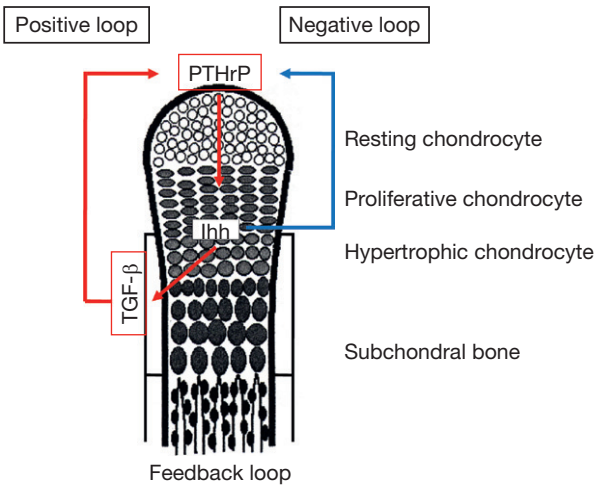

Figure 6 Signal pathway between periosteum and joint cartilage. Modified from Kronenberg, H. M. *Nature* **2003**, *423*, 332–336.

5.538.5.3. Signal Pathway Between Periosteum and Joint Cartilage

The periosteum releases various growth factors, including TGF-β, IGF-1, BMP-2, and integrins,[12] and has been suggested to be closely involved in the regulation and maintenance of the joint cartilage structure and extracellular matrix. Particularly, TGF-β released from the periosteum, PTHrP released from the resting layer present in the most superficial part of the joint cartilage, and Ihh released from the proliferative layer have been shown to form a feedback loop, leading to clarification on the control for signal pathway of joint cartilage by the periosteum (Figure 6).[22–30]

In the human phalanx model, cells were nonselectively captured by laser capture microdissection (LCM)[31] from three such areas as the side layer of the periosteum, the resting layers, and the hypertrophic layers of the joint cartilage (Figure 7). Then, serial changes in the expression of periosteum/cartilage-related genes (PTHrp, Ihh, TGF-β) were examined in the captured cells with RT-PCR to analyze the signal pathway between the periosteum and the joint cartilage. As a result, positive expressions of type TGF-β (side layer), PTHrp (resting layer), and Ihh (hypertrophic layer) were observed, and the positive feedback loop system was complete on the periosteal side, while it was incomplete on the nonperiosteal side (Figure 8).

5.538.6. Conclusion and Future Directions

In this study, a human phalanx model was prepared by attaching the periosteum to an osteoinductive biodegradable 3D polymer, which was P(LA-CL) with the incorporation of HA particles, in the shape of the human phalanx. Cultured chondrocytes seeded on PGA sheets were subsequently attached to both ends of the copolymer of P(LA-CL)with HA particles for the phalangeal regeneration. The model was implanted into nude mice, and the regeneration of phalanx and joint cartilage was induced. Areas with and without attachment of the

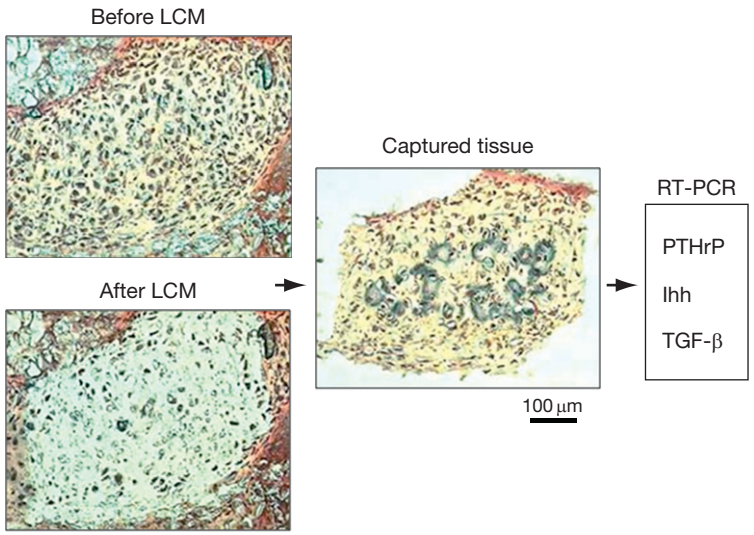

Figure 7 Method of laser capture microdissection.

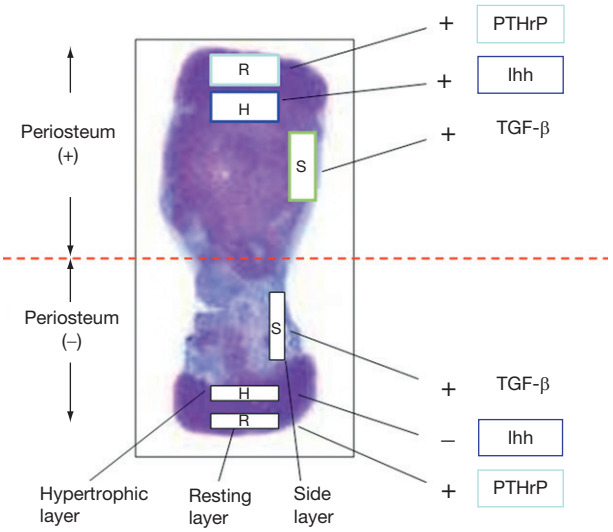

Figure 8 Gene expression using RT-PCR. Expression of PTHrp, Ihh, and TGF-β genes was examined at 20 weeks after implantation.

periosteum were prepared in each phalanx model (periosteal and nonperiosteal sides), and the involvement of the periosteum in the maturation process was evaluated. On gross examination, the 3D morphology of the phalanx was maintained more favorably on the periosteal side. On histological examination, bone formation was observed to proceed through an endochondral ossification mechanism. Expression of BSP on the periosteal side was remarkably higher than that on the nonperiosteal side. RT-PCR data suggested that expression of TGF-β, PTHrp, and Ihh was a central aspect of a feedback loop system that operated efficiently on the periosteal side, but incompletely on the nonperiosteal side.

From these results, it can be seen that the attached periosteum plays an important role in the induction of regeneration of the phalanx and joint cartilage in a human phalanx model. P(LA-CL) with the incorporation of HA particles promoted both osteogenesis and chondrogenesis with periosteum. Combination of the osteoinductive biodegradable 3D copolymer with periosteum was extremely useful for accelerating the human phalangeal regeneration. Future research will need to be directed at both donor and recipient transplantation sites in an autologous model. A functional network of blood vessels that can nourish the regenerated phalangeal tissue will need to be developed, either *in situ* at the defect site or in a donor site, which can be subsequently transferred as a 'free flap' using microvascular surgery. The latter approach will not only require good angiogenic development into the regenerated phalanx, but also need to have a primary pair of vessels of sufficient caliber for undertaking the microsurgical vascular connections. Further analysis of phalangeal regeneration techniques will allow functional and successful reproduction of the phalanx, with the goal of phalanx or phalangeal joint reconstruction for patients with phalangeal defects resulting from congenital or acquired diseases or traumatic injury.

References

1. Isogai, N.; Landis, W.; Vacanti, J. P. *J. Bone Joint Surg.* **1999**, *81A*, 306–316.
2. Isogai, N.; Landis, W. In *Methods of Tissue Engineering*; Atla, A., Lanza, R., Eds.; Academic Press: San Diego, 2001; pp 1041–1047.
3. Chubinskaya, S.; Isogai, N.; Landis, W. *Tissue Eng.* **2004**, *10*, 1204–1213.
4. Landis, W.; Jacquet, R.; Isogai, N. *Orthop. Clin. N. Am.* **2005**, *36*, 97–104.
5. Potter, K.; Isogai, N.; Landis, W. *Bone* **2006**, *38*, 350–358.
6. Honda, M.; Yada, T.; Ueda, M.; Kimata, K. *J. Oral Maxillofac. Surg.* **2000**, *58*, 767–775.
7. Watanabe, M.; Shinoka, T.; Tohyama, S.; *et al. Tissue Eng.* **2001**, *7*, 429–439.
8. Yamada, K.; Miyamoto, S.; Nagata, I.; *et al. J. Neurosurg.* **1997**, *86*, 1012–1017.
9. Yamada, K.; Miyamoto, S.; Takayama, M.; *et al. J. Neurosurg.* **2002**, *96*, 731–735.
10. Isogai, N.; Asamura, S.; Higashi, T.; *et al. Tissue Eng.* **2004**, *10*, 673–687.
11. Baht, G. S.; Hunter, G. K.; Goldberg, H. A. *Matrix Biol.* **2008**, *27*(7), 600–608.
12. O'Driscoll, S. W.; Fitzsimmons, J. S. *Clin. Orthop. Relat. Res.* **2001**, *391S*, S190–S207.
13. Kwon, D. S.; Spevak, M. R.; Fletcher, K.; Kleinman, P. K. *Am. J. Roentgenol.* **2002**, *179*, 985–988.
14. Szule, P.; Seeman, E.; Duboeuf, F.; Sornay-Rendu, E.; Delmas, P. *J. Bone Miner. Res.* **2006**, *21*, 1856–1863.
15. Fan, W.; Crawford, R.; Xiao, Y. *Bone* **2008**, *42*, 81–89.
16. Klagsbrun, M. *Meth. Enzymol.* **1979**, *58*, 560–564.
17. Pao, H.; Tao, J.; Xu, X.; Tang, R. *Langmuir* **2007**, *23*, 8972–8981.
18. Harris, N. L.; Rattray, K. R.; Tye, C. E.; *et al. Bone* **2000**, *27*, 795–802.
19. Fujiwara, R.; Mizuno, M. *Connect. Tissue* **2003**, *35*, 141–145.
20. Takai, H.; Ogata, Y. *Nihon Shishubyo Gakkai Kaishi* **2007**, *49*, 27–36.
21. Ganss, B.; Kim, R. H.; Sodek, J. *Crit. Rev. Oral Biol. Med.* **1999**, *10*, 79–98.
22. Alvarez, J.; Horton, J.; Sohn, P.; Serra, R. *Dev. Dyn.* **2001**, *221*, 311–321.
23. Faucheux, C.; Nicholls, B. M.; Allen, S.; Danks, J. A.; Horton, M. A.; Price, J. S. *Dev. Dyn.* **2004**, *231*, 88–97.
24. Bandyopadhyay, A.; Kubilus, J. K.; Crochiere, M. L.; Linsenmayer, T. F.; Tabin, C. J. *Dev. Biol.* **2008**, *321*(1), 162–174.
25. Goldring, M. B.; Tsuchimori, K.; Ijiri, K. *J. Cell. Biochem.* **2006**, *97*, 33–44.
26. de Crombrugghe, B.; Lefebvre, V.; Nakashima, K. *Curr. Opin. Cell Biol.* **2001**, *13*, 721–727.
27. Kronenberg, H. M. *Nature* **2003**, *423*, 332–336.
28. Provot, S.; Schipani, E. *Biochem. Biophys. Res. Commun.* **2005**, *328*, 658–665.
29. Eames, B. F.; de la Fuente, L. F.; Helms, J. A. *Birth Defects Res. C* **2003**, *69*, 93–101.
30. Ballock, R. T.; O'Keefe, R. J. *J. Bone Joint Surg.* **2003**, *85*(4), 715–725.
31. Jacquet, R.; Landis, W. *Anal. Biochem.* **2005**, *337*, 22–34.

5.539. From Tissue to Organ Engineering

A Atala, Wake Forest University School of Medicine, Winston-Salem, NC, USA

© 2011 Elsevier Ltd. All rights reserved.

5.539.1.	**Introduction**	548
5.539.2.	**Biomaterials**	548
5.539.2.1.	Naturally Derived Materials	549
5.539.2.2.	Acellular Tissue Matrices	549
5.539.2.3.	Synthetic Polymers	549
5.539.3.	**Cells for Use in Tissue Engineering**	549
5.539.3.1.	Embryonic Stem Cells	549
5.539.3.2.	Laboratory-Generated Stem Cells	550
5.539.3.3.	Amniotic Fluid and Placental Stem Cells	551
5.539.3.4.	Adult Stem Cells and Native Progenitor Cells	551
5.539.4.	**Cell Therapy with Injectable Substances**	551
5.539.4.1.	Bulking Agents	551
5.539.4.2.	Injectable Muscle Cells	552
5.539.4.3.	Endocrine Replacement	552
5.539.5.	**Tissue Engineering of Specific Structures**	553
5.539.5.1.	Urethra	553
5.539.5.2.	Bladder	554
5.539.5.3.	Kidney	556
5.539.5.4.	Male Reproductive Organs	557
5.539.5.5.	Female Reproductive Organs	558
5.539.5.6.	Blood Vessels	558
5.539.5.7.	Heart	558
5.539.5.8.	Liver	559
5.539.5.9.	Articular Cartilage and Trachea	559
5.539.6.	**Summary and Conclusion**	560
References		560

Glossary

Acellular matrix Collagen-rich scaffolds prepared by removing all cellular components from a donor tissue.

Adult stem cell An undifferentiated cell found in postnatal tissues that can self-renew as well as produce progeny that can differentiate into the various cell types that comprise the tissue.

Amniotic fluid stem (AFS) cell A multipotent cell type found in the amniotic fluid surrounding an embryo; AFS cells may be mesenchymal in origin and differentiation to neural, hepatic, osteogenic, and chondrogenic lineages, among others, has been demonstrated.

Embryonic stem (ES) cell A broadly multipotent cell type found in the inner cell mass of a blastocyst; ES cells can differentiate into nearly every cell type in the body.

Induced pluripotent stem (iPS) cell A somatic cell that has been dedifferentiated to a stem cell-like phenotype via the introduction of functional gene products involved in maintaining pluripotency.

Reproductive cloning The use of cloning procedures to produce a live offspring that is a genetic copy of an adult animal.

Therapeutic cloning The use of cloning procedures to produce a blastocyst *in vitro* in order to obtain embryonic stem cells for cell therapy or tissue engineering applications.

Abbreviations

AFPSC	Amniotic fluid and placental stem cell
AFS	Amniotic fluid stem
CDC	Centers for disease control
DNA	Deoxyribonucleic acid
ECM	Extracellular matrix
EliSPOT	Enzyme-linked immunosorbent spot assay
ES	Embryonic stem
FDA	Food and Drug Administration
FLM	Fluorescent latex microspheres
GIRK	G-protein-gated inwardly rectifying potassium
iPS	Induced pluripotent state
IFN	Interferon
MEF	Murine embryonic fibroblast
MMP	Matrix metalloproteinase
mtDNA	Mitochondrial DNA

PGA	Polyglycolic acid	**RNA**	Ribonucleic acid
PLA	Polylactic acid	**RT-PCR**	Reverse transcription polymerase chain reaction
PLGA	Poly(lactic-co-glycolic) acid	**SCNT**	Somatic cell nuclear transfer
RGD	Arginine-glycine-aspartate		

5.539.1. Introduction

Patients suffering from diseased and injured organs may be treated with transplanted organs. However, there is a severe shortage of donor organs that is worsening yearly. As modern medicine increases the human lifespan, the aging population grows, and the need for organs grows with it, as aging organs are generally more prone to failure. Scientists in the field of regenerative medicine and tissue engineering apply the principles of cell transplantation, material science, and bioengineering to construct biological substitutes that can prolong life by reducing mortality from these diseases. Therapeutic cloning, where the nucleus from a donor cell is transferred into an enucleated oocyte in order to extract pluripotent embryonic stem cells, offers a potentially limitless source of cells for tissue engineering applications. The stem cell field is also advancing rapidly, opening new options for therapy. This chapter reviews recent advances that have occurred in regenerative medicine and describes applications of these new technologies that offer promise of a longer life.

The field of regenerative medicine encompasses various areas of technology, such as tissue engineering, stem cells, and cloning. Tissue engineering, one of the major components of regenerative medicine, follows the principles of cell transplantation, materials science, and engineering toward the development of biological substitutes that can restore and maintain normal function. Tissue engineering strategies generally fall into two categories: the use of acellular matrices, which depend on the body's natural ability to regenerate for proper orientation and direction of new tissue growth, and the use of matrices with cells. Acellular tissue matrices are usually prepared by manufacturing artificial scaffolds, or by removing cellular components from tissues via mechanical and chemical manipulation to produce collagen-rich matrices.[1–4] These matrices tend to slowly degrade on implantation and are generally replaced by the extracellular matrix (ECM) proteins that are secreted by the ingrowing cells. Cells can also be used for therapy via injection, either with carriers such as hydrogels, or alone.

When cells are used for tissue engineering, a small piece of donor tissue is dissociated into individual cells. These cells are either implanted directly into the host, or are expanded in culture, attached to a support matrix, and then reimplanted into the host after expansion. The source of donor tissue can be heterologous (such as bovine), allogeneic (same species, different individual), or autologous. Ideally, both structural and functional tissue replacement will occur with minimal complications. The preferred cells to use are autologous cells, where a biopsy of tissue is obtained from the host, the cells are dissociated and expanded in culture, and the expanded cells are implanted into the same host.[4–12] The use of autologous cells, although it may cause an inflammatory response, avoids rejection, and thus, the deleterious side effects of immunosuppressive medications can be avoided.

Most current strategies for tissue engineering depend upon a sample of autologous cells from the diseased organ of the host. Aging itself is not a barrier to successful applications of engineered tissues, as cells can be expanded from young and old patients alike. However, for many patients with extensive end-stage organ failure, a tissue biopsy may not yield enough normal cells for expansion and transplantation. In other instances, primary autologous human cells cannot be expanded from a particular organ, such as the pancreas. In these situations, stem cells are envisioned as being an alternative source of cells from which the desired tissue can be derived. Stem cells can be derived from discarded human embryos (human embryonic stem cells), from fetal tissue, or from adult sources (bone marrow, fat, skin).

Therapeutic cloning has also played a role in the development of the field of regenerative medicine. This type of cloning, which has also been called nuclear transplantation and nuclear transfer, involves the introduction of a nucleus from a donor cell into an enucleated oocyte to generate an embryo with a genetic makeup identical to that of the donor. Stem cells can be derived from this source, which may have the future potential to be used therapeutically.

5.539.2. Biomaterials

For cell-based tissue engineering, the expanded cells are seeded onto a scaffold synthesized with the appropriate biomaterial. In tissue engineering, biomaterials replicate the biologic and mechanical function of the native ECM found in tissues in the body by serving as an artificial ECM. Biomaterials provide a three-dimensional space for the cells to form into new tissues with appropriate structure and function, and also can allow for the delivery of cells and appropriate bioactive factors (e.g., cell-adhesion peptides, growth factors), to desired sites in the body.[13] As the majority of mammalian cell types are anchorage-dependent and will die if no cell-adhesion substrate is available, biomaterials provide a cell-adhesion substrate that can deliver cells to specific sites in the body with high loading efficiency. Biomaterials can also provide mechanical support against *in vivo* forces such that the predefined three-dimensional structure is maintained during tissue development. Furthermore, bioactive signals, such as cell-adhesion peptides and growth factors, can be loaded along with cells to help regulate cellular function.

The ideal biomaterial should be biodegradable and bioresorbable to support the replacement of normal tissue without inflammation. Incompatible materials are destined for an inflammatory or foreign-body response that eventually leads to rejection and/or necrosis. Degradation products, if produced, should be removed from the body via metabolic pathways at an adequate rate that keeps the concentration of these degradation products in the tissues at a tolerable level.[14] The biomaterial should also provide an environment in which

appropriate regulation of cell behavior (adhesion, proliferation, migration, and differentiation) can occur such that functional tissue can form. Cell behavior in the newly formed tissue has been shown to be regulated by multiple interactions of the cells with their microenvironment, including interactions with cell-adhesion ligands[15] and with soluble growth factors. Since biomaterials provide temporary mechanical support while the cells undergo spatial reorganization into tissue, the properly chosen biomaterial should allow the engineered tissue to maintain sufficient mechanical integrity to support itself in early development, while in late development, it should have begun degradation such that it does not hinder further tissue growth.[13]

In general, three classes of biomaterials are used for engineering tissues: naturally derived materials (e.g., collagen and alginate), acellular tissue matrices (e.g., bladder submucosa and small intestinal submucosa), and synthetic polymers such as polyglycolic acid (PGA), polylactic acid (PLA), and poly(lactic-*co*-glycolic acid) PLGA). These classes of biomaterials have been tested with respect to their biocompatibility.[16,17] Naturally derived materials and acellular tissue matrices have the potential advantage of biological recognition. However, synthetic polymers can be produced reproducibly on a large scale with controlled properties such as strength, degradation rate, and microstructure.

5.539.2.1. Naturally Derived Materials

Collagen is the most abundant and ubiquitous structural protein in the body, and may be readily purified from both animal and human tissues with an enzyme treatment and salt/acid extraction.[18] Collagen implants, under normal conditions, degrade through a process involving phagocytosis of collagen fibrils by fibroblasts.[19] This is followed by sequential attack by lysosomal enzymes including cathepsins B1 and D. Under inflammatory conditions, the implants can be rapidly degraded largely by matrix metalloproteinases (MMPs) and collagenases.[19] However, the *in vivo* resorption rate of a collagen implant can be regulated by controlling the density of the implant and the extent of intermolecular cross-linking. The lower the density, the greater the space between collagen fibers and the larger the pores for cell infiltration, leading to a higher rate of implant degradation. Collagen contains cell-adhesion domain sequences (e.g., RGD) that may assist in retaining the phenotype and activity of many types of cells, including fibroblasts[20] and chondrocytes.[21]

Alginate, a polysaccharide isolated from seaweed, has been used as an injectable cell delivery vehicle[22] and a cell immobilization matrix[23] owing to its gentle gelling properties in the presence of divalent ions, such as calcium. Alginate is relatively biocompatible and approved by the Food and Drug Administration (FDA) for human use as wound dressing material. Alginate is a family of copolymers of D-mannuronate and L-guluronate. The physical and mechanical properties of alginate gel are strongly correlated with the proportion and length of polygluronic block in the alginate chains.[22]

5.539.2.2. Acellular Tissue Matrices

Acellular tissue matrices are collagen-rich matrices prepared by removing cellular components from tissues. The matrices are often prepared by mechanical and chemical manipulation of a segment of tissue.[1–4] The matrices slowly degrade upon implantation, and are replaced and remodeled by ECM proteins synthesized and secreted by transplanted or ingrowing cells.

5.539.2.3. Synthetic Polymers

Polyesters of naturally occurring α-hydroxy acids, including PGA, PLA, and PLGA, are widely used in tissue engineering. These polymers have gained FDA approval for human use in a variety of applications, including sutures.[24] The ester bonds in these polymers are hydrolytically labile, and these polymers degrade by nonenzymatic hydrolysis. The degradation products of PGA, PLA, and PLGA are nontoxic natural metabolites and are eventually eliminated from the body in the form of carbon dioxide and water.[24] The degradation rate of these polymers can be tailored from several weeks to several years by altering crystallinity, initial molecular weight, and the copolymer ratio of lactic to glycolic acid. Since these polymers are thermoplastics, they can be easily formed into a three-dimensional scaffold with a desired microstructure, gross shape, and dimension by various techniques, including molding, extrusion, solvent casting,[25] phase separation techniques, and gas foaming techniques.[26] Many applications in tissue engineering often require a scaffold with high porosity and ratio of surface area to volume. Other biodegradable synthetic polymers, including poly(anhydrides) and poly(ortho-esters), can also be used to fabricate scaffolds for tissue engineering with controlled properties.[27]

5.539.3. Cells for Use in Tissue Engineering

5.539.3.1. Embryonic Stem Cells

Human embryonic stem cells exhibit two remarkable properties: the ability to proliferate in an undifferentiated but pluripotent state (self-renewal), and the ability to differentiate into many specialized cell types.[28] They can be isolated by aspirating the inner cell mass from the embryo during the blastocyst stage (5 days postfertilization), and are usually grown on feeder layers consisting of mouse embryonic fibroblasts (MEFs) or human feeder cells.[29] More recent reports have shown that these cells can be grown without the use of a feeder layer[30] and can thus avoid the exposure of these human cells to mouse viruses and proteins. These cells have demonstrated longevity in culture by maintaining their undifferentiated state for at least 80 passages when grown using current published protocols.[31,32]

Human embryonic stem cells have been shown to differentiate into cells from all three embryonic germ layers *in vitro*. Skin and neurons have been formed, indicating ectodermal differentiation.[33–36] Blood, cardiac cells, cartilage, endothelial cells, and muscle have been formed, indicating mesodermal differentiation.[37–39] Pancreatic cells have been formed, indicating endodermal differentiation.[40] In addition, as further evidence of their pluripotency, embryonic stem cells can form embryoid bodies, which are cell aggregations that contain all three embryonic germ layers while in culture, and can form teratomas *in vivo*.[41]

5.539.3.2. Laboratory-Generated Stem Cells

In addition, stem cells for tissue engineering can be generated through cloning procedures. There has been tremendous interest in the field of nuclear cloning since the birth of Dolly in 1997, but frogs were the first successfully cloned vertebrates derived from nuclear transfer[42–45] but the nuclei were derived from nonadult sources. In the past 15 years, tremendous advances in nuclear cloning technology have been reported, indicating the relative immaturity of the field. Dolly was not the first cloned mammal to be produced via nuclear transfer; in fact, live lambs were produced in 1996 using nuclear transfer and differentiated epithelial cells derived from embryonic discs.[46] The significance of Dolly was that she was the first mammal to be derived from an adult somatic cell using nuclear transfer.[47] Since then, animals from several species have been grown using nuclear transfer technology, including cattle,[48] goats,[49] mice,[50] and pigs.[51,52]

Two types of nuclear cloning, reproductive cloning and therapeutic cloning, have been described, and a better understanding of the differences between the two types may help to alleviate some of the controversy that surrounds these technologies.[53,54] Banned in most countries for human applications, reproductive cloning is used to generate an embryo that has the identical genetic material as its cell source. This embryo can then be implanted into the uterus of a female to give rise to an infant that is a clone of the donor. On the other hand, therapeutic cloning is used to generate early stage embryos that are explanted in culture to produce embryonic stem cell lines whose genetic material is identical to that of its source. These autologous stem cells have the potential to become almost any type of cell in the adult body, and thus would be useful in tissue and organ replacement applications.[55] Therefore, therapeutic cloning, which has also been called somatic cell nuclear transfer, may provide an alternative source of transplantable cells. **Figure 1** shows the strategy of combining therapeutic cloning with tissue engineering to develop tissues and organs. According to data from the Centers for Disease Control (CDC), an estimated 3000 Americans die every day of diseases that could have been treated with stem cell-derived tissues[56,57] With current allogeneic tissue transplantation protocols, rejection is a frequent complication because of immunologic incompatibility, and immunosuppressive drugs are usually required.[55] The use of transplantable tissue and organs derived from therapeutic cloning may potentially lead to the avoidance of immune responses that typically are associated with transplantation of nonautologous tissues.[56]

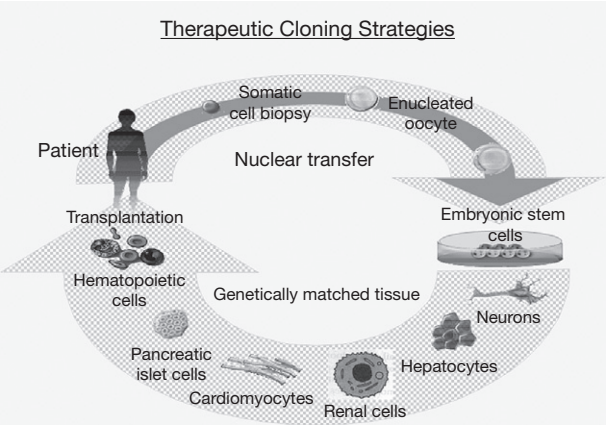

Figure 1 Strategy for therapeutic cloning and tissue engineering.

Although it looks promising, somatic cell nuclear transfer technology has certain limitations that require further improvements before therapeutic cloning can be applied widely in replacement therapy. Currently, the efficiency of the overall cloning process is low. The majority of embryos derived from animal cloning do not survive after implantation.[58–60] To improve cloning efficiency, further improvements are required in the multiple complex steps of nuclear transfer, such as enucleation and reconstruction, activation of oocytes, and cell cycle synchronization between donor cells and recipient oocytes.[61]

Recently, exciting reports of the successful transformation of adult cells into pluripotent stem cells through a type of genetic "reprogramming" have been published. Reprogramming is a technique that involves dedifferentiation of adult somatic cells to produce patient-specific pluripotent stem cells, without the use of embryos. Cells generated by reprogramming would be genetically identical to the somatic cells (and thus, the patient who donated these cells) and would not be rejected. Yamanaka was the first to discover that MEFs and adult mouse fibroblasts could be reprogrammed into an 'induced pluripotent state (iPS)'.[62] This group used MEFs engineered to express a neomycin resistance gene from the *Fbx15* locus, a gene expressed only in ES cells. They examined 24 genes that were thought to be important for embryonic stem cells and identified four key genes that, when introduced into the reporter fibroblasts, resulted in drug-resistant cells. These were Oct3/4, Sox2, c-MYC, and Klf4. This experiment indicated that expression of the four genes in these transgenic MEFs led to expression of a gene specific for ES cells. MEFs and adult fibroblasts were cotransduced with retroviral vectors, each carrying one of the four genes, and transduced cells were selected via drug resistance. The resultant iPS cells possessed the immortal growth characteristics of self-renewing ES cells, expressed genes specific for ES cells, and generated embryoid bodies *in vitro* and teratomas *in vivo*. When iPS cells were injected into mouse blastocysts, they contributed to a variety of cell types. However, although iPS cells selected in this way were pluripotent, they were not identical to ES cells. Unlike ES cells, chimeras made from iPS cells did not result in full-term pregnancies. Gene expression profiles of the iPS cells showed that they possessed a distinct gene expression signature that was different from that of ES cells. In addition, the epigenetic state of the iPS cells was somewhere between that found in somatic cells and that found in ES cells, suggesting that the reprogramming was incomplete.

These results were improved significantly by Wernig and Jaenisch in July 2007.[63] Fibroblasts were infected with retroviral vectors and selected for the activation of endogenous *Oct4* or *Nanog* genes. Results from this study showed that DNA methylation, gene expression profiles, and the chromatin state of the reprogrammed cells were similar to those of ES cells. Teratomas induced by these cells contained differentiated cell types representing all three embryonic germ layers. Most importantly, the reprogrammed cells from this experiment were able to form viable chimeras and contribute to the germline-like ES cells,

suggesting that these iPS cells were completely reprogrammed. Wernig *et al.* observed that the number of reprogrammed colonies increased when drug selection was initiated later (day 20 rather than day 3 posttransduction). This suggests that reprogramming is a slow and gradual process and may explain why previous attempts resulted in incomplete reprogramming.

It has recently been shown that reprogramming of human cells is possible.[64,65] Yamanaka showed that retrovirus-mediated transfection of *OCT3/4*, *SOX2*, *KLF4*, and *c-MYC* generates human iPS cells that are similar to hES cells in terms of morphology, proliferation, gene expression, surface markers, and teratoma formation. Thompson's group showed that retroviral transduction of *OCT4*, *SOX2*, *NANOG*, and *LIN28* could generate pluripotent stem cells without introducing any oncogenes (c-MYC). Both studies showed that human iPS were similar but not identical to hES cells.

Another concern is that these iPS cells contain three to six retroviral integrations (one for each factor), which may increase the risk of tumorigenesis. Yamanaka *et al.* studied the tumor formation in chimeric mice generated from Nanog-iPS cells and found 20% of the offspring developed tumors due to the retroviral expression of c-MYC.[66] An alternative approach would be to use a transient expression method, such as adenovirus-mediated system, since both Jaenisch and Yamanaka showed strong silencing of the viral-controlled transcripts in iPS cells.[66,67] This indicates that these viral genes are only required for the induction, not the maintenance, of pluripotency.

Another concern is the use of transgenic donor cells for reprogrammed cells in the mouse studies. Both studies used donor cells from transgenic mice harboring a drug resistance gene driven by *Fbx15*, *Oct3/4*, or *Nanog* promoters so that, if these ES cell-specific genes were activated, the resulting cells could be easily selected using neomycin. However, the use of genetically modified donors hinders clinical applicability for humans. To assess whether iPS cells can be derived from nontransgenic donor cells, wild-type MEF and adult skin cells were retrovirally transduced with Oct3/4, Sox2, c-MYC, and Klf4 and ES-like colonies were isolated by morphology alone, without the use of drug selection for *Oct4* or *Nanog*.[67] iPS cells from wild-type donor cells formed teratomas and generated live chimeras. This study suggests that transgenic donor cells are not necessary to generate iPS cells.

Although this is an exciting phenomenon, it is unclear why reprogramming adult fibroblasts and mesenchymal stromal cells have similar efficiencies.[62] It would seem that cells that are already multipotent could be reprogrammed with greater efficiency, since the more undifferentiated donor nucleus the better SCNT performs.[68] This further emphasizes our limited understanding of the mechanism of reprogramming, yet the potential for this area of study is exciting.

5.539.3.3. Amniotic Fluid and Placental Stem Cells

An alternate source of stem cells is the amniotic fluid and placenta. Amniotic fluid and the placenta are known to contain multiple partially differentiated cell types derived from the developing fetus. We isolated stem cell populations from these sources, called amniotic fluid and placental stem cells (AFPSC) that express embryonic and adult stem cell markers.[69] The undifferentiated stem cells expand extensively without feeders and double every 36 h. Unlike human embryonic stem cells, the AFPSC do not form tumors *in vivo*. Lines maintained for over 250 population doublings retained long telomeres and a normal karyotype. AFS cells are broadly multipotent. Clonal human lines verified by retroviral marking can be induced to differentiate into cell types representing each embryonic germ layer, including cells of adipogenic, osteogenic, myogenic, endothelial, neuronal, and hepatic lineages. In this respect, they meet a commonly accepted criterion for pluripotent stem cells, without implying that they can generate every adult tissue. Examples of differentiated cells derived from AFS cells and displaying specialized functions include neuronal lineage secreting the neurotransmitter L-glutamate or expressing G-protein-gated inwardly rectifying potassium (GIRK) channels, hepatic lineage cells producing urea, and osteogenic lineage cells forming tissue-engineered bone. The cells could be obtained either from amniocentesis or chorionic villous sampling in the developing fetus, or from the placenta at the time of birth. The cells could be preserved for self-use, and used without rejection, or they could be banked. A bank of 100,000 specimens could potentially supply 99% of the US population with a perfect genetic match for transplantation. Such a bank may be easier to create than with other cell sources, since there are approximately 4.5 million births per year in the United States.[69]

5.539.3.4. Adult Stem Cells and Native Progenitor Cells

One of the limitations of applying cell-based regenerative medicine techniques to organ replacement has been the inherent difficulty of growing specific cell types in large quantities. Even when some organs, such as the liver, have a high regenerative capacity *in vivo*, cell growth and expansion *in vitro* may be difficult. By studying the privileged sites for committed precursor cells in specific organs, as well as exploring the conditions that promote differentiation, one may be able to overcome the obstacles that limit cell expansion *in vitro*. For example, urothelial cells could be grown in the laboratory setting in the past, but only with limited expansion. Several protocols were developed over the past two decades that identified the undifferentiated cells, and kept them undifferentiated during their growth phase.[10,70–73] Using these methods of cell culture, it is now possible to expand a urothelial strain from a single specimen that initially covered a surface area of 1 cm^2 to one covering a surface area of 4202 m^2 (the equivalent of one football field) within 8 weeks.[10] These studies indicated that it should be possible to collect autologous bladder cells from human patients, expand them in culture, and return them to the donor in sufficient quantities for reconstructive purposes.[10,71–76] Major advances have been achieved within the past decade on the possible expansion of a variety of primary human cells, with specific techniques that make the use of autologous cells possible for clinical application.

5.539.4. Cell Therapy with Injectable Substances

5.539.4.1. Bulking Agents

Injectable bulking agents can be endoscopically used in the treatment of both urinary incontinence and vesicoureteral

reflux. The advantages in treating urinary incontinence and vesicoureteral reflux with this minimally invasive approach include the simplicity of this quick outpatient procedure and the low morbidity associated with it. Several investigators are seeking alternative implant materials that would be safe for human use.[77]

The ideal substance for the endoscopic treatment of reflux and incontinence should be injectable, nonantigenic, nonmigratory, volume stable, and safe for human use. Toward this goal long-term studies were conducted to determine the effect of injectable chondrocytes *in vivo*.[78] It was initially determined that alginate, a liquid solution of gluronic and mannuronic acid, embedded with chondrocytes, could serve as a synthetic substrate for the injectable delivery and maintenance of cartilage architecture *in vivo*. Alginate undergoes hydrolytic biodegradation and its degradation time can be varied depending on the concentration of each of the polysaccharides. The use of autologous cartilage for the treatment of vesicoureteral reflux in humans would satisfy all the requirements for an ideal injectable substance.

Chondrocytes derived from an ear biopsy can be readily grown and expanded in culture. Neocartilage formation can be achieved *in vitro* and *in vivo* using chondrocytes cultured on synthetic biodegradable polymers. In these experiments, the cartilage matrix replaced the alginate as the polysaccharide polymer underwent biodegradation. This system was adapted for the treatment of vesicoureteral reflux in a porcine model.[79] These studies showed that chondrocytes can be easily harvested and combined with alginate *in vitro*, the suspension can be easily injected cystoscopically, and the elastic cartilage tissue formed is able to correct vesicoureteral reflux without any evidence of obstruction.

Two multicenter clinical trials were conducted using this engineered chondrocyte technology. Patients with vesicoureteral reflux were treated at ten centers throughout the US. The patients had a similar success rate as with other injectable substances in terms of cure (**Figure 5**). Chondrocyte formation was not noted in patients who had treatment failure. It is supposed that the patients who were cured have a biocompatible region of engineered autologous tissue present, rather than a foreign material.[80] Patients with urinary incontinence were also treated endoscopically with injected chondrocytes at three different medical centers. Phase 1 trials showed an approximate success rate of 80% at follow-up 3 and 12 months postoperatively.[81] Several of the clinical trials involving bioengineered products have been placed on hold because of the costs involved with the specific technology. With a bioengineered product, costs are usually high because of the biological nature of the therapies involved. As with any therapy, the cost that the medical health care system can allow for a specific technology is limited. Therefore, the costs of bioengineered products have to be lowered for them to have an impact clinically. This is currently being addressed for multiple tissue-engineered technologies. As the technologies advance overtime, and the volume of the application is considered, costs will naturally decrease.

5.539.4.2. Injectable Muscle Cells

The potential use of injectable cultured myoblasts for the treatment of stress urinary incontinence has been investigated.[82,83] Myoblasts were labeled with fluorescent latex microspheres (FLM) in order to track them after injection. Labeled myoblasts were directly injected into the proximal urethra and lateral bladder walls of nude mice with a microsyringe in an open surgical procedure. Tissue harvested up to 35 days postinjection contained the labeled myoblasts, as well as evidence of differentiation of the labeled myoblasts into regenerative myofibers. The authors reported that a significant portion of the injected myoblast population persisted *in vivo*. Similar techniques of sphincteric derived muscle cells have been used for the treatment of urinary incontinence in a pig model.[84] The fact that myoblasts can be labeled and survive after injection and begin the process of myogenic differentiation further supports the feasibility of using cultured cells of muscular origin as an injectable bioimplant.

The use of injectable muscle precursor cells has also been investigated for use in the treatment of urinary incontinence due to irreversible urethral sphincter injury or maldevelopment. Muscle precursor cells are the quiescent satellite cells found in each myofiber that proliferate to form myoblasts and eventually myotubes and new muscle tissue. Intrinsic muscle precursor cells have previously been shown to play an active role in the regeneration of injured striated urethral sphincter.[85] In a subsequent study, autologous muscle precursor cells were injected into a rat model of urethral sphincter injury, and both replacement of mature myotubes and restoration of functional motor units were noted in the regenerating sphincteric muscle tissue.[86] This is the first demonstration of the replacement of both sphincter muscle tissue and its innervation by the injection of muscle precursor cells. As a result, muscle precursor cells may be a minimally invasive solution for urinary incontinence in patients with irreversible urinary sphincter muscle insufficiency.

5.539.4.3. Endocrine Replacement

Patients with testicular dysfunction and hypogonadal disorders are dependent on androgen replacement therapy to restore and maintain physiological levels of serum testosterone and its metabolites, dihydrotestosterone, and estradiol.[87,88] Currently available androgen replacement modalities, such as testosterone tablets and capsules, Depo-Provera injections, and skin patches may be associated with fluctuating serum levels and complications such as fluid and nitrogen retention, erythropoiesis, hypertension, and bone density changes.[89] Since Leydig cells of the testes are the major source of testosterone in men, implantation of heterologous Leydig cells or gonadal tissue fragments have previously been proposed as a method for chronic testosterone replacement.[90,91] These approaches, however, were limited by the failure of the tissues and cells to produce testosterone.

Encapsulation of cells in biocompatible and semipermeable polymeric membranes has been an effective method to protect against a host immune response as well as to maintain viability of the cells while allowing the secretion of desired therapeutic agents.[92,93] Alginate–poly-L-lysine-encapsulated Leydig cell microspheres were used as a novel method for testosterone delivery *in vivo*.[88] Elevated stable serum testosterone levels were noted in castrated adult rats over the course of the study, suggesting that microencapsulated Leydig cells

may be a potential therapeutic modality for testosterone supplementation.

5.539.5. Tissue Engineering of Specific Structures

Investigators around the world, including those in our laboratory, have been working toward the development of several cell types and tissues and organs for clinical application.

5.539.5.1. Urethra

Various strategies have been proposed over the years for the regeneration of urethral tissue. Woven meshes of PGA without cells[94,95] or with cells[96] were used to regenerate urethras in various animal models. Naturally derived collagen-based materials such bladder-derived acellular submucosa,[1] and an acellular urethral submucosa,[97] have also been tried experimentally in various animal models for urethral reconstruction.

The bladder submucosa matrix[1] proved to be a suitable graft for repair of urethral defects in rabbits. The neourethras demonstrated a normal urothelial luminal lining and organized muscle bundles. These results were confirmed clinically in a series of patients with a history of failed hypospadias reconstruction wherein the urethral defects were repaired with human bladder acellular collagen matrices (**Figure 2**).[98] The neourethras were created by anastomosing the matrix in an onlay fashion to the urethral plate. The size of the created neourethra ranged from 5 to 15 cm. After a 3-year follow-up, three of the four patients had a successful outcome with regard to cosmetic appearance and function. One patient who had a 15-cm neourethra created developed a subglandular fistula. The acellular collagen-based matrix eliminated the necessity of performing additional surgical procedures for graft harvesting, and both operative time and the potential morbidity from the harvest procedure were decreased. Similar results were obtained in pediatric and adult patients with primary urethral stricture disease using the same collagen matrices.[99] Another study in 30 patients with recurrent stricture disease showed that a healthy urethral bed (two or fewer prior urethral surgeries) was needed for successful urethral reconstruction using the acellular collage-based grafts.[100] More than 200 pediatric and adult patients with urethral disease have been successfully treated in an onlay manner with a bladder-derived collagen-based matrix. One of its advantages over nongenital tissue grafts used for urethroplasty is that the material is "off the shelf." This eliminates the necessity of additional surgical procedures for graft harvesting, which may decrease operative time, as well as the potential morbidity due to the harvest procedure.

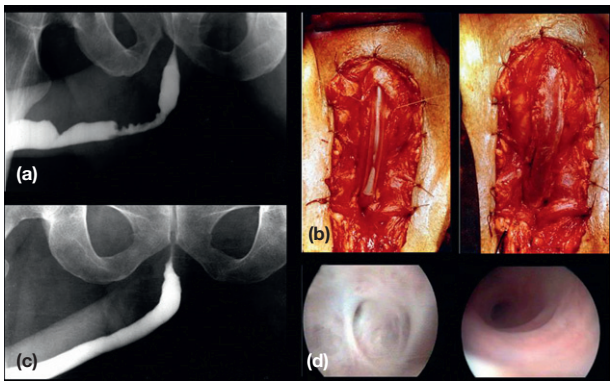

Figure 2 Tissue engineering of the urethra using a collagen matrix. (a) Representative case of a patient with a bulbar stricture. (b) During the urethral repair surgery, strictured tissue is excised, preserving the urethral plate on the left side, and matrix is anastamosed to the urethral plate in an onlay fashion on the right. The boxes in both photos indicate the area of interest, including the urethra, which appears white in the left photograph. In the left photograph, the arrow indicates the area of stricture in the urethra. On the right, the arrow indicates the repaired stricture. Note that the engineered tissue now obscures the native white urethral tissue in an onlay fashion in the right photograph. (c) Urethrogram 6 months after repair. (d) Cystoscopic view of urethra before surgery on the left side, and 4 months after repair on the right side.

The above techniques, using nonseeded acellular matrices, were applied experimentally and clinically in a successful manner for onlay urethral repairs. However, when tubularized urethral repairs were attempted experimentally, adequate urethral tissue regeneration was not achieved, and complications ensued, such as graft contracture and stricture formation.[101] Autologous rabbit bladder epithelial and smooth muscle cells were grown and seeded onto preconfigured tubular matrices. Entire urethra segments were resected and urethroplasties were performed with tubularized collagen matrices either seeded with cells, or without cells. The tubularized collagen matrices seeded with autologous cells formed new tissue that was histologically similar to native urethra. The tubularized collagen matrices without cells lead to poor tissue development, fibrosis, and stricture formation. These findings were confirmed clinically. A clinical trial using tubularized nonseeded SIS for urethral stricture repair was performed in eight evaluable patients. Two patients with short inflammatory strictures maintained urethral patency. Stricture recurrence developed in the other six patients within 3 months of surgery.[102] Other cell types have also been tried experimentally in acellular bladder collagen matrices, including foreskin epidermal cells and oral keratinocytes.[103,104] Vascular endothelial growth factor gene-modified urothelial cells have also been used experimentally for urethral reconstruction.[105]

The normal wound healing response to injury has been studied extensively, and this knowledge has been helpful in maximizing success for the engineering of tissues. At the time of tissue injury, cell ingrowth is initiated from the wound edges in order to cover the tissue defect. The cells from the edges of the native tissue are able to traverse short distances without any detrimental effects. If the wound is large, more than a few millimeters in distance or depth, increased collagen deposition, fibrosis, and scar formation ensue. Matrices implanted in wound beds are able to lengthen the distances that cells can traverse without initiating an adverse fibrotic response. However, these distances are also limited. The maximum distance that adjacent cells from the wound edge have to travel to create normal tissue over a biologic matrix is approximately 1 cm.[106] Tissue defects greater than 1 cm, that are treated with a matrix alone, without cells, usually have increased collagen deposition, increased fibrosis, and scar formation. Cell-seeded matrices implanted in wound beds are able to further lengthen the distance for normal tissue formation, without initiating an adverse fibrotic response.

Studies in the field of regenerative medicine have shown that very large defects, greater than 30 cm, can be successfully treated using cell-seeded scaffolds. This explains the described experimental and clinical results noted with urethral repair. Nonseeded matrices are able to replace urethral segments when used in an onlay fashion because of the short distances required for tissue ingrowth. However, if a tubularized urethral repair is needed, the matrices need to be seeded with autologous cells in order to avoid the risk of stricture formation and poor tissue development.

5.539.5.2. Bladder

Currently, gastrointestinal segments are commonly used as tissues for bladder replacement or repair. However, gastrointestinal tissues are designed to absorb specific solutes, whereas bladder tissue is designed for the excretion of solutes. Due to the problems encountered with the use of gastrointestinal segments, numerous investigators have attempted alternative materials and tissues for bladder replacement or repair.

Over the last few decades, several bladder wall substitutes have been attempted with both synthetic and organic materials. Synthetic materials that have been tried in experimental and clinical settings include polyvinyl sponge, Teflon, collagen matrices, Vicryl (PGA) matrices, and silicone. Most of these attempts have failed because of mechanical, structural, functional, or biocompatibility problems. Usually, permanent synthetic materials used for bladder reconstruction succumb to mechanical failure and urinary stone formation, and use of degradable materials lead to fibroblast deposition, scarring, graft contracture, and a reduced reservoir volume overtime.[7,107] Because of this, there has been an increase in the use of various collagen-based matrices for tissue regeneration. Nonseeded allogeneic acellular bladder matrices have served as scaffolds for the ingrowth of host bladder wall components. The matrices are prepared by mechanically and chemically removing all cellular components from bladder tissue.[3,4,108–110] The matrices serve as vehicles for partial bladder regeneration, and relevant antigenicity is not evident. However, in multiple studies using various materials as nonseeded grafts for cystoplasty, the urothelial layer was able to regenerate normally, but the muscle layer, although present, was not fully developed.[4,108,109,111–113] Studies involving acellular matrices that may provide the necessary environment to promote cell migration, growth, and differentiation are being conducted.[114] With continued bladder research in this area, these matrices may have a clinical role in bladder replacement in the future.

Cell-seeded allogeneic acellular bladder matrices were used for bladder augmentation in dogs.[4] The regenerated bladder tissues contained a normal cellular organization consisting of urothelium and smooth muscle and exhibited a normal compliance. Biomaterials preloaded with cells before their implantation showed better tissue regeneration compared with biomaterials implanted with no cells, in which tissue regeneration depended on ingrowth of the surrounding tissue. The bladders showed a significant increase (100%) in capacity when augmented with scaffolds seeded with cells, compared to scaffolds without cells (30%). The acellular collagen matrices can be enhanced with growth factors to improve bladder regeneration.[115]

It has been well established for decades that the bladder is able to regenerate generously over free grafts. Urothelium is associated with a high reparative capacity.[116] Bladder muscle tissue is less likely to regenerate in a normal fashion. Both urothelial and muscle ingrowth are believed to be initiated from the edges of the normal bladder toward the region of the free graft.[117,118] Usually, however, contracture or resorption of the graft has been evident. The inflammatory response toward the matrix may contribute to the resorption of the free graft. It was hypothesized that building the three-dimensional structure constructs *in vitro*, before implantation, would facilitate the eventual terminal differentiation of the cells after implantation *in vivo* and would minimize the inflammatory response toward the matrix, thus avoiding graft contracture and shrinkage. The dog study demonstrated a major difference between matrices used with autologous cells (tissue-engineered matrices) and those used without cells.[4] Matrices implanted with cells for bladder augmentation retained most of their implanted diameter, as opposed to matrices implanted without cells for bladder augmentation, in which graft contraction and shrinkage occurred. The histomorphology demonstrated a marked paucity of muscle cells and a more aggressive inflammatory reaction in the matrices implanted without cells. Epithelial-mesenchymal signaling is important for the differentiation of bladder smooth muscle.[119]

The results of initial studies showed that the creation of artificial bladders may be achieved *in vivo*; however, it could not be determined whether the functional parameters noted were caused by the augmented segment or by the intact native bladder tissue. To better address the functional parameters of tissue-engineered bladders, an animal model was designed that required a subtotal cystectomy with subsequent replacement with a tissue-engineered organ.[11] Cystectomy-only and nonseeded controls maintained average capacities of 22% and 46% of preoperative values, respectively. An average bladder capacity of 95% of the original precystectomy volume was achieved in the cell-seeded tissue-engineered bladder replacements. These findings were confirmed radiographically (**Figure 3**). The subtotal cystectomy reservoirs that were not reconstructed and the polymer-only reconstructed bladders showed a marked decrease in bladder compliance (10% and 42% total compliance). The compliance of the cell-seeded tissue-engineered bladders showed almost no difference from preoperative values that were measured when the native bladder was present (106%). Histologically, the nonseeded scaffold bladders presented a pattern of normal urothelial cells with a thickened fibrotic submucosa and a thin layer of muscle fibers. The retrieved tissue-engineered bladders showed a normal cellular organization, consisting of a trilayer of urothelium, submucosa, and muscle. Immunocytochemical analyses confirmed the muscle and urothelial phenotype. S-100 staining indicated the presence of neural structures.[11] These studies, performed with polyglocolic acid based-scaffolds, have been repeated by other investigators, showing similar long-term results in a large number of animals.[111,120] The strategy of using biodegradable scaffolds with cells can be pursued without concerns for local or systemic toxicity.[121] However, not all scaffolds perform well if a large portion of the bladder needs replacement. In a study using SIS for subtotal bladder replacement in dogs, both the unseeded and cell-seeded experimental groups showed graft

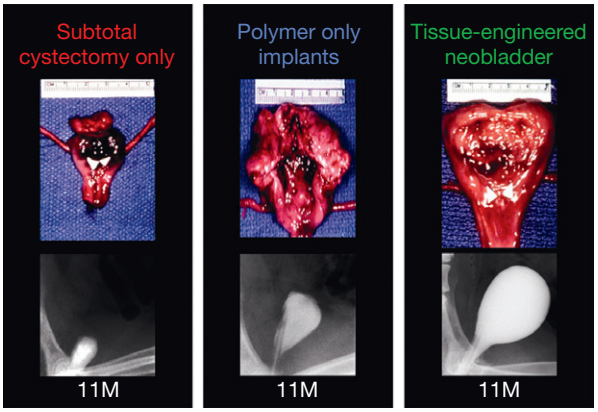

Figure 3 Gross specimens and cystograms at 11 months of the cystectomy-only, nonseeded controls, and cell-seeded tissue-engineered bladder replacements in dogs. The cystectomy-only bladder had a capacity of 22% of the preoperative value and a decrease in bladder compliance to 10% of the preoperative value. The nonseeded controls showed significant scarring with a capacity of 46% of the preoperative value and a decrease in bladder compliance to 42% of the preoperative value. An average bladder capacity of 95% of the original precystectomy volume was achieved in the cell-seeded tissue-engineered bladder replacements and the compliance showed almost no difference from preoperative values that were measured when the native bladder was present (106%).

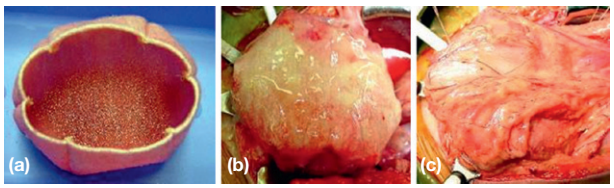

Figure 4 Construction of engineered bladder. (a) Scaffold material seeded with cells for use in bladder repair. (b) The seeded scaffold is anastamosed to native bladder with running 4–0 polyglycolic sutures. (c) Implant covered with fibrin glue and omentum.

shrinkage and poor results.[122] The type of scaffold used is critical for the success of these technologies. The use of bioreactors, in which mechanical stimulation is started at the time of organ production, has also been proposed as an important parameter for success.[123]

A clinical experience involving engineered bladder tissue for cystoplasty reconstruction was conducted starting in 1998. A small pilot study of seven patients was reported, using a collagen scaffold seeded with cells either with or without omentum coverage, or a combined PGA-collagen scaffold seeded with cells and omental coverage (**Figure 4**). The patients reconstructed with the engineered bladder tissue created with the PGA-collagen cell-seeded scaffolds with omental coverage showed increased compliance, decreased end-filling pressures, increased capacities, and longer dry periods overtime (**Figure 5**).[124] It is clear from this experience that the engineered bladders continued their improvement with time, mirroring their continued development. Although the experience is promising in terms of showing that engineered tissues can be implanted safely, it is just a start in terms of accomplishing the goal of engineering fully functional bladders. This was a limited clinical experience, and the technology is not yet ready for wide dissemination, as further experimental and clinical studies are required. FDA Phase 2 studies have now been completed.

An area of concern in the field of tissue engineering in the past was the source of cells for regeneration. The concept of creating engineered constructs involves initially obtaining cells for expansion from the diseased organ. However, it was not known until recently whether the cell population obtained for later autologous implantation was normal and would lead to normal tissue formation. For example, would the cells obtained from a neuropathic bladder lead to the engineering of another neuropathic bladder? Cultured neuropathic bladder smooth muscle cells possess and maintain different characteristics than normal smooth muscle cells *in vitro*, as demonstrated by growth assays, contractility, adherence tests, and microarray analysis.[125–127] However, when neuropathic smooth muscle cells were cultured *in vitro*, seeded onto matrices and implanted *in vivo*, the tissue-engineered constructs

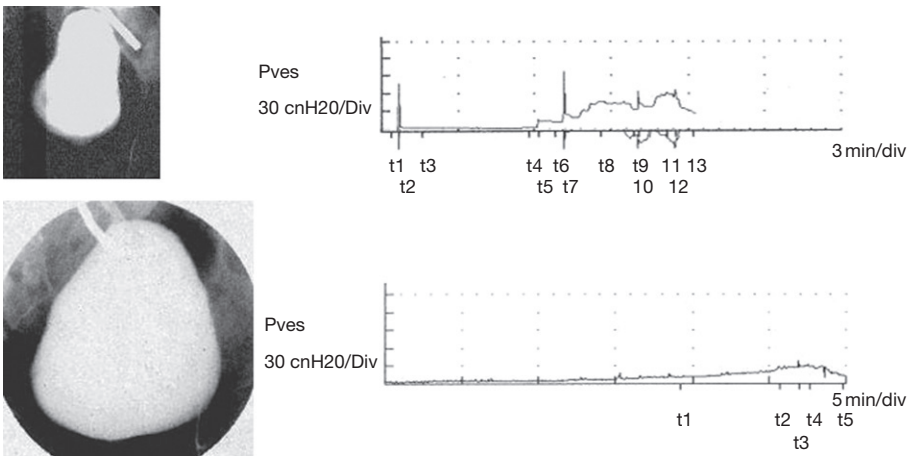

Figure 5 Cystograms and urodynamic studies of a patient before and after implantation of the tissue-engineered bladder. (a) Preoperative results indicate an irregular-shaped bladder in the cystogram (left) and abnormal bladder pressures as the bladder is filled during urodynamic studies (right). (b) Postoperatively, findings are significantly improved.

showed the same properties as the tissues engineered with normal cells.[128] The progenitor cells, which reside within stem cell niches within each organ, are responsible for new cell differentiation and tissue formation during the normal process of tissue regeneration due to natural turnover, aging, and tissue injury. It is known that genetically normal nonmalignant progenitor cells, which are the reservoirs for new cell formation, are programmed to give rise to normal tissue regardless of whether the niche resides in either normal or diseased tissues.[128–130] Therefore, although the mechanisms for tissue self-assembly and regenerative medicine are not fully understood, it is known that the progenitor cells are able to "reset" their program for normal cell differentiation. The stem cell niche and its role in normal tissue regeneration remains a fertile area of ongoing investigation.

5.539.5.3. Kidney

The kidney is a complex organ with multiple cell types, derived from combining anlagen and a complex functional anatomy that renders it one of the most difficult to reconstruct.[5,131] While the metanephros is responsible for the development of the proximal section of the nephrons, the ureteric bud forms the collecting ducts and distal structures. The large vessels of the kidney are induced from extrarenal tissues. Divergent embryologic origin converges to produce at least 26 distinct functional cells in the kidney.[132] Previous efforts in tissue engineering of the kidney have been directed toward the development of extracorporeal renal support systems made of biological and synthetic components[133–141] and these *ex vivo* renal replacement devices are known to be life-sustaining. However, there would be obvious benefits for patients with end-stage kidney disease if these devices could be implanted long term without the need for an extracorporeal perfusion circuit or immunosuppressive drugs.

We have explored the possibility of seeding an implantable biomaterial with a heterogeneous population of renal cells to evaluate function and viability. Atala *et al.* plated donor rabbit kidney cells, including distal tubules, glomeruli, and proximal tubules *in vitro* and after expansion, these were seeded onto biodegradeable PGA scaffolds and implanted subcutaneously into athymic mice. The implants consisted of individual cell types and a mixture of all three. When examined histologically, progressive formation and organization of the nephron segments within the polymer fibers was noted. Additionally, BrdU incorporation into the renal cell DNA was confirmed.[142] It was unclear if the tubular structures found on the scaffolds occurred *de novo* from the implanted cells or if they merely represented fragments of donor tubules that had survived intact the original dissociation and culture process. To further investigate this question, mouse renal cells were harvested and expanded in culture. Subsequently, a single cell suspension was created from the isolated cells, and these were seeded on biodegradable polymers and implanted into immunocompetent synergic hosts. In this experiment, renal epithelial cells reconstituted tubular structures *in vivo*. The analyses of the retrieved implants indicated that the renal epithelial cells first organized into a structure with a solid center. Next, canalization into a hollow tube could be seen at 2 weeks. Histologic examination with nephron-specific lactins revealed successful reconstitution of proximal tubules, distal tubules, loops of Henle, collecting tubules, and collecting ducts. These results clearly showed that single cell suspensions grown *in vitro* are capable of reconstituting tubule structures. The tubules contained homogenous cell types within each tubule.[143]

Further investigations by our group have demonstrated that renal tubular development from digested renal units is possible in the murine model as well. Joraku *et al.* developed an *in vitro* method for cultivation of renal cells that allowed for development of tubular structures. This technique involves digestion of the entire murine kidney followed by cultivation of the resulting cells in a specific renal media. Immunohistochemistry revealed cells expressing proximal and distal tubule markers as well as markers for glomerular and endothelial cells. When these cells were allowed to grow on rat-tail type 1 collagen, cells from the thick ascending loop of Henle stained positive for Tamm–Horsfall protein in an architectural pattern reminiscent of natural tubules.[144]

Yoo *et al.* evaluated whether murine renal cells grown *in vitro* could produce functional results *in vivo*. They harvested the cells, expanded them in culture and seeded them onto a tubular device constructed from polycarbonate. At one end of the tubular device was a silastic catheter, which terminated into a reservoir. The device was subcutaneously implanted into athymic mice. The implanted device demonstrated extensive vascularization in addition to glomerular formation and highly organized tubular architecture. Immunohistochemistry for alkaline phosphatase showed positivity in the proximal tubule-like structures. Osteopontin, which is secreted by the proximal and distal tubular cells and the cells of the thin loop of Henle, was found on immunocytochemical staining of the tubular sections. In addition, the ECM of the newly formed tubules stained uniformly positive for fibronectin. Importantly, fluid collected in the reservoir of the device. This fluid was yellow and the uric acid concentration was 66 mg dl^{-1} (as compared to 2 mg dl^{-1} in plasma). The creatinine concentration of the fluid (27.91 ± 7.56 mg dl^{-1}) was 8.2 times higher than that found in the serum (4.49 ± 0.08 mg dl^{-1}).[145] These studies demonstrate that single cells can form multicellular structures, become organized into functional renal units, and are capable of unidirectional excretion of solutes through production of a urine-like fluid.

Next, we applied the principles of both tissue engineering and therapeutic cloning in an effort to produce genetically identical renal tissue in a large animal model, the cow (*Bos taurus*).[146] Bovine skin fibroblasts from adult Holstein steers were obtained by ear notch, and single donor cells were isolated and microinjected into the perivitelline space of donor enucleated oocytes (nuclear transfer). The resulting blastocysts were implanted into progestin-synchronized recipients to allow for further *in vivo* growth. After 12 weeks, cloned renal cells were harvested, expanded *in vitro*, then seeded onto biodegradable scaffolds consisting of polycarbonate membranes and three collagen-coated cylindrical silastic catheters (**Figure 6(a)**). The ends of the three membranes of each scaffold were connected to catheters that terminated into a collecting reservoir. This created a renal neoorgan with a mechanism for collecting the excreted urinary fluid (**Figure 6(b)**). These devices were transplanted subcutaneously into the same steer from which the genetic material originated, and then retrieved 12 weeks after implantation.

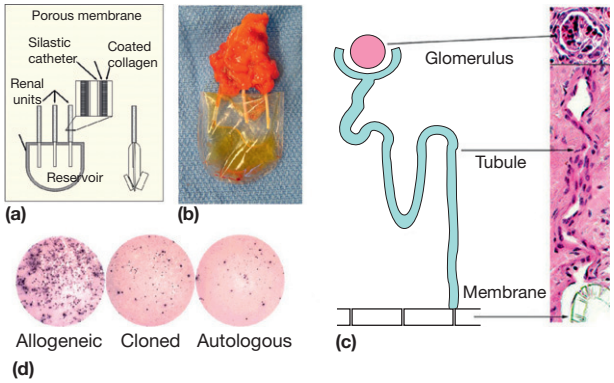

Figure 6 Combining therapeutic cloning and tissue engineering to produce kidney tissue. (a) Illustration of the tissue-engineered renal unit. (b) Renal unit seeded with cloned cells, 3 months after implantation, showing the accumulation of urine-like fluid. (c) Clear unidirectional continuity between the mature glomeruli, their tubules, and silastic catheter. (d) Elispot analyses of the frequencies of T cells that secrete IFN **FX** after stimulation with allogeneic renal cells, cloned renal cells, or nuclear donor fibroblasts. Cloned renal cells produce fewer IFNγ spots than the allogeneic cells, indicating that the rejection response to cloned cells is diminished. The presented wells are single representatives of duplicate wells.

Chemical analysis of the collected urine-like fluid, including urea nitrogen and creatinine levels, electrolyte levels, specific gravity, and glucose concentration, revealed that the implanted renal cells possessed filtration, reabsorption, and secretory capabilities. Histological examination of the retrieved implants revealed extensive vascularization and self-organization of the cells into glomeruli and tubule-like structures. A clear continuity between the glomeruli, the tubules, and the silastic catheter was noted (**Figure 6(c)**). Immunohistochemical analysis with renal-specific antibodies revealed the presence of renal proteins, RT-PCR analysis confirmed the transcription of renal-specific RNA in the cloned specimens, and Western blot analysis confirmed the presence of elevated renal-specific protein levels.

Since previous studies have shown that bovine clones harbor oocyte mitochondrial DNA,[147–149] the donor egg's mitochondrial DNA (mtDNA) was thought to be a potential source of immunologic incompatibility. Differences in mtDNA-encoded proteins expressed by cloned cells could stimulate a T cell response specific for mtDNA-encoded minor histocompatibility antigens when the cloned cells are implanted back into the original nuclear donor.[150] Maternally transmitted minor histocompatibility antigens in mice have been shown to stimulate both skin allograft rejection *in vivo* and cytotoxic T lymphocytes expansion *in vitro*[150] that could prevent the use of these cloned constructs in patients with chronic rejection of major histocompatibility matched human renal transplants.[151,152] We tested for a possible T cell response to the cloned renal devices using delayed-type hypersensitivity testing *in vivo* and EliSPOT analysis of interferon-γ secreting T cells *in vitro*. Both analyses revealed no evidence of a T cell response, indicating that rejection of cloned renal cells will not necessarily occur in the presence of oocyte-derived mtDNA (**Figure 6(d)**). This finding may represent a step forward in overcoming the histocompatibility problem of stem cell therapy.[152]

These studies demonstrated that cells derived from nuclear transfer can be successfully harvested, expanded in culture, and transplanted *in vivo* with the use of biodegradable scaffolds on which the single suspended cells can organize into tissue structures that are genetically identical to that of the host. These studies were the first demonstration of the use of therapeutic cloning for regeneration of tissues *in vivo*.

Investigations into the possibility of using other cell types to produce renal tissue have also been promising. Perin *et al.* have been able to induce AFPSC to differentiate into renal tissues. They labeled human AFPSC with a green fluorescent protein and microinjected the cells into developing murine embryonic kidneys. They found that the labeled cells assisted in forming both C- and S- shaped bodies, and the cells expressed RNA for early markers of renal development.[153] This study demonstrates that AFPSC can differentiate into renal lineages when cultured *in vitro* with renal precursors. Although it looks promising, further *in vivo* studies and functional assays are required prior to clinical applications with AFPSC. For more information on renal tissue engineering strategies, please see **Chapter 5.540, Kidney Tissue Engineering** in this book.

5.539.5.4. Male Reproductive Organs

Reconstructive surgery is required for a wide variety of pathologic penile conditions, including penile carcinoma, trauma, severe erectile dysfunction, and congenital conditions such as ambiguous genitalia, hypospadias, and epispadias. One of the major limitations of phallic reconstructive surgery is the availability of sufficient autologous tissue. Nongenital autologous tissue sources have been used for decades. Phallic reconstruction was initially attempted in the late 1930s, with rib cartilage used as a stiffener for patients with traumatic penile loss,[154,155] but this process produced unsatisfactory functional and cosmetic results. Silicone rigid prostheses were popularized in the 1970s and have been used widely.[156,157] However, biocompatibility issues have been a problem in selected patients.[158,159] Tissue transfer techniques with flaps from various nongenital sources such as the groin and forearm have been used for genital reconstruction.[160] However, operative complications such as infection, graft failure, and donor site morbidity are not negligible. Phallic reconstruction with autologous tissue, derived from the patient's own cells, may be preferable in selected cases.

One of the major components of the phallus is corporal smooth muscle. Initial experiments have shown that cultured human corporal smooth muscle cells may be used in conjunction with biodegradable polymers to create corpus cavernosum tissue *de novo*.[161] In a subsequent study, human corporal smooth muscle cells and endothelial cells seeded on biodegradable polymer scaffolds were able to form vascularized cavernosal muscle when implanted *in vivo*.[162] Later, in order to minimize any immune reactions that a synthetic biomaterial might cause, naturally derived acellular corporal tissue matrix with the same architecture as native corpora was developed. Acellular collagen matrices were derived from processed donor rabbit corpora using cell lysis techniques. Human corpus cavernosal muscle and endothelial cells were derived from donor penile tissue, and the cells were expanded *in vitro* and seeded on the acellular matrices. The matrices were covered with the appropriate cell architecture 4 weeks after implantation.[163]

In order to look at the functional parameters of the engineered corpora, acellular corporal collagen matrices were obtained from donor rabbit penis and autologous corpus cavernosal smooth muscle and endothelial cells were harvested, expanded, and seeded on the matrices. An entire cross-sectional segment of protruding rabbit phallus was excised, leaving the urethra intact. Cell-seeded matrices were interposed into the excised corporal space. Functional and structural parameters (cavernosography, cavernosometry, mating behavior, and sperm ejaculation) were followed, and histological, immunocytochemical, and Western blot analyses were performed up to 6 months after implantation. The engineered corpora cavernosa achieved adequate structural and functional parameters.[164] This technology was further confirmed when the entire rabbit corpora was removed and replaced with the engineered scaffolds. Most interestingly, mating activity in the animals with the engineered corpora appeared normal by 1 month after implantation. The presence of sperm was confirmed during mating, and was present in all the rabbits with the engineered corpora. The female rabbits mated with the animals implanted with engineered corpora and they conceived and delivered healthy pups. These studies demonstrate that penile corpora cavernosa tissue can be engineered. The engineered tissue is able to achieve adequate structural and functional parameters sufficient for erection, copulation, ejaculation, and conception in rabbits. Further studies will be needed to confirm the long-term functionality of these organs. In addition, further studies are needed to show that comparable human structures can also be engineered.

Patients with testicular dysfunction require androgen replacement for somatic development. Conventional treatment for testicular dysfunction consists of periodic intramuscular injections of chemically modified testosterone or, more recently, skin patch applications. However, long-term nonpulsatile testosterone therapy is not optimal and can cause multiple problems, including excessive erythropoiesis and bone density changes. To address the problem, a system was designed in which Leydig cells, which produce most of the testosterone in the male, were microencapsulated in an alginate–poly-L-lysine solution and injected into castrated animals. Serum testosterone was measured serially; the animals were able to maintain testosterone levels in the long term.[165] These studies suggest that microencapsulated Leydig cells may be able to replace or supplement testosterone in situations where anorchia or testicular failure is present. Microencapsulated Leydig cells offer several advantages. For example, the encapsulation process creates a semipermeable barrier between the transplanted cells and the host's immune system, and it allows for the long-term physiologic release of testosterone.

Other studies have shown that testicular prostheses created with chondrocytes in bioreactors could be loaded with testosterone, and that these prostheses could provide controlled testosterone release into the bloodstream when implanted. The prostheses were implanted in athymic mice with bilateral anorchia, and testosterone was released long term, maintaining the androgen level at a physiologic range.[166] One could envision combining the Leydig cell technology described above with engineered prostheses for the long-term functional replacement of androgen levels.

5.539.5.5. Female Reproductive Organs

Congenital malformations of the uterus may have profound implications clinically. Patients with cloacal exstrophy and intersex disorders may not have sufficient uterine tissue present for future reproduction. We investigated the possibility of engineering functional uterine tissue using autologous cells.[167] Autologous rabbit uterine smooth muscle and epithelial cells were harvested, then grown, and expanded in culture. These cells were seeded onto preconfigured uterine-shaped biodegradable polymer scaffolds, which were then used for subtotal uterine tissue replacement in the corresponding autologous animals. Upon retrieval 6 months after implantation, histological, immunocytochemical, and Western blot analyses confirmed the presence of normal uterine tissue components. Biomechanical analyses and organ bath studies showed that the functional characteristics of these tissues were similar to those of normal uterine tissue. Breeding studies using these engineered uteri are currently being performed.

Similarly, several pathologic conditions, including congenital malformations and malignancy, can adversely affect normal vaginal development or anatomy. Vaginal reconstruction has traditionally been challenging due to the paucity of available native tissue. The feasibility of engineering vaginal tissue *in vivo* was investigated.[168] Vaginal epithelial and smooth muscle cells of female rabbits were harvested, grown, and expanded in culture. These cells were seeded onto biodegradable polymer scaffolds, and the cell-seeded constructs were then implanted into nude mice for up to 6 weeks. Immunocytochemical, histological, and Western blot analyses confirmed the presence of vaginal tissue phenotypes. Electrical field stimulation studies in the tissue-engineered constructs showed similar functional properties to those of normal vaginal tissue. When these constructs were used for autologous total vaginal replacement, patent vaginal structures were noted in the tissue-engineered specimens, while the noncell-seeded structures were noted to be stenotic.[168]

5.539.5.6. Blood Vessels

Xenogenic or synthetic materials have been used as replacement blood vessels for complex cardiovascular lesions. However, these materials typically lack growth potential, and may place the recipient at risk for complications such as stenosis, thromboembolization, or infection.[169] Tissue-engineered vascular grafts have been constructed using autologous cells and biodegradable scaffolds and have been applied in dog and lamb models.[170–173] The key advantage of using these autografts is that they degrade *in vivo*, and thus allow the new tissue to form without the long-term presence of foreign material.[169] Application of these techniques from the laboratory to the clinical setting has begun, with autologous vascular cells harvested, expanded, and seeded onto a biodegradable scaffold.[174] The resultant autologous construct was used to replace a stenosed pulmonary artery that had been previously repaired. Seven months after implantation, no evidence of graft occlusion or aneurysmal changes was noted in the recipient.

5.539.5.7. Heart

In the United States, over 5 million people currently live with some form of heart disease, and many more are diagnosed each

year. While many medications have been developed to assist the ailing heart, the treatment for end-stage heart failure still remains transplantation. Unfortunately, as with other organs, donor hearts are in short supply, and even when a transplant can be performed, the patient must endure the side effects created by lifelong immunosuppression. Thus, alternatives are desperately needed, and the development of novel methods to regenerate or replace damaged heart muscle using tissue engineering and regenerative medicine techniques is an attractive option.

Cell therapy for infarcted areas of the heart is attractive, as these methods involve a rather simple injection into the damaged area of a patient's heart, rather than a rigorous surgical procedure, to complete. Various types of stem cells have been investigated for their potential to regenerate damaged or dead heart tissue in this manner. Skeletal muscle cells, bone marrow stem cells (both mesenchymal and hematopoietic), amniotic fluid stem cells, and embryonic stem cells have been used for this purpose. In this technique, cells are suspended in a biocompatible matrix that can range from simple normal saline to complex yet biocompatible hydrogels depending on the type of injection to be performed. The cells are either injected into the damaged area of the heart itself, or they are injected into the coronary circulation with the hope that they will home to the damaged area, take up residence there, and begin to repair the tissue. However, injectable therapies have been shown to be relatively inefficient, and cell loss is quite substantial. Newer methods of tissue engineering include the development of engineered "patches," which comprise cells adhered to a biomaterial that can theoretically be used to replace the damaged area of the heart. These techniques hold promise, but require further research into the optimal cell types and biomaterials for this purpose before they can be used extensively in the clinic (see Jawad *et al.*[175] for an excellent review of these methods).

However, the methods described above could only be used in cases where a relatively small section of heart muscle was damaged. In cases where a large area or even the whole heart has become nonfunctional, a more radical approach may be required. In these situations, the use of a bioartificial heart would be ideal, as rejection would be avoided and the problems associated with a mechanical heart (such as thromboembolus formation) would be abolished. To this end, Ott *et al.* recently developed a novel heart construct *in vitro* using decellularized cadaveric hearts. By reseeding the tissue scaffold that remained after a specialized decellularization process with various types of cells that make up a heart (cardiomyocytes, smooth muscle cells, endothelial cells, and fibrocytes) and culturing the resulting construct in a bioreactor system designed to mimic physiologic conditions, this group was able to produce a construct that could generate pump function on its own.[176] This study suggests that production of bioartificial hearts may one day be possible.

5.539.5.8. Liver

The liver can sustain a variety of insults, including viral infection, alcohol abuse, surgical resection of tumors, and acute drug-induced hepatic failure. The current therapy for liver failure is liver transplantation. However, this therapy is limited by the shortage of donors and the need for lifelong immunosuppressive therapy. Cell transplantation has been proposed as a potential solution for liver failure. The fact that the liver has enormous regenerative potential *in vivo* suggests that in the right environment, it may be possible to expand liver cells *in vitro* in sufficient quantities for tissue engineering.[177] Many approaches have been tried, including development of specialized media, coculture with other cell types, identification of growth factors that have proliferative effects on these cells, and culture on three-dimensional scaffolds within bioreactors.[177]

Extracorporeal bioartificial liver devices that use porcine hepatocytes have been designed and applied. These devices are designed to filter and purify the patient's blood as would the patient's own liver, and the blood is returned to the patient in a manner similar to kidney dialysis. Another cell-based approach is the injection of liver cell suspensions. This has been performed in animal models. Intraportal hepatocyte injection has also been used in patients with Crigler–Najjar Syndrome Type 1[178]; however, complications such as portal vein thrombosis and pulmonary embolism are major concerns, especially when large cell numbers are used.[179] Finally, cells including stem cells, oval progenitor cells, and mature hepatocytes have been seeded onto liver-shaped biocompatible matrices to engineer artificial, implantable livers. These have been tested in various animal models;[180,181] however, the transplantation efficiency as well as the functionality of these constructs must be improved substantially before the technology can be moved into the clinic.

5.539.5.9. Articular Cartilage and Trachea

Full-thickness articular cartilage lesions have limited healing capacity and thus represent a difficult management issue for the clinicians who treat adult patients with damaged articular cartilage.[182,183] Large defects can be associated with mechanical instability and may lead to degenerative joint disease if left untreated.[184,185] Chondrocytes were expanded and cultured onto biodegradable scaffolds to create engineered cartilage for use in large osteochondral defects in rabbits.[186] When sutured to a subchondral support, the engineered cartilage was able to withstand physiologic loading and underwent orderly remodeling of the large osteochondral defects in adult rabbits, providing a biomechanically functional template that was able to undergo orderly remodeling when subjected to quantitative structural and functional analyses.

Few treatment options are currently available for patients who suffer from severe congenital tracheal pathology, such as stenosis, atresia, and agenesis, due to the limited availability of autologous transplantable tissue in the neonatal period. Tissue engineering in the fetal period may be a viable alternative for the surgical treatment of these prenatally diagnosed congential anomalies, as cells could be harvested and grown into transplantable tissue in parallel with the remainder of gestation. Chondrocytes from both elastic and hyaline cartilage specimens have been harvested from fetal lambs, expanded *in vitro*, then dynamically seeded onto biodegradable scaffolds.[187] The constructs were then implanted as replacement tracheal tissue in fetal lambs. The resultant tissue-engineered cartilage was noted to undergo engraftment and epithelialization, while maintaining its structural support and patency. Furthermore, if native tracheal tissue is unavailable, engineered

cartilage may be derived from bone marrow-derived mesenchymal progenitor cells as well.[188]

5.539.6. Summary and Conclusion

Regenerative medicine efforts are currently underway experimentally for virtually every type of tissue and organ within the human body. As regenerative medicine incorporates the fields of tissue engineering, cell biology, nuclear transfer, and materials science, personnel who have mastered the techniques of cell harvest, culture, expansion, transplantation, as well as polymer design are essential for the successful application of these technologies to extend human life. Various tissues are at different stages of development, with some already being used clinically, a few in preclinical trials, and some in the discovery stage. Recent progress suggests that engineered tissues may have an expanded clinical applicability in the future and may represent a viable therapeutic option for those who would benefit from the life-extending benefits of tissue replacement or repair.

Acknowledgment

The author wishes to thank Jennifer L. Olson, Ph.D., for editorial assistance with this manuscript.

References

1. Chen, F.; Yoo, J. J.; Atala, A. *Urology* **1999**, *54*, 407–410.
2. Dahms, S. E.; Piechota, H. J.; Dahiya, R.; Lue, T. F.; Tanagho, E. A. *Br. J. Urol.* **1998**, *82*, 411–419.
3. Piechota, H. J.; Dahms, S. E.; Nunes, L. S.; Dahiya, R.; Lue, T. F.; Tanagho, E. A. *J. Urol.* **1998**, *159*, 1717–1724.
4. Yoo, J. J.; Meng, J.; Oberpenning, F.; Atala, A. *Urology* **1998**, *51*, 221–225.
5. Amiel, G. E.; Atala, A. *Urol. Clin. North Am.* **1999**, *26*, 235–246.
6. Amiel, G. E.; Komura, M.; Shapira, O.; *et al. Tissue Eng.* **2006**, *12*, 2355–2365.
7. Atala, A. *J. Urol.* **1998**, *159*, 2–3.
8. Atala, A. *Adv. Exp. Med. Biol.* **1999**, *462*, 31–42.
9. Atala, A. *BJU Int.* **2001**, *88*, 765–770.
10. Cilento, B. G.; Freeman, M. R.; Schneck, F. X.; Retik, A. B.; Atala, A. *J. Urol.* **1994**, *152*, 665–670.
11. Oberpenning, F.; Meng, J.; Yoo, J. J.; Atala, A. *Nat. Biotechnol.* **1999**, *17*, 149–155.
12. Yoo, J. J.; Park, H. J.; Lee, I.; Atala, A. *J. Urol.* **1999**, *162*, 1119–1121.
13. Kim, B. S.; Mooney, D. J. *Trends Biotechnol.* **1998**, *16*, 224–230.
14. Bergsma, J. E.; Rozema, F. R.; Bos, R. R.; Boering, G.; De Bruijn, W. C.; Pennings, A. J. *Biomaterials* **1995**, *16*, 267–274.
15. Hynes, R. O. *Cell* **1992**, *69*, 11–25.
16. Pariente, J. L.; Kim, B. S.; Atala, A. *J. Biomed. Mater. Res.* **2001**, *55*, 33–39.
17. Pariente, J. L.; Kim, B. S.; Atala, A. *J. Urol.* **2002**, *167*, 1867–1871.
18. Li, S. T. In *The Biomedical Engineering Handbook*; Bronzino, J. D., Ed.; CRC Press: Boca Raton, FL, 1995; pp 627–647.
19. Arora, P. D.; Manolson, M. F.; Downey, G. P.; Sodek, J.; McCulloch, C. A. G. *J. Biol. Chem.* **2000**, *275*, 35432–35441.
20. Silver, F. H.; Pins, G. *J. Long Term Eff. Med. Implants* **1992**, *2*, 67–80.
21. Sams, A. E.; Nixon, A. J. *Osteoarthr. Cartil.* **1995**, *3*, 47–59.
22. Smidsrod, O.; Skjak-Braek, G. *Trends Biotechnol.* **1990**, *8*, 71–78.
23. Lim, F.; Sun, A. M. *Science* **1980**, *210*, 908–910.
24. Gilding, D. In *Biocompatibility of Clinical Implant Materials*; Williams, D., Ed.; CRC Press: Boca Raton, FL, 1981; pp 209–232.
25. Mikos, A. G.; Lyman, M. D.; Freed, L. E.; Langer, R. *Biomaterials* **1994**, *15*, 55–58.
26. Harris, L. D.; Kim, B. S.; Mooney, D. J. *J. Biomed. Mater. Res.* **1998**, *42*, 396–402.
27. Peppas, N. A.; Langer, R. *Science* **1994**, *263*, 1715–1720.
28. Brivanlou, A. H.; Gage, F. H.; Jaenisch, R.; Jessell, T.; Melton, D.; Rossant, J. *Science* **2003**, *300*, 913–916.
29. Richards, M.; Fong, C. Y.; Chan, W. K.; Wong, P. C.; Bongso, A. *Nat. Biotechnol.* **2002**, *20*, 933–936.
30. Amit, M.; Shariki, C.; Margulets, V.; Itskovitz-Eldor, J. *Biol. Reprod.* **2004**, *70*, 837–845.
31. Reubinoff, B. E.; Pera, M. F.; Fong, C. Y.; Trounson, A.; Bongso, A. *Nat. Biotechnol.* **2000**, *18*, 399–404; [see comment; erratum in *Nat. Biotechnol.* **2000**, *18*(5), 559].
32. Thomson, J. A.; Itskovitz-Eldor, J.; Shapiro, S. S.; *et al. Science* **1998**, *282*, 1145–1147; [see comment; erratum in *Science* **1998**, *282*(5395), 1827].
33. Reubinoff, B. E.; Itsykson, P.; Turetsky, T.; *et al. Nat. Biotechnol.* **2001**, *19*, 1134–1140.
34. Schuldiner, M.; Eiges, R.; Eden, A.; *et al. Brain Res.* **2001**, *913*, 201–205.
35. Schuldiner, M.; Yanuka, O.; Itskovitz-Eldor, J.; Melton, D. A.; Benvenisty, N. *Proc. Natl. Acad. Sci. USA* **2000**, *97*, 11307–11312.
36. Zhang, S. C.; Wernig, M.; Duncan, I. D.; Brustle, O.; Thomson, J. A. *Nat. Biotechnol.* **2001**, *19*, 1129–1133.
37. Kaufman, D. S.; Hanson, E. T.; Lewis, R. L.; Auerbach, R.; Thomson, J. A. *Proc. Natl. Acad. Sci. USA* **2001**, *98*, 10716–10721.
38. Kehat, I.; Kenyagin-Karsenti, D.; Snir, M.; *et al. J. Clin. Investig.* **2001**, *108*, 407–414.
39. Levenberg, S.; Golub, J. S.; Amit, M.; Itskovitz-Eldor, J.; Langer, R. *Proc. Natl. Acad. Sci. USA* **2002**, *99*, 4391–4396.
40. Assady, S.; Maor, G.; Amit, M.; Itskovitz-Eldor, J.; Skorecki, K. L.; Tzukerman, M. *Diabetes* **2001**, *50*, 1691–1697.
41. Itskovitz-Eldor, J.; Schuldiner, M.; Karsenti, D.; *et al. Mol. Med.* **2000**, *6*, 88–95.
42. Gurdon, J. B. *J. Embryol. Exp. Morphol.* **1962**, *10*, 622–640.
43. Gurdon, J. B. *J. Hered.* **1962**, *53*, 5–9.
44. Gurdon, J. B. *Dev. Biol.* **1962**, *5*, 68–83.
45. Gurdon, J. B.; Elsdale, T. R.; Fischberg, M. *Nature* **1958**, *182*, 64–65.
46. Campbell, K. H.; Mcwhir, J.; Ritchie, W. A.; Wilmut, I. *Nature* **1996**, *380*, 64–66.
47. Wilmut, I.; Schnieke, A. E.; Mcwhir, J.; Kind, A. J.; Campbell, K. H. *Nature* **1997**, *385*, 810–813; [see comment; erratum in *Nature* **1997**, *386*(6621), 200].
48. Cibelli, J. B.; Stice, S. L.; Golueke, P. J.; *et al. Science* **1998**, *280*, 1256–1258.
49. Baguisi, A.; Behboodi, E.; Melican, D. T.; *et al. Nat. Biotechnol.* **1999**, *17*, 456–461.
50. Wakayama, T.; Perry, A. C.; Zuccotti, M.; Johnson, K. R.; Yanagimachi, R. *Nature* **1998**, *394*, 369–374.
51. Betthauser, J.; Forsberg, E.; Augenstein, M.; *et al. Nat. Biotechnol.* **2000**, *18*, 1055–1059.
52. De Sousa, P. A.; Dobrinsky, J. R.; Zhu, J.; *et al. Biol. Reprod.* **2002**, *66*, 642–650.
53. Colman, A.; Kind, A. *Trends Biotechnol.* **2000**, *18*, 192–196.
54. Vogelstein, B.; Alberts, B.; Shine, K. *Science* **2002**, *295*, 1237.
55. Hochedlinger, K.; Rideout, W. M.; Kyba, M.; Daley, G. Q.; Blelloch, R.; Jaenisch, R. *Hematol. J.* **2004**, *5*(Suppl. 3), S114–S117.
56. Lanza, R. P.; Cibelli, J. B.; West, M. D. *Nat. Biotechnol.* **1999**, *17*, 1171–1174.
57. Lanza, R. P.; Cibelli, J. B.; West, M. D.; Dorff, E.; Tauer, C.; Green, R. M. *Science* **2001**, *292*, 1299.
58. Hochedlinger, K.; Jaenisch, R. *Curr. Opin. Cell Biol.* **2002**, *14*, 741–748.
59. Rideout, W. M. 3rd.; Eggan, K.; Jaenisch, R. *Science* **2001**, *293*, 1093–1098.
60. Solter, D. *Nat. Rev. Genet.* **2000**, *1*, 199–207.
61. Dinnyes, A.; De Sousa, P.; King, T.; Wilmut, I. *Cloning Stem Cells* **2002**, *4*, 81–90.
62. Takahashi, K.; Yamanaka, S. *Cell* **2006**, *126*, 663–676.
63. Wernig, M.; Meissner, A.; Foreman, R.; *et al. Nature* **2007**, *448*, 318–324.
64. Takahashi, K.; Tanabe, K.; Ohnuki, M.; *et al. Cell* **2007**, *131*, 861–872.
65. Yu, J.; Vodyanik, M. A.; Smuga-Otto, K.; *et al. Science* **2007**, *318*, 1917–1920; 1151526.
66. Okita, K.; Ichisaka, T.; Yamanaka, S. *Nature* **2007**, *448*, 313–317.
67. Meissner, A.; Wernig, M.; Jaenisch, R. *Nat. Biotechnol.* **2007**, *25*, 1177–1181.
68. Blelloch, R.; Wang, Z.; Meissner, A.; Pollard, S.; Smith, A.; Jaenisch, R. *Stem Cells* **2006**, *24*, 2007–2013.
69. De Coppi, P.; Bartsch, G., Jr.; Siddiqui, M. M.; *et al. Nat. Biotechnol.* **2007**, *25*, 100–106.
70. Scriven, S. D.; Booth, C.; Thomas, D. F.; Trejdosiewicz, L. K.; Southgate, J. *J. Urol.* **1997**, *158*, 1147–1152.
71. Liebert, M.; Hubbel, A.; Chung, M.; *et al. Differentiation* **1997**, *61*, 177–185.
72. Liebert, M.; Wedemeyer, G.; Abruzzo, L. V.; *et al. Semin. Urol.* **1991**, *9*, 124–130.
73. Puthenveettil, J. A.; Burger, M. S.; Reznikoff, C. A. *Adv. Exp. Med. Biol.* **1999**, *462*, 83–91.
74. Freeman, M. R.; Yoo, J. J.; Raab, G.; *et al. J. Clin. Investig.* **1997**, *99*, 1028–1036.

75. Harriss, D. R. *Br. J. Urol*. **1995**, *75*(Suppl. 1), 18–26.
76. Nguyen, H. T.; Park, J. M.; Peters, C. A.; *et al*. *In Vitro Cell. Dev. Biol. Anim*. **1999**, *35*, 371–375.
77. Kershen, R. T.; Atala, A. *Urol. Clin. North Am*. **1999**, *26*, 81–94.
78. Atala, A.; Cima, L. G.; Kim, W.; *et al*. *J. Urol*. **1993**, *150*, 745–747.
79. Atala, A.; Kim, W.; Paige, K. T.; Vacanti, C. A.; Retik, A. B. *J. Urol*. **1994**, *152*, 641–643; discussion 644.
80. Diamond, D. A.; Caldamone, A. A. *J. Urol*. **1999**, *162*, 1185–1188.
81. Bent, A. E.; Tutrone, R. T.; Mclennan, M. T.; Lloyd, L. K.; Kennelly, M. J.; Badlani, G. *Neurourol. Urodyn*. **2001**, *20*, 157–165.
82. Chancellor, M. B.; Yokoyama, T.; Tirney, S.; *et al*. *Neurourol. Urodyn*. **2000**, *19*, 279–287.
83. Yokoyama, T.; Huard, J.; Chancellor, M. B. *World J. Urol*. **2000**, *18*, 56–61.
84. Strasser, H.; Berjukow, S.; Marksteiner, R.; *et al*. *Exp. Gerontol*. **2004**, *39*, 1259–1265.
85. Yiou, R.; Lefaucheur, J. P.; Atala, A. *Anat. Embryol*. **2003**, *206*, 429–435.
86. Yiou, R.; Yoo, J. J.; Atala, A. *Transplantation* **2003**, *76*, 1053–1060.
87. Machluf, M.; Orsola, A.; Atala, A. *World J. Urol*. **2000**, *18*, 80–83.
88. Machluf, M.; Orsola, A.; Boorjian, S.; Kershen, R.; Atala, A. *Endocrinology* **2003**, *144*, 4975–4979.
89. Santen, R.; Swerdloff, R. Clinical aspects of androgen therapy. In *Workshop Conference on Androgen Therapy: Biologic and Clinical Consequences*, Pennsylvania State: Philadelphia, PA, 1990.
90. Tai, J.; Johnson, H. W.; Tze, W. J. *Transplantation* **1989**, *47*, 1087–1089.
91. Van Dam, J. H.; Teerds, K. J.; Rommerts, F. F. *Arch. Androl*. **1989**, *22*, 123–129.
92. De Vos, P.; De Haan, B.; Van Schilfgaarde, R. *Biomaterials* **1997**, *18*, 273–278.
93. Tai, I. T.; Sun, A. M. *FASEB J*. **1993**, *7*, 1061–1069.
94. Bazeed, M. A.; Thuroff, J. W.; Schmidt, R. A.; Tanagho, E. A. *Urology* **1983**, *21*, 53–57.
95. Olsen, L.; Bowald, S.; Busch, C.; Carlsten, J.; Eriksson, I. *Scand. J. Urol. Nephrol*. **1992**, *26*, 323–326.
96. Atala, A.; Vacanti, J. P.; Peters, C. A.; Mandell, J.; Retik, A. B.; Freeman, M. R. *J. Urol*. **1992**, *148*, 658–662.
97. Sievert, K. D.; Bakircioglu, M. E.; Nunes, L.; Tu, R.; Dahiya, R.; Tanagho, E. A. *J. Urol*. **2000**, *163*, 1958–1965.
98. Atala, A.; Guzman, L.; Retik, A. B. *J. Urol*. **1999**, *162*, 1148–1151.
99. El-Kassaby, A. W.; Retik, A. B.; Yoo, J. J.; Atala, A. *J. Urol*. **2003**, *169*, 170–173; discussion 173.
100. El Kassaby, A.; Aboushwareb, T.; Atala, A. *J. Urol*. **2008**, *179*, 1432–1436.
101. De Filippo, R. E.; Yoo, J. J.; Atala, A. *J. Urol*. **2002**, *168*, 1789–1792; discussion 1792–1793.
102. Le Roux, P. J. *J. Urol*. **2005**, *173*, 140–143.
103. Fu, Q.; Deng, C. L.; Liu, W.; Cao, Y. L. *BJU Int*. **2007**, *99*, 1162–1165.
104. Li, C.; Xu, Y.; Song, L.; Fu, Q.; Cui, L.; Yin, S. *Urol. Int*. **2008**, *81*, 290–295.
105. Guan, Y.; Ou, L.; Hu, G.; *et al*. *Artif. Organs* **2008**, *32*, 91–99.
106. Dorin, R. P.; Pohl, H. G.; De Filippo, R. E.; Yoo, J. J.; Atala, A. *World J. Urol*. **2008**, *26*, 323–326.
107. Atala, A. *J. Urol*. **1995**, *156*, 338.
108. Probst, M.; Dahiya, R.; Carrier, S.; Tanagho, E. A. *Br. J. Urol*. **1997**, *79*, 505–515.
109. Sutherland, R. S.; Baskin, L. S.; Hayward, S. W.; Cunha, G. R. *J. Urol*. **1996**, *156*, 571–577.
110. Wefer, J.; Sievert, K. D.; Schlote, N.; *et al*. *J. Urol*. **2001**, *165*, 1755–1759.
111. Jayo, M. J.; Jain, D.; Wagner, B. J.; Bertram, T. A. *J. Urol*. **2008**, *180*, 392–397.
112. Kropp, B. P.; Sawyer, B. D.; Shannon, H. E.; *et al*. *J. Urol*. **1996**, *156*, 599–607.
113. Zhang, Y. *J. Urol*. **2008**, *180*, 10–11.
114. Chun, S. Y.; Lim, G. J.; Kwon, T. G.; *et al*. *Biomaterials* **2007**, *28*, 4251–4256.
115. Kikuno, N.; Kawamoto, K.; Hirata, H.; *et al*. *BJU Int*. **2009**, *103*, 1424–1428.
116. De Boer, W. I.; Schuller, A. G.; Vermey, M.; Van Der Kwast, T. H. *Am. J. Pathol*. **1994**, *145*, 1199–1207.
117. Baker, R.; Kelly, T.; Tehan, T.; Putnam, C.; Beaugard, E. *J. Am. Med. Assoc*. **1958**, *168*, 1178–1185.
118. Gorham, S. D.; French, D. A.; Shivas, A. A.; Scott, R. *Eur. Urol*. **1989**, *16*, 440–443.
119. Master, V. A.; Wei, G.; Liu, W.; Baskin, L. S. *J. Urol*. **2003**, *170*, 1628–1632.
120. Jayo, M. J.; Jain, D.; Ludlow, J. W.; *et al*. *Regen. Med*. **2008**, *3*, 671–682.
121. Kwon, T. G.; Yoo, J. J.; Atala, A. *J. Urol*. **2008**, *179*, 2035–2041.
122. Zhang, Y.; Frimberger, D.; Cheng, E. Y.; Lin, H. K.; Kropp, B. P. *BJU Int*. **2006**, *98*, 1100–1105.
123. Farhat, W. A.; Yeger, H. *World J. Urol*. **2008**, *26*, 301–305.
124. Atala, A.; Bauer, S. B.; Soker, S.; Yoo, J. J.; Retik, A. B. *Lancet* **2006**, *367*, 1241–1246.
125. Dozmorov, M. G.; Kropp, B. P.; Hurst, R. E.; Cheng, E. Y.; Lin, H. K. *J. Smooth Muscle Res*. **2007**, *43*, 55–72.
126. Hipp, J.; Andersson, K. E.; Kwon, T. G.; Kwak, E. K.; Yoo, J.; Atala, A. *BJU Int*. **2008**, *101*, 100–105.
127. Lin, H. K.; Cowan, R.; Moore, P.; *et al*. *J. Urol*. **2004**, *171*, 1348–1352.
128. Lai, J. Y.; Yoon, C. Y.; Yoo, J. J.; Wulf, T.; Atala, A. *J. Urol*. **2002**, *168*, 1853–1857; discussion 1858.
129. Faris, R. A.; Konkin, T.; Halpert, G. *Artif. Organs* **2001**, *25*, 513–521.
130. Haller, H.; De Groot, K.; Bahlmann, F.; Elger, M.; Fliser, D. *Kidney Int*. **2005**, *68*, 1932–1936.
131. Auchincloss, H.; Bonventre, J. V. *Nat. Biotechnol*. **2002**, *20*, 665–666.
132. Al-Awqati, Q.; Oliver, J. A. *Kidney Int*. **2002**, *61*, 387–395.
133. Aebischer, P.; Ip, T. K.; Miracoli, L.; Galletti, P. M. *ASAIO Trans*. **1987**, *33*, 96–102.
134. Aebischer, P.; Ip, T. K.; Panol, G.; Galletti, P. M. *Life Support Syst*. **1987**, *5*, 159–168.
135. Amiel, G. E.; Yoo, J. J.; Atala, A. *World J. Urol*. **2000**, *18*, 71–79.
136. Humes, H. D.; Buffington, D. A.; MacKay, S. M.; Funke, A. J.; Weitzel, W. F. *Nat. Biotechnol*. **1999**, *17*, 451–455.
137. Humes, H. D.; MacKay, S. M.; Funke, A. J.; Buffington, D. A. *Kidney Int*. **1999**, *55*, 2502–2514.
138. Ip, T. K.; Aebischer, P.; Galletti, P. M. *ASAIO Trans*. **1988**, *34*, 351–355.
139. Joki, T.; Machluf, M.; Atala, A.; *et al*. *Nat. Biotechnol*. **2001**, *19*, 35–39.
140. Lanza, R. P.; Hayes, J. L.; Chick, W. L. *Nat. Biotechnol*. **1996**, *14*, 1107–1111.
141. MacKay, S. M.; Funke, A. J.; Buffington, D. A.; Humes, H. D. *ASAIO J*. **1998**, *44*, 179–183.
142. Atala, A.; Schlussel, R. N.; Retik, A. B. *J. Urol*. **1995**, *153*.
143. Fung, L. C. T.; Elenius, K.; Freeman, M.; Donovan, M. J.; Atala, A. *Pediatrics* **1996**, *98*(Suppl.), S631.
144. Joraku, A.; Stern, K. A.; Atala, A.; Yoo, J. J. *Methods* **2009**, *47*, 129–133.
145. Yoo, J.; Ashkar, S.; Atala, A. *Pediatrics* **1996**, *98S*, 605.
146. Lanza, R. P.; Chung, H. Y.; Yoo, J. J.; *et al*. *Nat. Biotechnol*. **2002**, *20*, 689–696.
147. Evans, M. J.; Gurer, C.; Loike, J. D.; Wilmut, I.; Schnieke, A. E.; Schon, E. A. *Nat. Genet*. **1999**, *23*, 90–93.
148. Hiendleder, S.; Schmutz, S. M.; Erhardt, G.; Green, R. D.; Plante, Y. *Mol. Reprod. Dev*. **1999**, *54*, 24–31.
149. Steinborn, R.; Schinogl, P.; Zakhartchenko, V.; *et al*. *Nat. Genet*. **2000**, *25*, 255–257.
150. Fischer Lindahl, K.; Hermel, E.; Loveland, B. E.; Wang, C. R. *Annu. Rev. Immunol*. **1991**, *9*, 351–372.
151. Hadley, G. A.; Linders, B.; Mohanakumar, T. *Transplantation* **1992**, *54*, 537–542.
152. Yard, B. A.; Kooymans-Couthino, M.; Reterink, T.; *et al*. *Kidney Int*. **1993**, *39* (Suppl.), S133–S138.
153. Perin, L.; Giuliani, S.; Jin, D.; *et al*. *Cell Prolif*. **2007**, *40*, 936–948.
154. Frumpkin, A. P. *Am. Rev. Sov. Med*. **1944**, *2*, 14.
155. Goodwin, W. E.; Scott, W. W. *J. Urol*. **1952**, *68*, 903–908.
156. Bretan, P. N. In *Genitourinary Prostheses*; Montague, D. K., Ed.; WB Saunders: Philadelphia, PA, 1989; pp 1–5.
157. Small, M. P.; Carrion, H. M.; Gordon, J. A. *Urology* **1975**, *5*, 479–486.
158. Nukui, F.; Okamoto, S.; Nagata, M.; Kurokawa, J.; Fukui, J. *Int. J. Urol*. **1997**, *4*, 52–54.
159. Thomalla, J. V.; Thompson, S. T.; Rowland, R. G.; Mulcahy, J. J. *J. Urol*. **1987**, *138*, 65–67.
160. Jordan, G. H. *Urol. Clin. North Am*. **1999**, *26*, 1–13.
161. Kershen, R. T.; Yoo, J. J.; Moreland, R. B.; Krane, R. J.; Atala, A. *Tissue Eng*. **2002**, *8*, 515–524.
162. Park, H. J.; Yoo, J. J.; Kershen, R. T.; Moreland, R.; Atala, A. *J. Urol*. **1999**, *162*, 1106–1109.
163. Falke, G.; Yoo, J. J.; Kwon, T. G.; Moreland, R.; Atala, A. *Tissue Eng*. **2003**, *9*, 871–879.
164. Kwon, T. G.; Yoo, J. J.; Atala, A. *J. Urol*. **2002**, *168*, 1754–1758.
165. Machluf, M.; Atala, A. *Graft* **1998**, *1*, 31–37.
166. Raya-Rivera, A. M.; Baez, C.; Atala, A.; Yoo, J. J. *World J. Urol*. **2008**, *26*, 307–314.
167. Wang, T.; Koh, C.; Yoo, J. J. *Creation of an Engineered Uterus for Surgical Reconstruction*. American Academy of Pediatrics Section on Urology: New Orleans, LA, 2003.
168. De Filippo, R. E.; Yoo, J. J.; Atala, A. *Tissue Eng*. **2003**, *9*, 301–306.
169. Matsumura, G.; Miyagawa-Tomita, S.; Shin'oka, T.; Ikada, Y.; Kurosawa, H. *Circulation* **2003**, *108*, 1729–1734.
170. Shinoka, T.; Breuer, C. K.; Tanel, R. E.; *et al*. *Ann. Thorac. Surg*. **1995**, *60*, S513–S516.
171. Shinoka, T.; Shum-Tim, D.; Ma, P. X.; *et al*. *J. Thorac. Cardiovasc. Surg*. **1998**, *115*, 536–545; discussion 545–546.

172. Shinoka, T.; Shum-Tim, D.; Ma, P. X.; *et al*. *Circulation* **1997**, *96*(II), 102–107.
173. Watanabe, M.; Shin'oka, T.; Tohyama, S.; *et al*. *Tissue Eng.* **2001**, *7*, 429–439.
174. Shin'oka, T.; Imai, Y.; Ikada, Y. *N Engl J. Med*. **2001**, *344*, 532–533.
175. Jawad, H.; Ali, N. N.; Lyon, A. R.; Chen, Q. Z.; Harding, S. E.; Boccaccini, A. R. *J. Tissue Eng. Regen. Med*. **2007**, *1*, 327–342.
176. Ott, H. C.; Matthiesen, T. S.; Goh, S. K.; *et al*. *Nat. Med*. **2008**, *14*(2), 213–221.
177. Bhandari, R. N.; Riccalton, L. A.; Lewis, A. L.; *et al*. *Tissue Eng.* **2001**, *7*, 345–357.
178. Fox, I. J.; Chowdhury, J. R.; Kaufman, S. S.; *et al*. *N Engl J. Med*. **1998**, *338*, 1422–1426.
179. Nieto, J. A.; Escandon, J.; Betancor, C.; Ramos, J.; Canton, T.; Cuervas-Mons, V. *Transplantation* **1989**, *47*, 449–450.
180. Gilbert, J. C.; Takada, T.; Stein, J. E.; Langer, R.; Vacanti, J. P. *Transplantation* **1993**, *56*, 423–427.
181. Kaufmann, P. M.; Kneser, U.; Fiegel, H. C.; Kluth, D.; Herbst, H.; Rogiers, X. *Transplant. Proc*. **1999**, *31*, 1928–1929.
182. Hunter, W. *Clin. Orthop. Relat. Res.* **1995**, *317*, 3–6.
183. O'Driscoll, S. W. *J. Bone Joint Surg. Am.* **1998**, *80*, 1795–1812.
184. Buckwalter, J. A.; Lohmander, S. *J. Bone Joint Surg. Am*. **1994**, *76*, 1405–1418.
185. Buckwalter, J. A.; Mankin, H. J. *Arthritis Rheum*. **1998**, *41*, 1331–1342.
186. Schaefer, D.; Martin, I.; Jundt, G.; *et al*. *Arthritis Rheum*. **2002**, *46*, 2524–2534.
187. Fuchs, J. R.; Terada, S.; Ochoa, E. R.; Vacanti, J. P.; Fauza, D. O. *J. Pediatr. Surg.* **2002**, *37*, 1000–1006; discussion 1000–1006.
188. Fuchs, J. R.; Hannouche, D.; Terada, S.; Vacanti, J. P.; Fauza, D. O. *J. Pediatr. Surg.* **2003**, *38*, 984–987.

5.540. Kidney Tissue Engineering

L S Krane, T Aboushwareb, and A Atala, Wake Forest University School of Medicine, Winston-Salem, NC, USA

© 2011 Elsevier Ltd. All rights reserved.

5.540.1.	**Introduction**	564
5.540.2.	**Developmental Techniques**	564
5.540.3.	**Renal Progenitor Cells**	565
5.540.4.	**Cellular-Based Therapies**	565
5.540.5.	**Stem Cells for Use in Renal Tissue Regeneration**	567
5.540.5.1.	ES Cells	567
5.540.5.1.1.	Single-cell embryo biopsy	568
5.540.5.1.2.	Obtaining cells from arrested embryos	568
5.540.5.1.3.	Therapeutic cloning (SCNT)	568
5.540.5.1.4.	Altered nuclear transfer	569
5.540.5.2.	Reprogramming (iPS Cells)	569
5.540.5.3.	Amniotic-Fluid and Placenta-Derived Stem Cells	569
5.540.5.4.	Adult Stem Cells	570
5.540.6.	***In Situ* Kidney Development**	570
5.540.7.	**Renal Tubular Assist Devices**	571
5.540.8.	**Summary and Conclusions**	572
References		572

Glossary

Acellular matrix Collagen-rich scaffolds prepared by removing all cellular components from a donor tissue.

Adult stem cell An undifferentiated cell found in postnatal tissues that can self-renew as well as produce progeny that can differentiate into the various cell types that comprise the tissue.

Amniotic fluid stem (AFS) cell A multipotent cell type found in the amniotic fluid surrounding an embryo; AFS cells may be differentiated to hepatic, pancreatic, renal, cardiac, osteogenic, and chondrogenic lineages, among others.

Distal tubule The final segment of the nephron in the kidney, located between the loop of Henle and the collecting duct; regulates serum concentrations of potassium, sodium, and calcium as well as pH.

Embryonic stem (ES) cell A broadly multipotent cell type found in the inner cell mass of a blastocyst; ES cells can differentiate into nearly every cell type in the body.

Erythropoietin A glycoprotein cytokine hormone produced by the peritubular capillary endothelial cells in the kidney that controls erythropoiesis, or red blood cell production.

Glomerulus The basic filtration unit of the kidney; composed of a capillary tuft surrounded by Bowman's capsule and performs the first step in filtering blood to form urine. The rate at which blood is filtered through all of the glomeruli, and thus the measure of the overall renal function, is the glomerular filtration rate (GFR).

Loop of Henle The portion of the nephron that leads from the proximal straight tubule to the distal convoluted tubule; functions to create concentrated urine for excretion by forming an area of high sodium concentration deep in the medulla of the kidney, so that water present in the filtrate flows through aquaporin channels out of the collecting duct and is reabsorbed.

Metanephros An embryonic structure that becomes the permanent kidney in reptiles, birds, and mammals; develops by the tenth week of gestation in human embryos.

Nephron The basic structural and functional unit of the kidney; regulates the concentration of water and soluble substances like sodium salts by filtering the blood, reabsorbing what is needed, and excreting the rest as urine. The nephron also regulates blood volume and blood pressure, controls levels of electrolytes and metabolites, and regulates blood pH. In humans, a normal kidney contains 800 000 to 1 million nephrons.

Podocyte A cell with branching tentacle-shaped extensions that constitutes the barrier through which blood is filtered in the glomerulus of the kidney.

Proximal tubule The portion of the nephron of the kidney that leads from Bowman's capsule to the loop of Henle; regulates the pH of renal filtrate by exchanging hydrogen ions in the interstitium for bicarbonate ions in the filtrate; also responsible for secreting organic acids, such as creatinine and other bases, into the filtrate.

5.540.1. Introduction

Patients with renal disease were the first to benefit from transplantation, as the kidney was the first human organ to be replaced in 1955.[1] This transplant was performed from one identical twin to another. In the early 1960s, Murray, who later received the Nobel Prize for his work, transplanted a kidney from a nongenetically identical patient into another. This transplant, which overcame the immunologic barrier, marked a new era in medical therapy and opened the door for the use of transplantation as a means of therapy for different organ systems. Despite this, the problems that plagued early transplant surgeons still create difficulties today. Immunosuppressive medications are still required to prevent complications, their monitoring and controlling graft rejection can be difficult, and there is still a shortage of donor organs. These challenges have led physicians and scientists to seek alternatives in the relatively new fields of tissue engineering and regenerative medicine, and progress in these fields has paved the way for the development of new technologies for renal replacement therapy.

The difficulty in applying regenerative medicine techniques to the kidney is inherent in the complexity of the organ. Functionally, the kidney is responsible not only for waste elimination; it has endocrine properties as well. The primary role of the kidney is hemofiltration. The blood is filtered through a complex architectural system. The resulting ultrafiltrate is then concentrated in the renal tubules, which allow for the absorption and secretion of specific ions and water, thus maintaining appropriate intravascular concentrations of these components. In addition, the kidney produces erythropoietin (EPO), which is responsible for red blood cell production and adequate oxygenation of tissues. Renin is also secreted by the kidney and is a major factor in regulating blood pressure. The kidney activates vitamin D by converting the circulating 25-hydroxycholecalciferol into 1,25-dihydroxycholecalciferol, and it releases prostaglandins into the circulation. Attempts at complete renal tissue regeneration must provide these important functions in addition to filtration.

Embryologically, the kidney is derived from the integration of several primordial structures. While the metanephros is responsible for the development of the proximal section of the nephrons, the ureteric bud forms the collecting ducts and distal structures. The large vessels of the kidney are derived from extrarenal tissues. These divergent embryologic origins converge to produce at least 26 distinct functional cells in the kidney.[2] This heterogeneity creates difficulty with *in vitro* culture and in identifying potential renal stem or progenitor cells.

Despite these hurdles, there are several techniques currently being investigated for renal regenerative therapy. Some of these are based on embryology/developmental biology and others depend upon the identification of renal progenitor cells that could eventually be used for clinical applications. Still other techniques for renal regeneration or replacement are based on cell therapies. These include both the direct injection of certain cell types and the use of biomaterial scaffolds seeded with cells. This chapter will focus largely on the current status of cell-based therapies in renal regeneration, but it will also provide a brief overview of the other techniques.

5.540.2. Developmental Techniques

In mammalian embryonic kidney development, there are two successive steps leading to development of the metanephros. Initially, the ureteric buds are formed at the caudal end of the Wolffian ducts and subsequently the metanephric mesenchyme, induced by the ureteric buds, and the ureteric buds themselves interact with one another to produce the metanephros. The metanephros becomes the permanent kidney. These structures originate at day 11 of development (E11) in mice, at day 12 in rats (E12), between days 21 and 28 in pigs (E21–28), and during the fifth week of gestation in humans. Outgrowths arising from the distal end of the ureteric bud push radially into the surrounding metanephric mesenchyme. The metanephric mesenchyme differentiates into all tubular structures of the adult nephron, with the exception of the collecting system, which is derived from the ureteric bud.

To develop viable renal tissue for clinical application and tissue regeneration, transplantation of metanephroi has been attempted. Transplantation of metanephroi appears to have two significant promising factors promoting its future clinical usage. First, metanephric tissue appears to have decreased immunogenicity. Extensive literature has documented the lack of antigenicity and cotransmitters in metanephric tissue. Secondly, transplanted metanephroi have been successful in developing complex vascularization induced from host tissue. This would promote cellular survival in the host and allow development of tissues *in vivo*.

Renal anlagen transplanted into a host have demonstrated differentiation into renal tissue and functional capabilities including production of urine. In addition, the transplant was able to improve survival in anephric rodents. Initial studies demonstrating the feasibility of metanephroi transplantation were conducted by Woolf, who implanted pieces of E13–16 metanephroi into cortical tunnels fashioned in newborn mice.[3] Abrahamson was able to demonstrate survival and function of metanephroi transplanted subcapsularly in rats.[4] Rogers *et al.* were able to not only implant metanephroi outside the renal capsule in the omentum, but also performed a ureteroureterostomy, allowing for quantification of urine production.[5] Rogers *et al.* were also the first to demonstrate improved survival associated with metanephros transplantation. They implanted E15 rat metanephroi into the omentum of rats concurrent with a unilateral nephrectomy. Three weeks later, they performed ureteroureterostomy between the host ureter and the transplanted metanephroi in some of the rats. At 20 weeks following initial transplantation, they performed contralateral nephrectomy, forcing animals into end-stage renal disease (ESRD). They demonstrated a significant prolongation of life in the animals with the reconstructed excretory urinary tracts versus controls or those who received transplants without ureteroureterostomy.[6] Marshall and colleagues successfully transplanted rat metanephroi into the omentum and patches of retroperitoneal fat in the renal bed, adjacent to the circumflex iliac vessels and adjacent to the aorta/vena cava. They were able to demonstrate the presence of urinary cysts in all locations at 21 days posttransplantation. In renal units with urinary cysts, ureteroureterostomy was performed at this time point. When inulin clearance was measured 130 days

following ureteroureterostomy, the transplanted units contributed up to 11% of the total glomerular filtration rate (GFR).[7]

Integration of new nephrons into a diseased kidney could obviate the need for renal replacement therapy. Investigations into this possibility in an animal model have been promising. Woolf *et al.* implanted embryonic tissue into the renal cortex of newly born mice. They found that the donor tissue integrated into the host and generated new nephrons. In addition, the glomeruli of the donated tissue were vascularized by the host. Mature tubules and tubular extensions into the medulla were seen; however, it could not be confirmed that these nephrons connected to a collecting duct.[3] Rogers and colleagues performed a similar experiment, placing E15 rat metanephroi in adult male mice. They also found that nephron development and creation of a chimeric kidney occurred.[5] However, like Woolf, they could not verify that these nephrons connected to the collecting duct despite transplantation of a portion of the ureteric bud.[3,5]

5.540.3. Renal Progenitor Cells

Owing to the diverse nature of the kidney, identification of a single progenitor cell responsible for generating all of the cell types in the kidney is unlikely. However, because the majority of renal dysfunction results from disorders of either the tubules or the glomeruli, identifying the progenitor cells responsible for generating these structures could produce the most significant clinical impact. One method for identifying progenitor cells includes the recognition of specific cell surface markers. Bussolati and colleagues chose to determine whether CD133+ cells reside in the adult human renal parenchyma.[8,9] CD133 is expressed in hematopoietic and progenitor cells, and also in the embryonic kidney. This group observed that a CD133+ population was present and comprised approximately 0.8% of the total cell population within the renal cortex. These cells expressed Pax-2 but not CD-45 (a marker of the hematopoietic lineage) and cKit and CD90 (stem cell markers).[8] *In vivo*, these cells formed tubular-like structures following implantation into immunocompromised mice.[8] Following enzymatic digestion of rat kidneys, Plotkin and associates identified a single clone which expressed Sca-1, CD44, and CD34, the transcription factors Pod-1 and BF-2, and receptors for sonic hedgehog, BMP and retinoic acid. When these cells were injected subcapsularly following an ischemia/reperfusion injury, the isolated cells integrated into the peritubular capillaries and periphery of the papillae.[10] Gupta *et al.* enzymatically digested 4-week-old rat kidneys and cultured the resulting cellular suspension using culture methods similar to those used for bone marrow-derived cells. They identified a population of cells that were capable of >200 population doublings without senescence, and these cells expressed vimentin, Oct-4, and Pax-2, but did not express markers of either MHC class or markers of differentiated cells. When labeled cells from this study were reintroduced *in vivo*, they demonstrated integration into the renal architecture, but did not improve renal function following ischemia reperfusion injury.[9] The identification of renal cells, which can integrate into the renal parenchyma has implications for future therapies based on the replacement of nephrons. Integration of nephrons is especially promising for patients with progressive renal dysfunction to prevent ESRD.

Podocytes also present a novel model for understanding and identifying potential renal progenitor cells. Podocytes are postmitotic cells that lack the ability to reproduce, but are routinely found in the urine even in healthy individuals.[11] The number of cells lost in the urine exceeds that which would be expected for renal survival of 80 years. Therefore, it has been hypothesized that an inherent population of progenitor cells resides in the kidney and that these cells are capable of regenerating podocytes. Several groups have investigated the role of progenitor cells that may be involved in podocyte regeneration. Sagrinati and colleagues found a population of CD133+CD24+ cells that were localized opposite the vascular pole of Bowman's capsule. These parietal epithelial cells (PECs) were between 0.5% and 4% of the total cellular population, were maintained up to 90 population doublings, and expressed Oct-4 and BmI-1. When introduced *in vitro* following glycerol-induced rhabdomyolysis acute renal injury, these cells attenuated renal injury as measured by lower BUN levels 7–10 days following injection.[12]

Further investigations of the PEC by this group identified three subpopulations of these cells. A subset of undifferentiated cells only CD133/24+ was located at the urinary pole. A second transitional population of cells expressing CD133/24 and also nestin, complement receptor 1 (CR1), and podocalyxin (PDX) (all podocyte markers) were located between the urinary and the vascular pole. Continuous with the podocytes was a subset of cells that no longer expressed CD133/24, but were positive for nestin, CR1, and PDX.[13] *In vitro*, the only cells capable of differentiating into tubular cells were those that were CD133/24+ but not PDX+. To evaluate *in vivo* properties of these cells, an FSGS model of renal dysfunction was created with adriamycin infusion. The CD133/24+PDX− cells were able to reduce albuminuria and decreased glomerular and tubular quantitative injury in this model.[13] In another series of experiments, Appel *et al.* evaluated the CD133+ PECs and concluded that the PECs were capable of migration along the glomerular tuft to replace podocyte populations. They examined the cells at the base of the vascular pole adjacent to the podocytes and noted that only these cells were able to be stained with both PEC markers (claudin-1) and podocyte-specific markers (nestin, DDPIV, aminopeptidase A). A PEC-specific promotor (PDX) was identified which could be used to trace the migration of cells, and this experiment pointed to the recruitment of PEC by podocytes.[14]

Identification of renal progenitor cells is a substantial step forward in the understanding of the inherent regenerative capacity of the kidney. The ability to identify the subset of cells responsible for endogenous renal repair and expand these cells *in vitro* could have future therapeutic implications. Care must be taken in referring to these identified cells as renal stem cells, however. Currently, no group has demonstrated a population of cells which satisfy the strict definition of a 'stem cell,' which includes the ability to form clonal populations *in vitro*. In addition, this technology still needs refinement prior to clinical usage.

5.540.4. Cellular-Based Therapies

The functional heterogeneity and complex cellular architecture within the kidney present many challenges in the development of cellular therapies. These include the need to ensure precise

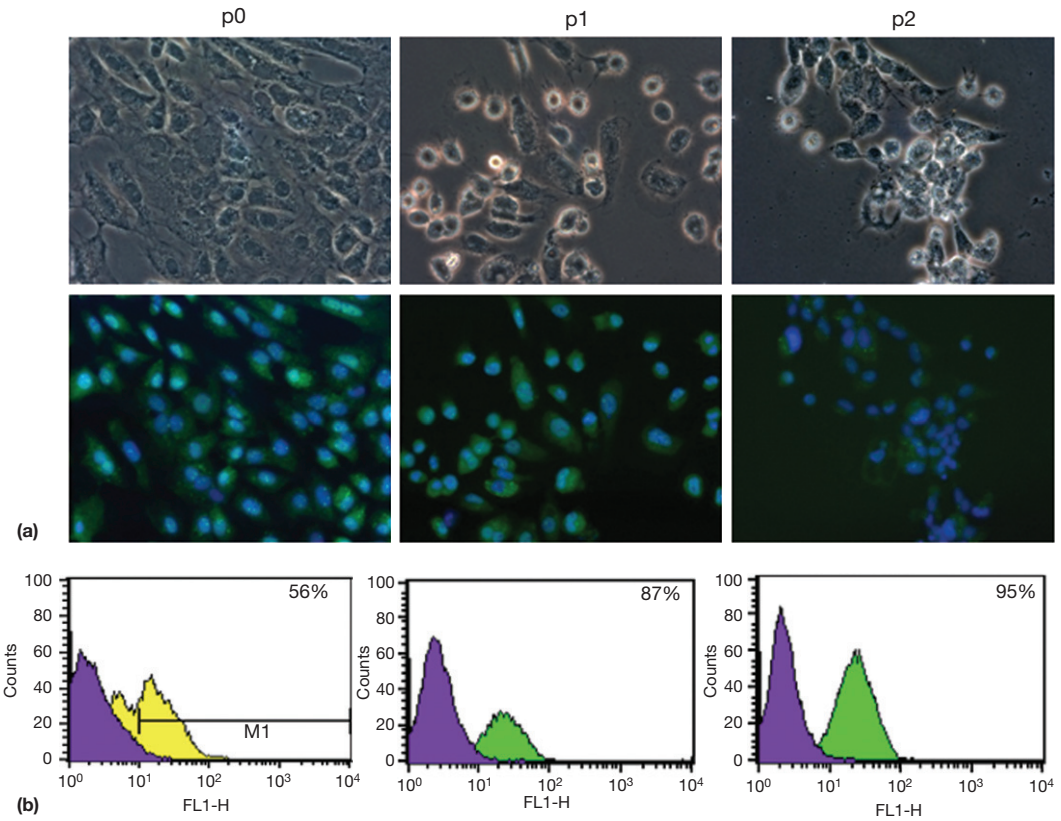

Figure 1 Isolation and characterization of EPO-producing cells. Rat primary renal cells were cultured according to previously established methods. (a) Subcultures through passage 2 and corresponding immunofluorescent staining with an anti-EPO antibody (400×). (b) FACs analysis of EPO expression through passage 2.

delivery of the cells, which allows homing to the necessary location, and the need to define exactly what type of cell should be delivered. While some groups have evaluated the possibility of using stem cells from various lineages, others have focused on the use of differentiated renal cells to improve function.

Isolation of a single cell type for reintroduction to the kidney may be an initial step in providing cellular therapies for renal dysfunction. One example of this type of therapy is the treatment of anemia associated with chronic renal dysfunction. Currently, patients with ESRD often require recombinant EPO injection in order to increase red blood cell counts, and recent research into alternatives to these injections has presented a novel platform for future clinical applications for cellular therapy. Isolation and culture of EPO-producing renal cells has been described by Aboushwareb *et al.*[15] The cells demonstrate increased EPO expression when exposed to hypoxic environments (Figures 1 and 2) (unpublished data, Aboushwareb *et al.*). These cells represent a potential lineage for future treatments of renal dysfunction-associated anemia. In another study on this topic, Bathlolomew and colleagues transfected baboon mesenchymal stem cells (MSC) with human EPO vectors and evaluated whether these cells were capable of *in vivo* EPO production. These cells could successfully produce EPO for up to 28 days in SCID mice and 137 days in baboons.[16] Targeting of anemia associated with renal dysfunction or other singular functions of the kidney may provide pathways to introduce cellular therapies for renal dysfunction.

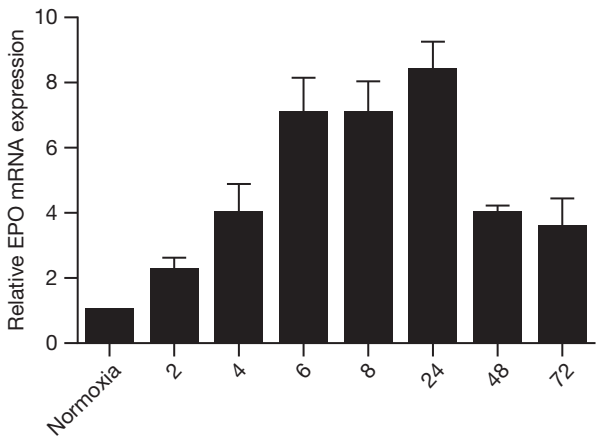

Figure 2 Time course of EPO gene expression in rat primary renal cells under 1% O_2 continuous hypoxia. Cells were allowed to grow in culture to 70% confluency. Following washing the cells and changing the medium, the culture plates were placed in continuous hypoxia from 2 up to 72 h. At the end points shown, total RNA was isolated from the cells relative EPO gene expression was quantified using real-time PCR. All the results were expressed relative to gene expression levels in normoxic samples. Result is expressed as mean ± SEM ($n = 5$).

Targeting of specific cells in the nephron could provide disease-specific cellular therapy. Patients may have either tubular dysfunction or podocyte dysfunction, and thus, each

patient requires a specific therapy based on pathology. Han and colleagues have found that primary rabbit proximal tubule cells are able to produce functional tubular units. Following enzymatic digestion of the cortex and removal of glomeruli, tubules were formed *in vitro* with luminal formation. Function was demonstrated with lucifer yellow, a fluorescent substrate of the *p*-aminohippurate (PAH) transport system transport.[17] In patients with tubular dysfunction, introduction of cultured tubules could direct therapy at the specific pathology of the disease.

Development of heterogenous populations of renal cells could also represent a potentially viable option for cellular therapy of renal disease. Joraku *et al.* developed an *in vitro* method for cultivation of mixed renal cells which allowed for the development of tubular structures (**Figure 3**). This technique involves digestion of the entire murine kidney, followed by cultivation of the resulting cells on rat-tail type 1 collagen. Upon histologic examination, cells from the thick ascending loop of Henle stained positive for Tamm–Horsfall protein.[18] This work was followed up by Souza *et al.* (unpublished data), who demonstrated the same phenomenon of self-assembly with isolated human kidney cells. These results further support the potential use of isolated and culture-expanded kidney cells for reassembling functional renal units within diseased kidneys. However, the published reports involving reintroduced adult renal cells have not yet demonstrated improvements in renal function resulting from this treatment, and the barrier of immune recognition has not been overcome either.[19]

5.540.5. Stem Cells for Use in Renal Tissue Regeneration

The cells used in regenerative medicine techniques can be autologous or heterologous in origin, and they can be either native cells or stem cells. In general, there are three broad categories of stem cells obtained from living tissue that are used for cell therapies. Embryonic stem (ES) cells are obtained through the aspiration of the inner cell mass of a blastocyst or, more recently, a single cell from this mass. Fetal and neonatal amniotic fluid and placenta may contain multipotent cells that may be useful in cell therapy applications. However, adult stem cells are usually isolated from organ or bone marrow biopsies. Stem cells are defined as having three important properties: the ability to self-renew, the ability to differentiate into a number of different cell types, and the ability to easily form clonal populations (populations of cells derived from a single stem cell). Many techniques for generating stem cells have been studied over the past few decades. Some of these techniques have yielded promising results, but others require further research.

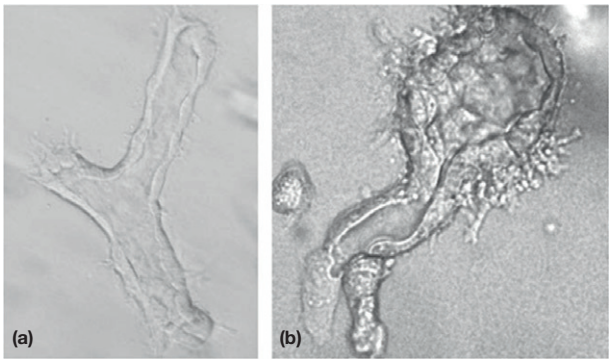

Figure 3 Murine primary renal cells form kidney-like structures *in vitro*. Primary murine renal cells were isolated, expanded in culture, and suspended in collagen. After 7 days of growth in the collagen matrix, the cells developed into three-dimensional structures that resemble tubules (a) and glomeruli (b).

5.540.5.1. ES Cells

In 1981, pluripotent cells were found in the inner cell mass of the human embryo, and the term 'human embryonic stem cell' was coined.[20] These cells are able to differentiate into all cells of the human body, excluding placental cells (only cells from the morula are totipotent, i.e., able to develop into all cells of the human body). These cells have great therapeutic potential, but their use is limited by both biological and ethical factors. The political controversy surrounding stem cells began in 1998 with the creation of human ES (hES) cells derived from discarded embryos. hES cells were isolated from the inner cell mass of a blastocyst (an embryo 5 days postfertilization) using an immunosurgical technique. Given that some cells cannot be expanded *ex vivo*, ES cells could be an ideal resource for regenerative medicine because of their fundamental properties: the ability to self-renew indefinitely and the ability to differentiate into cells from all the three embryonic germ layers. Skin and neurons have been formed, indicating ectodermal differentiation.[21–23] Blood, cardiac cells, cartilage, endothelial cells, and muscle have been formed, indicating mesodermal differentiation.[24–26] Pancreatic cells have been formed, indicating endodermal differentiation.[27] In addition, as further evidence of their pluripotency, ES cells can form embryoid bodies, which are cell aggregations that contain all the three embryonic germ layers while in culture, and can form teratomas *in vivo*.[28] These cells have demonstrated longevity in culture and can maintain their undifferentiated state for at least 80 passages when grown using current published protocols.[29,30]

Various researchers have shown that ES cells may be useful in renal regenerative medicine.[31] Schulinder *et al.* were able to induce differentiation of hES into cells that produce the renal-specific products renin and WT-1 using culture media including activin-A and HGF.[32] Kim and Dressler have evaluated whether murine ES cells could be cultured *in vitro* to renal precursor cells and mesoderm. By culturing the ES cells in activin-A, retinoic acid, and Bmp7, they were able to induce genetic expression of Pax-2 (a marker of intermediate mesoderm from which the renal epithelial cells arise), WT-1 (seen in high levels in podocytes), cadherin 6 (an early marker for proximal tubules), and lim1 (seen in intermediate mesoderm). These cells also formed tubule-like structures when introduced *in vivo* to cultured kidney rediments from 12.5-day embryonic mice.[33]

Vigneau and colleagues showed that ES expressing brachyury, an embryonic nuclear transcription factor, which possibly denotes mesoderm, may differentiate into renal progenitor cells in the presence of activin-A. When these cells were injected into a developing metanephros, they were incorporated into the blastemal cells of the nephrogenic zone. Additionally, after only

a single injection into the kidneys of live newborn mice, the cells were capable of integration into proximal tubules. At 7 months, there was no evidence of teratoma formation, and the cellular morphology and polarization appeared normal.[34]

In addition to the ethical dilemma surrounding the use of ES cells, their clinical application is limited because they represent an allogenic resource and thus have the potential to evoke an immune response. New stem cell technologies such as somatic cell nuclear transfer (SCNT) and induced pluripotent stem (iPS) cells promise to overcome this limitation.

5.540.5.1.1. Single-cell embryo biopsy

One major objection to hES cell research is that it results in the destruction of embryos. Thus, a method of isolating these cells without destroying the embryo would be advantageous. In 2006, Chung *et al.*[35] were the first authors to report the generation of mouse ES cell lines in this manner. Their method was based on a technique used to obtain a single-cell embryo biopsy for preimplantation genetic diagnosis. Cells were taken from eight-cell blastomeres rather than from blastocysts. The cells differentiated into derivatives of all the three embryonic germ layers *in vitro* and into teratomas *in vivo* as well. In addition, the mouse embryos that resulted from the biopsied blastomeres developed to term without a reduction in their developmental potential.

5.540.5.1.2. Obtaining cells from arrested embryos

hES cell lines can also be derived from arrested embryos.[36] During *in vitro* fertilization, only a small proportion of zygotes produced will develop and progress successfully to the morula and blastocyst stages. Over half of the embryos stop dividing[37,38] and are therefore considered dead embryos.[39] Such embryos have unequal or fragmented cells and blastomeres and are usually discarded. Not all the cells within these arrested embryos, however, are abnormal,[36,40] and these embryos might be a source of hES cells. More studies are needed to characterize the full proliferation and differentiation potential of ES cells derived from arrested embryos.

5.540.5.1.3. Therapeutic cloning (SCNT)

SCNT, or therapeutic cloning, entails the removal of an oocyte nucleus in culture, followed by its replacement with a nucleus derived from a somatic cell obtained from a patient. Following nuclear transfer, the gene expression pattern of the transferred nucleus must be reprogrammed to that similar to an early embryo. This is accomplished through DNA modifications including histone protein modification, cytosine methylation, and chromatin remodeling, and reengineering the framework of the normal methylation patterns. This is accomplished *in vitro* through a series of chemical signals or introduction of electric potentials.

At this point, it is extremely important to differentiate between the two types of cloning that exist – reproductive cloning and therapeutic cloning. Both involve the insertion of donor DNA into an enucleated oocyte to generate an embryo that has identical genetic material to its DNA source. Following this point, however, there are important differences in the ethical and scientific implications of the techniques. In reproductive cloning, the embryo that is produced using SCNT is implanted into the uterus of a pseudopregnant female to produce an infant that is a clone of the donor. A world-famous example of this type of cloning resulted in the birth of a sheep named Dolly in 1997.[41] However, there are many ethical concerns surrounding such practices, and as a result, reproductive cloning has been banned in most countries.

While therapeutic cloning also produces an embryo that is genetically identical to the donor, this process is used to generate blastocysts that are explanted and grown in culture, rather than *in utero*. ES cell lines can then be derived from these blastocysts, which are only allowed to grow up to a 100-cell stage. At this time, the inner cell mass is isolated and cultured, resulting in ES cells that are genetically identical to the patient. It has been shown that nuclear transferred ES cells derived from fibroblasts, lymphocytes, and olfactory neurons are pluripotent and can generate live pups after injection into blastocysts. This shows that the embryos generated from cells produced by SCNT have the same developmental potential as blastocysts that are fertilized and produced naturally.[42–47] In addition, the ES cells generated by SCNT are perfectly matched to the patient's immune system, and no immunosuppressants would be required to prevent rejection should these cells be used in regenerative medicine applications.

Although ES cells derived from SCNT contain the nuclear genome of the donor cells, mitochondrial DNA (mtDNA) contained in the oocyte could lead to immunogenicity after transplantation. To assess the histocompatibility of tissue generated using SCNT, Lanza *et al.* microinjected the nucleus of a bovine skin fibroblast into an enucleated oocyte.[48] Although the blastocyst was implanted (reproductive cloning), the purpose was to generate renal, cardiac, and skeletal muscle cells, which were then harvested, expanded *in vitro*, and seeded onto biodegradable scaffolds. These scaffolds were then implanted into the donor steer from which the cells were cloned to determine if cells were histocompatible. Analysis revealed that cloned renal cells showed no evidence of T cell response, suggesting that rejection will not necessarily occur in the presence of oocyte-derived mtDNA. This finding represents a step forward in overcoming the histocompatibility problem of stem cell therapy.

However, although promising, SCNT has certain limitations that require further improvement before its clinical application in addition to the ethical considerations regarding the potential of the resulting embryos to develop into clones if implanted into a uterus. In addition, this technique has not been shown to work in humans to date. The initial failures and fraudulent reports of nuclear transfer in humans reduced enthusiasm for human applications,[49–51] although it was recently reported that nonhuman primate ES cell lines were generated by SCNT of nuclei from adult skin fibroblasts.[52,53] In addition, before SCNT-derived ES cells can be used as clinical therapy, careful assessment of quality of the lines must be determined. For example, some cell lines generated by SCNT have contained chromosomal translocations and it is not known whether these abnormalities originated from aneuploid embryos or if they occurred during ES cell isolation and culture. In addition, the low efficiency of SNCT (0.7%) and the inadequate supply of human oocytes further hinder the therapeutic potential of this technique. Still, these studies renew the hope that ES cell lines could one day be generated from human cells to produce patient-specific stem cells with

the potential to cure many human diseases that are currently untreatable. Studies suggesting new uses for this technology are being published frequently, and these open the door for the development of many potential therapies related to these cells.[54]

5.540.5.1.4. Altered nuclear transfer

Altered nuclear transfer is a variation of SCNT in which a genetically modified nucleus from a somatic cell is transferred into a human oocyte. This embryo, which contains a deliberate genetic defect, is capable of developing into a blastocyst, but the induced defect prevents the blastocyst from implanting in the uterus. This process has the potential to generate customized hES cells from the blastocyst stage.[55] Human embryos with this genetic defect might lack the capacity to develop into viable fetuses, as a result of their inability to implant, thus providing a source of stem cells without destroying viable embryos. Proof of concept was obtained in mice by Meissner and Jaenisch[56] in 2006 using embryos lacking the *Cdx2* homeobox gene.

The viability of human embryos lacking the *CDX2* gene is unclear, as is whether this mutation restricts human developmental potential into certain lineages. While much research must be done before therapeutic strategies based on this technique could ever enter the clinic, at this time, hES cells derived from altered nuclear transfer can provide opportunities to study pluripotency in hES cells, without the need for destruction of viable embryos. The exact effects of CDX-2 gene knockout on the development of human embryos are not well known. The effects of this gene, however, have been thoroughly investigated in the gastric and intestinal epithelium.[57,58]

5.540.5.2. Reprogramming (iPS Cells)

Recently, reports of the successful transformation of adult cells into pluripotent stem cells through a type of genetic 'reprogramming' have been published. Reprogramming is a technique that involves dedifferentiation of adult somatic cells to produce patient-specific pluripotent stem cells. The advantage of this technique is that it obviates the need for creation of embryos. Cells generated by reprogramming would be genetically identical to the somatic cells (and thus, the patient who donated these cells) and would not be rejected. Yamanaka initially discovered that mouse embryonic fibroblasts (MEFs) and adult mouse fibroblasts could be reprogrammed into an 'induced pluripotent state (iPS)'.[59] These iPS cells were capable of immortal growth similar to the self-renewing characteristics of ES cells, expressed genes specific for ES cells, and generated embryoid bodies *in vitro* and teratomas *in vivo*. When iPS cells were injected into mouse blastocysts, they differentiated into several cell types. However, although iPS cells selected in this way were pluripotent, they were not identical to ES cells. Unlike ES cells, chimeras made from iPS cells did not result in full-term pregnancies. Gene expression profiles of the iPS cells showed that they possessed a distinct gene expression signature that was different from that of ES cells. In addition, the epigenetic state of the iPS cells was somewhere between that found in somatic cells and that found in ES cells, suggesting that the reprogramming was incomplete.

Wernig and Jaenisch significantly improved these results in July 2007.[60] In this study, DNA methylation, gene expression profiles, and the chromatin state of the reprogrammed cells were similar to those of ES cells. Teratomas induced by these cells contained differentiated cell types representing all mesoderm, ectoderm, and endoderm. Most importantly, the reprogrammed cells from this experiment were able to form viable chimeras and contribute to the germline like ES cells, suggesting that these iPS cells were completely reprogrammed.

It has recently been shown that reprogramming of human cells is possible.[61,62] Yamanaka generated human iPS cells that are similar to hES cells in terms of morphology, proliferation, gene expression, surface markers, and teratoma formation. Thompson's group showed that retroviral transduction of the stem cell markers *OCT4*, *SOX2*, *NANOG*, and *LIN28* could generate pluripotent stem cells. However, in both studies, the human iPS cells were similar but not identical to hES cells. Recent efforts by several researches have demonstrated successful creation of iPS in more than one animal model.[63,64] The porcine model is the most important of these due to its similarity to the human kidney. They each published retroviral transfection of cells with expression of stem cell markers. These are exciting potential preclinical models for future therapeutic direction.[65] Although reprogramming is an exciting phenomenon, our limited understanding of the mechanism underlying it currently limits the clinical applicability of the technique, but the future potential of reprogramming is quite exciting.

5.540.5.3. Amniotic-Fluid and Placenta-Derived Stem Cells

The amniotic fluid and placental membrane contain a heterogeneous population of cell types derived from the developing fetus.[66,67] Cells found in this heterogeneous population include MSC.[68,69] In addition, the isolation of multipotent human and mouse amniotic-fluid and placental-derived stem (AFPS) cells that are capable of extensive self-renewal and give rise to cells from all the three germ layers was reported in 2007.[70] AFPS cells represent approximately 1% of the cells found in the amniotic fluid and placenta. The undifferentiated stem cells expand extensively without a feeder cell layer and double every 36 h. Unlike hES cells, the AFPS cells do not form tumors *in vivo*. Lines maintained for over 250 population doublings retained long telomeres and a normal complement of chromosomes. AFPS cell lines can be induced to differentiate into cells representing each embryonic germ layer, including cells of adipogenic, osteogenic, myogenic, endothelial, neural-like, and hepatic lineages. In addition to the differentiated AFPS cells expressing lineage-specific markers, such cells can have specialized functions. Cells of the hepatic lineage secreted urea and α-fetoprotein, while osteogenic cells produced mineralized calcium. In this respect, they meet a commonly accepted criterion for multipotent stem cells, without implying that they can generate every adult tissue.

Amniotic fluid stem (AFS) cells represent a new class of stem cells with properties somewhere between those of embryonic and adult stem cell types, probably more agile than adult stem cells, but less so than ES cells. Unlike embryonic and iPS cells, however, AFPS cells do not form teratomas, and if preserved for self-use, avoid the problems of rejection. The cells

could be obtained either from amniocentesis or chorionic villous sampling in the developing fetus, or from the placenta at the time of birth. They could be preserved for self-use and used without rejection, or they could be banked. A bank of 100 000 specimens could potentially supply 99% of the US population with a perfect genetic match for transplantation. Such a bank may be easier to create than with other cell sources, since there are approximately 4.5 million births per year in the United States.

Since the discovery of the AFPS cells, other groups have published on the potential of the cells to differentiate to other lineages such as cartilage[71] and lung.[72] Perin and colleagues investigated if AFPS could differentiate into renal structures by labeling human cells and injecting them into murine embryologic renal tissues. The anlagen were cultured *in vitro* using a novel method to allow embryologic survival through 10 days in culture. The AFPS integrated in renal structures including C and S bodies. Reverse transcriptase polymerase chain reactions (rtPCR) demonstrated zona occludens-1, claudin, and glial-derived neurotrophic factor, all of which are early markers for renal differentiation and were not seen in AFPS not injected into the anlagen.[73] This study demonstrates that AFPS can differentiate into renal lineage when cultured *in vitro* with renal precursors. While this is promising, further *in vivo* studies and functional assays are required prior to clinical applications with AFPS.

5.540.5.4. Adult Stem Cells

Adult stem cells, especially hematopoietic stem cells, are the best understood cell type in stem cell biology.[74] However, adult stem cell research remains an area of intense study, as their potential for therapy may be applicable to a myriad of degenerative disorders. Within the past decade, adult stem cell populations have been found in many adult tissues other than the bone marrow and the gastrointestinal tract, including the brain,[75,76] skin,[77] and muscle.[78] Many other types of adult stem cells have been identified in organs all over the body and are thought to serve as the primary repair entities for their corresponding organs.[79] The discovery of such tissue-specific progenitors has opened up new avenues for research.

A notable exception to the tissue specificity of adult stem cells is the MSC, also known as the multipotent adult progenitor cell. This cell type is derived from bone marrow stroma.[80,81] Such cells can differentiate *in vitro* into numerous tissue types[82,83] and can also differentiate developmentally if injected into a blastocyst. Multipotent adult progenitor cells can develop into a variety of tissues, including neuronal,[84] adipose,[78] muscle,[78,85] liver,[86,87] lungs,[88] spleen,[89] and gut tissue,[81] but notably not bone marrow or gonads. There has been considerable research into the identification, characterization, and expansion of the renal multipotent progenitor cell.

5.540.6. *In Situ* Kidney Development

An attractive potential renal regenerative therapy would be a combination of several of the individual therapies discussed earlier. The ability to create a segment of functional kidney tissue *in vitro* and subsequently implant this into a patient with renal dysfunction would obviate the need for lifelong dialysis and for obtaining a suitable donor kidney. In addition, if such a construct could be seeded with autologous cells derived from the patient to be treated, there would be no need for immunosuppression. Previous studies have demonstrated that a bladder scaffold seeded with autologous cells can be transplanted *in vivo* with excellent results, even after 5 years of follow-up. While the kidney represents a more ambitious endeavor in terms of its more complex architecture and function, the promising results of the bladder regeneration study open the door for clinical use of this type of therapy for renal dysfunction.

One potential method for *in vitro* growth of kidney tissue involves the use of both biomaterial scaffolds and kidney cells. Heterogeneous cell populations could be seeded on an implantable biomaterial, and this construct could be cultured *in vitro* for some time to allow for cellular attachment and growth. Autologous cell populations for this purpose could be obtained with a renal biopsy. Atala *et al.* demonstrated the feasibility of this approach by plating donor rabbit kidney cells, including cells from the distal tubules, glomeruli, and proximal tubules *in vitro*. After expansion, these cells were seeded onto biodegradable polyglycolic acid (PGA) scaffolds and implanted subcutaneously into athymic mice. The implants consisted of either individual cell types or a mixture of all the three. When examined histologically, progressive formation and organization of the nephron segments within the polymer fibers was noted. Additionally, BrdU incorporation into the renal cell DNA was confirmed. However, it was unclear if the tubular structures found on the scaffolds formed *de novo* from the implanted cells or if they merely represented fragments of donor tubules which had survived the original dissociation and culture process intact. To further investigate this, mouse renal cells were harvested and expanded in culture. Subsequently, single isolated cells were seeded on biodegradable polymers and implanted in immune-competent synergic hosts. In this study, it was shown that renal epithelial cells reconstituted tubular structures *in vivo*. The analyses of the retrieved implants demonstrated that renal epithelial cells first organized into a structure with a solid center. Subsequently, canalization into a hollow tube could be seen at 2 weeks. Histologic examination with nephron-specific lactins revealed successful reconstitution of proximal tubules, distal tubules, loops of Henle collecting tubules, and collecting ducts. These results clearly showed that single-cell suspensions grown *in vitro* are capable of reconstituting into tubule structures. The tubules contained homogenous cell types within each tubule.

Yoo *et al.* evaluated murine renal cells grown *in vitro*.[90,91] They harvested the cells, expanded them in culture, and seeded them onto a tubular device constructed from polycarbonate. At one end of the tubular device was a silastic catheter, which terminated into a reservoir. The device was subcutaneously implanted into athymic mice. The implanted device demonstrated extensive vascularization in addition to glomerular formation and highly organized tubular architecture. Immunohistochemistry staining for alkaline phosphatase showed positivity in the proximal tubule-like structures. Osteopontin, which is secreted by the proximal and distal tubular cells and the cells of the thin loop of Henle, was found on immunocytochemical staining of the tubular sections. The extracellular

matrix of the newly formed tubules stained uniformly positive for fibronectin. The fluid collected from the reservoir was yellow and the uric acid concentration was 66 mg dl^{-1} (as compared to 2 mg dl^{-1} in plasma). The creatinine concentration of the fluid (27.91 ± 7.56 mg dl^{-1}) was 8.2 times higher than that found in the serum (4.49 ± 0.08 mg dl^{-1}). This demonstrates that single cells can form multicellular structures, become organized into functional renal units, and are capable of unidirectional excretion of solutes through a urine-like fluid.

Ross and colleagues have used a combination of renal scaffold and ES cells to induce *in vitro* formation of a kidney. Using a series of detergents, and following an intricate protocol to preserve physiologic pressure, they successfully decellularized a rat kidney as evidenced by histologic examination. At this point, ES cells from a GFP-labeled mouse were injected through either the ureter or renal artery, and the tissue was cultured *in vitro*. Without the use of differentiation agents, immunostains and rtPCR demonstrated Pax-2 (a critical factor in branching morphogenesis and is expressed in both the ureteric bud and induced metanephric mesenchyme) and Ksp-cadherin (an adhesion protein expressed by distal nephron tubular cells at later developmental stages).[92] Here, the decellularized extracellular matrix induces the differentiation of ESC and raises the possibility of using decellularized porcine kidneys, which have similar architecture to human kidneys, as a future clinical intervention.

To determine whether renal tissue could be formed using an alternative cell source, SCNT was performed to generate histocompatible tissues, and the feasibility of engineering syngeneic renal tissues *in vivo* using these cloned cells was investigated.[48] Renal cells from the cloned embryos were harvested, expanded *in vitro*, and seeded onto three-dimensional renal devices (Figure 4). The devices were implanted into the back of the same steer from which the cells were cloned and were retrieved 12 weeks later. This process produced functioning renal units. Urine production and viability were demonstrated after transplantation back into the nuclear donor animal. Chemical analysis suggested unidirectional secretion and concentration of urea nitrogen and creatinine. Microscopic analysis revealed formation of organized glomeruli and tubular structures. Immunohistochemical and RT-PCR analysis confirmed the expression of renal mRNA and proteins. These studies demonstrated that cells derived from nuclear transfer can be successfully harvested, expanded in culture, and transplanted *in vivo* with the use of biodegradable scaffolds on which the single suspended cells can organize into tissue structures that are genetically identical to that of the host. These studies were the first demonstration of the use of therapeutic cloning for regeneration of tissues *in vivo*.

5.540.7. Renal Tubular Assist Devices

Development of a renal tubular assist device (RAD) to attenuate hemofiltration has been another avenue of cellular therapy investigated. Humes and colleagues have designed an extracorporeal device, which works in concert with hemofiltration units. Here, proximal tubule cells are seeded in confluent monolayers in a multifiber bioreactor. When used for dialysis, blood is pumped through a conventional hemofilter. Following processing through this filter, the ultrafiltrate is again processed through the RAD. The filtered blood exiting the hemofilter enters the RAD through the extracapillary space port and then disperses throughout the fibers of the device. The hollow fiber membrane protects the cells lining the inner surface from immune-related attacks. The purpose of these devices is to supplement hemofiltration and attempt to replace the physiologic functions of the kidney that are not addressed with hemofiltration. Initial studies using porcine tubular cells demonstrated significantly improved ammonia excretion and elevated plasma levels of 1,25-dihydroxyvitamin D3 in dogs with acute uremia. Cells on the RAD demonstrated replicative capacity as they returned to baseline function 2 weeks following usage.[93]

A phase I/II trial of the RAD was performed in 10 ICU patients with acute renal failure associated with acute tubular necrosis. Proximal tubule cells for the RAD were derived from

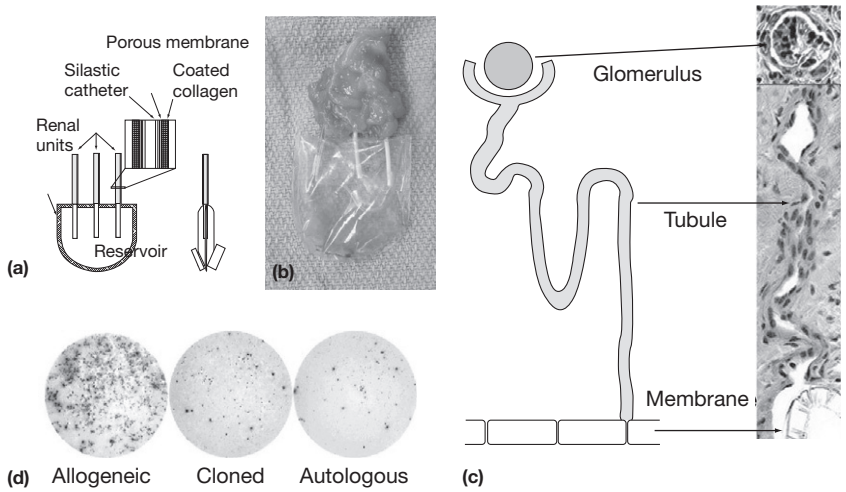

Figure 4 Production of kidney tissue by therapeutic cloning and regenerative medicine. (a) Illustration of the tissue-engineered renal unit. (b) Renal unit seeded with cloned cells, 3 months after implantation, showing the accumulation of urine-like fluid. (c) There was a clear unidirectional continuity between the mature glomeruli, their tubules, and the polycarbonate membrane. (d) ELISPOT analyses of the frequencies of T cells that secrete IFN-γ after primary and secondary stimulation with allogeneic renal cells, cloned renal cells, or nuclear donor fibroblasts.

the human kidney tissue that was intended for transplant but discarded due to anatomic or fibrotic concerns. These patients had significant other comorbidities with multiple concomitant illness and multiple organ failures. The most common adverse effects were hypovolemia, thrombocytopenia, and hyperglycemia. The RAD did appear to have an immunomodulatory effect, as there was a significant decline in IL-6, IL-10, and G-CSF. Despite high predicted 30-day mortality rates, 60% of patients survived for 30 days.[94] It is difficult to interpret efficacy from a phase I/II trial, so the results from a phase III, multicenter, randomized, controlled, open-label trial were reported recently. Here, 58 patients were randomized into two groups: 40 patients were treated with the RAD and hemofiltration versus 18 patients with hemofiltration alone. With a median treatment duration of 35.9 h, there was only one malfunction of an RAD. Patients receiving RAD renal supplementation were found to have an earlier recovery of renal function, although this was not statistically significant. Survival was significantly improved at 180 days in patients with RAD support. Using subgroup analysis, higher survival rates were noted for RAD patients for all sets of organ failure.[95] It is important to recognize that the patients enrolled in these studies are critically ill patients in the intensive care unit. Despite this, a substantive effect on survival and renal recovery was noted, paving the way for future investigations.

5.540.8. Summary and Conclusions

Renal regenerative therapy is an exceedingly complex endeavor due to the multiple functions of the kidney. However, as there is a shortage of donor kidneys and more patients progressing to ESRD, there is true hope for a significant clinical application. Through the use of methods described here, the future for renal regenerative therapy has great potential for clinical impact in the future.

Acknowledgment

The authors thank Dr. Jennifer L. Olson for editorial assistance with this chapter.

References

1. Guild, W. R.; Harrison, J. H.; Merrill, J. P.; Murray, J. *Trans. Am. Clin. Climatol. Assoc.* **1955**, *67*, 167–173.
2. Al-Awqati, Q.; Oliver, J. A. *Kidney Int.* **2002**, *61*, 387–395.
3. Woolf, A. S.; Palmer, S. J.; Snow, M. L.; Fine, L. G. *Kidney Int.* **1990**, *38*, 991–997.
4. Abrahamson, D. R.; St John, P. L.; Pillion, D. J.; Tucker, D. C. *Lab. Invest.* **1991**, *64*, 629–639.
5. Rogers, S. A.; Lowell, J. A.; Hammerman, N. A.; Hammerman, M. R. *Kidney Int.* **1998**, *54*, 27–37.
6. Rogers, S. A.; Hammerman, M. R. *Organogenesis* **2004**, *1*, 22–25.
7. Marshall, D.; Clancy, M.; Bottomley, M.; Symonds, K.; Brenchley, P. E.; Bravery, C. A. *Transplant. Proc.* **2005**, *37*, 194–197.
8. Bussolati, B.; Bruno, S.; Grange, C.; *et al. Am. J. Pathol.* **2005**, *166*, 545–555.
9. Gupta, S.; Verfaillie, C.; Chmielewski, D.; *et al. J. Am. Soc. Nephrol.* **2006**, *17*, 3028–3040.
10. Plotkin, M. D.; Goligorsky, M. S. *Am. J. Physiol. Renal Physiol.* **2006**, *291*, F902–F912.
11. Vogelmann, S. U.; Nelson, W. J.; Myers, B. D.; Lemley, K. V. *Am. J. Physiol. Renal Physiol.* **2003**, *285*, F40–F48.
12. Sagrinati, C.; Netti, G. S.; Mazzinghi, B.; *et al. J. Am. Soc. Nephrol.* **2006**, *17*, 2443–2456.
13. Ronconi, E.; Sagrinati, C.; Angelotti, M. L.; *et al. J. Am. Soc. Nephrol.* **2009**, *20*, 322–332.
14. Appel, D.; Kershaw, D. B.; Smeets, B.; *et al. J. Am. Soc. Nephrol.* **2009**, *20*, 333–343.
15. Aboushwareb, T.; Egydio, F.; Straker, L.; Gyabaah, K.; Atala, A.; Yoo, J. J. *World J. Urol.* **2008**, *26*, 295–300.
16. Bartholomew, A.; Patil, S.; MacKay, A.; *et al. Hum. Gene Ther.* **2001**, *12*, 1527–1541.
17. Han, H. J.; Sigurdson, W. J.; Nickerson, P. A.; Taub, M. *J. Cell Sci.* **2004**, *117*, 1821–1833.
18. Joraku, A.; Stern, K. A.; Atala, A.; Yoo, J. J. *Methods* **2009**, *47*, 129–133.
19. Kim, S. S.; Park, H. J.; Han, J.; *et al. Transplantation* **2007**, *83*, 1249–1258.
20. Martin, G. R. *Proc. Natl. Acad. Sci. USA* **1981**, *78*, 7634–7638.
21. Reubinoff, B. E.; Itsykson, P.; Turetsky, T.; *et al. Nat. Biotechnol.* **2001**, *19*, 1134–1140.
22. Schuldiner, M.; Eiges, R.; Eden, A.; *et al. Brain Res.* **2001**, *913*, 201–205.
23. Zhang, S. C.; Wernig, M.; Duncan, I. D.; Brustle, O.; Thomson, J. A. *Nat. Biotechnol.* **2001**, *19*, 1129–1133.
24. Kaufman, D. S.; Hanson, E. T.; Lewis, R. L.; Auerbach, R.; Thomson, J. A. *Proc. Natl. Acad. Sci. USA* **2001**, *98*, 10716–10721.
25. Kehat, I.; Kenyagin-Karsenti, D.; Snir, M.; *et al. J. Clin. Investig.* **2001**, *108*, 407–414.
26. Levenberg, S.; Golub, J. S.; Amit, M.; Itskovitz-Eldor, J.; Langer, R. *Proc. Natl. Acad. Sci. USA* **2002**, *99*, 4391–4396.
27. Assady, S.; Maor, G.; Amit, M.; Itskovitz-Eldor, J.; Skorecki, K. L.; Tzukerman, M. *Diabetes* **2001**, *50*, 1691–1697.
28. Itskovitz-Eldor, J.; Schuldiner, M.; Karsenti, D.; *et al. Mol. Med.* **2000**, *6*, 88–95.
29. Reubinoff, B. E.; Pera, M. F.; Fong, C. Y.; Trounson, A.; Bongso, A. *Nat. Biotechnol.* **2000**, *18*, 399–404.
30. Thomson, J. A.; Itskovitz-Eldor, J.; Shapiro, S. S.; *et al. Science* **1998**, *282*, 1145–1147.
31. Morizane, R.; Monkawa, T.; Itoh, H. *Biochem. Biophys. Res. Commun.* **2009**, *390*, 1334–1339.
32. Schuldiner, M.; Yanuka, O.; Itskovitz-Eldor, J.; Melton, D. A.; Benvenisty, N. *Proc. Natl. Acad. Sci. USA* **2000**, *97*, 11307–11312.
33. Kim, D.; Dressler, G. R. *J. Am. Soc. Nephrol.* **2005**, *16*, 3527–3534.
34. Vigneau, C.; Polgar, K.; Striker, G.; *et al. J. Am. Soc. Nephrol.* **2007**, *18*, 1709–1720.
35. Chung, Y.; Klimanskaya, I.; Becker, S.; *et al. Nature* **2006**, *439*, 216–219.
36. Zhang, X.; Stojkovic, P.; Przyborski, S.; *et al. Stem Cells* **2006**, *24*, 2669–2676.
37. Geber, S.; Sampaio, M. *Hum. Reprod.* **1999**, *14*, 782–786.
38. Hardy, K. In *Preimplantation Embryo Development*; Bavister, B., Ed.; Springer: New York, 1993; pp 184–199.
39. Landry, D. W.; Zucker, H. A. *J. Clin. Invest.* **2004**, *114*, 1184–1186.
40. Martinez, F.; Rienzi, L.; Iacobelli, M.; *et al. Hum. Reprod.* **2002**, *17*, 1584–1590.
41. Wilmut, I.; Schnieke, A. E.; Mcwhir, J.; Kind, A. J.; Campbell, K. H. *Nature* **1997**, *385*, 810–813.
42. Brambrink, T.; Hochedlinger, K.; Bell, G.; Jaenisch, R. *Proc. Natl. Acad. Sci. USA* **2006**, *103*, 933–938.
43. Eggan, K.; Baldwin, K.; Tackett, M.; *et al. Nature* **2004**, *428*, 44–49.
44. Hochedlinger, K.; Jaenisch, R. *Nature* **2002**, *415*, 1035–1038.
45. Mizobe, Y.; Kurino, S.; Sata, Y.; Mori, H.; Yoshida, M.; Miyoshi, K. *Anim. Sci. J.* **2010**, *81*, 453–460.
46. Yang, B. Z.; Yang, C. Y.; Li, R. C.; *et al. Reprod. Domest. Anim.* **2009**.
47. Yang, C. Y.; Li, R. C.; Pang, C. Y.; *et al. Anim. Reprod. Sci.* **2010**, *121*, 78–83.
48. Lanza, R. P.; Chung, H. Y.; Yoo, J. J.; *et al. Nat. Biotechnol.* **2002**, *20*, 689–696.
49. Hwang, W. S.; Roh, S. I.; Lee, B. C.; *et al. Science* **2005**, *308*, 1777–1783.
50. Hwang, W. S.; Ryu, Y. J.; Park, J. H.; *et al. Science* **2004**, *303*, 1669–1674.
51. Simerly, C.; Dominko, T.; Navara, C.; *et al. Science* **2003**, *300*, 297.
52. Byrne, J.; Pedersen, D.; Clepper, L.; *et al. Nature* **2007**, *450*(7169), 497–502.
53. Mitalipov, S. *Hum. Reprod.* **2007**, *22*, 2232–2242.
54. Pan, D.; Zhang, L.; Zhou, Y.; *et al. Sci. China Life Sci.* **2010**, *53*, 517–523.
55. Hurlbut, W. B. *Perspect. Biol. Med.* **2005**, *48*, 211–228.
56. Meissner, A.; Jaenisch, R. *Nature* **2006**, *439*, 212–215.
57. Benahmed, F.; Gross, I.; Gaunt, S. J.; *et al. Gastroenterology* **2008**, *135*, 1238–1247.
58. Vauhkonen, M.; Vauhkonen, H.; Sipponen, P. *Scand. J. Gastroenterol.* **2008**, *43*, 915–921.

59. Takahashi, K.; Yamanaka, S. *Cell* **2006**, *126*, 663–676.
60. Wernig, M.; Meissner, A.; Foreman, R.; *et al*. *Nature* **2007**, *448*, 318–324.
61. Takahashi, K.; Tanabe, K.; Ohnuki, M.; *et al*. *Cell* **2007**, *131*, 861–872.
62. Yu, J.; Vodyanik, M. A.; Smuga-Otto, K.; *et al*. *Science* **2007**, *381*(5858), 1917–1920.
63. Honda, A.; Hirose, M.; Hatori, M.; *et al*. *J. Biol. Chem.* **2010**, *285*(41), 31362–31369.
64. Tomioka, I.; Maeda, T.; Shimada, H.; *et al*. *Genes Cells* **2010**, *15*(9), 959–969.
65. Roberts, R. M.; Telugu, B. P.; Ezashi, T. *Cell Cycle* **2009**, *8*, 3078–3081.
66. Polgar, K.; Adany, R.; Abel, G.; Kappelmayer, J.; Muszbek, L.; Papp, Z. *Am. J. Hum. Genet.* **1989**, *45*, 786–792.
67. Priest, R. E.; Marimuthu, K. M.; Priest, J. H. *Lab. Investig.* **1978**, *39*, 106–109.
68. In't Anker, P. S.; Scherjon, S. A.; Kleijburg-Van Der Keur, C.; *et al*. *Blood* **2003**, *102*, 1548–1549.
69. Tsai, M. S.; Lee, J. L.; Chang, Y. J.; Hwang, S. M. *Hum. Reprod.* **2004**, *19*, 1450–1456.
70. De Coppi, P.; Bartsch, G., Jr.; Siddiqui, M. M.; *et al*. *Nat. Biotechnol.* **2007**, *25*, 100–106.
71. Kolambkar, Y. M.; Peister, A.; Soker, S.; Atala, A.; Guldberg, R. E. *J. Mol. Histol.* **2007**, *38*, 405–413.
72. Warburton, D.; Perin, L.; Defilippo, R.; Bellusci, S.; Shi, W.; Driscoll, B. *Proc. Am. Thorac. Soc.* **2008**, *5*, 703–706.
73. Perin, L.; Giuliani, S.; Jin, D.; *et al*. *Cell Prolif.* **2007**, *40*, 936–948.
74. Ballas, C. B.; Zielske, S. P.; Gerson, S. L. *J. Cell. Biochem.* **2002**, *85*(Suppl. 38), 20–28.
75. Jiao, J.; Chen, D. F. *Stem Cells* **2008**, *26*, 1221–1230.
76. Taupin, P. *Recent Pat. CNS Drug Discov.* **2006**, *1*, 299–303.
77. Jensen, U. B.; Yan, X.; Triel, C.; Woo, S. H.; Christensen, R.; Owens, D. M. *J. Cell Sci.* **2008**, *121*, 609–617.
78. Crisan, M.; Casteilla, L.; Lehr, L.; *et al*. *Stem Cells* **2008**, *26*, 2425–2433.
79. Weiner, L. P. *Meth. Mol. Biol.* **2008**, *438*, 3–8.
80. Devine, S. M. *J. Cell. Biochem. Suppl.* **2002**, *38*, 73–79.
81. Jiang, Y.; Jahagirdar, B. N.; Reinhardt, R. L.; *et al*. *Nature* **2002**, *418*, 41–49.
82. Caplan, A. I. *J. Cell. Physiol.* **2007**, *213*, 341–347.
83. Da Silva Meirelles, L.; Caplan, A. I.; Nardi, N. B. *Stem Cells* **2008**, *26*, 2287–2299.
84. Duan, X.; Chang, J. H.; Ge, S.; *et al*. *Cell* **2007**, *130*, 1146–1158.
85. Luttun, A.; Ross, J. J.; Verfaillie, C.; Aranguren, X.; Prosper, F. In *Current Protocols in Immunology*, John Wiley and Sons: Hoboken, NJ, 2006.
86. Ikeda, E.; Yagi, K.; Kojima, M.; *et al*. *Differentiation* **2008**, *76*, 495–505.
87. Mimeault, M.; Batra, S. K. *Stem Cell Rev.* **2008**, *4*, 27–49.
88. Nolen-Walston, R. D.; Kim, C. F.; Mazan, M. R.; *et al*. *Am. J. Physiol. Lung Cell. Mol. Physiol.* **2008**, *294*, L1158–L1165.
89. In't Anker, P. S.; Noort, W. A.; Scherjon, S. A.; *et al*. *Haematologica* **2003**, *88*, 845–852.
90. Atala, A.; Schlussel, R. N.; Retik, A. B. *J. Urol.* **1995**, *153*, 4.
91. Yoo, J.; Ashkar, S.; Atala, A. *Pediatrics* **1996**, *98S*, 605.
92. Ross, E. A.; Williams, M. J.; Hamazaki, T.; *et al*. *J. Am. Soc. Nephrol.* **2009**, *20*(11), 2338–2347.
93. Humes, H. D.; Buffington, D. A.; MacKay, S. M.; Funke, A. J.; Weitzel, W. F. *Nat. Biotechnol.* **1999**, *17*, 451–455.
94. Humes, H. D.; Weitzel, W. F.; Bartlett, R. H.; *et al*. *Kidney Int.* **2004**, *66*, 1578–1588.
95. Tumlin, J.; Wali, R.; Williams, W.; *et al*. *J. Am. Soc. Nephrol.* **2008**, *19*, 1034–1040.

5.541. Liver Tissue Engineering

B E Uygun and K Uygun, Harvard Medical School and Shriners Hospitals for Children in Boston, Boston, MA, USA
M L Yarmush, Harvard Medical School and Shriners Hospitals for Children in Boston, Boston, MA, USA; Rutgers University, Piscataway, NJ, USA

© 2011 Elsevier Ltd. All rights reserved.

5.541.1.	**Introduction**	575
5.541.1.1.	Liver Structure and Function	575
5.541.1.2.	Liver Failure	576
5.541.1.3.	Strategies for Replacement of Hepatic Function	577
5.541.2.	**Extracorporeal Liver Support Devices**	577
5.541.2.1.	Bioreactor Design	577
5.541.2.2.	Cell Source	578
5.541.3.	**Implantable Hepatic Support Systems**	580
5.541.3.1.	Direct Cell Transplantation	580
5.541.3.2.	Microcarrier and Encapsulated Systems	581
5.541.3.3.	Polymer Scaffolds	581
5.541.3.4.	Microfabrication for Liver Tissue	581
5.541.3.5.	Whole Liver Tissue Engineering	582
5.541.4.	**Conclusions and Future Directions**	583
References		583

Glossary

Acute liver failure Rapid development of severe complications after the first signs of liver disease, which indicates that the liver has sustained severe damage.
Bioartificial liver (BAL) device Artificial extracorporeal device designed to provide temporary support for liver functions during acute liver failure.
Chronic liver failure Diseased state of liver that involves progressive destruction of the liver parenchyma leading to fibrosis and cirrhosis.
Orthotopic liver transplantation Replacement of a diseased liver with a healthy allogenic organ.

Abbreviations

BAL	Bioartificial liver
DLM	Decellularized liver matrix
ECM	Extracellular matrix
ESC	Embryonic stem cell
hESC	Human embryonic stem cell
iPS cell	Induced pluripotent stem cell

5.541.1. Introduction

5.541.1.1. Liver Structure and Function

The liver is the largest solid organ of the body, constituting ~2–5% of the adult body weight. It is a dark reddish brown organ shaped like a cone. It lies below the diaphragm on top of the stomach in the thoracic region of the abdomen. It has two main and two accessory lobes conforming to peritoneal attachments and surface fissures. According to the functional vascular anatomy of the organ, it is divided into eight sectors and segments with independent afferent and efferent blood supply and biliary channels within collateral circulation within the segments. Structurally and histologically, the liver can be divided into four tissue systems[1]: intrahepatic vascular system, stroma, sinusoidal cells, and hepatocytes.

The intrahepatic vascular system comprises the hepatic artery, portal vein, hepatic vein, and biliary system. Because of its location in between the digestive tract and the rest of the body, the liver is provided with dual blood supply from portal vein and hepatic artery.[2,3] The portal blood passes through the periportal limiting plate of hepatocytes and enters into the sinusoids through venous inlets. Arterial blood in terminal branches of the arteries also flows into the sinusoids and gets mixed in with the portal blood. The outflow of the sinusoidal blood (75% portal, 25% arterial) is into the central hepatic vein. The hepatic vein emerges from the central hepatic vein within each lobule. Hepatic veins collected from different segments of the liver drain into the inferior vena cava at the posterior surface of the liver below the diaphragm.[4,5] The biliary system emerges from the biliary canaliculus, which is a bile capillary formed by intercellular space bound by two adjacent hepatocytes. The

canaliculi are interconnected and form an extensive polygonal network. The network of canaliculi reaches an ampulla-like extension called the Hering's canal, which is considered as the end of canaliculi and the beginning of the ductules. The ductules are followed by bile ducts, which gradually increase in size and collect to form the common bile duct exiting the liver.[6]

The stroma of the liver is differentiated as four different structures: liver capsule, perivascular connective tissue, Glisson's portal track, and reticular network. The liver extracellular matrix (ECM) is composed of collagens type I and III (large fibrils), IV (net structure), V and VI (small fibrils), glycoproteins (laminin and fibronectin), elastins, glycosaminoglycans and proteoglycans.[7] The capsule of the liver has an endothelial cell coating and a network of collagen and elastin fibers. The capsule has connections to the blood and lymph vessels as well as the bile duct. It is also closely connected to the liver parenchyma. The perivascular connective tissue, also called the Glisson's capsule, starts at the portal vein and extends into the parenchyma surrounding the interlobular vessels. The reticular network consists of lattice fibers, which lie on the hepatic cell plates and provide mechanical support to the sinusoids. In the portal tract, the perivascular connective tissue terminates in the connective tissue covering of the perivascular fibrous capsule. The continuous line of hepatocytes bordering the portal tract is called the limiting plate.

One of the cellular components of the liver are the sinusoidal cells (also called the nonparenchymal cells). These cells include endothelial cells, Kupffer cells, Ito cells, and Pit cells. Although they take up a smaller portion of the liver volume (6.5%), they constitute 30–40% of the total cell number. Endothelial cells form a large portion of the sinusoidal cells and they form the lining of the sinusoids. They are interspersed with pores that control filtering of components from the blood and regulate exchange of fluid and compounds between the sinusoidal blood and the hepatocytes. Endothelial cells also form and secrete cytokines and ECM as well as vasoactive substances and growth factors. Kupffer cells, also considered as liver resident macrophages, are found randomly distributed in the sinusendothelium. Their main function is phagocytosis. Other functions include pinocytosis, secretion of signaling molecules such as cytokines, and clearance of toxins.[8–11] Ito cells are also called fat-storing cells or stellate cells and they lie in the space of Disse. They are involved in regulation of the sinusoid width, and they regulate and secrete ECM. Pit cells are resident lymphocytes that are natural killer cells and they destroy tumor cells and foreign cells, as well as necrosed cells.

Hepatocytes are the parenchymal cells of the liver that are responsible for the functions of the liver. They are polygonal epithelial cells that are highly polarized. About 37% of the cellular surface area is sinusoidal surface and performs absorptive and secretory functions. About 12% of the cellular membrane faces the bile canaliculi and this area is the secretory pole of the cells. The remaining 50% of the cellular membrane is the smooth intercellular fissure, that is connected to the space of Disse. The space is sealed from bile canaliculi by tight junctions only allowing the exchange of water and cations. The rest of the junctions are intermediate junctions and desmosomes between adjacent hepatocytes. They contain gap junctions that facilitate intercellular exchange.

There are several descriptions of a functional liver unit due to the lack of defined appearance of structural lobules in a human liver. A classical central vein lobule resembles a hexagon with portal tracts in the corners. It consists of radially arranged plates of 15–20 hepatocytes between the central vein and the limiting plate. The hollow spaces between the liver cells plates form a network of sinusoids and space of Disse. In the central vein lobule, blood flows from the branches of hepatic artery and hepatic portal vein through liver sinusoids and it flows out to the central vein.

A portal vein lobule also resembles a hexagon, where the periportal region is in the center and the central veins form the limiting points. Blood flow is from the center to the periphery, and the bile flow is from the periphery to the center.

Liver acinus is defined as the functional unit of the liver determined by the microcirculatory architecture. At the center of the acinar unit, there is the portal vascular bundle with the terminal branches of the hepatic artery and portal vein. The central vein is at the periphery of the acinus towards which the sinuoids extends radially and drains off the blood. An acinus is also a secretory unit for the transport of the bile. Three or more acini form a complex acinus and constitute different metabolic zones arranged radially around the vessels. Each zone differs in the contents of their blood supply such that zone 1 hepatocytes, closest to the vessels, are exposed to the highest oxygen and nutrient supply. The toxic compound content of the blood in zone 1 is also the highest and damaging to the cells. Zone 2 has an intermediate blood supply and zone 3 being nearest to the central vein has the least oxygen and nutrient supply. The zonal variation of the blood supply brings about the zonal heterogeneity of hepatocyte metabolic functions.[12–14]

The liver performs many metabolic functions that are essential for the maintenance of the health of the human body. Due to its location between the digestive tract and the rest of the body, its two blood supply channels import a large variety of endobiotics and xenobiotics, including nutrients and toxic substances from the digestive system. The major role of liver is the regulation of metabolism at molecular, cellular, and organ level. This brings about a complex set of functions that are carried out by the liver. There are about 70 different functions made possible by approximately 500 reactions that take place in hepatocytes.[1]

The major metabolic functions of the liver can be categorized in 12 different areas. These include bilirubin metabolism, porphyrin metabolism, uptake of amino acids, carbohydrates, lipids, and vitamins and their subsequent storage, metabolic conversion, and release into the blood and bile. Part of its metabolic regulation activity comes from hormone production. Alcohol degradation, acid base balance, and trace element metabolism form another group of functions. Finally, biotransformation and detoxification of substances that enter the body by the liver is another essential liver function.

5.541.1.2. Liver Failure

The structural and functional integrity of the liver is vital to the health of the human body. Even though a healthy liver may regenerate from one-third of its volume, any major insult to the organ may result in liver failure that must be corrected

immediately. It is usually associated with increased levels of endogenous substances such as bilirubin, ammonia, lactate, glutamine, aromatic amino acids, free fatty acids, phenol, mercaptans, benzodiazepines, and proinflammatory cytokines.[1] The overload of toxins saturates detoxification pathways in the liver; which subsequently leads to accumulation of new toxins and progressively leads to liver failure.[15] Furthermore, accumulation of toxins may impair liver function due to hepatic necrosis and apoptosis. The liver failure may be acute or chronic, which may be due to several reasons. Hepatic encephalopathy, coagulopathy, jaundice, sepsis, kidney failure, and cholastasis are major complications of liver failure. In acute liver failure, the liver function decreases abruptly for which the most common reasons are intoxications (e.g., acetaminophen), viral infections, and hepatic ischemia.[16] Chronic liver failure occurs in the context of cirrhosis which happens due to chronic viral infections of the liver, excessive alcohol intake, or hereditary or autoimmune liver disorders. In the United States alone, about 30 million people undergo a liver disorder, with roughly 27 000 deaths due to liver disease being registered annually. Metabolic disorders of the liver such as nonalcoholic steatosis due to obesity will likely increase this number in the future.

5.541.1.3. Strategies for Replacement of Hepatic Function

Currently, the only definitive treatment for severe hepatic failure is orthotopic transplantation. However, a critical shortage of organs causes a growing deficit of ~4000 livers per year.[17] Extracorporeal liver support systems are intended for the support of liver functions during liver failure until a suitable donor is found. However, they are still in the experimental stage and have not yet made it to the bedside. Hepatocyte transplantation is an alternative way to treat patients with liver diseases[18–20] and years of laboratory and clinical studies have demonstrated its efficacy.[21–24] However, limited cell supply and minimal engraftment efficiency have traditionally limited this approach.[18,25,26] Finally, tissue engineering approaches offer tools to create implantable tissue systems, which is another alternative to organ transplantation. Each of these approaches will be discussed further in the text.

5.541.2. Extracorporeal Liver Support Devices

Extracorporeal liver support devices are intended for use to bridge liver failure patients for transplants and provide hepatic support until the liver recovers from an acute liver failure.[27] It can provide artificial or bioartificial support depending on whether or not cells are included in the design of the device. An artificial liver support device aims to replace the detoxification functions of the liver by using membrane separation techniques that involve adsorption by charcoal, anion, or cation exchange resins. The separation selectively removes toxins and regenerates the dialysate. Such devices that have been tested clinically include the liver dialysis device,[28,29] Molecular Adsorbent Recirculating System (MARS),[30,31] and The Prometheus.[32,33] However, these devices are still considered experimental because their efficacy has not been demonstrated in large clinical trials.[34]

A bioartificial liver (BAL) device aims to replace not only the detoxification functions but also the synthetic functions of the liver by incorporating cells into the design of the device. The device consists of a housing unit called the bioreactor where the cells are cultured. The two important factors that determine the efficacy of the device include the bioreactor design and the source of the cells used in the system. These two factors will be discussed in detail next.

5.541.2.1. Bioreactor Design

The bioreactor design in a BAL device is an important factor as it directly affects the function of the cells cultured in the BAL.[35,36] (see **Chapter 5.501, Scaffolds: Flow Perfusion Bioreactor Design**.) The design parameters for an ideal bioreactor include reduction of mass transfer resistances and elimination of substrate limitations so that the device can function at maximum efficiency and minimize the dead volume within the device, thereby reducing the effects of plasma dilution in the patient.[37] The general operation of a BAL device is such that hepatocytes are seeded in the bioreactor and the patient's blood or plasma is circulated through the device. The ideal bioreactor design should maximize mass transfer to the hepatocytes hence maximizing the delivery of oxygen, nutrients, and toxins from patient's blood to the hepatocytes. The treated blood or plasma is then returned to the patient. This task requires large surface area for mass transfer as well as uniform hepatocyte and flow distribution. Various design configurations have been used to achieve these goals.

Most devices tested clinically utilize hollow fiber cartridges in which the cells are loaded inside the cartridge and the patient's plasma or blood is circulated in the lumen.[38–40] Due to the large diameter of fibers used in these designs as well as the resistance to mass transport through the fibers, hollow fiber bioreactor design is associated with issues related to substrate limitations.[41–45] Hepatocytes are highly metabolically active cells with very high demand for oxygen. The design limitations described above for hollow fiber bioreactors necessitates the enhancement of oxygen delivery to the cells for survival and optimal function. Earliest attempts to enhance oxygen delivery to the cells involved incorporating hollow fibers as conduits for oxygenation that were shown to help hepatocytes express differentiated function over several weeks.[46–49] Later studies focused on increasing the oxygen delivery to the cells through the use of oxygen carriers in the perfusate such as red blood cells[50] or perfluorocarbons.[51,52]

Another bioreactor design in BAL devices is based on flat surface geometry in which the hepatocytes are attached on a flat surface. In such a design, it is easier to control the internal flow distribution and to adequately perfuse and oxygenate the cells. However, one problem with such a design is achieving a sufficient concentration of cells without increasing the dead volume in the bioreactor beyond what is physiologically possible. In a flat plate bioreactor, the chamber volume is directly proportional to the channel height, and decreasing the channel height to decrease the volume increases the shear stress exerted by the flow on the hepatocytes. In an attempt to adequately oxygenate pig hepatocytes and protect the cells from shear stress in a flat plate bioreactor, de Bartolo and coworkers cultured liver cells between two gas-permeable membranes

and showed that the cells maintained differentiated functions for 18 days under flow conditions.[53,54] A comparison of a radial flow flat plate design to a hollow fiber bioreactor revealed that cells achieved polarity faster and expressed higher hepatic functions in the radial flow flat plate bioreactor due to the maximal contact of hepatocytes with the fresh perfusate in the radial flow configuration. The radial flow design also permits scale up without sacrificing the survival and the function of the cells.[55]

Using microfabrication techniques, we developed a microchannel flat plate bioreactor with an internal gas permeable membrane through which oxygen is supplied (**Figure 1**).[56] The oxygen distribution was found to be sufficient to maintain high hepatocyte survival, and albumin and urea functions for 4 days of perfusion.[57–59] In addition, such a BAL device with an internal membrane oxygenator was shown to rescue animals undergoing fulminant hepatic failure induced by D-galactosamine.[60] Further improvement to this design was made by incorporating microgrooves on the substrate plate. Hepatocytes were seeded in the microgrooves to protect them from detrimental shear stress (**Figure 2**). With the microgroove design, the cell viability was much higher resulting in a more stable production of albumin and urea over a 4-day culture period when compared to the flat substrate bioreactors.[61] In order to increase the cellular capacity of the bioreactor without introducing oxygen deprivation, stacked microgrooved plates in a radial configuration were used in later studies.[62]

5.541.2.2. Cell Source

The cell mass required to support an animal model of hepatic failure has not been systematically determined. Prior studies have shown significant improvements in various parameters using as low as 2–3% of the normal liver mass of the animal.[54,63] Devices that have undergone clinical testing have used 6×10^9–1×10^{11} porcine hepatocytes[47,48,64] or 4×10^{10} C3A cells.[65] Recently, in a pig model of hepatic failure, a BAL containing as few as 6×10^8 pig hepatocytes (about 3–5% of the liver mass) significantly improved survival.[66]

Clinical improvements have also been seen in hepatocyte transplantation studies using less than 10% of the host's liver mass. Intrasplenic transplantation of 2.5×10^7 allogeneic rat hepatocytes (~5% of the rat liver mass) prolonged the survival and improved the blood chemistry of anhepatic rats.[67] In another study using reversibly transformed human hepatocytes, 5×10^7 cells were injected intrasplenically into 90% hepatectomized rats.[68] In a recent study on humans with acute liver failure, intrasplenic and intraarterial injections of human hepatocytes (ranging from 10^9 to 4×10^{10} per patient, i.e., 1–10% of the total liver mass) transiently improved blood chemistry parameters and brain function after a lag time of about 48 h, but did not improve survival.[69] The lag time before any benefit is observed may reflect the time required for the engraftment of the cells in the host liver. Better survival of the injected cells may be possible if they were seeded in prevascularized polymeric scaffolds.[70] The relatively low number of hepatocytes needed

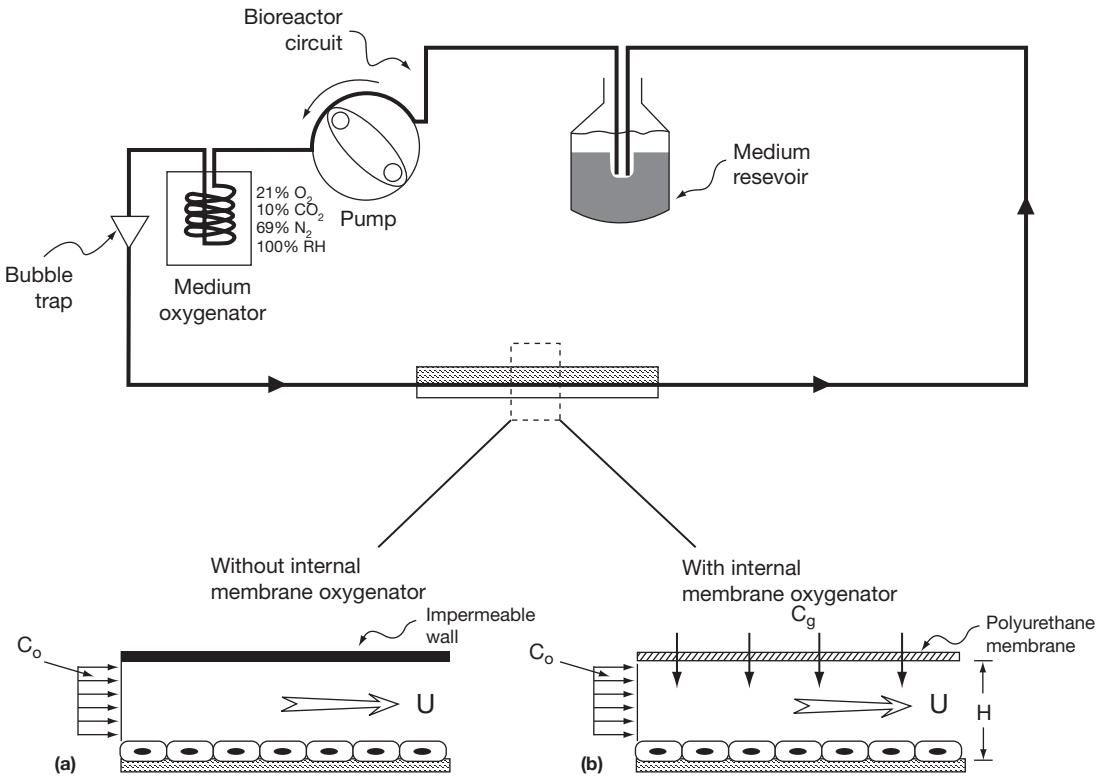

Figure 1 Schematic diagram of the bioartificial liver device for improved oxygen delivery. Flow circuit perfusion system and the bioreactors (a) with and (b) without internal membrane oxygenator. Reproduced from Tilles, A. W.; Baskaran, H.; Roy, P.; Yarmush, M. L.; Toner, M. *Biotechnol. Bioeng.* **2001**, *73*, 379–389, with permission from Wiley.

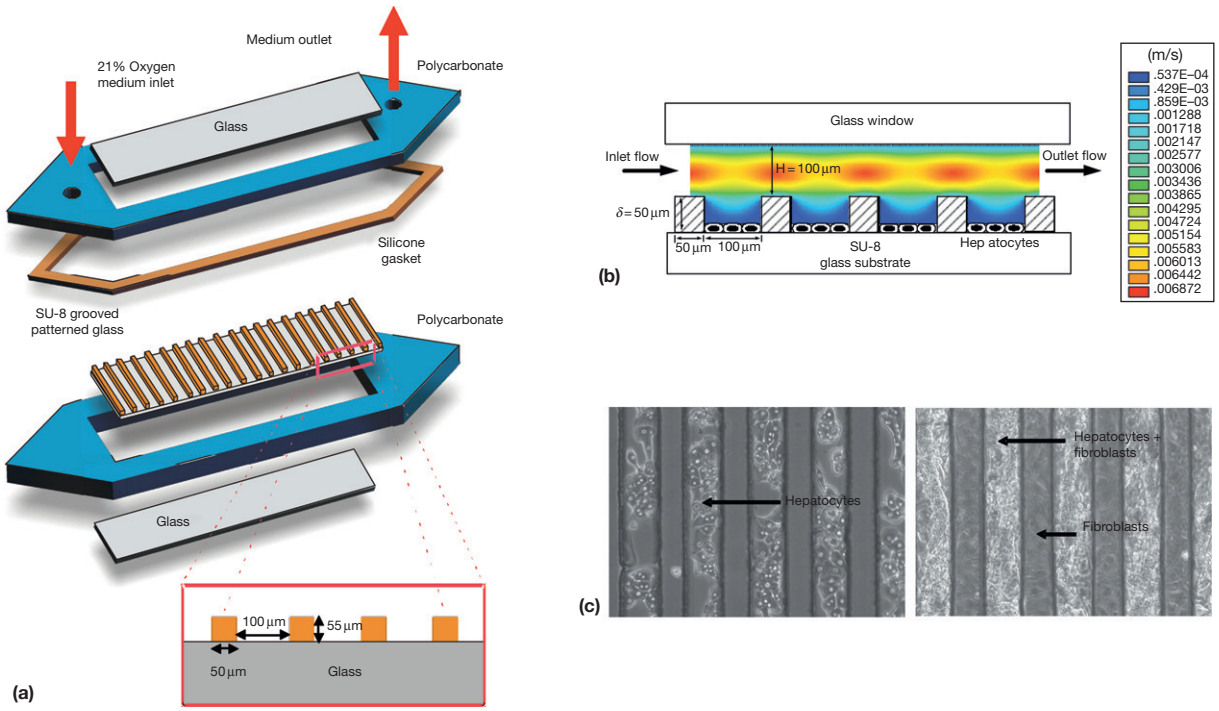

Figure 2 Bioartificial liver device designed for minimal shear stress. (a) Schematic representation of bioreactor with microgrooved glass substrate. (b) Contour plot of velocity vector field in channel of the microgrooved-substrate bioreactor using finite element analysis modeling for volumetric flow rate set at 0.7 ml min^{-1}. (c) Phase-contrast images of hepatocytes and hepatocytes/fibroblasts cultured on microgrooved substrate 1 day after seeding. Reproduced from Park, J.; Berthiaume, F.; Toner, M.; Yarmush, M. L.; Tilles, A. W. *Biotechnol. Bioeng.* **2005**, *90*, 632–644, with permission from Wiley.

for a therapeutic benefit suggests the possibility that the exogenously supplied hepatocytes may aid the regeneration of the native liver.[63] Considering that the cells in BAL devices do not survive for extended periods of treatment, cell sources chosen for BAL devices should be readily available in large numbers (see **Chapter 5.507, Tissue Engineering and Selection of Cells**).

Most clinically applied BAL support devices use primary porcine hepatocytes.[71] They are relatively easy to prepare in large quantities and show many of the differentiated functions of the primary adult human hepatopcytes.[72] Even though the safety and the efficacy of BAL devices using porcine hepatocytes have been demonstrated in preclinical trials,[55,60,73,74] significant improvement in patient survival has not been seen yet.[38,71,75] One disadvantage of using porcine hepatocytes is related to the immunological problems. Sustained exposure to xenogenic cells might result in anaphylactic reaction after 1 week.[76–78] In addition, there is also the risk of zoonosis including the transmission of porcine endogenous retrovirus (PERV), associated with the use of xenogeneic cells.[79]

An ideal cell type for use in a BAL device is the adult primary human hepatocyte because of the high number of differentiated liver functions demonstrated by this cell type. Primary adult human hepatocytes are isolated from discarded organs that are not found suitable for transplantation; hence they are usually in low supply and of low quality. In addition, primary adult hepatocytes are postmitotic and have no capacity to expand in culture to obtain sufficient numbers for use in a BAL device. Therefore, the shortage and the low quality of primary adult human hepatocytes limit the use of these cells in BAL devices.[80]

One alternative cell type is the human hepatocellular carcinoma cell line, HepG2. It is commonly used in the study of hepatocyte biology and has been shown to produce liver proteins including α-fetoprotein, albumin, α2-macroglobulin, α1-antitrypsin, transferrin, α1-antichymotrypsin, haptoglobin, ceruloplasmin, plasminogen, complement (C4), C3 activator, fibrinogen, α1-acid glycoprotein, α2-HS glycoprotein, β-lipoprotein, and retinol-binding protein.[81] A clonal derivative of HepG2, C3A cell line, is also used in BAL devices. It is selected for its strong contact inhibition of growth and increased albumin production in confluent cultures.[82,83] The ease of expansion to sufficient numbers and the display of a number of hepatic functions made them an attractive source of cells for use in bioartificial devices.[84] However, the low expression of phase I drug metabolizing enzymes compared to primary adult human cells makes them less attractive in detoxification properties desired in BAL support devices.[85,86]

Human fetal hepatocytes are an alternative source of human hepatocytes for use in BAL devices. Fetal hepatocytes, usually isolated from 22 to 24-week-old fetuses, still have the capacity to proliferate and, hence, they offer the possibility of being obtained in sufficiently high numbers for use in BAL devices. If the population doubling is not adequate, it is also possible to immortalize human fetal cells by SV40 or hTERT transformation.[87,88] Several studies report culture techniques to maturate fetal hepatocytes to display differentiated hepatic functions, which make them an attractive source for use in cell-based therapies for liver failure including BAL suppot.[89–92] However, ethical issues related to the use of fetal tissue as

well as the low availability of such a source necessitates the clonal expansion and generation of fetal hepatocyte cell lines that can match the functional capacity of adult primary hepatocytes.

An attractive cell source for generating human hepatocytes is the use of embryonic stem cells (ESCs). Human embryonic stem cells (hESCs) are pluripotent and they have the capacity for indefinite self-renewal when maintained under appropriate cell culture conditions. Given appropriate cues, they can form all three germ layers,[93–95] so they present as an invaluable cell source for cell-based therapies. ESC lines are derived from the inner cell mass of blastocyst stage embryos[93,96,97] and cultured on various types of feeder cells or suitable ECM under feeder-free conditions.[98,99] The pluripotency of hESCs is maintained in culture with knockout serum replacement and supplemental basic fibroblast growth factor.[100,101] The ethical issues related with the derivation and use of ESCs led to the generation of induced pluripotent stem (iPS) cells.[102] Generation of iPS cells involves introduction of pluripotency factors into adult somatic cells. The first studies used four transcription factors, Oct4, Sox2, c-Myc, and Klf4, which were introduced into adult mouse fibroblasts through retroviral transfection.[102] Through unknown mechanisms, these transcription factors reprogram the somatic cells into the pluripotent stage. Like hES cells, iPS cells have compact colony morphology and can be maintained in culture for prolonged periods. They express pluripotency markers such as Oct4, Nanog, SSEA-1, and they can differentiate *in vitro* and *in vivo* into three germ layers. One of the concerns about the use of iPS cells in cell therapies was the use of oncogenes, c-Myc and Klf4, to induce pluripotency. However, later studies showed that replacing c-Myc and Klf4 with Nanog and Lin-28 was also successful.[103] The use of small molecules such as valproic acid, a histone deacetylase inhibitor, instead of c-Myc and Klf4, has also been successful in inducing pluripotency in human fibroblasts.[104] Another concern about the use of iPS cells involves the use of viral transfection, which integrates viral genome into the recipient genome to deliver the pluripotency genes.[102] Recent studies have shown that gene delivery could be achieved by using the nonintegrating adenoviruses[105] or episomal vectors.[35,36] Given that the directed differentiation of iPS cells into the cell type of interest can be efficiently achieved, iPS cells are considered a safe and promising alternative to hESCs.

During recent years, there have been a number of reports on the hepatic differentiation of human ESCs. Protocols for directing the differentiation of ESCs into hepatocytes are usually based on signaling events in the early embryo, known to initiate specification of definitive endoderm.[106–108] Based on this understanding, treatment with growth factors in determined sequence has shown to direct ESCs to differentiate toward endoderm and further hepatic progenitors with some of the molecular characteristics of hepatocytes.[109–122] In the majority of settings, the resultant cells have morphological features similar to those of primary hepatocytes and most of the cells express liver-associated proteins. Our group's studies have contributed to this contemporary body of knowledge by showing that definitive endoderm can be produced through formation of embryoid bodies or by culturing mouse ESCs with collagen-sandwiched hepatocytes[123] and a more sophisticated coculture system, which has been demonstrated to differentiate ESCs into hepatocyte-like cells. However, existing concerns about these cells include the expression of many genes also expressed in the extra embryonic yolk sac. α-Fetoprotein, for example, is expressed in both the liver and the yolk sac.[108] To date, the majority of ESC hepatic differentiation protocols have produced cells with relatively immature hepatic characteristics despite rigorous enrichment protocols. Despite these issues, human ESCs are the most attractive cell type for the generation of hepatocytes with adult phenotype for use in BAL devices and other tissue engineering applications.

5.541.3. Implantable Hepatic Support Systems

The ultimate replacement of a failing liver is done by orthotopic transplantation. However, the shortage of available transplantable organs necessitates the search for other options to replace hepatic function. One straightforward alternative to organ transplantation is hepatocyte transplantation where the cells from a healthy donor are transplanted to a recipient with the failing organ with the expectation that the healthy cells will engraft in the recipient organ and provide the function of the failed organ. Besides the limited availability of healthy and functional hepatocytes, one major problem in cell transplantation is the low engraftment and survival of transplanted hepatocytes.[124] In order to overcome this issue, hepatocytes are transplanted within a carrier material in the form of encapsulation, microcarriers, or biodegradable scaffolds, which can protect the cells from the immune response of the recipient tissue by providing their own microenvironment; hence, increase their survival.[125] Furthermore, considering that the hepatocytes are highly metabolically active cells, there have been attempts to mimic the native liver architecture using tissue engineering and microfabrication techniques with the aim of providing perfusion for nutrient delivery and waste removal to enhance their survival and function.[126,127] Finally, development of a transplantable organ graft has been made possible by the use of a perfusion decellularized organ matrix as the scaffold which can be repopulated with liver cells.[128]

5.541.3.1. Direct Cell Transplantation

The first clinically successful case of hepatocyte transplantation was shown to treat Crigler–Najjar syndrome Type I, a metabolic liver disorder.[23] Crigler–Najjar syndrome results from the absence of uridine diphosphoglucuronate (UDP) glucuronosyltransferase activity, which is essential for the conjugation and excretion of bilirubin. Since hepatic architecture and function otherwise is normal in this metabolic syndrome, transplantation of hepatocytes was considered to be a safe and less invasive alternative to liver transplantation. Since that first clinical success, the clinical outcome of hepatocyte transplantation for acute and chronic liver failure and other metabolic diseases has been disappointing except when intended as a bridge to organ transplantation for patients with liver failure.[18,22,129,130] Several factors play a role in this poor outcome, including limited availability of high-quality cells and lack of suitable transplantation sites that can accommodate the required number of cells. Furthermore, the fate of transplanted

cells is dependent on their interactions with the microenvironment including the ECM, soluble factors such as cytokines and growth factors, and the immunological response of the host.[131] Hepatocyte engraftment is a low-efficiency process, transplantation of 3–5% host liver mass resulting in 0.5% engraftment of the host liver. The quality of the transplanted cells, the host liver architecture and ECM,[132] and the regeneration capacity of the host liver affect the engraftment efficiency.[133] Immune rejection by the host is another factor that affect the survival of the transplanted cells.[134]

5.541.3.2. Microcarrier and Encapsulated Systems

Hepatocyte attachment to microcarriers prior to transplantation is an alternative strategy to the direct injection of cells. The microcarriers offer ECM features on which the cells can attach and effect their survival and function. One of the earliest studies that report microcarrier-attached hepatocyte transplantation used collagen-coated microcarriers to host hepatocytes and their transplantation into Gunn rats, experimental models of Crigler–Najjar syndrome. The study showed the survival of hepatocytes for up to 2 months and display of function for 1 week.[135,136] When hepatocytes were attached to microcarriers made of chitosan/gelatin composite material, hepatocyte function was found to be at least 50% higher than those found in collagen-coated microcarriers.[137] The survival of C3A cells attached to porous collagen-coated polyethersulfone microcarriers into rats was about 95%, offering the possibility of transplantation of high concentrations of cells.[138]

A more promising approach in matrix-based hepatocyte transplantation is hepatocyte encapsulation. Encapsulation uses a thin spherical membrane around the cells that protects the cells from the immune response of the host tissue while creating a microenvironment that enhances the function of the transplanted cells[139] (see **Chapter 5.509, Cell Encapsulation**). Encapsulation also opens up the possibility of transplantation of xenogeneic cells due to the immunoprotection it provides.[140] An early study used a calcium–alginate–polylysine matrix to microencapsulate primary rat hepatocytes and transplanted the microcapsules in animal models of Crigler–Najjar syndrome. The microencapsulated cells were as effective as naked hepatocytes in lowering the bilirubin levels in the animals at 20 days of transplantation and the cells were not rejected.[141] Later animal studies also showed the immunoprotection of hepatocytes upon transplantation when the cells were encapsulated.[138,142–145] Another advantage of encapsulation is the possibility of cotransplantation of hepatocytes with nonparenchymal cells. The microenvironment created by the interactions between the hepatocytes and nonparenchymal cells within the capsule supports the function of hepatocytes and effects the long-term survival of the cells. Examples of such an approach include coculture of hepatocytes with bone marrow mesenchymal stem cells[146–148] and with Sertoli cells.[146–149]

5.541.3.3. Polymer Scaffolds

The ultimate goal of tissue engineering is to create structures that mimic the native organ architecture. Polymer scaffolds are tools of tissue engineering that provide the volume required to grow sufficient numbers of cells to recreate tissue architecture while featuring the ECM cues required for tissue organization. The polymer scaffold is desirably biodegradable so that the tissue may grow to replace the scaffold and support itself overtime.

Scaffolds have been used in the engineering of several tissues including, but not limited to, cartilage, bone, heart, blood vessels, and skin. Scaffolds used for liver tissue engineering serve as a vehicle for the delivery of hepatocytes, while allowing perfusion for nutrient delivery and waste removal to sustain the viability of the hepatocytes seeded inside. Moreover, it should be permissible to the growth of new blood vessels once transplanted for similar reasons.

One of the first examples of liver tissue engineering was shown using prevascularized polyvinyl alcohol discs. The discs were repopulated rat hepatocytes transplanted into animals for up to 1 year. Promisingly, even though initial cell engraftment was low, the discs contained viable cells after 1 year of transplantation.[150,151] Later studies focused on demonstrating optimal hepatocyte function and viability *in vitro* using tissue engineering culturing techniques. The first biomaterials that were tested for liver tissue engineering include those that are already approved for use in biomedical applications, such as polylactic acid (PLA), polyglycolic acid (PGA), and copolymers of lactic and glycolic acid (PLGA).[152] These materials are biodegradable, biocompatible, and can be fabricated into highly porous structures that may accommodate highly oxygen demanding hepatocytes.[153,154] Improved hepatocyte function due to spheroid formation has been shown in PLA-based discs[155–157] and PLA-based scaffolds.[158] A natural biopolymer, chitosan, has been the focus of several liver tissue engineering studies (see **Chapter 2.213, Chitosan**). Chitosan is a linear polysaccharide with randomly distributed β-(1-4)-linked D-glucosamine and *N*-acetyl-D-glucosamine units. It is a desirable material for biomedical applications because it is biodegradable, biocompatible,[159] and easy to chemically modify for manipulating its biological and mechanical properties.[160] Chitosan-based biomaterials that have been tested for hepatocyte culture and function so far include chitosan/alginate and chitosan/collagen blends,[161] galactosylated chitosan/alginate and galactosylated chitosan/alginate/heparin blends,[162,163] chitosan/galactosylated hyaluronic acid composites,[164] and nanofibrous galactosylated chitosan.[165] Recently, peptide-based biomaterials have drawn interest in tissue engineering applications. A well-defined synthetic hydrogel forming peptide, PuraMatrix™, was investigated for its capacity to support hepatocyte functions in a three-dimensional environment for rat[166] and porcine hepatocyte cultures.[167] Even though albumin and urea production as well as cytochrome P450 activities in PuraMatrix™ cultures were similar to those observed in collagen sandwich and Matrigel cultures, the advantage of using PuraMatrix™ was the possibility of achieving high functional capacity through the high-density cell cultures.[166] It also serves as a delivery vehicle for cell transplantation for which it has been shown to be highly effective in a number of animal models of liver failure.[168]

5.541.3.4. Microfabrication for Liver Tissue

Microfabrication techniques offer the skills to control the cellular microenvironment in cell culture and cocultures to mimic native tissue microarchitecture and subsequent cell

function in tissue engineering. Microfabrication techniques have thus far been used to create patterned cultures for cellular control and coculture[169–173] and molding for the construction of microvascular networks,[174] and for the assembly of three-dimensional networks for organ reconstruction[175–177] and development of microscale multiorgan systems for drug testing purposes.[178]

The leading work of Bhatia *et al*. revealed that the micropatterned coculture of hepatocytes with 3T3-J2 fibroblasts significantly improved the hepatocyte functions and the long-term maintenance of differentiated function using microfabrication techniques to create micropatterned surfaces for selective cell adhesion.[169–171] This work led to the fabrication of microscale culture systems of primary adult human hepatocytes that display highly differentiated drug metabolism functions (**Figure 3**).[173]

A successful culture of hepatocytes depends on the efficiency of nutrient delivery and waste removal in a tissue-engineered construct; which necessitates the presence of a vascular bed within the construct. One approach to reconstruct the artificial liver tissue is to build the tissue from ground up using microfabrication techniques. Even though it has not been realized so far, this promising approach involves a silicone or pyrex platform seeded with endothelial cells, with microchannels that allow continuous perfusion to form a well-sealed vascular network. Once the vascular network is established, the system is expected to be repopulated with hepatocytes and biliary epithelial cells to form the liver tissue.[179]

5.541.3.5. Whole Liver Tissue Engineering

The first generation tissue engineering materials have found limited use as they had limited ability to modulate the repair and regeneration of the host tissue. Consequently, material and host tissue interactions became an important consideration in the design of new materials such that the new generation materials should harness elements that regulate tissue regeneration by different mechanisms, such as controlling specific cell-binding interactions and responding to environmental cues.[180] In addition, since material microstructure has been found to play an important role for tissue morphogenesis,[181–183] three-dimensional aspects such as pore structure, surface area to volume ratio, texture, and surface topography that define material architecture have become other important design parameters.[184] Considering these design constraints, decellularized ECM represents an ideal material for tissue engineering applications as it retains the relevant aspects of the complex structure and chemical composition of the ECM[185] (see **Chapter 2.220, Extracellular Matrix as Biomimetic Biomaterial: Biological Matrices for Tissue Regeneration** and **Chapter 2.221, Decellularized Scaffolds**). Moreover, using a decellularization technique described recently for heart,[128] the native three-dimensional structure of the organ can also be preserved which will most likely provide the necessary architecture for optimal cell distribution and subsequent tissue morphogenesis. In addition, the scaffold obtained via perfusion decellularization will contain a perfusable vascular tree that facilitates *in vitro* perfusion and reconnection to the blood torrent – which has been observed in skin grafts –[186,187] and this can greatly enhance nutrient delivery and waste removal in the tissue-engineered construct.

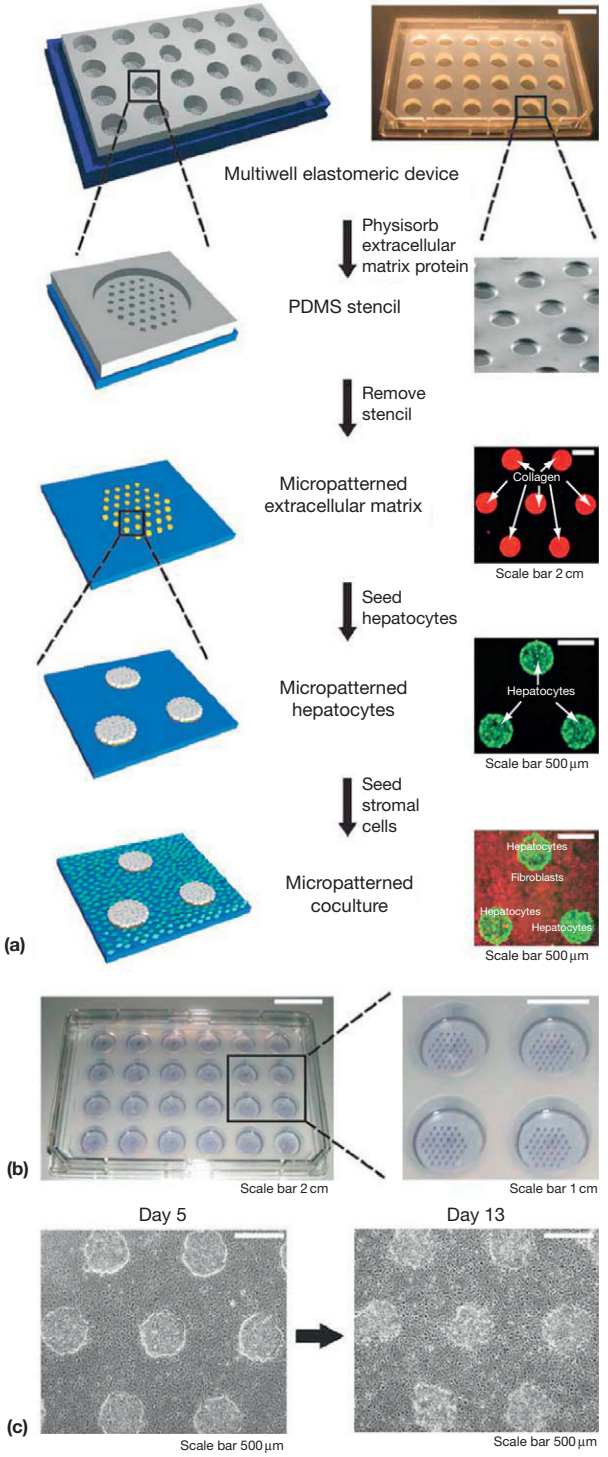

Figure 3 Preparation of microscale hepatocyte culture system. (a) Soft lithography process was used to fabricate microscale liver hepatocyte cultures in a multiwell format. A schematic of the process flow is shown next to the photomicrographs taken at each step (b) Photograph of a 24-well device with repeating hepatic microstructures (37 colonies of 500-μm diameter in each well), stained purple by 3-(4,5-Dimethylthiazol-2-yl)-2,5-diphenyltetrazolium bromide (c) Phase-contrast micrographs of micropatterned cocultures. Primary human hepatocytes arranged in ~500 μm collagen-coated islands surrounded with fibroblasts. Reproduced from Khetani, S. R.; Bhatia, S. N. *Nat. Biotechnol.* **2008**, *26*, 120–126, with permission from Nature Publishing Group.

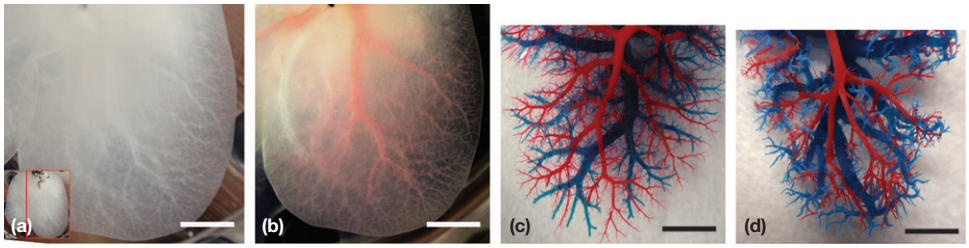

Figure 4 Decellularized liver matrix (DLM) scaffold retains intact lobular structure and vascular bed upon perfusion decellularization. (a) Representative photograph of decellularized left lateral and median lobes of rat liver, with the vascular tree visible. (b) The vascular tree, after perfusion with Allura Red AC dye. Corrosion cast model of left lobe of (c) a normal liver and (d) the DLM, portal (red) and venous (blue) vasculature. Scale bars (a and b) 10 mm (c and d) 5 mm. Reproduced from Uygun, B. E.; Soto-Gutierrez, A.; Yagi, H.; *et al*. *Nat*. *Med*. **2010**, *16*, 814–820.

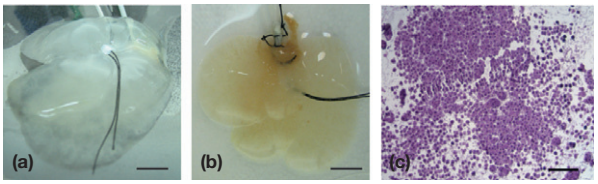

Figure 5 Repopulation of decellularized liver matrix (DLM) with adult primary hepatocytes. (a) Decellularized whole liver matrix, (b) the same liver after recellularization with about 50 million hepatocytes. (c) Hematoxylin and eosin staining of hepatocyte repopulated DLM. Scale bars, (a,b) 20 mm, (**c**) 100 μm. Reproduced from Uygun, B. E.; Soto-Gutierrez, A.; Yagi, H.; *et al*. *Nat*. *Med*. **2010**, *16*, 814–820.

Furthermore, traditional tissue engineering approaches for the development of transplantable liver grafts have, so far, been limited by oxygen and nutrient diffusion to thin two-dimensional structures, which are engrafted in highly vascularized regions.[166,167,188–190] Practical consideration of primary hepatocyte oxygen consumption requires that any hepatic mass, which is sufficient to provide metabolic function, should contain an extensive microvascular network and be connected to the blood supply; otherwise, the internal mass of the cells will suffer ischemic damage.[127,191,192]

Decellularization is an attractive technique for scaffold preparation in tissue engineering as the resulting material can potentially retain the architecture of the original tissue including the functional aspects of the native microvasculature.[193] The potential applications of decellularized matrix in tissue engineering have been demonstrated for a number of tissues including bladder,[194] artery,[195] esophagus,[196] myocardium,[197] skin,[187] and trachea[198] (see **Chapter 5.534, Skin Tissue Engineering**; **Chapter 5.539, From Tissue to Organ Engineering**; and **Chapter 5.527, Cardiovascular Tissue Engineering**). More recently, the Taylor group reported the decellularization of an entire heart through perfusion, preserving the original architecture and original microvascular network allowing for extensive recellularization.[128]

We have recently developed a transplantable liver graft using perfusion decellularized liver matrix (DLM).[199] The decellularization process preserved the structural and functional characteristics of the native microvascular network as shown by dye perfusion and corrosion cast molding (**Figure 4**). The preserved vasculature allowed subsequent recellularization with adult rat hepatocytes with over 90% efficiency (**Figure 5**). The *in vitro* perfusion culture of the recellularized liver graft showed that the graft supported liver-specific function at approximately 30% functional capacity of normal liver, including albumin secretion, urea synthesis, and cytochrome P450 expression *in vitro*. Furthermore, the recellularized liver grafts were transplanted in rats, supporting hepatocyte survival and function with minimal ischemic damage.

5.541.4. Conclusions and Future Directions

Liver is a highly metabolically active organ that has high oxygen and nutrient demands. Even though a healthy liver has the capacity to regenerate, damage to the organ may result in mortality if the hepatic function is not supported. As the current treatment methods for liver failure are limited, tissue engineering has offered tools for the development of alternative treatment options such as the provision of temporary support in terms of BAL devices, techniques to sustain long-term differentiated function of adult primary hepatocytes, and development of biomaterials as delivery vehicles of hepatocytes for cell transplantation. Furthermore, the tissue engineering tools have facilitated development of transplantable liver grafts from a wide range of synthetic and biological materials. Liver tissue engineering has also made use of microfabrication techniques to establish culture conditions that support long-term hepatic functions and it has led to studies to reconstruct liver tissue from ground up. However, so far, development of a transplantable liver graft using ground up techniques has not been successful mostly due to the complexity of the liver tissue architecture. Recently, use of whole organ scaffolds obtained by perfusion decellularization has drawn interest. The whole organ scaffold has the composition and the architecture of the native organ, which alleviates the need for reconstruction of the scaffold. It has already been shown that the hepatocytes display sustained function within the scaffold, and the presence of the vascular network facilitated its reconnection to the blood torrent *in vivo*. Future work in the development of a transplantable liver graft requires the addition of the nonparenchymal component of the liver, such as endothelial cells and the biliary epithelial cells, into the DLM scaffold.

References

1. Kuntz, E.; Kuntz, H. D. *Hepatology: Principles and Practice: History, Morphology, Biochemistry, Diagnostics, Clinic, Therapy*. Springer: Heidelberg, 2006.
2. Bismuth, H. In *Surgery of the Liver and Biliary Tract*; Blumgart, L. H., Ed.; Churchill Livingstone: Edinburgh, 1988.
3. Dawson, J. L.; Tan, K. C. *Anatomy of the Liver*. WB Saunders: London, 1992.

4. Ekataksin, W.; Kaneda, K. *Semin. Liver Dis.* **1999**, *19*, 359–382.
5. Sasse, D.; Spornitz, U. M.; Maly, I. P. *Enzyme* **1992**, *46*, 8–32.
6. Strazzabosco, M.; Fabris, L. *Anat. Rec. Hoboken.* **2008**, *291*, 653–660.
7. Greenwel, P.; Rojkind, M. *The Extracellular Matrix of the Liver*. Lippincott Williams and Wilkins: Philadelphia, PA, 2001.
8. Bouwens, L.; De Bleser, P.; Vanderkerken, K.; Geerts, B.; Wisse, E. *Enzyme* **1992**, *46*, 155–168.
9. Karpen, S. J.; Crawford, J. M. *Curr. Opin. Gastroenterol.* **1999**, *15*, 184–191.
10. Smedsrod, B.; De Bleser, P. J.; Braet, F.; *et al. Gut* **1994**, *35*, 1509–1516.
11. Toth, C. A.; Thomas, P. *Hepatology* **1992**, *16*, 255–266.
12. Gebhardt, R. *Pharmacol. Ther.* **1992**, *53*, 275–354.
13. Jungermann, K.; Kietzmann, T. *Annu. Rev. Nutr.* **1996**, *16*, 179–203.
14. Katz, N. R. *J. Nutr.* **1992**, *122*, 843–849.
15. Pascher, A.; Sauer, I. M.; Hammer, C.; Gerlach, J. C.; Neuhaus, P. *Xenotransplantation* **2002**, *9*, 309–324.
16. Batra, Y.; Acharya, S. K. *Indian J. Gastroenterol.* **2003**, *22*(Suppl. 2), S66–S68.
17. Punch, J. D.; Hayes, D. H.; Laporte, F. B.; Mcbride, V.; Seely, M. S. *Am. J. Transplant.* **2007**, *7*, 1327–1338.
18. Fox, I. J.; Roy-Chowdhury, J. *J. Hepatol.* **2004**, *40*, 878–886.
19. Navarro-Alvarez, N.; Soto-Gutierrez, A.; Kobayashi, N. *Curr. Opin. Organ Transplant.* **2007**, *12*, 652–658.
20. Strom, S. C.; Fisher, R. A.; Thompson, M. T.; *et al. Transplantation* **1997**, *63*, 559–569.
21. Chen, Y.; Kobayashi, N.; Suzuki, S.; *et al. Transplantation* **2005**, *79*, 1378–1385.
22. Fisher, R. A.; Strom, S. C. *Transplantation* **2006**, *82*, 441–449.
23. Fox, I. J.; Chowdhury, J. R.; Kaufman, S. S.; *et al. N. Engl. J. Med.* **1998**, *338*, 1422–1426.
24. Horslen, S. P.; Mccowan, T. C.; Goertzen, T. C.; *et al. Pediatrics* **2003**, *111*, 1262–1267.
25. Habibullah, C. M.; Syed, I. H.; Qamar, A.; Taher-Uz, Z. *Transplantation* **1994**, *58*, 951–952.
26. Nagata, H.; Nishitai, R.; Shirota, C.; *et al. Gastroenterology* **2007**, *132*, 321–329.
27. Carpentier, B.; Gautier, A.; Legallais, C. *Gut* **2009**, *58*, 1690–1702.
28. Ash, S. R. *Artif. Organs* **1994**, *18*, 355–362.
29. Ash, S. R.; Blake, D. E.; Carr, D. J.; Carter, C.; Howard, T.; Makowka, L. *Int. J. Artif. Organs* **1992**, *15*, 151–161.
30. Stange, J.; Mitzner, S. R.; Klammt, S.; *et al. Liver Transplan.* **2000**, *6*, 603–613.
31. Tan, H. K. *Ann. Acad. Med. Singapore* **2004**, *33*, 329–335.
32. Rifai, K.; Ernst, T.; Kretschmer, U.; *et al. J. Hepatol.* **2003**, *39*, 984–990.
33. Rifai, K.; Ernst, T.; Kretschmer, U.; Haller, H.; Manns, M. P.; Fliser, D. *World J. Gastroenterol.* **2006**, *12*, 940–944.
34. Krisper, P.; Stauber, R. E. *Nat. Clin. Pract. Nephrol.* **2007**, *3*, 267–276.
35. Yu, C. B.; Pan, X. P.; Li, L. J. *Hepatobiliary Pancreat. Dis. Int.* **2009**, *8*, 134–140.
36. Yu, J.; Hu, K.; Smuga-Otto, K.; *et al. Science* **2009**, *324*, 797–801.
37. Tilles, A. W.; Berthiaume, F.; Yarmush, M. L.; Tompkins, R. G.; Toner, M. *J. Hepatobiliary Pancreat. Surg.* **2002**, *9*, 686–696.
38. Ellis, A. J.; Hughes, R. D.; Wendon, J. A.; *et al. Hepatology* **1996**, *24*, 1446–1451.
39. Kamohara, Y.; Rozga, J.; Demetriou, A. A. *J. Hepatobiliary Pancreat. Surg.* **1998**, *5*, 273–285.
40. Watanabe, F. D.; Shackleton, C. R.; Cohen, S. M.; *et al. Transplant. Proc.* **1997**, *29*, 487–488.
41. Abu-Absi, S. F.; Seth, G.; Narayanan, R. A.; *et al. Artif. Organs* **2005**, *29*, 419–422.
42. Consolo, F.; Fiore, G. B.; Truscello, S.; *et al. Tissue Eng. C Meth.* **2009**, *15*, 41–55.
43. Hay, P. D.; Veitch, A. R.; Smith, M. D.; Cousins, R. B.; Gaylor, J. D. *Artif. Organs* **2000**, *24*, 278–288.
44. Kleinstreuer, C.; Agarwal, S. S. *Biotechnol. Bioeng.* **1986**, *28*, 1233–1240.
45. Piret, J. M.; Cooney, C. L. *Biotechnol. Bioeng.* **1991**, *37*, 80–92.
46. Flendrig, L. M.; La Soe, J. W.; Jorning, G. G.; *et al. J. Hepatol.* **1997**, *26*, 1379–1392.
47. Gerlach, J.; Trost, T.; Ryan, C. J.; *et al. Int. J. Artif. Organs* **1994**, *17*, 549–553.
48. Gerlach, J. C.; Encke, J.; Hole, O.; Muller, C.; Ryan, C. J.; Neuhaus, P. *Transplantation* **1994**, *58*, 984–988.
49. Jasmund, I.; Langsch, A.; Simmoteit, R.; Bader, A. *Biotechnol. Prog.* **2002**, *18*, 839–846.
50. Gordon, J.; Palmer, A. F. *Artif. Cells Blood Substit. Immobil. Biotechnol.* **2005**, *33*, 297–306.
51. Chen, G.; Palmer, A. F. *Biotechnol. Bioeng.* **2010**, *105*, 534–542.
52. Nahmias, Y.; Kramvis, Y.; Barbe, L.; Casali, M.; Berthiaume, F.; Yarmush, M. L. *FASEB J.* **2006**, *20*, 2531–2533.
53. De Bartolo, L.; Bader, A. *Ann. Transplant.* **2001**, *6*, 40–46.
54. De Bartolo, L.; Jarosch-Von Schweder, G.; Haverich, A.; Bader, A. *Biotechnol. Prog.* **2000**, *16*, 102–108.
55. Morsiani, E.; Galavotti, D.; Puviani, A. C.; *et al. Transplant. Proc.* **2000**, *32*, 2715–2718.
56. Tilles, A. W.; Baskaran, H.; Roy, P.; Yarmush, M. L.; Toner, M. *Biotechnol. Bioeng.* **2001**, *73*, 379–389.
57. Roy, P.; Baskaran, H.; Tilles, A. W.; Yarmush, M. L.; Toner, M. *Ann. Biomed. Eng.* **2001**, *29*, 947–955.
58. Roy, P.; Washizu, J.; Tilles, A. W.; Yarmush, M. L.; Toner, M. *Cell Transplant.* **2001**, *10*, 609–614.
59. Shito, M.; Kim, N. H.; Baskaran, H.; *et al. Artif. Organs* **2001**, *25*, 571–578.
60. Shito, M.; Tilles, A. W.; Tompkins, R. G.; Yarmush, M. L.; Toner, M. *J. Surg. Res.* **2003**, *111*, 53–62.
61. Park, J.; Berthiaume, F.; Toner, M.; Yarmush, M. L.; Tilles, A. W. *Biotechnol. Bioeng.* **2005**, *90*, 632–644.
62. Park, J.; Li, Y.; Berthiaume, F.; Toner, M.; Yarmush, M. L.; Tilles, A. W. *Biotechnol. Bioeng.* **2008**, *99*, 455–467.
63. Eguchi, S.; Lilja, H.; Hewitt, W. R.; Middleton, Y.; Demetriou, A. A.; Rozga, J. *J. Surg. Res.* **1997**, *72*, 112–122.
64. Rozga, J.; Holzman, M. D.; Ro, M. S.; *et al. Ann. Surg.* **1993**, *217*, 502–509.
65. Sussman, N. L.; Gislason, G. T.; Conlin, C. A.; Kelly, J. H. *Artif. Organs* **1994**, *18*, 390–396.
66. Cuervas-Mons, V.; Colas, A.; Rivera, J. A.; Prados, E. *Transplantation* **2000**, *69*, 337–344.
67. Arkadopoulos, N.; Lilja, H.; Suh, K. S.; Demetriou, A. A.; Rozga, J. *Hepatology* **1998**, *28*, 1365–1370.
68. Kobayashi, N.; Fujiwara, T.; Westerman, K. A.; *et al. Science* **2000**, *287*, 1258–1262.
69. Bilir, B. M.; Guinette, D.; Karrer, F.; *et al. Liver Transplant.* **2000**, *6*, 32–40.
70. Kim, S. S.; Kaihara, S.; Benvenuto, M. S.; Kim, B. S.; Mooney, D. J.; Vacanti, J. P. *Ann. Surg.* **1998**, *228*, 8–13.
71. Van De Kerkhove, M. P.; Hoekstra, R.; Chamuleau, R. A.; Van Gulik, T. M. *Ann. Surg.* **2004**, *240*, 216–230.
72. Fukuda, J.; Sakiyama, R.; Nakazawa, K.; *et al. Int. J. Artif. Organs* **2001**, *24*, 799–806.
73. Maringka, M.; Giri, S.; Bader, A. *Biomaterials* **2010**, *31*, 156–172.
74. Yamashita, Y.; Shimada, M.; Tsujita, E.; *et al. Cell Transplant.* **2002**, *11*, 379–384.
75. Demetriou, A. A.; Brown, R. S., Jr.; Busuttil, R. W.; *et al. Ann. Surg.* **2004**, *239*, 660–667; discussion 667-70.
76. Hasegawa, H.; Shimada, M.; Gion, T.; *et al. ASAIO J.* **1999**, *45*, 392–396.
77. Nyberg, S. L.; Amiot, B.; Hardin, J.; Baskin-Bey, E.; Platt, J. L. *Cell Transplant.* **2004**, *13*, 783–791.
78. Nyberg, S. L.; Yagi, T.; Matsushita, T.; *et al. Liver Transplan.* **2003**, *9*, 298–305.
79. Fruhauf, J. H.; Mertsching, H.; Giri, S.; Fruhauf, N. R.; Bader, A. *Liver Int.* **2009**, *29*, 1553–1561.
80. Ito, M.; Nagata, H.; Miyakawa, S.; Fox, I. J. *J. Hepatobiliary Pancreat. Surg.* **2009**, *16*, 97–100.
81. Kelly, J. H.; Darlington, G. J. *In Vitro Cell. Dev. Biol.* **1989**, *25*, 217–222.
82. Forte, T. M.; Mccall, M. R.; Knowles, B. B.; Shore, V. G. *J. Lipid Res.* **1989**, *30*, 817–829.
83. Sussman, N. L.; Kelly, J. H. *Am. J. Kidney Dis.* **1997**, *30*, S66–S71.
84. Enosawa, S.; Miyashita, T.; Saito, T.; Omasa, T.; Matsumura, T. *Cell Transplant.* **2006**, *15*, 873–880.
85. Mavri-Damelin, D.; Damelin, L. H.; Eaton, S.; Rees, M.; Selden, C.; Hodgson, H. J. *Biotechnol. Bioeng.* **2008**, *99*, 644–651.
86. Wilkening, S.; Stahl, F.; Bader, A. *Drug Metab. Dispos.* **2003**, *31*, 1035–1042.
87. Deurholt, T.; Van Til, N. P.; Chhatta, A. A.; *et al. BMC Biotechnol.* **2009**, *9*, 89.
88. Poyck, P. P.; Van Wijk, A. C.; Van Der Hoeven, T. V.; *et al. J. Hepatol.* **2008**, *48*, 266–275.
89. Begum, S.; Joshi, M.; Ek, M.; Holgersson, J.; Kleman, M. I.; Sumitran-Holgersson, S. *Cytotherapy* **2009**, *12*, 201–211.
90. Matsushita, T.; Nakano, K.; Nishikura, Y.; Higuchi, K.; Kiyota, A.; Ueoka, R. *Cytotechnology* **2003**, *42*, 57–66.
91. Ring, A.; Gerlach, J.; Peters, G.; *et al. Tissue Eng. C Meth.* **2010**, *16*(5), 835–845.
92. Schmelzer, E.; Triolo, F.; Turner, M. E.; *et al. Tissue Eng. A* **2010**, *16*, 2007–2016.
93. Amit, M.; Carpenter, M. K.; Inokuma, M. S.; *et al. Dev. Biol.* **2000**, *227*, 271–278.
94. Thomson, J. A.; Itskovitz-Eldor, J.; Shapiro, S. S.; *et al. Science* **1998**, *282*, 1145–1147.
95. Zwaka, T. P.; Thomson, J. A. *Stem Cells* **2005**, *23*, 146–149.
96. Evans, M. J.; Kaufman, M. H. *Nature* **1981**, *292*, 154–156.
97. Martin, G. R. *Proc. Natl. Acad. Sci. USA* **1981**, *78*, 7634–7638.
98. Klimanskaya, I.; Chung, Y.; Meisner, L.; Johnson, J.; West, M. D.; Lanza, R. *Lancet* **2005**, *365*, 1636–1641.
99. Skottman, H.; Dilber, M. S.; Hovatta, O. *FEBS Lett.* **2006**, *580*, 2875–2878.
100. Enver, T.; Soneji, S.; Joshi, C.; *et al. Hum. Mol. Genet.* **2005**, *14*, 3129–3140.
101. Schatten, G.; Smith, J.; Navara, C.; Park, J. H.; Pedersen, R. *Nat. Meth.* **2005**, *2*, 455–463.

102. Takahashi, K.; Yamanaka, S. *Cell* **2006**, *126*, 663–676.
103. Yu, J.; Vodyanik, M. A.; Smuga-Otto, K.; *et al*. *Science* **2007**, *318*, 1917–1920.
104. Huangfu, D.; Maehr, R.; Guo, W.; *et al*. *Nat. Biotechnol*. **2008**, *26*, 795–797.
105. Stadtfeld, M.; Nagaya, M.; Utikal, J.; Weir, G.; Hochedlinger, K. *Science* **2008**, *322*, 945–949.
106. D'amour, K. A.; Agulnick, A. D.; Eliazer, S.; Kelly, O. G.; Kroon, E.; Baetge, E. E. *Nat. Biotechnol*. **2005**, *23*, 1534–1541.
107. Kubo, A.; Shinozaki, K.; Shannon, J. M.; *et al*. *Development* **2004**, *131*, 1651–1662.
108. Zaret, K. S. *Curr. Opin. Genet. Dev.* **2001**, *11*, 568–574.
109. Asahina, K.; Fujimori, H.; Shimizu-Saito, K.; *et al*. *Genes Cells* **2004**, *9*, 1297–1308.
110. Basma, H.; Soto-Gutierrez, A.; Yannam, G. R.; *et al*. *Gastroenterology* **2009**, *136*, 990–999.
111. Brolen, G.; Sivertsson, L.; Bjorquist, P.; *et al*. *J. Biotechnol*. **2010**, *145*, 284–294.
112. Duan, Y.; Ma, X.; Zou, W.; *et al*. *Stem Cells* **2010**, *28*, 674–686.
113. Fair, J. H.; Cairns, B. A.; Lapaglia, M.; *et al*. *Surgery* **2003**, *134*, 189–196.
114. Gouon-Evans, V.; Boussemart, L.; Gadue, P.; *et al*. *Nat. Biotechnol*. **2006**, *24*, 1402–1411.
115. Lavon, N.; Yanuka, O.; Benvenisty, N. *Differentiation* **2004**, *72*, 230–238.
116. Loya, K.; Eggenschwiler, R.; Ko, K.; *et al*. *Biol. Chem.* **2009**, *390*, 1047–1055.
117. Rambhatla, L.; Chiu, C. P.; Kundu, P.; Peng, Y.; Carpenter, M. K. *Cell Transplant*. **2003**, *12*, 1–11.
118. Sharma, R.; Greenhough, S.; Medine, C. N.; Hay, D. C. *J. Biomed. Biotechnol*. **2010**, *2010*, 236147.
119. Song, Z.; Cai, J.; Liu, Y.; *et al*. *Cell Res*. **2009**, *19*, 1233–1242.
120. Soto-Gutierrez, A.; Kobayashi, N.; Rivas-Carrillo, J. D.; *et al*. *Nat. Biotechnol*. **2006**, *24*, 1412–1419.
121. Soto-Gutierrez, A.; Navarro-Alvarez, N.; Zhao, D.; *et al*. *Nat. Protoc.* **2007**, *2*, 347–356.
122. Teratani, T.; Yamamoto, H.; Aoyagi, K.; *et al*. *Hepatology* **2005**, *41*, 836–846.
123. Cho, C. H.; Parashurama, N.; Park, E. Y.; *et al*. *FASEB J.* **2008**, *22*, 898–909.
124. Smets, F.; Najimi, M.; Sokal, E. M. *Pediatr. Transplant*. **2008**, *12*, 6–13.
125. Mooney, D. J.; Vandenburgh, H. *Cell Stem Cell* **2008**, *2*, 205–213.
126. Carraro, A.; Hsu, W. M.; Kulig, K. M.; *et al*. *Biomed. Microdevices* **2008**, *10*, 795–805.
127. Kulig, K. M.; Vacanti, J. P. *Transpl. Immunol*. **2004**, *12*, 303–310.
128. Ott, H. C.; Matthiesen, T. S.; Goh, S.-K.; *et al*. *Nat. Med*. **2008**, *14*, 213–221.
129. Fitzpatrick, E.; Mitry, R. R.; Dhawan, A. *J. Intern. Med*. **2009**, *266*, 339–357.
130. Sgroi, A.; Serre-Beinier, V.; Morel, P.; Buhler, L. *Transplantation* **2009**, *87*, 457–466.
131. Allen, K. J.; Soriano, H. E. *J. Lab. Clin. Med*. **2001**, *138*, 298–312.
132. Kumaran, V.; Joseph, B.; Benten, D.; Gupta, S. *Gastroenterology* **2005**, *129*, 1643–1653.
133. Koenig, S.; Krause, P.; Schmidt, T. K.; *et al*. *Int. J. Radiat. Biol*. **2008**, *84*, 285–298.
134. Allen, K. J.; Mifsud, N. A.; Williamson, R.; Bertolino, P.; Hardikar, W. *Liver Transplant*. **2008**, *14*, 688–694.
135. Demetriou, A. A.; Levenson, S. M.; Novikoff, P. M.; *et al*. *Proc. Natl. Acad. Sci. USA* **1986**, *83*, 7475–7479.
136. Demetriou, A. A.; Whiting, J. F.; Feldman, D.; *et al*. *Science* **1986**, *233*, 1190–1192.
137. Li, K.; Wang, Y.; Miao, Z.; Xu, D.; Tang, Y.; Feng, M. *Biotechnol. Lett*. **2004**, *26*, 879–883.
138. Kinasiewicz, A.; Dudzinski, K.; Chwojnowski, A.; Werynski, A.; Kawiak, J. *Transplant. Proc.* **2007**, *39*, 2914–2916.
139. Orive, G.; Hernandez, R. M.; Gascon, A. R.; *et al*. *Nat. Med*. **2003**, *9*, 104–107.
140. Poncelet, A. J.; Denis, D.; Gianello, P. *Curr. Opin. Organ Transplant*. **2009**, *14*, 168–174.
141. Bruni, S.; Chang, T. M. *Biomater. Artif. Cells Artif. Organs* **1989**, *17*, 403–411.
142. Balladur, P.; Crema, E.; Honiger, J.; *et al*. *Surgery* **1995**, *117*, 189–194.
143. Hamazaki, K.; Doi, Y.; Koide, N. *Hepatogastroenterology* **2002**, *49*, 1514–1516.
144. Haque, T.; Chen, H.; Ouyang, W.; *et al*. *Biotechnol. Lett*. **2005**, *27*, 317–322.
145. Mei, J.; Sgroi, A.; Mai, G.; *et al*. *Cell Transplant*. **2009**, *18*, 101–110.
146. Liu, Z. C.; Chang, T. M. *Artif. Cells Blood Substit. Immobil. Biotechnol*. **2002**, *30*, 99–112.
147. Liu, Z. C.; Chang, T. M. *Int. J. Artif. Organs* **2003**, *26*, 491–497.
148. Shi, X. L.; Zhang, Y.; Gu, J. Y.; Ding, Y. T. *Transplantation* **2009**, *88*, 1178–1185.
149. Zheng, M. H.; Lin, H. L.; Qiu, L. X.; Cui, Y. L.; Sun, Q. F.; Chen, Y. P. *Cytotherapy* **2009**, *11*, 326–329.
150. Fiegel, H. C.; Kaufmann, P. M.; Bruns, H.; *et al*. *J. Cell. Mol. Med*. **2008**, *12*, 56–66.
151. Kaufmann, P. M.; Kneser, U.; Fiegel, H. C.; Kluth, D.; Herbst, H.; Rogiers, X. *Transplant. Proc.* **1999**, *31*, 1928–1929.
152. Davis, M. W.; Vacanti, J. P. *Biomaterials* **1996**, *17*, 365–372.
153. Mikos, A. G.; Sarakinos, G.; Lyman, M. D.; Ingber, D. E.; Vacanti, J. P.; Langer, R. *Biotechnol. Bioeng.* **1993**, *42*, 716–723.
154. Vacanti, J. P.; Morse, M. A.; Saltzman, W. M.; Domb, A. J.; Perez-Atayde, A.; Langer, R. *J. Pediatr. Surg.* **1988**, *23*, 3–9.
155. Torok, E.; Pollok, J. M.; Ma, P. X.; *et al*. *Cells Tissues Organs* **2001**, *169*, 34–41.
156. Torok, E.; Pollok, J. M.; Ma, P. X.; *et al*. *Dig. Surg.* **2001**, *18*, 196–203.
157. Torok, E.; Vogel, C.; Lutgehetmann, M.; *et al*. *Tissue Eng.* **2006**, *12*, 1881–1890.
158. Riccalton-Banks, L.; Liew, C.; Bhandari, R.; Fry, J.; Shakesheff, K. *Tissue Eng.* **2003**, *9*, 401–410.
159. Vandevord, P. J.; Matthew, H. W.; Desilva, S. P.; Mayton, L.; Wu, B.; Wooley, P. H. *J. Biomed. Mater. Res.* **2002**, *59*, 585–590.
160. Kim, I. Y.; Seo, S. J.; Moon, H. S.; *et al*. *Biotechnol. Adv.* **2008**, *26*, 1–21.
161. Elcin, Y. M.; Dixit, V.; Gitnick, G. *Artif. Organs* **1998**, *22*, 837–846.
162. Seo, S. J.; Choi, Y. J.; Akaike, T.; Higuchi, A.; Cho, C. S. *Tissue Eng.* **2006**, *12*, 33–44.
163. Seo, S. J.; Kim, I. Y.; Choi, Y. J.; Akaike, T.; Cho, C. S. *Biomaterials* **2006**, *27*, 1487–1495.
164. Fan, J.; Shang, Y.; Yuan, Y.; Yang, J. *J. Mater. Sci. Mater. Med.* **2010**, *21*, 319–327.
165. Feng, Z. Q.; Chu, X.; Huang, N. P.; *et al*. *Biomaterials* **2009**, *30*, 2753–2763.
166. Wang, S.; Nagrath, D.; Chen, P. C.; Berthiaume, F.; Yarmush, M. L. *Tissue Eng. A* **2008**, *14*, 227–236.
167. Navarro-Alvarez, N.; Soto-Gutierrez, A.; Rivas-Carrillo, J. D.; *et al*. *Cell Transplant*. **2006**, *15*, 921–927.
168. Navarro-Alvarez, N.; Soto-Gutierrez, A.; Chen, Y.; *et al*. *J. Hepatol*. **2010**, *52*, 211–219.
169. Bhatia, S. N.; Balis, U. J.; Yarmush, M. L.; Toner, M. *Biotechnol. Prog.* **1998**, *14*, 378–387.
170. Bhatia, S. N.; Balis, U. J.; Yarmush, M. L.; Toner, M. *FASEB J.* **1999**, *13*, 1883–1900.
171. Bhatia, S. N.; Yarmush, M. L.; Toner, M. *J. Biomed. Mater. Res.* **1997**, *34*, 189–199.
172. Cho, C. H.; Park, J.; Tilles, A. W.; Berthiaume, F.; Toner, M.; Yarmush, M. L. *Biotechniques* **2010**, *48*, 47–52.
173. Khetani, S. R.; Bhatia, S. N. *Nat. Biotechnol.* **2008**, *26*, 120–126.
174. Borenstein, J. T.; Weinberg, E. J.; Orrick, B. K.; Sundback, C.; Kaazempur-Mofrad, M. R.; Vacanti, J. P. *Tissue Eng.* **2007**, *13*, 1837–1844.
175. Baudoin, R.; Corlu, A.; Griscom, L.; Legallais, C.; Leclerc, E. *Toxicol. In Vitro* **2007**, *21*, 535–544.
176. Leclerc, E.; Furukawa, K. S.; Miyata, F.; Sakai, Y.; Ushida, T.; Fujii, T. *Biomaterials* **2004**, *25*, 4683–4690.
177. Tsang, V. L.; Bhatia, S. N. *Adv. Biochem. Eng. Biotechnol*. **2007**, *103*, 189–205.
178. Chao, P.; Maguire, T.; Novik, E.; Cheng, K. C.; Yarmush, M. L. *Biochem. Pharmacol*. **2009**, *78*, 625–632.
179. Ochoa, E. R.; Vacanti, J. P. *Ann. NY Acad. Sci*. **2002**, *979*, 10–26; discussion 35-8.
180. Lutolf, M. P.; Hubbell, J. A. *Nat. Biotechnol*. **2005**, *23*, 47–55.
181. Ghosh, K.; Ingber, D. E. *Adv. Drug Deliv. Rev.* **2007**, *59*, 1306–1318.
182. Ingber, D. E. *Circ. Res.* **2002**, *91*, 877–887.
183. Ingber, D. E. *Proc. Natl. Acad. Sci. USA* **2005**, *102*, 11571–11572.
184. Chan, G.; Mooney, D. J. *Trends Biotechnol*. **2008**, *26*, 382–392.
185. Gilbert, T. W.; Sellaro, T. L.; Badylak, S. F. *Biomaterials* **2006**, *27*, 3675–3683.
186. Rafii, S.; Lyden, D. *Nat. Med*. **2003**, *9*, 702–712.
187. Schechner, J. S.; Crane, S. K.; Wang, F.; *et al*. *FASEB J.* **2003**, *17*, 2250–2256.
188. Nahmias, Y.; Berthiaume, F.; Yarmush, M. L. *Adv. Biochem. Eng. Biotechnol*. **2007**, *103*, 309–329.
189. Ohashi, K.; Yokoyama, T.; Yamato, M.; *et al*. *Nat. Med*. **2007**, *13*, 880–885.
190. Soto-Gutierrez, A.; Navarro-Alvarez, N.; Rivas-Carrillo, J. D.; *et al*. *Transplantation* **2007**, *83*, 129–137.
191. Nahmias, Y.; Odde, D. J. *Nat. Protoc.* **2006**, *1*, 2288–2296.
192. Nahmias, Y.; Schwartz, R. E.; Hu, W. S.; Verfaillie, C. M.; Odde, D. J. *Tissue Eng.* **2006**, *12*, 1627–1638.
193. Badylak, S. F. *Biomaterials* **2007**, *28*, 3587–3593.
194. Yoo, J. J.; Meng, J.; Oberpenning, F.; Atala, A. *Urology* **1998**, *51*, 221–225.
195. Dahl, S. L.; Koh, J.; Prabhakar, V.; Niklason, L. E. *Cell Transplant*. **2003**, *12*, 659–666.
196. Nieponice, A.; Gilbert, T. W.; Badylak, S. F. *Ann. Thorac. Surg.* **2006**, *82*, 2050–2058.
197. Badylak, S. F.; Kochupura, P. V.; Cohen, I. S.; *et al*. *Cell Transplantation* **2006**, *15* (Suppl. 1), 29–40.
198. Macchiarini, P.; Jungebluth, P.; Go, T.; *et al*. *Lancet* **2008**, *372*, 2023–2030.
199. Uygun, B. E.; Soto-Gutierrez, A.; Yagi, H.; *et al*. *Nat. Med*. **2010**, *16*, 814–820.

5.542. Organ Printing

F Melchels, Queensland University of Technology, Brisbane, QLD, Australia
J Malda, Queensland University of Technology, Brisbane, QLD, Australia; University Medical Center Utrecht, Utrecht, The Netherlands
N Fedorovich and J Alblas, University Medical Center Utrecht, Utrecht, The Netherlands
T Woodfield, University of Otago Christchurch, Christchurch, New Zealand; University of Canterbury, Christchurch, New Zealand

© 2011 Elsevier Ltd. All rights reserved.

5.542.1. Introduction 588
5.542.1.1. Novel Scaffold Fabrication Methods in Tissue Engineering 588
5.542.1.2. Organ Printing 588
5.542.1.2.1. Rationale for developing organ-printing techniques 589
5.542.2. 2D Patterning and Cell Printing 591
5.542.2.1. Introduction 591
5.542.2.2. State of the Art 591
5.542.2.2.1. Techniques for patterning cell culture substrates 591
5.542.2.2.2. Examples of 2D substrate patterning studies for tissue engineering 593
5.542.2.2.3. Direct manipulation of cells 594
5.542.2.3. Translating 2D Approaches to 3D 595
5.542.3. 3D Organ-Printing Processes 596
5.542.3.1. Organ Printing Versus Book Printing 596
5.542.3.2. Overview of 3D Techniques 596
5.542.3.2.1. Inkjet printing 596
5.542.3.2.2. Robotic dispensing systems 598
5.542.3.2.3. Stereolithography 599
5.542.3.2.4. Robotic assembly 600
5.542.3.3. Developmental Phases and Components Associated with 3D Organ Printing 600
5.542.3.3.1. Preprocessing: design 600
5.542.3.3.2. Printing cell-laden 3D hydrogel constructs 601
5.542.3.3.3. Hydrogels: gels used and criteria for developing hydrogel carriers for cell and organ printing 601
5.542.3.3.4. Scaffold-free assembly: aggregates and cell-sheets 602
5.542.3.3.5. Printing of multiple cell populations and tissue equivalents 603
5.542.3.3.6. Postprocessing 603
5.542.4. Future Directions 603
5.542.4.1. Current Limitations in Organ Printing 603
5.542.4.2. Scale of Application 604
5.542.4.3. Tissue Complexity and Vascularization 604
5.542.5. Conclusions 604
References 604

Abbreviations

3DP	Three dimensional printing
AC	Alternating current
CAD	Computer-aided design
CAM	Computer-aided manufacture
CT	Computed tomography
DC	Direct current
DMD	Digital mirror device
ECM	Extracellular matrix
ITO	Indium tin oxide
LCD	Liquid crystal display
MAPLE-DW	Matrix-assisted pulsed laser evaporation direct write
MRI	Magnetic resonance imaging
MSC	Mesenchymal stem cell
NIH3T3	Mouse embryonic fibroblast cell line
PDMS	Poly(dimethylsiloxane)
PEG	Poly(ethylene glycol)
PEG-DA	Poly(ethylene glycol)diacrylate
PEG-DMA	Poly(ethylene glycol)dimethacrylate
PPO	Poly(propylene glycol)
PR	Photoresist
RGDS	Arginine–glycine–aspartic acid–serine
RhoA	Ras homolog gene family, member 1
RMPD	Rapid microproduct development
ROCK	Rho-associated, coiled-coil containing protein kinase 1
RP	Rapid prototyping

rps	Rotations per second	**TIPS**	Thermal-induced phase separation
SFF	Solid freeform fabrication	**UV**	Ultraviolet
SLS	Selective laser sintering	**VAC**	Alternating current voltage source
TCPS	Tissue culture polystyrene	**VSMC**	Vascular smooth muscle cell
TEC	Tissue-engineered construct		

5.542.1. Introduction

5.542.1.1. Novel Scaffold Fabrication Methods in Tissue Engineering

Any discussion on the development of tissues and organs requires an understanding of current tissue engineering approaches to fabricate porous three-dimensional (3D) scaffolds. The commonly adopted tissue engineering paradigm generally involves the seeding and culturing of cells in 3D porous scaffolds. The scaffold pore architecture plays an important role in cell seeding and tissue development, promoting homogenous cell spreading, cell differentiation, and host tissue ingrowth upon implantation. Traditional techniques to prepare such scaffolds include porogen leaching, phase separation, and gas foaming. Although parameters such as porosity and average pore size can be influenced by controlling processing parameters, the overall control of the scaffold architecture and its pore network is low. Most polymers used for tissue engineering scaffolds are hydrophobic, which particularly impedes the penetration of aqueous cell suspensions. Furthermore, foams fabricated using traditional techniques generally have low permeabilities and, therefore, slow diffusion of medium. This limits development of *in vitro* tissues to grafts of small cross-sections in static culture.[1,2]

These facts have driven the development of novel fabrication techniques for the preparation of tissue engineering scaffolds that provide more control over the scaffold design. One of these techniques is solid freeform fabrication (SFF), a computer-controlled additive fabrication of designed 3D constructs in a layer-by-layer process. Originally, SFF fabrication techniques were developed to create prototypes for purposes of designing new parts or products. Traditional prototyping methods involve laborious mould making and casting steps, while the ability to create an object within hours from a computer design by rapid prototyping (RP) significantly speeds up the development of products. In the biomedical field, these developments have led to the fabrication of aids for complex surgery[3] and patient-specific models for mould-assisted implant fabrication.[4] More recently, SFF techniques have been adopted for the preparation of medical implants, such as scaffolds for tissue engineering and regenerative medicine applications. The use of SFF is an attractive approach to producing scaffolds with customized external shape, and predefined and reproducible internal morphology. **Figure 1** gives a snapshot of techniques that have been applied in the preparation of porous scaffolds for tissue engineering – particularly polymer scaffolds – including SFF techniques. It also includes the characteristics of each method including the range of porosity and pore size that can be obtained, as well as the particular advantages and disadvantages of each technique, and a typical image of the scaffold microstructure.

Using SFF techniques, scaffold designs can be optimized with respect to mechanical properties and nutrient transport.[5] As SFF technologies are continuously evolving, fabrication costs are decreasing, and the properties of the manufactured parts are improving. For high-end applications, such as regenerative medicine, the relatively high cost per fabricated item justifies the use of SFF for the preparation of usable parts rather than prototypes. Following the early work of Sachs *et al.*[6,7] in 3D printing of biodegradable parts and, later, porous scaffolds, many SFF techniques have been used, modified and developed for tissue engineering over the last decade.[8] This has led to a significant improvement in the control over the design of 3D tissue engineering scaffolds.[9,10] Using SFF methods, it was shown that scaffold architecture influences mechanical properties,[11] oxygen gradients in culture,[12] engineered tissue composition,[13–15] and *in vivo* tissue ingrowth.[16] Although preparing scaffolds using SFF techniques has proven to be beneficial, major limitations still continue to hamper their application in tissue engineering. For example, the use of prefabricated scaffolds for tissue engineering does not allow for the precise placement of cells that is required to mimic the complex structural organization of natural tissues. Furthermore, seeding and culturing of prefabricated scaffolds is a very laborious process, and (pre)vascularization of the structures is a major challenge (see **Chapter 5.503, Biomaterials and the Microvasculature**).

5.542.1.2. Organ Printing

Organ printing adopts the principles of SFF fabrication to prepare tissue-engineered constructs (TECs) in an automated manner, but aims to include cells in the fabrication process itself. After pioneering experimental work on inkjet printing of biomaterials and cells by Boland *et al.*[17,18] and Derby *et al.*,[19,20] the term organ printing first appeared in 2003, being defined as "a rapid prototyping computer-aided 3D printing technology, based on using layer-by-layer deposition of cell and/or cell aggregates into a 3D gel with sequential maturation of the printed construct into perfused and vascularized living tissue or organ."[21] Additive manufacturing translates computer-aided design (CAD) to virtual cross-sections and then creates successive layers of cell-laden matrices with robotic computer-aided manufacturing (CAM) until the model is complete, with the aim of creating living tissue equivalents (**Figure 2**). The fundamental difference between organ printing and the preparation of cell-free tissue engineering scaffolds using SFF fabrication lies in the rationale that tissue formation is directed by the spatial placement of the cells themselves, rather than by the spatial architecture of a solid support structure.

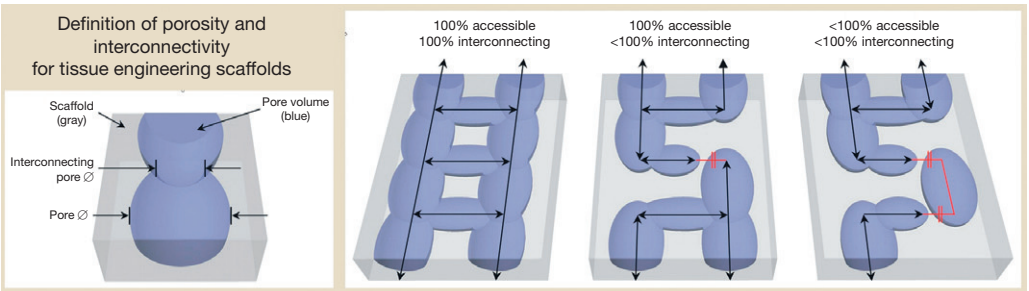

	Scaffold name	Porosity and size	Schematic	Advantage and disadvantages	Image
Conventional scaffolds	Particulate leaching	Porosity < 90% Pore size 5–600 μm		Adv: Simple and user friendly method, suitable with a range of biomaterials and no special equipment is needed. Disadv: Density differences result in nonuniform pore size distribution. Difficult to achieve full interconnectivity and large pore interconnections. Skinning effect on outside surfaces of scaffolds. Organic solvents typically required.	
	Thermally-induced phase separation (TIPS)	Porosity < 90% Pore size 5–600 μm	Homogeneous solution; Temperature; Spinodal decomposition; Polymer concentration	Adv: Simple method, suitable with a range of biomaterials and no special equipment is needed fully interconnecting pores and large pore interconnections can be fabricated if spinodal decomposition is achieved. Disadv: Skinning effect on outside surfaces of scaffolds. Organic solvents typically required.	
Nano-scale scaffolds	Electrospinning	Porosity < 90% Pore size <1–10 μm	High voltage; Polymer jet	Adv: Inexpensive method to produce nano-microfibers from a wide range of polymers. Excellent cell and tissue compatability for mesenchymal cells. By using ice crystals as a collector, scaffolds with large pores and significant volume may be fabricated.	
	Electrospinning onto ice crystals	Porosity < 95% Pore size 20–200 μm	High voltage; Polymer jet; Ice crystals	Disadv: Organic solvents often required, scaffolds with volume, and large pore size or thickness are difficult to manufacture except by using ice crystal technique which has the disadvantage that sublimation required that increases complexity of manufacture. Mechanical properties of electrospun fibers is generally poor.	
	Self-assembling nanofibers	Porosity < 95% Pore size 200–800 μm		Adv: Self-assembling system, typically in water and can be formed in the presence of cells, with bioactive functionality. Disadv: Relatively expensive to manufacture in significant quantities. Weak mechanical properties probably restrict this type of scaffold to soft tissues.	
Solid freeform fabrication (SFF) scaffolds	3D printing (3DP)	Porosity < 45–60% Pore size 45–1600 μm	Ink-jet head; Roller; Liquid adhesive; Powder bed; Powder delivery	Adv: SFF techniques have accurate control over pore size and interconnectivity over conventional/nanoscale approaches. The layer-by-layer process allows fabrication of complex and anatomically shaped structures. Disadv: Expensive machinery required, resolution limitations at lower pore sizes. Biomaterials need to come in powder form with controlled particle size.	
	Stereolithography	Porosity < 90% Pore size 20–1000 μm	Scanner system; Laser; Object being fabricated; Photopolymer	Adv: Accurate control over pore size and interconnectivity. Layer-by-layer process allows fabrication of complex and anatomically shaped structures. Disadv: Expensive machinery required. Polymers compatible with UV curing is required.	
	Selective laser sintering (SLS)	Porosity < 40% Pore size 30–2500 μm	Laser; Scanner system; Powder bed; Roller; Powder delivery; Fabrication piston	Adv: Accurate control over pore size and interconnectivity. Layer-by-layer process allows fabrication of complex and anatomically shaped structures. Disadv: Expensive machinery required. Resolution limitations at lower pore sizes. Biomaterials need to come in powder form with tight controlled particle size, mainly applicable to ceramic materials.	
	Fused deposition modelling/3D plotting	Porosity < 80% Pore size 100–2000 μm	x–y–z stage; Extrusion nozzle; Polymer melt or filament; Table	Adv: Accurate control over pore size and interconnectivity. Layer-by-layer process allows fabrication of complex pore architectures and anatomically shaped structures with good resolution. Disadv: Since the technique uses polymer melts, it is limited to thermoplastics. Low pore sizes difficult to achieve while maintaining high porosity.	
	Direct writing	Porosity < 90% Pore size 5–100 μm		Adv: Accurate control over pore size and interconnectivity. Layer-by-layer process allows fabrication of complex architectures with excellent resolution. Disadv: Expensive machinery required. Biomaterials used need to be able to form polyelectrolyte inks. Significant times are required to manufacture scaffolds with suitable thickness.	

Figure 1 Snapshot of techniques for preparing porous polymer scaffolds for tissue engineering, including some characteristics of each technique. Reproduced with permission from Dalton, P. D.; Woodfield, T.; Hutmacher, D. W. *Biomaterials* **2009**, *30*, 701–702.

5.542.1.2.1. Rationale for developing organ-printing techniques

Cell-based tissue engineering research may profit from design strategies that mimic the anatomical organization of cells, matrix, and bioactive molecules more closely than allowed for by currently used techniques. Such arrangement could contribute to graft functionality and achieve suitable mechanical properties for the engineered tissue.[22,23] For example, the complex zonal organization of articular cartilage is believed to be one of the reasons why over 20 years of cartilage tissue engineering research have not resulted in the consistency and effectiveness required for widespread clinical use.[24,25] The traditional concept of tissue engineering involves the seeding of cells into porous scaffolds, which are cultured *in vitro* to form new tissue. This strategy has proven to be unsuccessful, particularly for large vascularized tissues such as bone. The diffusion of nutrients into large tissue-engineered bone constructs and the slow rate of vascular growth, that is, 2 mm per month,[26] mean that the approach has limited chance of success as cell death occurs well before any blood supply can be established.

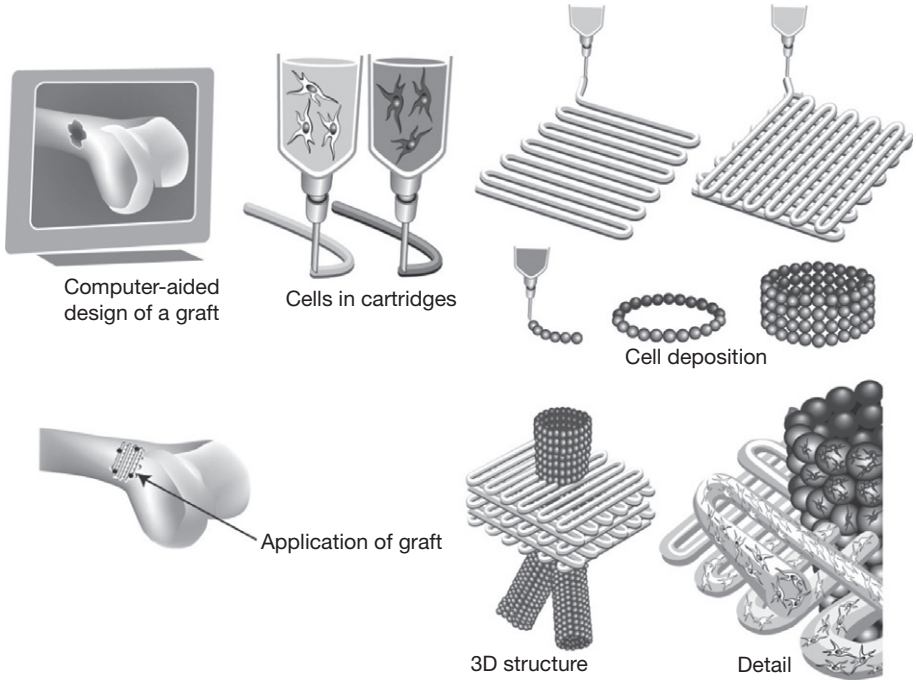

Figure 2 Approach to 3D organ printing. A designed graft is fabricated using a computer-controlled printing device from gels with structurally organized cells of different cell types. Reproduced with permission from Fedorovich, N. E.; Alblas, J.; De Wijn, J. R.; Hennink, W. E.; Verbout, A. J.; Dhert, W. J. A. *Tissue Eng.* **2007**, *13*, 1905–1925.

These findings, in combination with the relatively poor clinical translation of cell-based repair strategies to date, indicate that the current tissue engineering paradigm may have to be revised if more advanced progression toward creating tissues and organs is to take place. The four main justifications for pursuing an organ-printing approach are as follows.

First, the geometry and dimensionality of the cellular environment have a large influence on cell behavior. A number of studies have demonstrated the importance of a 3D structure on the behavior of cells in culture. For example, hepatocytes cultured as a monolayer on a collagen gel lose many of their liver-specific functions within a few days. However, when these same cells are overlaid with another layer of collagen gel to mimic the 3D structure of the liver, they retain many of their liver-specific functions for weeks in culture.[27] Also, it has been long known that chondrocytes dedifferentiate when cultured on flat surfaces,[28] whereas they retain their phenotype in 3D cultures. Although prefabricated porous scaffolds are 3D structures, seeded cells usually spread on scaffold walls or surfaces as they do on flat two-dimensional (2D) surfaces. So in practice, porous scaffolds often provide a 2D environment for cells, albeit with a high surface area in a 3D volume. In organ-printing techniques, the aim is to embed cells in a 3D artificial ECM to preserve phenotype and function, aiming to recreate the *in vivo* niche.

Secondly, traditional cell seeding techniques do not account for the spatial cellular organization of native tissues. Although cellular distributions and tissue formation can be influenced to some extent by controlling the scaffold architecture,[15] neither local variations in cell density, nor relative placement of different cell types can be well controlled when seeding prefabricated scaffolds. However, these parameters strongly influence cellular behavior and functionality of the engineered tissue. For example, stratified layers of chondrocytes harvested from different zones of native articular cartilage showed an increase in ECM production when compared to mixed controls.[22,29] Moreover, the chondrocytes in each layer retained their specific phenotypes. In another study, layered cartilage populations exhibited mechanical profiles that resembled the profile of native cartilage.[30] Hence, the relative placement of different cell types can modulate the way cells interact and influence each other's behavior. For example, there is evidence that endothelial cells promote differentiation of osteoprogenitors and osteoblastic cells. This was presented by many coculture studies,[31–34] wherein direct contact between the endothelial cells and osteoprogenitors was necessary for the increase in alkaline phosphatase activity and type I collagen synthesis to take place.[35] Cotransplanted endothelial cells enhanced bone marrow stromal-cell-mediated bone regeneration in an osseous defect.[36] In turn, bone marrow stromal cells influence endothelial cells by stabilizing blood vessel network formation *in vitro*.[33,37,38] For the formation of adequate blood vessels, stabilization of endothelial cells with other cell types is essential: smooth muscle cells[39,40] or fibroblasts[41] are indispensable, as long-term stabilization is ensured by association of the two cell types.[42–44]

This brings us to the third argument for using organ-printing techniques in making TECs. Neovascularization is a critical step in tissue engineering applications. Because diffusion enables sufficient supply of oxygen only over distances up to 100–200 μm, implantation of voluminous grafts of clinically relevant size without sufficient vascularity results

in hypoxic cells and cell death in the center of tissues.[45] Spontaneous vascular ingrowth of implants does occur, but at low speeds of typically tens of micrometers per day.[46] This has led to the successful use of TECs currently being limited to millimeter-scale or avascular tissues, such as skin or cartilage, in which postimplantation neovascularization from the host is sufficient to meet the demand for oxygen and nutrients.[47] Several strategies for enhancing vascularization are being investigated, including scaffold design, the inclusion of angiogenic factors, *in vitro* prevascularization, and *in vivo* prevascularization.[48] Organ-printing approach can be applied to each of these strategies, or a combination of them. Compared to tissue engineering using prefabricated scaffolds, the organ-printing approach has more potential for overcoming the problem of vascularization in thick tissue constructs through printing of an integrated vascular tree within the bioprinted tissue construct.[49,50] Endothelial cells can be deposited in a specific pattern between the cells that make up the engineered tissue, and the physiological fabrication conditions enable integration of patterned growth factors, such as vascular endothelial growth factor, without their being denaturated.

A fourth argument for following the organ-printing approach is one of logistics and economics. This is often disregarded by scientists but is a very important reason for the implementation of tissue engineering in clinical practice. Despite the widespread hype and significant investment, cell-based therapeutics have largely failed from both a clinical and financial perspective.[51] The developed tissue engineering products were not necessarily inferior to previous alternatives, but the improvement was not sufficient to justify the associated increase in costs.[52] It is critically important that newly developed tissue engineering products establish profitability to ensure continued investment from both the public and private sectors. A method for quantitatively estimating the chance of success of tissue engineering products is the headroom method, in which the effectiveness gap between the current best treatment and that which the new technology might plausibly achieve, is estimated.[53] The use of prefabricated scaffolds involves manual cell seeding and culturing processes. Such nonautomated tissue assembly is laborious and might be economically and logistically infeasible for clinical application on a large scale.[54,55] As organ printing is a fully automated tissue assembly process, it opens up a route to scalable and reproducible mass production of tissues and organ precursors.[56] Furthermore, implementing good manufacturing practices (GMP), quality control, and legislation are facilitated by the use of automated processes.

These arguments are a plea in the endeavor to develop organ-printing techniques for tissue engineering. Here, we present an overview of techniques and studies that support this development. This includes approaches that achieve defined cell organization, such as patterning of substrates and cells in 2D, and 3D assembly of cell-containing constructs.

5.542.2. 2D Patterning and Cell Printing

5.542.2.1. Introduction

Ultimately, for any pioneering work in cell printing, it is inherently easier to demonstrate proof-of-principle in 2D as opposed to 3D. Printing techniques that were initially developed in 2D and are now progressing toward 3D application are discussed in Section 5.542.3. Here, we discuss patterning and cell manipulation techniques that have been performed only in 2D so far.

Working in 2D has several specific advantages. Generally, higher resolutions and accuracies can be achieved, one has more control over the chemical and physical properties on a small scale, and imaging and characterization are easier. Patterning technologies can spatially control surface chemistry and topography at the micrometer level or even below. They can be designed to mimic the natural surroundings and regulatory microenvironments of cells *in vivo*, or to modify the microenvironment to study the cellular response (see Chapter 3.315, Biological Microelectromechanical Systems (BioMEMS) Devices).[57–59]

5.542.2.2. State of the Art

Numerous techniques can create cell patterns, either indirectly via patterning cell culture substrates or directly by patterning cells.

5.542.2.2.1. Techniques for patterning cell culture substrates

Photolithographic methods enable biomaterial scientists to alter surface properties at very high resolutions, at submicron scales. A well-developed set of tools, first developed for the electronics industry, has been translated and expanded to allow for studying cellular behavior on small scales on a variety of materials[60] with well-defined surface topographies[61] and spatially patterned proteins.[62] A scheme of how photolithography works is shown in Figure 3. First, a mask is created from a CAD on a chromium coated quartz (glass) plate by laser

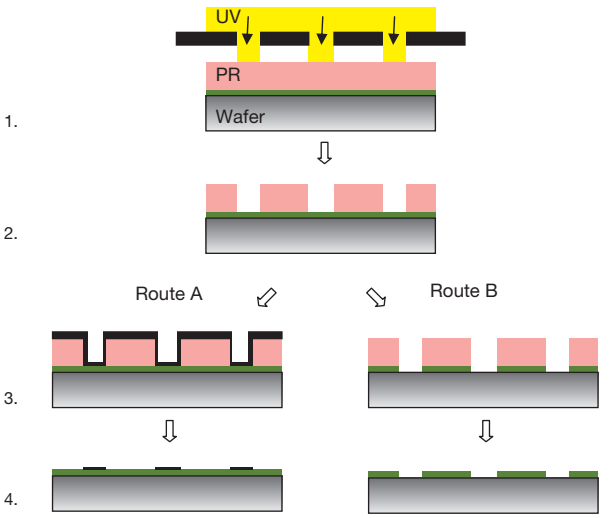

Figure 3 The photolithography process. 1. A flat substrate coated with photoresist (PR) is irradiated with UV light through a mask. 2. Developing of the wafer removes the (un)irradiated PR, leaving a pattern. In route A, the whole surface is coated with a (bio)active solution, and the pattern is exposed after lift-off of the remaining PR. In route B, a deeper layer of the substrate is etched with the pattern, after which the remaining PR is removed.

ablation. This mask is then used to illuminate a substrate spin-coated with a photosensitive polymer formulation – termed a photoresist (PR) – in a patterned manner. The UV-activated wafer is then 'developed' to dissolve either the illuminated parts (in the case of a negative-tone PR) or the not illuminated parts (for a positive-tone PR), thereby partly exposing the substrate. Then, two general routes can be followed. One is the etching-procedure, in which a layer on the substrate is removed by means of an etching solution, plasma or some kind of irradiation. Subsequently, the protected pattern is revealed by dissolution of the PR. In the other route, the total surface is first covered by a functional layer of metal or proteins for example. Then, the PR with the associated part of the functional layer is removed during a so-called 'lift-off ' process, leaving a patterned surface. The choice of the procedure to follow is often dictated by the chemistry of the substrate and functional patterning molecules.[63]

In the electronics industry, silicon is mostly used as the substrate material due to its finely tunable semiconductor properties and because it is atomically flat. For the purpose of imaging, transparent surfaces such as glass, tissue culture polystyrene (TCPS), and some (thin coatings of) metal oxides are preferred for cell studies. The applied patterned layers are often cell adhesive proteins or synthetic molecules containing cell adhesive peptide sequences. Several metal oxides show very different cell adhesive properties and have, therefore, also been used for patterned cell–substrate interaction studies.[64] The nonpatterned surface is usually backfilled with a second (passivating) solution. The passivation step is essential to limit the biofunctionalization to the printed areas.[63] Many passivating systems have been developed, most of them based on poly(ethylene glycol) (PEG). Photolithography can also be performed by direct writing with a laser beam, instead of by total irradiation using masks. Although the resolution is not as high and it takes more time to pattern a surface than can be done in a parallel fashion with a mask, this technique does have specific advantages. Heterogeneous patterns can be created by varying the exposure time, thereby influencing the ligand density.[65]

Photolithography gives researchers a set of tools to manipulate surfaces at very high resolutions, conferring on researchers the unique ability to study cell–substrate interactions on single cells in confined areas. A specific disadvantage of photolithography is the high cost associated with the necessary equipment and clean-room facilities. By transferring a pattern from a photolithography-fabricated silicon wafer to a polydimethylsiloxane (PDMS or silicone rubber) film, one can create a stamp to pattern material surfaces indirectly. This set of techniques, each of which uses stamps or channels fabricated in an elastomeric ('soft') material for pattern transfer, is referred to as soft lithography.[66] As one master wafer can be used to fabricate a large number of PDMS stamps, and the stamps can be reused, it greatly reduces costs. Furthermore, the stringent environmental requirements of photolithography do not apply. Also, the range of materials that can be patterned without the direct use of photoresists and UV irradiation is extended, particularly to delicate ligands such as peptides. Several techniques based on the soft lithography approach exist, of which the most commonly adopted is microcontact printing. As shown in **Figure 3**, a PDMS stamp is initially prepared by casting and curing of a prepolymer on a master, which usually is a silicon wafer, patterned using conventional photolithography. The stamp is inked with a solution containing the bioactive molecules to be printed, which (usually after drying) are transferred to the substrate. The nonprinted surface is then backfilled with a passivating solution. In many cases, the printed molecules are cell adhesion promoting proteins, such as fibronectin. As with photolithographic methods, here too the passivation step is essential to limit the biofunctionalization to the printed areas. An alternative soft lithography-based technique is microfluidic printing, which is also depicted in **Figure 4**. First, a stamp is brought into tight contact with the substrate, after which the patterning solution is introduced in the open channels (usually through capillary forces). After adsorption the stamp is removed, and the backfilling takes place. Although the patterns using this technique are restricted to continuous networks, it does have the advantage that simultaneous patterning with different molecular solutions is possible.[67] **Figure 4** gives an overview of the soft lithography-based techniques discussed above, while **Figure 5** shows an example of the application of microcontact printing to generate cell adhesive patterns on a cell non-adhesive background.

A strategy that bypasses the fabrication of silicon wafers in the clean room altogether and enables patterning in a very

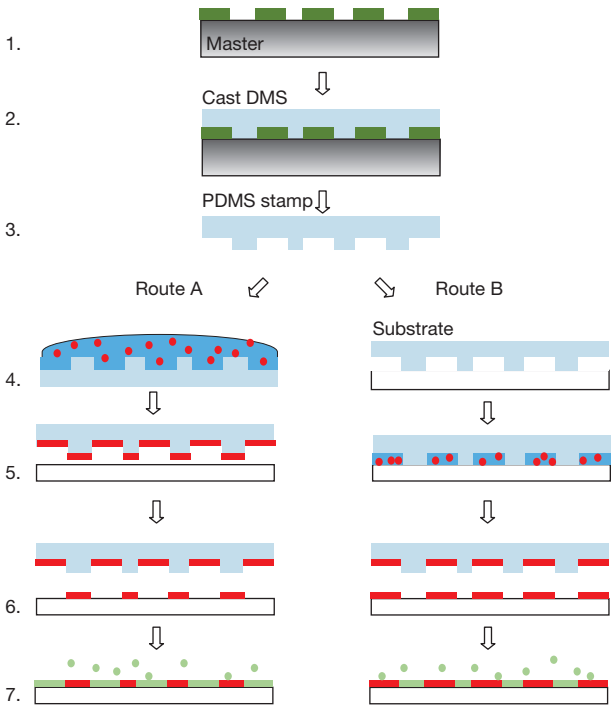

Figure 4 Principles of microcontact printing and microfluidic patterning. First, a 'master' wafer is created with conventional photolithography (1). DMS is cast on the master (2) and cured to create a PDMS stamp (3). In microcontact printing (route A), the stamp is coated with a bioactive compound (4 and 5), and the pattern is transferred to the substrate (6). In microfluidic printing (route B), the solution with the bioactive compound is introduced into the channels (6) after bringing the stamp in close contact to the substrate (5). For both methods, the final step is the backfilling of nonfunctionalized area with a cytophobic layer (7).

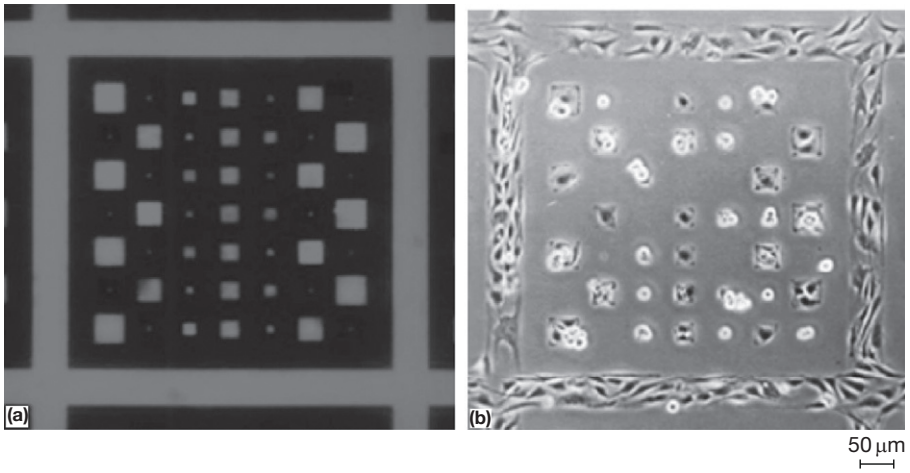

Figure 5 Example of microcontact printing. A gold surface was patterned into hydrophobic regions of alkanethiolate and hydrophilic regions of tri(ethylene glycol) terminated alkanethiolate. Fibronectin adsorbed specifically on the hydrophobic patches as visualized in (a) by antibody-bound fluorophores. (b) Bovine capillary endothelial (BCE) cells specifically bind to the fibronectin coated regions. Reproduced with permission from Kane, R. S.; Takayama, S.; Ostuni, E.; Ingber, D. E.; Whitesides, G. M. *Biomaterials* **1999**, *20*, 2363–2376.

inexpensive manner, is transparency-based photolithography. In this technique, the mask is generated by simply printing a pattern on a transparent overhead sheet, using a commercial inkjet or laser printer. Although the minimum feature size that can be accomplished is approximately 2 orders of magnitude larger than with conventional photolithography, it is still small enough (down to tens of micrometers) to make a valuable tool in fundamental cell biology studies[68], given that cells are typically 10–20 μm in size.

Yet another light-based patterning technique that allows for some control in the *z*-direction, makes use of two-photon polymerization to functionalize specific regions inside a transparent gel. In two-photon polymerization, the photoinitiator is excited by the (nearly) simultaneous absorption of two photons of relatively low intensity, which together introduce enough energy to initiate a chemical reaction. As a result, two-photon polymerization is a nonlinear optical process in which the reaction rate is proportional to the square of the laser intensity in contrast to a linear relationship, as in the case of single-photon polymerizations. This leads to more localized reactions. With this technique, Hahn *et al.*[69] locally modified a PEG-diacrylate (PEG-DA) hydrogel with acryl-PEG-peptide moieties, creating 3D cell-adhesive islets. Alternatively, they showed that low-molecular weight PEG-DA can be used to alter local cross-link density and, hence, transport and mechanical properties.

5.542.2.2.2. Examples of 2D substrate patterning studies for tissue engineering

As described previously, patterning technologies can spatially control surface chemistry and topography at the micrometer level and, therefore, they have the ability to control spatial cell distribution and study the effects of geometrical cues and spatial confinement on cellular behavior. Spatial concentration gradients prepared by modulating the spacing or width of photopatterned cell-adhesive peptide moieties influence cell alignment, morphology and motility. For example, Ito *et al.*[70] used photolithography to pattern a gradient in immobilized heparin, and cultured NIH3T3 cells in the presence of basic fibroblast growth factor. The cell proliferation was enhanced in a heparin density-dependent manner. The specific advantage of the patterning technique here is that a range of heparin densities can be tested at once, with nonimmobilized regions as an internal control. Chen *et al.*[71] used a similar technique to graft the thermoresponsive polymer poly(*N*-isopropylacrylamide-*co*-acrylic acid) to TCPS in a patterned manner, enabling the selective detachment of cells by cooling as a stimulus. In the same group, studies have also been performed on (micropatterned) photografting of pH-responsive polymers,[72] growth factors such as epidermal growth factor[73] and vascular endothelial growth factor,[74] cell-adherent proteins such as gelatin[75] and sugars such as β-galactose,[76] and sulfated hyaluronic acid for antithrombogenicity.[77]

Hahn *et al.*[57] used the simple and inexpensive transparency-based lithography approach to pattern otherwise non cell-adherent PEG hydrogel surfaces with the cell-adhesive arginine-glycine-aspartic acid-serine (RGDS) peptide sequences. The transparency of the hydrogel also enabled the construction of multiple layers of the patterned material.

The studies described above demonstrate the wide range of possibilities of functionalizing surfaces in a patterned manner, thereby preferentially influencing spatial cell distributions. The strength of high-resolution patterning techniques in relation to organ printing is exploited particularly when the behavior of the cells itself is influenced by altering their microenvironment. For example, Sarkar *et al.*[78] showed that the orientation of vascular smooth muscle cells (VSMCs), their F-actin fibers, and deposited fibronectin fibrils can be influenced by growing them in small-sized channels. For channels up to 50 μm in width, the cells were nearly 100% aligned, with a high aspect ratio of 12. Above 50 μm channel width, the aspect ratio and fiber alignment are decreased, and no preferred orientation is observed on nonpatterned surfaces. The structural organization of VSMC and their ECM is believed to play a crucial

role in the functionality of blood vessels of small diameter. The geometry of the cellular environment not only affects cell orientation, but also influences cell motility and shape. A study in which single cells were cultured on small adhesive islands of different shapes revealed a preferential focal point adhesion at sharp edges.[79] The deposition of synthesized fibronectin also took place particularly from these edges. The shaped islands, each measuring 900 μm^2 surface area, were prepared by microcontact printing of an alkanethiol on a gold-coated glass coverslip, followed by coating with fibronectin. Before the fibronectin coating step, the nonprinted area was made non-cell-adhesive by binding with PEG-alkanethiolate. Another strong example of geometry-driven manipulation of cellular behavior was presented by McBeath *et al.*,[80] using surfaces microcontact printed with fibronectin to prepare islets of different sizes. They showed that the differentiation of mesenchymal stem cells can be triggered by geometrical cues. The degree of cellular adhesion regulated the switch in MSC lineage commitment; the activation of the RhoA–ROCK pathway appeared to be instrumental in this switch. High activation of RhoA and ROCK led to osteogenic differentiation while low activity resulted in adipogenic differentiation, independent of cell shape.

5.542.2.2.3. Direct manipulation of cells

While the techniques and examples described above focus on the patterning of surfaces for the indirect manipulation of cell behavior, some of these techniques can be used for direct manipulation of cells as well. The use of UV and organic solvents prohibits the direct use of cells with most lithographic methods, but soft lithography techniques (microcontact printing in particular) can be used with cells. Using PDMS stamps prepared by photolithographic methods, patterns of cells can be transferred to a substrate. This form of microcontact printing is often referred to as cell stamping.[81] Cell stamping has also been performed on the surface of porous hydroxyapatite scaffolds.[82] Agarose hydrogel stamps were used for their low cell adhesion properties. Moreover, the hydrated surface ensured that the viability of cells adsorbed on stamps during the patterning process was maintained.

Laser-induced optical forces can be used in several ways for noncontact manipulation of particles 100 nm to 10 μm in diameter. One of these techniques is referred to as laser-guided direct writing, in which individual cells in suspension are guided to be deposited onto solid surfaces.[83] The optical force arises from a difference in the refractive indices of the cell and the medium it is suspended in. A laser beam that is directed off-center to the spherical cell is partially reflected and partially refracted to a different path, thereby transferring an impulse to the cell. By moving the target surface relative to the laser beam, arrays of cells are deposited. Although this ability to manipulate single cells in a noncontact manner is impressive, it has a number of limitations. Perhaps the major limitation is the low cell numbers that can be deposited, which makes it very difficult to upscale this technique for organ-printing purposes. Furthermore, it will be a challenge to retain the assembly of written cells, as they are only brought in physical contact with the substrate and do not necessarily bind to it directly.

Another cell manipulation technique that is laser-based, but works in a totally different manner, is matrix-assisted pulsed laser evaporation direct write (MAPLE DW), or simply laser printing.[84] In this technique, a layer of cells in medium is absorbed on the lower side of a quartz glass plate (**Figure 6**). A microscope objective is used to focus a laser beam on the plate, which results in a highly localized sharp temperature increase. This causes a small volume of liquid to vaporize and expel a jet of cell-containing medium, which is then deposited on a substrate. The excessive temperature during droplet generation does not appear to compromise cell viability, nor do printed cells express significantly higher levels of heat shock protein than nonprinted controls.[85] For the moment, laser printing works with cell-laden strips in a batch-wise manner; therefore, to reach high-throughput rates, a feeding mechanism for the continuous dispensing of cells will have to be established. Another challenge is to introduce hydrogels, or

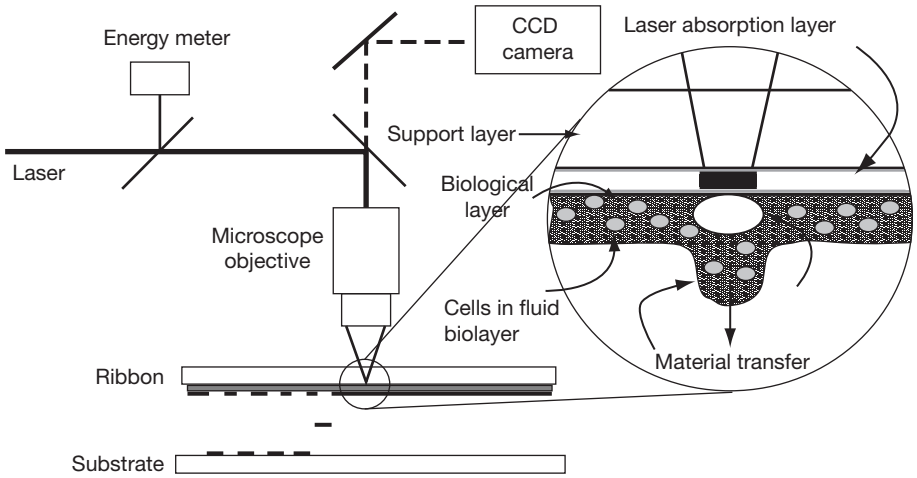

Figure 6 Schematic of a biolaser printing setup. A laser beam that is focused through a microscope objective heats up a small area on a metal or metal oxide absorption layer. The sudden localized temperature increase induces evaporation of a small volume of liquid in the biolayer, followed by expulsion of a drop of cell-containing liquid. Reproduced with permission from Barron, J. A.; Ringeisen, B. R.; Kim, H. S.; Spargo, B. J.; Chrisey, D. B. *Thin Solid Films* **2004**, *453*, 383–387.

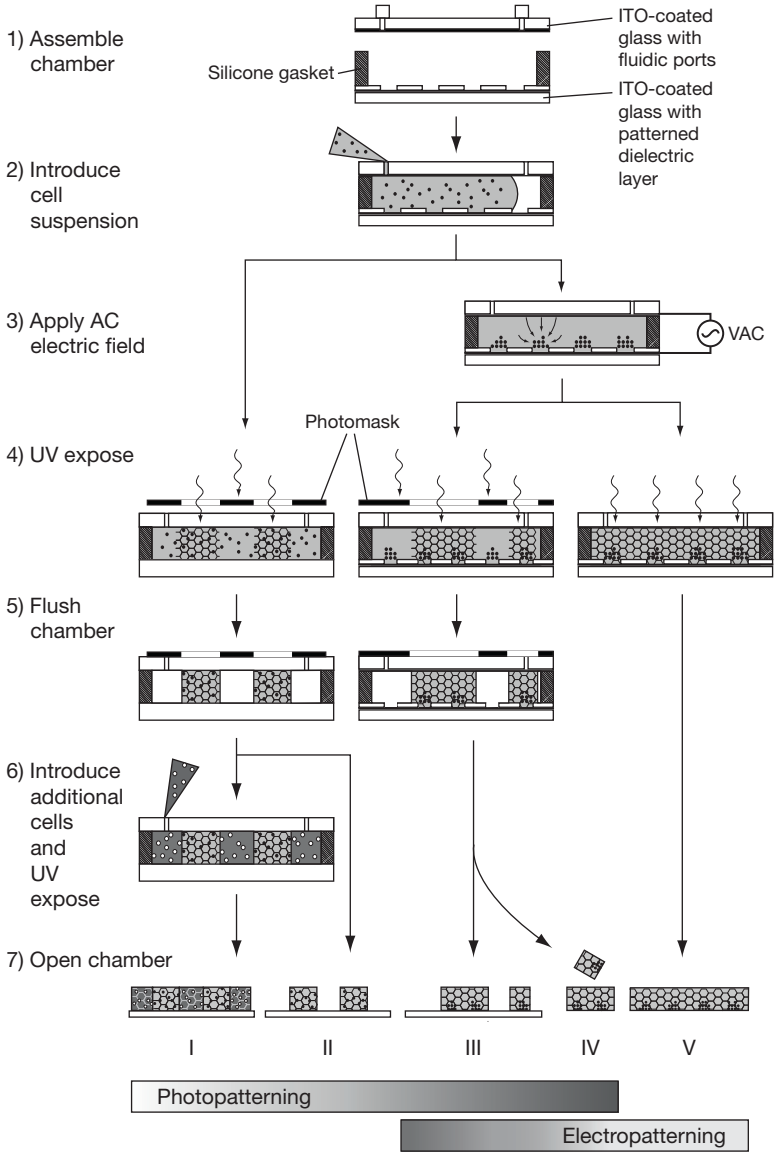

Figure 7 Schematic showing the versatility of the hydrogel photopatterning and cell electropatterning techniques for making hydrogel microstructures with encapsulated living cells. I, II. Photopatterned gels with randomly encapsulated (multiple types of) cells. III, IV. Photopatterned gel with clustered encapsulated cells on a substrate (III) or free-floating (IV). V. Free-floating unpatterned hydrogel with encapsulated cell clusters. Reproduced with permission from Albrecht, D. R.; Tsang, V. L.; Sah, R. L.; Bhatia, S. N. *Lab Chip* **2005**, *5*, 111–118.

some other form of support structure, to enable printing of stacked layers for organ-printing purposes.

Another cell manipulation approach is based on cell organization by dielectrophoretic forces and subsequent entrapment in a UV-sensitive hydrogel.[86] This combination of patterning techniques makes it possible to fabricate layered 3D matrices with variable cell and gel organization (Figure 7). It makes it possible to study the effects of volumetric cell density, nutrient transport, and paracrine signaling (i.e., signaling between adjacent cells). Microorganization of bovine chondrocytes patterned with this technique was shown to have direct biological consequences with respect to their synthetic activity. The cumulative quantity of deposited glucosaminoglycan matrix proteins per cell decreased in a dose-dependent manner with increase in the size of cell clusters, indicating that homogenous cell distribution at high cell densities is indeed more desirable for adequate ECM formation.[87]

5.542.2.3. Translating 2D Approaches to 3D

Microfabrication tools make it possible to understand how spatial presentation of regulatory signals, such as adhesive molecules and growth factors, tailors cell microenvironment and regulates cellular responses,[57,88] and help to uncouple some of the regulatory signals involved in cell–matrix interactions.[87] Cellular patterning techniques can easily control the degree of interaction between the two cell populations and allow of studying cellular interactions of different ratios.[89]

Recent technical developments have made it possible to perform patterning of adhesive sequences in 2D+, for example, by micromolding and stacking layered 2D structures.[58,69,90] Other approaches to generating microcontrolled materials make use of a photolithographic technique to pattern bioactivity of desired dimensions into a preformed, existing material.[91] A similar technique uses a 3D focused laser with higher intensities, with the aim of removing material through photoablation.[92] Using PEG-fibrinogen hydrogels, this technique allows for the 3D patterning of patterns/channels to promote and direct cell migration and assembly of 3D networks of cells.

Not all the 2D patterning and cell manipulation techniques described above have the potential to be translated to make 3D cellular constructs. Limitations can be either the possibility to upscale to dimensions relevant for organ printing, or that the used technique is inherently 2D. The most straightforward way to translate a 2D technique to 3D is to perform the 2D fabrication process repeatedly in a layer-by-layer fashion. Most photolithographic techniques rely, however, on the modification of nondegradable substrates such as gold, silicon, or glass with biofunctional molecules on their surfaces rather than producing full layers of functional biomaterials. Translation of this technique therefore requires labor-intensive production and coalignment of individual parts to achieve multilayered structures.[93] Introducing intricate shape and porosity into these structures is very challenging. This renders these techniques unsuitable for fast and efficient development of 3D tissues.

Lithography of cell-containing gels seems more promising for 3D application, such as shown by Hahn *et al.*[69] using a computer-controlled laser and two-photon polymerization. A similar opportunity for translation to 3D is found for electropatterned cell-containing hydrogels such as those presented by Albrecht *et al.*, by stacking prefabricated gel layers. In mask-based photolithography, particularly, the use of printed transparent overhead sheets is promising as these provide an easy and inexpensive way of making masks with dimensions relevant to organ printing. Actually, automated 3D photolithography has already been developed and first steps are being taken to apply stereolithography to organ printing, which is described in **Section 5.542.3.2.3**.

For the possibility of continuous cell deposition techniques to be used in 3D, the structural integrity of the cell layer is the main determinant. Other important factors are the throughput rate and the accuracy of positioning each layer in line with the previous one. Often, there is a trade-off between these two factors. Laser-guided direct writing has a very high accuracy as cells can be manipulated individually, but the throughput rates and scale of the application are far from being applicable to organ printing. Another obstacle is that cells need to be suspended in nonviscous media, which impedes the use of hydrogels. Finally, for making larger multilayered constructs, there will have to be a mechanism to fix the organization of cells being deposited by the laser. For the biolaser printing technique, upscaling seems to be less of a problem, but that could go at the cost of accuracy. The challenges here are the continuous feeding of the liquid film, fixation of a printed layer, and accurate printing of subsequent layers.

Many approaches have been attempted in 2D to investigate a proof-of-principle for the process, with the aim of translating it to 3D. In reality, however, very few approaches have been translated to 3D, or they have a number of limitations or shortcomings that impede their application in organ printing. Still, these developments may be suited to alternative tissue engineering and regenerative medicine applications on smaller tissues, or for drug screening.

5.542.3. 3D Organ-Printing Processes

5.542.3.1. Organ Printing Versus Book Printing

Cell and organ printing are often compared to the traditional book printing technique invented by Johannes Gutenberg in the fifteenth century.[56] In this analogy, five essential components are needed, which are summarized in **Table 1**

Although the analogy between traditional printing and organ printing stretches far, it is incomplete in the sense that traditional printing is only a 2D process, whereas the third dimension is essential for printing organs. Organs consist of multiple tissues, each having complex 3D architectures with spatial differences in cell types, cell densities, and composition of the ECM. Taking into account the 3D character of organ printing, the comparison of cell support structures to paper, particularly, is an imperfect one. Whereas paper is a preformed support structure for the printing of text, the support structure for cells in organ-printing applications has to be, in most cases, prepared in the printing process itself. Organ-printing techniques should therefore rely on the simultaneous dispensing or assembling of cells or cell aggregates and support materials, mostly hydrogels. This can be achieved using techniques based on a number of operating principles, which are introduced in the following sections.

5.542.3.2. Overview of 3D Techniques

Earlier, we discussed techniques for the direct manipulation of cells in 2D. Although some of these techniques could be, or have been, used to make multilayered constructs, many of them cannot be upscaled to fabricate large, 3D living structures. Most of the techniques to date that have shown potential to actually prepare such 3D structures can be roughly divided into two categories. They are jet-based techniques and robotic dispensing techniques, as summarized in **Table 2**.

5.542.3.2.1. Inkjet printing

The idea of being able to print live organs using a desktop printer is truly fascinating. The application of low-cost, everyday use Hewlett-Packard (HP) inkjet printers in the early studies of bioprinting perhaps added to the vision of a revolution at

Table 1 Components required for printing, comparing organ printing to traditional (book) printing

Traditional printing	*Organ printing*
Written text	Digital blueprint of organ
Printing press	Bioprinter
Moveable type	Cartridges or dispensers
Paper	Hydrogel or support structure
Ink	Cells or cell aggregates

Table 2 Overview of techniques for the computer-controlled fabrication of cell-laden hydrogel constructs for organ-printing purposes

Technique	*Gels*	*Cells*	*Gels + cells*
Inkjet printing			
Thermal Piezoelectrical	Boland *et al.*,[17,94] Roth *et al.*[95]	Wilson and Boland,[18] Xu *et al.*,[96,97] Saunders *et al.*[100]	Nishiyama *et al.*,[98] Xu *et al.*[99]
Robotic dispensing			
Mechanical			Smith *et al.*,[101] Khalil *et al.*,[102] Cohen *et al.*[103]
Pneumatic			Smith *et al.*,[101] Khalil *et al.*,[102] Yan *et al.*,[104] Wang *et al.*,[105] Fedorovich *et al.*,[106] Li *et al.*[107]
Stereolithography			Dhariwala *et al.*,[108] Arcaute *et al.*,[109] Lu *et al.*,[110] Arcaute *et al.*[111]

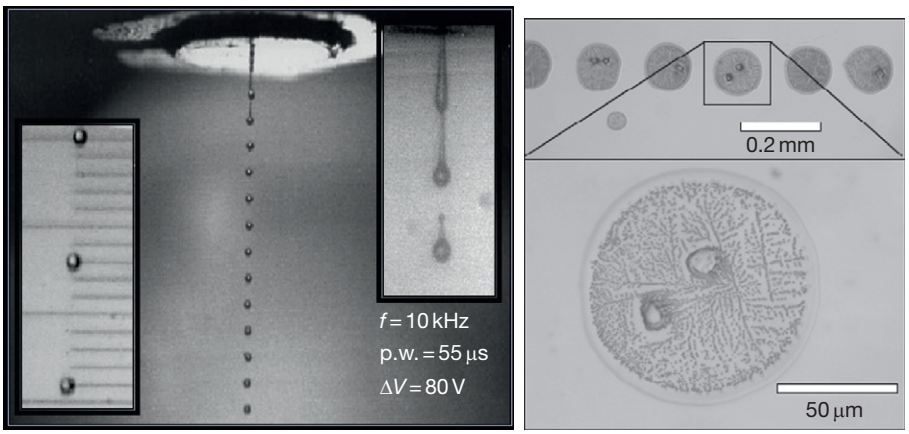

Figure 8 Inkjet printhead in action – a stroboscopic image showing the train of droplets being jetted from the orifice (left). Adapted from Reis, N.; Ainsley, C.; Derby, B. *J. Appl. Phys.* **2005**, *97*. Chondrocytes printed in alginate–agarose doplets (right). Reproduced with permission from Saunders, R.; Gough, J.; Derby, B. Deposition and immobilization of mammalian cells via piezoelectric drop-on-demand inkjet printing. In *Proceedings World Biomaterials Conference*, Amsterdam, The Netherlands, 2008.

hand.[17,18] Inkjet printing refers to the spatially controlled dispensing of a jet of small drops of liquid material through a small orifice (Figure 8). In thermal inkjet printing, small volumes of the printing fluid are vaporized by a microheater to create the pulse that expels droplets from the print head.[112] This could explain the significant cell death (26%) observed upon thermal inkjet printing of primary rat embryonic hippocampal and cortical cells,[113] although dehydration of the printed cells has also been suggested to have compromised the viability in this study. Alternatively, in piezoelectric-actuated inkjet printing, no heating is used for creating the pulse. Moreover, it allows for some control of the mechanical stress experienced by the cells during the printing process.[114] A recent thorough investigation of the influence of piezoelectric inkjet printing on the viability of a human fibroblast cell line reported no statistical difference in the viability of printed cell populations compared to unprinted controls, for optimized printing conditions.[100] Analysis of metabolic activity revealed no evidence for decreased functionality of printed cell populations.

To date, the predominant focus of studies in the literature related to inkjet printing of cells and gels is on 2D printing only. Generally, cells, either in culture medium or in a hydrogel precursor, are printed onto a sheet of collagen or a synthetic polymer that is used as biopaper.[17,18] A challenging barrier to overcome in translating inkjet printing to organ printing, is the fabrication of 3D structures. For this, a liquid-to-solid transition has to occur to make layering possible. The relatively low threshold for the viscosity of inkjet printing fluids, typically around 30 mPa s,[115] becomes a severe restriction. To date, the most commonly adopted system is that of sodium alginate and calcium ions (mostly from $CaCl_2$ solutions), which form a gel upon mixing. Boland *et al.*[94] have printed the less viscous $CaCl_2$ solution into a bath of sodium alginate to print the branched structure depicted in Figure 9. In their setup, a jet of $CaCl_2$ droplets is printed into a 100 μm liquid top layer, leading to local gel formation. After the printing of each layer, the object is moved down into the bath, leaving the next film of liquid exposed to the incoming jet. As the calcium ions diffuse into the surrounding sodium alginate solution to induce gelation outside the droplets, a characteristic hollow-shell structure is formed (Figure 9). Therefore, it is unlikely that this system could be used to print cell-containing gels.

Alternatively, Xu *et al.*[99] followed the opposite approach and printed drops of the more viscous alginate solution into a $CaCl_2$ solution. As the same phenomenon takes place in this situation, but in the opposite direction, it has proven a promising method to form alginate beads with encapsulated cells. Nishiyama *et al.*[98] followed the same approach to print alginate beads and rings containing viable cells. However, the

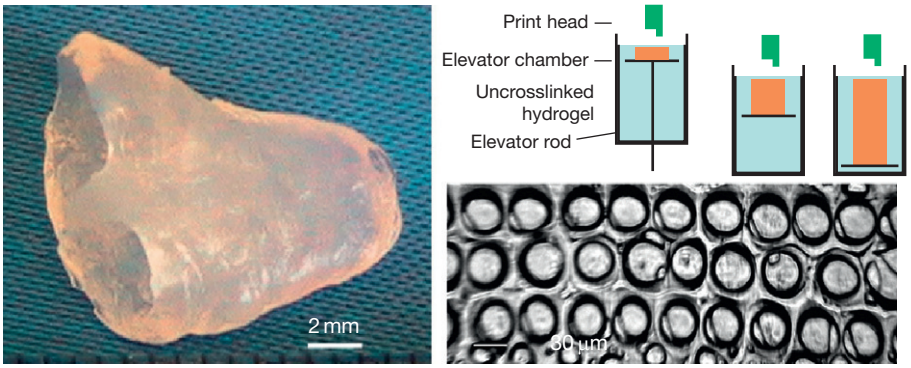

Figure 9 Alginate 3D structures prepared by thermal inkjet printing of a $CaCl_2$ solution into a sodium alginate pregel. Reproduced with permission from Boland, T.; Tao, X.; Damon, B. J.; *et al. Mater. Sci. Eng. C Biomim. Supramol. Syst.* **2007**, *27*, 372–376.

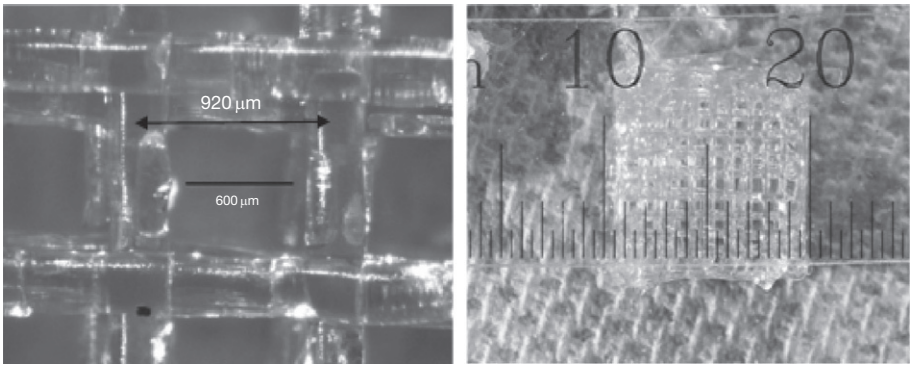

Figure 10 Close up image (a) and overall image (b) of alginate scaffold produced by pneumatic dispensing. Scale bars: 1 mm. Reproduced with permission from Khalil, S.; Nam, J.; Sun, W. *Rapid Prototyping Journal* **2005**, *11*, 9–17.

typical gelling behavior of the alginate/calcium system makes it impractical for printing robust, well-fused gel structures with encapsulated cells.

Although inkjet printing was the first technique reported to be associated with organ printing, it has shown limited development in the construction of organs since the introduction of the organ-printing concept. In their attempts to increase the chance of success of inkjet printing of complex 3D TECs, materials scientists are facing the difficult challenge of turning low-viscous solutions into strong, biocompatible materials.

5.542.3.2.2. Robotic dispensing systems

Although organ printing was first proposed to become a jet-based platform,[21] the most successful attempts to prepare cell-containing constructs have been via the use of dispensing-based systems (Table 2). Perhaps the simplest setup used so far has been one composed of a gantry robot with a syringe-based deposition tool.[103] Using this system, predesigned shapes were fabricated from alginate hydrogels, and cells could be printed in the hydrogels with a viability of $94 \pm 5\%$. Although external geometries of an intervertebral disk and a meniscus could be well reproduced with this system, the 1.2 mm diameter of the deposited strands provides only limited spatial control for placing cells and materials. Higher spatial resolutions are usually achieved by pneumatically actuated dispensers. Figure 10 provides an example of the accuracy of patterned pneumatic dispensing of a 3% sodium alginate solution into a 5% calcium chloride solution, causing instant gelling. The figure shows a stable alginate hydrogel structure built up from 0.2-mm-thick strands.

Khalil *et al.*[102] have combined several dispensing techniques in one multinozzle dispensing system, allowing dispensing of materials with a large range of properties. Table 3 summarizes the characteristics of the four different nozzle systems. Interestingly, a piezo-actuated inkjet dispenser is included in the system, enabling direct comparison of this technique with others. Here, the particular disadvantages of inkjet-based systems discussed earlier (low viscosity threshold and droplet-based dispensing) are reiterated. The solenoid-actuated micronozzle forms an attractive alternative as it provides the ability to deposit strands of material in a continuous method. Still, it has a much faster response and possibly more control over the dispensing than the pneumatic micronozzle. Finally, the pressurized miniextruder could be employed to deposit fibers of highly viscous materials such as thermoplastics. Unfortunately, the authors did not present a comprehensive study to compare the specific advantages and limitations of the dispensing systems. Theoretically, the combination of

Table 3 Characteristics and comparison of four different nozzle systems

Features	*Pressurized miniextruder*	*Solenoid micronozzle*	*Piezoelectric micronozzle*	*Pneumatic micronozzle*
Deposition mode	Continuous	Continuous/droplet	Droplet	Continuous/droplet
Operation/ control	Rotating screw gear via motor	Frequency pulse of voltage	Frequency pulse of voltage	Frequency pulse of air pressure
Key process parameters	Pressure and speed, temperature, material, nozzle diameter, deposition speed	Pressure, frequency pulse, material, nozzle diameter, deposition speed	Pressure, frequency pulse, material, nozzle diameter, deposition speed	Pressure, frequency pulse, material, nozzle diameter, deposition speed
Operating range limitations	Screw speed <1rps Temperature <150 °C *D*: 0.18–0.25 mm	*V*: 40 V(DC) *H*: (1–1200 Hz) *D*: (30, 50, 70 μm)	*H*: (0–20 000 Hz) *V*: (−100 to 100) *D*: (30, 50, 70 μm)	*H*: (0.01–14 Hz) Fluid *P*: (0–345 kPa) Valve *P*: (483–690 kPa)
Structure formation	Physical solidification	Physical solidification, chemical reaction	Physical solidification, chemical reaction	Physical solidification, chemical reaction
Advantages	Fast solidification, no solvents, strong structure, sterile environment	Room temperature, extrusion and droplets, sterile environment	Room temperature, micro-droplet depositions, controlled volume, sterile environment	Room temperature, high viscosity, extrusion and droplet, sterile environment
Disadvantages	Temperature, low melting material	Low viscosity, droplet controllability	Low viscosity, not continuous deposit	Droplet controllability, precision deposition

Source: Khalil, S.; Nam, J.; Sun, W. *Rapid Prototyping J.* **2005**, *11*, 9–17.

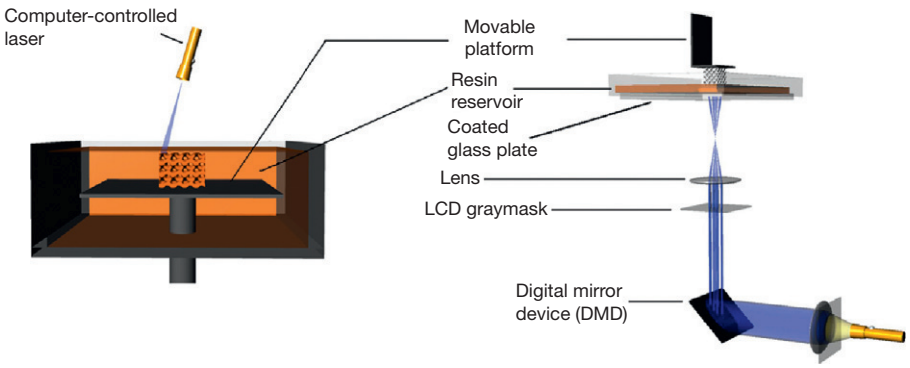

Figure 11 Schemes of two types of stereolithography setups. Left: A bottom-up system with scanning laser. Right: A top-down setup with digital light projection. Reproduced with permission from Melchels, F. P. W.; Feijen, J.; Grijpma, D. W. *Biomaterials* **2010**, *31*, 6121–6130.

extruding a thermoplastic (which is basically fused deposition modeling[11]) and plotting a cell-containing hydrogel in one structure could unite the favorable mechanical properties of prototyped solid scaffolds with the precise placement of cells seen in organ-printing techniques. So far, the employment of such a combination has not been reported.

In more recent years, several studies have been published on the robotic dispensing using pneumatic systems of gelatin-based formulations with encapsulated hepatocytes or neural cells,[97,104,105,107] and of several synthetic and natural hydrogels containing bone marrow stromal cells.[106] These successful attempts to encapsulate cells in structured hydrogels make it likely that pneumatic robotic dispensing systems will continue to play a large role in organ printing in the future.

5.542.3.2.3. Stereolithography

Stereolithography is another SFF technique that allows for creating computer-designed 3D hydrogel structures with encapsulated cells.[116] The working principle of stereolithography is based on the spatially controlled solidification of a liquid resin by photopolymerization (Figure 11). It is a layer-by-layer form of photolithography, where the pattern is created by the use of either a computer-controlled laser beam or a digital light projector. In the latter case, the instant creation of a pixelated light pattern is achieved using an array of millions of mirrors, which can be individually and independently rotated to an on or off state. The pattern is illuminated on the surface of a resin, which is then solidified to a defined depth. After photopolymerization of each layer, the supporting platform is moved away from the surface and the built layer is recoated with liquid resin. A pattern is then cured in this second layer. By controlling the depth of curing through light intensity and exposure time, good adherence to the preceding layer is ensured.

Various research groups have used water-soluble di(meth) acrylated poly(ethylene glycol) (PEG-D(M)A) precursors to create structured, cell-containing hydrogels by stereolithography. The first reported successful cell encapsulation using stereolithography made use of Chinese hamster ovary cells and PEG-DMA precursors.[108] Later, PEG-DMA constructs containing

encapsulated human dermal fibroblasts,[109] and PEG-DA gel structures containing marrow stromal cells[110] were reported. In all the cases, cells could be encapsulated at high densities: several millions of cells per milliliter. The cells showed good survival after fabrication of the construct, especially when peptides containing RGD sequences were incorporated in the gels.[109] In cell encapsulation based on photopolymerization, factors such as the choice of photoinitiator and its concentration, wavelength and intensity of the light source, and pH, all play a critical role.[117] Besides cells, ligands, ECM components, growth factors, and controlled release particles can also be patterned inside a single scaffold using stereolithography.[118]

Stereolithography is the SFF technique with the highest accuracy and precision; it is also the most versatile with respect to freedom of design. Additionally, the automated process and scale of application make it a promising technique for organ printing. Perhaps the major limitation of the technique is that to date, fully automated fabrication is possible with only one type of resin (or cell suspension) at a time. The ability to pattern multiple resins in a construct or even within a single layer has been demonstrated, but complex sequential polymerization and rinsing steps were required for each layer built.[109,118] A major technological challenge lies in developing an automated system to feed different resins and remove uncured resin,so that eventually different cell types can be patterned in specific locations in 3D.

5.542.3.2.4. Robotic assembly

A possible route to fabricate 3D TECs that is still in an early stage of development is via robotic assembly of designed microparts. This approach is based on the same concept as assembling a structure using small building-block units as in Lego.[10] By combining parts with different designs, porous structures with controllable pore sizes and porosities can be assembled, thereby influencing local mechanical and transport properties as well. An example of an assembly setup with four degrees of freedom and a shape-memory alloy-based microgripper is depicted in Figure 12.

Suitable microparts have been accurately fabricated by photolithography from SU-8 photoresist resin.[119] Although not biodegradable and therefore of limited use for tissue engineering purposes, cured SU-8 is a suitable cell substrate with mechanical properties comparable to poly(L-lactide) and therefore apt for proof-of-principle and *in vitro* cell culture studies. A second set of nondegradable microparts was fabricated using an acrylic resin with a rapid microproduct development (RMPD) process based on stereolithography. Since then, many stereolithography resins have been developed for the direct fabrication of biodegradable tissue engineering scaffolds.[116] It can therefore be expected that in the future, biodegradable microparts for robotic assembly with a wide range of physical properties will be fabricated for the engineering of a wide range of tissues.

The ability to seed the microparts with cells prior to scaffold assembly is what makes this technique particularly interesting for tissue engineering following the organ-printing approach. Different parts could be seeded with different cell types, or multiple cell types could be seeded on the microparts in a patterned manner using cell stamping techniques, as described in Section 5.542.2.2.3. The patterning of proteins on the microparts is another possibility. In these ways, cellular constructs can be fabricated with a controlled cellular organization. The biggest difference when comparing robotic assembly to inkjet or robotic dispensing systems is the 'biopaper' being solid parts as opposed to hydrogels in which cells are encapsulated. This makes the approach particularly interesting for the engineering of hard tissues, where load-bearing scaffolds are desirable. The robotic assembly of TECs is a complex process that requires the combined use of advanced technologies. It involves the use of precise robots, image analysis, and force feedback systems, different feeds of microparts preseeded with cells, and a sterile environment under physiological conditions. Perhaps this complexity is why it is less established than hydrogel-based printing and dispensing systems. Nevertheless, it is a promising approach for organ printing that deserves the attention of tissue engineers in the future.

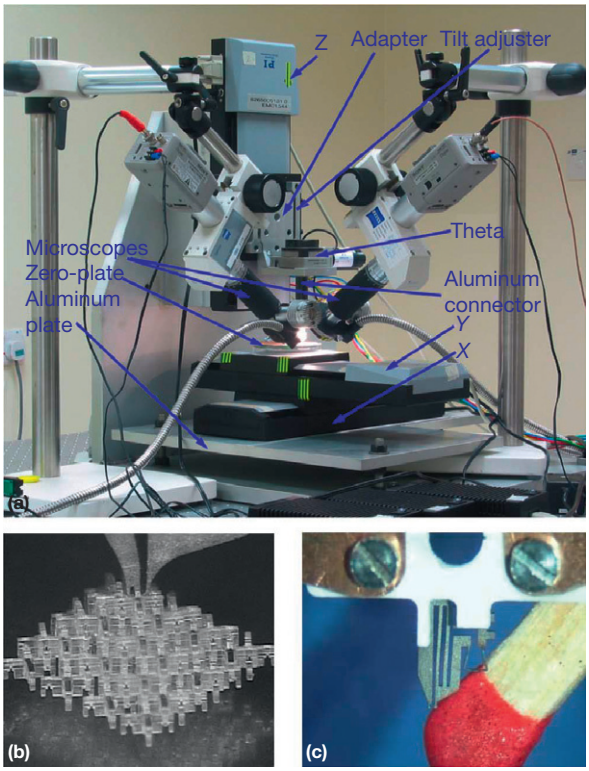

Figure 12 (a) Dedicated precision workstation for microassembly. (b) Whole scaffold can be lifted up by grasping one part, showing that microparts cleave together without glue or thermal treatment. (c) Shape memory alloy microgripper. Reproduced with permission from Zhang, H.; Burdet, E.; Poo, A. N.; Hutmacher, D. W. *IEEE Trans. Autom. Sci. Eng.* **2008**, *5*, 446–456.

5.542.3.3. Developmental Phases and Components Associated with 3D Organ Printing

5.542.3.3.1. Preprocessing: design

In order to fabricate organ constructs of anatomical shape and size, blueprints of the organ in the form of a CAD are the first requirement. Medical imaging techniques such as computed tomography (CT) and magnetic resonance imaging (MRI) can be used to get a digital image of an organ, or of a defect that is

to be tissue engineered. These digital images can be manipulated to serve as building instructions for the organ-printing process. Over the last few years, the combination of medical imaging and SFF techniques has found its way into the tissue engineering field. In the first reported uses, the fabricated parts served as moulds to prepare anatomically shaped implants.[120–122] Woodfield *et al.*[123] used CT data to directly fabricate anatomically shaped rabbit knee scaffolds using fused deposition modeling and a biodegradable polymer. The implants showed congruent articulation after a 5 week culturing period and subsequent *in vivo* implantation for 6 weeks. Cohen *et al.*[103] showed that they could fabricate a solid meniscus-shaped hydrogel structure designed from a CT scan, using the same device and hydrogel, as was used for cell-laden constructs. It is expected that the use of medical imaging will become standard practice in designing constructs to be fabricated by organ printing.

5.542.3.3.2. Printing cell-laden 3D hydrogel constructs

Printed cells are encapsulated homogeneously in printed hydrogel strands and overcome the current drawbacks of heterogeneous tissue development caused by inhomogeneous cell seeding and dispersion (see **Chapter 5.509, Cell Encapsulation**).[106] The cells, localized to separate layers by interlayered cross-linking, retain the printed architecture.[124] Furthermore, printing sustains high cell viability, and cells retain the ability to differentiate after printing.[106]

Most published studies on the automated printing of cell-laden hydrogel show proof-of-principle of construct fabrication and cell viability (see **Table 4**, **Section 5.542.3.3.3**). The first steps have now been taken to further develop these systems and understand the parameters that govern the processes. Smith *et al.*[125] studied the influence of processing parameters such as printing pressure and pen speed, and environmental factors such as humidity and stage heating on printed line widths and cell viability.

Although most of the used systems are still custom-built, in the last few years several systems have become commercially available (**Figure 13**), and more have been announced. The technological development of such systems will play a key role in the functionality of printed tissue and organ constructs.

5.542.3.3.3. Hydrogels: gels used and criteria for developing hydrogel carriers for cell and organ printing

Hydrogels are extremely hydrated polymer networks. Due to their high water content, they are highly biocompatible and can act as 3D supportive matrices to embed cells in organ printing[126] (**Table 4**). Hydrogels are built up of water-soluble polymers, either synthetic or natural, which swell in water due to cross-links as opposed to dissolving, thereby maintaining structural integrity. The cross-links between the polymer chains are either physical interactions or covalent bonds.

Hydrogels based on ECM polymers provide an adhesive surface for the cells, but their composition is unpredictable, and their mechanical properties and degradation rates are difficult to control. Synthetic hydrogels offer a higher lot-to-lot uniformity with a more controllable and reproducible scaffold structure, gel formation dynamics, degradation rates, and mechanical properties. Stimulus-responsive hydrogels are well suited for organ printing because gel formation can be controlled during and after the printing process. These types of materials form a gel in response to changes in their environment. Cross-linking can be initiated using physical stimuli such as changes in temperature, pH, and ionic environment, or can be chemically induced via enzymatic reaction, or exposure to UV light in the presence of a photoinitiator (photopolymerization). In general, hydrogels have good cytocompatibility. They can homogeneously incorporate and suspend cells, growth factors, and other bioactive compounds while allowing rapid diffusion of nutrients to, and metabolites from, incorporated cells. A major disadvantage of hydrogels is their low mechanical strength, which makes handling and *in vivo* application difficult. The low strength is because hydrogels consist predominantly of water, held in place by a relatively fragile polymer network.[127] Therefore, a popular approach in biofabrication is the improvement of the mechanical stability by modification of hydrogels with photosensitive sequences that result in covalent cross-linking. [128] Alternatively, various methods exist to prepare hydrogels with greatly improved mechanical properties and toughness, in particular. Among these are the use of slide-ring gels, double-network gels, and nanocomposite gels.[129] Future studies will show how, deriving advantage from the extraordinarily improved mechanical

Table 4 Hydrogels used for cell encapsulation in organ-printing and related techniques

Hydrogel	*Technique*	*Viability (%)*	*Proliferation*	*References*
Natural				
Collagen	Mech. dispensing	86[a] 46[b]	30% in 24 h	101
Gelatin	Pneum. dispensing	98	None (3 months)	105
Matrigel	Pneum. dispensing	99	None (2 weeks)	106
Agarose	Pneum. dispensing	93	None (2 weeks)	106
Alginate	Mech. dispensing	94	N/A	103
	Pneum. dispensing	91	None (2 weeks)	106
Synthetic				
PEG-DA	Stereolithography	65	N/A	108
PEG-PPO-PEG	Mech. dispensing	60	N/A	101
	Pneum. dispensing	84	>95% cell death in 3 days	106

[a]25 gauge needle.
[b]33 gauge needle.

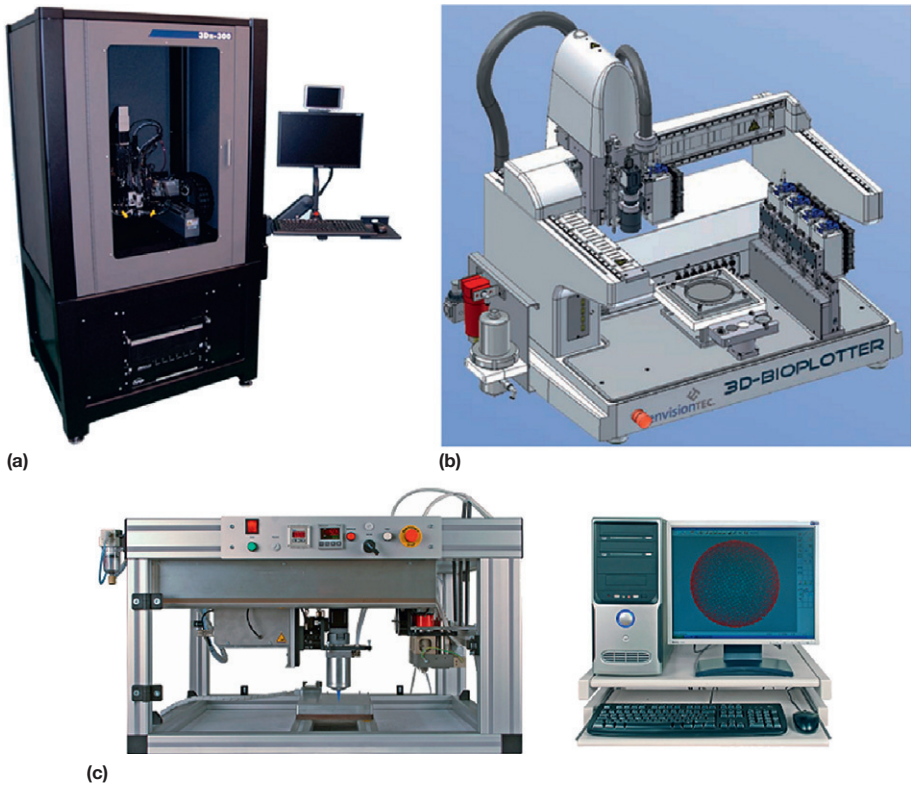

Figure 13 Commercially available robotic dispensing systems. (a) BioAssembly Tool (nScript, USA). (b) 3D-Bioplotter (Envisiontec, Germany). (c) BioScaffolder (SysEng, Germany).

properties, these novel approaches can be used for organ printing, in conjunction with cell encapsulation and printing techniques.

Unmodified synthetic hydrogel matrices commonly lack suitable binding sites for the cells to adhere to, and these gels are also limited in their ability to support cell differentiation. Modifications that have been applied to target cell functioning include incorporation of adhesive sequences (e.g., RGD; heparin-binding sites), and peptides coding for growth factors.[130,131]

Cell migration through extracellular matrices is a key step in morphogenesis and tissue regeneration. As hydrogels are molecular mazes with mesh sizes typically below 1 μm, the migration, and therefore proliferation and functioning of embedded cells as well, can be severely restricted by the polymer chains in hydrogels. Particularly, in covalently cross-linked hydrogels, embedded cells can remain viable, but show little proliferation.[106] Wang *et al.*[132] cultured hepatocytes in glutaraldehyde cross-linked 3D gelatin structures for as long as 3 months, without observing an increase in cell number. Cell proliferation functions could still be detected by the multiple nuclei and nearly separated cytoplasts, but full mitosis and proliferation were arrested by chemical cross-links induced by the glutaraldehyde treatment. For the engineering of some tissues, cell proliferation is indeed not desired. For example, chondrocytes tend to either proliferate (in a dedifferentiated state) or deposit matrix (in a differentiated state). Cartilage is a tissue containing only a low density of cells and in which functionality is derived mainly from its matrix composition.[24] Therefore, for the engineering of cartilage, differentiation and matrix production are preferred over proliferation.

In other cases, cell migration and proliferation are important for tissue formation. Cell migration often becomes possible after degradation of the polymer backbone in natural hydrogels. Migrating cells manipulate the balance of collagenase and inhibitors of collagenase to maintain a proteolytic environment that is localized near the cell but is inhibited farther away from the cell surface. PEG-based hydrogels with proteolytically sensitive cleavage sites have been developed that allow embedded cells to migrate through a synthetic hydrogel.[133,134] Alternatively, physically cross-linked hydrogels exist that enable nonproteolytic cell migration and outgrowth of fibroblast aggregates.[135] For successful organ printing, the suitability of the hydrogels used for cell migration, proliferation, differentiation, and tissue formation should be better addressed in the future.

5.542.3.3.4. Scaffold-free assembly: aggregates and cell-sheets

Directed self-assembly by inkjet printed cell-aggregates has been investigated, demonstrating assembly of cell aggregates into tubular structures upon printing in hydrogel matrices (see **Chapter 5.530, Medical Applications of Cell Sheet Engineering**).[136–138] Some researchers speculate that as long as the boundary conditions are met, the self-assembly potential of cells will organize tissue from homogeneous cellular mixtures. Therefore researchers (especially in vascular tissue engineering) have focused on scaffold- and template-free approaches to

engineer tissues composed of only cells and the secreted matrix. Scaffold- and template-free approaches state that initially strong material properties are nonessential and may even impede efficient organ biofabrication. In order to support cell or tissue spheroid fusion, many of these techniques rely on the use of supportive hydrogel matrices to sustain the spheroids,[49,50,136] which, by definition, implies that these approaches are not entirely scaffold-free. Current drawbacks of cell-sheet technology and aggregate printing are the low resolution and tissue thickness limitations. Furthermore, it is technically challenging to remove biopaper postfusion, and fusion of spheroids may take as long as a week, which can lead to nonuniform surfaces.[50]

Using an alternative multilayered cell-sheet approach, Lee *et al.*[124] investigated the effects of printing resolution on outgrowth and connectivity of neural cells dispensed in collagen gels. After 15 days of culture, neurons printed at 250 μm interdispensing distance still showed more sparsely distributed cell clusters with low neural connectivity through neurite outgrowth, compared to neurons printed at 150 μm interdispensing distance. For astrocytes, an increase in growth rate and influence on morphology was observed with decreasing interdispensing distance, with a minimum printing resolution of approximately 400 μm required for sufficient growth rate and morphology.

5.542.3.3.5. Printing of multiple cell populations and tissue equivalents

By incorporating several cell types at predetermined locations, cell-seeded implants that further mimic native tissues can be generated. It remains to be seen however whether printed tissues that follow native anatomy with respect to anatomical geometry and spatial organization are relevant for *in vivo* tissue formation. To validate this issue, tissue formation by distinct cell populations printed at defined locations within one construct was tested *in vitro* and *in vivo*. Recent data on the generation of such constructs underlines the potential feasibility and impact of this technology. For example, as a model for osteochondral grafts, chondrocytes and osteogenic multipotent stromal cells were printed, yielding a dual heterogeneous construct. Distinct ECM formation was observed in the different regions of the construct, which was associated with the type of cells deposited.

5.542.3.3.6. Postprocessing

The design characteristics of the scaffold have a major impact on nutrient delivery (see **Chapter 3.309, Fluid Mechanics: Transport and Diffusion Analyses as Applied in Biomaterials Studies**). The use of SFF techniques allows for the preparation of more regular scaffolds with increased permeability compared to the use of conventional techniques such as salt-leaching, phase separation/freeze-drying, and gas foaming processes. Furthermore, they enable the inclusion of some form of an artificial vascular system in the scaffold design.[5] Printed interconnected pores form channels through which the nutrients can diffuse, resulting in a significant increase in cell survival in the core of the graft. However, the use of SFF fabrication methods alone does not guarantee long-term cell survival as the transport of nutrients and oxygen can be compromised by tissue growth over time. This is where organ printing provides a fundamentally different strategy compared to solid-scaffold tissue engineering. In solid-scaffold tissue engineering, cells are seeded in the pore space of a scaffold. As the cells in the periphery of the scaffold are exposed to higher nutrient and oxygen concentrations, they proliferate more compared to cells seeded inside. In this way, they block pores and thereby reduce the transport of nutrients to the core of the scaffold, leading to hypoxia and, eventually, apoptosis, and necrosis.[139–141]

In the cell–gel structure printing approach, however, cells are embedded in the strands of the printed scaffold itself, and pore channels remain open for transport of medium. In this way, throughout a printed gelatin construct, hepatocytes have shown to remain 98% viable after 3 months of static culture.[105] It should be noted, however, that in this case, proliferation did not occur. Obviously, when cells proliferate and start growing outside the hydrogel strands also, blocking of pores could occur. However, if the right hydrogel material is chosen, cells will probably prefer to colonize the strands first.

In order to further optimize the architecture and encapsulate the cells inside the scaffold material itself, bioreactors that improve the transport of nutrients and oxygen in the maturation phase can be used. In particular, perfusion systems improve nutrient and oxygen delivery to the cells inside the engineered tissue (see **Chapter 5.501, Scaffolds: Flow Perfusion Bioreactor Design**).[142,143]

Furthermore, the printed construct should have sufficient mechanical properties to allow handling as well as maintenance of its integrity once implanted in the host. Mechanical properties are often disregarded in organ-printing studies; in many cases, 'handibility' is the only used measure. As stated earlier, a very large improvement is possible with the use of specific types of hydrogels. It has been shown that the mechanical properties of cell–gel constructs improve upon maturation, due to the production of ECM. The concert of mechanical loading and supplementing growth factors during bioreactor culture significantly enhances the quality and mechanical properties of the tissue formed.[144] Probably, the mechanical properties of as-printed cell–gel constructs have to be improved in order to allow for mechanical loading.

The increasing availability of predictive mathematical and physical models of cell and tissue behavior will provide further insight into the effects of nutrient limitation and mechanical stimulation.[142,145,146]

5.542.4. Future Directions

5.542.4.1. Current Limitations in Organ Printing

At the moment, it is still impossible to print a tissue or organ. The technology of organized deposition of cells by 3D plotting has just evolved toward fabrication of centimeter-scaled tissues. The *in vivo* performance of such constructs containing multiple cell types after implantation at ectopic and orthotopic locations will provide further answers to the quality and quantity of tissue formation within the printed grafts. It is especially important to investigate whether the imposed cell organization actually contributes to functional tissue formation once implanted. Other points of concern are the nature of tissue formation in the transition zone between different tissues, for example, the development of osteochondral constructs consisting of articular cartilage and bone, and

the interaction between implanted and host tissue. Many aspects of cellular behavior in printed constructs are dictated by the nature of the support matrix, and our understanding of cell–matrix interactions is still rather limited, making it difficult to predict cellular outcomes.

5.542.4.2. Scale of Application

Before the printing of whole organ substitutes is achieved, many hurdles will have to be overcome. One aspect will be the gradual upscaling of printed constructs. Going from the tens of millimeters scale that current work is focused on to the tens of centimeters scale of organs implies an increase by a factor of 1000 in material volume, numbers of cells, and construction time. With such upscaling, transport limitations and vascularization become increasingly difficult as well as important.

However, printing of millimeter-sized living constructs is already proving to be very useful as it provides model systems in the development of 3D tissue strategies for tissue regeneration.[23] The possible combinations of materials, cell types, bioactive molecules, other additives, and processing conditions are innumerable, and cell- and organ-printing techniques can provide a method for high-throughput screening similar to the screening of biomaterial–cell interactions, as reported earlier.[147] Presumably, upscaling will be of little use before such optimization studies have yielded specific conditions for the engineering of specific tissues. Moreover, the mechanisms of cell aggregate fusion and tissue morphogenesis will require more detailed studies on a small scale before being applied in the engineering of artificial organ constructs. Furthermore, printed 3D microtissues can be used as models for drug testing purposes or for studying disease processes. A printed 3D environment can provide a better model than 2D environments, which might make drug screening faster and more selective. Such printed microtissues can provide a valuable extra step in the development of drugs, by yielding extra information before expensive and complex preclinical and clinical trials are initiated.

5.542.4.3. Tissue Complexity and Vascularization

Whether tissue engineers can precisely recapitulate the most essential structure and functional features of natural tissues and organs, and how far they must try to imitate developmental morphogenesis are a matter of debate.[138] Organ printing is a powerful tool to study the effects of 3D organization and will further help to provide answers to whether anatomical tissue design is necessary to achieve more functional grafts.

Much of the future success in this field will relate to the types of tissues and organ structures that are targeted for regeneration. It is unclear whether tissue engineers will ever be able to have sufficient control over the cell and tissue assembly processes to recreate the extreme complexity observed within the human body, where the level of tissue organization ranges from nanoscale up to tens of centimeters. The major assumption in the current strategies is that the cells themselves will still be primarily responsible for generating the necessary ECM. While cell and organ printing provide a mechanism to potentially arrange cells, tissues, and support structures in an optimal 3D environment, with the necessary nutrients, growth factors, and ECM cues to support growth and regeneration, it is unlikely that even the most simple of tissues or organs could be completely regenerated *in vitro* or *in vivo* within the near future. Clearly, the development of bioreactor systems to provide a sufficient and controlled environment for nutrient supply and mechanical stimulus to mature tissue prior to implantation will go hand in hand with the development of organ-printing strategies.[148]

One of the major challenges in tissue engineering is the vascularization of constructs. Insufficient vascularization can lead to improper cell integration or cell death in TECs, and this might be one of the reasons why the extent of clinical applications in the field of tissue engineering is still limited.[48] The difficulty in achieving such vascularization in constructs engineered following the traditional approach of seeding prefabricated scaffolds is one of the main reasons to develop organ-printing techniques.[149]

5.542.5. Conclusions

Organ-printing techniques enable the production of living constructs with spatial variations along multiple axes with high geometric complexity. The level of control offered by these technologies in the development of printed tissues will allow tissue engineers to better study factors that modulate tissue formation and function, and provide them with a valuable tool to study the effect of anatomy on graft performance.[80,89] Different biofabrication technologies function at different scales of organization. Precise 2D microscale patterning techniques may help answer an increasing demand for *in vitro* models that capture more of the relevant tissue complexity than do traditional tissue engineering systems.[150] Cellular micropatterning has already been useful in the study of many diverse biological phenomena, including spatial control over cell attachment, spreading, influence of cell shape, and outgrowth of blood vessels.[72,77] Potentially, *in vitro* printed constructs will display important structural and functional characteristics of a natural tissue, and could be used as a model system to study tissue-level responses to molecular, mechanical, or genetic manipulations, or as a tool to study diseased cells and tissue development in pharmacological/toxicological screens[1,151] However, micropatterning tools are much too small to ultimately function as tissue equivalents for *in vivo* implantation. Organ-printing techniques, such as 3D printing and dispensing, are too crude for facilitating the microscale cell organization, but can, nevertheless, enable fast and efficient cell-laden scaffold formation. They are potentially the favored strategy for the construction of grafts for *in vivo* applications and their clinical translation. The current state of the art in the robotic fabrication of cell and tissue constructs is still very far from creating complex functional organs, but progress in this direction is being made. These developments can provide solutions to other problems and give answers to fundamental questions on tissue morphogenesis and cell functioning as well.

References

1. Freed, L. E.; Vunjak-Novakovic, G. *Adv. Drug Deliv. Rev.* **1998**, *33*, 15–30.
2. Ishaugriley, S. L.; Crane, G. M.; Gurlek, A.; *et al. J. Biomed. Mater. Res.* **1997**, *36*, 1–8.

3. Sarment, D. P.; Sukovic, P.; Clinthorne, N. *Int. J. Oral Maxillofac. Implants* **2003**, *18*, 571–577.
4. D'urso, P. S.; Earwaker, W. J.; Barker, T. M.; *et al. Br. J. Plast. Surg.* **2000**, *53*, 200–204.
5. Sachlos, E.; Czernuszka, J. T. *Eur. Cell. Mater.* **2003**, *5*, 29–40.
6. Giordano, R. A.; Wu, B. M.; Borland, S. W.; Cima, L. G.; Sachs, E. M.; Cima, M. J. *J. Biomater. Sci. Polym. Ed.* **1996**, *8*, 63–75.
7. Sachs, E.; Haggerty, J. S.; Cima, M. J.; Williams, P. A. *Three-Dimensional Printing Techniques*; Massachusetts Institute of Technology: Cambridge, MA, 1993.
8. Peltola, S. M.; Melchels, F. P. W.; Grijpma, D. W.; Kellomaki, M. *Ann. Med.* **2008**, *40*, 268–280.
9. Hollister, S. J. *Nat. Mater.* **2005**, *4*, 518–524.
10. Hutmacher, D. W. *Trends Biotechnol.* **2004**, *22*, 354–362.
11. Hutmacher, D. W.; Schantz, T.; Zein, I.; Ng, K. W.; Teoh, S. H.; Tan, K. C. *J. Biomed. Mater. Res.* **2001**, *55*, 203–216.
12. Malda, J.; Woodfield, T. B. F.; Van Der Vloodt, F.; *et al. Biomaterials* **2004**, *25*, 5773–5780.
13. Malda, J.; Woodfield, T. B. F.; Van Der Vloodt, F.; *et al. Biomaterials* **2005**, *26*, 63–72.
14. Miot, S.; Woodfield, T. B. F.; Daniels, A. U.; *et al. Biomaterials* **2005**, *26*, 2479–2489.
15. Woodfield, T. B. F.; Van Blitterswijk, C. A.; De Wijn, J.; Sims, T. J.; Hollander, A. P.; Riesle, J. *Tissue Eng.* **2005**, *11*, 1297–1311.
16. Williams, J. M.; Adewunmi, A.; Schek, R. M.; *et al. Biomaterials* **2005**, *26*, 4817–4827.
17. Boland, T.; Mironov, V.; Gutowska, A.; Roth, E. A.; Markwald, R. R. *Anat. Rec. A Discover. Mol. Cell. Evol. Biol.* **2003**, *272*, 497–502.
18. Wilson, W. C.; Boland, T. *Anat. Rec. A Discov. Mol. Cell. Evol. Biol.* **2003**, *272*, 491–496.
19. Limpanuphap, S.; Derby, B. *J. Mater. Sci. Mater. Med.* **2002**, *13*, 1163–1166.
20. Sachlos, E.; Reis, N.; Ainsley, C.; Derby, B.; Czernuszka, J. T. *Biomaterials* **2003**, *24*, 1487–1497.
21. Mironov, V.; Boland, T.; Trusk, T.; Forgacs, G.; Markwald, R. R. *Trends Biotechnol.* **2003**, *21*, 157–161.
22. Sharma, B.; Elisseeff, J. H. *Ann. Biomed. Eng.* **2004**, *32*, 148–159.
23. Woodfield, T. B.; Moroni, L.; Malda, J. *Comb. Chem. High Throughput Screen.* **2009**, *12*, 562–579.
24. Klein, T. J.; Malda, J.; Sah, R. L.; Hutmacher, D. W. *Tissue Eng. B Rev.* **2009**, *15*, 143–157.
25. Woodfield, T. B. F.; Bezemer, J. M.; Pieper, J. S.; Van Blitterswijk, C. A.; Riesle, J. *Crit. Rev. Eukaryot. Gene Expr.* **2002**, *12*, 209–236.
26. Grenga, T. E.; Zins, J. E.; Bauer, T. W. *Plast. Reconstr. Surg.* **1989**, *84*, 245–249.
27. Dunn, J. C. Y.; Yarmush, M. L.; Koebe, H. G.; Tompkins, R. G. *FASEB J.* **1989**, *3*, 174–177.
28. Benya, P. D.; Shaffer, J. D. *Cell* **1982**, *30*, 215–224.
29. Kim, T. K.; Sharma, B.; Williams, C. G.; *et al. Osteoarthritis Cartilage* **2003**, *11*, 653–664.
30. Ng, K. W.; Mauck, R. L.; Wang, C. C. B.; *et al. Cell. Mol. Bioeng.* **2009**, *2*, 386–394.
31. Guillotin, B.; Bourget, C.; Remy-Zolgadri, M.; *et al. Cell. Physiol. Biochem.* **2004**, *14*, 325–332.
32. Kaigler, D.; Krebsbach, P. H.; West, E. R.; Horger, K.; Huang, Y. C.; Mooney, D. J. *FASEB J.* **2005**, *19*, 665–667.
33. Rouwkema, J.; De Boer, J.; Van Blitterswijk, C. A. *Tissue Eng.* **2006**, *12*, 2685–2693.
34. Wang, D. S.; Miura, M.; Demura, H.; Sato, K. *Endocrinology* **1997**, *138*, 2953–2962.
35. Villars, F.; Guillotin, B.; Amedee, T.; *et al. Am. J. Physiol. Cell Physiol.* **2002**, *282*, C775–C785.
36. Kaigler, D.; Krebsbach, P. H.; Wang, Z.; West, E. R.; Horger, K.; Mooney, D. J. *J. Dent. Res.* **2006**, *85*, 633–637.
37. Fedorovich, N. E.; Haverslag, R. T.; Dhert, W. J. A.; Alblas, J. *Tissue Eng. A* **2010**, *16*, 2355–2367.
38. Kaigler, D.; Krebsbach, P. H.; Polverini, P. J.; Mooney, D. J. *Tissue Eng.* **2003**, *9*, 95–103.
39. Leung, B. M.; Sefton, M. V. *Ann. Biomed. Eng.* **2007**, *35*, 2039–2049.
40. Williams, C.; Wick, T. M. *Tissue Eng.* **2004**, *10*, 930–941.
41. Wenger, A.; Kowalewski, N.; Stahl, A.; *et al. Cells Tissues Organs* **2005**, *181*, 80–88.
42. Carmeliet, P. *Nat. Med.* **2000**, *6*, 389–395.
43. Korff, T.; Kimmina, S.; Martiny-Baron, G.; Augustin, H. G. *FASEB J.* **2001**, *15*, 447–457.
44. Levenberg, S.; Rouwkema, J.; Macdonald, M.; *et al. Nat. Biotechnol.* **2005**, *23*, 879–884.
45. Carmeliet, P.; Jain, R. K. *Nature* **2000**, *407*, 249–257.
46. Clark, E. R. C. *Am. J. Anat.* **1939**, *64*, 251–301.
47. Jain, R. K.; Au, P.; Tam, J.; Duda, D. G.; Fukumura, D. *Nat. Biotechnol.* **2005**, *23*, 821–823.
48. Rouwkema, J.; Rivron, N. C.; Van Blitterswijk, C. A. *Trends Biotechnol.* **2008**, *26*, 434–441.
49. Jakab, K.; Norotte, C.; Damon, B.; *et al. Tissue Eng. A* **2008**, *14*, 413–421.
50. Norotte, C.; Marga, F. S.; Niklason, L. E.; Forgacs, G. *Biomaterials* **2009**, *30*, 5910–5917.
51. Mcallister, T. N.; Dusserre, N.; Maruszewski, M.; L'heureux, N. *Regen. Med.* **2008**, *3*, 925–937.
52. Bouchie, A. *Nat. Biotechnol.* **2002**, *20*, 1178–1179.
53. Mcateer, H.; Cosh, E.; Freeman, G.; Pandit, A.; Wood, P.; Lilford, R. *J. Tissue Eng. Regen. Med.* **2007**, *1*, 343–349.
54. Archer, R.; Williams, D. J. *Nat. Biotechnol.* **2005**, *23*, 1353–1355.
55. Singh, P.; Williams, D. J. *J. Tissue Eng. Regen. Med.* **2008**, *2*, 307–319.
56. Mironov, V.; Kasyanov, V.; Drake, C.; Markwald, R. R. *Regen. Med.* **2008**, *3*, 93–103.
57. Hahn, M. S.; Taite, L. J.; Moon, J. J.; Rowland, M. C.; Ruffino, K. A.; West, J. L. *Biomaterials* **2006**, *27*, 2519–2524.
58. Khademhosseini, A.; Suh, K. Y.; Yang, J. M.; *et al. Biomaterials* **2004**, *25*, 3583–3592.
59. Underhill, G. H.; Chen, A. A.; Albrecht, D. R.; Bhatia, S. N. *Biomaterials* **2007**, *28*, 256–270.
60. Jacobs, J. W.; Fodor, S. P. A. *Trends Biotechnol.* **1994**, *12*, 19–26.
61. Singhvi, R.; Stephanopoulos, G.; Wang, D. I. C. *Biotechnol. Bioeng.* **1994**, *43*, 764–771.
62. Blawas, A. S.; Reichert, W. M. *Biomaterials* **1998**, *19*, 595–609.
63. Falconnet, D.; Csucs, G.; Grandin, H. M.; Textor, M. *Biomaterials* **2006**, *27*, 3044–3063.
64. Scotchford, C. A.; Ball, M.; Winkelmann, M.; *et al. Biomaterials* **2003**, *24*, 1147–1158.
65. Conrad, P. G.; Nishimura, P. T.; Aherne, D.; *et al. Adv. Mater.* **2003**, *15*, 1541–1544.
66. Xia, Y. N.; Whitesides, G. M. *Annu. Rev. Mater. Sci.* **1998**, *28*, 153–184.
67. Bernard, A.; Renault, J. P.; Michel, B.; Bosshard, H. R.; Delamarche, E. *Adv. Mater.* **2000**, *12*, 1067–1070.
68. Karp, J. M.; Yeo, Y.; Geng, W. L.; *et al. Biomaterials* **2006**, *27*, 4755–4764.
69. Hahn, M. S.; Miller, J. S.; West, J. L. *Adv. Mater.* **2006**, *18*, 2679–2684.
70. Ito, Y.; Hayashi, M.; Imanishi, Y. *J. Biomater. Sci. Polym. Ed.* **2001**, *12*, 367–378.
71. Chen, G. P.; Imanishi, Y.; Ito, Y. *J. Biomed. Mater. Res.* **1998**, *42*, 38–44.
72. Chen, G. P.; Ito, Y.; Imanishi, Y. *Macromolecules* **1997**, *30*, 7001–7003.
73. Chen, G. P.; Ito, Y. Y. *Biomaterials* **2001**, *22*, 2453–2457.
74. Ito, Y.; Hasuda, H.; Terai, H.; Kitajima, T. *J. Biomed. Mater. Res.* **2005**, *74A*, 659–665.
75. Heydari, M.; Hasuda, H.; Sakuragi, M.; Yoshida, Y.; Suzuki, K.; Ito, Y. *J. Biomed. Mater. Res.* **2007**, *83A*, 906–914.
76. Kang, I. K.; Kim, G. J.; Kwon, O. H.; Ito, Y. *Biomaterials* **2004**, *25*, 4225–4232.
77. Chen, G. P.; Ito, Y.; Imanishi, Y.; Magnani, A.; Lamponi, S.; Barbucci, R. *Bioconjug. Chem.* **1997**, *8*, 730–734.
78. Sarkar, S.; Dadhania, M.; Rourke, P.; Desai, T. A.; Wong, J. Y. *Acta Biomater.* **2005**, *1*, 93–100.
79. Brock, A.; Chang, E.; Ho, C. C.; *et al. Langmuir* **2003**, *19*, 1611–1617.
80. Mcbeath, R.; Pirone, D. M.; Nelson, C. M.; Bhadriraju, K.; Chen, C. S. *Dev. Cell* **2004**, *6*, 483–495.
81. Kane, R. S.; Takayama, S.; Ostuni, E.; Ingber, D. E.; Whitesides, G. M. *Biomaterials* **1999**, *20*, 2363–2376.
82. Stevens, M. M.; Mayer, M.; Anderson, D. G.; Weibel, D. B.; Whitesides, G. M.; Langer, R. *Biomaterials* **2005**, *26*, 7636–7641.
83. Odde, D. J.; Renn, M. J. *Trends Biotechnol.* **1999**, *17*, 385–389.
84. Barron, J. A.; Ringeisen, B. R.; Kim, H. S.; Spargo, B. J.; Chrisey, D. B. *Thin Solid Films* **2004**, *453*, 383–387.
85. Chen, C. Y.; Barron, J. A.; Ringeisen, B. R. *Appl. Surf. Sci.* **2006**, *252*, 8641–8645.
86. Albrecht, D. R.; Tsang, V. L.; Sah, R. L.; Bhatia, S. N. *Lab Chip* **2005**, *5*, 111–118.
87. Albrecht, D. R.; Underhill, G. H.; Wassermann, T. B.; Sah, R. L.; Bhatia, S. N. *Nat. Meth.* **2006**, *3*, 369–375.

88. Khademhosseini, A.; Langer, R.; Borenstein, J.; Vacanti, J. P. *Proc. Natl. Acad. Sci. USA* **2006**, *103*, 2480–2487.
89. Bhatia, S. N.; Balis, U. J.; Yarmush, M. L.; Toner, M. *FASEB J.* **1999**, *13*, 1883–1900.
90. Yeh, J.; Ling, Y. B.; Karp, J. M.; *et al. Biomaterials* **2006**, *27*, 5391–5398.
91. Luo, Y.; Shoichet, M. S. *Nat. Mater.* **2004**, *3*, 249–253.
92. Sarig-Nadir, O.; Livnat, N.; Zajdman, R.; Shoham, S.; Seliktar, D. *Biophys. J.* **2009**, *96*, 4743–4752.
93. Bettinger, C. J.; Borenstein, J. T.; Langer, R. S. *Mater. Res. Soc. Symp. Proc.* **2005**, *845*, 25–30.
94. Boland, T.; Tao, X.; Damon, B. J.; *et al. Mater. Sci. Eng. C Biomim. Supramol. Syst.* **2007**, *27*, 372–376.
95. Roth, E. A.; Xu, T.; Das, M.; Gregory, C.; Hickman, J. J.; Boland, T. *Biomaterials* **2004**, *25*, 3707–3715.
96. Xu, T.; Jin, J.; Gregory, C.; Hickman, J. J.; Boland, T. *Biomaterials* **2005**, *26*, 93–99.
97. Xu, W.; Wang, X. H.; Yan, Y. N.; *et al. J. Bioact. Compat. Polym.* **2007**, *22*, 363–377.
98. Nishiyama, Y.; Nakamura, M.; Henmi, C.; *et al.* In *The ASME International Conference on Manufacturing Science and Engineering*, American Society for Mechanical Engineers (ASME), New York, NY, 2007.
99. Xu, T.; Kincaid, H.; Atala, A.; Yoo, J. J. *J. Manuf. Sci. Eng. Trans. ASME* **2008**, *130*, 5.
100. Saunders, R. E.; Gough, J. E.; Derby, B. *Biomaterials* **2008**, *29*, 193–203.
101. Smith, C. M.; Stone, A. L.; Parkhill, R. L.; *et al. Tissue Eng.* **2004**, *10*, 1566–1576.
102. Khalil, S.; Nam, J.; Sun, W. *Rapid Prototyping J.* **2005**, *11*, 9–17.
103. Cohen, D. L.; Malone, E.; Lipson, H.; Bonassar, L. J. *Tissue Eng.* **2006**, *12*, 1325–1335.
104. Yan, Y. N.; Wang, X. H.; Xiong, Z.; *et al. J. Bioact. Compat. Polym.* **2005**, *20*, 259–269.
105. Wang, X. H.; Yan, Y. N.; Pan, Y. Q.; *et al. Tissue Eng.* **2006**, *12*, 83–90.
106. Fedorovich, N. E.; Dewijn, J. R.; Verbout, A. J.; Alblas, J.; Dhert, W. J. A. *Tissue Eng. A* **2008**, *14*, 127–133.
107. Li, S. J.; Yan, Y. N.; Xiong, Z.; Weng, C. Y.; Zhang, R. J.; Wang, X. H. *J. Bioact. Compat. Polym.* **2009**, *24*, 84–99.
108. Dhariwala, B.; Hunt, E.; Boland, T. *Tissue Eng.* **2004**, *10*, 1316–1322.
109. Arcaute, K.; Mann, B. K.; Wicker, R. B. *Ann. Biomed. Eng.* **2006**, *34*, 1429–1441.
110. Lu, Y.; Mapili, G.; Suhali, G.; Chen, S. C.; Roy, K. *J. Biomed. Mater. Res.* **2006**, *77A*, 396–405.
111. Arcaute, K.; Mann, B.; Wicker, R. *Acta Biomater.* **2010**, *6*, 1047–1054.
112. Derby, B. *J. Mater. Chem.* **2008**, *18*, 5717–5721.
113. Xu, T.; Gregory, C. A.; Molnar, P.; *et al. Biomaterials* **2006**, *27*, 3580–3588.
114. Reis, N.; Ainsley, C.; Derby, B. *J. Appl. Phys.* **2005**, *97*, 094903.
115. Seerden, K. A. M.; Reis, N.; Evans, J. R. G.; Grant, P. S.; Halloran, J. W.; Derby, B. *J. Am. Ceram. Soc.* **2001**, *84*, 2514–2520.
116. Melchels, F. P. W.; Feijen, J.; Grijpma, D. W. *Biomaterials* **2010**, *31*, 6121–6130.
117. Nicodemus, G. D.; Bryant, S. J. *Tissue Eng. B Rev.* **2008**, *14*, 149–165.
118. Mapili, G.; Lu, Y.; Chen, S. C.; Roy, K. *J. Biomed. Mater. Res. B Appl. Biomater.* **2005**, *75*, 414–424.
119. Zhang, H.; Burdet, E.; Poo, A. N.; Hutmacher, D. W. *IEEE Trans. Autom. Sci. Eng.* **2008**, *5*, 446–456.
120. Sodian, R.; Loebe, M.; Hein, A.; *et al. Asaio J.* **2002**, *48*, 12–16.
121. Sodian, R.; Fu, P.; Lueders, C.; *et al. Thorac. Cardiovasc. Surg.* **2005**, *53*, 144–149.
122. Naumann, A.; Aigner, J.; Staudenmaier, R.; *et al. Eur. Arch. Otorhinolaryngol.* **2003**, *260*, 568–575.
123. Woodfield, T. B. F.; Guggenheim, M.; Von Rechenberg, B.; Riesle, J.; Van Blitterswijk, C. A.; Wedler, V. *Cell Prolif.* **2009**, *42*, 485–497.
124. Lee, W.; Pinckney, J.; Lee, V.; *et al. NeuroReport* **2009**, *20*, 798–803.
125. Smith, C. M.; Christian, J. J.; Warren, W. L.; Williams, S. K. *Tissue Eng.* **2007**, *13*, 373–383.
126. Fedorovich, N. E.; Alblas, J.; De Wijn, J. R.; Hennink, W. E.; Verbout, A. J.; Dhert, W. J. A. *Tissue Eng.* **2007**, *13*, 1905–1925.
127. Johnson, J. A.; Turro, N. J.; Koberstein, J. T.; Mark, J. E. *Prog. Polym. Sci.* **2010**, *35*, 332–337.
128. Fedorovich, N. E.; Swennen, I.; Girones, J.; *et al. Biomacromolecules* **2009**, *10*, 1689–1696.
129. Kopecek, J. *J. Polym. Sci. A Polym. Chem.* **2009**, *47*, 5929–5946.
130. Hern, D. L.; Hubbell, J. A. *J. Biomed. Mater. Res.* **1998**, *39*, 266–276.
131. Lee, K. Y.; Peters, M. C.; Anderson, K. W.; Mooney, D. J. *Nature* **2000**, *408*, 998–1000.
132. Wang, S.; Foo, C. W. P.; Warrier, A.; Poo, M. M.; Heilshorn, S. C.; Zhang, X. *Biomed. Microdevices* **2009**, *11*, 1127–1134.
133. Raeber, G. P.; Lutolf, M. P.; Hubbell, J. A. *Biophys. J.* **2005**, *89*, 1374–1388.
134. West, J. L.; Hubbell, J. A. *Macromolecules* **1999**, *32*, 241–244.
135. Liu, B.; Lewis, A. K.; Shen, W. *Biomacromolecules* **2009**, *10*, 3182–3187.
136. Jakab, K.; Neagu, A.; Mironov, V.; Markwald, R. R.; Forgacs, G. *Proc. Natl. Acad. Sci. USA* **2004**, *101*, 2864–2869.
137. Mironov, V.; Reis, N.; Derby, B. *Tissue Eng.* **2006**, *12*, 631–634.
138. Mironov, V.; Visconti, R. P.; Kasyanov, V.; Forgacs, G.; Drake, C. J.; Markwald, R. R. *Biomaterials* **2009**, *30*, 2164–2174.
139. Lewis, M. C.; Macarthur, B. D.; Malda, J.; Pettet, G.; Please, C. P. *Biotechnol. Bioeng.* **2005**, *91*, 607–615.
140. Martin, I.; Padera, R. F.; Vunjak-Novakovic, G.; Freed, L. E. *J. Orthop. Res.* **1998**, *16*, 181–189.
141. Volkmer, E.; Drosse, I.; Otto, S.; *et al. Tissue Eng. A* **2008**, *14*, 1331–1340.
142. Radisic, M.; Malda, J.; Epping, E.; Geng, W.; Langer, R.; Vunjak-Novakovic, G. *Biotechnol. Bioeng.* **2006**, *93*, 332–343.
143. Wendt, D.; Stroebel, S.; Jakob, M.; John, G. T.; Martin, I. *Biorheology* **2006**, *43*, 481–488.
144. Mauck, R. L.; Nicoll, S. B.; Seyhan, S. L.; Ateshian, G. A.; Hung, C. T. *Tissue Eng.* **2003**, *9*, 597–611.
145. Sengers, B. G.; Oomens, C. W. J.; Baaijens, F. P. T. *J. Biomech. Eng. Trans. ASME* **2004**, *126*, 82–91.
146. Shipley, R. J.; Jones, G. W.; Dyson, R. J.; *et al. J. Theor. Biol.* **2009**, *259*, 489–502.
147. Hook, A. L.; Anderson, D. G.; Langer, R.; Williams, P.; Davies, M. C.; Alexander, M. R. *Biomaterials* **2010**, *31*, 187–198.
148. Martin, I.; Smith, T.; Wendt, D. *Trends Biotechnol.* **2009**, *27*, 495–502.
149. Visconti, R. P.; Kasyanov, V.; Gentile, C.; Zhang, J.; Markwald, R. R.; Mironov, V. *Expert Opin. Biol. Ther.* **2010**, *10*, 409–420.
150. Griffith, L. G.; Swartz, M. A. *Nat. Rev. Mol. Cell Biol.* **2006**, *7*, 211–224.
151. Choi, N. W.; Cabodi, M.; Held, B.; Gleghorn, J. P.; Bonassar, L. J.; Stroock, A. D. *Nat. Mater.* **2007**, *6*, 908–915.

6.601. Current and Projected Utilization of Total Joint Replacements

S M Kurtz, Exponent, Inc., Philadelphia, PA, USA; Drexel University, Philadelphia, PA
K L Ong, Exponent, Inc., Philadelphia, PA, USA
E Lau, Exponent Inc., Menlo Park, CA, USA
M T Manley, Homer Stryker Center for Orthopaedic Education and Research, Mahwah, NJ, USA

© 2011 Elsevier Ltd. All rights reserved.

6.601.1.	Introduction	1
6.601.2.	International Total Hip and Knee Implant Registries	2
6.601.3.	Public Data Sources for Orthopedic Implant Utilization in the United States	3
6.601.3.1.	National Hospital Discharge Survey	3
6.601.3.2.	Nationwide Inpatient Sample	3
6.601.3.3.	Medicare	4
6.601.4.	Current Utilization of Total Joint Replacements	4
6.601.5.	Projected Utilization of Total Joint Replacements	6
6.601.6.	Summary	7
References		8

Glossary

9th revision of the international classification of diseases, clinical modification (ICD-9-CM) Classification used in assigning codes to diagnoses and procedures associated with inpatient, outpatient, and physician office utilization in the United States.

National hospital discharge survey (NHDS) Annual survey conducted by the National Center for Health Statistics, representing a sample of hospitalization from non-Federal and non-military short-stay community hospitals throughout the United States.

National implant registry Repository of information collected on a national basis to quantify rates of surgeries for particular types of procedures and/or devices, which is used to provide feedback related to procedure outcomes.

Nationwide inpatient sample (NIS) Database of inpatient discharge data sampled from inpatient hospital visits in the United States.

Abbreviations

AAOS	American academy of orthopaedic surgeons
AHRQ	Agency of healthcare quality and research
CI	Confidence intervals
CMS	Center for medicare and medicaid services
HCUP	Healthcare cost & utilization project
LDS	Limited data set
LOS	Length of stay
NCHS	National center for health statistics
NHDS	National hospital discharge survey
NIS	Nationwide inpatient sample
THA	Total hip arthroplasty
THR	Total hip replacement
TJA	Total joint arthroplasty
TKA	Total knee arthroplasty

6.601.1. Introduction

Hip and knee joint replacement surgery is currently the standard of care for treating degenerative joint disease around the world. The prevalence of hip and knee arthroplasty in the United States has grown substantially since the 1990s.[1] Arthroplasty may involve total replacement of a diseased joint, or in the case of a hip fracture or single compartment knee arthritis, only one side of the joint may be surgically replaced by a partial joint prosthesis. The first time a joint is replaced, it is referred to as a primary procedure, but in the case of a failed surgery, it is necessary to perform a revision joint replacement. Considering both primary and revision procedures, over 1 million Americans benefited from partial and total joint replacement surgery in 2007. The different categories of primary and revision joint arthroplasty thus represent an established major platform for ongoing biomaterials advancement.

Because the cost, complications, and outcomes of revision joint replacement are generally worse than in primary surgery, there is great incentive to increase the longevity of joint replacements and to reduce the incidence of revisions. As a result, starting in the 1970s, orthopedic registries were developed in Scandinavia to track revisions on a national basis as a function of surgeon, patient, and implant characteristics.[2] In recent years, orthopedic registries have expanded across Europe, Canada, Australia, and New Zealand. Efforts to create a national orthopedic registry are still in the early stages in the United States. The sense of urgency surrounding a US arthroplasty

Table 1 Examples of international total joint registries

Starting year of available total joint registries data	*Register*	*Website*
1979	Swedish National Hip Arthroplasty Register	http://www.shpr.se/
1975	Swedish Knee Arthroplasty Register	http://www.knee.nko.se/
1987	Norwegian Arthroplasty Register	http://www.haukeland.no/nrl/
1999	Australian National Joint Replacement Registry	http://www.dmac.adelaide.edu.au/aoanjrr/
1994	Canadian Joint Replacement Registry	http://secure.cihi.ca/cihiweb/dispPage.jsp?cw_page=services_cjrr_e
1998	New Zealand National Joint Register	http://www.cdhb.govt.nz/NJR/
2003	England and Wales National Joint Registry	http://www.njrcentre.org.uk/

registry is compelling due to the anticipated future demand for joint arthroplasty. In the absence of a validated joint registry, administrative health care data in the United States represent a crucial resource in understanding the current and projected utilization of hip and knee replacements.

The purpose of this chapter is to provide a comprehensive review of the utilization of joint replacements and to discuss the implications of the future demand for surgeries in the field of biomaterials. As they are the earliest source of utilization data for joint replacement, international joint registries and validated administrative databases are first summarized and compared. The projected demand for joint replacements between 2010 and 2030 is also addressed. Finally, we review the limitations of the projection techniques and outline the economic implications of an escalating demand for joint replacement surgery in the future.

6.601.2. International Total Hip and Knee Implant Registries

International registries represent a well-established source of data regarding the current use of total joint replacement in Canada, Europe, and Australasia (Table 1). A registry is not merely a data repository containing basic clinical, patient, and implant data regarding the implantation and revision of total joint replacements. In countries in which an implant registry has been established, the data is also used as a tool to drive health care improvement by providing continuous feedback to the clinical community about procedure outcomes.

Orthopedic implant registries were first established in the 1970s in Sweden and later spread throughout Europe, Australia, and New Zealand. For example, the Swedish knee registry chronicles the growth of knee arthroplasty since the very beginnings of the procedure in the country (Figure 1). From the example of growth in Swedish total knee arthroplasty (TKA) utilization it may be appreciated that the characteristics and usage patterns of joint replacement vary considerably as a function of time. The temporal dimension greatly complicates comparisons among registries, which were established at different time periods and contain varying follow up. Thus, in the evaluation of clinical failure modes and their relationship to biomaterials across and between different registries, appreciation of the temporal variable is important.

If the long-term goal of a registry program is to improve the overall process of joint arthroplasty, tracking hospitalization outcomes (revisions, complications) is but the starting point

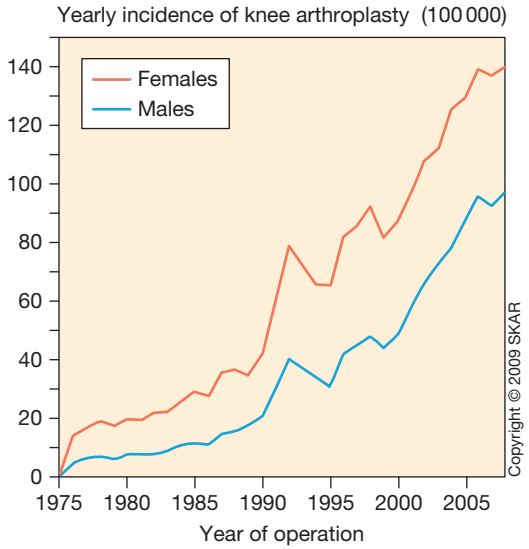

Figure 1 Annual incidence of knee arthroplasty in Sweden per 100 000 persons. Source: Swedish Knee Arthroplasty Register, Lund, Sweden.

for tracking the contribution joint arthroplasty makes to society. In its first 22 years of operation the Swedish hip registry focused on clinical metrics of surgery outcomes. However, since 2001, this registry has placed increasing emphasis on documenting improvement of the patients' quality of life following the surgery as well as the societal cost of performing the procedure. In many countries with a socialized health care system, including Sweden and Canada, the waiting time for surgery can be substantial. In Sweden, the mean wait time for total hip arthroplasty (THA) surgery was 312 days in 2007, whereas in Canada, the mean wait time was 182 days for THA. According to an economic analysis conducted by the Swedish hip registry, the societal cost for 1 year of wait time, incorporating lost productivity, is equivalent to the inpatient procedure cost of the surgery itself. Thus, the data from hip registries may be developed to drive changes in health care policy (e.g., reducing wait times in Sweden and Canada). Differences in health care delivery and access to joint replacement surgery cause wide variations in THA access between countries, as well as within countries over time. For example, within a country shifts in policy toward reducing wait times may increase the rate at which surgery is performed, even for a pool of patients that is not rapidly changing. Thus, policy shifts are but one example of the need for care

in extrapolating the current and projected utilization of hip and knee surgery outside of its national health care system.

Registries represent an important tool to evaluate the current use of total joint replacements in various countries, but they are by no means the only source of data regarding the utilization of surgical procedures. Large countries such as Germany and the United States currently do not have an operating hip and knee registry. Nationally representative administrative databases of countries without an operational registry are covered in the following section of this chapter. These databases can provide valuable and otherwise unavailable data regarding the current use of total hip and knee arthroplasty in the absence of a formal registry.

6.601.3. Public Data Sources for Orthopedic Implant Utilization in the United States

Even in countries with an established registry, administrative databases represent an important data source for total joint replacements. An administrative database may comprise a sampling of electronic hospital discharge records, or in the case of Medicare, the entire insurance claim history for individual patients. Total hip and knee procedures are identified in these databases according to the codes from the 9th Revision of the International Classification of Diseases, Clinical Modification (ICD-9-CM; see Table 2). Three public sources of administrative claims data for the United States are summarized in the following subsections.

6.601.3.1. National Hospital Discharge Survey

The National Hospital Discharge Survey (NHDS)[3] is an annual survey conducted by the National Center for Health Statistics (NCHS). Started in 1965, this survey program has continuously compiled a statistically representative sample of hospitalization from non-Federal and non-military short-stay community hospitals throughout the United States. As such, it is the oldest and most well-established inpatient discharge database in the country. Over the past decade, the number of hospitals included in NHDS has ranged from 430 to 490, with ~300 000 discharge records sampled per year. Information collected by NHDS includes patient demographics (e.g., age, gender), disease diagnosis, type of procedure performed, institutional characteristics, and resource utilization. Based on the information collected by the survey, national and regional estimates of characteristics of patients and surgical and nonsurgical procedures in hospitals of various bed sizes and types of ownership can be estimated using the provided sampling weights.

6.601.3.2. Nationwide Inpatient Sample

The Nationwide Inpatient Sample (NIS) is a larger and more recent database of inpatient discharge data in comparison with the NHDS.[4] Established in 1988 by the Healthcare Cost & Utilization Project (HCUP) of the Agency of Healthcare Quality and Research (AHRQ), the NIS has a far larger sample size in terms of both discharge records and number of hospitals. Compared to the NHDS, the NIS has 25 times more records with 5–8 million records per year and also includes twice the number of hospitals. The sampling of NIS captures 20% of inpatient hospital visits each year in the United States, and thus is well suited for studying national trends for rare diseases or for examining the epidemiology of diagnoses or procedures within minority subpopulations. The NIS also captures patient, payer, and hospitalization factors, as well as charges and cost information for the hospitalization, which can be used to evaluate the economic impact of procedures and diagnoses.

Table 2 Summary of ICD-9-CM codes for primary and revision total hip and knee replacement procedures

ICD9-CM-Code	*Description*	*Comments*
81.51	Primary total hip replacement	The type of bearing surface is coded, if known (00.74–0.77)
81.52	Partial hip replacement	This includes unipolar and bipolar hip prostheses; the type of bearing surface is coded, if known (00.74–0.77)
81.53	Revision of hip replacement, not otherwise specified	The type of bearing surface is coded, if known (00.74–0.77)
81.54	Primary total knee replacement	This code includes bicompartmental, tricompartmental, and unicondylar knee arthroplasty
81.55	Revision of knee replacement, not otherwise specified	
00.70	Revision of hip replacement, both acetabular and femoral components	Introduced 1 October 2005
00.71	Revision of hip replacement, acetabular component	Introduced 1 October 2005
00.72	Revision of hip replacement, femoral component	Introduced 1 October 2005
00.73	Revision of hip replacement, acetabular liner and/or femoral head only	Introduced 1 October 2005
00.74	Hip bearing surface, metal-on-polyethylene	Introduced 1 October 2005
00.75	Hip bearing surface, metal-on-metal	Introduced 1 October 2005
00.76	Hip bearing surface, ceramic-on-ceramic	Introduced 1 October 2005
00.77	Hip bearing surface, ceramic-on-polyethylene	Introduced 1 October 2006
00.80	Revision of knee replacement, total (all components)	Introduced 1 October 2005
00.81	Revision of knee replacement, tibial component	Introduced 1 October 2005
00.82	Revision of knee replacement, femoral component	Introduced 1 October 2005
00.83	Revision of knee replacement, patellar component	Introduced 1 October 2005
00.84	Revision of total knee replacement, tibial insert (liner)	Introduced 1 October 2005

6.601.3.3. Medicare

The 5% Medicare so-called Limited Data Set (LDS) is available from the Center for Medicare and Medicaid Services (CMS). The complete 5% dataset consists of seven components: hospital inpatient, hospital outpatient, home health agency, skilled nursing facility, hospice care, physician carrier (Part B), and durable medical equipment. A denominator file is also available that tracks the date of death or (more rarely) withdrawal by Medicare beneficiaries from the program. In the LDS, patients are uniquely identified by an encrypted Medicare beneficiary identification number that remains consistent across all parts of the database as well as over time. In this way, the utilization of healthcare resources by a patient can be tracked in different health care settings (i.e., both inpatient and outpatient), as well as in home hospice care, and during physician office visits.

6.601.4. Current Utilization of Total Joint Replacements

The number and prevalence of primary hip and knee replacement procedures have increased substantially in the United States between 1993 and 2006, most notably for primary TKA (Figure 2). The number of primary TKA and primary THA increased by 148% and 66%, respectively, during this period, corresponding to compound annual growth rates of 7.2% and 4.0%. The number of revision TKA and THA grew by 142% and 29%, respectively, with corresponding compound annual growth rates of 7.0% and 2.0%. Even after adjusting for population changes, the increase in procedure rates since 1993 was also evident, along with the slowdown in the prevalence of primary and revision THA and primary TKA between 2005 and 2006 (Figure 3).

To normalize the incidence of revision surgery, previous researchers from the Scandinavian registries have introduced the concept of a national revision burden, which is the ratio of revisions performed in a year to the total number of procedures (primary + revision). Using the 1993–2006 NIS dataset, the US mean revision burden of 16.2% (range 13.9–17.8%) for THA was approximately twice that for TKA (7.9%; range 7.3–8.4%; see Tables 3 and 4). The greater revision burden for THA compared to TKA is consistent with the relative revision burden in Canada which is 2.1 times greater than primary[6] and Finland which is 2.2 times greater.[7] The US mean revision burden for THA is also 65% greater than for TKA in Australia[8] and 78% greater than for Norway.[9]

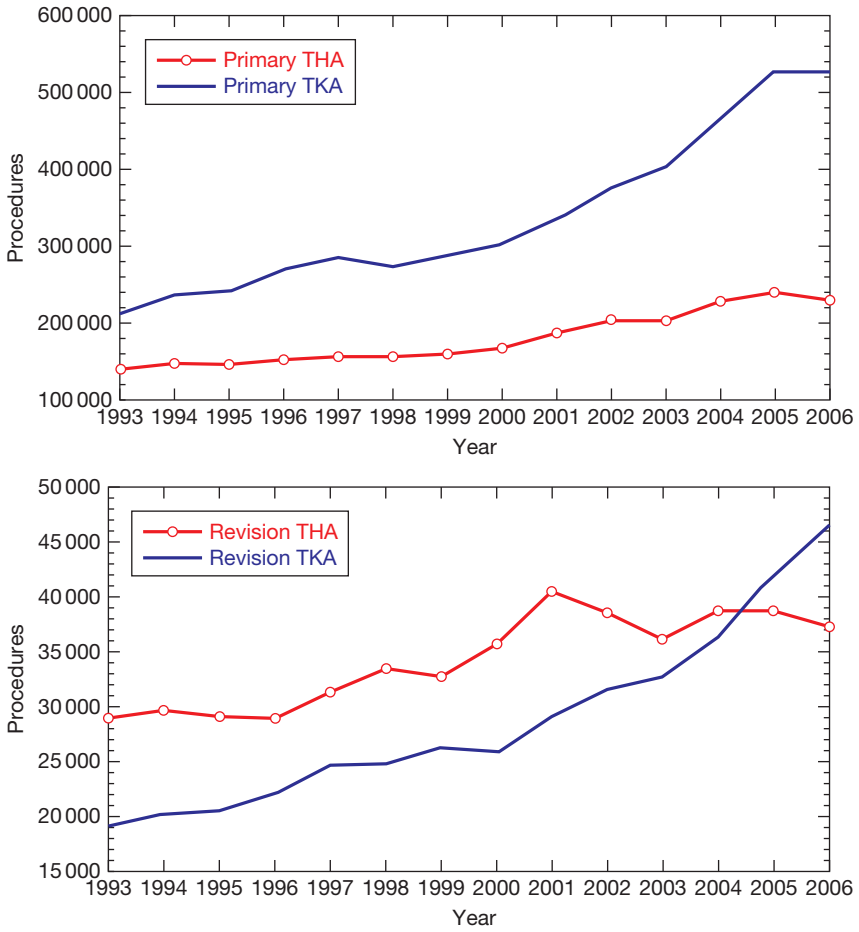

Figure 2 Annual number of primary (top panel) and revision (bottom panel) total hip arthroplasty and total knee arthroplasty in the United States. Note difference in *y*-axis scales.

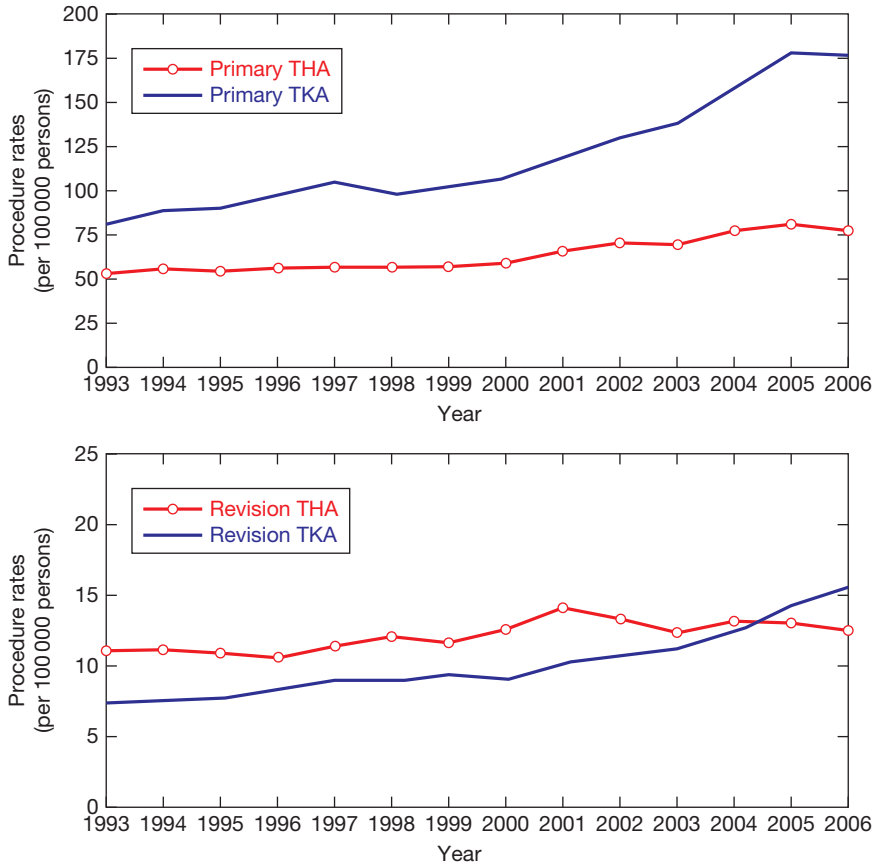

Figure 3 Annual incidence of primary (top panel) and revision (bottom panel) total hip arthroplasty and total knee arthroplasty in the United States per 100 000 persons.

Table 3 Mean revision burden for THA

Country	*Period*	*Revision burden (%)*	*Reference*
United States	1993–2006	16.2	Nationwide Inpatient Sample
Australia	2003–2007	15.7	Australian Orthopaedic Association – National Joint Replacement Registry
Canada	2002–2006	12.4	Canadian Institute for Health Information
Finland	1997–2006	17.3	National Agency for Medicines
Norway	1993–2007	14.6	The Norwegian Arthroplasty Register
Sweden	2003–2007	10.1	Swedish Hip Arthroplasty Register

Table 4 Mean revision burden for TKA

Country	*Period*	*Revision burden (%)*	*Source*
United States	1993–2006	7.9	Nationwide Inpatient Sample
Australia	2003–2007	9.5	Australian Orthopaedic Association – National Joint Replacement Registry
Canada	2002–2006	6.1	Canadian Institute for Health Information
Finland	1997–2006	7.9	National Agency for Medicine
Norway	1993–2007	8.2	Norwegian Arthroplasty Register
Sweden	1991–2003	4–7	Robertsson[5]

Overall, the THA revision burden in the United States is comparable to Australia[8] and Finland[7] (**Table 3**). Compared to the United States, the mean revision burden in Norway,[9] Canada,[6] and Sweden[10] are all lower. For TKA (**Table 4**), the US mean revision burden is comparable with the revision burdens of Norway[9] and Finland.[7] Compared to the United States, the knee revision burden is slightly lower in Canada[6] and in Sweden,[5] and slightly higher in Australia.[8]

In addition to revision procedures, the level of specificity in the ICD-9-CM codes makes it possible to perform national epidemiologic studies of postoperative complications in the US population. In a study by Kurtz *et al.*,[11] of periprosthetic infection between 1990 and 2004, the incidence of infection for both hip and knee arthroplasties in the United States nearly doubled from about 0.6% to 1.2%. The odds of infection increased annually at a rate of ~5% (odds ratio: 1.049; 95% confidence intervals (CI): 1.04–1.06). The length of stay (LOS) for infected TJAs was close to twice as long as for uninfected TJAs (2.21 times longer for THA, 95% CI: 2.18–2.23 times longer; and 1.87 times longer for TKA, 95% CI: 1.85–1.88 times longer) ($p < 0.0001$ for both). Furthermore, the ratio in LOS between infected and uninfected TJA has been on a widening trend between 1990 and 2004, with a rate of increase at 1.15% from year to year. The corresponding charge ratio for infected TJAs was also significantly greater ($p < 0.001$). This study highlighted an increasing trend of infected hip and knee arthroplasties in the United States. As demonstrated by the greater LOS and hospitalization charges/costs for infected TJA in this study and others,[12] the economic impact of deep infection is substantial. This infection research illustrates how administrative data from the NIS can be effectively used to quantify the national burden of specific total joint arthroplasty (TJA) complications, in addition to revision.

Recently, additional specificity provided in the ICD-9-CM procedure and diagnosis codes has greatly strengthened administrative databases as tools to examine national trends of TJA failure modes and revision strategies. In October 2005, based on a request from a group of orthopedic and health services researchers, the CMS and the NCHS implemented a series of changes to the ICD-9-CM diagnosis and procedure codes[13] (**Table 2**). These changes included new procedure codes that specify the THA bearing type, as well as new diagnosis and procedure codes to specify the cause of failure (e.g., dislocation, loosening, etc.) and type of component revised (e.g., acetabular component only, femoral component only, etc.) for revision THA. The availability of new bearing surface codes, revision diagnosis codes, and revision procedure codes provides an unprecedented opportunity to evaluate the comparative effectiveness of Total hip replacement (THR) bearing surfaces using administrative data.

Based on the new revision diagnosis and procedure codes, the epidemiology of revision THA was evaluated using the NIS database.[14] Based on a sample of 51 345 revision THA procedures spanning 1.25 years from October 2005 to December 2006, instability/dislocation was the most commonly reported cause of revision THA (22.5%), followed by mechanical loosening (19.7%) and infection (14.8%). All component revisions were most frequently reported (41.1%), followed by femoral component revision (13.2%), acetabular component revision (12.7%), isolated femoral head and acetabular liner exchange (12.6%), and arthrotomy (9.1%). Despite the increasing adoption of large diameter heads for THA over the recent years, this analysis indicated that dislocation remains the primary diagnosis reported for revision THA.

In summary, it can be seen that, based on data from administrative databases and national total joint registries, the current utilization of total joint replacements has been increasing over time. Despite the recognized success of these procedures, the number of revision procedures continues to increase for both THA and TKA. Minimizing revisions and complications continues to be a clinical concern and a major financial need.

6.601.5. Projected Utilization of Total Joint Replacements

Projections are important for guiding health care policy. In 2002, the American academy of orthopedic surgeons (AAOS) published projections of primary total hip and total knee replacement surgery through 2030, based on surgery rates calculated from the 1996 to 1999 hospitalization data from the NHDS and US Census projections for the next 30 years.[15] It is now clear that these projections by the AAOS underpredicted the expected utilization of primary TJA because the estimates of the surgery rates assumed a constant prevalence based on the average rate over the 4 years of the 1996–99 NHDS dataset and did not account for any year-to-year change in the rate itself. Thus, the projected growth in the number of hip and knee replacements in the AAOS model was fueled solely by the anticipated growth of the US population and was also limited to primary TJA without consideration for revision procedures. Since revision procedures place extensive additional demands on hospitals and surgeons and on medical costs, these should be considered in an analysis of projected future rates and population-based costs of arthroplasty procedures to the US health care system.

Motivated by the limitations in the prior projections, the authors used a much larger data source in the form of the NIS data, which has ~25 times more discharge records than the NHDS.[16,17] These projections[16] were based on 1990–2003 NIS data and the historical trajectory of surgery rates. They estimated the demand for primary THA to grow by 174%, from 208 600 in 2005 to 572 000 by 2030. The demand for primary TKA was also projected to grow more than sixfold, from 450 000 (95% prediction interval: 425 000–477 000) in 2005 to 3.48 million procedures (95% prediction interval: 2.95–4.14 million) by 2030. Revision TJA were also estimated to grow substantially from 40 800 to 96 700 for THA (an increase of 137%) and from 38 300 to 268 200 for TKA (an increase of 601%) between 2005 and 2030.

Following these initial projections, three additional years of NIS data (2004–2006) became available, allowing the comparison of previous projections with the recent NIS data, updating of the previous projections, and further demographic analysis of the projections. The previous projections[16] provided reasonably accurate estimates of the primary and revision TJA trends between 2004 and 2006,[17] particularly for revision TJA procedures, which were within the 95% CI of the previous projections. However, the previous projections underestimated the historical number of primary TJA procedures. Based on the additional 2004–2006 NIS data, the projections were reanalyzed, incorporating a 'variable rate' and a 'constant rate' approach to provide upper and lower prediction bounds, respectively. The 'variable rate' approach was consistent with the previous analysis, which allowed both the population and prevalence of surgery to vary over time. Conversely, the

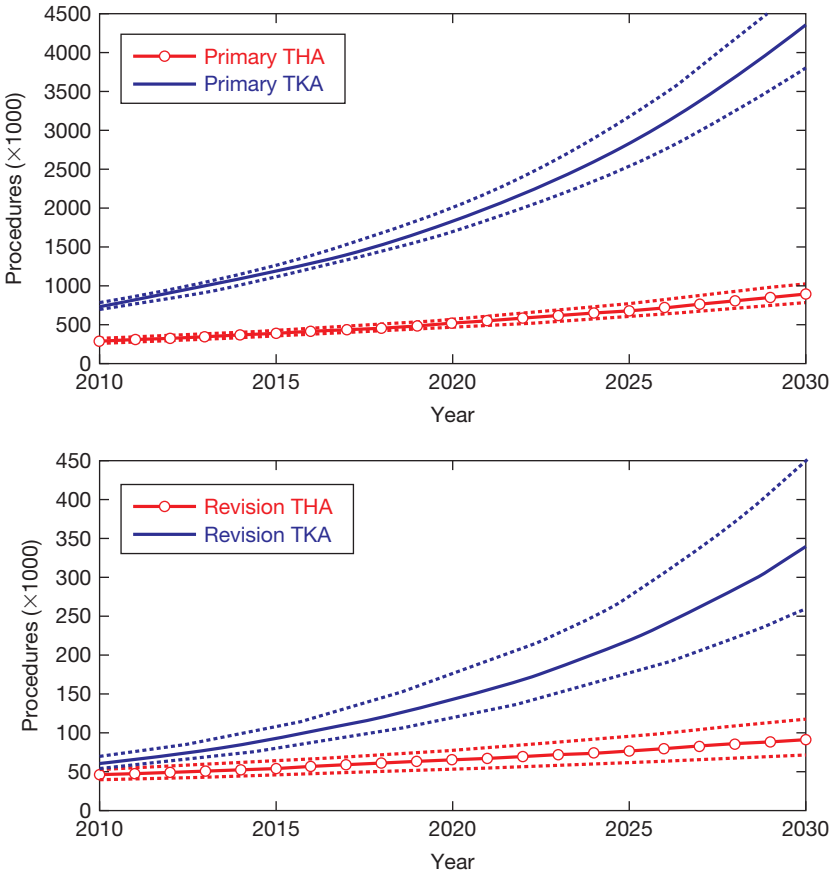

Figure 4 Projected annual demand for primary (top panel) and revision (bottom panel) total hip arthroplasty and total knee arthroplasty in the United States through the year 2030.

'constant rate' approach allowed the population to vary over time, but assumed that the future prevalence of surgery was constant, which was based on the average rate between 2004 and 2006.

Based on the updated projections,[17] the number of primary THA was predicted to increase from 229 900 procedures in 2006 to between 345 700 (constant rate) and 891 800 (variable rate) procedures in 2030 (Figure 4). Primary TKA was also predicted to increase from 524 600 procedures to between 792 200 (constant rate) and 4.34 million (variable rate) procedures over the same time period (Figure 4). Due to the relatively stable historical revision burden rates, the predicted demand for revision TJA is expected to be driven primarily by the increase in demand for primary procedures. Revision THA and TKA were projected to increase from 37 200 and 46 400 to 59 000 (constant rate)–91 400 (variable rate) and 64 600 (constant rate)–339 000 (variable rate), respectively, between 2006 and 2030. If the trajectory of surgery prevalence were to continue into the future, the demand for primary THA and TKA among younger patients, that is, patients <65 years old, will be projected to exceed 50% of all THA and TKA patients by 2011 and 2016, respectively. Younger patients will also be projected to exceed 50% of the revision TKA patient population by 2011. By 2030, the demand for TJA by younger patients aged <65 years will comprise 52% of primary THAs and 55–62% of primary or revision TKAs.

Based on the projected demand for primary and revision TJA, the corresponding economic impact in terms of hospitalization cost was also computed. By using the cost-to-charge ratio files provided in the NIS dataset to convert hospitalization charges to costs, the historical changes in average procedure costs were then projected for 2030. By combining the projected number of procedures and the projected costs for each procedure, the overall cost projections for primary and revision TJA were estimated. If the historical growth trajectory of procedure demand and costs continues, the overall cost for primary THA and TKA were projected to increase from $3.5 to $25.1 billion (95% CI: $14.9–40.4 billion) and from $7.0 to $92.9 billion (95% CI: $58.8–$144.6 billion), respectively (Figure 5). The economic burden for revision THA and TKA was also projected to increase from $712 million to $2.9 billion (95% CI: $1.1–$5.8 billion) and from $718 million to $13.9 billion (95% CI: $6.6–$27.1 billion), respectively.

6.601.6. Summary

In summary, the analyses of current and projected utilization for joint arthroplasty predict a massive anticipated demand for these procedures in the coming decades. However, the current economic and regulatory climate for health care

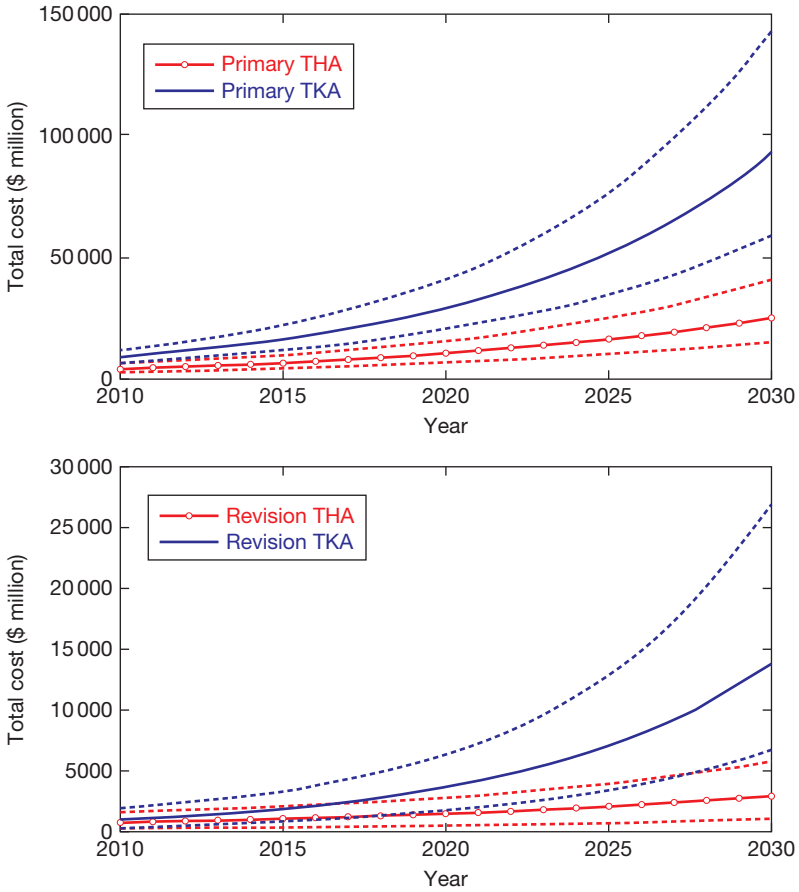

Figure 5 Projected annual cost of primary (top panel) and revision (bottom panel) total hip arthroplasty and total knee arthroplasty in the United States through the year 2030.

innovation is more challenging than ever before. New biomaterials for total joint replacement must be engineered to reduce widely recognized current complications such as loosening, dislocation, and infection for existing patient populations and to provide new functional capabilities to younger and more active patients. Technologies that only provide improved outcomes at 10+ years of service will require increased health economic justification. As scientists develop new biomaterials for the future joint replacement market, it is essential for commercial success that the studies to prove the cost effectiveness of these new technologies be designed and fully appreciated at the onset of the research and development phase in the product lifecycle.

References

1. Kurtz, S.; Mowat, F.; Ong, K.; Chan, N.; Lau, E.; Halpern, M. *J. Bone Joint Surg. Am.* **2005**, *87*, 1487–1497.
2. Malchau, H.; Herberts, P.; Ahnfelt, L. *Acta Orthop. Scand.* **1993**, *64*, 497–506.
3. National Center for Health Statistics. National Hospital Discharge Survey Description, 2009.
4. Agency for Healthcare Research and Quality. HCUP Databases. Healthcare Cost and Utilization Project (HCUP), 2008.
5. Robertsson, O. *J. Bone Joint Surg. Br.* **2007**, *89*, 1–4.
6. Canadian Institute for Health Information. Canadian Joint Replacement Registry (CJRR). 2007 Annual Report – Hip and Total Knee Replacements in Canada, 2008.
7. National Agency for Medicines. The 2006 Implant Yearbook on Orthopaedic Endoprostheses: Finnish Arthroplasty Register, 2008.
8. Australian Orthopaedic Association – National Joint Replacement Registry. Hip and knee arthroplasty, Annual report 2008.
9. The Norwegian Arthroplasty Register. Report 2008.
10. Swedish Hip Arthroplasty Register. Swedish Hip Arthroplasty Register, Annual Report 2007, 2008.
11. Kurtz, S. M.; Lau, E.; Schmier, J.; Ong, K. L.; Zhao, K.; Parvizi, J. *J. Arthroplasty* **2008**, *23*(7), 984–991.
12. Bozic, K. J.; Ries, M. D. *J. Bone Joint Surg. Am.* **2005**, *87*, 1746–1751.
13. Bozic, K. J.; Katz, P. P.; Showstack, J. A.; *et al*. The use of clinical and economic outcomes data to influence health policy in the United States: The case of total joint replacement, OREF Clinical Outcomes Research Award Paper. Presented at the 73rd Annual Meeting of the American Academy of Orthopaedic Surgeons, Chicago, IL, 2006.
14. Bozic, K. J.; Kurtz, S. M.; Lau, E.; Ong, K.; Vail, T. P.; Berry, D. J. *J. Bone Joint Surg. Am.* **2009**, *91*, 128–133.
15. Frankowski, J. J.; Watkins-Castillo, S. Primary Total Knee and Hip arthroplasty Projections for the US Population to the Year 2030, 2002.
16. Kurtz, S.; Ong, K.; Lau, E.; Mowat, F.; Halpern, M. *J. Bone Joint Surg. Am.* **2007**, *89*, 780–785.
17. Kurtz, S. M.; Lau, E.; Ong, K.; Zhao, K.; Kelly, M.; Bozic, K. J. *Clin. Orthop. Relat. Res.* **2009**, *467*(10), 2606–2612 [Epub Apr 10].

Relevant Websites

http://www.shpr.se/ – Swedish Hip Arthroplasty Register.
http://www.knee.nko.se/ – Swedish Knee Arthroplasty Register.
http://www.haukeland.no/nrl/ – The Norwegian Arthroplasty Register.
http://www.dmac.adelaide.edu.au/aoanjrr/ – The National Joint Replacement Registry (Australia).
http://www.cdhb.govt.nz/NJR/ – National Joint Register (New Zealand).
http://www.njrcentre.org.uk/ – National Joint Registry (UK).
http://www.cdc.gov/nchs/nhds.htm – National Hospital Discharge Survey (USA).
http://www.hcup-us.ahrq.gov/nisoverview.jsp – Overview of the Nationwide Inpatient Sample (NIS).
http://www.cms.hhs.gov/LimitedDataSets/ – Centers for Medicare & Medicaid Services.

6.602. Bone Cement

L D T Topoleski and R Rodriguez-Pinto, University of Maryland, Baltimore, MD, USA

© 2011 Elsevier Ltd. All rights reserved.

6.602.1.	**Introduction**	12
6.602.2.	**Bone Cement Chemistry**	12
6.602.3.	**Bone Cement Applications**	13
6.602.3.1.	Bone Cement in Surgery	13
6.602.3.2.	Potential Adverse Effects of Bone Cement	14
6.602.3.3.	Bone Cement as an Antibiotic Delivery System	15
6.602.4.	**Mechanical Properties of PMMA–Bone Cement**	15
6.602.4.1.	Overview	15
6.602.4.2.	Properties in the Nonsolid Phase	15
6.602.4.2.1.	Viscosity	15
6.602.4.3.	Structure of Solid Bone Cement	16
6.602.4.3.1.	Overall composition	16
6.602.4.3.2.	Molecular weight	16
6.602.4.3.3.	Porosity	16
6.602.4.3.4.	Radiopacifiers	17
6.602.4.4.	Properties in the Solid Phase	17
6.602.4.4.1.	Overview	17
6.602.4.4.2.	Static compressive properties	18
6.602.4.4.3.	Static tensile properties	18
6.602.4.4.4.	Shear strength	18
6.602.4.4.5.	Creep	18
6.602.4.4.6.	Fracture toughness	19
6.602.4.4.7.	Fatigue fracture	19
6.602.4.5.	Summary	24
6.602.5.	**Improving PMMA–Bone Cement**	24
6.602.5.1.	Introduction	24
6.602.5.2.	Chemical (‘or Internal’) Modifications	24
6.602.5.3.	Fiber Reinforcement	24
6.602.6.	**Summary and Concluding Remarks**	26
References		27

Glossary

Arthroplasty Surgery to relieve pain and restore range of motion by realigning or reconstructing a joint.

Bone cement A substance commonly used to hold implants in bone.

Curing Toughening or hardening of a polymer material by cross-linking of polymer chains.

Initiator A substance that initiates a chemical reaction.

Monomer A molecule that can combine with others to form a polymer.

Radicals Atoms, molecules, or ions with unpaired electrons on an open shell configuration.

Abbreviations

ASTM	American Society for Testing and Materials
HA	Hydroxyapatite
LVC	Low viscosity cement
MMA	Methylmethacrylate
MW	Molecular weight
OR	Operating room
PMMA	Poly(methyl methacrylate)
SEM	Scanning electron microscopy
UCS	Ultimate compressive strength
UHMWPE	Ultrahigh molecular weight polyethylene
UTS	Ultimate tensile strength

Symbols

E_t	Tensile modulus of elasticity, or Young's modulus
G	Energy release rate
J	Energy release rate
J_{Ic}	Critical energy release rate
K	Stress intensity factor
K_c	Fracture toughness
K_{Ic}	Mode I (opening mode) fracture toughness
M_n	Number average molecular weight
M_v	Viscosity average molecular weight
M_w	Weight average molecular weight
N	Number of cycles
S, σ	Stress

6.602.1. Introduction

The advent of acrylic bone cement, adapting dental acrylics to fix artificial hip joints in human bone, is certainly a watershed moment in the history of modern biomaterials. Total joint replacement has become one of the most successful, cost-effective operations in all of surgery.[1] In *The Well-Cemented Total Hip Arthroplasty: Theory and Practice*, Malchau and Breusch[2] write

> [Cemented total hip arthroplasty (THA)] is a method – if performed well – which is highly successful, reproducible and cost effective … a well-performed cemented THA still remains the treatment of choice for the average patients with osteoarthritis of the hip over the age of 60–65 with average activity. Younger patients and those with high demand activity will have to accept a higher chance of earlier failure irrespective of the mode of fixation and choice of implant.

The collaboration between Dr. Dennis Smith and Sir John Charnley that resulted in the first cemented prostheses revolutionized orthopedic surgery by enabling a long-term fixation of the metal and plastic components used as a treatment for arthritis that was previously unachievable.[3] Bone cement has been the most common means of fixation of artificial joints DiMaio.[4] The successful implementation of long-lasting internal devices, made from nonbiological materials, for example, artificial hips, was one of the inspirations for succeeding generations of biomaterials scientists and engineers that opened the doors to the myriad devices and strategies to replace the function of human tissue and organs that the world of biomaterials now offers.

Bone cement is made from a common polymer – poly (methyl methacrylate) (PMMA) – that is sold commercially under names like Plexiglas®, Perspex®, and Lucite®. It is not expensive and is available in many preformed geometries (e.g., sheets and rods). The main difference between the Plexiglas® we buy at the local home improvement store and orthopedic PMMA (bone cement) is how the material achieves its final form. Commercial acrylic pieces are generally formed under heat and pressure, in controlled conditions, and are homogeneous. Bone cement is formed by mixing prepolymerized beads and a liquid methyl methacrylate (MMA) monomer (**Section 6.602.2**). The combination of the two components results in a viscous, doughy mass that cures to the point of mechanical stability in 7–10 min. The cured bone cement is responsible for maintaining the integrity of the fixation of the prosthesis and transferring stresses from one side of the joint to the other. Thus, it is one of a very small group of load-bearing materials that are created directly in their service environment, and must maintain mechanical integrity from that time. Concrete is another example of such a material. (We might consider adhesives in this group as well, as most adhesives – glues, epoxies, etc. – are also formed '*in situ*.' Adhesives, however, have the specific purpose to hold structural materials together; admittedly, they are load-bearing, but without the accompanying structural materials, adhesives would have no structural role. Concrete and bone cement are independent structural materials.)

6.602.2. Bone Cement Chemistry

Acrylic bone cement is a form of PMMA, with essentially the same chemical composition as the commonly used 'industrial' transparent acrylics, known by the trade names Plexiglas®, Lucite®, or Perspex®. Bone cement is formed by the bulk polymerization of a liquid methyl methacrylate monomer (MMA – the liquid phase) and PMMA, or MMA copolymer-based beads (the powder phase). The process begins the creation of free radicals from the liquid MMA, by an initiator that is added to the powder phase (usually, dibenzoyl peroxide) and an activator that is added to the liquid phase (usually, *N*,*N*-dimethyl-*p*-toluidine). When the powder and liquid are mixed together, the initiator and activator react to form free radicals (eqn [I]), which then link to the MMA (eqn [II]), and generate polymer chains from the MMA (eqn [III]):

$$\mathrm{PMMA(C_6H_5COO{-}OOC_6H_5)} \rightarrow 2\mathrm{C_6H_5\text{-}(R^*)} + 2\mathrm{CO_2} \quad [\mathrm{I}]$$

$$R^* + \mathrm{MMA\,(CH_2{=}CCH_3)} \rightarrow R\text{-}\mathrm{MMA}^* + \mathrm{Heat} \quad [\mathrm{II}]$$

$$R\text{-}\mathrm{MMA}^* \rightarrow R\text{-}\mathrm{MMA\text{-}MMA}^* + \mathrm{Heat} \quad [\mathrm{III}]$$

where R^* is the free radical from the initiator. The polymerization reaction is exothermic, and the heat generated, and subsequent peak temperatures, depend on the cement composition, the cement mass, and the starting temperature of the components.[5–7] For additional details on the polymerization chemistry of bone cement, see Kuhn,[8] Lautenschlager *et al.*,[6] and Park.[5]

It is important to note that the polymerization of bone cement is really the polymerization of the liquid phase (MMA), which creates a solid matrix that binds the beads of the powder phase.[9,10] Often, an inorganic material is added to render the cured bone cement radiopaque, generally, $BaSO_4$ or ZrO_2. The radiopacifier is a component of the initial powder phase and also becomes embedded in the polymerized liquid. Air bubbles or voids may also form during the polymerization process, and thus, fully cured bone cement often consists of four distinct material phases: two polymer phases (prepolymerized beads and the polymerized monomer), the

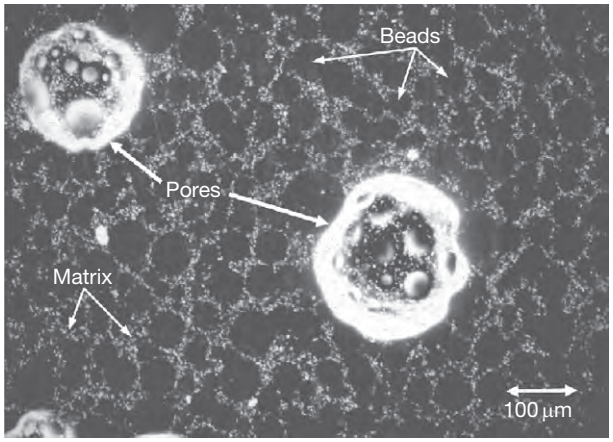

Figure 1 A polished cross-section of cured poly(methyl methacrylate) bone cement. The four major phases are present: Beads – which are from the original polymer powder, pores, polymerized monomer, and radiopacifier, in this case, $BaSO_4$. The polymerized monomer and radiopacifier are both contained in the matrix. The radiopacifier appears as tiny white specks that surround the dark circular cross-sections of the beads. The spherical beads are also seen lining the surfaces of the pores. Adapted from Topoleski, L. D. T.; Ducheyne, P.; Cuckler, J. M. *Biomaterials* **1993**, *14*(15), 1165–1172, used with permission.

radiopacifier, and voids (Figure 1). The mechanical and failure behavior of bone cement is likely to depend on the distribution and interaction of the phases within the bone cement mass.

The flow properties of bone cement change as the curing process progresses. Once the monomer has fully wetted the powder, the cement is in a predough stage and is in the least viscous state of curing. In the predough stage, the cement will stick to surgical gloves. The bone cement transforms into a nonsticky dough phase, as the surface monomer evaporates or polymerizes, and finally sets. Depending on initial temperature, bone cement may become solid in 7–12 min.[7] A user can control, to some extent, the length of the 'working time,' that is, time before the cement has hardened, by controlling the initial temperatures of the components (e.g., by storing them in a freezer or refrigerator). The fact that the bone cement has solidified, however, does not mean that the polymerization process is complete. Additional polymerization may continue for several weeks, and even then, not all of the monomers would have been converted.[11–16]

6.602.3. Bone Cement Applications

6.602.3.1. Bone Cement in Surgery

Bone cement is generally mixed in the operating room on an 'as needed' basis. Because the curing time is fast, the bone cement is usually not prepared until the whole surgery needed to permanently place a component of an artificial joint has been completed. The techniques used to introduce the bone cement into the bone depend on the location or component that is to be fixed, and the surgeon's preference and experience. The presence of voids, mentioned earlier, for example (Figure 1), was shown to reduce the fracture resistance of bone cement.[17,18] Therefore, most bone cement is subjected to a mixing environment that reduces the porosity. Initially, this was accomplished by centrifuging the liquid cement to separate the air from the polymer.[17] Mixing the cement in a bowl designed to create a vacuum proved to be a more favorable option;[18] it does not require transfer of the cement, the process takes place during mixing, not separately, thus giving the surgeon more time to work with the material, and eliminates the need for a centrifuge in the operating room (OR) (Figure 2).

Currently, to reduce porosity, most bone cement is mixed using various vacuum mixing systems. Many of the vacuum mixing systems are designed to release the mixed cement into a cartridge, which is then placed in what is essentially a caulking gun. If the cement is to be placed in a femur to fix the femoral component of an artificial hip joint, for example, the cement can be injected into the femoral canal. (This is generally done in a 'retrograde' fashion. The nozzle of the cement gun is placed into the distal or far end of the femoral canal, and the gun is withdrawn as the cement is injected distally to proximally.) The surgeon may opt to 'hand pack' the cement, as in the case of a tibial component of an artificial knee. In this case, the cement can be ejected from the cement gun onto the surgeon's hand and manipulated into the appropriate site. The state of the bone cement (predough, dough, etc.) when applied to the bone depends on the site of use, surgeon's preference, etc.

Once the cement is in place, the surgeon has a limited time to insert the device into the bone cement and ensure that the device is correctly placed and aligned. Although the time may be short, the surgeon must also ensure that the device does not move once it is in place, and must maintain a stable position until the bone cement is fully cured. The time from when the components of the bone cement are mixed until it is not possible to further manipulate either the prosthesis or bone cement is sometimes called the 'working time.' Once the cement has cured, its job is primarily structural – to hold the device in place permanently and facilitate load transfer from the device into the remaining bone. Bone cement fracture and/or loosening of the device within the cement mantle can lead to failure of the artificial joint and require a revision surgery. Thus, we discuss the mechanical properties of bone cement in detail in this chapter.

Radiographic examinations of patients with loosened prostheses may reveal a radiolucent line in the bulk of the cement, indicating that the cement has fractured. In the 15-year follow-up study by Kavanagh *et al.*,[19] cement fracture was identified as the 'most frequent mode of failure.' There are examples where cement fracture was indicated on a radiograph, yet the patient retained function of the prosthesis for over 3 years. A subsequent examination revealed that the extent of the cement fracture had escalated, the prosthesis had loosened, and revision surgery was necessary (Figure 3).[20]

The long-term success of a total joint prosthesis depends on the continued function of, and interaction between, each of the components comprising the prosthetic system. In a cemented total hip prosthesis, for instance, stress transfer from the pelvis to the femur is a function of the materials between the two bones (bone–PMMA–metal–UHMWPE–metal–PMMA–bone) and the interfaces between the materials. PMMA exhibits the lowest fracture toughness and ultimate tensile strength (UTS) of the materials.[21,22] (UHMWPE (ultra-high molecular



Figure 2 Elements of commercially available bone cement. Left: cement in the packaging, a case and single dose. Top: the packaged components of a single dose – 40 mg of polymer powder, 20 ml of monomer liquid. Right: the vacuum mixing chamber. Bottom: a different cement mixer and cement gun. Photographs provided courtesy of Stryker, Inc., used with permission.

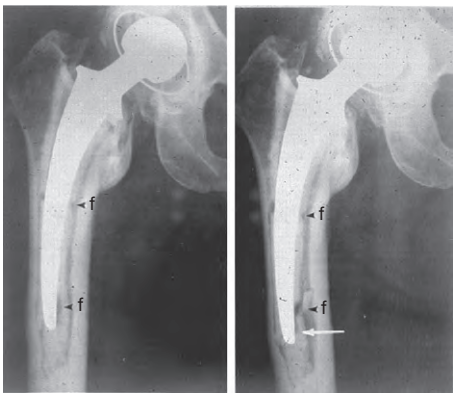

Figure 3 A set of radiographs of the same artificial hip joint taken ~3 years apart. (a) Fractures in the poly(methyl methacrylate) bone cement are evident (f), but at this point are not symptomatic. (b) The same patient 3 years later, where the progression of the fractures is evident. Bone cement fragments are penetrating the bone. Following this radiograph, the artificial hip was revised. Adapted from Topoleski, L. D. T.; Ducheyne, P.; Cuckler, J. M. *J. Biomed. Mater. Res.* **1990**, *24*, 135–154, used with permission.

weight polyethylene) is used as a low friction articulating surface, generally to prevent metal from articulating on metal, for example, as part of the acetabular component of a total hip prosthesis, or the tibial component of a total knee prosthesis.)

The relationship between interfacial integrity (stem/PMMA or bone/PMMA) and cement fracture is not well understood.[23] It has been postulated that maintaining the load-bearing capabilities of the metal stem–PMMA interface is critical to preventing fracture of the bone cement mantle,[24] or conversely, that the irregularity of the bone–PMMA interface is responsible for cracking of the bone cement.[25] The initiation of *in vivo* bone cement fractures remains an important topic of fundamental interest in orthopedic biomaterials.

Although we are concerned in this chapter with the use of bone cement, it is valuable to briefly discuss alternative means of fixation (which are discussed in more detail elsewhere in this text). As bone cement has been called the 'weak link' in artificial joint fixation, methods to fix joint components without cement have been used for some time.[26] Porous coatings on device surfaces provide a scaffold for bone to grow into the coatings and create a biological fixation, sometimes referred to as 'bone ingrowth.' Hence, not all artificial joints use bone cement fixation. Artificial joints may rely solely on bone ingrowth, may have some components cemented and others that are fixed by ingrowth, or may be completely cemented. The fixation method(s) may depend on the health of the patient's bones, the type of device implanted, and the surgeon's background and preferences. Therefore, we must recognize that not all artificial joints make use of cemented fixation.

6.602.3.2. Potential Adverse Effects of Bone Cement

There are a number of possible adverse effects from bone cement exposure, and the patient, the clinician, and the laboratory researcher working with bone cement are potentially susceptible. For example, methylmethacrylate exposure can cause skin reactions.[4] Surgical gloves do not protect the skin from MMA; in fact, MMA apparently easily penetrates the gloves.[27] When bone cement is delivered to the bone, there are potential thermal and chemical effects on the

contacting tissue.[28,29] The heat of the polymerizing bone cement, along with the release of MMA, may affect the tissue contacting the bone cement. There have been several reports of toxic effects from the MMA in humans and animals.[29–34]

Methylmethacrylate monomer may be released from the polymerizing cement into the surrounding tissues during mixing, manipulation, insertion, and curing of the bone cement.[28,29,35] The monomer release depends on the available monomer, which, in turn, depends on the polymerization rate.[5] For a given polymerization rate, the monomer release depends on the surface area of the cement mass. The cement mantle thickness does not affect the monomer release.[29] The adverse effects usually occur during or shortly after polymerization and, presumably, result from the availability of a relatively large amount of free monomer available before the reaction is completed.[15] The monomer may cause peripheral vasodilatation and hypotension when directly absorbed into the circulation.[35]

McLaughlin *et al.*[34] studied the mechanisms of MMA clearance from blood in dogs when the monomer was introduced by both simulated hip procedures or injection. They discovered that the monomer was almost completely cleared from the blood in <20 min. A measureable physiologic effect occurred only when the MMA exposure was between 30 and 40 times the amount available during total hip replacement. No foreign material was visible in the lungs of dogs receiving a low dose of injected monomer; dogs that received higher doses showed signs of pulmonary edema. The liver and spleen showed no evidence of monomer damage. Although monomer quantities released during surgery appear to be much lower than dangerous doses, reducing the amount of monomer released into a patient would seem to be advantageous in the long run.

6.602.3.3. Bone Cement as an Antibiotic Delivery System

One of the great advances in the application of biomaterials has been the use of materials, especially polymers, as drug delivery systems. Because total hip arthroplasties are susceptible to infection, one avenue to provide sustained delivery of antibiotics at the internal site of the operation is via the bone cement. Antibiotic-impregnated bone cement (also referred to as antibiotic-loaded bone cement) releases the antibiotic agent(s) into the surrounding tissue. There is some controversy as to the most effective use of antibiotic-loaded bone cement.[4,36–39] Furnes *et al.*[40] state that antibiotics in the bone cement give an added protection against infection over conventional antibiotic regimens. In revisions due to infection, for example, Gehrke[41] advocates the use of antibiotic-loaded bone cement.

Different investigators reached different conclusions on the effect of antibiotic loading on the mechanical properties of bone cement. One pivotal factor in how antibiotics may affect mechanical properties is how the antibiotic is mixed into the cement.[42] There are commercially available cements with the antibiotics premixed by the manufacturer; conversely, the antibiotic may be added and mixed during the cement preparation. Frommelt and Kühn[43] suggest that only the premixed cements retain appropriate mechanical properties. DeLuise and Scott[42] found that hand-mixing the antibiotic decreased the strength of the bone cement. In contrast, Lewis *et al.*[44] tested several mechanical properties of antibiotic-loaded bone cements mixed during preparation, and found no difference attributed to mixing method. Lewis and Bhattaram[45] examined the mechanical properties of three commercially available bone cements, available from the manufacturers both with and without antibiotics. They found that the addition of antibiotics did not affect the properties measured. Askew *et al.*[46] found no differences in bending modulus because of antibiotics, and also found that, after vacuum mixing, the antibiotics increased the porosity of the cement. Leone *et al.*[47] found that the reduction or increase in modulus depended on the type of antibiotic. Lewis[48] presents an excellent review of the literature on antibiotic-loaded bone cement, including compositions of commercially available cements and modeling of the elution kinetics, as well as details on the effect of antibiotic additives on the mechanical properties.

6.602.4. Mechanical Properties of PMMA–Bone Cement

6.602.4.1. Overview

The main function of bone cement is to transfer body weight under various service conditions (walking, standing, stair climbing, etc.) from the prosthesis to the bone. Therefore, the mechanical properties of bone cement will determine its success as a sold, structural material. In addition, as mentioned previously, bone cement is formed *in situ*, and its function will also depend on the properties when bone cement is in its nonsolid phase. The properties of bone cement in both its nonsolid and solid phases have enabled bone cement to perform its function admirably.[49]

6.602.4.2. Properties in the Nonsolid Phase

6.602.4.2.1. Viscosity

Polymerizing bone cement is a non-Newtonian fluid, which means that the viscosity is not constant as a function of time and shear rate. Viscosity cannot be determined independent of test method, and thus, for non-Newtonian fluids, the property 'viscosity' has no meaning. Viscosity calculations applied to fluids such as bone cement result in values termed the 'false-apparent viscosity' or 'apparent viscosity.' Because bone cement generally solidifies in about 10 min or less, apparent viscosity values depend on time, mass (volume), and test fixture geometry.[7,50]

Lewis[49] describes the 'ideal' bone cement as having a low and consistent value of apparent viscosity during the working time and, once the prosthesis was in its final location, polymerizes in a very short time. He provides a 'rule of thumb' that at 3 min after mixing, η should be $<100\ \text{Pa s}^{-1}$. Different cement formulations will achieve this viscosity at different strain rates.[49] Compositional factors that can influence the flow behavior of bone cements include the liquid monomer to powder ratio, the size of the solid polymer beads, the amount of radiopacifier, the amounts of initiator and accelerator, etc.[5,6]

The flow properties of bone cement can also be controlled to some extent by controlling the initial temperatures of the components before mixing. In general, chilling either or both the liquid and powder phase will lower the initial apparent viscosity and increase the working time[7] (**Figure 4**).

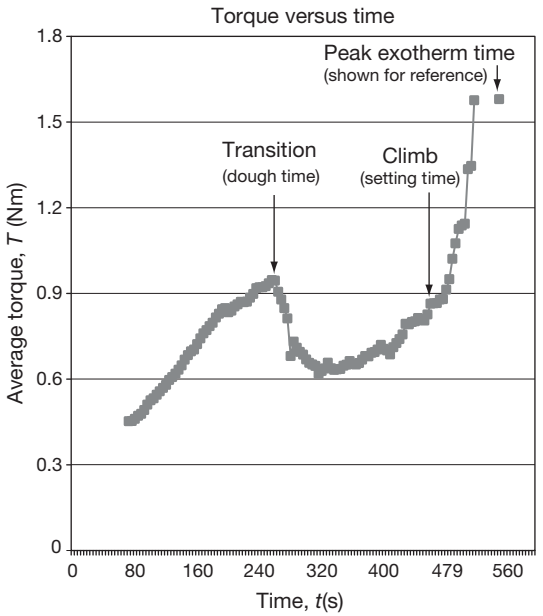

Figure 4 Torque versus time graph for curing poly(methyl methacrylate) (PMMA) bone cement. In this test, the torque resistance represents the changing viscous state of the curing bone cement. A relatively linear increase in resistance from the onset of testing (~80 s after mixing) reaches a peak at the Transition point, marking the onset of the dough phase. The torque values decrease because the material adheres less and less to the test chamber walls during the dough phase. The torque then increases again as the material starts to set. The point marked Climb indicates that the PMMA is completely set (the Setting Time) and the rapid torque increase occurs as the cement becomes solid. The setting time as determined by the peak exotherm temperature is shown for reference. From Sullivan, S. J.; Topoleski, L. D. T. *J. Biomed. Mater. Res. B Appl. Biomater.* **2007**, *81*(1), 224–230, used with permission.

6.602.4.3. Structure of Solid Bone Cement

6.602.4.3.1. Overall composition

The final solid bone cement generally consists of four distinct phases (if the cement is radiopaque): (1) The prepolymerized beads (from the powder component), (2) the polymer matrix (from the polymerization of the liquid MMA), (3) the radiopacifier, and (4) porosity (Figure 1). Pores may not be a material phase in the thermodynamic sense, but as a microstructural element, they contribute to the mechanical behavior of bone cement, and the designation 'phase' will be extended here to include porosity in bone cement. The relative amounts of each phase, and their distributions, will affect the properties of the bone cement.

6.602.4.3.2. Molecular weight

The molecular weight (MW) of a polymer can have a significant effect on its mechanical properties.[51–53] The two polymer phases of bone cement are polymerized under drastically different conditions – the prepolymerized beads are created under controlled factory conditions, and the matrix polymerizes within the bone. There is no reason to believe *a priori* that the MW or molecular chain entanglement of the two polymers is the same.

Lautenschlager *et al.*[6] reported several determinations of average MWs for bone cement: a number average (M_n) of $4.5–5.1 \times 10^3$ and a weight average (M_w) of 2.42×10^5 for cured bone cement. The number average for the powder (prepolymerized bead component) alone was $3.21–4.40 \times 10^4$. There was an apparent increase in the average MW during curing. This implies that the interbead matrix has a higher average MW than the prepolymerized beads. The result is unexpected as the polymerization of the matrix occurs through a 'run away' reaction, where an overabundance of initiator is added to the MMA (the initiator is mixed in with the powder). Many PMMA chains are initiated and they grow. For a fixed quantity of monomer, higher MWs are generally achieved by decreasing the number of polymer initiation sites. By saturating the monomer with initiators, the average MW is expected to stay low. Apparently, the interbead matrix manages to polymerize with a high average MW. It is possible that the interbead matrix polymer chains could raise the average MW, and yet not contribute extremely long chain polymers (MW of 1000 000 or greater) to the bulk polymer.[54] No attempt has been made to characterize the influence of the MW of each of the two polymer components on the fracture characteristics of bone cement.

In their discussion on the polymerization of bone cement, Lautenschlager *et al.*[6] noted:

> A most (desirable) feature in the context of set cement strength is a nearly complete interpenetration (entanglement) of preformed and newly formed chains after powder and liquid components are mixed. Boundaries of poor molecular interpenetration, created by the specific course of chemical events, are not necessarily visible in electron micrographs of set cement. Such defects can occur not only at undissolved bead/matrix interfaces, but also within what a typical scanning electron micrograph reveals as matrix material. The importance of weak molecular boundaries in the mass of the cement is their possible role in inducing localized microfractures.

Little is known about how the interaction between the two polymer phases affects the overall performance of bone cement, which would seem most relevant in the fracture properties. Numerous studies of fracture surfaces report observing bead 'pull-out' from the matrix polymer.[55,56] However, studies have shown that a decrease in MW in the beads (as the result of γ-irradiation) can lead to a decrease in the fracture resistance.[57] Other studies indicate that differences in MW can lead to differences in creep behavior.[58,59]

6.602.4.3.3. Porosity

We can roughly distinguish the types of pores found in fully polymerized bone cement as macropores (with a pore diameter >1 mm) or micropores (with a pore diameter <1 mm).[60] The pores may initiate, for example, from air initially adsorbed on powder constituents, including the radioopacifier, air trapped during mixing of the bone cement, evaporation of unreacted liquid monomer, and polymerization shrinkage.[12,20,49,56,61,62]

Centrifugation or vacuum mixing leads to a substantial reduction in porosity.[17,18] Centrifugation separates the air bubbles from the cement mass because of the different densities of the bubbles versus the cement material, and vacuum mixing eliminates or reduces the gasses in the cement environment by maintaining a vacuum. The amount of porosity

remaining in the solid cement mass depends on the mixing method and the initial temperature of the liquid monomer prior to mixing.[49]

The presence of pores in the cement may have an effect on the integrity of the cement mantle and hence on the life of the arthroplasty. The role of porosity in cement has been studied from different aspects, from reports of no effect on fracture toughness from reduced porosity,[25] to an optimum porosity content for fracture toughness,[63] to increased fatigue life in pore-reduced cements.[10,17,64,65]

From a mechanics point of view, spherical pores act to increase the local stresses by a factor of about 2.[66] Thus, pores may become initiation sites for fractures, and it follows that reducing porosity would reduce the likelihood of bone cement fracture. It is also possible that pores may play a role in blunting or diverting propagating cracks, thereby prolonging the life of the cement mantle by forming a larger damage zone and thus dispersing energy localized at the crack tip. Wang and Pilliar[63] indicated, based on maximizing the fracture toughness and plasticity effects, that an optimum pore density for bone cement could be defined; that is, there may be an effect of porosity on the fracture toughness of aged bone cement that is related to plasticizing effects of the aqueous aging. Topoleski *et al.*[20] showed that the porosity within the bone cement mass can interact with the propagating crack, but the link between the fracture mechanisms in bone cement and porosity has not yet been determined. Nonetheless, the current consensus is that the life of the cemented artificial joint will be extended by substantially reducing porosity.[49]

6.602.4.3.4. Radiopacifiers

Acrylic bone cements are invisible on radiographs, and hence, a radiopaque material is added to render the bone cement visible. Bone cements with radiopaque additives are termed radiopaque, and bone cements without such additives are termed radiolucent.

There are two commonly used radiopacifiers in commercial bone cement, $BaSO_4$ and ZrO_2. In general, $BaSO_4$ particles are roughly egg-shaped, ~1 μm or less in size. In contrast, ZrO_2 particles are larger and resemble cauliflower heads. In Charnley's[3] original paper introducing bone cement, he suggested using ~25% by weight $BaSO_4$ as a contrast agent. Currently, bone cements for total joint arthroplasty contain 10–15% by weight of either $BaSO_4$ or ZrO_2. More recently, applications of bone cements in spinal corrective surgery, such as kyphoplasty or vertebroplasty, use bone cements with up to 30% $BaSO_4$.[67–69]

Early studies on the effect of $BaSO_4$ addition on fracture toughness were inconsistent.[70] Beaumont[61] and Sih and Berman[71] attributed a decrease in bone cement fracture toughness to the addition of $BaSO_4$. Both Beaumont[61] and Wright and Robinson[56] indicated that $BaSO_4$ may act as a void initiator and therefore reduce the fracture performance of bone cement. Figure 5 illustrates voids that apparently nucleated around $BaSO_4$ particles.[20]

Barium sulfate is found in the interbead matrix phase of bone cement only, thus as much as one-sixth of the total matrix weight is $BaSO_4$. If $BaSO_4$ particles are essentially equivalent to pores, then the 'microporosity' of the PMMA matrix could be substantial, and may thus lead to reduced fracture toughness.

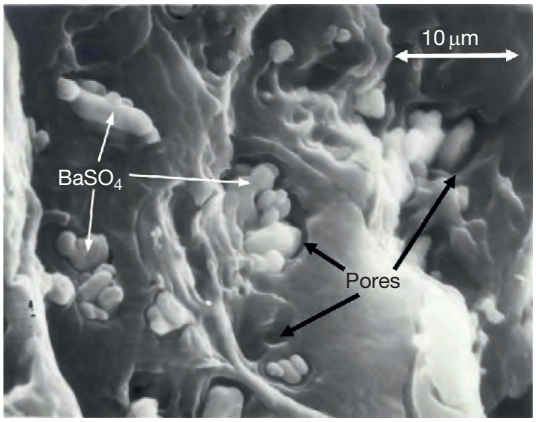

Figure 5 Scanning electron micrograph of a section from a fracture surface of cured PMMA bone cement. $BaSO_4$ particles, on the order of 1μm are not embedded in the polymer matrix, but rather appear to sit inside small pores. Adapted from Topoleski, L. D. T.; Ducheyne, P.; Cuckler, J. M. *J. Biomed. Mater. Res.* **1990**, *24*, 135–154, used with permission.

It is interesting that in one of the few studies to address the effect of testing environment on the fracture toughness of bone cement, Freitag and Cannon[70] noted an increase in fracture toughness for specimens tested in bovine serum, in contrast to specimens tested in air. The increase occurred only for bone cement containing $BaSO_4$. For bone cement without $BaSO_4$, fracture toughness was the same in both environments.

As the radiopacifier is added to the bone cement in the powder phase and ends up in the interbead matrix polymer, the distribution of the particles will depend on the mixing technique and the propensity for the particles to either disperse or to agglomerate. The radiopacifier will thus affect any mechanical processes that are influenced by the interbead matrix, especially fracture. Agglomerations of poorly dispersed $BaSO_4$ may reduce the fracture resistance of the bone cement by acting as crack initiation sites.[72] Molino and Topoleski[73] showed that $BaSO_4$ decreased fatigue crack velocity by creating a more favorable and longer crack propagation path through the interbead matrix polymer, resulting in longer fatigue lifetimes than in radiolucent cements of the same composition. Alternative methods to render bone cement radiopaque, such as reducing the size of the radiopaque particles,[74] may further allow researchers to improve the mechanical properties of cement while retaining the essential radiographic properties.

6.602.4.4. Properties in the Solid Phase

6.602.4.4.1. Overview

An artificial joint is subjected to a complex loading environment, and the ability of the bone cement to transfer loads from the prosthesis to the bone depends on the static or quasistatic responses to those loads. Similar to designing a bridge, the artificial joint system can best be designed when the mechanical properties of the constituents are well known and controlled. Bone cement generally behaves as a linear elastic material and tends to exhibit brittle fracture characteristics. Many of the common mechanical properties of bone cement have been determined for various conditions. Static or

quasistatic properties of materials are generally determined from the results of stress–strain tests. (Strictly speaking, most such mechanical tests measure load, or applied force, and deflection, or change in length. Stress and strain are calculated from the load and deflection data.) For a linear elastic material, the slope of the elastic portion of a stress–strain curve, whether the material is under compression, tension, or shear, is called the elastic modulus or Young's modulus. The highest stress the material attains before failure is called the ultimate stress. Note that the ultimate stress is not the fracture toughness, discussed below. Static compressive, tensile, and shear properties are generally obtained on regularly shaped specimens (cylinders, dog bones, etc.), using standard mechanics methods. There are at least two particularly valuable summaries of the mechanical properties of bone cement, those by Lewis[49] and Saha and Pal.[21,22] These excellent summaries lead to the same conclusion – that the reported properties of bone cement depend on how those properties were measured, from the formulation and mixing of the cement to the creation of test specimens and to the physical testing parameters. In a recent paper, Nottrott[75] showed that the environment in which test specimens were aged could have a significant effect on properties over the course of several years. Therefore, in comparing the results from different studies, we must take the testing procedures under consideration.

6.602.4.4.2. Static compressive properties

The values of the ultimate compressive strength (UCS) and Young's modulus (or modulus of elasticity, E_c) depend on the type of cement, and mixing, curing, and storage or aging conditions. The UCS values vary from 72.6 to 117.0 MPa and E_c varies from 1940 to 3180 MPa, as summarized in Lewis.[49] As the stress distribution in a cemented artificial joint depends, at least in part, on the properties of the constituent materials, the wide variations in UCS and E_c (over 60%) imply that the stress distribution in an artificial joint will depend on how the bone cement is created.

For a given mixing method, the bone cement formulation has the greatest influence on the results. As Lewis[49] states:

> The key parameters are: the quantities of stabilizers, initiators, and radiopacifiers; the presence or absence of a copolymer; the powder size and distribution; the ratio of bead to milled prepolymerized particles; and the rate of change of viscosity with time.

Lewis[49] also postulates that, for a given brand of cement, the mixing method has an important influence on the mechanical properties through its effect on the porosity. Clearly, the more porous the cement, the lower the density, and while the UCS increases with decreasing porosity, there is no clear relationship with compressive modulus.

6.602.4.4.3. Static tensile properties

Artificial knees and hips are subjected to compressive forces that arise from maintaining body weight in a variety of activities. At first glance, it would appear that no tensile stresses are obvious in an artificial joint system. Tensile stresses arise, for example, from bending forces, and also from the effects of local geometry (e.g., the irregular bone surface). As with the compressive properties, the values of the UTS and tensile modulus of elasticity (E_t) depend on the type of bone cement, the mixing and handling conditions, and the test procedures.

For a given cement type, whether or not the cement was mixed using a pore reduction method (centrifugation or vacuum mixing) was significant, with the UTS increasing as porosity decreased. UTS values vary from 23.6 to 49.2 MPa and E_t varies from 1583 to 4120 MPa, again as summarized in Lewis.[49] The variation in UTS is over 100%, and the variation in E_t is over 160%. The strain to failure ($\varepsilon_{max,t}$) ranged from 0.86 to 2.49, a change of 190%. The wide range of reported values again indicates that, because of variations in cement parameters, the stress distribution in an artificial joint system may be highly variable.

6.602.4.4.4. Shear strength

Shear strength of bone cement has not received as much attention as other properties. A summary of the results presented in Lewis[49] shows that the ultimate shear stress values range from 32 to 69 MPa, and are, as other static properties, influenced by cement type and preparation and testing parameters. Funk and Litsky[76] showed that the cement's shear modulus can have an effect of the shear stresses at the cement–bone interfaces, which will have a pivotal role in stress transfer to the bone, and thus, for example, bone remodeling.

6.602.4.4.5. Creep

Creep, and the related phenomenon of stress relaxation, are the results of the viscoelastic response of materials under either a prolonged load or deformation. Creep of a material can lead to a permanently altered geometry, and hence an altered stress environment. PMMA–bone cement, as an amorphous polymer, exhibits measurable creep, and its viscoelastic behavior will affect the overall structural behavior in an artificial joint system.[77]

Several studies have observed the creep behavior of bone cement both with static and dynamic loads. The creep of bone cement depends on the type of cement, preparation procedures, environment, and the testing conditions, including stress level and test type (i.e., static or dynamic, compressive of tensile).[77–79] A higher stress level will result in a higher creep rate, as will a higher temperature. Verdonschot and Huiskes[78] showed that bone cement creeps more readily under tensile loading than under compressive loading. Additional phases or additives may reduce the creep behavior of bone cement by effectively dividing the cement mass into smaller continuous segments. Both Pal and Saha[80] and Chwirut[77] showed that carbon-reinforced cement exhibits less creep deformation than nonreinforced cements.

Some researchers believe that some amount of creep may be beneficial to the implant, although an optimum creep level has not been established. Bone cement creep can result in subsidence of a femoral stem, effectively wedging the stem into the cement, and also reduce stress peaks in the cement mantle.[78,81,82] At some point, creep is no longer beneficial to the implant and may cause fracture of the cement mantle from excessive plastic deformation, which may result from microcracking around the pores.[77] Different cement parameters, such as the amount of porosity or residual monomer, the bead size in the powder phase, or cement formulation (such as adding an MMA-styrene copolymer or cross-linking agents)

can affect the creep of PMMA, as can test conditions, like temperature. For example, reducing porosity or increasing the bead size can increase creep resistance.[59,75,77,81,83,84]

6.602.4.4.6. Fracture toughness

The previous discussion of bone cement properties has addressed how the mechanical strength (UTS, UCS) is influenced by the environment, microstructure, and the method of curing. Stiffness or strength considerations, however, are not the only important factors in the bone–bone cement-prosthesis system. The ability of a material to resist crack growth requires the study of fracture mechanics.[71]

Although bone cement *in vivo* is subjected to a fatigue loading environment, the principles that govern static fracture, or the fracture toughness, of a material can be used to gain insight into the fatigue behavior. Thus, while improving the fracture toughness of bone cement may not directly translate to an improved fatigue resistance, studying the fracture mechanisms and material behavior during fracture toughness tests can guide future fatigue studies. In addition, the same fracture mechanics considerations that are used to predict and describe static fracture also apply to fatigue.

Two properties are generally used to describe the fracture resistance of a material: the energy release rate, G, and stress intensity factor, K. The energy release rate takes into account the energy involved in crack propagation and can be obtained from the work done on a cracked specimen. The stress intensity factor describes how the stress field is modified near the crack tip. The value of K is a function of the nominal stress, σ, and also the crack length, a. The general equation that describes the stress intensity factor is

$$K = Y\sigma\sqrt{a} \qquad [1]$$

where Y is a function of the crack size and geometry of the specimen. The equation states that the larger the flaw, or current crack length, the lower the stress needed to cause fracture. The value of the stress intensity factor at fracture is called the critical stress intensity factor, or fracture toughness, K_c. The fracture toughness is a simple relative value of the material's ability to resist crack propagation given the existence of an already sharp crack. Fracture toughness can therefore be characterized as a material's ability to resist further crack propagation or crack extension.[85] Another interpretation of fracture toughness is that it is a measure of the energy absorbed by a material prior to crack extension and is thereby related to the energy necessary for crack propagation. The Griffith[86] crack propagation criteria are based on the postulate that a crack can grow only if there is enough energy available to create a new crack surface area. It is important to understand that the presence of a critical quantity of energy is not a guarantee for crack growth. It is not correct to state that, given the energy necessary for crack growth, a crack *will* grow, only that a crack *can* grow; it may not.

Expressions for Y have been determined for many specimen geometries, making K_c usually straightforward to define.[87,88] The remarkable result of eqn [1] is that a material's fracture toughness value is independent of loading conditions, crack size, and specimen geometry, thus making fracture toughness a material property.

It is well known that the MW of a polymer, or the grain size in metals, affects fracture toughness.[53,87]

Fracture toughness tests require specimens with certain minimum dimensions (see, e.g., Broek[87] or ASTM E399) and that a sharp crack be introduced into the specimen (**Figure 6**). Different specimen geometries can be usedas, if the test requirements are met, the resulting data yield a material property that is independent of geometry. It is possible, therefore, to directly compare the published values of fracture toughness of various bone cements determined by different investigators. In his review paper, Lewis[49] reviewed the fracture toughness results from several different studies, conducted under a variety of conditions. The studies encompassed six different types of commercially available bone cements. The fracture toughness of the bone cements ranged from 1.03 to 2.32 MPa $m^{1/2}$. As a benchmark, the fracture toughness of commercial PMMA is roughly between 1 and 1.5 MPa $m^{1/2}$.[55,89] Thus, PMMA is not noted for its resistance to fracture. Fracture toughness tells only a part of the failure story; however, it is a starting point that must be augmented by a subsequent discussion of fatigue failure.

6.602.4.4.7. Fatigue fracture

Possibly, the most critical consideration for the integrity of the bone cement mantle itself is the fatigue behavior. Although other behaviors, like creep, may influence the overall success of the prosthesis, the artificial joint construct is subjected to fatigue loading, and gross or even undetected fatigue can cause failure of the prosthesis.[20,90] For example, microcracks that develop under cyclic loading can alter the modulus of the cement mantle, even if no gross fracture is present, and hence affect the stress transfer to the bone. The fatigue properties of bone cement received increased attention as researchers postulated and showed that fatigue was a primary cause of cement failure. Lewis[90] gives an excellent review of the details of different fatigue studies, with an emphasis on comparing/contrasting preparation methods, testing methods, and cement brands. It is difficult to compare/contrast fatigue results performed by different researchers, because there are many ways to conduct fatigue tests, and there is no material property, like fracture toughness, that completely characterizes the fatigue crack resistance of a material (**Figure 7**).

Few authors have examined specimens of PMMA that were retrieved from actual *in vivo* service. Williert *et al.*[91] examined only PMMA–bone interface surfaces of retrieved PMMA specimens to study the interface morphology of the bone cement. Topoleski *et al.*[20] performed a fractographic analysis of retrieved bone cement specimens, which failed *in vivo*, and compared and contrasted fracture surfaces created under known, controlled conditions. Rapid fracture surfaces, such as those created during a fracture toughness experiment, have a distinctly flat morphology, which was notably absent from the *in vivo* fracture surfaces. The identifying characteristic irregularity of the fatigue surfaces observed on both the controlled fractures and the retrieved specimens is the consequence of the fatigue crack damage zone characteristic of PMMA–bone cement.

There is a need for continued pursuance of bone cement fatigue knowledge. A brief summary of important concepts for consideration in fatigue testing of bone cement is presented in order to guide unfamiliar readers. The overview by

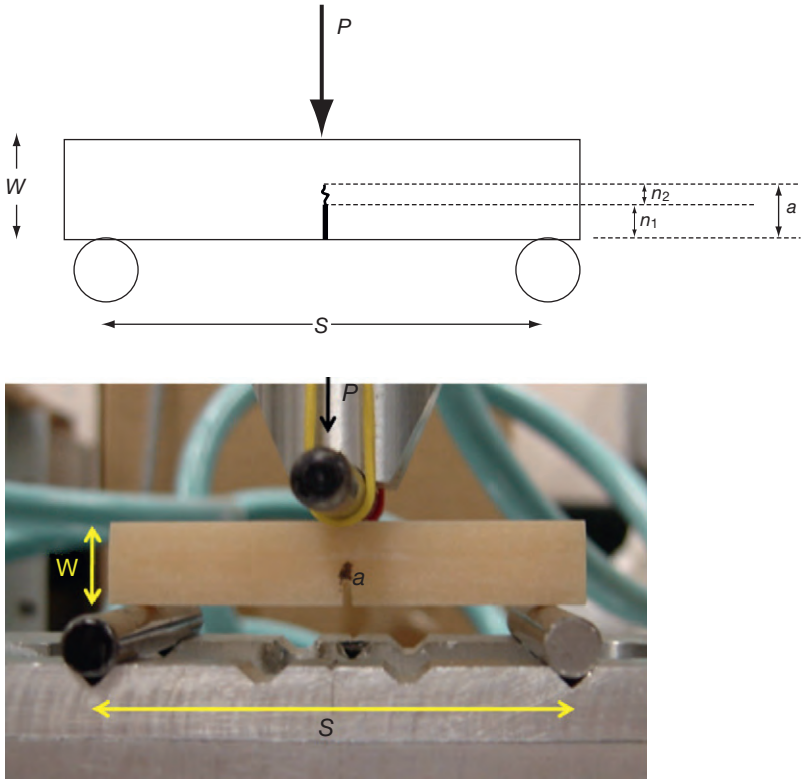

Figure 6 Top – a schematic of a three-point bending specimen for fracture toughness testing. A load (P) is centered between the two supporting fixtures, separated by span (S). An initial notch (n_1) is cut into the specimen, and then a further extension of the notch may be created by 'prefatiguing' a longer crack (n_2) from the initial notch. The total initial crack length (a) is the sum of the cut notch and the prefatigued crack ($n_1 + n_2$). The load at failure P, support span S, specimen height W, specimen depth B, and initial crack length a, are used to calculate the fracture toughness (K_{IC}) of the specimen using the equation $K_{IC} = \frac{PS}{BW^{3/2}}\left[2.9\alpha^{1/2} - 4.6\alpha^{3/2} + 21.8\alpha^{5/2} - 37.6\alpha^{7/2} + 38.7\alpha^{9/2}\right]$ where $\alpha = a/W$.[87] Broek[87] also gives an excellent summary of other potential geometries for fracture toughness testing, as well as the appropriate equations for calculating fracture toughness. Bottom – a photograph of a poly(methyl methacrylate) bone cement three-point bending specimen prior to loading for a fracture toughness test.

Krause *et al.*[92,93] or a text devoted specifically to fatigue analysis, such as Collins,[94] are more detailed sources of fatigue testing methodologies.

The fatigue or endurance limit of a material is defined as the stress level at which the material may undergo an infinite number of cycles, that is, may never break. An enormous amount of time is required to estimate the endurance limit of a material at a low testing frequency. A reliable model of stress (or strain) versus cycles to failure for bone cement, based on low cycle to failure testing, can reduce the time and expense of fatigue characterization. Krause *et al.*[92,93] present suggestions for statistical analysis of fatigue tests that may be useful for estimating the fatigue limit, by concentrating fatigue testing on failures that occur at <1 million cycles, and extrapolating to longer lifetimes. Fatigue data may be presented as lifetime, or cycles to failure for a given initial stress (based on the S–N or stress vs. cycles to failure curves), as probability of failure after a given number of cycles, or as crack growth rates (using, e.g., the Paris relationship[95]).

Because of the extensive time required to perform fatigue studies on any material, the loading frequency must optimize data production. Human gait analysis shows that the femur is loaded twice during each step, once at heal strike, and once at toe push-off, and the two loading peaks occur in a span of about 0.4 s.[96] The physiologic loading rate, therefore, for each step is two cycles per 0.4 s, or ~5 Hz. The twin loading peaks repeat with the next heal strike of the same foot, ~1 s later. A single fatigue test to 1 million cycles, at 5 Hz, requires ~2.5 days. A comprehensive series of fatigue tests would involve an inordinate amount of time. Higher frequencies may not be appropriate, however, because the fatigue properties of many polymers are sensitive to fatigue testing frequency, due primarily to thermal effects. Consideration of frequency sensitivity, service loading rates, and economics must be balanced. The highest frequency allowable, without changing the nature of the fatigue failure from that found *in vivo*, is the test frequency of choice.

Pilliar *et al.*[97] investigated the effect of test frequency on the results of fatigue tests in bone cement. They measured the effect of frequency on the temperature of the bone cement, and noted that below 10 Hz, there was no measured change in temperature with a change in test frequency; therefore, below 10 Hz, fatigue behavior of bone cement appears to be independent of thermal effects associated with increased test frequency.

Johnson *et al.*[98] published a study of the effect of test frequency and environment on the results of bone cement fatigue experiments. They performed tension fatigue tests at one stress level only, and their results, therefore, cannot be

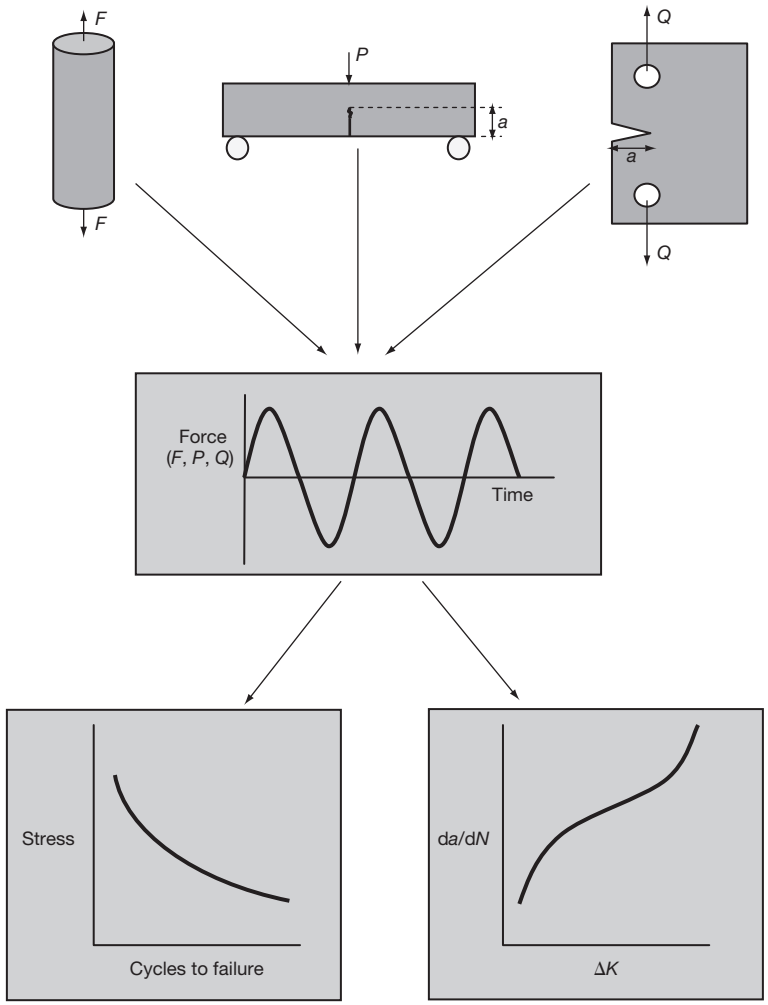

Figure 7 Fatigue specimens can take many forms, depending on the nature or amount of material available. The top row shows three commonly used specimens and test configurations. From left to right, simple tension (or compression), three-point bending, and compact tension (CT) specimens. Fatigue, or cyclic, loading is applied to the specimen, schematically depicted in the center row. The nature of the load cycle – maximum load, tension–tension versus tension–compression, loading frequency, etc. – depends on the goals of the particular study. The bottom row shows two common presentations of the fatigue data: (left) the stress versus cycles to failure, or *S–N*, curve, (right) and the crack velocity/cycle versus change in stress intensity (K), or da/dN versus ΔK, curve.

generalized. They reported an increase in fatigue life with increased testing frequency. They also reported a decrease in fatigue life in 37 °C saline versus an air and room temperature environment. Krause and coworkers[92,93,99] addressed the issue of consistency in fatigue testing of PMMA–bone cement. In their review, they state that comparisons between different studies are often difficult because of the myriad varieties of test conditions, cement preparation methods, test specimen geometry, and test methodology. They explicitly warn Krause *et al.*[92]:

> Readers of fatigue papers should be cautioned that conclusions presented are only valid for the parameters and test conditions tested. It is extremely dangerous and can be misleading to extrapolate test data conducted under one set of conditions to general conclusions. . .

In an effort to address this issue, Lewis and Nyman[100] suggested that standardized test conditions may be useful. For direct comparison of results for different conditions, especially for fatigue tests, the same test methods must be used; however, we must also recognize that different situations or scientific questions may require specific methods to determine an answer.

6.602.4.4.7.1. Effect of environment, differences between industrial PMMA and bone cement, and $BaSO_4$ addition

Jaffe *et al.*[101] investigated the effects of storing Simplex® and CMW® bone cements in bovine serum for up to 2 years on compressive fatigue life. They performed compression fatigue tests at 30 Hz, and determined the effect of storage to be negligible. Only one specimen of each storage treatment was tested at a given stress, however, and as fatigue testing is plagued by data scatter, it is difficult to extract fundamental conclusions from their work.

Beaumont and Young[55] compared the slow crack growth in both commercial PMMA (Perspex®) and PMMA–bone cement.

They did not perform dynamic fatigue studies, but measured instead the time to failure as function of a single, sustained load (static fatigue), at 20 °C in air and in water. Their data indicated that bone cement had better crack propagation resistance (lower crack velocities for a given stress intensity)and a higher fracture toughness than Perspex®. They also noted an environmental effect: an increase in propagation resistance for bone cement specimens tested in water versus bone cement tested in air.

The superior fracture properties of bone cement compared to Perspex® may be at first surprising, as Perspex® is generally polymerized under well-controlled conditions, and MWs can be high. In contrast, bone cement polymerization is uncontrolled and MWs are low compared to the industrial PMMA. For most polymers, including PMMA, fatigue fracture is dependent on MW,[51] and in the absence of MW information, fatigue data comparisons between the two forms of PMMA are difficult.

Beaumont and Young[55] also performed scanning electron microscopic fractography on their failed specimens. From observations of the bone cement fracture surfaces, they identified 'pull-out' of bead phase polymer from the surrounding matrix. The bead pull-out may explain the lower crack propagation velocities, and higher fracture toughness, of bone cement compared to Perspex®. Bead pull-out from the matrix requires energy that would otherwise be available to propagate a crack. As commercial PMMA is homogeneous, that is, there is no bead phase to pull out, that specific energy dissipation mechanism is absent.

Freitag and Cannon[89] performed the earliest cyclically loaded, tension-compression fatigue studies on bone cement. They investigated bone cement with and without the addition of 10% by weight $BaSO_4$. Their tests were performed at body temperature (37 °C) in a bovine serum bath and in air at room temperature. They showed that testing at 37 °C in serum increased the values of both fracture toughness and fatigue life over the respective values obtained in air at the ambient temperature. Their data relating the effect of $BaSO_4$ addition to the fracture properties of bone cement were inconclusive. Depending on the type of cement and the environment, the addition of $BaSO_4$ either increased or decreased the fracture toughness, but there was *no* observed effect on the fatigue behavior of the cement.

Wright and Robinson[56] compared fatigue crack propagation behavior in three different bone cements: a standard viscosity cement, a low viscosity cement (LVC), and carbon fiber-reinforced cement. They determined that there was no difference in crack propagation rates for standard bone cement compared to LVC. The addition of carbon fibers, however, reduced the crack propagation rate by an order of magnitude. Fractographic analysis of the standard and LVC cements indicated the separation of matrix and bead phases after fracture.

Krause *et al.*[93] performed an extensive series of fatigue tests examining three commercially available bone cements: Simplex P (Howmedica, Inc. Rutherford, NJ), Zimmer Regular (Zimmer, Inc. Warsaw, IN), and Zimmer LVC. They showed that there was no difference in the endurance limit between Zimmer Regular and Simplex P bone cements, but both had a significantly higher endurance limit than Zimmer LVC. They noted that the endurance limits estimated by their study were between 7 and 11 MPa. They reported that their endurance estimations were comparable to *in vivo* stresses for bone cement predicted by other investigators.

6.602.4.4.7.1.1. Porosity reduction Several studies have concentrated on the effect of porosity on the fatigue life of bone cement. Centrifugation and vacuum mixing are two techniques used to reduce the porosity inherent in bone cements hand mixed in the operating room. Burke *et al.*[17] (as well as Davies *et al.*[102,103]) showed that reduction of porosity in bone cements by centrifugation increased ultimate tensile strain, ultimate tensile stress, and fatigue life.

Rimnac *et al.*[25] argued that the fatigue life of a material encompasses the time for crack initiation plus the time for crack propagation through the material. Wright and Robinson[56] speculated that cracks in bone cement are readily initiated *in vivo*, and therefore, Rimnac *et al.*[25] suggested that crack propagation testing is more pertinent to the fatigue performance of bone cement than a test that does not differentiate between propagation and initiation. They based conclusions concerning fatigue crack propagation resistance of bone cement on fracture toughness test results. Fracture toughness is indeed a measure of a material's ability to resist crack growth or propagation, given a fully formed crack. A qualitative relationship between the fracture toughness and the fatigue life of a material generally exists; that is, materials with high fracture toughness tend to exhibit greater fatigue lives than materials with a lower fracture toughness, although there is no consistent functional relationship between fracture toughness and fatigue life of materials.[104] Rimnac *et al.*[25] found no difference in the fracture toughness of centrifuged (pore-reduced) and noncentrifuged bone cements.

The study by Rimnac *et al.*[25] motivated a series of 'Letters to the Editor' of *The Journal of Bone and Joint Surgery* written by Harris, Burke, Harrigan, Wixson and Lautenschlager, and Rimnac[105] in response. The controversy centered not on the results of the Rimnac *et al.*'s[25] study, but on the interpretation of the data and subsequent conclusion that porosity reduction in bone cement is inconsequential, as it does not affect crack propagation as measured by fracture toughness testing. Rimnac, in reply, maintained that because of the irregular surface of bone cement *in vivo*, cracks were readily initiated, and thus, fracture toughness is a relevant measure of failure resistance in bone cement.

6.602.4.4.7.1.2. Effects of notches and surface irregularities Davies *et al.*[102] began to address the question of the effect of surface irregularities on the fatigue life of porous (i.e., noncentrifuged) and centrifuged bone cements. They introduced surface flaws via composites of bovine trabecular bone or the addition of a 'sharp' notch, 0.25 mm deep. Their results indicated that the reduction of porosity was the dominant factor influencing the fatigue life of the specimens and not the introduction of surface irregularities. It is interesting that they reported an improvement in the fatigue life of both the centrifuged and noncentrifuged notched specimens over their nonnotched counterparts. Hamati *et al.*[106] also compared notched versus nonnotched specimens. They found that the notched specimens had a lower fatigue life at a given apparent applied stress.

An important concept of fracture testing is that stress intensity, a measure of energy available for crack propagation,

is the driving quantity in the fracture mechanics analysis of notched specimens. Notched and nonnotched specimens cannot be compared directly when tested at the same nominal stress, because stress may have no meaning in the case of the notched specimen if the notch is assumed to be a crack. The stress at a crack tip is theoretically infinite, regardless of the applied stress. The use of a notched specimen, in contrast to a nonnotched or smooth specimen, changes the condition of the test, and the comparison of notched and nonnotched specimens on the basis of a 'nominal stress' is inappropriate. At the very least, consideration of a stress concentration factor must be included in the analysis.

Topoleski *et al.*[10,65] presented results of the fatigue analysis of plain, pore-reduced, fiber-reinforced, and pore-reduced-fiber-reinforced bone cements from both nonnotched and notched specimens. The nonnotched specimens required both crack initiation and propagation time for failure, and were evaluated on the basis of nominal applied stress. The notched specimens required only the crack propagation time before failure, and were evaluated on the basis of nominal stress intensity. For both the nonnotched and notched cases, the pore-reduced cements exhibited higher fatigue lives at each stress level or stress intensity. Because the porosity reduction increased even the fatigue lives of the notched specimens, it was concluded that porosity enhances fatigue crack propagation resistance in bone cement; however, the effect of porosity reduction on the notched specimens decreased with decreasing nominal stress intensity and eventually vanished. It is therefore important to know the *in vivo* stresses and stress intensities in order to measure the efficacy of porosity reduction.

6.602.4.4.7.1.3. Porosity reduction: how does it work? It is reasonable to conclude from the published studies that porosity reduction does indeed enhance the fatigue life of bone cement. Two questions remain: (1) how? and (2) for actual *in vivo* stresses, is porosity reduction effective? Analytical and numerical approaches have been used to advance the answer to the second question, and have been summarized briefly[99]; however, the *in vivo* bone cement stresses remain an elusive piece of the cemented prosthesis puzzle and a potentially fruitful course for mechanics research.

The first question, how does porosity reduction enhance the fatigue performance of PMMA, is also unsettled; however, several investigators have begun to build a picture of the material mechanisms of porosity influence on bone cement fracture. Gharpuray *et al.*,[107] Gilbert *et al.*,[12,64] and Topoleski *et al.*[20] observed small cracks emanating from pores in bone cement during fatigue crack propagation. Lu and Topoleski[108] showed that the microcracks (to differentiate them from the primary crack) comprise part or all of the process zones associated with the propagating crack. Because fatigue crack propagation depends on the formation of microcracks, the way that ductile metals form a "plastic zone," or ceramics and concrete also form a process zone comprised of microcracks, then the apparent dependence of fatigue life on porosity content is explained: pores are sites where microcracks easily nucleate. As fatigue fracture is a low-energy phenomenon, the stress concentration effect of porosity may have a substantial effect compared to the stress intensity at the crack tip. Timoshenko and Goodier[66] give the solution for the maximum local stress around a spherical cavity, under uniform tension, as 45/22 $\sigma_{nominal}$. In the vicinity of a slowly advancing crack front, the stress concentration effect of the pore increases the material's stress and microcracks form in response. For the rapidly advancing crack, such as that in a fracture toughness test, the crack moves too fast to allow the development of microcracks; the crack tip fracture energy overwhelms the stress concentration contribution of the pores.

Topoleski *et al.*[20] showed that the fracture surfaces from fatigue cracks were irregular, due to microcracking in the process zone, and that the fracture surfaces formed during a fracture toughness test (rapid fractures) were flat, indicating that no microcracking occurred. The effects of porosity, therefore, may not be manifested during a test that produces a rapidly moving crack, like the fracture toughness test.

6.602.4.4.7.2. Failure mechanisms

There has been little work performed toward the understanding of crack growth mechanisms in bone cement. A fundamental procedure for investigating the fracture processes of a material is to examine fractured surfaces. Direct observation of the fracture surface characteristics or the microstructure of bone cement is rarely reported. The fracture surfaces from both slow and rapid fracture of industrially cured PMMA, conversely, have been studied in detail.[55,109–114] The surfaces of slow or fatigue fractured Plexiglas® are generally smooth, although Döll[110] showed that there is a smooth to rough transition in the surface appearance as the viscosity average MW (M_v) is decreased below about 163 000.

Few comparisons of the fracture surfaces of industrial PMMA and bone cement are documented. Beaumont and Young[55] showed that the slow fracture surface of Plexiglas® (high MW) had a smooth appearance, while the slow fracture surface of bone cement (lower MW), was irregular. Beaumont and Young[55] also noted that bone cement fatigue surfaces were 'rough,' but the Perspex® fatigue surfaces were 'smooth.' The contrast in fatigue surface morphology between the two forms of PMMA indicated that different mechanisms occurred during fatigue fracture. They mentioned possible fracture mechanisms, including particle pull-out and noting 'bunches of crazes' at the crack tip of Perspex®, indicating the nature of the process zone of the industrial form of PMMA. Kusy and Turner[113] examined the rapid fracture morphology of industrial PMMA specimens with varying MWs. They noted an absence of crazing below an M_v of 90 000, and observed glassy surfaces on specimens with $M_v < 60\,000$. The fracture surface morphology is highly dependent on MW, and hence the fracture mechanisms depend on MW also. The number average MW (M_n) of Simplex cement was reported as 89 700 by Rimnac *et al.*[25] ($M_v = 1.9\ M_n$, Kusy and Turner[113]), which would place bone cement above the M_v to form crazes proposed by Kusy and Turner.

Fatigue crack propagation, as well as quasistatic fracture properties, depends on MW.[109,110,114] Fracture toughness becomes independent of MW when $M_v > 40\,000$[109,111]; however, Kim *et al.*[111] showed that fatigue crack propagation continues to be influenced by MW even when $M_v > 1000\,000$. The morphology of fatigue fracture surfaces also likely depend on MW. Although bone cement is known to behave differently from industrial PMMA, and direct comparisons

between the two materials may not be relevant, the differences may be rooted in the different microstructures. Within each of the polymer phases of bone cement, the PMMA may be homogeneous like industrial PMMA. It follows that the surface morphology of fatigue fracture surfaces in bone cement are likely to be dependent on the MW of the two polymer phases.

The morphologies of fatigue and fast fracture surfaces of bone cement are distinct, and Freitag and Cannon[89] were able to identify the extent of a fatigue crack before catastrophic failure by observing the rough to smooth transition of the fracture surface. They reported that the fatigue surface of bone cement was 'textured,' as did Beaumont and Young,[55] and postulated a fracture mechanism based on the initiation and propagation of several 'microcracks,' leading to an irregular fracture surface. Fractographic studies support a simple generalization for PMMA–bone cement fracture surfaces: slow fractures (fatigue) produce rough or irregular fracture surfaces, while rapid fractures (produced during fracture toughness tests) produce smooth or cleaved fracture surfaces.[17,56,61,91,97,115]

The difference in fracture morphology indicates a different mechanism of failure. Topoleski *et al.*[20] and Lu and Topoleski[108] also investigated the damage zone of bone cement and observed that microcracking or a 'microcraze' shower preceded the crack tip. Microcracking can occur in PMMA (nonbone cement) if the MW is not high enough to develop crazes.[113,116] The coalescence of the microcracks is a mechanism for crack extension and the irregularity of the fatigue surface.

Because so little is known, fundamental research on the nature of bone cement fatigue failure mechanisms is crucial. Knowledge of the failure mechanisms is the tool to understand the role of bone cement in total joint failures, and is essential for applying creative alternate bone cement formulations with the intent to prevent failures.

6.602.4.5. Summary

Bone cement fracture can at least be linked to, if not directly responsible for, failures of total joint arthroplasties. There are two ways of evaluating the fracture properties of bone cement, fracture toughness measurements, and fatigue testing. Fracture toughness tests are, in general, an easier way to establish a quantitative evaluation of material fracture properties than fatigue tests because (1) fracture toughness is a material property, and independent of test protocol or specimen geometry; fatigue tests do *not* result in a unique material property, but are dependent on test methodology; (2) fewer specimens are required to characterize the fracture toughness of a material than to characterize the fatigue properties; and (3) fracture toughness tests do not require nearly as much time as fatigue. Fracture toughness embodies only one aspect of the fracture characterization of a material, however, and is related to a fast propagating, high energy crack. Fatigue, or subcritical, fracture is a lower energy phenomenon and requires a more extensive and sophisticated series of experiments than fracture toughness. If a material fails under fatigue or subcritical loading conditions, then fracture toughness alone is inadequate to understand or predict the failure behavior of the material; fatigue characterization is necessary.

6.602.5. Improving PMMA–Bone Cement

6.602.5.1. Introduction

Increasing the *in vivo* longevity of PMMA by improving the resistance to failure of the polymer has received some, albeit surprisingly little, attention. To improve bone cement, one can either replace current bone cements with new bone cements, that is, alter the chemical composition to create a better cement via an 'internal' modification, or modify existing bone cements using an additive 'external' force or agent. (Modifications of existing bone cement can also be applied to new bone cements, or new bone cements may be formulated to better take advantage of 'external' modifications; however, an understanding of any modification, internal or external, is fundamental to predicting efficacy of treatments, and has not yet been achieved.) Porosity reduction is an example of an external modification that has the apparent result of increasing the fatigue life of current cements.

To follow the discussion of bone cement failure, we will examine approaches to improving the failure resistance. First, a brief outline of two initial studies on chemically alternative cements, and second, a more extensive review of an external modification: the addition of a fiber-reinforcing phase to existing cements.

6.602.5.2. Chemical ('or Internal') Modifications

Weightman *et al.*[117] formulated a bone cement based on an *N*-butyl methacrylate monomer, replacing MMA. They noted that the *N*-butyl methacrylate-based material showed a higher ductility, a higher apparent fracture toughness, and a greater fatigue life. The concept of using butyl methacrylate was also investigated by Litsky *et al.*[118] They replaced the PMMA powder component of bone cement, rather than the liquid monomer component, with butyl methacrylate beads, and retained the MMA monomer. Their hypothesis was that local contact stresses are responsible for the initiation of total joint loosening, and reducing the cement modulus reduces the local contact stresses. Litsky *et al.*'s[118] preliminary studies showed clinical promise, but mechanical and failure characteristics are unknown and require further investigation.

There has been much research on replacing PMMA-based bone cements with other materials, for example, cements that contain hydroxyapatite (HA) that may allow the bone to biologically interact with the cement. A review of alternative cement materials is found elsewhere in this text. The reader of this chapter will find excellent reviews of the potential 'new' bone cements by Kenny and Buggy[119] and Lewis.[120]

6.602.5.3. Fiber Reinforcement

Different reinforcing fibers have been added to bone cement to try to improve the fracture resistance. Fibers include carbon,[22,97,121–126] Kevlar®,[127,128] PMMA,[129] polyethylene,[130,131] stainless steel,[61,132–134] titanium,[54,135] and zirconia.[136] At least one formulation, a carbon fiber-reinforced cement, was commercially available,[126] but its availability was short-lived.

An understanding of the interaction between the different materials in a total joint replacement is essential for success.

As fundamental understanding increases, and prostheses are used to facilitate a wider variety of patient needs and service functions, more exactly engineered materials will be required to ensure prosthesis longevity. Advances in fiber-reinforced composite engineering materials are indicative of the potential for tailoring material properties, and total joint fixation is ideal for composite materials applications. The addition of a reinforcing phase to bone cement, generally short fibers or whiskers, has been investigated only sporadically in the past. One advantage of adding a reinforcing fiber to bone cements is that currently used cements can be potentially reinforced with little or no alteration.

Knoell *et al.*[123] added between 0.67% and 5.87% by volume content (1–10% by weight. The percent fiber contents are reported as volume percents for consistency. Where the original source reports percent by weight, a conversion has been made from wt% to vol%, using the following values for densities: PMMA 1.2, carbon 1.75, and aramid (Kevlar®) 1.44 gm cm^{-3}) carbon fibers (~6 mm in length) to PMMA. They measured increases of up to 100% in the average Young's modulus for the reinforced PMMA. They were also among the first to report a decrease in peak curing temperature of the reinforced PMMA.

Pilliar *et al.*[97,124] incorporated 2% carbon fibers (6 mm length, 7 μm diameter) into bone cement. They measured a 50% improvement in tension–tension fatigue limit, an improved impact performance, and a 36% increase in UTS. Pilliar *et al.*[97,124] indicated that their reinforced PMMA had poor intrusion characteristics due to increased apparent viscosity and poor fiber distribution throughout the cement mass.

Wright and Trent[137,138] performed preliminary studies using PMMA reinforced with chopped aramid fibers. PMMA reinforced with 5.17% fibers (7% by weight) exhibited a 74% increase in fracture toughness over the plain PMMA. They were not able to produce reinforced PMMA with a fiber content >5% because of mixing and handling difficulties.

Beaumont[61] introduced glass beads into the PMMA mass. He measured a decrease in crack propagation velocity, as much as three orders of magnitude, with a 30% bead addition.

Very few investigators considered the use of metal fibers to reinforce PMMA. Metal fibers have an advantage over brittle carbon fibers because they can be ductile. Taitsman and Saha[139] used large diameter (0.5–1.0 mm) stainless steel and Vitallium *wires* as a reinforcing phase. Their concept was more like the inclusion of reinforcing bars in structural concrete than that of a fiber-reinforced composite material. They embedded 1, 2, or 3 wires in PMMA specimens and reported up to an 80% increase in tensile strength (with 3 embedded Vitallium wires), but noted that clinical applications of their wire reinforced cement were limited.

Fishbane and Pond[132] reinforced industrial grade PMMA (Plexiglas®) and PMMA–bone cement with stainless steel whiskers (0.5–1.0 mm length, 65 μm diameter; or 3–6 mm length, 90 μm diameter). They determined that the addition of fibers up to 6.5% improved the compressive strength of Plexiglas® by nearly 100%, but for the surgical grade PMMA realized only a 25% increase. Fishbane and Pond[132] postulated that the reason for the decreased performance of the surgical PMMA was "...due to limitations imposed by the (surgical) methacrylate preparation technique."

Kotha *et al.*[133] also reported an increase in the fracture toughness using stainless steel fibers. Kotha *et al.*[134] generated further improvements by treating the stainless steel fibers with a silane coupling agent. The increase was attributed to the enhanced adhesion between the coated fibers in contrast to the noncoated fibers.

Schnur and Lee[140] investigated the use of titanium (Ti) sheet, wire, mesh, and powder as a reinforcing phase. Their work is similar to that of Taitsman and Saha[139]; both investigated a system similar to reinforced concrete, rather than a composite bone cement. Schnur and Lee's goal was to increase the modulus of PMMA to that of cortical bone. An addition of 16%, 1 mm diameter wires (a total of 25 wires), increased the modulus of the PMMA by 380% and the maximum compressive stress by 75%. It is not clear, however, whether the modulus of PMMA must approach that of cortical bone for prosthesis success. Some bone cement researchers[118] have proposed the opposite, while others[71,140] argued that a reduction in PMMA modulus might be detrimental to the prosthesis.

Other studies of reinforced PMMA–bone cement have incorporated carbon/graphite or aramid fibers. Robinson *et al.*[141] tested both Zimmer Regular and Zimmer LVC reinforced with 2% volume of carbon fibers (1.5 mm in length, 10 μm diameter). Both reinforced cements exhibited an increase in fracture toughness of ~32% over their plain counterparts. Surface fractography revealed no evidence of fiber fracture, indicating that the increase in 'toughness' was due principally to fiber pull out. Subsequent work by Wright and coworkers[56,142] addressed fatigue crack propagation rates of carbon fiber-reinforced PMMA. An order of magnitude decrease in crack propagation velocity was measured for carbon fiber-reinforced cements.

Saha and Pal[22] tested PMMA reinforced with 0.67% carbon fibers (1% by weight; 6 mm length, 8 μm diameter) and PMMA reinforced with 1.61% and 3.82% aramid fibers (Kevlar-29®, 2 and 4% by weight; 12–13 mm length, unspecified diameter). The carbon fiber-reinforced PMMA showed a 20.5% increase in UCS, and the aramid fiber-reinforced cement showed increases of 19.5% and 28.7% for the 1.61 and 3.82 vol%, respectively. Saha and Pal emphasized two important consequences of the addition of fibers to PMMA: (1) the peak temperature of the reinforced PMMA was lower than the plain PMMA, which might help to reduce thermal necrosis of tissue surrounding the polymerizing PMMA, and (2) the addition of fibers decreased the workability of the cement. They noted, as did Pilliar *et al.*,[97] that uniform dispersion of fibers was difficult to obtain. Saha and Pal[22] machine-mixed carbon fibers with PMMA powder prior to the monomer addition in an attempt to improve fiber distribution in the reinforced PMMA. They claimed that the machine-mixed PMMA exhibited, in general, improved mechanical properties over their hand-mixed reinforced PMMA. The carbon fibers used in the two investigations were different, however. The fibers used in the machine-mixed study were 'dumbbell' shaped, contrasting with the cylindrically shaped fibers used in the hand-mixed study. The 'dumbbell' shape of the fibers probably increased the stress transfer between the fiber and the PMMA matrix, which led to an increase in the overall strength of the machine-mixed reinforced PMMA.

Ekstrand *et al.*[121] were able to fabricate carbon fiber-reinforced PMMA with fiber contents as high as 16.38% by volume (40% by weight) They used industrial composite fabrication techniques, however, which have limited or no clinical application. The primary contribution of their work showed that there was no contact between the carbon fibers and the PMMA after the composite was stored in distilled water for 30 days. They also showed that the ultimate flexural strength of the composite nearly tripled as the volume fiber content was increased from 5.87% to 16.38% (10–40% by weight).

Pourdeyhimi *et al.*[127] studied the effect of the fiber content on the fracture toughness of hand-mixed, reinforced, dental PMMA. They used aramid fibers from 0.82% to 5.17% by volume (1–7% by weight), and graphite from 0.67% to 5.87% by volume (1–10% by weight), and performed fracture toughness tests, calculating values for both K_{Ic} and J_{Ic}. (J_{Ic} is the critical value of a quantity J, calculated by the so-called J-integral, and is a measure of energy release rate for materials where plasticity effects at the crack tip are not negligible.[87]) For each type of fiber-reinforced cement, the fracture toughness increased with increasing fiber content. The aramid fiber specimens showed a greater increase than the carbon fiber specimens of the same volume fraction. The energy dissipated in the micromechanisms of failure was greater for the aramid fibers than for the carbon fibers. Dental PMMA is different from surgical PMMA, however. The dental PMMA may be heat-cured, and sometimes pressurized, before it is used. The techniques for creating a reinforced dental PMMA generally cannot be adopted to create a reinforced surgical PMMA. In a parallel study,[128] where reinforced dental and bone cements were both tested at 5.17% fiber content, the K_{IC} of the bone cement increased by 77%, and for the dental acrylic by 98% (the nonreinforced bone cement had a K_{IC} 33% greater than the nonreinforced dental acrylic).

Wagner and Cohn[143] and Pourdeyhimi and Wagner[130] investigated the performance of polyethylene (PE) fibers as a reinforcing phase. An increase in fracture toughness of about 24% was observed for 0.8%, 3.2%, and 5.6% fiber content (1%, 4%, and 7% by weight). Fracture toughness was not affected by fiber content after the initial addition of 0.8% fibers; the fracture toughness remained constant. They characterized the bonding between the fibers and the PMMA matrix as 'poor.' Their reported fractography showed fiber pull-out and fiber bending as energy absorption mechanisms contributed by PE fibers. It is difficult to explain why a fracture toughness plateau is reached, and fracture toughness does not improve with increasing fiber content. Yang *et al.*[131] also investigated PE fibers. They modified the surfaces of the PE fibers and determined that the treated fibers (with grafted MMA) produced a greater reinforcing effect than did the untreated PE fibers.

Topoleski *et al.*[10,54,65] determined the fracture toughness and studied the fatigue behavior of Ti-reinforced bone cement. They achieved >50% increases in fracture toughness with 5% fiber content. They also addressed the reinforced cement delivery and fiber distribution problems,[144] and were able to mix and deliver, with relative ease, a reinforced bone cement with a uniform fiber distribution. Fractography revealed fiber-matrix debonding, local fracture path change, and ductile fiber deformation and subsequent fracture as principal mechanisms of energy absorption. Analysis of the fatigue characteristics[10,65] revealed that for both notched and nonnotched reinforced specimens, the fatigue lives were increased by nearly an order of magnitude. The combination of porosity reduction *and* fiber reinforcement further increased the fatigue resistance.

Kotha *et al.*[134,135] also incorporated titanium fibers into bone cement. In their study, they heat-treated the fibers to produce a thin coating of titania on the fibers. They obtained an increase in fracture toughness of the reinforced bone cement of between 19% and 30%.

Gilbert *et al.*[129] reported an increase in the UTS and fracture toughness using PMMA fibers (a 'self-reinforced' cement). Their cement was a dental acrylic, however, and the fracture toughness of the reinforced acrylic was approximately equal to the fracture toughness of nonreinforced orthopedic bone cement. They claimed that the increase in fracture toughness was 50% for 'preferentially aligned fibers.' Further study is required to determine whether similar increases can be achieved in bone cement.

Very recently, Kane *et al.*[136] reported that the fatigue life of zirconia fiber-reinforced PMMA increased significantly over that of PMMA. They were able to incorporate up to 20% by the volume of zirconia fibers. The use of brittle ceramic fibers to reinforce bone cement is relatively new, and it will be interesting to pursue this avenue and investigate the reinforcing mechanisms.

6.602.6. Summary and Concluding Remarks

Artificial joints are an extremely successful medical treatment for people suffering from arthritis. Bone cement was one of the biomaterials essential to the success of artificial joints. There are many critical considerations to address to further improve bone cement and thereby improve cemented artificial joints. For instance, it is necessary to distinguish between fatigue crack initiation and fatigue crack propagation and their relative contribution to the fatigue life of bone cement. A greater understanding of the nature of bone cement, the material, is needed: how do the various phases influence failure? For instance, how does $BaSO_4$ alter bone cement properties and produce an apparent environmental interaction?; what are the material mechanisms contributing to fracture and can they be altered to increase failure resistance? The questions of where and why cement cracks initiate, whether an initiated crack must necessarily propagate to failure, and how bone cement interaction with other material components of the total joint prosthesis contributes to success or failure remain to be answered. By studying each component and then analyzing that component's contribution to the system behavior, a greater understanding of material-related mechanical failures of total joint prostheses is generated, and may eventually lead to failure elimination.

There is an ongoing effort to improve the fracture properties of bone cement, through both chemical modification, and the addition of a reinforcing phase, or to create bone cements with alternative formulations. Most of the published studies of fiber-reinforced bone cement involved measuring a material property with respect to the nonreinforced bone cement. Few of the papers have discussed the actual mechanisms of reinforcement. Among the material properties enhanced by the addition of a fiber-reinforcing phase are the ultimate strength,

fracture toughness, and fatigue crack propagation resistance of bone cement. To improve the properties of bone cement through the use of a fiber-reinforcing phase, it is clear that (1) a clinically workable cement must be engineered, and (2) the mechanisms of material property improvements in such a bone cement must be well characterized in order to produce the best possible bone cement. Advances in achieving both goals have received some recent attention; however, many aspects of fiber reinforcement remain unknown. Fiber material, dimensions, content, and delivery techniques must be further researched to produce reinforced cements with superior properties.

Acrylic bone cement appears to be a material that will continue to play a role in orthopedic treatments. Orthopedic research today is concentrated on several important avenues to improve artificial joint replacements, and relatively few investigators devote time to understanding and improving bone cement. The potential exists, however, to improve the performance of bone cement and thus continue to provide patients with better prostheses and higher quality of life.

References

1. Goodman, S. In *Presented in the Panel Discussion – Clinical Experience with Orthopaedic and Dental Biomaterials, 31st Annual Meeting Society for Biomaterials*, Pittsburgh, PA, 2006.
2. Malchau, H.; Breusch, S. In *The Well-Cemented Total Hip Arthroplasty: Theory and Practice*; Breusch, S., Malchau, H., Eds.; Springer Medizin Verlag: Berlin, 2005; pp 367–369.
3. Charnley J. *J Bone Joint Surg. Br*., 1960; *42-B*, 28–30.
4. DiMaio, F. R. *Orthopedics* **2002**, *25*(12), 1399–1409.
5. Park, J. *J. Biomed. Eng.* **1983**, *11*, 297–312.
6. Lautenschlager, E. P.; Stupp, S. I.; Keller, J. C. In *Functional Behavior of Orthopedic Biomaterials, Volume II: Applications*; Ducheyne, P., Hastings, G. W., Eds.; CRC Series in Structure-Property Relationships of Biomaterials; CRC Press: Boca Raton, FL, 1984; pp 88–119.
7. Sullivan, S. J.; Topoleski, L. D. T. *J. Biomed. Mater. Res. B Appl. Biomater.* **2007**, *81*(1), 224–230.
8. Kuhn, K.-D. In *The Well-Cemented Total Hip Arthroplasty: Theory and Practice*; Breusch, S., Malchau, H., Eds.; Springer Medizin Verlag: Berlin, 2005; pp 367–369.
9. Topoleski, L. D. T.; Ducheyne, P.; Cuckler, J. M. *Biomaterials* **1993**, *14*(15), 1165–1172.
10. Topoleski, L. D. T.; Rutledge, P.; Lu, X. *Cells Mater.* **1995**, *5*(3), 283–292.
11. Brauer, G. M.; Termini, D. J.; Dickson, G. *J. Biomed. Mater. Res.* **1977**, *11*, 577–607.
12. Gilbert, J. L.; Hasenwinkel, J. M.; Wixson, R. L.; Lautenschlager, E. P. *J. Biomed. Mater. Res.* **2000**, *52*(1), 210–218.
13. Haas, S. S.; Brauer, G. M.; Dickson, G. *J. Bone Joint Surg.* **1975**, *57-A*(3), 380–391.
14. Hasenwinkel, J. M.; Lautenschlager, E. P.; Wixson, R. L.; Gilbert, J. L. *J. Biomed. Mater. Res.* **2002**, *59*(3), 411–421.
15. Schoenfeld, C. M.; Conard, G. J.; Lautenschlager, E. P. *J. Biomed. Mater. Res.* **1979**, *13*(1), 135–147.
16. Vallo, C. I. *J. Biomed. Mater. Res.* **2002**, *63*(5), 627–642.
17. Burke, D. W.; Gates, E. J.; Harris, W. H. *J. Bone Joint Surg.* **1984**, *66-A*(8), 1265–1273.
18. Wixson, R. L.; Lautenschlager, E. P.; Novak, M. A. *J. Arthroplasty* **1987**, *2*(2), 141–149.
19. Kavanagh, B. F.; Dewitz, M. A.; Ilstrup, D. M.; Stauffer, R. N.; Coventry, M. B. *J. Bone Joint Surg.* **1989**, *71-A*(10), 1496–1503.
20. Topoleski, L. D. T.; Ducheyne, P.; Cuckler, J. M. *J. Biomed. Mater. Res.* **1990**, *24*, 135–154.
21. Saha, S.; Pal, S. *J. Biomed. Mater. Res.* **1984**, *18*, 435–462.
22. Saha, S.; Pal, S. *J. Biomech.* **1984**, *17*, 467–478.
23. Raab, S.; Ahmed, A. M.; Provan, J. W. *J. Biomed. Mater. Res.* **1981**, *15*, 159–182.
24. Jasty, M.; Maloney, W. J.; Bragdon, C. R.; O'Connor, D. O.; Haire, T.; Harris, W. H. *J. Bone Joint Surg.* **1991**, *73-B*(4), 551–558.
25. Rimnac, C. M.; Wright, T. M.; McGill, D. L. *J. Bone Joint Surg.* **1986**, *68-A*(2), 281–287.
26. Engh, C. A.; Bobyn, J. D. *Biological Fixation in Total Hip Arthroplasty*. Slack: Thorofare, NJ, 1985.
27. Darre, E.; Vedel, P.; Jensen, J. S. *Acta Orthop. Scand.* **1987**, *58*(3), 236–238.
28. Linder, L. *J. Bone Joint Surg.* **1977**, *59-A*(1), 82–87.
29. Linder, L. G.; Harthon, L.; Kullberg, L. *Clin. Orthop. Relat. Res.* **1976**, *119*, 242–249.
30. Convery, F. R.; Gunn, D. R.; Hughes, J. D.; Martin, W. E. *J. Bone Joint Surg.* **1975**, *57-A*(1), 57–64.
31. Bengtson, A.; Larsson, M.; Gammer, W.; Heideman, M. *J. Bone Joint Surg.* **1987**, *69-A*(1), 46–49.
32. Bayne, S. C.; Lautenschlager, E. P.; Greener, E. H. *Proc. Ann. Conf. Eng. Med. Biol.* **1973**, *15*, 201.
33. Stürup, J.; Nimb, L.; Kramhøft, M.; Jensen, J. S. *Acta Orthop. Scand.* **1994**, *65*(1), 20–23.
34. McLaughlin, R. E.; DiFazio, C. A.; Hakala, M.; *et al*. *J. Bone Joint Surg.* **1973**, *55-A*(8), 1621–1628.
35. Rijke, A. M.; Johnson, R. A.; Oser, E. R. *J. Biomed. Mater. Res.* **1977**, *11*(2), 211–221.
36. Bourne, R. B. *J. Arthroplasty* **2004**, *19*(4 Suppl. 1), 69–72.
37. Dunbar, M. J. *Orthopedics* **2009**, *32*(9), 662.
38. Hanssen, A. D. *J. Arthroplasty* **2004**, *19*(4 Suppl. 1), 73–77.
39. Jiranek, W. *Orthopedics* **2005**, *28*(Suppl. 8), s873–s877.
40. Furnes, O.; Havelin, L. I.; Espehaug, B. In *The Well-Cemented Total Hip Arthroplasty: Theory and Practice*; Breusch, S., Malchau, H., Eds.; Springer Medizin Verlag: Berlin, 2005; pp 103–106.
41. Gehrke, T. In *The Well-Cemented Total Hip Arthroplasty: Theory and Practice*; Breusch, S., Malchau, H., Eds.; Springer Medizin Verlag: Berlin, 2005; pp 348–358.
42. DeLuise, M.; Scott, C. P. *Orthopedics* **2004**, *27*(12), 1289–1291.
43. Frommelt, L.; Kühn, K.-D. In *The Well-Cemented Total Hip Arthroplasty: Theory and Practice*; Breusch, S., Malchau, H., Eds.; Springer Medizin Verlag: Berlin, 2005; pp 86–92.
44. Lewis, G.; Janna, S.; Bhattaram, A. *Biomaterials* **2005**, *26*(20), 4317–4325.
45. Lewis, G.; Bhattaram, A. *J. Biomater. Appl.* **2006**, *20*(4), 377–408.
46. Askew, M. J.; Kufel, M. F.; Fleissner, P. R., Jr.; Gradisar, I. A., Jr.; Salstrom, S. J.; Tan, J. S. *J. Biomed. Mater. Res.* **1990**, *24*(5), 573–580.
47. Leone, J.; Johnson, A.; Ziada, S.; Hashemi, A.; Adili, A.; de Beer, J. *J. Biomed. Mater. Res. B Appl. Biomater.* **2007**, *83*(1), 97–104.
48. Lewis, G. *J. Biomed. Mater. Res. B Appl. Biomater.* **2009**, *89B*(2), 558–574.
49. Lewis, G. *J. Biomed. Mater. Res.* **1997**, *38*(2), 155–182.
50. Wang, J. S.; Franzén, H.; Toksvig-Larsen, S.; Lidgren, L. *J. Appl. Biomater.* **1995**, *6*(2), 105–108.
51. Döll, W. *J. Mater. Sci.* **1975**, *10*, 935–942.
52. Rodriguez, F.; Cohen, C.; Ober, C. K.; Archer, L. A. In *Principles of Polymer Systems*, 5th ed.; Taylor and Francis: New York, 2003; Chapter 5, pp 177–208.
53. Sperling, L. H. *Introduction to Physical Polymer Science*. Wiley: New York, 1986.
54. Topoleski, L. D. T.; Ducheyne, P.; Cuckler, J. M. *J. Biomed. Mater. Res.* **1992**, *26*, 1599–1617.
55. Beaumont, P. W. R.; Young, R. J. *J. Biomed. Mater. Res.* **1975**, *9*, 423–439.
56. Wright, T. M.; Robinson, R. P. *J. Mater. Sci.* **1982**, *17*, 2463–2468.
57. Graham, J.; Pruitt, L.; Ries, M.; Gundiah, N. *J. Arthroplasty* **2000**, *15*(8), 1028–1035.
58. Deb, S.; Vazquez, B.; Bonfield, W. *J. Biomed. Mater. Res.* **1997**, *37*(4), 465–473.
59. Liu, C.; Green, S. M.; Watkins, N. D.; Gregg, P. J.; McCaskie, A. W. *J. Mater. Sci. Mater. Med.* **2002**, *13*(11), 1021–1028.
60. Wang, J. S.; Franzén, H.; Jonsson, E.; Lidgren, L. *Acta Orthop.* **1993**, *64*(2), 143–146.
61. Beaumont, P. W. R. *J. Mater. Sci.* **1977**, *12*, 1845–1852.
62. Schreurs, B. W.; Spierings, P. T.; Huiskes, R.; Slooff, T. J. *Acta Orthop.* **1988**, *59*(4), 403–409.
63. Wang, C. T.; Pilliar, R. M. *J. Mater. Sci.* **1989**, *24*, 3725–3738.
64. Gilbert, J. L.; Menis, D. W.; Smith, S. M.; Lautenschlager, E. P.; Wixson, R. W. In *Transaction of the 16th Annual Meeting, Society for Biomaterials*, Charleston, SC, 1990 p 130.
65. Topoleski, L. D. T.; Ducheyne, P.; Cuckler, J. M. *J. Biomed. Mater. Res.* **1995**, *29*, 299–307.
66. Timoshenko, S. P.; Goodier, J. N. In *Theory of Elasticity*, 3rd ed.; McGraw-Hill: New York, 1970; pp 396–398.

67. Lewis, G. *J. Biomed. Mater. Res. B Appl. Biomater.* **2006**, *76*(2), 456–468.
68. Phillips, F. M.; Todd Wetzel, F.; Lieberman, I.; Campbell-Hupp, M. *Spine* **2002**, *27*(19), 2173–2178.
69. Rodrigues, D. C.; Gilbert, J. L.; Hasenwinkel, J. M. *J. Biomed. Mater. Res. B Appl. Biomater.* **2009**, *91*(1), 248–256.
70. Freitag, T. A.; Cannon, S. L. *J. Biomed. Mater. Res.* **1976**, *10*, 805–828.
71. Sih, G. C.; Berman, A. T. *J. Biomed. Mater. Res.* **1980**, *14*, 311–324.
72. Demian, H. W.; Shalaby, S. W. U.S. Pat. 5,795,922, 1998.
73. Molino, L. N.; Topoleski, L. D. T. *J. Biomed. Mater. Res.* **1996**, *31*(1), 131–137.
74. Gomoll, A. H.; Fitz, W.; Scott, R. D.; Thornhill, T. S.; Bellare, A. *Acta Orthop.* **2008**, *79*(3), 421–427.
75. Nottrott, M. *Acta Orthop. Scand. Suppl.* **2010**, *81*(341), 1–27.
76. Funk, M. J.; Litsky, A. S. *Biomaterials* **1998**, *19*(17), 1561–1567.
77. Chwirut, D. J. *J. Biomed. Mater. Res.* **1984**, *18*(1), 25–37.
78. Verdonschot, N.; Huiskes, R. *J. Biomed. Mater. Res.* **1995**, *29*(5), 575–581.
79. Verdonschot, N.; Huiskes, R. *J. Biomed. Mater. Res.* **2000**, *53*(5), 498–504.
80. Pal, S.; Saha, S. *Biomaterials* **1982**, *3*(2), 93–96.
81. Norman, T. L.; Kish, V.; Blaha, J. D.; Gruen, T. A.; Hustosky, K. *J. Biomed. Mater. Res.* **1995**, *29*(4), 495–501.
82. Yetkinler, D. N.; Litsky, A. S. *Biomaterials* **1998**, *19*(17), 1551–1559.
83. Oysaed, H.; Ruyter, I. E. *J. Biomed. Mater. Res.* **1989**, *23*(7), 719–733.
84. Treharne, R. W.; Brown, N. *J. Biomed. Mater. Res.* **1975**, *9*(4), 81–88.
85. Irwin, G. R.; deWit, R. *J. Test. Eval.* **1983**, *11*(1), 56–65.
86. Griffith, A. A. *Philos. Trans. R. Soc. Lond.* **1921**, *221*, 163–198.
87. Broek, D. *Elementary Engineering Fracture Mechanics*. Martinus Nijhoff: Dordrecht, 1983.
88. Tada, H.; Paris, P. C.; Irwin, G. R. *The Stress Analysis of Cracks Handbook*. Del Research Corporation: Hellertown, PA, 1973.
89. Freitag, T. A.; Cannon, S. L. *J. Biomed. Mater. Res.* **1977**, *11*, 609–624.
90. Lewis, G. *J. Biomed. Mater. Res. B Appl. Biomater.* **2003**, *66*(1), 457–486.
91. Williert, H. G.; Mueller, K.; Semlitsch, M. *Arch. Orthop. Trauma. Surg.* **1979**, *94*, 265–292.
92. Krause, W. R.; Grimes, L. W.; Mathis, R. S. *J. Biomed. Mater. Res.* **1988**, *22*(A2), 179–190.
93. Krause, W. R.; Mathis, R. S.; Grimes, L. W. *J. Biomed. Mater. Res. Appl. Biomater.* **1988**, *22*(A3), 221–244.
94. Collins, J. A. *Failure of Materials in Mechanical Design. Analysis, Prediction, Prevention*. Wiley: New York, 1981.
95. Paris, P.; Erdogan, F. *J. Basic Eng. Trans. ASME* **1963**, *85*, 528–534.
96. Antonsson, E. K.; Mann, R. W. *J. Biomech.* **1985**, *18*, 39–47.
97. Pilliar, R. M.; Bratina, W. J.; Blackwell, R. A. In *Fatigue of Filamentary Composite Materials*; Reifsnider, K. L., Lauraitis, K. N., Eds.; ASTM: West Conshohocken, PA, 1977; pp 206–227; ASTM STP 636.
98. Johnson, J. A.; Provan, J. W.; Krygier, J. J.; Chan, K. H.; Miller, J. *J. Biomed. Mater. Res.* **1989**, *23*, 819–831.
99. Krause, W.; Mathis, R. S. *J. Biomed. Mater. Res.* **1988**, *22*(A1), 37–53.
100. Lewis, G.; Nyman, J. S. *J. Biomed. Mater. Res.* **2000**, *53*(6), 748–768.
101. Jaffe, W. L.; Rose, R. M.; Radin, E. L. *J. Bone Joint Surg.* **1974**, *56-A*, 1711–1714.
102. Davies, J. P.; O'Connor, D. O.; Burke, D. W.; Jasty, M.; Harris, W. H. *Clin. Orthop. Relat. Res.* **1988**, *229*, 156–161.
103. Davies, J. P.; O'Connor, D. O.; Greer, J. A.; Harris, W. H. *J. Biomed. Mater. Res.* **1987**, *21*, 719–730.
104. Hertzberg, R. W.; Manson, J. A. *Fatigue of Engineering Plastics*. Academic Press, Harcourt Brace Jovanovich: New York, 1980.
105. (1) Harris, W. H.; (2) Burke, D. W.; (3) Harrigan, T. P.; (4) Wixson, R. L. and Lautenschlager, E. P.; (5) Rimnac, C. M. *J. Bone Joint Surg. A* **1986**, *68*(7), 1125–1128.
106. Hamati, F. I.; Wixson, R. L.; Novak, M. A.; Lautenschlager, E. P. In *Transaction of the 33rd Annual Meeting of the Orthopaedic Research Society*, San Francisco, CA, 1987 p 226.
107. Gharpuray, V. M.; Keer, L. M.; Lewis, J. L. *J. Biomech. Eng.* **1990**, *112*, 22–28.
108. Lu, X.; Topoleski, L. D. T. *J. Biomed. Mater. Res. Appl. Biomater.* **2000**, *53*, 505–510.
109. Berry, J. P. In *Fracture Processes in Polymeric Solids, Phenomena and Theory*; Rosen, B., Ed.; Wiley: New York, 1964; pp 157–234.
110. Döll, W. In *Advances in Polymer Sciences: Crazing in Polymers*; Kausch, H. H., Ed.; Springer-Verlag: Berlin, 1983; Vol. 52/53, pp 105–168.
111. Kim, S. L.; Skibo, M.; Manson, J. A.; Hertzberg, R. W. *Polym. Eng. Sci.* **1977**, *17*, 194–203.
112. Kusy, R. P.; Turner, D. T. *J. Biomed. Mater. Res. Symp.* **1975**, *6*, 89–98.
113. Kusy, R. P.; Turner, D. T. *Polymer* **1977**, *18*, 391–402.
114. Wolock, I.; Newman, S. B. In *Fracture Processes in Polymeric Solids, Phenomena and Theory*; Rosen, B., Ed.; Wiley: New York, 1964; pp 235–290.
115. Markolf, K. L.; Amstutz, H. C. *Biomechanics* **1976**, *9*, 73–79.
116. Lu, X. In *Proceedings of the Binary Polymer Science Conference China Japan*, Beijing, China, 1983 pp 405–406.
117. Weightman, B.; Freeman, M. A. R.; Revell, P. A.; Braden, M.; Albrektsson, B. E. J.; Carlson, L. V. *J. Bone Joint Surg.* **1987**, *69-B*, 558–564.
118. Litsky, A. S.; Rose, R. M.; Rubin, C. T.; Thrasher, E. L. *J. Orthop. Res.* **1990**, *8*, 623–626.
119. Kenny, S. M.; Buggy, M. *J. Mater. Sci. Mater. Med.* **2003**, *14*, 923–938.
120. Lewis, G. *J. Biomed. Mater. Res. B Appl. Biomater.* **2008**, *84*(2), 301–319.
121. Ekstrand, K.; Ruyter, I. E.; Wellendorf, H. *J. Biomed. Mater. Res.* **1987**, *21*, 1065–1080.
122. Kim, H. Y.; Yasuda, H. K. *J. Biomed. Mater. Res.* **1999**, *48*(2), 135–142.
123. Knoell, A.; Maxwell, H.; Bechtol, C. *Ann. Biomed. Eng.* **1975**, *3*, 225–229.
124. Pilliar, R. M.; Blackwell, R.; McNab, I.; Cameron, H. U. *J. Biomed. Mater. Res.* **1976**, *10*, 893–906.
125. Saha, S.; Pal, S. *J. Biomed. Mater. Res.* **1983**, *17*(6), 1041–1047.
126. Saha, S.; Pal, S. *J. Biomed. Mater. Res.* **1986**, *20*(6), 817–826.
127. Pourdeyhimi, B.; Robinson, H. H., IV; Schwartz, P.; Wagner, H. D. *Ann. Biomed. Eng.* **1986**, *14*, 277–294.
128. Pourdeyhimi, B.; Wagner, H. D.; Schwartz, P. *J. Mater. Res.* **1986**, *21*, 4468–4474.
129. Gilbert, J. L.; Ney, D. S.; Lautenschlager, E. P. *Biomaterials* **1995**, *16*(14), 1043–1055.
130. Pourdeyhimi, B.; Wagner, H. D. *J. Biomed. Mater. Res.* **1989**, *23*, 63–80.
131. Yang, J. M.; Huang, P. Y.; Yang, M. C.; Lo, S. K. *J. Biomed. Mater. Res.* **1997**, *38*(4), 361–369.
132. Fishbane, B. M.; Pond, R. B. *Clin. Orthop. Relat. Res.* **1977**, *128*, 194–199.
133. Kotha, S. P.; Li, C.; Schmid, S. R.; Mason, J. J. *J. Biomed. Mater. Res.* **2004**, *70*(A3), 514–521.
134. Kotha, S. P.; Lieberman, M.; Vickers, A.; Schmid, S. R.; Mason, J. J. *J. Biomed. Mater. Res. A* **2006**, *76*(A1), 111–119.
135. Kotha, S. P.; Li, C.; McGinn, P.; Schmid, S. R.; Mason, J. J. *J. Mater. Sci. Mater. Med.* **2006**, *17*(12), 1403–1409.
136. Kane, R. J.; Yue, W.; Mason, J. J.; Roeder, R. K. *J. Mech. Behav. Biomed. Mater.* **2010**, *3*(7), 504–511.
137. Wright, T. M.; Trent, P. S. *Transplantation* **1977**, *5*, 395.
138. Wright, T. M.; Trent, P. S. *J. Mater. Sci. Lett.* **1979**, *14*, 503–505.
139. Taitsman, J. P.; Saha, S. *J. Bone Joint Surg.* **1977**, *59-A*, 419–425.
140. Schnur, D. S.; Lee, D. *J. Biomed. Mater. Res.* **1983**, *17*, 973–991.
141. Robinson, R. P.; Wright, T. M.; Burstein, A. H. *J. Biomed. Mater. Res.* **1981**, *15*, 203–208.
142. Wright, T. M.; Conelly, G. M.; Rimnac, C. M.; Hertzberg, R. W.; Burstein, A. H. In *Biomaterials and Biomechanics 1983*; Ducheyne, P., Van der Perre, G., Aubert, A. E., Eds.; Elsevier Science: Amsterdam, 1984; pp 67–72.
143. Wagner, H. D.; Cohn, D. *Biomaterials* **1989**, *10*, 139–141.
144. Ducheyne, P.; Topoleski, L. D. T.; Cuckler, J. M. U.S. Pat. 4,963,151, 1990.

6.603. Ultrahigh Molecular Weight Polyethylene Total Joint Implants*

E Oral, Massachusetts General Hospital, Boston, MA, USA; Harvard Medical School, Boston, MA, USA
S M Kurtz, Exponent, Inc., Philadelphia, PA, USA; Drexel University, Philadelphia, PA
O K Muratoglu**, Massachusetts General Hospital, Boston, MA, USA; Harvard Medical School, Boston, MA, USA

© 2011 Elsevier Ltd. All rights reserved.

6.603.1.	**Introduction**	29
6.603.2.	**General Properties and Processing of UHMWPE**	30
6.603.2.1.	Manufacture	30
6.603.2.2.	Structure–Property Relationships	31
6.603.3.	**The Effects of Sterilization and Early Developments**	32
6.603.4.	**Cross-linking Technologies**	33
6.603.4.1.	Early Experience with Cross-linking	33
6.603.4.2.	Radiation Cross-linking Followed by Thermal Treatment	34
6.603.4.2.1.	Formation of cross-links and wear reduction through cross-linking	34
6.603.4.2.2.	The effects of thermal treatment during or after irradiation on oxidation and wear	34
6.603.4.2.3.	Development of highly cross-linked total knees	37
6.603.4.2.4.	Mechanical and fatigue properties	38
6.603.4.3.	Sequential Irradiation and Annealing	38
6.603.5.	**Vitamin E-Stabilized, Radiation Cross-linked UHMWPE**	39
6.603.5.1.	The Rationale and Incorporation Methods	39
6.603.5.2.	Mechanism of Action Against Oxidation	39
6.603.5.3.	Diffusion of Vitamin E in UHMWPE	40
6.603.5.4.	Oxidative Properties	40
6.603.5.5.	Wear	41
6.603.5.6.	Peri-Prosthetic Effects	42
6.603.5.7.	Mechanical and Fatigue Properties	43
6.603.6.	**Other UHMWPEs with Clinical Potential**	43
6.603.6.1.	High-Pressure Crystallized UHMWPE with Stabilized Free Radicals	43
6.603.6.2.	Vitamin E-Blended, Irradiated, and Mechanically Annealed UHMWPE	44
6.603.6.3.	Surface Cross-linked UHMWPE	44
6.603.7.	**Conclusions and Future Directions**	46
References		46

Abbreviations

ASTM	American Society for Testing and Materials
CoCr	Cobalt/chromium alloy
EAB	Elongation at break
GUR	Granular UHMWPE Ruhrchemie
ISO	International Organization for Standardization
IV	Intrinsic viscosity
PMMA	Poly(methylmethacrylate)
POD	Pin-on-disc
TNF-α	Tumor necrosis factor α
Tween 80	Polysorbate 80; polyoxyethylene (20) sorbitan monooleate
UTS	Ultimate tensile strength
WF	Work to failure

Symbols

ΔK_i	Fatigue crack propagation resistance unit; stress factor range at crack inception (MPa $m^{1/2}$)
R_a	Surface roughness unit; arithmetical mean roughness (μm)

*Financial Disclaimer: The studies discussed here were performed by research funding in part from NIH/NIAMS AR051142, research grants from Biomet, Inc. (Warsaw, IN) and Zimmer, Inc (Warsaw, IN) and the William H. Harris Foundation. The laboratory and the department also received funding from royalties from Zimmer, Inc and Biomet, Inc.

**Dr. Muratoglu received royalties from Biomet, Inc and Zimmer, Inc. Dr. Oral received royalties from Zimmer, Inc.

6.603.1. Introduction

Joint arthroplasty, or the surgical reconstruction of diseased joints, has been practiced in the United States since the nineteenth century. It evolved from an osteotomy of the hip joint, performed by a physician from Pennsylvania

in 1826 to include the interposition of an implant material between the articulating surfaces of a reconstructed joint.[1] A variety of natural and metallic biomaterials were initially employed, including ivory, silver, rubber, wood, celluloid, and glass. By the early twentieth century, mold arthroplasties, in which an implant was molded over the surface of the femur to articulate against the natural acetabulum, were fabricated out of glass, ceramic, and metal including Vitallium™, a cobalt–chromium alloy.[2] The success of early arthroplasties was highly variable and spurred continuous innovations in surgical procedure, implant design, and biomaterials.

In contrast to hemiarthroplasty in which only one side of a diseased joint is surgically reconstructed, in total joint arthroplasty, both articulating surfaces of the joint are replaced. Contemporary total joint arthroplasty evolved from technology developed by McKee (in 1951) and Charnley (in 1958) for the artificial hip.[3,4] The most widely accepted implant configuration since this time comprises a metal component articulating against a polymeric component fabricated from ultra-high molecular weight polyethylene (UHMWPE). Although other bearing couples have been investigated during the past three decades, such as metal-on-metal or ceramic-on-ceramic total joint replacements, today metal-on-UHMWPE articulations are an international standard of care for degenerative joint disorders.[5] Worldwide, approximately 1.5 million UHMWPE components are implanted annually. In the United States alone, an estimated 800 000 total joint replacements are performed, representing healthcare costs of above 20 billion dollars.[6,7] Today, metal-on-UHMWPE total joint arthroplasty is an effective treatment modality providing immediate pain relief and remarkable restoration of mobility for patients with disabilities. Thus, UHMWPE is one of the most widely used biomaterials in the world.

Since the inception of metal-on-polyethylene joint implants in the 1960s, osteolysis (resorption of peri-prosthetic bone) triggered mainly by UHMWPE wear particles has been one of the major problems in total hip arthroplasty among instability/dislocation and infection.[8] Efforts to solve the wear problem in UHMWPE have spurred studies into the structure, morphology, and mechanical properties of the polymer. Among these developments, radiation cross-linking accompanied by thermal treatments to improve oxidative stability has successfully decreased wear in the first decade of service. Recently, several alternative antioxidant-stabilized UHMWPE bearing surfaces with improved mechanical properties have been introduced.

This chapter provides a review of the processing, manufacture, and sterilization methods and provides more detailed explanations of methods of cross-linking and the introduction of an antioxidant stabilizer in UHMWPE for total joint replacement. The first part of the chapter summarizes the structure and relevant properties of UHMWPE as well as processing conditions for total joint implants; the second part summarizes degradation mechanisms of UHMWPE; the third part reviews cross-linked UHMWPEs in clinical use. The final section reviews recently introduced and new UHMWPEs in development as alternative biomaterials for total joint arthroplasty.

6.603.2. General Properties and Processing of UHMWPE

6.603.2.1. Manufacture

Implant manufacturing process for implants fabricated out of UHMWPE starts with the resin powder. The resin powder, historically provided by only a handful of chemical manufacturers is converted to consolidated forms of stock either by bulk converters or on-site by medical implant manufacturers. Because the melt viscosity of UHMWPE is very low, it is not amenable to typical processing methods such as injection molding, and consolidation is done either by compression molding or ram extrusion.[9] Implants can then be machined from consolidated stock, or resin powder can be 'direct compression molded' into the final implant shape. In addition to direct compression molding and machining of converted stock material, there exists a hybrid UHMWPE manufacturing process used by Biomet known as HIP (hot isostatic pressing).[10] The multistep process begins with the manufacture of a cylindrical compact through cold isostatic pressing which expels most of the air. Subsequently, the compacted rods are sintered in a hot isostatic pressure furnace in a low oxygen pouch to prevent degradation. The resulting rod stock is essentially isotropic due to the hydrostatic sintering process and may be considered to be a compression molded form of the resin. Finished implants are then made by either turning or milling operations. In some cases, the resin converter may supply the stock in a shape that is a slight oversizing (preforming) of the finished implant. The mechanical and wear properties of UHMWPE may be significantly affected by the manufacturing processes, such as the temperature and pressure cycles during molding, and as such, these processes are proprietary.

The mechanical properties of consolidated UHMWPE vary as a function of the cooling rate,[11] which affects the crystallization kinetics and may lead to lower crystallinity at higher cooling rates. A slow cooling rate from 142 °C under nitrogen produced a compact that had a modulus of 475 MPa and a yield strength of 21.7 MPa, whereas water quenching from 200 °C produced a compact with a modulus of 213 MPa and a yield strength of 13.8 MPa. The variation in mechanical behavior with cooling rate of the melt may be attributed to differences in the quantity and morphology of the crystalline phase in UHMWPE. It is also known that while type 1 fusion defects (incomplete interparticle voids) can be removed by properly controlling the consolidation conditions, type 2 fusion defects (incomplete interparticle cohesion by self-diffusion) are common in UHMWPE. One major reason for the existence of structural defects in consolidated UHMWPE is the extremely slow diffusion of the ultra long polyethylene chains during consolidation. According to the Reptation Theory by[12] and the tube model of Doi–Edwards,[13] the motion of a single linear chain is described as restricted by the topological constraints ('tube') from the neighboring chains so that this chain can relax only along the tube axis. Dynamic thermal analysis of entangled UHMWPE (molecular weight, $3.6 \times 10^6\,g\,mol^{-1}$) showed a terminal relaxation time of 15 h at 180 °C,[14] much longer than the conventional processing time (usually less than 1 h at 190–250 °C). It was shown that prolonged exposure to high temperatures (~300 °C) can enhance the toughness of UHMWPE.[15]

The wear of UHMWPE components, which is a crucial clinically relevant macroscopic property for joint implants, depends upon surface roughness to an extent.[16] Off-the-shelf UHMWPE components vary in surface R_a from 0.28 to 0.89 μm. The polished metal counterfaces of orthopedic bearings, in contrast, vary in typical surface R_a from 0.01 to 0.02 μm. Because of the initial difference in surface roughness at the UHMWPE and metal counterfaces, the initial wear rate involves the removal of the larger 'macroscopic' asperities on the UHMWPE surface, whereas the long-term wear rate is governed by the 'microscopic' asperity size of the metal counterface. Thus, changes to the surface roughness of UHMWPE components may be expected to affect the initial wear rate.

6.603.2.2. Structure–Property Relationships

The nomenclature of UHMWPE has changed considerably in the past four decades, complicating the comparison and review of historical processing conditions. In the early 1960s, UHMWPE was classified as a form of high-density polyethylene (HDPE) among members of the polymer industry.[1] Thus, Charnley's earlier references to UHMWPE as HDPE are technically accurate for his time.[17] Today, HDPE is classified as linear polyethylene with a density $>0.940\,g\,cm^{-3}$ and having a molecular weight typically below $200\,000\,g\,mol^{-1}$, whereas UHMWPE is defined by ASTM D 4020 as a linear polyethylene with an average molecular weight >3.1 million $g\,mol^{-1}$[18] and >1 million $g\,mol^{-1}$ by ISO 11542. The two UHMWPE resins available today are designated GUR 1020 and GUR 1050 and have molecular weights of about 3.5 and 6 million $g\,mol^{-1}$, respectively.[19] Up until the early 1990s, this type of resin was produced only from what today we would consider the lower molecular weight UHMWPE (GUR 1020). To date, this compression molded low molecular weight UHMWPE is still the primary UHMWPE used in the European marketplace.

Two ram extruded resins, 1900 and 1900H, were supplied from Hercules Powder Company and Montell Polyolefins (Wilmington, DE, USA) until the disassembly of the production line in 2002. It has to be mentioned that the 1900 resin, which had a molecular weight in the range of 2–4 million $g\,mol^{-1}$, has a relatively high long-term success; implants that had been fabricated by direct compression molding of this resin showed higher survival rates because of their resistance to oxidation compared to implants fabricated from the conventional GUR resin of similar molecular weight.[20] As this resin was discontinued in 2002, implants fabricated from this material are not expected to be available for very long.

Variations between the material properties of consolidated Ticona and Montell resins have been explained by differences in the average resin particle size, the size distribution, and morphology of the resin particles.[21] GUR resins have a mean particle size of about 140 μm, whereas the mean particle size of Montell 1900 was around 300 μm. The subtle differences between the nascent particle morphology of the spheroid particles of the resin powders, when studied under a scanning electron microscope, revealed notably that the powder morphology in the Ticona resins was characterized by a fine network of submicron-sized fibrils which interconnected the microscopic spheroids.[1] These were attributed to the use of different catalysts and manufacturing processes, resulting in different polymer morphologies. For example, depending upon the processing conditions, the 1900 also exhibited spherulitic crystalline morphology,[22] whereas spherulites are not observed in Ticona resins, which have a lamellar crystalline morphology.[23] There is ongoing research at DSM (Netherlands) to reintroduce a Type 3 resin such as Himont 1900, a class of resin categorized by its molecular weight and catalyst residues.[19]

At the nanometer length scale, UHMWPE is a two-phase viscoplastic solid, consisting of crystalline domains embedded within an amorphous matrix (**Figure 1**). The crystalline phase of UHMWPE consists of folded rows of carbon atoms packed into lamellae, typically 10–50 nm in thickness and 10–50 μm in length. The crystalline morphology of UHMWPE encompasses a distribution of lamellar sizes within the polymer, although the typical interlamellar spacing is 50 nm, on the basis of small-angle X-ray scattering measurements.[24] The surrounding amorphous phase consists of randomly oriented and entangled polymer chains traversed by tie molecules which interconnect lamellae and provide resistance to mechanical deformation. Thus, at the nanometer length scale, UHMWPE is a complex composite material which can evolve over time in response to its mechanical, chemical, and thermal history.

The intrinsic viscosity (IV) of UHMWPE is related to the bulk impact strength and abrasive wear resistance after conversion to bulk form, although the relationships are nonlinear. The maximum impact strength was found to be between 16 and 20 IV, which is the equivalent to a molecular weight range of 2.4–3.3 million using the ASTM calculation for molecular weight.[1,19] As the IV increases, abrasive wear resistance increases, as measured by sand slurry testing, reaching a plateau for IV greater than 20. In *in vitro* wear studies using pin-on-disc (POD) apparatus, the wear of UHMWPE consolidated by compression molding varied between 7 and 10 mg million^{-1}-cycles of testing.[25,26]

Despite the successful use of additives such as antioxidants in many polymers used in food packaging, consumer applications, and other medical devices, additives in UHMWPE total joint implants are not common. This is due to some serious negative effects of historically used additives. Calcium stearate, which was used as a scavenger for catalyst particles left in the polymer as well as a release agent, was found in the oxidized portions of retrieved tibias accompanied by white banding, suggesting its involvement in oxidation.[27] Fusion defects and

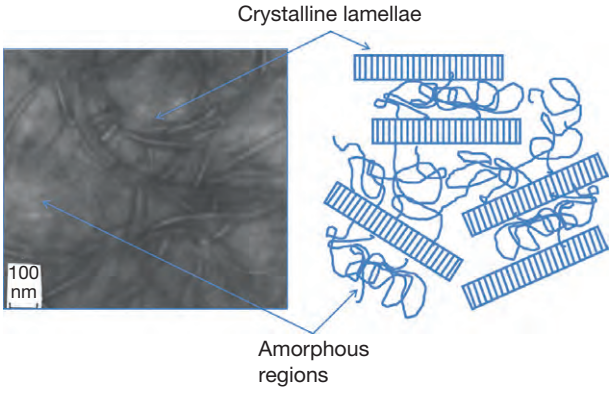

Figure 1 Polyethylene morphology.

internal microvoids could serve as stress concentrations and promote the nucleation of cracks and general reduction in the mechanical properties of the material, with deleterious consequences for the fatigue wear commonly observed in tibial bearings for total knee arthroplasty as a result of oxidation.[28–30] While the effects of consolidation parameters and the presence of calcium stearate at the grain boundaries on fusion defects could not be clearly identified, manufacturers opted to use resins with lowered calcium stearate concentrations (i.e., GUR 1020 and 1050). Another additive that was included in a modified UHMWPE in the 1970s was carbon fiber in an attempt to increase the modulus and mechanical strength of UHMWPE, thereby improving its longevity.[1] Despite showing some promise in the laboratory in terms of increased strength and pitting resistance, this carbon-reinforced UHMWPE (Poly II™) failed completely after short-term implantation *in vivo*.[31] It was revealed that carbon fibers, which were not well bonded to the polymer matrix, acted as crack nucleation sites and cracks propagated much faster in this material than in unreinforced polymer. Recently, the lipophilic natural antioxidant vitamin E was introduced in UHMWPE to improve its oxidation resistance in the long term.[32] This additive does not appear to affect the wear and mechanical properties of UHMWPE detrimentally, and we discuss the properties of vitamin E-stabilized UHMWPE in detail in the following sections.

6.603.3. The Effects of Sterilization and Early Developments

During the first three decades of UHMWPE as a joint arthroplasty material and as recently as 1995, UHMWPE was typically sterilized with a nominal dose of 25–40 kGy of gamma radiation in the presence of air. However, it was clearly shown that this sterilization process led to increased oxidation, accompanied by recrystallization, embrittlement, and general degradation of the mechanical integrity of the implant (**Figure 2**).[33] By 1998, all of the major orthopedic manufacturers in the United States were either sterilizing UHMWPE using gamma radiation in a reduced oxygen environment or sterilizing without ionizing radiation, using ethylene oxide or gas plasma. Today, gamma sterilization in inert atmosphere is a standard for implants using radiation sterilization. Implants, which are produced with reduced or no free radicals, as we discuss later, use nonionizing techniques of gas plasma or ethylene oxide gas sterilization. Gamma sterilization in inert gas has reduced the rate of oxidation of the implants in the high oxygen environment on the shelf before implantation.[34]

Sterilizing by ionizing radiation introduces oxidation potential into UHMWPE because of free radicals caused by the irradiation, and these radicals remain trapped in the material in the long term (**Figure 3**). The mechanism of generation and methods of reducing, eliminating, or stabilizing these free radicals are discussed in detail later in the chapter; however, the benefit of ionizing radiation over nonionizing sterilization methods should briefly be mentioned here. While increasing oxidation potential, radiation also induces cross-linking in the polymer, which significantly reduces the wear of UHMWPE as a function of increasing radiation dose.[35–37]

The need to compare the oxidative stability of UHMWPEs with different free radical and oxidation burdens brought about the development of *in vitro* preconditioning and accelerated aging methods.[1] From a variety of accelerated aging studies involving increased temperature, oxygen partial pressure, and in some cases, the addition of oxidizing media such as hydrogen peroxide, two testing methods have emerged as 'standard' preconditioning techniques. The first preconditioning method,[38] relied on thermally aging specimens in a standard air furnace at 80 °C for up to 23 days. The validation of the protocol was with gamma-sterilized UHMWPE (in air) prior to accelerated oxidation or shelf aging for up to 10 years. After 23 days of thermal aging, the maximum oxidation index in the specimens corresponded to that of 7–9 years of shelf aging. In the second method,[39] specimens were preconditioned under 5 atm of pure oxygen at 60 and 70 °C for up to 7 days.

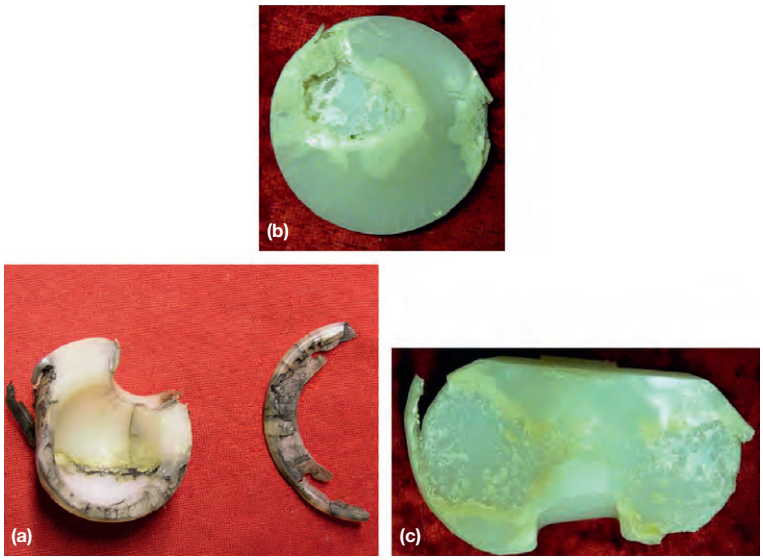

Figure 2 Examples of oxidative damage in hip (a), patella (b), and knee (c) components.

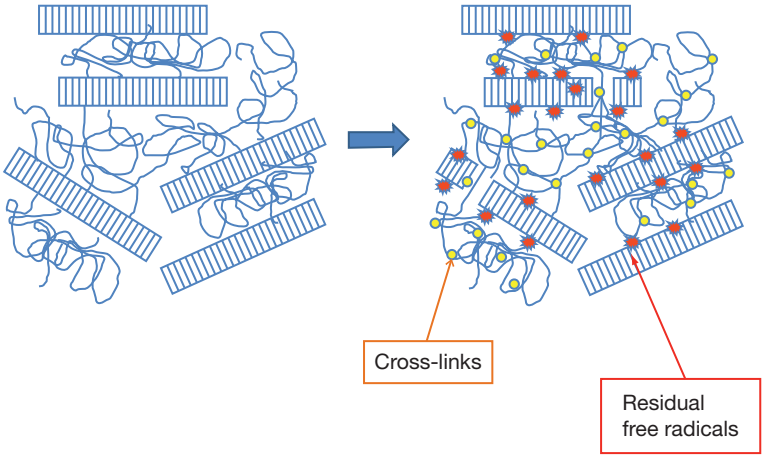

Figure 3 Induction of free radicals and cross-link in UHMWPE on irradiation.

The specimens preconditioned at 70 °C exhibited a subsurface oxidation peak, similar to that observed in retrieved components. Using this method, 1 week of preconditioning at 70 °C and 5 atm of pure oxygen resulted in oxidation equivalent to 5–10 years of ambient shelf aging. In subsequent research, 2 weeks was adopted as a 'standard' aging duration at 70 °C and 5 atm of oxygen.[9,40]

These early developments in accelerated aging protocols were designed to differentiate UHMWPE with and without the oxidative burden of residual free radicals from irradiation. These methods do not produce any difference between the newer generations of UHMWPE materials without free radicals or with substantially reduced oxidation potential. Oxidation-resistant materials have been introduced clinically relatively recently (irradiated and melted UHMWPEs since 1999, and vitamin E-stabilized and irradiated UHMWPEs since 2007); therefore, it is yet somewhat early to compare new *in vitro* accelerated aging methods to *in vivo* results. Nevertheless, several *in vitro* methods, including real-time aging in aqueous environment at body temperature,[41–43] thermal aging combined with cyclic loading,[44,45] and thermal aging combined with lipid absorption,[46] are being developed to differentiate between oxidatively more resistant UHMWPEs. These methods also attempt to better simulate the chemical and mechanical environment of the implants *in vivo*.

The level of oxidation in UHMWPE components can be determined using spectroscopic techniques. The oxidation cascade initiated by radiation-induced free radicals results finally in polymer degradation products, which are mainly carbonyl-containing species such as ketones, esters, and acids (Brach del Prever[47]; Costa[48]). Therefore, the area under the IR absorbance of the peak(s) in the 1680–1800 cm^{-1} range is used to quantify oxidation normalizing to an internal standard.[49]

Cross-linking polyethylene by using irradiation doses higher than sterilization dose (>40 kGy) was introduced to decrease the abrasive/adhesive wear of UHMWPE to decrease the incidence of peri-prosthetic bone loss, directly caused by UHMWPE wear debris. In the next section, we describe different cross-linking technologies and also the treatments addressing the oxidation burden introduced by radiation cross-linking.

6.603.4. Cross-linking Technologies

6.603.4.1. Early Experience with Cross-linking

In early developments, cross-linking of UHMWPE was performed by two different methods: radiation cross-linking and chemical cross-linking.[50–52] In the early 1970s, Oonishi *et al.* implanted UHMWPE acetabular cups that were cross-linked in the solid state using 1000 kGy of gamma radiation in the presence of air.[53–58] Oonishi implanted acetabular components made from this material and compared the wear rate to that in patients implanted with control UHMWPE, which were sterilized by ethylene oxide. The radiographic wear measurements showed average rates of steady-state linear head penetration of 0.006 mm $year^{-1}$ for 600 kGy-irradiated UHMWPE, compared to 0.098 mm $year^{-1}$ for ethylene oxide sterilized conventional UHMWPE.[59] In the 1970s, Grobbelaar *et al.* also investigated cross-linking of UHMWPE using up to 800 kGy of gamma radiation in the presence of a sensitizing environment such as acetylene.[60] They observed a 30% increase in the abrasion resistance of the cross-linked UHMWPE as measured by the sand-slurry method.

The use of polyethylenes cross-linked by silane chemistry was first proposed with the hypothesis that cross-linked UHMWPE would exhibit less creep and would contribute to decreased penetration in the early stage of implantation.[50,51,61] They showed a slightly improved creep resistance as well as improved wear resistance at high sliding velocities under unidirectional motion in cross-linked UHMWPE compared to un-cross-linked UHMWPE. They did not show any significant difference between the wear rates of uncross-linked and cross-linked UHMWPEs, but this was because of the lubrication and dynamic conditions they used, which were not in their more clinically relevant form at the time.[62–66,52,67] reported on the wear behavior of 22 mm diameter, silane cross-linked acetabular components, which were actually injection molded HDPE,[1] similar to the material described by Atkinson and Cicek.[50,51] Wroblewski's clinical and joint simulator studies showed remarkable agreement in the wear rates of the cross-linked polymer. After an initial 'bedding-in' penetration of 0.2–0.41 mm at 2 years, the subsequent average penetration rate (or wear rate) was 0.019 mm $year^{-1}$.

Clinical follow-up was at a minimum of 15 years with a maximum of 18.1 years with a total of 17 patients.[68]

Despite the evidence of improved wear resistance also with peroxide-cross-linked UHMWPE, its oxidative stability was of concern.[10,36] While these developments introduced cross-linking as a means of decreasing wear and creep in implant components, the large-scale use of cross-linked UHMWPE in joint implants started in 1999 after development of cross-linking and oxidative stabilization methods using radiation cross-linking.

6.603.4.2. Radiation Cross-linking Followed by Thermal Treatment

6.603.4.2.1. Formation of cross-links and wear reduction through cross-linking

Radiation cross-linking combined with thermal treatment emerged in the late 1990s as a technology to improve the wear and oxidation resistance of UHMWPE acetabular components.[35,36,69] The development of this technology during the past decade led to a series of new alternate UHMWPE bearing materials, including irradiated and melted, irradiated and annealed, sequentially irradiated and annealed, and irradiated and mechanically annealed UHMWPEs.

Understanding the wear mechanism of UHMWPE became central to the aim of improving the wear resistance of this polymer. The analysis of acetabular components retrieved during an autopsy or a revision operation showed that the highly worn areas were polished to a glassy finish on gross examination.[70] Upon investigation under a scanning electron microscope, numerous multidirectional scratches along with fine, drawn-out fibrils with a diameter of 1 μm or less oriented parallel to each other became apparent on the worn articular surfaces. These fibrils were thought to be the most likely source of the wear particles observed in periprosthetic osteolytic tissue.[71] Thus, wear appeared to occur mostly through the breakup of fibrils formed by large-strain plastic deformation and orientation of the surface. The fibrils were weakened in the transverse direction and subsequently ruptured during multidirectional motion of the hip. These *in vivo* findings were later reproduced *in vitro*[65,71,72] using wear testing devices. These researchers showed that the wear rate of UHMWPE increased markedly when the articulation was switched from a unidirectional to a multidirectional motion. The underlying mechanism in the orientation of the surface fibrils is the direction of motion. This orientation increases the strength of the fibrils in this direction and weakens them in the transverse direction. Hence, debris generation occurs easily when the direction of motion is altered.

During ionizing irradiation of UHMWPE, free radicals are formed, the most prevalent of which are the carbon free radicals resulting from the breakage of the C–H bonds[73] and these radicals are found in three forms: the alkyl, allyl, and polyenyl free radicals.[74–76] The polyenyl free radicals are formed especially at higher radiation doses.[77] Most of these free radicals recombine in the amorphous portion of the polymer,[78] where the chains are highly mobile. The reaction of a free radical generated by the cleavage of a C–H and C–C bond results in long-chain branching or Y-linkages by reacting with terminal vinyl groups (**Figure 4**). The recombination of two free radicals formed by the cleavage of C–H bonds on separate chains

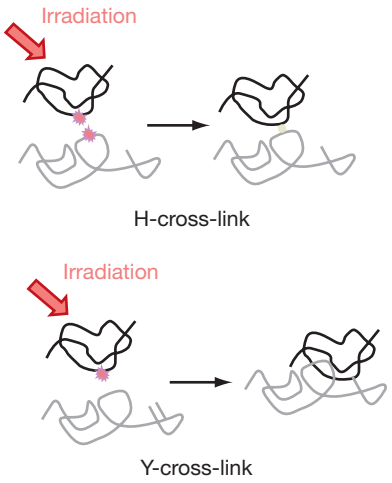

Figure 4 Schematics of cross-linked structures.

results in cross-linking through an H-linkage. The remaining free radicals are trapped in the highly ordered crystalline lamellae.[79,80] As the interchain distance is fixed at 4.1 Å between polyethylene chains in a crystal and the C–C bond distance is 1.5 Å,[81] interchain or intrachain cross-linking is highly unlikely. Therefore, free radicals travel along the crystal chains and encounter other free radicals to form a double bond or encounter the crystalline–amorphous interface. The decay of free radicals in the crystalline phase, therefore, is extremely slow, taking as long as several years.[82]

When oxygen is present in irradiated polyethylene, it reacts with the primary free radicals to form peroxy free radicals.[73,83–86] These peroxy radicals abstract a hydrogen atom from other polyethylene chains, creating primary free radicals, which can then react with oxygen to further this cascade.[87,88] When peroxy free radicals get hydrogenated, they form hydroperoxides, which are not stable and over time degrade into oxidation products, mainly ketones, esters, and acids.[89–93] The formation of these oxidation products is accompanied by chain scission and a decrease in the molecular weight of polyethylene, leading to deterioration of mechanical properties[94–96] (**Figure 5**).

Increasing the entanglement density of UHMWPE through melt-annealing was the first proposal to decrease the extent of surface deformation during articulation. However, quenching of the molten UHMWPE was not effective in maintaining what was thought to be a higher entanglement state of the polymer in the melt. This method was later modified by adding radiation cross-linking at above the melt temperature to lock in the entanglements in place. Later, it became clear that the increase in wear resistance of the polymer was not necessarily due to the increase in entanglement density but was due to the cross-linking. Hence, cross-linking was advanced as a means to impede the formation of surface fibrils and reduce the wear of UHMWPE. Cross-linking of UHMWPE molecules would decrease the chain mobility needed for the large-scale plastic deformation and hence slow down the surface fibril formation.

6.603.4.2.2. The effects of thermal treatment during or after irradiation on oxidation and wear

In first-generation cross-linked UHMWPEs widely available for clinical use,[97] postirradiation thermal treatment was used

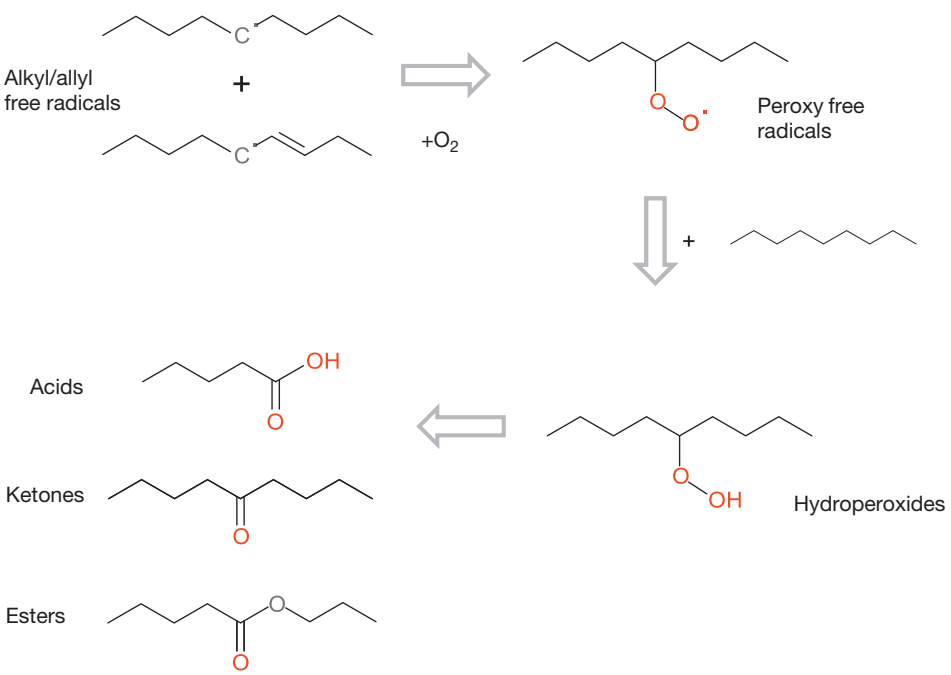

Figure 5 Oxidation cascade in polyethylene.

to increase the oxidation resistance to reduce or eliminate the residual free radicals trapped in the crystalline domains. One approach was to anneal the irradiated UHMWPE below its peak melting point,[98] reducing the free radical concentration by providing more energy to the free radicals and allowing them to recombine to some extent.[99] The free radicals were reduced by annealing, but the implant was also terminally gamma sterilized, which introduced additional free radicals. In the long term, there was significant oxidation in irradiated and annealed UHMWPE *in vivo*.[100–102] In spite of this, at intermediate follow-up (up to 8 years), the *in vivo* femoral head penetration rates with irradiated and annealed UHMWPE are less than those for conventional UHMWPE[103,104] and the clinical effects of this elevated oxidation are not yet manifested.[101] One study showed fatigue damage at the oxidized rim of explanted irradiated and annealed UHMWPE acetabular liners, although none was revised because of rim damage.[100]

The second approach was postirradiation remelting of the crystals to allow for the free radicals to recombine completely. This method reduced the radiation-induced residual free radical concentrations to undetectable levels as measured by electron spin resonance and resulted in very low measurable oxidation in accelerated aging tests.[105] At the same time, recrystallization was hindered by the newly formed cross-links, the crystallinity was reduced, and therefore, the fatigue strength of radiation cross-linked UHMWPE was further reduced.[106] The *in vitro* wear rate[36] and the penetration rates of remelted UHMWPE in the intermediate term (5–7 years) have been very low,[107] but there are some concerns about the increased incidence of rim fracture under impingement and adverse loading conditions because of the lowered fatigue strength of this material.[108–110]

Both gamma and electron beam (e-beam) irradiation have been used to cross-link UHMWPE.[35,105] While the cascade of events that leads to the formation of cross-links and residual free radicals are similar for both gamma irradiation and electron beam irradiation, there are still important differences between the two methods, specifically in terms of penetration of the effects of radiation and radiation dose rate achieved. Gamma irradiation sources are commonly on the basis of the artificial isotope of cobalt (^{60}Co) that generates gamma photons. While the penetration of gamma source into UHMWPE has no practical limitations, the activity level of the gamma source limits the radiation dose rate. With an electron beam, the radiation is in the form of accelerated, charged particles. The penetration of the effects of e-beam radiation is limited by the kinetic energy of the electron beam, measured in million electron volts (MeV). With a 10 MeV electron beam incident on a UHMWPE surface, radiation penetrates about 4–4.5 cm. The radiation dose rate that a commercial e-beam accelerator provides is about two orders of magnitude larger than that from a commercial gamma source.

Because of the high dose rate of irradiation to which the UHMWPE is exposed, adiabatic heating of UHMWPE is common during electron beam irradiation. Electron beam radiation offers a greater control of dose rate, which presented a means to control the temperature rise in UHMWPE during irradiation during the development of highly cross-linked UHMWPEs. This also meant that the polymer could be melted during irradiation. It was also shown that the rate of formation of H-linkages increased with increasing irradiation temperature, thus leading to increased cross-linking.[111] Radiation dose is energy per unit mass of the material being irradiated and it is measured in kGy units, or $kJ\,g^{-1}$. The specific heat of UHMWPE is $\sim 2.5\,kJ\,g^{-1}\,^{\circ}C$; using a radiation dose of 100 kGy, UHMWPE needs to be heated to at least 120 °C to achieve near complete melting of the crystalline domains

during irradiation. The efforts on using e-beam to melt the UHMWPE led to the development of warm irradiated UHMWPE, now used in the fabrication of some total hip and total knee components.[97] In the large-scale manufacturing of warm irradiated UHMWPE, a terminal melting step in an air convection oven is used to ensure that complete melting is achieved and that residual free radicals are eliminated. Surprisingly, warm irradiation of UHMWPE resulted in some unusual properties: Warm irradiated UHMWPE displays two distinct peak melting points, one near 115 °C and the other at 137 °C. This is an indication of a bimodal lamellae thickness distribution. Transmission electron microscopy of warm irradiated UHMWPE corroborated this finding, showing thick lamellae embedded in a matrix comprising smaller and thinner lamellae and the amorphous phase.[69] Warm irradiation and melting of UHMWPE also results in higher ductility and lower strength in comparison with irradiation without preheating and melting.[69]

As the absorbed radiation dose increased, the cross-link density increased with saturation behavior starting at around 100 kGy, beyond which increases in cross-link density decreased rapidly.[36] The multidirectional wear rate of UHMWPE was also shown to decrease with increasing radiation dose, also showing asymptotic behavior with saturating cross-link density. Studies of damaged surfaces of retrieved implants[70] showed that there exists a plasticity-induced damage layer on the articulating surface of implants.[112] As discussed above, increased plasticity results in orientation in the principal direction of motion with weakening in transverse directions. Radiation cross-linking decreases chain mobility and chain stretch; as a result, it decreases the plasticity of the polymer.[106,113–115] This is presumably a major mechanism by which wear was decreased through radiation cross-linking (**Figure 6**).

Investigations on the wear behavior of highly cross-linked UHMWPE on functional joint simulators followed the initial preclinical testing using pin-on-disc wear testers. To obtain more clinically relevant results, simulators have been designed for wear testing.[116–119] Simulators have been designed to match the *in vivo* wear rate, wear debris size, and shape of UHMWPE as well as the surface morphology observed in explanted components by replicating *in vivo* attributes such as component positioning, temperature, loading, and kinematics of normal gait,[120–124] all of which are known to affect the wear rate of UHMWPE. The simulator tests are typically carried out at 1–2 Hz, in bovine serum at 37–40 °C to simulate joint temperature. Wear is assessed gravimetrically and can be measured also by a volumetric method using a coordinate measuring machine, which can measure the three-dimensional shape of the articular surface. When measuring wear volumetrically, creep deformation of UHMWPE has to be separated from wear; this can be done by melting the component after testing is completed as UHMWPE has excellent shape memory and creep deformation can be eliminated by remelting the component (**Figure 7**[125]). Limitations of simulators are the choice of kinematics, which is usually limited to normal gait kinematics in contrast to a complex variety of activities of daily living. Another factor affecting wear in the simulator is the testing environment. While bovine serum is the accepted analog for synovial fluid, dilution of bovine serum with water to obtain protein concentrations relevant to *in vivo* conditions is commonly used. However, wear of conventional (gamma-sterilized) UHMWPE has been shown to increase with bovine serum dilution.[66] At high water concentration, nonphysiological wear mechanisms can dominate the wear process.[63] Other factors that may affect the outcome are surface finish of the metallic counterface, stress levels, and loading mode (dynamic vs. constant).[126]

Hip simulator studies of various designs with irradiated and melted UHMWPE all showed significantly improved wear resistance (60–90% decrease) in comparison with conventional UHMWPE. Some studies used gamma in air-sterilized UHMWPE and others used ethylene oxide or gas plasma-sterilized UHMWPE as controls. Note that the gamma-sterilized controls would have some cross-linking and thus would also have a lower wear rate than the controls sterilized by nonionizing methods. The hip simulator studies explored the influence of long-term use, artificial aging, presence of third-body particles, femoral head size, and, later, component

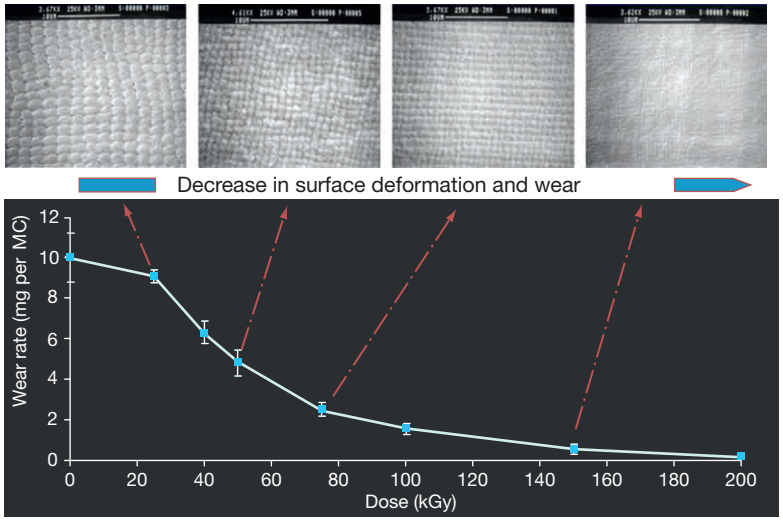

Figure 6 The effect of cross-linking on surface features and wear.

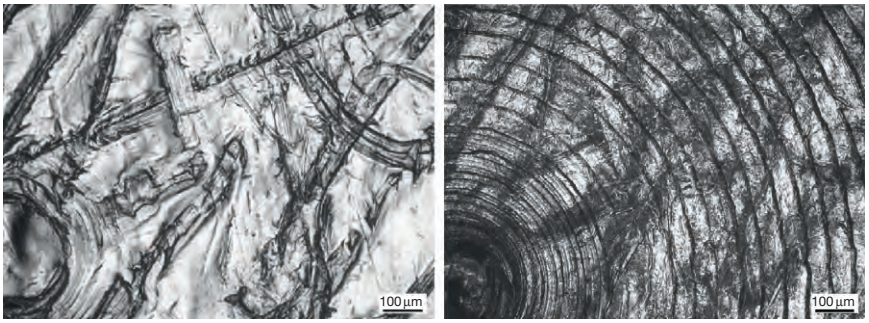

Figure 7 The recovery of surface deformation of cross-linked UHMWPE by melting.

placement on the wear of irradiated and melted UHMWPEs. Some studies were carried out to 30 million cycles, corresponding to 15–30 years of *in vivo* service of an average total hip patient.[35,66,69,125,127,128] These studies showed that the marked reduction in wear was not affected by the long-term testing and that there was no fatigue-induced wear. The addition of third-body particles, in the form of bone cement, increased the wear of both conventional and highly cross-linked UHMWPEs; yet the latter still exhibited better wear resistance. Standard artificial aging protocols did not oxidize the irradiated and melted UHMWPEs appreciably because of the improved oxidation resistance and as a result did not affect their wear rate.

The femoral head size is an important effect in that with larger heads the wear rate of conventional UHMWPE acetabular liners increases.[128] Even though there is an increase in the contact area and hence a reduction in contact stress, wear increases with head size because of the dominant increase in the distance traveled at every gait cycle. Historically, smaller heads, 22 to 28-mm-diameter femoral heads, had been used to minimize the wear of the liners. Yet, the disadvantage of smaller heads is the decrease in the stability and the range of motion of the joint.[129] Hip simulator studies also showed that interestingly, there was not any significant increase in the wear rate of UHMWPE when tested against larger femoral heads and the wear rate of an acetabular liner with an inner diameter of 46 mm and fabricated with irradiated and melted UHMWPE was lower than that of a 22-mm conventional UHMWPE acetabular liner.[128]

There have been a number of clinical trials comparing the *in vivo* performance of irradiated and melted UHMWPE to that of conventional UHMWPE acetabular liners.[130–132] Radiographic examination of the patients allows the measurement of femoral head penetration into the acetabular liner. The penetration for the first 1–2 years is mostly due to creep and wear, and beyond the second year of follow-up, penetration is attributed to mostly wear alone. All of these studies are showing markedly reduced wear rate with highly cross-linked UHMWPE beyond the second year of follow-up compared to the respective controls (regardless of sterilization method), corroborating the laboratory evidence of reduced wear.[69,128]

6.603.4.2.3. Development of highly cross-linked total knees

The development of highly cross-linked UHMWPE for use in tibial knee inserts followed the introduction of this material in total hips. Knee simulator studies on the wear behavior of irradiated and melted UHMWPE tibial knee inserts have been widely published.[133–139] These investigations focused on the effect of long-term testing, artificial aging, presence of third-body particles, implant design, and most importantly on malpositioning of the implants. The studies uniformly showed improved adhesive/abrasive wear with irradiated and melted UHMWPE in comparison with conventional gamma-in-air or -in-nitrogen sterilized UHMWPE tibial knee inserts of either cruciate retaining or posterior stabilized designs. Artificial aging of the test components was used to simulate long-term oxidation in the conventional UHMWPE and the testing of these components on the knee simulators showed delamination damage. When the irradiated and melted UHMWPE components were subjected to identical accelerated aging conditions and tested on the knee simulator, they showed no delamination or pitting.[138] In the presence of third-body particles, the highly cross-linked UHMWPE components still showed lower wear rate than conventional UHMWPE. Investigations also showed that the highly cross-linked UHMWPE exhibits better wear performance when it is articulated against surgically explanted femoral components that had been extensively damaged during *in vivo* service.[137]

In total knees, the malpositioning of components can seriously compromise not only the knee function but also the performance of the UHMWPE components used because of the altered stress state.[136] The highly cross-linked UHMWPE tibia inserts were also tested under certain worst-case scenarios. One is the circumstance of a tight posterior cruciate ligament (PCL), which would increase the roll back of the femoral component during flexion and apply high stresses to the posterior edge of the tibial component. Under these conditions, accelerated aged conventional UHMWPE tibial inserts showed massive delamination in less than 50 000 cycles of stair climbing, while the aged highly cross-linked components showed no delamination up to 500 000 cycles.[136]

Backside wear is another important factor that could affect long-term performance of total knees. Knee simulator studies also showed that the extent of backside wear decreases markedly with irradiated and melted UHMWPE in comparison with that observed in conventional UHMWPE.[138]

There have been a number reports on the *in vivo* performance of irradiated and melted UHMWPE based on changes observed on surgically explanted components.[140,141] Interestingly, the articular surfaces of the first retrievals were very

highly scratched and discolored. Plastic deformation due to third-body particles was the culprit despite an initial fear that the scratches were due to wear and the discoloration due to oxidation. We used the shape memory property of UHMWPE and showed by melting of the explants the elimination of the scratches and recovery of the original machining marks.[140] The discoloration was not due to the oxidation of the components but simply due to the absorption of the lipids from the synovial fluid.[140] While wear polishes the articular surface and removes the scratches and discoloration, in irradiated and melted UHMWPE scratches and discoloration accumulate, which points to the lack of wear in these components. Similar observations were also made with surgically retrieved tibial knee inserts that were made from irradiated and melted UHMWPE.[141]

While there have not been any published prospective, randomized clinical studies looking at highly cross-linked UHMWPE knees, one retrospective, case-matched series of 200 patients compared highly cross-linked knee implants with conventional knee implants at a follow-up of 6–7 years[142] and showed that there was a significant reduction in cases showing radiolucency (2 compared to 20 for control), and no revisions due to osteolysis in the highly cross-linked cohort. The irradiated and melted UHMWPE has been in clinical use around the globe for the past decade with more than two million implantations.[97]

6.603.4.2.4. Mechanical and fatigue properties

There are compressive and shear forces on UHMWPE during articulation, and there may be residual tensile stresses that arise from accumulated stress during repeated load cycles.[143] The reversal of stress direction causes fatigue cracks to initiate causing delamination, especially in total knee implants.[144,145] Therefore, besides wear, the second most important property change in UHMWPE induced by irradiation is its fatigue resistance. Fatigue testing is performed in cyclic tension on a compact tension specimen,[146] which is designed to concentrate applied stress at a notch tip with an existing crack. A stress factor at crack inception (ΔK_i) is calculated as a measure of fatigue crack propagation resistance. This is the stress factor range (dependent on the load ratio, sample geometry, and crack length), at which the crack growth rate exceeds 10^{-6} mm per cycle. The ΔK_i of unirradiated UHMWPE is reported as 1.6–2.0 MPa $m^{1/2}$.[26,147] The temperature at which the testing is performed (25 vs. 40 °C), the frequency used in the test, testing environment (air vs. water), and the crack initiation method are some factors that account for the variation in the results obtained from different laboratories.

With increasing cross-link density, the fatigue crack propagation (FCP) resistance decreases.[106,148] On the other hand, crack initiation resistance increases with cross-linking.[149] While irradiation alone decreases the FCP resistance, melting subsequent to irradiation further decreases the FCP resistance.[106] This decrease is again related to the decrease in the ductility of the materials and is also manifested in other mechanical properties such as the elongation to break. The tensile mechanical strength of UHMWPE is mainly dependent on its crystallinity and therefore, irradiation by itself does not adversely affect the strength. On the other hand, melting after or during irradiation decreases the crystallinity and therefore decreases the strength.[106] Recrystallization of the polymer chains is hindered by the presence of cross-links, and chain mobility and reptation needed for the lamellae to form are limited. However, the decrease in crystallinity results in an increase in compliance of the polymer, which is desirable in load-bearing applications as it decreases the contact stress.[150]

The fatigue strength may be decreasing with cross-linking and melting, but understanding the effects of these changes on implant performance is complicated by the design and use of the implants. Fatigue failures reported with irradiated and melted UHMWPE acetabular liners are rare; however, when they occur, these failures are primarily at the rim and almost always occur with steep shell placement.[108,109] While some occurrences of fracture were reported with acetabular liners,[110] none was reported with highly cross-linked tibial knee inserts.

Orthopedic implant manufacturers chose different radiation dose levels as the optimum for irradiation and melting. The debate continues between 100 kGy and 50 kGy as being the optimum dose levels. As we explained above, the beneficial effects of radiation cross-linking in terms of increasing the wear resistance decrease rapidly above 100 kGy. Thus, the optimum radiation dose rate for increasing wear resistance is around 100 kGy. At 50 kGy, some of the mechanical properties, such as toughness and elongation at break, are higher with a lower wear resistance compared to that at 100 kGy. The argument between 50 and 100 kGy is mainly how much reduction in wear is needed to prevent periprosthetic osteolysis. While there have been cases of osteolysis in 50 kGy irradiated and melted UHMWPE[151] clinically, we need long-term (beyond 10 years) clinical studies to determine the comparative incidence of periprosthetic osteolysis and loosening while using this and conventional UHMWPE.

6.603.4.3. Sequential Irradiation and Annealing

While the clinical significance of measured oxidation levels in highly cross-linked UHMWPE is not clear, it is clear that oxidized conventional UHMWPE gamma sterilized in air caused high incidence of wear and damage on total joint implants. It is also clear that a UHMWPE with residual free radicals has high oxidation and thus degradation potential. Therefore, a sequentially irradiated and annealed UHMWPE (X3™) was also developed to replace the irradiated and annealed UHMWPE (Crossfire™), which showed oxidation *in vivo*.[100,102] The hypothesis was that smaller doses of irradiation (30 kGy) followed by high temperature annealing below the melting point (at 130 °C) would lead to more effective reduction of free radicals and less oxidation potential. Also, in contrast to the original material, this annealed UHMWPE is sterilized by nonionizing gas plasma sterilization in order not to introduce an extra oxidative burden on the material. In one study, where X3 UHMWPE was compared to conventional, gamma-sterilized UHMWPE and 90 kGy irradiated and thermally annealed UHMWPE, the free radical content of X3 was low but detectable (9×10^{15} mg MC^{-1}).[152] In a separate test performed in our laboratory, the free radical content of two never implanted X3 acetabular liners from two different lots showed a substantial free radical signal. The free radical concentration of X3™ was 1.12×10^{15} spins per gram in comparison to 2.6×10^{15} and 4.3×10^{15} spins per gram for

conventional and Crossfire™ acetabular liners. The oxidation rate of this material *in vivo* and the effects of this oxidation in the properties are yet to be determined.

Hip simulator wear testing of 32 and 36 mm unaged X3 acetabular liners was performed for 10 million cycles in 50% fetal substitute alpha calf serum diluted by deionized water.[99,153] The wear rate of X3 was substantially reduced compared to gamma-sterilized UHMWPE tested for 5 million cycles. This study showed that the wear behavior of X3 is substantially better than that of conventional UHMWPE in its unaged state.

The main advantage of irradiation followed by annealing below the melting point is the retention of the crystallinity of radiation cross-linked UHMWPE as melting of the crystals is avoided. Thus, the mechanical properties and fatigue strength of this material would be substantially changed from that of the cross-linked state in contrast to irradiated and melted UHMWPE, whose fatigue strength is decreased around 30% by postirradiation melting. The crystallinity of X3 UHMWPE was reported to be about 62% before and after accelerated aging in a pressure vessel at 70 °C at 5 atm oxygen for 2 weeks, compared to 61.3% and 70.8%, respectively for conventional UHMWPE.[153] These suggest that the crystallinity of X3 is close to that of conventional UHMWPE. The ultimate tensile strength of X3 UHMWPE before and after aging was 56.7 and 56.3 MPa compared to 54.8 and 29.9 MPa, respectively, for conventional UHMWPE.[153]

The need to develop a wear- and oxidation-resistant cross-linked UHMWPE with improved fatigue properties led to the development of a second-generation cross-linked UHMWPE with antioxidant stabilization. The rationale behind the development of this material was that the residual free radicals from the radiation cross-linking could be stabilized by the antioxidant vitamin E, thus eliminating the need for postirradiation melting for oxidative resistance. This would lead to the retention of crystallinity and fatigue resistance. The next section is devoted to vitamin E-stabilized highly cross-linked UHMWPE.

6.603.5. Vitamin E-Stabilized, Radiation Cross-linked UHMWPE

6.603.5.1. The Rationale and Incorporation Methods

Vitamin E stabilization of UHMWPE was introduced as an alternative method to provide oxidation resistance without sacrificing some of the fatigue strength.[32] There are two methods by which vitamin E can be incorporated into radiation cross-linked UHMWPE. The first is blending of the liquid antioxidant with UHMWPE resin powder, consolidating the mixture by compression molding, and irradiating the consolidated blend for cross-linking.[154–157] Because vitamin E can act as a free radical scavenger during irradiation as well, the cross-linking efficiency of UHMWPE is lowered in the presence of vitamin E[156,157] and the vitamin E concentration in the blend is limited to less than about 0.3 wt%.[158] In addition, the radiation dose has to be optimized as it is necessary to expose a vitamin E blend to a higher dose irradiation than virgin UHMWPE to obtain a desired cross-linking or wear rate. Nevertheless, this vitamin E-stabilized UHMWPE is promising in decreasing oxidation of irradiated UHMWPE[155,159] and can have low wear rates if the vitamin E concentration and radiation dose are optimized.[156,158] Recently, medical grade UHMWPE resin supplier Ticona (Florence, KY) has announced its large-scale production of vitamin E-containing resin for various ultimate applications and a 0.1 wt% vitamin E-containing, 91-kGy irradiated UHMWPE acetabular cup was implanted in Switzerland in 2009.[160] The second approach, which we describe in detail in this chapter, is diffusing vitamin E into already consolidated and radiation cross-linked UHMWPE. Using this method, the amount of incorporated vitamin E is not limited by the cross-link density, but the saturation limit of the cross-linked polymer at body temperature, which is approximately 0.7 wt%. Total hip implants manufactured from 100-kGy irradiated, vitamin E-diffused, and terminally gamma-sterilized UHMWPEs have been clinically used since 2007. Prospective, randomized clinical studies, including an RSA study based at our institution, are underway.[161]

6.603.5.2. Mechanism of Action Against Oxidation

Vitamin E is the most abundant and effective chain-breaking antioxidant present in the human body.[162] The major physiological role of vitamin E is to react with free radicals in cell membranes and protect polyunsaturated fatty acids from degradation due to oxidation.[163] Oxidation of polyunsaturated fatty acids results in active free radicals (LOO•, LO•). The antioxidant activity of vitamin E (RRR-α-tocopherol *in vivo*) is due to hydrogen donation from the phenolic OH group on the chroman ring to a free radical on the oxidized lipid chain. Hydrogen abstraction results in a tocopheryl free radical, which can combine with another free radical. Therefore, tocopherol can theoretically prevent two peroxy free radicals from attacking other fatty acid chains and producing more free radicals.[164–166] Therefore, the cascading nature of oxidation is stopped, and oxidative damage can be prevented.

Oxidation reactions in polyethylene, which has a lipid-like molecular structure, also follow a similar mechanism of oxidation as lipids do *in vivo*.[87,91,167] In irradiated UHMWPE, the carbon free radicals resulting from the breakage of the C-H bonds are prevalent.[73] When oxygen is present in irradiated polyethylene, it reacts with the primary free radicals to form peroxy free radicals.[83–86] These peroxy radicals, in the absence of an antioxidant such as vitamin E, abstract a hydrogen atom from other polyethylene chains, creating new primary free radicals, which can then react with oxygen to further this chain of reactions.[87,88] When peroxy free radicals react with hydrogen, they form hydroperoxides, which are not stable, and degrade into oxidation products, mainly ketones, esters, and acids.[89,90,92,93] The formation of these oxidation products is accompanied by chain scission and a decrease in the molecular weight of polyethylene, deteriorating its mechanical properties.[94–96] In an irradiated polyethylene containing vitamin E, peroxy free radicals presumably abstract a hydrogen atom from vitamin E, forming hydroperoxides without the formation of new free radicals. Vitamin E is also effective in reacting with alkyl radicals,[168] but the reaction rate with peroxy free radicals is higher than that with any other radical.[164,166] The oxidation cascade in irradiated polyethylene is, therefore, hindered in the presence of vitamin E.

6.603.5.3. Diffusion of Vitamin E in UHMWPE

For vitamin E to be able to protect UHMWPE against oxidation, the antioxidant has to be distributed throughout the entire thickness of the component.[169] Polyethylene can be doped with vitamin E simply by allowing it to remain in a bath of pure or diluted vitamin E (**Figure 8(a)**). Because vitamin E is highly hydrophobic, it diffuses readily into polyethylene, especially at elevated temperature; however, on the application of this concept, there are several factors to be considered.

First, it is important not to melt the sample substantially during the diffusion process and thereby to avoid the loss of crystallinity during postirradiation melting, which causes a decrease in mechanical strength.[106] The melting range of UHMWPE starts at 100 °C with a peak melting point of about 140 °C; more crystallinity is lost as the diffusion temperature nears the peak melting point. Increased temperature also increases the surface concentration and the saturation concentration of vitamin E at the surface of UHMWPE.[170,171] Dimensional changes can occur both due to the thermal release of residual stresses from previous processing steps and due to the swelling of the surface with vitamin E. A slightly oversized preform can be processed and machined as a terminal step before sterilization to overcome changes in dimensions.

To obtain a uniform vitamin E concentration profile throughout components of various thicknesses, a two-step diffusion process at elevated temperatures below the melting point was developed involving doping of UHMWPE by soaking in vitamin E with subsequent homogenization at an elevated temperature below the melting point.[170] The doping step was restricted to 120 °C because there were significant volumetric and weight changes above this temperature. When a high surface concentration of vitamin E had been obtained, the homogenization of the surface vitamin E throughout the irradiated component could be achieved at a higher temperature below the melting point because there was no additional diffusion of vitamin E into the component.

A secondary effect of exposing the polyethylene to high temperature during doping and homogenization would be to decrease the amount of residual free radicals caused by radiation cross-linking. But, a terminal sterilization by gamma irradiation is used currently in clinically available implants prepared using this method, resulting in substantially detectable free radicals in this material (3.5×10^{16} spins per gram compared to 11.7×10^{16} spins per gram for 100-kGy irradiated UHMWPE;[42]). Despite the presence of these free radicals, vitamin E-stabilized UHMWPE has shown great oxidative stability when subjected to accelerated aging as discussed later.

During irradiation, vitamin E hinders cross-linking in UHMWPE as a function of increasing concentration.[156,157] In fact, at vitamin E concentrations above 0.3 wt%, the incremental increase in cross-link density by increasing the radiation dose is minimal and it is not possible to cross-link vitamin E-containing UHMWPE to the same level as that of 100-kGy irradiated and melted UHMWPE even at irradiation doses as high as 200 kGy.[158] The terminal gamma irradiation for sterilization causes a very small increase in cross-link density. At the same time, some vitamin E is grafted onto the polymer chain by the postdiffusion irradiation, preventing elution out of components;[172] therefore, it may be desirable to graft some of the vitamin E in the material.

6.603.5.4. Oxidative Properties

A major factor limiting the maintenance of the wear and mechanical properties of irradiated UHMWPEs *in vivo* is oxidation.[33] Oxidation is determined by spectroscopic techniques measuring carbonyl moieties on UHMWPE formed as a result

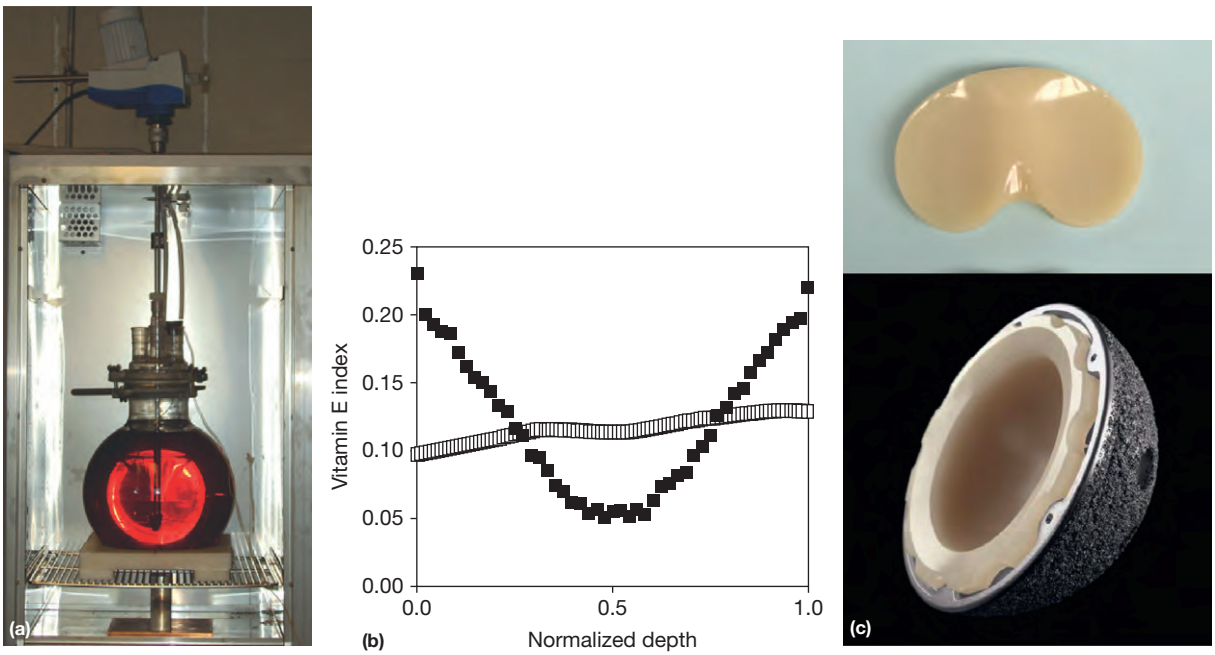

Figure 8 Benchtop pilot setup for vitamin E doping of UHMWPE (a); representative profiles of a component with a vitamin E-rich surface and a uniform vitamin E profile (b); vitamin E-diffused, radiation cross-linked joint implant components (c) (courtesy of Biomet).

of the decay of hydroperoxides.[173] Typically accelerated aging methods are used *in vitro* to compare the oxidative stability of various polyethylene formulations.[9] While accelerated aging is helpful in comparing the oxidation resistance and oxidation potential of different types of bearing materials, it cannot be used to predict the oxidation timeline or profile of a particular material *in vivo*.

Nevertheless, it has been shown in several types of accelerated aging studies, carried out at elevated temperatures and/or in the presence of pure oxygen under high pressure, that vitamin E-containing, irradiated polyethylene is more stable than gamma-sterilized or high-dose irradiated polyethylene.[32,106,154,155,159,174–176] It is proposed that this is due to the reaction of vitamin E with the primary free radicals on the polyethylene chains and also free radicals resulting from their reaction with oxygen. In a study looking specifically at the stabilizing effect of vitamin E in vitamin E-diffused, irradiated UHMWPE showed higher oxidative stability than unstabilized, irradiated UHMWPE over 7 months in air at room temperature and in water at 40 °C[42](showing similar trends at 36 months; **Figure 9**).[177]

As mentioned above, a cross-link density equivalent to that of 100-kGy irradiated and melted UHMWPE is desired because this material has been shown *in vitro* and *in vivo* to decrease wear significantly compared to conventional UHMWPE.[69,130] The studies discussed here were performed on UHMWPE with an initial radiation dose of 85–100 kGy and with a terminal gamma sterilization dose of ~25–40 kGy after vitamin E incorporation designed to obtain similar wear resistance to this predicate material.

6.603.5.5. Wear

Wear testing of vitamin E-diffused, 100-kGy irradiated UHMWPE on a custom-designed pin-on-disc tester in bovine serum showed that the wear rate was comparable to that of 100-kGy irradiated and melted UHMWPE.[32] In this study, accelerated aging at 80 °C for 5 weeks did not change the wear rate of this UHMWPE despite the fact that vitamin E was diffused only 0.5 mm into the surface of this sample and not throughout the entire thickness. This suggested that the wear region was within this surface layer protected by the vitamin E.

After the development of the diffusion method by doping followed by homogenization below the melting point, 5-mm thick acetabular liners were irradiated by 85-kGy gamma irradiation, doped with vitamin E, subsequently homogenized to obtain vitamin E throughout, and terminally gamma-sterilized. These acetabular liners (28- and 40-mm inner diameter) were wear-tested on a hip simulator against CoCr femoral heads using normal gait load and kinematics at 2 Hz in undiluted clean bovine serum for 5 million cycles and compared to conventional UHMWPE gamma sterilized in inert gas.[178] This study showed *in vitro* that under normal conditions, the wear reduction in vitamin E-diffused, highly cross-linked UHMWPE compared to conventional UHMWPE (**Figure 10**; 92% and 90% reduction in wear for 28- and 40-mm cups, respectively, compared to 28-mm conventional UHMWPE) was comparable to what was observed previously with irradiated and melted UHMWPE compared to conventional UHMWPE.[69,128] Similar results were observed when these liners were tested in undiluted bovine serum with third-body polymethyl methacrylate (PMMA) and barium sulfate particulate debris (72% and 75% reduction in wear for 28- and 40-mm cups, respectively, compared to 28-mm conventional). The results obtained from these hip simulator studies with vitamin E-diffused, irradiated highly cross-linked UHMWPE confirmed earlier studies that showed that the wear rate of highly cross-linked UHMWPEs was largely independent of femoral head size.[128]

There are concerns about the ability of highly cross-linked UHMWPEs to withstand especially two clinically adverse situations. One of these is the femoral neck impingement on the rim of an acetabular liner, most often because of the vertical placement of the shell with excessive anteversion.[109,110] There is increased concern for highly cross-linked UHMWPEs because of their initially lower fatigue strength than that of unaged conventional UHMWPE and the fact that larger head sizes with thinner polyethylene can now be used, thanks to the independence of the wear rate of highly cross-linked UHMWPEs from femoral head size.[128,179,180] In a clinically

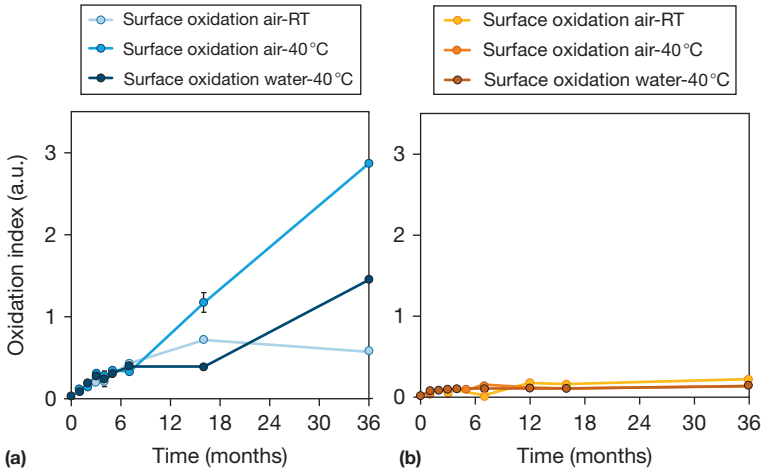

Figure 9 Oxidation levels of radiation cross-linked (unstabilized) (a) and vitamin E-diffused, radiation cross-linked UHMWPEs (b) after real-time aging for 3 years.

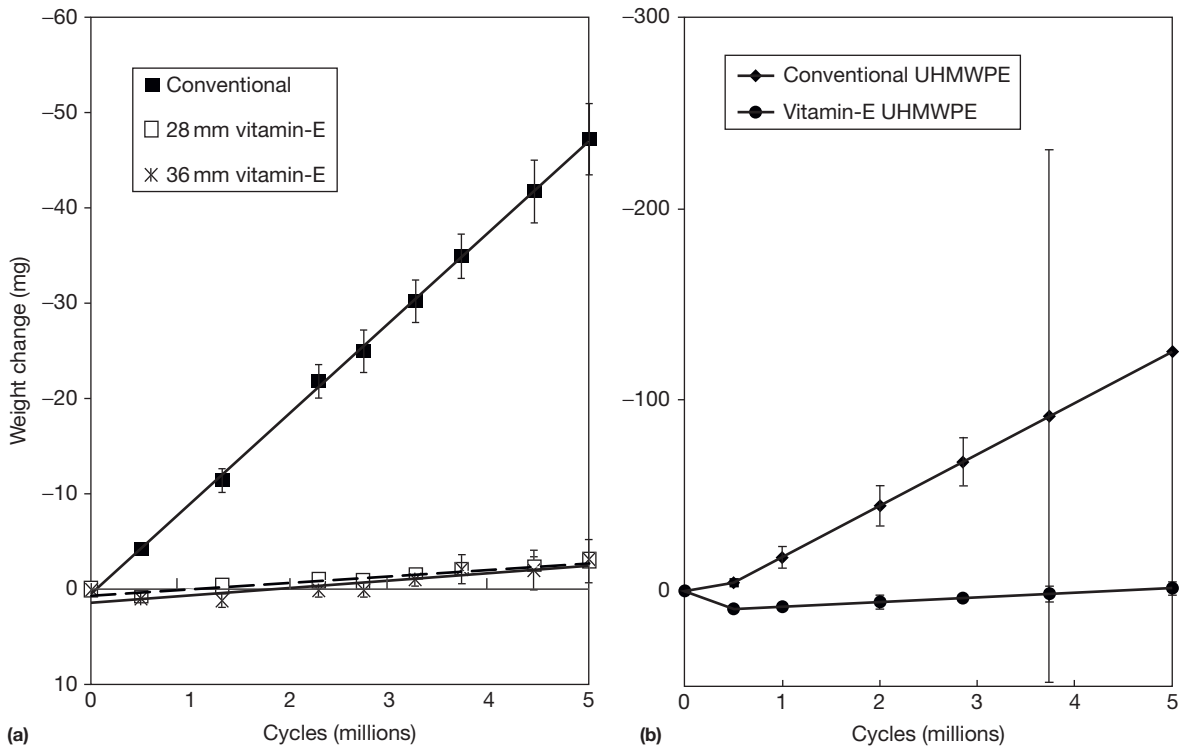

Figure 10 Hip (a) and knee (b) simulator wear data of unaged vitamin E-diffused, radiation cross-linked UHMWPE against conventional, gamma-sterilized UHMWPE in clean serum.

relevant device fatigue test involving the impingement of the rim of thin polyethylene liners by the neck of the femoral components, simulating the adverse case of vertical malpositioning of the implant, 3.7-mm-thick vitamin E-diffused, cross-linked acetabular liners with 28- and 40-mm inner diameter were loaded on the rim by the femoral neck for 2 million cycles. There were no fractures in any of the tested liners, including the conventional UHMWPE liners with 28 mm inner diameter used as controls. No apparent differences between unaged conventional UHMWPE and vitamin E-diffused, highly cross-linked UHMWPE were observed.[178]

6.603.5.6. Peri-Prosthetic Effects

Wear debris of conventional UHMWPE has been clearly associated with osteolysis and loosening of implants.[181,182] Currently, there is no conclusion on the differences in the biological activity of the wear debris from highly cross-linked UHMWPE compared to conventional UHMWPE. While the average particle size of highly cross-linked UHMWPEs appears to be smaller than that of conventional UHMWPE, the number of particles is also significantly lower. In addition, conventional UHMWPE has been associated with high oxidation not observed in irradiated and melted UHMWPE; therefore, the activity of the particles may not be the same.[183] In fact, there is recently one study showing that vitamin E-containing wear particles of uncross-linked UHMWPE reduced the biological response of cells *in vitro* as measured by tumor necrosis factor-α (TNF-α) production.[184] Vitamin E may also have a direct role in regulating immune response when associated with UHMWPE particles on the basis of an *in vitro* study indicating that vitamin E-stabilized unirradiated UHMWPE increased matrix metalloproteinase-9 secretion from granulocytes.[185]

Vitamin E is found in foods such as vegetable oils, nuts, seeds, whole grains, leafy green vegetables, and avocados.[186] The vitamin E commonly used for the stabilization of radiation cross-linked UHMWPE is produced synthetically and is certified to be at least 97% pure α-tocopherol. Both synthetic and natural vitamin E are regarded as safe for human consumption by the Food and Drug Administration as additives in prepared food in accordance with current good manufacturing principles.[187] There are no known adverse effects of the consumption of vitamin E naturally occurring in food. One major concern regarding vitamin E-stabilized UHMWPE involves its possible elution from the polymer *in vivo* and its local/ systemic effects. There was measurable elution of vitamin E from vitamin E-diffused UHMWPE aged in the laboratory in water at 40 °C for 3 years.[177] This was attributed to the surface vitamin E concentration being higher than the saturation concentration of vitamin E in early-phase vitamin E-diffused, irradiated UHMWPE at 40 °C. The concentration profile became uniform at a vitamin E level of ~0.7 wt% at 3 years, suggesting that this was the saturation concentration. Nevertheless, these components did not show any detectable oxidation at 3 years. To quantify the effects of complete elution on the oxidative stability of vitamin E-diffused cross-linked UHMWPE, a clinically irrelevant extraction procedure in boiling hexane was used,[172] after which some vitamin E remained in the samples. These samples were exposed to accelerated aging after extraction and did not

oxidize despite the removal of most of the vitamin E. This suggested that under clinically relevant conditions, the complete removal of vitamin E from the components was highly unlikely and that the components would be protected even under adverse conditions. In addition, currently clinically used components are prepared to have a more uniform concentration at around 0.7 wt% before sterilization, which would minimize the driving force for elution out of the components.

Regarding the peri-prosthetic effects of the elution of vitamin E from irradiated UHMWPE, Wolf *et al.*[188] have determined that there were no cellular cytotoxic or genotoxic effects of vitamin E extracted from a vitamin E-blended and terminally gamma-sterilized UHMWPE containing 0.8 wt% vitamin E *in vitro*. In a study investigating the local toxicity of vitamin E, an emulsifying agent (Tween 80™) was used to solubilize vitamin E in an aqueous solution, in order to simulate the mechanism of vitamin E transport conjugated to lipoproteins. In this study, 2 ml of this emulsion (10 mg of vitamin E) was injected to the knee joints of New Zealand white rabbits and the animals were sacrificed at 2 weeks ($n = 3$) and at 12 weeks ($n = 6$). The control knee was injected with the carrier solution without vitamin E. The findings were that regardless of the time *in situ*, the synovial tissue had a normal appearance at harvest and there were no signs of inflammation or sterile puss. The tissue of all control knees had the same unremarkable appearance.[189]

The effect of vitamin E on the device fixation of vitamin E-diffused, irradiated UHMWPE was investigated in a canine hip model.[189] A comparison between bony ingrowth (using histology) of cups with vitamin E-diffused, irradiated UHMWPE liners ($n = 14$) and irradiated, unstabilized UHMWPE liners ($n = 7$) showed no significant differences between the two groups after 3 months of implantation time.

6.603.5.7. Mechanical and Fatigue Properties

As mentioned above, there is a decrease in mechanical and fatigue strength of irradiated and melted UHMWPEs, caused both by cross-linking and the loss of crystallinity during melting, which quenches the residual free radicals.[105] The loss of crystallinity during postirradiation melting was avoided by doping irradiated UHMWPE with vitamin E.[106,178] Therefore, the ultimate tensile strength, yield strength, and fatigue crack propagation resistance were increased as well. The value for the ultimate tensile strength of 100 kGy irradiated and melted UHMWPE reported in the literature is ~35 MPa;[106] the ultimate tensile strength of vitamin E-diffused, irradiated UHMWPE was measured to be 46 MPa under the same testing conditions.[178]

The fatigue strength of surgical-grade UHMWPE is typically quantified by determining the resistance to fatigue crack propagation by cyclically loading a specimen designed to concentrate stresses at a crack tip (2008). The stress range that needs to be applied to propagate the crack at a rate of 10^{-6} mm per cycle is reported as a measure of the resistance to crack propagation. The values for unirradiated or gamma-sterilized UHMWPE, which has high fatigue resistance in its unaged state, have been reported as 1.4–2.0 MPa $m^{1/2}$.[32,149] In contrast, irradiated and melted highly cross-linked UHMWPEs had values of 0.55–0.69 MPa $m^{1/2}$ depending on the radiation dose.[32,149] The fatigue resistance of vitamin E-diffused, 100-kGy irradiated UHMWPE was 0.70–0.77 MPa $m^{1/2}$.[32,178] Also importantly, the strength of vitamin E-diffused, irradiated UHMWPE remained unchanged when exposed to accelerated aging, while that of conventional, gamma-sterilized UHMWPE deteriorated significantly.[106,178] While conventional UHMWPE has high fatigue strength in its unaged form before exposure to oxygen, its fatigue resistance is severely deteriorated due to oxidation, to as low as 0.19 MPa $m^{1/2}$.[106]

In summary, vitamin E-stabilized, highly cross-linked UHMWPE appears to be equivalent or better than irradiated and melted UHMWPE in terms of wear and oxidation resistance with improved fatigue resistance, as tested *in vitro*. Its clinical performance is yet to be determined.

6.603.6. Other UHMWPEs with Clinical Potential

The future goal of UHMWPE development is to remove the bearing surface material from being the bottleneck in the success and longevity of joint implants. While significant improvements have been made, the material can still be improved to allow for more anatomical designs and ease with more challenging surgery. Also, the average longevity of joint implants still falls short when it comes to a patient with degenerative joint disease requiring a primary joint replacement surgery in his or her 50s or younger age. Therefore, we would like to finally discuss some UHMWPEs that are still in laboratory development but have the potential of improving the outcome of joint surgery from a material perspective.

6.603.6.1. High-Pressure Crystallized UHMWPE with Stabilized Free Radicals

Polyethylene exhibits a hexagonal crystalline phase at elevated temperatures and pressures.[190] In this phase, which is only encountered at pressures in excess of 210 MPa, the individual chain stems are rotated at random phase angles with respect to each other, allowing for chains to slide past each other. The crystalline lamellae formed in this phase are called 'extended chain' crystals (ECC) and these crystals can grow to larger extent and also result in higher crystallinity.[190,191] This is believed to be a consequence of less hindered crystallization kinetics in the hexagonal phase compared with that in the orthorhombic phase.[190,191] High-pressure crystallization (HPC) of unirradiated GUR 1050 UHMWPE at above 160 °C and 300 MPa yielded ~70% crystalline UHMWPE, compared to 50–60% for conventional UHMWPE.[192] An increase in crystallinity of UHMWPE by HPC was shown to increase the resistance of UHMWPE to the propagation of fatigue cracks by about 25%[147] while no significant changes in ultimate tensile strength were observed.[193] Thus, HPC can be an important tool in improving the mechanical strength of wear and oxidation-resistant UHMWPEs.

It is believed that extended chain crystal growth occurs in the hexagonal crystalline phase. The stable hexagonal crystalline phase, as determined by *in situ* thermal analysis experiments, lies above about 210 °C and 340 MPa.[194,195] However, it has been shown that extended chain crystals can be obtained in a 'transitional' hexagonal phase above about 190 °C and

200 MPa.[196] In our studies with uncross-linked UHMWPE (GUR 1050, 6 Mg mol^{-1}), we were able to obtain extended chain crystals and increased crystallinity at 180 °C and 310 MPa.

In 1991, a high-pressure crystallized, gamma-sterilized UHMWPE known as Hylamer™ was marketed by the DePuy-DuPont Orthopaedics joint venture (Newark, DE, USA). Hylamer™ was prepared by hot isostatic pressing UHMWPE, leading to the formation of extended-chain crystallite morphology with thick (200–500 nm) lamellae and high crystallinity (65–71%).[197] Two members of this high-pressure crystallized UHMWPE family prepared by changes in the processing conditions included the Hylamer™ for use in acetabular liners and Hylamer™-M for use in tibial inserts. Because of increased crystallinity, the strength of Hylamer was higher than that of conventional UHMWPE, but its modulus was also increased, leading to increased contact stresses.[1,147] Wear simulation *in vitro* suggested that the wear rate of Hylamer was not significantly affected.[198] In contrast, the *in vivo* wear rates of Hylamer components turned out to be much higher than expected.[199–201] An analysis of the average wear rate, oxidation, and mechanical properties in retrieved Hylamer™ and conventional UHMWPE inserts of the same design[202] showed no statistically significant difference between the linear wear rates of the two materials, while the ultimate tensile strength and elongation to break appeared lower in the Hylamer™ components for a given level of oxidation, leading the authors to conclude that the impact of oxidation may be more detrimental to Hylamer™ than to conventional UHMWPE. This material was discontinued because of unacceptably high revision rates; however, the reason for this *in vivo* change in wear behavior was not clarified. Presumably, the highly crystalline Hylamer was more susceptible to oxidative degradation because it had less amorphous content and therefore, there was a greater percentage of tie molecules broken for a given level of oxidation.

On the basis of this hypothesis, we and others have continued working with HPC of UHMWPE as an alternative method for improving the fatigue strength of cross-linked UHMWPE. Our hypothesis was that if stabilized properly against oxidation, the HPC process could lead to improved strength without sacrifices in structural integrity. One approach was to high pressure crystallize UHMWPE first, and then increase its crystallinity and fatigue resistance.[192,203,204] The highly crystalline UHMWPE was then further irradiated for cross-linking. We found that despite obtaining satisfactory wear resistance with this material, the radiation dose rate had to be controlled to control crystalline population distribution and obtain improved mechanical properties.[205] This cross-linked UHMWPE with improved strength was then doped with vitamin E as described above for non-high-pressure crystallized UHMWPE for oxidative stability.[203]

A second approach was to high pressure crystallize cross-linked UHMWPE to improve its strength.[206,207] A third approach was to high pressure anneal cross-linked UHMWPE.[208] High-pressure annealing utilizes a pressurizing/heating route to the hexagonal phase without melting the irradiated UHMWPE. The mobility induced in the crystalline chains during the phase transformation allowed the recombination and elimination of residual free radicals. The increase in crystallinity and crystal size accompanying the hexagonal phase transformation was negatively correlated to increased cross-link density presumably because of increased cross-linking constraints decreasing the mobility of the chains. Nevertheless, there was a substantial increase in the strength of UHMWPEs cross-linked with 25–65 kGy.

Another idea was to induce mobility in UHMWPE chains during hexagonal phase transformation by using a plasticizer. Our hypothesis tested positive and vitamin E, which we used for this purpose, increased the crystallinity and fatigue strength of the resulting high-pressure crystallized UHMWPE.[26] Interestingly, there was a strong correlation between increased crystallinity and decreased wear for this material. A vitamin E-blended, radiation cross-linked UHMWPE showed significantly lower wear than conventionally cross-linked UHMWPE at similar cross-link density,[209] and it appears that there is a synergy between the presence of vitamin E during high-pressure crystallization and radiation cross-linking thereafter in preparing a crystalline and cross-linked amorphous structure leading to low wear and improved properties.

6.603.6.2. Vitamin E-Blended, Irradiated, and Mechanically Annealed UHMWPE

The mechanical deformation of irradiated UHMWPE followed by annealing below the melting point has been shown to eliminate detectable residual free radicals.[210,211] In addition, mechanical deformation can induce isotropic changes in UHMWPE where the mechanical strength in a preferred direction can be higher because of orientation.[212] Thus, a vitamin E-blended, radiation cross-linked, and mechanically deformed UHMWPE can have high oxidative resistance by two mechanisms: incorporation of vitamin E and decrease in the free radical burden by deformation. It can also have high mechanical properties. If it is used in its mechanically deformed state, these properties will be anisotropic, and if the original shape is recovered through a thermal treatment at the end (**Figure 11**[213]), they will be isotropic.

6.603.6.3. Surface Cross-linked UHMWPE

In uniformly cross-linked UHMWPEs, the mechanical properties are governed by the amount of cross-link density in the material. However, cross-linking is not needed all throughout the implant but at the articular surface. Therefore, it is desirable to limit cross-linking to a thin surface layer on the articular surface of the implant such that a majority of the implant remains at a low cross-link density and its mechanical properties remain unaltered. Surface cross-linking using controlled electron beam penetration has been reported.[214,215] However, this method is not feasible for use with curved surfaces and was not accurately controllable. Assuming a conservative *in vivo* linear femoral head penetration rate into highly cross-linked UHMWPE acetabular liners of 0.05 mm year^{-1},[130,216] it would take 40 years to wear through 2 mm of highly cross-linked UHMWPE surface. Thus, a surface cross-linked layer about 2 mm could be used for long-term wear resistance.

When UHMWPE is irradiated in the presence of vitamin E, its cross-linking is hindered with increasing vitamin E concentration[157] such that increased radiation exposure is necessary for vitamin E-containing UHMWPE to obtain wear resistance

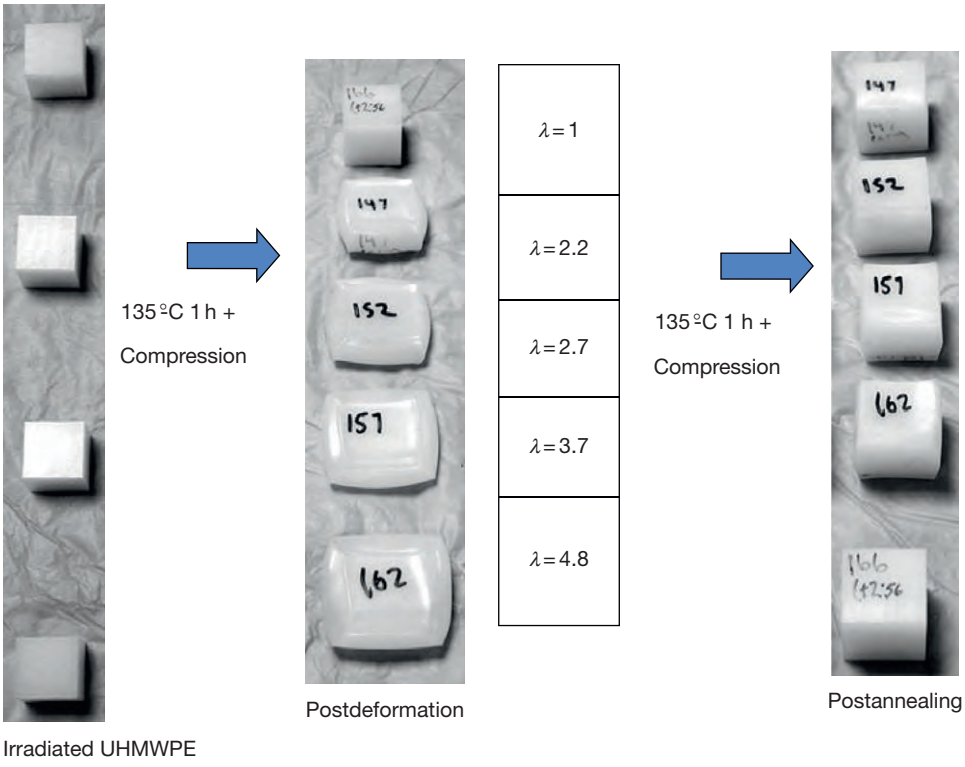

Figure 11 An example of the mechanical annealing process to eliminate residual free radicals.

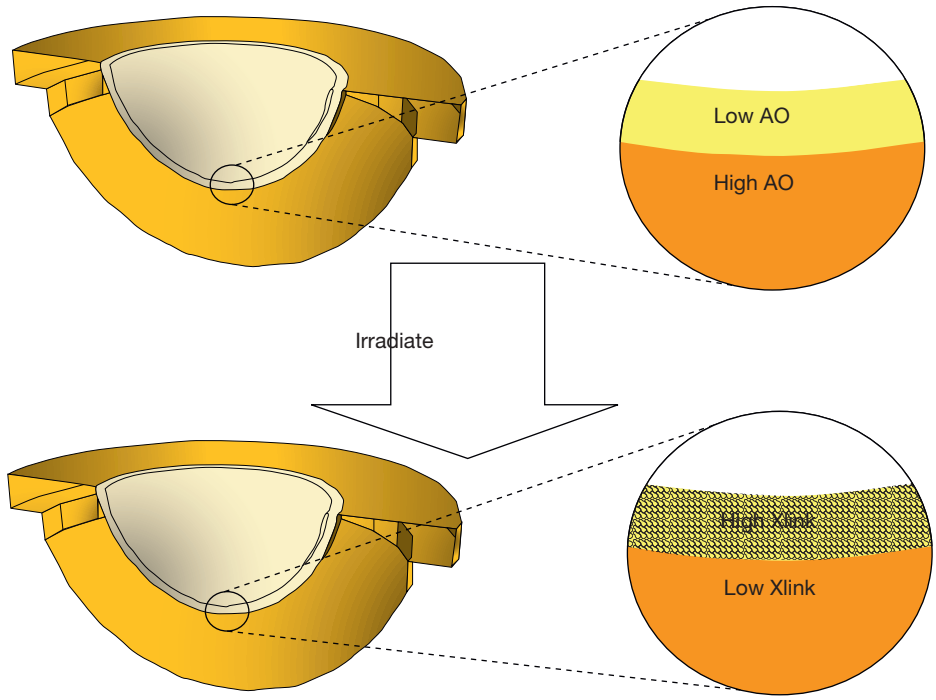

Figure 12 Surface cross-linked UHMWPE using a spatially controlled antioxidant (AO) concentration.

equivalent to that of virgin irradiated UHMWPE.[156,158] The advantage of this result is that cross-link density can be manipulated through spatially controlling vitamin E concentration during irradiation. On the basis of this result, we limited the cross-linking of the implant to the surface by using a low vitamin E concentration on the surface (~0.05 wt%) and a high vitamin E concentration in the bulk (~1 wt%) (Figure 12[217]).

Table 1 Comparison of the mechanical properties of radiation cross-linked UHMWPEs

	UTS (MPa)	*EAB (%)*	*WF (kJ m^{-2})*	*Impact strength (kJ m^{-2})*	*ΔK_i (MPa m$^{1/2}$)*
Conventional (25 kGy)	46 ± 2	376 ± 20	2237 ± 148	93 ± 3	1.19 ± 0.04
First-generation cross-linked (100 kGy + melting)	39 ± 3	225 ± 9	1206 ± 67	60 ± 2	0.54 ± 0.02
Second-generation cross-linked (100 kGy)	43 ± 2	256 ± 17	1240 ± 151	66 ± 2	0.72 ± 0.02
Third-generation surface cross-linked (2wt% + 100 kGy)	56 ± 3	422 ± 11	3091 ± 315	122 ± 1	1.24 ± 0.02

UTS, ultimate tensile strength; EAB, elongation-at-break; WF, work-to-failure; ΔK_i, stress factor range at fatigue crack inception.

This UHMWPE with a spatially controlled vitamin E concentration profile was prepared by either layered molding UHMWPEs with different concentration of vitamin E or by extracting the surface antioxidant from a UHMWPE molded with a uniform concentration of vitamin E. Using either method, we showed that high cross-linking could be achieved on the surface with low cross-link density in the bulk. This led, as expected, to higher overall fatigue strength. In fact, using a 2 wt% vitamin E blend in the bulk with 100 kGy subsequent irradiation resulted in impact strength and fatigue strength comparable to unaged, conventional, gamma-sterilized UHMWPE, virtually eliminating the effects of increasing the wear resistance by cross-linking from the mechanical properties (**Table 1**).

This material is promising as a bearing surface for all joints and can lead to reduced concern about the incidences of fracture of implants under high stresses. Another advantage of improving the fatigue resistance of UHMWPE is the ability to use thinner UHMWPE components, which may have the benefit of preservation of more bone stock and improving dislocation rates in hips by enabling the use of larger femoral heads.

6.603.7. Conclusions and Future Directions

Together with catheterization materials in cardiovascular surgery, UHMWPE is the most widely used biomaterial for long-term implantation. While joint replacement surgery is one of the most successful surgeries today, restoring function and quality of life to patients with debilitating degenerative joint disease, implant longevity is still wanting, especially for high-demand patients such as those with high BMI or young (age <55 years) patients with high activity levels. The development of UHMWPE technology is only one factor affecting clinical outcomes among those such as device design, patient comorbidity, and most notably, surgeon skill. However, the advances in UHMWPE technology are such that the material properties of UHMWPE are no longer the bottleneck in surgical outcome. Therefore, revisions due to UHMWPE-related failure such as particle-induced osteolysis or delamination-related instability are expected to decrease significantly in the coming decade. In the hip, highly cross-linked UHMWPEs have now become the standard-of-care as bearing surfaces.[5] It appears that radiation cross-linking has increased the wear resistance of UHMWPE[107,216] and is likely to decrease the incidence of osteolysis, at least in the first decade.[142] It also appears that using larger head sizes coupled with cross-linked UHMWPE has less of an effect in increasing wear rates than previously observed for conventional UHMWPE.[128,179,180] Combined with the belief that using larger head sizes results in less risk of dislocation,[129] there is a tendency to use thinner cross-linked UHMWPE components. This may increase the risk of adverse occurrences such as rim impingement, edge loading, and rim fracture, especially given the high prevalence of surgical malalignment in the hip (63%[218]). In the knee, the use of cross-linked UHMWPE is less common because of concerns of mechanical failure; therefore, there is still prevalent use of wear and oxidation-prone conventional UHMWPE. Improvements in the mechanical properties of wear-resistant cross-linked UHMWPEs would allow more widespread use of cross-linked UHMWPE[219] and presumably less incidence of wear, delamination, and instability.[135,220,221]

Furthermore, we are attempting to provide successful therapies for joint disease at progressively early stages of the diseases to maintain the health and function of the joint, as well as the quality of life of joint implant patients. Therefore, advance in polyethylene technology is expected to provide more flexibility in implant design such that more anatomical reconstruction of joints can be performed with the least amount of invasive interference.

Finally, the mechanical and tribological properties of UHMWPE favor its use as a bearing material in many joint replacement devices. This chapter has focused on acetabular liners for hip artroplasty and tibial bearings in knee arthroplasties because these comprise the largest number of joint implants and the improvements in bearing technology can be determined statistically in these two joints. However, UHMWPE is also used in buttons to resurface the patella in total knee arthroplasty, in sleeves to permit semiconstrained rotation in elbow and wrist arthroplasty designs, in counterfaces inserted into the glenoid in shoulder arthroplasty, and most recently, in total disc replacement surfaces in the spine. The discussion here is undoubtedly relevant for these devices as well, and developments in polyethylene technology are expected to positively affect the outcomes in these other joints albeit with some time lag.[222]

References

1. Kurtz, S. M.; Muratoglu, O. K.; Evans, M.; Edidin, A. A. *Biomaterials* **1999**, *20*(18), 1659–1688.
2. Smith-Petersen, M. *J. Bone Joint Surg. Br.* **1948**, *30B*(1), 59–75.
3. Charnley, J. *Lancet* **1961**, *1*, 1129–1132.
4. McKee, G.; Watson-Farrar, J. *J. Bone Joint Surg.* **1966**, *48-B*, 245–259.
5. Registry, C. J. R. *Hip and knee replacements in Canada. 2008*. Annual Report; 2008.
6. Kurtz, S.; Mowat, F.; Ong, K.; Chan, N.; Lau, E.; Halpern, M. *J. Bone Joint Surg.* **2005**, *87A*, 1487–1497.
7. Kurtz, S. M.; Ong, K.; Lau, E.; Mowat, F.; Halpern, M. *J. Bone Joint Surg. Br.* **2007**, *89*, 780–785.

8. Bozic, K.; Kurtz, S.; Lau, E.; Ong, K.; Vail, T.; Berry, D. *J. Bone Joint Surg.* **2009**, *91*, 128–133.
9. Kurtz, S., Ed.; In *UHMWPE Biomaterials Handbook*; London: Elsevier, 2009.
10. Gul, R. Ph.D. Thesis. Materials Science and Engineering, Massachusetts Institute of Technology, Cambridge, 1997.
11. Truss, R.; Han, K.; Wallace, J.; Geil, P. *J. Appl. Polym. Sci.* **1981**, *26*, 79–88.
12. deGennes, P. *Scaling Concepts in Polymer Physics*. Corenell University Press: Ithaca, 1979.
13. Doi, M.; Edwards, S. *The Theory of Polymer Dynamics*. Clarendon: Oxford, 1986.
14. Rastogi, S.; Lippits, D.; Peters, G.; Graf, R.; Yao, Y.; Spiess, H. *Nat. Mater.* **2005**, *4*, 635–641.
15. Fu, J.; Ghali, B.; Lozynsky, A.; Oral, E.; Muratoglu, O. *Polymer* **2010**, *51*(12), 2721–2731.
16. Cooper, J.; Dowson, D.; Fisher, J. *Wear* **1993**, *162–164*, 378–384.
17. Charnley, J. *Lancet* **1963**, *2*, 1379.
18. Coughlan, J.; Hug, D. In *Encyclopedia of Polymer Science and Engineering*; Mark, H., Bikales, N., Overberger, C., Menges, G., Kroschwitz, J., Eds.; Wiley: New York, 1986.
19. Kurtz, S. *From Ethylene Gas to UHMWPE Component: The Process of Producing Orthopaedic Implants*. UHMWPE Biomaterials Handbook. Elsevier: New York, 2009; pp 7–19.
20. Currier, B. H.; Currier, J. H.; Collier, J. P.; Mayor, M. B. *J. Biomed. Mat. Res* **2000**, *53*(number 2), 143–151.
21. Han, K.; Wallace, J.; Truss, R.; Geil, P. *J. Macromol. Sci. B Phys.* **1981**, *19*, 313–349.
22. Weightman, B.; Light, D. *Biomaterials* **1985**, *6*(3), 177–183.
23. Goldman, M.; Gronsky, R.; Ranganathan, R.; Pruitt, L. *Polymer* **1996**, *37*(14), 2909–2913.
24. Bellare, A.; Scnabblegger, H.; Cohen, R. *Macromolecules* **1995**, *17*, 2325–2333.
25. Gul, R.; McGarry, F.; Bragdon, C.; Muratoglu, O.; Harris, W. *Biomaterials* **2003**, *24*(19), 3193–3199.
26. Oral, E.; Ghali, B.; Muratoglu, O. In *Transactions of the 55th Annual Meeting of the Orthopaedic Research Society*, Las Vegas, NV, 2009.
27. Willie, B.; Gingell, D.; Bloebaum, R.; Hofmann, A. *J. Biomed. Mater. Res.* **2000**, *52*(3), 558–566.
28. Blunn, G. W.; Joshi, A. B.; Minns, R. J.; *et al. J. Arthroplasty* **1997**, *12*(3), 281–290.
29. Landy, M. M.; Walker, P. S. *J. Arthroplasty* **1988**, *3*(Suppl), S73–S85.
30. Sutula, L.; Collier, J.; Saum, K.; *et al. Clin. Orthop.* **1995**, *319*, 28–40.
31. Wright, T. M.; Astion, D. J.; Bansal, M.; Rimnac, C. M.; Insall, J. N.; Robinson, R. P. *J. Bone Joint Surg.* **1988**, *70A*, 926–932.
32. Oral, E.; Wannomae, K. K.; Hawkins, N. E.; Harris, W. H.; Muratoglu, O. K. *Biomaterials* **2004**, *25*(24), 5515–5522.
33. Premnath, V.; Harris, W.; Jasty, M.; Merrill, E. *Biomaterials* **1996**, *17*, 1741–1753.
34. Kurtz, S. M.; Hozack, W. J.; Purtill, J. J.; *et al. Clin. Orthop. Relat. Res.* **2006**, *453*, 47–57.
35. McKellop, H.; Shen, F.-W.; Lu, B.; Campbell, P.; Salovey, R. *J. Orthop. Res.* **1999**, *17*(2), 157–167.
36. Muratoglu, O. K.; Bragdon, C. R.; O'Connor, D. O.; *et al. Biomaterials* **1999**, *20*(16), 1463–1470.
37. Muratoglu, O. K.; Bragdon, C. R.; O'Connor, D. O.; *et al. Biomaterials* **2003**, *24*, 1527.
38. Sun, D.; Stark, C.; Dumbleton, J. *Development of an accelerated aging method for evaluation of long-term irradiation effects on UHMWPE Implants*. Meeting of American Chemical Society: Washington, DC, Division of Polymer Chemistry, 1994.
39. Sanford, W.; Saum, K. In *Transactions of the XXth Meeting of the Orthopaedic Research Society*, 1995; p 119.
40. ASTM, *Standard Guide for Evaluating the Extent of Oxidation in Ultra-high-mocular-weight polyethylene Fabricated Forms Intended for Surgical Implants*, ASTM International: West Conshohocken, PA, 2001; pp 1–4.
41. Goldman, M.; Lee, M.; Gronsky, R.; Pruitt, L. *J. Biomed. Mater. Res.* **1997**, *37*, 43–50.
42. Oral, E.; Rowell, S.; Muratoglu, O. *Biomaterials* **2006**, *27*, 5580–5587.
43. Rowell, S.; Oral, E.; Muratoglu, O. *J. Orthop. Res.* **2010**, 1–8.
44. Nabar, S.; Wannomae, K.; Muratoglu, O. In *Transactions of the 54th Annual Meeting of the Orthopaedic Research Society*, San Francisco, CA, 2008.
45. Rimnac, C. M.; Klein, R. W.; Burstein, A. H.; Wright, T.; Santner, T. In *40th Annual Meeting, Orthopaedic Reseach Society*, New Orleans, LA, 1994.
46. Oral, E.; Ghali, B.; Rowell, S.; Micheli, B.; Muratoglu, O. *Biomaterials* **2010**, *31*, 7051–7060.
47. Brach del Prever, E.; Crova, M.; Costa, L.; Dallera, A.; Camino, G.; Gallinaro, P. *Biomaterials* **1996**, *17*, 873–878.
48. Costa, L.; Luda, M. P.; Trossarelli, L.; Brach del Prever, E. M.; Crova, M.; Gallinaro, P. *Biomaterials* **1998**, *19*, 1371–1385.
49. Kurtz, S. M.; Muratoglu, O. K.; Gsell, R.; *et al. J. Biomed. Mater. Res. Appl. Biomater.* **2002**, *63*(1), 15–23.
50. Atkinson, J. R.; Cicek, R. Z. *Biomaterials* **1983**, *4*, 267–275.
51. Atkinson, J. R.; Cicek, R. Z. *Biomaterials* **1984**, *5*, 326–335.
52. Wroblewski, B.; Siney, P.; Fleming, P. *J. Bone Joint Surg.* **1999**, *81B*, 54–55.
53. Oonishi, H.; Clarke, I. C.; Yamamoto, K.; Masaoka, T.; Fujisawa, A.; Masuda, S. *J. Biomed. Mater. Res. A* **2004**, , *68*, 52–60.
54. Oonishi, H.; Kadoya, Y.; Masuda, S. *J. Biomed. Mat. Res.* **2001**, *58*(2), 167–171.
55. Oonishi, H.; Takayama, Y. In *The 17th Annual Meeting of the Society for Biomaterials*, Scottsdale, AZ, 1991.
56. Oonishi, H.; Takayama, Y.; Tsuji, E. *Radiat. Phys. Chem.* **1992**, *39*(6), 495–504.
57. Oonishi, H.; Takayama, Y.; Tsuji, E. *Marcel Dekker* **1995**, *2*, 1853–1868.
58. Shikita, T.; Oonishi, H.; Hashimoto, Y.; *et al.* In *Transactions of the 3rd Annual Meeting of the Society for Biomaterials*, 1977; Vol. 3, p 118.
59. Oonishi, H.; Kim, S.; Takao, Y.; Kyomoto, M.; Iwamoto, M.; Ueno, M. *J. Arthroplasty* **2006**, *21*(7), 944–949.
60. Grobbelaar, C. J.; DuPlessis, T. A.; Marais, F. *J. Bone Joint Surg.* **1978**, *60-B*(3), 370–374.
61. Atkinson, J. R.; Dowling, J. M.; Cicek, R. Z. *Biomaterials* **1980**, *1*, 89–96.
62. Bragdon, C.; O'Connor, D.; Lowenstein, J.; Jasty, M.; Syniuta, W. *Proc. Inst. Mech. Eng. H* **1996**, *210*, 157–165.
63. Liao, Y.-S.; Benya, P.; McKellop, H. *J. Biomed. Mater. Res.* **1999**, *48*(4), 465–473.
64. Saikko, V.; Ahlroos, T. *J. Biomed. Mater. Res.* **2000**, *49*(2), 147–154.
65. Wang, A. *WEAR* **2001**, *248*, 38–47.
66. Wang, A.; Essner, A.; Polineni, V.; Stark, C.; Dumbleton, J. H. *Tribol. Int.* **1998**, *31*, 17–33.
67. Wroblewski, B. M.; Siney, P. D.; Dowson, D.; Collins, S. N. *J. Bone Joint Surg.* **1996**, *78B*, 280–285.
68. Wroblewski, B.; Siney, P.; Fleming, P. *J. Bone Joint Surg. Br.* **2005**, *87B*, 1220–1221.
69. Muratoglu, O. K.; Bragdon, C. R.; O'Connor, D. O.; Jasty, M.; Harris, W. H. *J. Arthroplasty* **2001**, *16*(2), 149–160.
70. Jasty, M. J.; Goetz, D. D.; Lee, K. R.; Hanson, A. E.; Elder, J. R.; Harris, W. H. *J. Bone Joint Surg.* **1997**, *79A*, 349–358.
71. Bragdon, C. R.; O'Connor, D. O.; Lowenstein, J. D.; Jasty, M.; Syniuta, W. D. *Proc Instn Mech Engrs* **1995**, *210*, 157–165.
72. Wang, A.; Stark, C.; Dumbleton, J. H. *Eng. Med.* **1996**, *210*(3), 141–155.
73. Carlsson, D.; Chmela, S.; Lacoste, J. *Macromolecules* **1990**, *23*, 4934–4938.
74. Charlesby, A.; Libby, D.; Ormerod, M. *Proc. R. Soc. Lond.* **1961**, *A262*(130), 207.
75. Libby, D.; Ormerod, M.; Charlesby, A. *Polymer* **1960**, *1*, 212–218.
76. Ohnishi, S.; Sugimoto, S.; Nitta, I. *J. Chem. Phys.* **1962**, *37*, 1283–1288.
77. Lawton, E.; Balwit, J.; Powell, R. *J. Chem. Phys.* **1960**, *33*(2), 405–412.
78. Dole, M. *Free Radicals in Irradiated Polyethylene. The Radiation Chemistry of Macromolecules*, Academic Press: New York, 1972; pp 335–348.
79. Bhateja, S.; Duerst, R.; Aus, E.; Andrews, E. *J. Macromol. Sci. B Phys.* **1995**, *34*(3), 263–272.
80. Keller, A.; Ungar, G. *J. Phys. Chem.* **1983**, *22*(1/2), 155–181.
81. Peacock, A. J. *Handbook of Polyethylene*. Marcel Dekker: New York, 2000.
82. Jahan, M. S.; King, M. C.; Haggard, W. O.; Sevo, K. L.; Parr, J. E. *Radiat. Phys. Chem.* **2001**, *62*, 141–144.
83. Ohnishi, S.; Sugimoto, S.; Nitta, I. *J. Polym. Sci., A: Polym. Chem.* **1963**, *1*, 605–623.
84. Seguchi, T.; Tamura, N. *J. Phys. Chem.* **1973**, *77*(1), 40–44.
85. Carlsson, D.; Dobbin, C.; Wiles, D. *Macromolecules* **1985**, *18*, 2092–2094.
86. Kuzuya, M.; Kondo, S.; Sugito, M.; Yamashiro, T. *Macromolecules* **1998**, *31*, 3230–3234.
87. Al-Malaika, S. In *Atmospheric Oxidation and Antioxidants*; Scott, G., Ed.; Elsevier: Amsterdam, 1993; pp 45–82.
88. Rabek, J.; Ranby, B. *Photochemical Oxidation Reactions of Synthetic Polymers. ESR Applications to Polymer Research*. Almqvist-Wiksell Forlag AB: Stockholm, 1973.
89. Costa, L.; Luda, M. P.; Trossarelli, L. *Polym. Degrad. Stab.* **1997**, *55*, 329–338.
90. Costa, L.; Luda, M. P.; Trossarelli, L. *Polym. Degrad. Stab.* **1997**, *58*, 41–54.
91. Costa, L.; Luda, M. P.; Trossarelli, L.; Brach del Prever, E. M.; Crova, M.; Gallinaro, P. *Biomaterials* **1998**, *19*, 659–668.
92. Al-Malaika, S. *Adv. Polym. Sci.* **2004**, *169*, 121–150.

93. Assink, R.; Celina, M.; Dunbar, T.; Alam, T.; Clough, R.; Gillen, K. *Macromolecules* **2000**, *33*, 4023–4029.
94. Collier, J.; Sutula, L.; Currier, B.; *et al*. *Clin. Orthop.* **1996**, *333*, 76–86.
95. Costa, L.; Jacobson, K.; Bracco, P.; Brach del Prever, E. M. *Biomaterials* **2002**, *23*, 1613–1624.
96. Kurtz, S.; Hozack, W. J.; Marcolongo, M.; Turner, J.; Rimnac, C. M.; Edidin, A. *J. Arthroplasty* **2003**, *18*(7 Supp. 1), 68–78.
97. Kurtz, S. *Compendium of Highly Crosslinked UHMWPEs*. UHMWPE Biomaterials Handbook. Elsevier: New York, 2009; pp 291–308.
98. Ries, M.; Pruitt, L. *Clin. Orthop. Relat. Res.* **2005**, *440*, 149–156.
99. Essner, A.; Schmidig, G.; Herrera, L.; *et al*. In *Transactions of the 51st Annual Meeting of the Orthopaedic Research Society*, Washington, DC, 2005.
100. Currier, B. H.; Currier, J. H.; Mayor, M. B.; Lyford, K.; Collier, J. P.; Van Citters, D. W. *J. Bone Joint Surg.* **2007**, *89A*, 2023–2029.
101. Kurtz, S.; Austin, M.; Azzam, K.; *et al*. *J. Arthroplasty* **2010**, *25*(4), 614–625.
102. Wannomae, K.; Bhattacharyya, S.; Freiberg, A.; Estok, D.; Harris, W.; Muratoglu, O. *J. Arthroplasty* **2006**, *21*(7), 1005–1011.
103. Martell, J. M.; Verner, J. J.; Incavo, S. J. *J. Arthroplasty* **2003**, *18*(7 Suppl. 1), 9.
104. Rohrl, S.; Li, M.; Nilsson, K.; Nivbrant, B. *Acta Orthop.* **2007**, *78*(6), 739–745.
105. Muratoglu, O. K.; Merrill, E. W.; Bragdon, C. R.; *et al*. *Clin. Orthop. Relat. Res.* **2003**, *417*, 253–262.
106. Oral, E.; Malhi, A.; Muratoglu, O. *Biomaterials* **2006**, *27*, 917–925.
107. Digas, G.; Karrholm, J.; Thanner, J.; Herberts, P. In *53rd Annual Meeting of The Orthopaedic Society*, San Diego, CA, 2007.
108. Birman, M.; Noble, P.; Conditt, M.; Li, S.; Mathis, K. *J. Arthroplasty* **2005**, *20*(7), 87–92.
109. Halley, D.; Glassman, A.; Crowninshield, R. *J. Bone Joint Surg.* **2004**, *86A*(4), 827–830.
110. Tower, S. S.; Currier, J. H.; Currier, B. H.; Lyford, K. A.; Van Citters, D. W.; Mayor, M. B. *J. Bone Joint Surg. Am.* **2007**, *89*(10), 2212–2217.
111. Horii, F.; Zhu, Q.; Kitamaru, R.; Yamaoka, H. *Macromolecules* **1990**, *23*, 977–981.
112. Edidin, A. A.; Pruitt, L.; Jewett, C. W.; Crane, D. J.; Roberts, D.; Kurtz, S. M. *J. Arthroplasty* **1999**, *14*(5), 616–627.
113. Bergstrom, J. S.; Rimnac, C. M.; Kurtz, S. M. *J. Orthop. Res.* **2005**, *23*, 367–375.
114. Bradford, L.; Baker, D.; Ries, M. D.; Pruitt, L. A. *Clin. Orthop.* **2004**, *429*, 68–72.
115. Kurtz, S. M.; Rimnac, C. M.; Pruitt, L.; Jewett, C. W.; Goldberg, V.; Edidin, A. A. *Biomaterials* **2000**, *21*, 283–291.
116. Dumbleton, J.; Miller, D.; Miller, E. *Wear* **1972**, *20*, 165.
117. Scales, J.; Kelly, P.; Goddard, D. *Ann. Rheum. Dis.* **1969**, *28*(Suppl.), 30–35.
118. Shaw, J. A.; Murray, D. G. *Clin. Orthop.* **1973**, *94*, 15–23.
119. Walker, P.; Blunn, G.; Broome, D.; *et al*. *J. Biomech.* **1997**, *30*(1), 83–89.
120. Bergmann, G.; Graichen, F.; Rohlmann, A. *J. Biomech.* **1993**, *26*(8), 969–990.
121. Johnston, R. C.; Schmidt, G. L. *J Bone Joint Surg. Am.* **1969**, *51*(A), 1083.
122. Paul, J. P. *Proc. Inst. Mech. Eng.* **1966**, *181*(Pt 3F), 8–15.
123. Ramamurti, B.; Bragdon, C.; O'Connor, D.; *et al*. *J. Arthroplasty* **1996**, *11*, 845–852.
124. Ramamurti, B. S.; Estok, D. M.; Jasty, M.; Harris, W. H. *J. Orthop. Res.* **1998**, *16*(3), 365–369.
125. Muratoglu, O.; Oral, E.; Burroughs, B.; *et al*. In *Transactions of the 51st Annual Meeting of the Orthopaedic Research Society*, Washington, DC, 2005.
126. Haider, H. *Tribological assessment of UHMWPE in the knee*, UHMWPE Biomaterials Handbook. Kurtz S. New York: Elsevier, 2009; pp 381–408.
127. Endo, M.; Tipper, J.; Barton, D.; Stone, M.; Ingham, E.; Fisher, J. *Proc. Inst. Mech. Eng., H: J. Eng. Med.* **2002**, *216*(2), 111–122.
128. Muratoglu, O. K.; Bragdon, C. R.; O'Connor, D. O.; *et al*. *J. Arthroplasty* **2001**, *16*(8 suppl.), 24–30.
129. Cuckler, J.; Moore, K.; Lombardi, A., Jr.; McPherson, E.; Emerson, R. *Jounal Arthroplasty* **2004**, *19*(8 Suppl. 3), 41–44.
130. Digas, G.; Karrholm, J.; Thanner, J.; Herberts, P. *Acta Orthop.* **2007**, *78*(6), 746–754.
131. Engh, C., Jr.; Stepniewski, A.; Ginn, S.; *et al*. *J. Arthroplasty* **2006**, *21*(6-Suppl. 2), 17–25.
132. Garcia-Rey, E.; Garcia-Cimbrelo, E.; Cruz-Pardos, A.; Ortega-Chamarro, J. *J. Bone Joint Surg. Br.* **2008**, *90B*(2), 149–153.
133. Asano, T.; Akagi, M.; Clarke, I. C.; Masuda, S.; Ishii, T.; Nakamura, T. *J. Biomed. Mater. Res. B Appl. Biomater.* **2007**, *83*(2), 615–622.
134. Johnson, T.; Laurent, M.; Yao, J.; Blanchard, C. R. *Wear* **2003**, *255*, 1107–1112.
135. Muratoglu, O.; Mark, A.; Vittetoe, D.; Harris, W.; Rubash, H. *J. Bone Joint Surg.* **2003**, *85-A*(Suppl. 1), 7–13.
136. Muratoglu, O. K.; Bragdon, C. R.; O'Connor, D. O.; Perinchief, R.; Jasty, M.; Harris, W. H. *Clin. Orthop.* **2002**, *404*, 89–95.
137. Muratoglu, O. K.; Greenbaum, E.; Bragdon, C.; Jasty, M.; Freiberg, A.; Harris, W. H. *J. Arthroplasty* **2004**, *19*(1), 68–77.
138. Muratoglu, O. K.; Rubash, H. E.; Bragdon, C. R.; Burroughs, B. R.; Huang, A.; Harris, W. H. *J. Arthroplasty* **2007**, *22*(3), 435–444.
139. Muratoglu, O. K.; Bragdon, C. R.; Jasty, M.; O'Connor, D. O.; Von Knoch, R.; Harris, W. H. *J. Arthroplasty* **2004**, *19*(7), 887–897.
140. Muratoglu, O. K.; Burroughs, B. R.; Christensen, S. D.; Lozynsky, A. J.; Harris, W. H. In *Proceedings of 50th Orthopaedic Research Society*, San Francisco, CA, 2004.
141. Muratoglu, O. K.; Ruberti, J.; Melotti, S.; Spiegelberg, S.; Greenbaum, E.; Harris, W. H. *J. Arthroplasty* **2003**, *18*(7, Suppl. 1), 42–47.
142. Hodrick, J.; Severson, E.; McAlister, D.; Dahl, B.; Hofmann, A. *Clin. Orthop. Relat. Res.* **2008**, *466*, 2806–2812.
143. Sathasivam, S.; Walker, P. *J. Orthop. Res.* **1998**, *16*, 564–571.
144. Bartel, D. L.; Bicknell, V. L.; Wright, T. M. *J. Bone Joint Surg. Am.* **1986**, *68*(7), 1041–1051.
145. Bartel, D. L.; Rawlinson, J. J.; Burstein, A. H.; Ranawat, C. S.; Flynn, W. F. *Clin. Orthop. Rel. Res.* **1995**, *317*, 76–82.
146. ASTM E647-08, *Standard Test Method for Measurement of Fatigue Crack Growth Rates*. ASTM International: West Conshohocken, PA, 2008.
147. Baker, D. A.; Hastings, R. S.; Pruitt, L. *Polymer* **2000**, *41*(2), 795–808.
148. Pruitt, L. A. *Biomaterials* **2005**, *26*(8), 15.
149. Baker, D. A.; Bellare, A.; Pruitt, L. *J. Biomed. Mater. Res. A* **2003**, *66*, 146–154.
150. Plank, G.; Estok, D.; Muratoglu, O.; O'Connor, D.; Burroughs, B.; Harris, W. *J. Biomed. Mater. Res.* **2007**, *80B*, 1–10.
151. Leung, S. B.; Egawa, H.; Stepniewski, A.; Beykirch, S.; Engh, C. A., Jr.; Engh, C. A., Sr. *J. Arthroplasty* **2007**, *22*(6, Suppl. 2), 134–139.
152. Wang, A.; Zeng, H.; Yau, S.-S.; Essner, A.; Manely, M.; Dumbleton, J. *J. Phys. D Appl. Phys.* **2006**, *39*, 3213–3219.
153. Dumbleton, J.; D'Antonio, J.; Manley, M.; Capello, W.; Wang, A. *Clin. Ortho. Rel. Res.* **2006**, *453*, 265–271.
154. Bracco, P.; Brunella, V.; Zanetti, M.; Luda, M. P.; Costa, L. *Polym. Degrad. Stab.* **2007**, *92*, 2155–2162.
155. Kurtz, S.; Dumbleton, J.; Siskey, R.; Wang, A.; Manley, M. *J. Biomed. Mater. Res.* **2008**, *90A*, 549–563.
156. Oral, E.; Greenbaum, E. S.; Malhi, A. S.; Harris, W. H.; Muratoglu, O. K. *Biomaterials* **2005**, *26*(33), 6657–6663.
157. Parth, M.; Aust, N.; Lederer, K. *J. Mater. Sci. Mater. Med.* **2002**, *13*(10), 917–921.
158. Oral, E.; Godleski Beckos, C.; Malhi, A.; Muratoglu, O. *Biomaterials* **2008**, *29*, 3557–3560.
159. Lerf, R.; Zurbrugg, D.; Delfosse, D. *Biomaterials* **2010**, *31*, 3643–3648.
160. Mathys I. From http://www.efort.org/communications/Press%20Releases%20Industry%20for%20Media%20page/Mathys/EFORT%202010_vitamys.pdf.
161. Biomet, Inc. Biomet and Massachusetts General Hospital form strategic research alliance for REGENEREX™ AND E-POLY™ Technologies. Available at http://www.biomet.com/news/getFile.cfm?id=28&rt=inline&type=pr
162. Packer, L. *Am. J. Clin. Nutr.* **1991**, *53*, 1050S–1055S.
163. Packer, L.; Kagan, V. E. In *Vitamin E in Health and Disease*; Fuchs, J., Packer, L., Eds.; Marcel Dekker, Inc.,: New York, 1993; pp 179–192.
164. Burton, G.; Ingold, K. *J. Am. Chem. Soc.* **1981**, *103*, 6472–6477.
165. Burton, G. W.; Traber, M. G. *Annu. Rev. Nutr.* **1990**, *10*, 357–382.
166. Kamal-Eldin, A.; Appelqvist, L. *Lipids* **1996**, *31*(7), 671–701.
167. Esterbauer, H.; Gebicki, J.; Puhl, H.; Jurgens, G. *Free Radic. Biol. Med.* **1992**, *13*, 341–390.
168. Scott, G. In *Atmospheric Oxidation and Antioxidants*; Scott, G., Ed.; Elsevier: Amsterdam, 1993; pp 121–160.
169. Oral, E.; Wannomae, K.; Muratoglu, O. In *Transactions of the 51st Annual Meeting of the Orthopaedic Research Society*, Washington, DC, 2005.
170. Oral, E.; Godleski, C.; Muratoglu, O. In *Transactions of the 53rd Annual Meeting of the Orthopaedic Research Society*, San Diego, CA, 2007.
171. Wolf, C.; Maninger, J.; Lederer, K.; Fruhwirth-Smounig, H.; Gamse, T.; Marr, R. *J. Mater. Sci. Mater. Med.* **2006**, *17*, 1323–1331.
172. Oral, E.; Rowell, S.; Muratoglu, O. In *Transactions of the 52nd Annual Meeting of the Orthopaedic Research Society*. Chicago, IL, 2006.
173. Carlsson, D. J.; Brousseau, R.; Zhang, C.; Wiles, D. M. *Polym. Degrad. Stab.* **1987**, *17*, 303–318.
174. Costa, L.; Bracco, P.; Carpentieri, I.; Brunella, V.; Brach del Prever, E. In *Transactions of the 55th Annual Meeting of the Orthopaedic Research Society*, Las Vegas, NV, 2009.

175. Mallegol, J.; Carlsson, D.; Deschenes, L. *Nucl. Instrum. Meth. Phys. Res. B* **2001**, *185*, 283–293.
176. Yamamoto, K.; Yamaguchi, M.; Tani, M.; *et al*. *Appl. Phys. Lett.* **2004**, *85*(22), 5194–5196.
177. Rowell, S.; Oral, E.; Muratoglu, O. In *Transactions of the 55th Annual Meeting of the Orthopaedic Research Society*, Las Vegas, NV, 2009.
178. Oral, E.; Christensen, S.; Malhi, A.; Wannomae, K.; Muratoglu, O. *J. Arthroplasty* **2006**, *21*(4), 580–591.
179. D'Lima, D.; Hermida, J.; Chen, P.; Colwell, C. E., Jr. *Effect of Head Size & Crosslinking on Wear in Polyethylene Acetabular Components*. Joint Mechanics Laboratory Scripps Clinic: CA, 2001.
180. Livermore, J.; Ilstrup, D.; Morrey, B. *J. Bone Joint Surg.* **1990**, *72-A*, 518–528.
181. Ingham, E.; Fisher, J. *Proc. Instn. Mech. Engrs.* **2000**, *21*(H1), 21–37.
182. Sochart, D. H. *Clin. Orthop. Relat. Res.* **1999**, *363*, 135–150.
183. Costa, L.; Bracco, P.; Brach Del Prever, E. *Interact. Surg.* **2007**, *2*(3–4), 169–173.
184. Teramura, S.; Russell, S.; Ingham, E.; *et al*. In *Transactions of the 55th Annual Meeting of the Orthopaedic Research Society*, Las Vegas, NV, 2009.
185. Reno, F.; Bracco, P.; Lombardi, F.; Boccafoschi, F.; Costa, L.; Cannas, M. *Biomaterials* **2004**, *25*(6), 1001.
186. Sheppard, A. J.; Pennington, J. A.; Weihrauch, J. L. In *Vitamin E in Health and Disease*; Packer, L., Fuchs, J., Eds.; Marcel Dekker Inc: New York, 1993; pp 9–31.
187. FDA DoHaHS. Code of Federal Regulations 184. 1890: Direct Food Substances Affirmed as Generally Recognized as.Safe-[alpha]-tocopherols, 2004; Vol. 3(21), revised April 1.
188. Wolf, C.; Lederer, K.; Muller, U. *J. Mater. Sci. Mater. Med.* **2002**, *13*, 701–703.
189. Jarrett, B.; Cofske, J.; Rosenberg, A.; Oral, E.; Muratoglu, O.; Malchau, H. *J. Bone Joint Surg.* **2010**, *92*, 2672–2681.
190. Bassett, D. C.; Block, S.; Piermarini, G. *J. Appl. Phys.* **1974**, *45*, 4145.
191. Wunderlich, B.; Davidson, T. *J. Polym. Sci. A 2 Polym. Phys.* **1969**, *7*(12), 2043–2050.
192. Turell, M. E.; Schetter, P.; Bellare, A.; Thornhill, T. S. In *Transactions of the Annual Meeting of the Orthopedic Research Society*. New Orleans, LA, 2003; p 1409.
193. Bistolfi, A.; Turell, M. E.; Lee, Y.-L.; Bellare, A. In *Transactions of the 51st Annual Meeting of the Orthopaedic Research Society*, 2005; p 240.
194. Bassett, D.; Turner, B. *Nat. Phys. Sci.* **1972**, *240*, 146–148.
195. Kurelec, L.; Rastogi, S.; Meier, R.; Lemstra, P. *Macromolecules* **2000**, *33*, 5593–5601.
196. Maeda, Y.; Kanetsuna, H. *J. Polym. ScienceB Polym. Phys.* **1974**, *12*(12), 2551–2565.
197. Bellare, A.; Sun, D. C. In *24th Annual Meeting of the Society for Biomaterials*, San Diego, CA, 1998.
198. McKellop, H.; Lu, B.; Li, S. *Orthop. Res. Soc.* **1992**; *17*, 356.
199. Chmell, M.; Poss, R.; Thomas, W.; Sledge, C. *J. Arthroplasty* **1996**, *11*, 351–353.
200. Livingston, B. J.; Chmell, M. J.; Spector, M.; Poss, R. *J. Bone Joint Surg.* **1997**, *79A*(10), 1529–1538.
201. Wroblewski, B. M.; Siney, P. D.; Fleming, P. A. *J. Bone Joint Surg. Br.* **2003**, *85*(3), 376–379.
202. Collier, J.; Bargmann, L.; Currier, B.; Mayor, M.; Currier, J.; Bargmann, B. *Orthopaedics* **1998**, *21*(8), 865–871.
203. Oral, E.; Wannome, K.; Christensen, S.; Muratoglu, O. In *Transactions of the 51st Annual Meeting of the Orthopaedic Research Society*, Washington, DC, 2005.
204. Turell, M.; Bellare, A. *Biomaterials* **2004**, *25*, 3389–3398.
205. Oral, E.; Wannomae, K. K.; Rowell, S. L.; Muratoglu, O. K. *Biomaterials* **2007**, *28*(35), 5225–5237.
206. Oral, E.; Godleski Beckos, C.; Lozynsky, A.; Malhi, A.; Muratoglu, O. *Biomaterials* **2009**, *30*, 1870–1880.
207. Simis, K. S.; Bistolfi, A.; Bellare, A.; Pruitt, L. A. *Biomaterials* **2006**, *27*(9), 1688–1694.
208. Oral, E.; Godleski Beckos, C.; Muratoglu, O. *Polymer* **2008**, *49*, 4733–4739.
209. Oral, E.; Godleski Beckos, C.; Ghali, B.; Lozynsky, A.; Muratoglu, O. *J. Biomed. Mater. Res. B* **2009**, *90B*(2), 720–729.
210. Malhi, A.; Wannomae, K.; Christensen, S.; Godleski, C.; Muratoglu, O. In *Transactions of the 52nd Annual Meeting of the Orthopaedic Research Society*, Chicago, IL, 2006.
211. Muratoglu, O. K.; Wannomae, K.; Christensen, S.; Rubash, H. E.; Harris, W. H. *Clin. Orthop. Relat. Res.* **2005**, *438*, 158–164.
212. Kurtz, S. M.; Mazzucco, D.; Rimnac, C. M.; Schroeder, D. *Biomaterials* **2006**, *27*(1), 24–34.
213. Wannomae, K.; Micheli, B.; Lozynsky, A.; Muratoglu, O. In *Transactions of the 56th Annual Meeting of the Orthopaedic Research Society*, New Orleans, NV, 2010.
214. McKellop, H.; Shen, F. In *Transactions of the 46th Annual Meeting of the Orthopaedic Research Society*, Orlando, FL, 2000.
215. Muratoglu, O. K.; O'Connor, D. O.; Bragdon, C. R.; *et al*. *Biomaterials* **2002**, *23*, 717–724.
216. Manning, D. W.; Chiang, P. P.; Martell, J. M.; Galante, J. O.; Harris, W. H. *J. Arthroplasty* **2005**, *20*(7), 880–886.
217. Oral, E.; Ghali, B.; Muratoglu, O. In *Transactions of the 56th Annual Meeting of the Orthopaedic Research Society*, New Orleans, LA, 2010.
218. Malchau, H.; Bragdon, C.; Rubash, H.; Zurakowski, D.; Callanan, M. In *Proceedings of the Annual Meeting of the American Academy of Orthopaedic Surgeons*, New Orleans, LA, AAOS, 2010.
219. Jacofsky, D. *J. Arthroplasty* **2008**, *23*(7, Suppl. 1), 28–30.
220. Colizza, W. A.; Insall, J. N.; Scuderi, G. R. *J. Bone Joint Surg.* **1995**, *77*(11), 1713–1720.
221. Wright, T. M.; Bartel, D. L. *Clin. Orthop. Rel. Res.* **1986**, *205*, 67–74.
222. Ticona. Retrieved August 5, 2010, from http://ticona.com/home/products/uhmw-pe/gur_uhmw-pe__premium.htm.

6.604. Ceramic Prostheses: Clinical Results Worldwide

A F Kamath, G-C Lee, and J P Garino, University of Pennsylvania, Philadelphia, PA, USA

© 2011 Elsevier Ltd. All rights reserved.

6.604.1.	Introduction	51
6.604.2.	History	52
6.604.3.	Early Clinical Results	52
6.604.4.	Evolution of the Mechanical Properties of Alumina and the New Alumina Matrix Composite	52
6.604.5.	Proven Long-Term Clinical Stability	53
6.604.6.	Biocompatibility	54
6.604.7.	Current Manufacturing State of the Art	54
6.604.8.	Ceramic Component Failure	54
6.604.9.	Recent Clinical Reports of the Use of the Latest Generation of Alumina Ceramics	55
6.604.9.1.	United States Experience	55
6.604.9.2.	European Experience	56
6.604.9.3.	Asian Experience	56
6.604.10.	Statistical Observations of the Largest Ceramic Manufacturer Clinical Report Database (January 2000 to September 2009)	57
6.604.11.	Ceramic Component Squeaking	59
6.604.12.	The Beneficial Wear Properties of Alumina Ceramics Outweigh the Risk of Fracture	60
6.604.13.	Clinical Use of Ceramics in the Global Community	60
6.604.14.	Ceramics Allow Large Diameter Wear Couple with Little Wear Debris	61
6.604.15.	Conclusions	61
References		62

Abbreviations

ASTM	American Society for Testing and Materials
FDA	Food and Drug Administration
HMWPE	High-molecular-weight polyethylene
ISO	International Standards Organization
THA	Total hip arthroplasty
UHMWPE	Ultra-high-molecular-weight polyethylene

6.604.1. Introduction

Ceramics are inorganic, nonmetallic materials classified as bioresorbable, bioreactive, or bioinert based on *in vivo* characteristics. Bioinert ceramics, such as alumina and zirconia, have gained particular attention as orthopedic bearing materials with desirable *in vitro* and *in vivo* wear properties. The mechanical properties of ceramics – low wear and high stability – make their use especially suitable for high-demand applications such as total hip arthroplasty (THA).

During nearly four decades of clinical use, more than 6 million alumina orthopedic components have been implanted worldwide.[1] While promising clinical outcomes have been demonstrated in large-scale cohorts around the world, there have been concerns with regard to risks of fracture and audible squeaking.

The problem with ceramics, which has prevented higher surgeon adoption over the years, has been breakage. Issues with other bearings have resulted in continued improvements in ceramics. Breakage has been a historical problem with metallic components too; however, with improvements in manufacturing and metallurgy, this problem has been obviated in metals. Likewise, as successive generations of ceramic products are introduced to the market, the risk of fracture has been dramatically decreased, and the squeaking issue is now largely understood to be related to the total hip system used and not solely to a ceramic articulation.

Each successive generation of ceramics has seen improvements in manufacturing, quality control, and clinical application and utility. We spend some time detailing the history of ceramics and the subsequent improvements in the material over the years, to trace these sequential improvements in components. The fourth generation, the alumina matrix composite, has been available only for approximately 5 years now in any major capacity, and, with the increased use of this material, a clear reduction in the fracture rate has already been seen.

This chapter reviews the evolution of modern ceramics and concludes with the clinical experience worldwide, presenting a discussion of both outcomes and complications. Over the last decade, CeramTec AG (Plochingen, Germany) has emerged as the dominant manufacturer of medical-grade ceramics worldwide. Moreover, the vast majority of the world clinical results literature is based on ceramic materials manufactured by CeramTec. As such, and in the interest of space, we have decided to focus on the manufacturing data provided by CeramTec for this historical and manufacturing overview.

6.604.2. History

THA remains one of the most successful and durable procedures in orthopedic surgery. Yet, surgeons and engineers are continually seeking to improve this procedure, in both operative technique and implanted hardware/biomaterials.[2] Historically, it was the initial concern over catastrophic wear in early THA designs that prompted the introduction of ceramics in the early 1970s.

The first use of alumina (aluminum oxide, Al_2O_3) as a biomaterial in dental implants can be traced back to 1930.[3] The modern era of alumina ceramics was ushered in by Sandhaus in 1965, with the use of high alumina powder in dental implants.[4] The initial pioneering attempts to utilize ceramics as a means of reducing early problems of wear in THA were conducted in France under the direction of Dr. P.M. Boutin. Boutin first used alumina in orthopedic surgery in the early 1970s, when he successfully implanted total hip components made of alumina.[5] His efforts proved to be of limited success due to the difficulty in coupling alumina ceramics and metal components.

Like Boutin in France, the German government decided in the early 1970s to fund research focused on the development of alumina ceramic technology for the purpose of reducing wear in THA. This work resulted in the development of a medical-grade alumina ceramic material. Moreover, the project established modularity via the Morse taper concept: different materials could be matched according to function (e.g., alumina ceramic as a bearing material, and metal employed as a stem material).

Early pioneers selected alumina ceramics for a number of reasons. First, ceramics are extremely hard (over 2000 Vickers Pyramid units on the Smith and Sandland hardness scale[6]). In comparison, materials such as cobalt chrome and titanium exhibit hardness of less than 500 HV. Second, alumina ceramics are stable at high temperatures in aqueous environments. The hydrophilic surface in an aqueous environment allows for fluid lubricant to cover larger areas of the bearing surfaces than seen with metals. Finally, alumina ceramic has superior bioinertness in both bulk and particle scales when compared to metal and plastics materials in THA.

6.604.3. Early Clinical Results

Clinical results of the early high molecular weight polyethylene (HMWPE) cups against alumina ceramic ball heads were excellent.[7] The ceramic on plastic combination showed substantial reduction in wear debris over the traditional HMWPE cup on metal ball head systems.

Results of the early alumina-on-alumina ceramic designs were mixed, largely due to ceramic fractures and poorly designed acetabular and femoral components. Review of the French clinical series of 172 consecutive patients at more than 10 years follow-up included 15 acetabular cup revisions for aseptic loosening, as well as five component fractures.[8] A review of the German experience of 109 patients at minimum 10 years follow-up included 24 revisions for femoral component aseptic loosening and five fractured components.[9] The experience in the United States with monolithic cup and cementless stems (Mittelmeier design) was also unacceptable and led to the removal of the system from the market. Miller[10] (United States) followed the results of 102 patients and reported a 26% aseptic loosening rate for the femoral stem, with no fracture of any of the ceramic components in the first 3 years after implantation.

While early clinical experience with alumina ceramic components in THA had high rates of loosening, it is unclear whether it was directly related to the use of alumina ceramics. The first generation of alumina ceramics had a high incidence of fracture, partly related to the heterogeneity of industrial ceramic manufacturing processes and a lack of consensus standard for the materials. As a result of this early experience, a number of manufacturers who had entered the market discontinued their activities in the medical field. Nevertheless, the wear rate of these early alumina ceramic wear couples was low ($2.6\,\mu m\,year^{-1}$ for the cup; $5.4\,\mu m\,year^{-1}$ for the head) and showed promise when compared with metal against HMWPE; wear rates have only continued to improve over the last three decades.[11,12]

The problems of the 1970s became the focus of the orthopedic ceramic manufacturing efforts in the 1980s. Improved fixation of second-generation acetabular and femoral designs reduced the incidence of aseptic loosening; refinement of surgical indications, including implantation of ceramics in younger, active patients improved complication rates.[13] Finally, the aggressive efforts by the manufacturers to first standardize and then to continually improve alumina ceramics, coupled with improvements in THA design, were rewarded with lower fracture rates, decreased incidence of loosening, and improved implant survivorship.[13]

In the early 1990s, a separate effort in France centered upon zirconia ceramic (zirconium oxide) applications. Zirconia has improved strength and fracture toughness compared to alumina. Despite its improved mechanical properties over alumina, the material exhibits different degrees of stability depending on the conditions of use. Under the stress of high-temperature conditions in an aqueous environment, there can be transformation to a monoclinic phase from a tetragonal phase seen at room temperature. This phase transformation, accompanied by volume expansion of the transforming crystals, causes increased surface roughness and results in distinctly inferior wear characteristics. Furthermore, zirconia's inability to articulate against itself limits its versatility.[14] Accordingly, zirconia has now been largely abandoned in orthopedic surgery, including in THA systems.

6.604.4. Evolution of the Mechanical Properties of Alumina and the New Alumina Matrix Composite

In nearly four decades of ceramic use in THA, more than 6 million alumina ceramic components produced by CeramTec AG have been implanted in patients worldwide (CeramTec company data). The majority of these implanted components are alumina ceramic ball heads. The materials used in these alumina components have undergone improvements to enhance reliability *in vivo*. These improvements largely stem from the following: medical-grade processing conditions of the raw material, improved sintering techniques coupled with hot isostatic pressing, laser marking, and proof testing of finished components.[15]

In addition to these processing improvements, the development of ceramic materials to satisfy increasing physiologic demands, additional sizes, and increased longevity has resulted in higher strength composite ceramic materials. Recent iterations of ceramic components marketed in the United States include BIOLOX® *delta*, an alumina matrix composite produced by CeramTec AG. This product has improved upon biocompatibility, mechanical performance, and chemical and hydrothermal stability; importantly, it exhibits at least equivalent tribological characteristics when compared to the alumina ceramic materials currently in use.[16]

The basic foundation for this composite material dates back to the early 1970s, when companies began investigating transformation toughening to increase strength. The transformation, which involves addition of small zirconia particles homogeneously dispersed within the alumina matrix, presents a means to dissipate energy associated with a crack propagating in the microstructure. The compressive stress field generation in the vicinity of the transforming grain (due to volume increase) impedes crack propagation. This process increases the fracture toughness of the composite material. While this mechanism has been well known for many years, additional work was required before the zirconia-toughened materials could be reliably used as orthopedic load-bearing implants.

Subsequent work was carried out to enhance the long-term reliability of the zirconia-toughened alumina composites.[17] In addition to modified toughening techniques (e.g., *in situ* formation of elongated oxide crystals), hardness may be improved by alloying the material with chromium oxide, creating a solid solution within the basic alumina matrix. The distribution of chromium inside the alumina atomic lattice activates a colorizing effect similar to natural ruby. Properties of the successive generations of alumina and alumina matrix composite ceramics are illustrated in Table 1. Higher Young's modulus translates to increased stiffness (i.e., small deformation), and hardness is related to lower wear, while a low wetting angle ensures increased lubrication. Smaller grain size provides increased strength, and a high density provides for better surface finish. Figures 1–3 present other key mechanical properties of ceramics – stiffness, hardness, and flexural strength, respectively – in comparison with commonly used materials in orthopedic surgery.

Table 1 Mechanical properties of alumina and the alumina matrix composite

	1970s alumina	*1980s alumina*	*1990s alumina*	*Alumina matrix composite*
Strength (MPa)	400	500	580	1250
Hardness (HV)	1800	1900	2000	1925
Bending strength (MPa)	>450	>500	>550	>950
Wetting angle (°)	<50	<50	<50	<50
Microstructure (μm)	≤4.5	≤3.2	≤1.8	≤1.0
Density (g cm^{-3})	3.94	3.96	3.98	4.37
Young's modulus (GPa)	380	380	380	350
Laser marking	No	+	+	+
Hipped	No	–	+	+
Proof-tested	No	–	+	+
100% control	+	++	+++	+++
Suitable for ceramic–ceramic	+	++	+++	+++

HV, Vickers hardness scale.
Source: CeramTec AG company data.

6.604.5. Proven Long-Term Clinical Stability

The long-term stability of alumina ceramic components relates to both biocompatibility and bioinertness. Long-term retrieval analysis of 32 mm BIOLOX® ball heads against cemented polyethylene cups at more than 20 years confirmed a majority compliance with the original manufacturing specifications.[18,19] These analyses demonstrated no fretting corrosion

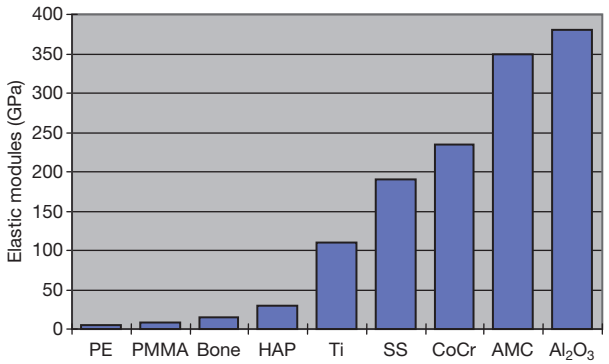

Figure 1 Comparison of stiffness. PE, polyethylene; PMMA, polymethylmethacrylate; HAP, hydroxyapatite; Ti, titanium; SS, stainless steel; CoCr, cobalt-chrome; AMC, alumina matrix composite; Al_2O_3, alumina. Source: CeramTec AG company data.

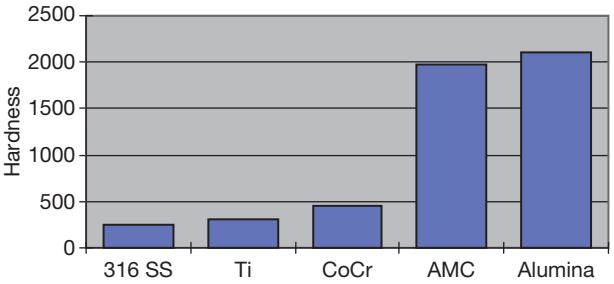

Figure 2 Hardness for different structural biomaterials. 316 SS, 316L stainless steel; Ti, titanium; CoCr, cobalt-chrome; AMC, alumina matrix composite. Source: CeramTec AG company data.

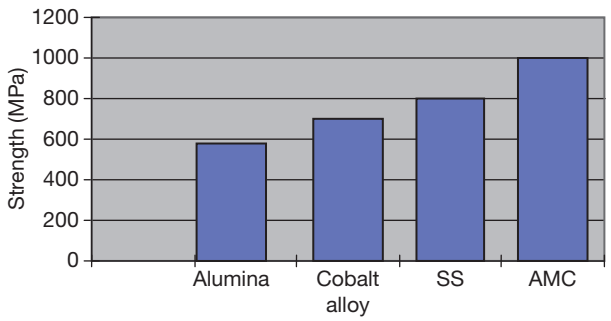

Figure 3 Comparison of flexural strength. SS, stainless steel; AMC, alumina matrix composite. Source: CeramTec AG company data.

or corrosion in the bore of the BIOLOX® heads and the tapers of their corresponding metal stems, and no degradation in strength. These findings contrast with the clinical findings of retrieved metal ball heads[20,21] and *in vitro* wear testing.[22] Consequently, the superior wear rates *in vitro* and stability *in vivo* of alumina ceramic ball heads have proven to be valuable characteristics in the quest for improved bearings in arthroplasty.

6.604.6. Biocompatibility

The search for alternative bearings is not new, and it is certainly not limited to ceramic couples. Alterative bearings include ceramic-on-ceramic/polyethylene, as well as metal-on-metal. Experimentation with these couples dates back over decades. Metal-on-metal couples, purported to be linked to malignancy and teratogenicity, have been under recent scrutiny for metal hypersensitivity, blood ion levels, and animal studies.[23] These concerns seen with metal couplings have not been borne out in ceramic bearings, making ceramics a more biocompatible option.

The testing of all materials to be used for permanent implants in the body has been standardized for several years. International Standards Organization (ISO) regulation 10993 outlines specific tests to be carried out depending on the intended use of the material. Because all ceramic components produced are permanent orthopedic implants, they are subjected to rigorous protocols: cytotoxicity testing of both solid and particulate material; sensitization, genotoxicity, chronic toxicity, and carcinogenicity evaluations; and short- and long-term implantation animal studies.

The particles generated by the different wear couples in orthopedic implants today have different levels of biological activity in the body. Ceramic wear debris has the lowest level of reactivity due to the size, shape, and chemical composition of the particles. This fact results in significantly lower osteolytic potential when compared to polyethylene, cross-linked polyethylene, and metal.[24–33] When this is combined with the lower volumetric wear rate of the ceramic-on-ceramic wear couple, a 100-fold reduction in biological activity and osteolytic potential is seen.[34] Even under microseparation conditions (contact of ball head/cup rim), the wear rate of the alumina ceramic-on-ceramic was 50 times less than that of metal-on-crosslinked polyethylene.[27,35] The concentration of wear particles in the periprosthetic tissues of loosened implants was 2–22 times lower with alumina ceramic than with metal-on-polyethylene.[25] Long-term clinical results with ceramic-on-ceramic THA confirm the excellent biocompatibility and reduced wear rate of ceramic-on-ceramic bearings.[24,25,36–38] The proven biocompatibility data are based largely on the track record of the largest alumina manufacturer, CeramTec AG, and the over 6 500 000 alumina and nearly 1 000 000 alumina matrix composite components implanted globally since 1973.

6.604.7. Current Manufacturing State of the Art

The quality of either alumina or the alumina matrix composites is defined by key processing parameters, and governed by regulations established by the American Society for Testing and Materials (ASTM) and by the ISO. These processes include obtention of high-purity raw material, medical-grade processing conditions, improved sintering techniques and hot isostatic pressing, laser marking, and proof testing. All these factors enhance the reliability of the ceramic components *in vivo*.[1]

Removal of impurities such as silicates and alkali oxides reduces glassy phases at the grain boundaries, improving corrosion resistance, mechanical strength, and fatigue properties. Sintering temperature is optimized to establish ideal grain size and distribution. This, in combination with hot isostatic pressing, provides a higher density. Laser marking is used to establish smoother surface conditions and prevent stress risers. Finally, proof testing is now carried out by most manufacturers of ceramic components around the world. This, along with verification of the chemical composition, grain size, density, surface finish, sphericity, dimensional compliance, and surface inspection using a dye penetrant, ensures the reliability of the components.

6.604.8. Ceramic Component Failure

There remain inherent risks of alumina ceramic use *in vivo*. While *in vitro* studies seek to minimize these risks, *in vivo* conditions can be quite different. For example, abnormally high loads may be placed on the component on account of trauma. Poor placement of the components, such as vertical cup placement, may impose abnormal loading conditions. Patient-related factors, such as poor bone density, high activity levels, and obesity can undermine component stability. Patient-related factors, as well as surgeon and material factors, can significantly affect the reliability and expected service life of the component.

In addition to individual components (e.g., acetabular cup, ball head, and femoral stem), the taper mating surface and its proper function are important to the eventual service life of present-day alumina ceramic components. Components must have identical mating taper surfaces, and mating surfaces must be protected during surgery, to prevent damage, and impacted properly in adequate axial alignment. **Table 2** captures the incidence of *in vivo* fractures of ceramic components reported historically **Table 2**.

Complications data demonstrate several trends. In the early years, two companies (Rosenthal and Friedrichsfeld) experienced unusually high failure rates on their products as a result of which they do not presently produce ceramic components. Overall, breakage of an alumina ceramic component is rare and actually lower than that of other procedural complications (e.g., stem breakage).[67] Furthermore, improvements in manufacturing process, surgical technique (i.e., cup position and minimizing impingement), and improved acetabular component design (i.e., elimination of lipped liners) have over time continually decreased the rate of catastrophic failure. Nevertheless, while they are rare, there are still instances when even modern ceramic bearings fail. Therefore, more study is needed to stratify specifically the breakages related to trauma, surgical technique, and a number of other conditions.

The higher mechanical properties of zirconia in ball heads did not translate into a lower rate of breakage, as had

Table 2 Fractures of alumina ceramic components (by date of implantation)

Author	*Year*	*Period implanted*	*Company or brand*	*Couple*	*Total implants*	*Number of fractures*	*Fractures (%)*
Boutin[39]	1981	1970–1972	Ceraver		373	28	7.5
Higuchi[40]	1995	1971–1991	Kyocera		847	3	0.3
Griss[41]	1981	1974–1978	Friedrichsfeld	c/c	130	9	6.9
Winter[42]	1992	1974–1979	Friedrichsfeld	c/c	100	8	8
Knahr[43]	1981	1974–1980	Rosenthal		75	8	10.6
Mittelmeier[9]	1985	1974–1983	BIOLOX		877	3	0.4
Heisel[44]	1987	1974–1986	BIOLOX		2536	5	0.2
Mittelmeier[45]	1992	1974–1992	BIOLOX		3149	3	0.10
Willmann[1]	1993	1974–1993	BIOLOX		1 000 000	240	0.02
Willert[2]	1996	1974–1995	BIOLOX		511 000	79	0.015
Knahr[46]	1987	1976–1979	Rosenthal	c/c	67	9	13.4
Trepte[47]	1985	1977	BIOLOX	c/c	41	0	0
Nizard[8]	1992	1977–1979	Ceraver	c/c	187	3	1.6
Boutin[48]	1988	1977–1985	Ceraver	c/c	560	3	0.54
Oonishi[49]	1992	1977–1991	Kyocera		10 000	0	0
Boutin[50]	1988	1979–1986	Ceraver		373	0	0
Rampoldi[51]	1984	1979–1982	BIOLOX		59	0	0
Holmer[52]	1993	1979–1987	BIOLOX	c/p	> 2000	0	0
Higgs[53]	1990	1980–1987	BIOLOX	c/c	337	1	0.29
Nevelos[54]	1993	1980–1989	BIOLOX		166	0	0
Cameron[55]	1991	1980–1990	BIOLOX	c/p	> 600	3	0.5
Bardos[56]	1990	1981–1986	BIOLOX		3500	0	0
Kern[57]	1990	1981–1989	BIOLOX	c/p	> 500	1	0.2
Peiró[58]	1991	1982–1989	BIOLOX	c/p	250	2	0.8
O'Leary[59]	1988	1982–1983	BIOLOX	c/c	69	0	0
Miller[10]	1986	1982–1984	BIOLOX	c/c	231	0	0
Hoffinger[60]	1991	1983–1984	BIOLOX	c/c	119	0	0
Israel[61]	1989	1983–1988	Keramed	c/p	491	1	0.2
Toni[62]	1990	1985–1987	Ostalox		82	2	2.4
Toni[62]	1989	1987	Ostalox		96	1	1.04
Toni[63]	1994	1987–1992	BIOLOX	c/p	615	0	0
Holmer[52]	1993	1987–1990	Zirconia	c/p	300	5	1.6
Callaway[64]	1995	1991–1993	BIOLOX	c/p	184	4	1.9
Hummer[65]	1995	1992–1995	Zirconia	c/p	189	2	1.05

c/c, alumina ceramic against ceramic; c/p, alumina ceramic against ultra-high-molecular-weight polyethylene (UHMWPE).
Note: Willmann[1] and Semlitsch[66] reported the experience of one company's alumina ceramic components (Feldmuhle/Cerasiv/CeramTec and their product trademark BIOLOX®). These articles state a number of failures, which may be duplicated in the individual clinician reports.
Source: CeramTec AG company data.

been originally anticipated. Even though there are only two series reported in the literature, the zirconia fracture rate is higher than that reported for current-day alumina.[64,65] The Callaway series, of note, used femoral stems produced by the Hospital for Special Surgery Dana Center, which has been criticized for a high breakage rate secondary to a substandard connecting taper.

6.604.9. Recent Clinical Reports of the Use of the Latest Generation of Alumina Ceramics

Several reports have described the clinical outcomes of THA implanted with current generation implants, fixation technology, surgical techniques, and modern alumina bearings. In over 61 644 cases reported from 2000 to 2008 in the medical literature, there have been a total of 21 fractured components (~0.034% fracture rate). In alumina-on-alumina THA cases in several clinical series, with follow-up of 3–20 years, no alumina bearing failures were encountered (Table 3). Thus, modern alumina THA bearings appear to be safe and reliable if used with implants of proven design and durability.[1,39,46,57]

6.604.9.1. United States Experience

D'Antonio and Capello presented a review of the 52 000 ceramic–ceramic hips implanted since the 2003 Food and Drug Administration (FDA) approval of Stryker ceramic hip arthroplasty products[68]: four acetabular fractures (0.008%) and nine head fractures (0.017%) were seen in the group. Further Stryker data comparing metal-on-polyethylene and ceramic–ceramic couples at greater than 7 years follow-up found a 7.5% revision rate in the control group (metal-on-polyethylene) versus a 2.7% revision rate for ceramic-on-ceramic.[69] There were no fractures in the ceramic cohort, while the control group experienced osteolysis and revisions attributable to wear. Capello *et al.* reported on 475 hips at an average 8 years of follow-up. Cortical erosions were less seen in the ceramic-on-ceramic hips than in the metal-on-polyethylene

Table 3 Clinical outcomes of total hip arthroplasty with alumina bearings since the year 2000

Year	*Author*	*Region*	*Follow-up (years)*	*Number of cases*	*Number of fractures*
2000	Boehler *et al.*[90]	Europe	6	243	0
2000	Bizot *et al.*[91]	Europe	>5	234	1
2000	Garino *et al.*[71]	United States	1–3	333	0
2001	Urban *et al.*[92]	United States	17–21	64	0
2001	Delaunay *et al.*[93]	Europe	5–10	133	0
2001	Bizot *et al.*[91]	Europe	<3	96	1
2001	Hamadouche *et al.*[94]	Europe	>18	118	0
2002	D'Antonio *et al.*[95]	United States	3	345	0
2002	Bierbaum *et al.*[96]	United States	4	514	0
2003	Hannauche *et al.*[97]	Europe	25	5500	8
2005	Capello *et al.*[70]	United States	4	514	0
2005	Kawanabe *et al.*[86]	Asia	7–21	215	0
2006	Murphy *et al.*[73]	United States	2–8	194	0
2006	Slack *et al.*[98]	Europe	13–15	116	0
2006	Park *et al.*[87]	Asia	4–7	357	2
2007	Lusty *et al.*[99]	Australia	5–7	301	0
2008	Koo *et al.*[85]	Asia	3–4	367	5
2008	Capello *et al.*[70]	United States	5	52 000+	4

Source: CeramTec AG company data.

group, and there was no aseptic loosening in the ceramic group. Overall, there was a <1% fracture rate requiring reoperation in the ceramic-on-ceramic hips.[70]

Garino cited no fractures at 3 years follow-up in 333 cases.[71] Murphy *et al.*, in a report on the Wright IDE trials, included 1709 hips in 1484 patients across 12 centers.[72] Minimum follow-up was 2 years after implantation of Transcend cups and various femoral stems. At average 8-year survival, there were four ceramic liner fractures (0.27%) and two reoperations for instability. While breakage issues have historically forced ceramics to lag with respect to head size, Murphy concluded that the relative lack of neck and liner options did not impede safe surgery with these components. Murphy *et al.* also reported no osteolysis and no dislocations at mean 4.3 years in 194 hips implanted with alumina-on-alumina bearings.[73] In a study looking at both Biolox Delta ceramic-on-ceramic and Biolox Delta ceramic on moderately cross-linked polyethylene, Hamilton *et al.* cited two ceramic liners that were chipped during insertion and two acetabular liner failures in the ceramic-on-ceramic group.[74]

6.604.9.2. European Experience

The reported European experience with an alumina-on-alumina combination showed a mean wear rate of 0.025 μm $year^{-1}$ and limited osteolysis up to 10 years after arthroplasty.[8,48,75–77] Hamadouche *et al.* saw no evidence of wear and no fractures at 18.5 years minimum follow-up.[78] When comparing 28 bilateral arthroplasties (one ceramic–ceramic and the others contralateral ceramic–polyethylene) at 20-year revision-free follow-up, Hernigou *et al.* saw more osteolysis/wear in the alumina-on-polyethylene hip than the alumina-on-alumina hip.[79] Aldrian *et al.* reviewed the mid-term results of Biolox ceramic-on-ceramic and Alpha Cera Fit Alphanorm (Lassnitzhohe, Austria) uncemented components in 107 hips at minimum 7 years follow-up[80]: three ceramic head fractures were seen; there were no radiographic signs of lysis or loosening. Nau *et al.* in Germany reported no osteolysis or loosening in 199 Cera Fit THA at mean follow-up time of 42 months.[81] Fenollosa *et al.* in Spain saw no osteolysis or component fracture in their series of 74 patients below the age of 50 years.[82] At greater than 7 years' survival, Lazzaro *et al.* reported no clinical or radiographic signs of loosening of the femoral component, and seven cases of acetabular cup loosening.[83]

6.604.9.3. Asian Experience

Poor results were seen with early Kyocera ceramic components in the Japanese population: 10-year survival rates of 75% for the acetabular component and 86% for the femoral component, and a mean polyethylene linear wear rate of 0.10 mm $year^{-1}$, radiographically.[84] Koo *et al.* cited five alumina head fractures for a 1.4% fracture rate.[85] Kawanabe *et al.* reported no fractures at 7–21 years' follow-up in 215 THAs.[86] Park *et al.* found two fractures in 357 patients at 4–7 years' follow-up.[87] Sugano *et al.* reviewed the use of navigation in performing cementless ceramic-on-ceramic THA in 59 hips at a mean of 6 years postoperatively.[88] The results were compared with 111 hips implanted without navigation: two revisions were performed in the group without navigation (one aseptic acetabular loosening and one ceramic liner fracture). Zhou *et al.* compared ceramic-on-ceramic with metal-on-polyethylene implants for cup migration; they found no increased cup migration in the ceramic-on-ceramic implant compared with the metal-on-polyethylene.[89]

As of December 2009, the US FDA had approved seven Pre-Market Approval applications and one Product Development Protocol submitted by orthopedic implant manufacturers who presently market alumina THA bearings within the United States (**Table 4**). Alumina-on-alumina THA bearings in the United States are classified by the FDA as class III devices.

Therefore, annual follow-up is required of all patients for a minimum of 5 years postsurgery, and a selected postmarket surveillance group must be followed for 10 years.

At the conclusion of 2009, more than 5500 patients were enrolled in clinical studies with alumina-on-alumina ceramic THA, with some follow-ups reaching the 10–12 year mark. Ongoing clinical studies in the United States show the improvements made in manufacturing and design over the years, which feature the use of cemented or cementless components (stem and acetabular shells) in conjunction with alumina ball heads with either an UHMWPE or an alumina shell insert. The alumina acetabular insert design is used in conjunction with a metal shell design with a taper that locks the ceramic insert in place. Both the insert and ball heads have no unsupported alumina ceramic edges, and all exposed alumina ceramic surfaces are polished. The only variable in the material design is the acetabular insert (either UHMWPE or alumina ceramic). This mating of current-day stem and shell designs with different wear couples is the basis for future designs.

Table 4 United States Food and Drug Administration approved Premarket applications

Company	*Premarket application*
Biomet	Alumina with direct locking of the insert (flush)
DePuy	Alumina with direct locking of the insert (flush)
DJO Orthopedics	Alumina with direct locking of the insert (flush)
Exactech	Alumina with direct locking of the insert (flush)
Smith & Nephew	Alumina with direct locking of the insert (flush)
Stryker	Alumina with protected ceramic insert (metal rim)
Wright Medical	Alumina with direct locking of the insert (flush)
Zimmer	Alumina with direct locking of the insert (flush)

Source: CeramTec AG company data.

6.604.10. Statistical Observations of the Largest Ceramic Manufacturer Clinical Report Database (January 2000 to September 2009)

An analysis of the CeramTec database related to the BIOLOX® family of ceramic components (January 2000 to September 2009) offers important insights into the complication rates related to implanted ceramics products. However, product failure data reported to CeramTec AG Medical Products Division may not accurately capture all failures, as not all events are reported to the manufacturer. Similar company databases were not able to capture unexpectedly high failure rates, such as with the yttrium-stabilized zirconia femoral heads made by the French company DesMarquest.[11] Nevertheless, it is important to evaluate large-scale company database reports for emerging trends. Conclusions from data analysis of the CeramTec database are given below:

Alumina bearing failures in THA are uncommon. A total of 2 420 000 alumina THA bearing components were manufactured from January 2000 to September 2009 (**Figure 4**). Based on the clinical reports received by the manufacturer, a clinical fracture rate of 0.020% occurred[100]; the overall probability of a ceramic component failure *in vivo* was therefore about 2 in 10 000.

Alumina failures can be related to specific adverse events. In the database, there were only 58 failed components files that contained sufficient information from which to draw firm conclusions as to the reason for failure. In each of these cases, the components failed after a single adverse event that might not ordinarily be associated with routine primary THA. These adverse events included trauma, cold immersion of the component after autoclaving, mismatch between the femoral head diameter and the acetabular insert, recurrent hip dislocations, and gross mal-positioning

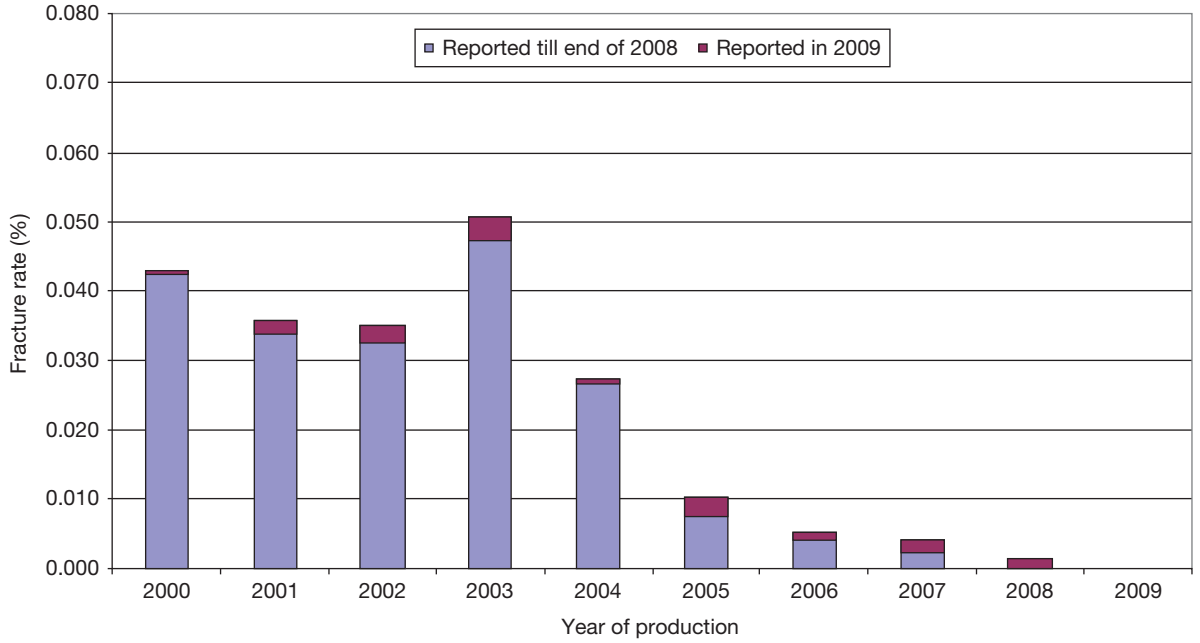

Figure 4 Fracture rate in CeramTec database according to year. Source: CeramTec AG company data.

of THA implants. While there may be an inherent risk of component fracture with routine conditions, it is clear that these components often fracture clinically, as a result of some event creating an overload condition.

Most in vivo failures of alumina THA occur early after implantation. Femoral heads manufactured from the historical alumina material and the new alumina matrix composites tend to fracture relatively early after surgery. Forty percent of the fractures had failed within 12 months of surgery; 60% had failed within 24 months, and 75% had failed within 36 months following implantation. These data suggest that, after 3 years, the risk of an alumina femoral head fracture *in vivo* is only 25% of the 0.02% overall incidence of failure (i.e., 0.004%) (**Figure 5**).

Alumina matrix composite is more reliable than previous alumina (in the short- to midterm). Future material improvements may continue to reduce the risk of failure of alumina components. Alumina matrix composites have even greater fracture toughness values and resistance to crack propagation when compared to traditional alumina.[8] The improvement in reliability offered by this new composite ceramic material is quite promising. In a comparison of the *in vivo* fracture rate between the alumina components (2.42 million implanted) and the alumina matrix composite components (570 000 implanted), the fracture rate reported to the manufacturer was reduced from 0.020% to 0.002% (CeramTec company data). This increase in short- to mid-term reliability is quite promising and requires further follow up.

Increasing femoral head diameter reduces the risk of fracture. The failures reported to CeramTec suggest that the risk of alumina femoral head fracture declined with increase in femoral head diameter. Larger diameter femoral heads were associated with a reduced risk of failure *in vivo* (**Figure 6**).

Alumina femoral head fracture rates can vary with the neck size. Among the 28 mm diameter alumina femoral heads, the fracture rate was influenced by the neck length design in the taper bore. The lowest risk of fracture was associated with a medium neck size, while the short and long neck lengths were associated with higher femoral head fracture rates (CeramTec company data).

The risk of failure of an alumina acetabular insert is quite small. One of the reported early issues with ceramic acetabular inserts involved the chipping of ceramic inserts intraoperatively when an alumina acetabular insert was seated into a metal shell. If it is not properly aligned with the metal shell, a piece of ceramic can chip off the insert edge.[40,52] This problem is technique related and associated with eccentrically placed insert impacted into a metal shell.[1,46,55] While only a small part of the edge is damaged by chipping, a significant stress riser is created in the material, and the chipped insert must be replaced with a new one. The rate of alumina insert damage during surgery as reported to CeramTec was relatively stable at 0.026% from January 2000 to September 2009 (CeramTec company data).

Implant design affects the performance of alumina bearings. Optimal load transfer from an alumina bearing to either a metallic femoral stem or an acetabular shell depends upon the load transfer area design, its material composition, roughness, morphology, and many other factors. At the present time, variables related to the design of these load transfer areas vary between the various implant manufacturers. The specific design of a given THA implant can influence the reliability of the alumina bearing components. The extent to which implant design variables contributed to the failures is unknown.

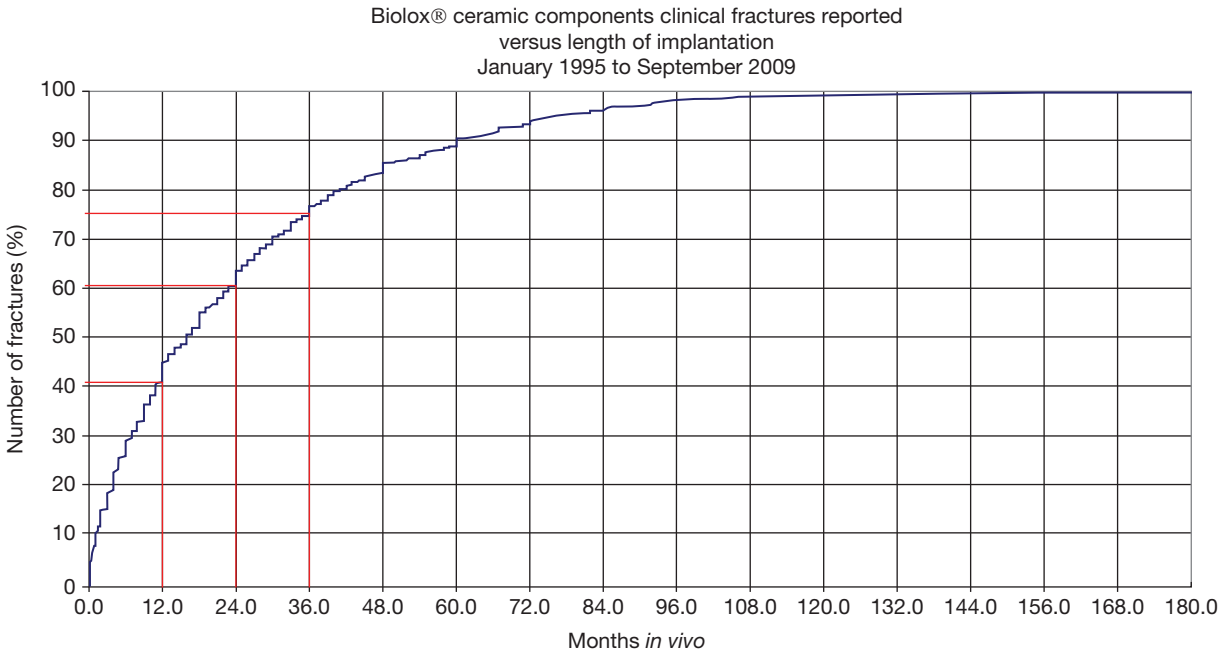

Figure 5 Percent of fractures as a function of time from implantation. Source: CeramTec AG company data.

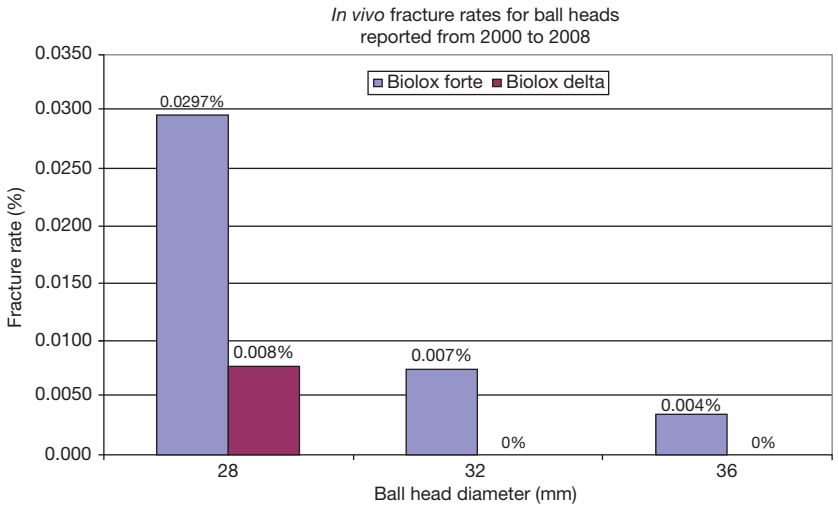

Figure 6 Femoral head fracture rate according to head diameter. Source: CeramTec AG company data.

6.604.11. Ceramic Component Squeaking

Complications such as articulation noise and, in particular, squeaking can create a degree of concern and discomfort in the patient. Much research has been devoted to clarify the mechanisms involved. Present data conclusions are as follows:

All hard-on-hard bearings are susceptible to the generation of articulation noises. The incidence of articulation noise is not unique to ceramic-on-ceramic bearings. Articulation noises have also been associated with metal-on-metal bearings and metal-on-metal resurfacing systems: for example, Back *et al.* noted a 3.9% rate of transient squeaking with metal-on-metal resurfacing replacements.[101]

The cause of squeaking may be multifactorial. Patient factors, such as muscle tension, weight, and height may be contributing factors. Taller and heavier patients tend to have a higher incidence of articulation noises. Surgical-related issues, such as placement of the implants and bone or tissue impingement, are also found to be important factors. Implant design issues – femoral stem and neck geometry, implant material, implant range of motion to mechanical impingement, the number of interfaces in a given design, shell deformation, and locking mechanism – all play a role.

The frequency of occurrence appears to be design related. A substantial difference in the frequency of these noises appears to be related to component design differences. Squeaking in ceramic taper locking modular shells with flush mounted ceramic insert designs has a reported incidence of less than 1%. In contrast, a design utilizing titanium encased and recessed ceramic liner appears to have a much higher incidence (2.7% to more than 11%). There appears to be a direct relationship between the type of femoral stem, the design of the neck, and the material used in the stem, and the incidence of squeaking. In one study, surgeons using one specific femoral stem design had a significantly higher incidence of squeaking when compared to other surgeons in the group who used the same acetabular modular system but with a femoral stem of a different design.[102]

Squeaking may be a temporary condition. Komistek analyzed under fluoroscopy a group of patients with documented complaints of squeaking following C–C hip replacements, and found that he could not reproduce squeaking in the audible range in any of these patients, under a variety of conditions mimicking activities of daily living.[103] Furthermore, in another study, Lee and Garino reported on a group of squeakers followed prospectively for a minimum of 5 years and found that, after the minimum follow-up period, 50% of patients had either had complete cessation of squeaking or had significant diminution of symptoms.[104] Thus, this type of acoustic phenomena following ceramic THA continues to be poorly understood and its clinical significance remains uncertain.

Squeaking has not been shown to be a predictor of clinical performance. There is no data available that indicates that one type of articulation noise, such as squeaking, compromises the mechanical integrity and clinical longevity of the implanted system. In most clinical studies, reports of squeaking following THA comprise a small portion of the patient population.

Studies utilizing the Ti alloy (TAl6V) with a C-taper include a 0.3% squeaking rate cited by Lusty *et al.*,[99] and a 0.97% rate in Mesko *et al.* in a report of 930 consecutive ceramic-on-ceramic hips.[105] According to D'Antonio, the highest reports of squeaking have involved the use of a femoral stem made of titanium–molybdenum–zirconium–iron with a V-40 tapered neck geometry.[102] These reports include the following: Restrepo *et al.*[106] at a 2.7% incidence; four of these Trident Stryker components underwent revision, and stripe wear was observed. Keurentjes in the Netherlands[107] reported a 20.9% incidence, and Jarrett *et al.* cited a 32.8% incidence of all noises and 10.7% squeaking incidence (4 of 14 reproducible squeaking).[108]

Walter *et al.* in Australia reported a 0.6% rate,[109] and Capello saw 0.8% squeaking rate in Stryker components.[70] Jarrett *et al.* also reported a 19.5% squeaking rate at less than 3 years.[110] Chang *et al.* in Korea described no squeaking in revision THA using third-generation CoC components

at average follow-up of 5.4 years.[111] Hamilton reported no squeaking at minimum 2 years follow-up in either Delta ceramic-on-ceramic or Delta ceramic on moderately cross-linked polyethylene.[74] Mai *et al.* reported a 17% rate of patient-perceived hip noise, with 10% rate of 'squeaking.'[112]

While squeaking is noted as a nuisance by most patients, few reports have linked nontraumatic squeaking to impending failure of the hip system. Our institutional experience on squeaking has been that most patients report squeaking as a waxing and waning condition that occurs during the first few years following THA, with eventual disappearance or diminution of symptoms. Most patients complained of no pain with this condition and had high levels of function postoperatively. Consequently, one must weigh the risks and benefits of revision for squeaking alone.

The indications for THA have been extended into younger age and/or high activity groups. These patients will place more rigorous environmental demands, both occupational and recreational, upon their THA. As a result of this, the longevity of existing THA systems in the market today is being redefined, and biomechanical testing has been useful in exploring this complication.[113,114] Articulation noises are not new phenomena; however, it appears that the specific noise described as 'squeaking' is the result of a number of factors. Proper classification of the sounds may be helpful in diagnosing their origin and clinical implication.

Table 5 Clinical wear rates of various wear couples

Material combination	*Annual wear (mm)*
Metal/UHMWPE[11]	0.2
Alumina/UHMWPE[11]	0.1
Alumina/Alumina (1980s)[32]	0.005
Alumina/Alumina (1990s)[115]	0.001

UHMWPE, ultra-high-molecular-weight polyethylene.
Source: CeramTec AG company data.

6.604.12. The Beneficial Wear Properties of Alumina Ceramics Outweigh the Risk of Fracture

While metal on UHMWPE has been the traditional benchmark for clinical wear, alternative bearings have positively influenced wear rates and offer options in the high-demand or young populations. Justification for ceramic bearings is made in the face of a relatively constant revision rate of THA in the United States despite advancing surgical techniques.[7] It is possible that the new generation of UHMWPE may be more sensitive to abrasive wear and might be 'protected' against this type of wear by the use of a ceramic ball head. Table 5 illustrates the difference between the bearing couple wear rates. It is important for the operating surgeon to carefully balance the risk of alumina ceramic complications against the gains achieved by the reduction of wear debris, particularly when the patient is younger and more active.

6.604.13. Clinical Use of Ceramics in the Global Community

The use of ceramics ball heads varies greatly by region (Figures 7 and 8). Perhaps the most important issue relates to the price differential between metal and ceramic ball heads. As an example, in the United States, the ceramic ball head list price is often greater than four times that of the same ball head sold in Europe, while metal ball head prices are more equivalent. This price differential may be the largest single contributing factor accounting for the different usage rates around the world. Another important factor that influences usage relates to the educational programs for orthopedic surgeons: some

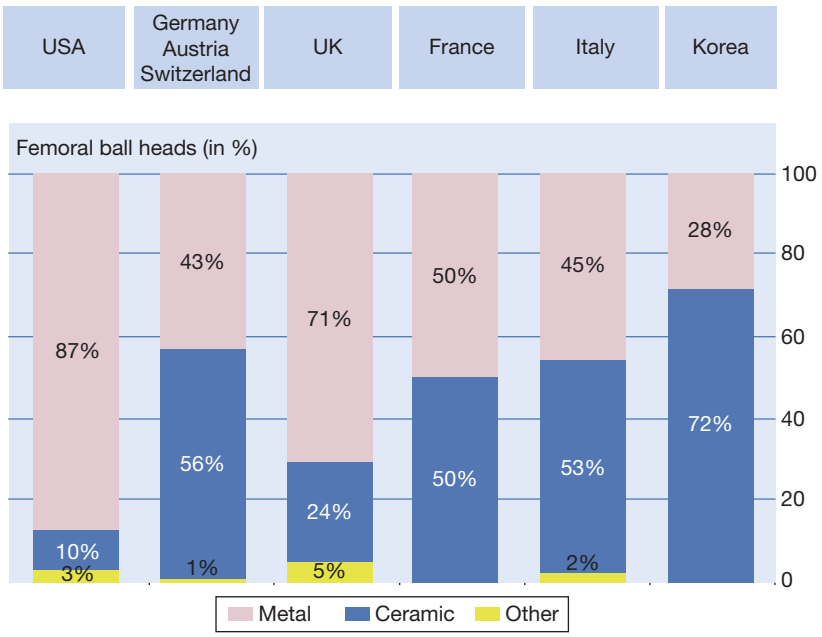

Figure 7 Femoral ball head usage by region. Source: Avicenne, BVmed, Eucomed, Global Markets Direct, and CeramTec (2007).

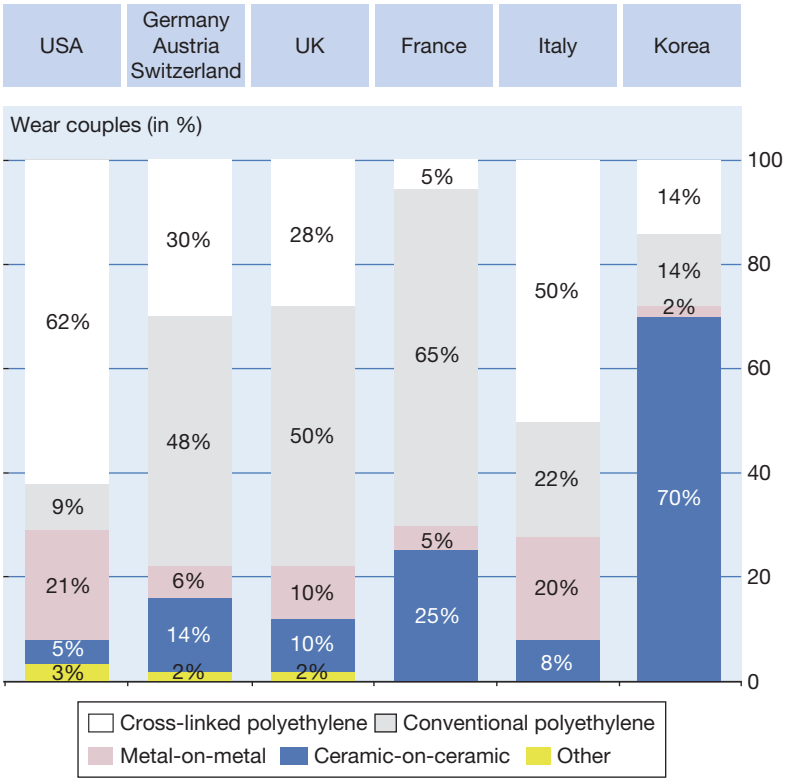

Figure 8 Wear couples by region. Source: Avicenne, BVmed, Eucomed, Global Markets Direct, and CeramTec (2007).

countries have endorsed usage of ceramics for many years, whereas in other areas, a rebirth of ceramics has been recognized only in the last decade or so.

6.604.14. Ceramics Allow Large Diameter Wear Couple with Little Wear Debris

The use of ceramic-on-UHMWPE or ceramic-on-ceramic articulation offers the possibility of large diameter wear couples. The use of these large wear couple sizes provides enhanced stability and range of motion with a negligible increase in the amount of wear debris. For example, a change of a 28-mm wear couple to a 32-mm wear couple in the same system (assuming a 2–1 head-to-neck ratio) provides an increase of nearly 7° in arc range of motion. The use of a 36-mm wear couple improves the range of motion by a total of 14° from the 28-mm couple (Figure 9).

The next generation of CeramTec ceramic components, the Delta Ceramax system manufactured by the Smith and Nephew company, is presently an investigational device and pending approval in the United States. No claims regarding safety and efficacy can be made, and preliminary data regarding excellent burst testing and wear properties must be fully evaluated in clinical trials. For example, burst testing for 28 mm ceramic inserts reveals inserts that exceed testing capacity at >247 kN; likewise, 36 mm inserts exceed testing capacity at >285 kN. The FDA requires a minimum of 46 kN.[116] As ceramics perform well under compression, the factory-assembled titanium band for the ceramic insert preloads the liner in a compressive manner; this feature significantly increases burst strength.

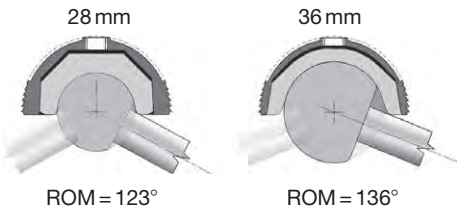

Figure 9 Implanting a larger wear couple diameter improves arc range of motion, and range of motion to impingement. Source: CeramTec AG company data.

6.604.15. Conclusions

Alumina THA bearings are the result of extensive improvements to the material, manufacturing processes, and implant design. Clinical experience during the last three decades has demonstrated the wear advantages of the alumina family of ceramics in reducing debris in THA, as well as the reliability and safety of modern alumina bearings. As an alternative to metal-on-polyethylene and metal-on-metal bearings in THA, modern alumina is safe, durable, reliable, and provides substantial benefits in wear reduction. Low *in vitro* and *in vivo* wear rates may outweigh the small risks of ceramic-associated complications.

The surgeon has to balance these risks of alumina failure and audible noise generation against the proven advantages of alumina. Reductions in wear have been seen when ceramics are coupled with UHMWPE or alumina ceramic. These may have long-term implications in the reduction of revision rates

in THA. Furthermore, the applications of THA in young, more active, and high-demand patients may be extended. Ceramics have permanently changed the alternative bearings options, both in the United States and worldwide.

References

1. Willmann, G. *Orthopaedics* **1997**, *4*, 269–276.
2. Willert, H. G. The effect of particle debris on the long term performance of artificial joints and possible improvements. In *The Hip Society Twenty Fourth Open Scientific Meeting*, Atlanta, GA, February 25, 1996.
3. Rock, M. Ger. Patent Drp No. 583589, 1933.
4. Sandhaus, S. Br. Patent No. 1083769, 1967.
5. Boutin, P. M. *Rev. Chi. Orthop.* **1972**, *58*, 229–246.
6. Smith, R. L.; Sandland, G. E. An accurate method of determining the hardness of metals, with particular reference to those of a high degree of hardness. In *Proceedings of the Institution of Mechanical Engineers;* 1922; Vol. I, pp 623–641.
7. Black, J. In *Performance of the Wear Couple Biolox Forte in Hip Arthroplasty*; Enke: Stuttgart, 1997; pp 2–10.
8. Nizard, R. S.; *et al. Clin. Orthop. Relat. Res.* **1992**, *282*, 53–63.
9. Mittelmeier, H. *Acta Orthop. Belg.* **1985**, *51*, 367.
10. Miller, E. H.; Heidt, R. S.; Welch, M. C.; *et al. Instr. Course Lect.* **1986**, *35*, 188–202.
11. Zichner, L. P.; Willert, H. G. *Clin. Orthop. Relat. Res.* **1992**, *282*, 86–94.
12. Lachiewicz, P. F.; Heckman, D. S.; Soileau, E. S.; Mangla, J.; Martell, J. M. *Clin. Orthop. Relat. Res.* **2009**, *467*(12), 3290–3296.
13. D'Antonio, J. A.; Sutton, K. *J. Am. Acad. Orthop. Surg.* **2009**, *17*(2), 63–68.
14. Cameron, H. In *Bone Implant Interface*; Mosby: St. Louis, MO, 1994; pp 203–262.
15. Bragdon, C. R.; Jasty, M.; Muratoglu, O.; Harris, H. *J. Arthroplasty* **2005**, *20*(3), 379–385.
16. Clarke, I. C. In *Biomechanics and Alternative Bearings in Joint Replacement*; Springer: Steinkopff, 2007; pp 33–45.
17. Chevalier, J.; Granjean, S.; Kunz, M.; Pezzotti, G. *Biomaterials* **2009**, *30*(29), 5279–5282.
18. Willmann, G.; Brodbeck, A.; Effenberger, H.; Mauch, C.; Nagel, J.; Dalla Pria, P. In *Bioceramics in Orthopaedics*, 3rd BIOLOX® Symposium Proceedings; Puhl, W., Ed.; Georg Thieme: Stuttgart, 1998; pp 13–18.
19. Willmann, G.; Richter, H. G.; Zweymüller, K. In *Bioceramics in Joint Arthroplasty*, 7th BIOLOX® Symposium Proceedings; Garino, J. P., Willmann, G., Eds.; Georg Thieme: Stuttgart, 2002; pp 94–96.
20. Clarke, I. C.; Manley, M. T. *J. Am. Acad. Orthop. Surg.* **2008**, *16*(Suppl 1), S86–S93.
21. Huo, M. H.; Parvizi, J.; Gilbert, N. F. *J. Bone Joint Surg. Am.* **2006**, *88*, 2100–2113.
22. Oonishi, H.; Clarke, I. C.; Good, V.; Amino, H.; Ueno, M. *J. Biomed. Med. Res.* **2004**, *70*, 523.
23. Jacobs, J. J.; Urban, R. M.; Hallab, N. J.; *et al. J. Am. Acad. Orthop. Surg.* **2009**, *17*(2), 69–76.
24. Bos, I.; Henssge, E. J.; Willmann, G. In *Die Keramikpaarung BIOLOX in der Hüftendoprothetik*; Puhl, W., Ed.; Enke: Stuttgart, 1996; pp 24–30.
25. Boehler, M.; Mochida, Y.; Bauer, T. W.; Salzer, M. In *Reliability and Long-term Results of Ceramics in Orthopaedics*, 4th BIOLOX Symposium Proceedings; Georg Thieme: Stuttgart, 1999; pp 57–59.
26. Fisher, J. *J. Bone Joint Surg. Br.* **2006**, *88B*(Suppl I), 7.
27. Fisher, J.; Galvin, A.; Tipper, J.; Stewart, T.; Stone, M.; Ingham, E. In *Bioceramics and Alternative Bearings in Joint Arthroplasty*, 10th BIOLOX® Symposium Proceedings; D'Antonio, J. A., Dietrich, M., Eds.; Steinkopff: Darmstadt, 2005; pp 21–24.
28. Fisher, J.; Nevelos, J.; Stewart, T. D.; Tipper, J. L.; Ingham, E. In *Bioceramics in Joint Arthroplasty*, 9th BIOLOX® Symposium Proceedings; Lazennec, J. Y., Dietrich, M., Eds.; Steinkopff: Darmstadt, 2004; p 45.
29. Granchi, D.; Ciapetti, G.; Amato, I.; *et al. Biomaterials* **2004**, *25*, 4037–4045.
30. Hatton, A.; Nevelos, J. E.; Matthew, J. B.; Fisher, I.; Ingham, E. *Biomaterials* **2003**, *24*, 1193–1204.
31. Heimke, G.; Willmann, G. In *Biomaterials Engineering and Devices. Human Applications*; Wise, D. L., *et al*., Eds.; Humana Press: Totowa, NJ, 2000; Vol 2, pp 223–251.
32. Henssge, E. J.; Bos, I.; Willmann, G. *J. Mater. Sci. Med.* **1994**, *5*, 657–661.
33. Sterner, T.; Schütze, N.; Saxler, G.; Jakob, F.; Rader, C. P. *Biomed. Technik* **2004**, *49*, 340–344.
34. Fisher, J.; Jin, Z.; Tipper, J.; *et al. Clin. Orthop. Rel. Res.* **2006**, *453*, 25–34.
35. Fisher, J.; Ingham, E.; Stone, M. H. *Hip Int.* **2003**, *13*(Suppl 2), S31–S35.
36. Bos, I.; Willmann, G. *Acta Orthop. Scand.* **2001**, *72*(4), 335–342.
37. Fritsch, E.; Remberger, K.; Mittelmeier, H. In *Die Keramikpaarung BIOLOX in der Hüftendoprothetik*; Puhl, W., Ed.; Enke: Stuttgart, 1996; pp 12–17.
38. Shishido, T.; Yamamoto, K.; Tanaka, S.; Masaoka, T.; Clarke, I. C.; Williams, P. *J. Arthroplasty* **2006**, *21*(2), 294–298.
39. Boutin, P. In *Proceedings of the Japanese Society of Orthopaedic Ceramic Implants*; Oonishi, H., Ooi, Y., Eds.; *Orthopedic Alumina Ceramic Implants*; 1981, Vol. 1, pp 11–19.
40. Higuchi, F.; Shiba, N.; Inoue, A.; *et al. J. Arthroplasty* **1995**, *10*(6), 851–854.
41. Griss, P.; Heimke, G. *Arch. Orthop. Trauma. Surg.* **1981**, *98*(3), 157–164.
42. Winter, M.; Griss, P.; Scheller, G.; *et al. Clin. Orthop.* **1992**, *282*, 73–80.
43. Knahr, K.; Salzer, M.; Plenk, H., Jr.; *et al. Biomaterials* **1981**, *2*(2), 98–104.
44. Heisel, J.; Schmitt, E. *Z. Orthop. Ihre Grenzgeb.* **1987**, *125*(5), 480–490.
45. Mittelmeier, H.; Heisel, J. *Clin. Orthop.* **1992**, *282*, 64–72.
46. Knahr, K.; Böhler, M.; Frank, P.; *et al. Arch. Orthop. Trauma. Surg.* **1987**, *106*(5), 297–300.
47. Trepte, C. T.; Gauer, E. F.; Gärtner, B. M. *Z. Orthop.* **1985**, *123*(2), 239–244.
48. Boutin, P.; Christel, P.; Dorlot, J. M.; *et al. J. Biomed. Mater. Res.* **1988**, *22*(12), 1203–1232.
49. Oonishi, H.; Aono, M.; Murata, N.; *et al. Clin. Orthop.* **1992**, *282*, 95–104.
50. Boutin, P.; Blanquaert, D. *Rev. Chir. Orthop.* **1981**, *67*(3), 279–287.
51. Rampoldi, A. *Ital. J. Orthop. Traumatol.* **1984**, *10*(3), 305–311.
52. Hølmer, P.; Nielsen, P. T. *J. Arthroplasty* **1993**, *8*(6), 567–571.
53. Higgs, R. J. *J. Bone Joint Surg.* **1990**, *72B*, 1101.
54. Nevelös, A. B.; Evans, P. A.; Harrison, P.; *et al. Proc. Inst. Mech. Eng. [H]* **1993**, *207*(3), 155–162.
55. Cameron, H. U. *J. Arthroplasty* **1991**, *6*(2), 185–188.
56. Bardos, D. I. In *Ceramics in Clinical Applications*; Vincenzini, P., Ed.; Elsevier: Amsterdam, 1987; pp 305–311.
57. Kern, S.; Schreiber, A.; Hilfiker, B. *Z. Orthop.* **1990**, *128*(5), 543–548.
58. Peiró, A.; Pardo, J.; Navarrete, R.; *et al. J. Arthroplasty* **1991**, *6*(4), 371–374.
59. O'Leary, J. F.; Mallory, T. H.; Kraus, T. J.; *et al. J. Arthroplasty* **1988**, *3*(1), 87–96.
60. Hoffinger, S. A.; Keggi, K. J.; Zatorski, L. E. *Orthopedics* **1991**, *14*(5), 523–531.
61. Israel, C.; Linke, R. *Beitr. Orthop. Traumatol.* **1989**, *36*(7), 310–312.
62. Toni, A.; Sudanese, A.; Ciaroni, D.; *et al. Chir. Organi Mov.* **1990**, *75*(1), 81–97.
63. Toni, A.; Lewis, C. G.; Sudanese, A.; *et al. J. Arthroplasty* **1994**, *9*(4), 435–444.
64. Callaway, G. H.; Flynn, W.; Ranawat, C. S.; *et al. J. Arthroplasty* **1995**, *10*(6), 855–859.
65. Hummer, C. D.; Rothman, H. R.; Hozack, W. J. *J. Arthroplasty* **1995**, *10*, 849–850.
66. Semlitsch, M.; Weber, H.; Steger, R. *Biomed. Technik.* **1995**, *40*, 347–355.
67. Castro, F. P.; Chimiento, G.; Munn, B. G.; *et al. J. Arthroplasty* **1997,** *12*(7), 765–771.
68. D'Antonio. Ceramic fracture: Past & present. Presentation at the Hip Society 2007 Meeting.
69. D'Antonio, J.; Capello, W.; Manley, M.; Naughton, M.; Sutton, K. *Clin. Orthop. Relat. Res.* **2005**, *436*, 164–171.
70. Capello, W. N.; D'Antonio, J. A.; Feinberg, J. R.; Manley, M. T.; Naughton, M. *J. Arthroplasty* **2008**, *23*, 39–43.
71. Garino, J. P. *Clin. Orthop. Relat. Res.* **2000**, *379*, 41–47.
72. Murphy, S. B.; Ecker, T.; Tannast, M.; *et al. Semin. Arthroplasty* **2006**, *17*(3), 120–124.
73. Murphy, S. B.; Ecker, T. M.; Tannast, M. *Clin. Orthop. Relat. Res.* **2006**, *453*, 97–102.
74. Hamilton, W. G.; McAuley, J. P.; Dennis, D. A.; Murphy, J. A.; Blumenfeld, T. J.; Politi, J. *Clin. Orthop. Relat. Res.* **2010**, *468*(2), 358–366.
75. Dorlot, J. M.; Christel, P.; Meunier, A. *J. Biomed. Mater. Res. A* **1989**, *23*(3 Suppl), 299–310.
76. Boehler, M.; Knahr, K.; Plenk, H., Jr.; Walter, A.; Salzer, M.; Schreiber, V. *J. Bone Joint Surg. Br.* **1994**, *76*, 53–59.
77. Prudhommeaux, F.; Hamadouche, M.; Nevelos, J.; Doyle, C.; Meunier, A.; Sedel, L. *Clin. Orthop.* **2000**, *379*, 113–122.
78. Hamadouche, M.; Boutin, P.; Daussange, J.; Bolander, M. E.; Sedel, L. *J. Bone Joint Surg. Am.* **2002**, *84A*(1), 69–77.
79. Hernigou, P.; Zilber, S.; Filippini, P.; Poignard, A. *Clin. Orthop. Relat. Res.* **2009**, *467*(9), 2274–2280.
80. Aldrian, S.; Nau, T.; Gillesberger, F.; Petras, N.; Ehall, R. *Hip Int.* **2009**, *19*(1), 36–40.

81. Nau, T.; Raschid, J.; Kirnbauer, W.; Schwischei, H.; Ehall, R. *Wien. Med. Wochenschr.* **2005**, *155*(3–4), 70–74.
82. Fenollosa, J.; Seminario, P.; Montijano, C. *Clin. Orthop. Relat. Res.* **2000**, *379*, 55–67.
83. Lazzaro, F.; Verdoia, C.; Gorla, P.; Balbino, C.; Benvenuti, R. *Chir. Organi Mov.* **1999**, *84*(4), 319–328.
84. Hasegawa, M.; Ohashi, T.; Tani, T. *Acta Orthop. Scand.* **2001**, *72*(5), 449–456.
85. Koo, K. H.; Ha, Y. C.; Jung, W. H.; Kim, S. R.; Yoo, J. J.; Kim, H. J. *J. Bone Joint Surg. Am.* **2008**, *90*, 329–336.
86. Kawanabe, K.; Tanaka, K.; Tamura, J.; *et al*. *J. Orthop. Sci.* **2005**, *10*(4), 378–384.
87. Park, Y. S.; Hwang, S. K.; Choy, W. S.; Kim, Y. S.; Moon, Y. W.; Lim, S. J. *J. Bone Joint Surg. Am.* **2006**, *88*(4), 780–787.
88. Sugano, N.; Nishii, T.; Miki, H.; Yoshikawa, H.; Sato, Y.; Tamura, S. *J. Bone Joint Surg. Br.* **2007**, *89*(4), 455–460.
89. Zhou, Z. K.; Li, M. G.; Borlin, N.; Wood, D. J.; Nivbrant, B. *Clin. Orthop. Relat. Res.* **2006**, *448*, 39–45.
90. Boehler, M.; Plenk, H.; Slazer, M. *Clin. Orthop. Relat. Res.* **2000**, *379*, 85–93.
91. Bizot, P.; Nizard, R.; Leronge, S.; *et al*. *J. Orthop. Sci.* **2000**, *5*(6), 622–627.
92. Urban, J. A.; Garvin, K. L.; Boese, C. K.; *et al*. *J. Bone Joint Surg. Am.* **2001**, *83A*(11), 1688–1694.
93. Delaunay, C.; Bonnonet, F.; North, J. *J. Arthroplasty* **2001**, *16*(1), 47–54.
94. Hamadouche, M.; Sedel, L. *J. Bone Joint Surg. Am.* **2000**, *82*(8), 1095–1099.
95. D'Antonio, J.; Capello, W.; Manley, M. *J. Arthroplasty* **2002**, *17*(4), 390–397.
96. Bierbaum, B. E.; Hozack, W. J.; Mesko, W.; *et al*. *Clin. Orthop. Relat. Res.* **2007**, *465*, 155–158.
97. Hannauche, D.; Tanaka, K.; Tamura, J.; *et al*. *J. Orthop. Sci.* **2005**, *10*(4), 378–384.
98. Slack, R.; Tindall, A.; Shetty, A.; *et al*. *J. Orthop Surg.* **2006**, *14*(2), 151–154.
99. Lusty, P. K.; Tai, C. C.; Sew-Hoy, R. P.; Walter, W. L.; Walter, W. K.; Zicat, B. A. *J. Bone Joint Surg. Am.* **2007**, *89*, 2676.
100. Heros, R.; Willmann, G. *Semin. Arthroplasty* **1998**, *9*(2), 114–122.
101. Back, D. L.; Dalziel, R.; Young, D.; Shimmin, A. *J. Bone Joint Surg. Br.* **2005**, *87*, 324–329.
102. D'Antonio. Ceramic bearings: Squeaking not a problem. Presentation at the American Association of Hip and Knee Surgeons 2009 Annual Meeting.
103. Komistek. In vivo determination and correlation of kinematics and sound for subjects having two different ceramic-on-ceramic THA. Presentation at the Orthopedic Research Society 2008 Annual Meeting.
104. Garino *et al*. What happens to the squeaky ceramic THA: Average 5-year follow-up. Presentation at the American Academy of Orthopedic Surgeons 2009 Annual Meeting.
105. Mesko *et al*. 3rd generation alumina-alumina THA: Has it met expectations? Presentation at the American Academy of Orthopedic Surgeons 2009 Annual Meeting.
106. Restrepo, C.; Parvizi, J.; Kurtz, S. M.; Sharkey, P. F.; Hozack, W. J.; Rothman, R. H. *J. Arthroplasty* **2008**, *23*, 643–649.
107. Keurentjes, J. C.; Kuipers, R. M.; Wever, D. J.; Schreurs, B. W. *Clin. Orthop.* **2008**, *466*, 1438.
108. Jarrett, C. A.; Ranawat, A. S.; Bruzzone, M.; Blum, Y. C.; Rodriguez, J. A.; Ranawat, C. S. *J. Bone Joint Surg. Am.* **2009**, *91*(6), 1344–1349.
109. Walter, W. L.; O'Toole, G. C.; Walter, W. K.; Ellis, A.; Zicat, B. A. *J. Arthroplasty* **2007**, *22*, 496.
110. Jarrett, C. A.; Ranawat, A.; Bruzzone, M.; Rodriguez, J.; Ranawat, C. *J. Arthroplasty* **2007**, *22*, 302.
111. Chang, J. D.; Kamdar, R.; Yoo, J. H.; Hur, M.; Lee, S. S. *J. Arthroplasty* **2009**, *24*(8), 1231–1235.
112. Mai, K.; Verioti, C.; Ezzet, K. A.; Copp, S. N.; Walker, R. H.; Colwell, C. W., Jr. *Clin. Orthop. Relat. Res.* **2010**, *468*(2), 413–417.
113. Chevillotte, C.; Trousdale, R. T.; Chen, Q.; Guyen, O.; An, K. N. *Clin. Orthop. Relat. Res.* **2010 Feb**, *468*(2), 345–350.
114. Taylor, S.; Manley, M. T.; Sutton, K. *J. Arthroplasty* **2007**, *22*(Suppl 3), 47–51.
115. Walter, A. *Clin. Orthop. Relat. Res.* **1992**, *282*, 31–46.
116. Food and Drug Administration. *Guidance Document for the Preparation of Premarket Notification for Ceramic Ball Hip Systems*, 1995 January 10.

Relevant Websites

http://www.ceramtec.com/index/advanced-ceramics/ – CeramTec AG.
http://www.arthroplastyjournal.org/search – Journal of Arthroplasty.
http://www.ejbjs.org/search.dtl – Journal of Bone and Joint Surgery.
http://www.clinorthop.org/index.html – Clinical Orthopaedics and Related Research.

6.605. Porous Coatings in Orthopedics

D H Kohn, University of Michigan, Ann Arbor, MI, USA

© 2011 Elsevier Ltd. All rights reserved.

6.605.1.	**Introduction**	65
6.605.1.1.	Objectives of Joint Replacement	65
6.605.1.2.	Objectives of Biological Fixation Using Porous Materials	66
6.605.2.	**Materials Used for Porous Coatings**	66
6.605.2.1.	Metals	66
6.605.2.1.1.	Cobalt-based alloys	67
6.605.2.1.2.	Titanium-based materials	67
6.605.2.1.3.	Tantalum	68
6.605.2.2.	Ceramics and Ceramic-Coated Metals	68
6.605.2.3.	Polymers	70
6.605.3.	**Properties of Porous-Coated Implants**	70
6.605.3.1.	Mechanical Properties	70
6.605.3.2.	Electrochemical Properties	71
6.605.4.	**Design and Characterization of Porous Materials**	72
6.605.5.	**Porous Coatings in Tissue Engineering**	73
6.605.6.	**Summary and Future Directions**	75
References		75

Abbreviations

Ac	Acicular
AC	Alternating current
BAA	Beta annealing and aging heat treatment
BCC	Body-centered cubic
COD	Crack opening displacement
CP Ti	Commercially pure titanium
DC	Direct current
DCPD	Dicalcium phosphate dihydrate
EA	Equiaxed
FCI	Fatigue crack initiation
FCC	Face-centered cubic
HA	Hydroxyapatite
HAT	Hydrogen alloying treatment
HCF	High cycle fatigue
HCP	Hexagonal close packed
HIP	Hot isostatic pressing
L	Lamellar
LFCP	Long fatigue crack propagation
MCP	Monocalcium phosphate
MCPH	Monohydrate calcium phosphate
N	Number of fatigue cycles
OCP	Octacalcium phosphate
PEG	Polyethylene glycol
PLGA	Polylactic–glycolic acid copolymer
RNA	Ribonucleic acid
SEM	Scanning electron microscopy
SFCP	Short fatigue crack propagation
STM	Scanning tunneling microscopy
STP	Standard temperature and pressure
TCP	Tricalcium phosphate

6.605.1. Introduction

6.605.1.1. Objectives of Joint Replacement

The clinical objectives of joint replacement are to relieve pain and increase mobility. To meet this objective, material choice and design decisions must provide as physiologic a strain as possible to the bone surrounding the prosthesis so that the integrity and functionality of the bone and implant are maintained over an expected service life of 10–15 years. Materials suited for joint replacements are those that are well-tolerated by the body and can withstand cyclic loading on the order of 10^7 cycles in an aqueous, protein enriched environment.

Total joint replacements are categorized by the mechanism of fixing the implant to the surrounding tissue. In general, implants are either cemented or cementless, referring to whether the implant is stabilized with a grouting agent or by direct contact between tissue and the implant surface. Problems with cemented implants, especially in younger patients, inspired cementless implants in which fixation is dependent upon tissues' ability to bond with the implant and maintain this bond over time.[1–5]

The design of joint replacements is geared toward maximizing interfacial bonding and stress transfer across the implant/tissue interface, within the constraints of using materials that can meet the mechanical demands and be tolerated biologically. Parameters dictating the success of porous-coated joint replacements (Figure 1) include the mechanical properties of the implant, coating, and implant/coating interface[6–10]; mechanisms of tissue attachment to the implant, including

the surface state of the implant and coating, and size, shape, and distribution of surface porosity[11–18]; the mechanical properties of the tissue, including stress and strain magnitude and distribution[19–21]; the elastic properties of the implant, coating and tissue, especially with respect to mediating relative motion and tissue adaptation[22–27]; initial stability and strategies to stimulate tissue ingrowth[28–34]; implant design[35–37]; and the biological response to the implant materials.[38,39]

6.605.1.2. Objectives of Biological Fixation Using Porous Materials

Cementless fixation is achieved by establishing an interference fit between the implant and surrounding tissue. Cementless implants are designed to minimize the time necessary for tissue integration and maximize interfacial stability. Ideally, the implant materials should elicit the formation of normal tissue at the surface and establish a continuous interface capable of supporting service loads over time.[40]

Cementless fixation may be achieved via surface active materials, surface textured materials, or porous-coated materials. Surface active materials lead to fixation through a chemical reaction between tissues and a bioactive implant surface.[41] With surface textured materials, bone grows onto the surface of a grooved or textured implant.[6,42,43] With porous-coated materials, bone grows into the pores of a three-dimensional (3D) porous or porous-coated material.[13,18]

Porous-coated prostheses provide fixation to bone by creating an interdigitation between bone and a porous 3D surface.[12,13,44] Porous-coated systems can lead to a higher bone/implant shear strength than other types of fixation,[12,45] resulting in a better stress transfer from the implant to the surrounding bone, a more uniform stress distribution between the implant and bone, and lower stresses in the implant.[44,46]

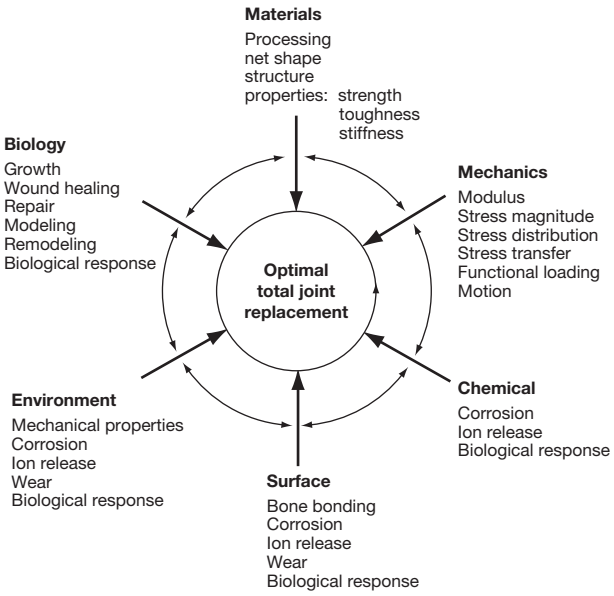

Figure 1 Schematic of interdependent factors affecting the success of porous-coated implants. Reproduced from Kohn, D. H.; Ducheyne, P. In *Medical and Dental Materials*; Williams, D. F., Ed.; VCH, Verlagsgesellschaft, FRG, 1992; pp 29–109, with permission.

6.605.2. Materials Used for Porous Coatings

Porous coatings have been fabricated from polymers – polytetrafluoro-ethylene,[47,48] polysulfone,[43,49] polyethylene,[50] and poly(methylmethacrylate),[51] ceramics – calcium aluminate[52] and alumina,[53,54] and metals – stainless steel,[55] cobalt-based alloys,[18] titanium-based alloys,[13] and tantalum.[56]

6.605.2.1. Metals

Implant materials may corrode and/or wear leading to the generation of particulate debris, which may elicit local and systemic responses. Although metals exhibit high strength and toughness, they are more susceptible to electrochemical degradation than ceramics or polymers. Therefore, a fundamental criterion for choosing a metallic implant material, especially one that will be used as a porous coating with a high surface area, is that the biological response it elicits is minimal. Because of the combined mechanical and environmental demands, metals currently used for porous coatings in orthopedics are limited to three classes: cobalt-based alloys, titanium-based materials, and tantalum. Each of these materials is well-tolerated by the body because of its passive oxide layer.

Porous metal coatings are manufactured from powdered microspheres,[18] fibers,[13] wires,[55] foams,[57] or other porous conglomerates,[58] which are mechanically or chemically bonded onto a dense metallic substrate to produce periodic or inhomogeneous porous surface geometries that vary in porosity and degree to which the porous medium is open or closed (**Figure 2**).

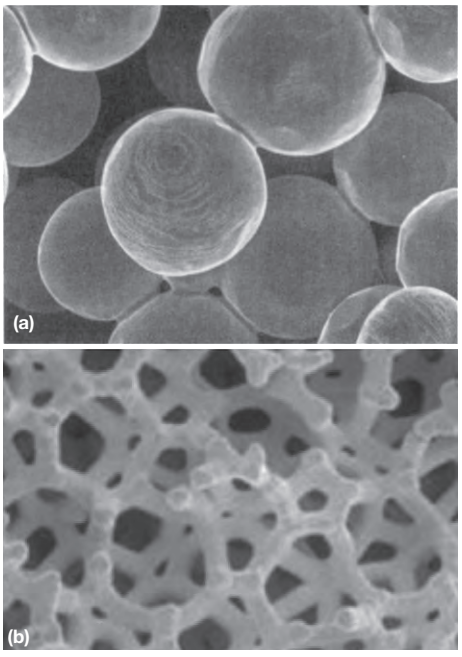

Figure 2 Images of porous metals used in orthopedics. (a) Scanning electron micrograph of porous surface made from titanium powder microspheres approximately 300 μm in diameter. Reproduced from Kohn, D. H.; Ducheyne, P. In *Medical and Dental Materials*; Williams, D. F., Ed.; VCH, Verlagsgesellschaft, FRG, 1992; pp 29–109, with permission. (b) Microstructure of Ta trabecular metal. Reproduced from Levine, B. *Adv. Eng. Mater.* **2008**, *10*, 788–792, with permission.

6.605.2.1.1. Cobalt-based alloys

Three cobalt alloys are used as orthopedic implants: Co–28Cr–6Mo, which is cast (ASTM F75), forged (ASTM F799), or wrought (ASTM F1537); Co–20Cr–15W–10Ni, which is wrought (ASTM F90); and Co–35Ni–20Cr–10Mo, which is wrought (ASTM F562) or forged (ASTM 961) (Table 1). The requirements for powdered coatings conform to those of cast Co–28Cr–6Mo (ASTM F1377).

Co–28Cr–6Mo alloys are cast at 1350–1450 °C and exhibit an inhomogeneous, large-grained, cored microstructure. The dendritic regions are Co-rich and the interdendritic regions are a combination of a Co-rich γ-phase, a Cr-rich $M_{23}C_6$ phase, where M is Co, Cr, or Mo, an M_7C_3 phase, and a Cr and Mo-rich σ-phase.[59] Co–28Cr–6Mo alloys exhibit a eutectic point at 1235 °C.[59] At temperatures above the eutectic, local melting of the solute-rich zones occurs. Cooling to below the eutectic yields a microstructure consisting of grain boundary σ, γ, and $M_{23}C_6$, which embrittle the alloy. Since the interdendritic phases reduce ductility and corrosion resistance, Co–28Cr–6Mo is solution annealed at 1225 °C, resulting in the transformation of σ to $M_{23}C_6$ and partial dissolution of the $M_{23}C_6$ phase.[60]

Wrought Co–Cr has an austenitic microstructure. Forging above 650 °C results in elongated grains, without recrystallization of the austenitic structure, whereas cold-working below 650 °C results in the formation of an ε-phase. Forging results in a smaller grain size and finer distribution of the block carbides than casting.

Co–35Ni–20Cr–10Mo also has a fine-grained austenitic microstructure. This alloy undergoes an allotropic phase transformation, from an HCP to an FCC structure at 650 °C. Similar to Co–28Cr–6Mo, the low-temperature FCC phase is retained upon cooling, with the transformation product existing only within narrow HCP bands. Aging within the two-phase field leads to the formation of a Co_3Mo precipitate in the HCP regions.

Porous-coated Co–Cr–Mo alloys are created by sintering powdered Co–Cr–Mo microspheres, 100–300 μm in diameter onto a Co–Cr–Mo substrate at 1200–1300 °C for 1–3 h. Alternatively, some coatings are formed by plasma-spraying irregular particles onto a substrate. Since sintering temperatures are above the eutectic point,[59] localized melting accelerates particle bonding. However, processing at temperatures in this range results in the formation of eutectic phases and grain boundary carbides, reducing ductility.

6.605.2.1.2. Titanium-based materials

The combination of high strength, resistance to electrochemical degradation, benign biological response, and relatively low modulus make titanium-based materials attractive for load-bearing applications. Commercially, pure titanium does not possess sufficient strength for orthopedic load-bearing applications, but it is used for porous coatings. Several titanium alloys provide sufficient strength and corrosion resistance: Ti–6Al–4V, wrought (ASTM F136) or cast (ASTM F1108); Ti–6Al–7Nb, wrought (ASTM F1295); Ti–13Nb–13Zr, wrought (ASTM F1713); Ti–15Mo, wrought (ASTM F2066) (Table 2). Several new Ti alloys have also been investigated: Ti–5Al–2.5Fe,[61] Ti–12Mo–6Zr–2Fe, and Ti–35Nb–7Zr–5Ta.[62] Of these alloys, Ti–6Al–4V is the most extensively characterized and used. Porous coatings are comprised of commercially pure Ti or Ti–6Al–4V (ASTM F1580).

At room temperature, Ti–6Al–4V is a two-phase α + β alloy. Above the β-transition temperature (975 °C), an allotropic phase transition occurs, transforming the microstructure to a single-phase body-centered cubic (BCC) β-alloy. Heat treating Ti alloys varies the relative amounts of α- and β-phases and morphologies, resulting in a variety of microstructures and

Table 1 Chemical composition (wt%) of cobalt–chromium alloys used in total joint replacement

Element	*Co–28Cr–6Mo*				*Co–20Cr–15W–10Ni*	*Co–35Ni–20Cr–10Mo*
	F75 (cast) + F1377 (powder)	*F799 (forged) + F1537 (wrought)*			*F90 (wrought)*	*F562 (wrought) + F961 (forged)*
		Low carbon	*High carbon*	*Dispersion strengthened*		
Cr	27.0–30.0	26.0–30.0	26.0–30.0	26.0–30.0	19.0–21.0	19.0–21.0
Mo	5.0–7.0	5.0–7.0	5.0–7.0	5.0–7.0		9.0–10.5
Ni	0.5 (max)	1.0 (max)	1.0 (max)	1.0 (max)	9.0–11.0	33.0–37.0
Fe	0.75 (max)	0.75 (max)	0.75 (max)	0.75 (max)	3.0 (max)	1.0 (max)
C	0.35 (max)	0.14 (max)	0.15–0.35	0.14 (max)	0.05–0.15	0.025 (max)
Si	1.0 (max)	1.0 (max)	1.0 (max)	1.0 (max)	0.4 (max)	0.15 (max)
Mn	1.0 (max)	1.0 (max)	1.0 (max)	1.0 (max)	1.0–2.0	0.15 (max)
W	0.2 (max)				14.0–16.0	
P	0.02 (max)				0.04 (max)	0.015 (max)
S	0.01 (max)				0.03 (max)	0.010 (max)
N_2	0.25 (max)	0.25 (max)	0.25 (max)	0.25 (max)		
Al	0.1 (max)			0.30–1.0		
Ti	0.1 (max)					1.0 (max)
B	0.01 (max)					0.015 (max)
La				0.03–0.2		
Co	Balance	Balance	Balance	Balance	Balance	Balance

Table 2 Chemical composition (wt%) of titanium and titanium alloys used in total joint replacement

Element	*c.p. Ti*	*Ti–6Al–4V*			*Ti–6Al–7Nb*	*Ti–13Nb–13Zr*	*Ti–15Mo*
	F1580 (powder)	*F136 (wrought)*	*F1108 (cast)*	*F1580 (powder)*	*F1295 (wrought)*	*F1713 (wrought)*	*F2066 (wrought)*
N_2	0.05 (max)	0.05 (max)	0.05 (max)	0.05 (max)	0.05 (max)	0.05 (max)	0.05 (max)
C	0.08 (max)	0.08 (max)	0.10 (max)	0.08 (max)	0.08 (max)	0.08 (max)	0.10 (max)
H_2	0.05 (max)	0.012 (max)	0.015 (max)	0.015 (max)	0.009 (max)	0.012 (max)	0.015 (max)
Fe	0.50 (max)	0.25 (max)	0.30 (max)	0.30 (max)	0.25 (max)	0.25 (max)	0.10 (max)
O_2	0.40 (max)	0.13 (max)	0.20 (max)	0.20 (max)	0.20 (max)	0.15 (max)	0.20 (max)
Cu				0.10 (max)			
Sn				0.10 (max)			
Y				0.005 (max)			
Ta					0.5 (max)		
Al		5.5–6.5	5.5–6.75	5.5–6.75	5.5–6.5		
V		3.5–4.5	3.5–4.5	3.5–4.5			
Nb					6.5–7.5	12.5–14.0	
Zr						12.5–14.0	
Mo							14.0–16.0
Ti	Balance	Balance	Balance	Balance	Balance	Balance	Balance

range of mechanical properties, depending on whether heat treatments were performed above or below the β-transition temperature and cooling rate.

Thermal treatments below the β-transition temperature produce recrystallized equiaxed microstructures, characterized by small (3–10 μm), rounded α-grains with aspect ratios near unity. This type of microstructure is recommended for Ti–6Al–4V implants (ASTM F136). Thermal treatments above the β-transition temperature lead to a variety of microstructures, depending on cooling rate in the $(\alpha+\beta)$ field. Slow cooling produces a lamellar microstructure, similar to that produced by casting and high-temperature sintering of porous coatings, and characterized by coarse (5–20-μm thick) parallel α-platelets. Lamellar microstructures may be refined via solution treatments above the β-transus and subsequent aging at a temperature high in the $(\alpha+\beta)$ phase field.[7,63,64] Titanium microstructures may also be refined by chemical alloying,[65–68] resulting in microstructures with α-grain sizes <1 μm, aspect ratios near unity and discontinuous grain boundary α, microstructural attributes which increase fatigue strength.

To produce sufficient energy to bond Ti microspheres or particles to a substrate, sintering temperatures in the range of 1200–1400 °C are necessary.[5] At these temperatures, bonding of titanium occurs by solid state diffusion. Temperatures in the 1200–1400 °C range are above the β-transition temperature of most Ti alloys used in medicine, leading to coarse lamellar microstructures. The notch-sensitivity of titanium, along with the lamellar microstructure and surface changes created by high-temperature sintering, lead to a significant reduction in fatigue strength of porous-coated Ti implants versus noncoated implants.

Fiber or wire mesh coatings may be bonded to the substrate using a combination of temperature and pressure. The use of pressure allows for lower sintering temperatures. Therefore, Ti–6Al–4V can be sintered at temperatures below the β-transition temperature,[69] resulting in the retention of an equiaxed microstructure. Other porous coatings, such as ones formed from powdered microspheres, become too dense when subjected to pressure, reducing the porosity below the minimum level necessary for bone ingrowth.

On average, bone only grows into 30% of the total available pore spaces in porous-coated implants and is limited to outer regions of porous coatings.[70] To provide porous surfaces with a higher degree of porosity, without compromising mechanical properties, open cell foams, some mimicking the architecture of trabecular bone, have been developed.[57] Starting with an organic foam shell precursor, metal, typically titanium or tantalum, is coated onto the pore surfaces using vapor deposition and sintered to the bulk implant, resulting in porosities of 60–80%.

6.605.2.1.3. Tantalum

Porous tantalum foams are developed from pyrolysis of an organic precursor into a vitreous carbon skeleton.[57] Subsequently, crystalline tantalum is deposited into the foam via chemical vapor deposition.[56] Modifying the thickness of the Ta layer controls stiffness, strength, and porosity. Nominally, physical properties of Ta foams are in the range of trabecular bone properties: stiffness 3 GPa, compressive strength 60 MPa.[71,72] The larger, more open and regular porosity can lead to bone ingrowth through the full thickness of the coating, filling as much as 80% of the pores and leading to higher fixation strength.[56] Applications of porous Ta include hip and knee arthroplasty, especially revision cases, treatment of osteonecrosis of the femoral head, spinal fusion cages, and use as a structural bone graft substitute.[73,74]

6.605.2.2. Ceramics and Ceramic-Coated Metals

Ceramics were originally used in medicine and dentistry because of their relative biological inertness compared to metals. Over time, emphasis has shifted toward bioactive ceramics, or ceramics that can form a chemical gradient and chemical bond with bone through surface dissolution and ion exchange. In addition to having the ability to bond to bone, ceramics are also used to deliver cells, proteins, and genes.

The most common bioceramic used in orthopedics is hydroxyapatite (HA; $Ca_{10}(PO_4)_6(OH)_2$). The motivation for using synthetic HA as a biomaterial stems from the hypothesis that a biomaterial with a composition similar to the mineral phase in bone will bond to bone. The crystal structure of HA is modified by ionic substitutions, which influence bone bonding. Most synthetic HA implants contain substitutions for the PO_4^{3-} and/or OH^- groups and vary from the ideal stoichiometry and Ca/P ratio of 1.67. For example, oxyhydroxyapatite, tricalcium phosphate, tetracalcium phosphate, and octocalcium phosphate have all been detected in commercially available apatite implants (**Table 3**).[75–78]

Bioactive ceramics exhibit low tensile strength and fracture toughness. Therefore, their use in bulk form is limited to applications in which only compressive loads are applied. Bioactive ceramics may be implanted in anatomic sites subjected to tensile stresses if they are used as a coating on a metal or ceramic implant[29] or strengthened via crystallization or reinforcing with a second phase.[79–82]

Calcium-phosphate coatings have been deposited onto porous metal implants to accelerate bone ingrowth, increase the strength of the prosthesis/bone interface, and shield tissues from metallic corrosion products.[29,70,83] The amount of bone ingrowth, strength of the ceramic/bone interface, degree of improvement in bond strength relative to noncoated metals and Ca-P solubility are variable, suggesting material and processing induced variance in the ceramic and metal, in addition to biological variability.[76,84]

Calcium-phosphate coatings are bonded to metallic implants via several techniques: sintering[75,76,85]; plasma-spraying[77,86]; ion beam and other sputtering techniques[87,88]; electrophoretic deposition[75,76]; sol–gel techniques[89]; pulsed laser deposition[90]; chemical vapor deposition[91]; and solution techniques.[92–95]

Table 3 Calcium-phosphate phases with corresponding Ca/P ratios

Name	*Formula*	*Ca/P ratio*
Hydroxyapatite (HA)	$Ca_{10}(PO_4)_6(OH)_2$	1.67
Fluorapatite	$Ca_{10}(PO_4)_6F_2$	1.67
Chlorapatite	$Ca_{10}(PO_4)_6Cl_2$	1.67
A-type carbonated apatite (unhydroxylated)	$Ca_{10}(PO_4)_6CO_3$	1.67
B-type carbonated hydroxyapatite (dahllite)	$Ca_{10-x}[(PO_4)_{6-2x}(CO_3)_{2x}](OH)_2$	$\geq$1.67
Mixed A and B-type carbonated apatites	$Ca_{10-x}[(PO_4)_{6-2x}(CO_3)_{2x}]CO_3$	$\geq$1.67
HPO_4-containing apatite	$Ca_{10-x}[(PO_4)_{6-x}(HPO_4)_x](OH)_{2-x}$	$\leq$1.67
Monohydrate calcium phosphate (MCPH)	$Ca(H_2PO_4)_2{\cdot}H_2O$	0.50
Monocalcium phosphate (MCP)	$Ca(H_2PO_4)_2$	0.50
Dicalcium phosphate dihydrate (DCPD)	$Ca(HPO_4){\cdot}2H_2O$	1.00
Tricalcium phosphate (TCP)	α- and β-$Ca_3(PO_4)_2$	1.50
Octacalcium phosphate (OCP)	$Ca_8H(PO_4)_6{\cdot}5H_2O$	1.33

Adapted from Segvich, S. J.; Luong, L. N.; Kohn, D. H. In *Biomaterials and Biomedical Engineering*; Ahmed, W., Ali, N., Öchsner, A., Eds.; Trans Tech Publications: Zurich, 2008, with permission.

During plasma-spraying, powder is sprayed onto the metal implant, with plasma temperatures as high as 10 000 °C. The ceramic particles form a loosely bonded coating on impact. Due to the rapid cooling of the particles, the temperature of the metal does not exceed 150 °C and the structure and properties of the bulk metal do not change. However, porosity and phase changes are induced in the ceramic, and mixtures of HA, TCP, and tetracalcium phosphate evolve from stiochiometric HA.[77]

During ion sputtering, an ion beam sputters off atoms from a target to form a thin coating on the porous metal. With electrophoretic deposition, the Ca-P coating is precipitated out of suspension onto the metal implant. Electrophoretic deposition is more conducive to coating the internal surfaces of a porous metal. Both sintering and electrophoretic deposition of apatite on titanium result in a phosphate-rich interfacial layer.[75] The interior of the coating is phosphate-depleted, resulting in a higher Ca/P ratio, the formation of tetracalcium phosphate and increased solubility.

An apatite layer can also be formed on an implant surface *in vitro* under STP conditions.[92,93,95–99] The use of biomineralization strategies to form 'bone-like mineral' *in vitro* is based on the concept that bioactive ceramics can bond to bone through a layer of bone-like apatite, which forms on some ceramic surfaces *in vivo* and is characterized as a carbonate-containing apatite with nanoscale crystallites.[100–103] It is therefore hypothesized that a requirement for a biomaterial to bond to bone is the formation of a biologically active bone-like apatite layer.[100–103]

The deposition of apatite onto an implant surface from solution is guided by the pH and ionic concentration of the microenvironment. Conditions conducive to heterogeneous nucleation will support epitaxial growth of mineral. To drive heterogeneous precipitation of mineral nuclei, the net energy between a nucleated precursor and the substrate must be less than the net energy of the nucleated precursor within the ionic solution.[93] The surface energy of an implant may be altered and functional groups that can chelate calcium ions may be created by grafting, self-assembled monolayers, irradiation, alkaline treatment, or hydrolysis.[95,97,99,104,105] Biomimetic strategies have been used to coat metals to accelerate osseointegration,[92,96,98,104,106] as well as glasses, ceramics, and polymers.[95,97,99,105,107,108]

The self-assembly of apatite within the pores of a porous or porous-coated implant enhances cell adhesion, proliferation, and osteogenic differentiation, as well as modulates cytoskeletal organization and cell motility *in vitro*.[109] When progenitor cells are transplanted on these materials, a larger and more spatially uniform volume of bone is regenerated.[110] An additional benefit of the biomimetic processing conditions is that growth factors can be incorporated into the coating without denaturing, enabling a dual conductive/inductive approach.[111–113]

Regardless of the technique used to coat an implant with bioactive ceramic, long-term stabilization and fixation strength frequently do not depend on the ceramic coating. The primary benefit of ceramic-coated porous metals is to accelerate the achievement of a steady-state interfacial strength. In addition to characterizing the ceramic/bone interface under functional loading, the mechanical integrity of the metal/ceramic interface must also be considered as a design parameter.

Different structures and compositions of Ca-P coatings result from different processing techniques. Ion exchange reactions at the interface between a ceramic surface and biological environment depend on a comprehensive set of physical/chemical properties, including particle size and shape, pore size, shape and distribution, phases present, crystallinity, coating thickness, hardness, stiffness, roughness, and surface area.[114] Differences in ceramic chemistry and structure lead to differences in biological response both *in vitro* (e.g., cell attachment and proliferation, protein synthesis, RNA transcription)[109,115,116] and *in vivo* (e.g., cell differentiation, amount and rate of bone formation, intensity, or duration of inflammatory response).[117–119] The collective data from numerous animal and human studies are that calcium-phosphate coatings with Ca/P ratios in the range 1.5–1.67, tricalcium phosphate and HA, respectively, result in the most beneficial tissue response.[114]

6.605.2.3. Polymers

Because of stress shielding of bone with stiff metallic implants, it is hypothesized that an isoelastic femoral stem or coating, which has a modulus similar to that of bone, will result in a more uniform stress distribution and better stress transfer across the implant/bone interface, reducing mechanically mediated bone resorption. Since most polymers are not mechanically suitable to be used as bulk load-bearing implants porous polymers, including polytetrafluoro-ethylene,[47,48] polysulfone,[43,49] and polyethylene,[50] have been used as coatings.

Coating metal implants with polymers could circumvent problems arising with porous metal coatings, including reduction in fatigue strength, stress shielding, and release of dissolution products. For example, polymer coatings have a lower modulus, are sintered to Ti–6Al–4V at temperatures below the β-transformation, and decrease the surface area of metal exposed to body fluids.[49] These advantages, however, are outweighed by the inability of the metal–polymer interface to withstand the stresses resulting from functional loading.

Although polymer coatings are used less extensively than metal or ceramic coatings, bone will grow into many polymers that are sufficiently inert and have a suitable porosity. The extent and time course of ingrowth depends on the location of implantation and mode of loading, but, at least from qualitative observations, the integrity of the polymer/bone interface can be as mechanically stable as a metal/bone interface. With the interest in degradable materials for tissue regeneration, porous polymers have experienced a renewed interest.

6.605.3. Properties of Porous-Coated Implants

To achieve bone ingrowth into the surface of an implant, high surface area coatings are used. The surface area of porous-coated implants is five to ten times greater than the surface area of noncoated, nontextured implants. Porous coatings have the potential to provide advantages of biological fixation, increased bone/implant shear strength, better stress transfer from the implant to the surrounding bone, and a more uniform stress distribution. However, the increased surface area does lead to potential, mechanical, and electrochemical disadvantages and design of porous-coated implants requires an understanding of the mechanical and electrochemical consequences of higher surface area materials. Reductions in fatigue and degradation resistance have been implicated in the failure of porous-coated implants.[120–122]

6.605.3.1. Mechanical Properties

Due to the long service life requirements of total joint replacements, the most critical mechanical property is high cycle fatigue strength. For many materials, 90% of the fatigue life is spent initiating a fatigue crack.[123] Thus, microstructural and compositional parameters inhibiting crack nucleation produce good high cycle fatigue strength. However, for materials with voids and geometric irregularities, especially notch-sensitive materials such as titanium, resistance to crack propagation is also a critical design parameter. Because of the microstructural and geometric changes brought about by the deposition of a porous coating onto an implant surface, the high cycle fatigue strength of porous metal implants is approximately 75% lower than the fatigue strength of uncoated total joint replacements[7,8,10,124,125] (**Table 4**).

The high ultimate and fatigue strengths make Co–Cr–Mo alloys suitable for joint reconstruction. However, the fatigue strength of porous-coated Co–Cr–Mo is only 180–250 MPa.[5,60,125] The high-temperature (1200–1300 °C) sintering treatment required to bond the coating to the substrate results in a microstructure similar to the microstructure of cast Co–Cr–Mo, which exhibits porosity and eutectic phases. Noncoated implants subject to the same sintering treatment have similar low fatigue strengths.[5,125] The lower fatigue strength of porous-coated Co–Cr–Mo implants can therefore be attributed to sintering, and postsintering treatments sufficient to refine cast microstructures are also applicable to porous-coated Co–Cr–Mo implants.[60,125]

The fatigue strength of Co–Cr–Mo alloys is controlled by the ability of the solute atoms C, Cr, and Mo to inhibit dislocation motion.[60] Solution annealing increases strength and ductility due to a reinforcing effect of the transformed carbides. However, prolonged annealing, such as during sintering treatments, results in more complete carbide dissolution and a decrease in fatigue strength.[60] Hot isostatic pressing (HIP-ing) increases the fatigue strength by reducing porosity and eliminating grain boundary carbides.[125]

The mechanical properties of $(\alpha+\beta)$ titanium alloys are dictated by the amount, size, shape, and morphology of the α-phase and the density of α/β interfaces.[114,126–128] Microstructures with a small α-grain size, a well dispersed β-phase, and a small α/β interface area, such as equiaxed and H_2-alloyed microstructures, resist fatigue crack initiation best and have the highest fatigue strengths (500–700 MPa),[8,67,127–129] because a small α-grain size decreases the slip length. Lamellar microstructures, which have a larger α/β surface area and more oriented colonies, have lower fatigue strengths (300–500 MPa), because slip is more easily transmitted from one plate to another. Hydrogen-alloying treatments break up the continuous grain boundary α and colony structure and produce a homogeneous microstructure consisting of refined α-grains in a matrix of discontinuous β, resulting in increased fatigue strength.[67]

Table 4 Fatigue strengths of porous-coated metals

Material	*Treatment*	*Fatigue strength (MPa)*	*Testing parameters*	*Authors*
Co–Cr–Mo	As cast	267	Reverse bending ($R=-1$); 167 Hz; $N=2\times10^7$	Georgette and Davidson[125]
	Sintered + HT[a]	177		
	Sintered + HIP + HT	255		
	Porous-coated, sintered + HT	193		
	Porous-coated, sintered + HIP + HT	234		
Ti–6Al–4V	Wrought	625	Reverse bending ($R=-1$); 50 Hz; $N=10^7$	Yue *et al.*[10]
	β-sintered	500		
	Porous-coated, β-sintered	200		
	Wrought	617	Reverse bending ($R=-1$); 167 Hz; $N=5\times10^7$	Cook *et al.*[124]
	β-sintered	377		
	Porous-coated, β-sintered	138		
	Wrought	668	Reverse bending ($R=-1$); 167 Hz; $N=5\times10^7$	Cook *et al.*[7]
	β-sintered	394		
	β-sintered + BAA-1[b]	488		
	β-sintered + BAA-2[b]	494		
	Porous-coated, β-sintered	140		
	Porous-coated, β-sintered + BAA-1	161		
	Porous-coated, β-sintered + BAA-2	162		
	Wrought	590	Reverse bending ($R=-1$); 100 Hz; $N=10^7$	Kohn and Ducheyne[8]
	β-sintered	497		
	β-sintered + HAT-1[c]	669		
	β-sintered + HAT-3[c]	643		
	β-sintered + BAA-3[b]	538		
	Porous-coated, β-sintered	218		
	Porous-coated, β-sintered + HAT-3	177		
	Porous-coated, β-sintered + BAA-3	233		

Modified from Kohn, D. H.; Ducheyne, P. In *Medical and Dental Materials*; Williams, D. F., Ed.; VCH: Verlagsgesellschaft, FRG, 1992; pp 29–109, with permission.

[a]Proprietary postsintering heat treatment.

[b]BAA = postsintering beta annealing and aging treatment: BAA-1 = 1250 °C, 2 h, slow cool; BAA-2 = 1250 °C, 2 h, slow cool/Ar cool/(α + β) anneal, 4 h, Ar cool BAA-3 = 1030 °C, 20 min, Ar quench/540 °C, 4 h, Ar quench.

[c]HAT = postsintering hydrogen-alloying treatments: HAT-1 = 850 °C, 0.5 h in H_2/650 °C, 16 h in vacuum; HAT-3 = 850 °C, 0.5 h in H_2/590 °C, 4 h in Ar/775 °C, 4 h in vacuum.

Since the fatigue life of porous-coated titanium alloys is governed by both the initiation and propagation of fatigue damage, the design of porous-coated implants must also account for mechanisms of fatigue crack propagation, which differ from those governing fatigue crack initiation. Microstructures with large grains and α/β interfacial areas have lower fatigue crack propagation rates and higher threshold stress intensities than fine-grained microstructures.

The reduced fatigue strength of porous-coated Ti is due to a combination of three factors: stress concentrations at the porous coating/substrate interface and within the porous coating: local stresses can be as high as 6X the applied stress[130]; changes in microstructure due to high-temperature sintering: resulting lamellar microstructures have a fatigue strength 20–40% lower than the fatigue strength of wrought, equiaxed Ti–6Al–4V[8,10,67,124,131]; and surface contamination from sintering.[10] Of these three factors, stress concentrations are the most critical.

As the stress concentration in a porous coating increases, the controlling stage of fatigue changes from crack initiation to short crack propagation to long crack propagation (**Figure 3**). As the governing stage of fatigue changes, the microstructure which maximizes the resistance to damage accumulation during that particular stage also changes. At low stress concentrations, crack initiation is the governing stage of fatigue and microstructures with small grains have the highest fatigue strength. At high stress concentrations, fatigue is governed by long crack propagation and coarse microstructures have the highest fatigue strength. At intermediate stress concentrations, such as the stress concentrations at sinternecks, there is no effect of microstructure, since fatigue life is equally dependent on crack initiation and crack propagation. Current porous coating designs lie in the crack propagation region of **Figure 3**. Reducing the stress concentrations at the porous coating/substrate interface will enable postsintering treatments to increase the fatigue strength of porous-coated titanium implants.

6.605.3.2. Electrochemical Properties

Corrosion and wear of implants are undesirable because of potential biological reactions to the degradation products

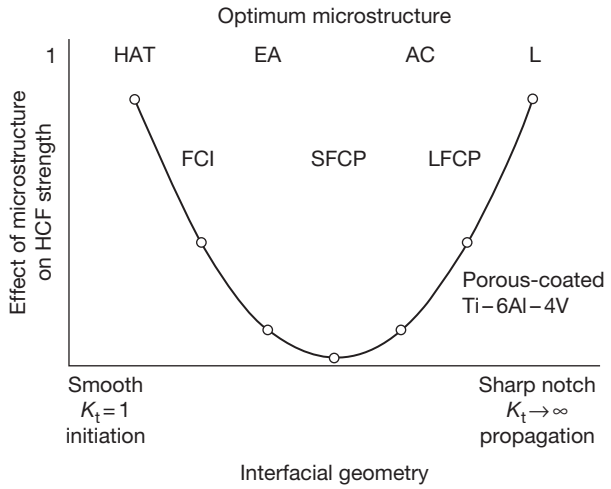

Figure 3 Schematic of Ti–6Al–4V high cycle fatigue (HCF) strength and governing stages of fatigue (FCI, fatigue crack initiation; SFCP, short crack propagation; LFCP, long fatigue crack propagation) as functions of microstructure (HAT, hydrogen alloy treated; EA, equiaxed; AC, acicular; L, lamellar) and interfacial geometry. Reproduced from Kohn, D. H.; Ducheyne, P. In *Medical and Dental Materials*; Williams, D. F., Ed.; VCH: Verlagsgesellschaft, FRG, 1992; pp 29–109, with permission.

and potential loss of implant structural integrity. For these reasons, metals used in implantology are in their passive state under typical physiological conditions and, theoretically, breakdown of passivity and transport of metal ions and electrons across the metal oxide should not occur.

Cobalt–chromium alloys are corrosion resistant because of their passive chromium oxide layer. Alloying with Mo further enhances corrosion resistance.[60] The inhomogeneous microstructure of cast Co–Cr–Mo makes it more susceptible to corrosion than the forged alloy,[132] due to the presence of Cr-depleted dendritic regions acting as the more anodic sites in a galvanic reaction. Wrought Co–Cr–Mo has a lower carbon content than cast Co–Cr–Mo and, as a result, a lower corrosion resistance.[132] However, the rest potentials of Co–Cr alloys are below the breakdown potential, and the breakdown potential exceeds the potential of the oxygen reduction reaction.[133] In addition to the increased surface area of porous-coated Co–Cr alloys, sintering causes microstructural changes that also decrease corrosion resistance behavior. For example, in sintered Co–Cr, corrosion preferentially occurs at grain boundaries and regions adjacent to carbides.[134] Both c.p. Ti and Ti–6Al–4V possess excellent corrosion resistance for a full range of oxide states and pH levels. The low dissolution rate and near chemical inertness of titanium dissolution products allow bone to osseointegrate with titanium.[133]

Even in their passive condition, however, metals are not inert, and passive dissolution occurs from the surfaces of metals used in orthopedics. Corrosion of a metal (oxidation/reduction reactions and the rate of these reactions) is dictated by thermodynamic driving forces and kinetics. Corrosion may be an independent process or act in concert with wear. Even if uncoupled, neither corrosion nor wear operates via a single or spatially uniform mechanism. For example, corrosion may occur globally over a large region of an implant surface or locally at sites of different surface or solution concentration. Under functional loading, which can involve relative motion, fretting or wear between components, corrosion can be mechanically assisted. Fretting corrosion, corrosion fatigue and stress corrosion cracking can accelerate the release of metal ions or particulates. Dynamic metal-on-metal contact can occur in metal–metal wear couples and in tapered connections in modular prostheses and these junctions are especially prone to corrosion, with elevated amounts of corrosion products detected in surrounding tissues.[135–137] If wear particles are generated, then there also exists the potential for these higher surface area particles to undergo dissolution.

Although the biological consequences are unknown, increased concentrations of metal ions occur locally and systemically in patients with metal implants, especially loose implants.[39,138–141] While discolored tissues adjacent to titanium implants are due to metal debris, the elemental ratios in the tissue are similar to those in the bulk alloy, suggesting that the debris represent wear particles rather than corrosion products.[142] Although wear debris present a large surface area for corrosion, it is the presence of wear debris that is the major contributor to systemic increases in titanium.[140] Corrosion products are more prevalent in tissues adjacent to Co–Cr implants, although these products are also associated with modular implants or loosening.[39] During wear accelerated corrosion, Co–Cr alloys can release large amounts of dissolution product during repassivation, due to solution supersaturation at the metal surface. Titanium, on the other hand, repassivates almost instantaneously through surface controlled oxidation kinetics. Titanium ion release that does occur is a result of the chemical dissolution of titanium oxide.

The increased surface area of porous-coated implants increases the potential for passive dissolution or mechanically-assisted degradation. Metal oxide dissolution in porous-coated implants creates several questions that are important to investigate: What material is released? How much is released? What reactions are release products involved in? What percent of the release products is excreted versus retained? If retained, where do these products accumulate? What biological responses result from the retained fraction?[39,143–145]

6.605.4. Design and Characterization of Porous Materials

The complex 3D surface geometry and micromechanical environment within porous materials make the design and characterization of porous-coated implants challenging. The interfaces between the porous coating and implant and porous coating and tissue (hard and soft) also need to be well characterized as part of an effective design approach. Many of the design principles for porous-coated implants translate into the design of porous scaffolds for tissue engineering. The success of both technologies depends on the ability of the microenvironment to help organize cell function in 3D porous media and allow functional tissue to grow and adapt. Understanding the interaction between porous biomaterials and tissue at different dimensional scales is therefore important, and a variety of experimental and analytical approaches are available to characterize this complex microenvironment.

Porous coatings are formed from bonded microspheres, fibers, plasma-sprayed particles, or foams, and can be either open or closed systems of ordered or random architecture. Quantifying architectural parameters and developing structure–property relations is critical, especially considering competing design objectives of maximizing porosity for transport, cellular invasion, and bone ingrowth, but also maximizing strength.

Stereology is well established in metallurgy and stereological principles were adapted for analysis of trabecular bone and other porous and granular media.[146,147] Briefly, test lines oriented at an angle θ are superposed onto planar sections of a porous coating consisting of domains that are defined as either material or void space. The mean intercept length is the average distance between two material/void interfaces measured along a line. When mean intercept length is plotted against direction, the data fit the equation of an ellipse in 2D and an ellipsoid in 3D. From 2D measures of the ratio of material voxels to total voxels and the number of intersections a test line makes relative to its total length, architectural parameters, such as volume fraction, surface-to-volume ratio, thickness, density, and separation can be calculated. The ratios of mean intercept length in orthogonal directions can provide an estimate of the degree of anisotropy. Connectivity of a porous structure and determination of whether a structure is open (connected pores) or closed cell (pores not connected) can be quantified via the determination of an Euler number.

Characterizing the mechanical properties of porous materials is more complicated than for dense, spatially homogeneous materials. Three levels of dimensional scale should be considered: structural properties or properties of the whole domain of material and voids; material properties or properties of individual microspheres, fibers, or struts of trabecular metal; and nanoscale properties or properties on the same dimensional scale as features of the material that interact with cells.

Characterizing the stiffness of porous coatings is important because local stiffness controls cell spreading, cytoskeletal mechanics, and cell differentiation,[148] ultimately affecting bone ingrowth. The stiffness of a porous coating also controls stress transfer, bone adaptation, and stability of the porous coating/tissue interface.[149,150] Gradients in stiffness between porous coatings and the underlying dense implant also affect porous coating/substrate bonding. At the structural-level, porous coatings may be anisotropic, which necessitates testing in multiple directions. Structural-level stiffness–strength relations follow a power law relationship with structural density and, for idealized models of cellular solids, closed form relations for the stiffness of open and closed cell structures exist.[151]

Anisotropic elastic constants of a porous coating/tissue interfacial zone can be predicted via a number of analytical techniques that provide values bounded by load and displacement boundary conditions.[25] The amount and distribution of bone ingrowth into a porous coating and subsequent bone adaptation depend on local strains,[152,153] which are dependent on material and tissue architecture within the implant/tissue interfacial zone.[150,154] Coating design, loading history, and relative motion also affect the amount of bone ingrowth.[27,154,155] Developing relations between local strain magnitude and amount and distribution of ingrown bone is challenging. Most studies focus on bone adaptation to implants on a global level, not accounting for porous coating architecture. However, local tissue distribution surrounding individual microspheres within a whole implant interface is poorly correlated with global mechanical fields. Global models by themselves, unless highly refined and computationally intensive, model the porous coating/tissue interface as a homogeneous bonded interface, and omit local details. Local models of isolated regions of a porous coating are valuable for predicting local stresses and strains, but are typically not linked to an analysis of the whole implant. Scaling local strains to actual tissue strains in relation to physiological loading is needed to establish the relationship between local interface tissue strains and amount of bone ingrowth.

Local models idealize porous coatings into regular, periodic microstructures consisting of idealized shaped unit cells and, in hierarchical analyses, are coupled with global continuum models.[150] Coupled global/local modeling shows that with increased depth of bone ingrowth, stress concentrations in both metal and tissue are reduced, reducing potential mechanical failure at the porous coating/tissue interface.[150,156] Moreover, strain fields around individual microspheres are inhomogeneous and peak strains in the interfacial zone are more than triple the strains predicted by global analyses, demonstrating the need for local analyses.

Because of the stress intensification in porous metals, crack initiation life is not a valid predictor of fatigue life. Therefore, a technique of detecting fatigue crack initiation and monitoring fatigue crack propagation is important for characterizing the mechanical response of porous coatings. In implementing a technique of monitoring fatigue damage in porous materials, several material characteristics must be considered: the complex surface geometry, the potential for damage to occur simultaneously at multiple, unknown sites, and the possibility of irregular crack contours.[157]

A technique of monitoring the structural integrity of a porous material should fulfill the following criteria[157]: (1) detect damage at any location at any time; (2) detect damage at multiple sites that are unknown *a priori*; (3) measure the dimensions of damage; (4) be sensitive, accurate, free of artifact, easily calibrated and implemented; (5) monitor the material continuously during loading; (6) monitor in real-time; (7) be nondestructive; and (8) be applicable to all materials and in all environments. Nondestructive techniques of detecting material flaws and measuring damage may be defined with respect to the physical parameter(s) of the material that the defects alter, and include techniques that measure alterations in mechanical, electrical, magnetic, thermal, acoustic, chemical and optical properties, and particle and wave parameters (**Table 5**).

In summary, a combination of experimental and analytical techniques introduced into biomaterials has yielded insights into the behavior of porous coatings as structural materials and as components of a biomaterial/tissue composite that are critical to the clinical success of porous-coated prostheses.

6.605.5. Porous Coatings in Tissue Engineering

Many of the strategies used to design porous-coated implants can be transferred to the design of porous scaffolds used in

Table 5 Summary of techniques to monitor material damage

Technique	*Advantages*[a]	*Disadvantages*[a]	*Minimum detectable damage zone (μm)*
Acoustic emission	1, 2, 4–8	3, 4	10
Barkhausen noise	1, 2, 5–7	3, 4, 8	–
Compliance/ COD	3, 5–8	1, 2, 4	25
Computed tomography	1–3, 7, 8	4–6	50
Eddy currents	1, 2, 7	3–6, 8	220
Exoelectrons	1, 2, 5–7	3, 4, 8	–
Holography	1, 2, 5–8	3, 4	–
Laser telemetry	3–8	1, 2	0.13
Metallography	2–4, 8	1, 5–7	O(μm)[b]
Microwaves	5–8	1–4	2500
Moire patterns	1, 2, 5–8	3, 4	10
Potential drop – DC	1, 3–7	2, 8	3
Potential drop – AC	1, 3–7	2, 8	10
Radiography	1–4, 6, 7	5, 8	25
SEM	2–4, 8	1, 5–7	0.01
STM	3,8	1, 2, 4–7	O(Å)[b]
Ultrasound	1, 2, 6–8	3–5	2100

Modified from Kohn, D. H. *Crit. Rev. Biomed. Eng.* **1995**, *22*, 221–306, with permission.
[a]Numbers refer to attributes (1)–(8) of damage monitoring techniques listed at Section 4. Numbers listed under advantages mean the technique can meet those requirements, while listings under disadvantages mean those particular requirements cannot be met.
[b]O = on the order of.

tissue engineering for controlling tissue growth. An ideal tissue substitute would satisfy the following design requirements, many of which are design requirements for porous-coated implants[94,158]: biocompatibility; osteoconductivity – it should provide an appropriate environment for attachment, proliferation, and function of osteoblasts or their progenitors, leading to the secretion of new bone; osteoinductivity – it should have the ability to incorporate factors that direct bone growth; sufficient porosity to allow transport and ingrowth of vascular tissue; mechanical integrity to support functional loads; controlled degradation into nontoxic species that are metabolized or excreted; and ability to be easily processed into irregular 3D shapes.

Bone regeneration can be achieved by culturing cells capable of expressing the osteoblast phenotype onto porous synthetic or natural materials that mimic structural and/or functional aspects of natural extracellular matrices. Materials that satisfy at least some of the design requirements for a bone substitute and support bone regeneration include titanium,[34,159] PLGA,[160] collagen,[161] polyphosphazenes,[162] polyurethanes,[163] polycaprolactone,[164] PEG,[165] poly-(propylene fumarate),[166] starch-based materials,[167] alginate,[168] silk,[169] bioactive glasses and glass ceramics,[115,116] HA, TCP, and coral,[119,161,170,171] HA/ and HA/TCP/collagen,[161] and polymer/apatite composites.[97,172–174] Analogous to the findings that the architecture and composition of a porous-coated total joint replacement control tissue ingrowth,[27,154] alterations in scaffold composition and structure can alter *in vitro* outcomes, including osteoblast or progenitor cell attachment and proliferation, collagen and noncollagenous protein synthesis and RNA transcription,[109,116,174–177] as well as *in vivo* outcomes, including progenitor cell differentiation to an osteoblast lineage, amount and rate of bone formation.[117,119,178]

In addition to their osteoconductive nature, porous and porous-coated biomaterials can be combined with inductive factors, to control cell proliferation, differentiation, and bone formation.[113,179,180] Osteoinductive properties can be integrated into a biomaterial by immobilizing proteins or peptides to the material surface via adsorption, cross-linking, covalent binding, or physical entrapment. Each of these immobilization techniques results in different loading efficiencies and different levels of protein retention, as well as influences the release profile of the molecule. Growth factors can be adsorbed to or dispersed over the surfaces of metal, ceramic, and polymer biomaterials, allowing these nonbiologically communicative materials to serve as delivery systems for molecules that can communicate with surrounding cells.[181,182] Although release kinetics are dependent on the material and protein, the general release profile of a surface adsorbed molecule is rapid release, followed by a slower release based on the chemical and/or physical attraction between the material and protein.[183,184] In some cases, a more sustained release or a pulsatile release is required for a growth factor to be effective. Controlled release of a growth factor can be achieved by incorporating the factor into the bulk of a polymer during polymerization and designing a release profile based on protein diffusion and/or material degradation.[185,186] Other means of incorporating proteins into the bulk of a material include using layer-by-layer assembly and adsorbing the protein into each layer deposited,[187] binding pellets together using a gel, with a growth factor adsorbed to the surface of the pellets,[188] using sol–gel techniques to create slow release protein carrier coatings,[189,190] and coprecipitating inorganic/organic coatings onto implants.[111,191]

In order to integrate drug delivery capabilities with other design variables for a porous-coated implant, methodologies that are amenable to encapsulating a drug to the surface of a material that can withstand mechanical loads would have the most impact. Growth factors and antibiotics have been incorporated onto titanium alloy implants by coprecipitating the proteins with calcium phosphate.[179,192] An important advantage to this approach is the ability to produce calcium-phosphate coatings at a physiological temperature, minimizing conditions that would change the biological activity of the factors. The mineral/protein coating can be as thick as 50 μm.[191] Biomolecules can be incorporated at different stages of calcium-phosphate nucleation and growth,[111,193] enabling spatial localization of the molecule through the apatite thickness and increasing protein loading. Coprecipitation therefore results in a more controlled release of biomolecules in comparison to adsorption, because the negatively charged protein has an affinity for the apatite matrix, rather than just a superficial association.[111,191] Techniques used to incorporate growth factors into bone-like mineral can also be used to incorporate genes.[112,194]

6.605.6. Summary and Future Directions

Over the past 40 years, porous-coated implants have been utilized clinically as an alternative to cemented implants, especially in younger and more active patients. In addition to total joint replacements, porous-coated implants are used for segmental defects and as spinal implants. Many of the design objectives learned over the last four decades may also be translated to tissue engineering. Conversely, tissue engineering strategies may come to fruition first when used to augment the function of an implant, rather than regenerate a tissue *de novo*.

The use of porous and porous-coated biomaterials is expected to expand and, although clinically successful, modifications to current technologies could increase the service life and expand the pool of patients with indications for use. There are several areas in which new materials, new designs, and new strategies of creating and maintaining tissue ingrowth could be achieved. New coating materials that have a combination of fatigue resistance and elastic match with bone, yet have sufficient porosity to facilitate transport and are biologically tolerable are needed. A second approach to improve mechanical integrity and cooptimize mechanical and transport properties to modify coating architecture. Architectural modifications include design of functionally graded materials, creation of open cell coatings, and development of optimization algorithms to design coatings in which material is distributed to meet dual objective functions of maximizing strength and maximizing permeability. Design and manufacturing of periodic, open microstructures can be achieved by solid free form fabrication methods, such as 3D fiber deposition, selective laser melting, 3D printing.[195–197]

Strategies to increase the magnitude and rate of bone ingrowth using material chemistry and biological approaches also parallel many strategies used in tissue engineering. In fact, advances in tissue engineering are likely to first arise in conjunction with established implantology approaches and materials. Use of nanomaterials, attachment of biological factors, and integration of drug delivery with implantology may each help enhance bone growth. A variety of cell functions, such as adhesion and intracellular signaling, are sensitive to surface features on the order of nanometers.[198] Creation of nanosized grains or nanoscale topologies on a microscale coating could therefore provide a porous-coated implant with the physical scale necessary to better influence biological function.

Attachment and delivery of proteins from implants is also being pursued.[189,190] Proteins, however, are subject to isolation and degradation. Proteins can also change conformation because they possess sections with varying hydrophobicities. Peptides can mimic the function of a protein while being smaller, cheaper, and less susceptible to degradation. Peptides have the potential for controlling initial biological activity, because they can contain specific target amino acid sequences and can permit control of hydrophilic properties through sequence design. Peptide sequences have been designed to mimic sections of ECM proteins,[199] and material-specific peptides have been discovered.[200]

Modifying surface chemistry and integration of biological molecules with materials to control cell function are important design modifications. By themselves, however, they are not sufficient for clinical function. A key to translating advances in nanotechnology, materials chemistry, and biomolecular surface engineering into the design of a clinically relevant implant is to integrate the nanoscale features needed to control cell function with a larger 3D implant that has the dimensions and bulk properties required to fulfill a desired clinical application.

References

1. Ducheyne, P. In *Functional Behavior of Orthopaedic Biomaterials*; Ducheyne, P., Hastings, G. W., Eds.; Applications; CRC Press: Boca Raton, FL, 1984; Vol. II, pp 163–169.
2. Haddad, R. J.; Cook, S. D.; Thomas, K. A. *J. Bone Joint Surg. Am.* **1987**, *69*, 1459–1466.
3. Hulbert, S. F.; Young, F. A.; Mathews, R. S.; Klawitter, J. J.; Talbert, C. D.; Stelling, F. H. *J. Biomed. Mater. Res.* **1970**, *4*, 433–456.
4. Lemons, J. E. *ASTM STP 953, Quantitative Characterization and Performance of Porous Implants for Hard Tissue Applications*; ASTM: West Conshohocken, PA, 1987.
5. Pilliar, R. M. *Clin. Orthop.* **1983**, *176*, 42–51.
6. Bourassa, P. L.; Yue, S.; Bobyn, J. D. *J. Biomed. Mater. Res.* **1997**, *37*, 291–300.
7. Cook, S. D.; Thongpreda, N.; Anderson, R. C.; Haddad, R. J., Jr. *J. Biomed. Mater. Res.* **1988**, *22*, 287–302.
8. Kohn, D. H.; Ducheyne, P. *J. Biomed. Mater. Res.* **1990**, *24*, 1483–1501.
9. Kohn, D. H.; Ducheyne, P.; Awerbuch, J. *J. Biomed. Mater. Res.* **1992**, *26*, 19–38.
10. Yue, S.; Pilliar, R. M.; Weatherly, G. C. *J. Biomed. Mater. Res.* **1984**, *18*, 1043–1058.
11. Albrektsson, T.; Branemark, P. I.; Hansson, H. A.; *et al. Ann. Biomed. Eng.* **1983**, *11*, 1–27.
12. Bobyn, J. D.; Pilliar, R. M.; Cameron, H. U.; Weatherly, G. C. *Clin. Orthop.* **1980**, *150*, 263–270.
13. Galante, J.; Rostoker, W.; Lueck, R.; Ray, R. D. *J. Bone Joint Surg.* **1971**, *53A*, 101–114.
14. Hacking, S. A.; Harvey, E. J.; Tanzer, M.; Krygier, J. J.; Bobyn, J. D. *J. Bone Joint Surg. Br.* **2003**, *85*, 1182–1189.
15. Healy, K. E.; Ducheyne, P. *Biomaterials* **1992**, *13*, 553–561.
16. Shannon, F. J.; Cottrell, J. M.; Deng, X. H.; *et al. J. Biomed. Mater. Res.* **2008**, *86A*, 857–864.
17. Taché, A.; Gan, L.; Deporter, D.; Pilliar, R. M. *Int. J. Oral Maxillofac. Implants* **2004**, *19*, 19–29.
18. Welsh, R. P.; Pilliar, R. M.; Macnab, I. *J. Bone Joint Surg.* **1971**, *53A*, 963–977.
19. Goldstein, S. A.; Matthews, L. S.; Kuhn, J. L.; Hollister, S. J. *J. Biomech.* **1991**, *24*(Suppl 1), 135–150.
20. Heck, D. A.; Nakajima, I.; Kelly, P. J.; Chao, E. Y. *J. Bone Joint Surg.* **1986**, *68A*, 118–126.
21. Lanyon, L. E.; Paul, I. L.; Rubin, C. T.; *et al. J. Bone Joint Surg.* **1981**, *63A*, 989–1001.
22. Andreykiv, A.; van Keulen, F.; Prendergast, P. J. *J. Biomech. Eng.* **2008**, *130*, 051015-1-11.
23. Engh, C. A.; Bobyn, J. D. *Clin. Orthop.* **1988**, *231*, 7–28.
24. Keaveny, T. M.; Bartel, D. L. *J. Biomech.* **1993**, *26*, 1355–1368.
25. Ko, C. C.; Kohn, D. H.; Hollister, S. J. *J. Mater. Sci. Mater. Med.* **1995**, *7*, 109–117.
26. Rohlmann, A.; Cheal, E. J.; Hayes, W. C.; Bergmann, G. *J. Biomech.* **1988**, *21*, 605–611.
27. Sumner, D. R.; Turner, T. M.; Urban, R. M.; Galante, J. O. *Clin. Orthop. Relat. Res.* **1992**, *276*, 83–90.
28. Bobyn, J. D.; McKenzie, K.; Karabasz, D.; Krygier, J. J.; Tanzer, M. *J. Bone Joint Surg.* **2009**, *91A*, 23–31.
29. Ducheyne, P.; Hench, L. L.; Kagan, A., II; Martens, M.; Bursens, A.; Mulier, J. C. *J. Biomed. Mater. Res.* **1980**, *14*, 225–237.
30. Jasty, M.; Bragdon, C.; Burke, D.; O'Connor, D.; Lowenstein, J.; Harris, W. H. *J. Bone Joint Surg. Am.* **1997**, *79*, 707–714.
31. Mikulec, L. J.; Puleo, D. A. *J. Biomed. Mater. Res.* **1996**, *32*, 203–208.
32. Pilliar, R. M.; Lee, J. M.; Maniatopoulos, C. *Clin. Orthop.* **1986**, *208*, 108–113.
33. Thomas, C. H.; Collier, J. H.; Sfeir, C. S.; Healy, K. E. *Proc. Natl. Acad. Sci.* **2002**, *99*, 1972–1977.

34. van den Dolder, J.; Bancroft, G. N.; Sikavitsas, V. I.; Spauwen, P. H.; Mikos, A. G.; Jansen, J. A. *Tissue Eng.* **2003**, *9*, 505–515.
35. Bobyn, J. D.; Pilliar, R. M.; Binnington, A. G.; Szivek, J. A. *J. Orthop. Res.* **1987**, *5*, 393–408.
36. Crowninshield, R. D.; Brand, R. A.; Johnston, R. C.; Milroy, J. C. *J. Bone Joint Surg.* **1980**, *62A*, 68–78.
37. Willie, B. M.; Yang, X.; Kelly, N. H.; *et al*. *J. Biomed. Mater. Res. B Appl. Biomater.* **2010**, *92*, 479–488.
38. Galante, J. O.; Lemons, J.; Spector, M.; Wilson, P. D., Jr.; Wright, T. M. *J. Orthop. Res.* **1991**, *9*, 760–775.
39. Jacobs, J. J.; Gilbert, J. L.; Urban, R. M. *J. Bone Joint Surg.* **1998**, *80A*, 268–282.
40. Ducheyne, P. *Ann. N. Y. Acad. Sci.* **1988**, *523*, 1–296.
41. Hench, L. L.; Splinter, R. J.; Allen, W. C.; Greenlee, T. K., Jr. *J. Biomed. Mater. Res. Symp.* **1972**, *2*, 117–141.
42. Lord, G.; Bancel, P. *Clin. Orthop.* **1983**, *176*, 67–76.
43. Spector, M.; Davis, R. J.; Lunceford, E. M.; Harmon, S. L. *Clin. Orthop.* **1983**, *176*, 34–41.
44. Pilliar, R. M.; Cameron, H. U.; Macnab, I. *Biomed. Eng.* **1975**, *10*, 126–131.
45. Cook, S. D.; Walsh, K. A.; Haddad, R. J., Jr. *Clin. Orthop.* **1985**, *193*, 271–280.
46. Huiskes, R. In *Functional Behavior of Orthopaedic Biomaterials*; Ducheyne, P., Hastings, G. W., Eds.; Applications; CRC Press: Boca Raton, FL, 1984; Vol. II, pp 121–162.
47. Homsy, C. A.; Cain, T. E.; Kessler, F. B.; Anderson, M. S.; King, J. W. *Clin. Orthop.* **1972**, *89*, 220–235.
48. Tullos, H. S.; McCaskill, B. L.; Dickey, R.; Davidson, J. *J. Bone Joint Surg.* **1984**, *66A*, 888–898.
49. DeMane, M.; Beals, N. B.; McDowell, D. L.; Georgette, F. S.; Spector, M. In *ASTM STP 953 Quantitative Characterization and Performance of Porous Implants for Hard Tissue Applications*; Lemons, J. E., Ed.; ASTM: West Conshohocken, PA, 1987; pp 315–329.
50. Klawitter, J. J.; Bagwell, J. G.; Weinstein, A. M.; Sauer, B. W.; Pruitt, J. R. *J. Biomed. Mater. Res.* **1976**, *10*, 311–323.
51. Rijke, A. M.; Rieger, M. R. *J. Biomed. Mater. Res.* **1977**, *11*, 373–394.
52. Klawitter, J. J.; Hulbert, S. F. *J. Biomed. Mater. Res. Symp.* **1971**, *2*, 161–229.
53. Briggs, E. P.; Walpole, A. R.; Wilshaw, P. R.; Karlsson, M.; Pålsgård, E. *J. Mater. Sci. Mater. Med.* **2004**, *15*, 1021–1029.
54. Walpole, A. R.; Xia, Z.; Wilson, C. W.; Triffitt, J. T.; Wilshaw, P. R. *J. Biomed. Mater. Res. A* **2009**, *90*, 46–54.
55. Ducheyne, P.; Martens, M.; Aernoudt, E.; Mulier, J.; De Meester, P. *Acta Orthop. Belg.* **1974**, *40*, 799–805.
56. Bobyn, J. D.; Stackpool, G. J.; Hacking, S. A.; Tanzer, M.; Krygier, J. J. *J. Bone Joint Surg. Br.* **1999**, *81*, 907–914.
57. Levine, B. *Adv. Eng. Mater.* **2008**, *10*, 788–792.
58. Hahn, H.; Palich, W. *J. Biomed. Mater. Res.* **1970**, *4*, 571–577.
59. Kilner, T.; Pilliar, R. M.; Weatherly, G. C.; Allibert, C. *J. Biomed. Mater. Res.* **1982**, *16*, 63–79.
60. Pilliar, R. M.; Weatherly, G. C. *CRC Crit. Rev. Biocompat.* **1986**, *1*, 371–403.
61. Merget, M.; Aldinger, F. In *Titanium, Science and Technology*; Lutjering, G., Zwicker, U., Bunk, W., Eds.; Deutsche Gesellschaft Fur Metallkunde: Oberursel, West Germany, 1985; pp 1393–1398.
62. Zardiackas, L. D.; Freese, H. L.; Kraay, M. J. *ASTM STP 1471, Titanium, Niobium, Zirconium, and Tantalum for Medical and Surgical Applications*; ASTM: West Conshohocken, PA, 2006.
63. Ducheyne, P.; Kohn, D.; Smith, T. S. *Biomaterials* **1987**, *8*, 223–227.
64. Eylon, D.; Froes, F. H.; Levin, L. In *Titanium, Science and Technology*; Lutjering, G., Zwicker, U., Bunk, W., Eds.; Deutsche Gesellschaft Fur Metallkunde: Oberursel, West Germany, 1985; pp 179–186.
65. Kerr, W. R.; Smith, P. R.; Rosenblum, M. E.; Gurney, F. J.; Mahajan, Y. R.; Bidwell, L. R. In *Titanium '80 Science and Technology*; Kimura, H., Izumi, O., Eds.; The Metallurgical Society of AIME: Warrendale, PA, 1980; pp 2477–2486.
66. Kohn, D. H.; Ducheyne, P. *J. Mater. Sci.* **1991**, *26*, 534–544.
67. Kohn, D. H.; Ducheyne, P. *J. Mater. Sci.* **1991**, *26*, 328–334.
68. Levin, L.; Vogt, R. G.; Eylon, D.; Froes, F. H. In *Titanium, Science and Technology*; Lutjering, G., Zwicker, U., Bunk, W., Eds.; Deutsche Gesellschaft Fur Metallkunde: Oberursel, West Germany, 1985; pp 2107–2114.
69. Ducheyne, P.; Martens, M. *Clin. Mater.* **1986**, *1*, 91–98.
70. Hofmann, A. A.; Bachus, K. N.; Bloebaum, R. D. *J. Arthroplasty* **1993**, *8*, 157–166.
71. Shimko, D. A.; Shimko, V. F.; Sander, E. A.; Dickson, K. F.; Nauman, E. A. *J. Biomed. Mater. Res. B Appl. Biomater.* **2005**, *73*, 315–324.
72. Zardiackas, L. D.; Parsell, D. E.; Dillon, L. D.; Mitchell, D. W.; Nunnery, L. A.; Poggie, R. *J. Biomed. Mater. Res.* **2001**, *58*, 180–187.
73. Levine, B. R.; Sporer, S.; Poggie, R. A.; Della Valle, C. J.; Jacobs, J. J. *Biomaterials* **2006**, *27*, 4671–4681.
74. Patil, N.; Lee, K.; Goodman, S. B. *J. Biomed. Mater. Res. B Appl. Biomater* **2009**, *89*, 242–251.
75. Ducheyne, P.; Van Raemdonck, W.; Heughebaert, J. C.; Heughebaert, M. *Biomaterials* **1986**, *7*, 97–103.
76. Ducheyne, P.; Radin, S.; Heughebaert, M.; Heughebaert, J. C. *Biomaterials* **1990**, *11*, 244–254.
77. Koch, B.; Wolke, J. G. C.; de Groot, K. *J. Biomed. Mater. Res.* **1990**, *24*, 655–667.
78. Segvich, S. J.; Luong, L. N.; Kohn, D. H. In *Biomaterials and Biomedical Engineering*; Ahmed, W., Ali, N., Öchsner, A., Eds.; Trans Tech Publications: Zurich, 2008.
79. Ioku, K.; Yoshimura, M.; Somiya, S. *Biomaterials* **1990**, *11*, 57–61.
80. Kitsugi, T.; Yamamuro, T.; Nakamura, T.; *et al*. *J. Biomed. Mater. Res.* **1986**, *20*, 1295–1307.
81. Knowles, J. C.; Bonfield, W. *J. Biomed. Mater. Res.* **1993**, *27*, 1591–1598.
82. Li, J.; Fartash, B.; Hermansson, L. *Biomaterials* **1995**, *16*, 417–422.
83. Chae, J. C.; Collier, J. P.; Mayor, M. B.; Surprenant, V. A.; Dauphinais, L. A. *J. Biomed. Mater. Res.* **1992**, *26*, 93–102.
84. Koeneman, J.; Lemons, J.; Ducheyne, P.; *et al*. *J. Appl. Biomat.* **1990**, *1*, 79–90.
85. de Groot, K. *Bioceramics of Calcium Phosphate*; CRC Press: Boca Raton, FL, 1983.
86. de Groot, K.; Geesink, R. G. T.; Klein, C. P. A. T.; Serekian, P. *J. Biomed. Mater. Res.* **1987**, *21*, 1375–1381.
87. Ong, J. L.; Harris, L. A.; Lucas, L. C.; Lacefield, W. R.; Rigney, E. D. *J. Am. Ceram. Soc.* **1991**, *74*, 2301–2304.
88. Wolke, J. G. C.; van Dijk, K.; Schaeken, H. G.; de Groot, K.; Jansen, J. A. *J. Biomed. Mater. Res.* **1994**, *28*, 1477–1484.
89. Chai, C. S.; Gross, K. A.; Ben-Nissan, B. *Biomaterials* **1998**, *19*, 2291–2296.
90. Garcia, F.; Arias, J. L.; Mayor, B.; *et al*. *J. Biomed. Mater. Res. (Appl. Biomat.)* **1998**, *43*, 69–76.
91. Gao, Y. In *Biomedical Materials – Drug Delivery, Implants and Tissue Engineering*; Neenan, T., Marcolongo, M., Valentini, R. F., Eds.; Materials Research Society: Warrendale, PA, 1999; pp 361–366.
92. Abe, Y.; Kokubo, T.; Yamamuro, T. *J. Mater. Sci. Mater. Med.* **1990**, *1*, 233–238.
93. Bunker, B. C.; Rieke, P. C.; Tarasevich, B. J.; *et al*. *Science* **1994**, *264*, 48–55.
94. Kohn, D. H. In *Biomedical Engineering and Design Handbook*, 2nd ed.; Kutz, M., Ed.; McGraw-Hill: New York, 2009; Vol. 1, pp 357–381.
95. Tanahashi, M.; Yao, T.; Kokubo, T.; *et al*. *J. Biomed. Mater. Res.* **1995**, *29*, 349–357.
96. Campbell, A. A.; Fryxell, G. E.; Linehan, J. C.; Graff, G. L. *J. Biomed. Mater. Res.* **1996**, *32*, 111–118.
97. Shin, K.; Jayasuriya, A. C.; Kohn, D. H. *J. Biomed. Mater. Res.* **2007**, *83A*, 1076–1086.
98. Wen, H. B.; de Wijn, J. R.; Cui, F. Z.; de Groot, K. *J. Biomed. Mater. Res.* **1997**, *35*, 93–99.
99. Wu, W.; Zhuang, H.; Nancollas, G. H. *J. Biomed. Mater. Res.* **1997**, *35*, 93–99.
100. Combes, C.; Rey, C. *Biomaterials* **2002**, *23*, 2817–2823.
101. Ducheyne, P. *J. Biomed. Mater. Res. Appl. Biomat.* **1987**, *21*(A2), 219–236.
102. Kokubo, T.; Takadama, H. *Biomaterials* **2006**, *27*, 2907–2915.
103. Nakamura, T.; Yamamuro, T.; Higashi, S.; Kokubo, T.; Ito, S. *J. Biomed. Mater. Res.* **1985**, *19*, 685–698.
104. Hanawa, T.; Kon, M.; Ukai, H.; Murakami, K.; Miyamoto, Y.; Asaoka, K. *J. Biomed. Mater. Res.* **1998**, *41*, 227–236.
105. Yamamoto, M.; Kato, K.; Ikada, Y. *J. Biomed. Mater. Res.* **1997**, *37*, 29–36.
106. Kohn, D. H. *Curr. Opin. Solid State Mater. Sci.* **1998**, *3*, 309–316.
107. Du, C.; Cui, F. Z.; Zhu, X. D.; de Groot, K. *J. Biomed. Mater. Res.* **1999**, *44*, 407–415.
108. Hong, S. I.; Lee, K. H.; Outslay, M. E.; Kohn, D. H. *J. Mater. Res.* **2008**, *23*, 478–485.
109. Leonova, E. V.; Pennington, K. E.; Krebsbach, P. H.; Kohn, D. H. *J. Biomed. Mater. Res. A* **2006**, *79A*, 263–270.
110. Kohn, D. H.; Shin, K.; Hong, S. I.; *et al*. In *Proceedings of the 8th International Conference on the Chemistry and Biology of Mineralized Tissues*; Landis, W. J., Sodek, J., Eds.; University of Toronto Press: Toronto, 2005; pp 216–219.
111. Luong, L. N.; Hong, S. I.; Patel, R. J.; Outslay, M. E.; Kohn, D. H. *Biomaterials* **2006**, *27*, 1175–1186.
112. Luong, L. N.; McFalls, K. M.; Kohn, D. H. *Biomaterials* **2009**, *30*, 6996–7004.
113. Segvich, S. J.; Smith, H. C.; Luong, L. N.; Kohn, D. H. *J. Biomed. Mater. Res. B* **2008**, *84B*, 340–349.

114. Kohn, D. H.; Ducheyne, P. In *Medical and Dental Materials*; Williams, D. F., Ed.; VCH: Verlagsgesellschaft, FRG, 1992; pp 29–109.
115. Ducheyne, P.; El-Ghannam, A.; Shapiro, I. *J. Cell. Biochem.* **1994**, *56*, 162–167.
116. El-Ghannam, A.; Ducheyne, P.; Shapiro, I. M. *J. Biomed. Mater. Res.* **1997**, *36*, 167–180.
117. Hartman, E. H. M.; Vehof, J. W. M.; Spauwen, P. H. M.; Jansen, J. A. *Biomaterials* **2005**, *26*, 1829–1835.
118. Krebsbach, P. H.; Kuznetsov, S. A.; Bianco, P.; Gehron-Robey, P. *Crit. Rev. Oral Biol. Med.* **1999**, *10*, 165–181.
119. Ohgushi, H.; Okumura, M.; Tamai, S.; Shors, E. C.; Caplan, A. I. *J. Biomed. Mater. Res.* **1990**, *24*, 1563–1570.
120. Cook, S. D.; Thomas, K. A. *J. Bone Joint Surg. Br.* **1991**, *73*, 20–24.
121. Jasty, M.; Bragdon, C.; Jiranek, W.; Chandler, H.; Maloney, W.; Harris, W. H. *Clin. Orthop. Relat. Res.* **1994**, *308*, 111–126.
122. Kohn, D. H.; Ducheyne, P.; Cuckler, J. M.; Chu, A.; Radin, S. *Med. Prog. Technol.* **1994**, *20*, 169–177.
123. Frost, N. E.; Marsh, K. J.; Pook, L. P. *Metal Fatigue*; Clarendon Press: Oxford, 1974.
124. Cook, S. D.; Georgette, F. S.; Skinner, H. B.; Haddad, R. J., Jr. *J. Biomed. Mater. Res.* **1984**, *18*, 497–512.
125. Georgette, F. S.; Davidson, J. A. *J. Biomed. Mater. Res.* **1986**, *20*, 1229–1248.
126. Margolin, H.; Williams, J. C.; Chesnutt, J. C.; Lutjering, G. In *Titanium '80 Science and Technology*; Kimura, H., Izumi, O., Eds.; The Metallurgical Society of AIME: Warrendale, PA, 1980; pp 169–216.
127. Peters, M.; Gysler, A.; Lutjering, G. In *Titanium '80 Science and Technology*; Kimura, H., Izumi, O., Eds.; The Metallurgical Society of AIME: Warrendale, PA, 1980; pp 1777–1786.
128. Stubbington, C. A.; Bowen, A. W. *J. Mater. Sci.* **1974**, *9*, 941–947.
129. Soltesz, S. M.; Smickley, R. J.; Dardi, L. E. In *Titanium, Science and Technology*; Lutjering, G., Zwicker, U., Bunk, W., Eds.; Deutsche Gesellschaft Fur Metallkunde: Oberursel, West Germany, 1985; pp 187–194.
130. Wolfarth, D.; Filiaggi, M.; Ducheyne, P. *J. Appl. Biomat.* **1990**, *1*, 3–12.
131. Lutjering, G.; Gysler, A. In *Titanium, Science and Technology*; Lutjering, G., Zwicker, U., Bunk, W., Eds.; Deutsche Gesellschaft Fur Metallkunde: Oberursel, West Germany, 1985; pp 2065–2083.
132. Devine, T. M.; Wulff, J. *J. Biomed. Mater. Res.* **1975**, *9*, 151–167.
133. Williams, D. F. In *Biocompatibility of Clinical Implant Materials*, Williams, D. F., Ed.; CRC Press: Boca Raton, FL, 1981; Vol. I, pp 9–44.
134. Placko, H. E.; Brown, S. A.; Payer, J. H. *J. Biomed. Mater. Res.* **1998**, *39*, 292–299.
135. Gilbert, J. L.; Buckley, C. A.; Jacobs, J. J. *J. Biomed. Mater. Res.* **1993**, *27*, 1533–1544.
136. Jacobs, J. J.; Urban, R. M.; Gilbert, J. L.; *et al. Clin. Orthop.* **1995**, *319*, 94–105.
137. Urban, R. M.; Jacobs, J. J.; Gilbert, J. L.; Galante, J. O. *J. Bone Joint Surg.* **1994**, *76A*, 1345–1359.
138. Bartolozzi, A.; Black, J. *Biomaterials* **1985**, *6*, 2–8.
139. Brien, W. W.; Salvati, E. A.; Betts, F.; *et al. Clin. Orthop.* **1992**, *276*, 66–74.
140. Jacobs, J. J.; Skipor, A. K.; Black, J.; Urban, R. M.; Galante, J. O. *J. Bone Joint Surg.* **1991**, *73A*, 1475–1486.
141. Sunderman, F. W., Jr.; Hopfer, S. M.; Swift, T.; *et al. J. Orthop. Res.* **1989**, *7*, 307–315.
142. Agins, H. J.; Alcock, N. W.; Bansai, M.; *et al. J. Bone Joint Surg.* **1988**, *70A*, 347–356.
143. Black, J.; Oppenheimer, P.; Morris, D. M.; Peduto, A. M.; Clark, C. C. *J. Biomed. Mater. Res.* **1987**, *21*, 1213–1230.
144. Brown, S. A.; Farnsworth, L. J.; Merritt, K.; Crowe, T. D. *J. Biomed. Mater. Res.* **1988**, *22*, 321–338.
145. Ducheyne, P.; Healy, K. E. *J. Biomed. Mater. Res.* **1988**, *22*, 1137–1163.
146. Cowin, S. C., Ed.; *Bone Mechanics Handbook*; CRC Press: Boca Raton, FL, 2001.
147. Underwood, E. E. *Quantitative Stereology*; Addison-Wesley: Reading, MA, 1970.
148. Engler, A. J.; Sen, S.; Sweeney, H. L.; Discher, D. E. *Cell* **2006**, *126*, 677–689.
149. Huiskes, R.; Hollister, S. J. *J. Biomech. Eng.* **1993**, *115*, 520–527.
150. Ko, C. C.; Kohn, D. H.; Hollister, S. J. *J. Oral Implantol.* **1992**, *18*, 220–230.
151. Gibson, L. J.; Ashby, M. S. *Proc. R. Soc. Lond.* **1982**, *A382*, 43–59.
152. Simmons, C. A.; Meguid, S. A.; Pilliar, R. M. *J. Orthop. Res.* **2001**, *19*, 187–194.
153. Crowninshield, R. D.; Maloney, W. J.; Wentz, D. H.; Levine, D. L. *Clin. Orthop. Relat. Res.* **2004**, *420*, 176–180.
154. Keaveny, T. M.; Bartel, D. L. *J. Biomech.* **1994**, *27*, 1147–1157.
155. Ramamurti, B. S.; Orr, T. E.; Bragdon, C. R.; Lowenstein, J. D.; Jasty, M.; Harris, W. H. *J. Biomed. Mater. Res.* **1997**, *36*, 274–280.
156. Peterson, C. D.; Hillberry, B. M.; Heck, D. A. *J. Biomed. Mater. Res.* **1988**, *22*, 887–903.
157. Kohn, D. H. *Crit. Rev. Biomed. Eng.* **1995**, *22*, 221–306.
158. Yaszemski, M. J.; Payne, R. G.; Hayes, W. C.; Langer, R. S.; Mikos, A. G. *Biomaterials* **1996**, *17*, 175–185.
159. Li, J. P.; Habibovic, P.; van den Doel, M.; *et al. Biomaterials* **2007**, *28*, 2810–2820.
160. Ishaug-Riley, S. L.; Crane, G. M.; Gurlek, A.; *et al. J. Biomed. Mater. Res.* **1997**, *36*, 1–8.
161. Krebsbach, P. H.; Mankani, M. H.; Satomura, K.; Kuznetsov, S. A.; Gehron-Robey, P. *Transplantation* **1998**, *66*, 1272–1278.
162. Laurencin, C. T.; El-Amin, S. F.; Ibim, S. E.; *et al. J. Biomed. Mater. Res.* **1996**, *30*, 133–138.
163. Gorna, K.; Gogolewski, S. *J. Biomed. Mater. Res.* **2003**, *67A*, 813–827.
164. Li, W. J.; Tuli, R.; Huang, X.; Laquerriere, P.; Tuan, R. S. *Biomaterials* **2005**, *26*, 5158–5166.
165. Nuttelman, C. R.; Tripodi, M. C.; Anseth, K. S. *J. Biomed. Mater. Res.* **2004**, *68A*, 773–782.
166. Payne, R. G.; McGonigle, J. S.; Yaszemski, M. J.; Yasko, A. W.; Mikos, A. G. *Biomaterials* **2002**, *23*, 4381–4387.
167. Marques, A. P.; Cruz, H. R.; Coutinho, O. P.; Reis, R. L. *J. Mater. Sci. Mater. Med.* **2005**, *16*, 833–842.
168. Alsberg, E.; Anderson, K. W.; Alberiuti, A.; Franceschi, R. T.; Mooney, D. J. *J. Dent. Res.* **2001**, *80*, 2025–2029.
169. Kim, H. J.; Kim, U. J.; Vunjak-Novakovic, G.; Min, B. H.; Kaplan, D. L. *Biomaterials* **2005**, *26*, 4442–4452.
170. Holtorf, H. L.; Sheffield, T. L.; Ambrose, C. G.; Jansen, J. A.; Mikos, A. G. *Ann. Biomed. Eng.* **2005**, *33*, 1238–1248.
171. Kruyt, M. C.; Dhert, W. J. A.; Yuan, H.; *et al. J. Orthop. Res.* **2004**, *22*, 544–551.
172. Attawia, M. A.; Devin, J. E.; Laurencin, C. T. *J. Biomed. Mater. Res.* **1995**, *29*, 843–848.
173. Murphy, W. L.; Kohn, D. H.; Mooney, D. J. *J. Biomed. Mater. Res.* **2000**, *50*, 50–58.
174. Thomson, R. C.; Yaszemski, M. J.; Powers, J. M.; Mikos, A. G. *Biomaterials* **1998**, *19*, 1935–1943.
175. Chou, Y. F.; Huang, W.; Dunn, J. C. Y.; Miller, T. A.; Wu, B. M. *Biomaterials* **2005**, *26*, 285–295.
176. Puleo, D. A.; Holleran, L. A.; Doremus, R. H.; Bizios, R. *J. Biomed. Mater. Res.* **1991**, *25*, 711–723.
177. Zreiqat, H.; Evans, P.; Howlett, C. R. *J. Biomed. Mater. Res.* **1999**, *44*, 389–396.
178. James, K.; Levene, H.; Parson, J. R.; Kohn, J. *Biomaterials* **1999**, *20*, 2203–2212.
179. Liu, Y. L.; Hunziker, E. B.; Layrolle, P.; de Bruijn, J. D.; de Groot, K. *Tissue Eng.* **2004**, *10*, 101–108.
180. Shea, L. D.; Smiley, E.; Bonadio, J.; Mooney, D. J. *Nat. Biotechnol.* **1999**, *17*, 551–554.
181. Ripamonti, U.; Ma, S.; Reddi, A. H. *Matrix* **1992**, *12*, 202–212.
182. Sumner, D. R.; Turner, T. M.; Urban, R. M.; *et al. J. Orthop. Res.* **2001**, *19*, 85–94.
183. Midy, V.; Rey, C.; Bres, E.; Dard, M. *J. Biomed. Mater. Res.* **1998**, *41*, 405–411.
184. Ziegler, J.; Mayr-Wohlfart, U.; Kessler, S.; Breitig, D.; Gunther, K. P. *J. Biomed. Mater. Res.* **2002**, *59*, 422–428.
185. Sheridan, M. H.; Shea, L. D.; Peters, M. C.; Mooney, D. J. *J. Control. Release* **2000**, *64*, 91–102.
186. Whang, K.; Tsai, D. C.; Nam, E. K.; *et al. J. Biomed. Mater. Res.* **1998**, *42*, 491–499.
187. Campbell, A. A.; Song, L.; Li, X. S.; *et al. J. Biomed. Mater. Res.* **2000**, *53*, 400–407.
188. Alam, M. I.; Asahina, I.; Ohmamiuda, K.; Takahashi, K.; Yokota, S.; Enomoto, S. *Biomaterials* **2001**, *22*, 1643–1651.
189. Adams, C. S.; Antoci, V., Jr.; Harrison, G.; *et al. J. Orthop. Res.* **2009**, *27*, 701–709.
190. Reiner, T.; Kababya, S.; Gotman, I. *J. Mater. Sci. Mater. Med.* **2008**, *19*, 583–589.
191. Liu, Y. L.; Layrolle, P.; de Bruijn, J.; van Blitterswijk, C.; de Groot, K. *J. Biomed. Mater. Res.* **2002**, *57*, 327.
192. Stigter, M.; de Groot, K.; Layrolle, P. *Biomaterials* **2002**, *23*, 4143–4153.
193. Azevedo, H. S.; Leonor, I. B.; Alves, C. M.; Reis, R. L. *Mater. Sci. Eng. C* **2005**, *25*, 169.
194. Kofron, M. D.; Laurencin, C. T. *Biomaterials* **2004**, *25*, 2637–2643.
195. Li, J. P.; de Wijn, J. R.; van Blitterswijk, C. A.; de Groot, K. *J. Biomed. Mater. Res. A* **2010**, *92*, 33–42.
196. Lin, C. Y.; Wirtz, T.; LaMarca, F.; Hollister, S. J. *J. Biomed. Mater. Res. A* **2007**, *83*, 272–279.
197. Ryan, G. E.; Pandit, A. S.; Apatsidis, D. P. *Biomaterials* **2008**, *27*, 3625–3635.
198. Stevens, M. M.; George, J. H. *Science* **2005**, *310*, 1135–1138.
199. Fujisawa, R.; Mizuno, M.; Nodasaka, Y.; Kuboki, Y. *Matrix Biol.* **1997**, *16*, 21.
200. Segvich, S. J.; Smith, H. C.; Kohn, D. H. *Biomaterials* **2009**, *30*, 1287–1298.

6.606. Biological Effects of Wear Debris from Joint Arthroplasties

T Ma, Stanford University, Stanford, CA, USA
S B Goodman, Stanford University Medical Center Outpatient Center, Redwood City, CA, USA

© 2011 Elsevier Ltd. All rights reserved.

6.606.1.	**Introduction**	80
6.606.2.	**Orthopedic Wear Debris**	80
6.606.3.	**Biologic Reactions of the Host to Wear Debris**	81
6.606.3.1.	Macrophages	81
6.606.3.2.	Osteoblasts and MSCs	82
6.606.3.3.	Osteoclasts	82
6.606.4.	**Other Factors Modulating the Biological Activity of Wear Particles**	83
6.606.4.1.	Genetic Contribution	83
6.606.4.2.	Endotoxin	83
6.606.4.3.	Implant Instability	83
6.606.4.4.	Pressure	83
6.606.5.	**New *In Vivo* Models and Development of Particle-Induced Osteolysis**	84
6.606.5.1.	Models of Continuous Delivery of Particles *In Vivo*	84
6.606.5.2.	Cell Trafficking in the Presence of Wear Particles	84
6.606.6.	**Therapeutic Strategies**	85
6.606.7.	**Conclusion**	85
References		85

Glossary

Osteolysis Lysis of bone, typically an active resorption of bone tissue by osteoclasts as part of an ongoing disease process.

Radiostereometric analysis A high precision method for measuring micromotions, such as the migration and wear, of orthopedic implants in the skeleton in three dimensions.

Single-nucleotide polymorphism A DNA sequence variation occurring when a single nucleotide, such as an A, replaces one of the other three nucleotide letters—C, G, or T in a certain stretch of DNA.

Synovitis Inflammation of the synovial membrane.

Synovium Synovium, also called synovial membrane, is the soft tissue that lines the non-cartilaginous surfaces of joints.

Abbreviations

ASGM1	Anti-asialo GM1 rabbit sera
BC	Bone cement
BSP	Bone sialoprotein
COX	Cyclooxygenase
hIL1Ra	Human interleukin-1 receptor antagonist
IL-1	Interleukin-1
ITAM	Immunoreceptor tyrosine-based activation motif
LPS	Lipopolysaccharides
mRNA	Messenger ribonucleic acid
M-CSF	Macrophage colony-stimulating factor
MSCs	Mesenchymal stem cells
NF-kB	Nuclear factor kappa B
NSAIDs	Nonsteroidal anti-inflammatory drugs
OCP	Osteoclast precursors
OPG	Osteoprotegerin
PAMPS	Pathogen-associated molecular patterns
PBMCs	Human peripheral blood monocytes
PGE2	Prostaglandin E2
RANK	Receptor activator of NF-kB
RANKL	Receptor activator of NF-kB ligand
RSA	Radiostereometric analysis
SCID	Severely combined immunodeficient
SNPs	Single nucleotide polymorphisms
TGF	Transforming growth factor
THR	Total hip arthroplasty
TiAlV	Titanium–aluminum–vanadium
TJA	Total joint arthroplasty
TJR	Total joint replacement
TKR	Total knee replacement
TLR	TOLL-like receptors
TNF-α	Tumor necrosis factor alpha
UHMWPE	Ultra-high-molecular-weight polyethylene
VEGF	Vascular endothelial growth factor

6.606.1. Introduction

Total joint replacement/arthroplasty (TJR/TJA) has been one of the most successful operations for patients with disabling arthritis. The 15-year survivorship of the total hip replacement (THR) and total knee replacement (TKR) is ~90% or higher using contemporary prostheses and techniques and judicious patient selection.[1] However, wear of TJRs is inevitable and as a result of excessive wear of the articulating surfaces, late failure has been the most common long-term complication of the procedure, which often requires revision surgery. On the other hand, the population is aging and the shifting demographics in the United States has prompted younger patients and those with more active life styles to undergo TJR. These facts have led to higher expectations of patients for the improved survivorship of TJR. Although technical advances have been associated with an increasing success rate of specific prostheses, the incidence of failures resulting from wear-related osteolysis requiring surgical revision may not be decreasing.[2] According to a recent report, a 10-year revision-free survival rate was observed in 90% of patients older than 70, but only 72% of patients younger than 50.[2] Wear between the primary bearing surfaces generally exhibits few clinical symptoms or signs until painful synovitis, fracture, structural failure, or loosening of the implant are noticed. Thus, when debris-associated chronic synovitis and osteolysis become notable, revision surgery including thorough debridement and replacement of worn and damaged components is indicated. At revision surgery, implant loosening is often accompanied by the formation of a fibrous chronic inflammatory membrane.[3] In this chapter, the characteristics of the bone–implant interface are reviewed, the biological effects of wear debris generated from wearing of TJRs are summarized, and the available nonsurgical treatments are discussed.

6.606.2. Orthopedic Wear Debris

Orthopedic implants must be integrated with host bone to function properly. However, formation of a fibrous membrane, as opposed to osseous integration is often accompanied by loosening of the implants.[4] Observation of the tissue surrounding loose prostheses has enhanced our understanding of the nature of the wear debris generated from the prosthesis. Histological observations show that retrieved periprosthetic tissue contains numerous particles of bone cement (BC), polyethylene, and metallic debris and that the generation of wear particles and the process of loosening are related[5,6] (**Figure 1**). The nature of the wear particles is dependent on the materials used in the prosthesis.[3,6,7] Studies in the 1980s and 1990s revealed that the majority of wear debris contained in the interface membrane of failed joint implants is polyethelene[8] and cementless prostheses generated more particles than cemented ones.[4] For a metal-on-polyethylene articulation, several hundreds of thousands of polyethylene particles may be generated during a single gait cycle.[9] Besides the quantity of generated particles, many factors influence the biological reactivity of particulates. *In vitro* studies established that the biologic response of the cells to wear particles is a function of the size, composition, surface roughness, and the quantity of particles.[8] The aspect ratio, the surface binding proteins may also influence the general biocompatibility.[8] Recently, alternative bearing surfaces designed to reduce the wear process have been introduced. These include highly cross-linked ultra-high-molecular-weight polyethylene (UHMWPE), ceramic-on-ceramic and metal-on-metal bearing surfaces. These new articulations have shown promise in reducing volumetric wear and it is hoped that the long-term complications of osteolysis will also be reduced.[8] However, recent analysis suggested that although the volumetric wear rate of highly cross-linked UHMWPE has been significantly decreased, the smaller sized highly cross-linked polyethylene particles may be more bioreactive.[10] When metal-on-metal wear is involved, the metallic particles are usually in the nanometer scale range and the resulting surface area of the particles is large.[11] In addition to generating particulate wear debris, metal-on-metal articulating surfaces can also produce other byproducts, mainly free metallic ions that can lead to chronic toxic and immune reactions such as a type IV T-cell-mediated immune response and pseudotumor formation.[8,12] In cases of ceramic wear debris, submicron-sized particulates of alumina and zirconia

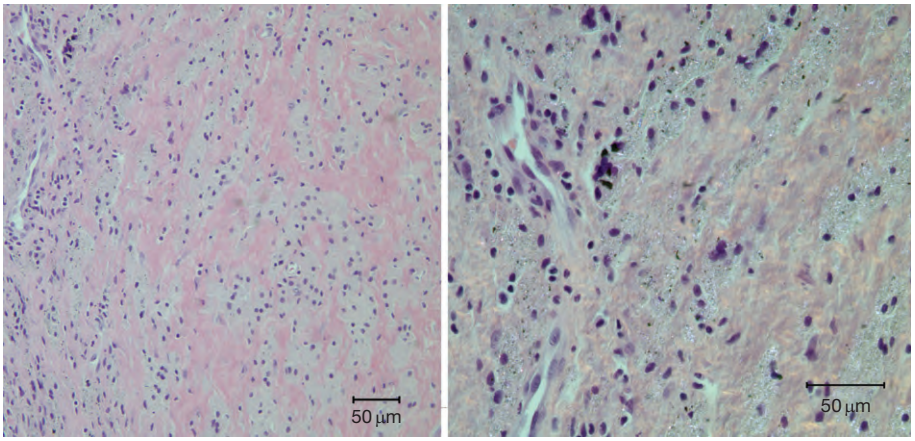

Figure 1 Photomicrograph of histological section from tissue retrieved from the granulomatous synovial capsular tissues demonstrating sheets of macrophages in a fibrovascular stroma. Left: Hematoxylin and eosin stain, light field and right: hematoxylin and eosin stain, polarized light field.
Note: Black metal particles and abundant granular white specks of polyethylene under polarized light can be seen.

can elicit a similar but usually less intense reaction to those seen with submicron-sized polymers and metal debris.[13,14] Overall, the wear rate of these newer bearing surfaces has been significantly reduced compared to conventional metal-on-polyethylene articulations. However, although the volumetric wear rates of the bearing surfaces are reduced, the characteristics of particles, including size, shape, and surface coating antigenic properties of the particles and host factors, all contribute to the complex process of osteolysis.[10,15–17]

6.606.3. Biologic Reactions of the Host to Wear Debris

The biological response of the host to wear debris occurs in a unique microenvironment in which a variety of host cells are exposed to continuously generated wear particles. The cellular response has been dominated by cells of the monocyte–macrophage lineage and many other cells are active participants. Cellular profiles from studying retrieved membranes surrounding the implant revealed the presence of macrophages, fibroblasts, lymphocytes, mesenchymal stem cells (MSCs), osteoblasts, and osteoclasts.[3,18,19] Current research has also identified molecules that are released by these cells that regulate the inflammatory processes elicited primarily by particles (**Figure 2**).

The role of the major cells implicated in the process of implant wear and the cellular response to wear debris and the biological factors involved in the regulation of these cells are reviewed in the following sections.

6.606.3.1. Macrophages

The presence of macrophages with phagocytosed wear particles has been universally reported in cases of failed TJR. To date, almost all the particles generated from wearing of prostheses, including metal particles, UHMWPE, PMMA, ceramics, and hydroxyapatite have been shown to activate macrophages.[20–23] Wear particles less than approximately 10 μm can be engulfed by macrophages,[24] which then become activated, and can activate other macrophages by means of autocrine and paracrine mechanisms. Furthermore, more macrophages are recruited to the site, thereby increasing the local macrophage population.[25,26] Activated macrophages release inflammatory mediators and disrupt the homeostatic balance between osteoclasts and osteoblasts. Activation of macrophages by particles can also occur without phagocytosis.[27] In the case of surface contact between particles and macrophages, multiple surface receptors (CD11b, CD14, TOLL-like receptors (TLRs)) on macrophages can interact with particles that are associated with specific proteins. The intracellular signaling transduction involves the activation of the mitogen-activated protein kinase cascade (JNK, MEK), leading to activation of transcription factor nuclear factor kappa B (NF-κB) and nuclear translocation, which upregulates gene expression mechanisms for proinflammatory cytokines and chemokines, the hallmarks of foreign body and chronic inflammatory reaction.[28] These cytokines and inflammatory mediators include interleukin-1 (IL-1), IL-6, IL-8, IL-11, prostaglandin E2 (PGE2), metalloproteinases, collagenase, receptor activator of NF-κB ligand (RANKL), macrophage

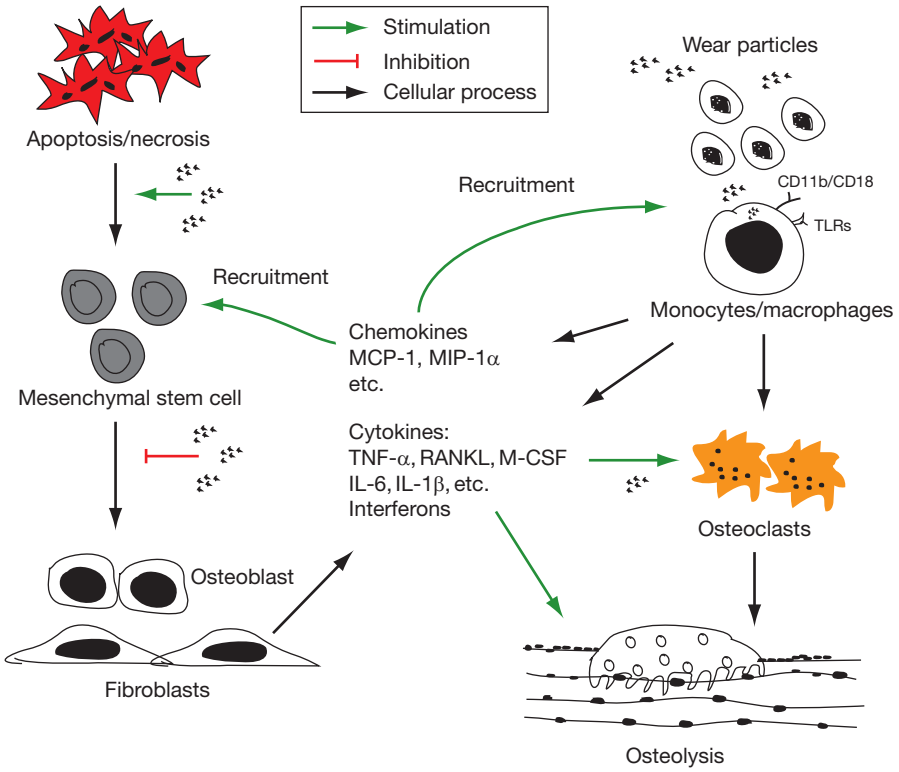

Figure 2 Diagram of the biological reactions associated with wear particles.

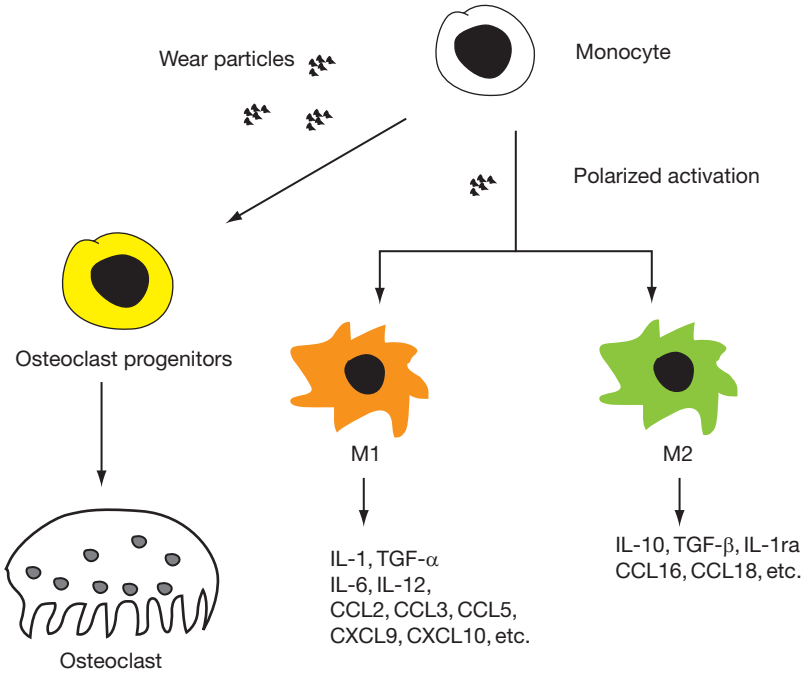

Involvement of monocyte/macrophages in periprosthetic osteolysis

Figure 3 Involvement of monocyte/macrophages in periprosthetic osteolysis. Monocytes are precursors to both macrophages and osteoclast precursors (OCPs). Wear debris induce the classically activated macrophages (M1) to secrete proinflammatory mediators and the release of reactive oxygen. In contrast, alternative activation of macrophages (M2) may contribute to granuloma fibrosis and bone remodeling.

colony-stimulating factor (M-CSF), vascular endothelial growth factor (VEGF), and tumor necrosis factor alpha (TNF-α).[8]

An emerging hypothesis for macrophage activation in osteolysis is that macrophages are heterogeneous cells and the heterogeneity of the undifferentiated circulating monocytes as well as the microenvironment may lead to polarized activation of macrophages. Following the initial exposure to wear particles, classically activated macrophages (M1) initiate a periprosthetic proinflammatory response, and this response subsequently transitions to a more prolonged, noninflammatory phase dominated by an alternative macrophage phenotype (M2) to form granulomas in an attempt to process nondegradable materials[29] (Figure 3). Studies comparing the periprosthetic tissue from revision TJR and synovium revealed elevated levels of chitotriosidase and CCL18, markers for alternative macrophage activation.[30–32]

6.606.3.2. Osteoblasts and MSCs

Osteoblasts are mainly responsible for the process of bone formation. Several studies have demonstrated reduced new bone formation in the presence of particles.[33] In cell culture studies, osteoblasts or osteoblast-like cells were able to phagocytose particles and release chemokines that trigger the migration of other cell types.[34] Particles also disrupt the osteoblast adhesive behavior, alter its gene expression profile, and induce apoptosis.[35,36] One mechanism by which osteoblasts communicate with osteoclasts is the production of cell membrane-associated RANKL and M-CSF. Interaction of RANKL with the receptor activator of nuclear factor κB (RANK) on mononuclear cells of the monocyte/macrophage lineage eventually leads to osteoclastogenesis. Particle-treated human primary osteoblasts produce high amounts of factors that induce osteoclastogenesis including RANKL and M-CSF-1.[10]

Recently, attention has shifted to the potential destructive effects of wear particles on osteoprogenitors as they differentiate to bone-forming cells. Adult MSC-like progenitor cells can be found in bone marrow as well as in adult trabecular bone.[37,38] During the life span of the prosthesis, bone marrow cells and the trabecula directly juxtaposed to bone are exposed to continuously generated particles. The biological function of these progenitor cells could be critically affected by increasing amounts of wear particles, potentially diminishing the pool of osteoblasts for bone formation and osseointegration. The mechanisms by which wear particles exert their impact on MSCs remain largely unknown. Recent studies showed that submicron-sized particles decrease the proliferation and viability of human MSCs, suppress gene expression of bone sialoprotein (BSP), and inhibit matrix mineralization.[39] Prolonged exposure of murine osteoprogenitor-like cells to titanium particles also reduced the viability of these cells by direct and indirect induction of apoptosis or necrosis.[40] With the diminished stem cell population and compromised stem cell function, the process of osseointegration and prosthesis fixation can be severely jeopardized.[41]

6.606.3.3. Osteoclasts

The differentiation, migration, and activation of osteoclasts have been implicated as the key step accelerating the degradation of bone.[3] Most inflammatory mediators released by macrophages and present at the bone–implant interface,

including PGE2, TNF-α, IL-1β, and M-CSF are potent stimulators of osteoclastogenesis.[42–44] The essential signaling for osteoclastogenesis is the interaction of RANKL and RANK. RANK, a member of the TNF receptor superfamily, is expressed on osteoclast precursors and mature osteoclasts. RANKL is expressed on the cell surface of osteoblasts, bone marrow stromal cells, fibroblasts, mammary epithelial cells, and activated T cells.[45] RANKL is active as a transmembrane molecule as well as a soluble monomer.[46] Following RANKL–RANK contact, multiple signaling molecules (TRAF6, NF-κB, AP-1, and NFAFc1) are activated. NFATc1 is absolutely required as the master regulator of osteoclasts.[47] Together with M-CSF, RANKL also activates the resorptive function and maintains the survival of mature osteoclasts.[48–50] RANKL or RANK deficient mice develop severe osteopetrosis as a result of complete deficiency in osteoclastogenesis.[49,51,52] Osteoprotegerin (OPG), a soluble decoy receptor of RANKL, blocks the RANKL–RANK coupling by competitively binding with RANK.[52–55] OPG is mainly produced by bone marrow stromal cells, dendritic cells, and monocytes/macrophages.[55,56] The molecular ratio of RANKL, RANK, and OPG expression has become an indicator for assessing bone remodeling. Studies using polyethylene and TiAlV wear particles and a human monocytic leukemic cell line showed that TiAlV and polyethylene particles induced the expression of RANK mRNA, and OPG mRNA expression increased transiently.[57] OPG levels in the joint fluid from failed total hip arthroplasty patients were much lower than those from patients with osteoarthritis.[58]

Osteoclastogenesis also requires costimulation via ITAM (immunoreceptor tyrosine-based activation motif) signaling receptors. When osteoclast precursors deficient of DAP12 and FcRγ, two ITAM-containing adaptor proteins were stimulated with RANKL and M-CSF, no multinucleated osteoclasts could be seen.[59,60]

Because osteoclasts have the ability to mobilize calcium from bone, initiate bone remodeling, and communicate with hematopoietic stem cells, they are referred as innate immune cells of bone by some researchers.[61–65] Murine osteoclast precursors express TLRs TLR1–TLR9 and *in vitro* studies showed that direct TLR stimulation inhibited osteoclast formation induced by RANKL.[66] Very little information is available on the role of TLRs on osteoclastogenesis *in vivo*. The interaction of osteoclasts and other innate immune receptors is currently an active research area.

6.606.4. Other Factors Modulating the Biological Activity of Wear Particles

6.606.4.1. Genetic Contribution

Clinical variation seen in patients with TJR suggests a potential genetic contribution. Minor variations in DNA sequence can result in subtle changes in gene expression, giving rise to altered susceptibility to osteolysis. Variation in specific genes for single nucleotide polymorphisms (SNPs) correlated with osteolysis after TJR in a cohort of 481 subjects (214 failed cemented THR, 267 radiologically intact implants).[67] A study conducted on a cohort of 609 subjects (268 patients with osteolysis, 341 nonosteolytic THR controls) suggested a positive association of the gene, FREZ, encoding a protein for Wnt signaling, with osteolysis.[68]

6.606.4.2. Endotoxin

The contribution of byproducts derived from bacteria to aseptic loosening has received considerable attention in recent years. Lipopolysaccharides (LPS), the classic endotoxin, has been shown to increase the biological activity of wear particles to induce osteolysis *in vitro* and *in vivo*.[69–75] Besides LPS, a collection of immunostimulatory molecules known as pathogen-associated molecular patterns (PAMPs) have been identified. The sources of PAMPs in patients with aseptic loosening and how crucial the PAMPs are to aseptic loosening remains unclear. Studies have suggested that one source of PAMPs could be the gram-positive bacteria containing biofilm attached to implants.[76,77] Other sources of PAMPs could be the systemic blood circulation[78] or the contamination of surgical implants.[79] Studies to evaluate the polymorphisms in the genes encoding the PAMP receptors and the risk of aseptic loosening will provide key information regarding this subject.[67,68]

6.606.4.3. Implant Instability

Recent studies have emphasized the importance of mechanical stability of implants in the generation of wear particles and aseptic loosening. Relative motion of the implant in bone triggers the formation of a fibrous membrane.[80,81] Such a membrane serves as a conduit for particles, cells, and other osteolytic mediators, inhibiting bone formation and enhancing bone erosion.[82–84] Clinical studies showed that cemented THRs with minor early subsidence rates (relative motion) using sensitive techniques such as radiostereometric analysis (RSA) will become loose clinically within 2 years.[85] However, whether relative motion of an implant precedes or follows the formation of a fibrous membrane is unknown.

6.606.4.4. Pressure

In general, cells can be perturbed by pressure in various manners. In the context of implant fixation, pressure can alter local bone remodeling, affecting new bone formation and osteolysis.[86] Clinically, when implants have subsided during loading, widening of the medullary canal, thinning of the cortex, and the presence of a bony pedestal distal to the implant can often be found as a result of profoundly altered distribution of mechanical forces. Under normal conditions, there is a thin layer of synovial fluid in the articulating surface that bathes the natural or replaced joint articulation. This fluid is distributed into the contiguous accessible areas of the joint, also known as the effective joint space, by each step during loading of the limb, much like a hydraulic piston. In the case of synovitis, increased fluid production within the joint causes increased intraarticular pressure during loading, which is transmitted to the joint space and contiguous areas. When synovitis occurs concurrently with increased numbers of wear particles, fluid containing wear particles, cellular infiltrates, proinflammatory factors, and other molecules can be introduced into the effective joint space.[87–89] This may be the reason for the observation of osteolysis remote from the source of particle generation, as seen in cases of polyethylene wear with widespread osteolysis around the femoral stem.

In vivo animal studies also confirmed that pressure alone can adversely alter bone remodeling.[90–93] In fact, particles and

mechanical forces such as hydrostatic pressure, cyclic stretch, or mechanical strain have been shown to be synergistic.[82,94,95] Although animal models are always somewhat different than the clinical situation, they do suggest that pressure can induce adverse bone remodeling in the absence of wear particles.

6.606.5. New *In Vivo* Models and Development of Particle-Induced Osteolysis

The ongoing production of wear debris may be asymptomatic clinically. When severe pain or other local symptoms such as swelling, poor function, or pathologic fracture are noticed long after joint replacement, periprosthetic osteolysis is often present to an extended degree. Newer alternative bearing surfaces are successful in reducing the particle load delivered to the local tissues, but to date, nonsurgical pharmacological methods to prevent or treat the adverse effects of wear particles are still not available. This fact has spawned new research efforts into the pathogenesis of particle disease in the hope that early nonsurgical intervention may prevent or delay the need for revision surgery. Several new *in vivo* models have emerged and information collected from these studies further pinpointed the biological pathways involved in wear particle disease (Table 1).

6.606.5.1. Models of Continuous Delivery of Particles *In Vivo*

Following THA, wear particles are generated continuously with usage of the joint. As a result, the local tissues are exposed to wear particles in an accumulative fashion over prolonged periods of time. For *in vivo* studies of particle disease, the majority of animal models have been applying one bolus/a single dose of particles, or multiple periodic injections of particles to an anatomical site, which is different from the clinical situation. Kim and colleagues made the first attempt to connect a diffusion pump with the knee joint containing an intramedullary femoral Kirschner wire in rats to deliver polyethylene particles to the knee joint continuously.[105,106,119] This novel model showed that continuous delivery of high-density polyethylene particles was associated with increased expression of TNF-α mRNA and radiographic osteolysis around the rod. Formation of an inflammatory periprosthetic membrane lined with osteoclasts was also found.

The group from Stanford University optimized and quantitated Kim's rat model using bench top experiments and converted and validated it into an *in vivo* murine model for studying the effects of continuous infusion of particles.[102–104,120] In the *in vitro* experiment, blue-dyed commercial polystyrene particles and retrieved clinically relevant UHMWPE particles were suspended in mouse serum at various concentrations and loaded into Alzet mini-osmotic pumps.[103] Pumps were attached to hollow titanium rods via vinyl tubing and the efflux from the rod was collected into a vessel. The number of particles contained in the collection vessel was quantitified at the 2- and 4-week time points. Delivery of both particle types was feasible when the pumps were loaded with concentrations of 10^9–10^{11} particles per pump, which are clinically relevant particle concentrations. Efficiency of delivery of polystyrene particles decreased with higher initial particle concentration; UHMWPE particle delivery increased slightly with increasing initial particle concentration. By the end of the 4 weeks, approximately one-third of the UHMWPE particles in the pump were delivered into the collection vessel. The same delivery system was then evaluated using explanted mice femora in organ culture to show that continuous intramedullary delivery of submicron-sized polymer particles using osmotic pumps is feasible.[102] Infusion of UHMWPE particles at concentrations of 2.60×10^{11} particles per ml for 2 weeks and 8.06×10^{11} particles per ml for 4 weeks both yielded significantly more bone loss radiographically compared to controls in which only mouse serum was infused. Finally, clinically relevant UHMWPE particles were infused to the femoral intramedullary space of live mice for 4 weeks using a subcutaneous implanted osmotic pump.[104] Continuous infusion of UHMWPE particles for 4 weeks led to reduced bone volume detected by microCT and altered alkaline phosphatase expression. The model has therefore proven useful in studying the biological processes associated with wear debris in a more clinically relevant scenario.

Table 1 Animal models currently used to study wear debris-induced inflammation

Species	*Model*	*Key references*
Mouse	Calvarial	96–98
Mouse	Air pouch	99–101
Mouse	Intramedullary implant with particles – femur	102–104
Rat	Intra-articular or intramedullary – femur	105–108
Rabbit	Intramedullary – femur	109–111
Rabbit	Harvest chamber – tibia	112–114
Dog	Pistoning implant – femoral condyle	82
Dog	Intramedullary – hip replacement	115–117
Sheep	Intra-articular injection – hip replacement	118

6.606.5.2. Cell Trafficking in the Presence of Wear Particles

Macrophages, foreign body giant cells, and osteoclasts are the primary cells carrying out phagocytosis and bone resorption. The common precursor of these cells are monocytes in the blood circulation. Whether the phagocytic cells/osteoclasts participating in osteolysis were derived from local monocytes population or migrated remote monocytes is an interesting question that pertains to the therapeutic strategy of particle disease. There have been a few recent studies to suggest that local wear debris may cause systemic migration of macrophages to the site of particle generation. One study injected the distal femora of nude mice with suspensions of Simplex BC or UHMWPE particles and delivered reporter murine RAW 264.7 macrophages, which stably expressed the bioluminescent reporter gene *fluc*, and the fluorescence reporter gene *gfp* intravenously through the tail vein. Trafficking of the labeled macrophages to the femora containing the particles was evaluated by bioluminescence imaging and compared to animals which only received saline in the femora.[121] Six to eight days after the animals were given the exogenous labeled macrophages in the tail vein, the bioluminescent signal of femora containing BC or UHMWPE particle suspensions increased significantly whereas the saline controls did not show this effect. Histological study confirmed the presence of large numbers of reporter macrophages within the medullary canal of

mice that also received the particles. Thus, BC and UHMWPE particles contained in the mouse femur were able to stimulate the systemic recruitment of macrophages. Manipulating the trafficking of systemic macrophages may be a therapeutic strategy to interfere with particle-induced periprosthetic osteolysis.

The trafficking of human peripheral blood monocytes (PBMCs) in the context of particle-associated periprosthetic osteolysis was also studied in a mouse–human (SCID-Hu) chimera model.[122] Human periprosthetic tissues harvested during revision surgery of aseptic periprosthetic loosening were placed into the quadriceps and paravertebral muscles of severely combined immunodeficient (SCID) mice. After a 30-day recovery period following the implantation, the engrafted tissue contained high levels of IL-1, TNF, and IL-6. Priming of the periprosthetic tissues before implantation with retroviruses encoding for human IL-1 receptor antagonist (hIL-lRa) decreased the total number of inflammatory cells and expression of IL-1 and TNF. In a separate study, the SCID mice underwent periodic intraperitoneal injection of anti-asialo GM1 rabbit sera (ASGM1) to deplete the mouse of the host macrophages and the human periprosthetic tissues harvested during revision arthroplasty surgery for aseptic loosening were placed the same way as previously described. Human PBMCs labeled with PKH2 fluorescent dye were then injected into the peritoneum of the same mice. Fourteen days later, the injected fluorescence labeled PBMC were found to traffic to the xenografts and were associated with increased expression of IL-1, IL-6, TNF-α, and RANK within the periprosthetic tissue.[123] This experiment once again confirmed that systemically administered blood monocytes can traffic to an area of particle-induced inflammation.

6.606.6. Therapeutic Strategies

Since aseptic loosening occurs in only a small fraction of patients who undergo TJR, current attempts for nonsurgical treatments has focused on existing pharmacologic approaches known to interfere with inflammation. Several candidate drugs are being considered based on their specific targets. Anti-inflammatory drugs, such as nonsteroidal anti-inflammatory drugs (NSAIDs), selective cyclooxygenase (COX) inhibitors (e.g., celecoxib), TNF antagonists (e.g., etanercept, infliximab, adalimumab), and IL-1 antagonists (e.g., Anakinra) may potentially have a role in curtailing the progression of osteolysis on a theoretical basis. However, the adverse effects of these drugs, especially the impairment to the immune system are of great concern. In this respect, one promising candidate for the nonsurgical treatment of osteolysis is the RANKL antagonist. This approach not only prevented wear-induced osteolysis in animal models,[124–127] but consistently demonstrated nonimmunosuppressive effects. Interestingly, a human recessive null mutation in RANKL led to clinical osteopetrosis but without adverse immunosuppressive effects, further demonstrating the potential of RANKL antagonists.

6.606.7. Conclusion

Wear particles from bearing surfaces and supporting materials of TJAs are inevitably generated with usage of the joint. The characteristics of the particles depend on the materials of the bearing surfaces and the overall design and function of the implant. These particles and their byproducts stimulate local and systemic biological reactions by the host to mount an inflammatory and foreign body reaction. Many cell types are active participants or modulators of these events. The cells communicate by the release of cytokines, chemokines, and other proinflammatory factors in a paracrine and autocrine fashion. Newer bearing couples reduce overall volumetric wear; however, the long-term clinical performance still needs to be evaluated. Newer pharmacological approaches may hold promise in mitigating osteolysis as an alternative nonsurgical treatment for selected patients if the prosthesis is still functioning well.

Acknowledgments

This work has been supported in part by the National Institute of Health, National Institute of Arthritis, Musculoskeletal and Skin Diseases, Grant #1R01AR055650.

References

1. Goodman, S. B.; Wright, T. *J. Am. Acad. Orthop. Surg.* **2008**, *16*(Suppl. 1), x–xi.
2. Marshall, A.; Ries, M. D.; Paprosky, W. *J. Am. Acad. Orthop. Surg.* **2008**, *16*(Suppl. 1), S1–S6.
3. Goodman, S. B.; Huie, P.; Song, Y.; *et al. J. Bone Joint Surg. Br.* **1998**, *80*, 531–539.
4. Gallo, J.; Kaminek, P.; Ticha, V.; Rihakova, P.; Ditmar, R. *Biomed. Pap. Med. Fac. Univ. Palacky Olomouc. Czech. Repub.* **2002**, *146*, 21–28.
5. Goodman, S. B.; Lind, M.; Song, Y.; Smith, R. L. *Clin. Orthop. Relat. Res.* **1998**, *352*, 25–34.
6. Santavirta, S.; Takagi, M.; Gomez-Barrena, E.; *et al. J. Long Term Eff. Med. Implants* **1999**, *9*, 67–76.
7. Goodman, S. B.; Trindade, M.; Ma, T.; Genovese, M.; Smith, R. L. *Clin. Orthop. Relat. Res.* **2005**, *430*, 39–45.
8. Jacobs, J. J.; Campbell, P. A.; Kontinnen, Y. T. *Am. Acad. Orthop. Surg.* **2008**, *16*(Suppl. 1), S49–S55.
9. McKellop, H. A.; Campbell, P.; Park, S. H.; *et al. Clin. Orthop. Relat. Res.* **1995**, *349*, 3–20.
10. Ingram, J. H.; Stone, M.; Fisher, J.; Ingham, E. *Biomaterials* **2004**, *25*, 3511–3522.
11. Doorn, P. F.; Campbell, P. A.; Worrall, J.; Benya, P. D.; McKellop, H. A.; Amstutz, H. C. *J. Biomed. Mater. Res.* **1998**, *42*, 103–111.
12. Ladon, D.; Doherty, A.; Newson, R.; Turner, J.; Bhamra, M.; Case, C. P. *J. Arthroplasty* **2004**, *19*, 78–83.
13. Catelas, I.; Petit, A.; Zukor, D. J.; Marchand, R.; Yahia, L.; Huk, O. L. *Biomaterials* **1999**, *20*, 625–630.
14. Catelas, I.; Huk, O. L.; Petit, A.; Zukor, D. J.; Marchand, R.; Yahia, L. *J. Biomed. Mater. Res.* **1998**, *41*, 600–607.
15. Shanbhag, A. S.; Kaufman, A. M.; Hayata, K.; Rubash, H. E. *J. Bone Joint Surg. Am.* **2007**, *89*, 1081–1089.
16. Campbell, P.; Ma, S.; Yeom, B.; McKellop, H.; Schmalzried, T. P.; Amstutz, H. C. *J. Biomed. Mater. Res.* **1995**, *29*, 127–131.
17. Green, T. R.; Fisher, J.; Matthews, J. B.; Stone, M. H.; Ingham, E. *J. Biomed. Mater. Res.* **2000**, *53*, 490–497.
18. Goldring, S. R.; Jasty, M.; Roelke, M. S.; Rourke, C. M.; Bringhurst, F. R.; Harris, W. H. *Arthritis Rheum.* **1986**, *29*, 836–842.
19. Perry, M. J.; Mortuza, F. Y.; Ponsford, F. M.; Elson, C. J.; Atkins, R. M. *Br. J. Rheumatol.* **1995**, *34*, 1127–1134.
20. Willert, H. G.; Bertram, H.; Buchhorn, G. H. *Clin. Orthop. Relat. Res.* **1990**, *258*, 108–121.
21. Haynes, D. R.; Rogers, S. D.; Hay, S.; Pearcy, M. J.; Howie, D. W. *J. Bone Joint Surg. Am.* **1993**, *75*, 825–834.
22. Horowitz, S. M.; Doty, S. B.; Lane, J. M.; Burstein, A. H. *J. Bone Joint Surg. Am.* **1993**, *75*, 802–813.

23. Harada, Y.; Wang, J. T.; Doppalapudi, V. A.; *et al*. *J. Biomed. Mater. Res.* **1996**, *31*, 19–26.
24. Trindade, M. C.; Lind, M.; Sun, D.; Schurman, D. J.; Goodman, S. B.; Smith, R. L. *Biomaterials* **2001**, *22*, 253–259.
25. Miyanishi, K.; Trindade, M. C.; Ma, T.; Goodman, S. B.; Schurman, D. J.; Smith, R. L. *J. Bone Miner. Res.* **2003**, *18*, 1573–1583.
26. Santerre, J. P.; Labow, R. S.; Boynton, E. L. *Can. J. Surg.* **2000**, *43*, 173–179.
27. Nakashima, Y.; Sun, D. H.; Trindade, M. C.; *et al*. *J. Bone Joint Surg. Am.* **1999**, *81*, 603–615.
28. Tuan, R. S.; Lee, F. Y.; Konttinen, Y. T.; Wilkinson, J. M.; Smith, R. L. *J. Am. Acad. Orthop. Surg.* **2008**, *16*(Suppl. 1), S42–S48.
29. Purdue, P. E. *Autoimmunity* **2008**, *41*, 212–217.
30. Koulouvaris, P.; Ly, K.; Ivashkiv, L. B.; *et al*. *J. Orthop. Res.* **2008**, *26*, 106–116.
31. Boven, L. A.; van Meurs, M.; Boot, R. G.; *et al*. *Am. J. Clin. Pathol.* **2004**, *122*, 359–369.
32. Boot, R. G.; Verhoek, M.; de Fost, M.; *et al*. *Blood* **2004**, *103*, 33–39.
33. Sacomen, D.; Smith, R. L.; Song, Y.; Fornasier, V.; Goodman, S. B. *J. Biomed. Mater. Res.* **1998**, *43*, 123–130.
34. Fritz, E. A.; Glant, T. T.; Vermes, C.; Jacobs, J. J.; Roebuck, K. A. *J. Biomed. Mater. Res. A* **2006**, *77*, 192–201.
35. Pioletti, D. P.; Takei, H.; Kwon, S. Y.; Wood, D.; Sung, K. L. *J. Biomed. Mater. Res.* **1999**, *46*, 399–407.
36. Kwon, S. Y.; Lin, T.; Takei, H.; *et al*. *Biorheology* **2001**, *38*, 161–183.
37. Noth, U.; Osyczka, A. M.; Tuli, R.; Hickok, N. J.; Danielson, K. G.; Tuan, R. S. *J. Orthop. Res.* **2002**, *20*, 1060–1069.
38. Tuli, R.; Tuli, S.; Nandi, S.; *et al*. *Stem Cells* **2003**, *21*, 681–693.
39. Wang, M. L.; Nesti, L. J.; Tuli, R.; *et al*. *J. Orthop. Res.* **2002**, *20*, 1175–1184.
40. Chen, F. H.; Rousche, K. T.; Tuan, R. S. *Nat. Clin. Pract. Rheumatol.* **2006**, *2*, 373–382.
41. Wang, M. L.; Tuli, R.; Manner, P. A.; Sharkey, P. F.; Hall, D. J.; Tuan, R. S. *J. Orthop. Res.* **2003**, *21*, 697–707.
42. Lam, J.; Takeshita, S.; Barker, J. E.; Kanagawa, O.; Ross, F. P.; Teitelbaum, S. L. *J. Clin. Invest.* **2000**, *106*, 1481–1488.
43. Ma, T.; Miyanishi, K.; Suen, A.; *et al*. *Cytokine* **2004**, *26*, 138–144.
44. Suda, K.; Udagawa, N.; Sato, N.; *et al*. *J. Immunol.* **2004**, *172*, 2504–2510.
45. Goldring, S. R. *Calcif. Tissue Int.* **2003**, *73*, 97–100.
46. Lum, L.; Wong, B. R.; Josien, R.; *et al*. *J. Biol. Chem.* **1999**, *274*, 13613–13618.
47. Takayanagi, H.; Kim, S.; Koga, T.; *et al*. *Dev. Cell* **2002**, *3*, 889–901.
48. Wong, B. R.; Josien, R.; Choi, Y. *J. Leukoc. Biol.* **1999**, *65*, 715–724.
49. Theill, L. E.; Boyle, W. J.; Penninger, J. M. *Annu. Rev. Immunol.* **2002**, *20*, 795–823.
50. Anderson, D. M.; Maraskovsky, E.; Billingsley, W. L.; *et al*. *Nature* **1997**, *390*, 175–179.
51. Teitelbaum, S. L.; Ross, F. P. *Nat. Rev. Genet.* **2003**, *4*, 638–649.
52. Li, J.; Sarosi, I.; Yan, X. Q.; *et al*. *Proc. Natl Acad. Sci. USA* **2000**, *97*, 1566–1571.
53. Yasuda, H.; Shima, N.; Nakagawa, N.; *et al*. *Proc. Natl Acad. Sci. USA* **1998**, *95*, 3597–3602.
54. Dougall, W. C.; Glaccum, M.; Charrier, K.; *et al*. *Genes Dev.* **1999**, *13*, 2412–2424.
55. Simonet, W. S.; Lacey, D. L.; Dunstan, C. R.; *et al*. *Cell* **1997**, *89*, 309–319.
56. Hofbauer, L. C.; Schoppet, M. *JAMA* **2004**, *292*, 490–495.
57. Baumann, B.; Rader, C. P.; Seufert, J.; *et al*. *Acta Orthop. Scand.* **2004**, *75*, 295–302.
58. Kim, K. J.; Kotake, S.; Udagawa, N.; *et al*. *J. Biomed. Mater. Res.* **2001**, *58*, 393–400.
59. Humphrey, M. B.; Lanier, L. L.; Nakamura, M. C. *Immunol. Rev.* **2005**, *208*, 50–65.
60. Koga, T.; Inui, M.; Inoue, K.; *et al*. *Nature* **2004**, *428*, 758–763.
61. Kollet, O.; Dar, A.; Shivtiel, S.; *et al*. *Nat. Med.* **2006**, *12*, 657–664.
62. Miller, S. C. *J. Cell Biol.* **1978**, *76*, 615–618.
63. Teitelbaum, S. L. *Am. J. Pathol.* **2007**, *170*, 427–435.
64. Kollet, O.; Dar, A.; Lapidot, T. *Annu. Rev. Immunol.* **2007**, *25*, 51–69.
65. Wu, Y.; Humphrey, M. B.; Nakamura, M. C. *Autoimmunity* **2008**, *41*, 183–194.
66. Kim, N.; Takami, M.; Rho, J.; Josien, R.; Choi, Y. *J. Exp. Med.* **2002**, *195*, 201–209.
67. Wilkinson, J. M.; Wilson, A. G.; Stockley, I.; *et al*. *J. Bone Miner. Res.* **2003**, *18*, 1995–2001.
68. Gordon, A.; Southam, L.; Loughlin, J.; *et al*. *J. Orthop. Res.* **2007**, *25*, 1665–1670.
69. Schwab, L. P.; Xing, Z.; Hasty, K. A.; Smith, R. A. *J. Biomed. Mater. Res. B Appl. Biomater.* **2006**, *79*, 66–73.
70. Akisue, T.; Bauer, T. W.; Farver, C. F.; Mochida, Y. *J. Biomed. Mater. Res.* **2002**, *59*, 507–515.
71. Cho, D. R.; Shanbhag, A. S.; Hong, C. Y.; Baran, G. R.; Goldring, S. R. *J. Orthop. Res.* **2002**, *20*, 704–713.
72. Bi, Y.; Seabold, J. M.; Kaar, S. G.; *et al*. *J. Bone Miner. Res.* **2001**, *16*, 2082–2091.
73. Daniels, A. U.; Barnes, F. H.; Charlebois, S. J.; Smith, R. A. *J. Biomed. Mater. Res.* **2000**, *49*, 469–478.
74. Skoglund, B.; Larsson, L.; Aspenberg, P. A. *J. Bone Joint Surg. Br.* **2002**, *84*, 767–773.
75. Tatro, J. M.; Taki, N.; Islam, A. S.; *et al*. *J. Orthop. Res.* **2007**, *25*, 361–369.
76. Greenfield, E. M.; Bi, Y.; Ragab, A. A. *J. Biomed. Mater. Res. B Appl. Biomater.* **2005**, *72*, 179–185.
77. Nelson, C. L.; McLaren, A. C.; McLaren, S. G.; Johnson, J. W.; Smeltzer, M. S. *Clin. Orthop. Relat. Res.* **2005**, *430*, 25–30.
78. Inada, K.; Endo, S.; Takahashi, K.; *et al*. *Microbiol. Immunol.* **1991**, *35*, 303–314.
79. Ragab, A. A.; Van De Motter, R.; Lavish, S. A.; *et al*. *J. Orthop. Res.* **1999**, *17*, 803–809.
80. Bragdon, C. R.; Jasty, M.; Greene, M.; Rubash, H. E.; Harris, W. H. *J. Bone Joint Surg. Am.* **2004**, *86A*(Suppl. 2), 105–117.
81. Soballe, K.; Hansen, E. S.; Brockstedt-Rasmussen, H.; Bunger, C. *J. Bone Joint Surg. Br.* **1993**, *75*, 270–278.
82. Bechtold, J. E.; Kubic, V.; Soballe, K. *J. Bone Joint Surg. Br.* **2002**, *84*, 915–919.
83. De Man, F. H.; Tigchelaar, W.; Marti, R. K.; Van Noorden, C. J.; Van der Vis, H. M. *J. Bone Joint Surg. Am.* **2005**, *87*, 1522–1533.
84. Bechtold, J. E.; Kubic, V.; Soballe, K. *Acta Orthop. Scand.* **2001**, *72*, 642–649.
85. Karrholm, J.; Herberts, P.; Hultmark, P.; Malchau, H.; Nivbrant, B.; Thanner, J. *Clin. Orthop. Relat. Res.* **1997**, *351*, 94–110.
86. Greenfield, E. M.; Bechtold, J. *J. Am. Acad. Orthop. Surg.* **2008**, *16*(Suppl. 1), S56–S62.
87. Schmalzried, T. P.; Kwong, L. M.; Jasty, M.; *et al*. *Clin. Orthop. Relat. Res.* **1992**, *260*, 60–78.
88. Willert, H. G.; Semlitsch, M. *J. Biomed. Mater. Res.* **1977**, *11*, 157–164.
89. Willert, H. G. *J. Biomed. Mater. Res.* **1977**, *11*, 157–164.
90. Aspenberg, P.; Herbertsson, P. *J. Bone Joint Surg. Br.* **1996**, *78*, 641–646.
91. Aspenberg, P.; Van der Vis, H. *Clin. Orthop. Relat. Res.* **1998**, *352*, 75–80.
92. Van der Vis, H. M.; Aspenberg, P.; Marti, R. K.; Tigchelaar, W.; Van Noorden, C. J. *Clin. Orthop. Relat. Res.* **1998**, *352*, 201–208.
93. Skoglund, B.; Aspenberg, P. *J. Orthop. Res.* **2003**, *21*, 196–201.
94. McEvoy, A.; Jeyam, M.; Ferrier, G.; Evans, C. E.; Andrew, J. G. *Bone* **2002**, *30*, 171–177.
95. MacQuarrie, R. A.; Fang Chen, Y.; Coles, C.; Anderson, G. I. *J. Biomed. Mater. Res. B Appl. Biomater.* **2004**, *69*, 104–112.
96. Carmody, E. E.; Schwarz, E. M.; Puzas, J. E.; Rosier, R. N.; O'Keefe, R. J. *Arthritis Rheum.* **2002**, *46*, 1298–1308.
97. Merkel, K. D.; Erdmann, J. M.; McHugh, K. P.; Abu-Amer, Y.; Ross, F. P.; Teitelbaum, S. L. *Am. J. Pathol.* **1999**, *154*, 203–210.
98. Ren, W.; Wu, B.; Mayton, L.; Wooley, P. H. *J. Orthop. Res.* **2002**, *20*, 1031–1037.
99. Wooley, P. H.; Morren, R.; Andary, J.; *et al*. *Biomaterials* **2002**, *23*, 517–526.
100. Yang, S. Y.; Mayton, L.; Wu, B.; Goater, J. J.; Schwarz, E. M.; Wooley, P. H. *Arthritis Rheum.* **2002**, *46*, 2514–2523.
101. Sud, S.; Yang, S. Y.; Evans, C. H.; Robbins, P. D.; Wooley, P. H. *Inflammation* **2001**, *25*, 361–372.
102. Ortiz, S. G.; Ma, T.; Regula, D.; Smith, R. L.; Goodman, S. B. *J. Biomed. Mater. Res. B Appl. Biomater.* **2008**, *87*, 440–446.
103. Ortiz, S. G.; Ma, T.; Epstein, N. J.; Smith, R. L.; Goodman, S. B. *J. Biomed. Mater. Res. B Appl. Biomater.* **2008**, *84*, 328–333.
104. Ma, T.; Huang, Z.; Ren, P. G.; *et al*. *Biomaterials* **2008**, *29*, 3738–3742.
105. Iwase, M.; Kim, K. J.; Kobayashi, Y.; Itoh, M.; Itoh, T. *J. Orthop. Res.* **2002**, *20*, 499–505.
106. Kim, K. J.; Kobayashi, Y.; Itoh, T. *Clin. Orthop. Relat. Res.* **1998**, *352*, 46–52.
107. Millett, P. J.; Allen, M. J.; Bostrom, M. P. *J. Bone Joint Surg. Am.* **2002**, *84A*, 236–249.
108. Howie, D. W.; Vernon-Roberts, B.; Oakeshott, R.; Manthey, B. *J. Bone Joint Surg. Am.* **1988**, *70*, 257–263.
109. Im, G. I.; Kwon, B. C.; Lee, K. B. *Biomaterials* **2004**, *25*, 269–275.
110. Lalor, P. A.; Namba, R.; Mitchell, S. L.; *et al*. *J. Long Term Eff. Med. Implants* **1999**, *9*, 261–272.
111. Sundfeldt, M.; Widmark, M.; Johansson, C. B.; Campbell, P.; Carlsson, L. V. *Acta Orthop. Scand.* **2002**, *73*, 416–424.
112. Goodman, S. B. *Acta Orthop. Scand. Suppl.* **1994**, *258*, 1–43.
113. Goodman, S. B.; Song, Y.; Chun, L.; Regula, D.; Aspenberg, P. *J. Bone Joint Surg. Br.* **1999**, *81*, 1069–1075.

114. Goodman, S. B.; Song, Y.; Yoo, J. Y.; *et al*. *J*. *Biomed*. *Mater*. *Res*. *A* **2003**, *65*, 454–461.
115. Shanbhag, A. S.; Hasselman, C. T.; Rubash, H. E. *Clin*. *Orthop*. *Relat*. *Res*. **1997**, *351*, 33–43.
116. Jones, L. C.; Frondoza, C.; Hungerford, D. S. *J*. *Bone Joint Surg*. *Br*. **2001**, *83*, 448–458.
117. Kraemer, W. J.; Maistrelli, G. L.; Fornasier, V.; Binnington, A.; Zhao, J. F. *J*. *Appl*. *Biomater*. **1995**, *6*, 225–230.
118. Coathup, M. J.; Blackburn, J.; Goodship, A. E.; Cunningham, J. L.; Smith, T.; Blunn, G. W. *Biomaterials* **2005**, *26*, 4161–4169.
119. Kobayashi, Y.; Kim, K. J.; Itoh, T. *J*. *Orthop*. *Sci*. **2005**, *10*, 62–69.
120. Ma, T.; Ortiz, S. G.; Huang, Z.; Ren, P.; Smith, R. L.; Goodman, S. B. *J*. *Biomed*. *Mater*. *Res*. *B Appl*. *Biomater*. **2009**, *88*, 250–253.
121. Ren, P. G.; Lee, S. W.; Biswal, S.; Goodman, S. B. *Biomaterials* **2008**, *29*, 4760–4765.
122. Yang, S. Y.; Nasser, S.; Markel, D. C.; Robbins, P. D.; Wooley, P. H. *J*. *Bone Joint Surg*. *Am*. **2005**, *87*, 1088–1097.
123. Zhang, K.; Jia, T. H.; McQueen, D.; *et al*. *Inflamm*. *Res*. **2009**.
124. Childs, L. M.; Paschalis, E. P.; Xing, L.; *et al*. *J*. *Bone Miner*. *Res*. **2002**, *17*, 192–199.
125. Clohisy, J. C.; Frazier, E.; Hirayama, T.; Abu-Amer, Y. *J*. *Orthop*. *Res*. **2003**, *21*, 202–212.
126. Ulrich-Vinther, M.; Carmody, E. E.; Goater, J. J.; *et al*. *J*. *Bone Joint Surg*. *Am*. **2002**, *84A*, 1405–1412.
127. Schwarz, E. M. *J*. *Am*. *Acad*. *Orthop*. *Surg*. **2008**, *16*(Suppl. 1), S72–S75.

6.607. Fretting Corrosion of Orthopedic Implants

N J Hallab, Rush University Medical Center, Chicago, IL, USA

© 2011 Elsevier Ltd. All rights reserved.

6.607.1.	**Introduction**	89
6.607.1.1.	Orthopedic Alloys	90
6.607.1.1.1.	Stainless steel alloys	90
6.607.1.1.2.	Cobalt–chromium alloys	90
6.607.1.1.3.	Titanium alloys	90
6.607.1.2.	Implant Junctions	90
6.607.1.2.1.	Screw–plate interface	90
6.607.1.2.2.	Modular junctions	90
6.607.2.	**Experimental Methods: Implant Fretting Corrosion**	91
6.607.2.1.	Methods: Oxide Layer Testing	91
6.607.2.2.	Methods: Modular Junction Fretting Testing	91
6.607.2.2.1.	Open circuit potential	91
6.607.2.2.2.	Metal release fretting corrosion testing	93
6.607.2.2.3.	Mechanical loading	93
6.607.2.2.4.	Short-term testing	93
6.607.2.2.5.	Long-term testing	93
6.607.3.	**Implant Fretting and Biocompatibility**	94
6.607.3.1.	Past Investigation of Fretting Corrosion Testing	94
6.607.4.	**Conclusions**	94
References		95

Abbreviations

AAS	Atomic absorption spectrophotometry
ALVAL	Aseptic lymphocyte vasculitis-associated lesion
ICP-MS	Inductively coupled plasma atomic emission mass spectroscopy
MAC	Mechanically assisted corrosion
OCP	Open circuit potential
THA	Total hip arthroplasty
TJA	Total joint arthroplasty
TJR	Total joint replacement

6.607.1. Introduction

Fretting corrosion, or mechanically assisted corrosion (MAC), occurs at modular junctions or connections of implant components and is produced by relatively small-scale (1–100 μm) motion between implant components induced by cyclic loading. This type of corrosion occurs in all types of alloys regardless of material couple (e.g., stainless steel/stainless steel, Co-alloy/Co-alloy, Co-alloy/titanium, titanium/titanium, etc.). Fretting of modular implant components commonly occurs in the modular connections of hip and knee implant in orthopedics.[1] Corrosion products are bioreactive and cause local inflammation that results in local bone loss (osteolysis), pain, and ultimately implant loosening. An in-depth analysis of this phenomenon is given elsewhere in this publication (see **Chapter 6.608, Implant Debris: Clinical Data and Relevance**). Inflammation from corrosion debris is proportional to the amount of debris and can thus occur slowly over time (decades) with little debris or can occur within months when there is aggressive fretting corrosion. This was the case in stainless steel (SS) intramedullary rods used for hip fracture fixation that demonstrated aggressive corrosion in the modular taper resulting in rapid bone loss and ultimately recall of the implant.[2] Fretting corrosion is dependent on amount of micromotion, the designs of modular connections, the alloy combination, and other factors that affect the mechanical or chemical environment of the implant, including surgical factors. For example, tibial inserts in total knee replacements have been shown to undergo over 100 μm of micromotion at low loads (<100 N) when 'locked' into place, creating an ideal site for the generation of fretting corrosion products.[3] Mechanical-load-induced motion results in increased rates of corrosion by deforming the protective oxide layer (which forms a barrier on the surface of metal implants) and thereby reducing the activation across the oxide. Furthermore, the oxide layer is also fractured and reformed (repassivation). Fretting corrosion is MAC at interfaces; if and when present, the mechanical abrasion of the oxide layer also leads to changes in solution composition at the interface, and may thereby further reduce the energy barrier for ion release and enhance corrosion.

The metals literature is clear: there is no 'crevice' corrosion with Co–Cr alloys and Ti alloys in the typical conditions of the body. Fretting corrosion is electrochemically determined in

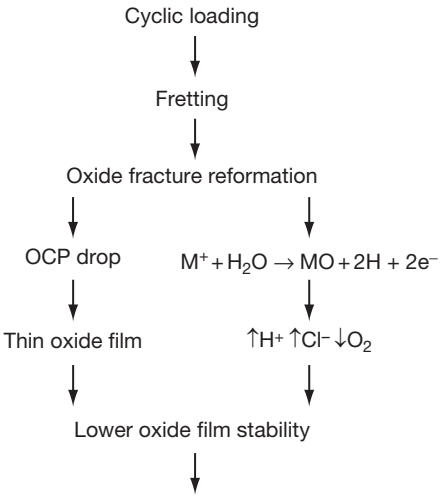

Figure 1 Schematic of the mechanically assisted corrosion (fretting corrosion) within modular junctions (connections) of implant components is shown. Upon repassivation of metal surfaces, a buildup of H^+ and Cl^-, and a lowering of the pH within the crevice environment occur.

that the oxidation reaction of the metallic species is energetically favored by the reduction in free energy associated with metal-oxide formation that results in the sequestration of O_2 from any available source (primarily H_2O). Repassivation of a metal surface at the interface environment results in a buildup of Cl^- and H^+ (lowers the pH). This MAC[4] model of modular junction fretting corrosion has been reported on and popularized by Gilbert *et al.*[1,4] and is schematically represented in Figure 1. An in-depth analysis of these phenomena is given elsewhere in this publication (see **Chapter 1.102, Metals for Use in Medicine**).

6.607.1.1. Orthopedic Alloys

While there are few new alloys that are designed to improve the fretting corrosion resistance of modular junctions (e.g., Zr–Nb alloys, Oxinium™ from Smith and Nephew, Memphis), the three principal metal alloys used in orthopedics over the past 25 years remain dominant, particularly in total joint replacement: (1) titanium alloys, (2) cobalt alloys, and (3) stainless steel alloys. Differences in strength, ductility, and hardness generally determine which of these three alloys is used for a particular implant component.

6.607.1.1.1. Stainless steel alloys

Orthopedic stainless steels, such as 316LV (i.e., ASTM F 138), include molybdenum to enhance the corrosion resistance of the grain boundaries, while chromium dissipated evenly within the microstructure allows the formation of chromium oxide (Cr_2O_3) on the surface of the metal. Stainless steels are surface treated (e.g., in nitric acid) to promote the growth and thickening of this passive oxide layer over the entire surface.[5–8]

6.607.1.1.2. Cobalt–chromium alloys

Cobalt–chromium implant alloys fall into one of two categories of biologic concern: those with nickel and those without; cobalt–nickel–chromium–molybdenum (CoNiCrMo), designated as ASTM F 562, and those without nickel, cobalt–chromium—molybdenum (CoCrMo), for example, ASTM F 75 and F 76.

6.607.1.1.3. Titanium alloys

While pure titanium is generally the most corrosion resistant of the implant metals, titanium alloy Ti–6Al–4V (ASTM F 136) is used for joint replacement components because of its needed superior mechanical properties in comparison to commercially pure titanium (cp Ti). The Ti–6Al–4V alloy microstructure is generally composed of a fine-grained HCP phase with a sparse distribution of the BCC phase to maintain strength and corrosion resistance.

6.607.1.2. Implant Junctions

6.607.1.2.1. Screw–plate interface

Corrosion is often observed in the connections of retrieved screw–plate interfaces and modular connections of joint replacement components. Investigations have shown that crevices formed at the screw plate junction are dependent on the geometry of the screw–plate interface and that preventing fretting corrosion may not be feasible through enhanced surgical technique. Screw–plate fretting is a common source of corrosion debris, although gross evidence of corrosion in screw–plate interfaces is rare.[9]

6.607.1.2.2. Modular junctions

Implant modularity is a primary design feature of modern total joint replacements. The vast majority of the >1 000 000 total joint replacements that are performed every year in North America are modular in design with components that press fit together using press-fit interlocking connections. These modular connections typically involve a tapered male–female junction between implant components, such as a Morse taper, consisting of a tapered shank and socket held together by interlocking ridges. In total hip replacement components, this connection is either metal to metal or metal to ceramic, with a tapered cone on the stem and a tapered bore in the head (Figure 2). This has been a mechanism of connection used in machine tooling for over a century and has been used in orthopedics for approximately 30 years. The more common forms of Morse taper modular junction in total hip replacements are made from cobalt–chromium–molybdenum (Co–Cr–Mo) alloys (ASTM F 75 or F 799) or titanium alloys (Ti–6Al–4V, ASTM F 136), and the heads which fit on these femoral stems comprise either Co-alloy, ceramic alumina (Al_2O_3), or ceramic zirconia (ZrO_2). Despite the geometry-specific interlocking mechanisms of these junctions, micromotion does occur. When body fluids penetrate this junction, MAC, that is, fretting corrosion, may occur, perturbing and disrupting the passive film layer.

Orthopedic alloys rely on the protective barrier of passive films to reduce oxidation (corrosion) from taking place. Since the electrical potential across the body-fluid–metal solution interface for these reactive metals can be 1–2 V and the distances are so small, the resulting electric field gradient across the oxide is very high, on the order of 10^6–10^7 V cm^{-1} (Figure 3). Particularly important to implants is the oxide film theory of Mott and Cabrera,[10] which states that oxide film growth depends on the electric field across the oxide. If the



Figure 2 Total hip replacement femoral components are shown where the head is press fitted onto the stem and secured only by tapping into place to form an interlocking at the 'Morse taper' modular junction. Courtesy of Bioengineering Solutions, Inc.

voltage potential across a metal–oxide–solution interface is decreased, then the oxide film thickness decreases by a reductive dissolution process resulting from electrochemical interactions that act to compensate and keep the electric field strength constant. Increasing the voltage across an interface will correspondingly increase the thickness of the film. In fact, oxide thickness is often determined by the 'anodization rate,' which is defined as the oxide thickness per volt.[11] If the interfacial potential of an implant interface is made sufficiently negative (or similarly if the pH of the solution is made low enough), then metal oxide films will no longer be thermodynamically stable and will undergo reductive dissolution, resulting in no barrier to active corrosion. These barrier oxide films are not flat, smooth, continuous sheets of adherent oxide covering the metal; they can be of needle[12] or dome[13] shapes. Several treatments are used to increase the barrier effect of protective oxide films, which include hot, concentrated nitric acid baths, boiling in distilled water,[14] and anodization. However, detailed investigations into how induced changes in oxide film structure maintain and protect the surface of orthopedic alloys *in vivo* remain incomplete.

6.607.2. Experimental Methods: Implant Fretting Corrosion

6.607.2.1. Methods: Oxide Layer Testing

Structural properties of protective oxide films intimately relate to the degree of fretting or corrosion resistance offered by metal surfaces. These structural properties include adhesion strength of the oxide to the substrate metal, hardness, thickness of the oxide, and the relative modulus of elasticity of oxide and substrate. One method to investigate these properties during and after oxide fracture is scratch testing. This technique has been extensively used by Gilbert *et al.*[15–17] to investigate oxide behavior where the components of a scratch test apparatus include piezoelectric actuators able to produce high-speed displacements of a nonconductive diamond stylus, all attached to a load cell to measure the force imposed on the diamond stylus (Figure 4). The stylus is lowered onto the specimen with a known force and displaces approximately 50 μm in 1–2 s to produce a controlled high-speed repeatable scratch. Both the force of the stylus and the potential voltage applied to the metal specimen can be varied and the resultant measured corrosion current(s) transients and repassivation time constants can be used to assess the repassivation behavior of various orthopedic alloys in different conditions (e.g., electrolytes). By scratching off a narrow band of oxide, the repassivation magnitudes and rates, the mechanical strength of the oxide layer, and the magnitudes and time constants associated with the potential and current transients created can all be studied on different materials and compared.

6.607.2.2. Methods: Modular Junction Fretting Testing

In vitro studies of modular junction fretting quantify the degree of fretting corrosion through electrochemical measurement and through measurement of weight loss of the implant under cyclic loading laboratory conditions (see Figure 4).[18] Fretting corrosion testing of modular junctions employs a combination of classical open circuit analysis and metal release immersion testing during mechanical loading.

6.607.2.2.1. Open circuit potential

Open circuit potential (OCP) analysis during mechanical loading represents the sum of thousands of chemical reactions at the interface, in the complicated environment of the multiple metals in an alloy/surface oxide and the proteinaceous serum electrolyte. An example of an experimental set-up for testing the head–neck junction of a total hip replacement is shown in Figure 5. The equilibrium external current (at 0 load) for this 'multielectrode system,' will reach steady state at near zero. Within an appropriate electrolyte (e.g., serum), one part of a modular component is used as a working electrode (WE) to measure the voltage (OCP) between the WE and a standard reference electrode (e.g., calomel or standard hydrogen electrode). A distal portion of the same component is sectioned or cut away from the area of interest to provide for an electron sink and is used as a counter electrode to measure the fretting corrosion current (I_{fret}). Alternatively, a similar material with equal surface area as the area of the implant that would have been in contact with the solution is often used. The testing chamber is filled with appropriate electrolyte (at 37 °C) and allowed to equilibrate for at least 24 h prior to loading. The electrolyte should fully cover the modular junctions to be tested but remain below any contact point(s) used to apply compression. Typically, the components may be wetted with electrolyte immediately prior to assembly, to simulate a worse case surgical scenario and facilitate fluid–crevice penetration within the period available for *in vitro* testing of the modular junctions.

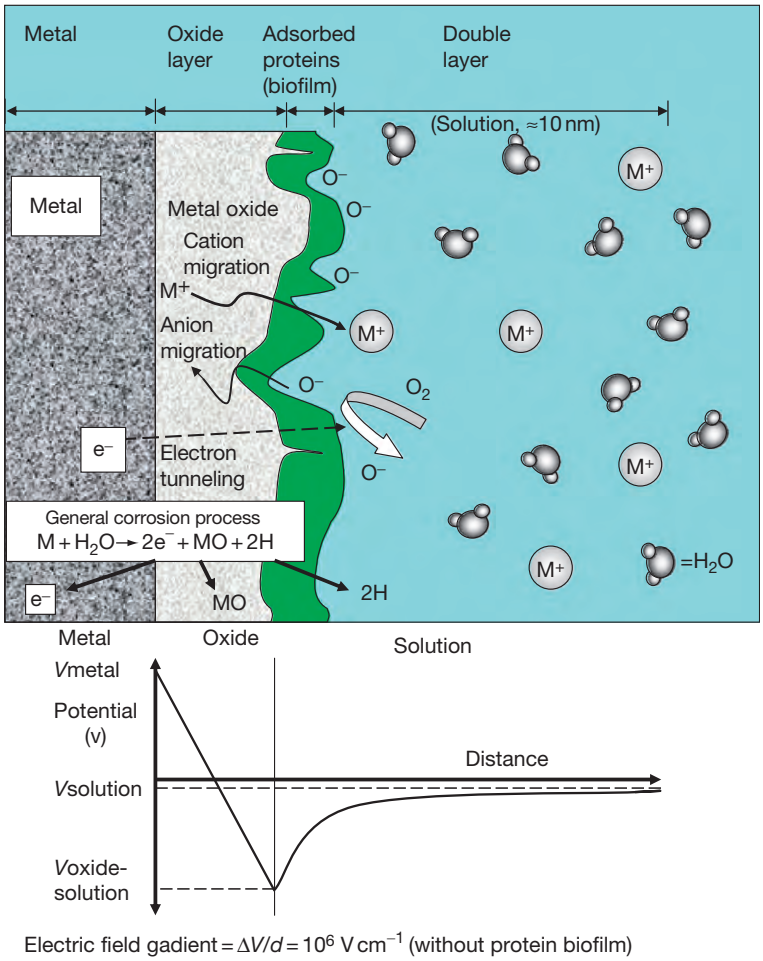

Figure 3 Orthopedic implant metal surfaces in contact with a biological environment are covered by an oxide layer followed by the adsorbed protein (biofilm) through which metal ions can pass into solution as shown.

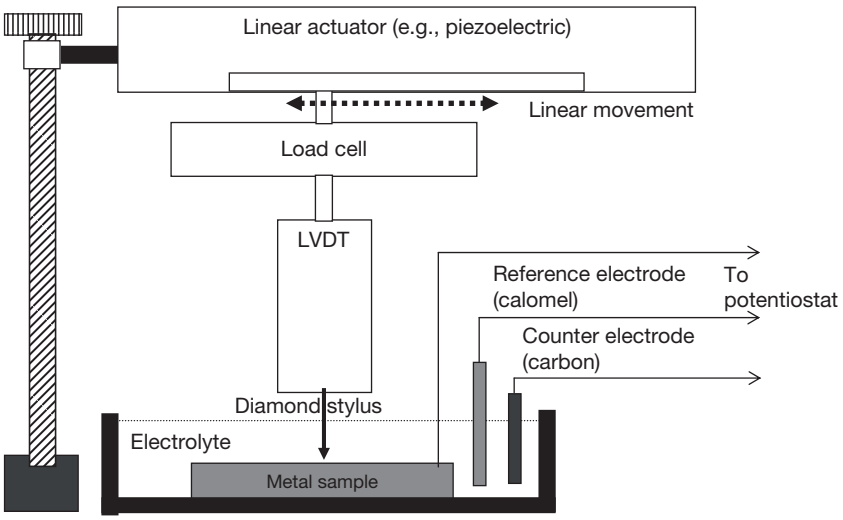

Figure 4 The components of a scratch test apparatus are shown that include piezoelectric, a nonconductive diamond stylus, a load cell to measure the force imposed on the diamond stylus, and a potentiostat to measure the voltage and current generated when the sample is scratched with a known force and displacement, for example, 50 μm in 1–2 s. The corrosion current(s) transients and repassivation time constants can be used to assess the repassivation behavior of various orthopedic alloys under different conditions (e.g., electrolytes).

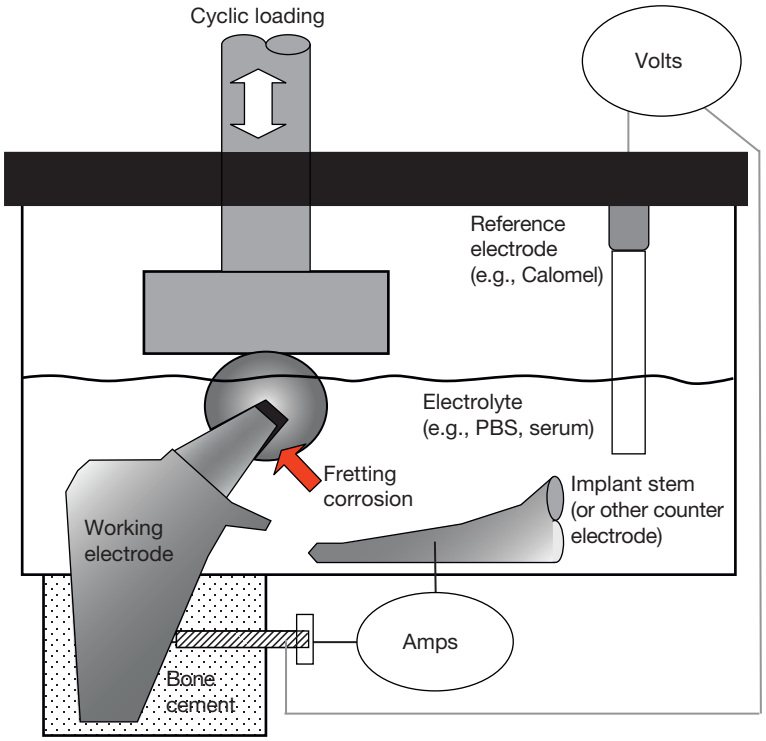

Figure 5 Fretting corrosion test chamber should ideally be air tight or have a 0.2 μm filtered connection to the environment to prevent bacterial contamination within the electrolyte. The modular component of the implant is embedded in bone cement and connected to a potentiostat for monitoring the (1) increase in current and (2) decrease in voltage that occur during fretting corrosion.

6.607.2.2.2. Metal release fretting corrosion testing

A direct test of metal released during fretting corrosion can be conducted using atomic absorption spectroscopy (AAS) and inductively coupled plasma atomic emission mass spectroscopy (ICP-MS) to quantify the concentration of ions released. These spectroscopic analysis techniques have high sensitivity (in parts per billion with proper experimental technique) but they cannot provide information about the valence state of the ions released.

6.607.2.2.3. Mechanical loading

Different mechanical loading environments can be used to simulate physiologic loading or to determine loading conditions at which fretting corrosion will start in different types of material couple or junction configurations. Sinusoidal loads are used to simulate cyclic *in vivo* loads. A typical loading environment for monitoring a total hip replacement modular junction involves simple uniaxial sinusoidal cyclic compression, with a 210 kg load (with a loading ratio of $R = 0.1$, 210–21 kg or 2060–206 N) applied at 1–5 Hz in a neutral anatomic position (following ASTM F 1404 guidelines) for $\sim 1 \times 10^6$ cycles. As a result of the muscle and weight balance biomechanics at the hip joint, a load of 210 kg simulates the average net physiologic load imposed on the femoral head by the cumulative muscle and weight component of a 70 kg individual.

6.607.2.2.4. Short-term testing

Short-term fretting corrosion tests are used to measure the initiation of fretting behavior. These tests are generally either scratch tests or actual mechanical loading of the implant junctions in a physiologically relevant electrolyte with electrochemical monitoring. Short-term testing is used to evaluate fretting associated with material design characteristics (such as alloy material, surface roughness, component tolerances, and surface treatments) and loading characteristics (such as load magnitudes, frequency, load pattern, etc).

6.607.2.2.5. Long-term testing

Long-term testing is used to evaluate how material design characteristics (such as alloy material, surface roughness, component tolerances, and surface treatments) and loading characteristics (such as load magnitudes, frequency, load pattern, etc.) affect fretting over the long term (i.e., typically >2 days of cyclic load testing at >1 Hz). Electrochemical monitoring of voltage drops and current increases associated with fretting induced by cyclic loading can be combined with other types of measurements of corrosion such as metal ion release within the electrolyte. Monitoring the voltage, current, and metal ion release requires state-of-the-art methods for assessing how specific designs and material affect modular and other types of implant junction fretting.

Longer term testing of fretting corrosion can involve the measurement of weight loss of the implant. This type of long-term testing is typically conducted by simulating a yearly loading regimen (>1 million cycles) and then measuring the subsequent weight loss and physical condition of the modular components. Past investigations involving the study of weight loss of modular head–neck junctions of total hip replacements

have indicated less than 5 mg of weight loss for a 5-million cycle test at average physiologic loads (e.g., 2100 N for a 70 kg person).[19,20] This matches the values of weight loss cycles measured in some Ti–6Al–4V alloy stem designs. This value of 1 mg year^{-1} likely represents the upper limit of what is physiologically tolerable without inducing inflammation, bone loss, and early loosening.[19,20]

6.607.3. Implant Fretting and Biocompatibility

6.607.3.1. Past Investigation of Fretting Corrosion Testing

Beginning in the late 1980s, there were reports of fretting corrosion occurring in the modular junctions of total hip replacement components, while concern about corrosion at connections of spinal rods began a little earlier.[21] Both mixed and similar metal couples were undergoing this type of corrosion attack, but there was greater modular junction fretting observed in hip replacements in mixed metal connections.[4,22]

While wear of articulating surfaces is the major source of released metal *in vivo*, many implant retrieval studies have implicated modular junction fretting as a significant source of released metal in total joint replacements that do not have metal-on-metal articulating bearings.[4,23–34] Some studies of implant retrievals have found some fretting corrosion in greater than 35% of cases where dissimilar metal junctions were used (e.g., Ti–6Al–4V to Co-alloy), and in only 7% of THA cases studied with same metal junctions (e.g., Co-alloy to Co-alloy).[28,34–36] Urban *et al*. reported that of 10 different taper designs in 25 retrieved hip arthroplasties, there was evidence of fretting corrosion in all 10 different taper designs (from six different manufacturers) with Co-alloy/Co-alloy, Co-alloy/Ti-alloy, and Co-alloy/$A1_2O_3$ couples.[25,37] Although less common, modular junction corrosion attack of titanium alloy stems also occurs. Thus, material type highly influences modular junction corrosion,[31] and this emphasizes the need to clearly evaluate new highly modular component materials (e.g., ceramic heads on highly modular stems in THA). It should be noted that the majority of heavily corroded modular junctions observed in past retrieval studies were so-called '6-degree taper' designs (see **Figure 6**), which have been phased out of modern implant designs.[28,34–36]

With the increasing popularity of highly modular implants and new types of materials used for articulating surfaces (such as ceramic heads in THA), the possibility of accelerated fretting corrosion requires further study (i.e., in Co-alloy heads).

Fretting corrosion is highly dependent on the composition of the electrolyte, that is, saline versus protein solutions.[18,38,39] While it has been generally established that decreased rates of fretting corrosion occur in protein solutions when compared to physiologic saline solutions, there are notable exceptions. In one study, serum proteins were shown to increase the corrosion (up to 61%, increasing anodic Tafel constants and decreasing cathodic Tafel constants) of stainless steel implant specimens, during electrochemical testing.[40] Similarly, the fretting corrosion of stainless steel plates and screws in protein solutions released increased amounts of Ni and Cr compared to that in saline.[41] Thus, the solubility of metals within the electrolyte media is intimately related to the electrolyte and the implant materials themselves.[42] Even small changes to the

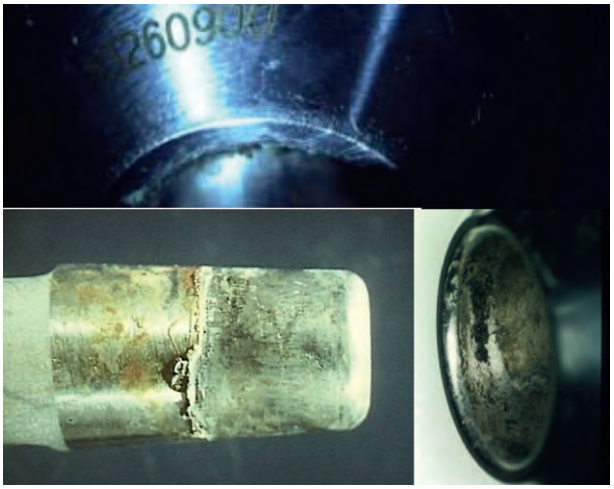

Figure 6 Previous generations of retrieved joint replacement components commonly showed corrosion around the rims of metal conical taper connections, that is, corrosion precipitates at the head–neck junction composed of $CrPO_4$ and other corrosion products. Courtesy of Prof. Robert Urban.

electrolyte can dramatically change fretting corrosion behavior; for example, rates of fretting corrosion in titanium alloy screw plates increased with the addition of soluble calcium to test electrolyte.[43] Generally however, testing in saline solutions (0.9% saline, Ringer's, Hank's Tyrode's, or 10% serum) provides identification of worst case environments even though they do not represent the 100% serum *in vivo* environment.

Both material-dependant surface chemistry and the surface roughness geometry (e.g., ridge design, tolerances, etc.) play a role in the amount of fretting corrosion. However, we have found that among femoral heads with similar geometrical/topographical characteristics (i.e., nearly identical *Ra* values, macroscopic geometry, and stem interface fit) material-dependent surface characteristics seem to dominate as a source of differential fretting corrosion behavior. When testing the fretting corrosion behavior of ceramic-to-metal and metal-to-metal modular junctions, we found that ceramic-to-metal modular junctions produce significantly less fretting and soluble metal debris than geometrically similar metal-to-metal modular junctions.[44] This was evaluated potentiodynamically where both a smaller voltage drop and recovery time were associated with the fretting of ZrO_2 heads on Co-alloy stems (compared to Co-alloy heads) (see **Figure 7**). However, there was little visual evidence of fretting corrosion after 5 million cycles at physiologic loads in serum (**Figure 8**).

6.607.4. Conclusions

Fretting corrosion of orthopedic implants remains a significant clinical problem that has yet to be mitigated in any targeted way. Currently, minimizing fretting corrosion involves (1) understanding the metallurgical processing variables, (2) minimizing the tolerances of modular connections, (3) understanding the surface chemistry and topography, and (4) using appropriate material selection. Surface treatments (e.g., nitriding,

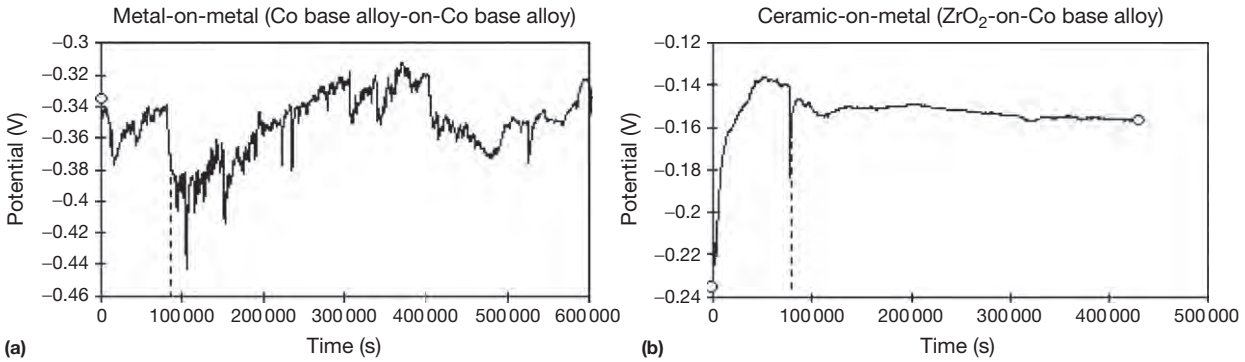

Figure 7 Potentiodynamic monitoring (open circuit potential, OCP) of (a) cobalt alloy and (b) zirconium oxide heads coupled to cobalt alloy stems (210 kg at 2 Hz). Dotted lines indicate onset of cyclic loading. Directly following loading, both configurations decreased in potential (voltage) by approximately 55 mV, indicative of fretting onset.

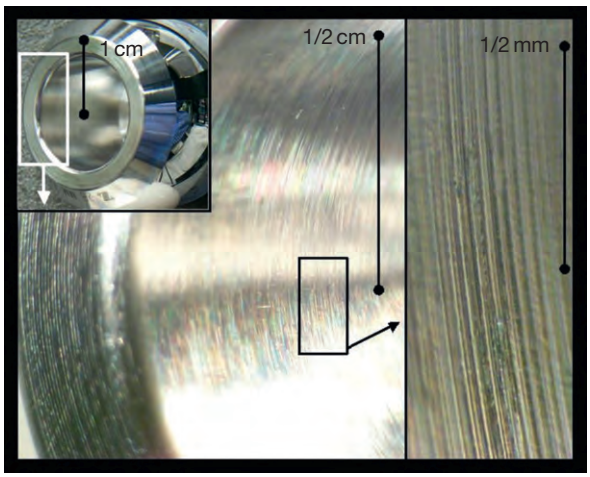

Figure 8 Photographs showing the inside of the modular connection of a Co-alloy femoral head (Zimalloy™, Zimmer, Inc., Warsaw, IN) after fretting corrosion testing for 5×10^6 cycles at 2200–220 N, 2 Hz. There was no observable damage at low magnification, but at high magnification slight degradation of some of the ridges within the taper are apparent. Note: Bars indicate scale.

ion implantation, etc.) can significantly reduce the magnitude of fretting corrosion of titanium alloys and other metal implant devices but to date have not been widely designed to specifically address fretting corrosion. There is an incomplete understanding of which corrosion mechanisms (electrochemical determinants), geometrical characteristics, and material alloy designs dominate *in vivo* fretting of current orthopedic implants. Modular junctions used in joint replacement components and internal fixation devices are now a pillar of modern orthopedic surgery and increasing in popularity. Thus, fretting corrosion is likely to grow as a problem associated with current orthopedic implant designs. Continued awareness of this issue within the orthopedic community and continued basic and clinical research to enhance our understanding of these phenomena are needed to engineer solutions targeted to eliminate implant micromotion or prevent mechanically aided corrosion, that is, fretting corrosion.

References

1. Gilbert, J. L.; Mehta, M.; Pinder, B. *J. Biomed. Mater. Res. B Appl. Biomater.* **2009**, *88*, 162–173.
2. Jones, D. M.; Marsh, J. L.; Nepola, J. V.; *et al. J. Bone Joint Surg. Am.* **2001**, *83A*, 537–548.
3. Parks, N. L.; Engh, G. A.; Topoleski, L. D.; Emperado, J. *Clin. Orthop.* **1998**, *356*, 10–15.
4. Gilbert, J. L.; Jacobs, J. In *Modularity of Orthopedic Implants*; Marlowe, D. E., Parr, J. E., Mayor, M. B., Eds.; American Society for Testing and Materials: Philadelphia, PA, 1997; pp 45–59; ASTM STP 1301.
5. Bundy, K. In *Bone Mechanics*; Cowin, S. C., Ed.; CRC Press: Boca Raton, FL, 1989; pp 160–184.
6. Park, J. B. *Biomaterials Science and Engineering*. Plenum Press: New York, 1984.
7. Silver, F. H.; Christiansen, D. L. *Biomaterials Science and Biocompatibility*. Springer: New York, 1999.
8. Jacobs, J. J.; Gilbert, J. L.; Urban, R. M. *J. Bone Joint Surg. Am.* **1998**, *80*, 268–282.
9. Cohen, J.; Lindenbaum, B. *Clin. Orthop.* **1968**, *61*, 167–175.
10. Cabrera, N.; Mott, N. F. *Physics* **1948**, *12*, 163–184.
11. Aladjem, A. *J. Mater. Sci.* **1973**, *8*, 688–704.
12. Fraker, A.; Ruff, A. W.; Yeager, M. *Corrosion Sci.* **1973**, *11*, 763–765.
13. Brown, G. M.; Thundat, T.; Allison, D. A.; Warmack, R. J. *J. Vac. Sci. Technol.* **1992**, *10*, 3001–3006.
14. Wishey, A.; Gregson, P. J.; Peter, L. M. *Biomaterials* **1991**, *12*, 470–473.
15. Gilbert, J. L.; Buckley, C. A.; Lautenachlager, E. P. In *Medical Applications of Titanium and Its Alloys: The Materials and Biological Issues*. American Society for Testing and Materials: Philadelphia, PA, 1996; pp 199–215; ASTM STP 1272.
16. Goldberg, J. R.; Gilbert, J. L. *J. Biomed. Mater. Res.* **1997**, *37*, 421–431.
17. Goldberg, J. R.; Gilbert, J. L. *Biomaterials* **2004**, *25*, 851–864.
18. Brown, S. A.; Simpson, J. P. *J. Biomed. Mater. Res.* **1981**, *15*, 867–878.
19. Viceconti, M.; Baleani, M.; Squarzoni, S.; Toni, A. *J. Biomed. Mater. Res.* **1997**, *35*, 207–216.
20. Viceconti, M.; Ruggeri, O.; Toni, A.; Giunti, A. *J. Biomed. Mater. Res.* **1996**, *30*, 181–186.
21. Aulisa, L.; di Benedetto, A.; Vinciguerra, A.; Lorini, G.; Tranquilli-Leali, P. *Biomaterials* **1982**, *3*, 246–248.
22. Cook, S. D.; Gianoli, G. J.; Clemow, A. J.; Haddad, R. J. J. *Biomater. Med. Devices Artif. Organs* **1983**, *11*, 281–292.
23. Fricker, D. C.; Shivanath, R. *Biomaterials* **1990**, *11*, 495–500.
24. Chandler, H. P.; Ayres, D. K.; Tan, R. C.; Anderson, L. C.; Varma, A. K. *Clin. Orthop.* **1995**, *319*, 130–140.
25. Urban, R. M.; Jacobs, J.; Gilbert, J. L.; *et al*. In *Modularity of Orthopedic Implants*; Marlowe, D. E., Parr, J. E., Mayor, M. B., Eds.; American Society for Testing and Materials: Philadelphia, PA, 1997; pp 33–44; ASTM STP 1301.
26. Gilbert, J. L.; Zarka, L.; Chang, E.; Thomas, C. H. *J. Biomed. Mater. Res.* **1998**, *42*, 321–330.
27. Xulin, S.; Ito, A.; Tateishi, T.; Hoshino, A. *J. Biomed. Mater. Res.* **1997**, *34*, 9–14.
28. Gilbert, J. L.; Buckley, C. A.; Jacobs, J. J. *J. Biomed. Mater. Res.* **1993**, *27*, 1533–1544.

29. Jacobs, J. J.; Skipor, A. K.; Doorn, P. F.; *et al*. *Clin. Orthop.* **1996**, *329*, S256–S263.
30. McCarthy, J. C.; Bono, J. V.; O'Donnell, P. J. *Clin. Orthop.* **1997**, *344*, 162–171.
31. Lieberman, J. R.; Rimnac, C. M.; Garvin, K. L.; Klein, R. W.; Salvati, E. A. *Clin. Orthop.* **1994**, *300*, 162–167.
32. McKellop, H.; Park, S. H.; Chiesa, R.; *et al*. *Clin. Orthop.* **1996**, *329*, S128–S140.
33. Huk, O. L.; Bansal, M.; Betts, F.; *et al*. *J. Bone Joint Surg. Br.* **1994**, *76*, 568–574.
34. Collier, J. P.; Surprenant, V. A.; Jensen, R. E.; Mayor, M. B.; Surprenant, H. P. *J. Bone Joint Surg. Am.* **1992**, *74B*, 511–517.
35. Mathiesen, E. B.; Lindgren, J. U.; Blomgren, G. G.; Reinholt, F. P. *J. Bone Joint Surg. Br.* **1991**, *73*, 569–575.
36. Collier, J. P.; Surprenant, V. A.; Jensen, R. E.; Mayor, M. B. *Clin. Orthop.* **1991**, *271*, 305–312.
37. Jacobs, J. J.; Skipor, A. K.; Patterson, L. M.; *et al*. *J. Bone Joint Surg. Am.* **1998**, *80*, 1447–1458.
38. Brown, S. A.; Merritt, K. *J. Biomed. Mater. Res.* **1981**, *15*, 479–488.
39. Brown, S. A.; Hughes, P. J.; Merritt, K. *J. Orthop. Res.* **1988**, *6*, 572–579.
40. Williams, R. L.; Brown, S. A.; Merritt, K. *Biomaterials* **1988**, *9*, 181–186.
41. Merritt, K.; Brown, S. A. *J. Biomed. Mater. Res.* **1988**, *22*, 111–120.
42. Bundy, K. J.; Kelly, R. G.; Brown, E. L.; Delahunty, C. M. *Biomaterials* **1985**, *6*, 89–96.
43. Montague, A.; Merritt, K.; Brown, S.; Payer, J. *J. Biomed. Mater. Res.* **1996**, *32*, 519–526.
44. Hallab, N. J.; Messina, C.; Skipor, A.; Jacobs, J. J. *J. Orthop. Res.* **2004**, *22*, 250–259.

6.608. Implant Debris: Clinical Data and Relevance

N J Hallab and J J Jacobs, Rush University Medical Center, Chicago, IL, USA

© 2011 Elsevier Ltd. All rights reserved.

6.608.1.	**Introduction**	97
6.608.2.	**Implant Debris Types: Particles and Ions**	98
6.608.2.1.	Particulate Debris	98
6.608.2.1.1.	Particle characterization	99
6.608.2.2.	Metal Ions (Soluble Debris)	99
6.608.2.2.1.	Metal ion release	99
6.608.3.	**Local Tissue Effects of Wear and Corrosion**	100
6.608.4.	**Systemic Effects of Wear and Corrosion**	103
6.608.4.1.	Systemic Particle Distribution	103
6.608.4.2.	Hypersensitivity	104
6.608.4.2.1.	Incidence of hypersensitivity responses among patients with metal implants	104
6.608.4.2.2.	Testing for metal sensitivity	105
6.608.4.3.	Carcinogenesis	106
6.608.5.	**Conclusions**	106
References		107

Abbreviations

ALVAL	Aseptic lymphocyte vasculitis-associated lesion
DAMP	Danger-associated molecular patterns
DTH	Delayed type hypersensitivity
IL-1β	Interleukin-1β
IL-6	Interleukin-6
IL-18	Interleukin-18
IL-33	Interleukin-33
LALLS	Low-angle laser light scattering
Metal-LTT	Metal-lymphocyte transformation test (proliferation assay)
NALP3/ ASC	Inflammasome complex of proteins
PAMP	Pathogen-associated molecular pattern
PGE_2	Prostaglandin E_2
PMMA	Polymethylmethacrylate
PTFE	Teflon (polytetraflouroethylene)
RANKL	Receptor activator of nuclear factor kappa beta ligand
ROS	Reactive oxygen species
SEM	Scanning electron microscopy
TEM	Transmission electron microscopy
THA	Total hip arthroplasty
TJA	Total joint arthroplasty
TJR	Total joint replacement
TNF-α	Tumor necrosis factor-alpha
UHMWPE	Ultra-high-molecular-weight polyethylene

6.608.1. Introduction

Over 1 000 000 total joint arthroplasties (TJA) are performed each year in the United States and the projected demand is much higher for the next decade.[1,2] While TJAs typically function successfully for an average of 15 years, such implant procedures still fail in the longer term, and there remains a problem of lasting success.[2,3] Over the long term, all implant debris cause a local inflammatory response that eventually results in bone loss and loss of implant fixation.[4] This inflammatory reaction can occur in 10% of these individuals at 10 years postsurgery and results in marked bone loss around the implant. This phenomenon of bone loss is called 'aseptic osteolysis' and results in pain and premature loosening of the orthopedic implants.[5–7] However, aseptic osteolysis generally only refers to bone loss around an implant that is radiographically visible on an X-ray, Figure 1. The degradation products of the orthopedic biomaterials, generated by wear and electrochemical corrosion, mediate this adverse effect. How this debris is produced via fretting corrosion is discussed elsewhere in this publication (**Chapter 6.607, Fretting Corrosion of Orthopedic Implants**). Debris may be present as particulate wear, colloidal nanometer-size complexes (specifically or nonspecifically bound to protein), free metallic ions, inorganic metal salts/oxides, or in an organic storage form such as hemosiderin. Particulate debris have an extremely large and specific surface area for a given mass of debris, which is available for interaction with the surroundings. This can cause or further increase chronic elevations in serum metal content due to degradation of the implant. This chapter will focus on biomaterial degradation (through wear and electrochemical corrosion), dissemination of the debris, and the consequent local and systemic effects. General mechanisms are discussed elsewhere in this publication (**Chapter 6.606, Biological Effects of Wear Debris from Joint Arthroplasties**).

6.608.2. Implant Debris Types: Particles and Ions

The debris from all orthopedic implants can only be one of two basic types: particles or soluble debris (metal ions). The difference between particles and ions blurs as the size of the particles decreases to the nanometer range, and they become 'soluble.' Typically, particulate wear debris (metal, ceramic, or polymers) range from 40 nm to 1 mm in size, while the so-called 'soluble debris' is limited to metal ions or nanoparticles that are too small to be distinguished from ions, and are bound to plasma proteins.



Figure 1 Periimplant aseptic osteolysis above the acetabular cup of a metal-on-polymer bearing total hip replacement. Inset shows a granuloma surrounding acetabular fixation screw, which is a common site for bone resorption due to the ease with which particles can migrate and cause inflammatory soft tissue and osteolysis. Courtesy of BioEngineering Solutions Inc.

6.608.2.1. Particulate Debris

Different types of joint arthroplasty produce different amounts of wear debris. These can be of different sizes and shapes, and are implant and material specific. For instance, hard-on-hard bearing couples, such as metal on metal hips replacements, generally produce smaller sized (submicron), fairly round debris whereas the traditional metal-on-polymer bearings produce larger (micron sized) debris and is more elongated in shape (Figure 2).

Implants with metal-on-poly bearings comprise polymer particles that generally fall into the size range of 0.23 to 1 μm, with little metallic debris. Other sources of metal debris include corrosion at metal-to-metal connections between modular components of orthopedic implants. Ultra-high-molecular-weight polyethylene (UHMWPE) wear debris, in periimplant tissues, have shown that 70–90% of recovered particulates were submicron, with their mean size being approximately 0.5 μm.[8–10] Highly cross-linked polyethylene,

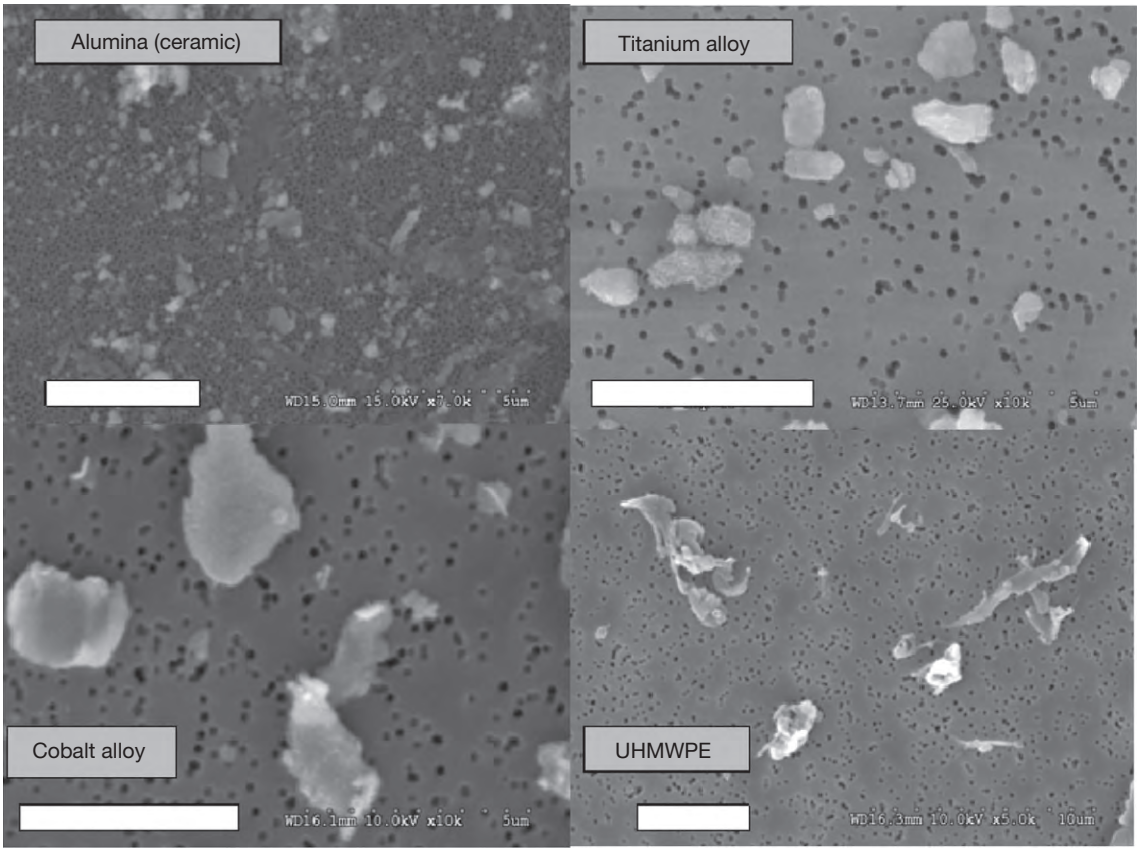

Figure 2 Implant debris from metal (cobalt alloy and titanium) and ceramic (alumina) debris are more rounded in comparison to polymeric (UHMWPE) debris which is more elongated in shape. Note: Bar = 5 μm. Courtesy of BioEngineering Solutions Inc.

used in current models of hip replacements, have demonstrated the production of smaller, and more rounded, debris in the submicron range and are as small as 0.1 μm in size.[11,12] Metal and ceramic bearings produce particles that are generally an order of magnitude smaller than the polymeric particles (at $\sim <0.05$ μm in diameter, i.e., in the nanometer range).

Histological analyses of periimplant tissues have identified different types and sizes of particles.[13–19]

Stainless steel: Stainless steel debris are found as closely packed, plate-like particle aggregates, occurring mostly at the steel screw–plate junctions. This debris contains particles of chromium compounds and range in size from 0.5 to 5.0 μm.[20]

Cobalt alloy: Cobalt alloy debris is a chromium–phosphate ($Cr(PO_4)\cdot 4H_2O$) hydrate-rich material termed 'orthophosphate,' and ranges in size from <1 to >500 μm.[20,21]

Titanium alloy: The degradation products observed in histologic sections of tissues adjacent to titanium-based alloys generally have the same elemental composition as the parent alloy, as opposed to the corrosion products of stainless steel and cobalt–chromium alloys used in implants.

6.608.2.1.1. Particle characterization

Traditionally, clinical analysis or particle characterization uses methods such as scanning electron microscopy (SEM) or transmission electron microscopy (TEM), both of which are number-based counting methods. These methods have biased our current understanding and have indicated that the majority of the wear (mass loss) from an implant comprises particles in the nanometer to submicron range. Such bias stems from the limited sampling of particles in tissues (100s–1000s) that are counted in image-based analysis techniques such as SEM. While newer analytical techniques, such as low-angle laser light scattering (LALLS) analysis, have the capability of sampling millions to billions of particles – as particles are counted as they pass in front of and scatter a laser light beam in proportion to their size – there is limited ability to use these more comprehensive assessments as a large amount of debris need to be analyzed. As millions of particles flow in front of a laser, in a LALLS analysis, the one-in-a-million large particle, which equals the mass of at least a million small particles, can be detected, and thus provides a more accurate accounting of the total debris.

The ability to comprehensively characterize implant debris is important as new designs and bearing surfaces are being used in both new and older implants. A multianalysis approach is necessary because a given amount of wear debris (weight loss from the implant) after a year of use could be attributed to the loss of a relatively few large particles, or hundreds of millions of small particles (e.g., $\sim 0.2\,mm^3$ volume loss after a million cycles of use could be from ~400 particles of 100 μm diameter or 400 million particles that are only 1 μm in diameter). The aforementioned bias of SEM techniques is limited to 'number-based' analysis, where, two very similar number-based distributions can look very different when analyzed on a 'volume-based' perspective. This is illustrated in **Figure 3**, a comparison of two samples A and B, where very different volume-based distributions are shown to look like very similar number-based distributions. Unfortunately, in the analysis of implant debris from tissues or simulator fluids there is usually <0.05 mg of debris which is insufficient for obtaining an accurate LALLS volume distribution and thus SEM and TEM analyses remain the standard methods used to characterize debris.

6.608.2.2. Metal Ions (Soluble Debris)

There is continuing clinical concern regarding the release of chemically active metal ions, which bind to proteins and remain in a solution and then disseminate to surrounding tissues, bloodstream, and remote organs. Normal serum levels of implant metals are as follows: 1–10 $ng\,ml^{-1}$ Al, 0.15 $ng\,ml^{-1}$ Cr, <0.01 $ng\,ml^{-1}$ V, 0.1–0.2 $ng\,ml^{-1}$ Co, and <4.1 $ng\,ml^{-1}$ Ti. These levels increase following TJA (**Table 1**). Particulate metallic wear debris contributes to this increase in metal concentrations in the serum because of the large surface area available for electrochemical dissolution.[14,17,18,20,21]

6.608.2.2.1. Metal ion release

Metal release from implants has always been of concern, because of both systemic and local effects. Increase in the levels of serum and urine Co and Cr are detected following successful total joint replacements of Co-alloy based components. Similarly, increased serum Ti and Cr concentrations are found in subjects with well-functioning Ti and/or Cr containing THR implants (**Table 1**).[14,22–25] An increase in Ni has been noted immediately following surgery; however, this increase is likely to be related to the use of stainless steel surgical instruments or the metabolic changes associated with the surgery itself.

Many factors can affect metal ion levels in the serum and urine of TJA patients, the most important of which is unintended metal wear. For example, increase in Ti levels, up to a hundred times higher than normal, has been reported in cases of failed metal-backed patellar components where unintended metal/metal articulation was the result of malpositioning of the implant or wear through of the polymer lining. However, in cases of excessive Ti-alloy wear and metal release, there was still no increase in the serum or urine levels of Al, V, or urine Ti levels. The second most important mechanism of metal release is mechanically assisted corrosion, or fretting corrosion, of the components of the modular implant that fit together, such as the head and neck junction of stems in a total hip arthroplasty, and has been associated with elevations in serum Co and urine Cr.[14,26,27] Another source of metal release is the general corrosion which takes place on any surface and increases in proportion to the surface area available, and where a porous coating on implant components gives rise to higher serum and urine chromium concentrations due to the larger surface area available for passive dissolution. Where does this metal circulate and accumulate? Homogenates of remote organs and tissue, obtained from people with living wills to donate their bodies for research upon death, have been found to have significant increases in Co and Cr concentrations in the heart, liver, kidney, spleen, and lymphatic tissue (**Table 1**). However, the majority of metal debris remains localized at the implant site and is most often 'kept' within the pseudocapsule that forms around a total joint implant which acts much like a joint capsule with pseudosynovial fluid in it as well. Increased levels of Ti, Al, and V in joint pseudocapsules have been found

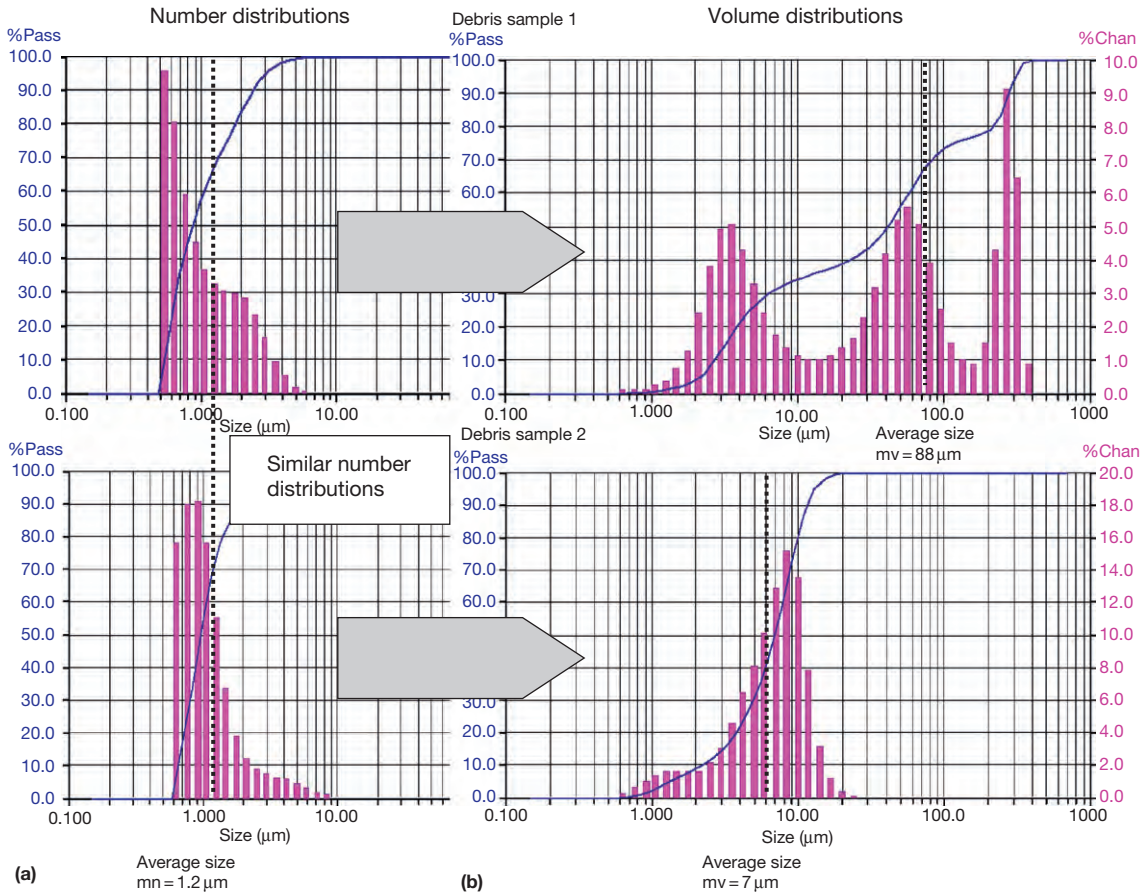

Figure 3 LALLS analyses of two implant debris samples using a (a) volume and (b) number distributions, demonstrates that similar number distributions and estimates of particle size can result from two very different sizes particles when analyzed using a volume distribution, which shows the size of the particle as a percent of the total volume. Note: The *x*-axis is particle diameter and the *y*-axis is (a) percentage of total number of particles in each size range and (b) the percentage of total mass in each size range. Courtesy of BioEngineering Solutions Inc.

with up to 200 ppm of Ti (six orders of magnitude greater than that of controls), 880 ppb of Al, and 250 ppb of V. Other filtering organs, such as the spleen, have been associated with increased Al levels and the liver has been found to contain enhanced Ti concentrations in people with failed titanium-alloy implants.[28]

6.608.3. Local Tissue Effects of Wear and Corrosion

Implant debris is the major determinant of the long-term performance of the implant because local inflammatory responses lead to bone erosion and implant loosening. The normal bone relies on the balance of bone formation and bone resorption forces (bone homeostasis), which involve the coordinated function of osteoblasts (bone building cells), osteoclasts (bone resorbing cells), and osteocytes (bone mechanotransduction and signaling network cells). If implant debris-induced inflammation causes a decrease in osteoblastic bone formation or an increase in osteoclastic bone resorption, the result will be a net loss of bone and osteolysis. Such bone loss (i.e., osteolysis) around an implant is the primary pathology that is associated with the local effects of the degradation of an orthopedic implant. This bone loss can occur as a diffuse cortical thinning or as focal cyst-like lesions. Particulate polymethylmethacrylate (PMMA) bone cement and old acetabular cups made of polytetraflouroethylene (PTFE) (Teflon) that produced massive amounts of implant debris were the first materials to be associated with osteolytic lesions. These were based on histological studies which demonstrated that the debris was associated with macrophages, giant cells, and a vascular granulation tissue. It is now known that osteolysis, in both loose and well-fixed uncemented implants, occurs due to particle debris generated by any material.[29,30]

Goldring *et al.*[31] were among the first to describe that the bone–implant interface in patients with loose total hip replacements is similar to the synovial-like membrane and that cells within the membrane have the capacity to produce bone resorbing factors such as prostaglandin E_2 (PGE_2) and collagenase. Such particle-induced osteolysis is less frequently associated with total knee arthroplasty than with total hip arthroplasty. It is unclear why this is so. However, factors such as implant/bone mechanical loading environment, differential mechanisms of hip and knee wear, and differences in interface barriers to migration of debris, have all been postulated to account for this apparent disparity.

Table 1 Approximate concentrations of metal in human body fluids and in human tissue with and without total joint replacements

		Ti	*Al*	*V*	*Co*	*Cr*	*Mo*	*Ni*
Body fluids (ng ml^{-1} or ppb)								
Serum	Normal	0.06	0.08	<0.02	0.003	0.001	[a]	0.007
	TJA	0.09	0.09	0.03	0.007	0.006	[a]	<0.16
Urine	Normal	<0.04	0.24	0.01	[a]	0.001	[a]	[a]
	TJA	0.07	0.24	<0.01	[a]	0.009	[a]	[a]
Synovial fluid	Normal	0.27	4.0	0.10	0.085	0.058	0.219	0.086
	TJA	11.5	24	1.2	10	7.4	0.604	0.55
Joint capsule	Normal	15.0	35	2.4	0.42	2.6	0.177	69
	TJA-F	399	47	29	14	64	4.65	100
Whole blood	Normal	0.35	0.48	0.12	0.002	0.058	0.009	0.078
	TJA	1.4	8.1	0.45	0.33	2.1	0.104	0.50
Body tissues (μg g^{-1})								
Skeletal muscle	Normal	[a]	[a]	[a]	<12	<12	[a]	[a]
	TJA	[a]	[a]	[a]	160	570	[a]	[a]
Liver	Normal	100	890	14	120	<14	[a]	[a]
	TJA	560	680	22	15200	1130	[a]	[a]
Lung	Normal	710	9830	26	[a]	[a]	[a]	[a]
	TJA	980	8740	23	[a]	[a]	[a]	[a]
Spleen	Normal	70	800	<9	30	10	[a]	[a]
	TJA	1280	1070	12	1600	180	[a]	[a]
Psuedocapsule	Normal	<65	120	<9	50	150	[a]	[a]
	TJA	39 400	460	121	5490	3820	[a]	[a]
Kidney	Normal	[a]	[a]	[a]	30	<40	[a]	[a]
	TJA	[a]	[a]	[a]	60	<40	[a]	[a]
Lymphatic tissue	Normal	[a]	[a]	[a]	10	690	[a]	[a]
	TJA	[a]	[a]	[a]	390	690	[a]	[a]
Heart	Normal	[a]	[a]	[a]	30	30	[a]	[a]
	TJA	[a]	[a]	[a]	280	90	[a]	[a]

Normal: subjects without any metallic prosthesis (not including dental); TJA: subjects with total joint arthroplasty.

Source: Dorr, L. D.; Bloebaum, R.; Emmanual, J.; *et al*. *Clin. Orthop. Relat. Res*. **1990**, *261*, 82–95; Jacobs, J. J.; Gilbert, J. L.; Urban, R. M. *J. Bone Joint Surg. [Am]* **1998**, *80*, 268–282; Jacobs, J. J.; Skipor, A. K.; Urban, R. M.; *et al*. *Trans. Orthop. Res. Soc*. (New Orleans) **1994**, 838; Michel, R.; Nolte, M.; Reich, M.; *et al*. *Arch. Orthop. Trauma Surg*. **1991**, *110*, 61–74; Stulberg, B. N.; Merritt, K.; Bauer, T. *J. Biomed. Mat. Res. Appl. Biomater*. **1994**, *5*, 9–16.

[a]Data not available.

One unavoidable fact is that all implant debris cause low-grade inflammation that can ultimately lead to implant failure. Exactly how this happens is still unclear. Over the past 40 years we have learnt that implant debris-induced inflammation is largely caused by macrophages which react to implant debris by upregulating proinflammatory transcription factors (e.g., NFκβ) that signal the production and secretion of inflammatory cytokines such as interleukin-1β (IL-1β), tumor necrosis factor-alpha (TNF-α), IL-6, and IL-8[29] (**Figure 4**). Prostaglandins (e.g., PGE_2) are known to be important proinflammatory intercellular messengers that are involved in osteolysis due to implant debris. Anti-inflammatory cytokines such as IL-10 modulate the inflammatory process and are a part and parcel of this pathology, but the degree to which a lack of anti-inflammatory factors can contribute to particle-induced inflammation remains largely unknown. Other factors involved with bone loss include the enzymes responsible for the catabolism of the organic component of bone, such as the matrix metalloproteinases, collagenase and stromelysin. Activated immune and bone cells can produce several mediators that are known to be involved in the stimulation of osteoclast differentiation and maturation, such as the receptor activator of nuclear factor kappa beta ligand (RANKL) (also referred to as osteoclast differentiation factor).

Implant debris is relatively sterile, inert, and does not 'look' like a pathogen in any molecularly recognizable way. How then does implant debris provoke an inflammatory response? In other words, how can extra- and intracellular mechanisms sense and respond to sterile, nonbiological material such as implant debris? While this question has remained largely unknown for the past half century, new discoveries in immunology have implicated the 'inflammasome,' the danger signaling pathway (**Figure 5**).[32]

The first of these recent discoveries was that of the pattern recognition receptors (PRRs), which were discovered in 1996, and are present in the membrane and cytosol of human immune cells, such as macrophages. These are the toll-like receptors (TLRs) which recognize specific bacterial glycoprotein patterns and are now called 'pathogen-associated molecular patterns' or PAMPs. The types of identified PAMP receptors now include TLRs,[33] mannose receptors (MR), and NOD-like receptors (NLRs).[34] These PRRs initiate events that activate the cell and induce the secretion of proinflammatory cytokines which then lead to a broader inflammatory response.

Similar to PAMPs, nonpathogenic stimuli were found to activate immune cells via a novel danger signal pathway. The key molecular components in this pathway were called the

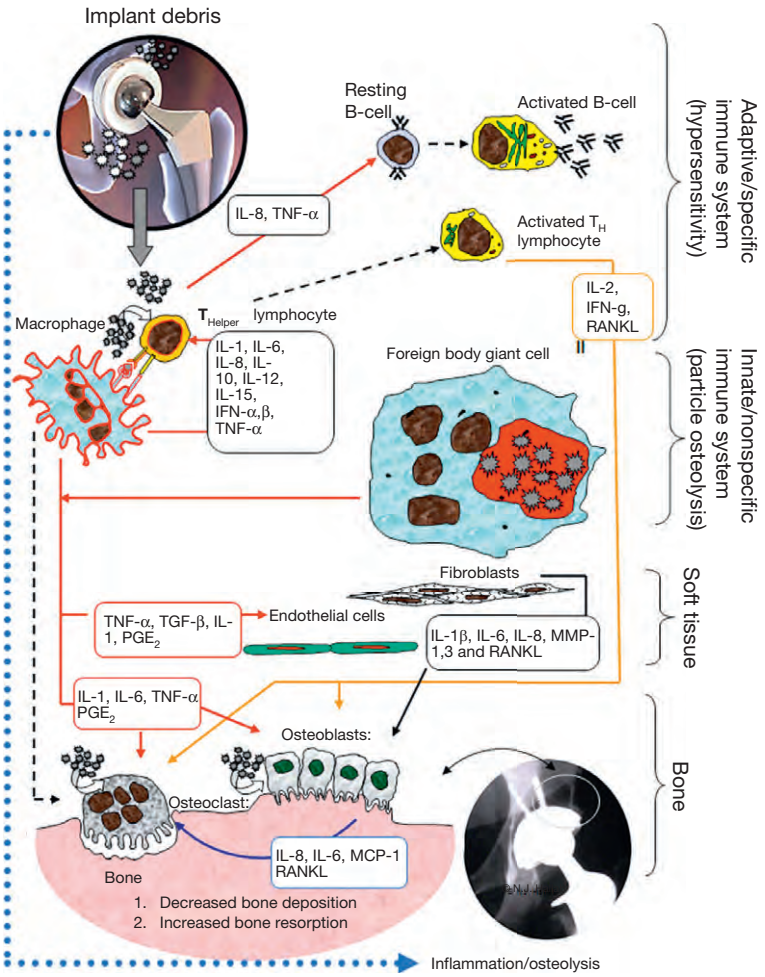

Figure 4 Numerous cytokines from periimplant cells reacting to implant debris can negatively affect bone turnover. IL-1, IL-6, and TNF-α are some of the most potent cytokines responsible for increasing bone loss and enhancing proinflammatory responses. Courtesy of BioEngineering Solutions Inc.

'inflammasome' and the signals that activate it were termed 'danger-associated molecular patterns,' or DAMPs.[35] So now there are PAMPs (pathogens) and DAMPs (something the cell recognizes as a danger signal that is causing or will most likely cause cell damage). Thus, this new paradigm for immune system activation now includes specific receptors that recognize both PAMPs and DAMPs.[36,37] This is important because the inflammasome pathway was the first pathway to explain how cells could transduce sterile, nonpathogen-derived stimuli (e.g., cell stress and cell necrosis) into an inflammatory response.[34,38] Other nonbiological-derived danger signals include such cell-damaging stimuli as UV light, particulate adjuvants present in modern vaccines[39,40] and, as it also turns out, implant debris.[41]

When particles activate the inflammasome pathway, cells release IL-1β, IL-18, IL-33, and other cytokines. This happens as follows:

Debris → Phagocytosis → Lysosome damage → ROS (reactive oxygen species) → Inflammasome (NALP3/ASC) → Caspase-1 → IL-1β (and other IL-1-family) cytokines (Figure 5).

Therefore, once ingested by immune cells, particles (or DAMPs, such as asbestos and implant debris, etc.) induce some degree of lysosomal destabilization. This lysosomal destabilization then causes an increase in NADPH (nicotinamide adenine dinucleotide phosphate-oxidase), and an associated increase in reactive oxygen species (ROS). This release comes from the protease- and acid-rich extreme environment inside lysosomes which is used to breakdown ingested particles/bacteria, etc. The release of the intracellular ROS species then activates the intracellular multiprotein 'inflammasome' complex which is composed of NALP3 (NACHT-, LRR-, and pyrin domain-containing protein 3) which is associated with ASC (apoptosis-associated speck-like protein containing a CARD domain).[34,42] This inflammasome activation then activates Caspase-1, which then converts cytokines such as IL-1β and IL-18 (and others) into their respective active forms. This illustrates the many steps that are involved in this relatively simple danger-signaling pathway and the many new potential points of pharmacological intervention to block this response to prevent particle-induced inflammation and osteolysis.

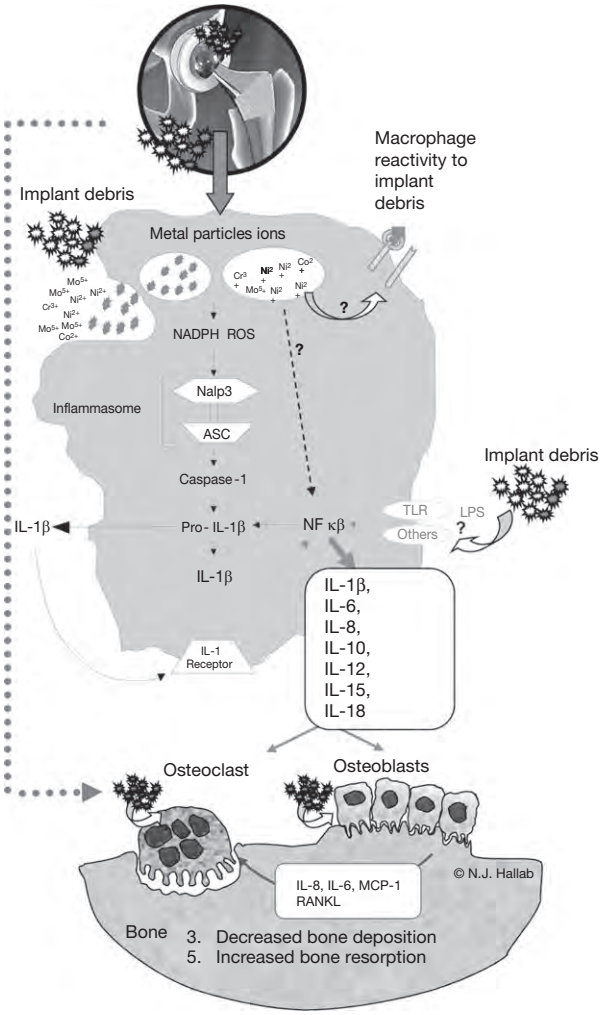

Figure 5 Metal-induced inflammasome activation occurs when soluble and/or particulate implant debris activate the Nalp3 inflammasome when chemicals inside intracellular compartments used to digest foreign material (such as phagosomal NADPH-induced reactive oxygen species and/or cathepsin B) leaks out of these compartments in an event called phagosomal destabilization. The inflammasome complex, Nalp3-ASC then induces the activation of caspase-1, which in turn allows mature IL-1β to be secreted. IL-1β is a very potent proinflammatory cytokine that exerts an autocrine and paracrine effect inducing a broader more potent inflammatory response (e.g., activation of NFκβ proinflammatory responses). Courtesy of BioEngineering Solutions Inc.

6.608.4. Systemic Effects of Wear and Corrosion

Implant surfaces and wear debris are always, to some degree, releasing chemically active metal ions into the surrounding tissues. While these metal ions, bound to serum proteins, may reside in local tissues, they are also transported via the bloodstream and the lymphatics to the remote organs. There is concern about this phenomenon because of the known, potential toxicity of the elements that are being used in modern orthopedic implant alloys: titanium, aluminum, vanadium, cobalt, chromium, and nickel. Metal toxicity can occur by altering (i) cell/tissue metabolism, (ii) host/parasite interactions, (iii) immunologic interactions, and (iv) by inducing chemical carcinogenesis.[43–47]

Cobalt and chromium are essential trace metals required for the normal function of some enzyme reactions. In excessive amounts, however, these elements are toxic. Excessive cobalt can lead to heart problems (cardiomyopathy), excess red blood cells (polycythemia), a decrease in thyroid functions (hypothyroidism), and to carcinogenesis. Excessive chromium has been linked to nephropathy, hypersensitivity, and carcinogenesis. Other metals such as nickel can cause skin rashes (eczematous dermatitis), hypersensitivity reactions, and cancer. Excessive vanadium exposure has been linked to heart and kidney dysfunction, hypertension, and depressive psychosis. Aluminum toxicity results in renal failure and anemia, bone softening (osteomalacia), and neurological problems. However, it is important to note that such effects generally apply only to excessively high levels of the soluble forms of these elements, and, most likely, do not apply to the levels of metals released due to implant degradation.

The association of metal release from orthopedic implants with any toxicity is conjectural since a cause-and-effect relationship has not yet been established. However, discovering any toxic effects is very difficult given the kinds of problems that are normally associated with the elderly, and thus, those expected to occur in any population of orthopedic patients.[48]

6.608.4.1. Systemic Particle Distribution

What determines the amount of wear debris accumulation in remote organs is not clearly understood. When there is an increase in the magnitude of particulate debris generated by a prosthetic device, there is a corresponding elevation in both the local and systemic burden of particles. Wear particles found systemically (found beyond the local environment of the implant periprosthetic tissue) are primarily in the submicron size range. There have been numerous cases where metallic, ceramic, or polymeric wear debris from hip and knee prostheses have been found in the regional and pelvic lymph nodes, along with gross dark staining by metallic debris, fibrosis (buildup of fibrous tissue), lymph node necrosis, and histiocytosis (abnormal function of tissue macrophages,). Metallic wear particles have been detected in the paraaortic lymph nodes in up to 70% of patients with total joint replacement components. It is unclear what the ramifications of this are, but traditional inflammatory responses to metallic and polymeric debris in lymph nodes includes the same responses that are seen locally, which are immune activation of macrophages and the associated production of cytokines.

Thus, lymphatic transport is, most likely, a major route for the dissemination of debris by which particles migrate via the perivascular lymph channels, either as free or phagocytosed particles within the macrophages. Within the lymph nodes, the disseminated particles are mostly submicron in size. However some metallic particles as large as 50 μm and polyethylene particles as large as 30 μm have also been found. These particles can travel further on to the liver and spleen where they are found within the macrophages or, in some cases, in nodules of inflammatory tissue granulomas throughout the organs. The size of these metallic particles is nearly an order of magnitude less in the liver and

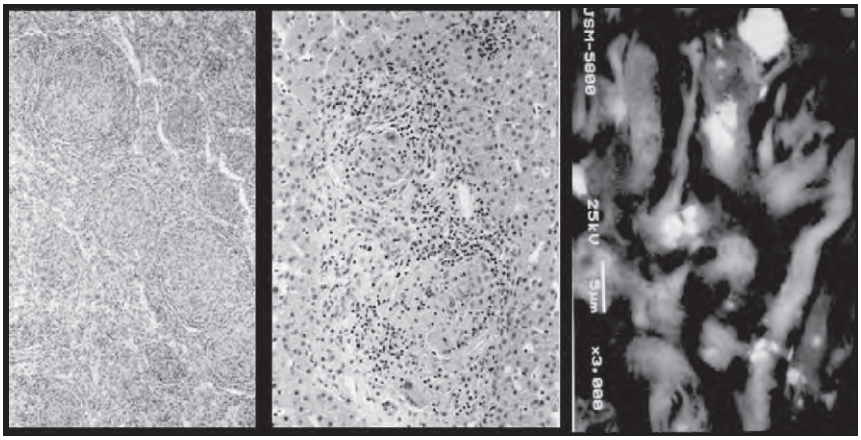

Figure 6 Soft tissue nodules of immune cells and tissue cells called epithelioid granulomas have been found to (a) occur within the portal tract of the liver (40×) and, (b) within the splenic parenchyma (15×). (c) The particles within these tissues have been identified as titanium alloy particles using backscattered SEM/EDS analysis of particles in a spleen (3000×). Courtesy of Prof Robert Urban.

spleen than that in lymph nodes, indicating that some additional filtration happens before the particles end up in the these organs. This is not alarming because the cells of liver, spleen, and lymph nodes normally accumulate small amounts of a variety of foreign materials without any apparent clinical manifestation. However, an excessive accumulation of particles can induce the formation of nodules of inflammatory tissue (granulomas) or granulomatoid lesions in the liver and spleen (Figure 6). The degree of reaction to these particles in the liver, spleen, and lymph nodes is probably modulated, as it is in other tissues by (1) the number of particles (dose), (2) their rate of accumulation, (3) the duration of their prescence, and (4) the biologic reactivity of the cells to these particles (size and materials composition). It is no surprise that metallic particles in the liver or spleen are more prevalent in subjects with previously failed arthroplasties compared to those with well-functioning primary joint replacements.

Diseases, which obstruct lymph flow through lymph nodes such as a metastatic tumor, or those which cause a generalized disturbance of circulation such as chronic heart disease or diabetes, may be expected to decrease particle migration to remote organs. Other pathologies, such as acute or chronic-active inflammation in the periprosthetic tissues may increase particle migration[29,48,49] by recruiting more immune cells to remove the debris.

6.608.4.2. Hypersensitivity

Some adverse responses to orthopedic biomaterials are subtle and continue to foster debate and investigation. One of these responses is 'metal allergy' or hypersensitivity to metallic biomaterials. Ions released from the implants, while not sensitizers on their own, can activate the immune system by forming complexes with native proteins. Polymeric wear debris is not easily chemically degraded *in vivo*, but has not been implicated in allergic type immune responses.[50–53] Metals that are accepted as allergens/sensitizers (haptenic moieties in antigens) include (but are not limited to) the following: beryllium, nickel, cobalt and chromium, tantalum, titanium, and vanadium. Nickel is the most common allergen in humans followed by cobalt and chromium, and nickel is still a prominent alloy in medical grade stainless steel (Table 2). Generally, there are more reports of hypersensitivity reactions associated with stainless steel and cobalt-alloy implants than with titanium-alloy components.[54–61]

Hypersensitivity to metals is common and affects about 10–15% of the population. Skin contact and ingestion of certain metals result in immune reactions such as eczema (skin hives, redness, and itching). Hypersensitivity reactions are associated with the adverse performance of metallic cardiovascular, orthopedic, and dental implants. Orthopedic implant associated hypersensitivity reactions (metal sensitivity or metal allergy) are generally associated with type IV delayed type hypersensitivity (DTH), a specific type of cell-mediated adaptive immune response. Over the past 20 years a growing number of case and group studies have linked immunogenic reactions with the adverse performance of metallic cardiovascular, orthopedic, and plastic surgical and dental implants, and clinical symptoms have lead directly to device removal. These symptoms include severe dermatitis (inflammation of the skin), urticaria (intensely sensitive and itching red round wheels on the skin), and/or vasculitis (patch inflammation of the walls of small blood vessels).

6.608.4.2.1. Incidence of hypersensitivity responses among patients with metal implants

The incidence of metal sensitivity among people with well-functioning implants is about twice as high as that of the general population at approximately 25% (vs. 10%, Figure 7). Moreover, the incidence of metal sensitivity in people fitted with a 'failing' implant (in need of revision surgery) or with a well-performing metal-on-metal articulating implant is approximately 50–60% (Figure 7). This increase in the prevalence of metal sensitivity among people with a failing metal-on-polymer prosthesis has prompted the speculation that such immunological processes may be a factor that contributes to implant loosening. Cohort studies over the past

Table 2 Approximate weight percent of different metals within popular orthopedic alloys

Alloy	*Ni*	*N*	*Co*	*Cr*	*Ti*	*Mo*	*Al*	*Fe*	*Mn*	*Cu*	*W*	*C*	*Si*	*V*
Stainless steel (ASTM F138)	10–15.5	<0.5	*	17–19	*	2–4	*	61–68	*	<0.5	<2.0	<0.06	<1.0	*
CoCrMo alloys														
(ASTM F75)	<2.0	*	61–66	27–30	*	4.5–7.0	*	<1.5	<1.0	*	*	<0.35	<1.0	*
(ASTM F90)	9–11	*	46–51	19–20	*	*	*	<3.0	<2.5	*	14–16	<0.15	<1.0	*
(ASTM F562)	33–37	*	35	19–21	<1	9.0–11	*	<1	<0.15	*	*	*	<0.15	*
Ti alloys														
CPTi (ASTM F67)	*	*	*	*	99	*	*	0.2–0.5	*	*	*	<0.1	*	*
Ti–6Al–4V (ASTM F136)	*	*	*	*	89–91	*	5.5–6.5	*	*	*	*	<0.08	*	3.5–4.5
45TiNi	55	*	*	*	45	*	*	*	*	*	*	*	*	*
Zr alloy (97.5% Zr, 2.5% Nb)	*	*	*	*	*	*	*	*	*	*	*	*	*	*

Note: Alloy compositions are standardized by the American Society for Testing and Materials (ASTM, Vol. 13.01).
*Indicates less than 0.05%.

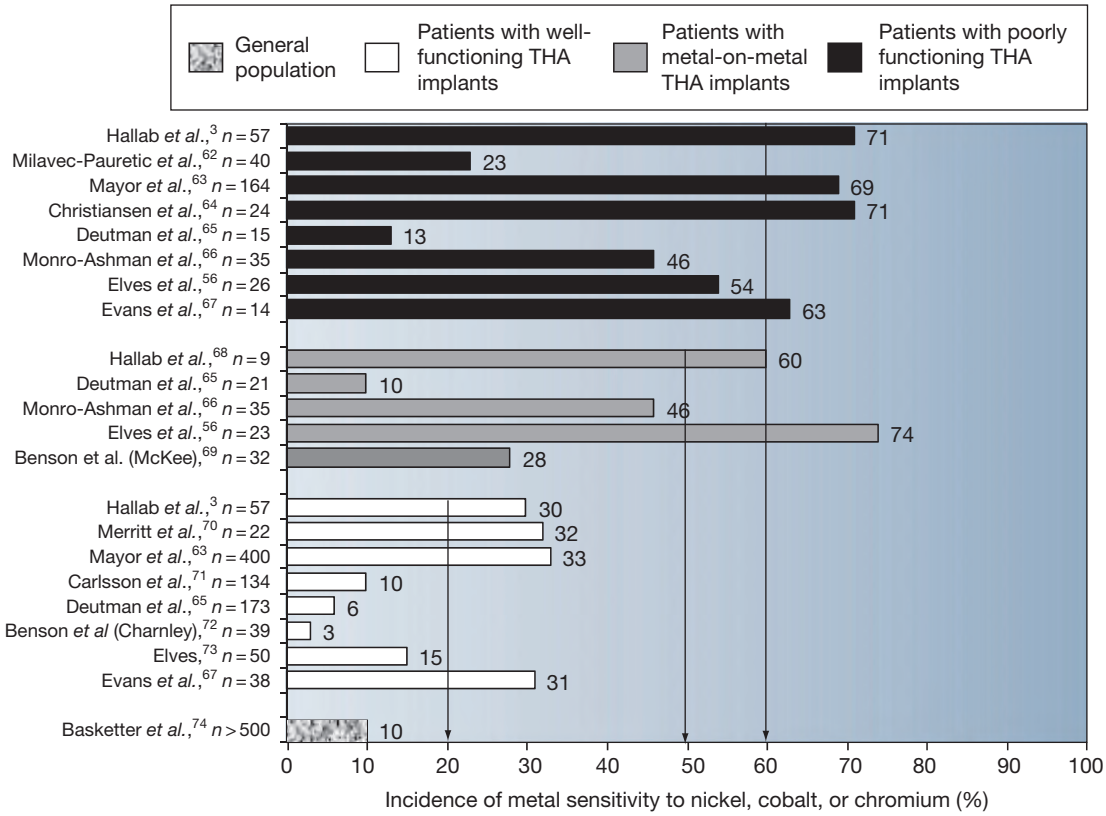

Figure 7 A compilation of investigations showing the averaged percentage of metal sensitivity among the general population, people with well-functioning implants, people with metal-on-metal implants, and people with failing implants (prior to getting them revised). Metal incidence rates include a positive response to allergy testing for nickel, cobalt, and/or chromium. All subjects were tested by means of a patch or metal-LTT (lymphocyte transformation test). Courtesy of Orthopedic Analysis LLC.

30+ years have, generally, indicated a correlation between metal implants and metal sensitivity,[50] clearly indicating that metal sensitivity can be a contributing factor to implant failure[60,75,76] (Figure 7).

Thus metal allergy testing ('metal-lymphocyte transformation test, metal-LTT') may be warranted in individuals with a history of metal allergy prior to receiving an implant. The importance of this line of investigation is growing, as the use of metallic spinal implants is increasing, as are the expectations of implant durability and performance.[77,78]

6.608.4.2.2. Testing for metal sensitivity

The time-related physical evidence associated with the symptoms of type IV allergic responses are severe enough to require

a revision of the arthroplasty in what is thought to be approximately 1–2% of all orthopedic patients. Diagnostic testing for metal allergy includes skin testing (i.e., so-called patch testing), and blood testing called metal-LTT. While patch commercial kits do exist for some metals,[76,79] there is continuing concern about sensitizing patients with patch testing[80] and doubts over how representative the dermal Langerhans cells are as proxies of periimplant antigen presenting cells.[81,82] The metal-LTT assesses the proliferative response of lymphocytes, obtained from peripheral blood by routine blood draw, to different metal antigens. Studies that have used both of these testing methodologies have shown similar incidence of metal sensitivity among patients with metal-containing total joint replacement implants.[53,83,84] This indicates that the adaptive immune system (i.e., lymphocytes) may be involved to a much larger degree in debris-induced inflammation than what has been previously attributed to the innate immune system alone (i.e., periimplant macrophages).

6.608.4.3. Carcinogenesis

The carcinogenic potential of implant debris remains an area of concern. Animal studies have documented that implant metals can act as carcinogens. Small increases in the incidence of rat sarcomas were found to correlate with high levels of serum cobalt, chromium, or nickel released from the metal implants. Additionally, lymphomas with some form of bone involvement were also more commonly found in rat models with metallic implants. Although not common, implant site tumors in dogs and cats – primarily osteosarcoma and fibrosarcoma – have been associated with stainless steel internal fixation devices.

Some epidemiological studies have implicated orthopedic implants in causing cancer 10–20 years after total hip replacement. However, recently, larger studies have found no significant increase in cancers such as leukemia or lymphoma, although these studies did not include individuals with higher serum concentration of metals such as those with a metal-on-metal prosthesis. The many differences between populations with and without implants that do not depend on the implant itself confound the interpretation of any epidemiological investigations.

It is still not known if metal release from orthopedic implants is carcinogenic because causality has not been established in human subjects, and, in fact, testing by the authors found that periimplant cells became toxic, prior to any DNA strand breaks, when tested with increasing concentrations of the metal ions found in implants.[85,86] The actual number of cases of tumors associated with orthopedic implants is probably underreported due to the frequency of tumors in the population that receive metal implants. However, compared to the number of devices implanted on a yearly basis (over 1 million), the incidence of cancer at the site of implantation is relatively rare. Continued monitoring and large long epidemiological studies are required to fully understand the associated risk.[87–90]

6.608.5. Conclusions

Total joint implants are a miracle of modern medicine, returning mobility, independence, and quality of life to millions of individuals every year. Implant debris is unavoidable and results in activation of the innate immune system, which in turn results in local inflammation that, over time, causes more bone loss than homeostatic mechanisms can keep up with. All of these lead to implant loosening, via aseptic osteolysis (**Figure 8**). When this reactivity is excessive, it may activate the adaptive immune system and result in an allergic response involving T-cells. New kinds of 'alternative' bearings that are being used in total joint implants, such as metal-on-metal articulating components, have resulted in new types of biological responses including lymphocyte-dominated granuloma-like lesions in the bone (termed ALVAL, for aseptic lymphocyte vasculitis-associated lesion), being found around some implants. This type of response seems to encompass the features of both the innate and the adaptive immune response,[91,92] and demonstrates that both innate (macrophage) and adaptive (T-lymphocyte) immune system reactivity can act to limit the lifetime of the current total joint replacement implants. Advances at the molecular and cellular level have increased our understanding of inflammatory bone loss. Treatment options ranging from diagnosing preexisting conditions of metal allergy (metal-LTT), general management of inflammation (e.g., NSAIDS) to selective blocking of cellular mediators (e.g., anti-IL-6, anti-TNF-α, IL-1β-receptor antagonist, etc.) are all part of the modern arsenal that is being used to help fight the problem of implant debris-induced inflammatory bone loss. There is increasing need for clinical studies to define the role of metal allergy, genetic susceptibility to particle-induced inflammation, general biological variability, and prosthesis-related factors in the pathogenesis of nonspecific and specific biological responses to implant debris.

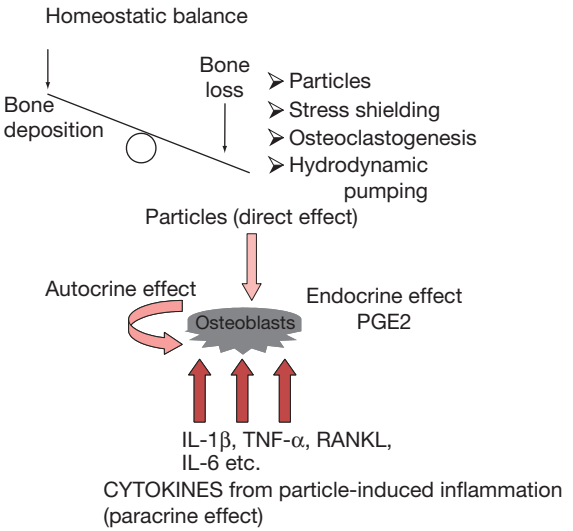

Figure 8 A number of factors can tip the scales away from bone homeostasis and towards net bone loss. Particle-induced inflammation is one of these factors and induces the release of potent cellular messages (inflammatory cytokines) which causes bone depositing cells called osteoblasts to stop producing bone and causes bone resorbing cells called osteoclasts to start increasing resorption. Over time, this results in a net bone loss and loosening of implants.

References

1. Hallab, N. *J. Clin. Rheumatol*. **2001**, *7*, 215–218.
2. Looney, R. J.; Schwarz, E. M.; Boyd, A.; *et al*. *Curr. Opin. Rheumatol*. **2006**, *18*, 80–87.
3. Hallab, N. J.; Anderson, S.; Stafford, T.; *et al*. *J. Orthop. Res*. **2005**, *23*, 384–391.
4. Willert, H. G.; Semlitsch, M. *J. Biomed. Mater. Res*. **1977**, *11*, 157–164.
5. Archibeck, M. J.; Jacobs, J. J.; Roebuck, K. A.; *et al*. *Instr. Course Lect*. **2001**, *50*, 185–195.
6. Arora, A.; Song, Y.; Chun, L.; *et al*. *J. Biomed. Mater. Res. A* **2003**, *64*, 693–697.
7. Jacobs, J. J.; Roebuck, K. A.; Archibeck, M.; *et al*. *Clin. Orthop. Relat. Res*. **2001**, *393*, 71–77.
8. Campbell, P.; Ma, S.; Yeom, B.; *et al*. *J. Biomed. Mater. Res*. **1995**, *29*, 127–131.
9. Jacobs, J. J.; Shanbhag, A.; Glant, T. T.; *et al*. *J. Am. Acad. Orthop. Surg*. **1994**, *2*, 212–220.
10. Maloney, W. J.; Smith, R. L.; Castro, F.; *et al*. *J. Bone Joint Surg. Am*. **1993**, *75*, 835–844.
11. Catelas, I.; Medley, J. B.; Campbell, P. A.; *et al*. *J. Biomed. Mater. Res. B Appl. Biomater*. **2004**, *70*, 167–178.
12. Scott, M.; Morrison, M.; Mishra, S. R.; *et al*. *J. Biomed. Mater. Res. B Appl. Biomater*. **2005**, *73*, 325–337.
13. Choma, T. J.; Miranda, J.; Siskey, R.; *et al*. *J. Spinal Disord. Tech*. **2009**, *22*, 290–296.
14. Jacobs, J. J.; Gilbert, J. L.; Urban, R. M. *J. Bone Joint Surg. Am*. **1998**, *80*, 268–282.
15. Punt, I. M.; Cleutjens, J. P.; de Bruin, T.; *et al*. *Biomaterials* **2009**, *30*, 2079–2084.
16. Punt, I. M.; Visser, V. M.; van Rhijn, L. W.; *et al*. *Eur. Spine J*. **2008**, *17*, 36–43.
17. Urban, R. M.; Hall, D. J.; Sapienza, C. I.; *et al*. *Trans. SFB* **1998**, *21*, 17.
18. Urban, R. M.; Jacobs, J. J.; Tomlinson, M. J.; *et al*. *J. Bone Joint Surg. [Am.]* **2000**, *82*, 457–476.
19. Van, O. A.; Kurtz, S. M.; Stessels, F.; *et al*. *Spine* **2007**, *32*, 223–229.
20. Urban, R. M.; Jacobs, J. J.; Sumner, D. R.; *et al*. *J. Bone Joint Surg. [Am.]* **1996**, *78A*, 1068–1081.
21. Urban, R. M.; Jacobs, J.; Gilbert, J. L.; *et al*. In *STP 1301 Modularity of Orthopedic Implants*; Marlowe, D. E., Parr, J. E., Mayor, M. B., Eds.; ASTM: Philadelphia, 1997; pp 33–44.
22. Dorr, L. D.; Bloebaum, R.; Emmanual, J.; *et al*. *Clin. Orthop. Relat. Res*. **1990**, *261*, 82–95.
23. Jacobs, J. J.; Patterson, L. M.; Skipor, A. K.; *et al*. *J. Biomed. Mater. Res*. **1999**, *48*, 385–391.
24. Michel, R.; Hoffman, J.; Loer, F.; *et al*. *Arch. Orthop. Trauma Surg*. **1984**, *103*, 85–95.
25. Stulberg, B. N.; Merritt, K.; Bauer, T. *Biomaterials* **1994**, *5*, 9–16.
26. Jacobs, J. J.; Silverton, C.; Hallab, N. J.; *et al*. *Clin. Orthop*. **1999**, *358*, 173–180.
27. Jacobs, J. J.; Skipor, A. K.; Patterson, L. M.; *et al*. *J. Bone Joint Surg. [Am.]* **1998**, *80*, 1447–1458.
28. Jacobs, J. J.; Gilbert, J. L.; Urban, R. M. In *Advances in Orthopaedic Surgery;* Stauffer, R. N., Ed.; Mosby: St. Louis, 1994; Vol. 2, pp 279–319.
29. Jacobs, J. J.; Hallab, N. J.; Urban, R. M.; Wimmer, M. A. *J. Bone Joint Surg. Am*. **2006**, *88*(Suppl. 2), 99–102.
30. Vermes, C.; Chandrasekaran, R.; Jacobs, J. J.; *et al*. *J. Bone Joint Surg. Am*. **2001**, *83*, 201–211.
31. Goldring, S. R.; Schiller, A. L.; Roelke, M.; *et al*. *J. Bone Joint Surg*. **1983**, *65A*, 575–584.
32. Caicedo, M. S.; Pennekamp, P. H.; McAllister, K.; Jacobs, J. J.; Hallab, N. J. *J. Biomed. Mater. Res. A* **2010**, *93*, 1312–1321.
33. Taguchi, T.; Mitcham, J. L.; Dower, S. K.; *et al*. *Genomics* **1996**, *32*, 486–488.
34. Mariathasan, S.; Monack, D. M. *Nat. Rev. Immunol*. **2007**, *7*, 31–40.
35. Martinon, F.; Petrilli, V.; Mayor, A.; *et al*. *Nature* **2006**, *440*, 237–241.
36. Medzhitov, R. *Nature* **2008**, *454*, 428–435.
37. Ting, J. P.; Willingham, S. B.; Bergstralh, D. T. *Nat. Rev. Immunol*. **2008**, *8*, 372–379.
38. Mariathasan, S.; Newton, K.; Monack, D. M.; *et al*. *Nature* **2004**, *430*, 213–218.
39. Dostert, C.; Petrilli, V.; Van, B. R.; *et al*. *Science* **2008**, *320*, 674–677.
40. Hornung, V.; Bauernfeind, F.; Halle, A.; *et al*. *Nat. Immunol*. **2008**, *9*, 847–856.
41. Caicedo, M. S.; Desai, R.; McAllister, K.; *et al*. *J. Orthop. Res*. **2008**, *27*, 847–854.
42. Petrilli, V.; Dostert, C.; Muruve, D. A.; *et al*. *Curr. Opin. Immunol*. **2007**, *19*, 615–622.
43. Beyersmann, D. *Toxicol. Lett*. **1994**, *72*, 333–338.
44. Britton, R. S. *Semin. Liver Dis*. **1996**, *16*, 3–12.
45. Goering, P. L.; Klaasen, C. D. *Hepatoxicity of Metals*. Academic Press: New York, 1995; pp 339–388.
46. Hartwig, A. *Toxicol. Lett*. **1998**, *102–103*, 235–239.
47. Luckey, T. D.; Venugopal, B. *Metal Toxicity in Mammals*. Plenum: New York, 1979.
48. Jacobs, J.; Goodman, S.; Sumner, D. R.; *et al*. In *Orthopedic Basic Science*; Buckwalter, J., Einhorn, T., Sheldon, S., Eds.; American Academy of Orthopedic Surgeons: Chicago, 1999; pp 402–426.
49. Vermes, C.; Glant, T. T.; Hallab, N. J.; *et al*. *J. Arthroplasty* **2001**, *16*, 95–100.
50. Hallab, N.; Merritt, K.; Jacobs, J. J. *J. Bone Joint Surg. Am*. **2001**, *83A*, 428–436.
51. Hallab, N. J.; Jacobs, J. J.; Skipor, A.; *et al*. *J. Biomed. Mater. Res*. **2000**, *49*, 353–361.
52. Hallab, N. J.; Mikecz, K.; Jacobs, J. J. *J. Biomed. Mater. Res*. **2000**, *53*, 480–489.
53. Hallab, N. J.; Mikecz, K.; Vermes, C.; *et al*. *J. Biomed. Mater. Res*. **2001**, *56*, 427–436.
54. Burt, C. F.; Garvin, K. L.; Otterberg, E. T.; *et al*. *J. Bone Joint Surg. Am*. **1998**, *80*, 952–960.
55. Cramers, M.; Lucht, U. *Acta Orthop. Scand*. **1977**, *48*, 245–249.
56. Elves, M. W.; Wilson, J. N.; Scales, J. T.; *et al*. *Br. Med. J*. **1975**, *4*, 376–378.
57. Gordon, P. M.; White, M. I.; Scotland, T. R. *Contact Dermat*. **1994**, *30*, 181–182.
58. King, J.; Fransway, A.; Adkins, R. B. *N. Engl. J. Med*. **1993**, *329*, 1583–1584.
59. Merle, C.; Vigan, M.; Devred, D.; *et al*. *Contact Dermat*. **1992**, *27*, 257–258.
60. Rostoker, G.; Robin, J.; Binet, O.; *et al*. *J. Bone Joint Surg*. **1987**, *69A*, 1408–1412.
61. Thomas, R. H.; Rademaker, M.; Goddard, N. J.; *et al*. *Br. Med. J*. **1987**, *294*, 106–107.
62. Milavec-Puretic, V.; Orlic, D.; Marusic, A. *Arch. Orthop. Trauma Surg*. **1998**, *117*, 383–386.
63. Mayor, M. B.; Merritt, K.; Brown, S. A. *The American Journal of Surgery* **1980**, *139*, 477–479.
64. Christiansen, K.; Holmes, K.; Zilko, P. J. *Ann. Rheum. Dis*. **1980**, *39*, 476–480.
65. Deutman, R.; Mulder, T. H.; Brian, R.; Nater, J. P. *J. Bone Joint Surg. Am*. **1977**, *59-A*, 862–865.
66. Munro-Ashman, D.; Miller, A. J. *Contact Dermatitis* **1976**, *2*, 65.
67. Evans, E. M.; Freeman, M. A.; Miller, A. J.; Vernon-Roberts, B. *J. Bone Joint Surg*. **1974**, *56-B*, 626–642.
68. Hallab, N. J.; Anderson, S.; Caicedo, M.; Skipor, A.; Campbell, P.; Jacobs, J. J. *J. Arthroplasty* **2004**, *19*, 88–93.
69. Benson, M. K.; Goodwin, P. G.; Brostoff, J. *British Medical Journal* **1975**, *4*, 374–375.
70. Merritt, K.; Brown, S. *International Journal of Dermatology* **1981**, *20*, 89–94.
71. Carlsson, A. S.; Macnusson, B.; Moller, H. *Acta Orthop. Scand*. **1980**, *51*, 57–62.
72. Benson, M. K.; Goodwin, P. G.; Brostoff, J. *British Medical Journal* **1975**, *4*, 374–375.
73. Elves, M. W.; Wilson, J. N.; Scales, J. T.; Kemp, H. B. *British Medical Journal* **1975**, *4*, 376–378.
74. Basketter, D. A.; Briatico-Vangosa, G.; Kaestner, W.; Lally, C.; Bontinck, W. J. *Contact Dermatitis* **1993**, *28*, 15–25.
75. Merritt, K.; Rodrigo, J. J. *Clin. Orthop. Relat. Res*. **1996**, *326*, 71–79.
76. Rooker, G. D.; Wilkinson, J. D. *J. Bone Joint Surg*. **1980**, *62B*, 502–505.
77. Black, J. *Prosthetic Materials*. VCH Publishers, Inc.: New York, 1996; pp 141–162.
78. Jacobs, J. J.; Goodman, S. L. In *Implant Wear: The Future of Total Joint Replacement*; Wright, T. M., Goodman, S. B., Eds.; American Academy of Orthopedic Surgeons: Rosemont, 1996; pp 41–44.
79. Hensten-Pettersen, A. In *Biological, Material, and Mechanical Considerations of Joint Replacements*; Morrey, B. F., Ed.; Raven Press: New York, 1993; pp 353–360.
80. Merritt, K.; Brown, S. *Acta Orthop. Scand*. **1980**, *51*, 403–411.
81. Korenblat, P. E. *Contact Dermatitis*, 2nd ed.; W.B. Saunders Company: Philidelphia, 1992.
82. Kuby, J. *Immunology*, 2nd ed.; W.H. Freeman and Company: New York, 1991.
83. Hallab, N. J.; Anderson, S.; Caicedo, M.; *et al*. *J. Arthroplasty* **2004**, *19*, 88–93.
84. Hallab, N. J.; Jacobs, J. J.; Black, J. In *Biomaterials and Engineering and Devices: Human Applications*; Wise, D. L., Ed.; Humane Press: Totowa, NJ, 2000.
85. Caicedo, M.; Jacobs, J. J.; Reddy, A.; *et al*. *J. Biomed. Mater. Res. A* **2007**.
86. Hallab, N. J.; Vermes, C.; Messina, C.; *et al*. *J. Biomed. Mater. Res*. **2002**, *60*, 420–433.
87. Gillespie, W. J.; Frampton, C. M.; Henderson, R. J.; *et al*. *J. Bone Joint Surg. Br*. **1988**, *70*, 539–542.
88. Matheisen, E. B.; Ahlbom, A.; Bermann, G.; *et al*. *J. Bone Joint Surg. [Br.]* **1995**, *77B*, 345–350.
89. Nyren, O.; Mclaughlin, J. K.; Anders-Ekbom, G. G.; *et al*. *J. Natl Cancer Inst*. **1995**, *87*, 28–33.
90. Visuri, T.; Koskenvuo, M. *Orthopedics* **1991**, *14*, 137–142.
91. Goodman, S. B.; Huie, P.; Song, Y.; *et al*. *J. Bone Joint Surg. Br*. **1998**, *80*, 531–539.
92. Park, Y. S.; Moon, Y. W.; Lim, S. J.; *et al*. *J. Bone Joint Surg. Am*. **2005**, *87*, 1515–1521.

6.609. Orthopedic Implant Use and Infection

V Antoci, Massachusetts General Hospital, Boston, MA, USA
J Parvizi, Thomas Jefferson University, Philadelphia, PA, USA

© 2011 Elsevier Ltd. All rights reserved.

6.609.1.	**Orthopedic Implants**	109
6.609.1.1.	New-Generation Biomaterials	109
6.609.1.2.	Orthopedic Complications	110
6.609.2.	**Periprosthetic Infection**	111
6.609.2.1.	Prevalence and Etiology	111
6.609.2.2.	Mechanisms and Routes of Infection	111
6.609.2.3.	Biofilms in Pathogenesis of Infection	112
6.609.2.4.	Biofilms and Multidrug Resistance	113
6.609.3.	**The Diagnostic Dilemmas**	114
6.609.3.1.	Markers of Infection	114
6.609.3.2.	Microbiology Assays	114
6.609.3.3.	Intraoperative Diagnosis	116
6.609.4.	**An Interjection on Orthopedic Trauma**	116
6.609.5.	**Classification Schemes for Implant Infection**	117
6.609.6.	**Management of Periprosthetic Infection**	119
6.609.6.1.	Surgical Approaches	119
6.609.6.2.	Antibiotic-Laden Bone Cements	120
6.609.6.3.	Self-Protective Implants	121
6.609.7.	**The Future of Implant Design in Orthopedic Infection**	121
6.609.8.	**Nanomolecular Permanent Modification of Biomaterials**	121
6.609.8.1.	Feasibility of the Concept	122
6.609.9.	**Conclusions**	123
References		123

Abbreviations

18F-FDG	18F-fluorodeoxyglucose
BAP	Biofilmassociated protein
BMP	Bone morphogenetic protein
CT	Computed tomography
ESR	Erythrocyte sedimentation rates
FDA	Food and Drug Administration (USA)
MESS	mangled extremity severity score
MIC	Minimum inhibitory concentrations
MRI	Magnetic Resonance Imaging
MRSA	Methicillin-resistant *S. aureus*
NSAID	Nonsteroidal Antiinflammatory Drug
PCR	Polymerase chain reaction
PET	Positron emission tomography
PIA	Polysaccharide intercellular adhesin/ hemagglutinin
RGD	Argineglycine-aspartate
sub-MIC	Subminimal inhibitory concentration

6.609.1. Orthopedic Implants

6.609.1.1. New-Generation Biomaterials

The age of bionic human beings is not too distant as implants are being popularized throughout the different areas of medicine.[1–3] The old system or tissue-based conservative approaches to treatment is slowly being phased out and replaced with aggressive surgical interventions that include the increasing use of biomolecular artificial implant components.[4–6] Implants, drugs, and innovative procedures have improved life expectancy from 49.2 years a century ago to over 78 years now.[7] In fact, according to recent data from a physician survey, the hip and knee replacement operation has been ranked number 10 on the list of most important medical innovations, ahead of NSAIDs, cardiac enzymes, and laparoscopic surgery, yet behind balloon angioplasty and MRI or CT scans.[8] Most implants in medicine are associated with orthopedics, with some form of fixation device in 40% and artificial joints in 12% of the people with implants.[9] Annually, over 800 000 new hip arthroplasties are performed worldwide, with 120 000 in the United States alone[10] and 43 000 in Canada.[11] Additionally, over 300 000 total knee replacements are performed per year in the United States,[12] adding up to over 1.5 million total joint replacements performed worldwide.[13]

The rapidly aging population has driven the demand for implants even higher. Specifically, in the United States during 1900s, only 3.1 million people were over 65 years of age; there are over 35 million people in that population group in 2006,

with a projected 60 million by 2020.[7] Currently, more than 3.2% of the population over 55 have an artificial joint and at least another 2% require one.[14] These numbers are only expected to increase as the aging population shows a high prevalence of osteoporosis, osteoarthritis, and degenerative bone conditions that promote the higher implant demand.[15] In addition to implant demand associated with aging, more than 35 million people experienced trauma in 2004, resulting in over 6 million fractures that required an implantable fixation device, with an estimated cost of $58.5 billion in 2004.[16,17] These numbers, when combined with the 200% increase in joint utilization between 1999 and 2002 alone,[18] suggest that implant applications will skyrocket over the next few decades.[19]

The $23 billion US medical implant industry is a witness to the sophistication and extensive research in implant engineering and design.[20] Implant designs have evolved with surgical experience and are now radically different from the original Charnley low friction hip.[21–23] Orthopedic implants are manufactured from a variety of materials that show biological compatibility and mechanical performance, good interface responses, and long-term reliability of the surface.[24] Industrial designs use stainless steel, titanium, polyethylene, ceramics, bioglass, and carbon, often in combination, to create a complex total joint replacement with separate components serving specific biomechanical and biological functions.[25–28] Of these, titanium and its alloys have often been a preferred material in orthopedic and dentistry applications as they possess great biocompatibility and exhibit minimal toxicity to host tissues.[29–34] Through the history of biomedical implants, simple, unprocessed alloys were used to create an implant that was relatively inert to the physiological milieu. Modern implants undergo blasting, coating, and modification of both surface topography and chemical characteristics in order to best adapt to the target tissue environment.[35–39] Additional surface modifications often focus on introducing biological agents directly onto the surface. Hydroxyapatite, calcium phosphate, arginine-glycine-aspartate (RGD), bone morphogenetic proteins (BMPs), or albumin have been used to further improve the specific functions of different implants.[35,40–44]

A drawback to these sophisticated implants, however, is the increase in research and development costs as well as the higher cost of implant production. Together, these result in the overall increase in joint replacement costs.[45] In 2003, the total cost of joint replacement amounted to over $1.4 billion for total hips and over $2.59 billion for total knees.[46–50] When considering that 15% of the US gross domestic product is allocated to health care, the rising costs of orthopedic implants affects everybody,[51] with more than 2/3 of the costs of joint replacement and 22% of trauma reimbursed through either Medicare or Medicaid.[17,52] A simpler, smarter design is necessary to decrease both costs and complications.

6.609.1.2. Orthopedic Complications

Joint replacement has been called the orthopedic success story by the American Academy of Orthopaedic Surgeons[53] with over 85% of patients satisfied with the results of surgery.[54] Perioperative mortality is less than 0.5% and prosthesis failure is about 10% at 10 years.[54,55] Despite that visible success, the rate of failure and the need for revision procedures have been increasing faster than the rate of primary replacement.[18] An obvious cause is that, as implants become more popular, both the number of patients and surgeons involved with joint replacements has been increasing rapidly. On the patient side, the inclusion of both younger and older patients has expanded into population groups that have an increased rate of complications.[45] The overall incidence of these complications appears to be gender dependent, with higher risks in the male patient population.[54] More importantly, prior revisions lead to a threefold increase in complications as compared to outcomes after the first revision.[56] Nevertheless, most comorbidities and preoperative function do not substantially change arthroplasty outcomes at 5 years.[57] Still, some, including obesity, are important patient-dependent factors that lead to additional complexity and even premature failure of the implant.[57–60] On the other side of the surgical table, the surgeon's experience and technique are crucial to the final outcome of surgery. Medicare data suggest that surgeons who themselves perform less than 12 operations a year and are in hospitals that see less than 25 joint replacements per year see the highest complication rates.[54,61,62] The rate of complications decreases as the number of surgeries increases and remains inversely proportional to the surgeon's experience.[63] In retrospect, over 17.5% of hips and 8.2% of knee implants are currently being revised due to complications, leading to substantial costs, disability, and patient discomfort.[18,52]

Most patients come back for revision due to pain (66%), dislocation or instability of the prosthesis (14%), infection (11%), trauma (5%), or immobility (4%).[64] Ultimately, the implant is a foreign body and is inextricably associated with complications due to foreign body reaction, inflammation, and poor host integration. The most common prosthesis-associated long-term complications of arthroplasty include aseptic loosening (30–40%), infection (0.5–7%), and osteolysis (5%).[65–70] Other nonsurgical complications after joint replacements include pulmonary embolism, pneumonia, myocardial infarction, cerebrovascular accidents, deep vein thrombosis, and others.[71] All these complications are currently being addressed in the clinic by improved technique and better indications for joint replacement. Still, no ideal or simple solution exists and such complications are only partially solved through treatments like peri- and postoperative antibiotics or stringent limitations imposed on the patient.[72–74]

Aseptic loosening produces pain and instability affecting the patient's quality of life. Improving implant design may significantly lower the incidence of aseptic loosening and osteolysis,[75–77] especially in cases where inflammation and immune system response may be the causative agents of loosening.[13] Specifically, the implant may erode to produce metal particles both surrounding the implant and also within phagocytosing immune cells to provide a mechanism for osteolysis and failure of the implant to integrate.[78,79] Once ingested into the cells, the lysozomes are unable to enzymatically degrade metals, leading to a cascade of cytokine release. Such release elicits a continuous inflammatory response that affects the immediate periprosthetic environment, endosteum, and bone tissue.[13] Several approaches from plasma coating to nanoscale surface fabrication attempt to decrease the amount of particulate matter and debris produced by the implant and thus decrease the cytotoxic effects of joint prosthesis.[80,81]

6.609.2. Periprosthetic Infection

The complications of aseptic loosening are minor when compared to another major problem associated with implant placement – an infected prosthesis. Over 2 million cases of hospital-acquired infection are reported annually in the United States, with more than half associated with implants.[82] Periprosthetic infection, one of the most dreaded complications in orthopedics, often results in repeat surgeries, patient distress and disability, and increased cost and utilization of medical resources.[83,84] Infection, despite being less prevalent than aseptic loosening, can lead to chronic systemic spread, osteomyelitis, possible tissue necrosis or amputation, and, in particularly difficult cases, even death.[85] It is important to realize that, at the end of the day, periprosthetic infections do not affect just the patient, but this dreadful complication impinges on society at large. As far back as 1989, the annual cost of infection exceeded $200 million.[85] More recent data show that joint revisions due to infection cost more than $50 000 per case; revision due to aseptic loosening is only about $16 000 and primary arthroplasty, about $8500. Financial analysis estimates that as little as 1% decrease in revision rate for total joint arthroplasty would save as much as $211 million in US health care costs.[18] Considering the costs of revisions, the additional hospital time and disability and the loss of the workforce due to sick leave, the costs of periprosthetic infection easily surpass $1 billion, with much higher costs to society at large.

6.609.2.1. Prevalence and Etiology

Despite the apparently decreasing incidence of infection from almost 7% in Charnley's experience[21] to less than 1% in high volume institutions,[86–88] recent data suggest that infection rates are greatly underestimated.[89–91] The inadequate reporting is related to the difficult diagnosis in the clinical setting.[89,92] Classically, microbiological sampling of the tissue was used to differentiate between aseptic and septic loosening. However, as our knowledge of infection has increased, it has become apparent that bacteria can escape detection either because they are not present in large enough numbers for diagnosis or they remain strongly adherent to the implant and thus are difficult to sample through ordinary microbiological methods.[91,93,94] Because of these difficulties, there is no gold standard test for diagnosis of periprosthetic infection and most physicians struggle with a combination of clinical and biochemical markers that inconsistently detect or misdiagnose infection. Data based on DNA detection using the polymerase chain reaction (PCR) suggest the possibility of infection presence in as many as 73% of revision cases. However, PCR is overly sensitive to contamination or proteic material and, thus, often produces a high rate of false positives.[89,95,96] Nevertheless, multiple studies have also found bacteria, bacterial components, and infection-associated immune responses associated with a disproportionately large number of implants retrieved during revision surgery.[89,97–100] Furthermore, the fact that antibiotic prophylaxis improves the outcomes of joint replacements and decreases the overall rate of complications including aseptic loosening and osteolysis supports the current understanding that infectious organisms may play a larger role than initially thought.[101]

Certain comorbidities further increase the risk of infection. Rheumatoid arthritis, diabetes mellitus, obesity, sickle-cell disease, psoriasis, poor diet, and a compromised immune system, as well as previous surgeries in the affected limb, are often linked to higher risks of implant-associated infection.[85,102–104] Rheumatoid arthritis, for example, is associated with a 2.6-fold increase in infection rates compared to osteoarthritis.[105] Also, revision surgeries lead to an almost threefold increase in infection risk.[55,106] Most of these conditions are associated with a depressed or compromised immune system which allows any chance contamination to develop into an overt infection. However, on the other side of the surgical table, as is the general case for complications, surgeon experience, antibiotic timing and dosing, surgery duration, especially if over 2.5 h,[106] operating-room traffic, and the complexity of reconstruction are all important factors determining the probability of infection.[85] Finally, in trauma, compound open fractures are at increased risk of deep wound infection and osteomyelitis, which is further compounded by the fact that over 30% osteosynthetic materials have a high risk of infection. In fact, virtually 100% of patients who undergo external fracture fixation develop pin tract infections.[107–110]

Periprosthetic infection is caused by the same infectious organisms that are found in hospital intensive care units or associated with trauma.[111] Most of these organisms are natural flora and become pathogenic by being introduced into deep tissues, thus bypassing skin defenses. Coagulase-negative staphylococci are the most prevalent organisms in orthopedic infection and are the causative organism in 30–67% of cases.[88,112,113] These include *Staphylococcus epidermidis*, *S. haemoliticus*, and over 30 other species of gram-positive bacteria. *S. aureus* is isolated in 12–23% of the cases, with other mixed flora found in 10–11%, streptococci in 9–10%, gram-negative bacilli in 3–6%, enterococci in 3–7%, and anaerobes in 2–4%[88,113]; these organisms are common contaminants on all indwelling implants, including heart valves, dental prosthesis, or catheters.[114–117] Interestingly, the prevalence of coagulase-negative staphylococci in orthopedic infection has been constantly decreasing with *S. aureus* slowly taking prevalence.[113] Even more importantly, *S. aureus*, *S. epidermidis*, and *Pseudomonas aeruginosa* are inherently efficient at adhering to and colonizing implant surfaces through expressing specific genetic elements for both quorum sensing and ultimately, biofilm formation.[118–122] The adherence and colonization of the implant surface greatly increases the recalcitrance of infection to treatment and thus, any implant that could inhibit adherence would decrease periprosthetic infection and its associated disability and cost. However, in devising such an implant, better understanding of the etiology and pathophysiology of infection is necessary to best map the angle of attack against the ravages of periprosthetic infection.

6.609.2.2. Mechanisms and Routes of Infection

Infection originates from bacterial contamination of the implant either during surgery or later through hematogenous transfer or local dissemination.[110] Each mechanism of infection initiation is important, even though surgical contamination is the most common route. Infection associated with surgical contamination manifests itself within the first 3 months after

surgery.[110,123] The importance of surgical contamination is documented by an infection rate of 1–5% that drops to less than 0.5–1% after improved prophylactic measures and superior sterility.[106,110,124] For that reason, the more stringent operating procedures in high-volume centers could be part of their success, while smaller centers without such capabilities tend to struggle.[55,125–127]

Late, acute onset of periprosthetic infection, often one year or more after surgery is attributed to hematogenous transfer/contamination.[128] Such transfer can occur during a urinary tract infection, dental work, or other minor surgery where bacteria can be introduced into the bloodstream. The possibility of infection through this route has led to a debate as to the use prophylactic antibiotics during minor surgery or dental procedures in patients with a previous implant.[129,130] Minor bacteremia that initiates in patients after such procedures may lead to contamination of the implant, which becomes a safe haven for the infectious organisms. Thus, current practice recommends prophylactic antibiotics in urological or extensive dental procedures for high-risk patients with artificial joints.[131,132]

In addition to hematogenous transfer, local dissemination from a contiguous focus is another important, yet often overlooked, mechanism of infection. When multiple prior surgeries or procedures are being performed on a limb,[106] bacterial contamination, even if not associated with an implant, may produce local chronic infectious foci.[108,133,134] Bacteria can remain encapsulated in a biofilm within the endosteum crevices without clinical manifestation.[135,136] Such biofilms, when disturbed by another surgical intervention, generate the seeders necessary for implant contamination.

In order to estimate the overall distribution of infection, recent data from 146 patients showed 70% of infection cases were chronic, 17%, acute postoperative; and 13%, acute hematogenous.[137] One study saw 45% of infections presenting early, 23% delayed, and 32% expressing late onset of periprosthetic infection,[138] with an average time from primary joint arthroplasty to diagnosis of infection of about 30–35 months.[137,139] In conclusion, no matter which mechanism bacteria use to get to the implant, bacterial colonization resulting in biofilm formation is an important culprit in infection survival and propagation that leads to the final implant failure. By preventing this colonization and inhibiting biofilm formation, implant infection could be inhibited, and thus the occurrence of periprosthetic infection strongly curtailed.

6.609.2.3. Biofilms in Pathogenesis of Infection

Implant-associated infection invariably involves the interplay between the infectious organism, the implant, and the host. Gristina *et al.* have formulated a 'race for the surface' hypothesis, where infection development competes with normal osseointegration, with the ultimate success of the implant dependent on the prevalent process.[140–142] Generally, with a successful sterile surgery and a host balance between integration and immune system response, arthroplasty is quite successful. However, the events that occur within bone to adapt to the presence of a new implant are also those that predispose the implant to bacterial colonization. In fact, the presence of an implant decreases by more than 10^5-fold the minimal dose of *S. aureus* that is necessary to create an abscess.[123] When the implant provides this safe heaven for bacterial colonization, osteomyelitis can be initiated with only 10–100 bacteria; normal bone would require millions of bacteria to induce the same degree of infection and bone destruction.[143,144] Thus, the presence of a foreign body allows other foreign organisms to mitigate their own existence in the shadow of a much larger intruder like the implant.

The physiological response to the introduction of the implant into tissue environment challenges the host immune system, which may further trigger a foreign body reaction.[78,145] During implantation, the prosthetic surface becomes coated with physiological fluids, serum, and tissue fragments, as well as fibronectin, vitronectin, and albumin.[123] Albumin has been shown to inhibit the activation of the immune system and prevent extracellular matrix deposition on the implant.[146,147] Local granulocytes in the immediate periimplant environment tend to be degranulated and lack superoxide production due to wear particle ingestion, and, thus, are unable to kill bacteria.[123,148] The lack of an efficient immune system in the presence of abundant extracellular proteins provides an advantage for bacterial adherence.[149–152] In fact, the coating proteins support successful bacterial colonization. Studies have shown that over 90% of *S. aureus* express either fibronectin binding proteins, fibrinogen binding proteins, or collagen binding proteins, with almost 60% of bacteria expressing a combination of all the three.[153] More worrisome, these genes were significantly more common in methicillin-resistant *S. aureus* (MRSA) than in susceptible strains.[153] Thus, bacteria introduced to the site of the implant can undergo rapid, yet reversible surface adhesion.

Specific signals are required for successful bacterial colonization and biofilm formation. These include biofilm-associated protein (BAP) in *S. aureus* and polysaccharide intercellular adhesin/hemagglutinin (PIA), which is encoded by the *ica* operon in *S. epidermidis*.[123,154] This colonization and biofilm formation are not random, but molecular decisions take place in response to the suitability of the local environment, availability of nutrients, and the relative absence of bactericidal agents.[133] As the decisions are made, the adherent bacteria either release from the surface in search of a new habitat or initiate proliferative cascades and matrix production. This proliferation and subsequent accumulation of bacteria on the biomaterial surface is specific to biofilms, so, for example, *S. epidermidis* strains not capable of biofilm formation will adhere to the surface but fail to accumulate.[123,155,156] Once attached and proliferating, production of signaling and quorum sensing molecules leads to communal regulation of signaling cascades, specific patterns of geometric organization, and housekeeping.[110,123,133,152]

In the biofilm, a variety of microbial strains and species can coexist in close proximity and exist in areas of widely varying metabolisms, both rich and poor nutrient environments, and bordering aerobic and anaerobic pockets.[152,157] Bacteria within biofilms, originally thought to maintain a low metabolic state, are, in fact, more active than free-floating planktonic organisms. This high metabolism is necessary for producing extracellular polysaccharides, signaling proteins, and toxins.[154] For example, *S. aureus* produces over 40 toxins including enterotoxins, coagulase, proteases, and hemolysins.[158,159]

Many of these toxins work alongside the inflammatory antibodies and cytokines released locally from immune cells to further augment the damage to the periprosthetic host environment.[160,161] Other components in the extracellular polysaccharide matrix include proteins and nucleic acids, making it hard to differentiate the remnants of matrix from live bacterial populations.[154]

The abundant extracellular polysaccharide production results in a 'sludge' that comprises 85% of the biofilm with cells accounting for only 15% content by volume.[133] This composition makes biofilms difficult to detect and differentiate from surface debris. Furthermore, the usual treatment strategies fail to penetrate this sludge. Despite its seeming simplicity, such structural arrangement confers superior functional complexity. Developed biofilm communities form mushroom-like structures that are able to extend into the surrounding environment, sense fluid movement, and respond to the bathing environment, similar to the higher eukaryotic organisms from phylum Cnidaria or Porifera that include sponges and Hydrozoa. Furthermore, such structures can actually migrate in response to shear stress along the material surface, or propagate by either separation of entire biofilm fragments or dispersion of single free-floating planktonic bacteria.[133] Such cycles of propagation lead to the chronicity of biofilm infections.

Infection associated with biofilms remains subclinical for extended periods of time, with only mild fever and slight bacteremia, as the planktonic bacteria are killed by the immune system. Local damage results in loosening of the prosthesis and osteolysis, but such symptoms are often difficult to identify and differentiate from aseptic loosening or associated foreign-body reaction. Ultimately, if undiagnosed, the growing and expanding biofilm may lead to osteomyelitis and life-threatening complications. More importantly, the biofilm can confer multidrug resistance that makes the infection difficult to eliminate, often requiring radical interventions.

6.609.2.4. Biofilms and Multidrug Resistance

Biofilms are notoriously difficult to treat and common antibacterial treatment strategies often fail. Antibiotics are often successful at killing cultures extracted from biofilms, yet the same antibiotics have minimum effect on bacteria adherent onto implants and hidden within the biofilm.[162,163] Several factors are commonly thought to be responsible for biofilm resistance, including (1) decreased fluid flow and antibiotic penetration, (2) varied metabolism across the biofilm structure and thus decreased susceptibility, and (3) possible resistance genes within the often heterogeneous bacterial population with rapid interchange of plasmids.[164] The usual theory invokes the slow penetration of antibiotics into the sludge that kills only the surface bacteria. Fluid channels that are abundant within the biofilm are limited in pore size and capillary movement, forcing antibiotics to only slowly diffuse and not equilibrate. The resulting concentration gradients create zones of stress for cells deeper in the biofilm, without reaching the MIC for the antibiotic.[133,150,165,166] Simultaneously, the same slow diffusion creates nutrient gradients within the biofilm with areas of nutrient depletion and starvation.[164,167–169] These niches result in bacteria with low metabolic rates that fail to respond to the sub-MIC concentration of antibiotic.[164,170,171] The microbial organisms are given time to adapt and survive, inducing genetic modification or gene transfer to acquire resistant phenotypes.[169,172] Despite this theorized propensity to acquire resistance, bacteria within biofilms are not normally more resistant to antibiotics than planktonic bacteria.[164]

Specifically, antibiotic resistance is usually developed when long-term selective pressure on a bacterial population provides a competitive advantage to those organisms able to survive in the presence of the antibiotic. This survival and hence resistance results from genetic mutation or gene acquisition from other organisms of the same or different species. The specific mechanism involves either (1) drug inactivation by specific enzymes as in β-lactamases, (2) alteration of the antibiotic target site such as change in the D-ala-D-ala sequence for vancomycin binding, (3) alteration of metabolic pathways as in common resistance to sulfonamides, or (4) reduced accumulation of the drug such as in acquisition of efflux pumps.[173] Typically, resistance is manifested only when the cells are exposed to increasing sub-MIC concentrations of an antibiotic that do not produce killing. The antibiotic then introduces a new selective pressure in the population and stimulates adaptation and evolutionary changes toward resistance. However, quite often, due to manipulation of normal metabolic machinery, resistant organisms are slow growers and thus are at a disadvantage under normal circumstances.[163,169,171,174]

However, recent data with floroquinolones question the assumed origin of biofilm resistance to antibiotics. Floroquinolones, in contrast to aminoglycosides, have been shown to quickly penetrate and equilibrate throughout the entire biofilm, killing most cells.[164] Paradoxically, the biofilm survives and regenerates.[164] To explain that phenomenon, Lewis *et al.* have proposed the concept of 'persisters,' that is, bacteria within the biofilm that may have altered metabolism and resist killing by drugs.[172] Persisters, in fact, have similar susceptibility to growth inhibition, but cannot be killed by normal antibiotic dosing.[164] As a result, biofilms would not be theoretically resistant in a microbiological assay as they would maintain similar MIC to normal flora. This phenomenon only emphasizes that MIC reflects a measurement of growth rather than killing. In the usual host environment where the bacteria are planktonic and the drug eliminates the bulk of the infectious population, the immune system is capable of eliminating the few persisters.[164] This scenario changes in biofilms where the sludge prevents immune cell penetration. Antibiotics eliminate the bulk of the biofilm and successfully inhibit further growth. However, a few persisters, though, manage to survive and, upon discontinuation of the drug, are then responsible for biofilm regeneration and long-term survival.[175] Very high antibiotic doses are usually required to eliminate persisters; such doses are often impossible to prescribe due to host toxicity. In fact, we have previously shown that antibiotics given at doses as high as 10× the MIC have minimal effect on preventing bacterial growth and colonization of titanium surfaces.[176] Other studies on urinary catheters have found the need for over 1000 times the MIC to eliminate colonizing bacteria.[177] Thus, to address the very foundation to the problem, bacterial adhesion must be inhibited as we have suggested in a proposed novel implant design that has a self-protective surface to inhibit bacterial colonization, inhibit biofilm

formation, and ultimately address the problem of periprosthetic infection, treatment, and prevention. The success of an implant with these properties can only be judged based on the current criteria for infection detection.

6.609.3. The Diagnostic Dilemmas

Despite extensive progress in implant designs, the diagnosis of periprosthetic infection remains the most elusive part of the entire clinical process. No universal criteria exist to determine and differentiate infection from aseptic loosening and osteolysis, and the entire process is based on the integration of clinical presentation, laboratory data, imaging modalities, and good, old-fashioned, judgment. The ultimate evidence of infection includes the identification of the infecting organism and morphological determination of biofilms on the implanted surface,[161] however, such evidence is often only obtained after the failure and removal of the implant. Modern serological tests, molecular techniques, and imaging modalities have varying sensitivities and specificities that depend on the individual laboratory, hospital, and chosen cutoff values for positive diagnosis. Parvizi *et al.* have previously proposed a diagnostic algorithm that includes both pre- and intraoperative tests and thus shows reasonable success in diagnosing periprosthetic infection.[92] However, improved predictive tests are needed with easier and earlier diagnosis and more specific differentiation between infection and aseptic conditions.

Clinical history and physical examination are critical for determining the risk of periprosthetic infection. A good history identifying the specific presentation, duration and localization of symptoms, predisposing factors, and response to treatments may render an early diagnosis. In fact, a diagnosis can be almost always confirmed in cases presenting with severe joint pain, fever, poor wound healing, erythema, drainage, sinus formation, and early implant failure.[89,178,179] Such presentation is more common for an early onset of infection occurring within the first few months after surgery.[123] Early short-term antibiotics may ameliorate the symptoms but leave a nidus of infection that ultimately leads to chronicity, premature implant failure, and delayed infection. As such, delayed infection, due to the chronic subclinical nature of biofilms on implant surfaces, presents in more than 75% of cases with nonspecific symptoms including minor hip pain, instability, and local inflammatory responses.[180] Owing to various presentations, clinical suspicion is an important factor in the ultimate diagnosis of periprosthetic infection, but confirmation of infection requires additional testing.

6.609.3.1. Markers of Infection

Radiographic studies allow for additional information that would not be easily obtained on physical examination. Radiographs can provide some nonspecific information about the local environment around the prosthesis; in cases of overt infection, periosteal reaction, bone cysts, and resorption may be visible (**Figure 1**). Even though radiographs complete another aspect of the clinical scenario, more specific tests are required for a better differential diagnosis. Another aid to diagnosis is serologic testing that is often easy to perform and provides preoperative information to aid in the diagnostic algorithm. Specifically, blood leukocyte count and differential is not sensitive or specific to periprosthetic infection,[123,181] whereas synovial fluid leukocyte count and differential is a rapid and accurate assay for predicting periprosthetic infection.[123] In fact, a knee synovial fluid leukocyte count of more than $1.7 \times 10^9\,l^{-1}$ and a differential of more than 65% neutrophils produced a sensitivity of 94% and 97%, with specificities of 88% and 98%, for detecting periprosthetic infection, respectively.[182] Erythrocyte sedimentation rates (ESR) and C-reactive protein have become very popular as an initial screening test of infection due to their high negative predictive values, even though they are generally nonspecific markers of inflammation.[92] Both of these markers normally rise after arthroplasty, with C-reactive protein returning to normal within 3 weeks; ESR, however, takes up to 6 weeks to reach normal values with some diurnal variation present even at that time.[89] Elevation of these markers after 3 months is considered abnormal and may indicate the development of periprosthetic infection. ESR values of more than $50\,mm\,h^{-1}$ produced a sensitivity of at least 79%, with a specificity of 78%.[183] Even values over 30 mm/Hr in some studies produced 82% sensitivity and 85% specificity.[184] C-reactive protein is generally a better predictor of infection, with levels of 1 mg/dL considered more than 96% sensitive and 92% specific for periprosthetic infection.[184] However, these predictive values have to be evaluated alongside the clinical history, eliminating other inflammatory conditions like inflammatory arthropathies, psoriasis, and gout that also produce elevated ESR and C-reactive protein. More recently, serum levels of interleukin-6 (IL-6) have been shown to correlate with infection.[89] IL-6 is produced by monocytes and macrophages, and serum levels above $10\,pg\,ml^{-1}$ have consistently predicted infection with a sensitivity of 100%, specificity of 95%, positive predictive value of 89%, negative predictive value of 100%, and accuracy of 97% against positive histopathology and culture.[185] Such results are superior to both ESR and C-reactive protein with the caveat that this was a limited study that examined only 17 patients with infection out of a 58-patient case–control study.[185]

6.609.3.2. Microbiology Assays

High clinical suspicion combined with elevated serological values provide a clear indication for joint aspiration and culture.[92] Microbiological culture of the aspirate is the most direct preoperative method to detect and identify the infectious organism.[186] The presence of bacteria after culture is thought to have high specificity for infection even though possibly low sensitivity. The test is flawed by the low retrieval rate of bacteria from culture when compared to more sensitive methods like PCR or other biomolecular techniques.[95,96,187,188] However with proper technique and sterile handling, the chance of contamination is very low and allows clear delineation of the patient population. The presence of bacteria correlates with periprosthetic infection with a predictive value for knees of 85%.[91,189] In fact, in the Rothman Institute experience, such culture of aspirated fluid showed 100% specificity and 100% positive predictive value.[92] The predictive value is much lower for hips, mainly due to the different anatomy and pathways of communication between the peri-implant space and the joint

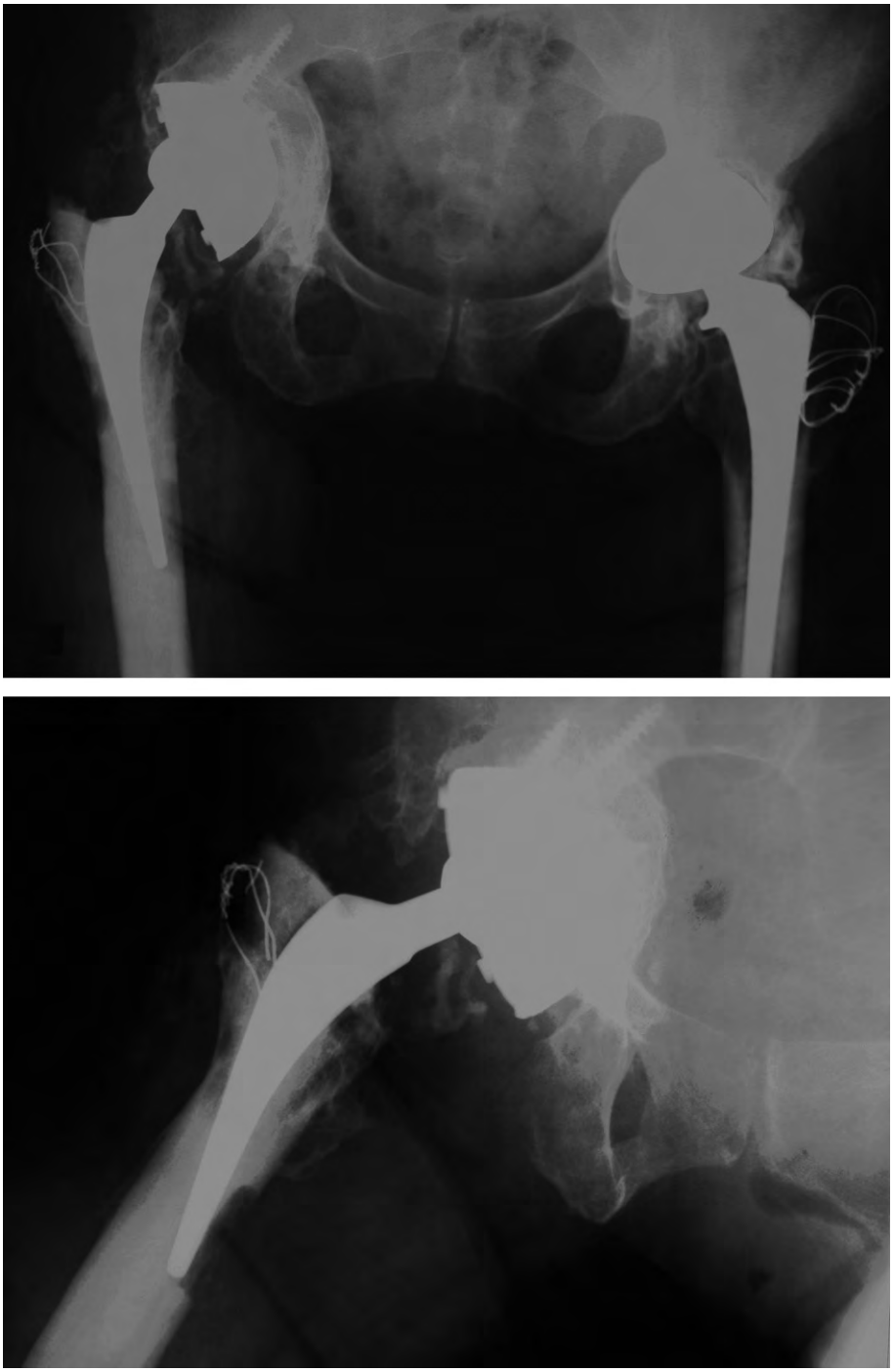

Figure 1 Failed implant. The patient presents with persistent hip pain, ESR 118 and CRP 4.3. Imaging (AP pelvis and hip shown) shows periosteal reaction, bone cysts, and implant loosening. The subsequent hip aspirate showed leukocytosis with a WBC count of 15 600 and a predominance of polymorphonuclear neutrophils (92%). The patient was taken to the OR with gross purulence observed upon opening the capsule and subsequent cultures were positive for *S. aureus*. A two-stage approach was taken with an antibiotic spacer initially and subsequent revision reimplantation.

synovium. Overall however, microbiological culture is not recommended as the single test for periprosthetic infection. Most authors agree on the utility of culture as a confirmatory test after clinical suspicion and serological tests have already indicated the probability of infection.[89,92,189] As a caveat to all of this, negative tests sometimes yield positive results when repeated, while antibiotic therapy within 2–3 weeks of aspiration drastically change the results, severely decreasing the chance of detecting true infections.[89,91,186,190] Therefore, in the presence of a strong clinical suspicion and positive serological test with no culture, advanced radionuclide imaging may provide another option.

More and more orthopedic surgeons employ radionuclide studies in their diagnostic algorithm by combining bone scintigraphy, technetium-99m, indium-111 scanning, or 18F-fluorodeoxyglucose (18F-FDG) imaging. Three-phase bone imaging by itself showed only 33% sensitivity and 86% specificity, with poor predictive value.[191] When using more specific antigranulocyte scintigraphy with monoclonal antibodies, a meta-analysis of over 522 implants showed a sensitivity as high as 90% and a specificity of 80%.[192] Technetium-99m sulfur colloid indium-111-labeled leukocyte bone scintigraphy gave a sensitivity of over 50% and a specificity of 95% in diagnosing infection.[193]

By comparison, fluorodeoxyglucose (FDG) positron emission tomography (PET) showed 95% sensitivity and 93% specificity for hip prosthesis-associated infection.[193] Yet another study showed 91% sensitivity and 72% specificity for diagnosing infection around the knee and 90% sensitivity, and 89% specificity around the hip.[194,195] Areas of infection involve inflammation and increased metabolism, especially relevant to glucose consumption. Immune system cells uptake the fluorodeoxyglucose which gets phosphorylated to deoxyglucose-6-phosphate and trapped in the cell long enough to be imaged by PET. However, again, PET is generally nonspecific and inflammatory conditions have to be ruled out in order to have any predictive value in the diagnosis of infection. Overall, radionuclide imaging is an exciting test but requires extensive resource utilization which is not easily available at most centers. Intraoperative tests and frozen sections represent a much more important component in the operating room.

Gram stain is probably the most common test performed intraoperatively that provides a specificity close to 100% but a sensitivity as low as 12–19%.[184,196,197] Unfortunately, bacteria, if in relatively low numbers, may escape the microscopic field and provide a false negative result. Intraoperative culture provides a better sensitivity, even though contamination during sampling may lead to a high rate of false positives.[89,198] More importantly, sampling techniques vary from surgeon to surgeon and the subsequent results confirm a high variability. Even with multiple samplings, sensitivity ranges from 65% to more than 94% with a high specificity of 96–100%.[92,184,196] Like gram stain, albeit having a slightly better sensitivity, cultures allow a high positive predictive value, and isolation of a single organism from multiple specimens almost always indicates a positive diagnosis of periprosthetic infection.

6.609.3.3. Intraoperative Diagnosis

When the culture results fail to confirm the presence of infection, frozen sections provide the last resort for ruling between the diagnosis of periprosthetic infection and aseptic loosening. Frozen sections associated with infection show the presence of inflammation and neutrophils. Because sampling and sections differ, sometimes lymphocytes or plasma cells are the only ones found, with few if any neutrophils.[89] For frozen sections with a polymorphonuclear lymphocyte count of more than 5 per 40x field, sensitivity reached 84–93% with a specificity of 77–96%.[199,200] By increasing the threshold to 10, specificity goes up to 85–98% at the cost of sensitivity dropping to 86%.[199,200] In the hands of other labs, though, 5 polymorphonuclear lymphocytes per field were associated with only 67% sensitivity and over 97% specificity in diagnosing infection.[201] Other inflammatory conditions may produce false-positive results and further skew the picture. Like other diagnostic tests, despite the fact that the criteria and thresholds for frozen sections are quite heterogeneous, five neutrophils per microscopic field combined with clinical suspicion is a good predictor of periprosthetic infection.

Therefore, after all tests, the final diagnosis is dependent on the complete picture and good clinical judgment. For instance, a strong clinical picture combined with less than three neutrophils per microscopic field is a strong indicator of infection, despite not exactly fulfilling the typical criteria in the literature. Many of the available tests are confirmatory or provide a good screening method, while none of them can be used as a single ultimate test for infection. Specific algorithms for diagnosis are helpful but do not apply to every patient.[92] Thus, a safe diagnosis relies on a combination of tests, science, judgment, and good predictive values.

6.609.4. An Interjection on Orthopedic Trauma

A diagnosis of infection is more direct in the orthopedic trauma setting and often can result in nonunion. Many times we see patients coming into the emergency department with complex open fractures and grossly contaminated wounds where the question of infection is brought up right at onset and a treatment protocol is automatically initiated before clinical decisions even start formulating themselves.

Trauma presents a unique situation wherein multiple biological systems are often affected and play an important role in final outcomes. The basic trauma assessment, even though superficially unrelated to a peripheral open fracture, has important details that direct subsequent management solutions and the specific approach. Basics of airway, breathing, and circulation provide information on the overall severity of trauma, initial mechanisms, and the energy of impact. Pending the stability of the patient, damage control orthopedics with external fixation in the operating room or even the trauma bay may take precedence over a fully orchestrated intervention. Various works have been done on assembling algorithms to direct initial trauma management.

The mangled extremity severity score (MESS)[202] attempts to combine patient information with the mechanism of injury and stability at presentation in order to predict the success of salvaging an injured extremity (**Table 1**). A younger patient with a simple fracture who is hemodynamically stable will typically do quite well compared to an elderly trauma victim with severely contaminated wounds and hemodynamic instability. A MESS score greater than 7 accurately predicts amputation in 100% of cases based on both prospective and retrospective data.

Gustilo and Anderson[203] have attempted to classify open fractures based on size, soft tissue characteristics, and overall contamination (**Table 1**). All these parameters usually play an important role in healing as well as infection complications. Grade I fractures are usually simple with a bone fragment breaking skin integrity but for all intense purposes they often act as close fractures (**Figure 2**). In contrast, grade III open fractures involve extensive soft tissue injury and sometimes

Table 1 Trauma classification of open fractures and mangled extremities

Gustilo classification of open fractures[a]		*Mangled extremity serverity score*[b]	
Type I		*Skeletal/soft tissue injury*	
Size	<1 cm	1. Low energy	Stab/simple fracture
Quality	Clean	2. Medium energy	Open fracture/dislocation
Soft tissue	Normal	3. High energy	Crush injury/close shot wound
Fracture	Typically simple	4. Very high energy	Includes gross contamination
Type II		*Limb ischemia (double if >6 h)*	
Size	>1 cm	1. Asymmetric pulse	
Quality	Clean-to-moderate contamination	2. Pulseless with diminished capillary refill	
Soft Tissue	Moderate crush	3. Cool, paralyzed, insensate	
Fracture	Usually comminuted	Shock	
Type III		1. Transient hypotension	
Size	>1 cm	2. Persistent hypotension	
Quality	Often high degree of contamination	Patient age	
Soft tissues	A. Adequate soft tissue coverage	0. Age <30 years old	
	B. Need for local or free flap	1. 30–50 years old	
	C. Arterial injury regardless of soft tissue injury	2. Age >50 years old	

[a]Adapted from Gustilo, R. B.; Merkow, R. L.; Templeman, D. *J. Bone. Joint. Surg.* **1990**, *72-A*, 299–304.
[b]Adapted from Johansen, K.; Daines, M.; Howey, T.; Helfet, D.; Hansen, S. T. *J. Trauma* **1990**, *30*(5), 568–572; discussion 572–573.

associated vascular injury. 24–70% of open fractures show growth based on derived microbiology data, even though likely 100% of open fractures are contaminated by bacteria, either foreign or normal skin flora. In the experience of Patzakis *et al.*,[204] simple fractures showed a rate of infection of 1.4% compared to 22.7% infection in grade III fractures, which mimics the data presented by Gustilo and Anderson[203] wherein up to 24% of complex open fractures were complicated by infection. Dellinger *et al.* supported that work through the finding that local fracture, requirement for blood transfussions, or polytrauma.[205] Antibiotic prophylaxis is nowadays initiated as soon as possible with cefazolin and augmented by gentamycin in grade III open fractures with addition of metronidazole in the case of soil/farm contamination. The duration of antibiotic treatment is less important, but 24–48 h seem appropriate. Radical debridement is usually as important as antibiotics, with all nonviable or potentially devascularized tissue being removed to minimize the necrotic area and therefore safe zone for bacterial growth.[206] Vascularity is the most important factor in determining infection and other complications after open fractures.[207]

Once infected, the presence of a foreign body, be it the intramedullary nail or the plate and screws, presents a unique and usettling problem. As already discussed, the predilection to biofilms as well as the immunosuppressed state in the immediate vicinity is further escalated by the presence of a fracture and instability. This is a different problem than the typical situation with joint replacements which will be discussed later – these implants can usually be removed with full functionality to the limb if the fracture integrity is somehow reestablished. Nevertheless, the same premise remains – an infection cannot be eradicated while infected hardware remains present.[208] Nevertheless, many orthopedic trauma surgeons believe that stability is more important than infection for ultimate fracture healing, and several studies, largely based on laboratory animal protocols,[209] support that hypothesis. As such, standard protocol usually dictates irrigation and debridement to minimize the bacterial load, suppressive antibiotics, with or without hardware exchange.[210] Reamed intramedullary nailing is usually the preferred method of fixation in long bone diaphyseal open fractures, even though external fixators are sometimes used for damage control.[211] Delayed conversion from external fixator to intramedullary nailing has been associated with increased risk of infection.[207] Nevertheless, Rightmire *et al.* report a rate of only 68% of infected complications with retained hardware after an open reduction and internal fixation progressing to union, with as many as 32% of cases requiring additional procedures. Even then, 38% of healed fractures required hardware removal for persistent infection, and another 21% developed a hardware associated infection later. Long-term suppressive antibiotics for more than 6 weeks after irrigation, improve the outcomes, but often fail in view of antibiotic resistance and resilient species. Based on DNA analysis, as many as 42% of fracture callus specimens show bacterial presence, with actual bacteria isolated from 14% of healing fractures.[212]

Such results remain unacceptable, and extensive work is underway to minimize those rates. This work has been used in civil fracture management, but becomes even more important in the battlefield setting, where military high energy gunshot wounds are automatically grade III. Even though fixation is the ultimate goal of management, the presence of the implant as a medium for bacterial survival is the unifying factor between trauma, spine, or arthroplasty.

6.609.5. Classification Schemes for Implant Infection

Attention to the timing of initial clinical presentation prompted a method of classifying periprosthetic infections as either early acute or late chronic.[213,214] This classification is based on several prospective and retrospective studies and introducing a couple of additional groups based on etiology and diagnosis.[139,215,216] Even though not complete, the



Figure 2 Open fractures. Gustilo *et al*. introduced an open fracture classification based largely on soft tissue injury. Type I fractures usually result from bone fragment disrupting the skin integrity, but the wounds are small and clearn, and the fracture is treated as close for all intense purposes (Top left: distal radius fracture with small overlying skin lac likely from small fragment penetration). Type II fractures have large skin wounds putting the patient at higher risk for contamination and subsequent infection (Top right: open ankle fracture with relatively clean wound). Type III fractures usually involve large soft tissue injuries and contamination. The differentiation between a IIIA and IIIB is dependent on the ability to close the wound and the requirement for skin graft/flaps (Bottom left: tibia and fibula fracture with large soft tissue defect over the anterior tibia). Type IIIC fractures are independent of soft tissue coverage but include vascular injury (Bottom right: ankle fracture dislocation with associated posterior tibial artery injury and absent pulses distally).

classification allows for a more pragmatic approach to diagnosis and subsequent treatment. Type I infections are identified as those clearly diagnosed by positive intraoperative culture obtained during revision surgery initially performed for aseptic loosening. Type II infections are acute, initiating within 4 weeks after implantation, associated with contamination during surgery, and presenting classical symptoms of fever, inflammation, and fluid/pus. Furthermore, type II can be separated into superficial (a) or deep (b) depending on the extension through the joint capsule. Type III infections are considered acute hematogenous in etiology due to the rapid deterioration of a previously normal joint. Onset usually starts later than 4 weeks with extension through the joint capsule. Finally, type IV infections are usually late, chronic infections that occur more than 4 weeks after primary implantation with sinus, induration, and joint involvement. Several of the groupings are relatively difficult to separate and do not hold validity in the current standard of practice. For example, classification as hematogenous infection may be difficult, as the presentation switches from acute to chronic depending on the duration of symptoms.[217,218] Later adaptations to this ranking system have changed the timing to define the breakdown between early and late infection at 6 weeks.[179] Furthermore, most of these classifications are overly simplistic and do not account for newer developments in the field of periprosthetic infection, including better understanding of biofilm biology, issues of drug resistance, and emerging challenges in diagnostic modalities. However, a discrete stratification of the patient population into groups provides a good scheme for developing a consistent strategy and standardizing the approach to periprosthetic infections.

6.609.6. Management of Periprosthetic Infection

The complexities associated with correct diagnosis is only the harbinger of the difficulties associated with successful treatment. Revision surgery is often indicated, although prosthesis retention with antibiotic therapy is a viable alternative in uncomplicated cases where acute presentation is within 4 weeks of initial surgery. Typically, the treatment of periprosthetic infection involves surgery with implant retrieval, extensive debridement and excision of contaminated tissue, one- or two-stage reimplantation, aggressive antibiotic therapy, and follow-up.[67,128,216,219–221] Long-term antibiotic suppression, arthrodesis, resection arthroplasty, and amputation are reserved for the extremely difficult case where other alternatives fail.

Currently, antibiotics are the only available noninvasive method for combating an active infection and are always used regardless of the chosen strategies.[222,223] However, once infection is established, common antibiotic combinations have limited effect.[188] Therefore, maximum impact is achieved only by prophylactic use of antibiotics before or during primary arthroplasty thereby allowing more stringent sterility measures. Perioperative antibiotics are now the standard and predosing is called for in patients with associated comorbidities. However, the antibiotics selection is often not the drug with best activity against adherent bacteria in biofilms.[128,224] The choice is complicated as, due to the involvement of biofilms in implant infections, common susceptibility tests are not good predictors of biofilm antibiotic efficacy.[225–227] Rifampin is the only antibiotic with well-documented activity against adherent biofilms; however, used alone, it induces resistance in as little as 24 h.[228,229] Rifampin in combination with fusidic acid showed 55% success against MRSA[230,231] and thus could be a more suitable choice. Another good choice is the quinolone antibiotics due to their capability to penetrate biofilms and equilibrate across the bacterial population. Both ciprofloxacin and ofloxacin are often used to treat bone or joint infections[128,134,231]; levofloxacin is even more effective, but data on efficacy in bone are still limited. When used after surgical debridement, ciprofloxacin in combination with rifampin produced a 100% cure rate in one study; only a 58% cure rate was measured with ciprofloxacin monotherapy.[82] Rifampin can also be combined with trimethoprim-sulfamethoxazole, minocycline, and linezolid, even though efficacy data are limited at this time.[87,88,128] The increasing risk of resistance development constantly requires strategy reevaluation and demands new drugs for the treatment of orthopedic infections. Linezolid, daptomycin, and tigecycline are three relatively new but promising drugs being currently explored for treatment of periprosthetic infections, albeit patient data are still insufficient for pertinent recommendations.

During the management of infection, both the identity and susceptibility of the infectious organisms should be determined soon after empiric therapy is initiated. Despite availability of new super-drugs, a basic algorithm suggests use of vancomycin for gram-positive organisms in acute or chronic infections, while cephazolin and gentamycin are recommended for hematogenous contamination.[137] Furthermore, third of fourth-generation cephalosporin alone or in combination with vancomycin are recommended for gram-negative and mixed flora.[137] Clindamycin or a combination of ampicillin with sulbactam are efficient against anaerobes.[228,229] Treatment should be continued for a minimum of 4–6 weeks, which also coincides with the typical period of revascularization.[139,228,229] At the same time, drug rotation is crucial in minimizing resistance,[232] so a varying antibiotic algorithm is favored rather than the constant prescription of a single drug like vancomycin. Such a strategy may decrease the risk of resistance by decreasing the selective pressure of a single drug.[233] Interestingly, recent hypothesis on antibiotic resistance actually recommend early prophylactic use despite the perceived unnecessary treatment. Such prophylactic strategy may prevent advanced infection and therefore prevent excessive late use of antibiotics, ultimately decreasing the total antibiotic pressure on the bacteria in our environment. Despite improved antibiotic strategies in the face of emerging resistance, periprosthetic infection often requires revision surgery.

6.609.6.1. Surgical Approaches

When everything else fails or the associated risks are too high, surgery has shown the best results at treating and ultimately eradicating the associated infection. Surgical intervention allows direct removal of the biofilm, further excision of contaminated tissue, and washing with antibiotic solutions in high local concentrations. During the early postoperative days, superficial infection without joint capsule involvement can be managed with soft tissue resection and debridement,

which allows implant salvage. Antibiotic-laden cement beads containing tobramycin or vancomycin are often used within the wound for up to 2 weeks.[216] Such cement beads maintain a high local antibiotic concentration inhibitory to bacterial growth while allowing the immune system to eliminate persisters. Intravenous antibiotics are continued for a duration of 4–6 weeks. This approach can yield very good results, with eradication reported in 26–71% of patients.[139,234] Delay in treatment, however, converts the early acute infection to a chronic status, with surgery and aggressive management necessary if symptoms persist for more than 2 weeks.[234]

Implant removal is always involved in more severe infections where the joint capsule is involved or symptoms have a late chronic presentation. Depending on the severity of infection, risk factors, and the surgeon's ability to cleanly excise the surrounding tissue, a one-stage or two-stage revision is performed. If the infection is (1) relatively mild, without sinus tracts or induration, and (2) the cultured organisms show simple flora susceptible to typical antibiotics, which is rare nowadays, then a one-stage procedure is possible with relatively good success.[179,215,235] The rate of reinfection after one-stage procedures varies from 8 to over 12%, allowing over 80% survival of the implant.[179,236] One-stage procedures are less involved and provide faster recuperation for the patient. Despite that, with the high risk and costs of reinfection, and the very limited indications for a one-stage procedure, two-stage exchange revision is currently the standard for many physicians in the United States.[179] After removal of the infected prosthesis with extensive debridement and soft tissue excision, an antibiotic cement spacer is used to help eradicate the remaining bacteria. A second surgery is used to remove the spacer and implant a new joint prosthesis. The specific timing for the procedures is not clearly defined and ranges from 3 to 6 months.[237–239] The system is very complex as biofilms are difficult to eradicate, so intraoperative aspiration and culture is recommended during the extraction of the spacer.[240] Comparison studies of two-stage versus one-stage procedures suggest an advantage to the two-stage revision with reinfection rates of 3–6%, even though another study documented up to 22% infection with delayed surgery.[179,241–243]

Despite improved treatment, the rate of infection is higher after revision surgery than primary joint arthroplasty. Such a conclusion emphasizes the critical role of a successful primary surgery, with maximum precautions taken to eliminate infection. The consequences of an aggressive infection are further amplified by additional complications associated with revision surgery. Extensive bone loss can take place, which precludes additional revisions, leaving no choice but arthrodesis or even amputation. However, considering that two-stage procedures are the management step just before amputation, antibiotic laden cements are currently considered the gold standard for local antibiotic delivery in cases of periprosthetic infection.[244]

6.609.6.2. Antibiotic-Laden Bone Cements

Antibiotics are crucial, along with surgical intervention, for the ultimate eradication of infection. However, given intravenously, antibiotics have poor diffusion to the implanted joint, especially when the environment is complicated by the associated injury, hematoma, and loss of vascular supply after surgery.[229] Therefore, antibiotics are often needed in concentrations many times higher than their MIC in order to be efficient against biofilm formation.[177] Such antibiotic concentrations, though, are impossible to maintain systemically due to toxicity and clearance issues. A carrier mechanism is necessary to bypass the systemic route and locally provide the drug in controlled, constant dosages. Such a carrier should be simple in design without additional complications and costs for either the patient or the surgeon.

Most experts agree that there is no ideal local delivery method for targeting antibiotics to the site of implant infection, even though bone cements now serve that role.[244–246] Originally used for stabilization and improved integration of the joint prosthesis, bone cements are being phased out by the popularity of cementless joint replacement.[247] However, materials like methyl-methacrylate and calcium-phosphate are quite pliable and easy to mix, mold, and otherwise manipulate, allowing them to be formed into spacers, intramedullary fixation nails, beads, and implant coatings.[248–252] Such applications for bone cements were investigated as early as the 1970s, with slow accumulation of data and clinical information in favor of clinical use.[253] The system is quite flexible and often allows mixing the antibiotic of choice right in the operating room. The form can be molded to the local anatomy with antibiotic concentrations adjusted for the individual patient infection and systemic clearance.[237]

Despite the initial success of antibiotic-laden bone cements and extensive applications and indications for their use, the FDA had not approved this local antibiotic delivery system until recently. The four forms of bone cement currently approved by the FDA include tobramycin SimplexP (Stryker Howmedica Osteonics, Mahwah, NJ), gentamycin Palacos® G (Biomet, Inc., Warsaw, IN), and gentamycin SmartSet GHV and MHV (DePuy Orthopaedics, Inc., Warsaw, IN). PROSTLAC with 1 g vancomycin and 3.6 g tobramycin (DePuy Orthopaedics, Inc., Warsaw, IN) is another system currently approved as a combination antibiotic therapy with reasonable gram-positive and gram-negative coverage. Industrialization of the process allows for reproducibility and standardization, eliminating inconsistent mixtures, and variations in texture or porosity. As a result, recent data from two-stage arthroplasty procedures further support use of antibiotic-laden bone cement as the best available management.

Unfortunately, while achieving supratherapeutic concentrations of antibiotic at the insertion site, antibiotic-laden cements are often associated with tissue toxicity due to the initial high antibiotic elution profile.[254–256] Multiple studies have clearly documented inhibition of bone cell proliferation and maturation, leading to possible inhibition of bone healing and osseointegration.[257] Several cases have even reported systemic toxicity associated with vancomycin and tobramycin-laden bone cements due to acute renal failure.[258] Such complications are mainly due to the pharmacokinetics of bone cements, which are difficult to control. The delivery of antibiotics depends on concentration gradients, which often fluctuate with the immediate host environment. That environment is inherently unstable due to local trauma in surgery, patient to patient anatomical differences, fluid flow, and changes in physiological electrolytes. Current elution data show an immediate burst of antibiotics to very high levels

within the first 24 h after implantation, which is followed by rapid depletion and exhaustion of antibiotics in the first days.[256,259,260] In fact, the cement material itself is a great biomaterial for bacterial colonization and propagation of biofilms.[261,262] The subsequent drop to sub-MIC concentration of antibiotic induces an environment conductive to resistance development within surviving persisters.[263–265] In addition, the popular methyl-methacrylate cement is highly exothermic during the curing process which may inactivate temperature sensitive antibiotics like vancomycin. Furthermore, no matter how efficient the local delivery systems may be, they themselves produce additional pain and disability, requiring more bone loss, prolonged lack of mobility, and additional surgery to replace the biomechanically inappropriate spacer with a true joint replacement. Thus, while these cements have proven to be powerful tools against established infection, their complications limit their utility.

6.609.6.3. Self-Protective Implants

New advances in biomaterials and biotechnology are rapidly visible in medical designs and stimulate the science behind novel concepts like 'smart' implants.[6,261,266] New implant coatings and direct surface modifications interact with cell surface proteins like integrins to modulate cell survival, proliferation, differentiation, and signaling.[267–270] They take advantage of current biomolecular concepts in order to target specific cellular responses at the cell signaling level.[267] However, industrial production of these biomaterials and their subsequent introduction into mainstream medicine has been hampered by the complexity of proposed technologies. Using classical methods in chemistry and engineering, synthesis of such materials is difficult to control and practically impossible to reproduce with uniform consistency.[262] To overcome limitations in research and development, new directives explore self-assembly and autonomous organization of molecules based on entropy.[271,272] A fresh approach requires nanoscale designs and robotics.[262] Such systems borrow and apply concepts developed in nature over many evolutionary eons. As an example, complex arrangements in the quaternary structure of proteins or self-assembly of membranes require simple physical interactions with reproducible products. Such interactions are often reversible and, thus, allow extensive modulation depending on the interplay and balance of involved molecules. Therefore, such complexes can be further modified to respond to external cues, like the change in acid-base balance or temperature, resulting in 'smart' biomaterials that monitor their environment.[262] Despite the application of such technology to further improve osseointegration, very little is done in the area of infection prevention.[267]

Currently, only a few applications have targeted incorporation of antibiotics into surface coatings directly deposited onto the implant.[273–275] Most of these applications build on the information learned from antibiotic-laden bone cements and provide an initial protective barrier for infection.[276–278] Current protocols include poly-D,L-lactide, calcium phosphate, or carbonated hydroxyapatite antibiotic coatings. Other direct techniques attempt to physically modify the surface for antibiotic adsorption or simply dip the implant in antibiotic producing a transient coating.[80,278–280] The coating is a local delivery system that provides targeted release into the periimplant space and allows use of high antibiotic concentrations while minimizing the risk of systemic toxicity. Still, these surface coatings are not radically different from antibiotic-laden bone cements, and, thus, they are associated with the same problems that affect elution technologies in general. Specifically, the release of antibiotics from the surface coating depends on concentration gradients, resulting in the initial burst of antibiotic with sub-MIC delivery at later times. Newer methods have attempted to improve control by introducing various biopolymers like ceramics and bioglasses.[27,281–283] These novel materials use improved assembly chemistry to control pore size and tortuosity to allow programmed release of the antibiotic over longer periods of time. Despite that, the duration of release is still limited, leaving the implant susceptible to late infection and contamination through hematogenous spread. Simultaneously, it is important to consider that late infection is often the most common presentation, and it is inherently difficult to treat.[220,284,285] Therefore, although elution technologies provide an excellent local antibiotic delivery system and represent an excellent strategy for the immediate postoperative period, they cannot deal with the more complex aspects of late periprosthetic infections. Even with newer, improved surface coatings, the issue of periprosthetic infection remains largely unsolved.

6.609.7. The Future of Implant Design in Orthopedic Infection

Even though immediate postoperative strategies help decrease the rate of acute infection, the most dreadful complications are often associated with late infection. The successful prevention and eradication of periprosthetic infection requires a more permanent solution for implant protection. Such technology should directly integrate biological defenses in the implant design, making protection feasible for the life of the replacement prosthesis.[128,286,287] Furthermore, the antibiotic dose should be controlled, specific against target microorganisms, and devoid of toxicity in both the immediate and distant host environment. Recent scientific progress in biomolecular interactions and nanoscale engineering provides new inspiration for medical implant designs that may have the potential to deal with infection.[6,262] Biodegradable thermoplastic elastomers with changing shape, biological sensors, and electroactive polymers that replace muscles provide a vast background for further development and translation into orthopedic implants.[265,266,288] A true cooperation between biology, chemistry, biomaterial science, and engineering can produce an implant that will resist bacterial colonization and thus prevent the survival of persisters within resistant biofilms.

6.609.8. Nanomolecular Permanent Modification of Biomaterials

In fact, we have been working on such a system that incorporates antibiotics not as a coating, but rather as a nanoscale permanent modification of the implant surface that makes the implant resistant to bacterial colonization.[289] We have

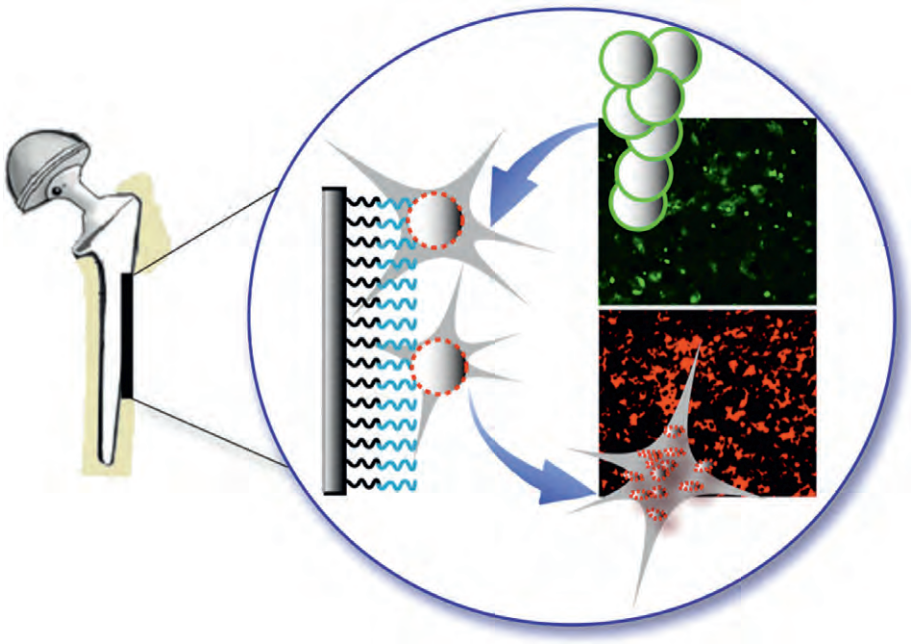

Figure 3 Smart implant. Antibiotic surfaces directly interact with their environment. Live bacteria coming in contact with the implant (SYTO® 9 green fluorescent nucleic stain) coming into contact with the surface die as a result of cell wall lysis (red fluorescent propidium iodide stain).

previously described the covalent attachment of antibiotics to the surface of titanium commonly used in surgical devices. We hypothesized that direct bonding of the antibiotics onto implant materials would provide a nanoscale stable surface that would prevent the aforementioned bacterial colonization and therefore prevent the progression of infection (Figure 3). We have, in multiple publications, presented the accomplishments of our group over the last 5 years in this regard.[176,290–292]

The chemistry was initially described for vancomycin but other antibiotics and biological compounds can be tethered using the same mechanism. In addition, the underlying surface is not limited to metallic materials but can easily be extended to silicone, plastic surfaces, synthetic vascular grafts, and potentially, ceramics, allowing extension of this technology for use in other medical fields such as plastics, vascular, cardiothoracic surgery, or general medicine. We have shown extensive antibiotic coverage on the surface and vancomycin remained present even after multiple challenges with very high bacterial counts. The antibiotic retained its bactericidal properties after linkage and showed potent and consistent activity when challenged with both *S. aureus* and *S. epidermidis*. Other currently available technologies attempt to prevent surface inhibition by including the antibiotic in an adsorbed or chemisorbed layer. The drug is then eluded from the material at variable kinetics dependent on concentration gradients, and may rapidly achieve levels that are toxic to the immediate bone environment.[257,293] The proposed antibiotic surface raises similar concerns due to the permanent nature of the modification, despite no perceived elution of antibiotics. Nevertheless, musculoskeletal cells showed normal colonization of the implant, indicating strong adherence and subsequent differentiation and maturation. Both osteoblastic and chondrocytic cell lines show normal morphology and metabolism capable of mineral or proteoglycan deposition respectively.

6.609.8.1. Feasibility of the Concept

A final test of feasibility involves testing in a mammalian system to simulate the clinical environment. The proposed vancomycin-modified rods inhibited microbial colonization of the surface, as observed by quantifying the adherent bacterial numbers. Furthermore, bone infection and the associated bone destruction was inhibited in the femora containing modified rods, while same implants supported normal fracture healing and bone repair. Interestingly, we have shown that both preoperative contamination of the implant during handling and the intraoperative contamination of the femoral canal can be effectively curtailed using the proposed implant. The material inhibits bacterial colonization at all stages in the clinical process. Furthermore, the vancomycin-modified implant showed such results under conditions that would typically lead to septicemia and shock in humans due to the high numbers of introduced bacteria.

These promising accomplishments continue to advocate for the potential use of antibiotic-modified implants in preventing and eradicating infection. The current data are far from complete but presents the necessary proof of principle that the technology is feasible and highly effective at controlling infection. The chemistry is simple and easy to reproduce, with the cost of reagents not exceeding $20 per synthesis. The antibiotic remains stable in the face of demanding environments and inhibits bacterial proliferation both *in vitro* and *in vivo*, while still allowing bone cell proliferation and adherence. In recent years, we have upscaled our technology to allow modification of plates, screws, and intramedullary nails used in clinical practice. The technology is currently being adapted for hip prosthesis to be used in canine and ovine models in order to closer approximate the human geometry. Additional animal experiments are in process in order to clarify the specific limits

of the surface with regard to bacterial dose, temporal survival *in vitro*, and osteointegration. We are encouraged by the early animal data and believe that this implant has great promise for use in clinical practice. In fact, the project anticipates the initiation of clinical trails in order to evaluate the efficacy of the proposed implant in its targeted application. With such exciting prospects, the current work has already set a pioneering template for a new generation of smart implants that use surface agents as a tool to control and alter the biomaterial–host interface. Such implants can truly shift the balance stated in Gristina's hypothesis,[162,170,294] allowing host cells to finally conquer the implant surface in defiance of quickly adapting infectious organism.

6.609.9. Conclusions

Joint replacement remains one of the most successful procedures in orthopedic surgery. There is a constantly rising demand for these procedures and, therefore, subsequent increase in the prevalence of complications. Despite immense progress in prosthesis design, periprosthetic infection remains one of the most common complications and one that has dreadful consequences that may lead to arthrodesis, amputation, and in rare cases, even death. The very nature of the implant and its propensity for bacterial colonization by small numbers of bacteria predisposes the implant to biofilm formation. Biofilms are resistant to available treatment strategies and, even when seemingly eradicated, leave behind persisting bacteria that are capable of reinitiating an infection long after the initial presentation. Furthermore, they complicate the diagnosis, with no clear-cut diagnostic assay or algorithm. Subjective decisions are usually required and they must take into account a panel of positive or negative tests and the clinical presentation. The inconsistent evaluation and variability in the present diagnostic algorithms make it difficult to standardize a diagnostic classification that would allow uniform management decisions. Revision surgery and antibiotics are quite successful, yet the risk of reinfection is more than tripled after such procedures. Even with successful treatment, the effort required to combat periprosthetic infections leads to more bone loss, excessive pain and disability, and immense cost for both the patient and the health care system at large. A new solution is needed to not only address the problem of infection by treating it, but prevent infection occurrence which would simultaneously improve all aspects of joint replacement. Smart implants and antimicrobial surfaces are the only answer that currently show reasonable success and that have immense potential. Perhaps, after more than a century of experimentation with joint replacements, the future is brighter than ever.

References

1. Greenland, S.; Finkle, W. D. *Ann. Epidemiol.* **2000**, *10*(4), 205–213.
2. Howe, L.; Palmer, P.; Barrett, V. *Br. Dent. J.* **1999**, *187*(11), 593–600.
3. Moradian-Oldak, J.; Wen, H. B.; Schneider, G. B.; Stanford, C. M. *Periodontol* **2006**, *2000*(41), 157–176.
4. Einhorn, T. A. *Clin. Orthop. Relat. Research*. **1998**, (355 Suppl.), S7–S21.
5. Herndon, J. H.; Davidson, S. M.; Apazidis, A. *J. Bone Joint Surg. Am.* **2001**, *83*(7), 1097–1105.
6. Lendlein, A.; Kratz, K.; Kelch, S. *Med. Device Technol.* **2005**, *16*(3), 12–14 PM:15871417.
7. Schoenborn, C.; Vickerie, J.; Powell-Griner, E. *Vital Health Stat.* **2006**, *370*, 1–32.
8. Fuchs, V.; Sox, C. *Health Aff.* **2001**, *20*(5), 30–42.
9. Moss, A. J.; Hamburger, S.; Moore, R. M.; Jeng, L. L. *Natl. Cent. Health Stats.* **1991**, *191*, 5–27.
10. White, L. M.; Kim, J. K.; Mehta, M. *Radiology* **2000**, *215*(1), 254–262.
11. *Canadian Joint Replacement Registry 2003 Annual Report*; Canadian Institute for Health Information, 2003.
12. Consensus Panel, N. I. H. *J. Bone Joint Surg. Am.* **2004**, *86*(6), 1328–1335.
13. Drees, P.; Eckardt, A.; Gay, R.; Gay, S.; Huber, L. *Nat. Clin. Pract. Rheumatol* **2007**, *3*(3), 165–167.
14. Fear, J.; Hillman, M.; Chamberlain, M. A.; Tennant, A. *Br. J. Rheumatol.* **1997**, *36*(1), 74–76.
15. Nordon, J. I. *Med. J. Aust.* **2005**, *182*(6), 312.
16. Anglen, J. *Tech. Orthopaedics.* **2002**, *17*(4), 506–514.
17. Soni, A. *Med. Expend. Panel Surv.* **2007**, *167*, 1–6.
18. Kurtz, S.; Mowat, F.; Ong, K.; Chan, N.; Lau, E.; Halpern, M. *J. Bone Joint Surg. Am.* **2005**, *87*, 1487–1497.
19. Birrell, F.; Johnell, O.; Silman, A. *Ann. Rheum. Dis.* **1999**, *58*(9), 569–572.
20. Freedonia Group 2005. Implantable Medical Devices to 2009. Strategic Report.
21. Charnley, J.; Eftekhar, N. *Br. J. Surgery.* **1969**, *56*(9), 641–649.
22. Charnley, J. *Clin. Orthop.* **1970**, (72), 7–21.
23. Lynch, M.; Esser, M.; Wroblewski, B. *J. Bone Joint Surg.* **1987**, *69B*, 355–359.
24. Hench, L. L. *Biomater. Med. Devices Artif. Organs* **1979**, *7*(2), 339–350.
25. Fruh, H. J.; Liebetrau, A.; Bertagnoli, R. *Orthopade* **2002**, *31*(5), 454–458.
26. Gough, J. E.; Notingher, I.; Hench, L. L. *J. Biomed. Mater. Res.* **2004**, *68*(4), 640–650.
27. Saravanapavan, P.; Jones, J. R.; Verrier, S.; *et al. Biomed. Mater. Eng.* **2004**, *14*(4), 467–486.
28. Shim, H. S.; Agarwal, N. K.; Haubold, A. D. *J. Bioeng.* **1976**, *1*(1), 45–50.
29. Giavaresi, G.; Fini, M.; Cigada, A.; *et al. J. Biomed. Mater. Res. A* **2003**, *67*(1), 112–120.
30. Krause, A.; Cowles, E. A.; Gronowicz, G. *J. Biomed. Mater. Res.* **2000**, *52*(4), 738–747.
31. Nishiguchi, S.; Fujibayashi, S.; Kim, H. M.; Kokubo, T.; Nakamura, T. *J. Biomed. Mater. Res. A* **2003**, *67*(1), 26–35.
32. Rohner, D.; Meng, C. S.; Hutmacher, D. W.; Tsai, K. T. *Int. J. Oral Maxillofac. Surg.* **2003**, *32*(4), 383–389.
33. Spriano, S.; Bosetti, M.; Bronzoni, M.; *et al. Biomaterials* **2005**, *26*(11), 1219–1229.
34. Williams, D. *Med. Device Technol.* **2001**, *12*(7), 8–11.
35. Bagno, A.; Di Bello, C. *J. Mater. Sci. Mater. Med.* **2004**, *15*(9), 935–949.
36. Kurella, A.; Dahotre, N. B. *J. Biomater. Appl.* **1920**, (1), 5–50.
37. Nanci, A.; Wuest, J. D.; Peru, L.; *et al. J. Biomed. Mater. Res.* **1998**, *40*(2), 324–335.
38. Ronold, H. J.; Lyngstadaas, S. P.; Ellingsen, J. E. *J. Biomed. Mater. Res. A* **2003**, *67*(2), 524–530.
39. Wojcik, S. M.; Puleo, D. A. *Biomed. Sci. Instrum.* **1997**, *33*, 166–171.
40. An, Y. H.; Bradley, J.; Powers, D. L.; Friedman, R. J. *J. Bone Joint Surg. Br.* **1997**, *79*(5), 816–819.
41. El Ghannam, A. R.; Ducheyne, P.; Risbud, M.; *et al. J. Biomed. Mater. Res. A* **2004**, *68*(4), 615–627.
42. Hansson, K. M.; Tosatti, S.; Isaksson, J.; *et al. Biomaterials* **2005**, *26*(8), 861–872.
43. Kim, H. W.; Knowles, J. C.; Salih, V.; Kim, H. E. *J. Biomed. Mater. Res. B Appl. Biomater.* **2004**, *71*(1), 66–76.
44. Ng, B. S.; Annergren, I.; Soutar, A. M.; Khor, K. A.; Jarfors, A. E. *Biomaterials* **2005**, *26*(10), 1087–1095.
45. Burns, L. *Health Aff.* **2006**, *25*, 241–251.
46. *OR Manager* **2001**, *17*(12), 1 8–10.
47. Berger, R. A.; Jacobs, J. J. *Am. Acad. Orthop. Surg. Bull.* **1996**, *44*(1), 1.
48. Ferdinand, M. *J. Healthc. Mater. Manage.* **1994**, *12*(11), 20–25.
49. Phillips, K. *J. Healthc. Resour. Manage.* **1995**, *13*(7), 40.
50. Wagner, M. *Mod. Healthc.* **1993**, *23*(4), 34.
51. Chen, L.; Evans, D.; Evans, T.; *et al. World Health Rep.* **2006**, *1*, 1–237.
52. Ong, K.; Mowat, F.; Chan, N.; Lau, E.; Halpern, M.; Kurtz, S. *Clin. Orthop. Relat. Res.* **2006**, *446*, 22–28.
53. Bren, L. *FDA Consum. Mag.* **2004**, *1335C*, 1.
54. NIH consensus statement on total knee replacement. *NIH Consens. State Sci. Statements* **2003**, *20*(1), 1–34.

55. Zhan, C.; Kaczmarek, R.; Loyo-Berrios, N.; Sangl, J.; Bright, R. *J. Bone Joint Surg. Am.* **2007**, *89*, 526–533.
56. Kinkel, S.; Kessler, S.; Mattes, T.; Reichel, H.; Kafer, W. *Z. Orthop. Ihre Grenzgeb.* **2007**, *145*(1), 91–96.
57. Lubbeke, A.; Katz, J.; Perneger, T.; Hoffmeyer, P. *J. Rheumatol.* **2007**, *34*(2), 394–400.
58. Amin, A.; Clayton, R.; Patton, J.; Gaston, M.; Cook, R.; Brenkel, I. *J. Bone Joint Surg. Br.* **2006**, *88*(10), 1321–1326.
59. Kim, Y.; Morshed, S.; Joseph, T.; Bozic, K.; Ries, M. *Clin. Orthop. Relat. Res.* **2006**, *453*, 142–146.
60. Vincent, H.; Vincent, K.; Lee, L.; Alfano, A. *Clin. Rehabil.* **2007**, *21*(2), 182–190.
61. Hervey, S.; Purves, H.; Guller, U.; Toth, A.; Vail, T.; Pietrobon, R. *J. Bone Joint Surg. Am.* **2003**, *85*(9), 1775–1783.
62. Solomon, D.; Losina, E.; Baron, J.; *et al. Arthritis Rheum.* **2002**, *49*(9), 2436–2444.
63. Feinglass, J.; Koo, S.; Koh, J. *Clin. Orthop. Relat. Res.* **2004**, *429*, 279–285.
64. Barrack, R.; McClure, J.; Burak, C.; Clohisy, J.; Parvizi, J.; Hozack, W. *Clin. Orthop. Relat. Res.* **2006**, *453*, 173–177.
65. Cierny, G., III; DiPasquale, D. *Clin. Orthop. Relat. Research.* **2002**, 23–28.
66. Dobzyniak, M.; Fehring, T.; Odum, S. *Clin. Orthop. Relat. Res.* **2006**, *447*, 76–78.
67. Duggan, J. M.; Georgiadis, G. M.; Kleshinski, J. F. *Infect. Med.* **2001**, *18*, 534–541.
68. Kim, Y. *J. Bone Joint Surg. Br.* **2005**, *87*, 623–627.
69. McPherson, E. J.; Woodson, C.; Holtom, P.; Roidis, N.; Shufelt, C.; Patzakis, M. J. *Clin. Orthop. Relat. Res.* **2002**, *1*, 8–15.
70. Puolakka, T. J.; Pajamaki, K. J.; Halonen, P. J.; Pulkkinen, P. O.; Paavolainen, P.; Nevalainen, J. K. *Acta Orthop. Scand.* **2001**, *72*, 433–441.
71. Alfonso, D.; Toussaint, R.; Alfonso, B.; Strauss, E.; Steiger, D.; Di Cesare, P. *Am. J. Orthop.* **2006**, *35*, 503–510.
72. Brems, J. J. *Instr. Course Lect.* **2002**, *51*, 29–39.
73. Clough, J. D. *Cleve. Clin. J. Med.* **2003**, *70*(4), 280.
74. Davenas, J.; Thevenard, P.; Philippe, F.; Arnaud, M. N. *Biomol. Eng.* **2002**, *19*(2–6), 263–268.
75. LeGeros, R.; Craig, R. *J. Bone Miner. Res.* **1993**, *8*, S583–S596.
76. Najafpour, H. D.; Suzina, A. H.; Nizam, A.; Samsudin, A. R. *Med. J. Malays.* **2004**, *59*, 121–122.
77. Stangl, R.; Pries, A.; Loos, B.; Muller, M.; Erben, R. G. *J. Biomed. Mater. Res. A* **2004**, *69*(3), 444–453.
78. Baumann, B.; Rader, C.; Seufert, J.; *et al. Acta Orthop. Scand.* **2004**, *75*(3), 295–302.
79. Kumazawa, R.; Watari, F.; Takashi, N.; Tanimura, Y.; Uo, M.; Totsuka, Y. *Biomaterials* **2002**, *23*(17), 3757–3764.
80. Hayakawa, T.; Yoshinari, M.; Nemoto, K. *Biomaterials* **2004**, *25*(1), 119–127.
81. Kawai, H.; Shibata, Y.; Miyazaki, T. *Biomaterials* **2004**, *25*(10), 1805–1811.
82. Darouiche, R. O. *N. Engl. J. Med.* **2004**, *350*(14), 1422–1429.
83. Barrack, R. L. *Clin. Orthop. Relat. Research.* **1995**, *319*, 209–214.
84. Gomez, J.; Rodriguez, M.; Banos, V.; *et al. Enferm. Infecc. Microbiol. Clin.* **2003**, *21*(5), 232–236.
85. Bozic, K.; Ries, M. *J. Bone Joint Surg. Am.* **2005**, *87*(8), 1746–1751.
86. Campoccia, D.; Montanaro, L.; Arciola, C. R. *Biomaterials* **2006**, *27*(11), 2331–2339.
87. Trampuz, A.; Zimmerli, W. *Curr. Opin. Investig. Drugs* **2005**, *6*, 185–190.
88. Zimmerli, W.; Trampuz, A.; Ochsner, P. E. *N. Engl. J. Med.* **2004**, *351*(16), 1645–1654.
89. Bauer, T.; Parvizi, J.; Kobayashi, N.; Krebs, V. *J. Bone Joint Surg. Am.* **2006**, *88* (4), 869–882.
90. Nelson, C.; McLaren, A.; McLaren, S.; Johnson, J.; Smeltzer, M. *Clin. Orthop. Relat. Res.* **2005**, *437*, 25–30.
91. Somme, D.; Ziza, J. M.; Desplaces, N.; *et al. Joint Bone Spine* **2003**, *70*(6), 489–495.
92. Parvizi, J.; Ghanem, E.; Menashe, S.; Barrack, R.; Bauer, T. *J. Bone Joint Surg. Am.* **2006**, *88*, 138–147.
93. Musso, A. D.; Mohanty, K.; Spencer-Jones, R. *Postgrad. Med. J.* **2003**, *79*(936), 590–593.
94. Reid, G.; Bailey, R. R. *NZ Med. Journal.* **1996**, *109*(1016), 41–42.
95. Tunney, M. M.; Patrick, S.; Curran, M. D.; *et al. J. Clin. Microbiol.* **1999**, *37*, 3281–3290.
96. Tunney, M. M.; Patrick, S.; Curran, M. D.; *et al. Meth. Enzymol.* **1999**, *310*, 566–576.
97. Bi, Y.; Collier, T.; Goldberg, V.; Anderson, J.; Greenfield, E. *J. Orthop. Res.* **2002**, *16*(2082), 2091.
98. Greenfield, E.; Bi, Y.; Ragab, A.; Goldberg, V.; Nalepka, J.; Seabold, J. *J. Biomed. Mater. Res. B Appl. Biomater.* **2005**, *72*, 179–185.
99. Padgett, D.; Silverman, A.; Sachjowicz, F.; Simpson, R.; Rosenberg, A.; Galante, J. *J. Arthroplasty* **1995**, *10*, 420–426.
100. Tarkin, I. S.; Henry, T. J.; Fey, P. I.; Iwen, P. C.; Hinrichs, S. H.; Garvin, K. L. *Clin. Orthop. Relat. Res.* **2003**, *414*, 89–94.
101. Espehaug, B.; Engesaeter, L.; Vollset, S.; Havelin, L.; Langeland, N. *J. Bone Joint Surg. Am.* **1997**, *79*, 590–595.
102. Berbari, E. F.; Hanssen, A. D.; Duffy, M. C. *Clin. Infect. Dis.* **1998**, (27), 1247–1254.
103. Garvin, K. L.; Hanssen, A. D. *J. Bone Joint Surg.* **1995**, *77A*, 1576–1588.
104. Wilson, M.; Kelley, K.; Thornhill, T. *J Bone Joint Surg. Am.* **1990**, *72*, 878–883.
105. Poss, R.; Thornhill, T.; Ewald, F. *Clin. Orthop. Relat. Res.* **1984**, *182*, 117–126.
106. Peersman, G.; Laskin, R.; Davis, J.; Peterson, M. *Clin. Orthop. Relat. Res.* **2001**, *392*, 15–23.
107. Mahan, J.; Seligson, D.; Henry, S. L.; Hynes, P.; Dobbins, J. *Orthopedics* **1991**, *14*(3), 305–308.
108. Raahave, D. *Acta Orthop. Scand.* **1976**, *47*, 28–35.
109. Stone, I. E.; Dodson, T. B.; Bays, R. A. *Plast. Reconstr. Surg.* **1993**, *91*(1), 64–68.
110. Trampuz, A.; Widmer, A. *Curr. Opin. Infect. Dis.* **2006**, *19*, 349–356.
111. CDC, *Am. J. Infect. Control* **1999**, *27*(6), 520–532.
112. Jansen, B.; Peters, G. *Urologe Ausg. A* **1991**, *30*(5), 306–309.
113. Rafiq, I.; Gambhir, A.; Wroblewski, B.; Kay, P. *Int. Orthop.* **2006**, *30*, 532–535.
114. Castillo, J. C.; Anguita, M. P.; Torres, F.; *et al. Am. J. Cardiol.* **2004**, *93*(9), 1185–1187.
115. Lee, R.; Moon, M. R. *J. Thorac. Cardiovasc. Surg.* **2003**, *125*(3), 725–727.
116. Rijnders, B. J.; Van Wijngaerden, E.; Peetermans, W. E. *Clin. Infect. Dis.* **2002**, *35*(9), 1053–1058.
117. Rijnders, B. J.; Van Wijngaerden, E.; Wilmer, A.; Peetermans, W. E. *Clin. Infect. Dis.* **2003**, *36*(6), 743–748.
118. Arciola, C. R.; Campoccia, D.; Gamberini, S.; Donati, M. E.; Montanaro, L. *Biomaterials* **2004**, *25*(19), 4825–4829.
119. Fluckiger, U.; Ulrich, M.; Steinhuber, A.; *et al. Infect. Immun.* **2005**, *73*(3), 1811–1819.
120. Kandemir, O.; Oztuna, V.; Milcan, A.; *et al. Clin. Orthop. Relat. Research.* **2005**, *430*, 171–175.
121. O'Gara, J. P.; Humphreys, H. *J. Med. Microbiol.* **2001**, *50*(7), 582–587.
122. Vandecasteele, S. J.; Peetermans, W. E.; Merckx, R.; Van Eldere, J. *J. Infect. Dis.* **2003**, *188*(5), 730–737.
123. Zimmerli, W. *Best Pract. Res. Clin. Rheumatol.* **2006**, *20*, 1045–1063.
124. Ritter, M. *Clin. Orthop. Relat. Res.* **1999**, *369*, 103–109.
125. Dimick, J.; Welch, H.; Birkmeyer, J. *JAMA* **2004**, *292*, 847–851.
126. Ritter, M. A.; Eitzen, H. E.; Hart, J. B.; French, M. L. *Clin. Orthop. Relat. Res.* **1980**, *153*, 204–209; PM:7449218.
127. Stewart, G.; Stewart, P.; Nott, M.; Long, G. *Aust. J. Rural Health* **2006**, *14*, 253–257.
128. Zimmerli, W.; Ochsner, P. E. *Infection* **2003**, *31*(2), 99–108.
129. Kingston, R.; Kiely, P.; McElwain, J. P. *J. Infect.* **2002**, *45*(4), 243–245.
130. Rose, R. *West Indian Med. J.* **2003**, *52*, 317–320.
131. Curry, S.; Phillips, H. *J. Arthroplasty* **2002**, *17*, 111–113.
132. Drangsholt, M. *J Bone Joint Surg. Am.* **1998**, *80*, 1394–1395.
133. Costerton, W.; Veeh, R.; Shirtliff, M.; Pasmore, M.; Post, C.; Ehrlich, G. *J. Clin. Investig.* **2003**, *112*(10), 1466–1477.
134. Trampuz, A.; Zimmerli, W. *Injury* **2006**, *37*, S59–S66.
135. Goodrich, L. *Vet. Clin. North Am. Equine Pract.* **2006**, *22*, 389–417.
136. Ninin, E.; Caroff, N.; Espaze, E.; *et al. Clin. Microbiol. Infect.* **2006**, *12*, 446–452.
137. Fulkerson, E.; Valle, C.; Wise, B.; Walsh, M.; Preston, C.; Di Cesare, P. *J. Bone Joint Surg. Am.* **2006**, *88*, 1231–1237.
138. Laffer, R.; Graber, P.; Ochsner, P.; Zimmerli, W. *Clin. Microbiol. Infect.* **2006**, *12*, 433–439.
139. Tsukayama, D.; Estrada, R.; Gustilo, R. *J Bone Joint Surg. Am.* **1996**, *78*, 512–523.
140. Gristina, A. G. *Science* **1987**, *237*(4822), 1588–1595.
141. Gristina, A. G.; Oga, M.; Webb, L. X.; Hobgood, C. D. *Science* **1985**, *228*(4702), 990–993.
142. Gristina, A. G.; Wagner, W.; Myrvik, Q. N.; Wagner, W.; Barth, E. In *High Performance Biomaterials – A Comprehensive Guide to Medical and Pharmaceutical Applications*; Szycher, M., Ed.; Technomic Publishing: Lancaster, Basel, 1991; pp 143–154.
143. Southwood, R.; Rice, J.; McDonald, P.; Hakendorf, P.; Rozenbilds, M. *J. Bone Joint Surg. Br.* **1985**, *67*, 229–231.
144. Southwood, R.; Rice, J.; McDonald, P.; Hakendorf, P.; Rozenbilds, M. *Clin. Orthop. Relat. Res.* **1987**, *224*, 33–36.
145. Wagner, C. N.; Shabaik, A. H. *J. Biomed. Mater. Res.* **1976**, *10*(5), 653–670.

146. Candlish, J. K. *Pathology* **1993**, *25*(2), 148–151.
147. Powers, K. A.; Kapus, A.; Khadaroo, R. G.; Papia, G.; Rotstein, O. D. *Surgery* **2002**, *132*(2), 391–398.
148. Zimmerli, W.; Lew, P.; Waldvogel, F. *J. Clin. Investig.* **1984**, *73*, 1191–1200.
149. Costerton, J. W.; Lewandowski, Z.; Caldwell, D. E.; Korber, D. R.; Lappin-Scott, H. M. *Annu. Rev. Microbiol.* **1995**, *49*, 711–745.
150. Costerton, J. W.; Stewart, P. S.; Greenberg, E. P. *Science* **1999**, *284*(5418), 1318–1322.
151. Donlan, R. M.; Costerton, J. W. *Clin. Microbiol. Rev.* **2002**, *15*(2), 167–193.
152. Stoodley, P.; Sauer, K.; Davies, D. G.; Costerton, J. W. *Annu. Rev. Microbiol.* **2002**, *56*, 187–209.
153. Wisniewska, K.; Garbacz, K.; Piechowicz, L. *Med. Dosw. Mikrobiol.* **2006**, *58*, 113–117.
154. Hall-Stoodley, L.; Stoodley, P. *Curr. Opin. Biotechnol.* **2002**, *13*, 228–233.
155. Konig, D. P.; Perdreau-Remington, F.; Rutt, J.; Stossberger, P.; Hilgers, R. D.; Plum, G. *Acta Orthop. Scand.* **1998**, *69*(5), 523–526.
156. Konig, D.; Schierholz, J.; Hilgers, R.; Bertram, C.; Perdeau-Remington, F.; Rutt, J. *Langenbecks Arch. Surg.* **2001**, *386*, 328–332.
157. Costerton, J. W.; Cheng, K. J.; Geesey, G. G.; *et al. Annu. Rev. Microbiol.* **1987**, *41*, 435–464.
158. Balaban, N.; Stoodley, P.; Fux, C.; Wilson, S.; Costerton, J.; Dell'Acqua, G. *Clin. Orthop. Relat. Res.* **2005**, *437*, 48–54.
159. Giacometti, A.; Cirioni, O.; Gov, Y.; *et al. Antimicrob. Agents Chemother.* **2003**, *47*(6), 1979–1983.
160. Leid, J.; Shirtliff, M.; Costerton, J.; Stoodley, P. *Infect. Immun.* **2002**, *70*, 6339–6345.
161. Stoodley, P.; Kathju, S.; Hu, F.; *et al. Clin. Orthop. Relat. Res.* **2005**, *437*, 31–40.
162. Gristina, A. G.; Hobgood, C. D.; Webb, L. X.; Myrvik, Q. N. *Biomaterials* **1987**, *8*(6), 423–426.
163. Stewart, P. S.; Costerton, J. W. *Lancet* **2001**, *358*(9276), 135–138.
164. Lewis, K. *Antimicrob. Agents Chemother.* **2001**, *45*, 999–1007.
165. Anwar, H.; Dasgupta, M. K.; Costerton, J. W. *Antimicrob. Agents Chemother.* **1990**, *34*(11), 2043–2046.
166. Costerton, J. W.; Lewandowski, Z.; DeBeer, D.; Caldwell, D.; Korber, D.; James, G. *J. Bacteriol.* **1994**, *176*(8), 2137–2142.
167. Bahar, G. *Mikrobiyol. Bül.* **2002**, *36*(3–4), 343–351.
168. Luppens, S. B.; Reij, M. W.; van der Heijden, R. W.; Rombouts, F. M.; Abee, T. *Appl. Environ. Microbiol.* **2002**, *68*(9), 4194–4200.
169. Neu, H. C. *Diagn. Microbiol. Infect. Dis.* **1989**, *12*(Suppl. 4), 109S–116S.
170. Gristina, A. G.; Naylor, P. T.; Myrvik, Q. N. *Infect. Dis. Clin. North Am.* **1990**, *4*(3), 391–408.
171. Neu, H. C. *Rev. Infect. Dis.* **1983**, *5*(Suppl 1), S9–S20.
172. Brooun, A.; Liu, S.; Lewis, K. *Antimicrob. Agents Chemother.* **2000**, *44*, 640–646.
173. Tenover, F. *Am. J. Med.* **2006**, *119*, 3–10.
174. Neu, H. C. *Am. J. Surg.* **1995**, *169*(Suppl. 5A), 13S–20S.
175. Roberts, M. E.; Stewart, P. S. *Microbiology* **2005**, *151*(Pt 1), 75–80.
176. Antoci, V., Jr.; Adams, C. S.; Hickok, N. J.; Shapiro, I. M.; Parvizi, J. *Clin. Orthop. Relat. Res.* **2007**, *461*.
177. Nickel, J. C.; Ruseska, I.; Wright, J. B.; Costerton, J. W. *Antimicrob. Agents Chemother.* **1985**, *27*(4), 619–624.
178. Hanssen, A. D.; Spangehl, M. J. *Clin. Orthop. Relat. Res.* **2004**, *420*, 63–71.
179. Toms, A.; Davidson, D.; Masri, B.; Duncan, C. *J. Bone Joint Surg. Br.* **2006**, *88*, 149–155.
180. Fitzgerald, R. J. *Orthopedics* **1995**, *18*, 833–835.
181. Rand, J.; Morrey, B.; Bryan, R. *Orthop. Clin. North Am.* **1984**, *15*, 491–504.
182. Trampuz, A.; Hanssen, A.; Osmon, D.; Mandrekar, J.; Steckelberg, J.; Patel, R. *Am. J. Med.* **2004**, *117*, 556–562.
183. Feldman, D.; Lonner, J.; Desai, P.; Zuckerman, J. *J. Bone Joint Surg. Am.* **1995**, *77*, 1807–1813.
184. Spangehl, M.; Masri, B.; O'Connell, J.; Duncan, C. *J Bone Joint Surg. Am.* **1999**, *81*, 672–683.
185. Di Cesare, P.; Chang, E.; Preston, C.; Liu, C. *J. Bone Joint Surg. Am.* **2005**, *87*, 1921–1927.
186. Williams, J. L.; Norman, P.; Stockley, I. *J. Arthroplasty* **2004**, *19*(5), 582–586.
187. Tunney, M. M.; Patrick, S.; Curran, M. D.; Ramage, G.; *et al. J. Clin. Microbiol.* **1999**, *37*(10), 3281–3290.
188. Tunney, M.; Dunne, N.; Einarsson, G.; McDowell, A.; Kerr, A.; Patrick, S. *J. Orthop. Res.* **2007**, *25*, 2–10.
189. Barrack, R.; Jennings, R.; Wolfe, M.; Bertot, A. *Clin. Orthop. Relat. Res.* **1997**, *345*, 8–16.
190. Bach, C. M.; Sturmer, R.; Nogler, M.; Wimmer, C.; Biedermann, R.; Krismer, M. *J. Arthroplasty* **2002**, *17*(5), 615–618.
191. Levitsky, K.; Hozack, W.; Balderston, R.; *et al. J. Arthroplasty* **1991**, *6*, 237–244.
192. Pakos, E.; Trikalinos, T.; Fotopoulos, A.; Ioannidis, J. *Radiology* **2007**, *242*, 101–108.
193. Pill, S.; Parvizi, J.; Tang, P.; *et al. J. Arthroplasty* **2006**, *21*, 91–97.
194. Zhuang, H.; Duarte, P.; Poudehnad, M.; *et al. J. Nucl. Med.* **2001**, *42*, 44–48.
195. Zhuang, H.; Chacko, T. K.; Hickeson, M.; *et al. Eur. J. Nucl. Med. Mol. Imaging* **2002**, *29*(10), 1328–1333.
196. Atkins, B.; Athanasou, N.; Deeks, J.; Crook, D.; Simpson, H.; Peto, T. *J. Clin. Microbiol.* **1998**, *36*, 2932–2939.
197. Della Valle, C.; Scher, D.; Kim, Y.; *et al. J. Arthroplasty* **1999**, *14*, 500–504.
198. Bauer, T. W.; Brooks, P. J.; Sakai, H.; Krebs, V.; Borden, L. *Orthopedics* **2003**, *26*(9), 929–930.
199. Lonner, J.; Desai, P.; Dicesare, P.; Steiner, G.; Zuckerman, J. *J. Bone Joint Surg. Am.* **1996**, *78*, 1553–1558.
200. Wong, Y.; Lee, Q.; Wai, Y.; Ng, W. *J. Arthroplasty* **2005**, *20*, 1015–1020.
201. Ko, P.; Ip, D.; Chow, K.; Cheung, F.; Lee, O.; Lam, J. *J. Arthroplasty* **2005**, *20*, 189–195.
202. Johansen, K.; Daines, M.; Howey, T.; Helfet, D.; Hansen, S. T. *J. Trauma* **1990**, *30*(5), 568–572 discussion 572-3.
203. Gustilo, R. B.; Anderson, J. T. *J. Bone Joint Surg. Am.* **1976**, *58*(4), 453–458.
204. Patzakis, M. J.; Wilkins, J. *Clin. Orthop Relat Res.* **1989**, *243*, 36–40.
205. Dellinger, E. P. *Rev. Infect. Dis.* **1991**, *13*(Suppl. 10), S847–S857.
206. Godina, M. *Plast. Reconstr. Surg.* **1986**, *78*(3), 285–292.
207. Zalavras, C. G.; Marcus, R. E.; Levin, L. S.; Patzakis, M. J. *Instr. Course Lect.* **2008**, *57*, 51–63.
208. Waldvogel, F. A.; Medoff, G.; Swartz, M. N. *N. Engl. J. Med.* **1970**, *282*(4), 198–206.
209. Worlock, P.; Slack, R.; Harvey, L.; Mawhinney, R. *Injury* **1994**, *25*(1), 31–38.
210. Rightmire, E.; Zurakowski, D.; Vrahas, M. *clin. Orthop. Relat. Res.* **2008**, *466*(2), 466–472.
211. Harwood, P. J.; Giannoudis, P. V.; van Griensven, M.; Krettek, C.; Pape, H. C. *J. Trauma* **2005**, *58*(3), 446–452; discussion 452–4.
212. Schmidt, A. H.; Jahangir, A. A. *J. Bone Joint Surg. Am.* **2009**, *91*(8), 2055–2066.
213. Fitzgerald, R. J. *Ann. NY Acad. Sci.* **1980**, *353*, 262–270.
214. Fitzgerald, R. J.; Nolan, D.; Ilstrup, D.; Van Scoy, R.; Washington, J. A., II; Coventry, M. *J. Bone Joint Surg. Am.* **1977**, *59*, 847–855.
215. Segawa, H.; Tsukayama, D.; Kyle, R.; Becker, D.; Gustilo, R. *J. Bone Joint Surg. Am.* **1999**, *81*, 1434–1445.
216. Tsukayama, D. T.; Goldberg, V. M.; Kyle, R. *J. Bone Joint Surg. Am.* **2003**, *85*, S75–S80.
217. Schmalzried, T.; Amstutz, H.; Au, M.; Dorey, F. *Clin. Orthop. Relat. Res.* **1992**, *280*, 200–207.
218. Silva, M.; Tharani, R.; Schmalzried, T. P. *Clin. Orthop. Relat. Res.* **2002**, *404*, 125–131.
219. Darouiche, R. O. *Clin. Infect. Dis.* **2003**, *36*(10), 1284–1289.
220. Hendriks, J. G.; van Horn, J. R.; van der Mei, H. C.; Busscher, H. J. *Biomaterials* **2004**, *25*(3), 545–556.
221. Lee, G. C.; Cushner, F. D. *Orthopedics* **2004**, *27*(Suppl. 6), s669–s673.
222. Kilgus, D. J.; Howe, D. J.; Strang, A. *Clin. Orthop. Relat. Research.* **2002**, *404*, 116–124.
223. Mohanty, S. S.; Kay, P. R. *J. Bone Joint Surg.* **2004**, *86*(2), 266–268.
224. Giulieri, S. G.; Graber, P.; Ochsner, P. E.; Zimmerli, W. *Infection* **2004**, *32*(4), 222–228.
225. Schwank, S.; Rajacic, Z.; Zimmerli, W.; Blaser, J. *Antimicrob. Agents Chemother.* **1998**, *42*, 895–898.
226. Widmer, A.; Frei, R.; Rajacic, Z.; Zimmerli, W. *J. Infect. Dis.* **1990**, *162*, 96–102.
227. Zimmerli, W.; Frei, R.; Widmer, A.; Rajacic, Z. *J. Antimicrob. Chemoterap.* **1994**, *33*, 959–967.
228. Frommelt, L. *Injury* **2006**, *37*, S87–S94.
229. Frommelt, L. *Orthopade* **2004**, *33*(7), 822–828.
230. Drancourt, M.; Stein, A.; Argenson, J.; Roiron, R.; Groulier, P.; Raoult, D. *J. Antimicrob. Chemoterap.* **1997**, *39*, 235–240.
231. Zimmerli, W.; Widmer, A.; Blatter, M.; Frei, R.; Ochsner, P. *JAMA* **1998**, *279*, 1537–1541.
232. Anderson, R. *Nat. Med.* **1999**, *5*, 147–149.
233. Sandiumenge, A.; Diaz, E.; Rodriguez, A.; *et al. J. Antimicrob. Chemoterap.* **2006**, *57*, 1197–1204.
234. Crockarell, J.; Hanssen, A.; Osmon, D.; Morrey, B. *J. Bone Joint Surg. Am.* **1998**, *80*, 1306–1313.
235. Lohmann, C.; Furst, M.; Niggemeyer, O.; Ruther, W. *Z. Rheumatol.* **2007**, *66*, 28–33.
236. Callaghan, J.; Katz, R.; Johnston, R. *Clin. Orthop.* **1999**, *369*, 139–143.

237. Anagnostakos, K.; Furst, O.; Kelm, J. *Antibiotic Impregnated PMMA Hip Spacers Curr. Status* **2006**, *77*(4), 628–637.
238. Durbhakula, S. M.; Czajka, J.; Fuchs, M. D.; Uhl, R. L. *J. Arthroplasty* **2004**, *19*(6), 768–774.
239. Yamamoto, K.; Miyagawa, N.; Masaoka, T.; Katori, Y.; Shishido, T.; Imakiire, A. *J. Orthop. Sci.* **2003**, *8*(6), 823–828.
240. Mont, M.; Waldman, B.; Hungerford, D. *J. Bone Joint Surg. Am.* **2000**, *82*, 1552–1557.
241. Colyer, R.; Capello, W. *Clin. Orthop.* **1994**, *298*, 75–79.
242. Elson, R. *Orthop. Clin. North Am.* **1993**, *24*, 761–767.
243. Garvin, K.; Gitzgerald, R. J.; Salvati, E.; *et al. Instr. Course Lect.* **1993**, *42*, 293–302.
244. Nelson, C. L. *Clin. Orthop. Relat. Res.* **2004**, *427*, 72–78.
245. Hoad-Reddick, D. A.; Evans, C. R.; Norman, P.; Stockley, I. *J. Bone Joint Surg. Br.* **2005**, *87*(2), 171–174.
246. McLaren, A. C. *Clin. Orthop. Relat. Res.* **2004**, *427*, 101–106.
247. Sanfilippo, J.; Austin, M. *Expert Rev. Med. Devices* **2006**, *3*, 769–776.
248. Diefenbeck, M.; Muckley, T.; HOfmann, G. *Injury* **2006**, *37*, S95–S104.
249. Mader, J. T.; Calhoun, J.; Cobos, J. *Antimicrob. Agents Chemother.* **1997**, *41*(2), 415–418.
250. Morimoto, Y.; Tatebayashi, S.; Imai, Y.; Kirita, T. *J. Oral Maxillofac. Surg.* **2005**, *63*(8), 1234–1238.
251. Paley, D.; Herzenberg, J. *J. Orthop. Trauma* **2002**, *16*, 723–729.
252. Taggart, T.; Kerry, R. M.; Norman, P.; Stockley, I. *J. Bone Joint Surg. Br.* **2002**, *84*(1), 70–72.
253. Buchholz, H.; Elson, R.; Engelbrecht, E.; Lodenkamper, H.; Rottger, J.; Siegel, A. *J. Bone Joint Surg. Br.* **1981**, *63*, 342–353.
254. Greene, N.; Holtom, P. D.; Warren, C. A.; *et al. Am. J. Orthop.* **1998**, *27*, 201–205.
255. McLaren, A. C.; Nelson, C. L.; McLaren, S. G.; DeCLerk, G. R. *Clin. Orthop. Relat. Res.* **2004**, *427*, 25–27.
256. Stevens, C. M.; Tetsworth, K. D.; Calhoun, J. H.; Mader, J. T. *J. Orthop. Res.* **2005**, *23*(1), 27–33.
257. Antoci, V., Jr.; Adams, C. S.; Hickok, N. J.; Shapiro, I. M.; Parvizi, J. *Clin. Orthop. Relat. Res.* **2007**, *462*.
258. Patrick, B.; Rivey, M.; Allington, D. *Ann. Pharmacother.* **2006**, *40*, 2037–2042.
259. Balint, L.; Koos, Z.; Horvath, G.; Szabo, G. *Orthopedics* **2006**, *29*, 432–436.
260. Garvin, K.; Feschuk, C. *Clin. Orthop. Relat. Res.* **2005**, *437*, 105–110.
261. Burny, F.; Donkerwolcke, M.; Moulart, F.; *et al. Med. Eng. Phys.* **2000**, *22*(7), 469–479.
262. Fairman, R.; Akerfeldt, K. *Curr. Opin. Struct. Biol.* **2005**, *15*, 453–463.
263. Dyce, J.; Olmstead, M. L. *Vet. Surg.* **2002**, *31*(6), 552–560.
264. Neut, D.; Van de, B. H.; Stokroos, I.; van Horn, J. R.; van der Mei, H. C.; Busscher, H. J. *J. Antimicrob. Chemother.* **2001**, *47*(6), 885–891.
265. Parvizi, J.; Antoci, V. J.; Hickok, N.; Shapiro, I. *Expert Rev. Med. Devices* **2007**, *4*, 55–64.
266. Lendlein, A.; Langer, R. *Science* **2002**, *296*(5573), 1673–1676; PM:11976407.
267. Hench, L. L.; Polak, J. M. *Science* **2002**, *295*(5557), 1014–1017.
268. Kroese-Deutman, H. C.; Ruhe, P. Q.; Spauwen, P. H.; Jansen, J. A. *Biomaterials* **2005**, *26*(10), 1131–1138.
269. Pihlainen, K.; Kostiainen, R. *J. Chromatogr. A* **2004**, *1033*(1), 91–99.
270. Schliephake, H.; Scharnweber, D.; Dard, M.; *et al. Clin. Oral Implants Res.* **2002**, *13*(3), 312–319.
271. Lehn, J. *Science* **2002**, *295*, 2400–2403.
272. Whitesides, G.; Grzybowski, B. *Science* **2002**, *295*, 2418–2421.
273. Lin, T.; Lu, F.; Conroy, S.; Sheu, M.; Su, S.; Tang, L. *Med. Device Technol.* **2001**, *12*, 26–30.
274. Radin, S.; Campbell, J. T.; Ducheyne, P.; Cuckler, J. M. *Biomaterials* **1997**, *18*(11), 777–782.
275. Radin, S.; Ducheyne, P.; Kamplain, T.; Tan, B. H. *Mater. Res.* **2001**, *57*(2), 313–320.
276. Ducheyne, P.; Van Raemdonck, W.; Heughebaert, J.; Heughebaert, M. *Biomaterials* **1986**, *7*(2), 97–103.
277. Stigter, M.; Bezemer, J.; de Groot, K.; Layrolle, P. *J. Control. Release* **2004**, *99*(1), 127–137.
278. Stigter, M.; de Groot, K.; Layrolle, P. *Biomaterials* **2002**, *23*(20), 4143–4153.
279. Dunn, D. S.; Raghavan, S.; Volz, R. G. *J. Biomed. Mater. Res.* **1993**, *27*(7), 895–900.
280. Lucke, M.; Schmidmaier, G.; Sadoni, S.; *et al. Bone* **2003**, *32*(5), 521–531.
281. Ducheyne, P. *J. Biomed. Mater. Res.* **1985**, *19*(3), 273–291.
282. Kovarik, R. E.; Haubenreich, J. E.; Gore, D. *J. Long Term Eff. Med. Implants* **2005**, *15*(6), 655–671.
283. Ohsawa, K.; Neo, M.; Okamoto, T.; Tamura, J.; Nakamura, T. *J. Mater. Sci. Mater. Med.* **2004**, *15*(8), 859–864.
284. Khardori, N.; Yassien, M. *J. Ind. Microbiol.* **1995**, *15*(3), 141–147.
285. Vinh, D. C.; Embil, J. M. *J. Long Term Eff. Med. Implants* **2005**, *15*(5), 467–488.
286. Parra-Ruiz, J.; Martinez, M.; Antelo-Lorenzo, R.; Hernandez-Quero, J. *J. Antimicrob. Chemother.* **2004**, *53*(5), 886–887.
287. Peck, K. R.; Kim, S. W.; Jung, S. I.; *et al. Chemotherapy* **2003**, *49*(4), 189–193.
288. Kim, J.; Nayak, S.; Lyon, L. *J. Am. Chem. Soc.* **2005**, *127*, 9588–9592.
289. Parvizi, J.; Wickstrom, E.; Zeiger, A. R.; *et al. Clin. Orthop. Relat. Res.* **2004**, *429*, 33–38.
290. Antoci, V.; Phillips, M. J.; Antoci, V., Jr.; Krackow, K. A. *J. Arthroplasty* **2009**, *24*.
291. Antoci, V., Jr.; King, S. B.; Jose, B.; *et al. J. Orthop. Res.* **2007***25*(7).
292. Parvizi, J.; Wickstrom, E.; Zeiger, A. R.; *et al. Clin. Orthop. Relat. Res.* **2004**, *429 Accessed 1912b*.
293. Kalteis, T.; Luring, C.; Gugler, G.; *et al. Z. Orthop. Ihre Grenzgeb.* **2004**, *142 Accessed 1911*.
294. Gristina, A. G.; Giridhar, G.; Gabriel, B. L.; Naylor, P. T.; Myrvik, Q. N. *Int. J. Artif. Organs* **1993**, *16*(11), 755–763.

6.610. Trends in Materials for Spine Surgery

M Marcolongo, S Sarkar, and N Ganesh, Drexel University, Philadelphia, PA, USA

© 2011 Published by Elsevier Ltd.

6.610.1.	**Introduction**	128
6.610.2.	**Anatomy and Physiology of the Spine**	128
6.610.2.1.	The Vertebral Column	128
6.610.2.2.	The Intervertebral Disc	129
6.610.2.3.	The Nucleus Pulposus	129
6.610.2.4.	The Annulus Fibrosus	129
6.610.2.5.	Intervertebral Disc Degeneration	130
6.610.3.	**Spinal Fusion**	131
6.610.3.1.	Metals for Spinal Cages and Interbody Spacers	132
6.610.3.2.	Polymers and Composites for Fusion Cages	132
6.610.3.3.	Wires, Tapes, and Cables in Spinal Fusion	133
6.610.3.4.	Pedicle Screws, Plates, Bands, and Rods for Fusion and Dynamic Stabilization	134
6.610.3.5.	Bioresorbable Materials for Spinal Fusion Implants	134
6.610.4.	**Total Disc Arthroplasty**	135
6.610.4.1.	Material Requirements	136
6.610.4.1.1.	Implant endplate	136
6.610.4.1.2.	Bone implant interface	136
6.610.4.1.3.	Bearing surfaces	136
6.610.4.1.4.	General material specifications	136
6.610.4.2.	Discontinued Artificial Discs	137
6.610.4.2.1.	Acroflex	137
6.610.4.3.	Currently Available Devices	137
6.610.4.3.1.	Charitè artificial disc	137
6.610.4.3.2.	ProDisc	138
6.610.4.3.3.	Maverick	139
6.610.4.3.4.	Flexicore	140
6.610.4.4.	Future Trends	140
6.610.5.	**Annulus Repair**	140
6.610.5.1.	Procedure	140
6.610.5.2.	Mechanical Role	140
6.610.5.3.	Reported Treatment Methods	141
6.610.5.3.1.	Suture techniques	141
6.610.5.3.2.	Sealant and bulking techniques	141
6.610.5.4.	Current Technologies	141
6.610.5.4.1.	Xclose™ tissue repair system	141
6.610.5.5.	Barrier Technologies	142
6.610.5.5.1.	Inclose™ surgical mesh system	142
6.610.5.5.2.	Barricaid® prosthesis	143
6.610.5.5.3.	SpineJet XL®	143
6.610.5.6.	Material Requirements	143
6.610.5.7.	Future Trends	144
6.610.6.	**Concluding Remarks**	144
References		144

Glossary

Discogenic back pain Discogenic back pain is also known as lumbar disc pain. The most frequent symptoms of discogenic back pain are lower back pain and spasms.

Fretting corrosion Fretting corrosion refers to corrosion damage at the asperities of contact surfaces. This damage is induced under load and in the presence of repeated relative surface motion and wear.

Hemangiomas An abnormal proliferation of blood vessels that may occur in any vascularized tissue.

Laminectomy Spine surgery that removea the portion of the bone arch on the dorsal surface of a vertebra.

Osteopenia A condition in which bone mineral density is lower than normal, but not low enough to be classified as osteoporosis.

Pseudo elasticity A reversible response to an applied stress, caused by a phase transformation between the austenitic and martensitic phases of a crystal.

Vertebroplasty and kyphoplasty Medical spinal procedures in which a material is injected through a small hole in the skin (percutaneously) into a fractured vertebra and hardens; the goal of the procedure is to relieve the pain caused by osteoporotic compression fractures.

Abbreviations

AF Annulus fibrosus
GAG Glycosaminoglycan
IVD Intervertebral disc
NP Nucleus pulposus
PG Proteoglycan
TDA Total disc arthroplasty

6.610.1. Introduction

The spine has two main purposes: (1) it must provide a strong mobile central axis to support the skeleton and (2) it must also provide protection for the delicate nerves that travel from the brain to the periphery. A balance between stability and flexibility are essential to achieve this dual purpose. Aging, injury, disease, and genetic conditions can disrupt this balance resulting in back pain with more than 60% of the population experiencing back pain throughout a lifetime.[1] Low back pain alone accounts for 2% of all US physician office visits.[2] Pain can be generated in the spine from damage to several anatomical elements including the vertebral bodies, intervertebral discs (IVDs), facet joints, dura of the nerve roots, ligaments, facia, and muscles.[3] Stabilization of the spine has been the major focus of surgical interventions to alleviate back pain.[4]

Interventional techniques have evolved from the earliest use of metal screws and plates to correct scoliosis adapted from peripheral extremity repair in the late 1950s.[5] Internal fixation of the spine using pedical screws was first introduced in 1959 by Boucher in Canada.[6] In the 1960s, the advent of bony fusion techniques greatly increased the success of these procedures and currently, advancements are still being made on materials choice and structural design of spinal internal fixation devices.[7] The IVD has also been a major focus in spinal procedures with the first surgeries on disc protrusion reported in 1934 by Mixter and Barr.[6] Current techniques in treating discogenic back pain include removal of disc material and replacement with prosthetic devices[8]; however, advances in knowledge of the IVD ultrastructure have led to recent investigations into the repair of individual IVD components, that is, nucleus replacements[9] and annulus repair technologies (see **Chapter 6.613, Nucleus Replacement**).[10] Recent advances in minimally invasive surgery have also made a large impact on spine surgery and the potential for novel therapies.

Most notable is the development of the vertebroplasty and kyphoplasty procedures developed in the late 1980s for the percutaneous treatment of vertebral fractures (see **Chapter 6.611, Injectable Bone Cements for Spinal Column Augmentation: Materials for Kyphoplasty/Vertebroplasty**).[11–13] The development of materials for spinal procedures has been greatly influenced by advances in technology that permit the visualization of spinal structures, innovations of novel surgical procedures, and a better understanding of the biology and structure of the native tissue. Early materials were adapted from procedures designed for the repair of bones and joints in the extremities; however, as more is understood about the unique structure and mechanical needs of the spine, novel materials are being developed for use in spine specific procedures. Tissue engineering and drug delivery have also motivated the development of new materials with porous and regenerative surfaces. This chapter outlines the current materials utilized in the major surgical interventions (spinal fusion, total disc replacement, and annulus repair) and spine pathologies as well as the future direction of material development.

6.610.2. Anatomy and Physiology of the Spine

6.610.2.1. The Vertebral Column

The human vertebral column or spine functions to transfer loads and bending moments of the head, trunk, and any external loads to the pelvis, allows sufficient physiological movement and flexibility of the upper body, and protects the spinal cord from dangers due to motion and trauma.[14] It also serves as protection to other vital internal organs and as a base of attachment for upper-body ligaments, tendons, and muscles. These functions help explain its form and structure.

The spine consists of 24 individual vertebrae, the sacrum, and the coccyx, and spans from the skull to the pelvis. The vertebrae are stacked on top of each other and are grouped into five distinct regions – there are 7 cervical vertebrae, 12 thoracic, 5 lumbar, 5 fused sacral, and 3 fused vertebrae that make up the coccyx (**Figure 1**). From posterior perspective, the spine appears to be straight, but lateral view shows four normal curves that mechanically serve to give the spinal column increased flexibility and shock-absorption ability.

The vertebral body is the primary weight bearing area, and adjacent vertebrae are connected by an IVD (**Figure 2**). The vertebral foramen is the large hole in the center of the vertebra that is surrounded by lamina, forming the spinal canal. The spinal cord runs through this opening and is protected by it. The spinous process protrudes from the central posterior region of the vertebra and acts as a connection point for ligaments. There

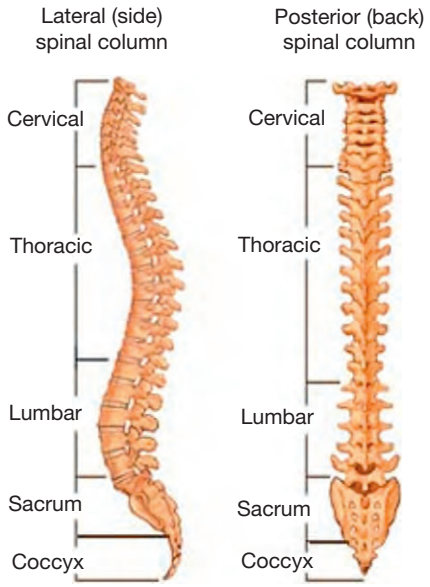

Figure 1 Regions of the human spine with respect to the vertebrae and corresponding intervertebral discs (http://healthbase.wordpress.com/2007/06/13/spinal-fusion-surgery/).

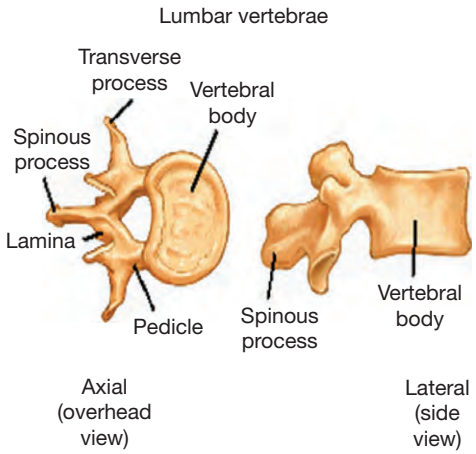

Figure 2 The lumbar vertebrae. Reproduced from Toida, T.; Kakinuma, N.; Toyoda, H.; Imanari, T. *Anal. Sci.* **1994**, *10*, 537–541.

are pairs of transverse processes which are orthogonal to the spinous process and provide attachment for the back muscles. There are also four facet joints on each vertebra that are found in pairs (one superior and one inferior), interlocking with adjacent vertebrae to provide stability to the spine. When osteoporosis occurs in the spine, vertebral collapse, or compression fractures, may occur (Figure 3.). Vertebral compression fractures may also be caused by hemangiomas, multiple myeloma, and osteolytic metastases.[15] Multiple fractures lead to a stooped or hunched posture, chronic pain, and loss of height.

6.610.2.2. The Intervertebral Disc

The IVD separates adjacent vertebrae and acts as a shock absorber, dissipating energy under loading. The disc is the largest avascular tissue in the human body requiring nutrients to enter and waste to be removed primarily through diffusion and fluid flow.[14] The disc structure is quite complex combining three distinct regions: the nucleus pulposus (NP), an inner gelatinous core; the annulus fibrosus (AF), a surrounding ordered fibrous structure; and the bony endplates that are partly cartilaginous and partly bony and serve as an interface between the disc and the vertebral bodies (Figure 4). The cellular content of the disc is very low, less than ~0.25% of tissue volume.[16] The extracellular disc matrix plays the main role in determining the mechanical properties of the disc.

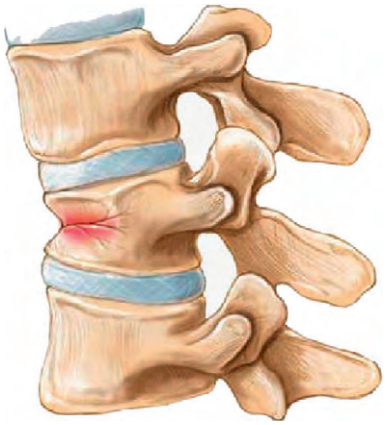

Figure 3 Vertebral compression fracture. Reproduced from Stryker-Interventional. 2008. Compression Fractures of the Spine. http://www.helpingbacks.com/spinalfractures.php.

6.610.2.3. The Nucleus Pulposus

The central NP region of the IVD is a gelatinous structure that is mostly water (77% of wet weight) but also contains a large constituent of proteoglycans (PGs) (14% of wet weight) which are composed of charged glycosaminoglycan (GAG) chains covalently attached to a protein core. Randomly organized collagen fibers are also present in the NP (about 4% of wet weight) and associate with the PGs to form a loose network.[17] Collagen fibers within the NP provide tensile strength while PGs create a large osmotic swelling pressure and draw water into the tissue (Figure 5). Charged groups on the GAG chains of the PGs carry with them mobile counter ions such as Na^+ which draw water into the tissue because of the osmotic imbalance generating a hydrostatic pressure within the NP.[18]

6.610.2.4. The Annulus Fibrosus

The AF of the IVD is a structure that serves to contain the gelatinous NP. The chemical composition of the AF comprises 65–90% wet weight of water, 50–70% dry weight of collagen, 10–20% dry weight of PGs, and noncollagenous proteins such as elastin.[19] The structure of the AF is laminate in nature, consisting of a minimum of 15 (posterior) and 25 (lateral) concentric layers. The layers are made up of type I collagen fibers which alternate in angles from 30° at the peripheral AF to 44° at the central AF with reference to the transverse plane of the disc (Figure 6). The concentric rings of the AF are referred to as lamellae, and the spaces between them as interlamellar septae.[19]

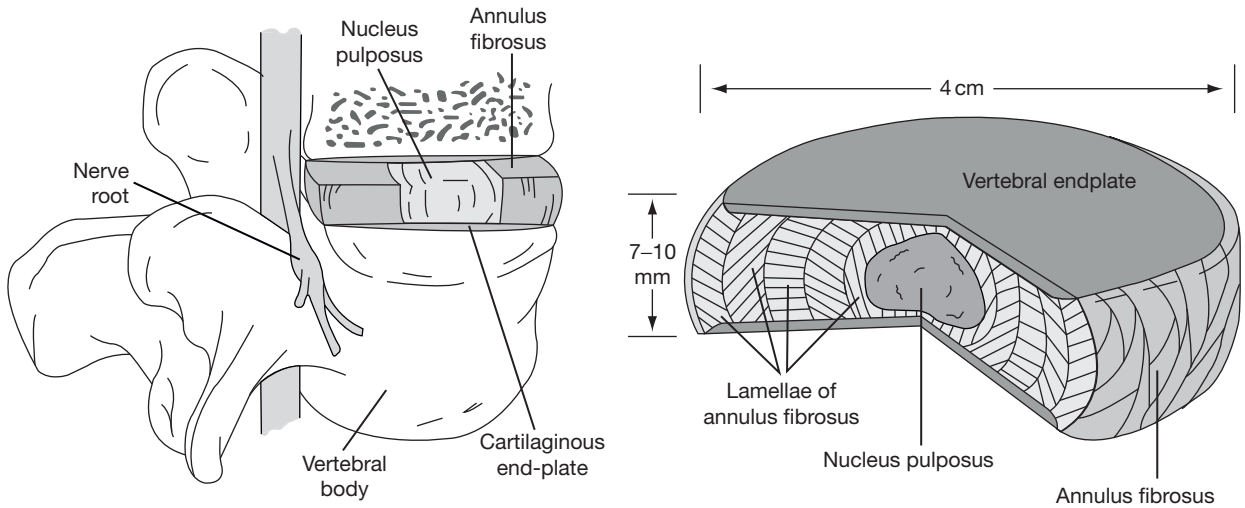

Figure 4 The intervertebral disc (IVD) location between adjacent vertebrae and the individual structures and average dimensions of the IVD. Reproduced from Raj, P. P.; Fipp, A. *Pain Practice* **2008**, *8*, 18.

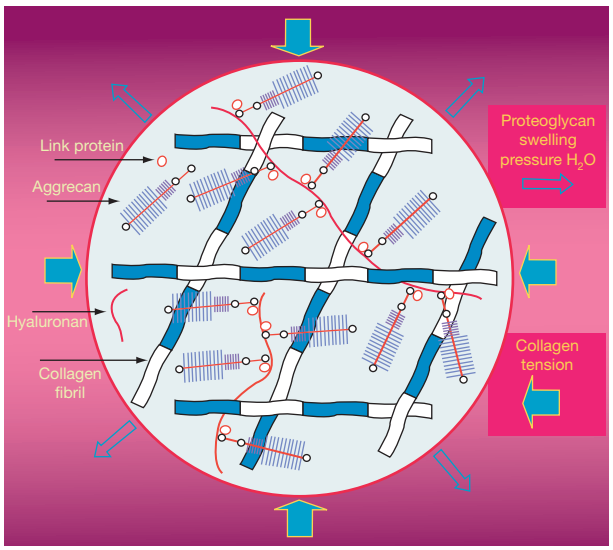

Figure 5 Constituents of the nucleus pulposus and subsequent development of hydrostatic pressure. Reproduced from Kiani, C.; Liwen, C.; Yao Jiong, W. U.; Yee, A. J.; Burton, B. Y. *Cell Res*. **2002**, *12*, 19–32.

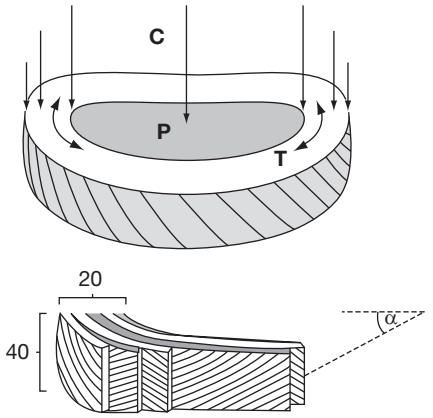

Figure 6 Load transfer in the intervertebral disc (IVD) and lamellar structure of the annulus fibrosus. When a compressive load (C) is placed on the IVD, a hydrostatic pressure (P) is generated in the NP and tensile stress (T) on the annulus. Lamella of the annulus has oblique collagen fibers in alternating directions. On average, there are 20 collagen lamellae in the annulus with approximately 40 collagen bundles per lamella. Reproduced from Adams, M.; Roughley, P. *Spine* **2006**, *31*, 2151.

Spinal compression generates a hydrostatic pressure in the NP that places the annulus into tension thereby resisting the applied load (Figure 6).[20] The AF has a very highly organized structure which results in complex anisotropic behavior with loading. The tensile, compressive, and shear properties of the AF differ in the axial, radial, and circumferential directions. The AF can be further divided into the inner and outer AF on the basis of the structural differences, the inner AF being subjected to higher hydrostatic pressures of the NP than the outer AF which is subject to tensile forces.

6.610.2.5. Intervertebral Disc Degeneration

The IVD of the spine is subject to degenerative changes induced by normal aging as well as injury, loading, or genetically induced accelerated disc degeneration.[21] The exact mechanism of IVD degeneration is not well understood; however, possible degenerative cascades have been proposed which lead to eventual changes in disc mechanical properties (Figure 7). Initial changes in the IVD are thought to be brought about by changes in the nutrient flow to and waste product flow out of the nucleus. Calcification of the cartilaginous endplates, the major route of nutrient supply to the disc, leads to harsh cellular environments, subsequently reducing matrix synthesis and increasing enzyme production further reducing PG and collagen content of the disc, in particular in the NP.[21,23,24] The loss of PGs in the NP has major effects on the load-bearing behavior of the disc, causing the osmotic pressure of the disc to fall and reducing the disc water content disrupting the NP's ability to behave hydrostatically under load. Loading can then

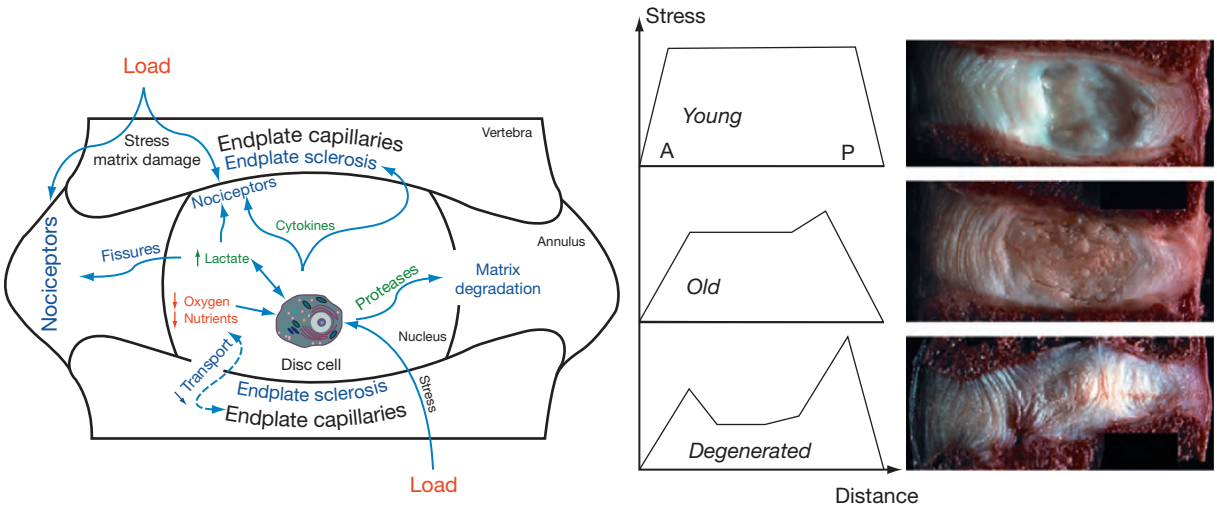

Figure 7 Cascade of events in intervertebral disc (IVD) degeneration[22] and changes in mechanical properties of the IVD with degeneration (Normal disc to degenerated disc from top to bottom). Reproduced from Adams, M. A.; Dolan, P.; McNally, D. S. *Matrix Biol*. **2009**, *28*, 384–389.

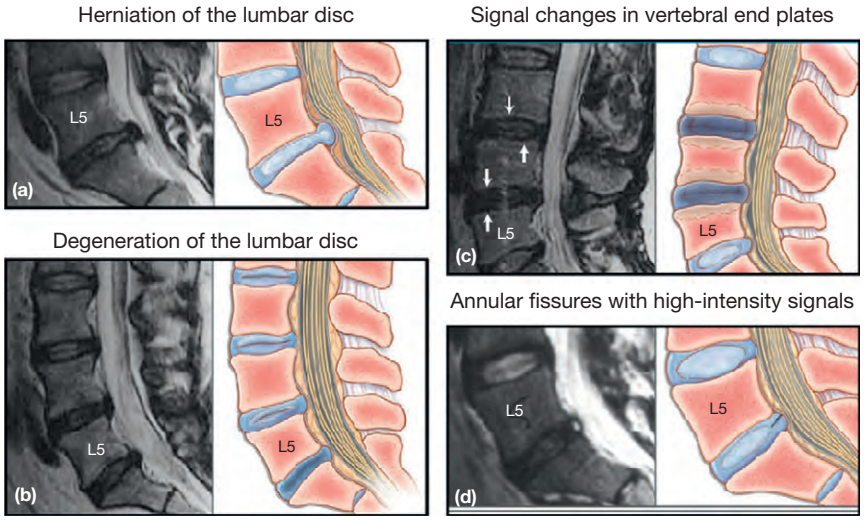

Figure 8 MRI and schematic images of intervertebral disc disruptions. (a) Herniation of the lumbar disc with extrusion of disc material found in 1–18% of asymptomatic subjects. (b) Degeneration of the lumbar disc increases with age and is found in 25–70% of asymptomatic subjects. (c) Signal changes in the vertebral endplates, found in 10% of asymptomatic subjects. (d) Disc with annular fissures seen in 14–33% of asymptomatic subjects. Despite high prevalence of these damage modes in healthy persons, these findings are often associated with serious back pain and are often treated with spinal fusion or disc replacement strategies. Adapted from Carragee, E. J. *N. Engl. J. Med*. **2005**, *352*, 1891–1898.

lead to inappropriate stress concentrations along the endplate and in the annulus with progressive changes as disc degeneration proceeds (Figure 7).

Changes in stress concentration can lead to damage of the AF as well as the endplates with stress concentrations being associated with discogenic pain.[17] Several manifestations of disc degeneration and damage can be visualized with MRI and are represented in Figure 8. Although these alterations in the IVD are prevalent in the asymptomatic population, disc disruptions have been associated with back pain and are targets for surgical interventions such as spinal fusion, total disc replacement, nucleus replacement, and annulus repair.[25]

6.610.3. Spinal Fusion

Spinal fusion and stabilization utilizes a wide range of devices such as screws, wires, artificial ligaments, and vertebral cages.[26] The instrumentation used in fusion surgery is designed to stabilize the spine during fusion and promote osseous fusion.[7] Material choice for these devices is therefore targeted toward the promotion of bone ingrowth, and immediate mechanical stabilization of the spine. Postoperative imaging and analysis of surgical success is also of importance in material choice for spinal fusion devices.[27] Early spinal fusion devices were based on metals commonly utilized in other orthopedic surgeries such as in hip implants.

Metals are still widely used in spine fusion implants today; however, advances have been made in implant design and material development in order to address the unique needs of the spine including maintenance of spine flexibility and to avoid the occurrence of adjacent area damage.

6.610.3.1. Metals for Spinal Cages and Interbody Spacers

The removal of the IVD in order to address discogenic back pain and disc herniation will lead to the loss of disc height and lead to spinal instability. Cage structures have been developed to assist in implanting allo- and autologous bone graft interbody spacers. These cages enhance stabilization of the spinal segment and prevent postoperative collapse.

The BAK™ interbody fusion system is a cage structure made of porous Ti–6Al–4V shell with a cavity for the placement of bone grafts (Figure 9).[28] This device is implanted centrally or bilaterally between the vertebral bodies.[28,29] The ends of this device are capped with ultrahigh molecular weight polyethylene (UHMWPE) plugs in order to contain the bone grafts and to minimize adhesion to surrounding nerves and blood vessels. The strength of the titanium material allows for the load bearing function of the spine and protection of the graft material while the implant design which incoroporates threading to stabilize the implant, and a hollow center to allow for bone delivery, achieves the other functions of this device. Metals, however, are subject to fatigue failure if the graft does not fuse; also the high modulus of metals can lead to stress shielding and eventual failure of the device to integrate into its surroundings.[26] See Table 1 for some common metals used in spine implants and their material properties.



Figure 9 The BAK cervical spinal fixation device. A threaded hollow titanium implant that allows bone grafts to be implanted within the shell to facilitate fusion. Ends are capped with UHMWPE to minimize adhesion. Reproduced from Martz, E. O.; Goel, V. K.; Pope, M. H.; Park, J. B. *J. Biomed. Mater. Res.* **1997**, *38*, 267–288.

Cobalt chrome has also been developed into a porous metal sponge for use in spinal surgery.[32] The porous structure was designed to match the structure of cancellous bone and the implant could be loaded axially up to 28.5 MPa. Problems arose, however, with metal ion release because of the high surface area imparted by the porous structure. Released metal ions may increase pain at the implant site and cause loosening of the implant and local bone resorption at the implant site.[33,34] Decreased pH levels at the implant site can be brought about by the inflammatory response and infection and may also have a deleterious effect on metallic implants causing fretting corrosion.[33,34]

6.610.3.2. Polymers and Composites for Fusion Cages

In order to address some of the drawbacks of metal fusion cages, composite materials have been developed and utilized in spinal cages. A cage made from a composite of poly ether ketone ether ketone ketone (PEKEKK) with pyrolytic carbon fibers interspersed within the polymer matrix was developed.[35] The material was molded to incorporate teeth located superiorly and inferiorly in order to resist expulsion (Figure 10). Material properties were modulated to better mimic those of bone in order to better support physiological loads as the graft material slowly integrates into the surgical site and in case the graft does not fuse. The cage was designed to have a Young's modulus of ~17 GPa, close to that of cortical bone.[35] This matched modulus decreases the likelihood of stress

Table 1 Material properties of common metals in spinal implants

Property	*316L SS (cold worked)*	*Wrought CoNiCrMo*	*Ti–6Al–4V*	*Pure Ti (Grade 4)*
ASTM designation[a]	F 138 (grade 2)	F 562 (cold worked and aged)	F 136	F 67
Density (g cm^{-3})[b]	7.9	9.2	4.5	4.51
Elastic modulus (GPa)[a]	193	220–234[b]	105	100
Yield strength (MPa)[c]	690	1586	795	483–655
Tensile strength (MPa)[c]	860	1793	860	550
Elongation (%)[c]	12	8	10	15
Fatigue strength (MPa) (10^7 cycles)[a]	310 (F55 cold worked)	500 (cold worked)	520 (forged, annealed)	240 (as fabricated)

[a]From Black.[30]

[b]From Park and Lakes.[31]

[c]ASTM F 138, ASTM F 562, ASTM F 136, and ASTM F 67.

Source: ASTM. *Annual Book of ASTM Standards*; ASTM: Philadelphia, PA, 1992; Park, J. B.; Lakes, R. S. *Biomaterials: An Introduction*; Springer: Berlin, 2007; Black, J. *Orthopaedic Biomaterials in Research and Practice*; Churchill Livingstone: New York, 1988; Martz, E. O.; Goel, V. K.; Pope, M. H.; Park, J. B. *J. Biomed. Mater. Res.* **1997**, *38*, 267–288.

shielding. An additional benefit of the nonmetallic implant is the ability to visualize the postoperative implant area because of the radiolucent property of the material.

Polyaryletherketones (PAEKs) are in the family of high temperature thermoplastic polymers and have been widely used for spinal cage implants after their introduction in the 1990s as an improvement over metal devices by Acromed (Cleveland, OH, now DePuy Spine, Raynham, MA).[36] PAEKs consist of an aromatic backbone molecular chain interconnected by ketone and ether functional groups. Specifically, poly (aryl-ether-ether-ketone), PEEK, and poly(aryl-ether-ketone-ether-ketone-ketone), PEKEKK, have been used in orthopedic and spinal implants. The chemical structure of PAEKs allows stability at high temperatures, exceeding 300 °C,[37] resistance to chemical and radiation damage,[38] compatibility with reinforcing agents such as glass and carbon fibers, and greater strength than even metals.[36] Mechanical and material properties for some PEEK formulations in comparison to other commonly used polymer materials are given in Table 2.[36] These materials are also radiolucent making them a good alternative to metallic spine biomaterials.

PEEK and PEKEKK were first used in the development of the Brantigan cage with 68% by weight carbon fiber reinforcement in a 2-year clinical trial beginning in 1989.[39] Clinical results were good with 100% interbody fusion identified. Interbody fusion could be identified because of the radiolucency of the PAEK materials which continued to be a major reason for the use of this material (Figure 11).[36,40]

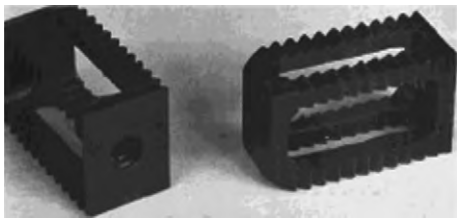

Figure 10 Carbon fiber composite cage made from Ultrapek. Reproduced from Martz, E. O.; Goel, V. K.; Pope, M. H.; Park, J. B. *J. Biomed. Mater. Res.* **1997**, *38*, 267–288.

In addition to carbon reinforced PEEK, neat PEEK is also utilized in the development of spinal cages and implants.[41–43] Studies have also been conducted to investigate the improvement of PEEK cages to incorporate accelerated fusion performance by adding bioactive materials such as hydroxylapatite or rhBMP-2.[41,43,44] Wear and fracture can be potential concerns with the use of PEEK as a load-bearing implant material; however, these concerns are not unique to PEEK. Although debris from wear has been noted in biopsies from carbon fiber PEEK cages, there has been no evidence of an inflammatory reaction making PAEK type materials promising in this application.[45] PEEK materials have also been investigated for other spine stabilization devices such as posterior dynamic stabilization devices[46] and total disc replacements.[36]

6.610.3.3. Wires, Tapes, and Cables in Spinal Fusion

Fusion of single or multiple spinal segments is also accomplished through the use of wires, tapes, and cables to secure adjacent bone segments. The most commonly used wire material is 316L stainless steel (Table 1).[26] Stainless steel is relatively strong, ductile, and relatively inexpensive. Stainless steel 316L is especially preferred because of its resistance to corrosion as a result of low carbon content (0.03% maximum) which prevents sensitization of the stainless steel. Nevertheless, even stainless steel 316L is susceptible to localized corrosion associated with a loss of the protective chromium oxide surface layer.[47] A concern in the use of metal wires for fixation is the possibility of neurological damage as well as concerns that the wire may cut through the bone if the bone is soft, which is especially the case in children.[26] As an alternative, polymer tapes have been introduced such as nylon and woven strands of polyethylene (Mersiline) for use in procedures on scoliotic children[48,49]

Table 2 Typical average physical properties of PEEK and CFR-PEEK structural composite biomaterials, compared with UHMWPE and polymethyl methacrylate (PMMA)

Property (ISO)	*Selected lavibio PEEK biomaterials (OPTIMALTI)*			*UHMWPE*	*PMMA*
	Unfilled (OPTIMALTI)	*30% (w/w) chopped carbon fiber reinforced (LTICA30)*	*68% (v/v) continuous carbon fiber reinforced (Endolign)*		
Polymer type	Semicrystalline			Semicrystalline	Amorphous
Molecular weight (10^6 g mol^{-1})	0.08–0.12	0.08–0.12	0.08–0.12	2–6	0.1–0.8
Poisson's ratio	0.36	0.40	0.38	0.46	0.35
Specific gravity	1.3	1.4	1.6	0.932–0.945	1.180–1.246
Flexural modulus (GPa)	4	20	135	0.8–1.6	1.5–4.1
Tensile strength (MPa)	93	170	>2000	39–48	24–49
Tensile elongation (%)	30–40	1–2	1	350–525	1–2
Degree of crystallinity (%)	30–35	30–35	30–35	39–75	Noncrystalline

Testing conducted at 23 °C.

6.610.3.4. Pedicle Screws, Plates, Bands, and Rods for Fusion and Dynamic Stabilization

Screws, plates, and rods are often used to augment spinal fusion. Screws placed in the pedicles or vertebral bodies act as anchor points for bands, rods and plates working together to restore spinal stability. The screw–bone interface is especially influential in the success of fixations. Surface treatments of metal implants of stainless steel[50] or titanium[51] have been utilized to increase fatigue life of the implants and promote better integration. Stainless steel fatigue strength is enhanced by the implantation of nitrogen ions by inducing the formation of extremely hard nitrides at the surface of the material while maintaining the bulk properties of the material.[26] Titanium can be modified by the introduction of bioactive titanate layers of, for example, sodium titanate, calcium titanate, or titanium oxide which induce apatite formation on the implant surfaces and have been demonstrated to enhance osteoinductivity as well as osteoconductivity for improved implant integration.[51]

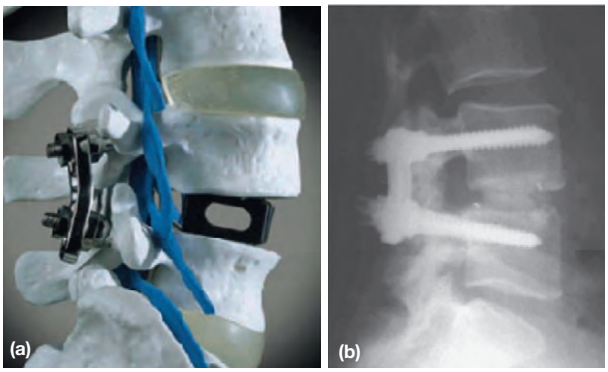

Figure 11 (a) Brantigan spine fusion cage and (b) lateral radiograph of a Brantigan cage with a solid fusion. (Note that the Brantigan cage has tantalum microspheres for visualization on radiographs.) Reproduced from Kurtz, S. M.; Devine, J. N. *Biomaterials* **2007**, *28*, 4845–4869.

Dynamic stabilization may be an alternative to fusion in some patients and may provide an improvement over fusion by altering load bearing and controlling abnormal motion while maintaining some flexibility. Dynamic stabilization devices incorporate a flexible ligament like component or other spring or mobile joint to allow motion in the spine while controlling movement such as flexion and extension. The diverse functionality of these devices often requires the use of both flexible polymeric materials and more rigid materials such as metals (Table 3).[7]

6.610.3.5. Bioresorbable Materials for Spinal Fusion Implants

Another key element in the successful stabilization of the spine in fusion surgeries is the restoration of the normal curvature of the spine. If the material system is too rigid, it becomes difficult to bend and twist to provide the appropriate curvature.

Table 3 Dynamic stabilization devices

Category and trade name	*Key features*
Pedicle screws and artificial ligaments	
Dynesys (Dynamic Neutralization System for the Spine); Zimmer Spine, Warsaw, Ind (18)	Semirigid artificial ligament system composed of titanium alloy pedicle screws and polycarbonaturethane spacers connected by polyster cords (artificial ligaments) that are placed under tension
Graf ligament; Surgicraft, Redditch, England (19)	Nonelastic polyester ligament looped around pedicle screws and placed under tension to prevent rotation while allowing some flexion; if tension is too high, hyperlordosis, foraminal narrowing, and nerve root impingement may result
IsoBar; Scient'x USA, Maitland, FL	Includes a mobile joint within metal rods
M-Brace; Applied Spine Technologies, New Haven, Conn	Implanted by using a minimally invasive technique
Stabilimax NZ; Applied Spine Technologies	Utilizes a dual spring mechanism
Dynamic Soft Stabilization System (20)	Elliptical metal coil connecting adjacent pedicle screws
Inter-spinour process decompression system	
Wallis ligament; Abbott Spine, Austin, Tex (21)	Interspinous process distraction device composed of a spacer held between spinous processes with Dacron tape
X STOP; St Francis Medical Technologies, Concord, NH (22)	Titanium device in two pieces, placed between adjacent spinous processes to hold spine in flexion; can be inserted by using a minimally invasive approach with a local anesthetic and is thus useful in elderly patients with degenerative spinal stenosis
Diam; Medtronic So famor Danek, Memphis, Tenn	H-shaped silicone device held in place by a mesh band and suture
Coflex; Paradigm Spine, New York, NY Posterior element replacement systems	U-shaped device that controls flexion and extension
Total Facet Arthroplasty System; Archus Orthopedics, Redmond, Wash	Consists of a sphere that slides along a curved plate anchored by pegs passing into the vertebral body
Total Posterior System; Impliant, Princeton, NJ	Posterior elements are removed and a plastic device is implanted and anchored with devices similar to pedicle screws

Note: Some of the devices listed may not yet have been approved by the FDA for clinical use.

Source: Zucherman, J. F.; Hsu, K. Y.; Hartjen, C. A.; *et al*. *Spine* **2005**, *30*, 1351; Senegas, J.; Etchevers, J. P.; Vital, J. M.; Baulny, D.; Grenier, F. *Rev. Chir. Orthop. Reparatrice Appar. Mot*. **1988**, *74*, 15; Sengupta, D. K. *The Lumbar Spine*; Lippincott, Williams & Wilkins: Philadelphia, PA, 2004; Vol. 1, pp 373–383; Graf, H. *Rachis* **1992**, *4*, 123–137; Stoll, T. M.; Dubois, G.; Schwarzenbach, O. *Eur. Spine J*. **2002**, *11*, 170–178; Senegas, J. *Eur. Spine J*. **2002**, *11*, 164–169.

Inducing an abnormal curvature may lead to stress induced osteopenia of the vertebral bodies and spinal degeneration in adjacent spinal levels.[26] This is, however, in contrast to the needs of a rigid system in order to promote the solid fusion process. Therefore, the use of a system whose rigidity decreases with time is desirable. Bioresorbable materials provide promise for such a system. Bioresorbable cages have stiffnesses comparable to those of bone, are radiolucent, and resorb over time.[52] These cages provide the additional benefits of eliminating risks associated with permanent implants such as implant removal on revision surgery. In addition, degradation of the polymer may allow for the incorporation of a drug release system into the implanted device.

The most commonly used biodegradable materials are polyesters derived from poly(α-hydroxy acids) such as poly (lactic acid) (PLA) and poly(glycolic acid) (PGA), and their isomers and copolymers. The chemical backbones of these materials are hydrolytically unstable, and the chains will degrade when placed in aqueous environments such as the body. PLA and PLGA degrade to lactic acid and glycolic acid respectively and are natural, biocompatible metabolic compounds. The strength and degradation rate of these polymers can be modified by the fabrication of copolymer systems. PGA degrades within months and is therefore used only in small amounts in copolymer systems, while PLA is more widely used in spinal implants. Chemical and physical properties of some commonly used PLA and PLA isomers are summarized in Table 4.

The polymer degradation kinetics and mechanical properties can be influenced by the polymer system utilized; however, the implant design and geometry itself has a large influence on the rates and types of degradation experienced by the implant. PLA devices degrade faster when they are less porous, less permeable, and have a bulkier design and wall thicknesses.[52] Sterilization of the implant can also have drastic effects on the physical and mechanical properties of the polymer. Many conventional sterilization techniques such as steam sterilization can cause melting of the polymer system and therefore cannot be utilized. Ionizing radiation is an alternative sterilization technique; however, this technique can also induce damage in the polymers causing changes in biocompatibility and biomechanical characteristics. Treatment with ethylene oxide or plasma sterilization provides better alternatives and shows limited effect on molecular weight and tensile strength of PLA-based materials.[53,54] Biocompatibility of PLA and related polymers has generally been demonstrated to be good with the absence of significant toxicity.[52] A local reduction in pH imparted by the degradation products, however, may be responsible for some adverse tissue reactions such as osteolysis and bone resorption around the implant.[55]

Table 4 Chemical and physical characteristics of PLLA and PLDLLA

	PLLA (literature)	*PLLA (own use)*	*70/30 PLDLLA (literature)*	*70/30 PLDLLA (own use)*
M_n ($g\,mol^{-1}$)		240 500		140 250
M_w ($g\,mol^{-1}$)		395 500		253 300
D (M_w/M_n)		1.64		1.81
Intr. visc. ($dl\,g^{-1}$)		2.68		1.57
Inh. visc. ($dl\,g^{-1}$)		2.42		1.45
Crystallinity (%)		13.0	Amorphous	Amorphous
T_g (°C)	60–65	64–67	55–60	60–62
T_m (°C)	173–178	180	Amorphous	Amorphous
Degr. time (min)	>24	36–48	12–18	>12

Reproduced from Wuisman, P.; Smit, T. H. *Eur. Spine J.* **2006**, *15*, 133–148.

Bioresorbable PLA plates have performed well in comparison to titanium plates in controlled clinical studies. In an original study by Nabhan *et al.*, bioresorbable plates made of L-lactic and D,L-lactic acid in the ratio of 80:20 in the INION S-1 Biodegradable Anterior Cervical Fusion System were investigated in a prospective randomized controlled study with 40 patients.[56] The bioresorbable plates in this study were designed to hydrolyze over the course of 2 years. Plates maintained 90% of their initial strength after 6 months, then continued to decrease slowly to 70% after 9 months, and continued to absorb after 2 years. The fusion incidence and rates of fusion were found to be comparable to those of titanium plates but with several added benefits associated with the use of a biodegradable polymer. Advantages of the PLA plates included the radiolucency of the plates which allowed visualization of the graft material giving reassurance that the plates had not migrated. The plates were also somewhat flexible and were able to be bent to match the vertebral contours of the patients. Gradual resportion of the plates may allow the fusion to gradually assume the role of structural support and enhance fusion rates while reducing stress shielding.[56]

6.610.4. Total Disc Arthroplasty

The first mode of treatment proposed for the treatment of the majority of patients who suffer from disc degeneration is nonoperative care. On the basis of carefully considered guidelines, surgical interventions are recommended in the event that conservative remedies do not address the clinical needs of the patient. Arthrodesis or spinal fusion is the traditionally accepted surgical intervention technique advocated in cases of isolated disc degeneration in the cervical or lumbar spine. The procedure involves the removal of a motion segment through the use of bone grafts and sometimes through internal fixation. Indications for the procedure are instability of a motion segment caused by traumatic injury or degeneration.[57] A successful fusion procedure eliminates motion that causes pain and offers the ability to restore intervertebral height and alignment.[58]

However, spinal fusion has its limitations, some of which include the following[41]:

- No significant improvement seen in the success rate of fusion procedures despite the advances made in terms of surgical techniques and instruments;
- Morbidities associated with bone graft harvests during the procedure;
- Accelerated adjacent level disc degeneration;

- Long postoperative recuperation times;
- Increased costs of fusion procedures.

Disc arthroplasty is a surgical procedure that has been getting a lot of attention in the spine community. The procedure aims to potentially eliminate a painful disc while preserving/restoring motion.[58] The goals of arthroplasty include successful pain relief and functional recovery, acceptable levels of morbidity associated with the procedure (equal to or less than those seen in fusion), shorter postoperative recuperation times, and easily implantable surgical techniques.[41] The biomechanical objectives of disc arthroplasty are the restoration of disc function to relieve abnormal stress or strain caused by degeneration. More importantly, it is essential that the procedure does not cause any detrimental biomechanical effects on surrounding structures within the motion segment and on adjacent levels.[41]

6.610.4.1. Material Requirements

In order to understand the material requirements, it is necessary to understand the biomechanics of disc arthroplasty. The following are some of the biomechanical parameters that might be considered while designing a total disc replacement implant[59]:

- Restoration of mobility while avoiding segmental instability;
- Restoration of correct spinal alignment;
- Protection of adjacent structures from overloading and resultant accelerated degeneration;
- Stability and wear properties of the device.

The material requirements for a TDA prosthesis are discussed according to each component of the artificial disc to be designed, along with some examples where possible.

6.610.4.1.1. Implant endplate

The vertebral endplate is subject to repetitive physiological loads, and therefore, a material chosen for this component needs to be durable enough to withstand such types of loads. Other aspects to be considered include the reactivity of the material, its modulus of elasticity, ultimate tensile strength, imaging characteristics, ease of manufacture, and cost.[57] Commonly used materials for endplates are stainless steel, cobalt–chromium alloys, and titanium alloys.[58]

Stainless steel implants are inexpensive to fabricate, show relatively low corrosion, and have high moduli of elasticity. Cobalt chromium alloys have properties in between those of steel and titanium alloys. Depending on the alloy, processing of the end product can be tuned to a wide range of strengths and ductility, thus making these alloys versatile in their applicability as implants. However, such implants are more expensive to manufacture.[58] Currently used prostheses have endplates made out of these types of alloys.

Titanium alloys are attractive as implant materials owing to their high biocompatibility. They are also more corrosion resistant than the other two types of alloys. Further, they yield fewer debris particles as detected by imaging with magnetic resonance. Their mechanical properties are closer to those of cancellous bone, but they have higher susceptibility to wear debris generation. Pure titanium implants have not been studied clinically, but titanium coatings are being used currently.

6.610.4.1.2. Bone implant interface

Attachment of an implant to the endplate can be achieved through the use of screws, serrations, or fins. These structures help insert the device, prevent early displacement, and facilitate long term stability. Long term attachment of the device can be facilitated by the presence of microstructured features on the surface of the implant in order to encourage bony ingrowth. Other options for inducing bony ingrowth include titanium spraying or meshes, calcium sulfate coatings, and hydroxyapatite coatings.[58]

6.610.4.1.3. Bearing surfaces

Special attention is to be paid while selecting materials for the bearing surfaces of the implant. The bearing surface usually determines the long term stability of a well-fixed TDA implant. The articulation of these surfaces must allow low friction motion, resist permanent deformation, and show good wear resistance (see Chapter 6.614, Wear: Total Intervertebral Disc Prostheses).

Typically, surgical intervention to correct disc degeneration is performed on patients between the ages of 35 and 50 years. In order to reduce incidence of revision surgeries, the estimated life of a prosthesis is proposed to be over 40 years. Taking into consideration the number and amplitude of load cycles a lumbar disc experiences in a year, it can be assumed that the average adult bends 125 000 (extension and flexion movements) annually and takes about 2 million steps (gait cycles), the device is expected to endure roughly 85 million cycles of loading during its lifetime without significant degeneration.[60] It is recommended that the device be tested for a 100 million cycles of loading. This hypothesis is made after taking into account the implant's capacity to resist fatigue, and immunologic response to wear particles including their toxicity.

UHMWPE is used as a bearing material in several implants owing to its low creep properties. Even though polyethylene shows wear debris in its use with other joints, animal studies of metal-on-polyethylene disc implants have not shown significant evidence of wear particles.[61,62]

6.610.4.1.4. General material specifications

Metals are considered to be good candidates for a total disc replacement device owing to their inherent high fatigue strength. Also, metal alloys have been shown to possess good biocompatibility.[57] On the other hand, nonmetallic materials such as polymers and elastomers are also good candidates because of the similarities between their mechanical properties and those of native disc tissue. Over a short period of time, the lower elastic moduli of nonmetals help replicate disc behavior adequately. However, in terms of a long term device, such materials tend to pose a challenge to develop. Overall, the need of the hour is to develop materials that demonstrate both biomechanical applicability and biocompatibility while being user friendly in a surgical environment.[63]

In order to meet the needs for an artificial disc, combinations of both metallic and nonmetallic components have been researched. In most cases, these take the form of metal–polymer–metal sandwiches, wherein the metal portion is used to improve fixation using screws/spikes or porous coatings to promote tissue ingrowth. The polymer component of the fixed implant can provide the flexibility seen in native discs.[57]

6.610.4.2. Discontinued Artificial Discs

6.610.4.2.1. Acroflex

The Acroflex artificial disc was developed in the 1970s by Arthur Stefee. The device represents a leap in the concepts and design of artificial discs.[39,62] The design of the disc comprises two porous metal end plates coated with titanium and fused to a hyperplastic polymer disc which is made up of a hexane based polyolefin rubber.[62,64] The design of the device is such that the vertebral bone is intended to grow into the titanium plates to ensure long term fixation, while the polymer disc is intended for restoration of flexibility and motion to the functional spinal unit.[39]

The Acroflex device had significant biomechanical advantages. It helped in the preservation of disc height and allowed semiconstrained motion in all modes including compression.[58]

Over the years, there have been three generations of the Acroflex disc developed. Each generation of the device successfully passed the mechanical testing protocols to which they were subjected, only to fail in the short term when implanted in a series of limited human clinical trials.[10,39]

6.610.4.2.1.1. First generation

The first generation of Acroflex was composed of CoCr alloy and polyethylene as the polymeric core cemented together and implanted through an anterior approach.[39] The disc was tested in cadaveric spines; however, concerns were raised regarding the bone–cement interface, and the device idea was subsequently abandoned.[62]

A cementless design was developed in the 1980s using titanium end plates with a double layer of sintered 250 μm beads to enhance long term fixation. In this version of the disc, the polymeric core was made out of a polyolefin rubber known as Hexsyn, manufactured by Goodyear for fatigue resistant biomedical applications.[39]

The device was subjected to preliminary mechanical testing, and despite some incidences of local material failure, the tests were judged to be successful. The next step was animal testing; however, the company was never able to obtain permission to carry out animal studies. Instead, on the basis of *in vitro* studies to study biocompatibility, a decision was made to proceed to human trials directly.[39]

The device was implanted in six patients and follow-up studies were conducted. However, in 1990 the FDA raised concerns of the use of Hexsyn, which contained 2-mercaptobenzothiazole, a potential carcinogenic.[57] The disc was eventually removed from the market.

6.610.4.2.1.2. Second generation

There is very little information available in the literature about the second generation of the Acroflex device (**Figure 12**). In this iteration of the design, the polymeric core was composed of a silicone elastomer and clinical trials were performed in eight patients. Data for this generation of studies are not available because of the controversies surrounding the use of the silicone gel in breast implants. Class action lawsuits had been filed against the manufacturer of the silicone (Dow Corning), making the developers of the disc hesitate to publish their findings.[62]

6.610.4.2.1.3. Third generation

The third generation of the Acroflex disc once again used a hexane based polyolefin rubber core. The endplate design was modified to reduce the profile to facilitate easier implantation. The endplates were made from a Ti–6Al–4V ELI alloy, coated with porous beads made of pure Ti.[10] Mechanical testing was performed on the device and concluded to be satisfactory. Debris testing was not undertaken as the disc had no articulating surfaces.[65]

Animal studies conducted on 20 baboons showed significant evidence of osteointegration into the porous coating after 6 months. There was one case of failure and histological reaction because of the presence of wear particles in one animal.[66]

Pilot human trials were conducted with two groups of patients, with subtle design differences in the endplate of the device. Both sets of trials did not yield significant results to conclude the success of the device.[10,66]

Eventually, even after three decades of changes to the design and materials used in the Acroflex artificial disc, the device did not achieve significant clinical success. The design concept of using a one piece nonarticulating artificial disc is very attractive, as it would mimic natural disc function very well. However, this is hindered by the complex loading environment seen in the spine. The device was successful in terms of achieving rapid osteointegration. The biggest hurdle to the success of the Acroflex artificial disc though was the designers' inability to find a suitable polymeric core material to meet the required needs for an artificial disc.[62]

6.610.4.3. Currently Available Devices

6.610.4.3.1. Charitè artificial disc

The Charitè Artificial Disc (marketed by DePuy Spine), unlike the Acroflex was designed with the goal of replicating the kinematics of the disc as opposed to the motion. The device

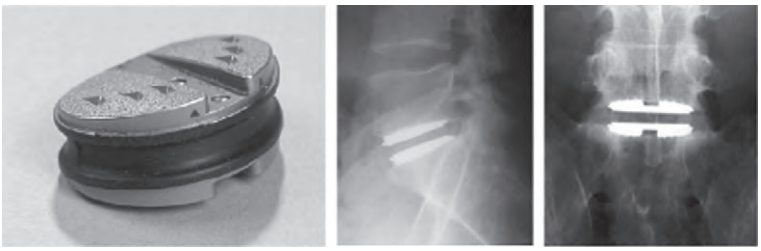

Figure 12 Second generation Acroflex implant with radiographic images post implantation. Reproduced from Melrose, J.; Smith, S. M.; Little, C. B.; Moore, R. J.; Vernon-Roberts, B.; Fraser, R. D. *Eur. Spine J.* **2008**, *17*, 1131–1148.

was designed by Kurt Shellnack M.D., and Karin Buttner-Janz M.D., Ph.D, who were affiliated at the time to the Charitè Center for Musculoskeletal Surgery at the University of Berlin.[67] The basic design of the device incorporates two metallic end plates made of cobalt-chromium alloy[57] which are attached to adjacent vertebral bodies, and articulate against a central polymeric core made up of UHMWPE.[67]

The UHMWPE core has two domed (convex) surfaces that help to articulate against the concave metallic endplates. The hypothesis is that in conditions of full flexion or tension, the core is free to translate or rotate when the polyethylene rim of the core contacts the metal rims of the endplates. The device is implanted through an anterior approach.[67] The device provides unconstrained motion during rotation, and semi constrained motion during flexion, extension, lateral bending, and translation, to some extent.[58]

The Charitè Aritficial disc has undergone four iterations in design since its inception and offers the largest and longest clinical trial of any existing artificial disc.[57,62] The rationale for choosing an UHMWPE core was because of the outstanding friction and fatigue properties of the material.

6.610.4.3.1.1. SB Charitè I and II

Only retrospective clinical data are available for the SB Charitè I and II, the first two generations of the device. The first two generations were made up of stainless steel endplates, which had protruding teeth for better fixation.[62] In the SB I disc, the end plates were circular and shaped like bottle caps, while in the SB II they were expanded by providing lateral wings to enhance contact with the vertebral end plates.[62] The SB I and II discs were implanted in 15 and 22 patients respectively and follow-up data obtained after a period of 17.5 years. Follow-up studies revealed a success rate of 87% (13/15) for the SB I disc, and 68% (15/22) for the SB II discs (**Figure 13**). The success was defined in terms of the absence of long term complications.[68]

The inventors performed mechanical testing on the devices and found that the height of the UHMWPE core was reduced by 10% during testing. They claimed that there was minimal wear and debris formation posttesting[67]; however, it has been seen that their claims are consistent with testing in a single direction, which produces far less wear particles than testing in multiple directions.

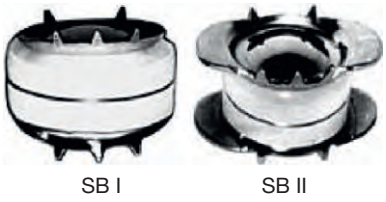

Figure 13 SB Charitè I and II.

6.610.4.3.1.2. SB Charitè III

Waldemar Link GmbH and Co. was the company that commercialized the Charitè artificial disc, resulting in the third generation SB Charitè III (**Figure 14**). Major changes were made to the endplate material, which was now constructed out of a proprietary CoCr alloy called VACUCAST (0.25% C, 28–20% Cr, 5.5–6.5% Mo, max 0.5% Ni, max. 0.5% Fe, 0.4–1% Si, 1% Mn, and the remaining 57.1–69% Co). The back of the alloy was 'satin' finished by corundum blasting, and the device was fitted with six sharp teeth to achieve fixation. The UHMWPE core design remained unchanged.[62]

There have been a number of clinical studies undertaken to document the performance of the SB Charitè III. In summary, most of these studies have demonstrated that the Charitè artificial disc has the potential to preserve motion and survive long term implantation in the body with good to excellent outcomes. However, cohort studies undertaken have shown variability in the complication and success rates of the device, which raises concerns regarding the repeatability and reproducibility of the procedure.

6.610.4.3.2. ProDisc

The ProDisc (Synthes Spine, Paoli, PA) also consists of metallic endplate with an UHMWPE core. Unlike the Charitè, the ProDisc is attached firmly to the inferior end plate through a locking mechanism. The convex surface of the polymer core articulates against the superior end plate. There have been two generations of the ProDisc, ProDisc I and II, but only the ProDisc II has been commercialized.[69]

The ProDisc has undergone the second largest clinical trial of any artificial disc after the Charitè. The ProDisc I had metallic endplates made of Ti alloy, whose back surfaces were plasma sprayed with a titanium coating to promote bone growth.[70] Follow-up reports for ProDisc I showed some procedure related complications. Minimal wear of the UHMWPE core was detected.[70]

Clinical studies on the ProDisc II have only been short term (17–31 months), with reports of positive outcomes. It is to be noted that the studies for ProDisc are more scientifically sound than the studies for the Chartité disc, which has only been retrospectively studied in Europe. Studies on the ProDisc

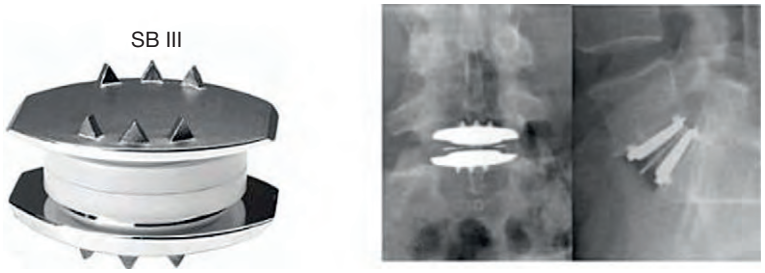

Figure 14 SB Charitè III, and radiographic image of the implanted device.



Figure 15 Components of the ProDisc. From left to right: superior endplate, polyethylene inlay, and inferior endplate. Source: Synthes Product Literature.

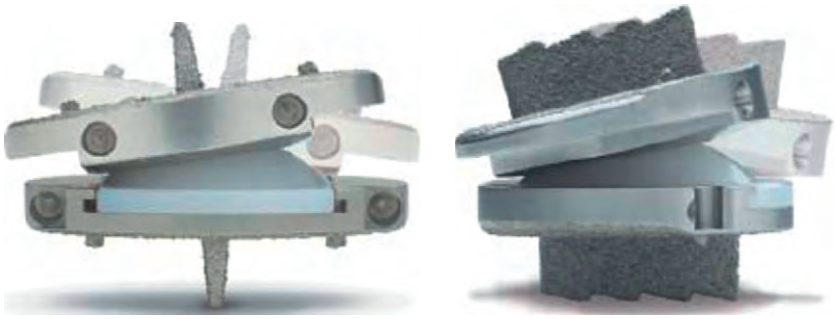

Figure 16 Front and side views of the ProDisc-L artificial disc. Source: Synthes Product Literature.



Figure 17 The Maverick artificial disc. Reproduced from Mathews, H.; Lehuec, J.; Friesem, T.; Zdeblick, T.; Eisermann, L. *Spine J*. **2004**, *4*, 268–275.

II however, are prospective and employ validated outcome measures such as the Oswestry Disability Index, which can be compared with alternative spine procedures (Figures 15 and 16).[62]

6.610.4.3.3. Maverick

The Maverick total disc replacement device was developed in 2001 by Medtronic Sofamor Danek (Figure 17). Initial prototypes were designed using alumina ceramic, but the commercially available device now features a two piece metal-on-metal design, which comprises superior and inferior endplates made of CoCr alloy. Bearing surfaces are made of CoCr alloy based on ultra low wear rates obtained in hip replacements. The endplates have been treated with hydroxyapatite to promote bone growth.[62]

Clinical trials of the Maverick disc began in 2002. Two-year follow-up results have been reported so far. Clinical success was reported in 75% of the patients. No revisions or device related complications were reported in this study. Mechanical testing on the disc showed good shock loading, and showed no mechanical damage after 10 million loading cycles. However, wear debris was produced, but the test methods were not published in the literature. On the basis of this, the life span of the device was predicted to be around 31.5 years *in vivo*, but this claim cannot be validated until further studies are conducted.[71,72]

To sum, the Maverick disc is a good alternative to metal-polymer-metal disc replacements that are currently available. Two-year follow-up studies and biomechanical testing have been reported. Metal-on-metal articulation produces less wear than metal-on-UHMWPE prostheses; however, it also produces metallic wear debris. This can be a cause for concern. Only further studies can tell if the Maverick disc will be clinically successful.

6.610.4.3.4. Flexicore

The Flexicore disc manufactured by Stryker Spine is the most constrained of lumbar discs and consists of four CoCr components: a superior and an inferior baseplate, a spherical head that attaches to the superior endplate, and a shield (Figure 18).[73]

The device is capable of supporting tensile loading because of the presence of the spherical head. It also contains mechanical stops in order to limit flexion/extension and lateral bending. The device endplates are coated with titanium plasma spray coating to promote bone growth. Mechanical testing has been conducted in tension, compression, and shear. The studies showed that the device is mechanically sound and has strength limits excessive to the load limits for the IVD. Wear testing showed that minimal or no wear damage was seen.[73]

The disc is undergoing a clinical trial at present, but the results are not expected for several years. The success of the Flexicore disc can only be determined when more clinical data become available.

6.610.4.4. Future Trends

The field of total disc replacement is a rapidly evolving area of new technologies and techniques, and great strides have been made in the development of spinal implants that are able to replicate and preserve motion in the IVD. The arena of total disc replacement has seen many leaps in terms of achieving short term benefits such as patient satisfaction and speed of recovery.

New implants are being designed, developed, and tested. The near future might hold answers regarding the long term benefits of using total disc replacements, especially the goal of reducing the incidence of adjacent segment degeneration. More comprehensive follow-up studies will reveal the future for these implants.

From a materials standpoint, there have been different design concepts explored. The use of all-metal implants and that of metal–polymer implants have been investigated. At this juncture, it is hard to say which system works better. Each type of design has its own inherent advantages and disadvantages; for example, the main issue with metal–polymer implants is the wear of the polymer core, which can cause early failure of the implant. The all metal implants show excellent wear resistance; however, the generation of wear debris is an issue of concern. The consequences of these wear particles and their corrosion solubility products are unknown at present. There might also be concerns regarding the maintenance of bony attachment with the degradation of bone tissue with age and osteoporosis with respect to these devices.

Nevertheless, the future holds a lot of promise for this field, and as more data are published on the available and developing implants, changes in design and materials can be conceptualized and implemented to meet the objective of achieving a successful implant that will meet all the needs of patients who require total disc replacement.

6.610.5. Annulus Repair

6.610.5.1. Procedure

The repair of the AF has seemed to be an intuitive idea for many researchers, but given the limitations posed by the current microscopic and endoscopic surgical techniques, this has not been attempted much. Advanced technologies are being developed to close annulus defects. These could also enhance the use of intradiscal prostheses which are contained by the AF. Efforts are also underway to develop devices that will support the annulus after a discectomy procedure.

6.610.5.2. Mechanical Role

The AF of the IVD is a structure that serves to contain the gelatinous central portion of the disc, the NP. The chemical composition of the AF comprises 65–90% water, 50–70% dry weight of collagen, 10–20% dry weight of PGs, and noncollagenous proteins such as elastin.[19]

The structure of the AF is laminate in nature, consisting of a minimum of 15 (posterior) and 25 (lateral) concentric layers. The layers are made up of type I collagen fibers which alternate in angles from 28° at the peripheral AF to 44° at the central AF with reference to the transverse plane of the disc. The concentric rings of the AF are referred to as lamellae, and the spaces between them as interlamellar septae.[19]

The AF has a very highly organized structure which results in complex anisotropic behavior. The tensile, compressive, and shear properties of the AF differ in the axial, radial, and circumferential directions. The AF can be further divided into the inner and outer AF on the basis of the structural differences, the inner AF being subjected to higher hydrostatic pressures of the NP than the outer AF which is subject to tensile forces.

Age related degradation of annulus tissue manifests in the form of annular tears and fissures, and can ultimately lead to



Figure 18 Components of the Flexicore artificial disc. Reproduced from Valdevit, A.; Errico, T. *Spine J.* **2004**, *4*, 276–288.

disc herniation.[74] Circumferential delamination and the formation of radial fissures can cause the extrusion of the NP material which is contained by the annulus.[13] This is referred to as disc herniation. Herniation can be defined as the localized displacement of disc material beyond the limits of the intervertebral disc space.[75] When this happens from the posterior region of the annulus, the release of chemical inflammatory signals can result in severe pain in the back.[13,76]

Degeneration of the annulus results in a transfer of load from the NP to the posterior portion of the annulus. To compensate for the added stress, the annulus tends to broaden, which often causes significant protrusion of the disc. This manifests in the form of circumferential disc bulging or focal herniation. Tissue remodeling in the posterior annulus is often accompanied by calcification and other changes that pose a challenge to the treatment of this issue.[77]

In the past, surgical intervention to reverse disc degeneration has focused on re-establishing disc height and geometry, while minimizing the flexibility of the disc. But recently, techniques that seek to retain or restore disc motion are being investigated in a bid to avoid the elimination of spinal segmental motion. Some of these include the replacement of the 'total disc' (i.e., the NP and a significant portion of the annulus) with a prosthetic implant. An alternative to this approach is to replace the NP while retaining a major part of the annulus.[78]

Studies have shown that an incision through the annulus can alter the mechanics of the involved disc. Hampton *et al.* showed that incisions made in the posterior annulus showed limited healing potential and the presence of a persistent defect could form a pathway for the leakage of nuclear fluid into surrounding perineural tissue.[76] This view was reinforced by other researchers who investigated annulotomy techniques in animal models. They found that a box type or window annulotomy technique produces a significantly weaker healing response than a slit or cruciate incision.[79,80]

On the basis of the results reported, it can be inferred that the AF has a limited capacity for regeneration after an annulotomy. On the basis of the type of annulotomy performed, the healing process leads to the formation of a thin layer of inferior fibrous tissue. The poor regenerative capacity may be due to the fact that the external repairs do not meet the needs of fiber recruitment to withstand the tensile forces applied to the annulus.[81,82] In order for the annulus to shift between axial loading and circumferential tension, it is necessary that the nucleus volume remains elastic, deformable, and contained. When the annulus suffers damage from an annulotomy or degradation, its ability to retain the nucleus is lowered.[19] In light of the above discussion, we can say that preservation of as much annular tissue as possible should be the goal during surgical interventions to treat disc degeneration.

6.610.5.3. Reported Treatment Methods

6.610.5.3.1. Suture techniques

There have been reports of closing annular defects with sutures after a microdiscectomy. The first instance of suture usage to close annular defects was reported by Yasargil in 1977, wherein he used 7-0 sutures to close a defect made to remove nucleus material. He reported that this method could help prevent adhesions in the annulus, but did not suggest any mechanism for the same. He tested his method on 105 patients, and recorded no reherniations, neurological impairment, or postoperative radiculopathy in them.[83]

Lehmann *et al.* have reported suture related techniques to close annular defects by using 4-0 sutures to close the flaps of the posterior longitudinal ligament, peridural membrane, and outer fibers of the annulus. In a study conducted in 152 patients, a larger percentage of patients who received sutures had less postsurgery pain compared to those who did not receive them; however, the result was not statistically significant. The investigators did not report on the incidence of reoperation or reherniation.[84]

Cauthen *et al.* have studied suturing of the annulus with a focus on reducing the rate of reoperations. He studied 254 patients and reported that there was a 21% chance of recurrent disc herniation when the patient did not receive sutures at 2 years. The use of one suture to perform microsurgical suturing showed a decreased recurrence rate of 10% while the use of more than one suture brought it down to as low as 5%.[85]

6.610.5.3.2. Sealant and bulking techniques

Biocompatible tissue adhesives have been used in many areas of the body containing soft tissue, for example, fascial hernias or cardiovascular procedures.[86,87] Such procedures, however, have not been extended to the AF because of the undesirable effects of adhesion that might occur with neural tissue in the vicinity. Instead, 'sealing' biomaterials, which are polymeric solutions that cure *in situ*, have been injected into the annulus.[88] In concept, these bulking hydrogels are intended to form a sealant which will take on the complex, irregular shape of the AF defect, and may bond strongly to the neighboring tissue around the defect. There have been no clinical reports of such a technique being applied to the annulus; instead, these types of biomaterials seem more applicable to nucleus replacement.[89,90]

6.610.5.4. Current Technologies

6.610.5.4.1. Xclose™ tissue repair system

The Xclose™ Tissue Repair System marketed by Anulex Technologies, Inc. is an FDA approved technology, and is recommended for reapproximation of soft tissue such as the AF after a discectomy procedure (**Figure 19**). The system consists of two tension band devices and one knot pusher. The device works by placing tension bands at the annulotomy site and securing them with tension bands.[78]

6.610.5.4.1.1. Material

All implanted components of the device are made up of polyethylene terephthalate.[78,91]

6.610.5.4.1.2. Procedure

All the components of the kit are provided in sterile conditions and preloaded on disposable delivery instruments. A tension band consists of a pair of nonabsorbable suture loops each of which is attached to a T-anchor. A third loop of suture with a pretied knot is then used to connect the two loops together, while facilitating the tightening of the tension band, which helps to draw the construct together and hence closes the defect in the tissue.[78]

Cadaveric experiments have been performed to study the use of the Xclose™ system. The results were presented at the annual

meeting of the Spine Arthroplasty Society in Berlin. The ability of the system to remain in place after cyclic loading of the repaired tissue was analyzed. A partial laminectomy was performed to make a posterior annular incision. A limited amount of nucleus was removed (~0.2 cm^3), and the incision was repaired using the Xclose™ system. Nine spinal units were tested in this study.[92]

Cyclic fatigue loading was performed, consisting of 20 K cycles of flexion–extension, 15 K cycles of lateral bending, and 5 K cycles of axial rotation. Calibrated digital macrophotography was used to assess the system's ability to keep the repaired tissue in place, and the knot slippage was measured to check for loosening of the suture knots.[78]

The study showed that all annulotomy defects remained closed and intact after 40 K cycles of loading. Post cyclic loading, the loosening in the system was minimal and knot slippage was measured to be 0.8 ± 0.7 mm. Also, the system did not migrate out of the annulus or pull out of the tissue.[92]

On the basis of the results of the study, we can infer that the Xclose™ system is a simple and effective method to close annular defects incurred during a discectomy. The materials used do not detrimentally affect the repaired tissue, and the system has shown stability upon cyclic loading. So far, the Xclose™ system has been implanted in over 6000 patients in the United States.[93]

The Xclose™ system is undergoing a Phase IV randomized clinical trial at present, but no clinical data are currently available. In 2009, the company also launched a Post Market Clinical study in which 750 patients from 34 facilities around the United States were enrolled.[93] On the basis of data from the clinical trials, more can be said about the materials that are used to construct the device and their role in the body post implantation. Until data from more long term studies *in vivo* are made available, the final understanding of this approach cannot be formulated.

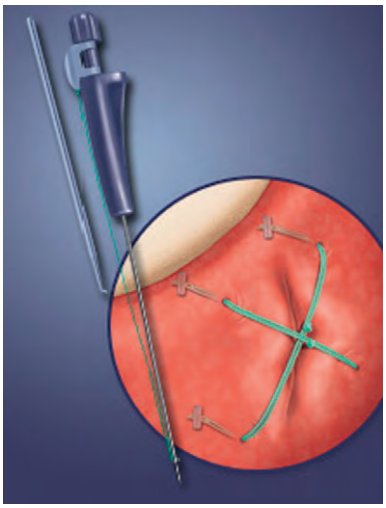

Figure 19 Schematic of the Xclose™ Tissue Repair System. Reproduced from http://www.anulex.com/anulex_technology/xclose.asp.

6.610.5.5. Barrier Technologies

6.610.5.5.1. Inclose™ surgical mesh system

The Inclose™ Surgical Mesh System is marketed by Anulex Technologies (Minnetonka, Minnesota) (**Figure 20**). The device is designed to act as a barrier and provide a scaffold for the repair of soft tissue such as the AF.[94] The surgical mesh implant is made up of a monofilament polymeric braid which is preloaded on a disposable delivery device.

6.610.5.5.1.1. Materials

The braided mesh is biocompatible, expandable, and composed of polyethylene terephthalate,[91] a commonly used polymer in medical devices.[75]

6.610.5.5.1.2. Procedure

The mesh is a low profile device which enables it to be inserted into the annulus in a minimally invasive manner. The device is inserted using a preloaded delivery device supplied with the kit. The system is secured in place using nonabsorbable surgical suture anchors.

The cylindrical device is mounted on a delivery instrument which allows it to extend in a circumferential direction to form a barrier by latching the cylinder ends together. The mesh device can be inserted into any tissue aperture, such as an annular defect, and once deployed into position, it can be tethered using sutures.[75]

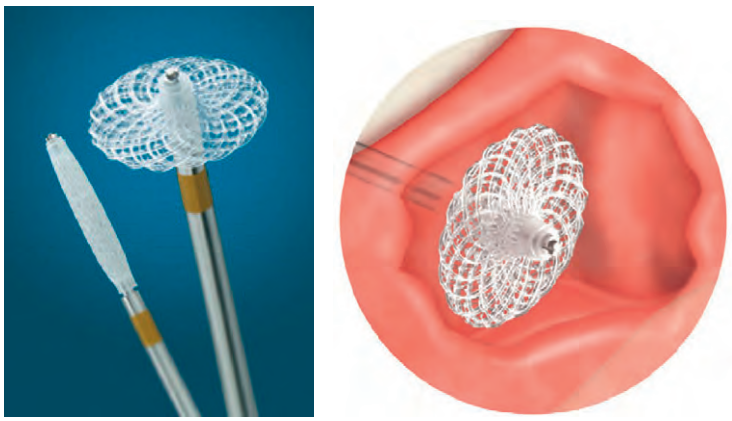

Figure 20 Inclose™ Surgical Mesh System and the configuration of the device post implantation (http://anulex.com/anulex_technology/inclose_us.asp).

6.610.5.5.1.3. Studies on the device

In vitro biomechanics studies were conducted using the device, and demonstrated that implantation of the Inclose™ system did not alter segmental spinal biomechanics. The study also showed that the implant position remained intact despite application of complex cyclic loading.[95] In theory, a stable spinal motion segment may be able to reduce risks of herniation in an adjacent disc by avoiding stress redistribution. Also, this study suggests that the repair of the annulus using such a device might indirectly avoid the need of nucleus material removal which is often a solution employed by surgeons to mitigate the effects of disc herniations.

Animal studies on intradiscal implants are faced with complications of downsizing the device in order to accommodate smaller tissue areas. In general, no animal models exist that can accurately represent the exact nature of disc space characteristics as seen in humans and correlate to human clinical use. Despite these limitations, animal models were designed to study the surgical implantation of the Inclose™ device and histological response to the PET mesh.

Peppelman *et al*. studied Inclose™ implantation in a Nubian goat model and showed that a lateral approach could be used to place the implant safely in the proximity of the annulus. When positioned and affixed properly, the implant remained intact over the course of 12 weeks, as seen using radiography. Also, the device was found to be incorporated histologically without any detrimental effects on the surrounding tissues.[96]

The device was studied after implantation in cadaveric and animal models. On the basis of a report submitted at the Spine Arthroplasty Society in Berlin in 2007, the studies demonstrated that the presence of wear particulates was minimal. Also, motion of the implant was negligible and it had no detrimental effects on spinal flexibility. Early findings showed that there were no recurrent herniations when the device was implanted.[97]

Early clinical use of the Inclose™ mesh device has shown promising results. Around 10 patients were implanted with the device after an endoscopic L4-L5 or L5-S1 discectomy. The implant was inserted with minimal disruption to the annulus, with access openings between 3 and 8 mm. There was inadequate length of follow up, because of which long term effects of the implant cannot be predicted yet. However, it was noted that the best technical results were obtained in patients with focal, protruded, and/or extruded disc herniations.[98]

6.610.5.5.2. Barricaid® prosthesis

The Barricaid® Prosthesis device is currently not clinically available in the United States. It is a device aimed at reconstruction of the annulus in the region of disc herniation. The Barricaid® implant works by forming a strong and flexible wall between the AF and NP, where it is implanted.

The salient features of the prosthesis include its ability to create a mechanical barrier that closes the annulus defect, while allowing more nucleus material to be retained in the disc. According to the manufacturers, the device can be implanted quickly, simply, and securely (Intrinsic Therapeutics).[104]

6.610.5.5.2.1. Material

The Barricaid® Prosthesis consists of a woven mesh made of polytetrafluoroethylene (PTFE) supported by a nitinol frame. The frame is made up of a nickel–titanium alloy base, which anchors the annulus and reinforces it while closing the defect.[104] The frame functions as a shape memory alloy, and exhibits pseudo elasticity (Intrinsic Therapeutics).

6.610.5.5.2.2. Procedure

The Barricaid® Prosthesis is implanted into the annulus through a small incision (5×10 mm defect) made on the posterior side, as part of a standard limited discectomy, just prior to wound closure (Intrinsic Therapeutics). The device covers a major portion of the medialateral distance in the posterior AF, and expands cephalad–caudad postinsertion.[75]

6.610.5.5.2.3. Studies on the device

In vitro biomechanical studies have been performed to evaluate the Barricaid® device, and they have demonstrated that the rate of recurrent herniations is decreased.[99] The ability of the device to withstand intradiscal pressure was demonstrated in a study by subjecting the device to complex applied loads, and measuring the intradiscal pressures.[100] The clinical use of the device was also tested, and the study demonstrated that compared to patients who were not implanted with the prosthesis, patients who received the device after a standard discectomy were seen to experience restoration in disc height lost because of the procedure.[101] However, the evaluation of the long term effects of the device in a clinical setting will require longer follow-up studies.

6.610.5.5.3. SpineJet XL®

The SpineJet HydroSurgery system is a novel technology that harnesses the power of water in medical applications such as surgery (**Figure 21**). The system comprises a controlled hair-thin supersonic stream of water that can be used as an effective cutting, ablation, and collection device. The advantage of such a system is that it has the power of laser technology and radiofrequency devices, but avoids the damage to tissue that such technologies cause.[102] The SpineJet XL is a percutaneous hydrodiscectomy device that can be used in the minimally invasive surgical intervention of intervertebral disc degeneration. The device aspirates tissue as it is being used, and can be used to remove cartilage and nucleus material.

The device is designed with four cutting surfaces. Annular thinning is accomplished using a windshield wiper motion to scrape the heel and toe of the device along the inner surface of the annulus. Lateral cutting sides are used to scrape cartilage off the endplates to increase the surface area for interbody lumbar fusion.[102]

The device is mainly used for the removal of NP, in order to perform spinal fusion. The system's use of cold fluid prevents thermal damage to tissue. The design of the device is such that it enables the removal of precise amounts of nucleus tissue without annular puncture or endplate damage.[102]

The device underwent a trial on 13 patients in 2008–2009.[103] Initial results suggested that percutaneous hydrodiscectomy could be a good alternative for the treatment of lumbar degenerative disc disease. However, more clinical data are required to properly assess the device before more widespread use.

6.610.5.6. Material Requirements

On the basis of the discussion of current materials/technologies, we can say that closure of an annulus defect using suture

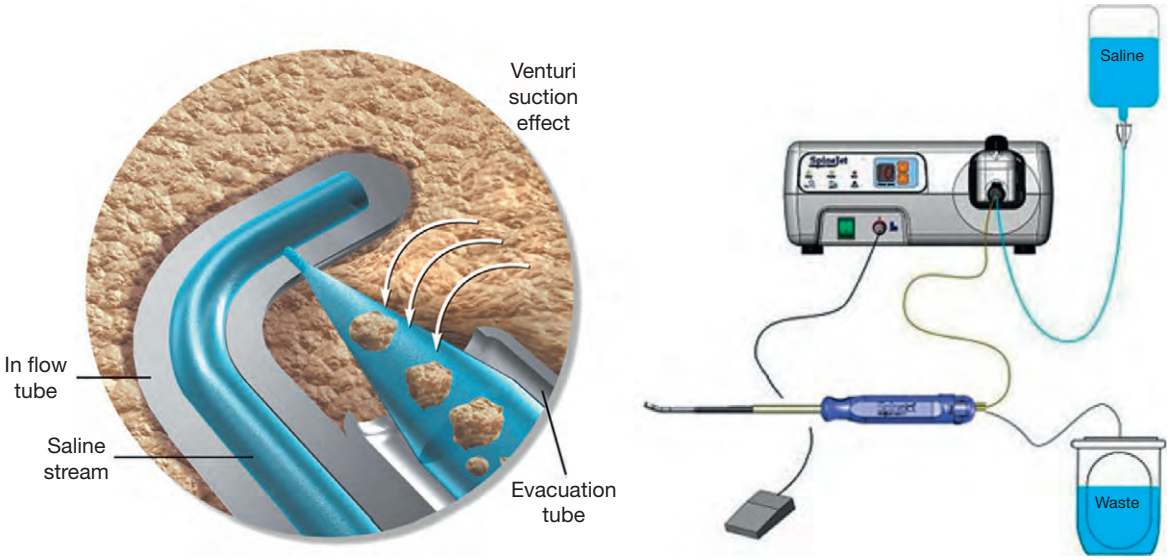

Figure 21 Schematic of the SpineJet XL hydrodiscectomy system and the complete setup.

approximations would require materials that are nonabsorbable, given the nature of an annular defect. With respect to the barrier type of technologies that have been developed so far, the material in question should be able to support the annulus appropriately on the basis of the biomechanical environments it is subject to, without the device getting damaged or causing damage to the annulus; that is, the material has to have mechanical properties matching those of the annulus. Any motion of the device due to functioning of the annulus should not generate any wear particles that might bring about adverse effects in the tissue. Further, considering that such types of techniques are limited by the method of implantation of the device, it is also required that the material in question has properties that enable molding it in a manner that facilitates easy and efficient implantation into the AF.

6.610.5.7. Future Trends

The field of annulus repair is still in its infancy, with data still being collected on implantation of devices that are currently available in the market. However, preserving the integrity of the annulus is an important consideration while repairing the intervertebral disc, as it is the only means of gaining access to the NP. On the basis of the discussion presented above, it is intuitive to try to preserve as much of the annulus as possible as the annulus is responsible for the mechanical properties of the disc. As more follow-up data become available, investigators can look to modifying the currently available technologies to refine their applicability, as well as lay the foundation for the design and development of newer devices that can be implanted minimally invasively, which will help retain the properties of the annulus while allowing access to the NP.

6.610.6. Concluding Remarks

Early spinal implants were based on metals because of the utility of metals in other orthopedic devices. The complex loading nature and function of the spine however necessitated the development of novel materials and techniques in surgical spine interventions. Composite materials and polymers have been utilized in spinal implants as an improvement over metals which do not have matching mechanical properties to the spinal anatomy and are subject to wear. A better understanding of spine anatomy, physiology, and pathophysiology has also led to the development of new materials with several materials being developed specifically for application in the spine. Failure of earlier devices has especially expanded the breadth of materials utilized in spinal interventions. Adjacent level disc degeneration with spinal fusion, expulsion of implant materials through surgical sites, and subsidence of implants into the endplates have driven the development of new surgical techniques and provided the impetus for the development of novel spine materials. This is especially illustrated by the development of *in situ* curing hydrogel and nonhydrogel nucleus replacements where materials were designed such that they could be delivered with minimal damage to the AF, a major way for nucleus replacement as well as the development of sealants for the AF itself. Another drive in materials for spine implants is the utilization of tissue engineering approaches. Tissue scaffolds that support nucleus and AF cell growth are under investigation; however, major limitations in nutrient supply to the implant after implantation must be addressed before tissue engineering approaches for the IVD can be realized.

References

1. Atlas, S. J.; Deyo, R. A. *J. Gen. Intern. Med.* **2001**, *16*, 120–131.
2. Martin, B. I.; Deyo, R. A.; Mirza, S. K.; *et al. JAMA* **2008**, *299*, 656–664.
3. Kuslich, S. D.; Ulstrom, C. L.; Michael, C. J. *Orthop. Clin. North Am.* **1991**, *22*, 181–187.
4. Benzel, E. C. *Biomechanics of Spine Stabilization*. American Association of Neurological Surgeons: Rolling Meadows, IL, 2001.
5. Knoeller, S. M.; Seifried, C. *Spine (Phila Pa 1976)* **2000**, *25*, 2838–2843.
6. Klenerman, L. *The Evolution of Orthopaedic Surgery*. RSM Press: Oxon, UK, 2002.
7. Rutherford, E.; Tarplett, L.; Davies, E.; Harley, J.; King, L. *Radiographics* **2007**, *27*, 1737.
8. Sakalkale, D. P.; Bhagia, S. A.; Slipman, C. W. *Pain Physician* **2003**, *6*, 195–198.
9. Coric, D.; Mummaneni, P. V. *J. Neurosurg. Spine* **2008**, *8*, 115–120.

10. Melrose, J.; Smith, S. M.; Little, C. B.; Moore, R. J.; Vernon-Roberts, B.; Fraser, R. D. *Eur. Spine J.* **2008**, *17*, 1131–1148.
11. Deramond, H.; Depriester, C.; Galibert, P.; Le Gars, D. *Radiol. Clin. North Am.* **1998**, *36*, 533–546.
12. Galibert, P.; Deramond, H.; Rosat, P.; Le Gars, D. *Neurochirurgie* **1987**, *33*, 166.
13. Thongtrangan, I.; Le, H.; Park, J.; Kim, D. H. *Neurosurg. Focus* **2004**, *16*, E13.
14. White, A. A.; Panjabi, M. M. *Clinical Biomechanics of the Spine*; Lippincott: Philadelphia, PA, 1990.
15. Lieberman, I. H.; Togawa, D.; Kayanja, M. M. *Spine J.* **2005**, *5*, 305S–316S.
16. Errington, R. J.; Puustjarvi, K.; White, I. R. F.; Roberts, S.; Urban, J. P. G. *J. Anat.* **1998**, *192*, 369–378.
17. Raj, P. P.; Fipp, A. *Pain Pract.* **2008**, *8*, 18.
18. Kiani, C.; Liwen, C.; Yao Jiong, W. U.; Yee, A. J.; Burton, B. Y. *Cell Res.* **2002**, *12*, 19–32.
19. Bron, J.; Helder, M.; Meisel, H.-J.; Van Royen, B.; Smit, T. *Eur. Spine J.* **2009**, *18*, 301–313.
20. Adams, M.; Roughley, P. *Spine* **2006**, *31*, 2151.
21. Roughley, P. J. *Spine (Phila Pa 1976)* **2004**, *29*, 2691–2699.
22. Masuda, K.; Lotz, J. C. *Tissue Eng. B Rev.* **2010**, *16*, 147–158.
23. Le Maitre, C.; Pockert, A.; Buttle, D.; Freemont, A.; Hoyland, J. *Biochem. Soc. Trans.* **2007**, *35*, 652–655.
24. Urban, J. P. G.; Smith, S.; Fairbank, J. C. T. *Spine* **2004**, *29*, 2700.
25. Carragee, E. J. *N. Engl. J. Med.* **2005**, *352*, 1891–1898.
26. Martz, E. O.; Goel, V. K.; Pope, M. H.; Park, J. B. *J. Biomed. Mater. Res.* **1997**, *38*, 267–288.
27. Vaccaro, A. R.; Singh, K.; Haid, R.; *et al. Spine J.* **2003**, *3*, 227–237.
28. Kuslich, S. D.; Bagby, G. The BAK interbody fusion system: Early clinical results of treatment for chronic low back pain. In *8th NASS Annual Meeting*. San Diego, USA, 1993; pp 175–176.
29. Matge, G. *Acta Neurochir.* **1998**, *140*, 1–8.
30. Black, J. *Orthopaedic Biomaterials in Research and Practice*. Churchill Livingstone: New York, 1988.
31. Park, J. B.; Lakes, R. S. *Biomaterials: An Introduction*; Springer: Berlin, 2007.
32. Waisbrod, H. *Arch. Orthop. Trauma Surg.* **1988**, *107*, 222–225.
33. Merritt, K.; Brown, S. A. *Biological Effects of Corrosion Products from Metals*. ASTM International: Philadelphia, PA, 1985; p 195.
34. Merritt, K.; Brown, S. A. *Clin. Orthop. Relat. Res.* **1996**, S233–S243.
35. McMillin, C. R.; Brantigan, J. W. *Soc. Adv. Mater. Process Eng.* **1993**, 582–590.
36. Kurtz, S. M.; Devine, J. N. *Biomaterials* **2007**, *28*, 4845–4869.
37. Hay, J. N.; Kemmish, D. J. *Polymer* **1987**, *28*, 2047–2051.
38. Katoozian, H.; Davy, D. T.; Arshi, A.; Saadati, U. *Med. Eng. Phys.* **2001**, *23*, 505–511.
39. Brantigan, J. W.; Steffee, A. D. *Spine (Phila Pa 1976)* **1993**, *18*, 2106–2107.
40. McMillin, C. R. *Soc. Adv. Mater. Process Eng.* **1993**, 591–598.
41. Cho, D.-Y.; Lee, W.-Y.; Sheu, P.-C. *Surg. Neurol.* **2004**, *62*, 378–385.
42. Ferguson, S. J.; Visser, J. M. A.; Polikeit, A. *Eur. Spine J.* **2006**, *15*, 149–156.
43. Toth, J. M.; Wang, M.; Estes, B. T.; Scifert, J. L.; Seim, H. B., III; Turner, A. S. *Biomaterials* **2006**, *27*, 324–334.
44. Mastronardi, L.; Ducati, A.; Ferrante, L. *Acta Neurochir.* **2006**, *148*, 307–312.
45. Togawa, D.; Bauer, T. W.; Brantigan, J. W.; Lowery, G. L. *Spine* **2001**, *26*, 2744.
46. Senegas, J. *Eur. Spine J.* **2002**, *11*, 164–169.
47. Lemons, J. E.; Lucas, L. C. *J. Arthroplasty* **1986**, *1*, 143–147.
48. Gaines, R. W., Jr.; Abernathie, D. L. *Spine* **1986**, *11*, 907.
49. O'Brien, J. P.; Stephens, M. M.; Prickett, C. F.; Wilcox, A.; Evans, J. H. *Clin. Orthop. Relat. Res.* **1986**, *203*, 168.
50. Liu, Y.; Njus, G. O.; Bahr, P. A.; Geng, P. O. *Spine* **1990**, *15*, 311.
51. Kokubo, T.; Yamaguchi, S. *Materials* **2009**, *3*, 48–63.
52. Wuisman, P.; Smit, T. H. *Eur. Spine J.* **2006**, *15*, 133–148.
53. Gogolewski, S.; Mainil-Varlet, P.; Dillon, J. G. *J. Biomed. Mater. Res.* **1996**, *32*, 227–235.
54. Nuutinen, J.-P.; Clerc, C.; Virta, T.; Tulamo, R. M.; Tormala, P. *J. Biomater. Sci. Polym. Ed.* **2002**, *13*, 1325–1336.
55. Jun, S.; Harold, A. *J. Appl. Biomater.* **1993**, *4*, 13–27.
56. Nabhan, A. M. D.; Ishak, B. C. M.; Steimer, O. M. D.; *et al. J. Spinal Disord. Tech.* **2009**, *22*, 155–161.
57. Bao, Q.; Mccullen, G.; Higham, P.; Dumbleton, J.; Yuan, H. *Biomaterials* **1996**, *17*, 1157–1167.
58. White, A.; Lawrence, J.; Grauer, J. In *Spinal Reconstruction: Clinical Examples of Applied Basic Science, Biomechanics and Engineering*, Informa Healthcare: New York, 2007; p 263.
59. Galbusera, F.; Bellini, C.; Zweig, T.; *et al. Eur. Spine J.* **2008**, *17*, 1635–1650.
60. Hedman, T. P.; Kostuik, J. P.; Fernie, G. R.; Heller, W. G. *Spine* **1991**, *16*, S256.
61. Cunningham, B.; Dmitriev, A.; Hu, N.; McAfee, P. *Spine* **2003**, *28*, S118.
62. Kurtz, S. M.; Edidin, A. A. *Spine Technology Handbook*. Academic Press: New York, 2006.
63. Edeland, H. *J. Biomed. Eng.* **1985**, *7*, 57.
64. Szpalski, M.; Gunzburg, R.; Mayer, M. *Eur. Spine J.* **2002**, *11*, 65–84.
65. Serhan, H. Personal Communication, 2005; DePuy Spine, Raynham, MA.
66. Cunningham, B.; Lowery, G.; Serhan, H.; *et al. Eur. Spine J.* **2002**, *11*, 115–123.
67. Büttner-Janz, K.; Hochschuler, S.; McAfee, P. *The Artificial Disc*. Springer: Berlin, 2003.
68. Putzier, M.; Funk, J.; Schneider, S.; *et al. Eur. Spine J.* **2006**, *15*, 183–195.
69. Delamarter, R.; Bae, H.; Pradhan, B. *Orthop. Clin. North Am.* **2005**, *36*, 301–313.
70. Tropiano, P.; Huang, R.; Girardi, F.; Cammisa, F., Jr.; Marnay, T. *J. Bone Joint Surg.* **2005**, *87*, 490.
71. Lehuec, J.; Kiaer, T.; Friesem, T.; Mathews, H.; Liu, M.; Eisermann, L. *Spine* **2003**, *28*, 346.
72. Mathews, H.; Lehuec, J.; Friesem, T.; Zdeblick, T.; Eisermann, L. *Spine J.* **2004**, *4*, 268–275.
73. Valdevit, A.; Errico, T. *Spine J.* **2004**, *4*, 276–288.
74. Hickey, D.; Hukins, D. *Spine* **1980**, *5*, 106.
75. Kenneth Yonemura, J. S.; Peppelman, W., Jr.; Griffith, S.; Davis, R,.; Cauthen, J. C., III. In *Spinal Reconstruction: Clinical Examples of Applied Basic Science, Biomechanics and Engineering*, 1st edn.; Kai-Uwe Lewandrowski, M. J. Y. E., Kalfas, I., Park, P., Mclain, R. F., Trantolo, D. J., Eds.; Informa Healthcare: New York, 2007.
76. Hampton, D.; Laros, G.; Mccarron, R.; Franks, D. *Spine* **1989**, *14*, 398–401.
77. Adams, M.; Mcnally, D.; Dolan, P. *J. Bone Joint Surg. Br.* **1996**, *78*, 965–972.
78. Griffith, S., Davis, R., Hutton, W., Eds.; In *Repair of the Anulus Fibrosus of the Lumbar Disc*; Raymedica, LLC: USA, 2007.
79. Ahlgren, B.; Lui, W.; Herkowitz, H.; Panjabi, M. *Spine* **2000**, *25*, 2165.
80. Ethier, D.; Cain, J.; Yaszemski, M.; *et al. Spine* **1994**, *19*, 2071.
81. Guerin, H.; Elliott, D. *J. Orthop. Res.* **2007**, *25*, 508–516.
82. Iatridis, J. C. P.; Weidenbaum, M. M. D.; Setton, L. A. P.; Mow, V. C. P. *Spine* **1996**, *21*(10), 1174–1184.
83. Yasargil, M. *Adv. Neurosurg.* **1977**, *4*, 81.
84. Lehmann, T. R.; Titus, M. K. Refinements in technique for open lumbar discectomy. In *Proceedings of the International Society for the Study of the Lumbar Spine (ISSLS)*, June 1997.
85. Cauthen, J. *Spinal Arthoplasty: A New Era in Spine Care*; Quality Medical: St. Louis, MO, 2005; pp 157–177.
86. Basu, S.; Marini, C.; Bauman, F.; *et al. Ann. Thorac. Surg.* **1995**, *60*, 1255.
87. Miyano, G.; Yamataka, A.; Kato, Y.; *et al. J. Pediatr. Surg.* **2004**, *39*, 1867–1870.
88. Haldimann, D. System for repairing inter-vertebral discs. US Patent App. 10/207,285, 2002.
89. Bao, Q.; Yuan, H. *Spine* **2002**, *27*, 1245.
90. Carl, A.; Ledet, E.; Yuan, H.; Sharan, A. *Spine J.* **2004**, *4*, 325–329.
91. Wilke, H.-J. P.; Neef, P. M. D.; Caimi, M. M. D.; Hoogland, T. M. D.; Claes, L. E. P. *Spine* **1999**, *24*, 755–762.
92. Bourgeault, C.; Beaubien, B. P.; Freeman, A. L.; Bentley, I.; Houfburg, R.; Griffith, S. L. In *Biomechanical Assessment of Anulus Fibrosus Repair with Sutureteth ered Tissue Anchors*. Proceedings of the 2007 Annual Meeting of the Spine Arthroplasty Society (SAS7), Berlin, Germany, May 2007.
93. Anulex Technologies, Inc. Completes Patient Enrollment Phase of Post Market Study and Announces the Treatment of over 6000 Patients with the Xclose™ Tissue Repair System, 2009. http://www.anulex.com/about_anulex/news_events.asp.
94. Anulex Technologies, Inc. Anulex Technologies Receives FDA 510(k) Clearance for the Inclose™ Surgical Mesh System. 2005 [Online].
95. Cunningham, B. C.; Hu, N. B.; Beatson, H.; McAfee, P. In *Fifth Global Symposium on Motion Preservation Technology*; Author, C. D., Ed.; Spine Arthroplasty Society: New York, 2005.
96. Peppelman, W. C.; Kraus, D. R.; Sherman, J.; Yonemura, K.; Griffith, S. L.; Cauthen, J. In *Feasibility Results of a Novel Annular Repair Device in a Goat Model*. World Spine III, Rio de Janeiro, Brazil, 2005.
97. Guillermo Bajares, A. P.; Diaz, Manuel; *et al. Spine Arthroplasty Soc.* **2007**, *7*.
98. Bajaras, G.; Perez-Olivia, A. In *Fifth Global Symposium on Motion Preservation Technology*; Spine Arthroplasty Society (SAS): New York, 2005.
99. Gorensek, M.; Vilendecic, M.; Eustacchio, S.; *et al. Spine J.* **2006**, *6*, 144.
100. Yeh, O.; Chow, S.; Small, M.; Einhorn, J.; Lambrecht, G. *Spine J.* **2006**, *6*, 146–147.
101. Emir Kamaric, O. Y.; Velagic, A.; Einhorn, J.; Osman, G.; Vilandecic, M.; Lambrecht, G. *Spine J.* **2005**, *5*, S178–S179.
102. HYDROCISION, The SpineJet System. 2010. http://www.hydrocision.com.
103. Han, H. J.; Kim, W. K.; Park, C. K.; Oh, S. H.; Lee, D. G.; Doh, E. S. *Kor. J. Spine* **2009**, *6*, 187–191.
104. Intrinsic Therapeutics, Inc. The Barricaid® Prosthesis: Optimizing Outcomes for Discectomy Patients. Available at http://www.intrinsic-therapeutics.com/barricaid_ard.shtml

6.611. Injectable Bone Cements for Spinal Column Augmentation: Materials for Kyphoplasty/Vertebroplasty

J J Verlaan, University Medical Center Utrecht, Utrecht, The Netherlands
M A Lopez-Heredia, University Medical Center Nijmegen, Nijmegen, The Netherlands
J Alblas and F C Oner, University Medical Center Utrecht, Utrecht, The Netherlands
J A Jansen, University Medical Center Nijmegen, Nijmegen, The Netherlands
W J A Dhert, University Medical Center Utrecht, Utrecht, The Netherlands

© 2011 Elsevier Ltd. All rights reserved.

6.611.1. Introduction 147
6.611.2. History of Spinal Column Augmentation with Injectable Bone Cements and Currently Accepted Indications 148
6.611.2.1. History 148
6.611.2.2. Currently Accepted Indications 149
6.611.2.2.1. Painful osteoporotic vertebral compression fractures 149
6.611.2.2.2. Painful metastatic/malignant vertebral body lesions 149
6.611.2.2.3. Traumatic fractures 149
6.611.3. Overview of Frequently Used Injectable Bone Cements for Spinal Augmentation 149
6.611.3.1. Acrylate Cements 150
6.611.3.1.1. Mixing phase 150
6.611.3.1.2. Initial propagation phase 150
6.611.3.1.3. Injection phase 150
6.611.3.1.4. Curing phase 150
6.611.3.2. CaP Cements 151
6.611.3.3. Composite Cements (Hybrid Acrylic/CaP Cements) 152
6.611.3.4. Miscellaneous Cements 153
6.611.4. Clinical Results of Spinal Column Augmentation with Injectable Bone Cements 154
6.611.4.1. Osteoporotic Vertebral Compression Fractures 154
6.611.4.2. Metastatic/Malignant Vertebral Body Lesions 155
6.611.4.3. Traumatic Fractures 155
6.611.5. Complications in Spinal Column Augmentation 155
6.611.5.1. Fracture Type 156
6.611.5.2. Duration of Symptoms 156
6.611.5.3. Instruments/Instrument Positioning/Spinal Anatomy 156
6.611.5.4. Viscosity of Cement Injected 157
6.611.5.5. Volume of Cement Injected 157
6.611.5.6. Mechanical/Thrombogenic/Thermal Properties of Cement 157
6.611.5.7. General Patient Health Characteristics 158
6.611.6. Future Directions and Conclusions 158
References 158

Abbreviations

CaP	Calcium phosphate
CaS	Calcium sulfate
CPC	Calcium phosphate cement
DmpT	*N*,*N*-Dimethyl-*p*-toluidine
KP	Kyphoplasty
PMMA	Polymethyl methacrylate
SF-36 PCS	Short form 36 physical component summary
VAS	Visual analog scale
VP	Vertebroplasty
Zn GPC	Zinc-based glass polyalkenoate cement

6.611.1. Introduction

In contemporary surgical practice, injectable bone cements are increasingly being used to treat a variety of pathological conditions of the spine including osteoporotic vertebral compression fractures, metastatic vertebral body lesions, and traumatic fractures. The principal goal of applying these injectable bone cements is to augment impaired bony structures in order to maintain or improve strength and stability of the spinal column. The first type of cement used in the spine,

PMMA (polymethyl methacrylate), was originally developed for completely different purposes in humans and used, for example, as the material for dental implants, ocular prosthetics, and later for implant fixation in artificial joints prosthetics. Currently, new injectable bone cements are designed specifically for application in the vertebral body. The clinical results obtained in the last decades by using PMMA bone cement in vertebroplasty (VP) and balloon kyphoplasty (KP) procedures have clearly established a demand for biomaterials better adapted to their function as vertebral body bone void filler. Many biomaterial research centers now focus on incorporating into new bone cements the features notably absent in PMMA, such as the properties for osseointegration, capability of remodeling, and mechanical characteristics better approximating that of cancellous bone.

This chapter aims to provide the reader with a brief introduction on the history of injectable bone cements for spinal column augmentation and discusses its currently accepted indications. Furthermore, an overview of frequently used injectable bone cements and their respective technical characteristics are described in detail followed by a summary of the clinical results obtained by this procedure. The clinical implications of cement leakage are discussed together with guidelines for bone cement handling to prevent this complication. A quick glance at possible future directions in the field of injectable bone cements for spinal column augmentation concludes this chapter.

6.611.2. History of Spinal Column Augmentation with Injectable Bone Cements and Currently Accepted Indications

6.611.2.1. History

The first published case of VP, a technique referring to the injection of bone cement into a vertebral body, dates back to 1987 when Frenchmen Galibert and Deramond treated a painful hemangioma, refractory to conservative medical treatment, by filling the intravertebral lesion with an injectable bone cement (PMMA) resulting in immediate and long-lasting relief of symptoms.[1] This paper is regarded as the index work on injectable bone cements for spinal column augmentation. However, the material used in this case had already been developed in 1928 and the process of polymerizing methyl methacrylate was invented as early as 1877 by Fittig and Paul. PMMA became commercially available in the year 1936 and is widely known to the public as an alternative to glass under the name plexiglas or perspex. The first clinical application of this material was in odontology where it was used to build dental implants. Following the observation by ophthalmologist Ridley during the Second World War that splinters of perspex from shattered aircraft cockpit canopies did not trigger an inflammation reaction in the eyes of wounded pilots, he made the material suitable for implantation in the form of artificial lenses, an operation he first conducted in 1949. Sir Charnley was among the first pioneers to use PMMA in orthopedic surgery to establish a bond between bone and implants in hip replacement surgery: a highly successful practice still in use today.[2]

Although the landmark paper by Galibert and Deramond, currently cited over 750 times, was followed by several other publications in French journals on this subject, VP as a new treatment for painful osteoporotic vertebral body fractures, did not gain momentum until the late 1990s when the first article in English was published by Jensen and coworkers.[3] Jacques Dion, a French Canadian and senior author of the article, became the pivotal link importing the French knowledge into North American medical practice. The year 1999 saw a large number of papers published on various topics related to VP including the expansion of indications to metastatic lesions; the first prospective trials; and the first descriptions of serious complications including infection, pulmonary embolism, and neurological deficits after extravasation of cement.[4–7] Around this time, the first critical notes on the (lack of) scientific evidence of the efficacy of injecting PMMA in the spinal column were also expressed.[8] Trout and Kallmes raised the question about whether VP caused incidental vertebral fractures but failed to reach strong conclusions due to insufficient quality of data available from the literature.[9] It has been estimated that over 1 million procedures have been performed worldwide.[10–12]

Meanwhile, in 2001 an alternative to VP, balloon KP, was described by Lieberman and coauthors.[13] In this technique, balloons were inserted in the vertebral body and inflated prior to injection of the cement. The potential benefits of this procedure consisted of improved restoration of vertebral body anatomy and a reduction in cement extravasation due to the creation of a cavity lined by higher density bone facilitating lower pressures needed to inject bone cement. Subsequent clinical studies have shown results comparable to VP with often lower rates of cement extravasation.[14]

Virtually all studies described above dealt with the treatment of painful osteoporotic vertebral compression fractures treated by injection of PMMA cement in the affected vertebral level. Notable exceptions published in the same timeframe were the studies by, among others, Nakano *et al*. in which painful osteoporotic vertebral compression fractures were treated by VP or balloon KP using calcium phosphate (CaP) cement instead of PMMA cement.[15–18] The rationale behind the use of CaP cement was the assumed superior biocompatibility, potentially leading to a more intimate bone–cement interface and subsequent remodeling of the biomaterial into bone by creeping substitution.[19]

In an attempt to combine the favorable characteristics of both PMMA (immediate stability) and CaP cement (superior osseointegration), some manufacturers have designed hybrid cements containing both materials.[20] To our best knowledge no clinical data on the performance of these hybrid cements is available from the literature and the application of these biomaterials must currently be regarded to be mostly in the experimental phase.[21]

Augmentation of the spinal column using either PMMA or CaP cement has, in combination with pedicle screw instrumentation, recently also become an adjunct to the surgical treatment of traumatic burst fractures of the spine. Proponents of this new indication for VP/balloon KP suggested this technique to be able to (partially) restore the anatomy of the intervertebral disk space thereby decreasing the chance for secondary deformity due to disk intrusion into the fractured vertebral body.[22]

6.611.2.2. Currently Accepted Indications

As can be concluded from the considerable media coverage and editorials that rapidly emerged following the publication of the first attempt at randomized controlled trials on VP and balloon KP in 2009, a debate is presently raging concerning the efficacy of augmenting the spinal column with injectable biomaterials for any of the indications stated above.[23–25] Notwithstanding the conflicting results gained from many studies conducted in the past two decades, augmentation of the spinal column with injectable biomaterials can presently be divided into the following main categories of indications for treatment:

1. painful osteoporotic vertebral compression fractures;
2. painful metastatic/malignant vertebral body lesions;
3. traumatic fractures.

6.611.2.2.1. Painful osteoporotic vertebral compression fractures

Most of the spinal augmentations with injectable bone cement are being performed due to painful osteoporotic vertebral compression fractures refractory to conservative medical treatment which mainly consists of bed rest and analgesics.[26] The natural history of these types of fractures is frequently benign with progressive resolution of symptoms 6–12 months after the onset of pain regardless of index treatment. It is the immediate and dramatic reduction of pain, typically within 24 h, giving VP or balloon KP the edge over nonoperative treatment strategies in the first 3 months of treatment.[27] Currently, the principal hypothesis explaining the beneficial effect of injecting bone cement into osteoporotic vertebral compression fracture holds that cement injected in the vertebral body stabilizes the fracture and the subsequent decrease in residual motion leads to a reduction of perceived pain.[28] Supporting this hypothesis, it has been demonstrated by many studies that painful vertebral bodies showing edema on magnetic resonance images, indicating unhealed vertebral body fractures, respond better to VP or balloon KP.[29] To prevent cement extravasation, the amount of bone cement injected has steadily decreased in the last decade without affecting the high success rates. It can be argued as to whether everdecreasing volumes of bone cement injected can still adequately stabilize a vertebral body fracture, in which case the 'stabilizing hypothesis' may ultimately prove to be incorrect. Alternative hypotheses claim the exothermic and polymerizing effects of curing PMMA to result in thermal and chemical destruction of nociceptors, respectively. These two hypotheses have been refuted by *in vivo* animal experiments showing little or no tissue necrosis or inflammatory response, after injection of PMMA cement.[19,30–32] Furthermore, by using CaP cement as bone void filler for osteoporotic vertebral compression fractures, Nakano *et al.*[18] demonstrated that this isothermic, nonpolymerizing biomaterial leads to identical results compared to PMMA cement when injected in the spinal column.

6.611.2.2.2. Painful metastatic/malignant vertebral body lesions

The first lesion to be treated by VP was a painful hemangioma. Many other pathologic lesions including metastatic spinal tumors and multiple myeloma have subsequently been shown to respond favorably to the injection of bone cements provided the pedicles and laminae were not affected and compression of the spinal cord was not present.[33] Spinal pain due to metastatic or hematological disease may be caused by a variety of factors and it has been suggested that they include (imminent) pathological fractures, chemical mediators, increased pressure within the bone, microfractures, overstretched periosteum, and compression of neural structures such as the spinal cord and roots.[34,35] Similar to the group of osteoporotic vertebral compression fractures, the exact mechanism by which augmentation of the spine with injectable bone cements achieves its beneficial effect in metastatic/malignant spinal disease has not been elucidated. It is possible that stabilization of the vertebral body after VP or balloon KP also underlies the relief of pain for this indication.[33] Deducing from the observation that tumor recurrence was rare in vertebral bodies treated with cement injection, some authors have suggested that PMMA has some antitumor properties. These properties could include cytotoxicity, hyperthermia, and local induction of ischemia. In a recently published review, Chi and Gokaslan[33] recommend VP or balloon KP in properly selected patients with painful pathologic fractures to be performed as early as possible. Furthermore, they speculate that newer more elastic biomaterials than those currently used may lower the risk for adjacent level collapse and reduce complication rates.

6.611.2.2.3. Traumatic fractures

Oner *et al.*[36] suggested that recurrent kyphosis after surgical treatment of traumatic thoracolumbar fractures resulted from improperly reduced endplate fractures. It was shown that intervertebral disks adjacent to the fractured segment could intrude through fractured endplates into the burst vertebral body thereby causing spinal deformity.[37] Hypothesizing that proper reduction of the endplates and subsequent augmentation of the vertebral body with bone cement could largely prevent this deformity, a technique was developed and subsequently tested to reduce fractured endplates in traumatic thoracolumbar burst fractures by pedicle screw fixation and balloon-assisted endplate reduction.[22] After optimal endplate reduction was achieved, the balloons were removed and the intravertebral void was filled with CaP cement. The choice for this filler material was based on the expected average age of patients with traumatic spine fractures, which is significantly lower (mean age ~35–40 years) compared to that of patients with osteoporotic vertebral compression fractures.[38]

6.611.3. Overview of Frequently Used Injectable Bone Cements for Spinal Augmentation

The biomaterials used for spinal column augmententation by VP or balloon KP require several characteristics including injectability, biocompatibility, and mechanical stability.[21] In selecting the biomaterial, a treating physician considers many parameters: patient condition, patient age, fracture configuration, selection of surgical technique, characteristics of the biomaterial, and environment of implantation site. In the next sections, the characteristics of the cements frequently used in, or with potential use for, VP and balloon KP are discussed.

6.611.3.1. Acrylate Cements

Virtually all cements commercially available for augmentation of the spinal column are based on PMMA, the synthetic polymer of methyl methacrylate. The monomer methyl methacrylate is an organic compound with the formula $CH_2=C(CH_3)CO_2CH_3$ (Figure 1(a) and 1(b)) which can be produced by several manufacturing routes. Fittig and Paul, two German physicists, were the first to invent, in 1877, the polymerization reaction leading to PMMA $(C_5O_2H_8)_n$ (Figure 2).

PMMA is a transparent material with a density of 1180 g l^{-1} and has good resistance against mechanical impact.[21] The melting and boiling temperatures are 130 °C (403 K) and 200 °C (473 K), respectively, while the material autoignites at 460 °C (733 K). The polymerization reaction of methyl methacrylate to form PMMA is initiated by benzoyl peroxide, while *N*,*N*-dimethyl-*p*-toluidine (DmpT) is used as a radical-forming activator. Before the bone cement can be injected in the spinal column, its ingredients, a powder (containing polymethyl powder, benzoyl peroxide, and often an opaque material such as barium sulfate to improve radiological visibility) and a liquid (methyl methacrylate and DmpT), must be mixed. In the ensuing process, benzoyl peroxide and DmpT react to produce benzoyl radicals which are highly reactive and readily bind to the C=C bond of methyl methacrylate. The radical-enhanced methyl methacrylate molecule subsequently starts the polymerization process by reacting with nearby nonradical methyl methacrylate molecules. The resulting (methyl methacrylate)$_n$ molecule retains its radical characteristics and continuous addition of new methyl methacrylate molecules leads to the formation of increasingly large chains of PMMA. The addition of each methyl methacrylate molecule to the developing chain is an exothermic process and can lead to temperatures of up to 100 °C (373 K) in the core of the polymerizing cement when the maximum number of reactions per time unit is reached.[39] As methyl methacrylate molecules eventually become rare in the increasingly viscous cement and radicals start to react with each other, self-extinguishing their reactivity, the chain-forming process decelerates and the chemical reaction peters out. The process from mixing the components to finalization of the polymerization reaction can be described in four functional phases:

1. mixing phase,
2. initial propagation phase,
3. injection phase,
4. curing phase.

6.611.3.1.1. Mixing phase

In this phase the components of the bone cement are combined and mixed into a low viscosity fluid; radicals form to start the polymerization process.

6.611.3.1.2. Initial propagation phase

During initial propagation, the number and length of (methyl methacrylate)$_n$ chains increase rapidly. The viscosity of the cement, although increasing, is still too low for safe injection.

6.611.3.1.3. Injection phase

Many polymer chains have now been formed resulting in a substantial increase in cohesion and simultaneously decreased adhesion within the bone cement. To assess whether the bone cement has entered the injection phase, many physicians probe or test the material qualitatively in what is sometimes, frivolously, called the 'toothpaste test' or 'spaghetti test' as the viscosities of these familiar products accurately resemble the ideal constitution for injection of bone cement into the spinal column.

6.611.3.1.4. Curing phase

The cement is not injectable anymore and now starts to radiate the heat generated by the exothermic polymerization reaction. Although the cement may appear fully hardened, the polymerization process is not complete for another 24 h.

The duration of each phase is highly variable and depends mainly on the temperature of the premixed bone cement components and ambient temperature of the operating theater or radiological suite.[40–42] This variability in duration of the various phases of the polymerizing cement poses a problem for physicians since it directly affects the time window available for safe injection.[43] It has been noted by many authors that a change of only a few degrees in ambient or cement component temperature may lead to substantial deviations in the duration of the injection phase.[44] Several *in vitro* studies have verified these observations and currently devices are being deployed to intraoperatively probe cement viscosity in real-time.[45]

Concerns have been expressed regarding the increased risk for adjacent level fractures after spinal augmentation with PMMA cement in osteoporotic vertebral compression fractures.[46] Although no study has proven that the occurrence of adjacent level fractures is directly related to a change of the mechanical and elastic characteristics of the spinal column after augmentation (as opposed to the natural history of an already weakened spine where the presence of one vertebral compression fracture is highly predictive for subsequent fractures) many clinical studies have, nonetheless, reported the phenomenon to occur frequently.[47] Moreover, *in vitro* studies assessing the stiffness (Young's modulus) of human cadaveric

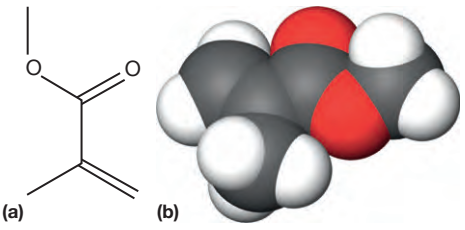

Figure 1 (a) Molecular structure of methyl methacrylate and (b) three-dimensional representation of methyl methacrylate.

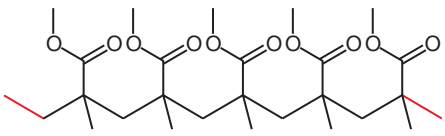

Figure 2 Molecular structure of polymethyl methacrylate.

vertebral specimens after VP or balloon KP using PMMA cement have demonstrated significant increases in stiffness after treatment compared to untreated control specimens.[48] The stiffness of PMMA cement has been shown in earlier biomechanical experiments to range somewhere between cortical and cancellous bone.[48] As a consequence, it has been hypothesized that the increase in stiffness resulting from cement augmentation may contribute to the failure of adjacent levels. Presently, some institutions are in the process of designing and testing PMMA cements with altered biomechanical properties to better approximate the compliancy of cancellous bone found in osteoporotic vertebral bodies, with the aim of reducing the adjacent level fracture rate.[49] Boger and coauthors added *N*-methyl-pyrrolidone to regular PMMA cement and found a significant decrease in Young's modulus, yield strength, and polymerization temperature while the handling time of the cement (i.e., injection phase) was increased by 200%.[50] It was suggested that this type of cement was promising, showing compliancy closer to cancellous bone, while simultaneously exhibiting favorable handling and thermal characteristics compared to unmodified PMMA cement. Other methods to reduce the stiffness of PMMA have been investigated and include increasing cement porosity by addition of ingredients such as hydrogels or oligomers.[51]

Alternative acrylic cement compositions, such as dimethacrylate-based cements, have been designed showing favorable biomechanical and biocompatible properties compared to regular PMMA cements.[52] Currently, most of these biomaterials continue to be studied in a meticulous way. Recent data suggest that the principles underlying their formulation may lead to enhanced clinical performance.[53]

6.611.3.2. CaP Cements

When performing spinal column augmentation with injectable bone cements, several material characteristics including injectability and moldability are required. Heini *et al.* compiled the requirements for materials in VP and KP (KP). This was later elaborated upon by Lewis.[21,54] These requirements can be subdivided into those intrinsically belonging to the material and the desired performance of the material and technique involved. CaP cements satisfy some of the requirements and this category of biomaterials is being considered useful for application in the spinal column. CaP materials have already been used for a long time in dentistry and maxillofacial surgery, but only recently in the field of spinal surgery.[55]

CaP cements are obtained by mixing a solid phase with a liquid phase, producing a paste that can be injected. Depending on the interaction between the solid and liquid phase and the particle distribution of the CaP powder used, there will be a variability in moldability and pressure filtering effect, the latter phenomenon referring to the undesired separation of the solid and liquid components when put under pressure, thereby greatly influencing injectability of the material.[56,57] For application in VP or balloon KP, CaP cement is preferentially tailored to mimic the viscous behavior of PMMA during injection, since this is considered the reference, without displaying the pressure filtering effect.[58] **Table 1** lists the CaP that can be found in several CaP cement compositions.

Table 1 Calcium phosphates that may be used in the solid phase of a calcium phosphate cement

Name	*Formula*	*Ca/P*
Monocalcium phosphate monohydrated	$Ca(H_2PO_4)_2 \cdot H_2O$	0.50
Monocalcium phosphate anhydrous	$Ca(H_2PO_4)_2$	0.50
Dicalcium phosphate dihydrate	$CaHPO_4 \cdot 2H_2O$	1.00
Dicalcium phosphate anhydrous	$CaHPO_4$	1.00
Octacalcium phosphate	$Ca_8H_2(PO_4)_6 \cdot 5H_2O$	1.33
α-Tricalcium phosphate	$Ca_3(PO_4)_2$	1.50
β-Tricalcium phosphate	$Ca_3(PO_4)_2$	1.50
Hydroxyapatite	$Ca_{10}(PO_4)_6(OH)_2$	1.67
Fluoroapatite	$Ca_{10}(PO_4)_6F_2$	1.67
Tetracalcium phosphate (TTCP)	$Ca_4(PO_4)_2O$	2.00

CaP cement holds distinct advantages over PMMA cement by having the potential to undergo resorption while also displaying osteoconductive properties. In recent *in vitro* studies the effect of CaP cements on vertebral body repair has been investigated.[59] Two types of calcium-based materials, namely CaPs and calcium sulfates (CaSs), are used in spinal applications (see also **Table 2**). CaS cements are sometimes considered not to have osteoconductive properties and, due to their fast dissolution characteristics, achieving adequate mechanical support in the spinal column is found to be more difficult.[60] In either case, CaP and CaS cements have demonstrated a superior biocompatibility profile *in vitro* compared to PMMA cements.[61] CaP cements are considered suitable scaffolds for bone substitution since they affect cellular function by virtue of their composition that is similar to the mineral phase of the bone.[62,63] CaP allows adhesion and differentiation of osteoblasts while CaP cements are injectable and can be molded to the defect they have to fill. CaP cements exhibit plasticity during their working period allowing the material to occupy the defect well in which they are injected.[64,65] In addition, by using different CaP powders, the dissolution/degradation and resorption behavior of CaP cements can be tailored. CaP cements are intended to be used as temporary scaffolds and the initial contact between cement and surrounding bone tissue is considered a key factor for the osseointegration and bone formation at the implantation site.[66] CaP cements are required to present a resorption behavior in synchrony with the bone formation.[67] CaP cements can be classified into four categories depending on the role and condition of the CaP solid and liquid components.[68,69] Among these, hydraulic cements are the most commonly used and usually the term cement refers to this category. Depending on the end solubility product, these CaP cements can be classified into two types: brushite or apatite cements.[58,70] Brushite cements contain less favorable mechanical properties but show faster biodegradability when compared to apatite cements.[71] Apatite CaP cements have been studied since the early 1970s and by the 1990s started to make inroads into reconstructive surgery.[72] When mixing CaP powder with the liquid phase, it will create a partial dissolution of the CaP, causing the creation of a paste with the liquid phase supersaturated with calcium and phosphorus ions, which then will reprecipitate, producing crystal growth and entanglement

Table 2 Commercially available cements for spine surgery

Cement type	*Product name (Company)*
PMMA	Spineplex® (Stryker-Howmedica); Corinplast (Corin); Simplex® P (Stryker-Howmedica); Palacos® LV (Zimmer/Heraeus Kulzer); Palacos® R (Zimmer/Heraeus Kulzer); CMW™ (CMW-DePuy); Codman Cranioplastic (CMW-DePuy); KyphX® (Kyphon); HV-R (Kyphon); Osteopal® (Heraeus Kulzer); Symphony™ VR (Advanced Biomaterial Systems); Osteobond (Zimmer)
Calcium phosphate	BSM/Biobon® (ETEX/Merck/Biomet/Lorenz Surgical); Biopex R® (Mitsubishi) BoneSave (Stryker); BoneSource (Orthofix/Stryker-Howmedica); ChronOS Inject (Synthes), MCPC (Biomatlante); Calcibon (Merck/Biomet); Eurovbone (F-H Orthopedics); Norian® SRS® (Norian/Synthes); Mimix (Lorenz Surgical); Cementek (Teknimed); Fracture Grout (Norian); Collagraft (Zimmer); KyphOs (Kyphon)
Calcium sulfate	BonePlast (Interpore Cross Int); MIIG® X3 (Wright Medical)
Composites	Cortoss (Orthovita), CAP (Kuraray)

Source: Heini, P. F.; Berlemann, U. *Eur. Spine J.* **2001**, *10*(Suppl. 2), S205–S213; Lewis, G. *J. Biomed. Mater. Res. B Appl. Biomater.* **2006**, *76*(2), 456–468.

providing the initial mechanical properties for the CaP cement. During this phase the CaP cement will be moldable. For CaP cement, solutions of 1–4 wt% Na_2HPO_4 are commonly used as the liquid phase.[69,73] The degree of supersaturation, pH and temperature of the mixture will dictate the endproduct, which can be resorbed and remodeled *in vivo*. Contrary to acrylic cements, CaP cements have the advantage that the setting phase is an isothermic process reducing the risk of thermal damage to surrounding tissues.[21,59] The phase formed after the reprecipitation of the CaP will dictate the resorption properties of the CaP cement.[74] Each phase presents a different solubility behavior.[75]

The injectability and mechanical properties of CaP cements can be changed by modifying the liquid-to-powder ratio, the type of liquid component or the use of a pore generator without affecting the final obtained CaP phase.[57,76,77] Porosity is found among the requirements for cements used in VP and balloon KP. After injection, CaP cements present a certain degree of microporosity depending on the dissolution–reprecipitation process which is related to the liquid-to-powder ratio used.[73] If the CaP cement is used by itself, comprising only the microporosity, it will take years for the material to degrade since it will do it by a layer-by-layer mechanism, even if it possesses the good chemical characteristics.[55] To increase the degradation between the material and the surrounding tissue, an increase in microporosity and/or the incorporation of a macroporous network could be used. This can be achieved by using various techniques.[78,79] However, it is important to remember that the mechanical properties of the CaP cement will come mainly from two sides, first from the dissolution–reprecipitation mechanism and further crystallization which creates the microporosity of the material and second from the contribution of additives or pore generators which will influence the macroporosity.

CaP cements can withstand compression forces of around 50 MPa after full crystallization which is within the ranges of human bone.[71,80] It has been reported that CaP cement loaded with particles, acting as pore generators or drug-delivery systems, can reduce compression values by 80% compared to cements not loaded with particles.[71,77] If particles are used for pore generator or drug delivery purposes, the mechanical properties will be dependent on the size, amount, and distribution of the particles in the cement, as well as their compositions.[55,71] An agglomeration of these particles should be avoided to not drastically reduce the mechanical properties of the cement.[81] The drug-delivery systems can be used to enhance the biological behavior and activity of CaP cement. Several studies have reported the use of growth factors and proteins in combination with this CaP cement.[82–85]

Surgical interventions of the spine are typically carried out under radiological guidance; therefore the material used must be radiopaque.[59] In contrast to acrylic cements, CaP cements are radiopaque once injected and fully crystallized. However, this action may take 1 day or more days depending upon the characteristics of the cement used. Improving the contrast characteristics of these cements in its early stage is important if CaP cements are aimed to be used in minimal invasive surgery. Tracking the material during the intervention is of high importance in order to avoid leakage of the material that may increase the risk of injuries or adverse effects.[86] Some common contrasting agents used are barium, iodine, tantalum, and tungsten.[87] Although this approach is relatively new for CaP cement, some groups have already explored this field.[88]

6.611.3.3. Composite Cements (Hybrid Acrylic/CaP Cements)

The goal of adding CaP additives to acrylic cements is to establish a compromise between the desired mechanical and biological properties.[89–91] These composite cements may be able to reduce stiffness, polymerization temperature, and potential monomer toxicity of PMMA while strengthening the bone–cement interface by creating a chemical bonding and changing the encapsulation of the acrylic cement to a direct contact with bone.[90,92,93] This type of cement has been developed quite recently and the interaction between the components is currently under research.[89,91] From the possible CaP candidates, hydroxyapatite (HA) has been most investigated due to the closest similarity of this material to the mineral phase of bone and its high stability.[94,95] However, there are also studies directing attention to other CaPs.[89,96] Bioactive glass has also been studied.[97] All these studies aim to provide a better characterization and understanding of the physical, chemical, mechanical, and biological behaviors of composite materials. It has been proven that the inclusion of CaP additives in the acrylic matrix does not modify the properties of the CaP. CaPs maintain their ability to promote bone ingrowth while the monomer concentration of the acrylic cements stays

Table 3 Factors affecting CaP–acrylic composite cement behavior

Molecular structure of CaP
Characteristics of the CaP (e.g., porous, thermally treated, doped, etc.)
Amount added
Particle size of the CaP
Fabrication process

stable.[96] When considering composites, understanding the properties related to the interaction between the phases will be essential to better understand the composite material, overall. In the case of the acrylic composites, this interaction will affect setting times, temperature, and mechanical properties. Table 3 shows the factors affecting the acrylate–CaP composites. The setting time of these composites will be affected mainly by the amount of CaP added while the exact type of CaP will only have a minor effect.[89,96] While PMMA by itself can reach temperatures up to 100 °C (373 K), the addition of CaP can reduce it to room temperature.[89,92,96] The addition of CaP will interfere with the polymerization of the acrylic cement and can therefore act as a heat absorber.[89] The mechanical behavior will be a complex interaction between the shape of the additive, and its dissolution and transformation properties as well as its distribution within the sample, amount within the sample, and the anisotropy created.[98] CaP particles may act as stress concentration factors or fracture energy absorbers, hence affecting the mechanical properties in several ways.[91] Some authors reported that the addition of CaP does not change the mechanical properties significantly, while others report an improvement or even a decrease in these properties.[90,95,96] These differences may be related to the type and size of the CaP and their bonding to the acrylic matrix. Standard ISO 5833 indicates that acrylic cements must present a minimum compressive, tensile, and bending strength of 70, 30, and 50 MPa, respectively.

Concerning porosity, acrylic cements by themselves have low porosity.[91,96,99] When the CaP is added, an important factor is the porosity and interconnectivity between the CaP particles. If particles are embedded in the acrylic matrix without contact to surrounding tissue, the properties of the CaP, and the reason for including them, will not be utilized. Here the CaP particle size and amount included will play a significant role, as it happens when loading a CPC with particles for pore generator or drug-delivery systems.[92,96] It has been demonstrated that including HA particles causes a void increment.[91] Therefore, CaP additives *per se* will have an effect on the pore size in the cement also. This effect will be related to the additive content and its wettability toward the acrylic material.[96] CaP materials are hydrophilic, so they are partially covered by the liquid monomer that later will polymerize with the powder polymer embedding the CaP into the acrylic matrix but without a strong interface.[89,95] Treated and untreated CaP additives (silinazed) have proven to have a different interaction with the acrylic matrix and influence the mechanical behavior of the composites.[95] However, these treatments may modify the hydrophobicity of the CaP additives, which could affect their biological properties. Thermal treatments affect the surface properties of CaP.[70] This approach could be used to increase the interaction of the CaP with the liquid monomer without affecting the biological properties of the CaP. Another approach that has been studied to modify the mechanical properties of this type of cement is the creation of a porous acrylic cement by preparing the PMMA with a biodegradable gel.[100,101] In this last approach, if combined with the loading of CaP particles, the structure will be affected on the mechanical properties due to the porous network and type, size, and amount of the particles included.[50,89] Acrylic cements with lower modulus are attractive since they allow better stress distribution in the filled vertebral body, thus potentially reducing the risk of fractures on the vertebrae adjacent to the operated sites.[102] In the case of using radiopaque agents for tracking the material during the surgical intervention, composite cements show a higher degree of complexity since the cement will be a three-phase composite system; hence the interaction of each component will not be one-to-one but one-to-two. Although studied to some extent by some groups the characterization of these three-phase systems is an area that needs to be researched further in order to fully validate the use of these composites.[91]

6.611.3.4. Miscellaneous Cements

Acknowledging the several drawbacks found in commonly used biomaterials for spinal augmentation (i.e., PMMA and CaP cement) consisting of difficult handling characteristics, thermal issues, potential for toxic reactions, mismatched Young's modulus, and limited mechanical strength, researchers have recently started to focus on entirely different materials to be used for this application.[21,103] Boyd and coauthors suggested aluminum-free, zinc-based glass polyalkenoate cements (Zn-GPC) to be a suitable alternative for use in VP.[104] In their recent work, comparing polymerization temperature, strength, Young's modulus, and biocompatibility of this cement formulation with three commercially available bone cements (two PMMA cements and one composed of resins and glass ceramic particles) it was found that, although setting times precluded clinical use in the current composition, thermal behavior of the new material was benign, its stiffness exhibited values similar to cancellous bone while biocompatibility was superior. The authors suggested Zn-GPC to be a suitable candidate material for further development as bone cement once the setting parameters were optimized. In recent studies by Perry *et al.*[105] two new biomaterials, polypropylene fumarate cement and CaS cement, were tested as alternatives for PMMA cement in a model for human cadaveric osteoporotic vertebral compression fractures treated by balloon KP. The authors concluded from their biomechanical tests, showing similar mechanical properties to PMMA, that both polypropylene fumarate and CaS were potential new candidates for this application. In 2004 Zhao and coworkers reported on the properties of a strontium-containing HA cement with surface treatment using methyl methacrylate to be used for VP and found favorable biomechanical results.[106] Other promising cement compositions include glass–ceramic-based cements.[52,107] The studies described in this section cover just a small selection of several biomaterials currently under study, but it can be expected that many more new biomaterials will be designed, tested and eventually qualify for clinical investigation in the near future. The prospect of the availability of biomaterials better adapted to

the needs of both the treating physicians, in terms of superior handling profiles, and patients, in terms of improved safety, efficacy, and biocompatibility, is encouraging.

6.611.4. Clinical Results of Spinal Column Augmentation with Injectable Bone Cements

6.611.4.1. Osteoporotic Vertebral Compression Fractures

In 1994 Gangi and coauthors described one of the first, small-scale, series of patients treated for various indications including osteoporotic vertebral body collapse and spinal metastasis treated with VP using PMMA cement.[108] They noted immediate relief of pain and absence of further vertebral body compression during follow-up in all. Jensen *et al.*[3] published a series of 47 spinal levels treated in 29 patients suffering from osteoporotic vertebral compression fracture and found relief of pain immediately after treatment. Identical results were reported by Martin and coworkers in their series of 68 levels treated in 40 patients with 80% of the patients experiencing substantially improved symptoms.[5] According to the authors, failures were related to insufficient pretreatment, clinical evaluation, and excessive injection of PMMA. In 2003 a prospective controlled trial was published by Diamond and coauthors, describing VP as a safe technique resulting in prompt relief of pain when compared to conservative medical treatment.[109] The same year a review was published, in which it was emphasized that this technique should be reserved for carefully selected patients who do not respond to conservative treatment.[110] In 2006, a review of the treatment of osteoporotic vertebral compression fractures by VP summarized 15 studies (11 prospective, 3 retrospective, and 1 controlled trial) containing a total of 1136 procedures in 793 patients.[111] The visual analog scale (VAS) for pain, a validated pain measuring tool, ranging from 0 to 10, with 0 meaning no pain and 10 the worst pain imaginable, improved from a mean of 7.8 to 3.1. The rate of complications ranged between 0.4% and 75.6%, and was frequently related to cement extravasation and included major adverse events. It was concluded that long-term, properly controlled trials were required to address the lack of sound scientific and clinical understanding of this technique. Hochmuth and coauthors performed yet another review on VP, describing the results from 30 studies and 2086 patients and, again, concluded that although spinal augmentation with PMMA cement seemed to dramatically improve symptoms in patients with osteoporotic vertebral compression fractures, randomized controlled trials were needed to confirm the efficacy of the procedure.[112]

In 2006 Bouza and coworkers published a review of the literature on balloon KP presenting the pooled clinical data of 26 previously published articles.[113] It was found that, although the methodological quality of the papers on which their review was based was generally low, balloon KP for the treatment of painful vertebral compression fractures led to significant improvements in pain intensity, vertebral height, sagittal alignment, functional capacity, and quality of life. The authors concluded the review suggesting that balloon KP was safe and effective. Hulme and coworkers, in their review of 69 articles published in the literature on the outcome of VP and balloon KP, refuted this claim, stating that definite proof of safety and efficacy of both procedures could not be obtained without comparative, blinded, randomized trials.[114] Taylor and coauthors found, in contrast again, Level III evidence to support balloon KP and VP as effective therapies in the management of patients with symptomatic osteoporotic vertebral compression fractures refractory to conventional medical therapy.[14] Moreover, balloon KP was suggested to offer a better profile with respect to adverse events than VP.

The first randomized controlled trial on this subject was the FREE trial published in the *Lancet* in 2009 describing the efficacy and safety of balloon KP compared with nonsurgical care for the treatment of osteoporotic vertebral compression fractures, metastatic spinal lesions, and multiple myeloma.[115] In this trial a total of 300 patients were enrolled and randomly assigned to receive balloon KP with PMMA cement or optimal nonsurgical care. A total of 266 patients completed the 1-month follow-up and a significant difference in SF-36 PCS was found between the two groups favoring the surgical intervention group. At 12 months, 38 out of 115 patients in the balloon KP group and 24 out of 95 in the nonoperative group had new or worsening vertebral fractures. It was concluded that balloon KP with PMMA cement was an effective and safe technique for patients with acute vertebral fractures. In the same year two studies were published in one issue of the *New England Journal of Medicine*.[10,11] These papers generally received a critical reception.[23,25] In the paper by Buchbinder and coauthors, a randomized, double-blind, placebo-controlled trial was performed to study the efficacy of VP using PMMA cement for the treatment of painful osteoporotic vertebral compression fractures in 78 patients. In this study patients were randomly assigned to receive regular VP or a sham operation in which the needle used to inject cement was not advanced in the vertebral body but rested upon the lamina but cement was not injected. During follow-up, the authors found no significant difference in perceived pain between the groups at any time-point while incidental vertebral fractures occurred in both groups (three in the VP group and four in the placebo group). The authors concluded that VP had no beneficial effect when compared to the sham procedure used. The study by Kallmes included a total of 131 patients who were assigned to undergo VP with PMMA cement ($n = 68$) or infiltration of the skin and periosteum with the possibility to crossover from either group at 1-month posttreatment. After 1 month no difference was found in disability scores or pain rating. At 3 months a significantly higher rate of crossover was found in patients from the control group than in the VP group. No incidental fractures were reported for any of the groups. The authors concluded that improvements in the VP study group were similar to improvements in the control group. Both studies have been criticized by virtue of a number of limitations: the low percentage of cases included from the total number of patients eligible; the improvement in pain after receiving treatment being unusually small for both the treatment and control arm, indicating that patients might have undergone inadequate or suboptimal VP procedures; the insufficient statistical power; the potential bias in patient selection; the inclusion of patients possibly not indicated for the treatment; and the sham not being a proper control.[23,25]

Studies describing the clinical results following VP using CaP cement to treat painful osteoporotic vertebral compression fractures are relatively rare.

Nakano and coauthors were, to our best knowledge, the first to describe the treatment of 65 osteoporotic vertebral compression fractures with VP using CaP cement.[18,116] Their results were indistinguishable from studies describing similar cohorts of patients treated with VP based on PMMA cement. Hillmeier and coauthors reported on the treatment of 102 patients with 192 osteoporotic vertebral compression fractures treated by balloon KP with PMMA cement in 138 cases and with CaP cement in 54 cases.[16] Again, the results were comparable for both groups and led to immediate, substantial, and long-term relief of pain in 89% of the patients. In 7% of all treated vertebral bodies cement leakage occurred, however, without clinical sequelae. Grafe *et al.*[15] performed a prospective comparative trial in which 20 patients received balloon KP with CaP cement and 20 patients with PMMA cement. After 3 years of follow-up, no differences were detected at any timepoint between the two groups. It was concluded that CaP cement was as effective as PMMA cement to achieve pain reduction and improvement of mobility in this category of patients. Furthermore, since CaP cement has the potential of being resorbed and replaced by new bone, they concluded this type of cement to be a promising alternative for PMMA cement especially in younger patients.

6.611.4.2. Metastatic/Malignant Vertebral Body Lesions

Metastatic vertebral body lesions and pathological fractures are exclusively being treated with VP or balloon KP in combination with PMMA cement. In 2003 Fourney and coworkers described the treatment of 97 vertebral levels in 56 patients with multiple myeloma ($n = 21$) or other primary malignancies ($n = 35$) by VP or balloon KP.[35] At a median follow-up length of 4.5 months, 84% of the patients noted marked or complete relief of pain while no patient was worse after treatment. Asymptomatic cement leakage was observed in six cases of VP; no cement leakage was observed in the KP group. The authors concluded that both procedures provided significant and durable pain relief in a high percentage of patients. In a recent review on cement injection for spinal metastases Heini and Pfäffli stated VP and balloon KP with PMMA cement to be extremely efficient procedures provided that treatment is restricted to osteolytic lesions in the presence of mechanically challenged bony structures. In a review of the literature, Bouza and coauthors reported on the pooled data of seven studies describing the clinical outcome of balloon KP with PMMA cement for the treatment of malignant spinal fractures and concluded, despite the limited methodological quality of the original studies, that balloon KP is a well-tolerated, relatively safe, and effective technique to provide early relief of pain and improved functional outcomes in this category of patients.[34]

6.611.4.3. Traumatic Fractures

Traumatic fractures of the spine are mostly seen in young and active individuals and bone void fillers used for vertebral body augmentation in this group of patients are likely to remain *in situ* for many decades and will be subjected to many load cycles.[117,118] Concerns on the detrimental long-term effects of acrylic cements in the spine, including short-term inflammation or thermal necrosis and long-term particle-induced osteolysis, have prompted researchers and clinicians to revert to alternative biomaterials. In 2005 Verlaan and coworkers reported on the application of CaP cement after pedicle screw fixation and balloon-assisted endplate reduction in a small series of 20 patients with traumatic thoracolumbar fractures.[119] It was found that the procedure was relatively undemanding for patients, a significant restoration of the vertebral body anatomy was achieved, and major complications were not observed except for an adjacent level fracture in one patient necessitating a secondary surgical intervention. All patients underwent elective removal of their pedicle instrumentation between 12 and 18 months posttrauma as part of the study protocol. At a minimum of 6 years follow-up it was found that recurrence of kyphosis had not occurred. Similar studies were published by Korovessis *et al.*[120] and Marco and Kushwaha,[121] respectively. In the series by Korovessis and coauthors, a total of 23 patients with thoracolumbar burst fractures underwent pedicle screw instrumentation followed by balloon KP with CaP cement and it was concluded after a minimum of 2 years follow-up that the technique provided excellent immediate reduction of posttraumatic kyphosis, provided significant spinal canal clearance, and restored vertebral body height of the fractured level. Marco and coauthors described a series of 38 patients with unstable thoracolumbar burst fractures with and without associated neurological deficits treated with short-segment pedicle screw fixation followed by transpedicular balloon-assisted endplate reduction and injection of CaP cement. It was concluded that the procedure led to maintained or improved neurological function in all patients with preexistent neurological deficits and a low rate of instrumentation failure or loss of correction. Maestretti and coauthors reported on a series of patients with traumatic thoracolumbar fractures treated with standalone (i.e., without pedicle screw fixation) balloon KP using CaP cement.[122] Although the clinical results were good, it was noted that CaP cement had distinctive biomechanical disadvantages compared to PMMA cement sometimes leading to loss of fracture correction and unpredictable resorption behavior. Currently, Blattert *et al.*[123] recommend against standalone treatment of traumatic thoracolumbar fractures by VP or balloon KP.

To our knowledge, only one article has been published on the treatment of traumatic thoracolumbar fractures treated by pedicle screw fixation and VP using PMMA cement.[124] In this work, Cho and coworkers report on a series of 70 patients of which 20 underwent VP additional to pedicle screw fixation and 50 underwent regular pedicle screw fixation.[124] The authors concluded from their work that reinforcement of the anterior column with VP using PMMA cement may achieve and maintain kyphosis correction and decrease instrument failure rate.

6.611.5. Complications in Spinal Column Augmentation

Within 2 years after the widespread use of VP with PMMA bone cement, the first descriptions of serious complications occurred. Two independent cases of symptomatic pulmonary embolism resulted from extravasation of bone cement into the pulmonary circulation.[6,7] Shortly after, it was found that the incidence of asymptomatic pulmonary embolism could

be as high as 87.9% and was predominantly related to an excessive volume of cement injected.[125,126] It is a currently accepted notion that during VP or balloon KP, leakage of cement into the surrounding soft tissue, venous circulation, or pulmonary system often goes unnoticed by both the physician and the patient. Complications arising from VP or balloon KP can be divided into categories of minor and major severity.[12] Minor complications include wound hematoma, superficial infection, rib fracture due to patient manipulation, needle malpositioning, and asymptomatic cement extravasation. These minor complications are responsible for an estimated 95–98% of all adverse events. Major complications include symptomatic pulmonary embolism, cement infection, symptomatic spinal cord or root compression, myocardial infarction, and death. Many studies have reported cement emboli to be present in the pulmonary circulation after augmentation of the spinal column by VP or balloon KP. In a recent meta-analysis of the literature, Lee *et al.*[12] reported on a total of 3078 cases of cement leakage found in 4097 patients treated with VP using PMMA leading to an unusually high leakage percentage of 75%. Symptomatic leakage of cement was, however, found in only 1.5% of cases reported. The number of asymptomatic versus symptomatic cement leakage after treatment with balloon KP was found to be 14% and 0.06%, respectively. The review by McGirt and coauthors confirmed these results and, moreover, reported neurological decline to occur in less than 1% of cases treated by VP and balloon KP.[127] These results raise the question as to why cement leakage is apparently tolerated so well by the majority of patients. It is currently, for example, not known what factors are involved or necessary for pulmonary embolism to become symptomatic after cement leakage has occurred. Patient-related factors, such as decreased pulmonary capacity and heart failure, may lead to a predilection for symptomatic pulmonary embolism but do not explain the actual occurrence since these highly prevalent conditions may be present in the asymptomatic group as well. Many reviews of the pertinent literature have, however, shown almost all complications, both of minor and major severity, to be related to leakage of bone cement. Two groups of factors have been identified to potentially influence the risk of adverse events following VP or balloon KP.

Factors increasing the risk of cement leakage are

1. fracture type,
2. duration of symptoms,
3. instruments/instrument positioning/spinal anatomy,
4. viscosity of cement injected,
5. volume of cement injected.

Factors not increasing the risk of cement leakage are

6. mechanical/thrombogenic/thermal properties of cement,
7. general patient health characteristics.

6.611.5.1. Fracture Type

Osteoporotic vertebral compression fractures are associated with less cement extravasation than malignant spinal lesions, which in turn are less prone to cement leakage than traumatic fractures.[128] The explanation for the differences may be found in the varying degree of fracture comminution, cortical disruption, and surrounding soft tissue damage for these three categories.[129] It is hypothesized that postural reduction and subsequent ligamentotaxis may decrease the risk of cement extravasation due to minimization of fracture gaps and (partial) restoration of the vertebral anatomy thereby facilitating unimpeded cement flow.[29]

6.611.5.2. Duration of Symptoms

It has been suggested that the duration of symptoms influences both clinical outcome and incidence of cement extravasation in osteoporotic vertebral compression fractures. It is generally accepted that the optimal window for treatment ranges approximately between 6 and 12 weeks after the onset of symptoms. Performing spinal augmentation at an earlier stage is, considering the generally benign nature of these lesions showing full resolution in the majority of patients, considered overtreatment while after 3 months the effect of postural reduction is diminished. The optimal timing of intervention for metastatic spinal disease or traumatic fractures by VP or balloon KP is unknown but, considering the natural history of the lesions in this category of patients, is rather on acute or emergency basis than elective.[121]

6.611.5.3. Instruments/Instrument Positioning/Spinal Anatomy

In order to minimize the resistance of bone cement to flow, short, large-diameter cement delivering needles are recommended, regardless of the type of biomaterial used. Assuming laminar flow of a liquid with a given viscosity through a tube, the following equation can be applied (nonalgebraic version of Poiseuille's law):

$$\text{Flow} = \text{Pressure}^{*}\text{diameter}^{4}/\text{viscosity}^{*}\text{length}$$

Assuming a limitation of the pressure that can be generated by human force using a manually operated syringe and assuming a lower threshold of viscosity needed for safe injection of the biomaterial in the vertebral body, shortening the length of the needle while increasing its diameter will increase flow. Since the increase in flow is proportional to needle diameter by the fourth power, it is clear that using large-bore needles optimally facilitates injection of higher viscosity cement. The topic of cement viscosity and flow in relation to cement extravasation is described in more detail elsewhere in this chapter. The optimal positioning of the needle(s) is considered to be close to the midline in the anterior third of the vertebral body. Deviating from this position may lead to uneven distribution of cement and increased risk for cement extravasation due to the proximity of venous structures (anterior vertebral venous plexus; intraspinal extradural venous plexus).[130] Unipedicular, bipedicular, or extrapedicular procedures are currently being performed for both VP and balloon KP and are showing identical results.[131] It can be argued that the utilization of the unipedicular approach would decrease the chance of instrument malposition by 50%. However, controlled clinical trials showing this theoretical advantage to lead to better clinical results and less cement extravasation or complications have

not been performed. Variations in patient anatomy, most notably small-diameter or aberrant pedicles, can lead to difficulties in proper access to the vertebral body and may, in case of pedicle wall fracture, increase the risk of false routes and subsequent leakage of cement.

6.611.5.4. Viscosity of Cement Injected

The viscosity of the bone cement injected in the spinal column is of utmost importance to achieve even flow and controlled distribution of the biomaterial in the vertebral cancellous bone. However, during polymerization of PMMA cement (or formation of HA crystals during setting in the case of calcium phophate cements), the viscosity increases slowly but exponentially with time from the moment of mixing the components until the fully cured state.[132] The interval in which bone cement can safely be injected is often called the working time or injection phase and is dependent on

- the initial ratio of ingredients (monomer-to-polymer in PMMA cement and ratio of liquid-to-CaP in CaP cement);[40,133]
- the presence of additives in PMMA cement or alternative solutions for CaP cement;[134,135]
- the temperature of the components before mixing;[136]
- the mixing process itself;[132]
- the temperature of the environment ('room temperature') during polymerization/setting;[136]
- considering the significant variations in working time under apparently identical circumstances: miscellaneous yet unidentified factors.[45]

By trial and error, clinicians have found, rather unscientifically, that the optimal viscosity for safe injection resembles that of toothpaste or spaghetti; cement of lower viscosity (before the injection phase) led to frequent extravasation while cement displaying higher viscosity (after the injection phase) substantially reduced injectability.[137] Baroud and coauthors quantified this observation using cements of different viscosities in an *in vitro* model of VP.[138] It was demonstrated that the highest viscosity cement stabilized flow and prevented extravasation but was no longer injectable using human force. An experimental study by Loeffel and coauthors, published in 2008, assessed distribution of PMMA cement in the vertebral body as a function of cement viscosity, bone porosity, and injection speed.[139] Their main conclusion was that viscosity was the key factor to reduce cement extravasation and should be adapted to each patient individually according to the degree of osteoporosis present. It was advised to use high-viscosity cement combined with high injecting speed to safely augment the vertebral body. The experimental work by Krebs and coworkers, investigating bone marrow fat embolism in an *in vivo* VP model, however, suggests that increasing cement viscosity and injection speed could lead to different, yet no less harmless, adverse events.[140,141]

6.611.5.5. Volume of Cement Injected

In the first decade following the invention of VP, near-complete filling of a vertebral body with bone cement was considered necessary for good clinical outcome. However, soon it was realized that smaller amounts of cement injected led to identical good results while substantially decreasing the occurrence of adverse events related to cement extravasation. Injection of 3–4 ml bone cement in the thoracic spine and of 4–6 ml cement in the lumbar spine is presently recommended by many authors and this practice has, thus far, been shown to yield the optimal compromise between clinical outcome and adverse events related to cement leakage.[142] No data are yet available on the efficacy and safety of spinal augmentation using even less cement.

6.611.5.6. Mechanical/Thrombogenic/Thermal Properties of Cement

Limited data are available on whether the contribution of bone cement to the development of pulmonary embolism after extravasation is by direct mechanical blockage of pulmonary vessels or by promotion of thromboembolic processes downstream. In multiple *in vitro* studies conducted by Cenni *et al.* it was demonstrated that several acrylic cements, when tested for hemolytic activity, antithrombotic properties, and the plasmatic phase of coagulation, did not seem to influence these parameters.[143–145] Further work by the same group showed that, in general, products released from acrylic cements were not able to elicit a specific immune or endothelial response.[146] The lack of thrombogenic activity in PMMA cement was confirmed by the work of Blinc and coauthors, adding that liquid components of this type of cement inhibited platelet aggegration and plasma clotting *in vitro*.[147] Concluding from these studies it seems plausible that mechanical blocking of the pulmonary circulation by cement particles, as opposed to chemical induction of thrombogenesis, is responsible for the development of pulmonary embolism when using PMMA cement. Large cement particle size (>2 mmr) in combination with preexistent risk factors for symptomatic pulmonary embolism can be hypothesized to constitute the key etiological factors for the occurrence of this complication.[86]

With respect to CaP cements and the occurrence of pulmonary embolism, two experimental *in vivo* studies have been conducted to test the hypothesis that extravasation of CaP cement into the venous circulation may result in uncontrolled activation of the coagulation cascade.[148,149] In the study by Bernards *et al.*,[148] CaP was injected directly into the venous system of 21 pigs to investigate any cardiopulmonary insults. An overall mortality of 13 out of 21 pigs was observed following a profound increase in pulmonary artery pressure and subsequent drop in left atrial and systemic blood pressure after cement injection. On autopsy, massive thromboemboli were found in the arterial pulmonary circulation and right ventricle. The authors hypothesized that semiliquid, curing CaP cement may have acted as a powerful scaffold for blood clot formation. Furthermore, it was suggested that the release of significant amounts of calcium in the circulation, being an important cofactor in the coagulation cascade, may have further stimulated the coagulation process.

The occurrence of neurological deterioration after leakage of cement into the spinal canal or neural foramina has been suggested to result from mechanical compression of neural structures (i.e., spinal cord, cauda equina, or neural roots)

or thermal damage. Currently, the damage by mechanical compression of neural structures, resulting from cement extravasation after VP or balloon KP, is undisputed and warrants immediate surgical decompression.[150] Patients in any of the three indication categories presenting with neurological deficits are not considered good candidates for spinal augmentation with injectable bone cements without additional surgical decompressive measures, since leakage of cement into the spinal canal may further compromise neurological function.

The often suggested possibility that local heat, produced during the exothermic polymerization of PMMA, may cause neural tissue damage has received considerable attention in recent *in vitro* and *in vivo* studies.[30,32,151] Several experimental investigations have demonstrated conductive and convective mechanisms by the circulation and flow of cerebrospinal fluid to effectively dispose of the excessive thermal energy generated by the curing cement. The heat effect of large quantities of polymerizing PMMA cement located in the spinal canal, however, was not studied and may still pose a considerable threat to neural tissue integrity. CaP cements set isothermically and concerns about thermal damage therefore do not apply.

6.611.5.7. General Patient Health Characteristics

Health hazards that are generally prevalent in the frail and elderly include hypertension, osteoporosis, diabetes mellitus, coronary artery disease, heart failure, coagulation disorders, and chronic obstructive pulmonary disease. These are obvious patient-related factors associated with an increased complication risk for virtually any surgical treatment and may account for, at least, some of the complications occurring after spinal augmentation including both minor and major events such as rib fracture, infection, hematoma, pulmonary embolism, and myocardial infarction.[12]

6.611.6. Future Directions and Conclusions

The number of articles published in basic scientific and clinical journals on injectable bone cements for spinal column augmentation has expanded immensely in the last decade. Despite all this work, no generally accepted explanations have emerged as to why augmenting the vertebral body leads, in general, to such good clinical results; whether adjacent fractures occur more frequently after augmentation of the spine; why cement leakage sometimes, but certainly not always, leads to serious complications. Acknowledging the logistic (study enrollment) and ethical (sham operations) difficulties in conducting randomized controlled trials to find an effect of VP or balloon KP, investigators could focus on well-controlled dose-dependent studies. In these studies the minimal amount of cement needed for adequate pain reduction could be established which could serve as a basis to support or refute the fracture stabilization theory and find the optimum balance between treatment effect and complication rate.

If augmentation of the spinal column indeed leads to pain reduction, by stabilization or other means, the next step would be to identify the key factors that determine success or failure. Considering the exceedingly large number of procedures of VP and balloon KP performed each year, establishing a registry (similar to the large total hip/knee replacement databases in worldwide use today) may help clinicians identify factors leading to the occurrence of adjacent level fractures and symptomatic pulmonary embolism, for example. Such analyses are generally useful for suggesting better performing biomaterial characteristics. It is a tempting concept that the biomechanical and biological properties of an ideal bone cement more closely match the individual patient requirements. Factors such as cement stiffness and capacity for osseointegration may be adapted to unique individual characteristics including easily quantifiable variables such as gender, age, and bone mineral density and further including more qualitative concepts such as activities of daily life, workload, risk of major intraoperative complications, and life expectancy. As the medical community is slowly gaining a better understanding of the specific needs for patients with spinal lesions, it is possible that, in time, more individualized vertebral bone void fillers may become available.

The last two decades have brought us promising new minimal invasive techniques and biomaterials to augment the spinal column of patients who otherwise would be confined to long-term immobilization and analgesics or subjected to major surgery. By virtue of sheer need, these techniques and biomaterials were introduced and became widely accepted. Well-controlled studies addressing safety and efficacy were not routinely performed. Continued progress in this exciting field should depend on rigorous scientific and clinical studies.

References

1. Galibert, P.; Deramond, H.; Rosat, P.; Le Gars, D. *Neurochirurgie* **1987**, *33*(2), 166–168.
2. Boss, J. H.; Shajrawi, I.; Dekel, S.; Mendes, D. G. *J. Biomater. Sci. Polym. Ed.* **1993**, *5*(3), 221–230.
3. Jensen, M. E.; Evans, A. J.; Mathis, J. M.; Kallmes, D. F.; Cloft, H. J.; Dion, J. E. *AJNR Am. J. Neuroradiol.* **1997**, *18*(10), 1897–1904.
4. Cortet, B.; Cotten, A.; Boutry, N.; *et al. J. Rheumatol.* **1999**, *26*(10), 2222–2228.
5. Martin, J. B.; Jean, B.; Sugiu, K.; *et al. Bone* **1999**, *25*(Suppl. 2), 11S–15S.
6. Padovani, B.; Kasriel, O.; Brunner, P.; Peretti-Viton, P. *AJNR Am. J. Neuroradiol.* **1999**, *20*(3), 375–377.
7. Perrin, C.; Jullien, V.; Padovani, B.; Blaive, B. *Rev. Mal. Respir.* **1999**, *16*(2), 215–217.
8. Jarvik, J. G.; Deyo, R. A. *AJNR Am. J. Neuroradiol.* **2000**, *21*(8), 1373–1374.
9. Trout, A. T.; Kallmes, D. F. *AJNR Am. J. Neuroradiol.* **2006**, *27*(7), 1397–1403.
10. Buchbinder, R.; Osborne, R. H.; Ebeling, P. R.; *et al. N. Engl. J. Med.* **2009**, *361*(6), 557–568.
11. Kallmes, D. F.; Comstock, B. A.; Heagerty, P. J.; *et al. N. Engl. J. Med.* **2009**, *361*(6), 569–579.
12. Lee, M. J.; Dumonski, M.; Cahill, P.; Stanley, T.; Park, D.; Singh, K. *Spine (Phila Pa 1976)* **2009**, *34*(11), 1228–1232.
13. Lieberman, I. H.; Dudeney, S.; Reinhardt, M. K.; Bell, G. *Spine* **2001**, *26*(14), 1631–1638.
14. Taylor, R. S.; Taylor, R. J.; Fritzell, P. *Spine (Phila Pa 1976)* **2006**, *31*(23), 2747–2755.
15. Grafe, I. A.; Baier, M.; Noldge, G.; *et al. Spine (Phila Pa 1976)* **2008**, *33*(11), 1284–1290.
16. Hillmeier, J.; Grafe, I.; Da Fonseca, K.; *et al. Orthopade* **2004**, *33*(8), 893–904.
17. Matsuyama, Y.; Goto, M.; Yoshihara, H.; *et al. J. Spinal Disord. Tech.* **2004**, *17*(4), 291–296.
18. Nakano, M.; Hirano, N.; Matsuura, K.; *et al. J. Neurosurg.* **2002**, *97*(Suppl. 3), 287–293.
19. Verlaan, J. J.; Oner, F. C.; Slootweg, P. J.; Verbout, A. J.; Dhert, W. J. *J. Bone Joint Surg. Am.* **2004**, *86A*(6), 1230–1238.
20. Dalby, M. J.; Di, S. L.; Harper, E. J.; Bonfield, W. *Biomaterials* **2001**, *22*(13), 1739–1747.

21. Heini, P. F.; Berlemann, U. *Eur. Spine J.* **2001**, *10*(Suppl. 2), S205–S213.
22. Verlaan, J. J.; van Helden, W. H.; Oner, F. C.; Verbout, A. J.; Dhert, W. J. *Spine* **2002**, *27*(5), 543–548.
23. Aebi, M. *Eur. Spine J.* **2009**, *18*(9), 1247–1248.
24. Kallmes, D. F.; Jarvik, J. G. *Lancet* **2009**, *373*(9668), 982–984.
25. Weinstein, J. N. *N. Engl. J. Med.* **2009**, *361*(6), 619–621.
26. Evans, A. J.; Jensen, M. E.; Kip, K. E.; *et al. Radiology* **2003**, *226*(2), 366–372.
27. Voormolen, M. H.; Mali, W. P.; Lohle, P. N.; *et al. AJNR Am. J. Neuroradiol.* **2007**, *28*(3), 555–560.
28. Heini, P. F.; Berlemann, U.; Kaufmann, M.; Lippuner, K.; Fankhauser, C.; van Landuyt, P. *Eur. Spine J.* **2001**, *10*(2), 164–171.
29. Koh, Y. H.; Han, D.; Cha, J. H.; Seong, C. K.; Kim, J.; Choi, Y. H. *Acta Radiol.* **2007**, *48*(3), 315–320.
30. Aebli, N.; Goss, B. G.; Thorpe, P.; Williams, R.; Krebs, J. *Spine* **2006**, *31*(15), 1674–1678.
31. Togawa, D.; Bauer, T. W.; Lieberman, I. H.; Takikawa, S. *Spine* **2003**, *28*(14), 1521–1527.
32. Verlaan, J. J.; Oner, F. C.; Verbout, A. J.; Dhert, W. J. *J. Biomed. Mater. Res.* **2003**, *67B*(1), 581–585.
33. Chi, J. H.; Gokaslan, Z. L. *Curr. Opin. Support. Palliat. Care* **2008**, *2*(1), 9–13.
34. Bouza, C.; Lopez-Cuadrado, T.; Cediel, P.; Saz-Parkinson, Z.; Amate, J. M. *BMC. Palliat. Care* **2009**, *8*, 12.
35. Fourney, D. R.; Schomer, D. F.; Nader, R.; *et al. J. Neurosurg.* **2003**, *98*(Suppl. 1), 21–30.
36. Oner, F. C.; van Gils, A. P.; Dhert, W. J.; Verbout, A. J. *Skeletal Radiol.* **1999**, *28*(8), 433–443.
37. Oner, F. C.; vd Rijt, R. H.; Ramos, L. M.; Groen, G. J.; Dhert, W. J.; Verbout, A. J. *Eur. Spine J.* **1999**, *8*(3), 194–198.
38. Knop, C.; Blauth, M.; Buhren, V.; *et al. Unfallchirurg* **1999**, *102*(12), 924–935.
39. Jefferiss, C. D.; Lee, A. J.; Ling, R. S. *J. Bone Joint Surg. Br.* **1975**, *57*(4), 511–518.
40. Baroud, G.; Bohner, M.; Heini, P.; Steffen, T. *Biomed. Mater. Eng.* **2004**, *14*(4), 487–504.
41. Debrunner, H. U.; Wettstein, A. *Arch. Orthop. Unfallchir.* **1975**, *81*(4), 291–299.
42. Lewis, G.; Mishra, S. R. *J. Biomed. Mater. Res. B Appl. Biomater.* **2007**, *81*(2), 524–529.
43. Krebs, J.; Ferguson, S. J.; Bohner, M.; Baroud, G.; Steffen, T.; Heini, P. F. *Spine (Phila Pa 1976)* **2005**, *30*(5), E118–E122.
44. Hansen, D.; Jensen, J. S. *J. Arthroplasty* **1990**, *5*(4), 287–290.
45. Boger, A.; Wheeler, K. D.; Schenk, B.; Heini, P. F. *Eur. Spine J.* **2009**, *18*(9), 1272–1278.
46. Baroud, G.; Vant, C.; Wilcox, R. *J. Long Term Eff. Med. Implants* **2006**, *16*(4), 265–280.
47. Lin, E. P.; Ekholm, S.; Hiwatashi, A.; Westesson, P. L. *AJNR Am. J. Neuroradiol.* **2004**, *25*(2), 175–180.
48. Berlemann, U.; Ferguson, S. J.; Nolte, L. P.; Heini, P. F. *J. Bone Joint Surg. Br.* **2002**, *84*(5), 748–752.
49. Boger, A.; Bisig, A.; Bohner, M.; Heini, P.; Schneider, E. *J. Biomater. Sci. Polym. Ed.* **2008**, *19*(9), 1125–1142.
50. Boger, A.; Bohner, M.; Heini, P.; Verrier, S.; Schneider, E. *J. Biomed. Mater. Res. B Appl. Biomater.* **2008**, *86B*(2), 474–482.
51. Puska, M. A.; Kokkari, A. K.; Narhi, T. O.; Vallittu, P. K. *Biomaterials* **2003**, *24*(3), 417–425.
52. Erbe, E. M.; Clineff, T. D.; Gualtieri, G. *Eur. Spine J.* **2001**, *10*, S147–S152.
53. Bae *et al.* (2010).
54. Lewis, G. *J. Biomed. Mater. Res. B Appl. Biomater.* **2006**, *76*(2), 456–468.
55. Bohner, M. *Eur. Spine J.* **2001**, *10*(Suppl. 2), S114–S121.
56. Habib, M.; Baroud, G.; Gitzhofer, F.; Bohner, M. *Acta Biomater.* **2010**, *6*(1), 250–256.
57. Khairoun, I.; Boltong, M. G.; Driessens, F. C.; Planell, J. A. *J. Mater. Sci. Mater. Med.* **1998**, *9*(8), 425–428.
58. Bohner, M.; Baroud, G. *Biomaterials* **2005**, *26*(13), 1553–1563.
59. Lieberman, I. H.; Togawa, D.; Kayanja, M. M. *Spine J.* **2005**, *5*(Suppl. 6), 305S–316S.
60. Glazer, P. A.; Spencer, U. M.; Alkalay, R. N.; Schwardt, J. *Spine J.* **2001**, *1*(6), 395–401.
61. Lazary, A.; Speer, G.; Varga, P. P.; *et al. J. Orthop. Res.* **2008**, *26*(5), 601–607.
62. Hartman, E. H.; Vehof, J. W.; Spauwen, P. H.; Jansen, J. A. *Biomaterials* **2005**, *26*(14), 1829–1835.
63. Huse, R. O.; Quinten, R. P.; Wolke, J. G.; Jansen, J. A. *Clin. Oral Implants Res.* **2004**, *15*(6), 741–749.
64. Anselme, K. *Biomaterials* **2000**, *21*(7), 667–681.
65. Denissen, H. W.; Kalk, W.; Veldhuis, A. A.; Van Den, H. A. *J. Prosthet. Dent.* **1989**, *61*(6), 706–712.
66. Gosain, A. K.; McCarthy, J. G.; Staffenberg, D.; Glat, P. M.; Simmons, D. J. *Plast. Reconstr. Surg.* **1996**, *97*(5), 1001–1013.
67. Daculsi, G.; Laboux, O.; Malard, O.; Weiss, P. *J. Mater. Sci. Mater. Med.* **2003**, *14*(3), 195–200.
68. Chow, L. C. *Monogr. Oral Sci.* **2001**, *18*, 148–163.
69. Ooms, E. M.; Wolke, J. G.; van de Heuvel, M. T.; Jeschke, B.; Jansen, J. A. *Biomaterials* **2003**, *24*(6), 989–1000.
70. Bohner, M.; Doebelin, N.; Baroud, G. *Eur. Cell Mater.* **2006**, *12*, 26–35.
71. Habraken, W. J.; Wolke, J. G.; Mikos, A. G.; Jansen, J. A. *J. Biomater. Sci. Polym. Ed.* **2006**, *17*(9), 1057–1074.
72. LeGeros, R. Z. *Clin. Mater.* **1993**, *14*(1), 65–88.
73. Habraken, W. J.; de Jonge, L. T.; Wolke, J. G.; Yubao, L.; Mikos, A. G.; Jansen, J. A. *J. Biomed. Mater. Res. A* **2008**, *87*(3), 643–655.
74. Schmitz, J. P.; Hollinger, J. O.; Milam, S. B. *J. Oral Maxillofac. Surg.* **1999**, *57*(9), 1122–1126.
75. Ishikawa, K.; Takagi, S.; Chow, L. C.; Ishikawa, Y.; Eanes, E. D.; Asaoka, K. *Dent. Mater.* **1994**, *10*(1), 26–32.
76. Habraken, W. J.; Zhang, Z.; Wolke, J. G.; *et al. Biomaterials* **2008**, *29*(16), 2464–2476.
77. Ruhe, P. Q.; Hedberg, E. L.; Padron, N. T.; Spauwen, P. H.; Jansen, J. A.; Mikos, A. G. *J. Bone Joint Surg. Am.* **2003**, *85A*(Suppl. 3), 75–81.
78. del Real, R. P.; Wolke, J. G.; Vallet-Regi, M.; Jansen, J. A. *Biomaterials* **2002**, *23*(17), 3673–3680.
79. Ruhe, P. Q.; Hedberg-Dirk, E. L.; Padron, N. T.; Spauwen, P. H.; Jansen, J. A.; Mikos, A. G. *Tissue Eng.* **2006**, *12*(4), 789–800.
80. Motoyoshi, M.; Ueno, S.; Okazaki, K.; Shimizu, N. *Int. J. Oral Maxillofac. Surg.* **2009**, *38*(4), 363–368.
81. Link, D. P.; van den Dolder, J.; Jurgens, W. J.; Wolke, J. G.; Jansen, J. A. *Biomaterials* **2006**, *27*(28), 4941–4947.
82. Bodde, E. W.; Kowalski, R. S.; Spauwen, P. H.; Jansen, J. A. *Tissue Eng. A* **2008**, *14*(1), 29–39.
83. Plachokova, A.; Link, D.; van den Dolder, D. J.; van den Beucken, J.; Jansen, J. *J. Tissue Eng. Regen. Med.* **2007**, *1*(6), 457–464.
84. Plachokova, A. S.; van den Dolder, J.; Stoelinga, P. J.; Jansen, J. A. *Clin. Oral Implants. Res.* **2007**, *18*(2), 244–251.
85. Ruhe, P. Q.; Hedberg, E. L.; Padron, N. T.; Spauwen, P. H.; Jansen, J. A.; Mikos, A. G. *J. Bone Joint Surg. Am.* **2003**, *85A* (Suppl. 3), 75–81.
86. Kim, Y. J.; Lee, J. W.; Park, K. W.; *et al. Radiology* **2009**, *251*(1), 250–259.
87. Sabokbar, A.; Fujikawa, Y.; Murray, D. W.; Athanasou, N. A. *J. Bone Joint Surg. Br.* **1997**, *79*(1), 129–134.
88. Wang, X.; Ye, J.; Wang, Y. *Acta Biomater.* **2007**, *3*(5), 757–763.
89. Beruto, D. T.; Mezzasalma, S. A.; Capurro, M.; Botter, R.; Cirillo, P. *J. Biomed. Mater. Res.* **2000**, *49*(4), 498–505.
90. Dalby, M. J.; Di, S. L.; Harper, E. J.; Bonfield, W. *J. Mater. Sci. Mater. Med.* **1999**, *10*(12), 793–796.
91. Vallo, C. I.; Montemartini, P. E.; Fanovich, M. A.; Porto Lopez, J. M.; Cuadrado, T. R. *J. Biomed. Mater. Res.* **1999**, *48*(2), 150–158.
92. Saito, M.; Maruoka, A.; Mori, T.; Sugano, N.; Hino, K. *Biomaterials* **1994**, *15*(2), 156–160.
93. Dalby, M. J.; Di, S. L.; Harper, E. J.; Bonfield, W. *Biomaterials* **2001b**, *22*(13), 1739–1747.
94. Castaldini, A.; Cavallini, A. *Biomaterials* **1985**, *6*(1), 55–60.
95. Harper, E. J.; Braden, M.; Bonfield, W. *J. Mater. Sci. Mater. Med.* **2000**, *11*(8), 491–497.
96. Canul-Chuil, A.; Vargas-Coronado, R.; Cauich-Rodriguez, J. V.; Martinez-Richa, A.; Fernandez, E.; Nazhat, S. N. *J. Biomed. Mater. Res. B Appl. Biomater.* **2003**, *64*(1), 27–37.
97. Heikkila, J. T.; Aho, A. J.; Kangasniemi, I.; Yli-Urpo, A. *Biomaterials* **1996**, *17*(18), 1755–1760.
98. Dalby, M. J.; Di, S. L.; Harper, E. J.; Bonfield, W. *Biomaterials* **2002**, *23*(2), 569–576.
99. Lewis, G. *J. Biomed. Mater. Res.* **1997**, *38*(2), 155–182.
100. Boger, A.; Bohner, M.; Heini, P.; Schwieger, K.; Schneider, E. *Acta Biomater.* **2008**, *4*(6), 1688–1693.
101. Bruens, M. L.; Pieterman, H.; de Wijn, J. R.; Vaandrager, J. M. *J. Craniofac. Surg.* **2003**, *14*(1), 63–68.
102. Boger, A.; Heini, P.; Windolf, M.; Schneider, E. *Eur. Spine J.* **2007**, *16*(12), 2118–2125.
103. Verlaan, J. J.; Oner, F. C.; Dhert, W. J. *Biomaterials* **2005**, *27*(3), 290–301.
104. Boyd, D.; Clarkin, O. M.; Wren, A. W.; Towler, M. R. *Acta Biomater.* **2008**, *4*(2), 425–431.

105. Perry, A.; Mahar, A.; Massie, J.; Arrieta, N.; Garfin, S.; Kim, C. *Spine J.* **2005**, *5*(5), 489–493.
106. Zhao, F.; Lu, W. W.; Luk, K. D. K.; *et al. J. Biomed. Mater. Res. B* **2004**, *69B*, 79–86.
107. Yamamuro, T.; Nakamura, T.; Iida, H.; *et al. Biomaterials* **1998**, *19*, 1479–1482.
108. Gangi, A.; Kastler, B. A.; Dietemann, J. L. *AJNR Am. J. Neuroradiol.* **1994**, *15*(1), 83–86.
109. Diamond, T. H.; Champion, B.; Clark, W. A. *Am. J. Med.* **2003**, *114*(4), 257–265.
110. Hendrikse, C. A.; Kalmijn, S.; Voormolen, M. H.; Verhaar, H. J.; Mali, W. P. *Ned. Tijdschr. Geneeskd* **2003**, *147*(32), 1553–1559.
111. Ploeg, W. T.; Veldhuizen, A. G.; The, B.; Sietsma, M. S. *Eur. Spine J.* **2006**, *15*(12), 1749–1758.
112. Hochmuth, K.; Proschek, D.; Schwarz, W.; Mack, M.; Kurth, A. A.; Vogl, T. J. *Eur. Radiol.* **2006**, *16*(5), 998–1004.
113. Bouza, C.; Lopez, T.; Magro, A.; Navalpotro, L.; Amate, J. M. *Eur. Spine J.* **2006**, *15*(7), 1050–1067.
114. Hulme, P. A.; Krebs, J.; Ferguson, S. J.; Berlemann, U. *Spine (Phila Pa 1976)* **2006**, *31*(17), 1983–2001.
115. Wardlaw, D.; Cummings, S. R.; Van, M. J.; *et al. Lancet* **2009**, *373*(9668), 1016–1024.
116. Nakano, M.; Hirano, N.; Ishihara, H.; Kawaguchi, Y.; Matsuura, K. *J. Neurosurg. Spine* **2005**, *2*(1), 27–33.
117. Oner, F. C.; Verlaan, J. J.; Verbout, A. J.; Dhert, W. J. *Spine* **2006**, *31*(Suppl. 11), S89–S95.
118. Verlaan, J. J.; Diekerhof, C. H.; Buskens, E.; *et al. Spine* **2004**, *29*(7), 803–814.
119. Verlaan, J. J.; Dhert, W. J.; Verbout, A. J.; Oner, F. C. *Spine* **2005**, *30*(3), E73–E79.
120. Korovessis, P.; Repantis, T.; Petsinis, G.; Iliopoulos, P.; Hadjipavlou, A. *Spine (Phila Pa 1976)* **2008**, *33*(4), E100–E108.
121. Marco, R. A.; Kushwaha, V. P. *J. Bone Joint Surg. Am.* **2009**, *91*(1), 20–28.
122. Maestretti, G.; Cremer, C.; Otten, P.; Jakob, R. P. *Eur. Spine J.* **2007**, *16*(5), 601–610.
123. Blattert, T. R.; Jestaedt, L.; Weckbach, A. *Spine (Phila Pa 1976)* **2009**, *34*(2), 108–114.
124. Cho, D. Y.; Lee, W. Y.; Sheu, P. C. *Neurosurgery* **2003**, *53*(6), 1354–1360.
125. Schmidt, R.; Cakir, B.; Mattes, T.; Wegener, M.; Puhl, W.; Richter, M. *Eur. Spine J.* **2005**, *14*, 466–473.
126. Yeom, J. S.; Kim, W. J.; Choy, W. S.; Lee, C. K.; Chang, B. S.; Kang, J. W. *J. Bone Joint Surg. Br.* **2003**, *85*(1), 83–89.
127. McGirt, M. J.; Parker, S. L.; Wolinsky, J. P.; Witham, T. F.; Bydon, A.; Gokaslan, Z. L. *Spine J.* **2009**, *9*(6), 501–508.
128. Mousavi, P.; Roth, S.; Finkelstein, J.; Cheung, G.; Whyne, C. *J. Neurosurg.* **2003**, *99*(1 Suppl.), 56–59.
129. Whyne, C. M.; Hu, S. S.; Lotz, J. C. *Spine* **2003**, *28*(7), 652–660.
130. Prymka, M.; Puhler, T.; Hirt, S.; Ulrich, H. W. *Unfallchirurg* **2003**, *106*(10), 860–864.
131. Tohmeh, A. G.; Mathis, J. M.; Fenton, D. C.; Levine, A. M.; Belkoff, S. M. *Spine* **1999**, *24*(17), 1772–1776.
132. Baroud, G.; Matsushita, C.; Samara, M.; Beckman, L.; Steffen, T. *J. Biomed. Mater. Res.* **2004**, *68B*(1), 105–111.
133. Hernandez, L.; Gurruchaga, M.; Goni, I. *J. Biomed. Mater. Res. B Appl. Biomater.* **2006**, *77*(1), 98–103.
134. Cheung, K. M.; Lu, W. W.; Luk, K. D.; *et al. Spine (Phila Pa 1976)* **2005**, *30*(Suppl. 17), S84–S91.
135. Gbureck, U.; Barralet, J. E.; Spatz, K.; Grover, L. M.; Thull, R. *Biomaterials* **2004**, *25*(11), 2187–2195.
136. Sullivan, S. J.; Topoleski, L. D. *J. Biomed. Mater. Res. B Appl. Biomater.* **2007**, *81*(1), 224–230.
137. Anselmetti, G. C.; Zoarski, G.; Manca, A.; *et al. Cardiovasc. Intervent. Radiol.* **2008**, *31*(5), 937–947.
138. Baroud, G.; Falk, R.; Crookshank, M.; Sponagel, S.; Steffen, T. *J. Biomech.* **2004**, *37*(2), 189–196.
139. Loeffel, M.; Ferguson, S. J.; Nolte, L. P.; Kowal, J. H. *Spine (Phila Pa 1976)* **2008**, *33*(12), 1352–1359.
140. Aebli, N.; Krebs, J.; Davis, G.; Walton, M.; Williams, M. J.; Theis, J. C. *Spine* **2002**, *27*(5), 460–466.
141. Aebli, N.; Krebs, J.; Schwenke, D.; Davis, G.; Theis, J. C. *Spine* **2003**, *28*(14), 1513–1519.
142. Cotten, A.; Dewatre, F.; Cortet, B.; *et al. Radiology* **1996**, *200*(2), 525–530.
143. Cenni, E.; Ciapetti, G.; Granchi, D.; Savarino, L.; Stea, S.; Corradini, A. *Biomaterials* **2001**, *22*(11), 1321–1326.
144. Cenni, E.; Granchi, D.; Ciapetti, G.; Savarino, L.; Corradini, A. *Biomaterials* **2002**, *23*(1), 305–311.
145. Cenni, E.; Granchi, D.; Pizzoferrato, A. *J. Biomater. Sci. Polym. Ed.* **2002**, *13*(1), 17–25.
146. Cenni, E.; Ciapetti, G.; Granchi, D.; *et al. J. Biomed. Mater. Res.* **2001**, *55*(1), 131–136.
147. Blinc, A.; Bozic, M.; Vengust, R.; Stegnar, M. *Thromb. Res.* **2004**, *114*(3), 179–184.
148. Bernards, C. M.; Chapman, J.; Mirza, S. In *50th Annual Meeting of the Orthopaedic Research Society [Paper No: 0254]*, 2004.
149. Krebs, J.; Aebli, N.; Goss, B. G.; *et al. J. Biomed. Mater. Res. B Appl. Biomater.* **2007**, *82*(2), 526–532.
150. Harrington, K. D. *J. Bone Joint Surg. Am.* **2001**, *83A*(7), 1070–1073.
151. Deramond, H.; Wright, N. T.; Belkoff, S. M. *Bone* **1999**, *25*(Suppl. 2), 17S–21S.

6.612. Biomaterials for Intervertebral Disc Regeneration

B Gantenbein-Ritter, University of Bern, Bern, Switzerland
D Sakai, Tokai University School of Medicine, Isehara, Kanagawa, Japan

© 2011 Elsevier Ltd. All rights reserved.

6.612.1.	**Overview of Intervertebral Repair: Current Strategies**	162
6.612.1.1.	Introduction	162
6.612.1.2.	Normal Disc Structure and Function: Disc Cells, Extracellular Matrix, Nutrition	162
6.612.1.3.	Aging and Degeneration: Pathophysiology, Effect on Function and Pain, Repair Capacity	162
6.612.1.4.	Current Treatment Options (Conservative, Fusion Surgery, Motion Preservation Techniques, and Devices)	162
6.612.1.5.	New Treatment Strategies in Research (Protein Injections, Gene Therapy, Cell Therapy)	163
6.612.2.	**Repair of the NP**	164
6.612.2.1.	The Pathobiology of the NP	164
6.612.2.2.	Current Therapeutic Strategies	164
6.612.2.3.	Candidate Biomaterials for Nucleus Repair	164
6.612.2.3.1.	Polymers and biological molecules	164
6.612.2.3.2.	Biomaterials for tissue-engineering methods in cell-based nucleus repair	165
6.612.2.4.	Overview of Nucleus Repair and Regeneration	165
6.612.2.5.	Biomaterials for Cell Scaffolds	165
6.612.2.6.	Future Perspectives	165
6.612.3.	**Repair for the AF**	165
6.612.3.1.	Development and Healthy Structure of the AF	165
6.612.3.2.	Surgical Strategies to Rescue the AF	166
6.612.3.3.	Nonbiodegradable Materials	166
6.612.3.4.	Biodegradable: Resorbable Materials	166
6.612.3.4.1.	Polymers	166
6.612.3.4.2.	Silk and other biomaterials	167
6.612.3.4.3.	Collagen fiber scaffolds (electrospinning)	167
6.612.3.5.	Future Perspective: The Biological AF Replacement	167
References		167

Glossary

Alginate The chemical compound sodium alginate is the sodium salt of alginic acid. Its empirical formula is $NaC_6H_7O_6$. It is a linear copolymer with homopolymeric blocks of (1–4)-linked β-D-mannuronate and its C_5 epimer α-L-guluronate residues, which are covalently linked together in different sequences or blocks. Sodium alginate is a 'gold-standard' for three-dimensional culture of disc cells from the nucleus pulposus (NP) and has been proposed for NP replacement.

Atelocollagen This the solubilized collagen revealed from enzymatic removal of telopeptides by proteolytic enzymes such as pepsin. Telopeptides are nonhelical portions of the collagen that molecule are located at the N- and C-terminal ends (9∼26 residues).

Bone morphogenic proteins (BMPs) A family of growth factors involved in the bone morphogenesis. BMPs interact with specific receptors on the cell surface, referred to as bone morphogenetic protein receptors (BMPRs). Signal transduction through BMPRs results in the mobilization of members of the SMAD family of proteins. The signaling pathways involving BMPs, BMPRs, and SMADs are important in the development of the heart, central nervous system, and cartilage, as well as postnatal bone development.

Discogenic phenotype A cell phenotype, which differs from the chondrogenic phenotype by the ratio of hualoronic acid to total collagen, which has been described to be about 29:1 according to Mwale *et al.*[1] The phenotype is furthermore distinguished from the chondrocyte phenotype by transcriptomics as shown recently by Minogue *et al.*[2]

Growth and differentiation factor-5 (GDF-5) It is a growth factor of the BMP family and is assumed to induce discogenic pathway on mesenchymal stem cells.

Mesenchymal stem cells Multipotent stromal cells that can be differentiated into different cell phenotypes of the mesenchyme such as bone, chondrocytes, adipocytes, and myocytes. These cells have anti-inflammatory action and active potential to migrate (known as homing) to the site of injury.

Nucleotomy Surgical removal of the native nucleus pulposus tissue.

PEG PEG, PEO, or POE refers to an oligomer or polymer of ethylene oxide. PEGs are prepared by polymerization of ethylene oxide and are commercially available over a wide range of molecular weights from 300 to

$10\,000\,000\ g\,mol^{-1}$. PEGs hydrogels have been used for disc regeneration.
POM Poly(1,8)-octanediol malate. It is a malic acid-based polyester, which is formed by polycondensation.
SMAD The SMAD proteins are homologs of both the *Drosophila* protein, *mothers* against *decapentaplegic* (MAD), and the *Caenorhabditis elegans* protein SMA. The name is a combination of the two.

Abbreviations
AF Annulus fibrosus
bFGF Basic fibroblast growth factor
DDD Degenerative disc disease
ECM Extracellular matrix
HA Hyaluronic acid
IVD Intervertebral disc
LBP Low back pain
NP Nucleus pulposus
PG Proteoglycan
TGFβ Transforming and growth factor β

6.612.1. Overview of Intervertebral Repair: Current Strategies

6.612.1.1. Introduction

The healthy spine is indeed the 'backbone' of our society. Healthy discs function as essential load-absorbers between all vertebrae, allowing bending, flexion, and torsion of the spine. As the global population ages, the incidence of intervertebral disc (IVD) degeneration and low back pain (LBP) increases. The occurrence of LBP has been associated in many cases with degenerative disc disease (DDD).[3,4] Given that disc degeneration is a cell-mediated response to progressive structural failure, new treatments that normalize disc cell homeostasis and restore full disc function are required. Here, we review recent studies that aimed to regenerate the IVD with comprehensive biomaterials.

6.612.1.2. Normal Disc Structure and Function: Disc Cells, Extracellular Matrix, Nutrition

The IVDs lie between the vertebral bodies and link them together. The height of all discs makes up about a third of the spine.[5–7] The IVD is a complex structure mainly composed macroscopically of two different tissues, the fibrous tissue, annulus fibrosus, (AF) and in the center the nucleus pulposus (NP); the AF is anchored to the cartilaginous endplates of the vertebral bodies and keeps the NP in position. The IVD is avascular, and there are, thus, steep gradients in the concentration of nutrients and metabolites from the blood supply at the disc's margins to the cells in the center of the disc.[5,8–10] Even in normal healthy animal discs, low oxygen and high lactic acid concentrations (and thus acidic pH levels) compared to the levels of blood plasma have been recorded. Thus, the 'niche' for disc-like cells of the NP is marked by low oxygen concentration, high lactic acid concentrations, and relatively high hydrostatic pressures.[11,12] A nonpathophysiological disc acts as a shock-absorbing organ and provides motion for the spine and maintains disc height; thus, the distance between two adjacent vertebral bodies is kept in a certain tolerance range. With a closer look, there are in fact four different tissue types, that is, from the outside to the inside: (1) the outer AF, a ring of highly oriented, densely packed collagen fibril lamellae, (2) the fibrocartilaginous inner AF, (3) the transition zone, a thin zone between the inner AF and the central NP, and (4) the vertebral endplates, initially comprising hyaline cartilage of which the cells resemble chondrocytes found in other hyaline cartilage.[13,14]

6.612.1.3. Aging and Degeneration: Pathophysiology, Effect on Function and Pain, Repair Capacity

There are two processes that change the mechanical properties of the extracellular structure of the IVD. The first is ageing and the second is genetic preposition, known as degenerative disc disease (DDD).[13,15–26] As we age, the disc undergoes major apparent structural rearrangements that become macroscopically evident from the color change to brown and an apparent water loss in the NP.[27] Also the NP becomes very fibrous in nature and the disc loses water content as seen on magnet resonance imaging (MRI).[21,22,28] One major biological change is the cell death of disc cells at a relatively early stage of our lifetime. It is hypothesized limiting nutrition overlaid over aging is a genetically predisposed IVD degeneration. This has been described as DDD. The evidence comes from twin studies, which demonstrate a high heritability for DDD (70%).[29,30]

6.612.1.4. Current Treatment Options (Conservative, Fusion Surgery, Motion Preservation Techniques, and Devices)

LBP is limiting the daily activities of about 80% of people of our modern society at least once in the lifetime and there is increasing evidence that it is directly associated with DDD.[31,32] There are a variety of disc replacement strategies out in the market; however, fusion is still considered the 'gold' standard for all cases that lack an alternative treatment.[33,34]

Although fusion rates of ~90% are achieved, early complication rates of up to 31% have been registered.[35] Most of these complications are local hematomas or superficial infections; however, deep wound infection rates of 1.9–20% are also documented in the literature.[36,37] With regard to the long-term outcome, a high reoperation rate of 21.5% was found in an 11-year follow-up study for instrumented fusion of the lumbar spine. Two-thirds of these cases were related to implant complications or pseudoarthritis.[38] Unfortunately, spinal fusion alters the normal biomechanics of the spine, and the loss of motion at the fused levels is compensated by increased

motion at other nonfused segments. As a result, a significant amount of additional load is placed on the discs and facet joints at the nonfused levels. One commonly observed (and usually long term) consequence of fusing spinal motion segments and thus increasing the forces on the adjacent levels has been adjacent segment disease (ASD). As adjacent mobile segments proximal to the fusion degenerate over time, the initial good results following posterior spinal fusion often degrade. Radiographic evidence of ASD has been reported with a prevalence of more than 30%.[39,40] Reoperation rates due to ASD or transition syndrome lie between 20 and 27% over 2–15 years postoperatively. Mechanistic disc prostheses all have their major drawbacks and are far from being perfect in terms of range of motion and longevity. Some of the disc replacements may even lead to disc degeneration of adjacent vertebral bodies, spinal stenosis, or hypertrophic facet arthropathy.[41,42] Thus, in the clinics, there is an urgent need to understand the mechanisms that lead to disc degeneration. Moreover, there is a need to develop good model systems for the disc, such as organ cultures, to understand pathological mechanisms and to test clinical treatment scenarios.[43–46]

6.612.1.5. New Treatment Strategies in Research (Protein Injections, Gene Therapy, Cell Therapy)

Two regenerative approaches for the early degenerative lumbar IVD that are currently debated include (1) injection of growth factors[47–51] and (2) application of autologous stem cells[52–58] (**Figure 1**) (see **Chapter 6.615, Intervertebral Disc**).

On the side of growth factors, insulin-like growth factor-1,[78,79] basic fibroblast growth factor (bFGF),[80–81] and growth factors of the transforming growth factor-β (TGF-β) superfamily, mainly bone morphogenic protein (BMP) 2 and 4 and TGF-β1, have been investigated.[82–86] A relatively recently identified growth factor of the BMP family is growth and differentiation factor-5 (GDF-5).[87] GDF-5 plays a major role in skeletal development and has been shown to promote proliferation and matrix synthesis of IVD cells. Gene expression of aggrecan and collagen type 2 of rat disc cells was significantly upregulated upon overexpression of rhGDF-5 by viral transfection, and also simply adding the substance to the media led to dose-dependent responses.[88,89] GDF-5 has also been identified as a potential candidate for restoring disc height in the rabbit degenerative model.[50] In fact, all of these growth factors seem to be able to reverse at least partially disc height loss as demonstrated for the annular stab rabbit degeneration model. The question remains whether growth factors would be successful for discs with larger dimensions and nutritional problems.[90]

Cytotherapy appears to be an extremely potential approach to regenerate the degenerating disc[91] (**Figure 1**). Autologous mesenchymal stem cells (MSCs) have intensively been investigated as promising candidates for regenerative medicine.[51,71,92–98] There are two major reasons for this; one is their multipotentiality to differentiate into different cell types of the mesenchyme, which promotes them as ideal candidates for regeneration of bone, cartilage, muscle, tendon, and potentially IVD tissue.[45,99,100] The second reason is that these cells can be relatively easily isolated from various tissues, such as the bone marrow or adipose tissue.[96,101–104]

The MSCs would be ideally supplied in a scaffold, which could be a kind of injectable hydrogel in the case of NP replacement.[105–109] Here, chitosan in combination with gelatin[110] or, alternatively, hyaluronan in combination of collagen type 2[60] could be very promising to differentiate stem cells toward the 'discogenic' phenotype. Atellocollagen type I was a successful

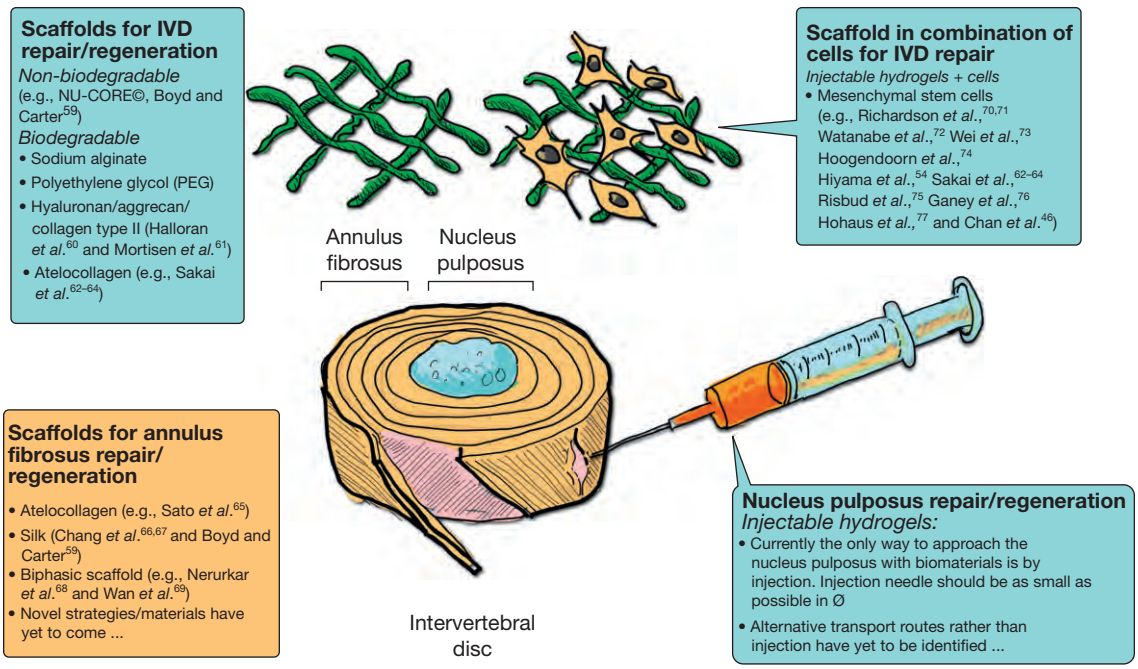

Figure 1 Overview of current regenerative approaches to rescue the intervertebrate disc from degeneration using a biomaterial scaffold with or without the injection of mesenchymal stem cells.

material to thrive stem cells toward discogenic phenotype or if NP cells are kept in hydrogels.[63,64] The definition of 'discogenic discs' to characterize differences between the phenotypes of NP cells and articular cartilage was completely lacking until recently. Some of these problems were addressed in recent comparative microarray studies to characterize the transcriptomes of the NP, the AF, and the articular chondrocyte phenotype in rat, dog, and human.[111–113] However, these recent studies also confirmed that the difference between the articular chondrocyte and the NP cell or a AF cell is only about a dozen genes, which show clear up or downregulation (in the order of >10 times difference). This finding, however, supports the old term of 'fibrocartilage,' which can be found in older text books on IVD tissue.

6.612.2. Repair of the NP

6.612.2.1. The Pathobiology of the NP

Developmentally, cells composing the NP are thought to originate from the notochord. At the beginning of the fourth week of embryonic period, somite undergoes a specialization to sclerotome, myotome, and dermatome (Table 1). Sclerotome becomes the future vertebrae. The mesenchymal tissue in the sclerotome forms a cylindrical column called perichordal tube that surrounds the notochord. Segmentation of the perichordial tube by aggregation of mesenchymal cells occurs to form dense perichordal discs. Then, chondrogenesis begins at the center of perichordal discs constricting the notochordal tissue passing through it, which eventually disappears in the vertebral bodies.[145,146] However, notochordal cells remain at the center which becomes the precursor of NP.[147] Classically, it has been documented that they are cells that contain large vacuoles interconnected with each other by gap junction to form cell clusters. However, in humans and several other species (e.g., chondrodystrophoid breed canines, cattle), these notochordal cells disappear earlier in life and chodrocyte-like mature NP cells from unknown origin take over. After the disappearance of notochordal NP cells remains chondrocyte-like cells of unknown origin, which produces more collagenous and less hydrated extracellular matrix (ECM) leading to aging or degeneration of the IVD and is often associated with LBP, spinal stenosis, and sciatica. Regarding the fact that species retaining notochordal NP cells for longer period of life rarely develops disc degeneration, understanding the molecular mechanism in the maintenance of notochordal and other NP cell populations may well provide key concepts to prevention of disc degeneration and regenerative strategies. It has been speculated that this morphological change in cells composing the NP is due to change in nutrition provided mostly by diffusion from the end plate. Hunter *et al.*[148] and Guehring *et al.*[149] have pointed out that notochordal cells are more metabolically active and more susceptible to nutrient deprivation compared to mature NP cells. They have also found that animal species with higher end plate porosity will retain the nucleus environment, which may prevent apoptosis of the notochordal cells.

6.612.2.2. Current Therapeutic Strategies

Treatment of disease resulting from disc degeneration includes surgical procedures, such as discectomy and spinal fusion; however, these procedures do not preserve the function of IVD. Moreover, they reduce the mobility of the associated spinal motion segment and increase the mechanical load and stresses on adjacent discs. Mobility preserving techniques using artificial disc and nucleus implants have been tested clinically to preserve mobility in cases of severely damaged discs (see **Chapter 6.614, Wear: Total Intervertebral Disc Prostheses**).

6.612.2.3. Candidate Biomaterials for Nucleus Repair

6.612.2.3.1. Polymers and biological molecules

There is an increasing demand for bioadsorbable polymers. One reason for this is that they can eliminate the potential for various implant-related complications resulting from stress shielding, corrosion, and release of wear debris. Polyglycolic acid (PGA) and poly-L-lactic acid are the two major bioabsorbable polymers. The former is metabolized to glycine

Table 1 Overview of biomaterials used for the repair of intervertebral disc, targeted for the nucleus pulposus (NP) and the annulus fibrosus (AF) or the entire disc (IVD)

Biomaterial class	*Biomaterial examples*	*Targeted tissue*	*Repair strategy*	*References*
Synthetic degradable polymers	Polylactides/glycolides	NP/AF	B	114–118
	Polycaprolactone	AF	B	69,119,120
	Polyurethanes		B	121–124
	Polyethylene glycol (PEG)	NP	B	125,126
Natural biopolymers	Collagen type 2	NP/AF	B	60,62–65,127–129
	Elastin	AF	B	59
	Fibrin/fibrinogen	NP/AF	B	117,119,130–132
	Silk	AF	B	59,66,67
	Alginates	NP	B	133–137
	Chitosan	NP	B	70,105,107,109,138,139
	Hyaluronic acid	NP	B	76
Calcium phosphates	TCP	IVD	F	116,140–142
Bioactive glasses		NP, AF	F, B	118
Composites/biopolymers/bioactive ceramics		IVD, NP, AF	B	115,116,121,143
Tissue-derived ECM and transplants	Disc organ explant	IVD	B	144

(F) denotes classical approach to achieve intervertebrate body fusion, (B) denotes biological repair approach to repair or regenerate tissue parts.

in about 4–6 weeks, but the latter is to L-lactate and takes 6–12 months to degrade. Inflammatory tissue reaction is seen more in PGA than in poly-L-lactic acid. Polymer biomaterials have advantages over the others because of their ease and flexibility of manufacturing, relative low cost, and availability in a wide range of properties.

Current approach for IVD repair was proposed to apply injectable hydrogels. A hydrogel is a relatively broad term referring to a gel that has water dispersed in various types of polymer network. Owing to the polymer network difference, the mechanical and biologic properties for various hydrogels can be very different.

6.612.2.3.2. Biomaterials for tissue-engineering methods in cell-based nucleus repair

Alginate, agarose, collagen gel, collagen sponges, and fibrin gels were used previously to hold cells in three-dimensional (3D) culture systems. Besides using these materials as *in vitro* culture scaffolds, they are further expected to be useful as candidates for cell-carriers in cell transplantation therapy for IVD degeneration or cell-holding scaffolds in IVD tissue engineering. Autologous or allogenic disc cell transplantation has been reported from multiple research groups as a major approach in delaying the progression of degeneration by restoring lost cells. In delivering donor cells to the IVD, the selection of an adequate cell-carrier is important. The generation of disc-like tissue using various scaffolds and tissue-engineering techniques also possesses the potential of becoming a new strategy for regenerating the nucleus (see **Chapter 6.613, Nucleus Replacement**).

6.612.2.4. Overview of Nucleus Repair and Regeneration

Nucleus replacement devices can be classified to either injectable or preformed implants. Injectable, *in situ* curing materials can be divided into uncontained or contained devices. Uncontained are adhesive hydrogels (e.g., NuCore or BioDisc) and nonadhesive nonhydrogels (e.g., Sinux). Contained devices are hydrogel (with no currently available device) or nonhydrogel devices (e.g., DASCOR, PNR, PDR). Preformed implants can be divided into nonarticulating or articulating implants. Nonarticulating implants are hydrogel (e.g., PDN-Solo, Hydraflex, NeuDisc, Aquarelle) or nonhydrogel (e.g., Newcleus, NeoDisc, Regain). Articulating implants can be divided based on whether they are made of same material of components (e.g., NUBAC) or different components.[139]

6.612.2.5. Biomaterials for Cell Scaffolds

Among various cell scaffolds such as alginate, agarose, collagen gel, collagen sponges, fibrin gels, PGA, and poly-L-lactic acid, not many have been broadly used clinically in other areas of human body.

Atelocollagen is a collagen gel that has an advantage in safety, as the antigenic telopeptide region has been removed by pepsin digestion and differential salt precipitation during purification. Atelocollagen is in liquid form at 41 °C, but gels after incubation at 37 °C. Atelocollagen composed of type I collagen purified from calf dermis is already in use by physicians for subcutaneous injection during cosmetic and plastic surgery. Atelocollagen can be obtained as collagen types I–IV, depending on the animal and organ from which it is purified. The results of a study culturing human NP cells in atelocollagen showed that it can provide 3D culture condition for human NP cells, as measured by cell proliferation and proteoglycan (PG) production and also generate NP like tissue *in vitro*. A similar combination of collagen type II hydrogel has been proposed which uses a combination of noncross-linked and enzymatically cross-linked, atelocollagen type II-based scaffolds containing varying concentrations of aggrecan and hyaluronan.[60,63,64] These authors found that cross-linking atelocollagen type II-based scaffolds did not cause any negative effects on cell viability or cell proliferation over a 7-day culture period. **Figure 2** shows the optical appearance of non-cell-seeded and cell-seeded scaffolds. They compared cross-linked and non-cross-linked collagen/aggrecan/hyaluran mixtures: collagen (C), collagen/hyaluronan (CH), mTGase cross-linked collagen/hyaluronan (xCH), collagen/aggrecan/hyaluronan (CAH), and mTGase cross-linked collagen/aggrecan/hyaluronan (xCAH) (**Figure 2**).

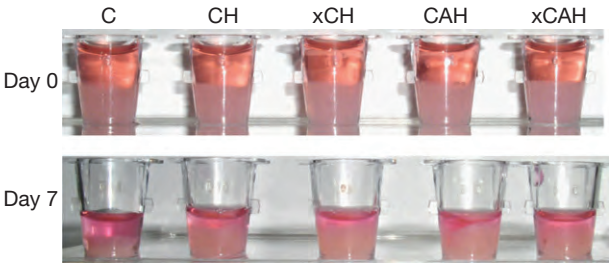

Figure 2 Acellular scaffolds (i.e., day 0) and nucleus pulposus cell-seeded scaffolds on culture day 7, on the top and bottom row, respectively. Progressing from left to right are the scaffold groups: collagen (C), collagen/hyaluronan (CH), mTGase cross-linked collagen/hyaluronan (xCH), collagen/aggrecan/hyaluronan (CAH), and mTGase cross-linked collagen/aggrecan/hyaluronan (xCAH). Reproduced from Halloran, D. O.; Grad, S.; Stoddart, M.; Dockery, P.; Alini, M.; Pandit, A. S. *Biomaterials* **2008**, *29*, 438–447, with permission from publisher.

6.612.2.6. Future Perspectives

Although many biomaterials have been tested in the laboratory or in the clinics, there has not been an ultimate solution for repair of the NP that lasts forever. The big challenge is to determine the appropriate pathology for the indication of each device or technique. Furthermore, since most of the nucleus replacement devices owe their function in intact AF, the repair/regeneration of the annulus remains a great consideration. Current strategies are to develop hydrogels that are thermo-responsive, for example, those that are in a fluid state at room temperature but are in a coiled and gel-like state at physiological temperature of 37 °C.[61]

6.612.3. Repair for the AF

6.612.3.1. Development and Healthy Structure of the AF

The IVD is confined by the two cartilage endplates and is composed of two distinct structures, the NP and the surrounding AF.[150,151] Although the two cartilage endplates

offer anatomical limitation to the vertebral bodies, morphology along the plate is distinguished by a central articular-like cartilage under the NP and a peripheral fibrocartilage appropriately associated with the AF. During embryogenesis, the AF develops from the mesenchyme, whereas the NP is derived from the notochord.[152] The AF consists of water (65–90%), collagen (50–70% dry weight), PGs (10–20% dry weight), and noncollagenous proteins (e.g., elastin).[153] The IVD has been recently described as tough, composite biomaterial which acts as a viscoelastic weight-bearing cushion and is a major contributor to the spinal flexibility and mechanical stability properties of the spine.[150] The AF is a structure, which surrounds the hyalinic PG-rich NP. The function of the AF in the young to middle-aged discs is to counteract the hydrostatic pressure of the NP and to prevent leakage.[13,154]

The need to find more satisfying repair strategies for the AF has been recognized only relatively recently.[155,156] The AF as a major component of the disc has been shifted to the current research focus.[155,157] It has been recently noticed that injection of needles, as it is done in discography, into the IVD can be a major risk for the onset of disc degeneration.[158] Carragee and his colleagues found strong evidence for discographic-induced disc degeneration at 10 years postoperative follow-up.

6.612.3.2. Surgical Strategies to Rescue the AF

Commercially, there are two implants to close the AF available. It is the Inclose© and the Xclose©, which can be seen as modified sutures with anchors.[155] However, these approaches try to contain the NP but cannot maintain the biological AF structure for the long term or stop AF degeneration. Barricaid© is another commercially available implant used in adjunction to discectomies that fully bridges the defect in the AF. This product reinforces the complete posterior annulus and could therefore even prevent contralateral herniation.

6.612.3.3. Nonbiodegradable Materials

Under this category fall the metals, ceramics, and polymers. To our knowledge, there were no metals successfully tested for the reconstruction of the AF till date, which lies in the nature of this complex and viscoelastic tissue. Metals are to stiff to fit the biomechanical needs for AF replacement. As for the ceramics, a combination has been applied to the IVD repair.[12,159–167] However, only few were tried for AF repair. Thus, none of these studies tried to rescue the AF for the long term but aimed to achieve fusion in the first place. As for the polymers, there were PDLLA/bioactive glass composite foams lately investigated to check cell attachment and phenotype.[114,115,168] These findings provide preliminary evidence for the use of PDLLA/bioactive glass composite scaffolds as cell-carrier materials for future treatments of IVDs with damaged AF region.

6.612.3.4. Biodegradable: Resorbable Materials

6.612.3.4.1. Polymers

More recently biodegradable malic acid-based polyester (poly [1,8] octanediol malate) (POM) was tested as a scaffold for AF replacement using rat IVD cells.[69,169] The POM was synthesized by mixing malic acid and 1,8-octanediol in the appropriate ratios. Recently, other hyaluronan-derived polymers were tested in female pigs[170]: two hyaluronan-derived polymeric substitute materials, that is, HYAFF 120, an ester, and HYADD 3, an amide, were injected into the NP of the lumbar spine of female pigs in which a nucleotomy had also been performed.

Hegewald and his colleagues[171] tested an absorbable PGA biomaterial, which was lyophilized with hyaluronic acid (HA) in bovine, lumbar spinal units. Hydrogels are recently good candidates for intervertebral disk replacement for NP tissue. However, for the AF, the hydrogel approach seems too less stiff and the elasticity is not ideal. In contrast to the NP, any material trying to move with the torsional and compressive deformation of the annulus might fail. It is known that if AF cells are cultured in hydrogels, such as alginate or matrigel, these cells become like NP cells over time.[172] Nevertheless, Shao and Hunter[108] created a scaffold from wet-spinned lyophilized alginate/chitosan. They found the AF cells growing in clusters and spread along the alginate/chitosan fibres. The cells

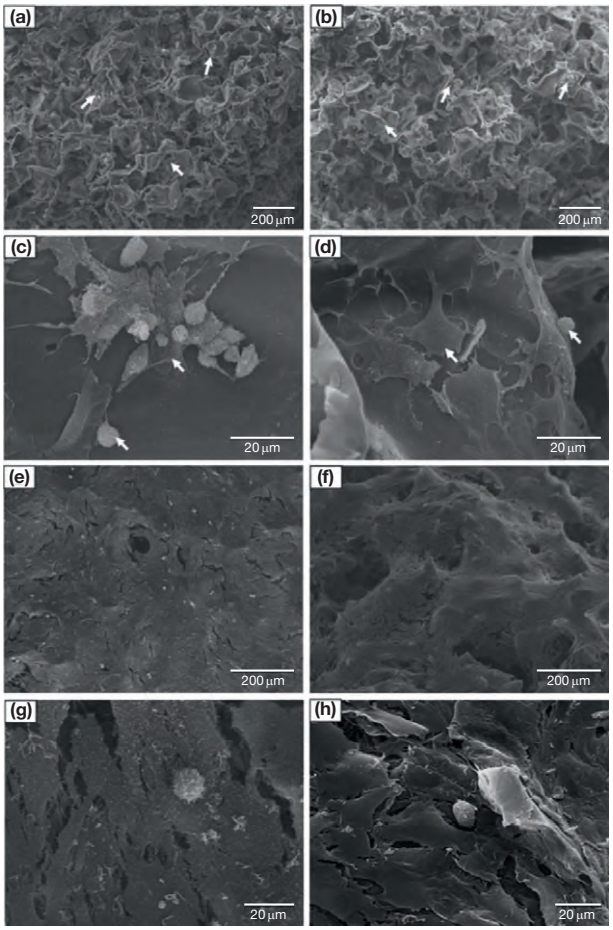

Figure 3 Scanning electron microscopy images of annulus fibrosus cells 24 h (a–d) or 14 days (e–h) after seeding onto nonmodified scaffolds (a, c or e, g) or modified scaffolds (b, d or f, h). Arrows indicate representative cells attached to porous silk scaffold. Reproduced from Chang, G.; Kim, H. J.; Kaplan, D.; Vunjak-Novakovic, G.; Kandel, R. A. *Eur. Spine J.* **2007**, *16*, 1848–1857, with permission from publisher.

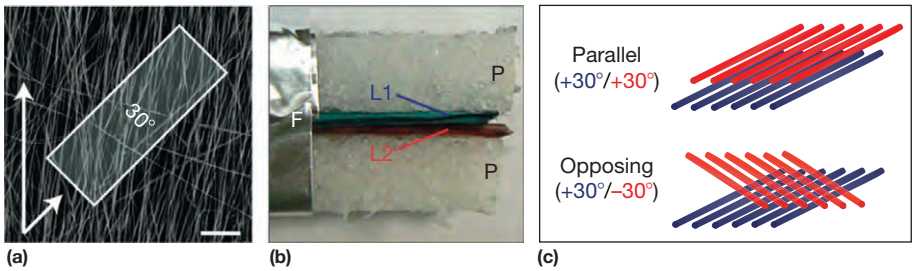

Figure 4 Fabrication of bilamellar tissue constructs. (a) Scaffolds were excised 30° from the prevailing fiber direction of electrospun nanofibrous mats to replicate the oblique collagen orientation within a single lamella of the annulus fibrosus. Scale bar: 25 μm. (b) At 0 weeks, mesenchymal stem cell-seeded scaffolds were formed into bilayers between pieces of porous polypropylene and wrapped with a foil sleeve. P, porous polypropylene; F, foil; L1/2, lamella 1/2. (c) Bilayers were oriented with either parallel (+30°/+30°) or opposing (+30°/−30°) fiber alignment relative to the long axis of the scaffold. Reproduced from Nerurkar, N. L.; Baker, B. M.; Sen, S.; Wible, E. E.; Elliott, D. M.; Mauck, R. L. *Nat. Mater.* **2009**, *8*, 986–992, with permission from the publishers.

expressed collagen I, II, and aggrecan. More elastic a biphasic scaffold to structurally and elastically simulate the AF tissue of the IVD was recently explored by Wan and his colleagues.[69] In this study, the outer phase of the scaffold was a ring-shaped demineralized bone matrix gelatin (BMG) extracted from cortical bone which mimics the type I collagen structure and ligamentous properties of outer AF. The inner phase of the scaffold was a bio-biomaterial poly(polycaprolactone triol malate) (PPCLM) orientated in concentric sheets and seeded with chondrocytes to recapitulate the inner layer of the AF, which is rich in type II collagen and PG.

6.612.3.4.2. Silk and other biomaterials

Silk has been proposed as a major biomaterial to be used as a suture or a tissue construct to close AF lesions and disc herniations.[59,67,173]

The chemical structure of silk is a polypeptide consisting of the amino acid Gly-Ser-Gly-Ala (Glycine-Sericine-Glycine-Alanine). In order to get a high medical grade silk of high biocompatibility and low allergenic reaction, the cocoons of the silk worm *Bombyx mori* (Lepidoptera: Bombycidae) are usually boiled for 30 min in low molar Na_2CO_3 solution and then rinsed with water to extract the contained Sericin, which has been identified to be a major allergen.[174] Sericin-free silk has been successfully applied in orthopedics for decades. Chang and his colleagues[66,67] investigated on different porosity of the silk scaffold for cell spreading and proliferation of AF cells. They also modified their scaffold by linking RGD peptides for better cell attachment. However, they did not find any significant difference in gene expression nor in cell spreading using this modification (Figure 3).

6.612.3.4.3. Collagen fiber scaffolds (electrospinning)

One of the major challenges, which is left for future tissue engineering of the AF, is not to dedifferentiate the cells in culture after *in vitro* culture. It is generally known that primary cells of NP or AF cells are cultured *in vitro* over longer passaging ($p > 6$) that these start to dedifferentiate.[175,176] The AF has a cell density of about 9×10^6 cells cm^{-3} in mature healthy subjects, this is about two times higher than that of the NP.[6,155,177,178]

Electrospun poly-ε-caprolactone has been studied by Nerurkar *et al.*[179] They report that cultured bovine AF cells became elongated over time and that these were aligned along the elongated cells aligned along the predominant fibers direction. Current approach is to electrospin the complex shape of the AF.[68] Figure 4 shows the principle how bilamellar tissue constructs can be formed from nano fibrous mats and how scaffolds are excised in a 30° angle from the prevailing fiber direction to replicate the collagen orientation within a single lamella of the AF.

6.612.3.5. Future Perspective: The Biological AF Replacement

Current approaches for a complete replacement of the IVD with a complete AF and NP seems difficult but may not be unachievable. Current *in vitro* approaches of tissue-engineered organs using stiffer materials such as tendon and AF could be successfully mimicked with biphasic biomaterials with high elastic modulus.[69,180] While 3D printing devices are emerging, which are able to print complex fixable shapes,[181–183] we might only be footsteps away to print a complete AF replacement polymer material along with mixed cells such as preconditioned MSCs.

References

1. Mwale, F.; Roughley, P.; Antoniou, J. *Eur. Cell. Mater.* **2004**, *8*, 58–63; discussion 63–64.
2. Minogue, B. M.; Richardson, S. M.; Zeef, L. A.; Freemont, A. J.; Hoyland, J. A. *Arthritis Res. Ther.* **2010**, *12*, R22.
3. Frymoyer, J. W.; Pope, M. H.; Clements, J. H.; Wilder, D. G.; MacPherson, B.; Ashikaga, T. *J. Bone Joint Surg. Am.* **1983**, *65*, 213–218.
4. Heliövaara, M. *Ann. Med.* **1989**, *21*, 257–264.
5. Urban, J. P.; Roberts, S. *Arthritis Res. Ther.* **2003**, *5*, 120–130.
6. Cassidy, J. J.; Hiltner, A.; Baer, E. *Connect. Tissue Res.* **1989**, *23*, 75–88.
7. Roberts, S.; Evans, H.; Trivedi, J.; Menage, J. *J. Bone Joint Surg. Am.* **2006**, *88* (Suppl. 2), 10–14.
8. Bibby, S. R.; Jones, D. A.; Ripley, R. M.; Urban, J. P. *Spine* **2005**, *30*, 487–496.
9. Bibby, S. R. S.; Yu, J.; Urban, J. P. G. In *Degenerative Disc Disease*; Gunzburg, R., Szpalski, M., Andersson, G. B., Eds.; Lippincott Williams Wilkins: Philadelphia, PA, 2004; pp 23–33.
10. Urban, J. P.; Smith, S.; Fairbank, J. C. *Spine* **2004**, *29*, 2700–2709.
11. Wuertz, K.; Godburn, K.; Neidlinger-Wilke, C.; Urban, J.; Iatridis, J. C. *Spine* **2008**, *33*, 1843–1849.

12. Das, D. B.; Welling, A.; Urban, J. P.; Boubriak, O. A. *Ann. N. Y. Acad. Sci.* **2009**, *1161*, 44–61.
13. Buckwalter, J. A. *Spine* **1995**, *20*, 1307–1314.
14. Hunter, C. J.; Matyas, J. R.; Duncan, N. A. *J. Anat.* **2004**, *205*, 357–362.
15. Nachemson, A. *Int. Orthop.* **1985**, *9*, 1–10.
16. Nachemson, A. In *Degenerative Disc Disease*; Gunzburg, R., Szpalski, M., Andersson, G. B., Eds.; Lippincott Williams Wilkins: Philadelphia, PA, 2004; pp 1–5.
17. Acaroglu, E. R.; Iatridis, J. C.; Setton, L. A.; Foster, R. J.; Mow, V. C.; Weidenbaum, M. *Spine* **1995**, *20*, 2690–2701.
18. An, H. S.; Anderson, P. A.; Haughton, V. M.; *et al. Spine* **2004**, *29*, 2677–2678.
19. Antoniou, J.; Steffen, T.; Nelson, F.; *et al. J. Clin. Investig.* **1996**, *98*, 996–1003.
20. Antoniou, J.; Mwale, F.; Demers, C. N.; *et al. Spine* **2006**, *31*, 1547–1554.
21. Benneker, L. M.; Heini, P. F.; Alini, M.; Anderson, S. E.; Ito, K. *Spine* **2005**, *30*, 167–173.
22. Benneker, L. M.; Heini, P. F.; Anderson, S. E.; Alini, M.; Ito, K. *Eur. Spine J.* **2005**, *14*, 27–35.
23. Dietemann, J. L. In *Degenerative Disc Disease*; Gunzburg, R., Szpalski, M., Andersson, G. B., Eds.; Lippincott Williams Wilkins: Philadelphia, PA, 2004; pp 75–89.
24. Ferguson, S. J.; Steffen, T. *Eur. Spine J.* **2003**, *12*(Suppl. 2), S97–S103.
25. Luoma, K.; Riihimaki, H.; Luukkonen, R.; Raininko, R.; Viikari-Juntura, E.; Lamminen, A. *Spine* **2000**, *25*, 487–492.
26. Boos, N.; Weissbach, S.; Rohrbach, H.; Weiler, C.; Spratt, K. F.; Nerlich, A. G. *Spine* **2002**, *27*, 2631–2644.
27. Dyer, D. G.; Dunn, J. A.; Thorpe, S. R.; *et al. J. Clin. Invest.* **1993**, *91*, 2463–2469.
28. Rajasekaran, S.; Naresh-Babu, J.; Murugan, S. *J. Magn. Reson. Imaging* **2007**, *25*, 410–418.
29. Battié, M. C.; Videman, T.; Kaprio, J.; *et al. Spine J.* **2009**, *9*, 47–59.
30. Battié, M. C.; Haynor, D. R.; Fisher, L. D.; Gill, K.; Gibbons, L. E.; Videman, T. *J. Bone Joint Surg. Am.* **1995**, *77*, 1662–1670.
31. Nachemson, A. L. *Clin. Orthop. Relat. Res.* **1985**, *200*, 266–278.
32. Andersson, G. B. *Lancet* **1999**, *354*, 581–585.
33. Cohen, S. P.; Larkin, T. M.; Barna, S. A.; Palmer, W. E.; Hecht, A. C.; Stojanovic, M. P. *Reg. Anesth. Pain Med.* **2005**, *30*, 163–183.
34. Mayer, H. M.; Korge, A. *Eur. Spine J.* **2002**, *11*(Suppl. 2), 85–91.
35. Fritzell, P.; Hägg, O.; Wessberg, P.; Nordwall, A.; Swedish Lumbar Spine Study Group. *Spine* **2002**, *27*, 1131–1141.
36. Weinstein, M. A.; McCabe, J. P.; Cammisa, F. P. *J. Spinal Disord.* **2000**, *13*, 422–426.
37. Klink, B. K.; Thurman, R. T.; Wittpenn, G. P.; Lauerman, W. C.; Cain, J. E. *Spine* **1994**, *19*, 1467–1470.
38. Martin, B. I.; Mirza, S. K.; Comstock, B. A.; Gray, D. T.; Kreuter, W.; Deyo, R. A. *Spine* **2007**, *32*, 382–387.
39. Etebar, S.; Cahill, D. W. *J. Neurosurg.* **1999**, *90*, 163–169.
40. Schlegel, J. D.; Smith, J. A.; Schleusener, R. L. *Spine* **1996**, *21*, 970–981.
41. Hanley, E. N.; Shapiro, D. E. *J. Bone Joint Surg. Am.* **1989**, *71*, 719–721.
42. Crawshaw, C.; Frazer, A. M.; Merriam, W. F.; Mulholland, R. C.; Webb, J. K. *Spine* **1984**, *9*, 195–198.
43. Gantenbein, B.; Grünhagen, T.; Lee, C. R.; van Donkelaar, C. C.; Alini, M.; Ito, K. *Spine* **2006**, *31*, 2665–2673.
44. Jünger, S.; Gantenbein-Ritter, B.; Lezuo, P.; Alini, M.; Ferguson, S. J.; Ito, K. *Spine* **2009**, *34*, 1264–1271.
45. Lee, C. R.; Iatridis, J. C.; Poveda, L.; Alini, M. *Spine* **2006**, *31*, 515–522.
46. Chan, S. C. W.; Gantenbein-Ritter, B.; Leung, Y. L.; Chan, D.; Cheung, K. M. C.; Ito, K. *Spine J.* **2010**, *10*(6), 486–496.
47. Masuda, K.; Oegema, T. R.; An, H. S. *Spine* **2004**, *29*, 2757–2769.
48. Masuda, K.; An, H. S. *Eur. Spine J.* **2006**, *15*(Suppl. 3), S422–S432.
49. Masuda, K.; Lotz, J. *Tissue Eng. B Rev.* **2010**, *16*(1), 147–158.
50. Chujo, T.; An, H. S.; Akeda, K.; *et al. Spine* **2006**, *31*, 2909–2917.
51. Feng, G.; Wan, Y.; Shen, F. H.; Li, X. *J. Orthop. Res.* **2009**, *27*, 814–819.
52. Paesold, G.; Nerlich, A. G.; Boos, N. *Eur. Spine J.* **2007**, *16*, 447–468.
53. Acosta, F. L.; Lotz, J.; Ames, C. P. *Neurosurg. Focus* **2005**, *19*, E4.
54. Hiyama, A.; Mochida, J.; Iwashina, T.; *et al. J. Orthop. Res.* **2008**, *26*, 589–600.
55. Leung, V. Y.; Chan, D.; Cheung, K. M. *Eur. Spine J.* **2006**, *15*(Suppl. 3), S406–S413.
56. O'Halloran, D. M.; Pandit, A. S. *Tissue Eng.* **2007**, *13*, 1927–1954.
57. Sakai, D.; Mochida, J.; Iwashina, T.; *et al. Spine* **2005**, *30*, 2379–2387.
58. Yoon, S. T. In *Degenerative Disc Disease*; Gunzburg, R., Szpalski, M., Andersson, G. B., Eds.; Lippincott Williams Wilkins: Philadelphia, PA, 2004; pp 133–138.
59. Boyd, L. M.; Carter, A. J. *Eur. Spine J.* **2006**, *15*(Suppl. 3), S414–S421.
60. Halloran, D. O.; Grad, S.; Stoddart, M.; Dockery, P.; Alini, M.; Pandit, A. S. *Biomaterials* **2008**, *29*, 438–447.
61. Mortisen, D.; Peroglio, M.; Alini, M.; Eglin, D. *Biomacromolecules* **2010**, *11*, 1261–1272.
62. Sakai, D.; Mochida, J.; Yamamoto, Y.; *et al. Biomaterials* **2003**, *24*, 3531–3541.
63. Sakai, D.; Mochida, J.; Iwashina, T.; *et al. Biomaterials* **2006**, *27*, 346–353.
64. Sakai, D.; Mochida, J.; Iwashina, T.; *et al. Biomaterials* **2006**, *27*, 335–345.
65. Sato, M.; Asazuma, T.; Ishihara, M.; *et al. J. Biomed. Mater. Res. A* **2003**, *64*, 248–256.
66. Chang, G.; Kim, H. J.; Vunjak-Novakovic, G.; Kaplan, D. L.; Kandel, R. *J. Biomed. Mater. Res. A* **2010**, *92*, 43–51.
67. Chang, G.; Kim, H. J.; Kaplan, D.; Vunjak-Novakovic, G.; Kandel, R. A. *Eur. Spine J.* **2007**, *16*, 1848–1857.
68. Nerurkar, N. L.; Baker, B. M.; Sen, S.; Wible, E. E.; Elliott, D. M.; Mauck, R. L. *Nat. Mater.* **2009**, *8*, 986–992.
69. Wan, Y.; Feng, G.; Shen, F. H.; Laurencin, C. T.; Li, X. *Biomaterials* **2008**, *29*, 643–652.
70. Richardson, S. M.; Hughes, N.; Hunt, J. A.; Freemont, A. J.; Hoyland, J. A. *Biomaterials* **2008**, *29*, 85–93.
71. Richardson, S. M.; Hoyland, J. A.; Mobasheri, R.; Csaki, C.; Shakibaei, M.; Mobasheri, A. *J. Cell. Physiol.* **2010**, *222*, 23–32.
72. Watanabe, T.; Sakai, D.; Yamamoto, Y.; *et al. J. Orthop. Res.* **2009**, *28*, 623–630.
73. Wei, A.; Tao, H.; Chung, S. A.; Brisby, H.; Ma, D. D.; Diwan, A. D. *J. Orthop. Res.* **2009**, *27*, 374–379.
74. Hoogendoorn, R. J.; Lu, Z. F.; Kroeze, R. J.; Bank, R. A.; Wuisman, P. I.; Helder, M. N. *J. Cell Mol. Med.* **2008**, *12*, 2205–2216.
75. Risbud, M. V.; Albert, T. J.; Guttapalli, A.; *et al. Spine* **2004**, *29*, 2627–2632.
76. Ganey, T.; Hutton, W. C.; Moseley, T.; Hedrick, M.; Meisel, H. J. *Spine* **2009**, *34*, 2297–2304.
77. Hohaus, C.; Ganey, T. M.; Minkus, Y.; Meisel, H. J. *Eur. Spine J.* **2008**, *17*(Suppl. 4), 492–503.
78. Osada, R.; Ohshima, H.; Ishihara, H.; *et al. J. Orthop. Res.* **1996**, *14*, 690–699.
79. Okuda, S.; Myoui, A.; Ariga, K.; Nakase, T.; Yonenobu, K.; Yoshikawa, H. *Spine* **2001**, *26*, 2421–2426.
80. Tolonen, J.; Grönblad, M.; Virri, J.; Seitsalo, S.; Rytömaa, T.; Karaharju, E. *Spine* **1995**, *20*, 271–276.
81. Nagano, T.; Yonenobu, K.; Miyamoto, S.; Tohyama, M.; Ono, K. *Spine* **1995**, *20*, 1972–1978.
82. Takae, R.; Matsunaga, S.; Origuchi, N.; *et al. Spine* **1999**, *24*, 1397–1401.
83. Masuda, K.; Imai, Y.; Okuma, M.; *et al. Spine* **2006**, *31*, 742–754.
84. Takegami, K.; Thonar, E. J.; An, H. S.; Kamada, H.; Masuda, K. *Spine* **2002**, *27*, 1318–1325.
85. Konttinen, Y. T.; Kemppinen, P.; Li, T. F.; *et al. J. Bone Joint Surg. Br.* **1999**, *81*, 1058–1063.
86. Tolonen, J.; Grönblad, M.; Vanharanta, H.; *et al. Eur. Spine J.* **2006**, *15*, 588–596.
87. Nakase, T.; Ariga, K.; Miyamoto, S.; *et al. J. Neurosurg.* **2001**, *94*, 68–75.
88. Cui, M.; Wan, Y.; Anderson, D. G.; *et al. Spine J.* **2008**, *8*, 287–295.
89. Wang, H.; Kroeber, M.; Hanke, M.; *et al. J. Mol. Med.* **2004**, *82*, 126–134.
90. Miyazaki, T.; Kobayashi, S.; Takeno, K.; Meir, A.; Urban, J.; Baba, H. *Tissue. Eng. A* 2009.
91. Yoon, S. T. *Spine J.* **2005**, *5*, 280S–286S.
92. Caplan, A. I. *J. Orthop. Res.* **1991**, *9*, 641–650.
93. Wei, H.; Vander Heide, R. S. *Am. J. Physiol. Heart Circ. Physiol.* 2008.
94. Pittenger, M. F. *Methods Mol. Biol.* **2008**, *449*, 27–44.
95. Chamberlain, G.; Fox, J.; Ashton, B.; Middleton, J. *Stem Cells* **2007**, *25*, 2739–2749.
96. da Silva Meirelles, L.; Caplan, A. I.; Nardi, N. B. *Stem Cells* **2008**, *26*, 2287–2299.
97. Chamberlain, J. S. *Nature* **2006**, *444*, 552–553.
98. Caplan, A. I. *Tissue Eng.* **2005**, *11*, 1198–1211.
99. Pittenger, M. F.; Mackay, A. M.; Beck, S. C.; *et al. Science* **1999**, *284*, 143.
100. Yamada, Y.; Yokoyama, S. I.; Fukuda, N.; *et al. Biochem. Biophys. Res. Commun.* **2006**, *353*, 182–188.
101. Zuk, P. A.; Zhu, M.; Mizuno, H.; *et al. Tissue Eng.* **2001**, *7*, 211–228.
102. Mitchell, J. B.; McIntosh, K.; Zvonic, S.; *et al. Stem Cells* **2006**, *24*, 376–385.
103. Lin, Y.; Luo, E.; Chen, X.; *et al. J. Cell. Mol. Med.* **2005**, *9*, 929–939.
104. Lee, S. H.; Derby, R.; Chen, Y.; Seo, K. S.; Kim, M. J. *Spine J.* **2004**, *4*, 614–618.
105. Alini, M.; Roughley, P. J.; Antoniou, J.; Stoll, T.; Aebi, M. *Eur. Spine J.* **2002**, *11*(Suppl. 2), S215–S220.
106. Berger, J.; Reist, M.; Mayer, J. M.; Felt, O.; Peppas, N. A.; Gurny, R. *Eur. J. Pharm. Biopharm.* **2004**, *57*, 19–34.
107. Mwale, F.; Iordanova, M.; Demers, C. N.; Steffen, T.; Roughley, P.; Antoniou, J. *Tissue Eng.* **2005**, *11*, 130–140.

108. Shao, X.; Hunter, C. J. *J. Biomed. Mater. Res. A* **2007**, *82*, 701–710.
109. Suh, J. K.; Matthew, H. W. *Biomaterials* **2000**, *21*, 2589–2598.
110. Yang, X.; Li, X. *Eur. Spine J.* **2009**, *18*, 1–9.
111. Lee, C. R.; Sakai, D.; Nakai, T.; *et al. Eur. Spine J.* **2007**, *16*, 2174–2185.
112. Rutges, J.; Creemers, L. B.; Dhert, W.; *et al. Osteoarthritis Cartilage* 2009.
113. Sakai, D.; Nakai, T.; Mochida, J.; Alini, M.; Grad, S. *Spine* **2009**, *34*, 1448–1456.
114. Helen, W.; Merry, C. L.; Blaker, J. J.; Gough, J. E. *Biomaterials* **2007**, *28*, 2010–2020.
115. Helen, W.; Gough, J. E. *Acta Biomater.* **2008**, *4*, 230–243.
116. Debusscher, F.; Aunoble, S.; Alsawad, Y.; Clement, D.; Le Huec, J. C. *Eur. Spine J.* **2009**, *18*, 1314–1320.
117. Sha'ban, M.; Yoon, S. J.; Ko, Y. K.; *et al. J. Biomater. Sci. Polym. Ed.* **2008**, *19*, 1219–1237.
118. Ellä, V.; Kellomäki, M.; Törmälä, P. *J. Mater. Sci. Mater. Med.* **2005**, *16*, 655–662.
119. Hutmacher, D. W.; Goh, J. C.; Teoh, S. H. *Ann. Acad. Med. Singapore* **2001**, *30*, 183–191.
120. Ambrosio, L.; De Santis, R.; Nicolais, L. *Proc. Inst. Mech. Eng. H* **1998**, *212*, 93–99.
121. Taksali, S.; Grauer, J. N.; Vaccaro, A. R. *Spine J.* **2004**, *4*, 231S–238S.
122. Lanir, Y.; Seybold, J.; Schneiderman, R.; Huyghe, J. M. *Tissue Eng.* **1998**, *4*, 365–378.
123. Langrana, N. A.; Parsons, J. R.; Lee, C. K.; Vuono-Hawkins, M.; Yang, S. W.; Alexander, H. *J. Appl. Biomater.* **1994**, *5*, 125–132.
124. Lee, C. K.; Langrana, N. A.; Parsons, J. R.; Zimmerman, M. C. *Spine* **1991**, *16*, S253–S255.
125. Vernengo, J.; Fussell, G. W.; Smith, N. G.; Lowman, A. M. *J. Biomed. Mater. Res. B Appl. Biomater.* **2008**, *84*, 64–69.
126. Cloyd, J. M.; Malhotra, N. R.; Weng, L.; Chen, W.; Mauck, R. L.; Elliott, D. M. *Eur. Spine J.* **2007**, *16*, 1892–1898.
127. Sakai, Y.; Ochi, M.; Uchio, Y.; Ryoke, K.; Yamamoto, S. *J. Biomed. Mater. Res. B Appl. Biomater.* **2005**, *73*, 355–360.
128. Sato, M.; Asazuma, T.; Ishihara, M.; *et al. Spine* **2003**, *28*, 548–553.
129. Sato, M.; Kikuchi, M.; Ishihara, M.; *et al. Med. Biol. Eng. Comput.* **2003**, *41*, 365–371.
130. Gruber, H. E.; Hoelscher, G. L.; Leslie, K.; Ingram, J. A.; Hanley, E. N. *Biomaterials* **2006**, *27*, 371–376.
131. Gruber, H. E.; Leslie, K.; Ingram, J.; Norton, H. J.; Hanley, E. N. *Spine J.* **2004**, *4*, 44–55.
132. Stern, S.; Lindenhayn, K.; Schultz, O.; Perka, C. *Acta Orthop. Scand.* **2000**, *71*, 496–502.
133. Guehring, T.; Urban, J. P.; Cui, Z.; Tirlapur, U. K. *Microsc. Res. Tech.* **2008**, *71*, 298–304.
134. Moon, S. H.; Nishida, K.; Gilbertson, L. G.; *et al. Spine* **2008**, *33*, 1850–1855.
135. Melrose, J.; Smith, S.; Ghosh, P. *J. Anat.* **2000**, *197*(Pt 2), 189–198.
136. Gruber, H. E.; Fisher, E. C.; Desai, B.; Stasky, A. A.; Hoelscher, G.; Hanley, E. N. *Exp. Cell Res.* **1997**, *235*, 13–21.
137. Maldonado, B. A.; Oegema, T. R. *J. Orthop. Res.* **1992**, *10*, 677–690.
138. Roughley, P.; Hoemann, C.; DesRosiers, E.; Mwale, F.; Antoniou, J.; Alini, M. *Biomaterials* **2006**, *27*, 388–396.
139. Di Martino, A.; Sittinger, M.; Risbud, M. V. *Biomaterials* **2005**, *26*, 5983–5990.
140. Jiang, L.-S.; Dai, L.-Y. *Eur. Spine J.* **2008**, *17*, 698–705.
141. Cosar, M.; Ozer, A. F.; Iplikcioglu, A. C.; *et al. J. Spinal Disord. Tech.* **2008**, *21*, 436–441.
142. Helder, M. N.; Knippenberg, M.; Klein-Nulend, J.; Wuisman, P. I. *Tissue Eng.* **2007**, *13*, 1799–1808.
143. Cunningham, B. W.; Atkinson, B. L.; Hu, N.; *et al. J. Neurosurg. Spine* **2009**, *10*, 300–307.
144. Ruan, D.; He, Q.; Ding, Y.; Hou, L.; Li, J.; Luk, K. D. *Lancet* **2007**, *369*, 993–999.
145. Parke, W. W. In *Rothman-Simone's The Spine*, 4th ed.; Herkowitz, H. N., Garfin, S. R., Eismont, F. J., Bell, G. R., Balderson, R. A., Eds.; WB Saunders: Philadelphia, PA, 1999; pp 3–27.
146. Kuzhupilly, R.; Bell, G. R. In *Developmental Spinal Anatomy*; Vaccaro, V. R., Betz, R. R., Zeidman, S. M., Batzdorf, U., Eds.; Mosby: Philadelphia, PA, 2003; pp 1–14.
147. Wolfe, H. J.; Putschar, W. G.; Vickery, A. L. *Clin. Orthop. Relat. Res.* **1965**, *39*, 205–212.
148. Hunter, C. J.; Matyas, J. R.; Duncan, N. A. *Tissue Eng.* **2003**, *9*, 667–677.
149. Guehring, T.; Wilde, G.; Sumner, M.; *et al. Arthritis Rheum.* **2009**, *60*, 1026–1034.
150. Humzah, M. D.; Soames, R. W. *Anat. Rec.* **1988**, *220*, 337–356.
151. Yu, J.; Tirlapur, U.; Fairbank, J.; *et al. J. Anat.* **2007**, *210*, 460–471.
152. Risbud, M. V.; Schaer, T. P.; Shapiro, I. M. *Dev. Dyn.* **2010**, *239*, 2141–2148.
153. Bruehlmann, S. B.; Rattner, J. B.; Matyas, J. R.; Duncan, N. A. *J. Anat.* **2002**, *201*, 159–171.
154. Adams, M. A.; Freeman, B. J.; Morrison, H. P.; Nelson, I. W.; Dolan, P. *Spine* **2000**, *25*, 1625–1636.
155. Bron, J. L.; Helder, M. N.; Meisel, H. J.; Van Royen, B. J.; Smit, T. H. *Eur. Spine J.* **2009**, *18*, 301–313.
156. Melrose, J.; Smith, S. M.; Little, C. B.; Moore, R. J.; Vernon-Roberts, B.; Fraser, R. D. *Eur. Spine J.* **2008**, *17*, 1131–1148.
157. Sun, D. D.; Leong, K. W. *Ann. Biomed. Eng.* **2004**, *32*, 92–102.
158. Carragee, E. J.; Don, A. S.; Hurwitz, E. L.; Cuellar, J. M.; Carrino, J.; Herzog, R. *Spine* **2009**, *34*, 2338–2345.
159. Stulík, J.; Krbec, M.; Vyskocil, T. *Acta Chir. Orthop. Traumatol. Cech.* **2002**, *69*, 288–294.
160. Matsumoto, S. *Hokkaido Igaku Zasshi* **2002**, *77*, 543–549, 551–556.
161. Agrillo, U.; Mastronardi, L.; Puzzilli, F. *J. Neurosurg.* **2002**, *96*, 273–276.
162. Kotani, Y.; Abumi, K.; Shikinami, Y.; *et al. Spine* **2002**, *27*, 929–935; discussion 935–936.
163. Xu, W.; Chen, A.; Feng, X.; Yin, W. *J. Huazhong Univ. Sci. Technolog. Med. Sci.* **2003**, *23*, 300–301.
164. Takahata, M.; Kotani, Y.; Abumi, K.; *et al. Spine* **2003**, *28*, 637–644; discussion 644.
165. Kai, T.; Shao-qing, G.; Geng-ting, D. *Spine* **2003**, *28*, 1653–1658.
166. Korinth, M. C.; Hero, T.; Mahnken, A. H.; Ragoss, C.; Scherer, K. *Biomed. Tech. (Berl)* **2004**, *49*, 356–363.
167. Li, H.; Zou, X.; Xue, Q.; Egund, N.; Lind, M.; Bünger, C. *Eur. Spine J.* **2004**, *13*, 354–358.
168. Wilda, H.; Gough, J. E. *Biomaterials* **2006**, *27*, 5220–5229.
169. Wan, Y.; Feng, G.; Shen, F. H.; Balian, G.; Laurencin, C. T.; Li, X. *Macromol. Biosci.* **2007**, *7*, 1217–1224.
170. Revell, P. A.; Damien, E.; Di Silvio, L.; Gurav, N.; Longinotti, C.; Ambrosio, L. *J. Mater. Sci. Mater. Med.* **2007**, *18*, 303–308.
171. Hegewald, A. A.; Knecht, S.; Baumgartner, D.; *et al. J. Orthop. Surg. Res.* **2009**, *4*, 25.
172. Alini, M.; Li, W.; Markovic, P.; Aebi, M.; Spiro, R. C.; Roughley, P. J. *Spine* **2003**, *28*, 446–454; discussion 453.
173. Fielding, J. W. *Clin. Orthop. Relat. Res.* **1992**, *284*, 10–13.
174. Ebner, H.; Kraft, D. *Wien. Klin. Wochenschr.* **1987**, *99*, 542–546.
175. Chou, A. I.; Reza, A. T.; Nicoll, S. B. *Tissue Eng. A* **2008**, *14*, 2079–2087.
176. Chou, A. I.; Bansal, A.; Miller, G. J.; Nicoll, S. B. *Spine* **2006**, *31*, 1875–1881.
177. Errington, R. J.; Puustjarvi, K.; White, I. R.; Roberts, S.; Urban, J. P. *J. Anat.* **1998**, *192*(Pt 3), 369–378.
178. Maroudas, A.; Stockwell, R. A.; Nachemson, A.; Urban, J. *J. Anat.* **1975**, *120*, 113–130.
179. Nerurkar, N. L.; Elliott, D. M.; Mauck, R. L. *J. Orthop. Res.* **2007**, *25*, 1018–1028.
180. Nesti, L. J.; Li, W. J.; Shanti, R. M.; *et al. Tissue Eng. A* **2008**, *14*, 1527–1537.
181. Fedorovich, N. E.; Swennen, I.; Girones, J.; *et al. Biomacromolecules* 2009.
182. Cui, X.; Boland, T. *Biomaterials* **2009**, *30*, 6221–6227.
183. Nishiyama, Y.; Nakamura, M.; Henmi, C.; *et al. J. Biomech. Eng.* **2009**, *131*, 035001.

6.613. Nucleus Replacement

M H Pelletier and W R Walsh, University of New South Wales, Randwick, NSW, Australia
P Ducheyne, University of Pennsylvania, Philadelphia, PA, USA

© 2011 Elsevier Ltd. All rights reserved.

6.613.1.	**Introduction**	172
6.613.1.1.	Intervertebral Disk	172
6.613.1.1.1.	Microbiology of the intervertebral disk	173
6.613.1.2.	Biomechanics	173
6.613.1.2.1.	Principle planes/rotations	173
6.613.1.2.2.	Evaluation of spinal motion	174
6.613.1.2.3.	Viscoelastic properties	174
6.613.2.	**Ageing and Disk Injury**	175
6.613.2.1.	Degenerative Disk Disease	175
6.613.2.1.1.	Causes of DDD	175
6.613.2.1.2.	Morphologic changes	175
6.613.2.1.3.	Biomechanical changes	175
6.613.2.1.4.	Microbiological changes	176
6.613.2.1.5.	Pain	176
6.613.2.2.	Herniation	176
6.613.2.2.1.	Causes	176
6.613.2.2.2.	Morphological/radiographic/soft tissue changes	176
6.613.2.2.3.	Changes in motion	176
6.613.2.2.4.	Microbiological changes	176
6.613.2.2.5.	Pain	176
6.613.3.	**Treatment Options**	176
6.613.3.1.	Conservative Treatment	177
6.613.3.2.	Discectomy	177
6.613.3.2.1.	Surgical procedure	177
6.613.3.2.2.	Outcome	177
6.613.3.2.3.	Radical versus limited discectomy	177
6.613.3.3.	Total Disk Arthroplasty	177
6.613.3.3.1.	Surgical technique	177
6.613.3.4.	Fusion	177
6.613.4.	**Nucleus Replacement**	178
6.613.4.1.	Solid Preformed Implants	178
6.613.4.2.	Preformed Hydrogel Implants	179
6.613.4.3.	Externally Inflated Implants	181
6.613.4.4.	Injectable Implants	182
6.613.4.5.	Scaffolds, Cells, Growth Factors, and Tissue Engineering Concepts	183
6.613.5.	**Considerations for Evaluating Nucleus Replacements *In Vitro* and *In Vivo***	184
6.613.5.1.	*In Vitro* Evaluation of Nucleus Replacement Performance	184
6.613.5.1.1.	Hydration/temperature	184
6.613.5.1.2.	Repeated testing	184
6.613.5.2.	*In Vivo* Studies: Animal Models	185
6.613.5.2.1.	Murine	185
6.613.5.2.2.	Leporine	185
6.613.5.2.3.	Porcine	185
6.613.5.2.4.	Canine	186
6.613.5.2.5.	Bovine	186
6.613.5.2.6.	Ovine	186
6.613.5.2.7.	Nonhuman primates	186
6.613.5.2.8.	Summary – animal models	187
6.613.6.	**Summary**	187
References		187

Abbreviations

BMPs	Bone morphogenetic proteins
CoCr	Cobalt chromium
CoCrMo	Cobalt–chromium–molybdenum
DDD	Degenerative disk disease
GDF	Growth and differentiation factor
HA	Hyaluronic acid
IGF	Insulin-like growth factor
MMP	Matrix metalloproteinase
NZ	Neutral zone
PDN	Prosthetic disk nucleus
PMMA	Polymethylmethacrylate
PVA	Polyvinyl alcohol
PVP	Polyvinyl pyrrolidone
ROM	Range of motion
TDR	Total disk replacement
TGF-β	Transforming growth factor-β

6.613.1. Introduction

Low back pain is a widespread social and economic problem with 70–85% of people experiencing severe pain some time in their life.[1] When surveyed, one in four adults reports pain within the 3 months preceding the appraisal.[2] For employers, mechanical low back pain is the fourth most expensive medical cost and the most costly musculoskeletal disorder[3] as well as the single largest cause of absence from work.[4]

Disk herniation and changes associated with degenerative disk disease (DDD) are the common causes of low back pain. Herniation of some nucleus tissue past the annular fibers can impinge on nearby nerves causing pain as well as paralysis. If conservative treatment is unsuccessful, a discectomy is commonly performed. In a limited discectomy, the extruded nuclear material as well as a small amount of nucleus that is still within the annulus is removed. In a radical discectomy, the nucleus is completely removed. If insufficient tissue is removed, there is a risk that the remaining nucleus will herniate through the same annular defect; however, removal of the entire nucleus, as in a radical discectomy, may result in instability and acceleration of degeneration.

DDD is a gradually progressing disease characterized by several stages. Early degenerative changes are typically associated with the decreasing ability of proteoglycan within the nucleus to bind water. This affects the capacity of the nucleus pulposus to distribute the intradiscal pressure to the annulus fibrosus as a homogeneous pressure. The depressurized disk is unstable and exhibits excessive motion in the middle stages of this disease. This can cause pain via the motion itself, impingement of the surrounding nerves, or may be chemically mediated. Later stages of the disease involve boney growths connecting the upper and lower vertebrae, limiting or eliminating motion at the affected level. When low back pain of this nature does not respond to conservative treatment, surgical intervention may be unavoidable. Fusion is the most commonly applied treatment for painful unstable disks. It involves the removal of the disk and placement of stabilizing hardware. Bone is encouraged to grow between the vertebrae to eliminate motion simulating the later stages of DDD. The procedure is broadly successful in relieving pain but alters the biomechanics of the spine such that motion that previously occurred at the treated level is transferred to adjacent levels, increasing the stresses and possibly accelerating degeneration in these levels. There are no options following a failed fusion other than another attempt of fusion.

Another option to treat painful disks is total disk replacement (TDR) where the disk is completely removed and a mechanical joint is placed. Motion is retained and this may spare adjacent disks from the excessive loads associated with fusion. This very new procedure is currently only applicable to a small number of patients and does have other drawbacks. Of primary concern is the invasive nature of the surgery. In addition, the motion created in TDR is often very simple and lacks the hysteresis seen in healthy disks. This nonphysiological motion can produce excessive pressure on facet joints, particularly if the implant is not placed properly. The TDR is still evolving, as a result of which it probably still has a limited life span in contrast to other articulating implants, has the potential to subside into the adjacent vertebral bodies, and generates wear particles with the associated problems of biological responses and osteolysis.

Problems associated with discectomy, fusion, and TDR have prompted a focus toward the origins of the disease and treating or replacing the nucleus pulposus tissue with a synthetic material that, ideally, would restore the mechanical function of the nucleus. It would be inserted during the early stages of DDD. Intervention at the early stages of DDD has the potential to stop the degenerative changes in the spine in their tracks and postpone, if not eliminate, the need for more drastic surgeries such as fusion or TDR. The material could be implanted in a minimally invasive manner following complete discectomy or could be used as an adjunct to minimal discectomy where a portion of herniated disk is removed while a portion of the nucleus still within the annulus is removed and replaced by the synthetic material.

This chapter explore the biomechanics of the spine in terms of evaluation, the current standard protocols for treating painful disks, and nucleus replacement materials that are currently being studied for clinical use.

6.613.1.1. Intervertebral Disk

There are three primary components of the intervertebral disk: the nucleus pulposus, the annulus fibrosus, and the endplates of the vertebrae above and below. The nucleus pulposus is a hydrated mass of gelatinous tissue in the center of the disk. The annulus fibrosus is a complex, layered, isotropic ring of fibers that attaches circumferentially to the endplates. Fiber orientation between layers of the annulus alternate orientation by ~30°. The endplates are attached to the boney body of the vertebrae via thin layers of hyaline cartilage similar to articular

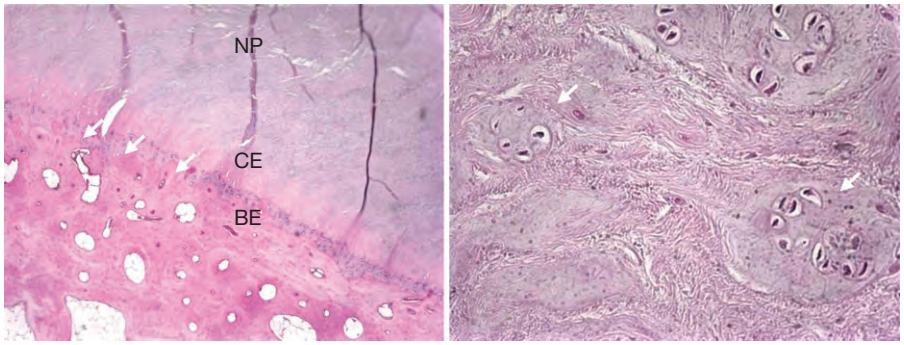

Figure 1 Left: 10× H&E stained section of the transition from nucleus to endplate. White arrows indicate row of densely packed chondrocytes. BE, boney endplate; CE, cartilagenous endplate; NP, nucleus pulposus. Right: 20× image of nucleus pulposus, arrows indicate chondrocytes.

cartilage. This layer is the cartilaginous endplate. Together the annulus and the endplates serve to contain the nucleus. In the healthy disk, an osmotic pressure gradient provides flow to the nucleus.

The intervertebral disk does not contain nervous tissue beyond the outer layers of the annulus fibrosus or the cartilaginous endplate of the vertebral body.[5,6] Blood supply to the vertebral bodies is provided by the precentral arteries which circumnavigate the body, venous return is provided via an external and internal plexus draining from the center of the vertebral body.[7] With no direct vascular supply, the intervertebral disk is the largest avascular component of the human body. The intervertebral disk relies entirely on diffusion for nutrition as well as elimination of waste products. Cells within the nucleus pulposus are sparse (Figure 1) and responsible for the maintenance of the extracellular matrix including proteoglycan.[8]

6.613.1.1.1. Microbiology of the intervertebral disk

Proteoglycans are mucopolysaccharides bound to protein, commonly found in connective tissues, and are plentiful in the nucleus. Proteoglycans are composed of glycosaminoglycans, which have strong water binding abilities. One example of a proteoglycan is aggrecan (Figure 2), which has an important physiochemical role in the maintenance of the hydration levels in articular cartilage with the ability to generate large osmotic pressures.[9] Due to their water binding ability, their spatial concentration correlates closely with water content of the disk.[10]

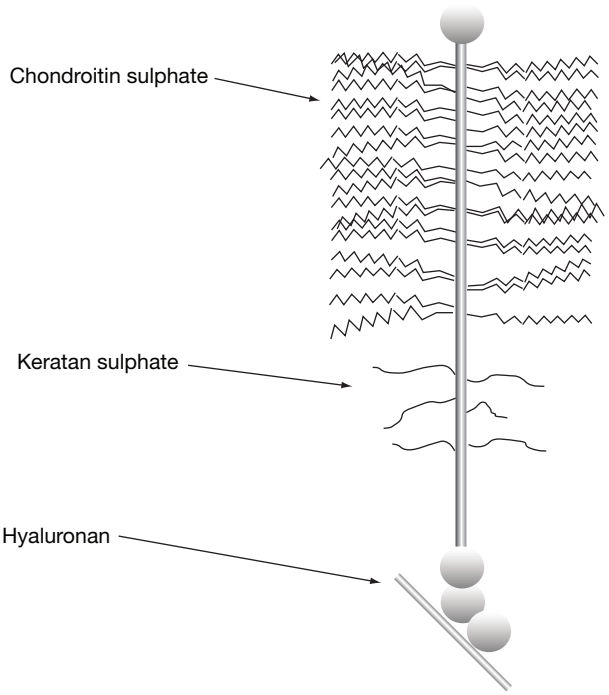

Figure 2 Structure of aggrecan.

6.613.1.2. Biomechanics

6.613.1.2.1. Principle planes/rotations

The intervertebral joints allow motion in 6 degrees of freedom. Translational motion is commonly described along the principal anatomical axes, in the sagittal, coronal, or transverse (axial) planes. Relative rotations between the vertebrae are described about three mutually perpendicular axes at the intersection of these planes (Figure 3). Flexion and extension of the spine occur around an axis perpendicular to the sagittal plane, left and right lateral bending occur around an axis perpendicular to the coronal plane, and left and right axial rotation occurs

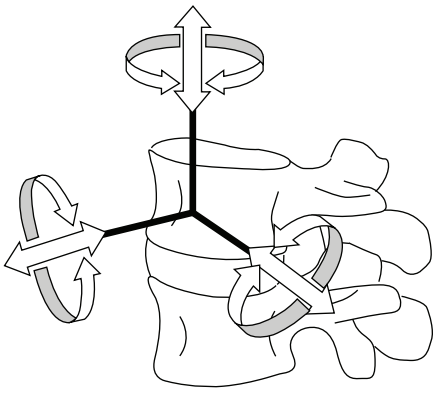

Figure 3 Mutually perpendicular axes for describing rotations and translations of vertebrae.

around an axis perpendicular to the transverse plane. These definitions can be applied to motions relative to the trunk but are more often applied relative to adjacent vertebrae.

6.613.1.2.2. Evaluation of spinal motion

Spinal motion in patients is commonly assessed in the clinical setting via simple range of motion (ROM) tests or radiographic imaging while passively or actively positioning the spine.[11] *In vitro* laboratory tests with cadaveric or animal spinal segments are used to more fully characterize the biomechanics of the spine.

Spinal motion testing can be carried out using either a stiffness protocol or a flexibility protocol. Ultimately, the best method depends on the goal of the test.[12–14] With an unconstrained flexibility protocol, a load is applied and the resulting motions are recorded; no center of rotation or motion path is prescribed. For a constrained stiffness protocol, a motion path or center of rotation is prescribed and forces are recorded. Many of the same values can be determined from either protocol and a load–displacement curve is created for both. Due to the difficulties of accurately reproducing the *in vivo* motion, a flexibility protocol is often employed.[15]

The application of pure moments for torsional tests eliminates off axis loads and allows a segment to determine its own center of rotation. The center of rotation changes throughout flexion and choosing a fixed center of rotation different to the center will affect results.[16] To carry out these tests, a motion segment, consisting of two vertebral bodies and the intervening disk, is mounted into a potting fixture, which is subsequently mounted into a testing machine (**Figure 4**).

These tests may be carried out with pulleys and weights;[17] however, computer controlled servo-hydraulic testing machines provide the ability to quickly change loads and allow the application of tightly controlled loading profiles. Biaxial testing machines may be fitted with special apparati[18] that allow pure moment application or more advanced systems may be employed that allow individual control of motion in all 6 degrees of freedom without adjusting the specimen.[19]

The result of this type of loading will produce a hysteresis curve. This can be divided into four segments as shown in **Figure 5** as loading+; loading from 0 to maximum torque, unloading+; from maximum torque to zero, loading−; the loading portion from 0 maximum negative torque, and unloading−; from maximum negative torque to zero.

Bending moments applied to the disk produce a stiffness curve that is nonlinear and steeper at higher loads than at lower ones. The overall angular rotation of the segment is known as the ROM. Stiffness is calculated from linear regions at the higher loads. The area of lower bending resistance is known as the neutral zone (NZ). There are variations on how this is calculated[18,20–23] but this is described qualitatively as a zone of laxity where a relatively small load will produce a large motion.

Axial load of the spine is shared between the facet joints and the intervertebral disk. Compressive loads directed through the vertebral body are transferred to the nucleus which distributes the force as a hydrostatic intradiscal pressure (**Figure 6**) across the inside of the annulus and the opposing endplate.[24,25]

Intradiscal pressures during activities of daily living have been shown to range between 0.1 MPa while lying prone to 2.3 MPa when lifting 20 kg weight with round, flexed back.[26] The nucleus is capable of opposing these pressures due to the previously mentioned ability to generate an osmotic pressure gradient. This pressure is essential for maintaining the stability of the spine.[27]

The thick collagen fiber bundles of the annulus fibrosus build gradually from the inner border with the nucleus. The organization of these bundles gradually builds as well, with the fibers arranged into individual concentric lamellae with alternating orientation of fibers.[28]

The integrity of this highly ordered and complex structured tissue is essential for maintaining the pressure on the nucleus pulposus.[29] Deformations of the annulus and nucleus are closely linked. The nucleus pulposus is relatively fluid and deforms toward the area of least compression.[30] Anterior rim lesions decrease the ability of the disk to resist bending and rotation. Concentric tears and radial tears have been shown to reduce the hysteresis response indicating an altered stress distribution.[31]

6.613.1.2.3. Viscoelastic properties

The balance between mechanical load and moisture content of the disk is dynamic. With prolonged compression, water is

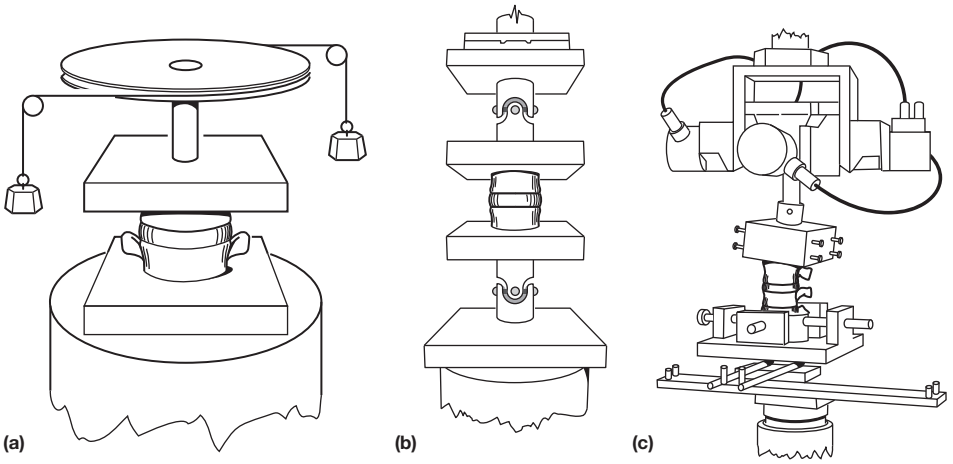

Figure 4 Examples (left to right) of pulley weighted system, system mounted in biaxial testing machine, system with full control of all degrees of freedom.

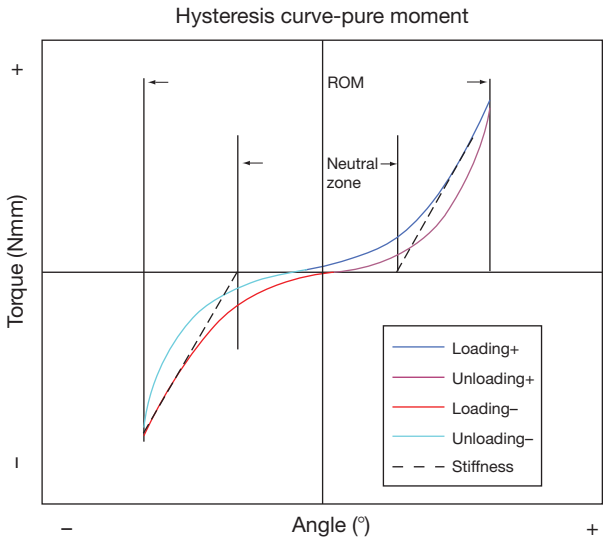

Figure 5 Typical hysteresis curve from torsional tests indicating commonly measured parameters of neutral zone, stiffness in the linear range of the loading curve and range of motion.

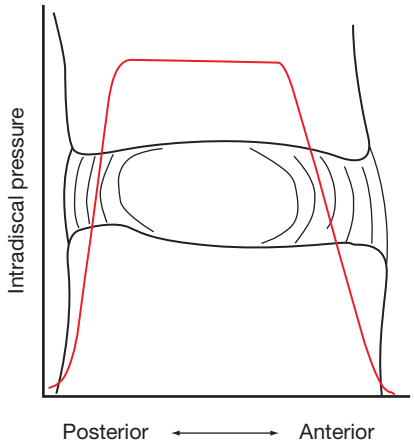

Figure 6 Pressure distribution across in the intervertebral disk.

driven out of the nucleus through the cartilaginous endplates and, to a lesser degree, the annulus fibrosus. This loss of fluid from the nucleus decreases intradiscal pressure requiring the annulus to bear more of the load.[32] *In vivo* the disks experience diurnal fluid transport during periods of sleep and waking by a volume of 1300 mm^3[33] corresponding to changes in disk height. Work by Iatridis *et al.*[34] quantified these properties in nucleus tissues, showing near fluid-like behavior under static loading with stress relaxation approaching zero, while dynamic modulus ranged from 7 to 20 kPa with loss angle ranging from 23 to 30°.

6.613.2. Ageing and Disk Injury

There are several conditions that may require intervention with respect to the intervertebral disk. Here, we will explore two of these: DDD and herniation.

6.613.2.1. Degenerative Disk Disease

DDD is characterized by many features that, given enough time, will play out naturally with aging. DDD is perhaps best described as an acceleration or exaggeration of these changes. From birth, the density of cells with notochordal origin in the intervertebral disk drops and approaches zero by ~6 years of age.[35]

Upon reaching skeletal maturity, the nucleus is populated by sparse chondrocyte-like cells with unknown origin. The disk at this point is completely avascular and completely reliant on diffusion and osmosis for obtaining nutrients and eliminating waste. This is a delicate system where the perimeter of the disk is important, and the rate of diffusion and osmosis is heavily influenced by mechanical loading.[36]

6.613.2.1.1. Causes of DDD

There are several risk factors for developing DDD. These include daily environmental factors such as driving vehicles with unsprung seats[37] and lifting very heavy objects,[38] especially in confined spaces.[39] There are also a number of morphological factors that affect the likelihood of developing DDD. Disks with low disk area in cross-section and large disk height are prone to larger motion, higher annular fiber stresses, and larger disk bulge, making them more likely to encroach on neural space.[40–42] Disks with concave endplates have a superior outcome, flat endplates do worse, and irregular endplates have the worst prognosis for DDD.[43,44] Several genetic factors have also been identified within certain populations[45–47] with hereditary effects explaining 47–66% of the degenerative changes.[48]

6.613.2.1.2. Morphologic changes

Following maturity of the disk, DDD is marked by specific morphological and microbiological changes. A healthy disk contains a moist nucleus pulposus, clear delineation between the annulus and vertebrae with rounded margins.

During the middle stages of DDD, the nucleus loses water content and becomes more fibrous.[49–51] Disk height decreases and the margins of the vertebrae above and below may develop osteophytes.[52,53] During more advanced stages, the nucleus will be considerably dehydrated with osteophytes (**Figure 7**) joining together, fusing the vertebral bodies around or through the intervertebral disk.[54]

6.613.2.1.3. Biomechanical changes

Accompanying the changes in the morphology of the disk are alterations in the motion of the spinal segments. Hypermobility has been seen in patients with back pain[55–57] as well as increased asymmetrical motion.[58,59]

A key cofactor of joint instability is the loss of intradiscal pressure, which accompanies DDD.[60] This loss of intradiscal pressure is due to the dehydration of the nucleus pulposus. The degenerate nucleus is less able to maintain its hydration resulting in increased NZ and ROM, and altered viscoelastic properties.[22,61–64]

The progression of DDD dictates that in the early and middle stages of degeneration, abnormal motion and motion in general are increased. In the later and final stages, the mobility decreases and may cease at the affected level completely.[65–67]



Figure 7 Sagittal radiograph of the lumbar spine, note increasing osteophytes from superior to inferior.

6.613.2.1.4. Microbiological changes

The loss of intradiscal pressure due to its dehydration is central to the degenerative process. The axial mechanics of the disk show a correlation between glycosaminoclycan content and decreased viscoelastic properties and increased NZ.[61] Lack of proteoglycan content decreases the ability of degenerated disks to maintain an osmotic pressure gradient.[64] Accompanying this are changes in the permeability of the boney endplates.[68]

6.613.2.1.5. Pain

Although pain is not invariably associated with DDD,[69] those patients who do experience pain often have a significantly decreased quality of life with local or radiating pain, increased analgesic intake and decreased mobility.[70] One cause of radiating pain in patients with DDD is impingement of nerve branches as they exit the spinal canal. This commonly affects the sciatic nerve and consequently is known as sciatica. In this condition, the decreased height of the disk and the associated changes in the facet joints lead to a smaller intervertebral foramen for the sciatic nerve to exit. Compression of this nerve presents as radiating leg pain with numbness, and possible weakness.[71] DDD may also cause to diffuse pain originating from the disk. The mechanism of this pain is not well understood although it may be chemically mediated.[72,73]

Segmental instability is also associated with lower back pain.[55] In the healthy spine, motion is kept within a pain free zone. It is believed that motion is increased to an extent that causes pain. If this motion is reduced back to the range of normal function, then pain is likely to be alleviated.[74]

6.613.2.2. Herniation

Although not necessarily a requisite for DDD, herniation of the nucleus pulposus beyond the confines of the annulus fibrosus is oftentimes associated with DDD and pain. Herniation may also serve as an injury that acts as an initiator for further degeneration of the disk, as many of the associated aspects such as morphology, microbiology, risk factors, etc., are similar.

6.613.2.2.1. Causes

As just stated, many of the risk factors for herniation are similar to those of DDD. The injury is usually caused by a high compressive or a high combination loading of the disk. Following from this, one of the risk factors is the lifting of heavy objects, with arms extended and while twisting.[75] Driving for extended periods is also associated with increased risk of herniation.[76,77] Disks with low area in cross-section and large disk height are prone to herniation.[78] Genetic factors also play a role.[79,80]

6.613.2.2.2. Morphological/radiographic/soft tissue changes

Herniations of the posterior annulus are the most common. In these cases, it is possible that herniated disk tissue can compress nerves exiting the intervertebral foramen causing weakness, tingling, or pain.

6.613.2.2.3. Changes in motion

An annular breach causes a loss of intradiscal pressure and similar biomechanical consequences to those of the dehydrated disk found in DDD. These include increased NZ and ROM and decreased viscoelastic properties.[22,61–64] Just as in DDD, the decreased intradiscal pressure and excessive motion increase the stresses on the annulus.[81,82] Over half of all herniations decrease in size over time with larger herniations more likely to regress than smaller ones.[83]

6.613.2.2.4. Microbiological changes

Failure of the annulus interferes with the normal diffusion in the disk similar to the way it does with endplate defects during DDD.[84,85] Herniated tissue is exposed to inflammatory mediators and becomes vascularized and may induce further vascularization toward the center of the disk.

6.613.2.2.5. Pain

The source of pain in herniated patients may be attributed to similar sources as those of DDD including those of chemical origin, mechanical overload, inflammatory mediators, or nerve effects,[86,87] but it is often associated with sciatica.[88]

6.613.3. Treatment Options

Treatment options for DDD include conservative treatment, discectomy, laminectomy, fusion, and TDR. Herniations are more commonly treated with less aggressive procedures, either conservatively or with discectomy. The treatment of nucleus replacement is at the horizon, but is not an established approach in the clinical armamentarium. The goal of all these procedures is to reduce or eliminate the source of the pain specific to each case. The treatments vary in invasiveness as well as the intended outcome and mechanism for relieving pain. They are chosen based on patients' symptoms, history, age, lifestyle, and the predicted outcome of the surgery.

6.613.3.1. Conservative Treatment

The current, initial treatment for both painful DDD and herniation is a conservative treatment involving initial rest followed by exercise to strengthen core spinal stabilization muscles. Nonsteroidal antiinflammatory drugs may be taken orally, and epidural, transforaminal, or interlaminar steroid injections may be prescribed for acute episodes of pain.[89–92] These treatments are aimed at decreasing inflammation but do not address the degeneration of the disk.

6.613.3.2. Discectomy

Discectomy is often the first course of surgical intervention for a herniated disk. Indications for discectomy are severe radiating pain which is unresponsive to conservative treatment for greater than 6 weeks, signs of neural deficit, and herniation as identified by discography or MR.[93,94]

6.613.3.2.1. Surgical procedure

Discectomy is the removal of the greater part, or a portion of the nucleus pulposus while leaving the majority of the annulus fibrosus intact. It can be performed as an open or an endoscopic procedure. A small window is made into the annulus and nucleus tissue is removed using a ronguer.[95]

6.613.3.2.2. Outcome

The outcome of the discectomy procedure is generally positive in terms of pain relief,[94,96,97] but this fades over time.[93,98] Patients show a high level of satisfaction and over 80% return to work rate although reoperation rates of around 15% are common.[98–101] However, revision discectomies have been shown to be just as effective at relieving pain and numbness.[97] Carragee *et al.*[102] have investigated the type of herniation and its effect on patient outcome. Annular competence as well as fragmentation of the herniated tissue was shown to be important for overall outcome.

6.613.3.2.3. Radical versus limited discectomy

One issue relating to the discectomy procedure is how much nucleus should be removed during the surgery (**Figure 8**). The radical removal of disk material decreases the possibility of reherniation by minimizing the chance that leftover disk material might become the source of another disk protrusion.[103,104] However, preserving as much disk material as possible shows better maintenance of hydration over the long term[105] and that radical discectomy is related to decreased disk height.[104,106]

6.613.3.3. Total Disk Arthroplasty

Implantation of a TDR involves the removal and replacement of the annulus fibrosus, nucleus pulposus, and generally the endplates of the adjacent vertebrae. A mechanical replacement is inserted into the void left by the disk. Implants marketed in the United States include the Charité III (Johnson & Johnson) constructed of cobalt chromium (CoCr) alloy endplates and a sliding PE insert and the ProDisc II (Synthes) composed of ultra high-molecular-weight polyethylene inlay sandwiched between upper and lower cobalt–chromium–molybdenum (CoCrMo) endplates.

As well as providing an earlier return to activities,[107,108] the major advantage of the TDR over fusion (discussed in following section) is the retention of motion at the affected level.[108–110] The retention of this motion requires less motion of the adjacent disk in comparison to fusion.[111] As mentioned previously, this excessive motion has been connected to degeneration at adjacent levels.[112] Total disk arthroplasty is still in an early phase of development and long-term studies to establish longevity and optimize design are lacking.[113–115]

6.613.3.3.1. Surgical technique

Implanting a disk replacement requires intensive surgery.[116,117] The implant is generally placed via an anterior approach, which requires the mobilization of the descending aorta and vena cava for L4–L5 and L3–L4 disk replacements. The endplates of the vertebral body are roughened or removed following the removal of the disk and the implant is placed.

Early[107,118] and midterm results are promising;[119] however, there are some drawbacks. The procedure is only applicable to a small portion of those with painful disks.[120] TDR also carries potential complications including damage to the genitourinary tract, injuries to the ganglia running along the anterior portion of the spine, and paralysis due to injuries to any of the nerves located along the anterior approach,[121] and vertebral split fractures.[122]

While these motion sparing implants have been shown to retain or even increase ROM quantity,[123,124] the quality is not necessarily retained.[125] This motion also generates wear particles, which have been associated with subsidence, migration, and adjacent fusion.[126–128]

6.613.3.4. Fusion

Intervertebral fusion involves surgery to induce a union between upper and lower vertebrae, thereby fusing the vertebrae. The goal of the surgery is to eliminate motion that may be causing pain. Spinal fusion is a well-established procedure that is applicable to a large portion of the patient population for a number of disorders.[129,130] Two common fusion techniques are posterolateral fusion and interbody fusion. Posterolateral fusion is achieved by placing bone graft between the transverse processes to eliminate motion between the posterior elements. Stabilizing hardware may also be used.

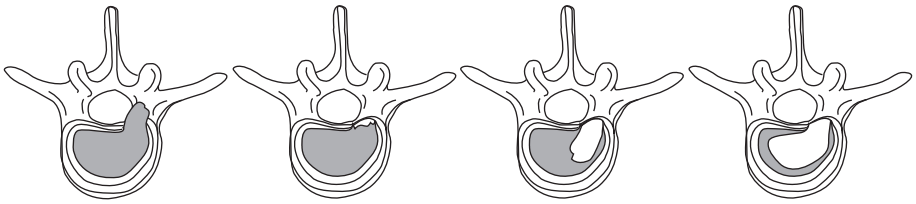

Figure 8 Nucleus present following (left to right): hernation, removal of herniated portion, limited discectomy, and aggressive discectomy.

Interbody fusion is achieved by placing graft between the vertebral bodies, often following discectomy. The objective is to form new bone between the vertebral bodies, through the endplates, and eliminate motion. Hardware generally used in this procedure may include fusion cages or pedicle screws, or bone graft alone may be used.[131]

Lumbar fusion has drawbacks, perhaps the most important being the extent to which it alters the biomechanics of the spine and, subsequently, the strains experienced in the surrounding tissues. Successful fusion results in either a significantly reduced amount of motion or no motion in the treated level. To maintain the overall ROM of the spine, the adjacent levels are required to compensate. This results in increased motion at these adjacent levels,[111,132] which induces increased stresses and intradiscal pressure,[132] which may, in turn, accelerate the degenerative process at these levels.

6.613.4. Nucleus Replacement

Replacing the nucleus pulposus has the potential to provide several benefits over traditional treatments. When compared to fusion, nucleus replacement has the advantages of being a minimally invasive procedure and retaining motion. In addition, there are few options after a failed fusion. However, if pain persists following nucleus replacement, TDR and fusion remain viable options for pain relief. Nucleus replacement most often uses the same surgical approach as discectomy, is generally no more invasive, and normally follows a discectomy. The retention of the endplates and annulus while replacing the nucleus with a material possessing viscoelastic properties similar to that of the healthy nucleus would be expected to reproduce more physiologic motion than TDR without the highly invasive anterior approach to the spinal column and the drawback of accumulating wear particles. In discectomy without nucleus replacement, there is no outward pressure applied to the endplates and inner annulus to place its fibers in tension. Without this pressure, the fibers bulge inward and are subjected to compressive forces between the endplates, and disk height is reduced.[106,133,134] With nucleus replacement, a discectomy would be performed to remove the ailing nucleus, and the nucleus replacement would be placed to restore disk height, avoiding further stenosis and associated pain generators. Ideally, this would decelerate the degenerative cascade and thereby postpone or prevent the need for more invasive interventions such as TDR and fusion.

Nucleus replacements require a patient to have largely intact and functioning annulus and endplates free from significant defects as well as healthy facet joints and greater than 5 mm disk height.[135] This excludes cases of advanced degeneration; significant loss of disk height may be difficult to restore. The ability to mimic the function of the intact nucleus is the ultimate goal of any nucleus replacement. An implanted material would need to resist expulsion through any fissure or injury, or through any incision or defect created during implantation. It would need to resist compressive forces between the vertebrae and be able to maintain properties through millions of cycles of loading/unloading produced through normal human activities of daily living.[134]

To date, several diverse designs have been conceived for nucleus replacement. They can be categorized into solid preformed implants, hydrogel preformed implants, externally inflated implants, and injectable implants.

6.613.4.1. Solid Preformed Implants

The first attempts at replacing the nucleus while maintaining the majority of the annulus were not entirely successful. In 1959 Harmon *et al.*[136] implanted spheres of a corrosion resistant alloy made of CoCrMo known as Vitallium®. This device was originally known as the Harmon sphere and was implanted after an open discectomy as a nucleus replacement but was eventually classified as a fusion device due to the spontaneous fusion occurring in some of its recipients.

A more extensive clinical evaluation was carried out by Fernstrom[137] and Reitz and Joubert[138] with respect to the use of metallic spheres as nucleus replacements. The Fernstrom ball was a simple stainless steel ball bearing, 16–10 mm in diameter, that was inserted through an annular incision following discectomy under local anesthetic. The device was implanted in over 100 patients, and although the results were acceptable, the significant difference in the mechanical properties of the native nucleus and stainless steel led to the subsidence of the ball into the vertebral body. Although the device was not successful, the concept of retaining the annulus and motion was explored. This, by itself, represented a meaningful advance.

The ball theme was modified by Gau *et al.*[139] who incorporated one or several balls which are hard, smooth, and non oxidizing into the design of a nucleus replacement (**Figure 9**). The balls were arranged into a cage in which they were freely movable. This design would likely limit the amount of subluxation into vertebral endplates but its size and shape would make it difficult to implant. Bryan *et al.*[140] created a unique shape and function in his peanut spectacle design. The device consisted of two peanut shaped shells containing resilient bodies.

Lawson *et al.* conceived two designs with anchorage to the inferior vertebrae. The first design was a flattened oval disk with convex surfaces (**Figure 10**). The bottom peg can be

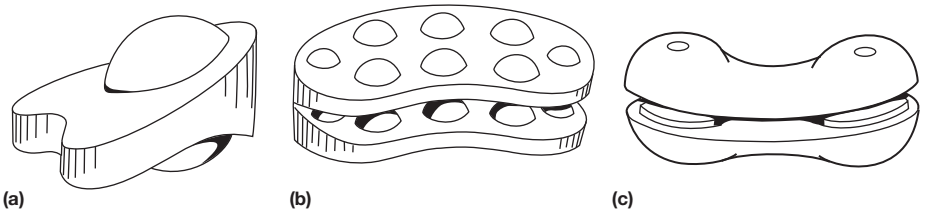

Figure 9 Interpretation of Gau's constrained ball design with one, and several spheres, Bryan's peanut spectacle design.

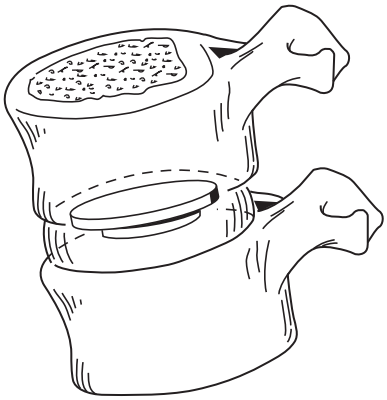

Figure 10 Interpretation of one of Lawson's inferiorly anchored design.

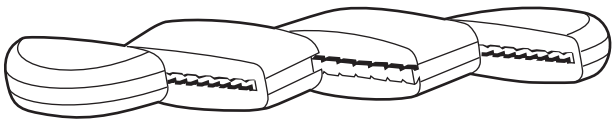

Figure 11 Interpretation of Felt's modular design.

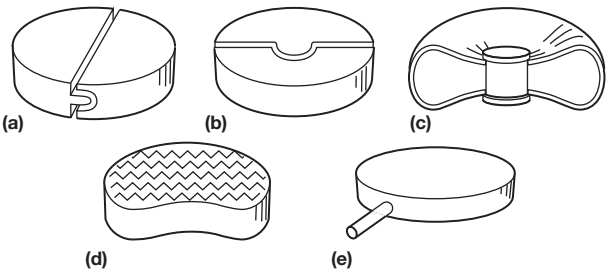

Figure 12 Interpretation of Ferree's multiple nucleus replacement concepts.

cemented.[141] The second design had a separate keel of porous metal for fixation and was free to rotate about this keel.[142]

In an effort to completely fill the disk space following discectomy while limiting the damage to the annulus, Felt *et al.*[143] outlined a modular nucleus replacement (Figure 11). The unassembled pieces were inserted through the posterior annulus and interlocked *in situ*. The inner cores are to be constructed of polyvinyl alcohol (PVA) while the outer shell would be constructed of a polymeric material. Ferree *et al.*[144] also perceived modular designs (Figure 12) as well as several other concepts, one unique design[145] incorporated an annular or donut shape.

Recently, Kettler *et al.*[146] have studied implants consisting of knitted titanium filaments *in vitro* following discectomy. Biomechanical testing revealed that intact ROM was nearly restored after implantation. However, in axial rotation and extension, the ROM increased slightly with the implant. ROM in flexion decreased. Some of these changes in motion could be affected by the large annulotomy, spanning nearly two-thirds anterior aspect. Although there was no extrusion of the device, cyclic testing did cause increased ROM in all loading planes.

Biomet EBI scheduled an IDE study for the Regain Lumbar Artificial Disc (Figure 13), and preliminary testing in baboons has been completed.[147] The device is constructed of pyrolytic

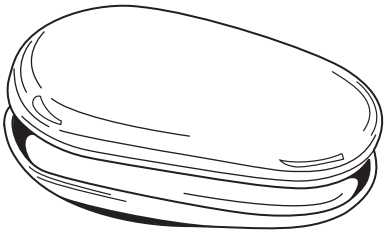

Figure 13 Depiction of regain lumbar nucleus replacement.

carbon, more detailed descriptions of carbon constructs can be found in **Chapter 1.107, Carbon and Diamond**; **Chapter 5.523, Carbon Nanotubes: Applications for *In Situ* Implant Sensors**; and **Chapter 3.330, Carbon Nanotube-Based Sensors: Overview**. The shape of the device has been carefully crafted so that it seats itself in a concave endplate while causing minimal subsidence. This makes patient selection based on endplate morphology an important factor for success of the implant. The 15–17 mm anterior incision required for insertion is likely to increase the likelihood of expulsion; however, this is offset by a shape designed to prevent migration. The device has been implanted in 10 patients and 3-month follow-up demonstrated increased disk height and decreased pain but no improvement in lumbar motion.[148]

6.613.4.2. Preformed Hydrogel Implants

Hydrogels are cross-linked macromolecular networks formed by hydrophilic polymers. As they are described in **Chapter 1.131, Superporous Hydrogels for Drug Delivery Systems**; **Chapter 1.132, Dynamic Hydrogels**; and **Chapter 3.329, Hydrogels in Biosensing Applications**, they will only be explained briefly with respect to nucleus replacement here. They are an attractive replacement material as they can be engineered to mimic the mechanical properties of the native nucleus, all while having a low level of immunogenicity. They have the ability to attract water and swell, thereby generating an osmotic pressure similar to what the native cells in the nucleus pulposus experience. Hydrogels are categorized as chemical or physical hydrogels, based on the type of bonding in the cross-links. Physical hydrogels are maintained by cohesion forces such as ionic bonding, hydrogen bonding, Van der Waals forces, and forces that arise during hydrophobic interactions. These can be produced by a number of methods including exposure to heating and cooling cycles.

Chemical, or permanent, bonds cannot be dissolved in water or solvents. This bond can be achieved by copolymerization of a monomer with a cross-linker, irradiation, free radical polymerization, thermal initiation, catalyzed initiation as well as other methods. The extensive control of cross-linking that can be achieved by chemical bonding is attractive. However, the toxic effects of residual monomers used for the hydrogel polymer synthesis are a potential drawback.[149]

Bao *et al.*[150] were among the first to use hydrogel as a substitute for nucleus replacement when proposing polyacrylonitrile hydrogels be implanted in a dehydrated state. Dehydration can decrease the implant size by more than half of its hydrated state. The isotropic swelling ability of the hydrogel permitted it to be inserted at a smaller size and to expand after insertion. In principle, this allowed a smaller annular defect to be created during the

procedure, and it provided the ability to generate a lifting pressure between the vertebrae after implantation.

After insertion, there is an annular defect and the path of least resistance will be in the direction of that defect. To counteract any possible extrusion effect, as well as annular bulging, the hydrogel may be preformed or otherwise constrained to promote expansion in the axial direction. Bao's design was intended for implantation in single or multiple preformed dehydrated pieces (Figure 14). A coiled design was later introduced to combat lateral bulging[151] while another version incorporated hydrogel pellets restrained by a woven bag.[152]

While the hydrophilic properties of hydrogels are initially appealing, the reversible nature of this water absorption may be a limitation. The implant is inserted in a tissue with limited fluid flow, which is in a diseased state, and in which water binding is compromised. Additionally, the deformational characteristics of hydrogels typically limit the ability to withstand bulging and expulsion.

One of the most used nucleus replacement to date has been the prosthetic disk nucleus (PDN) (RayMedica).[153–156] The PDN is a hydrogel core encased in a woven polyethylene jacket. The formed hydrogel pellet is a copolymer of polyacrylonitrile (nonhydrophylic) and polyacrylamide (hydrophilic) sustained by physical cross-links in a ratio that achieves a maximum of 80% water weight at full saturation. The hydrogel allows the implant to be dehydrated prior to implantation after which it regains hydration and increases disk height. The jacket limits the maximum expansion and radial bulge of the hydrogel. The device has been modified many times (Figure 15), reflecting the difficulty of optimizing this device with its underlying design principle. It was originally designed as a single implant then modified to include two, then the orientation was altered so that placement was lengthwise left to right rather than front to back, then a single, larger, and wedged implant was designed.[155,157–161]

Laboratory studies on motion segments have shown that following discectomy the PDN can restore compressive stiffness, viscoelasticity, disk height, and ROM *in vitro*.[162]

The PDN was first implanted in 1996, in Germany.[155,157] Results of early clinical trials showed a high rate of device migration.[153,156] Little data are available regarding longer term outcomes; however, a small series with follow up at 4 years showed subsidence in all cases although disk height and Oswestry scores remained improved for most patients, and none required surgical intervention.[163]

Patient selection now requires a minimum of 5 mm disk height, healthy endplates, and minimum diameter of the disk. The size of the implant requires an enlargement of the annulotomy formed to remove the nucleus. This is done by cutting an annular flap and suturing it back into position afterward.[154] The large annulotomy and the fact that the PDN does not fill the nucleus void completely are, however, significant drawbacks and have interfered with achieving a clinically effective device.

Replication Medical, Inc. developed NeuDisc.[164,165] NeuDisc produces controllable swelling of the hydrogel/fiber implant by internal restraint. The cylindrical implant also uses polyacrylomitrile hydrogel in a stacked design with layers of polyester fiber mesh interposed. The mesh restricts the radial bulge of the implant and therefore the outward bulge and pressure on the annulus. The implant is dehydrated and rolled for insertion (Figure 16) through the anterolateral annulus following discectomy and has successfully survived cyclic testing to 10 million cycles.[166,167] Clinical results are, as of yet, not available.

The axially directed lifting force is advantageous to increasing disk height but the incomplete filling of the nuclear space is nonphysiological and may lead to compression and inward bulging of annulus fibers.[168] In this context, it may be apparent that surgical placement is challenging.

Another company, Zimmer Spine developed NewCleus (Figure 17), a polycarbonate urethane elastomer with a spiral configuration.[169] The material absorbed up to 35% of its net weight in water once implanted. The spiral allows a small

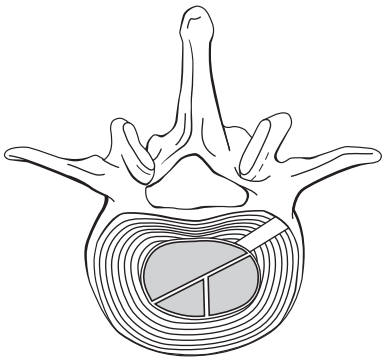

Figure 14 Interpretation of Bao's preformed hydrogel.

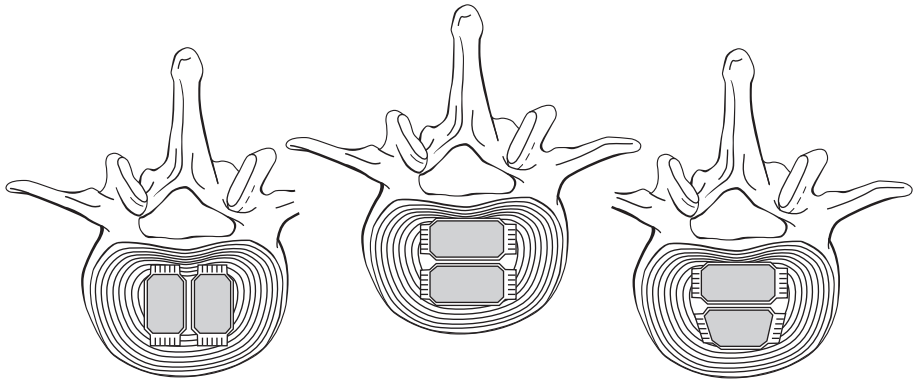

Figure 15 Different PDN designs and implanted positions.

incision relative to the size of the implant while having no fixed axis once implanted so that it does not need to be centrally located. Five patients have currently received the implant and, at 2 years, show improved postoperative pain and function with no signs of migration; however, there were some signs of changes in MRI signals in adjacent vertebrae potentially due to changes in loading.[135,169,170]

The Aquarelle hydrogel nucleus (Stryker Spine) is an unrestrained PVA bead (Figure 18) bound by physical cross-links.[171] It has been tested in two sizes; 0.1 and 0.3 cm^2 and is inserted through a 5 mm cannula using a lateral or posterior technique. Early tests in baboons revealed high extrusion rates, but no device related pathology at 2 years. The high extrusion rate of the implant may be due to the relatively high hydration at the time of implantation, requiring an annular defect similar to the implants size, as well as the rounded pill shape.

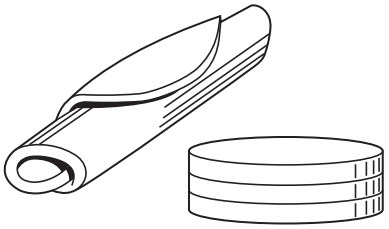

Figure 16 Depiction of NeuDisc rolled and dehydrated for implantation and in its hydrated state.

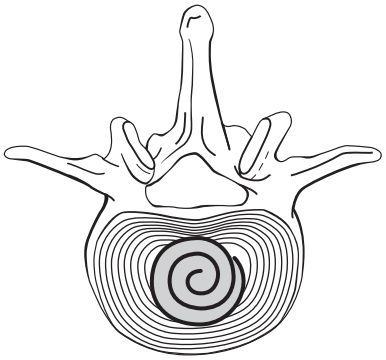

Figure 17 Diagram of implanted NewCleus.

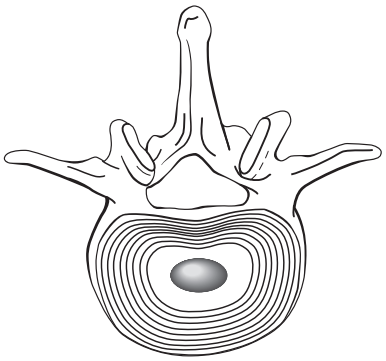

Figure 18 Diagram of implanted Aquarelle.

6.613.4.3. Externally Inflated Implants

Externally inflated implants require a smaller annular defect to insert than preformed implants while still achieving an inflated size that will prevent extrusion. The ability to be inflated decreases the need for the implant to generate a lifting force once implanted as they can be externally pressurized. Early designs that incorporate external filling include Froning's design[172] which used a plastic bladder implanted posterolaterally with anchorage to the endplates centrally, Krapiva's design[173] consisted of a flexible disk that was implanted in a hollow state and expanded *in situ* and then filled with a gel, and a variation of the coiled design by Baumgartner[174] which used a coiled elastic material with a central chamber that was filled with fluid (Figure 19).

More recently, Wardlaw *et al.*[175] has worked on a design similar to Froning's, with a woven outer or porous fabric bag containing hydrogel that allows the removal or addition of filler material after implantation. The outer bag is complex with several layers supporting transudative or ion transport. The outer surface would allow fibrous tissue ingrowth and water transport but not bone ingrowth.

The most current inflatable design is a continuation of the bag design (Figure 20)[176]; DASCOR® (Disc Dynamics, Inc.), which is an inflatable balloon delivered via a catheter and inflated with a polyurethane that is cured *in situ*. Following discectomy, the device is inserted and inflated to a desired level of vertebral distraction, the balloon is removed and another is placed which is filled with polyurethane activated with diisocyanate cross-linker that polymerizes in minutes (Figure 21).



Figure 19 Depiction of Baumgartner's inflatable device as it is implanted.

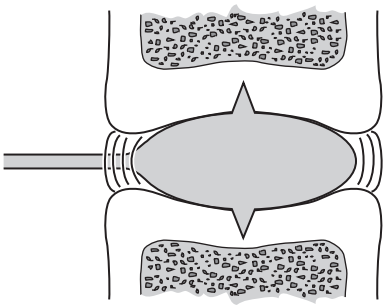

Figure 20 Variation of Bao's implantable design incorporating endplate spikes.

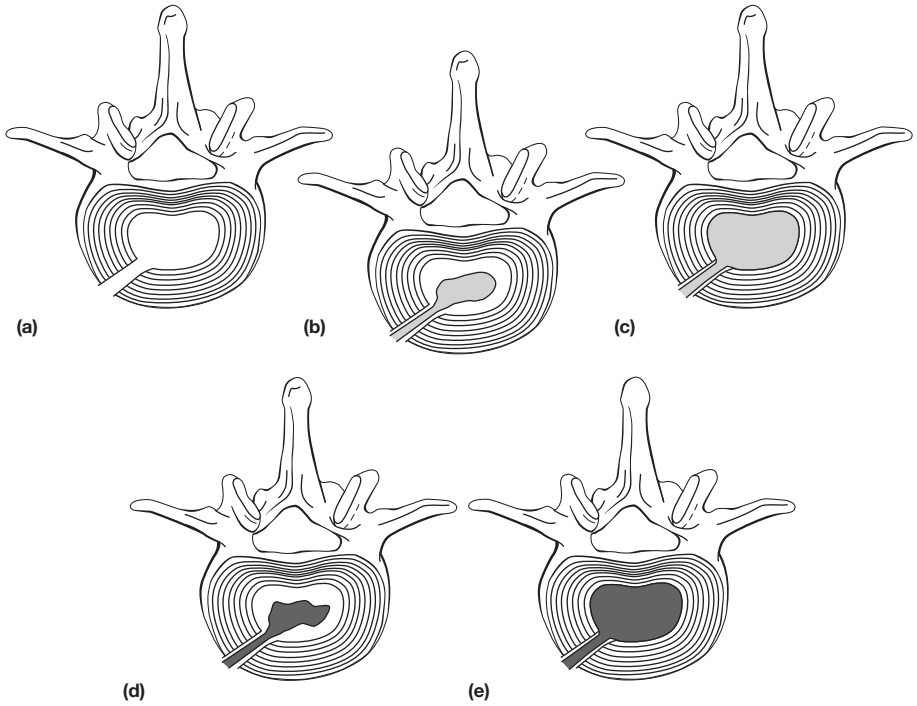

Figure 21 Implantation of the DASCOR device: (a) discectomy, (b) sizing/diagnostic catheter inserted, (c) balloon filled with contrast solution, (d) the final catheter inserted, and (e) mixed polymer injected, cured and the catheter is cut off.

Clinical studies with 2 years of follow up show decreased pain and increased function and maintenance of disk height.[177] Mechanical testing of cadaveric motion segments showed that the use of a cured polymer, restored mechanical properties better than the use of water.[178]

The use of an inflatable bag has the advantage of more completely filling the defect than preformed implants with a final shape that is unique to each patient. However, the constraining bag does not facilitate transport of nutrients, which may be a concern for the nutrition of residual disk tissue.

6.613.4.4. Injectable Implants

The first injected nucleus replacements were performed in 1956 by Cleveland *et al.*[179] injecting polymethylmethacrylate (PMMA) into the disk space following discectomy. PMMA is commonly used as bone cement in joint replacement arthroplasty. It is a relatively stiff polymer used to anchor the implants in the bone structure. This concept led to clinical results that were similar to fusion with arrested motion and pain. Yet, there was also some tissue damage arising from the exothermic reaction of the curing polymer.[180] Long-term (10–15 years) results were published and the procedure was less invasive than more traditional fusion although it had the same disadvantages as fusion.[181]

In 1962, Nachemson *et al.*[182] attempted to replace the nucleus with a more pliant material. In laboratory tests, vulcanizing silicone was injected into cadaveric disks after discectomy and showed some return to original properties. Unfortunately, after repeated testing, the rubber failed. The contribution from these studies is that these tests showed that the mechanics of the disk could be restored by replacing the nucleus tissue with a flexible material cured *in situ*.

In situ curing of an unconstrained nucleus replacement is an attractive idea, and the area is currently receiving a great deal of interest, particularly by using *in situ* setting hydrogels. By adjusting the ratio of PVA and polyvinyl pyrrolidone (PVP), hydrogels have shown the ability to return mechanical properties and height of the disk that are lost through denucleation.[183,184] Cloyd *et al.*[185] and Revell *et al.*[186] have shown that hydrogels based on hyaluronic acid (HA) have the ability to mimic modulus, Poisson's ratio, and stress relaxation properties of the nucleus. Leone *et al.*[187] have shown that hydrogels composed of modified polysaccharide cross-linked with diaminopropane also exhibit the thixotropic behavior of native nucleus tissue. This behavior was identified in the nucleus by Iatridis *et al.*[34,188] as the ability to behave as a liquid under certain mechanical conditions and as a solid under different conditions. Other researchers are working on adding clinically advantageous aspects such as radiopacity.[189,190]

The major advantage of using an injectable material is the small access required. The ability to inject through a small cannula or needle necessitates only a minute annular defect which will increase the maximum pressure that can be borne by the residual annulus.[191] Whereas the size of an inflated implant reduces the risk of extrusion, a material injected as a liquid and curing to a gel *in situ* has the ability to fully interdigitate with remaining tissue prior to curing. This intimate contact reduces the risk of extrusion and would theoretically function more like the intact nucleus.[184] There are several groups focusing on advancing these concepts. Patenting activity in this area is high with patents issued for injectable *in situ*

curing keratin hydrogels, hydrogels cross-linked by pH, temperature, exposure to moisture, for PVA/PVP combinations, and elastomers.[192–196] These materials are, however, still hydrogels, which will meet the same challenges as mentioned when describing the preformed hydrogels.

CryoLife, Inc. is developing an injectable hydrogel made from purified bovine albumin and glutaraldehyde called BioDisc. The material is injected following discectomy and eventually absorbs 63% liquid by volume. The unique makeup of the BioDisc allows covalent bonding to annular tissue. It is injected as a liquid and gels in 2 min with negligible exothermic reaction. Mechanical tests have shown restoration of disk height and stability in bovine specimens through 10 million cycles[197] and early results of a 10 patient trial have been positive for reduced pain and increased function.[198] One issue that may affect the results of the device is the toxicity of the activator agent, glutaraldehyde.[199,200]

Cohen *et al.*[201,202] have synthesized an injectable *in situ* nucleus replacement not based on hydrogel concepts. Viscoelastic behavior akin to that of the native nucleus is achieved using emulsion technology concepts. The DiscCell polymer emulsion cures in 5–7 min and is injected in a minimally invasive manner. Current work focused on establishing the biocompatibility of the material and the determination of the mechanical behavior under a range of physiologically relevant loading conditions. The material is radio-opaque making image guidance a useful tool to provide feedback on the amount of material injected and the placement of the material (**Figure 22**).

One can show that extended compressive loading will change the mechanics of the intervertebral disk *in vitro*; in fact, NZ and ROM are increased and disk height is lost. The injection of DiscCell, however, reverses these changes; that is, the disk height and NZ laxity are restored to conditions equal to or beyond the initial parameters.[203] These data support the notion to restore the biomechanics of disks in the middle stages of DDD and may obviate the need for discectomy completely.

SpineWave Inc. has developed an injectable nucleus device known as NuCore™. The protein polymer hydrogel is a copolymer of silk and elastin with one modified elastin block per mer for chemical cross-linking and two silk blocks and seven additional elastin blocks. The protein polymer is created through chemical DNA synthesis, produced by *Escherichia coli* through fermentation. The material is intended as a total or partial disk replacement, is mixed with hexamethylene diisocyanate cross-linker prior to injection, and cures *in situ* under pressure. The material has a working time of ~90 s, primary curing occurs in 5 min with full curing in 30 min. The hydrogel has the additional benefit of being adhesive to the residual disk tissue.[204]

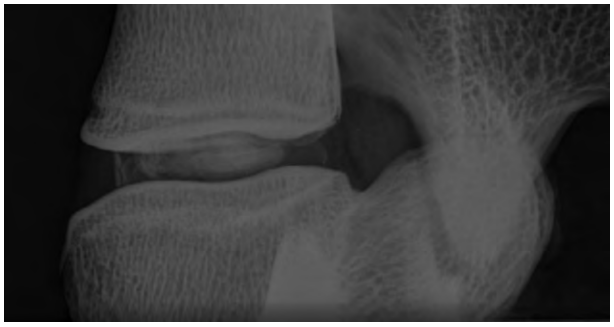

Figure 22 Sagittal radiograph of sheep disk with DiscCell implanted.

Pelletier *et al.*[205] have developed an ovine discectomy model to evaluate nucleus replacements involving the removal of the nucleus pulposus with a surgical shaver. This model has been employed with and without treatment with NuCore. At 52 weeks, results showed a high degree of biocompatibility and interdigitation with residual disk tissue, additionally treated levels showed decreased osteophyte formation in comparison to levels that received discectomy alone.

A 2 year follow-up on a pilot clinical trial[206] showed that treatment following discectomy and limited injection of synthetic material improved pain, function, and disability scores. Retention of disk height was superior when compared to published data on discectomy alone, showing the potential for nucleus replacement following discectomy to improve outcome over discectomy alone.

6.613.4.5. Scaffolds, Cells, Growth Factors, and Tissue Engineering Concepts

Several of the hydrogels described previously have been evaluated in terms of their ability to support cells from bone marrow and explanted intervertebral disk cells.[186,187,207,208] This provides the possibility of using the hydrogels as a scaffold for seeding the nucleus with cells capable of proliferation. Other materials have also been constructed as scaffolds for cells, Wilke *et al.*[209] evaluated a condensed collagen type I matrix but found that there was a significant problem with extrusion as the material did not cure, or increase in viscosity in any way after injection. Other scaffold materials have also been suggested including resorbable glycosaminoglycan molecules.[210]

Mizuno[211] harvested cells from sheep disks and constructed a scaffold of polyglycolic acid and polylactic acid, annulus fibrosus cells were pipette into the scaffold and allowed to attach for 1 day. Nucleus pulposus cells were suspended in alginate and injected into the center. The implants resembled disks histologically although this technology is far from clinical application. Work by Bron *et al.*[212] has shown the ability of dense collagen scaffolds to mimic the properties of the nucleus pulposus. While the collagen scaffold has lower energy dissipation, and gamma sterilization increased the shear moduli while decreasing swelling ability, the material has potential as a cell scaffold.

Various studies have addressed using growth factors to influence cell behavior in the intervertebral disk. Walsh *et al.*[213] have shown insulin-like growth factor-1 (IGF-1) to have some effect on the inner annular chondrocytes in degenerated disks and Gruber *et al.*[214] have shown IGF-1 to decreased apoptosis in low serum conditions. Many studies have looked into the effect of bone morphogenetic proteins (BMPs), important in the behavior of boney tissue, on intervertebral disk cells. The application of BMP-2 has been shown to increase chondrogenic phenotype, proteoglycan content, and aggrecan gene expression.[215–218] Similarly, BMP-7 has been shown to increase disk height, proteoglycan content

and metabolism, and production of collagen II.[219–221] Additionally, transforming growth factor-β (TGF-β) increases proteoglycan synthesis,[222] growth and differentiation factor-5 (GDF-5) stimulates aggrecan and collagen type II expression,[223,224] and matrix metalloproteinases (MMPs) influence proteoglycan content.[225]

Recent work by Hohaus *et al.*[226] used a canine model to demonstrate the possibility of implanting harvested autologous disk-derived chondrocytes into degenerated disks. Disk height was shown to correlate with the treatment. This has led to the use of adipose-derived stem cells as a source for chondrocyte-like cells. This work shows potential as a DDD therapy.

Sobajima *et al.*[227] have shown the ability of mesenchymal stem cells to survive as long as 24 weeks in a rabbit model. They pointed to limitations of attempting to implant the cells before a more complete understanding of the pathogenesis and pathophysiology of disk degeneration, the biochemical and physical signals needed to cause a stem cell to differentiate into a nucleus pulposus-like cell, and the specific mechanisms by which stem cells might exert beneficial stimulatory effects were known.

The results of these studies are promising, but the action of these therapies is not fully understood. This research is still at a very early stage and has many hurdles to pass. The factors have a sort lifespan with which to act and although they may utilize a natural signaling pathway, they do produce an unnatural influence. An increased proliferation of disk cells will use more resources in an already scarce environment. This may have a short-term benefit at a long-term cost. The initiator of degeneration is still unknown at this time. The degradation of the matrix of the nucleus pulposus and subsequent cell death may be a symptom and not the actual source of the problem. The source may be the inability to nourish the intervertebral cells due to changes in permeability and blood flow the endplates.

Simply increasing the population of cells in the nucleus may not be beneficial, as follows from the work by Kobayasi *et al.*[228] In this study, glycosaminoglycan accumulation was measured with cell populations at physiologic populations and at levels increased by a factor of 6. The result was an overall increase in glycosaminoglycan of 2–4% while the secretion per cell decreased by about 50%. In addition, apoptosis and cell death followed. Such data underscore current, inherent benefits for a synthetic approach to treat the nucleus pulposus. In fact, a nonliving nucleus replacement is not subject to apoptosis and does not require nourishment. Admittedly, wear and tear of a nonliving material would not be repaired, and changes in endplate condition may have an effect. Yet, the inherent ability to reconstitute function, this is mechanical function, at the time of placement represents a treatment advantage that cannot be matched by biological treatment concepts.

6.613.5. Considerations for Evaluating Nucleus Replacements *In Vitro* and *In Vivo*

Animal models can provide valuable information regarding local and systemic biocompatibility as well as potential functional performance of a nucleus replacement. The choice of the animal model is not trivial, as an inappropriate model may provide possibly confounding results. The model must be selected to address specific clinical questions and be technically feasible.

The evaluation of nucleus replacements prior to implantation, however, is vital to gain an understanding of the implant. ASTM is currently developing standard WK4863; *Standard Practice/Guide for the Mechanical Characterization of Lumbar Nucleus Devices*. This standard covers several mechanical tests to quantify static properties, creep behavior, ROM, and accelerated aging of nucleus replacements. The standard does not cover testing in biological tissues.

Testing with human cadaveric tissue or animal tissue can provide insight as to how a material behaves inside a loaded disk and how it affects the biomechanics of a motion segment. Spinal biomechanics, mechanical testing devices, and outcome measures have been covered previously; here, we explore some common considerations for testing of spinal segments in harvested tissues. The goal of *in vitro* studies is to gain information that can be related to *in vivo* tissue behavior, ideally by recreating *in vivo* conditions as closely as possible without sacrificing repeatability. Choosing boundary conditions and testing protocols that have temporal effects on a specimen may unduly affect the outcome of a laboratory study. The primary considerations include hydration of the disk, temperature, and effects induced by repeated testing.

6.613.5.1. *In Vitro* Evaluation of Nucleus Replacement Performance

6.613.5.1.1. Hydration/temperature

In life, the disk regularly exchanges over 1.2% of its volume in water during normal activities of daily living.[33] Nucleus tissue loses moisture in air, swells considerably in saline and is most stable when in a humid environment, such as a humidity chamber.[34] Common testing protocols include wrapping specimens in gauze or plastic wrap and moisturizing with saline, testing in a 37 °C saline bath, or in a humidity chamber. If the disk is placed in saline without preload, it swells by ~24% and remains static if wrapped in plastic and sprayed with saline.[33,229] The change is asymptotic and plateaus after ~7 h which corresponds to changes occurring in life.[33] These changes in hydration affect the biomechanical properties of the disk.[230,231]

Testing in air and moisturizing with sprayed saline provides a stable testing condition that will suffice for most tests.[19] The benefit of testing in a saline bath is that temperature can be more closely controlled to minimize artifact in measurements of biomechanics induced by the temperature dependent properties of spinal structures.[232,233] To offset the swelling of the nucleus, follower loads are often applied to provide a compressive load mimicking muscle forces.[234,235] When available, a humidity chamber provides a useful alternative to testing in a saline bath.[236,237]

6.613.5.1.2. Repeated testing

Specimens are commonly tested in sequence; intact, after discectomy, and after treatment with nucleus replacement. This is an efficient approach given that it allows for repeated measurements, and thus, that it enables to reduce the ultimate number of specimens needed. Unfortunately, it does not allow for randomization of treatment order. Allowing adequate recovery time between tests is important as work by

Johannessen *et al.*[238] and van der Veen *et al.*[239] have shown. When sheep disks were cycled through 10 000 400 N cycles, the mechanics of the disk were restored after 18 h; however, when pig disks were subjected to constant compressive loading for 15 min and allowed 30 min recovery, the mechanics were not restored.

In a very long-term study, repeated testing of spinal segments over 72 h, Wilke *et al.*[19] found steadily increasing ROM. This was shown to take place on a shorter time scale as well, with six repeated tests in three modes of bending over 6 h demonstrating steadily increasing ROM.[237] Testing of an additional specimen alongside treated specimens may help gauge the effects of a repeated testing protocol. An implant will have to overcome the effects of discectomy as well as tissue fatigue brought about by repeated tests.

6.613.5.2. *In Vivo* Studies: Animal Models

Few animals practice upright, bipedal walking as humans do. Nonhuman primates are capable of upright walking; however, upper limbs are often involved. Kangaroos often stand upright but their gait is distinctively different to the human gait; using all four limbs and tail at a slow gait, and two hind limbs in a hopping motion for high speed gait. Practical concerns regarding animal availability and caring facilities encourage the use of quadruped animals. One perceived disparity between the quadruped spine and the human spine is loading.

Quadrupeds do not stand upright and therefore gravity does not place the spine in constant axial load and the forces transferred due to vibration may be of a different nature. However, the loads placed on the lumbar spine are more complex than those generated by gravity alone, and surrounding musculature and ligaments generate loading which predominates axially.[240,241] Quadrupeds also show similar axial alignment of trabeculae within vertebral bodies[242] and signs of degeneration analogous to the human degenerative cascade.[243–245] Several animal models have served as models for the human spine and are applicable to *in vivo* evaluation of nucleus replacements (**Figure 23**).

6.613.5.2.1. Murine

The size of mice makes caring for them comparatively expedient, and the disks of both rats and mice have been shown to be scalable to the human, providing a useful model.[246] Lotz *et al.*[247,248] have shown the degenerative effects of mechanical loading on the mouse tail with a system of pins through the vertebral bodies. Similar devices exist for rats.[249] While these models are useful for investigating the degenerative cascade, these disks do not normally undergo significant compression or diurnal changes and they lack facet joints. Also, the mechanics of the tail do not correlate as well to a body weight adjusted human spine as lumbar levels.[250] The small size of the disk makes discectomy and implantation of a prosthetic nucleus difficult, thus they are less suitable for investigating nucleus replacements.

6.613.5.2.2. Leporine

Rabbits provide a medium-sized model for spinal devices. Grauer *et al.*[251] examined three-dimensional motion of the rabbit spine and have shown that is an acceptable model for representing the human spine although the NZ and ROM are somewhat greater than in the human. Degeneration may be induced mechanically,[252] via needle puncture,[253,254] or discectomy may be performed.[255]

The rabbit model has been extensively used to study the injection of cells into the intervertebral disk following aspiration of the nucleus pulposus.[227,256–259] Aspiration is commonly applied due to the difficulty of performing discectomy on the small disk, although traditional discectomy may be applied. Larson *et al.*[260] injected a hydrogel following discectomy with a micro-pituitary but few differences were noted between groups, likely influenced by a small sample size. Abbushi *et al.*[255] implanted a polyglycolic acid/hyaluronan scaffold following open discectomy and showed maintenance of disk height and improved MRI T1 signal compared to discectomy alone.

So *et al.*[261] has investigated a PVA hydrogel implant in the rabbit disk. This approach differed from previous models, as the implant was a sharpened rod that was inserted laterally through the disk and left proud following the removal of the transverse process and associated musculature. This procedure differed greatly from that which would be performed in the human. Despite this, the implant preserved disk height and delayed degenerative changes at 6 months.

6.613.5.2.3. Porcine

McLain *et al.*[262] compared the morphology of human and large animal L4 vertebrae finding the pig to be an acceptable match. Sheng *et al.*[263] evaluated the anatomy of several large animals and suggested that the thoracic and lumbar regions of the pig can be used as models for human. The intervertebral disk, although not as thick, is comparable if scaled by the size of adjacent vertebral bodies.[264]

Kaigle *et al.*[265] have shown that, in 50–60 kg 4-month-old pigs, an annular incision to the nucleus results in severe degeneration of the disk at 3-month follow up. Revell *et al.*[186] have utilized a porcine model to test two hyaluronan-derived polymeric substitutes that were injected after discectomy. Treated levels prevented fibrous tissue infiltration and endplate

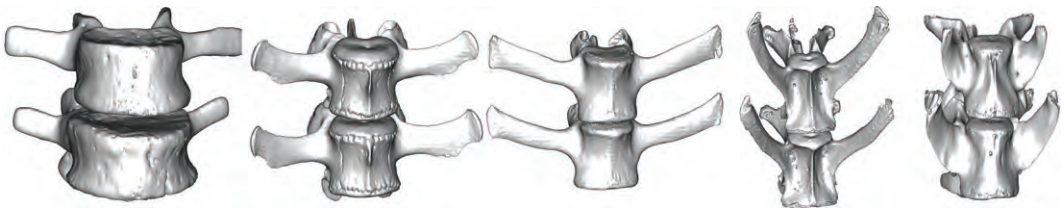

Figure 23 3D reconstructions of L3–L4 motion segments from computed tomography and micro computed tomography data, left to right: human, pig, sheep, rabbit, and rat. Images are not in the same scale.

disruption at 6 weeks. These pigs were 11 kg and were most likely immature. One difficulty in using immature pigs is that they quickly outgrow a normal human weight range.

Yingling *et al.*[266] advise that the porcine cervical spine shows similarities to the human in load and function and may serve as a substitute for the human lumbar spine. This model has been utilized by Drake *et al.*[267] to evaluate failure of motion segments but at present, has not been used for the evaluation of nucleus replacements.

Minipigs have also been used. The effects of nucleuotomy, nucleotomy with HA/sodium salt solution, chemonucleolysis with chymopapain, and annulus dissection on disk degeneration of minipigs have been described by Pfieffer *et al.*,[268] all of which could serve as prenucleus replacement models. Henriksson *et al.*[269] used 6-month-old 10–15 kg minipigs and transplanted mesenchymal stems cells after aspirating the nucleus. Cells were injected with and without a degradable amino acid based hydrogel carrier. Cells survived to the last 6-month time point.

6.613.5.2.4. Canine

The contributions of ligaments, posterior elements, and the intervertebral disk to the stability of a motion segment are similar between canines and humans. The torsional and axial mechanics are also similar but when normalized for scale, the canine properties are stiffer.[270] Ganey *et al.*[271] performed partial nucleotomy and injected HA, or HA and adipose-derived stem cells, finding the closest similarities in morphology between the intact and HA with cell treatment groups.

6.613.5.2.5. Bovine

The adult cow spine is difficult to relate to the adult human due to the fourfold increase in overall length. For this reason, and similarities in shape and structure, calf spines are often used.[272] They can be used on a limited basis as these similarities predominate in AR and LB, and facet joint orientation varies by as much as 107% at this level when compared to human.[273] Mean pedicle height is greater than for the human, as for most quadrupeds, but is an accepted model for the human lumbar spine.[263]

Wilke *et al.* have utilized this model to test a collagen matrix based scaffold nucleus replacement *in vitro*, demonstrating restored height and biomechanics following discectomy; however, extrusion was common.[209] More unique designs have also been tested in the calf model. Butterman *et al.*[274] used the calf spine, with posterior elements removed, in an investigational study to test a spring based, nonannulus sparing system, finding that spring stiffness was a primary determiniant of ROM in the reconstructed spine. Kettler *et al.*[146] have also used this model to test woven titanium filaments as a nucleus replacement, finding increased ROM in most directions. Yuksel *et al.*[197] treated denucleated calf motion segments with BioDisc which regained disk height and survived loading of 10 million cycles.

Calf spines are in a rapid phase of growth so *in vitro* tests are often more appropriate than *in vivo*. The cow tail has been suggested as a substitute due to similarities in microfibile organization,[275] ROM before scaling,[250] and intradiscal pressure under compressive load.[276] However, there are some limitations. The cow tail has differing creep characteristics,[250] and differences in cell phenotype and matrix contents,[277] as well as the limitations cited earlier for the rat spine. Currently this model has not been used to evaluate nucleus replacements.

6.613.5.2.6. Ovine

Wilke *et al.*[23,278] have studied the biomechanics and morphology of sheep and suggest that the sheep provides a useful model of the human spine, with qualitatively similar biomechanics. The vertebrae is taller and the disk height less, while facet joints and spinal canal are very similar to the human. The lumbar and thoracic regions show the closest match, and the lumbar spine is also useful for surgical training of discectomy for spinal surgeons.[279] The intervertebral disk itself has been shown to simulate the human in terms of construction and makeup,[280] with the proteoglycan content in the disk and endplate in sheep most closely matching that of human disks when compared to rats and cattle.[281] Easlyey *et al.*[282] evaluated the radiographic and biomechanical properties of the lumbar spine and found ROM and NZ as well as load sharing were in line with human published data.

Several models of degeneration have been applied to the sheep lumbar spine. Melrose *et al.*[283] found that nerve and blood vessel ingrowth is associated with proteoglycan depletion. Colloca *et al.*[62] performed stab incisions to the lateral annulus of sheep and identified a decreased viscoelastic response with time. This has also been shown to induce loss of disk height.[284] Fazzalari *et al.*[285] have used the sheep model to investigate the effect of annular tears on the biomechanics of the spine.

Meakin *et al.*[286] used the sheep disk to demonstrate the ability of a silicone rubber, uncured silicone and another elastic solid to reverse inward bulging of annulus fibers that occurs following nucleotomy. This is one of the principle functions of a nucleus replacement. An ideal Young's modulus was proposed for the implant near 3 MPa.

As described earlier, Pelletier *et al.*[287] used a surgical shaver to perform a nucleotomy on sheep lumbar disks and injected a hydrogel nucleus replacement. Results showed decreased osteophyte formation at 52 weeks when compared to discectomy alone.

6.613.5.2.7. Nonhuman primates

By virtue of their upright posture nonhuman primates are attractive as a model of the human spine. Baboons and macaque monkeys are well-established research models. Baboon lumbar spinal segments have similar compressive stiffness to the human, although glycosaminoglycan content differs. The macaque monkey represents one of the few naturally occurring examples of DDD. Nuckley *et al.* found that advanced degeneration was marked by osteophytes, loss of disk height, and changes in biomechanics that parallel the human progression of DDD in a study with animals of advanced age.[288]

Degeneration in baboons has been incited by injecting chondroitinase ABC to digest the nucleus resulting in bone marrow depletion and loss of disk height at 24 weeks,[289] but discectomy is more commonly applied.

Ledet *et al.*[290] examined the PDN in lumbar spine of three baboons. Two of these implants migrated and a revision was performed. It was found that there was a loss of disk height, endplate degeneration, subsidence, and sclerosis of adjacent

vertebrae. These complications were similar to those found in humans clinically, supporting the use of this model. Cook *et al.*[147] implanted six adult baboons with a solid preformed nucleus following discectomy finding no migration of the implant but some endplate changes. Allan *et al.*[171] implanted hydrogel beads in baboons following discectomy and although device related tissue responses were not present, extrusion occurred in one-third of cases. Cunningham *et al.*[291] implanted 14 mature baboons with DASCOR implants and found maintained motion but adjacent vertebral body changes in most levels at 12 months with no expulsion of implant.

6.613.5.2.8. Summary – animal models

Several animal models provide useful information regarding the performance of nucleus replacements. Smaller animal models may provide useful information regarding the biocompatibility of a material,[292] however relative size to the human disk is required to maintain the appropriate surgical procedure. The size of an annular defect relative to the overall disk size affects the recovery of the disk.[293] Smaller animals are also not suitable if residual tissue is present or the performance of the implant relies on diffusion. Smaller disks are at less of a disadvantage in terms of nutrition as distances are smaller and diffusion less of a challenge.[294] Although the scaled tissue properties of the disk are similar across species, the direct measures vary by orders of magnitude (**Figure 23**).[250]

While no animal model will perfectly substitute the human case, there are several models available that will aid in expanding the understanding of nucleus replacements. Nonhuman primates provide a good approximation; however, practical issues may preclude the use of these models. In this light, there are several useful quadrupedal models. The sheep and calf lumbar spines provide both accessible and acceptable surrogates to the human.[263]

While differences between discectomy alone, as well as the safety of nucleus replacements can be shown without preexisting pathology, the ideal animal model would apply nucleus replacement to treat a degenerative condition. There are few examples of naturally occurring DDD. The aged macaque, chondrodystrophoid dogs, and the sand rat represent a few. Present models of degeneration primarily use acute injury to accelerate degeneration. While this may increase repeatability and control over the extent of degeneration, it may not represent the diseased state. The exact initiator of degeneration is, as yet, not well understood and further progress in this regard will facilitate creating reproducible pathologies that more closely represent human DDD.

6.613.6. Summary

Nucleus replacement is the removal of the nucleus in the mid to early stages of DDD followed by replacement with a synthetic material. Replacement of the nucleus with a material possessing properties of a healthy nucleus would be expected to restore the biomechanics of the affected level, decelerate degenerative changes and relieve pain. If successful, nucleus replacement would postpone or preclude more drastic procedures, while still allowing them to be performed later if necessary.

Early attempts at nucleus replacement often resulted in fusion, but greater success followed from mimicking the properties of the healthy nucleus. Polymer technology has emerged as the means to achieve reliable nucleus replacement. Injectable polymers show promise due to the minimal disruption of the annulus and ability to interdigitate with remaining tissues making extrusion less likely. Although tissue engineering solutions with cells and growth factors can be added to the polymer concepts, there are, currently, inherent advantages to the synthetic route only, until further progress in cellular and biological treatments can address the imbalance with currently achievable functional outcomes.

References

1. Andersson, G. In *The Adult Spine: Principles and Practice*, 2nd ed.; Frymoyer, J. W., Ed.; Lippincott-Raven: Philadelpia, PA, 1997; Vol. 1, pp 93–141.
2. Deyo, R. A.; Mirza, S. K.; Martin, B. I. *Spine* **2006**, *31*(23), 2724–2727.
3. Goetzel, R. Z.; Hawkins, K.; Ozminkowski, R. J.; Wang, S. *J. Occup. Environ. Med.* **2003**, *45*(1), 5–14.
4. Maniadakis, N.; Gray, A. *Pain* **2000**, *84*(1), 95–103.
5. Fagan, A.; Moore, R.; Vernon Roberts, B.; Blumbergs, P.; Fraser, R. *Spine* **2003**, *28*(23), 2570–2576.
6. Ozawa, T.; Ohtori, S.; Inoue, G.; Aoki, Y.; Moriya, H.; Takahashi, K. *Spine* **2006**, *31*(21), 2418–2422.
7. Lockhart, R. D. *Anatomy of the Human Body*, 2nd ed.; Faber and Faber: London, 1965.
8. Cappello, R.; Bird, J. L.; Pfeiffer, D.; Bayliss, M. T.; Dudhia, J. *Spine* **2006**, *31*(8), 873–882; discussion 83.
9. Ishihara, H.; Warensjo, K.; Roberts, S.; Urban, J. P. *Am. J. Physiol.* **1997**, *272*(5 Pt 1), C1499–C1506.
10. Iatridis, J. C.; MacLean, J. J.; O'Brien, M.; Stokes, I. A. *Spine* **2007**, *32*(14), 1493–1497.
11. Frobin, W.; Brinckmann, P.; Leivseth, G.; Biggemann, M.; Reikeras, O. *Clin. Biomech. (Bristol, Avon)* **1996**, *11*(8), 457–465.
12. Goel, V. K.; Wilder, D. G.; Pope, M. H.; Edwards, W. T. *Spine* **1995**, *20*(21), 2354–2357.
13. Panjabi, M. M.; Brand, R. A., Jr.; White, A. A., 3rd *J. Biomech.* **1976**, *9*(4), 185–192.
14. Wilke, H. J.; Rohlmann, A.; Neller, S.; *et al. Spine* **2001**, *26*(6), 636–642.
15. Panjabi, M. M.; Kato, Y.; Hoffman, H.; Cholewicki, J.; Krag, M. *Spine* **2000**, *25*(21), 2748–2754.
16. Grassmann, S.; Oxland, T. R.; Gerich, U.; Nolte, L. P. *Spine* **1998**, *23*(10), 1155–1162.
17. Charriere, E. A.; Beutler, T.; Caride, M.; Mordasini, P.; Orr, T. E.; Zysset, P. K. *Eur. Spine J.* **2006**, *15*(1), 74–81.
18. Spenciner, D.; Greene, D.; Paiva, J.; Palumbo, M.; Crisco, J. *Spine J.* **2006**, *6*(3), 248–257.
19. Wilke, H. J.; Jungkunz, B.; Wenger, K.; Claes, L. E. *Anat. Rec.* **1998**, *251*(1), 15–19.
20. Gay, R. E.; Ilharreborde, B.; Zhao, K.; Zhao, C.; An, K. N. *Clin. Biomech. (Bristol, Avon)* **2006**, *21*(9), 914–919.
21. Johannessen, W.; Cloyd, J. M.; O'Connell, G. D.; Vresilovic, E. J.; Elliott, D. M. *Ann. Biomed. Eng.* **2006**, *34*(4), 687–696.
22. Lu, D. S.; Shono, Y.; Oda, I.; Abumi, K.; Kaneda, K. *Spine* **1997**, *22*(16), 1828–1834; discussion 34–35.
23. Wilke, H. J.; Kettler, A.; Claes, L. E. *Spine* **1997**, *22*(20), 2365–2374.
24. Adams, M. A.; Freeman, B. J.; Morrison, H. P.; Nelson, I. W.; Dolan, P. *Spine* **2000**, *25*(13), 1625–1636.
25. Buttermann, G. R.; Beaubien, B. P. *Spine* **2008**, *33*(20), 2134–2142.
26. Wilke, H. J.; Neef, P.; Caimi, M.; Hoogland, T.; Claes, L. E. *Spine* **1999**, *24*(8), 755–762.
27. Heuer, F.; Schmidt, H.; Klezl, Z.; Claes, L.; Wilke, H. J. *J. Biomech.* **2007**, *40*(2), 271–280.
28. Marchand, F.; Ahmed, A. M. *Spine* **1990**, *15*(5), 402–410.
29. Lee, S. H.; Derby, R.; Chen, Y.; Seo, K. S.; Kim, M. J. *Spine J.* **2004**, *4*(6), 614–618.
30. Fazey, P. J.; Song, S.; Monsas, S.; *et al. Clin. Biomech. (Bristol, Avon)* **2006**, *21*(5), 538–542.

31. Thompson, R. E.; Pearcy, M. J.; Barker, T. M. *Clin. Biomech. (Bristol, Avon)* **2004**, *19*(5), 448–455.
32. Martinez, J. B.; Oloyede, V. O.; Broom, N. D. *Med. Eng. Phys.* **1997**, *19*(2), 145–156.
33. Roberts, N.; Hogg, D.; Whitehouse, G. H.; Dangerfield, P. *Clin. Anat.* **1998**, *11*(1), 1–8.
34. Iatridis, J. C.; Setton, L. A.; Weidenbaum, M.; Mow, V. C. *J. Biomech.* **1997**, *30*(10), 1005–1013.
35. Pazzaglia, U. E.; Salisbury, J. R.; Byers, P. D. *J. R. Soc. Med.* **1989**, *82*(7), 413–415.
36. Walsh, A. J.; Lotz, J. C. *J. Biomech.* **2004**, *37*(3), 329–337.
37. Sakakibara, T.; Kasai, Y.; Uchida, A. *Occup. Med. (Lond.)* **2006**, *56*(7), 494–496.
38. Mariconda, M.; Galasso, O.; Imbimbo, L.; Lotti, G.; Milano, C. *Eur. Spine J.* **2006**, *12*, 12.
39. Brinckmann, P.; Frobin, W.; Biggemann, M.; Tillotson, M.; Burton, K. *Clin. Biomech. (Bristol, Avon)* **1998**, *13*(Suppl 2), S1–S36.
40. Lu, Y. M.; Hutton, W. C.; Gharpuray, V. M. *Spine* **1996**, *21*(19), 2208–2216; discussion 17.
41. Natarajan, R. N.; Andersson, G. B. *Spine* **1999**, *24*(18), 1873–1881.
42. Videman, T.; Levalahti, E.; Battie, M. C. *Spine* **2007**, *32*(13), 1406–1413.
43. Langrana, N. A.; Kale, S. P.; Edwards, W. T.; Lee, C. K.; Kopacz, K. J. *Spine J.* **2006**, *6*(3), 267–278.
44. Pappou, I. P.; Cammisa, F. P., Jr.; Girardi, F. P. *Spine J.* **2007**, *7*(1), 32–38.
45. Seki, S.; Kawaguchi, Y.; Mori, M.; *et al. J. Hum. Genet.* **2006**, *51*(12), 1063–1067.
46. Solovieva, S.; Lohiniva, J.; Leino-Arjas, P.; *et al. Eur. Spine J.* **2006**, *15*(5), 613–619.
47. Virtanen, I. M.; Noponen, N.; Barral, S.; *et al. J. Bone Miner. Res.* **2007**, *22*(5), 701–707.
48. Videman, T.; Battie, M. C.; Ripatti, S.; Gill, K.; Manninen, H.; Kaprio, J. *Spine* **2006**, *31*(6), 671–678.
49. Auerbach, J. D.; Johannessen, W.; Borthakur, A.; *et al. Eur. Spine J.* **2006**, *15*(Suppl 3), S338–S344.
50. Benneker, L. M.; Heini, P. F.; Anderson, S. E.; Alini, M.; Ito, K. *Eur. Spine J.* **2005**, *14*(1), 27–35.
51. Johannessen, W.; Auerbach, J. D.; Wheaton, A. J.; *et al. Spine* **2006**, *31*(11), 1253–1257.
52. Kumaresan, S.; Yoganandan, N.; Pintar, F. A.; Maiman, D. J.; Goel, V. K. *J. Orthop. Res.* **2001**, *19*(5), 977–984.
53. Thompson, J. P.; Pearce, R. H.; Schechter, M. T.; Adams, M. E.; Tsang, I. K.; Bishop, P. B. *Spine* **1990**, *15*(5), 411–415.
54. Miller, J. A.; Schmatz, C.; Schultz, A. B. *Spine* **1988**, *13*(2), 173–178.
55. Abbott, J. H.; Fritz, J. M.; McCane, B.; *et al. BMC Musculoskelet. Disord.* **2006**, *7*(45), 45.
56. Karadimas, E. J.; Siddiqui, M.; Smith, F. W.; Wardlaw, D. *J. Spinal Disord. Tech.* **2006**, *19*(7), 495–500.
57. Mok, N. W.; Brauer, S. G.; Hodges, P. W. *Spine* **2007**, *32*(19), E537–E543.
58. Al-Eisa, E.; Egan, D.; Deluzio, K.; Wassersug, R. *Spine* **2006**, *31*(3), E71–E79.
59. Barker, K. L.; Shamley, D. R.; Jackson, D. *Spine* **2004**, *29*(22), E515–E519.
60. Sato, K.; Kikuchi, S.; Yonezawa, T. *Spine* **1999**, *24*(23), 2468–2474.
61. Boxberger, J. I.; Sen, S.; Yerramalli, C. S.; Elliott, D. M. *J. Orthop. Res.* **2006**, *24*, 24.
62. Colloca, C. J.; Keller, T. S.; Moore, R. J.; Gunzburg, R.; Harrison, D. E. *Spine* **2007**, *32*(19), E544–E550.
63. Iatridis, J. C.; Setton, L. A.; Foster, R. J.; Rawlins, B. A.; Weidenbaum, M.; Mow, V. C. *J. Biomech.* **1998**, *31*(6), 535–544.
64. Johannessen, W.; Elliott, D. M. *Spine* **2005**, *30*(24), E724–E729.
65. Brown, M. D.; Holmes, D. C.; Heiner, A. D. *Spine* **2002**, *27*(9), 918–922.
66. Natarajan, R. N.; Williams, J. R.; Andersson, G. B. *Spine* **2004**, *29*(23), 2733–2741.
67. Tanaka, N.; An, H. S.; Lim, T. H.; Fujiwara, A.; Jeon, C. H.; Haughton, V. M. *Spine J.* **2001**, *1*(1), 47–56.
68. Benneker, L. M.; Heini, P. F.; Alini, M.; Anderson, S. E.; Ito, K. *Spine* **2005**, *30*(2), 167–173.
69. Kjaer, P.; Korsholm, L.; Bendix, T.; Sorensen, J. S.; Leboeuf-Yde, C. *Eur. Spine J.* **2006**, *15*(9), 1312–1319.
70. Zanoli, G.; Jonsson, B.; Stromqvist, B. *Acta Orthop.* **2006**, *77*(2), 298–306.
71. Schenk, P.; Laubli, T.; Hodler, J.; Klipstein, A. *Spine* **2006**, *31*(23), 2701–2706.
72. Igarashi, A.; Kikuchi, S.; Konno, S. *J. Orthop. Sci.* **2007**, *12*(2), 154–160.
73. Zhang, Y.; Kerns, J. M.; Anderson, D. G.; *et al. Am. J. Phys. Med. Rehabil.* **2006**, *85*(11), 865–871.
74. Panjabi, M. M. *J. Electromyogr. Kinesiol.* **2003**, *13*(4), 371–379.
75. Mundt, D. J.; Kelsey, J. L.; Golden, A. L.; *et al. Spine* **1993**, *18*(5), 595–602.
76. Postacchini, F.; Lami, R.; Pugliese, O. *Spine* **1988**, *13*(12), 1403–1406.
77. Scapinelli, R. *Acta Orthop. Belg.* **1993**, *59*(4), 371–376.
78. Kim, K. T.; Park, S. W.; Kim, Y. B. *Spine (Phila Pa 1976)* **2009**, *34*(24), 2674–2678.
79. Bhardwaj, R.; Midha, R. *Can. J. Neurol. Sci.* **2004**, *31*(4), 554–557.
80. Choy, D. S. *J. Clin. Laser Med. Surg.* **2000**, *18*(1), 29–32.
81. Tsantrizos, A.; Ito, K.; Aebi, M.; Steffen, T. *Spine* **2005**, *30*(19), 2129–2137.
82. Zhao, F.; Pollintine, P.; Hole, B. D.; Dolan, P.; Adams, M. A. *Spine* **2005**, *30*(23), 2621–2630.
83. Erly, W. K.; Munoz, D.; Beaton, R. *J. Comput. Assist. Tomogr.* **2006**, *30*(3), 486–489.
84. Nguyen-minh, C.; Riley, L., 3rd; Ho, K. C.; Xu, R.; An, H.; Haughton, V. M. *AJNR Am. J. Neuroradiol.* **1997**, *18*(3), 435–442.
85. Rajasekaran, S.; Babu, J. N.; Arun, R.; Armstrong, B. R.; Shetty, A. P.; Murugan, S. *Spine* **2004**, *29*(23), 2654–2667.
86. Aoki, Y.; Akeda, K.; An, H.; *et al. Spine* **2006**, *31*(21), E774–E780.
87. Inoue, G.; Ohtori, S.; Aoki, Y.; *et al. Spine* **2006**, *31*(13), 1433–1438.
88. Awad, J. N.; Moskovich, R. *Clin. Orthop. Relat. Res.* **2006**, *443*, 183–197.
89. Carette, S.; Leclaire, R.; Marcoux, S.; *et al. N. Engl. J. Med.* **1997**, *336*(23), 1634–1640.
90. Choi, S. J.; Song, J. S.; Kim, C.; *et al. Korean J. Radiol.* **2007**, *8*(2), 156–163.
91. Masala, S.; Massari, F.; Fabiano, S.; *et al. Cardiovasc. Intervent. Radiol.* **2007**, *30*(3), 426–432.
92. Schaufele, M. K.; Hatch, L.; Jones, W. *Pain Physician* **2006**, *9*(4), 361–366.
93. Mariconda, M.; Galasso, O.; Secondulfo, V.; Rotonda, G. D.; Milano, C. *Spine* **2006**, *31*(22), 2593–2599; discussion 600–601.
94. Osterman, H.; Seitsalo, S.; Karppinen, J.; Malmivaara, A. *Spine* **2006**, *31*(21), 2409–2414.
95. Jang, J. S.; An, S. H.; Lee, S. H. *J. Spinal Disord. Tech.* **2006**, *19*(5), 338–343.
96. Fountas, K. N.; Kapsalaki, E. Z.; Feltes, C. H.; *et al. Spine* **2004**, *29*(22), 2521–2524; discussion 5–6.
97. Papadopoulos, E. C.; Girardi, F. P.; Sandhu, H. S.; *et al. Spine* **2006**, *31*(13), 1473–1476.
98. Jensdottir, M.; Gudmundsson, K.; Hannesson, B.; Gudmundsson, G. *Acta Neurochir. (Wien.)* **2007**, *149*(1), 51–58; discussion 7–8.
99. Ronnberg, K.; Lind, B.; Zoega, B.; Halldin, K.; Gellerstedt, M.; Brisby, H. *Spine* **2007**, *32*(2), 256–261.
100. Smorgick, Y.; Floman, Y.; Millgram, M. A.; Anekstein, Y.; Pekarsky, I.; Mirovsky, Y. *Spine J.* **2006**, *6*(4), 380–384.
101. Weiner, B. K.; Dabbah, M. *J. Spinal Disord. Tech.* **2005**, *18*(6), 519–521.
102. Carragee, E. J.; Han, M. Y.; Suen, P. W.; Kim, D. *J. Bone Joint Surg. Am.* **2003**, *85A*(1), 102–108.
103. Carragee, E. J.; Spinnickie, A. O.; Alamin, T. F.; Paragioudakis, S. *Spine* **2006**, *31*(6), 653–657.
104. McGirt, M. J.; Eustacchio, S.; Varga, P.; *et al. Spine (Phila Pa 1976)* **2009**, *34*(19), 2044–2051.
105. Mochida, J.; Toh, E.; Nomura, T.; Nishimura, K. *J. Bone Joint Surg. Br.* **2001**, *83*(4), 501–505.
106. Brinckmann, P.; Grootenboer, H. *Spine* **1991**, *16*(6), 641–646.
107. Blumenthal, S.; McAfee, P. C.; Guyer, R. D.; *et al. Spine* **2005**, *30*(14), 1565–1575; discussion E387–E391.
108. Cunningham, B. W. *Spine J.* **2004**, *4*(6 Suppl), 219S–230S.
109. Chung, S. S.; Lee, C. S.; Kang, C. S.; Kim, S. H. *J. Spinal Disord. Tech.* **2006**, *19*(5), 307–311.
110. McAfee, P. C.; Geisler, F. H.; Saiedy, S. S.; *et al. Spine* **2006**, *31*(11), 1217–1226.
111. Auerbach, J. D.; Wills, B. P.; McIntosh, T. C.; Balderston, R. A. *Spine* **2007**, *32*(5), 527–536.
112. Huang, R. C.; Girardi, F. P.; Cammisa, F. P., Jr.; Tropiano, P.; Marnay, T. *J. Spinal Disord. Tech.* **2003**, *16*(5), 435–440.
113. Errico, T. J. *Clin. Orthop. Relat. Res.* **2005**, *435*, 106–117.
114. German, J. W.; Foley, K. T. *Spine* **2005**, *30*(16 Suppl), S60–S67.
115. Guyer, R. D.; Ohnmeiss, D. D. *Spine (Phila Pa 1976)* **2003**, *28*(15 Suppl), S15–S23.
116. Geisler, F. H. *Neurosurgery* **2005**, *56*(1 Suppl), 46–57; discussion 46–57.
117. Tropiano, P.; Huang, R. C.; Girardi, F. P.; Cammisa, F. P., Jr.; Marnay, T. *J. Bone Joint Surg. Am.* **2006**, *88*(Suppl 1 Pt 1), 50–64.
118. Bertagnoli, R.; Yue, J. J.; Shah, R. V.; *et al. Spine* **2005**, *30*(19), 2192–2199.
119. Lemaire, J. P.; Carrier, H.; Sari Ali el, H.; Skalli, W.; Lavaste, F. *J. Spinal Disord. Tech.* **2005**, *18*(4), 353–359.
120. Huang, R. C.; Lim, M. R.; Girardi, F. P.; Cammisa, F. P., Jr. *Spine* **2004**, *29*(22), 2538–2541.
121. Ikard, R. W. *Arch. Surg.* **2006**, *141*(10), 1025–1034.
122. Shim, C. S.; Lee, S.; Maeng, D. H.; Lee, S. H. *J. Spinal Disord. Tech.* **2005**, *18*(5), 465–469.

123. Denoziere, G.; Ku, D. N. *J. Biomech.* **2006**, *39*(4), 766–775.
124. Goel, V. K.; Grauer, J. N.; Patel, T.; *et al*. *Spine* **2005**, *30*(24), 2755–2764.
125. O'Leary, P.; Nicolakis, M.; Lorenz, M. A.; *et al*. *Spine J.* **2005**, *5*(6), 590–599.
126. Kurtz, S. M.; Peloza, J.; Siskey, R.; Villarraga, M. L. *Spine J.* **2005**, *5*(3), 344–350.
127. Punt, I. M.; Cleutjens, J. P.; de Bruin, T.; *et al*. *Biomaterials* **2009**, *18*, 18.
128. van Ooij, A.; Kurtz, S. M.; Stessels, F.; Noten, H.; van Rhijn, L. *Spine* **2007**, *32*(2), 223–229.
129. Mofidi, A.; Sedhom, M.; O'Shea, K.; Fogarty, E. E.; Dowling, F. *J. Spinal Disord. Tech.* **2005**, *18*(6), 479–484.
130. Potter, B. K.; Freedman, B. A.; Verwiebe, E. G.; Hall, J. M.; Polly, D. W., Jr.; Kuklo, T. R. *J. Spinal Disord. Tech.* **2005**, *18*(4), 337–346.
131. Lipson, S. J. *N. Engl. J. Med.* **2004**, *350*(7), 643–644.
132. Rao, R. D.; David, K. S.; Wang, M. *Spine* **2005**, *30*(24), 2772–2776.
133. Goel, V. K.; Nishiyama, K.; Weinstein, J. N.; Liu, Y. K. *Spine* **1986**, *11*(10), 1008–1012.
134. Meakin, J. R. *J. Mater. Sci. Mater. Med.* **2001**, *12*(3), 207–213.
135. Korge, A.; Nydegger, T.; Polard, J. L.; Mayer, H. M.; Husson, J. L. *Eur. Spine J.* **2002**, *11*(Suppl 2), S149–S153.
136. Harmon, P. H. *Am. J. Surg.* **1959**, *97*(5), 649–659.
137. Fernstrom, U. *Acta Chir. Scand. Suppl.* **1966**, *357*, 154–159.
138. Reitz, H.; Joubert, M. J. *S. Afr. Med. J.* **1964**, *38*, 881–884.
139. Gau, M. Intervertebral Nucleus Prosthesis and Surgical Procedure for Implanting the Same. United States Patent Office, 70337340b2, 2006.
140. Bryan, V. Peanut Spectacle Multi Discoid Thraco-Lumbar Disc Prosthesis. United States Patent Office, 6749635, 2004.
141. Lawson, J. Prosthetic Nucleus Replacement for Surgical Reconstruction of Intervertebral Discs and Treatment of Method. United States Patent Office, 6146422, 2000.
142. Lawson, K.; Timm, J. Keeled Prosthetic Nucleus. United States Patent Office, 6802863b2, 2004.
143. Felt, J. Interlocked Modular Disc Nucleus Prosthesis. United States Patent Office, 7267690b2, 2007.
144. Ferree, B. Artificial Intervertebral Disc Replacement Methods and Apparatus. United States Patent Office, 6419704b1, 2002.
145. Serhan, H.; Dooris, A. Annular Nucleus Pulposus Replacement. United States Patent Office, 7004971b2, 2006.
146. Kettler, A.; Kaps, H.; Haegele, B.; Wilke, H. *SAS J.* **2007**, *1*, 125–130.
147. Cook, S.; Salkeld, S.; Patron, L.; *et al*. *Spine J.* **2004**, *4*(5 Suppl), S80.
148. Alpizar-Aguirre, A.; Mireles-Cano, J. N.; Rosales-Olivares, M.; Miramontes-Martinez, V.; Reyes-Sanchez, A. *Cir. Cir.* **2008**, *76*(4), 317–321.
149. Li, J. In *Engineering Materials for Biomedical Applications*; Hin, T. S., Ed.; World Scientific: Singapore, 2004; p 1.
150. Bao, Q. B.; Higham, P. Hydrogel Intervertebral Disc Nucleus. United States Patent Office, 5047055, 1991.
151. Bao, Q. B.; Higham, P. A. Hydrogel Intervertebral Disc Nucleus. United States Patent Office, 5976186, 1999.
152. Bao, Q. B.; Higham, P. Hydrogel Bead Intervertebral Disc Nucleus. United States Patent Office, 5192326, 1993.
153. Bertagnoli, R.; Schonmayr, R. *Eur. Spine J.* **2002**, *11*(Suppl 2), S143–S148.
154. Bertagnoli, R.; Vazquez, R. J. *J. Spinal Disord. Tech.* **2003**, *16*(4), 398–404.
155. Ray, C. D. *Eur. Spine J.* **2002**, *11*(Suppl 2), S137–S142.
156. Shim, C. S.; Lee, S. H.; Park, C. W.; *et al*. *J. Spinal Disord. Tech.* **2003**, *16*(4), 324–330.
157. Klara, P. M.; Ray, C. D. *Spine* **2002**, *27*(12), 1374–1377.
158. Norton, B. K.; Sherman, T. N.; Bauer, L. J. Prosthetic Spinal Disc Nucleus Having Selectively Coupled Bodies. United States Patent Office, 6110210, 2000.
159. Ray, C.; Assell, R. Tapered Prosthetic Spinal Disc Nucleus. United States Patent Office, 6132465, 2000.
160. Ray, C.; Assell, R. Prosthetic Spinal Disc Nucleus Having a Shape Change Characteristic. United States Patent Office, 6602290b1, 2003.
161. Ray, C.; Dickhudt, E.; Ledoux, P.; Frutiger, B. Prosthetic Spinal Disc Nucleus. United States Patent Office, 5674295, 1997.
162. Wilke, H. J.; Kavanagh, S.; Neller, S.; Haid, C.; Claes, L. E. *J. Neurosurg.* **2001**, *95*(2 Suppl), 208–214.
163. Rosales-Olivares, L. M.; Perez-Viquez, A.; Miramontes-Martinez, V.; Alpizar-Aguirre, A.; Reyes-Sanchez, A. A. *Cir. Cir.* **2007**, *75*(1), 31–36.
164. Stoy, V. Spinal Nucleus Implant. United States Patent Office, 6264695b1, 2001.
165. Stoy, V.; Stehlicek, P.; Kozlova, Z.; Drunecky, K. Hydrogel Based Prosthetic Device for Replacing and Least a Part of the Nucleus of a Spinal Disc. United States Patent Office, 6726721b2, 2004.
166. Bertagnoli, R.; Sabatino, C. T.; Edwards, J. T.; Gontarz, G. A.; Prewett, A.; Parsons, J. R. *Spine J.* **2005**, *5*(6), 672–681.
167. Li, L. Prosthetic Apparatus and Method. United States Patent Office, 6764514b1, 2004.
168. Meakin, J. R.; Hukins, D. W. *J. Biomech.* **2000**, *33*(5), 575–580.
169. Husson, J. L.; Korge, A.; Polard, J. L.; Nydegger, T.; Kneubuhler, S.; Mayer, H. M. *J. Spinal Disord. Tech.* **2003**, *16*(4), 405–411.
170. Husson, J. L.; Baumgartner, W.; Freudiger, S. Intervertebral Prosthesis. United States Patent Office, 6660037, 2003.
171. Allen, M. J.; Schoonmaker, J. E.; Bauer, T. W.; Williams, P. F.; Higham, P. A.; Yuan, H. A. *Spine* **2004**, *29*(5), 515–523.
172. Froning, E. Intervertebral Disc Prosthesis and Instruments for Locating Same. United States Patent Office, 3875595, 1975.
173. Krapiva, P. Disc Replacement Method and Apparatus. United States Patent Office, 5645597, 1997.
174. Baumgartner, W. Intervertebral Prosthesis. United States Patent Office, 5171280, 1992.
175. Wardlaw, D. Intervertebral Disc Nucleus Prosthesis. United States Patent Office, 6402784b1, 2002.
176. Bao, Q. B.; Hudgins, R. G.; Felt, J. C.; Arsenyev, A.; Yuan, H. A. Intervertebral Disc Prosthesis. United States Patent Office, 7001431b2, 2006.
177. Ahrens, M.; Tsantrizos, A.; Donkersloot, P.; *et al*. *Spine* **2009**.
178. Tsantrizos, A.; Ordway, N.; Bao, C.; Yuan, H. *Spine J.* **2006**, *6*(5), 106S.
179. Cleveland, D. *J. Lancet* **1956**, *76*(10), 327–331.
180. Hamby, W. B.; Glaser, H. T. *J. Neurosurg.* **1959**, *16*(3), 311–313.
181. Hamburger, C.; Festenberg, F. V.; Uhl, E. *Spine* **2001**, *26*(3), 249–255.
182. Nachemson, A. *Bull. Hosp. Joint Dis.* **1962**, *23*, 130–143.
183. Joshi, A.; Fussell, G.; Thomas, J.; *et al*. *Biomaterials* **2006**, *27*(2), 176–184.
184. Joshi, A.; Mehta, S.; Vresilovic, E.; Karduna, A.; Marcolongo, M. *J. Biomech. Eng.* **2005**, *127*(3), 536–540.
185. Cloyd, J. M.; Malhotra, N. R.; Weng, L.; Chen, W.; Mauck, R. L.; Elliott, D. M. *Eur. Spine J.* **2007**, *28*, 28.
186. Revell, P. A.; Damien, E.; Di Silvio, L.; Gurav, N.; Longinotti, C.; Ambrosio, L. *J. Mater. Sci. Mater. Med.* **2007**, *18*(2), 303–308.
187. Leone, G.; Torricelli, P.; Chiumiento, A.; Facchini, A.; Barbucci, R. *J. Biomed. Mater. Res. A* **2007**, *6*, 6.
188. Iatridis, J. C.; Weidenbaum, M.; Setton, L. A.; Mow, V. C. *Spine* **1996**, *21*(10), 1174–1184.
189. Boelen, E. J.; Koole, L. H.; van Rhijn, L. W.; van Hooy-Corstjens, C. S. *J. Biomed. Mater. Res. B Appl. Biomater.* **2007**, *5*, 5.
190. Boelen, E. J.; van Hooy-Corstjens, C. S.; Bulstra, S. K.; van Ooij, A.; van Rhijn, L. W.; Koole, L. H. *Biomaterials* **2005**, *26*(33), 6674–6683.
191. Wang, J. L.; Tsai, Y. C.; Wang, Y. H. *Spine* **2007**, *32*(17), 1809–1815.
192. Ferree, B. Nucleus Augmentation with In Situ Formed Hydrogels. United States Patent Office, 6719797b1, 2004.
193. Marcolongo, M. Associating Hydrogels for Nucleus Pulposus Replacement in Intervertebral Discs. United States Patent Office, 7214245b1, 2007.
194. Milner, R.; Arrowsmith, P.; Millan, E. Intervertebral Disc Implant. United States Patent Office, 6187048b1, 2001.
195. Thomas, J.; Lowman, A.; Marcolongo, M. *J. Biomed. Mater. Res. A* **2003**, *67*(4), 1329–1337.
196. Zucherman, J.; Hsu, K.; Yerby, S.; Smith, R. Implantable Prosthetic or Tissue Expanding Device. United States Patent Office, 6783546b2, 2004.
197. Yuksel, U.; Walsh, S.; Curd, D.; Black, K. *Spine J.* **2002**, *2*, 47S–128S.
198. Wardlaw, D.; Craig, N. J.; Smith, F. W.; Singal, V. *J. Bone Joint Surg. Br* **2007**, *90B*(Suppl III), 529.
199. Boillot, C.; Perrodin, Y. *Ecotoxicol. Environ. Saf.* **2007**, *16*, 16.
200. Sano, L. L.; Krueger, A. M.; Landrum, P. F. *Aquat. Toxicol.* **2005**, *71*(3), 283–296.
201. Cohen, C.; Nazareth, G.; Arora, P.; Devore, D.; Ducheyne, P. Polymerizable reverse emulsions: A versatile platform for designing biomaterials with tunable mechanical properties. In *Orthopaedic Research Society 56th Annual Meeting*, New Orleans, LA, 2010.
202. Cohen, C.; Radin, A.; Ducheyne, P. Fatigue testing of an injectable polymer composite for nucleus pulposus augmentation. In *8th World Biomaterials Congress, Transactions of the 33rd Society for Biomaterials Meeting*, 2008; Vol. 4, p 2036, ISBN: 978-1-61567-080-2.
203. Pelletier, M. H.; Cohen, C. S.; Walsh, W. R. Biomechanics of mechanically degenerated discs restored through injection of a novel nucleus augmentation material. In *Orthopaedic Research Society 56th Annual Meeting*, New Orleans, Louisiana, 2010.
204. Boyd, L. M.; Carter, A. J. *Eur. Spine J.* **2006**, *15*(Suppl 3), S414–S421.
205. Pelletier, M. H.; Smitham, P. J.; Michael, D.; Carter, A.; Diwan, A.; Walsh, W. R. *In vivo* evaluation of novel protein polymer hydrogel for nucleus pulposus

replacement. In *53rd Annual Meeting of the Orthopaedic Research Society*, San Diego, CA, 2007.
206. Berlemann, U.; Schwarzenbach, O. *Eur. Spine J.* **2009**, *18*(11), 1706–1712.
207. Ferree, B. Treating Degenerative Disc Disease Through Transplantation of Allograft Disc and Vertebral Endplates. United States Patent Office, 6344058b1, 2000.
208. Goel, K.; Fournier, R. Bioartificial Intervertebral Disc. United States Patent Office, 6958078b2, 2005.
209. Wilke, H. J.; Heuer, F.; Neidlinger-Wilke, C.; Claes, L. *Eur. Spine J.* **2006**, *26*, 26.
210. Stone, K. R. Prosthetic Intervertebral Disc. United States Patent Office, 5108438, 1992.
211. Mizuno, H.; Roy, A. K.; Vacanti, C. A.; Kojima, K.; Ueda, M.; Bonassar, L. *J. Spine* **2004**, *29*(12), 1290–1297; discussion 7–8.
212. Bron, J. L.; Koenderink, G. H.; Everts, V.; Smit, T. H. *J. Orthop. Res.* **2008**, *7*, 7.
213. Walsh, A. J.; Bradford, D. S.; Lotz, J. C. *Spine* **2004**, *29*(2), 156–163.
214. Gruber, H. E.; Norton, H. J.; Hanley, E. N., Jr. *Spine* **2000**, *25*(17), 2153–2157.
215. Fei, Q. M.; Jiang, X. X.; Chen, T. Y.; *et al*. *Acta Biochim. Biophys. Sin. (Shanghai)* **2006**, *38*(11), 773–779.
216. Gilbertson, L.; Ahn, S. H.; Teng, P. N.; Studer, R. K.; Niyibizi, C.; Kang, J. D. *Spine J.* **2008**, *8*(3), 449–456.
217. Kim, D. J.; Moon, S. H.; Kim, H.; *et al*. *Spine* **2003**, *28*(24), 2679–2684.
218. Li, J.; Kim, K. S.; Park, J. S.; Elmer, W. A.; Hutton, W. C.; Yoon, S. T. *J. Orthop. Sci.* **2003**, *8*(6), 829–835.
219. An, H. S.; Takegami, K.; Kamada, H.; *et al*. *Spine* **2005**, *30*(1), 25–31; discussion 2.
220. Imai, Y.; Miyamoto, K.; An, H. S.; Thonar, E. J.; Andersson, G. B.; Masuda, K. *Spine* **2007**, *32*(12), 1303–1309; discussion 10.
221. Masuda, K.; Takegami, K.; An, H.; *et al*. *J. Orthop. Res.* **2003**, *21*(5), 922–930.
222. Nishida, K.; Kang, J. D.; Gilbertson, L. G.; *et al*. *Spine* **1999**, *24*(23), 2419–2425.
223. Li, X.; Leo, B. M.; Beck, G.; Balian, G.; Anderson, G. D. *Spine* **2004**, *29*(20), 2229–2234.
224. Wang, H.; Kroeber, M.; Hanke, M.; *et al*. *J. Mol. Med.* **2004**, *82*(2), 126–134.
225. Wallach, C. J.; Sobajima, S.; Watanabe, Y.; *et al*. *Spine* **2003**, *28*(20), 2331–2337.
226. Hohaus, C.; Ganey, T. M.; Minkus, Y.; Meisel, H. J. *Eur. Spine J.* **2008**, *13*, 13.
227. Sobajima, S.; Vadala, G.; Shimer, A.; Kim, J. S.; Gilbertson, L. G.; Kang, J. D. *Spine J.* **2008**, *8*(6), 888–896.
228. Kobayashi, S.; Meir, A.; Urban, J. *J. Orthop. Res.* **2008**, *26*(4), 493–503.
229. Pflaster, D. S.; Krag, M. H.; Johnson, C. C.; Haugh, L. D.; Pope, M. H. *Spine* **1997**, *22*(2), 133–139.
230. Race, A.; Broom, N. D.; Robertson, P. *Spine* **2000**, *25*(6), 662–669.
231. van Deursen, D. L.; Snijders, C. J.; Kingma, I.; van Dieen, J. H. *Spine* **2001**, *26*(23), 2582–2586.
232. Bass, C. R.; Planchak, C. J.; Salzar, R. S.; *et al*. *Spine* **2007**, *32*(16), E436–E442.
233. Hasberry, S.; Pearcy, M. J. *J. Biomed. Eng.* **1986**, *8*(1), 62–66.
234. Gardner-Morse, M. G.; Stokes, I. A. *J. Orthop. Res.* **2003**, *21*(3), 547–552.
235. Renner, S. M.; Natarajan, R. N.; Patwardhan, A. G.; *et al*. *J. Biomech.* **2006**, *13*, 13.
236. Goel, V. K.; Voo, L. M.; Weinstein, J. N.; Liu, Y. K.; Okuma, T.; Njus, G. O. *Spine* **1988**, *13*(3), 294–300.
237. Pelletier, M. H.; Walsh, W. R. Mechanical properties of spinal segments with humidity and temperature variation. In *17th Annual Meeting of the European Orthopaedic Research Society*, Madrid, Spain, 2008.
238. Johannessen, W.; Vresilovic, E. J.; Wright, A. C.; Elliott, D. M. *Ann. Biomed. Eng.* **2004**, *32*(1), 70–76.
239. van der Veen, A. J.; Mullender, M.; Smit, T. H.; Kingma, I.; van Dieen, J. H. *Spine* **2005**, *30*(18), E534–E539.
240. Arjmand, N.; Gagnon, D.; Plamondon, A.; Shirazi-Adl, A.; Lariviere, C. *Clin. Biomech. (Bristol, Avon)* **2009**, *1*, 1.
241. Takahashi, I.; Kikuchi, S.; Sato, K.; Sato, N. *Spine* **2006**, *31*(1), 18–23.
242. Smit, T. H. *Eur. Spine J.* **2002**, *11*(2), 137–144.
243. Bayliss, M. T.; Johnstone, B.; O'Brien, J. P. *Spine* **1988**, *13*(9), 972–981.
244. Maeda, S.; Kokubun, S. *Spine* **2000**, *25*(2), 166–169.
245. Park, C.; Kim, Y. J.; Lee, C. S.; *et al*. *Spine* **2005**, *30*(10), E259–E265.
246. Elliott, D. M.; Sarver, J. J. *Spine (Phila Pa 1976)* **2004**, *29*(7), 713–722.
247. Lotz, J. C.; Chin, J. R. *Spine* **2000**, *25*(12), 1477–1483.
248. Lotz, J. C.; Colliou, O. K.; Chin, J. R.; Duncan, N. A.; Liebenberg, E. *Spine* **1998**, *23*(23), 2493–2506.
249. MacLean, J. J.; Lee, C. R.; Grad, S.; Ito, K.; Alini, M.; Iatridis, J. C. *Spine* **2003**, *28*(10), 973–981.
250. Beckstein, J. C.; Sen, S.; Schaer, T. P.; Vresilovic, E. J.; Elliott, D. M. *Spine* **2008**, *33*(6), E166–E173.
251. Grauer, J. N.; Erulkar, J. S.; Patel, T. C.; Panjabi, M. M. *Eur. Spine J.* **2000**, *9*(3), 250–255.
252. Kroeber, M. W.; Unglaub, F.; Wang, H.; *et al*. *Spine* **2002**, *27*(23), 2684–2690.
253. Masuda, K.; Aota, Y.; Muehleman, C.; *et al*. *Spine* **2005**, *30*(1), 5–14.
254. Sobajima, S.; Kompel, J. F.; Kim, J. S.; *et al*. *Spine* **2005**, *30*(1), 15–24.
255. Abbushi, A.; Endres, M.; Cabraja, M.; *et al*. *Spine* **2008**, *33*(14), 1527–1532.
256. Gan, J. C.; Ducheyne, P.; Vresilovic, E.; Shapiro, I. M. *J. Biomed. Mater. Res.* **2000**, *51*(4), 596–604.
257. Iwashina, T.; Mochida, J.; Sakai, D.; *et al*. *Spine* **2006**, *31*(11), 1177–1186.
258. Okuma, M.; Mochida, J.; Nishimura, K.; Sakabe, K.; Seiki, K. *J. Orthop. Res.* **2000**, *18*(6), 988–997.
259. Sakai, D.; Mochida, J.; Iwashina, T.; *et al*. *Spine* **2005**, *30*(21), 2379–2387.
260. Larson, J. W.; Levicoff, E. A.; Chadderdon, R. C.; *et al*. Prevention of intervertebral disc degeneration after surgical discectomy using and injectable hydrogel as a nucleus pulposus prosthesis. In *51st Annual Meeting of the Orthopaedic Research Society*, Washington, DC, 2005.
261. So, K.; Takemoto, M.; Fujibayashi, S.; *et al*. *Spine* **2007**, *32*(15), 1586–1591.
262. McLain, R. F.; Yerby, S. A.; Moseley, T. A. *Spine* **2002**, *27*(8), E200–E206.
263. Sheng, S. R.; Wang, X. Y.; Xu, H. Z.; Zhu, G. Q.; Zhou, Y. F. *Eur. Spine J.* **2009**, *30*, 30.
264. Busscher, I.; Ploegmakers, J. J.; Verkerke, G. J.; Veldhuizen, A. G. *Eur. Spine J.* **2010**, *19*(7), 1104–1114.
265. Kaigle, A. M.; Holm, S. H.; Hansson, T. H. *Spine* **1997**, *22*(24), 2796–2806.
266. Yingling, V. R.; Callaghan, J. P.; McGill, S. M. *J. Spinal Disord.* **1999**, *12*(5), 415–423.
267. Drake, J. D.; Aultman, C. D.; McGill, S. M.; Callaghan, J. P. *Clin. Biomech. (Bristol, Avon)* **2005**, *20*(10), 1038–1045.
268. Pfeiffer, M.; Griss, P.; Franke, P.; *et al*. *Eur. Spine J.* **1994**, *3*(1), 8–16.
269. Henriksson, H. B.; Svanvik, T.; Jonsson, M.; *et al*. *Spine (Phila Pa 1976)* **2009**, *34*(2), 141–148.
270. Zimmerman, M. C.; Vuono-Hawkins, M.; Parsons, J. R.; *et al*. *Spine (Phila Pa 1976)* **1992**, *17*(2), 213–220.
271. Ganey, T.; Hutton, W. C.; Moseley, T.; Hedrick, M.; Meisel, H. J. *Spine (Phila Pa 1976)* **2009**, *34*(21), 2297–2304.
272. Wilke, H. J.; Krischak, S. T.; Wenger, K. H.; Claes, L. E. *Eur. Spine J.* **1997**, *6*(2), 129–137.
273. Cotterill, P. C.; Kostuik, J. P.; D'Angelo, G.; Fernie, G. R.; Maki, B. E. *J. Orthop. Res.* **1986**, *4*(3), 298–303.
274. Buttermann, G. R.; Beaubien, B. P. *Spine J.* **2004**, *4*(3), 265–274.
275. Yu, J.; Tirlapur, U.; Fairbank, J.; *et al*. *J. Anat.* **2007**, *210*(4), 460–471.
276. Ishihara, H.; McNally, D. S.; Urban, J. P.; Hall, A. C. *J. Appl. Physiol.* **1996**, *80*(3), 839–846.
277. Demers, C. N.; Antoniou, J.; Mwale, F. *Spine* **2004**, *29*(24), 2793–2799.
278. Wilke, H. J.; Kettler, A.; Wenger, K. H.; Claes, L. E. *Anat. Rec.* **1997**, *247*(4), 542–555.
279. Kalayci, M.; Cagavi, F.; Gul, S.; Cagavi, Z.; Acikgoz, B. *J. Clin. Neurosci.* **2005**, *12*(6), 673–675.
280. Reid, J. E.; Meakin, J. R.; Robins, S. P.; Skakle, J. M.; Hukins, D. W. *Clin. Biomech. (Bristol, Avon)* **2002**, *17*(4), 312–314.
281. Roberts, S.; Caterson, B.; Evans, H.; Eisenstein, S. M. *Histochem. J.* **1994**, *26*(5), 402–411.
282. Easley, N. E.; Wang, M.; McGrady, L. M.; Toth, J. M. *Proc. Inst. Mech. Eng. [H]* **2008**, *222*(6), 915–922.
283. Melrose, J.; Smith, S.; Little, C. B.; Kitson, J.; Hwa, S. Y.; Ghosh, P. *Spine* **2002**, *27*(16), 1756–1764.
284. Osti, O. L.; Vernon-Roberts, B.; Fraser, R. D. *Spine* **1990**, *15*(8), 762–767.
285. Fazzalari, N. L.; Costi, J. J.; Hearn, T. C.; *et al*. *Spine* **2001**, *26*(23), 2575–2581.
286. Meakin, J. R.; Reid, J. E.; Hukins, D. W. *Clin. Biomech. (Bristol, Avon)* **2001**, *16*(7), 560–565.
287. Pelletier, M.; Smitam, P.; Michael, D.; Carter, A.; Diwan, A.; Walsh, W. Nucleus pulposus replacement in a sheep model. In *12th Annual Scientific Meeting of the Australian & New Zealand Orthopaedic Research Society*, Canberra Hospital, Canberra, Australia, 2006.
288. Nuckley, D. J.; Kramer, P. A.; Del Rosario, A.; Fabro, N.; Baran, S.; Ching, R. P. *J. Orthop. Res.* **2008**, *26*(9), 1283–1288.
289. Malinin, T.; Brown, M. D. *Spine* **2007**, *32*(21), E603–E607.
290. Ledet, E.; Dirisio, D.; Tymeson, M.; *et al*. *Spine J.* **2002**, *2*(5), 1.
291. Cunningham, B.; Hu, N.; Beatson, H.; McAfee, P.; Yuan, H. *Spine J.* **2007**, *7*(5 Suppl 1), 156S–157S.
292. Chou, A. I.; Akintoye, S. O.; Nicoll, S. B. *Osteoarthr. Cartil.* **2009**, *17*(10), 1377–1384.
293. Elliott, D. M.; Yerramalli, C. S.; Beckstein, J. C.; Boxberger, J. I.; Johannessen, W.; Vresilovic, E. J. *Spine* **2008**, *33*(6), 588–596.
294. Lotz, J. C. *Spine* **2004**, *29*(23), 2742–2750.

6.614. Wear: Total Intervertebral Disc Prostheses

R Vicars, R Hall, and J Fisher, University of Leeds, Leeds, UK

© 2011 Elsevier Ltd. All rights reserved.

6.614.1.	**Introduction to Total Disc Prostheses**	192
6.614.1.1.	Back and Neck Pain	192
6.614.1.2.	Degenerative Disc Disease and TDR	192
6.614.2.	**Basic Anatomy and Biomechanics of the Spine**	193
6.614.2.1.	The Spine	193
6.614.2.2.	The Natural Disc and Associated Structures	194
6.614.2.3.	The FSU and Spine Biomechanics	194
6.614.2.3.1.	Cervical spine loading	194
6.614.2.3.2.	Lumbar spine loading	194
6.614.2.3.3.	Cervical spine motions	194
6.614.2.3.4.	Lumbar spine motions	195
6.614.2.3.5.	Shear loads and motions	195
6.614.2.3.6.	Instantaneous axis of rotation	195
6.614.2.4.	The Degenerated Disc and Associated Structures	195
6.614.3.	**TDR Surgery**	195
6.614.3.1.	Indications and Contraindications	195
6.614.3.2.	Access/Surgical Techniques	196
6.614.3.3.	Success	196
6.614.3.4.	Complications	197
6.614.3.5.	Revision	198
6.614.4.	**TDR Design**	198
6.614.4.1.	History and Evolution	198
6.614.4.2.	Material Selection	198
6.614.4.3.	Constraint	199
6.614.5.	**Evidence of TDR Wear**	199
6.614.6.	**TDR Wear Simulation**	199
6.614.6.1.	ISO and ASTM Standards	199
6.614.6.2.	Spine Wear Simulators	200
6.614.6.3.	Wear Simulation Validation	201
6.614.7.	**Wear of Metal–PE TDR**	201
6.614.8.	**Wear of Metal–Metal TDR**	202
6.614.9.	**Wear of Alternative Material TDR**	202
6.614.10.	**Biological Response to TDR Wear Debris**	203
6.614.10.1.	Biological Response to PE Debris in the Spine	203
6.614.10.2.	Biological Response to Metal Debris in the Spine	203
6.614.11.	**Conclusions**	203
References		203

Glossary

Degenerative disc disease (DDD) Degeneration of the intervertebral disc resulting in disc dehydration and shrinkage and a change in the biomechanical properties.

Facet joint The joints created by the articular processes of superior and inferior vertebrae. The facet joints are true synovial joints including a covering of cartilage and surrounded by synovium, also known as the zygopaphysial joints.

Functional spinal unit (FSU) The smallest component of motion in the spine, consisting of two vertebrae and the intervening intervertebral disc.

Intervertebral disc Soft tissue structure connecting adjacent vertebral bodies through a cartilage layer and consisting of a gel-like nucleus pulposus surrounded by collagen fiber bands.

Total disc replacement (TDR) Any replacement requiring complete (or near complete) removal of the natural intervertebral disc.

Trijoint complex The three joints providing articulation within each functional spinal unit. They are the two facet joints and the intervertebral disc.

Abbreviations

ALL	Anterior longitudinal ligament
AP	Anterior–posterior
AR	Axial rotation
ASTM	American Society for Testing and Materials
C1–C7	Cervical vertebrae 1–7
CFR-PEEK	Carbon fiber-reinforced PEEK
CoCrMo	Cobalt–chromium–molybdenum
COR	Center of rotation
DDD	Degenerative disc disease
DOF	Degree(s) of freedom
FDA	Food and Drug Administration (USA)
FE	Flexion–extension
FSU	Functional spinal unit
IAR	Instantaneous axis of rotation
IDE	Investigational device exemption
ISO	International Organisation for Standardisation
L1–L5	Lumbar vertebrae 1–5
LB	Lateral bending
LBP	Low back pain
NICE	National Institute for Clinical Excellence (UK)
PE	Polyethylene
PEEK	Polyaryletheretherketone
PEK	Polyaryletherketone
ROM	Range of motion
TDR	Total disc replacement
THR	Total hip replacement
TJR	Total joint replacement
TKR	Total knee replacement
UHMWPE	Ultrahigh-molecular-weight polyethylene
μCT	Microcomputer tomography

6.614.1. Introduction to Total Disc Prostheses

6.614.1.1. Back and Neck Pain

Back and/or neck pain affects 60–85% of individuals during their lifetime, in higher income countries.[1–3] In both conditions, 90% of individuals recover in a few weeks or months, while in ~5–10% cases, the pain develops into a chronically disabling disorder.[4,5]

Although back and neck pain are already a large social concern, their prevalence has seemingly increased in the post-war period, escalating even further in the past 2 decades.[6] One suggested reason for this is that jobs are becoming increasingly sedentary, and sitting for long hours is thought to exacerbate low back pain (LBP).[7] Conversely, these has also been a decrease in manual handling jobs, which has been suggested as another risk factor. Another school of thought suggests that the incidence of LBP itself has not increased but that a psychosomatic 'syndrome shift'[8] has occurred due to increased public awareness of LBP through media attention and government reports and increased reporting of symptoms due to dissatisfaction in daily life.[6]

Whether the increasing incidence is genuine or psychosomatic, the economic burden of back pain is substantial and increasing. The overall economic burden of back and neck pain includes health-care costs, out-of-work benefits, and production losses, estimated to be as high as $200 billion per year in the United States alone.[9] It is recommended that back and neck pain are first managed by structured exercise, manual therapy, or acupuncture, followed by pharmacological therapies and psychosocial management. Only when conservative methods have failed to provide relief, surgical referral is considered.

6.614.1.2. Degenerative Disc Disease and TDR

Back and neck pain have multifactorial etiologies, including systemic causes (such as malignancies and infection[10]), deformities (such as scoliosis and kyphosis), fractures (which may be a result of trauma or systemic disease such as osteoporosis), nerve root compression (which may be due to any of the preceding factors), muscle and ligament sprains, and degenerative disc disease (DDD).

DDD has been attributed to be a significant cause of chronic LBP,[11,12] even though a substantial proportion of healthy patients show evidence of some disc degeneration,[13] suggesting that DDD, in part, is just a natural progression of the aging process. Chronic neck pain is more commonly associated with mechanical injury of the disc, such as whiplash, after which degeneration is accelerated. The pain itself tends to arise from cervical radiculopathy, where the cervical nerve roots are compressed, or myelopathy, where the spinal cord is impeded by spinal stenosis, spondylolysis, or herniated disc, and as such, these are the indications for surgery, not the DDD.

For the past 25 years, the gold standard for the treatment of LBP from DDD and chronic neck pain has been spinal fusion (after conservative measures are exhausted), with an estimated 450 000 patients undergoing fusion procedures in the United States.[14] The aim of fusion surgery is to eliminate motion, thereby eliminating pain. Overall success rates for spinal fusion have varied widely from 32% to 99%,[15] and complications arise due to the suitability of graft materials, incidences of nonunion, and the technical difficulties of the procedure. In addition, it has been proposed that fusion of one joint may cause an acceleration of DDD at adjacent joints.[16–18]

In contrast to fusion, total disc replacement (TDR) aims at the preservation, rather than the elimination, of motion. The procedure involves excision of the disc (which itself may be causing pain), and it is thought that the restoration of near-normal biomechanics will reduce the risk of adjacent level disease.[12,19–21] TDRs have been used as implants in Europe for more than 20 years, yielding good short- to mid-term clinical results so far. Questions that arise regarding the long-term success of TDR focus primarily on the longevity of the device *in vivo*. In particular, there are concerns over wear of articulating devices in the spine, wear-induced osteolysis being the prime cause of late failure in other joint replacements.

6.614.2. Basic Anatomy and Biomechanics of the Spine

6.614.2.1. The Spine

The spine consists of a column of vertebrae, running from the base of the skull to the coccyx. These vertebrae are connected by the trijoint complexes, consisting of two facet joints and an intervertebral disc. In normal, healthy individuals, the spine is straight in the frontal plane, and consists of four curves in the sagittal plane. The cervical and lumbar regions are convex in the anterior, whereas the thoracic and sacral regions are convex in the posterior. It is thought that the cervical curve develops during infancy as we learn to support our heads, sit, and crawl, and the lumbar curve develops when we are learning to walk. The typical shape formed by these curves is thought to increase resistance to axial compression and enhance flexibility.[22] The spine has a number of biomechanical functions: protecting the spinal cord (and associated neural function), providing stability, facilitating mobility, and controlling the movement and coordination of the upper and lower extremities.[23]

The human spine consists of 33 vertebras, split into 5 regions: 7 cervical, 12 thoracic, 5 lumbar, 5 sacral (fused), and 3–4 coccyx (fused). Although all the vertebrae differ slightly in size and shape, they all share a common structure and features, with the exception of C1 and C2 (the Atlas and the Axis). A large block of bone, the vertebral body, lies at the anterior of the spine, from which the pedicles protrude to the posterior elements. The neural arch is formed by the laminae pars and the connections of the various processes: two transverse (right and left), four articular (superior and inferior: right and left), one spinous, two mamillary (right and left), and two accessory (right and left). The neural arch encloses the vertebral foramina, which are aligned to form the canal through which the spinal cord passes from the brain to the lumbar spine. Nerve roots extend from the spinal cord, passing through the intervertebral foramen created by the interlocking of the processes, to the rest of the body.

The vertebral body is the main weight-bearing component of the vertebra, having flat superior and inferior surfaces, and a core of trabecular bone. The vertebral body (and intervening discs) resists ~80% of the compressive load of the spine in the neutral position, the proportion decreasing with extension[24] and the load transferring to the posterior elements. The compressive strength of the lumbar vertebrae has been found by several authors to exceed 5000 N,[25] with L4 being able to exceed 8000 N.[26]

The pedicles are two pillars of bone projecting from the back of the vertebral body, connecting to the posterior elements. The posterior elements (processes) of the spine are all designed to provide stability and/or enable motion. The articular processes (of which there are four) are the only physical connections between each of the vertebrae, forming the facet joints. The spinous, transverse, accessory, and mamillary processes provide lever arms for effective muscle and ligament attachment. The laminae and pedicles connect the spinous processes to the vertebral body, allowing transmission of forces and so aiding stability and enabling motion of the vertebral body.

The subtle differences between the vertebrae are related to the differing loading demands placed on them, and so not surprisingly, vertebrae within the same region are more alike. The lumbar spine has larger vertebral bodies and larger articular processes, which enable better transference of the greater loads experienced at this level. The thoracic vertebrae are slightly smaller and have larger transverse processes that provide attachment for stabilizing muscles. The ribs also attach to the thoracic vertebrae, making the spine in this region more rigid, facilitating less movement and protecting the major organs. The spinous processes of the thoracic vertebrae are typically small, which reflects the limited flexion–extension of this region of the spine. The cervical vertebrae are smaller still, as they have much lower loads to support, only supporting the weight of the head and associated muscle action. The spinous and transverse processes are large so as to provide greater leverage for muscular attachments, which along with the less stable facet joints allow for the increased flexibility of the cervical spine.

The facet joints, otherwise known as the zygapophysial joints, are formed by the articulation of the articular processes. These joints are synovial, the surface of the facets covered by articular cartilage with synovial membranes and surrounded by a joint capsule. The purpose of the facet joints is to resist forward sliding and twisting of the vertebral bodies, preventing shear stresses being applied to the intervertebral discs. A significant amount of loading is apportioned to the facet joints, with estimates of the load borne from zero,[27] where the capsular ligaments are put under tension, to 45% of the compressive loading on the spine.[28] As such, they are subject to degeneration and are a possible source of back and neck pain.

The orientation of the facet joints varies throughout the spine and determines their mechanical importance at each level. The joints can be flat or curved, and oriented any way between 0 and 90° to the sagittal plane. Flat joints parallel to the sagittal plane resist rotation, whereas those perpendicular to it resist forward sliding. Those oriented between 0 and 90° to the sagittal plane will offer some resistance to both rotation and forward sliding. In curved joints, the degree of resistance depends on the proportion of surface area that is posterior facing, with 'C'-shaped joints offering more resistance than 'J'-shaped joints. In general, curved joints resist rotation, as they maximize the surface area contact between the joints.

The facet joints are of concern to TDR, as the motion of the disc is directly related to the facets. It is argued that unconstrained TDRs, such as the Charité (DePuy Spine, Raynham, MA), subject the facets (and posterior ligaments) to increased shear loads, as they have no inherent shear stability.[29,30] This increased loading may cause degeneration of the facet joints, leading to further instability and pain. The ProDisc (Synthes Spine Solutions, New York, NY) has been found to reduce facet joint loading when compared to the Charité,[31] although this study did not compare the two to normal physiological loads conditions. Conversely, unconstrained designs provide a physiological center of rotation (COR) and thus may prevent non-physiological loading of the facets[29,30] as well as transfer of the loading to other locations, such as the implant–bone interface, which may lead to implant loosening.[29] The nature of the effect of constraint with relation to facet joint degeneration is not yet clear,[32] but clinical studies have shown that facet joint degeneration is seen in more than 30% of TDR patients at 3-year follow-up, regardless of the choice of constraint[33] (see **Chapter 6.610, Trends in Materials for Spine Surgery**).

6.614.2.2. The Natural Disc and Associated Structures

Intervertebral discs are positioned between each of the non-fused vertebrae, facilitating motion between the vertebrae, supporting compressive loading, maintaining the height of the spinal column, and providing some flexibility and stability at the extremes of motion. The intervertebral disc is composed of three main parts: the nucleus pulposus, the annulus fibrosus, and the cartilaginous endplates.

The nucleus pulposus is the center of the disc and is composed of 70–90% water,[25] which is attracted to the nucleus by the presence of hydrophilic proteins known as proteoglycans. Collagen fibers are irregularly arranged throughout the nucleus, creating a firm, gel-like texture,[11] and mature cartilage cells known as chondrocytes exist in the voids between these fibers and the proteoglycans. The fluid, incompressible nature of the nucleus allows it to be deformed under pressure, and so allows transference of forces in all directions. It has the capacity to swell via the process of diffusion, which provides nutrients to the chondrocytes and also contributes to its compliance.

The annulus fibrosus forms the outer boundary of the disc, developing in concentric laminated bands around the nucleus. Collagen fibers are highly organized around the nucleus in lamellae, with the adjacent lamellae fibers oriented at 90° to each other. This structure allows the disc to resist tension in all directions,[24] which is particularly important at the extremes of motion.

The cartilaginous endplates provide attachment of the disc to the vertebral body. These endplates, which are ~1 mm thick, are composed of hyaline cartilage and fibrocartilage, similar to that seen in other articulating joints. This cartilage develops with age, with decreasing amounts of hyaline cartilage until it is virtually all fibrocartilage. These endplates attach directly to the inner annulus fibrosis, and so are strongly bound to the intervertebral disc, but are only weakly attached to the vertebral bodies. The outer annulus fibers anchor themselves directly to the vertebral body.

The intervertebral disc is often casually referred to as a shock absorber, but in order for this to be true, the disc must be able to dissipate energy. There are two possible mechanisms by which this can occur: elastic hysteresis during loading and unloading of the disc [34,35] and diffusion of water through the vertebral capillaries allowing transfer of heat energy.[11] Increases in loading rates reduce the ability of the disc to dissipate energy, thereby making it a less effective shock absorber, with high loading rates meaning that the disc has less time to 'recover.'

Although the intervertebral disc is capable of shock absorption, studies have shown that the contribution of the discs to shock absorption in the spine is minimal,[36] with the other soft tissue structures of the spine, particularly the muscles, being much more effective shock absorbers than the discs. However, the effect of replacing a minimal shock absorber with a completely rigid device has yet to be studied, but the development of elastomeric devices has originated from this concern.

6.614.2.3. The FSU and Spine Biomechanics

Consideration of 'healthy' spine biomechanics is important when defining parameters for any mechanical test. The loading and motion experienced by the lumbar spine have been much more complex to quantify than those in the hip and knee. The functional spinal unit (FSU) consists of two vertebrae and one intervertebral disc and is capable of six degrees of freedom (DOF).[25,37] A coordinate system has been adopted by both International Organisation for Standardisation (ISO) and American Society for Testing and Materials (ASTM) for spinal testing[37] where the *X*-, *Y*-, and *Z*-axes are defined in the anterior–posterior (AP), lateral, and superior–inferior directions, respectively. Lateral bending is described as rotation about *X*-axis, flexion/extension as rotation about *Y*-axis, and axial rotation as rotation about *Z*-axis.

The loads and motions vary significantly from FSU to FSU, with lumbar vertebrae experiencing higher loads but reduced motion compared to cervical vertebrae, but even within the same region, differences are significant. Idiosyncrasies are significant not only because the weight and activity levels of patients differ but also because vertebral recruitment patterns differ for any given motion.[38] Complexities also arise because motions are kinematically coupled, such as the coupling of translational motion and flexion–extension, and coupling of axial rotation and lateral bending.[39]

The spine is loaded not only by the head (in the case of the cervical) and upper body weight (in the case of the lumbar) but also by a complex group of muscles and ligaments that provide both stability and motion. The center of gravity of the upper torso lies anterior to the spine, and so these muscles and ligaments are in constant tension in order to retain an upright posture, and the muscles in the upper spine and neck must similarly support the head. As such, the spine is never fully unloaded, although it is partially unloaded in the prone position.

6.614.2.3.1. Cervical spine loading

The cervical spine experiences much smaller loading than the lumbar spine, supporting the weight of the head and associated musculature. These loads are usually up to three times the head weight, typically <200 N, but can reach up to 1200 N during everyday activities in which maximum muscle contraction occurs, for example, during contact sports or heavy lifting.[40]

6.614.2.3.2. Lumbar spine loading

Even in perceived inactivity such as standing and sitting, the lumbar spine experiences loads of between 1.5 and 2.0 times body weight.[41] Loading increases with increasing activity levels, so during level walking the compressive forces rise to more than three times the body weight in the lumbar spine.[42] Extremely high loads can be experienced during vigorous activity,[43] the extremes of motion,[43,44] and external load carriage[43,45–47] with loads in excess of five to six times the body weight.

6.614.2.3.3. Cervical spine motions

The motions in the cervical spine are on the whole much larger than those in the lumbar spine. Total ranges of motion for the cervical region are typically 120° flexion–extension, 80° lateral bending, and 140° axial rotation.[48] Maximum flexion–extension ranges between 15 and 25°, with lateral bending 5–12° and axial rotation 2–7°, except in the joint of the atlas/axis (C1–C2) where it is 40°.[25] The ranges of motion, observed in an *in vitro* study,[49] for C4–C5 and C5–C6, the most commonly operated cervical discs, are summarized in **Table 1**.

Table 1 Ranges of motion at C4–C5 and C5–C6

	Combined flexion/extension	*Total lateral bending*	*Total axial rotation*
C4–C5	7.3	5.4	3.6
C5–C6	10.1	4.6	2.8

Source: Goel, V. K.; Clark, C. R.; McGowan, S.; Goyal, S. *J. Biomech*. **1984**, *17*(5), 363–376.

6.614.2.3.4. Lumbar spine motions

The results of motion studies of the lumbar spine relative to the pelvis[42] show that peak flexion follows toe off, transferring to peak extension at heel strike. Lateral bending is directed toward the contralateral side and axial rotation toward the same side of heel contact. Increased cadence has been found to increase the magnitude of lateral bending, axial rotation, and flexion, but it decreases extension.[42] The above studies focus on the lumbar spine as a segment and so motion values are likely to be less than these figures suggest for a single FSU. Maximum flexion/extension angles have been found to be ~5°/3° at FSU L3/L4 and 4°/2° at L4/L5.[50] Another study has shown that although the maximum value of flexion/extension of an FSU for healthy patients *in vivo* was 6°, the average value was only 2.5°.[51]

6.614.2.3.5. Shear loads and motions

AP shear loads are important when considering TDR effects on the shear stability of the spine. Callaghan *et al.*[42] calculated the loads and moments experienced by the L4/L5 FSU during walking, finding that the lumbar spine underwent a significant anterior shear load during flexion–extension. Peak loading occurs at toe off, with a significant simultaneous anterior shear load of up to 200 N and a smaller lateral shear load directed toward the standing foot. Studies have shown that AP shear loads can be extremely large in cases of heavy lifting, approaching 1000 N.[45]

AP shear has also been measured in terms of the translation, with an anterior translation of 1.6 ± 0.3 mm and a posterior translation of 1.9 ± 0.3 mm in the cervical spine.[52] This translation is similar in the lumbar spine, with typical translations of 1–2.5 mm in both AP and lateral directions.[53,54]

6.614.2.3.6. Instantaneous axis of rotation

Another aspect important in the definition of motion of the spine, especially when referring to individual segments, is the instantaneous axis of rotation (IAR). This defines the point about which a body rotates in plane motion. The IAR can be summarized for all three rotations in the lumbar spine,[25] although changes at different levels of the spine and during motion.[29] The IARs alter significantly with DDD,[55,56] and one of the design criteria of TDR is to try to reproduce the IAR of the natural disc.

6.614.2.4. The Degenerated Disc and Associated Structures

Many studies have found decreased mobility of the spine with aging, but it is not clear whether this is due to degeneration, disease or as a result of decreasing activity.[25] Some degeneration appears to be part of the natural ageing process, and there are no definitive markers as to what constitutes disease.[24] Much of the literature has focused upon the disc as the primary cause of pain in the spine, whether this be due to the changes in the disc itself or the reduced ability of the disc to maintain normal biomechanics (possibly causing osteoarthritis in the facet joints) or the compression of veins and nerves because of changes in disc geometry.

With aging, the vertebral endplates become less porous and sclerotic, and inhibit the transfer of water and nutrients, resulting in metabolite accumulation and an increase in acidity. After the age of 30, there is a gradual change in the type and amount of proteoglycans within the disc nucleus.[57] This reduces the water content of the disc, meaning that it becomes dehydrated and shrinks, and reduces the effectiveness of the load transfer through the nucleus, increasing the load on the annulus.[58] This increased load can damage the annulus, resulting in radial fissures and tears, which may allow the disc nucleus to migrate through the tears, stimulating the sinuvertebral nerve and resulting in pain. If the nucleus transgresses completely through the annulus (disc herniation), it may compress a nerve root causing radicular pain that travels down the extremity in the distribution of that particular nerve, leading to chronic LBP associated with pain in the legs (Sciatica). Secondary to this, the nucleus, now being exposed, is recognized as 'foreign' by the body, inducing an inflammatory response.[59]

Another effect of the degenerating disc is that its loss of turgidity results in height loss and a narrowing of the neuroforamen, compressing nerve roots. This geometry change may also alter the biomechanics of the spine, compromising stability and increasing motion. The spinous processes adapt, resulting in hypertrophy, which can again narrow the vertebral foramen (spinal stenosis). An increasing amount of the compressive load must be taken by the facet joints, causing wear and inflammation. An impaired facet joint may no longer protect the disc from shear stress, and so disc degeneration is accelerated.

The spine is a cooperative system of elements, and degeneration of one component or at one level is closely followed by subsequent degenerations of components or at adjacent levels. It is therefore difficult to determine the initial cause of the degeneration, and so difficult to prevent entirely. Until this can be determined, treatments must exist to repair the spine once degeneration has begun.

6.614.3. TDR Surgery

6.614.3.1. Indications and Contraindications

Currently, TDR is still evolving, and clinical selection criteria for treatment are subject to ongoing discussion. TDR is typically recommended for the treatment of single-level symptomatic DDD in the lumbar spine for which fusion would be indicated in otherwise healthy, younger patients; it has extremely limited use for other spinal diseases, trauma, and deformities where instability is a problem (**Table 2**). Determining DDD is difficult as a significant number of asymptomatic patients have shown some evidence of DDD in radiographic examination.[13] Further, not all patients with established DDD can receive TDR due to the large number of contraindications to the technique. **Table 2** outlines the inclusion and exclusion criteria for the Charité disc Food and Drug Administration (FDA) trials; however, European clinical experience suggests broader applications of TDR. There

is no consensus as to whether patients with pathologies associated with DDD, such as facet joint osteoarthritis, spinal stenosis, and multisegmental pathology, should be accepted for TDR.[32] However, it has been reported that healthy facet joints and intact posterior musculature and ligaments are required for successful TDR.[60]

The indications are broader for cervical TDR, mainly because the surgical access is exactly the same as for TDR or fusion, and so it is not considered as risky as the procedure for lumbar TDR. However, complications may be deemed as more serious because of the closer proximity of the device to the spinal cord at this level, as well as the esophagus and the vessels serving the brain (Table 3).

TDR is generally indicated for patients younger than those typically seen for total hip replacement (THR), mean age 70 years, and total knee replacement (TKR), mean age 73 years.[61] The suggested age of TDR patients is between 18 and 60 years, optimally those under 50 years.[62] Elderly patients present further risk due to the prevalence of metabolic bone diseases, most commonly osteoporosis, which carry an increased likelihood of endplate subsidence and vertebral body fracture. The younger patients are likely to have a higher activity level than the majority of hip THR/TKR recipients, and live longer, placing increased demands on the endurance of the devices. In addition, failure of TDR is thought to be more serious than that of THR/TKR replacements, not only because of revision difficulties but also because of the proximity of the device to the neural network, and major organs and vessels.

Table 2 Inclusion and exclusion criteria for lumbar TDR

Inclusion criteria	*Exclusion criteria*
• Discogenic LBP with single-level DDD, proven by MRI or CT and/or discography • Age 18–60 years, optimally <50 • Minimum 6 months of unsuccessful conservative therapy • No signs of nerve root compression • The majority of the studies require preoperative Oswestry score of >40% and a VAS value of >40 mm	• Deformities • Tumors • Infection • Posttraumatic segments • Postoperative segments excluding postdiscectomy • Metabolic bone disease • Metal allergy • Pregnancy • Autoimmune disorders • Morbid obesity (BMI > 40)

Table 3 Inclusion and exclusion criteria for cervical TDR

Inclusion criteria	*Exclusion criteria*
• DDD with symptoms of radiculopathy and/or myelopathy, with or without neck pain • Compressive legion diagnosed by MRI, CT, or myelography • Age 18–65 years • Minimum 6 weeks of unsuccessful conservative therapy	• Ankylosing spondolytis, rheumatoid arthritis, ossification of PLL, or diffuse idiopathic skeletal hyperostosis • Insulin-requiring diabetes mellitus • Prior cervical spinal infection • Chronic steroid use • Morbid obesity (BMI > 40) • Pregnancy • Neck pain as the only symptom

Source: McAfee, P. C. *Spine J.* **2004**, *4*(Suppl. 6), 177S–181S.

6.614.3.2. Access/Surgical Techniques

The lumbar TDR procedure is most commonly performed with anterior access, having to pass the abdominal organs as well as major vessels to gain access to the disc space in the case of lumbar TDR, and the esophagus in the case of cervical TDR. Although the anterior approach involves close proximity to major organs, and dissection of the anterior longitudinal ligament (ALL), posterior spinal surgery would compromise the facet joints and further endanger the spinal cord. Lateral surgery is also an option[63,64] and means that both the posterior elements and the ALL can be preserved, but access is not possible at the lumbosacral joint.

The natural disc is partially or fully excised, and after appropriate sizing and preparatory work, the disc space is distracted. The metal endplates are positioned, along with the core (depending on the design), and then the disc space is retracted. The positioning and alignment of the disc is extremely important for the correct functioning of the device and for prevention of any adverse events such as dislocations (Figure 1).

The procedure itself presents its own surgical risks, regardless of the success of the actual device. Perioperatively, complications arise due to accidental damage to the greater vessels[65] and other factors consistent with any type of major surgery. Postoperative complications include spontaneous fusion,[66,67] persisting LBP,[65] vascular and neural complications,[30,65,68] infection,[65,69,70] and complications associated with damage to the presacral plexus such as retrograde ejaculation.[65,71]

6.614.3.3. Success

The clinical success of TDR is not well defined. Ultimately, the aim of TDR is elimination of pain while providing a normal, healthy range of motion (ROM). It also aims to reduce or eliminate increased incidence of adjacent level disease, without mechanical or design failure and be biocompatible, both in

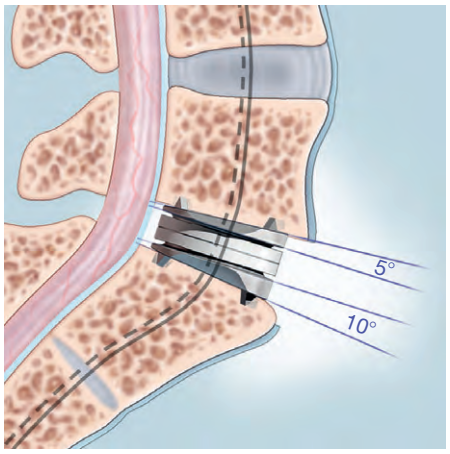

Figure 1 Placement of the total disc replacement within the disc space is of paramount importance for the biomechanical and clinical functioning of the device. Courtesy of DePuy International Ltd.

terms of base material reaction and secondary to any wear-related debris. If all of the preceding aims are achieved, the device will survive the remaining lifetime of the patient.

The clearest indicator of the success of a TDR is patient satisfaction, primarily with regard to pain relief and return to normal function. TDR has been shown to match the success of spinal fusion at least in terms of patient satisfaction. It has been shown to have advantages over fusion, including better and quicker back-to-work rates, presumably due to the increased mobility of the patient.

Investigational device exemption (IDE) trials have been performed for several TDRs, both lumbar (Table 4) and cervical (Table 5). The design of these trials was to prove equivalence to fusion, and as such, none can claim that the TDR is superior to fusion. However, all the TDRs that have undergone IDE trials have proven to be at least equivalent to their fusion counterpart and have often shown increased and more rapid back-to-work rates.

Good clinical outcomes increased from 63% in the beginning of the 1990s to 93% in 1997,[77] showing that improvement in surgical techniques and experience influence the outcome of surgery. High surgical volume has been associated with improved clinical outcomes for a number of clinical procedures including THR and TKR.[15] The Charité IDE study found that surgeons experienced in the technique reported a decrease in operative times, length of hospital stay, and rates of complications and neurological deterioration.[78,79]

6.614.3.4. Complications

Increased ROM has been evident in a number of studies in comparison to both fusion and preoperative states. Altered biomechanics have been shown to play a primary role in the development of accelerated DDD at adjacent levels.[25] Sixty-six percent of individuals implanted with the first-generation ProDisc device had ROM values within the range of 'normal' ROM, but did not restore the full ROM and was less successful than the Charité.[80] Twenty-four percent of patients had incidence of adjacent level degeneration, compared to 36% and 37% of patients reported for lumbar fusion.[17,18] Cadaveric studies have shown that the implanted Charité disc closely mimics the COR of the lumbar disc and it does not adversely affect the ROM at adjacent levels, whereas fusion results in a 'marked increase' in adjacent level motion.[81] Lumbar fusion patients have had a mean symptom-free period from adjacent segment degeneration of 13.1 years,[82] and so clearly long-term follow-up of TDR is needed to prove its worth against fusion.

Sagittal plane alignment has been associated with LBP and altered biomechanics for the past century.[83–85] It has been reported that correct lumbar lordosis increases spine strength (defined as the buckling load) by 34.4%[30] and that both hypo- and hyperlordosis are associated with LBP.[86] Altering the segmental angle of lordosis will alter the partitioning of the loading between the compressive axial component and the tangential shear component. Patients with decreased sacral inclination after lumbar fusion, defined as being $<35^{\circ}$, were found to have increased incidence of adjacent segment degeneration (from 8% to 47.8%).[17] Lumbar TDR restores lumbar and segmental lordosis closer to physiological values compared to fusion,[87] although it has been found that it decreases the lordosis at adjacent levels, which may cause loading alterations and degeneration.[86]

Facet joint degeneration is another concern if the biomechanics of the natural spine are altered. Fifty percent of patients treated with the Charité had progressive facet joint degeneration after 2 years,[88] and more than 30% of TDR patients have shown aggravated facet joint degeneration at the index level, with both the Charité and ProDisc.[33] Rousseau *et al.*[89] compared the effects of the ProDisc and the Charité on the facet joints, finding that the ProDisc decreased and the Charité increased the facet joint loading. Both cases result in alteration of the disc/facet load sharing, which explains why both discs are associated with facet degeneration. The surgical placement

Table 4 Patient satisfaction, VAS and ODI pain improvement scores, and return-to-work rates for lumbar fusion and TDR as reported in IDE studies

Time-point	*5 years Geisler* et al.[72]		*2 years Zigler* et al.[73]		*2 years Pettine and Donner*[74]
	Charité	*Fusion*	*ProDisc*	*Fusion*	*Maverick*
Patient satisfaction (%)	97	84	81	69	96
VAS pain score improvement	36.5	46.3	39	32	53.6
ODI score improvement	26.6	32.5	28.9	22.9	43
Return to work (%)	70	61	92.4	85.1	67

Table 5 Patient satisfaction, VAS and NDI pain improvement scores, and return-to-work rates for cervical fusion and TDR as reported in IDE studies

Time-point	*2 years Riew* et al.[75]		*2 years Murrey* et al.[76]		*2 years Riew* et al.[75]	
	Prestige	*Fusion*	*ProDisc*	*Fusion*	*Bryan*	*Fusion*
Patient satisfaction (%)	89.8	91.9	85.6	80.9	94.7	90.0
VAS pain score improvement	43	46	46	43	49	31
NDI score improvement	32.1	31.1	32.5	31.7	35.5	20.9
Return to work (%)	n/a	n/a	82.8	80	n/a	n/a

of the disc has a large effect on the load sharing of the facet joints,[90] and this must be studied further in order to improve surgical outcomes.

Mechanical failure of TDR has been due to fracture of the polyethylene (PE) component,[91] dislocation of the PE component,[92] and subsidence of the metal endplates into the vertebral endplates.[67,93,94] Improved designs, careful patient selection, and advanced surgical techniques have gone on to see that these failures are extremely rare. Vertebral body fracture has been reported in a few cases,[95,96] although it is rare as metabolic bone diseases such as osteoporosis are a contraindication to TDR. There are suggestions for the use of vertebroplasty with TDR to allow patients with metabolic bone diseases to be considered for TDR.[97,98] It has been shown to decrease the risk of subsidence (compared to historical controls) with no adverse effects. Further study of the suitability of vertebroplasty with TDR surgery is needed to identify whether the inclusion criteria could be expanded for these cases (see **Chapter 6.603, Ultrahigh Molecular Weight Polyethylene Total Joint Implants**).

All materials currently used in TDR have a proven history of biocompatibility in other implants, and so in the short-term have yielded few problems. However, long-term biocompatibility of TDR has yet to be proven. TDR implantation is a relatively new procedure compared with other joint replacements, and so we have not had the chance to present significant numbers of late failure due to wear. However, in more recent years, a number of studies have demonstrated both the potential for osteolysis[99,100] and, more importantly, clinical cases of osteolysis with TDR,[101–103] occurring from as little as 8 years after implantation.[102] Failure due to wear is potentially more serious in the spine, with the close proximity to vital organs and neural networks in comparison to other joint replacement. Repeated invasive surgery needs to be avoided, and so the segment is often fused with the prostheses left in place. As a result of this, few explanted TDRs are available for study.

With the development of TDR matching the evolution of THR/TKR, many of the problems have been overcome. Improved designs, careful material selection, and advanced surgical techniques have removed many of the concerns regarding endplate subsidence, fatigue failure, and dislocations. The current focus in TDR is ensuring its capacity for long-term success, including further investigation of its effect on the facet joints (and possible subsequent degeneration) and the role of wear and wear debris-induced osteolysis. It is imperative that access to explanted components and tissues be made available, both at revision and postmortem, so that the long-term success of both unsuccessful and successful devices can be monitored.

6.614.3.5. Revision

TDR cases requiring revision are comparable in number with THR/TKR, but more numerate than spinal fusion (**Table 6**). Revision operations of TDR are difficult due to the limited amount of bone in the vertebrae to attach the implant, and so it is preferable to ensure the long-term success of these devices and eliminate the need for revision. In the lumbar spine, revisions tend to be performed using posterior fusion, fusing the TDR in place so as to avoid the invasive anterior approach for a second time, which is further complicated by the presence of scar tissue.

Table 6 Comparison of revision rates of TDR, fusion, THR, and TKR

Procedure	*Revision rate (%)*	*Study*
Lumbar TDR	11.2	Kurtz *et al.*[104]
Anterior lumbar fusion	5.8	Kurtz *et al.*[104]
Posterior lumbar fusion	7.4	Kurtz *et al.*[104]
Cervical TDR	8.8–12.1	Anderson *et al.*[105] and Phillips *et al.*[106]
Anterior cervical fusion	3.1–5.0	Anderson *et al.*[105] and Phillips *et al.*[106]
THR	13.9	Kurtz *et al.*[104]
TKR	7.7	Kurtz *et al.*[104]

6.614.4. TDR Design

6.614.4.1. History and Evolution

TDR describes any procedure that involves excision of the anatomical disc and its replacement with a device that restores natural motion to some extent. TDR has lagged behind replacements of the peripheral joints, mainly due to the complex biomechanics and the surgical challenges that replacement presents. Although the most common types are the articulating discs, they have also included 'spring and hinge' designs, fluid-filled chambers, and elastomeric discs.[11]

Several 'spring and hinge' devices, similar to the articulating designs in the attachment to the vertebral body by spikes,[107] have been patented by inventors, but the articulating surfaces are substituted with a collection of miniature springs or a hinge design[108,109] that has an element of 'springy' flexibility. These designs allow limited motion, as well as some compliance, but have never been used clinically.

Elastomeric discs, such as those made of silicone and polyurethane, were designed as it was thought that these could be mechanically, if not chemically, similar to the anatomical disc.[11] The Bryan disc (Medtronic Sofamor Danek, Memphis, TN) uses elastomeric material, a polyurethane membrane that surrounds an articulating core, which means that the quality of motion still relies on the articulating parts. Lumbar discs have been more difficult to develop because of the increased loading demands of the lumbar spine; yet in 2008, several designs began to appear for use in the lumbar spine, including the CAdisc-L (Ranier Technology, Cambridge, UK) and Physio-L (Nexgen Spine, Inc., Whippany, NJ). The manufacturers of these discs claim that they provide a more physiological kinetics, in that they replicate the viscoelastic nature of the natural disc, provide some shock absorbency, and show little wear. These discs are yet to be independently tested *in vitro* as well as *in vivo*, but they can have great potential if these claims are proven true.

6.614.4.2. Material Selection

The most successful lumbar TDRs to date are those articulating designs that have, in part, developed from the successes of THR/TKR. Material selection (**Table 7**) in TDR has closely followed the use of materials in other joint replacements. Metal–PE bearings were used in the first articulating TDR (Charité, ProDisc) and have remained the most implanted devices, particularly in the lumbar spine. Metal–metal bearing combinations followed shortly after, with supporting evidence that these bearings could reduce wear in THR. More recently, other materials have been

Table 7 Summary of TDR devices and materials

Device name	*Manufacturer*	*L*	*C*	*Materials*
Charité	Link/DePuy Spine	•		CoCrMo–UHMWPE
ProDisc (-C or -L)	Synthes Spine	•	•	CoCrMo–UHMWPE
Maverick	Medtronic	•		CoCrMo–CoCrMo
Flexicore	Stryker Spine	•		CoCr–CoCr
Activ (-C or -L)	Aesculap	•	•	CoCrMo–UHMWPE
Mobidisc (-C or -L)	LDR	•	•	CoCrMo–UHMWPE
Kineflex	Spinal Motion	•	•	CoCrMo–CoCrMo
Prestige ST	Medtronic		•	Stainless steel–stainless steel
Prestige LP	Medtronic		•	Ceramic–ceramic
Cervicore	Stryker Spine		•	CoCrMo–CoCrMo
Secure-C	Globus Medical		•	CoCrMo–UHMWPE
Cerpass	Nu Vasive		•	Titanium–ceramic
Discover	DePuy Spine		•	Titanium–UHMWPE
Bryan	Medtronic		•	Titanium–UHMWPE and polyurethane core
NeoDisc	Nu Vasive		•	Silicone elastomer and textile
M6	Spinal Kinetics		•	Titanium plates polyurethane–UHMWPE core
Freedom	AxioMed	•		Titanium plates, polymer core
CADisc (-C or -L)	Ranier Technology	•	•	One-piece polyurethane
Physio-L	Nexgen Spine	•		Titanium plates, elastomeric core
Theken eDsic	Theken Disc	•		Titanium endplates, elastomeric core

used including polyether–ether–ketone (PEEK) and one-piece elastomeric materials that are thought to significantly reduce wear or eliminate it completely (see **Chapter 6.601, Current and Projected Utilization of Total Joint Replacements**).

6.614.4.3. Constraint

Articulating TDRs are often referred to as constrained (also referred to as fixed-bearing), semiconstrained, or unconstrained devices (also referred to as mobile bearing). This terminology relates to the DOF that the devices can support. All current TDRs (**Table 8**) provide three DOF: flexion–extension, lateral bending, and axial rotation. Various TDRs provide an additional one to two DOF for AP displacement and lateral displacement, often being referred to as unconstrained or semiconstrained. Only the TDRs that provide a full six DOF, including axial compression, can be said to be fully unconstrained, and these are currently limited to the elastomeric designs.

Increasing constraint leads to a more stable design and has inherent shear stability that is thought to protect the facet joints. However, it may lead to underuse of the facet joint, which could subsequently lead to degeneration. Decrease in constraint leads to a more physiological motion, with a mobile COR, but little shear stability, which means that the facet joints may be overloaded, again leading to degeneration.

Table 8 Summary of TDRs and their constraints

Device name	*FE*	*LB*	*AR*	*AP*	*LR*	*AC*
Charité	•	•	•	•	•	
ProDisc (-C or -L)	•	•	•			
Maverick	•	•	•			
Flexicore	•	•	•			
Activ (-C or -L)	•	•	•	•		
Mobidisc (-C or -L)	•	•	•	•	•	
Kineflex	•	•	•	•	•	
Prestige ST	•	•	•			
Prestige LP	•	•	•			
Cervicore	•	•	•			
Secure-C	•	•	•	•		
Cerpass	•	•	•			
Discover	•	•	•			
Bryan	•	•	•	•	•	•
NeoDisc	•	•	•	•	•	•
M6	•	•	•	•	•	•
Freedom	•	•	•	•	•	•
CADisc (-C or -L)	•	•	•	•	•	•
Physio-L	•	•	•	•	•	•
Theken eDsic	•	•	•	•	•	•

6.614.5. Evidence of TDR Wear

In the early use of TDR, radiographic measurements found no evidence that either PE wear[71] or osteolysis[80] had occurred after a mean follow-up of 8.7 years after ProDisc implantation and after a 10-year follow-up for the Charité disc.[110] However, more recently, with the increased number of implants exceeding short-term implantation, several studies have found that PE debris is accumulating around TDR in which the incidence of osteolysis has been reported.[103] Further *in vivo* monitoring of the wear process is essential in order to determine safe implantation times, increased risk factors, and additional complications resulting from the wear process.

Explanted components have shown evidence of wear. The volumetric wear of explants was studied using a microcomputer tomography (μCT) scanning technique.[111] The finding was an average height change of 0.2 mm over an average of 9.1 years, although this was a combination of wear and creep. Retrievals have also suffered from severe wear and even breakages of the PE cores,[112] although they have primarily been those early implants that were γ-sterilized in air. Study of explanted discs at postmortem would make it possible to ascertain whether these levels of wear are typical of well-functioning implants as well.

6.614.6. TDR Wear Simulation

6.614.6.1. ISO and ASTM Standards

The experience of THR/TKR wear studies and the biomechanical investigations of the spine have provided the basis for testing requirements as specified by both ISO 18192[113] and ASTM F 2423[114] for both the cervical (**Table 9**) and lumbar spine (**Table 10**). The loading profiles follow a sinusoidal pattern with the corresponding peaks clearly coincident with those seen in the work by Callaghan *et al.*[42] However, it is important to note that the Callaghan motion data are for a lumbar spinal

Table 9 ISO and ASTM input conditions for wear simulation of cervical TDR

Test profile	*ISO*		*ASTM*	
	Displacement control	*Load control*	*Displacement control*	*Load control*
Axial load	N/A	50–150 N (±3%)	N/A	100 N (±5%)
Flexion/extension	±7.5° (±0.5°)	N/A	±7.5° (±0.5°)	±2 Nm (±5%)
Lateral bending	±6° (±0.5°)	N/A	±6° (±0.5°)	±2 Nm (±5%)
Axial rotation	±4° (±0.5°)	N/A	±6° (±0.5°)	±4 Nm (±5%)

Table 10 ISO and ASTM input conditions for wear simulation of lumbar TDR

Test profile	*ISO*		*ASTM*	
	Displacement control	*Load control*	*Displacement control*	*Load control*
Axial load	N/A	600–2000 N (±3%)	N/A	1200 N (±5%)
Flexion/extension	6°/3° (±0.5°)	N/A	±7.5° (±0.5°)	±10 Nm (±5%)
Lateral bending	±2° (±0.5°)	N/A	±3° (±0.5°)	±10 Nm (±5%)
Axial rotation	±2° (±0.5°)	N/A	±6° (±0.5°)	±12 Nm (±5%)

segment, and not for an FSU, and so motion parameters may be exaggerated for simulator testing of a single FSU.

One crucial difference of the ASTM standard guide is that the suggested axial compressive load is static, which may lead to depletion of the lubricant between the bearing surfaces, and so resulting in unrealistically high wear rates.[114] Both standards state that displacement control be the preferred method of application for all three rotations, which ensures that the bearing is not displaced beyond its limits and so does not dislocate, and force control of the axial compressive load, which ensures that extreme contact forces are not generated. To date, there is no suggestion for the applications of AP or lateral shear loads, although these have been documented.[42,53] The application of AP shear loads in TKR wear simulation has been shown to affect wear performance, depending on implant type.[115] The same may be true in the spine, with additional shear loads altering the motion patterns and therefore cross-shear.

Both standards recommend a minimum of six active stations and one load-soak control station. The testing chambers should be isolated from each other such that the debris from each can be assessed independently and to prevent contamination from the surrounding environment. All stations are required to have control systems that maintain temperature at 37 °C, to a tolerance of ±2 °C[113] or ±3 °C.[114] Bovine serum lubricant is specified by both standards, although the protein concentration differs from $20\,g\,l^{-1}$ in the ASTM standard guide to $30\,g\,l^{-1}$ in the ISO 18192. The addition of antimicrobial agents is permitted to prevent degradation of the serum. These protein concentrations have been successfully used in THR/TKR simulator studies, and are considered analogous to the pseudosynovial fluid that is formed within the fibrous capsule that forms around these peripheral joint replacements.[116] However, the intervertebral discs are not synovial joints, and although it has been suggested that a similar fibrous capsule and pseudosynovial fluid are formed,[117] to date no *in vivo* studies have investigated the nature of this capsule. As such, the exact nature of the lubricant remains to be discovered.

6.614.6.2. Spine Wear Simulators

The increased use of TDR and the race for FDA approval for the US market has led to the development of wear testing standards and the development of commercial simulators based on these standards. There are currently five commercial simulator designs in use for TDR wear testing: Endolab Spine simulator (Rosenheim, Germany),[118] AMTI simulator (AMTI Boston, MA),[119] Bose Spinal disc fatigue/wear test instrument (Bose Corporation, Electroforce systems group, MN),[120] MTS Bionix[121] spine wear simulator (MTS systems corporation, MN), and ProSim 5DOF Spine Wear simulator (Simulation solutions, Manchester, UK).

Both the Endolab Spine simulator and the AMTI simulator incorporate four active DOF: flexion/extension, lateral bending, axial rotation, and axial compression, in accordance with ISO 18192[113] and ASTM F 2423.[114] The Bose and MTS Bionix simulators both claim to incorporate a full six DOF; however, the fifth and sixth DOF are only passive. The ProSim 5DOF Spine Wear simulator applies five active DOF, the fifth DOF being application of AP shear by either load or displacement (**Figure 2**). **Table 11** summarizes the ROM in each DOF for the five simulators discussed.

All the simulators are capable of producing the load motion profiles, with phase angles, as specified by the ISO 18192. Hydraulic actuators provide motions with a high degree of control and are used for four of the commercially available simulators. However, they are relatively high in cost and require effort to contain and maintain the fluid. Electromechanical actuators are used for all DOF in the ProSim 5DOF simulator and for one DOF in the AMTI simulator.

As well as the magnitude and phasing of the loads, the point at which the load is applied is likely to affect the wear pattern of TDR. The Endolab simulator applies the compressive force to the superior fixture, with all of the motions applied to the inferior fixture. The Bose, AMTI, MTS, and ProSim simulators apply the axial force and rotation to the inferior fixture, and the flexion–extension and lateral bending to the superior fixture. As TDR wear testing is still in its infancy, there is very little

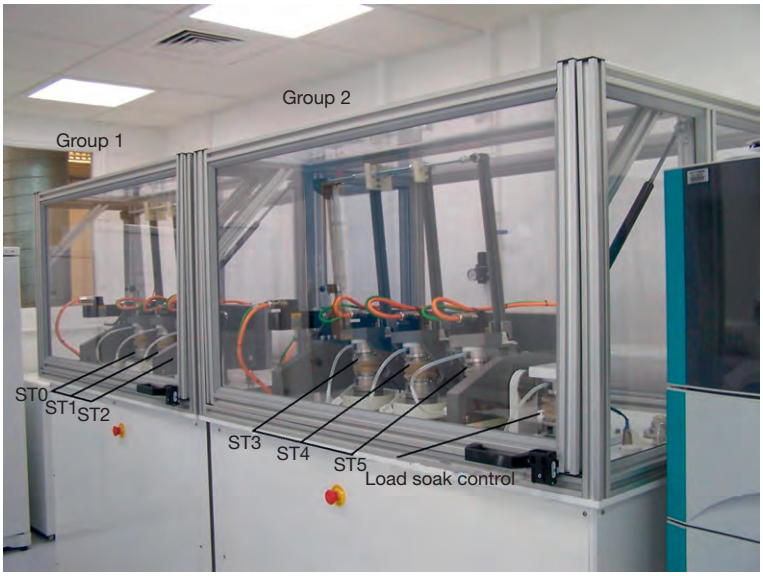

Figure 2 The ProSim Spine Wear Simulator, which comprises six wear and one load-soak station.

Table 11 Capabilities of spine wear simulators

	Endolab[118]	*AMTI*[119]	*Bose spinal*[120]	*MTS Bionix*[121]	*ProSim 5DOF*
X rot (LB)	Active +20°/−15°	Active ±7.5°	Active ±8° or 12 Nm	Active ±10° or 15 Nm	Active ±15°
Y rot (F/E)	Active +30°/−25°	Active ±7.5°	Active ±10° or 10 Nm	Active ±10° or 10 Nm	Active ±15°
Z rot (AR)	Active ±9°	Active ±2°	Active ±6° or 10 Nm	Active ±7.5° or 15 Nm	Active ±15°
X trans (APS)	N/A	N/A	Passive ±4 mm	Passive ±4.5 mm	Active ±5 mm or ±400 N
Y trans (LS)	N/A	N/A	Passive ±4 mm	Passive ±4.5 mm	Passive ±10 mm
Z trans (AC)	Active 5000 N	Active 900–1850 N	Active 2000 N	Active 4000 N or +12.7/−3.2 mm	Active 4000 N

validation to prove that the wear patterns produced by ISO 18192 (or any other loading profile) *in vitro* match those experienced *in vivo*.

Both ISO 18192 and ASTM F 2423 advise testing to be done over a minimum of 10MC (million-cycles), with analysis of test fluid and the core components over at least every 1MC. A definitive number of cycles experienced *in vivo* is as yet to be determined, but 10MC, incorporating a high safety factor, is suggested by ISO 18192 to exceed that required *in vivo*. In previous ISO standard hip studies, 1MC corresponds to the average number of steps per year, and the same could be considered for the spine. However, ASTM have approximated 125 000 significant motions within the spine per year,[114] and so 10MC would be equivalent to up to 80 years *in vivo*. Shorter test runs may be justified as wear in THR/TKR is accepted as steady state after the initial 'running in' period, and this has so far been the case for TDR.[99,122,123]

Measurement protocols currently consist of gravimetric and dimensional measurements, such as coordinate measurement. Other measurement methods to be considered are fluid displacement[124] and a relatively new dimensional method, μCT,[125] both of which have been used to measure wear of explants.

6.614.6.3. Wear Simulation Validation

To date, only a few attempts have been made to validate *in vitro* wear studies with explanted TDR. The ProDisc[126] and Charité[112] have both had *in vivo* and *in vitro* wear scars qualitatively examined, with the size of this attribute proving similar. However, key damage modes such as scratching and impingement were missing in the *in vitro* implants when compared to explants, suggesting that the simulator studies do not capture all *in vivo* conditions.

Height loss comparisons of *in vivo* and *in vitro* Charité suggest that 1MC of the ISO 18192 conditions equates to 5.6 years *in vivo* wear.[127] 1MC of ISO 18192 wear simulation in the lumbar spine (±95% confidence) has been shown to be equivalent to 0.5–1.5 years *in vivo* when comparing height loss alone.[128]

6.614.7. Wear of Metal–PE TDR

Independent four DOF wear tests of metal–PE TDR have shown wear rates to be 0.2–3 mg per MC in cervical implants and 10–20 mg per MC in lumbar devices (Table 12). These levels of wear represent up one-tenth of the wear seen in THR for the cervical case, but similar levels of wear are seen for the lumbar case in comparison to THR. These wear tests produce multidirectional motion on the surface of the PE.

Low cross-shear conditions, where the surface motion is reciprocating resulting in molecular orientation in the principal direction of motion, have been shown to reduce the wear rates in other joint replacements.[115,134] When only three DOF

Table 12 Summary of metal–PE wear rates published in the literature for cervical and lumbar discs

Study	Input conditions	Device	Mean wear rate (mg per MC)
Cervical TDR			
Grupp *et al.*[129]	4DOF	Activ-C	1.0 ± 0.1
Nechtow	4DOF	ProDisc-C	1.99 ± 0.15
Bushelow	4DOF	ProDisc-C	1.82 ± 0.11
Anderson *et al.*[130]	3DOF	Bryan	1.2
Dooris *et al.*[131]	3DOF	Discover	2.82[a]
Dooris *et al.*[131]	4DOF	Experimental	2.1–4.1
Lumbar TDR			
Vicars[128]	4DOF	ProDisc-L	12.7 ± 2.1
		Charité	12.2 ± 1.0
Nechtow *et al.*[122]	4DOF	ProDisc-L	16.59 ± 0.96
		Charité	19.35 ± 1.16
Rawlinson *et al.*[123]	4DOF	ProDisc-L	11.77
Bushelow *et al.*[132]	4DOF	ProDisc-L	9.19[a]
Grupp *et al.*[99]	4DOF	Activ-L	2.70 ± 0.30
Goreham-Voss *et al.*[133]	4DOF	ProDisc-L	16.1 ± 1.4
Nechtow *et al.*[122]	3DOF	ProDisc	0.35 ± 0.01
		Charité	-0.87 ± 0.76
Grupp *et al.*[99]	3DOF	Activ-L	0.14 ± 0.06
Goreham-Voss *et al.*[133]	4DOF (FE-LB in-phase)	ProDisc	6.0 ± 1.3
Vicars[128]	5DOF	ProDisc-L	11.6 ± 1.2
		Charité	22.3 ± 2.0

[a]Reported in mm^3 per MC, converted to mg per MC using PE density of 940 kg m^{-3}.

conditions, or conditions that result in low cross-shear conditions, are used, reductions in the wear rate are seen, with wear at least halved (to 6 mg per MC) to <1 mg per MC (**Table 11**).

AP and lateral shear conditions for wear testing of TDR are not currently specified. However, tests incorporating an additional DOF, AP shear, did not produce any increase in wear rate for the ProDisc.[128] Similar tests of the Charité resulted in a substantial increase in the wear rate (a twofold increase).[128] Motion studies have shown that the addition of the fifth DOF had little effect on the ProDisc motion, but with the Charité, both bearing surfaces were engaged, and so the increase in wear rate appears logical.[135] This study shows that it is also important to consider the effects of device design when comparing wear rates.

Such input-related changes in wear rates indicate that clinically relevant input conditions are important so as to ensure that *in vitro* wear simulations are producing clinically relevant wear rates. The PE wear regimes relating to cross-shear and pressure dependency that are seen in TKR are also present in TDR designs, and so input conditions must include perturbations that consider these phenomenon, as well as classical wear theory.

Cross-linked PE has been used in THR for many years, and has consistently shown reductions in wear rates,[136] and as such is now commonly used. The radiation levels at which TDR PE is sterilized (2.5–4MRads) produce some mild cross-linking, but no intentionally cross-linked PE devices are currently available. In addition to possible reductions in wear rates, cross-linking can increase the brittleness of the PE, thereby leading to increased surface damage due to other processes such as fatigue.

Table 13 Summary of metal–metal wear rates published in the literature for cervical and lumbar discs

Study	Input conditions	Device	Mean wear rate (mm^3 per MC)
Cervical			
Laureysen (SAS6)	3DOF	Kineflex	0.38
Kim (SAS6)	3DOF	M6	0.44
Anderson[137]	3DOF	Prestige	0.18
Lumbar			
Lee *et al.*[138]	3DOF	Experimental design	6.2–15.8
Bushelow *et al.*[139]	4DOF	Maverick	4.91

6.614.8. Wear of Metal–Metal TDR

Published wear rates of metal–metal cervical TDR are 0.1–0.5 mm^3 per MC, similar to those seen in THR (**Table 13**). Despite the low reported wear rates in cervical TDR, independently published wear studies of metal–metal lumbar TDR have shown discouraging results following the use of metal–metal bearing combinations. Wear rates are within the same order of magnitude as those for metal–PE devices, up to 15 mm^3 per MC. The increased load in lumbar TDR may be increasing the wear in comparison to cervical TDR, with the material wear properties conforming to classical wear theory.[140] These large wear rates in comparison to THR and the damage modes seen suggest that preferential lubrication regimes do not occur in metal–metal TDR.[141] These studies show that current metal–metal TDR devices do not produce the wear characteristics that have made metal–metal THR so popular, and so metal–metal bearings may not be suitable for TDR, at least in the lumbar region. Metal–metal wear rates have been shown to be highly dependent on design,[142] and so improved bearing design may lead to improvements in wear rates.

6.614.9. Wear of Alternative Material TDR

The risk of osteolysis with PE bearings, the high wear rate of metal–metal TDR, and the concerns related to the use of noncompliant materials have led to the development of alternative bearing materials. These materials include elastomers, polyaryletheretherketone (PEEK), carbon-reinforced PEEK (CRF-PEEK), and polyaryletherketone (PEK) (**Table 14**).

Although elastomeric discs were developed to be biomechanically similar to natural discs, an added advantage was that the absence of articulating parts would ensure the absence of wear. However, some of the designs that use elastomeric materials involve articulation within the bearing (such as the Bryan), while others involve some rubbing of material (such as NeoDisc). The NeoDisc has been shown to have similar wear rates to other cervical TDR. One-piece elastomeric bearings will not produce wear debris due to articulation, but material loss is still possible due to other factors such as fatigue, erosion, or third-body damage. As such, the effects of these materials both in mass and particulate form must be studied.

PEEK has been shown to be a promising material for artificial joints in THR and TKR,[145,146] producing much lower wear

Table 14 Summary of alternative bearing wear rates published in the literature for TDR

Study	*Input conditions*	*Device*	*Mean wear rate*
Elastomer/ textile[143]	3DOF	NeoDisc	0.56 mm^3 per MC
PEEK-PEEK[144]	3DOF	NUNEC	0.34 mg per MC[a]
PEEK-PEEK[144]	4DOF	NUNEC	0.41 mg per MC[a]
PEEK-PEEK[128]	4DOF	Activ-C	1.4 ± 0.4 mg per MC
CFR-PEEK[128]	4DOF	Activ-C	0.02 ± 0.02 mg per MC
PEK-PEK[128]	4DOF	Activ-C	0.8 ± 0.1 mg per MC

[a]Reported in mm^3 per MC, converted to mg per MC using PEEK density of 1320 $kg\,m^{-3}$.

rates than PE. Tests on PEEK have not shown any decrease in wear rate for the cervical TDR when compared to metal–PE devices. PEK showed a small reduction (50%), but carbon fiber-reinforced PEEK (CFR-PEEK) showed a substantial reduction in wear rates.[128] Further research into alternative bearing materials is necessary in order to reduce wear rates further.

6.614.10. Biological Response to TDR Wear Debris

Although all of the materials used in TDR have a history of successful use in other implants, there is little information as to the effect of these materials in spinal tissues such as the dura and pia mater, and whether wear particles, in particular, could breach these and enter the spinal fluid. Such complications would denote a significant contraindication to any TDR procedure that is capable of producing wear particles (see **Chapter 6.606, Biological Effects of Wear Debris from Joint Arthroplasties**).

6.614.10.1. Biological Response to PE Debris in the Spine

The biological response to PE debris in total joint replacement (TJR) has been well documented and shows that osteolysis and implant loosening lead to late-stage failure in THR and TKR. As such, research on metal–PE bearings has focused on the reduction in wear rates, achieved by improvement in design and/or enhancement of the material properties of the PE by cross-linking. Some have suggested that the lack of a synovial capsule in the spine may be beneficial, in that the PE debris is not contained and so the levels of PE particles do not exceed the osteolytic threshold.

In vitro wear simulations have shown that TDR wear debris has osteolytic potential,[99,100] and evidence of increased osteolytic cytokinanes has been seen clinically as well as in *in vivo* studies,[102,147,148] indicating that an osteolytic response is at least possible, if not likely, within the tissue. Clinical cases of osteolysis around TDR are now beginning to emerge, as early as 8 years after implantation.[101–103]

6.614.10.2. Biological Response to Metal Debris in the Spine

Metal-on-metal implants have been used in THR as the wear rates are much lower than with conventional PE, and the particles have been shown to be less biologically active than PE particles. However, there are long-term concerns regarding the accumulation of metal ions in the body, including concerns associated with genotoxicity and carcinogenesis. The wear rates of metal-on-metal TDR have shown to be much greater than in THR, and so the resulting wear debris is likely to be more damaging.

Studies of titanium debris within spinal tissues have shown that an osteolytic response is also possible with metal–metal devices in the spine.[147,149] Other studies of metal debris have shown that the dura mater, subdural space, nerve roots, and spinal cord were free of reaction in an animal model.[150] Further studies of this type are necessary to ensure the safety of metallic debris around the spine.

6.614.11. Conclusions

Wear studies of TDR are still in their infancy compared with those for THR and TKR. Wear rates have been shown to be comparable, despite the smaller motions experienced by most TDRs, to THR/TKR. Recent studies have investigated the effect of different input conditions, material selection, and device design on wear rates. Biological studies have shown that particles have similar characteristics, and complications due to these particles are at least as serious, when compared to THR/TKR.

Further wear simulation is required to investigate the effects of device design, material selection, and input conditions on the wear behavior of TDR. Monitoring of the wear process *in vivo* is essential to patient safety and to the tracking of the progress of wear *in vivo* and its relation to future complications. Further, clinical validations are essential to determine the appropriateness of *in vitro* wear simulation. Finally, biological studies of wear particles and their effect on the spine must also be accelerated to determine the likelihood of severe complications such as neurological damage and carcinogenesis.

References

1. Fejer, R.; Kyvik, K. O.; Hartvigsen, J. *Eur. Spine J.* **2006**, *15*, 834–848.
2. Frymoyer, J. W.; Cats-Baril, W. L. *Orthop. Clin. North Am.* **1991**, *22*(2), 263–271.
3. Rosen, M. *Back Pain – Report of a CSAG Committee on Back Pain*. Clinical Standards Advisory Group: London, 1994.
4. Cote, P.; Cassidy, J. D.; Carroll, L. *Spine* **1998**, *23*(15), 1689–1698.
5. Croft, P.; Papageorgious, A.; McNally, R. *Health Care Needs Assessment, Series 2*. Radcliffe Medical Press: Oxford, 1997; pp 129–181.
6. Croft, P. *BMJ* **2000**, *8*, 217–258.
7. Barnekow-Bergkvist, M.; Hedberg, G.; Janlert, U.; Jansson, E. *Spine* **1998**, *23*, 235–243.
8. Kissen, D. M. *J. Nerv. Ment. Dis.* **1963**, *136*, 34–42.
9. Katz, J. N. *J. Bone Joint Surg. Am.* **2006**, *88*(Suppl. 2), 21–24.
10. Wipf, J. E.; Deyo, R. A. *Med. Clin. North Am.* **1995**, *79*(2), 231–246.
11. Bao, Q. B.; McCullen, G. M.; Higham, P. A.; Dumbleton, J. H.; Yuan, H. A. *Biomaterials* **1996**, *17*(12), 1157–1167.
12. Errico, T. J. *Spine J.* **2004**, *4*(Suppl. 6), 151S–157S.
13. Boden, S. D.; Davis, D. O.; Dina, T. S.; Patronas, N. J.; Wiesel, S. W. *J. Bone Joint Surg. Am.* **1990**, *72*(3), 403–408.
14. Weinstein, J. N.; Denhoy, R.; Krishnan, A. Disruptive Medical Technologies. The next big thing in spine; North American Equity Research: JP Morgan, 2003.
15. Birkmeyer, J. D.; Stukel, T. A.; Siewers, A. E.; Goodney, P. P.; Wennberg, D. E.; Lucas, F. L. *N. Engl. J. Med.* **2003**, *349*(22), 2117–2127.
16. Gillet, P. *J. Spinal Disord. Tech.* **2003**, *16*(4), 338–345.
17. Kumar, M. N.; Baklanov, A.; Chopin, D. *Eur. Spine J.* **2001**, *10*(4), 314–319.

18. Park, P.; Garton, H. J.; Gala, V. C.; Hoff, J. T.; McGillicuddy, J. E. *Spine* **2004**, *29*(17), 1938–1944.
19. Anderson, P. A.; Rouleau, J. P. *Spine* **2004**, *29*(23), 2779–2786.
20. Neal, C. J.; Rosner, M. K.; Kuklo, T. R. *J. Neurosurg. Spine* **2005**, *3*(5), 342–347.
21. Regan, J. J. *Orthop. Clin. North Am.* **2005**, *36*(3), 323–340.
22. Kapandji, I. *The Physiology of the Joints: The Trunk and the Vertebral Column*. Churchill Livingstone: New York, 1974.
23. Harms, J., Tabasso, G., Eds.; In *Instrumented Spinal Surgery: Principles and Technique*; Georg Thieme Verlag: New York, 1999.
24. Adams, M.; Bogduk, N.; Burton, K.; Dolan, P. *The Biomechanics of Back Pain*. Churchill Livingstone: Edinburgh, 2002.
25. White, A. A.; Panjabi, M. M. *Clinical Biomechanics of the Spine*. Lippincott Williams & Wilkins: Philadelphia, PA, 1990.
26. Bell, G. H.; Dunbar, O.; Beck, J. S.; Gibb, A. *Calcif. Tissue Res.* **1967**, *1*, 75.
27. King, A. I.; Prasad, P.; Ewing, C. L. *Orthop. Clin. North Am.* **1975**, *6*(1), 19–31.
28. Farfan, H. F. *Mechanical Disorders of the Low Back*. Lea & Febiger: Philadelphia, PA, 1973.
29. Huang, R. C.; Girardi, F. P.; Cammisa, F. P., Jr.; Wright, T. M. *J. Spinal Disord. Tech.* **2003**, *16*(4), 412–417.
30. Lemaire, J. P.; Skalli, W.; Lavaste, F.; *et al*. *Clin. Orthop. Relat. Res.* **1997**, *337*, 64–76.
31. Patel, V. In *Spine Arthroplasty 5: Global Symposium on Motion Preservation Technology*, Spine Arthroplasty Society, New York, 2005.
32. Mayer, H. M. *J. Bone Joint Surg. Br.* **2005**, *87*(8), 1029–1037.
33. Shim, C. S.; Lee, S.-H.; Shin, H.-D.; *et al*. *Spine* **2007**, *32*(9), 1012–1018.
34. Bogduk, N. *Clinical Anatomy of the Lumbar Spine and Sacrum*. Elsevier Churchill Livingstone: Edinburgh, 2005.
35. Race, A.; Broom, N. D.; Robertson, P. *Spine* **2000**, *25*(6), 662–669.
36. Smeathers, J. E. *Curr. Orthop.* **1994**, *8*, 45–48.
37. Wilke, H. J.; Wenger, K.; Claes, L. *Eur. Spine J.* **1998**, *7*(2), 148–154.
38. Gatton, M. L.; Pearcy, M. J. *Clin. Biomech.* **1999**, *14*(6), 376–383.
39. Pearcy, M. J.; Tibrewal, S. B. *Spine* **1984**, *9*(6), 582–587.
40. Moroney, S.; Schultz, A.; Miller, J. *J. Orthop. Res.* **1988**, *6*, 713–720.
41. Callaghan, J. P.; McGill, S. M. *Ergonomics* **2001**, *44*(3), 280–294.
42. Callaghan, J. P.; Patla, A. E.; McGill, S. M. *Clin. Biomech.* **1999**, *14*(3), 203–216.
43. Rohlmann, A.; Claes, L. E.; Bergmann, G.; Graichen, F.; Neef, P.; Wilke, H. J. *Ergonomics* **2001**, *44*(8), 781–794.
44. Rohlmann, A.; Bergmann, G.; Graichen, F. *Eur. Spine J.* **1999**, *8*(5), 354–359.
45. Dennis, G. J.; Barrett, R. S. *Ergonomics* **2002**, *45*(10), 671–681.
46. Ferguson, S. A.; Gaudes-MacLaren, L. L.; Marras, W. S.; Waters, T. R.; Davis, K. G. *Ergonomics* **2002**, *45*(6), 399–414.
47. Kumar, S.; Moro, L. I. L.; Narayan, Y. *Ergonomics* **2003**, *46*(5), 502–517.
48. Lansade, C.; Laporte, S.; Thoreux, P.; Rousseau, M.-A.; Skalli, W.; Lavaste, F. *Spine* **2009**, *34*(26), 2900–2906.
49. Goel, V. K.; Clark, C. R.; McGowan, S.; Goyal, S. *J. Biomech.* **1984**, *17*(5), 363–376.
50. Auerbach, J. D.; Wills, B. P. D.; McIntosh, T. C.; Balderston, R. A. *Spine* **2007**, *32*(5), 527–536.
51. SariAli, E.-H.; Lemaire, J. P.; Pascal-Mousselard, H.; Carrier, H.; Skalli, W. *Eur. Spine J.* **2006**, *15*(10), 1501–1510.
52. Panjabi, M. P.; Summers, D.; Pelker, R. R.; Videman, T. M. D. P.; Friedlaender, G. E.; Southwick, W. O. *J. Orthop. Res.* **2005**, *4*(2), 152–161.
53. Campana, S.; deGuise, J. A.; Rillardon, L.; Mitton, D.; Skalli, W. *Eur. J. Orthop. Surg. Traumatol.* **2007**, *17*, 533–541.
54. Pearcy, M. J. *Acta Orthop.* **1985**, *56*(1), 1–45.
55. Gertzbein, S. D.; Seligman, J.; Holtby, R.; *et al*. *Spine* **1985**, *10*(3), 257–261.
56. Rolander, S. D. *Acta Orthop. Scand.* **1966**, *90*(Suppl.), 1–144.
57. Akeson, W. H.; Woo, S. Y. L.; Taylor, T. K. F.; Ghosh, P.; Bushell, G. R. *Clin. Orthop. Relat. Res.* **1977**, *129*, 133–139.
58. McNally, D. S.; Adams, M. A. *Spine* **1992**, *17*, 66–73.
59. Fujita, K.; Nakagawa, T.; Hirabayashi, K.; Nagai, Y. *Spine* **1993**, *18*, 1766–1773.
60. Geisler, F. H.; Blumenthal, S. L.; Guyer, R. D.; *et al*. *J. Neurosurg. Spine* **2004**, *1*(2), 143–154.
61. Chidambaram, R.; Cobb, A. G. EFORT – European Federation of National Associations of Orthopaedics and Traumatology (8th Congress. *J. Bone Joint Surg. Br Vol.* **2007**, *91B*, 152.
62. McAfee, P. C.; Fedder, I. L.; Saiedy, S.; Shucosky, E. M.; Cunningham, B. W. *Spine* **2003**, *28*(20), S153–S162.
63. Pimenta, L.; Arias Pesantez, C.; Oliviera, L.; Lhamby, J.; Schaffa, T.; Coutinho, E. In *Spine Arthroplasty Society 8: Global Symposium on Motion Preservation Technology*, Miami, FL, 2008.
64. Pimenta, L.; Guerreiro, L. In *Spine Arthroplasty 6: Global Symposium on Motion Preservation Technology*; Spine Arthroplasty Society: Montreal, QC, 2006.
65. NICE. *Interventional Procedures Programme: Prosthetic Intervertebral Disc Replacement*; National Institute for Clincal Excellence: London, 2004.
66. McAfee, P. C.; Cunningham, B. W.; Devine, J.; Williams, E.; Yu-Yahiro, J. *J. Spinal Disord. Tech.* **2003**, *16*(4), 384–389.
67. van Ooij, A.; Oner, F. C.; Verbout, A. J. *J. Spinal Disord. Tech.* **2003**, *16*(4), 369–383.
68. Brau, S. A. *Spine J.* **2002**, *2*, 216–223.
69. Kostuik, J. P. *Spine J.* **2004**, *4*(6 Suppl. 1), S289–S291.
70. Spivak, J.; Petrizzo, D. O. In *Spine Arthroplasty 6: Global Symposium on Motion Preservation Technology*, Spine Arthroplasty Society: Montreal, QC, 2006.
71. Tropiano, P.; Huang, R. C.; Girardi, F. P.; Cammisa, F. P., Jr.; Marnay, T. *J. Bone Joint Surg. Am.* **2005**, *87*(3), 490–496.
72. Geisler, F. H.; McAfee, P. C.; Banco, R. J.; *et al*. *SAS J.* **2009**, *3*(1), 17–25.
73. Zigler, J.; Delamarter, R. B.; Spivak, J.; *et al*. *Spine* **2007**, *32*(11), 1155–1162.
74. Pettine, K.; Donner, E. In *Spine Arthroplasty Society 8: Global Symposium on Motion Preservation Technology*, Miami, FL, 2008.
75. Riew, D.; Buchowski, J.; Sasso, R.; Zdeblick, T.; Metcalf, N. H.; Anderson, P. A. *J. Bone Joint Surg. Am.* **2008**, *90*, 2354–2364.
76. Murrey, D.; Janssen, M.; Delamarter, R. B.; *et al*. *Spine J.* **2009**, *9*(4), 275–286.
77. Cinotti, G.; David, T.; Postacchini, F. *Spine* **1996**, *8*, 995–1000.
78. Regan, J. J.; McAfee, P.; Guyer, R.; Blumenthal, S. L.; Geisler, F. H. In *Spine Arthroplasty 5: Global Symposium on Motion Preservation Technology*, Spine Arthroplasty Society: New York, 2005.
79. Regan, J. J.; McAfee, P. C.; Blumenthal, S. L.; *et al*. *Spine* **2006**, *31*(19), 2270–2276.
80. Huang, R. C.; Girardi, F. P.; Cammisa, F. P., Jr.; Tropiano, P.; Marnay, T. *J. Spinal Disord. Tech.* **2003**, *16*(5), 435–440.
81. Cunningham, B. W.; Gordon, J. D.; Dmitriev, A. E.; Hu, N.; McAfee, P. C. *Spine* **2003**, *28*(20), S110–S117.
82. Schlegel, J. D.; Smith, J. A.; Schleusener, R. L. *Spine* **1996**, *21*, 970–981.
83. Magora, A.; Schwartz, A. *Scand. J. Rehabil. Med.* **1980**, *12*, 47–52.
84. Splithoff, C. *J. Am. Med. Assoc.* **1953**, *152*(17), 1610–1613.
85. VonLackum, H. *J. Am. Med. Assoc.* **1924**, *82*, 1109.
86. Cakir, B.; Richter, M.; Kafer, W.; Puhl, W.; Schmidt, R. *Clin. Biomech.* **2005**, *20*(4), 357–364.
87. Chung, S. S.; Lee, C. S.; Kang, C. S.; Kim, S. H. *J. Spinal Disord. Tech.* **2006**, *19*(5), 307–311.
88. Phillips, F.; Diaz, R.; Pimenta, L. In *Spine Arthroplasty 5: Global Symposium on Motion Preservation Technology*, Spine Arthroplasty Society: New York, 2005.
89. Rousseau, M.-A.; Bradford, D. S.; Bertagnoli, R.; Hu, S. S.; Lotz, J. C. *Spine J.* **2006**, *6*(3), 258–266.
90. Dooris, A. P.; Goel, V. K.; Grosland, N. M.; Gilbertson, L. G.; Wilder, D. G. *Spine* **2001**, *26*(6), E122–E129.
91. Kurtz, S. M.; Van Ooij, A.; Ross, E. R. S.; *et al*. *Spine J.* **2006**, *7*(1), 12–21.
92. Mathew, P.; Blackman, M.; Redla, S.; Hussein, A. A. *Spine* **2005**, *30*(11), E311–E314.
93. Bertagnoli, R.; Yue, J. J.; Shah, R. V.; *et al*. *Spine* **2005**, *30*(19), 2192–2199.
94. Lemaire, J.-P.; Carrier, H.; Sari Ali, E.-H.; Skalli, W.; Lavaste, F. *J. Spinal Disord. Tech.* **2005**, *18*(4), 353–359.
95. Shim, C. S.; Lee, S.; Maeng, D. H.; Lee, S.-H. *J. Spinal Disord. Tech.* **2005**, *18*(5), 465–469.
96. Tropiano, P.; Huang, R. C.; Girardi, F. P.; Marnay, T. *J. Spinal Disord. Tech.* **2003**, *16*(4), 362–368.
97. Bertagnoli, R.; Yue, J. J.; Nanieva, R.; *et al*. *J. Neurosurg. Spine* **2006**, *4*(2), 85–90.
98. Yue, J. J.; Bertagnoli, R.; Fen-Mayer, A.; Lee, R.; Kirk, J.; Karg, A. In *Spine Arthroplasty 6: Global Symposium on Motion Preservation Technology*; Spine Arthroplasty Society: Montreal, QC, 2006.
99. Grupp, T. M.; Yue, J. J.; Garcia, R.; *et al*. *Eur. Spine J.* **2009**, *18*, 98–108.
100. Tipper, J. L.; Marsh, R.; Vicars, R.; *et al*. In *Spine Arthoplasty Society 9: Symposium on Motion Preservation Technology*, Spine Arthroplasty Society: London, 2009.
101. Devin, C. J.; Myers, T. G.; Kang, J. D. *J. Bone Joint Surg. Am.* **2008**, *90*(10), 2230–2234.
102. Punt, I.; Cleutjens, J. P. M.; de Bruin, T.; *et al*. *Biomaterials* **2009**, *30*, 2079–2084.
103. van Ooij, A. M.; Kurtz, S. M.; Stessels, F.; Noten, H.; van Rhijn, L. *Spine* **2007**, *32*(2), 223–229.
104. Kurtz, S. M.; Lau, E.; Ianuzzi, A.; *et al*. In *55th Annual Meeting of the Orthopaedic Research Society*; Orthopaedic Research Society: Las Vegas, NV, 2009.

105. Anderson, P. A.; Riew, D.; Sasso, R. In *SAS8 Global Symposium on Motion Preservation Technology 8th Annual Meeting*, Miami, FL, 2008.
106. Phillips, F.; Singh, K.; Shah, J.; An, H.; Goldberg, E.; Andersson, G. B. In *SAS8 Global Symposium on Motion Preservation Technology 8th Annual Meeting*; Spine Arthroplasty Society: Miami, FL, 2008.
107. Patil, A. A. Artificial Intervertebral Disc. U.S. Patent 4,309,777, Jan 12, 1982.
108. Baumgartner, W. Intervertebral Disk Prosthesis. U.S. Patent 5,320,644, Jun 14, 1994.
109. Hedman, T. P.; Kostuik, J. P.; Fernie, G. R.; Maki, B. E. Artificial Spinal Disc. U.S. Patent, Health & Research Services Inc., 4,759,769, 1988.
110. Lemaire, J.-P.; Carrier, H.; Sari-Ali, E.-H.; Skalli, W.; Lavaste, F. *J. Spinal Disord. Tech.* **2005**, *18*(4), 353–359.
111. Kurtz, S. M.; Van Ooij, A.; Peloza, J.; *et al*. In *Spine Arthroplasty 5: Global Symposium on Motion Preservation Technology*; Spine Arthroplasty Society: New York, 2005.
112. Kurtz, S. M.; van Ooij, A.; Ross, R.; *et al*. *Spine J.* **2007**, *7*(1), 12–21.
113. BS ISO 18192-1. Implants for surgery – wear of total intevertebral spinal disc prostheses – Part 1: Loading and displacement parameters for wear testing and corresponding environmental conditions for test, 2008.
114. ASTM F 2423-05. Standard Guide for Functional, Kinematic, and Wear Assessment of Total Disc Prostheses, 2005.
115. McEwen, H. M. J.; Barnett, P. I.; Bell, C.; *et al*. *J. Biomech.* **2005**, *38*, 357–365.
116. ASTM F 732-00. Standard Test Method for Wear Testing of Polymeric Materials Used in Total Joint Prostheses, 2003.
117. Bullough, P. G.; DiCarlo, E. F.; Hansraj, K. K.; Neves, M. C. *Orthop. Clin. North Am.* **1988**, *19*(3), 611–625.
118. Endolab Spine simulator. Retrieved July 21, 2006, from www.endolab.de.
119. AMTI-Boston 12 station Hip simulator model HS2-12-1000. Retrieved July 21, 2006, from http://www.amtiweb.com/brochures/hipknee.pdf#search=%22AMTI%20Boston%20simulator%22.
120. Bose Spinal wear simulator. Retrieved July 21, 2006, from www.bose-electroforce.com/products/moreinfo/MoreInfoSpinalDisc.html.
121. MTS Bionix spinal disc fatigue/wear simulator. Retrieved July 21, 2006, from http://www.mts.com/stellent/groups/public/documents/library/dev_002173.pdf.
122. Nechtow, W.; Hinter, M.; Bushelow, M.; Kaddick, C. In *Orthopaedic Research Society Meeting*, Chicago, IL, 2006.
123. Rawlinson, J. J.; Punga, K. P.; Gunsallus, K. L.; Bartel, D. L.; Wright, T. M. *J. Neurosurg. Spine* **2007**, *7*(2), 165–173.
124. Yamamoto, K.; Imakiire, A.; Masaoka, T.; *et al*. *Int. Orthop.* **2003**, *27*(5), 286–290.
125. Kurtz, S. M.; Peloza, J.; Siskey, R.; Villarraga, M. L. *Spine J.* **2005**, *5*(3), 344–350.
126. Wright, T. M.; Chen, D.; Kelly, N. In *Ninth Annual Global Symposium on Motion Preservation Technology*, The International Society for the Advancement of Spine Surgery: London, 2009.
127. Kurtz, S. M.; Ianuzzi, A.; Siskey, R.; *et al*. In *Spine Week 2008 Meeting*, Geneva, Switzerland, 2008.
128. Vicars, R. Ph.D. Thesis, *School of Mechanical Engineering*, University of Leeds: Leeds, 2009; p 186.
129. Grupp, T. M.; Meisel, H.-J.; Cotton, J. A.; *et al*. *Biomaterials* **2010**, *31*, 523–531.
130. Anderson, P.; Rouleau, J. P.; Bryan, V. E.; Carlson, C. E. *Spine* **2003**, *28*(20 S), S186–S194.
131. Dooris, A.; Hester, D.; Albert, T.; Ares, P. In *SAS7: Spine Arthroplasty Society Global Symposium on Motion Preservation Technology*, Berlin, Germany, 2007.
132. Bushelow, M.; Nechtow, W.; Walker, J.; Hinter, M.; Ochs, A.; Kaddick, C. In *Spine Arthroplasty Society 8: Global Symposium on Motion Preservation Technology*, Miami, FL, 2008.
133. Goreham-Voss, C.; Hyde, P. J.; Hall, R. M.; Fisher, J.; Brown, T. D. In *SAS10 – 10th Annual Global Symposium on Motion Preservation Technology*; Spine Arthroplasty Society: New Orleans, LA, 2010.
134. Kang, L.; Galvin, A. L.; Brown, T. D.; Fisher, J.; Jin, Z. M. *Proc. Inst. Mech. Eng. H J. Eng. Med.* **2008**, *222*(7), 1049–1064.
135. Vicars, R.; Chyuan Loo, F.; Goreham-Voss, C.; *et al*. In *ORS 2010*; Orthopaedic Research Society: New Orleans, LA, 2010.
136. Endo, M. M.; Barbour, P. S.; Barton, D. C.; *et al*. *Biomed. Mater. Eng.* **2001**, *11*(1), 23–35.
137. Anderson, P. A. *J. Neurosurg. Spine* **2004**, *2*(1), 202–210.
138. Lee, J. L.; Billi, F.; Sangiorgio, S. N.; *et al*. *Spine* **2008**, *33*(6), 597–606.
139. Bushelow, M.; Walker, J.; Coppes, J.; Hinter, M.; Nechtow, W.; Kaddick, C. *Spine J.* **2008**, *7*, 97S–98S.
140. Archard, J. F. *J. Appl. Phys.* **1953**, *24*, 981–988.
141. Shaheen, A.; Shepherd, D. E. T. *Proc. Inst. Mech. Eng. H J. Eng. Med.* **2007**, *221*, 621–627.
142. Goldsmith, A. A. J.; Dowson, D.; Isaac, G. H.; Lancaster, J. G. *Proc. Inst. Mech. Eng. H J. Eng. Med.* **2000**, *214*(1), 39–47.
143. Reah, C.; Lewis, D. In *SAS7: Spine Arthroplasty Society Global Symposium on Motion Preservation Technology*, Berlin, Germany, 2007.
144. Brown, T.; Bao, Q.-B.; Hallab, N. In *SAS 9: Ninth Annual Global Symposium on Motion Preservation Technology*; Spine Arthroplasty Society: London, 2009.
145. Scholes, S. C.; Inman, I. A.; Unsworth, A.; Jones, E. *Proc. Inst. Mech. Eng. H J. Eng. Med.* **2008**, *222*, 273–283.
146. Scholes, S. C.; Unsworth, A. *Proc. Inst. Mech. Eng. H J. Eng. Tribol.* **2009**, *223*, 13–25.
147. Cunningham, B. W.; Orbegoso, C. M.; Dmitriev, A. E.; *et al*. *Spine J.* **2003**, *3*(1), 19–32.
148. Hallab, N. J.; Cunningham, B. W.; Jacobs, J. J. *Spine* **2003**, *28*(20), S125–S138.
149. Chang, B.-S.; Brown, P. R.; Sieber, A.; Valdevit, A.; Tateno, K.; Kostuik, J. P. *Spine J.* **2004**, *4*(Suppl. 6), 239S–244S.
150. Rhalmi, S.; Charette, S.; Assad, M.; Coillard, C.; Rivard, C. *Eur. Spine J.* **2007**, *16*(7), 1063–1072.

Relevant Websites

http://en.wikipedia.org/wiki/Intervertebral_disc_arthroplasty – Wikipedia – Total Disc Replacement.
http://www.spine.org/Pages/Default.aspx – North American Spine Society.
http://journals.lww.com/spinejournal/pages/default.aspx – The Spine Journal.
http://www.eurospine.org/p31000409.html – EuroSpine, the Spine Society of Europe.
http://www.springerlink.com/content/101557/ – The European Spine Journal.

6.615. Intervertebral Disc

R D Bowles and L J Bonassar, Department of Biomedical Engineering, Cornell University, Ithaca, NY, USA

© 2011 Elsevier Ltd. All rights reserved.

6.615.1.	**Background**	208
6.615.1.1.	Spinal Fusion	208
6.615.1.1.1.	Bone grafts	208
6.615.1.1.2.	Synthetic bone grafts	209
6.615.1.1.3.	Demineralized bone matrix	209
6.615.1.1.4.	Growth factors and gene therapy	209
6.615.1.2.	Motion Preservation	209
6.615.1.2.1.	Total disc replacement	209
6.615.1.2.2.	Dynamic stabilization	209
6.615.1.2.3.	IVD transplantation	210
6.615.1.2.4.	Regenerative medicine and tissue engineering approaches to motion preservation	210
6.615.2.	**IVD Structure and Function**	210
6.615.2.1.	Extracellular Matrix	211
6.615.2.2.	Organization	211
6.615.3.	**IVD Preservation, Repair, and Regeneration**	211
6.615.3.1.	Nuclear Replacement	212
6.615.3.1.1.	Acellular	212
6.615.3.1.2.	Cellular	212
6.615.3.2.	Annular Repair	213
6.615.3.2.1.	Acellular	213
6.615.3.2.2.	Cellular	213
6.615.3.3.	Total Disc Replacement	214
6.615.4.	**Future Challenges**	216
References		217

Glossary

Allograft Transplanted tissue from the same species but from different individual.
Autograft Transplanted tissue obtained from self.
Discogenic Originating from the intervertebral disc.
Fibrocartilage Tissue having both cartilaginous and fibrous tissue properties usually containing both collagen type I and proteoglycans in varying proportions.
Herniation Protrusion of nucleus pulposus tissue through disruptions in the annulus fibrosus.
Hydrogel Colloidal gel containing water as liquid constituent.
In situ Latin for 'in the place.'
Notochordal Originating from the notochord structure in embryos from which the spinal column develops.
Osteoconductive Having the ability to promote the ingrowth of bone.
Osteogenic Having the ability to deliver bone-forming cells.
Osteoinductive Having the ability to promote the differentiation of undefined cells into osteoprogenitor cells.
Osteolysis Resorption of bone in response to disease state.
Proteoglycan Heavily glycosylated glycoprotein with one or more covalently bound glycosaminoglycan chains.
Radiculopathy Disease of the spinal nerve root or nerves.
Spinal stenosis Narrowing of the spinal canal.

Abbreviations

AF	Annulus fibrosus
BMP	Bone morphogenic protein
ECM	Extracellular matrix
FDA	Food and drug administration
IVD	Intervertebral disc
MSC	Mesenchymal stem cells
NP	Nucleus pulposus
PCL	Polycaprolactone
PEG	Polyethylene glycol
PGA	Polyglycolic acid
PLA	Polylactic acid
PLLA	Poly-L-lactide
PMMA	Poly(methyl methacrylate)
rhBMP	Recombinant human bone morphogenic protein
SIS	Small intestine submucosa
TDR	Total disc replacement
TE-TDR	Tissue-engineered total disc replacement

6.615.1. Background

Intervertebral disc (IVD) degeneration is a leading cause of disability in the developed world, with ~65 million people in the United States alone suffering from prolonged back pain.[1] Although, a direct connection between pain and IVD degeneration is not always evident, the vast majority of chronic spine ailments involve some amount of disc degeneration. Moreover, by age 50, more than 85% of the population will have some evidence of this disease.

Degenerative disc disease can lead to a number of pathological conditions that can cause pain and discomfort. Due to the proximity of the IVD to the nerve roots, protruding disc material can impinge the local nerve roots causing radiculopathy.[2] In addition, peripheral sensitization and neoinnervation of the nerve fibers located in the outer lamellae of the annulus fibrosus (AF) and endplate can result in pain due to disc degeneration, and altered mechanical stimuli.[3] Furthermore, disc degeneration and herniation are associated with inflammation and immune response that can lead to neuritis and increased sensitivity in the nerves.[4] Finally, alterations in the AF and nucleus pulposus (NP) composition and structure lead to hypermobility in the spine that can result in greater inflammation and stimulation of the sensitized nerves. One of the difficulties of treating pain resulting from the IVD is the complex interactions between the inflammation, innervation, hypermobilitiy, and stenosis observed in IVD pathology. These interactions are currently an active area of investigation, as they are not fully understood to date.

The cost of treatment of degenerative disc diseases and its associated symptoms is estimated to be in excess of $50 billion per year in the United States. Due to the prominence of this disorder, a number of materials are currently being used for the treatment of degenerative disc disease (**Table 1**). Because the primary presentation of these disorders is pain, surgical treatments are primarily palliative, with less, if any, focus on restoring function to the diseased tissue.

6.615.1.1. Spinal Fusion

One of the most common surgical treatments is partial or complete discectomy, in which the IVD is removed in an attempt to eliminate the source of the pain, whether the pain is caused by the impingement of the nerve root or discogenic in origin. In the case of complete discectomy, the spine must be stabilized through the fusion of the vertebral bodies. This allows the pain-inducing disc to be removed, but results in the loss of mobility at the operated motion segment. As a result, it is necessary for the remaining motion segments to provide the required flexibility to the spine. In addition, it is essential to maintain the anatomy of the spine to protect the integrity of the intertwined nervous system. This includes the disc space height that was originally maintained by the IVD.

This is accomplished by implanting autologous bone grafts, cadaveric allografts, or bone graft substitutes in the disc space in combination with rods, screws, plates, or cages. The hardware is designed to provide stabilization to the spine while the grafts are implanted to promote bone formation between the vertebral bodies during fusion. An optimal material used for spinal fusion will have an osteoconductive scaffold that promotes the ingrowth of bone, osteogenic capabilities that provide cells to the fusion site, and osteoinductive factors that promote the differentiation of progenitor cells into osteoblast cells. The materials currently used all have at least one of these properties and multiple materials are being combined to maximize these properties in many cases.

6.615.1.1.1. Bone grafts

Bone grafts were the first material choice in promoting a fusion between the vertebral bodies.[5] They provide the exact material that is desired in the disc space and in the case of autografts are osteogenic, osteoconductive, and osteoinductive. As a result, the material could be harvested from the patient and implanted in the disc space to promote fusion between the vertebral bodies while maintaining the disc space height formally maintained by the IVD. The two types of bone grafts available are autografts and allografts.

Autografts are obtained from the patient's own bone and are usually obtained from the iliac crest of the pelvis. Autografts provide the highest likelihood of fusion due to the presence of bone, osteoblasts, and bone morphogenetic proteins (BMPs). However, autografts can result in donor site morbidity and chronic pain at the harvest site.[6,7] In contrast, allografts are obtained from a human source other than the patient. This bone is acquired from tissue banks and circumvents the issues of donor site pain and morbidity but introduce the possibility of disease transmission. When used alone, allografts tend to underperform autografts in producing a successful fusion.[8–11] This is likely due to the lack of osetogenic cells and minimal osteoinductive factors contained in the allograft despite its osteoconductive scaffold. The allografts cells are purposefully removed during processing to reduce the likelihood of an immune response caused by the foreign cells.

Table 1 Current treatments for degenerative disc disease

Treatment	*Physical therapy*	*Partial discectomy*	*Spinal fusion*	*Total disc replacement*	*Dynamic stabilization*	*IVD transplant*	*Tissue-based regeneration*
Disease severity	Mild–moderate	Moderate–severe	Severe	Severe	Moderate–severe	Severe	Mild–severe
Biomaterials	NA	NA	Autograft bone, allograft bone, demineralized bone, matrix, growth factors	Metal/polyethylene articulating joint	Metal/polyethylene screws, cords, spacers, flexible rods, flexible screws	Allograft IVD	Broad range of hydrogels, fibrous materials, and cells

Currently, in an attempt to increase the likelihood of fusion, adult stem cells are being investigated as a possible way to overcome the lack of living cells in allografts.[12]

6.615.1.1.2. Synthetic bone grafts

Autografts and allografts are both limited in supply since they require a donor and donor site. Synthetic bone grafts, on the other hand, could mimic the properties of bone and provide a material to promote fusion while circumventing the autograft/allograft cons of supply, donor site morbidity, donor site pain, and disease transmission. Bone has both an organic (collagen type I) and inorganic (hydroxyapatite) component. Synthetic bone grafts attempt to mimic the compositional content of the bone, usually the inorganic component, to provide a biodegradable osteoconductive scaffold to promote fusion. This involves producing calcium containing crystalline solids with porosity similar to that of bone that will promote bone ingrowth.

A number of synthetic materials designed to mimic the properties of bone, including various ceramics, are being investigated for use in fusion procedures. These materials are osteoconductive but, similar to allografts, do not contain cells. For this reason, they are often used in combination with autografts as bone graft extenders. The most commonly used materials are coralline hydroxyapatite, β-tricalcium phosphate, and calcium sulfate.[13–15] The use of these materials as an extender allows for less autograft material to be harvested, thus decreasing the risk of donor site morbidity and pain (see **Chapter 6.612, Biomaterials for Intervertebral Disc Regeneration**).

6.615.1.1.3. Demineralized bone matrix

While allografts and synthetic bone grafts provide an osteoconductive scaffold, they fail to provide substantial osteoinductive proteins to stimulate bone growth. The combination of both osteoconductive and osteoinductive properties similar to that found in autografts can further promote fusion beyond what an osteoconductive scaffold can produce alone.

Used as a bone graft extender, demineralized bone matrix is obtained by removing the mineralized component of allograft bone by acid extraction. The resulting matrix is predominantly type I collagen in addition to various growth factors including BMPs. As a result, demineralized bone matrix is both osteoconductive and osteoinductive. However, the mechanical stiffness of demineralized bone matrix are much lower than that of bone and must be used in combination with a material that can provide the necessary structural strength when implanted. For this reason, the material is used primarily as a bone graft extender to introduce the osteoconductive proteins into the disc space.

6.615.1.1.4. Growth factors and gene therapy

Both autografts and demineralized bone matrix have osteoinductive proteins and demonstrate the ability of these proteins to stimulate bone growth. As a result, it is advantageous to develop techniques that allow these osteoinductive proteins to be utilized for spinal fusion in combination with techniques other than autografts and demineralized bone matrix. In addition, recombinant production of growth factors enables greater control of the types and concentrations of growth factors delivered to the fusion site.

A number of growth factors including BMPs have been shown to be osteoinductive. As a result, the use of recombinant forms of these proteins has been combined with osteoconductive materials to be utilized in spinal fusion surgeries. Human trials have shown increased success over autografts when using either recombinant human bone morphogenic protein 2 (rhBMP-2) or rhBMP-7 in combination with a number of carrier matrices including collagen sponges, collagen type I powder, allograft bone, and ceramic granules.[16–20] Overall, this provides a technique that is both osteoconductive and osteoinductive without requiring autograft harvesting.

One of the drawbacks of rhBMPs is their soluble nature and high doses need to be inserted in the carrier matrix to be effective over a sustained period of time. As a result, the associated cost of this type of procedure is quite high. One possible solution is to utilize gene therapy to introduce the osteoinductive BMPs to the fusion site. Such a technique allows sustained production of the BMPs at the fusion site without having to insert large amounts of rhBMP into the carrier. Currently, a number of animal studies are being performed to test the efficacy of such strategies and investigate the safety concerns related to gene therapy[21–23] (see **Chapter 5.522, Bone Tissue Engineering: Growth Factors and Cytokines**).

6.615.1.2. Motion Preservation

Despite the common use of spinal fusion for the treatment of various spinal complications, the procedure produces a number of deleterious consequences. First the fusion of the vertebral body results in a loss of motion at the fused site and often leads to adjacent-level degeneration thought to be caused by the altered mechanical loading at the adjacent levels.[24,25] For this reason, a number of devices have been designed to preserve the motion of the IVD at the operated level.

6.615.1.2.1. Total disc replacement

Similar to what is performed in the knee and hip, the first attempts to preserve motion as an alternative to fusing the vertebral bodies were total disc replacement (TDR) strategies. In this procedure, the entire disc is removed and replaced by an artificial joint containing an articulating surface designed to provide motion to the joint segment (**Figure 1**). The devices reaching clinical trial have contained either two metal alloy endplates with an ultra high molecular weight polyethylene articulating surface (Charité® and ProDisc®) or have a metal on metal design (Prestige®, Flexicore®, and Kineflex®). Currently, the Charité®, ProDisc®, and Prestige® have received food and drug administration (FDA) approval. Relatively short-term data indicates that these devices have been successful in reducing adjacent level degeneration[26,27]; however, it is unclear whether this will be true in the long term. Furthermore, it appears that these discs may suffer from polyethylene wear,[28,29] which could lead to osteolysis, dislodgement, and failure of the device. As a result, further investigation will need to be carried out to understand the long-term efficacy of the TDR strategy.

6.615.1.2.2. Dynamic stabilization

In addition to TDR, a new class of devices is currently being investigated for treatment of spinal disorders. These devices are designed to provide controlled motion at the disc level without

replacing the entire disc level. The devices attach to the posterior elements of the spine and are composed of some combination of screws, cords, spacers, flexible rods, and flexible screws. One example of such a system is the Dyneses® system, which has received FDA approval as an adjunct to spinal fusion surgeries but is not approved as a stand-alone device, although clinical trials are underway (Figure 2). The Dyneses® system is made of pedical screws, surgical polyurethane spacers, and polyethylene cords. This combination of parts is designed to maintain motion in a controlled manner that will decrease pain but allow motion similar to that of the healthy motion segment. Many similar devices can be imagined and quite a few are currently under investigation for the treatment of spinal disorders.[30,31]

6.615.1.2.3. IVD transplantation

In addition to using hardware to maintain motion and stability in the diseased spine, a novel technique of transplanting cadaveric IVDs is being investigated. The hypothesis behind this procedure is that the transplanted healthy native tissue will most accurately restore the complex function of the IVD to the spine while relieving the pain and circumventing the issues associated with using traditional metal/polyethylene materials. In this method, segments of the boney vertebral bodies are left on either end of the IVD in order to promote integration of the transplanted disc into the motion segment. The low vascularity of the IVD reduces the risk of tissue rejection and allows the procedure to be performed without immunosuppressant drugs.

IVD transplantation was originally investigated in canine[32–34] and primate[35,36] animal models and has now been tested in a small number of human patients.[37] Animal models showed that the transplanted discs were able to successfully integrate with the native tissue by 6 months and form functional motion segments after an initial period of hypermobility (2–4 months). However, despite forming functional motion segments, a loss of water and proteoglycans were observed in allografts from 6 to 24 months. In addition, nucleus cells had an irregular shape and mitochondrial swelling at 24 months. These findings indicate that the transplanted IVDs are capable of integrating and forming functional motion segments; however, they show signs of degeneration over time after implantation. Immune response was localized to the boney interfaces. Human trials in five patients have met with success as patients show no signs of significant pain at a 5-year follow-up. Radiologically, patients showed minimal disc height loss and a normal range of motion.

Overall, the animal models and early clinical results on IVD transplantation are promising. However, it will be important to carry out studies in a larger cohort of patients and investigate the long-term survival of the transplants. In addition, despite the apparent success of the procedure, IVD transplantation suffers from limited donor tissue, issues of size matching, and possible disease transmission. As a result, regenerative techniques are also being investigated for IVD tissue replacement.



Figure 1 Total disc replacement – Charité.

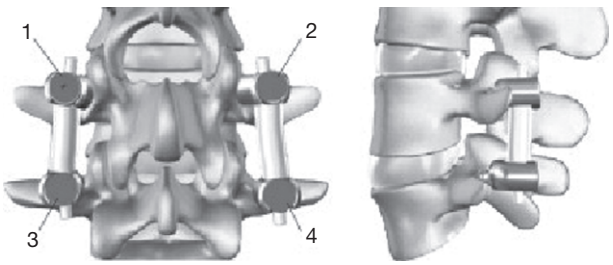

Figure 2 Dynamic stabilization – Dyneses system.

6.615.1.2.4. Regenerative medicine and tissue engineering approaches to motion preservation

Despite the development of TDR and dynamic stabilization devices, the long-term success that these devices will have in reducing adjacent segment degeneration remains unclear. While these devices are promising, it is likely that these devises will suffer from long-term failure modes (wear, fatigue, and loosening via osteolysis) similar to that of other traditional knee and hip polymer/metal implants. For these reasons, acellular and cellular tissue-based approaches that mimic the native IVD extracellular matrix (ECM) composition and architecture may be advantageous. The cellular component would allow the tissue to be remodeled and repaired over the life of the tissue while the ECM component could more accurately mimic the native IVD function than a metal–polymer implant. A tissue-based approach could create a treatment that could mimic this function, maintain mobility, and not suffer from the failure modes of wear, fatigue, and osteolysis. For this reason, the investigation of tissue-based approaches for the treatment of spinal disorders is actively being pursued (see Chapter 5.507, Tissue Engineering and Selection of Cells).

6.615.2. IVD Structure and Function

In order to understand the material design criteria involved in IVD repair, one must first be familiar with the complex structure and function of the native IVD. Grossly, the IVD is a composite tissue containing an outer AF, an inner NP, and the cartilage endplates.[38] Each of these regions is distinct in

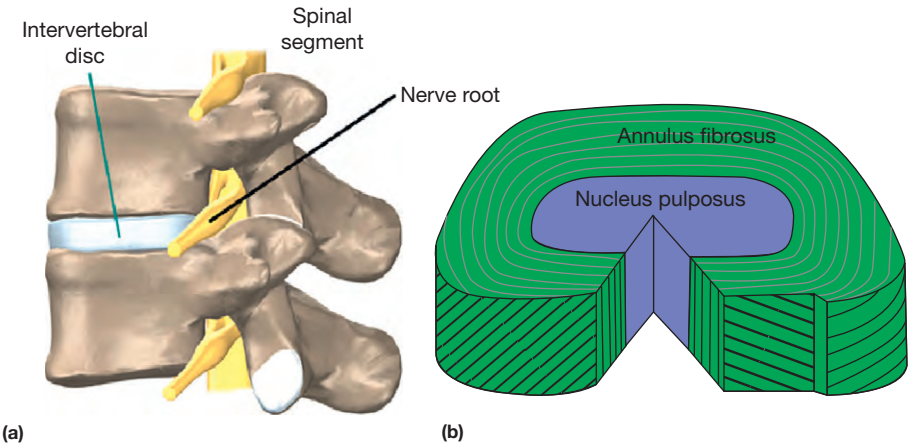

Figure 3 Intervertebral disc (IVD) structure. (a) IVD located in spine between vertebral bodies with the *cauda equina* (lumbar) or spinal cord (thoracic and cervical) running through the spinal canal posteriorly. Nerve roots exit from the spinal canal through the intervertebral foramen. (b) The IVD composed of the unorganized inner nucleus pulposus and outer highly organized annulus fibrosus. The annulus fibrosus is composed of lamellae and alternating collagen alignment (±28°) between each adjacent lamella.

composition, as well as organization, and work in concert to provide the mechanical function of the IVD (Figure 3).

The NP is an isotropic, unorganized, gelatinous material that is enclosed by the highly organized AF fibrocartilage on the side and the hyaline cartilage endplates on the top and bottom (Figure 3(b)). The encapsulation of the gelatinous NP by the AF allows the IVD to be both strong in compression while also withstanding complex tensile and shear forces in the AF region. Upon compression, the NP is pressurized as the AF resists the radial expansion of the NP. It is this pressurization that gives the IVD its high compressive stiffness.[39] In addition, during the bending and torsional movements of the spine, the complex collagen architecture of the AF bears the tensile loads.[40] It is this elegant function that one hopes to restore when selecting materials for IVD repair, and for this reason, it is advantageous to understand the material components and architecture that accomplish this naturally.

6.615.2.1. Extracellular Matrix

Overall, the key components of the IVD are water, collagens, proteoglycans, elastin, and cells with varying amounts and types located in the distinct IVD regions. The IVD is extremely hydrated with the AF and NP having a water content of ~65% and 80% of wet weight respectively.[41] In the AF, collagens make up 70% of the dry weight with 84% of that being collagen type I and 14% collagen type II at the outer AF.[42] In contrast, collagens only make up 20% of the dry weight of the NP with 80% of that being collagen type II. Proteoglycans follow the opposite trend with the percentage starting low in the AF and increasing until reaching 50% of the dry weight in the NP.[43]

Of these proteoglycans, the negatively charged large aggregating proteoglycans, aggrecan, and versican are found in the IVD with members of the small leucine-rich proteoglycan family (decorin, biglycan, lumican, and fibromodulin) also being present.[44,45] It is the negative charge of aggrecan that produces an affinity for water in the IVD via osmotic swelling and Donnan equilibrium. As a result, the high proteoglycan to collagen ratio produces the gelatinous nature of the NP and the low proteoglycan to collagen ratio and prevalence of type I collagen gives rise to the fibrous nature of the AF.

Finally, elastin is found in both the NP and AF.[46] The fibers are located predominately between the AF lamellae but are also found parallel to the collagen fibrils within the lamellae.

6.615.2.2. Organization

The degree of organization observed within the NP and AF is dramatically different. The NP has an unorganized collagen type II matrix dispersed within the proteoglycan-rich tissue. This unorganized state leads to the isotropic nature of the NP and its capacity for significant swelling when liberated from the surrounding AF. In contrast, the AF has a very organized collagen type I fiber structure. The AF is macroscopically segmented into lamellae surrounding the NP core. In each lamella, the collagen fibrils are highly aligned at an angle of ±28° to the transverse plane and this angle increases to 44° in the inner AF,[47,48] with the angle alternating in each successive lamella (Figure 3(b)). As a result, this organization leads to anisotropic mechanical properties and creates a tissue that is good at resisting the tensile loads observed in torsion and bending as well as withstanding the hoop stresses that occur during compression. Overall, this tissue produces a unique set of mechanical properties in compression, torsion, and bending that tissue-based approaches of repair will need to recreate to restore function to the diseased or injured IVD.

6.615.3. IVD Preservation, Repair, and Regeneration

By any measure, tissue-based IVD repair and tissue engineering is a relatively new field. Extracting broad trends from published data is quite challenging even with the small number of studies to date (~50 peer-reviewed manuscripts), since there is relatively little continuity in the cell types and materials used. The approaches can be broken down into NP, AF, and total disc repair.

6.615.3.1. Nuclear Replacement

The idea of nuclear replacement has received the most attention. This approach relies on the idea that replacing the herniated or diseased disc material will maintain or restore disc height and function to the spine. By replacing the NP, the disc height is restored and the AF fibers are placed back into tension, similar to that of a healthy disc. This type of intervention requires a healthy AF and, as a result, is a solution to an earlier stage of disease than used in spinal fusion and TDR. Currently, clinically available products are material based but research is being conducted on creating tissue-engineered material/cell solutions (Table 2) (see Chapter 6.613, Nucleus Replacement).

6.615.3.1.1. Acellular

Early attempts at nucleus replacement focused on acellular materials to restore disc height. The first attempt at nucleus replacement was conducted in 1955 by David Cleveland,[49] in which he replaced the NP after discectomy with methylmethacrylate. Aceular strategies continue to be investigated today and are at various stages of clinical evaluation. For a thorough analysis ofaceullar nuclear replacement, please see Chapter 6.613, Nucleus Replacement.

6.615.3.1.2. Cellular

Creating tissue-based strategies with a cellular component creates a tissue that can mature and repair over the life of the implant. As a result, this dramatically increases the theoretical limit for how long the treatment can be effective. The key to the successful development of a tissue-based strategy is in the proper selection of the material, cell source, and signaling. The NP has been a prime target for this type of therapy due to the isotropic unorganized structure of the tissue, which eliminates the need to worry about a complex tissue architecture during tissue development. Overall, the goal is to produce a tissue that is gelatinous in nature with high proteoglcyan content and type II collagen.

The choice of an animal source for IVD cells is challenging, as the time at which the cell population of the NP changes from notochordal to chondrocytic varies with species. Regardless of species chosen, it appears to be critical to ensure that cells are obtained from skeletally mature animals. To date, cells from seven species have been investigated for use in IVD regeneration, including murine,[50] lapine,[51] porcine,[52] ovine,[53,54] canine,[55] bovine,[55] and human.[56] It is highly likely that human cell sources will be required for clinical use; however, obtaining cells from the human IVD tissue may be difficult due to the diseased state of the tissue. As a result, the use of mesenchymal stem cells (MSCs) is being investigated. In fact, MSCs have been shown to take on a NP-like phenotype, both *in vitro* and after being injected into NP tissue[57,58] making them a suitable candidate for tissue-based NP replacement.

Disc degeneration results in decreased cell density in the NP and reduced cellular activity. As a result, one of the proposed treatments for NP degeneration is to simply inject cells into the NP without scaffolding material to promote *de novo* tissue formation in the NP of the degenerated disc. NP cells,[59] NP cells cocultured with MSCs,[60] MSCs,[61] chondrocytes,[62] and AF cells cocultured with MSCs[63] have all been investigated for NP injection. In general, cells were able to produce proteoglycan-rich matrix in the NP and delay degeneration in disc degeneration models. In a human trial, IVD cells were cultured and injected back into the NP after microdiscectomy surgery.[64] Patients receiving the treatment showed decreased pain at 2 years compared to those receiving no injection of cells after microdiscectomy. This data indicates that injecting cells into the NP may be able to delay degeneration in the IVD and be used as an adjunct to microdiscectomy to improve clinical outcomes.

While cell injection alone has shown potential to delay degeneration and promote *de novo* tissue formation, the use of a scaffolding material in concordance with the cells provides the additional ability to repressurize the NP by injecting the scaffold/cell material into the disc space. The isotropic gelatinous nature of the NP makes hydrogels a prime material candidate for NP tissue engineering. However, unlike acellular NP replacement, these materials must be deliverable in a noncytotoxic manner eliminating a number of hydrogels used in intradiscal implants. Wide ranges of scaffold materials have been used as substrates for cell culture. In general, NP cells have been cultured in hydrogels, with alginate[52–55] and gelatin[50] accounting for more than half of the studies published. Both materials appear to be well suited to maintaining NP cell phenotype and enabling proteoglycan synthesis, although significant accumulation of proteoglycan and collagen was not observed uniformly. Additional materials being utilized have been type II collagen,[65] hyaluranon composites,[66] calcium polyphosphate substrate,[67] type I atelocollagen,[61] and chitosan.[68]

While a large portion of this work has been done *in vitro*, a number of studies are available investigating the effectiveness of cell/material nuclear replacement *in vivo*. These studies have been conducted in degenerated animal lapine,[59] canine,[69] and murine[50] models. The results of the animal model *in vivo* studies have been promising, showing a delay in degeneration, restoration of disc height, and significant proteoglcyan-rich ECM. In addition to the animal studies, interim results of a human randomized trial have been reported. In this study,

Table 2 Nuclear replacement

	Acellular		*Cellular*	
	Intradiscal implants	*In situ* curable polymers	Cell only	Cell + scaffold
Goal	Restore/maintain disc height	Restore/maintain disc height, repressurize NP, minimally invasive	Restore/maintain disc height, repopulate lost cellularity to produce *de nove* tissue	Restore/maintain disc height, repressurize NP, repopulate lost cellularity to produce *de novo* tissue
Materials	Springs and hydrogels	Hydrogels, polyurethane, water/oil emulsion	Autologous disc cells, MSCs	Autologous disc cells, MSCs + hydrogels, type II collagen, hyaluronan composite, calcium polyphosphate, chitosan

autologous NP cells derived from therapeutic discectomy were cultured and delivered 12 weeks after discectomy in patients with chronic back pain.[70] Their data suggest MR imaging improvement consistent with increased proteoglycan matrix within the NP and a reduction in low back pain at 2 years when compared to controls. As a result, NP replacement may be a powerful adjunct to discectomy. However, it is important to note that this treatment must be conducted at an early enough stage that a functional AF is in place. Later stages of degeneration are unlikely to be treated by NP replacement alone.

6.615.3.2. Annular Repair

Due to the nature of disc herniation and the resulting disruption in the AF, it is necessary for the AF to be repaired to return proper mechanical function to the disc. In addition, the herniated region of the AF can allow the remaining NP or NP replacement to reherniate through the disruption. This can happen in up to 15% of patients after discectomy,[71–73] and unfortunately, the AF has a limited healing capacity and will only produce a thin biomechanically inferior tissue without intervention.[74] For this reason, it is a significant and relevant challenge to produce surgical treatments to repair the AF upon herniation (**Table 3**).

6.615.3.2.1. Acellular

The earliest attempts to repair the disrupted AF involved suturing the AF to provide both a barrier to reherniation and to promote healing. Unfortunately, few studies have been performed to study the effectiveness of suturing. In one of the few studies available, no significant increase in healing strength was observed as a result of direct annular repair.[75] In addition to suturing, a number of additional implants designed to close and act as barriers are being developed. These devices include sutures with anchors,[76] meshes,[77] and collagen poly(methyl methacrylate) (PMMA) injections.[78] However, currently there is little data to determine the effectiveness of these devices and they continue to suffer from the poor intrinsic healing of the AF, as they do not directly promote healing. For this reason, tissue-based approaches are also being investigated to promote a functional healing in the defect in addition to simply closing it.

6.615.3.2.2. Cellular

The goal of introducing cells into an annular defect is to promote the production of a functional tissue in the defect to both inhibit NP reherniation, as well as restore the mechanical properties of the AF. The creation of a functional engineered AF tissue is more difficult to produce than the NP due to its highly organized architecture and anisotropic mechanical properties. The tissue must not only contain the proper amounts of ECM, but they must also be organized properly to restore the mechanical function to the AF. The key organizational structures of importance are the high degree of alignment, the angle of alignment, and the alternating directions of alignment between lamellae. However, it must be noted that currently it is unknown as to what degree this organization needs to be recreated to successfully reduce the number of cases of reherniation and slow the progression of the disease state.

Cell selection for AF repair requires the selection of a cell that can produce a highly organized type I collagen ECM. The most likely candidates for use in AF repair strategies are the AF cells themselves or MSCs. However, once again autologous AF cells suffer from the diseased state of the tissue and diseased state of the resulting cells.[79] In addition, the availability of autologous AF cells varies greatly between patients and will likely require *in vitro* culture to expand to an adequate number of cells. These shortcomings may limit the effectiveness of these cells for clinical treatments. In comparison, MSC cells provide a more reliable cell source but are not without their own difficulties. Early work showed that MSCs differentiate into an NP-like phenotype and not an AF phenotype when cultured in hydrogels.[58,80] Nevertheless, the proper combination of scaffold and cell signaling that promotes an AF phenotype from MSCs may still be elucidated. In fact, more recent work has shown that when MSCs are placed on electrospun nanofibrous scaffolds the cells take up a more AF-like phenotype.[81,82] This may indicate scaffold selection as a key determiner of MSC phenotype and make proper material selection vital in producing a successful tissue-based approach to AF repair.

A number of scaffolds with a wide range of properties have been investigated for AF tissue engineering. Early work used scaffolds seeded with AF cells that lacked the structure necessary to promote collagen alignment and organization. These scaffolds included collagen type I/hyaluronan,[66] type I atellocollagen,[83] alginate,[51] type I collagen/glycosaminoglycan,[84] collagen sponges,[85] collagen gels,[85] fibrin gels,[85] polyglycolic acid/polylactic acid (PGA/PLA),[53] chitosan,[86] and electrospun poly-L-lactide (PLLA).[82] These constructs in general allowed for significant production of proteoglycans and collagen but the ECM development was still substantially lower than native values of ECM. In addition, no collagen organization was observed in these scaffolds.

Recently, focus has turned to culturing cells on scaffolds that promote tissue organization and alignment in the hope that an engineered AF tissue can be created that mimics the complex anisotropic function of the AF. This has been accomplished through the creation and use of aligned fibrous scaffolds. To date it has been achieved naturally with the use of small intestine submucosa (SIS),[87] with the self-assembly of contracted collagen gels,[88] and with the aligned electrospinning of polycaprolactone (PCL).[81] Each of these techniques has advantages and disadvantages for treating AF defects.

The SIS is obtained by processing small intestine to remove the mucosa layer. This results in a construct that contains oriented collagen fibers, proteoglycans, and trapped growth factors. This is ideal due to the similarity of the SIS ECM composition (aligned collagen and proteoglycans) and structure to the native AF. In addition, the trapped growth factors can be released and promote tissue development at the site of

Table 3 Annular repair

	Acellular	*Cellular*
Goal	Provide barrier to reherniation	Produce novel tissue in defect, provide barrier to reherniation
Materials	Anchored sutures, meshes, collagen PMMA injections	Autologous disc cells, MSCs + hydrogels, electospun nanofibrous scaffolds, chitosan, PGA/PLA, collagen sponges

implantation. SIS has been investigated for the repair of a number of tissues, including blood vessels, bladder defects, rotator cuffs, knee ligaments, and meniscus previously. The use of SIS for annular repair is relatively new but has shown promise in a sheep model by repairing AF defects and returning partial function to the IVD[89] (see **Chapter 5.524, Biomaterials for Replacement and Repair of the Meniscus and Annulus Fibrosus**).

Contracting collagen gels while controlling the boundary conditions has been shown to create aligned collagen fibrils and has been investigated for the repair of a number of tissues, including blood vessels, tendon, ligament, and cardiac tissue. The advantages of the technique are the production of aligned collagen architecture and aligned cells that are seeded throughout the tissue. However, contracted collagen gel tissues have notoriously week mechanical properties in contrast to the native AF. At early time points after implantation it may be difficult for an implanted collagen gel to withstand the mechanical loading imposed upon the aligned collagen gel. Conversely, the collagen nature of the scaffold may promote earlier integration of the tissue with the native AF and the high permeability of the collagen gel may promote the transport of nutrients into the developing tissue. This increased transport in the developing tissue may be especially important in the low nutrient environment present in the IVD and allow the tissue to mature into an integrated mechanically functional tissue after implantation.

Electrospinning allows scaffolds to be produced that have fibers of similar size to that of the collagen fibrils found in the AF. In addition, electrospinning can incorporate fiber alignment into the scaffold and has been used to create engineered tissues that contain lamellae with alternating $\pm 30^{\circ}$ fiber orientation.[81] These electrospun tissue structures developed tensile properties similar to that of native AF and showed promise for use in AF tissue engineering. However, the electrospinning process is not without its challenges. One of those challenges is the migration of cells into the electrospun scaffolds. Often, cells will fail to migrate to the center of the scaffold and will result in reduced tissue development at the center. Currently, a number of techniques are being studied to address these issues including the combination of composite electrospun materials that have differing degradation rates to encourage migration of cells into the scaffold.[90] In addition, a big question is how these organized fibrils will integrate with the endplate and vertebral bodies once implanted. Without integration and anchoring of the fiber structure, the fiber architecture will not be engaged and will fail to provide the mechanical function they are designed for. Further work is being conducted in the field to better understand how these electrospun scaffolds will integrate with the native tissue.

As can be seen, the amount of work done in the field of AF tissue engineering is limited and much of it has been *in vitro*. It will be important in the future direction of AF tissue engineering to understand how these strategies respond *in vivo* to the demands of AF defects. The major questions are centered on the ability of the repair strategies to confine the NP, the ability to restore pressurization capability to the IVD, and the ability to restore proper functioning to the AF in tension. Clearly, if these capabilities can be restored, it will have a profound effect on the treatment of disc herniation in the clinic.

6.615.3.3. Total Disc Replacement

A similarity exists between the IVD and a tire with the air of the tire being represented by the NP and the steel-belt reinforced rubber being represented by the AF. Furthermore, this similarity can be extended to the repair of the IVD as well. In certain situations, it will be advantageous to refill the air of the tire (nuclear replacement); in other situations, one may be able to patch a hole in the tire (AF repair), and finally, there are times when the entire tire must be replaced (TDR). It is the final situation, in which the herniation or degeneration of the AF is advanced enough that a sole NP or AF approach cannot be effective. It is for this reason that TDR is currently being investigated.

Artificial TDR has been recently introduced into clinical practice in the United States with the FDA approval of the previously discussed Charité device in 2004. The idea of a tissue-based composite disc was introduced with publication of the first tissue-engineered composite disc around the same time.[53] The idea that the entire IVD can be replaced by a tissue-engineered structure is an ambitious one due to the complex structure of the IVD; however, the early studies showed promising ECM and mechanical properties with a PLA/PGA/alginate composite. The major design criteria in developing a tissue-engineered total disc replacement (TE-TDR) are (1) designing a disc that can withstand the complex mechanical loading once implanted, (2) can recreate the mechanical function of the IVD, (3) can integrate with native tissues, and (4) can survive and develop in the nutrient-deprived disc space. These design criteria are complex and are even competing. The development of a mechanically stiff disc designed to withstand the complex loading will likely have low permeability properties and may make it difficult to get sufficient nutrient transport throughout the disc in the low nutrient disc environment. Conversely, a highly permeable disc that can provide better nutrient transport will be less stiff and may have trouble withstanding the mechanical loads. Currently, it is unknown what the proper balance of these competing properties will be in a successful TE-TDR.

To date, only four designs and five papers have been published on TE-TDRs. These TE-TDRs include an PGA/PLA (AF)/alginate (NP) composite,[53,54] an electrospun PLLA (AF)/hyaluronic acid (NP) composite,[82] a contracted collagen gel (AF)/alginate (NP) composite,[88] and an electrospun PCL (AF)/agarose (NP) composite.[91] The cell selection for these constructs has been either ovine IVD cells, bovine MSCs, or human MSCs. The material selection for each attempt has utilized a hydrogel for the NP, with a trend toward increasing hierarchical organization in the AF region (**Table 4**).

The first TE-TDR to be attempted was the PGA/PLA/alginate composite. The construct was seeded with ovine NP and AF cells in their respective regions of the disc. The alginate hydrogel provided an NP-like environment that maintained the rounded morphology of the NP cells once encapsulated. The AF region of PGA/PLA provided the gross morphology of the AF but contained none of the organization inherent in the native AF (**Figure 4(a)**). The scaffolds were implanted subcutaneously in the back of an athymic mouse for 4 months and produced proteoglycan composition similar to that of the native in the AF and NP. The constructs produced collagen to

Table 4 Tissue-engineered total disc replacement

	Mizuno et al.[53,54]	*Nesti* et al.[82]	*Bowles* et al.[92]	*Nerurkar* et al.[91]
Materials	AF – PGA/PLA NP – alginate	AF – electrospun PLLA NP – hyaluronic acid	AF – contracted collagen gel NP – alginate	AF – electrospun PCL NP – agarose
Cells	AF – ovine AF NP – ovine NP	AF – human MSC NP – human MSC	AF – ovine AF NP – ovine NP	AF – bovine MSC NP – bovine MSC
Organization	Composite disc	Composite disc with nanofibers of similar diameter to collagen	Composite disc with circumferentially aligned collagen fibrils in AF	Composite disc with multilamellar AF and alternating nanofiber alignment (±30°)

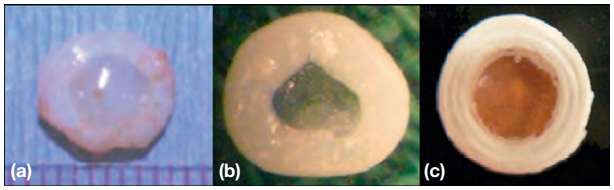

Figure 4 Tissue-engineered total disc replacements with (a) PGA/PLA annulus fibrosus (AF) and alginate nucleus pulposus (NP), (b) circumferentially aligned collagen fibril AF and alginate NP, and (c) multilamellae aligned electrospun polycaprolactone AF and agarose NP.

near native levels in the AF but not in the NP where it developed 10% of the native values. The collagen produced was properly localized with increased collagen type I in the AF and type II in the NP. In addition, the compressive mechanical properties were similar to that of the native sheep IVD. Overall, these studies demonstrated the feasibility of developing a TE-TDR that mimicked the compositional and compressive properties of the native IVD. However, with the lack of organization and architecture in the AF, and the failure to test the discs in anything but compression, it is unclear if this design could mimic the torsional and bending properties of the native IVD (see **Chapter 5.509, Cell Encapsulation**).

The second attempt to produce a TE-TDR utilized electrospun PLLA and hyaluronic acid seeded with human MSCs. This technique was similar to the previous attempt in that it used an unaligned AF regional scaffold and a hydrogel NP scaffold. However, the use of electrospun PLLA allowed the fibers to be of similar diameter to the native collagen fibrils in the AF region. In addition, the hyaluronic acid was injected into the electropsun PLLA to pressurize the NP region within the scaffold and place the electrospun fibers in tension similar to that of the native AF. Furthermore, the use of human MSCs is significant due to the clinical relevance of the cell source and begins to investigate their effectiveness in a TE-TDR.

The constructs were cultured for 28 days *in vitro* and the AF cells organized into concentric layers resembling the concentric lamellae of the AF while the NP remained amorphous in structure. ECM proteoglycan deposition was most prevalent in the AF region with a less pronounced deposition in the NP. Collagen types I and II also had the highest concentration in the AF region with least present in the NP region. This poor tissue development in the NP was likely due to the decreased cell content in the NP region of the scaffold after construction. Overall, the electrospun PLLA showed promising results for the AF region and tissue development; however, no mechanical testing was performed on the tissue to investigate the mechanical function of such an implant and it will be necessary to overcome the poor cellular density in the NP in the future.

Unlike the first two TE-TDR designs, the contracted collagen gel/alginate construct was the first to introduce collagen alignment into the AF region (**Figure 4(b)**). The technique produced an alginate NP region seeded with ovine NP cells and a type I collagen gel region seeded with ovine AF cells surrounding the NP region. During culture, the cells contract the collagen fibril network around the alginate NP. As a result of the physical boundary of the NP, the collagen fibrils aligned circumferentially around the alginate NP. In addition, the AF cells were elongated and circumferentially aligned between the type I collagen fibrils similar to native AF cells and the NP cells took on a rounded morphology similar to the native NP. This technique provides a method of producing a TE-TDR that has an architecture and organization similar to that of the native IVD in the AF and NP region. However, despite the circumferential alignment of the collagen fibrils, the technique currently fails to capture the ±28° collagen alignment observed in the successive AF lamellae. In addition, no mechanical testing or ECM composition analysis was performed in this study.

The most recent TE-TDR combines the previous strategies to produce the most complex TE-TDR to date (**Figure 4(c)**). The technique uses electrospun PCL to produce aligned PCL fibers at ±30° angles in each successive lamella. Once again this is done around a hydrogel NP region, which in this case was agarose. The cells selected were bovine MSCs because of the clinical promise of MSCs. The idea is that the complex PCL fiber architecture will lead to organized collagen development with the same alignment of the original scaffolding.

After 6 weeks of culture, collagen and proteoglycan production was observed in both the AF and NP region. It was observed that both AF cells and collagen production were organized in the ±30° direction of the underlying PCL scaffold. Despite the deposition of ECM over culture time, values for proteoglycans were <32% of the native values in both the AF and NP and were 5% of the native values for collagen in the AF. The collagen values were similar between native and the TE-TDR in the NP. As can be seen, the technique of using aligned electrospun fibers does help promote collagen organization similar to the native AF. However, it will be important to investigate how to promote greater ECM development to native value levels in these scaffolds.

The development of these TE-TDR strategies has shown initial promise at promoting varying levels of ECM composition and organization similar to the native IVD. However, despite the trend toward increasing AF organization and the

focus on mechanical properties of these implants, it is currently unknown what is needed for the successful implementation of such a device in the native disc space. Less attention is given to other design parameters such as the permeability of these scaffolds, a property that might prove extremely important in the limited nutrient environment of the disc space. A better understanding of how these TE-TDRs react in the native disc environment will be necessary to recognize what the proper balance of scaffold properties is that will promote successful tissue development and proper spinal function. These implants will need to withstand the mechanical loading, survive and develop, and integrate with the native tissue once implanted.

Recent work has begun to address these *in situ* questions using the contracted collagen gel/alginate TE-TDR.[92] The TE-TDRs were implanted into the lumbar and tail disc space of the rat and cultured for up to 6 months. These studies demonstrated that despite the much lower modulus of the collagen/alginate TE-TDR at the time of implantation compared to the native disc, the tissue was able to maintain a majority of the disc height over 6 months (78%). In addition, the tissue saw extensive deposition of proteoglycans and collagen and had integrated with the vertebral bodies and endplates. Furthermore, when the engineered motion segment was tested mechanically, it demonstrated similar compressive properties to the native disc. These results were the first that showed a TE-TDR could successfully form a mechanically functional tissue when implanted into the disc space. These results are especially intriguing due to the relatively low mechanical strength of the TE-TDRs at implantation. It is possible that the coupled highly permeable nature of the collagen and alginate TE-TDR allowed sufficient nutrient transport that promoted the tissue development and integration in the disc space. It will be important as this field moves forward, for more work to be done in the native disc space to understand how the TE-TDR properties (modulus, permeability, cell type, ECM composition, AF fiber organization, etc.) affect *in situ* tissue formation (see **Chapter 6.614, Wear: Total Intervertebral Disc Prostheses**).

6.615.4. Future Challenges

The clinical need for new treatments to IVD injury and disease is driving the development of novel material- and tissue-based solutions. Many of these solutions are designed to treat IVD disease and injury at varying stages of disease progression. These range from posterior dynamic stabilization of the spine to tissue-based TDR. With the wide range of disease stages presenting in the clinic and variability among patients, it is likely that this broad spectrum of treatments will be needed.

The most immediate impact in disease treatment will be seen in non-tissue-based solutions. These include posterior dynamic stabilization, nuclear replacement, and novel TDR devices. These devices can provide improved performance in current clinical treatments while avoiding the more difficult FDA hurdles faced by cellular-based approaches. With the large range of possibilities in material design and solutions for dynamic stabilization, nuclear replacement, and TDR devices, one expects a large number of products to begin to hit the market and enter clinical trials. The biggest hurdles will be proving the effectiveness of the treatments at reducing disease progression and pain while determining the most effective devices among the large variable space of possible designs.

In contrast to acellular approaches, the regulatory path for tissue-based approaches is more complex. In addition, as cells are introduced and the complexities of the treatments increase, the cost of producing the technology will increase as well. However, despite the hurdles, the upside of developing tissue-based technologies is large. Tissue-based solutions provide the opportunity to restore complete function to the IVD and produce treatments with longer life spans. It will be necessary for continued investment into tissue-based solutions to bring these technologies into common practice. As the technologies become more common and better understood, the regulatory hurdles will also decrease.

One of the great challenges to tissue-based treatments to disease is the large variable space available in material and cell selection. One must contemplate material, formulation, concentration, cross-linking agent, material organization, cell type, cell source, culture length, media type, cell signaling, etc. The variable space can be so large, it can be difficult to investigate the entire variable space and narrow down to the best solutions. This can become even more clouded when animal model variables and selection are introduced into the equation. In addition, these variables are rarely independent of one another, making it very difficult to process and understand the data and results that are produced. As this field continues to advance, techniques will need to be developed to help process these large amounts of data and interactions between variables. One possible solution is neural network analysis, which has been used to process the large input and output variable space of chondrogenesis in elastin-like polypeptides.[93] Applying techniques like neural network analysis may allow ideal solutions and better understandings of how material properties and tissue development parameters interact. As a result, this may lead to better design criteria for creating complex tissue-based treatments to IVD disease.

Despite progress in research on tissue-based solutions of IVD repair, there are still a number of major unknowns. One of these unknown variables applicable to all the tissue-based approaches is the long-term survival and durability of the treatments. Despite evidence that new tissue can be developed that resembles the native tissue, it is unclear what will happen to this tissue over time, especially in a diseased environment. This is principally true for TE-TDR technologies that will require relatively large tissues to be supplied with nutrients during maturation and long-term survival. It may be difficult for tissues to survive and mature relying on diffusion of nutrients from the AF periphery and endplates. As a result, it will be critical to assess the tissue response and ability to survive once implanted. The ideal situation will be that the tissue can mature and last for the entirety of the patient's life; however, shorter tissue survival does not eliminate the usefulness of tissue-based approaches. The ability to extend and delay the need for spinal fusion or TDR treatments by even just 5–10 years could dramatically improve the patient's outcome and quality of life. Therefore, it will be important to understand the lifespan of these technologies and how they fit into the long-term care and outcome of the patient treatment.

In addition to the challenges facing all tissue-based approaches, TE-TDR has an additional specific challenge.

These tissues must deliver in a way that allows the tissue to mature and integrate with the native tissue while maintaining the stability of the spine. As a result of the removal of the native IVD, the time after implantation and before integration leaves the vertebral column compromised. This provides a situation that could result in deleterious consequences if the vertebral column is not stabilized. For this reason, it is likely that TE-TDR strategies need to be developed in concert with stabilization techniques. Some possible solutions would be to use resorbable plates similar to those being investigated for use during fusion surgeries[94] or using posterior dynamic stabilization devices as an adjunct. These techniques would give time for the tissue to develop and integrate and could even act to augment mechanical properties during tissue development. Whatever the solution, it will be important to answer these questions of stabilization as more TE-TDR studies move toward *in vivo* implementation.

Despite these challenges, as our research and understanding of IVD repair and regeneration moves forward, great strides can be made toward improving the lives of those suffering from IVD related disease. As the field moves forward, the biomaterials used will continue to expand, new ideas for treatment will arise, and unforeseen challenges will present themselves. However, great hope lies in the continued research and investigation of tissue and non-tissue-based solutions to IVD disease.

References

1. Diwan, A. D.; Parvataneni, H. K.; Khan, S. N.; Sandhu, H. S.; Girardi, F. P.; Cammisa, F. P., Jr. *Orthop. Clin. North Am.* **2000**, *31*, 453–464.
2. Aota, Y.; Onari, K.; An, H. S.; Yoshikawa, K. *Spine (Phila Pa 1976)* **2001**, *26*, 2125–2132.
3. Lotz, J. C.; Ulrich, J. A. *J. Bone Joint Surg. Am.* **2006**, *88*(Suppl. 2), 76–82.
4. Shamji, M. F.; Allen, K. D.; So, S.; *et al*. *Spine (Phila Pa 1976)* **2009**, *34*, 648–654.
5. Nelson, M. A. *Proc. R. Soc. Med.* **1968**, *61*, 558–559.
6. Ahlmann, E.; Patzakis, M.; Roidis, N.; Shepherd, L.; Holtom, P. *J. Bone Joint Surg. Am.* **2002**, *84-A*, 716–720.
7. Silber, J. S.; Anderson, D. G.; Daffner, S. D.; *et al*. *Spine (Phila Pa 1976)* **2003**, *28*, 134–139.
8. An, H. S.; Lynch, K.; Toth, J. *J. Spinal Disord.* **1995**, *8*, 131–135.
9. Jorgenson, S. S.; Lowe, T. G.; France, J.; Sabin, J. *Spine (Phila Pa 1976)* **1994**, *19*, 2048–2053.
10. Tsuang, Y. H.; Yang, R. S.; Chen, P. Q.; Liu, T. K. *Taiwan Yi Xue Hui Za Zhi* **1989**, *88*, 989–994.
11. Zhang, Z. H.; Yin, H.; Yang, K. *Spine (Phila Pa 1976)* **1983**, *8*, 16–19.
12. Mclain, R. F.; Fleming, J. E.; Boehm, C. A.; Muschler, G. F. *J. Bone Joint Surg. Am.* **2005**, *87*, 2655–2661.
13. Chen, W. J.; Tsai, T. T.; Chen, L. H.; *et al*. *Spine (Phila Pa 1976)* **2005**, *30*, 2293–2297.
14. Korovessis, P.; Koureas, G.; Zacharatos, S.; Papazisis, Z.; Lambiris, E. *Eur. Spine J.* **2005**, *14*, 630–638.
15. Ransford, A. O.; Morley, T.; Edgar, M. A.; *et al*. *J. Bone Joint Surg. Br.* **1998**, *80*, 13–18.
16. Boden, S. D.; Kang, J.; Sandhu, H.; Heller, J. G. *Spine (Phila Pa 1976)* **2002**, *27*, 2662–2673.
17. Boden, S. D.; Zdeblick, T. A.; Sandhu, H. S.; Heim, S. E. *Spine (Phila Pa 1976)* **2000**, *25*, 376–381.
18. Dimar, J. R.; Glassman, S. D.; Burkus, K. J.; Carreon, L. Y. *Spine (Phila Pa 1976)* **2006**, *31*, 2534–2539; discussion 2540.
19. Johnsson, R.; Stromqvist, B.; Aspenberg, P. *Spine (Phila Pa 1976)* **2002**, *27*, 2654–2661.
20. Slosar, P. J.; Josey, R.; Reynolds, J. *Spine J.* **2007**, *7*, 301–307.
21. Alden, T. D.; Pittman, D. D.; Beres, E. J.; *et al*. *J. Neurosurg.* **1999**, *90*, 109–114.
22. Helm, G. A.; Alden, T. D.; Beres, E. J.; *et al*. *J. Neurosurg.* **2000**, *92*, 191–196.
23. Wang, J. C.; Kanim, L. E.; Yoo, S.; Campbell, P. A.; Berk, A. J.; Lieberman, J. R. *J. Bone Joint Surg. Am.* **2003**, *85-A*, 905–911.
24. Chiu, J. C.; Clifford, T.; Princenthal, R.; Shaw, S. *Surg. Technol. Int.* **2005**, *14*, 305–315.
25. Kumar, M. N.; Baklanov, A.; Chopin, D. *Eur. Spine J.* **2001**, *10*, 314–319.
26. Beaurain, J.; Bernard, P.; Dufour, T.; *et al*. *Eur. Spine J.* **2009**, *18*, 841–850.
27. Harrop, J. S.; Youssef, J. A.; Maltenfort, M.; *et al*. *Spine (Phila Pa 1976)* **2008**, *33*, 1701–1707.
28. Kurtz, S. M.; Van Ooij, A.; Ross, R.; *et al*. *Spine J.* **2007**, *7*, 12–21.
29. Van Ooij, A.; Kurtz, S. M.; Stessels, F.; Noten, H.; Van Rhijn, L. *Spine (Phila Pa 1976)* **2007**, *32*, 223–229.
30. Bozkus, H.; Senoglu, M.; Baek, S.; *et al*. *J. Neurosurg. Spine* **2010**, *12*, 183–189.
31. Mandigo, C. E.; Sampath, P.; Kaiser, M. G. *Neurosurg. Focus* **2007**, *22*, E9.
32. Frick, S. L.; Hanley, E. N., Jr.; Meyer, R. A., Jr.; Ramp, W. K.; Chapman, T. M. *Spine (Phila Pa 1976)* **1994**, *19*, 1826–1834; discussion 1834–1835.
33. Katsuura, A.; Hukuda, S. *Spine (Phila Pa 1976)* **1994**, *19*, 2426–2432.
34. Matsuzaki, H.; Wakabayashi, K.; Ishihara, K.; Ishikawa, H.; Ohkawa, A. *Spine (Phila Pa 1976)* **1996**, *21*, 178–183.
35. Luk, K. D.; Ruan, D. K.; Chow, D. H.; Leong, J. C. *Clin. Orthop. Relat. Res.* **1997**, *337*, 13–26.
36. Luk, K. D.; Ruan, D. K.; Lu, D. S.; Fei, Z. Q. *Spine (Phila Pa 1976)* **2003**, *28*, 864–869; discussion 870.
37. Ruan, D.; He, Q.; Ding, Y.; Hou, L.; Li, J.; Luk, K. D. *Lancet* **2007**, *369*, 993–999.
38. Humzah, M. D.; Soames, R. W. *Anat. Rec.* **1988**, *220*, 337–356.
39. Broberg, K. B. *Spine* **1983**, *8*, 151–165.
40. Hickey, D. S.; Hukins, D. W. *Spine (Phila Pa 1976)* **1980**, *5*, 106–116.
41. Roberts, S.; Beard, H. K.; O'brien, J. P. *Ann. Rheum. Dis.* **1982**, *41*, 78–85.
42. Eyre, D. R.; Muir, H. *Biochem. J.* **1976**, *157*, 267–270.
43. Eyre, D. R. *Int. Rev. Connect. Tissue Res.* **1979**, *8*, 227–291.
44. Melrose, J.; Ghosh, P.; Taylor, T. K. *J. Anat.* **2001**, *198*, 3–15.
45. Sztrolovics, R.; Alini, M.; Mort, J. S.; Roughley, P. J. *Spine (Phila Pa 1976)* **1999**, *24*, 1765–1771.
46. Yu, J.; Winlove, P. C.; Roberts, S.; Urban, J. P. *J. Anat.* **2002**, *201*, 465–475.
47. Cassidy, J. J.; Hiltner, A.; Baer, E. *Connect. Tissue Res.* **1989**, *23*, 75–88.
48. Marchand, F.; Ahmed, A. M. *Spine* **1990**, *15*, 402–410.
49. Cleveland, D. *Marquette Med. Rev.* **1955**, *20*, 62–64.
50. Gruber, H. E.; Johnson, T. L.; Leslie, K.; *et al*. *Spine (Phila Pa 1976)* **2002**, *27*, 1626–1633.
51. Chiba, K.; Andersson, G. B.; Masuda, K.; Thonar, E. J. *Spine (Phila Pa 1976)* **1997**, *22*, 2885–2893.
52. Baer, A. E.; Wang, J. Y.; Kraus, V. B.; Setton, L. A. *J. Orthop. Res.* **2001**, *19*, 2–10.
53. Mizuno, H.; Roy, A. K.; Vacanti, C. A.; Kojima, K.; Ueda, M.; Bonassar, L. J. *Spine* **2004**, *29*, 1290–1297; discussion 1297–1298.
54. Mizuno, H.; Roy, A. K.; Zaporojan, V.; Vacanti, C. A.; Ueda, M.; Bonassar, L. J. *Biomaterials* **2006**, *27*, 362–370.
55. Aguiar, D. J.; Johnson, S. L.; Oegema, T. R. *Exp. Cell Res.* **1999**, *246*, 129–137.
56. Sakai, D.; Mochida, J.; Yamamoto, Y.; *et al*. *Spine (Phila Pa 1976)* **2004**, *29*, 1515–1523.
57. Le Maitre, C. L.; Baird, P.; Freemont, A. J.; Hoyland, J. A. *Arthritis Res. Ther.* **2009**, *11*, R20.
58. Risbud, M. V.; Albert, T. J.; Guttapalli, A.; *et al*. *Spine (Phila Pa 1976)* **2004**, *29*, 2627–2632.
59. Okuma, M.; Mochida, J.; Nishimura, K.; Sakabe, K.; Seiki, K. *J. Orthop. Res.* **2000**, *18*, 988–997.
60. Watanabe, K.; Mochida, J.; Nomura, T.; Okuma, M.; Sakabe, K.; Seiki, K. *Connect. Tissue Res.* **2003**, *44*, 104–108.
61. Sakai, D.; Mochida, J.; Iwashina, T.; *et al*. *Spine (Phila Pa 1976)* **2005**, *30*, 2379–2387.
62. Gorensek, M.; Jaksimovic, C.; Kregar-Velikonja, N.; *et al*. *Cell. Mol. Biol. Lett.* **2004**, *9*, 363–373.
63. Kim, S.; Le Visage, C.; Tateno, K.; Sieber, A.; Kostuik, J.; Leong, K. *Spine J.* **2002**, *2*, 107S.
64. Hohaus, C.; Ganey, T. M.; Minkus, Y.; Meisel, H. J. *Eur. Spine J.* **2008**, *17*(Suppl. 4), 492–503.
65. Sun, Y.; Hurtig, M.; Pilliar, R. M.; Grynpas, M.; Kandel, R. A. *J. Orthop. Res.* **2001**, *19*, 1078–1084.
66. Alini, M.; Li, W.; Markovic, P.; Aebi, M.; Spiro, R. C.; Roughley, P. J. *Spine (Phila Pa 1976)* **2003**, *28*, 446–454; discussion 453.
67. Seguin, C. A.; Grynpas, M. D.; Pilliar, R. M.; Waldman, S. D.; Kandel, R. A. *Spine (Phila Pa 1976)* **2004**, *29*, 1299–1306; discussion 1306–1307.
68. Roughley, P.; Hoemann, C.; Desrosiers, E.; Mwale, F.; Antoniou, J.; Alini, M. *Biomaterials* **2006**, *27*, 388–396.
69. Ganey, T.; Libera, J.; Moos, V.; *et al*. *Spine (Phila Pa 1976)* **2003**, *28*, 2609–2620.
70. Meisel, H. J.; Siodla, V.; Ganey, T.; Minkus, Y.; Hutton, W. C.; Alasevic, O. J. *Biomol. Eng.* **2007**, *24*, 5–21.

71. Atlas, S. J.; Keller, R. B.; Wu, Y. A.; Deyo, R. A.; Singer, D. E. *Spine (Phila Pa 1976)* **2005**, *30*, 936–943.
72. Atlas, S. J.; Keller, R. B.; Wu, Y. A.; Deyo, R. A.; Singer, D. E. *Spine (Phila Pa 1976)* **2005**, *30*, 927–935.
73. Carragee, E. J.; Han, M. Y.; Suen, P. W.; Kim, D. *J. Bone Joint Surg. Am.* **2003**, *85-A*, 102–108.
74. Key, J. A.; Ford, L. T. *J. Bone Joint Surg. Am.* **1948**, *30A*, 621–630.
75. Ahlgren, B. D.; Lui, W.; Herkowitz, H. N.; Panjabi, M. M.; Guiboux, J. P. *Spine (Phila Pa 1976)* **2000**, *25*, 2165–2170.
76. Bourgeault, C.; Beaubien, B.; Griffith, S. *Biomechanical Assessment of Annulus Fibrosus Repair with Suture Tethered Anchors*. Spine Arthroplasty Society: Berlin, 2007.
77. Bajanes, G.; Perez, A.; Diaz, M. *One Year Follow Up of Discectomy Patients Who Received a Mesh to Repair the annulus fibrosus*. Spine Arthoplasty Society: Berlin, 2007.
78. Taylor, W. *Spine J.* **2006**, *6*, 48S–49S.
79. Gruber, H. E.; Ingram, J. A.; Norton, H. J.; Hanley, E. N., Jr. *Spine (Phila Pa 1976)* **2007**, *32*, 321–327.
80. Richardson, S. M.; Hughes, N.; Hunt, J. A.; Freemont, A. J.; Hoyland, J. A. *Biomaterials* **2008**, *29*, 85–93.
81. Nerurkar, N. L.; Baker, B. M.; Sen, S.; Wible, E. E.; Elliott, D. M.; Mauck, R. L. *Nat. Mater.* **2009**, *8*, 986–992.
82. Nesti, L. J.; Li, W. J.; Shanti, R. M.; *et al*. *Tissue Eng. A* **2008**, *14*, 1527–1537.
83. Sato, M.; Kikuchi, M.; Ishihara, M.; *et al*. *Med. Biol. Eng. Comput.* **2003**, *41*, 365–371.
84. Rong, Y.; Sugumaran, G.; Silbert, J. E.; Spector, M. *Tissue Eng.* **2002**, *8*, 1037–1047.
85. Gruber, H. E.; Stasky, A. A.; Hanley, E. N., Jr. *Matrix Biol.* **1997**, *16*, 285–288.
86. Dang, J. M.; Sun, D. D.; Shin-Ya, Y.; Sieber, A. N.; Kostuik, J. P.; Leong, K. W. *Biomaterials* **2006**, *27*, 406–418.
87. Le Visage, C.; Yang, S. H.; Kadakia, L.; Sieber, A. N.; Kostuik, J. P.; Leong, K. W. *Spine (Phila Pa 1976)* **2006**, *31*, 2423–2430; discussion 2431.
88. Bowles, R. D.; Williams, R.; Zipfel, W.; Bonassar, L. J. *Tissue Eng. A* **2009**, *16*, 1339–1348.
89. Ledet, E. H.; Jeshuran, W.; Glennon, J. C.; *et al*. *Spine (Phila Pa 1976)* **2009**, *34*, 1457–1463.
90. Baker, B. M.; Nerurkar, N. L.; Burdick, J. A.; Elliott, D. M.; Mauck, R. L. *J. Biomech. Eng.* **2009**, *131*, 101012.
91. Nerurkar, N. L.; Sen, S.; Huang, A. H.; Elliott, D. M.; Mauck, R. L. *Spine (Phila Pa 1976)* **2010**, *35*, 867–873.
92. Bowles, R. D.; Gebhard, H. G.; Hartl, R.; Bonassar, L. J. *NMR Biomed.* **2011**, doi: 10.1002/nbm.1651.
93. Nettles, D. L.; Haider, M. A.; Chilkoti, A.; Setton, L. A. *Tissue Eng. A* **2010**, *16*, 11–20.
94. Bindal, R. K.; Ghosh, S.; Foldi, B. *Neurosurgery* **2007**, *61*, 305–309; discussion 309–310.

6.616. Materials in Fracture Fixation

J M Lane and J E Mait, Hospital for Special Surgery, New York, NY, USA
A Unnanuntana, Siriraj Hospital, Mahidol University, Bangkok, Thailand
B P Hirsch, Hospital for Special Surgery, New York, NY, USA; Yale School of Medicine, New Haven, CT, USA
A D Shaffer and O A Shonuga, Hospital for Special Surgery, New York, NY, USA; Weill Cornell Medical College, New York, NY, USA

© 2011 Elsevier Ltd. All rights reserved.

6.616.1. Fracture Healing 220
6.616.1.1. Biological Requirements for Fracture Healing 220
6.616.1.2. Mechanical Requirements for Fracture Healing 221
6.616.2. Basic Requirements of Biomaterials for Fracture Fixation Device 221
6.616.2.1. Biocompatibility 221
6.616.2.2. Corrosion Resistance 221
6.616.2.3. Mechanical Properties 221
6.616.3. Devices Used in Fracture Fixation 222
6.616.3.1. Plate and Screw Fixation 222
6.616.3.1.1. Design rationale 222
6.616.3.1.2. Applications of biomaterials to plate and screw fixation 223
6.616.3.1.3. Advantages of plate and screw fixation 224
6.616.3.1.4. Limitations of plate and screw fixation 224
6.616.3.2. Intramedullary Fixation 225
6.616.3.2.1. Design rationale 225
6.616.3.2.2. The application of biomaterials in internal fixation 225
6.616.3.2.3. Advantages of intramedullary fixation 226
6.616.3.2.4. Limitations of intramedullary fixation 226
6.616.3.3. External Fixation 226
6.616.3.3.1. Design rationale 227
6.616.3.3.2. The application of biomaterials in external fixation 227
6.616.3.3.3. Advantages of external fixation 229
6.616.3.3.4. Limitations of external fixation 229
6.616.3.4. Structural Augmentation 229
6.616.3.4.1. Calcium phosphate ceramics 229
6.616.3.4.2. Glass ceramics 231
6.616.3.4.3. Polymers 232
6.616.3.4.4. Composites 232
References 232

Abbreviations

AO	Arbeitsgemeinschaft für osteosynthesefragen
AWGC	Apatite-wollastonite glass ceramics
BCP	Biphasic hydroxyapatite
BMP	Bone morphogenetic protein
CPCs	Calcium phosphate cements
DLC	Diamond-like carbon
IGF	Insulin-like growth factor
IL-1 / IL-6	Interleukins
LC-DCP	Limited contact–dynamic compression plate
LCP	Locking compression plates
LSP	Laser shock peening
PC-Fix	Point contact fixation plate
PDS	Polydioxanone
PGA	Poly-glycolic acid
PLA	Poly-L-lactic acid
PMMA	Polymethylmethacrylate
PTH	Parathyroid hormone
SRS	Skeletal repair system
TCP	Tricalcium phosphate
TGF-β	Transforming growth factor-β
TNF-α	Tumor necrosis factor-α
VEGF	Vascular endothelial growth factor

In the year 2000, worldwide, approximately 9 million people suffered from fractures.[1] There were several causes, ranging from high-energy trauma such as gunshot wounds, motor vehicle accidents, and contact sports to low-energy trauma such as falls from a standing height. Falls are the most common reasons for hospital admissions in the older age group and

account for 87% of fractures.[2] These fractures cause considerable financial, emotional, and psychological hardship – due to many factors such as pain, lack of mobility, lack of independence, and concomitant injuries. In addition, approximately 5–10% of fractures suffer complications such as mal- and nonunion. The goal of fracture treatment is to obtain fracture union, while restoring normal anatomy and function. Successful treatment of fractures depends on a thorough evaluation of the patient and formulation of a treatment plan tailored to their needs.

Generally, treatment of fracture is divided into nonoperative and operative management. Operative treatment is preferred in particular circumstances including open or displaced fractures and fractures involving weight-bearing bones, articular surfaces, or neurovascular structures. In the year 1990, approximately 3.6 million operations were performed in the United States to reduce and fix fractures.[3] The exact annual cost of these interventions is unknown. It is estimated that by the year 2050, the cost of treating osteoporosis-related fractures alone will be between $130 and $250 billion per year. Therefore, advances in fracture management that improve healing and reduce costs from complications, especially through the use of cutting edge implants, are important to society, both in terms of the human and financial costs.

In the setting of fractures, metallic alloys are commonly used to fabricate devices for both internal and external fixation. Internal fixation can be divided primarily into plate and screw fixation and intramedullary fixation. Understanding the link between the structure, material properties, and biological effects of fracture fixation devices in the context of fracture healing is essential to ensure safety and efficacy in clinical practice. Choosing appropriate biomaterials with correct balance between mechanical stability and preservation of an appropriate biological milieu is the key to obtain successful bone healing. This chapter discusses the fracture healing process and basic requirements of biomaterials used in fracture fixation devices. Common devices used in fracture fixation including plate and screw construct, intramedullary fixation, and external fixator are described in terms of their overall design and the application of their biomaterial properties in fracture fixation. Furthermore, we discuss synthetic bone graft substitutes that are being used as adjuvant biomaterials in fracture settings.

6.616.1. Fracture Healing

Fracture healing is a complex process that involves a unique, highly integrated sequence of events in which bone is restored to its original condition. Normal endochondral fracture repair proceeds along a continuum, with different overlapping stages beginning with inflammation and callus formation and ending with a remodeling phase. In the inflammatory phase of fracture healing, a hematoma is formed from the blood vessels ruptured by the injury. Inflammatory cells invade the hematoma and initiate degradation and removal of necrotic debris. A mixture of degranulating platelets, macrophages, leukocytes, histiocytes, and mast cells infiltrate the fractured area and amplify the initial inflammatory responses by elaborating additional proinflammatory cytokines and peptide signaling molecules that trigger and promote growth and repair, as well as begin to clean up necrotic debris.[4,5]

This cellular response is highly coordinated and involves a number of different cytokines and growth factors such as vascular endothelial growth factor (VEGF), tumor necrosis factor-α (TNF-α), bone morphogenetic proteins (BMPs), and interleukins-1 and -6. The reparative phase, which usually begins 4 or 5 days after injury, is characterized by the migration of mesenchymal stem cells, which subsequently differentiate into fibroblasts, chondroblasts, and osteoblasts, forming a soft tissue callus that is mostly cartilage. This soft tissue callus serves as a hypoxia-tolerant temporary scaffold for the formation of a bony callus that will replace it once vascular invasion occurs. As this process continues, multiple foci of cartilaginous formation merge to form a central plug. Proliferation of blood vessels within medullary spaces and periosteum helps direct the appropriate cells to fracture site and provides critical nutrients. Chondrocytes within the cartilaginous plug lead to hypertrophy and mineralize to become woven bone. At this stage, hard callus formation occurs, representing the penultimate stage of fracture healing. In the remodeling phase, woven bone is replaced by lamellar bone and the medullary canal is restored. The remodeling process at the fractured site begins during the middle of the reparative phase and continues long after the fracture has clinically healed. Although stages within the fracture healing process are somewhat distinctive from each other, these phases overlap one another making fracture healing a continuous process.

The capacity for bone to repair or regenerate after fracture is similar to the events that transpire during development in the growth plate: endochondral ossification and intramembranous ossification. Endochondral ossification is a process that results in healing primarily through cartilage formation, while intramembranous ossification occurs without a cartilage model. For intramembranous ossification, undifferentiated mesenchymal cells aggregate into layers. These cells differentiate into osteoblasts and deposit an organic matrix that mineralizes to form bone. This type of bone healing occurs without callus and resembles normal bone remodeling. The process of intramembranous bone healing is exceedingly slow and requires adequate stability until the fracture is healed. The process of fracture healing is closely related to the mechanical and biological environment at the fracture site including motion and oxygen tensions.[6] Motion or high strain (>2%) at the fracture site results in healing primarily through endochondral ossification, whereas stability or low strain (≤2%) promotes bone healing via intramembranous ossification.[7] Most fractures, however, heal through a combination of intramembranous and endochondral ossification.[8]

6.616.1.1. Biological Requirements for Fracture Healing

Numerous factors have been identified to play a major role in fracture healing. In addition to mechanical stability at the fracture site, there are vast requirements of biological factors for bone healing. These include skeletal progenitor cells, extracellular matrix, bone-forming cytokines, and intact vasculature. Understanding the cellular and molecular pathways that govern the process of fracture healing is important to determine the treatment options. In general, the biological methods of fracture repair can be categorized into three essential modalities: osteogenesis, osteoinduction, and osteoconduction. Osteogenesis is the formation of bone tissue by mesenchymal stem cells.[9] During fracture healing,

mesenchymal stem cells from surrounding tissues invade the fracture site, where they proliferate and differentiate into cartilage or bone. The recruitment and differentiation of mesenchymal stem cells into bone-forming cells at a fracture site are mediated by certain molecules or cytokines, such as insulin growth factors (IGFs), transforming growth factor-β (TGF-βs), and BMPs.[10] This molecular process that regulates recruitment and differentiation of the mesenchymal stem cells is called osteoinduction. Finally, osteoconductive materials serve as scaffolds upon which osteogenic and osteoinductive factors can function. These materials provide structural support for the ingrowth of perivascular soft tissue, osteoprogenitor cells, and microvasculature that supplies critical nutrients necessary for bone healing.[11] Some biological tissues such as the skeletal extracellular matrix provide two essential functions: osteoconduction and osteoinduction. Bone extracellular matrix serves not only as a scaffold, but also binds growth factors and cytokines that play critical roles in stem cell differentiation. Examples of osteoconductive biomaterials commonly used in fracture fixation include calcium phosphate cements (CPCs), hydroxyapatite, and tricalcium phosphate (TCP). Currently, these biomaterials are widely used as adjuvant devices for fracture fixation especially in the settings of poor bone quality such as in osteoporosis.

6.616.1.2. Mechanical Requirements for Fracture Healing

During the first stage of fracture healing, the method of immobilization determines the biological mechanism by which fracture healing will take place. In cases of fractures treated with rigid fixation (defined as fixation of a fracture that is permitted little deformation under load), where strain across the fracture site is less than 2% and the bone ends are aligned along their normal anatomic axis, intramembranous bone healing occurs.[158] The necrotic bone ends are invaded by neighboring osteons that subsequently bridge across the fracture ends in an accelerated type of bone remodeling. Examples of rigid fixation devices for fracture treatment include compression plating or interfragmentary compression screws. Stable fixation is defined as a fixation in which fracture fragments are kept within less than 10% strain during joint movement, thus allowing early painless mobilization. Where fractured bone fragments experience strain levels between 2% and 10%, endochondral bone healing occurs. There are several fixation techniques that employ stable fixation. These include casting, locking-plate fixation, intramedullary fixation, and external fixation. While the pioneers of internal fixation saw external callus formation as a sign of treatment failure in fracture healing, recent studies show that stable fixation and the endochondral bone healing are preferred.

6.616.2. Basic Requirements of Biomaterials for Fracture Fixation Device

The term biomaterials refers to all synthetic and natural materials that are used in clinical practice to replace, stabilize, or augment damaged tissue. To ensure the safety and functionality of the devices used in fracture fixation, orthopedic biomaterials must be biocompatible, resistant to corrosion, and have adequate mechanical strength.[8]

6.616.2.1. Biocompatibility

Biocompatibility is the ability of an implant material to function *in vivo* without eliciting detrimental local or systemic responses in the body.[8] Prior to their use in human fracture fixation, biomaterials undergo tissue and animal testing to determine their safety and efficacy. Biomaterials that elicit little or no host response such as cobalt–chromium metallic alloys can be thought of as inert materials. The importance of biocompatibility is demonstrated by the consequences of allergic reactions to nickel- and chromium-containing stainless steel implants. The biological rejection of an implant leads to an inflammatory response mediated by immune cells and can necessitate removal of the implant. Much of the research into new biomaterials is focused on improving biocompatibility of implants, avoiding unnecessary complications (see **Chapter 4.401, The Concept of Biocompatibility**; **Chapter 4.402, Biocompatibility and the Relationship to Standards: Meaning and Scope of Biomaterials Testing**; and **Chapter 3.319, Characterization of Nanoparticles in Biological Environments**).

6.616.2.2. Corrosion Resistance

Corrosion is the oxidative deterioration of metals. As a metal corrodes, its mechanical properties weaken, compromising its function as a fixation device. Although orthopedic implants are subject to a variety of corrosive effects, galvanic corrosion is of particular concern. Galvanic corrosion is an electrochemical process in which one metal corrodes preferentially for another when both metals are in electrical contact and immersed in a conductive medium. This type of corrosion most often takes place at the interface between plates and the screws that secure it to the bone. The corrosion not only damages the surface of orthopedic implants creating surface defects that can act as stress risers but also releases corrosion products to the adjacent structures, resulting in damage to surrounding soft tissues and impaired healing. Therefore, biomaterials used in fracture fixation devices must be corrosion resistant even in the highly reactive environment of body fluids. For example, titanium alloy is corrosion resistant *in vivo* due to an electrically isolating protective layer that forms on its surface.

6.616.2.3. Mechanical Properties

Design of an effective fracture fixation device requires attention to shape, mechanical, and material properties. Mechanical properties of orthopedic implants depend on several factors including stress and strain, isotropic and anisotropic behavior, viscoelasticity, and wear resistance. A discussion of all aspects of mechanical properties of the fixation devices is beyond the scope of this chapter and the reader is referred to other resources devoted to this subject for more information.

As mentioned earlier, the concept of rigid versus stable fixation is critical for the selection of fracture fixation devices as well as biomaterials. In order to heal properly and maintain its normal strength, bone needs to be subjected to dynamic stresses. As stainless steel is significantly stiffer than bone (~10 times stiffer), using stainless steel in rigid fixation devices can alter fracture remodeling and decrease bone density,

leading to regional osteoporosis.[8] This phenomenon, known as stress shielding, occurs when a fractured bone is shielded from normal stresses by its more rigid implant, attenuating the normal mechanical stimuli necessary to heal and maintain normal strength.[12]

Implants used for the treatment of fractures must control the amount of strain as well as rotational motion at the fracture site to achieve bone union. The currently available fracture fixation devices can be classified on the basis of their function as load-bearing and load-sharing constructs. Load-bearing constructs such as plates reduce the strain on healing bone – over time, the reduced strain can lead to local bone resorption adjacent to the plate. This can prove to be hazardous upon removal of the implant, as foci of ostepenic bone can act as stress risers, and may refracture at this location.[3,13] For this reason, if possible, implants should be load sharing, subjecting the bone to an optimal amount of stress and strain during the healing process. In general, the majority of intramedullary constructs and external fixation are considered as load-sharing devices. The concept of load bearing and load sharing is important and remains an active area of inquiry in fracture implant biomaterials.[14]

6.616.3. Devices Used in Fracture Fixation

6.616.3.1. Plate and Screw Fixation

Screws were likely first used in fracture fixation in the late 1840s. The French surgeons Cucuel and Rigaud reported utilizing screws to reduce and fix both sternal and olecranon fractures. In these early cases, screws were primarily used to reduce the fracture fragments and wires were used to secure the reduction.[4] By the late 1880s, this had evolved to the first reported use of plate and screw fixation when the surgeon Hansmann of Hamburg used a plate and special screws to reduce and fix complicated fractures.[4] These original plates and screws were ordinary steel, and by the early 1900s, corrosion-resistant vanadium steel was utilized for both plates and screws.

In 1949, the surgeon Danis published his treatise on osteosynthesis (the process of mechanically bringing the ends of a fractured bone close together), and he was the first to describe the mechanism of bone healing in rigid plate fixation of fractures.[4] A year after publication, a young surgeon from Switzerland, Dr. Maurice Müller visited Dr. Danis. The visit served as a source of inspiration to Dr. Müller, who went on to assemble and form the internal fixation study group – *Arbeitsgemeinschaft für Osteosynthesefragen*, commonly known as AO – that would revolutionize modern internal fixation.

Plates are ideally used in situations where their biological and mechanical properties make them well suited to the requirements of fracture healing. This is typically true in periarticular or metaphyseal fractures; oblique, comminuted, or segmental fractures; fractures in flat or small bones; rapidly healing fractures; or fractures in patients who have suffered pulmonary trauma or have extensive soft tissue or anatomical contraindications to other fracture fixation methods.[15]

6.616.3.1.1. Design rationale

Plate and screw constructs have a range of designs related to their biomechanical and biological properties. Ultimately, plates are used to provide stability, limiting the amount of strain a fracture experiences while avoiding interference with the biological needs of the fracture. When used in the correct clinical situation and applied with skill, plates are extremely useful in the treatment of fractures.

Plates have evolved a great deal structurally, with a diverse range of structures, mechanical properties, and materials. Bridge plates are used to bridge between comminuted or segmental fractures, serving as a splint. Dynamic compression plates use friction generated by screws to compress the plate to the bone, acting as a conduit to transfer loads between the bone ends.[16] Limited contact-dynamic compression plates (LC-DCP), point contact fixation plates (PC-Fix), and locking compression plates (LCPs) serve the same purpose but with less bone–plate contact. In the case of LCPs, no contact exists between the bone and plate.[17] Buttress plates are used at the end of long bones in periarticular regions, preventing axial forces from distorting the initial reduction.[18] The common denominator to plates is that they must be designed to provide stability, limiting strain at the fracture site to less than 10% while limiting the biological insult that they cause.

Additional design goals of plates include attempting to spread and reduce the loads encountered by plate–screw constructs equally across the screws and hence to the bone. Several aspects of plate design affect functionality. Plate length is an important consideration that affects forces experienced by the screws.[3,19] Plate contact surface area is another important characteristic of plates – a smaller bone–plate contact surface area has less negative effects on bone growth, vascularity, and bone healing.[20] Plate shape and profile play a role in the anatomic reduction of a fracture as well as its interactions with the surrounding soft tissue. Plates and screws that protrude into moving structures such as tendons and neurovascular bundles can cause complications.[21] Plate screw hole configuration influences the type of screws a plate can accept and screw density which affect biomechanical behavior. Plates with combination screw holes can accept both locking and nonlocking screws.

Screws are an integral part of plate screw constructs, and there is an equally diverse range of types of screws, which is beyond the scope of this chapter. The impact of biomaterials used in screws is an area of active research, yet to date, physical design factors have had a greater impact on the performance of screws than the materials used. Screw inner diameter, thread pitch, and working length have been shown to affect variables such as yield strength, screw pullout strength, torque resistance, and fatigue strength more than the material composition of the screws.[22] Inner diameter is the diameter of the part of the screw that does not include the threads. Thread pitch is the distance between adjacent threads. Working length is the length of the screw that is in contact with bone.

Of prime importance are two types of screws – locking-head and non-locking-head screws. Non-locking-head screws are screws that can be inserted at any angle into the plate/bone, and require incorporation into the bone in order to maintain compressive forces at the bone–plate interface. Locking-head screws lock into the plate because of its matching threads. The screws are fixed perpendicular to the plate providing angular stability and allowing it to act biomechanically as a single beam construct which increases its strength and resistance to

breakage.[23] Locked-plate–screw constructs also do not need compression at the bone–plate interface, which avoids disruption of periosteal vascularization.[3] On the horizon are polyaxial locking screws that combine the locking-head screw with a swiveling threaded bushing that deforms upon tightening the screw, locking the bushing and screw in place at the chosen angle.[24] The ability to choose screw orientation, reap the biomechanical benefits of angular stability, and eliminate plate–bone contact is extremely promising.

6.616.3.1.2. Applications of biomaterials to plate and screw fixation

Plates and screws used for fixation of fractures have a number of challenges and complications that the design and composition affect. Plates and screws can lead to stress shielding, bone resorption and inhibition of bone formation, local irritation and inflammation, vascular compromise, and infection via a variety of mechanisms. Additionally, over time, plates can break prior to complete fracture healing. Research aimed at avoiding these complications is active in areas such as alloys, surface treatments, and coatings.

The vast majority of plates and screws are made of metallic materials such as stainless steel and titanium. Both materials are relatively biocompatible and while Disegi and Eschbach report that stainless steel possesses bulk mechanical properties such as high strength and stiffness, low weight, ease of handling and manufacture, and cost effectiveness making it practical to use, titanium shares all of these properties. Between the two, stainless steel offers greater stiffness and strength than titanium, although both lead to excellent union rates. While titanium and stainless steel can produce stress shielding, stainless steel has pronounced effects since it eliminates many of the dynamic loads that bone would otherwise experience, and needs in order to maintain its strength.

These concerns led to the development of titanium plates, which have a lower modulus of elasticity. This tends to attenuate the effects of stress shielding, although not completely eliminating them. Titanium plates were additionally found to have superior fixation strength, screw torque-out strength, and fewer loose screws when compared to stainless steel plates in animal fracture models.[25] Titanium screws were shown to have longer fatigue life than stainless steel screws, and both constructs were shown to result in bone of equal strength at the end of healing.[22] Additionally, titanium is better visualized on radiographic and computed tomography images. Other materials such as biodegradable plates made from biopolymers such as poly-L-lactic acid (PLA) and poly-glycolic acid (PGA) have been tested, although concerns over their inferior fatigue life, reduced torque strength, and rapid degradation have led to recommendations that they are used for only non-weight-bearing, rapidly healing fractures such as maxillofacial and carpal/metacarpal fractures. Further research and development is warranted however as biopolymer plates and screws hold theoretical advantages such as diminished stress shielding with gradual load transfer to bone, reduced need for hardware removal, increased biocompatibility, and radiolucency.[26] Ultimately, research into newer alloys such as magnesium–calcium hybrids and nitinol (nickel–titanium) promises to eliminate some of the problems of stress shielding found in metallic alloys. Magnesium–calcium and nitinol both have a modulus of elasticity that is very close to that of bone. Nitinol is superelastic with shape-memory properties that may be beneficial to fatigue life and strain minimization.[27] Magnesium calcium alloys may be osteoconductive, and the products of degradation are utilized by normal biochemical pathways.[28]

Stainless steel, although corrosion resistant, does corrode with time. The release of nickel and chromium ions into surrounding tissue can cause irritation, inflammation, local microvascular compromise, type IV allergic-type hypersensitivity reactions, and decreased resistance to infection.[29,30] These reactions have been shown to cause decreases in implant strength, osteoblast cellularity, and bone apposition as well as increases in bone resorption.[31] Additionally, there are several case reports of rare connective tissue neoplasms such as angiosarcoma, fibrosarcoma, and osteosarcoma arising adjacent to stainless steel plates.[32–34] While titanium is widely viewed as more biocompatible than stainless steel, with less corrosion, titanium particles have some inhibitory effects on osteoblast cytoskeletal function, impairing adhesion, proliferation, and viability, however less so than stainless steel.[35,36] Although biopolymers do not exhibit as many problems with biocompatibility as metals, they have been shown to lead to reactions such as osteolysis, synovitis, and sterile sinus tract and abscess formation.[10] Alloys such as magnesium–calcium can also exhibit rapid degradation,[28] leading to serious magnesium or calcium toxicity that can negatively affect cardiac functioning. These complications are uncommon, however, with the vast majority of patients experiencing few to no side effects. Nevertheless, additional research is underway aiming to improve the suitability of these promising materials for use in plate and screw fixation.

Closely related to biocompatibility is infection resistance. Infection is a serious, oftentimes grave complication of internal fixation and can lead to premature implant removal, nonunion, sepsis, and potentially death. Avoidance of infection, therefore, is of paramount concern that should extend from the operating room to the design and manufacture of internal fixation devices. While showing more resistance to infection than stainless steel, titanium implants are still susceptible to wound infections.[23,37–39]

Arising from these concerns, several common surface treatments are being developed to improve biocompatibility, osteoblast proliferation, and viability, and decrease susceptibility to bacterial adherence and colonization. Improvement of the surface wettability characteristics of stainless steel by CO_2 laser leads to improved cell proliferation regarding osteoblast adherence, spread, and rate of growth.[40] UV irradiation of titanium surfaces, also leading to increased wettability, did not alter human osteoblast adhesion or function, but did reduce bacterial adhesion.[41] Production of microroughened ultrafine-grain pure titanium through the use of equal channel angular pressing showed better osteoblast compatibility over other titanium implant materials.[42] Laser shock peening (LSP) of magnesium–calcium alloys improved the corrosion profile, considerably slowing its degradation, as well as producing a surface effect analogous to microroughening which is favorable for osteoblast adherence and growth.[28] Lastly, increasing surface porosity of stainless steel and inducing surface hydrophobicity in titanium sheets by treatment with butanol were found to attenuate inflammatory responses to the materials *ex vivo*.[43]

Several surface coatings that improve biocompatibility are currently being tested. Phosphate-ion incorporated micro-roughened titanium surfaces showed significant increases in cell attachment and growth, with higher torque removal forces, and increased osteoblastic gene expression compared to untreated surfaces.[44] Tantalum and hydroxyapatite and multi-walled carbon nanotube composite coatings of titanium and stainless steel can lead to better cell–implant interactions and higher living cell densities.[45,46] Coating of titanium alloys with zeolite – a microporous aluminosilicate that can sequester ionic species – can improve their already excellent biocompatibility by reducing the amount of cytotoxic aluminum and vanadium ions an implant can release into surrounding tissue.[47] Processing Ti–13Nb–13Zr alloys with a mixture of minimal essential medium and hydrogen peroxide leads to a porous layer of hydroxyapatite and amino acids that favor the growth of osteoblasts, acclerating osseointegration.[48] Several coatings using collagen have been shown to improve cell adhesion and viability.[14,49]

Another problem with plates is local compromise of circulation. In addition to loss of vasculature associated with implantation, local tissue reaction to plates can have inflammatory effects that can compromise local soft-tissue microcirculation and can lead to local necrosis and nonunion. Compared to stainless steel wear debris, titanium wear particles produce a modest and transient amount of inflammation, with no microcirculatory compromise.[50] Finally, electrocoating stainless steel with a bovine serum albumin derivative showed better biocompatibility in terms of local microvascular sequale, improving healing and incorporation.[51]

Surface coatings also play a role in the prevention of infections. Hydroxyapatite-coated screws show a greater resistance to *Staphylococcus epidermidis* adherence,[52] and chitosan-coated screws and plates have been shown to be bacteriostatic.[53] Silver, silicon polymer, and silicon or nitrogen doped diamond-like carbon (DLC) coatings on implants have reduced bacterial adhesion to components, and have shown efficacy against strains of *Staphylococcus aureus* and *Staphylococcus epidermidis*.[54–56] Hydrogel coatings containing the antibiotic ciprofloxacin are being developed to prevent implant-associated infections in titanium devices.[57] Finally, several coatings that elute drugs, biological factors, and minerals have been investigated with the goal of improving the biological response to growth. PTH- and bisphosphonate-coated stainless steel screws increased pullout strength and energy as well as fixation.[58,59] Plates that elute recombinant human BMP 2 were able to induce new bone formation and heal large segmental bone defects.[60–62] Lastly, strontium-eluting implants are capable of simultaneously stimulating bone formation and inhibiting bone resorption.[44,63]

6.616.3.1.3. Advantages of plate and screw fixation

Plates are particularly advantageous in complex periarticular and metaphyseal fractures where biological, anatomic, and mechanical factors that lead to successful healing favor their use. Fractures in these areas require precise anatomic reduction and heal via intramembranous bone healing. Additionally, the location of the fractures precludes the bony fragments from generating large lever arms and mechanical forces for the plate to counteract, which increases the plate's lifespan. Finally, the excellent blood supply to periarticular regions makes them more resilient in the face of potential vascular compromise.

Anatomic considerations can weigh heavily in deciding if plate osteosynthesis is indicated. It is beneficial in fractures in small or flat bones such as acetabular, facial, or hand fractures. In these cases, reconstruction plates can be contoured, intraoperatively to fit the fracture anatomy. Anatomic considerations also play a role in fractures that are commonly treated with intramedullary nailing, such as intertrochanteric femoral fractures. In this setting, the fracture can compromise areas that the intramedullary nail relies upon, causing that mode of fixation to become unreliable. In this situation, plate fixation may be useful.

Lastly in patients with head injuries, trauma-related medical conditions such as acute respiratory distress syndrome, or patients with extensive concomitant soft-tissue injury requiring vascular repair, or staged repair, plating is a viable option.[64] In this setting, the process of installing a plate can be less physiologically demanding than intramedullary nailing, and with newer techniques such as minimally invasive plate osteosynthesis, may have many of the same benefits.

6.616.3.1.4. Limitations of plate and screw fixation

There are several drawbacks to plate osteosynthesis. Certain types of fractures are more prone to difficulties when repaired with plates, including diaphyseal fractures, transverse fractures, and fractures in weight-bearing bones. Additionally, the process of implantation of plates and their local effects can be harmful as the surgical approach can require extensive soft-tissue stripping.

Simple, transverse fractures occurring in the diaphyseal areas are an example of fracture type and location that can exhibit difficulty in healing when fixed with plates. This is exaggerated in weight-bearing bones. In these cases, the biomechanical and anatomic factors that favored plate osteosynthesis in periarticular and comminuted or oblique fractures are no longer present. The fracture has long bone ends on either side, but has a short gap, which presents long lever arms, and because of the small gap makes the intraoperative design of low strain environments difficult. High strain in this situation can lead to bone resorption as the bone seeks a way to minimize strain – by increasing the distance between fragments, relative motion causes less strain, allowing healing – albeit by fibrous not bony tissue. Additionally, the mechanical factors at play in this situation maximize forces on the plates, leading to screw toggling, loosening, and ultimately plate breakage.

Additionally, in weight-bearing bones, the effect of stress shielding on bone integrity is amplified, as many plate constructs are load bearing. Stress shielding, leading to bone resorption and stress risers, is the mechanism implicated in early refracture after removal of plates.[13] As plates are placed alongside the bone, but not directly in line with the axial stresses, if stability is not provided, bone will be resorbed to limit the strain. In the setting of segmental defects, this resorption may lead to a nonunion. Stress shielding and nonunions are adverse effects of many plating techniques, and one that has prompted vigorous research. The use of newer metallic alloys and the improvement of biopolymer plates on the horizon may help to eliminate this concern.[65]

Finally, plate osteosynthesis can put nearby neurovascular and moving soft tissue structures at risk. As it is external to the bone, prominent features of the plate may irritate soft tissue.

In the forearm where plate osteosynthesis is the primary method of internal fixation, first-generation plates have been reported to cause tendon irritation and rupture, along with nerve compression.[21,66] The development of low-profile plates and coatings leading to less friction is a promising solution to this problem.

6.616.3.2. Intramedullary Fixation

The concept of intramedullary fixation was introduced in the late 1800s and proved early that it was capable of restoring length, axial rotational, angular alignment, and obtaining union. Intramedullary fixation of fractures is the process of introducing a metal rod (often referred to as a 'nail') into the medullary canal of a long bone. Bircher is credited with the first use in which attempts were made to secure fixation of a fracture using intramedullary ivory pegs.[67] Since that time, the design, technique, and indications for its use have drastically changed, and intramedullary fixation is now considered the standard of care for the treatment of most diaphyseal lower extremity fractures.[4] The distinct advantage to the use of intramedullary fixation is in its intricate design, which allows the nail to share the load with the bone and allow for the indirect reduction of the fracture without exposure of the fracture site. By doing this, it potentially reduces substantial operative time with minimal risk of infection or nonunion.[68]

Intramedullary fixation was initially indicated for fractures of the long bones in which instability of length, rotation, and angulation was of concern.[69] It is considered the gold standard in the surgical fixation of subtrochanteric as well as femoral shaft fractures. As time progressed, the spectrum of intramedullary fixation reached out to encompass a broad range of fractures. While the majority of the literature regarding intramedullary fixation involves fractures of the femur, its use for the correction of both the tibia and humerus has increased dramatically. For example, intramedullary fixation has become a popular treatment for displaced mid-diaphyseal tibial fractures with minimal comminution. As seen with intramedullary fixation for femoral fractures, those of the tibia experience the same benefits of reduced infection rate and early ambulation.[70,71] Although its popularity for the use in fracture of the lower extremities has increased, the role of intramedullary fixation in humeral shaft fractures remains controversial. Bhandari *et al.* performed a meta-analysis of three clinical trials in which intramedullary fixation was compared to plates in patients with humeral shaft fractures. The authors found that plate and screws construct reduced the need for reoperation as well as the prevalence of shoulder impingement. However, there were no differences in the rate of nonunion, radial nerve palsy, or infection.[72,73]

6.616.3.2.1. Design rationale

The healing properties of intramedullary fixation are rooted in its inherent strength and rigidity.[9] The prosthesis acts as an internal splint that aids in the fracture stability, load sharing, and scaffolding, in which the fracture is able to heal. They have a proven track record in providing relative stability with high union rates but low rates of hardware failure, loss of alignment, or infection. This makes intramedullary fixation of fractures a valuable alternative in the armamentarium afforded to orthopedic surgeons.

Intramedullary nails can be classified by anatomical and functional names such as centromedullary, condylocephalic, and cephalomedullary nails.[2] Centromedullary nails, such as those of Kuntscher and Sampson, enter the bone in line with the medullary canal. During the 1940s, Kuntscher introduced a nonlocking nail to be used in diaphyseal fractures of long bones.[74] The nail was made from inert metal, had the cross-section design of a clover leaf, and had a slit-like opening. This design allowed for elastic compression, strength, stiffness, and the ability of the nail to adapt to the canal.[75,76] Condylocephalic nails enter the bone in the condyles of the metaphysis and usually reach the opposite end of the metaphyseal–epiphyseal area. Examples of condylocephalic nails include Ender and Hackenthall pins. This type of intramedullary nail is commonly used in pediatric fractures.[77] Cephalomedullary nails have a centromedullary portion, but also permit fixation up into the femoral head. Zickel nail and Gamma nail are examples of this type.

Addition of interlocking fixation to the intramedullary nails allows a longer working length to the nail and thereby ability to resist both axial and rotational deformation of the fracture. Interlocking fixation is defined as dynamic or static. Dynamic fixation controls bending and rotational deformation but allows axial loading at the fracture site, while static fixation controls rotation, bending, and axial load. Dynamic fixation can be used in fractures that are considered to be axially stable.

6.616.3.2.2. The application of biomaterials in internal fixation

Intramedullary fixation has a biomechanical advantage over plate and screw construct due in part to the shorter distance to the center of the medullary canal. The shorter the distance in which the bending forces act, the lower the moment is on the device.[69] The key to the success of the intramedullary nail is its stiffness, rigidity, and strength.[76] Rigidity is defined from a load–deflection curve for a given structure. Load–deflection curve is divided into elastic and plastic regions. Elastic region represents the ability of the implant to retain its structure after a given load. Once loads exceed the proportional limit, a plastic deformation occurs and the structure of the biomaterials is permanently changed. The slope in the elastic region of this curve reflects the stiffness of the biomaterials. As the slope of the elastic portion of the curve (stiffness) increases, the given structure becomes more rigid. As stiffness decreases, so does the rigidity, and the structure becomes more flexible (plastic). The point at which elastic becomes plastic is known as the proportional limit. It is at this point, that once exceeded, permanent deformation of the device takes place.[76] An intramedullary nail that is loaded beyond the proportional limit can lead to complications such as non or malunited fractures and breaking or deformation of the implant itself. For this reason, the ideal intramedullary fixation device would have a high proportional limit to minimize the potential of these complications.

The biomechanics of the intramedullary implant have a more prominent role in healing than do the biomaterials. Nonetheless, the material of the implant does add to the biomechanical properties. The intramedullary implants most frequently used are made out of stainless steel or titanium. The biomechanical properties of each are different. Titanium

implants are more flexible and have a higher proportional limit than stainless steel. They have an inherent elasticity because of which they can be substantially over bent to maintain a curvature.[78] Stainless steel implants are stiffer and lead to greater fracture stability. Mahar *et al.* demonstrated that when compared to one another in biomechanical testing, titanium nails provide greater fracture stability than a stainless nail. The author postulated that it is due to increased contact of the titanium in the medullary canal as compared to its stainless steel counterpart. The characteristics of the titanium nail allow for the needed flexibility to mold to the naturally curved medullary canal of the femur.

The geometry incorporated into the design of the intramedullary nail is the basis of the implants ability to share the load. Calculating both the area and the moments of inertia enables the computation of bending and torsional forces through the cross-section of the device. The stiffest design (most rigid) is an implant that has the material distributed further away from the bending or torsional axis. This would lead to greater resistance to bending and torsional forces of the intramedullary nail.[9,76] While those with the highest rigidity are able to withstand the greatest forces, it turns out that it is not optimal for fracture healing. Intramedullary nails that have a good balance between rigidity and allowing some movement at the fracture margins have proven to show superior results regarding fracture union.[9]

Prior to the development of the locking intramedullary nail, all intramedullary devices were considered to be dynamic. Intramedullary fixations are determined to be dynamic in nature when only one end (the proximal portion) is locked, thereby allowing the distal fragment to move about the intramedullary device. Current models have predrilled screw holes at either end of the implant that allow for potential static or dynamic locking of the device. In doing so, the proximal and distal fragments of the fracture are potentially fixed in both length and rotation. When statically locked, the intramedullary nail prevents the contact between the two main fragments of the fracture. This allows for rotational control of the epiphyseal–metaphysial fragment.[68] Dynamization of the intramedullary nail can lead to fracture shortening and rotation of the fracture fragments. As the proximal end remains locked, the distal portion acts as a splint. For this reason, dynamic fixation is recommended if sufficient contact between the two main fracture fragments is present or for those fractures that have failed to show healing at 4–6 months after the surgery.[79] Fully threaded distal locking screws are preferred as they have a decreased chance of backing out, requiring additional surgery. While the use of one screw is often adequate, two screws are used in cases of infraisthmal fractures, severely comminuted femoral fractures, or for those patients who will not be compliant with weight-bearing instructions.[79]

6.616.3.2.3. Advantages of intramedullary fixation

The design of the intramedullary prosthesis reduces fracture fragment motion but does not completely eliminate it leading to bridging callus healing. This allows for endochondral healing as opposed to intramembranous healing that is seen in cases of rigid fixation. The presence of motion across the fracture site stimulates vascular invasion as well as increased thermal, mechanical, chemical, and local environmental factors which are all key elements in regulating fracture healing.[76] Intramedullary fixation is load sharing, allowing for minimal stress shielding. As a result, disuse osteoporosis is minimized by allowing the weight-bearing status of patients to be advanced at a quicker rate (once callus formation is confirmed via radiographs) than with plates and/or external fixation.

The procedure of introducing an intramedullary fixation is innately more advantageous than its plating counterpart. By being minimally invasive, the surgeon does not have to expose the fracture site, leaving the blood clot (and it healing properties) intact as well as any callus formation.[69] By not disturbing the fracture site or the hematoma that surrounds it, the copious amounts of natural healing cells in the area of the fracture lead to rapid healing with abundant callus. The act of reaming the medullary canal, to allow for the proper fit of the prosthesis, has an impact on blood flow. It was originally postulated that the reaming interrupts the local blood supply, but was later determined that it in fact may stimulate a periosteal reaction and increase blood supply to the bone.[80,81] In addition, the spillage of the reamings may fill into the fracture site allowing it to act as a natural bone graft. The design and mechanical properties of the nail allow for load sharing, which leads to an increased union rate, rate of healing, and early mobilization. This directly corresponds to a shortened time in the hospital, accrued hospital costs, and exposure to iatrogenic ailments.[82]

6.616.3.2.4. Limitations of intramedullary fixation

While complications are minimal, they are not obsolete. Heavy emphasis is placed on experience of the surgeon. In general, there is always risk of infection and in the case of intramedullary fixation, it has the potential to be problematic. The prosthesis allows easy passage of the organism(s) along the full length of the bone. This often necessitates the usage of intravenous antibiotics and in some cases the removal of the instrumentation. Therefore, it is relatively contraindicated in patients with bone infections. Many patients have also complained about local irritation in the area of the distal or interlocking screw(s). While it is encouraged to keep the hardware intact until the fracture is completely healed, many patients insist on having the screws removed to relieve the pain. The soft tissue irritation could be caused by the design of the screw head or the loosening of the screw as a result of poor purchase into the bone. On rare occasions, there are reported cases of intramedullary hardware that is either deformed and/or breaking, which would necessitate further surgical intervention (**Figure 1**).

Cases of compartment syndrome, malreduction, nonunion, and neurovascular injury have been documented in the use of tibial intramedullary nails. The most common reported adverse event of intramedullary fixation in the tibia is the inability to obtain an anatomical reduction of the fracture. This leads to a rotational malalignment, which is usually well tolerated by the patient.[83,84] With use in the setting of humeral shaft fractures, damages to the radial, axillary, musculocutaneous and median nerves, brachial artery, as well as the rotator cuff, are all possible.

6.616.3.3. External Fixation

Orthopedic surgeons use a variety of strategies to manage fractures of the long bones and pelvis. One particular approach, termed external fixation, involves the stabilization of a fracture

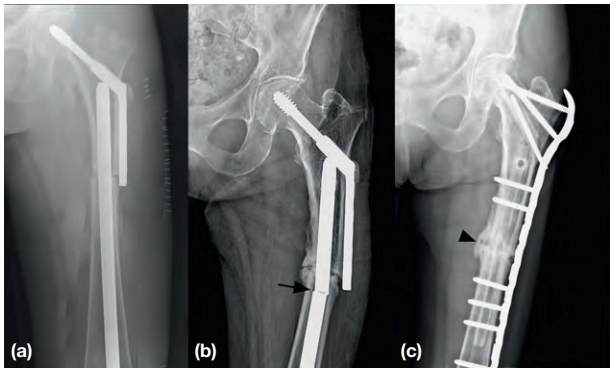

Figure 1 Radiographs demonstrating broken retrograde femoral nail. (a) Anteroposterior radiograph of the left femur showing proximal femoral shaft fracture at the tip of a dynamic hip screw fixation. Patient was treated with unlocked retrograde femoral nail. (b) 3-year post intramedullary fixation anteroposterior radiograph showing fracture of the intramedullary nail just distal to fracture site (arrow). (c) Revision surgery was performed with locking plate and intramedullary strut fibular allograft. This radiograph was taken 4 months after surgery and showed evidence of fracture healing (arrowhead).

site using a metal construct attached to the fracture fragments. The construct, called an external fixator, is primarily external to the skin but also enters the soft tissue envelope and interfaces directly with adjacent bone, maintaining its position to allow for fracture healing. The first modern use of external fixation dates back to the nineteenth century. Its originator is believed to be Joseph-François Malgaigne, a French surgeon who in 1843 used a percutaneous clamp to treat fractures of the patella.[85] In fact, his use of the device predated the development of plaster casts for fracture immobilization.[86] Since the time of Malgaigne, many developments in the design and composition of external fixators have been made and the use of this technique has become widespread within orthopedic surgery. Extensive research and development have brought about the use of external fixation for a wide variety of applications. These include limb lengthening, osteotomy, fusion, deformity correction, transportation of bone for defect reconstruction, and fracture fixation.[86] Among these procedures, the use of external fixation for fracture management remains its most common application.

6.616.3.3.1. Design rationale

While a countless number of configurations exist, all external fixators involve a pin or wire which penetrates skin and affixes to bone, a strut which is either bar-shaped or ring-shaped, and a connection between the two. Multiple iterations of this concept joined together comprise an external fixator. A pin is a metal portion of the construct which passes through the skin and soft tissue and into the bone. In Europe, pins are sometimes referred to as screws or nails. A full pin is one that penetrates the bone and soft tissue envelope on both sides of the extremity, connecting to the rest of the construct at both ends. These are sometimes termed through-and-through pins. A half-pin is a pin that only passes through soft tissue on one side of the extremity but engages both the near and far cortex of the bone in which it is placed. Full and half-pins are typically 2–6 mm in diameter.[86] A wire is a thinner version of a pin, usually less than 2 mm in diameter, which traverses bone and soft tissue and is attached to the rest of the construct on both sides of the limb. A wire is not nearly as stiff as a pin and is not inherently stable unless it is attached to the rest of the external fixator. A pin gripper is a component that attaches a pin or wire to the other portions of the construct. A bar is the element of the external fixator that connects the pin grippers to one another. A ring is similar to a bar and serves the same function, except that it is round, encircles the extremity, and runs perpendicular to the limb rather than parallel to it. A half-ring is also round and serves a function similar to that of a bar, but it does not completely encircle the extremity. Half-rings are used in parts of the body where a full ring could not practically incorporate the entire portion of the anatomy. This tends to be in more proximal portions of the extremities such as the upper thigh and the pelvis. An articulation is a component that connects one bar or ring to another.[4]

Several different configurations of external fixators exist (Figure 2). The choice of construct type depends on several factors, including the clinical scenario, location of the fracture site, and surgeon preference. A unilateral bar construct employs a bar connected to multiple pin grippers along with pins inserted into bone. This is considered the simplest design for external fixation. A bilateral bar external fixator contains a bar on both sides of the affected extremity, connected to full pins via pin grippers. These two bars are arranged in one spatial plane. A multiplanar construct uses pins or wires (connected to bars) oriented in two or more planes in order to increase overall stability of fractured bone. A ring external fixator employs circular bars oriented orthogonal to the affected extremity. Pins are then placed through the limb and connected on both ends to the ring fixator. Rings are then connected to one another by additional bars. This construct was developed and popularized by Russian orthopedic surgeons, including Ilizarov, whose name is often used to refer to the device.[87]

6.616.3.3.2. The application of biomaterials in external fixation

The goal of external fixation is to provide a stable construct that minimizes motion of fracture fragments in order to promote successful bone healing while avoiding infection. As such, orthopedic surgeons face a set of specific, well-characterized challenges in the application of this technique. The most common of these challenges include creating a strong, stabile construct to minimize gross motion at the fracture site, preventing loosening of pins from bone, and preventing infection at pin sites. Both the architectural design of the construct and the properties of biomaterials used in an external fixator play an important role in helping orthopedic surgeons address each of these challenges.

An external fixator must have sufficient stability such that it prevents gross motion about the fracture site that could disrupt the bony contact necessary for bone healing. Several geometric properties of the construct have a direct relationship to the rigidity of an external fixator. These include the number of pins used, the distance between each pin, the modulus of elasticity of each component, the number of distinct planes in which pins are placed, and most importantly pin diameter.[88] The distance between the bars of the external fixator and the involved limb has an inverse relationship to construct rigidity,

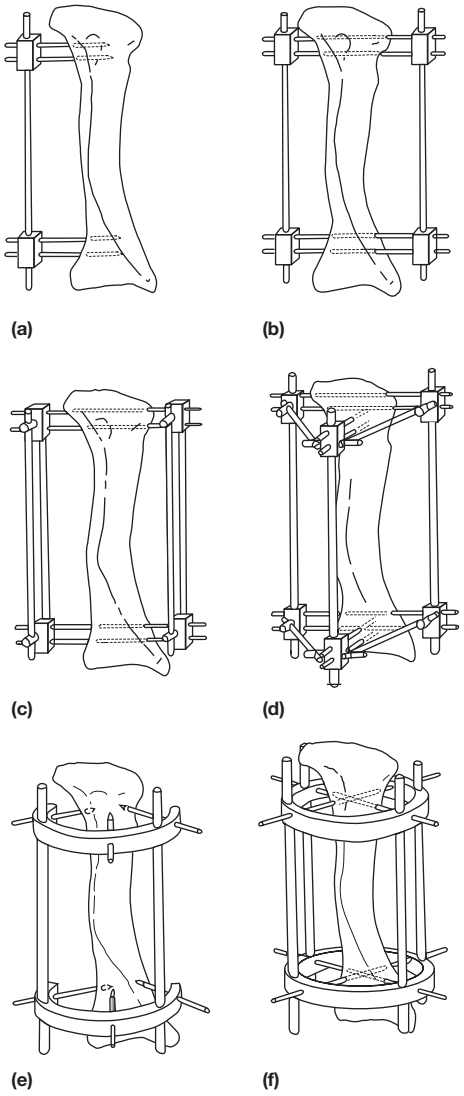

Figure 2 Basic configurations of external fixators: (a) unilateral bar, (b) bilateral bar, (c) quadrilateral multiplanar, (d) triangular multiplanar, (e) half ring, (f) full ring. Reproduced with permission from Stuart A. Green, MD (UC-Irvine).

that is, the closer the bar to the limb, the more rigid is the construct.[88,89] The type of pins used in external fixators has effects on construct rigidity. Stainless steel pins have a higher modulus of elasticity and are more fatigue resistant than titanium alloy pins, reducing the likelihood that they will fail.[86,90] The biomaterials used in bars and rings also affect the stability of external fixation. The stiffness of carbon fiber bars is approximately 15% greater than that of stainless steel tubes.[91] In addition, carbon fiber external fixator bars are radiolucent, meaning that they allow penetration by X-ray energy. This prevents them from obscuring the radiographs that are commonly used to assess fracture alignment in the external fixator during follow-up.

It should be noted that with respect to the overall structural integrity of the external fixator construct, there exists a tradeoff between rigid stabilization of the fracture site and stimulation of bone formation. Absolute rigidity of the construct ensures immobilization of fracture fragments so that movement does not compromise the constant bony contact that is essential for bone healing. However, an absolutely rigid external fixator will also shield the fracture site from compressive forces, detracting from stimulation of bone formation (stress shielding). To date, no data exist on the optimal ratio between absolute rigidity and flexibility that best allows for fracture healing in external fixation. In order to balance these opposing biomechanical principles, orthopedic surgeons rely on a feature of certain external fixators termed dynamization.[86] Dynamization refers to the process by which an external fixator acts to neutralize forces in the plane parallel to the fracture (often perpendicular to the extremity) while allowing for motion and compression in the axial direction, perpendicular to the fracture. Dynamization can be accomplished either by weight bearing on the extremity or by sequential adjustment of the pins of the external fixator to apply compression across the fracture site. Certain 'sliding' external fixators exist which allow pin gripper components to move along the bar to which they are attached, creating a dynamization.[92]

Loosening of the external fixators at the pin–bone interface presents a challenge because it can compromise the structural integrity of the fixator. Biomaterials play an important role in overcoming this obstacle. In particular, the coating of fixator pins with various materials has been investigated as a potential solution. As early as 1913, pins were coated with nickel and gold.[93–95] Since that time, many formulations of coatings have been investigated for their effect on pin loosening. Of all the different pin coatings in use today, hydroxyapatite has probably been the most widely studied. In both animals and humans, hydroxyapatite coating has been repeatedly shown to increase the strength of the interface between external fixation pin and bone, decreasing the likelihood of pin loosening.[96–98] Hydroxyapatite coating improves integration of bone with the metal implant by increasing bony ingrowth into the pin, hence increasing strength.[11,99] This property is of particular interest under the special circumstance in which patients with fractures in osteoporotic bone are treated with external fixation, as it is very difficult to prevent pin loosening in this patient population. Moroni and colleagues studied patients treated for wrist fractures with external fixation who were randomized to use either hydroxyapatite-coated pins or plain pins.[99] They found that the hydroxyapatite-coated pins demonstrated stronger pin–bone integration as measured by a statistically significant difference in the extraction torque necessary for removal. Moroni's findings suggest a unique role for hydroxyapatite in this clinical scenario. Both titanium and silver coatings have been investigated with regard to their potential to prevent pin loosening, but results have not been convincing enough to drive their use in clinical practice.[100–102] DLC, of considerable interest as a coating for prostheses, has gained attention for its potential to improve the pin–bone interface.[103,104] Early *in vitro* data suggest that the attachment of biological tissue to DLC-coated pins may be improved, but the coating has not been investigated in human trials for this purpose.[105]

Infection of external fixator pin sites, also termed pin sepsis, presents one of the considerable challenges in using this technique, occurring at a rate of up to 30%.[106] Pin sites are particularly vulnerable to infection because they provide a continuous

tract from the skin, which is universally colonized with many different types of bacteria. Pins made of different biomaterials have varying resistance to pin site infection. In comparison to stainless steel pins, titanium pins have better biocompatibility, better bony ingrowth, and have been shown in a randomized, prospective study to have lower rates of pin sepsis.[107] Of the coatings examined for this purpose, hydroxyapatite has been most extensively studied. Hydroxyapatite coatings have consistently been shown to be effective at decreasing rates of pin tract infection[98,108,109] and this may be related to its enhancement of osseointegration. Coating of external fixator pins with silver has also been investigated as a strategy for preventing pin sepsis. While silver coating was shown to be capable of preventing infection in animals and in human trials, concerns over leeching of silver into the blood precluded further consideration of its use for this purpose.[110,111] Antibiotic-based coatings, such as tobramycin-impregnated polymethylmethacrylate (PMMA) and combined minocycline/rifampin formulations, have been investigated in animal models and have shown efficacy in reducing pin site infection.[112,113] However, their utility in improving clinical outcomes in humans has not yet been demonstrated. As with pin loosening, the ability of DLC to prevent infection at pin sites has been studied and shown to be effective at reducing the number of bacterial colonies cultured from external fixation pins in an animal model.[105] These results have not yet been replicated in human subjects and so clinical use of this type of coating remains theoretical.

6.616.3.3.3. Advantages of external fixation

The application of external fixation has certain advantages. First, it allows for the rapid immobilization of a fracture in patients with significant soft tissue injury and damage to nearby arteries or nerves. In this setting, delicate repairs of these structures are carried out and require time to heal, during which the extremity must be immobilized. In addition, in cases with significant soft tissue damage, the soft tissue envelope may not be immediately amenable for open reduction of the fracture. If open surgery were to be undertaken in these cases, breakdown of the skin and soft tissues could cause internal hardware to be exposed. Exposure of internal hardware could lead to bacterial colonization of the implant and thus result in a serious infection of the limb. External fixation allows the surgeon to adequately immobilize the fracture during the time period necessary for the inflammation in the surrounding soft tissues to subside. External fixators are also advantageous in that they allow for constant adjustments to be made during the postoperative period in order to maximize bone healing. This may consist of moving fracture fragments into better alignment or even applying compressive forces across the fragment, as in dynamization.

There is currently newfound interest in expanding the traditional uses of external fixation, resulting, to some degree, from advances in biomaterials. Because of the advantages of external fixation, some surgeons believe that external fixation could play a role in the rescue of failure of internal fixation. This would be particularly useful in patients who are too sick to tolerate an extensive surgical procedure. In this scenario, external fixation could produce adequate fracture healing, albeit at the relatively minor cost of temporary inconvenience to the patient.

6.616.3.3.4. Limitations of external fixation

Limitations of external fixation include the significant skill level and training needed to place pins and create a stable construct. Development of this skill takes many years of training and is not widely possessed by nonresidency-trained orthopedic surgeons. External fixation is also difficult to employ across joints. Furthermore, external fixators require a high level of patient compliance in order to prevent compromise of the construct. Patients usually need to restrict their weight bearing on the affected extremity. If not kept clean, pin sites can quickly become infected. Some patients may find external fixators to be cumbersome and inconvenient.

6.616.3.4. Structural Augmentation

Over the past half-century, major advancements have been made in manufacturing fixation devices for the treatment of fractures. Despite these advancements, 5–10% of all annual fractures occurring in the United States show evidence of delayed or impaired healing,[114] emphasizing the need for methods of augmentation. The ability to provide stability at a fracture fixation site has significant effects on successful bone healing. Factors affecting fixation site stability include the patient's bone quality, initial extent of fracture displacement, and severity of fracture comminution.[115] As a result, several manufacturers have developed synthetic materials designed to stabilize comminuted bone fragments, facilitate load transfer in regions of metaphyseal fractures, and better secure internal fixation devices in the setting of poor bone quality.[115]

Although most fractures heal spontaneously, there are certain fractures in which structural augmentation has proven beneficial by reducing the risk of hardware-failure related impaction, facilitating early weight bearing, and improving overall clinical outcome.[116–120] Common examples of fractures requiring structural augmentation are those of the tibial plateau, vertebral bodies, and femoral intertrochanteric region. For example, unstable intertrochanteric fractures are routinely treated surgically with internal fixation using a fixed-angle sliding hip screw in an effort to facilitate early weight bearing; however, these devices are associated with mechanical failure rates as high as 16–23% with 76% of failure occurring due to collapse of the femoral neck-shaft angle into a varus position, causing extrusion or 'cut-out' of the hip screws from the femoral head.[121,122] In the past, an acrylic cement known as PMMA was routinely used for structural stabilization of the fixation construct, but this cement has failed to achieve wide clinical acceptance due to complications such as thermal necrosis, disturbance of healing, and difficulty of removal in the event of revision surgery.[123,124] Newer nonthermogenic ceramics have since been developed with capabilities of *in vivo* remodeling and replacement by host bone, while maintaining properties necessary for structural augmentation.[4,116] In this section, we discuss newer augmentation materials and their clinical applications: calcium phosphate ceramics, with subgroups of CPCs, hydroxyapatite, and TCP; glass ceramics; polymers; and composites.

6.616.3.4.1. Calcium phosphate ceramics

Calcium phosphate ceramics are highly oxidized mineral salts made into a polycrystalline structure by a process called sintering. Sintering fuses the compounds by heating to over 1000°C

Table 1 A comparison of mechanical properties between bone and selected ceramics[159–193]

	Examples of products	*Composition*	*Compressive strength (MPa)*	*Tensile strength (MPa)*	*Elastic modulus (GPa)*
Cancellous bone			5.5	3	1
Cortical bone			162	151	15
Calcium phosphate cement	Norian SRS	Carbonated hydroxyapatite (dahllite)	55	2.1	–
Coralline hydroxyapatite	ProOsteon	$Ca_5(PO_4)_3OH$	9.3	2.8	85
Glass	Bioglass	$Na_2O–CaO–SiO_2P_2O_5$	–	42	35
	AWGC	Apatite–wollastonite	–	215	118
Composite	Cortoss	Combeite reinforced Bis-GMA/Bis-EMA/ TEGDM A polymer resins	146	–	–
Polymer	Depuy 1, Palacos, Osteobond, Simplex P	PMMA	90	6.9	–

AWGC, apatite-wollastonite glass ceramic; Bis-EMA, bisphenol-a-ethoxy dimethacrylate; Bis-GMA, bisphenol-a-glycidyl dimethacrylate; Mpa, megapascal; GPa, gigapascal; PMMA, polymethylmethacrylate; TEGDMA, triethylene glycol dimethacrylate; –, no data available in the current literature.

Adapted from Gheduzzi, S.; Webb, J. J.; Miles, A. W. *J Mater. Sci. Mater. Med.* **2006**, *17*(5), 421–426; Moore, W. R.; Graves, S. E.; Brain, G. I. *ANZ J. Surg.* **2001**, *71*(6), 354–361.

and in the process, decreases the amount of unstable and weakly soluble calcium apatite in the scaffold.[4,125] Ceramics are generally considered to be chemically and biologically inert. Ceramics obtain these properties from the large heat of formation released during the sintering process; thus placing them in a very low energy and biocompatible state.[126] Ceramics are also generally known to be brittle and have poor tensile strength, limiting their use primarily to that of filling bone voids and restoring areas of bone loss resulting from fractures.[125] Nevertheless, calcium phosphate ceramics have proven useful in various orthopedic applications such as improving the mechanical holding strength of screws and conventional fixation devices.[115,125] These synthetic bone scaffolds have also been used as local delivery vehicles for growth factors, osteoprogenitor cells, and antibiotics.[4,127]

6.616.3.4.1.1. Calcium phosphate cements

Inorganic calcium and phosphate can be combined into an injectable paste to be delivered percutaneously into the cancellous bone of a fracture site in order to structurally augment bone healing.[128] Several injectable CPCs (Bone Source, Alpha-BSM, Biopex) are either in preclinical animal studies or human pilot studies, but none is as well established and documented in clinical use as Norian SRS (skeletal repair system; Norian Corp., Cupertino, CA).[129] It is a fast-setting cement that hardens within minutes *in vivo*, forming a carbonated mineral apatite known as dahllite.[4,125] Dahllite formation is 85–90% complete by 12 h with a composition and crystal morphology similar to that of mineralized bone.[128] It exhibits a higher maximum compressive strength and similar tensile strength as cancellous bone[128,130] (**Table 1**). Because of its crystalline structure, Norian SRS is resorbable over months and animal models have shown that it undergoes cell-mediated *in vivo* remodeling with replacement by host bone. Norian SRS is osteoconductive, but functions primarily in improving the mechanical stability of internal fixation devices in skeletal injuries, decreasing the time to full weight-bearing and total functional recovery.[4]

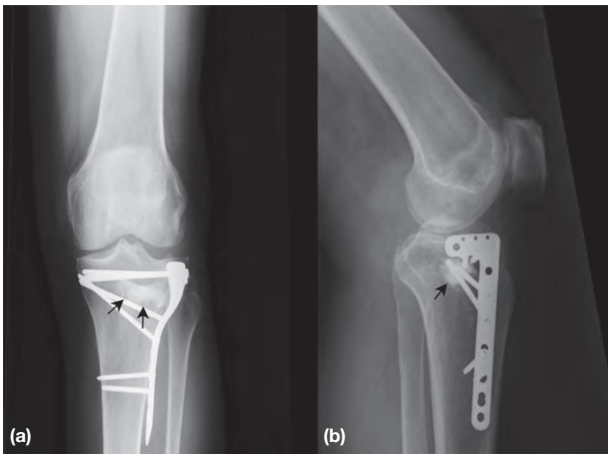

Figure 3 Radiographs demonstrating the application of calcium phosphate cement (Norian SRS). (a) An anteroposterior radiograph of the left knee showing the use of calcium phosphate bone cement (arrows) to fill the defect after tibial plateau fracture. (b) Bone cement can be used as an adjunct to increase the purchase of screws during fracture fixation (arrow). Courtesy of David L. Helfet, MD.

Unlike PMMA, Norian SRS is nonexothermic, eliminating the drawback of thermal necrosis.[119] As it is resorbable, it also eliminates the need for cement removal during revision surgery. The disadvantages of Norian SRS include its low tension and shear strength and an increased perioperative blood loss secondary to an increase in operating time.[115]

In regards to fracture healing in weight-bearing regions, CPCs have been applied as structural adjuncts in calcaneal, tibial plateau, and intertrochanteric fractures (**Figure 3**). Mattsson *et al.* augmented dynamic hip screw fixation of unstable intertrochanteric fractures by injecting approximately 20 ml of Norian SRS into the proximal femur using a curved needle. The goal of this approach was to achieve cement filling of the posteromedial gap with the intent of producing a mechanically

stable medial arch, which would provide load-sharing support between the bone and implant. At the 6-weeks postoperative period, patients in the augmented group had statistically significant lower global and pain scores, less pain after walking 50 ft, and better return of the activities of daily living. It is proposed that the more stable fixation in the augmented group reduced the pain of impaction during initial weight bearing, thus facilitating faster functional recovery. In the treatment of tibial plateau fractures, a similar void filling approach has been used along with only cancellous bone screws and temporary Kirschner wires to maintain reduction of the fracture. In this case, the cement was loaded and injected into the subchondral bone defect at the tibial plateau using a delivery gun. Results showed that patients treated with Norian SRS had less plateau depression at 1 year compared to patients treated with buttress-plating.[120] Additionally, Norian SRS has been suggested to permit early full weight bearing in the treatment of calcaneal fractures.[4] Callos (Skeletal Kinetics, Acumed LLC Hillboro, OR) is a next generation injectable CPC. It shares many of the same mechanical and biological properties as Norian SRS. It is non-exothermic, biocompatible, resorbable, and can be drilled and inserted with screws. Callos has superior tensile strength, flexural strength, and fracture toughness compared to Norian SRS.[131]

6.616.3.4.1.2. Hydroxyapatite

Crystalline hydroxyapatite is a slowly resorbing calcium phosphate ceramic that is very stable *in vivo* and has a resorbing rate of 5–15% per year.[132] The most relevant form of porous and highly crystalline hydroxyapatite currently in clinical use is manufactured by a simple hydrothermal exchange method, which converts weak calcium carbonate into mechanically superior hydroxyapatite. This crystalline hydroxyapatite is similar to human cancellous bone, exhibiting pore diameters in the range of 230–600 μm.[133] Several synthetic (Synatite, Cerapatite, permaOS, Orthoss) and biologic (Pro-Osteon, Endobon, Pyrost) hydroxyapatites are currently in clinical use. Of these, Pro-Osteon (Interpore, Irvine, CA) is the best known in regards to structural augmentation.[134–136] It is an effective osteoconductive material owing to its function as a matrix scaffold with an extensive interconnected pore system, which allows for bone ingrowth. The biocompatibility of Pro-Osteon and other coralline hydroxyapatites is demonstrated by a lack of local and systemic toxicity *in vivo* and its lack of eliciting a foreign body response.[137] A major disadvantage of this material is its lack of significant resorption, which prevents host bone replacement over time. Moreover, it also lacks osteoinductive properties, limiting its ability to facilitate new bone formation, and many investigators have reported problems of particle migration as a potential complication of using hydroxyapatites.[138]

The clinical applications of hydroxyapatite are mostly limited to serving as a bone graft substitute and coating of other biomaterials. For example, Healos (Depuy, Raynham, MA), is a highly porous and resorbable graft substitute composed of cross-linked type 1 bovine collagen coated with hydroxyapatite. This material can be soaked with concentrated bone marrow aspirate to deliver bone-forming stem cells to a localized area, thus enhancing bone healing.[139] In terms of fracture treatment in weight-bearing bone, Bucholz *et al.* examined the efficacy of ceramic hydroxyapatite in the treatment of split compression fractures of the tibial plateau in humans. After careful elevation of the depressed osteochondral fragments, the dimension of the cancellous defect was measured and an oversized block of coralline hydroxyapatite was approximately shaped to the dimensions of the defect. The newly shaped material was inserted into the void with insertion of additional variable-sized granules of Pro-Osteon. Standard interfragmentary screws and plates were used to stabilize the reduction. Functional knee joint assessments showed no difference between the Pro-Osteon group and control.[4] Similarly, Itokazu *et al.* have since conducted a study using Pro-Osteon for the augmentation of tibial plateau fractures with the exception of performing the procedure arthroscopically.[140]

6.616.3.4.1.3. Tricalcium phosphate

TCP, a fast-resorbing material, undergoes partial conversion to hydroxyapatite *in vivo*.[125] TCP is more porous than hydroxyapatite, thus giving it a faster resorbing rate, but rendering it weaker in compressive testing. TCP is found in two distinct crystalline configurations: α-TCP and β-TCP.[138] β-TCP is more stable and is a very biocompatible material. As TCP resorbs, new bone is formed simultaneously in the area previously occupied by the material. For this reason, TCP is ideally used in cases where resorption of implant material, with subsequent host bone replacement, is desired. Similar to hydroxyapatite, TCP is osteoconductive but not osteoinductive. Another disadvantage of TCP materials is that the parts that are converted to hydroxyapatite are slow to resorb, leaving unwanted fragments in place for years. TCP's unpredictable biodegradation profile has limited its clinical use. The effectiveness of ceramic TCP in treating fracture-related bony defects of the femur, tibia, and calcaneus has been studied with preliminary results indicating its viability as an alternative to cancellous bone grafts. It completely resorbs in 6–24 months, eliminates donor site morbidity, and exhibits an unlimited shelf-life in sterile vials.[141] The clinical applications of pure TCP ceramics such as Vitoss, β-Gran, OsteoPore TCP, and Ossaplast are limited. Composites, such as Graftys BCP, a porous biphasic (60% hydroxyapatite, 40% β-TCP) calcium phosphate ceramic, have wider clinical application in the extremities, spine, and pelvis because of their mechanical stability and ease of handling.[142] Graftys BCP is available as cones, wedges, cylinders, sticks, and granules.

6.616.3.4.2. Glass ceramics

Since the 1970s when Hench discovered Bioglass, several more glasses and glass ceramics have been found with similar ability to bind directly to living bone.[143] However, their weak mechanical properties have restricted their clinical applications to those of low load-bearing capacities. This material is bioactive in the sense that it binds bone by eliciting a response at the interface between material and tissue.[144] *In vitro* testing has shown that Bioglass undergoes a rapid multistage surface reaction, which forms a thin layer of biologically active hydroxy-carbonate apatite, the essential piece to its direct bond to bone.[145] Silicon-based glasses and glass ceramics currently in clinical use include Bioglass and apatite–wollastonite glass ceramics (AWGC), respectively. Bioglass (USBiomaterials, Alachua, FL) is made of SiO_2, Na_2O, CaO, and P_2O_5, while AWGC is composed of oxyapatite,

fluorapatite, and β-wollastonite. Bioactive glasses and bioactive glass ceramics mostly have the same composition, with the exception that P_2O_5 is slightly higher, and there is slightly less Na_2O in glass ceramics.[146] While both materials demonstrate good bonding with bone, AWGC is mechanically superior to Bioglass, thus allowing it to be used in stronger load-bearing applications such as vertebral prosthesis.[145] In granular form, Bioglass and AWGC can be used as bone filler for irregular shape defects. However, there are reports of difficulty in handling the granular forms and maintaining them within the defect. This has prompted a mixture of these materials with other products (i.e., glass–ceramic–fibrin mixture) to make them easier to handle and to facilitate retention within defects.

In clinical practice, the mechanical superiority of AWGC has allowed for its use in various load-bearing capacities such as in vertebral prosthesis, intervertebral disks, and iliac crest in dense bulk form. Dense and porous formulations of AWGC have also been applied as a bone spacer and filler in bulk or granular size.[147] Yamamuro *et al.* used AWGC as vertebral prosthetic replacement of thoracic and lumbar burst fractures.[148] He also applied it as prosthesis for the reconstruction of iliac crests that had undergone large autologous bone graft harvesting and were thus at risk for fracture. Due to its lack of mechanical strength, the clinical use of Bioglass has been limited to applications requiring low load-bearing capacities such as maxillofacial reconstruction and dental applications.[144]

6.616.3.4.3. Polymers

Of the multitude of biodegradable and resorbable organic compounds currently known, only a few possess the biocompatible and mechanical properties essential for use in internal fixation devices.[149] The most suitable and clinically relevant of these compounds are the self-reinforced polymers PLA, PGA, polydioxanone (PDS), and PLA–PGA copolymers. In clinical use, these polymers have been fabricated into mechanically stable implants such as pins, rods, screws, and plates for the purpose of fracture fixation. The emergence of resorbable polymeric implants stems from efforts to undo the long-term complications of metallic implants, which ultimately require surgical removal, exposing patients to potential surgical complications. These implants completely resorb, with subsequent host bone replacement.[149] Their function has been comparable with metallic fixation devices in regards to treatment outcomes and complication rate, making these polymers an attractive adjunct in treating weight-bearing fractures.[150] There are few technical difficulties associated with the use of polymers implants in fracture fixation, most notably the effort to prevent breakage of the implant as it is inserted into the fracture site. This may necessitate special instruments such as a torque screwdriver, drill-bits, and inserters of various sizes.[149] The major disadvantage of using polymers is a reported 7.9% rate of delayed noninfectious inflammatory tissue response requiring surgical drainage. Moreover, these polymer implants cost as much as fifteen times their metallic equivalent. In regards to weight-bearing application for fracture treatment, polymers are often combined with other biomaterials in order to form clinically relevant composites. An example of this is Plexur (Osteotech, Eatontown, NJ), a PLA–PGA copolymer scaffold that contains calcium, phosphate, and trace elements of matrix proteins. It is available in block, cylindrical, wedge, sheet, and granular form.[142] Plexur can be used as bone void filler or to improve purchase of implant materials such as screws.

6.616.3.4.4. Composites

Composite materials are composed of acrylic cements in combination with ceramics.[134] Similar to their constituents, they are biocompatible and bioactive and feature superior mechanical properties, which allows for diverse clinical applications.[129,135] A major advantage of using composites is that the combination of constituents allows it to demonstrate the superior mechanical properties of individual components, while each component can overcome the weaknesses of another. While there are many composites on the market, Cortoss (Orthovita, Malvern, PA) is one material that is well established in clinical use. It is a fast setting, low viscosity tetrapolymer reinforced with glass particles called combeite.[129,135] Similar to glass ceramics, it is available as injectable cement. Compared to PMMA, it has a lower curing temperature and features an optimal and constant viscosity, which minimizes the risk of leaking after placement. Its compressive strength of 211 MPa is over twice that of PMMA.[151]

Cortoss is undergoing clinical trial as a replacement for PMMA in vertebral augmentation, specifically percutaneous vertebroplasty and kyphoplasty.[129,135] It is also in preclinical testing as cement augmentation for proximal femoral fractures.[152] Cortoss serves as a good bone filler in these cases because it shares similar characteristics with human cortical bone. Similarly, Actifuse Synthetic Bone Graft (Apatech, Inc. Foxborough, MA), a silicate-substituted calcium phosphate composite, has also been used as bone void replacement after vertebral compression fracture and subsequent kyphoplasty.[153] Compared to traditional ceramics, silicon-substituted ceramics have shown an enhanced capacity for resorption and bone ingrowth in and around the implanted material.[154]

Fixation of osteoporotic fractures has always proven difficult due to poor bone quality. Cement augmentation of cannulated screws with side holes are currently in clinical use.[155] These screws allow bone cements (Norian SRS or Cortoss) to be injected through the cannula and into the cancellous bone surrounding the threads.[151,156,157] After the cement has hardened, the holding power of the screw is significantly increased. Because of its brittleness, Norian SRS has been known to easily crack, especially during screw insertion. However, drillable forms of Norian reinforced with copolymer fibers are also available. In the event that cannulated screws are not available, cement augmentation can still be achieved by injecting cement into the drill hole, followed by insertion of a standard screw prior to cement hardening.[156]

References

1. Shane, E. *N. Engl. J. Med.* **2010**, *362*(19), 1825–1827.
2. Canale, S. T. *Campbell's Operative Orthopaedics*. Mosby/Elsevier: Philadelphia, 2002.
3. Miller, D. L.; Goswami, T. *Clinical Biomechanics* **2007**, *22*(10), 1049–1062.
4. Browner, B. D. *Skeletal Trauma: Basic Science, Management, and Reconstruction*, Saunders/Elsevier: Philadelphia, 2009; Vol. 4.
5. McKibbin, B. *J. Bone Joint Surg. Br.* **1978**, *60B*(2), 150–162.
6. Hart, J. A.; Miller, M. D. *Miller Review of Orthopaedics*. Saunders/Elsevier: Philadelphia, 2008.

7. Perren, S. M. *J. Bone Joint Surg. Br.* **2002**, *84*(8), 1093–1110.
8. Wright, T. M.; Maher, S. A. In *Orthopaedic Basic Science: Foundations of Clinical Practice*, 3rd ed.; Einhorn, T. A., Buckwalter, J. A., O'Keefe, R. J., American Academy of Orthopaedic Surgeons, Eds.; American Academy of Orthopaedic Surgeons: Rosemont, IL, 2007; pp 65–85.
9. Allen, W. C.; Piotrowshi, G.; Burstein, A. H.; Frankel, V. H. *Clin. Orthop. Relat. Res.* **1968**, *60*, 13–20.
10. An, Y. H.; Friedman, R. J.; Powers, D. L.; Draughn, R. A.; Latour, R. A., Jr. *Clin. Orthop. Relat. Res.* **1998**, *355*, 300–311.
11. Anderson, D. E.; St-Jean, G.; Richardson, D. C.; *et al*. *Acta Orthop. Scand.* **1997**, *68*(6), 571–576.
12. Hidaka, S.; Gustilo, R. B. *J. Bone Joint Surg. Am.* **1984**, *66*(8), 1241–1243.
13. Kessler, S. B.; Deiler, S.; Schiffl-Deiler, M.; Uhthoff, H. K.; Schweiberer, L. *Arch. Orthop. Trauma Surg.* **1992**, *111*(2), 96–101.
14. Müller, M. E.; Perren, S. M.; Allgöwer, M., Eds. *Manual of Internal Fixation: Techniques Recommended by the AO-ASIF Group*, 3rd ed.; Berlin: Springer, 1995; (Arbeitsgemeinschaft für Osteosynthesefragen).
15. Tan, S. L.; Balogh, Z. J. *Injury* **2009**, *40*(7), 683–691.
16. Wagner, M. *Injury* **2003**, *34*(Suppl 2), B31–B42.
17. Perren, S. M. *Injury* **2001**, *32*(Suppl 2), B3–B9.
18. Nana, A. D.; Joshi, A.; Lichtman, D. M. *J. Am. Acad. Orthop. Surg.* **2005**, *13*(3), 159–171.
19. Rozbruch, S. R.; Muller, U.; Gautier, E.; Ganz, R. *Clin. Orthop. Relat. Res.* **1998**, *354*, 195–208.
20. Gardner, M. J.; *et al*. *J. Orthop. Trauma.* **2005**, *19*(9), 597–603.
21. Maschke, S. D.; *et al*. *Hand* **2007**, *2*(3), 144–150.
22. Chao, C. K.; Hsu, C. C.; Wang, J. L.; Lin, J. *Clin. Biomech. (Bristol, Avon)* **2007**, *22*(1), 59–66.
23. Gautier, E.; Perren, S. M.; Cordey, J. *Injury* **2000**, *31*(Suppl 3), C37–C44.
24. Cullen, A. B.; Curtiss, S.; Lee, M. A. *J. Orthop. Trauma* **2009**, *23*(7), 507–513.
25. Seligson, D.; Mehta, S.; Mishra, A. K.; *et al*. *Clin. Orthop. Relat. Res.* **1997**, *343*, 213–223.
26. Ciccone, W. J., II; Motz, C.; Bentley, C.; Tasto, J. P. *J. Am. Acad. Orthop. Surg.* **2001**, *9*(5), 280–288.
27. Kapanen, A.; Ryhänen, J.; Danilov, A.; Tukkanen, J. *Biomaterials* **2001**, *22*(18), 2475–2480.
28. Sealy, M. P.; Guo, Y. B. *J. Mech. Behav. Biomed. Mater.* **2010**, *3*(7), 488–496.
29. Savarino, L.; Maci, G. S.; Greco, M.; Baldini, N.; Giunti, A. *J. Biomed. Mater. Res. B. Appl. Biomater.* **2008**, *86B*(2), 389–395.
30. Hallab, N.; Jacobs, J. J.; Black, J. *Biomaterials* **2000**, *21*(13), 1301–1314.
31. Brown, S. A.; Devine, S. D.; Merritt, K. *Biomater. Med. Devices Artif. Organs* **1983**, *11*(1), 73–81.
32. Harrison, J. W.; McLain, D. L.; Hohn, R. B.; Wilson, G. P., III; Chalman, J. A.; MacGowan, K. N. *Clin. Orthop. Relat. Res.* **1976**, *116*, 253–257.
33. McDonald, D. J.; Enneking, W. F.; Sundaram, M. *Clin. Orthop. Relat. Res.* **2002**, *396*, 206–214.
34. Hinarejos, P.; Escuder, M. C.; Monllau, J. C.; Alvarez, P.; Lloreta, J.; Ballester, J. *Acta Orthop. Scand.* **2000**, *71*(3), 329–332.
35. Saldaña, L.; Vilaboa, N. *Acta Biomaterialia* **2010**, *6*(4), 1649–1660.
36. Pioletti, D. P.; Takei, H.; Kwon, S. Y.; Wood, D.; Sung, K. L. *J. Biomed. Mater. Res.* **1999**, *46*(3), 399–407.
37. Hierholzer, S.; Hierholzer, G.; Sauer, K. H.; Paterson, R. S. *Arch. Orthop. Trauma. Surg.* **1984**, *102*(3), 198–200.
38. Arens, S.; Schlegel, U.; Printzen, G.; Ziegler, W. J.; Perren, S. M.; Hansis, M. *J. Bone Joint Surg. Br.* **1996**, *78B*(4), 647–651.
39. Johansson, A.; Lindgren, J. U.; Nord, C. E.; Svensson, O. *Injury* **1999**, *30*(10), 651–657.
40. Hao, L.; Lawrence, J.; Phua, Y. F.; Chian, K. S.; Lim, G. C.; Zheng, H. Y. *J. Biomed. Mater. Res. B Appl. Biomater.* **2005**, *73*(1), 148–156.
41. Gallardo-Moreno, A. M.; Pacha-Olivenza, M. A.; Saldaña, L.; *et al*. *Acta Biomater.* **2009**, *5*(1), 181–192.
42. Park, J. W.; Kim, Y. J.; Park, C. H.; *et al*. *Acta Biomater.* **2009**, *5*(8), 3272–3280.
43. Nygren, H.; Hrustic, E.; Karlsson, C.; Oster, L. *J. Biomed. Mater. Res.* **2001**, *57*(2), 238–247.
44. Park, J. W.; Kim, Y. J.; Jang, J. H.; Kwon, T. G.; Bae, Y. C.; Suh, J. Y. *Acta Biomater.* **2010**, *6*(4), 1661–1670.
45. Lin, C.; Han, H.; Zhang, F.; Li, A. *J. Mater. Sci. Mater. Med.* **2008**, *19*(7), 2569–2574.
46. Balla, V. K.; Banerjee, S.; Bose, S.; Bandyopadhyay, A. *Acta Biomater.* **2010**, *6*(6), 2329–2334.
47. Bedi, R. S.; Beving, D. E.; Zanello, L. P.; Yan, Y. *Acta Biomater.* **2009**, *5*(8), 3265–3271.
48. Baker, M. A.; Assis, S. L.; Higa, O. Z.; Costa, I. *Acta Biomater.* **2009**, *5*(1), 63–75.
49. Xin, Y.; Jiang, J.; Huo, K.; Hu, T.; Chu, P. K. *ACS Nano* **2009**, *3*(10), 3228–3234.
50. Abarrategi, A.; García-Cantalejo, J.; Moreno-Vicente, C.; *et al*. *Acta Biomater.* **2009**, *5*(7), 2633–2646.
51. Tengvall, P.; Skoglund, B.; Askendal, A.; Aspenberg, P. *Biomaterials* **2004**, *25*(11), 2133–2138.
52. Arciola, C. R.; Montanaro, L.; Moroni, A.; Giordano, M.; Pizzoferrato, A.; Donati, M. E. *Biomaterials* **1999**, *20*(4), 323–327.
53. Greene, A. H.; Bumgardner, J. D.; Yang, Y.; Moseley, J.; Haggard, W. O. *Clin. Orthop. Relat. Res.* **2008**, *466*(7), 1699–1704.
54. Liu, C.; Zhao, Q.; Liu, Y.; Wang, S.; Abel, E. W. *Colloids Surf. B Biointerfaces* **2008**, *61*(2), 182–187.
55. Khalilpour, P.; Lampe, K.; Wagener, M.; *et al*. *J. Biomed. Mater. Res. B Appl. Biomater.* **2010**, *94*(1), 196–202.
56. Miola, M.; Ferraris, S.; Di Nunzio, S.; *et al*. *J. Mater. Sci. Mater. M Medial.* **2009**, *20*(3), 741–749.
57. De Giglio, E.; Cometa, S.; Ricci, M. A.; *et al*. *Acta Biomater.* **2011**, *7*(2), 882–891.
58. Wermelin, K.; Tengvall, P.; Aspenberg, P. *Acta Orthop.* **2007**, *78*(3), 385–392.
59. Hauser, J.; Koeller, M.; Bensch, S.; *et al*. *J. Biomed. Mater. Res. A* **2010**, *94*(1), 19–26.
60. Kirker-Head, C. A.; Gerhart, T. N.; Armstrong, R.; Schelling, S. H.; Carmel, L. A. *Clin. Orthop. Relat. Res.* **1998**, *349*, 205–217.
61. Vogelin, E.; Jones, N. F.; Huang, J. I.; Brekke, J. H.; Lieberman, J. R. *J. Bone Joint Surg. (Am.)* **2005**, *87*(6), 1323–1331.
62. Khan, W.; Kapoor, M.; Kumar, N. *Acta Biomater.* **2007**, *3*(4), 541–549.
63. Kraft, C. N.; Diedrich, O.; Burian, B.; Schmitt, O.; Wimmer, M. A. *J. Bone Joint Surg. Br.* **2003**, *85*(1), 133–141.
64. Ma, C. H.; Yu, S. W.; Tu, Y. K.; Yen, C. Y.; Yeh, J. J.; Wu, C. H. *Acta Orthop.* **2010**, *81*(3), 382–386.
65. Hanafusa, S.; Matsusue, Y.; Yasunaga, T.; *et al*. *Clin. Orthop. Relat. Res.* **1995**, *315*, 262–271.
66. Cohen, M. S.; Turner, T. M.; Urban, R. M. *Clin. Orthop. Relat. Res.* **2006**, *445*, 81–90.
67. Bong, M. R.; Koval, K. J.; Egol, K. A. *Bull NYU Hosp. Jt. Dis.* **2006**, *64*(3–4), 94–97.
68. Winquist, R. A.; Hansen, S. T. *J. Bone Joint Surg.* **1978**, *60*, 934.
69. Sims, S. H. *Orthop. Clin. North Am.* **2002**, *33*(1), 113–126.
70. Jenny, J. Y.; Jenny, G.; Kempf, I. *Acta. Orthop. Scand.* **1994**, *65*, 94–96.
71. Wiss, D. A.; Stetson, W. B. *Clin. Orthop. Relat. Res.* **1995**, *315*, 56–63.
72. Bhandari, M.; Devereaux, P. J.; Mckee, M.; *et al*. *Acta Orthop.* **2006**, *77*, 175–176.
73. Lin, J. *Clin. Orthop. Relat. Res.* **2002**, *403*, 213–220.
74. Le Vay, A. D. *J. Bone Joint Surg.* **1950**, *32*, 698.
75. Christensen, N. E. *Clin. Orthop. Relat. Res.* **1976**, *115*, 182–188.
76. Tarr, R. R.; Wiss, D. A. *Clinincal Orthop. Relat. Res.* **1986**, *212*, 10–17.
77. Roposch, A.; Linhart, W. E. *J. Pediatr. Orthop.* **2002**, *22*(4), 556–557.
78. Mahar, A. T.; Lee, S. S.; Lalonde, F. D.; Impelluso, T.; Newton, P. O. *J. Pediatr. Orthop.* **2004**, *24*(6), 638–641.
79. Winquist, R. A. *J. Am. Acad. Orthop. Surg.* **1993**, *1*(2), 95–105.
80. Kellam, J. F. *Orthopedics* **1985**, *8*, 1387–1388.
81. Pape, H. C.; Giannoudis, P. *J. Bone Joint Surg.* **2007**, *89*(11), 1421–1426.
82. Wu, C. C.; Lee, Z. L.; Shih, C. H. *J. Trauma* **1991**, *31*(3), 326–333.
83. Kahn, K. M.; Beals, R. K. *J. Trauma* **2002**, *53*, 549–552.
84. Puloski, S.; Romano, C.; Buckley, R.; *et al*. *J. Orthop. Trauma* **2004**, *18*, 397–402.
85. Bartonicek, J. *Arch. Orthop. Trauma Surg.* **2010**, *130*(11), 1385–1396.
86. Rockwood, C. A.; Green, D. P.; Bucholz, R. W. *Rockwood & Green's Fractures in Adults*; Lippincott, Williams & Wilkins: Philadelphia, PA, 2010; [database online].
87. Martinez, R. L.; Shampo, M. A.; Kyle, R. A. Ilizarov, G. A. *Mayo Clin. Proc.* **2002**, *77*(4), 304.
88. Rodriguez-Gonzalez, F.Á. *Biomaterials in Orthopaedic Surgery*; ASM International: Materials Park, OH, 2009.
89. Fragomen, A. T.; Rozbruch, S. R. *HSS J.* **2007**, *3*(1), 13–29.
90. Kasman, R. A.; Chao, E. Y. *J. Orthop. Res.* **1984**, *2*(4), 377–384.
91. Kowalski, M.; Schemitsch, E. H.; Harrington, R. M.; Chapman, J. R.; Swiontkowski, M. F. *J. Orthop. Trauma* **1996**, *10*(7), 470–475.
92. Matsushita, T.; Nakamura, K.; Ohnishi, I.; Kurokawa, T. *Med. Eng. Phys.* **1998**, *20*(1), 66–69.
93. Moroni, A.; Faldini, C.; Pegreffi, F.; Giannini, S. *J. Biomed. Mater. Res.* **2002**, *63*(1), 61–64.
94. Moroni, A.; Faldini, C.; Rocca, M.; Stea, S.; Giannini, S. *J. Orthop. Trauma* **2002**, *16*(4), 257–263.

95. Moroni, A.; Vannini, F.; Mosca, M.; Giannini, S. *J. Orthop. Trauma* **2002**, *16*(3), 189.
96. Augat, P.; Claes, L.; Hanselmann, K. F.; Suger, G.; Fleischmann, W. *J. Appl. Biomater.* **1995**, *6*(2), 99–104.
97. Magyar, G.; Toksvig-Larsen, S.; Moroni, A. *J. Bone Joint Surg. Br.* **1997**, *79*(3), 487–489.
98. Moroni, A.; Toksvig-Larsen, S.; Maltarello, M. C.; Orienti, L.; Stea, S.; Giannini, S. *J. Bone Joint Surg. Am.* **1998**, *80*(4), 547–554.
99. Moroni, A.; Faldini, C.; Marchetti, S.; Manca, M.; Consoli, V.; Giannini, S. *J. Bone Joint Surg. Am.* **2001**, *83A*(5), 717–721.
100. Bosetti, M.; Masse, A.; Tobin, E.; Cannas, M. *Biomaterials* **2002**, *23*(3), 887–892.
101. Coester, L. M.; Nepola, J. V.; Allen, J.; Marsh, J. L. *Iowa Orthop. J.* **2006**, *26*, 48–53.
102. Moroni, A.; Aspenberg, P.; Toksvig-Larsen, S.; Falzarano, G.; Giannini, S. *Clin. Orthop. Relat. Res.* **1998**, *346*, 171–177.
103. Butter, R. S.; Lettington, A. H. *J. Chem. Vapor Depos. (USA)* **1995**, *3*(3), 182–192.
104. Dearnaley, G.; Arps, J. H. *Surf. Coat. Technol.* **2005**, *200*(7), 2518–2524.
105. Smith, T. J.; Galm, A.; Chatterjee, S.; *et al. J. Orthop. Res.* **2006**, *24*(7), 1377–1383.
106. Parameswaran, A. D.; Roberts, C. S.; Seligson, D.; Voor, M. *J. Orthop. Trauma* **2003**, *17*(7), 503.
107. Pieske, O.; Geleng, P.; Zaspel, J.; Piltz, S. *J. Trauma* **2008**, *64*(5), 1275–1280.
108. Moroni, A.; Heikkila, J.; Magyar, G.; Toksvig-Larsen, S.; Giannini, S. *Clin. Orthop. Relat. Res.* **2001**, *388*, 209–217.
109. Pommer, A.; Muhr, G.; David, A. *J. Bone Joint Surg. Am.* **2002**, *84A*(7), 1162–1166.
110. Collinge, C. A.; Goll, G.; Seligson, D.; Easley, K. J. *Orthopedics* **1994**, *17*(5), 445–448.
111. Masse, A.; Bruno, A.; Bosetti, M.; Biasibetti, A.; Cannas, M.; Gallinaro, P. *J. Biomed. Mater. Res.* **2000**, *53*(5), 600–604.
112. Darouiche, R. O.; Mansouri, M. D.; Zakarevicz, D.; Alsharif, A.; Landon, G. C. *J. Bone Joint Surg. Am.* **2007**, *89*(4), 792–797.
113. Voos, K.; Rosenberg, B.; Fagrhi, M.; Seligson, D. *J. Orthop. Trauma* **1999**, *13*(2), 98–101.
114. Praemer, A.; Furner, S.; Rice, D. P. *Musculoskeletal Conditions in United States*; The American Academy of Orthopaedic Surgeons: Rosemont, IL, 1992.
115. Goodman, S. B.; Bauer, T. W.; Carter, D.; *et al. Clin. Orthop. Relat. Res.* **1998**, *348*, 42–50.
116. Einhorn, T. A. *J. Bone Joint Surg. (Am.)* **1995**, *77*(6), 940–956.
117. Horstmann, W. G.; Verheyen, C. C.; Leemans, R. *Injury* **2003**, *34*(2), 141–144.
118. Lobenhoffer, P.; Gerich, T.; Witte, F.; Tscherne, H. *J. Orthop. Trauma* **2002**, *16*(3), 143–149.
119. Mattsson, P.; Alberts, A.; Dahlberg, G.; Sohlman, M.; Hyldahl, H. C.; Larsson, S. *J. Bone Joint Surg. (Br.)* **2005**, *87*(9), 1203–1209.
120. Simpson, D.; Keating, J. F. *Injury* **2004**, *35*(9), 913–918.
121. Baumgaertner, M. R.; Curtin, S. L.; Lindskog, D. M.; Keggi, J. M. *J. Bone Joint Surg. (Am.)* **1995**, *77*(7), 1058–1064.
122. Davis, T. R.; Sher, J. L.; Horsman, A.; Simpson, M.; Porter, B. B.; Checketts, R. G. *J. Bone Joint Surg. (Br.)* **1990**, *72*(1), 26–31.
123. Harrington, K. D. *J. Bone Joint Surg. (Am.)* **1975**, *57*(6), 744–750.
124. Schatzker, J.; Ha'eri, G. B.; Chapman, M. *J. Trauma* **1978**, *18*(10), 732–735.
125. Finkemeier, C. G. *J. Bone Joint Surg. (Am.)* **2002**, *84A*(3), 454–464.
126. Cooke, F. W. *Clin. Orthop. Relat. Res.* **1992**, *276*, 135–146.
127. Lee, S. H.; Shin, H. *Adv. Drug Deliv. Rev.* **2007**, *59*(4–5), 339–359.
128. Constantz, B. R.; Ison, I. C.; Fulmer, M. T.; *et al. Science (New York, NY)* **1995**, *267*(5205), 1796–1799.
129. Lieberman, I. H.; Togawa, D.; Kayanja, M. M. *Spine J.* **2005**, *5*(6 Suppl), 305S–316S.
130. Rohl, L.; Larsen, E.; Linde, F.; Odgaard, A.; Jorgensen, J. *J. Biomech.* **1991**, *24*(12), 1143–1149.
131. Yetlinker, D. N.; Delany, D.; Constantz, B. R. In vitro and in vivo evaluation of two calcium phosphate cements. *Paper presented at Proceeding of the 50th Annual Meeting of the Orthopaedic Research Society*, San Francisco, USA, 2004.
132. Fleming, J. E., Jr.; Cornell, C. N.; Muschler, G. F. *Orthop. Clin. North Am.* **2000**, *31*(3), 357–374.
133. Bucholz, R. W.; Carlton, A.; Holmes, R. *Clin. Orthop. Relat. Res.* **1989**, *240*, 53–62.
134. Bostrom, M. P.; Lane, J. M. *Spine* **1997**, *22*(24 Suppl), 38S–42S.
135. Heini, P. F.; Berlemann, U. *Eur. Spine J.* **2001**, *10*(Suppl 2), S205–S213.
136. Holmes, R. E.; Bucholz, R. W.; Mooney, V. *J. Bone Joint Surg. (Am.)* **1986**, *68*(6), 904–911.
137. Jarcho, M. *Clin. Orthop. Relat. Res.* **1981**, *157*, 259–278.
138. Damien, C. J.; Parsons, J. R. *J. Appl. Biomater. Off. J. Soc. Biomater.* **1991**, *2*(3), 187–208.
139. Ploumis, A.; Albert, T. J.; Brown, Z.; Mehbod, A. A.; Transfeldt, E. E. *J. Neurosurg. Spine* **2010**, *13*(2), 211–215.
140. Itokazu, M.; Matsunaga, T.; Ishii, M.; Kusakabe, H.; Wyni, Y. *Arch. Orthop. Trauma Surg.* **1996**, *115*(1), 45–48.
141. McAndrew, M. P.; Gorman, P. W.; Lange, T. A. *J. Orthop. Trauma* **1988**, *2*(4), 333–339.
142. Engelhardt, S. A. *Bone graft materials in orthopaedics*. *Orthopaedic Product News* **2008**; May/June.
143. Kokubo, T. *Biomaterials* **1991**, *12*(2), 155–163.
144. Hench, L. L. *J. Am. Ceram. Soc.* **1991**, *74*, 1487–1510.
145. Best, S. M.; Porter, A. E.; Thian, E. S.; Huang, J. *J. Eur. Ceram. Soc.* **2008**, *28*(7), 1319–1327.
146. Rawlings, R. D. *Clin. Mater.* **1993**, *14*(2), 155–179.
147. Kokubo, T.; Kim, H. M.; Kawashita, M. *Biomaterials* **2003**, *24*(13), 2161–2175.
148. Yamamuro, T. In *An Introduction to Bioceramics*; Hench, L. L., Wilson, J., Eds.; World Scientific: Singapore, 1993; Vol. 1, pp 89–104.
149. Bostman, O. M. *J. Bone Joint Surg. (Am.)* **1991**, *73*(1), 148–153.
150. Leong, K. W. *Connect. Tissue Res.* **1995**, *31*(4), S69–S75.
151. Szpalski, M.; Gunzburg, R. *Bull. Hosp. Joint Dis.* **2001**, *60*(2), 84–88.
152. Beckmann, J.; Ferguson, S. J.; Gebauer, M.; Luering, C.; Gasser, B.; Heini, P. *Med. Eng. Phys.* **2007**, *29*(7), 755–764.
153. Hardenbrook, M. A.; Lombardo, S. R. *Neurosurg. Focus* **2006**, *21*(6), E9.
154. Hing, K. A.; Revell, P. A.; Smith, N.; Buckland, T. *Biomaterials* **2006**, *27*(29), 5014–5026.
155. Larsson, S. *Scand. J. Surg.* **2006**, *95*(2), 111–118.
156. Andreassen, G. S.; Hoiness, P. R.; Skraamm, I.; Granlund, O.; Engebretsen, L. *Arch. Orthop. Trauma Surg.* **2004**, *124*(3), 161–165.
157. Stankewich, C. J.; Swiontkowski, M. F.; Tencer, A. F.; Yetkinler, D. N.; Poser, R. D. *J. Orthop. Res.* **1996**, *14*(5), 786–793.
158. Aro, H. T.; Chao, E. Y. *Clin. Orthop. Relat. Res.* **1993**, *293*, 8–17.
159. Aro, H. T.; Kelly, P. J.; Lewallen, D. G.; Chao, E. Y. *Clin. Orthop. Relat. Res.* **1990**, *256*, 260–273.
160. Brinker, M. R.; O'Connor, D. P. In *Review of Orthopaedics*, 5th ed.; Miller, M. D., Ed.; Saunders/Elsevier: Philadelphia, PA, 2008; pp 1–20.
161. Brumback, R. J.; Uwagie-Ero, S.; Lakatos, R. P.; Poka, A.; Bathon, G. H.; Burgess, A. R. *J. Bone Joint Surg.* **1988**, *70*, 1453–1462.
162. Caja, V. L.; Moroni, A. *Clin. Orthop. Relat. Res.* **1996**, *325*, 269–275.
163. Disegi, J. A.; Eschbach, L. *Injury* **2000**, *31*(Suppl 4), 2–6.
164. Ducheyne, P.; Hench, L. L.; Kagan, A., II; Martens, M.; Bursens, A.; Mulier, J. C. *J. Biomed. Mater. Res.* **1980**, *14*(3), 225–237.
165. Egol, K. A.; Kubiak, E. N.; Fulkerson, E.; Kummer, F. J.; Koval, K. J. *J. Orthop. Trauma* **2004**, *18*(8), 488–493.
166. Firkins, P.; Hailey, J. L.; Fisher, J.; Lettington, A. H.; Butter, R. *J. Mater. Sci. Mater. Med.* **1998**, *9*(10), 597–601.
167. Gautier, E.; Sommer, C. *Injury* **2003**, *34*(Suppl 2), B63–B76.
168. Gheduzzi, S.; Webb, J. J.; Miles, A. W. *J. Mater. Sci. Mater. Med.* **2006**, *17*(5), 421–426.
169. Hayashi, K.; Matsuguchi, N.; Uenoyama, K.; Kanemaru, T.; Sugioka, Y. *J. Biomed. Mater. Res.* **1989**, *23*(11), 1247–1259.
170. Lewis, G.; Holland, D. *J. Orthop. Trauma* **1998**, *12*(1), 8–15.
171. Moore, W. R.; Graves, S. E.; Bain, G. I. *ANZ J. Surg.* **2001**, *71*(6), 354–361.
172. Moroni, A.; Cadossi, M.; Romagnoli, M.; Faldini, C.; Giannini, S. *J. Biomed. Mater. Res. B Appl. Biomater.* **2008**, *86B*(2), 417–421.
173. Moroni, A.; Caja, V. L.; Egger, E. L.; Trinchese, L.; Chao, E. Y. *Biomaterials* **1994**, *15*(11), 926–930.
174. Moroni, A.; Caja, V. L.; Maltarello, M. C.; *et al. J. Orthop. Trauma* **1997**, *11*(3), 154–161.
175. Moroni, A.; Faldini, C.; Giannini, S.; Wippermann, B. *Clin. Orthop. Relat. Res.* **2003**, *408*, 262–267.
176. Moroni, A.; Faldini, C.; Pegreffi, F.; Giannini, S. *Clin. Orthop. Relat. Res.* **2004**, *425*, 87–92.
177. Moroni, A.; Pegreffi, F.; Cadossi, M.; Hoang-Kim, A.; Lio, V.; Giannini, S. *Expert Rev. Med. Devices* **2005**, *2*(4), 465–471.
178. Moroni, A.; Pegreffi, F.; Hoang-Kim, A.; Tesei, F.; Giannini, S.; Wippermann, B. *J. Orthop. Trauma* **2008**, *22*(1), 37–42.

179. Moroni, A.; Rocca, M.; Faldini, C.; Stea, S.; Giardino, R.; Giannini, S. *Ann. Chir. Gynaecol.* **1999**, *88*(3), 198–204.
180. Moroni, M.; Privitera, G.; Lazzarin, A.; Celano, V.; Cavalli, G. *Quad. Sclavo Diagn.* **1976**, *12*(2), 207–214.
181. Saithna, A. *Injury* **2010**, *41*(2), 128–132.
182. Sarmiento, A.; Schaeffer, J. F.; Beckerman, L.; Latta, L. L.; Enis, J. E. *J. Bone Joint Surg. Am.* **1977**, *59*(3), 369–375.
183. Savarino, L.; Cenni, E.; Stea, S.; *et al*. *Biomaterials* **1993**, *14*(12), 900–905.
184. Savarino, L.; Stea, S.; Granchi, D.; *et al*. *J. Mater. Sci. Mater. Med.* **1998**, *9*(2), 109–115.
185. Schildhauer, T. A.; Bauer, T. W.; Josten, C.; Muhr, G. *J. Orthop. Trauma* **2000**, *14*(5), 309–317.
186. Smith, E. J.; Ward, A. J.; Watt, I. *Injury* **1993**, *24*(6), 411–415.
187. Stea, S.; Visentin, M.; Savarino, L.; *et al*. *J. Biomed. Mater. Res.* **1995**, *29*(6), 695–699.
188. Tandon, S. C.; Gregson, P. A.; Thomas, P. B. M.; Saklatvala, J.; Singanayagam, J.; Jones, P. W. *Injury* **1995**, *26*(7), 459–462.
189. Vasenius, J.; Helevirta, P.; Kuisma, H.; Rokkanen, P.; Tormala, P. *Clin. Mater.* **1994**, *17*(3), 119–123.
190. Wheeler, D. L.; Montfort, M. J.; McLoughlin, S. W. *J. Biomed. Mater. Res.* **2001**, *55*(4), 603–612.
191. Wood, G. W., II. In *Campbell's Operative Orthopaedics*, 11th ed.; Campbell, W. C., Canale, S. T., Beaty, J. H., Eds.; Mosby/Elsevier: Philadelphia, PA, 2008; pp 3017–3084.
192. Wright, T. M.; Goodman, S. B.; American Academy of Orthopaedic Surgeons, and National Institute of Arthritis and Metabolic Diseases. In *Implant Wear in Total Joint Replacement: Clinical and Biologic Issues, Material and Design Considerations: Symposium, Oakbrook, Illinois, October 2000*, 1st ed.; American Academy of Orthopaedic Surgeons: Rosemont, IL, 2001.
193. Xie, X. H.; Yu, X. W.; Zeng, S. X.; *et al*. *J. Mater. Sci. Mater. Med.* **2010**, *21*(7), 2165–2173.

6.617. Bone Tissue Grafting and Tissue Engineering Concepts

B D Boyan, M I Baker, C S D Lee, and A L Raines, Georgia Institute of Technology, Atlanta, GA, USA
A S Greenwald, Orthopaedic Research Laboratories, Cleveland, OH, USA
R Olivares-Navarrete and Z Schwartz, Georgia Institute of Technology, Atlanta, GA, USA

© 2011 Elsevier Ltd. All rights reserved.

6.617.1.	**Introduction**	238
6.617.2.	**Historical Overview**	238
6.617.2.1.	Ceramics and Glasses	238
6.617.2.1.1.	Calcium phosphates	246
6.617.2.1.2.	Calcium sulfate	246
6.617.2.1.3.	Bioactive glass	246
6.617.2.1.4.	Physical parameters of ceramics and bioactive glasses	246
6.617.2.2.	Polymers	247
6.617.3.	**Polymeric Bone Graft Substitutes to Tissue Engineering**	247
6.617.4.	**Bone Tissue Engineering**	247
6.617.4.1.	Tailoring Biomaterials for New Age Bone Grafts	248
6.617.4.1.1.	Anatomically specific shape and architecture	248
6.617.4.1.2.	Mechanical properties	248
6.617.4.1.3.	Degradation	248
6.617.4.1.4.	Surface chemistry and topographical cues	249
6.617.4.1.5.	Cellular adhesion	249
6.617.4.2.	New Age Bone Graft Approaches	249
6.617.4.2.1.	Implanting *in vitro* cultured tissues	249
6.617.4.2.2.	Delivering MSCs	249
6.617.4.2.3.	Osteoconduction	249
6.617.4.2.4.	Osteoinduction	250
6.617.5.	**Animal Models for Assessing Effectiveness of Bone Tissue Engineering Strategies**	250
6.617.5.1.	Calvarial Defects	250
6.617.5.2.	Maxillary Sinus Augmentation	251
6.617.5.3.	Analysis Methods for Cranial Defects	251
6.617.5.4.	Critical-Sized Segmental Defect	252
References		252

Glossary

Allografts Tissue harvested from one individual and implanted into another of the same species.

Amino acid motif A protein structural unit formed by a particular sequence of amino acids, often linked with a specific function.

Angiogenic factor Substance that contributes to the growth of new blood vessels.

Autograft Tissue from one site implanted in a second site in the same individual.

Bioreactor An apparatus or system that simulates a biological active environment.

Demineralized bone matrix (DBM) Bone that has been demineralized via acid extraction, leaving cell remnants, extracellular matrix, and a small amount of residual mineral.

Histomorphometrics The quantitative study of the organization and structure of a tissue.

Osseointegration The integration of the graft with the surrounding already existing bone.

Osteoconduction The ability of a material to serve as a scaffold on which osteoprogenitor cells in adjacent bone tissue can attach, migrate, proliferate, and synthesize and mineralize osteoid, resulting in new bone formation that is contiguous with existing bone.

Osteogenesis The events that cause bone tissue formation.

Osteoinduction The process by which materials or chemicals cause bone to form *de novo*, that is, unrelated to existing bone. The process involves recruitment of undifferentiated mesenchymal cells and their differentiation into cells of the osteochondral lineage. Osteoinduction is the result of osteogenesis.

Progenitor cells Cells that are committed to one or more lineages, but have not yet exhibited a differentiated phenotype. Osteochondroprogenitor cells are multipotent and may differentiate into chondrocytes or osteoblasts depending on their environment.

Retrovirus An RNA virus that contains reverse transcriptase, which allows it to transcribe RNA into DNA.

Xenograft Tissue from a donor of one species transplanted into a recipient/organism of another species, genus, or family.

6.617.1. Introduction

This chapter reviews current commercially available bone graft substitutes, future directions for bone tissue engineering, and how scientists use animal and *in vitro* models to assess bone graft effectiveness prior to clinical use. The history of bone tissue engineering is as long as humans have had bone injuries. Materials have included allografts, autografts, bone marrow, xenografts, processed bone, calcium phosphates, glass, synthetic polymers, and composites fabricated from among this eclectic group of component parts. Strategies have included *in vivo* recruitment of host cells, production of bone-like constructs *ex vivo*, and various forms of cell therapy. Many approaches work when used in small defects in otherwise healthy bone. The challenge for bone tissue engineering is to effect repair or regeneration of large defects in compromised patients.

6.617.2. Historical Overview

For years, scientists have worked with different materials to create bone graft substitutes that include three primary properties: osteoinduction, osteoconduction, and osteogenicity.[1] Osteoinduction refers to properties that stimulate undifferentiated cells to start differentiating into the bone-forming cell lineage, osteoblasts. In its simplest definition, osteoinductive materials cause bone to form in sites that would otherwise not form bone. Osteoconduction refers to properties that support migration and attachment of osteoblasts and osteoprogenitor cells, providing a substrate for bone ingrowth. An osteogenic material is one that supports new bone formation to a greater extent than would be expected by osteoconduction alone. Nonresorbable materials should result in osseointegration with the surrounding already existing bone. In contrast, resorbable materials should be replaced with bone, ideally as new bone formation occurs.

Autografts, grafts that are transplanted from one part of the body to another within the same individual, are considered to be the optimal material because they provide an osteoconductive surface and they contain osteoprogenitor cells that contribute to the osseointegration process.[2] Autografts are not osteoinductive as this property is defined earlier. Unlike osteoinductive materials, autografts are resorbed when implanted in nonorthotopic sites and new bone does not form.[3,4] Despite this, their osteogenic properties are sufficient in orthotopic sites to support osteogenesis in all but the most difficult cases. Autografts may require additional surgery, there may be loss of donor site sensitivity, quantity may be limited, and there may be pain and risk of infection.[1,5–7] Therefore, bone grafts alternatives started emerging including allografts (tissues/grafts from same species), xenografts (tissues/organs from different species), and synthetic and biological bone substitute materials not from donors.

Allografts are not as osteogenic as autografts but they do have several advantages over autografts. They can be used in large defect sites, there is no donor site morbidity, they are readily available, and they can be modified to be a composite bone graft. As allografts are derived from human donors, there is a risk of disease transmission, immunogenicity, and lack of uniformity in the products.[8,9] The most common allografts include frozen, freeze-dried, and demineralized bone. Most recently, the allograft concept has been extended to include bone that is minimally processed to remove immunogenic cells leaving a tissue that is enriched in progenitor cells.[10]

Demineralized bone matrix (DBM) is produced by acid extraction of human cortical bone leaving cell remnants, extracellular matrix (ECM), and a small amount of residual mineral.[11] DBM is osteoinductive due to the remaining growth factors after the acid extraction, in particular, bone morphogenic proteins (BMPs). When it is implanted in nonorthotopic connective tissues, DBM causes bone to form, satisfying the operative definition of osteoinductivity. Interestingly, BMPs are also present in nondemineralized allograft and autograft, but neither of these types of grafts are osteoinductive under the same experimental conditions as DBM. This suggests that factors other than simply the presence of BMPs play a role, including changes in matrix properties due to the acid extraction, removal of inhibitors, and differences in the initial biological response of peri-implant cells to the implanted materials.

Studies done with commercially available DBM and DBM combined with carriers have determined that there is variability in osteoinductivity between donor batches and tissue banks.[9,12–15] Currently, DBM is commercially available as dried powder, or in combination with gelatin, various hydrogels, lecithin, collagen, hyaluronic acid, bioglass, poly hydroxy acids, reverse copolymers, and calcium sulfate powder. DBM may be combined with carriers in the operating room or commercially to meet different clinical needs. Surgeons frequently premix DBM with autologous blood or autograft inside the operating room, to improve its biological activity and handling characteristics. They may also use it in combination with allograft to provide an osteoinductive stimulus. However, mixing DBM with different carriers can change its properties, in some cases causing particles to swell.

Ideal bone graft materials and substitutes should be osteoinductive, osteoconductive, biocompatible, bioresorbable, similar to bone structurally and mechanically, and must be cost-effective.[16] They should perform as well as autograft at least clinically. This goal may not always be met, but the bone graft material must accomplish the goal of supporting bone formation to a sufficient extent to restore function. There are now at least 200 forms of bone graft materials and substitutes that are approved for use in humans in the United States alone (**Table 1**). Because these materials often provide the scaffolding for bone tissue engineering, it is important to have an overview of their strengths and weaknesses. For the most part, the existing materials fit the tissue engineering concept of providing appropriate surfaces for the attachment, proliferation, and differentiation of osteoprogenitor cells into secretory osteoblasts. In the best of situations, they are osteogenic, recruiting cells in the osteoblast lineage to the site and enhancing their differentiation. A small subset is osteoinductive as well.

6.617.2.1. Ceramics and Glasses

Some of the ceramic-based bone substitutes clinically available are made of calcium phosphates, calcium sulfate, and bioactive

Table 1 Summary of typical bone graft substitutes that are commercially available – 2010

Company	*Commercially available product*	*Composition*	*Commercially available forms*	*Claimed mechanisms of action*	*Burdens of proof*	*FDA status*
AlloSource	AlloFuse™	Hear-sensitive copolymer with DBM	Injectable gel and putty	• Osteoconduction • Bioresorbable • Osteoinduction	• Case reports • Animal studies • Cell culture	510(k) cleared • Bone graft extender • Bone void filler
Biomet Osteobiologics	BonePlast®	Calcium sulfate with or without HA/CC composite granules	Various volumes of power and setting solution	• Osteoconduction • Bioresorbable	• Case reports • Animal studies	510(k) cleared • Bone void filler
	BonePlast® Quick Set	Calcium sulfate	Quick setting paste	• Osteoconductive • Bioresorbable	• Case reports • Animal studies	510(k) cleared • Bone void filler
	InterGro®	DBM in a lecithin carrier	Paste, putty, and mix with HA/CC composite granules	• Ostoconduction • Bioresorbable • Osteoinduction	• Case reports • Animal studies • Every lot tested for osteoinduction	510(k) cleared • Bone graft extender • Bone void filler
	ProOsteon® 500R	Coralline-derived HA/CC composite	Granular or black	• Osteoconduction • Bioresorbable	• Human studies • Case reports • Animal studies	510(k) cleared • Bone void filler
	CONDUIT® TCP Granules	100% β-TCP	Granules	• Osteoconduction • Bioresorbable	• Case reports • Animal studies	510(k) cleared • Bone void filler
DePuy Spine	HEALOS® Bone Graft Replacement	Mineralized collagen matrix	Variety of strip sizes	• Osteoconduction • Creeping substitution • Osteogenesis when mixed with bone marrow aspirate	• Peer-reviewed, published human studies • Case reports • Animal studies	510(k) cleared • Bone void filler: must be used with autogenous bone marrow
Exactech	Optecure®	DBM suspended in a hydrogel carrier	Dry mix kit delivered with buffered saline	• Osteoconduction • Bioresorbable • Osteoinduction • Osteogenesis when mixed with autogenous bone graft	• Human studies • Case reports • Animal studies • Every lot tested *in vivo* for osteoinduction	510(k) cleared • Bone graft extender • Bone void filler
	Optecure® + CCC	DBM and CCC suspended in a hydrogel carrier	Dry mix kit delivered with buffered saline	• Osteoconduction • Bioresorbable • Osteoinduction • Osteogenesis when mixed with autogenous bone graft	• Human studies • Case reports • Animal studies • Every lot tested *in vivo* for osteoinduction	510(k) cleared • Bone graft extender • Bone void filler
	Optefil®	DBM suspended in gelatin carrier	Injectable bone paste-dry powder ready to be hydrated	• Osteoconduction • Bioresorbable • Osteoinduction • Osteogenesis when mixed with autogenous bone graft	• Human studies • Case reports • Animal studies • Every lot tested *in vivo* for osteoinduction	510(k) cleared • Bone void filler

(*Continued*)

Table 1 (Continued)

Company	*Commercially available product*	*Composition*	*Commercially available forms*	*Claimed mechanisms of action*	*Burdens of proof*	*FDA status*
	Opteform®	DBM and cortical cancellous chips suspended in gelatin carrier	Formable putty or dry powder ready to be hydrated	• Osteoconduction • Bioresorbable • Osteoinduction • Osteogenesis when mixed with autogenous bone graft	• Human studies • Case reports • Animal studies • Every lot tested *in vivo* for osteoinduction	510(k) cleared • Bone void filler
	OpteMx®	HA/TCP biphasic combination	Granules, sticks, rounded wedges, wedges and cylinders in several sizes	• Osteoconduction • Bioresorbable • Compressive strength of 400 psi • Osteogenesis and limited osteoinduction when mixed with bone marrow aspirate	• Human studies • Case reports • Animal studies	510(k) cleared • Bone void filler
Integra Orthobiologics/ (IsoTis OrthoBiologics)	Accell Connexus®	DBM, Accell bone matrix, reverse phase medium	Injectable putty	• Osteoconduction • Bioresorbable • Osteoinduction	• Human studies • Case reports • Animal studies • Every DBM lot tested for osteoinduction	510(k) cleared Extremities, pelvis • Bone void filler extremities, pelvis, spine • Bone graft extender
	Accell Evo3™	DBM, Accell bone matrix, reverse phase medium	Injectable putty	• Osteoconduction • Bioresorbable • Osteoinduction	• Animal studies • Every DBM lot tested for osteoinduction	510(k) cleared Extremities, pelvis • Bone void filler extremities, pelvis, spine • Bone graft extender
	Accell TBM®	DBM, Accell bone matrix	Various sized strips	• Osteoconduction • Bioresorbable • Osteoinduction	• Human studies • Case reports • Animal studies • Every DBM lot tested for osteoinduction	510(k) cleared Extremities, pelvis • Bone void filler extremities, pelvis, spine • Bone graft extender
	DynaGraft II	DBM, reverse phase medium	Injectable putty	• Osteoconduction • Bioresorbable • Osteoinduction	• Human studies • Case reports • Animal studies • Every DBM lot tested for osteoinduction	510(k) cleared
	OrthoBlast II	DBM, cancellous bone, reverse phase medium	Injectable putty	• Osteoconduction • Bioresorbable • Osteoinduction	• Human studies • Case reports • Animal studies • Every DBM lot tested for osteoinduction	510(k) cleared Extremities, pelvis • Bone void filler extremities, pelvis, spine Bone graft extender
	Integra Mozaik™	80% highly purified β-TCP/20% highly purified type-1 collagen	Strip and putty	• Osteoconduction • Bioresorbable	• Human studies • Case reports • Animal studies	510(k) cleared Extremities, pelvis Bone void filler

Life Net Health	IC Graft Chamber®	DBM particles and cancellous chips	Lyophilized and packaged in various sizes within a delivery chamber	• Osteoconduction • Bioresorbable • Osteoinduction • Designed to be used with blood, PRP, or bone marrow to enhance DBM activity	• Animal studies • Case reports	• Regulated under CFR 1270 and 1271 as a human tissue and 510(k) cleared
	Optium DBM®	DBM combined with glycerol carrier	Formable putty (bone fibers) and injectable gel (bone particles)	• Osteoconduction • Bioresorbable • Osteoinduction	• Human studies • Case reports • Animal studies	510(k) cleared • Bone void filler
Medtronic Spinal & Biologics	INFUSE® Bone Graft	rhBMP-2 protein on an absorbable collagen sponge	Multiple kit sizes	• Bioresorbable carrier • Osteoinduction • Chemotaxis of stem cells; indirect osteogenesis	• Human studies (level I and level III data) • Case reports • Animal studies	• PMA approved for fusion with spinal cage • PMA approved for open tibia fractures with IM nail
	MasterGraft® Granules	Biphasic calcium phosphate (15% HA/85% β-TCP)	Granules	• Osteoconduction • Bioresorbable	• Animal studies • Case reports	510(k) cleared • Bone void filler
	MasterGraft® Matrix	Biphasic calcium phosphate and collagen	Compression-resistant block	• Osteoconduction • Bioresorbable	• Animal studies • Case reports	510(k) cleared • Bone void filler: must be used with autogenous bone marrow
Medtronic Spinal & Biologics	MasterGraft® Putty	Biphasic calcium phosphate and collagen	Moldable putty	• Osteoconduction • Bioresorbable	• Animal studies	510(k) cleared • Bone graft extender: must be used with autograft • Bone void filler: must be used with autogenous bone marrow and/or autograft and/or sterile water
	MasterGraft® Strip	Biphasic calcium phosphate (15% HA and 85% β-TCP) and collagen	Compression-resistant strip	• Osteoconduction • Bioresorbable	• Animal studies	510(k) cleared • Bone void filler: must be used with autogenous bone marrow
	Osteofil®DBM	DBM in porcine gelatin	Injectable paste and moldable strips	• Osteoconduction • Bioresorbable • Osteoinduction	• Animal studies • Case reports	510(k) cleared • Bone void filler
	Progenix™ Plus	DBM in type-1 bovine collagen and sodium alginate	Putty with demineralized cortical bone chips	• Osteoconduction • Bioresorbable • Osteoinduction	• Animal studies • Case reports	510(k) cleared • Bone graft substitute • Bone graft extender • Bone void filler
	Progenix™ Putty	DBM in type-1 bovine collagen and sodium alginate	Ready-to-use injectable putty	• Osteoconduction • Bioresorbable • Osteoinduction	• Animal studies • Case reports	510(k) cleared Extremities, pelvis • Bone graft substitute • Bone void filler spine • Bone graft extender: must be used with autograft bone
MTF/Orthofix	Trinity Evolution™	Viable cellular bone matrix	Multiple volumes available	• Osteogenesis • Osteoconduction	• Animal studies • Case reports	• Regulated under CFR 1270 and 1271 as a human tissue

(*Continued*)

Table 1 (Continued)

Company	*Commercially available product*	*Composition*	*Commercially available forms*	*Claimed mechanisms of action*	*Burdens of proof*	*FDA status*
MTF/Synthes	DBX®	DBM in sodium hyaluronate carrier	Paste, putty, mix, and strip	• Osteoconduction • Bioresorbable • Osteoinduction	• Human studies • Case reports • Animal studies	510(k) cleared • Bone graft extender • Bone void filler
NovaBone/MTF	NovaBone®	Bioactive silicate	Particulate, putty, and morsels	• Osteoconduction • Bioresorbable • Osteostimulation	• Published human studies • Case reports • Animal studies	510(k) cleared • Bone void filler
Orthovita	Vitoss®	100% β-TCP and 80% β-TCP/ 20% collagen and 70% β-TCP/ 20% collagen/10% bioactive glass	Putty, strip, flow, morsels, and shapes	• Osteoconduction • Bioresorbable • Bioactive/ osteostimulation • Osteogenesis and osteoinduction when mixed with bone marrow aspirate	• Published human studies (levels I and III) • Case reports • Animal studies	510(k) cleared • Bone void filler
Osteotech	GRAFTON® A-Flex®	DBM fiber technology	Round flexible sheet	• Osteoconduction • Osteoinduction • Incorporation/complete remodeling • Osteogenesis when mixed with bone marrow aspirate or autogenous bone graft	• Peer-reviewed published human studies (including levels I–II prospective studies) • Case reports • Animal studies • Every lot tested *in vivo* for osteoinduction	510(k) cleared • Bone graft substitute • Bone graft extender • Bone void filler
	GRAFTON® Crunch®	DBM fibers with demineralized cortical cubes	Packable graft	• Osteoconduction • Osteoinduction • Incorporation/complete remodeling • Osteogenesis when mixed with bone marrow aspirate or autogenous bone graft	• Peer-reviewed published human studies (including levels I–II prospective studies) • Case reports • Animal studies • Every lot tested *in vivo* for osteoinduction	510(k) cleared • Bone graft substitute • Bone graft extender • Bone void filler
	CRAFTON® Flex®	DBM fiber technology	Various sizes of flexible sheets	• Osteoconduction • Osteoinduction • Incorporation/complete remodeling • Osteogenesis when mixed with bone marrow aspirate or autogenous bone graft	• Peer-reviewed published human studies (including levels I–II prospective studies) • Case reports • Animal studies • Every lot tested *in vivo* for osteoinduction	510(k) cleared • Bone graft substitute • Bone graft extender • Bone void filler

	GRAFTON® Gel	DBM in a syringe	MIS and percutaneous injectable graft	• Osteoconduction • Osteoinduction • Incorporation/complete remodeling • Osteogenesis when mixed with bone marrow aspirate or autogenous bone graft	• Peer-reviewed published human studies (including levels I–II prospective studies) • Case reports • Animal studies • Every lot tested *in vivo* for osteoinduction	510(k) cleared • Bone graft substitute • Bone graft extender • Bone void filler
	GRAFTON® Matrix PLF	DBM fiber technology	Single and double troughs	• Osteoconduction • Osteoinduction • Incorporation/complete remodeling • Osteogenesis when mixed with bone marrow aspirate or autogenous bone graft	• Peer-reviewed published human studies (including levels I–II prospective studies) • Case reports • Animal studies • Every lot tested *in vivo* for osteoinduction	510(k) cleared • Bone graft substitute • Bone graft extender • Bone void filler
	GRAFTON® Matrix Scoliosis Strips	DBM fiber technology	Various sizes of strips	• Osteoconduction • Osteoinduction • Incorporation/complete remodeling • Osteogenesis when mixed with bone marrow aspirate or autogenous bone graft	• Peer-reviewed published human studies (including levels I–II prospective studies) • Case reports • Animal studies • Every lot tested *in vivo* for osteoinduction	510(k) cleared • Bone graft substitute • Bone graft extender • Bone void filler
	GRAFTON® Orthoblend Large Defect	DBM fibers with crushed cancellous chips	Packable graft	• Osteoconduction • Osteoinduction • Incorporation/complete remodeling • Osteogenesis when mixed with bone marrow aspirate or autogenous bone graft	• Peer-reviewed published human studies (including levels I–II prospective studies) • Case reports • Animal studies • Every lot tested *in vivo* for osteoinduction	510(k) cleared • Bone graft substitute • Bone graft extender • Bone void filler
	GRAFTON® Orthoblend small defect	DBM fibers with larger cancellous chips	Packable moldable graft	• Osteoconduction • Osteoinduction • Incorporation/complete remodeling • Osteogenesis when mixed with bone marrow aspirate or autogenous bone graft	• Peer-reviewed published human studies (including levels I–II prospective studies) • Case reports • Animal studies • Every lot tested *in vivo* for osteoinduction	510(k) cleared • Bone graft substitute • Bone graft extender • Bone void filler
Osteotech	GRAFTON Plus® Paste	DBM in a syringe	Injectable MIS graft, resists irrigation	• Osteoconduction • Osteoinduction • Incorporation/complete remodeling • Osteogenesis when mixed with bone marrow aspirate or autogenous bone graft	• Peer-reviewed published human studies (including levels I–II prospective studies) • Case reports • Animal studies • Every lot tested *in vivo* for osteoinduction	510(k) cleared • Bone graft substitute • Bone graft extender • Bone void filler

(*Continued*)

Table 1 (Continued)

Company	*Commercially available product*	*Composition*	*Commercially available forms*	*Claimed mechanisms of action*	*Burdens of proof*	*FDA status*
	GRAFTON® Putty	DBM fiber technology	Packable moldable graft	• Osteoconduction • Osteoinduction • Incorporation/complete remodeling • Osteogenesis when mixed with bone marrow aspirate or autogenous bone graft	• Peer-reviewed published human studies (including levels I–II prospective studies) • Case reports • Animal studies • Every lot tested *in vivo* for osteoinduction	510(k) cleared • Bone graft substitute • Bone graft extender • Bone void filler
Regeneration Technologies	BioSet™	DBM combined with natural gelatin carrier	Injectable paste, injectable putty, strips and blocks with cortical cancellous chips	• Osteoconduction • Bioresorbable • Osteoinduction	• Human studies • Case reports • Animal studies • Every lot tested *in vivo* for osteoinduction	510(k) cleared • Bone void filler
Smith & Nephew	VIAGRAF	DBM combined with glucerol	Putty, paste, gel, crunch, and flex	• Osteoconduction • Bioresorbable • Osteoinduction	• Animal studies	510(k) cleared • Bone void filler
Stryker Biotech	OP-1® Implant	rhBMP-7 with type-1 bone collagen	Lyophilized powder reconstituted with saline to form wet sand-like consistency	• Bioresorbable scaffold • Osteoinduction	• Human studies (level I data) • Case reports • Animal studies	• HDF approval for long bone nonunions
	OP-1® Putty	rgBMP-7 with type-1 bone collagen plus carboxymethylcellulose (putty additive)	Lyophilized powder reconstituted with saline to form wet sand-lime consistency	• Bioresorbable scaffold • Osteoinduction	• Human studies (level I data) • Case reports • Animal studies	• HDF approval for revision posterolateral lumbar fusion
Synthes	Calceon® 6	Calcium sulfate	Pellets	• Osteoconduction • Bioresorbable	• Animal studies	510(k) cleared
	chronOS®	β-TCP	Granules, blocks, and wedges	• Osteoconduction • Bioresorbable	• Animal studies	510(k) cleared • Bone void filler
	Norian® SRS®	Calcium phosphate	Injectable paste	• Osteoconduction • Bioresorbable	• Human studies • Case reports • Animal studies	510(k) cleared • Bone void filler
	Norian® SRS® Fast Set Putty	Calcium phosphate	Moldable putty	• Osteoconduction • Bioresorbable	• Human studies • Case reports • Animal studies	510(k) cleared • Bone void filler
Wright Medical Technology	ALLOMATRIX®	DBM with/without CBM in surgical grade calcium sulfate powder	Various volumes of injectable/formable putty	• Osteoconduction • Bioresorbable • Osteoinduction	• Human studies • Case reports • Animal studies • Cell culture	510(k) cleared • Bone void filler
	ALLOMATRIX® RCS	DBM with CACIPLEX™ technology in surgical grade calcium sulfate powder	Various volumes of formable putty	• Osteoconduction • Bioresorbable • Osteoinduction	• Animal studies	510(k) cleared • Bone void filler

	ALLOPURE™	Sterile femoral/tibial allograft	12 mm Evans wedge 6 mm Cotton wedge	• Osteoconduction	• Mechanical testing	• 100% derived from allograft tissue • Regulated under 21 CFR parts 1270 and 1271 as a human tissue
	CANCELLO-PURE® Wedges	Bovine bone	10 mm × 50 mm wedge 12 mm Evans wedge 6 mm Cotton wedge	• Osteoconduction	• Case reports • Animal studies	510(k) cleared • Bone void filler
	CELLPLEX®	β-TCP	Various sized granules	• Osteoconduction • Bioresorbable	• Case reports • Animal studies	510(k) cleared • Bone void filler
	IGNITE®	DBM in surgical grade calcium sulfate powder to be mixed with bone marrow aspirate	Percutaneous graft for problem fractures	• Osteoconduction • Bioresorbable • Osteoinduction	• Human studies • Case reports • Animal studies • Cell culture	510(k) cleared • Bone void filler
	MIIG® X3	High-strength surgical grade calcium sulfate	Minimally invasive injectable graft for compression fractures	• Osteoconduction • Bioresorbable	• Human studies • Case reports • Animal studies	510(k) cleared • Bone void filler
	OSTEOSET®	Surgical grade calcium sulfate	Various sized pellets	• Osteoconduction • Bioresorbable	• Human studies • Case reports • Animal studies	510(k) cleared • Bone void filler
	PRO-DENSE® Injectable Regenerative Graft	75% calcium sulfate and 25% calcium phosphate	Procedure kits, various volumes of injectable paste	• Osteoconduction • Bioresorbable • Dense bone regeneration	• Human studies • Case reports • Animal studies	510(k) cleared • Bone void filler
	PRO-STIM™ Injectable Inductive Graft	50% calcium sulfate, 10% calcium phosphate, and 40% DBM by weight	Procedure kits, various volumes of injectable paste/formable putty	• Osteoconduction • Bioresorbable • Osteoinduction	• Case reports • Animal studies	510(k) cleared • Resorbable calcium salt bone void filler device
Zimmer	CopiOs® Bone Void Filler	Dibasic calcium phosphate and type-1 collagen	Sponge and paste	• Osteoconduction • Accelerated healing versus autograft • Bioresorbable • Osteogenesis and osteoinduction when mixed with bone marrow aspirate	• Case reports • Animal studies	510(k) cleared • Bone void filler: must be used with autologous blood products like blood or bone marrow
	CopiOs® Cancellous Bone Graft	Bovine bone	Cancellous chips, cancellous cubes, and cortico-cancellous wedges	• Osteoconduction	• Case reports • Animal studies	510(k) cleared • Bone void filler
	Puros® DBM	Allograft DBM putty (putty with chips includes allograft chips from the same donor)	Putty and putty with chips	• Osteoconduction • Bioresorbable • Osteoinduction	• Every lot tested in an *in vivo* rat assay for osteoinductive potential demonstrating bone formation in an ectopic model	• 100% derived from allograft tissue • Regulated under 21 CFR parts 1270 and 1271 as a human tissue

glass. The idea of using ceramics as a material for bone grafts derived from the fact that bone mineral is a carbonate-substituted form of calcium hydroxyapatite (HA). Today, various forms of HA are used as bone graft substitutes. In some instances, they are derived from biological sources, including coral and bovine bone. In other cases, they are produced synthetically, resulting in materials that vary in calcium and phosphate content, the presence of other ions such as magnesium, fluoride, nickel and silica, and crystallinity, all of which can impact dissolution rates *in vivo*. Ceramics or glasses cannot be used for mechanical load-bearing applications because of their brittle nature. However, because their elastic modulus is similar to bone, they serve as coatings in composite grafts and as defect fillers where there is sufficient existing bone to carry the load or where other mechanical devices provide stability to the grafted site.

6.617.2.1.1. Calcium phosphates

Calcium phosphate materials are osteoconductive and are well integrated with surrounding bone.[17–19] Recently, there have been reports that some formulations of calcium phosphate materials are osteoinductive, based on the observation that bone can be found within the implant when particles are placed in muscle tissues.[20,21] A proposed mechanism in which calcium phosphates induce bone formation in a non-osseous environment is the adsorption of osteogenic molecules such as BMP-2 onto its surface, initiating bone formation. Differences in osteoinductivity were shown to be dependent on the location/proximity to the osteogenic environment.[20] The debate over whether this phenomenon is true osteoinduction has not been resolved, but it does raise important considerations for bone tissue engineering. It may not be necessary to produce a perfect material that provides scaffolding, bioactive molecules, and cells to achieve bone regeneration. The same goal may be achievable through engineering microenvironments that optimize the body's own regenerative process.

Common calcium phosphates include tricalcium and biphasic phosphate, calcium phosphate cements, and HA (coral-based or synthetic). Tricalcium phosphate $Ca_3(PO_4)_2$ (TCP), unlike other HA sintered ceramics, is resorbable *in vivo*[22] after stimulation of bone formation. TCP has a Ca:P molar ratio of 1.5 and it is less crystalline than HA with a Ca:P ratio of 1.67. High temperatures increase crystallinity of TCP creating α- and β-TCPs.[23] α-TCP is more soluble than β-TCP, but studies have shown comparable rates of degradation.[24] These crystalline TCPs are available in blocks, granules, powder form, or in combination with collagen and carboxymethylcellulose carriers to form pastes. Biphasic calcium phosphate is a composite of HA and β-TCP. It is more rapidly degradable than HA alone. Biphasic calcium phosphates in combination with HA and collagen are commercially available in granules, sticks, wedges, and cylinders and are used in posterior lumbar fusion mixed with autograft.[25]

Coralline HAs $Ca_{10}(PO_4)_6(OH)_2$ are derived from marine coral. The replamineform process is used to convert calcium carbonate found in natural mineral corals into calcium HA.[26] Modifications to the conversion process give commercial manufacturers the opportunity to control resorption rates and have more predictable products.[27] The final hybrid product will have a HA layer, which is resorbed slowly, and a carbonate core that once exposed, is resorbed rapidly allowing bone substitution.[11] The thickness of the HA layer will control the resorption rates. Synthetic HA differs from natural bone mineral in that it is more homogeneous in composition, has larger crystals, and crystals are more uniform. In general, synthetic HA degrades more slowly compared to the duration of the bone formation and remodeling process, raising concerns about the mechanical properties of the new bone at the treatment site. Synthetic HA is commercially available in dried powder, blocks, and in combination with collagen and cancellous bone chips, among other carriers.

Calcium phosphates that are enriched in carbonate to more closely approximate bone mineral[28,29] have also been developed as has silicated HA.[30] Whether these materials will prove more clinically useful as bone graft substitutes than other forms of calcium phosphate is not yet known.

6.617.2.1.2. Calcium sulfate

Calcium sulfate ($CaSO_4$), also known as plaster of Paris, is an osteoconductive crystalline substance used for bone void fillers and for cranial defects. Reports of *in vivo* use of calcium sulfate include deposition of cancellous host bone while the graft substance is resorbed.[31] Calcium sulfate is not suitable for structural support clinical applications due to its rapid biodegradability. Clinically, it is used in forms of pellets alone or in combination with other substances. Interestingly, as calcium sulfate dissolves, it acidifies the local environment resulting in antimicrobial action. Some of the calcium precipitates with local phosphate ions as HA, creating a microscaffold for osteoconduction within the defect.[32]

6.617.2.1.3. Bioactive glass

Bioactive glasses are considered highly reactive surfaces formed by melt or sol–gel techniques. Bioactive glass forms a hydroxycarbonated apatite layer when immersed in biological fluid, which enhances protein adsorption to the surface of the implant and integration with surrounding bone.[33,34] The rate of ion release from the bioglass surface is determined by the Ca:P ratio, composition, and microstructure. The initial reaction of some bioactive glasses with biological fluids causes local pH to increase[34]; some studies propose that this is beneficial to cell activity and HA production.[35] Clinically, the 45S5 form of bioglass has been used for bone defects, in restorative dentistry, and in craniofacial surgery. *In vitro* assays comparing osteoblast response to different bioglass formulations indicate that the phosphate content is an important variable.[36] Lower phosphate content, typical of the 45S5 bioglass that is used clinically, supports cell attachment and osteoblastic differentiation, whereas other forms of bioglass are less effective. Bioactive glass is currently available in sintered porous bulk or particulate form.

6.617.2.1.4. Physical parameters of ceramics and bioactive glasses

Bone's physical properties are important to its overall physiology. Because the early bone graft substitutes were not resorbable, the question of how the implants would be incorporated during the osseointegration process was critical to the overall success of the material. The goal was to produce a composite of graft and healthy new bone that would share the mechanical

load at the defect site. To do this required a pore size sufficiently large to permit ingrowth of blood vessels, ultimately surrounded by remodeled lamellar bone. A dogma was established that this meant a minimal pore size of 300 μm. The pore size consideration was taken into account not only when constructing ceramic blocks, but also when determining the size of spaces between particulate bone graft materials. More recent studies using biodegradable polymers indicate that pore size is not as critical a parameter if the material will stabilize clot formation and facilitate inward migration of osteoprogenitor cells and endothelial cells as it degrades.[37]

As experience with ceramic materials increased, care was taken to limit the number of blind alleys. This concept was supported by studies from Caplan and his colleagues showing that when porous ceramic cubes were implanted together with bone marrow-derived mesenchymal stem cells (MSCs) in muscle tissue, cells at the ends of blind alleys where oxygen tension was low differentiated into chondrocytes and adipocytes, whereas cells closer to the edges of the cubes where oxygen tension was high differentiated into osteoblasts.[38–40] The normal architecture of bone, particularly of trabecular bone, is one that provides for optimal exposure of osteoblasts to blood vessels. More recent ceramics have been designed to copy this architecture as much as possible. To accomplish this goal most effectively, manufacturers have used high temperatures to deorganify bovine bone, leaving the natural mineralized tissue architecture intact. At lower temperatures (300 °C), the mineral crystals also retain their physical properties (Bio-Oss, Geistlich Pharma Ag, Wolhusen, Switzerland), but there is also retention of minute levels of proteins including transforming growth factor β1 (TGFβ1) and BMP-2.[41] At higher temperatures (>1300 °C), the mineral becomes sintered and there is no retained organic component.[42]

6.617.2.2. Polymers

Nondegradable and biodegradable polymers are used for a variety of clinical applications today. Nondegradable polymers such as ultra high molecular weight polyethylene (UHMWPE) and poly methyl methacrylate (PMMA) are used as bearing surfaces in total joint arthroplasty and as acrylic cement for implant fixation, respectively. The success of these materials depends on osseointegration, and they are not intended to be replaced with bone.

Biodegradable polymers, depending on the clinical application, are replaced with bone, eliminating the need for an additional removal surgery, long-term biocompatibility issues, and the risk of stress shielding.[43] Biodegradable polymers used as suture materials[44,45] and as internal fixation devices[46] have been adapted for use in bone as 'bone void fillers,' which is a term used to define materials placed in bone voids that provide osteoconductive surfaces. Initial applications of these synthetic biodegradable polymers were in extraction sockets to stabilize the clot and facilitate bone growth.[47] More recently, they have been approved for use in orthopedic sites.[48,49] A goal of the biopolymers used as bone void fillers is that they degrade over the same time frame as new bone formation occurs. Polymers belonging to the polyhydroxy family including poly (L-lactide) and poly (D,L-lactide) (PLA), polyglycolide (PGA) and copolymers based on PLA and PGA, have been attractive because they degrade by hydrolysis, resulting in water and carbon dioxide. The degradation rates of PLA/PGA materials can be tuned by modifying the polymer chain length, the percent of each polymer type, the amount of cross-linking, and whether the L-form or the racemic mixture is used. There are two important drawbacks to PLA/PGA: the degradation products have the potential to acidify the local environment and cause inflammation, and the crystalline form of PLA may never completely degrade. These drawbacks have led investigators to develop alternative polymers for use in bone: polypropylene fumarate (PPF),[50] polycaprolactone (PCL),[51,52] tyrosine-derived polymers,[53] and polyanhydrides.[54]

6.617.3. Polymeric Bone Graft Substitutes to Tissue Engineering

Many of these materials were originally conceived in particulate form to be either space fillers or carriers of bioactive peptides. However, their polymeric properties were quickly co-opted as tissue engineering scaffolds, either as osteoconductive matrices or as substrates for *ex vivo* cell growth. Scaffold fabrication techniques such as gas foaming, phase separation, fiber meshing, three-dimensional (3D) printing (solid free form fabrication, SFF), and microsphere sintering have been reported in the literature.[55–58] These techniques permit controlling porosity and surface characteristics to target specific clinical use.

Hydrogels are a popular choice for tissue engineering scaffolds because their stiffness resembles that of biological soft tissues. They also provide highly swollen 3D scaffolds that allow diffusion of nutrients and cellular waste. Hydrogels can be made with flexible natural and synthetic polymers. Natural polymers used to make hydrogels include proteins (collagen, gelatin, and fibrin) and polysaccharides (hyaluronic acid, alginate). Synthetic polymers include poly (ethylene glycol) (PEG), poly (acrylic acid) (PAA), and polypeptides. Hydrogel scaffolds are being investigated for cartilage[59] and bone regeneration.[60]

More recently, composite materials that better simulate the intricate environment inside the host bone have been developed. These may include mineral plus a protein scaffold, a polymeric scaffold plus cells, a scaffold plus one or more bioactive agents, or a combination that has all three components. The goal is to achieve better integration and rapid and efficient bone regeneration. Gene therapy or the transfer of genetic information to cells can be done to enhance bone induction. In the next part of the chapter, we focus on the bone tissue engineering technologies that are currently being studied and reported in the literature.

6.617.4. Bone Tissue Engineering

Bone tissue engineering has evolved through the combination of biological and engineering approaches to overcome the shortages of existing bone graft materials. A critical consideration in developing effective 'new age' bone grafts is the diversity of biological, mechanical, and structural challenges that exist with each clinical application. For example, craniofacial reconstructions require a strategy that can conform to complex

geometries while matching the shape of the defect. Approaches for repairing nonunited fractures need to address excessive motion, fibrosis, and occasional infection. Spinal fusion needs to locally deliver osteoinductive signals to produce bone where none existed previously. Large segmental bone defects, >3 cm, are a particularly challenging problem and require consideration of high mechanical demands under complex load-bearing conditions, angiogenesis to address mass transport issues, and innervation. As a result of these distinct applications, it is unlikely that only one approach will be effective in replacing or regenerating all bone. Therefore, more than most other tissues substitutes, new age bone grafts will need to be tailorable for specific applications.

6.617.4.1. Tailoring Biomaterials for New Age Bone Grafts

An early clinical application of bone tissue engineering as we know it today was used to replace an avulsed distal phalanx of the thumb at the turn of the century.[61] Cells isolated from the periosteum were expanded, suspended in alginate, injected into a carved porous coral implant, and fixed with calcium chloride. Although the procedure demonstrated what the potential of combining cells and tailorable biomaterials can offer in improving bone replacement, preparing the engineered graft was more time consuming than a conventional bone autograft and was considered to be no more effective.[62] To make these kinds of implants effective clinically, engineers, biologists, and clinicians must consider the complexity of the final product, how quickly it can be assembled, and how difficult it is to use in surgery in addition to its ability to osseointegrate and regenerate the biomechanical and physiological properties of bone. Regardless of the approach, it is clear that tailoring biomaterials will play a critical role in achieving these goals. In the following sections, different adjustable properties and modifications of biomaterials for new age bone grafts are described, starting from macroscopic characteristics down to the cellular level.

6.617.4.1.1. Anatomically specific shape and architecture

Replication of the anatomical shape is a critical criterion for engineered bone grafts for craniofacial reconstruction and orthopedic applications where fitting the defect and joint conformity are required. Biomaterial architecture parameters such as pore size, density, and interconnectivity are also important as these have subsequent effects on local mechanical properties, mass transport, blood vessel invasion, and osteogenic behavior. Traditional methods of achieving appropriate shape and architecture have included carving, molding, and salt-leaching, but these methods can have minimal accuracy, reproducibility, or throughput. These shortcomings have led to significant interest in using medical imaging techniques such as magnetic resonance imaging and computed tomography to fabricate customized bone constructs. Recent advances in both computation topology design (CTD) and SFF have allowed for rapid prototyping of highly reproducible engineered bone grafts with a spatial resolution up to 25 μm.[63] SFF techniques build structures using a layer by layer additive process and have been used with a wide range of metals, polymers, and hydrogels. Scaffolds for engineered bone grafts can be fabricated directly or cast in a mold created with SFF techniques. Specific strut architectures and precise porosity have also been created with this technology to create desired anisotropic elasticity and permeability for new age bone grafts.[55]

Scaffold design has evolved to include components that mimic biological function. Electrospinning technology has made it possible to produce both random and oriented fiber polymer constructs that provide an ECM-like meshwork for cell attachment and differentiation.[64–66] These polymer meshes can also be made into fabric sheets that serve as a barrier, limiting epithelial cell down-growth in oral applications[67] or fibrous connective tissue ingrowth in segmental defect applications.[68] By combining a barrier with a biodegradable polymer scaffold, the tissue engineering application becomes one of guided tissue regeneration. This concept has been well accepted in dentistry and is now being adapted to orthopedic applications.

6.617.4.1.2. Mechanical properties

Because bone serves a dual function as a protective and weight-bearing structure, mechanical properties of new age bone grafts and how these properties change once implanted are critical considerations. Local mechanical properties such as modulus and viscosity are chosen not only to provide initial stability and protection to the damaged area but also to elicit the desired osteogenic response. Stiffer matrices facilitate stem cell differentiation down the osteogenic lineage, whereas softer matrices that mimic the mechanics of other tissues do not.[69] Therefore, scaffold mechanical properties can be varied by adjusting the local architecture or using different biomaterial compositions.[55,70] It is well established that bone remodeling is a function of mechanical loading due to Wolff's law, and effective bone regeneration strategies can take this attribute into account by mechanically stimulating viscoelastic tissue-engineered constructs under normal bone loading.[71]

6.617.4.1.3. Degradation

With the goal of new age bone grafts to increase the speed and quality of bone regeneration compared to traditional methods, the biomaterial used must eventually be replaced. To achieve this, the degradation rate must be such that cell migration, ECM remodeling, and tissue growth can occur while maintaining mechanical stability. The degradation products must also be biocompatible while eliciting minimal inflammation. Recent approaches have tried to tailor biomaterial degradation specifically to the expression profile of matrix metalloproteinase (MMP)-related and ECM-related genes during bone remodeling. This approach would allow scaffolds to better work temporally with resident stem cells and MMPs naturally expressed during bone regeneration by cross-linking a polymeric biomaterial with MMP-degradable peptides.[72,73]

New age bone grafts have also used scaffold degradation to control the release of stimulatory signaling molecules to promote bone regeneration.[74] BMPs have been released from solid constructs to enhance bone formation *in vivo*, and angiogenic factors have also been delivered to address mass transfer concerns.[75,76] Based on different scaffold degradation properties, the release kinetics of multiple factors can be manipulated to provide more robust tissue formation in new age bone grafts.[77]

6.617.4.1.4. Surface chemistry and topographical cues

Surface chemistry and roughness have well-defined influences on osteogenic behavior. Osteoblasts and stem cells respond to groves, ridges, wells, and other features at the micron and nanoscale.[78] For titanium implants and biomaterial surfaces, rougher hydrophilic interfaces elicit a stronger osteogenic response from osteoblasts[79,80] and MSCs,[81] whereas disordered nanotopographical features enhance stem cell spreading and subsequent osteogenesis.[82] New age bone grafts have focused on incorporating these findings into 3D scaffolds. HA-collagen and carbon nanotube polymer nanocomposities are examples of nanophase reinforcements that are able to increase bioactivity and mechanical properties of engineered grafts.[70] Other approaches aim to generate an enhanced osteogenic environment by recreating the topographical context of native ECM through engineered 3D nanofibrous matrices. Biological and synthetic polymers are electrospun into 3D matrices with high spatial interconnectivity, high porosity, and oriented fibers to direct cellular morphology and migration for *in vivo* bone regeneration.[70,83] Fiber diameter and alignment within these biomaterials can influence bone growth while mimicing the function of the periosteum.[84,85] The surface chemistry of these fibers can also be modified to promote direct nucleation and deposition of HA.[86] Surfaces of fibers and other biomaterials can be modified with other biological components such as glycosaminoglycans and heparin that can localize growth factors important for angiogenesis and bone formation.[70]

6.617.4.1.5. Cellular adhesion

Cellular adhesion via integrins not only influences osteoblast migration and spreading but also provides cellular signaling and influences cell behavior and osteogenesis. ECM components such as collagen and fibronectin are important in stimulating osteoblasts and directing bone growth. Although these proteins have been incorporated into various new age bone grafts, recent strategies have focused to mimic and enhance the therapeutic function of these tissue components. These biomimetic modifications of new age bone grafts have centered on creating peptide mimetics based on motifs found in collagen, fibronectin, and bone sialoprotein.[87–89] By adjusting the presentation and surface density of these peptides, osteoblast adhesion, migration, and differentiation can be tailored. These specific peptide sequences can also provide more direct stimulatory signaling while reducing infiltration of nonosteogenic-specific cells.

6.617.4.2. New Age Bone Graft Approaches

In 1989, a method was described to implant autologous marrow cells containing MSCs in combination with a porous ceramic material to repair large femoral defects in rats.[90] The addition of the marrow cells significantly improved bone formation over just the implanted ceramic alone and showed that delivering stem cells with biomaterials may have clinical applications in repairing bone defects. What is unknown is the mechanism these cells participated in to facilitate bone regeneration. The delivered marrow cells could have produced bone directly, attracted surrounding osteogenic cells to produce bone, or delivered soluble signals that initiated bone formation from uncommitted progenitor cells. It is also possible that the implanted cells would have performed even better if the cells and biomaterial were stimulated into producing tissue *in vitro* prior to implantation. In the years following, new age bone grafts have focused on using one or more of these distinct mechanisms to develop approaches that would better regenerate bone.

6.617.4.2.1. *Implanting* in vitro *cultured tissues*

Ideally, bone grafts that are optimized *in vitro* will be remodeled once implanted *in vivo*. Therefore, one approach has been to prime bone graft for quicker and enhanced osseointegration and bone regeneration. This has been particularly useful for graft integration where two tissues are involved, such as osteochondral grafts or tendon grafts. To improve osseointegration and graft function, current *in vitro* culture techniques aim to recreate the heterogeneous structure of bone interfaces such as the osteochondral transition and bone-soft tissue interfaces. To recreate these structures, mechanical, chemical, and biological gradients developed *in vitro* are often used. Perfusion and dynamic compression bioreactors have been created for anatomically shaped grafts to manipulate the local mechanical and chemical environment.[91] Controlled delivery of soluble factors from biomaterials and gradients of immobilized retrovirus can be used to recreate biological gradients.[75,92] These *in vitro* culture techniques act directly on seeded cells to enhance differentiation, proliferation, and subsequent tissue deposition and mineralization.

Interestingly, attempts to grow bone nodules *in vitro* for bone tissue engineering have been less successful. While it is possible to culture osteogenic cells on scaffolds in bioreactors, if the conditions support matrix mineralization, the constructs tend to form a calcified shell, resulting in a necrotic core.[93,94] This is due to reduced nutrient diffusion into the construct as well as reduced diffusion of waste products out of the construct. These tissue-engineered constructs may still have utility as mineralized templates as they present a 3D matrix containing bone-like HA.[95]

6.617.4.2.2. Delivering MSCs

Since Ohgushi *et al.*[96] showed that marrow cell delivery can improve bone formation over porous calcium phosphate, many new age bone grafts have attempted to deliver MSCs isolated from adult tissues to improve tissue regeneration. Although the exact mechanism of how these cells recreate bone *in vivo* is not completely understood, it is believed that these cells can either produce bone tissue directly or stimulate bone regeneration by recruiting surrounding progenitor cells. Adult stem cells for bone regeneration have been isolated from bone marrow, adipose tissue, synovium, and muscle[97]; they are able to modulate the immune response and have the ability to home to damaged tissues.[98] The effectiveness of stem cells in new age bone grafts can be enhanced by differentiating them toward the osteogenic lineage, genetic manipulation, and co-delivery with other cell types.[99,100]

6.617.4.2.3. Osteoconduction

As noted previously, osteoconduction refers to the ability of a material to serve as a scaffold on which bone cells can attach,

migrate, and grow and divide. Osteoconductive materials need to be adjacent to bone to 'conduct' bone cells and is generally reminiscent of electricity being conducted through conductive materials. Therefore, osteoconductive materials cannot form *de novo* bone at sites where bone previously did not exist such as the muscle. Current common clinical materials that actively use osteoconduction include terminally sterilized allografts and calcium phosphate synthetic substitutes.[101] New age bone grafts are able to tailor their osteoconductive properties by adjusting porosity, surface chemistry, topographical cues, and cellular adhesion sites.[70,78]

6.617.4.2.4. Osteoinduction

Osteoinduction is the process in which uncommitted progenitor cells in surrounding tissue are stimulated, undergo mitosis and osteogenesis, and form new bone. This process can occur not only in sites adjacent to the bone, but also in locations, such as the muscle, where the bone never existed previously. Because osteoconductive and osteogenic materials may have the same outcome as an osteoinductive material in the bone, the term 'osteoinductive' can only be applied to those materials that actually induce bone in nonbone tissues. Current clinical approaches that actively use osteoinduction include DBM produced by acid extraction of an allograft and recombinant human BMPs (rhBMPs)-2 and -7 on collagen sponges.[101] New age bone grafts aim to have biomaterials control the temporal and spatial delivery of osteoinductive factors like rhBMPs[75] or retroviral vectors increasing the expression of osteogenic genes[92] to provide a more localized bone formation while reducing the amount of osteoinductive molecules used.

6.617.5. Animal Models for Assessing Effectiveness of Bone Tissue Engineering Strategies

Bone tissue formation is mediated by a complex process orchestrated by osteoprogenitor cells and osteoblasts, which requires biochemical, biomechanical, and hormonal regulation by the body. Bone substitutes are used as treatments for bone healing and regeneration. Bone autografts are considered the gold standard to augment or enhance bone regeneration. However, autografts are limited by the size of the graft, in addition to high morbidity and painful extraction procedures and long recovery. Autografts, allografts, and xenografts usually result in an incomplete integration with the host tissue, mainly due to lack of vascularization. Infections and immune reactions are also associated with the use of allografts and xenografts.

Naturally derived and synthetic bone substitutes have been designed in order to avoid the limitations associated with standard treatments. Recently, tissue engineering has emerged with the potential to overcome the deficiencies that bulk materials have, integrating material science, mechanical engineering, and cell biology. These materials demonstrate biocompatibility and osteogenic potential in an *in vitro* environment. However, the complex cellular, biochemical, and systemic environments found in the body are impossible to replicate *in vitro*. Animal models are a powerful tool to evaluate bone grafting materials and their osteogenic potential, because the material will be exposed to several different cell types that can induce different tissue formations, encounter an aggressive local and systemic environment that may enhance graft outcome, and will experience a multitude of mechanical loads, factors impossible to reproduce *in vitro*.

The use of animal models to evaluate the potential healing capability of bone graft substitutes is critical in evaluation of their success. Mammalian animal species currently used in bone research include rat, rabbit, dog, sheep, pig, goat, and nonhuman primates, and some of the defect types commonly investigated include nongap fractures, segmental defects, cylindrical defects, and calvarial defects.[102] The numerous species and defect models available make selection of an appropriate defect model difficult. A number of factors need to be considered when choosing an *in vivo* model for research in bone tissue engineering.[102,103] Systemic factors such as age,[104,105] sex,[106] and hormone status[107] are known to play a significant role in bone repair and remodeling. It is therefore of importance to select a model that closely mimics both the physiological and pathophysiological conditions for the intended use.

Critical-size defects (CSDs) were originally defined as "the smallest size intraosseous wound in a particular bone and species of animal that will not heal spontaneously during the lifetime of the animal."[108] Later, this concept was redefined as "a defect that shows less than 10 percent bony regeneration during the animal lifetime."[109] A number of factors must be considered when selecting a specific animal species as a model system to evaluate bone substitutes. Selection criteria should include animal availability, size, age, sex, species phylogeny, metabolic and systemic conditions, cost of acquisition and care, size of operating field compared to size of defect, and postsurgery recovery time. Important factors for selecting the right CSD model are the anatomic location, bone structure, vascularization, presence of periosteum, physiological conditions, mechanical load, and pathophysiology.

6.617.5.1. Calvarial Defects

Calvarial defect models are important to test biomaterials and tissue-engineered constructs that will eventually be used in human defects in this area, common after trauma, degenerative diseases, or brain surgery. Age is particularly important, as it has been shown that the ability of animals to heal large calvarial defects is age-dependent.[110–112] Mice and rat models of calvarial defects are common, as they are easy to breed and husbandry is simple. However, they present a challenge due to a very small operating field and thin calvarial bones. Instead of surgical tools, dental burrs and drills are used to operate precisely in the confined space. An advantage of using these models is the availability of athymic models, which allow for study of materials from other species while limiting host graft rejection responses. Also, because of the ease of housing, these models are often used to examine the time course of bone formation and remodeling in the defect.

Defects in mice are typically 4 mm,[113–116] but smaller[117] and larger[117] defects can be found in the literature. In mice, a single defect is created in the center of the skull, although some studies have reported using bilateral parietal defects.[114] The size of the critical defect in mice varies widely depending on the age and strain used. Mouse models have been extensively used to characterize the ability of MSCs to repair calvarial defects. Bone marrow stromal cells with overexpression of

Runx2,[118] Osterix,[119] or BMP-7[117] have been used in this model, as have osteoblasts overexpressing Noggin.[120] The scaffolds used range from simple (gelfoam,[117] vitrigel,[121] or silk fibroin[117]) or more complex (combinations of RGD and MMP substrates in PEG hydrogels[113] or apatite-coated PLA/PGA scaffolds[120]). There is little uniformity in study endpoints, with the earliest ending after 2 weeks[116] and the longest extending to 6 months.[122] Most examine multiple time points, between 2 and 8 weeks.[114,120,121]

In rats, as in mice, there is no agreed-upon defect size. Defects used include 3.8 mm,[123] 5 mm,[124] 8 mm,[125,126] 8.8 mm,[127] and 9 mm.[128] Rats have also been used extensively for models of stem cell repair of calvarial defects, including muscle stem cells,[126] adipose-derived stem cells,[129,130] and MSCs.[125] Studies examine these cells grown on scaffolds such as polyglycolic mesh[126] or poly lactide-*co*-glycolic acid scaffolds.[130,131] Other studies focus on the effect of biomaterials on bone healing, using polylactic or polyglycolic acid[132,133] or bone substitutes (eggshell-derived,[134] bioactive glass[135]). A combination of scaffolds or cells and growth factors such as BMP-2[125,131,136,137] and VEGF[137] have also been studied using the rat calvarial defect model. Study endpoints vary, ranging from 4,[125] 6,[129] 8,[126] or 24,[127] but many studies examine bone formation at 12 weeks.[130,131,137] Experiments using the rodent models require inclusion of a control group as bone ingrowth occurs even in the absence of a scaffold or bone graft.[138]

Larger animal models are also used to test healing of calvarial defects. Rabbits are the most commonly used model in these types of defect studies, and study materials primarily in male animals. Defects are typically bilateral parietal circular or square defects between 10 and 15 mm.[139–141] Many materials have been examined in this defect, including PCL scaffolds,[142] resorbable polyethylene glycol hydrogels,[143] silica gels,[144] and bioactive synthetic bone and hyaluronic acid hydrogels.[145] Less commonly, a single mid-cortical defect is used,[146] but healing may be affected as this defect includes the sutures of the skull.

Dogs are less commonly used as experimental models in cranial defects. In one study, a 2 cm × 2 cm bone flap was created to test the efficacy of a mixture of β-TCP, calcium, collagen, and autologous bone fragments in bone healing.[147] The second study used combinations of DBM, platelet-rich plasma, and bone morphogenetic protein 2 to regenerate a 6 cm × 2 cm calvarial defect that crossed the sagittal suture.[148] Both studies examined bone formation 3 months after surgery.

Sheep defect models have a wide range of parameters. Some studies used 2 cm × 2 cm parietal defects,[149] one testing TCP-chitosan-collagen hydrogels and poly(L-lactide-*co*-glycolide).[150] However, usually multiple defects are created, which allows for testing of multiple substances in the same animal. A study testing HA composites[151] female, five 1.68 cm diameter defects-four in parietal, one in temporal bone, 1 year. In studies that specified sex, female animals were used. Studies examined healing time points of 6–14 weeks, up to 1 year.

Goats are a less-common large animal model, but one study examined healing of a single 2.2 cm diameter circular defect in the center of the cranial bone using poly lactide-*co*-glycolide/TCP/bone morphogenetic protein 2.[152]

Defects vary depending on the material, species, and location. A study outcome also depends on surgical technique. One study[123] demonstrated that the periosteum is crucial in bone repair; in that study, rat cranial defects did not heal from the defect edges but instead bone repair was found to originate from the periosteum. Another study found that as long as the periosteum is in contact with the implant material, the defect heals.[153] The question whether the defect involves only cranial bone or transverses sutures will also affect study outcome. For this reason, it is also important to accurately and thoroughly describe surgical procedures, as small variations in technique may influence experimental outcome.

6.617.5.2. Maxillary Sinus Augmentation

Sinus floor augmentations are used mostly to test particulate materials, including allogenic and autogenic bone, xenograft substitutes, synthetic biomaterials, or some combination of materials. More recently, growth factors have also been combined with these materials and examined in a sinus lift model.[154,155] Currently, autogenous bone is used as the gold standard as a bone substitute. The most common technique for animal models of maxillary sinus augmentation was described by Haas *et al.*[156] A crucial step in experimental design is the choice of the model. While larger species such as monkeys,[157–162] minipigs,[163] goats,[164] and sheep[165,166] have been used in such studies, they have several serious limitations. To achieve adequate statistical power, a large number of animals are necessary, and animal husbandry of these species is expensive. The majority of studies using this model only use a small number of animals, usually three to five animals per experimental variable, for their studies given these limitations. However, rabbits are a less costly alternative species and have been successfully used as a model in this type of defect.[167,168] Because of the ease of breeding and housing these animals, a larger sample size can be used for experiments. When larger animal models are used, bilateral defects are often created and both control and test materials implanted into the same animal. Typically, bone formation in maxillary sinus lift models is examined after periods ranging from 4 to 8 weeks, although some studies observe animals until 26 weeks postoperatively.[156]

6.617.5.3. Analysis Methods for Cranial Defects

Many studies examine the quality and quantity of new bone using histomorphometric analysis. Samples are either fixed in formalin and decalcified sections embedded in paraffin or undecalcified sections embedded in a plastic such as methyl methacrylate. Sections can be stained with hematoxylin and eosin to make quantitative measurements of defect area, total bone area, marrow area, fibrous tissue area, or void areas. Histological analysis is well accepted as an evaluation method for bone formation. However, it is limited in that many sections of each sample and many fields of each section must be analyzed in order to get an accurate representation of new bone growth. Sections can also be stained with antibodies conjugated to fluorescent molecules to determine the presence of several markers, including angiogenic factors. If cells are implanted, an *in vitro* imaging system can be used to track them after surgery. *In vivo* imaging systems can be used to quantify cells labeled with bioluminescence,[113,169] fluorescent proteins,[114,119,170] or quantum dots.[171]

For gross qualitative analysis, X-rays are used. However, images can only be related descriptively to one another. More recently, microcomputed tomography (μCT) has been used to quantify differences in bone formation. After the user determines a threshold of mineralization for bone, both 2D and 3D images are taken. This allows for calculation of bone volume density, bone surface density, and trabecular thickness. Additionally, contrast agents can be administered during the harvest process to quantify blood vessel formation. Studies comparing μCT and histology have found the results to correlate well.[172–174] The advantage of μCT is that it allows you to analyze the whole sample or a smaller portion of the sample nondestructively, leaving the bone intact for additional studies such as mechanical testing.

6.617.5.4. Critical-Sized Segmental Defect

One of the most commonly used animal models for bone tissue engineering research is the critical-sized segmental defect model. A CSD is defined as the minimum defect size that is incapable of complete healing without intervention.[103] Clinically, a defect is of critical size when complete healing has not occurred over a period of 6 months following injury. In general, the length of a critically sized defect should be at least 1.5 times the diameter of the selected bone,[175,176] although several studies indicate that a defect length of 2–2.5 times the diameter of the affected bone is necessary to create a critical-sized defect.[103]

Several animal species and anatomical locations are used in critical-sized segmental defect models. In the rat segmental defect model, a femoral defect between 5 and 10 mm is commonly used.[177] On account of the load-bearing nature of the rat femora, it is necessary to use either internal or external fixation to stabilize the defect. In rabbits, the defect sites typically used are the radius and ulna where fixation is not required and the typical critical-sized defect is 20 mm.[178] In canines, 20–25 mm defects of the radius, ulna, and femur are the most used.[179,180] In the large animal models of goats and sheep, the tibia is a common defect site and defect sizes in these animals range from 25 up to 50 mm.[181]

All of the aforementioned segmental defect models have been used to assess the bone-healing capability of various bone graft substitutes. Marks *et al.*[182] examined the healing capability of DBM in a rat segmental defect model and found that after 4 weeks, animals treated with DBM + antibiotic exhibited greater bone formation both radiographically and histologically compared to control animals and animals treated with antibiotic alone. Wojtowicz *et al.* coated PCL scaffolds with a short biomimetic peptide motif (GFOGER) and implanted coated and uncoated scaffolds into an 8 mm rat femoral segmental defect. After 12 weeks, it was observed that greater bone formation occurred in animals with GFOGER-coated PCL scaffolds compared to both empty defects and uncoated PCL scaffolds using both X-ray and micro-CT analysis techniques, although no difference in torsional strength of the newly formed bone was observed between the treatment groups.[183] Using a canine ulnar model, Itoh *et al.*[179] found that high doses of rhBMP-2 (160 or 640 μg) incorporated into PLGA/gelatin sponge scaffolds resulted in complete bridging of a 20-mm segmental bone defect 16 weeks postoperatively as assessed using radiographic and histological methods. The effect of a resorbable calcium phosphate paste on healing of a critically sized (30 mm) sheep tibial defect was examined by Bloemers *et al.*[184] Using both radiological and biomechanical torsion testing, it was found that at 12 weeks, animals treated with the resorbable calcium phosphate paste had more bone radiographically and exhibited a significantly higher torsional stiffness compared to animals that had been treated with autologous bone or with calcium phosphate particles.

These models have been referred to incorrectly as nonunion models because they fail to heal with bone. As they are used in the examples earlier, they are actually acute defects and as such, they test the ability of the tissue engineering approach to either enhance or retard the ingrowth of bone from the bone ends. This is particularly true if the preparation of the defect site includes removal of periosteum, thereby limiting the source of stem cells to the bone ends or to the muscle surrounding the defect. If the defect is allowed to heal in the absence of a graft, it will heal with fibrous connective tissue typical of nonunion, containing areas of fibrocartilage.[185] These chronic nonunions have also been treated effectively using injected MSCs[186] and injected BMP-7,[187] as well as by implanting PLA foams with adsorbed BMPs following resection of the nonbony tissue.[188]

Another model that is useful for the evaluation of the osteogenic capability of bone graft substitutes as well as their remodeling is the bone marrow ablation model. This model takes advantage of the rapid endosteal bone formation that occurs following injury to the marrow cavity of rat tibial bone.[189] In the rat ablation model, the bone marrows of rat tibias are flushed of cells. A blood clot and granulation tissue fill the marrow space over the first 3 days of healing. Primary bone begins to form on the endosteal surface by day 6 and eventually fills the marrow cavity. Remodeling of the newly formed bone occurs between days 12 and 25, resulting in resorption of the primary bone. By day 35 postablation, replacement of the primary bone with bone marrow is complete, resulting in the regeneration of normal tissue phenotype.[190] This process follows a well-documented timetable,[191,192] which makes it a very useful model for the study of normal bone repair and for the evaluation of extrinsic and intrinsic factors that may influence it. The enclosed environment of the marrow space restricts the distribution of test materials and localizes their effects, thus allowing the model to be useful for the study of the effects of biomaterials that have been designed for bone augmentation. Using the tibial marrow ablation model, our lab has found that hyaluronic acid in combination with DBM stimulates endosteal bone formation through increased vascularization of the ablated marrow space, suggesting that incorporation of hyaluronic acid with DBM may enhance osteogenesis in bone-healing applications (unpublished data). While the bone marrow ablation model can provide information on the rate of endosteal bone formation, its strength lies in the opportunity to assess graft remodeling.[190]

References

1. Perry, C. R. *Clin. Orthop. Relat. Res.* **1999**, *360*, 71–86.
2. Heyligers, I. C.; Klein-Nulend, J. *Cell Tissue Bank.* **2005**, *6*, 25–31.

3. Lian, J. B.; Tassinari, M.; Glowacki, J. *J. Clin. Invest.* **1984**, *73*, 1223–1226.
4. Lohmann, C. H.; Andreacchio, D.; Koster, G.; *et al. Arch. Orthop. Trauma Surg.* **2001**, *121*, 583–590.
5. Banwart, J. C.; Asher, M. A.; Hassanein, R. S. *Spine (Phila Pa 1976)* **1995**, *20*, 1055–1060.
6. Fleming, J. E., Jr.; Cornell, C. N.; Muschler, G. F. *Orthop. Clin. North Am.* **2000**, *31*, 357–374.
7. Summers, B. N.; Eisenstein, S. M. *J. Bone Joint Surg. Br.* **1989**, *71*, 677–680.
8. Poynton, A. R.; Lane, J. M. In *Bone Graft Substitutes*; Laurencin, C. T., Ed.; ASTM International: New Jersey, 2003.
9. Schwartz, Z.; Mellonig, J. T.; Carnes, D. L., Jr.; *et al. J. Periodontol.* **1996**, *67*, 918–926.
10. McAllister, B. S.; Haghighat, K.; Gonshor, A. *J. Periodontol.* **2009**, *80*, 679–686.
11. Boyan, B. D.; Mcmillan, J.; Lohmann, C. H.; Ranly, D. M.; Schwartz, Z. In *Bone Graft Substitutes*; Laurencin, C. T., Ed.; ASTM International: New Jersey, 2003.
12. Lee, Y. P.; Jo, M.; Luna, M.; Chien, B.; Lieberman, J. R.; Wang, J. C. *J. Spinal Disord. Tech.* **2005**, *18*, 439–444.
13. Peterson, B.; Whang, P. G.; Iglesias, R.; Wang, J. C.; Lieberman, J. R. *J. Bone Joint Surg. Am.* **2004**, *86-A*, 2243–2250.
14. Takikawa, S.; Bauer, T. W.; Kambic, H.; Togawa, D. *J. Biomed. Mater. Res. A* **2003**, *65*, 37–42.
15. Wang, J. C.; Alanay, A.; Mark, D.; *et al. Eur. Spine J.* **2007**, *16*, 1233–1240.
16. Greenwald, A. S.; Boden, S. D.; Goldberg, V. M.; Khan, Y.; Laurencin, C. T.; Rosier, R. N. *J. Bone Joint Surg. Am.* **2001**, *83-A*(Suppl. 2 Pt 2), 98–103.
17. Ripamonti, U. *J. Bone Joint Surg. Am.* **1991**, *73*, 692–703.
18. Ripamonti, U. *Biomaterials* **1996**, *17*, 31–35.
19. Yamasaki, H.; Sakai, H. *Biomaterials* **1992**, *13*, 308–312.
20. Cheng, L.; Ye, F.; Yang, R.; *et al. Acta Biomater.* **2010**, *6*, 1569–1574.
21. Yuan, H.; Yang, Z.; Li, Y.; Zhang, X.; De Bruijn, J. D.; De Groot, K. *J. Mater. Sci. Mater. Med.* **1998**, *9*, 723–726.
22. Winter, M.; Griss, P.; De Groot, K.; *et al. Biomaterials* **1981**, *2*, 159–160.
23. Termine, J. D.; Peckauskas, R. A.; Posner, A. S. *Arch. Biochem. Biophys.* **1970**, *140*, 318–325.
24. Wiltfang, J.; Merten, H. A.; Schlegel, K. A.; *et al. J. Biomed. Mater. Res.* **2002**, *63*, 115–121.
25. Fujibayashi, S.; Shikata, J.; Tanaka, C.; Matsushita, M.; Nakamura, T. *J. Spinal Disord.* **2001**, *14*, 214–221.
26. White, E.; Shors, E. C. *Dent. Clin. North Am.* **1986**, *30*, 49–67.
27. Shors, E. C. *Orthop. Clin. North Am.* **1999**, *30*, 599–613.
28. Ellies, L. G.; Nelson, D. G.; Featherstone, J. D. *J. Biomed. Mater. Res.* **1988**, *22*, 541–553.
29. Hing, K. A.; Best, S. M.; Tanner, K. E.; Revell, P. A.; Bonfield, W. *Proc. Inst. Mech. Eng. H* **1998**, *212*, 437–451.
30. Hing, K. A.; Revell, P. A.; Smith, N.; Buckland, T. *Biomaterials* **2006**, *27*, 5014–5026.
31. Coetzee, A. S. *Arch. Otolaryngol.* **1980**, *106*, 405–409.
32. Frenkel, S. R.; Simon, J.; Alexander, H.; Dennis, M.; Ricci, J. L. *J. Biomed. Mater. Res.* **2002**, *63*, 706–713.
33. Ducheyne, P.; Cuckler, J. M. *Clin. Orthop. Relat. Res.* **1992**, *276*, 102–114.
34. El-Ghannam, A.; Ducheyne, P.; Shapiro, I. M. *Biomaterials* **1997**, *18*, 295–303.
35. Silver, I. A.; Deas, J.; Erecinska, M. *Biomaterials* **2001**, *22*, 175–185.
36. Lossdorfer, S.; Schwartz, Z.; Lohmann, C. H.; Greenspan, D. C.; Ranly, D. M.; Boyan, B. D. *Biomaterials* **2004**, *25*, 2547–2555.
37. Whang, K.; Healy, K. E.; Elenz, D. R.; *et al. Tissue Eng.* **1999**, *5*, 35–51.
38. Boyan, B. D.; Caplan, A. I.; Heckman, J. D.; Lennon, D. P.; Ehler, W.; Schwartz, Z. *J. Orthop. Res.* **1999**, *17*, 246–255.
39. Dennis, J. E.; Konstantakos, E. K.; Arm, D.; Caplan, A. I. *Biomaterials* **1998**, *19*, 1323–1328.
40. Huibregtse, B. A.; Johnstone, B.; Goldberg, V. M.; Caplan, A. I. *J. Orthop. Res.* **2000**, *18*, 18–24.
41. Schwartz, Z.; Weesner, T.; Van Dijk, S.; *et al. J. Periodontol.* **2000**, *71*, 1258–1269.
42. Sogal, A.; Tofe, A. J. *J. Periodontol.* **1999**, *70*, 1053–1063.
43. Nair, L. S.; Laurencin, C. T. *Adv. Biochem. Eng. Biotechnol.* **2006**, *102*, 47–90.
44. Hermann, R. E.; Hertzer, N. R. *Arch. Surg.* **1970**, *100*, 71–75.
45. Ray, J. A.; Doddi, N.; Regula, D.; Williams, J. A.; Melveger, A. *Surg. Gynecol. Obstet.* **1981**, *153*, 497–507.
46. Bucholz, R. W.; Henry, S.; Henley, M. B. *J. Bone Joint Surg. Am.* **1994**, *76*, 319–324.
47. Brekke, J. H.; Olson, R. A.; Scully, J. R.; Osbon, D. B. *Oral Surg. Oral Med. Oral Pathol.* **1983**, *56*, 240–245.
48. Athanasiou, K. A.; Agrawal, C. M.; Barber, F. A.; Burkhart, S. S. *Arthroscopy* **1998**, *14*, 726–737.
49. Hutmacher, D.; Hurzeler, M. B.; Schliephake, H. *Int. J. Oral Maxillofac. Implants* **1996**, *11*, 667–678.
50. Yaszemski, M. J.; Payne, R. G.; Hayes, W. C.; Langer, R.; Mikos, A. G. *Biomaterials* **1996**, *17*, 2127–2130.
51. Hutmacher, D. W. *Biomaterials* **2000**, *21*, 2529–2543.
52. Hutmacher, D. W.; Schantz, T.; Zein, I.; Ng, K. W.; Teoh, S. H.; Tan, K. C. *J. Biomed. Mater. Res.* **2001**, *55*, 203–216.
53. Bourke, S. L.; Kohn, J. *Adv. Drug Deliv. Rev.* **2003**, *55*, 447–466.
54. Laurencin, C. T.; Gerhart, T.; Witschger, P.; *et al. J. Orthop. Res.* **1993**, *11*, 256–262.
55. Hollister, S. J. *Nat. Mater.* **2005**, *4*, 518–524.
56. Lin, H. R.; Kuo, C. J.; Yang, C. Y.; Shaw, S. Y.; Wu, Y. J. *J. Biomed. Mater. Res.* **2002**, *63*, 271–279.
57. Ma, P. X.; Choi, J. W. *Tissue Eng.* **2001**, *7*, 23–33.
58. Sherwood, J. K.; Riley, S. L.; Palazzolo, R.; *et al. Biomaterials* **2002**, *23*, 4739–4751.
59. Maher, S. A.; Mauck, R. L.; Rackwitz, L.; Tuan, R. S. *J. Tissue Eng. Regen. Med.* **2010**, *4*, 25–29.
60. Betz, M. W.; Yeatts, A. B.; Richbourg, W. J.; *et al. Biomacromolecules* **2010**, *11*, 1160–1168.
61. Vacanti, C. A.; Bonassar, L. J.; Vacanti, M. P.; Shufflebarger, J. *N. Engl. J. Med.* **2001**, *344*, 1511–1514.
62. Hentz, V. R.; Chang, J. *N. Engl. J. Med.* **2001**, *344*, 1547–1548.
63. Ballyns, J. J.; Bonassar, L. J. *J. Cell. Mol. Med.* **2009**, *13*, 1428–1436.
64. Ekaputra, A. K.; Prestwich, G. D.; Cool, S. M.; Hutmacher, D. W. *Biomacromolecules* **2008**, *9*, 2097–2103.
65. Ji, Y.; Ghosh, K.; Shu, X. Z.; *et al. Biomaterials* **2006**, *27*, 3782–3792.
66. Lin, A. S.; Barrows, T. H.; Cartmell, S. H.; Guldberg, R. E. *Biomaterials* **2003**, *24*, 481–489.
67. Yang, F.; Both, S. K.; Yang, X.; Walboomers, X. F.; Jansen, J. A. *Acta Biomater.* **2009**, *5*, 3295–3304.
68. Rai, B.; Oest, M. E.; Dupont, K. M.; Ho, K. H.; Teoh, S. H.; Guldberg, R. E. *J. Biomed. Mater. Res. A* **2007**, *81*, 888–899.
69. Engler, A. J.; Sen, S.; Sweeney, H. L.; Discher, D. E. *Cell* **2006**, *126*, 677–689.
70. Stevens, M. M. *Mater. Today* **2008**, *11*, 18–25.
71. Boerckel, J. D.; Dupont, K. M.; Kolambkar, Y. M.; Lin, A. S.; Guldberg, R. E. *J. Biomech. Eng.* **2009**, *131*, 084502.
72. Kim, S.; Chung, E. H.; Gilbert, M.; Healy, K. E. *J. Biomed. Mater. Res. A* **2005**, *75*, 73–88.
73. Kim, S.; Healy, K. E. *Biomacromolecules* **2003**, *4*, 1214–1223.
74. Athanasiou, K. A.; Singhal, A. R.; Agrawal, C. M.; Boyan, B. D. *Clin. Orthop. Relat. Res.* **1995**, *315*, 272–281.
75. Guldberg, R. E. *J. Bone Miner. Res.* **2009**, *24*, 1507–1511.
76. Oest, M. E.; Dupont, K. M.; Kong, H. J.; Mooney, D. J.; Guldberg, R. E. *J. Orthop. Res.* **2007**, *25*, 941–950.
77. Richardson, T. P.; Peters, M. C.; Ennett, A. B.; Mooney, D. J. *Nat. Biotechnol.* **2001**, *19*, 1029–1034.
78. Healy, K. E.; Guldberg, R. E. *J. Musculoskelet. Neuronal Interact.* **2007**, *7*, 328–330.
79. Schwartz, Z.; Kieswetter, K.; Dean, D. D.; Boyan, B. D. *J. Periodontal Res.* **1997**, *32*, 166–171.
80. Schwarz, F.; Wieland, M.; Schwartz, Z.; *et al. J. Biomed. Mater. Res. B Appl. Biomater.* **2009**, *88*, 544–557.
81. Olivares-Navarrete, R.; Hyzy, S. L.; Hutton, D. L.; *et al. Biomaterials* **2010**, *31*, 2728–2735.
82. Dalby, M. J.; Gadegaard, N.; Tare, R.; *et al. Nat. Mater.* **2007**, *6*, 997–1003.
83. Shin, M.; Yoshimoto, H.; Vacanti, J. P. *Tissue Eng.* **2004**, *10*, 33–41.
84. Bashur, C. A.; Shaffer, R. D.; Dahlgren, L. A.; Guelcher, S. A.; Goldstein, A. S. *Tissue Eng. A* **2009**, *15*, 2435–2445.
85. Guldberg, R. E.; Oest, M. E.; Dupont, K.; *et al. J. Musculoskelet. Neuronal Interact.* **2007**, *7*, 333–334.
86. Hartgerink, J. D.; Beniash, E.; Stupp, S. I. *Science* **2001**, *294*, 1684–1688.
87. Chung, E. H.; Gilbert, M.; Virdi, A. S.; Sena, K.; Sumner, D. R.; Healy, K. E. *J. Biomed. Mater. Res. A* **2006**, *79*, 815–826.
88. Keselowsky, B. G.; Collard, D. M.; Garcia, A. J. *Proc. Natl. Acad. Sci. USA* **2005**, *102*, 5953–5957.
89. Reyes, C. D.; Garcia, A. J. *J. Biomed. Mater. Res. A* **2003**, *65*, 511–523.
90. Ohgushi, H.; Goldberg, V. M.; Caplan, A. I. *Acta Orthop. Scand.* **1989**, *60*, 334–339.
91. Grayson, W. L.; Chao, P. H.; Marolt, D.; Kaplan, D. L.; Vunjak-Novakovic, G. *Trends Biotechnol.* **2008**, *26*, 181–189.
92. Phillips, J. E.; Burns, K. L.; Le Doux, J. M.; Guldberg, R. E.; Garcia, A. J. *Proc. Natl. Acad. Sci. USA* **2008**, *105*, 12170–12175.

93. Cartmell, S. H.; Porter, B. D.; Garcia, A. J.; Guldberg, R. E. *Tissue Eng.* **2003**, *9*, 1197–1203.
94. Sikavitsas, V. I.; Bancroft, G. N.; Mikos, A. G. *J. Biomed. Mater. Res.* **2002**, *62*, 136–148.
95. Byers, B. A.; Guldberg, R. E.; Garcia, A. J. *Tissue Eng.* **2004**, *10*, 1757–1766.
96. Ohgushi, H.; Goldberg, V. M.; Caplan, A. I. *J. Orthop. Res.* **1989**, *7*, 568–578.
97. Marot, D.; Knezevic, M.; Novakovic, G. *Stem Cell Res. Ther.* **2010**, *1*, 10.
98. Caplan, A. I. *J. Cell. Physiol.* **2007**, *213*, 341–347.
99. Grellier, M.; Granja, P. L.; Fricain, J. C.; *et al. Biomaterials* **2009**, *30*, 3271–3278.
100. Jabbarzadeh, E.; Starnes, T.; Khan, Y. M.; *et al. Proc. Natl. Acad. Sci. USA* **2008**, *105*, 11099–11104.
101. De Long, W. G., Jr.; Einhorn, T. A.; Koval, K.; *et al. J. Bone Joint Surg. Am.* **2007**, *89*, 649–658.
102. Muschler, G. F.; Raut, V. P.; Patterson, T. E.; Wenke, J. C.; Hollinger, J. O. *Tissue Eng. B Rev.* **2009**, *16*, 123–145.
103. Reichert, J. C.; Saifzadeh, S.; Wullschleger, M. E.; *et al. Biomaterials* **2009**, *30*, 2149–2163.
104. Egermann, M.; Goldhahn, J.; Schneider, E. *Osteoporos. Int.* **2005**, *16*(Suppl. 2), S129–S138.
105. Kloss, F. R.; Gassner, R. *Exp. Gerontol.* **2006**, *41*, 123–129.
106. Strube, P.; Mehta, M.; Baerenwaldt, A.; *et al. Bone* **2009**, *45*, 1065–1072.
107. Reinwald, S.; Burr, D. *J. Bone Miner. Res.* **2008**, *23*, 1353–1368.
108. Schmitz, J. P.; Hollinger, J. O. *Clin. Orthop. Relat. Res.* **1986**, *205*, 299–308.
109. Gugala, Z.; Gogolewski, S. *J. Orthop. Trauma* **1999**, *13*, 187–195.
110. Aalami, O. O.; Nacamuli, R. P.; Lenton, K. A.; *et al. Plast. Reconstr. Surg.* **2004**, *114*, 713–720.
111. Hobar, P. C.; Schreiber, J. S.; McCarthy, J. G.; Thomas, P. A. *Plast. Reconstr. Surg.* **1993**, *92*, 405–410.
112. Sirola, K. *Ann. Med. Exp. Biol. Fenn.* **1960**, *38*(Suppl. 2), 1–87.
113. Degano, I. R.; Vilalta, M.; Bago, J. R.; *et al. Biomaterials* **2008**, *29*, 427–437.
114. Dumas, A.; Moreau, M. F.; Gherardi, R. K.; Basle, M. F.; Chappard, D. *J. Biomed. Mater. Res. A* **2009**, *90*, 1218–1229.
115. Gupta, D. M.; Kwan, M. D.; Slater, B. J.; Wan, D. C.; Longaker, M. T. *J. Craniofac. Surg.* **2008**, *19*, 192–197.
116. Wan, D. C.; Kwan, M. D.; Gupta, D. M.; *et al. J. Craniofac. Surg.* **2008**, *19*, 1292–1301.
117. Zhang, Y.; Fan, W.; Ma, Z.; *et al. Acta Biomater.* **2010**, *6*, 3021–3028.
118. Zhao, Z.; Wang, Z.; Ge, C.; Krebsbach, P.; Franceschi, R. T. *J. Dent. Res.* **2007**, *86*, 1207–1211.
119. Tu, Q.; Valverde, P.; Li, S.; Zhang, J.; Yang, P.; Chen, J. *Tissue Eng.* **2007**, *13*, 2431–2440.
120. Wan, D. C.; Pomerantz, J. H.; Brunet, L. J.; *et al. J. Biol. Chem.* **2007**, *282*, 26450–26459.
121. Zhao, J.; Shinkai, M.; Takezawa, T.; Ohba, S.; Chung, U. I.; Nagamune, T. *J. Biosci. Bioeng.* **2009**, *107*, 318–323.
122. Seo, B. M.; Sonoyama, W.; Yamaza, T.; *et al. Oral Dis.* **2008**, *14*, 428–434.
123. Honma, T.; Itagaki, T.; Nakamura, M.; *et al. Oral Dis.* **2008**, *14*, 457–464.
124. Umoh, J. U.; Sampaio, A. V.; Welch, I.; *et al. Phys. Med. Biol.* **2009**, *54*, 2147–2161.
125. Stephan, S. J.; Tholpady, S. S.; Gross, B.; *et al. Laryngoscope* **2010**, *120*, 895–901.
126. Taub, P. J.; Yau, J.; Spangler, M.; Mason, J. M.; Lucas, P. A. *Plast. Reconstr. Surg.* **2009**, *123*, 1178–1185.
127. Itagaki, T.; Honma, T.; Takahashi, I.; Echigo, S.; Sasano, Y. *Anat. Rec. (Hoboken)* **2008**, *291*, 1038–1046.
128. Arnaud, E. *Childs Nerv. Syst.* **2000**, *16*, 659–668.
129. Bohnenblust, M. E.; Steigelman, M. B.; Wang, Q.; Walker, J. A.; Wang, H. T. *J. Craniofac. Surg.* **2009**, *20*, 340–346.
130. Yoon, E.; Dhar, S.; Chun, D. E.; Gharibjanian, N. A.; Evans, G. R. *Tissue Eng.* **2007**, *13*, 619–627.
131. Cowan, C. M.; Aghaloo, T.; Chou, Y. F.; *et al. Tissue Eng.* **2007**, *13*, 501–512.
132. Jung, U. W.; Song, K. Y.; Kim, C. S.; *et al. Biomed. Mater.* **2007**, *2*, S101–S105.
133. Montjovent, M. O.; Mathieu, L.; Schmoekel, H.; *et al. J. Biomed. Mater. Res. A* **2007**, *83*, 41–51.
134. Park, J. W.; Bae, S. R.; Suh, J. Y.; *et al. J. Biomed. Mater. Res. A* **2008**, *87*, 203–214.
135. Leu, A.; Stieger, S. M.; Dayton, P.; Ferrara, K. W.; Leach, J. K. *Tissue Eng. A* **2009**, *15*, 877–885.
136. Schwarz, F.; Ferrari, D.; Sager, M.; Herten, M.; Hartig, B.; Becker, J. *Clin. Oral Implants Res.* **2009**, *20*, 1219–1230.
137. Young, S.; Patel, Z. S.; Kretlow, J. D.; *et al. Tissue Eng. A* **2009**, *15*, 2347–2362.
138. Schmitz, J. P.; Schwartz, Z.; Hollinger, J. O.; Boyan, B. D. *Acta Anat. (Basel)* **1990**, *138*, 185–192.
139. Chen, K. Y.; Shyu, P. C.; Dong, G. C.; Chen, Y. S.; Kuo, W. W.; Yao, C. H. *Biomaterials* **2009**, *30*, 1682–1688.
140. Peters, D. A.; Courtemanche, D. J. *J. Craniofac. Surg.* **2009**, *20*, 2200–2204.
141. Yeom, H.; Blanchard, S.; Kim, S.; Zunt, S.; Chu, T. M. *J. Craniofac. Surg.* **2008**, *19*, 446–452.
142. Lam, C. X.; Hutmacher, D. W.; Schantz, J. T.; Woodruff, M. A.; Teoh, S. H. *J. Biomed. Mater. Res. A* **2009**, *90*, 906–919.
143. Humber, C. C.; Sandor, G. K.; Davis, J. M.; *et al. Oral Surg. Oral Med. Oral Pathol. Oral Radiol. Endod.* **2010**, *109*, 372–384.
144. Seol, Y. J.; Kim, K. H.; Kang, Y. M.; Kim, I. A.; Rhee, S. H. *J. Biomed. Mater. Res. B Appl. Biomater.* **2009**, *90*, 679–687.
145. Yeom, J.; Chang, S.; Park, J. K.; *et al. Tissue Eng. C Methods* **2010**, *16*, 1059–1068.
146. Pripatnanont, P.; Nuntanaranont, T.; Vongvatcharanon, S. *Int. J. Oral Maxillofac. Surg.* **2009**, *38*, 356–362.
147. Kishimoto, M.; Kanemaru, S.; Yamashita, M.; *et al. Laryngoscope* **2006**, *116*, 212–216.
148. Por, Y. C.; Barcelo, C. R.; Salyer, K. E.; *et al. J. Craniofac. Surg.* **2008**, *19*, 383–392.
149. Icekson, M.; Regev, E.; Neuman, R.; Margulis, A. *Cleft Palate Craniofac. J.* **2009**, *46*, 363–367.
150. Haberstroh, K.; Ritter, K.; Kuschnierz, J.; *et al. J. Biomed. Mater. Res. B Appl. Biomater.* **2010**, *93*, 520–530.
151. Gosain, A. K.; Riordan, P. A.; Song, L.; *et al. Plast. Reconstr. Surg.* **2004**, *114*, 1155–1163; discussion 1164–1165.
152. Yu, D.; Li, Q.; Mu, X.; Chang, T.; Xiong, Z. *Int. J. Oral Maxillofac. Surg.* **2008**, *37*, 929–934.
153. Thaller, S. R.; Kim, J. C.; Kawamoto, H. K. *Ann. Plast. Surg.* **1989**, *23*, 390–395.
154. Gruber, R. M.; Ludwig, A.; Merten, H. A.; Pippig, S.; Kramer, F. J.; Schliephake, H. *Clin. Oral Implants Res.* **2009**, *20*, 175–182.
155. Sicca, C. M.; Corotti, M. V.; Sgarbosa, S. H.; *et al. J. Biomed. Mater. Res. B Appl. Biomater.* **2008**, *86*, 188–196.
156. Haas, R.; Donath, K.; Fodinger, M.; Watzek, G. *Clin. Oral Implants Res.* **1998**, *9*, 107–116.
157. Hanisch, O.; Tatakis, D. N.; Rohrer, M. D.; Wohrle, P. S.; Wozney, J. M.; Wikesjo, U. M. *Int. J. Oral Maxillofac. Implants* **1997**, *12*, 785–792.
158. Hurzeler, M. B.; Quinones, C. R.; Kirsch, A.; *et al. Clin. Oral Implants Res.* **1997**, *8*, 476–486.
159. Hurzeler, M. B.; Quinones, C. R.; Kirsch, A.; *et al. Clin. Oral Implants Res.* **1997**, *8*, 401–411.
160. Kirker-Head, C. A.; Nevins, M.; Palmer, R.; Nevins, M. L.; Schelling, S. H. *Int. J. Oral Maxillofac. Implants* **1997**, *12*, 403–411.
161. Quinones, C. R.; Hurzeler, M. B.; Schupbach, P.; Arnold, D. R.; Strub, J. R.; Caffesse, R. G. *Clin. Oral Implants Res.* **1997**, *8*, 497–505.
162. Quinones, C. R.; Hurzeler, M. B.; Schupbach, P.; *et al. Clin. Oral Implants Res.* **1997**, *8*, 487–496.
163. Furst, G.; Gruber, R.; Tangl, S.; *et al. Clin. Oral Implants Res.* **2003**, *14*, 500–508.
164. Nevins, M.; Kirker-Head, C.; Wozney, J. A.; Palmer, R.; Graham, D. *Int. J. Periodontics Restorative Dent.* **1996**, *16*, 8–19.
165. Haas, R.; Mailath, G.; Dortbudak, O.; Watzek, G. *Clin. Oral Implants Res.* **1998**, *9*, 117–122.
166. Sauerbier, S.; Stubbe, K.; Maglione, M.; *et al. Tissue Eng. C Methods* **2010**, *16*, 1033–1039.
167. Asai, S.; Shimizu, Y.; Ooya, K. *Clin. Oral Implants Res.* **2002**, *13*, 405–409.
168. Watanabe, K.; Niimi, A.; Ueda, M. *Oral Surg. Oral Med. Oral Pathol. Oral Radiol. Endod.* **1999**, *88*, 26–32.
169. Lim, E.; Modi, K. D.; Kim, J. *J. Vis. Exp.* **2009**.
170. Remy, S.; Tesson, L.; Usal, C.; *et al. Transgenic Res.* **2010**, *19*, 745–763.
171. Terrovitis, J. V.; Smith, R. R.; Marban, E. *Circ. Res.* **2010**, *106*, 479–494.
172. Muller, R.; Van Campenhout, H.; Van Damme, B.; *et al. Bone* **1998**, *23*, 59–66.
173. Odgaard, A. *Bone* **1997**, *20*, 315–328.
174. Uchiyama, T.; Tanizawa, T.; Muramatsu, H.; Endo, N.; Takahashi, H. E.; Hara, T. *Calcif. Tissue Int.* **1997**, *61*, 493–498.
175. Bruder, S. P.; Kraus, K. H.; Goldberg, V. M.; Kadiyala, S. *J. Bone Joint Surg. Am.* **1998**, *80*, 985–996.
176. Cook, S. D.; Salkeld, S. L.; Brinker, M. R.; Wolfe, M. W.; Rueger, D. C. *J. Orthop. Trauma* **1998**, *12*, 407–412.
177. An, Y., Friedman, R., Eds.; In *Animal Models in Orthopedic Research*; CRC Press: Boca Raton, FL, 1999.
178. Shang, Q.; Wang, Z.; Liu, W.; Shi, Y.; Cui, L.; Cao, Y. *J. Craniofac. Surg.* **2001**, *12*, 586–593; discussion 594–595.
179. Itoh, T.; Mochizuki, M.; Nishimura, R.; *et al. J. Vet. Med. Sci.* **1998**, *60*, 451–458.

180. Segal, U.; Shani, J. *Vet. Comp. Orthop. Traumatol.* **2010**, *23*, 66–70.
181. Pluhar, G. E.; Turner, A. S.; Pierce, A. R.; Toth, C. A.; Wheeler, D. L. *J. Bone Joint Surg. Br.* **2006**, *88*, 960–966.
182. Marks, T.; Wingerter, S.; Franklin, L.; *et al. Biomed. Sci. Instrum.* **2007**, *43*, 194–199.
183. Wojtowicz, A. M.; Shekaran, A.; Oest, M. E.; *et al. Biomaterials* **2010**, *31*, 2574–2582.
184. Bloemers, F. W.; Blokhuis, T. J.; Patka, P.; Bakker, F. C.; Wippermann, B. W.; Haarman, H. J. *J. Biomed. Mater. Res. B Appl. Biomater.* **2003**, *66*, 526–531.
185. Heckman, J. D.; Boyan, B. D.; Aufdemorte, T. B.; Abbott, J. T. *J. Bone Joint Surg. Am.* **1991**, *73A*, 750–764.
186. Connolly, J. F.; Guse, R.; Tiedeman, J.; Dehne, R. *Clin. Orthop. Relat. Res.* **1991**, *266*, 259–270.
187. Cook, S. D.; Baffes, G. C.; Wolfe, M. W.; Sampath, T. K.; Rueger, D. C.; Whitecloud, T. S., 3rd. *J. Bone Joint Surg. Am.* **1994**, *76*, 827–838.
188. Agrawal, C. M.; Best, J.; Heckman, J. D.; Boyan, B. D. *Biomaterials* **1995**, *16*, 1255–1260.
189. Sasaki, T.; Watanabe, C. *Bone* **1995**, *16*, 9–15.
190. Schwartz, Z.; Doukarsky-Marx, T.; Nasatzky, E.; *et al. Clin. Oral Implants Res.* **2008**, *19*, 1233–1245.
191. Bab, I. A. *Bone* **1995**, *17*, 437S–441S.
192. Schwartz, Z.; Sela, J.; Ramirez, V.; Amir, D.; Boyan, B. D. *Bone* **1989**, *10*, 53–60.

6.618. Materials in Tendon and Ligament Repair

K Miller, J E Hsu, and L J Soslowsky, University of Pennsylvania, Philadelphia, PA, USA

© 2011 Elsevier Ltd. All rights reserved.

6.618.1.	**Introduction**	258
6.618.2.	**Basic Properties of Tendon and Ligament**	259
6.618.2.1.	Classification	259
6.618.2.2.	General Structure	259
6.618.2.3.	Composition	260
6.618.2.4.	Biomechanical Properties	261
6.618.2.5.	Effect of Mechanical Loading	262
6.618.2.6.	Tendon and Ligament Injury and Healing	262
6.618.2.7.	Summary	263
6.618.3.	**Augmentation of Scaffolds**	263
6.618.4.	**Animal Models in Tendon and Ligament Research**	265
6.618.4.1.	Choosing an Appropriate Animal Model	265
6.618.4.2.	Animal Models of Tendon Injury	266
6.618.4.3.	Animal Models of Ligament Injury	266
6.618.5.	**Graft Materials**	268
6.618.5.1.	Biologic Materials	268
6.618.5.1.1.	Collagen derivatives	268
6.618.5.1.2.	Polysaccharides: Chitin, chitosan, alignate, and hyaluronan	269
6.618.5.1.3.	Silk	270
6.618.5.1.4.	Xenograft	270
6.618.5.1.5.	Autograft/allograft	271
6.618.5.2.	Synthetic Materials	272
6.618.5.2.1.	Resorbable polyesters	272
6.618.5.2.2.	Nonresorbable materials	273
6.618.6.	**Clinical Application**	274
6.618.6.1.	Rotator Cuff	274
6.618.6.2.	Anterior Cruciate Ligament	275
6.618.6.3.	Suture Anchors	275
6.618.7.	**Summary**	276
References		276

Glossary

Allograft A tissue or organ obtained from one member of a species and grafted to a genetically dissimilar member of the same species.

Autograft A tissue or organ that is grafted into a new position on the body of the individual from which it was removed.

Gene therapy The application of genetic engineering to the transplantation of genes into human cells in order to cure a disease caused by a genetic defect.

Tendinopathy Clinical syndrome encompassing overuse tendon injuries characterized by pain, swelling, and impaired function.

Xenograft A graft obtained from a member of one species and transplanted to a member of another species.

Abbreviations

ACL	Anterior Cruciate Ligament
bFGF	Basic fibroblast growth factor
BMP	Bone morphogenetic proteins
ECM	Extracellular matrix
GAG	Glycosaminoglycan
HA	Hyaluronan
IGF-1	Insulin-like growth factor 1
MCL	Medial Collateral Ligament
MMP	Matrix metalloproteinase
MSCs	Mesenchymal stem cells
PCL	Poly-ε-caprolactone, Poly(caprolactone)
PDGF	Platelet derived growth factor
PDLLA	Poly-D, L-lactic acid
PDS	Polydioxanone
PET	Polyethylene terephthalate

PGA	Polyglycolic acid
PLAGA	poly(lactide-*co*-glycolide)
PLA	Polylactic acid
PLGA	polylactic-*co*-glycolic acid
PLLA	Poly-L-lactide, Poly-L-lactic acid
PTFE	Polytetrafluroethylene
QLV	Quasi-linear viscoelasticity
RGD	Arg-Gly-Asp
SIS	Small intestina submucosa
TGF-β	Transforming growth factor beta
UHMWPE	Ultrahigh molecular weight polyethylene
VEGF	Vascular endothelial growth factor

6.618.1. Introduction

Tendon and ligament disorders represent a large subset of musculoskeletal injuries that cause pain and functional disability for millions of individuals and account for a significant portion of health care costs.[1] Thirty to fifty percent of injuries in athletes are diagnosed as soft tissue injuries,[2] and this number will likely continue to rise. For example, reconstruction of the anterior cruciate ligament (ACL) of the knee after rupture is one of the most common procedures performed by orthopedic surgeons. The number of patients undergoing ACL reconstruction is increasing substantially, and although considered a relatively safe procedure, the need for subsequent knee surgery in these patients is not uncommon, especially in young and female patients.[3] In addition to the large percentage of the young and active affected by tendon and ligament disorders, the current population continues to be active at older ages. Large increases in visits from active elderly patients for musculoskeletal problems are expected to be seen in sports and occupational medicine clinics. Soft tissue injuries, such as rotator cuff tears, are becoming increasingly common in individuals over the age of 40. This is not only important in terms of long-term pain and disability caused by these conditions, but treating these musculoskeletal injuries will put increasing financial pressure on health care providers worldwide.[4]

Tendons and ligaments are soft tissue structures that are frequently injured as a result of acute trauma or chronic overuse. Sudden, severe loading, which can occur with athletic injuries or motor vehicle accidents, can lead to rupture of tendons or ligaments. For example, sudden rotational force applied to the knee with the foot planted in the ground can lead to acute rupture of the ACL or medial collateral ligament (MCL), common injuries that occur in young, active individuals. Excessive and repetitive loading of tendons, such as the rotator cuff tendons of the shoulder, can similarly lead to rupture. In addition, tendons are often subject to overuse injuries, collectively referred to as tendinopathies. Repetitive tendon motion can lead to microtrauma and pathologic changes within the substance of the tendon. Historically, these changes were described by the term 'tendinitis,' implying inflammation of the tendon[5–8]; however, histopathologic studies have shown that these tendons have pathologic degenerative lesions in the absence of inflammation.[9–11] Therefore, 'tendinosis,' or degeneration of the tendon, or even the more general term 'tendinopathy' may be more appropriate to describe these overuse tendon injuries.

Our understanding of the pathogenesis of these common tendon and ligament conditions continues to improve. However, current treatment regimens formulated on evidence-based medicine are limited, and outcomes are often suboptimal. The preferred and accepted treatment for overuse tendinopathy is unclear. Tendinopathy was traditionally treated with corticosteroids, and nonsteroidal antiinflammatory medications for inflammation that later was found to be, if anything, only transiently present. Results of other treatment modalities such as shock wave therapy, physical therapy, and eccentric strengthening protocols have provided inconsistent results.[12] Neither ACL nor rotator cuff tendon injuries spontaneously heal after acute injury. Although these common musculoskeletal injuries have accepted standards for surgical treatment, many challenges remain in treating recurrent or recalcitrant cases. ACL reconstructions can successfully be performed with local autograft or allograft but are limited by the morbidity associated with local autograft and the immunogenic and infectious complications from allograft. Rotator cuff tears are typically treated with direct repair, but chronic or massive tears not amenable to direct repair pose a significant challenge to the orthopedic surgeon. Furthermore, these repaired tendons and ligaments do not return to baseline structural and mechanical function after injury, repair, and healing and can be complicated by rerupture. Restoring this normal mechanical function after injury, healing, and repair remains a significant challenge. This underscores the importance of developing new therapeutic approaches to treat these injuries.

Fortunately, with recent advancements in tissue engineering, novel strategies aimed at restoring native tendon and ligament structure and function show a lot of promise in their ability to address these challenging problems. As cellular and biochemical mechanisms for tendon and ligament healing continue to be elucidated, identification of therapeutic targets and manipulation of these biochemical mediators may prove useful in improving the healing potential of these structures. Recent studies have used gene therapeutic methods to introduce growth factors to improve tissue healing and remodeling, while others have used cell therapy and the introduction of mesenchymal stem cells (MSCs) in an attempt to improve healing. Furthermore, combinations of biocompatible scaffolds with appropriate cell populations and biologic growth factors are being investigated, with the hope that recreating or enhancing the mechanical and biological environment will lead to tendon and ligament properties similar to or mechanically stronger than native tissue. Tissue engineering is a quickly emerging field with great potential and could soon revolutionize the treatment for a number of musculoskeletal conditions.

The aim of this chapter is to concisely review the fundamental aspects of synthetic and natural biomaterials used in tendon and ligament repair. The first section of this chapter will review the basic biomechanical properties of tendons and ligaments. While similar in gross appearance and in general

load-transmitting capacities, these structures differ significantly in functional, compositional, and structural properties. Understanding basic properties of tendons and ligaments is crucial in the creation of novel biomaterials that reproduce and augment their native properties. The following sections will review various methods and techniques required to test tendons and ligaments, including methods of augmentation and factors involved in choosing an appropriate animal testing model. The primary section of this chapter will review individual biologic and synthetic graft materials and describe the primary characteristics that make each a suitable material for tendon and ligament repair and healing. Finally, the current clinical application and experience with these biomaterials will be summarized.

6.618.2. Basic Properties of Tendon and Ligament

Tendons and ligaments are dense fibrous connective tissue structures that assist in the complex mechanical functions of the musculoskeletal system. From an anatomical and functional perspective, tendons transmit forces from muscle to bone and allow for dynamic joint and limb motion, while ligaments connect two bony structures to serve as static stabilizers of joint movement. Tendons can center the action of multiple muscles across a joint (e.g., Achilles tendon), as well as distribute the pull of one muscle to several bones (e.g., posterior tibial tendon). They also transmit the force produced by large muscle bodies through narrow fibro-osseous tunnels and can change the direction of pull across a joint. Each tissue has structural and mechanical properties that are specific for its anatomic location and function and are composed of a unique combination of water, collagen, proteoglycan, and other constituents. Furthermore, tendons and ligaments have viscoelastic properties that allow for both smooth movement during normal joint motion and resistance to excessive or abnormal joint displacement at high loads. Also of importance is the ability of these structures to adjust their biomechanical properties in response to mechanical loading. Studies have shown that exercise-related loading can improve properties of tendons and ligaments. Immobility can lead to quick deterioration of properties, making these structures more susceptible to injury and pathologic change. Excessive or repetitive motions can lead to tendon and ligament injury or rupture as well. A series of coordinated responses occur after injury, leading to a structurally and mechanically inferior structure (see **Chapter 5.525, Tissue Engineering Approaches to Regeneration of Anterior Cruciate Ligament**).

6.618.2.1. Classification

Because tendons and ligaments have different structural and material properties based on anatomic location and function, these structures can be classified in many different manners. Tendons are commonly classified based on the presence or absence of a surrounding synovial sheath, as this characteristic affects the healing capacity and ultimate structural and mechanical properties of tendon after injury. The soft tissue envelope and vascularity of sheathed tendons are fundamentally different than unsheathed tendons. Sheathed tendons are relatively avascular and get nutrition from the synovium. In unsheathed tendons, a much richer blood supply is able to reach the tendon around its surface, and therefore, these unsheathed tendons have a greater potential to heal. Ligaments are similarly grouped into intraarticular or extraarticular location based on the presence or absence of joint synovial fluid surrounding the structure. Intraarticular ligaments such as the ACL of the knee are surrounded by synovial fluid and have poor healing potential because of the limited vascularity and nutrition available to the ligament. This is in contrast to extraarticular ligaments such as the MCL which have a more extensive blood supply and therefore can heal spontaneously.

6.618.2.2. General Structure

Tendons and ligaments are dense fibrous connective tissue structures that are composed of closely packed collagen fibers arranged in a hierarchical fashion. In the tendon, rod-like collagen molecules align in a quarter-stagger array parallel to the longitudinal axis of the tendon to form a fibril, the smallest tendon structural unit (**Figure 1**).[13] Collagen fibrils form fibers that are bound by endotenon, a connective tissue that contains nerves, blood vessels, and lymphatics. The hierarchial structure continues with a group of collagen fibers forming a fiber bundle, a group of fiber bundles forming a fascicle, and a group of fascicles forming the tendon. Contiguous with the endotenon is the epitenon which covers the tendon unit and similarly carries nerves, blood vessels, and lymphatics.[14] A third layer of thin connective tissue, the paratenon, also covers the tendon, and in some anatomical sites is the synovial sheath. The paratenon and epitenon together form the peritendon which provides protection and reduces friction to allow for smooth gliding of the tendon along the bone and other adjacent soft tissue structures as they pass through areas of high mechanical stress. The basic hierarchical structure of a ligament is similar to that of a tendon. The thin connective tissue covering of a ligament, the epiligament, is analogous to the epitenon in a tendon, and similarly carries vasculature, lymphatic, and nerves. In their relaxed state, the collagen fibers of both tendons and ligaments form a typical wavy pattern, also referred to as a 'crimp,' when viewed under a polarized light microscope. This contributes to the nonlinear mechanical properties for all collagenous tissues. One key difference between tendons and ligaments is that collagen fibers do not run as parallel to the longitudinal axis of ligament as they do in a tendon, and intertwining of collagen fibers is more common than in a tendon.

Common to both these structures is the tendon–bone or ligament–bone junction, also called the enthesis. This is a complex area of transition in tendons and ligaments that plays an important role in their structural and mechanical properties. The morphology of this enthesis is similar between the two structures and can take on two different forms, direct and indirect insertions.[15] Indirect fibrous insertions such as the femoral insertion of the MCL have collagen fibers that anchor the tendon or ligament directly into the bone through calcified collagen fibers, also called Sharpey's fibers.[16] In direct fibrocartilaginous insertions, such as the supraspinatus tendon of the rotator cuff, a continuous change in tissue composition occurs in four zones. The composition of the first zone is the same as the midsubstance of tendon composed of aligned collagen fibers. Toward the second and third zones, the collagen type changes with progressively more type II and III collagen in the

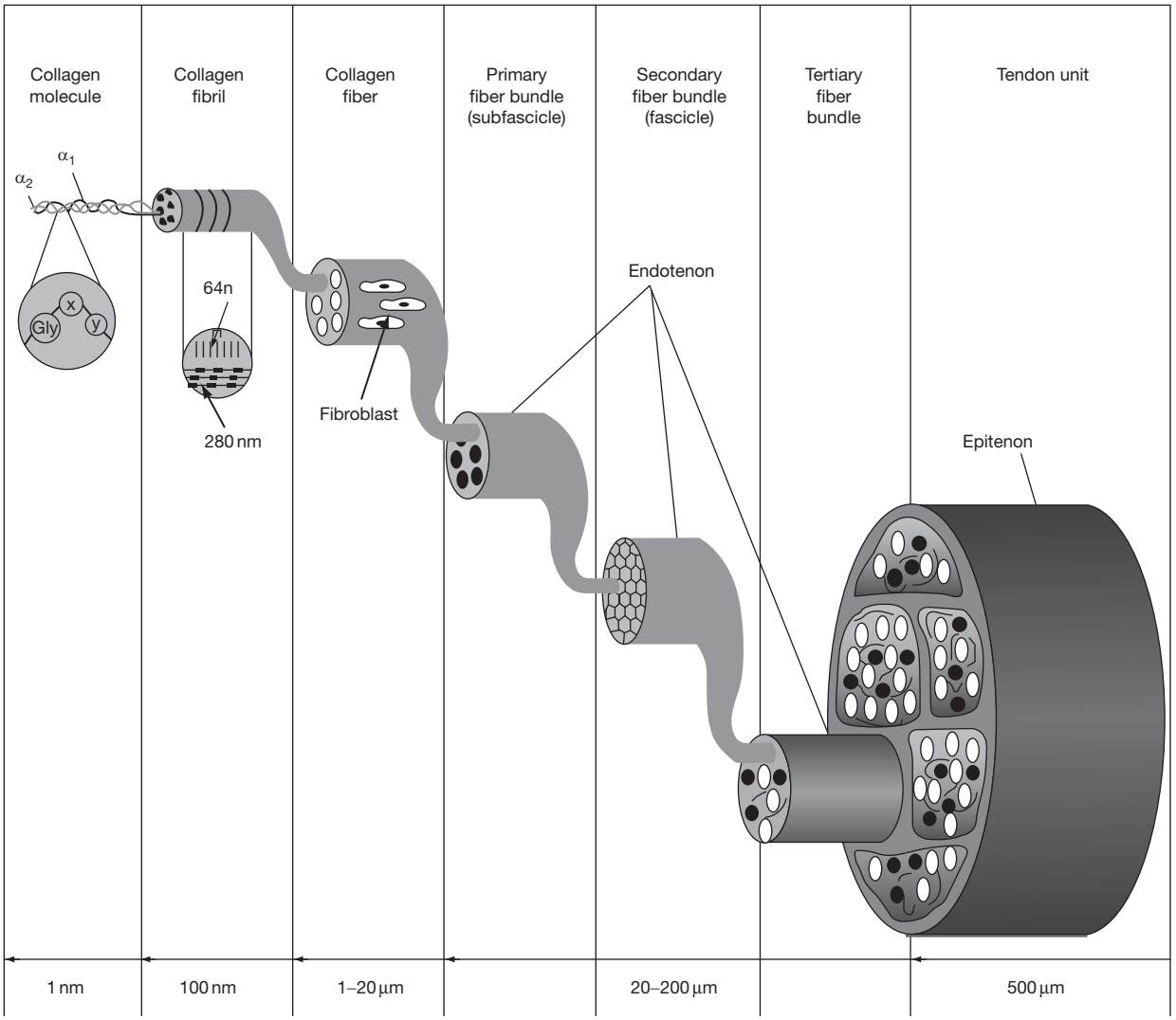

Figure 1 A schematic of multiunit hierarchical structure of the tendon. Reproduced from Wang, J. H. *J. Biomech*. **2006**, *39*, 1563–1582, with permission from Elsevier.

fibrocartilaginous second zone, and predominantly type II collagen in the mineralized fibrocartilage of the third zone. The fourth zone is bone and contains type I collagen and other minerals. This gradual transition and change in collagen composition helps to dissipate mechanical load at the enthesis, which is typically weaker in tension than the midsubstance of the tendon or ligament. On the opposite end of the enthesis in tendon is the myotendinous junction, in which collagen fibrils interdigitate with myofibroblasts, allowing for contractile proteins to exert their effect on tendon fibers.[17] This is the weakest point of the muscle–tendon unit.

6.618.2.3. Composition

Tendons and ligaments are composed of water, collagen, proteoglycans, glycoproteins, cells, and ground substance. Although the constituents are similar between the two structures, there are subtle differences that are important to differentiate in terms of their structural and mechanical properties. Water is the primary constituent of healthy tendon or ligament, accounting for about 60% of the wet weight. Of the dry weight, collagen is the primary component in both tendon and ligament and accounts for about 80% of the dry weight.[18] The content of water is lower and collagen is higher in tendon than in ligament. However, this varies not only between tendons and ligaments, but also between different anatomical and functional types of tendons and ligaments. Other constituents include elastin, proteoglycans, and a minimal amount of inorganic components. This overall composition allows these structures to have characteristics of tensile strength as well as elasticity.

Collagen contributes greatly to the tensile strength of tendon/ligament and comprises the majority of the dry mass of normal tendon. Individual collagen molecules consist of a triple chain helix with a characteristic tripeptide sequence which usually is glycine, proline, and hydroxyproline. These collagen molecules are synthesized in the endoplasmic reticulum of fibroblasts. They exist as procollagen chains which later

undergo multiple posttranslation modifications such as hydroxylation and glycosylation before reaching its typical triple helical structure. These collagen molecules are cross-linked by various enzymes in the extracellular matrix (ECM), such as lysyl oxidase.[19] This cross-linking increases the modulus of the tendon or ligament, and variations in cross-linking are responsible for the structural difference between the numerous different collagen types and their mechanical properties.[20] Both tendons and ligaments are primarily made of type I (> 90%) collagen, followed by type III and V collagen; ligaments contain more type III collagen than do tendons, which may be reflective of the increased metabolic activity in ligaments.[21] There are also minimal amounts of other collagen, notably type V collagen in vascular walls and type X collagen in mineralized fibrocartilage at the tendon/ligament enthesis. Type II collagen, predominantly found in cartilage, is also found in certain cartilaginous zones of tendons that undergo compression.

Glycoproteins are an integral part of the tendon and ligament ECM. Proteoglycans, which account for 1–5% of the dry weight of tendon and about 1% of the dry weight of ligament, are glycoproteins composed of a core protein attached to glycosaminoglycan (GAG) chains. GAGs are long linear carbohydrate side chains consisting of repeating disaccharide units. These side chains are highly negatively charged, a characteristic that is important in maintaining the hydration and viscoelastic behavior of tendon and ligament. The amount of proteoglycan present in these structures is largely dependent on whether the tendon or ligament is in a tension or compression-bearing location.[22,23] Proteoglycan content has been found to constitute a larger portion of the dry weight in compression-bearing regions than in tension-bearing regions. Larger aggregating proteoglycans, such as aggrecan, hold water within the fibrocartilage to resist compression, especially at the transition of ligament and tendon to bone.[22] Other smaller proteoglycans, particularly small leucine-rich proteoglycans such as decorin and biglycan, play a key role in the biologic activity and remodeling of tendons and ligaments.[24] Along with proteoglycans, there are numerous other glycoproteins in the ECM that contribute to the matrix structure. Elastin, which composes about 2% of the dry weight of tendon and a variable amount in ligament, is likely partially responsible for elasticity and return to a crimped configuration after loading.[25] Tenascin-C is a glycoprotein that interacts with collagen fibrils and is found in the tendon body as well as the enthesis and the myotendinous junction.[26] It is typically upregulated by mechanical loading of the tendon. Fibronectin is another important glycoprotein located on the collagen surface that attaches cells to various types of collagen and regulates cell migration and differentiation.[27] The role of these small and large proteoglycans and glycoproteins in tendon and ligament in the fundamental ECM processes continue to be elucidated.

Tendon fibroblasts, or tenocytes, and ligament fibroblasts represent the predominant cell type present in these structures, but like most types of connective tissue, these cells are few in number and not as abundant as the ECM. These spindle-shaped cells are oriented longitudinally between collagen bundles. Although tendons and ligaments have an overall low cellularity, these fibroblasts contain prominent cytoplasmic processes that allow for complex three-dimensional structural network and cell-to-cell communication via gap junctions with connexins 32 and 43.[28] As will be discussed in the following sections, tendons and ligaments respond to mechanical loading. The complex fibroblast structural network and cell-to-cell interactions are responsible for the changes in structural, compositional, and mechanical properties. When mechanically loaded, tendon and ligament cells alter gene expression and protein synthesis that lead to changes in ECM proteins such as collagen, proteoglycans, and other glycoproteins. Although the cellular mechanisms for mechanotransduction are still being elucidated, interactions between the actin cytoskeleton of fibroblasts, multiple cellular components such as integrins and membrane receptors, and the ECM help to detect changes in mechanical forces.[29,30] This leads to changes in gene expression and protein synthesis as a result of a cascade of cell-signaling events.[31] This complex array of interactions between tendon and ligament cells and their ECM allow these structures to respond and adapt to changes in mechanical loading conditions.

6.618.2.4. Biomechanical Properties

Tendons and ligaments must be able to transmit high tensile loads with minimal deformation. Structural properties describe the tensile capacity of the overall tendon structure and are therefore dependent on the size and shape of the tendon. Material properties, sometimes referred to as mechanical properties, describe the intrinsic quality of the tendon substance independent of its shape or size. These properties of tendon can be determined by mechanical tensile testing and are represented by the relationship between load and elongation (structural properties) and stress and strain (material properties).

Structural properties of tendon and ligament can be characterized by a load–elongation curve which typically has three major components. The toe region is the nonlinear portion at the base of the curve that is thought to be due in part to the recruitment and alignment of crimped collagen fibrils. The stiffness, defined by the slope of the curve between two defined points of elongation, increases throughout the toe region. Because collagen fibers are initially more highly aligned in the primary loading direction in tendon than in ligament, the toe region of the load–elongation curve for ligaments is typically larger, as more time is required to reorient the fibers in the direction of loading. Transition from the toe region to the linear region occurs as the tendon fibrils become aligned and oriented parallel to the longitudinal axis of the tendon. After the fibers are recruited and oriented in the longitudinal direction, the collagen fiber structure itself is being stressed. As opposed to the highly compliant toe region, the tendon exhibits much higher stiffness in the linear region of the curve. At a certain elongation, tearing of the collagen fibrils will begin to occur. This is represented by a reduction in the stiffness of the curve and signifies a transition from the linear region to the failure region. The highest load placed on the tendon before failure is the ultimate load, and the maximum elongation before failure is the ultimate elongation. Similarly, a stress–strain curve characterizes the mechanical properties of the tendon (Figure 2). Stress (the amount of force per unit of area) and strain (change in length relative to original length)

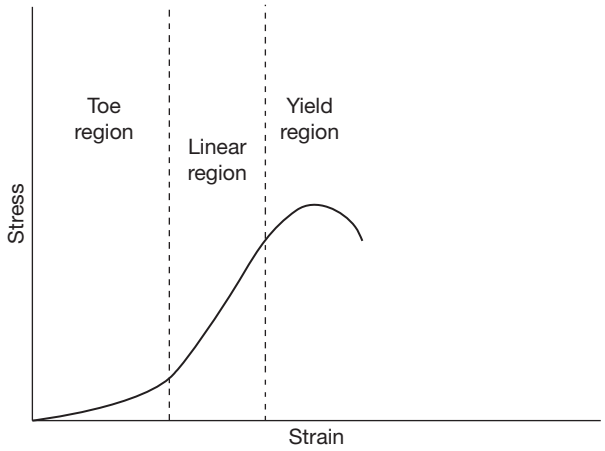

Figure 2 Stress–strain behavior of ligament showing the toe, linear, and yield regions. Reproduced from Freeman, J. W.; Woods, M. D.; Laurencin, C. T. *J. Biomech.* **2007**, *40*, 2029–2036, with permission from Elsevier.

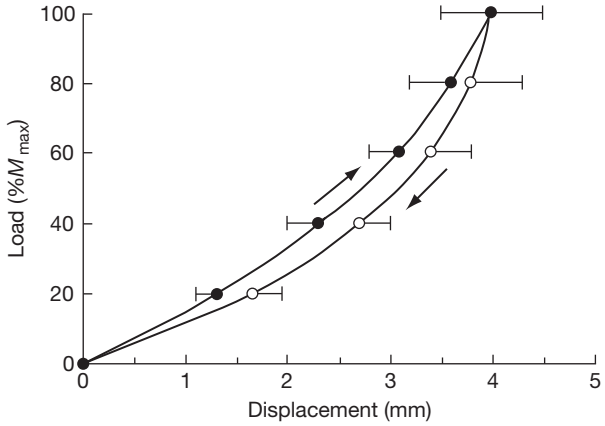

Figure 3 Load–displacement plots of tendon with arrows indicating loading and unloading directions. The area between the loading and unloading curves is the energy dissipated by viscous damping. Reproduced from Maganaris, C. N.; Paul, J. P. *J. Biomech.* **2000**, *33*, 1723–1727, with permission from Elsevier.

take geometry of the tissue into account. In a stress–strain curve, the elastic modulus is obtained by calculating the slope between two limits of strain. The tensile strength is the maximum stress achieved before failure, and the ultimate strain is the strain at failure.

An important characteristic of tendons and ligaments is their viscoelastic behavior, referring to the time and load-dependency of their mechanical behavior. This characteristic is thought to happen through the complex interaction of collagen, water, and other ECM constituents. These viscoelastic properties can be affected by changes in extracellular constituents, especially at low load stress states. Loading and unloading of the same specimen will result in different paths along a load–elongation curve (**Figure 3**). Hysteresis is a viscoelastic characteristic that refers to the amount of lengthening a tissue maintains during cyclic loading. On the curve, the hysteresis loop that is formed represents energy that is dissipated during the process. Two classic experimental characteristics of viscoelastic behavior are stress relaxation and creep. In a creep test, a specimen is subjected to a constant force and the deformation will gradually increase with time. In a stress relaxation test, a specimen is held at a constant elongation and the load will decrease with time as the tissue relaxes. A peak stress is still reached like in elasticity, but viscoelastic materials stress relax over time. Strain rate sensitivity is another characteristic of viscoelasticity. Tendons absorb more energy but are less effective in transferring load at low strain rates, but at high strain rates, tendons are less deformable and are more effective in moving large loads. This nonlinear behavior of tendon is important to take into account during experimental testing. Quasi-linear viscoelasticity (QLV) was developed as a method to model soft tissues such as tendons and ligaments. This model takes into account the nonlinear elastic response and time-dependency as separate functions in a general viscoelastic model. QLV is considered 'quasi-linear' as the material is assumed to be linear in its viscous time-dependent response; however, the deformation and instantaneous stress–strain behavior can be nonlinear. QLV can characterize the time-dependent and nonlinear behavior of tendons and ligaments and is an important tool in constitutive modeling in biomechanics of these structures.

6.618.2.5. Effect of Mechanical Loading

Mechanical and biochemical properties of tendons and ligaments have been shown to change in response to mechanical loading. Multiple studies have looked at the effect of mobilization and training while others have studied the effect of disuse and immobilization on tendon and ligament. In various investigations using mice, rabbit, and swine animal models, the structural and mechanical properties of tendon and ligament were higher in animals exposed to repetitive exercise compared to those that had no exercise.[32–36] Biochemical changes were evident as well, with increased collage deposition and upregulation of growth factors important in collagen synthesis and cell proliferation with exercise.[37,38] Repetitive and excessive mechanical loading, however, can become pathologic as evidenced by the clinical entity of tendinopathy. It is thought that repetitive loads lead to tendon microtrauma as well as production of inflammatory mediators, including PGE_2 and LTB_4.[39–41] Elevated levels of prostaglandins and leukotrienes produced in response to tissue damage contribute to further degeneration of tendon and tissue edema.[42,43] The effect of disuse on tendon is not so well studied, but the general conclusion from multiple studies is that immobilization of the tendon and ligament decreases stiffness and tensile strength, which occurs at a faster rate than the increase in structural properties seen with remobilization.[44–46]

6.618.2.6. Tendon and Ligament Injury and Healing

Following injury, tendons and ligaments undergo a reparative process that involves coordinated phases of inflammation, repairing/proliferation, and remodeling. The initial event in the inflammatory phase after injury involves the formation of a hematoma containing inflammatory cells, erythrocytes,

and platelets collected at the injury site. Resorption of necrotic debris ensues, and various chemotactic fibers recruit tendon fibroblasts to the area, and collagen synthesis and deposition begins as early as 3 days after injury. In the proliferative phase, these tendon fibroblasts continue to synthesize collagen as well as other ECM components into the wound site. The abundant amount of collagen tissue that is formed produces what appears like scar tissue by gross appearance between the two edges of the tendon or ligament. Histologically, the collagen matrix appears disorganized. Remodeling and realignment of fibroblasts and collagen fibers begins around three weeks after injury, presumably in response to stress along the longitudinal axis of the tendon. The end result is scar-like tendon tissue that is mechanically inferior to native tissue. Multiple studies have shown that after injury, these structures return to only a fraction of native strength.

Various growth factors and cytokines play a crucial role throughout this process. The primary growth factors that have been studied are insulin-like growth factor 1 (IGF-1), platelet-derived growth factor (PDGF), basic fibroblast growth factor (bFGF), vascular endothelial growth factor (VEGF), and transforming growth factor β (TGF-β). During the inflammatory phase, high expression of IGF-1 leads to proliferation and migration of fibroblasts to the healing tendon or ligament, which leads to increased proteoglycan and collagen production. Injection of this growth factor has been shown to accelerate functional recovery in rat Achilles tendon. PDGF is also present during the inflammatory phase and plays a role in cell migration and proliferation; it increases DNA synthesis in tendon fibroblasts and is required for fibroblast division and replication. bFGF and VEGF regulate cellular migration and proliferation and also promote angiogenesis. TGF-β has three isoforms, TGF-β1, TGF-β2, and TGF-β3, that each plays varying roles in the inflammatory and repair phases of tendon healing. While TGF-β1 promotes tissue fibrosis when overexpressed, TGF-β3 has been shown to improve tissue scarring. The roles of each of these cytokines and growth factors on inflammation, angiogenesis, cell differentiation and proliferation, and ECM synthesis are still being elucidated.

As previously discussed, exercise has beneficial effects on tendon and ligament properties, but the effect of mechanical loading on tendons and ligaments during healing after injury is not as clear. This is in large part due to concerns that motion may compromise the healing process, particularly at the insertion site. Animal studies investigating the role of early controlled mobilization after flexor tendon repair have suggested increases in mechanical properties and improved tendon excursion,[47,48] but similar studies in looking at passive motion after rotator cuff repair show no difference in mechanical properties and a detrimental effect on joint range of motion.[49] In chronic tendinopathy models, mechanical loading is thought to stimulate fibroblast proliferation and collagen synthesis.[50] Further investigations into the role of immobilization and mechanical loading on the postoperative management of tendon and ligament repair are necessary. Understanding the complex interactions between cytokines, growth factors, and the response of fibroblasts to mechanical loading during healing is difficult but crucial in determining the optimal regenerative milieu for future biologic therapies.

6.618.2.7. Summary

A thorough appreciation of tendons and ligament properties and healing is necessary when attempting to replicate native tissue with tissue-engineered constructs. Knowledge of the basic structural and mechanical properties of tendons and ligaments is important in the development and testing of new constructs. Also, understanding the components and mechanisms behind tendon and ligament healing can be helpful in determining targets for novel therapeutics. Biocompatible scaffolds should mimic the collagen fiber structure, while combinations of specific cell lines with growth factors may be able to assist in recapitulating the dynamic interaction that occurs between cells, their ECM, and their response to mechanical loading and injury.

6.618.3. Augmentation of Scaffolds

While tissue-engineered constructs can help promote tendon and ligament healing, biomaterials alone are insufficient to restore tissue to its preinjured state. Augmentation techniques are used to manipulate or supplement biomaterials to help bridge the gap between engineered structures and natural tissue. *In vitro* studies are an excellent way to optimize augmentation techniques before investing in preclinical or clinical studies and therefore are imperative to the advancement of biomaterials research. Mechanical testing by simple tensile testing, cyclic fatigue, and creep and stress relaxation testing can be combined with biochemical testing such as cell proliferation assays, evaluation of cytotoxic properties, or bioresorption studies. By minimizing confounding variables introduced with *in vivo* studies, these studies can assist in determining the optimal environment for biomaterial integration. Outcomes from *in vitro* studies can then be used to transition these augmentation techniques into *in vivo* models. Two broad categories of scaffold augmentation include various methods of mechanical stimulation and chemical stimulation, such as cell seeding, growth factor implantation, gene therapy, and scaffold surface modification (see **Chapter 3.312, Cell Culture Systems for studying Biomaterial Interactions with Biological Barriers**; **Chapter 3.313, Histological Analysis**; **Chapter 3.316, Immunohistochemistry**; **Chapter 3.321, Microarrays in Biomaterials Research**; **Chapter 5.501, Scaffolds: Flow Perfusion Bioreactor Design**; **Chapter 5.502, Engineering Scaffold Mechanical and Mass Transport Properties**; **Chapter 5.504, Effect of Substrate Modulus on Cell Function and Differentiation**; **Chapter 5.506, Effects of Mechanical Stress on Cells**; **Chapter 5.522, Bone Tissue Engineering: Growth Factors and Cytokines**; **Chapter 5.507, Tissue Engineering and Selection of Cells**; **Chapter 5.508, Scaffold Materials for hES Cell Culture and Differentiation**; **Chapter 5.509, Cell Encapsulation**; **Chapter 5.510, Engineered Bioactive Molecules**; **Chapter 5.511, Rotating-Wall Vessels for Cell Culture**; and **Chapter 5.512, *In Vivo* Bioreactors**).

The incorporation of cells into biologic scaffolds can improve its composition, structure, and biomechanical properties. This technique requires selection of a particular cell type that has the desired properties. Once procured, these cells can be

purified, cultured, and then seeded onto a scaffold *in vitro*. In tendon repair models, scaffolds have been seeded with many different cell types including MSCs, dermal fibroblasts, and tendon and ligament fibroblasts.[51–53] Once implanted into the injury site, these cell-seeded scaffolds can provide additional signals to encourage cell proliferation and tissue regeneration; provisional mechanical support is provided by the scaffold while native tissue ingrowth occurs. MSCs have recently garnered much interest as a target for cell therapy because of their ability to differentiate into certain lineages of tissue, including tendon, with the appropriate conditions and stimulus.[52,54] Tenocytes, the primary cell type in tendons, have been shown to significantly improve the mechanical properties of scaffolds in tendon repair.[51] Other studies have focused on using tenocytes and dermal fibroblasts in cell therapy; dermal fibroblasts are an attractive option as they are more accessible than tenocytes or MSCs and could potentially achieve similar results. Multiple studies have shown a positive effect of cell therapy on the biomechanical properties of biologic scaffolds.[52,53]

Because adhesion of a large number of cells to the scaffolds is integral to cell therapy, multiple methods of encouraging cell integration have been investigated. Increasing the porosity and surface area to volume ratio of the scaffold, such as that seen in nanofibrous membranes, produces a more hydrophilic material and can increase the cell seeding efficiency.[55] Another commonly used method involves coating the scaffold with a material known to be involved in cell adhesion. For example, various ECM glycoproteins, such as fibronectin, vitronectin, and laminin, contain the RGD (Arg-Gly-Asp) tripeptide cell-binding domain that attaches to integrins on the cell surface. Coating the surface of scaffolds with these glycoproteins may enhance cellular attachment, and a positive effect on cellular response and tissue regeneration may be seen.[56,57]

Local delivery of growth factors can potentially improve tendon and ligament healing by enhancing migration and proliferation of cells as well as the synthesis of tissue. Growth factors that have been well-characterized in tendon healing include IGF-1, TGF-β, bFGF, PDGF, and VEGF. During the initial inflammatory phase, PDGF-BB and bFGF stimulate cell proliferation and mitogenic responses,[58] while multiple isoforms TGF-β aid in wound healing through matrix deposition; specific isoforms of TGF-β have opposing effects in tissue fibrosis and scarring.[59,60] Bone morphogenetic proteins (BMPs), a subgroup of the TGF-β superfamily, can affect tissue differentiation and induction into tendon- and cartilage-like phenotypes. For example, BMP-12 has been shown to increase proliferation and expression of type I and III collagen in healing tendon.[61] VEGF can stimulate endothelial cell proliferation and angiogenesis to improve the blood supply and nutrition to healing tendon. Although the effect of these specific growth factors on tendon and ligament healing has not been fully elucidated, manipulation and regulation of these growth factors have great potential for enhancement of tissue healing.

Gene therapy is a technique by which an exogenous gene can be transferred into a host genome, allowing for sustained expression of specific cytokines or growth factors.[62] This technique uses viral vectors, such as adenoviruses or retroviruses, or nonviral methods, such as naked DNA or liposome to incorporate a specific gene of interest from the carrier to the host genome. Tendon and ligament fibroblasts can be transduced with particular growth factors known to be important in the healing process, with the hope that overexpression will lead to enhanced structural properties. The increase in cellular activity from cytokines or growth factors could result in more robust tendon and ligament repair constructs. One of the main limitations to gene therapy is that certain methods, particularly the use of viral vectors, are immunogenic and can cause a toxic or inflammatory host response. Another concern in gene therapy is insertional mutagenesis, or the chance that a tumor could be induced with incorrect DNA placement within the host genome.

Cross-linking is another chemical method which can play a significant role in achieving desired structural and material properties. Cross-linking of collagen is a natural posttranslational process that occurs in the ECM of tendons and ligaments which provides additional mechanical integrity to the collagen fiber structure. Various chemical and physical treatment, such as genipin,[63] can be used *in vitro* to affect the intramolecular and intermolecular cross-linking of collagen, and therefore, the solubility of collagen[64]; insoluble fibrils will provide a much stronger structure biomechanically. Manipulation of these cross-links can be performed in an attempt to match the properties of native tissue and be more suitable for implantation. The enzymatic degradation of collagen fibers by collagenases can also be reduced or suppressed, resulting in a mechanically stronger structure with increased number of cross-links.

Scaffolds can also be augmented by fibrin-based materials to promote cell proliferation and differentiation. Fibrin-based biomaterials are biocompatible, biodegradable and have an inherent affinity for biological surfaces. However, because it is mechanically weak and does not maintain a desired shape after *in vivo* implantation, it is usually paired with more mechanically robust structures in scaffolds such as synthetic polymers and used as a cell delivery-system to expedite tissue healing.[65,66] These materials can be prepared using a solution containing fibrinogen, fibronectin, thrombin, factor XIII, plasminogen, and aprotinin. Fibrinogen is a glycoprotein that is converted to fibrin monomers by thrombin; these monomers are then cross-linked by activated factor XIII to form a network of fibers. The rate at which the fibrin scaffold will be absorbed *in vivo* is determined by the ratio of plasminogen to aprotinin.[66]

Mechanical stimulation is a vital component of engineering tendon and ligament repair structures. In order to form well-organized ECM in load-bearing tissues, tendon and ligament fibroblasts must set forth appropriate mechanotransduction mechanisms. These complex mechanisms affect the type and amount of ECM produced, the release of cytokines and growth factors, and the morphology of cellular structures. It has been shown that the fibroblast response is dependent on the type of mechanical stimulation (cyclic strain, uniaxial tension, biaxial tension, shear stress), as well as magnitude and duration of mechanical loading.[67] For example, although native tendon and ligament is composed of predominantly type I collagen, tendons and ligaments subjected to compressive loading modify ECM synthesis and processing, leading to an increase in type II collagen synthesis and a resultant fibrocartilaginous phenotype. Increases in collagen production due to mechanical stimulation are concomitant with increase in matrix metalloproteinase (MMP) activity. MMPs, and other enzymes, are also synthesized in response to mechanical stimulation to

maintain balanced ECM remodeling. MMP activity degrades randomly-oriented scar tissue, which can be replaced with oriented collagen matrix. In addition to ECM synthesis, specific cell-signaling mechanisms also are activated during mechanical loading that induce the cytoskeletal reorganization important in maintaining the baseline elongated, spindle-like morphology of the tendon and ligament fibroblasts.[67,68]

6.618.4. Animal Models in Tendon and Ligament Research

With tissue engineering becoming a large part of research that is conducted in the tendon and ligament field, establishing and utilizing appropriate *in vitro* and *in vivo* preclinical models is a necessary step in the development and testing of new materials and techniques. Research utilizing human tissue, while providing information that directly correlates with the human condition, is limited by timing and availability of obtaining such samples for analysis. Commonly, human tissue can only be obtained during the end-stage chronic pathology rather than throughout disease progression. In addition, the methods by which to obtain tissue are typically invasive. In humans, disease progression is often evaluated radiographically or clinically by functional deterioration, which may not always correlate well with the actual disease process. It is impractical to study disease pathogenesis and response to treatment well in humans. The use of animal models allows for invasive evaluation at the tissue, cellular, and molecular level and avoids the limited and invasive nature of conducting human tissue research. These animal models allow the safety and efficacy of new materials and techniques to be tested in an *in vivo* model before translation into human trials.

6.618.4.1. Choosing an Appropriate Animal Model

Choosing an appropriate animal model for testing biomaterials involves consideration of a number of conditions that most appropriately addresses the specific research question at hand. Therefore, there is no one best model when speaking in general. Determining the most appropriate model involves finding an optimal integration of similar tissue properties and anatomy, analogous injury characteristics, pertinent outcome measures, and appropriate feasibility and cost. Clearly, the appropriate tissue and anatomy must be reproduced. Although tendons and ligaments share similar properties, they do have fundamental differences that require differentiation of the two for modeling.[69] The fact that ligaments have two bony attachments while tendons have one bony and one muscular attachment has implications not just on basic mechanical properties, but also on the appropriate evaluation of those properties such as preparation and gripping of tendon samples for mechanical testing. Anatomic location is also crucial. As mentioned previously, the presence or absence of surrounding synovial fluid or synovial tissue has implications on healing properties of the respective tissues. Intraarticular ligaments and intrasynovial tendons are surrounded by synovial fluid, which provides lubrication and also limits the healing potential of these structures as a consequence of a limited blood supply. Some structures in their native form may be considered extrasynovial, but after injury, would be considered intrasynovial (e.g., supraspinatus tendon). As will be discussed, the surrounding specific bony and soft tissue anatomy may be an important factor, especially when choosing a model for tendinopathy.

The various types of injuries and methods to reproduce them must be taken into account when selecting an appropriate animal model. Partial injuries and complete tears can occur, and complete injuries can be further subdivided into those that have gap formation and those that do not. These characteristics have specific implications on the treatment modality. Partial tears and complete tears with no gap formation, such as a partial MCL, may be amenable to nonsurgical treatment. Therefore, an appropriate animal model would study direct healing of tissue and evaluate methods to accelerate tissue healing. On the other hand, some injuries involve complete disruption of the tendon or ligament and gap formation, such as complete tears of the ACL of the knee or rotator cuff of the shoulder. Unlike the MCL, these injuries do not commonly heal spontaneously; instead, they commonly require surgical intervention. Therefore, the purpose of an animal model would be to evaluate the role of various surgical techniques and/or tissue-engineered constructs on tendon/ligament with gap formation. In general, evaluation of surgical manipulation and techniques is more accurate in large animal models. Methods of inducing tendinopathy include mechanical and chemically-induced models. Choosing an appropriate animal model should take into account the time and labor-intensive nature of mechanical loading, which best simulates the human condition. Chemical induction of injury is less invasive and easier than mechanical loading. However, it is dissimilar to what is thought to cause tendinopathy in humans. The chosen technique of injury must be easy, consistent and reproducible.

As mentioned previously, tendons and ligaments have a complex response to different mechanical loading conditions. Many studies have shown that postoperative activity or immobilization has an effect of tendon, ligament, and tendon/ligament-to-bone healing. Therefore, the ability to control this condition should be considered. Protective immobilization after tendon repair, such as rotator cuff repair, has been shown to be beneficial, and exercise too soon after surgery can be detrimental. In other circumstances such as flexor tendon injuries of the hand, postoperative motion after repair is necessary to prevent adhesion formation that will limit gliding of the tendon. Smaller animals should be used when control of postoperative activity level is required, as controlling the activity of larger animals is difficult.

The specific outcome measures should be taken into consideration when deciding on an animal model. Tissue properties can be assessed in a variety of ways, and each method has implications on the animal model to be used. The structural properties of the target tendon or ligament are usually of primary concern given the primary function of these structures. Larger samples from large animals are typically easier to test mechanically. Gripping of the bone attached to the tendon/ligament is generally less problematic than gripping soft tissue structures, such as the musculotendinous junction of the tendon. Other tissue properties, such as biological, biochemical, and molecular properties, also need to be taken into account.

Size consideration is also of paramount importance when taking these into account. Histologic sectioning is easier done on smaller animals. On the other hand, obtaining adequate quantities of RNA in small animals can be difficult given the low cellularity of tendon and ligament. Dependent on the techniques used to handle DNA, small animal models may not be optimal for these types of studies. A significant limitation that must be considered is the gene sequence information available for specific species; only the mouse genome has been completely sequenced.

Lastly, the financial cost and resources required to manage the animals must be taken into account. In general, although large animal models may sometimes offer more accurate manipulation and offer a better parallel to human anatomy and disease, the cost and resources needed to care for these animals is significantly more than that needed for small animals. This must be balanced with the need for the desired study sample size, as the cost of obtaining a minimal amount of large animals for an adequately powered study may be prohibitory.

6.618.4.2. Animal Models of Tendon Injury

An important distinction that must be made before choosing an appropriate animal model for tendons is whether the tendon to be modeled has the presence or absence of a synovial sheath. Flexor tendons of the hand, as well as the long head of the biceps and flexors of the foot, are intrasynovial tendons that are commonly used in animal modeling. These tendons are present in sheaths containing lubricating and nourishing synovial fluid. This fluid surrounds the tendon, and therefore, the blood supply to the tendon is more limited than in extrasynovial tendons.

Research using animal models of intrasynovial tendons has typically focused on scar and adhesion formation after tendon injury and repair. These peritendinous adhesions limit the normal gliding motion of tendons and lead to pain and functional disability in the human. Many different animal models including the chicken, rabbit, and dog have been used to replicate the intrasynovial tendon healing environment. Historically, an extrinsic healing mechanism prevailed, and these adhesions were thought to be important in providing cells and factors important in the healing process based on studies in canine flexor tendon.[70,71] However, these tendons were found to also heal by an intrinsic mechanism marked by cellular proliferation from the epitenon and endotenon.[72] Studies using the flexor tendons of rabbits showed tenoblastic activity and tendon healing without formation of adhesions.[73] More recent studies have investigated the role of early postoperative mobilization as a solution to adhesion formation and maintenance of normal flexor tendon excursion. Most commonly used in the canine model, a passive motion machine has been used to test the effect of activity level on healing flexor tendon and the formation of peritendinous adhesions.[74–76] The chicken and the rabbit have accessible flexor tendons that have been used to test the effect of certain growth factors on flexor tendon healing and adhesion formation, both by local delivery and by gene therapeutic methods.[77–80] These various animal models have been instrumental in testing the effects of various mechanical and biologic factors that affect flexor tendon healing.

Extrasynovial tendons have an inherently different healing environment than intrasynovial tendons. Because synovial fluid does not surround the tendon, blood supply is not an issue. The rotator cuff tendons, patellar tendon, and Achilles tendon are the most common extrasynovial tendons that have been modeled. Previous work has shown that the rat shoulder joint has anatomic similarities with the human shoulder joint. The supraspinatus tendon passes below the coracoacromial arch, similar to that in humans, making it a suitable animal model for studying rotator cuff tendons (**Figure 4**).[81] This rat supraspinatus is a well-established model, and the surgical accessibility of this tendon makes it a good target for testing the effect of various rotator cuff repair techniques. Although the rat model is the most established model for rotator cuff tendinopathy, the rabbit is also another model that has been used to study the supraspinatus.[82,83] Because the required bony anatomical features of the Achilles and patellar tendons do not need to match the human as specifically as the bony features adjacent to the rotator cuff, there are numerous animals, including mouse, rat, and rabbit, that could be acceptable to model these tendons, depending on the particular research questions to be asked.

Multiple animal models have been used to better understand the etiology and pathology of tendinopathy. Tendinitis and tendonosis in animal models can be induced by mechanical and by chemical means. As previously mentioned, the anatomic relationship of the bony architecture and the rotator cuff tendons in the rat shoulder are similar to that in a human. By using this relationship and by running rats on a declined treadmill, supraspinatus tendon injury can be created and used as a model for rotator cuff tendinosis.[84] The contribution of extrinsic causes can also be tested in the model using various methods to decrease the space between the overlying arch and the supraspinatus tendon.[85,86] This overuse supraspinatus model in the rat is one of the few animal models that utilizes active mechanical overloading for inducing tendinosis. Other mechanical means of inducing tendonosis include passive participation methods, such as utilizing electrical stimulation to cause muscle contraction in rabbit Achilles tendon and dropping a weight on exposed rat Achilles tendon.[87] Chemical means of inducing tendinosis have also been widely used. Using collagenase in animal models can reproduce many of the important traits seen in clinical tendinopathy, such as matrix degradation, increased cellularity, and increased vascularity.[88,89] By using this method, the pathogenesis of tendonosis has been studied,[89,90] and the effects of various treatment modalities have been evaluated.[91,92] Since the enzyme is degrading collagen fibers rather than causing mechanical damage, debate exists about whether this is a valid model for tendinosis since tissues tend to begin to heal after the initiation of the injury, rather than continue with the tendinopathic condition. Corticosteroids,[93,94] cytokines,[95] and prostaglandins[40,96] have also been used as chemical means to induce tendinopathy. Further work in characterizing these various animal models will lead to improved treatments and outcomes for tendinopathy.

6.618.4.3. Animal Models of Ligament Injury

The MCL and the ACL are two commonly injured structures that are typically studied with animal models. Because the MCL is

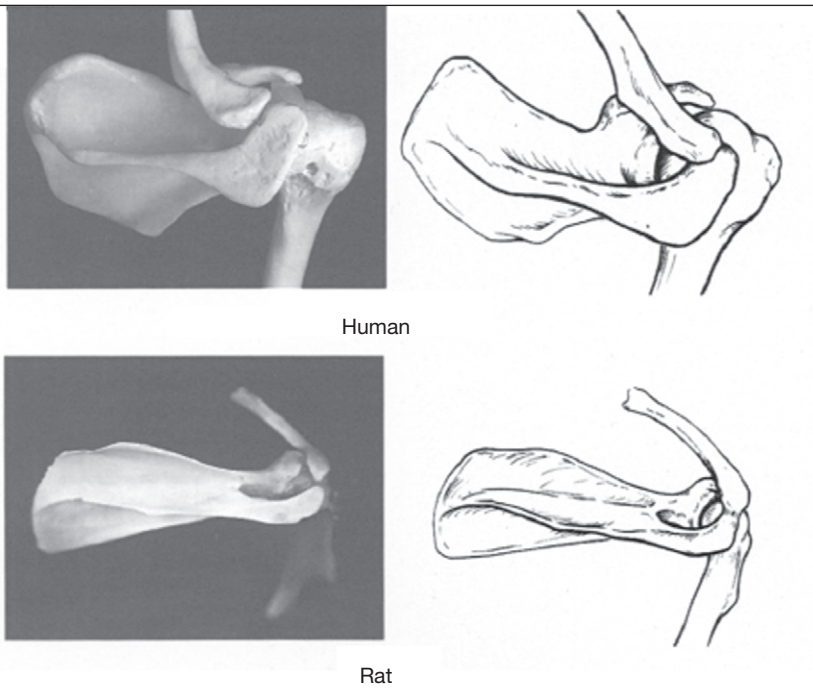

Photographs and schematics of the bony anatomy of the right human and rat shoulders from a postero-superior view demonstrating the similarity of the acromion projecting anteriorly over the humeral head to the clavicle.

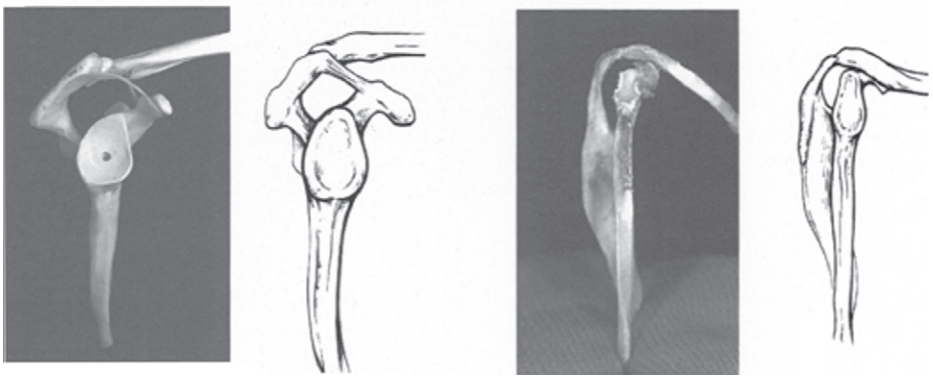

Photographs and schematics of the right human and rat shoulders from a lateral or "outlet" view with the humerus removed demonstrating the similar presence of an enclosed arch over the space for the supraspinatus tendon.

Figure 4 Comparison of human and rat shoulder bony anatomy from posterosuperior view and outlet view demonstrating enclosed arch over supraspinatus tendon in both cases. Reproduced from Soslowsky, L. J.; Carpenter, J. E.; Debano, C. M.; Banerji, I.; Moalli, M. R. *J. Shoulder Elbow Surg.* **1996**, *5*, 383–392, with permission from Elsevier.

extraarticular and the ACL is intraarticular, these two ligaments respond differently to injury. Smaller animals are typically used to model the MCL given its surgical accessibility. Larger animal models can be helpful in replicating the bony anatomic features that are important in the normal and reconstructed ACL.

The MCL is a structure that typically spontaneously heals in humans, and the response of ligament to healing and effects of growth factors on this healing are usually tested in animal models.[97,98] Testing the effects of growth factors on accelerating the healing process is also tested in animal models.[99,100] The rat and rabbit MCL have both been used as a model for MCL injuries due to low cost and ease of care, but some feel that the larger size of the rabbit allows for a more consistent and reproducible injury to the MCL.[98,101–103] Testing the effects of mobilization and immobilization on ligament healing has also been carried out using the rabbit model and has been significant in guiding the clinical treatment and rehabilitation after MCL injury.[46,104] The effects of various growth factors on the mechanical properties of the MCL are also commonly tested in this model. To show a clinically useful

result using the MCL, a significant improvement compared to a spontaneously healed ligament is necessary.

Animal models of the ACL, an intraarticular ligament, have typically focused on technical aspects of ligament reconstruction as well as tissue-engineered constructs to aide in ligament healing. Because ACL ruptures do not heal spontaneously and are not amenable to primary repair, the use of animal models to test new reconstructive techniques and novel biomaterials has grown. Collagenous or other biocompatible scaffolds with matrix amenable to cell seeding is a newer reconstructive option that is often tested in various models. Typically, larger animals are necessary to recreate the bony anatomy; in addition, a larger size is necessary to be able to consistently reproduce certain surgical techniques. The sheep, dog, and goat knee are often used to test new constructs, and results have been promising.[16,105–112]

6.618.5. Graft Materials

With the advent of tissue engineering, tendon and ligament grafts have transitioned from a primary role of mechanical stability to a multifaceted role integrating mechanical stability with active regeneration and incorporation of living tissue. Various biomaterials can act as scaffolds with properties conducive to cell infiltration and growth and can be organized into three main categories: biologic, synthetic resorbable, and synthetic nonresorbable. These scaffolds, regardless of type, must be nontoxic and biocompatible. Certain scaffolds possess specific characteristics, such as high porosity, which can be utilized to enhance cell infiltration and adherence. Other scaffolds have properties such as biodegradability that allow for temporary mechanical stability while functional remodeling of new tissue occurs around the scaffold. The goal of these constructs is to ultimately replicate the properties and characteristics of the native tissue particular to a specific anatomic site in a reliable and cost-effective manner (see **Chapter 4.401, The Concept of Biocompatibility**; **Chapter 4.402, Biocompatibility and the Relationship to Standards: Meaning and Scope of Biomaterials Testing**; **Chapter 4.403, The Innate Response to Biomaterials**; and **Chapter 4.404, Adaptive Immune Responses to Biomaterials**).

6.618.5.1. Biologic Materials

Biologic materials are protein-based ECM components derived from human or animal connective tissues. Biological scaffolds are advantageous in that their components are similar to that of native tissue, and they usually contain surface proteins the host body is familiar with. Biologic materials are naturally porous and provide space for cell attachment, proliferation, and migration. This porosity allows biologic scaffolds to interact more rapidly with host tissue than synthetic materials (see **Chapter 2.207, Extracellular Matrix: Inspired Biomaterials**; **Chapter 2.208, Artificial Extracellular Matrices to Functionalize Biomaterial Surfaces**; and **Chapter 2.209, Materials as Artificial Stem Cell Microenvironments**).

6.618.5.1.1. Collagen derivatives

Collagen derivatives are a popular research target for tendon and ligament tissue-engineering applications. Since tendon and ligament ECM is composed primarily of type I collagen, scaffolds developed with collagen derivatives most closely replicate the structural and mechanical properties of native tissue. Collagen is nontoxic and has minimal immunogenicity. Additionally, collagen provides mechanical strength to the tissue and is a logical choice for a base scaffold support structure. Collagen derivatives support cell adhesion and cell proliferation, making them more attractive than some synthetic materials. Cells can be nested in these scaffolds *in vitro*, encouraging rapid synthesis and reorganization of the injured tissue when implanted. Collagen can be processed several ways leading to the following derivatives: porous sponges, gels, and sheets. This section will briefly describe both historical and more recent research in the field of engineering collagen derivative constructs for tendon and ligament applications (see **Chapter 2.212, Silk Biomaterials**; **Chapter 2.218, Elastin Biopolymers**; **Chapter 2.213, Chitosan**; **Chapter 2.214, Hyaluronic Acid**; **Chapter 2.215, Collagen: Materials Analysis and Implant Uses**; **Chapter 2.216, Collagen–GAG Materials**; **Chapter 2.217, Fibrin**; **Chapter 2.220, Extracellular Matrix as Biomimetic Biomaterial: Biological Matrices for Tissue Regeneration**; **Chapter 2.221, Decellularized Scaffolds**; and **Chapter 2.222, Xenogenic Tissues and Biomaterials for the Skeletal System**).

Many studies have examined collagen gels as a potential scaffold material for tendon and ligament injuries. Collagen gels are usually seeded with cells and then cultured for a certain amount of time before implantation. MSCs are commonly used in collagen gel constructs but other cells such as dermal fibroblasts or tendon/ligament fibroblasts are also used. It has been observed that collagen gels encourage cell growth and that collagen substrates modify the morphology, migration, adhesion and differentiation of cells in certain conditions.[64] Cells seeded on collagen gels can cause contraction or shrinkage of the scaffold during culture. The amount of cell-induced gel contraction is dependent on the cell-to-collagen ratio.[113] The density of collagen is dependent on the amount of contraction. Fibroblast-seeded collagen gels can contract, causing the density of the collagen to drastically increase depending on the cell-to-collagen ratio. Gel contraction is thought to be the result of mechanical tension exerted by fibroblasts on collagen fibrils as opposed to cell–cell interactions.[64] Since the density of collagen is very high around cells and weak throughout the remainder of the gel, cell–collagen ratios are an important factor in designing appropriate scaffold materials. The rate and amount of gel contraction depends on a number of factors including quantity of serum in culture, number of cells, amount of collagen in cells, age of cells, and type of collagen.[64] Contraction can also be stimulated by growth factors or inhibited by excluding serum from culture. It is important to optimize culture conditions such as cell–collagen ratio before moving on to *in vivo* studies.

While collagen gels promote cellular activity, gels alone do not offer sufficient mechanical strength for effective repairs. In an attempt to increase the biomechanical properties of collagen gel structures, investigators began to add mechanical stimuli to collagen gels throughout the culture process. When cells are incubated in physically constrained collagen gels, they organize their ECM along the lines of tension created by the cell-mediated contraction of the gel.[54] It has been shown

that adding tensioned suture to the incubation setup aids in collagen gel attachment, contraction, and cell alignment.[113] Collagen gel contraction by cells significantly increases the structural biomechanics as well as the rates of improvement in material properties of repaired tendons in animal models.[54] This technique was later replaced with custom designed silicone dishes with anchor posts to replace the suture.[113] These anchor posts maintain axial strains on collagen gels[113] and the distance between the posts can be varied to allow for different gel aspect ratios. Larger aspect ratios demonstrate more highly aligned collagen gels.[114] Studies have also examined the effect of the cell-to-collagen ratios in gels and found that lower cell-to-collagen ratio constructs have a greater maximum force and maximum stress than repairs in rabbit patellar tendon defects using higher cellular concentrations.[115] Collagen gels can be integrated with other components or mechanically stimulated to improve mechanical properties of the scaffold and subsequently the repair constructs.

Collagen sponges are created by the lyophilization of collagen solutions and are porous three-dimensional structures. Before the lyophilization process, the size and structure of the pores can be modified by varying the pH concentration of collagen solution, temperature, or rate of freezing.[64] The porous nature of collagen sponges allows for better cell proliferation than collagen gels. Cell–sponge constructs can be created by applying the cell–collagen gel mixture to the surface of a type-I collagen sponge. These cell–sponge structures have been shown to improve the biomechanics and healing of tendon repairs in a rabbit patellar tendon model.[113,116,117] Constructs improve handling at the time of repair surgery, as they are much stiffer and have 10 times more collagen than previous collagen gel scaffolds.[116] These constructs significantly improve rabbit patellar tendon repairs along the range of *in vivo* loading when seeded with MSCs compared to the use of a gel–sponge composite alone.[116] The results from these construct studies are especially encouraging in that, for the first time, cell–gel–sponge repairs matched normal rabbit patellar tendon stiffness values up to peak *in vivo* forces.

Tensile mechanical stimulation has been applied to cell–sponge and cell–gel–sponge constructs in culture to try and improve repair mechanics. *In vitro* mechanical stimulation of cell–gel–sponge constructs significantly improved repair biomechanics after just 12 days in culture, despite the fact that collagen scaffold construct properties were not improved when tensile tested before implantation.[118] The tangent stiffness of cell–gel–sponge repairs have reached up to 25% beyond the threshold of normal rabbit patellar tendon peak *in vivo* forces, showing that mechanical stimulation in culture is an important tool in creating mechanically robust collagen biomaterials. A positive correlation has been demonstrated between linear stiffness and modulus for the in vitro collagen-derived construct and *in vivo* repair.[118] Further, the type, magnitude, and frequency of mechanical stimulation appropriate in culture for an optimized repair structure is dependent on the scaffold material. Additionally, some materials are more responsive to mechanical stimulation than others; cell–sponge constructs showed improved mechanical properties after being mechanically stimulated in culture, whereas cell–gel constructs did not.[119] This suggests that the collagen sponges, rather than collagen gel alone, facilitates cell response to mechanical stimulus.[119] Construct length has also been examined in both cell–gel and cell–sponge constructs. It was found that increasing construct length (distance between posts during cultures) increased construct linear stiffness and that longer, mechanically stimulated cell–sponge constructs had the highest *in vitro* stiffness overall.[114] *In vitro* studies can be used to optimize bioscaffold culture conditions such as mechanical stimulation, construct length, and aspect ratio. Many studies have demonstrated that it is possible to use *in vitro* predictors of *in vivo* outcome to expedite the development of biomaterial structures by reducing the time and cost of *in vivo* studies.

Growth factors can also be added to collagen-based scaffolds to encourage tissue healing. Specific growth factors can alter the biologic functions of cells seeded on scaffolds implanted in a tissue defect.[120] Growth factors accelerate many processes associated with healing including cell migration, proliferation, and collagen production in a scaffold that was originally mechanically weak. Specific dose–response relationships exist for each growth factor, so *in vitro* and *in vivo* studies are important in order to optimize the response desired for each implantation site.[120]

While there are many advantages to using collagen-derived constructs, they are not without their limitations. One disadvantage of collagen derivatives is the alteration of cell behavior. The different derivatives of collagen can have different effects on cell behavior, mechanical properties, and contraction. A disadvantage of seeding these collagen gels with cells is contraction or shrinkage of the scaffold during culture. Cells can reorganize collagen fibers in response to mechanical or chemical stimuli, causing scaffolds to shrink or lose their shape if the collagen is not stabilized throughout culture. Adding another material to improve mechanical properties or cell interactions with the collagen derivative can correct this limitation. Collagen-based constructs are subject to batch-to-batch variability, limiting the consistency and reproducibility of such structures. Collagen also does not offer comparable flexibility for modification as do biodegradable polymers.

6.618.5.1.2. Polysaccharides: Chitin, chitosan, alignate, and hyaluronan

Chitin is a one of the most abundant natural polysaccharides. It is a chemically inert linear polymer with high crystallinity.[121] It is plentiful, inexpensive, and biodegradable. Additionally, chitin has low immunogenicity and does not induce toxic reactions. Chitin enhances cellular proliferation and migration as well as accelerates wound healing.[122] Chitin scaffolds have also been shown to enhance collagen production at the repair site.[122] The pore size and thickness of the chitin fabric can be altered to control the mechanical strength of the construct. The diameter of fibers and density of chitin fabric can also be manipulated to control the degradation rate of the construct. Chitin is degraded by macrophages and decomposes more rapidly *in vivo* than other available scaffold materials. Since chitin fibers are partially absorbed early on and already possess low initial strength, chitin scaffolds must be supplemented with mechanically stronger materials in order to form an effective scaffold. For example, a braided combination of chitin and poly-ε-caprolactone (PCL) provides adequate initial strength to a rabbit Achilles tendon repair (see **Chapter 2.212,**

Silk Biomaterials; Chapter 2.218, Elastin Biopolymers; Chapter 2.213, Chitosan; Chapter 2.214, Hyaluronic Acid; Chapter 2.215, Collagen: Materials Analysis and Implant Uses; Chapter 2.216, Collagen–GAG Materials; Chapter 2.217, Fibrin; Chapter 2.220, Extracellular Matrix as Biomimetic Biomaterial: Biological Matrices for Tissue Regeneration; Chapter 2.221, Decellularized Scaffolds; and Chapter 2.222, Xenogenic Tissues and Biomaterials for the Skeletal System).[123]

Chitosan, alginate, and hyaluronan are resorbable polysaccharides with very similar properties to chitin. Chitosan is derived from chitin. Alginate is a nontoxic, noninflammatory polysaccharide derived from brown seaweed and can be processed in water. Hyaluronan (HA) is a repetitive linear GAG composed of *N*-acetyl-glucosamine and disaccharides of glucuronic acid. HA is a vital component of ECM, and its roles include interaction with proteoglycans and link proteins, facilitation of cell migration, differentiation, and adhesion, as well as eliciting electrostatic interactions with GAGs.[57] Like chitin, these materials produce a minimal foreign-body reaction and controllable mechanical and biodegradable properties. Chitosan, alginate, and hyaluronan alone possess low mechanical strength and can behave inconsistently with seeded cells. This problem may be ameliorated by combining them with other materials, or occasionally each other, to potentially increase strength and cell adhesion capabilities forming a more viable scaffold. For example, chitosan and alginate are commonly paired with agarose or hyaluronan to improve scaffold performance. Hyaluronan–chitosan scaffolds have also been shown to enhance fiber mechanical properties and improve adhesion to patellar tendon fibroblasts *in vitro* compared to chitosan scaffolds alone or a control group consisting of polyglactin 910.[124]

6.618.5.1.3. Silk

Silk is another potential biomaterial for tendon and ligament repair. It is biocompatible, degrades slowly and has attractive mechanical properties such as high strength and high elasticity.[125,126] The molecular structure and morphology of silk can be controlled through versatile processing and surface modification techniques.[125] Silk scaffolds can be made in many different shapes and forms. Silk grafts support cell adhesion, proliferation, and differentiation both *in vitro* and *in vivo* and promote tissue repair.[125] Additionally, woven silk scaffolds can be seeded with MSCs or modified with a peptide chain to increase collagen production. *In vitro* studies have shown that MSCs on silk scaffolds had robust proliferation and differentiation, while implantation of MSC scaffolds to repair ligament synthesized ECM and stimulated direct ligament-to-bone insertion.[112] Nanofibers or microporous silk sponges can also be incorporated into the silk mesh to prevent cells from leaking out of the scaffold.[112] This technique is exceptionally useful in that it creates a structure that mimics the ECM of ligament. Future studies will focus on increasing the strength and stiffness of these silk scaffolds (see Chapter 2.212, Silk Biomaterials; Chapter 2.218, Elastin Biopolymers; Chapter 2.213, Chitosan; Chapter 2.214, Hyaluronic Acid; Chapter 2.215, Collagen: Materials Analysis and Implant Uses; Chapter 2.216, Collagen–GAG Materials; Chapter 2.217, Fibrin; Chapter 2.220, Extracellular Matrix as Biomimetic Biomaterial: Biological Matrices for Tissue Regeneration; Chapter 2.221, Decellularized Scaffolds; and Chapter 2.222, Xenogenic Tissues and Biomaterials for the Skeletal System).

Hydrophilic silk scaffolds, comprising only protein and amino acids, have been used in some preclinical studies for ACL reconstruction.[127] The bundle size can be varied in hydrophilic scaffolds to allow differential diffusion of metabolites and nutrients with cell ingrowth, despite the lack of vasculature near the area of implantation.[127] In addition to supporting tissue ingrowth, hydrophilic silk grafts are mechanically strong and can be naturally resorbed by the body during tissue development. Small animal studies have shown that the bioresorption process of the hydrophilic silk is triggered by the ingrowth of cells as opposed to the presence of water in the case of the polyesters polylactic acid (PLA) and polyglycolic acid (PGA).[127] The stiffness of hydrophilic silk scaffolds is within the range of autograft and allograft tendons currently used for ACL replacements.[127] However, future work is still needed before this material can be implemented in the clinical setting, but *in vitro* and *in vivo* studies have demonstrated that hydrophilic silk scaffolds are mechanically robust and biocompatible.

6.618.5.1.4. Xenograft

Xenografts are transplantations of cells or tissues from one organism to another. ECMs derived from a variety of sources including small intestinal submucosa (SIS), dermis, and pericardium have been used as patches or grafts in tendon and ligament repair.[128] The most widely tested xenografts are the porcine SIS or porcine and bovine dermis. Because these xenografts can be highly immunogenic when implanted into the human body, these scaffolds must be processed thoroughly. This involves several steps including general cleaning, removal of lipid or fat deposits, disruption of cellular and DNA materials, cross-linking, and sterilization.[129] Any leftover noncollagen components may result in a host rejection response. These processes must be designed so that the natural collagen structure and mechanical properties of the tissue are not altered (see Chapter 2.212, Silk Biomaterials; Chapter 2.218, Elastin Biopolymers; Chapter 2.213, Chitosan; Chapter 2.214, Hyaluronic Acid; Chapter 2.215, Collagen: Materials Analysis and Implant Uses; Chapter 2.216, Collagen–GAG Materials; Chapter 2.217, Fibrin; Chapter 2.220, Extracellular Matrix as Biomimetic Biomaterial: Biological Matrices for Tissue Regeneration; Chapter 2.221, Decellularized Scaffolds; and Chapter 2.222, Xenogenic Tissues and Biomaterials for the Skeletal System).

6.618.5.1.4.1. Small intestinal submucosa

SIS biopolymer scaffolds are made up from the 100–200 μm thick interstitial ECM from the tunica submucosa layer. SIS scaffolds must undergo chemical processing to decrease cellular content before implantation. SIS is a thin translucent tissue that consists primarily of type I collagen and GAGs, such as chondroitin sulfate, heprain sulfate, and hyaluronan. It also contains growth factors such as TGF-β and VEGF which encourage growth and growth and differentiation of cells, while simultaneously providing integrity and strength to the scaffold throughout the healing process.[130] These scaffolds are mechanically strong, and their inherent porosity encourages a

reconstructive healing process by allowing cell infiltration. Mechanical studies have shown that porcine SIS scaffolds stretch considerably more than canine infraspinatus tendons before reaching maximum material properties and have linear moduli an order of magnitude lower than tendon.[128] Additionally, it has been reported that these scaffolds have a mean load to failure around 32–38 N.[131]

ECM scaffolds derived from porcine SIS have been used in a number of preclinical animal studies that have shown improvements in repair mechanical properties as well as formation of site-specific tissue.[132–136] Studies have shown that porcine SIS scaffolds can improve repair biomechanical and biochemical properties as well as histological appearance of a rabbit MCL and canine Achilles tendon.[132–134] Scaffolds rapidly degrade after implantation and are replaced by host tissue similar to that of normal uninjured tissue.[134] SIS grafts have also been used as interpositional grafts in canine infraspinatus, rat supraspinatus, and rabbit supraspinatus injury models with similar positive cell infiltration and tissue growth results.[128,135,136] Fibroblast-seeded, mechanically stimulated SIS scaffolds have induced changes in gene expression suggestive of tissue remodeling.[132] SIS scaffolds have also improved both the collagen fiber alignment and fibril diameter of repaired constructs.[137]

While some preclinical work has shown potential for these grafts, many animal studies have shown that porcine SIS grafts elicited a significant cellular and inflammatory response from the host and there is concern that SIS grafts do not possess adequate structural and material properties to support rotator cuff repairs.[138] Additionally, cross-linked SIS grafts have demonstrated delayed tissue degradation accompanied by repairs exhibiting little tissue organization, foreign-body giant cell presence, and a persistent inflammatory response.[128]

6.618.5.1.4.2. Dermis

Porcine and bovine dermis tissues have been used to create ECM grafts for tendon and ligament repair. Porcine dermal tissue grafts are acellular, cross-linked, collagen-based scaffolds. These scaffolds are primarily composed of type I collagen, some type III collagen, as well as a small amount of elastin. A porcine dermal scaffold was found to have a mean failure load of 128 N, bovine dermal grafts 70–76 N.[131] When implanted in a rat abdominal wall model, dermis xenografts were shown to cause low-grade chronic inflammation, fibrous encapsulation, and minimal scaffold degeneration.[128] After 112 days of implantation in mice, bovine dermal grafts were partially degraded, and the device had induced adipose connective tissue accumulation.[131] Porcine dermal grafts were not degraded at all after 112 days of implantation and were surrounded by thin, fibrous connective tissue.[131]

6.618.5.1.5. Autograft/allograft

An autograft is a tissue transplanted from one part of the body to another in the same individual. Autografts are appealing in that the use of the patient's own tissue eliminates the risk of rejection. Approximately 85–90% of ACL reconstruction patients have good-to-excellent results, with patellar tendon or hamstring autograft procedures currently being the most common choices for ACL reconstruction.[139] These grafts are chosen as they provide a high degree of stiffness and strength in the reconstructed structure. The main limitation to autograft is the associated donor site morbidity such as anterior knee pain after bone–patellar–bone autografts or weakened knee flexion with hamstring autograft. Allografts, or transplantation of tissue from a genetically nonidentical member of the same species as the recipient, are one potential solution. However, allografts have many complications including delayed biological incorporation, risk of disease transmission and tissue rejection. Human dermis and fascia lata have been used to create ECM grafts for rotator cuff repair augments. Human dermis is a highly elastic and tough layer of connective tissue located underneath the epidermis. Dermis is made primarily of type I and type III collagen, elastin fibers and contains growth factors, glycoproteins, and proteoglycans. Dermis can serve as a scaffold for tissue remodeling as its high collagen content provides a framework for tissue regeneration. Utilization of dermis requires processing to remove cellular components while preserving the native protein, collagen structure, vasculature, and biochemical composition before implantation.[129] Human dermis ECM grafts have been shown to stretch more than canine infraspinatus tendon before reaching its maximum material properties.[128] However, the linear region and elastic modulus of fascia lata ECM grafts are very similar to both canine infraspinatus and human supraspinatus tendons (see **Chapter 2.212, Silk Biomaterials**; **Chapter 2.218, Elastin Biopolymers**; **Chapter 2.213, Chitosan**; **Chapter 2.214, Hyaluronic Acid**; **Chapter 2.215, Collagen: Materials Analysis and Implant Uses**; **Chapter 2.216, Collagen–GAG Materials**; **Chapter 2.217, Fibrin**; **Chapter 2.220, Extracellular Matrix as Biomimetic Biomaterial: Biological Matrices for Tissue Regeneration**; **Chapter 2.221, Decellularized Scaffolds** and **Chapter 2.222, Xenogenic Tissues and Biomaterials for the Skeletal System**).[128]

Human dermis grafts are thicker and stiffer than other ECM grafts currently on the clinical market and have superior suture retention characteristics compared to porcine SIS grafts.[128] They have failure loads in the range of 157–229 N.[131] Human dermal ECM grafts induced chronic inflammation up to 8 weeks after implantation and encourage only minimal cell infiltration and partial material degradation at 16 weeks after implantation in a rat abdominal wall model.[128] However, interpositional implantation of human dermis ECM graft in a canine infraspinatus tendon injury model reported a structure that resembled tendon morphologically at 6 months[140] and a mouse model showed that grafts induced dense, partially organized collagenous connective tissue formation and graft degradation at 112 days postimplantation.[131,138] Tendons repaired with dermis grafts were mechanically stronger than tendons repaired without a graft; however, repaired tendons still have lower biomechanical capabilities than control tendons.[140] Additionally, human fascia lata patches possess comparable mechanical, chemical, and ultrastructural properties to tendon.[141]

Although biologic scaffolds provide an excellent platform for cell infiltration, they also have many disadvantages. Most apparent is their inferior mechanical properties, which may result in early failure of the device or repair. In addition, the biocompatibility of the material is variable dependent upon the source of the biomaterial, and inflammatory responses or

implant rejection can occur in the host body. Because of the undefined rate of degradation of these materials, predicting the repair construct timeline when using biologic scaffolds can be extremely difficult.

6.618.5.2. Synthetic Materials

Although biologic scaffolds can undergo various augmentation techniques to improve mechanical properties, synthetic materials have superior initial mechanical strength. Their biocompatibility, however, is inferior to biologic scaffolds, as the debris caused by synthetic scaffolds can cause a foreign-body response and lead to long-term complications. Synthetic materials are manufactured from chemical compounds and their mechanical, physical, and chemical properties can be controlled to create stronger and more consistent quality materials. Biodegradable synthetic polymers provide immediate stabilization to the repaired tissue while simultaneously acting as a scaffold for ingrowth and, eventually, replacement of tissue cells. Synthetic grafts eliminate the problems of graft harvest, offer no risk of disease transmission, and are readily available for implantation. Synthetic polymers are also advantageous in that they provide the ability to tailor mechanical properties and degradation kinematics to suit specific site requirements. They can also be fabricated into various shapes with a range of porosities. Current studies are investigating the use of synthetic grafts carrying cells, ECM or growth factors to promote tissue healing through a biodegradable scaffold (see **Chapter 1.122, Structural Biomedical Polymers (Nondegradable)**).

6.618.5.2.1. Resorbable polyesters

Polyesters are tough plastic materials with excellent fatigue and tear strength. This material is frequently used for tissue-engineering applications as it does not elicit a permanent foreign-body reaction and is reabsorbed into the body and replaced by natural tissue gradually. Additionally, the degradation products of many polyesters such as PGA, PLA, and polylactic-*co*-glycolic acid (PLGA) are naturally present in the human body. These polyesters also have good mechanical properties and many have been shown to improve tendon healing. However, future investigation is needed, as each polyester induces a different cellular response and has a different degradation profile.

6.618.5.2.1.1. Polyglycolic acid

Polyglycolide or PGA is the simplest linear, aliphatic polyester. PGA is a rigid material with high crystallinity, which is not soluble in most organic solvents. It is a biogradable polymer whose fibers exhibit high strength and modulus. PGA can be processed by extrusion, injection, or compression molding, similar to most polyesters. However, given its high sensitivity to hydrolytic degradation processing, conditions must be carefully monitored.[142] Processing techniques determine properties and degradation characteristics of PGA scaffolds. The degradation product, glycolic acid, is a natural metabolite but if absorbed at high concentrations, can cause local acid concentration accumulation, which may result in tissue damage. The rate of degradation in polyesters is determined by many factors including copolymer ratio, crystallinity, molecular weight, porosity, site of implantation, amount of residual monomer, configurational structure, morphology, and stresses.[142] PGA has an approximate strength of 7.0 GPa and degradation time of 6–12 months.[142] PGA can be woven or unwoven; however, woven scaffolds are more robust.[57]

Several *in vitro* and *in vivo* studies have suggested that both PGA and fellow polyester PLA are sufficiently biocompatible, but other studies have shown that PLA–PGA scaffolds may cause systemic or local reactions.[142] The main cause of concern for these polyesters is the potential for local reactions to acidic degradation and the release of small wear particles. Cell-seeded PGA scaffolds formed repair structures with adequate mechanical properties when implanted subcutaneously in nude mice.[143] A PGA–PET device has also been shown to provide adequate strength to use for tendon repairs, but have not demonstrated any notable advantages to currently available materials.[62]

6.618.5.2.1.2. Polylactic acid

Poly(L-lactic acid) (PLLA) has an approximate strength of 2.7 GPa and degradation time of over 24 months.[142] Lactic acid exists in two steroisomeric forms and the polymer derived from active L monomers are semicrystalline. The L-PLA isoform or PLLA is a slowly degrading and biocompatible polymer. The L-PLA isoform is more commonly used since its hydrolysis yields the L (+)-lactic acid which is a naturally occurring stereoisomer of lactic acid. L-PLA also has a higher mechanical strength and toughness than the D-PLA form. PLLA scaffolds have been used for rotator cuff repairs in animal models as interpositional devices for irreparable tears, reinforcement of suture repair line as well as augmentation with tendon–bone repair.[144] When used as an augmentation device, PLLA scaffolds reduced tendon retraction distance and improved stiffness and ultimate load of an infraspinatus tendon repair in a canine model at 12 weeks.[145] Felt PLLA grafts also improve tensile recovery of repairs[146]; however, PLA patches did not significantly improve ultimate strength in a goat model.[147]

6.618.5.2.1.3. Polylactic-co-glycolic acid

The material and degradation properties of polyesters can be altered by creating copolymers. PLGA, a copolymer composed of PGA combined with the more hydrophobic PLA, is very common. The hydrophobic nature of PLA limits the water uptake of the copolymer and reduces degradation. No linear relationship exists between the ratio of polyesters and physicomechanical properties of copolymers. The changes in copolymer properties are the result of changes in the rates of hydration and hydrolysis. This means that 50:50 copolymers will degrade more rapidly than either polymer individually.

The hydrophilicity of PLGA can be improved by plasma treatment or gelatin coating the scaffold.[148] PLGA and PCL (described below) have been coated with a gradient of calcium phosphate to augment tendon to bone healing in some studies and this form of augmentation will be discussed further in the following section. PLGA fibers braided together to form an ACL graft have demonstrated biocompatibility, healing and long-term mechanical strength when implanted in a rabbit model.[149,150] A scaffold consisting of three different continuous phases has recently been developed to mock the multitissue native insertion site and improve ligament-to-bone healing.[149,151–153] Phase A of the scaffold is composed of a

10:90 PLGA mesh for fibroblast culture and soft tissue formation, Phase B consists of 85:15 PLGA microspheres and is intended for fibrochondrocyte culture, while Phase C is composed of sintered PLGA 85:15 and bioactive glass microspheres for osteoblast culture and bone formation.[153,154] It has been shown that the innovative triphasic scaffolds form a fibro-cartilage-like interface and demonstrate the feasibility of the stratified scaffold for promoting ligament-to-bone healing.[153] Because the tendon and ligament enthesis is often the weakest area of a surgical repair and is most prone to fail, further investigation into using these multiphasic scaffolds to improve upon insertion site healing is of particular clinical importance.

6.618.5.2.1.4. Poly(caprolactone)

Poly(caprolactone) (PCL) is a semicrystalline polymer that degrades at a much lower rate than PLA. PCL is very popular as a base polymer for long-term drug delivery applications as it has a degradation time of two to three years.[142] The degradation rate can be altered by adding other copolymers and is one strategy for improving its potential as a bioscaffold. PCL is considered to be nontoxic. PCL has an approximate strength of 0.4 GPa and a degradation time of over 24 months.[142] PCL scaffolds have been developed that possess a calcium phosphate gradient between the top and bottom surface of the mat. A gradient in mineral composition within the construct has functional consequences in PCL and PLGA scaffolds, which lead to spatial gradients in mechanical properties and cell proliferation.[148] Mineralized PLGA scaffolds have lower strain in the loading direction at the mineralized end of the scaffold than the unmineralized end.[148] These graded constructs could significantly enhance tendon to bone healing, which remains a major obstacle in tendon and ligament healing in sites such as the rotator cuff and ACL.

6.618.5.2.1.5. Summary and general observations in polyesters

Current polyester biomaterial research for tendon and ligament applications is focused on finding the balance between scaffold degradability, rate of cell matrix production, structural integrity, and overall scaffold mechanical properties. Polymer composition and surface modification can have significant effects on both mechanical properties and degradation rates of scaffolds.[149] Changes in these properties also result in consequences for cell attachment morphology and growth rate.[149] Additionally, comparisons between polyesters found that braided PGA was the strongest scaffold followed by PLLA and poly(lactide-*co*-glycolide) (PLAGA).[149] It is important to remember that choosing an appropriate polyester scaffold material should be based on the intended target tissue's mechanical properties instead of simply choosing the strongest material available.

Studies have looked at augmenting polyester scaffolds by modifying the biomaterial surface with cell adhesion molecules to combat the hydrophilicity of polyesters that naturally support low levels of surface cell adhesion. Adding components such as fibrin or fibronectin to polyester scaffolds may increase the possibility for cell adhesion and organized tissue growth. Cells can be seeded onto a three-dimensional polyester scaffold to homogenously proliferate inside the graft and secrete their own ECM to form repair tissue. The biomaterial surface can be modified by precoating braided scaffolds with fibronectin in order to increase cell attachment efficiency and overall cell proliferation.[149] However, the magnitude of property changes after culture is dependent on the polyester material.[149] Fibronectin has a positive effect on matrix production and improved cell attachment on PLLA and PLAGA scaffolds. The mechanical strength of fibrin sponges increased after they were combined with cell-seeded PGA scaffolds.[155] Fibrin naturally encourages cell infiltration, but the addition of PGA increased resistance to compression in addition to forcing more free space inside the fibrin sponge allowing for increased cell infiltration.[155]

Cell-seeded polyester scaffolds have been shown to improve tendon and ligament repairs. In particular, knitted polyester scaffolds seeded with a cell–gel mixture can improve tissue repairs.[156] bMSCs can also be fabricated into a cell sheet and assembled into a knitted PLLA scaffold to create an incorporated structure that is stronger and more stretchable than previous structures.[156] The novel cell sheet technique was designed to improve the efficacy of cell seeding, as well as reduce inflammatory response of the polyester biomaterial. Growth factors can also be used to influence the maturation and homeostasis of the healing response in tendons and ligaments with polyester scaffolds. Further, growth factors can have an effect on cell division and even enhance tissue-healing response.[139]

Polyester scaffolds are not without their limitations. While the resorbable nature of polyesters is attractive, the concentration of degradation products is a major concern. Although the degradation products of polyesters are natural metabolites, a large concentration could cause adverse local or systemic reactions. Cell adhesion is vital to the engineering and repairing tendons and polyester's hydrophobic nature impedes this process. One potential solution to this limitation is surface modification with adhesive agents.[57]

6.618.5.2.2. Nonresorbable materials

Many attempts at synthetic grafts, composed of carbon fibers or bundled polyester fibers, have been characterized by chronic foreign-body inflammation, particle wear shedding into adjacent lymph nodes, graft rupture, and particle-induced synovitis. Synthetic nondegradable scaffolds provide a backbone to promote surrounding tissue ingrowth. These scaffolds use open fiber weaves in the hope that surrounding tissue would grow and incorporate into the scaffold forming a functional graft. Unfortunately, many studies using nondegradable synthetic scaffolds have shown that they cause significant inflammatory reactions and frequently rupture and fail.[143] In attempt to reduce the inflammatory response, fibroblasts were seeded on synthetic scaffolds, but with limited results.[143] The following briefly describes some studies on nonresorbable materials for tendon and ligament applications.

6.618.5.2.2.1. Carbon

Flexible carbon fiber implants were one of the initial attempts to step away from auto/allografts. Initial studies that used flexible carbon implants found that carbon fiber scaffolds induced the formation of tendon.[157] Carbon fiber grafts cause a reduction and even distribution of stress between the graft and soft tissue attachment and encourage ingrowth of

collagen into the implant. However, carbon wear particles migrate into the joint space and throughout the body after implantation of carbon scaffolds. Attempts were made to coat carbon structures with polymers or collagen to combat this problem with minimal success. A PLA coat was found to protect the graft from implantation but, the carbon implant stretched and ruptured, leading to poor long-term functional outcomes.[157] Focus has since shifted to other materials.

6.618.5.2.2.2. Polyethylene terephthalate

Polyethylene terephthalate (PET) implants are composites of four tightly woven polyester strips wrapped in a sheath of loosely woven velour and act as a scaffold for fibrous tissue ingrowth. The polyester coating of these scaffolds is designed to protect the graft from abrasion. PET has been used as a tendon graft in the form of suitably sized knitted velour prosthesis for implantation in the rat patellar ligament and tail tendon.[158] Implanted PET constructs are characterized by infiltration of large numbers of macrophages and foreign-body multinucleated giant cells.[158,159] Additionally, a capsule of fibrous tissue characterized by low collagen solubility has been found surrounding the PET structures. These grafts possess short-term strength initially but lack long-term stability.[139] Tissue repaired with PET grafts is more reminiscent of scar tissue formation than neoligament and exhibits disorderly collagen fibers.[158,160] Studies suggest that PET alone may not be suitable for ligament replacement.

PET has also been used in a graft attempting to combine the properties of permanent synthetic prothesis and a tissue-promoting scaffold. This graft consists of a PET mesh-like structure to promote tissue ingrowth through the intraarticular and extraarticular sections of ligament which is anchored between two bone plugs.[139] This graft has impressive maximum tensile strength; however, a study implanting the scaffold in ovine ACL found a large number of long-term graft ruptures.[161] Another two-part PET implant has been designed in an attempt to mimic the natural structure of ligaments. The intraosseous part of the graft is made of longitudinal fibers bound together by a transverse knitted structure while the intraarticular part comprises longitudinal parallel fibers twisted at 90°.[162] The twisted fibers should provide protection from shear forces by preorienting them in the appropriate direction for a right or left limb. This novel structure was designed to encourage tissue ingrowth from the porosity of PET fibers, ideally contributing to the viscoelasticity of the structure and providing protection from friction.[162] While this design has many promising features, no long-term data on its viability over time exist.

6.618.5.2.2.3. Polytetrafluoroethylene

Polytetrafluoroethylene (PTFE) grafts are composed of a single long fiber of expanded PTFE arranged into loops. The ultimate tensile strength of PTFE is about 3 times that of human ACL and extensive mechanical testing has shown it is one of the strongest potential synthetic graft materials in terms of material stability.[139] PTFE grafts are typically fixed at both ends and have been used to provide stability to ACL-deficient knees. Unfortunately, fixing the graft at both ends causes the graft to stress-shield the ligament. Stress-shielding prevents the ligament from developing proper mechanical strength. While these structures may provide positive short-term results, the long-term consequences will be poor due to wear and potential for rupture of the prosthesis.[139]

PTFE felt is made from 100% virgin PTFE fluorocarbon fiber and is acid-bleached. The cytotoxicity, haemolysis, and dissipation of material have not been shown to be different than currently used nonresorbable materials. It has adequate thickness and flexibility to be used in rotator cuff repairs.[163] PTFE felt has been used for covering irreparable tears of the rotator cuff and has been found to be effective for pain relief.[163] A study using PTFE to reconstruct defects in the infraspinatus tendon of beagle dogs found an ingrowth of fibrous tissue between PTFE fibers and adequate mechanical recovery of the tendon.[164] Foreign-body reactions were found at the margin of the PTFE-bone interface and remain a concern in using this material.

6.618.6. Clinical Application

Tissue engineering is an emerging field with considerable potential for the development of new therapeutics for tendon and ligament disorders. Rupture of the rotator cuff of the shoulder and ACL of the knee are two injuries which are attractive targets for tissue-engineered constructs. A biocompatible scaffold, responsive and robust cells for proliferation, and appropriate growth factors to stimulate reparative mechanisms are each important constituents for successfully developing an engineered ligament.[165] So far, *in vitro* and *in vivo* animal studies have been promising, but continued efforts are needed to translate these into clinically applicable solutions.

6.618.6.1. Rotator Cuff

Despite advances in surgical treatment and rehabilitation for rotator cuff tears, significant challenges still remain in the treatment of this disorder. Moderate to large rotator cuff tears do not heal spontaneously. Recurrent and chronic rotator cuff tears are difficult to treat, with limited options such as debridement with partial repair or muscle transfers as salvage procedures. Furthermore, failure rates after repair of large, chronic rotator cuff tears remain relatively high.[166–169] The recent development of synthetic and biologic augmentation devices and interpositional scaffolds are intended to improve and expand upon the current treatment options. The indications for use of these devices are not yet clearly defined but, in general, are limited to cases in which there is a high probability of suboptimal healing after primary repair, such as chronic or massive tears. They also can be used as interposition grafts for large tears in which only partial repair is attainable. These devices, typically made from ECM materials, provide a temporary mechanical support and act as a biologic scaffold for cellular proliferation. By mechanisms similar to the natural tendon healing response, these devices are remodeled by the host body and become incorporated into native healthy tissue. Many of these materials, including biodegradable polymers,[145,147,170] ECM[140,171] including SIS,[135,172–174] and chitin and chitosan-based material[124,175] have been tested in animal models with varying results.

Only a few devices, listed in **Table 1**, have been transitioned into the clinical setting, with devices composed of porcine

Table 1 List of commercially available bioabsorbable graft materials

Product	*Company*	*Type*	*Cross-linked*	*Irradiation*
Restore	DePuy (Warsaw, IN)	Porcine SIS	No	Electron beam
GraftJacket	Wright Medical (Arlington, TN)	Human dermis	No	N/a
TissueMend	Stryker Orthopaedics (Mahwah, NJ)	Fetal bovine dermis	No	N/A
CuffPatch	Arthrotek (Warsaw, IN)	Porcine SIS	Yes	Gamma
Permacol	Zimmer (Warsaw, IN)	Porcine dermis	Yes	Gamma
BioBlanket	Kensey Nash (Exton, PA)	Bovine dermis	Yes	Gamma
OrthoADAPT	Pegasus Biologics (Irvine, CA)	Equine pericardium	Yes	N/A

SIS most extensively studied.[128] This material is composed of 90% collagen, 5–10% lipids, and a small amount of glycoproteins and TGF-β.[136,176] Processing of porcine SIS has been studied extensively in *in vitro* and *in vivo* animal models to reduce the host cellular response.[177] Mechanical studies have shown that these grafts stretch considerably more than canine infraspinatus tendon before reaching maximum material properties and have linear moduli an order of magnitude lower than tendon.[128] Despite encouraging animal studies using porcine SIS, several studies have investigated the use of this material in augmentation devices for massive rotator cuff tears clinically with mostly unfavorable results. In a series of eleven patients using SIS as an augmentation device for massive rotator cuff tears, ten of eleven repairs were found to have failed by magnetic resonance imaging at 6 months.[178] Similarly, a prospective, randomized, controlled trial of 30 chronic two-tendon tears found a higher rate of failure in repairs using SIS as an augmentation device than those repairs with no augmentation.[179] Also, the porcine cellular elements in the porcine SIS devices used in these studies are thought to be the cause of a noninfectious inflammatory reaction that occurred in some patients in which the device was used.[174,179,180] Experience with human dermis ECM has been more favorable. When used as an interposition graft for massive rotator cuff tears, patients had significantly higher functional scores.[128,181] MRI scans showed failure of the graft in only three of the sixteen patients in the study. In another study of 17 patients with massive rotator cuff tears, human dermis ECM was used to augment repair. Similarly, patients had significantly improved functional scores, and three had recurrent tears. No patient had any adverse inflammatory reaction. These studies are promising but are limited by lack of proper controls. Further investigations are needed to determine whether rotator cuff regeneration and improved clinical outcomes is feasible using these materials.

6.618.6.2. Anterior Cruciate Ligament

Rupture of the ACL is one of the most common injuries to the knee, leading to pain, knee instability, and early arthritis. Ruptures of the ACL do not heal spontaneously, and in contrast to the rotator cuff tendon, the ACL is usually not amenable to direct repair. In appropriate patients, reconstruction of the ligament is performed. Various options are available to the surgeon for reconstruction of the ACL, the most common being local hamstring or bone–patellar–bone autograft and allograft.[182] Although results of ACL reconstruction using these tissues are generally favorable,[183,184] there are complications such as donor site morbidity using autograft, and immunogenic and infectious complications using allograft.[185,186] Because the prevalence of ACL injuries is expected to continue to rise, effort has gone into finding a suitable tissue-engineered construct to improve the reconstructive procedure and decrease the number of complications.

Currently, there have been no tissue-engineered constructs that have been tested *in vivo* in humans. Collagen has been the most widely studied material as a biocompatible scaffold[187,188] but has been found to have mechanical and immunogenic limitations.[189–191] Synthetic materials including silk[126,192] and biodegradable polymers[193] have also received attention as an attractive options due to their low cost and biocompatibility. Other modified biologic materials such as hyaluronic acid, chitosan, and alginate have been proposed as potential scaffold options.[194,195] Matching an appropriate cell source with the biocompatible scaffold is also important. ACL and patellar fibroblasts have been tested with various scaffolds,[187,188] but recently bone marrow stromal cells have presented themselves as an attractive candidate due to their relatively easy accessibility, robust renewal, and potential to differentiate.[196] Lastly, appropriate growth factors such as PDGF, TGF-β, FGF, and IGF-1 are important in stimulating cellular response and inducing collagen and proteoglycan synthesis. A number of these growth factors have been tested in various animal ACL models[197–199] as well as *ex vivo* in human tissue.[120,200]

6.618.6.3. Suture Anchors

The current standard for surgical repair and reconstruction of rotator cuff tears and ACL ruptures involves minimally invasive arthroscopic techniques. The role for arthroscopic fixation devices has expanded greatly. Options for suture anchors include metal and biodegradable materials, with the current trend leaning toward the use of biodegradable polymers.[201] The most common polymers currently used in suture anchors include PLLA, poly-D, L-lactic acid (PDLLA), PGA, polydioxanone (PDS), or a combination of these biomaterials. The material properties and rate of degradation and strength loss are the most clinically relevant characteristics of these materials. PGA degrades by both hydrolysis and enzymatic activity and when used *in vivo*, degrades more rapidly than PLA. The use of PGA has been thought to lead to inflammatory and lytic changes due complement cascade activation after enzymatic degradation, and therefore, has been used less in the clinical setting.[202,203] However, case reports of inflammatory reactions to PLLA anchors have also been reported.[204]

Current arthroscopic techniques also demand high strength suture material. Sutures using braided polyester or degradable PDS have been popular options, and new high strength sutures incorporating ultrahigh molecular weight polyethylene (UHMWPE) are available. The failure strength of these suture materials far exceeds the requirements to secure tissue into bone. Some sutures have been developed with a combination of materials to optimize properties of each. For example, UHMWPE and PDS have been used in combination – after degradation of the PDS, the material strength of UHMWPE remains, but with a lower profile. Although studying the properties of these suture and suture anchors is important, many other factors such as suture size and number, anchor design, and surgical technique ultimately dictate the final clinical outcome.

6.618.7. Summary

Tissue engineering has the potential to revolutionize the way we treat tendon and ligament disorders. Currently, autograft and allograft are most widely used in the augmentation or replacement of injured tissue. However, these options are not without associated morbidity and complications, therefore continued effort has been dedicated to applying biomaterials and tissue-engineering techniques to the enhancement of tendon and ligament healing. This requires a thorough understanding of the fundamental structural and material properties of these tissues. The effect of various chemical and mechanical manipulations on tendon and ligament properties and healing is important in creating and modifying novel biomaterials that best recreate native tissue properties. A multitude of mechanical, biochemical, and histologic assays can assist in testing the basic properties of materials *in vitro* and can assess various material augmentation methods. Once basic *in vitro* testing identifies an optimal combination of a specific material and augmentation methods, transitioning these biomaterials to a clinical setting requires preclinical studies utilizing animal models. Numerous animal models exist, and many factors must be taken into account in order to choose the animal model which best recreates the clinical scenario in a reproducible and cost-efficient manner. These include size of animal, anatomic similarity with the human, ability to recreate the injury, postoperative/injury management, and cost. Only after preclinical studies show encouraging results with regards to safety and efficacy can a device advance to clinical trials.

A wide variety of materials can be used in constructing a device to augment or replace tendon or ligament tissue. The chosen material not only needs to provide initial mechanical integrity, but should also function as a scaffold that is conducive to cell infiltration. Multiple methods of chemical and mechanical augmentation can then enhance the properties of these scaffolds, which must provide adequate initial strength before degradation in the body and replacement with native tissue. Biologic materials such as collagen most closely replicate the structural and mechanical properties of native tissue, and processing of these materials can reduce antigenicity and resultant inflammatory response. Many synthetic materials such as resorbable polyesters and other nonresorbable materials provide greater initial mechanical strength but are generally less biocompatible. Combinations of different materials based on their specific mechanical and biologic properties can enhance the overall structure and biologic response once implanted.

In general, clinical application of these devices has been limited. Chronic or massive rotator cuff tears and ACL tears are both common clinical problems that have been targets for healing enhancement with tissue-engineered constructs. Multiple preclinical animal studies using biodegradable polymers, ECM materials, and biologic implants have been promising, but the utility of these devices has yet to be proven in the clinical setting. Continued efforts into manipulating and enhancing these materials to improve cell infiltration, tissue proliferation, and mechanical integrity should be expected to result in the production of clinically successful devices capable of mimicking the mechanics and biologics of native tendon and ligament.

References

1. Praemer, A.; Furner, S.; Rice, D. P. American Academy of Orthopaedic Surgeons. *Musculoskeletal Conditions in the United States*. American Academy of Orthopaedic Surgeons: Park Ridge, IL, 1992.
2. Kannus, P. *Scand. J. Med. Sci. Sports* **1997**, *7*, 53–54.
3. Lyman, S.; Koulouvaris, P.; Sherman, S.; Do, H.; Mandl, L. A.; Marx, R. G. *J. Bone Joint Surg. Am.* **2009**, *91*, 2321–2328.
4. AAOS. *Burden of Musculoskeletal Diseases in the United States: Prevalence, Societal and Economic Cost*. American Academy of Orthopaedic Surgeons: Park Ridge, IL, 2008.
5. Clancy, W. G., Jr.; Neidhart, D.; Brand, R. L. *Am. J. Sports Med.* **1976**, *4*, 46–57.
6. Curwin, S.; Stanish, W. D. *Tendinitis: Its Etiology and Treatment*. Collamore: Lexington, MA, 1984.
7. Schepsis, A. A.; Leach, R. E. *Am. J. Sports Med.* **1987**, *15*, 308–315.
8. Leadbetter, W. B.; Mooar, P. A.; Lane, G. J.; Lee, S. J. *Clin. Sports Med.* **1992**, *11*, 679–712.
9. Astrom, M.; Rausing, A. *Clin. Orthop. Relat. Res.* **1995**, *316*, 151–164.
10. Khan, K. M.; Maffulli, N.; Coleman, B. D.; Cook, J. L.; Taunton, J. E. *Br. J. Sports Med.* **1998**, *32*, 346–355.
11. Sharma, P.; Maffulli, N. *J. Bone Joint Surg. Am.* **2005**, *87*, 187–202.
12. Andres, B. M.; Murrell, G. A. *Clin. Orthop. Relat. Res.* **2008**, *466*, 1539–1554.
13. Silver, F. H.; Freeman, J. W.; Seehra, G. P. *J. Biomech.* **2003**, *36*, 1529–1553.
14. Kastelic, J.; Galeski, A.; Baer, E. *Connect. Tissue Res.* **1978**, *6*, 11–23.
15. Benjamin, M.; Evans, E. J.; Copp, L. *J. Anat.* **1986**, *149*, 89–100.
16. Weiler, A.; Hoffmann, R. F.; Bail, H. J.; Rehm, O.; Sudkamp, N. P. *Arthroscopy* **2002**, *18*, 124–135.
17. Garrett, W. E., Jr. *Med. Sci. Sports Exerc.* **1990**, *22*, 436–443.
18. Riley, G. P.; Harrall, R. L.; Constant, C. R.; Chard, M. D.; Cawston, T. E.; Hazleman, B. L. *Ann. Rheum. Dis.* **1994**, *53*, 359–366.
19. Bailey, A. J.; Light, N. D. *Ciba Found. Symp.* **1985**, *114*, 80–96.
20. Thompson, J. I.; Czernuszka, J. T. *Biomed. Mater. Eng.* **1995**, *5*, 37–48.
21. Riechert, K.; Labs, K.; Lindenhayn, K.; Sinha, P. *J. Orthop. Sci.* **2001**, *6*, 68–74.
22. Berenson, M. C.; Blevins, F. T.; Plaas, A. H.; Vogel, K. G. *J. Orthop. Res.* **1996**, *14*, 518–525.
23. Vogel, K. G.; Koob, T. J. *Int. Rev. Cytol.* **1989**, *115*, 267–293.
24. Vogel, K. G.; Heinegard, D. *J. Biol. Chem.* **1985**, *260*, 9298–9306.
25. Butler, D. L.; Grood, E. S.; Noyes, F. R.; Zernicke, R. F. *Exerc. Sport Sci. Rev.* **1978**, *6*, 125–181.
26. Elefteriou, F.; Exposito, J. Y.; Garrone, R.; Lethias, C. *FEBS Lett.* **2001**, *495*, 44–47.
27. Williams, I. F.; Mccullagh, K. G.; Silver, I. A. *Connect. Tissue Res.* **1984**, *12*, 211–227.
28. Mcneilly, C. M.; Banes, A. J.; Benjamin, M.; Ralphs, J. R. *J. Anat.* **1996**, *189*(Pt 3), 593–600.
29. Wang, J. H.; Grood, E. S. *Connect. Tissue Res.* **2000**, *41*, 29–36.
30. Wang, N.; Ingber, D. E. *Biochem. Cell Biol.* **1995**, *73*, 327–335.
31. Janmey, P. A. *Curr. Opin. Cell Biol.* **1991**, *3*, 4–11.
32. Viidik, A. *Acta Orthop. Scand.* **1969**, *40*, 261–272.
33. Viidik, A. *Scand. J. Plast. Reconstr. Surg.* **1967**, *1*, 141–147.

34. Woo, S. L.; Gomez, M. A.; Amiel, D.; Ritter, M. A.; Gelberman, R. H.; Akeson, W. H. *J. Biomech. Eng.* **1981**, *103*, 51–56.
35. Michna, H. *Cell Tissue Res.* **1984**, *236*, 465–470.
36. Cabaud, H. E.; Chatty, A.; Gildengorin, V.; Feltman, R. J. *Am. J. Sports Med.* **1980**, *8*, 79–86.
37. Hansson, H. A.; Engstrom, A. M.; Holm, S.; Rosenqvist, A. L. *Acta Physiol. Scand.* **1988**, *134*, 199–208.
38. Curwin, S. L.; Vailas, A. C.; Wood, J. *J. Appl. Physiol.* **1988**, *65*, 2297–2301.
39. Khan, K. M.; Maffulli, N. *Clin. J. Sport Med.* **1998**, *8*, 151–154.
40. Langberg, H.; Skovgaard, D.; Karamouzis, M.; Bulow, J.; Kjaer, M. *J. Physiol.* **1999**, *515*(Pt 3), 919–927.
41. Denzlinger, C.; Rapp, S.; Hagmann, W.; Keppler, D. *Science* **1985**, *230*, 330–332.
42. Khan, M. H.; Li, Z.; Wang, J. H. *Clin. J. Sport Med.* **2005**, *15*, 27–33.
43. Sullo, A.; Maffulli, N.; Capasso, G.; Testa, V. *J. Orthop. Sci.* **2001**, *6*, 349–357.
44. Amiel, D.; Woo, S. L.; Harwood, F. L.; Akeson, W. H. *Acta Orthop. Scand.* **1982**, *53*, 325–332.
45. Woo, S. L.; Gomez, M. A.; Woo, Y. K.; Akeson, W. H. *Biorheology* **1982**, *19*, 397–408.
46. Woo, S. L.; Gomez, M. A.; Sites, T. J.; Newton, P. O.; Orlando, C. A.; Akeson, W. H. *J. Bone Joint Surg. Am.* **1987**, *69*, 1200–1211.
47. Wada, A.; Kubota, H.; Miyanishi, K.; Hatanaka, H.; Miura, H.; Iwamoto, Y. *J. Hand Surg. Br.* **2001**, *26*, 301–306.
48. Gelberman, R. H.; Manske, P. R.; Akeson, W. H.; Woo, S. L.; Lundborg, G.; Amiel, D. *J. Orthop. Res.* **1986**, *4*, 119–128.
49. Peltz, C. D.; Dourte, L. M.; Kuntz, A. F.; *et al. J. Bone Joint Surg. Am.* **2009**, *91*, 2421–2429.
50. Davidson, C. J.; Ganion, L. R.; Gehlsen, G. M.; Verhoestra, B.; Roepke, J. E.; Sevier, T. L. *Med. Sci. Sports Exerc.* **1997**, *29*, 313–319.
51. Cao, Y.; Liu, Y.; Liu, W.; Shan, Q.; Buonocore, S. D.; Cui, L. *Plast. Reconstr. Surg.* **2002**, *110*, 1280–1289.
52. Butler, D. L.; Awad, H. A. *Clin. Orthop. Relat. Res.* **1999**, S324–S332.
53. Ouyang, H. W.; Goh, J. C.; Thambyah, A.; Teoh, S. H.; Lee, E. H. *Tissue Eng.* **2003**, *9*, 431–439.
54. Young, R. G.; Butler, D. L.; Weber, W.; Caplan, A. I.; Gordon, S. L.; Fink, D. J. *J. Orthop. Res.* **1998**, *16*, 406–413.
55. Li, W. J.; Laurencin, C. T.; Caterson, E. J.; Tuan, R. S.; Ko, F. K. *J. Biomed. Mater. Res.* **2002**, *60*, 613–621.
56. Bokel, C.; Brown, N. H. *Dev. Cell* **2002**, *3*, 311–321.
57. Liu, Y.; Ramanath, H. S.; Wang, D. A. *Trends Biotechnol.* **2008**, *26*, 201–209.
58. Bagnaninchi, P. O.; Yang, Y.; El Haj, A. J.; Maffulli, N. *Br. J. Sports Med.* **2007**, *41*, e10; discussion e10.
59. Shah, M.; Revis, D.; Herrick, S.; *et al. Am. J. Pathol.* **1999**, *154*, 1115–1124.
60. Shah, M.; Foreman, D. M.; Ferguson, M. W. *J. Cell Sci.* **1995**, *108*(Pt 3), 985–1002.
61. Fu, S. C.; Wong, Y. P.; Chan, B. P.; *et al. Life Sci.* **2003**, *72*, 2965–2974.
62. Defranco, M. J.; Derwin, K.; Iannotti, J. P. *J. Am. Acad. Orthop. Surg.* **2004**, *12*, 298–304.
63. Sung, H. W.; Chang, W. H.; Ma, C. Y.; Lee, M. H. *J. Biomed. Mater. Res. A* **2003**, *64*, 427–438.
64. Chevallay, B.; Herbage, D. *Med. Biol. Eng. Comput.* **2000**, *38*, 211–218.
65. Thomopoulos, S.; Soslowsky, L. J.; Flanagan, C. L.; *et al. J. Shoulder Elbow Surg.* **2002**, *11*, 239–247.
66. Bensaid, W.; Triffitt, J. T.; Blanchat, C.; Oudina, K.; Sedel, L.; Petite, H. *Biomaterials* **2003**, *24*, 2497–2502.
67. Benhardt, H.; Cosgriff-Hernandez, E. *Tissue Eng. B Rev.* **2009**.
68. Hannafin, J. A.; Arnoczky, S. P.; Hoonjan, A.; Torzilli, P. A. *J. Orthop. Res.* **1995**, *13*, 907–914.
69. Amiel, D.; Frank, C.; Harwood, F.; Fronek, J.; Akeson, W. *J. Orthop. Res.* **1984**, *1*, 257–265.
70. Potenza, A. D. *Mil. Med.* **1962**, *127*, 34–47.
71. Potenza, A. D. *J. Bone Joint Surg. Am.* **1962**, *44A*, 49–64.
72. Abrahamsson, S. O.; Lundborg, G.; Lohmander, L. S. *Scand. J. Plast. Reconstr. Surg. Hand Surg.* **1989**, *23*, 199–205.
73. Matthews, P.; Richards, H. *J. Bone Joint Surg. Br.* **1974**, *56B*, 618–625.
74. Gelberman, R. H.; Botte, M. J.; Spiegelman, J. J.; Akeson, W. H. *J. Hand Surg. Am.* **1986**, *11*, 106–110.
75. Gelberman, R. H.; Woo, S. L.; Lothringer, K.; Akeson, W. H.; Amiel, D. *J. Hand Surg. Am.* **1982**, *7*, 170–175.
76. Takai, S.; Woo, S. L.; Horibe, S.; Tung, D. K.; Gelberman, R. H. *J. Orthop. Res.* **1991**, *9*, 705–713.
77. Tang, J. B.; Cao, Y.; Zhu, B.; Xin, K. Q.; Wang, X. T.; Liu, P. Y. *J. Bone Joint Surg. Am.* **2008**, *90*, 1078–1089.
78. Lou, J.; Manske, P. R.; Aoki, M.; Joyce, M. E. *J. Orthop. Res.* **1996**, *14*, 513–517.
79. Salti, N. I.; Tuel, R. J.; Mass, D. P. *J. Surg. Res.* **1993**, *55*, 411–415.
80. Chang, J.; Most, D.; Stelnicki, E.; *et al. Plast. Reconstr. Surg.* **1997**, *100*, 937–944.
81. Soslowsky, L. J.; Carpenter, J. E.; Debano, C. M.; Banerji, I.; Moalli, M. R. *J. Shoulder Elbow Surg.* **1996**, *5*, 383–392.
82. Matsumoto, F.; Uhthoff, H. K.; Trudel, G.; Loehr, J. F. *J. Orthop. Res.* **2002**, *20*, 357–363.
83. Uhthoff, H. K.; Seki, M.; Backman, D. S.; Trudel, G.; Himori, K.; Sano, H. *J. Shoulder Elbow Surg.* **2002**, *11*, 504–509.
84. Soslowsky, L. J.; Thomopoulos, S.; Tun, S.; *et al. J. Shoulder Elbow Surg.* **1999**, *2000*(9), 79–84.
85. Carpenter, J. E.; Flanagan, C. L.; Thomopoulos, S.; Yian, E. H.; Soslowsky, L. J. *Am. J. Sports Med.* **1998**, *26*, 801–807.
86. Soslowsky, L. J.; Thomopoulos, S.; Esmail, A.; *et al. Ann. Biomed. Eng.* **2002**, *30*, 1057–1063.
87. Lee, E. W.; Maffulli, N.; Li, C. K.; Chan, K. M. *Arch. Phys. Med. Rehabil.* **1997**, *78*, 399–404.
88. Silver, I. A.; Brown, P. N.; Goodship, A. E.; *et al. Equine Vet. J. Suppl.* **1983**, 1–43.
89. Williams, I. F.; Mccullagh, K. G.; Goodship, A. E.; Silver, I. A. *Res. Vet. Sci.* **1984**, *36*, 326–338.
90. Dahlgren, L. A.; Mohammed, H. O.; Nixon, A. J. *J. Orthop. Res.* **2005**, *23*, 84–92.
91. Kersh, K. D.; Mcclure, S. R.; Van Sickle, D.; Evans, R. B. *Vet. Comp. Orthop. Traumatol.* **2006**, *19*, 99–105.
92. Dahlgren, L. A.; Van Der Meulen, M. C.; Bertram, J. E.; Starrak, G. S.; Nixon, A. J. *J. Orthop. Res.* **2002**, *20*, 910–919.
93. Tatari, H.; Kosay, C.; Baran, O.; Ozcan, O.; Ozer, E. *Arch. Orthop. Trauma. Surg.* **2001**, *121*, 333–337.
94. Tatari, H.; Skiak, E.; Destan, H.; Ulukus, C.; Ozer, E.; Satoglu, S. *Arch. Phys. Med. Rehabil.* **2004**, *85*, 1470–1474.
95. Stone, D.; Green, C.; Rao, U.; *et al. J. Orthop. Res.* **1999**, *17*, 168–177.
96. Li, Z.; Yang, G.; Khan, M.; Stone, D.; Woo, S. L.; Wang, J. H. *Am. J. Sports Med.* **2004**, *32*, 435–440.
97. Chimich, D.; Frank, C.; Shrive, N.; Dougall, H.; Bray, R. *J. Orthop. Res.* **1991**, *9*, 37–47.
98. Frank, C. B.; Loitz, B.; Bray, R.; Chimich, D.; King, G.; Shrive, N. *J. Bone Joint Surg. Am.* **1994**, *76*, 403–412.
99. Batten, M. L.; Hansen, J. C.; Dahners, L. E. *J. Orthop. Res.* **1996**, *14*, 736–741.
100. Letson, A. K.; Dahners, L. E. *Clin. Orthop. Relat. Res.* **1994**, 207–212.
101. Frank, C.; Woo, S. L.; Amiel, D.; Harwood, F.; Gomez, M.; Akeson, W. *Am. J. Sports Med.* **1983**, *11*, 379–389.
102. Gomez, M. A.; Woo, S. L.; Amiel, D.; Harwood, F.; Kitabayashi, L.; Matyas, J. R. *Am. J. Sports Med.* **1991**, *19*, 347–354.
103. Walsh, S.; Frank, C. *J. Surg. Res.* **1988**, *45*, 159–166.
104. Walsh, S.; Frank, C.; Hart, D. *Clin. Orthop. Relat. Res.* **1992**, 277–288.
105. Weiler, A.; Peine, R.; Pashmineh-Azar, A.; Abel, C.; Sudkamp, N. P.; Hoffmann, R. F. *Arthroscopy* **2002**, *18*, 113–123.
106. Hunt, P.; Scheffler, S. U.; Unterhauser, F. N.; Weiler, A. *Arch. Orthop. Trauma. Surg.* **2005**, *125*, 238–248.
107. Ekdahl, M.; Nozaki, M.; Ferretti, M.; Tsai, A.; Smolinski, P.; Fu, F. H. *Am. J. Sports Med.* **2009**, *37*, 1522–1530.
108. Fleming, B. C.; Abate, J. A.; Peura, G. D.; Beynnon, B. D. *J. Orthop. Res.* **2001**, *19*, 841–844.
109. Papageorgiou, C. D.; Ma, C. B.; Abramowitch, S. D.; Clineff, T. D.; Woo, S. L. *Am. J. Sports Med.* **2001**, *29*, 620–626.
110. Zantop, T.; Ferretti, M.; Bell, K. M.; Brucker, P. U.; Gilbertson, L.; Fu, F. H. *Am. J. Sports Med.* **2008**, *36*, 2158–2166.
111. Fan, H.; Liu, H.; Toh, S. L.; Goh, J. C. *Biomaterials* **2009**, *30*, 4967–4977.
112. Fan, H.; Liu, H.; Wong, E. J.; Toh, S. L.; Goh, J. C. *Biomaterials* **2008**, *29*, 3324–3337.
113. Butler, D. L.; Juncosa-Melvin, N.; Boivin, G. P.; *et al. J. Orthop. Res.* **2008**, *26*, 1–9.
114. Nirmalanandhan, V. S.; Rao, M.; Shearn, J. T.; Juncosa-Melvin, N.; Gooch, C.; Butler, D. L. *J. Biomech.* **2008**, *41*, 822–828.
115. Juncosa-Melvin, N.; Boivin, G. P.; Galloway, M. T.; *et al. Tissue Eng.* **2005**, *11*, 448–457.
116. Juncosa-Melvin, N.; Boivin, G. P.; Gooch, C.; *et al. Tissue Eng.* **2006**, *12*, 369–379.

117. Juncosa-Melvin, N.; Shearn, J. T.; Boivin, G. P.; *et al*. *Tissue Eng*. **2006**, *12*, 2291–2300.
118. Shearn, J. T.; Juncosa-Melvin, N.; Boivin, G. P.; *et al*. *J. Biomech. Eng*. **2007**, *129*, 848–854.
119. Nirmalanandhan, V. S.; Dressler, M. R.; Shearn, J. T.; *et al*. *J. Biomech. Eng*. **2007**, *129*, 919–923.
120. Meaney Murray, M.; Rice, K.; Wright, R. J.; Spector, M. *J. Orthop. Res*. **2003**, *21*, 238–244.
121. Maeda, Y.; Jayakumar, R.; Nagahama, H.; Furuike, T.; Tamura, H. *Int. J. Biol. Macromol*. **2008**, *42*, 463–467.
122. Funakoshi, T.; Majima, T.; Suenaga, N.; Iwasaki, N.; Yamane, S.; Minami, A. *J. Shoulder Elbow Surg*. **2006**, *15*, 112–118.
123. Sato, M.; Maeda, M.; Kurosawa, H.; Inoue, Y.; Yamauchi, Y.; Iwase, H. *J. Orthop. Sci*. **2000**, *5*, 256–267.
124. Funakoshi, T.; Majima, T.; Iwasaki, N.; *et al*. *J. Biomed. Mater. Res. A* **2005**, *74*, 338–346.
125. Wang, Y.; Kim, H. J.; Vunjak-Novakovic, G.; Kaplan, D. L. *Biomaterials* **2006**, *27*, 6064–6082.
126. Altman, G. H.; Diaz, F.; Jakuba, C.; *et al*. *Biomaterials* **2003**, *24*, 401–416.
127. Horan, R. L.; Toponarski, I.; Boepple, H. E.; Weitzel, P. P.; Richmond, J. C.; Altman, G. H. *J. Knee Surg*. **2009**, *22*, 82–92.
128. Aurora, A.; Mccarron, J.; Iannotti, J. P.; Derwin, K. *J. Shoulder Elbow Surg*. **2007**, *16*, S171–S178.
129. Chen, J.; Xu, J.; Wang, A.; Zheng, M. *Expert Rev. Med. Devices* **2009**, *6*, 61–73.
130. Hodde, J. *Tissue Eng*. **2002**, *8*, 295–308.
131. Barber, F. A.; Herbert, M. A.; Coons, D. A. *Arthroscopy* **2006**, *22*, 534–538.
132. Gilbert, T. W.; Stewart-Akers, A. M.; Sydeski, J.; Nguyen, T. D.; Badylak, S. F.; Woo, S. L. *Tissue Eng*. **2007**, *13*, 1313–1323.
133. Liang, R.; Woo, S. L.; Takakura, Y.; Moon, D. K.; Jia, F.; Abramowitch, S. D. *J. Orthop. Res*. **2006**, *24*, 811–819.
134. Gilbert, T. W.; Stewart-Akers, A. M.; Simmons-Byrd, A.; Badylak, S. F. *J. Bone Joint Surg. Am*. **2007**, *89*, 621–630.
135. Dejardin, L. M.; Arnoczky, S. P.; Ewers, B. J.; Haut, R. C.; Clarke, R. B. *Am. J. Sports Med*. **2001**, *29*, 175–184.
136. Badylak, S. F.; Tullius, R.; Kokini, K.; *et al*. *J. Biomed. Mater. Res*. **1995**, *29*, 977–985.
137. Woo, S. L.; Takakura, Y.; Liang, R.; Jia, F.; Moon, D. K. *Tissue Eng*. **2006**, *12*, 159–166.
138. Valentin, J. E.; Badylak, J. S.; Mccabe, G. P.; Badylak, S. F. *J. Bone Joint Surg. Am*. **2006**, *88*, 2673–2686.
139. Mascarenhas, R.; Macdonald, P. B. *Mcgill. J. Med*. **2008**, *11*, 29–37.
140. Adams, J. E.; Zobitz, M. E.; Reach, J. S., Jr.; An, K. N.; Steinmann, S. P. *Arthroscopy* **2006**, *22*, 700–709.
141. Derwin, K. A.; Baker, A. R.; Spragg, R. K.; Leigh, D. R.; Farhat, W.; Iannotti, J. P. *J. Biomed. Mater. Res. A* **2008**, *84*, 500–507.
142. Gunatillake, P. A.; Adhikari, R. *Eur. Cell. Mater*. **2003**, *5*, 1–16; discussion 16.
143. Koski, J. A.; Ibarra, C.; Rodeo, S. A. *Orthop. Clin. N. Am*. **2000**, *31*, 437–452.
144. Derwin, K.; Baker, A. R.; Iannotti, J.; Mccarron, J. A. *Tissue Eng. B Rev*. **2009**.
145. Derwin, K. A.; Codsi, M. J.; Milks, R. A.; Baker, A. R.; Mccarron, J. A.; Iannotti, J. P. *J. Bone Joint Surg. Am*. **2009**, *91*, 1159–1171.
146. Aoki, M.; Miyamoto, S.; Okamura, K.; Yamashita, T.; Ikada, Y.; Matsuda, S. *J. Biomed. Mater. Res. B Appl. Biomater*. **2004**, *71*, 252–259.
147. Macgillivray, J. D.; Fealy, S.; Terry, M. A.; Koh, J. L.; Nixon, A. J.; Warren, R. F. *J. Shoulder Elbow Surg*. **2006**, *15*, 639–644.
148. Li, X.; Xie, J.; Lipner, J.; Yuan, X.; Thomopoulos, S.; Xia, Y. *Nano Lett*. **2009**, *9*, 2763–2768.
149. Lu, H. H.; Cooper, J. A., Jr.; Manuel, S.; *et al*. *Biomaterials* **2005**, *26*, 4805–4816.
150. Cooper, J. A.; Lu, H. H.; Ko, F. K.; Freeman, J. W.; Laurencin, C. T. *Biomaterials* **2005**, *26*, 1523–1532.
151. Moffat, K. L.; Sun, W. H.; Pena, P. E.; *et al*. *Proc. Natl Acad. Sci. USA* **2008**, *105*, 7947–7952.
152. Spalazzi, J. P.; Dagher, E.; Doty, S. B.; Guo, X. E.; Rodeo, S. A.; Lu, H. H. *J. Biomed. Mater. Res. A* **2008**, *86*, 1–12.
153. Moffat, K. L.; Wang, I. N.; Rodeo, S. A.; Lu, H. H. *Clin. Sports Med*. **2009**, *28*, 157–176.
154. Lu, H. H.; El-Amin, S. F.; Scott, K. D.; Laurencin, C. T. *J. Biomed. Mater. Res. A* **2003**, *64*, 465–474.
155. Hokugo, A.; Takamoto, T.; Tabata, Y. *Biomaterials* **2006**, *27*, 61–67.
156. Ouyang, H. W.; Toh, S. L.; Goh, J.; Tay, T. E.; Moe, K. *J. Biomed. Mater. Res. B Appl. Biomater*. **2005**, *75*, 264–271.
157. Jenkins, D. H. *J. Bone Joint Surg. Br*. **1978**, *60B*, 520–522.
158. Irie, K.; Kurosawa, H.; Oda, H. *J. Orthop. Res*. **1992**, *10*, 886–894.
159. Andrish, J. T.; Woods, L. D. *Clin. Orthop. Relat. Res*. **1984**, *183*, 298–302.
160. Arnoczky, S. P.; Warren, R. F.; Minei, J. P. *Am. J. Sports Med*. **1986**, *14*, 1–6.
161. Schindhelm, K.; Rogers, G. J.; Milthorpe, B. K.; *et al*. *Clin. Orthop. Relat. Res*. **1991**, *267*, 278–293.
162. Nau, T.; Lavoie, P.; Duval, N. *J. Bone Joint Surg. Br*. **2002**, *84*, 356–360.
163. Ozaki, J.; Fujimoto, S.; Masuhara, K.; Tamai, S.; Yoshimoto, S. *Clin. Orthop. Relat. Res*. **1986**, *202*, 173–183.
164. Kimura, A.; Aoki, M.; Fukushima, S.; Ishii, S.; Yamakoshi, K. *J. Bone Joint Surg. Br*. **2003**, *85B*, 282–287.
165. Petrigliano, F. A.; Mcallister, D. R.; Wu, B. M. *Arthroscopy* **2006**, *22*, 441–451.
166. Boileau, P.; Brassart, N.; Watkinson, D. J.; Carles, M.; Hatzidakis, A. M.; Krishnan, S. G. *J. Bone Joint Surg. Am*. **2005**, *87*, 1229–1240.
167. Galatz, L. M.; Ball, C. M.; Teefey, S. A.; Middleton, W. D.; Yamaguchi, K. *J. Bone Joint Surg. Am*. **2004**, *86A*, 219–224.
168. Gerber, C.; Fuchs, B.; Hodler, J. *J. Bone Joint Surg. Am*. **2000**, *82*, 505–515.
169. Romeo, A. A.; Hang, D. W.; Bach, B. R., Jr.; Shott, S. *Clin. Orthop. Relat. Res*. **1999**, *367*, 243–255.
170. Koh, J. L.; Szomor, Z.; Murrell, G. A.; Warren, R. F. *Am. J. Sports Med*. **2002**, *30*, 410–413.
171. Sano, H.; Kumagai, J.; Sawai, T. *J. Shoulder Elbow Surg*. **2002**, *11*, 166–173.
172. Konstantinovic, M. L.; Lagae, P.; Zheng, F.; Verbeken, E. K.; De Ridder, D.; Deprest, J. A. *BJOG* **2005**, *112*, 1554–1560.
173. Perry, S. M.; Gupta, R. R.; Van Kleunen, J.; Ramsey, M. L.; Soslowsky, L. J.; Glaser, D. L. *J. Shoulder Elbow Surg*. **2007**, *16*, S179–S183.
174. Zheng, M. H.; Chen, J.; Kirilak, Y.; Willers, C.; Xu, J.; Wood, D. *J. Biomed. Mater. Res. B Appl. Biomater*. **2005**, *73*, 61–67.
175. Funakoshi, T.; Majima, T.; Iwasaki, N.; *et al*. *Am. J. Sports Med*. **2005**, *33*, 1193–1201.
176. Badylak, S. F.; Record, R.; Lindberg, K.; Hodde, J.; Park, K. *J. Biomater. Sci. Polym. Ed*. **1998**, *9*, 863–878.
177. Derwin, K. A.; Baker, A. R.; Spragg, R. K.; Leigh, D. R.; Iannotti, J. P. *J. Bone Joint Surg. Am*. **2006**, *88*, 2665–2672.
178. Sclamberg, S. G.; Tibone, J. E.; Itamura, J. M.; Kasraeian, S. *J. Shoulder Elbow Surg*. **2004**, *13*, 538–541.
179. Iannotti, J. P.; Codsi, M. J.; Kwon, Y. W.; Derwin, K.; Ciccone, J.; Brems, J. J. *J. Bone Joint Surg. Am*. **2006**, *88*, 1238–1244.
180. Malcarney, H. L.; Bonar, F.; Murrell, G. A. *Am. J. Sports Med*. **2005**, *33*, 907–911.
181. Bond, J. L.; Dopirak, R. M.; Higgins, J.; Burns, J.; Snyder, S. J. *Arthroscopy* **2008**, *24*(403–409), e1.
182. Carey, J. L.; Dunn, W. R.; Dahm, D. L.; Zeger, S. L.; Spindler, K. P. *J. Bone Joint Surg. Am*. **2009**, *91*, 2242–2250.
183. West, R. V.; Harner, C. D. *J. Am. Acad. Orthop. Surg*. **2005**, *13*, 197–207.
184. Freedman, K. B.; D'amato, M. J.; Nedeff, D. D.; Kaz, A.; Bach, B. R., Jr. *Am. J. Sports Med*. **2003**, *31*, 2–11.
185. Crawford, C.; Kainer, M.; Jernigan, D.; *et al*. *Clin. Infect. Dis*. **2005**, *41*, 195–200.
186. Mahirogullari, M.; Ferguson, C. M.; Whitlock, P. W.; Stabile, K. J.; Poehling, G. G. *Clin. Sports Med*. **2007**, *26*, 625–637.
187. Dunn, M. G.; Liesch, J. B.; Tiku, M. L.; Zawadsky, J. P. *J. Biomed. Mater. Res*. **1995**, *29*, 1363–1371.
188. Bellincampi, L. D.; Closkey, R. F.; Prasad, R.; Zawadsky, J. P.; Dunn, M. G. *J. Orthop. Res*. **1998**, *16*, 414–420.
189. Caruso, A. B.; Dunn, M. G. *J. Biomed. Mater. Res. A* **2005**, *73*, 388–397.
190. Good, L.; Odensten, M.; Pettersson, L.; Gillquist, J. *Acta Orthop. Scand*. **1989**, *60*, 8–12.
191. Cartmell, J. S.; Dunn, M. G. *Tissue Eng*. **2004**, *10*, 1065–1075.
192. Altman, G. H.; Horan, R. L.; Lu, H. H.; *et al*. *Biomaterials* **2002**, *23*, 4131–4141.
193. Middleton, J. C.; Tipton, A. J. *Biomaterials* **2000**, *21*, 2335–2346.
194. Majima, T.; Funakosi, T.; Iwasaki, N.; *et al*. *J. Orthop. Sci*. **2005**, *10*, 302–307.
195. Cristino, S.; Grassi, F.; Toneguzzi, S.; *et al*. *J. Biomed. Mater. Res. A* **2005**, *73*, 275–283.
196. Van Eijk, F.; Saris, D. B.; Riesle, J.; *et al*. *Tissue Eng*. **2004**, *10*, 893–903.
197. Desrosiers, E. A.; Yahia, L.; Rivard, C. H. *J. Orthop. Res*. **1996**, *14*, 200–208.
198. Marui, T.; Niyibizi, C.; Georgescu, H. I.; *et al*. *J. Orthop. Res*. **1997**, *15*, 18–23.
199. Scherping, S. C., Jr.; Schmidt, C. C.; Georgescu, H. I.; Kwoh, C. K.; Evans, C. H.; Woo, S. L. *Connect. Tissue Res*. **1997**, *36*, 1–8.
200. Hankemeier, S.; Keus, M.; Zeichen, J.; *et al*. *Tissue Eng*. **2005**, *11*, 41–49.
201. Barber, F. A.; Herbert, M. A.; Coons, D. A.; Boothby, M. H. *Arthroscopy* **2006**, *22*(1063), e1–e9.

202. Ceonzo, K.; Gaynor, A.; Shaffer, L.; Kojima, K.; Vacanti, C. A.; Stahl, G. L. *Tissue Eng.* **2006**, *12*, 301–308.
203. Santavirta, S.; Konttinen, Y. T.; Saito, T.; *et al. J. Bone Joint Surg. Br.* **1990**, *72*, 597–600.
204. Freehill, M. Q.; Harms, D. J.; Huber, S. M.; Atlihan, D.; Buss, D. D. *Am. J. Sports Med.* **2003**, *31*, 643–647.

Relevant Websites

http://orthoinfo.aaos.org/main.cfm – American Academy of Orthopaedic Surgeons.
http://www.fda.gov/MedicalDevices/DeviceRegulationandGuidance/GuidanceDocuments/ucm073810.htm – Guidance for FDA Reviewers and Industry Medical Devices Containing Materials Derived from Animal Sources (Except for In Vitro Diagnostic Devices).
http://www.fda.gov/downloads/MedicalDevices/DeviceRegulationandGuidance/GuidanceDocuments/ucm081345.pdf – Guidance Document for the Preparation of Investigational Device Exemptions and Premarket Approval Applications for Intra-articular Prosthetic Knee Ligament Devices.
http://www.freepatentsonline.com/result.html?query_txt=Tendon+scaffolds&sort=relevance&srch=top&search= – List of current rendon scaffold patents.
http://www.freepatentsonline.com/result.html?query_txt=Ligament+scaffolds&sort=relevance&srch=top&search= – Listof current patents for ligament scaffolds.
http://www.physorg.com/search/?search=tendon%2C+ligament – PhysOrg search for tendon and ligament research and technology news.
http://www.biomaterials.org/publications.cfm – Society for Biomaterials.

6.619. Materials in Dental Implantology

B Al-Nawas, M O Klein, and W Wagner, University Medical Center Mainz, Mainz, Germany

© 2011 Elsevier Ltd. All rights reserved.

6.619.1.	**History and Development of Dental Implantology**	282
6.619.2.	**Indication and Procedure for Dental Implants**	283
6.619.2.1.	Functional Goal of Dental Implants	283
6.619.2.2.	Typical Indications	283
6.619.2.2.1.	Edentulous jaws	283
6.619.2.2.2.	Fixed partial denture	284
6.619.2.2.3.	Special indications	284
6.619.2.2.4.	Implant survival and success criteria	285
6.619.2.3.	General and Local Risk Factors	285
6.619.2.4.	Surgical Procedure	286
6.619.2.4.1.	Presurgical considerations	286
6.619.2.4.2.	Surgery	286
6.619.3.	**Tissue Reaction on Dental Implant Material**	288
6.619.3.1.	Bone (Enossal Part)	288
6.619.3.1.1.	Early interaction with noncellular components of the extracellular milieu	288
6.619.3.1.2.	Platelet activation and cytokine release	288
6.619.3.1.3.	Inflammation period, chemotaxis	289
6.619.3.1.4.	Osteoconduction and matrix synthesis, functional remodeling	289
6.619.3.2.	Soft Tissue (Mucosa and Epithelium)	289
6.619.3.3.	Experimental Methods	290
6.619.3.3.1.	Mechanical testing and modeling	290
6.619.3.3.2.	Cell culture methods	290
6.619.3.3.3.	Animal models	291
6.619.3.3.4.	Human histology	291
6.619.4.	**Implant Materials**	292
6.619.4.1.	Metal	292
6.619.4.2.	Ceramics	293
6.619.5.	**Surface Structure and Modifications**	293
6.619.5.1.	Macrostructure	293
6.619.5.2.	Physical Modification (Roughness)	293
6.619.5.3.	Chemical Modifications	294
6.619.5.4.	Clinical Impact of Surface Modifications	294
6.619.5.5.	Biofilm and Peri-implantitis	294
6.619.5.6.	Biofunctionalization	295
6.619.6.	**Implant Design**	296
6.619.6.1.	Principles in the Endosseal Part	296
6.619.6.2.	Future Developments	297
References		297

Glossary (from Laney[1])

Abutment Tooth, tooth root, or implant component that serves as support and/or retention for a dental prosthesis.

Bacterial leakage Colonization and release of bacteria at the interface of an oral implant abutment and implant.

Cutting torque Turning or twisting force produced by a rotary device (i.e., dental handpiece) to cut through a material such as bone.

Early implant loss Loss of an implant that occurs prior to implant osseointegration.

Early implant placement Early implant placement takes place 4–8 weeks following tooth extraction, providing sufficient time for soft tissue healing.

Early loading Placing of an implant into function or a load-bearing situation following a reduced period of healing after the initial placement. It is generally considered to be loading more than 48 h but less than 3 months after implant placement.

Immediate implant placement Implant placement immediately following extraction of a tooth.

Immediate loading Application of functional or nonfunctional load to an implant at the time of surgical placement or shortly thereafter; that is, generally considered to be loading within 48 h of implant placement.
Implant–abutment interface Surface forming a common boundary between the abutment and the implant (microgap).
Late implant loss Outcome related to the loss of an implant that occurred after implant osseointegration.
Late implant placement Implant placement at least 6 months following tooth extraction. The chosen time period should allow for sufficient bone regeneration of the extraction socket, and consequently, implant placement without bone augmentation procedure. Late implant placement bears the risk of bone atrophy in the orofacial direction, particularly in the anterior maxilla.
Microgap Microscopic space between two components, specifically between an implant and an abutment. It is usually considered to be a source of chronic irritation or contamination creating an inflammatory response.
Nonsubmerged healing Implant placement procedure incorporating a transmucosal extension for healing guidance. A special healing cap is required to extend the implant shoulder above the soft tissue level, allowing the suturing of wound margins around the implant neck/healing cap. This approach does not require a second surgical procedure and is often used in posterior implant sites. (One-stage implant placement).
Osseointegration Direct structural and functional connection between ordered, living bone and the surface of a load-carrying titanium implant.
Peri-implantitis Condition of inflamed peri-implant soft tissues, bone loss, and increased probing depth combined with exudation.
Permucosal seal Seal or tissue barrier at the base of the peri-implant sulcus provided by the epithelial tissue prevents the penetration of chemical and bacterial substances from the oral cavity to the internal environment of the peri-implant tissues.
Primary stability Clinically, implant immobility at the time of surgical placement, resulting from intimate contact of the implant with the bony walls of the osteotomy. Primary stability decreases with time as osseous remodeling occurs. It is distinct from secondary implant stability, which is the result of new bone formation and osseointegration.
Secondary stability Implant stability within its prepared bony site, created by osseointegration and the formation of new bone subsequent to loss of the bone initially in contact with the implant at the time of placement.

6.619.1. History and Development of Dental Implantology

The possible use of biomaterials in Oral and Maxillofacial Surgery dates back to pre-Christian times.[2,3] Early attempts to anchor 'artificial' teeth into the jaw bone are discussed in controversy.[4] The first trusted use of a biomaterial for the functional replacement of a tooth was performed by Maggiolo in 1807, who inserted a root form gold implant into an alveolar socket.[5] This procedure was repeated in 1887 using a platinum implant.[6] Younger was the first to describe the idea of the implant bed generation by transplanting teeth into artificially created bone cavities in 1886.[7] In his important work, Greenfield in 1913 described some principles of bone implant contact (secondary stability), and thus started with the idea of 'osseointegration'.[8]

At this time, some authors started to test different metals in animal experiments, first using histology to test biocompatibility[9]; the results for titanium in 1940 were described as positive.[10] In 1951, Leventhal[11] endorsed titanium as an ideal metal for use in fixation of bone fractures. He described what Brånemark later called 'osseointegration' when he placed titanium screws in rat femurs: 'At the end of 6 weeks, the screws were slightly tighter than when originally put in; . . . and at the end of 16 weeks, the screws were so tight that in one specimen the femur was fractured when an attempt was made to remove the screw.' Clinically in 1937, Strock used cobalt–chromium–molybdenum alloys ('vitallium') for tooth replacement[12] in alveolar sockets. His contribution was a description of a staged approach with a secondary fixation of the crown and an idea of the theoretical background of mechanical stability (primary stability) at the metal–bone interface. Despite various successful reports, these efforts remained case reports with unpredictable clinical success rates. During these times, many of the failures might have been caused by early loading or excessive mechanical stress and not by the material or the surgical technique that was used.

The replacement of a tooth by an artificial implant at the start of the last century was marked by the empirical search for the best implant area (subperiostal vs. enossal) and the best implant shape (extension vs. rotational-symmetric). Greenfield's cage-like implants in 1913[8] suffered from low surface contact with the bone. Dahl's subperiostal implants in 1948 led to excessive bone loss and have not been supported since the 1980s.[13] Blade implants were introduced by Linkow and Roberts[14] and became very popular for almost two decades. However, systematic research on long-term success rates was lacking. The majority of the blade implants were one-piece (implant and abutment), and had to be immediately loaded. This led to the clinical phenomenon of a peri-implant radiolucency called fibro-osseous integration. In these days, the majority of implant surgeons believed that a fibro-osseous connection had a 'shock-absorbing capacity' similar to the periodontal ligament around a natural tooth. At that time, advances in the understanding of implant biology were hampered by undeveloped histological methods. Beginning in 1976, Schroeder demonstrated that the pseudoligament was not the perpendicular orientation of fibers that is found around a natural tooth.[15] Thus, peri-implant radiolucencies were termed fibro-osseous encapsulation, indicating a pathological rather than an anatomical variation.

The scientific quantum leap is contributed to the orthopedic surgeon P. I. Branemark. In the 1950s, he performed vital blood flow microscopy in animals. The titanium cylinders he used were so difficult to remove from bone, that he thought they might withstand occlusal forces. He called this phenomenon 'osseointegration'[16] and developed the concept of unloaded healing of smooth titanium implants. On the basis of extensive preclinical and clinical experiments, he developed a helical implant, which had predictable success rates.[17,18] Characteristics of this system were a standardized surgical procedure, unloaded subgingival healing, and a helical implant with a smooth surface. The landmarks of the Branemark group consisted of the description of a standardized approach and the documentation of the long-term clinical outcome. This is an approach that continues to shape the academic work in implant dentistry and has led to the development of the so-called Branemark Implant System.

Almost simultaneously with the 'discovery' of osseointegration, Schroeder described the similar effect in transgingival, rough implants as 'functional ankylosis'.[19] Out of these results, a cylindrical implant with transgingival healing and a rough surface was developed,[20] known as the ITI implant (former bone fit implant), which also showed predictable implant success rates.[19,21–27] The primary clinical indication of these implants has been the functional rehabilitation of the edentulous mandible with implant placement in the regio interforaminalis.[17] The success of these systems in early days was partly based on the good bone quality in this area.

The first systematic approach to single-tooth replacement came from the University of Tubingen with a modification of the implant material. Two-piece aluminum oxide ceramic implants were used for immediate implantation.[28] After first positive results with respect to osseointegration,[29] fractures occurred, which led to the ceramic implant material being changed to metal titanium.[30,31] The implant has been widely used as the Frialit II implant.[29,31–34] The IMZ system (intramobile cylinder implant) played a key role in the systematic development of implantology. The basis of this system was the imitation of natural tooth mobility. Together with the Branemark system, it was one of the first implant systems with subgingival healing and with standardized, innercooled bone bed preparation.[35,36] Long-term studies with realistic assessment of success rates and a critical assessment of marginal bone remodeling/bone loss were available.[37–42]

So, in the early seventies of the last century, a treatment alternative with predictable and acceptable success rates for the restoration of edentulous jaws was available for the first time. This is reflected by several consensus statements in the description of the implant as a scientifically documented therapeutic option.[43–45] The goal of creating a means for a possible long-term oral, endosteal implant option on endosseous anchorage had been largely achieved. Only much later, the purely empirically verified, good success rates of implants in edentulous mandibles and for the single-tooth replacement were transferred to other indications. With the widening of the localization into the cancellous maxillary and vertically limited lateral mandible, the way was paved for masticatory rehabilitation of complex cases like severe atrophy or large jaw defects due to trauma or tumor.

6.619.2. Indication and Procedure for Dental Implants

6.619.2.1. Functional Goal of Dental Implants

The general property requirements for dental implants can be subdivided into biological and mechanical aspects:

- Biological properties (biocompatibility)
  - Nontoxic, noncancerogenic, nonteratogenic
  - Nonantigenic
  - Noninfectious, possibility to be sterilized
  - Biological stability
- Mechanical properties
  - Form stability
  - Mechanical toughness
  - Radio-opacity

Experiences from the last years have shown that dental implants have to be produced (and sold) at a market-adequate price. The ability to produce two-piece systems (endosseal part and supraconstruction) allows for unloaded healing and high flexibility regarding the prosthetic solutions. Prefabricated parts allow for high precision coupling of the elements during the entire process.

6.619.2.2. Typical Indications

6.619.2.2.1. Edentulous jaws

The first successful steps in dental implantology were initiated to rehabilitate patients with edentulous mandibles,[16,17,19,38,46–50] because in this situation, the classical denture often is insufficient due to progressive bone atrophy (**Figure 1**).[51] For these patients, implants help to 'carry' and stabilize the removable denture and are thought to prevent further progression of bone atrophy.[52,53] In the rehabilitation of the edentulous mandible, implants have already demonstrated very high survival rates of above 98% over 10–20 years and are promoted as the rehabilitation of choice compared to a conventional denture as a preventive measure for further bone loss.[54–58] Owing to the anatomical position of the inferior alveolar nerve, they are positioned in the interforaminal (anterior) region of the mandible. Earlier studies used six to four implants to support the denture. Quality of life (QoL)



Figure 1 Two implants in an edentulous mandible supporting a complete denture with a locator abutment.

studies have shown that patients already have a clear benefit with two implants supporting a mandibular overdenture compared to a conventional denture[59–66]; four implants compared to two implants do not change the QoL significantly.[67] Thus, the two implant rehabilitation of the mandible supporting an overdenture can be stated as a 'classical' solution nowadays. More comfort for the patient is provided by a fixed denture, which requires four to six implants.[68,69] Besides the higher number of implants needed for a fixed restoration compared to a removable one, this technique is more sensitive to patient-related factors and more cost intensive.[70] Prospective studies have shown that patients choose fixed or removable implant-supported prostheses for specific reasons, and that it is important to consider patient attitudes at the beginning of the therapy (**Figure 2**).[71]

The edentulous maxilla represents a far more complex situation. The anatomical proximity to the nasal cavity and the maxillary sinus limits the available bone area for dental implants. Esthetic demands and speech requirements are important for the planning of shape and position of the rehabilitation. This often makes the realization of a fixed solution more critical.[59,72–78] Owing to the increased bone softness of the maxilla, implant failure rates with smooth implant surfaces have been not as high as in the mandible.[79] Besides the speech and esthetic outcomes, palatal coverage is a crucial question for patients wearing a complete denture. In contrast to the high gain of QoL by restoring the mandible with two or more implants, the gain is less pronounced for the maxillary implant rehabilitation.[73]

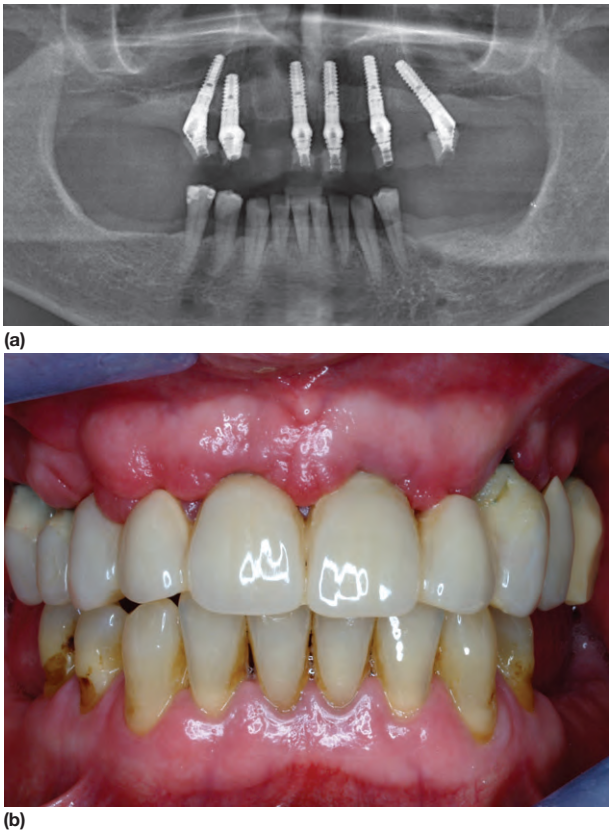

Figure 2 (a) Panoramic X-ray of six tilted implants in the maxilla to support a fixed denture and allow immediate loading; (b) intraoral situation with the provisional immediate restoration at the 6-month follow-up.

To overcome the limits of the anatomy in the maxilla as well as the mandible, tilted or angulated implants have been used to generate a larger area of support for the prosthesis by many groups using different implant systems.[80–91] The data on long-term outcomes of tilted implants, however, are still missing.[92]

A clear trend is seen in the indication 'edentulous mandible' for the use of small-diameter implants, but long-term data on low-diameter implants are rare[93–95] and the best supraconstruction in these cases still remains unclear.[65]

6.619.2.2.2. Fixed partial denture

The rehabilitation of single or more tooth gaps using implants requires different prerequisites in diagnosis, planning, and therapy compared to the fully edentulous jaw. In edentulous situations, bar constructions often allow mediation between the denture and the implant position, whereas in partial dentures, the direct connection of the implant to the crown using an abutment requires perfect positioning of the implant with respect to the future supraconstruction. Thus, especially in esthetically demanding cases, so-called backward planning is recommended; meaning that, after the planning of the supraconstructions (e.g., a wax up of the crowns), the ideal implant position is planned. Missing bone in this situation should be augmented.[96,97] Nevertheless, implants are overwhelmingly selected over a fixed bridge for the replacement of a single-tooth unit.[98]

The restoration can be either screwed on or cemented on the abutment. By using cemented crowns, the risk that residual cement in the crestal area leads to inflammation and bone loss may increase.[99] The increased possibility of removing the supraconstruction for cleaning and maintenance is an advantage of the screw-retained dentures.[100] Owing to the superior esthetical possibilities using full ceramic crowns, cementing is increasingly chosen by the dentists and has become more and more widespread.[101]

One open question in this field is the necessity to splint implants via supraconstructions together or to restore the crown individually. Especially when short implants (<8 mm) are in use, splinting seems to be preferred.[102] In many centers, the idea of splinting teeth to implants is still not followed, due to the fact that both have different mobility. The IMZ implant with its intramobile element was initially designed to overcome this problem.[42,50] Studies with other implant systems have shown that splinting teeth and implants together is possible, but a higher number of technical complications have to be expected.[103,104] Some systematic reviews have addressed the question of a possible distal cantilever in fixed partial denture.[105,106] Although some researchers are very cautious regarding this technique,[105] newer studies seem to indicate that despite minor technical problems such as screw loosening, the concept is rated a 'valid treatment modality'.[106,107]

6.619.2.2.3. Special indications

For the rehabilitation of tumor defects, extraoral anchorage of epitheses is needed. In these situations, dental implants inserted into extraoral bone sites have proven to be useful.[108–110]

The reported success rates in these indications are favorable, but extraoral skin seems to be more prominent for dermatitis than intraoral one for mucositis.[111–113] A well-established example is the implant-retained anchorage of hearing aids.[114] In concordance with the extraoral skin-penetrating epithesis implants, peri-implant abutment infections are known for this indication.

Particularly in the last years, skeletal orthodontic anchorage using dental implants or miniscrews has become an important issue. Positive results have been reported for short implants placed into the palate, which undergo classical Osseointegration.[115–117] The reported survival rates for miniscrews, which work with the principle of primary stability seem to be a little bit lower.[118–120] The potential of orthodontic anchorage continues to be a promising development.

6.619.2.2.4. Implant survival and success criteria

Several suggestions have been proposed on the question regarding how implant success can be obtained. The most tangible and objective criterion is implant survival (*in situ*), which is used in many studies, and therefore is a candidate for meta-analyses.[121] Implant survival rates of 90–100% are available for some systems for the last 10–20 years.[48,74,122–129] From a clinical point, it is clear that an implant can be *in situ*, but not successfully. Pain, persistent inflammation, progressive bone loss, probing depth, and mobility have been discussed as indicators of failure. Consequently, several respective criteria for success have been introduced, and at least one of them has been reported in a clinical study.[130,131] In more recent times, a critical discussion on these criteria has started. One major question is whether bone loss of 0.2 mm $year^{-1}$ is acceptable, and whether bone loss during the first year should be excluded.[130] Still no modern, fully accepted score for implant success is available. Rating implant outcomes seems to underestimate the prosthodontic outcome. Thus, reporting technical versus biological complications in conjunction with survival rates has increased.[100] Particularly in the anterior esthetically demanding zone, the esthetic outcome is of major importance. The former papilla score by Jemt[132] has been replaced by the more complex pink esthetic score,[133] which rates mucosal parameters, and the white esthetic score, which rates the crown esthetics.[134]

6.619.2.3. General and Local Risk Factors

As reported above, promising long-term results for well-established treatment sites with optimum bone quality, such as the interforaminal region of the lower jaw,[135] have led to a continuous expansion of indications and introduction of more aggressive treatment protocols like:

- implantation into augmented areas,
- immediate implantation following tooth extraction and/or,
- immediate loading of dental implants,

thereby defining potential risk factors for dental implant success.[136–139]

Furthermore, patients with limitations of tissue homeostasis and integrity, such as that which occurs after radiation therapy to the head and neck region or with impaired bone remodeling, and repair capacity under systemic medication (e.g., bisphosphonates) have been identified as challenging collectives for the treatment with dental implants.[140,141] Table 1 provides a synopsis over patient-related general and local risk factors affecting dental implant success.

Table 1 Dental implant success: patient-related parameters

Local factors	*Extended local factors*	*General constitution*
Bone parameters	Smoking	Diabetes mellitus
Quantity, quality	Radiation therapy	Immunodeficiency
Horizontal versus vertical deficit	Pathogenous microflora (parodontitis)	IL-1 polymorphism
Local versus augmented bone	Bad mouth hygiene, noncompliance	Systemic bisphosphonate medication
Alloplastic bone substitutes	Malocclusion, habits	
Soft tissue parameters		
Fixed versus mobile mucosa		

For instance, patients with generalized aggressive periodontitis showed higher implant failure rates (20%) when compared to healthy subjects (2%) or collectives with only chronic periodontitis (4%).[142] Another potential risk factor is diabetes mellitus (DM). In a recent systematic review, Javed and Romanos concluded that long-term high glucose levels (not well-adjusted DM) impair dental implant healing and successful osseointegration with higher failure rates, which could be avoided by correct adjustment of serum glucose levels.[143] To date, no serious scientific data provide evidence for higher implant failure rates in an osteoporotic collective.[144] However, concomitant bisphosphonate medication should be taken into account when an implant therapy is planned for these patients.[145,146]

Another potential risk factor for implant loss is radiation therapy. A recent systematic review by Ihde *et al.* identifies radiation therapy to the head and neck as a potential risk factor for implant failure.[147] The authors detected a 3–12-fold increased risk for implant loss when inserted into irradiated bone. They also defined a 'threshold' value above 50 Gy as a significant higher risk for subsequent to implant loss. In this study, no difference between the sequence of implantation and radiation could be observed.[147] Nevertheless, patients with considerable intraoral defects after ablative tumor surgery significantly benefit from functional rehabilitation through dental implants.[148–150] Other authors identified the time interval between radiation therapy and dental implantation as a potentially important cofactor for implant success. Schliephake and coworkers opine that radiation therapy has no relevant impact on implant success if dental implantation takes place at least 1 year after completing radiation therapy.[151] According to Jacobsson and coworkers, functional self-regeneration of the damaged tissue would provide sufficient implant healing and osseointegration capacities of the bone 1 year after radiation therapy.[152,153]

As a conclusion, the described host tissue limitations require an optimal treatment protocol as well as optimized implant properties to promote the endosseous healing cascade in order to achieve timely and stable osseointegration.

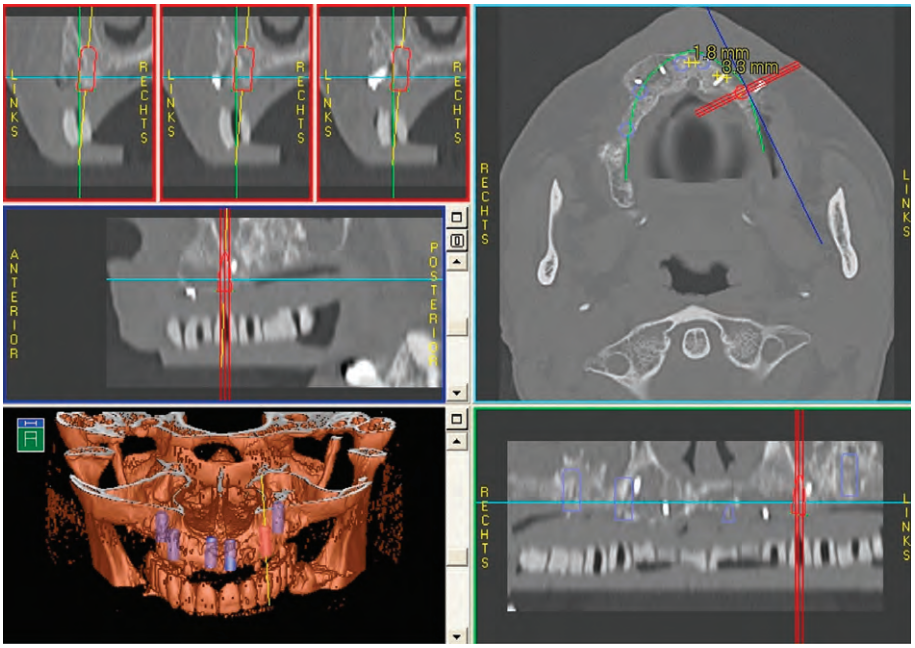

Figure 3 Example of a PC-based 3D planning tool showing the planning of six implants in the edentulous maxilla after lateral augmentation and sinus floor elevation.

6.619.2.4. Surgical Procedure

6.619.2.4.1. Presurgical considerations

After clinical and radiologic planning, there is a general consensus nowadays that before implant placement, prosthodontic planning should be done as well. This means that the type and details of the final restorations should be considered prior to implant placement (top–down planning). During the planning procedure, 3D-imaging and PC-based planning systems have become more and more important.[154–157] The assessment of the available alveolar bone prior to surgery particularly helps to plan augmentation procedures.[158] For this purpose, three-dimensional (3D) radiology or mechanical ridge mapping is used (**Figure 3**). Inactivity of the jaw bone after tooth extraction leads to resorption, which as a consequence leads to the necessity of bone augmentation before or at implant insertion.[51] The resorption processes immediately following tooth extraction have been a strong research focus. The major loss in alveolar crest width occurs within the first months after extraction.[159] In animal experiments, it was possible to prove that the bone adjacent to the sharpey fibers, which are connected to the tooth, is part of the periodontium. If the tooth is extracted, the periodontal structures, including this bundle bone, disappear.[160,161] Particularly, the thin buccal bone wall is susceptible to this physiologic remodeling (**Figure 4**).

To overcome this physiologic process, two options are currently being discussed: immediate implantation into the fresh extraction socket or early implantation after soft tissue healing (6–8 weeks).[162] Animal experiments show that the implant itself is not able to prevent buccal bone remodeling.[163] The dimension of the alveolar ridge and the implant diameter seem to be more important for the outcome than implant macro- or microstructure.[164–166] Perfect esthetic results after immediate implantation are possible but also depend on mucosal thickness,

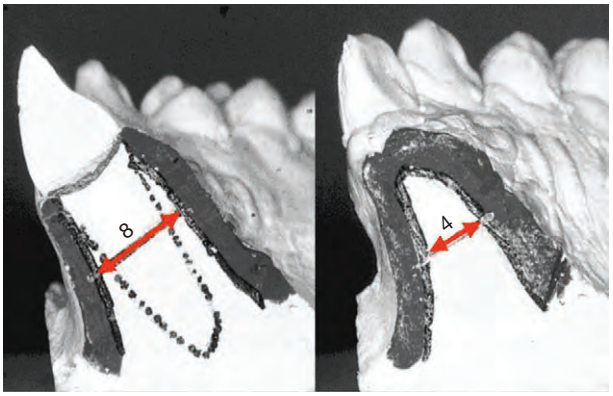

Figure 4 Model of the alveolar ridge remodeling after extraction with the typical loss of the buccal wall.

implant type and dimension, and implant positioning.[167,168] Systematic reviews show similar survival rates for immediate and early placed implants of about 95%, but early implant placement seems to be associated with a lower frequency of mucosal recession compared to immediate placement.[162]

6.619.2.4.2. Surgery

Under sterile conditions, a local anesthesia is applied and the crestal bone is exposed subperiostally. The setting includes a sterile drape for the patient's head and torso, sterile gloves for the surgeon, and a sterile rinsing/cooling solution; a full sterile draping of the patient and sterile gown do not seem necessary.[169] Using a drill guide as a direction indicator, the position of the implant in relation to the restoration (supraconstruction) can be controlled (**Figures 5–8**). In recent times, 3D-radiographic data are used to fabricate PC-planned

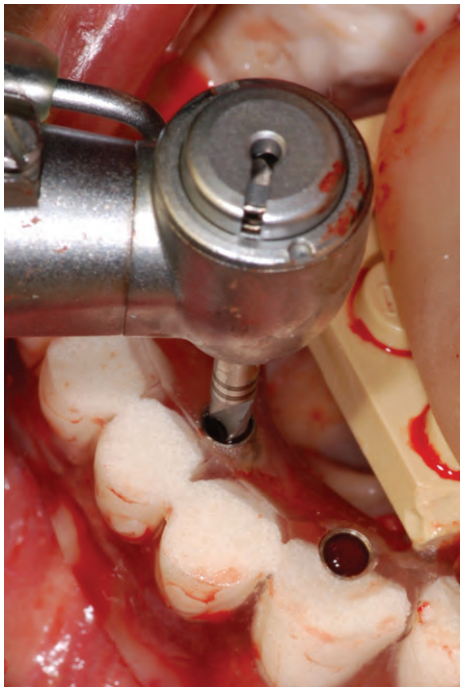

Figure 5 Use of a drill guide during implant insertion.

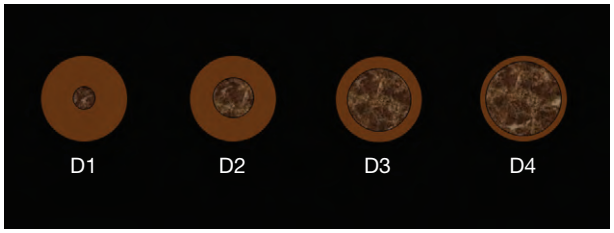

Figure 6 Bone classes in relation to the amount of cortical bone. Reproduced from Lekholm, U.; Zarb, G. A. In *Gewebeintegrierter Zahnersatz*; Branemark, P. I., Zarb, G. A., Eds.; Quintessenz: Berlin, 1985; pp 195–205.

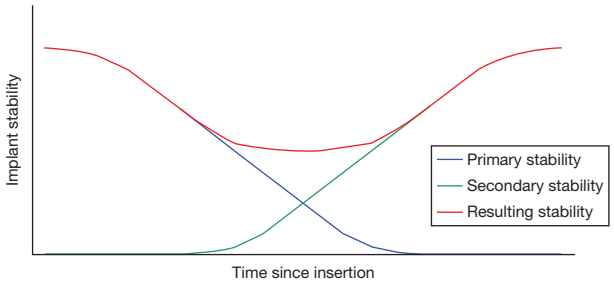

Figure 7 Time course of mechanical primary stability followed by biological secondary stability with a stability 'dip' within the first weeks.

surgical splints, thus allowing a more accurate realization of the preoperative plan and a reliable protection of critical anatomical structures.[170] It should, however, be noted that the deviation of the implant at the entry point into the bone can be up to 1–2 mm at the apex.[171]

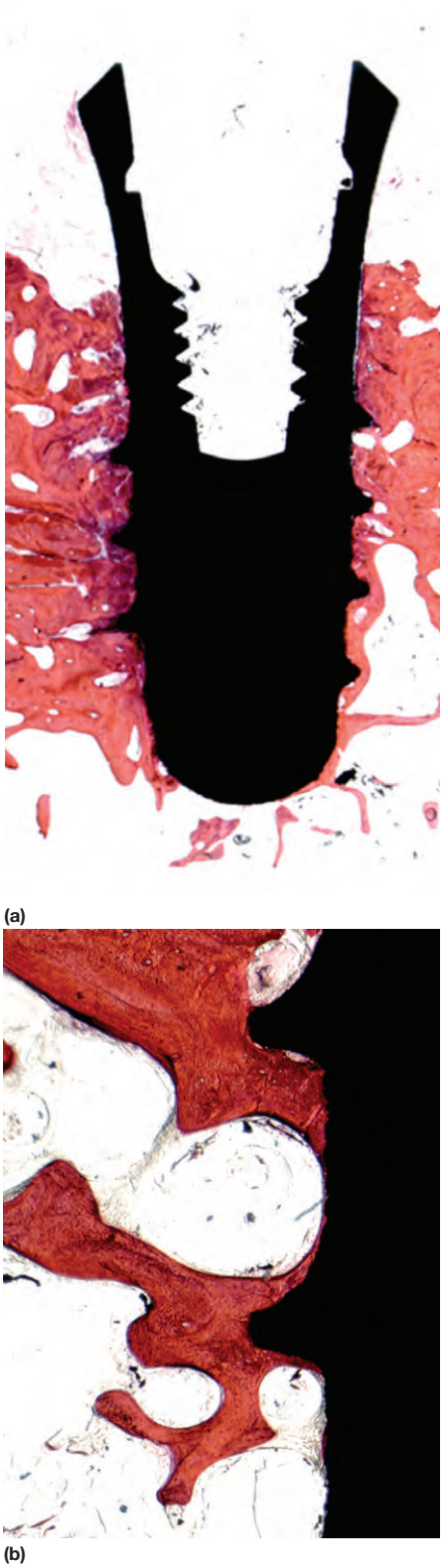

Figure 8 HE staining of an implant with sand blasted and etched surface showing osseointegration as a direct contact of bone to the biomaterial in the loaded situation. (a) Full aspect of the implant. Note that the typical bone implant contact area is 60–80%. (b) Detail showing the effect of loading on osseointegration with a dense contact in the thread area.

The drilling of the implant bed is done with increasing drill diameters until a congruent implant bed is prepared. *In vitro* studies indicate that cooling of the site is important,[172] especially if a surgical stent in 'modern' guided surgery is used.[173] Internal cooling was suggested by some researchers but does not seem to contribute to better outcomes.[36] The drills are either single or multiple use. It should be noted that heat production and signs of wear after sterilization and multiple use differ between the implant systems.[174,175] For some implant systems, zirconium drills are available. Recently, piezoelectric surgery has been used to prepare the implant bed, with positive results on early implant healing in animal models.[176] As one of the most important goals is achieving a sufficient primary stability, the last drilling steps mainly depend on the type of bone. The histology-based classification of bone 'quality' ranges from the types D1–D4 and is mostly concordant to the 'drilling feeling'.[177] Thus, the surgeon selects an adopted drilling procedure after the initial pilot drill, which is used for the full length of the planned implant. In hard bone, a nearly congruent bone bed will be prepared. Some implant systems allow tapping; in soft bone, underdimensioned drilling is used.[178,179] This adoption seems necessary, as missing primary stability of the implant leads to micromotions with impairment of sufficient osseointegration. On the other hand, exceedingly high primary stability (>50 N cm) is suspected to harm the crestal bone and lead to early implant failures or early crestal bone loss. This theory is challenged by the finding that rotationally unstable implants may osseointegrate despite the lack of primary stability,[180] and that some implant systems work with exceedingly high primary stability (<70 N cm) without overloading the crestal bone.[181] As primary stability is a prerequisite for early and immediate implant loading, future research on thread design and drilling procedure seems promising.

6.619.3. Tissue Reaction on Dental Implant Material

6.619.3.1. Bone (Enossal Part)

The term 'osseointegration' refers to successful, long-term endosseal dental healing. Per-Ingvar Brånemark defined osseointegration as "*direct* and *functional* apposition of *vital* bone at the implant surface under functional loading without establishment of a fibrous interface with maintenance of this connection under function."[17,182–184]

Successful osseointegration of a dental implant is a long-lasting *dynamic* process. After *de novo* bone formation at the dental surface ('modeling'), a lifelong physiologic turnover ('remodeling') takes place under functional implant loading.[185] Obligate preconditions for osseointegration are (1) careful surgery with minimal violation of the surrounding host tissue, (2) establishment of high primary stability with (3) prevention of infections and micromovements during the implant healing period, and in particular, (4) high biocompatibility of the dental surface with osteopromotive properties.[186] During or directly after implant insertion, the so-called primary stability is verifiable and depends on (1) mechanical bone quality, (2) bone quantity, (3) implant(macro-)design, and (4) insertion torque. High primary stability is a precondition for treatment strategies in the field of immediate or early loading.[187,188]

The healing cascade leading to stable osseointegration directly takes place at the implant surface by means of 'contact-osteogenesis'.[189,190] During surgical preparation of the implant cavity, the integrity of the bone is interrupted, which leads (after placement of the dental implant) to a defined sequence of biological events, resembling fracture healing. In detail, these events can be subdivided into

- hemorrhage into the defect with (unspecific) protein adsorption by the dental surface,
- platelet activation and degranulation,
- inflammation,
- recruitment, migration, and adhesion of osteogenic progenitor cells (*osteoconduction*),
- osteogenic proliferation,
- osteogenic differentiation with
- matrix synthesis,
- calcification (*de novo bone formation*), followed by lifelong
- bone remodeling at the implant surface.

This itemization implies that some fundamental processes with conditioning of the implant surface precede the adhesion of osteogenic cells at the implant surface.

6.619.3.1.1. Early interaction with noncellular components of the extracellular milieu

Initially, the implant surface interacts with blood components. For titanium (Ti) surfaces, H_2O molecules can lead to hydration of the titanium dioxide. Both anorganic compounds and proteins like fibrin or albumin are absorbed at the implant surface, thus modulating its biological response to the surrounding tissue. Protein interactions with the dental implant surface depend on their concentration, size, on the surrounding pH value, temperature and result in characteristic adsorption and desorption kinetics. Changes in protein conformation could result in impaired biological activity.[191,192] Both protein type and its conformation play a crucial role in modulating, for example, permissive cell adhesion via specific interactions with adhesion receptors as well as activation of further intracellular signal cascades.[191] **Chapter 4.405, Leukocyte–Biomaterial Interaction *In Vitro*** deals with the respective presentation of functional, adhesive RGD sequences.[193–196] As a short summary, proteins from the extracellular milieu serve as essential mediators of early biomaterial–host tissue interactions; initially, vitronectin, fibrinogen, and particularly fibronectin (FN), as well as the von Willebrand factor (vWF) seem to be of great importance.[192]

6.619.3.1.2. Platelet activation and cytokine release

Later in the process, an early, transient organic matrix is established on the biomaterial surface which is supplemented by further acellular and cellular blood components like fibrin (ogen), albumin, erythrocytes, and platelets. Particularly Ti surfaces as well as certain surface modifications bear highly thrombogenic properties.[197–199] Surface–platelet interactions play a crucial role in early biomaterial healing, as platelets are the first cellular components to interact with the above described transient matrix at the implant surface, and platelet activation with cytokine release[200] serves to promote biomaterial healing by stimulation migration, proliferation, and differentiation of osteogenic cells.[201,202] Well-investigated cytokines and growth factors are, for example, platelet-derived

growth factor (PDGF), vascular endothelial growth factor (VEGF), transforming growth factor beta (TGF-β) as well as vasoactive substances like serotonine and histamine.[203] Membrane-bound receptors interact with proteins absorbed at the implant surface, such as fibrin or vWF which are derived from vascular endothelial cells. These have an impact for platelet aggregation at the biomaterial surface with consecutive activation and degranulation. From the integrin receptor family, glycoprotein (gp) Ib-receptor modulates platelet binding at vWF and gpIIb/IIIa-receptor modulates platelet binding at fibrinogen/fibrin.[204] GpIIb/IIIa-mediated platelet interactions with fibrin absorbed at the implant surface are of especially great importance and can be further enhanced by chemical and structural implant surface modifications.[205] Respective investigations have shown that a rather rough microtopography of implant surfaces resulted in enhanced fibrin adsorption as well as enhanced platelet adhesion, aggregation, and activation.[197–199]

The above-mentioned cytokines PDGF and VEGF are stored in the platelet a-granules and released into the extracellular milieu after platelet activation.[206] Both cytokines (representing an abundance of other important mediators) are highly biologically relevant for implant and biomaterial healing. Especially for dental implant healing in compromised bony tissue (general and local risk factors), simultaneous neoangiogenesis plays a crucial role and is an obligate precondition for sufficient osteogenesis and osseointegration.[207,208] Furthermore, these cytokines are indispensable for osteogenic cell activation with subsequent osteoconduction and osteoinduction. Vascular endothelial growth factor-A (VEGF-A) stimulates early angiogenesis and osteogenesis by recruitment and activation of relevant hematopoietic and osteogenic cell populations.[208,209] Furthermore, VEGF promotes differentiation of osteogenic precursors,[210] not at least by stimulating the production of bone morphogenetic protein-2 (BMP-2) by endothelial cells.[211–213] A systematic review by Keramaris and coworkers emphasizes the value of VEGF for the treatment of critical size bony defects.[214]

Besides chemoattractive properties, PDGF stimulates proliferation of endothelial cells and osteogenic cells as well as osteogenic cell differentiation.[215–217] Successful treatment of periodontal defects with recombinant human PDGF has led to to its subsequent approval by the US Food and Drug Administration (FDA).[218] Finally, VEGF- and PDGF-mediated effects on osteogenic cells seem to be synergistic ones.[219,220] As already stated, platelet activation with consecutive degranulation and cytokine release can be modulated by surface properties like (micro-)topography, chemical composition, and surface charge.[221,222] Hong *et al.* identified titanium (Ti) as a highly thrombogenic substrate with enhanced platelet activation and PDGF release.[197] Further studies from Park and Kikuchi showed that a rough implant surface microtopography has a higher impact on platelet activation rather than the presence of calcium or phosphate ions.[199,223,224]

6.619.3.1.3. Inflammation period, chemotaxis

The implant surface maintains close contact with the blood coagulum, consisting of a loosely, 3D fibrin meshwork which directs both angiogenesis and osteogenic cell recruitment.[189,225] During the inflammation period, inflammatory cells like leucocytes migrate out of postcapillary venoles into the blood coagulum. Leucocytes, as well as the activated platelets and endothelial cells already mentioned, liberate cytokines, which promote the recruitment of further inflammatory cells. Low oxygenation of the early peri-implant compartment can serve as a chemotactic signal for mesenchymal and endothelial cells as well.[226,227] During the first 24–48 h, neutrophilic cells dominate, followed by monocytic cells like macrophages. As for platelets, rough titanium surfaces showed higher monocyte adhesion *in vitro*.[228]

6.619.3.1.4. Osteoconduction and matrix synthesis, functional remodeling

Finally, the liberated or secreted cytokines and growth factors such as VEGF, PDGF, and TGF-β[224,229] promote chemoattraction and recruitment of osteogenic cells,[202,230] which migrate from the local bone border through the peri-implant blood coagulum and the fibrin meshwork to the implant surface. This process of recruitment, migration, and adhesion of osteogenic cells is also called 'osteoconduction'[189] and plays a key role during implant healing. Initial osteogenic cell adhesion predominantly occurs at sites where fibrin adsorption on the implant surface has taken place. Later, osteogenic cells can produce their own adhesive environment (structural proteins like collagen type I α). Osteogenic cell adhesion is followed by cell proliferation and differentiation into mature, postmitotic osteoblasts. Osteoblasts produce a primarily nonmineralized organic bone matrix. The subsequent process of implant healing is referred to as '*de novo* bone formation' and results in calcification of the primary bone matrix via deposition of anorganic substrates and finally in a stiff connection between implant and surrounding bone.[189,231]

The initial deposition of vital bone at the implant surface is followed by early functional bone remodeling; multiple stress-induced adaptive cellular activities and interactions at the implant–bone interface result in directed formation of trabecular structures and in final bone maturation. This lamellar bone adapts to functional implant loading (chewing) and other peri-implant stimuli. At the end of this process, the osseointegration defined above occurs, with definitive close functional union between implant and bone. As vital tissue, peri-implant bone undergoes a permanent, lifelong functional remodeling.[232] **Figure 1** provides a schematic illustration of the activities of osteogenic cells and bone tissue during implant healing.

6.619.3.2. Soft Tissue (Mucosa and Epithelium)

In contrast to the extent of the literature regarding the bony healing, only few results on peri-implant soft tissues are published. There is, for the passage point of the implants through the mucosa, evidence that a higher roughness promotes plaque accumulation with bacterial invasion, thereby endangering the long-term development of a soft-tissue infection and subsequent lesion. A rather smooth surface, on the other hand, hinders epithelial cellular adhesion at the implant neck. It is postulated that cells adhere to the implant/abutment in the form of hemidesmosomes.[233] In cell culture experiments, both primary and secondary cultured gingival keratinocytes show an advantageous adhesion to smooth (polished)

compared to rough surfaces.[234,235] Only a few studies report on the basic material properties of the mucosal portion of dental implants.[236] Although the macroscopic structures of soft tissue seal at the implant and tooth are very similar, their morphology as well as the defense mechanisms are fundamentally different.[237] Micromorphologically, comparing the tooth and the implant's structural features, only the presence of hemidesmosomes, although to a lesser extent than the dentogingival seal, is described.[238] In contrast to the radial arrangement of collagen fibers in the cement at the attachment of natural teeth, collagen fibers at implants are found only circularly arranged with significantly fewer blood vessels.[239,240] As the epithelium junction around implants offers only a partial barrier against the penetration of bacteria from the oral cavity, perhaps due to functional adaptation, increased inflammatory cells, including T-cells, are found.[241,242] Similar to the bony attachment, glycoproteins seem to be important for the implant–mucosa connection.[243] The exact mechanism of the postulated soft tissue attachment has not yet been resolved. *In vitro* research of the fundamental mechanisms is difficult, as cell culture models do not allow mimicking of the complex structure of the epithelium and fibrous tissue.[244,245] Increasing evidence has been found that the soft tissue thickness has an influence on the bone remodeling around dental implants.[246]

6.619.3.3. Experimental Methods

6.619.3.3.1. Mechanical testing and modeling

Mechanical testing of dental implants has two central objectives. One is to study the influence of the implant macrostructure on primary stability in various bone densities, and the other is the stability of the implant abutment connection. The latter one classically is studied by mechanical testing.[247] The accepted method of fatigue testing is described in ISO/FDIS. 14801:2007 (**Figure 9**).

One method to determine the influence of the thread design on primary stability is photoelastic analysis. It helps to visualize critical stress points using a photoelastic, homogeneous, isotropic material. By studying the fringe pattern of polarized light, one can determine (visualize) the state of stress at various points in the material.[248,249] Photoelastic stress analysis was introduced into dentistry to evaluate different types of orthodontic movements.[250] Since then, the application of this method has started to be used in different areas of dental research, focusing on stress distribution.[251] It is an important tool for visualizing stress points. The main and inherent limitation of the method is its capacity to model the nonhomogeneous and anisotropic characteristics of bone and its limitation to qualitative data.[248]

The application of strain-gauge method on dental implants is based on the use of electrical resistance strain gauges. A strain gauge utilizes the property of electrical conductance's dependence on not only the electrical conductivity of a conductor, but also the conductor's geometry.[252,253] It mainly provides *in vitro* measurement strains under static and dynamic loads. *In vivo* studies were also developed to quantify the degree of stress that occurs in the bone around implants associated with fixed partial denture,[254] to measure strains involved in connecting implants to a natural tooth,[255] and to measure the force

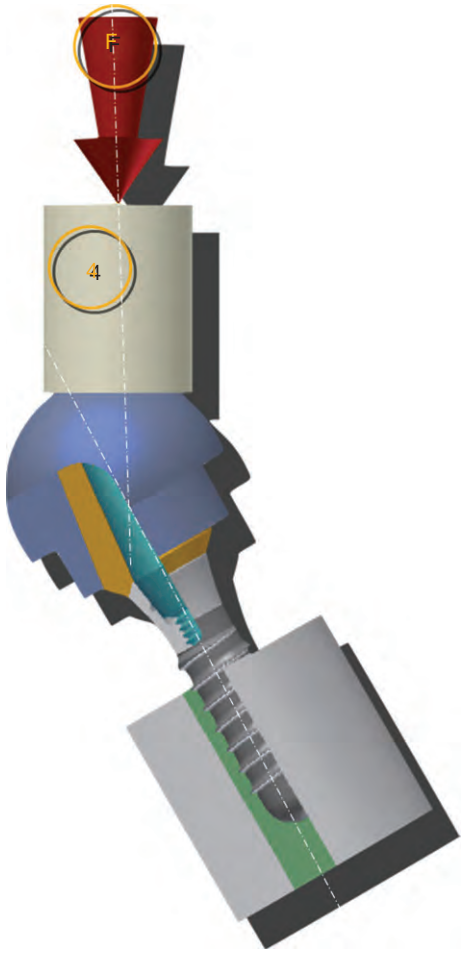

Figure 9 Schematic drawing of the fatigue testing setup due to ISO 14801 (4 = loading device, F = force applied in 30°.)

transmission onto implants supporting overdentures.[256] The limits of the *in vivo* use of the strain-gauge method are obvious, as it provides only the data regarding strain at the gauge.

The finite element analysis is based on the idea that a complex situation is divided into small elements which allow an estimation of the solution. Thus, it is a method whereby instead of seeking a direct solution function for the entire domain, one formulates the solution functions for its finite elements and combines them properly to obtain the solution to the entire structure.[257] By using computer-aided design software and engineering experience, the power of the finite element method is its versatility. The anistropic structure of bone and the wish for a 3D model, which are the limit of the method, are frequently solved by improved PC possibilities. The model is used for a variety of questions in dental implantology.[248]

6.619.3.3.2. Cell culture methods

Biocompatibility of various surface properties is primarily tested using cell culture models. They consist of cell (mainly osteogenic cells) visualization on the biomaterial surface employing methods based on scanning electron microscopy

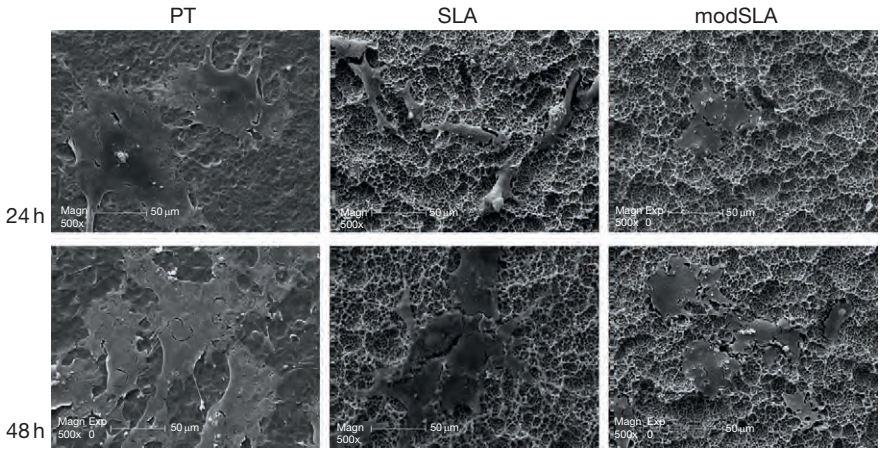

Figure 10 SEM image of osteoblast-like cells on different titanium surfaces (PT = machined; SLA = sandblasted & etched; modSLA = sandblasted & etched, hydrophilic) (Prof. Konerding, Department of Anatomy, University Medicine Mainz).

(SEM, Figure 10) or vital stainings. The interpretation of the cell shape provides first hints on the biocompatibility of the material. Visualization is completed by proliferation assays.[258] Different surfaces are tested using different cell populations like fibroblasts, chondrocytes, and osteoblast-like cells of different origin. The different origins of osteoblasts might be one cause for divergent results of these experiments. MG-63 cells have become a widely used cell line for these experiments.[259–266] The quantifications of osteogenic cell markers like osteocalcin, osteopontin, and alkaline phosphatase permit a conclusion as to the state of differentiation of these cells. Some groups are working on coculture models which might help to understand important interactions between the different cell types.[267,268]

6.619.3.3.3. Animal models

A better understanding of the human *in vivo* effects can be drawn from animal models.[269] Small animal models where implants are implanted into the tibia help to understand basic principles of the interactions between *in vivo* material and bone.[270–288] The results are based on histomorphometry, where bone–implant contact rates are measured after the classical sawing and grinding technique.[289] However, due to the mesenchymal bone and cortical structure of the bone, only minimal generalization to the human situation is possible. Moreover, it should be kept in mind that the unloaded situation does not really reflect the definition of osseointegration of a loaded implant. Another type of results is drawn by biomechanical testing of the implant–bone interface using reverse torque measurements.

Larger animal models allow simulation of a loading condition and are more similar to the clinical situation. Some groups are promoting a sheep model.[269,290–299] The majority of groups prefer a dog model, where the implants are inserted into the premolar region (Figure 11).[163,165,166,240,300–331] Quantification of the bone-to-implant contact is mainly done using the sawing and grinding technique followed by conventional staining. SEM analysis,[332] confocal laser scanning microscopy (CLSM),[331] and *in vivo* sequential staining are more rare.[333] More recently, µCT has been introduced as an additional method to study the bone–implant interface.[286] Direct comparison of conventional histology and micro-CT indicates a superiority of conventional histomorphometry over micro-CT, as the latter is hampered by deficits in the discrimination at the implant–tissue interface.[334] Noninvasive methods such as resonance frequency analysis[335] have been applied in animal models but seem not to reflect the clinical situation.[331,336–338] The classical bone-to-implant contact measurement shows the deficit of a static situation. To overcome this situation, bone ingrowth models[339] or dehiscence defect models[328,329] are common for some questions.

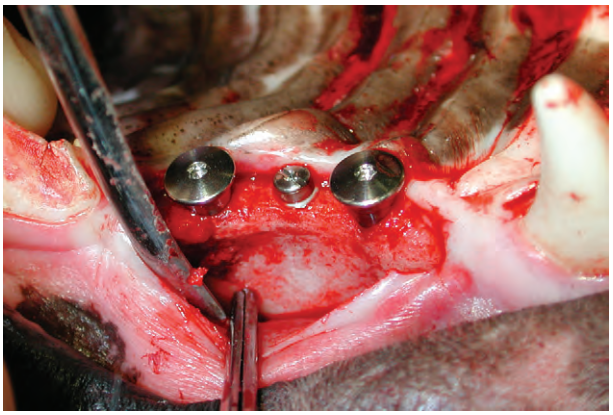

Figure 11 Intraoperative situs of the typical premolar area in a dog model. Note the narrow alveolar ridge after extraction of the premolars which allows the insertion of 3–4 small diameter implants.

6.619.3.3.4. Human histology

Human histologic specimens are rarely available. Some researches use retrieved implants in prospective studies,[340] which from an ethical point of view, might be considered drawing criticism. Implants retrieved from a clinical cause also allow long-term studies of dental implants in the human situation.[341] These results show a bone-to-implant contact area of about 60% for functioning implants (Figures 12 and 13).

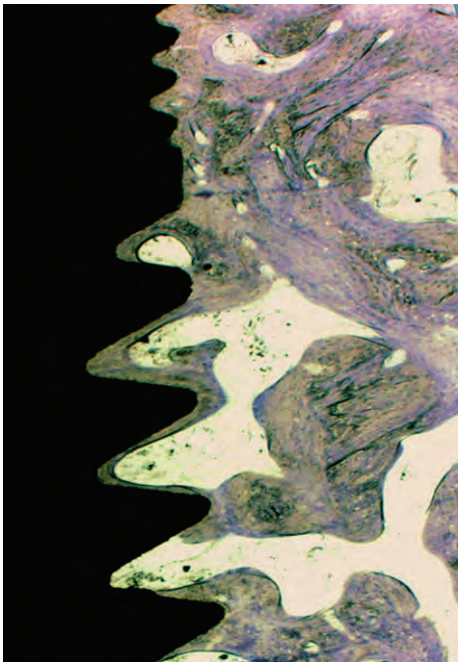

Figure 12 Human histology (toluidine blue) of a loaded TiO_2-blasted, fluoride-containing implant surface, which shows the dense contact in the microthreaded cortical area and a osseoconduction in the area of cancellous bone.

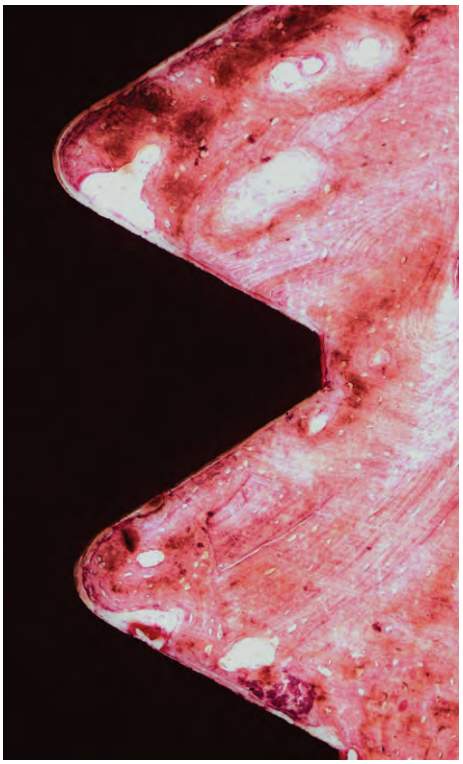

Figure 13 Human histology (HE staining) of a loaded zirconium oxide ceramic implant showing the promising osseointegration of this ceramic material.

6.619.4. Implant Materials

6.619.4.1. Metal

Despite the variety of materials used as biomaterials, titanium has been clinically established for use in dental implants. This is mainly due to its good tensile strength with relatively low weight and excellent corrosion resistance and because of the spontaneous formation of a passivating oxide layer. Both pure titanium and, more rarely, titanium alloys (Ti–6Al–4V and Ti–6Al–7Nb) are in use. Cp titanium and the alloy are defined by the American Society for Testing and Materials (ASTM F67). In older cell culture studies comparing alloy and pure titanium, no essential difference could be identified.[342] In a more recent work, when utilizing human osteoblasts on pure titanium in contrast to the alloy (Ti–6Al–7Nb), an improved proliferation rate and a higher activity of alkaline phosphatase as a measure of cell differentiation was reported for the pure Ti.[343] This is complemented by results from several *in vivo* studies, which demonstrate a superiority of the pure titanium on the osseous healing.[276,284,344] Titanium alloys are mainly used for diameter-reduced implants and orthodontic mini-implants.[345]

TiAlNb alloys are currently under investigation in preclinical studies.[346] Other alloys studied in animal models are Ti-75 (AlMoZrTi)[347] and TiAlNb[332] with positive results, and nitinol (Ni–Ti)[348] with negative results for osseointegration. In contrast to these experimentally used alloys, TiZr alloy is already commercially available for dental implants. This Ti alloy containing 50% zirconium is significantly harder and more tensile than the hardness of pure titanium and pure zirconium.[349] In a chondrocyte culture, TiZr showed positive results.[350] In a rat model, lower toxicity and higher biocompatibility of TiZr compared to Ti was reported,[351] which is also seen in a larger animal model.[352,353]

Regarding bone–implant interactions, currently the material 'Titan' and the macrostructure 'screw type' have been established clinically, whereas the microstructure and nanostructure are at the center of current research. In recent publications, the role and prevalence of Ti allergies have been discussed. The authors estimate a prevalence of 0.6% and propose cutaneous testing in patients who presented allergic symptoms after implant placement or suffered from unexplained implant failures.[354] However, the existence of Ti allergies and the role of testing are not generally accepted.

Tantalum (Ta) is one of the few nontitanium metals, which has been investigated for osseointegration in dental implantology. It has been shown to be bioactive and biologically bonds to bone. However, the relatively high cost of manufacture and an inability to produce a modular, pure Ta implant have limited its acceptance. Tantalum, especially porous variations, have been studied for use in orthopedics,[355] and positive findings for Ta have been seen in the cell culture.[356] TiTa alloys show promising biocorrosion parameters *in vivo* and would be more easy to produce.[357] Additionally, a Ta coating on Ti seems to increase biocompatibility in a cell culture.[358] Other metals have not yet revealed promising results; for example, CoCr implants show lesser osseointegration than TiAlV.[359]

6.619.4.2. Ceramics

Early and promising systematic data in implantology were derived from the Tuebinger immediate implant, which was made of aluminum oxide ceramic.[28,29] Despite its favorable osseointegration characteristics, fracture events after long-term use have outdated its use as dental implants. Because of this negative experience, for many years only metal implants were in use. However, in recent years, a recurrence of ceramic dental implants of favorable (white) color has taken place. Zirconium dioxide (zirconia) has shown favorable results in the osteoblastic cell culture.[360] The ceramic composite of zirconia–hydroxyapatite (TZ–2Y/25HA) has also been investigated in a single animal model.[361] The first *in vivo* experiments and clinical studies were done with single-piece implants with a rather smooth surface, as it was difficult to generate surfaces comparable to Ti on zirconium oxide.[362] As known from endodontic apical cones, the osseointegration was comparable to Ti or aluminum oxide.[363] The material primarily used is Y-TZP (tetragonal zirconia polycrystal), which is stabilized by yttrium oxide. In the unloaded animal experiment, the osseointegration of these rather smooth implants was positive.[281] By sandblasting the surface, the osseointegration of zirconia in a large animal model after loading is comparable to that of titanium.[364] This result has been reported by several other groups using different surface treatments, with the conclusion that in animal models, surface-modified zirconia implants can reach firm stability in bone.[282,293,365–371] As most of these implants are single-piece implants (with abutments directly connected to the implant), it is often necessary to reshape them. Despite some concerns about this procedure, Crown preparation did not influence the reliability of the one-piece ceramic implant from a mechanical point of view.[372] It should, however, be stated that in the clinical setting the success rates vary between 84% and 99%.[373–375] To date, no controlled clinical studies in humans regarding clinical outcomes or osseointegration are available. Thus, most researchers agree that zirconium oxide implants, although now available as two-piece implants with a rough surface, still cannot be recommended for routine use.[376] Y-TZP implants may have the potential to become an alternative to titanium implants, but long-term data in this field is lacking.[377]

6.619.5. Surface Structure and Modifications

6.619.5.1. Macrostructure

Macrostructures of dental implants have been developed empirically. Rotational symmetric screw and cylindrical designs have been favored by the clinicians. Finite element analysis is classically used to model stress distribution around different implant designs. In these models, screws have shown a more favorable stress distribution than cylinders.[378] One of the early ideas was that the design of the implant should not overload the crestal bone, thereby leading mechanical load to the apex of the implant. This has led to the progressive thread design of the Ankylos implant (formerly NM implant).[379,380] Another way to solve the problem of crestal overloading was the lack of threads in the neck region of the first-generation Astra standard implant.[122,381–383] The more or less rough 2D FEM analysis has been replaced by 3D models which include several material parameters of bone and implant.[384,385] Using these techniques, it is possible to optimize implant geometry with respect to platform shift and thread design.[386] It has been shown that the majority of stress distribution happens in the crestal part of the bone,[387] which promotes the use of short implants. On the other hand, clinical studies have shown that loading the crestal bone with microthreads leads to less pronounced bone remodeling in this area.[388,389]

As one major goal during implant insertion is to reach mechanical primary stability, the implant threads of modern dental implants are receiving more attention. The primary stability, especially in situations of critical bone quality, has been attempted to be optimized by modification of implant design. One suggested approach to enhance primary stability in critical bone quality is to choose a conical implant for insertion into a standard parallel-sided hole (underdimensioned drilling). The idea behind this approach is to induce controlled compressive forces in the cortical bone layer, as the implant is inserted.[390,391] Modern thread types are often intended to reach high primary stability even in soft bone.

6.619.5.2. Physical Modification (Roughness)

The implant surface is the area that is in direct contact with the body and is therefore mainly involved in implant healing. Therefore, one key target of various modifications is achieving high levels of biocompatibility. A prominent role is played by the already mentioned above. Owing to its high surface passivation by establishing an oxide film, corrosion resistance of titanium is achieved; this reduces the detachment and diffusion rate of ions or molecules on the surface and thus guarantees high chemical stability. In addition, it affects the adhesion and stability of coatings in the context of surface modification.[392] The 3–7 nm thick film consists mainly of TiO_2, but small amounts of TiO and Ti_2O_3 are also included.[393,394] After implant insertion, the oxide layer is modified in thickness, composition, and microstructure. In addition to the spontaneously formed natural oxide film, a variety of optional processing steps allow for more targeted modification of the implant surface. Primary surface treatments can be grouped into three methods[395]:

(a) Machining processes
The surfaces are macroscopically smooth; microscopically small groves can be seen along the working direction.

(b) Additive procedures
Application of material onto a surface is done either in the form of coatings with ceramic materials (mostly hydroxyapatite or calcium phosphate (CaP)) or produced by titanium plasma spray coating. This procedure gives a rough, relatively irregular shape with increased surface area. Other approaches closely related to biofunctionalization exist in the coating with functional protein ligands or cytokines (e.g., collagen or BMP and chemical modifications such as fluoride[396] or magnesium application).[288]

(c) Ablative procedures

These procedures include blasting the surface and/or acid treatment. For blasting, mainly Si, Al-(Al_2O_3), or titanium (TiO_2) particles are used. The surface is roughened with plastic deformation, and some small particles are embedded into the material. The size of the irregularities depends on various factors such as blast pressure, distance, time, and particle size. Acid etching also serves to increase the surface area or an increase in roughness. It leads to a more porous, but regular structure. It also adds to the process of cleaning the surface and the removal of blast residue. The extent of the etching process depends on the type and concentration of acid (H_2SO_4, HNO_3, HF, HCl), as well as temperature and duration time.[397]

The chemical composition of the surface results from both intentional and unintentional actions, and is also influenced by the various manufacturing and steps: often there are several organic pollutants such as hydrocarbons, fatty acids, or silicones. These come mainly from cleaning solutions or adsorbed molecules from the air. Etching, and grinding and abrasive residue, such as silicon, aluminum, or titanium, may also influence the chemical composition. Furthermore, increased temperatures, taking as an example, occur in the heat treatment effect on the elemental composition.[397]

6.619.5.3. Chemical Modifications

Anodic oxidation of titanium surfaces leads to different thickness of the oxide layer and a characteristic surface topography.[398] Animal experiments revealed positive bone reaction for these types of surfaces.[399,400] In comparison to an etched surface, the anodic oxidation revealed faster bone healing,[401] which has led to the development of two commercially available implant surfaces, which allow faster bone healing.[402,403]

Other experimental studies had focussed on the influence of surface hydrophilicity, for example, maintained by UV treatment.[326,339,404] Hydrophilic surface modifications show potential to support tissue integration of titanium dental implants.[405] Other groups have demonstrated positive osseocondictive effects for fluoride-modified surfaces.[325] Both hydrophilic and fluoride modifications are commercially available. Incorporation of Mg also seems to be favorable.[288]

6.619.5.4. Clinical Impact of Surface Modifications

A huge number of the experimental investigations have demonstrated that the bone response was influenced by the implant surface topography.[271,272,326,331,406–415] Smooth ($Sa < 0.5\,\mu m$) and minimally rough ($Sa\ 0.5–1\,\mu m$) surfaces showed less strong bone responses than rougher surfaces. Moderately rough ($Sa > 1–2\,\mu m$) surfaces showed stronger bone responses than rough ($Sa > 2\,\mu m$) in some studies. Owing to the various definitions of 'smooth' and 'rough' used by the different authors, it is very difficult to compare the results directly. The authors of a recent review conclude: "Surface topography influences bone response at the micrometer level. Some indications exist that surface topography influences bone response at the nanometer level. The majority of published papers present an inadequate surface characterization. Measurement and evaluation techniques need to be standardized. Not only height descriptive parameters but also spatial and hybrid ones should be used".[416] Interestingly, animal models demonstrate that in the presence of loading, the topographic dependency of the osteogenic activity at the interface is overruled by the loading-related bone response.[285,331,417]

Presuming optimal bone quality and healthy patients, dental implants with both minimally rough and rough surfaces have shown very high long-term survival rates.[25,79] However, in the compromised situation (e.g., following radiation therapy, bone augmentation, class D4 bone), the implant survival rate of machined implants is lower,[418] and it is still unclear which surface modification may lead to a higher clinical success rate.[25,122] Besides this aspect concerning the implant bed, surface topographical properties are a prerequisite for reduced healing time and are thus within the scope of *in vivo* studies.[402,419–425] The potential influence of a modified microstructure may be reflected by the high number of surface modifications which are commercially available. On the other hand, the clinical impact of these modifications is far from being clinically proven.

6.619.5.5. Biofilm and Peri-implantitis

The stable functional bone remodeling in the crestal part of the implant as a physiologic reaction ('biologic width') must be distinguished from a pathological loss of bone due to peri-implant inflammation. There is consent for the following definitions[426,427]:

Peri-implant disease: Collective term for inflammatory reactions in the tissues surrounding an implant.

Peri-implant mucositis: Presence of inflammation in the mucosa at an implant with no signs of loss of supporting bone.

Peri-implantitis: Besides inflammation in the mucosa, loss of supporting bone is found.

The diagnosis is made using probing (depth, the presence of bleeding on probing, suppuration) and radiographs to evaluate supporting bone levels around implants. There is strong evidence that poor oral hygiene, a history of periodontitis, and cigarette smoking are risk indicators for peri-implant bone loss due to peri-implant disease.[427] The prevalence of peri-implant disease is astonishingly high. In a systematic review, peri-implant mucositis occurred in approximately 80% of the subjects and in 50% of the implants. Peri-implantitis was found in 30–60% of the subjects and in 10–40% of implant sites.[426] The association with periodontitis is very important, as it is known that aggressive periodontitis[142] and bone loss[428,429] have a direct influence on peri-implant disease. Implants become colonized by periodontal pathogens originating from intraoral sources shortly after insertion.[430,431] However, *Staphylococcus aureus*[430] and Candida group[432] are also found at implants with peri-implant disease. Soft tissue integrity is a prerequisite to prevent bacterial colonization[433] but cannot prevent subgingival colonization.[434] The surface seems to have an effect on peri-implant disease as there is limited evidence showing that implants with relatively smooth (turned) surfaces are less prone to bone loss due to chronic infection than implants with rougher surfaces.[435] The current state of literature is more descriptive, rather than providing strong data, because animal models, such as the ligature model, are limited by the nonhuman flora in the mouth of the beagle dog.[436] *In vitro*,

it has been shown that an increase in surface roughness and surface-free energy facilitates biofilm formation on dental implant and abutment surfaces,[404] but does not directly lead to peri-implant disease in the human *in vivo* situation.[437] Surface chemistry and the design features of the implant–abutment configuration also play a significant role in biofilm formation.[438] The 'classical' process of biofilm formation on biomaterials plays an important role in this aspect. It includes an initial physicochemical interaction phase and a late molecular and cellular one.[439] Extensive work has been done in the theoretical background of this field, but few clinical steps to modify implant neck and/or abutment are available. One experimental way is to produce different surface types to prevent peri-implant disease, such as shaping memory alloys to prevent microleakage at the implant–abutment gap,[440] surface polishing,[441] ZrN coating,[442] and UV irradiation.[443] The other concept is disinfection or antibacterial coatings of abutments: Decontamination of the internal implant parts using 1% chlorhexidine gel seems to be effective for a 6-month period.[444] Experimental antibiotic delivery using different antibiotics and methods of delivery are also under investigation.[445–448] The possible role of biofunctionalization using different proteins in this context yet is unclear.[449,450]

6.619.5.6. Biofunctionalization

Because of its high biocompatibility and adjustable physicochemical properties, titanium (Ti) serves as a particularly favorable substrate for developing and testing new surface modifications.[190,451,452] As already stated above, current literature indicates that modifications of surface topography on a micrometer-scale supports both osteogenic cell activity *in vitro*[453,454] as well as bone response *in vivo*.[455] In some publications, alterations of surface-free energy with enhancement of hydrophilicity and consecutive *unspecific* protein precipitation also proved to enhance osteogenic cell response and osseointegration of dental implants.[339,456–458] In this context, *specific* biofunctionalization of dental implant surfaces with functional ligands has been identified as a consequent next step, but has yet only reached the level of *in vitro* or animal studies.[459] The biological value of functional extracellular matrix (ECM) ligands and solitaire cytokines/growth factors for bone regeneration and implant healing is beyond doubt (see **Chapter 4.403, The Innate Response to Biomaterials**). For respective clinical applications, cell adhesion peptides, such as collagen, FN, and RGD-sequences, and growth factors, such as members of the TGF-β superfamily (including the BMP family), are of special interest.[460]

In general, various approaches to immobilize biomolecules onto titanium surfaces exist.[460] *Physical adsorption* is a rather simple method with ideally no changes of protein conformation (and biological effects, respectively), but shows the disadvantage of an uncontrolled desorption from the surface. *Physical entrapment* strongly depends on the quality of the employed barrier system and bears the disadvantage of tearing or eroding with loss of biomolecules. *Covalent attachment*, for example, via silane chemistry, is sophisticated and time-consuming, but results in dense surface loading with low protein loss. However, changes in protein conformation could result in decreased presentation of functional receptor binding sites with consecutive impaired biological effectiveness.

As stated above, functional, biological ligands can be subdivided into *adhesion molecules* and into *cytokines or growth factors* such as BMP-2.[459]

Promising coatings to enhance *cell adhesion* are ECM peptides like collagen and FN, or ECM-peptide sequences such as the RGD (Arg-Gly-Asp) sequence, which directly affect osteogenic cell response via integrin-mediated signaling pathways.[460–463] The presentation of these biomolecules at the implant surface aims to accelerate peri-implant bone formation, to bridge small remaining gaps between implant and bone, and to improve the remodeling process.[464–466] In contrast to cytokines, where a rather transient immobilization with subsequent controlled release into the peri-implant environment might be favorable, adhesive molecules generally require long-term immobilization on the implant surface.[460] Another important issue in biomimetic implant coating is the preservation of the native protein conformation and biological activity. General approaches of biofunctionalization with adhesive molecules imply either physisorption directly on the metal surface or chemisorption over linker molecules.

Analogous to adhesion molecules, the estimated clinical benefit of (appropriate applied!) locally acting *cytokines or growth factors* at the bone–implant interface is beyond doubt.[467–470] Owing to its high osteoinductive potential, BMP-2 as a potent candidate for implant surface modifications is in the focus of intensive research activities.[471,472] However, ambiguous results of implant surfaces loaded with BMP-2 have at least challenged the clinical feasibility of various BMP-2 concentrations, delivery systems, or coatings.[473–476] The mode of immobilization on the implant surface as well as consecutive delivery from the implant surface are of particular significance for the biological effects of BMP-2. On the one hand, the concentration of BMP-2 must exceed the threshold levels for cellular activity;[190] on the other hand, the effectiveness of BMP-2 is strongly dose-dependent.[467,475] An overdose in the environment can trigger adverse effects like bone resorption or peri-implant inflammation.[473–475] It is known that BMPs also stimulate osteoclast recruitment, proliferation, and differentiation,[477] and that high dosage may result in local overexpression of BMP inhibitors such as noggin.[478]

For instance, Wikesjö *et al.* observed the effects of rhBMP-2 coated onto titanium porous surfaces. Different concentrations were used. On the one hand, rhBMP-2 *coated* surfaces resulted in significant higher vertical bone regeneration; on the other hand, the mean bone-to-implant contact was significantly higher for uncoated surfaces. Furthermore, high rhBMP-2 concentrations resulted in rather immature bone, peri-implant seroma formation, and extensive peri-implant bone remodeling.[475] Schliephake *et al.* found no additional benefit of BMP-2 *coated* onto collagen-modified titanium surfaces.[476] In a substantial study, Liu and coworkers assessed different BMP-2 delivery modes. The authors concluded that osteoconductivity was impaired when BMP-2 was present only as *superficially adsorbed* depot on CaP-coated or -uncoated surfaces.[473] An investigation by Becker *et al.* showed the highest bone-to-implant contact values for covalently immobilized rhBMP-2, followed by noncovalently immobilized rhBMP-2 and BMP-free surfaces.[468] As conclusion, an optimum modus of BMP-2 immobilization on the surface and delivery (if necessary at all) into the peri-implant environment still has to be clarified.

The review of the experimental surface alterations revealed that thin CaP coating technology can solve the problems associated with thick CaP coatings, while they still improve implant bone integration compared with noncoated titanium implants. Nevertheless, there is a lack of human studies in which the success rate of thin CaP-coated oral implants is compared with just roughened oral implants. No unequivocal evidence is available that suggests a positive effect on the implant bone integration of peptide sequences or growth factors coated on titanium oral implants. In contrast, the available literature suggests that BMP-2 coatings might even impede the magnitude of implant-to-bone response.[479]

6.619.6. Implant Design

6.619.6.1. Principles in the Endosseal Part

Successful treatment with dental implants is indispensably linked to a vital adjacent tissue situation. Both primary implant stability and a stable secondary osseointegration require a quantitatively and qualitatively sufficient hard tissue supply. Furthermore, high-leveled bone around the dental implant serves as a basis for a tight soft tissue margin fit with high esthetic implications ('soft tissue follows hard tissue'). On the other hand, well-placed and functionally loaded implants bear the potential of respective tissue maintenance or even regeneration and counteract atrophy and resorption kinetics.

As stated above, a mandatory precondition for successful dental implant healing is sufficient primary stability, which depends on implant macrodesign, mechanical bone quality, and adequate preparation of the implant bed. Secondary stability or osseointegration rather depends on implant surface microdesign, surface composition, and biological bone quality.

Conical implant designs as well as extended implant threads aim to increase primary stability especially in spongy D4 bone like in the maxillary side region. However, the insertion of conical implants requires more experience than the insertion of cylindrical-shaped ones. A practical compromise represents so-called 'hybrid-shaped' implants with a cylindrical apical part and a conical crestal part.

In a systematic meta-analysis by Kotsovilis *et al.*, the authors investigated the influence of implant length on implant survival.[121] They included eight studies on fully edentulous patients with overall implant survival rates of 97% for implants <8 mm, 95% for implants 8–10 mm, and 100% for implants >10 mm. They also included 12 studies on partly edentulous patients with overall implant survival rates of 97% for implants <8 mm, 97% for implants 8–10 mm, and 98% for implants >10 mm. As a result, it is admissible to insert dental implants <8 mm in clinical routine. However, the authors did not address the impact of different implant designs and abutment connections on the peri-implant bone loss with consecutive reduction of the functional length of a dental implant.

The impact of the ratio between length of the (inserted) implant and length of the prosthetic crown on peri-implant bone loss was analyzed in a systematic review by Blanes.[480] Two studies were included with a total number of over 450 investigated implants.[125,481] No negative impact of larger crown dimensions could be observed; generally, a crown to implant ratio up to two seems to be unproblematic.

An important criterion to assess implant success or to improve established implant systems is the stability of the crestal bone level. After insertion of a dental implant, certain clinically asymptomatic crestal bone defects are characteristic and occur in almost all cases.[482–484] Generally, these crestal bone changes occur during the early healing phase after implant placement.[485,486] These defects have to be differentiated from bone loss due to peri-implant inflammation. In addition to assessment of probing depth, radiographic evaluation is well employed to monitor marginal bone loss, resulting in differential success criteria. According to an older definition of Jahn and d'Hoedt, the mean mesial and distal angular bone defect should not exceed 30% of the endosseous part of the implant.[487] According to Albrektsson, after higher initial bone loss rates within the first year, additional vertical bone loss should be less than 0.2 mm year^{-1}.[488]

A variety of external, implant-related parameters to modulate alveolar peri-implant bone loss have been discussed. Both histomorphometric and radiographic analysis of animal models as well as recent clinical and radiographic observations of human collectives reported no significant differences in implant survival rates and marginal bone changes between submerged and nonsubmerged implant healing.[485,486,489–491] A variety of recent investigations identified the presence and location of an interface between implant and abutment (microgap) as an important variable for biological width and resulting crestal bone changes. Generally, changes of the marginal bone level are determined and initiated during the early healing phase after implant placement for one-piece nonsubmerged implants, or after abutment connection for two-piece implant configurations.[485,492] Furthermore, crestal bone changes around two-piece implants are significantly influenced by possible movements between implants and abutments, but not by the size of the microgap.[492,493] Finite element analysis revealed that the design of the implant–abutment interface has a profound effect upon the marginal bone stress state with advantages of conical interfaces compared to flat top interfaces.[494] In a histomorphometric study, Weng *et al.* could identify an internal taper abutment connection as advantageous for peri-implant crestal bone morphologies, compared to an external hex abutment connection.[495]

Another explanation for marginal bone loss could be bacterial colonization of the microgap.[496] Broggini and coworkers showed a significantly increased number of inflammatory cells for subcrestal located interfaces compared to supracrestal interfaces. Moreover, inflammatory cell accumulation below the original bone crest was significantly correlated with bone loss.[497]

In a canine animal model, for all two-part implants, nonsubmerged and submerged, the most coronal bone-to-implant contact was consistently located approximately 2 mm below the microgap.[486] As a clinical implication, supracrestal positioning of the microgap would minimize the amount of crestal bone loss.[485,498] Another strategy known as platform switching also yielded similar results. Platform switching involves repositioning the outer edge of the implant–abutment interface horizontally and inwardly by using healing abutments of a smaller diameter.[499–506]

The benefit of microstructured rough implant surfaces for the promotion of dental implant osseointegration and to sustain high-bone contact levels is well known.[507–510] Accordingly, subcrestal positioning of the border between the rough and smooth implant surfaces resulted in higher crestal bone loss.[485,511] Additional macroscopic modifications such as microthreads at the implant neck have been proven to maintain primary marginal bone levels.[388,389,512–514]

As a conclusion, adjustment of biological width with related crestal bone changes after dental implantation essentially depends on the following characteristic implant properties: macrodesign and surface microstructure as well as existence and positioning of the implant–abutment interface (microgap).

6.619.6.2. Future Developments

One clear clinical development is the challenge to avoid bone augmentations by using short or diameter-reduced implants.[515] The critical length of the implant in the bone (functional implant length) still has to be estimated. Clinical studies with 4- and 6-mm implants are ongoing. Reduced diameter implants are becoming more and more interesting, not only for the rehabilitation of the edentulous mandible,[516] but also in more challenging areas. Titanium alloys like TiZr will allow diameters smaller than 3.0 mm for use in the lower frontal area or the lateral incisor. In the esthetic area and for patients with concerns about metal, zirconium oxide implants will find their niche. Additionally, the development of custom-made CNC zirconia abutments is becoming more and more common. Three-dimensional imaging (cone beam CT) and the use of these techniques will allow better bidirectional planning, including the available bone volume and the planned supra construction. As long-term stability is a clear clinical goal, the 'fight' against peri-implantitis is an important topic. Modified abutments including better adhesion to the soft tissues and/or antibacterial properties are underdevelopment. Bone loss due to peri-implantitis is very difficult to be regained. Reosseointegration of the contaminated titanium surface is an issue of future research.

References

1. Laney, W. R. In *Glossary of Oral and Maxillofacial Implants*, 1st ed.; Broggini, N., Buser, D., Cochran, D. L., *et al*. Berlin: Quintessence Publishing, 2007.
2. Crubezy, E.; Murail, P.; Girard, L.; Bernadou, J. P. *Nature* **1998**, *391*(6662), 29.
3. Harris, J. E.; Pomitz, P. In *Mummies, Disease and Ancient Cultures*; Cockburn, A., Cockburn, E., Eds.; Cambridge: Cambridge University Press, 1955.
4. Becker, M. J. *Nature* **1998**, *394*(6693), 534.
5. Jourdan, M.; Maggiolo, M. *Le Manuel de l'Art du Dentiste*; Nancy: Edition originale, enrichie de 5 gravures; 1807.
6. Harris, H. A. *Bone Growth in Health and Disease: The Biological Principles Underlying the Clinical, Radiological, and Histological Diagnosis of Perversions of Growth and Disease in the Skeleton*. Oxford University Press: London, 1886.
7. Younger, W. I. *Pacific Med. Surg. J.* **1886**, *29*, 17.
8. Greenfield, E. J. *Dent. Cosmos.* **1913**, *55*, 364.
9. Zierold, A. A. *Arch. Surg.* **1924**, *9*, 365.
10. Boethe, R. T.; Beaton, L. E.; Davenport, H. A. *Surg. Gynecol. Obstet.* **1940**, *71*, 598–602.
11. Leventhal, G. *J. Bone Joint Surg.* **1951**, *33A*, 473–474.
12. Strock, A. E. *Am. J. Orthod.* **1939**, *25*, 467–477.
13. Garefis, P. N. *J. Prosthet. Dent.* **1978**, *39*(6), 670–677.
14. Linkow, L. I. *Oral Implantol.* **1972**, *2*(3), 190–205.
15. Schroeder, A. In *Orale Implantol*; Schroeder, A., Sutter, F., Krekeler, G., Eds.; Stuttgart: Thieme, 1988; pp 61–65.
16. Branemark, P. I.; Breine, U.; Adell, R.; Hansson, B. O.; Lindstrom, J.; Ohlsson, A. *Scand. J. Plast. Reconstr. Surg.* **1969**, *3*, 81–100.
17. Branemark, P. I.; Hansson, B. O.; Adell, R.; *et al*. *Scand. J. Plast. Reconstr. Surg. Suppl.* **1977**, *16*, 1–132.
18. Adell, R.; Lekholm, U.; Rockler, B.; Branemark, P. *Int. J. Oral Surg.* **1981**, *10*, 387.
19. Schroeder, A. *SSO Schweiz. Monatsschr. Zahnheilkd.* **1979**, *89*(11), 1136–1137.
20. Sutter, F.; Schroeder, A.; Straumann, F. *J. Oral Implantol.* **1983**, *10*(4), 535–551.
21. Schroeder, A.; Buser, D. A. *Shigaku* **1989**, *77*(SPEC), 1267–1288.
22. Ledermann, D.; Schroeder, A. *SSO Schweiz. Monatsschr. Zahnheilkd.* **1981**, *91*(5), 349–367.
23. Mericske-Stern, R.; Steinlin-Schaffner, T.; Marti, P. *Clin. Oral Implants Res.* **1994**, *5*(1), 9–18.
24. Behneke, A.; Behneke, N.; d'Hoedt, B.; Wagner, W. *Int. J. Oral Maxillofac. Implants* **1997**, *12*(6), 749–757.
25. Buser, D.; Mericske, S. R.; Bernard, J. P.; *et al*. *Clin. Oral Implants Res.* **1997**, *8*(3), 161–172.
26. Becker, W.; Becker, B. E.; Ricci, A.; *et al*. *Clin. Impl. Dent. Relat. Res.* **2000**, *2*(3), 159–165.
27. Behneke, A.; Behneke, N.; d'Hoedt, B. *Int. J. Oral Maxillofac. Implants* **2000**, *15*(5), 633–645.
28. Schulte, W.; Kleineikenscheidt, H.; Schareyka, R.; Heimke, G. *Dtsch. Zahnärztl. Z.* **1978**, *33*(5), 319–325.
29. Wagner, W.; Tetsch, P.; Bossler, L. *Dtsch. Zahnärztl. Z.* **1981**, *36*, 585–590.
30. d'Hoedt, B.; Lukas, D. *Z. Zahnärztl. Implantol.* **1987**, *III*, 6–14.
31. Noack, N.; Willer, J.; Hoffmann, J. *Int. J. Oral Maxillofac. Implants* **1999**, *14*(5), 748–755.
32. Gomez-Roman, G.; Schulte, W.; d'Hoedt, B.; Axman-Krcmar, D. *Int. J. Oral Maxillofac. Implants* **1997**, *12*(3), 299–309.
33. De Wijs, F. L.; Van Dongen, R. C.; De Lange, G. L.; De Putter, C. *J. Oral Rehabil.* **1994**, *21*(1), 11–26.
34. Nentwig, G. H. *Quintessenz* **1985**, *36*(8), 1411–1416.
35. Kirschner, H.; Bolz, U.; Michel, G. *Dtsch. Zahnärztl. Z.* **1988**, *39*, 802.
36. Addiere, R.; Watzek, G.; Plenk, H. *Int. J. Oral Maxillofac. Implants* **1993**, *8*, 83.
37. Haas, R.; Mensdorff-Pouilly, N.; Mailath, G.; Watzek, G. *Int. J. Oral Maxillofac. Implants* **1996**, *11*(5), 581–588.
38. Kirsch, A. In *Fünf Jahre IMZ-Implantat-System – Grundlagen, Methodik, Erfahrungen*; Franke, J., Ed.; München: Hanser, 1980.
39. Kirsch, A.; Ackermann, K. L. *Dent. Clin. North Am.* **1989**, *33*, 733.
40. De Wijs, F. L.; Cune, M. S.; De Putter, C. *J. Oral Rehabil.* **1995**, *22*(5), 319–326.
41. Weibrich, G.; Gnoth, S.-H.; Buch, R. S. R.; Müller, F.; Loos, A.; Wagner, W. *Mund Kiefer Gesichtschir.* **2001**, *5*, 120–125.
42. Dietrich, U.; Lippold, R.; Dirmeier, T.; Behneke, N.; Wagner, W. *Z. Zahnärztl. Implantol.* **1993**, *9*, 9–18.
43. Schnitman, P. A.; Shulman, L. B. *J. Am. Dent. Assoc.* **1979**, *98*(3), 373–377.
44. Schnitman, P. A., Shulman, L. B., Eds.; In *Proceedings of an NIH Harvard Consensus Development Conference 1978*. National Institute of Health (NIH) Harvard Consensus Development Conference, Bethesda, 1980.
45. Spiekermann, H. *Wissenschaftliche Stellungnahme der deutschen Gesellschaft für Zahn-, Mund- und Kieferheilkunde: Implantologie in der Zahnheilkunde*. [updated 1998; cited 2002 01.05.]. Available from: http://www.dgzmk.de/stellung/implantologie.pdf; 1998.
46. Ledermann, P. *Dtsch. Zahnärztl. Z.* **1979**, *34*(12), 907–911.
47. Branemark, P. I.; Svensson, B.; van Steenberghe, D. *Clin. Oral Implants Res.* **1995**, *6*(4), 227–231.
48. Astrand, P.; Ahlqvist, J.; Gunne, J.; Nilson, H. *Clin. Implant Dent. Relat. Res.* **2008**, *10*(4), 207–217.
49. Buser, D. A.; Schroeder, A.; Sutter, F.; Lang, N. P. *Int. J. Oral Maxillofac. Implants* **1988**, *3*(3), 173–181.
50. Koch, W. *Quintessenz* **1976**, *27*, 21.
51. Tallgren, A. *J. Prosthet. Dent.* **1975**, *27*, 120–132.
52. Kalk, W.; Denissen, H. W.; Kayser, A. F. *Int. Dent. J.* **1993**, *43*(5), 483–491.
53. Reddy, M. S.; Geurs, N. C.; Wang, I. C.; *et al*. *Int. J. Periodontics Restorative Dent.* **2002**, *22*(4), 315–321.
54. Hellem, S.; Karlsson, U.; Almfeldt, I.; Brunell, G.; Hamp, S. E.; Astrand, P. *Clin. Implant Dent. Relat. Res.* **2001**, *3*(1), 20–29.
55. Meijer, H. J.; Raghoebar, G. M.; Van't Hof, M. A.; Visser, A. *Clin. Oral Implants Res.* **2004**, *15*(4), 421–427.
56. Meijer, H. J.; Raghoebar, G. M.; Batenburg, R. H.; Vissink, A. *J. Clin. Periodontol.* **2009**, *36*(9), 799–806.
57. Vroom, M. G.; Sipos, P.; de Lange, G. L.; *et al*. *Clin. Oral Implants Res.* **2009**, *20*(11), 1231–1239.

58. Walton, J. N.; Glick, N.; Macentee, M. I. *Int. J. Prosthodont.* **2009**, *22*(4), 331–339.
59. Bergendal, T.; Engquist, B. *Int. J. Oral Maxillofac. Implants* **1998**, *13*(2), 253–262.
60. Kapur, K. K.; Garrett, N. R.; Hamada, M. O.; *et al. J. Prosthet. Dent.* **1998**, *79*(5), 555–569.
61. Awad, M. A.; Lund, J. P.; Dufresne, E.; Feine, J. S. *Int. J. Prosthodont.* **2003**, *16*(2), 117–122.
62. Awad, M. A.; Lund, J. P.; Shapiro, S. H.; *et al. Int. J. Prosthodont.* **2003**, *16*(4), 390–396.
63. Stricker, A.; Gutwald, R.; Schmelzeisen, R.; Gellrich, N. G. *Int. J. Oral Maxillofac. Implants* **2004**, *19*(6), 868–872.
64. Timmerman, R.; Stoker, G. T.; Wismeijer, D.; Oosterveld, P.; Vermeeren, J. I.; van Waas, M. A. *J. Dent. Res.* **2004**, *83*(8), 630–633.
65. Kleis, W. K.; Kammerer, P. W.; Hartmann, S.; Al-Nawas, B.; Wagner, W. *Clin. Impl. Dent. Relat. Res.* **2010**, *12*(3), 209–218.
66. de Grandmont, P.; Feine, J. S.; Tache, R.; *et al. J. Dent. Res.* **1994**, *73*(5), 1096–1104.
67. Meijer, H. J.; Raghoebar, G. M.; Batenburg, R. H.; Visser, A.; Vissink, A. *Clin. Oral Implants Res.* **2009**, *20*(7), 722–728.
68. Naert, I.; Quirynen, M.; van Steenberghe, D.; Darius, P. *J. Prosthet. Dent.* **1992**, *68*(6), 949–956.
69. Quirynen, M.; Naert, I.; van Steenberghe, D.; Nys, L. *J. Prosthet. Dent.* **1992**, *68*(4), 655–663.
70. DeBoer, J. *J. Prosthet. Dent.* **1993**, *69*(4), 386–390.
71. Feine, J. S.; de Grandmont, P.; Boudrias, P.; *et al. J. Dent. Res.* **1994**, *73*(5), 1105–1111.
72. Kaptein, M. L.; Hoogstraten, J.; de Putter, C.; de Lange, G. L.; Blijdorp, P. A. *Clin. Oral Implants Res.* **1998**, *9*(5), 321–326.
73. de Albuquerque, R. F., Jr.; Lund, J. P.; Tang, L.; *et al. Clin. Oral Implants Res.* **2000**, *11*(6), 555–565.
74. Ferrigno, N.; Laureti, M.; Fanali, S.; Grippaudo, G. *Clin. Oral Implants Res.* **2002**, *13*(3), 260–273.
75. Olsson, M.; Urde, G.; Andersen, J. B.; Sennerby, L. *Clin. Implant Dent. Relat. Res.* **2003**, *5*(Suppl 1), 81–87.
76. Balshi, S. F.; Wolfinger, G. J.; Balshi, T. J. *Clin. Implant Dent. Relat. Res.* **2005**, *7*(1), 24–31.
77. Cooper, L.; De Kok, I. J.; Reside, G. J.; Pungpapong, P.; Rojas-Vizcaya, F. *J. Oral Maxillofac. Surg.* **2005**, *63*(9 Suppl 2), 97–110.
78. Bergkvist, G.; Nilner, K.; Sahlholm, S.; Karlsson, U.; Lindh, C. *Clin. Impl. Dent. Relat. Res.* **2008**.
79. Adell, R.; Eriksson, B.; Lekholm, U.; Branemark, P. I.; Jemt, T. *Int. J. Oral Maxillofac. Implants* **1990**, *5*(4), 347–359.
80. ten Bruggenkate, C. M.; Sutter, F.; Oosterbeek, H. S.; Schroeder, A. *J. Prosthet. Dent.* **1992**, *67*(1), 85–93.
81. Agliardi, E. L.; Francetti, L.; Romeo, D.; Del Fabbro, M. *Int. J. Oral Maxillofac. Implants* **2009**, *24*(5), 887–895.
82. Krekmanov, L.; Kahn, M.; Rangert, B.; Lindstrom, H. *Int. J. Oral Maxillofac. Implants* **2000**, *15*(3), 405–414.
83. Aparicio, C.; Perales, P.; Rangert, B. *Clin. Implant Dent. Relat. Res.* **2001**, *3*(1), 39–49.
84. Fortin, Y.; Sullivan, R. M.; Rangert, B. R. *Clin. Implant Dent. Relat. Res.* **2002**, *4*(2), 69–77.
85. Calandriello, R.; Tomatis, M. *Clin. Implant Dent. Relat. Res.* **2005**, *7*(Suppl 1), S1–S12.
86. Krennmair, G.; Furhauser, R.; Krainhofner, M.; Weinlander, M.; Piehslinger, E. *Int. J. Oral Maxillofac. Implants* **2005**, *20*(6), 923–929.
87. Malo, P.; Nobre Mde, A.; Petersson, U.; Wigren, S. *Clin. Implant Dent. Relat. Res.* **2006**, *8*(4), 223–232.
88. Capelli, M.; Zuffetti, F.; Del Fabbro, M.; Testori, T. *Int. J. Oral Maxillofac. Implants* **2007**, *22*(4), 639–644.
89. Rosen, A.; Gynther, G. *J. Oral Maxillofac. Surg.* **2007**, *65*(5), 1010–1016.
90. Francetti, L.; Agliardi, E.; Testori, T.; Romeo, D.; Taschieri, S.; Fabbro, M. D. *Clin. Implant Dent. Relat. Res.* **2008**, *10*(4), 255–263.
91. Testori, T.; Del Fabbro, M.; Capelli, M.; Zuffetti, F.; Francetti, L.; Weinstein, R. L. *Clin. Oral Implants Res.* **2008**, *19*(3), 227–232.
92. Att, W.; Bernhart, J.; Strub, J. R. *J. Oral Maxillofac. Surg.* **2009**, *67*(11 Suppl), 60–73.
93. Morneburg, T. R.; Proschel, P. A. *Int. J. Oral Maxillofac. Implants* **2008**, *23*(2), 270–276.
94. Comfort, M. B.; Chu, F. C.; Chai, J.; Wat, P. Y.; Chow, T. W. *J. Oral Rehabil.* **2005**, *32*(5), 341–345.
95. Flanagan, D. *Implant Dent.* **2008**, *17*(2), 182–191.
96. Teughels, W.; Merheb, J.; Quirynen, M. *Clin. Oral Implants Res.* **2009**, *20*(Suppl 4), 134–145.
97. Buser, D.; Halbritter, S.; Hart, C.; *et al. J. Periodontol.* **2009**, *80*(1), 152–162.
98. Di Fiore, P. M.; Tam, L.; Thai, H. T.; Hittelman, E.; Norman, R. G. *J. Dent. Educ.* **2008**, *72*(3), 352–358.
99. Weber, H. P.; Kim, D. M.; Ng, M. W.; Hwang, J. W.; Fiorellini, J. P. *Clin. Oral Implants Res.* **2006**, *17*(4), 375–379.
100. Bragger, U.; Karoussis, I.; Persson, R.; Pjetursson, B.; Salvi, G.; Lang, N. *Clin. Oral Implants Res.* **2005**, *16*(3), 326–334.
101. Jemt, T. *Clin. Implant Dent. Relat. Res.* **2009**, *11*(4), 303–310.
102. Grant, B. T.; Pancko, F. X.; Kraut, R. A. *J. Oral Maxillofac. Surg.* **2009**, *67*(4), 713–717.
103. Brägger, U.; Aeschlimann, S.; Burgin, W.; Hammerle, C. H.; Lang, N. P. *Clin. Oral Implants Res.* **2001**, *12*(1), 26–34.
104. Olsson, M.; Gunne, J.; Astrand, P.; Borg, K. *Clin. Oral Implants Res.* **1995**, *6*(2), 114–121.
105. Zurdo, J.; Romao, C.; Wennstrom, J. L. *Clin. Oral Implants Res.* **2009**, *20*(Suppl 4), 59–66.
106. Aglietta, M.; Siciliano, V. I.; Zwahlen, M.; *et al. Clin. Oral Implants Res.* **2009**, *20*(5), 441–451.
107. Romeo, E.; Tomasi, C.; Finini, I.; Casentini, P.; Lops, D. *Clin. Oral Implants Res.* **2009**, *20*(11), 1278–1285.
108. Leonardi, A.; Buonaccorsi, S.; Pellacchia, V.; Moricca, L. M.; Indrizzi, E.; Fini, G. *J. Craniofac. Surg.* **2008**, *19*(2), 398–405.
109. Schlegel, K. A.; Schultze-Mosgau, S.; Eitner, S.; Wiltfang, J.; Rupprecht, S. *Int. J. Oral Maxillofac. Implants* **2004**, *19*(5), 716–720.
110. Westin, T.; Tjellstrom, A.; Hammerlid, E.; Bergstrom, K.; Rangert, B. *Otolaryngol. Head Neck Surg.* **1999**, *121*(1), 133–143.
111. Kwon, Y. D.; Karbach, J.; Wagner, W.; Al-Nawas, B. *Clin. Oral Impl. Res.* **2010**, *21*(3), 316–320.
112. Jacobsson, M.; Tjellstrom, A.; Fine, L.; Andersson, H. *Int. J. Oral Maxillofac. Implants* **1992**, *7*(4), 523–528.
113. Reyes, R. A.; Tjellstrom, A.; Granstrom, G. *Otolaryngol. Head Neck Surg.* **2000**, *122*(2), 272–276.
114. Tjellstrom, A.; Yontchev, E.; Lindstrom, J.; Branemark, P. I. *Otolaryngol. Head Neck Surg.* **1985**, *93*(3), 366–372.
115. Bernhart, T.; Freudenthaler, J.; Dortbudak, O.; Bantleon, H. P.; Watzek, G. *Clin. Oral Implants Res.* **2001**, *12*(6), 624–631.
116. Wehrbein, H.; Merz, B. R. *J. Esthet. Dent.* **1998**, *10*(6), 315–324.
117. Borbely, P.; Dunay, M. P.; Jung, B. A.; Wehrbein, H.; Wagner, W.; Kunkel, M. *J. Craniomaxillofac. Surg.* **2008**, *36*(1), 21–27.
118. Schätzle, M.; Mannchen, R.; Zwahlen, M.; Lang, N. P. *Clin. Oral Impl. Res.* **2009**, *20*(12), 1351–1359.
119. Wilmes, B.; Ottenstreuer, S.; Su, Y. Y.; Drescher, D. *J. Orofac. Orthop.* **2008**, *69*(1), 42–50.
120. Cho, H. J. *J. Calif. Dent. Assoc.* **2006**, *34*(10), 813–820.
121. Kotsovilis, S.; Fourmousis, I.; Karoussis, I. K.; Bamia, C. *J. Periodontol.* **2009**, *80*(11), 1700–1718.
122. Al-Nawas, B.; Kaemmerer, P.; Morbach, T.; *et al. Clin. Impl. Dent. Relat. Res.* **2010**, doi:10.1111/j.1708-8208.2009.00237.x.
123. Örtorp, A.; Jemt, T. *Clin. Implant Dent. Relat. Res.* **2009**, *11*(4), 311–322.
124. Landes, C. A.; Paffrath, C.; Koehler, C.; *et al. Int. J. Prosthodont.* **2009**, *22*(1), 20–32.
125. Blanes, R. J.; Bernard, J. P.; Blanes, Z. M.; Belser, U. C. *Clin. Oral Implants Res.* **2007**, *18*(6), 707–714.
126. Blanes, R. J.; Bernard, J. P.; Blanes, Z. M.; Belser, U. C. *Clin. Oral Implants Res.* **2007**, *18*(6), 699–706.
127. Meijer, H. J.; Raghoebar, G. M.; Van't Hof, M. A. *Int. J. Oral Maxillofac. Implants* **2003**, *18*(6), 879–885.
128. Ekelund, J. A.; Lindquist, L. W.; Carlsson, G. E.; Jemt, T. *Int. J. Prosthodont.* **2003**, *16*(6), 602–608.
129. Naert, I. E.; Duyck, J. A.; Hosny, M. M.; Van Steenberghe, D. *Clin. Oral Implants Res.* **2001**, *12*(3), 237–244.
130. Albrektsson, T.; Zarb, G.; Worthington, P.; Ericson, R. A. *Int. J. Oral Maxillofac. Implants* **1986**, *1*, 11.
131. Buser, D.; Bragger, U.; Lang, N. P.; Nyman, S. *Clin. Oral Implants Res.* **1990**, *1*(1), 22–32.
132. Jemt, T. *Int. J. Periodontics Restorative Dent.* **1997**, *17*(4), 326–333.
133. Furhauser, R.; Florescu, D.; Benesch, T.; Haas, R.; Mailath, G.; Watzek, G. *Clin. Oral Implants Res.* **2005**, *16*(6), 639–644.
134. Belser, U. C.; Grutter, L.; Vailati, F.; Bornstein, M. M.; Weber, H. P.; Buser, D. *J. Periodontol.* **2009**, *80*(1), 140–151.

135. Jemt, T.; Chai, J.; Harnett, J.; *et al*. *Int. J. Oral Maxillofac. Implants* **1996**, *11*(3), 291–298.
136. Nkenke, E.; Fenner, M. *Clin. Oral Implants Res.* **2006**, *17*(Suppl 2), 19–34.
137. De Rouck, T.; Collys, K.; Cosyn, J. *Int. J. Oral Maxillofac. Implants* **2008**, *23*(5), 897–904.
138. Aghaloo, T. L.; Moy, P. K. *Int. J. Oral Maxillofac. Implants* **2007**, *22*(Suppl), 49–70.
139. Esposito, M.; Grusovin, M. G.; Kwan, S.; Worthington, H. V.; Coulthard, P. *Cochrane Database Syst Rev.* **2006**, *16*(3), CD003607.
140. Klein, M. O.; Grötz, K. A.; Walter, C.; Wegener, J.; Wagner, W.; Al-Nawas, B. *Eur. Surg. Res.* **2009**, *43*(3), 269–275.
141. Madrid, C.; Sanz, M. *Clin. Oral Implants Res.* **2009**, *20*(S4), 87–95.
142. De Boever, A. L.; Quirynen, M.; Coucke, W.; Theuniers, G.; De Boever, J. A. *Clin. Oral Impl. Res.* **2009**, *20*(12), 1341–1350.
143. Javed, F.; Romanos, G. E. *J. Periodontol.* **2009**, *80*(11), 1719–1730.
144. Tsolaki, I. N.; Madianos, P. N.; Vrotsos, J. A. *J. Prosthodont.* **2009**, *18*(4), 309–323.
145. Shabestari, G. O.; Shayesteh, Y. S.; Khojasteh, A.; *et al*. *Clin. Impl. Dent. Relat. Res.* **2010**, *12*(3), 175–180.
146. Kasai, T.; Pogrel, M. A.; Hossaini, M. *J. Calif. Dent. Assoc.* **2009**, *37*(1), 39–42.
147. Ihde, S.; Kopp, S.; Gundlach, K.; Konstantinovic, V. S. *Oral Surg. Oral Med. Oral Pathol. Oral Radiol. Endod.* **2009**, *107*(1), 56–65.
148. Weischer, T.; Schettler, D.; Mohr, C. *Int. J. Oral Maxillofac. Implants* **1996**, *11*(6), 775–781.
149. Kovacs, A. F. *Head Neck* **2000**, *22*(2), 111–119.
150. McGhee, M. A.; Stern, S. J.; Callan, D.; Shewmake, K.; Smith, T. *Head Neck* **1997**, *19*(8), 659–665.
151. Schliephake, H.; Schmelzeisen, R.; Neukam, F. W.; Schierle, H. P.; Scheller, H. *Mund Kiefer Gesichtschir.* **1999**, *3*(Suppl 1), S106–S109.
152. Jacobsson, M.; Tjellstrom, A.; Thomsen, P.; Albrektsson, T.; Turesson, I. *Ann. Otol. Rhinol. Laryngol.* **1988**, *97*(4 Pt 1), 337–340.
153. Jacobsson, M. G.; Jonsson, A. K.; Albrektsson, T. O.; Turesson, I. E. *Plast. Reconstr. Surg.* **1985**, *76*(6), 841–850.
154. Johansson, B.; Friberg, B.; Nilson, H. *Clin. Implant Dent. Relat. Res.* **2009**, *11*(3), 194–200.
155. Danza, M.; Zollino, I.; Carinci, F. *J. Craniofac. Surg.* **2009**, *20*(4), 1086–1092.
156. Vazquez, L.; Saulacic, N.; Belser, U.; Bernard, J. P. *Clin. Oral Implants Res.* **2008**, *19*(1), 81–85.
157. Greenstein, G.; Cavallaro, J.; Romanos, G.; Tarnow, D. *J. Periodontol.* **2008**, *79*(8), 1317–1329.
158. Chen, L. C.; Lundgren, T.; Hallstrom, H.; Cherel, F. *J. Periodontol.* **2008**, *79*(3), 401–405.
159. Schropp, L.; Wenzel, A.; Kostopoulos, L.; Karring, T. *Int. J. Periodontics Restorative Dent.* **2003**, *23*(4), 313–323.
160. Araujo, M. G.; Lindhe, J. *J. Clin. Periodontol.* **2005**, *32*(2), 212–218.
161. Araujo, M. G.; Lindhe, J. *Clin. Oral Implants Res.* **2009**, *20*(6), 545–549.
162. Chen, S. T.; Buser, D. *Int. J. Oral Maxillofac. Implants* **2009**, *24*(Suppl), 186–217.
163. Araujo, M. G.; Wennstrom, J. L.; Lindhe, J. *Clin. Oral Implants Res.* **2006**, *17*(6), 606–614.
164. de Sanctis, M.; Vignoletti, F.; Discepoli, N.; Zucchelli, G.; Sanz, M. *J. Clin. Periodontol.* **2009**, *36*(8), 705–711.
165. Vignoletti, F.; de Sanctis, M.; Berglundh, T.; Abrahamsson, I.; Sanz, M. *J. Clin. Periodontol.* **2009**, *36*(8), 688–697.
166. Vignoletti, F.; Johansson, C.; Albrektsson, T.; De Sanctis, M.; San Roman, F.; Sanz, M. *J. Clin. Periodontol.* **2009**, *36*(3), 265–277.
167. Noelken, R.; Morbach, T.; Kunkel, M.; Wagner, W. *Int. J. Periodontics Restorative Dent.* **2007**, *27*(3), 277–285.
168. Covani, U.; Cornelini, R.; Barone, A. *Int. J. Oral Maxillofac. Implants* **2008**, *23*(5), 841–846.
169. Cardemil, C.; Ristevski, Z.; Alsen, B.; Dahlin, C. *Clin. Implant Dent. Relat. Res.* **2009**, *11*(4), 288–291.
170. Dreiseidler, T.; Neugebauer, J.; Ritter, L.; *et al*. *Clin. Oral Implants Res.* **2009**, *20*(11), 1191–1199.
171. Schneider, D.; Marquardt, P.; Zwahlen, M.; Jung, R. E. *Clin. Oral Implants Res.* **2009**, *20*(Suppl 4), 73–86.
172. Cordioli, G.; Majzoub, Z. *Int. J. Oral Maxillofac. Implants* **1997**, *12*(2), 186–193.
173. Misir, A. F.; Sumer, M.; Yenisey, M.; Ergioglu, E. *J. Oral Maxillofac. Surg.* **2009**, *67*(12), 2663–2668.
174. Chacon, G. E.; Bower, D. L.; Larsen, P. E.; McGlumphy, E. A.; Beck, F. M. *J. Oral Maxillofac. Surg.* **2006**, *64*(2), 265–269.
175. Ercoli, C.; Funkenbusch, P. D.; Lee, H. J.; Moss, M. E.; Graser, G. N. *Int. J. Oral Maxillofac. Implants* **2004**, *19*(3), 335–349.
176. Preti, G.; Martinasso, G.; Peirone, B.; *et al*. *J. Periodontol.* **2007**, *78*(4), 716–722.
177. Trisi, P.; Rao, W. *Clin. Oral Implants Res.* **1999**, *10*, 1–7.
178. Turkyilmaz, I.; Aksoy, U.; McGlumphy, E. A. *Clin. Implant Dent. Relat. Res.* **2008**, *10*(4), 231–237.
179. O'Sullivan, D.; Sennerby, L.; Jagger, D.; Meredith, N. *Clin. Implant Dent. Relat. Res.* **2004**, *6*(1), 48–57.
180. Balshi, S. F.; Wolfinger, G. J.; Balshi, T. J. *Int. J. Oral Maxillofac. Implants* **2007**, *22*(3), 467–471.
181. Irinakis, T.; Wiebe, C. *J. Oral Implantol.* **2009**, *35*(6), 283–288.
182. Albrektsson, T.; Branemark, P. I.; Hansson, H. A.; Lindstrom, J. *Acta Orthop. Scand.* **1981**, *52*(2), 155–170.
183. Branemark, P. I.; Adell, R.; Breine, U.; Hansson, B. O.; Lindstrom, J.; Ohlsson, A. *Scand. J. Plast. Reconstr. Surg.* **1969**, *3*(2), 81–100.
184. Linder, L.; Carlsson, A.; Marsal, L.; Bjursten, L. M.; Branemark, P. I. *J. Bone Joint Surg. Br.* **1988**, *70*(4), 550–555.
185. Joos, U.; Meyer, U. *Head Face Med.* **2006**, *2*, 19.
186. Berglundh, T.; Abrahamsson, I.; Lang, N. P.; Lindhe, J. *Clin. Oral Implants Res.* **2003**, *14*(3), 251–262.
187. Ostman, P. O.; Hellman, M.; Sennerby, L. *Clin. Implant Dent. Relat. Res.* **2005**, *7*(Suppl 1), S60–S69.
188. Ottoni, J. M.; Oliveira, Z. F.; Mansini, R.; Cabral, A. M. *Int. J. Oral Maxillofac. Implants* **2005**, *20*(5), 769–776.
189. Davies, J. E. *J. Dent. Educ.* **2003**, *67*(8), 932–949.
190. Puleo, D. A.; Nanci, A. *Biomaterials* **1999**, *20*(23–24), 2311–2321.
191. Kasemo, B.; Gold, J. *Adv. Dent. Res.* **1999**, *13*, 8–20.
192. Kieswetter, K.; Schwartz, Z.; Dean, D. D.; Boyan, B. D. *Crit. Rev. Oral Biol. Med.* **1996**, *7*(4), 329–345.
193. de Jonge, L. T.; Leeuwenburgh, S. C.; Wolke, J. G.; Jansen, J. A. *Pharm. Res.* **2008**, *25*(10), 2357–2369.
194. Geiger, B.; Bershadsky, A.; Pankov, R.; Yamada, K. M. *Nat. Rev. Mol. Cell Biol.* **2001**, *2*(11), 793–805.
195. Klein, M. O.; Reichert, C.; Koch, D.; Horn, S.; Al-Nawas, B. *Clin. Oral Implants Res.* **2007**, *18*(1), 40–45.
196. Ruoslahti, E. *Annu. Rev. Cell Dev. Biol.* **1996**, *12*, 697–715.
197. Hong, J.; Andersson, J.; Ekdahl, K. N.; *et al*. *Thromb. Haemost.* **1999**, *82*(1), 58–64.
198. Nygren, H.; Tengvall, P.; Lundstrom, I. *J. Biomed. Mater. Res.* **1997**, *34*(4), 487–492.
199. Park, J. Y.; Davies, J. E. *Clin. Oral Implants Res.* **2000**, *11*(6), 530–539.
200. Klein, M. O.; Kammerer, P. W.; Scholz, T.; *et al*. *Clin. Oral Impl. Res.* **2010**, *21*(3), 336–345.
201. Kark, L. R.; Karp, J. M.; Davies, J. E. *Clin. Oral Implants Res.* **2006**, *17*(3), 321–327.
202. Oprea, W. E.; Karp, J. M.; Hosseini, M. M.; Davies, J. E. *J. Craniofac. Surg.* **2003**, *14*(3), 292–300.
203. Pagel, C. N.; Sivagurunathan, S.; Loh, L. H.; Tudor, E. M.; Pike, R. N.; Mackie, E. J. *Biol. Chem.* **2006**, *387*(8), 1037–1041.
204. Buller, H. R.; Ten Cate, T. *Eur Heart J.* **1995**, *16*(Suppl L), 8–10.
205. Broberg, M.; Eriksson, C.; Nygren, H. *J. Lab. Clin. Med.* **2002**, *139*(3), 163–172.
206. Harrison, P.; Cramer, E. M. *Blood Rev.* **1993**, *7*(1), 52–62.
207. Huang, Y. C.; Kaigler, D.; Rice, K. G.; Krebsbach, P. H.; Mooney, D. J. *J. Bone Miner. Res.* **2005**, *20*(5), 848–857.
208. Kanczler, J. M.; Oreffo, R. O. *Eur. Cell Mater.* **2008**, *15*, 100–114.
209. Coultas, L.; Chawengsaksophak, K.; Rossant, J. *Nature* **2005**, *438*(7070), 937–945.
210. Grellier, M.; Ferreira-Tojais, N.; Bourget, C.; Bareille, R.; Guillemot, F.; Amedee, J. *J. Cell. Biochem.* **2009**, *106*(3), 390–398.
211. Bouletreau, P. J.; Warren, S. M.; Spector, J. A.; *et al*. *Plast. Reconstr. Surg.* **2002**, *109*(7), 2384–2397.
212. Peng, H.; Usas, A.; Olshanski, A.; *et al*. *J. Bone Miner. Res.* **2005**, *20*(11), 2017–2027.
213. Samee, M.; Kasugai, S.; Kondo, H.; Ohya, K.; Shimokawa, H.; Kuroda, S. *J. Pharmacol. Sci.* **2008**, *108*(1), 18–31.
214. Keramaris, N. C.; Calori, G. M.; Nikolaou, V. S.; Schemitsch, E. H.; Giannoudis, P. V. *Injury* **2008**, *39*(Suppl 2), S45–S57.
215. McCarthy, H. S.; Williams, J. H.; Davie, M. W.; Marshall, M. J. *J. Cell. Physiol.* **2009**, *218*(2), 350–354.
216. Sanchez-Fernandez, M. A.; Gallois, A.; Riedl, T.; Jurdic, P.; Hoflack, B. *PLoS One* **2008**, *3*(10), e3537.
217. Mezawa, M.; Araki, S.; Takai, H.; *et al*. *Gene* **2009**, *435*(1–2), 80–87.
218. Hollinger, J. O.; Hart, C. E.; Hirsch, S. N.; Lynch, S.; Friedlaender, G. E. *J. Bone Joint Surg. Am.* **2008**, *90*(Suppl 1), 48–54.

219. Tokuda, H.; Takai, S.; Hanai, Y.; *et al*. *Prostaglandins Leukot. Essent. Fatty Acids* **2007**, *77*(3–4), 187–193.
220. Tokuda, H.; Takai, S.; Hanai, Y.; *et al*. *J. Bone Miner. Metab*. **2008**, *26*(4), 335–341.
221. Chuang, W. H.; Lin, J. C. *J. Biomed. Mater. Res. A* **2007**, *82*(4), 820–830.
222. LaFayette, N. G.; Skrzypchak, A. M.; Merz, S.; Bartlett, R. H.; Annich, G. M. *ASAIO J.* **2007**, *53*(2), 159–162.
223. Kikuchi, L.; Park, J. Y.; Victor, C.; Davies, J. E. *Biomaterials* **2005**, *26*(26), 5285–5295.
224. Park, J. Y.; Gemmell, C. H.; Davies, J. E. *Biomaterials* **2001**, *22*(19), 2671–2682.
225. Cooper, L. F. *J. Prosthet. Dent*. **1998**, *80*(4), 439–449.
226. Anderson, J. In *Bone Engineering*; Davies, J. E., Ed.; Toronto: Em Squared, 2000; pp 81–93.
227. Arnold, F.; West, D. C. *Pharmacol. Ther*. **1991**, *52*(3), 407–422.
228. Soskolne, W. A.; Cohen, S.; Sennerby, L.; Wennerberg, A.; Shapira, L. *Clin. Oral Implants Res*. **2002**, *13*(1), 86–93.
229. Marx, R. In *Bone Engineering*; Davies, J. E., Ed.; Toronto: Em Squared, 2000; pp 447–453.
230. Graves, D. T.; Valentin-Opran, A.; Delgado, R.; Valente, A. J.; Mundy, G.; Piche, J. *Connect. Tissue Res*. **1989**, *23*(2–3), 209–218.
231. Davies, J. E. *Anat. Rec*. **1996**, *245*(2), 426–445.
232. Stanford, C. M.; Schneider, G. B. *Gerodontology* **2004**, *21*(2), 71–77.
233. Bollen, C. M. L.; Papaioannou, W.; van Eldere, J.; Schepers, E.; Quirynen, M.; van Steenberghe, D. *Clin. Oral Implants Res*. **1996**, *7*, 201–211.
234. Cochran, D. L.; Simpson, J.; Weber, H. P.; Buser, D. *Int. J. Oral Maxillofac. Implants* **1994**, *9*, 289–297.
235. Lauer, G.; Wiedmann-Al-Ahmad, M.; Otten, J. E.; Hubner, U.; Schmelzeisen, R.; Schilli, W. *Biomaterials* **2001**, *22*(20), 2799–2809.
236. Dietrich, M.; Arnold, W.; Grimm, W.-D. *Int. Poster J. Dent. Oral Med*. **2002**, *4*(4), 155.
237. Lindhe, J.; Berglundh, T. *Periodontology 2000* **1998**, *17*, 47–54.
238. Inoue, T.; Takeda, T.; Lee, C. Y.; *et al*. *Bull. Tokyo Dent. Coll*. **1997**, *38*(3), 187–193.
239. Comut, A. A.; Weber, H. P.; Shortkroff, S.; Cui, F. Z.; Spector, M. *Clin. Oral Implants Res*. **2001**, *12*(5), 433–440.
240. Berglundh, T.; Lindhe, J.; Ericsson, I.; Marinello, C. P.; Liljenberg, B.; Thomsen, P. *Clin. Oral Implants Res*. **1991**, *2*(2), 81–90.
241. Friedrich, R. E.; Plambeck, K.; Hellner, D.; Köhler, S.; Gbara, A.; Schmelzle, R. *Z. Zahnärztl. Implantol*. **1994**, *10*, 132–136.
242. Liljenberg, B.; Gualini, F.; Berglundh, T.; Tonetti, M.; Lindhe, J. *J. Clin. Periodontol*. **1996**, *23*(11), 1008–1013.
243. Chavrier, C.; Couble, M. L.; Hartmann, D. J. *Clin. Oral Implants Res*. **1994**, *5*(3), 117–124.
244. Tomakidi, P.; Fusenig, N. E.; Kohl, A.; Komposch, G. *J. Periodontal Res*. **1997**, *32*(4), 388–400.
245. Hildebrand, H. C.; Hakkinen, L.; Wiebe, C. B.; Larjava, H. S. *Histol. Histopathol*. **2002**, *17*(1), 151–163.
246. Linkevicius, T.; Apse, P.; Grybauskas, S.; Puisys, A. *Int. J. Oral Maxillofac. Implants* **2009**, *24*(4), 712–719.
247. Park, I. S.; Won, S. Y.; Bae, T. S.; *et al*. *Met. Mater. Int*. **2008**, *14*(2), 133–138.
248. Assuncao, W. G.; Barao, V. A.; Tabata, L. F.; Gomes, E. A.; Delben, J. A.; dos Santos, P. H. *J. Craniofac. Surg*. **2009**, *20*(4), 1173–1177.
249. Frocht, M. M. *Photoelasticity*, 1st ed.; Wiley: New York, 1962.
250. Zak, B. *Oesterr. Z. Stomatol*. **1935**, *35*, 22–37.
251. Akca, K.; Fanuscu, M. I.; Caputo, A. A. *J. Prosthodont*. **2008**, *17*(8), 616–620.
252. Glantz, P. O.; Rangert, B.; Svensson, A.; *et al*. *Clin. Oral Implants Res*. **1993**, *4*(2), 99–105.
253. Assif, D.; Marshak, B.; Horowitz, A. *J. Prosthet. Dent*. **1996**, *75*(3), 285–291.
254. Heckmann, S. M.; Karl, M.; Wichmann, M. G.; Winter, W.; Graef, F.; Taylor, T. D. *Clin. Oral Implants Res*. **2006**, *17*(3), 345–350.
255. Ormianer, Z.; Brosh, T.; Laufer, B. Z.; Shifman, A. *Implant Dent*. **2005**, *14*(1), 58–62.
256. Mericske-Stern, R.; Assal, P.; Buergin, W. *Clin. Oral Implants Res*. **1996**, *7*(4), 378–386.
257. Geng, J. P.; Tan, K. B.; Liu, G. R. *J. Prosthet. Dent*. **2001**, *85*(6), 585–598.
258. Bächle, M.; Kohal, R. J. *Clin. Oral Implants Res*. **2004**, *15*(6), 683–692.
259. Kieswetter, K.; Schwartz, Z.; Hummert, T. W.; *et al*. *J. Biomed. Mater. Res*. **1996**, *32*(1), 55–63.
260. Giuliani, N.; Pedrazzoni, M.; Passeri, G.; Girasole, G. *Scand. J. Rheumatol*. **1998**, *27*(1), 38–41.
261. Im, G. I.; Qureshi, S. A.; Kenney, J.; Rubash, H. E.; Shanbhag, A. S. *Biomaterials* **2004**, *25*(18), 4105–4115.
262. Nayab, S. N.; Jones, F. H.; Olsen, I. *Biomaterials* **2007**, *28*(1), 38–44.
263. Nebe, J. B.; Muller, L.; Luthen, F.; *et al*. *Acta Biomater*. **2008**, *4*(6), 1985–1995.
264. Nishimoto, S. K.; Nishimoto, M.; Park, S. W.; *et al*. *Int. J. Oral Maxillofac. Implants* **2008**, *23*(4), 675–680.
265. Feyerabend, F.; Siemers, C.; Willumeit, R.; Rosler, J. *J. Biomed. Mater. Res. A* **2009**, *90*(3), 931–939.
266. Shapira, L.; Halabi, A. *Clin. Oral Implants Res*. **2009**, *20*(1), 50–55.
267. Stahl, A.; Wenger, A.; Weber, H.; Stark, G. B.; Augustin, H. G.; Finkenzeller, G. *Biochem. Biophys. Res. Commun*. **2004**, *322*(2), 684–692.
268. Boda-Heggemann, J.; Regnier-Vigouroux, A.; Franke, W. W. *Cell Tissue Res*. **2009**, *335*(1), 49–65.
269. Pearce, A. I.; Richards, R. G.; Milz, S.; Schneider, E.; Pearce, S. G. *Eur. Cell Mater*. **2007**, *13*, 1–10.
270. Ungersbock, A.; Pohler, O.; Perren, S. M. *Biomed. Mater. Eng*. **1994**, *4*(4), 317–325.
271. Wennerberg, A.; Albrektsson, T.; Johansson, C.; Andersson, B. *Biomaterials* **1996**, *17*(1), 15–22.
272. Wennerberg, A.; Albrektsson, T.; Lausmaa, J. *J. Biomed. Mater. Res*. **1996**, *30*(2), 251–260.
273. Ivanoff, C. J.; Sennerby, L.; Johansson, C.; Rangert, B.; Lekholm, U. *Int. J. Oral Maxillofac. Surg*. **1997**, *26*(2), 141–148.
274. Meredith, N.; Shagaldi, F.; Alleyne, D.; Sennerby, L.; Cawley, P. *Clin. Oral Implants Res*. **1997**, *8*(3), 234–243.
275. Yan, W. Q.; Nakamura, T.; Kobayashi, M.; Kim, H. M.; Miyaji, F.; Kokubo, T. *J. Biomed. Mater. Res*. **1997**, *37*(2), 267–275.
276. Han, C. H.; Johansson, C. B.; Wennerberg, A.; Albrektsson, T. *Clin. Oral Implants Res*. **1998**, *9*(1), 1–10.
277. Johansson, C. B.; Han, C. H.; Wennerberg, A.; Albrektsson, T. *Int. J. Oral Maxillofac. Implants* **1998**, *13*(3), 315–321.
278. Konig, J. B.; Beck, T. J.; Kappert, H. F.; Kappert, C. C.; Masuko, T. S. *Ann. Anat*. **1998**, *180*(5), 471–475.
279. Sul, Y. T.; Johansson, C. B.; Albrektsson, T. *Int. J. Oral Maxillofac. Implants* **2002**, *17*(5), 625–634.
280. Sul, Y. T.; Johansson, C. B.; Jeong, Y.; Wennerberg, A.; Albrektsson, T. *Clin. Oral Implants Res*. **2002**, *13*(3), 252–259.
281. Scarano, A.; Di Carlo, F.; Quaranta, M.; Piattelli, A. *J. Oral Implantol*. **2003**, *29*(1), 8–12.
282. Sennerby, L.; Dasmah, A.; Larsson, B.; Iverhed, M. *Clin. Implant Dent. Relat. Res*. **2005**, *7*(Suppl 1), S13–S20.
283. Fernandes Ede, L.; Unikowski, I. L.; Teixeira, E. R.; da Costa, N. P.; Shinkai, R. S. *Int. J. Oral Maxillofac. Implants* **2007**, *22*(6), 886–892.
284. Stenport, V. F.; Johansson, C. B. *Clin. Implant Dent. Relat. Res*. **2008**, *10*(3), 191–199.
285. Vandamme, K.; Naert, I.; Vander Sloten, J.; Puers, R.; Duyck, J. *J. Periodontol*. **2008**, *79*(1), 150–157.
286. Kon, K.; Shiota, M.; Ozeki, M.; Yamashita, Y.; Kasugai, S. *Clin. Oral Implants Res*. **2009**, *20*(11), 1240–1246.
287. Palmquist, A.; Lindberg, F.; Emanuelsson, L.; Branemark, R.; Engqvist, H.; Thomsen, P. *J. Biomed. Mater. Res. B Appl. Biomater*. **2009**, *91*(1), 309–319.
288. Sul, Y. T.; Jonsson, J.; Yoon, G. S.; Johansson, C. *Clin. Oral Implants Res*. **2009**, *20*(10), 1146–1155.
289. Donath, K.; Breuner, G. *J. Oral Pathol*. **1982**, *11*, 318–326.
290. Ferguson, S. J.; Langhoff, J. D.; Voelter, K.; *et al*. *Int. J. Oral Maxillofac. Implants* **2008**, *23*(6), 1037–1046.
291. Vlaminck, L.; Gorski, T.; Huys, L.; Saunders, J.; Schacht, E.; Gasthuys, F. *Implant Dent*. **2008**, *17*(4), 439–450.
292. Langhoff, J. D.; Voelter, K.; Scharnweber, D.; *et al*. *Int. J. Oral Maxillofac. Surg*. **2008**, *37*(12), 1125–1132.
293. Franchi, M.; Bacchelli, B.; Giavaresi, G.; *et al*. *J. Periodontol*. **2007**, *78*(5), 879–888.
294. Schopper, C.; Moser, D.; Goriwoda, W.; *et al*. *Clin. Oral Implants Res*. **2005**, *16*(3), 357–368.
295. Franchi, M.; Bacchelli, B.; Martini, D.; *et al*. *Biomaterials* **2004**, *25*(12), 2239–2246.
296. Haas, R.; Baron, M.; Zechner, W.; Mailath-Pokorny, G. *Int. J. Oral Maxillofac. Implants* **2003**, *18*(5), 691–696.
297. Grizon, F.; Aguado, E.; Hure, G.; Basle, M. F.; Chappard, D. *J. Dent*. **2002**, *30*(5–6), 195–203.
298. Lucchini, J. P.; Aurelle, J. L.; Therin, M.; Donath, K.; Becker, W. *Clin. Oral Implants Res*. **1996**, *7*(4), 397–404.
299. Hure, G.; Donath, K.; Lesourd, M.; Chappard, D.; Basle, M. F. *Int. J. Oral Maxillofac. Implants* **1996**, *11*(4), 506–511.
300. Ehrl, P. A.; Reuther, J.; Frenkel, G. *Int. J. Oral Surg*. **1981**, *10*(Suppl 1), 93–98.

301. Branemark, P. I.; Adell, R.; Albrektsson, T.; Lekholm, U.; Lindstrom, J.; Rockler, B. *J. Oral Maxillofac. Surg.* **1984**, *42*(8), 497–505.
302. Deporter, D. A.; Friedland, B.; Watson, P. A.; *et al. J. Dent. Res.* **1986**, *65*(8), 1071–1077.
303. Deporter, D. A.; Watson, P. A.; Pilliar, R. M.; *et al. J. Dent. Res.* **1986**, *65*(8), 1064–1070.
304. Al-Sayyed, A.; Deporter, D. A.; Pilliar, R. M.; *et al. Clin. Oral Implants Res.* **1994**, *5*(3), 131–141.
305. Brosh, T.; Persovski, Z.; Binderman, I. *Int. J. Oral Maxillofac. Implants* **1995**, *10*(6), 729–735.
306. Ericsson, I.; Persson, L. G.; Berglundh, T.; Edlund, T.; Lindhe, J. *Clin. Oral Implants Res.* **1996**, *7*(4), 320–328.
307. Levy, D.; Deporter, D. A.; Pilliar, R. M.; Watson, P. A.; Valiquette, N. *Clin. Oral Implants Res.* **1996**, *7*(2), 101–110.
308. Cochran, D. L.; Hermann, J. S.; Schenk, R. K.; Higginbottom, F. L.; Buser, D. *J. Periodontol.* **1997**, *68*(2), 186–198.
309. Hermann, J. S.; Cochran, D. L.; Nummikoski, P. V.; Buser, D. *J. Periodontol.* **1997**, *68*(11), 1117–1130.
310. Abrahamsson, I.; Berglundh, T.; Glantz, P. O.; Lindhe, J. *J. Clin. Periodontol.* **1998**, *25*(9), 721–727.
311. Branemark, R.; Ohrnell, L. O.; Skalak, R.; Carlsson, L.; Branemark, P. I. *J. Orthop. Res.* **1998**, *16*(1), 61–69.
312. Cochran, D. L.; Schenk, R. K.; Lussi, A.; Higginbottom, F. L.; Buser, D. *J. Biomed. Mater. Res.* **1998**, *40*(1), 1–11.
313. Novaes, A. B., Jr.; Vidigal, G. M., Jr.; Novaes, A. B.; Grisi, M. F.; Polloni, S.; Rosa, A. *Int. J. Oral Maxillofac. Implants* **1998**, *13*(3), 422–427.
314. Moon, I. S.; Berglundh, T.; Abrahamsson, I.; Linder, E.; Lindhe, J. *J. Clin. Periodontol.* **1999**, *26*(10), 658–663.
315. Hermann, J. S.; Buser, D.; Schenk, R. K.; Higginbottom, F. L.; Cochran, D. L. *Clin. Oral Implants Res.* **2000**, *11*(1), 1–11.
316. Abrahamsson, I.; Zitzmann, N. U.; Berglundh, T.; Wennerberg, A.; Lindhe, J. *Int. J. Oral Maxillofac. Implants* **2001**, *16*(3), 323–332.
317. Hermann, J. S.; Buser, D.; Schenk, R. K.; Schoolfield, J. D.; Cochran, D. L. *Clin. Oral Implants Res.* **2001**, *12*(6), 559–571.
318. Hermann, J. S.; Schoolfield, J. D.; Schenk, R. K.; Buser, D.; Cochran, D. L. *J. Periodontol.* **2001**, *72*(10), 1372–1383.
319. Todescan, F. F.; Pustiglioni, F. E.; Imbronito, A. V.; Albrektsson, T.; Gioso, M. *Int. J. Oral Maxillofac. Implants* **2002**, *17*(4), 467–472.
320. Zitzmann, N. U.; Abrahamsson, I.; Berglundh, T.; Lindhe, J. *J. Clin. Periodontol.* **2002**, *29*(5), 456–461.
321. Abrahamsson, I.; Berglundh, T.; Sekino, S.; Lindhe, J. *Clin. Implant Dent. Relat. Res.* **2003**, *5*(2), 82–88.
322. Botticelli, D.; Berglundh, T.; Buser, D.; Lindhe, J. *Clin. Oral Implants Res.* **2003**, *14*(1), 35–42.
323. Araujo, M. G.; Sukekava, F.; Wennstrom, J. L.; Lindhe, J. *J. Clin. Periodontol.* **2005**, *32*(6), 645–652.
324. Schliephake, H.; Scharnweber, D.; Dard, M.; Sewing, A.; Aref, A.; Roessler, S. *J. Biomed. Mater. Res. B Appl. Biomater.* **2005**, *73*(1), 88–96.
325. Berglundh, T.; Abrahamsson, I.; Albouy, J. P.; Lindhe, J. *Clin. Oral Implants Res.* **2007**, *18*(2), 147–152.
326. Schwarz, F.; Ferrari, D.; Herten, M.; *et al. J. Periodontol.* **2007**, *78*(11), 2171–2184.
327. Schwarz, F.; Herten, M.; Sager, M.; Wieland, M.; Dard, M.; Becker, J. *Clin. Oral Implants Res.* **2007**, *18*(4), 481–488.
328. Schwarz, F.; Herten, M.; Sager, M.; Wieland, M.; Dard, M.; Becker, J. *J. Clin. Periodontol.* **2007**, *34*(1), 78–86.
329. Schwarz, F.; Sager, M.; Ferrari, D.; Herten, M.; Wieland, M.; Becker, J. *J. Clin. Periodontol.* **2008**, *35*(1), 64–75.
330. Yoo, J. H.; Choi, B. H.; Li, J.; *et al. Oral Surg. Oral Med. Oral Pathol. Oral Radiol. Endod.* **2008**, *105*(6), 702–706.
331. Al-Nawas, B.; Grötz, K. A.; Götz, H.; Duschner, H.; Wagner, W. *Clin. Oral Implants Res.* **2008**, *19*, 1–8.
332. Lavos-Valereto, I. C.; Wolynec, S.; Deboni, M. C.; Konig, B., Jr. *J. Biomed. Mater. Res.* **2001**, *58*(6), 727–733.
333. Rahn, B. V.; Bacellar, F. C.; Trapp, L.; Perren, S. M. *Aktuelle Traumatol.* **1980**, *10*(2), 109–115.
334. Schouten, C.; Meijer, G. J.; van den Beucken, J. J.; Spauwen, P. H.; Jansen, J. A. *Biomaterials* **2009**, *30*(27), 4539–4549.
335. Meredith, N.; Alleyne, D.; Cawley, P. *Clin. Oral Implants Res.* **1996**, *7*(3), 261–267.
336. Al-Nawas, B.; Wagner, W.; Grötz, K. A. *Int. J. Oral Maxillofac. Implants* **2006**, *21*, 726–732.
337. Brouwers, J. E.; Lobbezoo, F.; Visscher, C. M.; Wismeijer, D.; Naeije, M. *J. Oral Rehabil.* **2009**, *9*, 99.
338. Song, Y. D.; Jun, S. H.; Kwon, J. J. *Int. J. Oral Maxillofac. Implants* **2009**, *24*(1), 59–64.
339. Buser, D.; Broggini, N.; Wieland, M.; *et al. J. Dent. Res.* **2004**, *83*(7), 529–533.
340. Degidi, M.; Perrotti, V.; Strocchi, R.; Piattelli, A.; Iezzi, G. *Clin. Oral Implants Res.* **2009**, *20*(8), 778–781.
341. Vantaggiato, G.; Iezzi, G.; Fiera, E.; Perrotti, V.; Piattelli, A. *Implant Dent.* **2008**, *17*(2), 192–199.
342. Keller, J. C.; Stanford, C. M.; Wightman, J. P.; Draughn, R. A.; Zaharias, R. *J. Biomed. Mater. Res.* **1994**, *28*(8), 939–946.
343. Schmidt, C.; Ignatius, A. A.; Claes, L. E. *J. Biomed. Mater. Res.* **2001**, *54*(2), 209–215.
344. Wagner, W.; Valentin, A. H. *Z. Zahnärztl. Implantol.* **1987**, *3*, 48–52.
345. Morais, L. S.; Serra, G. G.; Muller, C. A.; *et al. Acta Biomater.* **2007**, *3*(3), 331–339.
346. Shapira, L.; Klinger, A.; Tadir, A.; Wilensky, A.; Halabi, A. *Clin. Oral Implants Res.* **2009**, *20*(6), 578–582.
347. Tao, C. Z.; Zhou, J.; Cheng, B. S.; Liu, Y.; Hao, L. *Shanghai Kou Qiang Yi Xue* **2000**, *9*(4), 218–221.
348. Takeshita, F.; Takata, H.; Ayukawa, Y.; Suetsugu, T. *Biomaterials* **1997**, *18*(1), 21–25.
349. Kobayashi, E.; Matsumoto, S.; Doi, H.; Yoneyama, T.; Hamanaka, H. *J. Biomed. Mater. Res.* **1995**, *29*(8), 943–950.
350. Tsuchiya, T.; Nakamura, A.; Oshima, Y.; *et al. Tissue Eng.* **1998**, *4*(2), 197–204.
351. Ikarashi, Y.; Toyoda, K.; Kobayashi, E.; *et al. Mater. Trans.* **2005**, *46*, 2260–2267.
352. Gottlow, J., Ed.; In Preclinical Data 23rd Annual Meeting of the Academy of Osseointegration (AO), Boston, 2008.
353. Kulakov, O. B.; Doktorov, A. A.; D'lakova, S. V.; Denisov-Nikol'skii Iu, I.; Grotz, K. A. *Morfologiia* **2005**, *127*(1), 52–55.
354. Sicilia, A.; Cuesta, S.; Coma, G.; *et al. Clin. Oral Implants Res.* **2008**, *19*(8), 823–835.
355. Bobyn, J. D.; Stackpool, G. J.; Hacking, S. A.; Tanzer, M.; Krygier, J. J. *J. Bone Joint Surg. Br.* **1999**, *81*(5), 907–914.
356. Ruckh, T.; Porter, J. R.; Allam, N. K.; Feng, X.; Grimes, C. A.; Popat, K. C. *Nanotechnology* **2009**, *20*(4), 45102.
357. Mareci, D.; Chelariu, R.; Gordin, D. M.; Ungureanu, G.; Gloriant, T. *Acta Biomater.* **2009**, *5*(9), 3625–3639.
358. Balla, V. K.; Banerjee, S.; Bose, S.; Bandyopadhyay, A. *Acta Biomater.* **2010**, *6*(6), 2329–2334.
359. Jinno, T.; Goldberg, V. M.; Davy, D.; Stevenson, S. *J. Biomed. Mater. Res.* **1998**, *42*(1), 20–29.
360. Depprich, R.; Ommerborn, M.; Zipprich, H.; *et al. Head Face Med.* **2008**, *4*, 29.
361. Li, J. *Biomed. Mater. Eng.* **1997**, *7*(6), 379–385.
362. Akagawa, Y.; Hosokawa, R.; Sato, Y.; Kamayama, K. *J. Prosthet. Dent.* **1998**, *80*(5), 551–558.
363. Schultze-Mosgau, S.; Schliephake, H.; Radespiel-Troger, M.; Neukam, F. W. *Oral Surg. Oral Med. Oral Pathol. Oral Radiol. Endod.* **2000**, *89*(1), 91–98.
364. Kohal, R. J.; Weng, D.; Bachle, M.; Strub, J. R. *J. Periodontol.* **2004**, *75*(9), 1262–1268.
365. Rocchietta, I.; Fontana, F.; Addis, A.; Schupbach, P.; Simion, M. *Clin. Oral Implants Res.* **2009**, *20*(8), 844–850.
366. Lee, J.; Sieweke, J. H.; Rodriguez, N. A.; *et al. J. Clin. Periodontol.* **2009**, *36*(7), 610–617.
367. Gahlert, M.; Rohling, S.; Wieland, M.; Sprecher, C. M.; Kniha, H.; Milz, S. *Clin. Oral Implants Res.* **2009**, *20*(11), 1247–1253.
368. Kohal, R. J.; Wolkewitz, M.; Hinze, M.; Han, J. S.; Bachle, M.; Butz, F. *Clin. Oral Implants Res.* **2009**, *20*(4), 333–339.
369. Depprich, R.; Zipprich, H.; Ommerborn, M.; *et al. Head Face Med.* **2008**, *4*, 30.
370. Depprich, R.; Zipprich, H.; Ommerborn, M.; *et al. Head Face Med.* **2008**, *4*, 25.
371. Hoffmann, O.; Angelov, N.; Gallez, F.; Jung, R. E.; Weber, F. E. *Int. J. Oral Maxillofac. Implants* **2008**, *23*(4), 691–695.
372. Silva, N. R.; Coelho, P. G.; Fernandes, C. A.; Navarro, J. M.; Dias, R. A.; Thompson, V. P. *J. Biomed. Mater. Res. B Appl. Biomater.* **2009**, *88*(2), 419–426.
373. Oliva, J.; Oliva, X.; Oliva, J. D. *Int. J. Oral Maxillofac. Implants* **2007**, *22*(3), 430–435.
374. Lambrich, M.; Iglhaut, G. *Z. Zahnärztl. Implantol.* **2008**, *24*, 182–191.
375. Mellinghoff, J. *Z. Zahnärztl. Implantol.* **2006**, *22*, 288–293.
376. Andreiotelli, M.; Wenz, H. J.; Kohal, R. J. *Clin. Oral Implants Res.* **2009**, *20*(Suppl 4), 32–47.
377. Wenz, H. J.; Bartsch, J.; Wolfart, S.; Kern, M. *Int. J. Prosthodont.* **2008**, *21*(1), 27–36.
378. Cook, S. D.; Weinstein, A. M.; Klawitter, J. J. *J. Biomed. Mater. Res.* **1982**, *16*, 875–885.
379. Nentwig, G. H. *Niedersächs. Zahnärztebl.* **1991**, *26*(11), 658–662.

380. Romanos, G. E.; Nentwig, G. H. *Int. J. Oral Maxillofac. Implants* **2000**, *15*(6), 831–836.
381. Arvidson, K.; Bystedt, H.; Ericsson, I. *Int. J. Oral Maxillofac. Implants* **1990**, *5*(2), 127–134.
382. Arvidson, K.; Bystedt, H.; Frykholm, A.; von Konow, L.; Lothigius, E. *Int. J. Oral Maxillofac. Implants* **1992**, *7*(3), 321–329.
383. Gotfredsen, K.; Holm, B.; Sewerin, I.; *et al*. *Clin. Oral Implants Res.* **1993**, *4*(2), 83–89.
384. Al-Sukhun, J.; Lindqvist, C.; Helenius, M. *J. Biomed. Mater. Res. A* **2007**, *80*(1), 247–256.
385. Karl, M.; Dickinson, A.; Holst, S.; Holst, A. *Eur. J. Prosthodont. Restor. Dent.* **2009**, *17*(2), 50–57.
386. Huang, H. L.; Hsu, J. T.; Fuh, L. J.; Tu, M. G.; Ko, C. C.; Shen, Y. W. *J. Dent.* **2008**, *36*(6), 409–417.
387. Huang, H. L.; Fuh, L. J.; Ko, C. C.; Hsu, J. T.; Chen, C. C. *Int. J. Oral Maxillofac. Implants* **2009**, *24*(3), 455–462.
388. Bratu, E. A.; Tandlich, M.; Shapira, L. *Clin. Oral Implants Res.* **2009**, *20*(8), 827–832.
389. Piao, C. M.; Lee, J. E.; Koak, J. Y.; *et al*. *J. Oral Rehabil.* **2009**, *36*(10), 748–754.
390. Sakoh, J.; Wahlmann, U.; Stender, E.; Al-Nawas, B.; Wagner, W. *Int. J. Oral Maxillofac. Implants* **2006**, *21*(4), 560–566.
391. Toyoshima, T.; Wagner, W.; Klein, M. O.; Stender, E.; Wieland, M.; Al-Nawas, B. *Clin. Impl. Dent. Relat. Res.* **2009**, *9*, 99 Epub ahead of print.
392. Textor, M.; Sittig, C.; Frauchiger, V.; Tosatti, S.; Brunette, D. M. In *Titanium in Medicine: Material Science, Surface Science, Engineering, Biological Responses and Medical Applications*; Brunette, D. M., Tengvall, P., Textor, M., Thomsen, P., Eds.; Heidelberg: Springer Verlag, 2001; pp 172–224.
393. Machnee, C. H.; Wagner, W. C.; Jaarda, M. J.; Lang, B. R. *Int. J. Oral Maxillofac. Implants* **1993**, *8*(5), 529–533.
394. Olefjord, I.; Hansson, S. *Int. J. Oral Maxillofac. Implants* **1993**, *8*(1), 32–40.
395. Al-Nawas, B.; Götz, H. *Clin. Implant Dent. Relat. Res.* **2003**, *5*(3), 176–183.
396. Ellingsen, J. E. *J. Mater. Sci. Mater. Med.* **1995**, *6*, 749–753.
397. Lausmaa, J.; Kasemo, B.; Rolander, U.; Bjursten, L. M.; Ericson, L. E.; Rosander, L.; *et al*. In *Surface Characterisation of Biomaterials*; Ratner, B. D., Ed.; Elsevier: Amsterdam, 1988; pp 161–174.
398. Kurze, P.; Krysmann, W.; Knöfler, W. *Z. Klin. Med.* **1986**, *41*, 219–222.
399. Larsson, C.; Thomsen, P.; Aronsson, B. O.; *et al*. *Biomaterials* **1996**, *17*(6), 605–616.
400. Kanagaraja, S.; Wennerberg, A.; Eriksson, C.; Nygren, H. *Biomaterials* **2001**, *22*(13), 1809–1818.
401. Gottlow, J.; Johansson, C.; Albrektsson, B.; Lundgren, K. A. *Appl. Osseoint. Res.* **2000**, *1*, 25–27.
402. Glauser, R.; Ruhstaller, P.; Windisch, S.; *et al*. *Clin. Implant Dent. Relat. Res.* **2005**, *7*(Suppl 1), S52–S59.
403. Graf, H.-L.; Geu, B.; Knöfler, W.; Hemprich, A. *Z. Zahnärztl. Implantol.* **2001**, *17*, 124–131.
404. Schwarz, F.; Sculean, A.; Wieland, M.; *et al*. *Mund Kiefer Gesichtschir.* **2007**, *11*(6), 333–338.
405. Schwarz, F.; Wieland, M.; Schwartz, Z.; *et al*. *J. Biomed. Mater. Res. B Appl. Biomater.* **2009**, *88*(2), 544–557.
406. Berglundh, T.; Abrahamsson, I.; Lang, N. P.; Lindhe, J. *Clin. Oral Implants Res.* **2003**, *14*(3), 251–262.
407. Lima, L. A.; Fuchs-Wehrle, A. M.; Lang, N. P.; *et al*. *Clin. Oral Implants Res.* **2003**, *14*(6), 669–679.
408. Marinho, V. C.; Celletti, R.; Bracchetti, G.; Petrone, G.; Minkin, C.; Piattelli, A. *Int. J. Oral Maxillofac. Implants* **2003**, *18*(1), 75–81.
409. Abrahamsson, I.; Berglundh, T.; Linder, E.; Lang, N. P.; Lindhe, J. *Clin. Oral Implants Res.* **2004**, *15*(4), 381–392.
410. Botticelli, D.; Berglundh, T.; Persson, L. G.; Lindhe, J. *J. Clin. Periodontol.* **2005**, *32*(5), 448–455.
411. Goransson, A.; Wennerberg, A. *Clin. Implant Dent. Relat. Res.* **2005**, *7*(1), 17–23.
412. Park, Y. S.; Yi, K. Y.; Lee, I. S.; Jung, Y. C. *Clin. Oral Implants Res.* **2005**, *16*(2), 156–160.
413. Shalabi, M. M.; Gortemaker, A.; Van't Hof, M. A.; Jansen, J. A.; Creugers, N. H. *J. Dent. Res.* **2006**, *85*(6), 496–500.
414. Wennerberg, A.; Hallgren, C.; Johansson, C.; Danelli, S. *Clin. Oral Implants Res.* **1998**, *9*(1), 11–19.
415. Wennerberg, A.; Ektessabi, A.; Albrektsson, T.; Johansson, C.; Andersson, B. *Int. J. Oral Maxillofac. Implants* **1997**, *12*(4), 486–494.
416. Wennerberg, A.; Albrektsson, T. *Clin. Oral Implants Res.* **2009**, *20*(Suppl 4), 172–184.
417. Buser, D.; Nydegger, T.; Oxland, T.; *et al*. *J. Biomed. Mater. Res.* **1999**, *45*(2), 75–83.
418. Jemt, T.; Chai, J.; Harnett, J.; *et al*. *Int. J. Oral Maxillofac. Implants* **1996**, *11*(3), 291–298.
419. Lazzara, R. J.; Porter, S. S.; Testori, T.; Galante, J.; Zetterqvist, L. *J. Esthet. Dent.* **1998**, *10*(6), 280–289.
420. Piattelli, A.; Corigliano, M.; Scarano, A.; Costigliola, G.; Paolantonio, M. *J. Periodontol.* **1998**, *69*(3), 321–327.
421. Roccuzzo, M.; Wilson, T. G., Jr. *Int. J. Oral Maxillofac. Implants* **2009**, *24*(1), 65–72.
422. Bornstein, M. M.; Hart, C. N.; Halbritter, S. A.; Morton, D.; Buser, D. *Clin. Implant Dent. Relat. Res.* **2009**, *11*(4), 338–347.
423. Roccuzzo, M.; Aglietta, M.; Bunino, M.; Bonino, L. *Clin. Oral Implants Res.* **2008**, *19*(2), 148–152.
424. Froberg, K. K.; Lindh, C.; Ericsson, I. *Clin. Implant Dent. Relat. Res.* **2006**, *8*(4), 187–197.
425. Jungner, M.; Lundqvist, P.; Lundgren, S. *Clin. Oral Implants Res.* **2005**, *16*(3), 308–312.
426. Zitzmann, N. U.; Berglundh, T. *J. Clin. Periodontol.* **2008**, *35*(8 Suppl), 286–291.
427. Heitz-Mayfield, L. J. *J. Clin. Periodontol.* **2008**, *35*(8 Suppl), 292–304.
428. Roos-Jansaker, A. M.; Renvert, H.; Lindahl, C.; Renvert, S. *J. Clin. Periodontol.* **2006**, *33*(4), 296–301.
429. Karoussis, I. K.; Salvi, G. E.; Heitz-Mayfield, L. J.; Bragger, U.; Hammerle, C. H.; Lang, N. P. *Clin. Oral Implants Res.* **2003**, *14*(3), 329–339.
430. Salvi, G. E.; Furst, M. M.; Lang, N. P.; Persson, G. R. *Clin. Oral Implants Res.* **2008**, *19*(3), 242–248.
431. Takanashi, K.; Kishi, M.; Okuda, K.; Ishihara, K. *Bull. Tokyo Dent. Coll.* **2004**, *45*(2), 77–85.
432. Karbach, J.; Callaway, A.; Kwon, Y.-D.; Röhrig, B.; D'Hoedt, B.; Al-Nawas, B. *Int. J. Oral Maxillofac. Implants* **2009**, *24*(3), 491–496.
433. Heuer, W.; Elter, C.; Demling, A.; *et al*. *J. Oral Rehabil.* **2007**, *34*(5), 377–382.
434. Quirynen, M.; Vogels, R.; Pauwels, M.; *et al*. *J. Dent. Res.* **2005**, *84*(4), 340–344.
435. Esposito, M.; Murray-Curtis, L.; Grusovin, M. G.; Coulthard, P.; Worthington, H. V. *Cochrane Database Syst Rev.* **2007**, *4*, CD03815.
436. Shibli, J. A.; Martins, M. C.; Lotufo, R. F.; Marcantonio, E., Jr. *Int. J. Oral Maxillofac. Implants* **2003**, *18*(3), 383–390.
437. Wennerberg, A.; Sennerby, L.; Kultje, C.; Lekholm, U. *J. Clin. Periodontol.* **2003**, *30*(1), 88–94.
438. Subramani, K.; Jung, R. E.; Molenberg, A.; Hammerle, C. H. *Int. J. Oral Maxillofac. Implants* **2009**, *24*(4), 616–626.
439. Katsikogianni, M.; Missirlis, Y. F. *Eur. Cell Mater.* **2004**, *8*, 37–57.
440. Pautke, C.; Kolk, A.; Brokate, M.; *et al*. *Int. J. Oral Maxillofac. Implants* **2009**, *24*(3), 477–483.
441. Barbour, M. E.; O'Sullivan, D. J.; Jenkinson, H. F.; Jagger, D. C. *J. Mater. Sci. Mater. Med.* **2007**, *18*(7), 1439–1447.
442. Grossner-Schreiber, B.; Teichmann, J.; Hannig, M.; Dorfer, C.; Wenderoth, D. F.; Ott, S. J. *Clin. Oral Implants Res.* **2009**, *20*(8), 817–826.
443. Gallardo-Moreno, A. M.; Pacha-Olivenza, M. A.; Saldana, L.; *et al*. *Acta Biomater.* **2009**, *5*(1), 181–192.
444. Paolantonio, M.; Perinetti, G.; D'Ercole, S.; *et al*. *J. Periodontol.* **2008**, *79*(8), 1419–1425.
445. Yao, C.; Webster, T. J. *J. Biomed. Mater. Res. B Appl. Biomater.* **2009**, *91*(2), 587–595.
446. Tang, L.; Zhao, C.; Xiong, Y.; Pan, C.; Wang, A. *Orthopedics* **2009**, *32*(5), 324.
447. Tamai, K.; Kawate, K.; Kawahara, I.; Takakura, Y.; Sakaki, K. *J. Orthop. Sci.* **2009**, *14*(2), 204–209.
448. Omori, S.; Shibata, Y.; Arimoto, T.; Igarashi, T.; Baba, K.; Miyazaki, T. *J. Dent. Res.* **2009**, *88*(10), 957–962.
449. Zhang, F.; Zhang, Z.; Zhu, X.; Kang, E. T.; Neoh, K. G. *Biomaterials* **2008**, *29*(36), 4751–4759.
450. Shi, Z.; Neoh, K. G.; Kang, E. T.; Poh, C.; Wang, W. *J. Biomed. Mater. Res. A* **2008**, *86*(4), 865–872.
451. Ellingsen, J. E.; Thomsen, P.; Lyngstadaas, S. P. *Periodontolgy 2006* **2006**, *41*, 136–156.
452. Feng, B.; Chen, J. Y.; Qi, S. K.; He, L.; Zhao, J. Z.; Zhang, X. D. *J. Mater. Sci. Mater. Med.* **2002**, *13*(5), 457–464.
453. Boyan, B. D.; Lossdorfer, S.; Wang, L.; *et al*. *Eur. Cell Mater.* **2003**, *6*, 22–27.
454. Zinger, O.; Zhao, G.; Schwartz, Z.; *et al*. *Biomaterials* **2005**, *26*(14), 1837–1847.
455. Wennerberg, A.; Albrektsson, T. *Clin. Oral Implants Res.* **2009**, *20*(Suppl 4), 172–184.
456. Schwarz, F.; Ferrari, D.; Herten, M.; *et al*. *J. Periodontol.* **2007**, *78*(11), 2171–2184.

457. Zhao, G.; Raines, A. L.; Wieland, M.; Schwartz, Z.; Boyan, B. *Biomaterials* **2007**, *28*(18), 2821–2829.
458. Zhao, G.; Schwartz, Z.; Wieland, M.; *et al*. *J. Biomed. Mater. Res. A* **2005**, *74*(1), 49–58.
459. Junker, R.; Dimakis, A.; Thoneick, M.; Jansen, J. A. *Clin. Oral Implants Res.* **2009**, *20*(Suppl 4), 185–206.
460. de Jonge, L. T.; Leeuwenburgh, S. C.; Wolke, J. G.; Jansen, J. A. *Pharm. Res.* **2008**, *25*(10), 2357–2369.
461. Ruoslahti, E. *Annu. Rev. Cell Dev. Biol.* **1996**, *12*, 697–715.
462. Geiger, B.; Bershadsky, A.; Pankov, R.; Yamada, K. M. *Nat. Rev. Mol. Cell Biol.* **2001**, *2*(11), 793–805.
463. Klein, M. O.; Reichert, C.; Koch, D.; Horn, S.; Al-Nawas, B. *Clin. Oral Implants Res.* **2007**, *18*(1), 40–45.
464. García, A. J.; Reyes, C. D. *J. Dent. Res.* **2005**, *84*(5), 407–413.
465. Schliephake, H.; Scharnweber, D.; Dard, M.; *et al*. *Clin. Oral Implants Res.* **2002**, *13*(3), 312–319.
466. Schliephake, H.; Scharnweber, D.; Dard, M.; Sewing, A.; Aref, A.; Roessler, S. *J. Biomed. Mater. Res. B Appl. Biomater.* **2005**, *73*(1), 88–96.
467. Hall, J.; Sorensen, R. G.; Wozney, J. M.; Wikesjö, U. M. *J. Clin. Periodontol.* **2007**, *34*(5), 444–451.
468. Becker, J.; Kirsch, A.; Schwarz, F.; *et al*. *Clin. Oral Investig.* **2006**, *10*(3), 217–224.
469. Schmidmaier, G.; Wildemann, B.; Cromme, F.; Kandziora, F.; Haas, N. P.; Raschke, M. *Bone* **2002**, *30*(6), 816–822.
470. Lind, M.; Overgaard, S.; Søballe, K.; Nguyen, T.; Ongpipattanakul, B.; Bünger, C. *J. Orthop. Res.* **1996**, *14*(3), 343–350.
471. Solheim, E. *Int. Orthop.* **1998**, *22*(6), 410–416.
472. Schliephake, H. *Int. J. Oral Maxillofac. Surg.* **2002**, *31*(5), 469–484.
473. Liu, Y.; Enggist, L.; Kuffer, A. F.; Buser, D.; Hunziker, E. B. *Biomaterials* **2007**, *28*(16), 2677–2686.
474. Liu, Y.; Huse, R. O.; de Groot, K.; Buser, D.; Hunziker, E. B. *J. Dent. Res.* **2007**, *86*(1), 84–89.
475. Wikesjö, U. M.; Qahash, M.; Polimeni, G.; *et al*. *J. Clin. Periodontol.* **2008**, *35*(11), 1001–1010.
476. Schliephake, H.; Aref, A.; Scharnweber, D.; Bierbaum, S.; Roessler, S.; Sewing, A. *Clin. Oral Implants Res.* **2005**, *16*(5), 563–569.
477. Chen, D.; Zhao, M.; Mundy, G. R. *Growth Factors* **2004**, *22*, 233–241.
478. Rosen, V. *Ann. NY Acad. Sci.* **2006**, *1068*, 19–25.
479. Junker, R.; Dimakis, A.; Thoneick, M.; Jansen, J. A. *Clin. Oral Implants Res.* **2009**, *20*(Suppl 4), 185–206.
480. Blanes, R. J. *Clin. Oral Implants Res.* **2009**, *20*(Suppl 4), 67–72.
481. Tawil, G.; Aboujaoude, N.; Younan, R. *Int. J. Oral Maxillofac. Implants* **2006**, *21*(2), 275–282.
482. Adell, R.; Lekholm, U.; Rockler, B.; *et al*. *Int. J. Oral Maxillofac. Surg.* **1986**, *15*(1), 39–52.
483. Berglundh, T.; Abrahamsson, I.; Lindhe, J. *J. Clin. Periodontol.* **2005**, *32*(9), 925–932.
484. Jung, Y. C.; Han, C. H.; Lee, K. W. *Int. J. Oral Maxillofac. Implants* **1996**, *11*(6), 811–818.
485. Hermann, J. S.; Buser, D.; Schenk, R. K.; Cochran, D. L. *J. Periodontol.* **2000**, *71*(9), 1412–1424.
486. Hermann, J. S.; Cochran, D. L.; Nummikoski, P. V.; Buser, D. *J. Periodontol.* **1997**, *68*(11), 1117–1130.
487. Jahn, M.; d'Hoedt, B. *Z. Zahnärztl. Implantol.* **1992**, *8*, 221–226.
488. Albrektsson, T.; Zarb, G.; Worthington, P.; Eriksson, A. R. *Int. J. Oral Maxillofac. Implants* **1986**, *1*(1), 11–25.
489. Garcia, R. V.; Kraehenmann, M. A.; Bezerra, F. J.; Mendes, C. M.; Rapp, G. E. *Clin. Oral Implants Res.* **2008**, *19*(10), 991–996.
490. Cecchinato, D.; Olsson, C.; Lindhe, J. *J. Clin. Periodontol.* **2004**, *31*(4), 299–308.
491. Astrand, P.; Engquist, B.; Anzén, B.; *et al*. *Clin. Implant Dent. Relat. Res.* **2002**, *4*(3), 115–127.
492. King, G. N.; Hermann, J. S.; Schoolfield, J. D.; Buser, D.; Cochran, D. L. *J. Periodontol.* **2002**, *73*(10), 1111–1117.
493. Hermann, J. S.; Schoolfield, J. D.; Schenk, R. K.; Buser, D.; Cochran, D. L. *J. Periodontol.* **2001**, *72*(10), 1372–1383.
494. Hansson, S. *Clin. Implant Dent. Relat. Res.* **2000**, *2*(1), 33–41.
495. Weng, D.; Nagata, M. J.; Bell, M.; Bosco, A. F.; de Melo, L. G.; Richter, E. J. *Clin. Oral Implants Res.* **2008**, *19*(11), 1141–1147.
496. Covani, U.; Marconcini, S.; Crespi, R.; Barone, A. *Implant Dent.* **2006**, *15*(3), 298–304.
497. Ferguson, S. J.; Broggini, N.; Wieland, M.; *et al*. *J. Biomed. Mater. Res. A* **2006**, *78*(2), 291–297.
498. Davarpanah, M.; Martinez, H.; Tecucianu, J. F. *Int. J. Oral Maxillofac. Implants* **2000**, *15*(6), 865–872.
499. Lazzara, R. J.; Porter, S. S. *Int. J. Periodontics Restorative Dent.* **2006**, *26*(1), 9–17.
500. Cappiello, M.; Luongo, R.; Di Iorio, D.; Bugea, C.; Cocchetto, R.; Celletti, R. *Int. J. Periodontics Restorative Dent.* **2008**, *28*(4), 347–355.
501. Hürzeler, M.; Fickl, S.; Zuhr, O.; Wachtel, H. C. *J. Oral Maxillofac. Surg.* **2007**, *65*(7 Suppl 1), 33–39.
502. Cochran, D. L.; Bosshardt, D. D.; Grize, L.; *et al*. *J. Periodontol.* **2009**, *80*(4), 609–617.
503. Jung, R. E.; Jones, A. A.; Higginbottom, F. L.; *et al*. *J. Periodontol.* **2008**, *79*(2), 260–270.
504. Canullo, L.; Goglia, G.; Iurlaro, G.; Iannello, G. *Int. J. Prosthodont.* **2009**, *22*(3), 277–282.
505. Prosper, L.; Redaelli, S.; Pasi, M.; Zarone, F.; Radaelli, G.; Gherlone, E. F. *Int. J. Oral Maxillofac. Implants* **2009**, *24*(2), 299–308.
506. Vigolo, P.; Givani, A. *Int. J. Oral Maxillofac. Implants* **2009**, *24*(1), 103–109.
507. Zechner, W.; Trinkl, N.; Watzak, G.; *et al*. *Int. J. Oral Maxillofac. Implants* **2004**, *19*(2), 216–221.
508. Hänggi, M. P.; Hänggi, D. C.; Schoolfield, J. D.; Meyer, J.; Cochran, D. L.; Hermann, J. S. *J. Periodontol.* **2005**, *76*(5), 791–802.
509. Botticelli, D.; Berglundh, T.; Persson, L. G.; Lindhe, J. *J. Clin. Periodontol.* **2005**, *32*(5), 448–455.
510. Stein, A. E.; McGlmphy, E. A.; Johnston, W. M.; Larsen, P. E. *Int. J. Oral Maxillofac. Implants* **2009**, *24*(5), 910–919.
511. Hämmerle, C. H.; Brägger, U.; Bürgin, W.; Lang, N. P. *Clin. Oral Implants Res.* **1996**, *7*(2), 111–119.
512. Shin, Y. K.; Han, C. H.; Heo, S. J.; Kim, S.; Chun, H. J. *Int. J. Oral Maxillofac. Implants* **2006**, *21*(5), 789–794.
513. Nickenig, H. J.; Wichmann, M.; Schlegel, K. A.; Nkenke, E.; Eitner, S. *Clin. Oral Implants Res.* **2009**, Epub ahead of print.
514. Abrahamsson, I.; Berglundh, T. *Clin. Implant Dent. Relat. Res.* **2006**, *8*(3), 107–113.
515. Esposito, M.; Grusovin, M. G.; Felice, P.; Karatzopoulos, G.; Worthington, H. V.; Coulthard, P. *Cochrane Database Syst Rev.* **2009**, *4*, CD003607.
516. Jofre, J.; Hamada, T.; Nishimura, M.; Klattenhoff, C. *Clin. Oral Implants Res.* **2010**, *21*(2), 243–249.

Relevant Websites

http://www.osseo.org/ – Academy of Osseointegration.
http://www.eao.org/ – European Association for Osseointegration.
www.iti.org – International Team for Implantology.

6.620. Dental Graft Materials

C Knabe, Philipps University Marburg, Marburg, Germany
P Ducheyne, University of Pennsylvania, Philadelphia, PA, USA
M Stiller, Charité – University Medical Center Berlin, Berlin, Germany

© 2011 Elsevier Ltd. All rights reserved.

6.620.1.	**Introduction**	305
6.620.2.	**Categories of Dental Grafting Materials**	306
6.620.2.1.	Hydroxyapatites	306
6.620.2.2.	TCP Ceramics	306
6.620.2.3.	Bioactive Glass 45S5	307
6.620.2.4.	Calcium Carbonate	307
6.620.2.5.	Biphasic HA TCP Materials	307
6.620.2.6.	Demineralized Freeze-Dried Bone Allografts and Mineralized Freeze-Dried Bone Allografts	307
6.620.2.7.	Polymer-Based Scaffolds for Craniofacial Tissue Engineering	308
6.620.2.8.	Bone Grafting Cements	309
6.620.2.9.	Combination of Bone Grafting Materials with Platelet-Rich Plasma	309
6.620.2.10.	Combined Use of Grafting Materials and Growth Factors or Other Biologicals	309
6.620.2.10.1.	Growth factors	309
6.620.2.10.2.	Enamel matrix derivative	310
6.620.3.	**Requirements and Novel Developments for Dental Graft Materials**	310
6.620.3.1.	Requirements for Dental Graft Materials	310
6.620.3.2.	Novel Developments for Dental Graft Materials	310
6.620.3.2.1.	Calcium alkali orthophosphate materials	310
6.620.3.2.2.	The effect of calcium-alkali-orthophosphate ceramics on the expression of the osteoblastic phenotype *in vitro*	311
6.620.3.2.3.	The effect of calcium alkali orthophosphates on bone formation and osteoblastic phenotype expression *in vivo*	312
6.620.3.2.4.	The effect of calcium alkali orthophosphate ceramics on cell adhesion and intracellular signaling mechanisms	314
6.620.3.2.5.	The effect of calcium alkali orthophosphate-based bone substitute cements on bone formation and osteogenic marker expression *in vivo*	314
6.620.3.2.6.	The effect of β-TCP particles with varying porosity on osteogenesis after sinus floor augmentation in humans	315
6.620.3.2.7.	Three-dimensional calcium-alkali-phosphate-based scaffolds for bone tissue engineering	318
6.620.4.	**Summary**	318
References		319

Abbreviations

BG45S5	Bioactive glass 45S5
BMP	Bone morphogenetic protein
CT	Computed tomography
DFDBAs	Demineralized freeze-dried bone allografts
FDA	Food and Drug Administration
HA	Hydroxyapatite
MFDBA	Mineralized freeze-dried bone allografts
PRP	Platelet-rich plasma
rhBMP	Recombinant BMP
TCP	Tricalcium phosphate
TMJ	Temporomandibular joint

6.620.1. Introduction

The use of oral implants has become a common treatment to replace missing or lost teeth.[1,2] When teeth are missing, the surrounding bone and soft tissue is challenged as a result of the natural resorptive process subsequent to extraction. Furthermore, the prosthodontic requirements for the design of the implant superstructure (rather than the bone volume available) dictate the position in which the dental implants have to be placed. This has been called 'restoration-driven' implant placement.[1,3–5] Consequently, resorption of the alveolar ridge after tooth extraction frequently mandates site development by augmentation before implants can be placed.[1,6–8]

The current gold standard for bone reconstruction in implant dentistry and craniomaxillofacila surgery is the use of autogenous bone grafts.[9–15] Among the various techniques to reconstruct or enlarge a deficient alveolar ridge, the concept of guided bone regeneration (GBR)[12] has become a predictable and well-documented surgical approach.[11] The need for localized ridge augmentation prior to the placement of dental implants has been one of the clinical indications for GBR.[12] At present, autogenous bone grafts are preferably combined with barrier membranes.[9,11,16] These autografts have been used to reduce the defect volume, thereby stabilizing the blood clot,[17] and to support the membrane as a space-maintaining device,

thus preventing their collapse into large defects.[12,13,18,19] Furthermore, augmentation of the maxillary sinus floor with autogenous bone grafts has become a well-established preimplantology procedure for alveolar ridge augmentation of the posterior maxilla.[20,21] The main disadvantages of autogenous bone grafts have been the need for an additional surgical site, increased donor site morbidity, insufficient volume of (intraorally) harvested bone, and the need to use general anesthesia for extraoral bone harvesting.[15,22–25] Using biodegradable bone substitutes as a membrane-supporting device would simplify GBR, as it avoids second-site surgery for autograft harvesting.[9,13] This is also true for sinus floor elevation procedures.[22,23,25] On account of the significant increase in dental implants placed and also in alveolar ridge augmentation procedures performed over the last two decades, there also has been an ever-increasing demand for adequate bone grafting materials for implant dentistry.

These bone substitute materials should undergo remodeling and substitution by newly formed functional bone tissue in view of placing dental implants in such augmented sites.[9,26–33] Bioactive calcium phosphate ceramics and bioactive glasses are candidate biomaterials which qualify as bone substitutes for this kind of application, as they are widely used in orthopedics.[34–38] Alloplastic bone substitute materials are superior to freeze-dried human allografts due to their safety in terms of disease transmission and immunological aspects.[9,24,39]

Among the ceramics most commonly investigated for use in bone regeneration are β-tricalcium phosphate (β-TCP),[36,37,40] hydroxyapatite (HA),[37,41–44] and bioactive glass.[34,35,45] All of these materials are biocompatible[37,38] and osteoconductive.[33–35,37,46–51] However, they differ considerably in the rate of resorption and in the rate of bone formation at their surface. Dense HA ceramics resorb very slowly compared to β-TCP[37,42,52] and bioactive glass.[34,35,50,53]

6.620.2. Categories of Dental Grafting Materials

As mentioned earlier, the majority of the dental grafting materials are calcium phosphate-based. Various HA- and TCP-based dental grafting materials[40,54–62] as well as bioactive glasses and glass ceramics[63–65] have been investigated and proposed as therapies to augment alveolar bone and to promote periodontal regeneration since the 1970s.

6.620.2.1. Hydroxyapatites

Numerous HA-based grafting materials were developed over the last decades. These include HAs, fluorohydroxyapatites, and apatites of coralline origin,[27,28,66–84] synthetic HAs[41] including nanocrystalline HAs such as an aqueous paste of synthetic nanoparticular HA[85–87] as well as bovine deproteinized bone xenograft particles.[88–94]

Most of these materials have been shown to be osteoconductive.[85–87,93,95,96] However, none of these materials exhibit a high biodegradability.[85–87,9697] Typical studies report excellent osteoconductivity.[18,30,70,71,86,87,93,97–110] In this regard, one of the porous bovine-derived HAs that closely resembles HA of bone, namely Bio-Oss™, has been extensively reported in the scientific literature. Its morphology resembles that of cancellous bone. Its excellent osteoconductive properties have been described in numerous *in vivo* preclinical and clinical studies.[18,30,70,71,93,97–112] It has been shown, however, that biopsies sampled 20 months after implantation in the human sinus floor still consisted of 29% residual grafting material, which showed close apposition to the newly formed bone.[97] With this material also three-dimensional (3D) cancellous blocks are available for the purposes of bone tissue engineering.

Various HA block grafts have also been proposed for reconstruction of contour and discontinuity defects in maxillofacial surgery by transplantation of HA-bone composite grafts[113–115] and for use as scaffolds in bone tissue engineering procedures.[116,117]

More recent developments include a peptide-modified HA[118–121] named PepGen P-15. P-15 is a highly conserved linear peptide with a 15 amino acid sequence identical to the sequence contained in the residues 766–780 of the α-chain of type I collagen. PepGen P-15 (Dentsply Friadent, Mannheim, Germany) is a combination of a bovine bone-derived hydroxypaptite with P-15. This material has been shown to accelerate bone formation at its surface at the early stages of wound healing; however, after 6 months, no difference compared to the native HA was noted.[120]

Another development is the use of a nanocrystalline HA embedded in a silica matrix, which is a synthetic HA produced by a sol–gel process in the presence of SiO_2. The use of this material is being advocated as a dental graft material, as it has been shown to exhibit good osteoconductivity and to support neovascularization.[85,122–125] However, it displays a limited biodegradability.[85]

6.620.2.2. TCP Ceramics

While early β-TCP ceramic products were plagued by insufficient phase purity and inhomogenous solubility characteristics, which led to varying biological and clinical outcomes, more recent improvements in β-TCP ceramics include products with a high phase purity (>99%) and homogenous solubility characteristics, so as to prevent premature separation of microparticles from the structural compound.[126] In the past, these types of microparticles have been shown to elicit inflammatory tissue responses.[126] Furthermore, the use of TCP particles with increased porosity (65% vs. 35% porosity) has been proposed in order to increase the biodegradability.[126–132] These particles exhibit a material structure with pores on different length scales micropores (size: <50 μm), mesopores (size: 50–100 μm), and macropores (size: 100–500 μm), designed to enhance the degradation process. This structure allows for a reduced bulk density. The microporosity allows circulation of biological fluids, increases the specific surface area, and thus accelerates the degradation process. The interconnectivity of the pores creates a capillary force that actively draws cells and nutrients in the center of the particles. The macroporosity is created to encourage the ingrowth of bone by permitting penetration of cells and vascularization.[126] Over the last decade, numerous studies have been published regarding the *in vivo* preclinical and clinical performance of TCP ceramic granules in implant dentistry, confirming the excellent osteoconductivity of various TCP ceramic products (**Figure 1**).[9,13,33,46,47,50,98,127,128,132–154] Long-term results in human patients were shown to be equal to those of autogenous bone grafts.[140,155] Recent developments also

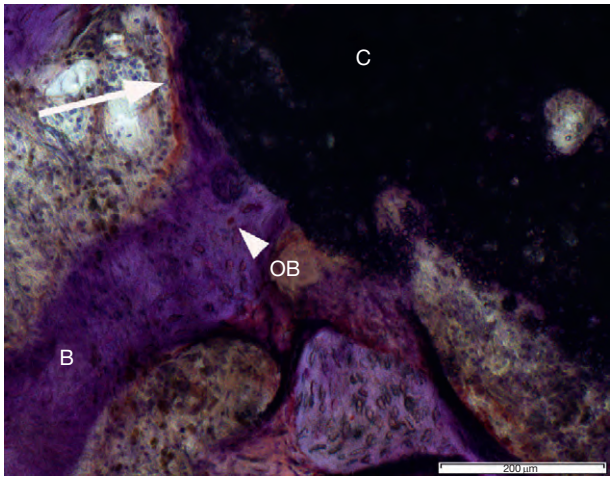

Figure 1 Resin-embedded human biopsy stained immunohistochemically for osteocalcin after deacrylation. The biopsy was sampled 6 months after augmentation of the sinus floor with β-tricalcium phosphate (β-TCP) particles (C) with 35% porosity. Intense staining of cells and unmineralized fibrous matrix (of the osteogenic mesenchym) lining the newly formed bony trabeculae (B) that are in contact with the TCP particle (C) is evident (arrow). OB (arrow head) – intensely stained osteoblast. These findings demonstrate the good bone-bonding properties of TCP. Furthermore, 6 months after implantation, bone formation and matrix mineralization are still actively progressing in the tissue surrounding the TCP particles. Undecalcified sawed section counterstained with hematoxylin. Bar = 200 µm.

include the clinical use of β-TCP block grafts in implant dentistry and maxillocraniofacial surgery.[156] Furthermore, the use of TCP ceramics with zinc or silica additives has been proposed with the goal to further enhance the osteogenic effect of TCPs as well as their mechanical properties.[157–159] Even more recently, a TCP putty-like material with kneadable properties has been introduced. It consists of pure, synthetic β-TCP granules of a wide range of particle sizes in a fermented sodium hyaluronate carrier. This material, however, does not set *in situ*, but with respect to surgical handling is advantageous over granules for a number of surgical uses. Furthermore, autologous blood or its derivates, bone marrow aspirate or bone chips as well as antibiotics can easily be added to the material prior to the surgical application (**Figure 2**).

6.620.2.3. Bioactive Glass 45S5

Bioactive glass (BG45S5) granules have been used for alveolar ridge augmentation and periodontal repair for more than a decade, and their excellent osteoconductivity, bone-bonding properties, and stimulatory effect on bone formation have been demonstrated by numerous *in vivo* preclinical and clinical studies since.[34,35,50,53,64,129,130,136,146,160–174] Among the various bone grafting materials used in implant dentistry, BG45S5 granules of a narrow size range were the first material, for which extensive and comprehensive histological data regarding their biodegradability derived from human biopsies were reported.[50,136,146] These biopsies were sampled at implant placement in clinical studies. Furthermore, the use of preexcavated granules has been proposed in order to even further enhance the osteogenic effect of BG45S5 granules of a narrow size range.[175]

6.620.2.4. Calcium Carbonate

Over the last two decades, a madroporic coralline calcium carbonate material (product name: Bio-coral) has been proposed as bone grafting material in implant dentistry, periodontology, and oral and maxillofacial surgery.[176–190] This material has been shown to exhibit good osteoconductive properties in combination with a limited biodegradability.[178,182] Furthermore, promising long-term clinical results have been demonstrated with respect to bony regeneration of infrabony periodontal defects.[189] More recently, this material has also been used for fabricating scaffolds for cell seeding and tissue engineering.[190,191]

6.620.2.5. Biphasic HA TCP Materials

Over the last 5 years, the use of synthetic biphasic HA TCP materials has been introduced for alveolar ridge augmentation. For these materials, a decreasing biodegradability has been demonstrated with increasing HA content.[192] A fully synthetic biphasic calcium phosphate consisting of a mixture of 60% HA and 40% of β-TCP (product name: Straumann Bone Ceramic) has been examined in *in vivo* animal and clinical studies. This material has been shown to display good osteoconductivity and support new bone formation.[100,103,192–196] Although this material has been shown to be not fully resorbable, it exhibited greater biodegradability than the bovine-derived HA material Bio-Oss; this, however, was associated with a less favorable bone-bonding behavior.[100]

6.620.2.6. Demineralized Freeze-Dried Bone Allografts and Mineralized Freeze-Dried Bone Allografts

Demineralized freeze-dried bone allografts (DFDBAs) and mineralized freeze-dried bone allografts (MFDBA) have been proposed as substitutes for autologous bone in implant dentistry, periodontology, and oral surgery for more than two decades.[162,164,168,197–230] These materials are inferior to synthetic materials in terms of risk of disease transmission and immunological challenges.[9,24,231] They have been widely used in the United States, while in several European countries, their use has not been approved for dental applications. Furthermore, conflicting results regarding their osteoconductivity and potential to support new bone formation in clinical settings have been reported.[199,218,223,225,228]

Schwartz *et al.*[223] showed that a wide variation in commercial bone bank preparations of DFDBA existed and that the ability to induce new bone formation also varied widely. In addition, commercial DFDBA differed in both size and ability to induce new bone formation, but the two were not related. The authors also pointed out that methods or assays for evaluating the ability of DFDBA to induce new bone should be developed and standardized.[223] In addition, these materials are not fully resorbable, even 4 years after implantation, residual grafting material was present in the human case.[225]

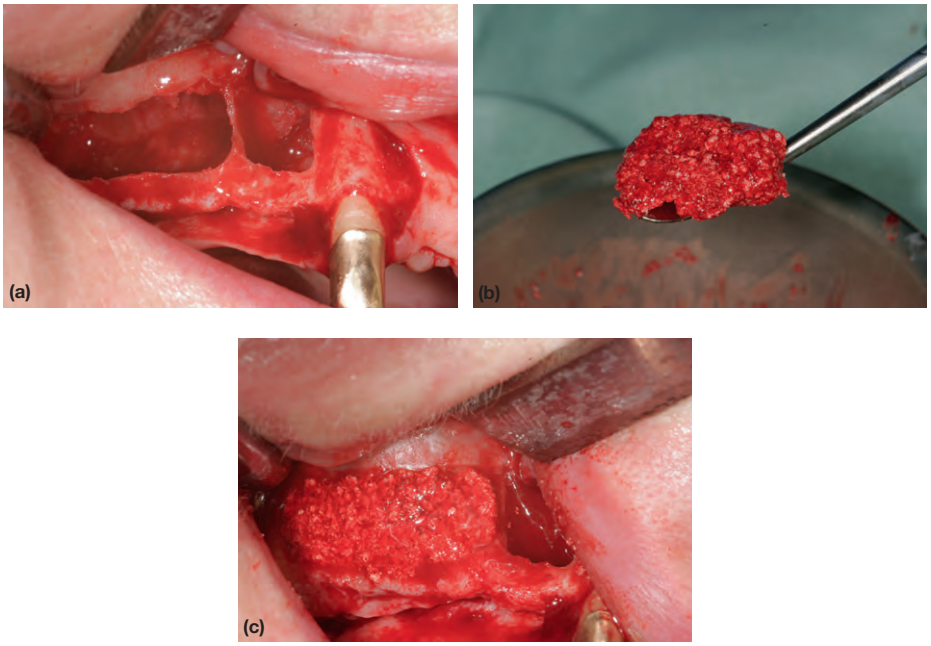

Figure 2 Clinical image of maxillary sinus floor augmentation using a tricalcium phosphate (TCP) putty material (a) sinus floor prior to augmentation, (b) TCP putty material which has been mixed with veinous blood, and (c) sinus floor after application of the TCP putty material.

6.620.2.7. Polymer-Based Scaffolds for Craniofacial Tissue Engineering

Over the last two decades, there have been increasing efforts to develop adequate scaffolds and concepts for bone-tissue engineering in the craniomaxillofacial domain.[232] However, only few of these concepts have reached the clinical arena so far.

In 2001, the 'bioseed oral bone' concept was introduced. Cell-fibrin constructs, that is, pellets made from polylactide, polyglycolide, and/or poly-*p*-dioxanon, which were coated with fibrin glue and cultured for 4–6 weeks with autologous periost-derived osteoblasts, were used for sinus augmentation of the severely resorbed posterior maxilla.[233–235] In clinical studies, this approach resulted in the formation of lamellar bone within 4 months after sinus floor augmentation, thereby providing a reliable basis for dental implant placement. The drawbacks of this approach were the high costs involved and the 4–6 week waiting period between the harvesting of the periosteum and the delivery of the cell-seeded pellets for sinus floor augmentation surgery. This concept, however, is one of the few tissue engineering approaches that has found somewhat wider clinical use in implant dentistry so far.

Hollister *et al.*[236–238] developed an image-based and integrated approach for engineering craniofacial scaffolds. This design/fabrication approach can create scaffolds with designed porous architecture to match craniofacial anatomy. These scaffolds were also designed to support bone regeneration for craniofacial reconstruction and, furthermore, to exhibit mechanical properties in the range of those of craniofacial tissue. Using image-based design (IBD) and computer software, precisely sized and shaped scaffolds created via selective laser sintering of polycaprolactone were developed for osseous tissue regeneration.[239] This way, polycaprolactone was used to create a condylar ramus unit (CRU) scaffold for application in temporomandibular joint (TMJ) reconstruction. These scaffolds were used successfully for the reconstruction of the mandibular ramus and TMJ in minipigs.[239] IBD and solid free-form (SFF) fabrication was also used to generate scaffolds that are load bearing and match patient and defect site geometry. Using this methodology, poly-L-lactic acid/HA composite scaffolds which were differentially seeded with fibroblasts transduced with an adenovirus expressing bone morphogenetic protein-7 (BMP-7) in the ceramic phase and fully differentiated chondrocytes in the polymeric phase were developed in order to regenerate osteochondral defects and, ultimately, the TMJ.[240]

3D polycaprolactone scaffolds with controlled microarchitecture were developed for fabricating customized cell-polymer constructs for the repair of calvarial defects using calvarial osteoblasts and mesenchymal progenitor cells in combination with these scaffolds and fibrin glue.[241,242] Furthermore, bone-marrow-coated polycaprolactone scaffolds were successfully used for the reconstruction of orbital and craniofacial defects in pigs.[243,244] More recently, polycaprolactone-20% TCP scaffolds were utilized in a pilot study in combination with platelet-rich plasma for the treatment of critical-sized defects of the mandible.[245] Also, a polycaprolactone-TCP/collagen scaffold loaded with recombinant BMP (rhBMP) was developed for the repair of calvarial bone defects, and the stimulation of healing within a rat calvarial defect was demonstrated.[246] Moreover, very recently, successful use of a customized polycaprolactone TCP scaffold fabricated by the rapid prototyping technology fused deposition modeling (CAD/CAM) for calvarial reconstruction in a human case was described.[247]

Hydrogels were proposed as scaffolds for craniofacial bone tissue engineering and delivery of stem cells and growth factors.[248–251] Very recently, calcium cement scaffolds with mesenchymal stem cells were developed for craniofacial tissue

engineering.[252,253] Furthermore, the use of rhBMP-2 loaded porous calcium phosphate cements was proposed for craniofacial tissue engineering.[254]

With most of these tissue engineering approaches, however, controlled clinical studies will have to follow for these concepts to proceed to the clinical arena.

Current research efforts in craniofacial tissue engineering also deal extensively with biomaterial matrices and scaffolds with controlled release of signaling cues for stem cells, and integrated tissue engineering approaches[255] as well as with 'guided interplay' between biomaterial scaffolds, growth factors, and local cell populations toward the restoration of the original architecture and function of complex tissues.[256,257] Furthermore, various approaches to pursue adequate vascularization of bioengineered constructs for repair of extensive discontinuity bone defects are being investigated.[258–263] This is in addition to optimizing pore-size distribution and pore-geometry of various scaffolds.

6.620.2.8. Bone Grafting Cements

To fill bone defects, currently available calcium phosphate bone grafting materials are mainly applied as granules. Bone substitutes with improved surgical handling properties include injectable and moldable calcium phosphate cements in paste or putty form that can be introduced into a bony defect with a spatula or injected with a syringe; they subsequently set *in situ*. These properties make this an intriguing group of materials for bone reconstruction, as by this way, these materials exhibit advantageous surgical handling properties for a number of surgical applications. Consequently, over the last two decades, the use of calcium phosphate-based cements and in a few cases, that of polymer-based cements, have been proposed for craniofacial bone grafting.[264–288] With most currently available cements, however, HA or calcium-deficient HA[289–292] is formed during setting, which limits their biodegradability.[289] This has initiated efforts to develop resorbable cements with improved biodegradability which form TCP or calcium alkali orthophosphates during setting.[261,293–298]

6.620.2.9. Combination of Bone Grafting Materials with Platelet-Rich Plasma

Numerous clinical and animal studies have explored the combined use of bone grafting materials and platelet-rich plasma [PRP] with the intent to enhance bone regeneration. The majority of the studies, however, failed to demonstrate an additional benefit when platelet-rich plasma [PRP] was used in addition to various bone grafting materials. As such, these studies did not show a significant improvement of clinical and histological outcomes.[279,280,299–302]

6.620.2.10. Combined Use of Grafting Materials and Growth Factors or Other Biologicals

6.620.2.10.1. Growth factors

Over the last two decades, numerous preclinical studies have explored the use of rhBMP-2 and -7 for bone regeneration in craniomaxillofacial applications.[254,303–321] Furthermore, absorbable collagen sponges and collagen sponges with incorporated HA and TCP particles were proposed as carriers for recombinant human BMP-2, -7, -10 as well as nerve growth factor β for use in craniofacial bone regeneration.[322–330] In addition, the use of recombinant human platelet-derived growth factor BB (rhPDGF-BB) and transforming growth factor β (TGF-β) have been investigated.[254,331]

Preclinical studies have shown that rhBMP-2 and -7 induces normal physiologic bone in clinically relevant defects in the craniofacial skeleton. The newly formed bone develops properties similar to those of the adjacent resident bone and allows placement, osseointegration/re-osseointegration, and functional loading of endosseous implants. Over the last 6 years also, some clinical reports and studies have been published.[263,303,304,332–337] A very visible report in this regard was the use of rhBMP-7 for preparing a customized vascularized tissue-engineered mandible, with the patient being used as a living bioreactor.[263,335] In this case, rhBMP-7 was combined with bovine-derived HA xenograft particles, bone morrow aspirate, and a titanium mesh shaped after the patient's mandible. However, further clinical studies optimizing dose and delivery technologies,[338,339] including the development of scaffolds with controlled release properties, as well as optimizing conditions for stimulation of bone growth, are needed. The use of rhBMP-2 and -7 for craniomaxillofacial application only received approval in Europe and by the US Food and Drug Administration (FDA) in 2005.[340] Furthermore, the aspect of the high costs involved in the use of these growth factors has had a somewhat limiting effect with respect to achieving wide clinical use in implant dentistry and other craniomaxillofacial applications.

In 2008, the FDA[341] published a safety review communication regarding the use of a PDGF-containing product 'Regranex' in cancer patients. An epidemiologic study that was performed to investigate the possibility of an increased risk of cancer in patients with diabetes who applied the product 'Regranex' (a topical medicine) directly to their foot and leg ulcers showed that the risk of death from cancer in patients who used three or more tubes of Regranex was 5 times higher than in those patients who did not use Regranex. However, the risk of getting new cancers among Regranex users was not increased compared to nonusers. As BMPs also enhance the vascularization of the regenerated tissue similar to PDGF, this FDA safety review communication raised major concerns with respect to the use of growth factors such as BMPs and PDGF for bone reconstruction and bone tissue engineering in tumor patients. It is useful to point out that tumor patients with major squamous cell carcinomas comprise a major patient population in maxillofacial surgery. This group of patients requires extensive surgery for bone reconstruction of the bone discontinuities arising from tumor resection in major portions of the mandible or maxilla. Thus, the question whether the use of growth factors for bone tissue regeneration in tumor patients increases the risk of relapse or metastases, warrants further investigation.

In 2008, the FDA[342] published a public health notification regarding life-threatening complications associated with recombinant human BMP application in cervical spine fusion, which involved airway obstruction and compression of major blood vessels and nervous structures in the head-neck region caused by extensive swelling, thereby resulting in patient

fatalities. Consequently, preclinical and clinical studies are needed to ensure that this type of complication can reliably be avoided when using BMPs for major mandibular or craniofacial bone reconstruction.

Recently, a β-TCP coated with recombinant human growth and differentiation factor 5 (rhGDF-5) was developed, and the results of a prospective, randomized multicenter clinical trial were recently reported. The authors investigated the potential benefit of rhGDF-5 coated onto β-TCP (rhGDF-5/β-TCP) to support bone formation after sinus floor augmentation.[343] rhGDF-5/β-TCP was found to be as effective for sinus floor augmentation as the control treatment with autologous bone, which was mixed with β-TCP. As very low amounts of anti-rhGDF-5 antibodies were transiently detected in some patients who received rhGDF-5, further investigations regarding efficacy and safety will be carried out in larger patient populations.[343]

6.620.2.10.2. Enamel matrix derivative

Some clinical and preclinical animal studies examined the combined use of various bone grafting materials and an enamel matrix derivative (EMD) for bone and periodontal regeneration.[221,331,344–346] In these studies, a trend was observed toward more bone formation and improvement in clinical outcomes, when EMD was combined with freeze-dried bone allograft, bovine-derived bone xenograft, and bioactive glass.[221,331,344–346] However, larger prospective controlled clinical trials are needed to confirm these findings.[221,345,346]

Evaluation of various dental grafting materials by comparing them with one another is fraught with uncertainty, as there are only few comparative animal and controlled clinical studies that compare several of these materials in the same study or in studies using identical study designs.[347] Furthermore, in order to ultimately prove the superiority of any of these materials or any of these tissue engineering approaches to any other materials/approaches or to autogenous bone graft as the gold standard, long-term, that is, 2-, 5-, and 10-year data from prospective controlled clinical studies would need to be provided, which is a gargantuan task. Such studies would need to show greater regenerated bone volume and higher survival rates for dental implants placed in areas augmented with these grafting materials or tissue engineering approaches, in comparison to areas in which autogenous bone, any other grafting material, or any other tissue engineering approach was used.

6.620.3. Requirements and Novel Developments for Dental Graft Materials

6.620.3.1. Requirements for Dental Graft Materials

As outlined earlier, over the last decade, the use of TCP and BG45S5 particles as alloplastic bone graft materials for alveolar ridge augmentation and sinus floor elevation procedures has received increasing attention in implant dentistry.[33,46,47,50,136,146,150,151,155] As also outlined earlier, the same is true for bovine deproteinized bone xenograft particles (product name: Bio-Oss®) that closely resemble the native HA of bone, have excellent osteoconductive properties, and exhibit a limited biodegradability.[18,30,70,71,97–110] Even with β-TCP, biodegradation has been reported to be incomplete 9.5 months after grafting in the human mandible.[47] Histologic examination of these biopsies revealed that 34% of the biopsy consisted of mineralized bone tissue and 29% of remaining β-TCP.[47] Biopsies sampled at 8 months after sinus floor augmentation consisted of 20% mineralized bone and 44% remaining β-TCP.[47] With respect to BG45S5 particles of a narrow size range, Tadjoedin *et al.*[50] reported that after grafting in the human sinus floor, BG particles appeared to resorb within 1–2 years. This was by dissolution rather than by osteoclastic activity.[50] It is useful to consider, though, that at those time points, these particles are no longer original glass, but calcium phosphate formed *in situ* out of the glass. When using mixtures of 80%, 90%, and 100% BG particles and 20%, 10%, and 0% autogenous bone, histomorphometric analysis of biopsies harvested at 4, 6, and 15 months showed that the grafts consisted of 27% mineralized bone tissue at 4 months, 36% bone at 6 months, and 42% bone at 15 months. The volume of the biologically transformed BG particles in the biopsies decreased from 29% at 4 months to 15% at 6 months and 8% at 15 months.[50] Thus, compared to the bone substitute materials which are currently clinically available,[47,50,85,97,100,136,146] there is a significant need for bone substitute materials that degrade more rapidly but still stimulate osteogenesis at the same time.[9,26–32] Particularly in non-load-bearing applications such as alveolar ridge augmentation, a biomaterial used as a bone substitute should be a temporary material serving as a scaffold for bone remodeling. The material must degrade in a controlled fashion into nontoxic products that the body can metabolize or excrete via normal physiological mechanisms.[37] Moreover, this substance should be resorbable and should undergo remodeling and substitution by newly formed functional bone tissue in view of placing dental implants in such augmented sites.[9,26–33] This has initiated an ever-increasing search for bioactive, rapidly resorbable bone grafting materials that exhibit good bone-bonding behavior by stimulating enhanced bone formation at the interface in combination with a high degradation rate. Another important consideration when using grafting materials for sinus floor and alveolar ridge augmentation is the stability of the height and volume of the regenerated bone over time. Consequently, with an ideal grafting material, reduction in height and volume should be minimal and should not exceed that in the presence of autogenous bone grafts. Furthermore, as outlined previously, dental graft materials have been most widely used as granules. However, because of the increasing number of surgical techniques and procedures used for bone regeneration in oral and craniomaxillofacial surgery, there has been a growing demand for resorbable bone grafting materials that can be either injected into defects in paste form or applied as putty that sets *in situ*. In addition, there is equal demand for biodegradable 3D blocks and scaffolds for bone tissue engineering purposes.

6.620.3.2. Novel Developments for Dental Graft Materials

6.620.3.2.1. Calcium alkali orthophosphate materials

Thus, considerable efforts have been undertaken to produce rapidly resorbable bone substitute materials that exhibit both excellent bone-bonding behavior by stimulating enhanced

bone formation and a high degradation rate. This has led to the development of a series of novel, bioactive, rapidly resorbable, glass ceramic calcium-alkali orthophosphate materials.[348–350] These are glassy/crystalline calcium alkali orthophosphates which exhibit stable crystalline $Ca_2KNa(PO_4)_2$ and $Ca_{10}[K/Na](PO_4)_7$ phases.[348–351] These materials were designed to exhibit a higher degree of biodegradability compared to TCP[348,349,352,353] and therefore could serve as excellent alloplastic materials. In fact, these materials have a higher solubility than TCP. Another approach to increase the solubility and biodegradability of calcium-orthophosphates is by adding diphosphates ($Ca_2P_2O_7$). Diphosphates have a higher solubility than orthophosphates and they are transiently formed *in vivo* during the mineralization process of the bone matrix. A number of *in vitro* and *in vivo* studies, which examined calcium phosphates to which diphosphates were added, yielded encouraging results.[354–357] This prompted Berger to synthesize a calcium alkali orthophosphate ceramic with a small portion of diphosphates.[358] He reported that there was an additional effect on the dissolution rate compared to that of the calcium-alkali-orthophosphate. At this time, 3D scaffolds have been fabricated from these calcium alkali orthophosphate ceramic materials, opening interesting perspectives for their use as tissue engineering scaffolds.

6.620.3.2.2. The effect of calcium-alkali-orthophosphate ceramics on the expression of the osteoblastic phenotype in vitro

In recent years, several studies examined the effect of rapidly resorbable calcium alkali orthophosphate bone substitute materials on the expression of osteogenic markers characteristic of the osteoblastic phenotype and compared this behavior to that of the currently clinically used materials β-TCP and BG45S5.

These studies showed that several calcium alkali orthophosphate materials supported osteoblast differentiation to a greater extent than did TCP.[128,290,291,359]

The composition of four of these calcium alkali orthophosphate grafting materials studied, GB14, GB9, GB9/25, and 352i, whose main crystalline phase is either the phase $Ca_2KNa(PO_4)_2$[348,349,351] or $Ca_{10}[K/Na](PO_4)_7$[358], is indicated in Tables 1 and 2. Glass ceramics GB14, GB9, and GB9/25 contain the crystalline phase $Ca_2KNa(PO_4)_2$.[348,349] They contain an amorphous phase, silica phosphate (GB9 and GB9/25), or magnesium potassium phosphate (GB14), respectively. Crystallization occurs spontaneously from the melt, and thus, these bioceramics can be fabricated easily. The dissolution rate of the calcium-alkali orthophosphates depends on the amount of added ions such as Na, K, or Mg. Importantly, GB 9/25[358] also contains a small portion of diphosphates ($Ca_2P_2O_7$), unlike GB9, which does not. This further increases the dissolution rate in comparison to this previously described GB9.[290,348,349,360]

More recently, it was demonstrated that the glass ceramic calcium alkali orthophosphate material GB9 had a significantly greater stimulatory effect on osteoblastic proliferation and differentiation when compared to β-TCP, preconditioned BG45S5, and other calcium-alkali-orthophosphate materials of varying composition, that is, GB14, GB9/25, and 352i (Table 1).[128,290,359] 45S5 discs were preconditioned by a two-step procedure, which resulted in the transformation of the BG surface into a crystalline, carbonated calcium phosphate apatite onto which serum proteins were adsorbed in a second step. Hence, the conditioning treatment of BG produced an *in situ*-formed calcium phosphate surface layer. Figure 3 shows that osteoblastic cells grown for 14 days on GB9 expressed significantly higher levels of the osteogenic markers type I collagen, alkaline phosphatase, osteopontin, osteonectin, and bone sialoprotein than when the same

Table 1 Description of novel calcium-alkali-orthophosphate ceramic bone substitute materials, TCP, and bioglass 45S5

GB14	*GB9*	*GB9/25*	*352i*	*β-TCP*	*Bioglass 45S5™*
Calcium-alkali-orthophosphate: $Ca_2KNa(PO_4)_2$ crystalline phase with a small amorphous portion containing magnesium potassium phosphate	Calcium-alkali-orthophosphate: $Ca_2KNa(PO_4)_2$ crystalline phase with a small amorphous portion containing silica phosphate	Diphosphate containing calcium-alkali-orthophosphate: $Ca_2KNa(PO_4)_2$ crystalline phase and $Ca_2P_2O_7$	Diphosphate containing calcium-alkali-orthophosphate: $Ca_{10}[K/Na](PO_4)_7$, crystalline phase with small addition of SiO_2	Tricalcium-phosphate $Ca_3(PO_4)_2$	(Bioactive glass45S5) Composition (wt%): SiO_2 45.0 CaO 24.5 P_2O_5 6.0 Na_2O 24.5

Table 2 Composition of novel calcium-alkali-orthophosphate ceramic bone grafting materials, TCP, and bioglass 45S5

Bone grafting materials	*CaO*	*P_2O_5*	*Na_2O*	*K_2O*	*MgO*	*SiO_2*
GB14 $Ca_{1.8}KMg_{0.4}Na(PO_4)_2$	30.67	43.14	9.42	14.32	2.45	
GB9 $Ca_2KNa(PO_4)_2 + Mg_2SiO_4$	32.25	40.81	8.91	13.54	2.57	1.92
GB9/25 $Ca_2KNa(PO_4)_2 + Mg_2SiO_4$ $Ca_2P_2O_7$	29.25	44.81	8.41	13.04	2.57	1.92
352i $Ca_{10}[K/Na](PO_4)_7 + SiO_2$	40–45	45–48	5–8	1–2	1–1.5	1–2
TCP $Ca_3(PO_4)_2$						
Bioglass 45S5	24.5	6.0	24.5			45.0

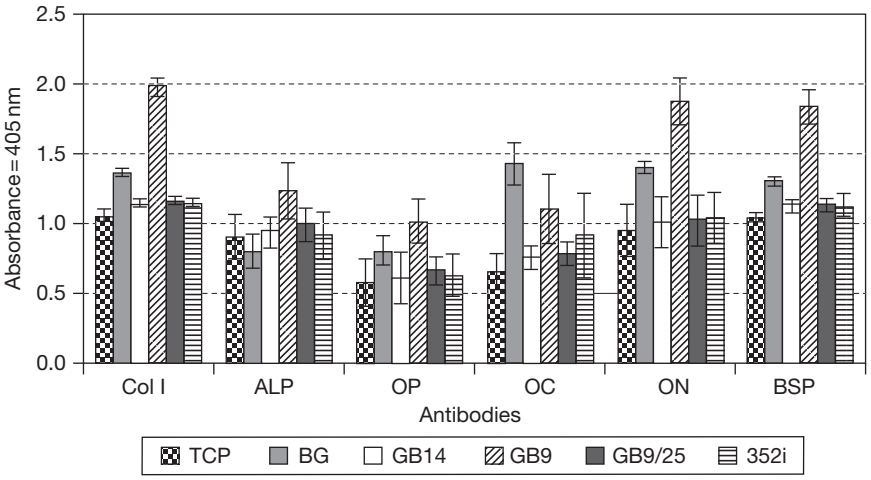

Figure 3 The temporal expression of osteogenic proteins by osteoblasts cultured on different calcium phosphate materials for 14 days. Intracellular protein expression by human osteoblasts is at 14 days of culture on tricalcium phosphate (TCP), bioactive glass 45S5 (BG) GB14, GB9, GB9/25, and 352i. Results are normalized to the internal control β-actin protein for each substratum. All values are mean±standard deviation of eight measurements. Col I, type I collagen; ALP, alkaline phosphatase; OP, osteopontin; OC, osteocalcin; ON, osteonectin; and BSP, bone sialoprotein.

cells were grown in parallel on β-TCP and BG 45S5. Furthermore, BG 45S5 and GB14 induced significantly greater expression of the majority of these osteogenic markers when compared to β-TCP.[128,163]

6.620.3.2.3. The effect of calcium alkali orthophosphates on bone formation and osteoblastic phenotype expression in vivo

Correlating *in vitro* data with *in vivo* phenomena is important in order to test the hypothesis that enhanced osteoblastic cell differentiation *in vitro* leads to more and more expeditious and more copious bone formation at the bone–biomaterial interface *in vivo*. This includes (1) correlating quantitative expression of the osteogenic markers *in vitro* with the amount of bone formed after bioceramics implantation and (2) quantifying the expression of these markers in histological sections obtained from *in vivo* experiments in comparison to the expression of the various markers *in vitro*. To this end, a study was performed in which the effect of the same selection of bioactive ceramics (Table 1) on the expression of osteogenic markers was studied *in vitro* as well as *in vivo*.[128–131,163,361] This required the development of an adequate hard tissue histology technique. Histological evaluation of the bone–biomaterial interface requires undecalcified poly(methylmethacrylate) (PMMA) sections. While various assays have been developed which permit studying the effect of calcium phosphate biomaterials on the expression of osteogenic markers *in vitro*,[290,291,359,362] there have been considerable difficulties to visualize the expression of these markers in undecalcified implant material containing sections of bone obtained from *in vivo* studies.[363] In recent years, a new technique has been developed that facilitates immunohistochemical analysis of osteogenic markers on undecalcified sawed sections of bone which contain ceramic implant materials.[129,364] This rendered it possible to study the effect of ceramic bone substitute materials on osteoblast differentiation and tissue maturation on *ex vivo* specimens by visualizing active osteoblasts in their different stages of differentiation at the bone–biomaterials interface. This experimental capability was in addition to visualizing the expression of various osteogenic markers in the mineralized and unmineralized extracellular matrix components.[129,130] Utilization of this hard tissue technology rendered it possible to study the effect of identical bioactive ceramics on the expression of osteogenic markers *in vitro* and *in vivo* and to test the aforementioned hypothesis.[130,163,298,361,365–367] In this study, calcium alkali orthophosphate ceramic bone substitute materials (Table 1) were implanted in the sheep mandible and sinus floor and compared to currently clinically used synthetic bone substitute materials (β-TCP, BG 45S5).[130,131,163] These materials were selected, because previous *in vitro* studies demonstrated that they stimulated greater differentiation of osteoblasts compared to cells grown on TCP ceramic.[128,290,359]

The various calcium phosphate materials with a particle size range of 300–355 μm were implanted in the sheep mandible for 1, 4, 12, and 24 weeks with the goal to regenerate critical size membrane-protected defects as described by von Arx *et al.*[9] Autogenous bone chips and empty defects, which were filled with collagen sponges, served as controls.[130,163,361] This study examined the aforementioned calcium alkali orthophosphate materials GB9 and GB14. As described previously, GB9, followed by GB14, displayed a significantly greater stimulatory effect on osteoblast proliferation and differentiation *in vitro* compared to TCP, BG 45S5, and other calcium alkali orthophosphates.[128,290,359] It was found that the *in vitro* findings correlated with enhanced bone formation and bone-particle-contact (i.e., bone-bonding behavior) *in vivo* (Figure 4(a) and 4(b)). This in its turn was associated with enhanced expression of type I collagen, osteopontin, osteocalcin, osteonectin, and bone sialoprotein *in vivo* (Figure 5(a) and 5(b)).[130,361] This was associated with a significantly greater decrease in particle area fraction over time, that is, a significantly greater biodegradation (Figure 4(c)).[130,361] Staining for tartrate-resistant

acid phosphatase showed that biodegradation of the various calcium alkali orthophosphates as well as TCP occurred by dissolution rather than by osteoclastic activity.[130,163,361] Furthermore, it is noteworthy that GB9 displayed a significantly greater bone-particle-contact than all other calcium phosphates after only 4 weeks (Figure 4(b)). By 12 weeks, the defects that were augmented using GB9 showed greater bone formation in comparison to those defects that were augmented with autogenous bone chips.[130,163] These findings are clinically very significant, by virtue of autogenous bone being the gold standard. BG 45S5 and TCP displayed good bone-regenerative capacities and bone-bonding behavior (Figures 4(a,b) and 6). However, the biodegradability was lower in comparison to GB9 (Figure 4(c)).[130,163]

With respect to augmentation of the ovine sinus floor, the materials GB9/25 and 352i were studied and compared to TCP. Among these materials, GB9/25 facilitated the greatest extent of bone formation (Figure 7(a)) in combination with the highest biodegradability (Figure 7(b)). This finding was in addition to a more enhanced effect on osteogenic marker expression (Figure 8).

The studies summarized here demonstrate that among the various bioceramic bone grafting materials studied, the calcium alkali orthophosphate material GB9 displayed the greatest stimulatory effect on osteogenesis *in vitro* and *in vivo*, in combination with a high biodegradability, and that in this it was followed by the materials GB14 (Figure 9) and GB9/25.

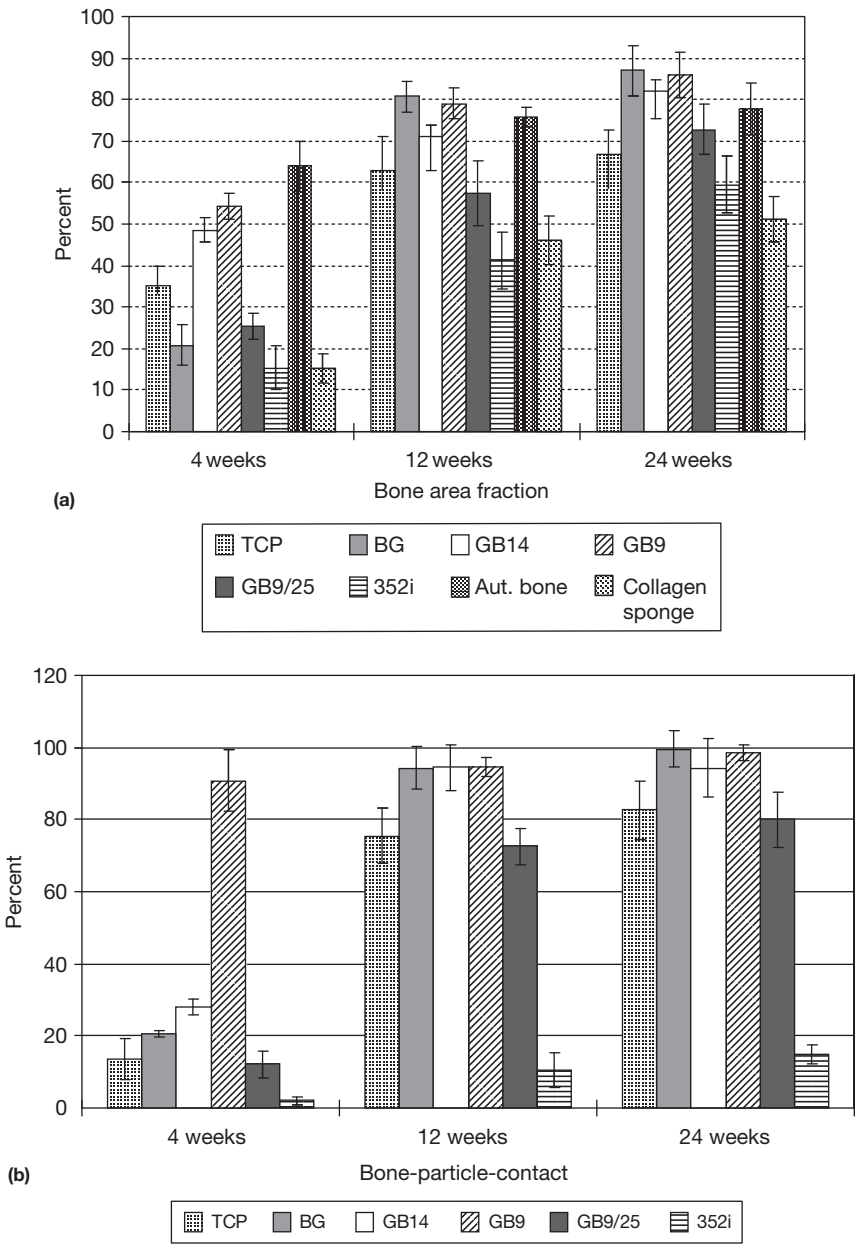

Figure 4 *(Continued)*

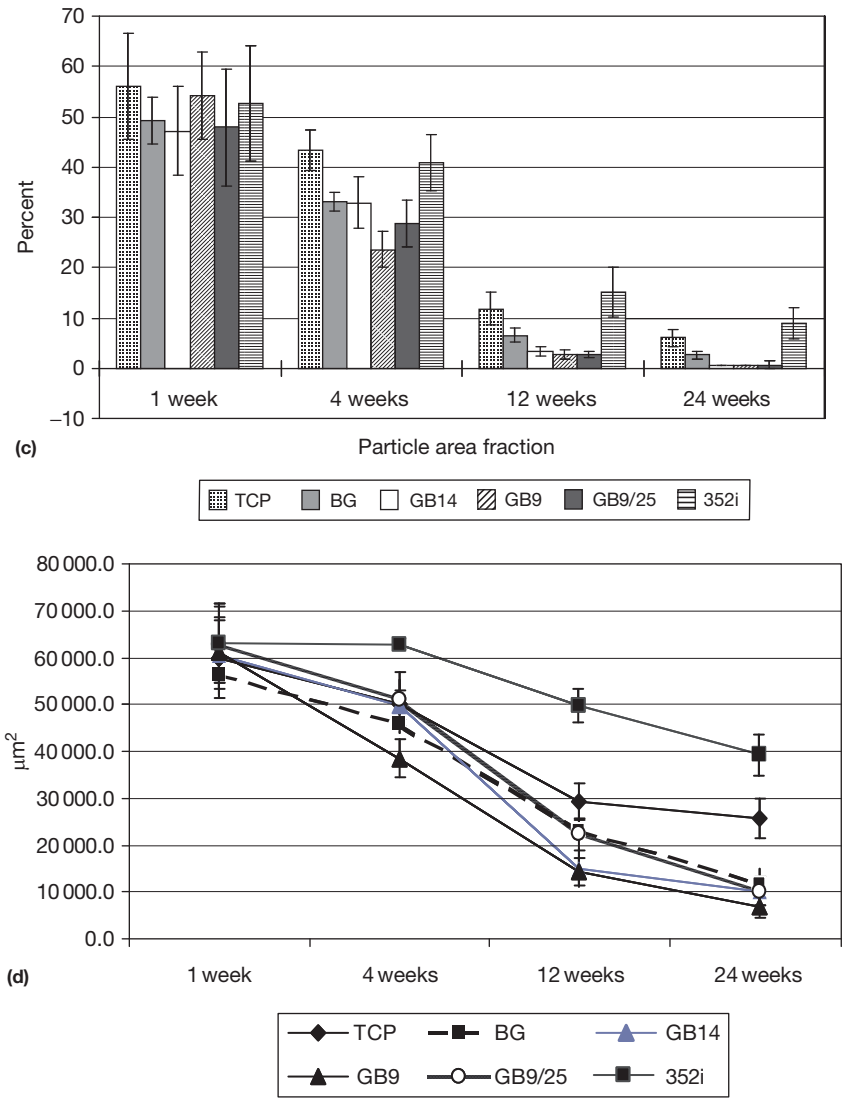

Figure 4 Histomorphometric results of mandibular defects augmented with various calcium phosphates after 1, 4, 12, and 24 weeks of implantation: (a) bone area fraction in the augmented defect area and (b) bone-particle-contact after 1, 4, 12, and 24 weeks of implantation. (c) Particle area fraction and (d) particle size. All values are mean±standard deviation of five measurements. TCP, tricalcium phosphate; BG, bioactive glass; aut. bone, autogenous bone chips; collagen, empty hole defects filled with a collagen sponge.

6.620.3.2.4. The effect of calcium alkali orthophosphate ceramics on cell adhesion and intracellular signaling mechanisms

Cell adhesion and intracellular signaling events which are associated with this stimulatory effect of some of the calcium alkali orthophosphate materials on osteogenesis *in vitro* and *in vivo* are not yet fully understood. Developing this understanding has been hampered by the inadequacy of the experimental techniques that could be used. Recently, however, new molecular biological methods have been brought to bear on similar problems of osteogenesis and they have been combined with insight generated using powerful surface analysis techniques. Consequently, we performed a series of experiments to study the mechanisms by which these novel bioactive bone substitutes stimulate the intracellular signaling pathways that regulate osteoblast differentiation and cell survival.[131,163,298,366,368] This included investigating (1) solution-mediated surface transformations, (2) serum protein adsorption events, (3) integrin-mediated cell adhesion mechanisms, and (4) intracellular signaling mechanisms. These studies are described in greater detail in **Chapter 1.114, Bioactivity: Mechanisms** to which the interested reader is referred here.

6.620.3.2.5. The effect of calcium alkali orthophosphate-based bone substitute cements on bone formation and osteogenic marker expression in vivo

Bone substitutes with improved surgical handling properties include moldable calcium phosphate cements in paste form that can be either introduced into a bony defect with a spatula or injected with a syringe; they subsequently set *in situ*, which makes them an attractive group of materials for bone reconstruction.[163,295] Over the past decade, various bioactive

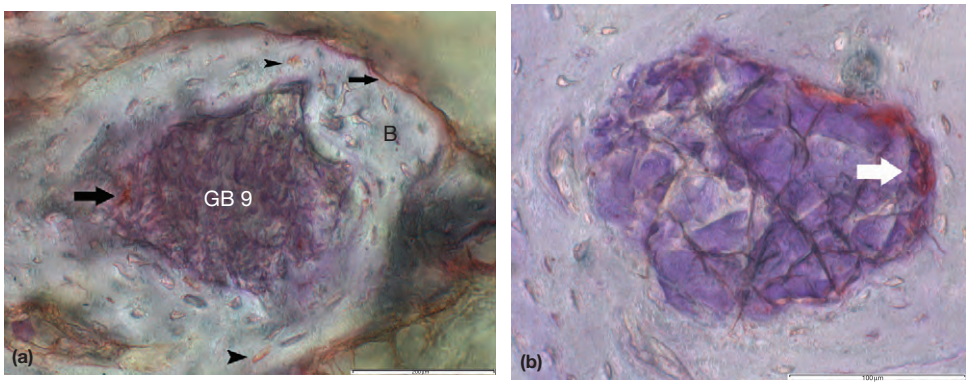

Figure 5 (a) Histomicrograph of GB9 particle 4 weeks after augmentation of a critical-size defect in the sheep mandible with GB9. Immunodetection of type I collagen in deacrylated sawed section of mandibular defect. Already after 4 weeks, the GB9 particle is almost fully covered by newly formed bone tissue. Strong staining of the newly formed bone matrix (B) in contact with the particle is present (block arrow). In addition, moderate cellular staining of osteocytes is visible (arrow heads). Moreover, strong staining of the osteoid and bone matrix lining the periphery of the newly formed bone is evident (small arrow). This is indicative that bone formation and matrix mineralization are actively progressing both at the surface of the degrading particle and on the periphery of the newly formed bone. These findings demonstrate the excellent bone-bonding and bone-regenerative capacities of the calcium alkali orthophosphate material GB9, which is capable of stimulating bone formation at its surface as early as 4 weeks after implantation. Undecalcified sawed section counterstained with hematoxylin. Bar = 200 μm. (b) Immunodetection of osteocalcin in deacrylated section of mandibular defect 12 weeks after implantation of GB9. Histomicrograph of residual GB9 particle fragment and surrounding bone tissue. In general, only very few particle fragments are present at 12 weeks. Areas with strong osteocalcin staining of cells and mineralized bone matrix (arrow) in contact with the degrading particle which displays new bone formation in its center are present. These findings show that after 12 weeks, bone formation, matrix mineralization, and particle degradation are still actively progressing at the surface of this degrading particle. Undecalcified sawed section counterstained with hematoxylin. Bar = 100 μm.

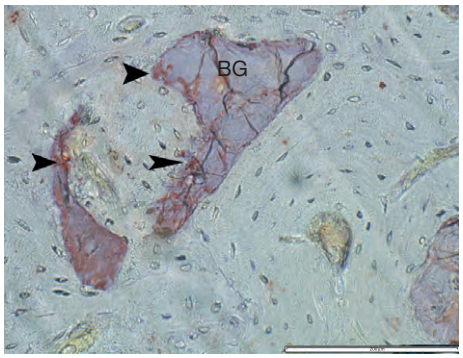

Figure 6 Immunodetection of bone sialoprotein in deacrylated section of mandibular defect 24 weeks after augmentation of a critical-size defect in the sheep mandible with BG45S5. Histomicrograph of residual excavated BG45S5 particle and surrounding bone tissue. Areas with strong osteocalcin staining of cells and mineralized bone matrix in contact with the particle are present (arrowheads). This shows that bone formation, matrix mineralization, and particle transformation are still actively progressing at the surface of the degrading particle 24 weeks after implantation. Undecalcified sawed section counterstained with hematoxylin. Bar = 200 μm.

calcium phosphate cements have been developed. In most cases, HA is formed during setting, which limits their biodegradability. More recent developments include cements which form calcium alkali phosphates during setting, which, as outlined previously, have been shown to have a stimulatory effect on osteogenesis *in vitro* and *in vivo*.[128,130,163,290] These cements are designed for higher biodegradability.[295] Thus, an animal study was performed to evaluate the effect of four calcium alkali orthophosphate cements as compared to TCP particles on osteogenesis *in vivo* after implantation in critical size effects in rabbit femora for 1, 3, 6, and 12 months.[261] Of the various bone substitute cements studied, the GB9 cement showed the best bone-bonding behavior and had the greatest stimulatory effect on bone formation and expression of osteogenic markers, while exhibiting the highest biodegradability.[261] After 12 months, the original trabecular structure of the rabbit femur was almost fully restored (Figure 10). The biodegradability of the GB9-cement, however, was lower than that of the TCP granules.[261] Hence, current efforts deal with increasing the porosity of the cement during setting in order to accelerate the biodegradation and studying moldable calcium-alkali-orthophosphate-based putty-like cements for restoring outer bony contours.[261,294]

6.620.3.2.6. The effect of β-TCP particles with varying porosity on osteogenesis after sinus floor augmentation in humans

By virtue of the importance to correlate findings from preclinical (animal) studies with data from clinical studies, a study was conducted in which the effect of various TCP particulate bone grafting materials with varying porosity on bone formation and osteogenic marker expression was examined in biopsies sampled 6 months after sinus floor augmentation in patients.[129,132,163] These studies demonstrated that greater porosity of the TCP particles (65% vs. 35% porosity) resulted in greater bone formation and particle degradation.[129,132,163] Moreover, 6 months after implantation of both types of β-TCP particles, bone formation and matrix mineralization was still actively progressing in the tissue surrounding the particles (Figure 1). Both TCP materials supported bone formation and exhibited excellent bone-bonding behavior (Figure 1).

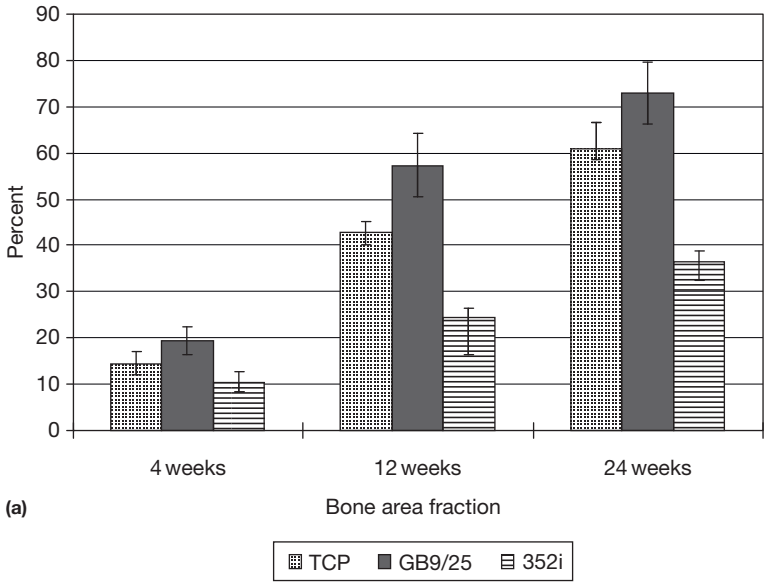

(a)

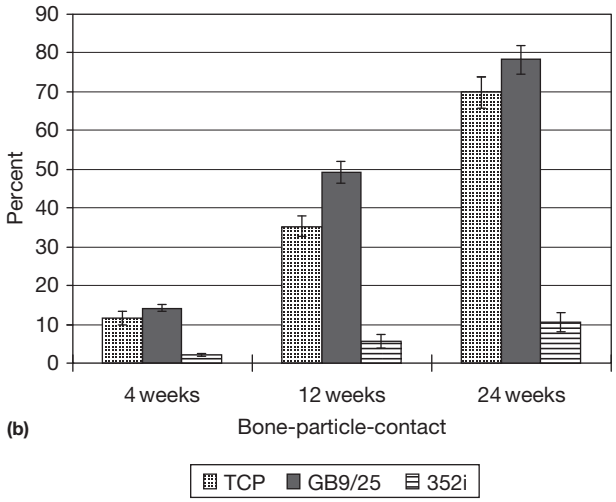

(b)

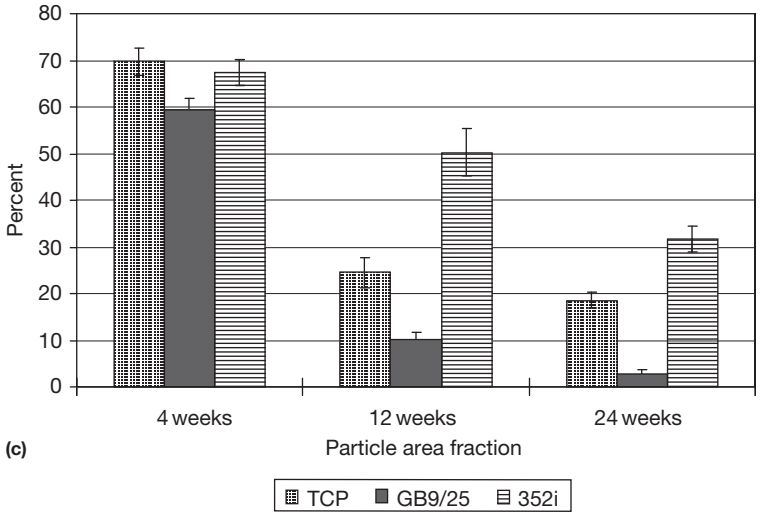

(c)

Figure 7 *(Continued)*

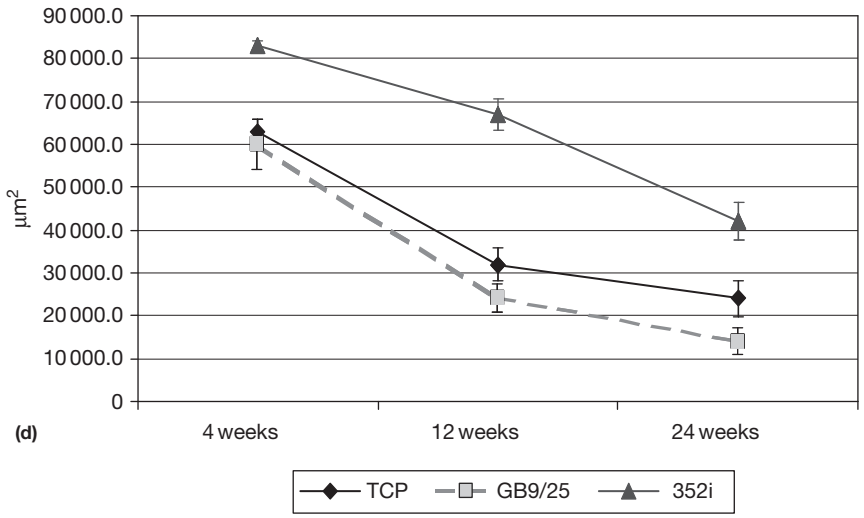

Figure 7 Histomorphometric results of the ovine sinus floor augmented with various calcium phosphates after 1, 4, 12, and 24 weeks of implantation: (a) bone area fraction in the augmented sinus; (b) bone-particle-contact after 4, 12, and 24 weeks of implantation; (c) particle area fraction; and (d) particle size. All values are mean±standard deviation of five measurements. TCP, tricalcium phosphate.

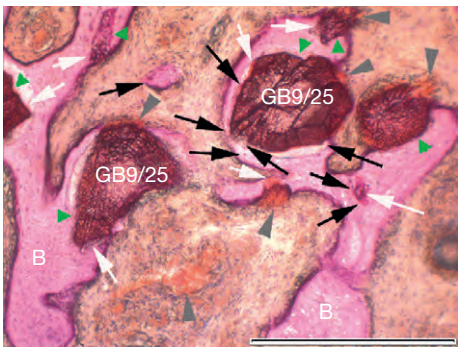

Figure 8 Histomicrograph of GB9/25 particles 3 months after implantation in the ovine sinus floor directly underneath the Schneiderian membrane. Immunodetection of osteopontin (OP) in deacrylated sawed section of the sinus floor. After 12 weeks, new bone formation (B) is visible at the surface of these particles (GB9/25) in combination with strong expression of OP in the mineralized bone matrix (white arrows) at the particle surface as well as in the not-yet mineralized fibrous matrix (gray arrowheads) in contact with the degrading particles and particle fragments. In addition, osteoblasts with strong OP expression (black arrows) are visible at the surface of these particle fragments which show excellent bone-bonding behavior (green arrowheads). These findings demonstrate the excellent bone-bonding and bone-regenerative capacities of the calcium alkali orthophosphate material GB9/25, which is capable of stimulating bone formation at its surface in this location underneath the Schneiderian membrane, that is, at a great distance from the original resident bone of the sinus floor. Undecalcified sawed section counterstained with hematoxylin. Bar = 320 µm.

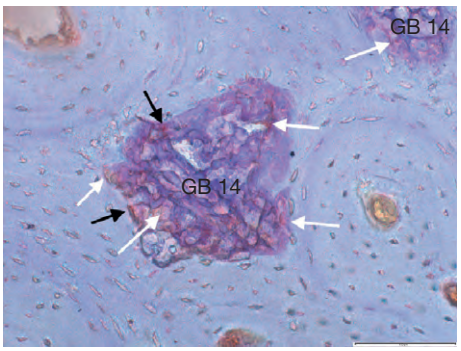

Figure 9 Immunodetection of bone sialoprotein in deacrylated section of mandibular critical-size defect 12 weeks after augmentation with GB14. Histomicrograph of residual GB14 particle fragments and surrounding bone tissue. Strong staining of osteoblasts (black arrows) is present at the particle surface in combination with moderate staining of the mineralized matrix (white arrows) in contact with these particles. This is indicative that after 12 weeks of implantation, bone formation, matrix mineralization, and particle degradation are still actively progressing at the surface of the degrading particles. Undecalcified sawed section counterstained with hematoxylin. Bar = 100 µm.

With the more porous particles, however, bone formation, osteogenic marker expression, and particle degradation had already reached a more advanced stage at 6 months. Consequently, a greater porosity appears to be advantageous for enhancing bone formation and particle degradation.[129,163] These studies provide a valuable insight into the performance of synthetic bone graft materials in the human case and can form the basis for designing controlled clinical studies and selecting appropriate model parameters. Such studies are needed to advancing new bone grafting materials to the clinic in an evidence-based fashion. This clinical study also confirms the validity of any animal model by correlating *in vivo* animal findings to those obtained from human biopsies. In fact, excellent correspondence between animal data and clinical findings suggests comparable *in vivo* response, a useful finding for any animal study.[129,130,163]

Current research efforts focus on dealing with efforts toward personalized medicine questions, in that the influence of age, gender, and hormone status-related parameters in 120 bone-regeneration patients (after sinus floor augmentation with TCP

bone grafting materials) are examined. Such studies have the potential to provide powerful predictive tools toward the therapeutic outcome in any future patient and thereby facilitate tailoring individual bone augmentation treatment regimens for individual patients. Additional research involves computed tomography (CT) and Synchroton-CT methodology for volumetric determination of the newly formed bone and the residual grafting material after sinus floor and alveolar ridge augmentation.[132] This is described in greater detail in **Chapter 3.304, Developments in High-Resolution CT: Studying Bioregeneration by Hard X-ray Synchrotron-Based Microtomography**.

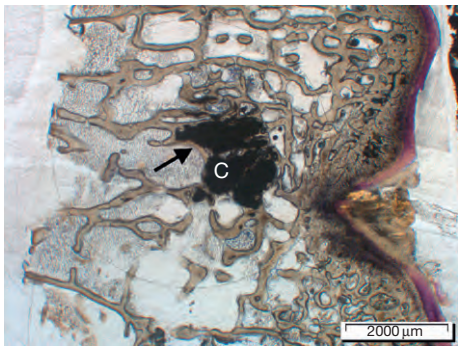

Figure 10 Histomicrograph of GB9 calcium alkali phosphate cement after 336 days after implantation in the rabbit femur. The defect area is circled. The highly cancellous original bone structure or the rabbit femur has been widely restored with only a very small amount of residual cement (C) being present which displays high bone-cement contact (arrow), that is, excellent bone-bonding behavior. Undecalcified sawed section stained with Giemsa surface staining. Bar = 2000 µm.

6.620.3.2.7. Three-dimensional calcium-alkali-phosphate-based scaffolds for bone tissue engineering

Current research also deals with optimizing 3D calcium-alkali-phosphate-based scaffolds[350] in which mesenchymal stem cells are cultured under perfusion bioreactor conditions for bone tissue engineering purposes, that is, repair of large segmental defects. This includes various approaches to achieve adequate angiogenesis. These scaffolds are fabricated from calcium alkali orthophosphates using a free form fabrication technique, that is, 3D printing as well as a method utilizing combustible polyurethane sponges as temporary templates (Schwartzwald–Somers-technique) (**Figure 11**).[350]

6.620.4. Summary

Insertion of dental implants has become a common treatment in modern dentistry. However, the resorptive processes following tooth extraction often mandate site development by alveolar ridge augmentation before implants can be placed. Although the current gold standard, namely autogenous bone grafts, serves this function, there has been an ever-increasing search for excellent synthetic bone grafting materials, in order to avoid second-site surgery for autograft harvesting.

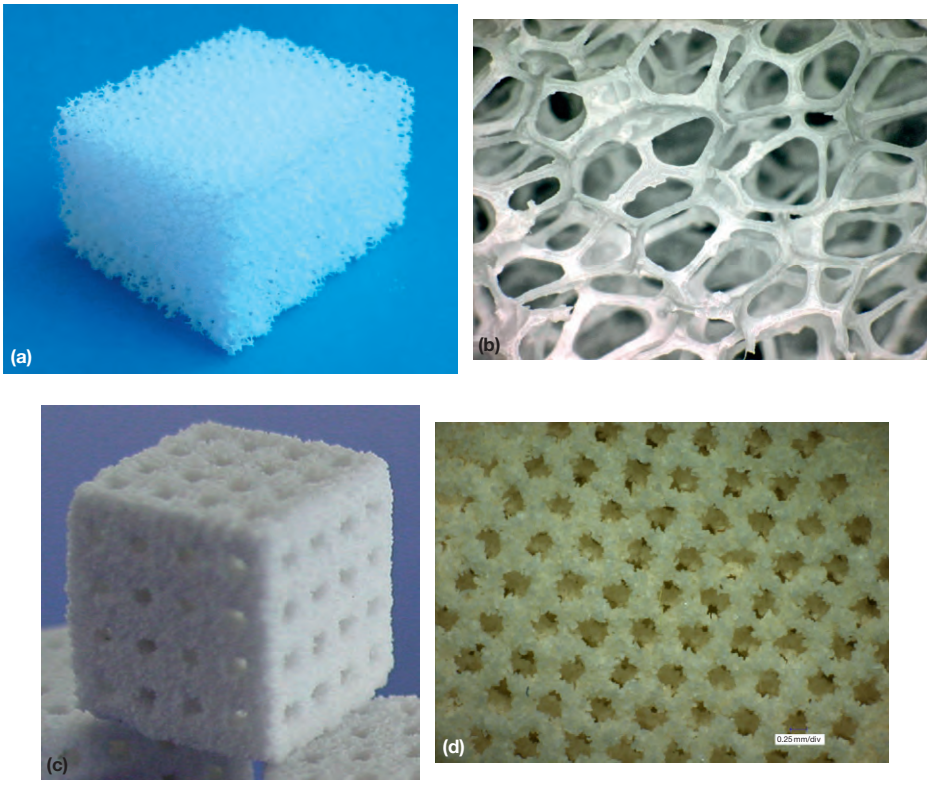

Figure 11 (a, b) Three-dimensional calcium-alkali-orthophosphate-based scaffold fabricated utilizing the Schwartzwald–Somers-technique, (magnification 50×), (c, d) 3D calcium-alkali-orthophosphate-based scaffold fabricated by 3D printing.

Furthermore, the significant increase in the number of dental implants placed and alveolar ridge augmentation procedures performed over the last two decades resulted in an ever-increasing demand for adequate bone grafting materials for implant dentistry.

Numerous bone grafting materials have been developed and studied since the late 1970s. The majority of these grafting materials are calcium phosphate-based materials. Various HA- and TCP-based dental grafting materials, as well as bioactive glasses and glass ceramics have been proposed for use in therapies to augment alveolar bone and to promote periodontal regeneration. These materials include synthetic as well as coralline and bovine-derived HAs, nanocrystalline or peptide-modified HAs, TCP ceramics, biphasic HA-TCPs, calcium carbonates, BG45S5, glass ceramics, and DFDBAs. Most of these materials have been shown to be osteoconductive but exhibit limited biodegradability. DFDBAs are inferior to synthetic materials in terms of the risk of disease transmission and immunological challenges. While for these DFDBAs a wide variation in commercial bone bank preparations of DFDBA and conflicting results regarding their osteoconductivity and potential to support new bone formation have been reported in combination with a low biodegradability, excellent osteoconductive properties have been demonstrated by numerous *in vivo* and clinical studies for one of the porous bovine-derived HAs that closely resembles the native HA of bone and whose morphology, in addition, resembles that of cancellous bone. This material, however, also exhibits only limited biodegradability. For other HAs, varying degrees of osteoconductivity and bone-bonding behavior have been reported. Both TCP ceramics and BG45S5 have been shown to possess excellent osteoconductivity, bone-regenerative capacity, and bone-bonding behavior in combination with a higher biodegradability than various HAs. More recently, injectable and moldable resorbable bone substitute cements as well as scaffolds for craniofacial bone tissue engineering have been developed. Furthermore, the combination of grafting materials with growth factors and other biologicals has been explored.

Compared to the bone substitute materials which are currently clinically available, there is a significant need for bone grafting materials that degrade more rapidly but at the same time stimulate osteogenesis. This prompted a search for bioactive, rapidly resorbable bone grafting materials that exhibit good bone-bonding behavior by stimulating enhanced bone formation at the interface. They also exhibit a high degradation rate. This led to the development of calcium alkali orthophosphate materials. Current research efforts include the optimization of resorbable bone grafting cements and of scaffolds for various tissue engineering approaches that integrate concepts to achieve adequate vascularization when restoring large segmental defects.

Acknowledgments

Support over the years from various agencies is gratefully acknowledged. Part of the work was supported by the German Research Foundation DFG (KN 377/2-1, KN377/3-1, KN377/5-1, KN377/8-1), the Osteology Foundation, Robert Mathys Foundation, and by the European Union (EFRE-ProFIT grants # 10136206, 10141914).

Furthermore, the authors thank the numerous colleagues who contributed to the work presented in this chapter. They are Prof. Dr. I. Shapiro, Dr. G. Berger, Dr. G. Gildenhaar, Prof. Dr. C. R. Howlett, Dr. A. Houshmand, Dr. Ch. Koch, Dr. A. Rack, Dr. A. Bednarek, Dr. S. Jonscher, Dr. K. Reiter, PD Dr. Ch. Müller-Mai, Dr. H. Renz, Dr. S. Radin, Ms. A. Kopp, Ms. I. Borchert, Mrs. K. Schulze-Dirksen, Ms. E. Rieger-Rüdiger, and Mrs. I. Schwarz.

References

1. Belser, U. C.; Mericske-Stern, R.; Bernard, J. P.; Taylor, T. D. *Clin. Oral Implants Res.* **2000**, *11*(Suppl. 1), 126–145; Review.
2. Bornstein, M. M.; Lussi, A.; Schmid, B.; Belser, U. C.; Buser, D. *Int. J. Oral Maxillofac. Implants* **2003**, *18*, 659–666.
3. Garber, D. A.; Belser, U. C. *Compend. Contin. Educ. Dent.* **1995**, *16*, 796; 798–802, 804.
4. Garber, D. A. *J. Am. Dent. Assoc.* **1995**, *126*, 319–325.
5. Taylor, T. D.; Belser, U.; Mericske-Stern, R. *Clin. Oral Implants Res.* **2000**, *11* (Suppl. 1), 101–107; Review.
6. Ganz, S. D.; Valen, M. *J. Oral Implantol.* **2002**, *28*, 178–183.
7. Winkler, S. *J. Oral Implantol.* **2002**, *28*, 226–229.
8. Eisig, S. B.; Ho, V.; Kraut, R.; Lalor, P. *J. Oral Maxillofac. Surg.* **2003**, *61*, 347–353.
9. von Arx, T.; Cochran, D. L.; Hermann, J. S.; Schenk, R. K.; Buser, D. *Clin. Oral Implants Res.* **2001**, *12*, 260–269.
10. von Arx, T.; Cochran, D. L.; Schenk, R. K.; Buser, D. *Int. J. Oral Maxillofac. Surg.* **2002**, *31*, 190–199.
11. Buser, D.; Dula, K.; Hess, D.; Hirt, H. P.; Belser, U. C. *Periodontol. 2000* **1999**, *19*, 151–163; Review.
12. Buser, D.; Dula, K.; Hirt, H. P.; Berthold, H. In *Guided Bone Regeneration in Implant Dentistry*; Buser, D., Dahlin, C., Schenk, R. K., Eds.; Quintessenz: Chicago, IL, 1994; pp 189–233.
13. Buser, D.; Hoffmann, B.; Bernard, J. P.; Lussi, A.; Mettler, D.; Schenk, R. K. *Clin. Oral Implants Res.* **1998**, *9*, 137–150.
14. Klijn, R. J.; Meijer, G. J.; Bronkhorst, E. M.; Jansen, J. A. *Tissue Eng. B Rev.* **2010**, *16*(5), 493–507.
15. Klijn, R. J.; Meijer, G. J.; Bronkhorst, E. M.; Jansen, J. A. *Tissue Eng. B Rev.* **2010**, *16*(3), 295–303; Review.
16. Buser, D.; Dula, K.; Hirt, H. P.; Schenk, R. *J. Oral Maxillofac. Surg.* **1996**, *54*, 420–432.
17. Friedmann, A.; Strietzel, F. P.; Maretzki, B.; Pitaru, S.; Bernimoulin, J. P. *Clin. Oral Implants Res.* **2002**, *13*(6), 587–594.
18. Hämmerle, C. H. F.; Chiantella, G. C.; Karring, T.; Lang, N. P. *Clin. Oral Implants Res.* **1998**, *9*, 151–162.
19. Kohal, R. J.; Mellas, P.; Hürzeler, M. B.; Trejo, P. M.; Morrison, E.; Caffesse, R. G. *J. Periodontol.* **1998**, *69*(8), 927–937.
20. Stricker, A.; Voss, P. J.; Gutwald, R.; Schramm, A.; Schmelzeisen, R. *Clin. Oral Implants Res.* **2003**, *14*, 207–212.
21. Timmenga, N. M.; Raghoebar, G. M.; van Weissenbruch, R.; Vissink, A. *Clin. Oral Implants Res.* **2003**, *14*, 322–328.
22. Kalk, W. W.; Raghoebar, G. M.; Jansma, J.; Boering, G. *J. Oral Maxillofac. Surg.* **1996**, *54*, 1424–1429.
23. Kaptein, M. L.; Hoogstraten, J.; de Putter, C.; de Lange, G. L.; Blijdorp, P. A. *Clin. Oral Implants Res.* **1998**, *9*, 321–326.
24. Orsini, G.; Ricci, J.; Scarano, A.; *et al. J. Biomed. Mater. Res.* **2004**, *68B*, 199–208.
25. Wheeler, S. L. *J. Oral Maxillofac. Surg.* **1997**, *55*, 1287–1293; Review.
26. Groeneveld, E. H. J.; van den Bergh, J. P. A.; Holzmann, P.; ten Bruggenkate, C. M.; Tuinzing, D. B.; Burger, E. H. *Clin. Oral Implants Res.* **1999**, *10*, 499–509.
27. Hürzeler, M. B.; Kirsch, A.; Ackermann, K. L.; Quinones, C. R. *Int. J. Oral Maxillofac. Implants* **1996**, *11*, 466–475.
28. Hürzeler, M. B.; Kirsch, A.; Ackermann, K. L.; Quiñones, C. R. *Int. J. Oral Maxillofac. Implants* **1996**, *11*(4), 466–475.
29. Lorenzetti, M.; Mozzati, M.; Campanino, P. P.; Valente, G. *Int. J. Oral Maxillofac. Implants* **1998**, *13*, 69–76.

30. Valentini, P.; Abensur, D. *Int. J. Periodontics Restorative Dent.* **1997**, *17*, 233–241.
31. Wallace, S. S.; Froum, S. J.; Tarnow, D. P. *Int. J. Periodontics Restorative Dent.* **1996**, *16*, 47–51.
32. Wetzel, A. C.; Stich, H.; Caffesse, R. G. *Clin. Oral Implants Res.* **1995**, *6*, 155–163.
33. Wiltfang, J.; Merten, H. A.; Schlegel, K. A.; *et al. J. Biomed. Mater. Res.* **2002**, *63*, 115–121.
34. Hench, L. L. *J. Am. Ceram. Soc.* **1998**, *81*, 1705–1728; Review.
35. Ducheyne, P. In *Hip Surgery: New Materials and Developments*; Sedel, L., Cabanela, M., Eds.; Martin Dunitz: London, 1998; pp 75–82.
36. Metsger, D. S.; Driskell, T. D.; Paulsrud, J. R. *J. Am. Dent. Assoc.* **1982**, *105*, 1035–1038; Review.
37. Yaszemski, M. J.; Payne, R. G.; Hayes, W. C.; Langer, R.; Mikos, A. C. *Biomaterials* **1996**, *17*, 175–185.
38. Hollinger, J. O.; Schmitz, J. P.; Mizgala, J. W.; Hassler, C. *J. Biomed. Mater. Res.* **1989**, *23*(1), 17–29.
39. Wenz, B.; Oesch, B.; Horst, M. *Biomaterials* **2001**, *22*(12), 1599–1606.
40. Saffar, J. F.; Colombier, M. L.; Detienville, R. *J. Periodontol.* **1990**, *61*, 209–216.
41. Ducheyne, P.; de Groot, K. *J. Biomed. Mater. Res.* **1991**, *15*, 441–445.
42. Eggli, P. S.; Muller, W.; Schenk, R. K. *Clin. Orthop. Relat. Res.* **1988**, *232*, 127–138.
43. Jarcho, M. *Clin. Orthop. Relat. Res.* **1981**, *157*, 259–278.
44. Daculsi, G.; Le Geros, R. Z.; Mitre, D. *Calcif. Tissue Int.* **1989**, *45*, 95–103.
45. Hench, L. L.; Paschall, H. A. *J. Biomed. Mater. Res.* **1973**, *7*, 25–42.
46. Schliephake, H.; Kage, T. *J. Biomed. Mater. Res.* **2001**, *56*, 128–136.
47. Zerbo, I. R.; Bronckers, A. L.; de Lange, G. L.; van Beek, G. J.; Burger, E. H. *Clin. Oral Implants Res.* **2001**, *12*, 379–384.
48. Merten, H. A.; Wiltfang, J.; Grohmann, U.; Hoenig, J. F. *J. Craniofac. Surg.* **2001**, *12*(1), 59–68.
49. Cordioli, G.; Mazzocco, C.; Schepers, E.; Brugnolo, E.; Majzoub, Z. *Clin. Oral. Implants Res.* **2001**, *12*, 270–278.
50. Tadjoedin, E. S.; de Lange, G. L.; Holzmann, P. J.; Kulper, L.; Burger, E. H. *Clin. Oral Implants Res.* **2000**, *11*, 334–344.
51. Davies, J. E. *Int. J. Prosthodont.* **1998**, *11*, 391–401.
52. Holmes, R. E.; Bucholz, R. W.; Mooney, V. *J. Orthop. Res.* **1987**, *5*(1), 114–121.
53. Schepers, E. J.; Ducheyne, P. *J. Oral Rehabil.* **1997**, *24*, 171–181.
54. Barney, V. C.; Levin, M. P.; Adams, D. F. *J. Periodontol.* **1986**, *57*(12), 764–770.
55. Chanavaz, M. *J. Oral Implantol.* **1990**, *16*(3), 199–209.
56. Desilets, C. P.; Marden, L. J.; Patterson, A. L.; Hollinger, J. O. *J. Craniofac. Surg.* **1990**, *1*(3), 150–153.
57. Hempton, T. J.; Fugazzotto, P. A. *Implant Dent.* **1994**, *3*(1), 35–37.
58. Hollinger, J. O.; Schmitz, J. P.; Mizgala, J. W.; Hassler, C. *J. Biomed. Mater. Res.* **1989**, *23*(1), 17–29.
59. Klein, C. P.; Driessen, A. A.; de Groot, K.; van den Hooff, A. *J. Biomed. Mater. Res.* **1983**, *17*(5), 769–784.
60. Misch, C. E.; Dietsh, F. *Implant Dent.* **1993**, *2*(3), 158–167; Review.
61. Riess, G.; Heide, H.; Köster, K.; Reiner, R. *Dtsch Zahnärztl. Z.* **1978**, *33*(4), 287.
62. Swart, J. G.; Feenstra, L.; Ponssen, H.; de Groot, K. *Ned. Tijdschr. Geneeskd* **1979**, *123*(33), 1421–1425.
63. Bunte, M.; Strunz, V. *J. Maxillofac. Surg.* **1977**, *5*(4), 303–309.
64. Schepers, E.; de Clercq, M.; Ducheyne, P.; Kempeneers, R. *J. Oral Rehabil.* **1991**, *18*(5), 439–452.
65. Strunz, V.; Bunte, M.; Stellmach, R.; *et al. Dtsch Zahnärztl. Z.* **1977**, *32*(4), 287–290.
66. Davis, W. H.; Hochwald, D.; Daly, B.; Owen, W. F., 3rd *J. Prosthet. Dent.* **1990**, *64*(5), 583–588; Review.
67. Ewers, R. *J. Oral Maxillofac. Surg.* **2005**, *63*(12), 1712–1723.
68. Haas, R.; Baron, M.; Zechner, W.; Mailath-Pokorny, G. *Int. J. Oral Maxillofac. Implants* **2003**, *18*(5), 691–696.
69. Hjorting-Hansen, E.; Worsaae, N.; Lemons, J. E. *Int. J. Oral Maxillofac. Implants* **1990**, *5*(3), 255–263.
70. Hürzeler, M. B.; Quinones, C. R.; Kirsch, A.; *et al. Clin. Oral Implants Res.* **1997**, *8*(5), 401–411.
71. Hürzeler, M. B.; Quiñones, C. R.; Kirsch, A.; *et al. Clin. Oral Implants Res.* **1997**, *8*(5), 401–411.
72. Krejci, C. B.; Bissada, N. F.; Farah, C.; Greenwell, H. *J. Periodontol.* **1987**, *58*(8), 521–528.
73. Noppe, C. *Quintessenz* **1987**, *38*(6), 1053–1063.
74. Otto, K.; Schopper, C.; Ewers, R.; Lambrecht, J. T. *Schweiz. Monatsschr. Zahnmed.* **2004**, *114*(10), 996–1002.
75. Prokic, B.; Lekovic, V.; Weingart, H.; Kleber, B. M. *Zahn Mund Kieferheilkd Zentralbl.* **1990**, *78*(7), 597–601.
76. Quiñones, C. R.; Hürzeler, M. B.; Schüpbach, P.; *et al. Clin. Oral Implants Res.* **1997**, *8*(6), 487–496.
77. Roos-Jansåker, A. M.; Renvert, H.; Lindahl, C.; Renvert, S. *J. Clin. Periodontol.* **2007**, *34*(7), 625–632.
78. Schopper, C.; Moser, D.; Wanschitz, F.; *et al. J. Long Term Eff. Med. Implants* **1999**, *9*(3), 203–213.
79. Small, S. A.; Zinner, I. D.; Panno, F. V.; Shapiro, H. J.; Stein, J. I. *Int. J. Oral Maxillofac. Implants* **1993**, *8*(5), 523–528.
80. Smiler, D. G.; Johnson, P. W.; Lozada, J. L.; *et al. Dent. Clin. North Am.* **1992**, *36*(1), 151–186.
81. Thompson, D. M.; Rohrer, M. D.; Prasad, H. S. *Implant Dent.* **2006**, *15*(1), 89–96.
82. Ripamonti, U. *J. Craniofac. Surg.* **1992**, *3*(3), 149–159.
83. Schopper, C.; Moser, D.; Wanschitz, F.; *et al. J. Long Term Eff. Med. Implants.* **1999**, *9*(3), 203–213.
84. Bertoli, F. *Dent. Cadmos* **1989**, *57*(1), 68–71.
85. Canullo, L.; Dellavia, C. *Clin. Implant Dent. Relat. Res.* **2009**, *11*(Suppl. 1), e7–e13.
86. Spies, C.; Schnürer, S.; Gotterbarm, T.; Breusch, S. *Z. Orthop. Unfall.* **2008**, *146*(1), 64–69.
87. Spies, C. K.; Schnürer, S.; Gotterbarm, T.; Breusch, S. *Arch. Orthop. Trauma. Surg.* **2009**, *129*(7), 979–988.
88. Al Ruhaimi, K. A. *Int. J. Oral Maxillofac. Implants* **2001**, *6*(1), 105–114.
89. Froum, S. J.; Tarnow, D. P.; Wallace, S. S.; Rohrer, M. D.; Cho, S. C. *Int. J. Periodontics Restorative Dent.* **1998**, *18*(6), 528–543.
90. Hämmerle, C. H.; Olah, A. J.; Schmid, J.; *et al. Clin. Oral Implants Res.* **1997**, *8*(3), 198–207.
91. Landi, L.; Pretel, R. W., Jr.; Hakimi, N. M.; Setayesh, R. *Int. J. Periodontics Restorative Dent.* **2000**, *20*(6), 574–583.
92. Schmid, J.; Hämmerle, C. H.; Flückiger, L.; *et al. Clin. Oral Implants Res.* **1997**, *8*(2), 75–81.
93. Tapety, F. I.; Amizuka, N.; Uoshima, K.; Nomura, S.; Maeda, T. *Clin. Oral Implants Res.* **2004**, *15*(3), 315–324.
94. Al Ruhaimi, K. A. *Int. J. Oral Maxillofac. Implants* **2000**, *15*(6), 859–864.
95. Busenlechner, D.; Tangl, S.; Mair, B.; *et al. Biomaterials* **2008**, *29*(22), 3195–3200.
96. Smeets, R.; Grosjean, M. B.; Jelitte, G.; *et al. Schweiz. Monatsschr. Zahnmed.* **2008**, *118*(3), 203–212.
97. Traini, T.; Degidi, M.; Sammons, R.; Stanley, P.; Piattelli, A. *J. Periodontol.* **2008**, *79*(7), 1232–1240.
98. Artzi, Z.; Kozlovsky, A.; Nemcovsky, C. E.; Weinreb, M. *J. Clin. Periodontol.* **2005**, *32*(2), 193–199.
99. Berglundh, T.; Lindhe, J. *Clin. Oral Implants Res.* **1997**, *8*(2), 117–124.
100. Cordaro, L.; Bosshardt, D. D.; Palattella, P.; Rao, W.; Serino, G.; Chiapasco, M. *Clin. Oral Implants Res.* **2008**, *19*(8), 796–803.
101. de Vicente, J. C.; Hernández-Vallejo, G.; Braña-Abascal, P.; Peña, I. *Clin. Oral Implants Res.* **2010**, *21*(4), 430–438.
102. Ferreira, C. E.; Novaes, A. B.; Haraszthy, V. I.; Bittencourt, M.; Martinelli, C. B.; Luczyszyn, S. M. *J. Periodontol.* **2009**, *80*(12), 1920–1927.
103. Froum, S. J.; Wallace, S. S.; Cho, S. C.; Elian, N.; Tarnow, D. P. *Int. J. Periodontics Restorative Dent.* **2008**, *28*(3), 273–281.
104. Gutwald, R.; Haberstroh, J.; Kuschnierz, J.; *et al. Br. J. Oral Maxillofac. Surg.* **2010**, *48*(4), 285–290.
105. Klinge, B.; Alberius, P.; Isaksson, S.; Jonsson, J. *J. Oral Maxillofac. Surg.* **1992**, *50*(3), 241–249.
106. Simunek, A.; Kopecka, D.; Somanathan, R. V.; Pilathadka, S.; Brazda, T. *Int. J. Oral Maxillofac. Implants* **2008**, *23*(5), 935–942.
107. Sohn, D. S.; Kim, W. S.; An, K. M.; Song, K. J.; Lee, J. M.; Mun, Y. S. *Implant Dent.* **2010**, *19*(3), 259–270.
108. van Steenberghe, D.; Callens, A.; Geers, L.; Jacobs, R. *Clin. Oral Implants Res.* **2000**, *11*(3), 210–216.
109. Yildirim, M.; Spiekermann, H.; Biesterfeld, S.; Edelhoff, D. *Clin. Oral Implants Res.* **2000**, *11*(3), 217–229.
110. Zitzmann, N. U.; Naef, R.; Schärer, P. *Int. J. Oral Maxillofac. Implants* **1997**, *12*(6), 844–852.
111. Jensen, S. S.; Broggini, N.; Hjørting-Hansen, E.; Schenk, R.; Buser, D. *Clin. Oral Implants Res.* **2006**, *17*(3), 237–243.
112. Valentini, P.; Abensur, D. J. *Int. J. Oral Maxillofac. Implants* **2003**, *18*(4), 556–560.
113. Schliephake, H.; Neukam, F. W.; Hutmacher, D.; Becker, J. *J. Oral Maxillofac. Surg.* **1994**, *52*(1), 57–63.
114. Schliephake, H.; Neukam, F. W.; Hutmacher, D.; Wüstenfeld, H. *J. Oral Maxillofac. Surg.* **1995**, *53*(1), 46–51; discussion 52.

115. Schliephake, H.; Neukam, F. W.; Hutmacher, D. *Fortschr. Kiefer Gesichtschir.* **1994**, *39*, 190–193.
116. Chu, T. M.; Hollister, S. J.; Halloran, J. W.; Feinberg, S. E.; Orton, D. G. *Ann. NY Acad. Sci.* **2002**, *961*, 114–117.
117. Chu, T. M.; Orton, D. G.; Hollister, S. J.; Feinberg, S. E.; Halloran, J. W. *Biomaterials* **2002**, *23*(5), 1283–1293.
118. Degidi, M.; Piattelli, M.; Scarano, A.; Iezzi, G.; Piattelli, A. *J. Oral Implantol.* **2004**, *30*(6), 376–383.
119. Hole, B. B.; Schwarz, J. A.; Gilbert, J. L.; Atkinson, B. L. *J. Biomed. Mater. Res. A* **2005**, *74*(4), 712–721.
120. Thorwarth, M.; Schultze-Mosgau, S.; Wehrhan, F.; Kessler, P.; Srour, S.; Wiltfang, J. *Biomaterials* **2005**, *26*(28), 5648–5657.
121. Thorwarth, M.; Wehrhan, F.; Srour, S.; *et al. Br. J. Oral Maxillofac. Surg.* **2007**, *45*(1), 41–47.
122. Abshagen, K.; Schrodi, I.; Gerber, T.; Vollmar, B. *J. Biomed. Mater. Res. A* **2009**, *91*(2), 557–566.
123. Götz, W.; Gerber, T.; Michel, B.; Lossdörfer, S.; Henkel, K. O.; Heinemann, F. *Clin. Oral Implants Res.* **2008**, *19*(10), 1016–1026.
124. Brandt, J.; Henning, S.; Michler, G.; Hein, W.; Bernstein, A.; Schulz, M. *J. Mater. Sci. Mater. Med.* **2010**, *21*(1), 283–294.
125. Heinemann, F.; Mundt, T.; Biffar, R.; Gedrange, T.; Goetz, W. *J. Physiol. Pharmacol.* **2009**, *60*(Suppl. 8), 91–97.
126. Peters, F.; Reif, D. *Materialwiss. Werkst.* **2004**, *35*, 203–207.
127. Bednarek, A. *Dissertation*; Charité University Medical Center: Berlin, Germany, 2010.
128. Knabe, C.; Houshmand, A.; Berger, G.; *et al. J. Biomed. Mater. Res. A* **2008**, *84*, 856–868.
129. Knabe, C.; Koch, C.; Rack, A.; Stiller, M. *Biomaterials* **2008**, *29*, 2249–2258.
130. Knabe, C.; Berger, G.; Gildenhaar, R.; *et al.* In (*Oral Presentation*) *Transactions of the 8th World Biomaterials Congress*, Amsterdam, The Netherlands, May 28–Jun 1, 2008 p 035.
131. Knabe, C.; Stiller, M.; Berger, G.; *et al.* In *Society for Biomaterials Transactions 2008 Translational Biomaterial Research Symposium*, Atlanta, GA, Sept 11–13, 2008 p 215.
132. Stiller, M.; Rack, A.; Zabler, S.; *et al. Bone* **2009**, *44*(4), 619–628.
133. Aguirre Zorzano, L. A.; Rodríguez Tojo, M. J.; Aguirre Urizar, J. M. *Med. Oral Patol. Oral Cir. Bucal* **2007**, *12*(7), E532–E536.
134. Artzi, Z.; Weinreb, M.; Givol, N.; *et al. Int. J. Oral Maxillofac. Implants* **2004**, *19*(3), 357–368.
135. Bornstein, M. M.; Chappuis, V.; von Arx, T.; Buser, D. *Clin. Oral Implants Res.* **2008**, *19*(10), 1034–1043.
136. Cordioli, G.; Mazzocco, C.; Schepers, E.; Brugnolo, E.; Majzoub, Z. *Clin. Oral Implants Res.* **2001**, *12*, 270–278.
137. Damron, T. A. *Nanomedicine (Lond.)* **2007**, *2*(6), 763–775; Review.
138. Fiorellini, J. P.; Kim, D. M.; Nakajima, Y.; Weber, H. P. *Int. J. Periodontics Restorative Dent.* **2007**, *27*(3), 287–294.
139. Horch, H. H.; Sader, R.; Pautke, C.; Neff, A.; Deppe, H.; Kolk, A. *Int. J. Oral Maxillofac. Surg.* **2006**, *35*(8), 708–713; *16*(7), 2343–2354.
140. Meyer, C.; Chatelain, B.; Benarroch, M.; Garnier, J. F.; Ricbourg, B. *Rev. Stomatol. Chir. Maxillofac.* **2009**, *110*(2), 69–75.
141. Nakajima, Y.; Fiorellini, J. P.; Kim, D. M.; Weber, H. P. *Int. J. Periodontics Restorative Dent.* **2007**, *27*(2), 151–159.
142. Ormianer, Z.; Palti, A.; Shifman, A. *Implant Dent.* **2006**, *15*(4), 395–403.
143. Suba, Z.; Takács, D.; Matusovicz, D.; Fazekas, A.; Szabó, G.; Barabás, J. *Fogorv. Sz.* **2006**, *99*(1), 21–28.
144. Suba, Z.; Takács, D.; Matusovits, D.; Barabás, J.; Fazekas, A.; Szabó, G. *Clin. Oral Implants Res.* **2006**, *17*(1), 102–108.
145. Szabó, G.; Suba, Z.; Hrabák, K.; Barabás, J.; Németh, Z. *Int. J. Oral Maxillofac. Implants* **2001**, *16*(5), 681–692.
146. Tadjoedin, E. S.; de Lange, G. L.; Holzmann, P. J.; Kulper, L.; Burger, E. H. *Clin. Oral Implants Res.* **2000**, *11*, 334–344.
147. Tetsch, J.; Tetsch, P.; Lysek, D. A. *Clin. Oral Implants Res.* **2010**, *21*(5), 497–503.
148. Uckan, S.; Deniz, K.; Dayangac, E.; Araz, K.; Ozdemir, B. H. *J. Oral Maxillofac. Surg.* **2010**, *68*(7), 1642–1645.
149. Velich, N.; Németh, Z.; Tóth, C.; Szabó, G. *J. Craniofac. Surg.* **2004**, *15*(1), 38–41.
150. Zerbo, I. R.; Zijderveld, S. A.; de Boer, A.; *et al. Clin. Oral Implants Res.* **2004**, *15*(6), 724–732.
151. Zijderveld, S. A.; Zerbo, I. R.; van den Bergh, J. P.; Schulten, E. A.; ten Bruggenkate, C. M. *Int. J. Oral Maxillofac. Implants* **2005**, *20*(3), 432–440.
152. Artzi, Z.; Weinreb, M.; Carmeli, G.; Lev-Dor, R.; Dard, M.; Nemcovsky, C. E. *Clin. Oral Implants Res.* **2008**, *19*(7), 686–692.
153. Németh, Z.; Suba, Z.; Hrabák, K.; Barabás, J.; Szabó, G. *Orv. Hetil.* **2002**, *143*(25), 1533–1538.
154. Szabó, G.; Huys, L.; Coulthard, P.; *et al. Int. J. Oral Maxillofac. Implants* **2005**, *20*(3), 371–381.
155. Zijderveld, S. A.; Schulten, E. A.; Aartman, I. H.; ten Bruggenkate, C. M. *Clin. Oral Implants Res.* **2009**, *20*(7), 691–700.
156. Yamauchi, K.; Takahashi, T.; Funaki, K.; Hamada, Y.; Yamashita, Y. *Int. J. Oral Maxillofac. Surg.* **2010**, *39*(10), 1000–1006.
157. Bohner, M. *Biomaterials* **2009**, *30*(32), 6403–6406; Review.
158. Komlev, V. S.; Mastrogiacomo, M.; Pereira, R. C.; Peyrin, F.; Rustichelli, F.; Cancedda, R. *Eur. Cell Mater.* **2010**, *19*, 136–146.
159. Lin, K.; Chang, J.; Shen, R. *Biomed. Mater.* **2009**, *4*(6), 065009 Epub.
160. Carmagnola, D.; Abati, S.; Celestino, S.; Chiapasco, M.; Bosshardt, D.; Lang, N. P. *Clin. Oral Implants Res.* **2008**, *19*(12), 1246–1253.
161. Galindo-Moreno, P.; Avila, G.; Fernández-Barbero, J. E.; Mesa, F.; O'Valle-Ravassa, F.; Wang, H. L. *Clin. Oral Implants Res.* **2008**, *19*(8), 755–759.
162. Hall, E. E.; Meffert, R. M.; Hermann, J. S.; Mellonig, J. T.; Cochran, D. L. *J. Periodontol.* **1999**, *70*(5), 526–535.
163. Knabe, C.; Ducheyne, P. In *Handbook of Bioceramics and Their Applications*; Kokubo, T., Ed.; Woodhead: Cambridge, UK, 2008; pp 133–164.
164. Lovelace, T. B.; Mellonig, J. T.; Meffert, R. M.; Jones, A. A.; Nummikoski, P. V.; Cochran, D. L. *J. Periodontol.* **1998**, *69*(9), 1027–1035.
165. Low, S. B. *Dent. Implantol. Update* **1998**, *9*(9), 65–67.
166. Nevins, M. L.; Camelo, M.; Nevins, M.; *et al. Int. J. Periodontics Restorative Dent.* **2000**, *20*(5), 458–467.
167. Norton, M. R.; Wilson, J. *Int. J. Oral Maxillofac. Implants* **2002**, *17*(2), 249–257.
168. Reynolds, M. A.; Aichelmann-Reidy, M. E.; Branch-Mays, G. L.; Gunsolley, J. C. *Ann. Periodontol.* **2003**, *8*(1), 227–265; Review.
169. Zamet, J. S.; Darbar, U. R.; Griffiths, G. S.; *et al. J. Clin. Periodontol.* **1997**, *24*(6), 410–418.
170. Ducheyne, P.; Bianco, P.; Radin, S.; Schepers, E. In *Bone-Bioactive Biomaterials*; Ducheyne, P., Kokubo, T., van Blitterswijk, C. A., Eds.; Reed Healthcare Communications: Leiderdorp, Netherlands, 1993; pp 1–12.
171. Ducheyne, P.; Qiu, Q. *Biomaterials* **1999**, *20*, 2287–2303; Review.
172. Effah, E.; Bianco, P.; Ducheyne, P. *J. Biomed. Mater. Res.* **1995**, *29*, 73–80.
173. El-Ghannam, A.; Ducheyne, P.; Shapiro, I. M. *J. Orthop. Res.* **1999**, *17*, 340–345.
174. Strunz, V.; Bunte, M.; Stellmach, R.; *et al. Dtsch Zahnärztl. Z.* **1976**, *31*(1), 69–70.
175. Radin, S.; Ducheyne, P.; Falaize, S.; Hammond, A. *J. Biomed. Mater. Res.* **2000**, *49*(2), 264–272.
176. Bottura, G.; Mongiorgi, R.; Valdrè, G.; *et al. Minerva Stomatol.* **1995**, *44*(1–2), 33–42.
177. Figueiredo, M.; Henriques, J.; Martins, G.; Guerra, F.; Judas, F.; Figueiredo, H. *J. Biomed. Mater. Res. B Appl. Biomater.* **2010**, *92*(2), 409–419.
178. Hippolyte, M. P.; Fabre, D.; Peyrol, S. *J. Parodontol.* **1991**, *10*(3), 279–286.
179. Molly, L.; Vandromme, H.; Quirynen, M.; Schepers, E.; Adams, J. L.; van Steenberghe, D. *J. Periodontol.* **2008**, *79*(6), 1108–1115.
180. Mongiorgi, R.; Valdrè, G.; Bertocchi, G.; *et al. Minerva Stomatol.* **1995**, *44*(1–2), 3–11.
181. Penel, G.; Pottier, E. C.; Leroy, G. *Bull. Group. Int. Rech. Sci. Stomatol. Odontol.* **2003**, *45*(2–3), 56–59.
182. Piattelli, A.; Podda, G.; Scarano, A. *Biomaterials* **1997**, *18*(8), 623–627.
183. Pretorius, J. A.; Melsen, B.; Nel, J. C.; Germishuys, P. J. *Int. J. Oral Maxillofac. Implants* **2005**, *20*(3), 387–398.
184. Sàndor, G. K.; Kainulainen, V. T.; Queiroz, J. O.; Carmichael, R. P.; Oikarinen, K. S. *Dent. Traumatol.* **2003**, *19*(4), 221–227.
185. Scarano, A.; Degidi, M.; Iezzi, G.; *et al. Implant Dent.* **2006**, *15*(2), 197–207.
186. Soost, F.; Reisshauer, B.; Herrmann, A.; Neumann, H. J. *Mund Kiefer Gesichtschir.* **1998**, *2*(2), 96–100.
187. Soost, F. *Chirurg* **1996**, *67*(11), 1193–1196.
188. Valdrè, G.; Mongiorgi, R.; Ferrieri, P.; Corvo, G.; Cattaneo, V.; Tartaro, G. P. *Minerva Stomatol.* **1995**, *44*(1–2), 55–68.
189. Yukna, R. A.; Yukna, C. N. *J. Clin. Periodontol.* **1998**, *25*(12), 1036–1040.
190. Zhu, H.; Schulz, J.; Schliephake, H. *Clin. Oral Implants Res.* **2010**, *21*(2), 182–188.
191. Mangano, C.; Piattelli, A.; Mangano, A.; *et al. Clin. Implant Dent. Relat. Res.* **2009**, *11*(Suppl. 1), e92–e102.

192. Jensen, S. S.; Bornstein, M. M.; Dard, M.; Bosshardt, D. D.; Buser, D. *J. Biomed. Mater. Res. B Appl. Biomater.* **2009**, *90*(1), 171–181.
193. Frenken, J. W.; Bouwman, W. F.; Bravenboer, N.; Zijderveld, S. A.; Schulten, E. A.; ten Bruggenkate, C. M. *Clin. Oral Implants Res.* **2010**, *21*(2), 201–208.
194. Friedmann, A.; Dard, M.; Kleber, B. M.; Bernimoulin, J. P.; Bosshardt, D. D. *Clin. Oral Implants Res.* **2009**, *20*(7), 708–714.
195. Jensen, S. S.; Yeo, A.; Dard, M.; Hunziker, E.; Schenk, R.; Buser, D. *Clin. Oral Implants Res.* **2007**, *18*(6), 752–760.
196. Dietze, S.; Bayerlein, T.; Proff, P.; Hoffmann, A.; Gedrange, T. *Folia Morphol. (Warsz)* **2006**, *65*(1), 63–65.
197. Anderegg, C. R.; Martin, S. J.; Gray, J. L.; Mellonig, J. T.; Gher, M. E. *J. Periodontol.* **1991**, *62*(4), 264–268.
198. Becker, W.; Schenk, R.; Higuchi, K.; Lekholm, U.; Becker, B. E. *Int. J. Oral Maxillofac. Implants* **1995**, *10*(2), 143–154.
199. Becker, W.; Urist, M.; Becker, B. E.; *et al. J. Periodontol.* **1996**, *67*(10), 1025–1033.
200. Becker, W.; Urist, M. R.; Tucker, L. M.; Becker, B. E.; Ochsenbein, C. *J. Periodontol.* **1995**, *66*(9), 822–828.
201. Blank, B. S.; Levy, A. R. *Int. J. Periodontics Restorative Dent.* **1999**, *19*(5), 481–487.
202. Boëck-Neto, R. J.; Gabrielli, M.; Lia, R.; Marcantonio, E.; Shibli, J. A.; Marcantonio, E., Jr. *J. Periodontol.* **2002**, *73*(3), 266–270.
203. Bowen, J. A.; Mellonig, J. T.; Gray, J. L.; Towle, H. T. *J. Periodontol.* **1989**, *60*(12), 647–654.
204. Brugnami, F.; Then, P. R.; Moroi, H.; Leone, C. W. *J. Periodontol.* **1996**, *67*(8), 821–825.
205. De Leonardis, D.; Garg, A. K.; Pedrazzoli, V.; Pecora, G. E. *J. Periodontol.* **1999**, *70*(1), 8–12.
206. Diès, F.; Etienne, D.; Abboud, N. B.; Ouhayoun, J. P. *Clin. Oral Implants Res.* **1996**, *7*(3), 277–285.
207. Froum, S.; Cho, S. C.; Rosenberg, E.; Rohrer, M.; Tarnow, D. *J. Periodontol.* **2002**, *73*(1), 94–102.
208. Fucini, S. E.; Quintero, G.; Gher, M. E.; Black, B. S.; Richardson, A. C. *J. Periodontol.* **1993**, *64*(9), 844–847.
209. Hanisch, O.; Lozada, J. L.; Holmes, R. E.; Calhoun, C. J.; Kan, J. Y.; Spiekermann, H. *Int. J. Oral Maxillofac. Implants* **1999**, *14*(3), 329–336.
210. Harasty, L. A.; Brownstein, C. N.; Deasy, M. J. *Periodontal Clin. Investig.* **1999**, *21*(1), 10–17.
211. Klepp, M.; Hinrichs, J. E.; Eastlund, T.; Schaffer, E. M. *J. Clin. Periodontol.* **2004**, *31*(7), 534–544.
212. Kohal, R. J.; Mellas, P.; Hürzeler, M. B.; Trejo, P. M.; Morrison, E.; Caffesse, R. G. *J. Periodontol.* **1998**, *69*(8), 927–937.
213. Kolerman, R.; Hirsh, A.; Shapira, L. *Refuat Hapeh Vehashinayim* **2001**, *18*(2), 24–32; 60.
214. Kübler, N. R.; Will, C.; Depprich, R.; *et al. Mund Kiefer Gesichtschir.* **1999**, *3*(Suppl. 1), S53–S60.
215. Landi, L. *Compend. Contin. Educ. Dent.* **1998**, *19*(12), 1221–1223; 1226–1230.
216. Olson, J. W.; Dent, C. D.; Morris, H. F.; Ochi, S. *Ann. Periodontol.* **2000**, *5*(1), 152–156.
217. Parashis, A.; Andronikaki-Faldami, A.; Tsiklakis, K. *Int. J. Periodontics Restorative Dent.* **2004**, *24*(1), 81–90.
218. Piattelli, A.; Scarano, A.; Corigliano, M.; Piattelli, M. *Biomaterials* **1996**, *17*(11), 1127–1131.
219. Piemontese, M.; Aspriello, S. D.; Rubini, C.; Ferrante, L.; Procaccini, M. *J. Periodontol.* **2008**, *79*(5), 802–810.
220. Reynolds, M. A.; Bowers, G. M. *J. Periodontol.* **1996**, *67*(2), 150–157.
221. Rosen, P. S.; Reynolds, M. A. *J. Periodontol.* **2002**, *73*(8), 942–949.
222. Rummelhart, J. M.; Mellonig, J. T.; Gray, J. L.; Towle, H. J. *J. Periodontol.* **1989**, *60*(12), 655–663.
223. Schwartz, Z.; Mellonig, J. T.; Carnes, D. L., Jr.; *et al. J. Periodontol.* **1996**, *67*(9), 918–926.
224. Schwartz, Z.; Somers, A.; Mellonig, J. T.; *et al. J. Periodontol.* **1998**, *69*(4), 470–478.
225. Simion, M.; Trisi, P.; Piattelli, A. *Int. J. Periodontics Restorative Dent.* **1996**, *16*(4), 338–347.
226. Trejo, P. M.; Weltman, R.; Caffesse, R. *J. Periodontol.* **2000**, *71*(12), 1852–1861.
227. Wallace, S. C.; Gellin, R. G.; Miller, M. C.; Mishkin, D. J. *J. Periodontol.* **1994**, *65*(3), 244–254.
228. Xiao, Y.; Parry, D. A.; Li, H.; Arnold, R.; Jackson, W. J.; Bartold, P. M. *J. Periodontol.* **1996**, *67*(11), 1233–1244.
229. Yamamichi, N.; Itose, T.; Neiva, R.; Wang, H. L. *Int. J. Periodontics Restorative Dent.* **2008**, *28*(2), 163–169.
230. Bowers, G. M.; Chadroff, B.; Carnevale, R.; *et al. J. Periodontol.* **1989**, *60*(12), 683–693.
231. Ouhayoun, J. P. 'Risques de transmission à l'homme de pathologies virale par de substituts oseux d'origine humaine ou animale'. In *Rapport sur l' état des recherches concernant les risques associés à l'utilisation à des fins thérapeutiques de produits d'origine humaine ou de produits et procédés de substitution*, Paris, Edition INSERM, 1995; pp 224–230.
232. Shaug, S. L.; Crane, G. M.; Miller, M. J.; Yasko, A. W.; Yaszemski, M. J.; Mikos, A. G. *J. Bone Miner. Res.* **1997**, *36*, 17–28.
233. Schimming, R.; Schmelzeisen, R. *J. Oral Maxillofac. Surg.* **2004**, *62*(6), 724–729.
234. Schmelzeisen, R.; Schimming, R.; Sittinger, M. *J. Craniomaxillofac. Surg.* **2003**, *31*(1), 34–39.
235. Schmelzeisen, R.; Schimming, R.; Sittinger, M. *Ann. R. Australas. Coll. Dent. Surg.* **2002**, *16*, 50–53.
236. Hollister, S. J.; Levy, R. A.; Chu, T. M.; Halloran, J. W.; Feinberg, S. E. *Int. J. Oral Maxillofac. Surg.* **2000**, *29*(1), 67–71.
237. Hollister, S. J.; Lin, C. Y.; Saito, E.; *et al. Orthod. Craniofac. Res.* **2005**, *8*(3), 162–173.
238. Feinberg, S. E.; Hollister, S. J.; Halloran, J. W. *Shanghai Kou Qiang Yi Xue* **2000**, *9*(1), 34–38.
239. Smith, M. H.; Flanagan, C. L.; Kemppainen, J. M.; *et al. Int. J. Med. Robot.* **2007**, *3*(3), 207–216.
240. Schek, R. M.; Taboas, J. M.; Hollister, S. J.; Krebsbach, P. H. *Orthod. Craniofac. Res.* **2005**, *8*(4), 313–319.
241. Schantz, J. T.; Hutmacher, D. W.; Lam, C. X.; *et al. Tissue Eng.* **2003**, *9*(Suppl. 1), S127–S139.
242. Schantz, J. T.; Teoh, S. H.; Lim, T. C.; Endres, M.; Lam, C. X.; Hutmacher, D. W. *Tissue Eng.* **2003**, *9*(Suppl. 1), S113–S126.
243. Rohner, D.; Hutmacher, D. W.; Cheng, T. K.; Oberholzer, M.; Hammer, B. *J. Biomed. Mater. Res. B Appl. Biomater.* **2003**, *66*(2), 574–580.
244. Rohner, D.; Hutmacher, D. W.; See, P.; *et al. Mund Kiefer Gesichtschir.* **2002**, *6*(3), 162–167.
245. Rai, B.; Ho, K. H.; Lei, Y.; Si-Hoe, K. M. *J. Oral Maxillofac. Surg.* **2007**, *65*(11), 2195–2205.
246. Sawyer, A. A.; Song, S. J.; Susanto, E.; *et al. Biomaterials* **2009**, *30*(13), 2479–2488.
247. Probst, F. A.; Hutmacher, D. W.; Müller, D. F.; Machens, H. G.; Schantz, J. T. *Handchir. Mikrochir. Plast. Chir.* **2010**, *42*(6), 369–373.
248. Betz, M. W.; Caccamese, J. F.; Coletti, D. P.; Sauk, J. J.; Fisher, J. P. *J. Biomed. Mater. Res. A* **2009**, *90*(3), 819–829.
249. Docherty-Skogh, A. C.; Bergman, K.; Waern, M. J.; *et al. Plast. Reconstr. Surg.* **2010**, *125*(5), 1383–1392.
250. Kretlow, J. D.; Young, S.; Klouda, L.; Wong, M.; Mikos, A. G. *Adv. Mater.* **2009**, *21*(32–33), 3368–3393.
251. Salinas, C. N.; Anseth, K. S. *J. Dent. Res.* **2009**, *88*(8), 681–692; Review.
252. Weir, M. D.; Xu, H. H. *J. Biomed. Mater. Res. B Appl. Biomater.* **2010**, *93*(1), 93–105.
253. Xu, H. H.; Zhao, L.; Weir, M. D. *J. Dent. Res.* **2010**, *89*(12), 1482–1488.
254. Jansen, J. A.; Vehof, J. W.; Ruhé, P. Q.; *et al. J. Control. Release* **2005**, *101*(1–3), 127–136.
255. Moioli, E. K.; Clark, P. A.; Xin, X.; Lal, S.; Mao, J. J. *Adv. Drug Deliv. Rev.* **2007**, *59*(4–5), 308–324; Review.
256. Mikos, A. G.; Herring, S. W.; Ochareon, P.; *et al. Tissue Eng.* **2006**, *12*(12), 3307–3339; Review.
257. Chan, W. D.; Perinpanayagam, H.; Goldberg, H. A.; *et al. J. Can. Dent. Assoc.* **2009**, *75*(5), 373–377.
258. Fuchs, S.; Hofmann, A.; Kirkpatrick, C. J. *Tissue Eng.* **2007**, *13*(10), 2577–2588.
259. Fuchs, S.; Jiang, X.; Schmidt, H.; *et al. Biomaterials* **2009**, *30*(7), 1329–1338.
260. Kirkpatrick, C. J. In *Proceedings BIOMED 2009, 15th International Biomedical Science and Technology Symposium*, Güzelyurt, Turkey, Aug 16–19, 2009 p 17.
261. Knabe, C.; Berger, G.; Gildenhaar, R.; *et al.* In *Transactions of the 36th Annual Meeting of the Society for Biomaterials USA*, Seattle, WA, Apr 21–24, 2010 p 10.
262. Tilkorn, D. J.; Bedogni, A.; Keramidaris, E.; *et al. Tissue Eng. A* **2010**, *16*(1), 165–178.
263. Warnke, P. H.; Springer, I. N.; Wiltfang, J.; *et al. Lancet* **2004**, *364*(9436), 766–770.

264. Aral, A.; Yalçin, S.; Karabuda, Z. C.; Anil, A.; Jansen, J. A.; Mutlu, Z. *Clin. Oral Implants Res.* **2008**, *19*(6), 612–617.
265. Bell, R. B. *Oral Maxillofac. Surg. Clin. North Am.* **2009**, *21*(2), 227–242; Review.
266. Bifano, C. A.; Edgin, W. A.; Colleton, C.; Bifano, S. L.; Constantino, P. D. *Oral Surg. Oral Med. Oral Pathol. Oral Radiol. Endod.* **1998**, *85*(5), 512–516.
267. Bohner, M.; Gbureck, U. *J. Biomed. Mater. Res. B Appl. Biomater.* **2008**, *84*(2), 375–385.
268. Brown, G. D.; Mealey, B. L.; Nummikoski, P. V.; Bifano, S. L.; Waldrop, T. C. *J. Periodontol.* **1998**, *69*(2), 146–157.
269. Cole, I.; Dan, N.; Anker, A. *Aust. NZ J. Surg.* **1996**, *66*(7), 469–472.
270. Ding, S. J.; Shie, M. Y.; Hoshiba, T.; Kawazoe, N.; Chen, G.; Chang, H. C. *Tissue Eng. A* **2010**, *16*(7), 2343–2354.
271. Fujimura, K.; Bessho, K.; Okubo, Y.; Segami, N.; Iizuka, T. *Clin. Oral Implants Res.* **2003**, *14*(5), 659–667.
272. Lew, D.; Farrell, B.; Bardach, J.; Keller, J. *J. Oral Maxillofac. Surg.* **1997**, *55*(12), 1441–1449; discussion 1449–1451.
273. Mazor, Z.; Peleg, M.; Garg, A. K.; Chaushu, G. *J. Periodontol.* **2000**, *71*(7), 1187–1194.
274. Nakadate, M.; Amizuka, N.; Li, M.; *et al. Microsc. Res. Tech.* **2008**, *71*(2), 93–104.
275. Reddi, S. P.; Stevens, M. R.; Kline, S. N.; Villanueva, P. *J. Craniomaxillofac. Trauma* **1999**, *5*(1), 7–12.
276. Shirakata, Y.; Setoguchi, T.; Machigashira, M.; *et al. J. Periodontol.* **2008**, *79*(1), 25–32.
277. Siniković, B.; Kramer, F. J.; Swennen, G.; Lübbers, H. T.; Dempf, R. *Int. J. Oral Maxillofac. Surg.* **2007**, *36*(1), 54–61.
278. Van Damme, P. A. *J. Craniomaxillofac. Surg.* **2005**, *33*(2), 75–78.
279. Wiltfang, J.; Kessler, P.; Buchfelder, M.; Merten, H. A.; Neukam, F. W.; Rupprecht, S. *J. Oral Maxillofac. Surg.* **2004**, *62*(1), 29–35.
280. Wiltfang, J.; Kloss, F. R.; Kessler, P.; *et al. Clin. Oral Implants Res.* **2004**, *15*(2), 187–193.
281. Wolff, K. D.; Swaid, S.; Nolte, D.; Böckmann, R. A.; Hölzle, F.; Müller-Mai, C. *J. Craniomaxillofac. Surg.* **2004**, *32*(2), 71–79.
282. Wright, S.; Bekiroglu, F.; Whear, N. M.; Grew, N. R. *Br. J. Oral Maxillofac. Surg.* **2006**, *44*(6), 531–533.
283. Arisan, V.; Ozdemir, T.; Anil, A.; Jansen, J. A.; Ozer, K. *Int. J. Oral Maxillofac. Implants* **2008**, *23*(6), 1053–1062.
284. Cavalcanti, S. C.; Pereira, C. L.; Mazzonetto, R.; de Moraes, M.; Moreira, R. W. *J. Craniomaxillofac. Surg.* **2008**, *36*(6), 354–359.
285. Habraken, W. J.; de Jonge, L. T.; Wolke, J. G.; Yubao, L.; Mikos, A. G.; Jansen, J. A. *J. Biomed. Mater. Res. A* **2008**, *87*(3), 643–655.
286. Kroese-Deutman, H. C.; Wolke, J. G.; Spauwen, P. H.; Jansen, J. A. *J. Biomed. Mater. Res. A* **2006**, *79*(3), 503–511.
287. Link, D. P.; van den Dolder, J.; van den Beucken, J. J.; *et al. J. Biomed. Mater. Res. A* **2009**, *90*(2), 372–379.
288. Zuo, Y.; Yang, F.; Wolke, J. G.; Li, Y.; Jansen, J. A. *Acta Biomater.* **2010**, *6*(4), 1238–1247.
289. Khairoun, I.; Boltong, M. G.; Driessens, F. C. M.; Planell, J. A. *Biomaterials* **1997**, *18*, 1535–1539.
290. Knabe, C.; Berger, G.; Gildenhaar, R.; *et al. J. Biomed. Mater. Res.* **2004**, *69A*, 145–154.
291. Knabe, C.; Berger, G.; Gildenhaar, R.; Howlett, C. R.; Markovic, B.; Zreiqat, H. *Biomaterials* **2004**, *25*, 335–344.
292. Ooms, E. M.; Wolke, J. G.; van der Waerden, J. P.; Jansen, J. A. *J. Biomed. Mater. Res.* **2002**, *61*, 9–18.
293. Cuisinier, F. J. G.; Wieber, A.; Tenenbaum, H.; van Landuyt, P.; Lemaitre, J. *J. Appl. Biomater. Biomech.* **2003**, *1*, 186–193.
294. Dombrowski, F.; Ploska, U.; Berger, G.; Gildenhaar, R.; Stiller, M.; Knabe, C. *Bioceramics Key Eng. Mater.* **2009**, *422–429*, 863–866.
295. Gildenhaar, R.; Berger, G.; Lehmann, E.; Knabe, C. *Key Eng. Mater.* **2008**, *361–363*, 331–334.
296. Jörn, D.; Gildenhaar, R.; Berger, G.; Stiller, M.; Knabe, C.; Schlau, S. *Biomaterialien* **2008**, *9*(3/4), 178.
297. Jörn, D.; Gildenhaar, R.; Berger, G.; Stiller, M.; Knabe, C. *Key Eng. Mater.* **2009**, *396–398*, 213–216.
298. Knabe, C.; Berger, G.; Gildenhaar, R.; Ducheyne, P.; Stiller, M. In Vicenzini, P., Ed.; *Advances in Science and Technology*; Trans Tech: Switzerland, 2010; Vol. 76, pp 214–223.
299. Broggini, N.; Hofstetter, W.; Hunziker, E.; *et al. Clin. Implant Dent. Relat. Res.* **2011**, *13*(1), 1–12.
300. Esposito, M.; Grusovin, M. G.; Rees, J.; *et al. Eur. J. Oral Implantol.* **2010**, *3*(1), 7–26; Review.
301. Mooren, R. E.; Dankers, A. C.; Merkx, M. A.; Bronkhorst, E. M.; Jansen, J. A.; Stoelinga, P. J. *Int. J. Oral Maxillofac. Surg.* **2010**, *39*(4), 371–378.
302. Klongnoi, B.; Rupprecht, S.; Kessler, P.; *et al. J. Clin. Periodontol.* **2006**, *33*(7), 500–509.
303. Costello, B. J.; Shah, G.; Kumta, P.; Sfeir, C. S. *Oral Maxillofac. Surg. Clin. North Am.* **2010**, *22*(1), 33–42; Review.
304. Davies, S. D.; Ochs, M. W. *Oral Maxillofac. Surg. Clin. North Am.* **2010**, *22*(1), 17–31; Review.
305. Hallman, M.; Thor, A. *Periodontol. 2000* **2008**, *47*, 172–192; Review.
306. Hanisch, O.; Sorensen, R. G.; Kinoshita, A.; Spiekermann, H.; Wozney, J. M.; Wikesjö, U. M. *J. Periodontol.* **2003**, *74*(5), 648–657.
307. Hanisch, O.; Tatakis, D. N.; Boskovic, M. M.; Rohrer, M. D.; Wikesjö, U. M. *Int. J. Oral Maxillofac. Implants* **1997**, *12*(5), 604–610.
308. Hanisch, O.; Tatakis, D. N.; Rohrer, M. D.; Wöhrle, P. S.; Wozney, J. M.; Wikesjö, U. M. *Int. J. Oral Maxillofac. Implants* **1997**, *12*(6), 785–792.
309. Leach, J. K.; Mooney, D. J. *Expert Opin. Biol. Ther.* **2004**, *4*(7), 1015–1027; Review.
310. Roldán, J. C.; Jepsen, S.; Miller, J.; *et al. Bone* **2004**, *34*(1), 80–90.
311. Roldán, J. C.; Jepsen, S.; Schmidt, C.; *et al. Clin. Oral Implants Res.* **2004**, *15*(6), 716–723.
312. Ruhé, P. Q.; Kroese-Deutman, H. C.; Wolke, J. G.; Spauwen, P. H.; Jansen, J. A. *Biomaterials* **2004**, *25*(11), 2123–2132.
313. Terheyden, H.; Jepsen, S.; Möller, B.; Rueger, D. *Laryngorhinootologie* **2001**, *80*(1), 47–51; German.
314. Terheyden, H.; Jepsen, S.; Vogeler, S.; Tucker, M.; Rueger, D. C. *Mund Kiefer Gesichtschir.* **1997**, *1*(5), 272–275.
315. Terheyden, H.; Knak, C.; Jepsen, S.; Palmie, S.; Rueger, D. R. *Int. J. Oral Maxillofac. Surg.* **2001**, *30*(5), 373–379.
316. Terheyden, H.; Menzel, C.; Wang, H.; Springer, I. N.; Rueger, D. R.; Acil, Y. *Int. J. Oral Maxillofac. Surg.* **2004**, *33*(2), 164–172.
317. Terheyden, H.; Warnke, P.; Dunsche, A.; *et al. Int. J. Oral Maxillofac. Surg.* **2001**, *30*(6), 469–478.
318. Wang, H. L.; Greenwell, H.; Fiorellini, J.; *et al. J. Periodontol.* **2005**, *76*(9), 1601–1622; Review.
319. Warnke, P. H.; Bolte, H.; Schünemann, K.; *et al. J. Craniomaxillofac. Surg.* **2010**, *38*(1), 54–59.
320. Warnke, P. H.; Wiltfang, J.; Springer, I.; *et al. Biomaterials* **2006**, *27*(17), 3163–3167.
321. Wikesjö, U. M.; Sorensen, R. G.; Kinoshita, A. *J. Clin. Periodontol.* **2004**, *31*(8), 662–670.
322. Arosarena, O. A.; Collins, W. L. *Otolaryngol. Head Neck Surg.* **2005**, *132*(4), 592–597.
323. Barboza, E. P.; Caúla, A. L.; Caúla Fde, O.; *et al. J. Periodontol.* **2004**, *75*(5), 702–708.
324. Bessa, P. C.; Casal, M.; Reis, R. L. *J. Tissue Eng. Regen. Med.* **2008**, *2*(2–3), 81–96; Review.
325. Dunn, C. A.; Jin, Q.; Taba, M., Jr.; Franceschi, R. T.; Bruce Rutherford, R.; Giannobile, W. V. *Mol. Ther.* **2005**, *11*(2), 294–299.
326. Letic-Gavrilovic, A.; Piattelli, A.; Abe, K. *J. Mater. Sci. Mater. Med.* **2003**, *14*(2), 95–102.
327. Smith, D. M.; Afifi, A. M.; Cooper, G. M.; Mooney, M. P.; Marra, K. G.; Losee, J. E. *J. Craniofac. Surg.* **2008**, *19*(5), 1315–1322.
328. Wikesjö, U. M.; Xiropaidis, A. V.; Thomson, R. C.; Cook, A. D.; Selvig, K. A.; Hardwick, W. R. *J. Clin. Periodontol.* **2003**, *30*(8), 715–725.
329. Wikesjö, U. M.; Xiropaidis, A. V.; Thomson, R. C.; Cook, A. D.; Selvig, K. A.; Hardwick, W. R. *J. Clin. Periodontol.* **2003**, *30*(8), 705–714.
330. Moore, J. C.; Matukas, V. J.; Deatherage, J. R.; Miller, E. J. *Int. J. Oral Maxillofac. Surg.* **1990**, *19*(3), 172–176.
331. Trombelli, L.; Farina, R. *J. Clin. Periodontol.* **2008**, *35*(Suppl. 8), 117–135; Review.
332. Esposito, M.; Grusovin, M. G.; Coulthard, P.; Worthington, H. V. *Int. J. Oral Maxillofac. Implants* **2006**, *21*(5), 696–710; Review.
333. Smeets, R.; Maciejewski, O.; Gerressen, M.; *et al. Oral Surg. Oral Med. Oral Pathol. Oral Radiol. Endod.* **2009**, *108*(4), e3–e12.
334. Springer, I. N.; Açil, Y.; Kuchenbecker, S.; *et al. Bone* **2005**, *37*(4), 563–569.
335. Warnke, P. H.; Springer, I. N.; Acil, Y.; *et al. Biomaterials* **2006**, *27*(7), 1081–1087.
336. Wikesjö, U. M.; Huang, Y. H.; Polimeni, G.; Qahash, M. *Oral Maxillofac. Surg. Clin. North Am.* **2007**, *19*(4), 535–551; vi–vii, Review.
337. Abu-Serriah, M. M.; Odell, E.; Lock, C.; Gillar, A.; Ayoub, A. F.; Fleming, R. H. *Br. J. Oral Maxillofac. Surg.* **2004**, *42*(5), 410–418.
338. Haidar, Z. S.; Hamdy, R. C.; Tabrizian, M. *Biotechnol. Lett.* **2009**, *31*(12), 1825–1835.

339. Haidar, Z. S.; Hamdy, R. C.; Tabrizian, M. *Biotechnol. Lett.* **2009**, *31*(12), 1817–1824; Review.
340. Food and Drug Administration, HHS. *Fed. Regist.* **2005**, *70*(81), 21947–21950.
341. FDA Communication of Jun 6, 2008: Follow-up to the Mar 27, 2008, Communication About the Ongoing Safety Review of Regranex (Becaplermin).
342. FDA Public Health Notification: Life-Threatening Complications Associated with Recombinant Human Bone Morphogenetic Protein in Cervical Spine Fusion, July 1, 2008.
343. Koch, F. P.; Becker, J.; Terheyden, H.; Capsius, B.; Wagner, W. *Clin. Oral Implants Res.* **2010**, *21*(11), 1301–1308.
344. Potijanyakul, P.; Sattayasansakul, W.; Pongpanich, S.; Leepong, N.; Kintarak, S. *J. Oral Implantol.* **2010**, *36*(3), 195–204.
345. Scheyer, E. T.; Velasquez-Plata, D.; Brunsvold, M. A.; Lasho, D. J.; Mellonig, J. T. *J. Periodontol.* **2002**, *73*(4), 423–432.
346. Velasquez-Plata, D.; Scheyer, E. T.; Mellonig, J. T. *J. Periodontol.* **2002**, *73*(4), 433–440; Erratum in *J. Periodontol.* **2002**, *73*(6), 684.
347. Merkx, M. A.; Maltha, J. C.; Stoelinga, P. J. *Int. J. Oral Maxillofac. Surg.* **2003**, *32*(1), 1–6.
348. Berger, G.; Gildenhaar, R.; Ploska, U. In Wilson, J., Hench, L. L., Greenspan, D. C., Eds.; *Bioceramics*; Butterworth-Heinemann: Oxford, UK, 1995; Vol. 8, pp 453–456.
349. Berger, G.; Gildenhaar, R.; Ploska, U. *Biomaterials* **1995**, *16*, 1241–1248.
350. Berger, G.; Mücke, U.; Harbich, K. W. In Ben-Nissan, B., Sher, D., Walsh, W. R., Eds.; *Key Engineering Materials*; Trans Tech: Zurich, Switzerland, 2003; Vols. 240–242, pp 469–472.
351. Schneider, M.; Gildenhaar, R.; Berger, G. *Cryst. Res. Technol.* **1994**, *29*, 671–675.
352. Berger, G.; Gildenhaar, R.; Ploska, U. In LeGeros, R. Z., LeGeros, J. P., Eds.; *Bioceramics*; World Scientific: Singapore, Malaysia, 1998; Vol. 11, pp 121–124.
353. Berger, G.; Gildenhaar, R.; Ploska, U.; Willfahrt, M. In Sedel, L. C., Rey, C., Eds.; *Bioceramics*; Elsevier Science: Oxford, UK, 1997; Vol. 10, pp 367–370.
354. Crawford, R.; *et al. J. Bone Joint Surg. Br.* **1999**, *81*, 552–554.
355. Sun, J. S.; *et al. J. Arthroplasty* **2003**, *18*(3), 352–360.
356. Sun, J. S.; *et al. J. Biomed. Mater. Res.* **1997**, *37*, 324–334.
357. Sun, J. S.; *et al. Artif. Organs* **1999**, *23*(4), 331–338.
358. Berger, G. In *Federal Institute for Materials Research and Testing (BAM) Annual Report*, BAM: Berlin, Germany, 2003; pp 34–43.
359. Knabe, C.; Stiller, M.; Berger, G.; *et al. Clin. Oral Implants Res.* **2005**, *16*, 119–127.
360. Knabe, C.; Gildenhaar, R.; Berger, G.; *et al. J. Mater. Sci. Mater. Med.* **1998**, *9*, 337–345.
361. Knabe, C.; Berger, G.; Gildenhaar, R.; *et al.* In *Transactions of the 32nd Annual Meeting of the Society for Biomaterials USA*, Chicago, IL, Apr 18–21, 2007 p 262.
362. El-Ghannam, A.; Ducheyne, P.; Shapiro, I. M. *J. Biomed. Mater. Res.* **1997**, *36*(2), 167–180.
363. Roeser, K.; Johansson, C. B.; Donath, K.; Albrektsson, T. *J. Biomed. Mater. Res.* **2000**, *51*, 280–291.
364. Knabe, C.; Kraska, B.; Koch, Ch.; Gross, U.; Zreiqat, H.; Stiller, M. *Biotech. Histochem.* **2006**, *81*, 31–39.
365. Knabe, C.; Berger, G.; Gildenhaar, R.; *et al.* In *Transactions of the 35th Annual Meeting of the Society for Biomaterials USA*, San Antonio, TX, Apr 22–25, 2009 p 262.
366. Knabe, C.; Kim, J.; Chen, C.; Meausoone, V.; Radin, S.; Ducheyne, P. In *Transactions of the 35th Annual Meeting of the Society for Biomaterials USA*, San Antonio, TX, Apr 22–25, 2009 p 359.
367. Knabe, C.; Berger, G.; Gildenhaar, R.; Ducheyne, P.; Stiller, M. In *Advances in Science and Technology*; Vicenzini, P., Ed.; Trans Tech Publications: Switzerland, 2010; Vol. 76, pp 214–223.
368. Kim, J.; Berger, G.; Gildenhaar, R.; Shapiro, I.; Ducheyne, P.; Knabe, C. In *Transactions 36th Annual Meeting of the Society for Biomaterials USA*. April 21–24, Seattle, Washington, USA, 2010; p 830.
369. Ohgushi, H.; Dohi, Y.; Susumu, T.; Tabata, S. *J. Biomed. Mater. Res.* **1993**, *27*, 1401–1407.

6.621. Biomaterials and Their Application in Craniomaxillofacial Surgery

C Szpalski and M McRae, New York University Medical Center, New York, NY, USA
G F Rogers, Children's Hospital Boston, Boston, MA, USA
J D Bumgardner, University of Memphis, Memphis, TN, USA
S M Warren, New York University Medical Center, New York, NY, USA

© 2011 Elsevier Ltd. All rights reserved.

6.621.1.	**Introduction**	326
6.621.2.	**Biomaterials and Implants in Craniomaxillofacial Surgery**	326
6.621.2.1.	Skeletal Fixation/Stabilization	326
6.621.2.1.1.	Metals and alloys	327
6.621.2.1.2.	Resorbable polymers	328
6.621.2.1.3.	Clinical application	329
6.621.2.2.	Skeletal Replacement and Augmentation	331
6.621.2.2.1.	Methyl methacrylate	332
6.621.2.2.2.	Silicone implants	332
6.621.2.2.3.	Hard tissue replacement (HTR)	332
6.621.2.2.4.	Porous polyethylene (MEDPOR™)	333
6.621.2.2.5.	Hydroxyapatite and bioactive glass	333
6.621.2.2.6.	Demineralized bone	334
6.621.2.3.	Cartilage Replacement	334
6.621.2.4.	Soft Tissue Replacement and Augmentation	334
6.621.2.4.1.	Collagen	334
6.621.2.4.2.	Dermal substitutes	334
6.621.2.4.3.	Hyaluronic acid	336
6.621.2.4.4.	Polymethylmethacrylate	336
6.621.2.4.5.	Poly-L-lactic acid	336
6.621.2.4.6.	Calcium hydroxyapatite-based dermal filler	336
6.621.2.4.7.	Fat	337
6.621.2.4.8.	Expanded polytetrafluoroethylene implants	338
6.621.2.4.9.	High-density polyethylene implants	338
6.621.3.	**Considerations and Future Applications**	339
References		339

Abbreviations

AATB	American Associate of Tissue Banks
ADRC	Adipose-derived regenerative cells
ASTM	A consensus standards organization, formally known as the American Society for Testing and Materials, but now referred to as ASTM International
BMPs	Bone morphogenetic proteins
CaHa	Calcium hydroxyapatite
CP	Commercially pure, used to designate a type of titanium
CT	X-ray computed tomography
DBM	Demineralized bone matrix
ECM	Extracellular matrix
ePTFE	Expanded polytetrafluoroethylene polymer
Et2Zn	Zinc(II) diethyldithiocarbamate, a catalyst used in polymerization of *p*-dioxanone
FDA	Food and Drug Administration
HA	Hyaluronic acid
HDPE	High-density polyethylene polymer
HTR	Hard tissue replacement, a copolymer of polymethylmethacrylate and polyhydroxymethylmethacrylate with a calcium phosphate coating
IGF-1	Insulin-like growth factor 1
IMF	Intermaxillary fixation
ISO	The International Standards Organization
MM	Methyl methacrylate
MMF	Mandibular-maxillary fixation
MRI	Magnetic resonance imaging
ORIF	Open reduction internal fixation
PDS	Polydioxanone polymer
PGA	Polyglycolic acid
PLA	Polylactic acid; can exist in dextrorotary (D) or levorotary (L) or racemic (equal parts D and L forms) stereoisomer forms; designated as poly-D-lactide, poly-L-lactide, and poly-DL-lactide, respectively
PLDA	Copolymer of poly-L-lactide and poly-D-lactide isomers

PLDLA	Copolymer of poly-L-lactide isomer and poly-D,L-lactide racemic forms
PLLA	Polymer or all poly-L-lactide isomers
PMMA	Polymethylmethacrylate
PRP	Platelet-rich plasma
SR	Self-reinforced polymer; special designation that refers to 70:30 PLDL copolymer that is specially processed to have highly oriented crystalline fibers in a polymer matrix
TGF	Transforming growth factor
VEGF	Vascular endothelial growth factor

6.621.1. Introduction

Since the origins of the specialty, craniomaxillofacial surgeons have relied on various biomaterials to stabilize, augment, repair, and replace biological tissues of the head and face. Materials currently used range from simple stainless steel wire to complex biological compounds that are designed to modulate cellular biology. While the application of various materials depends on the particular need and use, all of them share two general requirements. First, they must be biocompatible. Second, inorganic or alloplastic products must be prepared in a sterile environment or have the capacity to retain their physical properties when subjected to current sterilization procedures. These two basic requirements limit the number of materials that can be considered for use in craniomaxillofacial reconstruction.

Materials can generally be categorized into organic, that is, those deriving from a living organism, and inorganic. This clarity in material categorization has been blurred by the manufacture of synthetic 'organic-like' compounds that seek to replicate or stimulate living tissues. Organic material can be subclassified into autografts, allografts, and xenografts. An autograft is autologous tissue (i.e., self-derived) harvested and grafted on the same patient. In terms of reconstructive purposes, autogenous tissue is ideal for craniomaxillofacial surgery as it is biocompatible and inexpensive, and often possesses properties nearly identical to those of the deficient tissues. Autogenous material can be transferred without a vascular supply (graft), attached to a vascular pedicle (e.g., rotational flap), or be attached to a new blood supply (free tissue transfer). One of the advantages of autogenous grafts and flaps is that they become vascularized and fully incorporated into the recipient. This makes autogenous tissues durable and resistant to infection. Unfortunately, there is a limit to the quantity of autogenous tissue available. Furthermore, there is limited functional redundancy, and borrowing tissue from another area can have deleterious aesthetic and functional implications.

Allograft, or biological material from the same species, is an alternative to autogenous tissue. Allograft retailers capitalize on an economy of scale, enabling them to provide an almost unlimited supply of material. An allograft can become vascularized, although it tends to be less well vascularized and to incorporate to a lesser degree into recipient tissues than autografts. Thus, allografts serve as an option only when autograft is not available. Also, allografts have biocompatibility issues and will be rejected by the recipient's immune system unless they are decellularized. In addition, disease transmission (i.e., virus, prions, etc.) remains a concern. These significant issues have been addressed by altering or negating allograft tissue immunogenicity, or by modulating the host's immune response. Processed allograft materials are widely used in craniofacial reconstruction and will be reviewed later. Host immune modulation forms the basis for modern transplant surgery, the most recent application of which is facial transplantation; facial transplantation is beyond the scope of this text and will not be discussed. Recombinant technology allows the production of purified human proteins that have little immunologic reactivity and no risk of disease transmission.

Xenografts are biological materials derived from other species. Because sources of xenograft products are plentiful, they are an attractive option for reconstruction. However, the immune response to xenografts can be pronounced, and these tissues require processing to eliminate antigenic epitopes. In spite of xenogenic tissue processing, some patients experience a significant immune response to these materials. Moreover, xenogenic tissue processing can, unfortunately, alter the properties of the tissue and lessen its usefulness.

Nonorganic biomaterials also play an important role in craniomaxillofacial surgery. Some clinical needs, such as mandibular osteosynthesis, require material properties not found in biological tissues. In addition, there are many clinical applications where nonorganic products can effectively substitute for organic tissues. Biocompatible, nonorganic products must be nontoxic, nonimmunogenic, noninflammatory, and sterilizable. Additional specific considerations for nonorganic biomaterials to be used in craniomaxillofacial applications include modulability/flexibility to be shaped to meet the necessary geometry, potential to be stabilized/fixed in position, ability to restore proper tissue volumes for function and aesthetics, and capacity to resist infection. These materials include metals and alloys, plastics, and various synthetic polymers, and they have some distinct advantages over organic substrates. First, there is no concern regarding disease transmission. Second, the materials are plentiful. Third, the strength, contourability, and material properties can be engineered to fit the reconstructive needs. However, one major disadvantage of these materials is their inability to revascularize or fully incorporate into the host tissues; this results in an increased risk of infection and stress fracture. The choice of material depends on the application for which it is to be used.

6.621.2. Biomaterials and Implants in Craniomaxillofacial Surgery

6.621.2.1. Skeletal Fixation/Stabilization

Bone stabilization and osteosynthesis are fundamental to craniomaxillofacial reconstruction. Over the last three decades,

techniques have shifted from semirigid fixation using wires and suture, to rigid fixation using various plating systems. This transition has been propelled by the speed and ease of plate application as well as reduction in the incidence of nonunion and infection. Both metal and resorbable materials are now used for osteosynthesis.

Reported outcomes and rates of complications for metal and resorbable systems are similar. Nevertheless, resorbable plates are often used in pediatric patients to avoid plate migration as the craniofacial skeleton grows. For example, resorbable plates have largely replaced metal ones for craniosynostosis procedures for infants after several reports of intracranial migration after growth. However, the strength of metal systems may still be required for adult mandibular repair. Dorri *et al.* recently reviewed multiple clinical studies to compare resorbable and metal craniomaxillofacial implant systems for fracture management. The authors noted that there were no published randomized controlled clinical studies, that there was insufficient evidence for the effectiveness of resorbable systems over conventional titanium systems, and that trials needed to be undertaken.[1]

Implant materials must conform to certain basic requirements (e.g., adequate function, minimal side effects, and biocompatibility). Less obvious is the need for appropriate handling qualities, and the selection of the material and implant design depend on it. The plating system has five different functions: (1) protection, (2) compression, (3) tension band, (4) bridging, and (5) buttressing. Many different materials have been proposed to provide these functions and avoid implant failure under high mechanical load. Surgeons generally select the smallest plating system that will provide stable fixation under functional loads during the healing period. Larger plates are used when the fracture occurs across a longer osseous lever arm (e.g., the mandibular angle compared to the mandibular body), or in areas of comminution where bone contact or compression cannot be applied.

Miniplate osteosynthesis emerged in the late 1960s and capitalized on dynamic compression.[2] Analysis of the biomechanics and principles of tension banding in extremity fractures demonstrated that elevated tensile stress along the mandibular alveolar ridge could be neutralized by miniplates.[2] Champy described his method of mandibular fixation, which involved applying small plates to the superior border of mandibular angle fractures to offset tension stress, and in the neutral zone and body.[3] Stainless steel plates were later changed to titanium to improve strength.

With regard to the midface, small metallic plates have proved to have better potential to reestablish bony contours compared with direct wiring or suspension wiring techniques. Miniature and microplate systems have been developed with biocompatible metals such as titanium alloys. These plates have greatly facilitated reconstruction of comminuted, unstable fractures and reestablished normal facial projection and contour.[4] These plating systems have specialized instruments to assist in bending the plates; an improperly bent plate can exert undesirable forces on the bone and lead to loosening or malunion.

Oblique fractures can be stabilized without plates by placement of screws using a lag technique. Ideal situations include mandibular symphysal or oblique fractures of the zygoma.[5,6] This technique uses differential hole size – the hole in the near fragment is as wide as the outer thread diameter, while the hole in the distal fragment is the diameter of the screw body. Thus, the screw glides easily through the near fragment hole and begins to engage as it passes into the distal fragment. This creates progressive compression across the fracture as the screw is tightened.

6.621.2.1.1. Metals and alloys

The most common implant metals used for craniomaxillofacial fracture fixation are the alloys, 316L stainless steel, Co–Cr–Mo (Vitallium), and titanium.[7] They are biocompatible and strong, and can be contoured and shaped. Consequently, they have been used extensively for many applications in the head and neck. The composition, physical, mechanical, and corrosion properties are covered in detail in other chapters. A brief summary is provided here.

316L stainless steel is an iron-based alloy consisting of the following major elements: 17–19% Cr, 13–15 wt% Ni, 2.25–3.0 wt% Mo, 2.0 wt% (max) Mn, and 0.03 wt% (max) C. The 'L' designation refers to the low (< 0.03 wt%) carbon content of the alloy in comparison with the conventional 316 grade (0.08% C). The alloy is also referred to as ASTM F138 by ASTM International Standards Organization or as ISO 5832-1 [ASTM, ISO] by the International Standards Organization, ISO.. Chromium provides a corrosion-resistant chromium-oxide surface layer, and the addition of molybdenum enhances the oxide's resistance to chloride attack. While stainless steel, applied as plates and screws, was used in early craniomaxillofacial fracture fixation, it is not widely used currently for the same application. This is primarily because its high modulus ($E = 190$ GPa) makes it difficult to bend and contour it to fit complex craniofacial geometries.[7,8] Poor adaptation of the plates to the underlying bone makes them easily visible and palpable beneath facial soft tissues. Additionally, while stainless steel is highly corrosion-resistant, it shows some susceptibility to pitting corrosion *in vivo* as compared to either the Co–Cr–Mo or titanium alloys, despite the fact that the addition of Mo to the alloy composition is specifically intended to alleviate this issue. Stainless steel wires are still used though for temporary external fixation.[9] One early and still used method of bone stabilization after open reduction has been the placement of direct interosseous wiring (**Figure 1**). Wire osteosynthesis provides only semirigid fixation but has found use nearly everywhere in the craniofacial skeleton.

Co–Cr–Mo alloy (Vitallium® or ASTM F1537 or ISO 5832-12) is a high modulus alloy ($E \sim 230$ GPa) with a nominal composition of 26–30 wt% Cr, 5–7 wt% Mo, and the balance Co. Chromium alloy provides a highly corrosion-resistant chromium-oxide surface layer and exhibits higher corrosion-resistant properties than 316L stainless steel. This combination of high mechanical strength and excellent corrosion resistance make it useful in mandibular fixation where high fracture loading is typical. The high modulus of elasticity and strength of Co–Cr–Mo has also led to the development of micromesh sheets, which allow for versatility of design and coverage for large cranial defects.[10] However, the stiffness of the alloy also makes it difficult to shape and contour. Thus, special tools are required to fit plates and meshes to complex mandibular and cranial sites.[10] Potential for metal

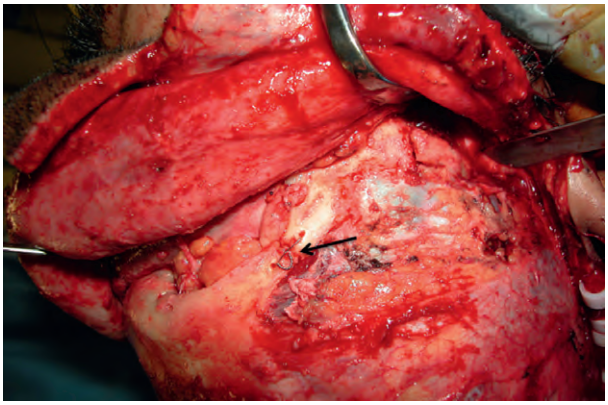

Figure 1 A 54-year-old man with orbitozygomaticomaxillary fracture. Intraoperative superior view of an interosseous wire placed across the frontozygomatic fracture (arrow). The placement of direct interosseous wires for bone stabilization provides only semirigid fixation. Note: A fracture of the zygomatic arch can also be seen.

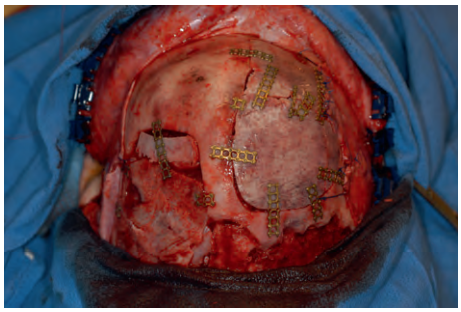

Figure 2 A 24-year-old man with titanium plates stabilizing a cranioplasty. Intraoperative view of various titanium plates holding multiple cranioplasty bone segments to the patient's skull.

hypersensitivity reactions to Co and Cr degradation/corrosion products has been a concern.[11]

Commercially pure (cp) titanium and titanium alloy (Ti–6Al–4V) are the predominant alloys used today in craniomaxillofacial bone fixation (Figure 2). These metals have a significantly lower modulus (E = 100–120 GPa] than stainless steel or Co–Cr–Mo alloys, making them much easier to shape and contour. CP Ti (also known as ASTM F67 or ISO 5832-2) is subcategorized into 4 grades depending on the content of oxygen, iron, and other trace elements. Higher grades depict increasing levels of oxygen (0.18–0.4 wt%), iron (0.2–0.5 wt%), and other trace elements, and are correlated with increasing mechanical strength (e.g., Grade 1 tensile strength = 240 MPa; Grade 4 tensile strength = 550 MPa). The Ti–6Al–4V alloy (ASTM F136 or ISO 5832-3) has a composition of 5.5–6.5 wt % Al and 3.5–4.5 wt% V. The addition of the Al and V alloying elements increases the modulus and high-cycle fatigue properties as compared to cp Ti. Titanium has a high affinity for oxygen, which results in the formation of a titanium oxide surface layer that has exceptional corrosion resistance and ability to osseointegrate.

Current craniomaxillofacial bone fixation systems come in a range of sizes that are generally referenced to diameter of screw (Figure 3). For example, a 2 mm plate is a plate that is



Figure 3 A 32-year-old man with midfacial fractures. Intraoperative view of a bioresorbable polymer plate across a midfacial fracture. The high-molecular-weight poly-a-hydroxy ester plates have been successfully used throughout the craniomaxillofacial skeleton. Note: metal arch bars have been temporarily placed on the teeth to restore normal occlusion.

used with 2-mm diameter screws. The thickness of the plates can range from <1.0 mm to >2.5 mm. Generally, larger diameter screws and thicker plates (e.g., >2 mm) are used for the highly loaded applications such as fractures of the mandible. These are still referred to sometimes in the literature as 'miniplate and screw' systems. The smaller diameter screws and thinner plates (e.g., <2.0 mm) are typically used in low load regions, such as the midface, orbit, and cranium, to limit palpability. Such thin plates and small diameter screws are still referred to sometimes as 'microplate and screw' systems in the literature. However, it is important to note that these designations are not standardized and there is significant variability among manufacturers.

Metal-based plate and screw systems are sometimes contoured to match craniomaxillofacial bone geometries with the aid of Al templates. The templates are pressed against the bone at the fixation site, and then using the molded template as a guide, the final fixation plate can be bent to the appropriate geometry.[10] Fixation systems for larger bones or bones that endure significant load, such as the mandible, often have screws that require tapping prior to insertion.[12] These tapped screws are typically used when bone thickness is >3 mm and biocortical fixation is required. In such applications, the excessive force and frictional heating that would occur without tapping the hole could lead to bone necrosis. Self-tapping screws are more applicable to bone <3 mm thick such as in the orbital rims, midface, and craniofacial skeleton. The thin bone in these regions coupled with the sharper threads on the self-tapping screws reduces the concern regarding frictional heating with insertion. It has been reported that non-self-tapping screws may be reinserted into their tapped holes without compromising stability, while self-tapping screws should not be reinserted if plate position requires adjustment.[12,13]

6.621.2.1.2. Resorbable polymers

Bioresorbable polymers are commonly used in the craniomaxillofacial region to effect bone stabilization or fracture fixation (Figure 4). These high-molecular-weight poly-alpha hydroxy esters include polylactic acid (PLA), polyglycolic acids (PGAs) and their copolymers, and polydioxanone. These materials have been successfully used as bioresorbable sutures or staples for upward of three decades.[14,15] The polymers degrade first

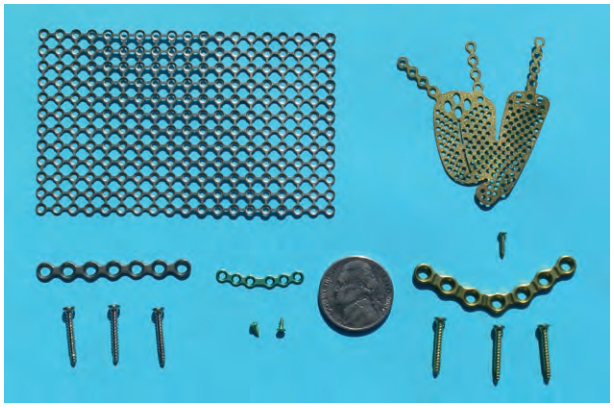

Figure 4 Plate and screw fixation system. Current titanium plate and screw systems for craniomaxillofacial bone fixation come in a range of sizes that are generally referenced to the screw diameter. (Plate and screws were kindly provided by BIOMET Microfixation, Jacksonville, FL, USA.)

by hydrolysis and then through metabolic processes. Once implanted, water and body fluids penetrate the implant and cause bulk hydrolysis of ester bonds in polymer chains, resulting in a decrease in polymer molecular weight, followed by a loss in mass and in mechanical properties. As hydrolysis continues, the material disintegrates/fragments and is ultimately metabolized into carbon dioxide and water or excreted in urine.[14–16]

Lactic acid is chiral and it exists in sterioisomeric forms that give rise to distinct polymers: poly-D-lactide, poly-L-lactide, and poly-D, L-lactide (racemic form from a mixture of D and L lactic acid). The D or L polylactides are optically active semicrystalline polymers, while the poly-D,L-lactide is optically inactive and amorphous. These sterioisomers may also be combined to form various copolymers such as poly-L-lactide–poly-D-lactide (poly (L/D) lactide or PLDA) or poly-L-lactide–poly-D,L-lactide (poly(L/DL) lactide or PLDLA). The pure poly-L-lactide (PLLA) can have high crystallinity, characterized by high strength (bending strengths of 240 MPa) and degradation times of three or more years.[14–16] When implanted as plates or screws, swelling and discharge from under thin subcutaneous tissues can occur.[17] The D,L-lactide polymer has low strength and degrades rapidly within a few months.[14,15] The combination of L-lactide and D,L- lactide make a copolymer with good strength with an intermittent degradation rate. For example, the 70:30 PLDLA polymer is 100% amorphous, and retains approximately 70% of its strength after 9 months, approximately 50% after 12 months, and undergoes complete degradation within 1.5–3 years.[15] Subjected to a solid-state extrusion process at 150 °C, the 70:30 PLDL material develops highly oriented crystal fibers within the polymer matrix, which increase its initial mechanical properties. This 'self-reinforced' (SR) polymer is reported to maintain its strength for 12–18 weeks, and be totally resorbed within 3 years.[18] Several commercial bioresorbable plates, screws, and mesh products are marketed based on the 70:30 PLDLA copolymer: MacroPore, Medtronic, MN; LactoSorb, Biomet Inc., IN; Fixsorb, BioPlate Inc., CA; Bionix, Bionix Development Corp, OH; Isosorb, Aesculap Implant Systems Inc. PA; Synthes Resorbable Fixation Systems, Synthes GmbH, Switzerland.

The PGA polymer is characterized as being highly crystalline, with a high melting temperature (~230 °C), good mechanical strength (~330 MPa), and low solubility in organic solvents. PGA suture, commercially available under the trade name Dexon™ S (Covidien, MSA), has been used since the 1970s. These sutures degrade rapidly and lose their mechanical strengths within 2–4 weeks after implantation.[14] Screws made of PGA were reported to lose their mechanical strengths within 6 weeks and to be completely resorbed within 1 year.[17,19] However, high rates of adverse tissue reactions to pure PGA materials, such as swelling, tissue drainage, and osteolysis have been reported as resulting from rapid degradation and buildup of acidic by-products.[17,19] PGA can be copolymerized with PLA to slow down the degradation rate compared to pure PGA; doping PLA into PGA, however, reduces the crystallinity and mechanical strength. The 82:18 PLLA/PGA copolymer (LactoSorb, Biomet) is reported to retain 70% of its strength for approximately 8 weeks and to be completely resorbed within 1 year.[19] An 85:15 PLLA/PGA copolymer has also been reported to have controlled rapid degradation properties with sufficient strength for pediatric craniofacial applications.[15] It is important to note that physicomechanical properties of PLA–PGA copolymers do not follow a linear relationship.

Polydioxanone, PDS, is a homopolymer of *p*-dioxanone prepared by polymerization in the presence of a Zinc(II) diethyldithiocarbamate, Et2Zn, catalyst.[14] It is considered a modification of PGA created by replacing one ester linkage for an ether linkage. This molecular alteration provides increased material flexibility while retaining good degradability. As a monofilament suture, it exhibits minimal to no tissue reaction. It loses 40% of its strength after 4 weeks, exhibits complete loss of mechanical properties after 8 weeks, and is totally resorbed by 4–6 months.[14,16] It has been used as fixation pins for unloaded fractures.

Resorbable plate and screw systems have screws that require tapping since the polymers are not as hard as bone. This can add time to surgery, and because pretapping does not always engage bone as well as self-tapping screws, fixation may not be as good in small mobile bone segments.[20,21] To overcome this issue, bioresorbable tacks have been developed.[22–24] The tacks may be placed by hand, or with a mallet or an automatic driver. However, if repositioning of plate and screws is needed, new drill holes may be made in the plates to allow screws to be optimally placed in bone. Also, if screws are damaged or broken during placement, they can be removed by burring through remnants and replaced with a new screw.[16] To adapt plates to bone geometries, they are heated above their glass transition temperatures (~55–70 °C) in water baths, with heat packs or other heating devices. *In situ* contouring may be achieved using electrocautery or thermal scalpels.[13]

6.621.2.1.3. Clinical application

6.621.2.1.3.1. External fixation

Initially, craniofacial surgeons used sutures, wires, occlusal splints, external fixators, and creative bone cuts to provide rigid fixation. For example, Gilmer first introduced his technique of mandibulomaxillary fixation in 1887 and the materials used were basic.[25] Wire ligatures were passed around the neck of available teeth and twisted clockwise until tight. By

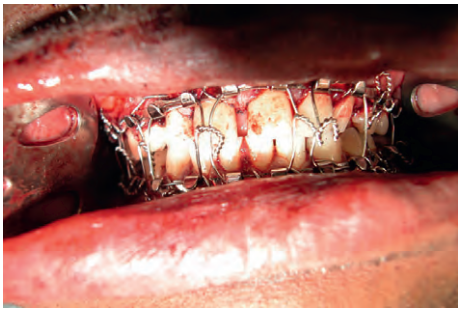

Figure 5 A 28-year-old man with maxillary and mandibular fractures. Erich arch bars can be secured to the upper and lower dental arches by passing wires around the neck of the available teeth and twisting clockwise until tight. Then, wires can be passed from the upper arch bar to the lower arch bar to establish centric occlusion.

attaching the upper wire to the lower wire, centric occlusion could be established (**Figure 5**).[25] The eyelet technique emerged as another technique of IMF. This method used a 24- or 26-gauge wire twisted around an instrument to make a loop.[27] A continuous wire loop has also been used. The technique of intermaxillary fixation used most commonly today uses stainless steel arch bars and wire. The stainless steel arch bar is contoured to the dental arch and affixed onto the dentition using 24-gauge wires that are twisted around individual teeth. One bar is placed on the lower and upper arch. Once the occlusion is set, the two bars are then tethered together by a series of wire loops placed between them. If there are not enough teeth, or if additional stability is needed, one can connect wires to the skeleton by passing the wires around the mandible, the zygoma, the pyriform rim, nasal spine, and infraorbital rim; this technique can be used anywhere in the face to provide additional bone stabilization.[28]

Closed reduction, particularly in edentulous patients, may be facilitated using intraoral splints. A Gunning splint is a prosthesis fabricated from models of edentulous maxillary and mandibular arches and aids in reduction and fixation of a fracture. Acrylic splints can be made by obtaining impressions of the arches. Using a stone model made from initial impressions, the model of the fractured side is sectioned and fit to the other side. The acrylic splint can now be made off these models. Holes are drilled so that it is wired to teeth, and reduction is achieved.[9]

External pin fixation is an effective method of fracture stabilization. It can be used in cases where there is significant bone loss, such as gun shot wounds, where bone grafting has been performed, or where rapid fixation is needed. Two or more pins are placed in the proximal and distal bone fragments and joined together using locking plates and bars.[28]

6.621.2.1.3.2. Open reduction internal fixation

Rigid internal fixation is designed to offset or negate functional forces that may impede fracture healing. Materials used for this application need to demonstrate durability, malleability, and biocompatibility. Metal wires, arch bars, and splints are still used as external fixation devices to stabilize fractures (i.e., nondisplaced or nongrossly comminuted fractures)[29] in combination with internal fixation systems. These internal fixation systems use a range of materials, from metals to resorbable polymer plates, screws, and mesh and pin systems.[18]

Carl Hansmann was the first to present a procedure for subcutaneous fixation of mandible bone fragments with a plate and screw system.[30] These were nickel-coated, came out through the skin, and were removed 4–8 weeks later. In 1907, Lambotte coined the term 'osteosynthesis.' He invented external fixation and many screws and plates made from silver, copper, brass, and aluminum.[31] Sherman is credited with applying the first self-tapping machine cut threads.[32] Although these plating systems were novel, mandibular-maxillary wire fixation (MMF) systems were still preferred because they had a lower incidence of pseudoarthrosis and they avoided the infections that were common with the internal fixation devices.[2]

One explanation for the increased complication rate with early plating systems is that they did not allow adequate approximation of the bone fragment. Collins was the first to develop a plate that allowed the fracture ends to be approximated.[33] The first true compression plate of the mandible was presented by Luhr.[26,34] The plates were Vitallium® and shaped like a half pipe around the lower body of the mandible. Compression plates allow a lateral moment of force that compresses the fracture together. The resultant frictional forces and load sharing reduce the size of the plate that is needed for stability. Spiessel of the Swiss Association for Internal Fixation modified plates of stainless steel, vitallium, and titanium.[35] Spiessel established a system that involves bicortical screws, an eccentric compression plate at the inferior border of the mandible, and a tension band at the superior border.[35]

Raveh introduced a locking plate system in 1980. Composed of titanium, the heads of screws locked into the holes of the plate. It was named the Titanium-coated Hollow Screw and Reconstruction Plate System.[36] The head of the screw was hollow, and a second smaller screw was inserted that pressed against the plate. This construct allowed the bone fragments to be stabilized without pressure from the plate. This technique has been replicated in other systems.[37]

With rigid internal fixation techniques, the need for MMF is limited. Rigid fixation is preferred in fractures with an unfavorable alignment, such as those at the angle of the mandible where the masseter and medial pterygoid cause displacement of the proximal mandible. Rigid fixation is also valuable when a patient has a condylar fracture and contrecoup fracture because it enables early mobilization. As a result, patients with condylar fractures and body fractures can start moving early toward ankylosis.

Numerous studies support the clinical benefits and relatively low complication rates with metallic and resorbable systems for craniofacial bone fixation.[15,19,21,38–43] In a comprehensive review, Rubin and Yaremchuk reported a low 6.6% incidence of infection and a 2% exposure rate from five clinical studies comprising 880 patients who received midfacial metal plates and screws.[39] Prominence (0.9%), pain (1.3%), and an overall 10.1% removal rate due to implant complications were reported. Studies on mandibular fracture plates also reported a similarly low 6.1% infection rate and very low incidence (<0.5%) of plate fracture loosening.[44] Infection and exposure rates increased to 14.3% and 14.9%, respectively, when plates were used for mandibular reconstruction after tumor resection

and adjuvant chemotherapy and/or radiation. Combined midfacial and mandibular data for 2659 patients reported an overall infection rate of only 7.4% and an exposure rate of 3.3% for metal fixation systems. Jack and coworkers reported similar complication rates (14%) in a series of 54 patients treated for more complex facial fractures with titanium plates and screws. Potter *et al*. observed that materials used for orbital reconstruction rarely became infected. The authors noted only one infection of metal meshes in two studies totaling 66 patients, and aesthetic outcomes were considered very good to excellent.[40]

While metal fixation systems provide excellent osteosynthesis, they can cause artifact with CT or MRI imaging, have been hypothesized to impair growth when used in children, and do not have sufficient long-term outcomes.[18,21,25] The artifacts created during radiological imaging or external radiation therapy for malignancy can be problematic, but they are fewer with titanium devices than with stainless steel or Co–Cro–Mo.[18] In children, it is unclear if the metal fixation devices interfere with bone and or brain growth. Additionally during this rapid growth period, the calvarial vault undergoes resorption from the inner aspect and deposition on the outer aspect. As this process occurs, there is a propensity of fixation plates to migrate or translocate from the ectocranial to the endocranial surface.[18,21] While the clinical consequences of this have not been noted, concern still exists about the long-term effects of deep metallic implants.[21] Other potential negative consequences include palpability, thermal sensitivity, and the need for subsequent removal of devices.[16,21]

Degradable implant systems were developed to overcome many of the issues related to metallic implants. The advantages of the degradable systems include the lack of need for device removal (especially for children) and, presumably, the lack of growth disturbance. Early resorbable plates and meshes were made of 100% PLLA, but their long degradation times (3–6 + years) and sterile foreign body were problematic.[45,46] Today, most common degradable systems are based on the PLLA-PDLLA or PLLA-PGLA systems. Agrawal *et al*. recently reported on a review of 19 clinical studies using resorbable mandibular plate systems. The studies comprised a total of 326 patients with 70:30 PLLA-PDLLA plates and screws, and 112 patients with screws only.[43] They noted that while the overall rate of removal for the resorbable devices (2–3%) was lower than that for metal devices, the former exhibited a 4–5% infection and were more likely to lose fixation and result in malunion than the latter. Eppley and Reilly[20] reported on 18 pediatric patients with facial fractures treated with 82:12 PLLA–PGLA (LactoSorb) systems. All of them healed with no complications and with total resorption of implants within 1 year. Yerit *et al*.[47] observed similarly good results in 13 pediatric patients treated with SR PLLA–PDLLA devices. Several studies found good clinical results with resorbable PLLA–PDLLA meshes in orbital rim repair, although some inflammation was noted even after 11 months due to the need to fold the mesh to obtain sufficient strength.[38] Bell and Kindsfater[21] retrospectively reviewed 59 patients with resorbable plates and found an overall complication rate of 6% (16 patients); this included 8 patients with infections (13%), 4 with malunions (7%), 2 with nonunions (3.3%), 3 with alterations in eyeball position (5%), and 1 patient with sterile abscess at 1 year. Holmes and coworkers reported an overall 12.8% (n = 14) complication rate in 164 patients treated with 70:30 PLLA–PDLLA devices.[15] This included 2 patients with minor erosion, 4 with intraoral exposure, 3 with fracture, and 5 with temporal or fronto-orbital swelling, which resolved over 3 months. They noted that improvements in surgical techniques may substantially reduce complication rates. They further suggested that good clinical and aesthetic outcomes had been obtained in preliminary studies using other implants such as a customized PLLA–PDLLA mesh for cranial repair, PLLA–PGLA tacks, and 85:15 PLDA–PGA fast resorbing screws and plates for pediatric patients.

Certain clinical situations clearly favor the use of either resorbable systems (e.g., pediatric stabilization) or metallic systems (e.g., mandibular stabilization). However, the advantages of one system over another are less clear for many applications. Dorri *et al*. recently published a Cochrane Database Systemic review of clinical studies to compare resorbable and metal craniomaxillofacial implant systems for facture management.[1] In their meta-analysis, the authors concluded that the lack of level I datas and randomized trials prevents adequate comparison between resorbable systems and conventional titanium systems. The lack of trials in their systematic review may be partly because of the ethical and methodological limitations of conducting such trials on humans. Fedorowicz and coworkers[48] carried out a similar Cochrane review to compare the effectiveness of bioresorbable fixation systems compared to titanium systems for orthognathic surgery. Based on their assessment of published clinical studies, they were also not able to determine any advantage of the resorbable systems compared to the titanium systems. These authors advised some caution in the interpretation of their results mainly because of the methodological limitations and poor reporting of the results of the trials. The best available studies seem to suggest that both fixation systems are similarly effective.

6.621.2.1.3.3. Extracellular matrix and growth factor-coated implants

The application of growth factors, such as bone morphogenic proteins (BMPs), to plating surfaces has shown promise with regard to improvement in bone healing.[49] BMPs are members of the TGF family of proteins, and there are at least 30 BMPs. BMPs are complex, and some studies have shown that BMPs also stimulate osteoclasts. Therefore, the net bone formation may be less with BMPs and it may be dose-dependent.[50] Other growth factors that have been tested on titanium implants include growth hormone, platelet-derived growth factor, and insulin-like growth factor.[51] This developing and promising area of implant technology is beyond the scope of this treatise.

6.621.2.2. Skeletal Replacement and Augmentation

Autogenous bone is a standard to which all biomaterials are compared.[52] Many of the most influential surgeons in the field continue to feel that autogenous bone is the best biomaterial for craniofacial reconstruction.[53,54] Advances in surgical technique have led to a decrease in morbidity and an increase in ease of harvest. Nevertheless, there are limitations to autogenous bone grafting. The most common bone graft donor sites are cranial bone, iliac bone, ribs, and tibia, and harvest of bone from these areas is associated with added operative time and

donor site morbidity. In addition, autogenous bone can be difficult to mold to meet the requirements of the craniofacial skeleton, and there can be significant and unpredictable resorption over time. Lastly, the supply of autogenous bone is limited, particularly in the pediatric population.

Given the limitations of autogenous bone graft, biomaterials have assumed a central role in oral and craniofacial bone replacement and augmentation. The most common recipients of facial implants are the cheek (malar, submalar, and midfacial), nose, jaw, and chin regions. While existing implants for these anatomic areas are biologically inert and nonbiodegradable, and elicit little inflammatory response, they tend to lack the plasticity for custom molding to fit the contours of the face.

6.621.2.2.1. Methyl methacrylate

First used in World War II for craniofacial reconstruction, poly (methylmethacrylate) (MM) is an acrylic-based resin that is strong and resistant to resorption.[55] MM is a colorless, odorless liquid that is made into a polymer. It is biologically inert. It has significant applications in the construction industry today, being used for casting, molding, and paints. It is inexpensive and easily accessible. Because MM does not integrate with the surrounding bone or develop a blood supply (**Figure 6**), it does not grow with the surrounding bone, can become dislodged if exposed to load, and is prone to infection.[56] Marchac *et al*. describe their experience with the use of MM in 98 patients over 21 years.[57] They document an infection rate of 9%, requiring removal of implant, with good or excellent results at long-term follow up of 85 out of 98 patients. Infection rates were higher when the nasal or frontal sinus was in contact with the implant during the operative procedure. Blum *et al*. noted a 23% complication rate with the use of MM. These complications were also noted in defects that communicated with the frontal sinus, were very large, or were associated with a history of infection or postoperative radiotherapy.[58]

6.621.2.2.2. Silicone implants

Silicone is a polymer of Si molecules described in the chapter by V. Hasirci. Implants designed from this material were used for cheek augmentation in the 1960s.[59] Silicon implants are inert and resist tissue ingrowth; instead, they become surrounded by a fibrous capsule.[60] Once formed, this capsule helps to maintain implant position.[61] Also, silicone is easy to handle, has minimal complications, and good overall patient satisfaction.[59] A recent study on techniques and materials used in rhinoplasty found that surgeries using silicone implants had overall shorter operation times compared with autologous grafts.[62] Another investigation recommended that silicone implants should not be used to create a caucasian nose in an Asian patient as this can cause protrusion of the implant.[63] Silicone implants have also been shown to be effective treatment options when reconstructing the orbital floor.[64]

While there are many benefits to silicone implants, they are not without limitations and problems. Silicone implants may be associated with increased bone resorption. Silicone implants used in mandibular reconstruction can cause a decrease in the volume of bone beneath the implants, possibly as a result of diminished circulation.[65] Further, it should also be noted that silicone implants can be associated with benign granulation which may be falsely diagnosed as a malignant tumor by radiograph.[66] Given this information, a physician should always question whether a patient has previously undergone any silicone implantation when interpreting radiographic images. Finally, silicone can degrade and fracture over time (**Figure 7**).

6.621.2.2.3. Hard tissue replacement (HTR)

Hard tissue replacement (HTR) is a porous polymeric composite of polymethylmethacrylate and polyhydroxyethyl methacrylate with a calcium hydroxide coating that acts to promote tissue ingrowth for implant stability. It has a 20–30% material porosity (150–350 μm), holds a negative surface charge (−8 to −15 mV), and has a compressive strength of 50 000 lb in^{-2} in particulate form and 5000 lb in^{-2} in molded form.[67] Porosity allows for some tissue ingrowth that helps stabilize the implant and prevent migration/dislodgement.

Eppley used a rabbit model to demonstrate osseous ingrowth into inlay implants extending up to 2000 μm.[68]

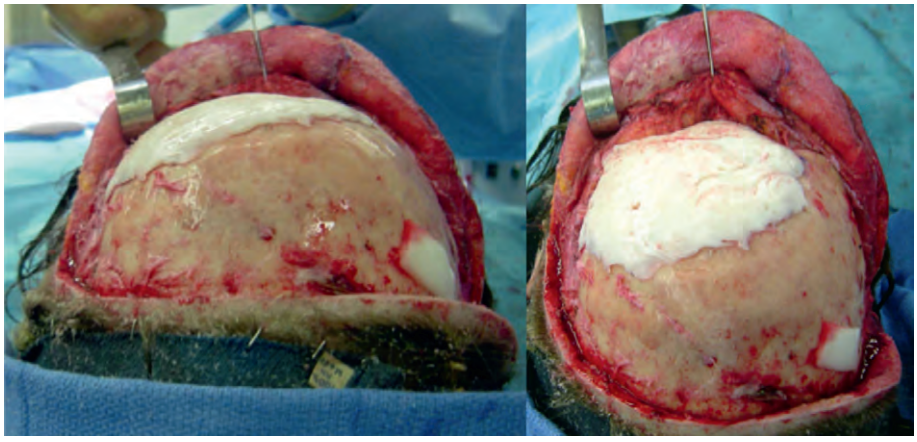

Figure 6 A 42-year-old female with left-sided coronal craniosynostosis. Intraoperative views of methylmethacrylate monomer applied to the frontal bone to correct forehead asymmetry. Methylmethacrylate is a colorless, odorless liquid that polymerizes into a strong inert solid that is resistant to resorption and does not incorporate into the bone.

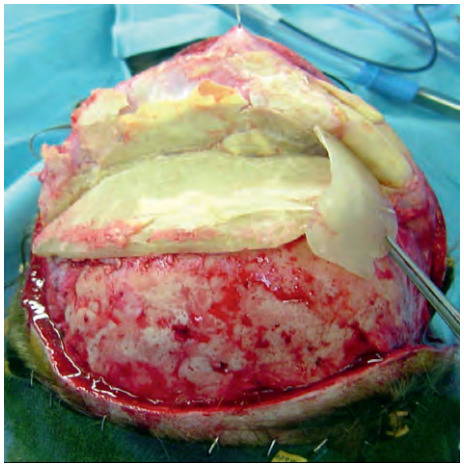

Figure 7 A 47-year-old female with a silicone implant placed 20 years earlier for correction of forehead contour deformity. Intraoperative view of a silicone implant 20 years after its placement showing the aging and fracture of silicone over time.

The onlay implants, however, exhibited more limited bony ingrowth, extending only up to 100–200 μm into the material. The material is considered osteoconductive and appears to resist infection. Guyuron reported good results using HTR to augment the orbit and temporal region in four patients to correct an hourglass facial deformity.[69] Eppley used prefabricated HTR from a computer-generated model in 14 patients to reconstruct large cranial defects (greater than 150 cm^2) with excellent results. In all these cases, the procedure was delayed for debridement and treatment of all sources of infection, and the frontal sinus was cranialized using pericranial flaps.[70]

6.621.2.2.4. Porous polyethylene (MEDPOR™)

MEDPOR™ Surgical Implants are manufactured from linear high-density polyethylene. MEDPOR™ allows for tissue growth into its interconnecting open pores. The average pore size is around 100 μm, and pores make up approximately 50% of the total implant volume. The firm material can be carved with a sharp instrument without collapsing the pore structure (**Figure 8**). Dougherty *et al.* reported ingrowth of vessels into the implants within 1 week and peripheral integration with bone at 3 weeks.[71]

Yaremchuk reported on a series of 370 porous polyethylene implants in 162 patients.[72,73] These implants were fixed in the subperiosteal plane with titanium screws. All implants were incorporated onto the native tissues without incident, and there was no implant extrusion or capsule formation. Reoperation rate was 10% and the infection rate was 3%. Porous polyethylene has found application in microtia reconstruction, nasal reconstruction, and throughout the craniofacial skeleton.[74] Like HTR, porous polyethylene molds can be made to fit the defect using CT imaging. It is considered osteoconductive due to the tissue and bone ingrowth into the material.

6.621.2.2.5. Hydroxyapatite and bioactive glass

Hydroxyapatite is a calcium phosphate ceramic, as is bioactive glass. These materials are described at great length in other chapters in this publication. Herein, we briefly describe their utility in craniomaxillofacial surgery. Hydroxyapatite is chemically similar to the mineral component of bone and hard tissues in mammals. It is a bioactive material that will support bone ingrowth and osseointegration. It has been used in orthopedic, dental, and maxillofacial applications and can be replaced with bone formation via osteoconduction.[75] This material is radiolucent and biocompatible. Hydroxyapatite cement consists of a calcium phosphate preparation comprised of tetracalcium phosphate and dicalcium phosphate anhydrous powders. When mixed with water, it isothermically forms a hydroxyapatite paste that can easily be shaped during application. The mixture sets in approximately 15–20 min and converts into a microporous material in 4 h.



Figure 8 Porous polyethylene chin implant. The firm nature of porous polyethylene allows intraoperative shaping without collapse of the pore structure. Note: The pore structure allows for some bony ingrowth.

Because it mimics the mineral component of the bone, this material has been made in various forms and has been extensively used in craniofacial surgery. It is important to keep in mind that dense hydroxyapatite does not have the mechanical strength, especially the fracture toughness, to allow its use in long-term load-bearing applications. Jackson *et al.* successfully used dense hydroxyapatite without complication to fill contour irregularities in 20 patients.[76] Burstein and coworkers have reported on 61 patients in whom hydroxyapatite was used for secondary craniofacial reconstruction: 31 for secondary orbitocranial defects after surgery for synostosis, 7 after surgery for hypertelorism, 10 for posttraumatic skull defects, and 13 for a variety of other facial skeletal defects. There was a 11% complication rate (four seroma, one drain cemented), but an excellent overall retention of implant volume with no recurrence of contour defects.[77] Byrd and colleagues reported the use of porous hydroxyapatite granules to augment the craniofacial skeleton in 200 patients over 8 years. They found favorable results in augmenting the perialar, maxilla, and glabellar area.[78]

Synthetic bioactive glass is a compound consisting of silicon oxide, sodium oxide, calcium oxide, and phosphate. Glass particles in various size ranges have been used: a size range from 300 to 355 μm and another from 90 to 710 μm.[79–83] Through a complex set of surface- and solution-mediated reactions, bioactive glass stimulates cell function, including the stimulation of osteoprogenitor cells to produce TGF-β, which makes the material osteogenic at the surface of glass particles.[84–86] Bioactive glass mixed with autogenous bone has been used in orbital floor fractures, maxillary sinus augmentation, and frontal sinus obliteration with promising results.[87,88]

It has proved useful to augment bone in preparation for titanium plating. Unfortunately, prefabricated bioactive glass ceramic implants made to date have not been proven to be more advantageous compared to other implants mentioned earlier, and are not widely used.[89]

6.621.2.2.6. Demineralized bone

Demineralized bone matrices (DBMs) are osteoinductive and, thus, can stimulate bone formation de novo. This material is prepared by acid demineralization of allograft bone. The remaining collagen and noncollagenous proteins, including growth factors and BMP, contain the osteoinductive components. DBMs are available in two different forms, as a paste or in small chips. Several different DBMs are commercially available, but each product has been shown to have a distinct osteoinductivity potential as a result of the differences in the preparation methods, storage, and donor specifications.[90] DBM is very pliable and can be easily molded to accommodate most defects. Based on their clinical observations, Salyer *et al.* conclude that demineralized perforated bone implants serve as osteoinductive centers.[91] These authors found that cortical demineralized perforated bone matrix caused no adverse tissue reactions and was capable of stimulating bone formation and remodeling. In large calvarial reconstructions, some areas had not been populated by living bone cells, although there were no signs of osseous resorption.

6.621.2.3. Cartilage Replacement

Autologous cartilage grafts are not new. Autologous cartilage harvested from the costal margin has been utilized in the treatment of microtia for decades.[92] Because the quantity of autogenous cartilage is limited, some researchers have focused efforts on manufacturing cartilage using cultured autologous human chondrocytes.[93] Yanaga and colleagues described a procedure where a 1 cm portion of the auricular concha was taken from a patient and placed in a serum that stimulates cell proliferation.[93] After only 4 weeks, cell counts were noted to be 1000 times larger than the number originally harvested. The autologous cells were then placed in a gel matrix and injected subcutaneously into areas requiring augmentation.[93] Surprisingly, cultured chondrocytes can be used to reconstruct complicated shapes.[94]

6.621.2.4. Soft Tissue Replacement and Augmentation

Reconstruction of the craniomaxillofacial soft tissue must be functional and aesthetic. Surgeons have used autologous grafts, allografts, and synthetic materials to reconstruct soft tissue defects. Depending on the type of defect and the size, as well as the patient preferences, one or multiple techniques may be required to address the soft tissue problem.

6.621.2.4.1. Collagen

Collagen is the most abundant protein in humans and the main structural support of the skin.[95] Collagen also acts as a scaffold for cell differentiation and proliferation. In the skin, fibroblasts secrete collagen and other proteins that form networks of extracellular matrices (ECMs); these ECMs are constantly being remodeled by collagenase and protease activity.[96] Many different physiologic changes occur in the skin during aging. One study suggested that advance-glycolitic end products, such as carboxymethyllysine, accumulate in the ECM and stimulate apoptotic pathways in fibroblasts, effectively reducing their cell count.[97] With fewer fibroblasts available, future collagen deposition is diminished and the overall thickness and strength of the ECMs is decreased. Aged or damaged fibroblasts have also been shown to produce up to 20% less collagen, further decreasing overall skin thickness and strength.[95] Thus, exogenous collagen augmentation may help restore soft tissue volume in aging skin and other conditions associated with soft tissue volume loss.

In the mid-1980s, bovine-derived collagen gained approval from the US Food and Drug Administration (FDA) for the correction of contour deficits in soft tissue.[95] Bovine collagen injections have been used to help correct wrinkles, such as glabelar lines, perioral lines, horizontal forehead lines, and crows' feet.[98] Despite its proven effectiveness in correcting contour defects in the aforementioned areas, bovine-derived collagen has unwanted side effects and relatively poor longevity. One problem is that compounds containing bovine-derived collagen can cause allergic reactions. Thus, it is suggested that a patient should have at least two allergy tests spaced 2 weeks apart before having bovine collagen treatment.[99] Furthermore, the life of a given treatment has been reported to be only a few months.[100] Zyplast™, a bovine collagen that is chemically cross-linked, is reported to last about 6 months due to its greater resistance to endogenous collagenases.[101] Chemically cross-linked bovine collagen has significantly better longevity and can last up to 24 months.[102] Recent advancements in collagen treatments have focused on human[103] and porcine-[104] derived collagen. While these options are reportedly less immunogenic than their bovine counterpart, the overall retention of the material is still quite limited. The poor longevity of injected collagen materials has prompted a move toward longer lasting dermal fillers, such as hyalorunic acid, calcium hydroxyapatite, and polylactic acid, in recent years.[105]

6.621.2.4.2. Dermal substitutes

Acellular human dermis is donated human skin that has been aseptically processed to remove the epidermis and the cells (that can lead to tissue rejection and graft failure) while preserving and stabilizing the remaining biochemical components and dermal matrix. This resulting framework (composed of collagen, elastin, protein, hyaloronan, proteoglycans, fibronectin, and vascular channels) is an intact acellular matrix of natural biological components that promotes rapid cellular repopulation and vascularization. The cadaver skin undergoes a strict comprehensive series of procedures as directed by the FDA, the American Association of Tissue Banks (AATB), and other regulatory bodies to assure its safety. The skin donors are prescreened and tested for transmissible diseases, and the grafts are harvested at the time of death. Microbiological cultures are performed on the tissue to assure the absence of bacterial and fungal pathogens. Once processed, histology and immunohistochemistry are performed on the dermal matrix to confirm that the material is acellular, has an intact basement membrane complex, and has retained most of the native collagen.

Acellular human dermis was originally developed and approved by the FDA as a skin substitute for burn victims. Nevertheless, it is now used more frequently for off-label uses in dental, orthopedic, urogenital, and plastic surgical reconstructive procedures. Currently, there are multiple commercially available acellular human dermis products, but the literature most commonly refers to Alloderm® (Lifecell, Branchburg, NJ).

6.621.2.4.2.1. Alloderm®

Since 1994, more then 1 million Alloderm® grafts have been implanted. This tissue has been used to repair soft tissue defects and is reported to support the revascularization and regeneration of tissue (www.lifecell.com) (**Figure 9**). Alloderm® has a shelf life of 2 years when stored at 1–10 °C and requires about 30 min for rehydration. Currently, it is used in many different reconstructive procedures, including implant-based breast reconstruction after mastectomy, abdominal wall reconstruction, and oncological head and neck reconstruction. Sclafani *et al*. compared the clinical results and longevity of Alloderm® to those of bovine cross-linked collagen, Zyplast® (Collagan Corp, Palo Alto, CA). These authors measured the persistence of the materials at 1, 3, 6, and 12 months after subdermal implantation (behind the ear) and found statistically better retention of Alloderm® (82.8%, 48.3%, 21.9%, and 20.2%, respectively) compared to Zyplast® (26.6%, 8.0%, 1.1%, and 0.9%) at all times. Biopsies taken at 12 months showed extensive ingrowth of mature blood vessels and fibroblasts in the Alloderm® specimens, but almost complete resorption of Zyplast® had occurred by 3 months. Although the volume retention of Alloderm was excellent, the authors still recommended overcorrection, given the observed loss of volume.[106]

The use of acellular dermal matrix has become increasingly popular as a substitute for donor connective tissue in oral surgery. Conventional wisdom now dictates that one should assess the quality of the underlying gingiva at the recipient site prior to hard tissue augmentation of autologous bone graft.

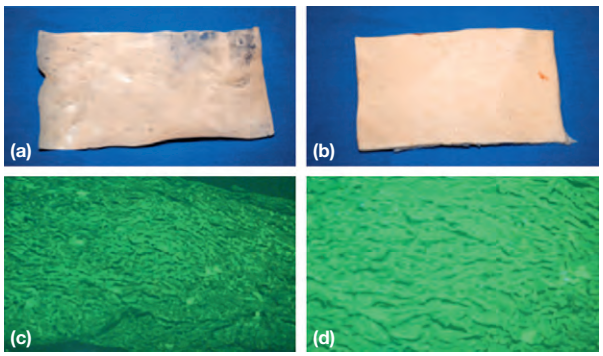

Figure 9 Gross and histologic images of Alloderm™ dermal matrix. Alloderm™ is human skin that has been aseptically processed to remove the epidermis and the cells (thereby reducing immunologic reaction) while preserving and stabilizing the remaining collagen components of the dermal matrix. (a) Dehydrated Alloderm™ (b) Alloderm™ after hydration (c) Alexa fluor stained Alloderm™ showing its intact acellular matrix of natural biological components serving as a framework for rapid cellular repopulation and vascularization (10×). (d) Higher power view of alexa fluor stained Alloderm™ (20×).

Alloderm® has been shown to improve graft survival and diminish the risk of graft exposure when used for soft tissue reconstruction of the gingival defect 12 weeks prior to the bone graft.[107]

The use of Alloderm® for secondary nasal reconstruction was successfully reported by Gryskiewicz in 2004. Nasal augmentation is important for correcting secondary deformities. The gold standard has been autogenous cartilage graft, but this technique has the drawback of donor site morbidity and irregularity of the cartilage graft, especially in patients who have had prior nasal procedures. In one report, 25 patients underwent dorsal augmentation of the nose using Alloderm® placed over autogenous cartilage grafts, including those used to reconstruct the nasal tip.[108] There was good patient satisfaction and only one patient had a partial extrusion. There was no resorption at 1 year, although nearly half of the patients had partial graft resorption (<50%) at 2 year follow-up. The latter observation led the authors to recommend overcorrection, particularly on the bony dorsum. Jackson *et al*. showed similar results using Alloderm® in secondary rhinoplasty to create a smooth nasal dorsum.[109] Sudarsan and coworkers used Alloderm® in combination with BioOss® (inorganic bone material) to treat Siebert's class I ridge deficiency.[110] Alloderm® acts as a barrier membrane to prevent the gingival tissue from contaminating the wound space and interfering with osteogenesis. This combination showed an increase in both bone and soft tissue volume after 6 months and 9 months of study.

Lastly in 1999, Rubin *et al*. showed that Alloderm® could be successfully used as a barrier and a reconstructive grafting material in occuloplastic interventions.[111] These authors used Alloderm® as a scaffolding for primary and secondary implant coverage, as a lid spacer graft, and for volume augmentation of the superior sulcus and other periorbital defects. Unpredictable resorption of the material did result in multiple revisions for some patients.

6.621.2.4.2.2. DermaMatrix

DermaMartix® (Synthes, West Chester, PA) is another acellular human dermis product available. DermaMartix® can be stored at room temperature and has a shelf life of 3 years and a rehydration time that is 10 times shorter than that required for Alloderm®. Nevertheless, Alloderm® seems to have a better elasticity than DermaMatrix®, making it more popular in breast reconstruction. Becker and coworkers compared DermaMatrix® and Alloderm® in immediate expander-based breast reconstruction procedures.[112] At 6 months, both materials were well incorporated into host tissue (grossly and histologically) and had equal vascularization. The most common complications were wound infection and the formation of seroma, although the complication rates were similar.

DermaMatrix® has been used in oculoplastic surgery. Lee *et al*. reported the use of DermaMatrix® for eyelid (lower eyelid retraction repair) and anophthalmic socket reconstruction.[113] The success of the surgery was gauged by the improvement of symptoms as well as the anophthalmic patient's ability to wear a prosthesis. Ten of the 13 patients were successfully treated in one operation; the remaining 3 patients had complex reconstructive needs that required more than one operation. At 3 months, the graft (typically 1×4 cm) demonstrated

neovascularization. The authors concluded that DermaMatrix® was a viable alternative to Alloderm® for oculoplastic surgery.

6.621.2.4.3. Hyaluronic acid

Hyaluronic acid (HA) is a polysaccharide and the most prevalent glycosaminoglycan in human dermis.[114] Therefore, this material would be a natural candidate for use as a dermal filler. Currently, HA is the most commonly used dermal filler, ranked second only to Botox™ in 2007 for its use in minimally invasive cosmetic procedures.[105] Age and sun damage decrease the amount of endogenous HA.[115,116] Restoring or replenishing HA can help correct volume deficits. A highly hydrophilic molecule, HA can bind many times its weight in water, further increasing the effective volume of the given treatment. HA was first approved by the FDA for use in correction nasolabial folds, but it has since been used to correct other areas prone to volume deficits such as the glabela crease, mental crease, ocular sulcus, and tear trough region.[105,117]

Despite the reported efficacy of HA to correct nasolabial folds and other facial volume deficits, HA too has been shown to have only temporary results. A recent study found that volume improvement from HA injected around the eye was evident even after 24 months and, in some cases, up to 36 months.[118] The longevity of HA has increased over the years by the creation of compounds of different molecular weights (1.5–2 million Da to 4–6 million Da) and different types of cross-linkages (e.g., 1,4-butandiol diglycidyl ether or divinyl sulfone).[114] There have been reports of allergic reactions to HA treatment, but this can be treated with injections of hyaluronidase to break down the HA.[119] This method can be used to correct misplacement or overinjection of HA.[120]

6.621.2.4.4. Polymethylmethacrylate

ArteFill™ is an injectable material that comprises 30–50 μm polymethylmethacrylate (PMMA) spheres suspended in bovine-derived collagen. This was the first permanent injectable filler approved by the FDA to improve nasolabial folds.[121] Once injected into the skin, PMMA cannot be broken down by enzymes or phagocytosis. Thus, PMMA treatment can persist for many years. Further, PMMA components are described to be completely encapsulated and do not migrate or spread apart.[122] Once injected into the subcutaneous tissue, PMMA microspheres promote fibroblast activation and act as a scaffold for collagen deposition.[123] Since obtaining FDA approval in 2006, PMMA treatment has proved to be a versatile dermal filler. It has been used to correct nasolabial folds, horizontal forehead lines, glabellar frown lines, shadowed lower lids, crow's feet wrinkles, facial wasting and cheek depressions, acne scars, traumatic scars, nose irregularities, lip enhancement, nipple augmentation, hand rejuvenation, and many other dermal lines and wrinkles.[121]

While the benefits of using permanent dermal fillers are obvious, the resulting complications may be as permanent. Unlike temporary and semipermanent fillers, permanent fillers and their complications are long-lived. Errors in technique, most notably, misplacement of the PMMA treatment (either too deep or too shallow), are common and can require subsequent treatments to amend the mistake. Also, permanent scarring, nodule formation, and granuloma formation is possible, albeit rare, following PMMA treatment.[121] Thus, the possibility of an uncorrectable negative result complicates the decision between temporary and permanent treatment options. Every patient should discuss his or her own goals and fears with the physician before deciding on a particular treatment option.

6.621.2.4.5. Poly-L-lactic acid

Poly-L-lactic acid (PLLA) is a synthetic biodegradable compound that has been approved by the FDA for use as an intradermal filler to help correct soft tissue defects associated with HIV. HIV-associated lipodystrophic syndrome is described as either a soft tissue volume loss or a soft tissue rearrangement and is a common and noticeable side effect of long-term antiretroviral drug use.[124] One study reported that lipodystrophy occurs in 20% of individuals using antiretroviral drugs and the most affected areas include the face, the buttocks, the legs, the arms, and the abdomen,[125] While both permanent and nonpermanent fillers have been used in the treatment of HIV-associated lipodystrophic syndrome, PLLA is one of the most promising. While results may still be seen in patients with severe facial lipoatrophy, the best results are reported in both younger and less lipoatrophic patients.[126] These results, and other similar findings, argue that patients should begin PLLA treatment on or before the first signs of facial lipoatrophy.[127] PLLA has also been shown to be a promising polymer for use in reconstructive surgery.

While it has not yet been approved in the United States, the use of PLLA as a cosmetic filler has gained popularity in Europe in recent years. As such, PLLA has been used to correct facial volume loss associated with the aging face.[128] Specifically, nasolabial folds and other age-related creases of the face have been the focus of PLLA treatment studies, with improvements lasting up to 25 months posttreatment.[129] Products such as New-Fill™ and Sculptra™ are being used to stimulate neocollagenesis and improve facial contours and folds. In a recent study, PLLA was found to have positive cosmetic results. Surgeons rated 55% of patients to have had good to excellent results, while 75% of the patients self-reported their results as good to excellent. There were a few negative findings, with 12.5% of patients reporting palpable nodules in their hands and 7.2% of reporting palpable nodules in their cheeks; however, these nodules were almost entirely nonvisible. Although only 68% of the patients in the aforementioned study would repeat the procedure again, PLLA appears to be promising for use in cosmetic surgery.[130]

PLLA is injected intradermally every 4–6 weeks to increase fibroblast number and collagen deposition.[131] Overall, PLLA injections are reported to be well tolerated, and there is little evidence of acute inflammation, tissue necrosis, or abscess formation. PLLA injections are associated with an increase in mononuclear macrophages, well-vascularized beds, and proliferating fibroblasts, findings that suggest an environment of remodeling and collagen deposition. As the PLLA polymer is broken down by the body, collagen deposition and overall volume have been shown to increase significantly.[132]

6.621.2.4.6. Calcium hydroxyapatite-based dermal filler

Radiesse™ is an aqueous gel of suspended calcium hydroxyapatite (CaHa) microspheres that has been approved by the FDA as a dermal filler. Radiesse™ has gained popularity in recent years as a nonsurgical treatment for nasolabial folds and for

improvement in volume loss in the face and hands.[133] Because this treatment is associated with some pain, the area is infiltrated with local anesthesia.[134] Some authors suggest premixing CaHa with lidocaine to reduce discomfort during and after injections.[135] Once injected into the treatment area, the aqueous gel is resorbed by the body. The resulting precipitating CaHa forms a matrix onto which new collagen deposition can take place. Histologic evaluations have demonstrated that the persistent localized CaHa lattices initiate an early macrophage response that is followed by a fibrotic response that lasts for up to 6 months after treatment. After 6 months, the CaHa matrix begins to lose form.[136] Another study reported obvious CaHa resorption and shape loss by 9 months and near complete resorption by 12 months.[137] One investigation compared CaHA to hyaluronic acid (HA) at 6, 9, and 12 months posttreatment. At 12 months, 79% of the CaHa treatments were still evident compared to the 43% of HA treatments. This study also showed that 30% more HA volume was needed to elicit the same results as the CaHa treatment.[138] While most of the literature supports treatment longevity of around 12 months, one study observed histologic remnants of CaHa injection up to 6 years after the treatment.[139] This information proves promising for the possibility of a longer lasting CaHa treatment. Caution must be exercised when examining patients who have previously had CaHa-based dermal fillers to prevent false interpretation of radiographic calcifications as evidence of malignancy.[140]

6.621.2.4.7. Fat

A great deal of the recent literature has focused on autologous fat grafting for the management of soft tissue volume depletion. Given its relative abundance and proximity to the surface of the skin, adipose tissue is thought to be an ideal filler for both age-related and pathologic volume deficits. This autologous tissue obviates the negative psychological impressions associated with synthetic implants and xenogenic fillers.[141] Furthermore, because the fat is harvested from and grafted into the same individual, there is no potential for immune rejection that can be associated with exogenous grafts (**Figure 10**). One of the major issues regarding fat grafts is the highly variable rate of resorption. Studies performed throughout the 1990s reported retention rates consistently in the range of 20–90%.[142–144] A more recent study in 2008 used computer topography to quantify cheek volume before autologous fat transfer and at 2 and 12 months posttreatment in HIV-positive individuals.[145] This population is reported to have minimal endogenous subcutaneous fat; therefore, possible biases are removed when evaluating treatment efficacy. This study found a significant increase in mean cheek volume after 2 months (2.93 cm^3) compared to mean pretreatment volume (1.57 cm^3). Interestingly, the study also reported an average increase of 0.33 cm^3 between 2 and 12 months. This study demonstrates that a single treatment with autologous fat can sustain for a minimum of 12 months and suggests that even at 12 months, there is little likelihood of resorption. While these

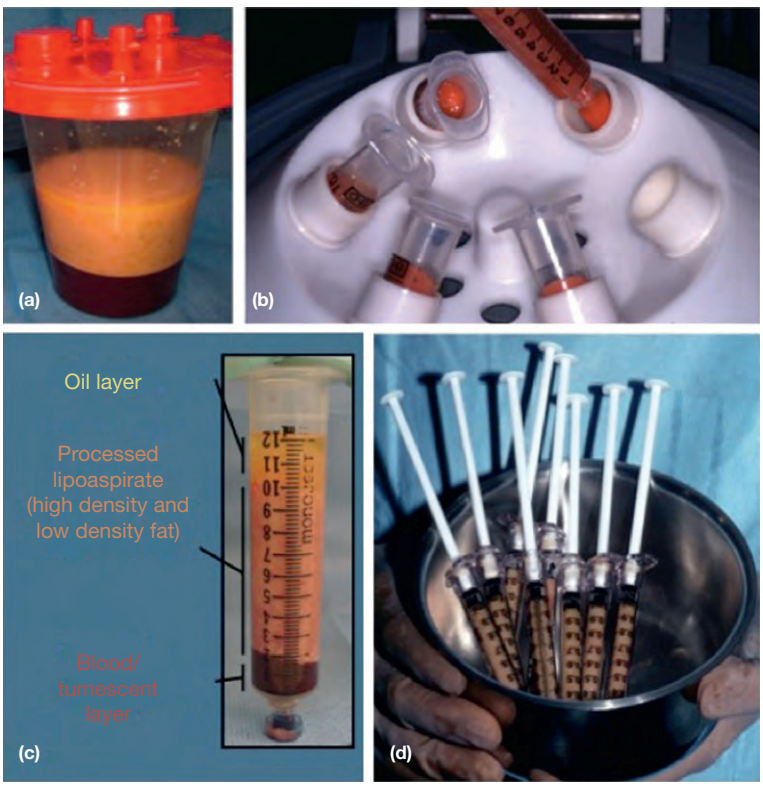

Figure 10 Human fat harvest and processing. After liposuction or syringe aspiration (a), centrifugation is used to separate the viable cell fraction (high-density cells) from nonviable cells (low-density cells) and oil as well as blood contained in the lipoaspirate (b). Following centrifugation, a gradient of lipoaspirate can be seen (c). The blood tumescent layer is discarded and the oil layer wicked away, leaving the processed lipoaspirate to be loaded into a 1-cm^3 syringe for reinjection (d).

results are impressive, other recent literature has not reported the same conclusion.[146] In 2009, Meier *et al*. injected 10.1 cm^3 into the midface region in eight patients. By 16 months post-treatment, on average there was only 3.3 cm^3 of grafted fat remaining (average graft retention was 31.8%).[147] Thus, more research in the field of fat grafting is needed to improve graft retention and equilibrate outcomes. The current literature focuses on the enhancement of grafting techniques, the addition of graft supplements to stimulate adipogenesis and increase individual cell size, and improvement in graft perfusion to prevent necrosis.

- Harvesting techniques

Techniques to harvest and implant fat vary greatly. While liposuction may take less time, it is generally agreed that syringe aspiration produces less trauma to the adipose tissue and improves cell survival.[148,149] The techniques for handling and implanting the lipoaspirate are less defined. The harvesting and processing techniques described and advocated by Coleman have gained wide acceptance in recent years; he harvests adipocytes using syringe aspiration and then uses centrifugation to separate the viable adipose cells (high-density fat) from nonviable cells (low-density fat), oil, and blood contained in the lipoaspirate. Studies using this technique report a greater number of total viable adipocytes and improved grafts survival after implantation.[150] Proper implantation of the fat is equally important and smaller grafts survive better than larger grafts.[151] As such, it is suggested that small droplets of fat are added through a cannula to different locations and in different planes of the subcutaneous space. A conservative approach should be taken, with small augmentations performed serially over time, to yield the most effective results.

- Improvement of fat graft survival

The physiologic demands of adipocytes require a critical amount of perfusion to prevent graft necrosis. Consequently, researchers are exploring ways of improving fat graft perfusion. The fate of an individual graft is determined in part by its ability to stimulate angiogenesis (the process of developing new vasculature from an existing vascular network) and vasculogenesis (the de novo creation of new vascular network).[152] Thanik and coworkers showed that human fat cells injected into the dorsum of nude tie2/lacz mice have both angiogenic and vasculogenic properties.[153] The presence of human-specific cytochrome c oxidace expression suggested that the perigraft vasculature was a human derivative and not merely a murine infiltrative vasculature. Although fat grafts are capable of creating their own vascular network, the size of any single fat droplet must be kept smaller than a specific radius to limit the likelihood of poor perfusion and graft necrosis. Thus, each fat droplet should optimally be limited to the size of a pea.[154]

Many studies have found promising results in augmentation of graft retention rates through the supplementation of different materials such as adipose-derived regenerative cells (ADRCs),[155] platelet-rich plasma (PRP),[156] and insulin-like growth factor (IGF-1).[157] The choice of the additive depends on the desired effect. For example, graft size and graft viability are both contingent upon the presence of a large population of viable mature adipocytes. Insulin, IGF-1, and other specific growth factors have been used to stimulate adipogenesis, the transformation of immature adipocytes to mature adipocytes.[157] To improve graft retention, additives that augment the mechanisms of angiogenesis and neovasculogenesis can be used. ADRCs contain populations of cells that are both multipotent and capable of secreting growth factors, such as VEGF, that have been proved to increase graft perfusion and survival.[155] Further research is needed to determine which of these combination treatments will yield higher rates of fat graft retention.

6.621.2.4.8. Expanded polytetrafluoroethylene implants

Another implant material that has been in use for several decades is expanded polytetrafluoroethylene (ePTFE). ePTFE is an ethylene monomer attached to four fluorine monomers. It has a more spongy feeling than denser silicone implants.[59] While technically simpler to use than silicone, ePTFE used for forehead reconstruction has been reported to have a relatively high rate of infection.[158] ePTFE has also been used to reconstruct the oral and maxillofacial region,[159] and the nasolabial fold and malolabial groove.[160] Surgeons like the pliability and durability of this material, and its ability to provide a solid anchor for soft tissue growth in the midface[161] While some studies support ePTFE for facial implantation, others have reported less favorable outcomes. One study that used ePTFE in the perioral region found the patients only moderately satisfied at a mean follow-up of 23 months: only 63% of these patients stated that they would have ePTFE for additional implants, and only 51% of these patients would recommend this type of implant to other patients. Further, the authors noted that there was histologic evidence of chronic inflammation in the ePTFE implants that were removed.[162] Another study in 2005 also surveyed patients about their ePTFE facial reconstructive experiences.[163] This study found that 10 of the 12 patients were satisfied with their ePTFE facial implant in all areas of the face but the lips. Furthermore, revision rates in the lips ranged from 1% to 100%. Redbord and colleagues found that 11 of the 85 ePTFE implants (33 patients) required removal – 4 were replaced with bigger ePTFE implants and 7 were completely removed for reasons such as malposition, localized swelling, or unnatural feel.[164] Reported complications with ePTFE implants include inflammation, extrusion, migration, shrinking, and hardening.[165] Thus, the suitability of ePTFE as a facial implant material is still debatable. The patient's goals and expectations, the area of restoration, and potential complications should be addressed before deciding on a ePTFE-based reconstruction.

6.621.2.4.9. High-density polyethylene implants

High-density polyethylene (HDPE) implants are firm, yet flexible, plastic that has pores to allow for some soft tissue and minimal bone ingrowth.[59] This material has been advocated for the correction of maxillonasal dysplasia (Binder's syndrome),[166] traumatic nasal deformity,[167] nasal valve collapse,[168] mandible reconstruction,[72,73] orbital trauma,[169] ear construction,[170] and other facial reconstruction. Because of its porosity, HDPE is more prone to infection than ePTFE or silicone. Consequently, preoperative antibiotic impregnation may be considered.[59] A recent study found that HDPE may not be as biologically inert as previously thought, and that a mild inflammatory response can occur.[171]

Cleft lip nasal reconstruction has also been successfully performed with HDPE. The characteristic spongy nature of this material allows tissue and vascular ingrowth, with good aesthetic outcomes and minimal complications.[172] A rabbit study demonstrated improved integration of HDPE into the host bed through the addition of basic fibroblast growth factor and epidermal growth factor.[173] These authors found a synergistic improvement in both the fibrous and vascular ingrowth into the HDPE implant, and noted very few complications.

6.621.3. Considerations and Future Applications

There are a wide array of treatment options for bone and soft tissue reconstruction. We have reviewed the basic principles and practices used in craniofacial reconstruction, and this treatise is by no means exhaustive. There is no one best solution for bone and soft tissue repair. Instead, physicians must devise a treatment plan that carefully weighs the benefits and pitfalls inherent in each surgical alternative and balances these considerations with the patient's condition and goals. Further research and biomaterial development should lead to better operative outcomes and the creation of more effective, safe treatment options to correct tissue losses associated with trauma, disease, and aging.

References

1. Dorri, M.; Nasser, M.; Oliver, R. Resorbable versus titanium plates for facial fractures. Cochrane Database System Review 21(1), 2009; CD007158.
2. Sauerbier, S.; Schn, R.; Otten, J.-E.; *et al*. *J. Craniomaxillofac. Surg.* **2008**, *36*, 251–259.
3. Champy, J. P. L.; Jaeger, J. H.; Wilk, A.; Gerber, J. C. *Rev. Stomatol. Chir. Maxillofac.* **1976**, *77*, 252–255.
4. Manson, P. N.; Glassman, D.; Vanderkolk, C.; Petty, P.; Crawley, W. A. *Plast. Reconstr. Surg.* **1990**, *85*, 711–717.
5. Frodel, J. L.; Marentette, L. J. *Arch. Otolaryngol. Head Neck Surg.* **1993**, *119*, 297–304.
6. Tiwana, P.; Kushner, G.; Alpert, B. *J. Oral Maxillofac. Surg.* **2007**, *65*, 1180–1185.
7. Dion, I.; Baquey, C.; Monties, J. R.; Havlik, P. *Biomaterials* **1993**, *14*(2), 122–126.
8. Dion, I.; Baquey, C.; Havlik, P.; Monties, J. R. *Int. J. Artif. Organs* **1993 Jul**, *16*(7), 545–550.
9. Peterson, L. J. *Principles of Oral and Maxillofacial Surgery*. Lippincott: Philadelphia, PA, 1992.
10. Leipziger, L. S.; Dufresne, C. R. In *Complex Craniofacial Problem: A Guide to Analysis and Treatment*; Dufresne, C. R., Carson, B. S., Zinreich, S. J., Eds.; Churchill Livingstone: New York, 1992; p 499.
11. Hallab, N. J.; Jacobs, J. J. *Bull. NYU Hosp. Jt. Dis.* **2009**, *67*(2), 182–188.
12. DeLacure, M. D.; Friedman, C. D. *Otolaryngol. Clin. North Am.* **1994**, *27*, 983–1000.
13. DeLacure, M. D.; Kuriakose, M. A. *Skull Base* **2002**, *12*, 103–106.
14. Hutmacher, D.; Hurzeler, M. B.; Schliephake, H. *Int. J. Oral Maxillofac. Implants* **1996**, *11*, 667–678.
15. Holmes, R. E.; Cohen, S. R.; Cronwall, G. B.; Thomas, K. A.; Kleinhenz, K. K.; Beckett, M. Z. *Clin. Plast. Surg.* **2004**, *31*, 393–406.
16. Suuronen, R.; Pohjonen, T.; Hietanen, J.; Lindqvist, C. *J. Oral Maxillofac. Surg.* **1998**, *56*, 604–614.
17. Suuronen, R.; Pohjonen, T.; Wessman, L.; Törmälä, P.; Vainionpää, S. *Clin. Mater.* **1992**, *9*, 77–84.
18. Havlik, R. J. In *Craniofacial Surgery; Science and Surgical Technique*; Lin, K. Y., Ogle, R,.C., Jane, J. A., Eds.; WB Saunders Co: Philadelphia, PA, 2002; p 132.
19. Suuronen, R.; Kallela, I.; Kindqvist, C. *J. Craniomaxillofac. Trauma* **2000**, *6*(19), 27.
20. Eppley, B. L.; Reilly, M. *J. Craniomaxillofac. Surg.* **1997**, *8*, 116–120.
21. Bell, B. R.; Kindsfater, C. S. *J. Oral Maxillofac. Surg.* **2006**, *64*, 31–39.
22. Eppley, B. L.; Pietrzak, W. S. *J. Craniofac. Surg.* **2006**, *17*, 11–14.
23. Cohen, S. R.; Holmes, R. E.; Amis, P.; Fitchner, H.; Shusterman, E. M. *J. Craniofac. Surg.* **2001**, *12*, 596–602.
24. Spanio, S.; Novack, E.; Gurunluoglu, R.; Shafighi, M.; Romansky, R.; Ninkovic, M. *Minerva Stomatol.* **2004**, *53*, 449–455.
25. Gilmer, T. *Arch. Dent.* **1887**, *4*, 388.
26. Luhr. Zur Stabilen Osteosynthese bei Unterkieferfrakturn. *Dtsch Zahnärztl Z* 223: 754, 1968.
27. Ivy, R. *J. Am. Med. Assoc.* **1922**, *79*, 295–297.
28. Howard, P.; Wolfe, S. A. *Ann. Plast. Surg.* **1986**, *17*, 391–407.
29. Stacey, D. H.; Doyle, J. F.; Mount, D. L.; Snyder, M. C.; Gutowski, K. A. *Plast. Reconstr. Surg.* **2006**, *117*, 48e–60e.
30. Hansmann, C. *Verh. Dtsch. Ges. Chir.* **1886**, *1886*, 134–136.
31. Lambotte, A. *Le traitement des fractures*. Masson: Paris, 1907.
32. Sherman, W. O. *Surg. Gynecol. Obstet.* **1912**, *14*, 629–634.
33. Collins, A. *J. Am. Med. Assoc.* **1920**, *74*, 950–951.
34. Danis, R. *Théorie et pratique de l'ostéosynthèse*. Masson: Paris, 1949.
35. Spiessl, B. *New Concepts in Maxillofacial Bone Surgery*. Springer: Berlin, 1976.
36. Raveh, J.; Stitch, H.; Sutter, F.; Greiner, R. *J. Oral Maxillofac. Surg.* **1984**, *42*, 281–294.
37. Herford, A.; Ellis, E. *J. Oral Maxillofac. Surg.* **1998**, *56*, 1261–1265.
38. Potter, J. K.; Ellis, E. *J. Oral Maxillofac. Surg.* **2004**, *62*, 1280–1297.
39. Rubin, J. P.; Yaremchuk, M. J. *Plast. Reconstr. Surg.* **1997**, *100*, 1336–1353.
40. Jack, J. M.; Stewart, D. H.; Rinker, B. D.; Vasconez, H. C.; Pu, L. L. *J. Craniofac. Surg.* **2005**, *16*, 726–731.
41. Eppley, B. L. *J. Oral Maxillofac. Surg.* **2005**, *63*, 385–391.
42. Moe, K. S.; Weisman, R. A. *Laryngoscope* **2001**, *111*, 1697–1701.
43. Agarwal, S.; Gupta, A.; Grevious, M.; Reid, R. R. *J. Craniofac. Surg.* **2009**, *20*, 331–339.
44. Yaremchuk, M. J. *Clin. Plast. Surg.* **1994**, *21*, 517–524.
45. Cordewener, F. W.; Bos, R. R.; Rozema, F. R.; Houtman, W. A. *J. Oral Maxillofac. Surg.* **1996**, *54*(1), 9–13; discussion 13-4.
46. Potter, J. K.; Ellis, E. *J. Oral Maxillofac. Surg.* **2004**, *62*, 1280–1297.
47. Yerit, K. C.; Hainich, S.; Enislidis, G.; *et al*. *Oral Surg. Oral Med. Oral Pathol. Oral Radiol. Endod.* **2005**, *100*(1), 17–24.
48. Fedorowicz, Z.; Nasser, M.; Newton, J. T.; Oliver, R. J. *Cochrane Database System Review* **2007**, *18*(2), CD006204.
49. Yoshida, K.; Bessho, K.; Fujimura, K.; *et al*. *J. Craniomaxillofac. Surg.* **1998**, *26*, 112–115.
50. Liu, Y.; Enggist, L.; Kuffer, A. F.; Buser, D.; Hunziker, E. B. *Biomaterials* **2007**, *28*, 2677–2686.
51. De Jonge, L. T.; Leeuwenburgh, S. C. G.; Wolke, J. G. A.; Jansen, J. A. *Pharm. Res.* **2008**, *25*, 2357–2369.
52. Tessier, P.; Kawamoto, H.; Matthews, D.; *et al*. *Plast. Reconstr. Surg.* **2005**, *116*, 6S–24S.
53. Wolfe, A. *Ann. Plast. Surg.* **1986**, *17*, 391–407.
54. Cho, Y.; Gosain, A. *Clin. Plast. Surg.* **2004**, *31*, 377–385.
55. Woodhall, B.; Spurling, R. G. *Ann. Surg.* **1945**, *121*, 649–668.
56. Manson, P. N.; Crawley, W. A.; Hoopes, J. E. *Plast. Reconstr. Surg.* **1986**, *77*, 888–904.
57. Marchac, D.; Greensmith, A. *J. Plast. Reconstr. Aesthet. Surg.* **2008**, *61*, 744–752.
58. Blum, K. S.; Schneider, S. J.; Rosenthal, A. D. *Pediatr. Neurosurg.* **1997**, *26*, 33–35.
59. Constantinides, M. S.; Galli, S. K.; Miller, P. J.; Adamson, P. A. *Facial Plast. Surg.* **2000**, *16*(1), 35–44.
60. Joseph, J.; Mohanty, M.; Mohanan, P. V. *J. Mater. Sci. Mater. Med.* **2010**, *21*(5), 1665–1676.
61. Poeppl, N.; Schreml, S.; Lichtenegger, F.; Lenich, A.; Eisenmann-Klein, M.; Prantl, L. *Aesthet. Plast. Surg.* **2007**, *31*(2), 133–139.
62. Jang, Y. J.; Yu, M. S. *Facial Plast. Surg.* **2010**, *26*(2), 93–101.
63. Wang, T. L.; Xue, Z. Q.; Yu, D. S.; *et al*. *Chin. Med. J. (Engl.)* **2009 Feb 5**, *122*(3), 296–300.
64. Chang, E. W.; Manolidis, S. *Facial Plast. Surg.* **2005 Aug**, *21*(3), 207–213.
65. Saleh, H. A.; Lohuis, P. J.; Vuyk, H. D. *Clin. Otolaryngol. Allied Sci.* **2002 Apr**, *27*(2), 129–132.
66. Gonales, E. *Oral Surg. Oral Med. Oral Pathol. Oral Radiol. Endod.* **2009**, *107*, e21–e23.
67. Gosain, A. K.; Persing, J. A. *J. Craniofac. Surg.* **1999**, *10*, 404–414.

68. Eppley, B. L.; Sadove, A. M.; German, R. Z. *Plast. Reconstr. Surg.* **1990**, *86*, 1085–1092.
69. Guyuron, B. *J. Craniomaxillofac. Surg.* **1990**, *18*, 187–191.
70. Eppley, B.; Kilgo, M.; Coleman, J. *Plast. Reconstr. Surg.* **2002**, *109*, 864–871.
71. Dougherty, W. R.; Wellisz, T. *J. Craniofac. Surg.* **1994**, *5*, 26–32.
72. Yaremchuk, M. *Plast. Reconstr. Surg.* **2003a**, *111*, 1818–1827.
73. Yaremchuk, M. *Plast. Reconstr. Surg.* **2003b**, *112*, 1422–1432.
74. Chen, C.-T.; Hu, T.-L.; Lai, J.-B.; *et al*. *J. Plast. Reconstr. Aesthet. Surg.* **2010**, *63*(2), 257–264.
75. Ducheyne, P.; Qiu, Q.-Q. *Biomaterials* **1999**, *20*, 2287–2303.
76. Chim, H.; Gosain, A. *J. Craniofac. Surg.* **2009**, *20*, 29–33.
77. Burstein, F. D.; Cohen, S. R.; Hudgins, R.; Boydston, W.; Simms, C. *Plast. Reconstr. Surg.* **1999**, *104*, 1270–1275.
78. Byrd, H. S.; Hobar, P. C. *Clin. Plast. Surg.* **1996**, *23*, 315–326.
79. Schepers, E.; DeClercq, M.; Ducheyne, P.; Kempeneers, R. *Oral Rehabil.* **1991**, *18*, 439–452.
80. Schepers, E. J. G.; Ducheyne, P.; Barbier, L.; Schepers, S. *Impl. Dent.* **1993**, *2*, 151–156.
81. Schepers, E.; Ducheyne, P. *J. Oral Rehabil.* **1997**, *24*, 171–181.
82. Wilson, J.; Low, S. B. *J. Appl. Biomater.* **1992**, *3*, 123–129.
83. Lovelace, T. B.; Mellonig, J. T.; Meffert, R. M.; Jones, A. A.; Nummikoski, P. V.; Cochran, D. L. *J. Periodontol.* **1998**, *69*, 1027–1035.
84. El-Ghannam, A. E.; Ducheyne, P.; Shapiro, I. *Biomaterials* **1997**, *18*, 295–303.
85. Price, N.; Bendall, S. P.; Frondoza, C.; Jinnah, R. H.; Hungerford, D. S. *J. Biomed. Mater. Res.* **1997**, *37*, 394–400.
86. Ducheyne *et al*. (1997).
87. Cordioli, G.; Mazzocco, C.; Schepers, E.; Brugnolo, E.; Majzoub, Z. *Clin. Oral Implants Res.* **2001**, *12*, 270–278.
88. Aitasalo, K.; Kinnunen, I.; Palmgren, J.; Varpula, M. *J. Oral Maxillofac. Surg.* **2001**, *59*, 1390–1395.
89. Gosain, A.; Riordan, P.; Song, L.; *et al*. *Plast. Reconstr. Surg.* **2004**, *114*, 1155–1163.
90. Wang, J. C.; Alanay, A.; Mark, D.; *et al*. *Eur. Spine J.* **2007**, *16*(8), 1233–1240.
91. Salyer, K. E.; Gendler, E.; Squier, C. A. *Plast. Reconstr. Surg.* **1997**, *99*, 1721–1726.
92. Boudard, P.; Benassayag, C.; Dhillon, R. S.; Bebear, J. P.; Portmann, M. *Arch. Otorhinolaryngol.* **1989**, *246*(5), 349–352.
93. Yanaga, H.; Yanaga, K.; Imai, K.; Koga, M.; Soejima, C.; Ohmori, K. *Plast. Reconstr. Surg.* **2006**, *117*(6), 2019–2030; discussion 2031-2.
94. Farhadi, J.; Fulco, I.; Miot, S.; *et al*. *Ann. Surg.* **2006**, *244*(6), 978–985.
95. Baumann, L. *Clin. Plast. Surg.* **2006**, *33*, 587–596.
96. Jinnin, M. *J. Dermatol.* **2010**, *37*, 11–25.
97. Obrenovich, M.; Monnier, V. *Sci. Aging Knowledge Environ.* **2005**, *2005*, pe3–pe.
98. Goldberg, D. *J. Cosmet. Laser Ther.* **2009**, *11*, 240–247.
99. Lowe, N.; Maxwell, C. A.; Patnaik, R. *Dermatol. Surg.* **2005**, *31*, 1616–1625.
100. Baumann, L. *J. Cosmet. Dermatol.* **2004**, *3*, 249–250.
101. Rostan, E. *Facial Plas. Surg. Clin. North Am.* **2007**, *15*, 55–61.
102. Baumann, L. S.; Shamban, A. T.; Lupo, M. P.; *et al*. *Dermatol. Surg.* **2007**, *33*, S128–S135.
103. Hotta, T. *Plast. Surg. Nurs.* **2004**, *24*, 14–19.
104. Landau, M. *J. Drugs Dermatol.* **2008**, *7*, 236–240.
105. Carruthers, J.; Cohen, S.; Joseph, J.; Narins, R.; Rubin, M. *J. Drugs Dermatol.* **2009**, *8*, 335–350.
106. Sclafani, A. P.; Romo, T., III; Jacono, A. A.; McCormick, S. A.; Cocker, R.; Parker, A. *Arch. Facial Plast. Surg.* **2001**, *3*(2), 101–103.
107. Ruiz-Magaz, V.; Hernández-Alfaro, F.; Díaz-Carandell, A.; Biosca-Gómez-de-Tejada, M. J. *Med. Oral Patol. Oral Cir. Bucal.* **2010**, *15*(1), e61–e64.
108. Gryskiewicz, J. M. *Plast. Reconstr. Surg.* **2005 Dec**, *116*(7), 1999–2004.
109. Jackson, I. T.; Yavuzer, R. *Plast. Reconstr. Surg.* **2001**, *107*(2), 553–558; discussion 559–60.
110. Sudarsan, S.; Arun, K. V.; Priya, M. S.; Arun, R. *J. Indian Soc. Periodontol.* **2008**, *12*(3), 73–78.
111. Rubin, P. A.; Fay, A. M.; Remulla, H. D.; Maus, M. *Ophthalmology* **1999 Nov**, *106*(11), 2091–2097.
112. Becker, S.; Saint-Cyr, M.; Wong, C.; *et al*. *Plast. Reconstr. Surg.* **2009**, *123*(1), 1–6; discussion 107–8.
113. Lee, E. W.; Berbos, Z.; Zaldivar, R. A.; Lee, M. S.; Harrison, A. R. *Ophthal. Plast. Reconstr. Surg.* **2010 May-Jun**, *26*(3), 153–154.
114. Lupo, M. *Semin. Cutan. Med. Surg.* **2006**, *25*, 122–126.
115. Ghersetich, I.; Lotti, T.; Campanile, G.; Grappone, C.; Dini, G. *Int. J. Dermatol.* **1994**, *33*, 119–122.
116. Bernstein, E. F.; Underhill, C. B.; Hahn, P. J.; Brown, D. B.; Uitto, J. *Br. J. Dermatol.* **1996**, *135*, 255–262.
117. de Maio, M. *Aesthet. Plast. Surg.* **2004**, *28*, 295–300.
118. Lambros, V. *Aesthet. Surg. Quart.* **2009**, *29*, 174–179.
119. Soparkar, C. N. S.; Patrinely, J. *Ophthalmic Plast. Reconstr. Surg.* **2005**, *21*, 151–153.
120. Brody, H. *Dermatol. Surg.* **2005**, *31*, 893–897.
121. Lemperle, G.; Knapp, T.; Sadick, N.; Lemperle, S. *Aesthet. Plast. Surg.* **2010**, *34*, 264–272.
122. Lemperle, G.; Morhenn, V.; Pestonjamasp, V.; Gallo, R. *Plast. Reconstr. Surg.* **2004**, *113*, 1380–1390.
123. Hilinski, J.; Cohen, S. *Facial Plast. Surg.* **2009**, *25*, 114–119.
124. Hammond, E.; McKinnon, E.; Nolan, D. *Clin. Infect. Dis.* **2010**, *51*, 591–599.
125. Puttawong, S.; Prasithsirikul, W.; Vadcharavivad, S. *Med. J. Med. Assoc. Thai.* **2004**, *87*, 605–611.
126. Fitzgerald, R.; Vleggaar, D. *J. Drugs Dermatol.* **2009**, *8*, s5–s14.
127. Narciso, P.; Bucciardini, R.; Tozzi, V.; *et al*. *AIDS Res. Hum. Retroviruses* **2009**, *25*, 979–987.
128. Vleggaar, D. *Dermatol. Surg.* **2005**, *31*, 1511–1517.
129. Narins, R. S.; Baumann, L.; Brandt, F. S.; *et al*. *J. Am. Acad. Dermatol.* **2010**, *62*, 448–462.
130. Palm, M.; Woodhall, K.; Butterwick, K.; Goldman, M. *Dermatol. Surg.* **2010**, *36*, 161–170.
131. Perry, C. *Am. J. Clin. Dermatol.* **2004**, *5*, 361–366.
132. Gogolewski, S.; Jovanovic, M.; Perren, S. M.; Dillon, J. G.; Hughes, M. K. *J. Biomed. Mater. Res.* **1993**, *27*, 1135–1148.
133. Lizzul, P.; Narurkar, V. *J. Drugs Dermatol.* **2010**, *9*, 446–450.
134. Bank, D. *J. Drugs Dermatol.* **2009**, *8*, 1122–1126.
135. Marmur, E.; Green, L.; Busso, M. *Dermatol. Surg.* **2010**, *36*, 309–315.
136. Marmur, E.; Phelps, R.; Goldberg, D. *J. Cosmet. Laser Ther.* **2004**, *6*, 223–226.
137. Lemperle, G.; Morhenn, V.; Charrier, U. *Aesthet. Plast. Surg.* **2003**, *27*, 354–366.
138. Moers-Carpi, M.; Tufet, J. *Dermatol. Surg.* **2008**, *34*, 210–215.
139. Shumaker, P. R.; Sakas, E. L.; Swann, M. H.; Greenway, H. T. *Dermatol. Surg.* **2009**, *35*, 375–379.
140. Valiyaparambil, J.; Rengasamy, K.; Mallya, S. M. *Br. Dent. J.* **2009**, *207*, 211–212.
141. Appel, J. Z.; Alwayn, I. P.; Cooper, D. K. *Prog. Transplant.* **2000**, *10*, 217–225.
142. Ersek, R. A. *Plast. Reconstr. Surg.* **1991**, *87*, 219–227.
143. Fournier, P. F. *Dermatol. Surg.* **2000**, *26*, 1117–1128.
144. Coleman, S. R. *Aesthet. Plast. Surg.* **1995**, *19*, 421–425.
145. Fontdevila, J.; Serra-Renom, J.; Raigosa, M.; *et al*. *Aesthet. Surg. Quart.* **2008**, *28*, 380–386.
146. Carey, D.; Liew, S.; Emery, S. *AIDS Rev.* **2008**, *10*, 116–124.
147. Meier, J.; Glasgold, R.; Glasgold, M. *Arch. Facial Plast. Surg.* **2009**, *11*, 24–28.
148. Coleman, W. P. *Dermatol. Clin.* **1999**, *17*, 891–898.
149. Gonzalez, A.; Lobocki, C.; Kelly, C.; Jackson, I. *Plast. Reconstr. Surg.* **2007**, *120*, 285–294.
150. Pu, L. L. Q.; Coleman, S.; Cui, X.; Ferguson, R. E. H.; Vasconez, H. *Plast. Reconstr. Surg.* **2008**, *122*, 932–937.
151. Coleman, S. R. *Clin. Plast. Surg.* **1997**, *24*, 347–367.
152. Risau, W. *Nature* **1997**, *386*, 671–674.
153. Thanik, V. D.; Chang, C. C.; Lerman, O. Z.; *et al*. *Plast. Reconstr. Surg.* **2009**, *124*, 74–81.
154. Horl, H. W.; Feller, A. M.; Biemer, E. *Ann. Plast. Surg.* **1991**, *26*, 248–258.
155. Zhu, M.; Zhou, Z.; Chen, Y.; *et al*. *Ann. Plast. Surg.* **2010**, *64*, 222–228.
156. Nakamura, S.; Ishihara, M.; Takikawa, M.; *et al*. *Ann. Plast. Surg.* **2010**, *65*(1), 101–106.
157. Yuksel, E.; Weinfeld, A. B.; Cleek, R.; *et al*. *Reconstr. Surg.* **2000**, *106*(2), 373–382.
158. Wong, J. *Facial Plast. Surg. Clin. North Am.* **2010**, *18*, 71–77.
159. Niamtu, J. *Oral Maxillofac. Surg. Clin. North Am.* **2005**, *17*, 29–39.
160. Verret, D. J.; Leach, J. L.; Gilmore, J. *Arch. Facial Plast. Surg.* **2006**, *8*, 423–425.
161. Steinsapir, K. *Plast. Reconstr. Surg.* **2003**, *111*, 1727–1737.
162. Wall, S.; Adamson, P.; Bailey, D.; van Nostrand, A. *Arch. Facial Plast. Surg.* **2003**, *5*, 320–324.
163. Cox, S. *Dermatol. Surg.* **2005**, *31*, 1613–1615.
164. Redbord, K.; Hanke, C. W. *Dermatol. Surg.* **2008**, *34*, 735–743.
165. Hanke, C. *Dermatol. Surg.* **2002**, *28*, 901–908.

166. Seyhan, T.; Kircelli, B.; Caglar, B. *Aesthet. Plast. Surg.* **2009**, *33*, 661–665.
167. Chen, C.-T.; Hu, T.-L.; Lai, J.-B.; Chen, Y.-C.; Chen, Y.-R. *J. Plast. Reconstr. Aesthet. Surg.* **2010**, *63*(2), 257–264.
168. Ramakrishnan, J.; Danner, C.; Yee, S. *Otolaryngol. Head Neck Surg.* **2007**, *136*, 357–361.
169. Eski, M.; Sahin, I.; Deveci, M.; Turegun, M.; Isik, S.; Sengezer, M. *J. Craniofac. Surg.* **2006**, *17*, 1059–1064.
170. Romo, T.; Reitzen, S. *Facial Plast. Surg.* **2008**, *24*, 120–128.
171. Gosau, M.; Draenert, F.; Ihrler, S. *J. Biomed. Mater. Res. B Appl. Biomater.* **2008**, *87*, 83–87.
172. Romo, T.; Choe, K.; Sclafani, A. *Arch. Facial Plast. Surg.* **2003**, *5*, 175–179.
173. Soparkar, C.; Wong, J.; Patrinely, J.; Appling, D. *Ophthalmic Plast. Reconstr. Surg.* **2000**, *16*, 337–340.

6.622. The Effect of Substrate Microtopography on Osseointegration of Titanium Implants

Z Schwartz, A L Raines, and B D Boyan, Georgia Institute of Technology, Atlanta, GA, USA

© 2011 Elsevier Ltd. All rights reserved.

6.622.1.	Introduction	343
6.622.2.	*In Vitro* Studies	344
6.622.3.	Mechanisms Mediating the Microtopography Effect	346
6.622.4.	*In Vivo* Studies	349
6.622.5.	Summary	350
References		351

Abbreviations

1α,25 $(OH)_2D_3$	1α,25-Dihydroxy vitamin D_3
Ang-1	Angiopoietin 1
BIC	Bone to implant contact
BMP-2	Bone morphogenetic protein 2
Cox	Cyclooxygenase
CSR	Cumulative success rate
DAG	Diacylglycerol
EGF	Epidermal growth factor
ERK1/2	Extracellular regulated kinase
FGF-2	Fibroblast growth factor 2 (basic fibroblast growth factor)
GFOGER	Glycine-phenylalanine-hydroxyproline-glycine-glutamate-arginine
KRSR	Lysine-arginine-serine-arginine
KSSR	Lysine-serine-serine-arginine
LPA	Lysophosphatidic acid
MAPK	Mitogen-activated protein kinase
MSC	Mesenchymal stem cell
OPG	Osteoprotegerin
PA	Phosphatidic acid
PC	Phosphatidylcholine
PGE_1	Prostaglandin E_1
PGE_2	Prostaglandin E_2
PKC	Protein kinase C
PLD	Phospholipase D
RANK	Receptor activator of nuclear factor κ B
RANKL	Receptor activator of nuclear factor κ B ligand
RGD	Arginine-glycine-aspartic acid
TGF-β_1	Transforming growth factor β_1
VEGF-A	Vascular endothelial growth factor A

6.622.1. Introduction

The first events after an implant comes in contact with tissues are due to interactions of the biological environment with the implant surface. Upon implantation, the implant surface is coated with an adsorbed layer of proteins, ions, sugars, and lipids present in the blood and tissue fluid. The onset of the biological reactions, as well as the particular response pathways in the bone surrounding the implant, depends strongly on a variety of surface properties, including topography, chemistry, charge, and tension (Figure 1). This chapter focuses on the role that the microtopography of the surface has in modulating cell behavior at the bone–implant interface.

It has been understood for some time that bone tends to form on rough surfaces, whereas fibrous connective tissue forms on smooth surfaces.[1–5] To capitalize on this empirical observation, implant manufacturers designed surfaces that had porous coatings with the intent to promote bony ingrowth. The results have been less than anticipated, in part because the microtopography of the surface that was sensed by individual cells was perceived by them as smooth.[1] More recently, investigators have examined microroughness effects and have noted that R_a values of 4–5 μm tend to enhance osteogenic differentiation both *in vitro*[6] and *in vivo*.[7]

In general, dental implants are produced by machining titanium rods. Machined surfaces are macroscopically smooth, although microscopic irregularities exist. These microscopic grooves and pits are the result of the machining operation and have dimensions in the micron range. Although there are minor differences in the microroughness and appearance of machined surfaces,[8–10] they have not been proved to be of clinical significance.[9]

In order to increase the implant surface in contact with bone and interaction with the bone formation process, most manufacturers modify the titanium surfaces, applying several surface treatments or coatings (see Chapter 1.112, Calcium Phosphate Coatings and Chapter 1.113, Bioactive Layer Formation on Metals and Polymers). One approach is to increase the surface roughness by grit blasting.[11] Implants can be blasted with silica, alumina, glass, or titanium particles, which erode the substrate and form an irregular surface with pits and depressions of various sizes.[12] The size of the irregularities depends on various factors such as the size and material of the blasting particles, the pressure used, the blasting time, and the distance from the blasting nozzle. Some blasted particles can remain embedded in the implant surface. This is an undesirable occurrence as the embedded particles can be released later in the biological environment, causing activation of phagocytes. To minimize this occurrence,

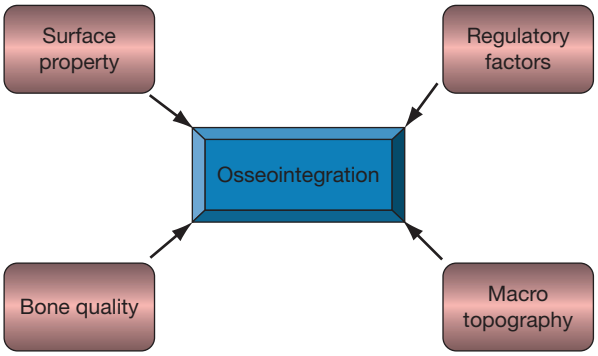

Figure 1 Schematic illustrating the various surface features that influence osseointegration.

meticulous postblasting cleaning procedures are used, such as chemical etching.[13]

Chemical etching is also used to increase the surface roughness of oral implants.[14] It can be applied after machining or grit blasting, further increasing the complexity of the surface microstructure.[15,16] While most chemical etching uses one acid, a dual etching procedure using HCl and H_2SO_4 has also been used.[17] This treatment results in small regular pits on the implant surface, doubling the surface area of the implant.[17]

Another treatment that increases surface microroughness is plasma spraying. In this process, individual titanium particles are suspended in a plasma torch and projected onto the implant.[18,19] During this process, local melting typically occurs, resulting in a surface that is characterized by depressions and protrusions with extremely irregular regions as well as relatively smooth areas.

Not only does the surface topography at the micron and submicron scale affects cell response, but features at the nanoscale have also been demonstrated to influence cell behavior (see **Chapter 4.409, Surfaces and Cell Behavior** and **Chapter 1.129, Engineering the Biophysical Properties of Basement Membranes into Biomaterials: Fabrication and Effects on Cell Behavior**).[20–23] The primary nonmineral component of bone, type I collagen, consists of fibers of approximately 300 nm in length and 0.5 nm in width. The mineral hydroxyapatite crystals in bone are generally around 50 nm in length and 5 nm in diameter.[24] Research suggests that features at the nanoscale may in fact aid in new bone formation at the tissue–implant interface. In one study, it was shown that composite materials possessing nanophase surface structural features comparable to natural bone (i.e., grain sizes in the nanometer range) support greater osteoblast adhesion and mineral deposition compared to conventional ceramics.[25]

To understand the role of surface microroughness on osseointegration, *in vitro* studies have been conducted to evaluate the mechanisms by which the micron-scale topographical features of an implant mediate their effects on bone cell behavior. *In vivo* studies have been conducted to determine if surface microarchitecture has an effect clinically on the relative success of a particular implant design. Investigators have begun to resolve the difficulties in characterizing implant surfaces where nanostructure is imposed upon microscale topography,[26] but it is not yet understood what influence features at this level will have on cell and tissue response.

6.622.2. *In Vitro* Studies

Osteoblast attachment to materials, and their proliferation, extracellular matrix synthesis, and differentiation are sensitive to the microtopography of the surface.[27] On titanium surfaces with microrough rugosities, osteoblasts assume a more differentiated morphology. Attachment is reduced on these surfaces in comparison with tissue culture polystyrene or smooth titanium surfaces. In addition, those cells that do attach exhibit reduced proliferation. In contrast, these cells show increased markers of osteoblastic differentiation. The cells exhibit increased levels of alkaline phosphatase-specific activity and osteocalcin, and they produce factors that are known to modulate osteoclastic activity,[28] as described below. Moreover, osteoblast phenotypic expression and the levels of regulatory factors in the conditioned media are modulated by the vitamin D metabolite $1\alpha,25(OH)_2D_3$ ($1\alpha,25$-dihydroxy vitamin D_3) in a manner that is synergistic with surface roughness.[29] Osteoblast response to BMP-2 also depends on surface features[30] and fetal rat calvarial cells are regulated by BMP-2 and dexamethasone under similar culture conditions.[31] Moreover, normal human osteoblasts are regulated by 17β-estradiol in a roughness-dependent manner.[32]

These observations indicate that the microstructural features of an implant surface modulate bone formation, and suggest the hypothesis that microtopography might be a factor regulating osteogenesis on bone surfaces as well. Studies examining the response of human MG63 osteoblast-like cells to the surfaces of dentin and bone wafers support this observation (see **Chapter 2.210, Bone as a Material**). When these cells are cultured on dentin or bone wafers, they exhibit reduced proliferation and increased differentiation in comparison with cells grown on tissue culture polystyrene.[33,34] This surface effect is further enhanced when the wafers are treated with osteoclasts. It is clear that part of the effect of osteoclastic resorption is due to biochemical conditioning of the surface and not simply to removal of mineral. If only 3% of a dentin surface is removed via osteoclastic resorption, the effect on osteoblasts is greater than that caused by demineralization of the entire surface with tetracycline. It has been shown that osteoclasts deposit attachment factors during the resorptive process.[35] However, at least part of the osteoclastic response is microtopography dependent. Resorption of mineral leaves a complex micro- and nanotopography that can be modeled using titanium substrates (**Figure 2**).

Surface-dependent changes in osteoblast physiology can result in altered paracrine regulation in peri-implant tissues (**Figure 3**). Many of the factors produced in increased amounts by osteoblast-like cells grown on microrough titanium surfaces are known to regulate bone remodeling by differentially affecting osteoblasts and osteoclasts. As surface microroughness increases, levels of PGE_1 and PGE_2 in the conditioned medium also increase.[36] The amount of PGE_2 produced also appears to be sensitive to the method used to fabricate microtextured surfaces[37] and to the osteoblast-like cell model.[38] Monocytes also exhibit increased PGE_2 production on Ti surfaces in comparison with plastic, but increases due to LPS stimulation are not dependent on microarchitecture.[39]

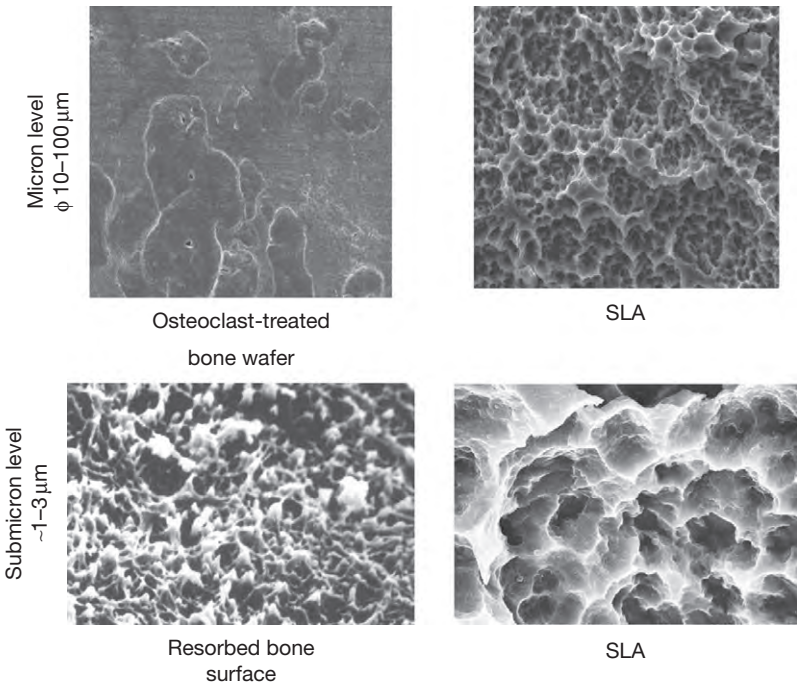

Figure 2 Scanning electron micrograph images showing the similarities between osteoclast resorbed bone surfaces and sandblasted, acid-etched titanium surfaces. Reproduced with permission from Davies JE, Hosseini MM. In *Bone Tissue Engineering*; Davies, J. D., Ed.; Toronto, Canada: Em Squared, Inc., 2000, with permission from Springer.

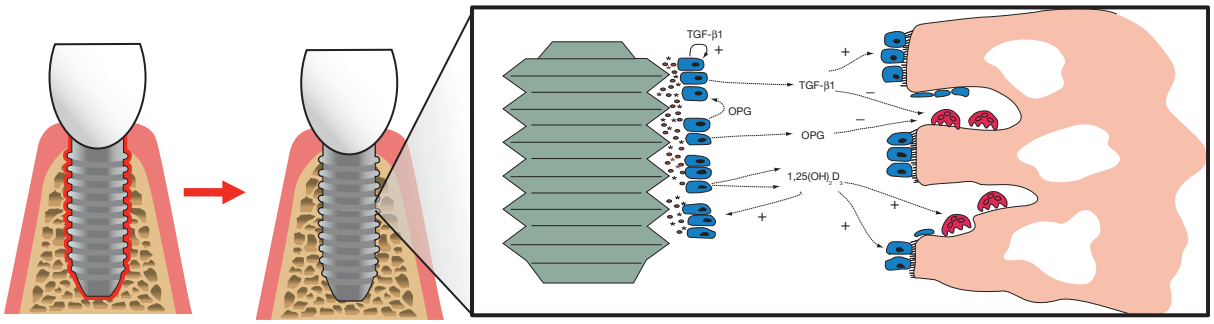

Figure 3 Processes involved in osseointegration. Events at the implant surface, including osteoprogenitor cell attachment, proliferation, and differentiation, lead to release of local regulatory factors in the peri-implant space. These factors contribute to the recruitment of osteoblast-progenitors on the endosteal bone surface and suppression of osteoclast formation and activity. Studies also show that implant materials placed at one site in bone can affect bone formation at distal sites, supporting the hypothesis that factors are released locally that become systemic.

PGE_2 stimulates osteoclastic activity at high levels, but it is required at low levels for osteoblast activity.[40,41] The elevated prostaglandins that are seen in cultures grown on rough microtopographies appear to be required for enhanced osteogenesis as inhibition of prostaglandin production by indomethacin blocks the increase in osteoblast phenotypic expression on these substrates.[42] Moreover, $1\alpha,25(OH)_2D_3$ stimulates PGE_2 production by MG63 cells only when they are grown on the rougher surfaces and this stimulatory effect is dose dependent and synergistic with the surface effect.[43]

Growth factor production and storage are regulated as well, as shown in studies using TGF-β1 as a model. TGF-β1 stimulates proliferation of mesenchymal cells and enhances the production of extracellular matrix, particularly of type I collagen.[36] It is synthesized in latent form and stored in the extracellular matrix together with a binding protein termed latent TGF-β binding protein. When MG63 cells are cultured on Ti surfaces of increasing roughness, most of the TGF-β1 produced is in latent form, and the amount increases on surfaces with rough microtopographies.[36] The regulation of TGF-β1 production on Ti surfaces depends on the osteoblast-like cell model used.[37,38] In studies using MG63 osteoblast-like cells as the model, the distribution of TGF-β1 between the matrix and the conditioned media of the cells is affected. On rougher surfaces, there is a greater incorporation of TGF-β1 into the matrix.[44] This is important for later bone remodeling because osteoclasts release TGF-β1 during the resorption phase and activate it. Once activated, TGF-β1 can act on the osteoclast to downregulate its activity.

The amount of TGF-β1 produced by osteoblasts cultured on Ti is modulated in a surface-dependent manner by factors that regulate osteogenesis and subsequent bone resorption. 17β-Estradiol has no effect on the TGF-β1 content of the media of MG63 cells grown on smooth Ti surfaces but when these cells are cultured on rougher microtopographies, 17β-estradiol causes a dose-dependent increase in the levels of TGF-β1.[33,34] The vitamin D metabolite $1\alpha,25(OH)_2D_3$ causes a similar effect.[29] $1\alpha,25(OH)_2D_3$ does not alter TGF-β 1 levels in cultures grown on smooth Ti, but it increases TGF-β1 levels in the media of cells grown on rougher surfaces and the effect is dose dependent.[29]

In vivo, it is likely that immune cells interact with implant surfaces before osteoblast-progenitor cells migrate onto the implant surface (see **Chapter 4.403, The Innate Response to Biomaterials**). Ti surface topography affects these cells as well. Macrophage and monocyte attachment and spreading, and BMP-2 expression are increased on microrough titanium.[39,45] Thus, the behavior of cells grown on surfaces with rough microarchitectures is altered both with respect to their basal production of autocrine factors and with respect to their ability to produce these factors in response to hormonal regulation. Moreover, the response is to increase production of factors that promote early stages of bone formation and retard osteoclastic resorption.

These studies suggest that other factors that modulate osteoclastogenesis might be modulated as well. To test this, an examination of osteoblast-dependent regulation of osteoclasts via receptor activator of nuclear factor κ B (RANK) ligand (RANKL) was initiated (see Khosla[46] for a review of the RANKL regulatory system). Osteoblasts retain RANKL on their plasma membranes. When RANKL binds its receptor RANK on osteoclasts, osteoclastic resorption is activated. To control this phenomenon, osteoblasts also produce a decoy receptor termed osteoprotegerin (OPG), which binds to RANKL, preventing it from interacting with RANK. If the regulatory stimulus now favors osteoclasts but excess OPG is present, the osteoblast may also produce soluble RANKL (sRANKL), which can then bind the OPG, leaving membrane-associated RANKL to interact with RANK on the osteoclasts. Thus, excess OPG would favor osteogenesis over bone resorption. When grown on titanium substrates with rough microtopographies, MG63 cells produce higher levels of OPG and this is further increased by $1\alpha,25(OH)_2D_3$ in a synergistic manner, but no change occurs in the expression of sRANKL.[47]

In addition to regulating osteoblast attachment, morphology, differentiation, and local factor production, Ti implant roughness also modulates the production of angiogenic factors by osteoblasts.[48] Clinically, the success of implanted materials in orthopedics and dentistry is dependent not only on bone apposition at the implant–tissue interface, but also on the establishment of a vascular supply in the peri-implant bone to allow for the delivery of oxygen and nutrients, as well as systemic hormones and osteoblast-progenitor cells. Angiogenesis, the sprouting of new capillary blood vessels from the preexisting vasculature, is a critical process during embryonic development and in several physiological conditions, including the formation of new bone and bone fracture healing,[49,50] as well as during bone regeneration and osseointegration of implanted materials.[51] This suggests that materials that support peri-implant bone formation may support angiogenesis as well as osteogenesis.

Both MG63 cells and normal human osteoblasts secrete several proangiogenic growth factors into their conditioned medium, including vascular endothelial growth factor A (VEGF-A), basic fibroblast growth factor (FGF-2), and epidermal growth factor (EGF).[48] When these cells are cultured on smooth Ti, secretions of VEGF-A, FGF-2, and EGF are increased compared to cells cultured on tissue culture polystyrene. On microrough Ti substrates, there is a further increase in secretion of these proangiogenic growth factors. The production of angiopoietin-1 (Ang-1), a marker of later stages of angiogenesis, was not affected by Ti implant microtopography. The increased production of proangiogenic growth factors by MG63 cells cultured on Ti substrates with a rough microtopography resulted in increased endothelial tubule formation in both Matrigel® and fibrin gel angiogenesis assays,[48] suggesting that implant surface roughness may directly enhance neovascularization as well, potentially resulting in greater clinical success of implanted materials. Recently, it was found that the receptor $\alpha_2\beta_1$ integrin regulates the expression of proangiogenic growth factors.[48]

Most studies examining the osteogenic potential of implant surfaces *in vitro* have used cells that are either immature osteoblasts or osteoblast cell lines.[52–54] However, the first group of mesenchymal cells to colonize the implant surface must be able to migrate through the peri-implant clot, and are likely to be multipotent progenitor cells.[55,56] Mesenchymal stem cell (MSC) differentiation to an osteoblast phenotype is sensitive to implant surface microstructure.[57] MSCs cultured on Ti substrates exhibited osteoblast characteristics indicated by a reduction in cell number and increases in alkaline phosphatase-specific activity, osteocalcin, OPG, and TGF-β1. In addition, MSCs cultured on smooth Ti substrates displayed increased mRNA levels of RUNX2 and integrins α_2 and β_1 relative to tissue culture polystyrene controls.[57] These increases were further enhanced in MSC cultures on microrough Ti substrates. In the same study, a coculture model was developed in which conditioned media from MG63 cells cultured on both smooth and microrough Ti substrates resulted in the osteogenic differentiation of MSC cultures.[57] Taken together, these data demonstrate that surface microstructure is able to direct MSCs toward an osteoblast lineage without the use of osteogenic growth factors in the culture media, and that differentiated osteoblasts cultured on implant surfaces with microrough rugosities create a sufficient environment for osteogenic differentiation of surrounding MSCs.

6.622.3. Mechanisms Mediating the Microtopography Effect

Prostaglandin plays an important role in mediating the effects of surface microtopography on osteoblast physiology. As noted above, the amount of PGE_1 and PGE_2 released into the conditioned media by MG63 osteoblast-like cells increases as surface microroughness increases.[36] Blocking prostaglandin production with the general cyclooxygenase (Cox) inhibitor indomethacin also blocks the increase in markers typical of mature osteoblasts. Both constitutive Cox-1 and inducible Cox-2 are involved, as inhibitors specific to only one form of the enzyme fail to block all prostaglandin-dependent responses.[58]

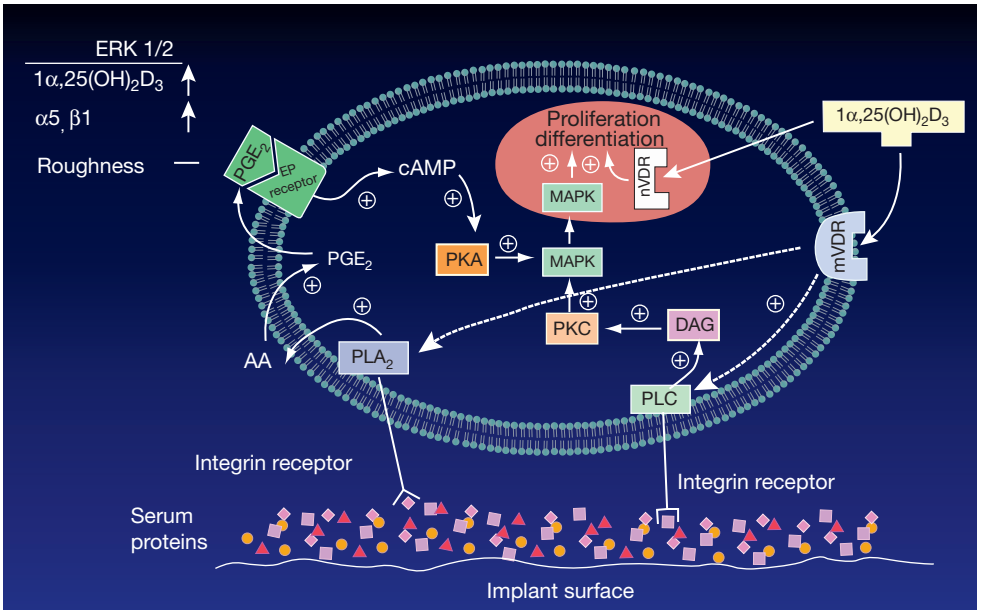

Figure 4 Integrin- and $1\alpha,25(OH)_2D_3$-mediated signaling and the interaction of the two pathways on osteoblasts grown on titanium surfaces.

Cells that are attachment dependent interact with their substrate through a number of mechanisms, including specific binding of integrins to components of the extracellular matrix, as well as to proteins adsorbed on the substrate surface (Figure 4). Part of the effect of surface microroughness on BMP-2 production by J774A.1 macrophages is mediated by the β_1 integrin and to a lesser extent by the β_3 integrin.[45] One of the integrins that mediates the binding of osteoblasts to proteins containing the arginine-glycine-aspartic acid (RGD) motif is $\alpha_5\beta_1$.[59] This binding initiates a signaling cascade resulting in new gene expression and protein synthesis. The signaling cascades initiated by integrin binding include protein kinase C (PKC)-dependent phosphorylation, culminating in mitogen-activated protein (MAP) kinase activation.[60] Part of the effect of $1\alpha,25(OH)_2D_3$ on osteoblasts is also mediated via this signaling pathway,[60] which may explain why MG63 cells respond in a synergistic manner to this vitamin D metabolite when they are cultured on microrough topographies.

To test this hypothesis, confluent cultures of MG63 cells were cultured for 24 h on smooth ($R_a < 0.6\,\mu m$) and rough (R_a 4–5 μm) titanium disk surfaces in the presence and absence of 10^{-8} M $1\alpha,25(OH)_2D_3$. One half of the cultures were treated with the MAP kinase inhibitor PD98059, which is specific for the ERK1/2 (extracellular regulated kinase) family of MAP kinases. The results of this study show that the decrease in cell number and increase in osteocalcin levels observed on rough surfaces are not regulated in this manner although the enhanced response to $1\alpha,25(OH)_2D_3$ is via ERK1/2. In contrast, the increase in alkaline phosphatase-specific activity on rough surfaces is due in part to ERK1/2, as is the stimulatory effect of $1\alpha,25(OH)_2D_3$ on this enzyme activity.[60] Thus, phenotypic expression due to surface microtopography may be modulated by multiple interacting pathways.

Recently, it was shown that MG63 cells exhibit increased phospholipase D (PLD) activity on sandblasted Ti surfaces and inhibition of PLD by 2,3-diphosphoglyceric acid reduced alkaline phosphatase-specific activity and osteocalcin production,[61] suggesting that PLD may also play a role in osteoblast differentiation on rough Ti substrates.

The main function of PLD is to hydrolyze membrane phosphatidylcholine (PC) to generate the precursor signaling molecules phosphatidic acid (PA) and choline.[62] PA can also be converted to lipid second messengers, such as lysophosphatidic acid (LPA) and diacylglycerol (DAG), which mediate the functional role of PLD. PA can be metabolized to DAG by PA phosphatase, which recruits PKC to the membrane to activate it.[63–65] This raises the possibility that changes in PLD activity might mediate the effects of surface microstructure on osteoblasts via PKC. To test this, PLD expression and activity in MG63 cells cultured on smooth and microstructured Ti substrates were examined.[66] PLD activity was inhibited using RNA interference for the PLD isoforms PLD1 and 2. The results of the study showed that inhibition of both PLD isoforms reduced surface roughness-dependent increases in osteoblast differentiation and reduced PKC activity, suggesting that PLD is upstream of PKC in mediating osteoblast response to surface microstructure. It was further shown that PLD2 is the primary isoform involved in this process.[66]

Osteoblasts assume distinct morphologies depending on the architectural features of their substrates. On microrough surfaces, as long as the peak-to-peak distance is less than the length of the cell body,[67] the cell bodies become more cuboidal, and anchor themselves to the surface through long dendritic filopodia.[1] In contrast, on the smoother surfaces, the cells flatten and spread, resulting in a fibroblastic appearance. The cell morphology correlates with the physiological behavior of the cells. On smooth surfaces, prostaglandin synthesis is low, TGF-β1 levels are low, alkaline phosphatase-specific activity is low, and osteocalcin levels are low, whereas proliferation rates are relatively high in comparison with cells cultured on rougher surfaces.[36] Moreover, these parameters are either not affected by $1\alpha,25(OH)_2D_3$ or the effect of the

hormone is minimal, supporting a fibroblastic phenotype. In contrast, on rougher surfaces, proliferation is reduced and the other parameters are increased, including responsiveness to $1\alpha,25(OH)_2D_3$, supporting a mature secretory osteoblast-like phenotype.[33,34]

It is not yet clear if the change in morphology precedes the expression of a more mature physiology or if the differentiation of the cell is activated by another yet-unidentified factor and the cell now responds differently to the surface microarchitecture. Observations suggest that the architecture of the surface forces the cells to adapt their morphology and this is translated to the cell through the integrin receptor system.[68] In subsequent experiments, cells were cultured on smooth and microrough Ti disks that were coated with polyethylene glycol (PEG) grafted to poly-L-lysine (PLL-*g*-PEG) to prevent nonspecific adhesion of serum proteins.[69] The experiment was conducted in three formats: cells were cultured on (a) PLL-*g*-PEG alone, and PLL-*g*-PEG on which a subset was modified to exhibit an RGD peptide; (b) PLL-*g*-PEG surfaces containing varying concentrations of the RGD peptide up to the concentration tested under format (a); and (c) PLL-*g*-PEG as defined in subset (a) in the presence of a soluble competing RGD peptide. The results of this study[69] indicate that MG63 cells will attach to PLL-*g*-PEG and those that do so exhibit the physiology of a mature osteoblast. Perhaps the most important observation is that inclusion of the RGD peptide on the surface restores the cells to the immature phenotype noted on smooth surfaces and tissue culture plastic, whereas inclusion of the inactive RDG peptide has no effect.[69]

The combination of osteoblast-specific peptide adhesive ligands with rough implant surface microtopographies could potentially enhance early osteoblast attachment and differentiation to better promote osseointegration and improve long-term implant fixation. It is unlikely that any one mimetic is responsible for all responses of osteoblasts on a functionalized surface. Integrin-mediated cell adhesion to extracellular matrix proteins initiates a cascade of intracellular signaling events that serve to direct cell differentiation and function.[68] Osteoblasts express several integrin subunits, including α_1, α_2, α_3, α_4, α_5, α_6, α_v, β_1, and β_3.[70–72] On tissue culture polystyrene, osteoblasts primarily express $\alpha_5\beta_1$ integrins.[73] However, when grown on Ti substrates, expression of α_2 and β_1 integrin subunits is increased,[74] indicating that the surface roughness-dependent differentiation of osteoblasts may be mediated specifically through $\alpha_2\beta_1$ signaling. Studies using antibodies to $\alpha_5\beta_1$, the integrin that binds RGD in fibronectin, and $\alpha_2\beta_1$, the integrin that binds type I collagen, indicate that the former is responsible for attachment and proliferation, but differentiation is mediated by the latter.[75,76] This suggests that combinations of peptide mimetics may be more effective than materials that are functionalized with a single motif.

To test this hypothesis, MG63 osteoblast-like cells were cultured on microrough Ti implant surfaces coated with a combination of peptide motifs: RGD to target $\alpha_5\beta_1$ integrin signaling, and a lysine-arginine-serine-arginine (KRSR) peptide sequence that is hypothesized to target transmembrane proteoglycans present on osteoblasts.[77] In addition, microrough Ti implant surfaces were coated with a lysine-serine-serine-arginine (KSSR) peptide sequence that is not known to target osteoblast binding. The results of the study demonstrated again that Ti surface coating with RGD increased osteoblast attachment but reduced osteoblast differentiation. In a similar manner, surfaces coated with either KRSR or a combination of RGD/KRSR inhibited overall osteoblast differentiation compared to uncoated, microrough Ti surfaces, as seen by reduced levels of alkaline phosphatase-specific activity, and levels of osteocalcin, PGE_2, and TGF-β_1. Conversely, surface coating with KSSR promoted a differentiated osteoblast phenotype with reduced cell number and increases in alkaline phosphatase activity and levels of osteocalcin and PGE_2 compared to uncoated surfaces. These data indicate that a combination of rough surface microarchitecture and surface functionalization with mimetic peptide sequences may further enhance osteoblast differentiation, although further study is needed to determine the mechanism by which KSSR mediates its effect.[78]

The $\alpha_2\beta_1$ integrin recognizes and binds the glycine-phenyalalanine-hydroxyproline-glycine-glutamate-arginine (GFOGER) motif present on residues 502–507 of the α_1(I) chain of type I collagen.[79,80] To examine whether the GFOGER peptide motif promoted osteoblast attachment and differentiation, biomolecular surface coating of GFOGER was done on glass and Ti substrates and the response of osteoblasts was examined both *in vitro* and *in vivo*.[81]

Tissue culture polystyrene dishes were coated with a 300 Å titanium layer via electron beam evaporation. The GFOGER peptide sequence was passively adsorbed onto the Ti surfaces. The results of the study showed that bone marrow stromal cell adhesion on GFOGER-coated Ti substrates was significantly higher compared to substrates coated with RGD peptide motif, and cells cultured on GFOGER-coated surfaces displayed higher mRNA transcript levels of Runx2, osteocalcin, and bone sialoprotein compared to cells cultured on uncoated Ti substrates.[81] Examination of osteoblastic differentiation showed that surface coating with the GFOGER peptide motif increased alkaline phosphatase-specific activity as well as calcium content *in vitro*, relative to uncoated controls.[81]

To evaluate the performance of the GFOGER peptide motif *in vivo*, osseointegration in a rat tibia cortical bone model was quantified on GFOGER-coated smooth Ti surfaces using histomorphometry and pull-out mechanical testing. After 4 weeks, greater bone mineral was observed along GFOGER-coated Ti implants versus type I collagen-coated and -uncoated controls and quantification of bone to implant contact (BIC) revealed a greater than twofold increase in BIC in GFOGER-coated Ti substrates versus -uncoated controls. Pull-out force of GFOGER-coated implants was also significantly higher compared to that of both uncoated and type I collagen-coated implants.[81] These results suggest that direct targeting of the $\alpha_2\beta_1$ integrin on osteoblasts promotes cell adhesion and osteoblast maturation *in vitro* and promotes osseointegration *in vivo*. It is important to note that in this study, only smooth Ti substrates were examined and the effect of implant microroughness and GFOGER surface coating is not known.[81]

Responses to the surface also depend on the state of maturation of the cell in the osteoblast lineage. Numerous cell lines and primary cell cultures have been examined in this model, from the multipotent fetal rat calvarial cells to the osteocyte cell line MLO-Y4.[31,82] These experiments indicate that as cells become more mature, the stimulatory effect of the microrough surface on differentiation becomes attenuated. However, it is

only on rough surfaces and only in the presence of BMP-2 that fetal rat calvarial cells are able to establish three-dimensional nodules that form minerals in a physiologically relevant manner.[31] Why this is the case is not yet clear. The results support *in vivo* observations that a material can affect cells directly on the surface as well as cells distal to the biomaterial,[83] indicating that the extracellular signaling factors released by the cells in direct contact with the material are sensed by other cells in the microenvironment, and potentially systemically as well.

6.622.4. *In Vivo* Studies

It has been difficult to definitely determine the relative clinical value of specific surface morphologies because of the confounding variables of surface chemistry, surface energy, and clinician expertise, and the inherent variability of the human patient population. Recently, Albrektsson and Wennerberg[84] reviewed the literature related to topographic and chemical properties of implants and concluded that moderately rough surfaces, defined as having S_a values between 1 and 2 μm, exhibited 'stronger bone responses' than either smoother or rougher surfaces. Some studies have reached similar conclusions, but other studies have reached quite different conclusions. A representative sample is described here.

In a meta-analysis published in 1999, evaluation of clinical data revealed that predictably high success rates can be achieved for implants with both rough and smooth titanium surfaces. When studies were clustered by specific indications or patient populations, rough-surfaced implants had significantly higher success rates compared to implants with smoother surfaces except in the cases of single tooth replacement where success rates were comparable. However, in the partially edentulous patient group, titanium implants with rough surfaces had significantly higher success rates in the maxilla than in the mandible.[85] A multicenter study compared 247 dual acid-etched (HCl/H_2SO_4) and 185 machined-surfaced implants implanted in various bone qualities in 97 patients. It was found that at 36 months, the cumulative success rates (CSRs) were 95% for the dual acid-etched and 86.7% for the machined-surfaced implants.[86]

Several studies have addressed various types of surface roughness (**Figure 5**) and their effects on human bone formation. A comparison of the BIC at 6 months was conducted for dual acid-etched and machined commercially pure titanium implant surfaces in 11 patients. Two-surfaced titanium microimplants were manufactured. One side received the rough surface modification and the opposite side maintained a machined surface. In each patient, one test implant was placed in the posterior maxilla during conventional dental implant surgery. Histologic analysis following 6 months of unloaded healing indicated that the mean BIC values for the rough surfaces were $72.96 \pm 25.13\%$ and BIC values for the smooth surfaces were $33.98 \pm 31.04\%$.[17] A similarly designed study examined the relationship between the actual BIC and the expected BIC after 6 months of nonloaded healing using both rough and machined implant surfaces. The investigators found that the actual BIC for rough surfaces was greater than expected, whereas the actual BIC for the machined surface was generally lower than expected.[87]

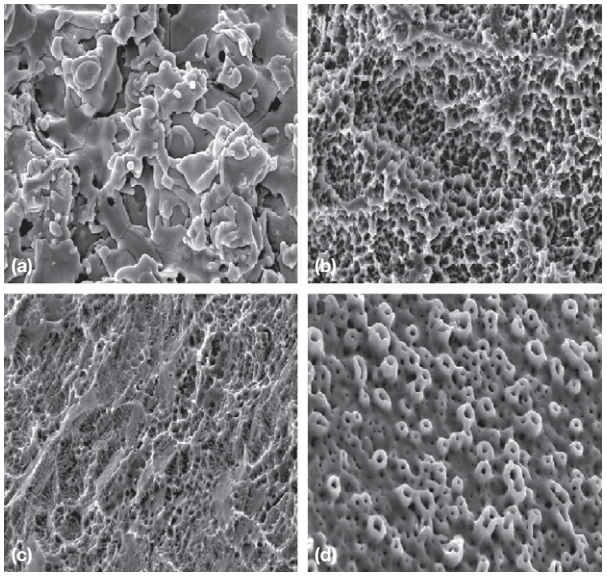

Figure 5 Scanning electron micrographs showing the different microrough morphologies on the surfaces of four commercially available dental implants: (a) titanium plasma-sprayed (TPS) surface; (b) sandblasted and acid-etched Ti surface (SLA®, Institut Straumann AG, Switzerland); (c) acid-etched Ti (Osseotite®, Biomet 3*i*, Palm Beach Gardens, FL); and (d) phosphate-enriched Ti oxide (TiUnite®, Nobel BioCare, Sweden).

The response of human bone tissue to oxidized and turned (machined) titanium surfaces has also been examined.[88] Twenty patients received one oxidized and one turned microimplant each during implant surgery. After a mean healing period of 6.6 months in the maxilla and 3.5 months in the mandible, the microimplants and surrounding tissue were removed. Histomorphometric evaluation demonstrated significantly higher BIC for the oxidized implants. Whether this was due to the fact that the oxidized implants have greater surface area because of the micron-scale TiO_2 cones produced during fabrication, or to the roughness itself, is not known. Moreover, significantly more bone was found inside the threaded area for the oxidized implants, whether placed in the maxilla or mandible, supporting a number of studies indicating that macroroughness is also a factor in osseointegration.

Placement of dental implants is often done under adverse conditions. Several articles have examined the influence of surface roughness on clinical outcomes when the implant is placed in poor quality bone, augmented ridge, or sinus. In a meta-analysis examining the cumulative success rate of 2614 machined-surfaced implants and 2288 dual etched-surfaced implants, the machined-surfaced implants had a 4-year CSR in all bone sites of 92.7%. For the implants placed in good bone, the 4-year CSR was 93.6% compared with the 4-year CSR in poor (soft) bone of 88.2% ($P < 0.05$). However, for rougher dual-etched implants in all sites, their overall 4-year CSR was 98.4% in good bone, and 98.1% in poor bone.[89] Another study compared the overall survival rate of 78 machined and 80 sandblasted, acid-etched implants that were inserted in an augmented bone of a reconstructed atrophied maxilla. The implants were followed between 20 and 67 months postimplantation. Fifteen machined implants, but only two

sandblasted, acid-etched implants, were lost. The overall survival rate for the machined implants was 81% and for the sandblasted, acid-etched implants 98%.[90]

A recent published systematic review analyzed the data from 43 human studies with a minimum of 20 interventions and a minimum follow-up period of 1-year loading of implants placed in sinuses augmented with the lateral window technique. The results pointed out that rough-surfaced implants have a significantly higher survival rate than machine-surfaced implants when placed in grafted sinuses. However, there was no statistical difference between different types of rough-surfaced implants.[91]

Custom-made microimplants with two different surface topographies were used to compare the effect of machined and microtextured surfaces on BIC in augmented human maxillary sinuses.[92] After 6 months of submerged healing, the microimplants were removed with the surrounding bone. Histologic analysis revealed that the mean BIC was significantly greater on the microtextured surfaces ($72 \pm 17\%$) compared to machined surfaces ($38 \pm 19\%$).

Other *in vivo* studies support the hypothesis that rough implant surfaces enhance osseointegration. Significant increases in pull-out strength between weeks 5 and 8 were noted with dual-etched Ti implants, and these increases were maintained.[93] Removal torque values (RTVs) of dual acid-etched and titanium plasma-sprayed (TPS) implants attained at 2 months postimplantation were comparable to those achieved only after 3 months of healing by the machined implants.[94] This may reflect higher BIC on the rougher surfaces. In order to compare the effectiveness of machined and acid-etched implants on BIC following short healing times in human posterior maxillas, custom-made microimplants were placed in 11 patients and allowed to integrate for 2 months. Histologic analysis of the surrounding bone showed that the BIC on the dual acid-etched side was 47.8%, significantly higher than the BIC on the machined side of 19%.[95] Moreover, the BIC on the dual acid-etched side was higher than that found in a previous study even after 6 months on the machined side (33.98%).[17]

It has been advocated that after implant placement, surgical sites should be undisturbed for at least 3–6 months to allow uneventful wound healing, thereby enhancing osseointegration between the implant and bone. The rationale behind this approach is that implant micromovement caused by functional force around the bone–implant interface during wound healing may induce fibrous tissue formation rather than bone leading to clinical failure.[96] Use of implants with microrough surfaces may permit clinicians to reduce or even eliminate the preplacement healing period. Histomorphometric analysis of bone surrounding two immediate loaded dual-etched implants implanted in the mandible and retrieved after 4 months of function showed high levels of BIC ranging from 78% to 85%.[97]

This case report led several groups of researchers and clinicians to redefine the minimum healing time needed before loading a rough surface dental implant. In a prospective multicenter study evaluating loading of 429 dual-etched implants 2 months after placement, only seven implants were lost at 2 years postloading. Six of these implants were identified prior to loading. The cumulative implant survival rate was 98.5% at 12.6 months. The cumulative postloading implant survival rate was 99.8% at 10.5 months.[98] Similar results were found when other groups examined the survival rates of sandblasted, acid-etched implants restored as early as 6 weeks after implant placement surgery. Out of 329 implants, three were lost prior to abutment connection. The success rate for these implants, 2 years after restoration, was 99.3%.[99]

In a paper published recently, sandblasted, acid-etched implants were placed in molar and premolar areas of the mandible according to a one-stage protocol and were loaded 2 or 6 weeks after implantation. After 1 year, the implant survival rate was 98.8%. Two test implants and one control implant rotated at time of abutment connection and were left unloaded for 12 additional weeks and then loaded. Loading the implants as early as 2 weeks did not appear to jeopardize osseointegration in the posterior mandible.[100]

Patient smoking is often attributed to the failure of dental implants to achieve osseointegration. An interesting meta-analysis examined the outcomes of clinical studies that monitored the performance of 2609 machined-surfaced and 2274 dual acid-etched implants and also isolated the effect of smoking. Among the machined implant surfaces, the 3-year CSR was 92.8% for nonsmokers and 93.5% for smokers while the 3-year CSR for dual acid-etched implants was found to be 98.4% for nonsmokers and 98.7% for smokers, resulting in no significant differences between smokers and nonsmokers. There was, however, a clinically relevant difference observed between the two implant types.[101]

6.622.5. Summary

Increased surface roughness of dental implants enhances the process of osseointegration. It increases bone formation and increases BIC in all types of bone, resulting in elevated RTVs. In preparing histologic sections of implants with their surrounding bone, the weak point when smooth surfaces are used is at the implant–bone interface. However, if rough surfaces are used, the weak point is inside the bone and not at the implant–bone interface (**Figure 6**). Surface roughness elevated the cumulative success rate of implants implanted in adverse conditions such as augmented ridges and sinuses and areas of poor bone such as posterior maxilla, and in some cases abolished the deleterious effect of smoking. A growing number of clinical studies suggest

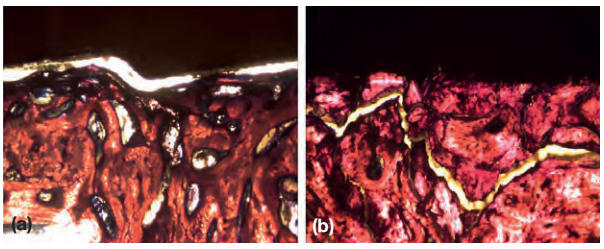

Figure 6 Histologic micrographs of the bone–titanium surface interface showing the fracture plane caused by sectioning: (a) smooth-surfaced implant; (b) rough-surfaced implant. Sections are stained with hematoxylin and eosin.

that early and immediate loading of rough-surfaced implants may lead to predictable osseointegration. However, it is important to note that these studies provide short-term results based only on radiographic observations and clinical mobility. Before we adopt new surgical and prosthetic guidelines, longer and broader studies are needed. Most recent research has examined the effect of surface roughness on bone healing around implants *in vivo* and the influence of surface roughness on osteoblasts *in vitro*. In a recent study, it was found that changing surface chemistry by submerging an implant in an isotonic NaCl solution following acid etching to avoid contamination with molecules from the atmosphere significantly increased osteoblast differentiation *in vitro* and BIC *in vivo*.[102]

Acknowledgments

The authors acknowledge the support of the ITI Foundation (Waldenburg, Switzerland), the National Institutes of Health (AR052102 and T32 GM08433), and the Georgia Tech/Emory Center for the Engineering of Living Tissues (Georgia Institute of Technology, Atlanta, Georgia).

References

1. Brunette, D. M. *Exp. Cell Res.* **1986**, *167*, 203–217.
2. Chehroudi, B.; Gould, T. R.; Brunette, D. M. *J. Biomed. Mater. Res.* **1989**, *23*, 1067–1085.
3. Chehroudi, B.; Gould, T. R.; Brunette, D. M. *J. Biomed. Mater. Res.* **1990**, *24*, 1203–1219.
4. Cochran, D. L.; Nummikoski, P. V.; Higginbottom, F. L.; Hermann, J. S.; Makins, S. R.; Buser, D. *Clin. Oral Implants Res.* **1996**, *7*, 240–252.
5. Thomas, K. A.; Cook, S. D. *J. Biomed. Mater. Res.* **1985**, *19*, 875–901.
6. Schroeder, A.; Buser, D. A. *Shigaku* **1989**, *77*, 1267–1288.
7. Martin, J. Y.; Schwartz, Z.; Hummert, T. W.; *et al. J. Biomed. Mater. Res.* **1995**, *29*, 389–401.
8. Mohammadi, S.; Wictorin, L.; Ericson, L. E.; Thomsen, P. *J. Mater. Sci. Mater. Med.* **1995**, *6*, 435–444.
9. Olefjord, I.; Hansson, S. *Int. J. Oral Maxillofac. Implants* **1993**, *8*, 32–40.
10. Wennerberg, A.; Albrektsson, R.; Andersson, B. *Int. J. Oral Maxillofac. Implants* **1993**, *8*, 622–633.
11. Gotfredsen, K.; Nimb, L.; Hjorting-Hansen, E.; Jensen, J. S.; Holmen, A. *Clin. Oral Implants Res.* **1992**, *3*, 77–84.
12. Le Guehennec, L.; Soueidan, A.; Layrolle, P.; Amouriq, Y. *Dent. Mater.* **2007**, *23*, 844–854.
13. Esposito, M. In *Titanium in Medicine*; Brunette, D. M., Tengvall, P., Textor, M., Thomsen, P., Eds.; Springer: Berlin, 2001.
14. De Leonardis, D.; Garg, A. K.; Pecora, G. E. *Int. J. Oral Maxillofac. Implants* **1999**, *14*, 384–391.
15. Buser, D.; Nydegger, T.; Oxland, T.; *et al. J. Biomed. Mater. Res.* **1999**, *45*, 75–83.
16. Hure, G.; Donath, K.; Lesourd, M.; Chappard, D.; Basle, M. F. *Int. J. Oral Maxillofac. Implants* **1996**, *11*, 506–511.
17. Lazzara, R. J.; Testori, T.; Trisi, P.; Porter, S. S.; Weinstein, R. L. *Int. J. Periodontics Restorative Dent.* **1999**, *19*, 117–129.
18. Pilliar, R. M. *Implant Dent.* **1998**, *7*, 305–314.
19. Steinemann, S. G. In *Oral Implantology*; Schroeder, A., Sutter, F., Buser, D., Krekler, G., Eds.; Georg Thieme: Stuttgart, 1991.
20. Webster, R. J.; Ergun, C.; Doremus, R. H.; Siegel, R. W.; Bizios, R. *Biomaterials* **2000**, *21*, 1803–1810.
21. Webster, R. J.; Ergun, C.; Doremus, R. H.; Siegel, R. W.; Bizios, R. *J. Biomed. Mater. Res.* **2000**, *51*, 475–483.
22. Webster, R. J.; Seigel, R. W.; Bizios, R. *Scr. Mater.* **2001**, *44*, 1639–1642.
23. Webster, R. J.; Siegel, R. W.; Bizios, R. *Biomaterials* **1999**, *20*, 1221–1227.
24. Fung, Y. C. *Biomechanics: Mechanical Properties of Living Tissue*. Springer: Berlin, 1993.
25. Liu, H.; Slamovich, E. B.; Webster, T. J. *J. Biomed. Mater. Res. A* **2006**, *78*, 798–807.
26. Svanborg, L. M.; Andersson, M.; Wennerberg, A. *J. Biomed. Mater. Res. B Appl. Biomater.* **2010**, *92*, 462–469.
27. Boyan, B. D.; Batzer, R.; Kieswetter, K.; *et al. Scanning Electron Microsc. (Cell & Materials)* **1995**, *39*, 323–335.
28. Schwartz, Z.; Lohmann, C. H.; Oefinger, J.; Bonewald, L. F.; Dean, D. D.; Boyan, B. D. *Adv. Dent. Res.* **1999**, *13*, 38–48.
29. Boyan, B. D.; Batzer, R.; Kieswetter, K.; *et al. J. Biomed. Mater. Res.* **1998**, *39*, 77–85.
30. Ong, J. L.; Cardenas, H. L.; Cavin, R.; Carnes, D. L., Jr. *Int. J. Oral Maxillofac. Implants* **1997**, *12*, 649–654.
31. Boyan, B. D.; Bonewald, L. F.; Paschaliz, E. P.; *et al. Calcif. Tissue Int.* **2002**, *71*, 519–529.
32. Lohmann, C. H.; Tandy, E. M.; Sylvia, V. L.; *et al. J. Biomed. Mater. Res.* **2002**, *62*, 204–213.
33. Boyan, B. D.; Lossdorfer, S.; Wang, L.; *et al. Eur. Cell Mater.* **2003**, *24*, 22–27.
34. Boyan, B. D.; Schwartz, Z.; Lohmann, C. H.; *et al. J. Orthop. Res.* **2003**, *21*, 638–647.
35. Dean, D. D.; Muniz, O. E.; Rodriquez, I.; *et al. Arthritis Rheum.* **1991**, *34*, 304–313.
36. Kieswetter, K.; Schwartz, Z.; Hummert, T. W.; *et al. J. Biomed. Mater. Res.* **1996**, *32*, 55–63.
37. Mustafa, K.; Rubinstein, J.; Lopez, B. S.; Arvidson, K. *Clin. Oral Implants Res.* **2003**, *14*, 50–56.
38. Lohmann, C. H.; Dean, D. D.; Bonewald, L. F.; Schwartz, Z.; Boyan, B. D. *J. Bone Joint Surg. Am.* **2002**, *84A*, 411–419.
39. Soskolne, W. A.; Cohen, S.; Sennerby, L.; Wennerberg, A.; Shapira, L. *Clin. Oral Implants Res.* **2002**, *13*, 86–93.
40. Atkin, I.; Dean, D. D.; Muniz, O. E.; *et al. J. Bone Miner. Res.* **1992**, *7*, 863–875.
41. Dean, D. D.; Schwartz, Z.; Muniz, O. E.; *et al. Bone Miner.* **1992**, *17*, 172–176.
42. Sisk, M. A.; Lohmann, C. H.; Cochran, D. L.; *et al. Clin. Oral Implants Res.* **2001**, *12*, 52–61.
43. Schwartz, Z.; Dennis, R.; Bonewald, L. F.; *et al. Bone* **1992**, *13*, 51–58.
44. Schwartz, Z.; Lohmann, C. H.; Sisk, M.; *et al. Biomaterials* **2001**, *22*, 731–741.
45. Takebe, J.; Champagne, C. M.; Offenbacher, S.; Ishibashi, K.; Cooper, L. F. *J. Biomed. Mater. Res. A* **2003**, *64*, 207–216.
46. Khosla, S. *Endocrinology* **2001**, *142*, 5050–5055.
47. Lossdorfer, S.; Schwartz, Z.; Wang, L.; *et al. J. Biomed. Mater. Res. A* **2004**, *70*, 361–369.
48. Raines, A. L.; Olivares-Navarrete, R.; Wieland, M.; Cochran, D. L.; Schwartz, Z.; Boyan, B. D. *Biomaterials* **2010**, *31*, 4909–4917.
49. Duvall, C. L.; Taylor, W. R.; Weiss, D.; Wojtowicz, A. M.; Guldberg, R. E. *J. Bone Miner. Res.* **2007**, *22*, 286–297.
50. Geris, L.; Gerisch, A.; Sloten, J. V.; Weiner, R.; Oosterwyck, H. V. *J. Theor. Biol.* **2008**, *251*, 137–158.
51. Abshagen, K.; Schrodi, I.; Gerber, T.; Vollmar, B. *J. Biomed. Mater. Res. A* **2009**, *91*, 557–566.
52. Dalby, M. J.; Gadegaard, N.; Curtis, A. S.; Oreffo, R. O. *Curr. Stem Cell Res. Ther.* **2007**, *2*, 129–138.
53. Dalby, M. J.; McCloy, D.; Reobertson, M.; *et al. Biomaterials* **2006**, *27*, 2980–2987.
54. Dalby, M. J.; McCloy, D.; Robertson, M.; Wilkinson, C. D.; Oreffo, R. O. *Biomaterials* **2006**, *27*, 1306–1315.
55. Caplan, A. I. *J. Pathol.* **2009**, *217*, 318–324.
56. Caplan, A. I.; Dennis, J. E. *J. Cell Biochem.* **2006**, *98*, 1076–1084.
57. Olivares-Navarrete, R.; Hyzy, S. L.; Hutton, D. L.; *et al. Biomaterials* **2010**, *31*, 2728–2735.
58. Boyan, B. D.; Lohmann, C. H.; Sisk, M.; *et al. J. Biomed. Mater. Res.* **2001**, *55*, 350–359.
59. Howell, D. S.; Dean, D. D.; Woessner, J. F.; Pita, J. C.; Carreno, M. R.; Muniz, O. E. *Calcif. Tissue Int.* **1984**, *36*, 463.
60. Schwartz, Z.; Lohmann, C. H.; Vocke, A. K.; *et al. J. Biomed. Mater. Res.* **2001**, *56*, 417–426.
61. Kim, M. J.; Choi, M. U.; Kim, C. W. *Biomaterials* **2006**, *27*, 5502–5511.
62. Holbrook, P. G.; Pannell, L. K.; Daly, J. W. *Biochim. Biophys. Acta* **1991**, *1084*, 155–158.
63. Becker, K. P.; Hannun, Y. A. *Cell Mol. Life Sci.* **2005**, *62*, 1448–1461.
64. Houle, M. G.; Bourgoin, S. *Biochim. Biophys. Acta* **1999**, *1439*, 135–149.
65. Nishizuka, Y. *Nature* **1984**, *308*, 693–698.
66. Fang, M.; Olivares-Navarrete, R.; Wieland, M.; Cochran, D. L.; Boyan, B. D.; Schwartz, Z. *J. Biomed. Mater. Res. A* **2010**, *93*(3), 897–909.

67. Brunette, D. M. *Int. J. Oral Maxillofac. Implants* **1988**, *3*, 231–246.
68. Garcia, A. J. *Biomaterials* **2005**, *26*, 7525–7529.
69. Tosatti, S.; Schwartz, Z.; Campbell, C.; *et al*. *J. Biomed. Mater. Res. A* **2004**, *68*, 458–472.
70. Gronthos, S.; Simmons, P. J.; Graves, S. E.; Robey, P. G. *Bone* **2001**, *28*, 174–181.
71. Moursi, A. M.; Globus, R. K.; Damsky, C. H. *J. Cell Sci*. **1997**, *110*(Pt 18), 2187–2196.
72. Siebers, M. C.; Ter Brugge, P. J.; Walboomers, X. F.; Jansen, J. A. *Biomaterials* **2005**, *26*, 137–146.
73. Gronowicz, G.; McCarthy, M. B. *J. Orthop. Res.* **1996**, *14*, 878–887.
74. Raz, P.; Lohmann, C. H.; Turner, J.; *et al*. *J. Biomed. Mater. Res. A* **2004**, *71*, 217–225.
75. Keselowsky, B. G.; Collard, D. M.; Garcia, A. J. *Biomaterials* **2004**, *25*, 5947–5954.
76. Olivares-Navarrete, R.; Raz, P.; Zhao, G.; *et al*. *Proc. Natl. Acad. Sci. USA* **2008**, *105*, 15767–15772.
77. Cardin, A. D.; Weintraub, H. J. R. *Arteriosclerosis* **1989**, *9*, 21–32.
78. Bell, B. F.; Schuler, M.; Tosatti, S.; Textor, M.; Schwartz, Z.; Boyan, B. D. Osteoblast response to titanium surfaces functionalized with extracellular matrix peptide biomimetics. *Clin. Oral Implants Res.* 2011, doi:10.1111/j.1600-0501.2010.02074.x.
79. Knight, C. G.; Morton, L. F.; Onley, D. J.; *et al*. *J. Biol. Chem.* **1998**, *273*, 33287–33294.
80. Knight, C. G.; Morton, L. F.; Peachey, A. R.; Tuckwell, D. S.; Farndale, R. W.; Barnes, M. J. *J. Biol. Chem.* **2000**, *275*, 35–40.
81. Reyes, C. D.; Petrie, T. A.; Burns, K. L.; Schwartz, Z.; Garcia, A. J. *Biomaterials* **2007**, *28*, 3228–3235.
82. Lohmann, C. H.; Bonewald, L. F.; Sisk, M. A.; *et al*. *J. Bone Miner. Res.* **2000**, *15*, 1169–1180.
83. Braun, G.; Kohavi, D.; Amir, D.; *et al*. *Clin. Oral Implants Res*. **1995**, *6*, 1–13.
84. Albrektsson, T.; Wennerberg, A. *Int. J. Prosthodont*. **2004**, *17*, 536–543.
85. Cochran, D. L. *J. Periodontol*. **1999**, *70*, 1523–1539.
86. Khang, W.; Feldman, S.; Hawley, C. E.; Gunsolley, J. *J. Periodontol*. **2001**, *72*, 1384–1390.
87. Trisi, P.; Lazzara, R.; Rao, W.; Rebaudi, A. *Int. J. Periodontics Restorative Dent*. **2002**, *22*, 535–545.
88. Ivanoff, C. J.; Widmark, G.; Johansson, C.; Wennerberg, A. *Int. J. Oral Maxillofac. Implants* **2003**, *18*, 341–348.
89. Stach, R. M.; Kohles, S. S. *Implant Dent*. **2003**, *12*, 87–96.
90. Pinholt, E. M. *Clin. Oral Implants Res*. **2003**, *14*, 584–592.
91. Wallace, S. S.; Froum, S. J. *Ann. Periodontol*. **2003**, *8*, 328–343.
92. Trisi, P.; Marcato, C.; Todisco, M. *Int. J. Periodontics Restorative Dent*. **2003**, *23*, 427–437.
93. Baker, D.; London, R. M.; O'Neal, R. *Int. J. Oral Maxillofac. Implants* **1999**, *14*, 722–728.
94. Klokkevold, P. R.; Johnson, P.; Dadgostari, S.; Caputo, A.; Davies, J. E.; Nishimura, R. D. *Clin. Oral Implants Res*. **2001**, *12*, 350–357.
95. Trisi, P.; Lazzara, R.; Rebaudi, A.; Rao, W.; Testori, T.; Porter, S. S. *J. Periodontol*. **2003**, *74*, 945–956.
96. Adell, R.; Lekholm, U.; Rockler, B.; Branemark, P. I. *Int. J. Oral Surg*. **1981**, *10*, 387–416.
97. Testori, T.; Szmukler-Moncler, S.; Francetti, L.; *et al*. *Int. J. Periodontics Restorative Dent*. **2001**, *21*, 451–459.
98. Lazzara, R. J.; Porter, S. S.; Testori, T.; *et al*. *J. Esthet. Dent*. **1998**, *10*, 280–289.
99. Cochran, D. L.; Buser, D.; Ten Bruggenkate, C. M.; *et al*. *Clin. Oral Implants Res*. **2002**, *13*, 144–153.
100. Luongo, G.; Di Raimondo, R.; Filippini, P.; Gualini, F.; Paoleschi, C. *Int. J. Oral Maxillofac. Implants* **2005**, *20*, 84–91.
101. Bain, C. A.; Weng, D.; Meltzer, A.; Kohles, S. S.; Stach, R. M. *Compend. Contin. Educ. Dent*. **2002**, *23*, 695–699; 702, 704 passim; quiz 708.
102. Buser, D.; Broggini, N.; Wieland, M.; *et al*. *J. Dent. Res.* **2004**, *83*, 529–533.

6.623. Materials in Fixed Prosthodontics for Indirect Dental Restorations

I Naert, K.U.Leuven, Leuven, Belgium

© 2011 Elsevier Ltd. All rights reserved.

6.623.1.	**General Introduction**	354
6.623.2.	**Indirect Restorations**	354
6.623.2.1.	Metallic Restorations	354
6.623.2.1.1.	Lost-wax casting	354
6.623.2.1.2.	Spark erosion	355
6.623.2.1.3.	Grinding	356
6.623.2.1.4.	Selective laser melting	356
6.623.2.2.	Dental Ceramics	356
6.623.2.2.1.	Introduction	356
6.623.2.2.2.	Dental porcelains	357
6.623.2.2.3.	Processing of dental porcelains	357
6.623.2.2.4.	Properties of dental porcelain	358
6.623.2.2.5.	Classification of modern dental ceramics	358
6.623.2.3.	Ceramo-Metals	358
6.623.2.3.1.	Introduction	358
6.623.2.3.2.	Choice of ceramo-metal alloys	359
6.623.2.4.	All-Ceramic Restorations: High-Strength Core Ceramics	361
6.623.2.4.1.	Introduction	361
6.623.2.4.2.	Core materials	361
6.623.2.5.	CAD–CAM in Dentistry	363
6.623.2.5.1.	Definition	363
6.623.2.5.2.	CAD–CAM concepts in dentistry	363
6.623.2.5.3.	CAD–CAM components	363
6.623.2.5.4.	Materials to be processed on dental CAD–CAM devices	364
6.623.2.5.5.	Processing	364
6.623.2.5.6.	Reflections	364
References		365

Glossary

Bridge Restoration that replaces one or more missing teeth and that is supported by neighboring teeth or by implants. Also coined fixed (partial) dental prosthesis (F(P)DP).

Cantilever A cantilevered artificial tooth or pontic attached toward neighboring tooth abutments.

Direct restoration Mode of manufacturing chair side by the dentist in a moldable consistency (e.g., composite, amalgam).

Indirect restoration Mode of manufacturing by a dental lab or production unit (e.g., cast or milled from an alloy or ceramic blank).

Inlay Partial restoration not covering the tooth cusps.

Onlay Partial restoration covering the tooth cusps.

Post-and-core Root canal post, cast with the tooth core to build the basis of a devitalized tooth.

Precision attachment Patrix (male) and matrix (female) device that fits precisely the one into the other aiming at replacing, for example, cast claps in removable partial dentures to guarantee retention to the latter.

Pyroplastic flow A characteristic of a material by overheating, for example, the flow of the molten glass.

Resin-bounded Mode of connection (micromechanical) of a restoration during cementation by means of a composite luting cement after pretreatment of the tooth and restoration by acid-etching.

Veneer Restoration that covers, for example, tooth tissue, metal, or ceramic and is used to restore the shape and the esthetics of a tooth or its replacement.

Abbreviations

BCC Body-centered cubic
CAD Computer-aided design
CAM Computer-aided manufacturing
cpTi Commercial pure titanium
EDM Electrical discharge machining
HCP Hexagonal close-packed
HIP Hot Isostatic Pressed
SLM Selective laser melting
STL Standard transformation language

6.623.1. General Introduction

Historically, the clinical disciplines involved to restore or to replace missing teeth are on the one hand named conservative or operative dentistry where moldable materials named fillings are put into tooth cavities (direct restorations), while on the other hand are named prosthodontics where cast/grinded crowns, bridges, and (removable) dentures (indirect restorations/prostheses) are made. Today there is a shift in the European dental schools to bring these activities under one and the same umbrella of restorative dentistry.

This chapter deals with the indirect (fixed) restorations used during clinical activities to restore damaged and/or missing teeth, in order to replace oral function in its broadest sense (chewing, speaking, swallowing, esthetics, social well-being). This means that to manufacture these devices, a third player, namely a dental laboratory/device, is involved. More and more of the latter are chair-side produced and the term semi-direct has been introduced as well. Contrary to prostheses that replace some (partial prostheses) or all teeth (full prostheses or dentures) and that must be taken out at least daily to be able to maintain the supporting oral structures, restorations are dental material devices that are permanently fixed onto teeth or implants and cannot be removed by the patients themselves (inlays, onlays, crowns, and bridges).

6.623.2. Indirect Restorations

As mentioned in the general introduction, indirect restorations need some laboratory handling or at least are not directly manufactured without any additional tool/machine, before the final restoration can be handed-over to the dentist.

6.623.2.1. Metallic Restorations

Four main techniques are used in dentistry to produce metal crowns as well as for frameworks for bridges; lost-wax casting, spark erosion, grinding, and more recently selective laser melting (SLM).

6.623.2.1.1. Lost-wax casting

6.623.2.1.1.1. Introduction

The production of cast metallic restorations, such as crowns, bridges, inlays, cast posts-and-cores in the dental laboratory is traditionally carried out by the *lost-wax casting* technique. The technique can be found back beyond 3000 BC, but it was not used in dentistry until Taggart in the early 1900s first developed the lost-wax casting technique by the use of gold alloys. Over the last century, for the manufacturing of removable partial dentures, the gold alloys were gradually replaced by cobalt–chromium (CoCr) alloys during the 1950s. At the end of the twentieth century, titanium made its entrée after its successful indication in implant dentistry. Owing to more esthetic demands of patients in the Western population, full metal crowns became the exception rather than the rule and are used only for indications were esthetics are of no concern (posterior area/cast post-and-cores) or when large occlusal forces are acting onto the teeth such as in patients suffering from bruxism, a disorder (during night) or bad habit (during daytime) characterized by grinding and clenching of the teeth leading to excessive wear or fracture of weakened teeth. Substructures/frameworks, that later on are porcelain veneered (see Section 6.623.2.3.1), are currently widely used, although also there ceramic-based substructures are rapidly gaining importance.

The basic principles of the lost-wax casting consists of a wax pattern that is molded of the desired shape, and this pattern is invested in a refractory investment. The wax is then removed by melting and burning, leaving behind a cavity of the desired tooth anatomy. This cavity can be filled with molten metal, so that the metal corresponds to the shape of the original wax pattern. The full clinical and technical events, used over decades in the production of cast dental restorations are as follows: tooth preparation, impression taking, model pouring, wax-up of the pattern, investing the wax pattern, wax burnout and heating, melting and casting the alloy, finishing and polishing, heat treatments, and eventually luting of the restoration onto the teeth. Thus it can be seen that many different materials are involved in the production of a metal casting. These include impression materials, model and die materials, waxes, investment materials, casting alloys, and luting cements. Attention will be focused on the materials that are used and the requirements that are placed upon them for the restorations themselves and not on a detailed description of the various clinical and practical stages involved.

6.623.2.1.1.2. Noble and precious metal alloys

These alloys are very resistant to corrosion (noble) and are expensive (precious). They consist of eight elements that have a number of features in common. The noble metals are considered to be made up of gold, platinum, rhodium, iridium, ruthenium, and osmium, whereas silver and palladium are generally referred to as the precious metals.[1]

6.623.2.1.1.2.1. High-gold alloys Their high precious metal content (gold, silver, platinum, and palladium) must not be <75% and the pure gold content in excess of 60%. These alloys can be classified into four distinct groups: type I (soft), type II (medium), type III (hard), and type IV (extra hard). Type I and II alloys are best suited for one-surface inlays (type I) in low-stress situations and for most multiple-surface inlays (type II). Their indications are fully taken over by direct composites/indirect ceramics today. Type III alloys can be used for all inlays, onlays, full-coverage crowns and short-span bridges, cast posts-and-cores because of their greater strength. Type IV alloys are used for cast posts-and-cores and long-span bridges.

6.623.2.1.1.2.2. Medium- and low-gold alloys In the 1970s, due to the rapid rise in the prices of noble metals manufacturers produced many new alloys with a reduced gold content. Some of these may be classified as *medium-gold alloys*, with the gold content varying from 40 to 60%. Compositions of a representative commercial example are presented in Table 1. The palladium and silver contents were increased to compensate for the reduced gold content, while the copper content is in the range of 10–15%. Palladium is added to counteract the tendency of silver to tarnish. The medium-gold alloys are recommended for the same indications as type III and IV high-gold alloys. Their ductility tends to be lower than that of the type IV high-gold alloys. They are very suitable for long-span prostheses and may be used for implant-supported prostheses and posts-and-cores as well.

Table 1 Composition, physical, and mechanical properties of a representative commercial example of a medium-gold alloy (Medior 3®, Cendres & Métaux SA, Biel, Switzerland)

Composition	*Au*	*Pd*	*Ag*	*Cu*	*Zn*	*Ru*
	55%	5.95%	26%	10.9%	2.1%	0.05%
Physical properties		*Melting range*		*Density*		*Young's modulus*
		875–920 °C		13.6 g cm^{-3}		106 kN mm^{-2}
Mechanical properties		*Vickers hardness*		*0.2% proof stress (N mm^{-2})*		*Elongation (%)*
As cast		295		865		4.0
Soft		170		435		35.0
Hardened		280		815		4.5

The *low-gold alloys* tend to have lower mechanical properties than the medium-gold alloys, and are recommended as an alternative to type III high-gold alloys. These alloys are extensively used for posts-and-cores, where the white color does not present a problem as the casting will be covered with another material.

Although, in general, the medium-gold alloys are a suitable alternative to the type IV high-gold alloys, and the low-gold alloys for type III high-gold alloys, one problem with these alloys is that their properties are more variable from one alloy to the other than for each of the four types of high-gold alloy series. The biocompatibility of these alloys appears to be good, and corrosion does not seem to be a problem, even with the two-phase low-gold copper-free alloys.

6.623.2.1.1.2.3. Silver–palladium alloys These alloys were introduced in the 1960s as an alternative to the high-gold alloys, and are also called 'white gold.' Ag–Pd alloys contain predominantly silver with significant amounts of palladium. The palladium improves the resistance to corrosion and helps to prevent tarnish, which is common with silver. Alloys with reduced silver content and increased palladium content have properties similar to those of the type IV high-gold alloys. Nevertheless, their use for long-span prostheses is generally contraindicated. This may be associated with the high casting temperatures for these alloys, which is the second most notable feature of this material. Although they are highly biocompatible, tarnishing does occur with these alloys.

6.623.2.1.1.3. Base metal alloys

Base metal alloys do not contain noble and precious alloys.

6.623.2.1.1.3.1. Cobalt–chromium alloys CoCr alloys were first introduced to the dental profession in the 1930s, and since then have effectively replaced the type IV high-gold alloys for the manufacturing of removable partial denture frameworks, and therefore will not be further dealt with. However, these materials gain anew popularity when milled out of blanks or laser melted from powder particles in the manufacturing of restoration on teeth and implants (see **Section 6.623.2.3.2.5**).

6.623.2.1.1.3.2. Titanium alloys The interest in titanium-based castings for (removable) and fixed prosthodontics came about at the same time as the development of titanium dental implants. Titanium has a number of attractive features such as high strength with low density and excellent biocompatibility. Clinically two forms of titanium have received the most interest. One is the commercially pure form of titanium (cpTi) and the other is an alloy of titanium–6% aluminum–4% vanadium.

6.623.2.1.1.3.3. Commercially pure titanium The term commercially pure titanium (cpTi) is applied to unalloyed titanium and designates several grades (1–4) containing minor amounts of impurity elements, such as carbon, iron, and oxygen. The amount of oxygen can be controlled at various levels to provide increased strength. Titanium is allotropic, with a hexagonal close-packed (HCP) structure (α) at low temperatures and a body-centered cubic (BCC) structure (β) above 882 °C. cpTi is in fact an alloy of titanium with up to 0.5% oxygen. The oxygen is in solution so that the metal is single phase. Oxygen, nitrogen, and carbon have a greater solubility in the HCP structure of the α-phase than in the cubic form of the β-phase. These elements form interstitial solid solutions with titanium and help to stabilize the α-phase. Transition elements such as niobium, molybdenum, and vanadium act as β-stabilizers. The elastic modulus of cpTi is 110 GPa, which is half that of stainless steel or CoCr alloy. The tensile properties of cpTi depend significantly on the oxygen content.

6.623.2.1.1.3.4. Titanium–6% Aluminum–4% Vanadium When aluminum and vanadium are added to titanium in only small quantities, the strength of the alloy is increased over that of cpTi. Aluminum is considered to be an α-stabilizer with vanadium acting as a β-stabilizer. When these are added to titanium the temperature at which the α–β transition occurs is depressed such that both the α- and β-forms can exist at room temperature. Thus, Ti–6% Al–4% V has a two-phase structure of α and β grains. While cpTi should not be used in situations where the tensile stress may exceed 175 MPa, for the Ti–6% Al–4% V, the fatigue limit is approximately 450 MPa. Castability does present a serious problem with these alloys. All castings need to be carried out in a vacuum or an inert atmosphere, which requires special casting equipment, because of its reactivity to oxygen. Hence, other forms of processing titanium for dental prostheses are also used such as grinding or laser melting (see **Section 6.623.2.5.4.1**).

6.623.2.1.2. Spark erosion

The spark erosion technique also know as electrical discharge machining (EDM) is utilizing base metal alloys and was first reported in dentistry in 1982. Mostly used for precision attachments, which are double structures in the fixed-removable (implant) prostheses, as well as for Ti single crowns in combination with, for example, outer grinding (Procera Ti crowns,

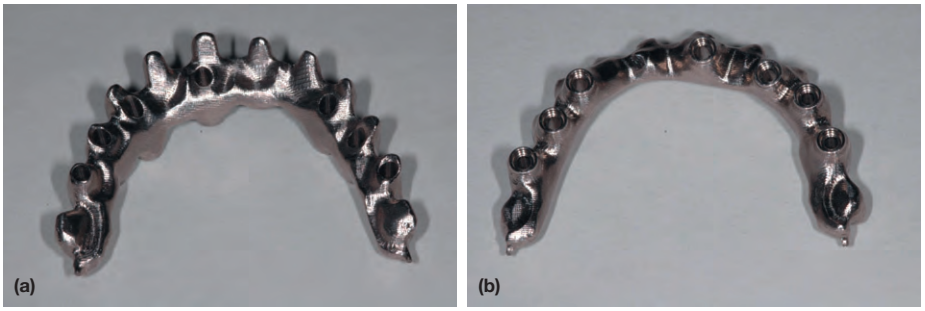

Figure 1 Milled Ti-substructure for an implant supported fixed full prosthesis top (a) and bottom (b) view. Courtesy by ES-Healtcare, Hasselt, Belgium.

Nobelpharma AB, Göteborg, Sweden.[2] In fact, it is a noncontact removal process using a series of electrical sparks per coping to erode material from a work piece in a liquid medium under carefully controlled conditions. The total time to erode, for example, one Ti coping is about 10 min. Because EDM is a thermal or melting process, conductivity and melting point of the metal or alloy are the key factors determining the amount of electrical energy required. EDM machines for dental applications have an output ranging between 10 and 30 A. Currently this technique is overruled by grinding.

6.623.2.1.3. Grinding

Construction data produced with the CAD software are converted into grinding strips for the Cam-processing and finally loaded into a grinding device. Processing devices are distinguished by means of the number of grinding axes: 3-, 4-, and 5-axis grinding devices.

6.623.2.1.3.1. Three-axis grinding devices

This type of grinding device has 3° of movement in the three spatial directions. Thus, the mill path points are uniquely defined by the *X*-, *Y*-, and *Z*- values. The calculation time is therefore minimal. Grinding of subsections, axis divergences, and convergences, however, is not possible.

6.623.2.1.3.2. Four-axis grinding devices

In addition to the three spatial axes, the tension bridge for the component can also be turned infinitely variably. As a result, it is possible to adjust bridge constructions with a large vertical height displacement into the usual mold dimensions and thus save material and grinding time.

6.623.2.1.3.3. Five-axis grinding devices

With a 5-axis grinding device there is also, in addition to the three spatial dimensions and the rotatable tension bridge (4th axis), the possibility of rotating the grinding spindle (5th axis). This enables the grinding of complex geometries with subsections, as for example, lower jaw bridge on converging abutment teeth, or also crown and bridges substructures that, as a result of anatomically reduced formation, demonstrate converging areas in the exterior of the frame.

It should be noted that the quality of the restoration does not necessarily increase with the number of processing axes. The quality results much more from the result of the digitalization, data processing, and production process (**Figure 1(a)** and **1(b)**).

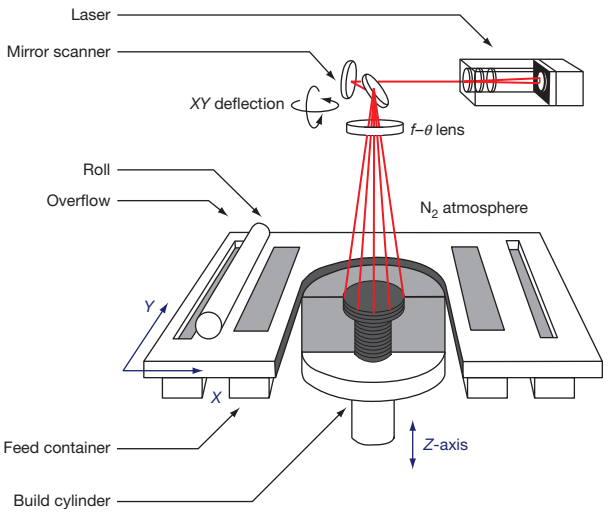

Figure 2 Overview of the basic principles of selective laser melting technology. Courtesy by Vandenbroucke, B. PhD. Thesis, K.U.Leuven, 2008.

6.623.2.1.4. Selective laser melting

The latest production technology use in dentistry is the generative production method which is a special CAD–CAM method, in contrast to grinding technology, that does not work by subtracting, but rather by adding material. **Figure 2** depicts a scheme of the basic features of SLM technology.[3] In the dental field, there are some areas of application for which this technology is already applied for single metal crown copings and in implant dentistry for substructure fabrication. In the production centers, the so-called laser sintering devices are used to produce crowns and bridge frames from CrCo, Ti, and its alloys. Since the productivity of such devices is very high, dental restorations can be produced very cost-effectively. Basically, geometries are conceivable with this technology that cannot be realized with grinding technology (**Figure 3(a)** and **3(b)**).

6.623.2.2. Dental Ceramics

6.623.2.2.1. Introduction

Dental porcelain dates back to 1774, when A. Duchateau considered the possibility of replacing his ivory teeth with porcelain ones. The most important indication of dental porcelain is in the construction of veneers, inlays, crowns, and for layering of metal or ceramic substructures where the esthetic qualities of

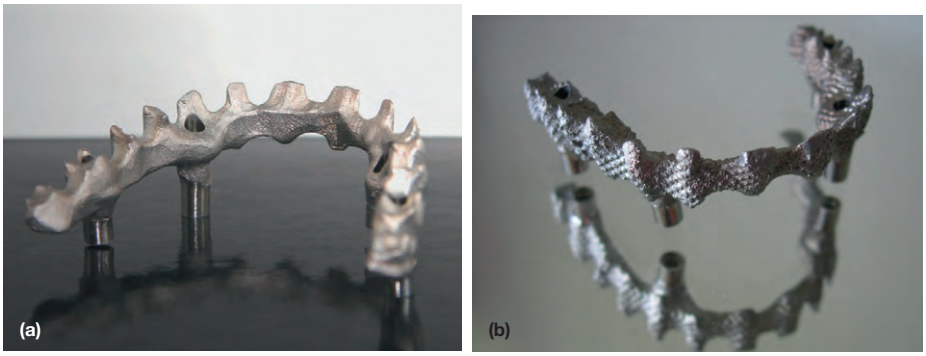

Figure 3 Selective laser melted substructure (Ti) for porcelain veneering (a) and for composite resin veneering (b). Basically, geometries (to mechanically retain the resin) are conceivable with this technology that cannot be realized with grinding technology. Courtesy by Layerwise, Leuven, Belgium.

the porcelain still are superior to that of any other substitute for enamel and dentine, such as dental composites.

Porcelains were the first materials used in the construction of the historical porcelain jacket crown. The latter is today replaced by the all-ceramic restorations because of its high fracture incidence and poor fit (see below). Many new materials did appear on the market over recent years that are described as porcelains, but are in fact very different forms of ceramic when compared with the early porcelains. It is now more appropriate to use the more general description of *dental ceramics*, within which the *dental porcelains* are but one group of materials.[4]

6.623.2.2.2. Dental porcelains

The earliest dental porcelains were mixtures of kaolin, feldspar, and quartz, and were quite different for earthenware, stoneware, and domestic porcelain. It was not until 1838 that E. Wildman produced dental porcelain with the translucency and shades that well matched those of natural teeth. The compositions for domestic porcelain are 50, 20–25, and 25–30% kaolin, quartz, and feldspar, respectively. For dental porcelains, these are 0, 25, and 65%, respectively, which are thus quite different from each other. For dental porcelains, the kaolin was omitted and could be considered to be a feldspathic glass with crystalline inclusions of silica. Kaolin is a hydrated aluminum silicate ($Al_2O\ 2SiO_2\ 2H_2O$) and acts as a binder in domestic porcelains. Quartz remains unchanged during the firing process and acts as a strengthening agent. It is present as a fine crystalline dispersion throughout the glassy phase that is produced by the melting of the feldspar. The feldspar fuses when it melts, forming a glass matrix. The feldspars are mixtures of potassium alumino-silicate ($K_2O\ Al_2O_3\ 6SiO_2$) and sodium alumino-silicate, also known as *albite* ($Na_2O\ Al_2O_3\ 6SiO_2$). Feldspars are naturally occurring substances, so the ratio between the potash (K_2O) and the soda (Na_2O) will vary somewhat. This affects the properties of the feldspar, in that the soda tends to lower the fusion temperature and the potash increases the viscosity of the molten glass. Typical oxide composition of a dental porcelain is; 63, 17, 7, 7, 4, and 2 wt% for silica, alumina, boric oxide, potash, soda, and other oxides, respectively.[5]

Dental porcelain powders are mixtures with additional metal oxides that are fused and then quench the molten mass in water. The resultant product is known as a *frit*, and the process as *fritting*. A consequence of the rapid cooling is that large internal stresses build up in the glass, resulting in extensive cracking. This material can be ground very easily to produce a fine powder for use by the dental technician. Besides, metal oxides, which provide the wide variety of colors of the porcelain, are added too. For example, oxides of iron, copper, titanium, and cobalt act as a brown, green, yellowish-brown, and blue colors, respectively.

6.623.2.2.3. Processing of dental porcelains

The production of the historically – no any longer used – porcelain crown (jacket crown), involves three technical stages namely: compaction, firing, and glazing. It will be used to explain the procedure because the principles remain the same when firing, for example, veneer porcelain onto a substructure (see below).

6.623.2.2.3.1. Compaction

To veneer the jacket crown, the porcelain mixture of powder and water is applied onto the die coated with a platinum foil to support the porcelain during firing in the oven. This follows in a number of ways such as: by spatulation, by brushing, by whipping, or vibrating, all of which are aimed at compacting the powder. The objective of these condensation techniques is to remove as much water as possible. Then the substrate is brought to the furnace. Conventionally, three basic types of porcelain powder are used. These are an opaque shade to mask the color of the underlying structure (e.g., tooth core). Then a dentine shade is applied and finally an enamel shade. A binder helps to hold the particles together as the material is very fragile in this so-called *green state*.

6.623.2.2.3.2. Firing

Initially, the porcelain is heated slowly in the open entrance to the furnace. This is carried out in order to evacuate excess water to avoid steam forming. Once the compact has been dried, it is placed in the furnace and the binders are burnt out. Some contraction occurs during this stage. A large contraction takes place during this phase (~20 vol%), and the resultant material is virtually nonporous. If the porcelain should remain in the furnace for too long, it will lose form due to *pyroplastic flow* (flow of the molten glass) and will become highly glazed.



Figure 4 An example of a finished jacket crown.

A very slow cooling rate is essential in order to avoid the possibility of cracking or crazing.

6.623.2.2.3.3. Glazing

There will always be some porosity in the porcelain, with small air voids being exposed at the surface. These will favor adhesion of bacteria and oral fluids and act as potential sites for the plaque build-up. To avoid this, the surface is glazed to produce a smooth, shiny, and closed outer layer. An example of a finished jacket crown is shown in Figure 4.

6.623.2.2.4. Properties of dental porcelain

Dental porcelain is chemically very stable, and does not deteriorate with time. The thermal conductivity and the coefficient of thermal expansion are similar to those of enamel and dentine. Thus in the presence of a good marginal seal, marginal percolation is less likely to be a problem. Although the compressive strength of dental porcelain is high (350–550 MPa), its tensile strength is very low (20–60 MPa). The material, being primarily a glass, and thus very esthetic, lacks any fracture toughness. The maximum strain that a glass can withstand is $<0.1\%$. Glasses are extremely sensitive to the presence of *surface microcracks*, and this represents one of the major drawbacks in the use of dental porcelain. The answer is to provide a high-strength support for the porcelain and nowadays a number of different systems became available (see Sections 6.623.2.2.5 and Sections 6.623.2.4).

6.623.2.2.5. Classification of modern dental ceramics

One of the most serious drawbacks with the early dental porcelains described above was their lack of strength and toughness, which seriously limited their use. To overcome the problem, there are two possible solutions. One solution is to provide the dental porcelain with support from a stronger substructure. The other option is to produce ceramics, which are stronger and tougher.[5] In this context, it is possible to consider dental ceramics to fall into three categories based on the nature of the *supporting* structure:

- Ceramo-metals
- Reinforced ceramic core systems
- Resin-bonded ceramics

In each case, the idea is to provide a high-strength supporting structure for the veneering ceramic providing the esthetic finish. Obviously, the ideal ceramic would have both the strength and the esthetics to perform both functions. In case of the ceramo-metal restoration, the esthetic veneering ceramic is supported by a strong and tough metal. This system is considered in detail in the next section dealing with metal-bounded ceramics. In the case of the reinforced ceramic core systems, the support for the esthetic veneering ceramic is provided by another ceramic material, which has the necessary high strength and toughness but may lack the desired esthetics. The various options using this approach are explored in the chapter dealing with all-ceramic restorations. In case of the resin-bonded ceramic, the support of the ceramic is provided by the tooth structure itself by bonding the esthetic ceramic directly to the enamel and dentine. In this instance, the ceramic provides the necessary esthetics and the strength is provided by the ability to bond to the tooth tissues. For resin-bonded ceramic restorations, success depends on the *quality of the bond*, since bond failure will lead to a loss of support of the ceramic restoration and eventually result in fracture of the ceramic restoration. This approach only became possible with the advent of enamel- and dentine-bonding procedures.

6.623.2.3. Ceramo-Metals

6.623.2.3.1. Introduction

A major limitation with the dental porcelains such as the feldspathic glasses was their lack of strength. For ceramic restorations the presence of microcracks on the fitting surface is a major source of weakness. A possibility to overcome the latter is bonding the ceramic to a metal substrate such that these microscopic cracks are effectively eliminated, with the consequence that the structure is considerably stronger. This is the basic premise behind the metal-bonded system also called ceramo-metal restorations. The significant breakthrough came by Weinstein *et al.*, in 1962, where they explained how it is possible to get a feldspathic glass to bond to an alloy surface by the inclusion of leucite crystals. The latter were added so as to ensure that the coefficient of thermal expansion of the ceramic closely matched that of the metal (see Section 6.623.2.3.2).

The crown/bridge consists of a cast metal coping/substructure onto which a veneering ceramic is fired (Figure 5(a) and 5(b)). If a proper bond is created, then the internal cracks are eliminated as the metal presents a barrier to the propagation of cracks by virtue of its high fracture toughness. One of the most likely modes of failure with this system is the separation of the ceramic from the metal due to an interfacial breakdown of the ceramo-metal bond. The success of the system depends upon the quality of this bond. An important contributory factor to the ability to bond the ceramic to the metal is the degree for a mismatch between the coefficients of expansion of the ceramic and the metal. If the mismatch is too great then stresses will build up during the cooling process after firing. These stresses can be sufficient to result in crazing or cracking of the ceramic.[5] The issues of the bond and the coefficients of expansion both require careful consideration. Three mechanisms are involved in the bond: mechanical retention, compression fit, and chemical bonding.

The composition of the ceramic for ceramo-metal restorations needs to be different from that of the ceramic used for all-ceramic restorations. The coefficient of thermal expansion (α) of the feldspathic glasses used in the construction of the porcelain jacket crowns is 7–8 ppm $^{\circ}C^{-1}$. This is far too low to be

compatible with the alloys, which are in the region of 14–16 ppm °C^{-1}. This mismatch would give rise to serious problems due to excessive differential shrinkage on cooling. The best combination of metal and ceramic is one where the coefficient of expansion of the ceramic is only slightly lower than that of the metal.[6] In fact the flexural strength of the ceramics used for ceramo-metal restorations is only of the order of 30–50 MPa. Hence the ceramic build-up on the metal framework should not be too thick as this can lead to ceramic fractures when loaded in the mouth. The general recommendation is that the ceramic thickness should not exceed 1–1.5 mm.

An increase in the number and size of the leucite crystals can occur when firing the ceramic onto the metal. In case of multiple firings, this will increase the coefficient of expansion of the ceramic. Such an increase can compromise the compatibility of the metal and the ceramic.

6.623.2.3.2. Choice of ceramo-metal alloys

The requirements for alloys used in the metal-bonded ceramic system are somewhat different from those for the all-metal constructions. As it is necessary to fire ceramic onto the surface of the metal, its high melting temperature must be higher than the sintering temperature for the ceramic. If the melting temperature of the metal is too close to the firing temperature of the ceramic, partial melting of thin sections of the coping may occur, or the coping may deform. Especially in the construction of long-span bridges, the metal must have a high elastic modulus and high yield stress. The resultant high stiffness of the bridge structure will prevent the occurrence of excessively high strains (that the ceramic cannot cope with) on occlusal loading. In addition, a low stiffness of the metal framework can result in distortion due to the differential contraction stresses that are generated on cooling after porcelain firing. Formerly, only high-gold alloys were available, but, with the rising cost of gold, a variety of alternative alloys have been developed, which may be classified as high-gold, gold–palladium, high-palladium, palladium–silver, nickel–chromium alloys, or cpTi.[7]

6.623.2.3.2.1. High-gold alloys

For the high-gold alloys, the melting temperature is raised by the addition of platinum and palladium, both of which have a high melting temperature. Compositions of a representative commercial example are presented in Table 2.

6.623.2.3.2.2. Gold–palladium alloys

The performance of Au–Pd alloys is comparable to that of the high-gold alloys in terms of castability, accuracy of fit, and corrosion resistance. Compositions of a representative commercial example are shown in Table 3.

6.623.2.3.2.3. High-palladium alloys

These alloys are primarily palladium, with small additions of other elements, such as copper, gallium, and tin and have become very popular in the last 30 years. The alloys are contraindicated for long-span bridges because the sag resistance can be poor due to excessive creep on ceramic firing.

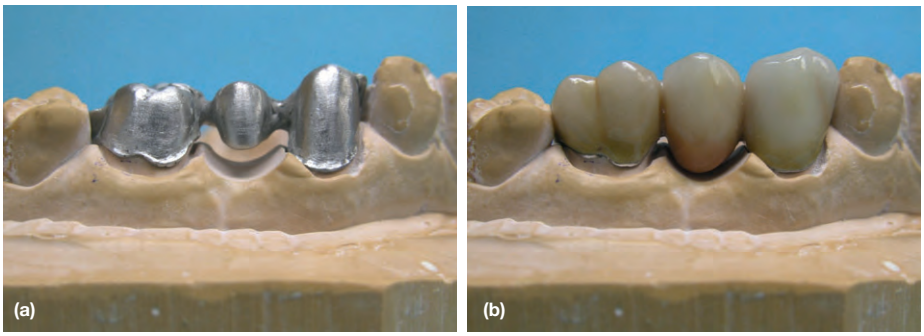

Figure 5 Metal substructure for porcelain veneering (a) and de porcelain veneered three-unit posterior bridge (b).

Table 2 Composition, physical, and mechanical properties of a representative commercial example of a high-gold alloy for porcelain veneering (BioEthic®, Cendres & Métaux SA, Biel, Switzerland)

Composition	*Au*	*Pt*	*Zn*	*Rh*	*Ta*	*In*	*Sn*	*Ag*	*Ir*
	86.7%	10.75%	1.5%	0.4%	0.3%	0.2%	0.1%	0.03%	0.02%

Physical properties	*Melting range*	*Density*	*Young's modulus*	*Coefficient of thermal expansion*
	1030–1150 °C	18.9 g cm^{-3}	88 kN mm^{-2}	(25–500 °C) 14.5 μm mK^{-1} (25–600 °C) 14.8 μm mK^{-1}

Mechanical properties	*Vickers hardness*	*Tensile strength (N mm^{-2})*	*0.2% proof stress (N mm^{-2})*	*Elongation (%)*
As cast	190	550	435	5.5
Soft	95	350	180	29.5
Hardened	220	655	525	6.0
After firing	220	655	525	6.5

6.623.2.3.2.4. Palladium–silver alloys

The Pd–Ag alloys have the most favorable elastic modulus of all of the precious metal alloys, producing castings with low flexibility and a reduced tendency to sag on porcelain firing. Owing to the presence of high amounts of silver, there is concern that porcelain discoloration may occur. The composition and the properties of such a representative alloy are presented in Table 4.

6.623.2.3.2.5. Cobalt–chromium alloys

The CoCr alloys are very stiff as their elastic modulus can be some 2.5–3 times higher than that of the high-gold alloys. They are indicated for the construction of long-span bridges as they provide greater rigidity, and because of the high melting temperature, there is less potential for sag during firing. Those days CAD–CAM produced frameworks may overcome this shortcoming. Also clinical experience would indicate that the ceramic to metal bond is not as reliable as for the other alloys although this is improved by gaining more experience over the years. The biocompatibility of Ni–Cr alloys, formerly used, has long been a matter of concern because of allergy reactions. That is why Ni-free alloys came into the market. Four to six percent wolfram was additionally added. The compositions of such an alloy are shown in Table 5.

6.623.2.3.2.6. Commercially pure titanium

Titanium has become popular for ceramo-metal restorations because of its good corrosion resistance, excellent biocompatibility, low weight, and relatively low cost compared to the

Table 3 Composition, physical, and mechanical properties of a representative commercial example of low-gold alloy (Esteticor Prisma®, Cendres & Métaux SA, Biel, Switzerland)

Composition	*Au*	*Pd*	*Ag*	*In*	*Ga*	*Ru*
	6.0%	75.0%	6.5%	6.0%	6.0%	0.5%

Physical properties	*Melting range*	*Density*	*Young's modulus*	*Coefficient of thermal expansion*
	1120–1310 °C	11.6 g cm^{-3}	120 kN mm^{-2}	(25–500 °C) 13.9 μm mK^{-1}(25–600 °C) 14.3 μm mK^{-1}

Mechanical properties	*Hardness*	*Tensile strength (N mm^{-2})*	*0.2% proof stress (N mm^{-2})*	*Elongation (%)*
As cast	255	880	545	34.5
After firing	250	850	550	40.0

Table 4 Composition, physical, and mechanical properties of a representative commercial example of palladium–silver alloy for porcelain veneering (Esteticor Actual®, Cendres & Métaux SA, Biel, Switzerland)

Composition	*Pd*	*Ag*	*Sn*	*Ru*
	53.6%	37.6%	8.6%	0.2%

Physical properties	*Melting range*	*Density*	*Young's modulus*	*Coefficient of thermal expansion*
	1190–1270 °C	11.2 g cm^{-3}	122 kN mm^{-2}	(25–500 °C) 14.8 μm mK^{-1}(25–600 °C) 15.1 μm mK^{-1}

Mechanical properties	*Hardness*	*Tensile strength (N mm^{-2})*	*0.2% proof stress (N mm^{-2})*	*Elongation (%)*
As cast	240	775	525	17.0
After firing	225	785	520	24.5

Table 5 Composition, physical, and mechanical properties of a representative commercial example of a cobalt–chromium alloy for porcelain veneering (Wirobond® C, BEGO GmbH, Bremen, Germany)

Composition	*Co*	*Cr*	*Mo*	*W*	*Si*	*Fe*	*Ce*	*C*
	61%	26%	6%	5%	1%	0.5%	0.5%	max 0.02%

Physical	*Melting range*	*Density*	*Young's modulus*	*Coefficient of thermal expansion*
	1270–1380 °C	8.5 g cm^{-3}	210 kN mm^{-2}	(25–500 °C) 14.0 μm mK^{-1}(20–600 °C) 14.2 μm mK^{-1}

Mechanical properties	*Hardness*	*Tensile strength (N mm^{-2})*	*0.2% proof stress (N mm^{-2})*	*Elongation (%)*
As cast	–	914	480	12
After firing	310	920	493	15

precious metal alloys. When titanium is cast, a reaction layer with a thickness of 50–100 μm forms on the surface of the casting due to an interaction between the titanium and the refractory investment. Even if the casting problems can be avoided by producing the restorations using an alternative technique, such as spark erosion and copy-grinding, titanium has a high chemical reactivity and if taken above 800 °C during porcelain firing, this gives rise to a thick oxide coating, with the consequence of a weak bond to the ceramic. The bonding of the ceramic to cpTi is problematic and the bond strength is not as good as that obtained to the alloys. Unlike the alloys described above, titanium has a coefficient of expansion of 9.6 ppm $°C^{-1}$. Thus the leucite-containing ceramics developed for the ceramo-metal alloys are inappropriate and it is important that ceramics specially designed for use with cpTi are used.[8]

6.623.2.4. All-Ceramic Restorations: High-Strength Core Ceramics

6.623.2.4.1. Introduction

Land, in the early 1900s, and others since then had shown that one of the problems with the porcelain jacket crown was that the porcelain would fracture from the fit surface outward. Some improvements in the strength of porcelain were achieved by the introduction of vacuum-firing furnaces, but the search was on for a core material that would provide the necessary strength and toughness to prevent fractures arising from cracks propagating from the fit surface of the crown.

Since ceramics tend to fail at the same critical strain of 0.1%; one means of achieving an increase in fracture strength is to increase the elastic modulus of the material. If, at the same time, the propagation of cracks is made more difficult such that a greater strain can be supported, a higher strength ceramic will result. The flexural strengths of a number of ceramics are: 800–900, 400–750, 640, and 420–520 MPa for hot-pressed silicon and carbide, partially sintered zirconia, and alumina 98% pure, respectively. Alumina and zirconia are white and strong and therefore these ceramics are now used in a number of dental ceramic systems.

McLean and Hughes, in the mid-1960s developed a core material based on the reinforcement of a feldspathic glass with alumina, commonly referred to as the alumina-reinforced porcelain jacket crown. Since then, other systems have been developed. A major contributor to the development of glass ceramics was Dicor (Dentsply Int, York, PA). This was a glass-ceramic material composed of 70% tetrasilicic fluormica crystals precipitated in 30% glass matrix and is no longer available today. In the 1980s, the glass-infiltrated high-strength ceramic *cores* were developed (In-Ceram, Vita), and in the 1990s, the pure alumina core made its first appearance (e.g., Procera AllCeram, Nobel Biocare). Recently yttria-stabilized zirconia for the fabrication of cores for crown and bridge framework was introduced.

6.623.2.4.2. Core materials

6.623.2.4.2.1. Silica-based ceramics

The alumina-reinforced feldspathic core introduced in the early 1960s consists of a feldspathic glass containing 40–50% alumina. The alumina particles are far stronger than the glass, and are more effective at preventing crack propagation than quartz and act as crack stoppers. Whereas the flexural strength of feldspathic porcelain is, at best, some 60 MPa, this is raised to 120–150 MPa for the aluminous core porcelains. In the construction of a crown, the opaque shade is made with an aluminous core porcelain. It is still necessary to use the weaker dentine and enamel shades of the feldspathic veneering porcelains. The main indication of the alumina-reinforced porcelain jacket crown, but today hardly used anymore, was for the restoration of the anterior teeth.

Ivoclar Vivadent (Schaan, Liechtenstein) developed the lithium disilicate glass ceramic (SiO_2–Li_2O) (IPS Empress 2, Ivoclar Vivadent) in the 1990s. It is fabricated through a combination of the lost-wax and heat-pressed techniques. A glass-ceramic ingot of the desired shade is plasticized at 920 °C and pressed into an investment mold under vacuum and pressure. IPS Empress 2 has improved flexural strength by a factor of 3 over the original IPS Empress which is a leucite-reinforced glass ceramic (SiO_2–Al_2O_3–K_2O), and can be used for three-unit bridges in the anterior area as well. The framework is veneered with fluoroapatite-based veneering porcelain (IPS Eris; Ivoclar Vivadent), resulting in a semitranslucent restoration with enhanced light transmission. IPS e.max Press (Ivoclar Vivadent) was introduced in 2005 as an improved press-ceramic material compared to IPS Empress 2. It also consists of a lithium disilicate pressed glass ceramic, but its physical properties and translucency are improved through a different firing process.

6.623.2.4.2.2. Infiltration ceramics

The addition of alumina to the feldspathic glass during the prefritting process limits the amount of alumina that can be incorporated to about 40–50 vol%. An alternative approach has been adopted in a new system called In-Ceram (Vita Zahnfabrik, Bad Säckinge, Germany). This core material has an alumina content of ~85%. The procedure consists of a ceramic core that is formed onto a refractory die from a fine slurry of alumina powder by a process known as slip-casting. After the die has dried it is sintered for 10 h at 1120 °C. The melting temperature of alumina is too high to produce full densification of the powder by liquid-phase sintering and only solid-phase sintering occurs. Consequently, the coping thus created is only just held together at the contact points between the alumina particles and a porous structure is the result. The strength of this porous core is only about 6–10 MPa. The porous structure is then infiltrated with a *lanthanum* glass, which has a low viscosity when fired at 1100 °C for 4–6 h. The molten glass is able to penetrate into the pores, producing a dense ceramic, the reason why these are also called glass-infiltrated high-strength ceramics. The esthetics and functional form are then achieved by veneering the core with conventional feldspathic veneering porcelains. Very high flexural strength values (400–500 MPa) have been claimed for this core ceramic, which makes this system suitable for anterior and posterior crowns, with excellent results. Several attempts have also been made at producing anterior cantilever and posterior three-unit bridges, which is a highly ambitious use of ceramics, but show considerable promise.

A similar approach has been adopted with *spinel* ($MgAl_2O_4$) replacing the alumina. The InCeram–Spinel offers superior esthetics over the InCeram–Alumina at a slightly reduced flexural strength (~350 MPa) and is recommended for inlays and anterior crowns.

The InCeram–Zirconia is based on the InCeram–Alumina, but with the addition of 33 wt% *zirconia* and produces a ceramic core with a strength of some 700 MPa. Its drawback is that the combination of a glass, alumina, and zirconia means that this core material is very opaque and not popular those days.

6.623.2.4.2.3. Pure alumina cores (see Chapter 1.105, Alumina)

There are several systems on the market that offer pure alumina cores. The potential advantages are increased strength and superior translucency compared with the glass-infiltrated core materials. A production example, of for example, the Procera AllCeram core (Nobelbiocare, Gothenburg, Sweden), involves producing a die from the impression, digitizing the geometry of the desired coping using specially designed computer software, and transferring this information down a modem to a centralized plant. This is all done by a designated dental laboratory. The coping is produced by a special process, which involves sintering 99.5% pure alumina at 1600–1700 °C such that it is fully densified. The coping is then returned to the dental laboratory for building on the crown's esthetics using compatible feldspathic veneering porcelain. The flexural strength of the Al_2O_3 core materials is in the order of 700 MPa and thus similar to that achieved with the InCeram–Zirconia. One of the potential benefits of producing a pure alumina core is that the *translucency* is improved compared to that of the glass-infiltrated alumina composite structures.

6.623.2.4.2.4. Zirconia core systems (see Chapter 1.106, Zirconia as a Biomaterial)

The reason zirconia became popular those days is due to the high strength of this material, which is in excess of 1000 MPa. The actual material used is yttria-stabilized zirconia and the yttria plays a very important function, although it is only there in a small amount (~3.0 mol%). Under normal circumstances, zirconia forms a stable monoclinic crystal structure at room temperature, but the addition of a small amount of yttria results in the formation of a metastable tetragonal crystal structure at room temperature. When a small defect such as a crack is present, it progresses through the material due to the localized stress at the crack tip being relieved by crack growth. As mentioned earlier, the way to improve ceramics is to prevent cracks from growing and in the case of yttria-stabilized zirconia, when the stress at the crack tip reaches a certain level, the metastable tetragonal crystal structure of zirconia transforms to the more stable monoclinic form. This stress-induced change in structure is accompanied by an expansion of the material, which causes the crack tip to close up and thus prevent it from advancing. Hence, it is very difficult for a crack to advance through an yttria-stabilized zirconia ceramic. In fact, the material is not only very strong but also very tough by comparison with other ceramics. It is this particular feature of zirconia that makes it possible to contemplate using this material not only as a core for crowns but also for bridge frameworks.

Until CAD–CAM became available it was inconceivable to consider the use of zirconia (ZrO_2) as a material for the construction of crowns and bridges, largely because a zirconia powder would not densify until reaching a temperature in excess of 1600 °C, making it impractical as a dental laboratory material. Because zirconia is so strong and tough, the most common approach used to deal with this is a technique often referred to as 'soft' machining. In this method, the restoration is machined from a porous blank, which is easy to machine and once the desired shape has been achieved the coping is fired in a furnace to cause the material to densify. The shrinkage that occurs, typically some 20 vol%, is taken care of during the computer-aided design process. The result is a very close-fitting, white core or bridge framework (**Figure 6**).

On the short run, zirconia-ceramic bridges exhibited a similar 3-year survival rate to ceramo-metal.[9] Chipping of the veneering porcelain seems to be higher in zirconia- versus ceramo-metal-veneered restorations. Although zirconia-based restorations are widely used those days, their susceptibility to hydrothermal degradation remains elusive. CAD–CAM machined surfaces initially exhibited superior hydrothermal degradation resistance, but deteriorated at a faster rate upon prolonged autoclave treatment compared with ground and grit-blasted surfaces. The accelerated hydrothermal degradation of CAD–CAM surfaces is attributed to the machining damage and the absence of surface compressive stresses in the fully sintered material. Clinical relevance for surface treatments of zirconia frameworks in terms of hydrothermal and structural stabilities still has to be addressed.[10]

6.623.2.4.2.5. Drawback of high-strength core systems

One drawback with all the high-strength core systems described above is that none of them are amenable to acid etching to produce a micromechanically retentive surface, although some bonding with the cementing medium will arise due to the roughness of the surface from processing. Since the fit surface is made up largely of alumina and/or zirconia rather than silica, no coupling agents are currently available that can effectively bond the core to resins. Without

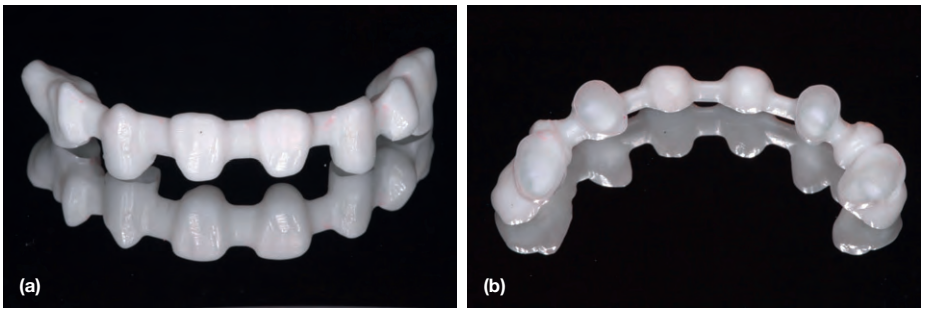

Figure 6 An example of a ZrO_2-milled substructure of a eight-unit bridge on teeth to be veneered with porcelain top (a) and bottom (b) view.

an effective coupling agent or an ideal micromechanically retentive surface, these systems cannot be resin-bonded to the tooth tissues and will not derive the added benefit associated with resin-bonded ceramic restorations. The reinforced core ceramic restoration must rely primarily on the strength and toughness of the core material and appropriate design in terms of retention and resistance of the tooth preparation to resist the forces of occlusion. However, recent work has shown that gridblasting the core with 50 µm grid at 1 bar combined with an adhesive luting cement (Panavia Ex and 21, Kuraray) do form a stable bond in time with the tooth enamel. This is why ZrO_2 is currently being explored to adhesively bond wings.[11]

The introduction of CAD–CAM technology to manufacture copings and bridge frames has been having a profound influence on the choice of the materials used. The next paragraph will deal with the principles of CAD–CAM generated restorations in dentistry.

6.623.2.5. CAD–CAM in Dentistry

6.623.2.5.1. Definition

The term CAD–CAM does not provide any information on the method of fabrication. All CAD–CAM systems consist of three components:

- A digitalization tool/scanner that transforms the geometry into digital data that can be processed by the computer.
- Software that processes data and, depending on the application, produces a data set for the product to be fabricated.
- A production technology that transforms the data set into the desired product.

6.623.2.5.2. CAD–CAM concepts in dentistry

Depending on the location of the CAD–CAM devices, three different production concepts are available: chair-side production, laboratory production, and centralized fabrication in a production center.[12]

6.623.2.5.2.1. Chair-side production

All components of the CAD–CAM system are located in the dental surgery. Fabrication of dental restorations can thus take place chair side without a laboratory procedure. The digitalization instrument is an intraoral camera, which replaces a conventional impression with elastomers in most situations. This saves time and offers the patient indirectly fabricated restorations at one appointment. An example is the Cerec® System (Sirona, Gemany). Since the Cerec® system functions with water cooling, a variety of materials can be processed, from glass-ceramics to high-performance oxide ceramics. Scientific literature reported success rates for CAD–CAM produced inlays of 90% after 10 years and 85% after 12 and 16 years.[13,14] Historically, this system was the first CAD–CAM system in dentistry and is currently available in its third generation.

6.623.2.5.2.2. Laboratory production

This variant of production is equivalent to the traditional working sequence between the dentist and the laboratory. The dentist sends the impression to the laboratory where a master cast is fabricated first. The remaining CAD–CAM production steps are carried out completely in the laboratory. With the assistance of a scanner, three-dimensional data are produced on the basis of the master die. These data are processed by means of dental design software. After the CAD-process, the data are transferred to a grinding device that produces the real geometry in the dental laboratory. Finally, the exact fit of the framework can be evaluated and, if necessary, corrected on the basis of the master cast. The ceramist carries out the veneering of the frameworks in a powder-layering technique.[15,16]

6.623.2.5.2.3. Centralized production

The third option of computer-assisted production of dental prostheses is centralized production in a grinding center. In this variation, it is possible for satellite scanners in the dental laboratory to be connected with a production center via the Internet. Data sets produced in the dental laboratory are sent to the production center for the restorations to be produced with a CAD–CAM device. Finally, the production center sends the restoration to the responsible laboratory. Thus, production components 1 and 2 take place in the dental laboratory, while the third one takes place in the production center.[17] As a result, the configuration of the restoration remains in the hands of the dental technician. The benefit of outsourcing CAM production is found in its small investment requirement, since only the digitalization tool and software have to be purchased, while still assuring a high-quality production process.

In addition, this procedure results in greater independence, since there is no relation to a particular production technology (e.g., grinding technology). It must, however, be noted that presently almost all CAD–CAM systems are only available as closed systems. In other words, if one acquires a scanner from one manufacturer, this implies, in the case of a closed system, that there is only access to that manufacturer's processes and line of products. Many production centers also offer, to smaller laboratories without a scanner, the possibility of sending the master cast to the production center for scanning, designing, and fabrication. The additional veneering of the frameworks for prosthetic restorations is still carried out in the dental laboratory.

6.623.2.5.3. CAD–CAM components

6.623.2.5.3.1. Scanner

In the area of dentistry, the term scanner implies data collection tools that measure the jaw and tooth structures three-dimensionally and transform them into digital data sets. Basically there are two different scanning possibilities, optical and mechanical. The latter is not much in use in the market today. The basis of the optical scanner is the collection of three-dimensional structures in, for example, a triangulation procedure or other. Here, the source of light (e.g., laser) and the receptor unit are in a definite angle in their relationship to one another. Through this angle the computer can calculate a three-dimensional data set from the image on the receptor unit.[18] Either white light projections or a laser beam can serve as a source of illumination. Until recently, dental scanners were aimed at scanning the plaster die or model. Recently, laboratories have been offered the possibility to scan the impression directly eliminating the plaster cast as an important potential source of error by means of the so-called conoscopic holographic principle (NobelProcera scanner, Nobel Biocare, Zürich, Switzerland). A further simplification in CAD–CAM production consists of intraoral data collection (intraoral

scanning) or the so-called 'digital impression taking.' This means a digitalization of what is now only an analog step through an elastomer impression technique transferred into a plaster cast or die. This could lead to an additional improvement in quality and cost reduction. Currently these systems have become available in the market (e.g., Lava Cos, 3MEspe).

6.623.2.5.3.2. Design software

Special software is provided by the manufacturers for the design of various kinds of dental restorations.[19] The software of CAD–CAM systems presently available in the market is continuously being improved. The data of the construction can be stored in various data formats, often standard transformation language (STL) data.[18] Many manufacturers, however, use their own data formats, specific to that particular manufacturer, with the result that data of the construction programs are not compatible with each other.

6.623.2.5.4. Materials to be processed on dental CAD–CAM devices

6.623.2.5.4.1. Metals

At present, titanium, titanium alloys, and chrome cobalt alloys are processed using dental grinding devices. The grinding of precious metal alloys has been shown to be of no economic interest, due to the high metal attrition and the high material costs.

6.623.2.5.4.2. Resin materials

On the one hand, resin materials can be used for the grinding of lost-wax frames for casting technology; on the other hand, it is possible to use resin materials directly as crown and bridge frameworks for long-term provisional or for full anatomical long-term temporary prostheses.

6.623.2.5.4.3. Silica-based ceramics

Grindable silica-based ceramic blocks are offered by several CAD–CAM systems for the production of inlays, onlays, veneers, partial crowns, and full crowns (fully anatomical, anatomically partially reduced). A machinable feldspathic porcelain Vita Mark II (VITA Zahnfabrik, Bad Sackingen, Germany), introduced in 1991 for the CAD–CAM CEREC 1 system (Siemens AG, Bensheim, Germany), has improved strength and finer grain size (4 μm) as compared to the Vita Mark I. It is primarily composed of SiO_2 (60–64%) and Al_2O_3 (20–23%) and can be etched with hydrofluoric acid to create micromechanical retention for adhesive cementation with composite resin cements. In addition to monochromatic blocks, various manufacturers now offer blanks with multicolored layers (Vitablocs TriLuxe (Vita), IPS Empress CAD Multi (IvoclarVivadent)), for the purpose of full anatomical crowns. Owing to their higher stability values, lithium disilicate ceramic blocks are particularly important in this group; they can be used for full anatomical anterior and posterior crowns, for copings in the anterior and posterior region, and for three-unit bridge frameworks in the anterior region due to their high mechanical stability of 360 MPa.[20] Glass ceramics are particularly well suited to chair-side application as a result of their translucent characteristics, similar to that of natural tooth structure; they provide esthetically pleasing results even without veneering. As a result of their relatively high portion of glass, these ceramics are, in contrast to oxide ceramics, etchable with hydrofluoric acid and thus can be inserted very well using adhesive systems.[21]

6.623.2.5.4.4. Infiltration ceramics

Grindable blocks of infiltration ceramics are processed in a porous, chalky condition and then infiltrated with lanthanum glass. All blanks for infiltration ceramics originate from the Vita In-Ceram system (Vita) and are offered in three variations. Vita In-Ceram Alumina (Al_2O_3), is suitable for crown copings in the anterior and posterior region, three-unit bridge frameworks in the anterior region.[22] Vita In-Ceram Zirconia (70% Al_2O_3, 30% ZrO_2), is suitable for crown copings and three-unit bridge frameworks in the posterior region. VITA In-Ceram Spinell ($MgAl_2O_4$), has the highest translucency of all oxide ceramics and is thus recommended for the production of highly esthetic anterior crown copings, in particular in vital abutment teeth and in the case of young patients.

6.623.2.5.4.5. Oxide high-performance ceramics

At present, aluminum and zirconium oxide are offered as blanks for CAD–CAM technology.

6.623.2.5.5. Processing

Processing can take place in different density stages.

Green stage processing: Is used on a blank without heat treatment, that is, an object pressed from ceramic powder and binding agents. Since there was no presintering, the object is as soft as chalk. This permits very easy processing, but results, due to the low degree of stability, in great problems in transport and application. Processing is by means of carbide metal grinders without liquid cooling. The green stage has an open porosity, and in firing a 25% linear shrinkage is to be expected. At present, zirconium oxide is not processed as a green stage in any of the CAD–CAM systems on the market.

White stage processing: As a result of the thermal pretreatment, the organic compressing additives have vanished and the blank has an adequate stability. As a result of presintering, the white body has already had shrinkage of approximately 5%. In the case of CAD–CAM production of objects from white bodies, the subsequent shrinkage of some 20% (linear) must be taken into consideration. Processing of white stage can be either with carbide metal grinders without water cooling or with diamond grinders with liquid cooling.[17,23]

Processing in hot isostatic pressing condition: Some systems also process zirconium oxide in HIP (hot isostatic pressed) condition with diamond tools and water cooling. The advantages are: no sinter shrinkage, as a result no sinter distortions, no sinter furnace necessary, and no additional time needed for sintering procedure. The disadvantages are: devices with high rigidity and stability necessary, longer grinding times, resulting in lower utilization of devices, high wear of the cutters.[24,25]

Figure 7 depicts an overview of the different steps in CAD–CAM and its technologies used in dentistry today.[3]

6.623.2.5.6. Reflections

The quality of dental prostheses has improved significantly by means of standardized production processes. This makes very efficient quality management possible. It changed dental laboratories from craftsmanship to modern computerized production centers. CAD–CAM technology has made it

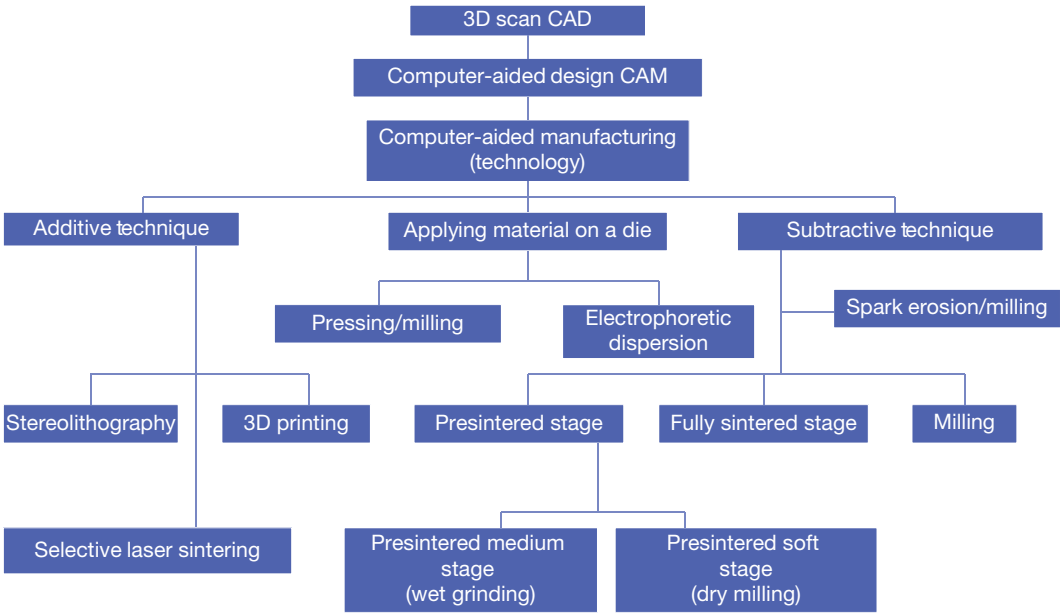

Figure 7 Overview of the different steps in CAD–CAM and its technologies used in dentistry today. Courtesy by Vandenbroucke, B. PhD. Thesis, K.U. Leuven, 2008.

possible to machine interesting new materials such as the high-performance ceramics and titanium with high accuracy. However, the high investment for machines might overextend the budget of smaller laboratories and some applications are limited due to software and production procedures. Overall, CAD–CAM technology has already changed dentistry and will replace more and more of the traditional techniques in fabricating dental restorations.

References

1. Leinfelder, K. F. *J. Am. Dent. Assoc.* **1997**, *128*, 37–45.
2. Andersson, M.; Bergman, B.; Bessing, C.; Ericson, G.; Lundquist, P.; Nilson, H. *Acta Odontol. Scand.* **1989**, *47*, 279–286.
3. Vandenbroucke, B. PhD. Thesis, K.U.Leuven, 2008, p 274.
4. Wildgoose, D. G.; Johnson, A.; Winstanley, R. B. *J. Prosthet. Dent.* **2004**, *91*, 136–143.
5. Van Noort R, *Introduction to Dental Materials*. Mosby Elsevier: London, 2007.
6. Johnson, A. J.; van Noort, R.; Stokes, C. W. *Dent. Mater.* **2006**, *22*, 330–337.
7. Bagby, M.; Marshall, S. J.; Marshall, G. W. *J. Prosthet. Dent.* **1990**, *63*, 21–25.
8. Wang, R. R.; Welsch, G. E.; Monteiro, O. *J. Biomed. Mater. Res.* **1999**, *46*, 262–270.
9. Sailer, I.; Gottnerb, J.; Känel, S.; Hämmerle, C. *Int. J. Prosthodont.* **2009**, *22*, 553–560.
10. Kim, J. W.; Covel, N. S.; Guess, P. C.; Rekow, E. D.; Zhang, Y. *J. Dent. Res.* **2010**, *89*, 91–95.
11. Kern, M.; Barloi, A.; Yang, B. *J. Dent. Res.* **2009**, *88*, 817–822.
12. Beuer, F.; Schweiger, J.; Edelhoff, D. *Br. Dent. J.* **2008**, *10*, 505–511.
13. Reiss, B. *Int. J. Comput. Dent.* **2006**, *9*, 11–22.
14. Sjögren, G.; Molin, M.; van Dijken, J. W. *Int. J. Prosthodont.* **2004**, *17*, 241–246.
15. Lüthy, H.; Filser, F.; Loeffel, O.; Schumacher, M.; Gauckler, L. J.; Hammerle, C. H. *Dent. Mater.* **2005**, *21*, 930–937.
16. Raigrodski, A. J. *Pract. Proced. Aesthet. Dent.* **2005**, *7*, 249–256.
17. Reich, S.; Wichmann, M.; Nkenke, E.; Proeschel, P. *Eur. J. Oral Sci.* **2005**, *113*, 174–179.
18. Mehl, A.; Gloger, W.; Kunzelmann, K. H.; Hickel, R. *J. Dent. Res.* **1997**, *76*, 1799–1807.
19. Reiss, B. *Int. J. Comput. Dent.* **2007**, *10*, 69–75.
20. Sorensen, J. A.; Cruz, M.; Mito, W. T.; Raffeiner, O.; Meredith, H. R.; Foser, H. P. *Pract. Periodontics Aesthet. Dent.* **1999**, *11*, 95–106.
21. Sorensen, J. A.; Munksgaard, E. C. *Eur. J. Oral Sci.* **1995**, *103*, 186–189.
22. Vult von Steyern, P.; Jonsson, O.; Nilner, K. *Int. J. Prosthodont.* **2001**, *14*, 379–384.
23. Sailer, I.; Feher, A.; Filser, F.; Gauckler, L. J.; Lüthy, H.; Hämmerle, C. H. *Int. J. Prosthodont.* **2007**, *20*, 383–388.
24. Tinschert, J.; Natt, G.; Mautsch, W.; Augthun, M.; Spiekermann, H. *Int. J. Prosthodont.* **2001**, *14*, 231–238.
25. Tinschert, J.; Natt, G.; Mautsch, W.; Spiekermann, H.; Anusavice, K. J. *Oper. Dent.* **2001**, *26*, 367–374.

6.624. Cardiac Patch with Cells: Biological or Synthetic

P Akhyari, University of Düsseldorf, Düsseldorf, Germany
M Barth, German Cancer Research Center, Heidelberg, Germany
A Lichtenberg, University of Düsseldorf, Düsseldorf, Germany

© 2011 Elsevier Ltd. All rights reserved.

6.624.1. Native Myocardium: Unique Tissue Properties 368
6.624.1.1. Anatomical Considerations 368
6.624.1.2. Anisotropic Architecture of the Heart 368
6.624.1.3. Coronary Blood Flow 368
6.624.1.4. Electrophysiological Integration 368
6.624.1.5. Physiologic Cellular and ECM Turnover 369
6.624.2. Clinical Indications for Myocardial Patch Repair 370
6.624.2.1. Congenital Malformations 370
6.624.2.1.1. Atrial septal defect 370
6.624.2.1.2. Ventricular septal defects and tetralogy of Fallot 370
6.624.2.1.3. Hypoplastic left heart syndrome and functional single ventricle 371
6.624.2.2. Acquired Heart Disease 372
6.624.2.2.1. Coronary heart disease 372
6.624.2.2.2. Dilatative myocardial dysfunction 372
6.624.2.2.3. Other forms of cardiomyopathy 373
6.624.3. Patch Materials in Current Clinical Use 373
6.624.3.1. Autologous Pericardium 373
6.624.3.2. Xenogenic and Decellularized Xenogenic Pericardium 374
6.624.3.3. Synthetic Polymers 374
6.624.4. Experimental Synthetic Polymers 375
6.624.5. Strategies for Myocardial Tissue Engineering 375
6.624.5.1. *In Vitro* Construction of 3D Structures with Cardiomyogenic Characteristics 376
6.624.5.2. Commonly Used Cell Sources 376
6.624.5.3. Solid or Gelling Scaffold Components: Some Considerations 377
6.624.5.4. From Diffusion to Perfusion 377
6.624.5.5. Controlled Stimulation by a Cellular Workout Program 379
6.624.5.6. Pacing for a Better Cardiac Patch 380
6.624.6. *In Vivo* Maturation of a Cardiac Patch 381
6.624.6.1. Experimental Transmural Ventricular Replacement 381
6.624.6.2. Experimental Ventricular Support by Patch Material 383
6.624.7. Scientific Frontiers 385
6.624.8. Clinical Relevance and Perspectives 386
6.624.9. Summary 386
References 386

Abbreviations

ASD	Atrial septal defect
CHD	Coronary heart disease
DNA	Deoxyribonucleic acid
EC	Endothelial cell
ECM	Extracellular matrix
ESC	Embryonic stem cell
HOCM	Hypertrophic obstructive cardiomyopathy
iPS	Induced pluripotent stem cells
LAD	Left anterior descending artery
MI	Myocardial infarction
MMP	Matrix metalloprotease
PEG	Poly(ethylene glycol)
PEUU	Polyester urethane urea
PGA	Poly(glycolic acid)
PTFE	Polytetrafluoroethylene
RGD	Arginine-glycine-aspartic acid
RVOT	Right ventricular outflow tract
VSD	Ventricular septal defect

6.624.1. Native Myocardium: Unique Tissue Properties

6.624.1.1. Anatomical Considerations

The human heart consists of four chambers that are functionally organized in two different units. Each unit consists of an atrium, a ventricle, and two heart valves that ensure the unidirectional blood flow through the heart. In the human body, the blood flow passes through a circuit where a pulmonary circulation and a systemic circulation are arranged in a serial order. The venous blood that returns from the peripheral organs, such as musculature, gastrointestinal organs, and the brain, is directed via the venous system toward the right atrium. Blood that returns after capillary passage through the myocardium itself also arrives in the right atrium where the pooled blood volume enters the cardiac cavity. Further blood flow leads through the tricuspid valve into the right ventricle, from where blood is ejected through the pulmonary valve into the pulmonary artery and the branching vessels. After gas exchange in the pulmonary system, the oxygen-saturated blood returns into the left atrium, which fulfill the function of a blood pooling cavity, similar to the right atrium. Through the mitral valve, a further transport of the blood takes place, first into the left ventricle and from there through the aortic valve into the aorta and the main systemic arteries.

6.624.1.2. Anisotropic Architecture of the Heart

A specific anisotropic arrangement of the myocardial fibers accounts for a highly efficient contractile function of the heart. The contraction of cardiomyocytes as well as their multicellular aggregates is potentiated by the spatial distribution and orientation of the individual myocardial fibers, which display a twisted assembly. There has been an ongoing debate on the functional role of the specific anatomical design of the heart and the history of scientific disquisition on the helical structure of the myocardial muscle is long lasting with current pertinence.[1] The unique structural plan of the heart that already exists throughout the prenatal development and persists during the postnatal life is characterized by an anisotropy, a distinct feature of the myocardium that helps to generate a level of myocardial force that may not be explained by the power of the myocardial subunits (e.g., cardiomyocytes or myocardial fibers) and their collective wrap up on isolated examination. What certainly works as perfect as an ingenious natural solution to the need for a robust circulatory pump has proven inaccessible to most sophisticated human endeavor, aiming at the creation of a homologous copy of the heart. This fascinating organ derives its attraction from the well-tuned interplay between the different anatomical and functional units that each may become the focus of congenital malfunction or alternatively may also be prone to acquired degeneration in later life. Recently, a new perspective on the anatomical assembly of the heart was generated by an extensive preparation work on explanted hearts that revealed the striking finding of a single muscle band constituting the complex cardiac structure through helical windings and loops forming the different chambers and allowing their coordinated function.[2] It is astonishing how challenging the seemingly simple uncoding of the anatomy of an organ may be, in spite of the collaborative approach by modern medical specialties and in spite of the availability of most advanced technical recourses.[3]

Some aspects of cardiac anatomy and physiology that deserve particular consideration in the context of tissue engineering and regeneration are highlighted in the following sections of this chapter. These are not intended as a comprehensive and structured discussion of the macroscopic and histological anatomy of the heart *per se*. More importantly, those basic subjects that are related to the main topics of the later Sections 6.624.4–225.7 are briefly mentioned, along with matters that are substantial for the explanation of the highlighted experimental work and their results.

6.624.1.3. Coronary Blood Flow

The working heart muscle derives its own nutrition and oxygen supply through the coronary vessels that originate from two different main vessels, the right and the left coronary artery. In case of a healthy adult person, the blood volume that passes through the coronary vasculature (coronary blood flow) is about 250 ml min^{-1}. At the same time, the total blood volume that is transported through the heart (cardiac output) ranges between 4 and 6 l min^{-1} at rest. Hence, the coronary perfusion accounts for about 5% of total body circulation, although the relative myocardial mass in relation to the whole body weight accounts for about 0.5% only. The main effectors in the coronary system are the capillaries, which densely surround cardiomyocytes and thereby provide a sufficient support of oxygen and nutrition as well as prohibiting an accumulation of metabolic products in the same way. According to the constantly high metabolic state of cardiomyocytes, an extensive capillary network is necessary for the prevention of undersupply. Hence, the average distance between two neighboring capillaries lies beneath 20 μm.[4,5] The combination of a dense vascular network with a relatively large perfusion volume results in a highly efficient gas and substrate exchange. In view of this background, the perfusion status of the myocardium appears excessive in relation to the supply of other organs in the human body. However, the high energetic demand of the cardiac muscle is dependent on such a high level of organ perfusion for an optimal functional performance. These are only some spotlights shed on the broad landscape of physiological supply conditions in the native myocardial tissue; any engineered cardiac patch will have to match up with this natural gold standard in terms of perfusion.

6.624.1.4. Electrophysiological Integration

In the native heart, the concerted function of the different myocardial regions is facilitated by a specialized system that allows rapid and interference-resistant impulse propagating throughout the heart along a specific anatomical path, the conduction system. The establishment of such a functional network requires the presence of specific cells embedded in adopted extracellular structures, each with its own particular biochemical and biomechanical features. The His–Purkinje system fulfills a wide range of criteria that are necessary for successful accomplishment of the task of impulse propagation in an active organ, such as the heart. Purkinje cells represent a great

example of the unique properties of the involved cells. Unlike other cardiac cells, unique physical dimensions (e.g., a long axis of up to 200 mm), a specific orientation of cell communication channels with special molecular features concerning their cell–cell junctions, a spatial relation to the extracellular matrix (ECM), and many more detailed specifications characterize the conducting cells.[6,7] Furthermore, the installation of a hierarchic order with a superior pace setting unit (as represented by the sinus node) and downstream regulatory units (atrioventricular node, His bundles) not only requires a delicately graduated pattern of morphological cell development for each subunit, but also involves a comprehensive arrangement for a functional integration of this system within the working myocardium. Moreover, the conduction system governs the rate of the cardiac cycles in a manner that is physiologically integrated with the activity level of the whole organism. There are a large number of independent or interrelated pathways that link the cardiac electrophysiology to systemic regulatory pathways, and the complexity of these naturally well-balanced arrangements, a subject that is reflected by a recent scientific field termed system biology, may remain out of reach for current and near-future technical options that are available in the laboratory.[8] The ultimate goal of cardiac tissue engineering that is defined by the creation of a cardiac patch that can entirely incorporate into the recipient's heart will have to have ready the appropriate tools to address the question of a complete electrophysiological integration.

6.624.1.5. Physiologic Cellular and ECM Turnover

For a long time, the heart and the constituting contractile cell fractions have been regarded as incapable of an innate regeneration. However, the discovery of a distinct cardiac cell type that exhibits cell cycle activity and may give rise to mature cardiomyocytes has attracted much attention in the very recent years.[9,10] Subsequently, other progenitor and stem cell characteristics have been proposed for a number of other cell types in the adult human body, giving rise to the hope for the possibility of a cardiac regeneration that enables the recovery of impaired organ function.

It is estimated that under physiological circumstances, a constant – although quantitatively very low – rate of cardiomyocyte regeneration exists, by which a compensation for the simultaneously occurring cell death may be achieved. The herein involved regulatory mechanisms ensure a balanced order of cell turnover, maintaining the quantity and functional quality of the working cardiomyocytes as well as those levels for the noncardiomyocytes. The implications of this cellular turnover may hardly be overestimated and currently, more questions are generated than resolved with respect to the regulatory pathways and the options for a therapeutic intervention. One of the early and extensively evaluated topics in cardiovascular medicine covers the significant contributions of the cardiac fibroblasts to the cardiac ECM constitution and remodeling.[11–13] In this context, it is worthwhile to recognize the full role of the ECM of the native heart, which is not merely a space dividing scaffold but also a significant contributor to the biomechanical performance of the heart and a distinct actor and cooperator in the process of regulation of cardiomyocyte function.[14–16] A wide range of different components are embedded in the entire network of the ECM. There are structural proteins, most prominently fibrillar collagens and elastins, with a predominantly biomechanical role, whereas other proteins, such as the constituents of basal lamina, primarily have an impact on cell adhesion properties and thereby regulate the degree of cell–matrix interaction. In the latter group, collagen type IV, laminin, and fibronectin are well-recognized promoters of cell adhesion. Hence, the addition of the components of the basal lamina significantly enhances the functional outcome of three-dimensional (3D) cultures of cardiac cells *in vitro*.[17] In contrast, a number of functional counter players exist, such as tenascin C or thrombospondin, to allow a fine tuning of cell adhesion properties of the native ECM depending on the activation of different signaling pathways. Furthermore, ECM-associated proteins, such as osteopontin (OPN), are recently recognized as differentially expressed components that are critically involved in pathological changes leading to degeneration and calcification of cardiovascular structures.[18] The presence of OPN is associated with different pathological changes, such as viral myocarditis or postmyocardial infarction remodeling, and a cross talk with other ECM regulating systems is suspected. However, the full range of the different interactions of ECM-associated proteins, such as OPN,[19] remains to be elucidated in future studies. An important group of cardiac ECM components is represented by proteoglycans, which are structurally composed of one or more glycosaminoglycan (GAG) chains covalently bound to a (core) protein. Their physical properties are of paramount importance in biomechanically challenged tissues where a dynamic change of compressive forces occurs. As a general filling matrix, also called ground substance, proteoglycans are generally present in the connective tissue of different organs and are capable of building complexes with other ECM components, such as collagens. Furthermore, proteoglycans have a relatively large binding capacity for extracellular H_2O and cations, such as Ca^{2+}, which underlines their functional role in regulating extracellular water and electrolyte homeostasis.[20] The aforementioned tenascin-C is recently shown to play a role in myocardial remodeling after ischemic injury, and it is most likely that many (if not all) of the different components of the cardiac ECM have an impact on the physiologic cellular and extracellular turnover of the heart, as well as on the remodeling pattern after myocardial injury.[21]

Because of ECM-linked biomechanical cues, interactions between the ECM, ECM producing cardiac fibroblasts, and coronary endothelial cells are expected, which in turn may act on cardiomyocytes by a series of bioactive messengers.[22] Conclusively, cardiomyocytes are strongly dependent on their cellular and extracellular environment. Endothelial cells and cardiac fibroblasts are well-known teammates in maintaining and supporting cardiomyocyte morphology and function, both *in vivo* and *in vitro*.[23] A dysfunction of either of the former cell types has deleterious effects on the natural fate of cardiomyocytes and may lead to a global functional impairment of the heart, and ultimately to cardiac failure. Coronary microangiopathy and cardiac fibrosis are only two of many pathological developments, in which a misbalance in noncardiomyocyte regulation impairs cardiomyocyte function in a direct or indirect manner with significant downstream effects.

The challenge of the old paradigm that used to neglect any regenerative capacity in the adult mammalian heart depicts the importance of a deeper understanding of the mechanisms that

direct regeneration under physiological or pathological conditions. Furthermore, functional properties, such as the electrophysiological integration of the cardiac cells, are sensitive products of perfect structural arrangements.

The *in vitro* generation and *in vivo* guidance of a cardiac patch imperatively warrant a high level of control of the development and the integration of all, cardiomyocytes and non-cardiomyocytes as well as their functional interplay within a physiological extracellular environment.

6.624.2. Clinical Indications for Myocardial Patch Repair

6.624.2.1. Congenital Malformations

A series of anomalies with a wide range of severity demand a surgical repair and the use of external patch material is often mandatory. Along the relatively young history of pediatric cardiac surgery, different strategies for the correction of the most common cardiovascular malformations have been established. In parallel to the development and refinement of surgical techniques, a continuous evaluation of different materials for their use as a functional and long-lasting surgical patch has been taking place.

According to their anatomical implementation, patch implants designed for reconstruction of vascular structures may be distinguished from those that are used for replacing myocardial (intracardiac) structures. Among the vast number of isolated congenital cardiac defects and their combinations, the most common anomalies and the surgical approaches using patch materials will be briefly outlined in the following. The development and the clinical use of vascular patch materials are discussed in other chapters of this work.

6.624.2.1.1. Atrial septal defect

A structural defect in the muscular wall that separates the left from the right atrial cavity is called atrial septal defect (ASD). Simple forms of an ASD are described by an isolated defect in the central region of the septal wall. A small to mid size ASD may be closed by a direct suture during open heart surgery, representing an exceptionally safe procedure with excellent long-term results. In recent years, many centers have adopted transcatheter device implantation techniques as a routine intervention for most of ASD patients with high success rates, although complications necessitating operative correction may impact the overall outcome.[24] However, large ASDs, usually with a diameter larger than 20–25 mm, may be optimal candidates for primary operative patch repair, and modern surgical strategies involving a less invasive access, for example, via right anterolateral minithoracotomy lead to high satisfaction for both, the patient and the surgical team.[25] The interatrial and the interventricular septal wall are mostly muscular structures that nevertheless have little contractile contribution to the overall pump function of the heart, although this view has been challenged for the interventricular wall.[26] As a consequence, noncontractile patch material of synthetic (e.g., polytetrafluoroethylene (PTFE) or Dacron) or biological (fresh or glutaraldehyde-fixed autologous pericardium) origin may be used for ASD repair with an excellent short-term outcome and almost no limitations in the longer term. Hence, the outcome of pediatric patients with a successful ASD repair is not limited by the characteristics of the patch material and the overall long-term survival of these patients matches that of the general population. Even in cases when ASD is accompanied by other malformations needing surgical correction and even when xenogenic pericardial material is used, long-term durability turns out favorable. In a clinical series of 60 patients, the 15-year freedom from patch failure has been reported to range around 92%.[27]

More complex cases may present as a rather superior (cranial) or inferior (caudal) location of the ASD within the septal wall. These cases frequently include additional defects along the atrioventricular continuity (partial atrioventricular septal defect) or they may be associated with any other abnormal development affecting the superior vena cava or the pulmonary veins (superior sinus venosus). But even under these circumstances, the reconstruction of the atrial septal wall and the correction of the vascular blood flow may yet be well managed using the above-mentioned patch materials. However, considering the low blood flow velocity and the flow pattern in the atrial cavities and in venous vasculature, a cardiac patch at these implant sites are at a potential risk for thrombosis. This is of particular importance for the design of an optimal biomaterial for the reconstruction of such complex ASD malformations.

Moreover, associated defects of the atrioventricular valve(s) may need the use of valve reconstruction techniques or the implantation of valvular prosthesis, if a reconstruction cannot be achieved. Special considerations in designing and manufacturing of heart valves are discussed in other chapters.

6.624.2.1.2. Ventricular septal defects and tetralogy of Fallot

The most common congenital anomaly among all born alive babies is a ventricular septal defect (VSD), which can occur in the superior, membranous part (so-called perimembranous defect) or in the inferior, muscular region of the septal wall. As for an ASD, a combination of this anomaly with other malformations, such as the tetralogy of Fallot or common arterial trunk, is possible and common. Also an association with other systemic conditions, such as trisomy 21 (Down syndrome) is recognized. The combined incidence of a VSD, whether as an isolated defect or part of a syndrome, reaches roughly half of all congenital heart defects.[28] VSD of muscular type, particularly if of smaller size, may undergo spontaneous closure in the first years of life, but a multifocal presence or a large VSD with significant shunting volume may urge for an early intervention because of progressive heart failure. Moreover, a persisting VSD that permits a significant blood volume to shunt from the high pressure left ventricle to the low pressure right ventricle may represent an indication for patch repair even in the absence of any symptoms in order to prevent the late development of pulmonary vascular disease (pulmonary hypertension and right ventricular hypertrophy).

VSD repair involves the implantation of a patch via a right atrial, a right ventricular, or alternatively, a pulmonary artery incision, depending on the location of the defect. Because of the high pressure gradients across the ventricular septum, strong synthetic patch materials are preferred to autologous pericardium or conventional biological solutions that are

commercially available today. Using this approach, some theoretical limitations may arise from the fact that the surgical repair takes place at a very young age and somatic growth might overload the small patch in the long term. Also, thrombembolic events and the risk of infection may be listed as theoretical drawbacks. However, in the clinical setting, growth-associated problems as well as neurological complications due to left heart embolic events are very rare, and other prophylactic measures, for example, to prevent an infective endocarditis are only recommended during the initial 6 months after patch repair,[29] when the autologous endothelialization of the implant material is yet underway. In specialized centers, a low operative risk is expected for uncomplicated cases, usually in the range of very few percents. Additional risks derive from concomitant defects or other conditions, such as pulmonary hypertension in patients with a long-standing history of VSD.

A relatively frequent syndrome that consists of (1) a VSD, (2) a right ventricular outflow tract (RVOT) stenosis, (3) a so-called overriding aorta with an anatomic dislocation with respect to the ventricular septum plane, and (4) right ventricular hypertrophy was named after a French physician, Etienne-Louis Arthur Fallot, who was among the first to report on this anomaly.

Unlike the initial situation in isolated cases of ASD or VSD, the combination of RVOT stenosis and VSD leads to a right-to-left shunt in the Fallot babies. This way, the shunting blood volume with low oxygen saturation circumvents the pulmonary circulation and enters directly the systemic circulation. As a result, peripheral arterial oxygen saturation is diminished and these babies appear morphologically as cyanotic, which is generally referred to as blue baby syndrome. Varying extents of the involved defects are observed and correlate with the phenotypic presentation as well as the degree of symptoms and also the level of risk for the life of the diseased. Similarly, the management of the tetralogy of Fallot patients may vary significantly depending on the individual constellation. As a general rule, the corrections of the VSD and the RVOT obstruction are main therapy goals. In both steps, often a patch reconstruction is employed (**Figure 1**). Regarding the VSD, similar considerations as mentioned above will govern the strategy, although reconstruction in the setting of Fallot might become more challenging because of the abnormal anatomical constellation of the aorta with a shift toward the RVOT. The reconstruction of the latter is frequently performed by using a synthetic patch to augment the narrowed outflow tract. When the pulmonary valve and a considerable segment of the pulmonary artery are also stenotic, the use of further implants, such as an allogenic donor valve conduit (so-called homograft), optionally with an additional prosthetic extension may be considered.

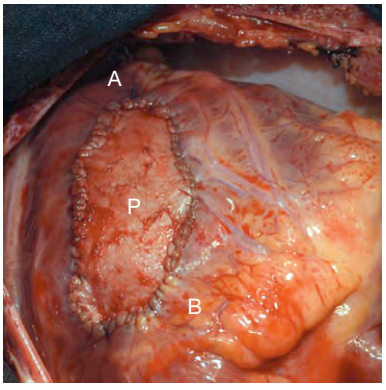

Figure 1 Intraoperative image demonstrates the anterior cardiac aspect after the implantation of a large pericardial patch (P) to reconstruct the obstructed right ventricular outflow tract. A indicates the apex of the heart and B indicates the base of the heart. Image provided by Dr. T. Loukanov.

Considering the complex nature of this syndrome and the large extent of the operative steps involved in the complete reconstruction, the initial outcome is remarkably satisfactory with a low operative risk of about 3% and a late survival rate of greater than 90% after 25 years.[30] However, the use of different implant materials (VSD patch, RVOT patch with or without homograft) and the accumulation of their individual risks (thrombosis, restenosis, degeneration and calcification, etc.) contributes to long-term morbidity and mortality.[31] Therefore, a further improvement of overall outcome for this patient cohort may be achieved by novel surgical strategies involving the use of superior biomaterials.

However, for the isolated patching of a VSD or an ASD, the currently achieved outcome with available synthetic materials leaves hardly any margin for a further improvement. Any future trend in the development of novel materials will have to consider both, the limited clinical need and tiny potential for a further clinical improvement by superior implant materials and the necessary financial and manpower investment in the engineering process and application-related resources for the use of novel cardiac patch materials.

6.624.2.1.3. Hypoplastic left heart syndrome and functional single ventricle

In some very complex malformations, one of the two ventricular chambers is severely underdeveloped (hypoplastic). Under these circumstances, the fetal and early postnatal circulation can be managed by the single functional ventricle only because of physiological fetal shunts, for example, the arterial duct connecting the pulmonary with the systemic circulation, or because of further concomitant defects, for example, a VSD. Either anatomical constellation resulting in a functional single ventricle represents a serious and life-threatening malformation that warrants best current therapy in order to provide considerable survival chances for the newborn. Different strategies have been developed to create a circulatory situation that permits the survival of the neonate period and the early infancy to reach an age and a body size that allows for more definite surgical therapy (staged procedures). However, despite the significant improvements in surgical techniques resulting in better outcome with regard to early survival, all currently applied strategies are mainly of palliative nature and no cure has become available for this group of severe malformations. A detailed description of the various anatomical pictures and a detailed surgical approach for their respective correction certainly goes beyond the scope of this chapter. However, it is important to understand that an early and comprehensive surgical intervention is necessary for the affected babies to survive. This involves the use of patch materials to reconstruct intracardiac and extracardiac structures, such as the ventricular septum, or the ascending aorta. In a very general way, the surgical goal is defined by an

optimal structural preservation and functional employment of the single developed ventricle for the maintenance of the systemic circulation, while a passive blood flow from the caval veins to the pulmonary vasculature (Fontana circulation) remains as the best available situation in the face of the severely hypoplastic morphology of the other ventricle. The challenging surgical plan may be abstracted in one single sentence, yet its completion takes up to a few repetitive operations over a time course of several years. Staged surgical interventions and frequent hospitalizations may amplify the general disadvantages of the currently available patch materials, thus contributing to a negative impact on the overall patient outcome. Hence, the risk of outgrowth of the installed patches or conduits, or the rate of thrombotic events and infections, is of particular concern in patients after an operative therapy for this kind of severe cardiac defects. Moreover, the late complications of an impaired cardiac output and the resulting high rate of congestive heart failure have a tremendous impact, both on freedom from reoperation and total survival.[32] Although the absolute number of babies born alive with a functional single ventricle is fairly low (a substantial proportion of severe cardiac malformations are prenatally lethal), the severity of the clinical impact imperatively calls for sustained efforts in developing a strategy for a cure. Notably, more than for any other patient group a cardiac transplantation is the only therapy that comes close to a cure.[33,34] An alternative approach that aims at the recreation of the dysfunctional ventricular parts will depend on the availability of a significant amount of additional contractile tissue, and may offer the perspective of not only an improved long-term prognosis including higher survival rates but also a normal level of quality of life.

6.624.2.2. Acquired Heart Disease

6.624.2.2.1. Coronary heart disease

Coronary heart disease (CHD) is a degenerative process that affects a large proportion of the population worldwide. A number of risk factors associated with the development of CHD have been identified and some of them have become accessible to medical therapy, for example, arterial hypertension, diabetes, and disorders of lipid metabolism, while others may be controlled by modifying patterns of daily behavior, which are collectively referred to as lifestyle issues. However, a number of further factors remain unknown or untreated, for example, genetic disposition. Hence, despite the growing amount of knowledge on the development and progression of CHD, the complications of this disease pose an unbowed burden on the individual patient and the whole community. The typical complications of CHD include the acute myocardial infarction (MI) with subsequent loss of contractile tissue and adverse myocardial remodeling, the development of ischemic cardiomyopathy on further progression, and also the occurrence of associated arrhythmia or thromboembolic events. Congestive heart failure represents the end stage of CHD, and also occurs as a consequence of other cardiac pathologies. To prevent the development of end-stage heart failure, a large armamentarium has been developed and proven effective for the treatment of CHD, including pharmacological, interventional, and surgical options. And yet, in a significant number of patients the development of end-stage heart failure cannot be prevented. Heart transplantation and mechanical assist device implantation remain as last therapeutic options for these very ill patients. Cell transplantation and other methods have been investigated as novel options to augment the myocardial contractile activity, but until today no success of a broad clinical relevance has been achieved. A myocardial patch has been suggested as an ideal solution for many currently untreatable chronic cardiac conditions and especially as a cure for localized ischemic injuries, for example, as a replacement part for post-MI dysfunctional regions of the heart. But unfortunately, until today the idea of a contractile myocardial tissue fragment has not been accessible to humankind bioengineering.

Another challenging situation currently without a perfect solution is the rupture of recently infarcted myocardial tissue. Following an acute MI, an inflammatory process is triggered by the factors released from the necrotic tissue. The loss of contractile cells and the acute injury diminish the active contractile performance of the heart. In parallel, a vicious circle of hypoxia and marked inflammatory infiltration of the myocardium leads to a dramatic reduction of the biomechanical strength of the myocardium, which reaches a maximum impact a few days after the initial infarction, typically within the first 2 weeks. A rupture of myocardial tissue, often in ventricular septal region, is one of the most critical complications of an acute MI. In contrast to a congenital type of VSD, post-MI VSDs are very difficult to manage and even in the modern era of cardiac surgery a high risk of mortality shadows the perspectives of the concerned patient. There are two different explanations for this unfavorable outcome. (1) An acute onset of a VSD is hemodynamically poorly tolerated because of the absence of any adaptation time for the circulatory system and the involved physiological mechanisms of compensation. (2) As mentioned before, following an MI, localized tissue necrosis and inflammation not only weaken the ischemic area of infarcted myocardium but also reduce the biomechanical strength of the adjacent areas, which translates into an extremely fragile tissue on surgical exposure and manipulation. Hence, endeavors for suturing a cardiac patch for direct repair are often frustrating and sometimes end up even abortive.

In the setting of a post-MI-VSD, some characteristics of an ideal cardiac patch are of paramount importance: (1) instant availability, (2) durability under a high range of dynamic mechanical loading, (3) resistance to the hostile biological milieu that is present in the acute ischemic setting, and (4) pronounced compatibility of the passive biomechanical features of the patch with those of the surrounding myocardium, for example, pliability and elasticity, for an optimal fit after implantation. However, because an ideal cardiac patch that fulfills all of these criteria does not exist, the same patch materials that are used for the reconstruction of chronic (e.g., congenital) VSD are also used for the repair of post-MI-VSD in the acute clinical setting.

6.624.2.2.2. Dilatative myocardial dysfunction

Idiopathic dilatative cardiomyopathy (DCM) is a term to describe a condition in which the cardiac function is significantly impaired because of a structural alternation of the heart with dilated chambers and no otherwise diagnosed reason for the observed functional impairment. Depending on the underlying cause, other forms of cardiomyopathy, such as toxic, inflammatory, or endocrine types, are distinguished.

If a specific cause is identified, a specific treatment, for example, anti-inflammatory and antiviral therapy, or correction of an endocrine dysregulation, may be initiated to support the symptomatic cardiocirculatory therapy. However, only limited therapeutic options may be offered on the diagnosis of an advanced cardiac impairment, and a prevention of further disease progression by conservative means of heart failure treatment represents the first line therapy. When end-stage heart failure develops, only heart transplantation or the implantation of a mechanical assist device remains as a further option. This progression affects up to half of all patients diagnosed with DCM and thus the underlying disease represents a significant medical problem.[35] Similar as for ischemic cardiomyopathy, also for this entity of cardiac disease a few novel strategies that are guided by the spirit of regenerative medicine have been investigated, including cell transplantation and scaffold-based cell and gene therapy.[36]

In the clinical arena, however, a surgical approach other than transplantation or ventricular assist device implantation could not be established so far.

6.624.2.2.3. Other forms of cardiomyopathy

A morphological development that is contrary to the situation in dilatative forms of cardiomyopathy may be observed in some hereditary syndromes, because of an unphysiologic hypertrophy of the myocardial tissue (hypertrophic obstructive cardiomyopathy, HOCM) or because of the deposition of excessive amounts of abnormal substrates (e.g., in amyloidosis). There is a large heterogenic group of cardiomyopathies that share common morphological features of nondilated but yet dysfunctional ventricles, but may be distinguished by a wide range of histopathological and molecular biological characteristics with different associated genetic disorders and systemic diseases.[37–40] In case of mainly cardiac localized tissue alterations, for example, subaortic septal hypertrophy and left ventricular apical hypertrophy, surgical or interventional options for the reduction of the pathologic myocardial mass have been applied with considerable success. In case of primary systemic conditions with secondary cardiac manifestation, a targeted treatment for the underlying disease may be the best option when available.[41,42] However, therapy strategies aiming at reversing morphological organ alterations and thereby restoring myocardial function often show little success when large parts of the organ are affected, particularly at later stages of the disease.[42] Thus, the prevention of disease progression and fatal complications (e.g., implantation of an internal cardioverter-defibrillator to prevent death from ventricular arrhythmia) represents the main principles of current therapy.

In some systemic conditions, such as amyloidosis, even cardiac transplantation can offer no cure, but remains palliative because the same pathological changes reoccur within the donor organ over time.[43,44] Further rare entities of nondilatative cardiomyopathies include infections pathologies and enzyme-deficiency-based storage disorders.[41,42]

The role of surgical or catheter-based interventions is largely depending on the specific type and the localization of the pathologic changes, for example, systemic versus local cardiac manifestation. A total replacement of dysfunctional parts of the myocardial tissue or even the whole organ can only lead to sustained cardiac improvement when a postoperative degeneration is effectively prevented. Unfortunately, many of the different syndromes associated with a progressive cardiac dysfunction appear only moderately accessible to current therapeutic options and thus even a total replacement of the heart by orthotopic transplantation cannot promise a substantial long-lasting benefit for the patient. Given the aforementioned diverse features of the numerous disease forms, a potential impact of a living cardiac patch, even if one day available, for the therapy of the majority of non-dilatative cardiomyopathies is largely unclear.

6.624.3. Patch Materials in Current Clinical Use

6.624.3.1. Autologous Pericardium

There are numerous situations where a congenital or acquired defect warrants coverage by an implant material that ideally displays the same characteristics as the surrounding native tissue. Autologous pericardium has been successfully employed in various cardiac surgical procedures for a long time. In general, the surgical access to the heart and proximal vascular structures is created by an incision to the pericardial sac after entry into the thoracic cavity and preparation through the extrapericardial structures (e.g., thymus or retrosternal adipose tissue). Irrespective of ventral (that is median sternotomy) or lateral (e.g., anterolateral thoracotomy) surgical access, a considerable area of the pericardial tissue may be exposed, which may be sacrificed for the achievement of crucial reconstructive goals, for example, enlargement of a vascular stricture or closure of a septal defect. The only delicate structures that must be preserved and deserve minituous caution during the preparation are the phrenic nerves that run laterally on both sides of the pericardial sac. As a consequence, the entire anterior part of the pericardial sac may be harvested as a valuable biological material.

There are many advantages that support the use of autologous pericardium in the setting of congenital as well as adult cardiac surgery: (1) the availability of the material without the need of additional surgical trauma for the harvesting of the tissue; (2) the instant availability in case of the use of native pericardium; the application of a fixation step by using glutaraldehyde (varying concentrations and corresponding incubation times) may cause minor delay, which may be without relevance, if proper planning of the order of the surgical steps has taken place prior to the procedure; (3) because of the autologous origin, no immunological reaction or clinically relevant inflammatory process is expected on implantation; (4) because of the biological origin and particularly because of the fact that native pericardium is a living tissue, a certain benefit regarding the risk of infection has been anticipated for this material and autologous pericardium is favored for the reconstruction of abscess cavities in the setting of surgery for infective endocarditis; (5) the easy access and preparation avoid additional time-consuming efforts for a tissue harvesting by the surgical team, and the involved instrumentation and media are ubiquitously available. Also, intraoperatively harvested tissue is sterile and needs no further treatment to avoid an infection. Hence, from the economic point of view, autologous pericardium represents the most favorable solution when a patch material is needed in cardiac surgical procedures;

(6) the passive biomechanical strength of pericardium integrated with the dense tissue structure results in suitability as a patch material in the pulmonary as well as in the systemic circulation; (7) the low incidence of bleeding from suture holes in a pericardial patch (in contrast to some synthetic counterparts); and (8) finally, the potential for remodeling and possible growth is an attractive advantage of autologous pericardium.

Because the heart is surrounded by pericardial tissue, an *in situ* use of pericardium may be feasible for specific reconstructive procedures, although a convincing amount of data supporting the superiority of an *in situ* or a pedicled pericardial patch to a free graft does not exist.[45] The question regarding the necessity of a fixation prior to implantation may be regarded in a controversial way by different institutions and surgeons. In general, a more or less advanced cross-linking of all protein structures, involving all cellular and extracellular components, is achieved by the incubation of native pericardium in a glutaraldehyde solution with varying concentrations of 0.5% up to several percentage over a time period of several minutes up to 15 or 30 min. This leads to a reduced elasticity of the material and also causes the later patch implant to be prone to calcification in the long term. Moreover, the toxicity of glutaraldehyde necessitates a thorough washout of the fixation solution before implantation. In turn, the risk of dilatation is reduced by a fixation, particularly, when the patch is exposed to high pressures *in vivo*, for example, in the systemic arterial circulation or in the left ventricular wall structures.[46]

As the native pericardium mainly consists of interstitial cells, no dynamic contractile activity may be expected for this tissue material. Experimental studies have demonstrated that a transformation of these interstitial cells from a quiescent fibroblast-like phenotype to a more activated myofibroblastoidal form may take place on stimulation by mechanical or biochemical cues. Hence, a certain remodeling process is expected for nonfixed pericardium when used as a cardiac or vascular patch. Glutaraldehyde fixation results in a widely inert material that will remain purely passive and also will not permit a relevant *de novo* repopulation for a later myogenic function.

As a consequence of the aforementioned issues, pericardial patches are widely used in congenital and adult cardiac surgery, where an enlargement of cardiac or vascular structures by a biocompatible material is necessary. Autologous pericardium is also used for repair of structures that are injured by an infective or inflammatory process. One classical indication for the use of autologous or xenogenic pericardium is the reconstruction of annular structures that are affected by an abscess formation in the context of infective endocarditis.[47] In other settings, when the ventricular outflow tract is replaced, a gain in the global ventricular contractile function may only be achieved by the support of existing native myocardium through the operative procedure, for example, by an enlargement of the RVOT, or by the correction of a regurgitation or shunt pathology, for example, as part of the correction of the tetralogy of Fallot. Under either circumstance, pericardial patch materials have proven long-lasting durability of several to many years, which is correlated by high rate of freedom from re-intervention.[48,49]

A disadvantage of the use of autologous pericardium is related to the postoperative adhesions that involve cardiac structures and the surrounding tissue. The pericardial surface that faces the heart usually is less susceptible to excessive adhesions, and a partial or near-complete closure of the pericardial sac at the end of the operation is an effective method that some surgeons rely on as a safety measure for a possible future reoperation. The partial resection of autologous pericardium always includes the compromise associated with increased adhesions in that particular area.

6.624.3.2. Xenogenic and Decellularized Xenogenic Pericardium

The need for an off-the-shelf material that is characterized by an unlimited and ubiquitous availability has inspired the exploration of an animal source for the manufacture of appropriate surgical materials. Bovine pericardial tissue (donor animal: cow) and equine pericardium (donor animal: horse) are commercially available materials that are subjected to a fixation process during their industrial processing. Unlike autologous pericardium, the fixation-mediated cross-linking of the donor cell antigens is of paramount importance for the immunological tolerance of these xenogenic implants in a human recipient. Unfortunately, the use of commercial xenogenic tissues is associated with a pronounced calcification, which may be explained by a chronic process due to the strong immunological cross-species barrier. When considering the use of xenogenic pericardial patches, degenerative events and calcification have to be weighed with respect to the advantage of a ready-to-use material with no donor-site-related concerns for the recipient.

Recently, the decellularization of different natural tissues has resulted in the production of several novel biomaterials, of which a few have entered commercial distribution as bioimplants in different surgical fields, although their role in the field of cardiac surgery has not been defined, yet. Today, bovine and equine pericardia are commercially available for human surgical application.[50,51] However, the use of decellularized xenogenic materials in the cardiovascular surgical field has suffered a tremendous loss of credibility after reports on limited durability and increased rates of failure in the setting of heart valve implants made of decellularized animal tissue.[52,53] The underlying problem of complete antigen removal without major destruction of the ECM is the major hurdle for the broad introduction of decellularized xenogenic biomaterials into clinical practice. While some studies with focus on the reconstruction of abdominal or musculoskeletal structures allow for diverse conclusions on the outcome of the currently commercially available decellularized materials,[50,51] caution is indicated when a cardiovascular structure has to be replaced, as a failure of these structures has potentially life threatening consequences for the recipient.[52]

6.624.3.3. Synthetic Polymers

For many years, chemically produced polymers have been used in surgical procedures. Suture material and patch materials are today widely used across all surgical specialties. For cardiovascular procedures, synthetic polymer materials made of Dacron

and PTFE are the most popular implants, either as vascular grafts or as cardiac patch implants.

A long-standing history of application found the ground for the safe and routine use of Dacron. On implantation, a stable persistence of highly pressure-resistant Dacron materials guarantees reliable long-term structural survival and maintained function. As a drawback of Dacron, a pronounced nonspecific inflammatory reaction to the implant (foreign body reaction) is observed, that causes excessive adhesions at the interface between the implant and the recipient (host) tissue. Furthermore, Dacron ranges among the most rigid synthetic materials, which impacts the overall compliance of cardiac chambers or vascular segments that are reconstructed with Dacron materials. In this sense, PTFE (also, Gore-Tex®) has some advantages over Dacron. On reoperation, technical difficulties arising from adhesions around graft material are less intense and at the same time, a microporous structure allows a higher level of interaction between the implant and the surrounding recipient tissue by the permissive character toward migrating interstitial cells. A favorable increase in elastic characteristics is paralleled with some tendency for bleeding of needle holes.

Although novel synthetic materials with markedly improved characteristics are under current experimental investigation (see Section 6.624.4), the current clinically available synthetic materials display major disadvantages when compared to their biological counterparts: (1) as a nonviable material, Dacron, PTFE, and other polymers do not support any growth tendency – a significant limitation in the pediatric cardiac surgery; (2) because of the long-term persistence *in vivo*, an elevated risk of infection with the need for challenging reoperative procedures threatens the recipient in the long term; (3) as with all current cardiac patch materials in clinical use, there is no active participation in the contractile function of the heart; (4) when implanted at intracardiac sites with direct contact with the blood circulation, an elevated risk of thrombosis and embolic events impacts the clinical outcome of pediatric and adult patients which may be managed by temporary anticoagulation or antiplatelet medication – each with its own associated risks for bleeding complications.

6.624.4. Experimental Synthetic Polymers

With the advent of technical advances in chemical engineering, the first generation polymers are most likely to be abandoned by novel materials that fulfill a number of essential criteria for a truly bioactive material. Biodegradability has already been realized with the introduction of poly-lactic and poly-glycolic acid materials. However, the exact control over the speed of polymer degradation has continuously been in the focus of experimental work. Beyond the speed of ECM degradation, a cell-responsive pattern of ECM turnover has been desired for novel synthetic ECM materials. One interesting approach lies in the use of enzymatically degradable poly (ethylene glycol) (PEG) hydrogels. By introducing specific amino acid sequences that are susceptible to cellular matrix metalloproteases (MMPs), a more physiologic cell migration pattern has been demonstrated for PEG.[54,55] In other circumstances, the introduction of bioactive peptides that specifically trigger integrin-dependent cellular responses has been proven as a promising tool to direct various basic cell characteristics, such as cell phenotype, cell migration, cell division, and differentiation.[56,57] In a study with a cardiac progenitor cell line, the use of an engineered ECM based on PEG, including MMP-sensitive domains, arginine-glycine-aspartic acid (RGD) containing domains, and integrin-responsive domains, has resulted in an enhanced cell differentiation toward cardiac cells, improving differentiation markers on the RNA and protein level.[58] Most interestingly, a cell driven release of matrix-bound molecules may also be successfully applied using PEG. By such an 'enzymatically accessible' addition of growth factors, the site-specific release of desired factors within the recipient organism, dependent on the site of cell invasion, becomes feasible.[59] Although the majority of the published studies so far have focused on wound healing or angiogenesis, myocardial engineering and regeneration is certainly an area that may benefit from the application of such smart bioactive ECM materials.[60] Using basically the same approach, the delivery of matrix-bound DNA with a controlled release pattern *in vivo* may become feasible in order to achieve a targeted local gene delivery without using viral vectors.[61,62] The use of an ECM-bound delivery of DNA not only offers the advantage of a greater spatial control of gene delivery, but may also enhance the degree of efficacy.[63] With a similar level of enthusiasm, the control over a wide range of physical characteristics of novel synthetic materials has become accessible. Using polymers and copolymers containing polyesters, polypeptides, poly (amino urethane), and chitosan, a number of synthetic materials may be produced with a thermoresponsive or a pH-sensitive physical state (for review refer to Nguyen and Lee[64]). The possibility of controlling the conditionally regulated solid to gel transition of a specific material *in vivo* paves new avenues for a variety of pharmaceutical and bioengineering applications. As an example, the injection of a liquid- or gel-based mixture of ECM and cells into a region of infarcted myocardium may result in higher cell retention, if the applied ECM material provides a temperature and/or pH transition to a solid phase under the *in vivo* conditions, thereby successfully immobilizing the injected cells at the site of delivery. This may further improve the results of previously applied, less controllable ECM components that have been used for cell delivery to injured or ischemic myocardial regions.[65] The advantage of tailored responsiveness to pH and temperature variations paired with bioactive molecular cues make these novel ECM materials attractive components for bioengineering purposes, particularly for soft tissue engineering using demanding cell types, such as skeletal myoblasts, cardiomyocytes, and their respective progenitors.

6.624.5. Strategies for Myocardial Tissue Engineering

The evident need for an alternative to some currently unsatisfactory therapy options in the cardiovascular field has inspired a growing scientific community to develop strategies for *in vitro* or *in vivo* organ engineering or regeneration, respectively. Over the past two decades, the scientific field of tissue engineering has experienced a dramatic progress in quantitative measures as well as with respect to the complexity of the involved

techniques. Studies with the focus on generation of a cardiac tissue surrogate with the ability for a later use as a patch started in the mid-1990s as rather simple 3D cell culture units and emerged as multifaceted and complex arrangements of multiple cellular and extracellular components in the recent years. In the following sections, different general strategies for the repair of malfunctioning myocardium or myocardial defects are highlighted. Representative models of a cardiac patch or a tissue analog that already have been demonstrated to be successful *in vivo* will be discussed along with further *in vitro* results that hold a lot of promise for a successful *in vivo* application in the future.

When a summary of the past achievements in cardiac tissue engineering is to be drawn, a categorization of different experimental series and models becomes necessary. Notably, a large number of published reports describe a 3D beating structure that has been achieved through the *in vitro* application of a cell suspension on a porous scaffold material, or alternatively by mixing cells with solidifying liquid ECM components *in vitro*.[17,66–71] A complete discussion of all related reports goes beyond the scope of this publication. Therefore, the focus in the following sections is directed toward some of the *in vitro* models that result in a structure with the potential use as a cardiac patch. A series of other investigations that follow the innovative idea of guided tissue regeneration, thereby strictly relying on the *in vivo* present local milieu, are discussed in the Section 6.624.6. Finally, a large number of further novel interventions for the treatment of irreversible myocardial injury have been recently introduced, with some remarkable preliminary success. However, in the majority of these approaches, a cardiac patch may not be generated *in vitro* or *in vivo* and the so far anticipated therapeutic effects may rather be derived from an indirect change of the natural fate of the cardiac disease. Hence, Section 6.624.7 only sheds a light on some of these alternative approaches, their current advances, and controversies.

6.624.5.1. *In Vitro* Construction of 3D Structures with Cardiomyogenic Characteristics

The laboratory manufacture of cardiac tissue has been one of mankind's dreams for many years. Early *in vitro* cell studies were restricted by primitive technical tools and the lack of a deeper cell and molecular biological understanding of the basic requirements of cultured cardiac cells.[72–75] The advent of biotechnological methods for the production of enzymes, complex culture media, and growth factors resembles an important prerequisite for the isolation and culture of demanding primary cell types, such as primary adult cardiomyocytes.[76] Additional advances in biochemical engineering allowing the production of increasingly biocompatible scaffold materials led to the first opportunity of *in vitro* construction of 3D cell cultures. With the dawn of the last decade of the past century, a growing body of knowledge about the crucial principles of *in vitro* development of 3D cell cultures formed the fundament for a novel discipline that was termed tissue engineering.[67,77,78] The principles of tissue engineering were applied to different organ systems and preliminary experimental results give rise to hope for a novel universal solution in therapy of various disorders.[79] Similarly, the engineering of a bioartificial cardiac patch was anticipated for the cure of both acquired and congenital heart disease.[66,71]

In parallel, 3D cardiac cell cultures were suggested as a substitute for animal models in the development and testing of novel pharmaceutical products.[17,70] Some of the involved pioneering experiments were conducted by surgical institutions, driven by the hope for a potential surgical utilization of the engineered tissue as a cardiac patch, which has been among the top goals of the investigators ever since.[79,80]

The first generation of cardiac tissue engineering models may be characterized by a few common features: a 3D physical structure was generated *in vitro* by the joint culture of isolated cells within a porous scaffold[66,71,80] or a consolidating solution of liquid scaffold components.[17,81] Collagen- and gelatin-based porous scaffolds have been commercially available for many years and a routine clinical application of these materials for the control of diffuse bleeding underlines their general biocompatibility and harmless use in humans. When mixed primary cardiac cells are cultured in an extracellular environment that is mainly constituted of collagen and gelatin, early beating activity and ultrastructural evidence of reconstituted contractile elements may be observed without any sophisticated auxiliary instruments, for example, bioreactors and mechanical simulators.[81] In parallel, synthetic polymer scaffolds were introduced as a controlled degradation pattern, and a definite composition supported their implementation in many laboratories.[82] In most experiments, a successful *in vitro* processing was defined by the ability to demonstrate basic morphological features of native cardiac tissue. When cardiomyocytes were employed, the retention of the contractile activity and some rudimentary electrophysiological features were further advocates of an advanced overall maturation of the novel tissue surrogate, suggesting the option of a future use of these constructs as cardiac patch implants.

6.624.5.2. Commonly Used Cell Sources

With the introduction of a robust cell source, such as fetal or neonatal hearts of rodent or chicken donors, a cell population that contains large numbers of cardiomyocytes became accessible. These cardiomyocytes have been preferred for cardiovascular research purposes for a long time.[83,84] They display a sustained high contractile activity *ex vivo* and a relatively low susceptibility to injury and death during the isolation process and the subsequent culture period under the artificial *in vitro* conditions. These cardiomyocyte populations become adherent to most simple materials (such as standard tissue culture dishes) even after a harsh enzymatic isolation (e.g., using trypsin), and they resume spontaneous contractile activity shortly after plating, typically resulting in beating activity in a significant proportion of the cultures soon after 24–72 h.[85] Taken together, these cardiomyocytes are strongly reliable actors *in vitro* and they may fulfill their mission and continue to demonstrate reliable function despite many constraints present under standard *in vitro* conditions. Consequently, when the choice of an appropriate ECM for the establishment of a 3D culture has to be made, a wide range of biomaterials may fulfill the basic criteria for the culture of these cardiomyocytes.

However, in most models the isolated primary cell population contains not only cardiomyocytes but also noncardiomyocytes, for example, cardiac fibroblasts, endothelial cells, and vascular smooth muscle cells. In various more recent experiments, a regulatory effect of the noncardiomyocytes on some important characteristics of the developing 3D construct and the embedded cardiomyocytes has been demonstrated.[23] Hence, cell culture techniques for specific modification of the cardiomyocyte fraction in the finally seeded cell population have been introduced early in the history of cardiac tissue engineering, all aiming at a targeted modification of specific characteristics of the developing cardiac patch.[86,87] Moreover, the effect of total cell density on the overall functional outcome of multicellular organizations of cardiomyocytes has been described decades ago[85] and more recently confirmed for *in vitro* seeded scaffolds.[71,80,88] The underlying mechanisms have been subject to studies on the cellular and molecular level, and among other issues, a critical role for spatial cell–cell communication, as well as interactions via paracrine pathways, have been suggested.[89–92] With improved protocols for the generation and selection of embryonic stem cell (ESC)-derived cardiomyocytes, the next level of cardiac tissue engineering has been entered. Although substantial ethical concerns have accompanied the scientific exploration of ESC-derived cells, their advent has – for the first time in the young history of cardiac tissue engineering – defined a specific investigative path with a potentially allogenic cardiac patch on the horizon. Although meanwhile a few technical hurdles, most prominently the tumorogenic risk on implantation, have cut down on the initial enthusiasm about ESC-derived cells, the proof of principle that has been delivered for a rodent and also for a human ESC-derived cardiac patch deserves particular attention. In an astonishing work that has somewhat revolutionized the field of regenerative medicine, a novel entity of autologous cells with an apparently unbound capacity for self-renewal and differentiation to various tissue-specific cell types has been produced by the *in vitro* manipulation of adult somatic cells. These man made cells were termed induced pluripotent stem cells (iPS) and have taken over as the anticipated protagonists in the cardiac tissue engineering scene. Their use is favored because of the circumvention of ESC and the associated ethical problems. However, with the first notice of a certain risk for the development of teratomas *in vivo*, a series of questions have been raised that are now common tasks for groups working on ESC and iPS.[93,94]

6.624.5.3. Solid or Gelling Scaffold Components: Some Considerations

Those models of tissue engineering that rely on a solid starter scaffold have been mostly limited by a heterogeneous spatial cell distribution. This warrants further manipulation and optimization in order to improve cell distribution.[80,95,96] The general principles that may govern the decision making process are comparable to those that direct the engineering approach of other organ systems or tissue fragments. The pore size of solid scaffolds is obviously a fundamental factor that may limit maximum medium convection and cell suspension penetration, although some other factors, such as the hydrophilic character of the material and the cell size, also have an impact on the initial cell seeding result. A pore size of 50–500 μm has been used successfully in previous reports.[23,86] However, some authors have noticed an optimization on cell seeding enhancing steps, such as the application of a mild centrifugal force of the seeding of the scaffolds under medium convective flow.[86,96,97] The herein described modification steps are simple and yet effective tools for improving the overall cell distribution, but on the other hand their effectiveness stems from the shortcomings of the basic setup prior to the modification. Moreover, the occurrence of scattered cell clusters within singular cavities of the scaffold and the need for the employment of further gelling scaffold materials (such as Matrigel™) for the entrapment of the cells in large scaffold pore structures[23,86] are typical phenomena associated with the use of solid scaffold materials and their predefined pore structures. In contrast, models consisting of a casting of initially liquid cell and matrix components that aggregate on mixing generally result in a more homogeneous cell distribution.[17] Beyond morphological changes, functional outcome is significantly influenced by the various characteristics of the scaffold, and most importantly, the biomechanical features and the electrophysiological performance of a cardiac patch are partially determined by the employed scaffold.[98] Early models of cardiac tissue engineering employed basic woven or knitted polymers or biological ECM materials of solid (gelatin, collagen) and liquid or gelling characteristics (collagen type I, fibrin, basement membrane extract). When biomechanical features are considered, solid polymers and biological ECM materials that are used for tissue engineering purposes outrange the cellular impact on the overall tissue performance in the initial culture phase. However, in the later culture period, for example, after 2–4 weeks, applying biomechanical testing reveals the impact of the cellular components within the cultures and the variation of parameters such as maximum tensile strength and elasticity.[95] On the microscopic level, this change in biomechanics correlates with (1) a degradation of the initial ECM material, (2) a *de novo* synthesis of natural ECM components by the embedded cells, and (3) a proliferation of oriented cells with an increasing level of cell–cell and cell–ECM adhesion. When liquid or gelling ECM materials are used, the initial overall physical strength is generally lower than in solid-scaffold-based cultures. Hence, the development of cell-derived biomechanical features becomes detectable at an earlier stage, and also active force measurements may become readily successful as early as 2 or 3 days after initiation of the cultures when the appropriate cell sources (e.g., neonatal rat cardiomyocytes) are used.[17,99]

Furthermore, the composition of the seeding cell suspension grossly correlates to the initially achieved cell composition in the condensated construct and cell size or cell shape is not a major determinant of the spatial positioning of the seeded individual cell types. This way, several different cell types with varying physical characteristics may be entrapped in a uniformly scattered order within a 3D scaffold.[23,87,100]

6.624.5.4. From Diffusion to Perfusion

However, diffusion capacity limits the maximum tissue depth in cardiac patches that are engineered according to either principle, and malnutrition and hypoxia may decrease viability of

the core regions of a growing cardiac patch.[71,96,101] For models that use higher initial cell densities resulting in a compact multicellular aggregate, a maximum tissue depth of ~100–200 μm has been proposed by multiple authors. At the most extreme, scaffold-free cardiomyocyte multilayer cultures that are produced by a method referred to as cell sheet engineering may experience diffusion limitations at a very low thickness of the assembly, resulting in a maximum thickness of even less than 100 μm.[101] However, a cardiac patch is unlikely to ever develop the desired active forces for an *in vivo* augmentation of cardiac function, neither will it withstand the forces that are periodically loaded on the various myocardial wall regions *in vivo*, unless the present dramatic limitations on the physical patch dimensions are overcome by novel modifications to the current manufacturing approaches, particularly the limitations regarding the tissue thickness. To this end, a larger thickness of the growing tissue may be achieved by several methods, including (1) targeting a lower cellular density in the final patch, (2) using a scaffold with larger average pores, (3) installing a medium convection system or even a true perfusion via a vascular network, and (4) addition of further cell types, such as endothelial cells and interstitial cells. Concepts of the category (1) and (2) may result in a thicker tissue, but functional results are expected to deteriorate because the scaffold characteristics are likely to overweigh the impact of the inoculated cells.

Following concept (3), a series of bioreactors have been tested by various groups in order to increase the quality of *in vitro* engineered cardiac patches. In early trials, a medium convection at the outer surfaces of the patch resulted already in an improved outcome.[71] Cell viability, total cellular content, and cardiac differentiation markers were improved and these effects may even be further enhanced by the installation of a true perfusion. However, a truly physiologic perfusion pattern depends on an enormous capillary capacity, and a capillary density as it is present *in vivo* may not be achievable *in vitro* because of assumable technical limitations. Notably, the average distance of capillary vessels in the native myocardial tissue ranges in the order of only 15–20 μm.[102] Yet far away from this ideal level of perfusion, a single central vessel in a 3D cardiomyocyte construct may provide the structural platform for a significant improvement in cell viability and function when culture medium is pumped through it.[103] Using disruptive imaging techniques, a spatial correlation of viability with perfusion level may become visible, which demonstrates the striking beneficial effect of relatively simple modifications to an *in vitro* model. Needless to say, along with and even beyond the pure survival of cardiomyocytes, a wide range of functional parameters are strongly dependent on tissue perfusion.[104] Hence, the extension of a central vessel to multiple vessels has been attempted in several studies.[105–107] A cardiac patch that is based on a porous synthetic material containing several scaffold-penetrating channels has been seeded with cardiomyocytes to result in improved spatial cell distribution and preservation of markers of mature cardiomyocytes. However, despite the apparent positive changes regarding the nutrition and oxygen supply in the core regions of the 2-mm-thick cardiac patches, a compact cellular mass of considerably larger depth than 100 μm is difficult to achieve, even in the instance of the use of channeled scaffolds.[105] As a next logical step, more delicate structures have been evaluated for their suitability as substitutes for a vascular network. Branching and collecting ensembles of interconnected tubular structures with smallest diameters created in the range of 60–120 μm have been proven accessible to *in vitro* reendothelialization techniques.[108] Apparently, the ongoing technological progress continuously pushes the limits for miniaturization of biocompatible structural components, such as vascular networks and ECM patterns.[109] Experiments of micropatterned scaffolds have not only extended our understanding of the interrelation of morphology and function but also have opened a new path to the *in vitro* manipulation and generation of multicellular living substrates.[108–112] Whether this trend in experimental downscaling will be guided by a continuous transfer of the involved technology into clinical practice remains speculative. From the clinical view, in the case of a channeled cardiac patch some limitations that may be experienced in replacing a blood barrier function bearing structure (e.g., septal wall between two ventricular chambers or the free ventricular wall) have to be addressed. More challenging, in the case of a miniaturized vascular tree, a connection of all channels to one single network and the linking of this network to the blood circulation warrant further novel strategies before these constructs may be evaluated *in vivo* in long-term studies. In spite of these concerns, the convincing principles that are highlighted by these experiments have set new standards for the generation of a bioartificial cardiac patch.

Another approach that aims at establishing functional tissue perfusion is based on the preservation and employment of an intact native vasculature network after the selective removal of the surrounding cellular components. This method has been developed over the past two decades and has spread among various disciplines as decellularization.[113] However, the field of myocardial tissue engineering has been granted little attention, when compared to similar scientific work with a focus on other tissue types or organ systems, e.g., urological tissue engineering or heart valve tissue engineering.[114–117] But recently, decellularization has experienced a revival as a magic tool to bypass the tremendous problems that currently limit soft tissue engineering concepts. By controlled application of a series of balanced detergent solutions, a disruption of cell–cell and cell–ECM junctions is possible with acceptable changes to the ECM. This principle has been applied to many tissues and organ fragments, including urinary bladder, small intestinal submucosa, skeletal muscle, arterial vessels, and heart valves.[118–121] In a recent study, the perfusion of a rodent heart with detergent solutions resulted in a decellularized whole heart that consequently served as a template for cardiac tissue engineering. By multifocal injection of neonatal rat cardiomyocytes, macroscopic contractile activity may be achieved that contributes to detectable force generation. This preliminary model of a tissue engineered whole heart has been characterized on the histological, the molecular biological, and the electrophysiological level and the *in vitro* results boost the enthusiasm about the future of cardiac tissue engineering. Most importantly, this model already comprises a vascular network of high quality in terms of vessel distribution throughout the scaffold (**Figure 2**). Moreover, a smooth and gradual reduction of the vessel diameter leading on the arterial side from the millimeter scaled aorta down to micrometer scaled capillaries and returning on the venous side from the capillaries to the right atrium are major advantages of the native developmental origin of decellularized scaffolds.[122]

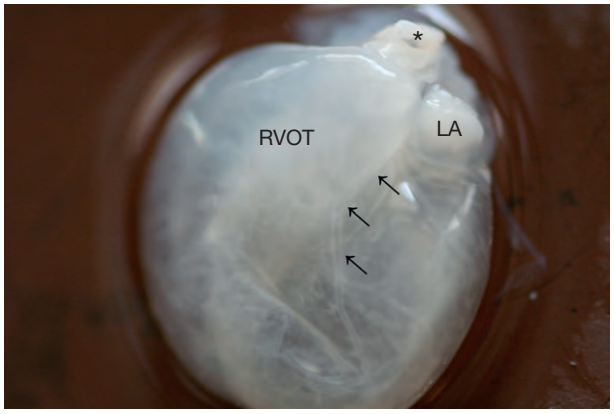

Figure 2 Macroscopic view of a detergent-decellularized rat heart with preserved macrovasculature. Ascending aorta is labeled with asterisks; arrows indicate the left anterior descending artery (LAD). LA, left atrial appendage; RVOT, right ventricular outflow tract.

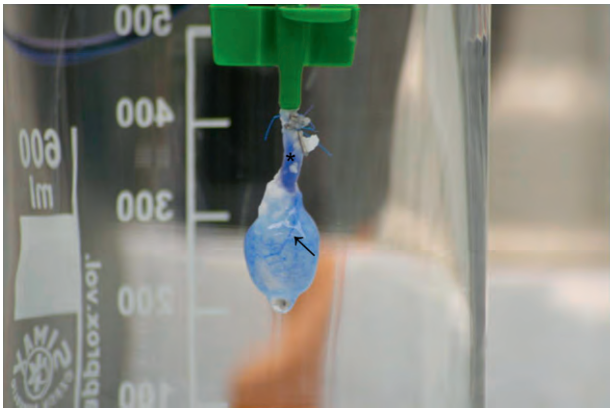

Figure 3 Gross evaluation of the patency of coronary macrovasculature. The ascending aorta (asterisk) is intubated with a canula and a dye solution is injected to perfuse the coronary vascular system in an antegrade fashion to demonstrate the preserved coronary macrovasculature. Arrow indicates the left anterior descending artery (LAD).

However, attention must be directed to maintain patency of the capillary structures, as they may be obstructed by cellular debris during the washing out process along the decellularization. A practical evaluation may be performed by perfusion of the coronary system by indicator dye injection into the aortic root of the decellularized heart (**Figure 3**). However, a quantitative assessment of the microvasculature patency is more challenging and warrants a considerable amount of investigative labor in order to establish valid and reproducible results. Also, a thrombotic occlusion during the subsequent transluminal repopulation (e.g., application of endothelial cells through the coronary vasculature) or during *in vivo* perfusion with whole blood has to be prevented, and more detailed studies have to prove the reproducibility and efficacy of maintained perfusion under *in vivo* conditions.[123–125] However, the proof of concept is there[122] and data from related studies on decellularized cardiovascular implants suggest the feasibility of innate anti-thrombotic measures through modification of decellularization protocols. To this end, a decellularized myocardial ECM ranges among the top candidate scaffolds for the creation of a cardiac patch, as it fulfills several general prerequisites: (i) biocompatibility, (ii) biomechanical stability, (iii) vascularization, and (iv) the potential of biological interaction and remodeling.[116] Ongoing studies will ultimately prove the *in vivo* value of this approach.

According to yet other strategies with the aim to overcome size limitations in cardiac patch engineering, the *in vitro* formation of capillary-like structures by endothelial cells and their progenitors is promoted. Using a liquid scaffold and a mixture of cardiac and endothelial cells, a spontaneous *in vitro* reorganization of both major cell types has been observed by different groups.[23,126] Endothelial cell-derived tubular structures that may resemble primitive capillary-like structures have been observed in synthetic as well as in biological scaffolds during *in vitro* culture. Although the respective structures represent single entities in loose and scattered localization without a uniform continuity, they have been regarded as surrogates of a vascular prearrangement with the option of finalizing maturation on *in vivo* application.[126] The latter issue is demonstrated by trials involving a cardiac implantation model in rodents,[100] which are further discussed in **Section 6.624.5.2**. But irrespective of the possibility of an eventual connection of these primitive capillaries to the systemic circulation, there is a growing body of evidence supporting the hypothesis that a wide range of biological effects on cardiomyocytes and interstitial cells may be triggered by the endothelial cell fraction in a growing cardiac patch. The addition of EC supports the maintenance of a differentiated status, represents a prosurvival factor, and increases functional performance of cardiac patches.[23,127] Surprisingly, although different biological and synthetic scaffold materials with varying microstructure have been employed, the effect of this strategy on the outcome in terms of optimized cell viability and contractile activity was comparably high, suggesting an independent protective role for cocultures of EC in a cardiac patch.

6.624.5.5. Controlled Stimulation by a Cellular Workout Program

'Form follows function.' This often cited basic principle proves valid for a wide range of remodeling processes on the cellular, tissue, and organ level *in vivo*. The most acknowledged examples concerning muscular tissue are hypertrophy on an increased level and the adverse process, hypotrophic degeneration, which occurs after withdrawal of a minimal level of physiological stimulation. Adopting this principle for cardiac tissue engineering purposes, an increasing number of different stimulation modes have been applied in order to control the morphology and function of an *in vitro* engineered cardiac patch construct. Highly effective stimulation of a cardiac patch may be achieved by passive mechanical loading.[87,95,100] In most experimental settings, a periodical loading and unloading of the cardiac patch has been maintained over a period of 7–14 days. In analogy to the physiologically occurring range, most of the past experiments involved a frequency and strain rate that varied between 1 and 2 Hz and 5 and 20%, respectively, depending on the cell donor species.[95,128]

The induced multifaceted effects of mechanical stimulation that are collectively referred to as hypertrophy include a higher content for contractile elements, an increased capacity for aerobic metabolism as determined by increased mitochondrial density, intensified cell–cell and cell–ECM junctions, a reorganization of the cytoskeleton elements, an altered pattern of ECM turnover, and many more.[87,100] In a cardiac patch, an increased level of passive mechanical strength and higher levels of active force generation encourage the use of mechanical stimulation. Furthermore, a structural maturation may be proposed because of the fact that *de novo* ECM production is increased in a stimulated cardiac patch in addition to a spatial cell orientation that is coordinated by the applied mechanical stress. Furthermore, the simple physical agitation of the patch causes a periodical spatial shift of soluble components in the culture medium, which may increase substrate exchange in core parts of a cardiac patch. On the molecular level, markers of mature cell phenotype may be preserved by mechanical stimulation, thus supporting the suitability of a hereby conditioned patch for a successful *in vivo* use.[129,130] Adding to the complexity, when a cardiac patch is stimulated, the primary effects on the cardiomyocytes may be further modulated by paracrine factors that are released from the adjacent noncardiomyocytes.[131,132] Thus, the ultimately achieved optimization covers structural, biomechanical, and electrophysiological maturation, along with further characteristics, such as increased functional response to physiological stimulations, for example, β-adrenergic agents. Under the appropriate level of stimulation, these tremendous effects join in concert to elevate the performance of engineered cardiac patches with macroscopic dimensions. Taking advantage of mechanical stimulation, a series of successful and standard defining experiments have been performed, where *in vitro* cardiac patches from neonatal rat cardiomyocytes were generated. Because of technical issues, a transformation of the physical shape of the same constructs from a rectangular patch to a circular or oval ring was achieved and further modifications by introducing rodent or human ESC-derived cardiomyocytes were performed, each with a high level of success.[133,134] Particularly, the introduction of ESC-derived cells demands a highly instructive environment for a maintained and even improved level of differentiation *in vitro* as well as *in vivo*.[133–135] Mechanical stimulation and other means of guidance of cellular growth and differentiation are tremendously helpful, if not being mandatory components of a successful *in vitro* generation of a cardiac patch.[136,137] The application of cyclic mechanical strain improves the spatial distribution of cells within the ECM, leads to cellular hypertrophy, and also enhances the synthesis of ECM components.[95] These three components of tissue remodeling have been in the center of previous studies on myocardial tissue engineering using mechanical stimulation. The hereof-resulting alternations of tissue characteristics are numerous. Obviously, the overall active (i.e., contractile) force is increased because of enhanced expression of contractile elements by the embedded cardiomyocytes and also by a qualitative shift of the contractile proteins.[138] But passive tissue characteristics are also changed because of the enhanced ECM production under mechanical stimulation.[95] Furthermore, both spatial cell distribution and alignment as well as the presence and distribution of ECM have an impact on the development of cell–cell adhesion complexes, which in turn may influence the contractile tissue activity via mechanical and electrophysiological cues. The complex setting of different tissue characteristics that are altered through mechanical stimulation is yet not fully understood. On the basis of current knowledge, it appears reasonable to assume that the benefits of mechanical stimulation during *in vitro* culture of bioartificial myocardial patch structures, for example, via application of cyclical bidirectional tensile stress to the tissue, are limited by a maximum efficacy range at a certain setting of stimulation (e.g., frequency of cycles per time, proportional displacement of tissue, or maximum force applied at each cycle, configuration of stimulation vs. resting phases, etc.). One of the challenges in myocardial tissue engineering lies in the determination of the optimal parameters of stimulation for every specific combination of cellular and extracellular components. Unfortunately, because of the wide range of the different cell sources and ECM materials in current use, only limited data transfer between different published models of myocardial tissue engineering is possible. The use of different bioreactor systems allowing multiple qualities of stimulation further adds to the complexity of this field.[138]

However, a growing body of evidence suggests the feasibility of further potentiating of *in vitro* generated cardiac patches by the addition of further stimulation modalities.[139] From the current perspective, the ultimate goal is the creation of a fully controlled culture environment that is capable of mimicking various aspects of the organ-specific local milieu that exists *in vivo*. This paradigm has been referred to as the biomimetic approach to tissue engineering.[140,141] The magic tool that may allow investigators to install the anticipated high standards is represented by bioreactor systems that allow simultaneous multimodal stimulation of the growing cardiac patch. Among the top candidates for potent modalities, mechanical stimulation and electrical stimulation are the most explored in cardiac tissue engineering.

6.624.5.6. Pacing for a Better Cardiac Patch

The second modus of stimulation that has resulted in an improved outcome of cardiac patches consists of periodical application of electrical stimulation. In several studies using electrical stimulation, a cardiac patch containing spontaneously contractile cardiomyocytes has served as a solid platform for investigation. Whether field stimulation or direct current application is used, in either case distinct morphological changes and an altered functional performance may be observed *in vitro*. As for the case of mechanical stimulation, the overall response covers a wide range of biological responses that lead to a profound modification of the cardiac patch, including changes in cell morphology, functional integration, and supracellular organization.[70] Electrical stimulation has proven effective in improving the coordinated conduction of action potentials throughout a 3D cardiac patch.[130] An almost doubled impulse propagation velocity was achieved in parallel with an enhanced expression pattern for key proteins of gap junctions, for example, connexin-43.[142] Further structural elements, such as desmosomes and adherens junctions or specific features of mature sarcomeres, such as of *Z*-bands, have been subject to several studies and their presence has been more pronounced in cardiac patches that were produced under electrically or mechanically

stimulated conditions.[88,100] However, the identification of molecular cues for the *de novo* formation of cell–cell junctions in stimulated cardiac patches, most importantly the formation of functional gap junctions, also speaks in favor of the electrical stimulation.[143] Moreover, an improvement of the electrophysiological capacity on the subcellular level has been observed, which has been linked to preservation of a mature and functional sarcoplasmatic reticulum and thereby to maintenance of physiological intracellular calcium handling during excitation as well as relaxation.[144] All of the above-mentioned aspects of cardiac patch maturation by electrophysiological stimulation will gain further importance on a shift of the employed cell source from robust neonatal cardiomyocytes to more delicate cell types or cell entities with a predetermined differentiation fate but not with a fully accomplished terminal differentiation process yet, for example, cardiomyocytes derived from ESC or induced pluripotent stem cells (iPS).

6.624.6. *In Vivo* Maturation of a Cardiac Patch

A tissue engineered cardiac construct that is designed for an *in vivo* utilization as a cardiac patch has to be capable of robust *in vitro* development and also has to survive the *in vivo* milieu after implantation. Hence, in a conceptual way amphibian adoptive capacities are warranted. However, none of the currently presented models convincingly fulfills all of the involved criteria for a distortion-free transition from *in vitro* culture to *in vivo* integration. Ischemic injury, immunologically triggered damage, inappropriate speed of structural remodeling, instable cellular composition, and functional incompatibilities significantly diminish the *in vivo* benefit of a cardiac patch. The following sections are intended as a recollection of the current experience with the observed events *in vivo* after implantation of a cardiac patch and its consequences. In this context, a distinction between two different groups of cardiac tissue engineering models is made. In contrast to a total replacement of cardiac tissue by a patch (**Section 6.624.5.1.**), other models of a structurally supported implantation, for example, by surface superpositioning to the ventricular free wall (**Section 6.624.5.2**), involve a distinct functional setting, and therefore, the discussion of these two families of *in vivo* models is separated.

6.624.6.1. Experimental Transmural Ventricular Replacement

A partial replacement of the myocardial tissue over the full thickness represents a challenging intervention with respect to both surgical technique and perioperative management of the patient. On the long term, the restoration of cardiac function by the implanted material and the associated changes in biomechanics, global geometry, and local milieu are expected to be of major relevance. Tissue engineered cardiac patches hold the promise of an ideal implant that may overcome several limitations of the currently available materials for the use in the clinical arena.

In one of the pioneering *in vivo* studies, a transmural defect in the RVOT of rats was patched with gelatin scaffolds that were implanted as plain biomaterial or after seeding with fetal or neonatal cardiomyocytes. The results on this study documented the feasibility of a small animal model for the study of a partial myocardial replacement. Although the use of gelatin was associated with a considerable inflammatory response, a persistence of the initially seeded cells was suggested. With the degradation of the patch over 12 weeks, a gradual thinning of the implant was noted, which was somewhat prevented by a preimplantation cell seeding. Also an endocardial endothelialization and a neovascularization of the patch were observed after 4 weeks.[145] Using the same model, a comparative study of three scaffold materials for generation of an autologous cardiac patch seeded with smooth muscle cells was conducted with specific focus on the morphological *in vivo* development of the patches.[146] A composite polymer, consisting of poly(caprolactone) and L-lactic acid, was proven superior to porous gelatin or polyglycolic acid (PGA) scaffolds as determined by maintained macroscopic integrity, apparently greater cell accommodation, and a favorable ECM *de novo* synthesis. However, the level of the *in vivo* occurring angiogenesis was comparable.

Since the spread of these and similar reports, different groups have introduced an increasing number of studies that use a full thickness myocardial replacement. Rats have represented the lower end of the size scale of the employed species, whereas large animal models also appear feasible and may offer distinct advantages over small animal models. Because of the wide range of combinatory possibilities between various cell types, different scaffold models, and preparation strategies, a direct comparison may not be appropriate. However, some data have been confirmed by independent studies. In most of the so far published experiments, a gradual formation of vascular networks that penetrate the cardiac patch has been documented. The scaffold properties have an impact on the *in vivo* vascularization, and although an overall benefit of the vascularization is anticipated, such development may be on the basis of adverse events, such as inflammation, and probably related to the utilized scaffold.[145] However, the inoculated cell population also impacts on the *in vivo* vascularization of a cardiac patch and thus may indirectly contribute to structural and functional outcome.[147] In parallel with *in vivo* angiogenesis, a cellular repopulation is observed with ingrowth of activated interstitial cells (i.e., myofibroblasts), smooth muscle cells, endothelial cells, and cell entities that display a partially differentiated phenotype. These findings lead to a topic that has ever since been guided by the question of the underlying mechanisms of angiongenesis and a search for the source of the cells that migrate into a cardiac patch. Using cell-labeling techniques, the survival of the initially seeded cells (i.e., donor cells) in a cardiac patch has been demonstrated for cardiomyocytes and noncardiomyocytes in small and large animal models.[145–147] However, there is no such agreement regarding the recipient cells, which appear in a cardiac patch after a certain time, usually 2–4 weeks *in vivo*. A delay in the repopulation and angiogenesis of central patch regions has led some authors to favor the theory of continuously ingrowing cells from the adjacent native myocardium across the patch margins toward the patch center.[148,149] However, in studies involving the implantation of a noncardiac patch, the scattered pattern of new cardiomyogenic cells on explantation and their predominant localization in the vicinity of scaffold-embedded vessels have been advocates for the hypothesis of a circulating

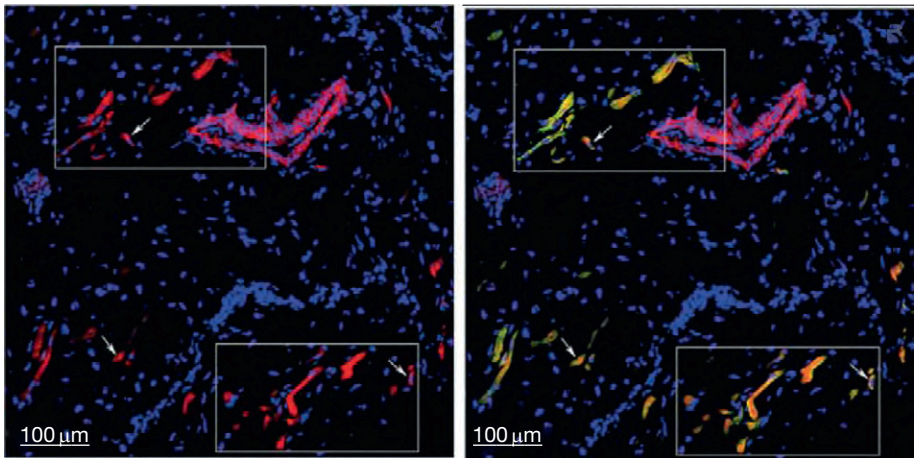

Figure 4 Autologous, noncardiac patches after cardiac implantation for one month. Immunohistochemistry shows premature cardiomyocytes (green, myosin heavy chain; and smooth muscle-α-actin indicated by arrows) of varying size around a mesenteric artery (red, smooth muscle-α-actin). (a) shows staining for muscle-α-actin (red) with nuclear counterstaining by DAPI (blue). Colocalization of yellow color (in b) results from overlapping green and red signals. Adapted from Tudorache, I.; Kostin, S.; Meyer, T.; *et al. Eur. J. Cardiothorac. Surg.* **2009**, *36*, 306–311; discussion 311.

cell source[150] (Figure 4). Irrespective of their original source, *in vivo* repopulating cells contribute to the development of a cardiac patch and their frequency appears to vary with different initially present scaffolds and cell components. The history of *in vivo* studies on cardiac patches comprises a shift from more primitive but robust cell sources (e.g., neonatal rat cardiomyocytes) to more delicate cell sources with the perspective of a future clinical application. Hence, mesenchymal stem cells have been studied on several occasions for their potential as progenitors of mature cardiomyocytes. Unfortunately, the available amount of data is yet too small, with a varying experimental framework and heterogeneous levels of cell characterization in each report further complicating a clear conclusion. Hence, controversial results are available regarding the potential of mesenchymal stem cells to give rise to cardiomyocytes.[147,148,151] More interestingly, in several studies the analysis of ingrowing cell types has indicated that cells with phenotype characteristics of cardiomyocytes may be observed over time within the implanted cardiac patch, even in the instance of an initially acellular implant.[149,150,152,153] The contribution to the overall outcome after a cardiac patch implantation harboring cardiomyocytes as opposed to non-cardiomyocytes has been studied on different morphological levels, including (i) the extent of patch vascularization, (ii) alternations in the physical dimensions of the patch, (iii) the source of the overall ventricular dimensions, (iv) functional ventricular performance, and many more. In general, a superior effect of cell-seeded patches over plain scaffolds is expected with respect to morphology on the macroscopic and microscopic level. The hallmarks of the better outcome are defined by an attenuation of the ventricular dilatation, prevention of patch thinning, and aneurysm formation and by the *de novo* synthesis of ECM components and microvascular structures along with a balanced repopulation throughout the patch vicinity.[147,151,154,155] These elements of a favorable outcome have been observed in synthetic biomaterials as well as biological scaffolds[153,155] and may be enhanced by the addition of cells to the patch. The ultimate goal of a functional improvement is determined by further parameters, such as the global (ventricular) and regional (patch areal) contractility and relaxation patterns, as well as the resulting force and pressure indices. Few recent studies have included sophisticated diagnostic algorithms to address a number of these questions.[148,149,156] In the limited number of studies that have been performed to date, the superiority of novel biomaterials over conventional patch materials (e.g., Dacron) has been proved with respect to several core parameters[146] including regional systolic function in the area of the implanted cardiac patch and a partial recovery of electrophysiological activation levels at the implant site.[149,156] Using even more biocompatible implants, such as an autologous patch of noncardiac origin but with preserved native vasculature, an elegant setup for the study of cardiomyocyte regeneration along with a tool for the successful surgical management of regional myocardial defects has been introduced.[150] This effect is probably related because of a spontaneous *in vivo* repopulation of cardiac patches by different cell types, including myogenic cells, although specific markers of differentiated cardiomyocytes (α-sarcomeric actinin, α-myosin heavy chain, specific Troponin isomers, presence and distribution pattern of specific cell adhesion proteins, developmentally altered nuclear expression, etc.) are infrequently analyzed (Figure 4).[148,150,153] In some studies and under different experimental settings, even opposing evidence has been gathered regarding the *de novo* generation of cardiomyocytes in MSC-seeded cardiac patches.[147] Hence, the quantitative range of the *in vivo* cardiac regeneration in an implanted full thickness patch varies considerably, even within reported series on the same scaffold material.[149,153,157,158] However, some fundamental benefits in terms of qualitative changes in patch morphology are commonly observed that speak in favor of the concept of guided tissue regeneration, that is, achievement

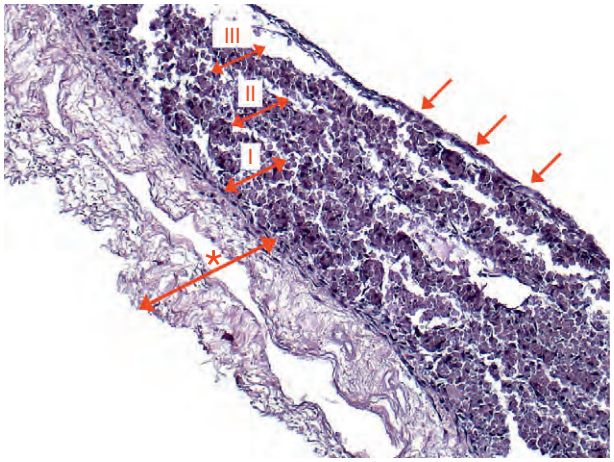

Figure 5 Cell sheet engineering and vascularized biological matrix. Neonatal rat cardiomyocyte cell sheets were cultured on a three-dimensional, vascularized biological matrix (decellularized porcine intestinal submucosa) to result in a single vital and vascularized myocardial patch. I–III indicate three cell sheets stocked over the vascularized (asterisk) ECM. Single headed arrows indicate an outer lining of *de novo* grown cells with myofibroblastoid phenotype. H&E staining, magnification: 50×. Image provided by Dr. Hilfiker.

of a functional benefit with an implant that experiences significant remodeling and final maturation after the implantation. In order to support this process, the scaffold alone may not be the most potent solution. Further improvement may be achieved through the *in vitro* addition of autologous cellular cues with the inherent potential of cardiomyogenic regeneration.

Unfortunately, on review of the reported effects of cell seeding and the choice of a specific cell type or cell differentiation level, the available functional data are even more diverse and difficult to interpret, a situation that may be compared to the obstacle in the meta-analysis of cell transplantation studies. So far, the effect of seeding of uncommitted mesenchymal stem cells may be questioned, whereas the initiation of a cardiac lineage commitment may result in an improvement of global ventricular function and measurable pressure indices.[147,151,159] Advanced cell seeding techniques and *in vitro* conditioning are major fields of future optimization (**Figure 5**).[101,147] Future strategies are likely to employ current *in vitro* techniques for controlled cardiomyocyte differentiation and angiogenesis in the setting of stem or progenitor cell seeded cardiac patches for a transmural myocardial reconstruction. Of particular interest is that an evaluation of the model *per se* has to be performed, as the currently available data are based on surgery in different animal species (i.e., rat, dog, or pig) on healthy or experimentally injured (i.e., with prior ischemic infarction) hearts. The bottleneck for *in vivo* applications will most likely be the establishment of a functional vascular network that is connected with the systemic circulation in order to supply the patch with sufficient metabolic substrates for increased biomechanical strength, high cellular density, and differentiation level. All of the latter parameters are hallmarks of functional performance and have to be coordinated in a single multifaceted biological system.

6.624.6.2. Experimental Ventricular Support by Patch Material

In contrast to the applications that are outlined in the previous section, the herein described models involve a cardiac patch that is primarily intended as a transport vehicle for cell transfer purposes. In other words, the following models described here are in a way an extension of cell transplantation studies. Obviously, all of these experiments involve a preserved continuity of all cardiac structures. In this sense, we are dealing with cardiac patch models that serve as supporting structures (as opposed to patches for a reconstruction by tissue replacement). The indication for a supporting patch is the treatment of an ischemic myocardial area (acute setting)[160] or a postischemic myocardial scar area[126,161,162] and application is performed by superpositioning of the patch onto the target myocardial region and fixation by suturing or gluing (e.g., with fibrin glue).

The idea of using a cardiac patch as transport vehicle is on the basis of the observation that the majority of cells are lost during other implantation procedures and a very low fraction, generally less than 10%, experience an acute engraftment. Further diminishing of the cell number is attributed to the hostile environment, which affects the isolated and unprotected cells in a direct manner. Thus, the concept of patch-mediated cell transfer was introduced. Initial studies using porous scaffolds confirmed the efficacy of patch implantation for sustained delivery of cardiac cells and prevention of adverse remodeling of ischemic hearts,[66,80] along with the demonstration of interstitial cell repopulation and vascular sprouting phenomena from the surrounding myocardial tissue. Interestingly, similar effects were described for cardiac patches where skeletal myoblasts were used instead of cardiac cells.[162] In a series of continuously optimized experiments, the engraftment, survival, *in vivo* vascularization, and continued functional performance of cardiac patches made of collagen-based scaffolds and cardiac cells were successfully demonstrated in small animal models of MI by LAD ligation.[100,126,163]

On the morphological level, embedded primary cardiomyocytes were organized in a compact and oriented pattern and maintained a high level of differentiation. This has been interpreted as an indicator of advanced culture maturation. As outlined in **Section 6.624.7**, such *in vitro* casted patches provide a highly homogeneous and compact microarchitecture, which turns them to be a particularly suitable tool for a supporting application where the ultimate biomechanical strength is somewhat less limiting.

In most studies, the epicardial implantation of a cardiac patch led to a significantly improved cardiac function as opposed to untreated hearts, and this had an impact on the overall animal survival. By using elaborate techniques in extensive series of experiments, the evidence for a functional integration of a cardiac patch with the host myocardium was demonstrated on the electrophysiological level.[100] Also, a maintained contractile activity has been demonstrated, which supports the hypothesis of partial contribution of active biomechanical performance to the overall benefit of a cardiac patch. When significant numbers of endothelial cells are mixed with the cardiac cells, the resulting patch will experience an accelerated *in vivo* vascularization, which is regarded as a key

component of favorable long-term development for the patch and the overall organ function. Recently, further modifications to the preparation protocols of a cardiac patch have been introduced to promote an intensified and accelerated *in vivo* angiogenesis.[164] Some modifications are based on the intrinsic capacity of the recipient organism; that is, in the clinical setting the patient's body is to act as an ideal bioreactor. In such a staged concept of tissue engineering, parts of the final tissue are implanted and preincubated at a remote location in the recipient organism in order to initiate a prevascularization or partial interstitial repopulation of the tissue, before explantation and further *in vitro* processing of the tissue can take place. After the final preparation is completed, the mature implant tissue is transferred to the target body site, for example, the posterior ventricular wall of the heart. Further scientific interest and considerable clinical attention has been attracted by another concept that is on the basis of the engineering of cell monolayers that can be detached from the culture dish and stacked on each other to form a multilayered, 3D cell culture. This concept that is referred to as cell sheet engineering has become available through chemical engineering advances and the advent of thermoresponsive polymers that can change their surface characteristics from hydrophilic to hydrophobic, depending on the temperature that they are exposed to. The fascinating advantage of this technology lies in the elimination of the need for enzymatic solutions for detachment of cell assemblies from the culture substrate. This is particularly of interest in the culture of cell entities with high degree of cell–cell adhesions, for example, cardiomyocytes that functionally depend on intact gap junctional connections. Using neonatal rat cardiomyocytes as a spontaneously beating cell source, this technology has been shown to result in beating 3D constructs with remarkably reproducible results and stable performance over time.[165,166] Even more interesting, some experimental reports demonstrate signs of electrophysiological integration of cell sheets within the implant site after the application to a recipient's heart.[167] Following this report, the involved technology has been applied to many cell types to enable regenerative therapy in the context of various organ systems. In the context of heart disease, the quest for the ideal cell source still goes on. A potential solution may be the acceptance of noncardiomyogenic cells as the therapeutic cell type, which has led some groups to apply interstitial cells or endothelial cells for ischemic or dilatative cardiomyopathies.[168] After the partially satisfying results of clinical trials performing myoblast cell transplantation for ischemic heart disease, the use of these cells in the form of multilayered cell sheet constructs has gained experimental attention recently,[36,169] and consecutive clinical attention may lead to a multicenter clinical trial that may in near future resume to evaluate the clinical relevance of cell sheet engineering in combination with skeletal myoblasts. However, beyond skeletal myoblasts further adult cells, such as mesenchymal stem cells, and also other progenitor or stem cells are regarded as candidate sources for the generation of a living cardiac patch.[170] Scientific debate is currently concentrated around the functional integration of cell sheets after their cardiac implantation, that is, (1) electrophysiological integration without the initiation of ectopic potentials; (2) biomechanical integration; and (3) rapid access of the sheet-enclosed cells to the tissue supplying vascular network *in vivo*.[171,172]

Other exciting developments include the use of stem or progenitor cells with the potential to generate autologous cardiomyocytes.[173] The latter option is a crucial one, because the optimal use of this technology remains unclear despite the numerous advantages of cell sheet engineering (e.g., better functional state of the cell components due to the omission of aggressive enzymes, physiological orientation and polarization of cells within the initial assembly, omission of artificial ECM materials, and more physiological ratio of cellular to extracellular components). As a matter of fact, it remains yet unclear whether an available adult cell source, that is, skeletal muscle, will clinically prove as sufficiently appropriate to initiate a true turn in the fatal cascade of heart failure which is observed in the setting of an ischemic or dilatative cardiomyopathy. Clinical trials certainly will be needed to shed some light on the clinical value of cell sheets as cardiac patch implants.

Whereas cell sheets are initially based on cellular components only, the exact opposite concept to achieve a cardiac patch is described by a cell free ECM material that becomes repopulated *in vivo* after implantation, for example, onto the region of a MI. In this setting, the implant material may fulfill mechanical function by preventing a progressive dilatation of postinfarction scar tissue. By choosing appropriate biomaterials with certain biodegradation kinetics and favorable bioinstructive characteristics, an ideal patch material may induce a local regenerative remodeling of the host tissue. Different groups using various ECM materials have evaluated such a concept. In a recent report, polyester urethane urea has been used as a cell free cardiac patch material after a subacute MI.[174] The application of this elastomeric and biodegradable material resulted in functional and histological improvement over time, leading to a diminished deterioration of left ventricular function as well as increased myogenic protein mass in the infarct region (**Figure 6**), which may be related to an increase in smooth muscle cell proliferation in response to the patch implantation. Also, a new vascularization at the vicinity of the biomaterial was observed (**Figure 7**). As indicated in **Section 6.624.4**, the bioactive action of modern biomaterials may be further enhanced by addition of functional bioactive molecules, such as gene encoding DNA, ECM degrading enzymes, and specific growth factors.[59] In another recent report, clinically relevant degradation patterns have been demonstrated for composite synthetic materials, with gradually released products being soluble and nontoxic. Future chemical engineering advances may provide further degrees of freedom, integrated in one single synthetic ECM material.

However, despite the apparently unbound options for some of the aforementioned models to promote comprehensive *in vivo* integration of a cardiac patch, competing experimental setups have resulted in partially divergent results, particularly with respect to stem cell homing, survival, and differentiation.[160,175] Therefore, the elucidation of the crucial factors that lead to a wide diversification of the individual outcome of similar experiments deserves a high priority setting in the upcoming investigative engagements. Finally, the general suitability of a supportive, patch-based cell therapy for the treatment of conditions other than ischemic cardiac disease may be defined in a more precise way,[36] once the underlying mechanisms are better understood.

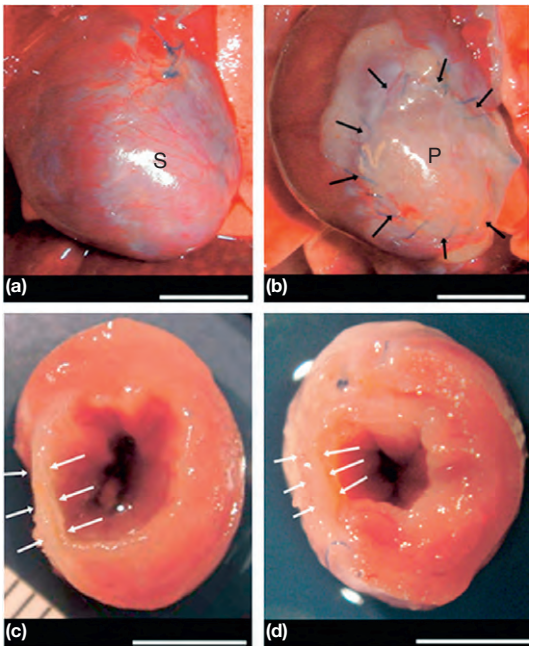

Figure 6 Implantation of a biodegradable polyester urethane urea (PEUU) material to prevent adverse postmyocardial infarction (MI) remodeling of the left ventricle. Control animals experienced scar formation and subsequent thinning of the respective LV wall region (a, c). The PEUU biomaterial (P in image b) was implanted onto the MI area to result in an enforced LV wall after 8 weeks, as demonstrated by cross-sectional view images (d). Black arrows point to the implanted PEUU patch (b), and white arrows indicate the infarcted anterior wall (c, d). Scale bar: 55 mm. P, the patch implanted area; S, the infarcted scar. Adapted from Fujimoto, K. L., Tobita, K., Merryman, W. D., *et al. J. Am. Coll. Cardiol.* **2007**, *49*, 2292–2300.

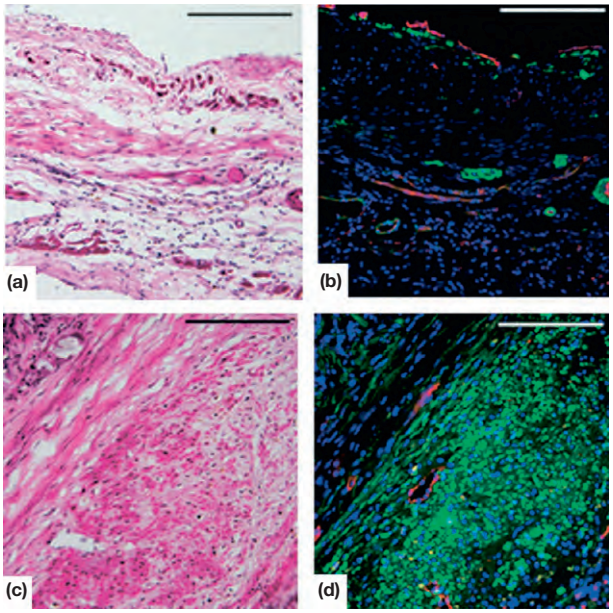

Figure 7 Histological evaluation of post-infarction myocardial tissue (a, b) and polyester urethane urea (PEUU) patched (c, d) myocardial wall 8 weeks after implantation shows a dense repopulation of the biomaterial resulting in a *de novo* tissue generation (c), where increased smooth muscle actin is apparent (green, α-smooth muscle actin) (d). Also, new microvascular structures that stain positive for endothelial markers (such as CD31, red) are observed within the formerly acellular patch. Nuclear staining appears blue. Scale bars are 200 μm. Adapted from Fujimoto, K. L., Tobita, K., Merryman, W. D., *et al. J. Am. Coll. Cardiol.* **2007**, *49*, 2292–2300.

6.624.7. Scientific Frontiers

The *in vitro* creation of a cardiac patch, the ultimate goal of the scientific field of cardiac tissue engineering, has experienced considerable progress over the past two decades. Above the so far achieved bioengineered tissue products, the extent of knowledge and insight into the cell biological events that govern the *in vitro* maturation and *in vivo* integration of cell seeded biomaterials are of great value for the ongoing and future experimental work.

Our understanding of the complexity of cell–cell and cell–ECM interactions even in the most simple 3D culture models has led us to reevaluate our knowledge about the natural developmental process of tissue formation. In fact, a number of biological events that occur during early native development are of crucial importance for the *in vitro* culture of 3D multicellular cultures.[176] Hence, the development of increasingly complex bioreactor systems that allow for the controlled *in vitro* mimicking of *in vivo* conditions with respect to a variety of parameters has become a scientific field of its own. One of the future challenges in cardiac tissue engineering will be the designing and engineering of bioreactor systems that provide maximum control over numerous culture conditions and also allow for the online and noninvasive monitoring of vital parameters in the developing culture.

In the field of cardiac patch engineering, the importance of cell type diversity has become evident. Hence, the role of multifunctional bioreactor systems has gained further importance. The need for cell types other than the cardiomyocyte fraction or the progenitors is even more urgent in studies that involve clinically more relevant progenitor or stem cell populations. It appears necessary to apply more than one single cell population in order to create a functional cardiac patch;[23] more interestingly, an increase in the complexity of the employed cell population may result in an advanced differentiation status and a higher functional outcome.[177] Thus, a successful approach for bioengineering of a cardiac patch includes the careful choice of a number of cell types and also will have to consider a well-planned sequence of introduction of theses cells into the developing tissue construct.[177]

One of the most relevant limitations to current bioengineering approaches to create a clinically useful cardiac patch concerns the cell source for the creation of a sufficient amount of autologous cardiomyocytes or their functional substitutes. Beyond the aforementioned ESC and iPS, other cell sources for obtaining pluripotent stem cells have been suggested in recent studies.[178,179] However, despite the discovery of different adult stem cell entities, some of them available in the adult human body, no method has provided the necessary quantity and quality of cells that are needed for the creation of a cardiac patch of significant size and function. Hence, novel concepts of cell harvesting, amplification, and preimplant conditioning

are most warranted for future successful application of a cardiac patch.

As outlined in Section 6.624.8, perfusion remains a problem in most of the current experimental models of myocardial tissue engineering and until today, no clinically relevant solution has been suggested to overcome the boundaries that are defined by diffusion limits. While some of current approaches involve cutting-edge biomedical and engineering sciences,[108,110] others rediscover principles that have already been applied decades ago.[180–182] It appears unpredictable whether a completely *in vitro* engineered or *in vitro* modified vascular network will prove successful in the long-term perfusion of a cardiac patch in a potentially pathological environment, such as an ischemic heart.[101,108,110,122] However, it remains unchallenged that a functional perfusion system is necessary, and thus, further improvements of available concepts or the development of novel strategies will be subjects of future investigation.

A series of *in vivo* studies have demonstrated the impact of a postimplantation remodeling on the morphological and functional development of a cardiac patch. A clinically relevant concept of cardiac patch engineering has to recognize the possible mechanisms of both beneficial and adverse graft remodeling *in vivo*. The preservation of the morphological and functional features of a cardiac patch translates into patient safety and overall success of the concept. Moreover, further gains in function and a physiological maturation on the morphological level characterize a superb outcome in the long term. Evidence from previous studies suggests the involvement of a large number of factors that affect the *in vivo* maturation of a cardiac patch. The complexity of the *in vivo* regulation and the numerous cross talk possibilities of these biological mediators question the feasibility of a successful therapeutic manipulation at a single factor level. Instead, a large group of single events and their mediators may be influenced, hoping for a desired overall outcome. One of the most relevant biological complexes is referred to as the postimplantation inflammatory response and many studies have focused on a therapeutic modulation.[16] Some preliminary studies that aimed at the *in vitro* modulation of the fate of a tissue engineered patch have employed single cytokines or a defined mixture to enhance the functional outcome, and it appears likely that more complex protocols involving a sequence of multiple factors with varying concentrations over time will lead to higher success rates in terms of morphological and functional maturation.[164]

6.624.8. Clinical Relevance and Perspectives

The field of tissue engineering has fascinated basic science investigators to the same degree as clinicians and a therapeutic implementation of laboratory grown tissues and organs has been predicted years ago. However, as with many other scientific fields, the optimism of the first few years has been challenged by a series of limitations and problems that were encountered in the following era of detailed *in vivo* studies. Notably, other previous concepts of end-stage heart failure have been developed and clinically introduced with a tremendous amount of effort and guided by a major wave of scientific and public enthusiasm.[183,184] The frustration on the investigator's side and the public disappointment about the long-term limitations of the concept of dynamic cardiomyoplasty are only two of the many recent examples for the demanding process of a successful bench-to-bedside transfer of a therapeutic approach to end-stage heart failure.[185–187] A bioengineered cardiac patch that is designed to change the fate of heart failure is yet far away from mankind's access.

Moreover, the clinician's point of view regarding the real demand for a bioengineered cardiac patch has not always been consistent with the predicted problems that have been driving the laboratory engagements. For instance, a contractile bioengineered cardiac patch may in theory represent the optimal solution for the repair of an ASD or a VSD, but considering the excellent clinical long-term outcome of synthetic patch materials, it is questionable whether a similar reproducibility and long-term durability will be achieved by a bioengineered patch. In addition, the laboratory manufacturing of such a cardiac patch will certainly need a vast amount of investment in terms of personal and material resources, which will have to be rewarded by a superior clinical outcome and thus also by a long-term benefit on the economic level.

The currently most exciting frontier is defined by experimental work to increase the maximum tissue thickness and to enhance the level of the actively generated contractile force by 3D bioengineered cardiac structures. These strategies, when paired with a clinically relevant cell source and effective *in vivo* maturation guiding mechanisms, ultimately may result in a concept with a realistic clinical perspective that can stand the competition from relatively cheap and ubiquitously available synthetic biomaterials already available on market.

6.624.9. Summary

In the young history of cardiac tissue engineering, significant improvements have been introduced, and the turnover rate in the applied models and concepts has been remarkably high. Early models of a bioengineered cardiac patch consisted of porous materials made of simple polymers or biological materials such as collagen and alginate, which were seeded with suspensions of primary cardiac cells to result in a contractile 3D structure. With growing experience, a diversification of the employed cells with a trend toward more immature progenitor or stem cells was paralleled with the introduction of decellularized biological scaffolds as well as novel synthetic scaffolds that were produced according to sophisticated biochemical engineering methods. Further input to this field was granted by the application of advanced bioreactor systems that provide an increasing level of control over major culture conditions *in vitro*. The induction and maturation of a vascular network, the introduction of a clinically relevant cell source, and the validation of the entire elements of a cardiac patch in an appropriate preclinical model are further challenges that the current cardiac tissue engineering field is confronted with.

References

1. Buckberg, G. D. *Eur. J. Cardiothorac. Surg.* **2006**, *29*(Suppl. 1), S2–S3.
2. Torrent-Guasp, F.; Buckberg, G. D.; Clemente, C.; Cox, J. L.; Coghlan, H. C.; Gharib, M. *Semin. Thorac. Cardiovasc. Surg.* **2001**, *13*, 301–319.

3. Buckberg, G. D.; Mahajan, A.; Jung, B.; Markl, M.; Hennig, J.; Ballester-Rodes, M. *Eur. J. Cardiothorac. Surg.* **2006**, *29*(Suppl. 1), S165–S177.
4. Korecky, B.; Hai, C. M.; Rakusan, K. *Can. J. Physiol. Pharmacol.* **1982**, *60*, 23–32.
5. Steinhausen, M.; Tillmanns, H.; Thederan, H. *Pflugers Arch.* **1978**, *378*, 9–14.
6. Pieperhoff, S.; Borrmann, C.; Grund, C.; Barth, M.; Rizzo, S.; Franke, W. W. *Eur. J. Cell Biol.* **2010**, *89*, 365–378.
7. Rubart, M.; Zipes, D. In *Heart Disease*; Braunwald, E., Zipes, D. P., Libby, P., Eds.; W.B. Saunders: Philadelphia, PA, 2001; Vol. 1, pp 659–699.
8. Yu, H.; Gao, J.; Wang, H.; *et al. Circ. Res.* **2000**, *86*, 1062–1068.
9. Beltrami, A. P.; Barlucchi, L.; Torella, D.; *et al. Cell* **2003**, *114*, 763–776.
10. Messina, E.; De Angelis, L.; Frati, G.; *et al. Circ. Res.* **2004**, *95*, 911–921.
11. Brilla, C. G.; Reams, G. P.; Maisch, B.; Weber, K. T. *Eur. Heart J.* **1993**, *14*(Suppl. J), 57–61.
12. Butt, R. P.; Bishop, J. E. *J. Mol. Cell. Cardiol.* **1997**, *29*, 1141–1151.
13. Goldspink, G. *J. Anat.* **1999**, *194*(Pt 3), 323–334.
14. Dokos, S.; Smaill, B. H.; Young, A. A.; LeGrice, I. J. *Am. J. Physiol. Heart Circ. Physiol.* **2002**, *283*, H2650–H2659.
15. Cushing, M. C.; Liao, J. T.; Anseth, K. S. *Matrix Biol.* **2005**, *24*, 428–437.
16. Dobaczewski, M.; Gonzalez-Quesada, C.; Frangogiannis, N. G. *J. Mol. Cell. Cardiol.* **2010**, *48*, 504–511.
17. Eschenhagen, T.; Fink, C.; Remmers, U.; *et al. FASEB J.* **1997**, *11*, 683–694.
18. Klingel, K.; Kandolf, R. *Semin. Thromb. Hemost.* **2010**, *36*, 195–202.
19. Singh, M.; Foster, C. R.; Dalal, S.; Singh, K. *J. Mol. Cell. Cardiol.* **2010**, *48*, 538–543.
20. Bereczki, E.; Santha, M. *Connect. Tissue Res.* **2008**, *49*, 129–132.
21. Nishioka, T.; Onishi, K.; Shimojo, N.; *et al. Am. J. Physiol. Heart Circ. Physiol.* **2010**, *298*, H1072–H1078.
22. Ratajska, A.; Campbell, S. E.; Cleutjens, J. P.; Weber, K. T. *J. Lab. Clin. Med.* **1994**, *124*, 408–415.
23. Caspi, O.; Lesman, A.; Basevitch, Y.; *et al. Circ. Res.* **2007**, *100*, 263–272.
24. Sarris, G. E.; Kirvassilis, G.; Zavaropoulos, P.; *et al. Eur. J. Cardiothorac. Surg.* **2010**, *37*(6), 1285–1290.
25. Moritz, A.; Ozaslan, F.; Dogan, S.; Abdel-Rahman, U.; Aybek, T.; Wimmer-Greinecker, G. *J. Interv. Cardiol.* **2005**, *18*, 523–527.
26. Saleh, S.; Liakopoulos, O. J.; Buckberg, G. D. *Eur. J. Cardiothorac. Surg.* **2006**, *29*(Suppl. 1), S126–S138.
27. Kirali, K.; Mansuroglu, D.; Ozen, Y.; *et al. Asian Cardiovasc. Thorac. Ann.* **2003**, *11*, 135–138.
28. Hoffman, J. I.; Kaplan, S. *J. Am. Coll. Cardiol.* **2002**, *39*, 1890–1900.
29. Nishimura, R. A.; Carabello, B. A.; Faxon, D. P.; *et al. Circulation.* **2008**, *118*, 887–896.
30. Park, C. S.; Lee, J. R.; Lim, H. G.; Kim, W. H.; Kim, Y. J. *Eur. J. Cardiothorac. Surg.* **2010**, *38*(3), 311–317.
31. Hickey, E. J.; Veldtman, G.; Bradley, T. J.; *et al. Eur. J. Cardiothorac. Surg.* **2009**, *35*, 156–164; discussion 164.
32. Barron, D. J.; Kilby, M. D.; Davies, B.; Wright, J. G.; Jones, T. J.; Brawn, W. J. *Lancet* **2009**, *374*, 551–564.
33. Miyamoto, S. D.; Pietra, B. A.; Chan, K. C.; *et al. Pediatr. Cardiol.* **2009**, *30*, 419–425.
34. DiBardino, D. J.; McElhinney, D. B.; Marshall, A. C.; Bacha, E. A. *Pediatr. Cardiol.* **2008**, *29*, 251–257.
35. Towbin, J. A.; Lowe, A. M.; Colan, S. D.; *et al. JAMA* **2006**, *296*, 1867–1876.
36. Kondoh, H.; Sawa, Y.; Miyagawa, S.; *et al. Cardiovasc. Res.* **2006**, *69*, 466–475.
37. Marcus, F. I.; McKenna, W. J.; Sherrill, D.; *et al. Circulation* **2010**, *121*, 1533–1541.
38. Dubrey, S. W.; Falk, R. H. *Prog. Cardiovasc. Dis.* **2010**, *52*, 336–346.
39. Fressart, V.; Duthoit, G.; Donal, E.; *et al. Europace* **2010**, *12*(6), 861–868.
40. Shah, J. S.; Hughes, D. A.; Tayebjee, M. H.; MacFadyen, R. J.; Mehta, A. B.; Elliott, P. M. *J. Inherit. Metab. Dis.* **2007**, *30*, 88–95.
41. Pierre-Louis, B.; Kumar, A.; Frishman, W. H. *Cardiol. Rev.* **2009**, *17*, 31–35.
42. Biolo, A.; Ribeiro, A. L.; Clausell, N. *Prog. Cardiovasc. Dis.* **2010**, *52*, 300–316.
43. Dubrey, S. W.; Burke, M. M.; Khaghani, A.; Hawkins, P. N.; Yacoub, M. H.; Banner, N. R. *Heart* **2001**, *85*, 202–207.
44. Kristen, A. V.; Sack, F. U.; Schonland, S. O.; *et al. Eur. J. Heart Fail.* **2009**, *11*, 1014–1020.
45. Corno, A. F.; Laks, H.; George, B.; Williams, R. G. *Ann. Thorac. Surg.* **1987**, *43*, 443–444.
46. Kreutzer, C.; Kreutzer, G. O.; De, C. M. R.; *et al. Semin. Thorac. Cardiovasc. Surg. Pediatr. Card. Surg. Annu.* **1999**, *2*, 65–76.
47. Sheikh, A. M.; Elhenawy, A. M.; Maganti, M.; Armstrong, S.; David, T. E.; Feindel, C. M. *J. Thorac. Cardiovasc. Surg.* **2009**, *138*, 69–75.
48. Bacha, E. A.; Scheule, A. M.; Zurakowski, D.; *et al. J. Thorac. Cardiovasc. Surg.* **2001**, *122*, 154–161.
49. David, T. E. *J. Heart Valve Dis.* **1998**, *7*, 13–18.
50. Barber, F. A.; Aziz-Jacobo, J. *Arthroscopy* **2009**, *25*, 1233–1239.
51. Gaertner, W. B.; Bonsack, M. E.; Delaney, J. P. *J. Gastrointest. Surg.* **2007**, *11*, 1275–1285.
52. Simon, P.; Kasimir, M. T.; Seebacher, G.; *et al. Eur. J. Cardiothorac. Surg.* **2003**, *23*, 1002–1006; discussion 1006.
53. Ruffer, A.; Purbojo, A.; Cicha, I.; *et al. Eur. J. Cardiothorac. Surg.* **2010**, *38*(1), 78–85.
54. Benton, J. A.; Fairbanks, B. D.; Anseth, K. S. *Biomaterials* **2009**, *30*, 6593–6603.
55. Raeber, G. P.; Lutolf, M. P.; Hubbell, J. A. *Biophys. J.* **2005**, *89*, 1374–1388.
56. Adelow, C.; Segura, T.; Hubbell, J. A.; Frey, P. *Biomaterials* **2008**, *29*, 314–326.
57. Lee, S. T.; Yun, J. I.; Jo, Y. S.; *et al. Biomaterials* **2010**, *31*, 1219–1226.
58. Kraehenbuehl, T. P.; Zammaretti, P.; Van der Vlies, A. J.; *et al. Biomaterials* **2008**, *29*, 2757–2766.
59. Guan, J.; Stankus, J. J.; Wagner, W. R. *J. Control. Release* **2007**, *120*, 70–78.
60. Ehrbar, M.; Zeisberger, S. M.; Raeber, G. P.; Hubbell, J. A.; Schnell, C.; Zisch, A. H. *Biomaterials* **2008**, *29*, 1720–1729.
61. Chang, W. Y.; Hsiao, Y. C.; Shau, M. D. *J. Biomater. Sci. Polym. Ed.* **2010** [Epub ahead of print].
62. Trentin, D.; Hubbell, J.; Hall, H. *J. Control. Release* **2005**, *102*, 263–275.
63. Kwon, J. S.; Park, I. K.; Cho, A. S.; *et al. J. Control. Release* **2009**, *138*, 168–176.
64. Nguyen, M. K.; Lee, D. S. *Macromol. Biosci.* **2010**, *10*, 563–579.
65. Kofidis, T.; Lebl, D. R.; Martinez, E. C.; Hoyt, G.; Tanaka, M.; Robbins, R. C. *Circulation* **2005**, *112*, I173–I177.
66. Li, R. K.; Jia, Z. Q.; Weisel, R. D.; Mickle, D. A.; Choi, A.; Yau, T. M. *Circulation* **1999**, *100*, II63–II69.
67. Cima, L. G.; Vacanti, J. P.; Vacanti, C.; Ingber, D.; Mooney, D.; Langer, R. *J. Biomech. Eng.* **1991**, *113*, 143–151.
68. Freed, L. E.; Vunjak-Novakovic, G. *In Vitro Cell. Dev. Biol. Anim.* **1997**, *33*, 381–385.
69. Akins, R. E.; Boyce, R. A.; Madonna, M. L.; *et al. Tissue Eng.* **1999**, *5*, 103–118.
70. Bursac, N.; Papadaki, M.; Cohen, R. J.; *et al. Am. J. Physiol.* **1999**, *277*, H433–H444.
71. Carrier, R. L.; Papadaki, M.; Rupnick, M.; *et al. Biotechnol. Bioeng.* **1999**, *64*, 580–589.
72. Carrel, A.; Burrows, M. T. *J. Exp. Med.* **1911**, *13*, 387–396.
73. Carrel, A.; Lindbergh, C. A. *Science* **1935**, *81*, 621–623.
74. Simms, H. S.; Stillman, N. P. *J. Gen. Physiol.* **1937**, *20*, 603–619.
75. Carrel, A. *JAMA* **1983**, *250*, 1085.
76. Borg, T. K.; Rubin, K.; Lundgren, E.; Borg, K.; Obrink, B. *Dev. Biol.* **1984**, *104*, 86–96.
77. Vacanti, J. P.; Morse, M. A.; Saltzman, W. M.; Domb, A. J.; Perez-Atayde, A.; Langer, R. *J. Pediatr. Surg.* **1988**, *23*, 3–9.
78. Langer, R.; Vacanti, J. P. *Science* **1993**, *260*, 920–926.
79. Fuchs, J. R.; Nasseri, B. A.; Vacanti, J. P. *Ann. Thorac. Surg.* **2001**, *72*, 577–591.
80. Leor, J.; Aboulafia-Etzion, S.; Dar, A.; *et al. Circulation* **2000**, *102*, III56–III61.
81. Souren, J. E.; Schneijdenberg, C.; Verkleij, A. J.; Van Wijk, R. *In Vitro Cell. Dev. Biol.* **1992**, *28A*, 199–204.
82. Freed, L. E.; Vunjak-Novakovic, G.; Biron, R. J.; *et al. Biotechnol. NY* **1994**, *12*, 689–693.
83. Harary, I.; Farley, B. *Science* **1960**, *131*, 1674–1675.
84. Agrell, I. P.; Gabbay, M. *Exp. Cell Res.* **1973**, *82*, 131–136.
85. Harary, I.; Farley, B. *Science* **1960**, *132*, 1839–1840.
86. Dar, A.; Shachar, M.; Leor, J.; Cohen, S. *Biotechnol. Bioeng.* **2002**, *80*, 305–312.
87. Fink, C.; Ergun, S.; Kralisch, D.; Remmers, U.; Weil, J.; Eschenhagen, T. *FASEB J.* **2000**, *14*, 669–679.
88. Guo, X. M.; Zhao, Y. S.; Chang, H. X.; *et al. Circulation* **2006**, *113*, 2229–2237.
89. He, X. Q.; Chen, M. S.; Li, S. H.; *et al. Mol. Cell. Biochem.* **2010**, *339*(1–2), 89–98.
90. Ryan, P. L.; Foty, R. A.; Kohn, J.; Steinberg, M. S. *Proc. Natl. Acad. Sci. USA* **2001**, *98*, 4323–4327.
91. Radisic, M.; Park, H.; Martens, T. P.; *et al. J. Biomed. Mater. Res. A* **2008**, *86*, 713–724.
92. Naito, H.; Melnychenko, I.; Didie, M.; *et al. Circulation* **2006**, *114*, I72–I78.
93. Cox, J. L.; Rizzino, A. *Exp. Biol. Med. (Maywood)* **2010**, *235*, 148–158.
94. Robbins, R. D.; Prasain, N.; Maier, B. F.; Yoder, M. C.; Mirmira, R. G. *Curr. Opin. Organ Transplant.* **2010**, *15*, 61–67.
95. Akhyari, P.; Fedak, P. W.; Weisel, R. D.; *et al. Circulation* **2002**, *106*, I137–I142.
96. Carrier, R. L.; Rupnick, M.; Langer, R.; Schoen, F. J.; Freed, L. E.; Vunjak-Novakovic, G. *Tissue Eng.* **2002**, *8*, 175–188.

97. Carrier, R. L.; Rupnick, M.; Langer, R.; Schoen, F. J.; Freed, L. E.; Vunjak-Novakovic, G. *Biotechnol. Bioeng.* **2002**, *78*, 617–625.
98. Yin, L.; Bien, H.; Entcheva, E. *Am. J. Physiol. Heart Circ. Physiol.* **2004**, *287*, H1276–H1285.
99. Kofidis, T.; Akhyari, P.; Wachsmann, B.; *et al. Tissue Eng.* **2003**, *9*, 517–523.
100. Zimmermann, W. H.; Melnychenko, I.; Wasmeier, G.; *et al. Nat. Med.* **2006**, *12*, 452–458.
101. Hata, H.; Bar, A.; Dorfman, S.; *et al. Eur. J. Cardiothorac. Surg.* **2010**, *38*(4), 450–455.
102. Rakusan, K.; Korecky, B. *Growth* **1982**, *46*, 275–281.
103. Kofidis, T.; Lenz, A.; Boublik, J.; *et al. Biomaterials* **2003**, *24*, 5009–5014.
104. Radisic, M.; Yang, L.; Boublik, J.; *et al. Am. J. Physiol. Heart Circ. Physiol.* **2004**, *286*, H507–H516.
105. Radisic, M.; Deen, W.; Langer, R.; Vunjak-Novakovic, G. *Am. J. Physiol. Heart Circ. Physiol.* **2005**, *288*, H1278–H1289.
106. Maidhof, R.; Marsano, A.; Lee, E. J.; Vunjak-Novakovic, G. *Biotechnol. Prog.* **2010**, *26*(2), 565–572.
107. Radisic, M.; Park, H.; Chen, F.; *et al. Tissue Eng.* **2006**, *12*, 2077–2091.
108. Wang, G. J.; Ho, K. H.; Hsu, S. H.; Wang, K. P. *Biomed. Microdevices* **2007**, *9*, 657–663.
109. Badie, N.; Satterwhite, L.; Bursac, N. *Ann. Biomed. Eng.* **2009**, *37*, 2510–2521.
110. Khademhosseini, A.; Eng, G.; Yeh, J.; *et al. Biomed. Microdevices* **2007**, *9*, 149–157.
111. Badie, N.; Bursac, N. *Biophys. J.* **2009**, *96*, 3873–3885.
112. Cimetta, E.; Pizzato, S.; Bollini, S.; Serena, E.; De Coppi, P.; Elvassore, N. *Biomed. Microdevices* **2009**, *11*, 389–400.
113. Badylak, S. F. *Transpl. Immunol.* **2004**, *12*, 367–377.
114. Lichtenberg, A.; Tudorache, I.; Cebotari, S.; *et al. Biomaterials* **2006**, *27*, 4221–4229.
115. Lichtenberg, A.; Tudorache, I.; Cebotari, S.; *et al. Circulation* **2006**, *114*, I559–I565.
116. Akhyari, P.; Kamiya, H.; Gwanmesia, P.; *et al. Eur. J. Cardio-thoracic Surg.* **2010**, *38*, 539–546.
117. Schultheiss, D.; Gabouev, A. I.; Cebotari, S.; *et al. J. Urol.* **2005**, *173*, 276–280.
118. Borschel, G. H.; Dennis, R. G.; Kuzon, W. M., Jr. *Plast. Reconstr. Surg.* **2004**, *113*, 595–602; discussion 603–594.
119. Borschel, G. H.; Huang, Y. C.; Calve, S.; *et al. Tissue Eng.* **2005**, *11*, 778–786.
120. Farhat, W. A.; Chen, J.; Haig, J.; *et al. Biomed. Mater.* **2008**, *3*, 025015.
121. Hudson, T. W.; Zawko, S.; Deister, C.; *et al. Tissue Eng.* **2004**, *10*, 1641–1651.
122. Ott, H. C.; Matthiesen, T. S.; Goh, S. K.; *et al. Nat. Med.* **2008**, *14*, 213–221.
123. Kasimir, M. T.; Weigel, G.; Sharma, J.; *et al. Thromb. Haemost.* **2005**, *94*, 562–567.
124. Zhou, J.; Fritze, O.; Schleicher, M.; *et al. Biomaterials* **2010**, *31*, 2549–2554.
125. Bar, A.; Dorfman, S. E.; Fischer, P.; *et al. Cardiovasc. Res.* **2010**, *85*, 806–813.
126. Zimmermann, W. H.; Schneiderbanger, K.; Schubert, P.; *et al. Circ. Res.* **2002**, *90*, 223–230.
127. Narmoneva, D. A.; Vukmirovic, R.; Davis, M. E.; Kamm, R. D.; Lee, R. T. *Circulation* **2004**, *110*, 962–968.
128. Zimmermann, W. H.; Fink, C.; Kralisch, D.; Remmers, U.; Weil, J.; Eschenhagen, T. *Biotechnol. Bioeng.* **2000**, *68*, 106–114.
129. Park, H.; Bhalla, R.; Saigal, R.; *et al. J. Tissue Eng. Regen. Med.* **2008**, *2*, 279–287.
130. Radisic, M.; Park, H.; Shing, H.; *et al. Proc. Natl. Acad. Sci. USA* **2004**, *101*, 18129–18134.
131. van Wamel, A. J.; Ruwhof, C.; van der Valk-Kokshoorn, L. J.; Schrier, P. I.; van der Laarse, A. *Arch. Biochem. Biophys.* **2000**, *381*, 67–73.
132. van Wamel, A. J.; Ruwhof, C.; van der Valk-Kokshoorn, L. J.; Schrier, P. I.; van der Laarse, A. *Mol. Cell. Biochem.* **2002**, *236*, 147–153.
133. Gwak, S. J.; Bhang, S. H.; Kim, I. K.; *et al. Biomaterials* **2008**, *29*, 844–856.
134. Shimko, V. F.; Claycomb, W. C. *Tissue Eng. A* **2008**, *14*, 49–58.
135. Akasha, A. A.; Sotiriadou, I.; Doss, M. X.; *et al. Cell. Physiol. Biochem.* **2008**, *22*, 665–672.
136. Serena, E.; Figallo, E.; Tandon, N.; *et al. Exp. Cell Res.* **2009**, *315*, 3611–3619.
137. Tandon, N.; Cannizzaro, C.; Chao, P. H.; *et al. Nat. Protoc.* **2009**, *4*, 155–173.
138. Kensah, G.; Gruh, I.; Viering, J.; *et al. Tissue Eng. C Meth.* **2011**, *17*, 463–473.
139. Chiu, L. L.; Iyer, R. K.; King, J. P.; Radisic, M. *Tissue Eng. A* **2008**. [Epub ahead of print].
140. Ingber, D. E.; Mow, V. C.; Butler, D.; *et al. Tissue Eng.* **2006**, *12*, 3265–3283.
141. Radisic, M.; Park, H.; Gerecht, S.; Cannizzaro, C.; Langer, R.; Vunjak-Novakovic, G. *Philos. Trans. R. Soc. Lond. B Biol. Sci.* **2007**, *362*, 1357–1368.
142. Radisic, M.; Fast, V. G.; Sharifov, O. F.; Iyer, R. K.; Park, H.; Vunjak-Novakovic, G. *Tissue Eng. A* **2009**, *15*, 851–860.
143. Bursac, N.; Loo, Y.; Leong, K.; Tung, L. *Biochem. Biophys. Res. Commun.* **2007**, *361*, 847–853.
144. Liu, J.; Fu, J. D.; Siu, C. W.; Li, R. A. *Stem Cells* **2007**, *25*, 3038–3044.
145. Sakai, T.; Li, R. K.; Weisel, R. D.; *et al. J. Thorac. Cardiovasc. Surg.* **2001**, *121*, 932–942.
146. Ozawa, T.; Mickle, D. A.; Weisel, R. D.; Koyama, N.; Ozawa, S.; Li, R. K. *Circulation* **2002**, *106*, I176–I182.
147. Chen, C. H.; Wei, H. J.; Lin, W. W.; *et al. Cardiovasc. Res.* **2008**, *80*, 88–95.
148. Potapova, I. A.; Doronin, S. V.; Kelly, D. J.; *et al. Am. J. Physiol. Heart Circ. Physiol.* **2008**, *295*, H2257–H2263.
149. Kochupura, P. V.; Azeloglu, E. U.; Kelly, D. J.; *et al. Circulation* **2005**, *112*, I144–I149.
150. Tudorache, I.; Kostin, S.; Meyer, T.; *et al. Eur. J. Cardiothorac. Surg.* **2009**, *36*, 306–311; discussion 311.
151. Wei, H. J.; Chen, S. C.; Chang, Y.; *et al. Biomaterials* **2006**, *27*, 5409–5419.
152. Badylak, S.; Obermiller, J.; Geddes, L.; Matheny, R. *Heart Surg. Forum* **2003**, *6*, E20–E26.
153. Badylak, S. F.; Kochupura, P. V.; Cohen, I. S.; *et al. Cell Transplant.* **2006**, *15*(Suppl. 1), S29–S40.
154. Ozawa, T.; Mickle, D. A.; Weisel, R. D.; *et al. J. Thorac. Cardiovasc. Surg.* **2002**, *124*, 1157–1164.
155. Ozawa, T.; Mickle, D. A.; Weisel, R. D.; *et al. Cell Transplant.* **2004**, *13*, 169–177.
156. Ota, T.; Gilbert, T. W.; Badylak, S. F.; Schwartzman, D.; Zenati, M. A. *J. Thorac. Cardiovasc. Surg.* **2007**, *133*, 979–985.
157. Badylak, S. F. *Ann. NY Acad. Sci.* **2002**, *961*, 302–304.
158. Ota, T.; Gilbert, T. W.; Schwartzman, D.; *et al. J. Thorac. Cardiovasc. Surg.* **2008**, *136*, 1309–1317.
159. Wei, H. J.; Chen, C. H.; Lee, W. Y.; *et al. Biomaterials* **2008**, *29*, 3547–3556.
160. Simpson, D.; Dudley, S. C., Jr. *Curr. Stem Cell Res. Ther.* **2009**, *4*, 210–223.
161. Giraud, M. N.; Ayuni, E.; Cook, S.; Siepe, M.; Carrel, T. P.; Tevaearai, H. T. *Artif. Organs* **2008**, *32*, 692–700.
162. Siepe, M.; Giraud, M. N.; Pavlovic, M.; *et al. J. Thorac. Cardiovasc. Surg.* **2006**, *132*, 124–131.
163. Zimmermann, W. H.; Didie, M.; Wasmeier, G. H.; *et al. Circulation* **2002**, *106*, I151–I157.
164. Dvir, T.; Kedem, A.; Ruvinov, E.; *et al. Proc. Natl. Acad. Sci. USA* **2009**, *106*, 14990–14995.
165. Shimizu, T.; Yamato, M.; Isoi, Y.; *et al. Circ. Res.* **2002**, *90*, e40.
166. Sekine, H.; Shimizu, T.; Yang, J.; Kobayashi, E.; Okano, T. *Circulation* **2006**, *114*, I87–I93.
167. Haraguchi, Y.; Shimizu, T.; Yamato, M.; Kikuchi, A.; Okano, T. *Biomaterials* **2006**, *27*, 4765–4774.
168. Kobayashi, H.; Shimizu, T.; Yamato, M.; *et al. J. Artif. Organs* **2008**, *11*, 141–147.
169. Hoashi, T.; Matsumiya, G.; Miyagawa, S.; *et al. J. Thorac. Cardiovasc. Surg.* **2009**, *138*, 460–467.
170. Miyahara, Y.; Nagaya, N.; Kataoka, M.; *et al. Nat. Med.* **2006**, *12*, 459–465.
171. Asakawa, N.; Shimizu, T.; Tsuda, Y.; *et al. Biomaterials* **2010**, *31*, 3903–3909.
172. Haraguchi, Y.; Shimizu, T.; Yamato, M.; Okano, T. *J. Tissue Eng. Regen. Med.* **2010**, *4*, 291–299.
173. Bel, A.; Planat-Bernard, V.; Saito, A.; *et al. Circulation* **2010**, *122*, S118–S123.
174. Fujimoto, K. L.; Tobita, K.; Merryman, W. D.; *et al. J. Am. Coll. Cardiol.* **2007**, *49*, 2292–2300.
175. Fukuhara, S.; Tomita, S.; Nakatani, T.; *et al. Circ. J.* **2005**, *69*, 850–857.
176. Gerecht-Nir, S.; Radisic, M.; Park, H.; *et al. Int. J. Dev. Biol.* **2006**, *50*, 233–243.
177. Darland, D. C.; Massingham, L. J.; Smith, S. R.; Piek, E.; Saint-Geniez, M.; D'Amore, P. A. *Dev. Biol.* **2003**, *264*, 275–288.
178. Guan, K.; Nayernia, K.; Maier, L. S.; *et al. Nature* **2006**, *440*, 1199–1203.
179. Vrana, K. E.; Hipp, J. D.; Goss, A. M.; *et al. Proc. Natl. Acad. Sci. USA* **2003**, *100*(Suppl. 1), 11911–11916.
180. Vineberg, A. *Can. Med. Assoc. J.* **1954**, *71*, 281–282.
181. Vineberg, A.; Lwin, M. M. *Surg. Gynecol. Obstet.* **1973**, *137*, 565–578.
182. Vineberg, A.; Pifarre, B.; Kato, Y. *Can. Med. Assoc. J.* **1963**, *88*, 499–504.
183. Chachques, J. C.; Grandjean, P.; Schwartz, K.; *et al. Circulation* **1988**, *78*, III203–III216.
184. Chachques, J. C.; Grandjean, P. A.; Tommasi, J. J.; *et al. Life Support Syst.* **1987**, *5*, 323–327.
185. Benicio, A.; Moreira, L. F.; Bacal, F.; Stolf, N. A.; Oliveira, S. A. *Ann. Thorac. Surg.* **2003**, *76*, 821–827; discussion 827.
186. Chachques, J. C. *Eur. J. Cardiothorac. Surg.* **2009**, *35*, 201–203.
187. Misawa, Y.; Mott, B. D.; Lough, J. O.; Chiu, R. C. *J. Heart Lung Transplant.* **1997**, *16*, 585–595.

6.625. Long-Term Implantable Ventricular Assist Devices (VADs) and Total Artificial Hearts (TAHs)

A Kumar, Boston Scientific Corporation, Boston, MA, USA
P S Khanwilkar, World Heart Corporation, Utah, UT, USA

© 2011 Elsevier Ltd. All rights reserved.

6.625.1.	**Introduction**	389
6.625.1.1.	Evolution of VADs and TAHs	389
6.625.1.2.	Anatomical and Physiological Considerations	390
6.625.2.	**Configuration**	390
6.625.3.	**LVAD Evolution**	392
6.625.3.1.	First-Generation LVADs	393
6.625.3.2.	Rotary Axial Pumps	395
6.625.3.3.	Rotary Centrifugal Pumps	396
6.625.3.3.1.	Rotary centrifugal pumps using hydrodynamic suspension	397
6.625.3.3.2.	Rotary centrifugal pumps using full magnetic levitation	397
6.625.4.	**Partial Circulatory Support VADs**	399
6.625.5.	**Total Artificial Heart**	400
6.625.6.	**Conclusions**	402
References		402

Abbreviations

bpm	Beats per minute
BTR	Bridge-to-recovery
BTT	Bridge-to-transplant
CAD	Computer-aided design
CFD	Computational fluid dynamics
CPB	Cardiopulmonary bypass
HDE	Humanitarian device exemption
HF	Heart failure
IDE	Investigational device exemption
INTREPID trial	Investigation of nontransplant eligible patients who are inotrope dependent
LMWH	Low molecular weight heparin
LV	Left ventricle
MCS	Mechanical circulatory support
NHLBI	National heart, lung and blood institute
REMATCH	Randomized evaluation of mechanical assistance for the treatment of congestive heart failure
RV	Right ventricle
TAH	Total artificial heart
TET	Transcutaneous energy transmission
VAD	Ventricular assist device

6.625.1. Introduction

6.625.1.1. Evolution of VADs and TAHs

Long-term implantable ventricular assist devices (VADs) and total artificial hearts (TAHs) have been under development since the late '60s as therapies for late-stage heart failure (HF), a debilitating and deadly malaise that affects millions worldwide. HF accounts for ~7% of death (mortality rate of 1 in 5) from cardiovascular diseases, affects 4.8 million Americans with 500 000 new Americans diagnosed every year and is the leading cause of death in the United States and the rest of the world.[1,2] These staggering figures give us an estimate of the magnitude and impact of HF on the society and the motivation for proliferating research and development initiatives from both academia and industry, to address this challenge.[3]

HF may be caused by coronary atherosclerosis, hypertension, viral or idiopathic cardiomyopathy, or congenital defects. The pathogenesis of chronic HF is a complex process that involves a series of morphological and molecular alterations of the myocardium ('remodeling'). Causes such as myocardial infarction, myocarditis, or genetic defects, can initiate cardiac insufficiency. This is followed by several pathophysiological compensatory mechanisms that cause additional stress on the weakening heart, leading to HF, a positive feedback mechanism. A primary component of such a mechanism is the volumetric expansion of the heart in order to provide adequate blood flow, a deficiency that weakens the heart muscle and leads to further volumetric expansion, resulting in a significantly enlarged heart. This is termed congestive HF – as the heart grows to 'congest' the chest.

Although traditional medical therapy (defibrillator implantation, biventricular pacing) provides a temporary solution to manage and control the seemingly unstoppable progression of HF to end-stage, until now, transplantation has been the only effective treatment for most end-stage HF patients. But a severely limited supply of donor hearts has meant that only about 3000 persons receive transplants each year worldwide while about 15% die waiting for a donor heart.[4,5]

This gap and the increasing need for a longer-term solution (an alternate to a heart transplant) was recognized in the 1960s by the US government thanks to early efforts by pioneering clinical researchers that showed the promise for mechanical circulatory support (MCS). The Artificial Heart Program was set up and run by the National Heart, Lung, and Blood Institute (NHLBI) with a goal to fund and foster the development of two types of MCS for long-term implantable use: ventricular assist devices (VADs) and total artificial hearts (TAHs). A Ventricular Assist Device or VAD in short, circulates blood through the host's circulatory system to compensate for the otherwise poor circulation provided by the recipient's failing heart which is left intact, while a TAH replaces the natural heart.

Since its inception in 1962, by Dr. Domingo Liotta of the Baylor College of Medicine in Houston, the VAD has been used to complement the function of a human heart, either as a 'bridge-to-transplant' (BTT) for patients with ailing heart waiting for a natural donor heart or sometimes as a 'permanent' implant (the so-called DT indication).[6,7] There is a fledgling new indication for VADs called bridge-to-recovery (BTR) in which, after VAD implant and support, native cardiac function of the recipient recovers ('reverse remodeling') and removal of the device is possible without subsequent support due to stable restoration of the natural heart pumping function.[8]

The NHLBI program has spawned the development and growth of a global industry comprised of many VAD/TAH academic institutions and companies not only in the US, but in Europe, Japan, and other locations. There are now several VADs and TAHs that have been approved by regulatory agencies for commercial sale and distribution in these locations, and ~10 000 implants with these devices have been performed worldwide to date, with the number increasing significantly every year. Use of LVADs has predominated, with the TAH being used to date in less than a thousand patients. Randomized and controlled clinical trials have shown that VADs provide significant improvement in the quality of life and survival of patients with HF.[2,9]

Further development continues – several companies are now developing MCS devices to provide short- or long-term support to reduce their size, improve safety and reduce adverse events, and optimize performance and ease-of-use. The use of computer-aided design (CAD) and its application complemented by computational fluid dynamics (CFD) has resulted in the development of some ingenious and novel 'smart' devices with potentially superior performance. These next-generation devices are presently being clinically evaluated.

This chapter outlines the need for MCS devices and focuses on long-term (multimonth to multiyear) implantable MCS devices, since challenges with these are most relevant from a biomaterials perspective. We provide an overview of generations of VADs that have seen some clinical use, emphasizing so-called left VADs (LVADs). LVADs support the failing left ventricle, which supplies oxygenated blood to the body and does the most work and typically fails more often than the right ventricle. Key devices representative of each generation are described, including a summary of their design configuration, technological innovations, especially biomaterials related, development status, clinical results, and future plans. The intent is to provide a representative overview to promote an understanding of the field and the various technologies, rather than provide an exhaustive and detailed summary description of every MCS device ever developed. Given their predominant clinical use, long-term implantable LVADs are the primary focus, while TAHs are also described.

6.625.1.2. Anatomical and Physiological Considerations

The anatomy of a human heart reveals two sides (left and right), each side having two chambers: an atrium and a ventricle. Each atrium collects incoming blood and helps provide it to the corresponding ventricle which actively pumps it for circulation through the pumping circuit: the right ventricle pumps deoxygenated blood into the lungs, and the left ventricle pumps oxygenated blood into the body, as illustrated in **Figure 1**. The basic mechanics underlying the functioning of a human heart is such that the ventricles act as unidirectional positive displacement pumps with a pulsatile motion alternating between filling (diastole) and ejection (systole) phases. The blood flow for each phase is regulated by inflow (mitral and tricuspid) and outflow (pulmonary and aorta) valves for the right and left sides, respectively. A normal functional adult heart ejects about 60 cm^3 of blood in each stroke and controls cardiac output by primarily varying the heart rate which can range from 40 beats per minute (bpm) at rest to 180 bpm during exercise.

Although VADs were designed to assist the right ventricle (RVAD), the left ventricle (LVAD), or both ventricles (BiVAD), this chapter focuses on the LVAD, which is shown schematically implanted in a human in **Figure 2(a)**. **Figure 2(b)** depicts an implanted TAH. About 15–30% of LVAD implants are reported to need right ventricular support.[10] However, this is usually clinically alleviated with short-term measures like nitric oxide or a temporary (multiday) RVAD such as the external Thoratec VAD or the Levitronix CentriMag VAD.[11,12] The authors have estimated that the clinical need for mechanical circulatory support can be provided by devices in the proportions of: 80% LVADs, 15% BiVADs, and 5% TAHs.

LVADs are designed to support blood circulation when the LV is no longer able to meet the body's systemic perfusion needs, presuming that the RV normally supports an adequate load, owing to its adaptability to elevated preload and after load changes. An LVAD may be implanted in the upper abdomen, chest, or inside the pericardium either extraventricular or transventricular. The inflow for long-term LVADs is typically from the apex of the left atrium via a cannula to the pump, and the outflow of the pump is connected to the ascending aorta via a graft.

Based on various mechanical and physiological performances, an ideal VAD would be expected (1) to provide sufficient cardiac output and complement an ailing heart so as to allow patients to return to their daily activities; (2) to have a low risk of thromboembolism, damage to and activation of blood components, driveline and pump infection, (3) to have a low incidence of malfunction; (4) to be easily implantable and also removable; and lastly (5) to fit well in the human anatomy which usually translates to a small size.

6.625.2. Configuration

The basic configuration of a pulsatile VAD has three components; (1) an electrically driven electromechanical pump,

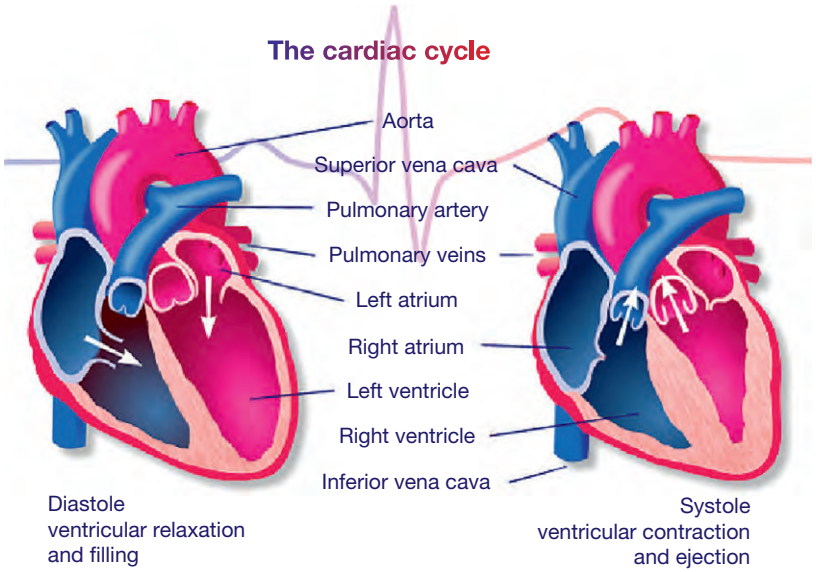

Figure 1 The normal Cardiac Cycle. *Source:* http://www.xaraxone.com/FeaturedArt/mar04/html/05.htm

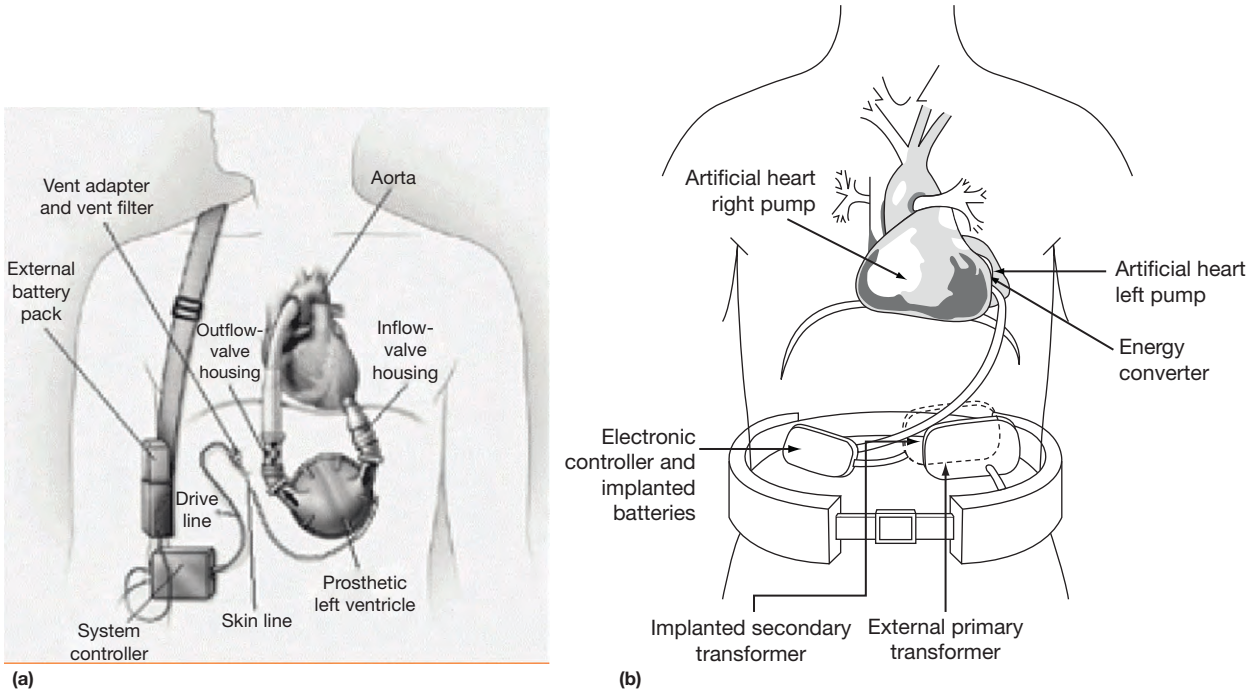

Figure 2 (a) Left ventricular assist device. (b) Total artificial heart.

(2) an electronic controller, and (3) a power supply. The pump weighs ~1.5 pounds typically made of biocompatible titanium with the flexing components made of biocompatible polyurethane. The circumferential acceleration of blood is achieved by controlled electric currents passing through coils contained in the pump housing that apply forces to an electromagnetic actuator that rotates and/or translates. This mechanism in turn squeezes a plastic blood sac to provide systole with the lack of a squeezing action being the diastolic phase of the LVAD's beat; the direction of blood flow is controlled by a pair of unidirectional valves embedded in the LVAD, the same types used when a natural heart valve is replaced (e.g., valves from pigs' hearts or ones made of metal and plastic).

A VAD could be classified in numerous ways based on (a) the mechanics of its pump: (1) volume or positive displacement or pulsatile, (2) rotary or continuous flow encompassing axial flow, or centrifugal pumps, (b) pump location (para corporeal, implantable, or extracorporeal): (c) intended clinical use (temporary, bridge-to-decision, recovery, transplant, or destination): (d) support provided (left – LVAD, right – RVAD,

or both ventricles – BiVAD): and (e) surgical approaches (percutaneous, subcostal, laparaotomy, sternotomy, thoracotomy). The first classification pulsatile and rotary pumps is how they are described going forward.

Table 1 shows the different types of LVADs (pulsatile, and so-called 'continuous flow') as well as TAHs and highlights a few representative pulsatile VADs that have played a pioneering role in developing the field.

The electronic controller is typically a microprocessor chip-based set of digital and analog electronics component that adjusts functions of the pump, such as pumping speed and provides diagnostic, alarms, alerts, and communications to an external monitor.

The power supply for the pump is by two external batteries, via a cable through the abdomen, carried in underarm holsters or a waist pack. A few efforts have been made to transmit electric power across the skin in a transformer-like arrangement; typically, one pair of coils is permanently implanted below the skin and the other is strapped over the skin with the electromagnetic coupling between the two coils allowing power transfer. This transcutaneous energy transmission (TET) technology has seen very limited clinical use and still needs additional improvements prior to further use in the clinical setting.

6.625.3. LVAD Evolution

The developmental evolution of LVADs dates back to early cardiopulmonary bypass (CPB) machines and experiments in the late 1950s, during which artificial hearts were implanted in dogs. Both TAHs and heart assist devices have achieved significant development and clinical milestones since then. Starting in the 1980s, these advancements in technology and refinements in implantation paved the way for the development of innovative and novel devices, gradually overcoming the shortcomings of earlier versions. LVAD design has made tremendous advances over the last decade, reducing size, increasing durability, and eliminating noise and vibration.

The first-generation pulsatile pumps were designed to emulate the natural heart. As a result, they were bulky, large, needed heart valves, consumed much power, and suffered from high noise and vibration. As Table 1 shows, they either suffered from limited life or high complication rates.

A new paradigm for long-term blood pumping with MCS was provided by the high-speed rotary Hemopump developed and clinically used in the mid-1980s. This device, despite being commercially unsuccessful, demonstrated that there were no discernible worse outcomes associated with the direct pumping of blood with a rotary pump as compared to a pulsatile pump. This provided the incentive for the development of next-generation rotary pumps to pump blood directly while being immersed in blood.

These long-term implantable rotary pumps have also evolved over three generations beyond the first-generation pulsatile pumps. From second-generation pumps (axial flow pumps supported by mechanical bearings) that proved that long-term circulatory support provided by rotary pumps was viable and accepted well by the human body, to third-generation pumps (centrifugal pumps supported by hydrodynamic bearings) to fourth-generation pumps (centrifugal pumps whose rotor is

Table 1 A summary of available cardiac devices highlighting their advantages and disadvantages

Thoratec	
Indications	Right, left, or biventricular support
Advantages	Fits in a wide range of patient sizes (body surface area 0.73–2.5 m^2)
	Pump can be changed without invasive surgery
	Can replace the entire function of the supported ventricle
Disadvantages	Need for strict anticoagulation with risk of bleeding or thromboembolism
	Large lines crossing the skin with a high risk of infection
	Limited patient mobility
	Not approved for home use
HeartMate	
Indications	Left ventricular support
Advantages	No need for anticoagulation
	Portability of controller and batteries permits good patient mobility and hospital discharge
	Can replace the entire function of the supported ventricle
Disadvantages	Driveline crossing the skin poses a risk of infection
	Left ventricle support only
	Does not fit in patients with body surface area $\leq$1.5 m^2
Novacor	
Indications	Left ventricular support
Advantages	Portability of controller and batteries permits good patient mobility and hospital discharge
	Can replace the entire function of the supported ventricle
Disadvantages	Need for strict anticoagulation with higher risk of bleeding or thromboembolism
	Driveline crossing the skin poses a high risk of infection
	Left ventricle support only
	Does not fit in patients with body surface area $\leq$1.5 m^2
Continuous-flow pumps	
Indications	Left ventricular support
Advantages	Small size permits greater patient mobility
	Quiet
	Fit in a wide range of patient body habitus
Disadvantages	Need anticoagulation; risk of bleeding and thromboembolism unknown
	May not replace the entire function of the supported ventricle
	Nonpulsatile flow
	Still in early clinical trials
Total artificial hearts	
Indications	Advanced biventricular dysfunction
	Pulmonary hypertension?
	Cardiac tumors?
Advantages	Complete replacement of the heart function
Disadvantages	Need anticoagulation; risk of bleeding or thromboembolism
	Due to the size of equipment, they only fit in patients with larger body habitus
	Still in early clinical trials

Source: DeBakey, M. E. *Ann. Thorac. Surg.* **2005**, *79*, S2228–S2231.

suspended completely using magnetic levitation), VAD technology has developed by leaps and bounds. Because the clinical development cycle time is extensive, today there are second, third, and fourth-generation VADs undergoing clinical trials concurrently.

The earliest LVAD was reported in 1961 by Dennis *et al.* and the strategy was to employ a roller pump to off-load LV by receiving blood from RA and in turn return it to femoral artery.[13] Although the device was supposed to have supported 12 patients for 4–17 h, no significant support to recovery was observed. Since then, several researchers and developers had made progress toward VAD and TAH that are fully implantable. In 1963, DeBakey developed the first implantable pulsatile VAD using unidirectional ball valves that bypassed the heart between the left atrium and the descending thoracic aorta.[14] The implanted VAD consisted of two coaxial tubes: the blood flowed through an inner biocompatible Dacron tube surrounded by a rigid outer tube. Blood was then pumped by pneumatically increasing the transluminal pressure causing the flexible inner tube to narrow. A second patient, supported for 10 days with an extracorporeal version of this device, became the first patient to be supported to recovery with a VAD.

Later in 1969, Cooley *et al.* performed the first successful BTT using a TAH demonstrating the possibility to support the patient's circulation until a donor heart became available (Figure 3).

Worldwide attention was focused on the University of Utah in 1982 when Barney Clark, received a Jarvik-7 TAH intended for long-term use. Despite an in-hospital stay with numerous complications, this implant was followed by William Schroeder, Murray Haydon, and Jack Burcham who fared a little better. In 1998, two LVAD systems were approved by the FDA and used for bridge-to-transplantation. The HeartMate™ VE pump (Thoratec Laboratories Corp., Pleasanton, CA) and Novacor™ (WorldHeart, Ottawa, Canada) were evaluated in the United States for permanent mechanical circulatory support in the REMATCH (Randomized Evaluation of Mechanical Assistance for the Treatment of Congestive Heart Failure) and INTREPID trial (Investigation of nontransplant eligible patients who are inotrope dependent) (Figure 4).[7]

These early pioneering clinical successes fueled the development of second-generation devices, such as the HeartMate II shown below. The HeartMate II was the first second-generation pump to be approved in 2008 for a BTT indication, a milestone followed by its 2010 approval for DT (Figure 5).

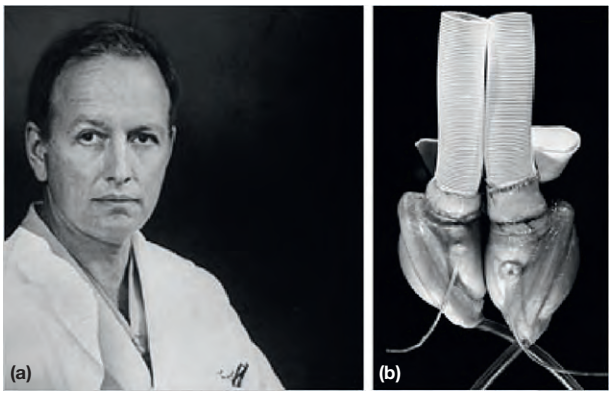

Figure 3 (a) Dr. Denton A. Cooley and (b) the total artificial heart used for the first successful bridge-to-transplant.

6.625.3.1. First-Generation LVADs

Positive/volume displacement pumps mimic the action of the human ventricles to pump blood. These could further be classified based on the mechanism by which they eject blood as pneumatic or electric. The valves incorporated into these VADs may either be bioprosthetic that offers superior biocompatibility, while suffering from poor longevity or of durable, mechanical valve with thrombogenic potential.

The most widely used and studied first-generation VADs include HeartMate® I[15] (originally developed by Thermo Cardiosystems, Inc., Waltham, MA and acquired by Thoratec Corporation of Pleasanton, CA) and the Novacor® LVAS (originally developed by Novacor Medical of Oakland, CA and later acquired by WorldHeart Corporation of Salt Lake City, Utah by way of Baxter HealthCare and Edwards LifeSciences).

The HeartMate I LVAD is available either as implantable pneumatic (IP-portable power unit on a console) that is used as bridge-to-heart transplant or, a more refined vented electric model (XVE), developed after REMATCH trial success that is currently approved for both BTT and DT use in the United States.[16,17] Both HeartMate pumps use titanium alloys and Cardioflex® polyurethane with advanced fabrication technology. The device has textured blood-contacting surfaces (textured titanium, textured blood sac) that reduces stroke and thrombus formation and does not require anticoagulant therapy benefiting patients that poorly tolerate these drugs.[18,19] A comparative study versus home inotropic infusion therapy reveals that this device certainly improves the quality of life and survival rate of patients (Figure 6).[20]

The Novacor and the HeartMate™ LVASs are both intracorporeal LVADs. Both incorporate porcine valves and have portable controllers that permit the patient to be discharged from the hospital and to be more ambulatory.[15,21] The HeartMate I is estimated to have been implanted in 5000 patients and the Novacor in 1800 patients worldwide.

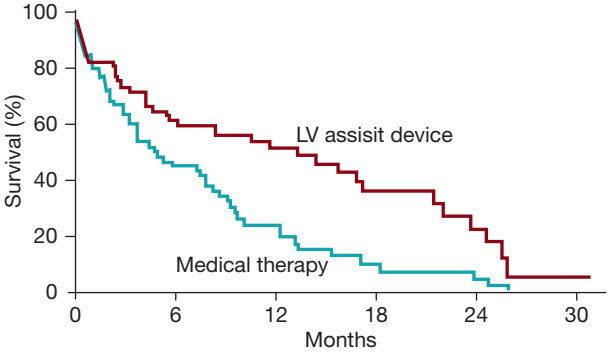

Figure 4 An outcome of survival of patients in the randomized evaluation of mechanical assistance for the treatment of congestive heart failure trial. The results reveal an obvious increase in survival of patients with end-stage heart failure. Reproduced with permission from Rose, E.A. *et al.* Long-term mechanical left ventricular assistance for end-stage heart failure. *N. Engl. J. Med.*, **2001**, *345*(20), 1435–1443.

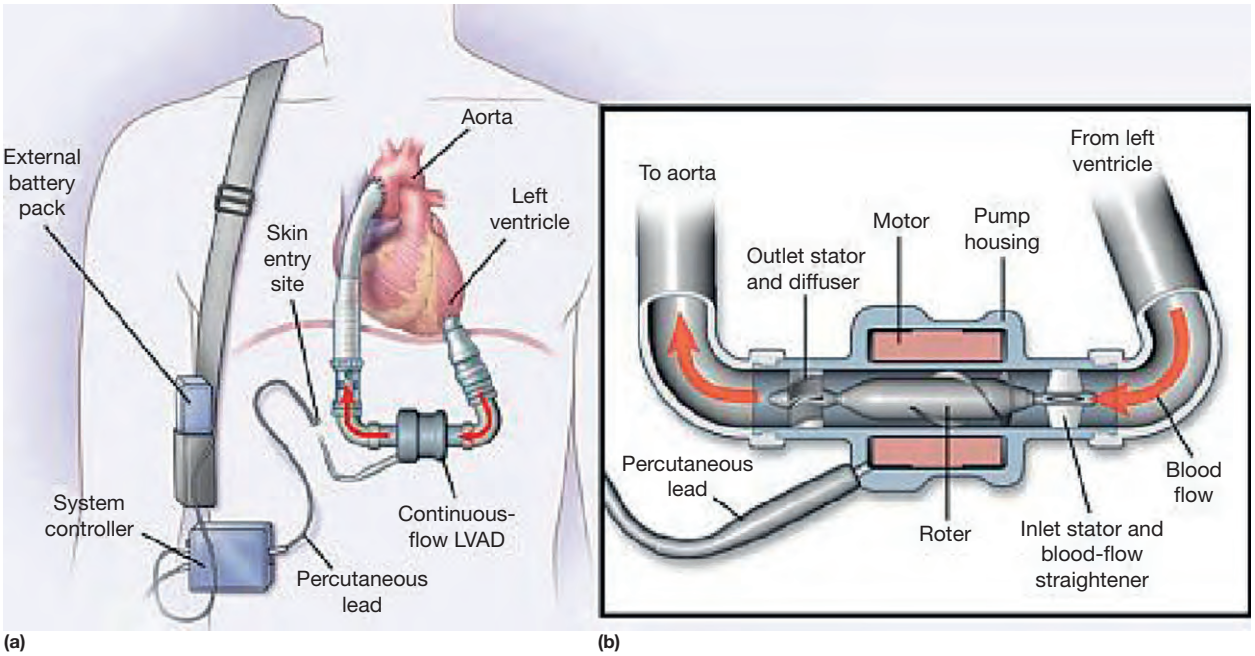

Figure 5 (a) Schematic of patient implanted with the HMII and (b) a close-up cross-section of HeartMate II.

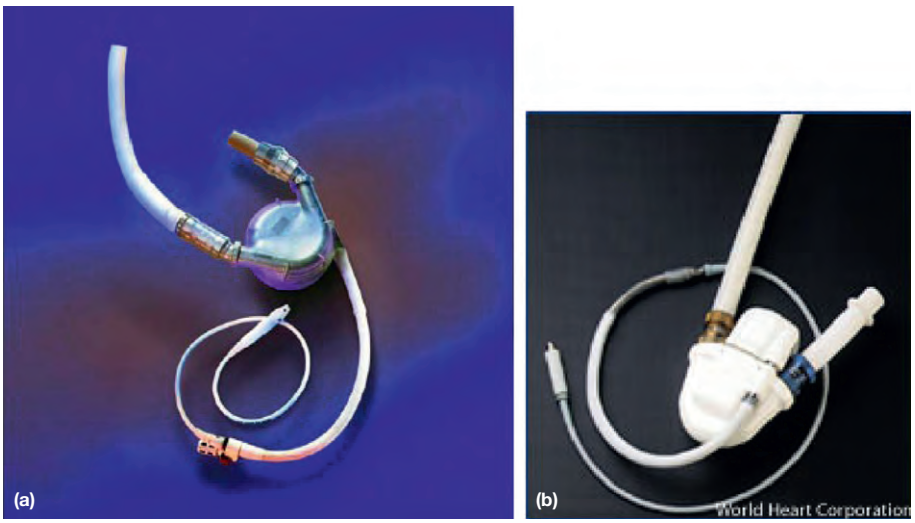

Figure 6 (a) Thoratec HeartMate I XVE pump. (b) Novacor LVAD blood pump.

The Novacor LVAS had the distinction of supporting a patient for more than 6 years with a single device, and was approved for BTT in the United States, and is CE Marked in Europe as well as approved in Japan.

As a historical footnote, it is worthwhile to mention the Arrow LionHeart™ (LionHeart Ventricular Assist System; Arrow International, Reading, PA) whose manufacture and distribution has been discontinued. The LionHeart was a pulsatile LVAD and was notable for its use of transcutaneous wireless power transmitter (TET – transcutaneous energy transfer). In Europe, the CUBS trial (Clinical Utility Baseline Study) evaluated its use as a permanent implant and it obtained the CE Mark. The LionHeart™ received an Investigational Device Exemption from the US FDA in 2001 and was undergoing Phase I human clinical trials in the United States until it was discontinued in 2006. Since it did not employ a vent tube for exchange of air, unlike its predecessors, and achieved it via an implanted compliance chamber, coupled with its use of a TET for power and data transmission across the skin, it eliminated the need for a percutaneous cable. While this certainly helped address the driveline infection issue, the trade-off was increased volume and number of separate implantable components, and the need to periodically (once every 2 weeks) prime the supple compliance chamber with working gas through an access port (shown in Figure 7), due to its gradual dissipation through the synthetic membrane.

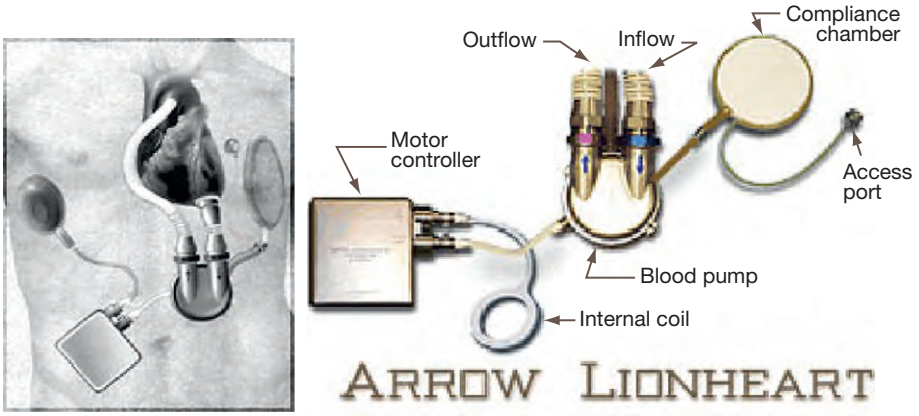

Figure 7 Arrow LionHeart™ (LionHeart Ventricular Assist System; Arrow International, Reading, PA).

The Berlin Heart Group (Berlin Heart AG, Berlin, Germany) produces and sells the EXCOR pulsatile VAD. This external device comes in a variety of sizes selected depending on patient needs, and has been used primarily in adults as a short-term support and more predominantly in newborns and infants with cardiac failure. The EXCOR VAD has received an HDE from the US FDA for this latter niche application.

While offering several advantages, the first-generation VAD suffered from serious drawbacks such as bulkiness (pump, driving console), noise, limited life due to mechanical wear and breakdown, high incidence of adverse events, and non-physiologically high systolic pressure that could result in elevated calcification and hence eventually to valve failure.

6.625.3.2. Rotary Axial Pumps

The pitfalls of first-generation volume displacement pumps were overcome to some extent with the 'second-generation' axial pumps.[17,22] Axial pumps were anticipated to be less obtrusive, of low noise and less prone to driveline infections due to reduced driveline diameter, increased flexibility, and less stiffness of the percutaneous cable. Furthermore, these pumps are driven by impellers that operate on a continuous basis using rotary pump technology. With speeds typically up to 12 000–15 000 rpm, these could generate higher flow rates at lower pressure (up to 10 l min^{-1}), without the need for a valve.[22,23] Initially, concerns were raised about the possibility that such speeds might lead to hemolysis of blood, but soon was discarded when the Hemopump was successfully used in a clinical setting.[24] The Hemopump thus set the stage for further evaluation of other types of axial flow pumps.[16,17,25–29]

Key second-generation pumps include the HeartMate II LVAD[23] (Thoratec), the DeBakey- MicroMed VAD® (MicroMed Cardiovascular, Houston, TX), and the Jarvik 2000 (Jarvik Heart, Inc., New York, NY). MicroMed's device uses an impeller/inducer with six blades and eight magnets, enclosed in a titanium tube and is capable of pumping up to 10 l min^{-1}, and is identical to the HeartMate II in many respects. Based on NASA-developed technology, the DeBakey's compelling features are its size, which is anatomically designed for fit even in the pediatric populace for which it has obtained FDA approval as a BTT, and an implantable ultrasonic flowmeter



Figure 8 HeartMate II left ventricular assist device.

to allow better patient monitoring and device speed adjustment.[25,27] The DeBakey VAD has been redesigned several times due to thrombotic issues leading to several changes in blood-contacting coatings. and the latest version is being evaluated under a CE Mark trial in Europe (Figure 8).

The Jarvik 2000, also known as the Flowmaker®, has the advantage of requiring no cannulation and potentially decreased thromboembolic events due to its design that is presently being qualified. It is 2.5 cm wide, 5.5 cm long, and weighs 85 g. The pump speed can be tuned by an analog controller on the basis of symptoms and individual requirements offering a unique biofeedback mechanism for the patients. The entire casing is of titanium with the pump suspended on ceramic bearings.[26] This device has the distinction of having supported a patient for more than 7 years and is presently in a US BTT clinical trial having received a CE Mark in Europe. The Jarvik 2000 is being adapted and miniaturized for use in the pediatric population (Figure 9).

Overall the second-generation VADs offers effective circulatory support and durability, less extensive and invasive surgical procedures hence postoperative complications, and reduction in pocket infections. Based on the above facts demonstrated through controlled clinical trials, HeartMate® II has been approved by FDA as BTT therapy and more recently for DT as well.[16] The main disadvantages of these devices are the intense anticoagulation regimens to treat embolic complications,

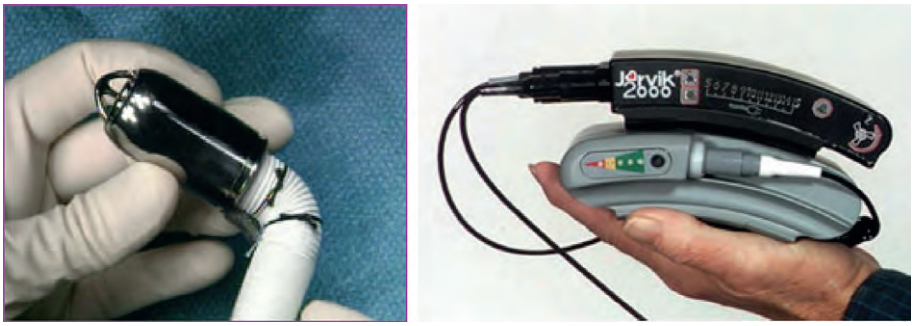

Figure 9 Jarvik 2000 also known as Flowmaker.

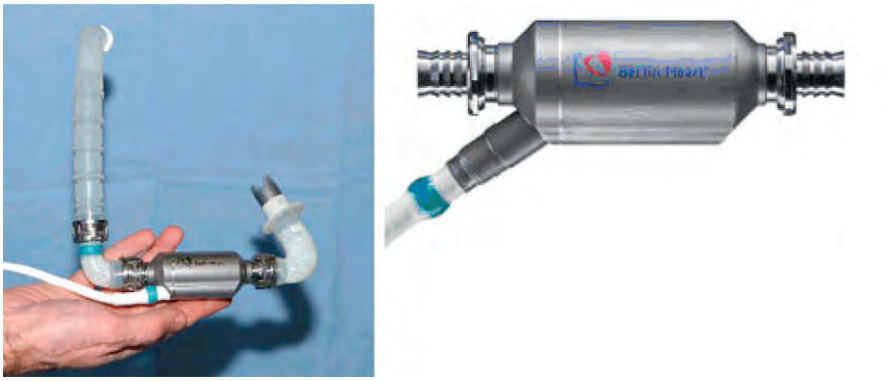

Figure 10 BerlinHeart Incor ventricular assist device.

bleeding, and the activation of undesirable blood constituents such as von Willebrand's factor.[30]

Since these pumps traditionally rely on mechanical bearings to suspend the rotor spinning at high speeds, the BerlinHeart Incor VAD incorporates an axial flow pump with a fully magnetically levitated suspension. The Incor® LVAD is an impeller device developed by the Berlin Heart Group (Berlin Heart AG, Berlin, Germany).[31] The pump is 30 mm in diameter, 12 cm in length, and weighs 200 gms. Blood enters the device through a cannula and passes the inducer and the flow is driven by an impeller that is held in suspension by magnets (both permanent and active electromagnets) and can develop a flow of up to 7 l min^{-1} with motor speeds of 5000–10 000 rpm. The clinical investigation of this device began in 2002 and the results showed a dramatic reduction in infection rate, with a significant increase in thromboembolism.[32] A retrospective study revealed that the long inflow cannula in the design yielded better clinical outcomes than a short one (138 patients – short length of inflow cannula and 78 with long inflow cannula) and a lower incidence of embolism.[31–33] A 2004–2005 study to evaluate BTT potential of the device revealed its feasibility for long-term use using a combination of LMWH (Heparin) and antiplatelet therapy as an alternative to oral anticoagulants. The study also revealed that, out of 10 patients, 6 patients successfully received transplants and 4 patients died – the last death occurred after 405 days of INCOR implantation. The autopsy indicated the causes of death to be sepsis, intestinal hemorrhage, acute right ventricular failure, and one major stroke.[34] A total of 500 patients worldwide have been implanted with the INCOR VAD (Figure 10).

6.625.3.3. Rotary Centrifugal Pumps

Centrifugal pumps are regarded as the next stage of evolution of VADs.[35] Although similar to axial pumps, in that they are rotary pumps, the rotor of a centrifugal pump is shaped so as to cause the blood to move circumferentially along the outer rim of the pump housing and be ejected. Centrifugal VADs have been found to improve myocardial function and be beneficial to end-organ functioning through pulsatile perfusion.[16,31,36] Due to its different pressure-flow characteristics compared to an axial flow pump, a centrifugul pump may be physiologically better suited for adults than an axial flow pump: it provides greater pulsatility in flow, and a more physiologic response to changing preload. The key area of distinction for the centrifugal pumps is how their single moving part, the impeller, is supported. Earlier designs such as the EVAHeart (Pittsburgh, PA) employ solid mechanical bearings, while next-generation centrifugal blood pumps either employ the blood itself to suspend the spinning impeller in a hydrodynamic suspension (HeartWare HVAD, VentrAssist's VentraCor, and the Arrow CorAide). The culmination of centrifugal blood pump technology has resulted in fourth-generation pumps (Terumo DuraHeart, Thoratec HeartMate III, WorldHeart Levacor) whose impellers are completely magnetically levitated inside the pump cavity.

These pumps stay suspended with magnetic levitation, providing a smooth, uniform, and unrestricted flow path to blood, and eliminate contact of the spinning rotor with the housing, thereby theoretically eliminating any wear on the impeller blades and mechanical friction resistance.

6.625.3.3.1. Rotary centrifugal pumps using hydrodynamic suspension

The VentrAssist™ LVAD (Ventracore, Chatswood, NSW, Australia) was a recently developed third-generation centrifugal blood pump with hydrodynamic suspension.[35] Its only moving part, an impeller, consists of four small blades that are embedded with permanent magnets. The combined dynamic interplay of fluid, bearing, and gravitational forces prevents the impeller from contacting the housing. The VentrAssist™ weighs 298 g and is made of titanium. It is ~60 mm in diameter and is suitable for use both in children and adults (Figure 11).

Recent studies have shown the device's ability to perform in BTT therapy.[24,37,38] The initial pilot study was conducted on four DT and five BTT patients in 2003. Having acquired considerable patient-years of experience (7 years), the safety and efficacy profile displayed no embolic events, minimal sepsis/infections and reportedly remarkable performance even in complex cases.[37,39] This pilot study instigated a phase II trial that led to its CE mark approval in the European Union. The overall performance was exceptional with over 70% of patients who achieved early hospital discharge, with better functional status and compliance. To corroborate the survival to transplant or the continued support while the patient was still on transplant wait list, a US multicenter, pilot study to BTT was conducted and the results showed a statistically and clinically significant improvement in the quality of life and functional status, with adverse effects similar to the current LVADs, while certainly being better than pulsatile LVADs.[40] The study was terminated early by Data Safety Monitoring Board because its interim analysis criteria for study discontinuation requirement had been fulfilled.[40] Further investigation of the device was not feasible owing to the company's lack of funds and subsequent dissolution.

The Arrow CorAide VAD (centrifugal pump, hydrodynamic suspension) was also CE Marked in Europe, but its owner exited the VAD space, and there are no further reports of any future development as both the CorAide and the LionHeart have been mothballed. This attrition leaves the Heartware HVAD as the only clinically used pump in this category.

The HVAD™ (Heartware Inc.,) consists of a small continuous flow rotary centrifugal pump with a hydrodynamic bearing design with a unique feature of its size that could be accommodated within the pericardial space near the left ventricle. This design obviates the need for an abdominal dissection. The impeller is suspended via a combination of passive magnetic and active hydrodynamic bearings. This reduces the mechanical strain on the pump and therefore its wear. The integrated design contains two motor stators for single-motor fault protection to increase reliability. A thin blood film generated by the bearings eliminates physical contact between the housing and the impeller during normal operation.[41,42] Since its implantation in March 2006, HVAD™ has undergone clinical evaluations in Europe and Australia and a US BTT trial consisting of 150 patients completed its enrollment in February 2010. After a 6-month follow-up for the last patient enrolled in August 2010, it is anticipated that a BTT PMA submission will occur by year-end 2010, with approval following earliest in mid-late 2011. A DT trial for HVAD with 450 patients randomized 2:1 to the HMI or II has been recently conditionally approved by the FDA (Figure 12).

6.625.3.3.2. Rotary centrifugal pumps using full magnetic levitation

The two devices in this category in clinical development are the Duraheart VAD (Terumo Cardiovascular), and the Levacor VAD (WorldHeart Corporation). Both these devices have a similar configuration, including a 'flat' inlet to the centrifugal pump that allows the pump to be implanted in the upper abdomen of even small patients. In comparison, the third-generation pumps described above have a traditional inlet to their centrifugal pump, one that is at right angles to the pump body. While this somewhat simplifies the blood flow path design, it is possible it may compromise anatomic fit and position of the third-generation pumps, including that of the inlet cannula. The flat inlet of the fourth-generation pumps described here may avoid this potential problem.

The DuraHeart™ VAD comprises an implantable pump with several components to augment its function.[43] The ingenuity of the device is attributed to the magnetically levitating centrifugal rotary pump (impeller with 3 positional sensors)

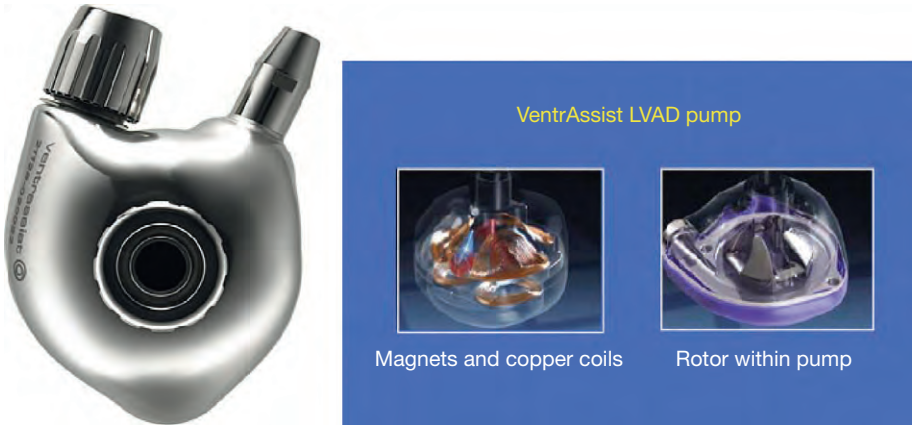

Figure 11 The VentrAssist™ left ventricular assist device (Ventracore, Chatswood, NSW, Australia).



Figure 12 HVAD Heartware, Inc.



Figure 13 DuraHeart™.

with a thin outflow conduit (Vascutek Gelweave™) that exits the skin and connects to the controller that controls and monitors the system status. The pump comprises an upper housing with the levitation system and the impeller, and bottom housing with an external-drive motor. The device has been fabricated with an active magnetic levitation of the impeller coupled with hydrodynamic bearings to support impeller levitation in case of failure of the magnetic levitation system. This design provides flow rate of 2–8 l min^{-1}, with rotor speeds of 1200–2400 rpm. The flow rate can be programmed to vary with physiological changes. DuraHeart™ with its combination of centrifugal pump and magnetic levitation technology was the first such device to reach clinical trial.[43] The pump is implanted in an abdominal pocket. The magnetic levitation of the impeller is designed so as to eliminate friction by allowing a wide gap between blood-contacting surface areas, and to enable blood to flow unimpeded, through the pump in a smooth nonturbulent fashion.

The DuraHeart™ pump has the dimensions of diameter 72 mm, thickness 45 mm, and weighs ~540 g. The displacement volume is 196 ml, that is, 30–50% smaller than the pulsatile pumps. The total horizontal length is ~50–60% shorter than that of axial flow LVADs.[44]

The DuraHeart™ LVAS (Figure 13) is currently being studied in a Pivotal US trial for BTT, a multicenter, nonrandomized study that involves 140 patients. The study is meant to evaluate the safety and efficacy in sustaining patients awaiting transplant and who are more prone to end-stage HF. The DuraHeart™ LVAS carries a CE Mark and is currently available for sale in European countries.[45] Furthermore, the company has completed enrollment for clinical trial in Japan.

The Levacor™ VAD was initially developed by MedQuest Products, Inc., a spin-off of the University of Utah's decades-long contributions to the MCS field, and is now being commercialized by WorldHeart Corporation (Salt Lake City, UT). The device incorporates an ultracompact, bearingless rotary centrifugal pump that is implanted in the peritoneal space. The rotor which acts as an impeller is completely magnetically levitated, ensuring the lack of contact with the housing under any normally encountered operating condition and thereby virtually minimizing thrombosis, damage to blood components, lack of heat, wear and mechanical damage. The inflow cannula is titanium while the outflow graft consists of 12 mm woven collagen sealed polyester anastomosed to the ascending aorta.[46] Its initial clinical evaluation was in Europe in 2006, with anticipated BTT/BTR outcomes in a shorter-term in-hospital setting: after 3 months of support, both patients' natural hearts recovered. To promote recovery of the natural heart, blood flow provided by the Levacor VAD was slowly reduced while the load on the natural heart was gradually increased. The unique maglev technology allowed the Levacor VAD to provide flow rates as low as 1.3 l min^{-1} for weeks at a time to each patient to promote recovery. Both of these devices were explanted after recovery was deemed to be stable. Now 4 years later, both patients are leading a normal device-free life at home.

Subsequently, the system underwent further development to enhance its suitability for longer-term applications and out-of-hospital use. Pump refinements included: a biocompatible coating on the blood-contacting surfaces to further enhance device performance, hermetic sealing of the motor/electronics cavity, a modular pump lead with implanted connector to permit replacement of the percutaneous lead without pump replacement, and an external connector that allows the distal extension cable to be quickly replaced, without surgery, either prophylactically or in case of damage.

Compact, lightweight, and ergonomic controller and battery packs were developed. The controller incorporates a rechargeable reserve battery to support pump operation during exchange of the primary power source. This reduces the number of separate modules to be carried by the recipient, and mitigates the possibility of pump stoppage due to accidental power source disconnection. The controller also provides the ability for the physician to set three different pump speeds, and the patient to then select any of these speeds depending on their condition and activity level.

A pivotal US trial evaluating this device for a BTT in 160 patients was initiated in January 2010, with 8 patients implanted in 4 centers through June 2010. the Levacor™ VAD is expected to be evaluated as an alternative to heart transplant and in future probably as a BTR. Potentially, due to its use of the simplest magnetic levitation allowed by physical laws combined with other innovations, the Levacor™ VAD could last and provide MCS for many years longer than other blood pumps (Figure 14, Table 2).[47]

6.625.4. Partial Circulatory Support VADs

While most devices have focused on providing full and complete support to the circulation, a hypothesis has emerged that, in order to support less-sick HF patients, a much smaller, less-invasive, more user-friendly device that only has to provide partial circulatory support (from 0 to 2.5–4 l min^{-1}) would be needed.

Several such devices are in early development (HeartWare MVAD, WorldHeart MiVAD, Orqis Medical Exceleras) and only one (Circulite Synergy) has been clinically evaluated to date.

The Synergy® micro-pump (Circulite, Inc., Hackensack, NJ, USA) measures roughly the size of an 'AA' battery. The device incorporates a combination of axial, centrifugal, and orthogonal flow paths with a single-stage impeller powered by an integrated brushless micro-electric motor. With the following dimensions: diameter 14 mm, length 49 mm, and weight of only 25 g, Synergy® can pump up to 3 l min^{-1}. The pump design features both a combination of magnetically and hydrodynamically levitated and stabilized rotor, that is sealed and a self-washing flow path that is designed to minimize the risk of thrombus formation in or around the rotor. The



Figure 14 Levacor™ ventricular assist device.

Table 2 RCP product comparison

Device	*Type*	*Weight*	*Size*	*Comments*	*Current status*
HeartWare™	TG, CCF, HDL, ML	145 g	50 mm diameter, 50 ml DV	Pericardial placement 2000–3000 rpm Up to 101 min^{-1}	Approved in Europe BTT trial in progress in the USA
Duraheart™	TG, CCF, ML, HDL (backup)	540 g	72 mm diameter, 45 mm height 180 ml DV	1200–2400 rpm 2–81 min^{-1}	Approved in Europe BTT trial in progress in the USA
Levacor™	TG, CCF, ML	440 g	38 mm anteroposterior dimension	Flow rate 0–101 min^{-1} 6.51 min^{-1} at 100 mmHg and 2500 rpm	Awaiting Pivotal Trial in the USA as BTT
Incor®	CAF	200 g	30 mm diameter, 120 mm length 80 ml DV	5000–10 000 rpm 51 min^{-1} against 100 mmHg	Approved in Europe
Synergy®	HDL, ML	25 g	14 mm diameter, 49 mm length	2–31 min^{-1}	Safety and performance evaluation in progress in Europe

Abbreviations: BTT, bridge-to-transplantation; CAF, continuous axial flow; CCF, continuous centrifugal flow; DV, displacement volume; HDL, hydrodynamic levitation; ML, magnetic levitation; TG, third generation

power console weighs ~3.3 pounds and the dual battery pack powers the device for ~16–18 h. The controller provides the patient with information on the battery status and also alerts the patient to any change that requires attention. With continued research and innovation, the company also intends to expand the Synergy platform with a fully implantable system with physiological feedback, in the near future. The device also comes with a built-in 'fail-safe' mechanism in case of accidental power disconnects, augmented by the patient's native cardiac flow.

CircuLite's development of *Synergy* is backed by established proof-of-concept in ongoing clinical studies and 8 years of engineering at the Helmholtz Institute in Aachen, Germany, one of the world's pioneering centers for blood pump technology development, in collaboration with Katholieke Universiteit in Leuven, Belgium and is specifically designed for long-term use in NYHA Class IIIb/early IV patients (INTERMACS 4–6) (**Figure 15**).

6.625.5. Total Artificial Heart

It has been man's immense quest to find a synthetic replacement for the human heart that could virtually eliminate the need for heart transplant. With the accrued advancements in science and technology over five decades, a TAH in clinical use is now a reality.

A TAH is, in design and operation, similar to VADs, but replaces the heart and presents many more challenges than simply to complement the failing ventricle. The challenge lies in positioning both the ventricular pumps in the abdomen. While developing earlier models, the top portions of the natural heart's atria were left in place when the heart's components were removed, to facilitate suturing the TAH into position. These portions of the atria provided the natural electric stimuli so that the TAH's speed could increase during exercise and slow during rest.

Despite its earlier start, TAH evolution has not progressed as rapidly as LVADs. The only FDA approved TAHs today are the C7–70 pneumatically driven TAH made by SynCardia Systems Inc. (Tucson, AZ, USA) and the electro-hydraulically driven AbioCor TAH commercialized by Abiomed Corp (Danvers, MA).

Some of the earliest pioneering work was done by Cardiowest™ (which was itself a successor to first Kolff Associates and then Symbion, both of Salt Lake City, UT). Nonprofit CardioWest was acquired by for-profit SynCardia Systems Inc., and its device, the C7–70 TAH was approved by the FDA in 2009 following a decade of clinical study, for use in BTT for patients with irreversible end-stage biventricular failure. The recent innovation is its conditional approval of the Freedom ™ driver for investigational device exemption (IDE) clinical study and it is the first-ever US portable driver designed to power the SynCardia temporary TAH inside and outside the hospital by the FDA in March 2010. The device driver weighs 13.5 lbs including two onboard batteries, designed to be charged via a standard electrical outlet and a power adaptor. The entire console could be carried in a shoulder bag or backpack. The driver is designed with a 'dark cockpit,' meaning the driver only sends an alarm when something requires the user's attention. The Freedom ™ driver is intended for use as a BTT in clinically stable cardiac transplant-eligible candidates who are implanted with the TAH (**Figure 16**). The Syncardia TAH costs about $125 000 and about $18 000 a year to maintain.[48]

Like the thoratec implantable VAD, and SynCardia Temporary Heart System, the Jarvik-7 TAH (named after Dr. Robert Jarvik and developed by the University of Utah and Symbion under the leadership of Dr. Willem Kolff, and later named the Symbion TAH) was also pneumatically driven. This device in its refined form is the present-day Syncardia System; so it is useful to describe it here.

It consists of two ventricular pumps joined together and requires a portable console (Big Blue) for power. The ventricle is ellipsoid shaped and is made of polyurethane that has a sac that pushes the blood from the inlet to the outlet valve as it is deflated and inflated by air on the nonblood side of the sac. Air is pulsed through the ventricular air chambers at rates of 40–120 bpm. The artificial heart is fastened to the heart's natural atrium by cuffs (Dacron™ felt). The drive-lines are made of reinforced polyurethane tubing. The outlet lines exiting the skin are covered with velour-covered Silastic™ to ensure stability, durability and also encourage tissue growth (minimal scarring). The power console is pretty large and heavy as that of a household refrigerator. In case of emergency or power failure, the system is also backed up by a rechargeable battery and includes on-board compressed air tanks (modified scuba type) for use during transport. Controls in the console regulate pump rate, pumping pressure, and other essential functions.[49]

Unlike the pneumatically powered devices described above, Abiomed devised an electrohydraulically driven, fully implantable device, the AbioCor® TAH, with transcutaneous energy delivery system (TET). This device is still in investigational use under a humanitarian device exemption (HDE) approved by the FDA. In a limited set of patients, who



Figure 15 The Synergy® micropump (Circulite, Inc., Hackensack, NJ, USA).



Figure 16 The only FDA-approved driver for powering the total artificial heart in the United States is the 418-lb hospital driver nicknamed 'Big Blue' shown alongside the Freedom™ driver system in a portable backpack for in-home use. Reprinted with permission from SynCardia Systems, Inc.

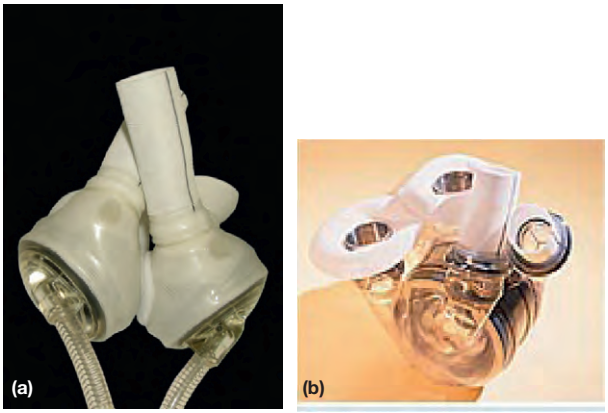

Figure 17 (a): Total artificial heart – Jarvik-7. (b): The AbioCor total artificial heart.

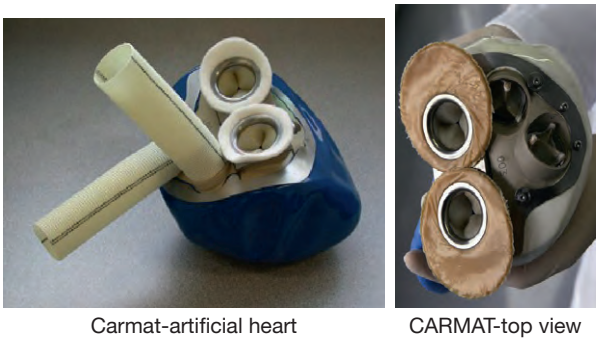

Figure 18 Total artificial heart developed by Carmat SAS.

have no other treatment options, the device is reported to have been found safe and beneficial with end-stage HF. Its uniqueness lies in the design of a mechanism that enables both systoles to occur sequentially. The AbioCor® system comprises a TAH, implanted TET, controller, battery, and cables. An energy converter in the replacement heart helps both the pumps keep blood flowing normally. The Energy Converter contains silicone hydraulic fluid in a sealed compartment that is separated from the right and left chambers by flexible membranes. A pump in the energy converter pushes the fluid against the membranes, causing the pumps to empty and fill (Figure 17).[50,51]

However, both the available TAHs have drawbacks; the former is bulky and obtrusive, while the latter could lead to stroke.

A recent TAH under early development by Carmat SAS, the company founded by professor Carpentier and EADS, Europe's aerospace and defense giant, promises to overcome these hurdles by utilizing 'pseudo-skin' of biosynthetic, microporous materials, and the power source, by implanting a titanium receiver in the skull that would channel energy sent through the skin (noninvasively) from a battery to the heart. The second would work by generating electricity through the skin between two transformers, one inside and one outside the body. The battery is likely to last for between 5 and 16 h, after which it would have to be recharged to prevent the artificial heart stopping. Equipped with 'smart' motors and unlike previous artificial hearts, this one detects the body's activity level (and therefore how much oxygen it requires) and changes its pace accordingly. This new design is likely to be available for clinical use by 2013 (Figure 18).[52]

While traditional TAH designs in clinical use and under development have focused on positive displacement pumps that inherently provide pulsatility, early work is being done by other researchers to install two rotary pumps back-to-back as ventricular replacements in a TAH configuration. These results are too early but it is a possibility that such a configuration might find greater use than the traditional 'pulsatile' devices.

6.625.6. Conclusions

The LVAD has been a remarkable technology that has bridged the void between conventional medical therapy and cardiac transplantation. With increasing number of people diagnosed with heart diseases, and ratio of aging population increasing every year, constraints in donor heart availability, VAD options that aim to support patients with late-stage HF as an alternative to a heart transplant are on the rise. The LVADs have certainly had a positive impact in its role of reducing hospitalization as well as improving the functional status and quality of life of patients. With ongoing research in improving design and performance, the newer LVADs promises to be patient-friendly, durable and minimally invasive to implant or explant, and potentially offer a safety and efficacy profile much superior to earlier-generation devices.

The future of LVADs, when complemented with gene therapy could culminate in a permanent 'dream' cure, wherein the device takes over the heart's functions providing the cardiac stem cells with a conducive environment to regenerate [REF].

With emerging technological advances, there certainly is likelihood for a slew of devices that will provide safe and effective therapy to less-severe HF patients. These devices will need to be significantly refined, smaller, and easier-to-use than the marketed ones.

In the long-term, it is clear to the authors that the answer to the biological question of HF will need to be answered by biological solutions that involve disciplines such as tissue engineering and genetic engineering.

Acknowledgments

The authors would like to acknowledge the contributions of Vivek Srinivasan and Priya Nayar for their diligent work toward the extensive research, sourcing and compilation, and editing of the information needed for this chapter.

References

1. AHA, Our guide to current statistics and the supplement to our Heart & Stroke Facts. In *Heart Disease & Stroke Statistics*; 2010.
2. Roger, V. L.; Weston, S. A.; Redfield, M. M.; *et al*. *JAMA* **2004**, *292*, 344–350.
3. Douglas, P.; Morgan, C.; Lee, H.; Foster, K. R. *IEEE Technol. Soc. Mag.* **2004**, *23*(2), 23–27.
4. Franco, K. L. *J. Card. Surg.* **2001**, *16*, 178–192.
5. "Waiting list activity" and "cadaveric transplant". Transplant Statistics. Scientific Registry of Transplant Recipients, 11/01/2001.
6. Moskowitz, A. J.; Rose, E. A.; Gelijns, A. C. *Ann. Thorac. Surg.* **2001**, *71*(Suppl. 3), S195–S198.
7. Rose, E. A.; Moskowitz, A. J.; Packer, M.; *et al*. *Ann. Thorac. Surg.* **1999**, *67*, 723–730.
8. Wohlschlaeger, J.; Schmitz, K. J.; Schmid, C.; *et al*. *Cardiovasc. Res.* **2005**, *68*, 376–386.
9. Frazier, O. H.; Rose, E. A.; Oz, M. C.; *et al*. *J. Thorac. Cardiovasc. Surg.* **2001**, *122*, 1186–1195.
10. Percentage of Patients Who Experience Right Ventricular DysfunctionAfter Implantation of a Left Ventricular Assist Device, http://www.syncardia.com/Medical-Professionals/lvads-and-rv-dysfunction.html.
11. Dang, N. C.; Topkara, V. K.; Mercando, M.; *et al*. *J. Heart Lung Transplant.* **2006**, *25*(1), 1–6.
12. Bhama, J. K.; Kormos, R. L.; Toyoda, Y.; Teuteberg, J. J.; McCurry, K. R.; Siegenthaler, M. P. *J. Heart Lung Transplant.* **2009**, *28*, 971–976.
13. Dennis, C.; Hall, D. P.; Moreno, J. R.; *et al*. *Acta Chir. Scand.* **1962**, *123*, 267–269.
14. DeBakey, M. E. *Ann. Thorac. Surg.* **2005**, *79*, S2228–S2231.
15. Goldstein, D. J. In *Cardiac Assist Devices*; Goldstein, D. J., Oz, M. C., Eds.; Futura: New York, 2000.
16. Frazier, O. H.; Delgado, R. M., III; Kar, B.; *et al*. *Tex. Heart Inst. J.* **2004**, *31*, 157–159.
17. Griffith, B. P.; Kormos, R. L.; Borovetz, H. S.; *et al*. *Ann. Thorac. Surg.* **2001**, *71*, 116–120.
18. Lazar, R. M.; Shapiro, P. A.; Jaski, B. E.; *et al*. *Circulation* **2004**, *109*(20), 2423–2427.
19. Fries, D.; Innerhofer, P.; Streif, W.; *et al*. *Ann. Thorac. Surg.* **2003**, *76*(5), 1593–1597.
20. Aaronson, K.; Eppinger, M.; Write, S.; Pagani, F. D. *J. Heart Lung Transplant.* **2001**, *20*(2), 241.
21. Ramasamy, N.; Vargo, R. L.; Kormos, R. L.; Portner, P. M. In *Cardiac Assist Devices*; Goldstein, D. J., Oz, M. C., Eds.; Futura: New York, 2000.
22. Song, X.; Throckmorton, A. L.; Untaroiu, A.; *et al*. *ASAIO J.* **2003**, *49*, 355–364.
23. Burke, D. J.; Burke, E.; Parsaie, F.; *et al*. *Artif. Organs* **2001**, *25*, 380–385.
24. Wampler, R. K.; Baker, B. A.; Wright, W. M. *Cardiology* **1994**, *84*, 194–201.
25. Goldstein, D. J. *Circulation* **2003**, *108*, 272–277.
26. Westaby, S.; Banning, A. P.; Jarvik, R.; *et al*. *Lancet* **2000**, *356*, 900–903.
27. Wieselthaler, G. M.; Schima, H.; Hiesmayr, M.; *et al*. *Circulation* **2000**, *101*, 356–359.
28. Miller, L. W.; Pagani, F. D.; Russell, S. D.; *et al*. *N. Engl. J. Med.* **2007**, *357*, 885–896.
29. Feller, E. D.; Sorensen, E. N.; Haddad, M.; *et al*. *Ann. Thorac. Surg.* **2007**, *83*, 1082–1088.
30. Ulrich, G.; Claudia, H.; Friedhelm, B.; *et al*. *Eur. J. Cardiothorac. Surg.* **2008**, *33*, 679–684.
31. Schmid, C.; Tjan, T. D.; Etz, C.; *et al*. *J. Heart Lung Transplant.* **2005**, *24*, 1188–1194.
32. Schmid, C.; *et al*. *J. Heart Lung Transplant.* **2008**, *27*, 253–260.
33. Hetzer, R.; *et al*. *Eur. J. Cardiothorac. Surg.* **2004**, *25*, 964–970.
34. Meuris, B.; Arnout, J.; Vlasselaers, D.; *et al*. *Artif. Organs* **2007**, *31*(5), 402–405.
35. Pagani, F. D. *Semin. Thorac. Cardiovasc. Surg.* **2008**, *20*, 255–263.
36. Osorio, J. *Nat. Rev. Cardiol.* **2010**, *7*(7), 360.
37. Esmore, D. S.; Kaye, D.; Salamonsen, R.; *et al*. *J. Heart Lung Transplant.* **2008**, *27*, 479–485.
38. Esmore, D.; Kaye, D.; Spratt, P.; *et al*. *J. Heart Lung Transplant.* **2008**, *27*, 579–588.
39. Esmore, D.; *et al*. *Eur. J. Cardiothorac. Surg.* **2007**, *32*, 735–744.
40. Boyle, A. J.; *et al*. In *Presented at the 58th annual meeting of the American College of Cardiology*, March 30, 2009.
41. Slaughter, M. S.; *et al*. *Tex. Heart Inst. J.* **2009**, *36*, 12–16.
42. Tuzun, E.; *et al*. *Tex. Heart Inst. J.* **2007**, *34*, 406–411.
43. Nishinaka, T.; *et al*. *Circulation* **2006**, *70*, 1421–1425.
44. Morshuis, M.; El-Banayosy, A.; Arusoglu, L.; *et al*. *Eur. J. Cardiothorac. Surg.* **2009**, *35*, 1020–1028.
45. Nojiri, C. In *International Society for Heart and Lung Transplantation 2008 Annual Meeting*, Boston, MA, April 12, 2008.
46. Pitsis, A. A.; *et al*. *Hell. J. Cardiol.* **2006**, *47*, 368–376.
47. New Utah-Made Vad Implanted In Idaho Man. April 8, 2010. Available from: http://www.unews.utah.edu/p/?r=040810-3#Media_Contacts.
48. Ashton, J. Man goes home with "total artificial heart". CBS Evening News May 21. Available from:http://www.cbsnews.com/stories/2010/05/21/eveningnews/main6507572.shtml.
49. Arabia, F. A.; Copeland, J. G.; Smith, R. G.; *et al*. *Artif. Organs* **2001**, *23*(2), 204–207.
50. 2010. Available from: http://www.heartreplacement.com/abiocore.html.
51. 2009. Available from: http://www.abiomed.com/products/heart_replacement.cfm.
52. Sage, A. Scientists develop artificial heart that beats like the real thing. cited 2010; Available from:http://www.timesonline.co.uk/tol/life_and_style/health/article5026788.ece.
53. Nemeh, H. W.; Smedira, N. G. *Cleve. Clin. J. Med.* **2003**, *70*(3), 223–233.
54. DiGiorgi, P. L.; Reel, M. S.; Thornton, B.; *et al*. *J. Heart Lung Transplant.* **2005**, *24*, 200–204.

6.626. Cardiac Valves: Biologic and Synthetic

S Browne, S Brody, and A Pandit, National University of Ireland, Galway, Ireland

© 2011 Elsevier Ltd. All rights reserved.

6.626.1.	Introduction	403
6.626.2.	Native Heart Valve Structure	404
6.626.3.	Current Treatments	405
6.626.4.	Ideal Scaffold	406
6.626.5.	Synthetic Scaffolds	406
6.626.6.	Decellularized Heart Valve Scaffolds	412
6.626.7.	Naturally Derived Biomaterials of Nonvalvular Origin	417
6.626.8.	Conclusion	423
References		423

Abbreviations

α-SMA	Alpha smooth muscle actin
ECM	Extracellular matrix
EDTA	Ethylenediaminetetraacetic acid
eNOS	Endothelial nitric oxide synthases
FDA	The United States Food and Drug Administration
GAGs	Glycosaminoglycans
MMPs	Matrix metalloproteinases
MSCs	Mesenchymal stem cells
P4HB	Poly-4-hydroxybutyrate
PERV	Porcine endogenous retrovirus
PGA	Polyglycolic acid
PGs	Proteoglycans
PHA	Polyhydroxyalkanoate
PLA	Polylactic acid
PLGA	Poly(lactic-*co*-glycolic acid)
PLLA	Poly-L-lactide
PTFE	Polytetrafluoroethylene
PVA	Polyvinyl alcohol
SDS	Sodium dodecyl sulfate
VECs	Valvular endothelial cells
VICs	Valvular interstitial cells

6.626.1. Introduction

Heart valve disease is a significant cause of mortality worldwide. It occurs when one or more of the valves in the heart are stenosed, restricting the flow of blood, or when one or more of the valves become insufficient, failing to make a tight enough seal during diastole, allowing backflow. While the aortic valve is the most commonly affected valve; valvular disease may occur in any of the valves of the heart likely because of the high pressures to which it is exposed. The major complication of valvular heart disease is cardiac failure resulting from a change in the myocardium induced by pressure or volume overload of the chambers upstream or downstream of the diseased valve. In 2006, the American Heart Association reported that in the United States alone, heart valve disease accounted for 21 386 deaths, and of these deaths, 13 752 deaths were attributed to aortic valve disease, and it was listed as a contributory factor in an additional 27 380 deaths.[1]

Although surgical valve repair is available, in most advanced cases implantation of a prosthetic heart valve, which may be either mechanical or biological in nature, is the preferable option. These prosthetic valves, although extensively used, have a number of problems associated with them, including requiring the patients to undergo anticoagulation treatment for the remainder of their lives. Thus far, a nonthrombogenic, noncalcific prosthetic valve that is capable of maintaining sufficient mechanical properties and hemodynamic flow, and exhibits appropriate fatigue properties, has yet to be fabricated. Current prosthetic designs do not have the necessary potential for growth and healing and are therefore unsuitable for implantation into young patients. The fact that heart valve design has remained virtually unchanged for the last 30 years suggests that the current valves are probably as advanced as they can become, and a new approach must be considered. Researchers have in recent times focused on the use of tissue engineering to achieve this goal. It has been suggested that an optimal heart valve replacement would contain regenerating interstitial cells to provide sufficient turnover of extracellular matrix (ECM), endothelial cells to provide an antithrombogenic element, and a suitable scaffold biomaterial with both appropriate mechanical properties to mimic the native valves and an optimized degradation rate to provide a medium in which the interstitial cells and endothelial cells can repopulate and replace it.[2]

The aortic heart valve facilitates the flow of blood from the left ventricle to the aorta, where it supplies the peripheral blood vessels, through a complex mechanism of opening and closing in an unrelenting, extremely demanding environment over a wide range of hemodynamic conditions.[3] The valve opens and closes 100 000 times every day which amounts to approximately 3 billion cycles over the life time of the average adult.[4,5] With over 8000 l of blood passing through the aortic valve and being pumped out of the heart each day, the physiological demands on the aortic valve are particularly harsh.

Biaxial mechanical analysis of the aortic valve cusp by Christie *et al*. has quantified the strain in the radial and circumferential directions. At a tension of 60 N m^{-1}, strains in the radial and circumferential directions are 75% and 12%, respectively.[6] Billiar *et al*. presented similar results following the application of physiologically relevant strain ratios to both the circumferential and radial axes of valve cusps.[7]

The primary cell types found in the aortic valve are valvular endothelial cells (VEC) and valvular interstitial cells (VIC). VECs form a confluent layer on the fibrosal and ventricular surfaces of the valve cusp. They function primarily in maintaining a nonthrombogenic surface, while it is thought that they play a role in regulating the activity of the VICs,[8] which are present in the underlying spongiosa layer. VICs function mainly in maintaining valve structure and producing ECM.[9] Both cell types have previously been seeded on scaffolds; however, concerns do exist as to the number of available cells. To this end, a number of alternative cell types have also been considered. These include human saphenous vein endothelial cells,[10,11] ovine circulating endothelial progenitor cells,[12] and ovine carotid artery endothelial cells,[13] which have all been assessed for their potential in fulfilling the role of VICs. Meanwhile, human neonatal fibroblasts,[14] human myofibroblasts,[15] ovine myofibroblasts,[13] human aortic myofibroblasts,[16] and neonatal rat smooth muscle cells[17] have all had their ability to fulfill the ECM-producing role of VICs characterized. In addition to functionally replacing VICs and VECs, cells seeded onto a scaffold must be available in clinically relevant quantities, while being free of contamination and pathogens of any type.

Two approaches have historically been taken in the design of scaffolds: the traditional approach and the tissue guided regeneration approach.[18] The traditional approach, which shows the most promise, involves *in vitro* seeding of cells on a scaffold often in the presence of the appropriate signals. These signals may include forces such as shear stresses, growth factors, cytokines, and topography, or a combination of two or more of these. Of these, the application of physiologically representative shear forces seems particularly critical during *in vitro* cell culture.[19,20] In a somewhat related field, studies have shown that preseeding vascular grafts with endothelial cells improves their long-term patency[21] and reduces thrombogenicity.[22] This finding is also relevant in the field of valvular tissue engineering. The development of a fully confluent endothelial cell layer and the regeneration of native ECM are the two critical attributes of a scaffold for valve replacement.[23] With the appropriate signals present, cells will ideally adhere to, proliferate on, and infiltrate the heart valve scaffold. This will result in the deposition of native ECM prior to implantation. The alternative method, guided tissue regeneration, has a similar concept but a different approach. It involves the implantation of a scaffold which will be autologously reseeded by the adjacent host tissue through cell migration or circulating stem or progenitor cells.[24] The benefits associated with this approach include the lack of preseeding and conditioning usually associated with the traditional approach, and the lower risk of an immunogenic reaction which has been associated with allogenic or xenogenic cells used to repopulate scaffolds *in vitro* in the traditional approach.

Synergraft™ (Cryolife, USA) conducted the most widely reported study which utilized the guided tissue engineering approach. The scaffolds were implanted into four male children in 2001. Two of the valves were prepared from noncoronary segments of aortic root while the other two were prepared from pulmonary roots. All valves were cryopreserved and then thawed out, under strict company protocol, prior to implantation. The xenogenic collagen matrix of the scaffold valve provoked a strong inflammatory response in humans that was nonspecific early on and followed by a lymphocyte reaction at 1 year. This trial resulted in death of all but one of the patients.[25] So while the guided tissue approach may seem advantageous when compared with the traditional approach, and has shown some success in animals,[26] human trials have failed. In fact, there is currently no scientific evidence to suggest that following human implantation heart valve scaffolds will be recellularized.[27] Many researchers are very skeptical of this approach, doubting its relevance and efficacy. It has been described as 'highly speculative and highly unlikely' by Stock and Schenke-Layland.[24] While the growth of endothelial monolayers on vascular grafts implanted in animals has been demonstrated,[28] it has thus far proved very different with grafts implanted in humans. Even in the case of Synergraft™, where implants survived for up to 1 year, *in vivo* scaffolds remained acellular.[25] The growth of an endothelial cells layer, and hence the maintenance of a nonthrombogenic layer on implanted scaffolds in the vascular system, is vital in heart valve replacement therapies. In addition, the repopulation of the scaffolds with native cells is vital for ECM deposition and remodeling. Mounting evidence suggests that the most clinically relevant approach to heart valve replacement therapy is utilization of the traditional tissue engineering approach, that is, the *in vitro* seeding of cells onto a scaffold, followed by *in vitro* conditioning, and finally implantation *in vivo*.

6.626.2. Native Heart Valve Structure

In a process known as valvuloseptal morphogenesis, the valves of the heart are derived from embryonic mesenchymal outgrowths, referred to as endocardial cushions.[29] Two valves are formed in the atrioventricular canal and two are formed in the ventricular outflow tract. The two valves in the atrioventricular canal are trileaflet and bileaflet, while the valves in the ventricular outflow tract are both trileaflet (the pulmonary and aortic arterial valves). It had been thought that valves were simple, passive structures whose role in maintaining unidirectional flow was controlled by changes in pressure across the valves.[30] This belief in passive valve function led to the design of passive valve replacement prosthesis, namely, mechanical valves and decellularized xenografts and homografts. However, it has since been established that valves are not merely passive structures, and that in fact they have a far more complex structure, which positions them ideally for their specialized role in the microenvironment in which they are present.[31] It is this realization that has led researchers to consider current treatment outdated, and to pursue an alternate route in which they attempt to replace diseased valves with valves that have both a similar structure and composition.

6.626.3. Current Treatments

The field of heart valve replacement began in the 1950s, with the first successful human implantation taking place as early as 1952.[32] Since then, over 100 models of prosthetic heart valves have been developed and used with varying degrees of success. The two main classifications of valves are mechanical valves composed entirely of synthetic materials and biological valves, fabricated from biological tissue (bioprosthetic). The split between the types of valves used is quite even, with 55% of implanted valves being mechanical and 45% being biological.

Major advances in both biomedical engineering and biomaterials science have facilitated the design and manufacture of very efficient mechanical heart valves with a life span of approximately 25 years. Early designs of mechanical valves were mainly ball and cage valves, progressing then onto tilting and bileaflet tilting disk valves. The opening and closing of these valves is purely a passive phenomenon, with the occluding apparatus (ball or disks) moving in response to the changes in pressure and blood flow within the heart and associated vessels. However, they are associated with thrombolytic therapy and thrombosis, and require the patient to undergo lifelong anticoagulation treatment, which has a number of associated complications. Other limitations include the risk of infective endocarditis, and the risk of failure or separation of valvular components, which may become embolised.[33]

Bioprosthetic valves may be composed from either animal-derived tissue (xenograft) or human-derived tissue (homograft). Xenografts are typically composed of bovine or porcine tissue, and mounted on a synthetic supporting frame (usually PTFE (polytetrafluoroethylene)) allowing it to be sewn into place. Valves are typically treated with glutaraldehyde to increase durability and to ensure decellularization, reducing the risk of immune rejection. The advantages of xenografts include the widespread availability of valves and the superior flow through them as they exactly mimic the architecture of native valves, as well as obviate the need for anticoagulation therapy. However, progressive tissue deterioration has been associated with xenografts resulting in a short life span of 10–15 years,[34] meaning that they are not suitable for use in younger patients. Also, they are susceptible to calcification in young patients and are therefore only implanted in elderly patients. Homografts may be either cryopreserved cadaveric valves or healthy valves from heart transplant patients. As with xenografts, the architecture matches that of the native valves with natural blood flow preserved and hence the valves perform well compared with mechanical valves with a low rate of thromboemoblic complications.[35] The valve contains living, viable cells, which is of course not the case with either mechanical valves or xenografts, and this leads to increased biocompatibility. However, it is still inadequate as a replacement for diseased valves.[36] There exists the risk of damage to the valves because of chronic rejection of the implant, with the foreign tissue and cells provoking an immune response. Although little evidence exists of acute rejection, there have been reports of rapid failure of homograft valves implanted into infants.[37] A further drawback of homograft valves is the lack of donor valves available.

It is clear that although major advances have been made in the field of heart valve replacement, each prosthetic valve designed has major flaws associated with it. A major underlying flaw is that nonliving prostheses lack the ability to grow and repair themselves. An ideal valve would be biocompatible with the capacity for both growth and regeneration.[38] In order to achieve this, researchers have moved toward the fabrication of a living, functional valve as a replacement for diseased valves. Current strategies in the field of tissue engineered heart valves involve the seeding of the appropriate cell types onto a scaffold, preconditioning in the presence of the correct signals, and implantation. The task of current researchers is to identify the appropriate cells and scaffold biomaterials to use, as well as the ideal preconditioning environment, or signals, necessary to fabricate the ideal heart valve replacement scaffold (Figure 1).

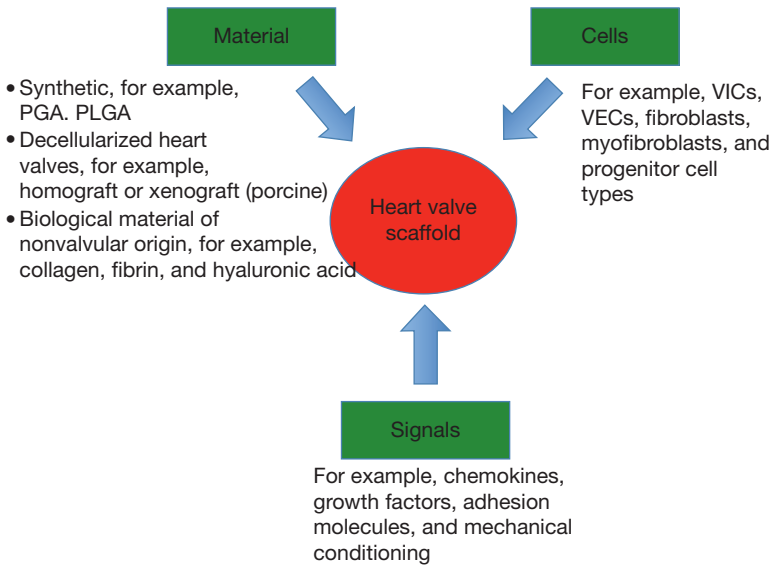

Figure 1 Components necessary for the fabrication of the ideal heart valve replacement scaffold.

6.626.4. Ideal Scaffold

There are many properties which a tissue engineering scaffold must possess to succeed following implantation. There are some which are common to all scaffolds, such as providing guidance for new tissue growth and organization, regulation of cellular behavior such as adhesion, proliferation, migration, and differentiation, all while maintaining the correct phenotype. As cells infiltrate the scaffold, ECM will be deposited, and the scaffold must degrade at a similar rate to facilitate replacement by native tissue. In particular, an ideal scaffold for heart valve replacement would be capable of the following:

- Withstanding the dynamic conditions in which it is implanted over the life span of the patient, in particular, be sufficiently elastic to maintain a tight seal during the diastole phase of the cycle; that is, it should have the appropriate mechanical properties.
- Mimicking the micro- and macroarchitecture of the native heart valve; mechanical properties of the heart valve are related to collagen fiber and elastin fiber microarchitecture, and the structural orientation of collagen fibers influences cellular orientation and mechanical properties.
- Incorporating nanotopography similar to that of the native aortic heart valve basement membrane to ensure the development of a confluent layer of endothelial cells. This will be critical to maintain a nonthrombogenic surface, with cellular growth and orientation significantly influenced by nanotopography.
- Supporting the adhesion, proliferation, and phenotypic expression of VICs and VECs or whichever cell type that has been identified and chosen to replicate the previously stated functions.
- Degrading (without releasing cytotoxic breakdown products) at a rate similar to that at which the ECM is being deposited, allowing for its replacement by a composition similar to that of native valves, while maintaining the ability of the construct to withstand the high pressure environment and maintain a tight seal during diastole, preventing backflow.

6.626.5. Synthetic Scaffolds

As with all biomaterial applications, synthetic scaffold materials offer a wide range of benefits not possible with biologically based materials, such as greater control over numerous scaffold parameters such as mechanical properties, degradation rates, fabrication, reproducibility, and geometrical design specifications. Similarly, sourcing of the raw material for synthetic scaffolds is usually a much simpler process than acquiring material for biological scaffolds. Synthetic scaffold biomaterials also have a much longer shelf life than biological biomaterials, which is an important factor for valve prosthesis, and they are known to initiate less of an immune response, with no possibility of the remaining cellular materials causing graft rejection (**Figure 2**). Unlike biological scaffold biomaterials, synthetic biomaterials contain no epitopes bound to cellular adhesion receptors. This limits any possible immunogenic reactions *in vivo*. There are a large number of processes used in polymer scaffold fabrication, including weaving, meshing, porogen leaching, emulsion freeze-drying, expansion in high pressure gas, 3D-printing, phase separation, and stereolithography.[39] By exploiting these techniques, synthetic scaffolds may be specifically designed to have specific, biologically relevant, porosities, mechanical properties, and surface topographies (**Table 1**).[61]

Shinoka *et al.* pioneered initial synthetic scaffold designs in the mid-to late-1990s.[41–43] Composites of poly(lactic-*co*-glycolic acid) (PLGA) layered with nonwoven PGA were studied. In most cases, scaffolds were seeded with autologous arterial cells and implanted *in vivo*, in an ovine pulmonary model. Although the cusps were thicker and less flexible than native cusps, overall results were quite favorable.[41] Seeded cells were shown to persist in the scaffold structure 6 weeks after implantation. Histological examination of the scaffold postmortem revealed a cellular architecture and tissue structure similar to that *in vivo*, although there was an inflammatory response and some complications due to infection in the animal.[42] As PGA is a biodegradable, relatively biocompatible, well-characterized biomaterial which has been approved for human implantation by the FDA (The United States Food and Drug Administration), its use as an independent scaffold for heart valve replacement design would have been favorable. However, when its mechanical properties were compared to those of the native heart valve it was deemed excessively stiff.[39,40,42,62] As a result, alternative biomaterials had to be investigated. Materials, which have been investigated thus far, include P4HB, PLA, PLLA, PHA, PVA, and PGA copolymers.

A method to improve the mechanical performance of PGA was investigated by dip coating the PGA scaffold in P4HB.[12,13,47–50] Contradictory evidence exists with regard to the success of this method, with Hoerstrup *et al.*[13,48] and Perry *et al.*[49] reporting synchronous opening and closing, pliable and mobile cusps, and mechanical properties comparable to those of the native valve, while Kadner *et al.* found that although

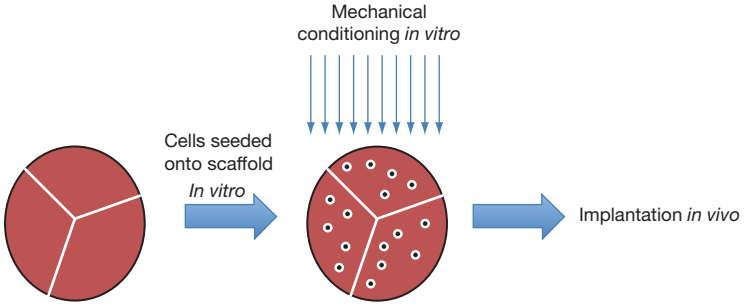

Figure 2 Typical approach taken to prepare heart valve prosthesis for implantation.

Table 1 Synthetic biomaterials tested for heart valve scaffold applications

Scaffold composition	*Cell population(s)*	*Mechanical forces/signals utilized*	*Model, time period*	*Structure, function, and degradation*	*Cell response, ECM deposition*	*Study limitations*	*Reference*
Nonwoven PGA or PHA or P4HB	Ovine carotid artery smooth muscle cells, endothelial cells, and fibroblasts	Continuous laminar flow	*In vitro*, 8 days in static culture, subsequently tested for 1 h in continuous flow	Trileaflet vavles formed from PHA and P4HB Surface morphology of all scaffolds after 1 h of continuous flow was similar	Cells formed confluent layers on the PHA and P4HB scaffold Initially cell numbers on the PGA scaffold were higher Collagen production was highest on the PGA scaffold	Nonwoven PGA cannot maintain a predefined structure	39
Nonwoven PGA mesh	Ovine femoral artery endothelial cells and fibroblasts	–	*In vivo*, allogenic ovine pulmonary valve model for up to 8 weeks	No evidence of stenosis, trivial regurgitation Increase in tensile strength	Increased ECM deposition (collagen and elastin)	High stiffness if implanted prematurely, but prolonged incubation causes degradation	40
PLGA woven mesh surrounded by nonwoven PGA	Ovine femoral artery endothelial cells and fibroblasts	–	*In vivo*, three autologous and four allogenic ovine pulmonary valve models for up to 21 days	Valve cusps were thicker and less flexible than native cusps, but had similar tensile strength prior to implantation Autologous cusps maintained size and shape; showed no stenosis; trivial regurgitation Allogenic cusps showed significant shrinkage	Constructs had 30% of the collagen content of the native valve at 7 days Constructs resembled native tissue histoligically 1 day postimplantation	Not fully investigated	41
PLGA woven mesh and nonwoven PGA	Ovine femoral artery endothelial cells and ovine femoral artery fibroblasts and smooth muscle cells	–	*In vivo*, autologous pulmonary model for up to 11 weeks	At 6 weeks cusps were thicker than native cusps Tensile strength was similar to that of the native cusp By 11 weeks, stenosis and regurgitation had not developed; 6 weeks postimplantation, PGA had almost fully degraded	Elastin and collagen fibers were expressed At 11 weeks collagen content was similar to that of the native valves Von Willebrand factor was expressed by the endothelial cells	Long-term cusp thickening may lead to functional problems	42
PLGA woven mesh sandwiched between nonwoven PGA mesh sheets	Ovine femoral artery endothelial cells and fibroblasts Ovine subdermal fibroblasts	–	*In vivo*, autologous pulmonary model for up to 10 weeks	At 10 weeks dermal cell-seeded cusps were thicker than native cusps Dermal cell-seeded cusps had lower mechanical tensile strength than arterial-seeded cusps and native pulmonary cusps Complete degradation of PGA at 10 weeks	Elastin and collagen fibers were expressed in all constructs Variation in elastin fiber organization was observed Endothelial cells expressed von Willebrand factor	Polygalactin degradation and cellular phenotypic expression, other than von Willebrand factor expression, were not investigated	43

(*Continued*)

Table 1 (Continued)

Scaffold composition	*Cell population(s)*	*Mechanical forces/signals utilized*	*Model, time period*	*Structure, function, and degradation*	*Cell response, ECM deposition*	*Study limitations*	*Reference*
PGA layered with a copolymer of PGA and PLA	Human dermal fibroblasts and bovine aortic endothelial cells Ovine aortic valve VICs and VECs	–	*In vitro* up to 14 days	Initially, scaffold was easily torn and stretched when gently handled Later scaffolds were stronger and stiffer	Initially fibroblasts or VICs covered the surface of the scaffold and these were then covered with a layer of endothelial cells In both cases endothelial cells did not infiltrate and capillaries were not formed	Functionality testing not complete	44
Inner layer of PGA and PLA fibers surrounded by an outer layer of PGA fibers	Ovine carotid artery endothelial cells and myofibroblasts	–	*In vivo*, ovine pulmonary valve model for up to 9 weeks (preseeded *in vitro* for 20 days)	Cusps were thicker and stiffer than the native valve cusps Polymer mesh fibers remained visible at 9 weeks	Endothelial cells formed a confluent layer on the surface and reduced thrombogenicity compared to unseeded cusps	Three of the seven animals experienced post operative valve insufficiency Inflammatory cells were identified at the implantation site at 9 weeks	45
Copolymer of PGA and PLA	Endothelial cells, smooth muscle cells and fibroblasts from ovine femoral arteries	–	*In vivo*, nine autologous and four allogenic ovine pulmonary valve models for up to 11 weeks	Thickness greater than that of the native cusp Tensile strength increased over time	Confluent layer of endothelial cells developed Development of ECM including collagen	Inflammatory response and mild regurgitation in allogenic valves PGA exhibits high stiffness	46
Nonwoven PGA coated with P4HB	Human umbilical cord cells	Continuous laminar flow	*In vitro*, up to 21 days	Constructs had similar uniaxial stress response to native pulmonary valves, but constructs were less pliable and less distensible Multiple breakages and fragmentation of scaffold	Collagen types I and III were deposited At 3 weeks cell/DNA content was higher than that of the native cusp	Stiffness of construct may limit *in vivo* functionality	47
PGA nonwoven mesh dip coated in P4HB, fabricated by welding techniques	Human marrow stromal cells	Pulsatile flow	*In vitro*, 7 days in static culture followed by 14 days in a pulsatile flow bioreactor	Synchronous opening and closing Cusps were intact, mobile and pliable Mechanical properties were comparable to native valves multiple hydrolytic breakage and fragmentation of polymer fibers	Cells grew to confluence, expression of α-SMA and vimentin and deposition of GAGs and collagen types I and III	Fragmentation may cause distal blockages	48
PGA nonwoven mesh dip coated in P4HB	Ovine aortic VECs and circulating endothelial progenitor cells	VEGF TGF-β1 basic fibroblast growth factor (bFGF)	*In vitro*, 1–8 days in static culture	Not reported	Cell proliferation increased in response to bFGF and VEGF TGF-β1 induced endothelial-to-mesenchymal transdifferentiation	Expression of VIC markers other than α-SMA not investigated	12

PGA coated with P4HB	Ovine MSCs	Pulsatile flow	*In vitro*, up to 3 weeks	Cusps coated uniformly Effective stiffness of the construct was similar to that of the native cusp At 3 weeks, residual polymer fibers remained	Cells were found throughout the full thickness of the cusps	Cellular phenotype and expression postseeding were not characterized	49
PGA nonwoven mesh dip coated in P4HB Fabricated by welding techniques	Autologous ovine carotid artery myofibroblasts and endothelial cells	Pulsatile flow for 14 days preconditioning	*In vivo*, Ovine pulmonary valve model for up to 20 weeks	Tensile strength was 130% that of native tissue at 20 weeks Complete polymer drgradation at 8 weeks	180% native valve collagen content at 8 weeks 150% of native valve DNA content, 140% of GAG content after 20 weeks Elastin detected at 6 weeks	Increase in inner diameter of constructs Moderate regurgitation at 16–20 weeks	13
PGA coated with P4HB	Ovine carotid artery medial cells and endothelial cells	Pulsatile flow *in vitro* for 14 days prior to implantation	*In vivo*, Autologous ovine pulmonary position for up to 20 weeks	Not reported	Expression of collagen types I and III was detected Myofibroblasts retained phenotypic expression Elastin was detected at the ventricular side	Valve function and mechanical properties not reported	50
Layers of PHO and PGA films	Ovine carotid artery endothelial cells and myofibroblasts	–	*In vivo*, autologous ovine pulmonary valve models for up to 24 weeks	No thrombus formation and mild nonprogressive valvular regurgitation Molecular loss of the PHA was observed but degradation time exceeds 6 months	Cellular and ECM contents increased over 24 weeks	The long degradation time is deemed an obstacle	46
Nonwoven PGA and PLLA (50:50)	Ovine carotid artery smooth muscle cells	Uniaxial cyclical three-point flexure at physiological frequency	*In vitro*, Up to 3 weeks	At 3 weeks, cyclic flexure had increased scaffold stiffness by 429% to 978±228 MPa	Flexure increased cellular infiltration, decreased cellular necrosis, and increased collagen expression	Elastin was not produced	51
Flat nonwoven sheets of PGA and PLLA fibers	Ovine bone marrow MSCs	–	*In vivo*, seeded *in vitro* in a rotating culture vessel for 4 weeks and autologous pulmonary valve model for up to 4 months	Prior to implantation scaffold stiffness was 50% that of the native valve At 24 weeks, scaffold tensile strength was 30% of the initial value Burst strength at the same stage exceeded the target strength for pulmonary valve substitute	Similar ECM organization to that of the native valve cusp Collagen fibers were found on the fibrosal surface and elastin was found on the ventricular surface GAGs were found in the remainder of the cusp	Explanted cusps were thicker than native cusps Incomplete coaptation of the valve cusps and mild regurgitation	52
Porous PHA	Ovine carotid artery vascular cells	–	*In vitro*, 4 days in static culture	Cusps opened and closed synchronously under pulsatile flow prior to seeding	Cells attached to the scaffold forming a confluent layer Cells also grew into pores	Short culture time Cellular behavior not fully characterized Pulsatile flow only applied prior to seeding No elastin formation	53

(*Continued*)

Table 1 (Continued)

Scaffold composition	*Cell population(s)*	*Mechanical forces/signals utilized*	*Model, time period*	*Structure, function, and degradation*	*Cell response, ECM deposition*	*Study limitations*	*Reference*
Porous PHA	Ovine carotid artery cells	Pulsatile flow	*In vitro*, 1, 4, and 8 days in a bioreactor under pulsatile flow	Not reported	Cells initially grew into the pores Confluent layers of cells formed on the surface orientated in the direction of flow Collagen and GAGs were expressed	No elastin expression	54
Porous PHA	Ovine jugular vein endothelial cells and a mixed population of ovine carotid artery cells	–	*In vivo*, allogenic ovine pulmonary valve model up to 17 weeks	Synchronous opening and closing Similar stress–strain response and morphology to that of the native valve at 17 weeks	ECM surrounding the implant was rich in collagen and GAGs but not elastin	Confluent intact endothelial lining not achieved	55
PVA with grafted PLA side chains	Porcine aortic VICs	–	*In vitro*, 1 day in static culture	Degradation, mass erosion profile, and hydrophobicity can be controlled	Ability of VICs to attach was demonstrated	Cellular behavior not fully characterized	56
Polyethylene glycol (PEG)-containing RGD and/or PHSRN (a fibronectin-derived peptide sequence)	Porcine aortic VICs	–	*In vitro*, up to 7 h in static culture	Not reported	RGD and PHSRN only slightly improved VIC proliferation	VIC adhesion not deemed adequate	57
Porous PCL coated with varying concentrations of chitosan (0.5–2%)	Human fetal lung fibroblasts	–	*In vitro*, up to 1 week	PCL scaffold morphology is minimally affected by the chitosan coating Chitosan adsorption remained stable for the duration of the experiment	Chitosan coating significantly improved cellular adhesion and proliferation	Cellular expression and phenotype not investigated	58
Multilayer PLA fibers using a cast and thermal fixation	Adult bone marrow-derived stem cells	Pulsatile flow	*In vivo*, ovine pulmonary valve model up to 8 weeks	Mobile but thickened leaflets	Layered neotissues with endothelialized surfaces ECM analysis at 8 weeks showed higher values for DNA, collagen, and GAGs compared to native valves	Small sample numbers No elastin expression	59
POSS–PCU	(Platelets)	Pulsatile flow	*In vitro*, up to 31 days	Minimal calcification The tensile strength remained unchanged following exposure to the pulsatile flow	Low platelet adherence to surface	VIC, VEC adhesion not assessed	60

the scaffolds did show a similar uniaxial response to that of the native pulmonary valve cusp, they did not match the mechanical properties of native valves as they were less pliable and less distensible.[47] Both Kadner *et al*. and Hoerstrup *et al*. noted multiple mechanical failures such as breakages and fragmentation *in vitro* which raise major concerns regarding suitability of this scaffold *in vivo*. Dvorin *et al*. examined the use of growth factor signaling to induce transdifferentiation of endothelial cells seeded onto the same scaffold. Ovine aortic VECs and circulating endothelial progenitor cells were seeded onto the scaffold, and through vascular endothelial cell growth factor (VEGF) and transforming growth factor beta (TGF-β) signaling, endothelial-to-mesenchymal transdifferentiation was induced.[12]

Recently, Englemayr *et al*.[51] and Sutherland *et al*.[52] have investigated the use of a number of copolymers of nonwoven PGA and poly-L-lactide acid (PLLA) for heart valve applications. Following 3 weeks of cyclic flexure *in vitro*, scaffold integrity remained intact, stiffness increased fourfold, infiltration of ovine carotid smooth muscle cells increased, and collagen was expressed.[51] The scaffold was seeded with ovine bone marrow mesenchymal stem cells (MSCs) and implanted in an autologous model. The construct functioned for 4 months, although incomplete coaptation and mild regurgitation were reported, possibly because of the thickness of the valve cusps observed following retrieval.[52] A major finding from this study was, in addition to the formation of a confluent endothelial layer on the scaffold, the site-appropriate phenotype assumed by the MSCs and the structural appearance of the scaffold. Structural remodeling created three distinct layers in the construct which were equivalent to the fibrosa, spongiosa, and ventricular layers of the native heart valve.[52,63]

Porous polyhydroxyalkanoate (PHA) has been characterized by Sodian *et al*. as a scaffold biomaterial using both *in vivo* and *in vitro* studies.[39,54,55] Scaffolds have been seeded with mixed populations of ovine carotid artery cells for both *in vitro* and *in vivo* studies. Confluent layers of cells were formed *in vitro* on the surface of the biomaterial and grew into the scaffold pores. However, when this scaffold was transferred *in vivo*, it failed to form a confluent endothelial cell lining. ECM expressed *in vivo* was rich in collagen and glycosaminoglycans (GAGs), although it lacked elastin. PGA demonstrated favorable properties when it was compared with PHA and P4HB. It was found that when compared to PHA and P4HB, the PGA scaffold induced the greatest initial cellular proliferation and the greatest overall collagen expression.[39]

The integration of cells within a synthetic biomaterial is a major challenge considering the delicate and specific environment that cells are accustomed to *in vivo*. Furthermore, promoting ECM production from these integrated cells to replace the synthetic biomaterial as it degrades is required to ensure the maintenance of scaffold integrity. Qzawa *et al*. fabricated and investigated the use of a copolymer sponge fabricated from PCLA (ε-caprolactone-*co*-L-lactide reinforced with poly-L-lactide fabric). It showed promising integration with only the fibrous polylactic acid (PLA) component of the PCLA remaining 8 weeks postimplantation. The scaffold had been successfully endothelialized, in the presence of the preseeded smooth muscle cells ensuring the presence of elastin in the deposited ECM.[64] Nuttelman *et al*. seeded VICs on a synthetic polyvinyl alcohol (PVA)–PLA scaffold. The tissue-like elasticity and high water content of the hydrogel seemed to suggest that it would be a suitable biomaterial to fabricate a heart valve scaffold. It was thought that its combined degradation profile, hydrophobicity, and ability to photo-cross-link would optimize cellular behavior. While VIC attachment was achieved, the cell proliferation rate and, as a result, the level of ECM deposition were considered insufficient.[56]

A recent study by Schmidt *et al*. investigated the combination of sandwich structured PLA scaffolds seeded with adult stem cells and minimally invasive surgery.[59] The valve was delivered using a crimping and delivery system. The implanted valves showed good performance *in vivo* following minimally invasive implantation, with leaflet movement and sufficient opening and closing. The presence of collagen in the outer layers was confirmed, while cells of the leaflet surface layer expressed endothelial nitric oxide synthases (eNOS) and α-smooth muscle actin (α-SMA), resembling the pattern of native valve endothelial cells. The relative success of this study could prove to be an important step in the movement toward a minimally invasive surgical technique for valve replacement.

A major issue with replacement valves has been calcification, a complex phenomenon induced by a large number of both mechanical and biochemical factors. Recent work has focused on the fabrication of novel polymers with anticalcification properties as biomaterials. Ghanbari *et al*. tested the calcification-resistance efficacy and other mechanical and surface properties of a new nanocomposite polymeric material (polyhedral oligomeric silsesquioxane–poly(carbonate-urea) urethane; POSS–PCU).[60] They found that after incubation in a calcium solution in a specifically designed *in vitro* physiological pulsatile system for 31 days, this new polymer had considerably less calcification when compared with polyurethane and bovine pericardium sample, and also that the mechanical properties showed no deterioration. This work shows that specifically designed novel polymers with tailored surface and mechanical properties hold promise for use as cardiac valve replacement biomaterials.

Long-term mechanical properties of synthetic scaffold biomaterials can change as the polymer degrades and the biomaterial is, ideally, replaced by native ECM. For example, it has been shown that when elastomeric polymers are placed under long-term cyclic strain *in vivo* they undergo irreversible deformation.[65] PHA had been suggested as an optimal scaffold owing to its flexibility and some promising *in vitro* results.[54] However, the work of Sodian *et al*. has shown that the rate of degradation and replacement by native tissue *in vivo* is not sufficient to retain its mechanical properties.[55] This is a common theme, with many materials offering a wide range of properties, but as yet none has been identified with the ideal set of properties. Synthetic materials, while offering many advantages such as great control over scaffold parameters, also have disadvantages. Their potential to induce a toxic response when releasing degradation products is a considerable and major limitation. Although a great many *in vitro* and *in vivo* studies are carried out to assess the toxicity of synthetic biomaterials and the associated degradation products, little can be predicted until the biomaterial is implanted in a human patient. These limitations and other uncertainties associated with the use of synthetic materials are fuelling the drive toward a solution using a biological alternative.

6.626.6. Decellularized Heart Valve Scaffolds

The use of decellularized heart valves as replacement for diseased valves is quite intuitive, with the first human clinical use of aortic valve allografts being reported in 1956 by Murray.[66] Allografts implanted into the descending aorta demonstrated durability, retained the ability to open and close correctly, and, furthermore, did not calcify. Indeed, it was thought originally that decellularized valves were viable and integrated with the host tissue. However, work by Gall *et al*. showed the absence of an endothelial layer and only very few fibroblasts present on the biomaterial years after implantation.[67] Because of issues regarding the supply of cadaveric allografts, research focused on xenografts, mainly of porcine origin. Xenografts are much more widely available. However, they are also associated with many more complications than homografts, such as cross-species contamination. Therefore, even more care must be taken to ensure complete removal of all cells or cell remnants from the scaffold. Ideally techniques to decellularize the scaffold should remove all cells and cellular debris from the tissue without causing damage to the surrounding ECM architecture, inhibiting the growth of seeded cells, or causing immunogenic reactions or calcification (**Table 2**; see **Chapter 2.221, Decellularized Scaffolds**).[24]

There is a great need to completely decellularize xenografts to ensure no cross-species contamination. In the presence of porcine cells or cell remnants, interaction occurs between the naturally occurring Gal α-1-3 Gal β-1-4 GlcNAc-R (α-Gal) antibodies in humans and α-Gal epitopes on porcine cells. This leads to an inflammatory response and the rejection of the implanted valve construct. Indeed, this failure to completely remove cell remnants was linked with the failure of Synergraft™ *in vivo*. Studies have revealed traces of the α-Gal epitope in the cusps of the valve, which may be a factor in its failure.[78] The porcine endogenous retrovirus (PERV) must also be considered when working with porcine-derived tissue, as a number of previous studies have shown human cell line and primary endothelial cell infection with PERV.[71,85–87] To ensure no cross-species contamination and ultimate rejection of the scaffold, it is essential that all cells or cell fragments are completely removed from the scaffold prior to implantation. Currently implanted valves are not susceptible to this type of rejection as glutaraldehyde treatment ensures complete cellular removal.[88]

Initially, studies focused on the use of freeze-drying as a technique to remove cellular remnants on heart valve and also to provide a porous matrix for cellular growth. It was hypothesized that freeze-drying would remove cell remnants and provide a porous surface, while at the same time preserving the ECM microarchitecture and thus the native valvular mechanical properties. However, because of the high water content of the native valve cusps, ice build-up during the freeze-drying procedure caused the native ECM of the scaffold to collapse. Freeze-drying failed to preserve the native ECM structure, thus negating the reason for using decellularized valves. The technique also failed to create a porous surface, which would restrict the infiltration of seeded cells into the scaffold. Further, preparation of the surface by wiping it with cotton wool was necessary to improve endothelial cell adhesion. Also, the danger of cross-species contamination was not removed as the removal of cells or cellular debris could not be confirmed.[89]

In vitro studies utilizing human fibroblasts and vascular endothelial cells were performed on the scaffold to assess any potential in *in vivo* use. It was found that while the fibroblasts did not reach physiologic densities during the experiments, endothelial cells did form confluent layers.[68]

Numerous alternative methods to decellularize native heart valves have also been investigated. These methods are usually detergent or enzyme based. Various combinations and concentrations of the following reagents have been utilized: ethylenediaminetetraacetic acid (EDTA), trypsin, RNase, DNase, (enzymatic), and Triton® X-100 and sodium dodecyl sulfate (SDS, detergent).[71,90,91]

Reider *et al*. compared three very standard methods of decellularization. They attempted to decellularize porcine, aortic, and pulmonary heart valve roots using three separate protocols followed by DNase and RNase treatment: trypsin–EDTA, SDS, and detergent-based Triton X-100. Treatment with EDTA-trypsin and SDS failed to completely decellularize the heart valves, while cell growth on the SDS-treated tissue was inhibited. This is due to the failure to wash away residual ionic-detergents. Triton X-100 treatment was deemed the best as following this treatment, the most favorable results for human cell attachment were observed in *in vitro* cell seeding studies. Although not as big a concern as complete cell removal, decellularization by trypsin and EDTA does not eliminate all active matrix metalloproteinases (MMPs).[91] Exposure to active MMPs for too long affects the microarchitecture and integrity of the ECM structure of the valve. However, the MMP activity decreases and eventually stops on a decellularized scaffold. A combination of enzymatic and detergent-based treatment successfully removed PERV and cellular components from aortic heart valves. This technique involved successive washes in 0.1% trypsin solution, hypotonic and hypertonic Triton X-100, DNase solution, and RNase solution, and rinses in Hank's solution in succession.[92]

Ideally, any decellularization technique would have minimal effects on the native valvular architecture and mechanical properties of the valve. However, this is very rarely the case. For example, longer incubations in trypsin can lead to improved decellularization of heart valves; however, adverse disruption to the ECM bundles is often caused.[93] Furthermore, the collagen triple helix can be disrupted and the elastin network can become swollen by SDS treatment.[93] An important area in which few studies have been carried out is the effect of the various decellularization techniques on the mechanical properties of valve scaffolds. However, a study by Dohmen *et al*. investigated ovine myofibroblasts and carotid artery endothelial cells seeded *in vitro* onto porcine decellularized heart valves and implanted into an ovine model. Following postimplantation at 6 months, the scaffold demonstrated both favorable mechanical properties and functional characteristics. Mechanical integrity was maintained while the seeded cells were still proliferating with no PERV sequences detected in the heart valve tissue or blood.[71]

Bertipaglia *et al*. took an approach that, although seemingly obvious in nature, has not been fully exploited. Usually, cells of a nonvalvular origin are seeded onto a decellularized scaffold, with the idea that they replace the functions of the VECs and VICs, which have been removed. However, in this case Bertipaglia *et al*. seeded cells from the heart valve onto

Table 2 Decellularized heart valves tested for heart valve scaffold applications

Scaffold composition	*Cell population(s)*	*Mechanical forces/ signals utilized*	*Model, time period*	*Structure, function, and degradation*	*Cell response, ECM production*	*Study limitations*	*Reference*
Freeze-dried porcine pulmonary valves	Human dermal fibroblasts and human umbilical vein endothelial cells	–	*In vitro*, up to 20 days in static culture	Freeze-drying created cavities	Fibroblast cell density was low and no cells were found on unperforated scaffolds Fibroblasts were metabolically active and adhered to the scaffold Endothelial cells formed a confluent layer	Freeze-drying created an impervious crust on the scaffold surface	68
Porcine aortic heart valves treated with 1% TX, RNase, and DNase	Human saphenous vein endothelial cells	–	*In vitro*, up to 3 days in static culture	Loose ECM structure	Confluent layer of endothelial cells on surface	Presence of immunostimulating cell remnants could not be excluded	10
Porcine aortic heart valves treated with Tris-buffer, PMSF protease inhibitor, DNase, RNase, trypsin, and phospholipases	Human dermal fibroblasts	Pulsatile flow	*In vitro*, up to 8 weeks, half in static and half in dynamic conditions	Good preservation of region specific achitecture	48% of average nuclear cell density after 8 weeks Detectable collagen expression reported	Cytoplasmic elements only partially extracted	14
Porcine aortic heart valves treated with either TX, cholate, and nucleases or *N*-cetylpyridinium and nucleases	Human dermal fibroblasts	–	*In vivo*, subdermal rat implantation of unseeded scaffold *In vivo*, seeded scaffold in static culture	Both treatments removed most cells while preserving endothelium basal membranes, ECM texture (collagen fibril bands), and mechanical properties Calcification was significantly reduced by TX-cholate treatment	Cells grew in patchy aggregates on the scaffold surface and infiltrated the scaffold Intercellular and cell–matrix contact was observed	Cellular behaviors only assessed by SEM and TEM Mechanical properties based only on uniaxial tests	69
Porcine pulmonary vaves treated with 0.1% deoxycholic acid	Ovine saphenous and jugular vein endothelial cells	–	*In vivo*, cell seeding in static culture for 7 days and then implanted in an autologous ovine pulmonary model for up to 6 months	No cusp tearing, perforation, fibrous tissue, or deformation observed at 6 months	Confluent cells at the commissures but only islands in the middle of the cusp Fibroblast migration observed at 3 and 6 months	Only islands of endothelial cells developed and no cells were seen at the free edges Calcification found at suture lines	70
Porcine pulmonary heart valves treated with 0.5% trypsin/0.2% EDTA	Ovine right carotid artery myofibroblasts and endothelial cells	–	*In vivo*, static cultured for 18 days and implanted in an autologous model for up to 6 months	Not reported	Collagen, GAG, and elastin contents similar to those of native valves No PERV detectable at 6 months in the construct or the blood	Decellularization procedure did not remove all PERV from the scaffold	71

(*Continued*)

Table 2 (Continued)

Scaffold composition	*Cell population(s)*	*Mechanical forces/ signals utilized*	*Model, time period*	*Structure, function, and degradation*	*Cell response, ECM production*	*Study limitations*	*Reference*
Porcine aortic valves treated with TX, Sodium deoxycholate (NaDC), and benzonase, and pretreated with fibronectin	Porcine aortic valve VICs	–	*In vitro*, static culture for up to 15 days	Good ultrastructural preservation	Cellular infiltration of scaffold Trace levels of smooth muscle myosin expressed Evidence of collagen and elastin generation	Nucleic acid detected post-decellularization	72
Porcine aortic valves treated with 0.5% trypsin and coated in a copolymer of 82% P3HB and 18% P4HB	Mouse fibroblasts	–	*In vivo*, allogenic porcine aortic and pulmonary model for up to 3 months	Valves in aortic position were functional and clinical signs of valve dysfunction were not demonstrated	Complete endothelial cell lining was formed and collagen was deposited	Inflammation was evident in both locations and in the pulmonary location valve was 'severely obliterated'	73
Porcine aortic and pulmonary valves treated with TX, NaDC, DNase, and RNase	Human saphenous vein endothelial cells Human saphenous vein myofibroblasts	–	*In vitro*, static culture endothelial cells up to 5 days Myofibroblasts up to 10 days	Not reported	Confluent layer of endothelial cells formed Confluent layer of endothelial cells formed	Effects of this decellularization technique on mechanical properties and structure not investigated	15
Porcine pulmonary valves treated with trypsin/EDTA	Ovine carotid artery endothelial cells and myofibroblasts	–	*In vitro*, static culture for up to 9 days	Structure comparable to that of the native porcine and ovine valves; well defined layers, collagen on the fibrosal layer, and elastin in the ventricular layer	Confluent endothelial lining developed Expression of α-SMA, myosin, calponin, and h-caldesmon detected	Complete valvular cell phenotypic expression not replicated by seeded cells	74
Porcine aortic valves treated with EDTA, gentamisin, DNase, RNase, and either 1% TX or 0.5% trypsin	Porcine descending thoracic aorta endothelial cells	–	*In vitro*, static culture for up to 10 days	Both treatments caused a loss of collagen density and GAGs and an increase in intercellular space Trypsin caused further loss of chondroitin sulfate (CS), laminin, and fibronectin	Endothelial cells covered 80% of the surface of the TX treated cusp Cells expressed vWf, fibronectin, laminin, and CS	Neither treatment completely removed cells from the aortic wall	75
Porcine aortic valves decellularized by TX, NaDC, and endonuclease	Porcine aortic valve VICs	Serum deprivation	*In vitro*, static culturte for up to 4 weeks	Not reported	Serum deprivation increased VIC numbers and infiltration rates At 4 weeks, cellular density was similar to that of the native valve	Preliminary study, endothelial response, and effects on mechanical properties also need to be considered	76

Porcine heart valves decellularized by 0.5% TX, 0.5% SDS, 0.5% Igepal CA-630®, and RNase	Human umbilical vein endothelial cells	–	*In vitro*, static culture for up to 24 h	Decellularization removed cells without affecting collagen and elastin contents	Endothelial cells grew to confluence on the scaffold The seeded scaffold did not cause platelet activation	Platelet adhesion experiments carried out in static culture	77
Porcine pulmonary vavles decellularized by 0.5% TX, 0.5% NaDC, 0.5% Igepal CA-630® and nucleases	Human umbilical vein endothelial cells	–	*In vitro*, static culture for up to 24 h	Decellularized cusps were totally cell free	A confluent monolayer was achieved on the surface of the decellularized scaffold and in the presence of platelet rich plasma, no platelet activation occured	Decellularization inhibits, but does not elininate, migration of monocytes into the scaffold	78
Ovine pulmonary valves treated with 0.5% trypsin and 0.2% EDTA	Ovine carotid artery endothelial cells and myofibroblasts	–	*In vivo*, autologous pulmonary model for up to 12 weeks	Moderate cusp thickening was observed Valve insufficiency was not observed	*In vitro* cell seeding was patchy and incomplete *In vivo* scaffolds developed a confluent endothelial cell lining at 4 weeks Positive procollagen staining demonstrated ECM synthesis	Subvalvular calcifications found on all tissue engineered constructs	79
Ovine pulmonary valves decellularized by 0.5% NaDC and 0.5% SDS	Ovine jugular vein endothelial cells	Pulsatile flow	*In vitro*, pulsatile flow bioreactor for up to 36 h	Basement membrane remained intact following decellularization	Confluent endothelial cell monolayers formed at moderate flow rates ($0.5\,l\,min^{-1}$) At higher and lower flow rates cellular proliferation and metabolic activity decreased Cells retained expression of vWf and eNOS	Valvular functionality within the bioreactor not reported	80
Ovine pulmonary valves decellularized by 0.5% NaDC and 0.5% SDS	Ovine jugular vein endothelial cells	Pulsatile flow	*In vitro*, pulsatile flow bioreactor for up to 36 h	Basement membrane was retained following decellularization Ultimate force, stiffness, ultimate strain, and ultimate stress decreased	Endothelial cells reached confluence forming a monolayer and maintaining expression of vWf High endothelial cell metabolic activity was maintained	ECM production was not addressed	81
Human aortic and pulmonary heart valves treated by agitation in 0.5% Trypsin/0.2% EDTA	Human saphenous vein endothelial cells	–	*In vitro*, preseeded, and cultured in a bioreactor for up to 10 days	Tissue integrity post-decellularization was superior in aortic valves than in pulmonary valves	Positively stained endothelial cells present on both sides	Cellular behavior, including expression, not fully analyzed	82

(*Continued*)

Table 2 (Continued)

Scaffold composition	*Cell population(s)*	*Mechanical forces/ signals utilized*	*Model, time period*	*Structure, function, and degradation*	*Cell response, ECM production*	*Study limitations*	*Reference*
Porcine aortic heart valves fixed with GTA alone or EDC–NHS and a hyaluronidase inhibitor followed by GTA cross-linking	–	–	*In vitro*, cyclic fatigue and buckling	EDC–NHS scaffolds with a preserved GAG content had a reduced rate of buckling when compared with GTA-fixed valves which do not retain GAGs The buckling patterns mimicked that of fresh, untreated cusps subjected to similar bending curvatures	GAGs were preserved within the scaffold using EDC–NHS cross-linking but not with the GTA alone	Cellular viability/ proliferation not assessed	83
Porcine pulmonary valves decellularized using NaDC, sodium dodecyl sulfate, Trypsin–EDTA, or Trypsin–detergent–nuclease	–	–	*In vitro*	Histological examination revealed no remaining cells and no significant differences in the ECM histoarchitecture in any group LSM detected significant ECM alterations in all groups except NaDC group with an almost completely preserved ECM	–	Compared to GTA-fixed tissue significantly increased immune responses, and thrombo-genicity were observed in all protocols No cellular testing	84

a decellularized scaffold. This explores the potential ability to take patients own cells, expand them *in vitro*, then seed them onto a decellularized scaffold, and implant them back into the patient. Results were quite promising with cells retaining their phenotype and penetrating the scaffold after an incubation period of 15 days. However, further analysis revealed an unequal, unrepresentative cellular distribution within the scaffold.[72]

The use of different cell types to repopulate decellularized valves is widespread, as a number of cells have demonstrated a potential to replace the functions of VECs and VICs. Human saphenous vein endothelial cells have been reported to completely recellularize decellularized valvular scaffolds,[10] thus replacing the VECs. They have been seeded successfully in conjunction with myofibroblasts on decellularized porcine aortic and pulmonary roots.[15] A confluent monolayer of endothelial cells was formed on the scaffold surface with active collagen synthesis by the myofibroblasts.[15] In addition, the behavior of neonatal fibroblasts on decellularized scaffolds has also been characterized. Following 8 weeks of culture in a dynamic pulsatile fluid flow bioreactor, cells were deemed to have attached, migrated into the scaffold, and remained viable. Studies at 1, 2, and 4 weeks of leaflets cultured statically demonstrated that the human fibroblasts were mitotic and synthesized human ECM proteins.[14]

Another approach which has been examined is that of decellularizing native heart valves and then coating them to improve mechanical properties and cellular infiltration. This has been investigated by Grabow *et al.*[94] and Stamm *et al.*[73] who have coated decellularized porcine aortic valves with forms of PHB in order to improve the mechanical properties. The hybrid valves demonstrated superior tensile strength and suture retention strength, and showed good fluid dynamic performance. At 12 weeks postimplantation, confluent endothelial cell layers were formed on the scaffolds and collagen was deposited; however, there was evidence of inflammation.[73] *In vitro* mechanical testing of decellularized scaffolds has found that the decellularization technique alone stiffens the valve cusp by 74–128 MPa and increases tensile strength by 11–17 MPa. These values are further increased by coating with PHB.[94] Fibronectin was also considered as a coating for decellularized heart valves. However, although the fibronectin enhanced cellular infiltration, it did not improve scaffold mechanical integrity.[72]

Development of effective decellularization protocols requires the establishment of a perfect balance between both the adequate removal of cellular elements and the preservation of the native ECM architecture. It is difficult to find a protocol that is harsh enough to completely decellularize the valve, but not too harsh as to damage the structure. For example, Zeltinger *et al.*[14] and Bertipaglia *et al.*[72] developed decellularization techniques which maintained cusp integrity, but failed to remove all cellular remnants. Treatments investigated by Grauss *et al.*[75] included EDTA, gentamicin, DNase, RNase, and either 1% Triton X-100 or 0.5% trypsin. These resulted in a complete loss of cellular structures from the valve cusp (but not the root), but caused damage to the ECM with a loss of collagen density, GAGs, chondroitin sulfate (CS), fibrin, and laminin from the tissue and increased intercellular space.

An area which has not yet been thoroughly investigated is the effect of GAGs on heart valve performance. Current glutaraldehyde-treated valves do not retain GAGs as they do not contain the amine functionality necessary for cross-linking by aldehydes.[95] Shah *et al.* investigated the role of GAGs in buckling of *in vitro* cross-linked heart valves by comparing carbodiimide cross-linked valves (which retain GAGs) and glutaraldehyde cross-linked valves, which do not.[83] They attached a hyaluronidase inhibitor (neomycin trisulfate) to the carbodiimide cross-linked valves to ensure that GAGs were not digested. They found that the carbodiimide cross-linked valves with the hyaluronidase inhibitor underwent reduced buckling compared with glutaraldehyde-treated valves. Hence, they concluded that the stabilization of GAGs may improve the durability of bioprosthetic valves.

Zhou *et al.* compared a number of decellularization protocols and their effects on 3D ultrastructure, immunogenicity, and thrombogenicity.[84] They compared four different protocols: sodium deoxycholate (NaDC), sodium dodecyl sulfate, trypsin/EDTA, and trypsin–detergent–nuclease. Using histology and two-photon laser scanning microscopy (LSM), they found that the NaDC group had an almost completely preserved ECM architecture. However, when compared with glutaraldehyde fixed valves, significantly increased immune responses and thrombogenicity were observed. This highlights the difficulty that while there are protocols which will perform some functions very well (i.e., cell removal, maintenance of ECM architecture), it has thus far proved impossible to establish a protocol which will deliver the perfect scaffold.

The decellularization of native heart valves for use as scaffolds seems like an ideal scenario: a preformed, natural scaffold ideally designed to direct tissue ingrowth. However, there are a number of issues associated with their use. The complete removal of cellular remnants from xenografts is of vital importance to ensure that no possibility of cross-species contamination exists. However, this has not yet been achieved.[14] In addition, in general, studies will focus on the valve cusp and neglect the valve root which contains different cell types such as smooth muscle cells.[15] The continued presence of cellular remnants leads to immune reactions, calcification, and, as a result, graft rejection. Indeed, calcification has been detected on decellularized heart valves following retrieval postimplantation.[69,70,79] As stated, the benefits of decellularized heart valves as scaffolds are plentiful. However, given that thus far researchers have failed to identify an appropriate technique to completely decellularize valves without damaging their structure or mechanical properties, it seems that alernative roots need to be explored. Hence, the use of natural biomaterials of a nonvalvular origin has in recent years gained prominence among researchers.

6.626.7. Naturally Derived Biomaterials of Nonvalvular Origin

Many natural biomaterials derived from various species and organs have been considered as potential scaffolds for the creation of the ideal heart valve implant. The list of natural biomaterials which have been investigated for heart valve scaffold design includes, but is not limited to, collagen, chitosan, small intestinal submucosa (SIS), hyaluronic acid (HA), fibrin, and CS (**Table 3**; see **Chapter 2.211, Polymers of Biological Origin**).

Table 3 Natural biomaterials tested for heart valve scaffold applications

Scaffold composition	*Cell population(s)*	*Mechanical forces/signals utilized*	*Model, time period*	*Structure, function, and degradation*	*Cell response, ECM deposition*	*Study limitations*	*Reference*
Fibrin gel with various concentrations of aprontonin	Human aortic myofibroblasts	–	*In vitro*, 1 month in static culture	20, 15, and 5 $\mu g\,ml^{-1}$ aprontonin caused no degradation, degradation at 3 weeks and degradation at 1 week	Multilayers of cells surrounded by ECM Collagen production increased with aprontonin concentration	Poor mechanical properties are associated with fibrin gel	16
Fibrin gel cross-linked either with poly-L-lysine or by mechanical fixation	Human aortic myofibroblasts	–	*In vitro*, 50 days in static culture	Construct was sutureable but stiffness was too low for implantation Shrinkage was lowest on the poly-L-lysine boarder fixed tissue	Well-developed ECM with organized collagen bundles Cell proliferation was optimal on the poly-L-lysine border fixed group	High degree of shrinkage and poor mechanical stiffness	96
SIS or SIS coated with fibronectin	Human dermal neonatal fibroblasts	–	*In vitro*, up to 4 weeks	SIS thickness (not including the cell layer) did not change	Minimal cellular infiltration Collagen type I production was highest in fibronectin-coated SIS	Lack of cellular infiltration and insufficient thickness of scaffold may reduce mechanical properties	97
Photopolymerized methacrylated hyaluronic acid (HA)	Porcine aortic VICs	–	*In vitro*, up to 5 days in static culture	Cross-linking did not affect the ability of fibronectin to bind with HA	VICs readily proliferated and formed confluent monolayers within 4 days	Mechanical properties and VIC infiltration not investigated	57
Methacrylated (HA) or methacrylated (HA)–PEG gels	Porcine aortic VICs	–	*In vitro*, up to 6 weeks in static culture	Addition of PEG to the gels reduced swelling PEG increased degradation time of the methacrylated HA from 2 days to more than 1 week	HA degradation products increased VIC proliferation VICs expressed ECM including elastin	Mechanical response and ability to support VECs not yet addressed	98
HA gel cross-linked with divinyl sulfone and surface treated with UV light	Neonatal rat aortic smooth muscle cells	–	*In vitro*, up to 6 weeks in static culture	Not reported	Significant expression of elastin was found Collagen expression plateau reached at 4 weeks ECM formed a homogenous layer at the cell–HA interface	Collagen synthesis was deemed insufficient and mechanical properties were not investigated	17
Collagen type I derived from bovine skin	Porcine thoracic aorta smooth muscle cells or human ascending aorta smooth muscle cells	–	*In vitro*, up to 28 days in static culture	Scaffold contraction prevented by a specially designed seeding ring	Porcine cells developed in layers which were separated by newly formed ECM including collagen, proteoglycans and ECM proteins thrombospondin 1 and fibronectin	Sufficient numbers of human cells were not isolated to complete experiments; results are therefore limited to porcine cellular behavior	99

Collagen sponge (Actifoam, Coetica, France)	Human VICs	–	*In vitro*, up to 51 days	Not reported	Phenotypic VIC expression of vimentin, α-SMA, and myosin was retained VICs demonstrated long interconnecting extensions indicating cell communication	VIC expression of prolyl-4-hydroxylase and desmin was reduced on the scaffold Poor cellular attachment to the scaffold during initial 24 h	100
Collagen type I	Porcine aortic VICs or porcine aortic smooth muscle cells	–	*In vitro*, up to 10 days in static culture	Both cell types caused gel compaction Protein degradation was seen in smooth muscle cell cultures, but protein synthesis was observed in VIC cultures	Both cell types had 70% viability GAG content in VIC cultures was initially lower, by day 6 similar GAG contents were seen in both cultures	Effects of mechanical forces on cellular behavior not considered	101
Collagen type I – 1%, 2%, and 5% w/v fabricated by rapid prototyping	Human aortic VICs	–	*In vitro*, up to 28 days in static culture	Not reported	Highest cell proliferation was on 1% collagen, and 2% and 5% demonstrated similar proliferation rates Good cellular infiltration	VIC expression on the scaffold was not investigated	102
Collagen type I	Neonatal human dermal fibroblasts	–	*In vitro*, up to 6 weeks in static culture	Similar collagen fiber alignment and geometry to that of the native valve cusp and root	Cell viability and infiltration were high and cellular orientation was similar to that of the collagen fibers Elastin and other structural proteins were not produced by the cells	Although gross collagen fiber alignment is similar to that of native valves, failure mechanisms differ suggesting differing microstructures	103
Collagen type I hydrogels	Porcine aortic VICs and VECs	Steady flow	*In vitro*, up to 96 h	High degree of collagen alignment of collagen fibers on the scaffold surface exposed to flow	Incomplete endothelial layer formed Endothelial cells orientated perpendicular to flow Cell numbers decreased upon exposure to flow but protein expression increased	Mechanical properties of the scaffold were not considered and a confluent endothelial cell layer was not formed	20
Collagen type I coated with Matrigel™ (Collaborative Research, USA)	Porcine thoracic aorta endothelial cells and porcine heart valve myofibroblasts	–	*In vitro*, up to 6 weeks in static culture	Not reported	15% of myofibroblasts infiltrated the scaffold Types of proteoglycans produced and their distribution resembled that of the native heart valve	Behavior of endothelial cells not fully characterized Inherent scaffold proteoglycan content was not investigated	104
Collagen type 1 coated with Matrigel	Porcine thoracic aorta endothelial cells and porcine heart valve myofibroblasts	–	*In vitro*, up to 6 weeks in static culture	Not reported	Myofibroblasts and endothelial cells lined both surfaces Collagen type I was expressed; fibers had smaller diamters, but a similar architecture to that of the native heart valve Proteoglycans and chondroitin/dermatan sulfate were expressed	Minor myofibroblast infiltration (5%); confluent endothelial layer was not formed	104
		–					105

(*Continued*)

Table 3 (Continued)

Scaffold composition	*Cell population(s)*	*Mechanical forces/signals utilized*	*Model, time period*	*Structure, function, and degradation*	*Cell response, ECM deposition*	*Study limitations*	*Reference*
Collagen fiber – collagen gel composite or hyaluronic gels coated with collagen and fibronectin	Neonatal rat aortic smooth muscle cells		*In vitro*, up to 8 weeks on collagen composites and up to 3 weeks on HA gels	On collagen composites, the gel contracted and collagen fibers became aligned; stiffness, extensibility, and failure strength were 5 MPa, 14%, and 1.1 MPa Branched collagen fiber bundles were also formed on the collagen composites	On collagen composites, an elastin sheath had formed around the fiber bundles at 5 weeks On HA gel, elastin was produced at 1 week and collagen at 2 weeks and a 12-μm thick basement membrane formed between the cell and HA gel layers	Preliminary study prior to fabrication of a composite valve	
Chitosan or chitosan–collagen IV films	Bovine aortic VECs	–	*In vitro*, 7 days in static culture	Not reported	VEC adhesion to uncoated chitosan was superior to PHA, similar to PLGA, and inferior to gelatin coatings Chitosan–collagen IV films further enhanced cell growth	Chitosan has been considered only as a material for coating heart valve prosthesis	106
Collagen type I or collagen type I – chondroitin sulfate (CS) composite	Porcine mitral VICs and porcine mitral VECs	–	*In vitro*., up to 28 days	Both scaffolds contracted during culture ≈24% of the CS was eluted from the collagen–CS scaffold CS increases porosity of the collagen scaffold	VICs infiltrated both scaffolds Confluent layers of VECs grew on the collagen–CS scaffolds and VECs on the collagen scaffolds were not confluent Phenotypic cellular expression and ECM production were evident on both scaffolds	Mechanical properties of the collagen gel scaffold not considered	107
Fibrin gel	Ovine-carotid-artery-derived cells	Mechanical conditioning	*In vitro*, 12 days in a bioreactor	Construct demonstrated intact and flexible tissue consisting of three leaflets attached to and continuous with a conduit wall The valve leaflets demonstrated synchronous opening and closing during the entire *in vitro* culture period	Dynamic conditioning increased cell attachment/alignment and expression of α-SMA enhanced deposition of ECM proteins, including types I and III collagen, fibronectin, laminin, and CS	Mehcanical testing not performed	108
Collagen gel	VICs	Cyclic mechanical strains	*In vitro*, 48 h	Not reported	The effect of cyclic strain magnitude on cellularity was negligible GAG and PG synthesis by VICs is regulated by cyclic stretching conditions	No mechanical testing performed	

The advantages that these natural biomaterials offer over synthetic biomaterials, and in some cases over decellularized heart valves, are numerous. They include inherent cell compatibility, and a topography and microarchitecture with which cells are familiar.[109] In addition to the usual scaffold characterization studies, such as those of cell–scaffold interactions and construct mechanical testing, research on natural scaffolds also often includes the optimization of scaffold isolation techniques, sterilization, preservation, and degradation studies.[109]

Collagen comprises 50% of the dry weight of the aortic valve cusp.[110] With it being the principal structural component of the cusp and a nonimmunogenic material compared with other structural proteins,[111] its choice as a biomaterial for scaffold fabrication is not surprising. Indeed, collagen has previously demonstrated its suitability as a biomaterial for scaffold design. Scaffolds have been fabricated from type I collagen derived from bovine skin and seeded with porcine heart valve myofibroblasts, and porcine aortic endothelial cells, mimicking the functions of the VICs and VECs, respectively. The cells infiltrated into the scaffold, with the seeded myofibroblasts expressing ECM and the development of an endothelial cell layer.[112] Taylor *et al*. assessed VIC behavior following seeding on collagen sponge scaffolds.[100] VICs seeded on the scaffolds expressed phenotypic markers, remained viable, and proliferated for up to 4 weeks. One of the primary limitations associated with the use of collagen foams and gels as biomaterials is poor mechanical properties. As a result, *in vivo* analysis of collagen foams and gels as scaffolds for heart valve replacement has not yet been assessed. In an attempt to overcome this limitation, Shi *et al*. formed composite heart valve scaffolds composed of collagen fibers and collagen gel. Following 8 weeks in static culture, elastin had been deposited on the scaffold by neonatal rat aortic smooth muscle cells and formed sheaths around the collagen bundles.[105] Improved mechanical properties were also observed, with stiffness and strain having reached 5 MPa and 14%, respectively (see **Chapter 2.215, Collagen: Materials Analysis and Implant Uses**).

Gupta *et al*. assessed the effect of cyclic mechanical strain on GAG and proteoglycan (PG) formation by VICs and chordate interstitial cells.[113] These cells were seeded separately within collagen gels and subjected to various strain rates at a fixed frequency of 1.16 Hz. They found that there were numerous differences in the cells subjected to different strain rates, and hence they concluded that GAG and PG synthesis is regulated by the cyclic strain conditions. They concluded that cyclic strain conditions (which these cells would experience *in vivo*) cause an upregulation of specific GAGs and PGs that are usually present in abundance in the native tissue where these particular cell types are present. This suggests an important role for GAGs and PGs in conditioning heart valves for the demanding *in vivo* environment.

Chitosan, formed from the structural polysaccharide chitin found in crustaceans, has previously been investigated as a potential scaffold in many applications including cartilage, liver, and heart valve tissue engineering.[106,114,115] Advantages of chitosan as a scaffold include minimal foreign body reaction, mild processing conditions, controllable degradation, structural similarity to GAGs, and the presence of many hydroxyl and amino functional groups, which allow the functionalization of the scaffold, allowing the fabrication of bioactive scaffolds.[114] Specifically related to valve scaffold fabrication, it has been shown that chitosan can support the growth of VECs. Indeed, in comparative studies with standard tissue culture conditions, gelatin, poly-L-lactide-*co*-glycolide, and PHA, chitosan was considered as good as, or better than, all substrates other than tissue culture plastic in terms of optimizing the attachment of VECs, as well as proliferation and morphology. Although coating chitosan with proteins failed to improve VEC adhesion, chitosan–collagen type IV films improved VEC proliferation and morphology better than chitosan alone. These initial studies have demonstrated the usefulness of chitosan, which can therefore be considered as a suitable candidate for the fabrication of heart valve scaffold (see **Chapter 2.213, Chitosan**).[106]

Fibrin, a fibrous protein involved in clot formation of blood, promotes cellular migration, proliferation, and matrix synthesis through the release of platelet-derived growth factor and TGF-β;[116] it can also serve as a reservoir for cell mediators, such as bioactive peptides, gene vectors for gene therapy, alternative growth factors, and proteins.[117–119] Fibrin gels seeded with human aortic myofibroblasts dissolve within 2 days, which is too short a period to allow for cellular infiltration and tissue formation. However, it has been suggested that degradation rates could be regulated by cross-linking, or the addition of aprotinin.[16] Fabrication techniques for fibrin scaffolds have also been investigated;[96,120] injection molding was used to create heart valve constructs from fibrin gel, which was supplemented with aprotinin, to improve degradation rate, and chemically fixed with poly-L-lysine. The constructs were seeded with human aortic myofibroblasts and cultured *in vitro*. Following 4 weeks, a uniform cell distribution was found and a well-developed ECM with well-organized collagen bundles was formed. However, fibrin gel has two main limitations associated with it that limit its potential for heart valve scaffold design: shrinkage of the gel and, as with many natural biomaterials, a low initial mechanical stiffness (see **Chapter 2.217, Fibrin**).

Flanagan *et al*. investigated the effect dynamic culture conditions had on the phenotype, attachment, proliferation, and ECM expression of cells seeded on a fibrin scaffold.[108] Scaffolds were placed in a bioreactor chamber where the pulse-rate was increased from 5 b.p.m. to 10 b.p.m after 6 days, and a pressure gradient of 20 mm H_2O was maintained across the valve leaflets. They found that when compared to stirred controls, dynamically conditioned scaffolds exhibited enhanced attachment/alignment and the presence of α-SMA, as well as increased expression of ECM proteins such as collagen type I and III, fibronectin, laminin, and CS. Although no elastin was detected, this study demonstrates that identification of the ideal dynamic conditions may lead to the production of autologous fibrin-based heart valve replacements.

HA has been considered for heart valve scaffold fabrication because of its role in embryonic heart valve formation. As a component of the cardiac jelly present during heart morphogenesis, it may have a substantial influence on valvular cellular behavior when used as a scaffold biomaterial.[98] It is nonimmunogenic, nonthrombogenic, and may be cross-linked through various mechanisms to create hydrogel structures.[121–124] Its relevance for cardiac valve applications was demonstrated by seeding VICs on HA scaffolds. The VICs exhibited an increased production of the structural protein elastin, remained viable for up to 6 weeks, infiltrated the HA hydrogel, and demonstrated

an increased proliferation in the presence of the HA degradation products.[98] Techniques have also been developed to cross-link HA scaffolds with ultraviolet light to improve cellular attachment.[125] However, as is a common theme, the primary limitation of HA in the design of heart valve scaffolds is its poor mechanical properties. As a result, it has been utilized more often as a biomaterial in composite scaffolds. HA was cross-linked using divinyl sulfone to fabricate a nondegradable spongiosa-like biomaterial, which was embedded within an elastin gel to fabricate an aortic valve scaffold. The nondegradable biomaterial was thought to be more capable of withstanding the physically demanding *in vivo* conditions. Neonatal rat smooth muscle cells were seeded onto the composite constructs and onto tissue culture plastic, with the components of the deposited ECM being examined. The composite biomaterial induced the cells to proliferate more rapidly and over longer time periods (4 weeks) than those on tissue culture plastic (2–3 weeks). Cells grown on the composite scaffold deposited an unusual matrix rich in elastin at the scaffold–cell interface. This deposited elastin was found to be organized into fenestrated sheets and loose elastin fibers, structures that were also isolated from the elastin matrix of the ventricularis layer of porcine aortic valve cusps.[17] This could lead to the fabrication of mechanically relevant scaffolds (see **Chapter 2.214, Hyaluronic Acid**).

Shi *et al*. took a different approach to that of many researchers in that they attempted to form a biomimetic, composite scaffold. Collagen bundles, elastin sheets, and GAG gel matrix, formed by cross-linking hylauronan with divinyl sulfone, were stacked together in an attempt to mimic the structure of the native valve. Collagen bundles were embedded into the gel which was constrained in the longitudinal direction, thus aligning the collagen bundles and optimizing mechanical properties which are often the main limitations with biological scaffolds of nonvalvular origin. Elastin sheets were formed adjacent to the collagen bundles and on top of the GAG gel, by neonatal aortic fibroblasts which were in culture for more than 4 weeks.[105]

When compared with synthetic and decellularized valves, natural scaffolds offer many advantages. Unlike synthetic biomaterials, natural scaffold biomaterials are derived from nature and contain natural cellular adhesion sites and inherent cell stimuli such as growth factors. In addition, their degradation products are nontoxic. In fact, some biomaterials such as elastin and hyaluronan have degradation properties with beneficial stimulatory effects on cells. They are less likely to initiate toxic immune responses. Unlike decellularized heart valve scaffolds, natural materials investigated for heart valve scaffold design are acellular; so the application of harsh decellularization techniques, which may affect the structural integrity and cellular adhesion properties, is not necessary. Also, the inflammatory reaction and other consequences associated with incomplete decellularization are of no concern. Although natural scaffolds would appear to be the optimal choice in heart valve scaffold design and many biomaterials have been investigated to date, none has fulfilled all of the requirements of an optimal heart valve scaffold, and none has been trialed *in vivo*. The main criterion in which these natural biomaterials often fall short is that of mechanical properties, which often falls far short of what is necessary *in vivo*. Current researchers should focus on attempting to alter the mechanical properties of biological scaffolds through novel cross-linking, compositional changes, or the use of combinatorial scaffolds, as, if this hurdle can be overcome, natural biomaterials offer many more advantages than synthetic or decellularized scaffolds.

Another approach that could yield dividends for researchers is to take a sequential approach to scaffold fabrication (**Figure 3**). By drawing inspiration from natural developmental

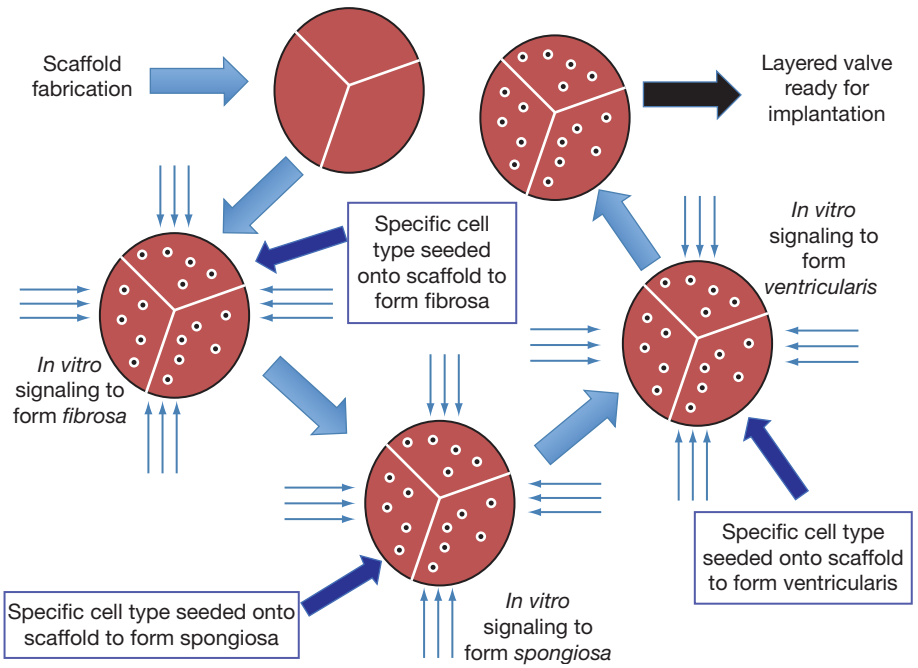

Figure 3 Schematic of fabrication of sequentially layered heart valve scaffold. At each stage an appropriate cell signal must be present to guide the correct formation of the desired layer.

processes, where a distinct sequence is followed, a biologically relevant scaffold could be fabricated. It is up to current researchers to identify the optimal cell types, and signals required to recreate the three distinct layers present in valves: the fibrosa, the spongiosa, and the ventricularis. By sequentially ordering the seeding of these cells and the application of specific signals, a layered scaffold similar to that of native valves could be fabricated.

6.626.8. Conclusion

The field on heart valve replacement is one which started off very promisingly with the great success of utilizing mechanical and bioprosthetic valves. However, the stagnation in the field is evident from the fact that valve design has changed very little since this early success story. As stated, although currently used clinically, mechanical and bioprosthetic valves are far from ideal. Although clinically available prostheses do greatly improve quality of life and life expectancy, they are associated with a number of problems such as thrombosis, hemolysis, and calcification, requiring patients to undergo lifelong antithrombosis therapy, with the mechanical and bioprosthetic valves having an expected lifetime of about 25 and 15 years, respectively. The major flaw associated with these valves is their lack of integration with the native tissue and capacity to repair and grow to match the needs of the patient. Hence, a large number of researchers have attempted to fabricate scaffolds which can be seeded with the appropriate cell type(s) *in vitro*, conditioned, and then implanted *in vivo*, where the idea is that they will degrade and be replaced by functional native tissue. Three main biomaterial approaches have been taken in the fabrication of these scaffolds: synthetic materials, decellularized valves, and natural materials of a nonvalvular origin. Each of these approaches has its associated advantages and disadvantages, and as yet, none has reached the clinic.

Synthetic biomaterials have the potential to be tailored to match the mechanical properties of native valves. However, this can quickly change when the biomaterial degrades *in vivo* and the effect of the degradation products *in vivo* on human patients cannot always be accurately predicted from *in vivo* animal models. Other problems which have been reported following implantation include scaffold shrinkage,[41] fragmentation,[48] thickening,[42] failure to coapt,[13,45,52] poor extensibility,[40,47] and failure to achieve a confluent endothelial cell lining.[55]

Decellularized valves provide a native scaffold architecture for cells to repopulate. Again however, there are a number of problems associated with decellularization procedures. Some methods fail to completely remove cellular remnants, while others are too severe and can affect the architecture and structural integrity of the ECM. A failure to completely decellularize these scaffolds prior to implantation leads to inflammation, while calcification is also associated with these scaffolds.

Natural scaffolds have none of the problems associated with synthetic or decellularized scaffold. There is no issue with toxic breakdown products or the effects of incomplete decellularization. In fact, these scaffolds demonstrate many of the requirements of the ideal scaffold biomaterial, such as mimicking the macro- and microarchitecture of the native valves, incorporating nanotopography similar to that of the native aortic heart valve basement membrane, supporting the adhesion of many appropriate cell types (VICs and VECs), and degrading without the release of toxic breakdown products. However, where they fail is in the mechanical properties of the biomaterial, as the scaffolds usually possess mechanical properties of orders of magnitude less than those of native valves, and in consequence would fail in the demanding *in vivo* environment. This is the reason that no natural scaffold of a nonvalvular origin has been assessed *in vivo* as yet. However, if this, admittedly crucial, limitation can be overcome, then natural scaffolds seem like the ideal replacements to promote regeneration of cardiac valves.

Acknowledgments

The authors wish to acknowledge Anthony Sloan for editorial support, and the support provided by Science Foundation Ireland under Grant No. 07/SRC/B1163.

References

1. Lloyd-Jones, Donald; Adams, Robert J.; Brown, Todd M.; *et al*. *Circulation* **2010**, *121*, e46–e215.
2. Farivar, R. S.; Filsoufi, F.; Adams, D. H. *J. Thorac. Cardiovasc. Surg.* **2003**, *125*, 306–314.
3. Yacoub, M. H.; Kilner, P. J.; Birks, E. J.; Misfeld, M. *Ann. Thorac. Surg.* **1999**, *68*(Suppl. 3), S37–S43.
4. Thubrikar, M. J. In *The Aortic Valve*, CRC: Boca Raton, FL, 1990; pp 23–24.
5. Howard, I. C.; Patterson, E. A.; Yoxall, A. *J. Med. Eng. Technol*. **2003**, *27*, 259–266.
6. Christie, G. W.; Barratt-Boyes, B. G. *Ann. Thorac. Surg.* **1995**, *60*, 195–199.
7. Billiar, K. L.; Sacks, M. S. *J. Biomech. Eng.* **2000**, *122*, 23–30.
8. Mulholland, D. L.; Gotlieb, A. I. *Cardiovasc. Pathol*. **1997**, *6*, 167–174.
9. Filip, D. A.; Radu, A.; Simionescu, M. *Circ. Res*. **1986**, *59*, 310–320.
10. Bader, A.; Schilling, T.; Teebken, O. E.; *et al*. *Eur. J. Cardiothorac. Surg.* **1998**, *14*, 279–284.
11. Gulbins, H.; Goldemund, A.; Anderson, I.; *et al*. *J. Thorac. Cardiovasc. Surg.* **2003**, *125*, 592–601.
12. Dvorin, E. L.; Wylie-Sears, J.; Kaushal, S.; Martin, D. P.; Bischoff, J. *Tissue Eng.* **2003**, *9*, 487–493.
13. Hoerstrup, S. P.; Sodian, R.; Daebritz, S.; *et al*. *Circulation* **2000**, *102*(19, Suppl. 3), III44–III49.
14. Zeltinger, J.; Landeen, L. K.; Alexander, H. G.; Kidd, I. D.; Sibanda, B. *Tissue Eng.* **2001**, *7*, 9–22.
15. Rieder, E.; Kasimir, M. T.; Silberhumer, G.; *et al*. *J. Thorac. Cardiovasc. Surg.* **2004**, *127*, 399–405.
16. Ye, Q.; Zund, G.; Benedikt, P.; *et al*. *Eur. J. Cardiothorac. Surg.* **2000**, *17*, 587–591.
17. Ramamurthi, A.; Vesely, I. *Biomaterials* **2005**, *26*, 999–1010.
18. Mendelson, K.; Schoen, F. J. *Ann. Biomed. Eng.* **2006**, *34*, 1799–1819.
19. Butcher, J. T.; Penrod, A. M.; Garcia, A. J.; Nerem, R. M. *Arterioscler. Thromb. Vasc. Biol*. **2004**, *24*, 1429–1434.
20. Butcher, J. T.; Nerem, R. M. *Tissue Eng.* **2006**, *12*, 905–915.
21. Magometschnigg, H.; Kadletz, M.; Vodrazka, M.; *et al*. *J. Vasc. Surg.* **1992**, *15*, 527–535.
22. Schneider, P. A.; Hanson, S. R.; Price, T. M.; Harker, L. A. *J. Vasc. Surg.* **1990**, *11*, 365–372.
23. Durbin, A. D.; Gotlieb, A. I. *Cardiovasc. Pathol*. **2002**, *11*, 69–77.
24. Stock, U. A.; Schenke-Layland, K. *Biomaterials* **2006**, *27*, 1–2.
25. Simon, P.; Kasimir, M. T.; Seebacher, G.; *et al*. *Eur. J. Cardiothorac. Surg.* **2003**, *23*, 1002–1006; discussion 1006.
26. Ruiz, C. E.; Iemura, M.; Medie, S.; *et al*. *J. Thorac. Cardiovasc. Surg.* **2005**, *130*, 477–484.
27. Vesely, I. *Circ. Res*. **2005**, *97*, 743–755.
28. Bordenave, L.; Remy-Zolghadri, M.; Fernandez, P.; Bareille, R.; Midy, D. *Endothelium* **1999**, *6*, 267–275.

29. Eisenberg, L. M.; Markwald, R. R. *Circulation* **1995**, *77*, 1–6.
30. Copper, T.; Napolitano, L. M.; Fitzgerald, M. J. T.; *et al*. *Arch. Surg*. **1966**, *93*, 767–771.
31. Yacoub, M. H.; Kilner, P. J.; Birks, E. J.; Misfeld, M. *Ann. Thorac. Surg*. **1999**, *68*, S37–S43.
32. Hufnagel, C. A.; Harvey, W. P.; Rabil, P. J.; McDermott, T. F. *Surgery* **1952**, *35*, 673–683.
33. Vongpatanasin, W.; Willis, L. D.; Lange, R. A. *N. Engl. J. Med*. **1996**, *335*, 407–416.
34. Hammermeister, K. E.; Sethi, G. K.; Henderson, W. G.; Oprian, C.; Kim, T.; Rahimtoola, S. *N. Engl. J. Med*. **1993**, *328*, 1289–1296.
35. Mitchell, R. N.; Jonas, R. A.; Schoen, F. J. *Ann. Thorac. Surg*. **1995**, *60*, S108–S113.
36. Angell, W. W.; Oury, J. H.; Lamberti, J. J.; Koziol, J. *J. Thorac. Cardiovasc. Surg*. **1989**, *98*, 48–55.
37. Majani, B.; Mee, R. B.; Ratliff, N. B. *J. Thorac. Cardiovasc. Surg*. **1998**, *115*, 111–117.
38. Nugent, H. M.; Edelman, E. R. *Circ. Res*. **2003**, *92*, 1068–1078.
39. Sodian, R.; Hoerstrup, S. P.; Sperling, J. S.; *et al*. *ASAIO J*. **2000**, *46*, 107–110.
40. Shinoka, T. *Artif. Organs* **2002**, *26*, 402–406.
41. Shinoka, T.; Breuer, C. K.; Tanel, R. E.; *et al*. *Ann. Thorac. Surg*. **1995**, *60* (Suppl. 6), S513–S516.
42. Shinoka, T.; MA, P. X.; Shum-Tim, D.; *et al*. *Circulation* **1996**, *94*(Suppl. 9), II164–II168.
43. Shinoka, T.; Shum-Tim, D.; Ma, P. X.; *et al*. *Circulation* **1997**, *96*(Suppl. 9), II102–II107.
44. Zund, G.; Breuer, C. K.; Shinoka, T.; *et al*. *Eur. J. Cardiothorac. Surg*. **1997**, *11*, 493–497.
45. Kim, W. G.; Cho, S. K.; Kang, M. C.; Lee, T. Y.; Park, J. K. *Int. J. Artif. Organs* **2001**, *24*, 642–648.
46. Stock, U. A.; Mayer, J. E., Jr. *J. Long Term Eff. Med. Implants* **2001**, *11*, 249–260.
47. Kadner, A.; Hoerstrup, S. P.; Tracy, J.; *et al*. *Ann. Thorac. Surg*. **2002**, *74*, S1422–S1428.
48. Hoerstrup, S. P.; Kadner, A.; Melnitchouk, S.; *et al*. *Circulation* **2002**, *106*(12, Suppl. 1), I143–I150.
49. Perry, T. E.; Kaushal, S.; Sutherland, F. W.; *et al*. *Ann. Thorac. Surg*. **2003**, *75*, 761–767; discussion 767.
50. Rabkin, E.; Hoerstrup, S. P.; Aikawa, M.; Mayer, J. E., Jr.; Schoen, F. J. *J. Heart Valve Dis*. **2002**, *11*, 308–314; discussion 314.
51. Engelmayr, G. C., Jr.; Rabkin, E.; Sutherland, F. W.; Schoen, F. J.; Mayer, J. E., Jr.; Sacks, M. S. *Biomaterials* **2005**, *26*, 175–187.
52. Sutherland, F. W.; Perry, T. E.; Yu, Y.; *et al*. *Circulation* **2005**, *111*, 2783–2791.
53. Sodian, R.; Sperling, J. S.; Martin, D. P.; *et al*. *Tissue Eng*. **2000**, *6*, 183–188.
54. Sodian, R.; Hoerstrup, S. P.; Sperling, J. S.; *et al*. *Ann. Thorac. Surg*. **2000**, *70*, 140–144.
55. Sodian, R.; Hoerstrup, S. P.; Sperling, J. S.; *et al*. *Circulation* **2000**, *102*(19, Suppl. 3), III22–III29.
56. Nuttelman, C. R.; Henry, S. M.; Anseth, K. S. *Biomaterials* **2002**, *23*, 3617–3626.
57. Masters, K. S.; Shah, D. N.; Walker, G.; Leinwand, L. A.; Anseth, K. S. *J. Biomed. Mater. Res. A* **2004**, *71*, 172–180.
58. Mei, N.; Chen, G.; Zhou, P.; *et al*. *J. Biomater. Appl*. **2005**, *19*, 323–339.
59. Schmidt, D.; Dijkman, P. E.; Driessen-Mol, A.; *et al*. *J. Am. College Cardiol*. **2010**, *56*(6), 510–520.
60. Ghanbari, H.; Kidane, A. G.; Burriesci, G.; Ramesh, B.; Darbyshire, A.; Seifalian, A. M. *Acta Biomater*. **2010**, *6*(11), 4249–4260; doi:10.1016/j.actbio.2010.06.015.
61. Shi, G.; Wang, C.; Lu, N.; Wang, S.; Bei, J. *Polym. Adv. Technol*. **2002**, *13*, 227.
62. Breuer, C. K.; Mettler, B. A.; Anthony, T.; Sales, V. L.; Schoen, F. J.; Mayer, J. E. *Tissue Eng*. **2004**, *10*, 1725–1736.
63. Badylak, S. F. *Circulation* **2005**, *111*, 2715–2716.
64. Ozawa, T.; Mickle, D. A.; Weisel, R. D.; *et al*. *Cell Transplant*. **2004**, *13*, 169–177.
65. Webb, A. R.; Yang, J.; Ameer, G. A. *Expert Opin. Biol. Ther*. **2004**, *4*, 801–812.
66. Murray, G. *Angiology* **1956**, *7*, 466–471.
67. Gall, K. L.; Smith, S. E.; Willmette, C. A.; O'Brien, M. F. *Ann. Thorac. Surg*. **1998**, *65*, 1032–1038.
68. Curtil, A.; Pegg, D. E.; Wilson, A. *J. Heart Valve Dis*. **1997**, *6*, 296–306.
69. Spina, M.; Ortolani, F.; Messlemani, A. E.; *et al*. *J. Biomed. Mater. Res. A* **2003**, *67*, 1338–1350.
70. Dohmen, P. M.; Ozaki, S.; Nitsch, R.; Yperman, J.; Flameng, W.; Konertz, W. *Med. Sci. Monit*. **2003**, *9*, 97–104.
71. Leyh, R. G.; Wilhelmi, M.; Walles, T.; *et al*. *J. Thorac. Cardiovasc. Surg*. **2003**, *126*, 1000–1004.
72. Bertipaglia, B.; Ortolani, F.; Petrelli, L.; *et al*. *Ann. Thorac. Surg*. **2003**, *75*, 1274–1282.
73. Stamm, C.; Khosravi, A.; Grabow, N.; *et al*. *Ann. Thorac. Surg*. **2004**, *78*, 2084–2092; discussion 2083–2092.
74. Schenke-Layland, K.; Riemann, I.; Opitz, F.; Konig, K.; Halbhuber, K. J.; Stock, U. A. *Matrix Biol*. **2004**, *23*, 113–125.
75. Grauss, R. W.; Hazekamp, M. G.; Oppenhuizen, F.; van Munsteren, C. J. *Eur. J. Cardiothorac. Surg*. **2005**, *27*, 566–571.
76. Cushing, M. C.; Jaeggli, M. P.; Masters, K. S.; Leinwand, L. A.; Anseth, K. S. *J. Biomed. Mater. Res. A* **2005**, *75*, 232–241.
77. Kasimir, M. T.; Weigel, G.; Sharma, J.; *et al*. *Thromb. Haemost*. **2005**, *94*, 562–567.
78. Kasimir, M. T.; Rieder, E.; Seebacher, G.; *et al*. *J. Heart Valve Dis*. **2006**, *15*, 278–286; discussion 286.
79. Steinhoff, G.; Stock, U.; Karim, N.; *et al*. *Circulation* **2000**, *102*(19, Suppl. 3), III50–III55.
80. Lichtenberg, A.; Cebotari, S.; Tudorache, I.; *et al*. *J. Heart Valve Dis*. **2006**, *15*, 287–293; discussion 284–293.
81. Lichtenberg, A.; Tudorache, I.; Cebotari, S.; *et al*. *Biomaterials* **2006**, *27*, 4221–4229.
82. Cebotari, S.; Mertsching, H.; Kallenbach, K.; *et al*. *Circulation* **2002**, *106*(12, Suppl. 1), I63–I68.
83. Shah, S. R.; Vyavahare, N. R. *Biomaterials* **2008**, *29*(11), 1645–1653.
84. Zhou, J.; Fritze, O.; Schleicher, M.; *et al*. *Biomaterials* **2010**, *31*(9), 2549–2554.
85. Martin, U.; Winkler, M. E.; Id, M.; *et al*. *Xenotransplantation* **2000**, *7*, 138–142.
86. Patience, C.; Takeuchi, Y.; Weiss, R. A. *Nat. Med*. **1997**, *3*, 282–286.
87. Wilson, C. A.; Wong, S.; Muller, J.; Davidson, C. E.; Rose, T. M.; Burd, P. *J. Virol*. **1998**, *72*, 3082–3087.
88. Moza, A. K.; Mertsching, H.; Herden, T.; Bader, A.; Haverich, A. *J. Thorac. Cardiovasc. Surg*. **2001**, *121*, 697–701.
89. Curtil, A.; Pegg, D. E.; Wilson, A. *Cryobiology* **1997**, *34*, 13–22.
90. Wilson, G. J.; Courtman, D. W.; Klement, P.; Lee, J. M.; Yeger, H. *Ann. Thorac. Surg*. **1995**, *60*(Suppl. 2), S353–S358.
91. Brenner, S.; Schulz, T.; Schenke-Layland, K.; Opitz, F.; Halbhuber, K. J.; Stock, U. In *Advances in Tissue Engineering and Biology of Heart Valves*. Florence, Italy, Sept 15–18, 2004; p 101.
92. Gu, C. H.; Liu, W. Y.; Yi, D. H.; *et al*. *Zhonghua Yi Xue Za Zhi* **2005**, *85*, 1827–1830.
93. Galili, U. *Biochimie* **2001**, *83*, 557–563.
94. Grabow, N.; Schmohl, K.; Khosravi, A.; *et al*. *Artif. Organs* **2004**, *28*, 971–979.
95. Lovekamp, J. J.; Simionescu, D. T.; Mercuri, J. J.; Zubiate, B.; Sacks, M. S.; Vyavahare, N. R. *Biomaterials* **2006**, *27*(8), 1507e18.
96. Jockenhoevel, S.; Zund, G.; Hoerstrup, S. P.; *et al*. *Eur. J. Cardiothorac. Surg*. **2001**, *19*, 424–430.
97. Cimini, M.; Boughner, D. R.; Ronald, J. A.; Johnston, D. E.; Rogers, K. A. *J. Biomed. Mater. Res. A* **2005**, *75*, 895–906.
98. Masters, K. S.; Shah, D. N.; Leinwand, L. A.; Anseth, K. S. *Biomaterials* **2005**, *26*, 2517–2525.
99. Rothenburger, M.; Vischer, P.; Volker, W.; *et al*. *Thorac. Cardiovasc. Surg*. **2001**, *49*, 204–209.
100. Taylor, P. M.; Allen, S. P.; Dreger, S. A.; Yacoub, M. H. *J. Heart Valve Dis*. **2002**, *11*, 298–306; discussion 297–306.
101. Butcher, J. T.; Nerem, R. M. *J. Heart Valve Dis*. **2004**, *13*, 478–485; discussion 476–485.
102. Taylor, P. M.; Sachlos, E.; Dreger, S. A.; Chester, A. H.; Czernuszka, J. T.; Yacoub, M. H. *Biomaterials* **2006**, *27*, 2733–2737.
103. Neidert, M. R.; Tranquillo, R. T. *Tissue Eng*. **2006**, *12*, 891–903.
104. Rothenburger, M.; Volker, W.; Vischer, P.; Glasmacher, B.; Scheld, H. H.; Deiwick, M. *Tissue Eng*. **2002**, *8*, 1049–1056.
105. Shi, Y.; Ramamurthi, A.; Vesely, I. *Biomed. Sci. Instrum*. **2002**, *38*, 35–40.
106. Cuy, J. L.; Beckstead, B. L.; Brown, C. D.; Hoffman, A. S.; Giachelli, C. M. *J. Biomed. Mater. Res. A* **2003**, *67*, 538–547.
107. Flanagan, T. C.; Wilkins, B.; Black, A.; Jockenhoevel, S.; Smith, T. J.; Pandit, A. S. *Biomaterials* **2006**, *27*, 2233–2246.
108. Flanagan, T. C.; Cornelissen, C.; Koch, S.; *et al*. *Biomaterials* **2007**, *28*(23), 3388–3397.
109. Schmidt, C. E.; Baier, J. M. *Biomaterials* **2000**, *21*, 2215–2231.
110. Vesely, I. *J. Biomech*. **1998**, *31*, 115–123.
111. Chevallay, B.; Herbage, D. *Med. Biol. Eng. Comput*. **2000**, *38*, 211–218.
112. Rothenburger, M.; Volker, W. *ASAIO J*. **2002**, *48*, 586–591.
113. Gupta, V.; Tseng, H.; Lawrence, B. D.; Grande-Allen, K. J. *Acta Biomater*. **2009**, *5*(2), 531–540.
114. Suh, J. K.; Matthew, H. W. *Biomaterials* **2000**, *21*, 2589–2598.

115. Elcin, Y. M.; Dixit, V.; Gitnick, G. *Artif. Organs* **1998**, *22*, 837–846.
116. Sierra, D. H. *J. Biomater. Appl.* **1993**, *7*, 309–352.
117. Hubbell, J. A. *Curr. Opin. Biotechnol.* **1999**, *10*, 123–129.
118. Hubbell, J. A. *Biotechnology NY* **1995**, *13*, 565–576.
119. Lewis, K. B.; Teller, D. C.; Fry, J.; Lasser, G. W.; Bishop, P. D. *Biochemistry* **1997**, *36*, 995–1002.
120. Jockenhoevel, S.; Chalabi, K.; Sachweh, J. S.; *et al. Thorac. Cardiovasc. Surg.* **2001**, *49*, 287–290.
121. Crescenzi, V.; Francescangeli, A.; Renier, D.; Bellini, D. *Biopolymers* **2002**, *64*, 86–94.
122. Smeds, K. A.; Pfister-Serres, A.; Miki, D.; *et al. J. Biomed. Mater. Res.* **2001**, *54*, 115–121.
123. Baier Leach, J.; Bivens, K. A.; Patrick, C. W., Jr.; Schmidt, C. E. *Biotechnol. Bioeng.* **2003**, *82*, 578–589.
124. Ramamurthi, A.; Vesely, I. *J. Biomed. Mater. Res. A* **2002**, *60*, 195–205.
125. Ramamurthi, A.; Vesely, I. *J. Biomed. Mater. Res. A* **2003**, *66*, 317–329.

6.627. Drug-Eluting Stents

S Garg, M Magro, and P W Serruys, Erasmus Medical Center, Rotterdam, The Netherlands

© 2011 Elsevier Ltd. All rights reserved.

6.627.1.	**Introduction**	428
6.627.2.	**The Need for Coronary Stents: Problems with Baloon Angioplasty and Bare-Metal Stents**	428
6.627.3.	**Development of DESs**	429
6.627.4.	**First Generation DESs**	430
6.627.4.1.	Sirolimus-Eluting Stent	430
6.627.4.2.	Paclitaxel-Eluting Stent	432
6.627.4.2.1.	TAXUS express versus TAXUS liberté	433
6.627.5.	**Benefits of DES**	433
6.627.6.	**Risks of DES**	433
6.627.7.	**Second Generation DES**	434
6.627.7.1.	Zotarolimus-Eluting Stents	435
6.627.7.2.	Everolimus-Eluting Stent	435
6.627.7.3.	Second Generation DES Versus BMS	436
6.627.7.4.	Second Generation DES Versus First Generation DES	437
6.627.7.5.	Second Generation DES Versus Second Generation DES	437
6.627.8.	**New Drug-Eluting Stents**	438
6.627.8.1.	DES with Biodegradable Polymers	438
6.627.8.1.1.	Biolimus A9-eluting DES with biodegradable polymers	438
6.627.8.1.2.	Sirolimus-eluting DES with biodegradable polymers	439
6.627.8.1.3.	Paclitaxel-eluting DES with biodegradable polymers	439
6.627.8.2.	Polymer-Free DES	440
6.627.8.2.1.	BioFreedom biolimus A9-eluting stent	440
6.627.8.2.2.	VESTAsyn sirolimus-eluting stent	440
6.627.8.2.3.	YUKON: sirolimus-eluting stent	441
6.627.8.3.	DES Made from New Metal Alloys	441
6.627.8.3.1.	TAXUS element	441
6.627.8.3.2.	PROMUS element	442
6.627.8.4.	Nitinol Stents	442
6.627.8.4.1.	Lesions in small vessels	442
6.627.8.4.2.	Lesions in bifurcation	443
6.627.8.4.3.	Lesions due to vulnerable plaque	444
6.627.9.	**Less Successful Medications on DES**	444
6.627.10.	**Conclusions**	445
References		445

Abbreviations

BMS	Bare-metal stents
CAD	Coronary artery disease
CE	Conformité Européenne
DES	Drug-eluting stent
E-ZES	Endeavor Zotarolimus-eluting stent
EES	Everolimus-eluting stent
FDA	Food and Drug Administration
FIM	First In Man
IVUS	Intravascular ultrasound
mTOR	Mammalian target of rapamycin
OCT	Optical coherence tomography
PCI	Percutaneous coronary intervention
PES	Paclitaxel-eluting stent
POBA	Plain old balloon angioplasty
QCA	Quantative coronary angiography
R-ZES	Resolute Zotarolimus-eluting stent
SES	Sirolimus-eluting stent
ST	Stent thrombosis
TLR	Target lesion revascularization
TVR	Target vessel revascularization

6.627.1. Introduction

The prevalence of ischemic heart disease is rising in line with increasing longevity of population, and the increased frequency of obesity, diabetes, and other coronary risk factors. Coupled with this is a lower threshold to investigate patients with symptoms suggestive of coronary artery disease (CAD), thereby increasing the importance of establishing an optimal form of treatment for patients with obstructive coronary lesions. Historically, owing to the problems associated with plain old balloon angioplasty (POBA) and the initial coronary stents, coronary artery bypass surgery was the preferred treatment in all but the simplest patient. In the past decade, new coronary stents have been developed which have revolutionized the ability to treat complex coronary lesions by percutaneous means. This chapter, after reviewing the problems associated with POBA and bare-metal stents (BMS), describes the first and second generation of drug-eluting stents (DESs), before finally reviewing some of the newer permanent stents which are currently being evaluated in on-going clinical trials.

6.627.2. The Need for Coronary Stents: Problems with Baloon Angioplasty and Bare-Metal Stents

The concept of wiring a diseased coronary artery and restoring luminal patency by means of a percutaneous approach has gone through extensive developments and advances since its first application in man by Andreas Grüntzig in 1977.[1] It has revolutionized the way we treat CAD and brought about a major shift from surgical to percutaneous intervention in all but the most severe and diffuse forms of the disease.[2]

POBA, the first form of percutaneous coronary intervention (PCI) relied on compression of atherosclerotic plaque through mechanical dilatation by balloon inflation. This process often caused vessel injury with tearing of the media. While chronic sequele in the form of vascular shrinkage (mediated by myofibroblasts, smooth muscle cells, and their proteoglycan and collagen secretions as well as elastic recoil) was a major concern, more sinister complications including abrupt vessel closure instigated the need for further development or alternatives of this technology.[3–5]

The use of a prosthetic device to improve vessel patency after POBA had already been proposed by Charles Dotter in 1964.[6] Two decades later, Puel implanted the first coronary stent – the Wallstent, a self-expanding metallic mesh.[7] The ability of such a device to cause and maintain a larger acute gain in luminal diameter proved to be key for its success, and the reason stents are implanted in the majority of PCIs performed today. The first stents to be implanted however were associated with a significant thombogenic risk which resulted in an 18% subacute stent thrombosis (ST) rate.[8] Measures to counteract this phenomenon, which included the introduction of complex anticoagulation regimens, resulted in an excess of vascular bleeding complications, and subsequent prolongation of hospitalization which altogether marred the initial successful results of the stenting concept when compared to POBA.[9]

Refinements in the stent system as seen in the landmark BENESTENT (BElgian NEtherlands STENT) (Figure 1)[10] and STRESS (STent REStenosis Study)[11] trials, as well as proof of the importance of adequate stent deployment,[12] redirected favorable light on the coronary stenting concept. Additionally, evidence that stenting was safe without need for anticoagulation through improvement in stent expansion and apposition, and with the use of dual antiplatelet therapy (DAPT), led to the exponential and widespread use of these early devices (Figure 2).[13–15]

The initial strengths and enthusiasm with the safer acute outcomes of stainless steel, cobalt–chromium alloy, and nitinol based stent implantation however met with what was described as the Achilles heel of BMS – in-stent restenosis (Figure 3). Neointimal growth mediated by smooth muscle hyperplasia and extracellular matrix produced significant luminal narrowing that peaked between 1 and 6 months after stent deployment.[16–18] As much as 20–40% of patients in whom

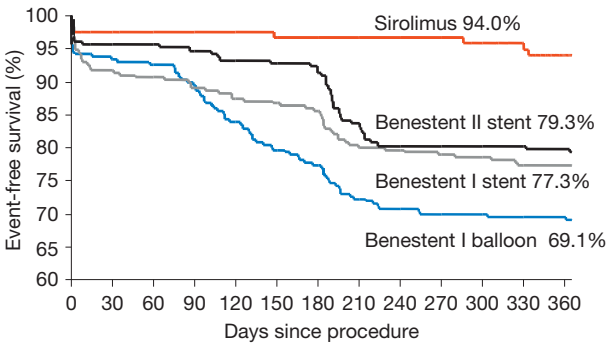

Figure 1 The improved event-free survival in the Benestent I and II trials with the use of a bare-metal stent (Benestent I stent) or a heparin coated stent (Benestent II) compared to only balloon angioplasty (Benestent balloon).[10] Event-free survival however is considerably greater with a sirolimus-eluting stent.

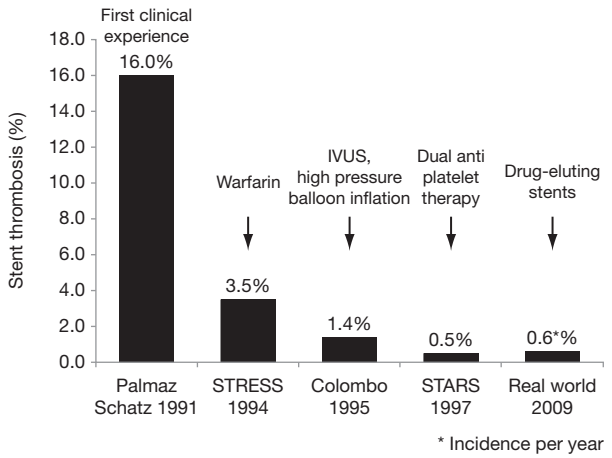

Figure 2 Temporal changes in the incidence of stent thrombosis following introduction of adjunct phamacotherapy, increased awareness of the importance of technique when implanting coronary stents, and the change from the use of bare-metal to drug-eluting stents. Adapted from Colombo, A.; Hall, P.; Nakamura, S.; *et al*. *Circulation* **1995**, *91*, 1676–1688; Leon, M. B.; Baim, D. S.; Popma, J. J.; *et al*. *N. Engl. J. Med*. **1998**, *339*, 1665–1671; Schatz, R. A.; Baim, D. S.; Leon, M.; *et al*. *Circulation* **1991**, *83*, 148–161; Fischman, D. L.; Leon, M. B.; Baim, D. S.; *et al*. *N. Engl. J. Med*. **1994**, *331*, 496–501; Wenaweser, P.; Daemen, J.; Zwahlen, M.; *et al*. *J. Am. Coll. Cardiol*. **2008**, *52*, 1134–1140.

these BMS were implanted, especially diabetic patients, those with small vessels and long lesions, presented with recurrence of anginal symptoms and angiographic restenosis (>50% diamenter stenosis). Restenosis rates, especially those confined to the stented part of the vessel (not including the 5 mm peristent segment) decreased dramatically after 6–12 months and this is attributable to replacement of the smooth muscle cells by a fibrotic matrix that halted further thickening of the neointimal layer.

Research efforts focusing on the neointimal proliferation phenomenon led to development of vascular brachytherapy, which employed beta or gamma sources to reduce in-stent restenosis.[19–22] Despite being shown to be effective in reducing recurrent stenosis by 30–70%, logistic problems associated with implementation of the treatment, recurrence of restenosis after 4 years[23] and the evolving concepts of using safer pharmacological agents instead of radiation, led to the downfall of this reparative technique.

Intravenous or oral antiproliferative, anti-inflammatory, or immunomodulatory agents failed to effectively reduce the neointimal hyperplasia in humans.[24] Attempts to increase local drug delivery by administration through porous angioplasty balloons also failed.[25,26] The possibility to link these bioactive substances to the stent surface itself and its release from the stent to the endothelium was then explored – DESs were born.

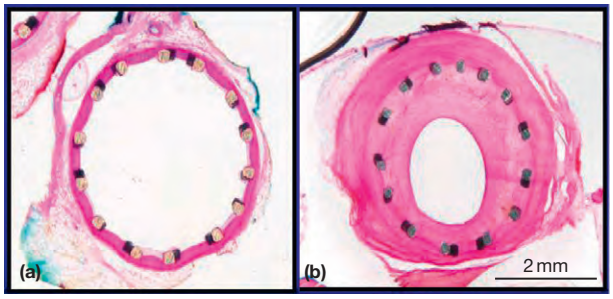

Figure 3 (a) Stent implantation in the porcine model demonstrating development of significant neointimal hyperplasia at follow-up (b).

6.627.3. Development of DESs

The first drug to be applied to coronary stents was in fact heparin, which was intuitively chosen to counter the thrombogenicity of BMS. Heparin-coated stents such as BX-Velocity Carmeda-coated stent (Johnson & Johnson, Warren, NJ), the Wiktor Hepamed-coated stent (Medtronic, Inc, Minneapolis, MN), and the Jostent Corline-coated stent (Jomed International AB, Helsingborg, Sweden) had their drug covalently bonded to the device, thereby significantly prolonging its presence on the stent.

Multiple drugs classes and types which inhibit restenosis by interference in pathways of inflammation and neointimal proliferation have been explored. These drugs can be classified as anti-inflammatory and/or immunomodulatory agents, antiproliferative agents, inhibitors of smooth muscle cell migration or extracellular matrix production, or promoters of healing and endothelialisation (**Table 1**).

The macrocylic lactone or 'limus' family of drugs which includes sirolimus, everolimus, biolimus A9, zotarolimus, tacrolimus, and pimecrolimus has been studied (**Figures 4** and **5**). The first four bind to the FKBP 12 binding protein which subsequently binds to the mammalian target of rapamycin (mTOR) and in doing so blocks the cell cycle mainly of the smooth muscle cell from the G1 to the S phase. Tacrolimus and pimecrolimus, on the other hand, bind to FKBP506 and form a complex which subsequently inhibits the calcineurin receptor, leading to decreased cytokine expression on the cell surface membrane. This results in inhibition of T cell activation and lower smooth muscle cell selectivity. Paclitaxel (**Figure 6**) is a nonlimus drug that stabilizes microtubules and thereby inhibits cell division in the G0/G1 and G2/M phases. It has also been applied to stents and thoroughly studied.

Table 1 A list of the various agents that were tested for potential application to drug-eluting stents

Anti-inflammatory, immunomodulators	*Antiproliferative*	*Smooth muscle cell migration inhibitors, extracellular matrix modulators*	*Promoters of healing and reendothelialization*
Limus family (sirolimus, everolimus, zotarolimus, biolimus A9, pimecrolimus)	Limus family (sirolimus, everolimus, zotarolimus, biolimus A9, pimecrolimus)	Batimastat	BCP671
Paclitaxel	Paclitaxel	Prolyl hydroxylase inhibitors	Vascular endothelial growth factor
Tacrolimus	Actinomycin D	Halofuginone	Estradiols
Cyclosporine	Methotrexate	C-proteinase inhibitors	Nitric oxide donors
Dexamethasone	Angiopeptin	Probucol	Endothelial progenitor cell antibodies
M-prednisolone	Vincristine		Biorest
Biorest	Mitomycine		Advanced coatings
Interferon gamma-1b	Statins		
Mycophenolic acid	CMYC antisense		
Mizorbine	RestenASE		
Tranilast	2-Chlorodeoxyadenosine		
	Proliferating cell nuclear antigen ribozyme		

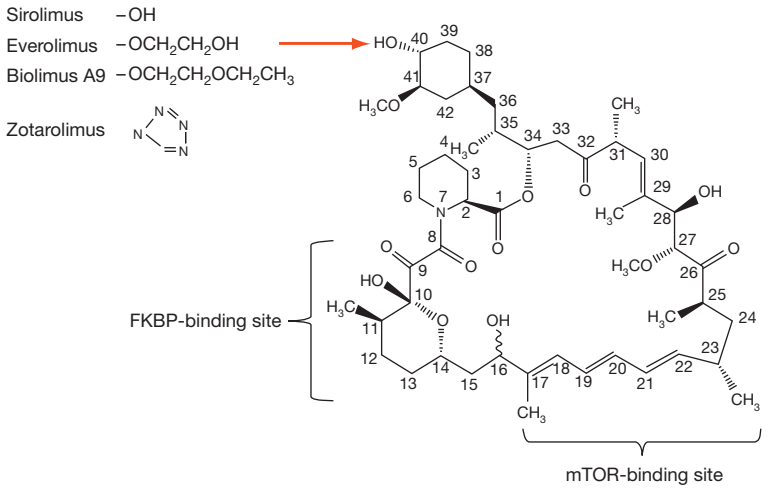

Figure 4 The macrocylic lactone or 'limus' family of antiproliferative agents. The different agents are derived following modifications to the macrocylic ring as shown. Their common mode of action includes binding to the FK-binding protein 12 (FKBP12), which in turn inhibits the mammalian target of rapamycin (mTOR) pathway. This subsequently prevents the down regulation of the cell division kinase inhibitor $p27^{kip1}$, thereby inhibiting cell division between phases G1 and S1 of the cell cycle.

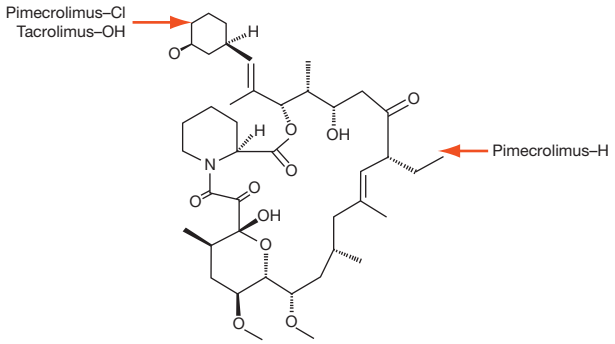

Figure 5 The chemical structure of tacrolimus and pimecrolimus.

Presently, only four DESs have been approved for use by the Food and Drug Administration (FDA). The first two DESs that were developed, the sirolimus-eluting and paclitaxel-eluting stent, are collectively known as first generation DESs, while the newer zotarolimus-eluting and everolimus-eluting stents are known as second generation DESs.

6.627.4. First Generation DESs

6.627.4.1. Sirolimus-Eluting Stent

Sirolimus was the first 'limus' agent to be used on a coronary stent (Figure 4). This macrolide antibiotic, produced by *Streptomyces hygroscopicus* has potent antifungal and antimitotic properties. It was discovered in Easter Island (Rapa Mui) in the South Pacific during an expedition in 1975 and was originally named rapamune to reflect its place of discovery. This highly lipophilic macrolytic lactone inhibits mTOR and exhibits potent antiproliferative and immunosuppressive effects. The first clinical application was as an immunosuppressive in renal transplant patients following FDA approval in 1999. The first sirolimus-eluting stent (SES) was the Cypher stent, developed by Cordis Corporation, Warren, NJ. It consisted of sirolimus in a concentration of 140 $\mu g\,cm^{-2}$, incorporated in an amalgam of two biostable polymers, with the polymer/drug matrix then applied onto the tubular 316L stainless steel BX-Velocity stent (Tables 2–4).

Both fast release stents with drug release in <15 days and slow-release stents with ≥ 28 days drug release were developed and tested in the 'First in Man' (FIM) study in 1999 in Sao Paulo, Brazil and Rotterdam, the Netherlands. Angiographic and intravascular ultrasound (IVUS) results from the 45 patients who were studied showed remarkable suppression of in-stent neointimal hyperplasia, which continued out to 4 years of follow-up (Figure 7).[27–29]

The pivotal RAVEL study (RAndomised study with the sirolimus-eluting VElocity balloon-expandable stent in the treatment of patients with de novo native coronary artery Lesions) evaluated the Cypher SES by randomizing 238 patients with relatively low-risk lesions to treatment with SES or BMS. At 1-year follow-up the rate of binary stenosis was 0.0 and 26.6% for patients treated with Cypher SES and BMS, respectively.[30] These results were subsequently confirmed in the much larger SIRIUS trial (SIRolImUS-coated BX-Velocity balloon-expandable stent in the treatment of patients with de novo coronary artery lesions) that enrolled 1058 patients with more complex lesions than were seen in RAVEL. Significantly lower rates of target lesion revascularization (TLR) and major adverse cardiovascular events (MACE) following treatment with the Cypher SES were demonstrated when compared to BMS controls at 9-month, 2-year, and 5-year follow-up.[31–33] The Cypher stent was thus the first DES to receive Conformité Européenne (CE)-mark in April 2002 and was subsequently approved by the FDA in 2003.

Performance of the Cypher stent has been also assessed in 'off-label' situations and specific subgroups of patients such as diabetic patients,[34,35] and those presenting with ST-elevation myocardial infarction.[36,37] In addition, it has been assessed in patients with different lesion types including chronic total occlusions,[38,39] saphenous vein grafts,[40,41] lesions in small coronary vessels,[42,43] and complex lesions.[44,45]

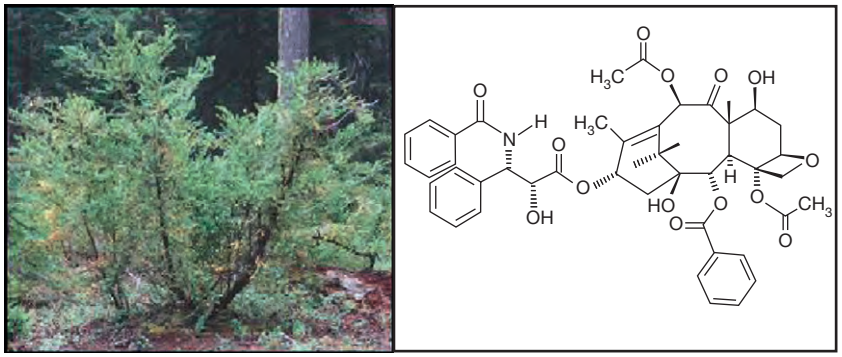

Figure 6 The antiproliferative agent paclitaxel, which is obtained from (a) the Pacific Yew tree, *Taxus brevifolia*. (b) The chemical structure of paclitaxel.

Table 2 Specifications of the first and second generation drug-eluting stents

Stent	*Drug (concentration)*	*Polymer*	*Polymer thickness (μm)*	*Release kinetics (28 days) (%)*	*Metal*	*Strut thickness (μm)*	*Crimped profile (mm)*[a]	*Max cell circumference/ diameter (mm)*[a]
CYPHER	Sirolimus (140 μg cm^{-2})	Polyethelyne-*co*-vinyl acetate and PBMA	12.6	80	SS	140	1.198	9.5/3.0
TAXUS Express	Paclitaxel (100 μg cm^{-2})	Poly(styrene-*b*-isobutylene-*b*-styrene)	16	<10	SS	132	1.245	11.9/3.8
TAXUS Liberté	Paclitaxel (100 μg cm^{-2})	Poly(styrene-*b*-isobutylene-*b*-styrene)	16	<10	SS	97	1.219	13.7/4.4
Endeavor	Zotarolimus (100 μg cm^{-2})	Phosphorylcholine	4.1	95[b]	CoCr	91	1.130	19.8/6.3
Resolute	Zotarolimus (100 μg cm^{-2})	BioLinx (C10, C19, polyvinyl pyrrolidinone	4.1	85[c]	CoCr	91	1.130	19.8/6.3
Xience V	Everolimus (100 μg cm^{-2})	PVDF+HFP+PBMA	7.6	80	CoCr	81	1.055	12.6/4.0

SS, stainless steel; CoCr, cobalt–chromium; PVDF-HFP, poly vinylidene fluoride *co*-hexafluoropropylene; PBMA, poly-*n*-butyl methacrylate.
[a]Based on a 3-mm stent.
[b]Drug release at 14 days.
[c]Drug released at 60 days.

Table 3 Comparison of the composition of different stent platform alloys

	Elemental composition (wt%)			
	316L stainless steel	Platinum–chromium alloy	L605 cobalt–chromium alloy	MP35N cobalt–chromium alloy
Iron	64	37	3.0[a]	1.0[a]
Platinum		33		
Cobalt			52	34
Chromium	18	18	20	20
Nickel	14	9	10	35
Tungsten			15	
Molybdenum	2.6	2.6		9.75
Manganese	2.0[a]	0.05[a]	1.5	0.15[a]
Titanium				1.0[a]

[a]Maximum.

Irrespective of clinical situation, when compared with BMS, the use of SES results in significant reductions in angiographic in-stent late loss; in-stent angiographic stenosis; and repeat revascularization at both short- and long-term 5-year follow-up, with results consistent across numerous different patient and lesion types. Furthermore, meta-analyses of patient data from the initial approval trials reaffirm the sustained advantage of SES over BMS in terms of reduced repeat revascularization, together with comparable rates of death and MI at long-term follow-up.[46–50]

Table 4 Comparison of the radio-opacity, strut thickness, radial strength, acute recoil, and conformability of different stent platforms

Stent	*Endeavor*	*Xience V*	*Cypher*	*TAXUS Liberté*	*TAXUS Element*
Stent platform	Cobalt–chromium	Cobalt–chromium	Stainless steel	Stainless steel	Platinum–chromium
Strut thickness (μm)	91	81	140	96	81
Radio-opacity ($g\,cm^{-3}$)		9.1		8.0	9.9
Radial strength[a] ($N\,mm^{-1}$)	0.14	0.11	0.17	0.24	0.26
Recoil[b] (% recoil)	5.1	4.6	3.4	2.8	3.0
Conformability[c] ($N\,mm^{-1}$)	0.06	0.30	1.00	0.09	0.04

[a]Amount of radial force required to reduce the diameter of a deployed stent (higher values preferred).
[b]Percentage of the stent diameter which decreases after balloon deflation (lower values preferred).
[c]Measure of the ability of the stent to naturally conform to the vessel (lower values preferred).

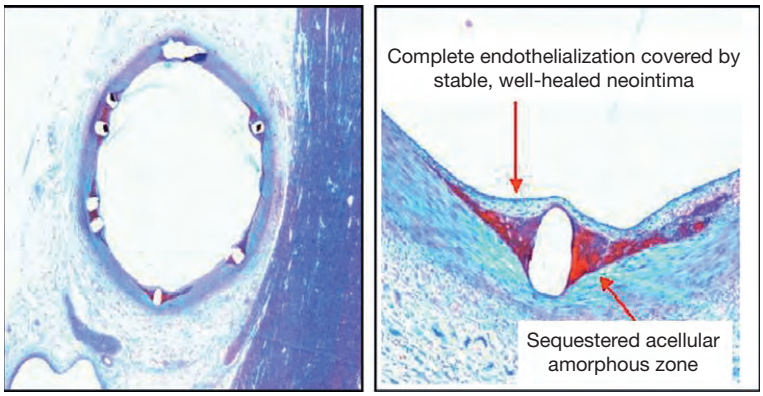

Figure 7 Sirolimus-eluting stent implantation in a porcine model demonstrating complete endothelialization of the stent struts without the development of significant neointimal hyperplasia.

Registries have also evaluated the performance of the Cypher stent in a 'real-world' setting. The first of these registries was the single-center RESEARCH (Rapamycin Eluting Stent Evaluated at Rotterdam Cardiology Hospital) registry, which enrolled 508 consecutive patients, who were treated with the Cypher SES irrespective of lesion complexity. Running concurrently with the RESEARCH registry was the multicenter ARTS-II (Arterial Revascularization Therapies Study) registry, which assessed the Cypher stent in 607 patients with two and three vessel CAD. Results from both registries at short and long-term follow-up, which now extends to 4 and 5 years for the respective RESEARCH and ARTS-II registries, mirror those from other registries, and the aforementioned randomized studies and meta-analyses, by continuing to demonstrate significantly lower rates of MACE and TLR following the use of the Cypher SES compared to historical BMS controls.[51–55]

6.627.4.2. Paclitaxel-Eluting Stent

Paclitaxel is a highly lipophilic diterpenoid compound that was first discovered in the pacific yew tree *Taxus brevifolia* in 1963 (Figure 6). This agent shifts the cytoskeletal equilibrium toward assembly, thereby inhibiting cell division in the G0/G1 and G2/M phases, which leads to reduced vascular cell proliferation, cell migration, cytokine and growth factor release and activity, interference with secretory processes, antiangiogenic effects, and impaired signal transduction.[56] At high doses, paclitaxel produces mitotic arrest in the G2/M phases of the cell cycle and promotes apoptosis. Conversely, at the low doses that are used on the paclitaxel-eluting stent (PES), paclitaxel affects the G0-G1 and G1-S phases, resulting in cytostasis without cell death. The first TAXUS PES (Boston Scientific, Natick, MA) consisted of paclitaxel contained within a polyolefin derivative biostable polymer coated on the stainless steel NIR platform. A slow-release (SR) formulation with an 18-μm thick coat, a moderate release (MR) with a 7-μm coat, and a fast release with 4-μm coat shed 8, 22, and 50% of the paclitaxel within 30 days, respectively. The difference in release was achieved by changing the polymer to drug ratio while maintaining the same paclitaxel concentration ($1\,\mu g\,mm^{-2}$).[57] The TAXUS PES has been evaluated in the TAXUS series of trials which have enrolled different patient and lesion types:

- The TAXUS I trial, a FIM phase I feasibility study with 61 randomized patients, reported a 3% MACE rate versus 10% in BMS at 1 year. Patients in the PES group had no TLR or binary stenosis, proving that paclitaxel effectively inhibited neointinal proliferation.[58]
- The TAXUS II study randomized 536 patients to treatment with BMS or SR PES, and BMS or MR PES. The reduction in percentage neointimal hyperplasia as measured by IVUS at 6 months was 7.8% for SR and 7.8% for MR versus 23.2% and 20.5% for control BMS.[59] These results provided the foundation for the sustained reduction in TLR of 4.5 and 10.3% for the MR PES and SR PES, respectively, (BMS 18.4%, BMS vs. PES $p < 0.001$) out to 5 years.[60] Of note, the MR formulation which was not subsequently used for

commercialization showed a better antirestenotic effect than the SR formulation at 5 years.

- TAXUS III tested the fast release PES in 28 patients with in-stent restenosis. At 6 months, the in-stent late loss was 0.54 mm with a neointimal hyperplasia volume of 20.3 mm^3, and a subsequent MACE rate was 29%. Overall results suggested that PES was a potentially efficacious treatment in those with in-stent restenosis.[61]
- The platform of the PES was changed from the NIR platform to less rigid Express platform (Table 2) and this combination was studied in the TAXUS IV study, which randomized 1326 patients with noncomplex CAD to treatment with the TAXUS Express stent or Express BMS. TVR at 9 months was significantly lower in the PES group (12.1% vs. 4.7%; $p < 0.0001$) and this advantage was maintained through to 5 years (27.4% vs. 16.9%; $p < 0.0001$), despite comparable annual TVR rates for BMS and PES between years 1 and 5 (4.1% per year vs. 3.3% per year, respectively, $p = 0.16$).[62,63]
- TAXUS V randomized 1156 patients, over half of whom had complex coronary lesions not studied in earlier PES trials, to treatment with PES ($n = 557$) and BMS ($n = 579$). Consistent with earlier studies, use of PES lead to significantly lower rates of angiographic stenosis, TLR, and TVR at 9 months, with comparable rates of death, MI, and ST. The benefit in favor of PES was maintained out to 5-year follow-up; however, PES was also associated with higher rates of MI (9.3% vs. 5.6%, $p < 0.05$) and definite/probable ST (2.4% vs. 1.5%, $p < 0.05$).[64,65]
- TAXUS VI also randomized 446 patients with long complex lesions to treatment with either PES or the Express BMS. At 9-month follow-up, use of PES led to significantly lower rates of binary stenosis, TLR, and TVR, while the overall MACE rate was similar. Subsequent 5-year follow-up demonstrated the sustained antirestenotic effect of PES on TLR (14.6% vs. 21.4%, $p = 0.03$); however, a significantly higher rate of non-TLR was also seen in the PES group (10.9% vs. 5.1%, $p = 0.03$). Rates of ST and MACE were similar.[66,67]

In a fashion similar to the SES, the TAXUS PES has been assessed in an unrestricted single-center registry, which used the PES as the default stent for all PCI in 576 consecutive 'real-world' patients. Two-year results from the T-SEARCH registry (Taxus Stent Evaluated at Rotterdam Cardiology Hospital) demonstrate similar efficacy in terms of suppression of neointimal growth and reduction of restenosis when compared to historical controls treated with SES.[68,69] In addition, patient level meta-analysis of the initial PES approval trials has confirmed the comparable safety and superior efficacy of PES, in relation to BMS, up to 4-year follow-up.[49,50]

6.627.4.2.1. TAXUS express versus TAXUS liberté

The TAXUS PES Express stent was the first PES approved by the FDA; however, it was subsequently replaced by the TAXUS PES Liberté stent, which was designed to be more deliverable and conformable, and to provide a more homogenous drug distribution.[70] Both stents utilized an identical polymer, dose of paclitaxel and release kinetics; however, the Liberté stent had a more uniform cell geometry allowing more enhanced and uniform drug delivery; thinner struts (97 vs. 132 μm); a smaller profile; and different stents designs depending on stent diameter (two cell stent for diameters 2.25–2.5 mm and three cell stent for diameter >2.75 mm) (Tables 2–4).

The superiority of the newer Liberté stent was confirmed by the multicenter noninferiority TAXUS ATLAS clinical trial. The study enrolled 871 patients treated with the TAXUS Liberté stent, who were compared to historical controls treated with the TAXUS Express-SR stent from the TAXUS IV and V trials.[70] In spite of similar inclusion criteria, patients with the Liberté stent received treatment for significantly more complex baseline lesions, however,the primary endpoint of 9-month TVR achieved the prespecified criteria for noninferiority (Express 7.0% vs. Liberté 8.0%, $p = 0.049$). There were no significant differences in other clinical outcomes.

Two subsequent studies, the TAXUS ATLAS Small Vessels study and the TAXUS ATLAS Long Lesions study, have also confirmed improved outcomes up to 3-year follow-up with the newer Liberté stent, specifically in patients with lesions treated with a single 2.25 mm TAXUS Express stent, and in patients with lesions 26–34 mm in length treated with a single 38 mm TAXUS Express stent.[71,72]

6.627.5. Benefits of DES

The previous discussion highlights the clear benefit DESs have over BMS in terms of reducing the risk of restenosis, which has been demonstrated in multiple randomized trials, and reaffirmed by meta-analyses. Results from the largest meta-analysis thus far, which included over 18 000 patients from 38 DES trials, indicated a reduction in TLR of 70% ($p < 0.0001$) with the use of SES, and 58% ($p < 0.001$) with the use of PES, when compared to BMS, which is up to 4-year follow-up.[49] This corresponded to a number needed to treat to prevent a single revascularization of only seven and eight patients for SES and PES, respectively. Encouragingly, consistent results have also been demonstrated in numerous other meta-analyses.[46–48,50] Importantly, these impressive results are not only confined to randomized studies which enrolled patients treated for 'on-label' indications, but have also been seen in registries, and randomized controlled trials which have included patients receiving DES for complex or 'off-label' indications.[52,73,74]

6.627.6. Risks of DES

- Restenosis

Despite the marked reduction in restenosis rates with the use of DES as compared to the use of POBA and BMS, clinically driven TLR remains common. These events which hinder the efficacy profile of the stents are even more common in real-world practice as has been consistently shown by registry data. Stenting in patients with diabetes, in those lesions at ostial locations, in small vessels, in lesions requiring long stented segments or stent overlap, and in the treatment of in-stent restenosis has been associated with a higher risk of repeat TVR. Restenosis in these high risk situations cannot be attributed to excessive neointimal proliferation alone, and in fact, failure of stenting in these situations is more likely to

be due to a combination of factors such as operator chosen stenting strategy, patient and lesion characteristics, as well as physical characteristics of the stent, including scaffolding/recoil. Inadequate stent expansion, incomplete apposition, strut fracture, geographical miss, and lesion calcification may all contribute to vessel recoil and inadequate drug elution to the vessel wall.[75,76]

- Stent thrombosis

ST is not unique to DES and in fact, as mentioned earlier, it has been a major problem since the first BMS were implanted. Although rare, it is a devastating, unpredictable event which carries significant morbidity and mortality.[77,78] The partial or complete clogging of the artery with thrombus results in the commonest mode of presentation, being symptoms typical of an acute coronary syndrome including ST-elevation MI.

In the DES era, concerns over the possible increased risk of ST compared to the earlier rates experienced with BMS led to collaborative efforts to investigate this issue. To assist in this assessment, large-scale registries and meta-analysis were performed, the majority of which employed the standardized definitions proposed by the Academic Research Consortium,[79] and reported no overall difference in rates of ST between DES and BMS. Of note, division of ST according to its timing indicated comparable rates of early (<30 days), and late (30 days to 1 year) ST; however, DESs were associated with significantly higher rates of very late (>1 year) ST (Table 5).[47–50,80]

The annual risk of ST seen in post marketing surveillance registries was ~0.2%, rising to 0.5% in trials of multivessel PCI.[81–84] Of importance, rates of ST at the different time points post DES implantation vary significantly as exemplified by the Dutch Stent registry (437/21009 patients with documented ST) where 32.0%, 41.2%, 13.3%, and 13.5% (146) of ST events occurred acutely, subacutely, early, and late.[85] Furthermore, registry data from the Rotterdam–Bern group (8146 patients), the SCAAR registry (21 717 patients), and from Pinto Slottow's *et al.* registry (8000 patients) have all indicated that the risk of very late ST persists at an annual rate of between 0.36% and 0.6% per year out to at least 5 years after DES implantation.[86–91] In addition, the results at 2-year follow-up from both the ARRIVE and STENT registry also suggest that the risk of ST is higher in those patients treated with DES for 'off-label' compared to 'on-label' indications.[92,93]

Numerous potential causes have been implicated as a risk factor for a ST event.[85,86,91,94] The possible increased thrombogenicity of DES as compared to BMS was attributed to lack of vessel endothelialization, vascular toxicity, and hypersensitivity reactions. A recent small scale study suggested stent malapposition as a more frequent finding in DES, whereas disease progression with neointimal rupture was more common in BMS.[95] Procedure related factors, such as stent under sizing, lesion length >28 mm, dissection, multiple stent implantation, stenting at bifurcations, calcification, and small vessel diameter, and most notably early cessation of DAPT, have been associated with development of early/late, but not very late, ST.[85,94] Renal failure and previous brachytherapy seem to be more important in very late ST.

Currently, efforts are underway to reduce the risk of ST, utilizing the vast acquired knowledge of factors which have been implicated in its occurrence. As discussed in the rest of this chapter, the development of newer stents with new stent platforms, new stent designs, and safer drug release mechanisms aims to decrease the inherent thrombogenicity of the stent itself. Coupled with these changes, are developments in imaging techniques that help better identify features implicated in precipitating ST, such as malapposition and dissections in the acute phase, thereby allowing immediate correction, which could potentially help in reducing ST events. Finally with respect to DAPT, investigations are underway to establish the optimal duration of DAPT, the full potential of new antiplatelet agents such as prasugrel and ticagrelor, and the optimal treatment of patients with antiplatelet resistance.

6.627.7. Second Generation DES

The previously discussed safety concerns that emerged with the first generation DES prompted the development of newer coronary stents, which utilized more biocompatible polymers, aimed more specifically at mimicking the endothelial lining in order to prevent thrombotic complications. In addition, these newer stents moved away from stent platforms using 316L stainless steel, and instead used cobalt–chromium, an alloy with improved radio-opacity and superior radial strength, thereby allowing thinner stent struts (Tables 2–4). Notably, previous studies of bare-metal and drug-eluting stainless steel

Table 5 Rates of overall, early, late, and very late stent thrombosis from recent meta-analyses comparing drug-eluting stents to bare-metal stents

Reference	*Stent (number of patients)*		*Longest follow-up (years)*	*Overall ST (DES vs. BMS)*	*Early ST (DES vs. BMS)*	*Late ST (DES vs. BMS)*	*Very late ST (DES vs. BMS)*
ST defined according to Academic Research Consortium definitions							
Spaudling *et al.*[48]	SES (878)	BMS (870)	4	3.6% vs. 3.3%	0.5% vs. 0.5%	0.3% vs. 1.3%[a]	2.8% vs. 1.7%
Stettler *et al.*[49]	SES (4643)	BMS (4003)	4	HR 1.00	HR 1.02	HR 1.14	HR 1.43
Stettler *et al.*[49]	PES (4327)	BMS (4003)	4	HR 1.38	HR 0.95	HR 1.61	HR 3.57
Mauri *et al.*[47]	PES (1400)	BMS (1397)	4	3.2% vs. 3.5%	0.5% vs. 0.5%	0.9% vs. 0.9%	1.8% vs. 2.1%
ST defined according to protocol							
Stone *et al.*[50]	SES (878)	BMS (870)	4	1.2% vs. 0.6%	0.5% vs. 0.1%	0.1% vs. 0.5%	0.6% vs. 0.0%[a]
Kastrati *et al.*[46]	SES (2486)	BMS (2472)	5	HR 1.09	–	–	0.6% vs. 0.05%[a]
Stone *et al.*[50]	PES (1755)	BMS (1758)	4	1.3% vs. 0.9%	0.5% vs. 0.6%	0.2% vs. 0.1%	0.7% vs. 0.2%[a]

Difference nonsignificant unless indicated. BMS, bare-metal stent; SES, sirolimus-eluting stent; PES, paclitaxel-eluting stent; ST, stent thrombosis; HR, hazard ratio.
[a] $p < 0.05$.

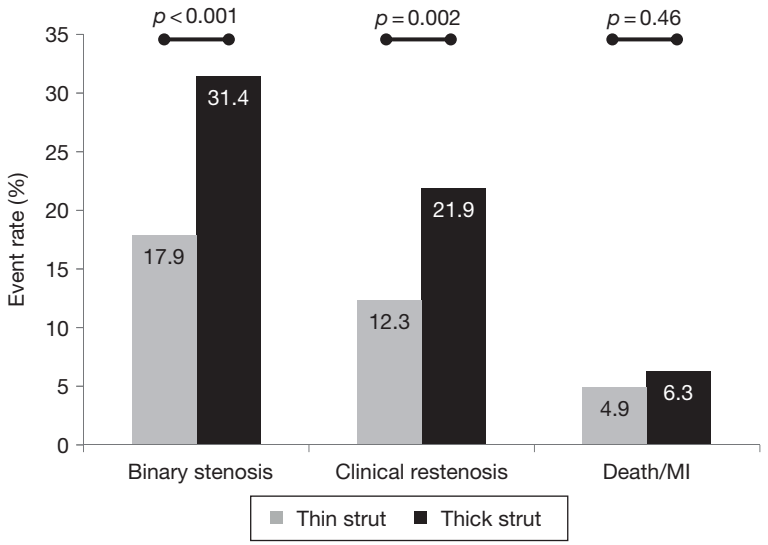

Figure 8 The rate of binary restenosis (diameter stenosis ≥50%) at 6-month follow-up together with the rate of clinical restenosis and death/myocardial infarction at 1-year follow-up among patients treated with bare-metal stents with thin or thick struts in the ISAR-STEREO-2 trial. Adapted from Pache, J.; Kastrati, A.; Mehilli, J.; *et al*. *J. Am. Coll. Cardiol*. **2003**, *41*, 1283–1288.

stents have indicated that stent strut thickness has a significant adverse impact on long-term rates of restenosis and clinical outcomes (Figure 8).[70–72,96,97] Therefore, reducing strut thickness not only has distinct potential advantages with respect to outcomes, but also allows devices to be of lower profile, improving overall stent deliverability. The second generation DES comprise the Endeavor (Medtronic, Santa Rosa, CA) zotarolimus-eluting stent (E-ZES), the Resolute (Medtronic) zotarolimus-eluting stent (R-ZES) and the XIENCE V everolimus-eluting stent as described below.

6.627.7.1. Zotarolimus-Eluting Stents

- Endeavor stent (Medtronic, Santa Rosa, CA)

This cobalt–chromium stent has a strut thickness of 91 μm, and is loaded with 100 μg cm^2 of the macrocylic lactone zotarolimus. The drug is released in a rapid fashion such that 95% is eluted within 14-days of implantation, release of which is facilitated by a 4.1-μm thick permanent 'biomimetic' phosphorylcholine polymer which is biostatic and biocompatible, being a natural component of the cell membrane (Tables 2–4). The superior biocompatibility of the polymer is suggested by studies which demonstrate less inflammation with this polymer compared to the methacrylate polymer found on the Cypher SES; in addition, animal and *in vivo* studies using angioscopy and optical coherence tomography (OCT) both demonstrate a greater endothelial coverage of struts, potentially as a result of less inflammation, with E-ZES compared to SES, and PES (Figure 9).[98–101]

The first clinical evaluation of the stent took place in the 100 patient single-arm ENDEAVOR I study. At 12 months, in-stent late loss and binary restenosis were 0.61 mm and 5.4%, respectively. Clinic event rates were low, with two TLRs, one MI, and one definite/probable ST at 1 year, and only one further TLR and no additional MIs or ST events were reported up to 5-year follow-up.[102,103] More extensive assessment of E-ZES has taken place in randomized comparisons with BMS, and first generation DES as described in Sections 6.627.7.3 and 232.7.4, respectively.

- Resolute ZES (Medtronic, Santa Rosa, CA)

The Resolute ZES (R-ZES) uses the same stent platform and dose of antiproliferative agent as that found on the Endeavor stent; however, zotarolimus release is controlled by the BioLinx polymer – a blend of three different polymers: the hydrophobic C10 polymer to control drug release; the biocompatible and hydrophilic C19 polymer; and polyvinyl pyrrolidone to allow an early burst of drug release (Table 2 and Figure 10).[104] The polymer prolongs drug release, such that at least 85% of the zotarolimus is released within 60 days, with the remainder being released within 180 days. The prolonged drug elution is aimed at matching the delayed healing times seen in complex lesions.

The first assessment of the R-ZES took place in the 139 patient, single-arm RESOLUTE study. At 9-month follow-up, angiographic in-stent late loss was 0.22 mm, which was notably less than the ≈0.6 mm consistently seen with the E-ZES. Rates of MACE, TLR, and any definite/probable ST were 8.6%, 0.7%, and 0.0%, respectively at 12-month follow-up, and 11.6%, 1.6%, and 0.0%, respectively at 3-year follow-up.[105–107] The R-ZES has also been assessed in a large randomized study as described in Section 6.627.7.5.

6.627.7.2. Everolimus-Eluting Stent

- XIENCE V

The cobalt–chromium EES stent has a strut thickness of 81 μm, and is coated with a 7.6-μm thick, nonerodable, copolymer of poly vinylidene fluoride *co*-hexafluoropropylene (PVDF-HFP), and poly *n*-butyl methacrylate (PBMA) (Tables 2–4, and Figure 11). The polymer facilitates the elution of the sirolimus analog, everolimus over 120 days. Of note,

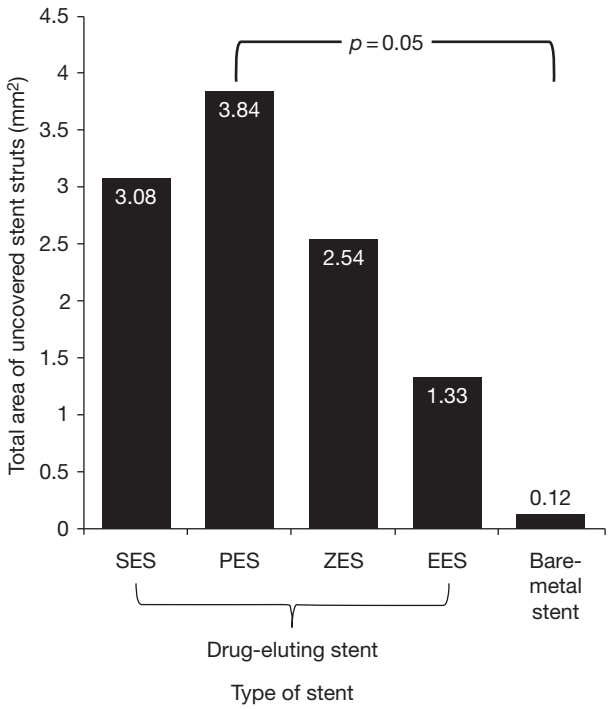

Figure 9 The difference in total area of stent struts that have not been endothelialized according to stent type at 1 month in a rabbit model. SES, sirolimus-eluting stent; PES, paclitaxel-eluting stent; ZES, Endeavor zotarolimus-eluting stent; EES, everolimus-eluting stent. Adapted from Joner, M.; Nakazawa, G.; Finn, A. V.; *et al. J. Am. Coll. Cardiol.* **2008**, *52*, 333–342.

preclinical studies have demonstrated more rapid endothelialization in rabbit iliac arteries implanted with an EES when compared to that with SES, PES, and E-ZES (Figure 9).[99]

The FUTURE I[108,109] and FUTURE II[110] studies were the first to demonstrate the feasibility of using everolimus on a DES, and subsequent trials, as indicated below, include randomized studies comparing EES with BMS, PES, and R-ZES.

- Xience PRIME™ (Abbott Vascular, Santa Clara, CA)

The Xience PRIME EES, which represents the newest development of the Xience® V stent, has recently gained regulatory approval in Europe. This modified EES has a CoCr platform; however, this is mounted on a new enhanced stent delivery system that enables the stent to be more flexible and deliverable. Furthermore, the stent balloon has higher rate burst pressures, and shorter balloon tapers to minimize the risk of edge dissections. The stent is being evaluated in the prospective, multicenter, nonrandomized SPIRIT PRIME study in 500 patients at 75 hospital centers, with the aim of gaining US FDA approval.

6.627.7.3. Second Generation DES Versus BMS

The ENDEAVOR II and SPIRIT FIRST trials were the first respective randomized evaluations of E-ZES and EES, with BMS as the comparator. The ENDEAVOR II trial enrolled 1197 patients (E-ZES = 598, BMS = 599) and demonstrated significantly lower rates of in-stent late loss (0.61 vs. 1.03 mm, $p < 0.001$),

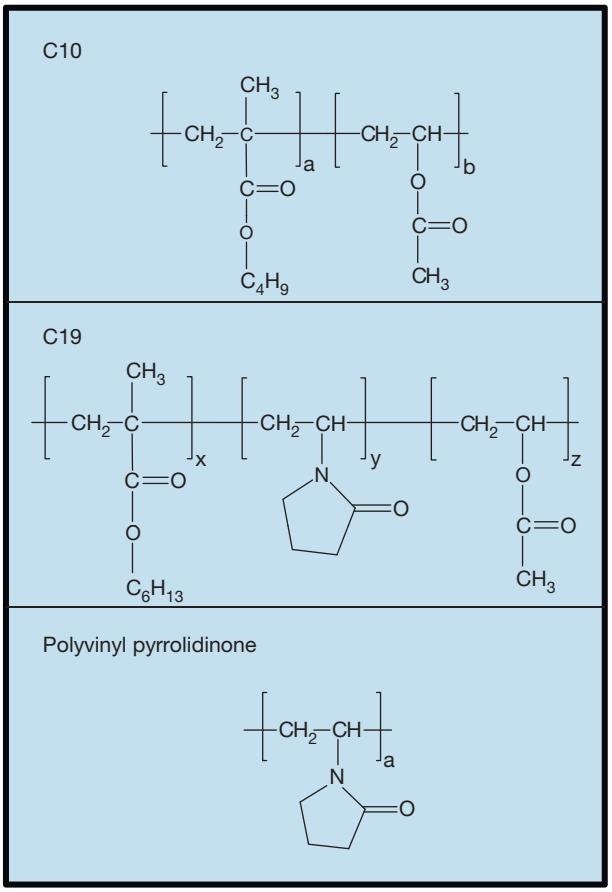

Figure 10 The chemical structure of the three components of the BioLinx polymer on the Endeavor Resolute stent. The hydrophobic C10 polymer is based on hydrophobic butyl methacrylate to provide adequate hydrophobicity for zotarolimus. The hydrophilic C19 polymer is manufactured from a mixture of hydrophobic hexyl methacrylate, and hydrophilic vinyl pyrrolidinone and vinyl acetate monomers, to provide enhanced biocompatibility. The hydrophilic polyvinyl pyrrolidinone increases the initial drug burst and enhances biocompatibility.

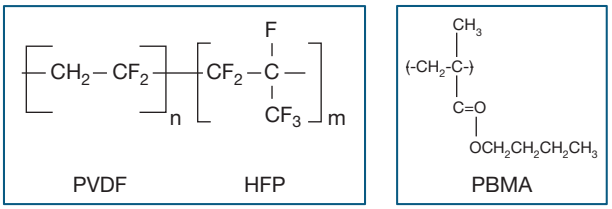

Figure 11 The structure of the Xience V everolimus-eluting stent polymer which is a copolymer of poly vinylidene fluoride *co*-hexafluoropropylene (PVDF-HFP), and poly *n*-butyl methacrylate (PBMA).

binary in-stent restenosis (9.4% vs. 33.5%, $p < 0.001$), TLR (4.6% vs. 11.8%, $p < 0.001$), and target vessel failure (TVF; a composite of cardiac death, MI attributable to the target vessel, and clinically driven TLR) (7.9% vs. 15.1%, $p < 0.001$) at 9-month follow-up, with additional clinical follow-up at 5 years indicating a sustained benefit in favor of E-ZES with respect to TLR and TVF.[111,112] Mortality and rates of MI and ST were comparable at all time points. Of note, unlike long-term

follow-up of the SIRIUS and TAXUS II study,[33,60] there was no reduction with time in the absolute difference in TLR between E-ZES and BMS (Δ7.2% at 1 year, Δ8.8% at 5 years).

The smaller SPIRIT FIRST study enrolled 56 patients (EES = 27, BMS = 29) and demonstrated superior performance of EES at 6-month and 5-year follow-up with respect to similar angiographic, and clinical endpoints as assessed in the ENDEAVOR II study.[113,114]

6.627.7.4. Second Generation DES Versus First Generation DES

After establishing their superiority over BMS, both second generation DESs have been compared to the first generation DES. While E-ZES has been compared in different randomized trials to both PES and SES, EES has only been compared to PES. Overall results with E-ZES have been inconsistent, while a clear benefit in favor of EES has been shown in its comparison with PES.

- E-ZES versus SES

The comparison of E-ZES and SES has taken place in the randomized ENDEAVOR III study which enrolled 436 patients (E-ZES = 323 and SES = 113) and the SORT-OUT III study which randomized 2332 patients (E-ZES ($n = 1162$) and SES ($n = 1170$)).[115–117] At short-term follow-up, results of both studies suggested superiority of SES. Notably, the ENDEAVOR III study failed to reach its noninferiority primary endpoint of in-stent late loss at 8-month follow-up (E-ZES 0.34 mm vs. SES 0.13 mm, $p < 0.001$); however, despite this, rates of TLR, mortality and TVF were similar in the stent groups. In contrast, in the SORT-OUT III study at both 9- and 18-month follow-up, significant differences in favor of SES were observed with respect to MI, TLR, and ST. Results at long-term follow-up of the ENDEAVOR III study suggest a more sustained antiproliferative effect with E-ZES compared with SES. Specifically at 5 years, the absolute difference in TLR between E-ZES and SES was 1.6% (E-ZES 8.1% vs. SES 6.5%) compared to an absolute difference at 9 months of 2.8%. Rates of ST remained similar in both groups throughout follow-up, although neither study was powered for this endpoint.

- E-ZES versus PES

The ENDEAVOR IV study randomized 1548 patients to E-ZES ($n = 773$) and PES ($n = 775$).[118] The study demonstrated noninferiority of E-ZES compared to PES with respect to the primary endpoint of TVF (E-ZES 6.6% vs. PES 7.2%); no significant differences were noted in other clinical endpoints at 1-year, with results maintained through to 3-year follow-up.[119] Similar to the ENDEAVOR III study, there was a reduction with time in the absolute difference in TLR between E-ZES and PES from 1.3% at 1 year to 0.5% at 3 years. Angiographic follow-up at 8 months demonstrated an in-stent late loss of 0.67 and 0.42 mm for E-ZES and PES, respectively ($p < 0.001$).

In summary, the comparison of E-ZES with first generation DES have shown similar results, with significantly inferior values for late loss observed on angiographic follow-up at between 6 and 8 months; however, this has not translated into any significant differences in clinical endpoints. Moreover, at long-term follow-up a reduction in the absolute difference between E-ZES and the comparator stent has been seen, which may suggest absence of the 'late catch-up' phenomena with E-ZES.

With respect to ST, no study has been adequately powered to detect differences, and consequently the results of the PROTECT study, anticipated in 2011, are eagerly awaited. This study has randomized 8800 'all-comers' patients to treatment with either the E-ZES or SES, and will report a primary endpoint of definite/probable ST at 3-year follow-up.[120]

- EES versus PES

EES has been compared to PES in several randomized studies which have enrolled increasingly complex patients ranging from those with up to two *de novo* lesions in the SPIRIT II study,[121–125] to the unrestricted all-comers population in the COMPARE study.[126] Irrespective of patient complexity or follow-up period, angiographic and clinical outcomes have been superior in those treated with EES. Specifically, in the SPIRIT II and SPIRIT III study in-stent late loss at 6 and 8 months, respectively, was significantly lower with EES.[125,127] Longer angiographic follow-up has only been performed in the SPIRIT II study, and this demonstrated evidence of delayed late loss with EES such that there was no longer a significant difference in in-stent late loss at 2 years.[121] Nevertheless, despite this observation, clinical outcomes at 3- and 4-year follow-up in the SPIRIT II study remained consistent with those seen at 6-month and 1-year follow-up, with numerically lower rates of cardiac death, MI, TLR, and overall MACE with EES. Similarly, at 3-year follow-up in the SPIRIT III study, treatment with EES led to significantly lower rates of TVF, target lesion failure, and MACE.[128] More extensive assessment of EES has taken place in the SPIRIT IV, which randomized 3690 patients (EES = 2458, PES = 1229), and represents the largest randomized trial comparing two DESs, and the COMPARE study, which recruited 1800 patients (EES = 897, PES = 903) and was the first randomized all-comers trial of the EES.[126,129] Both studies demonstrated significantly superior efficacy and safety with EES compared to PES. In addition, while nonsignificantly lower rates of ST have been observed in the SPIRIT II and III studies, the SPIRIT IV and COMPARE studies were the first to demonstrate a significant reduction in ST between two DES. At 12-month follow-up, rates of definite/probable ST for EES and PES were 0.29% versus 1.06% ($p = 0.003$), and 0.7% versus 2.6% ($p = 0.002$) in the SPIRIT IV and COMPARE studies, respectively.

6.627.7.5. Second Generation DES Versus Second Generation DES

The only data comparing two second generation DES come from the RESOLUTE All-Comers Trial. This study, which randomized 2300 patients to treatment with the R-ZES or EES, had an all-comers design, such that one-third of the population enrolled presented with ST-elevation MI, and two-thirds had at least one off-label indication.[130] The study achieved its prespecified criterion for noninferiority of the primary endpoint of target lesion failure (a composite of cardiac death, MI attributable to the target vessel, and clinically driven TLR) at 12-month follow-up (R-ZES 8.2% vs. EES 8.3%, $p_{\text{noninferiorty}} < 0.001$). In addition, the study also achieved its powered angiographic

endpoint of percent diameter stenosis at 13-month follow-up (R-ZES 21.7% vs. EES 19.8%, $p_{\text{noninferiorty}} = 0.04$). All other clinical endpoints were similar in both groups, including rates of ST, which were reassuringly low despite the complexity of the patient population.

6.627.8. New Drug-Eluting Stents

There is no doubt that the introduction of the DES revolutionized the practice of interventional cardiology. The first generation DESs undeniably offered distinct advantages over their BMS predecessors; however, safety concerns emerged with their use in the more diverse patient populations encountered in routine clinical practice. These concerns subsequently prompted development of second generation DES which had more biocompatible polymers, and results have so far been impressive, albeit at only medium-term follow-up.[122,131] The problem of ST persists however, and focus has now turned to developing newer DESs which utilize newer types of polymer. Of note, current first and second generation DESs use nonerodable polymers, which remain exposed to the coronary artery environment long after their useful function has been served, and consequently have been implicated in causing persistent arterial wall inflammation, and delayed vascular healing, both of which may play a role in precipitating ST and delayed restenosis.[99,132–135]

Advances in polymer technology have led to the development of DESs which have polymers that biodegrade into inert monomers over 6–9 months, or DESs which are completely polymer free. A final extension to these new developments is the concept of completely biodegradable stents which are discussed in.

A robust method of classifying this heterogeneous group of new stents, many of which are still undergoing preclinical and/or early FIM studies, has not yet been determined, but for simplicity, in the following discussion they are grouped according to the type of polymer. Of note, those stents utilizing new stent platforms such as platinum–chromium and nitinol are covered separately.

6.627.8.1. DES with Biodegradable Polymers

This represents the largest group of new DESs, with numerous devices undergoing current clinical evaluation, and some already commercially available in Europe. In theory, immediately after implantation these devices function similar to conventional DES; however, after polymer breakdown, they speculatively may offer the safety benefits of BMS. Short-term results from these stents have been encouraging; however, in the absence of long-term data it is not possible to definitively state that this technology will lead to improved clinical outcomes, most notably with respect to improved safety.

There are many challenges remaining for this new polymer technology, which include among others, establishing the optimal biocompatibility, composition, formulation, and degradation time of the polymer. In addition, attention must be paid to the pharmacokinetics of the antiproliferative agent released by the degradation of the polymer, and the variation in polymer degradation time which can be affected by production factors such as the use of long polymer chains, decreased polymer hydrophobicity, and greater polymer crystalinity, together with physical and biological environmental factors.[136] Evidence indicates that polymer breakdown can be associated with a significant inflammatory reaction which at times can create an acidic environment; moreover, complications may also occur as a result of a persistent immune response to monomer breakdown products.[137] These uncertainties reiterate the need for continued research, with clinical outcomes assessed at long-term follow-up.

The most prominent DESs with biodegradable polymers include those eluting biolimus A9, sirolimus, and paclitaxel, as described below.

6.627.8.1.1. Biolimus A9-eluting DES with biodegradable polymers

The most widely studied DESs with biodegradable polymers elute the highly lipophillic macrocyclic lactone biolimus A9, which is an analog of sirolimus that inhibits T cell and smooth muscle cell proliferation. The main difference between biolimus A9 and rapamycin is replacement of hydrogen by alkoxy-alkyl group at 40-O position, increasing its lipophilicity (Figure 4). The drug has been combined on several different stent platforms with an abluminal poly-lactide polymer, which biodegrades completely within 6–9 months of stent implantation (Figure 12). The abluminal location of the drug/polymer matrix is aimed at further improving overall safety, by allowing more targeted tissue release, and reducing systemic exposure.

- Biomatrix™ stent (Biosensors, Morges, Switzerland)

The stainless steel BioMatrix Flex™ stent (Figure 12) was initially evaluated in the 120 patient FIM STEALTH I trial which randomized patients to the biolimus-eluting stent (BES) or a BMS. At 6 months, angiographic follow-up rates of in-stent late lumen loss and angiographic stenosis were significantly lower with BES.[138] Results at 5-year follow-up from a subgroup of 32 patients demonstrate low rates of overall MACE, and importantly no episodes of ST.[139]

More recent evaluation took place in the all-comers noninferiority LEADERS study, which randomized 1707 patients to treatment with BioMatrix BES or the Cypher SES. At 9-month follow-up, BES was shown to be noninferior with respect to the primary endpoint of MACE, a composite of cardiac death, MI, and ischemia driven TVR (9% vs. 11%, $p_{\text{noninferiority}} = 0.003$, $p_{\text{superiority}} = 0.39$),[140] with results subsequently maintained at 12- and 24-month follow-up.[141,142] The stent's PLA polymer is expected to have completely biodegraded by 9 months (Figure 12), and therefore, even though the study is not adequately powered to detect differences in ST events, it is promising to observe the occurrence of less very late ST events (>1 year) with BES (0.2% vs. 0.5%).[142] Further data in support of the biodegradable polymer concept were obtained in an OCT substudy, which demonstrated a higher rate of near complete (>95%) strut coverage with BES when compared to the Cypher SES at 9-month follow-up (89.3% vs. 63.3%, $p = 0.03$).[143]

- Nobori™ stent (Terumo, Japan)

The Nobori™ stent is very similar to the BioMatrix Flex stent, utilizing the same polymer, antiproliferative agent, and stent platform; however, the delivery system, delivery balloon,

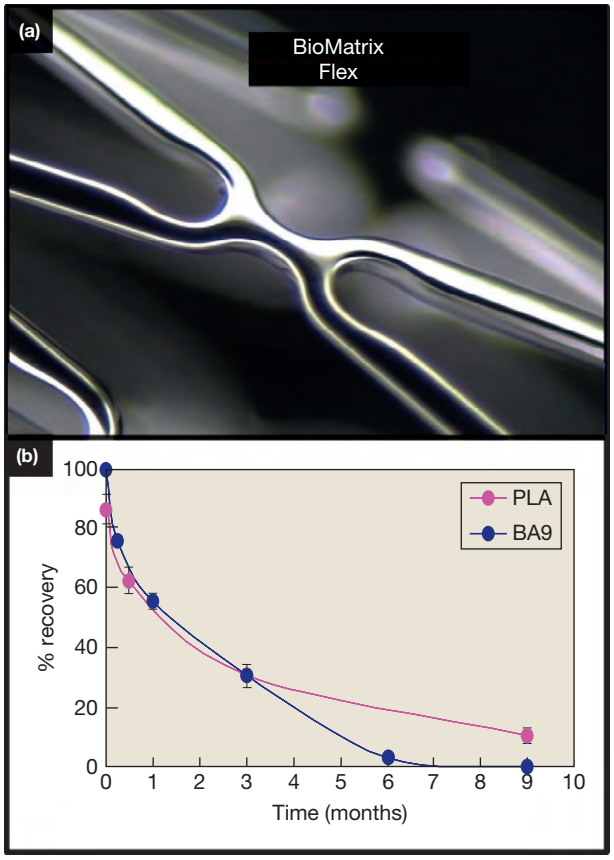

Figure 12 The BioMatrix Flex stent. (a) The stainless steel BioMatrix Flex stent. (b) The elution pattern of Biolimus A9 (BA9) and the corresponding biodegradation pattern of the poly-lactic acid (PLA) polymer.

and the stent coating process are different. In the NOBORI CORE study, which randomized 99 patients to treatment with the Nobori BES or the Cypher SES, there was no significant difference in 9-month angiographic in-stent late lumen loss (0.10 vs. 0.12 mm, $p = 0.66$).[144]

In the larger Nobori I study, 243 patients were randomized to treatment with either the Nobori™ stent ($n = 153$) or the TAXUS PES stent ($n = 90$). At 9 months, the Nobori stent was shown to be noninferior, and subsequently superior to the PES with respect to late loss (0.11 vs. 0.32 mm, $p_{\text{noninferiority}} < 0.001$, $p_{\text{superiority}} = 0.001$). In addition, the rate of ARC defined ST at 9-month follow-up was also lower with the Nobori stent (0.0% vs. 2.2%).[145] Encouragingly no episodes of very late ST have been reported in any study assessing the Nobori stent, which in total have enrolled over 3000 patients. Clinical evaluation continues in large-scale randomized trials comparing the stent to the EES in the COMPARE 2 ($n = 2700$ patients) and BASKET PROVE 2 ($n = 2400$ patients) studies, and to the Cypher Select SES in SORT-OUT IV study ($n = 2400$ patients).[146]

- Axxess™ stent (Devax Inc., Lake Forest, CA, USA)

The Axxess stent is a BES which is made of nitinol and designed specifically for bifurcation lesions. It is described in Section 6.627.8.4.2.

6.627.8.1.2. Sirolimus-eluting DES with biodegradable polymers

- NEVO™ Stent (Cordis, Warren, NJ, USA)

The NEVO™ stent is an open-cell, cobalt–chromium stent, with a PLGA biodegradable polymer which facilitates elution of sirolimus. The stent is unique in its design as the polymer and sirolimus are contained within reservoirs, which eliminate the need for a surface polymer coating, and subsequently reduce tissue-polymer contact, by over 75%. This stent design was previously used on the durable polymer, paclitaxel-eluting CoStar stent (Conor MedSystems, Palo Alto, CA). Unfortunately, despite promising initial results,[147–149] the CoStar stent failed to develop following disappointing results from the CoStar II study,[150] where it was shown not to be noninferior to the TAXUS PES with respect to clinical outcomes in terms of MACE (CoStar 11.0% vs. PES 6.9%, $p = 0.005$), and angiographic outcomes such as in-stent late loss (CoStar 0.49 mm vs. PES 0.18 mm, $p < 0.0001$). The failure of the stent was attributed to several factors including changes in the manufacturing process during the trial that may have affected the paclitaxel release kinetics and the small number of patients in the earlier studies. Perhaps of greatest relevance was that the dose of paclitaxel, which was reduced in an attempt to maximize long-term safety, may have been too low to inhibit neointimal hyperplasia. Learning from this, the NEVO stent has the same sirolimus dose and release kinetics as found on the Cypher SES, thus ensuring that drug elution is complete within 90 days.

The stent has so far only been evaluated in the NEVO-RES I study, which was a randomized, multicenter, noninferiority study comparing the NEVO™ stent to the TAXUS™ Liberté PES stent in 394 patients with single *de novo* coronary artery lesions. At 6-month angiographic follow-up, the primary endpoint of in-stent late lumen loss was significantly lower in patients treated with the NEVO stent (0.13 vs. 0.36 mm, $p < 0.0001$); a superiority which was preserved irrespective of diabetic status, lesion length, or vessel diameter.[151] Clinical endpoints at both 6 and 12 months were numerically lower in the NEVO treated group, although these differences did not reach significance. The rate of ST was 0.0% and 1.1% ($p = 0.24$) in patients treated with the NEVO and PES stent, respectively.

A more extensive evaluation of the NEVO stent is in the currently enrolling NEVO-II study, which will randomize 2500 'all-comers' in a 2:1 ratio to treatment with either the NEVO™ stent (1667) or the Xience V EES (883) stent, with a primary endpoint of target vessel failure at 12 months, and angiographic follow-up in a subset of patients planned at 13 months. Similarly, the NEVO-III will enroll 1300 US patients in a nonrandomized registry.

6.627.8.1.3. Paclitaxel-eluting DES with biodegradable polymers

- JACTAX™ stent (Boston Scientific, Natick, MA, USA)

The JACTAX™ Liberté PES stent is a stainless steel PES stent, which utilizes a novel abluminal PLA biodegradable polymer, known as the Juxtaposed Abluminal Coating technology (JAC™). This polymer, which is fully resorbed within 6–9 months and controls the release of paclitaxel over 90 days,

has a microdrop structure such that the 16 mm JACTAX™ stent has 2700 microdots, each containing 3.4 ng of polymer (total 9.2 μg, Figure 13). The thickness of the polymer (≤1 μm) is ~18 times less than that found on the TAXUS Liberté stent, while the corresponding polymer mass is 100 times less.

The JACTAX™ stent is currently being evaluated with a coating of either low (LD) or high dose (HD) paclitaxel. The JACTAX HD FIM study[152] has recently reported 9-month clinical and angiographic results among a cohort of 103 patients treated with the JACTAX HD stent, who were compared to 217 historical matched controls treated with the TAXUS Liberté stent from the ATLAS study.[70] The primary endpoint of MACE achieved the prespecified criterion for noninferiority; moreover there were no deaths, Q-wave MIs, or ST during follow-up. Finally, there were also no significant differences in the angiographic endpoints of in-stent late loss (0.33 vs. 0.39 mm, $p = 0.36$) and binary restenosis (5.2% vs. 9.2%, $p = 0.22$).

Clinical evaluation of the JACTAX™ LD stent is currently on-going in the JACTAX LD DES Trial, which is randomizing 130 patients to treatment with either the JACTAX™ LD stent or the TAXUS Liberté stent; the primary endpoint is MACE at 9-month follow-up. Additional studies are planned to evaluate this new polymer technology on different stent platforms including a platinum–chromium alloy (Element™ stent platform, Boston Scientific, Natick, USA) and in combination with everolimus on the JacPro™ stent (Boston Scientific, Natick, USA).[153]

6.627.8.2. Polymer-Free DES

Nonpolymeric stents offer the potential advantages of avoiding the long-term adverse effects of a polymer, improved healing, and an improvement in the integrity of the stent's surface because no polymer is present that can be peeled off the struts. Several different techniques are available to enable drug elution from stents in the absence of a polymer:

(1) The bioactive substance can be directly attached to the stent surface using covalent bonding, or crystallization–chemical precipitation on the stent surface.
(2) The bioactive agent can be dissolved in a nonpolymeric biodegradable carrier on the stent surface.
(3) The bioactive agent in its pure form can be impregnated into the porous surface of the stent, or the stent's body.

A brief over view of the available polymer-free stents is given below.

6.627.8.2.1. BioFreedom biolimus A9-eluting stent

This BioFreedom (Biosensors, Morges, Switerzland) 316L stainless steel stent elutes biolimus A9 without the presence of a polymer. Preclinical studies in the porcine model have reported lower injury scores; fewer struts with fibrin, granulomas, and giant cells; significantly lower percentage diameter stenosis; and greater endothelialization with the BioFreedom stent when compared to SES at 180-day follow-up.[154]

The only clinical trial performed so far enrolled 75 low-risk patients with *de novo* lesions, who were randomized to treatment with either a standard dose BioFreedom stent (15.6 μg mm^{-1}), a low dose BioFreedom stent (7.8 μg mm^{-1}), or a TAXUS PES. At 4-month angiographic follow-up, the in-stent late loss was 0.08, 0.12, and 0.37 mm for the standard dose BioFreedom stent, low dose BioFreedom stent, and TAXUS PES, respectively (Standard dose vs. TAXUS $p < 0.001$; low dose vs. TAXUS $p = 0.002$). At 4-month follow-up, there were no MACE or ST events with either the standard dose BioFreedom stent or the TAXUS PES. Clinical evaluation in larger patient populations is on-going.[155]

6.627.8.2.2. VESTAsyn sirolimus-eluting stent

The VESTAsyn SES (MIV Therapeutics, Atlanta, GA) is a polymer-free stainless stent which has a nanothin, microporous, hydroxyapatite surface coating impregnated with 55-μg dose of sirolimus (Figure 14(a) and 14(b)). Sirolimus is eluted over 90 days, while the hydroxyapatite remains stable over the first 4 months, before completely dissolving around 9–12 months after stent implantation. Preclinical studies indicate that the low dose of sirolimus, which is made possible by the hydroxyapatite platform, results in reduced signs of delayed vascular healing, suggesting less local toxicity, and a faster healing response.[156]

Primary evaluation of the stent took place in the 15 patients of the VESTAsync I FIM study.[157] At 4- and 9-month angiographic follow-up, effective reductions in late loss and intimal hyperplasia were observed, with no evidence of 'late-catch' seen on quantitative coronary angiography (QCA) or IVUS. Up to 3-year follow-up, the only clinic event was a single TLR.[158] Needless to say, randomized trials in more complex patient populations are planned, including the VESTAsyncII study which will enroll 75 patients randomized 3:1 to either

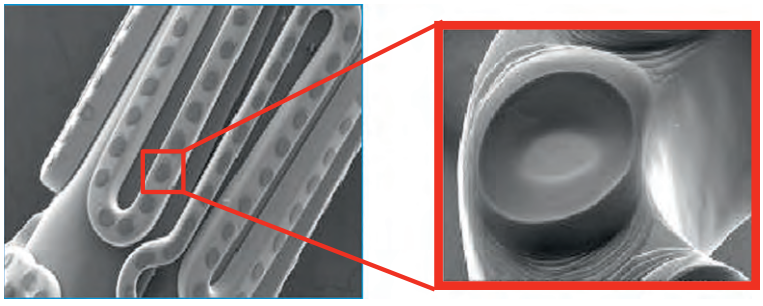

Figure 13 Scanning electron microscopy of the JACTAX paclitaxel-eluting stent. The image and insert demonstrate the microdrop structure of the Juxtaposed Abluminal Coating in use on the stent. Courtesy of Boston Scientific, Natick, USA.

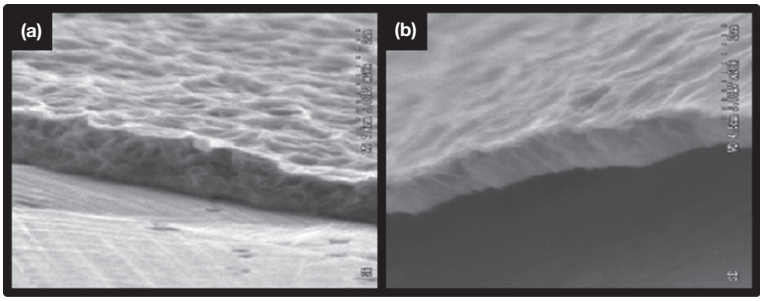

Figure 14 The polymer-free VESTAsyn stents have a (a) rough surface because of their hydroxyapatite coating; however this is (b) smoothed over following the addition of 0.6-μm coating of sirolimus.

the VESTAsyn SES or a control BMS, with a primary endpoint of late loss at 8-month follow-up.[158]

6.627.8.2.3. YUKON: sirolimus-eluting stent

The stainless steel YUKON SES (Translumina, Germany) was the first and consequently now the most extensively studied polymer-free DES. The stent has a microporous surface, with pores that are 2-μm deep and effectively function as a drug reservoir removing the need for a polymer.[159] Uniquely, the dose of sirolimus is customized in the cath lab, just prior to stent implantation, in a coating process taking ~8 min. Initial studies have established that the optimal concentration of rapamycin to prevent restenosis and TLR is 2%.[160]

After complete drug release, the remaining microporous surface appears to favor the adhesion of endothelial cells, a hypothesis initially suggested by angiographic follow-up data,[161] and now confirmed by OCT, which has demonstrated significantly greater neointimal thickening and stent strut coverage with the YUKON stent compared to SES at 3-month follow-up.[162] Clinical studies including both registry and randomized data demonstrate noninferiority of a YUKON stent eluting 2% rapamycin when compared with PES out to 1-year follow-up.[163,164]

Observation data extending out to 2-year follow-up have indicated that the YUKON stent is less susceptible to delayed restenosis than the conventional DES. Of note, Byrne *et al.* reported a significantly lower change in late loss between 6 and 8 months and 2 years for the YUKON stent, when compared with SES and PES (YUKON 0.01 ± 0.42 mm, SES 0.17 ± 0.50 mm, and PES 0.13 ± 0.50 mm, $p < 0.001$).[165] This important finding has also been observed during similar 2-year follow-up of the ISAR-TEST 2 and ISAR-TEST-3 studies, both of which randomized patients to treatment with polymer-free stents, or either conventional polymer or biodegradable polymer DES.[166–169] Collectively these results suggest that polymer-free stents may not be subject to the 'late-catch' phenomenon which has been reported with permanent polymer DES, and appears to be worse in those stents eluting macrocylic lactone derived antiproliferative coatings.[121,170,171]

6.627.8.3. DES Made from New Metal Alloys

Two new DESs, the PROMUS Element and the TAXUS Element (Boston Scientific, Natick, MA), both utilizing a platinum–chromium alloy have recently gained C.E mark approval. This new stent alloy, whose composition is compared to other stent platforms in Table 3, offers several distinct advantages over conventional stent materials. Platinum is two times more dense than iron or cobalt, malleable, corrosion resistant, and fully incorporated into the platinum–chromium alloy. Consequently the platinum–chromium stent offers the advantages of increased radio-opacity and thinner stent struts, which as previously discussed confer distinct advantages in terms of potential reductions in restenosis and improved clinical outcomes (Figure 8);[70–72,96,97] however, these must be balanced with the potential reduction in radial force and increase in acute recoil. However, encouraging initial bench mark studies have indicated that despite thinner struts, the platinum–chromium alloy stent has better radial strength, lower acute recoil, and better vessel conformability compared to conventional stent platforms; Table 4. In addition, rates of uncovered stent struts have been shown to be lower with the Element stent when compared with the stainless steel Liberté and Express stents at 14 days.

6.627.8.3.1. TAXUS element

The TAXUS Element stent (Figure 15) has a poly(styrene-*b*-isobutylene-*b*-styrene) polymer, which facilitates controlled elution of paclitaxel (concentration 1 $\mu g\,mm^{-2}$) in an identical pattern to that seen on the stainless steel TAXUS Liberté and Express stent. The TAXUS Element is currently being assessed in the PERSEUS (A Prospective Evaluation in a Randomized Trial of the Safety and Efficacy of the use of the TAXUS Element Paclitaxel Eluting Coronary Stent System for the Treatment of De Novo Coronary Artery Lesions) clinical trial program, which includes the following features:[172,173]

- The PERSEUS Workhorse trial randomized 1262 patients, with lesions <28-mm long, in vessels between 2.75–4.00 mm in diameter, to treatment with the TAXUS Element ($n = 942$) or the TAXUS Express PES ($n = 320$).[172] At 12-month clinical follow-up, the rate of TVF, the primary endpoint, was Element 5.6% and Express 6.1%, which met the prespecified criterion for noninferiority. The secondary endpoint, percent diameter stenosis at 9-month angiographic follow-up also met the prespecified criterion for noninferiority. In addition, no significant differences were seen between stents with respect to late loss (Element 0.34 ± 0.55 mm vs. Express 0.26 ± 0.52 mm, $p = 0.33$), or other the clinical points such as MACE, mortality, MI, and ST.
- The PERSEUS Small vessel trial compared the TAXUS Element stent to historical BMS controls in patients with

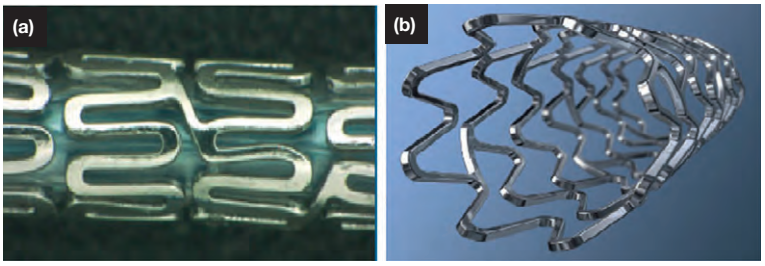

Figure 15 The platinum–chromium Element stent crimped (a) and expanded (b). Courtesy of Boston Scientific, Natick, USA.

lesions which were <20 mm long, in vessels between 2.25–2.75 mm in diameter.[173] Overall, the study enrolled 224 patients treated with the Element stent, who were compared to 125 lesion-matched historical controls treated with a BMS from the TAXUS IV study. Results at 9-month follow-up demonstrated a significantly lower in-stent late loss (the primary endpoint) with the Element stent compared to the BMS stent (0.38 ± 0.51 vs. 0.80 ± 0.53 mm, $p < 0.001$). At 12-month follow-up, the rates of target lesion failure and MACE were both significantly lower with the Element stent, while safety endpoints and ST were comparable between both stents.

6.627.8.3.2. PROMUS element

The PROMUS Element stent has a PBMA primer coating, a PVDF-HFP polymer, and is loaded with 1 μg mm^{-2} of everolimus, 87% of which is eluted within 90 days of stent implantation. No clinical data are available at present; however, the stent is undergoing evaluation in the PLATINUM clinical trial program comprising the following studies:[153]

- The fully enrolled multicenter PLATINUM Workhorse noninferiority study which randomized 1532 patients to treatment with the PROMUS Element or PROMUS Xience V EES stent (Boston Scientific, Natick, M). Results are expected in late 2010.
- The single-arm PLATINUM Small vessel study which will enrol 94 patients with lesions in vessels between 2.25 and 2.5 mm.
- The single-arm PLATINUM Long lesion study which will enrol 102 patients with lesions between 24 and 34 mm in length.
- The single-arm PLATINUM QCA study which will assess QCA in 100 patients at 9-month follow-up.

6.627.8.4. Nitinol Stents

In recent times, there has been increasing interest in the use of nitinol as a platform for coronary stents. Nitinol, which is an alloy of nickel and titanium, has shape memory property, which has resulted in its use in self-expanded coronary stents that have been specifically designed for dedicated coronary lesions such as those in small vessels, those at bifurcations, and those due to vulnerable plaque. In addition, the alloy also has other notable properties which make it favorable for use as a coronary stent platform, namely it is biocompatible, fatigue resistant, and has superelastic properties, which allow it to withstand large amounts of recoverable strain.

Historically, the early stents to be implanted in coronary arteries were self-expanding stents;[7] however, they were eventually replaced by balloon-expandable stents which are currently the preferred type of stents. Of note, self-expanding stents offer important advantages over conventional balloon-expandable stents which include a lower incidence of edge dissections; reduced rates of side-branch occlusion and no-reflow; positive remodeling; and reduced immediate vessel wall injury which may lead to a reduction in neointimal hyperplasia and a larger vessel lumen.[174–176]

Despite these potential advantages, there are some drawbacks of self-expanding stents which are related to their delivery systems and properties:

- *Delivery systems*: Self-expanding stents are housed within a delivery catheter that ensures stent security; however, these catheters can be cumbersome to use, and have an associated learning curve. The delivery profile of these stents is dictated by strut dimensions, as opposed to the balloon profile as in balloon-expandable stents.
- *Mechanical properties*: The continued outward radial force that self-expanding stents exert even after deployment leads to negative chronic recoil, and results in a larger vessel at follow-up. This phenomenon can make matching stent size to vessel size difficult. Secondly, self-expanding stents foreshorten on expansion and/or can move forward because of spring movements when the stent is released from the delivery system; these properties can make accurate placement difficult.

Recently reductions in strut thickness, improvements in delivery systems, and the addition of a drug coating have lead to increased interest in self-expanding stents for the treatment of the following types of lesion.

6.627.8.4.1. Lesions in small vessels

The use of balloon-expandable stents to treat lesions in small diameter coronary arteries is associated with a risk of edge dissection, owing to the high pressures required for optimal stents implantation. Ample evidence exists relating inadequate stent strut apposition, and stent expansion to a subsequent increased risk of restenosis and ST.[134] As stated previously, self-expandable stents offer the advantage of minimizing baro-trauma and the risk of edge dissections, and therefore have a potential role in the treatment of small vessel lesions.

The Cardiomind Sparrow™ (Cardiomind Inc, Sunnyvale, CA) is a small profile nitinol self-expanding stent that is designed specifically for treating lesions in coronary vessels with a diameter of between 2.00 and 2.75 mm (**Figure 16(a)**).

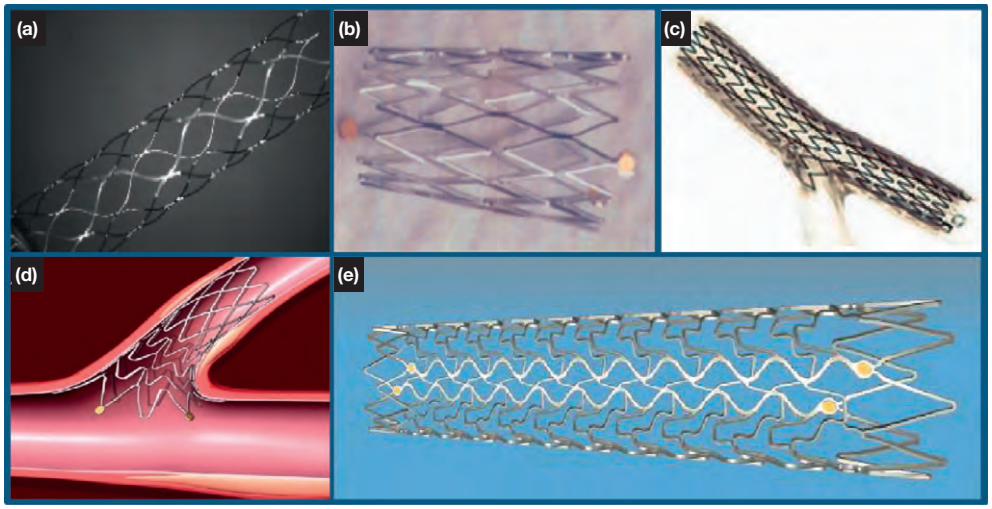

Figure 16 Self-expanding nitinol stents (a) The CardioMind Sparrow stent, (b) Axxess bifurcation stent, (c) Stentys bifurcation stent, (d) Capella side-branch stent, and (e) the vProtect® Luminal Shield stent.

The stent, which has a strut thickness of 61 μm, is preloaded on a 0.014″ guidewire, with 2–3 cm of radio-opaque guidewire at the distal end enabling positioning within the vessel. A dedicated delivery system is used to deploy the stent. The uncoated stent has been assessed in the CARE I feasibility study, which recruited 21 patients with *de novo* lesions in vessels 2.0–2.5 mm in diameter. A 13% rise in the in-stent volume index was observed at 6 months, together with a binary restenosis rate of 20%. There was no ST at 30 days, and two MACE events occurred through to 24-month follow-up. These patients have subsequently been compared to a group of historical controls, treated under the same inclusion and exclusion criteria, but with implantation of a balloon-expandable stent. Results demonstrate a significantly lower in-stent late lumen loss (0.73 vs. 1.11 mm, $p = 0.04$), and intimal hyperplasia volume obstruction (31.9% vs. 39.9%, $p < 0.001$) with the Cardiomind stent.[177,178]

The next-generation Sparrow stent has a strut thickness of 67 μm and is coated with a 4-μm thick layer of sirolimus at a dose of 6 $\mu g\,mm^{-1}$, and an 8-μm thick layer of biodegradable PLA/PGLA polymer. It is currently being assessed in the CARE-II study that will randomize 220 patients with lesions ≤20 mm in length, in vessels between 2.00 and 2.75 mm in diameter to treatment with the bare-metal Cardiomind Sparrow™, the drug coated Cardiomind Sparrow™, or a BMS. Interim results at 8-month follow-up are expected in 2010.[179]

6.627.8.4.2. Lesions in bifurcation

Bifurcation lesions remain a challenging lesion subset for today's interventional cardiologist. Discussion continues over the optimal number of stents to implant and the stenting technique to use; however, the wide anatomical variation in bifurcation lesions suggests that no optimal strategy suitable for all will be established. In view of these ongoing issues, some dedicated bifurcation stents have been developed, some of which utilize nitinol in view of its ability to conform more optimally to angulated coronary anatomy, compared to conventional balloon-expandable stents.[180,181]

The following are three such stents:

- Axxess™ (Devax, Irvine, CA)

This conical nitinol stent has a strut thickness of 152 μm, and is coated with a biodegradable PLA polymer, which degrades over 6–9 months, and release the macrocylic lactone biolimus A9 (Figure 16(b)). The stent is released by withdrawing a covering sheath, and is ideally placed at the level of bifurcation carina, allowing easy access to both distal branches, which can be stented if required. The stent has been assessed in the DIVERGE (Drug-Eluting Stent Intervention for Treating Side Branches Effectively) registry which recruited 302 patients who were followed-up for 9 months. Of note, additional stent implantation was required in 64.7% of patients. At 9-month angiographic follow-up, in-stent late loss was 0.29 mm in both branches, while the rates of binary in-stent restenosis were 2.3% and 4.8% in the main-branch and side-branch, respectively. Clinical event rates at follow-up were low with a rate of MACE of 7.7%, TLR 6.4%, and ST 1%.[182]

- StenTys™ (Stentys, SAS, France)

This paclitaxel-eluting self-expanding stent is made of a z-shaped mesh linked by small interconnections (Figure 16(c)). It consists of a preformed main-branch stent with side ports to facilitate access to the side-branch. Uniquely, the stent struts can be disconnected with the use of an angioplasty balloon; therefore, an opening for the side-branch can be created anywhere in the stent after it is implanted; the disconnected struts can subsequently scaffold the ostium of the side-branch. Evaluation of the stent has been performed in the OPEN (Stentys coronary bifurcation stent system for the percutaneous treatment of *de novo* lesions in native bifurcated coronary arteries) study which enrolled 40 patients and reported a low rate of additional stent implantation (main-branch 9%, side-branch 13%). Angiographic follow-up at 6 months demonstrated a late loss of 0.83 mm and a binary in-stent restenosis rate of 25% and 14% in the main- and side-branch, respectively. The rates of MACE, death, MI, and TLR were 5.1%, 0.0%, 2.5%, and 2.5%, respectively.[183,184]

- Cappella Sideguard™ (Cappella Inc, Auburndale, MA)

This nitinol stent is shaped like a trumpet (Figure 16(d)), to allow excellent conformability to vessel anatomy and is designed for bifurcation lesions with significant side-branch disease. It is implanted in the ostium of the side-branch, and facilitates conventional stent implantation in the main-branch without restriction. The stent has been evaluated in the 93 patient Sideguard I and II FIM studies. Encouraging at 12-month follow-up, angiographic in-stent late loss in this bare-metal stent was 0.21 and 0.58 mm in the main- and side-branch, respectively. With respect to clinical outcomes, the rates of cardiac death were 1.2%, MI 3.6%, and TLR 7.2%.[185,186]

6.627.8.4.3. Lesions due to vulnerable plaque

Data indicate that unstable presentations such as MIs are commonly the result of a disruption of thin-cap fibroatheromas (TCFAs).[187] It follows that preemptive treatment of these lesions involves preventing cap rupture, and promoting endothelialization. The very nature of these thin-cap lesions indicates that the high deployment pressures required for implantation of a balloon-expandable stent are undesired. Advantageously, self-expanding stents do not induce vessel injury during implantation, thereby minimizing the risk of embolizing necrotic material and thrombus distally. In the long-term, the lack of strut penetration into necrotic core may reduce the risk of ST, which may occur through the substantially delayed arterial healing that occurs when struts penetrate necrotic core.[188,189] The vProtect® Luminal Shield (Prescient Medical, Inc., Doylestown, PA) is a self-expanding nitinol stent (Figure 16(e)) which has been shown in animal studies to promote vascular healing, and importantly, achieve complete endothelialization of the stented segment within 7 days.[190] Encouragingly, data from the FIM study has demonstrated that the 'shield' can induce plaque remodeling, and has a positive vascular healing profile as demonstrated on IVUS. The randomized SECRITT I (Santorini Criteria for Investigating and Treating Thin Capped Fibroatheroma Trial) is currently evaluating the safety and feasibility of stenting a vulnerable plaque with the vProtect® Luminal Shield compared with a medically treated, nonstented (control) group.[191]

6.627.9. Less Successful Medications on DES

Apart from the drugs that have made it on to mainstream workhorse DES in catheterization labs around the world and those which are currently being tested, many have been tried with less than satisfactory results. The following are three such examples:

- Tacrolimus

Tacroliumus (FK506) (Figure 5) is a water-insoluble macrolide immunosuppressant produced by *Streptomyces tsukubaensism*, whose drug formulation (Prograf) is commonly used to prevent allograft rejection after organ transplantation. Its inhibitory effect, which is greatest on smooth muscle cells rather than endothelial cells, is mediated by means of its cytostatic effect, holding cells in their G_0 or resting phase.

In the Janus tacrolimus-eluting stent (Sorin Biomedica Cardio, Saluggia, Italy), the drug is embedded in reservoirs on the outer stent surface that allow release of the drug toward the vessel wall only. The stent also has an integrated thromboresistant carbofilm coating the whole stent surface. The largest assessment of the stent took place in the JUPITER-II trial, which randomized 332 patients to treatment with either the Janus tacrolimus-eluting stent or a carbofilm coated BMS. Despite a low frequency of clinical outcomes, which were nevertheless comparable between groups, angiographic results were disappointing, with no significant differences seen in the mean in-stent late lumen loss (tacrolimus-eluting stent 0.65 ± 0.47 vs. BMS 0.66 ± 0.53 mm).[192]

Further studies of DES-eluting tacrolimus include the evaluation of the MAHOROBA stent (Kaneka, Osaka, Japan), which had a cobalt–chromium stent platform and eluted tacrolimus from a bioabsorbable polymer (poly-DL-lactide-coglycolide). In the 47 patient FIM study, a 4-month in-stent late loss of 0.99 ± 0.46 mm and an IVUS determined in-stent % volume obstruction of $34.8 \pm 15.8\%$ reconfirmed the absence of any clinical advantage with use of this drug.[88,89]

- Pimecrolimus

Although pimecrolimus (Figure 5) is part of the 'Limus' family, it does not block mTOR, and therefore it has limited effects that are mediated through an anti-inflammatory action on endothelial proliferation. The FIM study with 15 patients showed a high rate of angiographic restenosis (61%), mean late loss (1.44 mm), and TLR (53%) at 6 months.[193] Further assessment of this drug took place in the ProLimus trial, which evaluated a cobalt–chromium pimecrolimus-eluting stent with a biodegradable polymer. The study enrolled 61 patients with relatively simple coronary lesions and had a MACE rate of 18% at 6 months, which actually achieved the study's primary endpoint of a 6-month MACE rate below 20%. Nevertheless, the late loss was 1.11 ± 0.65 mm, the rate of binary restenosis was 32.7% and the rate of TLR was 32.8%, thereby demonstrating an overall inferior antirestenotic effect of the pimecrolimus stent, compared to results from other established DESs.[194]

Pimecrolimus has also been combined with other antiproliferative agents with the hope that a synergistic effect would ultimately improve its overall neointimal inhibitory effect. The GENESIS trial randomized 246 patients to treatment with the PES CoStar stent ($n = 49$, Conor Medsystems, Menlo Park, CA); the SymBio stent, which eluted a combination of pimecrolimus and paclitaxel ($n = 97$); and the pimecrolimus-eluting Corio stent ($n = 100$).[195] The trial was prematurely suspended with the in-stent late lumen loss being significantly lower with the CoStar compared to either the SymBio or Corio stent (PES 0.58 ± 0.58 mm vs. PES/pimecrolimus 0.96 ± 0.73 mm and PES 0.58 ± 0.58 mm vs. pimecrolimus 1.40 ± 0.67 mm, $p < 0.001$ for both comparisons).

These results were consistent with other studies of the pimecrolimus-eluting stent, and thus are more reflective of the lack of efficacy of pimecrolimus rather than a lack of benefit in the use of dual DESs. Of note, the benefit of dual drug elution has been suggested by results of the ISAR-TEST 3 study, which demonstrated comparable clinical outcomes and a durable antirestenotic efficacy out to 2 years with a polymer-free stent eluting a combination of sirolimus and the antioxidant probucol, when compared to SES and E-ZES.[166,168]

- Estradiols

Experimental studies have suggested that estradiols can improve vascular healing, reduce smooth muscle cell migration and proliferation, and promote local angiogenesis.[196–198] In addition, animal data have indicated that local delivery of estradiol can inhibit neointimal hyperplasia, and also promote endothelial repair and recovery.[199–202]

The feasibility of using 17-β-estradiol to inhibit restenosis in humans was first assessed in the EASTER study, which enrolled 30 patients who received a 17-β-estradiol BiodivYsio (Biocompatibles Ltd., London, UK) stent in a *de novo* coronary lesion. Similar to the preclinical data, results were encouraging with a 6-month in-stent and in-segment late loss of 0.57 and 0.32 mm, respectively, and only one repeat revascularization.[203]

These promising results were further assessed in the ETHOS I study, which randomized 95 patients to treatment with a BMS ($n = 32$), a moderate-release estradiol-eluting stent ($n = 31$), or a slow-release estradiol-eluting stent ($n = 32$).[204] Despite good tolerability of the stent, the study disappointingly demonstrated no advantage from the use of the oestradiol stent over the BMS at 6-month follow-up. In particular, there were no significant differences between the three groups in the intravascular endpoints of neointimal hyperplasia volume, volumetric plaque burden, and in-stent volume obstruction; the angiographic endpoints of in-stent binary restenosis and in-stent late loss; and the clinical endpoints of TLR and MACE.

This lack of benefit from using a 17-β-estradiol-coated stent has been subsequently confirmed in two additional randomized trials.[205,206] Airoldi *et al.* randomized 108 patients to treatment with an estrodiol-eluting stent ($n = 54$) or a phosphorylcholine-coated stent ($n = 54$) and observed no between stent differences with respect to angiographic or clinical outcomes at 1-year follow-up.[206] In the ISAR-PEACE study, which is the largest evaluation of 17-β-estradiol-eluting stents, 508 patients with *de novo* lesions were randomized to treatment with a polymer-free estradiol plus rapamycin stent or a polymer-free rapamycin stent alone.[205] Angiographic follow-up at 6–8 months and clinical follow-up at 12 months failed to demonstrate any advantage with the addition of estradiol to a rapamycin-eluting stent.

6.627.10. Conclusions

Coronary stents have undisputedly revolutionized the treatment of patients with CAD; however, an element of concern remains regarding their long-term safety. In an effort to address some of these concerns, second generation DESs were developed and they have already demonstrated an overall improvement in the outcomes seen with the first generation DESs. Currently, a vast number of new stent designs are being evaluated and only time will tell if these newer stents will lead to further meaningful improvements in clinical outcomes and safety. A step further from stent implantation is the concept of restoring normal vascular function through the use of devices which completely biodegrade. This exciting new concept of completely biodegradable implants is explored in the next chapter.

References

1. Gruntzig, A. *Lancet* **1978**, *1*, 263.
2. Serruys, P. W.; Morice, M. C.; Kappetein, A. P.; *et al*. *N. Engl. J. Med*. **2009**, *360*, 961–972.
3. De Feyter, P. J.; De Jaegere, P. P.; Serruys, P. W. *Am. Heart J*. **1994**, *127*, 643–651.
4. Gruntzig, A. R.; Senning, A.; Siegenthaler, W. E. *N. Engl. J. Med*. **1979**, *301*, 61–68.
5. Sigwart, U.; Urban, P.; Golf, S.; *et al*. *Circulation* **1988**, *78*, 1121–1127.
6. Dotter, C. T.; Judkins, M. P. *Radiology* **1989**, *172*, 904–920.
7. Sigwart, U.; Puel, J.; Mirkovitch, V.; Joffre, F.; Kappenberger, L. *N. Engl. J. Med*. **1987**, *316*, 701–706.
8. Serruys, P. W.; Strauss, B. H.; Beatt, K. J.; *et al*. *N. Engl. J. Med*. **1991**, *324*, 13–17.
9. Van Domburg, R. T.; Foley, D. P.; De Jaegere, P. P.; *et al*. *Heart* **1999**, *82*(Suppl. 2), II27–II34.
10. Serruys, P. W.; De Jaegere, P.; Kiemeneij, F.; *et al*. *N. Engl. J. Med*. **1994**, *331*, 489–495.
11. Fischman, D. L.; Leon, M. B.; Baim, D. S.; *et al*. *N. Engl. J. Med*. **1994**, *331*, 496–501.
12. Colombo, A.; Hall, P.; Nakamura, S.; *et al*. *Circulation* **1995**, *91*, 1676–1688.
13. Barragan, P.; Sainsous, J.; Silvestri, M.; *et al*. *Cathet. Cardiovasc. Diagn*. **1994**, *32*, 133–138.
14. Cutlip, D. E.; Leon, M. B.; Ho, K. K.; *et al*. *J. Am. Coll. Cardiol*. **1999**, *34*, 698–706.
15. Schomig, A.; Neumann, F. J.; Kastrati, A.; *et al*. *N. Engl. J. Med*. **1996**, *334*, 1084–1089.
16. Gordon, P. C.; Gibson, C. M.; Cohen, D. J.; Carrozza, J. P.; Kuntz, R. E.; Baim, D. S. *J. Am. Coll. Cardiol*. **1993**, *21*, 1166–1174.
17. Hoffmann, R.; Mintz, G. S.; Dussaillant, G. R.; *et al*. *Circulation* **1996**, *94*, 1247–1254.
18. Karas, S. P.; Gravanis, M. B.; Santoian, E. C.; Robinson, K. A.; Anderberg, K. A.; King, S. B., III. *J. Am. Coll. Cardiol*. **1992**, *20*, 467–474.
19. Leon, M. B.; Teirstein, P. S.; Moses, J. W.; *et al*. *N. Engl. J. Med*. **2001**, *344*, 250–256.
20. Teirstein, P. S.; Massullo, V.; Jani, S.; *et al*. *N. Engl. J. Med*. **1997**, *336*, 1697–1703.
21. Waksman, R.; Cheneau, E.; Ajani, A. E.; *et al*. *Circulation* **2003**, *107*, 1744–1749.
22. Waksman, R.; White, R. L.; Chan, R. C.; *et al*. *Circulation* **2000**, *101*, 2165–2171.
23. Leon Mb, T. P.; Moses, J. W. *Circulation* **2004**, *110*, 405.
24. Lefkovits, J.; Topol, E. J. *Prog. Cardiovasc. Dis*. **1997**, *40*, 141–158.
25. Camenzind, E.; Bakker, W. H.; Reijs, A.; *et al*. *Circulation* **1997**, *96*, 154–165.
26. Kutryk, M. J.; Foley, D. P.; Van Den Brand, M.; *et al*. *J. Am. Coll. Cardiol*. **2002**, *39*, 281–287.
27. Rensing, B. J.; Vos, J.; Smits, P. C.; *et al*. *Eur. Heart J*. **2001**, *22*, 2125–2130.
28. Sousa, J. E.; Costa, M. A.; Abizaid, A.; *et al*. *Circulation* **2001**, *103*, 192–195.
29. Sousa, J. E.; Costa, M. A.; Abizaid, A. C.; *et al*. *Circulation* **2001**, *104*, 2007–2011.
30. Morice, M. C.; Serruys, P. W.; Sousa, J. E.; *et al*. *N. Engl. J. Med*. **2002**, *346*, 1773–1780.
31. Moses, J. W.; Leon, M. B.; Popma, J. J.; *et al*. *N. Engl. J. Med*. **2003**, *349*, 1315–1323.
32. Weisz, G.; Leon, M. B.; Holmes, D. R., Jr.; *et al*. *J. Am. Coll. Cardiol*. **2006**, *47*, 1350–1355.
33. Weisz, G.; Leon, M. B.; Holmes, D. R., Jr.; *et al*. *J. Am. Coll. Cardiol*. **2009**, *53*, 1488–1497.
34. Baumgart, D.; Klauss, V.; Baer, F.; *et al*. *J. Am. Coll. Cardiol*. **2007**, *50*, 1627–1634.
35. Sabate, M.; Jimenez-Quevedo, P.; Angiolillo, D. J.; *et al*. *Circulation* **2005**, *112*, 2175–2183.
36. Spaulding, C.; Henry, P.; Teiger, E.; *et al*. *N. Engl. J. Med*. **2006**, *355*, 1093–1104.
37. Valgimigli, M.; Campo, G.; Percoco, G.; *et al*. *JAMA* **2008**, *299*, 1788–1799.
38. Rahel, B. M.; Laarman, G. J.; Kelder, J. C.; Ten Berg, J. M.; Suttorp, M. J. *Am. Heart J*. **2009**, *157*, 149–155.
39. Suttorp, M. J.; Laarman, G. J.; Rahel, B. M.; *et al*. *Circulation* **2006**, *114*, 921–928.
40. Vermeersch, P.; Agostoni, P.; Verheye, S.; *et al*. *J. Am. Coll. Cardiol*. **2006**, *48*, 2423–2431.

41. Vermeersch, P.; Agostoni, P.; Verheye, S.; *et al*. *J. Am. Coll. Cardiol*. **2007**, *50*, 261–267.
42. Ardissino, D.; Cavallini, C.; Bramucci, E.; *et al*. *JAMA* **2004**, *292*, 2727–2734.
43. Menozzi, A.; Solinas, E.; Ortolani, P.; *et al*. *Eur. Heart J*. **2009**, *30*, 2095–2101.
44. Kelbaek, H.; Klovgaard, L.; Helqvist, S.; *et al*. *J. Am. Coll. Cardiol*. **2008**, *51*, 2011–2016.
45. Kelbaek, H.; Thuesen, L.; Helqvist, S.; *et al*. *J. Am. Coll. Cardiol*. **2006**, *47*, 449–455.
46. Kastrati, A.; Mehilli, J.; Pache, J.; *et al*. *N. Engl. J. Med*. **2007**, *356*, 1030–1039.
47. Mauri, L.; Hsieh, W. H.; Massaro, J. M.; Ho, K. K.; D'agostino, R.; Cutlip, D. E. *N. Engl. J. Med*. **2007**, *356*, 1020–1029.
48. Spaulding, C.; Daemen, J.; Boersma, E.; Cutlip, D. E.; Serruys, P. W. *N. Engl. J. Med*. **2007**, *356*, 989–997.
49. Stettler, C.; Wandel, S.; Allemann, S.; *et al*. *Lancet* **2007**, *370*, 937–948.
50. Stone, G. W.; Moses, J. W.; Ellis, S. G.; *et al*. *N. Engl. J. Med*. **2007**, *356*, 998–1008.
51. Daemen, J.; Kukreja, N.; Van Twisk, P. H.; *et al*. *Am. J. Cardiol*. **2008**, *101*, 1105–1111.
52. Lemos, P. A.; Serruys, P. W.; Van Domburg, R. T.; *et al*. *Circulation* **2004**, *109*, 190–195.
53. Serruys, P. W.; Daemen, J.; Morice, M. C.; *et al*. *EuroIntervention* **2008**, *3*, 450–459.
54. Serruys, P. W.; Ong, A. T. L.; Morice, M.-C.; *et al*. *EuroIntervention* **2005**, *1*, 147–156.
55. Serruys, P. W.; Onuma, Y.; Garg, S.; *et al*. *J. Am. Coll. Cardiol*. **2010**, *55*, 1093–1101.
56. Sollott, S. J.; Cheng, L.; Pauly, R. R.; *et al*. *J. Clin. Invest*. **1995**, *95*, 1869–1876.
57. Baim, D. S., Ed. In *Grossman's Cardiac Catheterisation, Angiography, and Intervention*; Lippincott Williams & Wilkins: Philadelphia, PA, 2006.
58. Grube, E.; Silber, S.; Hauptmann, K. E.; *et al*. *Circulation* **2003**, *107*, 38–42.
59. Colombo, A.; Drzewiecki, J.; Banning, A.; *et al*. *Circulation* **2003**, *108*, 788–794.
60. Silber, S.; Colombo, A.; Banning, A. P.; *et al*. *Circulation* **2009**, *120*, 1498–1504.
61. Tanabe, K.; Serruys, P. W.; Grube, E.; *et al*. *Circulation* **2003**, *107*, 559–564.
62. Ellis, S. G.; Stone, G. W.; Cox, D. A.; *et al*. *J. Am. Coll. Cardiol. Interv*. **2009**, *2*, 1248–1259.
63. Stone, G. W.; Ellis, S. G.; Cox, D. A.; *et al*. *N. Engl. J. Med*. **2004**, *350*, 221–231.
64. Ellis, S. G.; Cannon, L.; Mann, T.; *et al*. *Am. J. Cardiol*. **2009**, *104*, 135D; Abstract presentation at Transcatheter Cardiovascular Therapeutics, San Francisco, Sept 22, 2009.
65. Stone, G. W.; Ellis, S. G.; Cannon, L.; *et al*. *JAMA* **2005**, *294*, 1215–1223.
66. Dawkins, K. D.; Grube, E.; Guagliumi, G.; *et al*. *Circulation* **2005**, *112*, 3306–3313.
67. Grube, E.; Dawkins, K.; Guagliumi, G.; *et al*. *EuroIntervention* **2009**, *4*, 572–577.
68. Daemen, J.; Keiichi, T.; Kristensen, S. D.; *et al*. *EuroIntervention* **2006**, *2*, 330–337.
69. Ong, A. T.; Serruys, P. W.; Aoki, J.; *et al*. *J. Am. Coll. Cardiol*. **2005**, *45*, 1135–1141.
70. Turco, M. A.; Ormiston, J. A.; Popma, J. J.; *et al*. *J. Am. Coll. Cardiol*. **2007**, *49*, 1676–1683.
71. Turco, M. A. *Am. J. Cardiol*. **2009**, *104*, 141D –141D.
72. Turco, M. A.; Ormiston, J. A.; Popma, J. J.; *et al*. *JACC Cardiovasc. Interv*. **2008**, *1*, 699–709.
73. Douglas, P. S.; Brennan, J. M.; Anstrom, K. J.; *et al*. *J. Am. Coll. Cardiol*. **2009**, *53*, 1629–1641.
74. Kirtane, A. J.; Gupta, A.; Iyengar, S.; *et al*. *Circulation* **2009**, *119*, 3198–3206.
75. Castagna, M. T.; Mintz, G. S.; Leiboff, B. O.; *et al*. *Am. Heart J*. **2001**, *142*, 970–974.
76. Takebayashi, H.; Kobayashi, Y.; Mintz, G. S.; *et al*. *Am. J. Cardiol*. **2005**, *95*, 498–502.
77. Holmes, D. R.; Kereiakes, D.; Garg, S.; *et al*. *J. Am. Coll. Cardiol*. **2010**, *56*, 1357–1365.
78. Serruys, P. W.; Daemen, J. *Circulation* **2007**, *115*, 1433–1439; discussion 1439.
79. Cutlip, D. E.; Windecker, S.; Mehran, R.; *et al*. *Circulation* **2007**, *115*, 2344–2351.
80. Daemen, J.; Spaulding, C.; Jacob, S.; Boersma, E.; Varenne, O.; Serruys, P. *EuroIntervention* **2007**, *3*, 392–399.
81. Iakovou, I.; Schmidt, T.; Bonizzoni, E.; *et al*. *JAMA* **2005**, *293*, 2126–2130.
82. Kuchulakanti, P. K.; Chu, W. W.; Torguson, R.; *et al*. *Circulation* **2006**, *113*, 1108–1113.
83. Park, D. W.; Park, S. W.; Park, K. H.; *et al*. *Am. J. Cardiol*. **2006**, *98*, 352–356.
84. Urban, P.; Gershlick, A. H.; Guagliumi, G.; *et al*. *Circulation* **2006**, *113*, 1434–1441.
85. Van Werkum, J. W.; Heestermans, A. A.; Zomer, A. C.; *et al*. *J. Am. Coll. Cardiol*. **2009**, *53*, 1399–1409.
86. Daemen, J.; Wenaweser, P.; Tsuchida, K.; *et al*. *Lancet* **2007**, *369*, 667–678.
87. James, S. K.; Wallentin, L.; Lagerqvist, B. *EuroIntervention* **2009**, *5*, 501–504.
88. Onuma, Y. Incidence of late stent thrombosis up to 5 years after implantation of drug eluting stents in clinical practice. Presentation at European Society of Cardiology Meeting, Barcelona, Aug 31, 2009.
89. Onuma, Y.; Serruys, P.; Den Heijer, P.; *et al*. *Eur. Heart J*. **2009**, *30*, 1477–1485.
90. Pinto Slottow, T. L.; Steinberg, D. H.; Roy, P. K.; *et al*. *Am. J. Cardiol*. **2008**, *102*, 298–303.
91. Wenaweser, P.; Daemen, J.; Zwahlen, M.; *et al*. *J. Am. Coll. Cardiol*. **2008**, *52*, 1134–1140.
92. Brodie, B. R.; Stuckey, T.; Downey, W.; *et al*. *JACC Cardiovasc. Interv*. **2008**, *1*, 405–414.
93. Lasala, J. M.; Cox, D. A.; Lewis, S. J.; *et al*. *EuroIntervention* **2009**, *5*, 67–77.
94. Lasala, J. M.; Cox, D. A.; Dobies, D.; *et al*. *Circ. Cardiovasc. Interv*. **2009**, *2*, 285–293.
95. Lee, C. W.; Kang, S. J.; Park, D. W.; *et al*. *J. Am. Coll. Cardiol*. **2010**, *55*, 1936–1942.
96. Kastrati, A.; Mehilli, J.; Dirschinger, J.; *et al*. *Circulation* **2001**, *103*, 2816–2821.
97. Pache, J.; Kastrati, A.; Mehilli, J.; *et al*. *J. Am. Coll. Cardiol*. **2003**, *41*, 1283–1288.
98. Awata, M.; Nanto, S.; Uematsu, M.; *et al*. *J. Am. Coll. Cardiol*. **2008**, *52*, 789–790.
99. Joner, M.; Nakazawa, G.; Finn, A. V.; *et al*. *J. Am. Coll. Cardiol*. **2008**, *52*, 333–342.
100. Kim, J.-S.; Jang, I.-K.; Fan, C.; *et al*. *JACC Cardiovasc. Interv*. **2009**, *2*, 1240–1247.
101. Kim, J. W.; Seo, H. S.; Park, J. H.; *et al*. *J. Am. Coll. Cardiol*. **2009**, *53*, 1653–1659.
102. Meredith, I. T.; Ormiston, J.; Whitbourn, R.; *et al*. *EuroIntervention* **2005**, *1*, 157–164.
103. Meredith, I. T.; Ormiston, J.; Whitbourn, R.; Kay, I. P.; Muller, D.; Cutlip, D. E. *Catheter. Cardiovasc. Interv*. **2009**, *74*, 989–995.
104. Meredith, I. T.; Worthley, S.; Whitbourn, R.; *et al*. *EuroIntervention* **2007**, *3*, 50–53.
105. Meredith, I. *Am. J. Cardiol*. **2009**, *104*, 153D–154D.
106. Meredith, I.; Worthley, S.; Whitbourn, R.; *et al*. *EuroIntervention* **2010**, *5*, 692–697.
107. Meredith, I. T.; Worthley, S.; Whitbourn, R.; *et al*. *JACC Cardiovasc. Interv*. **2009**, *2*, 977–985.
108. Costa, R. A.; Lansky, A. J.; Mintz, G. S.; *et al*. *Am. J. Cardiol*. **2005**, *95*, 113–116.
109. Grube, E.; Sonoda, S.; Ikeno, F.; *et al*. *Circulation* **2004**, *109*, 2168–2171.
110. Tsuchiya, Y.; Lansky, A. J.; Costa, R. A.; *et al*. *Am. J. Cardiol*. **2006**, *98*, 464–469.
111. Fajadet, J.; Wijns, W.; Laarman, G. J.; *et al*. *Circulation* **2006**, *114*, 798–806.
112. Fajadet, J.; Wijns, W.; Laarman, G. J.; *et al*. *EuroIntervention* **2010**, *6*(5), 562–567.
113. Serruys, P. W.; Ong, A. T.; Piek, J. J.; *et al*. *EuroIntervention* **2005**, *1*, 58–65.
114. Wiemer, M.; Serruys, P. W.; Miquel-Hebert, K.; *et al*. *Catheter. Cardiovasc. Interv*. **2010**, *75*, 997–1003.
115. Kandzari, D.; Mauri, L.; Popma, J.; *et al*. ENDEAVOR III: 5 year final outcomes, Presentation at the American College of Cardiology Scientific Sessions, Atlanta, GA, Mar 14–16, 2010.
116. Kandzari, D. E.; Leon, M. B.; Popma, J. J.; *et al*. *J. Am. Coll. Cardiol*. **2006**, *48*, 2440–2447.
117. Rasmussen, K.; Maeng, M.; Kaltoft, A.; *et al*. *Lancet* **2010**, *375*, 1090–1099.
118. Leon, M. B.; Mauri, L.; Popma, J. J.; *et al*. *J. Am. Coll. Cardiol*. **2010**, *55*, 543–554.
119. Leon, M. B.; Nikolsky, E.; Cutlip, D. E.; *et al*. *JACC Cardiovasc. Interv*. **2010**, *3*(10), 1043–1050.
120. Camenzind, E.; Wijns, W.; Mauri, L.; *et al*. *Am. Heart J*. **2009**, *158*(902–909), e5.
121. Claessen, B. E.; Beijk, M. A.; Legrand, V.; *et al*. *Circ. Cardiovasc. Interv*. **2009**, *2*, 339–347.
122. Garg, S.; Serruys, P. W.; Onuma, Y.; *et al*. *J. Am. Coll. Cardiol. Interv*. **2009**, *2*, 1190–1198.
123. Garg, S.; Surruys, P. W.; Miquel-Hebert, K.; on behalf of the SPIRIT 11 Investigators. *Catheter Cardiovasc. Interv*. **2010**.
124. Ruygrok, P.; Desaga, M.; Van Den Branden, F.; *et al*. *EuroIntervention* **2007**, *3*, 315–320.
125. Serruys, P. W.; Ruygrok, P.; Neuzner, J.; *et al*. *EuroIntervention* **2006**, *2*, 286–294.
126. Kedhi, E.; Joesoef, K. S.; Mcfadden, E.; *et al*. *Lancet* **2010**, *375*, 201–209.

127. Stone, G. W.; Midei, M.; Newman, W.; *et al*. *JAMA* **2008**, *299*, 1903–1913.
128. Stone, G. W. The XIENCE V – PROMUS everolimus-eluting stent: Comprehensive update of the clinical trial program. Presentation at Transcatheter Cardiovascular Therapeutics, Sept 21, 2009. Available online www.tctmd.com/txshow.aspx?tid=939082&id=84006&trid=938634 (accessed Oct 28, 2009).
129. Stone, G. W.; Rizvi, A.; Newman, W.; *et al*. *N. Engl. J. Med*. **2010**, *362*, 1663–1674.
130. Serruys, P. W.; Silber, S.; Garg, S.; *et al*. *N. Engl. J. Med*. **2010**, *363*, 123–135.
131. Hamm, C. 5 years later and more than 20,000 patients studied: The ENDEAVOR clinical programme. Presentation at EuroPCR, Barcelona, May 19–22, 2009. Available online www.europcronline.com/fo/lecture/view_slide.php?idCongres=5&id=7617 (accessed Jun 20, 2009).
132. Finn, A. V.; Kolodgie, F. D.; Harnek, J.; *et al*. *Circulation* **2005**, *112*, 270–278.
133. Finn, A. V.; Nakazawa, G.; Joner, M.; *et al*. *Arterioscler. Thromb. Vasc. Biol*. **2007**, *27*, 1500–1510.
134. Garg, S.; Serruys, P. W. *Expert Rev. Cardiovasc. Ther*. **2010**, *8*, 449–470.
135. Wilson, G. J.; Nakazawa, G.; Schwartz, R. S.; *et al*. *Circulation* **2009**, *120*(141–9), 1–2.
136. Waksman, R.; Pakala, R. *EuroIntervention* **2009**, *5*, F36–F42.
137. De Jong, W. H.; Eelco Bergsma, J.; Robinson, J. E.; Bos, R. R. *Biomaterials* **2005**, *26*, 1781–1791.
138. Grube, E.; Hauptmann, K.-E.; Buellesfeld, L.; Lim, V.; Abizaid, A. *EuroIntervention* **2005**, *1*, 53–57.
139. Esteves, V.; Abizaid, A.; Costa, R.; *et al*. *EuroIntervention* **2010**, *6*(Suppl. H), H28.
140. Windecker, S.; Serruys, P. W.; Wandel, S.; *et al*. *Lancet* **2008**, *372*, 1163–1173.
141. Garg, S.; Sarno, G.; Serruys, P. W.; *et al*. *EuroIntervention* **2010**, *6*, 233–239.
142. Klauss, V. LEADERS: Two-year follow-up from a prospective randomized trial of biolimus A9-eluting stents with a bioabsorbable polymer vs. sirolimus-eluting stents with a durable polymer. Presentation at Transcatheter Cardiovascular Therapeutics, San Francisco, Sept 22, 2009.
143. Barlis, P.; Regar, E.; Serruys, P. W.; *et al*. *Eur. Heart J*. **2010**, *31*, 165–176.
144. Ostojic, M.; Sagic, D.; Beleslin, B.; *et al*. *EuroIntervention* **2008**, *3*, 574–579.
145. Chevalier, B.; Silber, S.; Park, S.-J.; *et al*. *Circ. Cardiovasc. Interv*. **2009**, *2*, 188–195.
146. Chevalier, B. The NOBORI biolimus-eluting stent: Comprehensive update of the clinical trial program. Presentation at Transcatheter Cardiovascular Therapeutics, San Francisco, Sept 21, 2009. Available online www.tctmd.com/txshow.aspx?tid=939082&id=84010&trid=938634 (accessed Nov 29, 2009).
147. Dawkins, K. D.; Verheye, S.; Schuhlen, H.; *et al*. *EuroIntervention* **2007**, *3*, 82–88.
148. Kaul, U.; Gupta, R. K.; Mathur, A.; *et al*. *Indian Heart J*. **2007**, *59*, 165–172.
149. Serruys, P. W.; Sianos, G.; Abizaid, A.; *et al*. *J. Am. Coll. Cardiol*. **2005**, *46*, 253–260.
150. Krucoff, M. W.; Kereiakes, D. J.; Petersen, J. L.; *et al*. *J. Am. Coll. Cardiol*. **2008**, *51*, 1543–1552.
151. Abizaid, A. The NEVO RES Elution I study: A randomised multicenter comparison of the NEVO reservoir-based Sirolimus eluting-stent with the TAXUS Liberte Paclitaxel-eluting stent: First presentation of the 12-month outcomes. Presentation at EuroPCR, Paris, France, May 25–28, 2010. Available online http://www.pcronline.com/Lectures/2010/The-NEVO-RES-Elution-I-study-a-randomised-multicentre-comparison-of-the-NEVO-reservoir-based-Sirolimus-eluting-stent-with-the-TAXUS-Liberte-Paclitaxel-eluting-stent-first-presentation-of-12-month-outcomes (accessed May 29, 2010).
152. Grube, E.; Schofer, J.; Hauptmann, K. E.; *et al*. *JACC Cardiovasc. Interv*. **2010**, *3*, 431–438.
153. Dawkins, K. D. The Element stent technology. Presentation at EuroPCR, May 25–28, 2010. Available online www.pcronline.com/Lectures/2010/The-ELEMENT-stent-technology (accessed May 29, 2010).
154. Tada, N.; Virmani, R.; Grant, G.; *et al*. *Circ. Cardiovasc. Interv*. **2010**, *3*, 174–183.
155. Grube, E. BioFreedom first in man progress report. Presentation at Transcatheter Cardiovascular Therapeutics, San Francisco, Sept 24, 2009. Available online www.tctmd.com/txshow.aspx?tid=941378&id=84088&trid=938634 (accessed Nov 10, 2009).
156. Van Der Giessen, W. J.; Sorop, O.; Serruys, P. W.; Peters-Krabbendam, I.; Van Beusekom, H. M. M. *JACC Cardiovasc. Interv*. **2009**, *2*, 284–290.
157. Costa, J. R., Jr.; Abizaid, A.; Costa, R.; *et al*. *J. Am. Coll. Cardiol. Interv*. **2009**, *2*, 422–427.
158. Abizaid, A. The MIV VESTASYNC polymer-free sirolimus-eluting stent program (micorporous hydroxyapatite surface). Presentation at Transcatheter Cardiovascular Therapeutics, San Francisco, Sept 21, 2009. Available online http://www.tctmd.com/txshow.aspx?tid=939088&id=84036&trid=938634 (accessed Oct 10, 2009).
159. Wessely, R.; Hausleiter, J.; Michaelis, C.; *et al*. *Arterioscler. Thromb. Vasc. Biol*. **2005**, *25*, 748–753.
160. Hausleiter, J.; Kastrati, A.; Wessely, R.; *et al*. *Eur. Heart J*. **2005**, *26*, 1475–1481.
161. Dibra, A.; Kastrati, A.; Mehilli, J.; *et al*. *Catheter. Cardiovasc. Interv*. **2005**, *65*, 374–380.
162. Moore, P.; Barlis, P.; Spiro, J.; *et al*. *JACC Cardiovasc. Interv*. **2009**, *2*, 437–444.
163. Mehilli, J.; Kastrati, A.; Wessely, R.; *et al*. *Circulation* **2006**, *113*, 273–279.
164. Ruef, J.; Storger, H.; Schwarz, F.; Haase, J. *Catheter. Cardiovasc. Interv*. **2008**, *71*, 333–339.
165. Byrne, R. A.; Iijima, R.; Mehilli, J.; *et al*. *JACC Cardiovasc. Interv*. **2009**, *2*, 291–299.
166. Byrne, R. A.; Kastrati, A.; Tiroch, K.; *et al*. *J. Am. Coll. Cardiol*. **2010**, *55*, 2536–2543.
167. Byrne, R. A.; Kufner, S.; Tiroch, K.; *et al*. *Heart* **2009**, *95*, 1489–1494.
168. Byrne, R. A.; Mehilli, J.; Iijima, R.; *et al*. *Eur. Heart J*. **2009**, *30*, 923–931.
169. Mehilli, J.; Byrne, R. A.; Wieczorek, A.; *et al*. *Eur. Heart J*. **2008**, *29*, 1975–1982.
170. Aoki, J.; Abizaid, A. C.; Ong, A. T.; Tsuchida, K.; Serruys, P. W. *EuroIntervention* **2005**, *1*, 235–255.
171. Raber, L. SIRTAX-LATE: Five-year clinical and angiographic follow-up from a prospective randomized trial of sirolimus-eluting and paclitaxel-eluting stents. Presentation Transcatheter Cardiovascular Therapeutics, San Francisco, Sept 22, 2009.
172. Kereiakes, D.; Cannon, L. A.; Feldman, R.; *et al*. TAXUS PERSEUS – A novel platinum chromium, thin-strut TAXUS Element stent for the treatment of de novo coronary stenoses. Presentation at i2summit, ACC, Atlanta, GA, Mar 15, 2010.
173. Kereiakes, D. J.; Cannon, L. A.; Feldman, R. L.; *et al*. *J. Am. Coll. Cardiol*. **2010**, *56*, 264–271.
174. Hirayama, A.; Kodama, K.; Adachi, T.; *et al*. *Catheter. Cardiovasc. Interv*. **2000**, *49*, 401–407.
175. Joner, M.; Nakazawa, G.; Bonsignore, C.; *et al*. *EuroIntervention* **2010**, *5*, 737–744.
176. Konig, A.; Schiele, T. M.; Rieber, J.; Theisen, K.; Mudra, H.; Klauss, V. *Catheter. Cardiovasc. Interv*. **2002**, *56*, 478–486.
177. Abizaid, A. CardioMind stent. Presentation at Transcatheter Cardiovascular Therapeutics, San Francisco, Sept 24, 2009. Available online www.tctmd.com/txshow.aspx?tid=939038&id=81898&trid=938634 (accessed Jan 26, 2010).
178. Chamie, D.; Costa, J. R., Jr.; Abizaid, A.; *et al*. *JACC Cardiovasc. Interv*. **2010**, *3*, 191–202.
179. Botelho, R. The CARDIOMIND Sparrow DES program (CARE II): A bioabsorbable polymer sirolimus-eluting 'micro-stent'. Presentation at Transcatheter Cardiovascular Therapeutics, San Francisco, Sept 21, 2009. Available online http:www.tctmd.com/txshow.aspx?tid=939086&id=84612&trid=938634 (accessed Oct 16, 2009).
180. Kaneda, H.; Ikeno, F.; Lyons, J.; Rezaee, M.; Yeung, A. C.; Fitzgerald, P. J. *Cardiovasc. Intervent. Radiol*. **2006**, *29*, 413–419.
181. Tanaka, N.; Martin, J. B.; Tokunaga, K.; *et al*. *AJNR Am. J. Neuroradiol*. **2004**, *25*, 604–607.
182. Verheye, S.; Agostoni, P.; Dubois, C. L.; *et al*. *J. Am. Coll. Cardiol*. **2009**, *53*, 1031–1039.
183. Verhey, S. The Stentys self-expanding stent: Design specification and clinical trial results. Presentation at Transcatheter Cardiovascular Therapeutics, Sept 21, 2009. Available online www.tctmd.com/txshow.aspx?tid=938900&id=83230&trid=938634.
184. Verheye, S.; Grube, E.; Ramcharitar, S.; *et al*. *EuroIntervention* **2009**, *4*, 566–571.
185. Doi, H.; Maehara, A.; Mintz, G. S.; Dani, L.; Leon, M. B.; Grube, E. *Am. J. Cardiol*. **2009**, *104*, 1216–1221.
186. Hauptman, K. Bifurcation management using Cappella technology. Presentation at EuroPCR, Paris, France, May 25–28, 2010. Available online www.pcronline.com/index.php/Lectures/2010/Bifurcation-management-using-Cappella-technology (accessed May 30, 2010).
187. Virmani, R.; Kolodgie, F. D.; Burke, A. P.; Farb, A.; Schwartz, S. M. *Arterioscler. Thromb. Vasc. Biol*. **2000**, *20*, 1262–1275.
188. Farb, A.; Burke, A. P.; Kolodgie, F. D.; Virmani, R. *Circulation* **2003**, *108*, 1701–1706.
189. Joner, M.; Finn, A. V.; Farb, A.; *et al*. *J. Am. Coll. Cardiol*. **2006**, *48*, 193–202.
190. Granada, J. F.; Pomeranz, M.; Heringes, J.; Odess, I. *EuroIntervention* **2007**, *3*, 416–419.
191. Ramcharitar, S.; Gonzalo, N.; Van Geuns, R. J.; *et al*. *Nat. Rev. Cardiol*. **2009**, *6*, 374–378.
192. Morice, M. C.; Bestehorn, H. P.; Carrie, D.; *et al*. *EuroIntervention* **2006**, *2*, 45–52.
193. Ormiston, J. A.; Webster, M. W.; Schwartz, R. S.; *et al*. *JACC Cardiovasc. Interv*. **2009**, *2*, 1017–1024.
194. Verheye, S.; Sarno, G.; Muller, R.; *et al*. *EuroIntervention* **2009**, *5*, 233–238.

195. Verheye, S.; Agostoni, P.; Dawkins, K. D.; *et al*. *JACC Cardiovasc. Interv.* **2009**, *2*, 205–214.
196. Brouchet, L.; Krust, A.; Dupont, S.; Chambon, P.; Bayard, F.; Arnal, J. F. *Circulation* **2001**, *103*, 423–428.
197. Dai-Do, D.; Espinosa, E.; Liu, G.; *et al*. *Cardiovasc. Res.* **1996**, *32*, 980–985.
198. Geraldes, P.; Sirois, M. G.; Bernatchez, P. N.; Tanguay, J. F. *Arterioscler. Thromb. Vasc. Biol*. **2002**, *22*, 1585–1590.
199. Chandrasekar, B.; Nattel, S.; Tanguay, J. F. *J. Am. Coll. Cardiol*. **2001**, *38*, 1570–1576.
200. Chandrasekar, B.; Sirois, M. G.; Geoffroy, P.; Lauzier, D.; Nattel, S.; Tanguay, J. F. *Thromb. Haemost*. **2005**, *94*, 1042–1047.
201. Chandrasekar, B.; Tanguay, J. F. *J. Am. Coll. Cardiol*. **2000**, *36*, 1972–1978.
202. New, G.; Moses, J. W.; Roubin, G. S.; *et al*. *Catheter. Cardiovasc. Interv.* **2002**, *57*, 266–271.
203. Abizaid, A.; Albertal, M.; Costa, M. A.; *et al*. *J. Am. Coll. Cardiol*. **2004**, *43*, 1118–1121.
204. Abizaid, A.; Chaves, A. J.; Leon, M. B.; *et al*. *Catheter. Cardiovasc. Interv.* **2007**, *70*, 654–660.
205. Adriaenssens, T.; Mehilli, J.; Wessely, R.; *et al*. *J. Am. Coll. Cardiol*. **2007**, *49*, 1265–1271.
206. Airoldi, F.; Di Mario, C.; Ribichini, F.; *et al*. *Am. J. Cardiol*. **2005**, *96*, 664–667.

6.628. Vascular Grafts

A A Ucuzian, Loyola University of Chicago, Maywood, IL, USA
H P Greisler, Loyola University of Chicago, Maywood, IL, USA; Edward J. Hines Jr. V.A. Hospital, Hines, IL, USA

© 2011 Elsevier Ltd. All rights reserved.

6.628.1. Introduction 450
6.628.2. Materials Used for Vascular Grafts: Current Clinical Experience 450
6.628.2.1. Autogenous Vein and Artery: The Gold Standard Material 450
6.628.2.1.1. Veins 450
6.628.2.1.2. Arteries 451
6.628.2.2. Synthetic Grafts 451
6.628.2.2.1. Expanded polytetrafluoroethylene 451
6.628.2.2.2. Polyethylene terepthalate 452
6.628.2.2.3. Endovascular surgery 452
6.628.3. Host Responses to Implanted Biomaterials 453
6.628.3.1. Host–Material Interfacial Processes 453
6.628.3.1.1. Protein adsorption 453
6.628.3.1.2. Platelet deposition 453
6.628.3.1.3. Inflammation and immunology 454
6.628.3.1.4. Endothelialization 454
6.628.3.1.5. Mesenchymal cell infiltration 455
6.628.3.1.6. Biomechanics 456
6.628.4. Improving Clinical Outcomes and Future Concepts 456
6.628.4.1. Systemic Pharmacotherapy 456
6.628.4.1.1. Acetylsalicylic acid 456
6.628.4.1.2. Clopidogrel 457
6.628.4.1.3. Statins 457
6.628.4.1.4. Warfarin 457
6.628.4.2. Coating and Surface Modification 457
6.628.4.2.1. Surface passivation 457
6.628.4.2.2. Heparin-bonding 458
6.628.4.2.3. Graft endothelialization 458
6.628.4.2.4. Drug-eluting stents and graft 460
6.628.4.3. Optimization of Biomechanical Biocompatibility 460
6.628.5. Gene Therapy 461
6.628.6. Tissue-Engineered Blood Vessels 461
6.628.6.1. General Concepts 461
6.628.6.2. Hydrogel-Based TEBVs 461
6.628.6.3. Bioresorbable TEBVs 462
6.628.6.4. Self-Assembled TEBVs 464
6.628.6.5. Decellularized Vessel Scaffolds 464
6.628.6.6. Final Remarks 464
References 464

Glossary

Biocompatibility The biologic compatibility of an implanted material to the host, affected by host responses such as protein adsorption, inflammation, biomechanics, endothelialization, and mesenchymal cell infiltration.

Bioresorbable Pertaining to the incorporation of a material into the native host tissue, mediated by host inflammatory, hydrolytic, and phagocytic mechanisms.

Graft endothelialization The process by which an endothelial monolayer covers a prosthetic surface, secondary to anastomotic ingrowth, transmural angiogenesis, and endothelial progenitor cell deposition.

Heparin-bonded grafts Grafts covalently linked to heparin for the purposes of promoting antithrombotic and antiproliferative effects.

Polyurethane Polymer consisting of a chain of organic units joined by urethane (carbamate) links.

Saphenous vein A major vein of the lower extremity which is commonly used as a conduit for peripheral and coronary bypasses.

Tissue-engineered blood vessel An broad conceptual title for any nonautologous vessel created *ex vivo* or induced *in vivo* using a variety of bioengineering and cell biologic techniques.

Abbreviations

ADP	Adenosine diphosphate
ASA	Acetylsalicylic acid
bFGF	Basic fibroblast growth factor
CABG	Coronary artery bypass graft
DLC	Diamond-like carbon
ePTFE	Expanded polytetrafluoroethylene
EC	Endothelial cell
ECM	Extracellular matrix
EPC	Endothelial progenitor cell
GA	Gluteraldehyde
GP	Glycoprotein
HMG-CoA reductase	3-Hydroxy-3-methylglutaryl-coenzyme A reductase
HUV	Human umbilical vein
ICAM	Intercellular adhesion molecule
IL	Interleukin
LIMA	Left internal mammary artery
LTB4	Leukotriene B4
MB-lectin	Mannose-binding lectin
MMP	Matrix metalloprotease
PAF	Platelet-activating factor
PDGF	Platelet-derived growth factor
PDS	Polydiaxonone
PEG	Polyethylene glycol
PEO	Polyethylene oxide
PET	Polyethylene terepthalate
PG910	Polyglactin 910
PGA	Polyglycolide
PGS	Poly(glycerol sebacate)
PLA	Polylactic acid
PLCA	Polycaprolactone
PLGA	Poly(lactic-*co*-glycolic acid)
PU	Polyurethane
SMC	Smooth muscle cell
TEBV	Tissue-engineered blood vessel
TGF-β	Transforming growth factor-β
TNF	Tumor necrosis factor
uPA	Urokinase-type plasminogen activator
VEGF	Vascular endothelial growth factor
vWF	von Willebrand factor

6.628.1. Introduction

Since their first use in 1906 by Goyanes to repair a popliteal arterial aneurysm, native autogenous vessels have served as the gold standard material in the treatment of many vascular diseases. They function as bypass conduits for aneurysmal defects and stenoses in the peripheral or coronary vascular system, as patches for the closure of arteriotomies or as conduits for the creation of arteriovenous fistulae for patients receiving hemodialysis. However, a significant percentage of patients lack suitable autogenous vessels for use in vascular interventions due to intrinsic vascular disease or because they have been used in previous vascular procedures. For these patients, alternative grafts most commonly comprising synthetic polymers are used. While these have generally been suitable for the bypass of larger vessels, their long-term success in bypasses of arteries of smaller caliber (<4 mm) has been limited. For this reason, strategies that utilize the knowledge of vascular cell biology and injury response, protein and molecular biology, and biomaterials and bioengineering sciences have focused on improving the long-term patency of alternatives to autogenous vessels. This chapter begins with a discussion of the clinical efficacy of autogenous vessels in comparison to the most commonly utilized synthetic materials used in vascular procedures, expanded polytetrafluoroethylene (ePTFE), and polyethylene terepthalate (PET). It then discusses the interactions between the host and the material at circulatory, perivascular, and anastomotic interfaces, which generally account for the inferior performance of currently available synthetic grafts. It concludes with a discussion of some of the strategies employed to improve the long-term efficacy of synthetic grafts by modulating host–biomaterial interactions, including a description of methodologies utilized for the construction of tissue-engineered blood vessels (TEBVs).

6.628.2. Materials Used for Vascular Grafts: Current Clinical Experience

6.628.2.1. Autogenous Vein and Artery: The Gold Standard Material

6.628.2.1.1. Veins

Under most circumstances, native vessels provide for the highest rates of long-term primary patency (continuous patency without any interventions such as angioplasty or rebypass of the graft to maintain patency), secondary patency (patency maintained by a thrombectomy of the graft), and limb salvage. Among the options for harvested autogenous vessels, the greater saphenous vein is the most commonly utilized for both peripheral and coronary vascular applications and provides the standard by which the efficacy of all other materials utilized for peripheral vascular procedures are compared (discussed in Section 6.628.2.2.1).[1,2] In addition to the greater saphenous vein, veins of the upper extremity such as the cephalic and basilic veins have also demonstrated superior

results compared with prosthetics when ipsilateral saphenous veins are not present or suitable. In a study of 740 patients receiving distal bypasses with arm vein versus prosthetic graft, the 3-year primary patency rates for arm vein in femoral to below knee popliteal artery bypasses and femoral to tibial bypasses were 73% and 68%, respectively, while patency rates for prosthetic grafts were 55% and 41%, respectively. Similar benefits were seen in overall limb salvage.[3,4]

Cryogenically preserved allogenic human umbilical veins (HUV) supported by an external polyester mesh were introduced by Dardik as a biological alternative for small caliber vascular bypasses. Interestingly, while being associated with increased graft thrombosis and amputation rates compared to ePTFE and saphenous vein within the first 30 postoperative days, HUV conduits have demonstrated superior patency compared with ePTFE at 5 years.[5,6] Notably, superior patency rates with HUV were dependent on the creation of a distal arteriovenous fistula. Because of concerns related to technical difficulties in handling and suturing HUV and fistula creation, and of potential late degeneration and aneurysm formation, HUV has not presented itself as a viable alternative for vascular reconstructions to most vascular surgeons. As a result of FDA guidelines regarding tissue donor eligibility in response to fears of communicable disease transmission, the manufacture of HUV has all but ceased.[7]

6.628.2.1.2. Arteries

Autogenous arterial grafts such as the left internal mammary artery (LIMA), radial artery, and gastroepiploic artery, most commonly used in coronary revascularization, have also demonstrated success compared to prosthetic grafts, with some evidence of superiority even to saphenous vein in coronary bypasses.[8] Early and recent studies have demonstrated the superiority of the internal mammary artery conduit in comparison with saphenous vein for coronary artery bypass, with 10-year patency rates of 85% versus 61%, respectively, and an increased 20-year survival compared to saphenous vein.[9,10] Excellent patency rates similar to those in the early studies have been demonstrated in radial artery conduits in coronary revascularization of roughly 89%, 93%, and 93% at 4, 7, and 10 years.[11] While, speculative, potential explanations for the superior patency rates of arterial grafts in comparison to vein grafts may be attributable to improved platelet resistance and differential vasoactive responses of the endothelium and arterial media to circulatory mechanical stresses, which may contribute toward limiting the intimal hyperplastic response (discussed below).[12,13]

While the patency of arterial conduits in the coronary vasculature is generally superior or noninferior to the saphenous vein, it is important to note that patency rates are dependent on not only the conduit, but also the target vessel, the side of the vasculature, the timeline of follow-up, the vessel hemodynamic and biomechanical characteristics, and patient comorbidities. Improvements in statin therapy, antiplatelet therapy, and medical management over the last two decades may have improved short-term outcomes of saphenous vein grafts, although randomized trials of long-term efficacy of these drug regimens on coronary graft patency are, surprisingly still lacking.[8,14–16] In addition, the use of the radial and gastroepiploic arteries remains somewhat controversial due to the morbidities associated with radial artery harvest and the technical challenges of gastroepiploic artery harvest, unknown long-term complications and cardiac event-free survival rates, and histologic characteristics, which affect their vasoactivity and competition for blood flow. Thus, radial and gastroepiploic arteries remain secondary choices after the availability of LIMA and saphenous vein conduits has been exhausted.[17–19]

6.628.2.2. Synthetic Grafts

Primarily used in bypasses of the arterial vasculature outside of the coronary vascular system, products comprising ePTFE and PET are most commonly used when suitable autogenous vessels are lacking. Their hydrophobic and crystalline structures prevent hydrolytic degradation, making these products relatively durable for use in bypassing vessels of medium to large caliber such as the aorta. However, due to the lack of an endothelium, the absence of histologic and molecular properties, which minimize platelet adherence and regulate cellular phenotypic characterization, as well as their mismatched compliance profiles in comparison to the native vasculature, these materials are prone to thrombosis and intimal hyperplasia. This section discusses the clinical experience associated with these common materials used for vascular grafts.

6.628.2.2.1. Expanded polytetrafluoroethylene

As indicated by its name, ePTFE is a polymer of carbon and fluorine, which comprise nodes of material connected by fibrils. The extruded material undergoes a forcible expansion, which results in a final structure that is microporous in nature, with most clinically used ePTFE grafts having an average internodal distance of 30 μm. ePTFE is relatively resistant to dilatation and can be implanted without preclotting with blood, its electronegative surface providing some benefits as it acts to minimize its interaction with surrounding tissues *in vivo*.[20]

However, ePTFE is far from inert and induces numerous host responses, and its relative stiffness is likely to exacerbate the intimal hyperplastic response. These characteristics are key contributors to its poor longer term results. The inferiority of ePTFE in comparison to native vessel conduits such as the saphenous vein is most pronounced in the bypass of more distal targets. However, while bypass of the femoral artery to the popliteal artery above the knee with ePTFE has demonstrated comparable rates of patency in comparison to saphenous vein within the first year or two, it is apparent that the intermediate to longer term results of these more proximal bypasses are also less successful. In a study of patients receiving bypass grafts predominantly for claudication, the primary 5-year patency of bypasses from the femoral artery to the popliteal artery above the knee utilizing the saphenous vein was 77.2% versus 57.4% for bypasses utilizing ePTFE.[21] Differences in patency rates for the saphenous vein compared with ePTFE in above knee bypasses were significant as early as 3 years post bypass. The patency for vein bypasses to the popliteal artery below the knee was 64.8% at 5 years, demonstrating the diminishing patency rates even for native vessel conduits for bypasses of greater distances, which cross the

knee articulation. In addition to their greater length and the flexion induced by the knee, these longer bypasses are commonly needed in patients with more advanced disease and are anastomosed to smaller diameter and less healthy recipient arteries. Similar trends were seen in patients in this study who received bypasses for critical ischemia of the lower extremity. These results are consistent with data from other meta-analyses, which demonstrate 5-year patency rates for ePTFE bypasses to the popliteal artery above the knee to be as low as 39% versus 73% for saphenous vein.[5] Long-term results of infrapopliteal bypasses (bypasses to the tibial or peroneal artery) with ePTFE are even less successful. In a meta-analysis of 43 studies, pooled estimates for the 5-year primary patency, secondary patency, and limb salvage rates of infrapopliteal bypasses with ePTFE were 30.5%, 39.7%, and 55.7%, respectively.[22]

Alterations in the geometric structure of ePTFE grafts with an interpositioned vein cuff at the site of the anastomosis has been reported to improve graft patency and the intimal hyperplastic response.[23] These results are theoretically attributable to the presence of a venous endothelium at the anastomosis, improved vein compliance, and the creation of a larger anastomosis. The literature provides little clarification on the mechanisms of this effect. Interestingly, animal studies have suggested that alterations of anastomosis hemodynamics may not account for these improved results.[24] While previous evidence in animals had suggested that cuffing grafts with ePTFE did not improve graft patency, early results of clinical trials of precuffed ePTFE vascular grafts have demonstrated 1-year primary patency, secondary patency, and limb salvage rates for below knee popliteal bypasses of 83.5%, 94.7%, and 94.4%, respectively.[25–27] This may suggest that hemodynamic modifications secondary to the increased size of the anastomosis may indeed account for improvements in graft patency. Longer-term results are required to further elucidate the efficacy and mechanisms of venous and synthetic graft cuffs on bypass patency.

6.628.2.2.2. Polyethylene terepthalate

First introduced in the 1930s and patented by Dupont as Dacron in 1950, PET has become a staple in peripheral vascular reconstructions most commonly involving the aorta. It is a polyester fiber that is available in both woven and knitted conformations. While the multifilament over and under weave of the woven PET limits its porosity, the knitted conformation introduced by Debakey allows for a more porous structure, which is thought to augment tissue incorporation and vascular healing.[28] In order to minimize extravasation of blood through the pores, the increased porosity of knitted PET has required the use of extracellular matrix (ECM) coatings such as gelatin, albumin, or collagen, or a preclotting period with blood prior to implantation in order to fill the interstices with fibrin clot.[20] Additionally, the velour finish of knitted grafts, which add loops of yarn at right angles to the surface of the graft, is thought to promote tissue integration by increasing the surface area for the binding of cells and the surrounding tissue and fibrin coagulum. Whether these theoretical advantages have made any significant impact on the clinical patency of PET grafts is unclear.

While knitted PET has been suggested to be prone to dilatation, the clinical implications have not been commonly observed in practice. With this exception, few clinically significant differences among the different formulations of PET and ePTFE have been demonstrated. One randomized control trial comparing the patency of knitted gelatin-coated PET, knitted collagen-coated PET, and ePTFE demonstrated patency rates of 77%, 78%, and 79%, respectively at 8 years for aortoiliac bypasses.[29] Similarly, PET and ePTFE demonstrate comparable patency rates to one another when used for femoro-femoral, axillo-femoral, or femoro-popliteal bypasses.[30–32] This said, due to cost considerations, easier handling, and surgeon habit, the standard use of PET has been reserved for aortic reconstructions, while ePTFE remains the material of choice for infrainguinal bypasses.

6.628.2.2.3. Endovascular surgery

Increasingly, endovascular treatments such as balloon angioplasty of stenotic lesions have been utilized as therapeutic strategies for peripheral vascular disease. The recent BASIL trial compared amputation-free survival in patients receiving balloon angioplasty versus surgery for infrainguinal stenoses with a mean follow-up of 5.5 years.[33] Among other conclusions, the study suggested that balloon angioplasty may be superior to prosthetic grafts in relation to amputation-free survival, especially in patients not expected to live beyond 2 years. More recently, self-expanding stent-grafts, primarily comprising a nitinol (a Ni–Ti alloy) stent supported by ePTFE, are being placed in conjunction with balloon angioplasty. The utilization of metal alloys with polymeric substances is likely to complicate the host response to these endovascular procedures. Studies comparing the results of such strategies to the long-term patency rates of standard synthetic grafts implanted by the open approach are ongoing and have become an area of intense study. A recent randomized control trial of 100 limbs in 86 patients was performed to compare the performance of stent-grafts to above knee surgical bypass with synthetic grafts for superficial femoral artery occlusive disease.[34] The stent-graft group demonstrated a primary patency of 81%, 72%, and 63% while the surgical group demonstrated a primary patency of 84%, 77%, and 64% at 6, 12, and 24 months, respectively ($p = 0.716$). The secondary patency rates were also not significantly different. Importantly, while patency rates between less severe versus more severe occlusive lesions at 24 months did not significantly differ in either of the two treatment groups, there was a trend toward improved outcomes in higher severity lesions when treated with fem-pop bypass with synthetic graft versus angioplasty and stent-graft (67% vs. 47%, respectively, for primary patency rates). Longer term and larger trials are required to determine if this is a true difference and how the long-term patency of stent-grafts compare with both synthetic and autogenous conduits.

In addition to infrainguinal bypasses, endovascular approaches to aortic reconstructions with aortic stent-grafts are becoming increasingly common and preferred in anatomically appropriate cases. A detailed review of these important methods is beyond the scope of this chapter; however, excellent reviews can be found in the literature.[35]

To summarize, while proponents of endovascular approaches point to potential benefits such as minimization of time in the operating room, less invasive wounds, reductions in procedural morbidity and mortality, and reduced costs and lengths

of stay, further data on long-term patency rates, limb salvage, mortality, morbidity, and health-care costs are necessary to determine the optimal treatment choice.

6.628.3. Host Responses to Implanted Biomaterials

After implantation into the host, vascular devices initiate blood–material and tissue–material interfacial processes, which are a constellation of normal adaptive responses to vascular injury and foreign devices. These processes begin almost immediately upon establishment of circulatory flow and continue over time based on the specific nanostructural and chemical properties of the biomaterials that comprise the device.

The histology of the native vessel comprises a quiescent endothelial monolayer, a basement membrane, internal elastic lamina, a vasoactive arterial media comprised primarily of smooth muscle cells (SMCs), collagen and elastin, the external elastic lamina, and the adventitia. (**Figure 1**) Synthetic grafts used to bypass vessels of smaller diameters are prone to failure in large part due to the absence of these native histologic features, which are critical to the long-term durability of autogenous native vessel conduits. Specifically, a quiescent endothelium provides for antithrombogenic properties, proper mechanotransduction of shear stresses and cyclic strain from pulsatile bloodflow in part by nitric oxide synthase signaling, and limited SMC proliferation rates. Quiescent SMCs, in turn, allow for proper cell–ECM interactions, which respond to mechanical and chemical stimuli to remodel the matrix and provide proper vessel compliance and elasticity. In the absence of such dynamic histologic functionality in most commonly utilized synthetic vascular grafts, host responses such as protein adsorption, platelet deposition and fibrin coagulum formation, inflammation, and mesenchymal cell infiltration are left unchecked and, consequently, often lead to graft thrombosis and intimal hyperplasia.

Strategies such as the systemic delivery of pharmacotherapeutic agents, the development of new or surface modified biomaterials, and the engineering of biological alternatives that possess the components of the native vasculature are all aimed at minimizing the injurious host responses at the material–circulation and material–tissue interfaces. This section discusses in detail the host responses to implanted biomaterials in the context of common vascular graft biomaterials. This is followed by a discussion of current and potential future advances aimed at improving the outcomes of vascular reconstructions in patients lacking autogenous conduits by modulating these host responses.

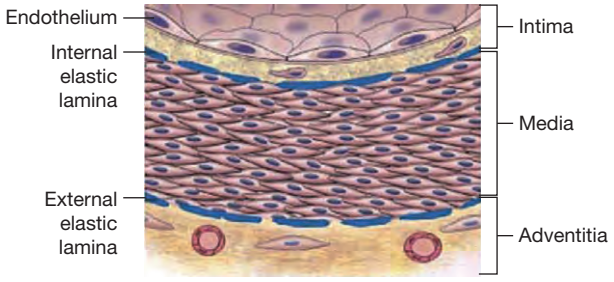

Figure 1 Representation of the vessel. Reproduced from Brewster, L. P.; Brey, E. M.; Greisler, H. P. *Adv. Drug Deliv. Rev.* **2006**, *58*, 604–629, with permission from Elsevier.

6.628.3.1. Host–Material Interfacial Processes

6.628.3.1.1. Protein adsorption

Almost immediately after the establishment of circulatory flow, protein adsorption to the biomaterial surfaces occurs in a manner dependent on both the intrinsic properties of the material itself and the concentration and diffusion coefficients of blood proteins. Thus, the most abundant and mobile proteins such as albumin, IgG, LDL, HDL, fibrinogen, and others are among the earliest adsorbed to the graft surfaces. Over the next 30–60 min after establishment of flow, however, protein adsorption continues on the biomaterial surface as determined by the Vroman effect.[36] This is characterized by the dynamic interchange between proteins initially adsorbed on the biomaterial surface with higher affinity proteins whose binding properties are dependent on their intrinsic 3D conformational and electrochemical properties, as well as the nanostructural irregularity and electrochemical activity of the biomaterial itself.[37]

Protein–surface interactions after adsorption can further alter the surface properties of the biomaterials, actively modulate the deposition of platelets, inflammatory cells, and coagulation cascade proteins, or alter the structure of the adsorbed proteins themselves. Atomic force microscopic analysis of fibrinogen bound to titanium (Ti), for example, has demonstrated alterations in the conformation of bound fibrinogen in comparison to unbound fibrinogen.[38] Such altered structural conformations of bound proteins demonstrate the specificity of protein interactions with the composition of the biomaterial, and may suggest a proximate mechanism for the way in which specific biomaterials can differentially activate downstream host responses.

6.628.3.1.2. Platelet deposition

The tendency of biomaterials to adhere platelets and promote their aggregation and activation prior to fibrin coagulum formation is a critical component with respect to the biocompatibility of vascular grafts. Clearly, thrombus formation not only leads to acute graft failures as seen in conduit thromboses, but also serves as a scaffold for mesenchymal and inflammatory cell infiltration prior to the formation of atherosclerotic plaques and intimal hyperplastic lesions.

After intimal injury, platelet adherence *in vivo* occurs via binding of the platelet surface glycoprotein (GP) receptor complexes to exposed subendothelial ECM proteins such as collagen or von Willebrand factor (vWF) bound to collagen.[39] The interaction between these glycoproteins with vWF bound to the exposed subendothelium or to endothelial cell (EC) surfaces activates platelets and causes the release of α-granule products such as fibrinogen, β-thromboglobulin, thrombospondin, vWF and fibronectin, and increases the local concentrations of serotonin, epinephrine, and adenosine diphosphate (ADP), among others. This degranulation serves to propagate platelet aggregation and activation. The formation of the prothrombinase complex on activated platelets mediated by the extrinsic coagulation pathway facilitates thrombin formation and subsequent fibrin generation.[39] Other factors released,

including platelet-derived growth factor (PDGF), platelet factor 4, and thromboxane A2, act to further modulate the subsequent inflammatory response, as well the mesenchymal cell infiltrative response.

The impact of these glycoproteins on the direct adherence of platelets to specific biomaterial surfaces remains unclear. However, the interaction of GPIIb/IIIa with the adsorbed RGD peptide sequences of fibrinogen and fibronectin appears to be an important mediator of platelet deposition onto artificial surfaces, and there is evidence of a direct correlation of fibrinogen adsorption to platelet adherence.[37,40–42] In addition, fiberoptic analyses have demonstrated wide variability in platelet adherence to several synthetic and metallic biomaterials, with woven polymeric PET demonstrating the greatest amount after 5 min in an *ex vivo* perfusion system.[43] Genetic expression patterns of platelets circulating in *ex vivo* flow systems containing tantalum stents demonstrate increased expression of CD62p (P-selectin) and CD63 expression within a few minutes of perfusion compared to platelets circulating in systems without stents, pointing to the universality of this problem as regards many biomaterials.[44]

Platelet deposition contributes to graft failure not only by the formation of an occlusive or lumen narrowing thrombus, but also by the induction of potential alterations in drug release kinetics from drug carrying polymer coatings as utilized in drug-eluting stents in both peripheral and coronary endovascular procedures. Drug deposition within developed thrombi have been shown to alter local drug concentrations, which may have the effect of limiting or increasing their bioavailability and efficacy.[45]

6.628.3.1.3. Inflammation and immunology

The inflammatory and immunologic responses to implanted vascular grafts can lead to direct tissue damage mediated by leukocytes and their released products, and may contribute to the initiation, remodeling, and progression of intimal hyperplasia.

The activation of complement is a key component of the innate immune response, which occurs via the classical pathway mediated by antigen or C1q binding to antigen, the alternative pathway mediated by activated complement components binding directly to the foreign body surface, or the mannose binding (MB)-lectin pathway. Biomaterials activate complement primarily via the classical and alternative pathway, and the degree of complement activation appears to be dependent on the type of biomaterial used. Complement activation assayed by C5a generation has been shown to be significantly greater in patients with implanted PET compared to ePTFE via the classical pathway as well as the alternative pathway.[46] All complement pathways converge on the formation of C3 convertase, which catalyzes downstream cleavages and generation of C5a, C3b, C3a, and other products, which have effector functions that include peptide mediation of inflammation, phagocyte and other leukocyte recruitment, and opsonization.[47–49] Thus the activation of complement can have significant downstream effects by propagating inflammation, inducing anaphylactoid reactions, and potentially promoting graft thromboses.[50,51]

In response to complement activation and generated C5a, leukotriene B4 (LTB4), platelet activating factor (PAF) and other chemokines, and deposited fibrin coagulum, neutrophils are recruited early in inflammation and produce products of oxygen metabolism and proteases that contribute to tissue and biomaterial injury. If an endothelium is present, neutrophil integrin receptors and sulfated sialyl-Lewis receptors bind to EC intercellular adhesion molecules (ICAM) and P- and E-selectins. The demonstration that pyrolytic carbon does not induce expression of these adhesion proteins on ECs has suggested its potential utility as a coating for PET synthetic prostheses.[52] It is important to note, however, that factors present *in vivo* modulate EC and neutrophil interactions on the biomaterial surface. These include products of platelet degranulation, complement activation, and macrophage activation, such as interleukin-1 (IL-1), tumor necrosis factor (TNF), LTB4, PAF, and C5a, which have been demonstrated to increase adhesiveness between neutrophils and ECs, and these are likely to serve to promote leukocyte adherence to the endothelium either surrounding the graft or growing on the graft.[53–55]

Macrophages, which are either resident in the tissues or derived from circulating monocytes, also comprise part of the early response to vascular grafts. Monocytes are recruited to implanted grafts by numerous chemokines and macrophage recruiting mediators from various sources including the regenerating endothelium, and platelets and other macrophages, as well by the fibrin coagulum and complement products.[53,56–63] These activated macrophages produce inflammatory mediators such as IL-1, TNF, and others, which propagate the host response to wound healing, the reaction to foreign materials, and the remodeling of pseudointimal and atherosclerotic plaques on the surface of grafts. The materials themselves may also induce inflammatory reactions as evidenced by the PET-mediated induction of TGF-β release by macrophages, an effect that may alter EC proliferation rates and modulate the healing and injury response after bypass.[64]

Dendritic cells and other antigen presenting cells link the innate immunologic response to the antigen specific and T cell-mediated adaptive response. The role of specific T cell responses to implanted biomaterials is still unclear.[65] Emerging literature, however, has explored the role of biomaterial surfaces as enhancers of adaptive immunity and investigated the role of biomaterials on dendritic cell maturation and phenotype.[66] Similarly, the role of regulatory T cells in the response to vascular graft implantation remains largely unknown.

6.628.3.1.4. Endothelialization

A quiescent endothelial monolayer provides a nonthrombogenic and mechanotransductive surface, which is thought to be critical to the prevention of synthetic SMC activity that leads to the intimal hyperplastic response after vascular injury (**Figure 2**).[67] However, this effect is partially dependent on the phenotypic characterization of the endothelium, as an endothelium activated by injury may function to promote thrombosis or intimal hyperplasia by the upregulation and release of adhesion receptors, vWF, tissue factor, endothelin-1, PDGF, and other EC products.[68,69]

It is likely that the inability of humans to promptly generate a functional endothelium and establish normal histological archeology in the coronary and peripheral vascular system after graft implantation or intravascular intervention impacts the long-term patency of synthetic vascular grafts.[70]

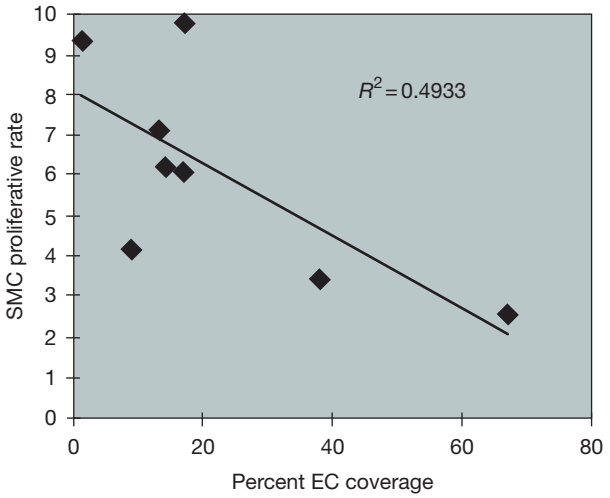

Figure 2 Smooth muscle cell proliferation, showing decreases with increased percent of reendothelialization *in vivo* using a canine carotid artery balloon angioplasty model. Reproduced from Zarge, J. I.; Huang, P.; Husak, V.; *et al*. *J. Vasc. Surg.* **1997**, 25, 840–848; discussion 848–849, with permission from Elsevier.

This phenomenon is not simply a function of insufficient EC proliferation, as the cessation of EC ingrowth ~1–3 cm from the edges of vascular anastomoses is seen even in the presence of elevated EC mitotic activity at these points on standard ePTFE grafts (30 μm internodal distance).[71–73] Interestingly, the utilization of more porous ePTFE (60 μm internodal distance) has been associated with increased EC coverage of the grafts in some animal models, probably as a result of transmural angiogenic mechanisms.[72,74–77] Thus, the endothelialization of vascular grafts is a function of spontaneous transanastomotic endothelial pannus ingrowth, angiogenic mechanisms, and, probably, the deposition and differentiation of endothelial progenitor cells (EPCs) onto the deendothelialized surface within the circulation.

While the specific effects of particular biomaterials on EC proliferation, turnover, and functionality, remain confusing, with the existence of a variety of contradictory studies, sufficient literature does suggest that EC–biomaterial interactions in general contribute to the biocompatibility of vascular grafts.[69] For example, one study compared the production of prostacylin, an inhibitor of platelet aggregation, by the endothelium generated *in vivo* on polyglactin 910 (PG910), PET, and polydiaxonone (PDS) grafts that had been interposed into rabbit aortas and later explanted and perfused under *ex vivo* flow conditions. After 1 month, the endothelium generated on PDS and PG 910 demonstrated significantly less prostacyclin production in response to arachidonic acid compared to normal aorta, while prostacyclin production by the endothelium of PET did not differ from normal aorta. By 3 months, all groups demonstrated prostacylin production equal to normal aorta.[78] How the apparent delay in normal endothelial function affects the long-term patency of the implanted material is a critical question as patency exceeded 90% in all groups up to 6 months. However, the increased incidence of atherosclerosis, thrombosis, and intima/media ratios in prostacyclin receptor knockout mice suggests that it is probably an important factor in synthetic graft longevity.[79]

Additionally, biomaterials may induce the release of growth factors from ECs, which can modulate mesenchymal cell mitogenesis and the subsequent intimal hyperplastic response. For example, *in vitro* data has demonstrated that PET induces release of the SMC mitogen basic fibroblast growth factor (bFGF) by ECs.[80] In addition, inflammatory and other cells in contact with specific biomaterials may modulate EC growth on vascular grafts. For example, macrophages cultured in the presence of PET have been shown to release greater amounts of TGF-β compared to macrophages cultured in the absence of biomaterial,[64] a significant observation as TGF-β may inhibit angiogenesis *in vitro*,[81] and stimulate the recruitment of inflammatory cells *in vivo*.

6.628.3.1.5. Mesenchymal cell infiltration

The infiltration of SMCs, fibroblasts, and cardiomyocytes onto the luminal surface of implanted grafts in the peripheral and coronary vasculature is an early event in the development of intimal hyperplasia, which is the primary cause of intermediate-term failures of vascular interventions utilizing both stents and bypass conduits.[1,82–85] The intimal hyperplastic response and formation of plaques are the pathologic consequences of the body's healing response either to iatrogenic injuries to the established endothelium and vascular tissue acquired during interventions or to implanted tissues, which lack the normal architecture of vascular tissue.[86–90] The injury response to angioplasty exemplifies the pathogenesis of intimal hyperplasia, which is common to the process in all vascular implants. The response to injury starts early, with a conversion of a subpopulation of SMCs from a 'contractile' to a 'synthetic' phenotype during the first 24 h after injury. These synthetically active SMCs demonstrate an increased responsiveness to mitogenic and chemotactic factors such as PDGF and FGF secreted in part by activated platelets and ECs, and have an increased ability to secrete their own growth factors when in the active cell cycle.[91,92] Observations that SMCs and fibroblasts from thrombosed vein grafts demonstrate higher proliferation rates in response to PDGF-BB and are more resistant to heparin-mediated attenuation of proliferation suggest the importance of these specific subpopulations of mesenchymal cells.[93] Indeed, a prospective study of SMCs harvested from vein segments used as conduits for revascularization in patients found that SMCs taken from veins that went on to develop graft failure were relatively less responsive *in vitro* to the antiproliferative effects of heparin.[94]

Thus, SMCs migrate and proliferate, and invade from the arterial media to the disrupted intraluminal area of injury, resulting in the formation of a 'pseudointima' within the first couple of weeks after injury. Over the next several weeks to months, continued synthetic behavior by SMCs contributes to the deposition of ECM proteins and further propagation and remodeling of the intraluminal pseudointimal lesion. After 2–3 months, in contrast to the earlier synthetic behavior, 'contractile' SMCs may contribute to the restenotic process by inducing contractile properties on the arterial wall, inducing further vessel narrowing by inward remodeling, which leads ultimately to an occlusive lesion.[95] Thus, while the initial synthetic response leads to the development and remodeling

of the pseudointimal lesion, both 'synthetic' and 'contractile' SMCs are likely to contribute to the eventual failure of angioplasty. While the utilization of stents and synthetic grafts in endovascular or open surgical approaches can serve to minimize the inward remodeling process due to their relative rigidity, stents and grafts are still prone to the formation of the initial restenotic pseudointimal hyperplastic lesions as a result of the injury response. Thus a significant factor in the long-term patency of any implanted vascular device is its ability to minimize this injury response.

6.628.3.1.6. Biomechanics

Circulatory shear stresses and cyclic strains impact the biocompatibility of vascular grafts almost immediately after the establishment of flow. These external mechanical factors interact with material surfaces and significantly impact cell signaling responses, SMC and EC phenotypic changes, and alterations in mitotic indices and cytoskeletal reorganizations. For example, direct comparisons of platelet activation by coated or uncoated stainless steel stents have demonstrated that the thrombogenicity profiles of these materials were significantly dependent on the flow patterns to which they were exposed.[96] Similarly, rates of shear stress can affect platelet content on vascular grafts. Higher rates of shear may increase platelet deposition on bypass conduits, but they may also cause dislodgment of adherent platelets depending on the amount of time that the high shear rates are maintained.[97] Similar results have been demonstrated on various metallic alloys such as titanium (Ti) and diamond-like carbon (DLC).[43]

Local hemodynamic conditions also significantly affect EC phenotypic behavior including cellular alignment and mitotic index.[98–101] Increased EC pinocytosis and prostacyclin production under both pulsatile and steady shear conditions, and increased endothelin production under low shear[102–104] can have significant effects on the healing, thrombotic, and endothelial regenerative processes, which are thought to modulate graft patency. In addition, flow related shear stresses impact the efficacy of cell seeding strategies utilized in the development of tissue-engineered or biohybrid grafts (discussed below). Rotational shear stresses (both high and low rates) have been shown to induce significant EC desquamation from fibronectin-coated ePTFE grafts in an *ex vivo* flow system.[105] Hydrogel coatings containing ECs in cell seeding experiments have demonstrated improved EC retention rates in response to pulsatile *ex vivo* flow compared to fibronectin-coated grafts.[106]

The biomechanical effects of circulatory flow are translated to the cellular level according to the intrinsic biomechanical and viscoelastic properties of the vascular implants themselves. Thus, the compliance and elasticity of various biomaterials can significantly impact the phenotypic and proliferative properties of vascular cells adherent to the surface or involved in the healing response. In one study, two composite partially bioresorbable PG910/polypropylene aortic grafts differing only in their nonresorbable polypropylene elasticity properties were implanted in rabbits. By 1–2 months, the PG910 component was bioresorbed, and the differential mechanical properties of the explanted prostheses/tissue complexes in each of the groups were determined by the elastic property of the remaining nonresorbed polypropylene. Cell proliferation rates within the inner capsule of the aortic graft was significantly higher at later time points in the higher compliance grafts, and this correlated with increased inner capsule thickness. These results demonstrate the apparent relationship between cellular activity and the intrinsic deformative properties of biomaterials implanted in circulatory flow conditions.[107]

6.628.4. Improving Clinical Outcomes and Future Concepts

The phenomena of protein adsorption, platelet deposition and thrombogenesis, graft endothelialization, and inflammatory and mesenchymal cell injury responses described above affect the long-term patency and efficacy of grafts and stent-grafts. Several systemic and locally applied strategies to modulate these processes have been investigated more recently in conjunction with tissue engineering strategies, in order to improve the long-term efficacy of current and investigational biomaterials. The following is a discussion of these strategies.

6.628.4.1. Systemic Pharmacotherapy

With the exception of anatomic limitations to the adequacy of inflow or outflow of revascularization targets, the thrombotic and restenotic failures of vascular grafts are local manifestations of the systemic processes, described above, that have long been targeted by systemic pharmacologic therapy. These include the use of warfarin, antiplatelet medications such as aspirin, clopidogrel, and dipyridamole, ACE inhibitors, statins and others.[108,109]

6.628.4.1.1. Acetylsalicylic acid

One of the oldest and most ubiquitous medications, acetylsalicylic acid, or aspirin (ASA), is a staple of therapy in patients with peripheral and coronary vascular disease. Its efficacy, as well as the currently less commonly used dipyridamole, in improving the outcomes of coronary and peripheral open and endovascular revascularizations is also well established. Early studies after coronary artery bypass grafting (CABG) demonstrated that ASA administration started prior to CABG significantly improved the early patency rates of saphenous vein grafts.[110] A large overview of 60 randomized trials including ~8000 patients demonstrated that ASA or ASA with dipyridamole significantly improved graft patency in all vascular interventions including coronary artery grafts, coronary angioplasty, peripheral arterial bypasses, and hemodialysis shunts or fistulae.[111] In addition, there was a significant reduction of ~25% in the risk of having a 'vascular event,' defined as nonfatal myocardial infarction, nonfatal stroke, or vascular death. In this and other studies, there appears to be no significant difference in the effects of ASA on vascular occlusion if the regimen is started before operation or soon after.[112] Of note, benefits of ASA or dipyridamole on coronary graft patency have not been demonstrated in studies where treatment was initiated 3 or more days after operation,[113,114] while some studies have suggested increased intraoperative bleeding and perioperative blood transfusion requirements in patients receiving ASA preoperatively.[115]

Interestingly, more recent systematic reviews of the literature and randomized control trials have brought into question some of the conclusions of these earlier studies. These studies have suggested that the efficacy of ASA in infrainguinal bypass patency is more pronounced in patients receiving synthetic bypass grafts, with less clear benefits in patients receiving vein grafts.[116–118] However, most consensus statements still recommend antiplatelet therapy with ASA soon after operation for its likely benefits on the patency of at least some bypasses, improvements in patient morbidity and mortality, and generally low complication and side effect profile.[119] Similar benefits are seen in peripheral arterial endovascular procedures utilizing percutaneous angioplasty with one meta-analysis demonstrating ~60% reductions in all endovascular restenoses up to 12 months postprocedure in patients who started an antiplatelet regimen including ASA prior to the procedure.[120] The use of stents in these cases was limited and further studies evaluating these effects with newer generation stents are warranted.

6.628.4.1.2. Clopidogrel

Recently, newer antiplatelet medications such as clopidogrel which target GPIIb/IIIA receptor activation and platelet aggregation by interfering with cell surface ADP receptors have been investigated in various outcome studies comparing ASA alone with ASA with clopidogrel. The benefits of this therapy in improving graft patency is unclear. A recent trial comparing clopidogrel alone to combination therapy with clopidogrel and ASA did not demonstrate any significant differences in patency rates for LIMA or saphenous vein grafts at 1 or 12 months after coronary artery bypass.[14] The role of combination therapy or monotherapy in the prevention of prosthetic graft thrombosis or restenosis in open and in endovascular peripheral interventions is even less clear. A study that demonstrated that ASA alone does not sufficiently attenuate arachidonic acid-induced platelet aggregation longer than 5 postoperative days after CABG suggests that alternate medications may be beneficial, at least in some cases.[121] For example, one study demonstrated that in patients who have postoperative thrombocytosis, combination therapy with ASA and clopidogrel may have increased benefits compared with ASA alone in maintaining CABG patency.[122] The potential for increased hemorrhagic complications should be seriously considered when evaluating the literature on clopidogrel and similar medications. The utilization of targeted approaches with systemic therapy such as the fusion of platelet integrin receptor (GPIIb/IIIa) ligands to antiplatelet drugs may have some benefit in minimizing systemic complications.[123]

6.628.4.1.3. Statins

Statins, which are a broad family of drugs that lower cholesterol by inhibiting HMG-CoA reductase, have a clear role in reducing hypercholesterolemia and cardiac mortality. In addition to this important benefit, their utility in preventing vascular graft failure has been suggested by some studies.[124] One such study, which analyzed 338 infrainguinal bypasses demonstrated that statin drug use was an independent factor associated with increased graft patency up to 17 months.[125] Further analyses on the effects of statin therapy on autogenous and synthetic graft primary and secondary patency, and limb salvage are needed.

6.628.4.1.4. Warfarin

Data on the efficacy of anticoagulation with vitamin K antagonists are less conclusive for most arterial bypasses. However, a recent meta-analysis demonstrated that the use of anticoagulation with vitamin K antagonists may provide more benefit in venous bypass graft patency compared with ASA therapy.[126] Benefits of vitamin K antagonists in comparison to ASA in prosthetic graft patency, however, were not demonstrated in this study. Separate studies with similar endpoints have found conflicting results, suggesting that, overall, those with prosthetic bypasses benefited from therapeutic levels of warfarin therapy.[127] The conflicting results exemplified by these studies, and the risks of fatal intracranial hemorrhages, higher transfusion requirements, as well as other minor bleeding events associated with the combinatorial use of warfarin with ASA, has led to the general practice of consideration of use of warfarin only in patients with high risk infrainguinal bypasses.[108,128]

6.628.4.2. Coating and Surface Modification

The coating of synthetic grafts with various synthetic and natural polymers, hydrogels, and ECM proteins, is a strategy that allows for the local delivery of drug, cell, and gene therapy. The utilization of bioresorbable polymer coatings as seen in newer generation drug-eluting stents further allows for the release or delivery of the therapeutic agent of interest while minimizing the long-term consequences of foreign material reactions. The following section discusses several past, current, and investigational graft coating and surface modification strategies that have been studied.

6.628.4.2.1. Surface passivation

The coating of grafts with several natural and synthetic materials alters the active binding sites on graft surfaces, and modifies the electrochemical and hydrophobic properties that contribute to protein and cell adhesion to biomaterial surfaces. For example, carbon coating of ePTFE vascular grafts has been shown to decrease surface thrombogenicity due to its negative charge and hydrophobic nature, and demonstrated reduced platelet deposition on graft surfaces.[129] Histologic assessment of several graft materials in a carotid artery patch model in sheep has suggested that the intimal hyperplastic response in fluoropassivated PET and carbon-lined ePTFE was reduced in comparison to gelatin-coated PET.[130] Specific semiconductive properties of amorphous silicon carbide and magnesium alloy, novel biomaterials utilized to coat metallic stent surfaces, have been shown to be associated with lower rates of platelet adhesion, platelet activation, and fibrin formation compared to uncoated stainless steel stents.[131] The use of albumin as a graft coating material, while demonstrating some encouraging results preliminarily, did not translate to clear benefits in improved graft patencies when applied clinically.[132]

More recent attempts to coat graft surfaces with synthetic hydrogels and polymers that are relatively resistant to cell and protein attachment offer a new potential direction for this strategy. Polyethylene glycol (PEG), otherwise known as polyethylene oxide (PEO), has been used for surface modification because of its relative hydrophilicity, flexibility, nontoxicity,

and nonimmunogenicity,[133] and has been demonstrated to reduce both protein and platelet adhesion when coated onto hydrophobic surfaces.[134] These effects may be dose-dependent, however, as higher concentrations of PEG coatings on ePTFE have demonstrated increases in surface platelet adhesion, in addition to increased albumin adsorption and decreased fibrinogen adsorption.[135] Sulfonated PEO-grafted polyurethane (PU) (PU-PEO-SO(3)) was used to coat PU vascular grafts and was found to have beneficial effects on surface platelet adhesion and thrombosis in a canine model.[136] To date, however, the benefits of many of these passivation strategies in the absence of other therapeutic interventions remain unclear after translation into the clinical realm.[133] Interactions among inflammatory, immunologic, and protein and cell adhesion effects of PEG and other such materials may be critical to their potential benefits as nonthrombogenic coating surfaces.[50]

6.628.4.2.2. Heparin-bonding

The modification of graft surfaces with the antithrombotic agent heparin has been an attractive strategy in improving graft patency. Early studies in animals demonstrated its utility in decreasing thrombogenesis and thromboembolic events and improving graft patency.[137138] In addition to its antithrombotic effects, which can mitigate immediate thrombus formation after graft implantation and alter the ECM of the early pseudointima, observations that heparin modulates SMC protease expression, proliferation, and migration rates after arterial injury may also suggest that it inhibits the intimal hyperplastic response.[139] In one study using a baboon aortoiliac bypass model, heparin-coated ePTFE grafts demonstrated decreased acute platelet deposition, as well as decreased perianastomotic pseudointimal proliferation and reduced pseudointimal area 4 weeks after implantation compared to controls.[140]

In our lab, silyl-heparin adsorbed onto a carbon-coated ePTFE graft in a canine aortoiliac bypass demonstrated significantly less platelet adherence, acutely with a trend toward longer term (7 days) reductions in platelet adherence and improved graft patency in the heparin-coated grafts.[141] Of note, 8% of preimplantation heparin activity was found to be active after 2 h, and only 2% of preimplantation activity remained at 7 days. Interestingly, the utilization of PEG hydrogels as a cross-linking agent for silyl-heparin bonding of ePTFE grafts led to significant differences in aggregated long-term graft patencies versus uncoated controls (7 days and 30 days), as well as a significant reduction in platelet deposition and intraluminal thrombus formation as far as 30 days after implantation versus controls.[142] Heparin activity in this group at 7 days was ~5% of preimplant heparin activity, and was present as late as 30 days postimplantation. The quantitative roles of increased heparin activity versus the potential passivation of the surface by PEG in the improved long-term patency results are not clear. More recent studies have investigated modalities of altering heparin release kinetics from PEG-DA (diacrylate) hydrogels in order to affect SMC synthetic activity.[143] By modifying both PEG-DA molecular weights and concentrations, optimal release kinetics led to a reduction in SMC proliferation rates and the upregulation of contractile markers associated with lower levels of synthetic activity. Controlled release strategies such as this can improve future formulations of heparin-bonded or releasing grafts.

Recent clinical investigations have begun to evaluate the patency rates of heparin-bonded ePTFE grafts. One year results of the PEPE II trial demonstrated patency rates of 83% in femoro-above knee popliteal bypasses for heparin-bonded ePTFE grafts, and the 1 year primary patency rates of 74% and 79% in femoro-below knee popliteal and femoro-infrapopliteal bypasses, respectively, were encouraging.[144] Another study of 350 patients demonstrated 92% primary patency rates for both above and below knee femoro-popliteal bypass and 79% for femoro-infrapopliteal bypasses at 1 year with heparin-bonded ePTFE.[145] Similarly encouraging results were found at 2 years with 83% primary patency rates for both femoro-above and below knee popliteal bypasses and 69% for femoro-infrapopliteal bypasses. Patency rates of heparin-bonded grafts at each time point were not significantly different from those of bypasses with autogenous saphenous vein. Other studies have demonstrated comparable results after 2 years follow-up.[146–148] Longer-term results have suggested that heparin-bonding may provide its most significant benefits for use in infragenicular bypass procedures compared to uncoated ePTFE 2–3 years after implantation. A recent study demonstrated ~71% primary patency rates at 3 and 4 years for femoro-below knee popliteal bypasses and ~50% patency at 5 years for femoro-infrapopliteal bypasses.[149] Clinical investigations, which have shown that implantation of heparin-bonded ePTFE grafts for lower extremity bypass is not associated with any markers of systemic alterations in hemostasis or antiheparin antibodies up to 6 weeks after implantation, suggest that these grafts have a good systemic biocompatibility.[150] Further randomized head-to-head trials comparing graft patency and limb salvage to uncoated grafts and autogenous saphenous vein in infrainguinal bypasses may be warranted. In addition, while ePTFE is the predominant graft of choice for infrainguinal bypasses, studies that have shown significantly improved primary patency rates in heparin-bonded PET compared to uncoated ePTFE at 3 years and near significant improvements at 5 years (46% vs. 35% for heparin-bonded PET vs. ePTFE, respectively; $p < 0.055$) suggest that direct comparisons between heparin-bonded PET and heparin-bonded ePTFE may be warranted.[151]

6.628.4.2.3. Graft endothelialization

For reasons discussed earlier, the induction of endothelialization on biomaterial blood-contacting surfaces is thought to be critical to establishing the long-term biocompatibility of vascular grafts. Early observations in animal models suggested that ePTFE grafts with larger pore sizes (60 μm internodal distance) compared with standard ePTFE (30 μm internodal distance) demonstrated increased EC coverage on the luminal surface. This has led to the general belief that a significant component of vascular endothelialization results from transmural angiogenic mechanisms, which consequently seed the luminal surface of the graft.[72,74–77] Increased porosity, while likely beneficial in promoting endothelialization, has also been shown to decrease the compliance of implanted grafts by promoting fibrovascular infiltration into the wall of both PET and ePTFE.[72,77] Thus, the dual effects of graft pore size on both mechanical biocompatibility and vascular healing capacity may or may not work in concert to improve graft performance.

Alternative strategies that can augment more rapid graft endothelialization in available and investigational prostheses

may prove useful.[20,152] These strategies can be broadly separated into two categories: (1) the *in vivo* augmentation of transmural angiogenesis, spontaneous anastomotic endothelialization, and EPC incorporation utilizing locally or systemically delivered drugs such as angiogenic growth factors[153–156]; and (2) the seeding of ECs or EPCs onto the graft surface via natural and synthetic polymeric coatings with or without adjunctive angiogenic growth factors prior to implantation.[157–160]

A fairly large body of investigational literature has focused on the utilization of hydrogels and polymers as drug delivery vehicles for the purpose of promoting angiogenic ingrowth and endothelialization. One group demonstrated that bFGF delivered from a gelatin coating on porous polyurethane grafts implanted in rats provided for improved endothelialization when compared with controls.[161] In our lab, ePTFE grafts (60 μm intermodal distances) coated with fibrin glue containing FGF-1 and heparin were placed in infrarenal aortas of rabbits. At 28 days, grafts treated with fibrin containing FGF-1 demonstrated extensive transmural capillary infiltration, seen neither in untreated controls, nor in controls treated with fibrin devoid of FGF-1.[162] This strategy, however, can be tempered by the nonspecific effects of growth factors or polymers in inducing SMC or fibroblastic infiltration and an intimal hyperplastic response. In other studies, the delivery of angiogenic growth factors has resulted in poor rates of endothelialization. For example, one group found that while fibrin delivery of vascular endothelial growth factor (VEGF) after carotid artery injury in a porcine model did not affect patency or endothelialization, treatment with fibrin, in the presence or absence of VEGF, resulted unexpectedly in an increased narrowing at the proximal anastomosis, an increased SMC infiltration, and intimal hyperplasia compared to controls.[163] These deleterious effects may be a consequence of the prothrombotic or prointimal hyperplastic effects of fibrin and/or a direct or indirect activation of SMC activity by VEGF.[164,165] Strategies that can improve graft endothelialization while minimizing these unwanted side effects are under investigation. *In vitro* observations that FGF-1 and 500 U ml of heparin released from fibrin hydrogels increase EC proliferation while decreasing SMC proliferation may provide one avenue for improvement.[166] Our lab has investigated the use of designer FGF-1-derived growth factors, created by site-directed mutagenesis, which possess some characteristics that are more clinically advantageous compared to wild-type FGF-1. These include relative thrombin resistance for improving bioavailability, heparin independence, and relative EC specificity.[167–172]

It is important to note that while *in vitro* data may initially prove promising, interactions between cell, drug, biomaterial, and host responses may affect the activity or the release kinetics of the therapeutic agent once implanted. bFGF has been found to bind specifically to fibrinogen and fibrin, impacting its release kinetics from fibrin-based drug delivery coatings and subsequent drug activity.[173] Indeed, it has been shown that the binding of bFGF to fibrinogen can affect the expression of EC urokinase-type plasminogen activator (u-PA), an important mediator of angiogenesis.[174,175] Strategies that try to control for drug release kinetics and cell–drug–polymer interactions may provide for more predictable host responses *in vivo*. The covalent binding of VEGF to fibrin or PEG hydrogels modified to contain tethering sites for the growth factor allows for cell-demanded matrix degradation and drug release, which have appeared to lead to more normal appearing microvasculatures *in vivo*.[176,177] The fusion of collagen binding domains to growth factors or designer growth factors can similarly improve bioavailability and cell-demanded drug release for utilization in collagen hydrogel delivery systems.[153] Thus, proper control of drug release kinetics is likely to be a critical element in hydrogel or polymer-based graft coating systems that aim to induce graft endothelialization by inducing transmural angiogenesis.

In contrast to the *in vivo* induction of graft endothelialization, the seeding of synthetic vascular grafts with ECs prior to implantation can be advantageous as it does not rely on the capacity of the host tissue to endothelialize the surface. Animal studies have provided hope for the efficacy of this strategy. Autologous ECs embedded within fibrin glue containing both FGF-1 and heparin were locally delivered to canine carotid arteries after balloon angioplasty. Carotid arteries treated with ECs in the fibrin glue demonstrated decreased pseudointimal formation at 30 days following procedure, in comparison to controls (**Figure 3**).[67]

A primary challenge of cell seeding strategies is preventing the loss of seeded ECs after exposure to physiologic shear

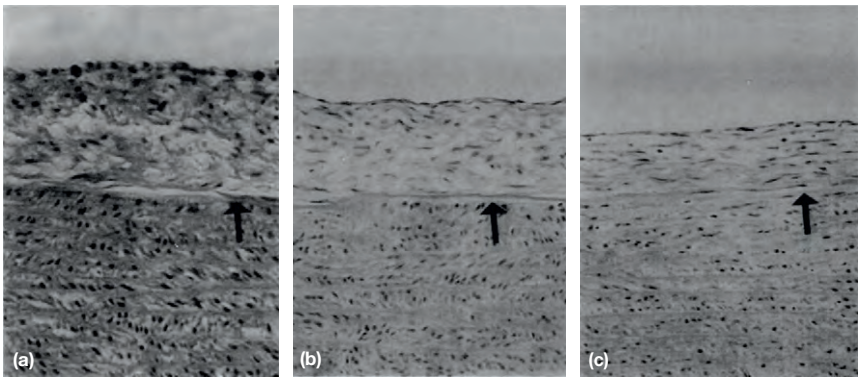

Figure 3 H&E photomicrographs of longitudinal sections of balloon-injured canine carotid arteries (Mag., 25×). Note the decreased pseudointimal formation in balloon-injured carotid artery treated with FG/FGF-1/heparin plus endothelial cell. Arrows indicate internal elastic lamina. Reproduced from Zarge, J. I.; Huang, P.; Husak, V.; *et al*. *J. Vasc. Surg*. **1997**, 25, 840–848; discussion 848–849.

stresses within the circulation. Numerous strategies have been employed to address this limitation. The coating of graft surfaces with various adhesion peptides, ECM proteins, and hydrogels is one such strategy. Coating of endovascular stents and vascular grafts with fibronectin and poly-L-lysine, or linking integrin ligand peptide sequences such as RGDV and YIGSR to polymeric coatings can significantly increase EC adhesiveness under both static and dynamic flow conditions.[154,178–181] The utility of RGD and heparin coatings, both alone and in combination, has been demonstrated on poly(carbonate-urea) urethane grafts, with significantly improved EC retention after stringent washings.[182] ePTFE covalently linked to fibronectin either via gluteraldehyde (GA) or sulfosuccinimidyl-4-(*p*-maleimidophenyl) butyrate (SMPB) has been shown to be significantly more effective in promoting cellular adhesion compared to uncoated ePTFE.[183] Increases in cell adhesion seen in fibronectin–GA-linked grafts compared to fibronectin–SPMB-linked graft groups were attributable to increased availability of RGD binding sites in the fibronectin–GA group.

Many other strategies for improving EC adhesion and growth on biomaterial surfaces have also been studied. These include the alteration of electrochemical surface properties by the implantation of negative silver ions,[184] coating of surfaces with a polyamino-acid urethane copolymer,[185] and cross linking of bFGF to collagen matrices.[186] The utilization of fibrin-based composite matrices as a coating with growth factors has also been shown to support the differentiation of seeded EPCs to nitric oxide-producing ECs on coated ePTFE and PET.[187]

As in methodologies used for *in vivo* tissue induction, strategies that augment *ex vivo* EC seeding and growth may be limited by nonspecific effects on other circulatory or vascular cells, which limit graft biocompatibility. Thus, cell specificity in cell adhesion strategies is desirable in promoting endothelialization while limiting the deposition of platelets or the adhesion of migrated SMCs onto the graft surface after implantation of the graft *in vivo*. REDV, another fibronectin peptide sequence, has been demonstrated *in vitro* to be relatively specific for EC adhesion, perhaps attributable to $\alpha 4\beta 1$ integrin receptors, which have been shown to be present on ECs, but not on platelets.[188–190] In addition, while increasing EC adhesiveness by surface modification may be beneficial in improving graft endothelialization, it has also been found that increasing adhesiveness to material surfaces can attenuate endogenous ECM production by SMCs, ECs, and fibroblasts, which may be required for proper tissue formation in tissue engineering strategies.[191]

Recently, long-term results of endothelialized ePTFE grafts used clinically as infrainguinal bypass conduits were reported. ECs were harvested from autologous subcutaneous veins and seeded onto grafts with a fibrin glue. 153 above knee femoro-popliteal, 155 below knee femoro-popliteal, and 33 femoro-infrapopliteal bypasses were performed with EC-coated ePTFE grafts.[192] Five-year patency rates were found to be 68% and 71% for femoro-above knee popliteal and femoro-below knee popliteal bypasses, respectively, and 61%, overall, at 10 years (59% and 64% for above knee and below knee, respectively). Fifty-two and thirty-six percent patency rates were seen in femoro-infrapopliteal bypasses at 5 and 10 years, respectively. While it was not possible to know the source of ECs because of the study design, explanted grafts after graft failure did demonstrate the presence of an endothelium on the lumens of the grafts. These results are encouraging, as they demonstrate the availability of autogenous ECs for graft seeding, and the feasibility of the strategy, as well as the apparent efficacy in comparison to historic controls. Further investigations into the functionality of autogenous ECs harvested from diabetic and vasculopathic patient populations, as well as improvements in cell harvest, culture, and seeding techniques are likely to promote the widespread use of this strategy in peripheral and coronary vascular procedures. Randomized control trials directly comparing endothelialized synthetic grafts versus uncoated grafts would provide further evidence as to the efficacy of this strategy.

6.628.4.2.4. Drug-eluting stents and graft

New generations of drug-eluting stents and grafts are being commonly used in the coronary vasculature; and they are also being investigated for use in the peripheral circulation. Although a thorough review of drug-eluting stents and grafts is beyond the scope of this chapter, it is to be noted that the delivery of numerous drug families, which aim at minimizing graft thrombogenicity, intimal hyperplasia, and inflammation from polymer coatings have been tested. In the peripheral vasculature, sirolimus-eluting polyurethane-based grafts used for arteriovenous fistulae in hemodialysis, patients have demonstrated encouraging, albeit nonsignificant, early benefits in improving stenosis secondary to intimal hyperplasia.[193] Polyurethane grafts with a polymer coating containing nitric oxide have demonstrated improved thromboresistance and patency compared to controls in limited animal studies,[194] and the delivery of nitric oxide from polyurethane-based polymers has been demonstrated in some studies to decrease platelet adhesion and SMC proliferation, and increase endothelialization.[195] Recent studies that evaluated the release of monoclonal antibodies targeted at GPIIb/IIIa platelet receptors from L-polylactic acid (L-PLA)-coated stents demonstrated a decreased platelet uptake compared to bare nitinol stent controls, highlighting a potential for the future utilization of monoclonal antibody therapy in the next generation intravascular prostheses.[196] New generations of investigational stents and grafts that utilize bioresorbable polymers to deliver therapeutic agents are becoming increasingly attractive for the minimization of the longer term responses to the foreign body (discussed below).

6.628.4.3. Optimization of Biomechanical Biocompatibility

The relative noncompliance of available synthetic grafts is thought to be one of the key factors in their propensity for inducing the intimal hyperplastic response.[152] For this reason, the development of synthetic polymers with more elastomeric properties has generated interest in order to improve compliance mismatches between native vessels and anastomosed grafts.[197] This is exemplified by synthetic polyurethanes. Comprising three monomeric components including a hard domain diisocyanate, a chain extender, and a soft domain (commonly polyol), polyurethanes provide flexibility and strength profiles dependent on the relative percentage of the polymer in each of its monomeric units.

While early attempts at utilizing polyurethane as a vascular graft demonstrated a good biocompatibility for infragenicular bypasses, unacceptable occlusion rates and reports of hydrolytic instability of poly(ester) and poly(ether) urethanes has limited its clinical use.[198–200] Newer generation grafts made of poly(carbonate)-based PUs have demonstrated improved hydrolytic and oxidative stability due to the elimination of ether linkages.[201] In addition to their more compliant characteristics, observations in rats that poly(carbonate)-based PUs appear to demonstrate earlier endothelialization and reduced intimal hyperplasia compared to ePTFE may offer another potential advantage to PU as a graft material.[202]

Polyetherurethaneurea-based PUs have been tested clinically as vascular access grafts for patients receiving hemodialysis. A comparison between PU grafts and ePTFE grafts used for hemodialysis access demonstrated that patency rates for polyurethane grafts did not differ significantly from patency rates of ePTFE grafts (44% vs. 36% primary patency rates at 12 months for PU vs. ePTFE grafts, respectively).[203,204] Similarly, 2-year patency rates of PU grafts are comparable to ePTFE.[205,206] However, due to the manufacture of PU grafts with pore sizes of 15 μm, these 'self-sealing' grafts have offered the advantage of earlier access because of the increased rates of hemostasis early after cannulation compared with ePTFE. Notably, a more recent study has demonstrated that while primary patency rates were equivalent between the PU-based grafts and brachial artery–basilic vein fistulae, achieving equivalent secondary patency rates necessitated an increased graft surveillance and endovascular procedures in PU-based grafts.[207] The authors of this study have cautioned that the need for a more vigilant surveillance and the increased risk of graft infections should be balanced with the benefits of earlier access when choosing PU-based hemodialysis grafts.

6.628.5. Gene Therapy

While progress in the field of gene therapy in medicine and cardiovascular disease has been slow in general, the strategic genetic modification of host cells that respond to vascular grafts or of cells seeded in or on tissue-engineered constructs provides theoretical opportunities for improving the biocompatibility of vascular grafts.[208] Adenoviral delivery of β-interferon has been demonstrated to decrease SMC proliferation *in vitro* and to reduce the intima/media ratio *in vivo* in a porcine balloon injury artery model.[209] The overexpression of endothelial nitric oxide synthase (eNOS) by intraluminal viral delivery in vein grafts has limited the intimal hyperplastic response in an animal model, though the mechanism of this effect was not clear.[210] Interesting results in a carotid artery injury model in rabbits demonstrated that EPC transplantation onto the luminal surface of injured arteries improved endothelialization rates and the neointimal hyperplastic response.[211] Further, the transplantation of EPCs transduced *ex vivo* with eNOS further reduced the intimal hyperplastic response after injury. The utility of polymers as gene delivery vehicles offers an exciting path for future investigations.[212,213] One study demonstrated that the coating of metallic stents with hydrogels carrying naked plasmid DNA encoding VEGF accelerated endothelialization of the stents in a rabbit balloon angioplasty model.[214]

Clinical applications have to this point been limited. However, the finding that the inhibition of the transcription factor E2F with transfected decoy oligodeoxynucleotides using therapeutic ultrasound minimized neointimal formation in a rat carotid artery injury model has offered hope.[215] However, clinical results in humans in both peripheral and coronary revascularizations have appeared to be less promising than predicted from the preclinical animal studies.[216,217]

6.628.6. Tissue-Engineered Blood Vessels

Vascular tissue engineering is a somewhat amorphous field that utilizes knowledge of vascular biology to engineer tissues resembling native vascular structures. The investigational concepts in the creation of a TEBV are founded on molecular and cellular biology, biomaterials science, bioengineering, and clinical sciences. The following section presents a focused discussion on the basic concepts and strategies involved in the creation of a TEBV.

6.628.6.1. General Concepts

While the methodologies described in the literature for the development of a TEBV can seem infinitely variable, they are founded on one ultimate goal: the organization of a structure comprising cells and ECM that mimics the biological functionalities of a native blood vessel, including mechanotransduction and vasoactivity and the maintenance of vessel wall and hemodynamic homeostasis. The way these structures are cellularized, the methodologies and materials used to construct or direct the deposition of ECM, and the strategies used to allow for the proper cell–matrix interactions requisite to the aforementioned biological functionalities are theoretically endless. However, as introduced in the section discussing graft endothelialization, the broad strategic categories include (1) the implantation of cells, materials, and drugs *in vivo*, utilizing the host body as a living bioreactor, which formulates the final structure after implantation; (2) the complete creation of a biological blood vessel *ex vivo* prior to implantation; or (3) a combination of both strategies. The sourcing of the cellular component, the materials utilized as scaffolds or drug delivery vehicles, and the nature of the genetic and protein level manipulations are fundamental and exciting territories in the field of tissue engineering. In addition, due to the advent of bioresorbable materials, the engineering of blood vessels from bioresorbable polymers, which incorporate entirely into the host tissue as a result of normal vascular healing, has become a possibility. The following discussion focuses on hydrogel-based TEBVs, self-assembled TEBVs, bioresorbable TEBVs, and TEBVs constructed from decellularized vessels.

6.628.6.2. Hydrogel-Based TEBVs

Natural hydrogel polymers such as fibrin, collagen, alginate, hyaluronan, as well as synthetic hydrogels such as PEG and polyvinyl alcohol are commonly used in tissue engineering as scaffolds or components of scaffolds for TEBVs.[218] The first credited attempt at the creation of a TEBV by Weinberg and Bell in 1986 utilized a collagen hydrogel scaffold constructed

as a tubular structure with layers of ECs, SMCs, and fibroblasts.[219] While poor burst strengths, a common limitation to hydrogel-based TEBVs, necessitated the use of sleeves comprising PET for mechanical support, these investigators demonstrated the feasibility of TEBV creation utilizing hydrogels as scaffolds.

Fibrin has also been utilized as a scaffold for TEBVs and has demonstrated its own advantages and disadvantages. In comparison to collagen hydrogels, fibrin has been found to promote an increased native collagen production by entrapped fibroblasts and SMCs, suggesting its ability to support the matrix remodeling processes involved in host tissue incorporation after implantation.[220] The presence of deposited elastin in fibrin hydrogels as compared to collagen hydrogels also suggests beneficial effects on cell-mediated matrix remodeling processes, which affect construct biomechanics.[221,222] Implantation of fibrin-based TEBVs into lamb external jugular veins demonstrated endogenous collagen and elastin deposition by SMCs in the arterial media, which orientated circumferentially in a direction perpendicular to the circulatory blood flow.[223] Interestingly, these TEBVs gained mechanical strength and vasoactivity comparable to that of native blood vessels after 15 weeks *in vivo*. Fibrin-coated vascular prostheses have been evaluated in animal models for coronary artery bypass.[224] While early results were encouraging, with patency up to 12–22 days, thrombus formation and platelet deposition as well as degradation of the hydrogel after the first 2 weeks limited the efficacy of these prostheses. As in collagen-based constructs, the mechanical strength of fibrin-based TEBVs in general remains a significant limitation and often requires the use of synthetic polymers, such as a polyvinylidene fluoride mesh, to improve their mechanical stability.[225]

Several modifications to hydrogel-based TEBVs have been developed in order to improve the mechanical strength of the constructs. These include chemical modifications that regulate the degradation of the hydrogel matrix, induce the cellular deposition of endogenous matrix proteins such as collagens and elastins, and promote covalent cross-linking among ECM fibers. For example, mechanical properties of fibrin-based TEBVs can be modified by the addition of plasmin inhibitors such as aprotinin, cross-linking agents such as Factor VIII, and media supplements such as insulin and TGF-β, which induce endogenous matrix deposition by embedded cells.[226,227] The use of media supplements such as retinoic acid and ascorbic acid has been shown to promote SMC elastin and collagen mRNA and protein expression within type I collagen tubular constructs.[228] This was associated with an increased TEBV tensile strength and a decreased stiffness compared to untreated TEBVs. Finally, TEBVs can be constructed in layers varied by the composition of the ECM and cellular component, with each layer performing separate functions. For example, fibrin-based TEBVs with an inner layer containing a lower concentration of fibrinogen to support SMC vasoactivity, and an outer cell-free layer comprising a higher concentration of fibrinogen for mechanical stability demonstrated significantly improved burst strengths compared to single layer constructs while maintaining vasoreactivity.[229]

Mechanical preconditioning with cyclic strain bioreactors has also been efficacious in improving the structural integrity of hydrogel-based TEBVs. In collagen-based constructs, this has been shown to be attributable in part to the modulation of cell and matrix organization, as well to the alteration of the expression of matrix metalloproteases (MMPs).[230,231] Recent studies have also demonstrated that the application of incremental cyclic distention from 5 to 15% significantly improved tensile strength, tensile modulus, and collagen deposition per cell in fibrin-based TEBVs.[232] In addition, a direct comparison of the mechanics of fibrin, collagen, and fibrin–collagen TEBVs showed that the mechanical properties of the TEBV were dependent not only on the application of mechanical strain, but also on the composition of the hydrogel scaffold.[233] Linear modulus was directly associated with collagen content, and gel compaction, which was associated with improved tensile strength, was augmented by the addition of fibrin. This study also found that cyclic mechanical strain not only augmented the tensile strength and gel compaction of collagen–fibrin TEBVs, but also decreased cellular proliferation. The effects of mechanical strain on cellular phenotype are further exemplified by increased levels of vWF, nitric oxide, SMC α-actin, and SMC myosin heavy chain in mechanically conditioned collagen/PLGA TEBVs containing ECs and SMCs compared with statically cultured TEBVs.[234] In addition, this study demonstrated that mechanical strain affected cellular orientation, with embedded cells aligning radially in mechanically conditioned TEBVs in contrast to the random alignment of statically cultured TEBVs.

6.628.6.3. Bioresorbable TEBVs

Bioresorbable materials can serve as temporary scaffolds for vascular prostheses, which incorporate into the native tissue, or as polymeric vehicles from which drugs can be eluted with controlled kinetics. Implanted devices comprising these materials, such as drug-eluting stents, can serve their functional purpose for the time it is required and then histologically 'disappear,' theoretically minimizing the long-term inflammatory and injury responses, and the potential for graft infection. As a scaffold for a TEBV, bioresorbable materials can serve as 'smart' materials that are modified to promote native tissue infiltration after implantation. Knowledge of the resorption kinetics of specific bioresorbable materials based on the intrinsic properties of the materials being used is critical to controlling host–material interactions, which lead to tissue incorporation.[235–238] The study of the histologic, immunologic, inflammatory, and other biologic mediators, which modulate the resorption kinetics of these biomaterials, is a field of intense study and should serve to provide optimal polymer constructs both for TEBV creation and for the delivery of drugs to interventional sites.

The conceptual utility of these biomaterials has been acknowledged for some time. Early studies with polyglycolic acid (PGA) demonstrated its regenerative capacity in comparison to PET. PGA prostheses implanted into rabbit aortas were found to have significantly more intramural and luminal surface myofibroblastic and endothelial cellular infiltration in comparison to PET.[239,240] Similarly, grafts of PDS and polyglactin 910 (PG910) demonstrated mesenchymal and EC infiltration, and even small amounts of PET woven into or around the absorbable polymer inhibited this process.[241] In addition, the rates of collagen deposition in both PG910 and PDS grafts were greater than that of PET, and appeared to parallel the

kinetics of cellular proliferation, tissue thickening, and the resorption of PG910 and PDS grafts.[242,243] Coincident mesenchymal cell infiltration with macrophage-mediated degradation of the bioresorbable material suggested the association of the two processes, and implied that the differential cellularization capacity of bioresorbable materials is, at least in part, attributable to their susceptibility to macrophage-mediated degradation.[76] This is consistent with *in vitro* data, which demonstrated that media conditioned by macrophages cultured in the presence of PG910 were significantly more mitogenic for ECs compared with negative controls or media conditioned by macrophages cultured in the presence of PET. In fact, media conditioned by macrophages cultured in the presence of PET did not demonstrate any significant EC mitogenicity compared with negative controls.[61,244] Thus, while inflammatory and mesenchymal cell infiltrative processes may be detrimental to the long-term biocompatibility of vascular grafts, they are also likely to be beneficial in the incorporation of bioresorbable vascular grafts. This highlights the importance of developing proper methodologies for the regulation of the kinetics and magnitude of these processes in order to fully realize the advantages and benefits of these materials.

While these early studies were encouraging, the increased prosthetic compliance coincident with endogenous cell repopulation potentially compromised the biomechanical biocompatibility of these TEBVs.[245] At 6–36 weeks postimplantation, the compliance of distal and proximal sections of PG910 grafts was found to be greater than that of midportions of the grafts, with compliance increasing significantly over time in the proximal portion of the grafts, and nonsignificantly in other portions. These changes were preceded by myofibroblastic changes and macrophage-mediated phagocytosis, suggesting that the histologic changes preceded the changes in graft biomechanics. Thus the cellular response to the materials probably affects significant consequences, which may lead to the undesirable sequelae of aneurysm formation and longer-term compliance mismatches.[245]

Several strategies have been employed in order to impart more strength to bioresorbable TEBVs. Altering the components of grafts by adding nonresorbable or more slowly resorbable materials is one such strategy.[246] At explantation, compounded resorbable PG910 and nonresorbable polypropylene grafts implanted in rabbits were found to withstand burst pressures exceeding those of perianastomotic native aorta, and no aneurysms were found up to the latest explant time point of 2 months.[247] Of note, only the nonresorbable polypropylene was present after 2 months. Biochemical and histologic data were suggestive of a functioning endothelium at the time of explant. Partially bioresorbable grafts comprising PG910/polypropylene or PDS/polypropylene were implanted into a canine model for up to 1 year and compared to PET or ePTFE controls.[248] Over the 1 year period, combined patency rates of partially bioresorbable grafts were significantly greater than those of nonresorbable grafts. Additionally, no aneurysms were found in any of the explanted grafts. Increased inner capsule EC and myofibroblastic infiltration and collagen deposition paralleled the kinetics of material resorption. The observation that varying the elasticity of the polyprolene component of PG910/polyprolene bicomponent grafts impacts the extent of cell infiltration and matrix deposition highlights the importance of the biomechanical contribution of the nonresorbable material to cellular activity.[107] Interestingly, it was shown that increased inner capsule mitotic index and thickness correlated with graft formulations with greater compliance.

Other bicomponent bioresorbable and partially bioresorbable grafts have also been investigated. PGA/polyhydroxyalkanoate copolymeric scaffolds with and without seeded carotid artery ovine cells were implanted into the aortas of lambs.[249] While all acellular polymeric graft controls were occluded by 5 months, TEBVs demonstrated 100% patency, no aneurysm formation, collagen levels and elastin content similar to those of native aorta, and vWF positive ECs along the luminal surface. More recently, investigators utilized a tubular scaffold comprising an inner and outer porous polylacticglycolic acid (PLGA) layer with a polyurethane layer in between.[250] They were seeded with bone marrow stromal cells (BMSCs) and, after a 7-day culture period, they were implanted into canine abdominal aortas. The results of the study did not demonstrate any dilatation up to 3 months after implantation. Additionally, α-SMA and VWF staining cells and collagen were seen in the grafts at explants, and the burst strengths of the explants were approximately the equivalent of 1200 mmHg.

The addition of mechanical conditioning may further augment the mechanical biocompatibility of bioresorbable grafts. The implantation of a TEBV comprising a PGA scaffold and endogenous collagen deposited by seeded SMCs into swine demonstrated the feasibility of the creation of a suturable construct that can withstand physiologic pressures *in vivo* after a period of mechanical preconditioning in bioreactors *in vitro*.[251] More recently, a TEBV was constructed by the incorporation of a bioresorbable macroporous poly(L/D)lactide 96/4 mesh into the wall of a fibrin-based graft containing SMCs and fibroblasts. The constructs were seeded with ECs and then made to undergo a 21-day mechanical conditioning period in a dynamic strain bioreactor.[252] In this model, while cell proliferation and endogenous collagen deposition increased within the wall during the conditioning period, the graft demonstrated burst strengths capable of withstanding supraphysiologic pressures.

One caveat to the selection of materials that increase construct burst strength, however, is that the differential compliance characteristics of various materials may lead to stiffer constructs without adequate compliance. This can affect the intimal hyperplastic response and the long-term durability of the TEBVs. Additionally, the components of the scaffold matrix can affect the deposition of elastin, the critical ECM component affecting elasticity, within the TEBV from seeded cells. One study compared the viscoelastic properties of bioresorbable TEBVs composed of either rigid PLGA or elastomeric poly (glycerol sebacate) (PGS).[253] It was shown that while the addition of SMCs within the scaffold increased the burst strengths of all constructs, the elastic modulus of PLGA-based constructs was significantly greater than that of native arteries or of PGS-based constructs and demonstrated no elastic deformation compared to PGS. Additionally, PGS-based constructs were found to contain less collagen and increased elastin in comparison to PLGA-based constructs. Therefore, a balance between compliance, elasticity, and burst strength must be achieved utilizing proper copolymeric formulations in order to optimize mechanical biocompatibility.

Some clinical experiences with bioresorbable grafts have provided encouraging results. Because current prosthetic materials cannot grow proportional to the growth of the native tissue during child development, bioresorbable TEBVs are especially useful in the pediatric population. TEBVs comprising a composite PGA/poly-4-hydroxybutyrate (P4HB) scaffold were seeded with vascular cells and implanted in the pulmonary arteries of a growing lamb model in which body size doubled over a 2-year period.[254] The TEBVs demonstrated a 30% increase in diameter and a 45% increase in length over time, with concomitant increases in collagen, proteoglycan, and cellular content. In addition, there was no evidence of thrombus formation, calcification, stenosis, suture dehiscence, or aneurysm in any of the grafts. However, a decreased elasticity and an absence of elastin in the TEBVs in comparison to native pulmonary arteries was noted.

In 2001, a TEBV comprising a bioresorbable polycaprolactone (PCLA)/PLA tubular scaffold seeded with autogenous cells were implanted into the pulmonary artery of a 4-year old child with pulmonary artery atresia.[255] At 7-month follow up, the patient was doing well, with no evidence of aneurysm formation or graft occlusion. Subsequent efforts utilized autologous bone marrow cells as a cell source to seed hybrid scaffolds of a copolymer of PLA and PCLA with a PGA reinforcement. These were implanted as vascular conduits in a clinical study of 23 patients with a 6-year follow-up.[256,257] Computed tomography studies did not demonstrate evidence of aneurysmal dilation and there was only one case of graft stenosis, which was successfully treated with angioplasty. With evidence of growth of the vessel conduit over the time period, these results provided encouraging initial clinical experiences. The investigators have received IRB approval and are hoping to begin clinical trials in the Unites States in the near future.

In the coronary vasculature, a fully bioresorbable stent comprising a poly-L-lactic acid backbone and a coating of poly-D-L-lactic acid containing the antiproliferative agent everolimus has recently been implanted in the first-in-human trials, with promising tolerance and clinical results up to 24 months.[258–260] At 2 years, there were no cardiac deaths, no revascularizations of the target lesion due to ischemia, and no stent thromboses. Additionally, there was evidence of tissue incorporation and vasomotion at the stented site and the adjacent coronary artery in response to vasoactive agents. This trial is ongoing, and continued encouraging results may provide the source for a potential revolution in the endovascular treatment of coronary and peripheral vascular stenoses.

6.628.6.4. Self-Assembled TEBVs

A promising strategy for TEBV construction, which has been tested in human subjects, is the self-assembly strategy described by L'Heureux *et al*.[261] Human SMCs are cultured with ascorbic acid and serve as a cellular sheet, which is wrapped around a tubular support to produce the media of the vessel. A second sheet generated by cultured human fibroblasts is then wrapped around the media to provide the vessel adventitia. After a period of culture, the tubular support is removed and ECs are seeded onto the lumen of the TEBV. This methodology is advantageous as it avoids the use of any foreign materials, and relies on the cellular components to provide the ECM scaffold. Implantation of these cell-assembled TEBVs in a canine model demonstrated tissue incorporation with intact endothelium, vasa vasorum, and an arterial media containing α-SMA positive SMCs as well as elastin and collagen.[262] Mechanical stability was demonstrated up to 8 months after implantation. Implantation in a limited number of human subjects for hemodialysis access has demonstrated encouraging early results, although long-term aneurysmal dilatation may appear to be a potential limitation for this strategy.[263,264]

6.628.6.5. Decellularized Vessel Scaffolds

Decellularized veins and arteries are a potential scaffold for TEBVs, and have the obvious advantage of possessing intact native vascular ECM structures.[265,266] Animal experiments have demonstrated some success with this methodology. Explanted decellularized grafts seeded with ECs and implanted in animal models have demonstrated EC lined lumens at the time of explant with repopulating SMCs after 4 weeks.[267,268] Of note, 89% of grafts seeded with ECs prior to implantation remained patent at 4 weeks, with only 29% of unseeded grafts remaining patent over the same time period. A decellularized cryopreserved human vein allograft, which was seeded with autologous ECs in a bioreactor, was implanted in a human patient for iliac vein reconstruction. This demonstrated the feasibility of this approach, although the tissue-engineered graft failed after 4 months.[269]

6.628.6.6. Final Remarks

While various alternatives to available synthetic grafts have been developed and investigated, a single commercially mass-produced product has yet to be introduced to the market. However, advances in the field of vascular tissue engineering have brought this endeavor closer than ever to patient care. As most of the current methodologies described in this chapter require several weeks to months, optimization of TEBV construction and synthetic graft modification will be required in order to produce a viable, cost-effective product for broad clinical use.

References

1. Klinkert, P.; Schepers, A.; Burger, D. H.; Vanbockel, J. H.; Breslau, P. J. *J. vasc. surg.* **2003**, *37*, 149.
2. Klinkert, P.; Van Dijk, P. J.; Breslau, P. J. *Ann. Vasc. Surg.* **2003**, *17*, 486–491.
3. Faries, P. L.; Arora, S.; Pomposelli, F. B., Jr.; *et al. J. Vasc. Surg.* **2000**, *31*, 50–59.
4. Faries, P. L.; Logerfo, F. W.; Arora, S.; *et al. J. Vasc. Surg.* **2000**, *32*, 1080–1090.
5. Johnson, W. C.; Lee, K. K. *J. Vasc. Surg.* **2000**, *32*, 268–277.
6. Mamode, N.; Scott, R. N. *Cochrane Database Syst. Rev.* **2000**; CD001487.
7. Dardik, H. *J. Am. Coll. Surg.* **2006**, *203*, 582–583.
8. Buxton, B.; Tatoulis, J.; Fuller, J. *Heart Lung Circ.* **2005**, *14*(Suppl. 2), S14–S17.
9. Goldman, S.; Zadina, K.; Moritz, T.; *et al. J. Am. Coll. Cardiol.* **2004**, *44*, 2149–2156.
10. Lytle, B. W.; Loop, F. D.; Cosgrove, D. M.; Ratliff, N. B.; Easley, K.; Taylor, P. C. *J. Thorac. Cardiovasc. Surg.* **1985**, *89*, 248–258.
11. Tatoulis, J.; Buxton, B. F.; Fuller, J. A.; *et al. Ann. Thorac. Surg.* **2009**, *88*, 23–29; discussion 29-30.
12. John, L. C. *Ann. Thorac. Surg.* **2009**, *87*, 331–338.
13. Komori, K.; Inoguchi, H.; Kume, M.; Shoji, T.; Furuyama, T. *Surgery* **2002**, *131*, S249–S255.

14. Gao, C.; Ren, C.; Li, D.; Li, L. *Ann. Thorac. Surg.* **2009**, *88*, 59–62.
15. Kulik, A.; Chan, V.; Ruel, M. *Expert Opin. Drug Saf.* **2009**, *8*, 169–182.
16. Kulik, A.; Ruel, M. *Expert Opin. Drug Saf.* **2009**, *8*, 559–571.
17. Kobayashi, J. *Circ. J.* **2009**, *73*, 1178–1183.
18. Sasaki, H. *J. Card. Surg.* **2008**, *23*, 398–407.
19. Suma, H.; Tanabe, H.; Takahashi, A.; *et al. Circulation* **2007**, *116*, I188–I191.
20. Xue, L.; Greisler, H. P. *J. Vasc. Surg.* **2003**, *37*, 472–480.
21. Pereira, C. E.; Albers, M.; Romiti, M.; Brochado-Neto, F. C.; Pereira, C. A. *J. Vasc. Surg.* **2006**, *44*, 510–517.
22. Albers, M.; Battistella, V. M.; Romiti, M.; Rodrigues, A. A.; Pereira, C. A. *J. Vasc. Surg.* **2003**, *37*, 1263–1269.
23. Kissin, M.; Kansal, N.; Pappas, P. J.; Defouw, D. O.; Duran, W. N.; Hobson, R. W., 2nd *J. Vasc. Surg.* **2000**, *31*, 69–83.
24. Norberto, J. J.; Sidawy, A. N.; Trad, K. S.; *et al. J. Vasc. Surg.* **1995**, *21*, 558–566.
25. Alcocer, F.; Jordan, W. D., Jr.; Wirthlin, D. J.; Whitley, D. *Vascular* **2004**, *12*, 318–324.
26. Gulkarov, I.; Malik, R.; Yakubov, R.; *et al. Vasc. Endovasc. Surg.* **2008**, *42*, 561–566.
27. Ruckert, R. I.; Tsilimparis, N.; Lobenstein, B.; Witte, J.; Seip, G.; Storck, M. *J. Vasc. Surg.* **2009**, *49*, 1203–1209; e3.
28. Wesolowski, S. A.; Fries, C. C.; Karlson, K. E.; De Bakey, M.; Sawyer, P. N. *Surgery* **1961**, *50*, 91–96.
29. Prager, M. R.; Hoblaj, T.; Nanobashvili, J.; *et al. Surgery* **2003**, *134*, 80–85.
30. Jensen, L. P.; Lepantalo, M.; Fossdal, J. E.; *et al. Eur. J. Vasc. Endovasc. Surg.* **2007**, *34*, 44–49.
31. Johnson, W. C.; Lee, K. K. *J. Vasc. Surg.* **1999**, *30*, 1077–1083.
32. Robinson, B. I.; Fletcher, J. P.; Tomlinson, P.; *et al. Cardiovasc. Surg.* **1999**, *7*, 214–218.
33. Bradbury, A. W.; Adam, D. J.; Bell, J.; *et al. Health Technol. Assess.* **2010**, *14*, 1–210; iii–iv.
34. Mcquade, K.; Gable, D.; Hohman, S.; Pearl, G.; Theune, B. *J. Vasc. Surg.* **2009**, *49*, 109–115; 116 e1–9; discussion 116.
35. Reilly, L. M.; Chuter, T. A. *J. Cardiovasc. Surg.* **2009**, *50*, 447–460.
36. Vroman, L. *Ann. N. Y. Acad. Sci.* **1987**, *516*, 300–305.
37. Roohk, H. V.; Pick, J.; Hill, R.; Hung, E.; Bartlett, R. H. *Trans. Am. Soc. Artif. Intern. Organs* **1976**, *22*, 1–8.
38. Keere, I. V.; Willaert, R.; Hubin, A.; Vereecken, J. *Langmuir* **2008**, *24*, 1844–1852.
39. Jennings, L. K. *Am. J. Cardiol.* **2009**, *103*, 4A–10A.
40. Beumer, S.; Ijsseldijk, M.; De Groot, P.; Sixma, J. *Blood* **1994**, *84*, 3724–3733.
41. Greisler, H. P.; Klosak, J. J.; Steinam, S.; *et al. ASAIO Trans.* **1989**, *35*, 561–563.
42. Nagai, H.; Handa, M.; Kawai, Y.; Watanabe, K.; Ikeda, Y. *Thromb. Res.* **1993**, *71*, 467–477.
43. Schaub, R. D.; Kameneva, M. V.; Borovetz, H. S.; Wagner, W. R. *J. Biomed. Mater. Res.* **2000**, *49*, 460–468.
44. Gutensohn, K.; Beythien, C.; Bau, J.; Meinertz, T.; Kuehnl, P. *Thromb. Res.* **1997**, *86*, 49–56.
45. Balakrishnan, B.; Dooley, J.; Kopia, G.; Edelman, E. R. *J. Control. Release* **2008**, *131*, 173–180.
46. Shepard, A. D.; Gelfand, J. A.; Callow, A. D.; O'Donnell, T. F., Jr. *J. Vasc. Surg.* **1984**, *1*, 829–838.
47. Carroll, M. C. *Vaccine* **2008**, *26*(Suppl. 8), I28–I33.
48. Chenoweth, D. E. *Ann. N. Y. Acad. Sci.* **1987**, *516*, 306–313.
49. Henderson, L. W.; Chenoweth, D. *Blood Purif.* **1987**, *5*, 100–111.
50. Gorbet, M. B.; Sefton, M. V. *Biomaterials* **2004**, *25*, 5681–5703.
51. Nilsson, B.; Ekdahl, K. N.; Mollnes, T. E.; Lambris, J. D. *Mol. Immunol.* **2007**, *44*, 82–94.
52. Cenni, E.; Granchi, D.; Arciola, C. R.; *et al. Biomaterials* **1995**, *16*, 1223–1227.
53. Bevilacqua, M. P.; Pober, J. S.; Wheeler, M. E.; Cotran, R. S.; Gimbrone, M. A., Jr. *J. Clin. Invest.* **1985**, *76*, 2003–2011.
54. Lackie, J. M.; De Bono, D. *Microvasc. Res.* **1977**, *13*, 107–112.
55. Tonnesen, M. G.; Smedly, L. A.; Henson, P. M. *J. Clin. Invest.* **1984**, *74*, 1581–1592.
56. Bar-Shavit, R.; Kahn, A.; Fenton, J. W., II; Wilner, G. D. *J. Cell Biol.* **1983**, *96*, 282–285.
57. Deuel, T. F.; Senior, R. M.; Huang, J. S.; Griffin, G. L. *J. Clin. Invest.* **1982**, *69*, 1046–1049.
58. Dicorleto, P. E.; De La Motte, C. A. *J. Clin. Invest.* **1985**, *75*, 1153–1161.
59. Greisler, H. *ASAIO Trans.* **1988**, *34*, 1051–1059.
60. Greisler, H. P. *Ann. Vasc. Surg.* **1990**, *4*, 98–103.
61. Greisler, H. P.; Dennis, J. W.; Endean, E. D.; Ellinger, J.; Friesel, R.; Burgess, W. *J. Vasc. Surg.* **1989**, *9*, 588–593.
62. Kay, A. B.; Pepper, D. S.; Ewart, M. R. *Nat. New Biol.* **1973**, *243*, 56–57.
63. Marder, S. R.; Chenoweth, D. E.; Goldstein, I. M.; Perez, H. D. *J. Immunol.* **1985**, *134*, 3325–3331.
64. Greisler, H. P.; Petsikas, D.; Cziperle, D. J.; Murchan, P. M.; Henderson, S. C.; Lam, T. M. *Cardiovasc. Surg.* **1996**, *4*, 169–173.
65. Rodriguez, A.; Voskerician, G.; Meyerson, H.; MacEwan, S. R.; Anderson, J. M. *J. Biomed. Mater. Res. A* **2008**, *85*, 556–565.
66. Babensee, J. E. *Semin. Immunol.* **2008**, *20*, 101–108.
67. Zarge, J. I.; Huang, P.; Husak, V.; *et al. J. Vasc. Surg.* **1997**, *25*, 840–848; discussion 848–849.
68. Anggrahini, D. W.; Emoto, N.; Nakayama, K.; *et al. Cardiovasc. Res.* **2009**, *82*, 143–151.
69. Mcguigan, A. P.; Sefton, M. V. *Biomaterials* **2007**, *28*, 2547–2571.
70. Mikucki, S. A.; Greisler, H. P. *Semin. Vasc. Surg.* **1999**, *12*, 18–26.
71. Clowes, A. W.; Gown, A. M.; Hanson, S. R.; Reidy, M. A. *Am. J. Pathol.* **1985**, *118*, 43–54.
72. Clowes, A. W.; Kirkman, T. R.; Reidy, M. A. *Am. J. Pathol.* **1986**, *123*, 220–230.
73. Reidy, M. A.; Clowes, A. W.; Schwartz, S. M. *Lab Invest* **1983**, *49*, 569–575.
74. Clowes, A. W.; Kohler, T. *J. vasc. surg.* **1991**, *13*, 734.
75. Greisler, H. P.; Dennis, J. W.; Endean, E. D.; Ellinger, J.; Buttle, K. F.; Kim, D. U. *Circulation* **1988**, *78*, I6–I12.
76. Greisler, H. P.; Ellinger, J.; Schwarcz, T. H.; Golan, J.; Raymond, R. M.; Kim, D. U. *Arch. Surg.* **1987**, *122*, 715–721.
77. Hirabayashi, K.; Saitoh, E.; Ijima, H.; Takenawa, T.; Kodama, M.; Hori, M. *J. Biomed. Mater. Res.* **1992**, *26*, 1433–1447.
78. Greisler, H. P.; Klosak, J. J.; Mcgurrin, J. F.; *et al. J. Cardiovasc. Surg.* **1990**, *31*, 640–645.
79. Arehart, E.; Gleim, S.; Kasza, Z.; Fetalvero, K. M.; Martin, K. A.; Hwa, J. *Curr. Med. Chem.* **2007**, *14*, 2161–2169.
80. Cenni, E.; Verri, E.; Granchi, D.; *et al. J. Biomater. Sci. Polym. Ed.* **1999**, *10*, 891–900.
81. Baird, A.; Durkin, T. *Biochem. Biophys. Res. Commun.* **1986**, *138*, 476.
82. De Mel, A.; Jell, G.; Stevens, M. M.; Seifalian, A. M. *Biomacromolecules* **2008**, *9*, 2969–2979.
83. McArthur, C. S.; Sheahan, M. G.; Pomposelli, F. B., Jr.; *et al. J. Vasc. Surg.* **2003**, *37*, 1181.
84. Nikkari, S. T.; Clowes, A. W. *Ann. Med.* **1994**, *26*, 95.
85. Ramdev, P.; Rayan, S. S.; Sheahan, M.; *et al. J. Vasc. Surg.* **2002**, *36*, 969.
86. Allaire, E.; Clowes, A. W. *Ann. Thorac. Surg.* **1997**, *63*, 582.
87. Bendeck, M. P.; Zempo, N.; Clowes, A. W.; Galardy, R. E.; Reidy, M. A. *Circ. Res.* **1994**, *75*, 539–545.
88. Boyle, E. M., Jr.; Lille, S. T.; Allaire, E.; Clowes, A. W.; Verrier, E. D. *Ann. Thorac. Surg.* **1997**, *63*, 885.
89. Hedin, U.; Roy, J.; Tran, P. K.; Lundmark, K.; Rahman, A. *Thromb. Haemost.* **1999**, *82*(Suppl 1), 23.
90. Nakatani, M.; Takeyama, Y.; Shibata, M.; *et al. Cardiovasc. Pathol.* **2003**, *12*, 40–48.
91. Sjolund, M.; Rahm, M.; Claesson-Welsh, L.; Sejersen, T.; Heldin, C. H.; Thyberg, J. *Growth Factors* **1990**, *3*, 191.
92. Thyberg, J. *Int. Rev. Cytol.* **1996**, *169*, 183.
93. Kenagy, R. D.; Fukai, N.; Min, S. K.; Jalikis, F.; Kohler, T. R.; Clowes, A. W. *J. Vasc. Surg.* **2009**, *49*, 1282–1288.
94. Refson, J. S.; Schachter, M.; Patel, M. K.; *et al. Circulation* **1998**, *97*, 2506–2510.
95. Zhang, W. D.; Bai, H. Z.; Sawa, Y.; *et al. J. Vasc. Surg.* **1999**, *30*, 169.
96. Kolandaivelu, K.; Edelman, E. R. *J. Biomed. Mater. Res. A* **2004**, *70*, 186–193.
97. Badimon, L.; Badimon, J. J.; Turitto, V. T.; Fuster, V. *Ann. N. Y. Acad. Sci.* **1987**, *516*, 527–540.
98. Davies, P. F.; Remuzzi, A.; Gordon, E. J.; Dewey, C. F., Jr.; Gimbrone, M. A., Jr. *Proc. Natl Acad. Sci. USA* **1986**, *83*, 2114–2117.
99. Flaherty, J. T.; Pierce, J. E.; Ferrans, V. J.; Patel, D. J.; Tucker, W. K.; Fry, D. L. *Circ. Res.* **1972**, *30*, 23–33.
100. Levesque, M. J.; Liepsch, D.; Moravec, S.; Nerem, R. M. *Arteriosclerosis* **1986**, *6*, 220–229.
101. Reidy, M. A.; Langille, B. L. *Exp. Mol. Pathol.* **1980**, *32*, 276–289.
102. Davies, P. F.; Dewey, C. F., Jr.; Bussolari, S. R.; Gordon, E. J.; Gimbrone, M. A., Jr. *J. Clin. Invest.* **1984**, *73*, 1121–1129.
103. Frangos, J. A.; Eskin, S. G.; Mcintire, L. V.; Ives, C. L. *Science* **1985**, *227*, 1477–1479.
104. Sharefkin, J. B.; Diamond, S. L.; Eskin, S. G.; Mcintire, L. V.; Dieffenbach, C. W. *J. Vasc. Surg.* **1991**, *14*, 1–9.
105. Greisler, H. P.; Johnson, S.; Joyce, K.; *et al. Arch. Surg.* **1990**, *125*, 1622–1625.
106. Gosselin, C.; Vorp, D. A.; Warty, V.; *et al. J. Surg. Res.* **1996**, *60*, 327–332.
107. Zenni, G. C.; Gray, J. L.; Appelgren, E. O.; *et al. ASAIO J.* **1993**, *39*, M496–M500.

108. Dagher, N. N.; Modrall, J. G. *Semin. Vasc. Surg.* **2007**, *20*, 10–14.
109. Henke, P. *Semin. Vasc. Surg.* **2009**, *22*, 245–251.
110. Goldman, S.; Copeland, J.; Moritz, T.; *et al. Circulation* **1988**, *77*, 1324–1332.
111. Antiplatelet Trialists' Collaboration. *Br. Med. J.* **1994**, *308*, 159–168.
112. Weber, M.; Von Schacky, C.; Lorenz, R.; *et al. Klin. Wochenschr.* **1984**, *62*, 458–464.
113. Pantely, G. A.; Goodnight, S. H., Jr.; Rahimtoola, S. H.; *et al. N. Engl. J. Med.* **1979**, *301*, 962–966.
114. Sharma, G. V.; Khuri, S. F.; Josa, M.; Folland, E. D.; Parisi, A. F. *Circulation* **1983**, *68*, II218–II221.
115. Sethi, G. K.; Copeland, J. G.; Goldman, S.; Moritz, T.; Zadina, K.; Henderson, W. G. *J. Am. Coll. Cardiol.* **1990**, *15*, 15–20.
116. Brown, J.; Lethaby, A.; Maxwell, H.; Wawrzyniak, A. J.; Prins, M. H. *Cochrane Database Syst. Rev.* **2008**; CD000535.
117. McCollum, C.; Alexander, C.; Kenchington, G.; Franks, P. J.; Greenhalgh, R. *J. Vasc. Surg.* **1991**, *13*, 150–161; discussion 161–162.
118. Watson, H. R.; Skene, A. M.; Belcher, G. *Br. J. Clin. Pharmacol.* **2000**, *49*, 479–483.
119. Dunning, J.; Versteegh, M.; Fabbri, A.; *et al. Eur. J. Cardiothorac. Surg.* **2008**, *34*, 73–92.
120. Dorffler-Melly, J.; Koopman, M. M.; Prins, M. H.; Buller, H. R. *Cochrane Database Syst. Rev.* **2009**.
121. Bednar, F.; Osmancik, P.; Hlavicka, J.; Jedlickova, V.; Paluch, Z.; Vanek, T. *J. Thromb. Thrombolysis* **2009**, *27*, 394–399.
122. Kayacioglu, I.; Gunay, R.; Saskin, H.; *et al. Heart Surg. Forum* **2008**, *11*, E152–E157.
123. Vyas, S. P.; Vaidya, B. *Expert Opin. Drug Deliv.* **2009**, *6*, 499–508.
124. Samson, R. H. *Vasc. Endovasc. Surg.* **2008**, *42*, 352–366.
125. Henke, P. K.; Blackburn, S.; Proctor, M. C.; *et al. J. Vasc. Surg.* **2004**, *39*, 357–365.
126. Dorffler-Melly, J.; Buller, H. R.; Koopman, M. M.; Prins, M. H. *Cochrane Database Syst. Rev.* **2003**; CD000536.
127. Brumberg, R. S.; Back, M. R.; Armstrong, P. A.; *et al. J. Vasc. Surg.* **2007**, *46*, 1160–1166.
128. Johnson, W. C.; Williford, W. O.; Corson, J. D.; Padberg, F. T., Jr. *Vascular* **2004**, *12*, 362–368.
129. Tsuchida, H.; Cameron, B. L.; Marcus, C. S.; Wilson, S. E. *J. Vasc. Surg.* **1992**, *16*, 643–649; discussion 649–650.
130. Ao, P. Y.; Hawthorne, W. J.; Vicaretti, M.; Fletcher, J. P. *Eur. J. Vasc. Endovasc. Surg.* **2000**, *20*, 241–249.
131. Hansi, C.; Arab, A.; Rzany, A.; Ahrens, I.; Bode, C.; Hehrlein, C. *Catheter. Cardiovasc. Interv.* **2009**, *73*, 488–496.
132. Al-Khaffaf, H.; Charlesworth, D. *J. Vasc. Surg.* **1996**, *23*, 686–690.
133. Jordan, S. W.; Chaikof, E. L. *J. Vasc. Surg.* **2007**, *45*, A104–A115.
134. Llanos, G. R.; Sefton, M. V. *Evaluation of thrombogenicity. J. Biomed. Mater. Res.* **1993**, *27*, 1383–1391.
135. Zhang, Q.; Wang, C.; Babukutty, Y.; Ohyama, T.; Kogoma, M.; Kodama, M. *J. Biomed. Mater. Res.* **2002**, *60*, 502–509.
136. Han, D. K.; Park, K.; Park, K. D.; Ahn, K. D.; Kim, Y. H. *Artif. Organs* **2006**, *30*, 955–959.
137. Ritter, E. F.; Fata, M. M.; Rudner, A. M.; Klitzman, B. *Plast. Reconstr. Surg.* **1998**, *101*, 142–146.
138. Ritter, E. F.; Kim, Y. B.; Reischl, H. P.; Serafin, D.; Rudner, A. M.; Klitzman, B. *Surgery* **1997**, *122*, 888–892.
139. Clowes, A. W.; Clowes, M. M.; Kirkman, T. R.; Jackson, C. L.; Au, Y. P.; Kenagy, R. *Circ. Res.* **1992**, *70*, 1128.
140. Lin, P. H.; Chen, C.; Bush, R. L.; Yao, Q.; Lumsden, A. B.; Hanson, S. R. *J. Vasc. Surg.* **2004**, *39*, 1322–1328.
141. Laredo, J.; Xue, L.; Husak, V. A.; Ellinger, J.; Greisler, H. P. *Am. J. Surg.* **2003**, *186*, 556–560.
142. Laredo, J.; Xue, L.; Husak, V. A.; *et al. J. Vasc. Surg.* **2004**, *39*, 1059–1065.
143. Beamish, J. A.; Geyer, L. C.; Haq-Siddiqi, N. A.; Kottke-Marchant, K.; Marchant, R. E. *Biomaterials* **2009**, *30*, 6286–6294.
144. Hugl, B.; Nevelsteen, A.; Daenens, K.; *et al. J. Cardiovasc. Surg.* **2009**, *50*, 195–203.
145. Daenens, K.; Schepers, S.; Fourneau, I.; Houthoofd, S.; Nevelsteen, A. *J. Vasc. Surg.* **2009**, *49*, 1210–1216.
146. Dorrucci, V.; Griselli, F.; Petralia, G.; Spinamano, L.; Adornetto, R. *J. Cardiovasc. Surg.* **2008**, *49*, 145–149.
147. Peeters, P.; Verbist, J.; Deloose, K.; Bosiers, M. *J. Cardiovasc. Surg.* **2006**, *47*, 407–413.
148. Wallusch eck, K. P.; Bierkandt, S.; Brandt, M.; Cremer, J. *J. Cardiovasc. Surg.* **2005**, *46*, 425–430.
149. Losel-Sadee, H.; Alefelder, C. *J. Cardiovasc. Surg.* **2009**, *50*, 339–343.
150. Heyligers, J. M.; Lisman, T.; Verhagen, H. J.; Weeterings, C.; De Groot, P. G.; Moll, F. L. *J. Vasc. Surg.* **2008**, *47*, 324–329; discussion 329.
151. Devine, C.; McCollum, C. *J. Vasc. Surg.* **2004**, *40*, 924–931.
152. Sarkar, S.; Salacinski, H. J.; Hamilton, G.; Seifalian, A. M. *Eur. J. Vasc. Endovasc. Surg.* **2006**, *31*, 627–636.
153. Brewster, L. P.; Washington, C.; Brey, E. M.; *et al. Biomaterials* **2008**, *29*, 327.
154. Cho, E. H.; Yang, Y. I.; Mun, C. W.; Kim, J. K. *J. Biomater. Sci. Polym. Ed.* **2005**, *16*, 775–790.
155. Gosselin, C.; Vorp, D. A.; Warty, V.; *et al. J. Surg. Res.* **1996**, *60*, 327.
156. Tassiopoulos, A. K.; Greisler, H. P. *J. Biomater. Sci. Polym. Ed.* **2000**, *11*, 1275–1284.
157. Gray, J. L.; Kang, S. S.; Zenni, G. C.; *et al. J. Surg. Res.* **1994**, *57*, 596–612.
158. Greisler, H. P.; Cziperle, D. J.; Kim, D. U.; *et al. Surgery* **1992**, *112*, 244–254; discussion 254–255.
159. Gulbins, H.; Pritisanac, A.; Uhlig, A.; *et al. Ann. Thorac. Surg.* **2005**, *79*, 2119–2126.
160. Suggs, L. J.; Mikos, A. G. *Cell Transplant.* **1999**, *8*, 345–350.
161. Doi, K.; Matsuda, T. *J. Biomed. Mater. Res.* **1997**, *34*, 361–370.
162. Greisler, H. P.; Cziperle, D. J.; Kim, D. U.; *et al. Surgery* **1992**, *112*, 244.
163. Walpoth, B. H.; Zammaretti, P.; Cikirikcioglu, M.; *et al. J. Thorac. Cardiovasc. Surg.* **2007**, *133*, 1163–1170.
164. Fillinger, M. F.; O'Connor, S. E.; Wagner, R. J.; Cronenwett, J. L. *J. Vasc. Surg.* **1993**, *17*, 1058.
165. Mcneil, P. L.; Muthukrishnan, L.; Warder, E.; D'Amore, P. A. *J. Cell Biol.* **1989**, *109*, 811–822.
166. Kang, S. S.; Gosselin, C.; Ren, D.; Greisler, H. P. *Surgery* **1995**, *118*, 280.
167. Brewster, L.; Brey, E. M.; Addis, M.; *et al. Am. J. Surg.* **2006**, *192*, 589–593.
168. Brewster, L. P.; Brey, E. M.; Tassiopoulos, A. K.; *et al. Am. J. Surg.* **2004**, *188*, 575–579.
169. Erzurum, V. Z.; Bian, J. F.; Husak, V. A.; *et al. J. Vasc. Surg.* **2003**, *37*, 1075.
170. Shireman, P. K.; Xue, L.; Maddox, E.; Burgess, W. H.; Greisler, H. P. *J. Vasc. Surg.* **2000**, *31*, 382.
171. Xue, L.; Shireman, P. K.; Hampton, B.; Burgess, W. H.; Greisler, H. P. *J. Surg. Res.* **2000**, *92*, 255.
172. Xue, L.; Tassiopoulos, A. K.; Woloson, S. K.; *et al. J. Vasc. Surg.* **2001**, *33*, 554.
173. Sahni, A.; Odrljin, T.; Francis, C. W. *J. Biol. Chem.* **1998**, *273*, 7554–7559.
174. Sahni, A.; Sahni, S. K.; Simpson-Haidaris, P. J.; Francis, C. W. *J. Thromb. Haemost.* **2004**, *2*, 1629–1636.
175. Sahni, A.; Sporn, L. A.; Francis, C. W. *J. Biol. Chem.* **1999**, *274*, 14936.
176. Ehrbar, M.; Djonov, V. G.; Schnell, C.; *et al. Circ. Res.* **2004**, *94*, 1124–1132.
177. Zisch, A. H.; Lutolf, M. P.; Ehrbar, M.; *et al. FASEB J.* **2003**, *17*, 2260–2262.
178. Jun, H. W.; West, J. *J. Biomater. Sci. Polym. Ed.* **2004**, *15*, 73–94.
179. Jun, H. W.; West, J. L. *Tissue Eng.* **2005**, *11*, 1133–1140.
180. Taite, L. J.; Yang, P.; Jun, H. W.; West, J. L. *J. Biomed. Mater. Res. B Appl. Biomater.* **2008**, *84*, 108–116.
181. Wang, G. X.; Deng, X. Y.; Tang, C. J.; *et al. Artif. Cells Blood Substit. Immobil. Biotechnol.* **2006**, *34*, 11–25.
182. Krijgsman, B.; Seifalian, A. M.; Salacinski, H. J.; *et al. Tissue Eng.* **2002**, *8*, 673–680.
183. Vallieres, K.; Petitclerc, E.; Laroche, G. *Macromol. Biosci.* **2007**, *7*, 738–745.
184. Sato, H.; Tsuji, H.; Ikeda, S.; Ikemoto, N.; Ishikawa, J.; Nishimoto, S. *J. Biomed. Mater. Res.* **1999**, *44*, 22–30.
185. Wang, C.; Zhang, Q.; Uchida, S.; Kodama, M. *J. Biomed. Mater. Res.* **2002**, *62*, 315–322.
186. Wissink, M. J.; Beernink, R.; Poot, A. A.; *et al. J. Control. Release* **2000**, *64*, 103–114.
187. Sreerekha, P. R.; Krishnan, L. K. *Artif. Organs* **2006**, *30*, 242–249.
188. Hubbell, J. A.; Massia, S. P.; Desai, N. P.; Drumheller, P. D. *Biotechnology* **1991**, *9*, 568–572.
189. Massia, S. P.; Hubbell, J. A. *J. Biol. Chem.* **1992**, *267*, 14019–14026.
190. Rodenberg, E. J.; Pavalko, F. M. *Tissue Eng.* **2007**, *13*, 2653–2666.
191. Mann, B. K.; Tsai, A. T.; Scott-Burden, T.; West, J. L. *Biomaterials* **1999**, *20*, 2281–2286.
192. Deutsch, M.; Meinhart, J.; Zilla, P.; *et al. J. Vasc. Surg.* **2009**, *49*, 352–362; Discussion 362.
193. Schuman, E.; Babu, J. *Vascular* **2008**, *16*, 269–274.
194. Fleser, P. S.; Nuthakki, V. K.; Malinzak, L. E.; *et al. J. Vasc. Surg.* **2004**, *40*, 803–811.
195. Jun, H. W.; Taite, L. J.; West, J. L. *Biomacromolecules* **2005**, *6*, 838–844.
196. Yin, T.; Wang, G.; Ruan, C.; Guzman, R.; Guidoin, R. *J. Biomed. Mater. Res. A* **2007**, *83*, 861–867.

197. Jordan, S. W.; Haller, C. A.; Sallach, R. E.; Apkarian, R. P.; Hanson, S. R.; Chaikof, E. L. *Biomaterials* **2007**, *28*, 1191–1197.
198. Marois, Y.; Paris, E.; Zhang, Z.; Doillon, C. J.; King, M. W.; Guidoin, R. G. *Biomaterials* **1996**, *17*, 1289–1300.
199. Santerre, J. P.; Labow, R. S.; Duguay, D. G.; Erfle, D.; Adams, G. A. *J. Biomed. Mater. Res.* **1994**, *28*, 1187–1199.
200. Zhang, Z.; Marois, Y.; Guidoin, R. G.; *et al*. *Biomaterials* **1997**, *18*, 113–124.
201. Edwards, A.; Carson, R. J.; Szycher, M.; Bowald, S. *J. Biomater. Appl.* **1998**, *13*, 23–45.
202. Jeschke, M. G.; Hermanutz, V.; Wolf, S. E.; Koveker, G. B. *J. Vasc. Surg.* **1999**, *29*, 168–176.
203. Glickman, M. H.; Stokes, G. K.; Ross, J. R.; *et al*. *J. Vasc. Surg.* **2001**, *34*, 465–472; discussion 472–473.
204. Jefic, D.; Reddy, P. P.; Flynn, L. M.; Provenzano, R. *Nephrol. News Issues* **2005**, *19*, 44–47.
205. Kiyama, H.; Imazeki, T.; Kurihara, S.; Yoneshima, H. *Ann. Vasc. Surg.* **2003**, *17*, 516–521.
206. Matsuda, H.; Miyazaki, M.; Oka, Y.; *et al*. *Artif. Organs* **2003**, *27*, 722–727.
207. Kakkos, S. K.; Andrzejewski, T.; Haddad, J. A.; *et al*. *J. Vasc. Surg.* **2008**, *47*, 407–414.
208. Brewster, L. P.; Brey, E. M.; Greisler, H. P. *Adv. Drug Deliv. Rev.* **2006**, *58*, 604–629.
209. Stephan, D.; San, H.; Yang, Z. Y.; *et al*. *Mol. Med.* **1997**, *3*, 593–599.
210. Ohta, S.; Komori, K.; Yonemitsu, Y.; Onohara, T.; Matsumoto, T.; Sugimachi, K. *Surgery* **2002**, *131*, 644–653.
211. Kong, D.; Melo, L. G.; Mangi, A. A.; *et al*. *Circulation* **2004**, *109*, 1769–1775.
212. Fishbein, I.; Alferiev, I.; Bakay, M.; *et al*. *Circulation* **2008**, *117*, 2096–2103.
213. Ye, Y. W.; Landau, C.; Willard, J. E.; *et al*. *Ann. Biomed. Eng.* **1998**, *26*, 398–408.
214. Van Belle, E.; Tio, F. O.; Chen, D.; Maillard, L.; Kearney, M.; Isner, J. M. *J. Am. Coll. Cardiol.* **1997**, *29*, 1371–1379.
215. Hashiya, N.; Aoki, M.; Tachibana, K.; *et al*. *Biochem. Biophys. Res. Commun.* **2004**, *317*, 508–514.
216. Alexander, J. H.; Hafley, G.; Harrington, R. A.; *et al*. *JAMA* **2005**, *294*, 2446–2454.
217. Conte, M. S.; Bandyk, D. F.; Clowes, A. W.; *et al*. *J. Vasc. Surg.* **2006**, *43*, 742–751; discussion 751.
218. Lee, K. Y.; Mooney, D. J. *Chem. Rev.* **2001**, *101*, 1869–1879.
219. Weinberg, C. B.; Bell, E. *Science* **1986**, *231*, 397.
220. Grassl, E. D.; Oegema, T. R.; Tranquillo, R. T. *J. Biomed. Mater. Res.* **2002**, *60*, 607.
221. Long, J. L.; Tranquillo, R. T. *Matrix Biol.* **2003**, *22*, 339.
222. Ross, J. J.; Tranquillo, R. T. *Matrix Biol.* **2003**, *22*, 477.
223. Swartz, D. D.; Russell, J. A.; Andreadis, S. T. *Am. J. Physiol. Heart Circ. Physiol.* **2005**, *288*, H1451–H1460.
224. Hasegawa, T.; Okada, K.; Takano, Y.; Hiraishi, Y.; Yoshida, Y.; Okita, Y. *ASAIO J.* **2005**, *51*, 725–729.
225. Tschoeke, B.; Flanagan, T. C.; Cornelissen, A.; *et al*. *Artif. Organs* **2008**, *32*, 800–809.
226. Grassl, E. D.; Oegema, T. R.; Tranquillo, R. T. *J. Biomed. Mater. Res. A* **2003**, *66*, 550.
227. Yao, L.; Swartz, D. D.; Gugino, S. F.; Russell, J. A.; Andreadis, S. T. *Tissue Eng.* **2005**, *11*, 991–1003.
228. Ogle, B. M.; Mooradian, D. L. *J. Biomech. Eng.* **2002**, *124*, 724–733.
229. Yao, L.; Liu, J.; Andreadis, S. T. *Pharm. Res.* **2008**, *25*, 1212–1221.
230. Engbers-Buijtenhuijs, P.; Buttafoco, L.; Poot, A. A.; *et al*. *Biomaterials* **2006**, *27*, 2390.
231. Nerem, R. M.; Seliktar, D. *Annu. Rev. Biomed. Eng.* **2001**, *3*, 225–243.
232. Syedain, Z. H.; Weinberg, J. S.; Tranquillo, R. T. *Proc. Natl. Acad. Sci. USA* **2008**, *105*, 6537–6542.
233. Cummings, C. L.; Gawlitta, D.; Nerem, R. M.; Stegemann, J. P. *Biomaterials* **2004**, *25*, 3699–3706.
234. Jeong, S. I.; Kim, S. Y.; Cho, S. K.; *et al*. *Biomaterials* **2007**, *28*, 1115–1122.
235. Blindt, R.; Hoffmeister, K. M.; Bienert, H.; *et al*. *Int. J. Artif. Organs* **1999**, *22*, 843–853.
236. Lafont, A.; Li, S.; Garreau, H.; Cornhill, F.; Vert, M. *J. Biomed. Mater. Res. B Appl. Biomater.* **2006**, *77*, 349–356.
237. Zilberman, M.; Nelson, K. D.; Eberhart, R. C. *J. Biomed. Mater. Res. B Appl. Biomater.* **2005**, *74*, 792–799.
238. Zilberman, M.; Schwade, N. D.; Eberhart, R. C. *J. Biomed. Mater. Res. B Appl. Biomater.* **2004**, *69*, 1–10.
239. Greisler, H. P. *Arch. Surg.* **1982**, *117*, 1425–1431.
240. Greisler, H. P.; Kim, D. U.; Price, J. B.; Voorhees, A. B., Jr. *Arch. Surg.* **1985**, *120*, 315–323.
241. Greisler, H. P.; Schwarcz, T. H.; Ellinger, J.; Kim, D. U. *J. Vasc. Surg.* **1986**, *3*, 747–756.
242. Greisler, H. P.; Cabusao, E. B.; Lam, T. M.; Murchan, P. M.; Ellinger, J.; Kim, D. U. *ASAIO Trans.* **1991**, *37*, M472–M475.
243. Greisler, H. P.; Petsikas, D.; Lam, T. M.; *et al*. *J. Biomed. Mater. Res.* **1993**, *27*, 955–961.
244. Greisler, H. P.; Henderson, S. C.; Lam, T. M. *J. Biomater. Sci. Polym. Ed.* **1993**, *4*, 415–430.
245. Greisler, H. P.; Joyce, K. A.; Kim, D. U.; Pham, S. M.; Berceli, S. A.; Borovetz, H. S. *J. Biomed. Mater. Res.* **1992**, *26*, 1449–1461.
246. Greisler, H. P.; Endean, E. D.; Klosak, J. J.; *et al*. *J. Vasc. Surg.* **1988**, *7*, 697–705.
247. Greisler, H. P.; Kim, D. U.; Dennis, J. W.; *et al*. *J. Vasc. Surg.* **1987**, *5*, 572–583.
248. Greisler, H. P.; Tattersall, C. W.; Klosak, J. J.; Cabusao, E. A.; Garfield, J. D.; Kim, D. U. *Surgery* **1991**, *110*, 645–654; discussion 654–655.
249. Shum-Tim, D.; Stock, U.; Hrkach, J.; *et al*. *Ann. Thorac. Surg.* **1999**, *68*, 2298–2304; discussion 2305.
250. Zhang, L.; Zhou, J.; Lu, Q.; Wei, Y.; Hu, S. *Biotechnol. Bioeng.* **2008**, *99*, 1007–1015.
251. Niklason, L. E.; Gao, J.; Abbott, W. M.; *et al*. *Science* **1999**, *284*, 489.
252. Tschoeke, B.; Flanagan, T. C.; Koch, S.; *et al*. *Tissue Eng. A* **2009**, *15*, 1909–1918.
253. Crapo, P. M.; Wang, Y. *Biomaterials* **2010**, *31*, 1626–1635.
254. Hoerstrup, S. P.; Cummings Mrcs, I.; Lachat, M.; *et al*. *Circulation* **2006**, *114*, I159–I166.
255. Shin'oka, T.; Imai, Y.; Ikada, Y. *N. Engl. J. Med.* **2001**, *344*, 532–533.
256. Shin'oka, T.; Matsumura, G.; Hibino, N.; *et al*. *J. Thorac. Cardiovasc. Surg.* **2005**, *129*, 1330–1338.
257. Shinoka, T.; Breuer, C. *Yale J. Biol. Med.* **2008**, *81*, 161–166.
258. Ormiston, J. A.; Serruys, P. W.; Regar, E.; *et al*. *Lancet* **2008**, *371*, 899–907.
259. Ormiston, J. A.; Webster, M. W.; Armstrong, G. *Catheter. Cardiovasc. Interv.* **2007**, *69*, 128–131.
260. Serruys, P. W.; Ormiston, J. A.; Onuma, Y.; *et al*. *Lancet* **2009**, *373*, 897–910.
261. L'Heureux, N.; Paquet, S.; Labbe, R.; Germain, L.; Auger, F. A. *FASEB J.* **1998**, *12*, 47–56.
262. L'Heureux, N.; Dusserre, N.; Konig, G.; *et al*. *Nat. Med.* **2006**, *12*, 361.
263. L'Heureux, N.; McAllister, T. N.; De La Fuente, L. M. *N. Engl. J. Med.* **2007**, *357*, 1451–1453.
264. McAllister, T. N.; Maruszewski, M.; Garrido, S. A.; *et al*. *Lancet* **2009**, *373*, 1440–1446.
265. Schaner, P. J.; Martin, N. D.; Tulenko, T. N.; *et al*. *J. Vasc. Surg.* **2004**, *40*, 146–153.
266. Yu, X. X.; Wan, C. X.; Chen, H. Q. *J. Mater. Sci. Mater. Med.* **2008**, *19*, 319–326.
267. Amiel, G. E.; Komura, M.; Shapira, O.; *et al*. *Tissue Eng.* **2006**, *12*, 2355–2365.
268. Borschel, G. H.; Huang, Y. C.; Calve, S.; *et al*. *Tissue Eng.* **2005**, *11*, 778–786.
269. Teebken, O. E.; Puschmann, C.; Rohde, B.; *et al*. *VASA* **2009**, *38*, 60–65.

6.629. Cerebrospinal Fluid Shunts

R Bayston, University of Nottingham, Nottingham, UK; Nottingham University Hospitals QMC, Nottingham, UK

© 2011 Elsevier Ltd. All rights reserved.

6.629.1.	**Introduction**	470
6.629.2.	**Hydrocephalus**	470
6.629.3.	**Treatment of Hydrocephalus**	470
6.629.3.1.	Shunting	470
6.629.3.2.	Early Shunts: Biomaterials and Biocompatibility	470
6.629.3.3.	The Next Stage	471
6.629.3.4.	State-of-the-Art Shunts	472
6.629.4.	**Biocompatibility of Silicone Shunts**	473
6.629.5.	**Infective Complications**	473
6.629.5.1.	Causative Bacteria	473
6.629.5.2.	Source of the Infecting Bacteria	474
6.629.5.3.	Incidence of Shunt Infection	474
6.629.6.	**Treatment of Shunt Infections**	474
6.629.6.1.	Biofilms and Other Reasons for Treatment Failure	474
6.629.6.2.	Treatment Regimens	475
6.629.7.	**Prevention of Shunt Infections**	475
6.629.7.1.	Surgical Technique	475
6.629.7.2.	Prophylactic Antibiotics	475
6.629.8.	**Antimicrobial Shunt Catheters**	475
6.629.8.1.	Principles of Antimicrobial Biomaterials for Shunting	475
6.629.8.2.	Coated Catheters	476
6.629.8.3.	Impregnated Catheters	476
6.629.8.4.	Biological Importance of the Boundary Layer	476
6.629.9.	**Evaluation of Antimicrobial Catheters**	476
6.629.9.1.	Broth Culture Test	477
6.629.9.2.	Roll Plate Test	477
6.629.9.3.	Zone Plate Test	477
6.629.9.4.	Serial Plate Transfer Test	477
6.629.9.5.	Time to Kill Assay	477
6.629.9.6.	*In Vitro* Challenge	478
6.629.9.7.	*In Vivo* Testing	478
6.629.10.	**Application of *In Vitro* Tests to Existing Shunt and EVD catheters**	478
6.629.10.1.	Hydrogel: Coated Catheters	478
6.629.10.2.	Admixed/Impregnated Catheters	478
6.629.10.3.	Impregnated Catheters	478
6.629.10.4.	Silver: Processed Catheters	479
6.629.11.	**Clinical Studies on Antimicrobial Shunt and EVD catheters**	479
6.629.11.1.	Hydrogel: Coated Catheters	479
6.629.11.2.	Admixed/Impregnated Catheters	479
6.629.11.3.	Impregnated Catheters	479
6.629.11.4.	Silver: Processed Catheters	479
6.629.12.	**Conclusions**	479
References		480

Glossary

Antibiotics Drugs that are used to inhibit or kill bacteria in the treatment or prevention of infection.

Biofilm A functional community of microorganisms attached to a surface or interface and integrated in a self-produced polysaccharide matrix. Biofilm infections are characterized by their failure to respond fully to antibiotic treatment.

Cerebral ventricles Spaces within the brain, one on each side, and two centrally, that are filled with cerebrospinal fluid that circulates from one to the other.

Cerebrospinal fluid A clear watery fluid produced inside the ventricles of the brain.

External ventricular drainage A temporary means of draining excess cerebrospinal fluid from the cerebral ventricles into a sterile collecting bag at the bedside.

Hydrocephalus A pathological accumulation of cerebrospinal fluid in the ventricles of the brain, usually caused by obstruction.

Shunts Devices usually made from silicone and consisting of tubes and a valve mechanism to control rate and direction of flow. They are inserted to drain excess cerebrospinal fluid from the cerebral ventricles to another body site, commonly the abdomen.

Staphylococcus A group of common bacteria found on human skin and elsewhere. *Staphylococcus aureus* is often pathogenic, causing would infections, septicaemia, etc. The others, termed coagulase negative, are usually harmless except when an implanted biomaterial or device is present.

Abbreviations

CFU	Colony–forming units
CNS	Central nervous system
CoNS	Coagulase negative staphylococci
CSF	Cerebrospinal fluid
CT	Computerised tomography
DNA	Deoxyribonucleic acid
EVD	External ventricular drainage
LP	Lumbar-peritoneal
NPH	Normal pressure hydrocephalus
ScCO2	Supercritical carbon dioxide
TDMAC	Tridodecylammonium chloride
VA	Ventriculo-atrial
VP	Ventriculo-peritoneal

6.629.1. Introduction

Cerebrospinal fluid shunts are used to treat hydrocephalus, caused by raised pressure in the brain. They are intended to remain in place for life. A more temporary measure is external ventricular drainage (EVD), used for acute rises in pressure such as those due to trauma or hemorrhage. Before the 1950s, no reliable treatment was available for hydrocephalus and many people either died or lived with very serious mental and physical disabilities, but then shunts became widely used and their complications soon appeared. Infection remains the most serious of these despite advances in antibiotic prophylaxis and surgical techniques, and this has led to the development of antimicrobial biomaterials for use in both shunts and EVDs. Laboratory evaluation of such devices requires insight into the microbiological, surgical, and biomaterials aspects of the problems.

6.629.2. Hydrocephalus

This condition is due to the accumulation of cerebrospinal fluid (CSF) in the ventricles of the brain, leading to increased pressure, with damage to the nervous tissue and reduction of essential blood supply. The accumulation arises due to blockage of the flow pathways, as CSF continues to be produced at an undiminished rate. The pathways can become blocked as a result of congenital anomaly such as spina bifida, meningitis, brain tumor, hemorrhage, or trauma, and hydrocephalus can appear at any age. A relatively newly recognized form, normal pressure hydrocephalus (NPH), affects the elderly.

6.629.3. Treatment of Hydrocephalus

6.629.3.1. Shunting

Though attempts to treat hydrocephalus with drugs have been made, the mainstay is surgical insertion of a device to divert CSF from the cerebral ventricles to another body site, where it can be reabsorbed. These devices, or shunts, consist of a catheter inserted into the cerebral ventricles, leading out through a burr-hole in the skull, under the scalp, and then subcutaneously to either the heart or the abdomen (Figure 1). Somewhere in the system there is usually a valve to regulate pressure or flow rate or both, and this can be placed either at the distal end of the catheter or about 15 cm from the proximal end, so that it lies behind the ear.

6.629.3.2. Early Shunts: Biomaterials and Biocompatibility

Before the 1950s, there was no satisfactory treatment for hydrocephalus and those with it either died within weeks or months, or lived with severe mental and physical disability, usually in institutions. The need to allow accumulated CSF to escape was realized centuries ago, and attempts to release it by trepanning or drilling holes in the skull were made. In 1898, a silver wire with a U-shaped cross-section was used in two patients to drain the CSF from the lumbar spinal part of the central nervous system (CNS) (which is usually in continuity with the cerebral ventricles) to the peritoneal cavity.[1] Both patients treated in this way died soon afterwards. Later, tubes were inserted into the ventricles in the same manner as modern shunts. These were originally made of either natural rubber or silver. The latter was chosen because of its presumed antiseptic properties. Hartwell in 1910 (cited by Haynes[2]) used silver wire to form a conduit from the cerebral ventricle to the abdomen in a child who lived for 2 years before dying due to fracture of the wire in the neck. At autopsy, a fibrin sheath had formed around the wire, producing a tubular fibrin conduit along which CSF had presumably flowed. Natural rubber tubing was used by Kauch in 1905[3] and this was also used by Heile in 1914.[4] Polyethylene tubing was used by Ingraham *et al.* in 1948.[5] The history of shunting is reviewed extensively by Aschoff *et al.*[6] Almost all attempts ended in failure, largely due to obstruction at the distal end

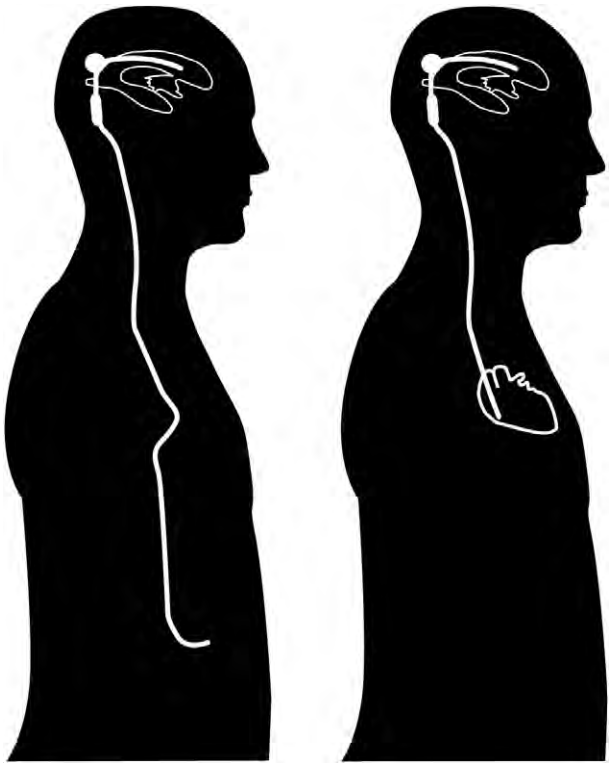

Figure 1 Routes of shunting for hydrocephalus. The shunts collect cerebrospinal fluid (CSF) from the ventricles in the brain. The fluid then flows through the circular reservoir and then through a valve that controls rate of drainage and prevents backflow. From there, the two routes differ. In (a), the ventriculoperitoneal (VP) shunt, the catheter lies subcutaneously over the ribs and enters the abdominal cavity, where the CSF is discharged and is reabsorbed into the bloodstream. In (b), the ventriculoatrial (VA) shunt, the catheter enters a neck vein and then, via the superior vena cava, discharges CSF into the right atrium of the heart, directly into the blood stream.

in the peritoneal cavity. The abdominal cavity is occupied by the small and large intestines, the latter of which contains enormous numbers of bacteria. If perforation of the colon occurs, perhaps due to ingestion of a sharp object, then the perforation is usually sealed very effectively by the large omentum, a membranous organ in the peritoneal cavity that has been referred to as 'the policeman of the abdominal cavity.' If any infective or inflammatory agent appears in the peritoneal cavity, the greater omentum moves to isolate and engulf it. The presence of a tube of natural rubber, polyethylene, or other poorly biocompatible materials in the peritoneal cavity attracts the attention of the omentum and the end of the tube is sealed, thus occluding it and stopping CSF drainage.[7] The peritoneal cavity is thus a critical site in terms of biocompatibility.

Valved shunts were being used on an experimental basis in the 1940s, but they were still made from natural rubber and while they functioned satisfactorily in a mechanical sense, they were not clinically successful. In addition, they could not be sterilized, a problem that unfortunately often still becomes apparent late in implant or biomaterial development.

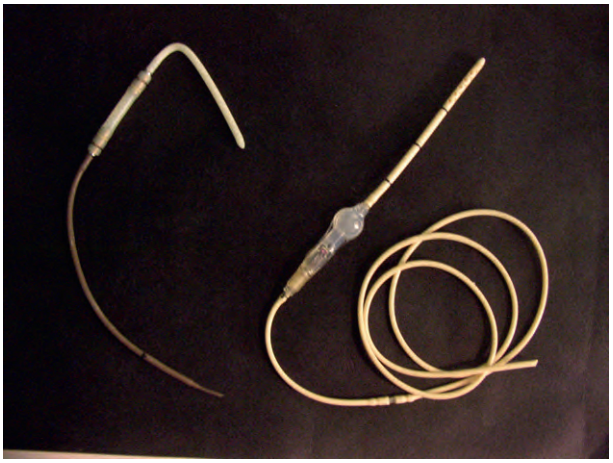

Figure 2 Shunts for hydrocephalus management. The original Holter shunt, with an angled ventricular catheter, two valves in series inside a silicone housing, and a tapered distal catheter for ventriculoatrial shunting. A modern shunt with a straight, graduated ventricular catheter that can be bent, leading to a magnetic step mechanism controlling the valve setting, which can be readjusted externally by a magnetic device without further surgery. The lower catheter is long, for insertion into the peritoneal cavity.

6.629.3.3. The Next Stage

The two problems to be overcome were biocompatibility and sterilization, and these were solved by John Holter in the 1950s. Holter was an American engineering technician whose son was born with spina bifida, a congenital anomaly that is usually accompanied by hydrocephalus. No treatment was available, but after discussing the problem with the surgeons, Holter constructed a valved shunt from silicone, then a new electrical insulating material (Figure 2). This could be sterilized, and silicone was soon found to be biocompatible. Unfortunately, Holter's son did not benefit from this development, but it paved the way for development of modern hydrocephalus shunts, all of which are made from silicone. An early development was to add barium sulfate to the silicone before extrusion so that the shunt catheters would be radio-opaque, allowing their location and inspection by radiography. Though early attempts were made to shunt into various body sites such as the fallopian tube, ureter, gall bladder, sagittal sinus and mastoid cavity,[8–11] and not just the abdomen or heart, it is the attempts to shunt into the abdomen and the heart that eventually proved most successful. With the adoption of silicone for shunt construction, the biocompatibility problems associated with the peritoneal cavity were largely, though not completely, overcome. However, the widespread use of these shunts in the heart ventriculoatrial (VA) was soon curtailed by the emergence of thrombus formation around the catheter in the right cardiac atrium.[12,13] This often caused shunt occlusion, but fragments of clot also broke away and were deposited in the vascular system of the lungs, often causing serious, potentially life-threatening pulmonary embolism.[14,15] This led to a decline in the use of VA shunts, and ventriculoperitoneal (VP) shunts are now predominant. Occasionally, for specific reasons, shunting by other routes is adopted, such as into the pleural space around the lungs, or from the spinal CSF space into the peritoneal cavity

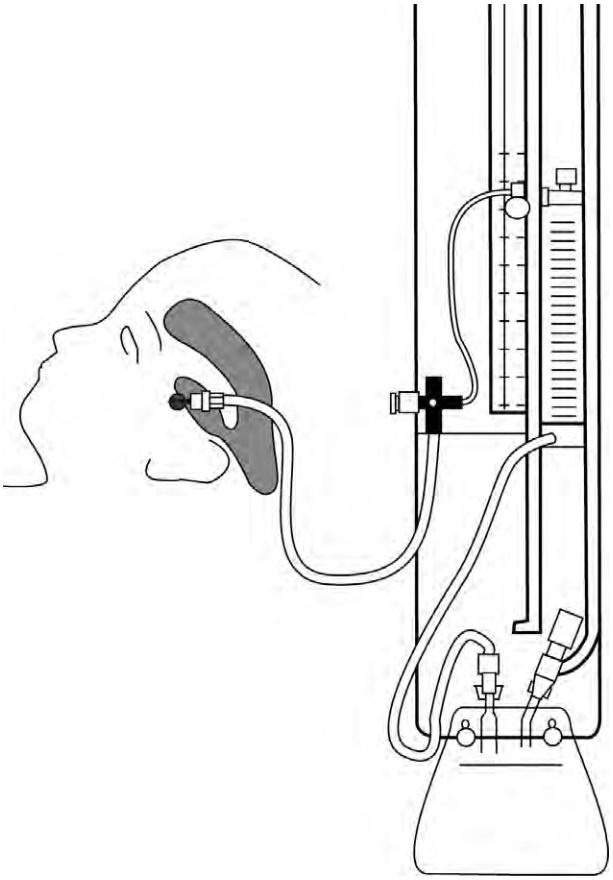

Figure 3 External ventricular drainage. The ventricular catheter is similar to that in a shunt, and drains cerebrospinal fluid from the ventricles in the brain. The catheter is connected to a drainage set with a manometer to adjust the height relative to the ventricles, and hence the rate of drainage. The fluid is collected into a sterile plastic bag at the bedside.

(lumbar–peritoneal, LP shunts). Temporary shunts for management of raised intracranial pressure are also often used in acute settings. These drain CSF from the cerebral ventricles using a catheter identical to permanent shunts, but the CSF is then collected in a bag at the bedside (Figure 3). Such EVD is used for a few days or for 2–3 weeks and is replaced by permanent shunting if the need for CSF drainage persists.

6.629.3.4. State-of-the-Art Shunts

The design of shunts has changed many times since Holter, though his design was used till 1990. The existence of a number of different designs perhaps suggests that the optimal one has not yet been achieved. In functional terms, the current clinical problems are overdrainage and the fact that it is impossible to predict the 'setting' of the valve for each individual. Most valves are supplied in low, medium, or high pressures, loosely equating to the CSF pressure that will result from their use. However, 'normal' CSF pressure ranges from 80 mm to about 150 mm water depending on age and other factors. If it is drained too rapidly, the cerebral ventricles will 'deflate,' and the surface of the brain will be pulled away from the overlying membranes, causing bleeding.[16,17] This collection of blood, a subdural hematoma, presses on the brain and causes malfunctions such as severe headache, convulsions, vomiting, and loss of consciousness. It usually requires surgical drainage. If the valve overdrains later and more slowly, the ventricles can collapse to the point where they are virtually invisible on CT scanning (Figure 4), a condition known as slit ventricles.[18] This paradoxically leads to increased intracranial pressure as the shunt catheter is no longer in the correct position in the ventricles.[19] Overdrainage is often referred to as siphoning, but the fluid mechanics of the phenomenon are ill-understood, and whether it is siphoning is debated. However, there does seem to be some connection between overdrainage and the length of the distal catheter from the valve to the peritoneal

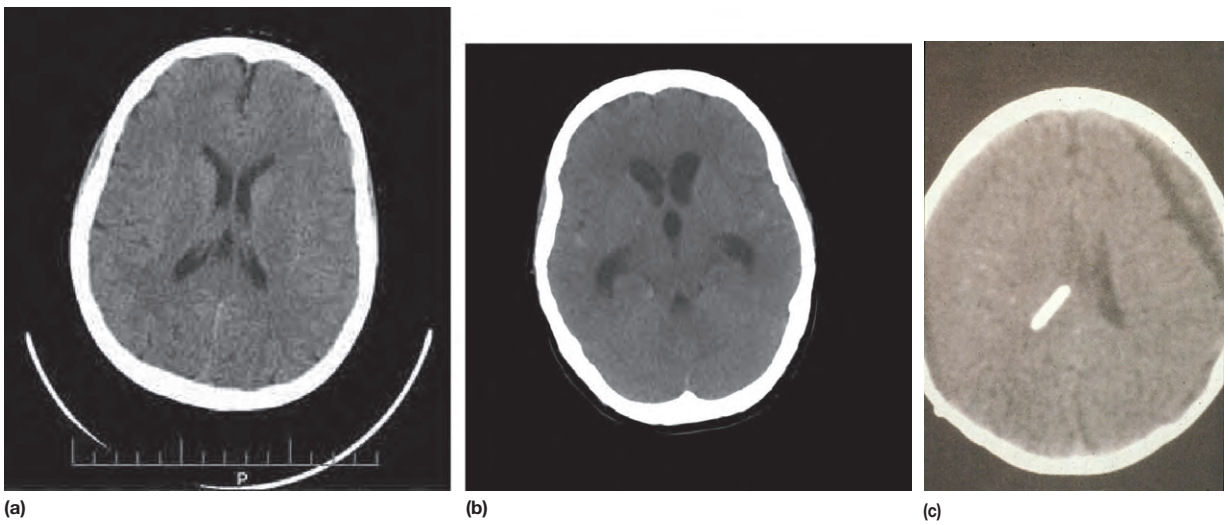

Figure 4 Computerized tomogram (CT) scans showing normal ventricles (a), enlarged ventricles in hydrocephalus (b), and reduced (slit) ventricles due to overdrainage (c).

cavity. One way in which overdrainage might be prevented is to place an 'antisiphon device' in the shunt system distal to the valve mechanism. Various types of devices are in use, but the one in which the CSF is diverted, if flow rate increases suddenly, into a much narrower pathway can slow the rate of flow and possibly arrest siphoning. Such devices appear to be successful in some patients but not in others and the mechanisms of overdrainage are still unclear. Certainly, changing the valve to one with a higher 'pressure' does not necessarily have any effect on overdrainage. The problem of predicting the CSF flow rate suitable for an individual patient, that is, the choice of a low, medium or high 'pressure' valve setting, has been solved by the introduction of the so-called programmable, or adjustable, valves (**Figure 2**). These contain a magnetic device that can be manipulated noninvasively at any time after surgical insertion of the shunt by means of another magnetic device placed on the scalp over the valve. The setting of the valve can then be changed according to the demands of the situation; if a patient shows signs of underdrainage after shunt insertion, the setting can be lowered to allow more CSF flow, and vice versa. In addition, the requirements of many patients change after shunt insertion, and these can also be accommodated without further surgery.[20,21] Currently, the factor limiting the more extensive use of such devices is their cost, but this has to be set against the cost of further admissions to hospital and more operations. Future developments in valve design will include biofeedback so that the valve will automatically respond to changes in CSF pressure, and telemonitoring and control of an individual patient's valve function.

6.629.4. Biocompatibility of Silicone Shunts

Medical grade heat-vulcanized silicone is highly biocompatible compared to natural rubber or polyethylene. However, after insertion, a fibrin sheath usually appears around the extracranial parts of the shunt tubing. This sheath is not usually attached to the silicone and does not interfere with its function. In some patients, usually after a few years, the fibrin sheath calcifies and this calcific layer attaches to the silicone and erodes the material, causing distortion and friability.[22] It is therefore responsible for local pain, and shunt failure due to catheter fracture, and it makes removal of defective catheters extremely difficult. Calcification has been blamed on the barium sulfate filler used in most shunt catheters; yet, the evidence for this is weak and it is also seen in shunts that do not contain barium sulfate (**Figure 5**). Nevertheless, in response to physician pressure, shunt tubing without barium sulfate is now being supplied. The reason for calcification is obscure, but it could be due to collection of blood around the catheter after surgical insertion. Calcification has also been shown to occur experimentally around longfixed catheter segments but not around small unfixed segments, suggesting that repeated tissue damage over time due to body movements over a fixed catheter might have a role.[23] Silicone allergy is very rare, but it does seem to occur occasionally.[24] Whether this is mainly due to patient predisposition or to some allergic property of silicone is unclear, but some cases reported are convincing. In particular, reports of persistent failure of shunts in the absence of infection or mechanical obstruction where replacement with an 'extracted' silicone shunt has solved the problem indicate that some extractable agent might be responsible.[25,26] It has been suggested that the small amount of residual uncross-linked silicone might in some individuals be allergenic, and this is presumably the agent that is extracted to make the shunts nonallergenic in the case reports. Fully cross-linked silicone is unlikely to be allergenic, though degradation due to lipid adsorption or mechanical damage might make reactive microparticles available. Another possible cause of allergic reaction to silicone shunts is adsorbance of contaminants such as latex proteins during insertion.[27]



Figure 5 A removed Holter shunt valve showing extensive surface calcification. The valve was made from plain silicone without barium sulfate filler.

6.629.5. Infective Complications

6.629.5.1. Causative Bacteria

As with any implantable device, infection is a possible complication. Soon after shunts began to be used for treatment of hydrocephalus, infection was reported.[28] At first the nature of the infection was unclear, but it soon became apparent that the hitherto harmless skin commensal *Staphylococcus epidermidis* was responsible for most cases. The genus *Staphylococcus* is divided for medical purposes into two groups. The first, consisting of one species, *S. aureus*, produces an enzyme, coagulase, and is therefore 'coagulase positive.' Members of this species were known to cause infection, and could easily be distinguished from the remainder (coagulase-negative staphylococci, CoNS) by the coagulase test. The CoNS were considered to be nonpathogenic and were generally disregarded, which is why it took so long to determine the cause of shunt infections. We now know that CoNS, of which *S. epidermidis* is by far the commonest, cause the majority of shunt infections. Shunt isolates of CoNS have been characterized[29] though the nomenclature has now changed.

6.629.5.2. Source of the Infecting Bacteria

In a modern operating theater with ordinary plenum ventilation, the theater air and environment are not a significant source of bacteria that infect shunts, and virtually all are caused by bacteria that inhabit the patient's skin.[30–32] Before any operation, the patient's skin at the surgical site is disinfected using antiseptics. The most effective is a solution of povidone iodine (a compound of polyvinylpyrrolidone and iodine) in alcohol. However, even when skin is prepared twice with this, viable skin bacteria survive in the sweat glands and hair follicles.[33] When the incision is made through the skin, they contaminate the surgical field and then gain access to the shunt tubing. Those that remain on the outside are usually phagocytosed and killed by the cellular immune system after closure, but those on the inside of the tubing are safe from host defenses. They attach to the silicone tubing and begin to change their phenotype and develop biofilms.[34–36] A few shunt infections are the result of skin abrasion over the shunt at a later date and another cause is perforation of an abdominal organ such as the colon or bladder by the distal catheter.[37] Sometimes this protrudes from the anus or urethra. However, though the catheter tubing obviously becomes contaminated and has to be removed, serious infection rarely results.

In EVD, the infecting bacteria might arise from the patient, the medical or nursing staff, or the environment and can gain access to the ventricular catheter at any time but especially during CSF sampling or collection bag change. While the infecting bacteria are similar to those in shunts, the proportion of Gram-negative bacteria such as *Escherichia coli* and *Klebsiella pneumoniae* is higher. Also, *Acinetobacter baumannii* is a bacterium that is particularly prevalent in intensive care units, where many EVDs are used. It is multiresistant and persists in the environment.[38]

6.629.5.3. Incidence of Shunt Infection

The infection rate in shunts varies considerably from one institution to another, and this might be due to different types of institutions, different patient populations, and different diagnostic criteria. There are also differences within institutions over time, and 'spikes' of infection arise and fade inexplicably in most. One factor is thought to be the routine change of junior medical or nursing staff at certain times of the year, and this does seem to influence infection rates.[39] However, the main difference is that between adults and older children and infants <6 months of age when shunted. In the former group, rates of 2–5% are not unusual, whereas in the infant group, rates of over 15% have been reported.[31,40] The 'average' rate often cited in the literature is 10%.[41]

6.629.6. Treatment of Shunt Infections

6.629.6.1. Biofilms and Other Reasons for Treatment Failure

The reasons for the great difficulty in treating shunt infections with antibiotics, to which the CoNS were usually very susceptible, were not understood earlier. In 1961, Cohen and Callaghan found that the intravenous antibiotics, which they usually used to treat staphylococcal infections, were failing to treat shunt infections, and this seemed to be because the drugs were not penetrating into the CSF in sufficient quantities.[42] The CNS is a privileged, protected area and we now know that most antibiotics when given intravenously do not penetrate into the CSF in healthy people. *S. epidermidis* does not cause sufficient inflammatory response in the CNS to open up the blood–CSF barrier, as would happen in the more acute forms of meningitis. While this was the explanation for the failure of intravenous antibiotic treatment, the infections were not eradicated even when antibiotics were introduced directly into the cerebral ventricles. The reason became apparent when shunts that had been removed for intractable infection were examined.[34] The offending bacteria were found to be confined to the inner surfaces of the shunt tubing. Moreover, they were adherent to the silicone, and they grew as microcolonies that produced a substance that appeared to hold them together and possibly to protect them from antibiotics. This 'mucoid substance' was found to stain with alcian blue, suggesting that it was a polysaccharide, and it reacted with fluorescent-labeled antiserum, showing that it was antigenic. This was in fact the first published demonstration of a biofilm in a medical device setting. At least 140 000 papers have now been published on biofilms in medical devices, and the significantly decreased susceptibility of bacteria when growing in a biofilm is now appreciated. While there may be more than one reason for this, in staphylococcal biofilms, the assumption that the 'mucoid substance,' now known as polysaccharide intercellular adhesin or exopolymer, is able to significantly impede access of antibiotics to the bacteria in the biofilm is known to be incorrect.[43,44] The penetration of antibiotics into bacterial biofilms has also been modeled mathematically.[45] Bacteria are able to adhere by means of specific adhesins to host proteins coating the biomaterial surface. Examples of these are the binding proteins for fibronectin and fibrinogen. Once adhesion has taken place, the bacteria begin to modify their metabolism, under genetic control, and to produce exopolymer. By the time the biofilm is fully developed in 1 or 2 weeks, the bacterial phenotype has undergone such modification that they are 500–1000 times less susceptible to antibiotics.[46–48] During this time, genes responsible for rapid multiplication and production of cell wall material, enzymes, toxins, etc. are downregulated, and those responsible for exopolymer production and stress response, a bacterial survival mechanism, are upregulated. The bacteria enter a dormant phase (**Figure 6**), with energy generation and transport drastically reduced.[49] Antibiotics act on bacteria by inhibiting cellular processes, and the three main groups of antibiotics inhibit cell wall synthesis (penicillins, cephalosporins, and vancomycin), protein synthesis (gentamicin, clindamycin, tetracyclines), and DNA replication (quinolones). As the biofilm bacteria do not synthesize much cell wall material, proteins, or enzymes, nor replicate their DNA, the antibiotics have no target sites and become therapeutically irrelevant. This is probably the most important mechanism explaining treatment failure in biofilm infections. Therefore, in view of the pharmacological problem of getting the antibiotics to the bacteria in the shunt, and their insusceptibility to all but concentrations toxic to the patient, the treatment of shunt infections must include total surgical removal of the infected device.

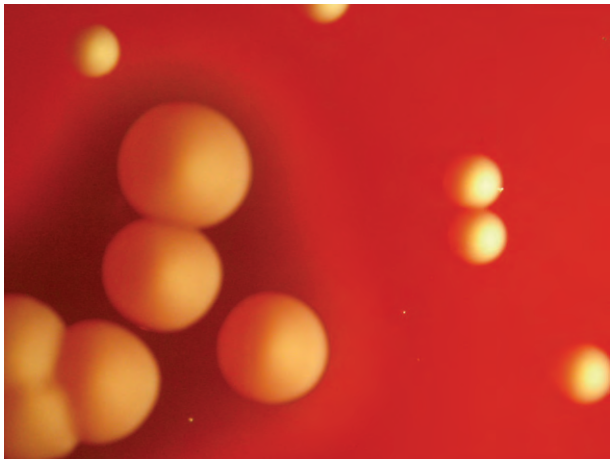

Figure 6 Small colony variants of *Staphylococcus aureus* on blood agar medium. The large bacterial colonies are the parent strain, and the small colonies are the resistant variants. Note the absence of enzyme activity around the small colonies. The image is not color-enhanced. Magnification ×200.

6.629.6.2. Treatment Regimens

As soon as possible after the diagnosis of shunt infection, the shunt system should be removed. The hydrocephalus is then managed by an EVD, with excess CSF draining through a collecting system into a bag. Antibiotics are also given, and many doctors prefer to include direct administration into the CSF.[50] The EVD is itself a source of infection as it represents a direct access to the CNS for bacteria from the scalp or the environment, and careful management is required. After the infection in the cerebral ventricles has been eradicated, typically after 10–14 days, the EVD can be removed and a new shunt inserted. Guidelines for treatment of shunt infections have been published,[51] and if these are followed, relapse of the infection is unlikely. However, relapse or a second infection are serious problems where guidelines are not followed, and the repeated surgery and infection cycle leads to diminished mental and physical ability with a poor overall outcome and possibly to death.[52]

6.629.7. Prevention of Shunt Infections

6.629.7.1. Surgical Technique

In any modern operating theater, a ritual involving scrupulous cleaning of surgeon's hands, gloving, gowning, and the use of caps and masks and sterile instruments is routine. Any break in this ritual often leads to a higher risk of infection. Some surgeons have applied the ritual more rigidly and have claimed that measures such as limiting the number of people in the theater, inserting shunts first thing in the morning, and introduction of ultraclean air systems are responsible for their reduction in infection rate.[53] However, so long as the usual ritual is maintained, the extra measures themselves are unlikely to be responsible, in view of the source of the infecting bacteria. Advocates of such enhanced systems often apply them rigorously, and it is probably this that is responsible. The Hawthorne effect, where the fact that changes are being made or a study or an audit is being carried out leads to improvement in infection rates irrespective of the nature of the changes,[54] is a powerful influence, but it must be regularly reinforced or the effect will diminish with time as personnel become accustomed. The effect can be exploited by constructing a protocol of procedures, none of which might be evidence-based but all of which appear sensible, and applying it rigorously with frequent personalized feedback of results. This is often called 'bundling' to describe the grouping together of such procedures. Bundling alone has been reported to reduce the incidence of shunt and EVD infections.[55,56] However, the effect is volatile, often disappearing when personnel change or lose interest.

6.629.7.2. Prophylactic Antibiotics

It is common practice in most types of surgery to administer an intravenous antibiotic, usually a cephalosporin, about 30 min before the first incision is made. This is to ensure adequate tissue concentrations of the antibiotic so that any bacteria reaching the operation site are killed or inhibited, and prevented from causing an infection. However, as the blood–CSF barrier is not patent in the absence of inflammation (and it is hoped that those to be shunted do not have ventriculitis), the intravenous antibiotics do not penetrate into the CSF in significant quantities to be effective.[50,57] Many trials and studies have been carried out to determine whether the use of prophylactic antibiotics reduces shunt infection, but a meta-analysis[58] has shown that there is no significant benefit unless the infection rate is >15%. In addition, published infection rates with an average of 10% are all from centers where antibiotics are used. The benefit from prophylactic antibiotics in shunt surgery is therefore doubtful. In EVD, prophylactic antibiotics are used in two ways. Firstly, they are given as in shunt surgery to prevent infection at the time of the insertion of the device. Secondly, some centers prefer to continue prophylaxis throughout the period of EVD. Studies have shown that the latter does not reduce infection but risks encouraging infection with resistant Gram-negative bacteria such as *Pseudomonas aeruginosa* and *E. coli*.[59,60]

6.629.8. Antimicrobial Shunt Catheters

6.629.8.1. Principles of Antimicrobial Biomaterials for Shunting

There have been many attempts to produce experimental antimicrobial biomaterials, mainly for use in catheters. Most have shown some antimicrobial activity in laboratory tests but few have been commercialized, and of those that have, few have been clinically successful. The two main types of antimicrobial catheters are coated and impregnated catheters, which are coated or impregnated with one or more antimicrobial agents. The differences between the two are clinically very important. Coating is, as the term suggests, the application of the agent to the catheter surface, either passively or by some bonding process, while impregnation consists of dispersing the agent throughout the biomaterial.

The required duration of antimicrobial activity and its activity against a range of microorganisms is determined by the

intended use of the catheter, and the known period of risk of infection. In the case of CSF shunts, the period of risk is during and immediately after the surgical procedure,[30] though once bacteria have attached to the shunt surface they take longer to kill.[61] Therefore, at least 2 weeks of sustained activity are desirable, and this must be directed against the main bacterial causes, that is the staphylococci and propionibacteria. In the case of EVDs, the activity is required for the duration of EVD use, which can be 3 weeks or more. The antimicrobial activity must cover not only the staphylococci but preferably also the Gram-negative pathogens such as *E. coli*, *K. pneumoniae*, and *A. baumannii*. In addition, EVDs are often used in cases of hemorrhage or trauma, when the CSF contains blood and clot breakdown products that coat the inside of the catheter. This can increase the chances of bacterial attachment, and it can also obliterate a bioactive surface.

6.629.8.2. Coated Catheters

These can be manufactured by various means including dipping, spraying, or coextrusion. Any process that is confined to the line of sight cannot access the inner surface of the catheter, and some catheters have shown disappointing results in clinical trials because of this.[62–64] However, the main reason for the failure of coated catheters is the lack of any depot effect, coupled with the usually rapid wash-off of the agent in flow conditions. The deposition of a host-derived conditioning film can also reduce the activity.[65] Preclinical testing must include these factors to approach clinical predictiveness. The antimicrobials used to coat catheters experimentally have ranged from antibiotics and antiseptics to silver. Some of the antiseptics and bonding agents, such as chlorhexidine[66] and tridodecylmethylammonium chloride (TDMAC),[67] are too neurotoxic for use in shunts and EVDs although their use has been suggested.[68] Silver coatings for catheters used in the urinary tract or for vascular access have included silver salts and metallic silver, deposited by ion beam. They have not been used in the CNS. Another approach consists of coating the catheter in a hydrogel such as polyvinylpyrrolidone, which swells on soaking in water to become a very hydrophilic layer. This is said to reduce bacterial attachment, and if antibiotics are dissolved in the water used for soaking, they are said to be released after implantation to reduce infection risk even further.[69]

6.629.8.3. Impregnated Catheters

Impregnation is far more difficult to achieve than coating, unless one includes admixing of powders prior to extrusion. Ideally, impregnation should disperse the antimicrobial as molecules, or at least nanoparticles, rather than granules. Impregnation is a postmanufacture process, and the antimicrobial agents must be introduced into the polymer matrix by some means. The exception is one form of silver impregnation in which metallic silver particles compounded with the polymer are then admixed into the main bulk of the polymer before extrusion.[70] This has been used for silicone and polyurethane EVD catheters.[71] Antimicrobials such as antibiotics have been impregnated into silicone using a solvent-swelling process.[72] This depends on the antimicrobial being soluble in the solvent, and the solvent being able to swell the matrix of the cross-linked silicone. The antimicrobial is dissolved in the solvent, and the silicone catheter is immersed in the solution. Within a few minutes, the silicone swells to approximately twice its volume, imbibing the solution. After complete swelling, the solvent is removed by evaporation, leaving the molecules of antimicrobial evenly dispersed throughout the silicone, which returns to its original volume and shape. In order to be clinically effective, the antimicrobial must be capable of migrating through the silicone. Most antimicrobials such as penicillins, cephalosporins, gentamicin, and vancomycin will not migrate, and even if they are introduced by some means, they will remain in the polymer without exerting any antimicrobial effect. These agents are also insoluble in the usual swelling solvents, of which chloroform is the most used, and a clear relationship can be developed between the solubility of the proposed antimicrobial in chloroform and the rate of its migration through the silicone.[73,74]

Metallic silver, being insoluble in swelling agents such as chloroform, cannot be impregnated in this way. However, a method by which metallic silver nanoparticles can be impregnated into silicone using a swelling agent has been developed.[75] In this method, silver is complexed with organic compounds such as glymes in anaerobic conditions. The organosilver complex is then solubilized in supercritical carbon dioxide ($scCO_2$), which also swells the silicone matrix under these conditions. As with the chloroform-based method, the organometallic complexes are left behind when the $scCO_2$ is removed and the silicone matrix returns to its original volume. The organic material then has to be removed as it is toxic, and this is done by reducing the complex with hydrogen and flushing out the organic residues with $scCO_2$. The effect is to leave nanoparticles (20–200 nm) of metallic silver dispersed throughout the silicone.[76] Nanoparticles are known to have much greater chemical and biological activity than the corresponding larger particles, and they can be expected to generate silver ions, on which antimicrobial activity depends, at a far greater rate. There is currently no clear information on whether the nanoparticles or their ions can migrate through silicone in the same way as organic antimicrobials.

6.629.8.4. Biological Importance of the Boundary Layer

The interface between the catheter and the CSF passing through it is critical, as it is here that any bacteria accessing the catheter lumen will attach. In order for an antimicrobial catheter to be clinically effective, the boundary layer must maintain a concentration of antimicrobial sufficient to kill the bacteria for long enough in flow conditions. As we established earlier, this must be for at least 2 weeks in shunts and over 3 weeks in EVDs. As the CSF flow removes antimicrobial ions or molecules constantly from the catheter surface, this concentration must be replenished by migration from the matrix to maintain activity (**Figure 7**).

6.629.9. Evaluation of Antimicrobial Catheters

It would appear from the above that any evaluation must include an assessment of bacterial attachment and time to kill, and include the effect, if any, of a protein conditioning film.

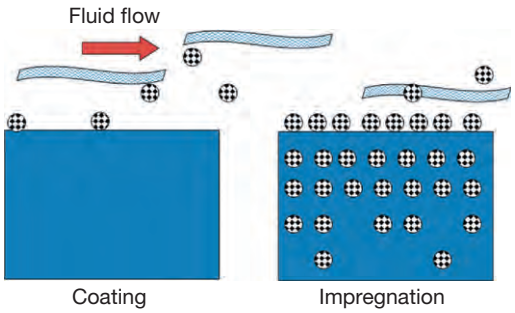

Figure 7 Comparison of the behavior of antimicrobial coatings and impregnation. As the cerebrospinal fluid flows over the antimicrobial surface, molecules of the antimicrobial are washed out of the boundary layer and removed. Eventually, no antimicrobial activity remains on the coated surface, but the boundary layer of the impregnated biomaterial remains full of antimicrobial molecules due to replenishment by diffusion from the matrix.

Demonstration of prevention of colonization after repeated bacterial challenge in flow conditions at 37 °C is also required. However, a variety of other tests have been applied.

6.629.9.1. Broth Culture Test

Here a segment of test catheter is added to a fluid ('broth') culture of test bacteria and incubated overnight. The numbers of surviving bacteria are compared to those before incubation. Any antimicrobial activity shown is against planktonic, that is unattached, bacteria and this is of questionable clinical relevance. Also, the activity depends on the antimicrobial agents being released from the catheter into the culture medium in sufficient quantity to kill or inhibit the test bacteria. If they do this, there is very little likelihood that useful activity would extend much beyond the 24-h test period in the absence of extremely high loading. The method is easy, inexpensive, and uninformative.

6.629.9.2. Roll Plate Test

A segment of a catheter is immersed in a suspension of test bacteria to allow them to attach to its surface. After removal, it is incubated in nutrient medium and then removed, rinsed, and rolled over the surface of a plate of solid culture medium. After incubation of this medium, colonies are counted and compared to those from a plain control catheter. While this assesses the ability of the catheter to kill attached bacteria, it gives no information about the duration of the effect. Also, only the outer surface is sampled, and where this method has been used in clinical trials the results have been flawed as most catheter-related infections begin on the luminal surface.[77]

6.629.9.3. Zone Plate Test

This consists of placing a segment of catheter on the surface of an agar plate that has been seeded with test bacteria. After incubation, the diameter of any zone of inhibition surrounding the catheter is measured. A zone of more than 18 mm has been taken as an indication that the catheter is likely to show clinical efficacy.[78] This test tells us whether a catheter has any activity at all, and can be used as a screen. However, it tells us nothing about duration of activity, nor does it test the effect of flow conditions. Also, some catheters that do not rely on release of water-soluble agents, such as silver-processed catheters, will not show any effect in this test.



Figure 8 Serial Plate Transfer Test, showing three segments of an antimicrobial shunt catheter after incubation on an agar plate seeded with staphylococci. The catheters had been transferred from plate to plate for 7 days.

6.629.9.4. Serial Plate Transfer Test

This initially appears to be very similar to the zone plate test, but it introduces an assessment of duration of activity. After demonstrating a zone of inhibition as in the zone plate test, the test segments are marked so that the same arc of the circumferential surface is presented to the agar surface on each occasion (Figure 8). The segments are then transferred to a fresh seeded agar plate and incubated overnight. Again, any zone of inhibition is measured and the segments are transferred until no more zone of inhibition is seen. Whereas the Zone Plate test can give a zone of inhibition from a small amount of antimicrobial on the catheter surface that would be removed in minutes in a flow system, a Serial Plate Transfer test that shows inhibition for several days or longer relies on a maintained antimicrobial boundary layer.[72] The longest durations of activity in the Serial Plate Transfer test are seen in impregnated biomaterials, where inhibition zones can persist for more than 250 days.[79] Even so, the test is no more than a screen for duration; it tells us nothing about actual protection against bacterial colonization in flow conditions.

6.629.9.5. Time to Kill Assay

This assay is known as the tK100, as it determines the time taken by an antimicrobial biomaterial to kill 100% of bacteria attached to its surface.[80] Test catheter and plain control catheter segments are immersed separately in a bacterial suspension for 1 h to allow attachment. They are then removed and rinsed to remove unattached bacteria, and immersed in a nutrient

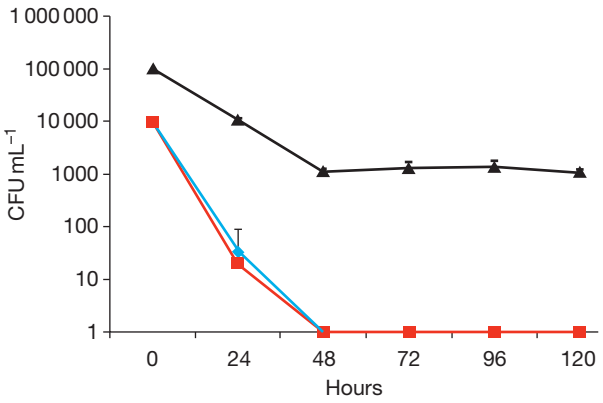

Figure 9 tK100 results to show persistence of bacteria in the plain control (▲) compared to the antimicrobial material (■). The activity is shown in colony-forming units per milliliter (CFU per milliliter) of surviving bacteria that are attached to the material surface. All bacteria attached to the antimicrobial material are nonviable by 48 h.

medium and incubated at 37 °C. The concentration of the medium is titrated for each test bacterium to allow bacterial survival on the plain catheter surface but not significant growth in the surrounding fluid; otherwise, constant reseeding of the segments will invalidate the test. Three segments are removed at intervals, rinsed, and sonicated to remove attached bacteria, and the viable bacteria in the sonicate are counted. Typically, the counts from the plain control segments remain constantly high while for a successful antimicrobial catheter, they will reach zero in 2–4 days. It is important to include sufficient catheter segments to allow for further testing after this period to rule out recovery and regrowth. The results of this assay (Figure 9) show that the time taken to kill attached bacteria is much longer than that taken to kill their planktonic counterparts, which can be killed in a few hours.

6.629.9.6. *In Vitro* Challenge

Here the catheters are tested in flow conditions at 37 °C by repeated challenge with bacteria.[72,80] Typically, plain control and antimicrobial catheters are perfused with nutrient medium at 20 ml h^{-1} (the normal CSF production rate) for 42 days. A suspension of test bacteria is injected into each catheter on the first day, and viable bacteria are counted in the effluent daily for the next 13 days. Control catheter counts increase and remain high, but if the counts have by then fallen to zero in the antimicrobial catheters, a new set of plain control catheters is set up and both are rechallenged. The process is repeated until the antimicrobial catheters become colonized. Counting the bacteria in the effluent can be criticized as not giving information about biofilm formation on the luminal surface of the catheters, but in practice it proves to be a reliable indicator.

6.629.9.7. *In Vivo* Testing

The insertion of a segment of antimicrobial catheter subcutaneously or into the muscle of an animal, and injecting bacteria around it, is a commonly used *in vivo* model,[81] but it is so uninformative and clinically irrelevant as to be unethical. *In vivo* testing that gives clinically useful results is very difficult for shunts and EVDs. Several hydrocephalic animal models are available, but the only one that gives the opportunity to use a full-size shunt to treat hydrocephalus is the dog. In this model, the dog is made hydrocephalic by obstructing the CSF pathways in the brain.[82] The test shunt can then be inserted in the same way as for human hydrocephalus. The model has been validated for shunting but so far has not been used to evaluate antimicrobial shunts or EVDs, almost certainly because of the high cost of the initial surgery, the shunting, and animal maintenance.

6.629.10. Application of *In Vitro* Tests to Existing Shunt and EVD catheters

6.629.10.1. Hydrogel: Coated Catheters

A catheter with a hydrogel coating is commercially available (Bioglide, Medtronic, Minneapolis, USA). According to the manufacturer's instructions, catheters were soaked in solutions of various antibiotics. They were then removed, blotted dry, and tested by the Serial Plate Transfer test.[83] Despite high concentrations of antibiotic, all except one showed no zones after day 2. The exception, rifampicin, failed by day 9, but this antibiotic cannot be used alone as resistance readily appears. Using the *in vitro* challenge test, all catheters colonized immediately. Further testing showed that, contrary to company assurances, the internal surfaces were not coated with hydrogel, explaining why the catheters could not have shown protective activity in the *in vitro* challenge.

6.629.10.2. Admixed/Impregnated Catheters

The method of manufacture of the rifampicin- and minocycline-processed EVD catheter (Ventriclear, Cook, Bloomington, USA) is unclear, but it appears to be a hybrid of admixture and impregnation. The minocycline appears to be released very rapidly,[84] leaving the rifampicin to act alone after a few days. The catheter behaves well in the Serial Plate Transfer test against staphylococci and *E. coli*, but the activity against the latter is lost if the catheter is first soaked for 5 days, probably due to the early loss of minocycline.

6.629.10.3. Impregnated Catheters

A shunt catheter impregnated with rifampicin and clindamycin is commercially available (Bactiseal, Codman, Raynham, USA), and an EVD version is also available. The antimicrobials are introduced by the solvent-swelling method and are distributed throughout the polymer. On testing by the Serial Plate Transfer method, the catheters show inhibition for ~50 days.[80] The tK100 assay shows that the catheters kill all attached bacteria by 48–52 h with no regrowth,[61] and these results are not affected by prior soaking of the catheters. No colonization appears after three consecutive challenges in the *in vitro* challenge test, with failure on the fourth challenge at 42 days. The catheter is active against Gram-positive shunt and EVD pathogens such as staphylococci, but not against Gram-negative bacteria.

6.629.10.4. Silver: Processed Catheters

An EVD catheter impregnated with nanoparticulate silver is commercially available (Silverline, Spiegelberg, Hamburg, Germany). The catheter is available in either silicone or polyurethane. The silver nanoparticles are apparently admixed prior to extrusion. In view of the wide antimicrobial spectrum of silver ions, the catheter is claimed to protect against infection by both Gram-positive and Gram-negative bacteria and fungi. Not surprisingly in view of its mode of action, the catheter gives no zones of inhibition in the Serial Plate Transfer test,[85] but in this case, this does not necessarily mean that it has not antimicrobial activity. On testing the silicone catheter using the tK100 assay,[86] *S. epidermidis* was killed within 72 h but *S. aureus* was not eradicated. On testing against *E. coli*, the bacteria appeared to be eradicated within 48 h but then regrew at 72 h. While the mechanism of antimicrobial action of silver is debated, it has been suggested that, at low concentrations, silver ions cause nonfatal damage to bacteria from which they can recover. There was no activity in the tK100 assay against *P. acnes*. No antimicrobial activity was shown by these catheters in the *in vitro* challenge. Scanning backscattered electron microscopy showed that the silver particles were ~500 nm in diameter, and it is possible that more activity could be achieved if they were <200 nm, that is, true nanoparticles.

6.629.11. Clinical Studies on Antimicrobial Shunt and EVD catheters

6.629.11.1. Hydrogel: Coated Catheters

One clinical trial has been published on the use of these catheters for EVD.[63] The catheters were soaked in bacitracin, an antibiotic with activity against most Gram-positive bacteria. No significant difference was seen in infection rates between plain and hydrogel-coated catheter groups, as suggested by the Serial Plate Transfer test and *in vitro* challenge results.

6.629.11.2. Admixed/Impregnated Catheters

One trial on Ventriclear catheters for use in EVD has been published.[87] The infection rate in the Ventriclear group was 1.3% compared to 9.4% in those receiving plain catheters ($p = 0.002$). This was mainly due to there being no infections due to staphylococci in the Ventriclear group, but there were two due to Gram-negative bacteria, confirming the validity of the results of the tK100 assay on these catheters.

6.629.11.3. Impregnated Catheters

Ten clinical trials of Bactiseal shunt catheters have been carried out in various parts of the world.[88–97] The trials are of varying design and quality, most not being the standard randomized controlled double-blind model. This might be for several reasons: the Bactiseal catheters are orange in color and cannot be 'blinded' against a white plain catheter; and the catheters have become widely used, so that ethical issues arise regarding possible randomization to the plain catheter, which could be considered inferior. Nevertheless, with one exception, use of the impregnated catheters was associated with a reduction in shunt infection rate, and in four cases this reached statistical significance and in two failed to do so because of small numbers. The average reduction in infection rate in the statistically significant trials was 80%. A study carried out by the UK Cambridge Shunt Registry[98] showed a 36% reduction in infection rate compared to controls ($p = 0.048$), but the study involved almost 2000 patients from most neurosurgery units in United Kingdom, and there were no diagnostic criteria for shunt infection other than the surgeon's opinion. Infection could therefore have been overdiagnosed. A recent German study[89] examined the cost-effectiveness of the antimicrobial shunt catheters, taking into account the increased cost of the catheters and the costs of treating an infection, and found that their use in 197 children and adults resulted in a saving of $50 000. Another study from United States[99] showed that factors leading to higher medical costs were reduced when antimicrobial catheters were used.

The Bactiseal EVD catheter has been available for a shorter period, and while trials are under way, only one has been published.[100] There was a reduction in positive CSF cultures from 31.8% in the plain catheter group to 2.1% in the Bactiseal group ($p = 0.003$). The results of more extensive trials are awaited.

6.629.11.4. Silver: Processed Catheters

Silver coatings in various forms have been used in catheters for vascular access and urinary use for some time, but the clinical results are very variable and seem to be influenced by the length of time that the catheters are in place. Silver nanoparticle impregnation offers theoretical advantages based on significantly greater ionization, and a catheter containing these has been tested as a central venous access catheter.[101] The catheters were in place for relatively short periods, and the reasons for catheterization were different in control and test groups, but the authors reported a significant reduction in infection rate with the use of the silver catheters. In a prospective study using retrospective selected controls, Lackner *et al.*[71] showed a significant reduction in infection rate, from 25% to 0%, though there was no difference in numbers of EVD catheters colonized by bacteria. The clinical significance of catheter colonization, that is bacteria growing inside the catheter in the absence of symptoms of infection, is unknown.

6.629.12. Conclusions

Infections associated with shunting and EVD are serious and potentially life threatening, and conventional measures such as prophylactic antibiotics are not very effective in reducing the risk while introducing the additional risks of side effects and resistance.

Various antimicrobial catheters have been proposed with the aim of killing any bacteria that reach the device on insertion or during use, but testing methods vary. While some take into account the biological and clinical factors, some others give clinically misleading data. Most proposed devices have not shown clinical benefit. Those that have are impregnated with antimicrobial(s) rather than being coated. Antimicrobial-impregnated shunt catheters have proved to be very successful,

and while there has been less clinical experience with similar EVD catheters, results suggest that they may also be useful. Silver nanoparticle-impregnated EVD catheters have recently been introduced, and early data suggest that these may be useful but more studies are needed.

References

1. Ferguson, A. H. *NY Med. J.* **1898**, *67*, 902–1008.
2. Haynes, I. S. *Ann. Surg.* **1913**, *57*, 449–484.
3. Kauch, J. Die Abteilung für Bakteriologie und experimental Therapie der deutschen Medizinischen. In *Ausstellung auf der Welltausstellung zu St Louis I ABT*, 1905; p xxxvi, 593–613.
4. Heile, B. *Arch. Clin. Chir.* **1914**, *105*, 501–506.
5. Ingraham, F. D.; Matson, D. D.; Alexander, E.; Woods, R. P. *J. Neuropathol. Exp. Neurol.* **1948**, *7*, 123–143.
6. Aschoff, A.; Kremer, P.; Hashimi, B.; Kunze, S. *Neurosurg. Rev.* **1999**, *22*, 67–93.
7. Bayston, R.; Spitz, L. *Z. Kinderchir.* **1977**, *34*, 339–345.
8. Drachter, A. *Zbl. Chir.* **1925**, *52*, 2776–2777.
9. Heile, B. *Zbl. Chir.* **1925**, *52*, 2229–2236.
10. Nosik, W. A. *J. Neurosurg.* **1950**, *7*, 236–239.
11. Payr, E. *Arch. Clin. Chir.* **1908**, *87*, 801–885.
12. Landouceur, D.; Giroux, M. *Pediatr. Neurosurg.* **1994**, *20*, 68–72.
13. Schmaltz, A. A.; Huenges, R.; Heil, R. P. *Br. Heart J.* **1980**, *43*, 241–243.
14. Fagan, E. T.; Jennings, G. L. *Aust. N. Z. J. Med.* **1978**, *8*, 426–427.
15. Piatt, J. H.; Hoffman, H. J. *Childs Nerv. Syst.* **1989**, *5*, 29–31.
16. He, X. S.; Zhang, X. *J. Neurol. Neurosurg. Psychiatr.* **2005**, *76*, 367.
17. Sharma, R. R.; Mahopatra, A.; Pawar, S. J.; Sousa, J.; Athale, S. D. *Pediatr. Neurosurg.* **1999**, *31*, 150–154.
18. Sgouros, S.; Malluci, C.; Walsh, A. R.; Hockley, A. D. *Pediatr. Neurosurg.* **1995**, *23*, 127–132.
19. Browd, S. R.; Gottfried, O. N.; Ragel, B. T.; Kestle, J. R. W. *Pediatr. Neurol.* **2006**, *34*, 171–176.
20. Ahn, E. S.; Bookland, M.; Carson, B. S.; Weingart, J. D.; Jallo, G. I. *Childs Nerv. Syst.* **2007**, *23*, 297–303.
21. Kay, A. D.; Fisher, A. J.; O'Kane, C.; Richards, K. K.; Pickard, J. D. *Br. J. Neurosurg.* **2000**, *14*, 535–542.
22. Boch, A.-L.; Hermelin, E.; Sainte-Rose, C.; Sgouros, S. *J. Neurosurg.* **1998**, *88*, 975–982.
23. Eymann, R.; Meyer, U.; Kiefer, M. In *Brain Edema X1V*; Cernicki, Z., Baethmann, A., Ito, U., Katayama, Y., Kuroiwa, T., Mendelow, D., Eds.; Acta Neurochirurgica Supplementum; Springer-Verlag: Wien, 2009; Vol. 106, pp 91–93.
24. Snow, R. B.; Kossovsky, N. *Surg. Neurol.* **1989**, *31*, 209–214.
25. Ellis, M. J.; Kazina, C. J.; Del Bigio, M. R.; McDonald, P. J. *J. Neurosurg. Pediatr.* **2008**, *1*, 237–239.
26. VandeVord, P. J.; Gupta, N.; Wilson, R. B.; *et al. Biomaterials* **2004**, *25*, 3853–3860.
27. Niggemann, B.; Bauer, A.; Jendroska, K.; Wahn, U. *J. Allergy Clin. Immunol.* **1997**, *100*, 849–850.
28. Anderson, F. M. *J. Neurosurg.* **1959**, *16*, 551–557.
29. Holt, R. J. *J. Clin. Pathol.* **1970**, *22*, 475–482.
30. Bayston, R.; Lari, J. *Dev. Med. Child Neurol.* **1974**, *32*(Suppl. 6), 16–22.
31. Pople, I. K.; Bayston, R.; Hayward, R. D. *J. Neurosurg.* **1992**, *77*, 29–36.
32. Raahave, D. *Acta Chir. Scand.* **1974**, *140*, 585–593.
33. Selwyn, S.; Ellis, H. *Br. Med. J.* **1972**, *1*(5793), 136–140.
34. Bayston, R.; Penny, S. R. *Dev. Med. Child Neurol.* **1972**, *27*(Suppl. 14), 25–28.
35. Fux, C. A.; Quigley, M.; Worel, A. M.; *et al. Clin. Microbiol. Infect.* **2006**, *12*, 331–337.
36. Guevara, J. A.; Zuccaro, G.; Trevisan, A.; Denoya, C. D. *J. Neurosurg.* **1987**, *67*, 438–445.
37. Gupta, S. K.; Jaiswal, A. K.; Kumar, S. *J. Clin. Neurosci.* **2005**, *12*, 966–967.
38. Guardadao, A. R.; Blanco, A.; Asensi, V.; *et al. J. Antimicrob. Chemother.* **2008**, *61*, 908–913.
39. Borgbjerg, B. M.; Gjerris, F.; Albeck, M. J.; Borgesen, S. E. *Acta Neurochir. (Wien)* **1995**, *136*, 1–7.
40. Renier, D.; Lacombe, J.; Pierre-Kahn, A.; Sainte-Rose, C.; Hirsch, J.-F. *J. Neurosurg.* **1984**, *61*, 1072–1078.
41. Duhaime, A.-C. *Clin. Pediatr.* **2006**, *45*, 705–713.
42. Callaghan, R. P.; Cohen, S. J.; Stewart, G. T. *Br. Med. J.* **1961**, *1*, 860–863.
43. Gordon, C. A.; Hodges, N. A.; Marriott, C. *J. Antimicrob. Chemother.* **1988**, *22*, 667–674.
44. Nichols, W. W.; Dorrington, S. M.; Slack, M. P. E.; Walmsley, H. L. *Antimicrob. Agents Chemother.* **1988**, *32*, 518–523.
45. Nichols, W. W.; Evans, M. J.; Slack, M. P. E.; Walmsley, H. *J. Gen. Microbiol.* **1989**, *135*, 1291–1303.
46. Evans, R. C.; Holmes, C. J. *Antimicrob. Agents Chemother.* **1987**, *31*, 889–894.
47. Mah, T.-F. C.; O'Toole, G. A. *Trends Microbiol.* **2001**, *9*, 34–39.
48. Nickel, J. C.; Ruseska, I.; Wright, J. B.; Costerton, J. W. *Antimicrob. Agents Chemother.* **1985**, *27*, 619–624.
49. Proctor, R. A. *Drug Resist. Updat.* **1998**, *1*, 227–235.
50. Arnell, K.; Enblad, P.; Wester, T.; Sjölin, J. *J. Neurosurg.* **2007**, *107*(3 Suppl. Pediatrics), 213–219.
51. Bayston, R.; de Louvois, J.; Brown, E. M.; Hedges, A. J.; Johnston, R. A.; Lees, P. *Br. J. Hosp. Med.* **1995**, *53*, 368–373.
52. Vinchon, M.; Dhellemmes, P. *Childs Nerv. Syst.* **2006**, *22*, 692–697.
53. Choux, M.; Genitori, L.; Lang, D.; Lena, G. *J. Neurosurg.* **1992**, *77*, 875–880.
54. McCarney, R.; Warner, J.; Iliffe, S.; van Haselen, R.; Griffin, M.; Fisher, P. *BMC Med. Res. Methodol.* **2007**; doi: 10.1186/1471-2288-7-30.
55. Choksey, M. S.; Malik, I. A. *J. Neurol. Neurosurg. Psychiatr.* **2004**, *75*, 87–91.
56. Dasic, D.; Hanna, S. J.; Bojanic, S.; Kerr, R. S. C. *Br. J. Neurosurg.* **2006**, *20*, 296–300.
57. Müller, C.; Netland, A.; Dawson, A. F.; Andrew, E. *J. Antimicrob. Chemother.* **1980**, *6*, 279–283.
58. Brown, E. M.; de Louvois, J.; Bayston, R.; Hedges, A. J.; Johnston, R. A.; Lees, P. *Lancet* **1994**, *344*, 1547–1551.
59. Alleyne, C. H.; Mahmood, H.; Zabramski, J. *Neurosurgery* **2000**, *47*, 1124–1129.
60. Korinek, A. M.; Reina, M.; Boch, A. L.; Rivera, A. O.; De Bels, D.; Puybasset, L. *Acta Neurochir. (Wien)* **2005**, *147*, 39–46.
61. Bayston, R.; Ashraf, W.; Bhundia, C. *J. Antimicrob. Chemother.* **2004**, *53*, 778–782.
62. Haxhe, J. J.; D'Hoore, W. *J. Hosp. Infect.* **1998**, *40*, 166–168.
63. Kaufmann, A. M.; Lye, T.; Redekop, G.; *et al. Can. J. Neurol. Sci.* **2004**, *31*, 506–510.
64. Wilcox, M. H.; Kite, P.; Dobbins, B. *J. Hosp. Infect.* **1998**, *38*, 322–324.
65. Hetrick, E. M.; Schoenfisch, M. H. *Chem. Soc. Rev.* **2006**, *35*, 780–789.
66. Maki, D. G.; Stolz, S. M.; Wheeler, S.; Mermel, L. A. *Ann. Intern. Med.* **1997**, *127*, 257–266.
67. Connors, J. P.; Ferguson, T. B.; Roper, C. L.; Weldon, C. S. *Ann. Surg.* **1975**, *1181*, 735–741.
68. Hamilton, A. J.; Orozco, J.; Narotam, P.; Bowersock, T. *Neurosurgery* **1997**, *40*, 1043–1049.
69. Boelens, J. J.; Tan, W. F.; Dankert, J.; Zaat, S. A. J. *J. Antimicrob. Chemother.* **2000**, *45*, 221–224.
70. Bechert, T.; Böswald, S.; Lugauer, S.; Regenfus, A.; Greil, J.; Guggenbichler, J.-P. *Infection* **1999**, *27*(Suppl. 1), S24–S29.
71. Lackner, P.; Beer, R.; Broessner, G.; *et al. Neurocrit. Care* **2008**, *8*, 360–365.
72. Bayston, R.; Grove, N.; Siegel, J.; Lawellin, D.; Barsham, S. *J. Neurol. Neurosurg. Psychiatr.* **1989**, *52*, 605–609.
73. Bayston, R. Ph.D. Thesis, University of Nottingham, Nottingham, UK, 1979.
74. Hansen, C. M. *Hansen Solubility Parameters*, 2nd ed.; CRC Press: Boca Ratan, FL, 2000; ISBN 10: 0-8493-7248-8.
75. Webb, P. B.; Parsons, A. J.; Marr, P. C.; Gidda, H. S.; Howdle, S. M. *Pure Appl. Chem.* **2000**, *72*, 1347–1355.
76. Furno, F.; Morley, K. S.; Wong, B.; *et al. J. Antimicrob. Chemother.* **2004**, *54*, 1019–1024.
77. Sherertz, R. J.; Heard, S. O.; Raad, I. I. *J. Clin. Microbiol.* **1997**, *35*, 641–646.
78. Bassetti, S.; Hu, J.; D'Agostino, R. B.; Sherertz, R. J. *Eur. J. Clin. Microbiol. Infect. Dis.* **2000**, *19*, 612–617.
79. Bayston, R.; Fisher, L.; Weber, K. *Biomaterials* **2009**, *30*, 3167–3173.
80. Bayston, R.; Lambert, E. *J. Neurosurg.* **1997**, *87*, 247–251.
81. Hart, E.; Azzopardi, K.; Taing, H.; *et al. J. Antimicrob. Chemother.* **2010**, *65*, 974–980.
82. Bayston, R.; Brant, C.; Dombrowski, S. M.; *et al. Cerebrospinal Fluid Res.* **2008**, *5*, 17. doi:10.1186/1743-8454-5-17.
83. Bayston, R.; Bhundia, C.; Ashraf, W. *J. Neurosurg.* **2005**, *102*(Pediatr 2), 207–212.
84. Stevens, E. A.; Palavecino, E.; Sherertz, R.; Shihabi, Z.; Couture, D. A. *J. Neurosurg.* **2009**; doi:10.3171/2009.10.jns09565.
85. Secer, H. I.; Kural, C.; Kaplan, M.; *et al. Pediatr. Neurosurg.* **2008**, *44*, 444–447.
86. Bayston, R.; Vera, L.; Mills, A.; Ashraf, W.; Stevenson, O.; Howdle, S. M. *J. Antimicrob. Chemother.* **2010**, *65*, 258–265.

87. Zabramski, J. M.; Whiting, D.; Darouiche, R. O.; *et al*. *J. Neurosurg*. **2003**, *98*, 725–730.
88. Aryan, H. E.; Meltzer, H. S.; Park, M. S.; Bennett, R. L.; Jandial, R.; Levy, M. L. *Childs Nerv. Syst*. **2005**, *21*, 56–61.
89. Eymann, R.; Chehab, S.; Strowitzki, M.; Steudel, W.-I.; Kiefer, M. *J. Neurosurg. Pediatr*. **2008**, *1*, 444–450.
90. Govender, S. T.; Nathoo, N.; van Dellen, J. R. *J. Neurosurg*. **2003**, *99*, 831–839.
91. Hayhurst, C.; Cooke, R.; Williams, D.; Kandasamy, J.; O'Brien, D. F.; Mallucci, C. L. *Childs Nerv. Syst*. **2008**, *24*, 557–562.
92. Kan, P.; Kestle, J. *Childs Nerv. Syst*. **2007**, *23*, 773–777.
93. Parker, S. L.; Attenello, F. J.; Sciubba, D. M.; *et al*. *Childs Nerv. Syst*. **2009**, *25*, 77–83.
94. Pattavilakom, A.; Xenos, C.; Bradfield, O.; Danks, R. A. *J. Clin. Neurosci*. **2007**, *14*, 526–531.
95. Ritz, R.; Roser, F.; Morgalla, M.; Dietz, K.; Tatagiba, M.; Will, B. E. *BMC Infect. Dis*. **2007**, *7*, 38.
96. Sciubba, D. M.; Noggle, J. C.; Carson, B. S.; Jallo, G. I. *Pediatr. Neurosurg*. **2008**, *44*, 91–96.
97. Sciubba, D. M.; Stuart, R. M.; McGirt, M. J.; *et al*. *J. Neurosurg*. **2005**, *103*(Suppl. 2), 131–136.
98. Richards, H. K.; Seeley, H. M.; Pickard, J. D. *J. Neurosurg. Pediatr*. **2009**, *4*, 389–393.
99. Sciubba, D. M.; Lin, L.-M.; Woodwoarth, G. F.; McGirt, M. J.; Carson, B.; Jallo, G. I. *Neurosurg. Focus* **2007**, *22*, 1–4.
100. Tamburrini, G.; Massimi, L.; Caldarelli, M.; Di Rocco, C. *Acta Neurochir. (Wien)* **2008**, *150*, 1049–1056.
101. Böswald, M.; Lugauer, S.; Regenfus, A.; *et al*. *Infection* **1999**, *27*(Suppl. 1), S56–S60.

6.630. Biomaterials for Spinal Cord Repair

M D Baumann, J C Stanwick, I E Donaghue, and M S Shoichet, University of Toronto, Toronto, ON, Canada

© 2011 Elsevier Ltd. All rights reserved.

6.630.1.	**An Introduction to Spinal Cord Injury**	483
6.630.1.1.	Anatomy of the Spinal Cord	484
6.630.1.2.	The Tissue Response to SCI	484
6.630.1.3.	Animal Models of SCI	485
6.630.1.3.1.	Small animal models	485
6.630.1.3.2.	Large animal models	486
6.630.1.4.	Current Treatment Strategies and Clinical Trials	486
6.630.2.	**Biomaterials for Drug Delivery**	487
6.630.2.1.	Hydrogels	488
6.630.2.1.1.	Control of drug release	489
6.630.2.2.	Polymeric Particles	489
6.630.3.	**Biomaterials for Cell Delivery**	490
6.630.3.1.	Nerve Guidance Channels	490
6.630.3.2.	Scaffolds	492
6.630.4.	**Future Outlook**	492
References		493

Abbreviations

BSCB	Blood-spinal cord barrier
BMSC	Bone marrow stromal cell
cAMP	Cyclic adenosine monophosphate
CSGP	Chitosan–glycerol phosphate
CNS	Central nervous system
CSF	Cerebrospinal fluid
DNA	Deoxyribonucleic acid
EC	Endothelial cell
ECM	Extracellular matrix
FDA	Food and Drug Administration (USA)
GM-1	Monosialotetrahexosylganglioside
HA	Hyaluronan
HAMC	Hyaluronan/methyl cellulose
HPMC	Hydroxypropyl methyl cellulose
MC	Methyl cellulose
MMA	Methyl methacrylate
MPSS	Methylprednisolone sodium succinate
NGF	Nerve growth factor
NSPCs	Neural stem/progenitor cells
NYU	New York University
OSU	Ohio State University
PACA	Poly(alkyl cyanoacrylate)
PAN/PVC	Poly(acrylonitrile)/poly(vinyl chloride)
PCL	Poly(ε-caprolactone)
PDMS	Poly(dimethyl siloxane)
PEG	Poly(ethylene glycol)
PHB	Poly(α-hydroxy butyrate)
PGA	Poly(glycolic acid)
PHEMA	Poly(2-hydroxyethyl methacrylate)
PLA	Poly(lactic acid)
PLGA	Poly(lactic-*co*-glycolic acid)
PLLA	Poly(L-lactic acid)
PNS	Peripheral nervous system
PP	Polypyrrole
PTFE	Poly(tetrafluorethylene)
PVDF	Polyvinylidene fluoride
SCI	Spinal cord injury

6.630.1. An Introduction to Spinal Cord Injury

Spinal cord injury (SCI) is devastating, resulting in lifelong disability. The physical, emotional, and economic costs are real and burdensome for the individual, their families, and society. Current treatment options for SCI are limited to delivery of methylprednisolone, decompressive surgery, and rehabilitation, each of which results in only modest functional recovery. Biomaterials will play a prominent role in future treatments for SCI because they enable localized drug delivery, provide physical support to regenerating tissue, and enhance survival of transplanted cells. These strategies are part of the treatment paradigm known as tissue engineering or regenerative medicine. In Sections 6.630.1.1–6.630.1.3, the complex anatomy of the spinal cord is introduced and animal models of SCI are reviewed. Current treatment methods and clinical trials are discussed in Section 6.630.1.4. Localized spinal drug delivery from hydrogels and polymeric particles is described in Section 6.630.2 and nerve guidance channels and scaffolds for cell delivery are elucidated in Section 6.630.3. These innovative strategies are enabled by the development of materials with desirable physical, chemical, and biological properties.

6.630.1.1. Anatomy of the Spinal Cord

The brain and spinal cord together make up the central nervous system (CNS) and are two of the most complex organs in the human body. The spinal cord serves as the communication pathway between the brain and the peripheral nervous system (PNS) and also coordinates reflex responses without the involvement of the brain. A cross-section of the spinal cord in the thoracic region is shown in **Figure 1**. Moving outward from the center of the spinal cord is the butterfly shaped gray matter, which contains motor and sensory neuron cell soma. The surrounding white matter contains myelinated axons which carry messages to and from the brain. The spinal cord is tightly wrapped by the pia mater, a highly vascularized connective tissue. The intrathecal space separates the pia mater from the arachnoid membrane and is filled with cerebrospinal fluid (CSF). The CSF cushions the spinal cord and brain against sudden motion and provides nutrition to the CNS while simultaneously removing metabolic byproducts. CSF is acellular, with an osmolarity and a salt composition similar to serum but with far lower protein content. The arachnoid and dura mater are the second and third of the three meninges and together contain the CSF and spinal cord. Lastly, the epidural space between the dura and inner surface of the vertebra is filled with fatty tissue, which supports and cushions the CNS.

An important feature of the spinal cord is the blood–spinal cord barrier (BSCB), which lines blood vessels within the cord and consists of endothelial cells and astrocytes. The BSCB protects the spinal cord from changes in the biological and chemical environment of the periphery, including fluctuations in the concentration of ions, small molecules, and growth factors. The filtering action of the BSCB restricts systemic drug delivery to the CNS to low molecular weight compounds, excluding therapeutic antibodies and proteins. Localized delivery methods, including the use of biomaterials to localize drug release, have been studied.

6.630.1.2. The Tissue Response to SCI

Traumatic SCI is described as resulting from compression or laceration (transection) of the cord. In both cases, damage results in necrotic cell death and severing of axons from the cell soma. The permanence of SCI is the result of differences in the wound healing response in the spinal cord relative to other soft tissue, including the PNS as described in **Chapter 5.531, Peripheral Nerve Regeneration**. While it was long believed that axons in the CNS were fundamentally incapable of regenerating, this was disproved in the early 1980s by Aguayo and colleagues who showed that CNS retinal neurons can regenerate within peripheral nerve grafts, but not beyond the graft into the CNS tissue.[1] This significant finding suggested that manipulation of the chemical and biological environment around the injury could serve as a powerful strategy to treat CNS damage.

Axonal regeneration is prevented in the CNS by the inhibitory environment. Specifically, glial cells at the CNS injury site produce a large number of inhibitory factors that limit axonal regeneration, including myelin-associated glycoprotein,[2,3] chondroitin sulfate proteoglycans,[4] and NogoA.[5] The potency of the inhibitory chemical environment present after CNS injury is evident in the hours following axotomy, during which severed CNS axons develop new growth cones that extend into very short distances before stabilizing and then receding in a process known as abortive sprouting.[6] Axonal regeneration in compression injury has been enhanced through the delivery of neuroregenerative factors (see **Section 6.630.2**). In transection injury, regeneration has been encouraged through the use of hydrogels or nerve guidance tubes which act as physical guides for regenerating tissue (see **Sections 6.630.2.1 and 6.630.3.1**, respectively).

After SCI, the primary mechanical insult is followed by a biochemical secondary injury which results in further loss of function. The cascade is initiated by the inflammatory response which results in increased production of growth factors, cytotoxic proteins, free radicals, and nitric oxides.[7] First ischemia

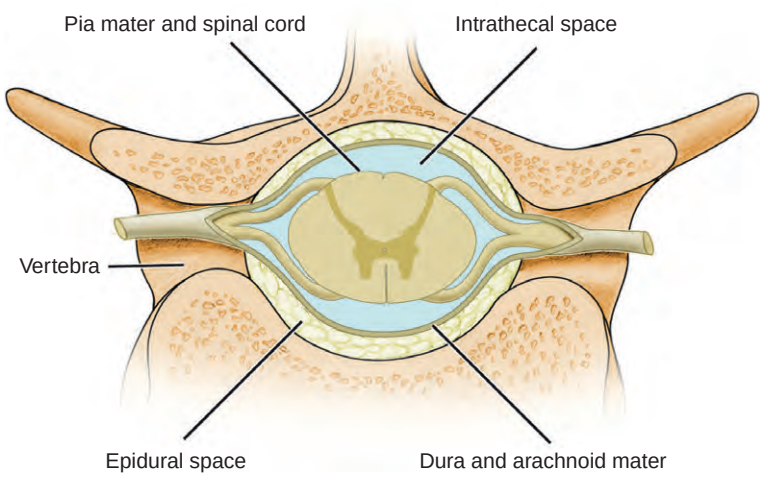

Figure 1 Gross anatomy of the spinal cord. Neural tissue is protected by the vertebrae, dura, arachnoid, and pia mater. Cerebrospinal fluid flows through the intrathecal space. The dorsal and ventral roots carry sensory and motor information, respectively, from and to the periphery. Image copyright (2005) by Michael Corrin.

and then hypoxia appear in the gray matter[8] with accompanying production of free radicals and lipid peroxidation which damage the fatty acids of cell membranes. These processes drive neurons and oligodendrocytes to apoptosis for weeks after injury and increase the volume of injured tissue, resulting in a spindle-shaped cystic cavity. This lesion is eventually isolated from healthy tissue by reactive astrocytes which migrate to the lesion and form a glial scar.[7] The duration and complexity of secondary processes in SCI suggest that there is no magic bullet for repair. Biomaterials can be used either to achieve simultaneous and sustained delivery of multiple pharmaceutics or to promote tissue regeneration using cell scaffolds.

6.630.1.3. Animal Models of SCI

6.630.1.3.1. Small animal models

Treatment strategies are tested in different injury models to determine safety and efficacy according to the therapeutic target. For example, a cellular transplant may initially be tested in a hemisection model to prove efficacy and later in a compression model which closely mimics human SCI. The safety and performance of the corresponding cell delivery scaffold will likewise be evaluated in both injury models. Rats are a common, low-cost mammalian model that offers better working size for spinal surgery and device implantation than mice. Rat models of SCI fall into three categories: *transection* models involve cutting all or part of the spinal cord, *contusion* models quickly crush the cord with measured force,[9] and *compression* models compress the cord for a defined time.[10] These models are illustrated in Figure 2. Each model may be *acute*, where treatment is initiated immediately after injury, or *chronic*, where the treatment is delivered during a second surgery 4–6 weeks after injury. Acute models are used to assess neuroprotection and/or neuroregeneration, while chronic models can test only the latter.

Compression models produce astrogliosis and also mimic the residual displacement of the spinal column similar to that seen in human SCI.[9] In the model developed by Rivlin and Tator,[11] the cord is exposed by laminectomy and a modified aneurysm clip creates the injury as a function of both closing force and duration of compression. Force is simultaneously applied to both the dorsal and ventral aspects of the cord, as in human SCI.[12] The model has previously been used to study the pathology of secondary injury[13] and the importance of surgical decompression following injury, the latter of which is now a clinical practice option.[14] More recently, clip compression has been used to evaluate neuroprotective agents[15,16] and a novel biomaterial-based drug delivery strategy.[17] Variants on balloon compression, a technique in which injury severity is related to both the pressure of an inflated angioplasty balloon and its period of application, are also in current use. The balloon is inflated intrathecally or epidurally, being introduced into the intervertebral canal via laminectomy[18] or an intervertebral foramen.[19] The least invasive balloon compression models reach the spinal cord by lumbar puncture, causing minimal extraneous tissue damage and facilitating medical imaging by eliminating surgical artifacts.[19]

Contusion models produce a cystic cavity, axotomy, and demyelination through a defined force or displacement of the cord. Reviews by Park[20] and Kwon[21] describe how secondary injury increases the severity of SCI in the days postinjury and is the target of neuroprotective strategies. Multiple contusive models are in current use, most notably the New York University (NYU) Impactor[22] and Ohio State University (OSU) Impactor.[23] The NYU device impacts the cord with a defined force whereas the OSU Impactor produces a defined cord displacement. In both cases, the contusion is accomplished quickly, with the force applied and removed within 1 s. Two criticisms of contusive injury models are the asymmetric application of force (dorsal only) and short duration of compression.[11] These features are not present in human SCI and may be problematic for clinical trials based on data collected in a contusion model.

Transection models are used extensively to evaluate the efficacy of a regenerative therapeutic approach. This model

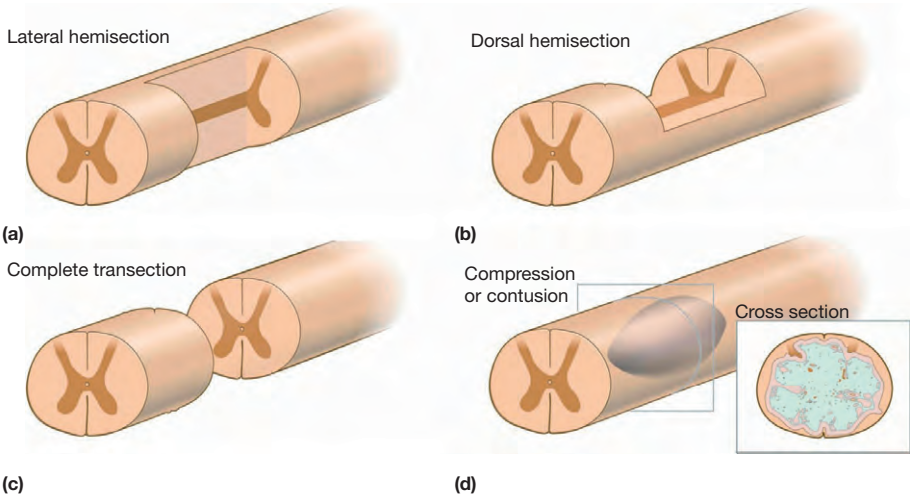

Figure 2 Animal models of spinal cord injury: (a, b) hemisection models cut sections of the spinal cord to produce specific functional deficits; (c) transection models create a gap between the rostral and caudal portions of the spinal cord; and (d) compression/contusion models mimic human spinal cord injury by creating a fluid-filled cyst. Image copyright (2006) by Michael Corrin.

can provide unambiguous proof of regeneration if a therapy leads to functional recovery and then the observed recovery is lost after resection. Hemisection leads to defined neurological deficits; thus, hemisection models are used when specific neuronal tracts are of interest. Dorsal hemisection cuts the sensory tracts in the dorsal horns while lateral hemisection disrupts both motor and sensory function. The main limitation of the hemisection model is the difficulty in accurately reproducing the injury and the consequent interanimal variability. Although transection does not accurately reflect the injury most often sustained by the individual (unless by stabbing or gunshot wound) or the pathophysiology of secondary injury, these injuries are useful for understanding the regenerative effect of experimental interventions.

6.630.1.3.2. Large animal models

The same models of SCI – compression, contusion, and transection – are also used in larger animals. Cats, dogs, and nonhuman primates, especially, are valued for functional neuroanatomy which more closely matches human structure and thus presents a more realistic scale of the injury. Promising therapies often progress from a rat model to a larger animal once the additional complexity and cost of the study can be justified. For example, data collected in an acute contusion model in the cat prompted the evaluation of methylprednisolone in multiple clinical trials, and the eventual use for treatment of human SCI. The preclinical data showed that so-called mega doses of methylprednisolone delivered within a short time of injury preserved the conduction velocity and amplitude of evoked potentials relative to controls.[24–26] Electrophysiology is an accepted predictor of injury severity (or recovery of function) and correlated well with locomotor assessment in the cat.[27]

More recently, acute application of the polymers poly (ethylene glycol) (PEG) and Poloxamer 488 was evaluated in naturally occurring, neurologically complete canine SCI. Outcome measures included pain perception, proprioceptive limb placement, locomotor testing, and electrophysiology.[28,29] In many ways, this model comes closest to what a surgeon might encounter in the clinic: unscheduled presentation; varied etiology, severity, and location; and a potentially demanding surgical timeframe. Though these factors understandably introduce variability into the study, positive outcomes may be more easily translated to the clinic because efficacy must be greater than the (large) interanimal variability. The disconnect between the controlled environment of a laboratory induced injury and often unknown character of real world SCI has been cited as a contributing factor to the high number of failed clinical trials in the field.[30]

Perhaps because of this fact, the use of nonhuman primate models is increasing, although there is not yet proof that a positive outcome in a 'clean' laboratory SCI in a nonhuman primate is a better predictor of efficacy for human SCI than the aforementioned feline, canine, or even rodent models. Much of this work is in Macaque monkeys, focused on the anti-NogoA family of antibodies first developed by Martin Schwab and coworkers. A recently completed a Phase I trial sponsored by Novartis examined anti-NogoA delivery over different periods between 1 and 28 days at participating European and Canadian hospitals. A Phase II trial is now being planned. The Macaque model used was an acute cervical hemisection which allowed testing of the forelimbs in tasks such as grasping and reaching.[31,32] Cervical injuries are the most common location of human SCI.[33]

6.630.1.4. Current Treatment Strategies and Clinical Trials

No device, drug, or cell therapy has shown significant functional recovery in a comprehensive clinical trial after SCI despite several trials.[30] Methylprednisolone sodium succinate (MPSS) was investigated in five clinical trials and adopted as a standard of care on the basis of modest functional recovery, but its continued use is debated because of an array of serious side effects.[34] These side effects are severe enough that the high dose arm of the most recent clinical trial was discontinued, a study in which MPSS was delivered intravenously for 48 h.[35] The modest functional benefit observed at lower intravenous doses and incidence of side effects at higher dosing suggest that localized delivery of MPSS, bypassing the BSCB, may achieve greater MPSS concentration at the injury site and increase function with fewer side effects. GM-1 ganglioside is a neuroprotective agent that was evaluated in over 700 patients with results similar to MPSS, showing a statistically insignificant trend toward improved function.[36] Modest functional benefit was observed at the lower dose and significant side effects were found at the higher dose, resulting in termination of this arm of the study. In this study, GM-1 was delivered intravenously over up to 8 weeks.[36] Current clinical studies are summarized in **Table 1**.

Cethrin is a Rho agonist which completed a Phase I/IIa safety trial in 2009 and entered Phase IIb, although this trial was terminated in early 2010. Cethrin is notable as the first use of a bioengineered delivery strategy. Cethrin is a bacterially derived kinase inhibitor coupled to a transport sequence which allows the molecule to pass from the epidural space, through the dura mater and arachnoid, to the intrathecal space and spinal cord. This route uses extra-dural administration where a fibrin matrix is used to deliver Cethrin on the dura mater; however, the concentration of Cethrin in the spinal cord has not been published.

Anti-NogoA, an anti-inhibitory neuroregenerative molecule, entered a Phase 1 clinical trial in 2006. Anti-NogoA was delivered clinically by continuous intrathecal infusion via an external pump; however, complications, likely due to infection, required multiple bolus injections over the course of the study. Anti-NogoA will enter a Phase II clinical trial.

Cell therapy holds great promise for treatment of SCI and will be the focus of more clinical trials as the technology matures. Two cellular treatments have been rigorously evaluated to date: the Procord trial for autologous macrophages[37] and a pilot study for bone marrow stromal cell (BMSC) injection.[38] The Procord trial did not progress and efficacy was not an endpoint of the BMSC trial. Geron currently has an embryonic stem-cell-derived oligodendrocyte precursor cell trial planned, with the view that the oligodendrocytes will save axons from degeneration. Cell therapy strategies face several key challenges for success: (1) defined starting cell population, (2) survival of transplanted cells, and (3) defined differentiation profile.

Biomaterials for the treatment of SCI are poised to grow as the advantages of drug delivery systems which reduce systemic

Table 1 Summary of select current clinical studies for spinal cord injury

Approach	*Description*	*Current stage of clinical trial*
Delivery of therapeutics		
Anti-NogoA	A monoclonal antibody that overcomes neurite outgrowth inhibition caused by NogoA. Delivered by osmotic pump or repeated bolus delivery by lumbar puncture	Phase I
Cethrin®	A Rho antagonist that promotes neuroprotection and neuroregeneration. Administered to the dura of the injured spinal cord with a fibrin sealant	Phase IIb – suspended
Minocycline	A broad spectrum antibiotic that has demonstrated neuroprotection in animal models. Injected intravenously	Phase I/II
Fampridine®	A voltage-dependent potassium channel blocker that improves sensory and motor function. Delivered intravenously or orally	Phase III
Cell-based therapies		
Procord®	Autologous macrophages that elevate the release of protective molecules. Delivered by injection onto the spinal cord	Phase II – suspended
Bone marrow stromal cells	Contains pluripotent cells that release growth factors to improve regeneration. Delivered by transplantation onto the spinal cord	Phase II

side effects and bypass the BSCB are recognized. The shift from repurposed small molecules with limited BSCB permeability (e.g., MPSS, minocycline) to larger and impermeable molecules (e.g., anti-NogoA) will accelerate this trend. The clinical use of cell-seeded scaffolds in other tissues[39,40] will drive clinical investigation of this strategy after SCI. Biomaterials which enhance cell survival or direct differentiation in the CNS are currently being developed.

6.630.2. Biomaterials for Drug Delivery

Strategies for delivering drugs to the injured spinal cord are categorized as either systemic or local. The primary obstacle to systemic drug delivery is the BSCB. A compounding problem for spinal drug delivery is that with the exceptions of methylprednisolone,[41] GM-1 ganglioside,[42] minocycline,[43] and cAMP moderators,[44] a majority of molecules proposed to treat SCI are high-molecular-weight proteins. These biomacromolecules generally possess short serum half-lives and can act nonspecifically (e.g., as mitogens), which further complicates systemic delivery. Local delivery of therapeutic molecules using biomaterials circumvents the BSCB and denaturation in serum by delivering the drug payload directly to the spinal cord, most often as a drug-loaded hydrogel injected into the epidural or intrathecal space. The possibility of systemic side effects and toxicity are likewise reduced by local delivery.[45]

The utility of a biomaterials strategy for localized release stems from the ability to deliver a sustained release formulation from a single injection. Sustained release is common for both neuroprotective and neuroregenerative molecules: in the latter case, efficacy is often improved when drug delivery is continued up to 28 days. This is currently only clinically possible from indwelling catheter and pump systems, although the method is not approved for use after SCI. These systems are initially appealing because they afford excellent control of the drug concentration delivered to the epidural fat or intrathecal space via a catheter over a period of weeks as shown in **Figure 3**. Both implanted and external pumps are available; however, external pumps are more susceptible to infection.[46,47] Significant drawbacks include the risk of scarring and compression of the spinal cord by an intrathecal catheter, chronic inflammatory response to the implanted pump, and the risk of infection when using an external infusion pump.[48]

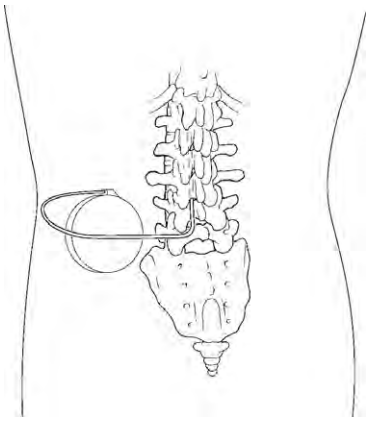

Figure 3 Infusions pumps may be implanted under the skin in a patient's abdomen and a catheter tunneled subcutaneously into the epidural or intrathecal space. Models used in animal studies are often powered by osmotic pressure whereas those in clinical use are powered by batteries or pressurized propellant. Image copyright (2006) by Michael Corrin.

The bolus injection of an appropriately formulated sustained release device is an attractive alternative to both the minipump/catheter and single bolus injection because it removes the risk of chronic catheter scarring, can be minimally invasive, and attenuates the host inflammatory response and risk of infection.

Among biomaterials strategies tested in compression/contusion models, the large majority are classified as epidural bolus delivery, such as injection of polymer hydrogels, liposomes, and combinations thereof.[49–51] In instances where a laminectomy is performed (i.e., in all injury models save balloon compression and as part of surgical decompression), gels may be applied directly to the exposed dura. Fibrin sealant has been used in this manner,[52,53] as have been foamed gelatin (e.g., Gelfoam)[54–56] and collagen.[57,58] Drugs released into the epidural space must cross the dura and arachnoid mater and

the fluid-filled intrathecal space before reaching the spinal cord. Various investigators also exploit intrathecal injection of a drug delivery system. This route affords greater localization than epidural delivery but requires puncturing the dura and arachnoid mater. One strategy is the injection of drug-loaded microparticles which are distributed throughout the intrathecal space by CSF flow. So long as the particles are too large to pass through the arachnoid granulations, the valves through which CSF drains to the venous blood, they can sustain release to the brain and spinal cord. This approach has been demonstrated using the analgesic Baclofen, where therapeutic concentrations were maintained for up to 30 days from 30-μm PLGA particles.[59–61] Another option is dispersing drug-loaded particles in a hydrogel, such as hyaluronan/methyl cellulose blend (HAMC) and injecting the resulting composite into the intrathecal space at the site of injury.[62] The drug can also be delivered from the HAMC hydrogel alone.[15,62,63] Localizing the drug payload on a specific area of the cord should avoid systemic side effects and other nonspecific effects elsewhere in the CNS and reduce the overall required dose.

Other biomaterials based drug delivery strategies have been developed on the basis of transection models of SCI, which may be modified to work with compression injuries in the future. Treating compression injury is important because 70% of clinical SCI is by compression.[64] Examples include photo-cross-linkable PEG,[65,66] fibrin gels,[67,68] and liposome or microparticle loaded agarose.[69,70]

6.630.2.1. Hydrogels

Many treatment strategies use hydrogels as a drug delivery device or scaffold for cell growth. Hydrogels are polymer matrices swollen by osmotic pressure and held together by intermolecular entanglement, reversible physical binding, or chemical cross-linking.[71] Forces of physical binding include hydrogen bonding, hydrophobic junction formation, and electrostatic attraction. Water content varies widely, from 40% in poly (2-hydroxyethyl methacrylate) gels to over 99% in the weakest agarose gels. Hydrogels, such as the one described in **Figure 4**, are the method of choice to achieve localization and spatial control of drug release within the intrathecal space because many are easily formulated to be injectable, can be gelled by various stimuli, and their high water content favors biocompatibility.[72] The extent of cross-linking of biodegradable polymers controls swelling.[72,73] Cell adhesion to the hydrogel can be intrinsic, such as with collagen (cell adhesive)[74] or agarose (noncell adhesive),[75] or modified through addition of cell-adhesive peptides.[76] In hydrogels with very high water content, drugs can be delivered at concentrations comparable to those used in infusion pumps, or a controlled release technology such as drug-loaded particles[62,70,77] or liposomes[69,78,79] can be incorporated.

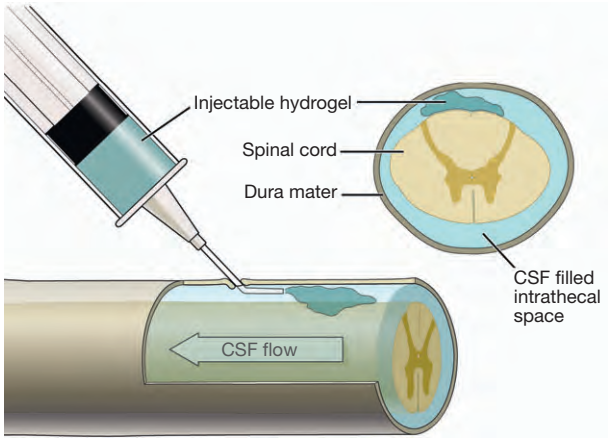

Figure 4 A hydrogel of hyaluronan and methylcellulose used for local and sustained drug delivery to the injured spinal cord. This fast-gelling, injectable hydrogel allows for a minimally invasive mode of treatment. Image copyright (2005) by Michael Corrin.

Both physical and covalently cross-linked hydrogels can be applied to the treatment of SCI. Physical gels generally offer milder cross-linking conditions and simplicity of use, and lack the possible toxicity associated with covalent coupling agents used *in situ*. Among physical gels which form by thermal means, inverse thermal-gelling polymers are most flexible because the subzero temperature needed for fast gelation of traditional materials is avoided. For example, agarose has been used as an *in situ* gelling epidural drug delivery system where gelation was triggered by flooding the injection site with air cooled by dry ice.[69,70] This type of system is less applicable intrathecally, where the gel is separated from the environment by the dura and arachnoid and subzero temperatures are likely to damage these tissues. Other polymers which gel on cooling include carrageenan and gelatin, among other polysaccharides.[80,81] Prominent inverse thermal-gelling polymers are methylcellulose, hydroxypropyl methylcellulose (HPMC), and chitosan–glycerol phosphate systems (CSGP). The cellulosic materials gel on heating as the water of hydration is lost, exposing hydrophobic portions of the backbone which then associate to form hydrophobic junctions. Gelation of MC in water occurs between 40 and 50 °C and HPMC between 75 and 90 °C.[82] Increasing the ionic strength of MC/HPMC solutions lowers the gelation temperature by reducing the number of free solvent molecules in the system through the salting out effect. This effect has been exploited for intrathecal drug delivery where methylcellulose formulated with anionic hyaluronan quickly forms a physical gel on exposure to body temperature.[15] CSGP solutions also gel as temperature is increased and the water of hydration is lost. In this case, gelation is a function of facilitated hydrophobic interactions and hydrogen bonding between chitosan chains.[83,84] Physical gels can also be formed through ionic interactions, most commonly between an anionic polymer such as alginate, gellan, or carrageenan, and divalent cations.[85] These gels can be stable *in vivo* and have been used for drug delivery.[86,87] Ionic gelation can be very fast, potentially making these materials difficult to use *in vivo*. A double barreled syringe or temporary loading of ions in liposomes may improve ease of use.[88]

Chemically cross-linked hydrogels are of interest because they allow greater flexibility to manipulate physical and biological properties than typically possible in physical cross-linking. For drug delivery, a polymer is modified with synthetic functional groups with the goal of enabling (or enhancing) gelation, improving *in vivo* stability, or imbuing specific enzymatic susceptibility. For example, the biocompatible, biodegradable, angiogenic, and anti-inflammatory nature of

hyaluronan drives synthetic efforts.[89–91] PEG and PEG–poly (lactic acid) block copolymers are also of interest. In these cases, the PEG backbone is nondegradable and cross-linking produces stable hydrogels.[92] Degradability is conferred by inclusion of PLA.[93] Some methods of chemical cross-linking, such as ionizing radiation and those requiring toxic organic solvents, are obviously incompatible with *in situ* gelation.[94] Photoinitiated radical cross-linking is most promising because the reactions are (a) fast, (b) proceed in water, (c) do not require a small molecule cross-linker, which can be toxic, and (d) can take place at physiological temperatures. Glycidyl methacrylate[90,95–97] and other acrylates[98,99] are most often used. Primary concerns are the choice and quantity of initiator with regard to toxicity, cross reactivity between the cross-linking chemistry and drugs in the hydrogel, and the potential for local heating during cross-linking. In addition, if the gel is rendered opaque by addition of drug-loaded particles or liposomes, it may not be possible to reliably photopolymerize the sample. A second cross-linking chemistry which has received significant interest is the grafting of thiol functional groups to create reversible disulfide bonds.[100,101] This chemistry is applicable to epidural use but the relatively slow rate of cross-linking, ~10 min, makes it unsuitable for intrathecal injection where CSF flow can dilute the pregel.

Overall, both physical and covalently cross-linked gel can be designed for spatial control of drug release in the intrathecal space. Physical gels are valued for the selection of biocompatible polymers, ease of fabrication, and absence of cross-linkers, initiators, or risk of gel–drug reactivity during cross-linking. The stability of chemically cross-linked gels, however, can be greater than that of physical gels.

6.630.2.1.1. Control of drug release

Bulk release is the simplest form of drug delivery from hydrogels and is a diffusive process often well described by Fick's law, wherein the fraction of drug released is linear with root time for the first 75% of drug released.[73,102] In this instance, the gel is formed in the presence of, or soaked in, a concentrated solution of the target drug so that the hydrogel bound solvent contains the molecule of interest. Drug release is completed quickly because the polymer chains present a minimal physical barrier, and drug diffusivity is similar to the rate observed in water. Exceptions are found when the hydrogel is highly cross-linked or the drug interacts with the hydrogel, either by electrostatic or hydrophobic interactions.[103,104] The period of drug release depends on molecular weight, diffusive path length, and sample geometry,[102] but is often reported to be 6–72 h *in vitro*.[16,62,77,105] This compares favorably to drug clearance from the intrathecal space after bolus injection of a drug solution, where the entire volume of CSF is turned over every 4–6 h.[106] A subset of bulk release is the suspension of poorly soluble drug particles in the hydrogel. In this case, release is limited by the rate of drug dissolution at the particle surface, and is prolonged relative to Fickian diffusion.[103,107,108] Bulk release is useful for the delivery of neuroprotective molecules which are required in the first weeks after injury.

Therapeutic molecules can also be incorporated into the hydrogel structure as part of the polymer backbone or as a pendant graft.[100,105,109] Incorporation into the backbone results in drug release only upon hydrogel degradation and is not suitable for use in the intrathecal space, where the partly degraded hydrogel with remaining drug load is likely to be removed from the injection site by CSF flow. Binding a drug to the polymer backbone *via* a hydrolytically cleavable linkage is useful when very specific release kinetics are required or it is not practical to delay release using particles/liposomes.[105,110,111]

6.630.2.2. Polymeric Particles

The ability of solid polymers to segregate drugs from the environment and control their *in vivo* release has led to their use in the delivery of peptides,[112] proteins, including neurotrophins;[113] DNA,[114] and many small molecules.[115–117] Solid polymer controlled drug release devices take many forms, with micro- and nanoparticles thoroughly studied because of their versatility in application.[118] Drug release from particles can be controlled by matrix degradation, passive diffusion, or a combination of the two. Degradative mechanisms are further subdivided into bulk degradation and surface erosion. In addition, the role of device fabrication technology, surface area to volume ratio, polymer structure, presence of excipients, and drug loading all play a part in governing drug release. In **Figure 5**, increasing the drug load is seen to increase surface porosity, accelerating drug release (and particle degradation). The size of particles used in epidural formulations is not restricted, but those of 40 μm and smaller are desirable for intrathecal delivery because they are likely to be injectable[92] and therefore minimally invasive.

Both synthetic and natural polymers find application as particulate delivery systems: in many cases the desired release profile informs polymer choice. Among synthetic polymers, poly(ortho esters), poly(hydroxyesters), poly(phosphazenes), and poly(ε-caprolactone) (PCL) are the most frequently cited.[22,23] Poly(anhydride) degradation by surface erosion and enzymatic degradation of polypeptides are also well known. Polymers of natural origin used to fabricate particles include chitin, poly(L-lysine), and alginate.[119,120] Fabrication of natural polymer-based particles often exploits the polyelectrolyte nature of these materials for drug encapsulation and particle formation. Particles of poly(lactic-*co*-glycolic acid) (PLGA) are especially important because the family of PLGA copolymers has been widely investigated for drug delivery, hydrophilic and hydrophobic drugs can be encapsulated using similar techniques,[117,121] and release of many molecules can be sustained for 30 days.[121,122] Additionally, PLGA is degraded by hydrolysis with well-characterized degradation products.[123] This degradation mechanism is expected to predominate when particles are injected intrathecally. When particles are prepared by double emulsion, the release kinetics, encapsulation efficiency, and particle size can be tailored by adjusting polymer concentration, molecular weight, copolymer ratio, solvent removal rate, drug loading, and surfactant concentration.[124,125]

With regard to the biocompatibility of PLGA in the CNS, the tissue response after epidural application is likely to parallel that in adipose tissue, where a thin fibrotic capsule can form around the polymer.[126] There are few reports of polymeric particle injection into the intrathecal space, and these indicated that PLGA was well tolerated.[59–61] This result is in accordance with the general literature, where PLGA and poly(alkyl cyanoacrylate) (PACA) particles are most thoroughly studied. PACA

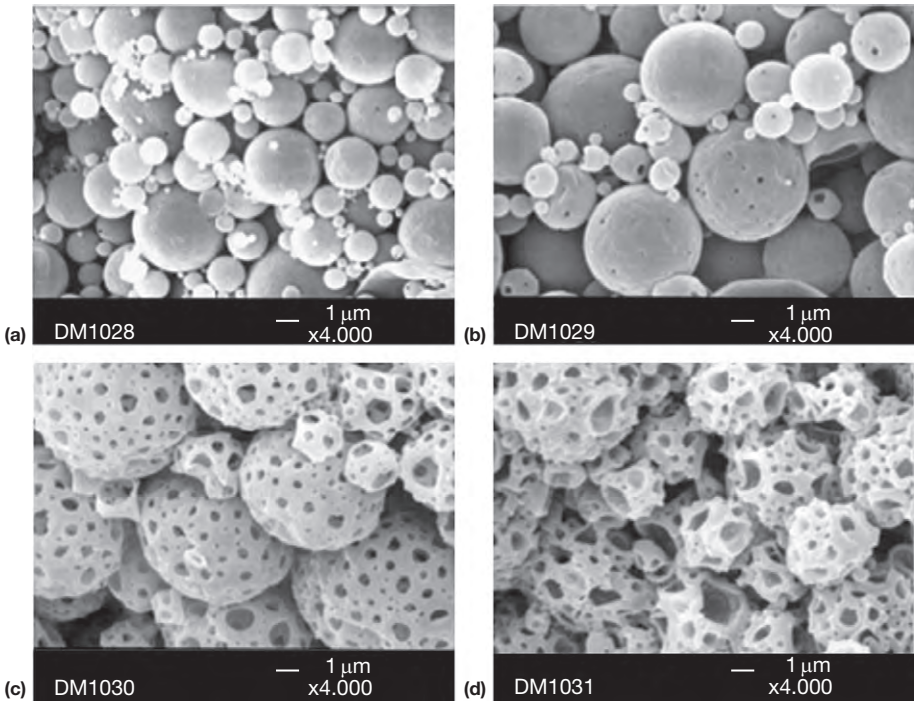

Figure 5 Electron microscope photographs of poly(lactic-*co*-glycolic acid) (50:50) microparticles prepared by the w/o/w solvent evaporation with increasing nominal drug loadings of (a) 0, (b) 1, (c) 5, and (d) 10% (w/w). Reproduced from Witschi, C.; Doelker, E. *J. Control. Release* **1998**, *51*(2–3), 327–341, with permission from Elsevier.

is clinically approved for *intra venous* use, but these particles degrade within hours[127] and are unlikely to sustain release sufficiently after SCI. Detailed studies of how injected particles are distributed in the intrathecal space, the local tissue response, and clearance mechanisms are needed to support the use of particulate biomaterials for spinal drug delivery.

6.630.3. Biomaterials for Cell Delivery

Biomaterials play a key role in strategies to encourage regeneration of native tissue by providing physical support and a controlled environment for repair. Nerve guidance channels, which aim to bridge nerve gaps after transection injury, have been developed on the basis of successes in the PNS.[128] The importance of polymeric scaffolds as fillers of tissue defects and as a transplantation matrix for cell delivery is increasing, encouraged by advances in other areas of tissue engineering.[129–131]

6.630.3.1. Nerve Guidance Channels

Nerve guidance channels, or conduits, are designed to assist in SCI repair by protecting and guiding nerve regeneration through the bridging of nerve gaps.[128] As such, key design criteria for nerve guidance channels are sufficient porosity for neurite ingrowth, cell adhesion, and mechanical strength. Nerve guidance channels may also be biodegradable, electrically active, enclose an internal matrix, or incorporate longitudinally parallel microchannels or fibers.[132–135]

Nerve guidance channels may be implanted for physical support alone after SCI, or seeded with cells in a combination therapy. The purpose of cell transplantation is to promote axonal regeneration and remyelination. Cell types that are transplanted include neural stem/progenitor cells (NSPCs), Schwann cells, and olfactory ensheathing glial cells.[136–138] Olfactory ensheathing glial cells have been delivered alone and with Schwann cells to promote axonal regeneration and functional improvement.[139,140] Schwann cells alone have been shown to provide a conducive environment for axonal regeneration when used in nerve guidance channels in the transected spinal cord.[141] However, in order to prove lasting functional recovery, the long-term survival of these cell types must be better understood.[142]

The appropriate polymeric biomaterial for nerve guidance channels must be biocompatible, nontoxic, and elicit only a minimal inflammatory response.[143] An example of a nondegradable material is poly(acrylonitrile)/poly(vinyl chloride) (PAN/PVC), which has been used in the delivery of Schwann cells and olfactory ensheathing glia.[128] As PAN/PVC is not cell adhesive, PAN/PVC channels were filled with Schwann cells suspended in Matrigel, resulting in partial regeneration but limited recovery.[137] Matrigel is derived from a mouse sarcoma and includes extracellular matrix (ECM) proteins and growth factors.[144] The inclusion of cyclic AMP (cAMP) to the Schwann cell/Matrigel PAN/PVC guidance channel promoted greater tissue regeneration and functional recovery.[44]

A second nondegradable polymer is poly(2-hydroxyethyl methacrylate) (PHEMA).[128] This is an attractive material for SCI therapy, as it is biocompatible and nontoxic.[142] It has tunable mechanical properties, and is the only polymer to date that has been fabricated as a nerve guidance channel with an elastic modulus corresponding to that of native spinal

cord tissue.[145] With the addition of an internal matrix such as collagen, fibrin, Matrigel, or methylcellulose, PHEMA has been shown to support axonal regeneration in injured rat spinal cords.[134] The surface charge of this polymer can be modified by the addition of quaternary amine groups or a second methacrylate subtype to promote cell adhesion.[141] In addition, it can incorporate bioactive compounds or functional concentration gradients to direct neurite outgrowth.[128,141]

The formation of nerve guidance channels from biodegradable polymers is of current interest because they do not require surgical removal. The majority of this class of biomaterials are natural polymers.[128] One such natural polymer, collagen, has been fabricated into guidance channels using chemical cross-linkers. Collagen has been approved by the FDA for use in the PNS as a nerve guide.[128] Collagen nerve conduits have also been modified with ECM proteins and peptide sequences to provide directional guidance.[146] Agarose scaffolds, with and without the addition of brain-derived neurotrophic factor, were found to guide axonal regeneration in a hemisection spinal cord model.[147] The natural polymers alginate and chitosan have also been used with seeded cells in transected spinal cord models.[141] Chitosan, introduced in **Chapter 2.213, Chitosan**, exhibits tunable properties through varying its acetyl group content and has been used to transplant peripheral nerve grafts and NSPCs into the injured rat spinal cord, showing increased axonal regeneration.[136,148,149] Tissue bridges formed in chitosan tubes seeded with brain-derived NSPCs were thicker than those formed in identical tubes seeded with spinal-cord-derived NSPCs. Both cell types formed tissue bridges that were thicker than those in animals which received chitosan tubes alone.[136] The tissue bridge can be easily observed through the transparent chitosan tube in **Figure 6**. Poly(α-hydroxy butyrate) (PHB) enhanced axonal regeneration in rat cervical spinal cord hemisection.[142] Partial regeneration and limited recovery were shown in rat models after the delivery of Schwann cells wrapped in PHB.[128]

Desirable synthetic polymers include poly(α-hydroxyacids), of which poly(glycolic acid) (PGA) and PCL have been approved by the FDA for PNS nerve regeneration.[128] Unlike poly(D,L-lactic acid), poly(L-lactic acid) (PLLA) has been used in nerve guidance channels without tube collapse, but has more rapid degradation.[141,142] PLGA has been shown to support neurite outgrowth to a greater extent than PCL and PLA.[141] A multichannel PLGA scaffold seeded with Schwann cells supported robust axonal growth but resulted in the formation of a rim of fibrous tissue surrounding the regenerated neurons. Subsequent investigations showed that a smaller channel diameter reduced the amount of fibrous tissue, yet it has not been pursued further.[141] Electrically active polymers such as poly(tetrafluorethylene) (PTFE), polypyrrole (PP), and polyvinylidene fluoride (PVDF) may be used to deliver electrical stimuli.[133,150,151] This approach is interesting as it has been shown that electrical stimulation results in increased neurite outgrowth.[152]

Many nerve guidance channels are designed to promote cell adhesion through either nonspecific or specific cell-surface receptors.[128] Nonspecific physical adhesion can be improved by changing the surface charge or increasing surface roughness. Specific cell–polymer adhesion can be achieved by functionalizing the conduit with ECM proteins such as laminin or fibronectin, or derived protein sequences such as RGD, YIGSR, or IKVAV.[153,154] The inclusion of an internal matrix can prevent tube collapse and improve bioactivity.[128] Multiple channels, longitudinally oriented fibers, or hydrogels have been used in this capacity.[128] An open path design using the internal matrix as minimal structural support was shown to improve regenerative capacity.[155] This demonstrates not only the importance of good cell–polymer adhesion, but also sufficient porosity for cell penetration.

An improvement in axon alignment can be achieved through the fabrication of microgrooves or the addition of cell-adhesive proteins or nanofibers.[141] Micro- and nanofibers synthesized by electrospinning, self-assembly, or phase-separation provide a large surface area for cell contact as well as spatial cues to promote nerve alignment.[152] Precise microtopographical features to control axon growth can be created using soft lithography, and most commonly using the nondegradable material poly(dimethyl siloxane).[152] These features influence axonal growth and direction by mimicking the microenvironment of the ECM; however, PDMS tubes are limited by poor permeability of nutrients across the wall structure.

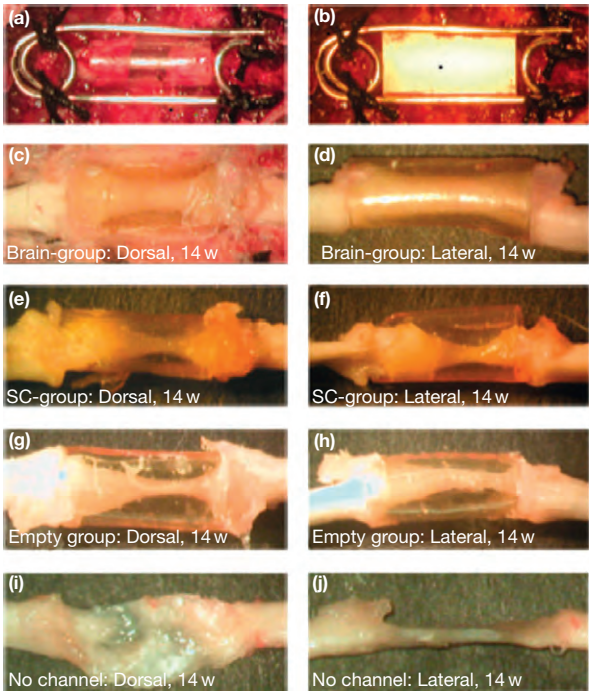

Figure 6 Surgical procedure for extramedullary chitosan channel implantation after spinal cord transection (a and b). At 14 weeks, gross appearance of the implanted channel (c–h) or spinal cord transection alone (i and j), from the dorsal and lateral aspects. In each panel, rostral is on the left. (a) Dorsal view of the transected spinal cord stumps placed within the transparent chitosan channel. The gap between the stumps is ~3.5 mm. (b) The spinal fusion with wire for spinal stabilization and the expanded polytetrafluoroethylene membrane placed on the dorsal aspect of the channel for prevention of scar invasion. (c–h) There is a tissue bridge inside the channels in the brain (c and d), spinal cord (e and f), and empty-channel groups (g and h). The brain group has the thickest bridge (c and d). In the no channel group, there is a pale connective tissue between the stumps (i and j). Reproduced with permission from Nomura, H., *et al*. *Tissue Eng. A* **2008**, *14*(5), 649–665.

6.630.3.2. Scaffolds

Polymer biomaterials are also used as scaffolds for cell transplantation to the injury site where they can fill defects and promote tissue repair, distributing cells throughout the injury. Because scaffolds are commonly used as cell carriers or to encourage host cell ingrowth, it is critical to consider cell–material interactions. High porosity is essential for cell attachment, allows for tissue vascularization, and will improve implant stability through the integration of scaffold and surrounding tissue.[141] However, high porosity materials may also exhibit weaker mechanical properties and faster degradation rates if the material is biodegradable. Successfully engineered scaffolds to be used in cell delivery have mimicked the cell microenvironment, or 'niche.'[156] The primary cells of interest are Schwann cells, neural stem/progenitor cells (NSPCs), and olfactory ensheathing glia.[128] Genetically modified cells that overexpress neurotrophic factors have also been pursued in a variety of combinatorial strategies.[157] An early example is the transplant of fibroblasts genetically modified to secrete NGF in collagen matrices applied to a hemisection model of SCI, resulting in neurite outgrowth from multiple neurite populations.[158] Scaffolds seeded with NSPCs provide platforms for cell differentiation, and potential for repair of large defects.[142] Coculture of NSPCs and endothelial cells (ECs) is being explored to enhance tissue survival by promoting development of vasculature.[156] For example, a scaffold seeded with brain ECs and neural progenitor cells implanted in a hemisection model of SCI promoted angiogenesis and BSCB formation.[159]

The most commonly used materials for SCI repair scaffolds are hydrogels.[128] Hydrogels, described in detail in **Section 6.630.2.1**, permit cell migration and nutrient exchange with the surroundings. Hydrogel structure mimics the native ECM and can be fabricated with varying elasticity and degradation rates to balance proliferation and differentiation of transplanted cells and/or in growth of host cells.[128,141]

ECM-derived hydrogels include collagen and hyaluronan (HA).[141] Collagen is thermoresponsive and gels at physiological temperatures. Therefore, it can be used for injectable polymer delivery and can incorporate cells. HA has been used as a matrix for embryonic spinal cord tissue in the transected spinal cord, but has also been used as a drug delivery scaffold when delivered as a physical blend with MC (see **Section 6.630.2**).[141] HA combined with cultured embryonic spinal tissue transplanted into the gap after spinal cord transection resulted in slight functional recovery.[142] HA and MC have also been shown to decrease the host inflammatory response relative to saline controls when injected into the intrathecal space.[143] Large-scale purification and sterilization of natural materials such as collagen are challenging however, and synthetic materials have been modified to include bioactive compounds similar to natural polymers.[156]

A wide range of synthetic polymers have been used as scaffolds for SCI because of the ease of purification and processing, and because their mechanical properties are more easily controlled. PEG has demonstrated neuroprotective properties *in vitro* and has been thoroughly examined as a polymer to control cell function.[142,143] PEG is attractive because, although it is not intrinsically cell adhesive, it can be modified with proteins and peptides to promote specific cell adhesion and differentiation.[143] PLA, PGA, and PLGA have also been investigated.[141] It has been shown that PLGA supports NSPC viability and proliferation. PLGA scaffolds seeded with NSPCs in a hemisection model showed persistent functional improvement for up to 1 year.[141] PLGA scaffolds seeded with murine neural stem cells were reported to significantly improve functional recovery. PLGA is undesirable for use in the spinal cord because it is more brittle than the spinal cord and degrades to acidic end products.[142] Scaffolds have also been fabricated to more closely mimic ECM through three-dimensional biochemical patterning and the inclusion of directionally guiding fibers.[128] Three-dimensional fibrin scaffolds are promising for neural stem cell differentiation and transplantation.[141]

Nondegradable polymers have also been used as membranes in encapsulated cell therapy.[143] In this approach, cells are protected from the host immune response by a polymeric membrane, facilitating use of nonautologous sources. Cells have been encapsulated in hollow fiber and microspherical membranes using polymers such as PAN/PVC, PHEMA–MMA, and alginate/poly(lysine), which were selected for their biocompatibility and processability. The challenge in encapsulated cell therapy is achieving a balance between effective nutrient, waste, and cell product exchange, while also shielding the cells from the host immune response. It has also been difficult to encapsulate therapeutically relevant numbers of cells.[143]

Through biochemical and structural modifications, it may be possible to control the behavior of exogenous or endogenous stem cells within scaffolds.[156] The microscale scaffold architecture of the ECM can be replicated and used to bias the fate of transplanted NSPCs. The mechanical properties, such as the elastic modulus, can also be manipulated to influence cell fate.[156,160] The biomimetic ECM can be chemically modified with bioactive molecules, such as proteins or derived peptide sequences, to promote cell adhesion or growth factors to induce proliferation and differentiation.[156] Both the scaffold material itself and the incorporation of bioactive factors can be used to direct cell differentiation.[142]

In on-going studies, biomaterials that promote cell survival, cell differentiation, and cell integration with the host tissue are being developed. Here, the biomaterials provide both the structural and chemical environment for survival and delivering factors, such as chondroitinase *abc*, to promote cell integration with the existing tissue.[161]

6.630.4. Future Outlook

Almost 30 years have passed since David and Aguayo demonstrated the regenerative potential of CNS axons and still no effective cure has been developed to overcome SCI. Translating positive results in animal models into the clinical setting has proven to be a significant challenge. There is clearly no 'magic bullet' that will overcome SCI. Instead combination strategies are now being pursued.

Biomaterials provide an opportunity to achieve greater efficacy for both therapeutic and cell delivery. For delivery of therapeutic molecules, biomaterials have been designed to achieve local and sustained release at the injured spinal cord, thereby overcoming the limitations of current delivery strategies. These new methods promise to achieve greater efficacy of

current molecules while also facilitating the release of multiple factors at different rates.

For the delivery of cells, biomaterials allow the codelivery of factors that promote survival and host tissue integration – two areas that have limited the efficacy of cell delivery. By providing an environment conducive to cell survival, biomaterials have already shown a significant benefit.[162] Moreover, biomaterials allow codelivery of therapeutic molecules and cells, thereby providing multiple strategies to promote repair in the complex spinal cord.

Biomaterials allow the combination of previously independent treatment strategies. For instance, an appropriately designed biomaterial could deliver a cocktail of neuroprotective/neuroregenerative molecules and stem cells, while providing a chemical and mechanical environment conducive to nerve guidance and regeneration. Through the development of clinically relevant biomaterials, it may be possible to achieve improved efficacy in the treatment of SCI.

References

1. David, S.; Aguayo, A. J. *Science* **1981**, *214*(4523), 931–933.
2. McKerracher, L.; David, S.; Jackson, D. L.; Kottis, V.; Dunn, R. J.; Braun, P. E. *Neuron* **1994**, *13*(4), 805–811.
3. Mukhopadhyay, G.; *et al*. *Neuron* **1994**, *13*(3), 757–767.
4. Fawcett, J. W.; Asher, R. A. *Brain Res. Bull*. **1999**, *49*(6), 377–391.
5. Bandtlow, C. E.; Schwab, M. E. *Glia* **2000**, *29*(2), 175–181.
6. Schwab, M. E.; Bartholdi, D. *Physiol. Rev.* **1996**, *76*(2), 319–370.
7. Hausmann, O. N. *Spinal Cord* **2003**, *41*(7), 369–378.
8. Amar, A. P.; Levy, M. L. *Neurosurgery* **1999**, *44*(5), 1027–1039; discussion 1039–1040.
9. Rivlin, A. S.; Tator, C. H. *Surg. Neurol*. **1978**, *10*(1), 38–43.
10. Grill, R. J. *Exp. Neurol*. **2005**, *196*(1), 1–5.
11. Poon, P. C.; *et al*. *Spine* **2007**, *32*(25), 2853–2859.
12. Fehlings, M. G.; Tator, C. H.; Linden, R. D. *Electroencephalogr. Clin. Neurophysiol*. **1989**, *74*(4), 241–259.
13. Guha, A.; *et al*. *Paraplegia* **1987**, *25*(4), 324–339.
14. Fehlings, M. G.; Perrin, R. G. *Injury* **2005**, *36*(Suppl. 2), B13–B26.
15. Gupta, D.; Tator, C. H.; Shoichet, M. S. *Biomaterials* **2006**, *27*(11), 2370–2379.
16. Kang, C. E.; *et al*. *Tissue Eng. A* **2009**, *15*(3), 595–604.
17. Jimenez Hamann, M. C.; *et al*. *Exp. Neurol*. **2003**, *182*(2), 300–309.
18. Martin, D.; *et al*. *J. Neurosci. Res.* **1992**, *32*(4), 539–550.
19. Purdy, P. D.; *et al*. *Am. J. Neuroradiol*. **2003**, *24*(2), 177–184.
20. Park, E.; Velumian, A. A.; Fehlings, M. G. *J. Neurotrauma* **2004**, *21*(6), 754–774.
21. Kwon, B. K.; Oxland, T. R.; Tetzlaff, W. *Spine* **2002**, *27*(14), 1504–1510.
22. Gruner, J. A. *J. Neurotrauma* **1992**, *9*(2), 123–128.
23. Bresnahan, J. C.; *et al*. *Exp. Neurol*. **1987**, *95*(3), 548–570.
24. Hall, E. D.; Braughler, J. M. *J. Neurosurg*. **1982**, *57*(2), 247–253.
25. Hall, E. D.; Wolf, D. L.; Braughler, J. M. *J. Neurosurg*. **1984**, *61*(1), 124–130.
26. Braughler, J. M.; Hall, E. D. *J. Neurosurg*. **1983**, *59*(2), 256–261.
27. Braughler, J. M.; *et al*. *J. Neurosurg*. **1987**, *67*(1), 102–105.
28. Laverty, P. H.; *et al*. *J. Neurotrauma* **2004**, *21*(12), 1767–1777.
29. Shapiro, S. A.; *et al*. *Neurosurgery* **2004**, *55*(2), 707.
30. Tator, C. H. *Neurosurgery* **2006**, *59*(5), 957–982; discussion 982–987.
31. Freund, P.; *et al*. *Behav. Neurosci*. **2009**, *29*, 983–996.
32. Freund, P.; *et al*. *Nat. Med*. **2006**, *12*, 790–792.
33. Sekhon, L. H.; Fehlings, M. G. *Spine (Phila Pa 1976)* **2001**, *26*(24 Suppl.), S2–S12.
34. Hawryluk, G. W. J.; *et al*. *Neurosurg. Focus* **2008**, *25*(5).
35. Hurlbert, R. J. *J. Neurosurg*. **2000**, *93*(1), 1–7.
36. Geisler, F. H.; *et al*. *Spine* **2001**, *26*(24 Suppl.), S87–S98.
37. Baptiste, D. C.; Fehlings, M. G. *J. Neurotrauma* **2006**, *23*(3–4), 318–334.
38. Pal, R.; *et al*. *Cytotherapy* **2009**, *11*(7), 897–911.
39. Atala, A.; *et al*. *Lancet* **2006**, *367*(9518), 1241–1246.
40. Roughley, P.; *et al*. *Biomaterials* **2006**, *27*(3), 388–396.
41. Bracken, M. B.; *et al*. *J. Neurosurg*. **1998**, *89*(5), 699–706.
42. Young, W. In *Neural Regeneration and Transplantation*; Seil, F. J., Ed.; *Frontiers of Clinical Neuroscience*; Alan R. Liss, Inc.: New York, 1989; Vol. 6, pp 157–169.
43. Wells, J. E.; *et al*. *Brain* **2003**, *126*(Pt 7), 1628–1637.
44. Pearse, D. D.; *et al*. *Nat. Med*. **2004**, *10*(6), 610–616.
45. Zhong, Y.; Bellamkonda, R. V. *J. R. Soc. Interface* **2008**, *5*, 957–975.
46. Coumans, J. V.; *et al*. *J. Neurosci*. **2001**, *21*(23), 9334–9344.
47. Namiki, J.; Kojima, A.; Tator, C. H. *J. Neurotrauma* **2000**, *17*(12), 1219–1231.
48. McCall, T. D.; MacDonald, J. D. *Neurosurgery* **2006**, *59*(3), 634–640; discussion 634–640.
49. Mantripragada, S. *Prog. Lipid Res*. **2002**, *41*(5), 392–406.
50. Paavola, A.; *et al*. *Int. J. Pharm*. **2000**, *199*(1), 85–93.
51. Paavola, A.; *et al*. *Pharm. Res*. **1998**, *15*(3), 482–487.
52. Dergham, P.; *et al*. *J. Neurosci*. **2002**, *22*(15), 6570–6577.
53. Baptiste, D. C.; Tighe, A.; Fehlings, M. G. *Expert Opin. Investig. Drugs* **2009**, *18*(5), 663–673.
54. Novikova, L. N.; Novikov, L. N.; Kellerth, J. O. *J. Comp. Neurol*. **2002**, *452*(3), 255–263.
55. Castellanos, D. A.; *et al*. *Cell Transplant*. **2002**, *11*(3), 297–307.
56. Li, L. X.; *et al*. *J. Neurobiol*. **1994**, *25*(7), 759–766.
57. Houweling, D. A.; *et al*. *Exp. Neurol*. **1998**, *153*(1), 49–59.
58. Houweling, D. A.; *et al*. *Neurosci. Lett*. **1998**, *251*(3), 193–196.
59. Lagarce, F.; *et al*. *Int. J. Pharm*. **2005**, *298*(1), 68–79.
60. Lagarce, F.; *et al*. *Eur. J. Pharm. Biopharm*. **2005**, *61*(3), 171–180.
61. Lagarce, F.; *et al*. *Eur. J. Pharm. Biopharm*. **2005**, *59*(3), 449–459.
62. Baumann, M. D.; *et al*. *J. Control. Release* **2009**, *138*(3), 205–213.
63. Jimenez Hamann, M. C.; Tator, C. H.; Shoichet, M. S. *Exp. Neurol*. **2005**, *194*(1), 106–119.
64. Norenberg, M. D.; Smith, J.; Marcillo, A. *J. Neurotrauma* **2004**, *21*(4), 429–440.
65. Piantino, J.; *et al*. *Exp. Neurol*. **2006**, *201*(2), 359–367.
66. Burdick, J. A.; *et al*. *Biomaterials* **2006**, *27*(3), 452–459.
67. Taylor, S. J.; McDonald, J. W., 3rd; Sakiyama-Elbert, S. E. *J. Control. Release* **2004**, *98*(2), 281–294.
68. Taylor, S. J.; Sakiyama-Elbert, S. E. *J. Control. Release* **2006**, *116*(2), 204–210.
69. Jain, A.; *et al*. *Biomaterials* **2006**, *27*(3), 497–504.
70. Chvatal, S. A.; *et al*. *Biomaterials* **2008**, *29*(12), 1967–1975.
71. Fried, J. R. *Polymer Science and Technology*, 2nd ed.; Prentice Hall: Upper Saddle River, NJ, 2003.
72. Peppas, N. A.; *et al*. *Eur. J. Pharm. Biopharm*. **2000**, *50*(1), 27–46.
73. Peppas, N. A.; Merrill, E. W. *J. Polym. Sci. A Polym. Chem*. **1976**, *14*(2), 441–457.
74. Park, I. S.; *et al*. *Key Eng. Mater*. **2007**, *324–342*, 333–336.
75. Bellamkonda, R. V.; *et al*. *J. Biomed. Mater. Res*. **1995**, *29*(5), 663–671.
76. Shu, X. Z.; *et al*. *J. Biomed. Mater. Res. A* **2004**, *68A*(2), 365–375.
77. Leach, J. B.; Schmidt, C. E. *Biomaterials* **2005**, *26*(2), 125–135.
78. Ruel-Gariepy, E.; *et al*. *Eur. J. Pharm. Biopharm*. **2004**, *57*(1), 53–63.
79. Ruel-Gariepy, E.; *et al*. *J. Control. Release* **2002**, *82*(2–3), 373–383.
80. Coviello, T.; *et al*. *J. Control. Release* **2007**, *119*(1), 5–24.
81. Tabata, Y.; Ikada, Y. *Adv. Drug Deliv. Rev.* **1998**, *31*(3), 287–301.
82. Sarkar, N. *J. Appl. Polym. Sci*. **1979**, *24*(4), 1073–1087.
83. Ruel-Gariepy, E.; *et al*. *Int. J. Pharm*. **2000**, *203*(1–2), 89–98.
84. Chenite, A.; *et al*. *Biomaterials* **2000**, *21*(21), 2155–2161.
85. Ruel-Gariepy, E.; Leroux, J. C. *Eur. J. Pharm. Biopharm*. **2004**, *58*(2), 409–426.
86. Gombotz, W. R.; Wee, S. F. *Adv. Drug Deliv. Rev.* **1998**, *31*(3), 267–285.
87. Tonnesen, H. H.; Karlsen, J. *Drug Dev. Ind. Pharm*. **2002**, *28*(6), 621–630.
88. Westhaus, E.; Messersmith, P. B. *Biomaterials* **2001**, *22*(5), 453–462.
89. Masters, K. S.; *et al*. *Biomaterials* **2005**, *26*(15), 2517–2525.
90. Leach, J. B.; *et al*. *Biotechnol. Bioeng*. **2003**, *82*(5), 578–589.
91. Vercruysse, K. P.; Prestwich, G. D. *Crit. Rev. Ther. Drug Carrier Syst*. **1998**, *15*(5), 513–555.
92. Katayama, Y. *Prolonged Release of BDNF from PLG Microspheres Dispersed Within a PEG Hydrogel*; University of Toronto: Toronto, 2003.
93. Zhang, Y.; *et al*. *Int. J. Pharm*. **2010**, *386*(1–2), 15–22.
94. Hennink, W. E.; van Nostrum, C. F. *Adv. Drug Deliv. Rev.* **2002**, *54*(1), 13–36.
95. Jia, X. Q.; *et al*. *Macromolecules* **2004**, *37*(9), 3239–3248.
96. Oudshoorn, M. H. M.; *et al*. *Polymer* **2007**, *48*(7), 1915–1920.
97. Bencherif, S. A.; *et al*. *Biomaterials* **2008**, *29*(12), 1739–1749.
98. Ossipov, D. A.; Piskounova, S.; Hilborn, J. *Macromolecules* **2008**, *41*(11), 3971–3982.
99. Kim, M. R.; Park, T. G. *J. Control. Release* **2002**, *80*(1–3), 69–77.
100. Cai, S.; *et al*. *Biomaterials* **2005**, *26*(30), 6054–6067.
101. Prestwich, G. D.; Kuo, J. *Curr. Pharm. Biotechnol*. **2008**, *9*(4), 242–245.
102. Crank, J. *The Mathematics of Diffusion*; Clarendon Press: Oxford, 1956.
103. Wang, Y.; *et al*. *J. Control. Release* **2009**, *140*(3), 218–223.

104. Liu, J.; Li, L. *J. Biomed. Mater. Res. A* **2007**, *83A*(4), 1103–1109.
105. Tian, W. M.; *et al*. *J. Control. Release* **2005**, *102*(1), 13–22.
106. Yaksh, T. L., Ed.; In *Spinal Drug Delivery*; Elsevier: New York, 1999; p 614.
107. Lapitsky, Y.; Kaler, E. W. *Soft Matter* **2006**, *2*(9), 779–784.
108. Kipp, J. E. *Int. J. Pharm.* **2004**, *284*(1–2), 109–122.
109. Hoffman, A. S.; *et al*. *J. Biomed. Mater. Res.* **2000**, *52*(4), 577–586.
110. Davis, K. A.; Anseth, K. S. *Crit. Rev. Ther. Drug Carrier Syst.* **2002**, *19*(4–5), 385–423.
111. Prabaharan, M. *J. Biomater. Applic.* **2008**, *23*(1), 5–36.
112. Sinha, V. R.; Trehan, A. *J. Control. Release* **2003**, *90*(3), 261–280.
113. Yun, Y. H.; *et al*. *Biomaterials* **2004**, *25*(1), 147–157.
114. Siepmann, J.; Gopferich, A. *Adv. Drug Deliv. Rev.* **2001**, *48*(2–3), 229–247.
115. Betancourt, T.; Brown, B.; Brannon-Peppas, L. *Nanomedicine* **2007**, *2*(2), 219–232.
116. Feng, S. S.; *et al*. *Curr. Med. Chem.* **2004**, *11*(4), 413–424.
117. Okada, H.; Toguchi, H. *Crit. Rev. Ther. Drug Carrier Syst.* **1995**, *12*(1), 1–99.
118. Couvreur, P.; Puisieux, F. *Adv. Drug Deliv. Rev.* **1993**, *10*(2–3), 141–162.
119. Bhavsar, M. D.; Amiji, M. M. *Expert Opin. Drug Deliv.* **2007**, *4*(3), 197–213.
120. Andrianov, A. K.; Payne, L. G. *Adv. Drug Deliv. Rev.* **1998**, *34*(2–3), 155–170.
121. Jain, R. A. *Biomaterials* **2000**, *21*(23), 2475–2490.
122. Soppimath, K. S.; *et al*. *J. Control. Release* **2001**, *70*(1–2), 1–20.
123. Bazile, D. V.; *et al*. *Biomaterials* **1992**, *13*(15), 1093–1102.
124. Li, M.; *et al*. *Int. J. Pharm.* **2008**, *363*, 26–39.
125. Yeo, Y.; Park, K. *Arch. Pharm. Res.* **2004**, *27*(1), 1–12.
126. Patrick, C. W., Jr.; *et al*. *Tissue Eng.* **2002**, *8*(2), 283–293.
127. Vauthier, C.; Labarre, D.; Ponchel, G. *J. Drug Target.* **2007**, *15*(10), 641–663.
128. Straley, K. S.; Foo, C. W. P.; Heilshorn, S. C. *J. Neurotrauma* **2010**, *27*(1), 1–19.
129. Homma, A.; *et al*. *Bioorg. Med. Chem.* **2009**, *17*(13), 4647–4656.
130. Klein, A. W. *Facial Plast. Surg. Clin. North Am.* **2001**, *9*(2), 205–218; viii.
131. Hoemann, C. D.; *et al*. *Osteoarthr. Cartil.* **2005**, *13*(4), 318–329.
132. Oudega, M.; *et al*. *Biomaterials* **2001**, *22*(10), 1125–1136.
133. Valentini, R. F.; *et al*. *Brain Res.* **1989**, *480*(1–2), 300–304.
134. Tsai, E. C.; *et al*. *Biomaterials* **2006**, *27*(3), 519–533.
135. Krych, A. J.; *et al*. *Acta Biomater.* **2009**, *5*(7), 2551–2559.
136. Nomura, H.; *et al*. *Tissue Eng. A* **2008**, *14*(5), 649–665.
137. Xu, X. M.; *et al*. *J. Comp. Neurol.* **1995**, *351*(1), 145–160.
138. Moon, L. D. F.; *et al*. *Restor. Neurol. Neurosci.* **2006**, *24*(3), 147–161.
139. Bunge, M. B.; McKerracher, L.; Doucet, G.; Rossignol, S. In *Progress in Brain Research*; Elsevier: New York, 2002; Chapter 19, p 275.
140. Fouad, K.; *et al*. *J. Neurosci.* **2005**, *25*(5), 1169–1178.
141. Madigan, N. N.; *et al*. *Respir. Physiol. Neurobiol.* **2009**, *169*(2), 183–199.
142. Nomura, H.; Tator, C. H.; Shoichet, M. S. *J. Neurotrauma* **2006**, *23*(3–4), 496–507.
143. Shoichet, M. S. *Macromolecules* **2010**, *43*(2), 581–591.
144. Baatout, S.; *et al*. *Rom. J. Intern. Med.* **1996**, *34*(3–4), 263–269.
145. Dalton, P. D.; Flynn, L.; Shoichet, M. S. *Biomaterials* **2002**, *23*(18), 3843–3851.
146. Yao, L.; *et al*. *J. Biomed. Mater. Res. A* **2010**, *92*(2), 484–492.
147. Stokols, S.; Tuszynski, M. H. *Biomaterials* **2006**, *27*(3), 443–451.
148. Zahir, T.; *et al*. *Cell Transplant.* **2008**, *17*(3), 245–254.
149. Nomura, H.; *et al*. *Neurosurgery* **2008**, *63*(1), 127–141.
150. Schmidt, C. E.; *et al*. *Proc. Natl. Acad. Sci. USA* **1997**, *94*(17), 8948–8953.
151. Fine, E. G.; *et al*. *Biomaterials* **1991**, *12*(8), 775.
152. Yu, L. M. Y.; Leipzig, N. D.; Shoichet, M. S. *Mater. Today* **2008**, *11*(5), 36–43.
153. Suzuki, M.; *et al*. *J. Neurosci. Res.* **2003**, *72*(5), 646–659.
154. Tong, Y. W.; Shoichet, M. S. *Biomaterials* **2001**, *22*(10), 1029–1034.
155. Wong, D. Y.; *et al*. *J. Neurotrauma* **2008**, *25*(8), 1027–1037.
156. Williams, C. A.; Lavik, E. B. *Regen. Med.* **2009**, *4*(6), 865–877.
157. Lu, P.; Tuszynski, M. H. *Exp. Neurol.* **2008**, *209*(2), 313.
158. Tuszynski, M. H.; *et al*. *Exp. Neurol.* **1996**, *137*(1), 157.
159. Rauch, M. F.; *et al*. *Eur. J. Neurosci.* **2009**, *29*(1), 132–145.
160. Leipzig, N. D.; Shoichet, M. S. *Biomaterials* **2009**, *30*(36), 6867–6878.
161. Lee, H.; McKeon, R. J.; Bellamkonda, R. V. *Proc. Natl. Acad. Sci. USA* **2009**, *107*(8), 3340–3345.
162. Ballios, B. G.; Cooke, M. J.; van der Kooy, D.; Shoichet, M. S. *Biomaterials* **2010**, *31*(9), 2555–2564.

6.631. Keratoprostheses

M A Princz and H Sheardown, McMaster University, Hamilton, ON, Canada

© 2011 Elsevier Ltd. All rights reserved.

6.631.1.	**The Cornea and the Need for Corneal Replacement**	495
6.631.1.1.	Keratoprosthesis	496
6.631.1.2.	Dohlman–Doane KPro	496
6.631.1.3.	Osteoodonto KPro	496
6.631.1.4.	Seoul-Type KPro	496
6.631.1.5.	AlphaCor KPro	497
6.631.1.6.	BIOKPro	497
6.631.1.7.	SupraDescemetic KPro	497
6.631.1.8.	Aachen KPro	497
6.631.1.9.	Other KPro Materials Developments	497
6.631.1.10.	Biological Enhancement of KPros	497
6.631.2.	**Conclusion**	498
References		498

Abbreviations

AM	Amniotic membrane
D-KPro	Dohlman-Doane KPro
EGF	Epidermal growth factor
FAP	Fibronectin adhesion promoting peptide
HA	Hydroxyapatite
KPro	Keratoprosthesis
NVP	N-vinyl pyrrolidinone
OOKP	Osteodonto KPro
PAA	Poly(acrylic acid)
PDMS	Poly(dimethyl siloxane)
PEG	Poly(ethylene glycol)
PFPE	Perfluoropolyether
PHEA	Poly(hydroxy ethyl acrylate)
PHEMA	Poly(hydroxyethyl methacrylate)
PMMA	Poly(methyl methacrylate)
PNIPAAM	Poly(*N*-isopropyl acrylamide)
PTFE	Polytetrafluoroethylene
PVA	Poly(vinyl alcohol)
RGD	Arginine-glycine-aspartic acid
RGDS	Arginine-glycine-aspartic acid-serine
SDKP	SupraDescemetic KPro
S-KPro	Seoul KPro
TGF-β	Transforming growth factor beta
YIGSR	Tyrosine-isoleucine-glycine-serine-arginine

6.631.1. The Cornea and the Need for Corneal Replacement

The cornea is the transparent window at the front of the eye which acts as both the main refractive component of the eye and as a physical barrier, protecting the interior ocular components.[1] It consists of three cellular layers, the epithelium, the stroma, and the endothelium separated by Bowman's and Descemet's membranes, respectively. The epithelium consists of five to seven layers of corneal epithelial cells and is primarily responsible for providing the barrier function of the cornea. The stroma, the thickest corneal layer and its main structural element, consists of a highly hydrated (~80%) collagen network and relatively few keratocytes. The endothelial layer consists of a single layer of cells, organized hexagonally. It is mainly responsible for the regulation of corneal hydration.

As the cornea refracts light onto the retina, any damage or opacification of the organ will result in vision impairment or blindness.[2] According to the World Health Organization, vision loss due to corneal disease, trauma, scarring, or ulceration constitutes the second leading cause of blindness,[3] affecting more than 10 million people worldwide, primarily in the third world.[4] Estimates suggest that 1.5–2 million new cases of corneal blindness occur annually as a result of cornea trauma or ulceration.[4]

In the developed world, the most successful treatment for cornea blindness is corneal allograft surgery, or penetrating keratoplasty, involving the replacement of the diseased or damaged corneal tissue with donor tissue. An 80% success rate has been reported in the 2 years following the surgery;[4] however, this rate falls to 65% 5 years post surgery[5] with additional complications and lower success rates associated with specific disease states.[1] Furthermore, there is a risk of disease transmission with corneal allograft surgery, particularly HIV and hepatitis.[6] With a shortage of donor tissue, surgical wait times average 2 years in North America. These times are expected to increase mainly due to an aging population[4] and the increased popularity of laser *in situ* keratomileusis (LASIK) surgery, which renders the cornea unsuitable for donation.[6] An artificial corneal replacement therefore represents an attractive alternative to donor tissue in the developed world and may be the only option in developing countries.[2]

An artificial corneal replacement must be transparent, with a refractive index similar to that of the native tissue, nontoxic and able to interact and preferably integrate with the surrounding corneal cells and tissue. Furthermore, it must be sufficiently strong to withstand intraocular pressure, and for maintaining cellular viability, it has been suggested that oxygen and nutrient diffusion are desired.[1,2,6,7] Current artificial cornea devices are either considered as keratoprostheses (KPros), which are made from synthetic polymers with or without biological components, or as tissue-engineered corneal equivalents, typically made from natural polymers and an appropriate biological component.[7] The focus of this chapter will be KPro, including those that are currently used clinically and those that are under development.

6.631.1.1. Keratoprosthesis

Synthetic KPro devices have the advantage of being available off the shelf as well as reducing the risk of disease transmission associated with allograft surgery.[2] Current clinically available KPro are designed either as collar button devices, also referred to as the optical stem with skirt implant, or as core and skirt devices in order to promote device integration.[8] The former design consists of two plates joined by a transparent optical core, while the latter design has a transparent optical core surrounded by a porous skirt used to anchor the device into the stroma. In addition to transparency, it is desirable for the optical core to be sufficiently short to avoid anterior chamber penetration.[9] Anchorage segments must be flexible, matching the properties of the native tissue where possible and sufficiently strong to permit suturing.[8] In many designs, the porosity and pore size of the skirt is sufficient to permit cellular infiltration, cell interactions, and extracellular matrix deposition.[6] It has also been suggested that the anterior surface of a KPro should encourage epithelialization to promote tear interactions and minimize the risk of bacterial infection. However, epithelial downgrowth should be avoided as this can lead to device extrusion.[7]

Early KPros were fabricated from gold, quartz, and glass and were associated with a high incidence of device extrusion.[9,10] The observation during World War II that certain polymers were relatively benign in the eye, led to the introduction of a second generation of KPros fabricated from synthetic polymers. While poly(methyl methacrylate) (PMMA)[10] was the first to be used, polymers, including polytetrafluoroethylene (PTFE), polybutylenes:polypropylene, polyurethane, Dacron, poly(2-hydroxyethyl methacylate) (PHEMA), and poly(dimethyl siloxane) (PDMS), have also been examined in artificial cornea applications.[2,10] Failure of these devices is often the result of their inability to interact sufficiently with the host tissue, resulting in stromal melting and epithelial thinning and ultimately extrusion of the device from the eye as well as such complications as aqueous humor leakage, infection, retroprosthetic membrane formation, retinal detachment, and glaucoma.[6,7,11]

6.631.1.2. Dohlman–Doane KPro

The Dohlman–Doane KPro (D-KPro) is a US Food and Drug Administration-approved PMMA collar button device that sandwiches the corneal tissue between two plates which has been implanted in over 190 eyes since the 1990s.[12,13] There are two prototypes: type I is utilized for patients with good ocular surface hydration, while type II is intended for use in patients with such ocular surface diseases as dry eye, ocular mucous membrane pemphigoid, or Stevens–Johnson syndrome.[12,13]

Clinical results with this device have been quite promising and it is currently one of the most used artificial cornea devices. Following implantation in 63 eyes between 1990 and 1997, six devices required replacement, while ten devices were permanently removed.[14] Complications associated with the D-KPro were glaucoma (46%), retroprosthetic membrane formation (37%), tissue melting (29%), retinal detachment (19%), and endophthalmitis (8%). Although visual acuities between 20/20 and 20/200 were achieved immediately following the surgical procedure, in 42% of patients, this improvement in vision was subsequently lost due to device complications.

Ongoing work has led to improved design as well as better surgical and postoperative care regimens including treatment with anti-inflammatory agents, contact lens bandages, or antibiotics. This resulted in a lower incidence of device extrusion and improved visual acuity.[15,16] Furthermore, there have been no reports of occurrences of endophthalmitis, reoperations, dislocations, or extrusions of implanted 25 D-KPros as of 2005.[17]

6.631.1.3. Osteoodonto KPro

The Osteoodonto KPro (OOKP) was developed based on the observation of tissue interactions with tooth components; it is composed of a PMMA optic, secured to a haptic made from a tooth root belonging to the patient or a compatible donor.[18] Synthetic OOKP devices have also been fabricated using aluminum oxide, hydroxyapatite (HA) ceramic, and glass ceramic.[19] However, degradation of corals, HA-based materials, tooth, and bone was rapid and may not be suitable for the ocular environment; hence more chemically stable materials are necessary.[19] Long-term studies in 224 eyes between 1973 and 1999 demonstrated 85% retention over 18 years with few complications[18]; however, there are concerns of increased intraocular pressure and resorption of the bone, due to chronic inflammation, which loosens and leads to the eventual failure of the device.[19,20]

6.631.1.4. Seoul-Type KPro

The Seoul-type KPro (S-KPro) is of the collar button design and consists of a PMMA optic, surrounded by a polyurethane or polypropylene skirt. It is secured to the cornea using monofilament polypropylene haptics; these are secured to the sclera.[21] Although *in vivo* studies in animals showed better performance of the polypropylene device, fibroblast integration, collagen deposition, and corneal neovascularization, with mild tissue necrosis and inflammation, were observed with both versions of the device.[22] However, in short-term human trials with the polypropylene prototype, tissue melting around the skirt was noted.[21] Other complications included retroprosthetic membrane formation, retinal detachment, glaucoma, and endophthalmitis.[21] In long-term implantations, visual rehabilitation for about 32 months could be achieved. However,

instances of tissue melting and exposure of the skirt after ~13 months were noted. Furthermore, retinal detachment occurred following S-KPro exchange, attributed to poor vitrectomy techniques.[23] However, given that preliminary *in vivo* tests showed promising results, it may be that improvement in surgical techniques may enhance the long-term success of this prototype.[24]

6.631.1.5. AlphaCor KPro

The AlphaCor KPro is a core and porous skirt design, all composed of poly (hydroxyethyl methacrylate) (PHEMA).[9] As of February 2006, 322 AlphaCor KPro devices have been implanted in the United States, Europe, and Australia resulting in 416 patient years of experience.[25] The high retention of this device after 1 year at 80% is attributable to the integration of stromal fibroblasts into the porous skirt. Observed complications include tissue melting, retroprosthetic membrane formation, optic damage, and in some cases, opacification due to calcification.[25,26] Extracted devices show evidence of stromal cell integration, although chronic inflammation was also observed.[27–29] Omission of the second-stage surgical procedure whereby the implant is exposed to the external surface of the eye, resulted in improved KPro outcomes, including longer device (14–38 months) tolerance, despite the lack of a functional endothelium. The effect of this surgical alteration on corneal hydration is as yet unknown.[30]

6.631.1.6. BIOKPro

There are three prototypes to the BIOKPro device with type I consisting of a PMMA optic core and types II and III comprising silicone with a polyvinylpyrrolidone coating. In all cases, the devices have porous PTFE haptics.[31] However, generally, this device has shown disappointing results when implanted. While BIOKPro I demonstrated tissue integration through keratocyte migration and collagen production,[32] glaucoma, tissue necrosis, device extrusion, endophthalmitis, lens dislocation, and retroprosthetic membrane formation were noted in 11 devices implanted over 5 years.[33] Only 36% of the devices were retained. BIOKPro II showed better short-term clinical success with increased keratocyte integration and few corneal complications.[34] Although this version was also more successful in long-term studies, with only a 38% failure rate, instances of skirt exposure, retroprosthetic membrane formation, endophthalmitis, and device extrusion remained.[31] Further design changes including a smaller optic and larger skirt resulted in the BIOKPro III.[35] However, human implantation results were disappointing, with only one of the seven devices remaining intact.

6.631.1.7. SupraDescemetic KPro

The SupraDescemetic KPro (SDKP) can be fabricated from PMMA, or copolymers of PHEMA with MMA (PHEMA–MMA) or *N*-vinylpyrrolidinone (PHEMA–NVP).[36] While not yet tested in humans, animal trials to date have shown promising results. Implantation in seven rabbit corneas demonstrated that these KPros were well tolerated after 8 weeks; there was no evidence of inflammation in five eyes and only mild inflammation in the remaining two eyes, and no cases of retinal detachment.[36] Subsequent implantation, also in rabbits, was also promising with 100% of the PHEMA–MMA, 80% of the PMMA, and 60% of the PHEMA-NVP devices remaining transparent.[37] Furthermore, deposited collagen was observed in the device skirt.[37] Implantation was also performed in feline corneas. In this model, device extrusion was observed in all cases between 15 and 150 days. However, these results may not be representative of those that would be achieved in humans as felines demonstrate complete cornea regeneration, which is not possible in humans.[38]

6.631.1.8. Aachen KPro

The Aachen KPro is made of silicone rubber, whose design boasts of easy surgical handling and flexibility.[39] Although not widely tested *in vivo*, this model has shown positive results in limited testing. Following short-term implantation in ten patients, there were no occurrences of retinal detachment and clear visual acuity in four eyes, although edema was observed in three eyes.[39] The type II Aachen KPro, with immobilized fibronectin for increased cellular attachment, was implanted as a temporary implant prior to retinal surgery or corneal grafting.[40,41] It also allows for intraocular pressure measurements in porcine eyes.[42]

6.631.1.9. Other KPro Materials Developments

Improvements in materials and better understanding of the factors that influence biocompatibility have been the subject of ongoing research projects to improve on KPro success. An interpenetrating polymer network of PDMS and poly(*N*-isopropylacrylamide) (PNIPAAM) has been fabricated to combine the mechanical strength, transparency, wettability, and glucose permeability of these two materials for ophthalmic applications.[43] While preliminary cell testing was positive, further evaluation in a KPro model is necessary to demonstrate the impact of these factors on *in vivo* success. Other porous materials, specifically polybutylene, polypropylene (80:20), poly(ethylene terephthalate), and PTFE, intended for application as a KPro, were evaluated in rabbit cornea stroma over 12 weeks.[44] PTFE demonstrated decreased inflammation and stromal cell migration; the incidence of edema and neovascularization were similar among the different materials.[44] A poly(ethylene glycol)/poly(acrylic acid) (PEG/PAA) interpenetrating polymer network hydrogel, with glucose permeability comparable to the human cornea, was evaluated over 2 weeks in rabbit stromas and was well tolerated in nine out of ten eyes.[45,46] Further development in fabrication led to the usage of photolithography to form a patterned skirt of poly(2-hydroxyethyl acrylate) (PHEA) around the PEG/PAA core.[47]

6.631.1.10. Biological Enhancement of KPros

The incorporation of biological components including collagen, fibronectin and laminin, and oligopeptides into KPro devices, has been suggested as a method to render the devices more compatible and to enhance the interactions of the devices with host cells and tissue.[6,7]

To aid with epithelialization and tissue integration, collagen type I was tethered to a PEG/PAA hydrogel. Somewhat

surprisingly, corneal epithelial migration and wound healing rates were decreased.[46] The authors attributed this to the leaching of antimicrobial compound from the hydrogel as well as improper surgical technique and the choice of collagen that did not properly mimic the corneal basement membrane.[46] Elsewhere, a poly(vinyl alcohol) (PVA) hydrogel with tethered collagen demonstrated enhanced epithelialization *in vitro*,[48] but required modification with an amniotic membrane (PVA-AM) for epithelialization, reduced inflammation, and opacification *in vivo*.[49]

Among the more successful models in helping to understand the biological effects of materials implanted into the cornea is a corneal onlay model developed by the CSIRO group in Australia. These corneal onlays were fabricated from porous perfluoropolyether (PFPE) and were coated with collagen type I and demonstrated enhanced epithelialization in four feline corneas for 39 days.[50] Similarly, porous polycarbonate membranes coated with collagen type I, collagen type IV, or laminin showed enhanced corneal epithelial cell migration and adhesion *in vivo*, although coating with fibronectin, endothelial extracellular matrix, hyaluronic acid, or chondroitin sulfate resulted in materials that did not support epithelialization.[51]

PHEMA-MAA-PEG hydrogels were fabricated with extracellular matrix components: fibronectin, laminin, substance P, and insulin-like growth factor; or peptide sequences such as Arginine-Glycine-Aspartic acid (RGD) or fibronectin adhesion-promoting peptide (FAP), in particular, enhanced epithelialization significantly.[52] Previous work showed that tethered FAP and laminin had better epithelial adhesion compared to fibronectin.[53] Corneal epithelial cell adhesion was also demonstrated to increase in *in vitro* testing on PHEMA hydrogels through tethering of Arginine-Glycine-Aspartic acid-Serine (RGDS) and Tyrosine-Isoleucine-Glycine-Serine-Arginine (YIGSR) cell adhesion peptides.[54] Incorporation of growth factors, including epidermal growth factor (EGF) and transforming growth factor beta (TGF-β), have also been used to manipulate epithelialization.[7] Specifically, EGF was tethered to PDMS through a PEG spacer to improve epithelialization of the surface, which was found to rely heavily on the underlying surface chemistry.[55–57] Tethered TGF-β2 was also demonstrated to enhance epithelialization and to hinder stromal cell adhesion.[58]

6.631.2. Conclusion

The past decade has seen significant advances in the development of corneal substitutes. Extremely promising results have been obtained with the synthetic artificial corneas, with the availability of a number of different prototypes. As a result, replacement of corneal tissue with artificial substitutes, while not commonplace, is certainly possible. The development of new tissue-engineered prototypes will only serve to enhance the potential of these systems for restoring the sight of visually compromised patients.

References

1. Chirila, T. A.; Hicks, C. R.; Dalton, P. D.; *et al*. *Prog. Polym. Sci*. **1998**, *23*, 447–473.
2. Griffith, M.; Hakim, M.; Shimmura, S.; *et al*. *Cornea* **2002**, *21*, S54–S61.
3. Whitcher, J. P.; Srinivasan, M.; Upadhyay, M. P. *Bull. World Health Organ*. **2001**, *79*, 214–221.
4. Carlsson, D. J.; Li, F.; Shimmura, S.; Griffith, M. *Curr. Opin. Ophthalmol*. **2003**, *14*, 192–197.
5. Sit, M.; Weisbrod, D. J.; Naor, J.; Slomovic, A. R. *Cornea* **2001**, *20*, 129–133.
6. Griffith, M.; Li, F.; Lohman, C.; Sheardown, H.; Shimmura, S.; Carlsson, D. J. In *Scaffolds in Tissue Engineering*; Ma, P., Ellsieff, J., Eds.; CRC: Boca Raton, FL, 2003; pp 413–423.
7. Duan, D.; Klenkler, B. J.; Sheardown, H. *Expert Rev. Med. Devices* **2006**, *3*, 59–72.
8. Khan, B.; Dudenhoefer, E. J.; Dohlman, C. H. *Curr. Opin. Ophthalmol*. **2001**, *12*, 282–287.
9. Hicks, C.; Crawford, G.; Chirila, T.; *et al*. *Prog. Retin. Eye Res*. **2000**, *19*, 149–170.
10. Chirila, T. V. *Biomaterials* **2001**, *22*, 3311–3317.
11. Lloyd, A. W.; Faragher, R. G. A.; Denyer, S. P. *Biomaterials* **2001**, *22*, 769–785.
12. Ilhan-Sarac, O.; Akpek, E. K. *Curr. Opin. Ophthalmol*. **2005**, *16*, 246–256.
13. Dudenhoefer, E. J.; Nouri, M.; Gipson, I. K.; *et al*. *Cornea* **2003**, *22*, 424–428.
14. Yaghouti, F.; Nouri, M.; Abad, J. C.; Power, W. J.; Doane, M. G.; Dohlman, C. H. *Cornea* **2001**, *20*, 19–23.
15. Aquavella, J. V.; Qian, Y.; McCormick, G. J.; Palakuru, J. R. *Am. J. Ophthalmol*. **2005**, *140*, 1032–1038.
16. Subhransu, R.; Khan, B. F.; Dohlman, C. H.; D'Amico, D. J. *Arch. Ophthalmol*. **2002**, *120*, 559–565.
17. Aquavella, J. V.; Qian, Y.; McCormick, G. J.; Palakuru, J. R. *Cornea* **2006**, *25*, 656–662.
18. Falcinelli, G.; Falsini, B.; Taloni, M.; Colliardo, P.; Falcinelli, G. *Arch. Ophthalmol*. **2005**, *123*, 1319–1329.
19. Viitala, R.; Franklin, V.; Green, D.; Liu, C.; Lloyd, A.; Tighe, B. *Acta Biomater*. **2009**, *5*, 438–452.
20. Liu, C.; Paul, B.; Tandon, R.; *et al*. *Semin. Ophthalmol*. **2005**, *20*, 113–128.
21. Kim, M. K.; Lee, J. L.; Wee, W. R.; Lee, J. H. *Arch. Ophthalmol*. **2002**, *120*, 761–766.
22. Kim, M. K.; Lee, J. L.; Wee, W. R.; Lee, J. H. *Br. J. Ophthalmol*. **2002**, *86*, 809–814.
23. Kim, M. K.; Lee, S. M.; Lee, J. L.; *et al*. *Cornea* **2007**, *26*, 546–551.
24. Lee, S. M.; Kim, M. K.; Oh, J. Y.; *et al*. *Invest. Ophthalmol. Vis. Sci*. **2008**, *49*, 4407–4411.
25. Hicks, C. R.; Crawford, G. J.; Dart, J. K.; *et al*. *Cornea* **2006**, *25*, 1034–1042.
26. Hicks, C. R.; Crawford, G. J.; Tan, D. T.; *et al*. *Cornea* **2003**, *22*, 583–590.
27. Chow, C. C.; Kulkarni, A. D.; Albert, D. M.; Darlington, J. K.; Hardten, D. R. *Cornea* **2007**, *26*, 1004–1007.
28. Coassin, M.; Zhang, C.; Green, W. R.; Aquavella, J. V.; Akpek, E. K. *Am. J. Ophthalmol*. **2007**, *144*, 699–704.
29. Chalam, K. V.; Chokshi, A.; Agarwal, S.; Edward, D. P. *Cornea* **2007**, *26*, 1258–1260.
30. Ngakeng, V.; Hauck, M. J.; Price, M. O.; Price, F. W. J. *Cornea* **2008**, *27*, 905–910.
31. Alio, J. L.; Mulet, M. E.; Haroun, H.; Merayo, J.; Ruiz Moreno, J. M. *Br. J. Ophthalmol*. **2004**, *88*, 1585–1589.
32. Legeais, J. M.; Renard, G.; Parel, J. M.; Serdarevic, O.; Mei-Mui, M.; Pouliquen, Y. *Exp. Eye Res*. **1994**, *58*, 41–51.
33. Legeais, J. M.; Renard, G.; Parel, J. M.; Savoldelli, M.; Pouliquen, Y. *Arch. Ophthalmol*. **1995**, *113*, 757–763.
34. Legeais, J. M.; Renard, G. *Biomaterials* **1998**, *19*, 1517–1522.
35. Hollick, E. J.; Watson, S. L.; Dart, J. K.; Luthert, P. J.; Allan, B. D. *Br. J. Ophthalmol*. **2006**, *90*, 1146–1151.
36. Stoiber, J.; Fernandez, V.; Kaminski, S.; *et al*. *Arch. Ophthalmol*. **2004**, *122*, 1850–1855.
37. Stoiber, J.; Fernandez, V.; Lamar, P. D.; *et al*. *Cornea* **2005**, *24*, 467–473.
38. Acosta, A. C.; Espana, E. M.; Stoiber, J.; *et al*. *Cornea* **2006**, *25*, 1830–1838.
39. Langefeld, S.; Kompa, S.; Redbrake, C.; Brenman, K.; Kirchhof, B.; Schrage, N. F. *Graefes Arch. Clin. Exp. Ophthalmol*. **2000**, *238*, 722–726.
40. Kompa, S.; Langefeld, S.; Kirchhof, B.; Brenman, K.; Schrage, N. *Int. J. Artif. Organs* **2000**, *23*, 345–348.
41. Kompa, S.; Redbrake, C.; Langefeld, S.; Brenman, K.; Schrage, N. *Int. J. Artif. Organs* **2001**, *24*, 110–114.
42. Krug, A.; Kompa, S.; Schrage, N. F. *Int. J. Artif. Organs* **2002**, *25*, 238–342.
43. Liu, L.; Sheardown, H. *Biomaterials* **2005**, *26*, 233–244.
44. Wu, X. Y.; Tsuk, A.; Leibowitz, H. M.; Trinkaus-Randall, V. *Br. J. Ophthalmol*. **1998**, *82*, 569–576.

45. Myung, D.; Farooqui, N.; Waters, D.; *et al*. *Curr. Eye Res.* **2008**, *33*, 29–43.
46. Myung, D.; Farooqui, N.; Zheng, L. L.; *et al*. *J. Biomed. Mater. Res. A* **2009**, *90*, 70–81.
47. Myung, D.; Duhamel, P. E.; Cochran, J. R.; Noolandi, J.; Ta, C. N.; Frank, C. W. *Biotechnol. Prog.* **2008**, *24*, 735–741.
48. Miyashita, H.; Shimmura, S.; Kobayashi, H.; *et al*. *J. Biomed. Mater. Res. B Appl. Biomater.* **2006**, *76*, 56–63.
49. Uchino, Y.; Shimmura, S.; Miyashita, H.; *et al*. *J. Biomed. Mater. Res. B Appl. Biomater.* **2007**, *81*, 201–206.
50. Evans, M. D.; Xie, R. Z.; Fabbri, M.; *et al*. *Invest. Ophthalmol. Vis. Sci.* **2000**, *41*, 1674–1680.
51. Sweeney, D. F.; Xie, R. Z.; Evans, M. D.; *et al*. *Invest. Ophthalmol. Vis. Sci.* **2003**, *44*, 3301–3309.
52. Jacob, J. T.; Rochefort, J. R.; Bi, J.; Gebhardt, B. M. *J. Biomed. Mater. Res. B Appl. Biomater.* **2005**, *72*, 198–205.
53. Wallace, C.; Jacob, J. T.; Stoltz, A.; Bi, J.; Bundy, K. *J. Biomed. Mater. Res. A* **2005**, *72*, 19–24.
54. Merrett, K.; Griffith, C. M.; Deslandes, Y.; Pleizier, G.; Sheardown, H. *J. Biomater. Sci. Polym. Ed.* **2001**, *12*, 647–671.
55. Klenkler, B. J.; Griffith, M.; Becerril, C.; West-Mays, J. A.; Sheardown, H. *Biomaterials* **2005**, *26*, 7286–7296.
56. Klenkler, B. J.; Sheardown, H. *Biotechnol. Bioeng.* **2006**, *95*, 1158–1166.
57. Klenkler, B. J.; Chen, H.; Chen, Y.; Brook, M. A.; Sheardown, H. *J. Biomater. Sci. Polym. Ed.* **2008**, *19*, 1411–1424.
58. Merrett, K.; Griffith, C. M.; Deslandes, Y.; Pleizier, G.; Dube, M. A.; Sheardown, H. *J. Biomed. Mater. Res.* **2003**, *67A*, 981–993.

6.632. Retina Reconstruction

M Saint-Geniez, Harvard Medical School, Boston, MA, USA
S L Tao and J T Borenstein, The Charles Stark Draper Laboratory, Inc., Cambridge, MA, USA
B T Tucker, University of Iowa, Iowa City, IA, USA
I M Herman, Tufts University School of Medicine, Boston, MA, USA
P A D'Amore and M J Young, Harvard Medical School, Boston, MA, USA

© 2011 Elsevier Ltd. All rights reserved.

6.632.1. The Retina 502
6.632.1.1. Basic Structure and Function of the Neurosensory Retina 502
6.632.1.2. The RPE–BrM Complex 503
6.632.1.3. Blood Supply of the Retina 503
6.632.2. Ocular Diseases Associated with Retinal Degeneration 504
6.632.2.1. Age-Related Macular Degeneration 504
6.632.2.2. Retinal Degeneration 505
6.632.3. Retinal Reconstruction 505
6.632.3.1. Transplantation Success and Failure 505
6.632.3.2. Retinal Transplantation 505
6.632.4. Challenges in Retina Reconstruction 505
6.632.4.1. Rationale 505
6.632.4.2. Retinal Pigment Epithelium 506
6.632.4.3. Bruch's Membrane 506
6.632.4.4. Choriocapillaris 506
6.632.4.5. Neuronal Regeneration of the Adult Nervous System: Regeneration in the Central Nervous System Versus Peripheral Nervous System 507
6.632.4.6. Interdependence 507
6.632.5. Scaffold Biocompatibility 508
6.632.5.1. Material 508
6.632.5.2. Physical Constraint of the Subretinal Space 508
6.632.5.3. Mechanical Properties 509
6.632.6. Scaffold Fabrication 509
6.632.6.1. Micro- and Nanotopography 510
6.632.6.2. Microfabricated Scaffolds 510
6.632.6.3. 3D Scaffolds 512
6.632.6.4. Surface Modification of Scaffolds 513
6.632.6.5. Controlled Release 514
6.632.6.6. The CNS Environment 514
6.632.7. Conclusions 515
References 515

Abbreviations

AMD	Age-related macular degeneration
BrM	Bruch's membrane
CAD	Computer-aided design
CC	Choriocapillaris
CNS	Central nervous system
CNTF	Ciliary neurotrophic factor
CNV	Choroidal neovascularization
EC	Endothelial cells
ECM	Extracellular matrix
ESC	Embryonic stem cells
GA	Geographic atrophy
GC	Ganglion cell
GCL	Ganglion cell layer
INL	Inner nuclear layer
iPSC	Induced pluripotent stem cells
MAG	Myelin-associated glycoprotein
MEMS	Microelectromechanical systems
MMP-2	Matrix metalloprotease-2
NPC	Neural progenitor cell
OMgp	Oligodendrocyte myelin glycoprotein
ONL	Outer nuclear layer
OS	Outer segment
PCL	Polycaprolactone
PDMS	Poly(dimethyl siloxane)
PEG	Poly(ethylene glycol)
PGS	Poly(glycerol sebacate)
PKC	Protein kinase C
PLA	Poly(lactic acid)
PLCL	Poly(lactic-*co*-caprolactone)

PLGA	Poly(lactic-*co*-glycolic acid)	**RP**	Retinitis pigmentosa
PLLA	Poly(L-lactic acid)	**RPC**	Retinal progenitor cell
PMMA	Poly(methyl methacrylate)	**RPE**	Retinal pigment epithelium
PR	Photoreceptor	**SEM**	Scanning electron microscopy
PVA	Poly(vinyl alcohol)	**UV**	Ultraviolet

6.632.1. The Retina

The retina is a critical component of the vertebrate visual system, which comprises the ocular globe and the subsequent subcortical and cortical targets in the brain. In the following sections, we describe the three main components of the retinal structure: the neuronal cells, the retinal pigment epithelium (RPE)–Bruch's membrane (BrM) complex, and the vascular networks that are intricately organized to ensure vision.

6.632.1.1. Basic Structure and Function of the Neurosensory Retina

After entering through the cornea, light is focused by the lens and is sensed by a thin laminated neural tissue on the back of the eye called the retina (Figure 1). The light stimulus is initially processed by the photoreceptors (PRs) in the outer nuclear layer (ONL), which are interestingly placed at the end of the light path, thus requiring the photons to travel through the entire thickness of the retina before being sensed. It is for this reason that some primates and birds of prey have developed a specialized region known as the macula.

PRs are highly specialized neurons able to detect light and transform it into an electrochemical impulse. They possess a unique compartmentalized, modified cilia, called outer segment (OS), that contains the light-sensitive machinery and enzymes necessary for phototransduction. PRs are divided into two cell types: rods and cones. Rods are highly light sensitive, with a slow response time course, and are therefore responsible for achromatic night vision. In contrast, cones are less light sensitive, but they are fast and color sensitive, and therefore mediate daylight vision. Once the PRs are activated, they signal to the inner nuclear layer (INL), which contains intermediary neurons (bipolar, horizontal, and amacrine cells) and glia cells (the Müller cells), through the release of the neurotransmitter, glutamate. Finally, the sensory stimulus is collected by the ganglion cells (GCs) in the ganglion cell layer (GCL), whose long axons bundle together to form the optic nerve, which extends to the brain. In some vertebrates, including humans, the retina contains a unique region with specialized topography and organization called the macula, which is responsible for

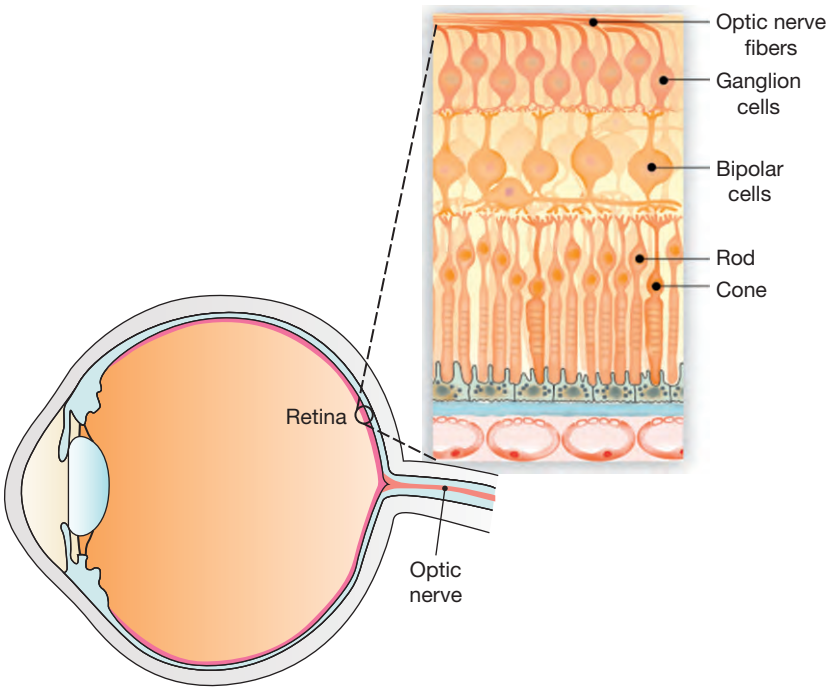

Figure 1 Schematic representation of the human eye. Illustration of a sagittal section of the eye, showing the cornea, the lens, and the retina, and of the retina structure. The human retina is a laminated neuronal tissue composed of distinct layers. From the innermost to the outermost layers, they include the ganglion cell layer (GCL) containing the GCs that give rise to the optic nerve fibers, the inner nuclear layer (INL) containing the intermediary neurons, the outer nuclear layer (ONL) comprising the photoreceptor cell bodies, and the retinal pigment epithelium (RPE). ONL, INL, and GCL are separated by synapses-rich layers called the plexiform layers (inner and outer).

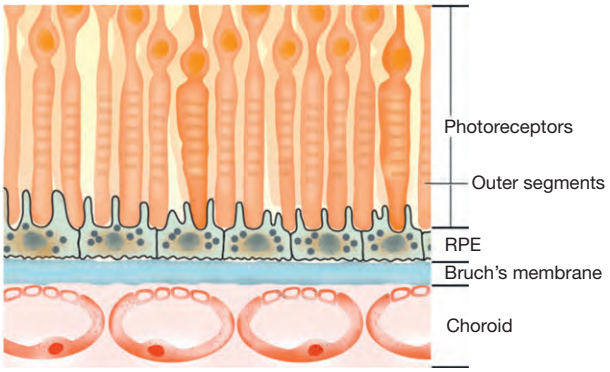

Figure 2 Organization of the outer retina. Schematic representation of the outer retina consisting of the photoreceptor's cell bodies and outer segments, of the retinal pigment epithelium (RPE) layer, and of Bruch's membrane. The outer segment is avascular, but its nutrients and oxygen supply are ensured by the choroidal vasculature located underneath the RPE layer.

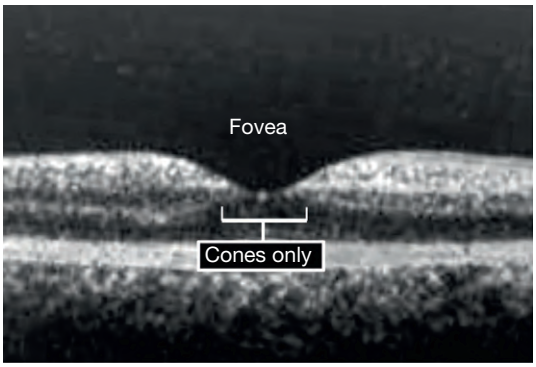

Figure 3 Optical coherence tomography image of a human fovea. The fovea corresponds to the pit at the center of the macula region. This highly specialized region contains mostly cone photoreceptors and is responsible for high-acuity vision. Courtesy of Dr. Ahad Fazelat, Massachusetts General Hospital, Boston, MA.

high-acuity vision. This specialized function is due to the high density of cone PRs, particularly in the fovea, a small pit 1 mm in diameter at the center of the macula (Figure 2).

6.632.1.2. The RPE–BrM Complex

The RPE constitutes the outermost cell layer of the retina. The apical membrane of this highly specialized and polarized pigmented epithelium faces the PRs' OS, while the basal side lies against a thick connective tissue, called the BrM, adjacent to the choroidal vasculature (Figure 3). The RPE has crucial functions in the normal eye as well as in pathological conditions. In the normal healthy eye, the RPE serves as the site of the outer retinal barrier. As the interface between the PRs and choroidal circulation, they are vital for the maintenance of the flow of water and ions, for protection against oxidative damage, for retinoid metabolism, and for the phagocytosis of the OS discs shed during the visual process.[1–4] RPE cells have been shown to secrete a variety of growth factors, including pigment epithelium-derived growth factor (PEDF) and vascular endothelial growth factor (VEGF), matrix metalloproteinases (MMP-9, MMP-2) and their inhibitors (TIMP-1, TIMP-3), and a wide

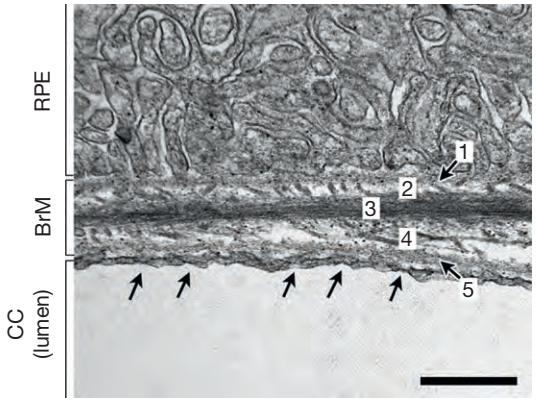

Figure 4 Ultrastructure of Bruch's membrane (BrM). Electron micrograph of the back of the eye of an adult mouse revealing the pentalaminar structure of the BrM: (1) retinal pigment epithelium basement membrane, (2) inner collagenous zone, (3) middle elastic layer, (4) outer collagenous layer, and (5) basement membrane of the choriocapillaris (CC). Endothelial fenestrations are indicated by arrows. Scale bar = 0.5 μm.

repertoire of cytokines.[1] These secreted molecules play an important role in RPE differentiation, maintenance of the endothelial cells (ECs) of the choriocapillaris (CC), and survival of PRs.[5]

Like most epithelium, RPE phenotype and function are intimately regulated by its interaction with the extracellular matrix (ECM) environment, in particular with BrM. BrM is a collagen-rich elastic lamina, with a thickness of 1–4 μm, depending on the retinal region, interposed between the basal surface of the RPE and the CC. BrM is classically described as a pentalaminar structure composed of the basal membranes of the RPE on the one side and CC on the other side, two collagenous layers, and one semicontinuous elastin layer (Figure 4). BrM serves as a critical physical and biological barrier, controlling the water and metabolic exchange between circulation and the outer retina. It regulates not only the diffusion of biomolecules and oxygen from the choroidal vasculature to the RPE and PR, but also the critical removal of waste products and membranous components of PR OSs produced during the visual cycle.

6.632.1.3. Blood Supply of the Retina

The retina is one of the most metabolically demanding tissues in the body. Therefore, maintenance of proper metabolic function and oxygen supply is crucial for retinal homeostasis and function. The retina is supplied by two independent vascular beds, the retinal vasculature proper and the choroidal circulation perfusing the inner and outer portions of the retina. These vascular beds exhibit extremely distinct morphologic and functional properties. The inner retinal vasculature is lined with ECs with tight junctions, making the vessels impermeable and constituting the inner blood–retinal barrier. In contrast, the walls of the CC endothelium are highly fenestrated, particularly on the side facing the RPE (fenestrations of the CC are shown in Figure 4). The anatomical organization of these two circulations is also highly dissimilar. The retinal vasculature has a classic anatomical organization, with the main veins and arteries extending radially from the optic nerve toward the periphery and dividing into smaller vessels extending into

the INL. The choroidal vasculature forms a mesh characterized by high blood flow, necessary to support the PR oxygen consumption.[6] In addition to its vascular functions as blood provider, the choroidal vasculature serves other critical roles: it is involved in the thermoregulation of the retina and in the lymphatic-like drainage of the debris and waste products produced by the PR and RPE.[7]

6.632.2. Ocular Diseases Associated with Retinal Degeneration

6.632.2.1. Age-Related Macular Degeneration

Age-related macular degeneration (AMD) is a complex disease and the leading cause of blindness in the elderly population of industrialized countries.[8] AMD currently affects more than 1.75 million individuals in the United States and, with the aging of the population, this number is predicted to reach 3 million by 2020.[9] AMD affects the macular region of the retina, which is responsible for fine vision.

Early AMD is characterized by a spectrum of ocular anomalies often indistinguishable from the normal aging process of the eye. These changes in the outer retina include the presence of drusen (yellowish deposits) localized under the RPE or within the BrM and pigmentation changes (hyper- and hypopigmentation, Figure 5(a)). From this asymptomatic stage, the disease can progress to advanced or late AMD that is diagnosed in its dry (geographic atrophy (GA)) and wet forms. GA, which can be associated with progressive and severe visual loss, presents with localized degeneration of the RPE, atrophy of the overlying PRs and the underlying CC (Figure 5(b)).[10] GA often develops in the macular area just outside the fovea and gradually progresses into the foveal center in its late stage. A patient's visual problems are directly related to the development of visual blind spots (scotomas) within his or her central visual field. The prevalence of GA is about 3.5% in people over 75, with the rate increasing to 22% at age 90.[11] Histopathological studies of eyes with GA show isolated areas of RPE loss, and it is speculated that the loss of CC is secondary to the absence of RPE.[12–14] Wet AMD, which appears to arise from dry AMD in 10–35% of patients according to the study,[15] is characterized by the growth of highly permeable vessels from the choroidal vasculature into the subretinal space. Fundus imaging of advanced cases of wet AMD shows subretinal blood and fluid in the macular region (Figure 5(c)).

The etiology of AMD appears to be highly multifactorial, with definitive genetic and environmental components such as primary RPE aging, oxidative stress, and complement pathway alterations.[16] Despite recent significant research discoveries, particularly related to the contribution of the complement pathway,[17,18] the disease pathogenesis is relatively poorly understood. Over the last 20 years, various strategies have been developed to reduce choroidal neovascularization and subretinal edema. Available treatments for wet AMD include photodynamic therapy, antiangiogenic therapy using anti-VEGF reagents (Lucentis® and Avastin® from Genentech), vitreoretinal surgery, and steroid administration. Unfortunately, current treatments are limited to the vascular pathologies associated with AMD, and no pharmacological or surgical therapeutic option exists for the treatment of retinal cell loss.

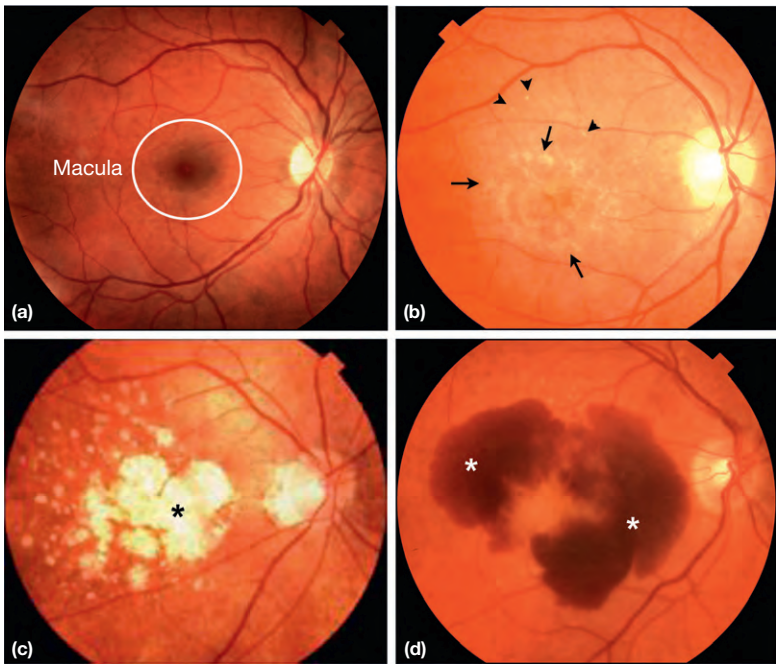

Figure 5 Color fundus photographs representing the different stages and types of age-related macular degeneration (AMD). (a) Normal fundus. The macular region is indicated by a circle. (b) Fundus of a patient with early AMD. Multiple small, medium-sized, hard drusen are seen here (arrowheads). Some confluent drusen with poorly defined edges are present temporally (arrows). (c) Case of advanced geographic atrophy. The loss of retinal pigment epithelium and choroidal atrophy can be clearly observed over the macula (black asterisk). (d) Fundus of advanced wet AMD showing a large polymorphic area of subretinal hemorrhage (white asterisks). Courtesy of Dr. Ahad Fazelat and Dr. Kam Lashkari, Massachusetts General Hospital, Boston, MA.

6.632.2.2. Retinal Degeneration

Heritable retinal degenerations such as retinitis pigmentosa (RP), Stargardt disease, and Usher syndrome are most often caused by one out of nearly 200-single-point mutations. These typically affect the rod PR, although cone and RPE mutations have also been described. Regardless of the primary genetic defect, the end result is PR cell death, with vision loss being an inevitable consequence. The tight coupling of PR and RPE cells, both metabolically and morphologically, makes repair through transplantation particularly challenging.

6.632.3. Retinal Reconstruction

6.632.3.1. Transplantation Success and Failure

While the prospect of using progenitor cells to repair the diseased central nervous system (CNS) has generated unprecedented interest in the field of neuroscience, the idea of using transplants of living tissues to replace organs that are no longer functional is a very old one. Historically, however, transplants exchanged between two members of a species routinely failed, and the reasons for the failure were unknown until the 1940s. At that time, Sir Peter Medawar, working on the problem of providing skin grafts for soldiers wounded in World War II, discovered that the destruction of transplanted tissues was dependent upon an immune response generated by the recipient against the so-called transplantation antigens expressed on the graft. These seminal observations laid the groundwork for the field of transplantation biology. It is no accident that within 20 years of Medawar's discoveries, the first successful solid organ transplants (kidneys) were conducted in human beings. By the 1980s, kidney, heart, liver, and bone marrow transplants were being performed routinely in humans, with a high rate of success.

Yet, despite the clinical successes, transplantation is not currently an option for many organs and tissues. CNS tissue, in particular, presents formidable technical and biological challenges with regard to successful transplantation. The demonstration that retinal grafts placed in the brain of neonatal hosts survive, develop, and make functional connections with the host brain[19] prompted investigators to attempt orthotopic retinal transplantation.[20] Because ectopic retinal transplants made functional connections, it was anticipated that achieving local connectivity in the retina would be relatively straightforward. Unfortunately, this has not been the case. The past 15 years of research on intraocular transplantation has yielded only scant evidence of integration between grafted neural tissue and the host retina. However, the recent demonstration by our group[21,22] and others[23,24] that progenitor cells can be isolated from the retina and ciliary margin suggests that the goal of functional PR replacement may finally be within reach.

6.632.3.2. Retinal Transplantation

We have recently demonstrated that neural progenitor cells (NPCs) derived from the hippocampus of mature rats can integrate with the mature, diseased retina.[25] While this is an essential requirement for functional neural reconstitution, morphological integration alone is not sufficient. An appropriate differentiation into retinal cells is also required. Despite showing very interesting morphological evidence of differentiation, hippocampal progenitor cells did not achieve full retinal-specific differentiation, as evidenced by the expression of retinal markers. Therefore, our next step was to obtain progenitor cells from the neuroretina,[22,26] with the rationale that retinal progenitor cells (RPCs) would be predisposed to differentiate into retinal neurons, particularly PRs. This supposition has been borne out by experimental studies in which we have shown that multipotent, self-renewing progenitor cells can indeed be isolated from the postnatal mammalian neuroretina. Importantly, these cells can be expanded greatly in culture prior to transplantation. When grafted back into mature, diseased hosts, they differentiate into cells of the PR lineage, as evidenced by the expression of the retinal- and PR-specific markers recoverin and rhodopsin.[22,26]

Previous experimental work in the field of intraocular retinal transplantation has relied on subretinal or intravitreal injection of either dissociated cells or tissue microaggregates, and it is now clear that these methods typically give rise to disorganized or incorrectly localized grafts. Studies of RPE cells have highlighted the importance of cellular continuity and polarity with respect to graft outcome.[27] In response to these concerns, investigators have begun isolating and transplanting organized sheets of RPE.[28–31] In addition, biodegradable polymers have been used as a substrate to obtain organized sheets of RPE for transplantation.[32] The ability of biodegradable polymer–progenitor cell composites to generate healthy, normal tissue has been shown in a number of settings, including bone,[33] cartilage,[34] and other tissue types.[35–37]

6.632.4. Challenges in Retina Reconstruction

6.632.4.1. Rationale

Ocular diseases such as AMD and RP lead ultimately to the degeneration of the PR cell layer and irreversible visual loss. At present, PR and/or RPE loss is untreatable and vision cannot be rescued. One of the most promising therapies for late-stage retinal degenerations involves the delivery of stem or progenitor cells to the outer retina, where limited cellular replacement has been shown to be possible in animal models.[38–40] Although bolus injection of stem cells has been sufficient to provide proof of principle for stem cell integration, it can also result in disorganized and incorrectly localized grafts. Therefore, in clinical situations where cell population has been severely depleted and the local laminar retinal architecture disrupted, a mechanism will be needed to confer organization to the grafted cells. Tissue engineering is founded on the basic principle that environmental cues can condition cell behaviors such as differentiation and functions. The clinical use of tissue engineering in the retina will depend on the ability to achieve the desired cell phenotype (PR and RPE) in a predictable and reproducible manner. Although the mere presence of certain stem cells may have beneficial effects, such as neuroprotection of PRs, on the retina, it remains highly improbable that formation of functional retinal tissue will be achieved simply by the delivery of cells. Harnessing the full regenerative potential of stem cells will most likely require additional attention to many detailed aspects of the complex and dynamic relationship

between the graft and the recipient microenvironment. Although no recipe for retinal reconstruction is currently established, recent advances in retinal development and materials science have shown that improved cellular assembly and organization are foreseeable with the precise coordination of physical, spatial, biochemical, and physiological cues.

6.632.4.2. Retinal Pigment Epithelium

As described earlier, AMD is characterized by the initial degeneration of the outer retina, including cellular changes in the RPE and the CC.[41] As the RPE layer is the primary support for both CC and PR,[1] the idea of replacing dysfunctional RPE using cell-based therapy is particularly attractive.[42] Successful RPE transplantation approaches need to address two major challenges: cell source selection and mode of delivery. Numerous cellular sources (fetal or adult autologous RPE) have been tested in various animal models and prospective clinical trials with very variable outcomes in terms of cell survival, organization, and vision rescue (reviewed in Binder *et al.*[43,44]). One of the main challenges in the use of stem cell-derived or native RPE for transplantation lies in the importance of delivering a monolayer instead of cell suspension. *In vitro* studies have clearly demonstrated that full maturation and proper polarization of RPE cells is a long process requiring weeks of culture after the cells have achieved full confluency.[45–47] While it is possible that a healthy ocular environment could accelerate RPE polarization compared to *in vitro* conditions, previous attempts at subretinal injections of RPE suspensions have shown to form abnormal epithelial layers and large clumps.[48] It is also important to note that although the intact retina constitutes an immune-privileged site,[49,50] alteration of the RPE monolayer in AMD can lead to allogenic transplantation failure,[51] particularly in wet AMD.[52,53] This observation supports the use of syngeneic cells to avoid the need of long-term immunosuppressive treatments.[54] Over the past decade, stem/progenitor cell transplantation as a means of inducing tissue reconstruction and functional regeneration has garnered extensive interest in the field of regenerative medicine. Significant advances have been made in the development of protocols for differentiation of RPE-like cells from embryonic stem cells (ESCs),[46] which have demonstrated the ability to halt PR loss in animal models of retinal degeneration.[55] However, clinical use of hESC is limited by ethical and immunological concerns. One significant achievement came in 2007, when the first stem cells were produced from adult tissue.[56] Unlike embryonic cells or tissue-specific progenitors, these induced pluripotent stem cells (iPSCs) offer the promise of creating patient-specific stem cells that obviate the need for chronic immunosuppression and eliminate the risk of immunorejection of the grafted cells. Recently, RPE cells have been successfully derived from mouse and human iPSCs.[57,58] Transplantation of iPS-derived RPE cell suspensions in an Royal College Surgeons (RCS) rat model of retinal dystrophy (similar to RPE-dependent RP) efficiently prevented PR death and improved visual function. However, some of the effects observed may not be directly attributable to the grafted cells but rather to macrophage infiltration secondary to graft rejection.[59] In addition, histological analysis demonstrated that the transplanted cells failed to form a proper monolayer,[59] again supporting the concept of cellular sheet transplantation.

6.632.4.3. Bruch's Membrane

The failure of most clinical trials using RPE cell therapy could be explained in part by the fact that AMD changes are not limited to the cellular components of the outer retina, but also affect the structure of BrM. Despite the fact that the more prominent anomalies associated with AMD are localized at the site of BrM, the critical role of this membrane in the success of cell-based therapy has been highly underestimated.[60] Although increased thickness and alteration of the BrM permeability have been reported as part of the normal aging process,[61,62] the accumulation of lipids and extracellular material beneath the RPE and in the BrM (also called drusen) is particularly predominant in AMD patients. As an acellular membrane, BrM functions are regulated by both its structure and molecular composition, and it has been proposed that by limiting the diffusion of water-soluble protein,[63,64] drusen formation and deposit accumulation contribute to RPE dysfunction. Studies have shown that changes in BrM precede the degeneration of the cellular component of the outer retina,[65,66] suggesting that an accelerated or exaggerated alteration of BrM may be responsible for the subsequent macular degeneration and disease onset. *In vitro* analyses have revealed that the culture of human RPE on BrM collected from aged or AMD patients drastically changes their behavior, gene expression profile,[67–69] and phagocytic activity.[70] BrM reconstruction is particularly difficult due to the lack of knowledge on BrM deposition[71,72] and turnover.[73] Some studies are exploring the option of BrM rejuvenation or, more precisely, resurfacing using enzymatic and chemical methods to remove the detrimental deposit on the matrix and improve RPE graft survival.[74] However, the clinical applicability of such an approach appears strongly limited. In addition, it appears to be clear that the transplantation of RPE as a cell suspension is unlikely to be as efficient as a preformed monolayer. Therefore, efforts are currently focused on the use of natural or bioengineered scaffolds for the transplantation of the RPE monolayer and BrM replacement. The majority of endogenous supports tested for the culture and transplantation of RPE have been isolated from ocular tissue such as lens capsule, Descemet's membrane (basement membrane of the corneal ECs), and the inner limiting membrane of the retina, with the exception of the amniotic membrane. While the results have been encouraging, problems associated with mechanical integrity have limited the success of this approach.

6.632.4.4. Choriocapillaris

The development of the adult choroidal and retinal microcirculatory systems represents a tightly regulated, highly coordinated process, where primordial microvascular networks are emergent from vasculogenic and angiogenesis-dependent processes. Indeed, the neural retina has a remarkable complexity and a significant metabolic demand, including a stringent requirement for heat dissipation. The choroidal microcirculation, an innovative plexus and 'heat exchanger,' achieves its fully functional status by the recruitment and local differentiation of vascular and cooperating nonvascular cells. Highly dependent upon local concentrations of metabolites and diffusible survival or growth factors, cell–cell and cell–matrix

interactions, the remodeling of the choroidal microvasculature contributes to the pathologic remodeling observable during aging.

Postnatally, and throughout adult life, nascent vessels are born, pruned, and stabilized, each event being driven and sustained via cell- and ECM-dependent signaling cascades that are not well understood. It has been suggested that once the preliminary endothelial tube is formed, vessel stabilization and maturation are initiated as ECs recruit mural cell precursors, which differentiate locally into pericytes (PCs).[75] Furthermore, the ECM produced and remodeled by proliferating and migrating ECs has also been postulated to provide a permissive or instructive role in signaling microvascular morphogenesis. Additionally, there is also recent evidence that suggests that there is partnering between nonvascular (glial) and vascular cells within the retina.[76] Astrocytes have been demonstrated to transiently express VEGF as they migrate across the GCL, preceding the formation of the superficial layer of retinal microvessels. Müller cells also express VEGF and may also participate in the microvascular morphogenetic events required to form the deeper retinal microcirculatory components. And, just as these complex cell- and matrix-dependent remodeling events are presumed to initiate and sustain the physiologic vasculature, metabolic demands and/or pathologic neuronal or vascular activity can comparably cause 'physiologic hypoxia,' which is detected by astrocytes and Müller cells.[76,77] It has been proposed that a lack of oxygen transfer to an area initially stimulates hypoxia-inducible factor 1 (HIF-1), which then induces the transcription of other angiogenic molecules, such as VEGF, insulin-like growth factor 1 (IGF-1), platelet-derived growth factor (PDGF), and hepatocyte growth factor (HGF), as mitogens, vasopermeability agents, and chemoattractants for EC.[78] Targeted disruption of a single allele of VEGF causes embryonic lethality in mice, with diminished angiogenesis and blood island formation.[79] VEGF binding to its specific receptor tyrosine kinase, VEGFR-2, induces receptor dimerization and phosphorylation. Subsequent tyrosine phosphorylation signaling activates several effector proteins, including protein kinase C (PKC), phospholipase-Cγ, and Ras GTPase-activating protein.[80] These factors and signaling cascades act to initiate the angiogenic cascade. In turn, these events have sparked anti-VEGF therapeutic strategies.

Blinding diseases such as AMD or neovascular glaucoma are believed to be consequences of this aberrant signaling among microvascular cells, plasma components, immune surveillance cells, and components of the nervous system, all of which contribute to the inception and etiology of aberrant angiogenic responses or pathologic angiogenesis. There are considerable gaps in our understanding of the 'angiogenic switch' that is responsible for inducing pathologic angiogenesis during AMD. Remarkably, of the nearly 2 million new cases that are reported every year in the United States, roughly 200 000 will develop wet AMD (http://nih.gov). These data are significantly compounded by the realization that there are likely to be nearly 3 million citizens who have AMD, but remain undiagnosed. Pathological changes in the choroidal microvasculature yield an invasive and proliferative endothelium, and recurrent rounds of endothelial migration and growth yield the pathologic angiogenesis observed during wet AMD.

6.632.4.5. Neuronal Regeneration of the Adult Nervous System: Regeneration in the Central Nervous System Versus Peripheral Nervous System

Following axotomy, the distal segment of the severed axon undergoes Wallerian degeneration. This is the process by which the distal part of the severed axon, which no longer has contact with its cell body, undergoes degeneration and subsequent removal.[81] During this process, there is an immune response that stimulates the infiltration of leukocytes and macrophages, which act to remove the degenerating myelin sheet via phagocytosis.[81]

Although the presence and rate of Wallerian degeneration are roughly the same in both the CNS and the peripheral nervous system (PNS), differences that are very important to axonal regeneration exist in these processes. In the CNS, myelin removal is slow and inefficient, and myelin debris, which contains a variety of inhibitory proteins, remains in the injury site for extended periods of time.[82] The injury site in the CNS is also plagued by the formation of a glial scar, which has also been shown to contain growth inhibitory molecules.[83,84] In contrast, axotomy of PNS neurons stimulates the complete removal of the myelin sheet, and Schwann cells change from their normal state of myelination, begin to proliferate, and form bands of Büngner, which act as basal lamina tubes providing guidance tracts for regenerating axons.[85] The Schwann cells of the distal nerve stump begin to release a variety of cell adhesion, ECM, and neurotrophic molecules in an attempt to provide a permissive environment for axonal regeneration.[81,85] During Wallerian degeneration in the CNS, oligodendrocytes do not change from a myelinating to a proliferating state, and the formation of structures such as the bands of Büngner does not occur. Unlike the PNS, there is a lack of permissive molecules such as nerve growth factor (NGF) and laminin that are secreted after CNS injury in the adult.[81,86]

It has long been known that CNS neurons, unlike PNS neurons, CNS neurons lack the ability to achieve significant amounts of axonal regeneration following injury.[87–90] However, when provided with the appropriate environmental conditions, CNS neurons have been shown to regenerate.[88,91–94] These findings suggest that the marked difference in regenerative capacity between CNS and PNS neurons is largely due to different environmental factors. Specifically, the adult CNS is faced with an inhibitory environment, which is created by the presence of inhibitory molecules associated with the myelin sheath and glial scar, and a lack of permissive molecules such as laminin and NGF associated with the Schwann cells of the PNS.[91,93,95]

6.632.4.6. Interdependence

As mentioned in the first paragraph, the survival of the neuronal cell in the retina is highly dependent on both the support cell such as RPE and the vascular system. Therefore, survival of transplanted retinal neurons (from stem cells or progenitor cells) would be particularly difficult if the main cellular and vascular support systems (i.e., the RPE and CC) were lost or become dysfunctional. This interdependence appears particularly critical in a complex disease such as ADM where anomalies and cellular loss are not confined to one retinal layer.

A widely investigated approach to tissue engineering in the retina is the design of novel scaffolds on which stem or progenitor cells can be cultured. Scaffolds provide structural support and direct cell behavior, and subsequently promote survival and integration when transplanted to the subretinal space. For transplantation into the eye, scaffolds must at least be biocompatible and mechanically stable. Recent advances in materials processing technology have enabled the design of materials to be tuned so as to mimic the normal developmental microenvironment. The incorporation of these properties provides the framework for efforts to regulate the behavior of the transplanted cell population and to orchestrate the host response.

6.632.5. Scaffold Biocompatibility

6.632.5.1. Material

For retinal reconstruction, the scaffold must be biocompatible in terms of both donor cells during culture and the host tissue following transplantation. Therefore, the materials of choice must not be appreciably immunogenic or cytotoxic, and they must neither elicit a chronic inflammatory response nor degrade into toxic by-products (see Volume 4: Biocompatibility). A variety of both natural and synthetic materials have been implanted and examined for compatibility in the subretinal space in conjunction with applications ranging from cell transplantation to drug delivery and retinal prostheses.

Natural polymers, or biopolymers, are a result of a polymerization process that takes place in nature in living organisms. These polymers are isolated from raw materials, such as donor tissue, and can also be postchemically modified. The use of natural polymers allows the creation of a scaffold that closely mimics the ECM of the targeted tissue. A variety of natural polymers constitute the matrix environment of the retina. For example, hyaluronan (HA) and several HA-binding proteins are key to the complex organization of the interphotoreceptor matrix located between the outer limiting membrane of the retina and the apical border of the RPE,[96] whereas in the RPE basement membrane and BrM, polymers such as collagen, elastin, laminin, and fibronectin are dominant.[73] Natural polymer matrices can be decellularized and left intact for direct use as scaffolds in cell support, or individual components of the ECM may be extracted for use in scaffold fabrication. Examples of intact biological matrices used as scaffolds in retinal tissue engineering include Descemet's membrane, amniotic membrane, BrM, and anterior lens capsule.[67,74,97–100] Examples of extracted ECM components used as scaffolds include collagen, gelatin, and fibrinogen.[101,102] Although natural materials have drawbacks, including lot-to-lot variability and immunogenicity associated with animal-derived products, these materials, in general, have been well tolerated *in vivo* in the subretinal space in the short term.

Synthetic polymers offer advantages over natural polymers in terms of synthetic flexibility and consistent reproducibility. Traditionally, scaffold biodegradability has been a necessary property to achieve full integration of an engineered construct, with the supportive role of the scaffold diminishing and transferring back to the host as the scaffold is resorbed (see **Chapter 4.401, The Concept of Biocompatibility**). The most widely used, and therefore widely studied, biodegradable polymers for implantation are based on poly(glycolide) (PGA), poly(L-lactide) (PLLA), poly(D,L-lactide) (PDLLA), poly(ε-caprolactone) (PCL), or their combinations (see **Chapter 1.123, Degradable Polymers**).

Although polymer properties are highly dependent on composition, form factor, and fabrication process, PGA-based polymers, including poly(lactide-*co*-glycolide) (PLGA), are known, in general, to possess relatively short degradation times (2–12 months). PLGA degrades by hydrolysis of its ester linkages in the presence of water to produce lactic acid and glycolic acid monomers. These monomers are normal byproducts of the body, and easily metabolized with minimal systemic toxicity. The degradation mechanism of PCL follows the same principles as those of PLGA. However, its hydrophobic nature and α-hydroxy acid structure make PCL a very slow-degrading polymer (two years or greater), especially at high molecular weights.

Synthetic polymers that have been implanted in the mammalian subretinal space have included both nondegradable polymers (poly(methyl methacrylate) (PMMA),[103] polyimide, parylene, poly(vinyl pyrrolidone) (PVP), polyethylene glycol (PEG),[104] poly(butyl methacrylate), and poly(ethylene-*co*-vinyl acetate) (EVAC)[105]) and biodegradable polymers (PLGA,[106,107] PCL,[108] and poly(glycerol sebacate) (PGS)[109,110]), depending on the particular application. Due to the differences in experimental design, animal model, and time course, there are varied reports of material compatibility in the subretinal space with regard to maintenance of the normal anatomy of the retina or the degree to which reactions were incited around the implant itself. However, the clinical application of fast-degrading polymers to retinal engineering may be limited. In the volume-limited subretinal space, the production and buildup of acidic degradation species by fast-resorbing PLGA have shown neural–retinal toxicity, thereby compromising retinal tissue repair.[106,111] Although a number of novel fast-degrading polymers are currently in development and under investigation, slow or nondegrading polymers may ultimately result in fewer physiological disturbances after transplantation.

6.632.5.2. Physical Constraint of the Subretinal Space

The physical constraint of the retinal space presents a formidable challenge to functional transplantation strategies. The neural retina averages ~250 μm in thickness, yet has a thickness of 100 μm in the central fovea, while the BrM has a thickness of only 5 μm.[111] The PRs derive their oxygen supply and nutrients from the choroidal circulation, which therefore necessitates transport of these molecules across the BrM and the RPE layer. The subretinal extracellular space between the PRs and the apical RPE is extremely thin; the thickness of any material substrate implanted within this space is therefore an important consideration. Scaffolds should be thin enough to allow a relevant diffusion pathway for the exchange of metabolites and nutrients between the retina and the CC, and at the same time sufficiently so to avoid physical distortion of the overlying PR layer after transplantation.

It has been demonstrated that the use of thin scaffolds increases the ease of delivery and reduces the risk of trauma, while allowing the scaffold to rest flat against the retina. This serves to enhance integration with the host. However, the

decreased volume of material also effectively limits the number of cells that can be delivered by the scaffold. A thickness of 5 μm was found to be the overall compromise between thinness and ease of physical handling and manipulation capabilities.

6.632.5.3. Mechanical Properties

The mechanical behavior of the native retina is characterized by a short elastic phase (Young's elastic modulus = 0.1 MPa) followed by a wide plastic phase range of 73.5% where irreversible deformation, but no tearing, can occur.[112] It is necessary for the retina to maintain a low level of elasticity in order to prevent retinal retraction, detachment, or visual distortion in conditions such as hypotony or myopic elongation. The retina's high degree of plasticity acts as a compensatory mechanism, providing a protective factor against tear formation. While a potential retinal transplant composite must be similar enough to natural tissue to handle potentially damaging stress and strain perturbations, it must also demonstrate a level of strength and stiffness amenable to surgical manipulation and implantation.

Natural polymers, such as gelatin and collagen, and hydrogels demonstrate poor mechanical properties, which can make them difficult to handle during transplantation and unpredictable in the presence of cells due to contractile-mediated gel shrinkage. Attempts to improve the mechanical properties of polymer gels for transplantation have been made with methods such as controlled cross-linking, where the level of cross-linking and substrate stiffness is tunable. However, when cross-linked collagen was used for transplantation, it was found to damage the retina. It is unclear, though, whether this may have been due to its mechanical properties, scaffold thickness, overall poor permeability, or inability to degrade.[102]

Biodegradable synthetic polymers may better provide the necessary mechanical properties to withstand the transplantation procedure. PLLA/PLGA membranes (Young's modulus = 9 MPa, strain at failure of 15%), though theoretically capable of delivering healthy cells,[107] have in some instances had the problem of stiffness and been damaging to the retina when implanted in the subretinal space of pigs.[111] Other polymers such as PCL and PGS have been successfully implanted in the subretinal space of mice with relative ease. Although the elastic moduli of these transplanted materials remained high, 280 and 2 MPa, respectively, in comparison to native retina, it is possible that the thin form factor of these constructs decreases the apparent stiffness to which tissue responds. Both materials maintained a strain at failure >110%, but with PGS acting as a completely elastic material, and PCL having a plastic phase of 92%, similar to the plasticity found in native retinal tissue (Figure 6).

In addition to the gross mechanical properties required for host transplantation, the apparent local stiffness may also play a substantial role in donor cell behavior (see Chapter 5.504, Effect of Substrate Modulus on Cell Function and Differentiation). Matrix elasticity is increasingly recognized as a key factor in cellular processes. Focal adhesions, the bridge between a material substrate and the cell cytoskeleton, are considered mechanosensory, and they change size and shape in response to the mechanical environment.[113,114] In response to local stiffness, cells rearrange their cytoskeletal filaments and

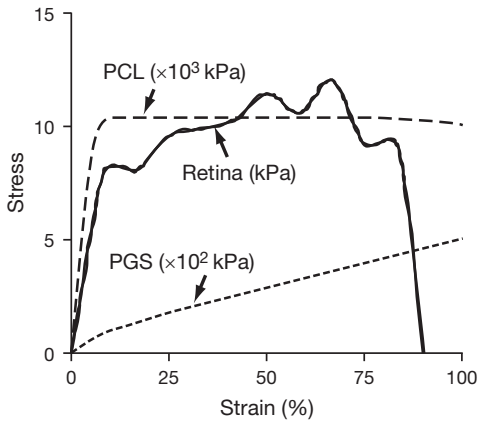

Figure 6 Example of a stress–strain curve for polycaprolactone (PCL), polyglycerol sebacate, and porcine retina. Porcine retina tested at a strain rate of 2 mm min^{-1} with data kindly provided by Dr. Gregor Wollensak[112]; 10 mm × 5 mm PCL (80 000 MW) scaffold 6 μm thick tested at a strain rate of 10 mm min^{-1} (adapted from Sodha, S.; Wall, K.; Redenti, S.; Klassen, H.; Young, M. J.; Tao, S. L. *J. Biomater. Sci. Polym. Ed.* **2011**, *22*, 443–456); 12 mm × 6 mm poly(glycerol sebacate) scaffold 45 mm thick tested at a strain rate of 2 mm min^{-1} (adapted from Neeley, W. L.; Redenti, S.; Klassen, H.; *et al. Biomaterials* **2008**, *29*, 418–426).

reorient their molecular machinery. Substrate stiffness influences the amount of traction force a cell exerts, and subsequently, the degree to which the cell adheres, spreads, and proliferates.[115,116] Furthermore, substrate stiffness has a fundamental effect on cellular differentiation. It has been proposed that matrix elasticity directs cell fate via nonmuscle myosin II. Myosin II, in conjunction with focal adhesions and the cytoskeleton, is thought to act as a cellular mechanosensor to detect substrate elasticity and, in turn, influence cellular lineage specification.[117] Undifferentiated stem cells grown on polymer gels mimicking the elasticity of a given tissue were found to express proteins for the cell type present in that particular tissue. As one of the softest tissues in the body, endogenous neural tissue has an elastic modulus of ~500 Pa. Recent studies have identified a range of 100–1000 Pa as being the optimal stiffness for neurogenic cell differentiation.[117,118] Mesenchymal stem cells, as well as neural stem/progenitor cells cultured on these 'soft' matrices (<1000 Pa), have been shown to develop neural morphology and express various neural markers.[117–119]

However, the mode by which cells mechanically respond to their environment will likely be substantially different between planar substrates and a three-dimensional (3D) material. In order to alter cell behavior and response with respect to mechanosensory response to a material scaffold, the scaffold may be altered not only by changing the biomaterial of choice, but also by modifying its thickness, structure, porosity, and topography.

6.632.6. Scaffold Fabrication

A biomaterial scaffold could promote the organization of grafted cells into defined layers, such as is seen in the normal retina. As long as there is adequate adhesion, culturing cells on a polymer scaffold results in a composite implant that, unlike

bolus injections, possesses an inherent structural organization. The most common methods of polymer scaffold fabrication include solvent casting and melt molding. During solvent casting, a polymer is dissolved in a solvent and cast into the desired mold. When the solvent evaporates, the polymer is left behind, taking on the shape of the mold. In melt molding, on the other hand, the polymer is brought to temperatures above its melt temperature (crystalline polymers) or its glass transition (amorphous polymers) to form a liquid for casting. Standard solvent casting of polymers (e.g., PCL) gives typical thicknesses of ~70 to upwards of 700 μm.[120–122] Melt molding under compression thicknesses can provide a thickness >50 μm while combined compression and biaxially stretching membranes are 5–30 μm in thickness; when combined with spin casting, they are <10 μm in thickness.[123–125] Implantation of polymer scaffolds of thickness greater than that of the retina have been found to significantly increase the incidence of retinal trauma and detachment during the transplantation procedure.

6.632.6.1. Micro- and Nanotopography

If surface topography and architecture are changed, a material may better mimic native guidance cues, thereby influencing cell response.[107] In a physiological environment, cells respond to micro- and nanometric topologies such as fibrous and porous materials formed by components of the ECM (see **Chapter 4.413, Patterned Biointerfaces**). Response to nanotopographic features (such as grooves, pores, pits, and pillars), though variable from cell type to cell type, has been reported in almost all mammalian cells and expertly reviewed in the literature (see **Chapter 4.409, Surfaces and Cell Behavior**).[126–129]

A highly utilized method to introduce topography is scaffold porosity. Pores can easily be incorporated into a scaffold during the solvent-casting or melt-molding process through introduction of a porogen, and subsequent leaching. Depending on the concentration and porogen used, this method can create a randomly open network within the scaffold, with the size of the porogen dictating the size of the pores. Other techniques of forming randomly open networks of pores include phase separation and foaming. The use of pores to introduce topography was first demonstrated in the context of the retina by Lavik and coworkers.[107,130] PLGA scaffolds, ~0.3 mm thick, were fabricated by phase-inversion casting and solid–liquid phase separation to contain pores ranging from 50 to 200 μm in diameter (**Figure 7(a)**). The use of the microporous composite graft not only increased the rate of retinal progenitor cell survival, but also promoted differentiation of RPCs, as evidenced by the induction of changes in morphology and gene expression.

Another approach to creating porosity is by electrospinning, a process that forms nanofibers through an electrically charged jet of polymer solution. Electrospinning can be used to create nanofibers ranging from <3 nm to >1 μm; however, this process remains dependent on jet stability (due to solvent viscosity, surface tension, and vapor pressure). Also, electrospinning essentially produces one infinitely long fiber, which is collected in an unordered mesh and is difficult to manipulate into higher order architectures other than uniaxial alignment (**Figure 7(b)**). It has been shown that electrospun nanofibers composed of laminin and PCL, as well as PLGA, promoted sufficient cell adhesion transplantation of isolated PR layers and retinal progenitor populations. Both of these composites developed large populations of recoverin- and rhodopsin-labeled PRs after transplantation.[131,132]

Nanotemplating is a simple method that can be used to nanostructure biodegradable materials without the use of organic solvents, pressure assistance, or custom instrumentation.[133] Templating entails synthesis of a desired material within the pores of a membrane.[134] Using a template of aligned and ordered pores produces ordered nanowire arrays perpendicular to the attached substrate (**Figure 7(c)**). Tao and Desai[133] demonstrated that template synthesis can be used as a fast and inexpensive method to form perpendicularly oriented high aspect ratio (>1:10) nanowire and nanofiber arrays from biodegradable and biocompatible polymers, including PLGA, PCL, and PLCL, without the use of organic solvents, pressure assistance, or custom instrumentation. Immunohistochemical analysis revealed that scaffold topology influenced protein expression levels. Only RPCs cultured on nanowire PCL demonstrated evidence of differentiation by expression of the bipolar cell marker PKC, the PR marker recoverin, and the rod PR marker rhodopsin. When transplanted subretinally in $Rho^{-/-}$ mice, RPCs cultured on nanowire PCL migrated into the retina ONL and INL, and developed an apparent cell polarity with early PR-like morphology and expression of recoverin.[108]

6.632.6.2. Microfabricated Scaffolds

However, in order to create an appropriate framework for the complex cellular organization of the retina, more sophisticated

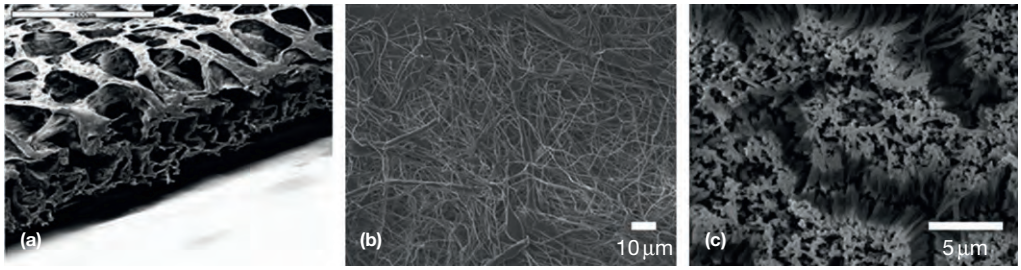

Figure 7 (a) A porous poly(lactic-*co*-glycolic acid) (PLGA) scaffold prepared using the solid–liquid phase separation technique. Reprinted from Lavik, E. B.; Klassen, H.; Warfvinge, K.; Langer, R.; Young, M. J. *Biomaterials* **2005**, *26*, 3187–3196. (b) An electrospun nanofiber PLGA scaffold. Reprinted from Tucker, B. A.; Redenti, S. M.; Jiang, C.; *et al. Biomaterials* **2010**, *31*, 9–19. (c) A poly(ε-caprolactone) scaffold containing nanowires. Reprinted from Tao, S. L.; Desai, T. A. *Nano Lett.* **2007**, *7*, 1463–1468.

fabrication approaches are needed. Microelectronic process engineering developed due to the rapid growth of the integrated circuit industry. Traditionally, microelectromechanical systems (MEMS) research has been used to produce functional devices on the micron scale, such as sensors, switches, filters, and gears, from silicon, the dominant material used throughout the integrated circuit industry. These devices are fabricated by the repeated application of unit process steps such as thin-film deposition, photolithography, and etching. The adaptation of microfabrication is an alternative method of fabricating scaffolds developed recently for retinal reconstruction to tailor spatial control over porosity and topography. Microfabrication techniques and the independent control of feature size and shape may provide a more uniform and precise method for creating retinal scaffolds. These micropatterned substrates can theoretically be designed to influence initial cell attachment and spreading, and allow the maintenance of differentiated cell phenotype throughout culture. The ability to culture tissue with proper anatomical organization and function could potentially result in a greater chance for reestablishing PR connections with the host.

In the microfabrication of scaffolds, a 2D feature layout is created utilizing computer-aided design software and printed into a photomask. The pattern is transferred to a substrate (typically silicon) via photolithography. During photolithography, a substrate is spin-coated with a photosensitive polymer (positive or negative) resist layer and exposed to UV light from a mask aligner through the photomask. If a negative photoresist is used, the photoresist is cross-linked when exposed to light. On the other hand, a positive photoresist is cleaved when exposed to light. During development, photoresist cross-linked to the substrate surface remains, while un-cross-linked or cleaved photoresist areas are washed away. While standard photolithography has a resolution of ~0.5–1 μm, it is possible to achieve sub-100-nm resolution using methods such as e-beam, ion beam, and dip-pen lithography. The pattern can then be transferred into the substrate material using a wet or dry etch process (Figure 8).

The hard patterned substrate can be used as a master mold in the process known as soft lithography to create a robust inverse replica in a soft elastomer poly(dimethyl siloxane) (PDMS). And, if maintained in a controlled environment, both the master mold and PDMS mold can potentially be used for limitless rounds of replication (Figure 8).

Utilizing microfabrication processes and soft lithography in combination with modified polymer processing techniques, such as spin-assisted solvent casting and nanotemplating techniques, polymer thin-film scaffolds can be structured precisely, simply, rapidly, and at low cost without the further use of specialized microfabrication equipment. A number of strategies utilizing MEMS base and nanotechnology have been developed to create micro- and nanostructured scaffolds for directing retinal cell behavior.[103,109,124,125,135,136]

One approach to the use of microfabrication is to form a transplantable thin-film scaffold containing regularly spaced through pores. Micropatterned scaffolds 6 μm thin were fabricated to contain through pores 11 μm in diameter with an interpore distance of 63 μm using a dual process of photolithography and reactive ion etching on a PMMA substrate.[103] Both nonporous and porous PMMA demonstrated full

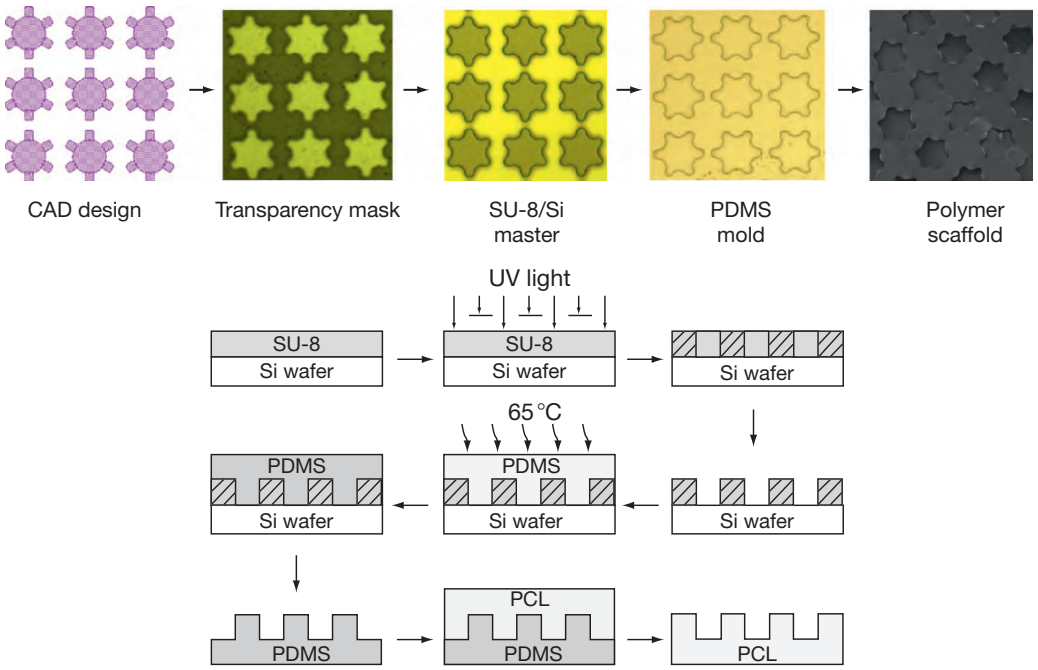

Figure 8 Schematic of thin-film polymer scaffold fabrication. Adapted from Sodha, S.; Wall, K.; Redenti, S.; Klassen, H.; Young, M. J.; Tao, S. L. *J. Biomater. Sci. Polym. Ed.* **2011**, *22*, 443–456; Steedman, M. R.; Tao, S. L.; Klassen, H.; Desai, T. A. *Biomed. Microdevices* **2010**, *12*, 363–369. SU-8 negative photoresist is spin-cast onto a silicon wafer and exposed to UV light through a negative mask. Unexposed areas are not cross-linked and developed away, and poly(dimethyl siloxane) (PDMS) is cured on the wafer. After peeling the PDMS mold from the wafer, a polymer, such as polycaprolactone, is spin-cast on the mold and peeled from the surface.

biocompatibility with RPCs in culture *in vitro*. Although RPC adherence and survival were nearly identical on both types of scaffolds in culture, transplantation with nonporous scaffolds showed limited RPC retention. The porous topography, however, allowed for RPC adherence through transplantation to the posterior eye for up to 4 weeks. The enhanced RPC attachment to porous scaffolds also provided a cytoarchitectural microenvironment permissive of eventual cell migration into the host retinal layers.[103] It seems probable that a mechanism of cell anchorage involved the insertion of individual cells or their processes into pores. RPCs embedded into pores remained attached to the scaffold during transplantation while also serving as an anchorage point for the surrounding RPCs through cell to cell contacts.

The concept of a tailored pore structure was further demonstrated in the use of PGS scaffolds. Using micromolding of a PDMS master, a PGS scaffold 50 μm thick, with an average pore size of 50 μm and an interpore distance of 200 μm, was fabricated. Though these pores were much larger than the size of a cell, this scaffold yielded a similar increase in terms of RPC survival,[109] and the mRPCs adherent to PGS differentiated toward mature phenotypes as evidenced by changes in mRNA, protein levels, and enhanced sensitivity to glutamate. Transplanted composites demonstrated long-term mRPC survival and cells that had migrated exhibited mature marker expression in host retina. Adhesion of RPCs to polymer scaffolds during the process of subretinal transplantation demonstrated the utility of a regular porous surface topography.

Another approach has been the use of guidance cues, particularly groove–ridge substrates, to direct differentiation and alignment of progenitor and PR cells. Tezcaner and Hicks[135] created both thin (10 μm) and thick (100 μm) groove–ridge substrates by solvent casting a blend of PLGA/poly (3-hydroxybutyrate-*co*-hydroxyvalerate) onto micropatterned silica templates. The scaffolds contained a final pattern dimension of 20 × (21 or 42) × 20 μm (groove width, ridge width, ridge height). When seeded with primary pig PRs, the cells displayed a preference for attachment to the groove structures as compared to ridges. The degree of alignment was found to be more than 90%. Similarly, polystyrene has also been cast onto micropatterned silicon wafers to create nondegradable scaffolds with a pattern dimension of 16 × 13 × 4 μm (groove width, ridge width, ridge height), which were subsequently seeded with human NPCs (hNPCs) isolated from 16- to 18-week fetal cortex.[136] No differences in proliferation or differentiation were found between micropatterned and nonpatterned substrates. However, hNPCs cultured on the micropatterned substrates were aligned in the direction of the micropattern (~90% within 10° of perfect alignment) compared with the cells cultured on the nonpatterned substrates. Furthermore, hNPC migration was directed in alignment with the micropatterned substrates. With the integration of high-resolution microfabrication processes, scaffolds for retinal transplantation can be fabricated with groove–ridge patterns in the submicron range, well below the size of an individual cell.[125] Rather than utilizing microfabricated topography to simply direct cell–cell and cell–substrate organization, it may be possible to direct the organization of individual cell machinery and function (Figure 9).

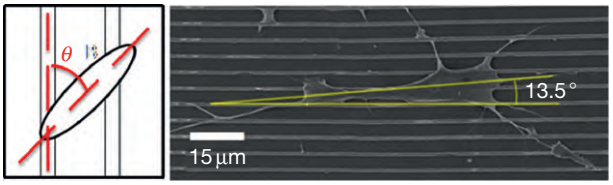

Figure 9 θ is the angle between the center axis of a cell and the vector along the direction of a ridge−groove. A cell preferentially aligns along a groove–ridge pattern. Courtesy of Chi Wan Ko, MIT University, Boston, MA.

6.632.6.3. 3D Scaffolds

Although it is possible to laminarly organize cells and direct alignment utilizing microfabricated planar substrates, the 3D structure and organization of the retina must be taken into account when considering its reconstruction. The retina is a highly ordered tissue consisting of stacked cell layers, and within the layers, there is the arrangement of neurons of the same type in orderly arrays, or mosaics. Mosaics are the earliest detectable patterned units during retinal development. Modeling and statistical analysis have shown that the spacing of like cells within the layer is nonrandom, and this spacing is a minimal distance by which the cells avoid being closer to one another than a given distance, usually comparable to several cell body diameters.[137,138] The spacing in the PR layer determines the ability of the retina to resolve fine spatial detail. In the PR layer, the inner segments of both rods and cones exhibit a hexagonal form and are regularly arranged in a honeycomb fashion – each cone or rod surrounded by six other cones or rods, respectively. The rod density is maximal at 150 000 rods per mm^2 and decreases to 30 000–40 000 cells per mm^2 toward the retinal periphery. The rod to cone ratio in the retina is 20:1 at the location with the highest rod density.[139] The rod diameter increases from 3 μm in the area with the highest rod density to 5.5 μm in the periphery and it is ~40 μm in length,[140] In a simplified two-compartment model, the retina is seen to be composed of two monostratified epithelial-like layers facing each other by their apical surfaces, and forming separate homeostatic compartments. The outer layer is formed of RPE cells, while the inner layer is composed of Müller cells. PR inner and outer segments alone reside within the outer compartment while the remaining neural elements (three sheets of neurons and their interconnections) are embedded in the inner compartment.[141] In a clinical situation, an engineered retina should maintain the transplanted cells within the ONL, and at the same time allow for the formation of OSs across the scaffold and interphotoreceptor space for invagination by RPE without being limited by the duration of scaffold degradation.

Utilizing the same microfabrication processes as described above, a 3D scaffold with an appropriate orientation can be built by aligning and bonding individually designed planar scaffolds. The encapsulation scaffolds were designed to be <30 μm in thickness with a centralized chamber for cell retention, and two porous membranes allowing for bidirectional molecule diffusion and graft–host cell communication. One example is described by Sodha *et al.*[125] (Figure 10). The assembled scaffold, with 200 μm diameter circular cell

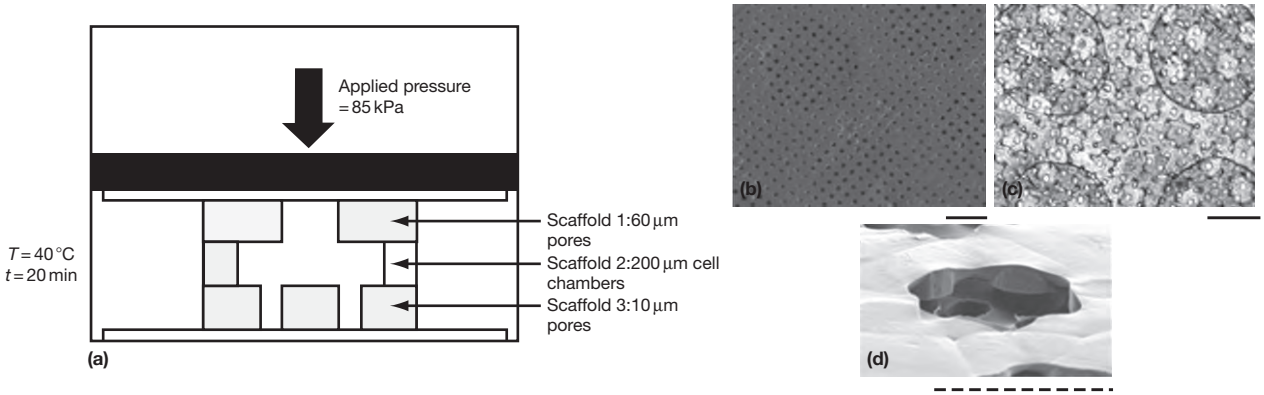

Figure 10 Thermal bonding to produce a three-dimensional (3D) polycaprolactone structure. (a) Scaffolds were aligned and stacked, and placed in a custom pressure vessel under constant pressure and temperature. (b) Scanning electron microscopy (SEM) image of a 3D scaffold from a 10-μm-diameter pore side. (c) Bright-field image of a 3D scaffold from a 60-μm pore side. (d) SEM image of a 3D scaffold from a 60-μm pore side. Black scale bar = 100 μm. Dashed scale bar = 50 μm. Reprinted from Sodha, S.; Wall, K.; Redenti, S.; Klassen, H.; Young, M. J.; Tao, S. L. *J. Biomater. Sci. Polym. Ed.* **2011**, *22*, 443–456.

holding chambers acts as a protective cell environment (Figure 10(a)). Each chamber was capable of holding ~600 cells by volume, assuming the cells were spherical, with a radius of 10 μm (Figure 10(b) and 10(c)). The 10-μm-diameter circular pores were designed as a potential interface between the transplanted cells and the host RPE. This pore architecture was based on previous studies, where individual cells could extend processes across a 10-μm pore, without migration of the cell body.[103] The 60-μm hexagonal star-shaped pores were designed as the neural retinal interface (Figure 10(c)). This pore architecture was designed to allow a possible migratory pathway, as demonstrated in previous studies,[109] while providing appropriate spacing of cells into a patterned unit, and adequate contact guidance for alignment in the *z*-direction. In this manner, the 3D scaffold combines the multiple requirements previously outlined. It is able to hold a number of cells in close proximity within a centralized chamber to lessen the effects of cell shearing, while retaining an appropriately thin form factor. It is highly porous and allows for diffusion as well as potential cell interactions from both sides (toward the neural retina and toward the RPE). The device can additionally serve as an organized framework to support cell adhesion, organization, and migration, and also as a barrier to prevent infiltration of surrounding cells.

6.632.6.4. Surface Modification of Scaffolds

The surface chemistry of a scaffold material may be patterned to change the surface energy of the material or to attach bioactive molecules (e.g., ECM proteins) in controlled orientation. The ability to chemically functionalize the scaffold surface provides a means for tuning interactions between cells and the artificial environment. The use of unmodified biocompatible polymers, which do not contain cell-binding domains, suffices for most cell-based studies. However, many materials are easily chemically modified to achieve cell-binding or activation characteristics for more directed material–cell interaction.

As many polymers are hydrophobic, a simple method of enhancing cell adhesion can be an alteration in the surface energy of the material, such as oxygen plasma or acid treatment to increase hydroxyl groups at the surface.[142] Surface chemistry can further include the simple adsorption or covalent attachment of ECM proteins (e.g., laminin, fibronectin, collagen IV, and heparin sulfate, singly or in combination) to the surface of the material. These simple methods of modifying the surface of a substrate can significantly influence cell adherence and differentiation.[74,143]

Similar to topography, scaffold chemistry can be modulated to form micro- and nanopatterns that can be used to control individual cell shape and adhesion patterns. Methods for precise chemical patterning of scaffolds include microfluidic printing and, more commonly, microcontact. Briefly, microfabrication processing is utilized to produce a PDMS mold with the desired pattern features. The 'inking' solution, comprising the desired proteins or molecules, is allowed to adsorb to the surface of the PDMS microstamp in the case of microcontact printing. The microstamp is then pressed against the substrate or scaffold with force. When the microstamp is removed, the molecules remain printed on the substrate. In the case of microfluidic printing, the PDMS stamp is brought into complete contact with the substrate, and the inking solution is allowed to flow through the open network created between the PDMS and substrate. By activating both the substrate and molecule prior to microcontact printing, permanent patterns of covalent linkages may also be formed. The shape and dimension of the transferred pattern, and the promotion of adhesion or repulsion by the molecules, will determine cellular shape and organization.

Lu *et al.*[144–146] patterned PLGA scaffolds with 50-μm circular islands of PEG/poly(lactic acid) (PLA) spaced 10 μm apart, as well as the inverse, PEG/PLA scaffolds with 50-μm circular islands of PLGA. In both instances, the repulsive PEG/PLA circles suppressed adhesion of D407 RPE cells, while the cells preferentially attached to the PLGA domains. However, while individual cells adherent to circles of PLGA were able to spread, they remained isolated in position in number. In contrast, cells adherent to contiguous PLGA increased in cell number over time and were seen to extend a number of cell processes for cell–cell interaction. Lee *et al.*[98,147] were able to utilize

microcontact and microfluidic printing, in addition to synthetic polymers, to prepare chemical micropatterns on human lens capsule tissue. The pattern was designed for a 2–10-μm-wide ring of cell repulsive poly(vinyl alcohol) (PVA) to enclose a 15–50-μm hexagonal space of unmodified lens capsule. RPE cells were able to selectively adhere to the cytoadhesive lens capsule region within the PVA ring. However, it was found that a 20-μm hexagon retained the highest cell density without clumping. Furthermore, these cells were able to spread across the PVA barriers with time and form the appropriate morphology of an RPE monolayer. This method of chemical modification may be an alternative method to enhance initial cell attachment and spreading, and to allow the maintenance of differentiated cell phenotype throughout culture and transplantation.

6.632.6.5. Controlled Release

The development and differentiation of cells during retinal reconstruction will also likely depend on a number of soluble growth factors. For example, retinoic acid, taurine, S-laminin, sonic hedgehog, activin, ciliary neurotrophic factor (CNTF), and a variety of additional neurotrophins have all been implicated in the differentiation of rod PR cells. In addition to directing donor cell response, methods to modulate the host environment may also be necessary to promote the integration of the transplanted construct. For example, in a diseased eye where immune privilege is disrupted, restoration of immune privilege through delivery of immunosuppressive or anti-inflammatory factors may be an important strategy for promoting the immunologic success of tissue-engineered constructs in the future (see **Chapter 4.419, Vaccine and Immunotherapy Delivery**).

Currently, delivery of therapeutics to the back of the eye is often performed by intraocular injection to the vitreous chamber, which requires frequent and large doses to account for clearance. Intravitreal implants and microparticle injections have been developed to provide sustained release; however, posterior to anterior convection still prevents adequate concentrations to the back of the eye. Many of the polymers utilized in scaffold fabrication are also well suited for use as long-term drug delivery systems. The rate of release is dependent on a number of factors including load concentration and distribution, surface area to volume ratio of the implant, diffusion, and polymer degradation rate. In particular, PCL has been demonstrated in an implantable system to the subretinal space for controlled delivery up to at least 1 month.[105] Therefore, therapeutic molecules could possibly be integrated into the scaffold during fabrication and processing to provide sustained, controlled, and localized delivery to the posterior segment after transplantation of the construct.

Tucker and coworkers[131] developed an effective PLGA scaffold to deliver stem cells as well as the enzyme MMP-2. The inability of the adult mammalian retina to regenerate can be partly attributed to the expression of injury-induced inhibitory ECM and cell adhesion molecules. In particular, PR degeneration stimulates deposition of neurocan and CD44 at the outer limits of the dystrophic retina, where they act as a barrier against cellular migration and axonal extension. Local delivery of MMP-2 has the potential to promote controlled degradation of CD44 and neurocan to reduce the inhibitory glial barrier and allow for the integration of donor cells. The PLGA scaffold was fabricated by two-phase electrospinning to produce a highly porous interwoven mat of PLGA fibers ranging from 100 to 5000 nm in diameter interlaced with picoliter domains of active MMP-2. As compared to control polymers, the controlled release of MMP-2 from the polymer scaffold was able to enhance stem cell integration and repopulation of the retina ONL while preserving retinal architecture and stem cell function.[131]

In the body, tissues are formed to maintain order, organization, and optimization of function. This is particularly demonstrated in the retina where the prevalent arrangement of cells into layers and arrays is a key element for efficient visual processing. The collective mechanisms controlling the building process and maintenance of this intricate architecture *in vivo* are still relatively unknown. Yet, recent *in vitro* experiments have demonstrated that numerous biochemical and physical cues can individually direct organization to a degree. To gain an understanding of how these mechanisms collectively confer organization, fundamental studies in which these components are varied systematically must be examined. With the capability of specifically directing stem cell behavior in a predictable manner, engineered tissues may prove a novel approach to retinal repair.

6.632.6.6. The CNS Environment

As noted earlier, it is postulated that the extracellular environment of the CNS is unfavorable for cellular integration and axonal regeneration, making functional recovery after CNS injury limited. The major inhibitory components of the CNS environment are derived from either the myelin sheath or the glial scar. Apart from the retinal GC axons housed within the optic nerve, myelin is absent within the retina proper, and as such the inhibitory molecules nogo, myelin-associated glycoprotein (MAG), and oligodendrocyte myelin glycoprotein (OMgp) that are found within the myelin sheath are also absent. However, atrophy-associated glial scarring, as in the case of retinal degenerative diseases such as RP and AMD, produces both a chemical and physical barrier to cellular migration and neurite extension.

The glial scar is formed in a process known as reactive gliosis, whereby the infiltration of reactive astrocytes and or glial cells into the injury site causes the formation of a physical barrier along with the accumulation of inhibitory molecules such as the chondroitin sulfate proteoglycans and other glycoproteins.[148,149] These molecules, which include neurocan, brevican, phosphocan, NG2, tenascin, chondroitin sulfate, and CD44, are known to inhibit axonal regeneration. For instance, NG2 has been shown to be responsible for inhibiting sensory neuron regeneration into the dorsal root entry zone,[150] neurocan and phosphocan inhibit the regeneration of adult cortical and retinal ganglion neurons,[149,151] and CD44 and neurocan block donor–host cell integration following subretinal transplantation.[131,152,153] Like many other inhibitory ECM molecules, chondroitin sulfates exert their inhibitory effects via activation of RhoA and its downstream effector Rho kinase ROCK.[151] Inhibition of this signaling pathway via the C3 exoenzyme or the use of the chemical inhibitor specific to ROCK,

Y-27632, allows the cell to overcome glial scar-induced inhibitory effects.[151,154] Many other methods to overcome inhibition by chondroitin sulfates have also been explored. For instance, the use of chondroitinase ABC, an enzyme that removes the glycosaminoglycan side chains of chondroitin sulfates rendering them inactive, has seen some success in stimulating cellular integration following transplantation of Müller cell-derived progenitors.[155] Similarly, degradation of both neurocan and CD44 via induction and/or delivery of active MMP-2 has been shown to enhance cellular integration and retinal ONL repopulation following RPC transplantation.[131,152,153] Conversely, chemical and/or genetic inhibition/removal of MMP-2 was shown to completely eliminate cellular migration and axonal extension in this model.[131,152,153] To date, specific receptors for this class of molecules have been elusive, and thus, experimental attempts to stimulate regeneration via receptor inhibition have not been possible.

As a result of this work, there now is a strategy for removing inhibitory barriers in the degenerated CNS, including the retina, and permitting the establishment of new connections following transplantation, be they of stem cell origin, solid tissue, or other yet to be developed techniques.

6.632.7. Conclusions

It should now be apparent that retinal reconstruction is a complicated prospect. Multiple tissue types, from multiple embryological origins, are impacted in retinal injury or degeneration. This makes tissue engineering a requisite approach for repair of the diseased retina. Important concerns relate to the biocompatibility of scaffold material, BrM integrity, CNS connectivity, and the formidable challenge of replicating the blood supply from the CC. Diseases affecting the macula (such as AMD) present further design and biological challenges. The aging of the population will likely lead to an even higher prevalence of AMD and other retinal diseases associated with increased age. Therefore, while many challenges remain and a huge unmet need for retinal repair exists, tissue engineering offers hope for millions afflicted by these diseases.

References

1. Strauss, O. *Physiol. Rev.* **2005**, *85*(3), 845–881.
2. Rizzolo, L. J. *Int. Rev. Cytol.* **2007**, *258*, 195–234.
3. Nguyen-Legros, J.; Hicks, D. *Int. Rev. Cytol.* **2000**, *196*, 245–313.
4. Bok, D. *J. Cell Sci. Suppl.* **1993**, *17*, 189–195.
5. Steinberg, R. H. *Doc. Ophthalmol.* **1985**, *60*(4), 327–346.
6. Wangsa-Wirawan, N. D.; Linsenmeier, R. A. *Arch. Ophthalmol.* **2003**, *121*(4), 547–557.
7. Nickla, D. L.; Wallman, J. *Prog. Retin. Eye Res.* **2010**, *29*(2), 144–168.
8. Jager, R. D.; Mieler, W. F.; Miller, J. W. *N. Engl. J. Med.* **2008**, *358*(24), 2606–2617.
9. Friedman, D. S.; *et al. Arch. Ophthalmol.* **2004**, *122*(4), 564–572.
10. Dunaief, J. L.; Dentchev, T.; Ying, G.-S.; Milam, A. H. *Arch. Ophthalmol.* **2002**, *120*(11), 1435–1442.
11. Sunness, J. S. *Mol. Vis.* **1999**, *5*, 25.
12. Sarks, J. P.; Sarks, S. H.; Killingsworth, M. C. *Eye* **1988**, *2*(Pt 5), 552–577.
13. McLeod, D.; Grebe, R.; Bhutto, I.; Merges, C.; Baba, T.; Lutty, G. *Invest. Ophthalmol. Vis. Sci.* **2009**, *50*, 4982–4991.
14. Lutty, G.; Grunwald, J.; Majji, A. B.; Uyama, M.; Yoneya, S. *Mol. Vis.* **1999**, *5*, 35.
15. Green, W. R. *Mol. Vis.* **1999**, *5*, 27.
16. Ambati, J.; Ambati, B.; Yoo, S.; Ianchulev, S.; Adamis, A. *Surv. Ophthalmol.* **2003**, *48*, 257–293.
17. Lotery, A.; Trump, D. *Hum. Genet.* **2007**, *122*(3–4), 219–236.
18. Gehrs, K.; Jackson, J.; Brown, E.; Allikmets, R.; Hageman, G. *Arch. Ophthalmol.* **2010**, *128*(3), 349.
19. Klassen, H.; Lund, R. D. *Proc. Natl. Acad. Sci. USA* **1987**, *84*(19), 6958–6960.
20. Coffey, P. J.; Whiteley, S. J.; Lund, R. D. *Prog. Brain Res.* **2000**, *127*, 489–499.
21. Kanno, H.; *et al. Am. J. Physiol. Cell Physiol.* **2003**, *284*(4), C988–C998.
22. Shatos, M. A.; *et al. Invest. Ophthalmol. Vis. Sci.* **2003**, *44*(6), 2477–2486.
23. Tropepe, V.; *et al. Science* **2000**, *287*(5460), 2032–2036.
24. Ahmad, I.; Dooley, C. M.; Thoreson, W. B.; Rogers, J. A.; Afiat, S. *Brain Res.* **1999**, *831*(1–2), 1–10.
25. Young, M. J.; Ray, J.; Whiteley, S. J.; Klassen, H.; Gage, F. H. *Mol. Cell. Neurosci.* **2000**, *16*(3), 197–205.
26. Shatos, M. A.; Rios, J. D.; Tepavcevic, V.; Kano, H.; Hodges, R.; Dartt, D. A. *Invest. Ophthalmol. Vis. Sci.* **2001**, *42*(7), 1455–1464.
27. Lund, R. D.; Coffey, P. J.; Sauve, Y.; Lawrence, J. M. *Ophthalmic Res.* **1997**, *29*(5), 305–319.
28. Castillo, B. V., Jr.; Little, C. W.; del Cerro, C.; del Cerro, M. *Curr. Eye Res.* **1995**, *14*(8), 677–683.
29. Castillo, B. V., Jr.; *et al. Exp. Neurol.* **1997**, *146*(1), 1–9.
30. Little, C. W.; Cox, C.; Wyatt, J.; del Cerro, C.; del Cerro, M. *Exp. Neurol.* **1998**, *149*(1), 151–160.
31. Little, C. W.; *et al. Invest. Ophthalmol. Vis. Sci.* **1996**, *37*(1), 204–211.
32. Giordano, G. G.; *et al. J. Biomed. Mater. Res.* **1997**, *34*(1), 87–93.
33. Yaszemski, M. J.; Payne, R. G.; Hayes, W. C.; Langer, R.; Mikos, A. G. *Biomaterials* **1996**, *17*(22), 2127–2130.
34. Mooney, V.; Saal, J. A.; Saal, J. S. *Clin. Symp.* **1996**, *48*(4), 1–32.
35. Hadlock, T.; Elisseeff, J.; Langer, R.; Vacanti, J.; Cheney, M. *Arch. Otolaryngol. Head Neck Surg.* **1998**, *124*(10), 1081–1086.
36. Hadlock, T. A.; Cheney, M. L. *Facial Plast. Surg.* **1998**, *14*(3), 179–184.
37. Carrier, R. L.; *et al. Biotechnol. Bioeng.* **1999**, *64*(5), 580–589.
38. Klassen, H. J.; *et al. Invest. Ophthalmol. Vis. Sci.* **2004**, *45*(11), 4167–4173.
39. Lamba, D. A.; Gust, J.; Reh, T. A. *Cell Stem Cell* **2009**, *4*(1), 73–79.
40. Osakada, F.; *et al. Nat. Biotechnol.* **2008**, *26*(2), 215–224.
41. Nowak, J. Z. *Pharmacol. Rep.* **2006**, *58*(3), 353–363.
42. da Cruz, L.; Chen, F. K.; Ahmado, A.; Greenwood, J.; Coffey, P. *Prog. Retin. Eye Res.* **2007**, *26*(6), 598–635.
43. Binder, S.; *et al. Invest. Ophthalmol. Vis. Sci.* **2004**, *45*(11), 4151.
44. Binder, S.; Stanzel, B. V.; Krebs, I.; Glittenberg, C. *Prog. Retin. Eye Res.* **2007**, *26*(5), 516–554.
45. Sonoda, S.; Spee, C.; Barron, E.; Ryan, S. J.; Kannan, R.; Hinton, D. R. *Nat. Protoc.* **2009**, *4*(5), 662–673.
46. Idelson, M.; *et al. Cell Stem Cell* **2009**, *5*(4), 396–408.
47. Dunn, K. C.; Aotaki-Keen, A. E.; Putkey, F. R.; Hjelmeland, L. M. *Exp. Eye Res.* **1996**, *62*(2), 155–169.
48. Lund, R. D.; *et al. Proc. Natl. Acad. Sci. USA* **2001**, *98*(17), 9942–9947.
49. Streilein, J. W.; Ma, N.; Wenkel, H.; Ng, T. F.; Zamiri, P. *Vis. Res.* **2002**, *42*(4), 487–495.
50. Streilein, J. W.; Ohta, K.; Mo, J. S.; Taylor, A. W. *DNA Cell Biol.* **2002**, *21*(5–6), 453–459.
51. He, S.; Wang, H. M.; Ogden, T. E.; Ryan, S. J. *Graefes Arch. Clin. Exp. Ophthalmol.* **1993**, *231*(12), 737–742.
52. Algvere, P. V. *Acta Ophthalmol. Scand.* **1997**, *75*(1), 1.
53. Algvere, P. V.; Berglin, L.; Gouras, P.; Sheng, Y.; Kopp, E. D. *Graefes Arch. Clin. Exp. Ophthalmol.* **1997**, *235*(3), 149–158.
54. Enzmann, V.; Faude, F.; Wiedemann, P.; Kohen, L. *Acta Anat. (Basel)* **1998**, *162*(2–3), 178–183.
55. Vugler, A.; *et al. Exp. Neurol.* **2008**, *214*(2), 347–361.
56. Takahashi, K.; *et al. Cell* **2007**, *131*(5), 861–872.
57. Buchholz, D. E.; *et al. Stem Cells* **2009**, *27*(10), 2427–2434.
58. Hirami, Y.; *et al. Neurosci. Lett.* **2009**, *458*(3), 126–131.
59. Carr, A. J.; *et al. PLoS ONE* **2009**, *4*(12), e8152.
60. Shiragami, C.; Matsuo, T.; Shiraga, F.; Matsuo, N. *Br. J. Ophthalmol.* **1998**, *82*(9), 1056–1062.
61. Ramrattan, R. S.; van der Schaft, T. L.; Mooy, C. M.; de Bruijn, W. C.; Mulder, P. G.; de Jong, P. T. *Invest. Ophthalmol. Vis. Sci.* **1994**, *35*(6), 2857–2864.
62. Moore, D. J.; Hussain, A. A.; Marshall, J. *Invest. Ophthalmol. Vis. Sci.* **1995**, *36*(7), 1290–1297.
63. Bird, A. C. *Br. J. Ophthalmol.* **1992**, *76*(3), 166–168.
64. Starita, C.; Hussain, A. A.; Pagliarini, S.; Marshall, J. *Exp. Eye Res.* **1996**, *62*(5), 565–572.

65. Pauleikhoff, D.; Harper, C. A.; Marshall, J.; Bird, A. C. *Ophthalmology* **1990**, *97*(2), 171–178.
66. Marshall, G. E.; Konstas, A. G.; Reid, G. G.; Edwards, J. G.; Lee, W. R. *Br. J. Ophthalmol.* **1992**, *76*(10), 607–614.
67. Del Priore, L. V.; Tezel, T. H. *Arch. Ophthalmol.* **1998**, *116*(3), 335–341.
68. Cai, H.; Del Priore, L. V. *Curr. Eye Res.* **2006**, *31*(2), 181–189.
69. Gullapalli, V. K.; Sugino, I. K.; Van Patten, Y.; Shah, S.; Zarbin, M. A. *Exp. Eye Res.* **2005**, *80*(2), 235–248.
70. Sun, K.; Cai, H.; Tezel, T. H.; Paik, D.; Gaillard, E. R.; Del Priore, L. V. *Mol. Vis.* **2007**, *13*, 2310–2319.
71. Olson, M. D. *Invest. Ophthalmol. Vis. Sci.* **1979**, *18*(4), 329–338.
72. Takei, Y.; Ozanics, V. *Invest. Ophthalmol.* **1975**, *14*(12), 903–916.
73. Booij, J.; Baas, D.; Beisekeeva, J.; Gorgels, T.; Bergen, A. *Prog. Retin. Eye Res.* **2010**, *29*(1), 1–18.
74. Tezel, T. H.; Del Priore, L. V.; Kaplan, H. J. *Invest. Ophthalmol. Vis. Sci.* **2004**, *45*(9), 3337–3348.
75. Kutcher, M. E.; Herman, I. M. *Microvasc. Res.* **2009**, *77*(3), 235–246.
76. Saint-Geniez, M.; *et al. PLoS ONE* **2008**, *3*(11), e3554.
77. Zhang, Y.; Porat, R. M.; Alon, T.; Keshet, E.; Stone, J. *Brain Res. Dev. Brain Res.* **1999**, *118*(1–2), 135–145.
78. Kvanta, A. *Acta Ophthalmol. Scand.* **2006**, *84*(3), 282–288.
79. Ferrara, N.; *et al. Nature* **1996**, *380*, 439–442.
80. Das, A.; McGuire, P. G. *Prog. Retin. Eye Res.* **2003**, *22*(6), 721–748.
81. Stoll, G.; Jander, S.; Myers, R. R. *J. Peripher. Nerv. Syst.* **2002**, *7*(1), 13–27.
82. George, R.; Griffin, J. W. *Exp. Neurol.* **1994**, *129*(2), 225–236.
83. Klapka, N.; *et al. Eur. J. Neurosci.* **2005**, *22*(12), 3047–3058.
84. Ribotta, M. G.; Menet, V.; Privat, A. *Acta Neurochir. Suppl.* **2004**, *89*, 87–92.
85. Fu, S. Y.; Gordon, T. *Mol. Neurobiol.* **1997**, *14*(1–2), 67–116.
86. Fenrich, K.; Gordon, T. *Can. J. Neurol. Sci.* **2004**, *31*(2), 142–156.
87. Aguayo, A. J.; David, S.; Bray, G. M. *J. Exp. Biol.* **1981**, *95*, 231–240.
88. David, S.; Aguayo, A. J. *Science* **1981**, *214*(4523), 931–933.
89. Aguayo, A. J.; *et al. Philos. Trans. R. Soc. Lond. B Biol. Sci.* **1991**, *331*(1261), 337–343.
90. Filbin, M. T. *Nat. Rev. Neurosci.* **2003**, *4*(9), 703–713.
91. Azanchi, R.; Bernal, G.; Gupta, R.; Keirstead, H. S. *J. Neurotrauma* **2004**, *21*(6), 775–788.
92. Fairless, R.; Barnett, S. C. *Int. J. Biochem. Cell Biol.* **2005**, *37*(4), 693–699.
93. Kuffler, D. *P. R. Health Sci. J.* **2000**, *19*(3), 241–252.
94. Klapka, N.; Muller, H. W. *J. Neurotrauma* **2006**, *23*(3–4), 422–435.
95. Fouad, K.; Schnell, L.; Bunge, M. B.; Schwab, M. E.; Liebscher, T.; Pearse, D. D. *J. Neurosci.* **2005**, *25*(5), 1169–1178.
96. Hollyfield, J. G. *Invest. Ophthalmol. Vis. Sci.* **1999**, *40*(12), 2767–2769.
97. Kiilgaard, J. F.; Wiencke, A. K.; Scherfig, E.; Prause, J. U.; la Cour, M. *Acta Ophthalmol. Scand.* **2002**, *80*(1), 76–81.
98. Lee, C. J.; *et al. Arch. Ophthalmol.* **2002**, *120*(12), 1714–1718.
99. Tezel, T. H.; Kaplan, H. J.; Del Priore, L. V. *Invest. Ophthalmol. Vis. Sci.* **1999**, *40*(2), 467–476.
100. Thumann, G.; Schraermeyer, U.; Bartz-Schmidt, K. U.; Heimann, K. *Curr. Eye Res.* **1997**, *16*(12), 1236–1238.
101. Gabrielian, K.; *et al. Graefes Arch. Clin. Exp. Ophthalmol.* **1999**, *237*(3), 241–248.
102. Bhatt, N. S.; *et al. Am. J. Ophthalmol.* **1994**, *117*(2), 214–221.
103. Tao, S.; *et al. Lab Chip* **2007**, *7*(6), 695–701.
104. Montezuma, S. R.; Loewenstein, J.; Scholz, C.; Rizzo, J. F., 3rd. *Invest. Ophthalmol. Vis. Sci.* **2006**, *47*(8), 3514–3522.
105. Beeley, N. R.; *et al. J. Biomed. Mater. Res. A* **2006**, *76*(4), 690–698.
106. Alfaro, D. V.; Liggett, P. E.; Mieler, W. F.; Quiroz-Mercado, H.; Jager, R. D.; Tano, Y. *Age-Related Macular Degeneration: A Comprehensive Textbook*; Lippincott Williams: Philadelphia, PA, 2006.
107. Lavik, E. B.; Klassen, H.; Warfvinge, K.; Langer, R.; Young, M. J. *Biomaterials* **2005**, *26*(16), 3187–3196.
108. Redenti, S.; *et al. J. Ocul. Biol. Dis. Infor.* **2008**, *1*(1), 19–29.
109. Neeley, W. L.; *et al. Biomaterials* **2008**, *29*(4), 418–426.
110. Redenti, S.; *et al. Biomaterials* **2009**, *30*(20), 3405–3414.
111. Singh, S.; Woerly, S.; McLaughlin, B. J. *Biomaterials* **2001**, *22*(24), 3337–3343.
112. Wollensak, G.; Spoerl, E. *Retina* **2004**, *24*(6), 967–970.
113. Ingber, D. *Curr. Opin. Cell Biol.* **1991**, *3*(5), 841–848.
114. Geiger, B.; Bershadsky, A. *Cell* **2002**, *110*(2), 139–142.
115. Pelham, R. J., Jr.; Wang, Y. *Proc. Natl. Acad. Sci. USA* **1997**, *94*(25), 13661–13665.
116. Discher, D. E.; Janmey, P.; Wang, Y. L. *Science* **2005**, *310*(5751), 1139–1143.
117. Engler, A. J.; Sen, S.; Sweeney, H. L.; Discher, D. E. *Cell* **2006**, *126*(4), 677–689.
118. Saha, K.; *et al. Biophys. J.* **2008**, *95*(9), 4426–4438.
119. Leipzig, N. D.; Shoichet, M. S. *Biomaterials* **2009**, *30*(36), 6867–6878.
120. Tang, Z. G.; Black, R. A.; Curran, J. M.; Hunt, J. A.; Rhodes, N. P.; Williams, D. F. *Biomaterials* **2004**, *25*(19), 4741–4748.
121. Lu, C. H.; Lin, W. J. *J. Biomed. Mater. Res.* **2002**, *63*(2), 220–225.
122. Ng, K. W.; *et al. Tissue Eng.* **2001**, *7*(4), 441–455.
123. Tiaw, K. S.; Teoh, S. H.; Chen, R.; Hong, M. H. *Biomacromolecules* **2007**, *8*(3), 807–816.
124. Steedman, M. R.; Tao, S. L.; Klassen, H.; Desai, T. A. *Biomed. Microdevices* **2010**, *12*(3), 363–369.
125. Sodha, S.; Wall, K.; Redenti, S.; Klassen, H.; Young, M. J.; Tao, S. L. *J. Biomater. Sci. Polym. Ed.* **2011**, *22*, 443–456.
126. Yim, E. K.; Leong, K. W. *Nanomedicine* **2005**, *1*(1), 10–21.
127. Martinez, E.; Engel, E.; Planell, J. A.; Samitier, J. *Ann. Anat.* **2009**, *191*(1), 126–135.
128. Kriparamanan, R.; Aswath, P.; Zhou, A.; Tang, L.; Nguyen, K. T. *J. Nanosci. Nanotechnol.* **2006**, *6*(7), 1905–1919.
129. Bettinger, C. J.; Langer, R.; Borenstein, J. T. *Angew. Chem. Int. Ed. Engl.* **2009**, *48*(30), 5406–5415.
130. Tomita, M.; Lavik, E.; Klassen, H.; Zahir, T.; Langer, R.; Young, M. J. *Stem Cells* **2005**, *23*(10), 1579–1588.
131. Tucker, B. A.; *et al. Biomaterials* **2010**, *31*(1), 9–19.
132. Pritchard, C. D.; *et al. Biomaterials* **2010**, *31*(8), 2153–2162.
133. Tao, S. L.; Desai, T. A. *Nano Lett.* **2007**, *7*(6), 1463–1468.
134. Martin, C. R. *Science* **1994**, *266*(5193), 1961–1966.
135. Tezcaner, A.; Hicks, D. *J. Biomed. Mater. Res. A* **2008**, *86*(1), 170–181.
136. Blong, C. C.; *et al. J. Neurosci. Res.* **2010**, *88*(7), 1445–1456.
137. Galli-Resta, L. *Trends Neurosci* **2002**, *25*(12), 638–643.
138. Galli-Resta, L.; Leone, P.; Bottari, D.; Ensini, M.; Rigosi, E.; Novelli, E. *Prog Retin Eye Res* **2008**, *27*(3), 260–283.
139. Galli-Resta, L.; Novelli, E.; Kryger, Z.; Jacobs, G. H.; Reese, B. E. *Eur. J. Neurosci.* **1999**, *11*(4), 1461–1469.
140. Curcio, C. A.; Sloan, K. R.; Kalina, R. E.; Hendrickson, A. E. *J. Comp. Neurol.* **1990**, *292*(4), 497–523.
141. Sisak, S.; Banin, E.; Blumenthal, E. Z. *Med. Hypotheses* **2004**, *62*(5), 808–816.
142. Tezcaner, A.; Bugra, K.; Hasirci, V. *Biomaterials* **2003**, *24*(25), 4573–4583.
143. Thomson, H. A.; Treharne, A. J.; Walker, P.; Grossel, M. C.; Lotery, A. J. *Br. J. Ophthalmol.* **2011**, *95*(4), 563–568.
144. Lu, L.; Garcia, C. A.; Mikos, A. G. *J. Biomater. Sci. Polym. Ed.* **1998**, *9*(11), 1187–1205.
145. Lu, L.; Yaszemski, M. J.; Mikos, A. G. *Biomaterials* **2001**, *22*(24), 3345–3355.
146. Lu, L.; *et al. Biomaterials* **1999**, *20*(23–24), 2351–2361.
147. Lee, C. J.; Blumenkranz, M. S.; Fishman, H. A.; Bent, S. F. *Langmuir* **2004**, *20*(10), 4155–4161.
148. McKeon, R. J.; Schreiber, R. C.; Rudge, J. S.; Silver, J. *J. Neurosci.* **1991**, *11*(11), 3398–3411.
149. McKeon, R. J.; Jurynec, M. J.; Buck, C. R. *J. Neurosci.* **1999**, *19*(24), 10778–10788.
150. Zhang, J. C.; *et al. Mol. Cell. Neurosci.* **2001**, *17*(3), 444–459.
151. Monnier, P. P.; Sierra, A.; Schwab, J. M.; Henke-Fahle, S.; Mueller, B. K. *Mol. Cell. Neurosci.* **2003**, *22*(3), 319–330.
152. Tucker, B.; Klassen, H.; Yang, L.; Chen, D. F.; Young, M. J. *Invest. Ophthalmol. Vis. Sci.* **2008**, *49*(4), 1686–1695.
153. Zhang, Y.; Klassen, H. J.; Tucker, B. A.; Perez, M. T.; Young, M. J. *J. Neurosci.* **2007**, *27*(17), 4499–4506.
154. Dergham, P.; Ellezam, B.; Essagian, C.; Avedissian, H.; Lubell, W. D.; McKerracher, L. *J. Neurosci.* **2002**, *22*(15), 6570–6577.
155. Singhal, S.; *et al. Stem Cells* **2008**, *26*(4), 1074–1082.

6.633. Development of Contact Lenses from a Biomaterial Point of View – Materials, Manufacture, and Clinical Application

N Efron, Queensland University of Technology, Kelvin Grove, QLD, Australia
C Maldonado-Codina, The University of Manchester, Manchester, UK

© 2011 Elsevier Ltd. All rights reserved.

6.633.1.	**Introduction**	519
6.633.2.	**General Properties of Hydrogel Materials of Relevance to Contact Lenses**	520
6.633.2.1.	Optical Transparency	520
6.633.2.2.	Mechanical Properties	520
6.633.2.3.	Surface Properties	521
6.633.2.4.	Water Content	522
6.633.2.5.	Oxygen Permeability	522
6.633.2.6.	Fluid and Ion Permeability	522
6.633.2.7.	Refractive Index	523
6.633.2.8.	Swell Factor and Dimensional Stability	523
6.633.3.	**Conventional Hydrogel Contact Lens Materials**	523
6.633.3.1.	Historical Development	523
6.633.3.2.	Polymeric Formulations	523
6.633.3.3.	High Water Content Hydrogel Lenses	525
6.633.3.4.	Strategies for Enhancing Lens Comfort	525
6.633.4.	**Silicone Hydrogel Contact Lens Materials**	527
6.633.4.1.	The Drive for Increased Corneal Oxygenation	527
6.633.4.2.	The Challenge of Incorporating Silicone into Hydrogel Materials	527
6.633.4.3.	The Launch of Silicone Hydrogel Lenses	528
6.633.4.4.	Surface Treatments	528
6.633.4.5.	Material Modulus of Elasticity	528
6.633.4.6.	Lens Edge Design	528
6.633.4.7.	'Second Generation' Silicone Hydrogel Lenses	528
6.633.4.8.	Optimizing Surface Characteristics	528
6.633.5.	**Classification of Soft Contact Lens Materials**	530
6.633.6.	**Soft Contact Lens Manufacture**	530
6.633.6.1.	Lathe Cutting	530
6.633.6.2.	Spin Casting	531
6.633.6.3.	Cast Molding	532
6.633.6.4.	Reproducibility and Quality of Mass-Produced Lenses	532
6.633.7.	**Clinical Ramifications of Polymer and Manufacturing Developments**	534
6.633.7.1.	Polymer Developments: Enhanced Corneal Oxygenation	536
6.633.7.2.	Manufacturing Developments: Planned Lens Replacement	538
6.633.8.	**Conclusions**	539
Appendix A.	**Classification of Soft Lens Materials**	539
A.1.	FDA Classification System	539
A.2.	ACLM Classification System	539
A.3.	BS EN ISO 18369-1: 2006	540
A.3.1.	Example	540
References		540

Glossary

Conjunctiva Clear transparent vascularized protective tissue layer that covers the white sclera of the eye. The conjunctiva also lines the inside of the eyelids.

Conjunctival flap formation Deep folds in the conjunctiva caused by pressure from the edge of a soft contact lens, resulting in a flap of tissue.

Conjunctival staining Disruption of the superficial epithelial layer of the conjunctiva, as revealed by an orange dye (fluorescein) that is inserted into the eye. Fluorescein fills spaces created by tissue damage, and the pooled dye displays a bright green fluorescence when illuminated with blue light, revealing the location of tissue damage.

Contact lens A clear, transparent shell-like optical appliance that is placed on the front of the eye to correct errors of refraction of the eye.
Cornea The clear transparent tissue at the front of the eye through which light passes to form an image at the back of the eye.
Corneal staining Disruption of the superficial epithelial layer of the cornea, as revealed by an orange dye (fluorescein) that is inserted into the eye. Fluorescein fills spaces created by tissue damage, and the pooled dye displays a bright green fluorescence when illuminated with blue light, revealing the location of tissue damage.
Endothelial cell density The number of endothelial cells per unit area of the endothelial surface.
Endothelial polymegethism Change in appearance of the endothelium, whereby the cells in this layer display a large variation in cell size.
Endothelium Single layer of highly metabolically active cells at the back of the cornea. The cells all appear to be of uniform size and display, and characteristic hexagonal shape.
Epithelium Superficial layer of cellular tissue of an organ, such as the cornea.
Epithelial microcysts Small cystic spheres that form within the corneal epithelium, when subjected to hypoxic stress.
Epithelial oxygen uptake The movement of oxygen into the cornea, from either the atmosphere in front of the eye, or the aqueous humor (the fluid inside the eye).
Fluorescein staining A term describing the use of fluorescein to reveal the presence of tissue damage in the cornea or conjunctiva (see 'corneal staining' and 'conjunctival staining').
Microbial keratitis Inflammation of the cornea caused by infection with microorganisms. This inflammatory process can result in opaque scar formation on the cornea, thus impeding the passage of light into the eye, resulting in partial or complete vision loss.
Mucin balls Small spherical balls of mucin, derived from mucin in the tear layer, that form between the back of the lens and front of the cornea, during lens wear.
Myopia Nearsightedness, whereby the image of a distant object in space is focused in front of the light-sensing retina at the back of the eye. This is corrected using minus powered ophthalmic lenses.
Papillary conjunctivitis An inflammation of the vascular mucous tissue on the inside of the eyelid, caused by irritation of the front surface of the contact lens, especially of the lens surface if contaminated with deposits.
Prelens tear film The thin layer of tears that covers the cornea and conjunctiva of the eye.
Presbyopia The reducing ability of the eye to focus on close objects, caused by a thickening and loss of flexibility of the lens inside the eye.
Stroma Forms the bulk of the middle of the cornea, consisting of collagen fibrils and mucopolysaccharide ground substance.
Superficial epithelial arcuate lesions (SEALs) Arc-shaped lesion of the superficial tissue of the cornea, occurring at the surface of the cornea. This is a transient form of tissue damage that is self-limiting; that is, it heals by itself within 24 h if the lenses are removed.
Trial fitting The process of sequentially applying contact lenses with different characteristics (curvature, diameter, thickness, material, etc.) to the eye and assessing lens behavior on the eye (stabilized position, movement with blink, etc.) until a lens fitting of satisfactory performance is achieved.
Xerogel The anhydrous polymer from which soft lenses may be made; water needs to be added to turn the xerogel into a functional hydrogel.

Abbreviations

ACLM	Association of Contact Lens Manufacturers (United Kingdom)
AFM	Atomic force microscopy
AMA	Alkyl methacrylate
BMA	Butyl (probably isobutyl) methacrylate
BS	British Standards
CMA	Cyclohexyl methacrylate
Dk	Oxygen permeability (diffusivity [D] × solubility [k])
Dk/t	Oxygen transmissibility (Dk divided by thickness [t])
DAA	Diacetone acrylamide
DMA	*N*,*N*-dimethyl acrylamide
EEMA	Ethoxyethyl methacrylate
EGDMA	Ethylene glycol dimethacrylate
EN	European Norm
EWC	Equilibrium water content
FDA	Food and Drug Administration
FM0411M	Methacryloyloxyethyl iminocarboxyethyloxypropyl poly (dimethylsiloxy)-butyldimethylsilane
GlyMA	Glyceryl methacrylate
GMA	Glyceryl methacrylate
HEMA	Hydroxyethyl methacrylate
HOB	2-hydroxybutyl methacrylate
IBM	Isobornylmethacrylate
ISO	International Standardization Organization
M3U	Bis(methacryloyloxyethyl iminocarboxy ethyloxypropyl) poly(dimethylsiloxane)-poly (trifluoropropylmethylsiloxane) poly (methoxy-poly[ethyleneglycol] propylmethylsiloxane)
MAA	Methacrylic acid
MMA	Methyl methacrylate
MPDMS	Monofunctional polydimethylsiloxane
NCVE	*N*-carboxyvinyl ester
NPDC	National Patent Development Corporation

NVP	*N*-vinyl pyrrolidone	**SF_{rad}**	Radial swell factor
PBVC	Poly(dimethysiloxy) di (silylbutanol) bis (vinyl carbamate)	**SIA**	Siloxanyl acrylate
		SIMA	Siloxanyl methacrylate
PC	Phosphoryl choline	**TAIC**	1,3,5-triallyl-1,3,5-triazine-2,4,6(1H,3H,5H)-trione
PDMS	Polydimethyl siloxane		
pHEMA	Poly(hydroxyethyl methacrylate)	**TEGDMA**	Tetraetheleneglycol dimethacrylate
PLTF	Prelens tear film	**TPVC**	Tris-(trimethyl siloxysilyl) propylvinyl carbamate
PMMA	Polymethyl methacrylate		
PVP	Polyvinyl pyrrolidone	**TRIS**	Tris(trimethylsiloxy)-methacryloxy-propylsilane
SEALs	Superior epithelial arcuate lesions		
SEM	Scanning electron microscopy	**USAN**	United States assigned name
SF	Swell factor	**VA**	Vinyl acetate
SF_{ax}	Axial swell factor	**VMA**	*N*-vinyl-*N*-methylacetamide

6.633.1. Introduction

Soft contact lenses have had a massive impact on the global contact lens market since their introduction into the market in the early 1970s. Over the past 50 years, the number of soft contact lenses being prescribed around the world has steadily increased, and it is mainly the sale of soft contact lenses which is responsible for an industry which is estimated to be worth around US$8 billion annually (this figure does not include the sale of contact lens solutions). A recent survey has indicated that soft lenses currently make up over 92% of all new contact lens fittings worldwide.[1]

The saturation of the contact lens market with soft lenses has occurred primarily for two reasons. First, soft lenses provide wearers with what they see as the two most important requirements for successful contact lens wear – good vision and good comfort. Rigid lenses, which were originally made from glass (between 1888 and 1940) and later from polymethyl methacrylate (PMMA) or silicone acrylate materials, are uncomfortable to wear. They are now seldom fitted to new patients and are rapidly becoming obsolete.[2] The major obstacle as far as rigid lenses are concerned is generally accepted as being their lack of comfort and, in particular, their initial discomfort.[3] Figure 1 illustrates the demise in rigid lens fitting over the past 40 years in Australia – a country in which fitting trends have been well documented over this period.

Second, advances in manufacturing technology have directed the industry toward soft lenses and, still further, toward the concept of disposability. In view of the above, rigid contact lenses will not be discussed in this chapter.

Contact lens materials are good examples of biomaterials; indeed, they are classed as a medical device in most countries. Biomaterials manufactured for use as contact lenses must not only satisfy the requirements of not having toxic or injurious effects for safe use within the eye, but additionally they must also have very specific characteristics, such as being transparent (and remain so on-eye), comfortable, and relatively cheap to manufacture.

This chapter will review the properties and characteristics of the materials which are used to manufacture soft contact lenses, provide some of the history of development of these materials, introduce the nomenclature used to categorize contact lens materials, describe current approaches to contact lens

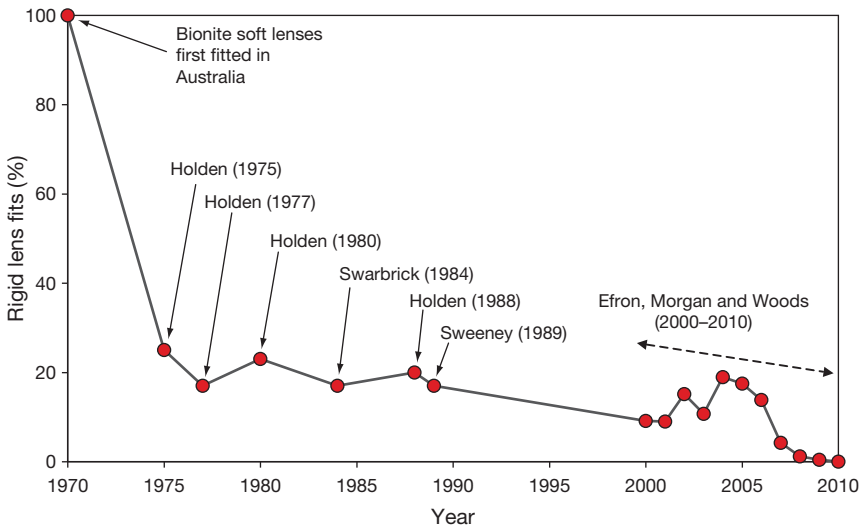

Figure 1 Decline in rigid contact lens new fits, as a proportion of all contact lenses fitted, between 1970 and 2010.

manufacture, and highlight the clinical implications of these developments.

6.633.2. General Properties of Hydrogel Materials of Relevance to Contact Lenses

The ocular environment places significant demands on the performance of hydrogels as biomaterials. These materials must have the following properties:

- maintain a stable, continuous tear film;
- be permeable to oxygen in order to maintain normal corneal metabolism;
- be permeable to ions in order to maintain on-eye movement;
- be comfortable;
- provide clear, stable vision.

These essential properties are expanded upon below.

6.633.2.1. Optical Transparency

A hydrogel to be used as a contact lens material needs to be transparent in order to achieve maximal visual performance. The light transmittance properties of polymers can be categorized as being transparent, translucent, or opaque. Transparent polymers are those that you can see through, translucent polymers are those that you cannot see through but allow light to pass through, and opaque polymers are those that neither permit you to see through nor allow light to pass through. Usually, the optical clarity of contact lens materials is expressed as the percentage of transmission of the visible electromagnetic spectrum. Hydrogels which are useful as contact lens materials transmit over 90% of light in the visible part of the spectrum.

When a hydrogel loses its transparency, it is likely to be due to microphase separation of water. This is due to regions of differing refractive index being formed within the gel. Hydrogels that show this type of behavior – typically synthesized by making copolymers with large blocks or segments of hydrophobic and hydrophilic monomers rather than randomly dispersing them – do have advantages in terms of enhanced strength and permeability performance.

If the phase separation is limited (e.g., the phase size is shorter than the wavelength of light), transparent materials can still be obtained. Some hydrogels are known to lose their transparency when heated, and this is an important consideration as there is an increase in temperature from lens packaging to eye. Additionally, some lens wearers still thermally disinfect their lenses although this approach is seldom used at the present time.

6.633.2.2. Mechanical Properties

The mechanical properties of hydrogel contact lenses are fundamentally important because they are directly related to factors such as comfort, visual performance, fitting characteristics, physiologic impact, durability, and handleability of the lenses.

In the hydrated state, most hydrogels are soft and flexible. When they are allowed to dehydrate, they become hard and brittle. Lower water content polymers tend to become more hard and brittle than higher water content materials. Because they are hydrophilic, hydrogels take up water, which causes them to become soft with elastic properties (the water acts as a plasticizer).

Unlike perfectly elastic materials which deform under stress but return to their original size and shape when the stress is released, hydrogels are viscoelastic. This means that they deform time dependently when a stress is applied to them and recover time dependently when the stress is removed. Theoretically, this can result in permanent deformation of the material.

One of the main difficulties in characterizing the mechanical properties of a contact lens is that there is no single property measurement which will accurately reflect its 'in use' situation. Contact lens hydrogels typically do not demonstrate a yield point. The strength of a hydrogel gives some indication of the behavior of the material during handling, while the modulus indicates the extent to which the eyelid will deform it and has an impact on the fitting characteristics of the lens. Rigid lens materials have a relatively high modulus (in the region of 10^3 MPa) whereas soft lens materials have a much lower value when in the hydrated state. The advantage of a lower value associated with greater comfort can be offset by poor visual performance.

New generation silicone hydrogel lenses have a higher tensile modulus (1.1–1.4 MPa) compared with conventional hydrogels (0.2–0.6 MPa). The higher moduli of silicone hydrogel materials have certain clinical implications which are discussed in more detail in Section 6.633.4.

The generally poor mechanical strength (including tear strength) of soft lenses is arguably the main reason why they have relatively short lifetimes. This problem has been somewhat overcome by the introduction of disposable lenses, which essentially means that the majority of soft lenses no longer need to last more than a day, 2 weeks, or a month depending on their intended replacement schedule.

Several factors can affect the mechanical properties of a hydrogel material and these can be broadly divided into (a) material composition factors and (b) polymer processing factors. Examples of material composition factors include changing the comonomers used in the hydrogel preparation. If the hydrogel is not a homopolymer, then increasing the relative amount(s) of physically stronger component(s) will lead to an increase in the final mechanical strength of the material. This may have the effect of altering the mechanical strength by increasing the stiffness of the backbone polymer by, for example, replacing acrylates with methacrylates, or it may alter the hydrophilicity of the polymer by, for example, replacing hydroxyethyl methacrylate (HEMA) with methacrylic acid (MAA). In general, as the equilibrium water content (EWC) of a hydrogel increases, its modulus decreases.

The mechanical properties of a hydrogel are dependent on the cross-link density in the system. In general, the strength of a hydrogel increases with increasing cross-link density, particularly when in the swollen state where physical entanglements are low. Cross-link density can be increased by the addition of larger amounts of cross-linking agent. Although increasing the cross-link density within a hydrogel network is beneficial in relation to its mechanical properties, it must also be considered that changes to other properties of the polymer will occur. The swelling capacity of the hydrogel is likely to be reduced with increasing cross-link density, and hence, its oxygen

permeability will also be reduced which is undesirable in a contact lens material. A balance of all the properties of a polymer is critical to its end application.

Polymer processing factors which can affect the mechanical properties of a hydrogel essentially refer to the fact that hydrogel materials are highly sensitive to the processing and fabrication conditions to which they are subjected. Lenses made by different methods of manufacture will undergo very different material processing – particularly polymerization. These different material processing steps may have an effect on the mechanical properties of the resultant lens. For example, lathed lenses are formed from solid buttons of dehydrated material. The buttons are usually bulk polymerized over relatively long periods.

Thermal initiators that have low activation energies are often used, thereby allowing water baths or ovens to be set to relatively low temperatures. This type of polymerization is likely to lead to a polymer structure consisting of longer chains (higher molecular weights) and, therefore, more chain entanglements.

In the cast-molding process, a small amount of monomer is placed between two casts to directly form the lens. The polymerization process is typically very fast which is one of the reasons why this is the method of choice for bulk (disposable) lens manufacture (see Section 6.633.6.3). Rapid polymerization times are likely to produce shorter chains, more chain ends, and less efficient cross-links.

6.633.2.3. Surface Properties

The surface characteristics of a hydrogel lens will directly affect its interactions with the tear film and consequently its biocompatibility in the ocular environment. 'Wettability' is used to describe the tendency for a liquid to spread on to a solid surface, and *in vivo* wettability in a contact lens context implies the ability of the tear film to spread and maintain itself over a contact lens surface. *In vivo* wettability is a key measure of clinical performance because the success of any contact lens is considered to be related to its ability to support a stable tear layer in the eye. General clinical consensus is that failure to meet this requirement is likely to result in a lens which is uncomfortable, has reduced visual performance, and deposits rapidly. The quality of the prelens tear film (PLTF) will also have an effect on the friction between the eyelid and the lens surface. This in turn is thought to be important in the etiology of physiologic responses such as contact lens-related papillary conjunctivitis. The issue of wettability has received considerable attention since the introduction of silicone hydrogel materials at the turn of the century, in view of the potentially poor wettability of untreated lenses manufactured from this material.

In vivo wettability is generally assessed using a range of relatively crude clinical tests which have been used for several decades. These include tear film break-up time (with or without the presence of fluorescein stain), interferometric techniques, and various techniques based around specular reflection. Unfortunately, these methods frequently fail to adequately differentiate between lens surface types, even when relatively different lens surfaces are evaluated.

On the other hand, laboratory measures of wettability are well established and are better at differentiating lens surfaces. Wettability in relation to contact lenses has traditionally been assessed *in vitro* using the sessile drop technique and measuring the contact angle of the drop with the surface to which it is applied (Figure 2). Figure 3 shows the contact angles of a conventional hydrogel and a silicone hydrogel. Note that the contact angle of the silicone hydrogel is considerably larger than that of the conventional contact lens. However, it is important to bear in mind that the wettability of a given surface depends on a number of factors including the surface tension of the test liquid and as such, it is a property of a liquid–solid combination rather than of the solid surface alone.

The contact angles obtained for a lens–liquid combination are highly methodologically dependent[4,5] and any reporting of contact angles should include experimental details such as the method itself, the probe liquid, and prior treatment of the material under test.

The sessile drop and the captive bubble techniques give discrepant results for a single sample because a different type of contact angle is measured in each technique: an advancing-type contact angle is measured in the sessile drop technique and a receding-type contact angle is measured in the captive bubble technique.

The receding contact angle obtained *in vitro* is especially relevant when considering the performance of a contact lens *in vivo*. The advancing angle corresponds more to the establishment of the tear film which is assisted mechanically by the eyelid. Conversely, the receding angle is thought to be important in the stability of the tear film between blinks.

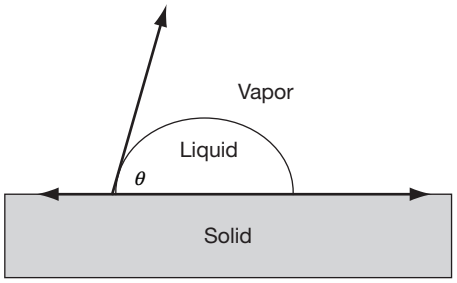

Figure 2 Schematic representation of the sessile drop technique showing the contact angle (θ) measured when a drop is placed on a solid surface. Adapted from Maldonado-Codina, M.; Efron, N. In *Contact Lens Practice*, 2nd ed.; Efron, N., Ed.; Butterworth-Heinemann/Elsevier: Maryland Heights, MO, 2010; p 72.



Figure 3 Sessile drop contact angle images of a conventional hydrogel lens (left) and a silicone hydrogel lens (right). Note the larger contact angle for the silicone hydrogel material. Reprinted with permission from Maldonado-Codina, M.; Efron, N. In *Contact Lens Practice*, 2nd ed.; Efron, N., Ed.; Butterworth-Heinemann/Elsevier: Maryland Heights, MO, 2010; p 73.

6.633.2.4. Water Content

The EWC of a hydrogel lens is defined as follows:

$$\text{EWC} = \frac{\text{Weight of water in polymer}}{\text{Total weight of hydrated polymer}} \times 100$$

The EWC of a hydrogel may vary depending on the environmental conditions. For example, pH, tonicity, and temperature may alter the EWC of a hydrogel. Increased temperature is an important consideration because there is a significant increase in temperature when a contact lens is taken from its packaging solution (normally at room temperature) and placed on the eye. Most contact lens hydrogels will undergo a small change in EWC when placed in solutions of different pH and osmolality, but these changes will be most pronounced in ionic lens materials.

The surface EWC of a contact lens can be measured using a soft contact lens refractometer.[6] This is a simple hand-held optical instrument which can be readily used in the clinical setting. More sophisticated electronic versions of this instrument are also available.[7] The principle underlying the capacity of a refractometer to determine contact lens water content is the inverse relationship between refractive index and EWC of hydrogel materials. The measured refractive index of a contact lens is converted to percent water which is read directly from the internal scale. This approach does assume that dehydrated hydrogels have the same refractive index, which is not strictly true. However, errors due to small differences between hydrogel polymers in respect of refractive indices are clinically inconsequential.

Difficulties are also encountered with this instrument when attempting to measure the EWC of silicone hydrogel lenses. These lenses have a lower refractive index compared to conventional hydrogels and their EWC is overestimated with the soft contact lens refractometer. Additionally, as it is *surface* EWC which is being measured with this instrument, it is unknown what effect the surface coatings on some of these lenses have on the final result.

British and ISO (the International Organization for Standardization) Standards specify both thermogravimetric and refractive index methods as valid techniques for measuring the EWC of a hydrogel lens.[8,9] The thermogravimetric method involves measuring the weight of a lens in the hydrated state and then remeasuring the lens in the completely dehydrated state. The disadvantages of this method are that it is time consuming and essentially destroys the lens.

6.633.2.5. Oxygen Permeability

As the cornea receives most of its oxygen from the atmosphere, the oxygen transmissibility profile of a contact lens is one of its most important properties. Oxygen permeability is a property of the material itself and is described as the *Dk*, where *D* is the diffusivity of the material and *k* is the solubility of the material. Oxygen permeability of a hydrogel will vary with temperature.

Oxygen permeability is essentially governed by EWC in conventional hydrogels. This relationship is on the basis of the ability of oxygen to pass through the water rather than through the material itself. The relationship between EWC and oxygen permeability has been found to be[10]:

$$Dk = 1.67e^{0.0397\text{EWC}}$$

where e is the natural logarithm (**Figure 4**).

In order to calculate the amount of oxygen which will move from the anterior to the posterior surface of a lens, the oxygen permeability (*Dk*) is divided by the thickness of the lens (*t*). The units of *Dk* and *Dk/t* are as follows[8,9]:

$$(Dk) \text{ in } Dk \text{ units} = 10^{-11}(\text{cm}^2 \times \text{ml O}_2)/(\text{s} \times \text{ml} \times \text{hPa})$$

$$(Dk/t) \text{ in } Dk/t \text{ units} = 10^{-9}(\text{cm} \times \text{ml O}_2)/(\text{s} \times \text{ml} \times \text{hPa})$$

6.633.2.6. Fluid and Ion Permeability

The development of silicone hydrogel materials has highlighted the importance of the so-called 'hydraulic permeability' or water transport of a contact lens material. Essentially, a

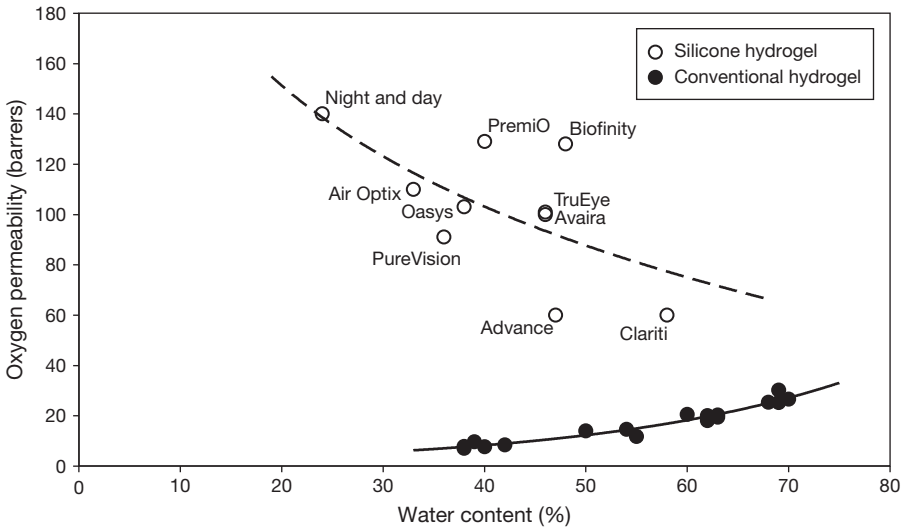

Figure 4 Relationship between oxygen permeability and equilibrium water content for conventional hydrogel lenses (solid curve) and silicone hydrogels (dashed curve).

minimum level of hydraulic (as well as ionic) permeability is necessary to maintain adequate lens movement. This is important in allowing the postlens tear film to reform between blinks, thus reducing the likelihood of these quite elastic lenses from binding to the cornea. Water is able to move through a hydrogel in a way quite different from the movement of sodium ions, that is, it is more difficult for sodium ions to travel through the gel, as in order to do so they must be accompanied by a shell of water.[11] In the eye, the sodium ion permeability of contact lens materials is particularly important as it is a major constituent of the tear film. Sodium ion transport is impeded in gels with a water content below 20%.

6.633.2.7. Refractive Index

Ideally, a hydrogel fabricated for contact lens materials should have a refractive index similar to that of the cornea, that is, near to 1.37. The variation of refractive index with EWC in conventional hydrogels is almost linear, with most hydrogel refractive indices falling within 1.46–1.48 at 20% water content and 1.37–1.38 at 75% water content, that is, the refractive index decreases with increasing water content. Because of this relationship, it is possible to calculate the refractive index of a hydrogel if its EWC is known (and vice versa), which is the basis for the use of the soft contact lens refractometer, as discussed in Section 6.633.2.4.

It is unlikely that a relationship between refractive index and water content will hold for all silicone hydrogel lenses on the market as many are fabricated on the basis of completely different material chemistries. British and ISO Standards recommend the use of an Abbe refractometer to measure the refractive index of a hydrogel contact lens.[8,9] However, other more automated instruments have been used for the assessment of hydrogel lens refractive index.[7,12,13]

6.633.2.8. Swell Factor and Dimensional Stability

The dimensional stability of a hydrogel lens refers to its ability to maintain its original dimensions under various conditions. It is dependent on any factor that will change the water content of the hydrogel or the *swelling* behavior of the hydrogel. Factors that influence the swell factor of a hydrogel include temperature, pH, and tonicity. The swelling behavior of a hydrogel is particularly important during the manufacture of contact lenses in the dry state, for example, when a soft contact lens is lathed. During the lathing process, a smaller, steeper lens of greater power is made so that when it is hydrated, it swells to the required dimensions and power required. It is vital, therefore, that the swell factors of the material are accurately known. The swell factor is described by the following relationship:

$$\text{Swell factor (SF)} = \text{Wet dimension/dry dimension}$$

Initially, it was thought that a hydrogel material swelled isotropically. Over time, it was found that the consistently anomalous swelling behavior of hydrogels could only be explained by specifying two swell factors. These swell factors are those in the diameter and axial (thickness) directions. From these, the value of the radial swell factor of a contact lens can be calculated using the following equation:

$$SF_{rad} = (SF_{dia})^2/SF_{ax}$$

where SF_{rad} is the radial swell factor, SF_{dia} is the diametral swell factor, and SF_{ax} is the axial swell factor.

6.633.3. Conventional Hydrogel Contact Lens Materials

Hydrogel materials can be conveniently divided into two groups: (1) conventional hydrogel materials (now sometimes referred to as low *Dk* materials) and (2) silicone hydrogels (high *Dk* materials). This section will discuss conventional hydrogel materials.

6.633.3.1. Historical Development

Hydrogel lenses were developed as a result of the extraordinary pioneering efforts of Professor Otto Wichterle (Figure 5) and colleagues in the Institute of Macromolecular Chemistry of the Czechoslovak Academy of Sciences in Prague in the mid-1950s. Essentially, Wichterle was working on the synthesis of a new material that he hoped could be used for implantation into the human body. That material was poly(hydroxyethyl methacrylate) or pHEMA.[14] Wichterle soon realized that the material had potential applications in the manufacture of contact lenses, but he was prevented from researching such a project by the directors of the Institute, who perceived this work as being a petty distraction from fundamental studies in chemistry. He was forced to carry out his experiments at home. Despite such difficult circumstances, he successfully managed to produce the first spun-cast lens (made from his son's toy construction set) in 1961.[15] The enormity of his breakthrough for the contact lens industry cannot be overstated.

6.633.3.2. Polymeric Formulations

HEMA (Figure 6) is made by polymerizing 2-hydroxyethyl methacrylate monomer with a cross-linker such as ethylene glycol dimethacrylate (EGDMA) (Figure 6). Most of the hydrophilic behavior of HEMA is due to the presence of the hydroxyl

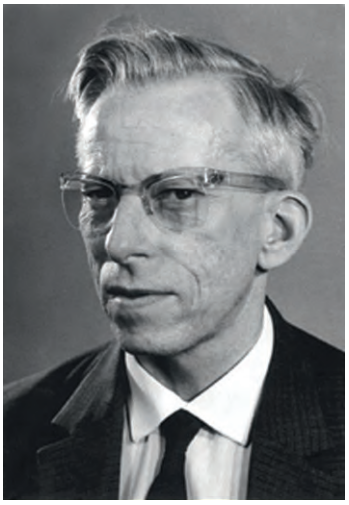

Figure 5 Otto Wichterle.

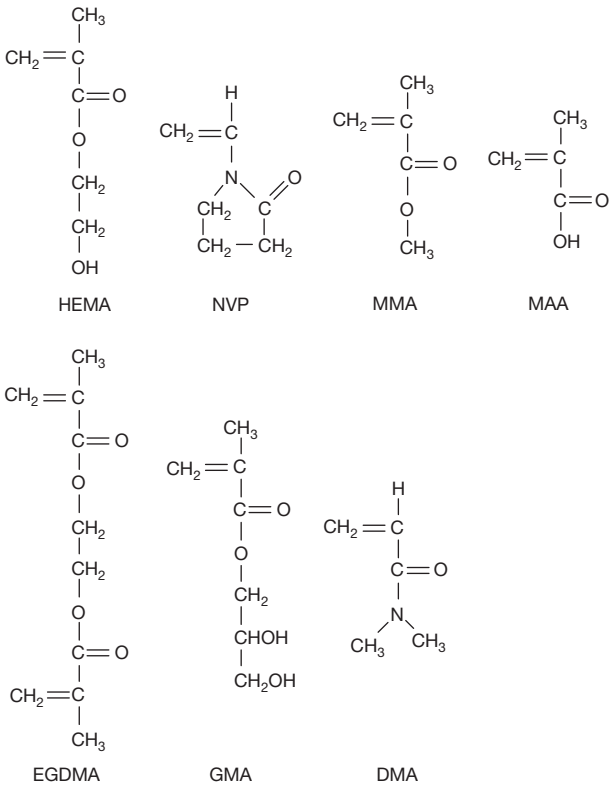

Figure 6 Some of the monomers used in conventional hydrogel lens materials. HEMA, hydroxyethyl methacrylate; NVP, *N*-vinyl pyrrolidone; MMA, methyl methacrylate; MAA, methacrylic acid; EGDMA, ethylene glycol dimethacrylate; GMA, glyceryl methacrylate; DMA, *N*,*N*-dimethyl acrylamide. Adapted from Maldonado-Codina, M.; Efron, N. In *Contact Lens Practice*, 2nd ed.; Efron, N., Ed.; Butterworth-Heinemann/Elsevier: Maryland Heights, MO, 2010; p 75.

group (OH) at the end of the monomer. At this location in the resultant polymer, hydrogen bonding with water molecules occurs, causing them to be drawn into the polymer matrix. The result is that contact lenses made from pHEMA contain approximately 40% water in the fully hydrated state.

Lenses fabricated from pHEMA were first distributed in Western Europe in 1962 but sales were disappointing. In 1965, the National Patent Development Corporation (NPDC) bought the licence for the American rights to the technology from the Czechs. This was subsequently sold on to Bausch & Lomb who at that time manufactured ophthalmic equipment and spectacle lenses. Bausch & Lomb significantly refined Wichterle's spin-casting process and finally obtained approval from the Food and Drug Administration (FDA) for their pHEMA lenses in 1971. This time, the lenses quickly became very popular – both practitioners and patients enjoyed the benefits of increased comfort, reduced adaptation time, and easier fitting procedures. With time, more and more companies developed their own pHEMA lenses; however, it soon became clear that these lenses were not problem-free. Most of these problems stemmed from the fact that the lenses caused hypoxia but other problems relating to solution toxicity and lens spoliation were also common.

Contact lens manufacturers, therefore, had two possible avenues to follow to increase the oxygen transmissibility of lenses: develop 'hyper-thin' lenses or develop materials with higher water contents. Producing lenses which were thinner was a relatively straight forward matter for lens designers and several such lenses were launched, for example, the Hydrocurve thin lens (Soft Lenses, Inc.) in 1977 and subsequently the O3 Series (Bausch & Lomb). These lenses were in the region of 0.035–0.06 mm in thickness which was less than half the thickness of the original Bausch & Lomb pHEMA lenses.

Developing materials with higher EWC led to the successful development of HEMA copolymers. One of the first successful copolymerizations was with *N*-vinyl pyrrolidone (NVP) (Figure 6). The amide (N–C=O) moiety is very polar and two molecules of water can become hydrogen bonded to it. NVP-based copolymers lose the slippery 'feel' of pHEMA and consequently can feel quite rubbery. These copolymers also tend to have relatively high evaporation rates of water which may be seen as a problem for lens stability and comfort. This occurs because the amide group does not bind water as strongly as a hydroxyl group. In addition, these polymers are significantly more temperature-sensitive than pHEMA-based materials; that is, their parameters tend to change with increasing or decreasing temperature. This is important when removing a lens from its packaging (at room temperature of, say, 20 °C) and inserting it into the eye (~33 °C); that is, lens parameters may change on-eye.

NVP-based lenses have also been associated with increased toxic reactions to the corneal epithelium – observed as patches of 'staining' on the corneal surface, which are observed clinically with the aid of fluorescein dye[16] – and decreased comfort when used in conjunction with solutions containing higher levels of polyhexanide.[17,18] This does not mean that polyhexanide-based solutions cannot be used with NVP-containing lenses, rather the interaction should be born in mind if any significant corneal staining or discomfort symptoms arise – these can usually be treated simply by changing the solution to one containing a lower level of polyhexanide or one free from polyhexanide.

Methyl methacrylate (MMA) is the material from which rigid contact lenses are originally made, that is, PMMA (Figure 6). When MMA and NVP are copolymerized, a completely new material is obtained with very different characteristics to the HEMA/NVP (also known as HEMA/VP) copolymers. Depending on their composition, contact lenses made from MMA/VP copolymers can contain 60–85% water. MMA is very hydrophobic but is useful in soft lens hydrogels as it gives the resultant polymers increased mechanical strength.

Another hydrophilic monomer that has been very successfully used in contact lens hydrogels is MAA (Figure 6). When added to a soft lens polymer formulation, it results in a soft lens with ionized groups (negatively charged) within the polymer matrix, allowing the lens to absorb more water. The higher the amount of MAA, the higher the EWC of the resulting polymer. Amounts of MAA in the region of 1.5–2.5% will increase the water content of a HEMA material into the mid-water content range of 50–60%, thereby allowing oxygen permeability to increase significantly.

Once HEMA/MAA lenses have been manufactured, they need to be ionized (i.e., the hydrogen atom in the carboxyl group is removed). The conversion of the carboxyl group (CO_2H) to the more hydrophilic ionized form (the carboxylate anion, CO_2^-) produces an increase in water content. This is commonly achieved by washing the lenses in sodium

bicarbonate solution or buffered saline and is referred to as 'expanding the matrix.' Unfortunately, using MAA to increase the water content of a polymer also has its disadvantages. These include the following:

1. A lens which is extremely sensitive to changes in tonicity.[19] The Na^+ ions present in saline solution have the effect of 'shielding' the carboxylate anions. In hypotonic solutions (e.g., pure water), as these shielding ions are present to a far lesser degree, more chain repulsion will occur, which increases the swelling of the network and consequently the EWC of the material. In hypertonic solutions, the reverse situation occurs and the material network shrinks, causing its EWC to decrease.
2. A pH-sensitive lens.[20] If the pH of the solution in which the lens is immersed is decreased (i.e., the hydrogen ion concentration is increased), the carboxylate anions are more shielded and the network becomes less expanded. This will cause a decrease in the lens EWC.
3. A very significant level of protein buildup both on the lens surface and within the lens matrix.[21,22] However, it is the biological activity of deposited proteins such as lysozyme which is thought to be most relevant in biocompatibility issues such as contact lens-related papillary conjunctivitis and comfort; that is, protein which remains active (as opposed to becoming denatured) is thought to be biocompatible. The protein deposited on HEMA/MAA lenses has been found to denature to a significantly lower degree compared to other lens materials.[23]
4. Dimensional instability when the lens is heat disinfected.

Glyceryl methacrylate (GMA) is more hydrophilic than HEMA because of the fact that the monomer contains two hydroxyl groups (**Figure 6**). This monomer has been used in contact lens materials in two main ways. The first method has used GMA in combination with MMA to produce materials which have water contents in the range of 30–42%. These materials are thought to be stiffer and stronger than pHEMA hydrogels but their oxygen permeabilities are not ideal for in-eye use.

The second method has been to use GMA in combination with HEMA to produce a high water, nonionic contact lens material (up to ~70% has been possible). These contact lenses are said to be 'biomimetic,' that is, they are claimed to improve biocompatibility by imitating the hydrophilic properties of mucin. Manufacturers also suggest that these lenses show a low rate of dehydration and a rapid rate of rehydration, that is, they have good 'water balance ratios.' In addition, the materials are thought to be relatively deposit resistant and seem to be relatively insensitive to pH changes in the range of pH 6–10. An example of such a lens is the hioxifilcon A material used in the Clear 1 Day lenses manufactured by Clearlab. Another example of a so-called 'biomimetic' lens is the Proclear lens (Coopervision) which contains phosphoryl choline (PC) and HEMA. PC is said to mimic the natural chemistry of cell membranes.

6.633.3.3. High Water Content Hydrogel Lenses

In the early days of soft lens development, de Carle[24] proposed that if the EWC of hydrogel lenses could be sufficiently increased, then these lenses could be worn successfully on an overnight or continuous basis. He developed the first extended wear lens to be distributed in the United Kingdom known as Permalens.[24] The lens material had an EWC of 71% and was made from a HEMA/VP/MAA copolymer. In 1981, the lens was given FDA approval for 'extended wear' of up to 30 days along with another lens, the Hydrocurve II (Wesley Jessen).

Slowly, other lenses were given approval for extended wear during the 1980s but along with the increase in demand for these lenses, so too came an increase in complications. In 1989, studies were published which showed that the risk of microbial keratitis was 5–15 times greater for extended wear than daily wear.[25,26] As a result, the FDA recommended that extended wear be limited to six consecutive nights and with that, the enthusiasm for extended wear died down – that is, until the emergence of silicone hydrogel lenses in the late 1990s.

Table 1 lists some of the most common hydrogel lenses on the market and groups them into their appropriate FDA classification. See Appendix A for details on the classification of hydrogels.

6.633.3.4. Strategies for Enhancing Lens Comfort

In recent years, so-called 'enhanced' hydrogel daily disposable lenses have been developed, such as 1 Day Acuvue Moist (Johnson & Johnson), Focus Dailes with AquaComfort (CIBA Vision), and SofLens daily disposable (Bausch & Lomb). These lenses utilize techniques of macromolecular entrapment and/or release of hydrophilic surface-active polymers at the lens surface in order to improve end-of-day comfort by stabilizing the PLTF.

The Focus Dailes with AquaComfort lens is manufactured from nelfilcon A which essentially consists of a cross-linked functionalized polyvinyl alcohol (PVA) macromer with the addition of nonfunctionalized PVA.[27]

PVA and polyvinyl pyrrolidone (PVP) are common soluble polymeric components in comfort drops and artificial tears and have a viscous consistency at elevated concentrations and molecular weights giving them good surface spreading characteristics. The 1 Day Acuvue Moist lens is manufactured from the etafilcon A polymer (HEMA/MAA) together with the incorporation of small concentrations of low-molecular-weight PVP into the ionic material network.

The Focus Dailies 'enhanced' lenses contain more unfunctionalized PVA than the original lenses. Unfunctionalized PVA is a non-cross-linked PVA macromer of a carefully selected molecular size which does not take part in the polymerization process and which is added to the monomer mix before polymerization. No imbibing step after the lens is polymerized is required. This unfunctionalized PVA macromer is thus free to elute from the lens into the tear film throughout the day with each blink. This PVA is thought to emerge from the lens matrix as 'strands' at the lens surface and it is this effect together with the effect of soluble PVA in the tear film which is what is referred to as the 'surface modification' of these lenses. The released PVA may improve lens comfort by decreasing the surface tension of the tears, or by mimicking mucin, found naturally in the tear film.[28]

In the 1 Day Acuvue Moist lens, the PVP is 'locked' into the lens matrix and is not released from the lens during wear. The PVP is adsorbed on to the preformed lens surface after manufacture from solution. The lens packaging states that the lenses

Table 1 Conventional soft (hydrogel) lenses

Name	*Manufacturer/supplier*	*Principal components*	W *(%)*	*USAN nomenclature*
FDA Group I (<50% EWC <0.2% ionic content)				
Biomedics 38	Coopervision	HEMA	38	Polymacon
CD	Ultra Vision	HEMA	38	Polymacon
Cibasoft	CIBA Vision	HEMA	38	Tefilcon-A
Classic	CIBA Vision	HEMA, VP, MMA	43	Tetrafilcon-A
CSI	CIBA Vision	GMA, MMA	38	Crofilcon-A
Durasoft	CIBA Vision	HEMA, EEMA, MAA	30	Phemfilcon-A
Frequency 38	CooperVision	HEMA	38	Polymacon
Hydron Z4/Z6	Coopervision	HEMA	38	Polymacon
Ultra Vision 38	Ultra Vision	HEMA	38	Polymacon
Medalist 38	Bausch & Lomb	HEMA	38	Polymacon
Menicon Soft	Menicon	HEMA, VA, PMA	30	Mafilcon-A
Omega 38	Ultra Vision	HEMA	38	Polymacon
Optima 38	Bausch & Lomb	HEMA	38	Polymacon
Sauflon 38	Sauflon	HEMA	38	Polymacon
Seelite 38	Coopervision	HEMA	38	Polymacon
SeeQuence	Bausch & Lomb	HEMA	38	Polymacon
Soflens 38	Bausch & Lomb	HEMA	38	Polymacon
Softspin	Bausch & Lomb	HEMA	38	Polymacon
FDA Group II (>50% EWC <0.2 ionic content)				
Actisoft 60	Coopervision	GlyMA	60	Hioxifilcon-A
Excelens	CIBA Vision	PVA, MMA	64	Atlafilcon
ES 70	Coopervision	AMA, VP	70	–
Focus Dailies	CIBA Vision	PVA	69	Nefilcon-A
Gentle Touch	CIBA Vision	MMA, DMA	65	Netrafilcon-A
Igel 67	Ultra Vision Optics	MMA, VP, CMA	67	Xylofilcon-A
Omniflex	Coopervision	MMA, VP	70	Lidofilcon-A
Medalist 66	Bausch & Lomb	HEMA, VP	66	Alphafilcon-A
Permaflex	CIBA Vision	MMA, VP	74	Surfilcon-A
Precision UV	CIBA Vision	MMA, VP	74	Vasurfilcon-A
Proclear	Coopervision	HEMA, PC-HEMA	62	Omafilcon-A
Rythmic	Coopervision	MMA, VP	73	Lidofilcon
Sauflon-55	Sauflon	HEMA, VP	55	–
Soflens One Day	Bausch & Lomb	HEMA, NVP	65	Hilafilcon-A
Softlens 66	Bausch & Lomb	HEMA, VP	66	Alphafilcon-A
FDA Group III (<50% EWC <0.2 ionic content)				
Accusoft	Ophthalmos	HEMA, PVP, MAA	47	Droxifilcon-A
Comfort Flex	Capital Contact Lens	HEMA, BMA, MAA	43	Deltafilcon-A
Durasoft 2	CIBA Vision	HEMA, EEMA, MAA	38	Phemefilcon-A
Soft Mate II	CIBA Vision	HEMA, DAA, MAA	45	Bufilcon-A
FDA Group IV (>50% EWC >0.2 ionic content)				
Acuvue	Johnson & Johnson	HEMA, MAA	58	Etafilcon-A
Durasoft 3	CIBA Vision	HEMA, EEMA, MAA	55	Phemefilcon-A
Focus 1–2 Week	CIBA Vision	HEMA, PVP, MAA	55	Vifilcon-A
Focus Monthly	CIBA Vision	HEMA, PVP, MAA	55	Vifilcon-A
Frequency 55	Coopervision	HEMA, MAA	55	Methafilcon-A
Hydrasoft	Coopervision	HEMA, MAA	55	Methafilcon-A
Hydrocurve II/3	CIBA Vision	HEMA, DAA, MAA	55	Bufilcon-A
1 Day Acuvue	Johnson & Johnson	HEMA, MAA	58	Etafilcon-A
Permalens	CIBA Vision	HEMA, VP, MAA	71	Perfilcon-A
Softcon	CIBA Vision	HEMA, PVP, MAA	55	Vifilcon-A
Surevue	Johnson & Johnson	HEMA, MAA	58	Etafilcon-A
Ultraflex 55	Coopervision	HEMA, MAA	55	Ocufilcon-D

HEMA, 2-hydroxyethyl methacrylate; VP, *N*-vinyl pyrrolidone; PVP, polyvinyl pyrrolidone (i.e., graft copolymer); MAA, methacrylic acid; MMA, methyl methacrylate; BMA, butyl (probably isobutyl) methacrylate; AMA, alkyl methacrylate; CMA, cyclohexyl methacrylate; EEMA, ethoxyethyl methacrylate; DMA, *N*,*N*-dimethyl acrylamide; DAA, diacetone, acrylamide; GMA, glycidyl, methacrylate; GlyMA, glyceryl, methacrylate; VA, vinyl acetate.

USAN, United States Adopted Name Council. Many USAN equivalents exist: for example, Hefilcon (Unilens, Miracon); Deltafilcon (Amsoft, Aquasoft, Aquasight, Metrosoft, Soft Form, Softics, Softflow, Softact); Lidofilcon (CV 70, Genesis 4, Hydrosight 70, Q&E 70, Lubrisof. PDC 70, N&N 70); Tefilcon (Cibathin, Torisoft, Softint, Bisoft); Metafilcon (Kontur, Metro 55, Biomedics 55, Mediflex 55, Omniflex 55); Polymacon (CustomEyes 38, Vesoft, Versaflex, Synsoft, Cellusoft). Polymacon has become used as a generic term for polyHEMA and Lidofilcon for NVP-MMA copolymers. The SoftLens 2000 database (adp Consultancy, Bristol, UK) provides clinically relevant information and brand equivalents on soft lenses in various modalities. Reprinted with permission from Efron, N.; Maldonado-Codina, C. In *Contact Lens Practice*, 2nd ed.; Efron, N., Ed.; Butterworth-Heinemann/Elsevier: Maryland Heights, MO, 2010; pp 78–79.

are packaged in 'buffered saline with povidone.' Povidone is another name for PVP. PVP is quite polar and it is likely to be relatively strongly attracted to the etafilcon material, potentially providing a mechanism for its retention on the lens surface. The persistence of the PVP at the lens surface during wear has been verified by Ross *et al.*[29] who have also described the PVP as being in a predominantly 'looped structure' across the lens surface.

PVP decreases the coefficient of friction of the lens surface compared to its original counterpart. These changes are thought to improve comfort by reducing lens–lid interaction on blinking or, in much the same way as the Focus Dailies lens, by mimicking mucin found naturally in the tear film.

The new SofLens daily disposable lens is modified by the adsorption of Tetronic 1107 – a hydrophilic surface-active polymer composed of ethylene oxide/propylene oxide block copolymer – on to the lens surface. The Tetronic at the surface lowers the coefficient of friction of the lens but it has been shown to be progressively lost from the surface during wear.[29] It is likely, therefore, that the Tetronic is held by weak forces at the lens surface, which would explain the least in-eye persistence of the three 'enhanced' lenses.[29]

6.633.4. Silicone Hydrogel Contact Lens Materials

6.633.4.1. The Drive for Increased Corneal Oxygenation

When Holden and Mertz[30] defined the critical oxygen levels in order to avoid corneal edema for daily and extended wear, they concluded that 24 Barrer per centimeter was the oxygen transmissibility required for daily wear and 87 Barrer per centimeter was that required for overnight wear. These values were reevaluated by Harvitt and Bonanno[31] who found that the minimum oxygen transmissibility required to avoid anoxia throughout the entire cornea was 35 Barrer per centimeter for the open eye and 125 Barrer per centimeter for the closed eye.

From inspection of the relationship between the EWC and the *Dk* of conventional hydrogels (Figure 4), it is obvious that there is an upper limit to how much oxygen permeability can be attained simply by increasing the EWC of conventional hydrogel materials. A hydrogel with a theoretical EWC of 90% and a central thickness of 0.1 mm would have an oxygen transmissibility in the region of 60 Barrer per centimeter which still falls far short of that required to avoid additional overnight corneal edema. Such a lens would need to be in the region of 0.06 mm thickness which is unrealistic both from a manufacturing and a clinical point of view.[32]

6.633.4.2. The Challenge of Incorporating Silicone into Hydrogel Materials

As reducing the thickness of lenses made from conventional hydrogels was not an option for achieving success in extended wear, polymer scientists had to come up with an altogether new kind of material. That material was silicone. Incorporating silicone into contact lens materials was not a new concept when scientists began trying to produce silicone hydrogels. Indeed, the first material to be used in contact lenses was silicone dioxide (glass). Additionally, silicone rubber (polydimethyl siloxane, PDMS) (Figure 7) has been used with limited success as a contact lens material in the form of silicone elastomer lenses. These lenses have not become popular mainly because of lens tightening and surface wettability problems (PDMS is extremely hydrophobic).[33] PDMS has an oxygen permeability in the region of 600 Barrer but is unwettable by tears, deposits high degrees of lipid, and needs to be surface treated. Surface treatments of silicone elastomer lenses have not been particularly successful in the past because Si–O chains have a tendency to rotate very easily and any hydrophilic parts of a newly treated surface tend to disappear inside the polymer.

Silicon, however, has been very successfully incorporated into rigid lens materials, and it was this development which has proven to be a key milestone in the subsequent development of silicone hydrogel materials. The first siloxane-based rigid lens material merged the properties of MMA with the increased oxygen performance of silicone rubber.[34,35]

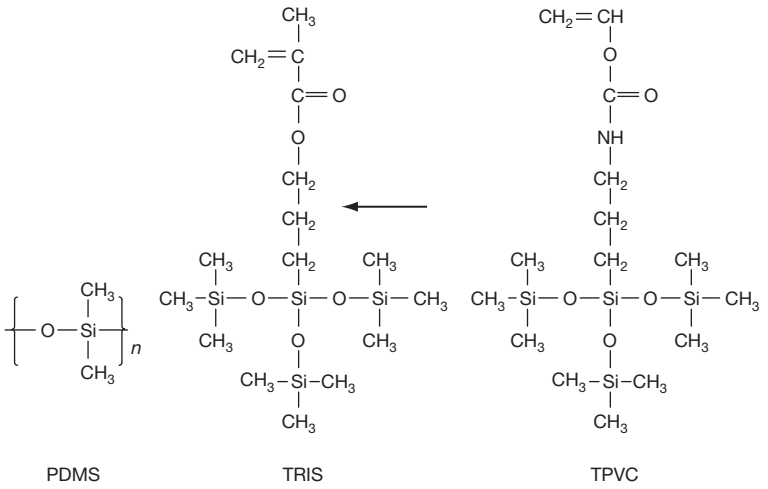

Figure 7 Silicone-based materials. PDMS, polydimethyl siloxane; TRIS, tris(trimethylsiloxy)-methacryloxy-propylsilane; TPVC, carbamate-substituted TRIS. Adapted from Maldonado-Codina, M.; Efron, N. In *Contact Lens Practice*, 2nd ed.; Efron, N., Ed.; Butterworth-Heinemann/Elsevier: Maryland Heights, MO, 2010; p 79.

The resultant siloxymethacrylate monomer was tris(trimethylsiloxy)-methacryloxy-propylsilane (Figure 7) and is more commonly referred to as TRIS.

The patent literature shows that combining silicone with conventional hydrogel monomers has been a goal for polymer scientists since the late 1970s. The biggest obstacle to this approach, however, is that silicone is hydrophobic and poorly miscible with hydrophilic monomers resulting in opaque, phase-separated materials. In order to solve this problem, two main approaches have been utilized.[11] The first approach involves the insertion of polar groups into the TRIS molecule in order to aid its miscibility with hydrophilic monomers.[36,37]

The second approach is that of utilizing macromers. These are large monomers formed by preassembly of structural units that are designed to bestow particular properties on the final polymer.[11] Figure 4 demonstrates the relationship between *Dk* and EWC for silicone-containing hydrogels based on TRIS, highlighting the benefits of increased oxygen performance.

6.633.4.3. The Launch of Silicone Hydrogel Lenses

The first two silicone hydrogels were launched in the late 1990s – the PureVision lens (Bausch & Lomb) and the Focus Night & Day lens (CIBA Vision). Both were licensed for 30 days of continuous wear. The PureVision lens (balafilcon A) has an EWC of 36% and an oxygen transmissibility of 110 Barrer per centimeter (at −3.00D). The exact compositions of these materials are proprietary but the USAN-registered components of the balfilcon A material show that it is based on a carbamate-substituted TRIS-based material known as TPVC (Figure 7). The TPVC is then copolymerized with NVP to form the balafilcon material.

The Focus Night & Day lens (lotrafilcon A) has an EWC of 24% and an oxygen transmissibility of 175 Barrer per centimeter (at −3.00D) and is said to be 'biphasic.' Tighe[11] describes the lens as being a fluoroether macromer copolymerized with TRIS and DMA (*N*,*N*-dimethyl acrylamide) in the presence of a diluent. Its biphasic structure means that oxygen and water permeability channels are not reliant on each other. The silicone-containing phase allows passage of oxygen while the water phase primarily allows the lens to move.

6.633.4.4. Surface Treatments

Without further treatment both of these lenses would be unsuitable for wear because of the fact that the resultant material surfaces are very hydrophobic. In order to overcome this problem, both lenses are surface treated using gas plasma techniques. High-energy gases or gas mixtures (the plasma) are used to modify the lens surface properties without changing the bulk properties. The result for the balafilcon lens is that surface wettability is gained via plasma oxidation which produces glassy silicate islands on the lens surface.

The lotrafilcon lens is coated with a dense 25-nm-thick coating. Both resultant surfaces have low molecular mobility which minimizes the migration of hydrophobic silicone groups to the surface. However, despite these surface modifications, wettability problems with these lenses have been reported. It is generally accepted that these lenses have inferior wettability compared to conventional hydrogels which occurs as a result of the hydrophobic interaction of silicone with the tear film.

6.633.4.5. Material Modulus of Elasticity

Another important difference between these materials and conventional hydrogels is that they have significantly greater elastic moduli. Such mechanical characteristics mean that the lenses are easy to handle but have also been implicated in the etiology of a number of clinical complications.[38] These include higher incidences of superficial epithelial arcuate lesions (SEALs), mucin balls, and contact lens papillary conjunctivitis, especially with continuous wear of these lenses.[39] The stiffness of the material may contribute to the mechanical irritation of the lens rubbing against the conjunctiva of the upper eyelid producing a localized response.

6.633.4.6. Lens Edge Design

The design of the lens, and in particular the edges, may also impact ocular compatibility. It has also been suggested that the design of the lens edge in conjunction with the mechanical properties of silicone hydrogel lenses may be responsible for increased conjunctival staining and conjunctival epithelial flaps observed with these lenses.[40] A knife-point edge or chisel-shaped edge may cause more conjunctival staining and flap formation than a round edge by 'carving' into the conjunctival tissue.[41] It has been proposed that certain edge designs incorporating localized increases in posterior edge lift, reduced peripheral thickness, or peripheral channels may reduce the pressure on the conjunctiva.[41]

6.633.4.7. 'Second Generation' Silicone Hydrogel Lenses

In an attempt to improve on the problems encountered with the early silicone hydrogels, manufacturers have engaged in a program of research aimed at manufacturing silicone hydrogel lenses with improved mechanical and surface characteristics. This has resulted in the gradual emergence of 'second generation' silicone hydrogel lenses such as Acuvue Advance, Acuvue Oasys, TruEye, Avaira, Biofinity, and Clariti. Table 2 compares the properties of all the silicone hydrogel lenses currently on the market.

The main advantage of these 'second generation' silicone hydrogels compared to the early silicone hydrogels is that they have increased water contents and reduced moduli, and they do not need to be surface treated. The mechanical and surface properties can be thought of as being 'in between' those of conventional hydrogels and the early silicone hydrogels. Results of clinical studies indicate that there may be a lower incidence of contact lens-induced papillary conjunctivitis (CLPC) with these lenses.[42]

6.633.4.8. Optimizing Surface Characteristics

Some of the lenses in Table 2 are based on materials containing TRIS-like components. Acuvue Advance and Acuvue Oasys are on the basis of Tanaka's original patent (following it's expiration after 25 years) using a modified TRIS molecule, a silicone macromer, and hydrophilic monomers such as HEMA and DMA. Alcohol is used as a solvent to aid the miscibility of these ingredients and is then extracted following polymerization. High-molecular-weight PVP is the internal wetting agent (the 'Hydraclear') used in these lenses, which is entangled and

Table 2 Currently available silicone hydrogel lenses

Brand name	*PureVision*	*Focus Night & Day*	*O_2 Optix*	*Avaira*	*Biofinity*	*Acuvue Advance*	*Acuvue Oasys*	*TruEye*	*PremiO*	*Clariti*
Manufacturer	Bausch & Lomb	CIBA Vision	CIBA Vision	CooperVision	CooperVision	Johnson & Johnson	Johnson & Johnson	Johnson & Johnson	Menicon	Sauflon
USAN[a]	Balafilcon A	Lotrafilcon A	Lotrafilcon B	Enfilcon A	Comfilcon A	Galyfilcon A	Senofilcon A	Narafilcon A	Asmofilcon A	–
Water content (%)	36	24	33	46	48	47	38	46	40	58
Oxygen permeability (Barrers)[b]	91	140	110	100	128	60	103	100	129	60
Modulus (MPa)	1.50	1.52	1.00	0.50	0.75	0.43	0.72	0.66	0.91	0.50
Surface treatment	Plasma oxidation	Plasma coating	Plasma coating	None (internal wetting agent, undisclosed)	None (internal wetting agent, undisclosed)	None (internal wetting agent, PVP)	None (internal wetting agent, PVP)	None (internal wetting agent, PVP)	Plasma treatment	None (wetting process not disclosed)
Principal monomers[c]	NVP, TPVC, NCVE, PBVC	DMA, TRIS, siloxane monomer	DMA, TRIS, siloxane monomer	NVP, VMA, IBM, TAIC, M3U, FM0411M, HOB	NVP, VMA, IBM, TAIC, M3U, FM0411M, HOB	MPDMS, DMA, HEMA, EGDMA, siloxane macromer, PVP	MPDMS, DMA, HEMA, siloxane macromer, TEGDMA, PVP	MPDMS, DMA, HEMA, siloxane macromer, TEGDMA, PVP	SIMA, SIA, DMA, pyrrolidone derivative	Not disclosed

PVP, polyvinyl pyrrolidone; MPDMS, monofunctional polydimethylsiloxane; DMA, *N*,M-dimethylacrylamide; HEMA, hydroxyethyl methacrylate; EGDMA, ethyleneglycol dimethacrylate; TEGDMA, tetraethyleneglycol dimethacrylate; TRIS, trimethyl siloxysilyl; NVP, *N*-vinyl pyrrolidone; TPVC, tris-(trimethyl siloxysilyl) propylvinyl carbamate; NCVE, *N*-carboxyvinyl ester; PBVC, poly(dimethysiloxy) di (silylbutanol) bis (vinyl carbamate); VMA, *N*-vinyl-*N*-methylacetamide; IBM, isobornyl methacrylate; TAIC, 1,3,5-triallyl-1,3,5-triazine-2,4,6(1*H*,3*H*,5*H*)-trione; M3U, bis(methacryloyloxyethyl iminocarboxy ethyloxypropyl)-poly(dimethylsiloxane)-poly(trifluoropropylmethylsiloxane)-poly(methoxy-poly[ethyleneglycol] propylmethylsiloxane); FM0411M, methacryloyloxyethyl iminocarboxyethyloxypropyl-poly(dimethylsiloxy)-butyldimethylsilane; HOB, 2-hydroxybutyl methacrylate; SIMA, siloxanyl methacrylate; SIA, siloxanyl acrylate.

[a]United States Adopted Name.

[b]Manufacturer-reported values.

[c]Partly from Jones, L.; Dumbleton, K. Contact lens fitting today. Silicone hydrogels Part 1: Technological developments. *Optometry Today*, November 18, 2005, 23–29. Reprinted with permission from Efron, N.; Maldonado-Codina, C. In *Contact Lens Practice*, 2nd ed.; Efron, N., Ed.; Butterworth-Heinemann/Elsevier: Maryland Heights, MO, 2010; p 81.

therefore 'entrapped' within the lens matrix, and allows them to be manufactured without requiring a surface treatment.[43,44] The PVP essentially works by shielding the silicone from the tear film at the lens interface.

The Biofinity lens (comfilcon A) is not based on TRIS chemistry. It comprises solely silicon-containing macromers and requires no surface treatment or wetting agent. The patents surrounding the material refer to a monofunctional macromer (containing only one double bond which takes part in the polymerization process) being combined with another rubber-like siloxy macromer resulting in a material with much longer chains (higher molecular weight) compared to the other silicone hydrogels.[45,46] The patents also discuss other hydrophilic monomers which are presumably the key to why these materials do not need to be surface treated. The material chemistry of this lens provides a higher than expected oxygen transmissibility for its water content. The introduction of these 'second generation' lenses has also seen a significant rise in the number of silicone hydrogel lenses being prescribed on a daily wear basis.

6.633.5. Classification of Soft Contact Lens Materials

There are three main classification systems for soft contact lens materials. Two are well established: the UK Association of Contact Lens Manufacturers (ACLM) classification system and the US Food and Drug (FDA) classification system. A third classification system has been put forward in a British and International Standard.[8,9] These classification systems are expanded upon in Appendix A.

6.633.6. Soft Contact Lens Manufacture

Three techniques can be employed to manufacture soft contact lenses – lathe cutting, spin casting, and cast molding. As medical devices that rest against the highly sensitive eyeball, contact lenses need to be of the highest quality in terms of their physical construction. As devices that correct optical defocus, the optical quality of contact lenses must also be of the highest order. At the same time, it must be recognized that companies will only manufacture contact lenses if they are profitable; the dominant forces in the market dictate that these high-quality products must be delivered at minimal cost, and one consequence of this is a simplification of lens parameters to streamline the high-volume process.

A key requisite of any technology employed to manufacture a medical appliance is that the final product is safe, predictable, and of high quality, so that it meets the intended need. The three technologies discussed below have been developed to meet these requirements.

6.633.6.1. Lathe Cutting

This process essentially involves the use of a special contact lens lathe to cut an anhydrous cylindrical button of material (xerogel) into the required shape, and then hydrating this to form the finished soft lens. Lathe manufacture ranges from labor-intensive, manual-based cutting systems to sophisticated and fully automated manufacturing lines, depending on the capital budget or skill levels available. Even with the use of automation, however, the number and variability of manufacturing steps, which are necessary for lathe cutting, means that manufacturing soft lenses using this technology is necessarily more expensive than that using spin casting or cast molding.

Therefore, lathe cutting is generally reserved for the production of custom-ordered or extreme range lenses that contain design features not amenable to mass production, such as lenses of high spherical power and/or high toric power, and more recently, aberration-correcting soft lenses for keratoconus.[47]

The raw xerogel is supplied to the lens manufacturer in the form of 'rods' or 'buttons.' A rod is a solid cylindrical piece of xerogel, about 16 mm in diameter and 400 mm long. The rod is then sliced, tangentially to the long axis, into buttons about 10 mm thick. More commonly, the xerogels are fabricated and supplied in button form. When this occurs, buttons have usually been pretrimmed to a industry standard size so that it can be machined in most of the available lathes.

The button is first secured to a back surface lathe in a clamp or 'collet,' and this assembly is set spinning at a high rate (typically 8000–12000 rpm) about its central axis. A diamond-tipped tool cuts the posterior surface lens shape into the button. A second diamond tool advances from the side to reduce the diameter to the required size. The surface is rendered smooth by either fine machining or polishing. Modern sophisticated lathes are capable of cutting xerogel surfaces to a tolerance of 8–15 nm. Such smooth surface finishing precludes the need for polishing and is preferred when nonspherical surface geometries are being generated. This approach also serves to preserve the consistency of one surface to the next. The dimensions of the lathed surface are calculated to allow for eventual expansion when the xerogel is later hydrated.

The button is removed from the collet and the cut posterior surface of the button is mounted onto a support tool of a front surface lathe, using low melting point wax. It is essential during this process that the button is mounted and fixed in an absolutely concentric and level aspect to the support tool in order to minimize unwanted prism being introduced by the front surface cutting. A diamond-tipped tool cuts the anterior surface down to the required thickness, and the surface is smoothed. The most advanced lathes now offer 'W' axis cutting options that can generate rotationally nonsymmetric surfaces while the primary front surface is being cut. Polishing tools may be used to smooth the lens edge, although some advanced lathes obviate this step.

After inspecting and measuring all relevant dry lens parameters, the lens is hydrated in normal, unpreserved saline until it is fully equilibrated and impurities have been extracted. The hydrated lens is reinspected for final wet parameter conformity, sealed in small glass vials and autoclaved at 120 °C for 15 min to effect sterilization. Advances in lathing technology and computer-controlled processing have led to the development of semiautomatic systems whereby stacks of buttons are automatically fed into lathes; however, even this technology cannot match the mass-production capabilities of cast molding.

Figure 8 is a schematic flow diagram illustrating the process of manufacturing a soft contact lens using lathe cutting technology.

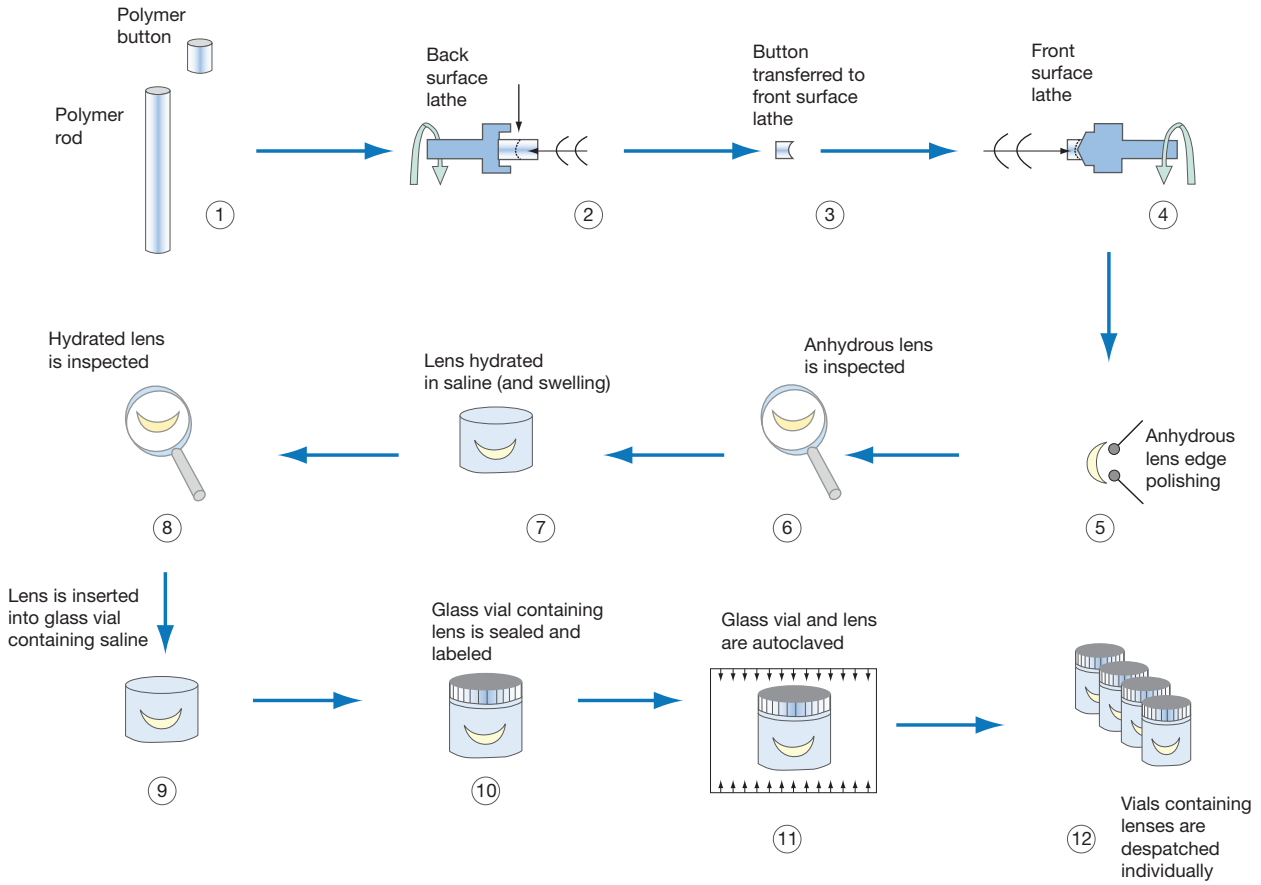

Figure 8 The process of manufacturing a soft contact lens by lathe cutting. (1) The dry polymer is supplied as a rod or button. (2) A polymer button is placed on a lathe; the button spins and a diamond knife is advanced toward the button to generate the lens back surface. (3) The button is released from the back surface lathe. (4) The button is mounted on a front surface lathe with adhesive wax; the button spins and a diamond knife is advanced toward the button to generate the lens front surface. (5) The dry lens is removed from the lathe and the edges are polished. (6) The lens is inspected at 10× magnification. (7) The dry lens is placed in saline to hydrate the lens, which swells to its final soft lens form. (8) The hydrated soft lens is inspected at 10× magnification. (9) The soft lens is inserted into a glass vial containing saline. (10) The glass vial is sealed and labeled. (11) The sealed glass vial containing the lens is sterilized in an autoclave. (12) The individual glass vials are despatched. Reprinted with permission from Efron, N.; Newman, S. In *Contact Lens Practice*, 2nd ed.; Efron, N., Ed.; Butterworth-Heinemann/Elsevier: Maryland Heights, MO, 2010; p 87.

6.633.6.2. Spin Casting

In this process, a convex 'male-shaped' stainless steel tool, or 'insert,' is produced on a high-precision engineering lathe and lapped to provide an accurate surface that matches the dry dimensions of the proposed anterior surface of the contact lens (Figure 9). Modern nonferrous materials are also suitable for producing the mold tool and these materials can be generated on 'nano-accurate' single point turning lathes. These lathes can cut mold tools to a surface finish which renders polishing unnecessary. The final surface shape of the master mold tool is verified using interferometry or other similar noncontact measuring methods. Any given tool is used to make millions of molds.

The steel tool is impressed against heated liquid polypropylene or polyvinyl chloride (PVC), which then cools and sets to form a solid plastic concave female mold. A series of about eight tools is used to produce eight molds simultaneously. The molding methods and tooling used must be very accurate in

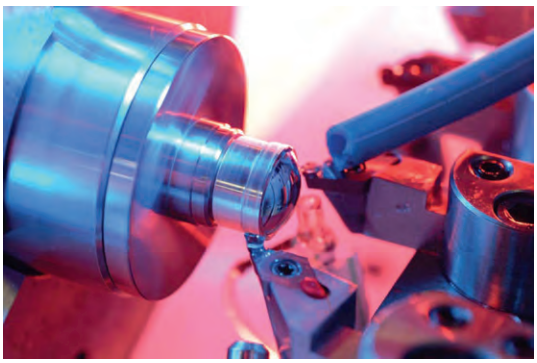

Figure 9 A male-shaped stainless steel tool being cut to shape using a high precision lathe. This tool will be used to form female molds. Reprinted with permission from Efron, N.; Newman, S. In *Contact Lens Practice*, 2nd ed.; Efron, N., Ed.; Butterworth-Heinemann/Elsevier: Maryland Heights, MO, 2010; p 89.

order to preserve the concentricity of the resultant plastic part. Any molding run out will create unwanted prism in the lens during the spinning process. This sort of injection cast molding is generally conducted in a controlled environment. It is imperative for a spin cast manufacturing process to control the level of potential contaminants to a minimum as it is an open molding system.

The xerogel lens form is created by pouring liquid monomers into the concave molds, which spin at a high rate about the central mold axis.

This spinning takes place in a controlled atmosphere of carbon dioxide or similar oxygen deprived atmosphere. This is necessary as the spin mold is an open system and thus exposes one surface of the lens (posterior) to air as it is being cured. Oxygen in air is a natural scavenger of the initiator and will ultimately inhibit the polymerization process.

The speed of rotation, combined with both the mold tool shape and monomer dose, ultimately determines the final lens parameters. The shape of the back surface is governed by centrifugal force generated by the rate of spin of the mold, surface tension and friction forces between the mold and polymer, and the effects of gravity. A greater speed of rotation of the mold will result in more polymer mass being shifted toward the lens periphery, and more negative lens power. Because of this system of manufacture, certain process controls such as monomer dosing must be more accurate than those found in full cast molding of contact lenses.

As the mold spin rate stabilizes, ultraviolet radiation and/or heat is introduced to initiate polymerization. The lens is removed from the mold, and the mold is discarded. Certain spinning processes hydrate the lens in the original plastic mold, which is never removed. Such a process has been proven advantageous and cost-effective for the mass production of daily lenses.

Other spinning systems still require that the edges of the lens are polished and that the lens be inspected, hydrated, reinspected, packaged, and autoclaved. Spin casting can produce a much higher output volume than lathe cutting, and in the latest systems, can match the high volume of lenses that can be produced by cast molding. The primary restriction of spin cast manufacture lies in its inability to generate a fully formed edge from the posterior to anterior surface; however, sophisticated design modeling, combined with accurate tooling, has largely mitigated this limitation. The process of spin casting is illustrated in Figure 10.

6.633.6.3. Cast Molding

Cast molding has become the dominant technology in high-volume lens manufacture. As with spin casting, a series of highly polished steel tools is used to fabricate polypropylene molds; however, matching male and female molds are required for cast molding. Again, modern nonferrous materials are suitable for producing the mold tool and can be generated to extremely fine levels of accuracy and surface finish. These master tools are used to make millions of male and female molds (Figure 11).

The variations found in different manufacturing facilities around the world, however, attest to significant development in challenging this norm. Modern molding machines can create reproducible results (a critical requirement for the high-volume production of contact lenses, particularly daily disposable lenses) with higher numbers of tools. Some machines can successfully carry as high as 36 cavities (18 males and 18 females) in one mold base. Molding parameters, tool accuracy, cooling, and balancing are critical if this is to be successful. The manufacturer will seek a balance between output and accuracy with the molding process.

Cast molding generally takes place in a continuous, automated production line (Figure 12). Monomer in liquid form is introduced into a concave female mold, which defines the shape of the lens front surface. An ultraviolet-transparent male mold is mated to the female mold and the two are clamped together in a carefully controlled environment.

The contact lens edge is formed when the two sides of the mold come together. There is considerable science and art in the control of the polymerization process and the pressure that is applied to the mold to form the lens. A crucial aspect of this process is to arrange for the excess polymer (so-called 'flash') to be squeezed out while leaving the edge intact.

Once the polymer is encapsulated in the mold, it is 'cured'– a process in which the assembled molds are exposed to either UV light or thermal radiation, or a combination of both, to effect polymerization so as to form the dry contact lens. Most cast-molding processes are designed so that when the dry lens is removed from the mold there is no need to polish the edge. The molds are disassembled and discarded, and the lens that is released from the molds – still in rigid form – is hydrated in saline.

Inspection is undertaken either manually (Figure 13) or using automated video-based computer-controlled image analysis. Finally, the lens blister packs are sealed, labeled (Figure 14), autoclaved, and packaged in boxes. Figure 15 is a flow diagram of the cast-molding process.

It should be recognized that the above descriptions are highly simplified accounts of sophisticated engineering processes. Various manufacturers have introduced a number of unique variations, such as wet-state polymerization, the employment of reusable glass molds,[48] and use of the male half of the mold for final lens packaging. Also, toric and bifocal lenses can be manufactured using either spin-casting or cast-molding technology by engineering the master tools to contain the desired lens forms; these design elements will then be faithfully transposed to the molds and then to the final lens.

6.633.6.4. Reproducibility and Quality of Mass-Produced Lenses

Practitioners who prescribe lenses, and patients who wear lenses, need to be assured of the reproducibility of lenses that have been manufactured using mass-production techniques. Young *et al.*[49] determined the reproducibility of 24 lenses in three lens powers (−1.00D, −3.00D, and −6.00D) of eight common frequent replacement spherical soft contact lens types. They found that the mean power of all the lenses was higher than their labeled powers, although all were within the tolerance ranges. Reproducibility was observed to be worse for all lenses at higher powers. All but two lens types had mean diameters within tolerance. A slight reduction of optical quality at high powers was noted. Measures of back optic zone radius, center thickness, and overall diameter showed reasonably good repeatability.

In a similar study conducted on three brands of daily disposable contact lenses, Efron *et al.*[50] found that 450 lenses

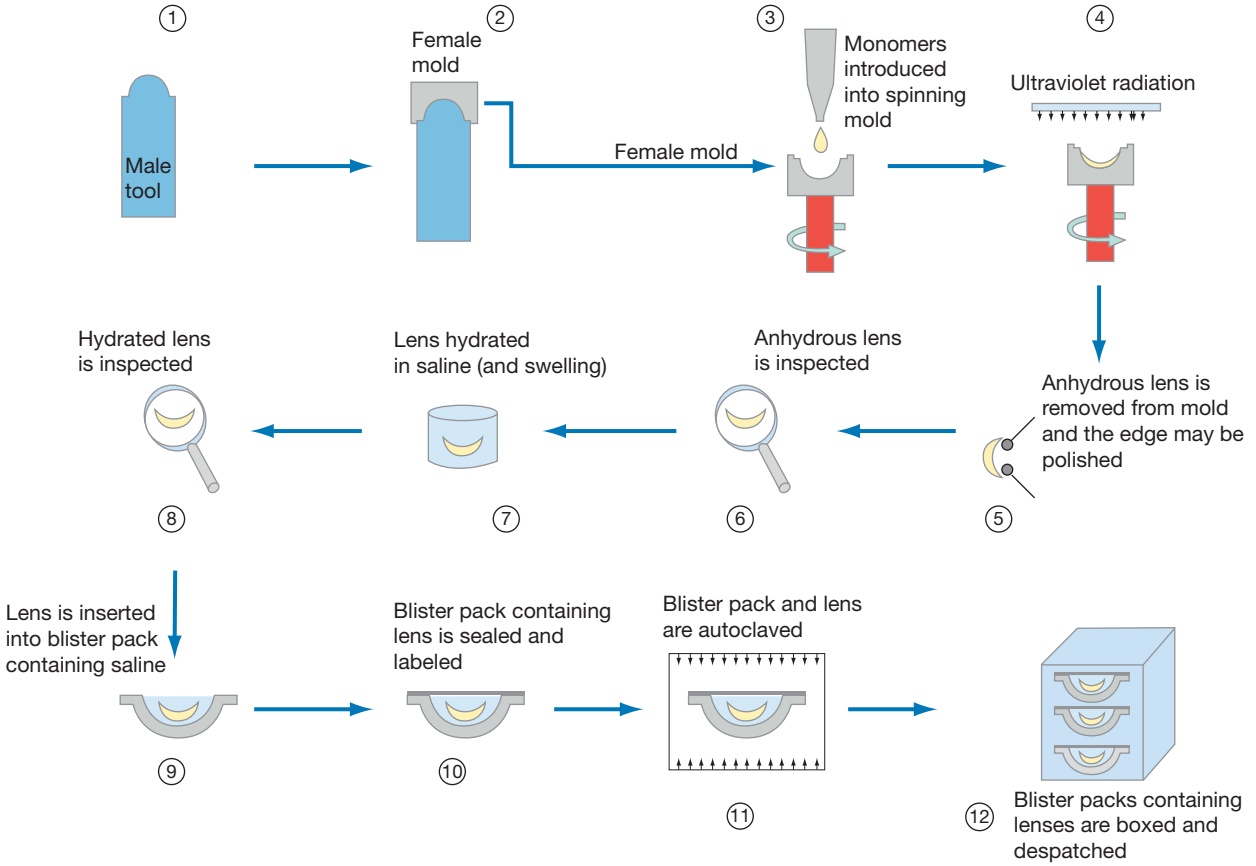

Figure 10 The process of manufacturing a soft contact lens by spin casting. (1) A male tool is machined from stainless steel; the contour of the tool head will define the shape of the anterior lens surface. The same tool is used to make millions of molds. (2) A female mold is made by pressing the male tool into molten polypropylene, which cools and sets. (3) The female mold is mounted, with the concavity facing upward, in a spindle that spins about the lens axis, and liquid monomers are introduced into the spinning mold. (4) The monomers in the spinning mold are irradiated with ultraviolet light to initiate lens polymerization. (5) The dry lens is removed from the mold, the lens edge is polished, and the mold is discarded. (6) The edge of the dry lens is inspected at 10× magnification. (7) The dry lens is placed in saline, which hydrates the lens, causing it to swell to its final soft lens form. (8) The hydrated soft lens is inspected at 10× magnification. (9) The soft lens is inserted into a blister pack containing saline. (10) The blister pack is sealed with a special foil, and a label is stuck onto this. (11) The sealed blister pack containing the lens is sterilized in an autoclave. (12) The individual blister packs are inserted into packages, typically in multiples of either three or six lenses. Reprinted with permission from Efron, N.; Newman, S. In *Contact Lens Practice*, 2nd ed.; Efron, N., Ed.; Butterworth-Heinemann/Elsevier: Maryland Heights, MO, 2010; p 89.

of −3.00D in power displayed an overall high degree of accuracy and reproducibility. They concluded that, with a single inconsequential exception, all measured parameters were found to fall well within clinically acceptable limits for providing wearers of these lenses with consistent vision and fit.

Efron and Veys[51] examined the quality of three types of early generation disposable lenses and observed a high prevalence of nicks, tears, roughness, and blemishes. At the time, other authors reported similar findings.[52–54] These studies accorded a valuable service to the contact lens industry in the early 1990s as they focused attention on the importance of the quality of mass-produced lenses, especially edge quality. Advances in cast-molding manufacturing technology over the past two decades, fuelled by the attention drawn to the above issues, have led to a substantial overall improvement in lens quality.

At a microscopic, subclinical level, it can be observed that different manufacturing techniques can have a significant effect on the finished lens surface. Fine concentric rings can often be seen on the surface of soft lenses that have been manufactured by lathe cutting; these 'lathe marks' are often visible under high magnification using the slit-lamp biomicroscope. Using atomic force microscopy, Bhatia *et al.*[55] observed that the surface of unused cast-molded lenses varied from smooth to rough with surface features unique to the polymers and manufacturing process.

Maldonado-Codina and Efron[56] investigated the impact of manufacturing method and material composition on the surface characteristics of five types of hydrogel contact lenses: three pHEMA lenses, each manufactured by a different technique, namely, lathing, spin casting, and cast molding, a HEMA/MAA cast-molded lens, and a HEMA/glycerol methacrylate cast-molded lens. Front and back lens surfaces were examined using scanning electron microscopy (SEM) and atomic force microscopy (AFM). The surfaces of the lathed lenses were covered in lathing/polishing marks. In general, at a microscopic level, the anterior surface appeared rougher. All three cast-molded lenses

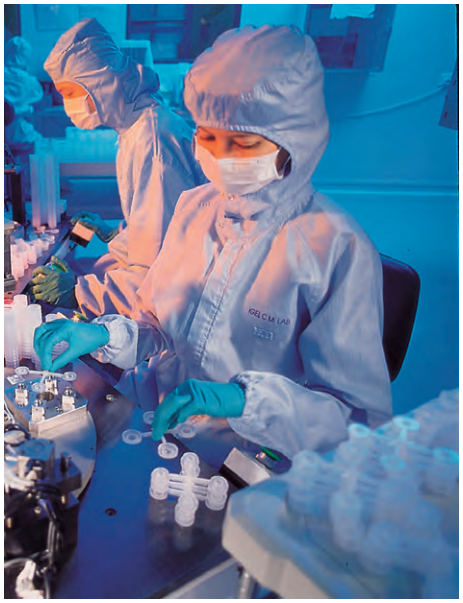

Figure 11 Polypropylene molds being prepared for lens for casting.



Figure 12 Automated production line for cast-molding soft contact lenses.



Figure 13 Manual inspection of contact lens quality. Reprinted with permission from Efron, N.; Newman, S. In *Contact Lens Practice*, 2nd ed.; Efron, N., Ed.; Butterworth-Heinemann/Elsevier: Maryland Heights, MO, 2010; p 90.

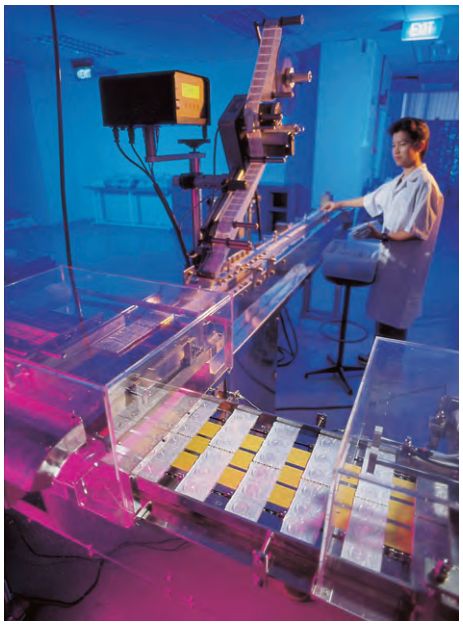

Figure 14 Automated contact lens labeling. Reprinted with permission from Efron, N.; Newman, S. In *Contact Lens Practice*, 2nd ed.; Efron, N., Ed.; Butterworth-Heinemann/Elsevier: Maryland Heights, MO, 2010; p 90.

had more processing debris than the lathed and spun-cast pHEMA lenses. Overall, the surfaces of the lathed lens were 'rougher' than those of the cast-molded lens. Maldonado-Codina and Efron[56] concluded that surface topographies of hydrogel contact lenses are dependent on method of manufacture. They also noted that cast-molded lenses are associated with apparently 'stickier' surfaces, which may be indicative of surface degradation during the manufacturing process.

Maldonado-Codina and Efron[57] measured high- and low-contrast visual acuity, and the level of protein deposition, in patients wearing HEMA lenses made by three manufacturing methods. They found that spun-cast HEMA lenses deposited less protein than cast-molded or lathed HEMA lenses; however, the differences in the amount of protein deposited did not affect visual function.

The impact of manufacturing method on the PLTF of soft HEMA contact lenses was also investigated by Maldonado-Codina and Efron.[56] Manufacturing method was found to have only a minor effect on the quality and stability of the PLTF in HEMA lenses. The authors concluded that PLTF structure is likely to be more related to material and patient characteristics than manufacturing method.

6.633.7. Clinical Ramifications of Polymer and Manufacturing Developments

As with all developments in the field of biomaterials, technological innovations and improvements are ultimately driven by the needs of clinicians working in the specific fields

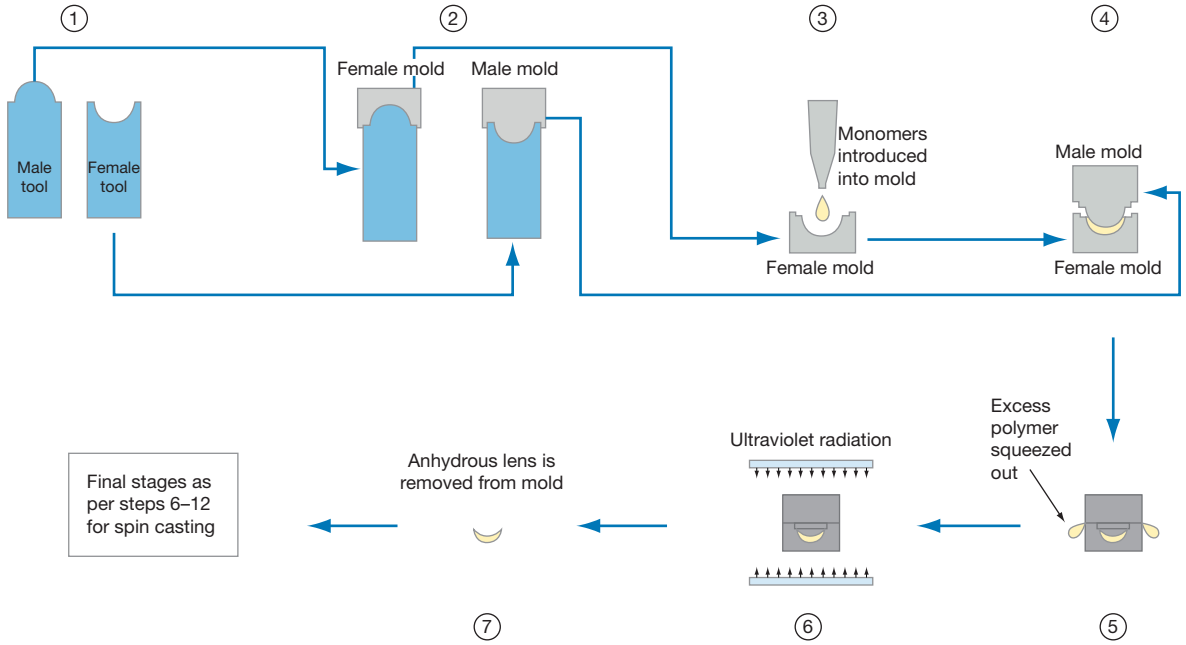

Figure 15 The process of manufacturing a soft contact lens by cast molding. (1) Male and female tools are machined from stainless steel; the contour of the male tool head will define the shape of the anterior lens surface, and the contour of the female tool head will define the shape of the posterior lens surface. The same tools are used to make millions of molds. (2) Male and female molds are made by pressing the tools into molten polypropylene, which cools and sets. (3) The female mold is mounted on a conveyer belt, with the concavity facing upward, and liquid monomers are introduced into the concavity. (4) The male mold is registered over the female mold and the two molds are clipped together. (5) Excess polymer is squeezed out from the sides of the mold. (6) The monomers inside the mold assembly are irradiated with ultraviolet light to initiate lens polymerization. (7) The dry lens is removed from the mold and the molds are discarded. The final stages of lens production are essentially the same as for spin casting, which is illustrated in steps 6–12 in **Figure 10**. Reprinted with permission from Efron, N.; Newman, S. In *Contact Lens Practice*, 2nd ed.; Efron, N., Ed.; Butterworth-Heinemann/Elsevier: Maryland Heights, MO, 2010; p 91.

to which the biomaterials relate. In the early stages of the development of soft contact lenses (i.e., throughout the 1970s and 1980s), two critical problems adversely impacted upon the biocompatibility of contact lenses: insufficient oxygenation of the cornea to sustain normal metabolic processes during lens wear, and problems relating to the buildup of deposits on the lens (and absorbed into the lens matrix) over time.

This section will provide an overview of ramifications of developments in polymer chemistry and manufacturing technology that have essentially solved the problems of poor corneal oxygenation and long-term deposit buildup. Although evidence had slowly been accumulating in the ophthalmic literature throughout the 1970s and 1980s of the imperative of developing soft lenses that could alleviate hypoxia and avoid deposit formation, the definitive work to address this issue was the celebrated 1985 report that became known as the 'Gothenburg study.'[58] This landmark publication is one of the most highly cited papers in the field of contact lenses. It provided a clear rationale of the imperative of solving these two problems, and pointed toward the likely solutions.

The Gothenburg study – so named because the research was undertaken in Gothenburg, Sweden – assessed the effects of long-term extended wear of soft contact lenses on the human cornea. This was achieved by examining 27 patients who had worn a high water content hydrogel contact lens in one eye only for an average of 62 ± 29 months (mean $\pm$ standard deviation). The other eye, which was either emmetropic or amblyopic, acted as a control. Thus, any difference between the two eyes could be attributed to the long-term effects of soft lens extended wear.

The lens-wearing eye showed a 14.8% reduction in epithelial oxygen uptake ($p < 0.001$), a 5.6% reduction in epithelial thickness ($p < 0.05$), a 2.3% reduction in stromal thickness ($p < 0.05$), the induction of epithelial microcysts, and a 22.0% increase in endothelial polymegethism ($p < 0.001$). Endothelial cell density was unaffected by extended lens wear. No interocular differences in any of these physiological characteristics were found in a matched control group of anisometropic and amblyopic subjects who did not wear contact lenses, which validated the use of the contralateral eye as a control in this experiment.

The patients ceased lens wear for up to 1 month and recovery of corneal function was monitored during this period. Epithelial oxygen uptake and thickness recovered within 33 days of lens removal. The number of microcysts increased over the first 7 days, but decreased thereafter; some microcysts were still present 33 days after lens removal. Recovery from stromal thinning had not occurred after 33 days following lens removal. There was a slight reduction in polymegethism in some patients, but overall this was not statistically significant. These findings establish (1) that the extended wear of hydrogel lenses induces significant changes in all layers of the cornea; (2) that lens wear suppresses aerobic epithelial metabolism, which may compromise the epithelial barrier to infection; and (3) that changes to the stroma and endothelium are long lasting.

The authors of the Gothenburg study concluded – on the basis of the outcome a regression analysis of the data – that lens-induced effects on corneal physiology can be minimized by fitting lenses that (1) are more frequently removed, (2) have greater oxygen transmissibility, (3) are more regularly replaced, and (4) are more mobile on the eye.[58] This conclusion became the blueprint for contact lens development over the next quarter of a century, and to this day remains the single most important set of doctrines governing technological refinements in the field.

The first requirement – that lenses should be more frequently removed – was easily solved by advising those using lenses on an extended wear basis (i.e., wearing lenses continuously day and night) of the imperative of wearing lenses continuously for no more than 30 days. This now represents standard advice worldwide, and is entrenched in legislation in the United States via directives from the FDA. In the early days of extended wear, it was thought that it might be possible to use lenses on an extended wear basis indefinitely, but it was gradually realized (and confirmed by the Gothenburg study) that the longer lenses were worn continuously, the greater was the adverse physiological impact.

The second requirement – that lenses have greater oxygen transmissibility – was a far more difficult problem to address, as it pointed toward the need to develop new materials with an oxygen permeability approaching an order of magnitude greater than existed at the time of the Gothenburg study. The answer to this was the development of silicone hydrogel materials, as discussed in Section 6.633.4. The clinical ramification of the introduction of these materials is discussed below in Section 6.633.7.

The requirement that contact lenses should be more regularly replaced – the third edict of the Gothenburg study – pointed toward the need to develop manufacturing processes that would allow mass production of high-quality contact lenses. The inventor of soft contact lenses, Otto Wichterle, had attempted to fabricate lenses using cast molding, but was unhappy with the resultant quality of the lens edge, so he developed an alternative spin-casting technique.[14] It was not until the mid-1980s that cast molding became commercially viable, and this heralded the development of regular replacement disposable lenses. The cast-molding manufacturing process has been discussed in Section 6.633.6.3, and clinical impact of this technology is discussed in Section 6.633.7.

The fourth requirement of the Gothenburg study – that lenses should be more mobile on the eye – relates to the need to constantly flush out debris that accumulates behind a contact lens during wear. At the time of the Gothenburg study, increased lens mobility was the only strategy possible to enhance tear exchange beneath the lens surface. However, other strategies are possible, so this requirement, which has yet to be solved, is perhaps better stated today as a need for greater postlens tear exchange.

The requirement for a greater postlens tear exchange is especially critical for overnight wear, when metabolic byproducts, tear-film components such as lipid and mucin, and naturally desquamating epithelial cells accumulate in the postlens tear film and form a potential 'breeding ground' for microorganisms, leading to an increased risk of inflammation and infection.[25,26] Various strategies for increasing greater postlens tear exchange have been investigated, such as (a) introducing channels, patterns, or grooves in the posterior surface of the lens, to act as conduits of hydraulic flow;[59,60] (b) designing lenses to facilitate a form of pumping action, whereby the lens would move closer to, and further from, the plane of the cornea; or (c) introducing fenestrations (small holes) in the lens.[61] While theoretical models point toward an enhancement of postlens tear exchange using these strategies, practical solutions remain elusive.

6.633.7.1. Polymer Developments: Enhanced Corneal Oxygenation

Arguably, the question of corneal oxygenation has been the most important driver of technological developments in the contact lens field. In fact, this problem was signaled at the very time a contact lens was fitted for the correction of myopia. This was in 1889; a 25-year-old medical student named August Müller (1864–1949) submitted the results of his final year project, entitled 'Brillenglüser und Hornhautlinsen' (Spectacle Lenses and Cornea Lenses), to the University of Kiel in Germany.[62] As can be seen from Figure 16, Müller wore spectacles to correct high myopia.

In what must have been perceived as a bold and perhaps dangerous experiment, Müller fitted himself with large, thick glass lenses (known as 'haptic' lenses); however, he was only able to wear them for half an hour, and provided the following graphic description of his experience:

> Gradually, about a quarter of an hour after insertion, a sensation of pressure and burning appeared, which could not be localized exactly. After a further quarter of an hour, the sensation became so agonizing that I had to remove the lenses. Upon their removal, the violent pain immediately stopped and a short while after I could use the eyes again.

Müller was so disappointed with the results of his experiments that he gave up the idea of becoming an eye specialist and went on to practice as an orthopedic surgeon.[62]

This pioneering work signaled the beginning of the battle to develop contact lenses that could be worn comfortably and continually for many hours. As it turned out, Müller was

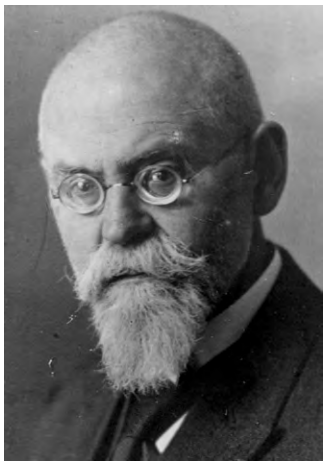

Figure 16 August Müller.

entirely correct in ascribing the failure of his own lens-wearing experiments to "... a disturbance of nourishment of corneal tissue." Unlike all other tissues in the body, the cornea does not contain blood vessels (so that it can remain optically transparent); therefore, in order to respire normally, it must obtain oxygen directly from, and eliminate carbon dioxide directly to, the atmosphere. Although he did not know it at the time, Müller's haptic lenses prevented this necessary exchange of respiratory gases.

If a contact lens blocks off the normal oxygen supply, the corneal epithelium will become hypoxic and will begin to respire anaerobically. This leads to a buildup of lactic acid, which diffuses into the corneal stroma, creating an osmotic force that draws in water. The cornea then develops edema and becomes less transparent, and the eye becomes uncomfortable. Carbon dioxide that is prevented by a contact lens from escaping from the corneal surface dissolves in the tears forming carbonic acid (Figure 17). The resulting acidosis compromises the physiological integrity of the cornea to a small extent – but the effects of hypoxia are far more critical.[63]

The solution to the problem of hypoxia is to design contact lenses that maximize corneal oxygenation during lens wear, as explained in Section 6.633.2.5. Because soft contact lenses completely cover the cornea, the only option for preventing hypoxia is to use soft materials that are permeable to oxygen. As explained in Section 6.633.2.5, the ease with which oxygen can diffuse through a contact lens (defined by the term 'oxygen transmissibility') is a function of the oxygen permeability of the hydrogel material from which the lens is made and the thickness of the lens. A thinner lens provides less resistance to oxygen flow; however, nothing much can be done about lens thickness, because a lens must have a certain thickness profile to achieve the desired optical power for vision correction. Furthermore, if a lens is made too thin, it will fall apart. This leaves material oxygen permeability as the only variable, and the introduction of silicone hydrogel materials this century has essentially solved this problem.

During the waking hours, silicone hydrogel lenses supply the cornea with enough oxygen to avoid excessive edema.[64] However, there is a small but significant minority of patients who need or desire to sleep in lenses, due to the convenience of being able to wake up, either in the morning or in the middle of the night, and have instantly clear vision. As well, sleeping in lenses for an extended period obviated the need for routine daily lens cleaning and maintenance, which is necessary for all daily wear lenses with the exception of daily disposable lenses (see Section 6.633.7.2).

Whereas oxygen reaches the cornea during open eye wear by diffusing from the atmosphere, through the lens to the cornea, the closed eyelid blocks off this oxygen supply when the eyes are closed. The rich plexus of capillary vessels in the conjunctiva on the inside of the eyelid (the superior palpebral conjunctiva) becomes the main source of oxygen for the cornea during sleep; however, the partial pressure of oxygen in the superior palpebral conjunctiva is about one-third of that in the atmosphere.[65] Therefore, the oxygen supply to the cornea is markedly reduced during sleep.

Many changes can be observed in the cornea in association with chronic low level hypoxia and edema, as they occur during sleep. The most critical of these chronic changes is a structural and metabolic weakening of the corneal epithelium. An intact epithelium provides a vital defense against invasion by potentially pathogenic microorganisms that could either enter the eye by chance or in a lens wearer, via contaminated fingers and/or contact lens storage solutions. Opportunistic pathogenic microorganisms – such as pseudomonas aeruginosa or acanthamoeba – can invade the epithelium and establish a potentially sight-threatening corneal infection.

Recent epidemiological studies have demonstrated that, despite the introduction of highly oxygen permeable silicone

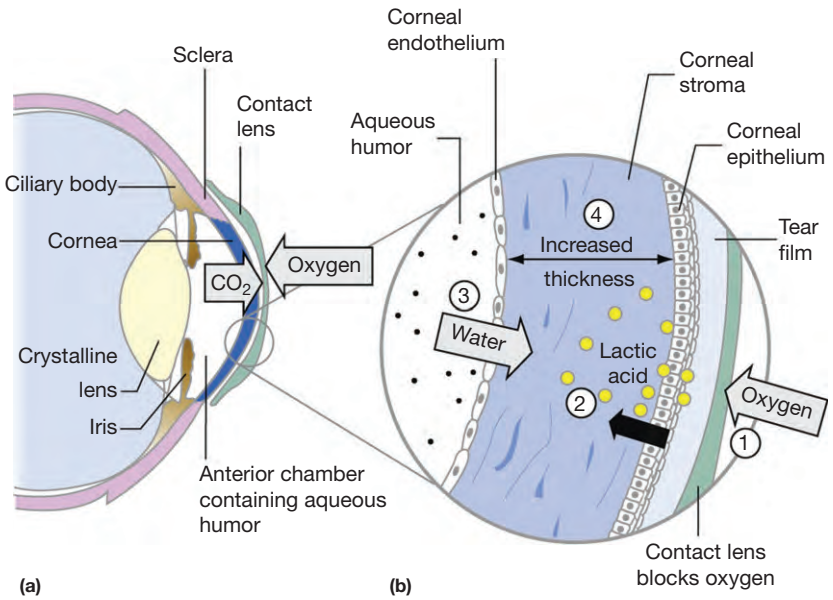

Figure 17 (a) Cross-section of an eye wearing a contact lens, which impedes ingress of oxygen into, and the egress of carbon dioxide from, the cornea. (b) The contact lens blocks oxygen supply to the cornea (1), causing lactic acid to accumulate in the stroma (2). This draws in water (3), leading to stromal edema (4). Adapted from Efron, N. *Biol. Sci. Rev.* **1997**, *9*, 29–31.

hydrogel contact lenses, the incidence of severe corneal infections (microbial keratitis) with extended wear silicone hydrogel lenses is about five times greater than for daily hydrogel lens wear.[66] Accordingly, overnight lens wear is discouraged by many eye care practitioners. Certainly, those who do sleep in lenses must be informed of the extra risks of adverse complications. If a problem is encountered and treatment is delayed, the consequent infection can be extremely painful and lead to some loss of sight (although true 'blindness' is extremely rare). Most of the sensational reports that occasionally appear in newspapers describing problems with contact lenses can be traced to patients sleeping in lenses.

Notwithstanding concerns about extended contact lens wear as outlined above, there is now an abundance of evidence demonstrating the health benefits of silicone hydrogel lenses for daily contact lens wear.[42,67] This lens material has essentially eliminated hypoxia-related contact lens complications, making daily contact lens wear a healthy vision correction option.

Most of the problems encountered today relating to contact lens wear can be traced to patient noncompliance, whereby lens wearers fail to adhere to advice and guidelines offered by their practitioners or the lens manufacturers. Noncompliant behaviors include improper lens maintenance, failing to replace lenses according to the prescribed replacement frequency, or sleeping in lenses designed for daily wear only.

6.633.7.2. Manufacturing Developments: Planned Lens Replacement

'Planned replacement' refers to lens replacement at intervals from 1 day to 12 months and therefore, includes all 'disposable lenses,' which are defined as lenses replaced at least monthly. The first disposable lenses were released internationally in the mid-1980s. The acceptance of disposability by practitioners and patients has been one of the most significant changes in the worldwide contact lens market over the past two decades. By 2005, UK practitioners were fitting 99% of their new soft lens patients with disposable lenses, compared with 61% 10 years before.[68]

The rationale for the planned replacement of soft contact lenses is simple: cleaner lenses should produce fewer adverse ocular effects. A significant proportion of clinical problems relating to the wear of soft contact lenses can be attributed to deposition on the lens surface with tear-derived substances. Contact lens deposits result in reduced acuity, comfort, and wettability and increased inflammatory complications such as papillary conjunctivitis and acute red eye.[69]

All soft contact lenses suffer gradual spoliation from the environment and tear-film components over time. Daily cleaning and periodic protein removal can slow this rate of deposition but not prevent its occurrence. By ensuring that soft lenses are replaced at a suitable predetermined interval, one of the most enduring medical management axioms – that of prevention being better than cure – is brought to bear. In practice, patients who replace lenses regularly report fewer symptoms and exhibit less physiological changes in most instances,[70–75] compared with patients who do not replace lenses regularly. Specific benefits arise from the use of planned replacement lenses;[76] these are so compelling that any decision not to prescribe soft lenses on this basis requires special justification, such as parameter and/or design unavailability, and should be a comparatively rare event.

While the need to clean and disinfect multiuse soft lenses is self-evident, a powerful argument for prolonging the life of lenses with elaborate lens care systems emerged in the early days of soft lenses because of their relatively high cost of production. By the start of the 1980s, soft lenses were becoming the preferred option in many countries. To achieve the then lens life norm of at least a year, a minimum of three lens care product types were needed. Daily cleaners were used to remove loose deposits and microorganisms from the lens surface; disinfecting solutions were used to kill any remaining microorganisms; and protein removal treatments were used to reduce the buildup of tear proteins on the lens surface. The ongoing cost of these products was often found to be more than that of the contact lenses themselves.

Planned replacement lenses (excluding daily disposable lenses) still need high standards of lens care to ensure safe wear, but the shorter replacement cycles allow some scope for simplification. It should not be necessary to deproteinize lenses changed at least monthly. In cases where lens surface spoliation is a problem with monthly replacement, shortening the replacement interval to 2 weeks or even 1 day is likely to be a superior option – at least in terms of patient convenience and therefore compliance – than adding a protein removal step to the care regime.

While mechanical daily cleaning, rinsing, and disinfection are still essential in the care of 2-weekly and monthly replacement lenses, in most cases these functions can be effectively achieved with a single lens care product, namely a multipurpose solution.[77] Daily disposable lenses, which are discarded each day following lens removal, by definition require no lens maintenance.

Because planned replacement lenses are supplied in multipacks, it follows that the loss or damage of a lens should not, in most cases, be an inconvenience to a patient. Practices fitting disposable lenses are also likely to have numerous trial lenses, and even stocks of the more popular parameters, on the premises, which enable rapid replacement if lens loss or damage occurs.

Planned replacement protocols require patients to return at regular intervals for fresh lenses. Aftercare visits can be scheduled to coincide with lens collection, which is a further benefit of prescribing this modality. However, regular repurchasing does not necessarily imply compliance with the wearing schedule.[78,79]

Prior to the introduction of disposable lenses, practitioners maintained sets of 'trial lenses' which were used to assess the fit of a lens on a given patient, and then cleaned and reused on subsequent patients. In the case of disposable lenses, new diagnostic or trial lenses are used with each patient, and disposed of thereafter. This eliminates the risk of cross-infection from a previous wearer of the lens. It also has the advantages of eliminating the time-consuming chore of trial lens cleaning, disinfection, and storage.

With the ready availability of a comprehensive stock of trial lenses, it is nearly always possible to undertake a lens-wearing trial on a prospective disposable lens patient with the required lens parameters, especially with respect to lens power. This was not the case prior to the introduction of disposable lenses,

when practitioners could only maintain a trial set with a limited range of parameters. Trial fitting with a lens with parameters that closely match the requirement of the patient allows for a realistic subjective impression of lens wear and assists the practitioner to accurately assess the fit of what is likely to be the final lens specification in many instances. For certain specialist fittings, such as presbyopia, trial fitting is more meaningful if the appropriate lens powers for the refractive condition of the patient are used.

By the very nature of planned replacement, it is straightforward to modify the prescription of a patient, particularly with respect to changes in refractive error. From a practice management viewpoint, it is advisable to carry out the annual aftercare appointment prior to the dispensing of the next supply of lenses for the patient. Any alteration in lens power can then be made without the need to exchange unwanted lenses.

There are probably no clinical disadvantages in prescribing planned, as opposed to unplanned, replacement lenses. However, there are some points to bear in mind that may have negative implications. The potential for practitioner and patient noncompliance with the designated replacement frequency is ever present.[80]

Provided lens fitting, aftercare, and patient education are of a good standard, there are no compelling reasons for avoiding planned replacement, as long as the required parameters are available.

With any lens replaced at least monthly, it is not practical for each lens to be inspected in detail, either prior to insertion or in the eye of the patient. For planned replacement to be successful, it is a requirement that lenses are sufficiently consistent in quality such that the patient will not notice any change in comfort, fit, or visual acuity from lens to lens. Certainly, the various types of molding systems used to produce most disposable lenses are developed on the principle of building quality into the product, as the traditional manual methods previously used by manufacturers to examine conventional lenses would not be cost-effective with a mass-produced lens.

Wider quality issues are also important when the patient is using many lenses each year. Consistency of packaging and labeling are of great significance when the patient is supplied with unopened packages. If patients find that some blister packs are empty or dry, or contain more than one lens, their confidence in the product is likely to be reduced.

Notwithstanding the above considerations, the recent literature is free of descriptions of complications attributable to poor disposable lens quality; nevertheless, patients should be advised to inspect visually all lenses prior to insertion and discard any lenses exhibiting surface or edge defects, or lenses that are persistently uncomfortable, cause significant eye redness, or provide poor vision.

6.633.8. Conclusions

Soft contact lenses have come a long way since the pioneering efforts of Professor Otto Wichterle in the late 1950s in terms of material, design, and the way they are manufactured. Thick pHEMA lenses which were replaced every few years are now a thing of the past.

Hypoxia-related problems with conventional hydrogels were alleviated to some degree by reducing the thickness of the lenses and/or utilizing more hydrophilic monomers. However, these materials still fell far short of the oxygen requirements needed for truly safe continuous wear.

Although the various hypoxia-related problems associated with contact lens wear appear to have been resolved with the new breed of silicone hydrogel materials, a number of mechanical and surface material-related complications still remain, despite the introduction of 'second generation' silicone hydrogel polymers. Future development of soft contact lens materials is likely to concentrate on trying to resolve the issues of inflammation and infection, improving lens comfort, enhancing postlens tear exchange, and improving surface wettability.

The three primary methods of manufacturing soft contact lenses are lathe cutting, spin casting, and cast molding. The technique of cast molding has become the dominant form of soft contact lens manufacture, because it is capable of producing sufficient quantities of high-quality lenses so as to meet the intense clinical demand for affordable planned replacement and disposable lens-wearing modalities. Modern soft lens manufacturing techniques produce lenses of high quality and good reproducibility.

Planned contact lens replacement, especially in the form of disposable soft lenses, has transformed contact lens practice over the past two decades. This approach is clearly justified in terms of clinical performance, increased convenience, and practice profitability. With the increasing popularity of daily disposable lenses, it is likely that this lens type will be used with greater frequency, and it may not be long before all contact lenses are supplied on this basis. Indeed, we predict that by the year 2020, the vast majority of contact lenses will be daily disposable products made of advanced silicone hydrogel materials.

Appendix A. Classification of Soft Lens Materials

A.1. FDA Classification System

The FDA classification system for soft lens materials is shown in Table A.1. The classification system has four groups. The main drawback with this system is that different materials containing different monomers can be classified within the same material group.

A.2. ACLM Classification System

The ACLM classification has two main groups: *focon* for rigid lens materials and *filcon* for soft lens materials. Each group is further subdivided depending on how much ionizable

Table A.1 FDA classification system for soft lens materials

Group	*Material*
I	Low water content (<50%), nonionic polymers
II	High water content (>50%), nonionic polymers
III	Low water content (<50%), ionic polymers
IV	High water content (>50%), ionic polymers

Table A.2 FDA classification system for soft lens materials

Group	*Material*
1a	Essentially poly 2-HEMA, but ≤0.2% by weight of any ionizable chemical (e.g., MA)
1b	Essentially poly 2-HEMA, but >0.2% by weight of any ionizable chemical
2a	A copolymer of 2-HEMA and/or other hydroxyalkylmethacrylates, dihydroxyalkylmethacrylates, and alkylmethacrylates, but ≤0.2% by weight of any ionizable chemical
2b	As in group 2a, but >0.2% by weight ionizable chemicals
3a	A copolymer of 2-HEMAwith an *N*-vinyl lactam and/or an alkyl acrylamide but ≤0.2% by weight of any ionizable chemical
3b	As in group 3a, but >0.2% by weight of ionizable chemicals
4a	A copolymer of alkyl methacrylate and *N*-vinyl lactam and/or an alkyl acrylamide, but ≤0.2% by weight of any ionizable chemical
4b	As in group 4a but >0.2% by weight of ionizable chemical
5	Soft lens materials formed from polysiloxanes

Table A.3 BS EN ISO hydrogel suffix groups

Group suffix	*Material*
I	Low water content, nonionic: materials which contain less than 50% water and 1% or less (expressed as mole fraction) of monomers that are ionic at pH 7.2
II	Medium and high water content, nonionic: materials which contain 50% water or more and 1% or less (expressed as mole fraction) of monomers that are ionic at pH 7.2
III	Low water content, ionic: materials which contain less than 50% water and greater than 1% (expressed as mole fraction) of monomers that are ionic at pH 7.2
IV	Medium and high water content, ionic: materials which contain 50% water or more and greater than 1% (expressed as mole fraction) of monomers that are ionic at pH 7.2

monomer is present in the material. The classification system is shown in Table A.2.

A.3. BS EN ISO 18369-1: 2006

The specific classification of a contact lens or contact lens material is given as a six-part code as follows:

(prefix) (stem) (series suffix) (group suffix) (*Dk* range) (modification code)

For soft lens materials, the classification denotes whether the material is ionic and the range in which the water content of the material lies. The presence or absence of surface modifications is also indicated.

The prefix is a term assigned to a material to designate a specific chemical formulation. Use of this prefix, which is administered by the United States Adopted Names (USAN) Council, is optional for all countries other than the United States.

Two types of *stems* are used. The filcon stem is affixed to the prefix and is applied for materials which contain <10% water by mass (hydrogel materials). Focon is applied to materials containing <10% water by mass (i.e., nonhydrogel materials).

Table A.4 BS EN ISO hydrogel *Dk* groups

Group	Dk *range*
0	<1 *Dk* unit
1	1–15 *Dk* units
2	16–30 *Dk* units
3	31–60 *Dk* units
4	61–100 *Dk* units
5	101–150 *Dk* units
6	151–200 *Dk* units
7 etc.	Increasing in increments of 50 *Dk* units

The *Series suffix* is also administered by the USAN council, and is used in cases in which the original ratio of the monomers of an existing contact lens polymeric material is changed to make a new material. In this case, the capital letter 'A' is added after the stem designation. Subsequent changes in monomer ratio are designated by the next letter of the alphabet. These letters are used to differentiate copolymers of unchanged monomer units, but with different ratios.

The Group suffix, represented by a Roman numeral, indicates the range of water content and ionic character of the material (Table A.3).

Table A.4 shows how the *oxygen permeability* of the materials is classified.

The *Modification* code, designated by a letter 'm' denotes whether the lens has a surface modification which renders the surface characteristics different from that of the bulk material. Such treatments include plasma treatment, acid/base hydrolysis, and incorporation of a material which migrates to the surface. Certain types of tinted lenses may also be considered surface modified. In the case of an unmodified surface, this suffix is omitted.

A.3.1. Example

In order to demonstrate the BS EN ISO classification system, the Acuvue 2 lens would be classified as follows:

Prefix – eta
Stem – filcon
Series suffix – A
Group suffix – IV
Dk range – 1
Modification code – none

The lens can, therefore, be classified *as* (*etafilcon A*) (IV) (1).

References

1. Morgan, P. B.; Woods, C. A.; Tranoudis, I. G.; *et al*. *Contact Lens Spectr*. **2010**, *25*(2), 30–36.
2. Efron, N. *Cont. Lens Anterior Eye* **2010**, *33*, 245–252.
3. Polse, K.; Graham, A.; Fusaro, R.; *et al*. *Contact Lens Assoc. Ophthalmol. J*. **1999**, *25*, 152–158.
4. Maldonado-Codina, C.; Morgan, P. B. *J. Biomed. Mater. Res. A* **2007**, *83*, 496–502.
5. Read, M. L.; Morgan, P. B.; Kelly, J. M.; Maldonado-Codina, C. *J. Biomater. Appl*. **2010**.
6. Efron, N.; Brennan, N. A. *Optician* **1987**, *194*(5117), 29–41.

7. González-Méijome, J. M.; López-Alemany, A.; Lira, M.; *et al*. *J. Biomed. Mater. Res. B Appl. Biomater.* **2007**, *80*, 184–191.
8. BSI. Ophthalmic optics – Contact lenses. Part 1. Vocabulary, classification system and recommendations for labelling specifications. BS EN ISO 18369-1:2006, 2006a.
9. BSI. Ophthalmic optics – Contact lenses. Part 4. Physicochemical properties of contact lens materials. BS EN ISO 18369-4:2006, 2006b.
10. Morgan, P. B.; Efron, N. *Cont. Lens Anterior Eye* **1998**, *21*, 3–6.
11. Tighe, B. In *Silicone Hydrogels: Continuous Wear Contact Lenses*; Sweeney, D. F., Ed.; Butterworth-Heinemann: Maryland Heights, MO, 2004; pp 1–27.
12. Lira, M.; Santos, L.; Azeredo, J.; *et al*. *Cont. Lens Anterior Eye* **2008**, *31*, 89–94.
13. Nichols, J. J.; Berntsen, D. A. *Ophthal. Physiol. Opt.* **2003**, *23*, 517–525.
14. Wichterle, O.; Lim, D. *Nature* **1960**, *185*, 117–118.
15. Wichterle, O.; Lim, D. Method for producing shaped articles from three dimensional hydrophilic high polymers. Czeskoslovenska Akademie Ved. US Patent 2,976,576, 1961.
16. Morgan, P. B.; Maldonado-Codina, C. *Cont. Lens Anterior Eye* **2009**, *32*, 48–54.
17. Jones, L.; Jones, D.; Houlford, M. *Cont. Lens Anterior Eye* **1997**, *20*, 23–30.
18. Jones, L.; MacDougall, N.; Sorbara, L. G. *Optom. Vis. Sci.* **2002**, *79*, 753–761.
19. McCarey, B. E.; Wilson, L. A. *Contact Intraocul. Lens Med. J.* **1982**, *8*, 158–167.
20. McKenney, C. *J. Brit. Contact Lens Assoc. (Trans. BCLA Annual Clinical Conference)* **1990**, *13*, 46–51.
21. Maissa, C.; Franklin, V. J.; Guillon, M.; *et al*. *Optom. Vis. Sci.* **1998**, *75*, 697–705.
22. Sack, R. A.; Jones, B.; Antignani, A.; *et al*. *Invest. Ophthalmol. Vis. Sci.* **1987**, *28*, 842–849.
23. Suwala, M.; Glasier, M. A.; Subbaraman, L. N.; *et al*. *Eye Contact Lens* **2007**, *33*, 138–143.
24. de Carle, J. T. Hydrophilic Polymers and Contact Lenses Manufactured Therefrom. GB Patent 1,385,677, 1975.
25. Poggio, E. C.; Glynn, R. J.; Schein, O. D.; *et al*. *N. Engl. J. Med.* **1989**, *321*, 779–783.
26. Schein, O. D.; Glynn, R. J.; Poggio, E. C.; *et al*. *N. Engl. J. Med.* **1989**, *321*, 773–778.
27. Winterton, L. C.; Lally, J. M.; Sentell, K. B.; *et al*. *J. Biomed. Mater. Res. B Appl. Biomater.* **2007**, *80*, 424–432.
28. Mahomed, A.; Ross, G.; Tighe, B. In Contact lenses and comfort enhancers: In vivo and in vitro release of soluble PVA. *Poster presented at the BCLA International Conference and Exhibition, May 21–23, 2004*, Birmingham, UK, 2004.
29. Ross, G.; Mann, A.; Tighe, B. In *Poster presentation at the BCLA International Conference and Exhibition*, May 31–June 3, 2007, Manchester, UK, 2007.
30. Holden, B. A.; Mertz, G. W. *Invest. Ophthalmol. Vis. Sci.* **1984**, *25*, 1161–1167.
31. Harvitt, D. M.; Bonanno, J. A. *Optom. Vis. Sci.* **1999**, *76*, 712–719.
32. Holden, B. A.; Sweeney, D. F.; Seger, R. G. *Clin. Exp. Optom.* **1986**, *69*, 103–107.
33. Josephson, J. E.; Caffery, B. E. *Am. J. Optom. Physiol. Opt.* **1987**, *64*, 958–959.
34. Gaylord, N. Oxygen Permeable Contact Lens Composition Methods and Article of Manufacture. Polycon Lab. Inc. US Patent 3,808,178, 1974.
35. Gaylord, N.G. Methods of Correcting Visual Defects: Compositions and Articles of Manufacture Useful Therein. Syntex USA. US Patent 4,120,570, 1978.
36. Künzler, J.; Ozark, R. Fluorosilicone Hydrogels. US Patent 5,321,108, 1994.
37. Tanaka, K.; Takahashi, K.; Kanada, M.; *et al*. Copolymer for soft contact lens, its preparation and soft contact lens made therefrom. US Patent 4,139,513, 1979.
38. Dumbleton, K. A. *Eye Contact Lens* **2003**, *29*, S186–S189.
39. Skotnitsky, C.; Sankaridurg, P. R.; Sweeney, D. F.; *et al*. *Clin. Exp. Optom.* **2002**, *85*, 193–197.
40. Loftstrom, T.; Kruse, A. *Contact Lens Spectr.* **2005**, *20*(9), 42–44.
41. Back, A. Contact lenses and methods for reducing conjunctival pressure in contact lens wearers; CooperVision Inc., 2006.
42. Maldonado-Codina, C.; Morgan, P. B.; Schnider, C. M.; *et al*. *Optom. Vis. Sci.* **2004**, *81*, 911–921.
43. Maiden, A. C.; Vanderlaan, D. G.; Turner, D. C.; *et al*. Hydrogel with internal wetting agent; Johnson & Johnson Vision Care Inc., 2002.
44. McCabe, K. P.; Molock, F. F.; Hill, G. A.; *et al*. Biomedical devices containing internal wetting agents. Johnson & Johnson Vision Care Inc. US Patent 6,822,016, 2004.
45. Iwata, J.; Hoki, T.; Ikawa, S. Long wearable soft contact lens; Asahi Aime Co Ltd., 2005.
46. Iwata, J.; Hoki, T.; Ikawa, S.; *et al*. Silicone hydrogel contact lens; Asakikasei Aime Co. Ltd and CooperVision Inc., 2006.
47. Marsack, J. D.; Parker, K. E.; Applegate, R. A. *Optom. Vis. Sci.* **2008**, *85*, E1172–E1178.
48. Hough, T. *Contact Lens Spectr.* **1998**, *13*, 42–44.
49. Young, G.; Lewis, Y.; Coleman, S.; Hunt, C. *Cont. Lens Anterior Eye* **1999**, *22*, 127–135.
50. Efron, N.; Morgan, P. B.; Morgan, S. L. *Int. Contact Lens Clin.* **1999**, *26*, 168–173.
51. Efron, N.; Veys, J. *Int. Contact Lens Clin.* **1992**, *19*, 8–18.
52. Holden, B. A.; Sulaiman, S.; Cornish, R. In *Acuvue 'Imperfections' Study*. Discussion paper presented at the 25th/30th Jubilee Conference of the Netherlands Association of Contact Lens Specialists (ANVC) and the Netherlands Optometric Association (OVN), Maastricht, Holland, November 16–18, 1991.
53. Lowther, G. E. *Contact Lens Spectr.* **1991**, *5*, 41–43.
54. Wodis, M.; Hodur, N.; Jurkus, J. *Int. Contact Lens Clin.* **1990**, *17*, 96–102.
55. Bhatia, S.; Goldberg, E. P.; Enns, J. B. *Cont. Lens Assoc. Ophthalmol. J.* **1997**, *23*, 264–269.
56. Maldonado-Codina, C.; Efron, N. *Clin. Exp. Optom.* **2005**, *88*, 396–404.
57. Maldonado-Codina, C.; Efron, N. *Optom. Vis. Sci.* **2004**, *81*, 442–454.
58. Holden, B. A.; Sweeney, D. F.; Vannas, A.; *et al*. *Invest. Ophthalmol. Vis. Sci.* **1985**, *26*, 1489–1501.
59. Lin, M. C.; Soliman, G. N.; Lim, V. A.; *et al*. *Optom. Vis. Sci.* **2006**, *83*, 874–878.
60. Weidemann, K. E.; Lakkis, C. *Optom. Vis. Sci.* **2005**, *82*, 498–504.
61. Miller, K. L.; Polse, K. A.; Radke, C. J. *Invest. Ophthalmol. Vis. Sci.* **2003**, *44*, 60–67.
62. Pearson, R. M.; Efron, N. *Surv. Ophthalmol.* **1989**, *34*, 133–141.
63. Efron, N.; Ang, J. H. B. *Optom. Vis. Sci.* **1990**, *67*, 512–521.
64. Morgan, P. B.; Brennan, N. A.; Maldonado-Codina, C.; *et al*. *J. Biomed. Mater. Res. B Appl. Biomater.* **2010**, *92*, 361–365.
65. Efron, N.; Carney, L. G. *Invest. Ophthalmol. Vis. Sci.* **1979**, *18*, 93–95.
66. Morgan, P. B.; Efron, N.; Hill, E. A. *Br. J. Ophthalmol.* **2005**, *89*, 430–436.
67. Covey, M.; Sweeney, D. F.; Terry, R.; *et al*. *Optom. Vis. Sci.* **2001**, *78*, 95–99.
68. Morgan, P. B.; Efron, N. *Cont. Lens Anterior Eye* **2006**, *29*, 59–68.
69. Jones, L.; Mann, A.; Evans, K.; *et al*. *Optom. Vis. Sci.* **2000**, *77*, 503–510.
70. Marshall, E.; Begley, C.; Nguyen, C. *Int. Contact Lens Clin.* **1992**, *19*, 55–60.
71. Nilsson, S. *Cont. Lens Anterior Eye* **1997**, *20*, 119–128.
72. Nilsson, S.; Montan, P. *Contact Lens Assoc. Ophthalmol. J.* **1994**, *20*, 97–101.
73. Poggio, E. C.; Abelson, M. *Contact Lens Assoc. Ophthalmol. J.* **1993**, *19*, 95–102.
74. Porazinski, A.; Donshik, P. *Contact Lens Assoc. Ophthalmol. J.* **1999**, *25*, 142–147.
75. Pritchard, N.; Fonn, D.; Weed, K. *Contact Lens Assoc. Ophthalmol. J.* **1996**, *22*, 53–59.
76. Ehlers, W. H.; Donshik, P. C.; Suchecki, J. K. *Ophthalmol. Clin. North Am.* **2003**, *16*, 341–352.
77. Franklin, V. *Cont. Lens Anterior Eye* **1997**, *20*, 63–68.
78. Claydon, B.; Efron, N. *Ophthal. Physiol. Opt.* **1994**, *14*, 356–364.
79. Dumbleton, K.; Richter, D.; Woods, C.; *et al*. *Optom. Vis. Sci.* **2010**, *87*, 131–139.
80. Dumbleton, K.; Woods, C.; Jones, L. *Eye Contact Lens* **2009**, *35*, 164–171.

6.634. Bioartificial Kidney

C Pino, Innovative Biotherapies, Ann Arbor, MI, USA
H D Humes, Innovative Biotherapies, Ann Arbor, MI, USA; University of Michigan, Ann Arbor, MI, USA

© 2011 Elsevier Ltd. All rights reserved.

6.634.1. Overview of Renal Replacement 544
6.634.1.1. Ultrafiltration and Small-Solute Clearance 544
6.634.1.2. Tubular Reabsorption and Secretion 544
6.634.1.3. Metabolic and Endocrine Function 545
6.634.2. Membranes for Small-Solute Clearance 545
6.634.2.1. Dialysis 545
6.634.2.2. Hemofiltration 547
6.634.2.3. Advancements in Membrane Technology 548
6.634.3. Renal Epithelial Cell Therapy 550
6.634.3.1. Device Design and Fabrication 550
6.634.3.1.1. Renal assist device 550
6.634.3.1.2. Bioartificial renal epithelial cell system 551
6.634.3.2. Metabolic Replacement 551
6.634.3.2.1. *In vitro* evaluation of the RAD 551
6.634.3.2.2. *In vitro* evaluation of the BRECS 552
6.634.3.3. Immunomodulation 553
6.634.4. Preclinical Evaluation of Bioartificial Kidney 554
6.634.4.1. Acute Renal Failure 554
6.634.4.2. End-Stage Renal Disease 554
6.634.5. Clinical Evaluation of Bioartificial Kidney 554
6.634.5.1. Acute Renal Failure 555
6.634.5.1.1. Phase I clinical studies of the RAD 555
6.634.5.1.2. Phase II clinical studies of the RAD 555
6.634.5.2. End-Stage Renal Disease 556
6.634.6. Future Prospects 556
6.634.6.1. Microelectromechanical System and Extracellular Fluid Volume Sensing 556
6.634.6.2. Wearable Artificial Kidney 557
6.634.6.3. Implantable Artificial Kidney 557
References 557

Glossary

Hemodialysis membrane A synthetic membrane used in dialysis, which is used to separate toxins from the blood through a diffusion-dominated process.

Hemofiltration membrane A synthetic membrane used in filtration of the blood to remove toxins in a process dominated by hydraulic pressure.

High-flux membrane A membrane used in hemofiltration, with larger pores and higher hydraulic conductivity than conventional membranes, which allows for the removal of higher molecular weight toxins.

Synthetic membrane A fabricated structure that allows for the separation of mixtures. Conventional membranes accomplish this separation based on molecular size, as lower molecular weight species are able to pass through pores in the membrane.

Abbreviations

AKI	Acute kidney injury
APACHE	Acute physiology, age, chronic health evaluation
ARDS	Adult respiratory distress syndrome
ARF	Acute renal failure
AT-1	Acetylated tubulin
ATN	Acute tubular necrosis
BAHF	Bioartificial hemofilter
BRECS	Bioartifical renal epithelial cell system
CPB	Cardiopulmonary bypass
CRI	Chronic renal injury
CRP	C-reactive protein
CRRT	Conventional renal replacement therapy
CVVH	Continuous veno-venous hemofiltration

EC	Endothelial cell
ECF	Extracellular fluid
ECS	Extracapillary space
ECM	Extracellular matrix
EDM	Esophageal Doppler monitoring
ESRD	End-stage renal disease
FDA	Food and Drug Administration
GHS	Glutathione
HD	Hemodialysis
HDF	Hemodiafiltration
HF	Hemofiltration
HLB	Hydrophilic/lipophilic balance
IHC	Immunohistochemistry
IL	Interleukin
MEMS	Microelectromechanical systems
MODS	Multiorgan dysfunction syndrome
MOF	Multiple organ failure
PD	Peritoneal dialysis
RAD	Renal assist device
REC	Renal epithelial cell
SCD	Selective cytopheretic device
SIRS	Systemic inflammatory response syndrome
SNM	Silicon nanopore membrane
TNF	Tumor necrosis factor
UF	Ultrafiltrate
WEBAK	Wearable bioartificial kidney
ZO-1	Zona occludens-1

6.634.1. Overview of Renal Replacement

The kidneys are vital organs, which play critical excretory and regulatory roles in maintaining water and electrolyte homeostasis in the body. In addition, the kidneys provide an essential endocrine function as they secrete important signaling molecules that interact with the cardiovascular, skeletal, and immune systems. As one of the most highly specialized, vascularized, and metabolically active tissues in the body, the demands placed on the kidneys cause organ failure at a rate higher than rates for many of the other vital organs of the body. The kidney was the first organ to be successfully transplanted, and a kidney transplant is one of the most common and effective transplantation surgeries performed in the world. However, global shortages of donor kidneys have proven to be a major barrier to the treatment of kidney disease, leaving millions of chronic kidney disease patients without total functional replacement.

The kidney was the first organ to have its function partially substituted by an artificial device. Current dialysis therapies, including hemodialysis (HD), peritoneal dialysis (PD), hemofiltration (HF), and hemodiafiltration (HDF), replace the blood filtration function of the kidney by removing waste products and excess electrolytes using artificial or natural semipermeable membranes. All these methodologies address water and electrolyte-balance functional replacement of the kidney. However, they fail to provide for the lost endocrine function. The long and storied history of medical technologies for kidney function replacement gives hope that a bioartifical kidney will be the first tissue-engineered device to fully replace a complex organ's function.

6.634.1.1. Ultrafiltration and Small-Solute Clearance

The basic functional element of the kidney is the nephron. There are approximately 1 million nephrons in each human kidney. Each nephron comprises three major parts, as shown in Figure 1: the glomerulus, the tubule, and the collecting duct. The glomerulus consists of a tuft of small, highly permeable capillaries interposed between the afferent and efferent arterioles and located inside a hollow structure called the Bowman's capsule. The Bowman's capsule opens out into a series of tubules – the proximal tubule, loop of Henle, distal tubule – and then into the collecting duct, all of which are lined by a continuous layer of epithelial cells.

The first step in the excretory process of the nephron is the generation of an ultrafiltrate (UF) of plasma across the glomerulus into the Bowman's space. The glomerulus is designed to provide efficient ultrafiltration of as much as one-third of the plasma entering it, removing waste products of metabolism from the circulation but retaining important circulating components such as albumin. This high rate of ultrafiltration across the glomerular capillary results from hydraulic pressure generated by the heart and vascular tone of the preglomerular and postglomerular arterioles and from the high hydraulic permeability of the glomerular capillary wall. To achieve the required semipermeability characteristics and extremely high ultrafiltration rates, the glomerular membrane evolved into a complex structure comprising a specialized fenestrated endothelium, a charged basement membrane, and highly differentiated epithelial cells called podocytes. Together, these components impart to the glomerular membrane its extraordinary characteristics, currently unmatched by artificial membranes.

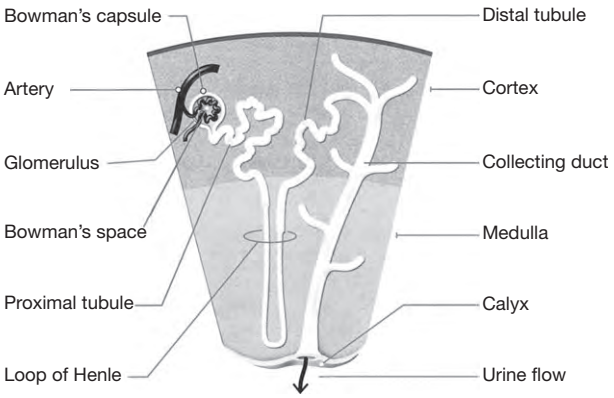

Figure 1 Anatomy of a nephron. Reprinted with permission from Tiranathanagul, K.; Humes, H. D. In *Cellular Transplantation: From Laboratory to Clinic*; Emerich, D. F., Halberstadt, C., Eds.; Academic: San Diego, 2007, with permission from Elsevier.

6.634.1.2. Tubular Reabsorption and Secretion

The UF is modified in two ways: by reabsorption and by secretion while passing through the series of tubules and the collecting duct. Reabsorption refers to the removal of a substance or water from the UF, whereas secretion refers to the addition of a substance to the UF. The different tubular segments and the collecting duct make various contributions to these processes. In normal human kidneys, ultrafiltration by the glomerulus produces approximately 130 l day^{-1}; daily urinary volume is roughly 2 l. Thus, more than 98% of the glomerular UF is reabsorbed by the renal tubules. The bulk of reabsorption, 50–65%, occurs along the proximal tubule. As in glomerular filtration, fluid movement across the renal proximal tubule cell is governed by physical forces. Unlike the fluid transfer across the glomerular capillary wall, however, tubular fluid flux is principally driven by osmotic and oncotic pressures rather than hydraulic pressure. Renal proximal tubule fluid reabsorption is based on active Na^+ transport, requiring the energy-dependent Na^+/K^+-ATPase located along the basolateral membrane of the renal tubule cell to promote a small degree of osmotic difference (2–3 mOsml kg^{-1} H_2O) across the renal tubule, sufficient to drive isotonic fluid reabsorption due to the very high diffusive water permeability of the renal tubule cell membrane. Once across the renal proximal tubule cell, the transported fluid is taken up by the peritubular capillary bed because of the high oncotic pressure gradient that results from the high rate of protein-free filtrate formed in the proximate glomerular capillary bed. As can be appreciated, an elegant system has evolved in the nephron to filter and reabsorb large amounts of fluid in bulk to attain high rates of metabolic product excretion while maintaining regulatory salt and water balance. When functioning properly, all kidney components work together to ensure the removal of toxic compounds from plasma while retaining useful components (e.g., glucose and proteins), maintaining appropriate fluid volumes, controlling the levels of ions, and regulating the function of other organs in the body. It is also important to note that evolution ensured that the kidney fulfills its role even under stress, during conditions of high toxin load. As a result, only a small portion of the overall excretory capacity of the kidneys is required under normal conditions and for sustaining life.

6.634.1.3. Metabolic and Endocrine Function

The kidney is responsible for the secretion of hormones that are critical in maintaining hemodynamics (renin, angiotension II, prostaglandins, nitric oxide, endothelin, and bradykinin), red blood cell production (erythropoietin), and bone metabolism (1,25-$(OH)_2$-vitD_3 or calcitriol).[1] It synthesizes glutathione (GSH) and free-radical scavenging enzymes and provides gluconeogenic and ammoniagenic capabilities.[2,3] Catabolism of low-molecular-weight proteins, including peptide hormones, cytokines, and growth factors, is also accomplished by the kidney.[4] The kidney also has a less-recognized immunoregulatory function. The mammalian renal proximal tubule cells are immunologically active. They are antigen-presenting cells[5] that have costimulatory molecules[6] that synthesize and process a variety of inflammatory cytokines.[6,7] The roles of the renal tubule cells in GSH metabolism,[2] regulation of vitamin D, and production and catabolism of multiple cytokines[1] are critical to immunoregulation to maintain tissue integrity and host defense under stress conditions.[8]

6.634.2. Membranes for Small-Solute Clearance

Filtration by the glomerulus is the first step in the excretory process in normal kidney. The glomerulus removes solutes from the blood by convective transport. Then, in the tubules of the nephron, solutes are removed or reclaimed based on diffusion. The water and solute balance function of the kidney is practically replaced by conventional dialysis or filtration. In these processes, synthetic membranes are used to selectively remove water and solutes based on diffusive or convective transport. In HD, where solute removal from the blood is driven by a concentration gradient of the solute across a membrane, the process is dominated by diffusion. However, solute transfer also occurs, to a lesser extent, convectively by a process of ultrafiltration, where water and solutes move across the membrane.[9] This process is leveraged further in HF, where pores in semipermeable membranes allow water and solutes across the membrane independent of the concentration gradient, and predominantly on the hydraulic pressure gradient across the membrane, which mimics the filtration function of the nephron. HDF combines HD and HF processes, where both diffusion and hydraulic pressure are used as driving forces.

6.634.2.1. Dialysis

Dialysis is a process of removing toxins and metabolic byproducts from the bloodstream based on diffusion and, to a lesser extent, ultrafiltration across a membrane. Dialysis is currently carried out by either HD or PD. In HD, blood exits the body through a catheter, and heparinized silicone tubing delivers the blood to the dialysis unit (**Figure 2**).

$$J/L_pS = \left[\left(P_{dialysate} - P_{blood}\right) - \left(\pi_{dialysate} - \pi_{blood}\right) = P_{effective}\right] \quad [1]$$

Equation [1] describes this process, where J is the flux of the solute across the semipermeable membrane, L_p is the permeability of the membrane to the solute, S is the surface area, $P_{dialysate}$ and P_{blood} are hydraulic pressures, and $\pi_{dialysate}$ and π_{blood} are oncotic pressures, the dominant diffusive driving forces. Within the dialyzer, blood interacts with a semipermeable membrane, which allows for small solutes such as urea, creatinine, potassium, and phosphorous to pass through, while retaining blood cells and critical large proteins such as albumin and immunoglobulin (**Figure 3**). Dialysate, the fluid that flows opposite the blood on the other side of the semipermeable membrane, is an aqueous solution with various concentrations of solutes that dictate the driving force to remove, retain, or add to solute concentrations in the blood. Movement of the solute is directed from high concentration to low concentration. For example, excess bicarbonate can be added to the initial dialysis solution to insure that bicarbonate moves according to this concentration gradient from the high concentration of bicarbonate in dialysate to the lower concentration in blood, resulting in a total net movement of bicarbonate into blood.

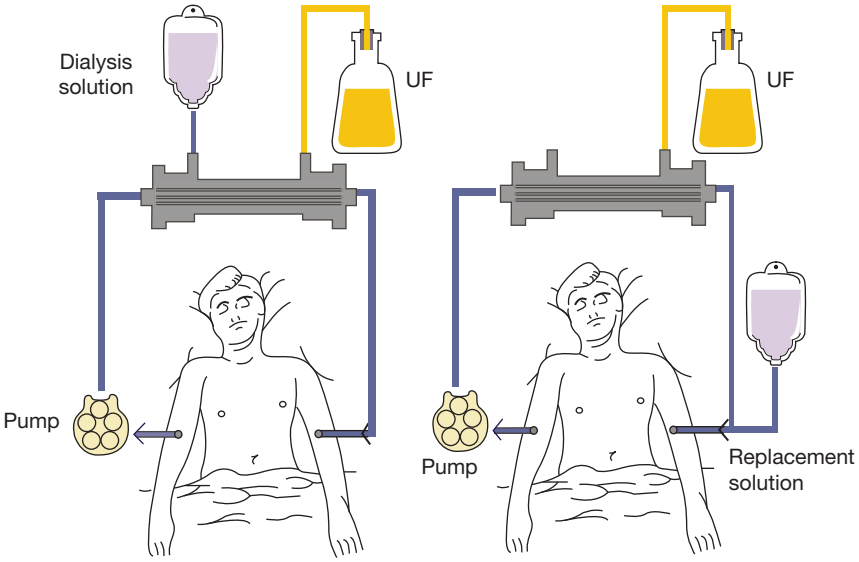

Figure 2 Schematic representations of hemodialysis (left) and hemofiltration (right).

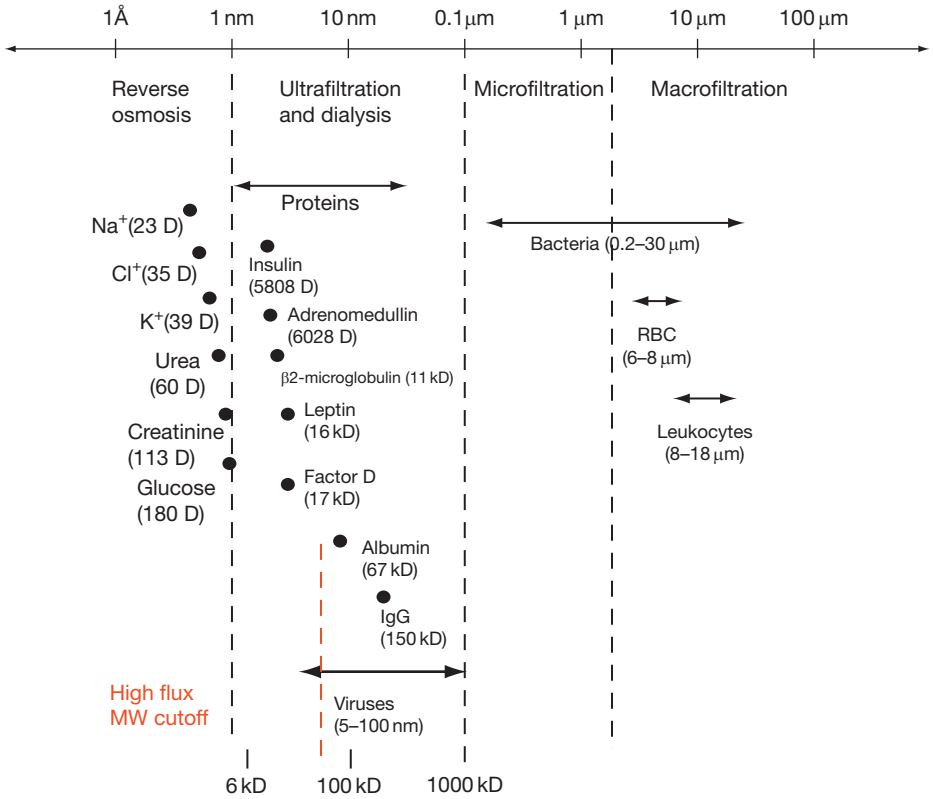

Figure 3 Separation methods: macrofiltration, microfiltration, ultrafiltration, and reverse osmosis, with molecules, pathogens, and cells of interest to dialysis technologies.

Graham first introduced the idea of substituting the clearance function of the kidney by the use of a semipermeable membrane to remove small solutes and water.[10] The first human HD treatment with collodion tube membranes, a cellulose-based material, allowed for the concentration of small solutes in dialysate.[11] Kolff and Berk later used a long cellophane tube spirally wrapped around a cylinder that rotated in a stationary dialysate bath.[12] There were several later designs of dialyzers, including coil and parallel flow dialyzers, before the widespread use of hollow-fiber dialyzers as

the current formulation for HD treatment.[13] The original development of hollow-fiber dialyzers in the 1960s utilized regenerated cellulose as the principal membrane material.

Membrane materials for separation processes are diverse, ranging from metals and ceramics to polymers. Critical to the choice of materials for current dialysis membranes, biocompatibility with blood is a major concern, as well as cost and manufacturing. Synthetic polymers have been the dominant membrane materials used for separation processes due a combination of these factors (see **Chapter 1.122, Structural Biomedical Polymers (Nondegradable)**). The most common polymers in the manufacturing of synthetic membranes are nondegradable polymers, cellulose derivatives, nitrates, esters; polysulfones; polyacrylonitrile derivatives; polyamides; polyimides; polyolefins such as polyethylene, polypropylene, or polyvinylchloride; and fluorinated polymers such as polytetrafluoroethylene and polyvinylidine fluoride.

Biocompatibility of HD membranes with blood is complex and depends on material properties that influence multiple failure mechanisms when in contact with blood, such as hemolysis, clotting, inflammation, and membrane fouling. The material properties that determine biocompatibility also play critical roles in governing separation kinetics. Solute partitioning is affected by hydrophobic/hydrophilic balance (HLB) and surface charges, which are also involved in chemical resistance and binding affinity. When many high molecular weight molecules, such as proteins, adsorb to a membrane's surface, this phenomenon is called membrane fouling. In general, high surface hydrophilicity favors better wettability and decreases fouling (see **Chapter 2.204, Peptoids: Synthesis, Characterization, and Nanostructures**).

Many membrane polymers are grafted, custom modified, or produced as copolymers to improve their properties.[14] For example, concerns about the bioincompatibility of widely used cellulose membranes stemmed from the hydroxyl groups within the cellulose structure. This led to the development of another membrane material, called modified cellulose, with improved biocompatibility. The hydroxyl groups in these modified membranes were masked either by replacing them with other chemical structures, such as acetyl derivatives, or by bonding with potentially advantageous compounds, such as vitamin E or heparin. The use of vitamin E-bonded membranes was recently developed to further improve biocompatibility and minimize HD-associated oxidant stress, thereby modifying the excessive inflammatory state of end-stage renal disease (ESRD).[15]

Current commercially available hemodialyzers are listed in **Table 1**, along with their constituent polymers.

6.634.2.2. Hemofiltration

HF is the ultrafiltration of the blood utilizing a pressure difference to drive water and solutes across a semipermeable membrane and into the filtrate compartment. This can be accomplished by applying a positive pressure to the blood

Table 1 Commercially available hemodialyzers and their respective materials

Company	*Product name*	*Material*	*Chemical structure*
Fresenius	Optiflux	Polysulfone	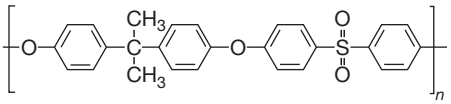
Baxter	CA	Cellulose acetate	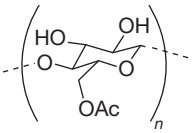
Baxter	CAHP, DICEA	Cellulose diacetate	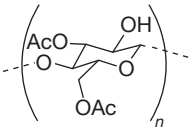
Baxter	CT, Exeltra	Cellulose triacetate	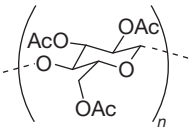
Baxter	Xenium	Proprietary polymer	NA
Gambro	Polyflux H, S, L, 2H	Polamix – a proprietary polymer	NA
Gambro	Evodial	Heparin-surface grafted hydrogel	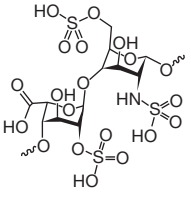

compartment or a negative pressure to the filtrate compartment. Because this process is solely dependent on convection and not diffusion, the resulting filtrate consists of both small and large molecular weight solutes in contrast to dialysate where larger molecular weight solutes are limited due to slow diffusion. Solute movement due to hydraulic pressure driving forces can be expressed in the equation:

$$J/L_pS = [(P_{filtrate} - P_{blood})] \quad [2]$$

In this equation, J is the flux of the solute across the semipermeable membrane, Lp is the permeability of the membrane to the solute, S is the surface area, and $P_{filtrate}$ and P_{blood} are hydraulic pressures.

No dialysate solution is used in HF; rather, the filtrate is collected and discarded, and ultrapure replacement solution is administered to the patient to maintain water/solute balance, as shown in comparison to dialysis in Figure 2.

In order for the artificial hemofilter to replicate the ability of the kidney glomerulus to efficiently remove blood toxins, the artificial membrane permeability must be high enough to permit pressure-driven ultrafiltration flux of the toxins, while retaining the important high molecular weight molecules such as proteins. Ultrafiltration removes water and effectively clears solutes that are within the molecular weight cutoff of the membrane. In contrast, clearance by diffusion depends on concentration gradients and solute mobility. As a result, diffusion is ineffective for the removal of large and/or highly dilute solutes.

Both diffusive and convective processes occur during traditional HD, but most solute movement is achieved via diffusion. Recognition of the inherent limitations in diffusive transport has led to the development of membranes with high hydraulic permeability and therapeutic extracorporeal modalities for renal failure, including HDF and HF in which blood cleansing is achieved via convective HF rather than diffusive HD. Removal of uremic toxins, predominantly by the convective process, has several distinct advantages because it initiates the glomerular process of toxin removal with increased clearance of higher molecular weight solutes and removal of all solutes (up to its molecular weight cutoff) at the same rate. Distinct differences are apparent between diffusive and convective transport across a semipermeable membrane. The clearance of a molecule by diffusion is inversely correlated with the size of the molecule (eqn [3]):

$$D = \frac{K_B T}{6\pi\mu R_H} \quad [3]$$

where D is a molecule's diffusion coefficient ($m^2\,s^{-1}$), which is inversely related to the Stokes–Einstein hydrodynamic radius (R_H). K_B is the Boltzman constant, T is temperature in Kelvin, and μ is the viscosity of the transport media.

In contrast, clearance of a solute by convection depends only on the molecular weight cutoff of the membrane. The bulk movement of water carries passable solutes along with it in approximately the same concentration as in the fluid, allowing for the removal of even dilute toxins.

Current commercially available hemofilters are listed in Table 2, along with their constituent polymers.

6.634.2.3. Advancements in Membrane Technology

Besides improvements in biocompatibility, HD membranes have been developed to better reproduce the physiologic process of glomerular ultrafiltration. It has long been recognized that dialysis membrane clearance was based on concentration differences rather than convective separation of small solutes and low-molecular-weight proteins from large serum proteins and blood elements. In an attempt to replicate glomerular ultrafiltration and removal of 'middle molecules,' synthetic membranes with larger pore sizes and higher water permeability compared to cellulosic membranes were developed. These so-called high-flux membranes are prepared with hydrophobic base materials, including polyacrylonitrile, polysulfone, polyethersulfone, or polymide, with various hydrophilic components. These have supplemented cellulosic membranes owing to manufacturing processes that can mass produce membranes with wide ranges of hydraulic permeabilities for various treatment modalities.[16]

Pore size is another critical issue in hemofilter design. Conventional polymeric membranes are typically cast or spun from polymers in solution, resulting in a dispersion of pore sizes and geometries in a single fiber or sheet that causes incomplete molecular weight cutoff in convective transport. New techniques using a nanocontrol spinning procedure could help solve this problem by producing high-flux membranes in which

Table 2 Commercially available hemofilters and their respective materials

Company	*Product name*	*Material*	*Chemical structure*
Fresenius	Ultraflux F400	Polysulfone	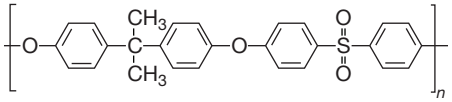
Minntech	Renaflo II	Polysulfone	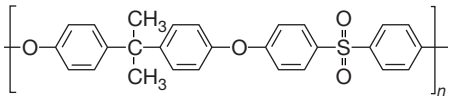
Gambro	Prismaflex M150	Polyacrylonitrile	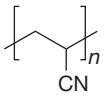

the porosity of the inner layer is finely controlled at the nanoscale level, resulting in an increased number of pores while the spectrum of pore diameters is narrowed and concentrated near the desired values.[17] However, polymeric membranes are basically thick and require high hydraulic pressure gradients to produce UF when compared to the glomerulus.

Based upon this technology, the main focus of recent membrane development has been to increase pore size while sharpening the molecular weight cutoff of high-flux membranes to maximize removal of low-molecular-weight proteins. This direction is based upon the idea that removal of a distinct class of uremic toxins, such as β2-microglobulin, factor D, leptin, and adrenomedullin (**Figure 3**), while minimizing the loss of albumin, could improve treatment outcomes of patients with ESRD. Further work has evolved with superflux or protein-leaking membranes. These membranes provide greater clearances for low-molecular-weight proteins and small protein-bound solutes, such as homocysteine and advanced glycation end products, but with significantly higher loss of albumin than high-flux dialysis membranes. The overall benefits for patients on chronic HD still require more extensive evaluation.[18] Nonmembrane-related determinants of dialyzer performance, including fiber bundle configuration, spacing, and sterilization techniques, also deserve further study.[19]

Current polymer membranes used in dialysis and ultrafiltration have been extensively studied. The pores in such membranes are formed by extrusion and solvent-casting techniques. The geometry and surface chemistry of the pores arise from the chemistry of the polymers and the fluid dynamics of the casting process. In general, the hollow-fiber membranes are fairly thick or employ a multilayer scaffold for mechanical support, and have a distribution of pore sizes rather than a regular array of uniform pores. Pores in conventional polymeric membranes tend to be roughly cylindrical, have a round orifice terminating in a larger channel, or have a structure resembling an open-cell sponge. Extensive descriptions of porous structures used in commercial ultrafiltration and microfiltration have been published.[14,20] It is not clear whether any of these structures provide optimal geometries for membrane filtration, for two reasons. First, a wide dispersion in pore sizes within a membrane leads to imperfect retention of molecules larger than the mean pore size of the membrane. This problem is remedied in practice by engineering the mean pore size of the membrane to be so small that negligibly few pores are large enough to allow passage of a solute above the desired molecular weight cutoff of the membrane. This solution, however, has the undesired effect of reducing the mean pore size in the membrane and thus reducing the hydraulic permeability of the membrane. Engineering narrower pore size distributions ameliorates this dilemma, allowing sharper transitions from passage to retention and maximizing the mean pore size of the membrane.

Second, the round shape of conventional pores dictates a fourth-power dependence of hydraulic permeability on pore radius:

$$\frac{Q}{\Delta P} = \frac{\pi r^4}{8uL} \qquad [4]$$

where Q denotes volumetric flow, P is hydrostatic pressure, r is the radius of the pore, μ is viscosity, and L is the length of the pore, which may or may not be the same as the thickness of the membrane. A pore that is slit-shaped allows steric hindrance to solute passage dictated by the smallest critical dimension of the pore, while increasing hydraulic permeability by a factor of the long dimension of the pore:

$$\frac{Q}{\Delta P} = \frac{wh^3}{12uL} \qquad [5]$$

where w is the long dimension of the slit, h is the thickness of the slit, and L is again the length of the pore. Consequently, it might be predicted that filtration structures with parallel slit-shaped pores might have superior performance when compared to structures with round pores. With that in mind, it is interesting but speculative to note that natural selection has produced filtration structures with elongated, slit-shaped geometries in the kidney.

Turning from steric hindrance to electrostatic effects, it has long been argued that the glomerular filtration barrier imposes an electrostatic restriction on solute passage.[21] This function has been variously attributed to the proteins within the slit diaphragm, the glomerular basement membrane, and the glycocalyx of the glomerular endothelial cell (EC).[22] At physiologic pH, many materials, such as glass, have an anionic surface charge, which can be neutralized at lower pH or possibly increased at higher pH. The net charge density on a microfluidic substrate in contact with an aqueous solution gives rise to an electrical double layer in the aqueous solution. This shielding layer is commonly known as the Debye layer or electrical double layer. For nanometer-scale pores, the thickness of the electrical double layer is in the same order of magnitude as the pore size itself and can contribute to the rejection of charged solutes by the pore.

Although HF can be achieved successfully with purely artificial membranes, new research in biomaterials and tissue engineering holds promise for significant future improvements. Modern membranes are used reliably all over the world in countless HD, HF, and HDF procedures. Typically, membranes are used in the form of hollow-fiber modules and are based on cellulose or synthetic polymers, including polysulfone, polyacrylonitrile, and polyamide, used as such or modified with a variety of agents.[23–25] A major limitation of current membrane technology is diminution of filtration rate owing to protein deposition on the membrane and thrombotic occlusion of the hollow fibers. These problems reduce the durability of the filtration membrane. Current technology introduces considerable advances in a number of areas, including biocompatibility and consistency of pore size. However, there is much room for improvement in the performance of current membranes. Conventional membranes remove solutes only on the basis of molecular size, whereas the glomerulus also employs charge selectivity by the basement membrane. This nonselective nature of conventional membranes is another limitation to overcome. One possible solution to this problem is the growth of basement membrane cells on the hemofilter membrane. Another approach is the design of 'smart' membranes that have selective transport characteristics and contain a predetermined number and size of nonpassive nanoengineered pores that have specific interactions with solutes and solvents at the atomic level.[26]

A membrane composed of slit-shaped pores can separately regulate steric and electrostatic hindrance with extremely high hydraulic permeability. These insights into structure–function relationships in the kidney have motivated the design and construction of a silicon membrane with slit-shaped pores, the dimensions of which approximate the dimensions of the glomerular slit diaphragm. Silicon nanopore membranes (SNMs) with 10–100 nm × 45 μm slit pores were designed and fabricated at the Cleveland Clinic Foundation and Case Western Reserve University. Initial hydraulic characterization of these membranes has been completed.[27] Silicon chips bearing 1 × 1 mm arrays of approximately 10^4 slit pores were fabricated via sacrificial layer techniques.[28] The pore structure is defined by deposition and patterning of a polysilicon film on the silicon wafer. The critical submicron pore dimension is defined by the thickness of a sacrificial SiO_2 layer, which can be grown with unprecedented control to within ±1 nm. The oxide layer is etched away in the final processing step to create the porous polysilicon membrane. The hydraulic permeability to gas, deionized water, and phosphate-buffered saline (PBS) of these novel membranes was tested in a custom-engineered ultrafiltration cell. Gas flow data were well fitted by transitional flow models, consistent with pore sizes approximating the mean free path of the gas molecule. Liquid flow was almost perfectly predicted by conventional Navier–Stokes predictions.

Rejection of charged proteins in solution by SNMs was examined in the same ultrafiltration cell. Briefly, solutions of three proteins (carbonic anhydrase, 25 kDa, bovine serum albumin (BSA), 66 kDa, and sweet potato amylase, 200 kDa) in 1× PBS (150 mM) and 10× PBS (1500 mM) were subjected to ultrafiltration by SNMs. Even for membranes with pore sizes much larger than the molecular radii of the proteins, some rejection of the proteins by the membrane was observed, but this effect was abrogated in high ionic strength solutions, strongly suggesting an electrostatic barrier to passage. Further definition of steric and electrostatic barriers to passage is an area of active research.

6.634.3. Renal Epithelial Cell Therapy

Improvements in membrane biocompatibility have reduced inflammatory reactions, but off-the-shelf polymeric materials still induce a cascade of biochemical events leading to blood coagulation, thrombus formation, and frequently complement activation and inflammation (see **Chapter 4.401, The Concept of Biocompatibility**). Thus, anticoagulation, most commonly the systemic administration of heparin, is required to solve these problems. The use of anticoagulants, however, may lead to additional complications such as hemorrhage, and therefore researchers are trying to improve anticoagulation therapy by finding alternative antithrombotic agents, such as hirudin,[29] and methods of administration, such as direct incorporation onto the polymeric membrane.[30]

The incorporation of a confluent cell monolayer on a synthetic membrane may provide a solution to the membrane/blood compatibility problems and form the basis for the development of a bioartificial hemofilter (BAHF). In addition to improved biocompatibility, a bioartificial membrane is inherently better suited to replicate glomerular filtration and thus provide a complete functional replacement for the glomerulus.

Owing to the relative clinical success of HD treatments and the complexity inherent in tissue engineering for kidney replacement, the literature is devoid of promising efforts to develop a BAHF. Nevertheless, the feasibility of the BAHF concept is supported by many existing studies. For example, the endothelial seeding of synthetic vascular grafts may inhibit long-term deposition of platelets and formation of thrombus,[31] and improve long-term patency after implantation.[32] In addition, the antithrombotic properties of endothelialized grafts may be further improved by ECs engineered to secrete anticoagulation factors.[33] Accordingly, ECs engineered to express an anticoagulant factor could be utilized to coat vascular grafts and stents,[34,35] and semipermeable membranes and thus improve long-term performance *in vivo*. The same approaches can be extended to improve the patency of endothelialized HF membranes.

The disease state arising from renal failure is the result of more than just the loss of blood volume regulation and the clearance of small solutes and toxins, which are replaced by conventional dialysis therapy. Survival rates of renal transplant recipients far exceed those of dialysis patients awaiting transplant,[36] suggesting that the other metabolic and endocrine functions of the kidney not replaced by dialysis account for the poor outcomes of patients receiving conventional dialysis treatment. A new approach using renal progenitor/stem cells to form a monolayer in tissue-engineered devices to supplement or replace the metabolic, endocrine, and immunomodulatory functions of the kidneys when used in conjunction with dialysis addresses these shortcomings (see **Chapter 2.209, Materials as Artificial Stem Cell Microenvironments**).

6.634.3.1. Device Design and Fabrication

6.634.3.1.1. Renal assist device

The tissue engineering of a bioartificial renal tubule as a cell therapy device to replace reclamation, metabolic, and endocrine functions of the kidney component is an approach that utilizes living cells supported on appropriate synthetic scaffolds (see **Chapter 5.501, Scaffolds: Flow Perfusion Bioreactor Design**; **Chapter 5.522, Bone Tissue Engineering: Growth Factors and Cytokines**; **Chapter 5.539, From Tissue to Organ Engineering** and **Chapter 5.540, Kidney Tissue Engineering**).[37] Because the scaffolding material provides the required physical support for the tubule cells, it should not degrade considerably over the life of the bioartificial construct. Furthermore, it should permit the unhindered transport of solutes reclaimed by the tubule cells on one side to the filtered blood circulating at the other side, provide a large surface area to facilitate this mass transport, be compatible with blood, and not leach cytotoxic products into the circulation. Therefore, a bioartificial tubule can be constructed utilizing renal tubule progenitor cells[38,39] cultured on semipermeable polymeric hollow-fiber membranes (polysulfone) on which an extracellular matrix has been layered to enhance the attachment and growth of the epithelial cells.[40] These hollow-fiber synthetic membranes not only provide the architectural scaffold for these cells but also allow for differentiated vectorial transport

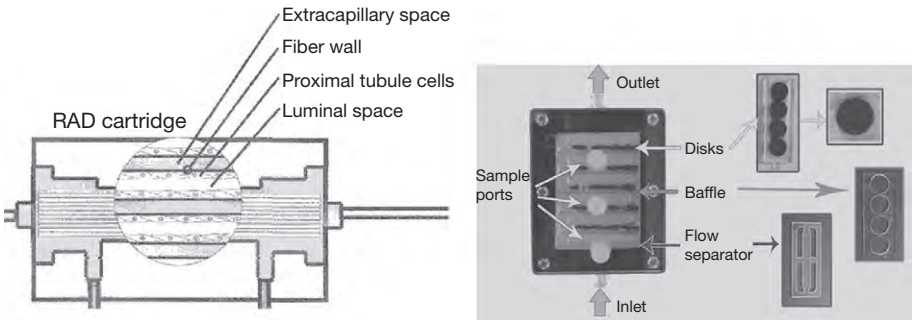

Figure 4 Designs of the renal assist device (RAD) and the bioartificial renal epithelial cell system (BRECS).

and metabolic and endocrine activity and provide immunoprotection, as has been observed in the long-term implantation of the bioartificial pancreas in a xenogeneic host.[41] With appropriate membranes and biomatrices, immunoprotection of cultured progenitor cells can be achieved concurrent with long-term functional performance as long as conditions support tubule cell viability.[37] The technical feasibility of an epithelial cell system derived from cells grown as a monolayer along the luminal surface of a single polymeric hollow fiber, called a bioreactor, has been achieved, as shown on the left in Figure 4.[42]

6.634.3.1.2. Bioartificial renal epithelial cell system

A major obstacle to the widespread adoption of renal cell therapy is the lack of a cryopreservable system to enable distribution, storage, and therapeutic use at point-of-care facilities. The bioartificial renal epithelial cell system (BRECS), shown on the right in Figure 4, is the first all-in-one culture vessel, cryostorage device, and cell therapy delivery system.

The BRECS was designed with the capability to support up to tenfold more cells in less than one-third of the volume of previous renal assist device (RAD) designs, along with the capacity to cryopreserve the full unit in order to facilitate distribution. The polysulfone hollow fibers used as the scaffold in previous RAD designs were limited in cell attachment surface area, and were prone to fracture during cryopreservation and reconstitution, a critical element for storage and distribution of a cell therapy device. The cell-seeding scaffold for the BRECS, niobium-coated carbon disks (Cytomatrix, Woburn, MA), was selected based on its biologically inert, nonbiodegradable and favorable thermomechanical properties for cryopreservation. Cell culture media containing oxygen and nutrients was perfused through and around the porous disks housed within the BRECS. Growth of adequate cell numbers to achieve a therapeutic impact was possible due to the disks' high surface area. High porosity (80–90%) allowed for sufficient, homogeneous delivery of oxygen and nutrients to the cells on the disks through a balance of convective and diffusive flows across and through the scaffold. The other BRECS components, the polycarbonate housing, the gasket, nuts, bolts, and access ports, were carefully selected and thoroughly tested for the ability to withstand cryogenic temperatures, while still maintaining an uncompromised, sterile internal BRECS environment. The BRECS casing consisted of a top lid and a bottom chambered piece, which defined the internal volume where the cell-covered disks were loaded. A single gasket (ethylene propylene diene monomer) was used to tightly seal the pieces together when assembled with external nuts and bolts (Figure 4). The inlet and outlet of the BRECS were standard polycarbonate female luers, which connect with male luers of tubing lines that deliver externally pumped perfusion media. To enable sampling of the BRECS for cell assessment, three sterile sampling ports were integrated into the lid. To insure a homogenous flow profile across the BRECS, a flow separator was used at the inlet, and a set of flow baffles was used to direct a significant amount of the flow directly through each cell-covered disk. At tested flow rates, no significant pressure drop was measured across the BRECS, demonstrating that incorporation of the BRECS into an extracorporeal circuit would not restrict flow. Perfusion was visualized using dilute dye showing a uniform flow distribution throughout the BRECS. During *in vitro* perfusion, all the components remained intact, with no indication of degradation over 6 months.

6.634.3.2. Metabolic Replacement

6.634.3.2.1. In vitro evaluation of the RAD

In vitro experiments have tested transport and metabolic functions of the RAD, utilizing porcine renal proximal tubule progenitor cells grown intraluminally within these cartridges with membrane surface areas of 97 cm^2 to 0.7 m^2, resulting in a device containing up to 10^8–10^9 cells.[43] Porcine cells were used because the pig is currently considered the best source of organs for both human xenotransplantation and immunoisolation cell therapy due to its anatomic and physiologic similarities to human tissue and the relative ease of breeding pigs in large numbers. The nonbiodegradability and pore size of the hollow fibers allow the membranes to act as scaffolds for the cells and as immunoprotective barriers as well. Studies of the RAD have demonstrated that the confluent monolayer cells exhibited morphological characteristics (e.g., apical microvilli, endocytic vesicles, and tight junctional complexes) typical for differentiated tubule epithelia, as well as differentiated active transport properties, differentiated metabolic activities, and important endocrine processes.[43] In particular, these *in vitro* studies demonstrated the ability of the RAD to actively transport sodium, glucose, bicarbonate, and organic anions. The RAD also reabsorbed significant amounts of water in response to oncotic and osmotic pressure gradients.

Vectorial transport of sodium and water across the monolayers was assessed by perfusion of the lumen and the

extracapillary space (ECS) with calibrated flows of culture media and measurement of timed collections of media from each flow. The RAD was tested to see if transport could be increased by creating an oncotic driving force across the monolayer, and if that increase could be abrogated by ouabain (a specific inhibitor of Na^+/K^+-ATPase), the enzyme responsible for the bulk of sodium transport across the luminal surface of the cell. Results suggested that the transport was an active process, rather than passive flow governed by Starling forces across a semipermeable membrane. To increase the oncotic pressure, BSA was added to the ECS perfusate, followed by addition of ouabain as well. As expected, the transport was active and mediated by Na^+/K^+-ATPase.[43] The metabolic characteristics of the cultured proximal tubule cells and the transport of glucose, bicarbonate, and GSH were explored and the data expressed in terms of fractional reabsorption accomplished by the RAD. For each molecule, fractional excretion was measured in the absence or presence of a known inhibitor of an enzyme essential for the reabsorption. In the case of glucose, the compound phlorizin was used; for bicarbonate, a carbonic anhydrase inhibitor (acetazolamide) was used; and for GSH, an inhibitor of γ-glutamyl transpeptidase (acivicin) was used. In each case, there was evidence of active transport and specific inhibition.[43]

In addition, renal proximal tubule cells cultured in the RAD or in culture plates maintained their ability to synthesize and excrete ammonia (a function critical for the maintenance of acid–base homeostasis in the body), produce 1,25-$(OH)_2$-$vitD_3$ (the active form of vitamin D), and, through metabolic degradation and transport of its constituent amino acids, remove GSH from the perfusate. It is thus evident that the RAD has the ability to replicate the major differentiated transport, and the metabolic and secretory functions performed by the healthy renal proximal tubule.

6.634.3.2.2. In vitro *evaluation of the BRECS*

Similar *in vitro* evaluation was undertaken with the BRECS. Cell viability and metabolic activity were confirmed in the BRECS by measuring lactate production and oxygen consumption (Figure 5). Both metrics of metabolism were consistent throughout the duration of perfusion culture, with an interpolated total cell number of 2×10^8 cells. The average oxygen consumption rate of 2–3 nmol O_2/min 10^6 cells is similar to previously reported values for metabolically active cells.[37] To determine if RECs in BRECS maintained renal differentiated phenotypic characteristics over time in perfusion culture, human REC-seeded disks from BRECS units were processed for immunohistochemical (IHC) analysis of selected renal cell differentiated markers acetylated tubulin (AT-1) and zona occludens (ZO-1). AT-1, a marker for apical central cilia of proximal tubule cells, exhibited regular staining in central regions of cells grown on disks (Figure 5, bottom left and middle). ZO-1, a marker for epithelial tight junctions, displayed strong expression along the surface of the cells. ZO-1-positive tight junctions and punctate AT-1-positive central cilia are indicative of polarized epithelium and were evident in all the disks tested.

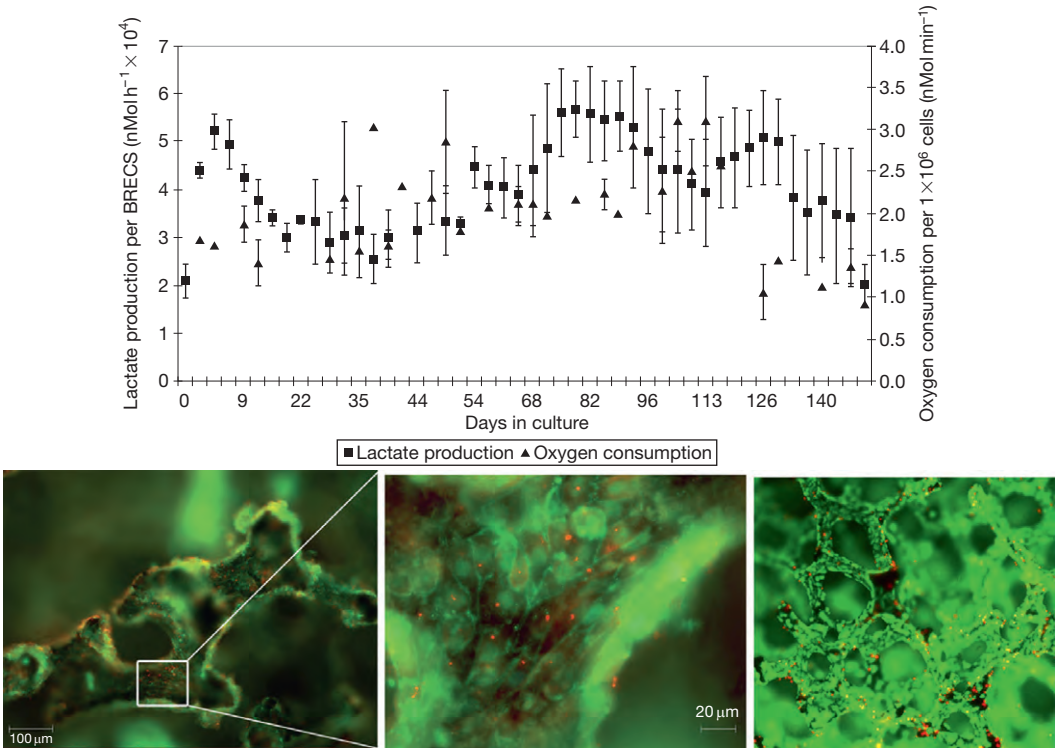

Figure 5 *In vitro* evaluation of the BRECS. Metabolic activity of renal cells was evaluated by measuring lactate production and oxygen consumption (top panel). Immunohistochemical analysis demonstrated that renal cells maintain a differentiated state with the expression of tight junction protein ZO-1 (green) and a central cilia protein, AT-1 (red, left and center panels). Cells maintain high viability both during culture and after reconstitution of cryopreserved BRECS, as demonstrated by a stain of living cells with fluorescein diacetate (green) and dead cells with propidium iodide (red, right panel).

A nondestructive GSH degradation assay was chosen to assess specific renal cell catabolic function in the BRECS units over time. Exogenous GSH was supplemented in the BRECS perfusion media, and metabolic degradation of GSH was measured over a 60-min period. GSH degradation rates in BRECS remained stable, ranging between 600 and 1200 nmol/h/BRECS over a 90-day period, indicative of sustained differentiated renal cell function in the device.

To assess the cryopreservation of RECs in the BRECS units, studies were conducted on single cryopreservable disks. In initial studies, many cryopreservation media performed well with hardy lamb and pig REC cells. However, human REC cells were more susceptible to lower viability after thaw. Of the commercially available and Food and Drug Administration (FDA)-approved cryopreservation media tested, postthaw cell retention and subsequent cell metabolic activity was highest with CryoStor 10 (#640222, Biolife Solutions, Bothell, WA). Immediate postcryopreservation cell retention was optimized when HTS-Purge solution (#637112, Biolife Solutions, Bothell, WA), a hypothermic solution used to prepare cells for the extreme conditions of cryopreservation, was utilized as a precryopreservation rinse buffer. An average cell retention of greater than 90% was achieved on porcine ($n = 4$) and lamb ($n = 2$) REC-seeded disks. Furthermore, this cryopreservation procedure yielded an average cell viability of approximately 90% for human REC-seeded disks (Figure 5, far right).

6.634.3.3. Immunomodulation

Our research group is now focused on the role of the kidney as an immunomodulatory organ and the possibility of renal bioreplacement therapy for the systemic treatment of inflammatory dysregulation. Current renal replacement therapy has poor patient prognosis due to the acute tubular necrosis (ATN) that results in the loss of the kidney's immunoregulatory function. Cell therapy is a potential approach to provide immunomodulation. Loss of immunoregulation results in a propensity to develop systemic inflammatory response syndrome (SIRS), sepsis, multiple organ failure (MOF), and a high risk of death because of systemic immunologic or inflammatory imbalance (Figure 6). Activation and release of inflammatory proteins from circulating activated leukocytes and imbalance between pro- and anti-inflammatory proteins are provoked and aggravated by kidney cell injury and possibly by dialysis. These conditions play a central role in the proinflammatory state in acute kidney injury (AKI) with SIRS and/or MOF.

SIRS is a catastrophic sequela of a variety of clinical insults and is usually present with AKI. In the past decade, a large constellation of data has provided new insights into the inflammatory response that seems to underlie the MOF syndrome. There are now data linking patient outcome to initial plasma levels of tumor necrosis factor (TNF)-α, interleukin (IL)-6, and other proinflammatory cytokines.[44–46] Septic shock is an acute syndrome that is characterized by hypotension, coagulopathy, and eventual MOF, primarily due to ischemic tissue injury. This disorder is associated with dramatic elevations in inflammatory cytokines, including TNF-α, IL-1β, IL-6, IL-8, and interferon-γ.[2] This reactive and uncontrolled inflammatory response results in the adverse hemodynamic and metabolic disturbances in septic shock. In the event of a loss of balance between pro- and anti-inflammatory mediators, the patient may proceed to cardiovascular collapse if proinflammatory processes are excessive, or develop profound immunosuppression with increased risk of recurrent or continuing infection if the anti-inflammatory cascade overreacts.[45,46]

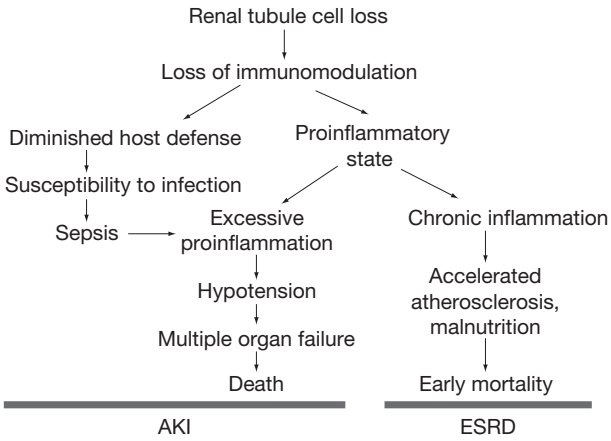

Figure 6 Schematic representation of the sequences of inflammatory dysregulation in acute kidney injury (AKI) and end-stage renal disease (ESRD). The intervention of renal cell therapy may interrupt the pathophysiologic spiral that leads to death in AKI, and may possibly interrupt the chronic proinflammatory state of patients with ESRD. Reprinted from Song, J. H.; Humes, H. D. *Semin. Dial.* **2009**, *22*, 603–609.

The disorder of ESRD is characterized by immune dysregulation presenting with clinical and biological immune deficiency despite chronic activation of immunocompetent cells, especially circulating neutrophils and monocytes.[47] This immune dysregulation develops in patients with chronic renal injury (CRI) prior to the initiation of chronic dialysis therapy, although dialysis causes further inflammatory activation.[48] This chronic inflammatory disease state is characterized by both neutrophil and monocyte dysfunction. Neutrophil phagocytosis and microbe killing are reduced in ESRD patients compared to normal individuals in the presence of spontaneous neutrophil and monocyte activation and reactive oxygen species generation.[49–51] High levels of proinflammatory cytokine serum levels, including IL-6, TNF-α, and IL-1β, are found in ESRD patients, with high levels of production observed in isolated monocytes in these patients.[51] In fact, serum levels of IL-6 correlate well with IL-6 production rates of isolated monocytes from individual ESRD patients.[52,53]

The clinical ramifications of this dysregulated immune state in CRI and ESRD have profound implications. The neutrophil dysfunction translates into the fact that infection is the second most common cause of death in HD patients, approaching 25% of the annual mortality rate.[54] This rate of infection complication is not diminished with a higher dialysis dose or high-flux membrane utilization.[55] Mortality due to sepsis occurs approximately 250-fold more commonly in these patients compared to the general population.[56] The chronic proinflammatory state, as reflected by elevated biomarkers, specifically C-reactive protein (CRP) and IL-6, as well as activation of circulating leukocytes,[57–60] is also highly correlated with accelerated atherosclerosis and early mortality in ESRD patients. Cardiovascular disease processes account for roughly 50% of the annual

mortality rates in Europe and the United States. In fact, the discrepancy between the vascular and chronologic ages of ESRD patients reflects the accelerated atherosclerotic process that develops in these patients.[61]

The immune dysregulated state of CRI and ESRD is also manifested in other ways. ESRD patients exhibit high rates of autoimmune diseases and neoplasia. They demonstate cutaneous anergy in delayed hypersensitivity reactions and respond poorly to vaccination.[62] An improved understanding of these immunologic processes should provide insight into new approaches to treating this immunologic disturbance.

Leukocytes are major contributors to the pathogenesis and progression of many clinical inflammatory disorders, including acute and chronic renal failure. Many therapeutic approaches are under investigation to limit the activation and tissue accumulation of leukocytes at sites of inflammation so that tissue destruction and disease progression can be minimized.[63,64] A synthetic membrane device with the ability to bind and inhibit activated leukocytes along a continuous renal replacement extracorporeal circuit has been developed and is called the selective cytopheretic inhibitory device (SCD). This device incorporates a low-velocity and low-shear-force blood path around a bundled collection of dialysis hollow fibers. In conjunction with regional citrate anticoagulation, this coupling of events within the device results in the sequestration of activated leukocytes in conjunction with a low ionized-calcium (Ca_i) environment due to citrate in the blood circuit to inhibit the release of inflammatory and destructive enzymes and cytokines from the membrane-bound neutrophils and monocytes.[65,66]

Other clinical inflammatory disorders, including SIRS, ischemia/reperfusion injury and adult respiratory distress syndrome (ARDS), are also strong candidate disease states for treatment with renal cell therapy or selective cytopheretic inhibition.[63,64] A large number of therapeutic approaches are under investigation to limit the activation and tissue accumulation of leukocytes at sites of inflammation in order to minimize tissue destruction and disease progression. For example, cardiopulmonary bypass (CPB) is a strong inducer of SIRS, with activation of complement and coagulation systems, and stimulation of cytokine production, and lung and kidney damage can be ameliorated during CPB surgery with the use of leukocyte-depletion filters.[67] Disruption of the activation process of circulating leukocytes may limit microvascular damage and multiorgan dysfunction.

6.634.4. Preclinical Evaluation of Bioartificial Kidney

6.634.4.1. Acute Renal Failure

A bioartificial tubule unit is clearly feasible when conceived as a combination of living cells supported on polymeric substrata, which act as scaffolds for the cells. Renal tubule progenitor cells can be cultured on the biomatrix-coated hollow-fiber membranes of a standard high-flux hemofilter. Dialysate from a conventional dialysis circuit can be passed into the bioartificial tubule as a nutrient and oxygen source for the cells grown on the membrane. The membrane is both water- and solute-permeable, allowing for differentiated vectorial transport and metabolic and endocrine activity provided by the cells, and processed dialysate is discarded. Immunoprotection of cultured progenitor cells is achieved concurrent with long-term functional performance as long as conditions support tubule cell viability.[9] Large-animal studies using an RAD consisting of renal proximal tubule progenitor cells have demonstrated that this device replaces filtration, transport, metabolic, and endocrine functions of the kidney in acutely uremic dogs, following bilateral nephrectomies.[43,68,69] A series of additional animal experiments investigated the impact of treatment with this device on the high mortality of sepsis complicated by AKI. Studies in both dogs and pigs have demonstrated that RAD treatment in a bioartificial kidney circuit improves cardiovascular performance associated with changes in cytokine profiles and confers a significant survival advantage in septic or endotoxin animal models.[70–72]

A noncell therapy, immunomodulatory approach was taken using an SCD, a standard polysulphone HF cartridge (F40, Fresenius AG, Bad Hamburg, Germany) set up in series with an HD circuit. The proprietary circuit[66] was designed to diminish the shear stress (SS) of blood along the hollow fibers from greater than arterial SS ($>30\,\text{dynes}\,\text{cm}^{-2}$) in the first cartridge, to levels below venular SS ($<1\,\text{dynes}\,\text{cm}^{-2}$) in the SCD cartridge to provide an environment for leukocyte adherence.[73] The SCD was evaluated in a porcine model of *Escherichia coli*-induced septic shock and demonstrated increased survival time for SCD-treated groups,[74] along with an ability to lower neutrophil activity (serum myeloperoxidase and CD11b cell-surface expression) and diminish neutrophil tissue invasion.[65]

6.634.4.2. End-Stage Renal Disease

A cell therapy approach to ESRD has a number of technical challenges due to the critical requirement of a durable cell therapy for chronic application. One approach by our group is a wearable bioartifical kidney (WEBAK), utilizing the BRECS and sorbent technology to regenerate peritoneal dialysate to improve therapy for ESRD. Similar to the use of the RAD and BRECS in acute renal failure (ARF), dialysate is used as a nutrient and oxygen source for the cells in the BRECS. A large-animal model was developed to evaluate these BRECS units using PD. PD catheters were placed in 40-kg sheep ($n = 5$). One week postop, 1–2 l of dialysate was infused into the abdomen, followed by continuous PD via catheter connection to the BRECS. In three sheep, the BRECS was used for 6–14 days; in two other sheep, a BRECS unit was not added due to catheter obstruction or peritonitis. No changes in hemodynamics were observed. Oxygen consumption increased by an average of 16% in the BRECS sheep, with a maximum of 63%, compared to *in vitro* averages. When placed into the extracorporeal circuit where PD fluid was the source for nutrients and O_2 delivery, the cells had consistently gluconeogenic properties. Glucose levels increased within the BRECS to an average of $30\,\text{mg}\,\text{dl}^{-1}$.[75] These initial findings are promising as cell durability is critical in cell therapies for chronic applications such as ESRD.

6.634.5. Clinical Evaluation of Bioartificial Kidney

AKI affects up to 200 000 people in the United States annually, and approximately 5% of all long-term hospital patients.

The development of AKI in a hospitalized patient results in a five- to eightfold higher risk of death.[76] The cause of death subsequent to AKI is generally the development of SIRS, frequently secondary to bacterial infection or sepsis, resulting in cardiovascular collapse and ischemic damage to vital organs, and culminating in MOF.[77]

In the United States, 452 000 patients were listed as having ESRD by the 2005 USRDS database, of whom 324 826 were receiving maintenance dialysis.[36] The prevalence of ESRD in the United States is rising by approximately 8% annually.[36,78] The financial cost of dialysis is immense, estimated at USD 64 614/HD patient/year and USD 47 384/PD patient/year. In contrast, transplant patients cost an average of USD 22 142/patient/year.[36,78] The higher cost of maintenance dialysis compared with transplantation does not translate into better results; annual mortality for patients listed for transplant and awaiting a kidney is 6.3%, compared with only 3.8% for patients listed for transplant who do receive a kidney. These statistics compare favorably with the 16.7% annual mortality for ESRD patients not listed for transplant.[79] Transplantation, despite its advantages in terms of cost, morbidity, and mortality, is severely limited by the scarcity of donor organs. In 2006, there were over 300 000 patients on dialysis and 72 983 patients on the kidney waiting list. Only 4096 renal transplants were performed in the first quarter of 2006, based on the Organ Procurement and Transplantation data as of 9 June 2006.

Current dialysis therapies are suboptimal for both AKI and ESRD. These therapies do not meet the medical need to reduce mortality from AKI. Even in ESRD, the outcomes of patients receiving chronic dialysis therapy are still disappointing, with an annual mortality exceeding 25%, on average, and a drastically shortened life expectancy of only 5 years.[36] Several groups have reported that the survival of critically ill patients with AKI could be improved by intensifying the dose of renal replacement therapy,[80–82] but the initial excitement generated by these reports has waned following studies demonstrating that dialysis dose is not closely related to outcomes.[83–85]

6.634.5.1. Acute Renal Failure

The pathophysiology of AKI is due to toxic and/or ischemic damage to the lining epithelium of the renal tubules, which promotes acute organ failure. If the patient can be maintained over the subsequent 7–10 days, the renal epithelium has the ability to regenerate and repair the organ. Extracorporeal cell therapy was implemented to bridge the patient from regenerative repair to baseline health. Renal epithelial cell therapy during an episode of AKI, in conjunction with HF, provides more complete renal replacement therapy as compared to dialysis treatment alone.

6.634.5.1.1. Phase I clinical studies of the RAD

Encouraging preclinical animal data led to an FDA-approved phase I/II clinical trial to evaluate the safety and efficacy of the RAD on ten critically ill patients with ARF and multiorgan dysfunction syndrome (MODS) who were receiving continuous venovenous hemofiltration (CVVH).[86] The predicted hospital mortality rates for these patients, as assessed with acute physiology, age, chronic health evaluation (APACHE) III scores, averaged 85%. The devices used in this study were seeded with human renal proximal tubule cells isolated from kidneys donated for cadaveric transplantation but found to be unsuitable for transplantation due to anatomic or fibrotic defects. The RAD perfusion pump system was connected in series to a CVVH extracorporeal pump system, following the principle tested in the preclinical animal studies, but with a minor adaptation of the circuit to maintain the original CVVH prescription in terms of blood flow rate from the patient and UF rate from the hemofilter.

The results of this clinical trial demonstrated that the experimental treatment could be delivered safely under study protocol guidelines for up to 24 h when used in conjunction with CVVH. The clinical data also indicate that the RAD maintains and exhibits viability, durability, and functionality in this clinical setting. Cardiovascular stability of the patients was maintained, and increased native kidney function, as determined by elevated urine outputs, which was temporally correlated with RAD treatment. The device also demonstrated differentiated metabolic and endocrinologic activity, with ammoniagenesis, GSH reclamation, and endocrinologic conversion of 25-OH-vitD$_3$, to the active form 1,25-(OH)$_2$-vitD$_3$.[87] All but one treated patient with more than a 3-day follow-up showed improvement, as assessed by acute physiologic scores. Six of the 10 treated patients survived past 28 days with kidney function recovery, although only 1 was expected to survive by the predicted mortality scoring system. Of interest, plasma cytokine levels suggested that RAD therapy produces dynamic and individualized responses in patients, depending on their unique pathophysiologic conditions. For the subset of patients who had excessive proinflammatory levels, RAD treatment resulted in significant declines in granulocyte colony-stimulating factor, IL-6, IL-10, and especially IL-6/IL-10 ratios, suggesting a greater decline in IL-6 compared to IL-10 levels and a less proinflammatory state.

6.634.5.1.2. Phase II clinical studies of the RAD

These favorable phase I/II trial results led to an FDA-approved, randomized, controlled, open-label phase II investigation at ten clinical sites to determine whether this cell therapy approach alters patient mortality.[88] Fifty-eight patients (age 18–80 years) with ARF requiring conventional renal replacement therapy (CRRT) in the intensive care unit (ICU) were randomized (2:1) to receive CVVH and RAD ($n = 40$) or CRRT alone ($n = 18$). The primary endpoints were all-cause mortality at days 28, 90, and 180, time to recovery of renal function, time to ICU and hospital discharge, and safety. Baseline demographics and clinical characteristics were well balanced between treatment groups. Mean SOFA renal organ dysfunction subscores were 2.9 and 2.7 in the RAD and CRRT groups, respectively. Acute physiology and chronic health evaluation (APACHE) II scores were slightly, but not significantly, higher in the CRRT-alone group. By most key clinical laboratory parameters, the RAD group had higher degrees of disease severity and MOF than the CRRT-alone group (but no significant differences). A higher proportion of patients in the RAD group completed the study (21 of 40, 53%) compared to patients who received CRRT alone (4 of 18, 22%). Median time on RAD therapy was 35.9 h with a range of 1.8–72.1 h. At day 28, the mortality rate was 33% in the RAD group and 61% in the CRRT group ($p = 0.082$); these 28-day results did not reach statistical

significance. Survival through day 180, however, was significantly improved in the RAD group ($p = 0.034$), and the Cox hazard ratio indicated that the risk of death was approximately 50% of that observed in the CRRT-alone group. By day 28, 21 (53%) of the 40 patients in the RAD group had recovered renal function, ten (25%) had died before renal recovery, eight (20%) remained on renal support, and one (3%) had withdrawn consent. In the CRRT-alone group, a lower proportion of patients had recovered renal function (5 of 18, 28%) by day 28, a higher proportion had died prior to recovery (9 of 18, 50%), and a similar proportion remained on renal support (4 of 18, 22%) compared to the RAD group. Subgroup analyses, including severity of illness (SOFA and APACHE scores), number of organ failures and presence of sepsis at study entry were evaluated. Consistently higher survival rates at 28 days were observed in the RAD group compared to the CRRT-alone group, regardless of the number of organ failures (Figure 7). The incidence of sepsis in the two groups was high, at 73 and 67% in RAD and CRRT-alone groups, respectively. RAD therapy decreased the mortality rate in the patients with sepsis from 67% in the CRRT-alone group to 34%. Of note, patients with five or more failed organs had a 60% mortality rate in the RAD group compared to a 100% rate in CRRT alone. Thus, it appears from these small sample sizes that RAD treatment effects may be more pronounced with greater illness severity at baseline. These promising data suggest that the addition of renal tubule cell therapy to CVVH results in a substantive clinical impact on survival, and that RAD treatment demonstrates an acceptable safety profile.

6.634.5.2. End-Stage Renal Disease

Though the WEBAK has not yet been evaluated in clinical studies for long-term use in ESRD, clinical studies with renal cell therapy paired with CRRT in an extracorporeal circuit have shown promise in the treatment of ARF. As noted previously, ESRD patients on CRRT are at high risk for cardiovascular and infectious diseases. A recent clinical trial failed to show survival benefit from increased doses of HD above what is now standard care.[89] This suggests that there are important metabolic derangements not adequately treated with conventional dialysis treatment. Data from the survival of renal transplant recipients, which far exceed those from the survival of age-, sex-, and risk-matched controls awaiting transplant, also suggest that there is some metabolic function provided by the kidney that transcends this organ's filtration function. Patients with ESRD display elevated levels of CRP (an emerging clinical marker) and proinflammatory cytokines, including IL-1, IL-6, and TNF.[57,58,90] All of these parameters are associated with enhanced mortality in ESRD patients. Specifically, IL-6 has been identified as a single predictive factor closely correlated with mortality in HD patients.[57] Although all ESRD patients could conceivably benefit from a bioartificial kidney, patients in the inflammatory stage who display elevated levels of certain markers of chronic inflammation (most notably IL-6 and CRP) would likely benefit most and will be the target population for clinical study in the near future. Clinical translation from preclinical studies will address long-term cell durability, biocompatibility, and administration protocols.

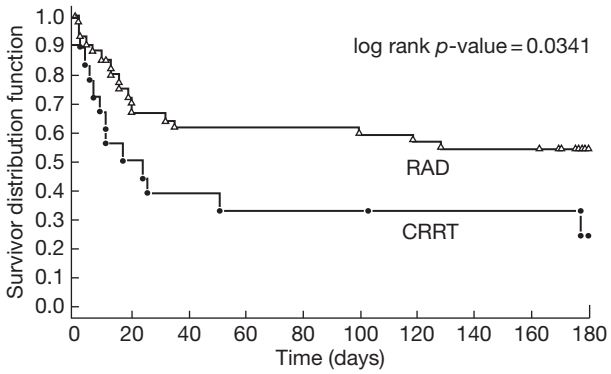

Figure 7 Kaplan–Meier estimates of survival of patients treated with either RAD cell therapy or conventional renal replacement therapy (CRRT). Reprinted from Tumlin, J.; Wali, R.; Williams, W.; *et al. J. Am. Soc. Nephrol.* **2008**, *19*, 1034–1040.

The SCD may provide a novel approach to the immune dysregulation in ESRD. Accordingly, our group has recently evaluated the SCD in a group of chronic HD patients with elevated CRP values. The SCD was placed in series with a hemodialyzer cartridge in a conventional dialysis pump system. Fifteen chronic HD patients were treated for 4 h under standard HD and SCD therapy to ameliorate leukocyte activation. Leukocyte activation parameters were assessed before, during, and after treatment with flow cytometry, along with blood cytokines before and after standard and SCD dialysis therapy. During SCD treatment, multiple leukocyte activation parameters were altered. SCD treatment also lowered proinflammatory cytokines and elevated anti-inflammatory cytokines. Ongoing studies are evaluating dose response effects and the mechanism of action of this device. This approach may be further tested in clinical studies as an innovative intervention to ameliorate the chronic proinflammatory state of ESRD and retard the accelerated atherogenesis associated with chronic renal failure.[91]

6.634.6. Future Prospects

Conventional renal replacement therapies are continuing to advance in the areas of increased feedback control of HD and HF for automated dialysis, ease of use for home treatment, and miniaturization for ambulatory treatments. The promise of renal cell therapy for both acute and chronic applications also opens up new avenues for advances, including implantable bioartificial kidneys.

6.634.6.1. Microelectromechanical System and Extracellular Fluid Volume Sensing

Critical to the success of an automated dialysis platform is online real-time estimation of extracellular fluid (ECF) volume, a complex engineering problem in its own right. Esophageal Doppler monitoring (EDM), pulmonary-artery catheters, and peripheral waveform analysis all provide measures of central hemodynamic parameters. Bioimpedance and hematocrit monitoring may provide estimates of changes in blood volume. Various volume estimation techniques have been deployed in

outpatient maintenance HD.[92] Blood volume monitors have yielded mixed results in clinical trials. An implanted right ventricular pressure monitor appeared to provide valuable clinical information over and above clinical judgment in a very small series.[93]

Ideally, a bioartificial kidney suitable for long-term use in ESRD patients would be capable of performing continuously, like the native kidney, to reduce risks from fluctuations in volume status, electrolytes, and solute concentrations and to maintain acid–base and uremic toxin regulation. As in ARF, cell therapy currently can be administered only intermittently. These additional functions require the eventual design and manufacture of a compact implantable or wearable bioartificial kidney. The advent of silicon bulk and surface micromachining offers hope for the development of such a device.[94] Microelectromechanical systems (MEMS) have traditionally referred to miniature components integrating sensors, actuators, and electronics (see **Chapter 3.315, Biological Microelectromechanical Systems (BioMEMS) Devices**).[95] These devices are produced using many of the same microfabrication techniques as those used to manufacture integrated circuits on silicon substrates. This manufacturing strategy enables the mass production of miniature, high-performance, mechanical, fluidic, and optical components that can be integrated with electronics at low unit cost. These technologies allow the fabrication of pores, beams, gears, and pressure sensors and the patterned deposition of cells in engineered micro- and nanoenvironments. Surface micromachining has been used to provide capillary-like conduits for blood flow in hepatocyte tissue cultures, and micropatterning has been used to control cell growth and differentiation.[96,97]

The telemetric application of MEMS sensor technology to hemodialytic systems has two component requirements: (1) sensing and (2) data transmission. If no internal power source is to be used, external powering of the system becomes a requirement, as well. This can be accomplished via inductive coupling, using radiofrequency transmission from an external source, the charging of a capacitor located on the implanted MEMS chip, and the releasing of the energy to power the MEMS chip and circuit in order to transmit sensed data to an external receiving source. An alternate, and even simpler, scheme is suitable for capacitive MEMS sensors, where changes in the sensing parameter can be translated into capacitance variations of the MEMS sensor. In such cases, the MEMS sensor can be configured into a passive tank circuit that is composed of the variable capacitor and a fixed inductor. This tank circuit exhibits a characteristic resonant frequency that varies as the capacitance changes. An external probe can be used to detect the resonant frequency of the implanted sensor without the use of any circuit in the implanted chip. Millimeter-scale continuous-reading wireless probes have been demonstrated for use within deep tissues, and could be adapted for continuous monitoring of hemodynamic parameters, permitting closed-loop cardiovascular feedback for autonomous HF systems.[98]

6.634.6.2. Wearable Artificial Kidney

The fill volume and footprint of cartridge-based artificial kidney devices continue to become more portable, which allows for future incorporation into a wearable dialysis system. Though no current wearable dialysis system exists, recent advancements in pump miniaturization and technology to reduce the volume of regenerated dialysate during continuous PD are important steps to an engineered solution.[99–102] In this regard, the durability of current cell-based therapy suggests that this therapy could be maintained for at least 6 months in a continuous PD circuit without need for replacement, ideal for a chronic use application such as ESRD.[75]

6.634.6.3. Implantable Artificial Kidney

The aforementioned extracorporeal BRECS is the first step toward a fully implantable artificial kidney. As the technical aspects of the durability of cells are being assessed in the BRECS, an initial proof of concept of the implantable artificial kidney was undertaken. An implantable BAHF to initiate new tissue formation with a capillary bed surrounding synthetic hollow fibers without EC lining was successfully fabricated and implanted. UF draining into an artificial bladder in a rat with protein permselective properties was produced from this implant device.[103] Long-term biocompatibility of the implantable artificial kidney and maintenance of the associated capillary bed are key technical hurdles to be addressed. Although research into the ideal implantable artificial kidney is ongoing, this is a promising future approach.

References

1. Stadnyk, A. W. *FASEB J.* **1994**, *8*, 1041–1047.
2. Deneke, S. M.; Fanburg, B. L. *Am. J. Physiol.* **1989**, *257*, L163–L173.
3. Tannen, R. L.; Sastrasinh, S. *Kidney Int.* **1984**, *25*, 1–10.
4. Maack, T. In *Handbook of Physiology*; Windhager, E. E., Ed.; Oxford University Press: New York, 1992; pp 2039–2118.
5. Bishop, G. A.; Waugh, J. A.; Hall, B. M. *Transplantation* **1988**, *46*, 303–310.
6. Wahl, P.; Schoop, R.; Bilic, G.; *et al. J. Am. Soc. Nephrol.* **2002**, *13*, 1517–1526.
7. Prodjosudjadi, W.; Gerritsma, J. S.; Klar-Mohamad, N.; *et al. Kidney Int.* **1995**, *48*, 1477–1486.
8. Humes, H. D. *Semin. Nephrol.* **2000**, *20*, 71–82.
9. Colton, C. K.; Henderson, L. W.; Ford, C. A.; Lysaght, M. J. *J. Lab. Clin. Med.* **1975**, *85*, 355–371.
10. Graham, T. *Philos. Trans. R. Soc. Lond.* **1854**, *144*, 177–228.
11. Haas, G. *Kilin. Wochenschr.* **1888**, *1923*, 70.
12. Kolff, W.; Berk, H. *Acta Med. Scand.* **1944**, *117*, 121–134.
13. Clark, W. R. *Semin. Dial.* **2000**, *13*, 309–311.
14. Zeaman, L. J.; Zydney, A. L. *Microfiltration and Ultrafiltration, Principles and Applications*; Marcel Dekker Inc.: New York, 1996.
15. Libetta, C.; Zucchi, M.; Gori, E.; *et al. Kidney Int.* **2004**, *65*, 1473–1481.
16. Hoenich, N. A.; Katopodis, K. P. *Contribut. Nephrol.* **2001**, *133*, 81–104.
17. Ronco, C.; Nissenson, A. R. *Blood Purif.* **2001**, *19*, 347–352.
18. Ward, R. A. *J. Am. Soc. Nephrol.* **2005**, *16*, 2421–2430.
19. Ward, R. A.; Leypoldt, J. K.; Clark, W. R.; Ronco, C.; Mishkin, G. J.; Paganini, E. P. *Semin. Dial.* **2001**, *14*, 160–174.
20. Dunleavy, M. *Med. Device Technol.* **1996**, *7*(14–16), 18–21.
21. Deen, W. M.; Satvat, B.; Jamieson, J. M. *Am. J. Physiol.* **1980**, *238*, F126–F139.
22. Bjornson, A.; Moses, J.; Ingemansson, A.; Haraldsson, B.; Sorensson, J. *Am. J. Physiol.* **2005**, *288*, F748–F756.
23. Deppisch, R.; Gohl, H.; Smeby, L. *Nephrol. Dial. Transplant.* **1998**, *13*, 1354–1359.
24. Hancock, L. F.; Fagan, S. M.; Ziolo, M. S. *Biomaterials* **2000**, *21*, 725–733.
25. Vienken, J.; Diamantoglou, M.; Henne, W.; Nederlof, B. *Am. J. Nephrol.* **1999**, *19*, 355–362.
26. Nissenson, A. R.; Ronco, C.; Pergamit, G.; Edelstein, M.; Watts, R. *Blood Purif.* **2005**, *23*, 269–274.

27. Fissell, W. H.; Manley, S.; Westover, A.; Humes, H. D.; Fleischman, A. J.; Roy, S. *ASAIO J*. **2006**, *52*, 221–227.
28. Lopez, C. A.; Fleischman, A. J.; Roy, S.; Desai, T. A. *Biomaterials* **2006**, *27*, 3075–3083.
29. Fareed, J.; Lewis, B. E.; Callas, D. D.; Hoppensteadt, D. A.; Walenga, J. M.; Bick, R. L. *Clin. Appl. Thromb. Hemost.* **1999**, *5*(Suppl. 1), S45–S55.
30. Seifert, B.; Romaniuk, P.; Groth, T. *Biomaterials* **1997**, *18*, 1495–1502.
31. Schneider, P. A.; Hanson, S. R.; Price, T. M.; Harker, L. A. *J. Vasc. Surg.* **1988**, *8*, 229–235.
32. Kadletz, M.; Magometschnigg, H.; Minar, E.; *et al. J. Thorac. Cardiovasc. Surg.* **1992**, *104*, 736–742.
33. Chen, D.; Riesbeck, K.; Kemball-Cook, G.; *et al. Transplantation* **1999**, *67*, 467–474.
34. Dichek, D. A.; Neville, R. F.; Zwiebel, J. A.; Freeman, S. M.; Leon, M. B.; Anderson, W. F. *Circulation* **1989**, *80*, 1347–1353.
35. Wilson, J. M.; Birinyi, L. K.; Salomon, R. N.; Libby, P.; Callow, A. D.; Mulligan, R. C. *Science* **1989**, *244*, 1344–1346.
36. United States Renal Data System, USRDS 2006 annual data report: Atlas of end-stage renal disease in the United States. National Institutes of Health and National Institute of Diabetes, Digestive and Kidney Diseases Eds., Bethesda, 2006.
37. Nikolovski, J.; Gulari, E.; Humes, H. D. *Cell Transplant.* **1999**, *8*, 351–364.
38. Humes, H. D.; Cieslinski, D. A. *Exp. Cell Res.* **1992**, *201*, 8–15.
39. Humes, H. D.; Krauss, J. C.; Cieslinski, D. A.; Funke, A. J. *Am. J. Physiol.* **1996**, *271*, F42–F49.
40. Timpl, R.; Rohde, H.; Robey, P. G.; Rennard, S. I.; Foidart, J. M.; Martin, G. R. *J. Biol. Chem.* **1979**, *254*, 9933–9937.
41. O'Neil, J. J.; Stegemann, J. P.; Nicholson, D. T.; *et al. Transplant. Proc.* **1997**, *29*, 2116–2117.
42. MacKay, S. M.; Funke, A. J.; Buffington, D. A.; Humes, H. D. *ASAIO J.* **1998**, *44*, 179–183.
43. Humes, H. D.; MacKay, S. M.; Funke, A. J.; Buffington, D. A. *Kidney Int.* **1999**, *55*, 2502–2514.
44. Pinsky, M. R.; Vincent, J. L.; Deviere, J.; Alegre, M.; Kahn, R. J.; Dupont, E. *Chest* **1993**, *103*, 565–575.
45. Munoz, C.; Carlet, J.; Fitting, C.; Misset, B.; Bleriot, J. P.; Cavaillon, J. M. *J. Clin. Investig.* **1991**, *88*, 1747–1754.
46. Astiz, M.; Saha, D.; Lustbader, D.; Lin, R.; Rackow, E. *J. Lab. Clin. Med.* **1996**, *128*, 594–600.
47. Descamps-Latscha, B. *Curr. Opin. Nephrol. Hypertens.* **1993**, *2*, 883–891.
48. Descamps-Latscha, B.; *et al*. In *Replacement of Renal Function by Dialysis*; Jacobs, C., *et al*. Eds.; Kluwer Academic: Boston, 1996.
49. Anding, K.; Gross, P.; Rost, J. M.; Allgaier, D.; Jacobs, E. *Nephrol. Dial. Transplant.* **2003**, *18*, 2067–2073.
50. Yoon, J. W.; Pahl, M. V.; Vaziri, N. D. *Kidney Int.* **2007**, *71*, 167–172.
51. Sela, S.; Shurtz-Swirski, R.; Cohen-Mazor, M.; *et al. J. Am. Soc. Nephrol.* **2005**, *16*, 2431–2438.
52. Girndt, M.; Köhler, H.; Schiedhelm-Weick, E.; Schlaak, J. F.; Meyer zum Büschenfelde, K. H.; Fleischer, B. *Kidney Int.* **1995**, *47*, 559–565.
53. Girndt, M.; Sester, U.; Kaul, H.; Köhler, H. *J. Am. Soc. Nephrol.* **1998**, *9*, 1689–1696.
54. Bloembergen, W. E.; Stannard, D. C.; Port, F. K.; *et al. Kidney Int.* **1996**, *50*, 557–565.
55. Allon, M.; Depner, T. A.; Radeva, M.; *et al. J. Am. Soc. Nephrol.* **2003**, *14*, 1863–1870.
56. Sarnak, M. J.; Jaber, B. L. *Kidney Int.* **2000**, *58*, 1758–1764.
57. Bologa, R. M.; Levine, D. M.; Parker, T. S.; *et al. Am. J. Kidney Dis.* **1998**, *32*, 107–114.
58. Zimmermann, J.; Herrlinger, S.; Pruy, A.; Metzger, T.; Wanner, C. *Kidney Int.* **1999**, *55*, 648–658.
59. Girndt, M.; Sester, U.; Sester, M.; Kaul, H.; Köhler, H. *Nephrol. Dial. Transplant.* **1999**, *14*, 2807–2810.
60. Heine, G. H.; Ulrich, C.; Seibert, E.; *et al. Kidney Int.* **2008**, *73*, 622–629.
61. Stenvinkel, P.; Ketteler, M.; Johnson, R. J.; *et al. Kidney Int.* **2005**, *67*, 1216–1233.
62. Descamps-Latscha, B.; Jungers, P.; Witko-Sarsat, V. *Blood Purif.* **2002**, *20*, 481–484.
63. Kaneider, N. C.; Leger, A. J.; Kuliopulos, A. *FEBS J.* **2006**, *273*, 4416–4424.
64. Maroszynska, I.; Fiedor, P. *Ann. Transplant.* **2000**, *5*, 5–11.
65. Ding, F.; Song, J. H.; Lou, L.; *et al. J. Am. Soc. Nephrol.* **2008**, *19*, 458A.
66. Humes, H. D. Selected cytopheresis device and related methods thereof. U.S. Patent WO2009/02981, June 4, 2009.
67. Gu, Y. J.; de Vries, A. J.; Boonstra, P. W.; van Oeveren, W. *J. Thorac. Cardiovasc. Surg.* **1996**, *112*, 494–500.
68. Humes, H. D.; Buffington, D. A.; MacKay, S. M.; Funke, A. J.; Weitzel, W. F. *Nat. Biotechnol.* **1999**, *17*, 451–455.
69. Humes, H. D.; Fissell, W. H.; Weitzel, W. F.; *et al. Am. J. Kidney Dis.* **2002**, *39*, 1078–1087.
70. Fissell, W. H.; Dyke, D. B.; Weitzel, W. F.; *et al. Blood Purif.* **2002**, *20*, 55–60.
71. Fissell, W. H.; Lou, L.; Abrishami, S.; Buffington, D. A.; Humes, H. D. *J. Am. Soc. Nephrol.* **2003**, *14*, 454–461.
72. Humes, H. D.; Buffington, D. A.; Lou, L.; *et al. Crit. Care Med.* **2003**, *31*, 2421–2428.
73. Kroll, M. H.; Hellums, J. D.; McIntire, L. V.; Schafer, A. I.; Moake, J. L. *Blood* **1996**, *88*, 1525–1541.
74. Ding, F.; Song, J.; Lou, L.; *et al. J. Am. Soc. Nephrol.* **2009** (abstract).
75. Rojas, A.; Hageman, G.; Lou, L.; *et al*. Animal model of a wearable bioartificial kidney using peritoneal dialysis. ASAIO 2009 Annual Meeting (abstract).
76. Schrier, R. W.; Wang, W. *N. Engl. J. Med.* **2004**, *351*, 159–169.
77. Breen, D.; Bihari, D. *Kidney Int.* **1998**, *66*, S25–S33.
78. Neilson, E. G.; Hull, A. R.; Wish, J. B.; Neylan, J. F.; Sherman, D.; Suki, W. N. *J. Am. Soc. Nephrol.* **1997**, *8*, S1–S4.
79. Wolfe, R. A.; Ashby, V. B.; Milford, E. L.; *et al. N. Engl. J. Med.* **1999**, *341*, 1725–1730.
80. Ronco, C.; Bellomo, R.; Homel, P.; *et al. Lancet* **2000**, *356*, 26–30.
81. Saudan, P.; Niederberger, M.; De Seigneux, S.; *et al. Kidney Int.* **2006**, *70*, 1312–1317.
82. Schiffl, H.; Lang, S. M.; Fischer, R. *N. Engl. J. Med.* **2002**, *346*, 305–310.
83. Bouman, C. S.; Oudemans-Van Straaten, H. M.; Tijssen, J. G.; Zandstra, D. F.; Kesecioglu, J. *Crit. Care Med.* **2002**, *30*, 2205–2211.
84. Gillum, D. M.; Dixon, B. S.; Yanover, M. J.; *et al. Clin. Nephrol.* **1986**, *25*, 249–255.
85. Tolwani, A. J.; Campbell, R. C.; Stofan, B. S.; Lai, K. R.; Oster, R. A.; Wille, K. M. *J. Am. Soc. Nephrol.* **2008**, *19*, 1233–1238.
86. Humes, H. D.; Weitzel, W. F.; Bartlett, R. H.; *et al. Kidney Int.* **2004**, *66*, 1578–1588.
87. Thomas, M. K.; Lloyd-Jones, D. M.; Thadhani, R. I.; *et al. N. Engl. J. Med.* **1998**, *338*, 777–783.
88. Tumlin, J.; Wali, R.; Williams, W.; *et al. J. Am. Soc. Nephrol.* **2008**, *19*, 1034–1040.
89. Eknoyan, G.; Beck, G. J.; Cheung, A. K.; *et al. N. Engl. J. Med.* **2002**, *347*, 2010–2019.
90. Kimmel, P. L.; Phillips, T. M.; Simmens, S. J.; *et al. Kidney Int.* **1998**, *54*, 236–244.
91. Humes, H. D.; Sobota, J. T.; Ding, F.; Song, J. H. The Rad Investigator Group. *Blood Purif.* **2010**, *29*, 183–190.
92. Dasselaar, J. J.; Huisman, R. M.; de Jong, P. E.; Franssen, C. F. *Nephrol. Dial. Transplant.* **2005**, *20*, 2043–2049.
93. Braunschweig, F.; Kjellstrom, B.; Soderhall, M.; Clyne, N.; Linde, C. *Nephrol. Dial. Transplant.* **2006**, *21*, 176–183.
94. Fissell, W. H.; Humes, H. D.; Roy, S.; Fleischman, A. *J. Am. Soc. Nephrol.* **2002**, *13*, 602A.
95. Roy, S.; Ferrara, L. A.; Fleischman, A. J.; Benzel, E. C. *Neurosurgery* **2001**, *49*, 779–797; discussion 797–778.
96. Chen, C. S.; Mrksich, M.; Huang, S.; Whitesides, G. M.; Ingber, D. E. *Biotechnol. Prog.* **1998**, *14*, 356–363.
97. Kaihara, S.; Borenstein, J.; Koka, R.; *et al. Tissue Eng.* **2000**, *6*, 105–117.
98. Talman, J. R.; Fleischman, A. J.; Roy, S. *IEEE Trans. Biomed. Eng.* **2006**, *53*, 538–546.
99. Gura, V.; Davenport, A.; Beizai, M.; Ezon, C.; Ronco, C. *Am. J. Kidney Dis.* **2009**, *54*, 104–111.
100. Ronco, C.; Davenport, A.; Gura, V. *Hemodial. Int.* **2008**, *12*(Suppl. 1), S40–S47.
101. Davenport, A.; Gura, V.; Ronco, C.; Beizai, M.; Ezon, C.; Rambod, E. *Lancet* **2007**, *370*, 2005–2010.
102. Gura, V.; Ronco, C.; Nalesso, F.; *et al. Kidney Int.* **2008**, *73*, 497–502.
103. Tiranathanagul, K.; Dhawan, V.; Lytle, I. F.; *et al. ASAIO J.* **2007**, *53*, 176–186.

Relevant Websites

http://www.advancedrenaleducation.com/
http://baxter.com/products/renal/hemodialysis/index.html

http://www.fmc-ag.com/internet/fmc/fmcag/neu/fmcpub.nsf/Content/Product_Portfolio
http://www.fmc-ag.com/internet/fmc/fmcag/neu/fmcpub.nsf/Content/Dialysis_Compact_2004_0
http://www.fresenius.se/internet/fag/com/faginpub.nsf/Content/History+of+Dialysis
http://gambro.com/int/
http://www.hdcn.com/ch/hist/
http://minntech.com/renal/products/index.html
http://www.kidneyschool.org
http://www.medscape.com/nephrology
http://www.nlm.nih.gov/medlineplus/tutorials/kidneyfailure/htm/_no_50_no_0.htm

6.635. Surgical Adhesion and Its Prevention

P Godara and B Milthorpe, University of Technology, Sydney, NSW, Australia

© 2011 Elsevier Ltd. All rights reserved.

6.635.1.	**Introduction**	561
6.635.2.	**Formation of Adhesions and Major Areas of Concern**	562
6.635.2.1.	Pathophysiology of Adhesion Formation	562
6.635.2.2.	Peritoneum and Urinary and Reproductive	564
6.635.2.2.1.	Peritoneum	564
6.635.2.2.2.	Urinary and reproductive	564
6.635.2.3.	Tendon, Ligament, and Joint	565
6.635.2.4.	Pericardium	565
6.635.3.	**Barriers to Adhesion: Current Clinical Practice**	565
6.635.3.1.	Solid Barriers (Membranes/Mechanical Barriers)	565
6.635.3.1.1.	Resorbables	565
6.635.3.1.2.	Nonresorbables	565
6.635.3.2.	Resorbable Spray-on, Gel, and Liquid Barriers	567
6.635.3.2.1.	Spray-on	567
6.635.3.2.2.	Gel	567
6.635.3.2.3.	Liquid	567
6.635.3.3.	Nonbarrier Methods	567
6.635.3.3.1.	Hybrid systems	567
6.635.3.3.2.	Transgene/drug/pharmacologic agent therapies	567
6.635.4.	**Barriers to Adhesion: Current Research**	568
6.635.5.	**Uses for Adhesion**	569
6.635.6.	**Discussion**	570
6.635.6.1.	Complications of Barrier Films	570
6.635.6.1.1.	Inflammation	570
6.635.6.1.2.	Nutrient deprivation	570
6.635.6.1.3.	Potential late adhesion development	570
6.635.6.2.	Design of New Barrier Films	570
6.635.6.2.1.	Drug-eluting barrier materials to reduce inflammation and increase fibrinolysis	570
6.635.6.2.2.	Allow penetration of nutrients and removal of waste (MW > 1 M)	570
6.635.6.2.3.	Bioresorbable, but does not form microscopic pieces on degradation (inflammatory)	570
6.635.6.3.	Technique and Assessment	570
6.635.6.4.	Summary	570
References		571

Glossary

Adhesiolysis Removal of adhesions (by dissolution).
Anastomosis Surgically made joint in an organ or tissue.
Fibrinolysis Dissolution of fibrin gel (by enzymes).
Peritoneal cavity Nominally the same as the peritoneum, but often implying the whole abdominal cavity.
Peritoneum The gap between the peritoneal membrane inner surfaces (outer surfaces of the relevant organs).

Abbreviations

FDA Food and Drug Administration (USA)
PTFE Poly(tetrafluoroethylene)
TGF-β Tissue-derived growth factor-beta
tPA Tissue plasminogen activator
USD United States Dollars
VEGF Vascular endothelial growth factor

6.635.1. Introduction

There are a number of organs and tissues that move significantly with respect to the surrounding structures. The intestines and visceral organs, the female reproductive organs, tendons, the heart, lungs, muscles, skin, and the brain are some of the major organs that have significant movement. For most of these organ systems, movement is vital to proper function, and the body has

developed several structures, including serous membranes, adventitia, and fascia layers, to allow this movement.

Adhesions are collagenous, fibrous structures that result from the body's wound-healing system and tether the moving organ to the surrounding tissue, or surround an organ, such as the intestine, and constrict it. The net effect of the adhesion can range from mild to catastrophic. Unfortunately, it is not possible to predict which adhesions will have severe to catastrophic effects on organ function.

Although adhesions may occur naturally from inflammatory disease, most adhesions are the result of surgical intervention, especially abdominal surgery. Ellis[1] gives a highly readable account of the history of the development of interest in surgical adhesions, their potential causes, and the effects on patients and society. According to Ellis, the rate of serious complications requiring reoperation is fairly small, generally around 1–9% (also see Grant *et al.*[2]), although there is a high degree of variability depending on operation type, and complications may take many years or decades to show up. However, abdominal operations are so common that one report[3,4] estimated that the total cost of adhesiolysis in the United States in 1988 alone was over USD1 billion, rising to USD1.3 billion by 1994! This does not include the cost of litigation.

Recently, Park *et al.*[5] in their study reported a 4.6% rate of serious complications following colorectal surgery. However, adhesion formation of all degrees of severity would appear to be in the high 90% range.[6] Not surprisingly, there have been many attempts to develop techniques and materials to prevent or reduce the occurrence of adhesions. One major approach is the use of (bio)materials as barriers to the development of fibrous adhesions between the serous membrane and the organ. This chapter examines some of the materials, and other approaches, used for adhesion prevention.

What is the benefit/advantage of using barrier biomaterials to prevent adhesion formation? The prevailing assumption from all the reviews and studies would appear to be that physical prevention of fibrous scar formation between the organ and the surrounding membrane will prevent the serious complications that are associated with a relatively low proportion of cases of actual fibrous adhesion formation. The prevailing practice is also to use resorbable materials (see **Section 6.635.3.1.1**), although there are some nonresorbable materials that have been used (**Section 6.635.3.1.2**).

There are a number of materials in clinical use and many more experimental composite materials, mostly centering around a limited set of base polymers. Both clinical and animal studies have increased our knowledge and understanding, and have led to improved surgical techniques and methods to reduce the overall level of adhesions.[5]

It is interesting to note that adhesions are not necessarily bad in abdominal surgery. Ellis[1] reports that previous experimental data on rats show that adhesions are a necessary source of revascularization of ischemic areas of the bowel. Indeed, retrospective analysis[7] of a number of studies involving a resorbable barrier shows an improvement in the rate of higher severity adhesions but no statistical improvement in serious complications. However, there is a statistical increase in abscess formation and anastomotic leakage, and the authors conclude that the anastomosis should not be covered by the barrier.

Zawaneh and Putnam[8] have provided a significant review, up to 2007 of the field of biomaterials for adhesion and seroma prevention. This chapter does not intend to repeat their work, and readers are referred to the review for details. This chapter will rather look at the more recent work (mainly 2007–2009), mostly animal studies, with some overview to enable an appropriate understanding of the context.

Although the concept of adhesion barriers and prevention is deceptively simple, the many decades of work on the subject have not yielded the desired outcome of prevention of serious sequelae from adhesions following surgery.[9]

> ... adhesions still remain a significant, unresolved postoperative complication. (Lim *et al.*, 2009)

6.635.2. Formation of Adhesions and Major Areas of Concern

6.635.2.1. Pathophysiology of Adhesion Formation

Adhesion formation is a natural, if unwelcome, consequence of the body's wound-healing response. Early events following wounding involve filling of the wound site with a fibrin clot. This clot, initially, is a weak hydrogel that fills space and is designed to prevent further loss of blood. As a hydrogel, it also allows invasion by the cells of the innate immune system (mainly neutrophils and granulocytes) to clean out the wound. As the wound-healing process continues, macrophages invade the clot and begin removing debris and bacteria. Finally, fibroblasts and cells from the regenerating local tissue invade, once the inflammatory (wound cleaning) phase has abated. The fibrin clot is eventually removed by fibrolytic enzymes and by the invading cells as relevant local tissue is regenerated.

Stiffening of the clot due to cross-linking occurs mechanically relatively early, and then as fibrinolysis occurs, the clot becomes less and less stiff. In the ideal case, fibrinolysis should be well advanced prior to fibroblast invasion.

Fibrin also acts as a sink, when whole, and as a source, as it is lysed, for a large number of growth factors that regulate the inflammatory process and for revascularization of the resolving tissue.

In the nonideal case, fibroblasts arrive in the clot while the inflammatory process is still under way and before substantial net fibrinolysis can occur. Under these circumstances, the fibroblasts receive information on the local mechanical and biochemical environment. In terms of biochemical environment, a fibrin clot is neutral, and therefore, it is reasonable to conjecture that the fibroblasts will tend to follow the local mechanical cues, and not the local tissue regeneration biochemical cues, which are usually too remote on a biochemical gradient basis to affect cellular behavior. The result will, therefore, be a scar, with collagen fibers oriented mostly to resist the local mechanical stress. An adhesion is formed where this scar tissue surrounds or adheres to an organ that moves (visceral organs, female reproductive organs, heart, tendons, brain). If the adhesion prevents necessary movement of the organ, or by constriction causes organ failure, a pathological condition is created.

Invasion by fibroblasts and regeneration of tissue is a natural competition. In the case of abdominal surgery, the

regenerating tissue of interest is the mesothelial layer that lines the inside of the peritoneal membrane. Coverage of damaged areas of mesothelium with new cells would appear to be essential to the prevention or limitation of adhesions.[1] This would appear to occur fairly quickly, with most damaged areas recovering in 3–7 days.[10] The timeline for fibroblast appearance in the fibrin clot is also around 1 day to 1 week.[10,11]

Figure 1 outlines the competitive processes and approximate timelines in the wound-healing system. The crucial time would appear to be around days 3–5 during which if fibrinolysis is sufficiently advanced, indicating mesothelial repair, adhesions will not form. If inflammation or irritation continues and the regrowth of the mesothelial layer is inhibited, then the conditions are set for adhesions to form. For more detailed descriptions of the associated biochemical factors and cellular invasion, the reader is referred to Thompson *et al.*,[12] diZerega and Campeau,[10] and Cheong *et al.*[11]

Irritants prolong the inflammatory stage, as demonstrated by the problems of powder on surgical gloves, first, talc, and then starch, in enhancing adhesions in abdominal surgery.[1]

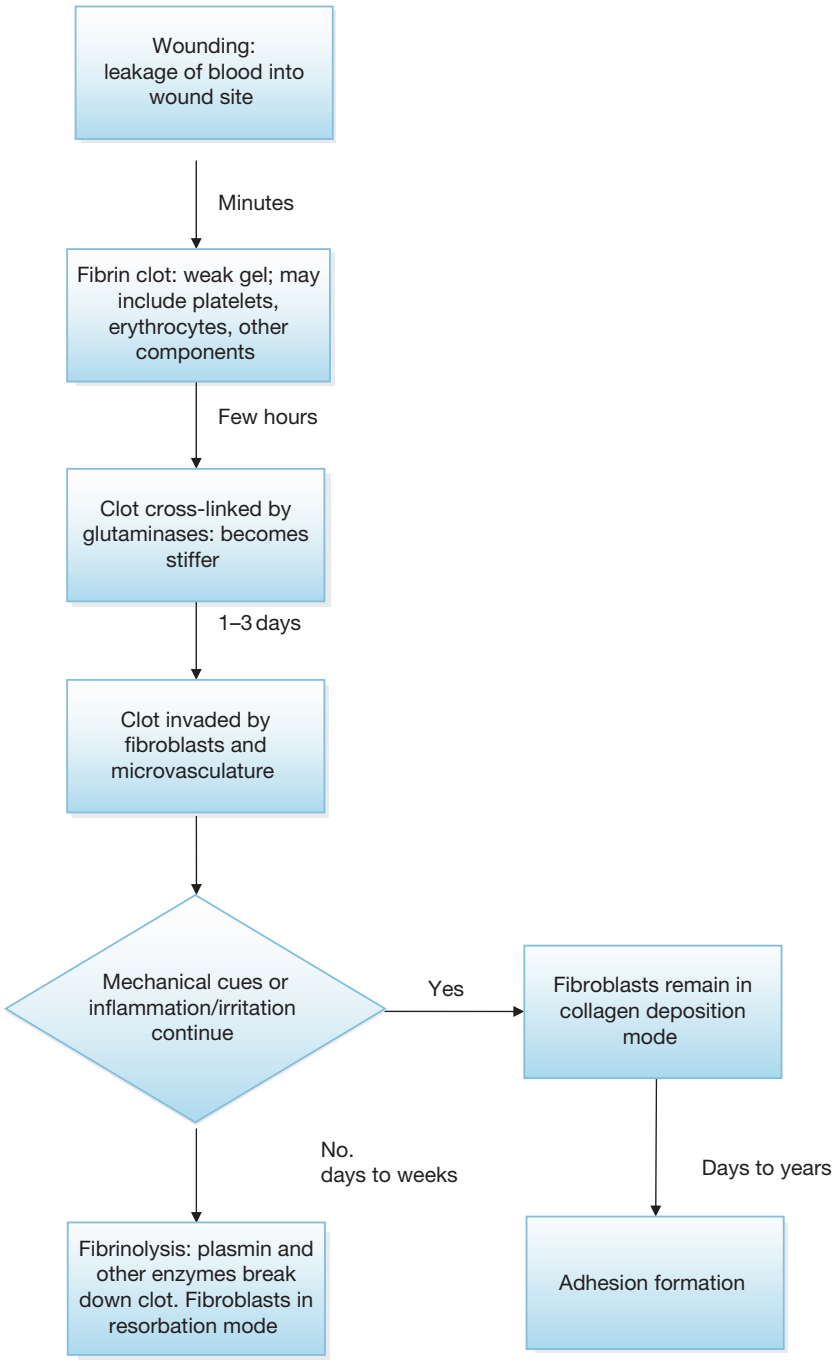

Figure 1 Flowchart, with approximate timeline, of the repair or adhesion development pathways.

Other irritants, such as sutures, would also appear to have a significant effect, and Ellis notes the final recommendation to avoid attempting to suture the damaged mesothelium and underlying membrane to reduce the deficit in the layer.

With prolonged irritation comes prolonged inflammation, addition to the fibrin clot (through increased vascular permeability), reduced fibrin degradation (through reduced tissue plasminogen activator (tPA) concentration[12]), and reduced mesothelial cell recovery. This means that fibrinolysis will not have proceeded far enough for the mechanical cues to the fibroblasts to be reduced and to cause them to gene-switch to resorption rather than collagen deposition. Mechanical stimulation has been shown to be a significant factor in the switch by fibroblasts between collagen deposition (strained) and matrix resorption (unstrained).[13]

Other tissues, such as the pleura, the dura mater/arachnoid mater/pia mater around the brain, and the pericardium are serous membranes that perform comparably to the pericardium. The tendon is surrounded by a synovial membrane that also performs a similar set of functions. In all these situations, wounding either by surgery, trauma, or infection can lead to adhesion formation by very similar mechanisms.

It should be noted again here that adhesions and scar tissue contain vasculature and can provide necessary nutrition to the organs to which they adhere[1] if the local vasculature has been damaged by the surgery. Indeed, Ellis[14] earlier proposed that ischemia, rather than wounding *per se*, was the cause of adhesions. Ischemia may still be a major cause of adhesions, as the lack of oxygen in the region will prolong the inflammatory response and provide cytokines that encourage vascular ingrowth through the repairing mesothelial layer.

Readers interested in more detail on wound healing, fibroproliferative diseases, and tissue regeneration may find the following general references useful:

Eming *et al.*[15] review the association of an advanced and active immune system on tissue regeneration;

Levin[16] takes a geometry-based overview of regeneration and sounds some warnings about attempting to micromanage regeneration that could well be applicable to attempts to control adhesions; and

Fusi[17] provides a generalized mathematical model that may be applied to wound healing and fibroproliferative disorders.

6.635.2.2. Peritoneum and Urinary and Reproductive

6.635.2.2.1. Peritoneum

The peritoneal cavity (abdominal cavity or coelum) contains, largely, the visceral organs including the liver, stomach, small and large intestines, and associated smaller organs. In women, the uterus, Fallopian tubes, and ovaries also protrude into the peritoneal cavity.

The peritoneal membrane (peritoneum) is a serous membrane that performs the functions of separating the visceral organs from the bulk of the body and each other, providing lubrication for the movement of the visceral organs,[18] and providing nutrition to the outer layers of the visceral organs and preventing the vasculature from connecting between the main part of the body and the moving visceral organs. As a serous membrane, it has a layer of connective tissue with a single cell thickness of mesothelial cells that secrete a lubricating liquid into the space between the layers. As most of the organs in the peritoneal cavity are coated with peritoneum, the peritoneum effectively provides the lubricated surface that allows the organs to move within the cavity.

The healing of the peritoneum is different from the process of general wound healing of the tissues or epidermal epithelium of the skin in that the areas of the peritoneum that have lost cells rapidly repopulate all over the denuded surface from precursor cells.[10] Major body tissues and skin epithelium repopulate from the edge of the wound only.

As mentioned in the previous section, the area of the denuded surface is also associated with a fibrin clot and the general wound-healing process, which may lead to fibrous tissue formation instead of tissue regeneration. The formation of an adhesion, in effect a bridge of tissue between the underlying layers of tissue, prevents the restoration of the original mesothelial layer. The opposite is also the case with a restored mesothelium preventing adhesions. The complexity of the competition between these processes in the early postoperative phase may well be the cause for a number of authors such as Tulandi[19] to conclude that aspects of the healing process are still unclear.

What is clear, however, is that complications due to adhesions in the peritoneal cavity may be severe, including obstruction of the small intestine (by forming a ring around the intestine and preventing peristalsis), and pelvic and intra-abdominal pain; that these complications may not occur until many years postoperatively[1,19]; and that these complications are sufficiently common and their intervention sufficiently costly to require the development of methods to reduce them.

A variety of approaches have been made in attempting to understand the causes of adhesion and complications. In terms of breadth of cause, Vural *et al.*[20] examined the role of neutrophils in adhesion formation, as these cells are major initiators of the inflammatory response, whereas Cahill and Redmond[21] have proposed anti-VEGF therapy in order to reduce the formation of blood vessels in the fibrin clot/adhesion and therefore the severity and longevity of the adhesion. Ellis[1] remains a strong promoter of tPA therapy, and there is some evidence that long and extensive abdominal surgery can result in lowered tPA levels in the peritoneal fluid.[22,23]

Cheung *et al.*[24] have conducted a recent review of adhesion prevention methods and clinical outcomes. Their conclusion is equivocal, citing expense and higher rates of complications for one material barrier, despite that barrier performing best in reducing adhesions at the site of surgery.

6.635.2.2.2. Urinary and reproductive

The top of the bladder and, in females, the uterus, Fallopian tubes, and ovaries, have peritoneal membrane surfaces. Gynecological surgery has been associated with fibrous adhesions affecting the small bowel as well as the reproductive organs. Conversely, an association between infertility and adhesions has been known for many years.[19] Adhesions from surgery in the lower abdomen can interfere significantly with egg translation to the Fallopian tube. The problems of specialization are commented upon by Tulandi, who remarks that gynecologists seem to forget that later onset bowel obstruction, a potentially fatal complication, could be associated with the gynecological surgery.

Nappi *et al.*[25] have reviewed a large number of techniques related to gynecological surgery and minimization of complications and equivocally concluded that there are benefits to the uses of barrier materials, liquids, or drug treatments at the time of operation.

In an interesting aside, Sjosten *et al.*,[26] using a rabbit model, found that starch granules placed in the vagina could lead to adhesions in the lower abdomen, as the granules were able to travel through the uterus and Fallopian tubes and then into the peritoneal cavity. This unlikely route to adhesion development gives cause for thought about other routes for inflammatory particles to reach the peritoneum, especially with the recent prevalence of nanoparticles that may be taken up by a number of cell types.

6.635.2.3. Tendon, Ligament, and Joint

Tendons connect the muscle body to the bone on which the muscle acts. As tendons must be able to move considerable distances, relatively, as the muscle body contracts, they lie within a synovial sheath structure that provides both lubrication and nutrition to the tendon.

The major repairs to tendons are usually those of the hand and the Achilles tendon at the ankle. Tendon reconstruction often is required following trauma to the hand or wrist, or as a result of 'snapping' of the Achilles tendon during exercise. Fibrous adhesions are a common complication of tendon repair,[27] and there have been a large number of studies on ways to prevent or minimize such adhesions, as they affect movement of the associated bone and, hence, the overall function of the associated joint.

The most common treatment to attempt to prevent adhesions is by use of passive movement. However, this is not always practicable, and the strength of the tendon repair is not always sufficient to allow passive movement over the whole range of motion of the joint. In addition, there seems to be some variation in the likelihood of adhesion formation with different styles of repair of the tendon and the tendon sheath, and the size of the deficit in the tendon sheath.

Ligaments and joints are also subject to adhesion formation in the synovial space after trauma or surgery. The degree of damage to the synovial membrane and time of immobilization are two of the major contributors.[28]

A number of barrier materials have been tried in tendon and joint repair in animal models with limited results. These include pericardium,[29,30] oxidized regenerated cellulose,[31] hyaluronic acid derivatives,[32] intestinal submucosa,[33] carboxymethylcellulose,[34] PTFE and e-PTFE,[35] hydroxyapatite and alumina,[36] and others listed by Ozturk *et al.*[37] Few have made it to clinical trial or clinical use.

6.635.2.4. Pericardium

The pericardium is the membrane surrounding the heart. Adhesions between the pericardium and the heart tissue are mainly due to open-heart surgery. Although adhesion-related complications are relatively rare, complications associated with reopening of the pericardium are more common and potentially life-threatening. Adhesions from previous surgery obscure the heart and graft structures, and dissection of the adhesions may lead to accidental damage to the grafts or to the heart muscle. Mortality rates from iatrogenic damage to the graft or the heart may range up to 56% with an incidence rate of 4–9% of reoperations.[38]

The number of coronary operations is increasing with the aging population and increasing longevity. Consequently, there is a need for systems to reduce adhesions in the pericardium if the reoperation rate is on the order of 10%.[38]

Recent experimental work has looked at a number of approaches, including carboxymethyl chitosan,[39] oxidized regenerated cellulose (Interceed®),[38] and hyaluronic acid derivatives.[40] All show reduced numbers or density of adhesions with the use of a barrier material. The current alternative for pericardial applications is pharmaceutical, with investigations including keratinocyte growth factor, an activator of mesothelium regeneration,[41] and chymase inhibitor, which reduces the activation of TGF-β1, an activator of fibroblasts and fibrosis.[42] Whether either of these approaches will attain clinical acceptance is still unknown.

6.635.3. Barriers to Adhesion: Current Clinical Practice

Barriers that physically separate serosal surfaces aim to prevent the occurrence of tissue adhesion after surgery. Currently, there are only two FDA-approved clinical membrane products, Interceed® (Johnson & Johnson) and Seprafilm® (Genzyme Corp), that are available for use for adhesion prevention.[43]

An overview of current resorbable and nonresorbable barrier methods including solid membrane/mechanical barriers, spray-on, gel and liquid barriers is presented. Emerging nonbarrier therapies such as those employing pharmacologic agents have also been included, but methods such as drainage and dissection techniques, and surgical and mechanical treatments are outside the scope of this chapter.

6.635.3.1. Solid Barriers (Membranes/Mechanical Barriers)

6.635.3.1.1. Resorbables

6.635.3.1.1.1. Polysaccharide-based

Table 1 lists recent work with resorbable barrier materials manufactured from cross-linked polysaccharides.

6.635.3.1.1.2. PEG-based (polyethylene glycol)

Polyethylene glycol-based resorbable barrier materials have been used in a variety of forms. Table 2 lists the recent studies.

6.635.3.1.1.3. Other polymers

Although polysaccharide- and PEG-based materials predominate in barrier applications, some other common biomaterial polymers are also used, as shown in Table 3.

6.635.3.1.1.4. Other

Among the resorbable solid barriers, there are some barriers made from animal tissue, listed in Table 4.

6.635.3.1.2. Nonresorbables

6.635.3.1.2.1. Polytetrafluoroethylene

Polytetrafluoroethylene (Teflon®) has been used in a large number of medical applications and elicits a very small inflammatory response. This has seen its continued use as a barrier

Table 1 Polysaccharide-based materials

Base material	*Product name*	*Manufacturer*	*Description*	*Application/procedure*
Hyaluronic acid	CMHA-SX or Carbylan-SX	Carbylan Biosurgery Inc.	Chemically modified, *in situ* cross-linkable derivative of hyaluronan	Pericardiotomy[40] Cecum–abdominal wall[56] Uterine horn[56]
Carboxymethyl cellulose (CMC)	Seprafilm	Genzyme Corp.	Made from chemically modified sodium hyaluronate and CMC	Ovarian and Fallopian tube laparatomy[57] Peritoneal laparatomy[57] Peritoneal midline incision[6] Ileostomy closure[58] Cecum–abdominal wall[59] Cecal abrasion[60] Radical colorectal resection[5]
	N/A	N/A	Made from Fe^{3+} cross-linked CMC	Achilles tendon abrasion[34]
Chitosan	N/A	N/A	Polypropylene mesh coated with a chitosan membrane	Cecal abrasion, parietal peritoneum incisions[46]
Cellulose	Interceed®	Johnson & Johnson	Made from oxidized regenerated cellulose	Achilles tendon repair[31] Pericardial excision[38]

Table 2 Polyethylene glycol-based materials

Base material	*Product name*	*Manufacturer*	*Description*	*Application/procedure*
Polyethylene glycol	Poloxamer 407	N/A	Composed of two hydrophilic PEG blocks separated by a hydrophobic poly(propylene glycol) block	Uterine horn devascularization and serosal injury[61]
	N/A	N/A	Comb-like polymers with pendent polyethylene glycol and polylactide side chains	Intra-abdominal serosal defects (peritoneal wall, intestine, liver)[62]
	N/A	N/A	Poly(L-lactic acid) and polyethylene diblock copolymer films	Cecum–peritoneal wall defects[63]

Table 3 Other polymeric materials

Base material	*Product name*	*Manufacturer*	*Description*	*Application/procedure*
Polylactic acid (PLA)	SurgiWrap™	Macropore Biosurgery	PLA film	Cecum–abdominal wall[59]
Poly(lactic-*co*-glycolic acid) (PLGA)	N/A	N/A	Electrospun nanofibrous membranes	Uterine horn and abdominal wall[64]
Polyglactin910/polydioxanon	Ethisorb®	Ethicon	Composite of polyglactin910 and polydioxanon	Abdominal wall closure[65]
Poly(3-hydroxybutyrate-*co*-3-hydroxyhexanoate) (PHBHHx)	N/A	N/A	PHBHHx dissolved in various nonharmful organic solvents, forms a porous structured film *in situ*	Intra-abdominal[66]
Polyester	PX	Covidien	Polyester–collagen composite	Ventral hernia[67]

Table 4 Other materials

Base material	*Product name*	*Manufacturer*	*Description*	*Application/procedure*
Human amniotic membrane (HAM)	N/A	N/A	Glycerol-cryopreserved human amniotic membrane	Abdominal wall closure[65]
Human peritoneal membrane	N/A	Community Tissue Services	Human peritoneal membrane	Ventral hernia[67]

material (Table 5), even though it must be sutured in place and removed by a subsequent surgery.

6.635.3.1.2.2. Polypropylene

Polypropylene is a widely used polymer in the production of prosthetic materials due to its low cost and *in situ* nondegradation. A number of commercially available meshes generally used intraperitoneally for intra-abdominal hernia repair are given in Table 6.

There are a number of problems associated with mesh use. The implant can undergo pronounced *in situ* shrinkage.[44] Seroma and hematoma formation can occur between the

Table 5 Polytetrafluoroethylene

Base material	*Product name*	*Manufacturer*	*Description*	*Application/ procedure*
Polytetrafluoroethylene (PTFE)	N/A	Proxy Biomedical	Compressed PTFE	Ventral hernia[67]
	N/A	N/A	Composite of human peritoneal membrane and compressed PTFE	Ventral hernia[67]
	GORE-TEX®	W.L. Gore & Associates	Porous thermomechanically expanded PTFE	Laminectomy[68]
Expanded polytetrafluoroethylene (e-PTFE)	GORE PRECLUDE® MVP®	W.L. Gore and Associates	Expanded polytetrafluoroethylene (e-PTFE)	Craniotomy[69]

Table 6 Coated polypropylene

Brand name	*Description*	*Manufacturer*
C-Qur™ Mesh	PP mesh with an omega-3 fatty acid absorbable coating	Atrium Medical Corp.
Dynamesh® IPOM	Woven composite PP and polyvinylidene fluoride mesh	FEG Textiltechnik mbH
Proceed™	PP mesh with a layer of polydioxanone polymer film and a layer of absorbable oxidized regenerated cellulose	Ethicon, Johnson & Johnson
Prolene®	PP mesh	Ethicon, Johnson & Johnson
Parietex™ Composite	Polyester mesh with a layer of absorbable collagen–polyethylene glycol–glycerol	Covidien Healthcare
Parietene™ Composite	PP mesh with a layer of absorbable collagen–polyethylene glycol–glycerol	Covidien Healthcare
TiMESH®	PP mesh with a titanium surface	GfE Medizintechnik GmbH
Ultrapro®	PP mesh with an absorbable polyglycolide/e-caprolactone coating	Ethicon, Johnson & Johnson

Table 7 Other

Base material	*Product name*	*Manufacturer*	*Description*	*Application/procedure*
Small intestinal submucosa	N/A	N/A	Porcine small intestinal submucosa	Patellar tendon defect[33]
Polyvinyl alcohol and CMC	A-Part®	Aesculap	40-μm thick membrane made of PVA and CMC in various ratios	Cecum–abdominal wall[50]

mesh and the abdominal wall. Mesh migration to neighboring organs can occur. Intraperitoneal mesh use can induce an inflammatory reaction, which can lead to excessive fibrosis and adhesion formation,[45] and direct contact between the mesh and the intestinal loops can promote enterocutaneous fistulas and visceral erosions.[46] Resistant infection and postoperative pain have also been reported.

The polypropylene base mesh/membrane is often coated with a biocompatible absorbable material in an attempt to limit direct contact between the polypropylene and the peritoneal surface. The aim of the coating is to resorb when it is no longer required to reduce the amount of foreign material left in the body. The coating can take the form of a gel, film, or membrane.

Comparative studies have explored the differences between the commercially available meshes.[43,45] A reduction in adhesion formation is seen with a reduction in polypropylene and a change in pore size.[47] Currently, no ideal mesh is available.[48]

6.635.3.1.2.3. Other

Table 7 lists a couple of other partially or nonresorbable membranes that have been trialed.

6.635.3.2. Resorbable Spray-on, Gel, and Liquid Barriers

Barriers may also be applied as gelling sprays, direct sprays, or as viscous liquids, as this reduces the amount of work required to get the barrier in place. However, there are problems with the length of time the barrier remains in place and the specificity of placement.

6.635.3.2.1. Spray-on

Table 8 lists recent work with spray-on gelling liquids.

6.635.3.2.2. Gel

There are a substantial number of gels available and a lot of recent work as shown in Table 9.

6.635.3.2.3. Liquid

Liquid barriers are largely based on corn starch (icodextrin) and hyaluronic acid (Table 10).

6.635.3.3. Nonbarrier Methods

6.635.3.3.1. Hybrid systems

There has been little recent reported work on drug-delivering barrier systems (Table 11).

6.635.3.3.2. Transgene/drug/pharmacologic agent therapies

Table 12 lists a variety of other agents, used to try to limit adhesion formation, from pharmaceuticals to gene therapy.

Table 8 Spray-on barriers

Base material	*Product name*	*Manufacturer*	*Description*	*Application/procedure*
Hyaluronic acid	CMHA-SX or Carbylan-SX	Carbylan Biosurgery Inc.	Chemically modified, *in situ* cross-linkable derivative of hyaluronan	Pericardiotomy[40] Cecum–abdominal wall[56] Uterine horn[56]
Polyethylene glycol	SprayGel™ Adhesion Barrier	Confluent Surgical	Composed of two PEG solutions, which cross-link upon application at the site to form a gel	Loop ileostomy[70]

Table 9 Gels

Base material	*Product*	*Manufacturer*	*Description*	*Application/procedure*
CMC and PEG	Intercoat Gel Oxiplex®/SP Oxiplex®/AP MediShield™	FzioMed, Inc.	Made from CMC, PEG, and $CaCl_2$	Pelvic lesions[71] Laminectomy[68]
Hyaluronic acid	Hyaloglide®	Fidia Advanced Biopolymers	Made from hyaluronic acid and utilizes an auto-cross-linking process	Flexor tendon repair[72]
	Hyalobarrier® GEL × ENDO	Fidia Advanced Biopolymers	Made from hyaluronic acid and utilizes an auto-cross-linking process	Laparoscopic myomectomy[73]
	Intergel	Lifecore Biomedical Inc.	Made from cross-linking carboxylate groups on the HA molecules by chelation with ferric ions to make a 0.5% ferric hyaluronate gel	Abdominal colorectal surgery, ileostomy reversal[74]
	Incert®-S	Anika Therapeutics	Composed of chemically cross-linked pure hyaluronic acid	Uterine horn[75]
Sodium CMC	Poly(p-dioxanone)/ NaCMC/Tranilast	Polymed (Tranilast) Hercules (CMC) BENECEL (CMC)	Tranilast was combined with a CMC gel and encapsulated using poly(p-dioxanone) for a sustained release	Sidewall abrasion, uterine horn abrasion, laminectomy, tendon[43]
Chitosan	N/A	N/A	Made from chitosan, hyaluronic acid and chemically modified 1,2-butylene oxide	Cecal abrasion[76]
Carboxymethyl chitosan	N/A	Dayang Chemicals Co (CMC powder)	Made from carboxymethyl chitosan	Percardiotomy[39]

Table 10 Liquids

Base material	*Product*	*Manufacturer*	*Description*	*Application/procedure*
Icodextrin derived from cornstarch	ADEPT®	Innovata plc	4% Icodextrin solution	Adhesive small intestine occlusion[77]
Hyaluronic acid	Sepracoat® (formerly HAL-C™)	Genzyme Corp.	Composed of chemically derived sodium hyaluronate and carboxymethyl cellulose	Abdominal wall defect[78]

Table 11 Drug-delivery films

Agent	*Product*	*Manufacturer*	*Description/mode of delivery*	*Application/procedure*
Insulin	N/A	N/A	Ibuprofen-loaded poly(L-lactic acid) and polyethylene diblock copolymer films used for defect repair	Cecum–peritoneal wall defects[63]

6.635.4. Barriers to Adhesion: Current Research

While a number of techniques have been employed to address unwanted postsurgical tissue adhesion, a great deal of attention has been paid to barrier methods. It has been attested that compared with other materials or substances used for the reduction or elimination of adhesion, barrier products are the only effective products currently available.[19,23] In spite of this fact, it should be noted that there still remains no unequivocally effective method, be it a surgical technique, pharmacological agent, material or barrier, to prevent adhesion formation.[19]

There are a number of limitations and concerns associated with current barriers. Many of the products are only suitable for specific anatomical locations, and outside of these areas have been shown to cause further complications. They are also dependent on application through particular surgical methods, and are not always suitable for minimally invasive laparoscopic procedures, which may be preferred.

Table 12 Gene and soluble drug delivery

Agent	*Product*	*Manufacturer*	*Description/Mode of delivery*	*Application/Procedure*
Smad7	pTRE-m2*Smad7*	N/A	Delivered to peritoneal cavity via a nonviral ultrasound-microbubble-mediated naked gene transfection system	Cecum and parietal peritoneum abrasions[79]
Melatonin	N/A	Details not given	Postsurgical daily single dose via orogastric gavage	Pinealectomy followed by cecum incision[80]
Kombucha mushroom	Kombucha fermented tea	N/A	Intraoperative intraperitoneal administration	Intestinal and peritoneal defects[81]
Neurokinin-1 receptor antagonist	CJ-12-255	Pfizer	Intraoperative intraperitoneal administration (intraperitoneal lavage)	Peritoneal side wall defects[82]
Metformin and atorvastatin	Metformin (Glucophage®); Atorvastatin (Lipitor®)	Merck Sante SAS; Pfizer	Oral delivery starting on the day of surgery	Uterine horn[83]
Keratinocyte growth factor	Recombinant human keratinocyte growth factor	Sigma	Solution in saline, injected into pericardial cavity postoperatively	Pericardial cavity (abrasion, blood instillation, and desiccation)[84]
Chymase inhibitor	Suc-Val-Pro-Phe^{p} $(OPh)_2$	Details not given	Solution in saline, sprayed topically into pericardial cavity	Epicardium abraded[42]

Barriers that are nonresorbable may require a second surgery to remove the implant. If the implant is not sufficiently anchored, it may move *in situ*, potentially resulting in further complications. Nonresorbable barriers can also degrade over time, and this breakdown can litter the area with aggravating debris.

Methods that utilize human tissue contain the risk of cross-infection, which in turn limits their use.

Ideally, a barrier should possess characteristics and prerequisites such as being inert to the surrounding tissue, with excellent biocompatibility; promoting fibrinolysis prior to fibroblast invasion; not encouraging clot formation which in turn will prevent/reduce fibroblast reaction; reliably avoiding the formation of adhesions; adhering to the desired tissue for as long as required[49]; possessing good handling characteristics[50]; being applicable to a number of anatomical sites; and being applicable by both open and laparoscopic procedures.[49]

Even if all these criteria are suitably satisfied, a shortcoming of barrier methods that will remain will be reliance on the surgeon for predicting potential sites of adhesion and subsequent placement of the barrier.[51]

The current approach for barriers is focused on one of two options, to make modifications to preexisting products in the hope of improvement, or for the use of new materials,[52] which have often been used in other *in situ* applications. These approaches are tested using various animal models (usually small animals), with different injury types attempting to mimic clinical surgical procedures. These models have variable degrees of trauma, with and without blood exposure. Comparison between studies can be difficult due to subjective grading systems used to gauge adhesion,[53] and reported results are sometimes found to be contradictory.

The use of small animal models, while practical from a laboratory point of view, does not necessarily provide accurate clinical predictions with success[49] for a number of reasons. There are differences in surgical procedures, and methods such as abrasion, incisions, and electrocautery are used to mimic surgical injury. Differences in scale and physiological forces also exist between small animals (mice, rats, and rabbits) and humans. The desire to eliminate some of these factors has led researchers toward porcine and canine models, particularly for pelvic surgery. While there is an increase in organ size, allowing more similarities in surgical procedure, there are the drawbacks of comparing the human anatomy with that of four-legged animals.

6.635.5. Uses for Adhesion

Adhesions and the process of adhesion formation are not necessarily always deleterious. There are a number of occasions where the formation of an adhesion may be necessary or may be utilized for beneficial purposes.

Many medical devices that are not directly bonded to bone require fixation in position, as migration around the body may cause significant problems. Pacemakers, heart valves, hernia reinforcement, and breast implants are probably the most common implants requiring fixation. Lack of fixation allows movement within the body, and many early devices failed because of the lack of appropriate fixation in one anatomical position. Although not intuitive, devices implanted in any of the planes between organs or tissues are not constrained in their ability to move in that plane. General body motion results in uneven forces on the device and consequent motion within the body.

Large diameter blood vessels, especially those made from Dacron® velour, utilize the body's chronic inflammatory reaction to the material to develop scar tissue analogous to adhesions elsewhere. This helps seal the graft and anchor it into position.

In the peritoneal region, adhesions are central to the use of meshes to reinforce weak areas prone to herniation. The development of a strong collagenous matrix on the tissue side of the mesh is essential to prevent the abdominal wall from failing and extruding the mesh and the viscera.

As mentioned previously, adhesions, or at least the associated vasculature, may be required to provide nutrients to the healing bowel.[1] This aspect of adhesion formation should not be overlooked when examining the clinical use of adhesion barriers.

6.635.6. Discussion

From the available literature, adhesion barriers do work to reduce the number and severity of adhesions in most clinical applications, generally without increasing the incidence of complications or producing new complications. There is the exception of use around the anastomosis site in bowel surgery where barrier materials may slow or impede healing. The rate of severe complications does not appear to be altered by the use of barrier materials, and one must question the tacit assumption that the severe complications are directly related to the adhesions.

At least for cardiac surgery, the complications appear to be related to the severity of the adhesions and not to the long-term sequelae. Adhesion barriers should do well in this situation, even if they do not reduce complication rates for abdominal surgery.

6.635.6.1. Complications of Barrier Films

Adhesion barrier materials are largely seen to be benign. However, there are some potential complications arising from their use in surgery.

6.635.6.1.1. Inflammation

The degradation of most resorbable biomaterials is by random hydrolysis of the bulk material. This results in the material losing strength well before it begins to lose mass. A consequence of this loss of strength is that the material should break up into pieces, especially in a mechanically active environment. Little work appears to have been done on this aspect of material degradation, although Ishii and coworkers[54] have demonstrated fragmentation of nanofibers of poly-L-lactic acid in an animal model.

Particles of polymeric material, especially around 0.1–1 μm size, contribute highly to macrophage activation,[55] so it is conceivable that the degradation of resorbable barrier materials may well result in inflammation as the material breaks up into small pieces late in the life of the barrier.

6.635.6.1.2. Nutrient deprivation

Most barriers are relatively thick, greater than 200 μm, and even the hydrogels will restrict diffusion of oxygen and nutrients. Where provision of nutrients to the wound site is dependent on the serosal (e.g., peritoneal) fluid or where the local vasculature has been compromised by surgery, the barrier material may well act as a barrier to nutrition and oxygen and thereby restrict the ability of the local tissue to heal. This scenario would lead to the finding of Zeng *et al.*[7] of increased leakage of anastomoses when covered by barrier materials.

6.635.6.1.3. Potential late adhesion development

A sufficiently robust inflammatory response to degrading barrier material may also generate local damage to the mesothelial layer and therefore cause renewed conditions conducive to adhesion development.

6.635.6.2. Design of New Barrier Films

In the design of barrier materials, the long-term goals of the material, its short- and long-term behavior, and the body's response need to be included in an interrelated manner.

Some criteria for the design of new materials are discussed in the following sections.

6.635.6.2.1. Drug-eluting barrier materials to reduce inflammation and increase fibrinolysis

Adhesions require a fibrin clot in which to develop and are exacerbated by the inflammatory response to the wound. Several researchers have proposed using anti-inflammatory, and even anticancer, drugs to reduce inflammation as an antiadhesion strategy (see **Section 6.635.3.3.2**). Profibrinolytic drugs, such as tPA which converts plasminogen to the enzyme plasmin that lyses cross-linked fibrin gels, can also reduce the mechanical stiffness or remove the fibrin clot. A drug-elution strategy from the adhesion barrier material that encourages fibrinolysis at around day 3–5 and has an anti-inflammatory effect at the same time as well as when the material is in the final stages of degradation could be a potential step forward in reducing complications.

6.635.6.2.2. Allow penetration of nutrients and removal of waste (MW > 1 M)

As nutrition is an essential function of the serous fluid (e.g., peritoneal fluid) pumped into the peritoneum, reduction in the diffusion barrier properties of the membrane while maintaining the cell-excluding properties is another strategy. This could be achieved by increasing the permeability of the membrane to a molecular weight of 1 million Daltons or more, and decreasing the thickness of the material.

6.635.6.2.3. Bioresorbable, but does not form microscopic pieces on degradation (inflammatory)

An alternative strategy for dealing with the long-term degradation behavior of the barrier materials is to make them surface eroding, rather than bulk eroding. This may be difficult for hydrogels, unless the mechanism of degradation is related to the surface activity of the material.

6.635.6.3. Technique and Assessment

Appropriate animal and (retrospective) clinical trials need to be undertaken to evaluate the use of barrier materials for inhibiting long-term complications. This will require the development of an animal model that simulates the conditions that lead to severe complications in humans.

In addition, assay systems that look at the entire degradation behavior of the materials and not just the first few days' behavior will need to be employed.

6.635.6.4. Summary

In summary, most resorbable barrier materials work to reduce adhesion formation. However, in abdominal surgery, there are severe complications that may occur months or years after surgery, the incidence of which does not seem to be affected by the use of adhesion barriers. We should question the

assumption that all severe complications arise as a direct result of those adhesions and look for a more complete understanding of the processes leading to bowel obstruction, as these should modify the strategy for the design of the material. New technologies and new materials should also be investigated if the benefits of adhesion barriers are to be increased to include late-onset complications.

However, barrier materials have a clinical use now in situations where the number and severity of adhesions is important (heart surgery, and protection of the uterus and Fallopian tubes). Most barrier materials would appear to be reasonably safe for use if used in the appropriate settings.

References

1. Ellis, H. *Colorectal Dis*. **2007**, *9*(Suppl. 2), 3–8.
2. Grant, H. W.; Parker, M. C.; Wilson, M. S.; *et al*. *J. Pediatr. Surg*. **2006**, *41*, 1453–1456.
3. Ray, N. F.; Denton, W. G.; Thamer, M.; Henderson, S. C.; Perry, S. *J. Am. Coll. Surg*. **1998**, *186*, 1–9.
4. Ray, N. F.; Larsen, J. W., Jr.; Stillman, R. J.; Jacobs, R. J. *Surg. Gynecol. Obstet*. **1993**, *176*, 271–276.
5. Park, C. M.; Lee, W. Y.; Cho, Y. B.; *et al*. *Int. J. Colorectal Dis*. **2009**, *24*, 305–310.
6. Lim, R.; Morrill, J. M.; Lynch, R. C.; *et al*. *J. Gastrointest. Surg*. **2009**, *13*, 35–41 discussion 41-42.
7. Zeng, Q.; Yu, Z.; You, J.; Zhang, Q. *World J. Surg*. **2007**, *31*, 2125–2131; discussion 2132.
8. Zawaneh, P. N.; Putnam, D. *Tissue Eng. B Rev*. **2008**, *14*, 377–391.
9. Liakakos, T.; Thomakos, N.; Fine, P. M.; Dervenis, C.; Young, R. L. *Dig. Surg*. **2001**, *18*, 260–273.
10. Dizerega, G. S.; Campeau, J. D. *Hum. Reprod. Update* **2001**, *7*, 547–555.
11. Cheong, Y. C.; Laird, S. M.; Li, T. C.; Shelton, J. B.; Ledger, W. L.; Cooke, I. D. *Hum. Reprod. Update* **2001**, *7*, 556–566.
12. Thompson, J. *Dig. Surg*. **1998**, *15*, 153–157.
13. Eckes, B.; Zweers, M. C.; Zhang, Z. G.; *et al*. *J. Investig. Dermatol. Symp. Proc*. **2006**, *11*, 66–72.
14. Ellis, H. *Proc. R. Soc. Med*. **1962**, *55*, 599–600.
15. Eming, S. A.; Hammerschmidt, M.; Krieg, T.; Roers, A. *Semin. Cell Dev. Biol*. **2009**, *20*, 517–527.
16. Levin, M. *Semin. Cell Dev. Biol*. **2009**, *20*, 643–645.
17. Fusi, L. *Math. Comput. Modell*. **2009**, *50*, 1474–1494.
18. Gray, H. *Gray's Anatomy*. Running Press: Philadelphia, 1901.
19. Tulandi, T. *Hum. Reprod. Update* **2001**, *7*, 545–546.
20. Vural, B.; Canturk, N. Z.; Esen, N.; *et al*. *Hum. Reprod*. **1999**, *14*, 49–54.
21. Cahill, R. A.; Redmond, H. P. *World J. Gastroenterol*. **2008**, *14*, 4861–4866.
22. Brokelman, W. J.; Holmdahl, L.; Janssen, I. M.; *et al*. *J. Surg. Res*. **2009**, *151*, 89–93.
23. Reed, K. L.; Stucchi, A. F.; Becker, J. M. *J. Surg. Res*. **2009**, *152*, 175–177.
24. Cheung, J. P.; Tsang, H. H.; Cheung, J. J.; Yu, H. H.; Leung, G. K.; Law, W. L. *Asian J. Surg*. **2009**, *32*, 180–186.
25. Nappi, C.; Di Spiezio Sardo, A.; Greco, E.; Guida, M.; Bettocchi, S.; Bifulco, G. *Hum. Reprod. Update* **2007**, *13*, 379–394.
26. Sjosten, A. C.; Ellis, H.; Edelstam, G. A. *Hum. Reprod*. **2000**, *15*, 1573–1577.
27. Khanna, A.; Friel, M.; Gougoulias, N.; Longo, U. G.; Maffulli, N. *Br. Med. Bull*. **2009**, *90*, 85–109.
28. Brunelli, G.; Longinotti, C.; Bertazzo, C.; Pavesio, A.; Pressato, D. *J. Orthop. Res*. **2005**, *23*, 1377–1382.
29. Milthorpe, B. K.; Schindhelm, K.; Howlett, C. R.; Hall, P. J.; Rogers, G. J. *Biomaterials* **1991**, *12*, 577–583.
30. Sungur, N.; Uysal, A.; Kocer, U.; *et al*. *J. Trauma* **2006**, *61*, 1467–1472.
31. Temiz, A.; Ozturk, C.; Bakunov, A.; Kara, K.; Kaleli, T. *Int. Orthop*. **2008**, *32*, 389–394.
32. Tanaka, T.; Zhao, C.; Sun, Y. L.; Zobitz, M. E.; An, K. N.; Amadio, P. C. *J. Hand Surg. Am*. **2007**, *32*, 876–881.
33. Karaoglu, S.; Fisher, M. B.; Woo, S. L.; Fu, Y. C.; Liang, R.; Abramowitch, S. D. *J. Orthop. Res*. **2008**, *26*, 255–263.
34. Zhang, C. L.; Tian, W. M.; Cui, F. Z. *Curr. Appl. Phys*. **2005**, *5*, 411–416.
35. Hanff, G.; Hagberg, L. *J. Hand Surg. Am*. **1998**, *23*, 658–664.
36. Siddiqi, N. A.; Hamada, Y.; Ide, T.; Akamatsu, N. *J. Appl. Biomater*. **1995**, *6*, 43–53.
37. Ozturk, A. M.; Yam, A.; Chin, S. I.; Heong, T. S.; Helvacioglu, F.; Tan, A. *J. Biomed. Mater. Res. A* **2008**, *84*, 1120–1126.
38. Bicer, M.; Bayram, A. S.; Gurbuz, O.; *et al*. *J. Int. Med. Res*. **2008**, *36*, 1311–1318.
39. Daroz, L. R. D.; Lopes, J. B.; Dallan, L. A. O.; Campana, S. P.; Moreira, L. F. P.; Stolf, N. A. G. *Rev. Bras. Cir. Cardiovasc*. **2008**, *23*, 480–487.
40. Connors, R. C.; Muir, J. J.; Liu, Y.; *et al*. *J. Surg. Res*. **2007**, *140*, 237–242.
41. Lopes, J. B.; Dallan, L. A. O.; Moreira, L. F. P.; *et al*. *Acta Cir. Bras*. **2009**, *24*, 82–86.
42. Soga, Y.; Takai, S.; Koyama, T.; *et al*. *J. Card. Surg*. **2007**, *22*, 343–347.
43. Cui, H.; Gensini, M.; Kataria, R.; *et al*. *Biomed. Mater*. **2009**, *4*, 15001.
44. Berrevoet, F.; Fierens, K.; De Gols, J.; *et al*. *Hernia* **2009**, *13*, 23–27.
45. Schreinemacher, M. H.; Emans, P. J.; Gijbels, M. J.; Greve, J. W.; Beets, G. L.; Bouvy, N. D. *Br. J. Surg*. **2009**, *96*, 305–313.
46. Paulo, N. M.; de Brito e Silva, M. S.; Moraes, A. M.; *et al*. *J. Biomed. Mater. Res. B Appl. Biomater*. **2009**, *91*, 221–227.
47. Schug-Pass, C.; Sommerer, F.; Tannapfel, A.; Lippert, H.; Kockerling, F. *Surg. Endosc*. **2009**, *23*, 487–495.
48. Emans, P. J.; Schreinemacher, M. H.; Gijbels, M. J.; *et al*. *Ann. Biomed. Eng*. **2009**, *37*, 410–418.
49. Ferland, R.; Mulani, D.; Campbell, P. K. *Hum. Reprod*. **2001**, *16*, 2718–2723.
50. Jaenigen, B. M.; Weis, C.; Odermatt, E. K.; Hopt, U. T.; Obermaier, R. *J. Biomed. Mater. Res. B Appl. Biomater*. **2008**, *89B*, 293–299.
51. Lundorff, P.; Van Geldorp, H.; Tronstad, S. E.; *et al*. *Hum. Reprod*. **2001**, *16*, 1982–1988.
52. Tulandi, T.; Al-Shahrani, A. *Curr. Opin. Obstet. Gynecol*. **2005**, *17*, 395–398.
53. Darmas, B. *J. Wound Care* **2008**, *17*, 405–408; 411.
54. Ishii, D.; Ying, T. H.; Mahara, A.; *et al*. *Biomacromolecules* **2009**, *10*, 237–242.
55. Ingham, E.; Fisher, J. *Biomaterials* **2005**, *26*, 1271–1286.
56. Liu, Y.; Shu, X. Z.; Prestwich, G. D. *Fertil. Steril*. **2007**, *87*, 940–948.
57. Leitao, M. M., Jr.; Natenzon, A.; Abu-Rustum, N. R.; *et al*. *Gynecol. Oncol*. **2009**, *115*, 204–208.
58. Kawamura, Y. J.; Kakizawa, N.; Tan, K. Y.; *et al*. *Tech. Coloproctol*. **2009**, *13*, 211–214.
59. Ersoy, E.; Ozturk, V.; Yazgan, A.; Ozdogan, M.; Gundogdu, H. *J. Gastrointest. Surg*. **2009**, *13*, 282–286.
60. Emre, A.; Akin, M.; Isikgonul, I.; Yuksel, O.; Anadol, A. Z.; Cifter, C. *Clinics (Sao Paulo)* **2009**, *64*, 363–368.
61. West, J. L.; Hubbell, J. A. *Biomaterials* **1995**, *16*, 1153–1156.
62. Hsieh, S. R.; Chang, C. J.; Way, T. D.; Kwan, P. C.; Hung, T. W. *J. Fluoresc*. **2009**, *19*, 733–740.
63. Lee, J. H.; Go, A. K.; Oh, S. H.; Lee, K. E.; Yuk, S. H. *Biomaterials* **2005**, *26*, 671–678.
64. Lee, Y. W.; Chu, B.; Lee, Y. G.; *et al*. *J. Korean Surg. Soc*. **2009**, *76*, 73–80.
65. Kesting, M. R.; Wolff, K. D.; Mucke, T.; *et al*. *J. Biomed. Mater. Res. B Appl. Biomater*. **2009**, *90*, 930–938.
66. Dai, Z. W.; Zou, X. H.; Chen, G. Q. *Biomaterials* **2009**, *30*, 3075–3083.
67. Jin, J.; Voskerician, G.; Hunter, S. A.; *et al*. *J. Surg. Res*. **2009**, *156*, 297–304.
68. Kurt, G.; Cemil, B.; Celik, B.; Durdag, E.; Erdem, O.; Ceviker, N. *Neurocirugía* **2009**, *20*, 360–366.
69. Chappell, E. T.; Pare, L.; Salehpour, M.; Mathews, M.; Middlehof, C. *Surg. Neurol*. **2009**, *71*, 126–128.
70. Tjandra, J. J.; Chan, M. K. Y. *Dis. Colon Rectum* **2008**, *51*, 956–960.
71. Schonman, R.; Corona, R.; Bastidas, A.; Mailova, K.; Koninckx, P. R. *J. Minim. Invasive Gynecol*. **2009**, *16*, 188–194.
72. Riccio, M.; Battiston, B.; Pajardi, G.; *et al*. *J. Hand Surg. Eur. Vol*. **2009**, *35*(2), 130–138.
73. Mais, V.; Bracco, G. L.; Litta, P.; Gargiulo, T.; Melis, G. B. *Hum. Reprod*. **2006**, *21*, 1248–1254.
74. Tang, C. L.; Jayne, D. G.; Seow-Choen, F. A.; Ng, Y. Y.; Eu, K. W.; Mustapha, N. *Ann. Surg*. **2006**, *243*, 449–455.
75. Haney, A. F.; Doty, E. *Fertil. Steril*. **1998**, *70*, 145–151.
76. Wei, C. Z.; Hou, C. L.; Gu, Q. S.; Jiang, L. X.; Zhu, B.; Sheng, A. L. *Iran. Polym. J*. **2009**, *18*, 355–364.
77. Catena, F.; Ansaloni, L.; Lauro, A.; Ercolani, G.; D'Alessandro, L.; Pinna, A. *Trials* **2008**, *9*, 74, doi:10.1186/1745-6215-9-74.
78. Van't Riet, M.; Van Steenwijk, P. J. D.; Bonthuis, F.; *et al*. *Ann. Surg*. **2003**, *237*, 123–128.
79. Guo, H.; Leung, J. C.; Cheung, J. S.; Chan, L. Y.; Wu, E. X.; Lai, K. N. *Br. J. Surg*. **2009**, *96*, 1323–1335.

80. Ersoz, N.; Ozler, M.; Altinel, O.; *et al*. *J*. *Gastroenterol*. *Hepatol*. **2009**, *24*(11), 1763–1767.
81. Maghsoudi, H.; Mohammadi, H. B. *Indian J*. *Surg*. **2009**, *71*, 73–77.
82. Reed, K. L.; Stucchi, A. F.; Leeman, S. E.; Becker, J. M. *Ann*. *N*. *Y*. *Acad*. *Sci*. **2008**, *1144*, 116–126.
83. Yilmaz, B.; Aksakal, O.; Gungor, T.; *et al*. *Reprod*. *Biomed*. *Online* **2009**, *18*, 436–442.
84. Lopes, J. B.; Dallan, L. A. O.; Campana-Filho, S. P.; *et al*. *Eur*. *J*. *Cardiothorac*. *Surg*. **2009**, *35*, 313–318.

6.636. Suture Material: Conventional and Stimuli Responsive

A J Dart and C M Dart, University of Sydney, Camden, NSW, Australia

© 2011 Elsevier Ltd. All rights reserved.

6.636.1.	**Introduction**	574
6.636.2.	**Properties of Suture Materials**	574
6.636.2.1.	Tensile Strength	574
6.636.2.2.	Tissue Absorption	574
6.636.2.3.	Cross-Sectional Diameter	575
6.636.2.4.	Coefficient of Friction	575
6.636.2.5.	Knot Security and Strength	575
6.636.2.6.	Elasticity	575
6.636.2.7.	Plasticity	575
6.636.2.8.	Memory	575
6.636.2.9.	Handling	575
6.636.2.10.	Tissue Reactivity	575
6.636.2.11.	Origin and Physical Configuration	576
6.636.2.12.	Capillarity	576
6.636.2.13.	Fluid Absorption	576
6.636.2.14.	Ease of Removal and Color	576
6.636.3.	**Sutures**	576
6.636.3.1.	Absorbable Suture Materials	576
6.636.3.1.1.	Surgical gut	576
6.636.3.1.2.	Polyglactin 910 (coated Vicryl, Vicryl Rapide, and coated Vicryl Plus)	578
6.636.3.1.3.	Polyglycolic acid (Dexon, Dexon II)	578
6.636.3.1.4.	Poliglecaprone (Monocryl)	578
6.636.3.1.5.	Polydioxanone	579
6.636.3.1.6.	Polyglycolide–trimethylene carbosnate (Maxon)	579
6.636.3.1.7.	Caprosyn	579
6.636.3.2.	Nonabsorbable Suture Materials	579
6.636.3.2.1.	Silk (Mersilk, Perma-Hand)	579
6.636.3.2.2.	Polybutester (Novafil)	579
6.636.3.2.3.	Braided polyester (Mersilene, Ethibond, Surgidac)	581
6.636.3.2.4.	Nylon (Ethilon, Monosof, Nurolon, Surgilon, Supramid)	581
6.636.3.2.5.	Polypropylene (Prolene, Surgilene)	581
6.636.3.2.6.	ePFTE (Gore-Tex CV4)	582
6.636.3.2.7.	Stainless steel	582
6.636.3.3.	Other Sutures	582
6.636.3.3.1.	Barbed suture (Quill SRS, Monderm, Coveidin)	582
6.636.4.	**Staples**	583
6.636.4.1.	Skin Staples	583
6.636.4.1.1.	Nonabsorbable staples (Proximate, Royal Autosuture)	583
6.636.4.1.2.	Absorbable staples (Insorb)	583
6.636.4.2.	Ligatures	583
6.636.4.3.	Stapling Devices in Abdominal and Thoracic Surgery	584
6.636.5.	**Surgical Needles**	585
6.636.5.1.	Anatomy of a Needle	585
6.636.5.2.	Point Types	585
6.636.5.3.	Body Types	586
6.636.5.4.	Selection of Needles	586
6.636.6.	**Conclusions**	586
References		587

Abbreviations

ATSM	American Society for Testing Materials
EEA	End-to-end anastomosing
ePFTE	Polytetrafluoroethylene
GIA	Gastrointestinal anastomosis
ILA	Intestinal linear anastomosis
LDS	Ligation and dividing stapler
PDS	Polydioxanone suture
TA	Thoracoabdominal
USP	United States Pharmacopeia

6.636.1. Introduction

Suture materials play an important role in wound repair by providing support to healing tissues. Closure of skin wounds is only one application of suture material. Sutures are used for closure of fascia, hemostasis, intestinal anastomosis and enterotomy, urogenital tract surgery, surgery of the musculoskeletal system, vascular surgery, ocular surgery, plastic surgery, and neurosurgery, amongst other applications. Selection of a suture material should be based on an understanding of the physical and biological properties of the material, assessment of the wound, the healing rate of different tissues, and the patient's physical condition. Too often, selection has been governed by the personal preference and training experience of the surgeon and by economic reasons. Continued technological improvement in suture materials has seen an increase in the variety of sutures available. At the same time, there has been a refinement in suture needles leading to a greater range of options with more tissue-specific applications. The development of surgical staples and various tissue adhesives has also provided an alternative to sutures for wound closure. The challenge for surgeons now is to comprehend the enormous choice available and stay abreast of new developments.

The general performance of a suture material is based on its physical properties, handling characteristics, and biological properties. The ideal suture material could be utilized for any purpose and would be characterized by good handling characteristics, have good knot security and tensile strength, would be sterile, nonelectrolytic, nonferromagnetic, noncapillary, nonallergenic, and noncarcinogenic, and would not provide a medium for bacterial growth. It should be resistant to shrinkage and absorbed with minimal tissue reaction, easy to sterilize without alterations to its properties and be economical to use.[1]

There is no ideal suture material. A compromise on the selection of the best suture material for a specific application is made by the surgeon and is based on the circumstances. The selection of suture material will be influenced by the age, weight, and health status of the patient and the site of the wound. Tissue varies throughout the body in thickness, elasticity, speed of healing, and the tendency to scar. Concurrent diseases such as diabetes, heart disease, dermatitis, and the systemic use of medications such as steroids may affect healing. The presence of infection and individual wound characteristics may all influence the choice of suture material. Surgeons should aim to select a material that has a high strength to diameter ratio, is of consistent diameter, sterile, pliable, and has optimal tissue acceptance and predictability of performance.

6.636.2. Properties of Suture Materials

6.636.2.1. Tensile Strength

Tensile strength is defined by the US Pharmacopeia (USP) as the weight necessary to break a suture divided by the cross-sectional area of the suture.[2–4] The relationship between the weight necessary to break a suture and the suture's diameter is not linear.[5] Tensile strength can be measured using either dry or wet sutures. The tensile strength of wet sutures is more clinically relevant, given that sutures are implanted into tissue comprised of extracellular fluid. Effective tensile strength is an additional measurement that evaluates the tensile strength of a looped and knotted suture. Effective tensile strength will vary with suture material and knot type.[5–7] A suture should have and maintain adequate tensile strength for its specified purpose.[4]

6.636.2.2. Tissue Absorption

Absorption is a characteristic that refers to the ability of the body to degrade the suture over time. Absorbable sutures lose tensile strength as they undergo degradation and absorption. Nonabsorbable sutures are resistant, although susceptible, to degradation and, therefore, maintain their tensile strength longer. Generally speaking, absorbable sutures are often defined as sutures that lose most of their tensile strength within 60 days after implantation, while nonabsorbable sutures maintain their tensile strength for more than 60 days. However, the loss of tensile strength is independent of absorption.[8] For example, an absorbable suture may lose tensile strength rapidly but be absorbed slowly. Most foreign materials will eventually undergo some degree of degradation over time. The use of absorbable or nonabsorbable sutures and their rates of absorption are particularly relevant to the development of suture-related complications such as wound dehiscence, suture sinus formation and granulomas.[9]

Absorbable sutures are most commonly used in deeper tissues from where they are fully absorbed and are unlikely to cause long-term complications. Nonabsorbable sutures are most commonly used in the skin where they can be removed after they have completely supported healing.[10] Nonabsorbable sutures may be used in deeper tissues when there is systemic disease or impaired healing and extended support is required. Common situations where wound healing may be delayed include diabetes, corticosteroid therapy, malnutrition, stress, and systemic disease. If nonabsorbable sutures are used in these cases it is preferable that these be placed such that the sutures can be removed when healing is complete in order to avoid suture sinua formation.

6.636.2.3. Cross-Sectional Diameter

When selecting suture size, the smallest diameter required, according to the estimated tension on the suture line and natural tissue strength, is recommended.[3] A suture does not need to be stronger than the sutured tissues. Selecting the smallest diameter required will minimize trauma as the suture passes through tissue and will reduce the amount of foreign material left in the wound. The number of sutures placed will depend on the suture pattern. The aim is to appose the skin edges with the minimum number and the smallest diameter of sutures.

The most commonly used standard for recording suture size is that of the USP which denotes dimensions in a numerical scale. Suture diameters are specified in a descending grade when followed by 0 such that 2-0 is larger than 5-0. However, once the 0 is dropped suture size increases numerically such that number 3 suture is larger than number 1.

6.636.2.4. Coefficient of Friction

The coefficient of friction is a measure of how easily a suture passes through tissue[8] and relates to the amount of tissue trauma a suture causes. Smooth surfaces cause less trauma and are particularly relevant in delicate tissues like the eye. However, smoother sutures require greater tension to ensure good apposition of tissues and have lower knot security.

6.636.2.5. Knot Security and Strength

The least reliable component of any suture is the knot.[3] A knot should hold securely without fraying or cutting. Knot strength is determined by calculating the force necessary to make a knot slip or break.[2,8] This measure is directly proportional to the coefficient of friction. A knot stays tied because of the friction produced by one throw of the knot acting on another. A suture material with a high coefficient of friction has good knot security but tends to be abrasive and experiences unwelcome resistance or drag when being pulled through tissues.[11]

Knot security reflects that characteristic of a suture which allows it to be tied securely with a minimum number of throws per knot.[12] For safety, a knot should be tied with at least three throws with 3 mm ends. Extra throws should be employed when sutures with smoother surfaces are used so that the knot holds securely without fraying, cutting, or slipping.

Effective tensile strength denotes the force a suture strand can withstand before it breaks after it is knotted. Greater effective tensile strength acts to minimize the risk of wound dehiscence; however, the tensile strength of the knotted suture should not greatly exceed the tensile strength of the tissue.

Irrespective of the knot configuration and material, the weakest point in a surgical suture is the knot and the weakest point is the point immediately adjacent to the knot. The reduction in tensile strength may be 35–95%, depending on the suture material used.[7,13,14] When functional biomechanics are considered this is not surprising, given the effects of slippage of suture material through the knot and the unavoidable suture elongation that occurs as the knot is formed and tightened.

Due to excessive relative wound tension on the knot and the concern for suture failure due to knot slippage, there is a tendency to overcome these concerns by tying excessively tight knots. However, if tied too tight, surgical knots can cause local tissue necrosis, inhibit fibroblast proliferation, and cause excessive tissue overlap, which may all lead to reduced strength in the healed wound.[15]

A surgical knot represents the highest density of foreign material within a suture and the volume of the knot is directly related to the amount of surrounding inflammatory reaction.[13] If minimizing the inflammatory reaction is integral to wound healing and minimal scarring, the surgeon should minimize knot sizes without compromising the tensile strength of the suture line. This may mean selecting a different suture type.

6.636.2.6. Elasticity

Elasticity is the ability of a material to stretch during wound edema and return to its original length after the edema subsides.[8] Elasticity is a desirable property for a suture material. High elasticity allows the suture to stretch as wounds swell without cutting through the tissue edges and then to regain its normal shape and length as swelling subsides. This maintains good tissue apposition throughout healing.

6.636.2.7. Plasticity

Plasticity and elasticity are interrelated. Plasticity is defined as the capacity of a suture to stretch with wound edema but remain permanently altered or deformed after edema subsides.[2,8] Like elastic sutures, sutures with high plasticity do not cut through the tissue edges as a wound swells. However unlike elasticity, plasticity is generally an undesirable characteristic. Sutures with high plasticity may become too loose when swollen wounds return to normal, leading to impaired wound healing and wound dehiscence.

6.636.2.8. Memory

Memory is the capacity of a suture to assume a stable linear configuration after removal from packaging and after stretching. Sutures with greater memory are not pliable. This results in a suture with poor surgical handling characteristics and poor knot security.[5]

6.636.2.9. Handling

Elasticity, plasticity, and memory all contribute to handling quality or flexibility of the suture material.[3] The material should handle comfortably and naturally. Silk is the standard by which other sutures are compared because of its exceptional handling and ease of knot tying.[3,10] Flexible sutures are indicated for ligating vessels or performing continuous sutures while less flexible sutures like wire are not suitable for these purposes.

6.636.2.10. Tissue Reactivity

All suture materials are foreign materials and may elicit a tissue response, usually inflammation, which interferes with wound healing and potentially increases the risk of infection.[3]

The severity and duration of the reaction are related to the type, quantity, origins, and presentation of the suture.[5,16] An ideal suture material should be nonelectrolytic, noncapillary, nonallergenic, and noncarcinogenic, thus minimizing tissue reaction.

6.636.2.11. Origin and Physical Configuration

The USP has defined and standardized caliber which denotes dimensions from fine to coarse.[2] The caliber of a suture, as defined by the USP, is determined in millimeters and its size is expressed in a numeric scale where 10-0 is the smallest and 7 is the largest. Zero is the baseline average size suture. The smaller the caliber of the suture the more zeros. For example, 10-0 is the smallest size available and has a finer diameter than a 4-0 suture. Sutures larger than 1-0 are numbered 1–7. USP 7 is the largest suture available.

Suture material may be either natural or synthetic. Natural fibers such as surgical gut and silk cause a more intense inflammatory reaction compared to synthetic materials such as polypropylene. Sutures may be single stranded (monofilament) or multistranded (multifilament). Monofilament sutures are strong, have low tissue drag, are less likely to harbor infection, and are associated with significantly lower wound infection rates compared to multifilament sutures.[8,9] However, the handling characteristics of monofilament sutures are not as good as those of the multifilament sutures. Multifilament sutures can be braided or twisted, which improves handling but also increases tissue reactivity and infection by virtue of its increased capillarity.[12] Bacteria can be protected in the crevices of braided sutures, thus escaping phagocytosis.

6.636.2.12. Capillarity

Capillarity is the ability of sutures to spread liquid along their length and this becomes important when bacteria are present. Neutrophils and macrophages are too large to enter the interstices of the fibers, and so infection may persist even in the presence of systemically administered antimicrobials. Monofilaments show no capillarity while multifilament sutures have variable capillarity which is related to their composition. A braided nylon suture could harbor up to three times as many bacteria as a monofilament nylon suture.[9] Braided polyester has capillarity and the potential to promote the spread of infection while braided silk, coated with wax, does not do so.[17] Coating a suture with teflon, silicone, wax, paraffin-wax, and calcium stearate can reduce its capillarity and its coefficient of friction.

6.636.2.13. Fluid Absorption

Fluid absorption is different from capillarity but both contribute to an increased risk of bacterial contamination and its spread. Chromic gut and plain gut sutures, which are both monofilament sutures with no capillarity, have the highest fluid absorption.[17] The chemical nature and physical structure of a suture determine the level of fluid absorption; however, the chemical nature appears to be more important than the physical structure.[9] Natural sutures have greater capacity to absorb fluid compared to synthetic sutures which are more hydrophobic. Nevertheless, generally speaking, multifilament sutures have higher fluid absorption than monofilament sutures.[9]

6.636.2.14. Ease of Removal and Color

Sutures come dyed or undyed. Dying makes the suture more visible and easier to remove. Where removal is not necessary, undyed sutures may be less conspicuous.

6.636.3. Sutures

Suture material may be absorbable or nonabsorbable, natural or synthetic, monofilament or multifilament, according to its composition and structure. Absorbable sutures are generally defined as materials that lose their tensile strength within 60 days of implantation.[18] Natural materials are absorbed through enzymatic degradation, while newer synthetic absorbable sutures are absorbed by nonenzymatic hydrolysis. During nonenzymatic hydrolysis, the polymers are divided into monomers by direct water cleavage and the monomers are metabolized to carbon dioxide and water.[19] The advantage of the new synthetic sutures is that their rates of absorption during the process of nonenzymatic hydrolysis are not affected by the presence of inflammation or infection.[20]

Nonabsorbable suture materials are those materials that are not significantly degraded after implantation. These sutures are normally used where extended support is required. The preference is usually toward synthetic materials, which are less reactive than natural fibers. Natural fibers invoke a more significant inflammatory reaction.

The use of absorbable sutures can be beneficial when suture support is required only for a short time or when removal of the sutures is likely to be painful or difficult due to its anatomical location. Monofilament nonabsorbable sutures are preferred to multifilament varieties, particularly when infection may be a problem. The capillarity of multifilament suture increases the attraction and retention of bacteria thereby increasing the risk of infection and the subsequent development of draining sinus tracts from the wound.

6.636.3.1. Absorbable Suture Materials (Table 1)

6.636.3.1.1. Surgical gut

Surgical gut comes in many varieties and can be plain, chromic, or fast absorbing. These are natural absorbable multifilament sutures and are prepared from purified connective tissue derived from either the submucosa of sheep intestines or the serosal layer of bovine intestines. Strands of, mostly, purified collagen are twisted together to form sutures. Surgical gut was an early standard in surgery but has lost favor today because it has poor tensile strength and knot security compared to the newer synthetic suture materials.[12] In Europe, it is no longer used because of the risk of bovine spongiform encephalitis. Although it is predominantly collagen, surgical gut invokes a moderate inflammatory reaction in tissues that is probably associated with miscellaneous muscle fibers and mucoprotein that are also present within the suture.[21] It is broken down rapidly by a combination of enzymatic degradation and

Table 1 Characteristics and applications of absorbable suture materials

Suture type	*Strand*	*Raw material*	*Properties*	*Use*	*Disadvantages*
Surgical gut	Multifilament				
Plain (Gut)		Ovine intestinal submucosa or serosa of bovine intestine	Absorbed quickly by proteases. Retains strength for 7 days. Fully absorbed by 14 days Invokes moderate inflammatory reaction	Rarely	Sets up an inflammatory reaction Absorption increased in infected tissues Short holding time
Chromic (chromic gut)		Same as plain but treated with chromium salts to improve strength and decrease reactivity	Absorbed more slowly Retains strength for 14 days and absorbed at 21 days	Good handling characteristics Used in rapidly healing tissues like subcutaneous tissue May be desirable where inflammatory reactions and fibrous tissue are desired	Inflammatory reaction Poor knot security Variable absorption rate Loss of tensile strength High capillarity Occasional reaction
Polyglactin 910 (Vicryl)	Braided multifilament	Copolymer of glycolic and lactic acid coated with calcium stearate	Retains 65% of strength at 2 weeks and loses all strength at 3 weeks	Easier to handle than gut, minimal tissue reaction, higher strength, and can be used in infected wounds	May cut through friable tissue
Vicryl			Absorption by hydrolysis complete at 60–90 days		
Vicryl Rapide		Polyglactin 910 partially hydrolyzed in buffer	50% of tensile strength lost at 7–14 days and absorbed at 21 days	Designed to mimic performance of gut without the inflammatory reaction	
Polyglycolic acid (Dexon, Dexon II)	Braided multifilament	Synthetic homopolymer of glycolic acid. Dexon II is coated with polycaprolate	Retains 89% of strength at 7 days, 63% at 14 days 17% at 21 days and absorbed at 90–120 days by hydrolysis	Similar properties to Vicryl. Wide variety of uses in normal and contaminated tissues. Useful for cesarean and intestinal anastomosis	Breakdown enhanced in urine and oral cavity. Uncoated form has high coefficient of friction
Poliglecaprone 25 (Monocryl)	Monofilament	Copolymer of glycolide and epsilon-caprolactone	Looses 30–40% of strength at 14 days, no strength at 3 weeks and absorbed at 90–120 days by hydrolysis	Easy to handle, good knot security, and minimal tissues reactivity. General tissue approximation	Should not be used in area of delayed healing
Polydioxanone (PDS II)	Monofilament	Polymer of paradioxanone	Retains 74% of tensile strength at 2 weeks and 25% at 6 weeks. Absorbed at 6–7 months by hydrolysis	Used where approximation of tissues needed for extended periods. Useful in infected tissues	Poor knot security and poor handling characteristics because of stiffness and memory
Polyglycolide–trimethylene carbonate (Maxon)	Monofilament	Copolymer of glycolic acid and trimethylene	Retains tensile strength for 42–92 days compared to 64–80 days for PDS. Absorbed by hydrolysis at 6 months	Better knot security than PDS II. Similar applications to PDS II	Poorer handling characteristics compared to PDS II
Caprosyn (caprosyn)	Monofilament	Composite of glycolide, caprolactone, trimethylene carbonate and lactide	Retains 50–60% tensile strength at 5 days and 0% at 3 weeks. Fully absorbed by 56 days	Superior handling, tensile strength, and knot security compared to gut and greater resistance to infection	Short retention time confined its use to plastic surgery, obstetrics and gynecology where rapid absorption and minimal scarring are important

phagocytosis. Plain gut also attracts small lymphocytes which enhance absorption.[22,23] The rate of absorption is significantly increased in the presence of infection and in tissues with high levels of proteolytic enzymes.[24]

Plain gut is an untreated preparation that retains its strength for 7 days and is fully absorbed in 10–14 days. Chromic gut is tanned with chromic salts to reduce the tissue reaction and to delay its breakdown. This treatment increases the holding time to ~14 days and delays absorption to 21 days. Chromic gut is difficult to handle, has a tendency to fray and has poor knot security when wet.[1] It is important to place four throws at the start of a continuous suture and five throws at the end.[25] Fast absorbing plain gut is heat treated to increase its rate of absorption; however, this also reduces suture strength compared to similar gauge, plain gut. It is commonly used in epidermal suturing where sutures are required for only 5–7 days and suture removal is difficult. Gut is generally inexpensive, making it economically attractive, but has now largely been superseded by newer synthetic absorbable sutures that have fewer complications.

6.636.3.1.2. Polyglactin 910 (coated Vicryl, Vicryl Rapide, and coated Vicryl Plus)

Vicryl was the second synthetic absorbable suture introduced after Dexon (polyglycolic acid). Vicryl is a synthetic, braided, absorbable suture made of polyglactin 910, a copolymer of L-lactide (10%) and glycolide (90%), and is coated with calcium stearate (**Figure 1**). Vicryl is sterilized by ethylene oxide. It comes in both clear and dyed forms. Vicryl is similar to Dexon in many of its characteristics. It has a greater initial tensile strength than surgical gut but is only marginally stronger than Dexon. This difference is clinically insignificant. Vicyl retains 50–65% of its tensile strength at 2 weeks, but by 3 weeks has no residual strength.[9,26] It elicits a minimal inflammatory reaction with complete absorption occurring by hydrolysis in 60–90 days. It has good handling characteristics and size to strength ratio, making it suitable for use in a variety of tissues, including infected wounds.[26] It comes in a range of sizes.

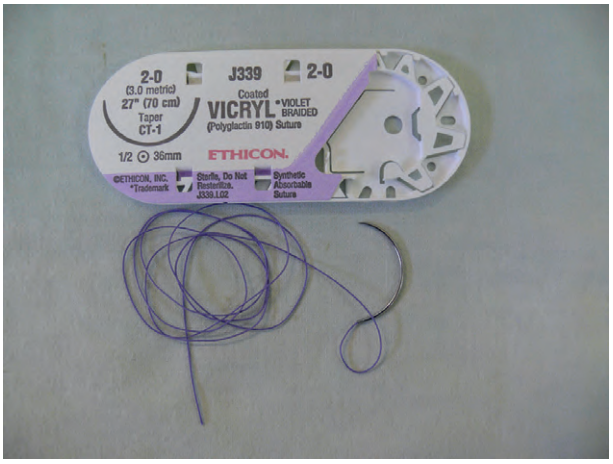

Figure 1 Polyglactin 910 is a commonly used absorbable braided multifilament suture which has better handling characteristics and is stronger than surgical gut.

Vicryl Rapide is a synthetic, absorbable, multifilament suture derived from polyglactin 910 that is partially hydrolyzed in a buffer solution and sterilized with gamma radiation. This processing enhances its absorption.[9] It has approximately 66% of the initial tensile strength of coated Vicryl.[27] It loses its tensile strength much faster than Vicryl and is used in the oral cavity as it will start to slough in 7–10 days.[1] In other tissues, strength is lost in 7–14 days and its absorption is complete by 21 days. It was designed to mimic the performance characteristics of surgical gut without inciting the inflammatory reaction associated with gut. It is suitable for tissues that heal with a rapid increase in tensile strength and long-term support is not required, such as in the gastrointestinal and urinary tracts.[1]

Coated Vicryl Plus employs a coating of the antimicrobial Triclosan which is thought to inhibit bacterial colonization of the braided suture and thus minimize the pain associated with subclinical infection.[8,9] It is often used in pediatric surgery because its antibacterial properties reduce the effects of pain in infants.

6.636.3.1.3. Polyglycolic acid (Dexon, Dexon II)

Polyglycolic acid was the first commercially available absorbable synthetic suture. It is a braided, synthetic absorbable suture made from a synthetic homopolymer of glycolic (hydroacetic) acid.[26] Dexon II has a coating of polycaprolate which enhances its handling characteristics by reducing the coefficient of friction. Polyglycolic acid is initially stronger than surgical gut but has less tensile strength compared to other synthetic absorbable sutures. It retains 89% of its tensile strength at 7 days, 63% at 14 days, 17% at 21 days, and is completely absorbed by 90–120 days.[28] Dexon loses its functional properties faster and has a lower knot breaking strength compared to Vicryl.[9]

Dexon is broken down by hydrolysis rather than enzymatic breakdown, thus leading to less tissue reaction and delayed absorption compared to surgical gut. The end products of breakdown do not provide growth materials for bacteria.[29,30] Polyglycolic acid has been reported to be unsuitable for use in the oral cavity or in the presence of infected urine as the alkaline pH increases its rate of breakdown.[29,30] It is suitable for use where extended approximation of tissues under stress is not required, such as intestinal anastomosis or a cesarean section.[31,32]

6.636.3.1.4. Poliglecaprone (Monocryl)

Poliglecaprone is a synthetic monofilament absorbable suture made of a copolymer of glycolide and ε-caprolactone. The lubricant coating decreases the coefficient of friction. It is available in the dyed or the undyed form. It is one of the strongest absorbable suture materials available, allowing the selection of suture sizes that are one to two times smaller than would ordinarily be chosen.[8,33] However, it rapidly loses its strength after implantation.[24] Dyed monocryl retains 30–40% of its tensile strength at 2 weeks whereas undyed monocryl retains only 25% at 2 weeks. By 3 weeks, there is no residual strength, absorption is by hydrolysis and is complete by 90–120 days.[9]

Monocryl elicits minimal tissue reaction, has good knot security and excellent handling characteristics as it lacks stiffness, and has less memory compared to other synthetic

absorbable sutures. Compared to Vicryl Rapide in a subcuticular closure, monocryl resulted in significantly smaller, less reactive scars, and a reduced tendency to produce hypertrophic scar formation.[34] It is recommended for general soft tissue approximation, including subcutaneous closures.

6.636.3.1.5. Polydioxanone

Polydioxanone (PDS II) is a synthetic, absorbable, monofilament suture made from a polymer of paradioxanone (Figure 2). It has greater initial tensile strength than polyglycolic acid and polyglactin 910 but has the poorest knot security of all the synthetic absorbable sutures.[24] The suture retains 74% of its tensile strength after 2 weeks, 50% after 4 weeks, and 25% after 6 weeks. There is minimal absorption by 90 days and absorption is not complete until 6–7 months after implantation.[9] This retention of strength after implantation is an advantage over other synthetic absorbable sutures and is useful wherever extended approximation of tissues (up to 6 weeks), under tension, is required.[35] PDS II is stiff and more difficult to handle than Dexon or Vicryl, but slides easily through tissue. PDS II was developed to improve the handling characteristics of the original form. It has low reactivity and maintains integrity in infected tissues and in urine and is often used in bladder surgery.[36] Its long retention time may act as a nidus for calculus formation in patients with a history of urinary calculi. However, it is suitable for use in a wide variety of tissues.[1]

6.636.3.1.6. Polyglycolide–trimethylene carbosnate (Maxon)

Maxon is a synthetic, absorbable, monofilament copolymer of glycolide and trimethylene carbonate. It has better handling properties than polyglactin 910 and polypropylene but is considered more difficult to handle than polydioxanone.[37,38]. Maxon is reported to have better knot security than PDS II.[38] It has greater initial tensile strength after implantation than most other absorbable sutures, but after implantation, the decrease in tensile strength is 81% at 14 days, 59% at 28 days, and 30% at 42 days, which is similar to PDS II.[12,39] On an average, Maxon retains its tensile strength for 42–92 days compared to 64–80 days for PDS II.[9] It is absorbed by hydrolysis like the other synthetic absorbable sutures and, like PDS II, loss of tensile strength occurs well before there is a significant reduction in mass. Absorption is complete by 6 months.[8]



Figure 2 Polydioxanone is a commonly used absorbable monofilament suture useful in infected tissues where approximation of tissues for extended periods is desired. However, it is stiff and has poor handling characteristics and knot security.

6.636.3.1.7. Caprosyn

Caprosyn is a monofilament, synthetic, absorbable suture prepared from polyglytone 6211 synthetic polyester which is composed of glycolide, caprolactone, trimethylene carbonate, and lactide.[40] This recently developed suture material undergoes rapid absorption. Caprosyn retains a minimum of 50–60% of knot strength at 5 days postimplantation and a minimum of 20–30% of knot strength at 10 days. All of its tensile strength is lost by 21 days after implantation and it is fully absorbed by 56 days. Caprosyn has been compared to chromic gut.[40] Caprosyn is superior in tensile strength to chromic gut but has comparable resistance to wound disruption. Caprosyn has far superior handling characteristics, better tissue approximation, and improved knot security. Caprosyn and chromic gut are absorbed at a similar rate but caprosyn has a greater resistance to infection. It is designed for plastic surgery, obstetrics and gynecology, and urology, where the benefits of rapid absorption and minimal scarring may be important.

6.636.3.2. Nonabsorbable Suture Materials (Table 2)

6.636.3.2.1. Silk (Mersilk, Perma-Hand)

Silk was introduced in the late 1800s as an alternative to gut. It is a natural nonabsorbable braided suture, produced by silkworm larvae, and made of protein filaments. These are braided for ease of handling and dyed for greater visibility. Silk evokes an inflammatory response that is second only to surgical gut and has significant capillarity. Silk may be coated by immersion in oil, wax, or silicone. Coating silk reduces capillarity at the expense of knot security.[18] Silk has superb handling characteristics and is the benchmark for comparison of handling characteristics of other suture materials. It has higher initial tensile strength compared to gut but is not as strong as most of the synthetic sutures. It retains 50% of tensile strength at 1 year and complete absorption may occur by 2 years.[9,24] Its braided configuration allows blood and serum to accumulate between its fibers and this predisposes it to infection and tissue ingrowth. Along with its tendency to produce an inflammatory reaction, it has also been shown to enhance the development of *Staphylococcal* spp. infection by up to 1000 times.[24] It may cause ulceration if used in the intestine or other hollow viscera and predisposes to calculi formation in the bladder and bile duct.[41] It is often used as a stay suture for retraction during surgery and for cutaneous surgery around the lips and eyelids.[2,5,12]

6.636.3.2.2. Polybutester (Novafil)

Polybutester is formed from a monofilament of polybutylene terephthalate and polytetramethylene ether glycol.[1,24] It was designed to combine the advantages of polypropylene and polyester. It has greater strength, less stiffness, and a lower coefficient of friction than either polypropylene or nylon.[12] It displays good handling characteristics and knot security

Table 2 Characteristics and applications for nonabsorbable suture materials

Suture type	*Strand*	*Raw material*	*Properties*	*Use*	*Disadvantages*
Silk (Mersilk, Permahand)	Braided multifilament	Protein filaments spun by silkworm larvae. May come coated in wax, silicone or immersion in oil	Looses 50% tensile strength at 1 year and complete absorption by 2 years	Excellent handling characteristics but invokes a marked inflammatory response. High capillarity. Used in ophthalmic surgery and as stay sutures	Not for use in contaminated tissues or intestinal anastomosis. Enhances infection in tissues
Polybutester (Novafil)	Monofilament	Copolymer of polybutylene terephthalate and polytetramethylene ether glycol	No appreciable loss of tensile strength. Designed to combine advantages of polypropylene and polyester	Excellent strength, elastic, good handling characteristics, good knot security while eliciting little tissue reaction. Useful in tendons and slow healing tissues	
Polyester (Mersilene, Ethibond, Surgilene, Surgidac)	Braided multifilament	Synthetic material made from condensation and polymerization. May be coated with polybutilate	Tensile strength second only to metallic sutures. No appreciable loss of strength. Good handling and knot security	Used to support slow healing tissues	Noncoated forms have high coefficient of friction. Not to be used in contaminated tissues, expensive
Nylon (Ethilon, Nurolon, Dermalon, Monsof, Supramid, Monosol, Surgilon)	Monofilament or multifilament	Polyamide thermoplastic made from hexamethylenediamine and adipic acid	Monofilament retains 72% of tensile strength after implantation and lose up to 50% by 2 years. Multifilament looses all strength by 6 months. Absorbed by hydrolysis	Inert, excellent elasticity makes it excellent in skin. Low capillarity and hydrolyses to antibacterial products so good in contaminated tissues	Poor handling characteristics, significant memory, and poor knot security. Multifilament forms have improved handling characteristics
Polypropylene (Prolene)	Monofilament	Catalytic polymerization of polypropylene	Retains tensile strength after implantation. Low tissue reactivity, least thrombogenic of all sutures. High plasticity	Excellent for skin and often used in vascular surgery	Poor knot security and poor handling characteristics
ePFTE Gore-Tex CV4	Monofilament	Polytetrafluroethylene	Retains tensile strength and is not degraded	Excellent handling characteristics	
Stainless steel	Monofilament or multifilament	Chromium and molybdenum alloy	Biologically inert and offers the greatest strength of all suture materials	Commonly used in orthopedic surgery and tendon and ligament repair Useful in slow healing or infected tissues	Can cut through tissues so not useful in highly mobile sites, poor handling characteristics

while eliciting only minimal tissue reaction.[42] As it is a monofilament it is less likely to harbor bacteria. It has a high degree of elastic stretch under low loads, thus offering distinct advantages over other nonabsorbable sutures.[43] It is able to stretch to 50% of its original length at a load of 25% of its breaking point.[12,43] This elasticity provides clinical advantages as it allows substantial swelling without cutting into tissue and maintains tissue approximation throughout healing. Polybutester is suitable for repair of tissues such as tendons where its elastic properties may be an advantage, particularly in the early phases of healing.[1]

6.636.3.2.3. Braided polyester (Mersilene, Ethibond, Surgidac)

Polyester is a nonabsorbable multifilament suture material formed by condensation polymerization (Figure 3). It may come coated with polybutilate (Ethibond) or in the uncoated (Mersilene) form. The uncoated forms have a high coefficient of friction and drag through tissue. The coated form was developed to overcome this problem but the coating has been noted to crack after implantation and may induce inflammatory reactions.[2,9,27] Braided polyesters were developed to induce minimal tissue reactivity while maintaining the good handling properties of braided multifilament sutures. While showing reduced tissue reactivity compared to other multifilament sutures, these braided polyesters do not match the inert qualities of other synthetic nonabsorbable monofilament sutures.[1] They generally show poor knot security, particularly the coated forms, with five throws suggested as a minimum number.[1] Braided polyesters are stronger than silk or gut and are second in tensile strength only to metal sutures.[44] They lose little tensile strength over time. They are more expensive than most other sutures and provide no significant advantages over other less expensive sutures, and so are not commonly used. Braided polyesters should not be used in the presence of contamination and infection as bacteria may become trapped between the fibers and isolated from phagocytic cells, leading to draining sinus tracts.

Ethibond suture material has a polybutilate coating which improves the handling characteristics and reduces the high coefficient of friction compared to uncoated forms. Polyester sutures show no significant loss of tensile strength over time.

6.636.3.2.4. Nylon (Ethilon, Monosof, Nurolon, Surgilon, Supramid)

Nylon is a synthetic, nonabsorbable, monofilament made of a chemically inert polyamide thermoplastic made from hexamethylenediamine and adipic acid.[1] It is available as either a monofilament (Ethilon, Monosof) or as a multifilament (Nurolon, Surgilon, Supramid) suture. The monofilament form is far more common and less susceptible to infection (Figure 4). The monofilament retains 72% of its tensile strength immediately after implantation, after which the degradation stabilizes.[45,46] It will lose up to 30–50% of its tensile strength by 2 years due to progressive hydrolysis over time.[1,9,47] Owing to nylon's chemically inert characteristics and slow hydrolysis, it induces less of an inflammatory reaction than polyglycolic acid sutures.[45] It maintains a high level of elasticity after implantation in tissue, an important consideration if tissue edema and inflammation develop. These properties make nylon the most commonly used skin suture.[10] The main disadvantages of nylon are its poor handling characteristics and knot security.[35] Nylon has significant memory and is not very pliable making it difficult to work with. Alcohol-soaked monofilaments improve handling. Multifilament forms tend to have improved handling characteristics and knot security, but at the expense of capillarity.[27]

Supramid is a twisted multifilament, polymerized caprolactam enclosed in a smooth sheet of proteinaceous material. It has superior tensile strength compared to other nylon products but tends to have poorer knot security.[24]

6.636.3.2.5. Polypropylene (Prolene, Surgilene)

This product is a synthetic, nonabsorbable, monofilament suture made by the catalytic polymerization of polypropylene (Figure 5). Polypropylene has the greatest tensile strength of all synthetic nonabsorbable suture materials and no appreciable reduction in strength after implantation.[47,48] It has low tissue



Figure 3 Polyester suture is a braided multifilament, nonabsorbable suture with tensile strength second only to metallic sutures. Polyester is commonly used to support slow healing tissues.

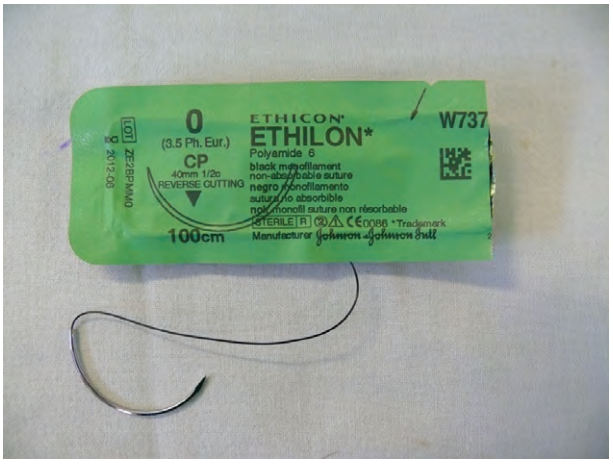

Figure 4 Nylon is a nonabsorbable monofilament suture which is most commonly used for skin closure. It has excellent elasticity, low capillarity, and hydrolyses to antibacterial products so is useful in contaminated tissues. However, it has poor handling characteristics, significant memory, and poor knot security.

reactivity and is the least thrombogenic suture material, and is, therefore, often used in vascular surgery.[49] Polypropylene has high plasticity and is useful in accommodating wound edema or swelling without cutting through the skin; however, once it is stretched it does lose its form. It has a very smooth surface giving it a low coefficient of friction; however, this feature along with high memory contributes to lower knot security.[27] If the knots are set firmly, polypropylene will flatten where strands cross each other and provide greater knot stability and greater knot strength. The longevity without significant loss of tensile strength, its resistance to infection and low tissue reactivity make it a suitable suture for the skin.[20]

6.636.3.2.6. ePFTE (Gore-Tex CV4)

Gore-Tex CV4 is a synthetic, nonabsorbable monofilament suture made from polytetrafluroethylene that has been expanded to produce a porous microstructure that is 50% air by volume. This suture is white in color and provokes minimal tissue response with cellular ingrowth. The tensile strength does not change *in vivo*. It is soft and supple, affording excellent handling characteristics. Gore-Tex CV4 does not degrade in the presence of infection and is not subject to the action of tissue enzymes.[9]

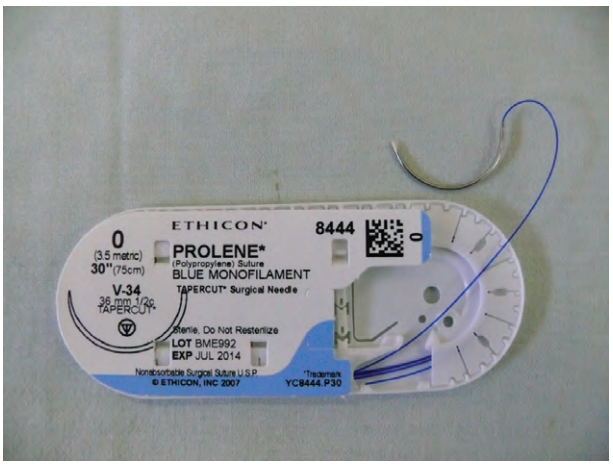

Figure 5 Polypropylene is a nonabsorbable monofilament suture that is commonly used in skin. It retains tensile strength after implantation and has low tissue reactivity making it the least thrombogenic of all sutures and useful for vascular surgery. It has high plasticity, poor handling characteristics, and poor knot security.

6.636.3.2.7. Stainless steel

Stainless steel is an alloy of chromium and molybdenum, available as either a monofilament or a multifilament suture. It is biologically inert and offers the greatest strength of all the suture materials.[27] It is most commonly used in orthopedic surgery but has also been used in tendon or ligament repair. It is used in contaminated and infected wounds such as abdominal wall hernias following wound infection in horses.[1,29,50,51] Stainless steel sutures have a tendency to cut through tissue and have poor handling characteristics.[35] Movement over the ends of the knot can cause tissue necrosis.[26]

6.636.3.3. Other Sutures

6.636.3.3.1. Barbed suture (Quill SRS, Monderm, Coveidin)

This is a knotless, synthetic suture that is available in a variety of nonabsorbable and absorbable materials; however, to date, all sutures are monofilaments. The first approved barbed suture was a bidirectional barbed polydioxanone. From that time onwards, bidirectional barbed suture has also become available in poliglecaprone 25, and is now available as a nonabsorbable suture in nylon and polypropylene.

Barbed sutures are effective due to their bidirectional fixation within the wound. The barbs are arranged around the suture, in opposite directions, on each side of a short retainer free segment. This is achieved by a micromachining technique that cuts barbs into the monofilament fibers around the circumference in a helical pattern. The barbs are separated by a distance of 0.88–0.98 mm. Closure begins at the midpoint of the wound and the suturing extendsin two directions

Table 3 Suggested suture selection for specific tissues

Skin	Monofilament nonabsorbable sutures such as nylon, polypropylene, and polybutester are recommended. Alternatively, the monofilament absorbable sutures with longer retention times such as polydioxanone or polyglycolide–trimethylene carbonate may be used where removal of sutures may be difficult. Stainless steel staples save time in larger incisions Avoid reactive or high capillarity sutures
Subcutis	Any of the synthetic absorbable sutures. Where approximation of tissues is required only for a short time polyglycolic acid or polyglactin 910 are commonly used. Where longer retention time for slower healing tissues then polydioxanone or polyglycolide–trimethylene carbonate may be used
Fascia	Synthetic, absorbable sutures with are recommended. Applications for subcuticular tissues apply. If prolonged strength is required, synthetic nonabsorbable sutures can be used but run the risk of suture sinus formation if contaminated. They should be placed so that they can be easily removed if needed
Muscle	Synthetic absorbable or nonabsorbable sutures may be used. Nylon and polypropylene are recommended for use in cardiac muscle because of their superior mechanical properties
Hollow viscus	Polyglycolic acid, polyglactin 910, polydioxanone, polyglycolide–trimethylene carbonate, poliglecaprone 25, caprosyn, and monofilament nonabsorbable sutures may be used in viscera. Polyglycolic acid is generally considered unsuitable for the bladder because it loses its tensile strength faster in urine. Polydioxanone may act as a nidus for calculi production because of its long half-life
Tendon	Nylon and stainless steel are often recommended. Polydioxanone, polyglycolide–trimethylene carbonate and polybutester may also be used where adhesion formation associated with prolonged presence of suture is a potential complication
Blood vessel	Polypropylene is the least thrombogenic of all sutures and is recommended. Nylon and coated polyester have also been used
Nerve	Nylon and polypropylene are used because they have the least tissues reactivity

with needles swaged onto each end. Barbs within the suture distribute tension evenly across the wound, thus eliminating the need for knots.[9] This material facilitates the use of a continuous suturing technique rather than the simple interrupted sutures in deeper tissue layers, thereby increasing the ease, speed, and economy of placement. As the barbs cannot slip backward, they do not leave gaps in areas of tension, allowing subcuticular closure with fewer primary buried sutures and significant time saving.

Owing to a decrease in the effective diameter during micromachining, generally, a barbed suture is rated as equivalent to 1 USP suture size greater than its conventional equivalent. So a 2-0 barbed suture will rate as a 3-0 conventional suture. However, it is worth noting that conventional sutures lose tensile strength at and around the knots while a barbed suture is knotless and is not predisposed to weak areas. When corrected for size, a barbed suture demonstrates equal, if not better, *in vivo* wound breaking strengths compared to conventional monofilament sutures.[13] Furthermore, elimination of the knot reduces the amount of foreign material within the wound and tissue reaction. The holding power and apposition of tissue are improved because the tension is distributed more evenly across the suture. This is expected to create a more watertight seal and can avoid uneven healing across the suture line.[13]

More recently, a unidirectional barbed suture has been released, which has a loop at the distal end for initial suture fastening. There is some conjecture that necrosis of the tissue at the loop end could limit the wound strength of this configuration of suture. Currently available barbed sutures are produced only in a limited number of suture materials and in limited suture and needle sizes.

6.636.4. Staples

Tissue staples provide a quick and effective alternative to manual suturing.[52] They are used in procedures such as gastrointestinal surgery, liver and lung resection, and reproductive surgery but may have wider applications. Skin staplers place individual rectangular-shaped sutures in a single row while staples used in other tissues place at least a double row of staples in a staggered 'B' configuration.[27] Stapling instruments reduce tissue handling, decrease surgery time, minimize contamination, provide secure visceral, vascular, and dermal closures, and preserve blood supply.[24] However, they may be ineffective if used on excessively thick tissues, and provide ineffective haemostasis in large blood vessels.[1]

6.636.4.1. Skin Staples

Skin staples come in both nonabsorbable and absorbable forms.

6.636.4.1.1. Nonabsorbable staples (Proximate, Royal Autosuture)

These staples are made of stainless steel and have the highest tensile strength. An additional advantage is that they come with low tissue reactivity.[12] Metal staples come in two sizes, regular (4.8–6.1 mm) and wide (6.5–7 mm), and are discharged from lightweight cartridges (Figure 6). Prior to application they have a straight cross member and straight or curved legs. After discharge, the cross member is bent over, thus crimping it at two sites and bringing the legs together to form a rectangular shape that is narrower than the original staple.[53] They provide a faster method of closure compared to sutures and evert wound edges without strangulation of tissue, thereby reducing the incidence of cross hatch scarring.[9,54] Staples may provide a superior cosmetic result in some circumstances and have a lower incidence of complications in contaminated wounds.[9]

6.636.4.1.2. Absorbable staples (Insorb)

This staple is made of an absorbable copolymer, consisting predominantly of polylactide and a lesser component of polyglycolide. These subcuticular staples provide a novel method of skin closure. They lose 60% of their holding strength within 2 weeks and have a half-life of 10 weeks.[53] They produce less severe inflammation at 7–21 days after surgery compared to subcuticular suture or stainless steel skin staples.[55] They are useful in contaminated wounds where, compared to Vicryl sutures, they have a lower incidence of infection.[8] Many studies have produced variable results when comparing the performance of absorbable and stainless steel staples with respect to wound infection.[9]

6.636.4.2. Ligatures

Instruments for vascular ligations are designed for vascular bundles that can be compressed to 5 or 7 mm. The device is pistol-shaped and, when activated, fires two stainless steel, titanium, or absorbable copolymer staples. The device transects the vessel between the two staples. These U-shaped staples come in two sizes, regular and wide. Regular staples are 5.79 mm wide and 5.23 mm tall, closing to a width of 5.33 mm. Wide staples are 8 mm wide and 7.22 mm tall,



Figure 6 Autosuturing devices contain stainless steel staples useful for skin closure. These staples have high tensile strength and low tissue reactivity and provide faster closure of surgical wounds. After discharge, the cross member of the original staple is bent over crimping it at two sites bringing the legs together to form a shape that is narrower than the original staple.

with a final closure width of 7.3 mm. Regular staples are set 6.35 mm apart and the wide staples are set 9.53 mm apart. Vascular clips are useful in procedures which require rapid or extensive vascular occlusion, such as during splenectomies or in intestinal resections where extensive ligation of mesenteric vessels may be required. The vessel should be isolated from the surrounding tissue to allow the most effective discharge of the device. If double ligation is required or if the vessel cannot be crushed to 7.5 mm the advantage of the ligatures (LDS) may be lost.

6.636.4.3. Stapling Devices in Abdominal and Thoracic Surgery

These devices come as disposable or reusable instruments that create an inverted or everted tissue closure that is secured by two or more rows of B-shaped stainless steel, titanium, or, occasionally, absorbable staples. The B-shaped configuration is noncrushing while compressing tissues, thereby creating some hemostasis without necrosis.

The GIA (gastrointestinal anastomosis) or ILA (intestinal linear anastomosis) devices come with disposable cartridges that fire two double rows of staggered titanium staples (Figure 7). The staple lines are set 3.5 mm apart and the device cuts between the second and third rows of staples, creating an incision length 8 mm short of the last staple at the distal end.[53,56] The GIA cartridges come in a variety of sizes, including 50, 60, 80, and 90 mm lengths (Figure 8), while the ILA cartridges are available in 52 and 100 mm lengths. Staples are 4.0 mm wide and come in 4.8 and 3.8 mm leg lengths that compress to 2.0 and 1.5 mm, respectively.[53] Discharge of the device results in an inverting, side-to-side anastomosis of two hollow organs such as the small intestine. However, these devices have also been used to resect diseased tissues in various organs, including the lung and intestine. The device is placed across the junction between the healthy and diseased tissues to seal both sides with a double row of staples. The diseased portion of tissue can be removed safely without leakage of body fluids. The sealed stump of the healthy tissue can then be oversewn, if required, to reinforce the seal.

Circular stapling devices are also available for intestinal anastomosis. The end-to-end anastomosing (EEA) devices contain 4-mm-wide staples with 4.8-mm leg length that close down to a height of 2.0 mm. Reusable staple devices are straight and come in lengths of 25, 28, and 31 mm. A circular cartridge is attached to the arm and these are available in diameters of 25, 28.6, and 31.6 mm with knife diameters of 15, 18, and 21.2 mm, respectively. Single use curved EEA devices come with circular cartridge diameters of 21.3, 25, 28.7, 31.6, and 34.1 mm and with knife diameters of 11.5, 15, 18, 21.2, and 23.6 mm.[53] The appropriate size of instrument for the lumen is gauged by ovoid sizers which can also be used to stretch the intestine. Once the correct diameter is determined, the device is passed into the lumen of the intestine, and the two edges of the intestine to be anastomosed are secured around the cartridge using a purse string suture. The device fires a circumferential double row of B-shaped titanium staples creating an inverted anastomosis between the two ends. The redundant tissue inside the staple line is removed simultaneously by the knife.

The TA (thoracoabdominal) staplers fire two or more rows of B-shaped titanium staples to seal the thoracic and abdominal organs. Cartridge sizes are 30, 55, or 90 mm for reusable devices and 30, 45, 60, and 90 mm for disposable devices. The cartridges generally fire two rows of staples; however, the 90 mm cartridges are also available with three or four rows of staples. The staples are 4.0 mm in width but have a leg length of 4.8 and 3.5 mm, closing down to 2 and 1.5 mm, respectively. The cartridges come in a U-shaped configuration that can be inserted into a long-handled device, allowing access to difficult areas (Figure 9). These devices are available with rotating and articulating heads which further improve access in tight areas.[57] The device does not automatically cut, however, after

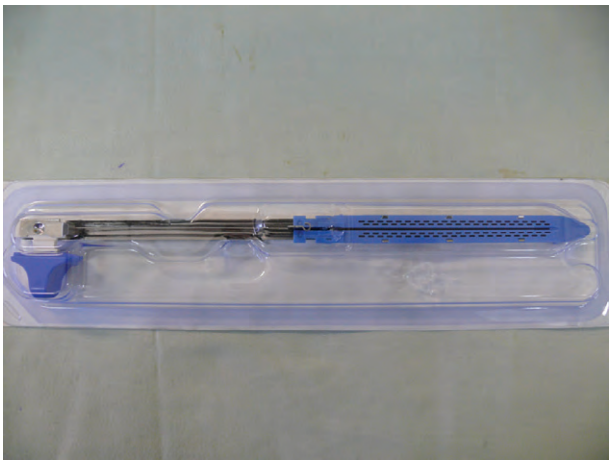

Figure 7 The disposable cartridges for the gastrointestinal anastomosing device contain two rows of staples either with 3.8 or 4.8 mm leg lengths. The staples are set 3.5 mm apart. When fired the staples compress to 1.5 and 2.0 mm, respectively. A blade cuts between the second and third rows of the staples creating a stoma 8 mm short of the last staple.



Figure 8 The gastrointestinal anastomosing (GIA) device comes in a variety of lengths with disposable cartridges that result in an inverting side-to-side anastomosis of tow hollow organs such as small intestine. They can also be used to resect and remove diseased tissues without leakage of body fluids.



Figure 9 The thoracoabdominal (TA) staplers come in a variety of sizes. The cartridges usually fire two rows of staples; however, the 90 mm cartridges are also available with three or four rows of staples. The devices come with a leg length of 3.8 or 4.8 mm closing down to 1.5 and 2 cm, respectively. The design of the handles allow access to difficult areas and devices are available with rotating and articulating heads further improving access to tight area.

discharging the staples; the instrument head can be used as a guide for transection, particularly in inaccessible areas.[53]

6.636.5. Surgical Needles

Needles are manufactured from stainless steel alloys which have excellent resistance to corrosion.[58] All true stainless steels contain a small amount of chromium which allows a thin protective surface layer of chromium oxide to form when the steel is exposed to oxygen. Maraging stainless steel with nickel provides a combination of high strength and toughness. The basic principle of maraging centers around strengthening the martenistic matrices so that the planes of atoms in the stainless steel are prevented from sliding over each other. A high nickel maraging stainless steel like S45500 is composed of 7.5–9.5% nickel, 0.8–1.4% titanium, and 11–25% chromium. High nickel maraging stainless steel is used to create surgical needles with greater strength and ductility. These needles show greater resistance to bending and breakage than stainless steel needles without nickel.

Surgical needles have a distinctive anatomy and characteristics such as shape, size, point, and method of suture attachment. Ideally, needles should be made of high quality stainless steel and be suitable to meet the needs of the surgery. They should be of the smallest diameter required to penetrate the tissue without bending, be able to be passed through both sides of the incision with minimal tissue trauma, be sharp enough to penetrate tissue with minimal resistance, be stable in the needle holder, and be sterile and corrosion resistant to minimize chances of infection. Some needles may be coated with silicone to enhance passage through tissue. When selecting a needle the surgeon should consider the thickness and accessibility of the tissue to be sutured, the importance of attaining a good cosmetic result, and the size of the suture material.[9,41]

6.636.5.1. Anatomy of a Needle

Needles have distinct features. The needle point is the portion of the needle that extends from the tip to the maximum cross-section of the body. The body incorporates most of the needle length. The importance of the body is that it is the point of engagement between the needle and needle holder during the transmission of force from the needle to the tip. Diameter, radius, geometry, and the material of the needle are all features of the body that determine bending moment, ultimate moment, surgical yield moment, and needle ductility.

Needles are available as eyed needles where the suture needs to be threaded onto the needles or as swaged needles where the suture is attached to the end. A channel swage is where the needle is created with a channel into which the suture is introduced and the channel is crimped on the suture. The swage, in this configuration, is wider than the body of the needle. A drill swage is where the material is removed from the center of the needle and the needle is crimped onto the suture. In this case, the swage is of a smaller diameter than the body of the needle. Swaged needles are less traumatic to tissues, easier to handle, and are always sharp because they are used once and then discarded.[41]

Eyed needles are reusable and less expensive than swaged needles, but cause greater trauma during suture placement. The larger diameter of the eye compared to the body of the needle and the need to loop a double strand of suture creates substantial trauma as the suture is pulled through the tissue. This effect is compounded when the needle becomes dull with reuse. The eye may be closed or French. A closed eye may be round, oblong, or square. A French eye is open to the end of the needle through a slit with ridges that catch and hold the suture in place. Increased handling of suture when threading a nonswaged needle can weaken the suture, or cause fraying or damage. Nonswaged needles are also less likely to become unthreaded during suturing compared to swaged needles.

Each needle is identified by various measurements. Chord length is the direct linear distance from the point of the curved needle to the swage (bite width). The needle length is the distance measured along the needle from the point to the swage. Needle length is the measurement supplied on suture packages. The radius is the distance from the body of the needle to the center of the circle along which the needle curves. The diameter is the thickness of the needle.

6.636.5.2. Point Types

The ability of the needle to penetrate tissue depends on the shape of the point and body of the needle.[41]

- Cutting

  A cutting needle has at least two, opposing, cutting edges because the point is usually triangular. Cutting needles are designed for penetration through dense, irregular, and relatively thick tissues. They are ideal for skin sutures. Conventional cutting needles have three cutting edges arranged in a triangle. The third cutting edge is on the inner or concave curvature.

  Reverse cutting needles are the same as conventional cutting needles except that the third cutting edge is on the

outside or convex curvature. These needles are stronger than the conventional cutting needles and have a lower chance of cutting through the edge of the tissue. They are designed for tough tissues but are also beneficial for cosmetic and ophthalmic surgery because, by cutting, they cause minimal trauma.

The taper cut needle combines the reverse cutting design at the point with a round shaft that is useful in delicate fibrous tissue.

Side-cutting needles have two cutting edges on each side of the needle and flat convex and concave surfaces. This maximizes passage through tissues while minimizing trauma.

The special K needle is similar to the taper cut needle but has a shorter and stronger cutting tip, making it useful in tough dense tissues such as cartilage.

- Taper point

  This is a round body needle with a sharp point that passes through tissue by stretching rather than cutting. These needles are not suitable for tissues that are hard to penetrate. They are usually used on nonfibrous soft tissues like abdominal viscera to minimize risk to adjacent vessels and nerves. The sharpness of the point is determined by the taper ratio (8–12.1) and tip angle (20–35°). Sharper needles have higher taper ratios and lower tip angles.
- Beveled, conventional, and cutting edge needles

  These needles are designed to repair lacerations. The angle of presentation of the cutting edge is decreased and this enhances the sharpness. They are composed of a stainless steel (ASTM 45500) that is heat treated after the curving process which enhances their resistance to bending. They are reported to have superior performance characteristics over conventional cutting edge needles.[59]
- Blunt point needles

  The point of these needles is blunt and rounded making them suitable for tissues like the kidneys or liver. This needle dissects tissues rather than cutting them.

6.636.5.3. Body Types

When choosing a needle shape, wound depth, size, and accessibility are the factors that should be considered.

- Straight

  This body type is used where tissue is easily accessed and the needle can be manipulated by hand, such as for skin, tendon, and gastrointestinal tract repair. It is also useful for nerve and vessel microsurgery.
- Half-curved ski

  This body type is not commonly used. It has a straight body and curved point such that the straight body does not follow the curved point making it difficult to handle.
- Curved

  This body type is commonly used and is useful in tight spaces. The path of the needle through tissues is predictable, optimizing passage through tissues. It comes in a variety of curves (quarter-inch, three-eighths-inch, half-inch, and five-eighths-inch). The three-eighths-inch is commonly used for skin closure while the half-inch is designed for tight spaces. The tighter the curve the greater the wrist manipulation that is required by the surgeon to place the suture.
- Compound curved

  This is an unusual needle with a tight 80° curvature at the tip which becomes a 45° curvature through the remainder of the body. It was originally designed for ophthalmic surgery but is now sometimes employed in microvascular surgery to approximate vessels.

6.636.5.4. Selection of Needles

There is no standardized sizing system for needles. Factors that should be considered when choosing a needle include:

- the hole made by the needle should only be large enough to permit suture passage so the needle does not weaken the tissue;
- the design and diameter of the needle should result in minimal tissue damage while minimizing the risk of needle breakage;
- the needle should have the appropriate size, shape, and diameter to permit rapid, accurate, and precise suturing.

In tissues that are easy to penetrate, a taper needle is usually sufficient, while cutting needles are typically reserved for tougher tissues. Cutting needles are usually used for the skin while taper needles are more suited to other tissues such as subcutaneous tissues and visceral organs such as the intestine.[41]

The length, diameter, and curvature of the needle will influence the surgeon's ability to place a suture and will be determined by the accessibility of the tissues. With swaged needles, the needle diameter will usually be preselected by the supplier according to the suture size. Needles are passed through tissues using needle holders. The jaws of the needle holder should be appropriate for the size of the needle to ensure that the needle is held securely to prevent rocking, turning, and twisting but at the same time there should not be excessive force which can cause bending or breakage of the needle.

6.636.6. Conclusions

Suture materials play an important role in wound repair by providing support to healing tissues. The number of options available to the surgeon has increased over the past 30 years. There is no ideal suture material available and the surgeon must make a decision based on scientific principles rather than by anecdote or tradition. Assessment of the wound, the healing properties of the tissues, and the patient's physical condition need to be matched to the physical and biological properties of the materials available. While the number of materials available has increased, within the variety of absorbable and nonabsorbable sutures available, there is a relatively consistent and stable range of established materials that cover most of the applications. With experience and excellent technical execution, different methods of closure may achieve similar high-quality results. However, with continued technological advances in suture materials, needles, and alternative approaches to wound closure, the challenge for the surgeon will be to stay abreast of new technology.

References

1. Tan, R. H. H.; Bell, R. J. W.; Dowling, B. A.; Dart, A. J. *Aust. Vet. J.* **2003**, *81*, 140–145.
2. Bloom, B. S.; Goldberg, D. *J. Cosmet. Laser Ther.* **2007**, *9*, 41–45.
3. Meyer, R. D.; Antonini, C. J. In *Compendium of CME in Dentistry*; Jamesburg Dental Learning Systems Co., 1989; pp 360–368.
4. Moy, R. L. *J. Dermatol. Surg. Oncol.* **1972**, *18*, 785–795.
5. Bennett, R. G. *J. Am. Acad. Dermatol.* **1988**, *18*, 619–637.
6. Rodheaver, G. T.; Thacker, J. G.; Edlich, R. F. *Surg. Gynecol. Obestet.* **1981**, *153*, 835–841.
7. Tera, H.; Aberg, C. *Acta Chir. Scand.* **1977**, *143*, 75–83.
8. Ammirati, C. T. In *Advances in Dermatology*; James, W. D., Ed.; Mosby: St. Louis, 2002; Vol. 18, pp 313–318.
9. Hochberg, J.; Meyer, K. M.; Marion, M. D. *Surg. Clin. North Am.* **2009**, *89*, 627–641.
10. Hochberg, J.; Murray, G. F. In *Textbook of Surgery*, 15th ed.; Sabiston, D. C., Ed.; Saunders: Philadelphia, 1992; pp 253–263.
11. Trimbos, J. B. *Obestet. Gynecol.* **1984**, *64*, 274–280.
12. Moy, R. L.; Waldmann, B.; Hein, D. W. *J. Dermatol. Oncol.* **1992**, *18*, 785–795.
13. Greenberg, J. A.; Clarke, R. M. *Rev. Obstet. Gynecol.* **2009**, *2*, 146–148.
14. Tera, H.; Aberg, C. *Acta Chir. Scand.* **1976**, *142*, 1–7.
15. Stone, I. K.; von Fraunhofer, A.; Masterson, B. J. *Surg. Gynecol. Obstet.* **1986**, *163*, 448–452.
16. Moy, R. L.; Lee, A.; Zalka, A. *Am. Fam. Physician* **1991**, *44*, 2123–2128.
17. Dumitriu, S. In *Polymeric Biomaterials*; Dimitriu, S., Ed.; CRC Press: London, 2002; p. 512.
18. Stashak, T. S.; Ytrurraspe, D. J. *Proc. Am. Assoc. Equine Pract.* **1979**, *24*, 369–382.
19. Steckel, R. R. In *Current Practice of Equine Surgery*; Auer, J. A., Stick, J. A., Eds.; Lippincott: Philadelphia, 1990; pp 50–55.
20. Stoloff, D. R. *Vet. Med. Rep.* **1991**, *3*, 53–58.
21. Apt, L.; Costenbader, F. D.; Parks, M. M.; Albert, D. G. *Arch. Opthalmol.* **1960**, *63*, 30–35.
22. Reiter, D. *Otolaryngol. Clin. North Am.* **1995**, *28*, 1069–1077.
23. Wu, T. *Aust. Fam. Physician* **2006**, *35*, 492–496.
24. Boothe, H. W. In *Textbook of Small Animal Surgery*, 2nd ed.; Slatter, D. H., Ed.; Saunders: Philadelphia, 1993; pp 204–212.
25. Rosin, E.; Robinson, G. M. *Vet. Surg.* **1989**, *18*, 269–273.
26. Bellenger, C. R. *Comp. Contin. Educ. Pract. Vet.* **1982**, *4*, 507–515.
27. Niles, J.; Williams, J. *In Pract.* **1999**, *21*, 308–320.
28. Outlaw, K. K.; Vela, A. A.; O'Leary, J. P. *Am. Surg.* **1998**, *64*, 348–354.
29. Campbell, J. R.; Marks, A. *In Pract.* **1985**, *7*, 72–75.
30. DeNardo, G. A.; Brown, N. O.; Trenka-Benthin, S.; Manfra Marretta, S. *J. Am. Anim. Hosp. Assoc.* **1996**, *3*, 164–172.
31. Ellison, G. W. In *Current Techniques in Small Animal Surgery*, 4th ed.; Bojrab, M. J., Ellison, G. W., Slocum, B., Eds.; Williams and Wilkins: Philadelphia, 1998; pp 245–258.
32. Larson, R. F. *N. Z. Vet. J.* **1978**, *26*, 258–259.
33. Runk, A.; Allen, S. W.; Mahaffey, E. A. *Vet. Surg.* **1999**, *28*, 466–471.
34. Niessen, F. B.; Spauwen, P. H.; Kon, M. *Ann. Plast. Surg.* **1997**, *39*, 254–260.
35. Smeak, D. D. In *Current Techniques in Small Animal Surgery*, 4th ed.; Bojrab, M. J., Ellison, G. W., Slocum, B., Eds.; Williams and Wilkins: Philadelphia, 1998; pp 19–27.
36. Schiller, T. D.; Stone, E. A.; Gupta, B. S. *Vet. Surg.* **1993**, *22*, 208–212.
37. Knoop, M.; Lunstead, B.; Thiede, A. *Langenbecks Arch. Chir.* **1987**, *371*, 13–28.
38. Kawcak, C. E.; Baxter, G. M. *Vet. Clin. North Am.* **1996**, *12*, 195–205.
39. Katz, A. R.; Mukherjee, D. P.; Kaganov, A. L.; Gordon, S. *Surg. Gynecol. Obstet.* **1985**, *161*, 213–222.
40. Pineros-Fernandez, A.; Drake, D. B.; Rodeheaver, P. A.; Moody, D. L.; Edlich, R. F.; Rodeheaver, G. T. *J. Long Term Eff. Med. Implants* **2004**, *14*, 359–368.
41. Blackford, L. W.; Blakford, J. T. In *Equine Surgery*, 2nd ed.; Auer, J., Stick, J., Eds.; Saunders: Philadelphia, 1991; pp 91–103.
42. Huber, D. J.; Egger, E. L.; James, S. P. *Vet. Surg.* **1999**, *28*, 260–268.
43. Rodheaver, G. T.; Nesbit, W. S.; Edlich, R. F. *Ann. Surg.* **1986**, *204*, 193–199.
44. Herrmann, J. B. *Am. Surg.* **1971**, *37*, 209–217.
45. Moloney, G. E. *Br. J. Surg.* **1961**, *48*, 528–530.
46. Postlethwaite, R. W. *Ann. Surg.* **1970**, *171*, 892–898.
47. Bellenger, C. R.; Meek, M. A. *Aust. Vet. J.* **1990**, *3*, 81–85.
48. Boothe, H. W. *Comp. Contin. Educ. Pract. Vet.* **1998**, *20*, 155–163.
49. Campbell, E. J.; Bailey, J. V. *Vet. Surg.* **1992**, *21*, 355–361.
50. Tulleners, E. P.; Donawick, W. J. *J. Am. Vet. Med. Assoc.* **1983**, *182*, 1377–1379.
51. Varma, V.; Lumb, M. W.; Johnson, L. W.; Ferguson, H. L. *Am. J. Vet. Res.* **1981**, *42*, 571–574.
52. Doran, R. E.; Allen, D. *Comp. Contin. Educ. Pract. Vet.* **1987**, *9*, 854–860.
53. Tobias, K. M. *Vet. Surg.* **2007**, *36*, 341–349.
54. Lubowski, D.; Hunt, D. *Aust. N. Z. J. Surg.* **1985**, *55*, 405–406.
55. Fick, J. L.; Novo, R. E.; Kirchhof, N. *Am. J. Vet. Res.* **2005**, *66*, 1975–1984.
56. Pavletic, M. M. *Comp. Contin. Educ. Small Anim. Pract.* **1990**, *12*, 1724–1741.
57. Pavletic, M. M.; Schwartz, A. *Vet. Clin. North Am. Small Anim. Pract.* **1994**, *24*, 247–278.
58. Szarmach, R. R.; Livingston, J.; Edlich, R. F. *J. Long Term Eff. Med. Implants* **2003**, *13*, 155–170.
59. Kaulbach, H. C.; Towler, M. A.; McClelland, W. A.; Povinelli, K. M.; Becker, D. G.; Cantrell, R. W. *J. Emerg. Med.* **1990**, *8*, 253–263.

6.637. Staple Line Reinforcement Materials

H H G Witjes and W A Draaisma, Meander Medical Centre, Amersfoort, The Netherlands
M Gagner, Florida International University, Miami, FL, USA
E C J Consten, Meander Medical Centre, Amersfoort, The Netherlands

© 2011 Elsevier Ltd. All rights reserved.

6.637.1.	**Introduction**	589
6.637.2.	**Staple Line Reinforcement**	590
6.637.2.1.	Etiology of Anastomotic Complications	590
6.637.2.2.	Buttress Material Properties	590
6.637.3.	**Reinforcement Materials**	590
6.637.3.1.	Absorbable Material	590
6.637.3.1.1.	Fibrin glue	590
6.637.3.1.2.	Cellulose	590
6.637.3.1.3.	Polyglycolic acid/trimethylene carbonate	590
6.637.3.1.4.	Polysaccharidic polyglycuronates biopolymers	591
6.637.3.2.	Semiabsorbable Material	591
6.637.3.3.	Nonabsorbable Material	591
6.637.4.	**Discussion**	591
References		592

Glossary

Anastomosis Artificial connection between parts of the gastrointestinal tract.
Buttressing materials Specific developed materials to support the healing of an anastomosis.
Laparoscopy Endoscopy of the abdominal cavity. Used for diagnostic goals and therapeutic surgical procedures (surgical resections).
Staple line reinforcement Strengthening of the newly created anastomosis (the staple line).

Abbreviations

BPS Bovine Pericardium Strips, (Peri-strips Dry®)
GI Gastrointestinal
PGA Polyglycolic acid
PTFE Polytetrafluoroethylene
SIS Small intestinal submucosa

6.637.1. Introduction

Intestinal resections and reconstruction by anastomosis are one of the most common procedures performed in abdominal surgery. The anastomosis can be either hand-sewn or stapled. Multiple studies have demonstrated that the complications associated with stapled anastomosis versus hand-sewn anastomosis seem comparable.[1] As complications associated with intestinal anastomosis have significant consequences, staple line reinforcement techniques have been developed to strengthen the anastomosis when this is performed with a stapled technique. Owing to the success of the use of staple line reinforcement in lung resections, varieties of studies have adapted this concept for GI resection. Morbidity and mortality after GI anastomosis is mainly due to anastomosis leakage. Leak rates may vary from 7% to 13%, and mortality following this complication can range from 6% to 40% because of abdominal sepsis and multiple organ failure. Formation of abscesses and fistulae because of dehiscence are also considered major complications and are often difficult to treat.[2,3]

Staple line reinforcement techniques have been shown to increase the burst pressure of the stapled anastomosis and, furthermore, to reduce the risk of hemorrhage. Despite several studies that have been performed regarding the use of these reinforcement materials, no final answers have been found for the prevention of leaks. However, no large prospective comparative studies have been performed up till now in order to prove the advantage of reinforcement of stapled anastomoses. Moreover, several materials are currently available and these materials are all accompanied by their individual approach. Thus, no consensus exists among surgeons who therefore remain divided in their opinion if stapled anastomosis or staple lines should be reinforced with buttress materials, have to be oversewed, or do not have to be reinforced at all.

This chapter aims to summarize the available literature on staple line reinforcement techniques after GI resections and provides an overview of the currently available evidence of the advantages and disadvantages of the usage of these materials.

6.637.2. Staple Line Reinforcement

6.637.2.1. Etiology of Anastomotic Complications

Anastomotic complications, whether they occur after hand-sewn or stapled anastomosis, are severe complications that can lead to life-threatening conditions of the patient. Several studies have shown that the incidence of the major complications associated with anastomotic formation (which is anastomotic leakage, hemorrhage, fistula formation, and abscess) are comparable between hand-sewn and stapled anastomosis.[1] Therefore, the use of staple armentarium for GI reconstruction after resection seems to increase, as they are easy to use and may save time.

Many causes of anastomotic leaks can be identified, but they mainly fall into two categories: mechanical and ischemic factors. Overall, leaks are more likely to occur when the intraluminal pressure exceeds the strength of the tissue and the staple line, resulting in a leak. Classically, anastomotic leakage occurs in the first 5–7 days postoperatively and is due to tissue ischemia. This may occur when the wound healing is between the inflammatory and fibrosis phases. Early leaks, in the first several postoperative days, are usually due to the mechanical failure of the staple line or technical hand-sewn anastomotic method flaws.[2]

6.637.2.2. Buttress Material Properties

Application of reinforcement material in the staple line is thought to moderate the tension of the staple line because it acts as a neutralization plate. Furthermore, the buttressing material seals off the staple holes and narrows the spaces between each staple. Thus, leakage, bleeding, and tearing at the staple line may be reduced.[4]

The buttress material is generally made up of two regions, one of which serves primarily to secure the buttress material to the stapler prior to actuation, and one of which serves primarily to form the improved seal. The buttress material is adapted to be stably positioned upon the staple cartridge or anvil components of the stapler prior to, or at the time of, use.

6.637.3. Reinforcement Materials

Different forms of staple line reinforcement are available. Reinforcement methods are material applied exogenously to the staple line or incorporated into the staple line. Reinforcement materials can be non-, semi-, or absorbable.

6.637.3.1. Absorbable Material

6.637.3.1.1. Fibrin glue

Fibrin glue is a material applied directly to the staple line. Fibrin sealants have been used to achieve hemostasis and tissue adhesion in surgical specialties. It contains fibrinogen, fibronectin, factor XIII, thrombin, ionized calcium, and aprotinin. In the presence of calcium, thrombin facilitates the activated factor XIII to polymerize the fibrin monomers to form an insoluble fibrin clot. The process mimics the last step of the coagulation cascade and is independent of the patient's coagulation status.

The process of fibrinolysis breaks down the fibrin glue material. New fibrin sealant materials with added antifibrinolytic agents are developed to slow down the material degradation. Most available sealants contain human plasma products and bovine-derived components and thus carry the potential but very rare risk of seroconversion.[5]

There are different types of fibrin sealant available on the market, and three are mentioned below:

1. Tisseel VH®/Tissucol® Fibrin Sealant (Baxter International, Inc., IL, USA)
   This sealant is mainly applied as an adjunct to hemostasis in procedures concerning parenchymatous organs and cardiopulmonary surgery. It is also applied as a sealant during the closure of several types of anastomoses and staple lines after gastric sleeve resection. This adjunct is completely resorbed during wound healing within 10–14 days.[6]
2. Vivostat® Autologous Fibrin Sealant (Vivolution, DK)
   Vivostat® is currently being used in a wide range of abdominal procedures, including liver and colorectal surgery.[6]
3. LifeSeal™ (LifeBond Ltd., Israel)
   This mixed sealant is applied to anastomosis staple line junctures in the GI tract and, thus, may fortify the attachment leading to a reduction of leakage.[6]

6.637.3.1.2. Cellulose

Cellulose was originally developed as a wound dressing. It is synthesized by *Acetobacter xylinum* and has a nonwoven, multilayered three-dimensional structure that is not found in synthetic polymeric materials. The manufacturing process ensures that the product is nonpyrogenic and biocompatible. This biosynthesized cellulose has been processed into a resorbable form. It demonstrates a fluid-holding capacity up to 100 times its dry weight and is four times stronger than organic fibers.

The available cellulose product is made by Xylos® (Xylos Corp., Langhorne, USA).[6]

6.637.3.1.3. Polyglycolic acid/trimethylene carbonate

Biodegradable polymers have proved to be of significance in medical applications. Polymers prepared from glycolic acid and lactic acid have found a multitude of uses in the medical industry, starting with the biodegradable sutures first approved in the 1960s. Since that time, many products have been accepted for use as medical devices. The ideal polymer has mechanical properties that match the application, remaining sufficiently strong until the surrounding tissue has healed and does not invoke an inflammatory or toxic response. It should be metabolized in the body after fulfilling its purpose and is easily processable into the final product form.

An example of bioabsorbable polyglycolic acid (PGA) is Seamguard® (W.L. Gore & Associates, Flagstaff, AZ, USA). This is made of a porous fibrous structure composed of poly copolymer. It retains measurable strength for 4–5 weeks and is completely absorbed within 6 months. The Seamguard is formed like a sleeve to be fitted over the stapler arm. After firing, a slipknot suture is pulled to unravel the sutures that secure the strips that hold the sleeve in place. It is available for both open and endoscopic procedures.[6,7]

6.637.3.1.4. Polysaccharidic polyglycuronates biopolymers

This buttressing material is made of highly purified fractions from calcium alginates, originating from seaweeds, with documented hemostatic and healing properties. The product available with this material is called FOREseal™ (Laboratoires Brothier, Nanterre, France) and is only to be used in pulmonary resections.

It consists of preformed coated knitted bioabsorbable sheets held into the form of sleeves sized to fit onto the forks of the surgical stapler. The sleeve preserves as a large strip of material, intended to overlap to the lung parenchyma widely, beyond both sides of the reinforced staple line.[6]

6.637.3.2. Semiabsorbable Material

C-seal® (Colon-seal) (Polyganics BV, The Netherlands).

The C-seal is a biodegradable synthetic fragmentable colorectal drain developed to protect anastomotic leakage in colorectal anastomosis. The C-seal is a single-use device, designed for circular stapler devices. It is stapled to the inner lining of the anastomosis. As a result, the anastomosis is protected and sealed for 10–15 days. The degraded material will be secreted from the body together with the GI contents. C-seal is still in its development stage.[6,8]

Bovine Pericardium Strips, Peri-strips Dry® (BPS) (Synovis Life Technologies, Inc., St. Paul, MN, USA)

BPS comprises two vacuum-dried strips of biological tissue derived from bovine pericardium. It is biocompatible and acellular but is semiabsorbable because of the glutaraldehyde treatment in the manufacturing process. It is designed to provide adequate strength while promoting angiogenesis and cellular ingrowth. A polydioxanone synthetic absorbable gel, an adhesive hydrogel, is applied to the inner surface of both stapler arms after which the stapler is positioned over the bovine pericardium strips and locked. With the bovine pericardium facing the tissue, the stapler device is fired and the tissue is cut after which the stapler can be removed. The remaining material will be incorporated by host tissue after healing. BPS can be used for reinforcement of staple lines during pulmonary, mesentery, and GI procedures.[6]

Porcine Small Intestinal Submucosa (SIS), Surgisis® Staple Line Reinforcement (Cook Biotech, Inc., West Lafayette, IN, USA)

SIS is an acellular xenograft. The material provides a bioscaffold for tissue growth. Following implantation, tissue adjacent to the SIS matrix begins to invade the SIS matrix. SIS is gradually replaced as the host system reinforces and rebuilds the weakened site. The body's tissue grows completely into the surgical site while SIS maintains the needed tissue support. It can be applied for many purposes such as lung and gastric resections and pelvic floor reconstructions.[6,9]

6.637.3.3. Nonabsorbable Material

ePTFE, Seamguard staple line reinforcement material® (W.L. Gore & Associates, Flagstaff, AZ, USA).

This product is made of expanded polytetrafluoroethylene and is intended to be used as a prosthesis for surgical repair of soft tissue deficiencies using linear surgical staplers. It was the first synthetic material used for staple line buttressing. The material is constructed like a sleeve that can be slid over the jaws of the stapling device, without the need for additional fixing to the stapler before firing. After firing, the material is released from the arms by pulling a ripcord. If necessary, the excess material can be trimmed. The use of ePTFE has been shown to have an effect in pulmonary resection, but there are no studies confirming the advantage of ePTFE in GI resection.[6]

6.637.4. Discussion

The use of staplers during reconstruction after GI resection seems to have increased in the past years as it is easy to use and generally shortens operating time. The ultimate goal, however, was to reduce the incidence of major complications associated with the formation of an intestinal anastomosis because the risk of technical failures was thought to be minimized, which is relatively high during hand-sewn anastomosis. A decrease in incidence of these severe complications, that is, anastomotic leakage and hemorrhage, ultimately may result in less postoperative morbidity, surgical reinterventions, and mortality. Several studies, however, have shown comparable results postoperative outcomes after hand-sewn versus stapled anastomosis.[1–3,10] Although these studies were carried out properly, it has to be taken into account that a difference between these techniques may still be present but may be small, necessitating prospective studies with large patient populations undergoing standardized surgical procedures. Such a study has not been performed up till now.

Staple line reinforcement techniques were developed[9,11] because anastomotic leakage and severe bleeding from the site of the staple line or anastomosis can be life threatening.

Several reports in the literature support the burst pressure as the most important factor in assessing the quality of a fresh intestinal suture.[12] Data support that staple line reinforcement increases the burst pressures.[13–16] This may suggest prevention or at least a reduced rate of postoperative leaks and bleeding. Polytetrafluorethylene (PTFE) was the first synthetic material used for staple line buttressing. Although popular with some surgeons, there are no randomized controlled trials evaluating its effectiveness in GI surgery. This accounts, however, for all studies performed on the possible advantages of staple line reinforcement materials as they mostly are carried out retrospectively and concern studies in small patient populations. The use of nonabsorbable staple line reinforcement materials in a contaminated environment during GI reconstruction may raise the question if this may lead to an increase in indolent infection, fistula formation, and erosion. As various small pilot studies suggest a reduction in complications after the use of absorbable staple line reinforcement materials, this has not led to any hesitancy regarding the use of these materials.[9,11,17] Consequently, absorbable staple line reinforcement is applied worldwide for many indications.

Another frequently applied method for reducing the risk of postoperative hemorrhage is an exogenous suspended material as fibrin glue. This is mainly used in obesity surgery such as gastric sleeve resection where fibrin glue is used as a hemostatic

agent. Unfortunately, there are no clinical or animal comparative studies specifically addressing whether hemorrhage was actually reduced by the use of fibrin sealant. A review article about the applications of fibrin sealant in surgery demonstrated that fibrin sealants help to strengthen the stapled or sutured anastomosis and seal microscopic leaks at the anastomosis, but no data exist if morbidity is reduced after surgery in clinical studies.[5] Fibrin glue promotes the formation of granulation tissue and changes its composition by increasing the density of fibroblasts that occur with angioblasts.[18] The pathways, by which fibrin glue accelerates granulation tissue formation, as well as vessel density, are unknown. Silecchia *et al.* have reported data from a rather small randomized prospective clinical trial, assessing safety and efficacy of fibrin glue, suggesting that the use of fibrin sealant in laparoscopic Roux-Y gastric bypass may be beneficial in reducing the reintervention rate for major perioperative complications.[19] Unequivocal beneficial data, however, are lacking.

Regarding absorbable staple line reinforcement materials, two separate prospective studies have been published.[20,21] One of these studies investigated Seamguard in gastric resections as part of bariatric procedures and showed a significant reduction in blood loss. No differences were seen for leakage at intra- and postoperative testing. Another study concerned a pilot study of 30 patients in which all anastomosis were performed with a linear stapler, reinforced with Seamguard.[22,23] Consistent with the former study, no differences were seen in the incidence of anastomotic leakage in this small population. Recently, Chen *et al*. also described no reduction in leak rates after reinforcement of the staple line. In his conclusion, he reported, just as in the previous studies, a decrease in hemorrhage.[24] Buttressing the staple line is also used during pancreatic resection with the objective to reduce pancreatic leakage from the staple line. Reports suggest that Seamguard® may decrease pancreatic fistulas in distal pancreatic resections as postoperative leakage was reduced.[4,25,26] Conversely, other recent studies found an increase in pancreatic fistulas after pancreatic resection with staple line reinforcement with absorbable materials.[27,28] Although these studies seem to conflict, it has to be emphasized that they suffer from major methodological flaws. To determine definitive conclusions, prospective trials are needed with large patient numbers to detect possible small differences.

We performed an extensive literature review and found no large comparative studies on the use of staple line reinforcement materials. Although no conclusions could be drawn regarding the effect of these techniques on a possible reduction of anastomotic or staple line leakage, it does seem beneficial in reducing the risk of postoperative bleeding. Two small studies routinely using bioabsorbable Seamguard® during laparoscopic colorectal resection showed a significant reduction in staple line bleeding sites.[22,23] Therefore, the incidence of GI hemorrhage may be minimized with the use of staple line reinforcement during, for example, gastric sleeve resection or the transection of large vessels during laparoscopic surgery.[29,30] Regarding anastomotic leakage, several small studies have been published, but they all could not provide clear data on a possible reduction of this complication.

This chapter has provided an overview of all currently available materials to reinforce staple lines during the construction of anastomoses or transection of organs and vessels. Furthermore, the literature has been reviewed on possible clinical relevant advantages of these materials during GI surgery. As no high-level prospective studies exist, it remains unclear at this moment if staple line reinforcement reduced the incidence of anastomotic leakage. However, the use of these materials, especially fibrin glue, does seem to minimize the risk of bleeding from the anastomotic or transection site.

References

1. Lustosa, S. A.; Matos, D.; Atallah, A. N.; Castro, A. A. *Cochrane Database Syst. Rev.* **2001**, CD003144.
2. Baker, R. S.; Foote, J.; Kenmeter, P.; Brady, R.; Vroegop, T.; Serveld, M. *Obes. Surg.* **2004**, *14*(10), 1290–1298.
3. Wassner, J. D.; Yohai, E.; Heimlich, H. *Surgery* **1977**, *82*(3), 395–399.
4. Yamamoto, M.; Hayashi, M. S.; Nguyen, N. T.; Nguyen, T. D.; McCloud, S.; Imagawa, D. K. *Arch. Surg.* **2009**, *144*, 894–899.
5. Martin-Lee, M. G.; Jones, D. *Surg. Innov.* **2005**, *12*(3), 203–213.
6. The manufacture's IFU (information for use) literature.
7. Consten, E. C. J.; Dakin, G. F.; Robertus, J. L.; Bardaro, S.; Milone, L.; Gagner, M. *Surg. Endosc.* **2008**, *22*, 1188–1193.
8. Kolkert, J. L. P.; Havenga, K.; ten Cate Hoedemaker, H. O.; Ploeg, R. J. In *Annual Meeting Proceedings NVvH*, Veldhoven, May 10–11, 2007.
9. Yo, L. S. F.; Consten, E. C. J.; Quarles van Ufford, H. M. E.; Gooszen, H. G.; Gagner, M. *Dig. Surg.* **2006**, *23*(5–6), 283–291.
10. Moran, B. J. *Br. J. Surg.* **1996**, *83*(7), 902–909.
11. Consten, E. C. J.; Gagner, M. *Surg. Technol. Int.* **2004**, *13*, 59–63.
12. Downey, D. M.; Harre, J. G.; Dolan, J. P. *Obes. Surg.* **2005**, *15*(10), 1379–1383.
13. Arnold, W.; Shikora, S. A. *Obes. Surg.* **2005**, *15*(2), 164–171.
14. Hagerman, G. F.; Gaertner, W. B.; Ruth, G. R.; Potter, M. L.; Karulf, R. E. *Dis. Colon Rectum* **2007**, *50*(6), 1–8.
15. Morton, J. M.; Lucktong, T. A.; Trasti, S.; Farrell, T. M. *J. Gastrointest. Surg.* **2004**, *8*(1), 127–131.
16. Pinheiro, J. S.; Correa, J. L.; Cohen, R. V.; Novaes, J. A.; Schiavon, C. A. *Surg. Obes. Relat. Dis.* **2006**, *2*(3), 397–399.
17. Nguyen, N. T.; Longoria, M.; Chalifoux, S.; Wilson, S. E. *Surg. Technol. Int.* **2005**, *14*, 107–111.
18. Becker, J. C.; Beckbauer, M.; Domschke, W.; Herbst, H.; Pohle, T. *Gastrointest. Endosc.* **2005**, *61*(4), 560–567.
19. Silecchia, G.; Boru, C. E.; Mouiel, J.; *et al. Obes. Surg.* **2006**, *16*(2), 125–131.
20. Jones, W. B.; Myers, K. M.; Traxler, B.; Bour, E. S. *Am. Surg.* **2008**, *74*, 462–468.
21. Saber, A. A.; Scharf, K. R.; Turk, A. Z.; Elgamal, M. H.; Martinez, R. L. *Obes. Surg.* **2008**, *18*, 525–529.
22. De la Portilla, F.; Zbar, A. P.; Rada, R.; *et al. Tech. Coloproctol.* **2006**, *10*(4), 335–338.
23. Franklin, M. E., Jr.; Ramila, G. P.; Treviño, J. M.; *et al. Surg. Laparosc. Endosc. Percutan. Tech.* **2006**, *16*(6), 411–415.
24. Chen, B.; Kiriakopoulos, A.; Tsakayannis, D.; Wachtel, M. S.; Linos, D.; Frezza, E. E. *Obes. Surg.* **2009**, *19*, 166–172.
25. Jimenez, R. E.; Mavanur, A.; Macaulay, W. P. *J. Gastrointest. Surg.* **2007**, *11*, 345–349.
26. Thaker, R. I.; Matthews, B. D.; Linehan, D. C.; Strasberg, S. M.; Eagon, C.; Hawkins, W. G. *J. Gastrointest. Surg.* **2007**, *11*, 59–65.
27. Ferrone, C. R.; Warshaw, A. L.; Rattner, D. W.; *et al. J. Gastrointest. Surg.* **2008**, *12*, 1691–1698.
28. Guzman, E. A.; Nelson, R. A.; Kim, J.; *et al. Am. Surg.* **2009**, *75*, 954–957.
29. Franklin, M. E., Jr.; Berghoff, K. E.; Arellano, P. P.; Trevino, J. M.; Abrego-Medina, D. *Surg. Laparosc. Endosc. Percutan. Tech.* **2005**, *15*(1), 9–13.
30. Nguyen, N. T.; Longoria, M.; Welbourne, S.; Sabio, A.; Wilson, S. E. *Arch. Surg.* **2005**, *140*(8), 773–778.

6.638. Biomaterials for Hernia Repair

C Hollinsky, KH Floridsdorf, Vienna, Austria

© 2011 Elsevier Ltd. All rights reserved.

6.638.1.	**Introduction**	594
6.638.1.1.	Why Are Biomaterials Essential in Hernia Surgery?	594
6.638.1.2.	Limitations of Biomaterials in the Field of Hernia Surgery	594
6.638.2.	**History of Biomaterials in Hernia Surgery**	594
6.638.2.1.	Initially Used Materials	594
6.638.2.2.	Averseness to Biomaterials	594
6.638.2.3.	Acceptance of Biomaterials	595
6.638.3.	**Materials Used in Hernia Surgery**	595
6.638.3.1.	Synthetic Fiber Polymers	595
6.638.3.1.1.	Polypropylene (e.g., Marlex®, Prolene®)	595
6.638.3.1.2.	Polyester	595
6.638.3.1.3.	Polytetrafluorethylene	596
6.638.3.1.4.	Polyvinylidene fluoride	596
6.638.3.1.5.	Composite meshes	596
6.638.3.2.	Biological Materials	596
6.638.4.	**Hernia Surgery with Prostheses**	597
6.638.4.1.	Inguinal Herniae	597
6.638.4.1.1.	Open techniques with mesh	597
6.638.4.1.2.	Laparoscopic techniques (TAPP and TEP)	597
6.638.4.2.	Ventral Hernia Repair	598
6.638.4.2.1.	Open mesh techniques	598
6.638.4.2.2.	Laparoscopic technique (IPOM)	598
6.638.4.3.	Hiatus Hernia Repair with Mesh	599
6.638.5.	**Forces Acting on Hernia Meshes**	599
6.638.5.1.	Biomaterial Reinforces a Closed Defect	599
6.638.5.2.	Biomaterial Covers Defect	599
6.638.6.	**Requirements for Hernia Meshes**	599
6.638.6.1.	Physical Stability to Tissue Secretions	600
6.638.6.2.	Biocompatibility	600
6.638.6.3.	No Carcinogenicity	600
6.638.6.4.	Tensile Strength	600
6.638.6.5.	Elasticity	601
6.638.6.6.	Thickness and Bending Properties	601
6.638.6.7.	Mesh Weight	601
6.638.6.8.	Surface Properties	601
6.638.6.8.1.	Mesh coating	601
6.638.6.8.2.	Microhooks	601
6.638.6.8.3.	Antiadhesive coat	602
6.638.6.9.	Mesh to Hernia Size Relation	602
6.638.6.9.1.	Surgical techniques with closure of the hernia	602
6.638.6.9.2.	The mesh overlaps the defect	602
6.638.6.10.	Costs of Meshes	602
6.638.7.	**Mesh Fixations**	602
6.638.7.1.	Nonabsorbable Devices	602
6.638.7.1.1.	Suture	602
6.638.7.1.2.	Hernia stapler	602
6.638.7.1.3.	Spiral tacker	603
6.638.7.2.	Absorbable Fixation Systems	603
6.638.7.2.1.	Absorba tack	603
6.638.7.2.2.	Microhooks	603
6.638.7.2.3.	Fibrin glue	603
6.638.7.2.4.	Suture	603
6.638.8.	**Potential Complications of Hernia Meshes**	603
6.638.8.1.	Perioperative Complications	603

6.638.8.1.1. Rejection 603
6.638.8.1.2. Infection 603
6.638.8.2. Chronic Complications 603
6.638.8.2.1. Hernia recurrence 603
6.638.8.2.2. Chronic pain 603
6.638.8.2.3. Stiffening of the abdominal wall 603
6.638.9. Conclusion and Future Perspectives 603
6.638.9.1. Further Developments 603
6.638.9.2. Conclusion 603
References 604

Glossary

Bioprostheses A prostheses made of biological material.
Elasticity It is the physical property of a material when returning to its original shape after the stress (typically arising from external forces) that made it to deform is removed.
Intraperitoneal Within the peritoneal cavity, the area that contains the abdominal organs.
Laparoscopy An operation performed in the abdomen or pelvis through small incisions (usually 0.5–1.5 cm) with the aid of a camera.
Tensile strength The tensile strength of a material is the maximum amount of tensile stress that it can take before failure.

6.638.1. Introduction

6.638.1.1. Why Are Biomaterials Essential in Hernia Surgery?

Billroth stated as early as in 1878, "If we could artificially produce tissues of the density and toughness of fascia and tendon, the secret of the radical cure of hernia would be discovered."[1] The grandmaster of surgery realized – more than a 100 years ago – that abdominal wall herniae were poorly reinforced by mere closure or the use of endogenous tissue. Recurrence rates of more than 50% for ventral herniae[2,3] and 15% for groin hernia[4] – reported in the recent published literature – clearly illustrate the problem of hernia treatment without the use of a foreign body for reinforcement.

Polymeric synthetics such as polypropylene or polyester possess the qualities demanded by Billroth and are being successfully used for the treatment of groin and ventral herniae for about 20 years now. By the use of surgical techniques with mesh reinforcement, recurrence rates in groin hernia surgery have been reduced to 1–2%[5,6] and those for ventral hernia surgery to about 10%.[2,7]

6.638.1.2. Limitations of Biomaterials in the Field of Hernia Surgery

In addition to their advantages these meshes cause, in part, very unpleasant foreign body reactions, which may culminate in stiffening of the abdominal wall in rare cases. The patients are then unable to perform simple activities of daily living such as tying their shoelaces. Klinge *et al.*[8,9] recognized the problem of meshes of the first generation, whose pore size was too small. This caused extensive scar plates, which rendered the ventral abdominal wall immobile. A subsequent advancement were meshes with a pore size of at least 1 mm, which caused the scar to be bridged with loose connective tissue (also known as the bridging phenomenon)[9–11] (**Figure 1**). The mobility of the abdominal wall was not limited by this procedure. Therefore, meshes with large pores are given preference, especially in the treatment of ventral abdominal wall herniae.

6.638.2. History of Biomaterials in Hernia Surgery

6.638.2.1. Initially Used Materials

In 1889, Witzel used silver wire meshes for abdominal wall herniae. However, due to the severity and high rate of complications (such as perforation of the bowel, skin necrosis, etc.), these foreign materials proved as unsuccessful as rubber sponges or stainless steel wire meshes.[12,13] It was in the middle of the twentieth century that synthetic materials such as nylon started to be employed for hernia closure. In 1952 Cumberland reported on the use of 'meshes' for herniae.[14] The first large application studies concerning the use of polyester and polypropylene meshes were published by Usher and coworkers in 1959.[15,16] However, this mesh reinforcement surgery was not widely accepted at that time and was rarely used. It was Irvin Lichtenstein in the United States who developed his own surgical method in 1989, using polypropylene for tissue reinforcement.[17] Shortly afterwards, laparoscopic groin hernia procedures employing synthetic implants were developed.[18]

6.638.2.2. Averseness to Biomaterials

Owing to potential complications such as wound infection or chronic pain, herniologists at the time initially adopted a very skeptical approach toward synthetic implants.[19,20] The latter were rated as hazardous foreign materials which, in the worst case, might cause cancer. Such fears have been clearly disproved in the last few years.[21,22]

6.638.2.3. Acceptance of Biomaterials

It was realized that implantation of foreign material provides the required tissue reinforcement for hernia surgery. Since the introduction of laparoscopy in the early 1990s, meshes are being increasingly used for various open as well as laparoscopic surgical procedures. Hernia recurrence rates have been markedly reduced by these procedures and the acceptance of the meshes increased rapidly. Currently, more than three-fourths of operations for abdominal wall herniae are performed by the use of mesh reinforcement.[23] Worldwide about 25 million hernia operations and nearly 20 million mesh implantations are performed per year (Table 1).

6.638.3. Materials Used in Hernia Surgery

6.638.3.1. Synthetic Fiber Polymers

As regards hernia meshes which have been used million-fold in the last 20 years, those of the first generation were replaced by recent ones. The first meshes were very close knit and had a pore size of >800 μm. This led to the formation of scar plates, which markedly reduced mobility, especially in cases of herniae in the anterior abdominal wall.[8] Klinge and coworkers[9–11] established the formation of connective tissue around the threads – which were a foreign body – as the reason for this phenomenon (Figure 1). Therefore, meshes with pore sizes of 1.5 mm or more were produced: these had a larger distance between the individual threads. The so-called bridging phenomenon prevented the formation of extensive scar tissue. Limitations in mobility such as those reported for synthetic meshes could be avoided by this approach.

The formation of scar plates also led to shrinkage of the meshes, followed by folding and waving of the meshes, and occasionally resulted in insufficient hernia repair.

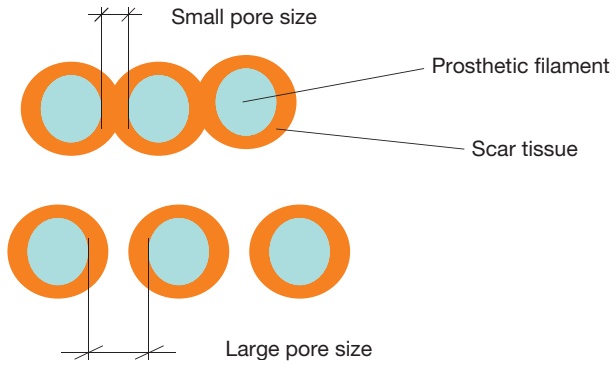

Figure 1 Diagram showing the scarring process provoked by the different pore sizes of the meshes. With small pores a continues scar plate occur.

Table 1 Hernia operations per year

USA	1 000 000
Europe	1 000 000
Worldwide	25 000 000

Such shrinkage of meshes of the first generation could be largely reduced and even avoided by the use of modern meshes with large pores.

In histological specimens one finds foreign body tissue reactions which, in the early phase, were marked by a monocyte-dominated acute form of inflammation. These were followed by chronic foreign body reactions, which were primarily granulomatous in nature.[24]

6.638.3.1.1. Polypropylene (e.g., Marlex®, Prolene®)

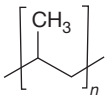

The most frequently used meshes in hernia surgery today are those made of polypropylene. Many companies produce hernia meshes made of polypropylene, which is an economical material. About 100 different designs, manufactured with different quantities of material, pore sizes, and elastic properties are offered in the market. Polypropylene meshes are largely monofilamentous (Figure 2), whereas polyester meshes usually possess a multifilamentous thread structure (Figure 2). The microporosity of the multifilamentous structure is about 10 μm. This thread design was presumed to be the reason for the high infection rates registered in earlier studies.[25] However, this hypothesis was disproved in recent investigations comprising large case numbers, because no difference in infection rates was found between monofilamentous and multifilamentous synthetics.[26,27]

Monofilamentous polypropylene meshes, which were used by Usher as early as in 1962,[15] are still used today. To achieve better ductility and elasticity, the initially woven meshes were replaced with knitted constructions. Modern polypropylene meshes are very stable and are associated with a low rate of accompanying inflammation.[28,29]

Nevertheless, polypropylene causes adhesion to intestinal organs. Therefore, contact with these organs should be painstakingly avoided.[30,31] In some techniques, polymeric meshes are introduced in the abdominal cavity in order to reinforce the abdominal wall. These are provided with a special antiadhesive coat,[32] ensuring satisfactory ingrowth of the polypropylene layer in the abdominal wall[33] on the one hand, and preventing adhesion of the mesh to abdominal organs such as the bowel or stomach[34,35] on the other.

6.638.3.1.2. Polyester

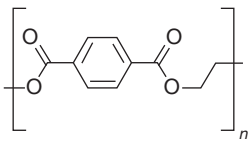

Multifilamentous mesh constructions made of ethylene glycol and terephthalate are highly flexible and also provide a high degree of mechanical stability.[36] They were rarely used in the past (almost exclusively in France) because a study published in 1998[37] advised against the use of polyester meshes due to their instability and the formation of fistulas. However, this statement was not confirmed in many recent studies.[27,36]

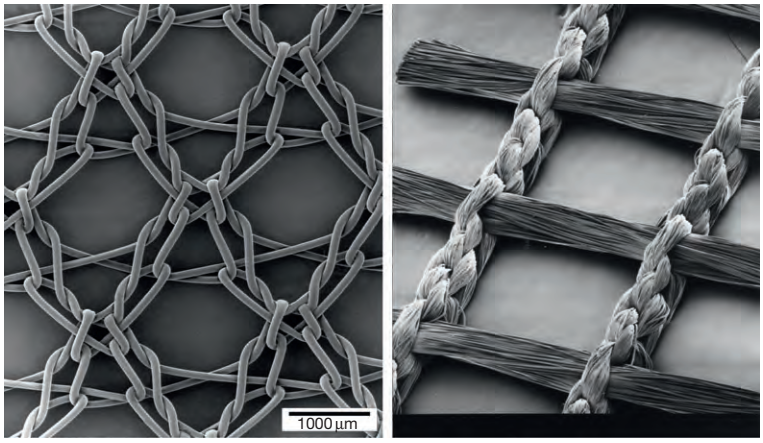

Figure 2 Electron microscopic view of a polypropylene mesh (left side) versus a polyester mesh (right side).

Currently, polyester and polypropylene are considered equally suitable for use in hernia surgery.

6.638.3.1.3. Polytetrafluorethylene

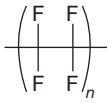

This product is available as a film and is therefore associated with poor healing, marked shrinkage of the scar, and a high propensity for infection. It is rather firm and not very elastic. Complete integration into host tissue does not occur. Rather, a scarred capsule is formed around the implant.[38] The prosthesis' poor ingrowth behavior is attributed to its film-like structure, its hydrophobic surface, and the negatively charged polytetrafluorethylene (PTFE). Anchorage in the surrounding tissue did not occur even after several years. However, as this material was shown to possess antiadhesive properties in a few studies, the films were initially used in intraperitoneal location. However, they were gradually ousted from the market by competitor products (such as polyester or polypropylene meshes with an antiadhesive coat) for this indication as well.

Besides, these 'meshes' were disproportionately expensive and were therefore rarely used from the very start.

6.638.3.1.4. Polyvinylidene fluoride

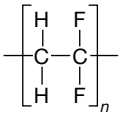

Hernia meshes made of polyvinylidene fluoride (PVDF) are being used to an increasing extent in the last few years. PVDF, an inert material, is being used as suture material for a long time now. It is marked by a high degree of biocompatibility – similar to that of polypropylene or polyester. In some studies it was shown that, due to its low rate of inflammatory and fibrotic foreign body reactions and low shrinkage after implantation, PVDF serves as a useful alternative to conventional materials such as polypropylene and polyester.[39,40]

6.638.3.1.5. Composite meshes

The concept underlying this mesh made of a combination of nonabsorbable and absorbable material is self-evident. After implantation one initially achieves a high degree of mesh stability. After absorption of one component, only a small quantity of residual foreign material remains. These meshes are usually composed of combinations of polypropylene and absorbable polyglactin (Vypro II) or absorbable poly-L-lactic acid. However, after absorption the meshes cause a significant foreign body reaction. Therefore, the overall reaction of the body to these synthetic materials is not markedly different from that of meshes composed of a single component.

In order to achieve better biocompatibility, polypropylene meshes are coated with a very thin layer of titanium (TiMesh). In the recent published literature, opinions about the advantages of this titanium coat are diverse as to whether this alteration of the surface does actually cause better tissue tolerance.[24,41]

6.638.3.2. Biological Materials

A disadvantage of all polypropylene meshes is the impossibility of mesh implantation in an infected wound. Synthetic materials are extremely susceptible to bacteria because the latter adhere to the mesh structures and form an impermeable biofilm for the body's immunological defense and for antibiotic treatment.[25] Therefore, infected meshes have to be removed in many cases. The film-like structure of polytetraflourethylene meshes renders them inaccessible to treatment with local or systemic antibiotics in case of infection, and the meshes have to be removed in nearly all cases. On the other hand, modern large-pore meshes can be successfully overcome by the body's own defense and treated by antibiotics in case of bacterial infection. They can be retained in more than one half of cases.

Biological meshes were developed to achieve reinforcement even in cases of infected or potentially infected wounds, because they are associated with a much higher degree of tolerance to infection.

Biological meshes have been used for the past few years and in very rare cases of groin herniae. They can be obtained from various donors: porcine, bovine, or human. All cellular

elements are removed from tissue rich in collagen, especially the skin, the pericardium or the intestinal submucosa, so that only the intact collagen and elastin framework remains. The following biological meshes are currently available:

Alloderm® is produced from foreign human skin (chemically unchanged)
Veriats® consists of acellular bovine pericardium
Peri Guard® is also obtained from the bovine pericardium (chemically modified)
Permacol® contains reinforced porcine collagen
Surgisis® is produced from the acellular freeze-dried tissue matrix of porcine submucosa.

In order to prevent rapid degradation of meshes by collagenases, the collagen framework of some meshes is altered or linked differently through chemical processes. This is achieved by blocking the collagenase-binding sites, which renders the prostheses capable of withstanding degradation and absorption by the body for a longer period of time than untreated bioprostheses. Chemically pretreated prostheses are known as cross-linked bioprostheses and differ from untreated non-cross-linked bioprostheses. The higher resistance of cross-linked bioprostheses to collagenases[42,43] as well as the rapid degeneration of non-cross-linked (Surgisis®) prostheses[44,45] have been proven in several studies.

Regardless of chemical pretreatment, after a certain period of time the implant becomes integrated in the host tissue. The structure of the prosthesis is markedly altered by this process, which is hence known as remodeling.

The clinical value of biological meshes cannot be estimated at the present time, because degradation of the implant and ingrowth of collagenic connective tissue for hernia reinforcement are still difficult to assess. Degradation of the mesh prior to the formation of adequate connective tissue causes hernia recurrence. Likewise, mechanical stabilities after several months or years are currently unknown. Therefore, at the present time these meshes can only be used as tissue reinforcement in cases of infected wounds. As biological meshes cost about 10 times more than synthetic meshes, the bioprostheses will be used in carefully selected cases in the next few years as well.

6.638.4. Hernia Surgery with Prostheses

Today about two-thirds of all abdominal wall herniae are treated with mesh reinforcement and the numbers are increasing. This is especially because suture techniques lead to high tension at the suture base, which frequently causes the suture to tear out of tissue and leads to recurrence of abdominal wall hernia. In addition to markedly lower recurrence rates, mesh reinforcement techniques permit early load bearing and cause chronic pain in very rare cases.

6.638.4.1. Inguinal Herniae

6.638.4.1.1. Open techniques with mesh

6.638.4.1.1.1. Lichtenstein

The procedure named after Irvin Lichtenstein is the most frequently used surgical technique for groin hernia throughout the world. As early as in 1986 Lichtenstein and Shulman[17] realized the advantages of mesh reinforcement through tension-free hernia treatment and therefore named it the 'tensionless' technique. The gap in the groin is not closed with sutures, as was done earlier, but is covered with synthetic material. The foreign body reaction induced by polypropylene – a foreign body – leads to the formation of a resilient scar plate. Recurrence rates could thus be significantly reduced from 15% to 1–2% (Figure 3).

6.638.4.1.1.2. Plug and patch repair

This technique was modified by Rutkow and Robbins[46] in that the gap was additionally narrowed by the use of an umbrella-like plug (Figure 4). A synthetic mesh is then introduced between the internal and external musculature, as in the Lichtenstein technique. This procedure is especially popular in the United States.

6.638.4.1.2. Laparoscopic techniques (TAPP and TEP)

Following the introduction of laparoscopy at the start of the 1990s, laparoscopic techniques were also developed from the treatment of groin hernia. Flat placement of a synthetic mesh measuring about 15 cm × 10 cm in the preperitoneal space (Figure 5), between the peritoneum and the musculature, became widely accepted. The hernia is not closed under tension but is covered with synthetic material, as is done in the Lichtenstein procedure. This tensionless technique is given preference in cases of surgery for hernia recurrence and also for bilateral groin herniae.[47] Depending on the access used to approach the preperitoneal space, a distinction is made between the transabdominal preperitoneal (TAPP) and the

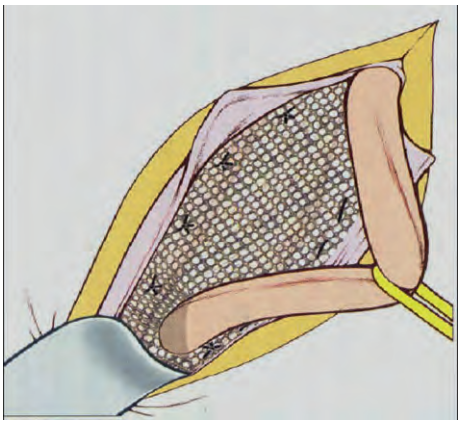

Figure 3 The Lichtenstein technique.

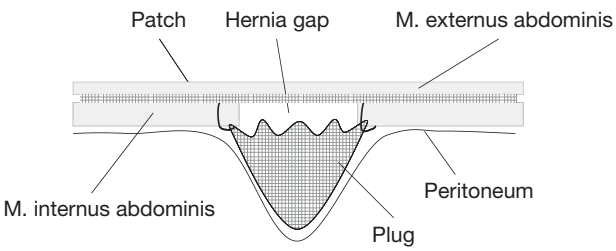

Figure 4 The Rutkow technique.

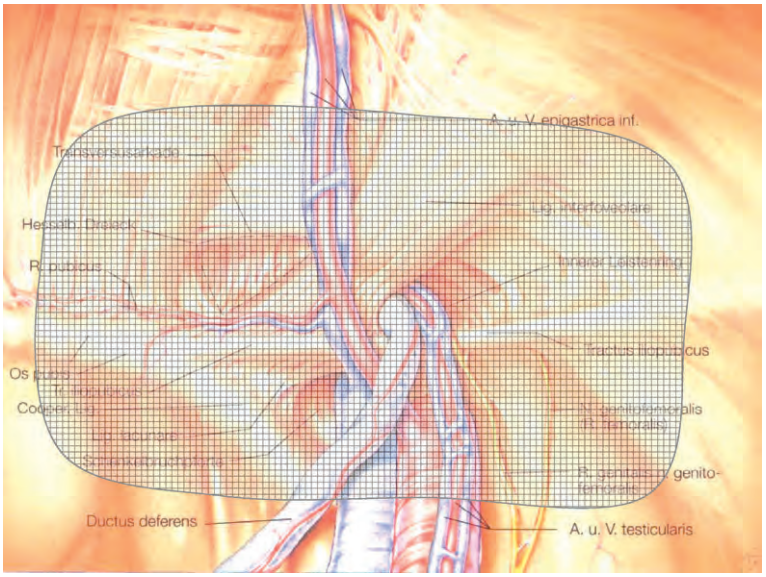

Figure 5 The laparoscopic view of a groin region. All possible groin defects are covered with a 15 cm × 10 cm mesh.

total extraperitoneal (TEP) technique. The advantage of the laparoscopic technique is especially the low degree of surgical trauma (small incisions of only 5 mm), because of which the patients are able to fully withstand loads after a mere 10 or 14 days.

6.638.4.2. Ventral Hernia Repair

6.638.4.2.1. Open mesh techniques

Treatment of the anterior abdominal wall is a much greater problem than treatment of groin hernia. This is clearly demonstrated by recurrence rates, which are about 50% after the suture technique and about 15% after mesh reinforcement[2,7] – which is still much higher than the recurrence rate of about 1% for groin herniae after the TAPP technique.[5,6] This may be explained by the fact that ventral herniae achieve enormous dimensions of up to 20 cm or may be composed of huge hernia sacs containing several intestinal loops (Figure 6). The mesh reinforcements required in cases of such large herniae are not only advantageous, but may also cause limitation of movement – as was true for meshes of the first generation – or even stiffening of the anterior abdominal wall. Large-pored meshes were developed to counteract this problem. Due to the bridging phenomenon they do not impair the mobility of the abdominal wall after implantation. Additionally, these herniae are usually highly susceptible to infection because of the large wound surface. Therefore, quite often it is necessary to remove the infected synthetic mesh. As these herniae cause major problems for the surgeon, a wide range of techniques are used for this condition, depending on the type of hernia and the patient's characteristics.

6.638.4.2.1.1. Onlay technique

By this technique the mesh is fixed to the anterior rectus sheath. The procedure is advantageous because it is very simple to perform, but is associated with a high rate (~15%) of infection



Figure 6 Huge ventral hernia reaching the knees of the patient.

of the foreign body.[48] The recurrence rate of 15% is an additional disadvantage as opposed to alternative techniques.[48]

6.638.4.2.1.2. Sublay technique

Due to the problems of the onlay technique, the sublay technique is given increasing preference. The mesh is introduced between the rectus muscle and the posterior rectus sheath and thus reinforces the midline. However, due to the position of the mesh, this rather laborious surgical technique is marked by a lower recurrence rate than the onlay technique.[48–50]

6.638.4.2.2. Laparoscopic technique (IPOM)

In the last few years, laparoscopic treatment of incisional herniae by the use of special meshes has been established as an

equally effective surgical technique as open procedures.[51–53] The meshes are fixed to the peritoneum by the laparoscopic technique (intraperitoneal onlay mesh) and bridge the abdominal wall defect on the side facing intraperitoneal pressure (Figure 7). As polyester, polypropylene, or other polymeric materials cause massive adhesions to abdominal organs,[30,31] these synthetics are coated with an antiadhesive layer (Figure 7). The coating may be made of porcine collagen for instance, and is absorbed after about 10 days. As a neoperitoneum will have formed by this time, adhesions to abdominal organs are avoided to a large extent.[33,54,55] Especially in cases of so-called Swiss cheese incisional herniae, which are usually composed of several small herniae, the scar tissue between the hernia gaps persists and holds the mesh in position like an abutment. However, large herniae may cause the mesh to bulge and are therefore commonly treated by open techniques.

The low degree of tissue trauma is an advantage of the Intraperitoneal onlay technique (IPOM); it is also associated with a low rate of wound infection and minimal postoperative pain.[51–53] A disadvantage at the current time is the possibility of the mesh becoming adherent to the abdominal organs despite the antiadhesive coat, because of its intraperitoneal position.[56]

6.638.4.3. Hiatus Hernia Repair with Mesh

In cases of large diaphgramatic herniae, reinforcement is achieved by adaptation of the diaphragm using a mesh. As the very sensitive esophagus and stomach are directly adjacent to the mesh in this region, even self-coated meshes are rarely used at the present time.[57] Due to rapid advancements in mesh technology, synthetic meshes will probably conquer this field as well.

6.638.5. Forces Acting on Hernia Meshes

The forces acting on this mesh are of various intensities, depending on the surgical method used. A basic distinction is made between two techniques, namely whether the mesh is used in addition to closure of the hernia for reinforcement of tissue, or whether the defect is merely covered with the mesh.

6.638.5.1. Biomaterial Reinforces a Closed Defect

After closure of the hernia the mesh is placed in order to reinforce the tissue (e.g., the onlay technique) or between the layers of the abdominal wall (e.g., sublay technique). However, closure of the hernia causes high tension on the hernia margins. Horizontal forces are especially strong in cases of ventral hernia because of the oblique muscles of the abdominal wall (external oblique muscles, internal oblique muscles, and transverse muscles of the abdomen). Thus, the linea alba is able to withstand horizontal loads of 10 N mm^{-2}, but vertical loads of only 5 N mm^{-2} until rupture occurs.[58] Due to the mesh, the load on the scar or the midline is shared by the polymer mesh. Recurrence rates have been markedly reduced by this approach.[2,7] However, as the majority of meshes were found to withstand loads of 100–200 N cm^{-1} when a strip of mesh was exposed to tensile loads (according to DIN 53587) – these values being well above their physiological load-bearing capacity – failure of the construction always causes mesh tear-off rather than rupture of the material. As the mesh is fixed on muscle or fascia, shear forces by far exceed the fixation strength of the mesh during mesh tear-off (Figure 8).

6.638.5.2. Biomaterial Covers Defect

By this technique the defect is not closed but merely covered with a mesh. This approach has been very successfully employed in laparoscopic groin hernia surgery (TAPP or TEP technique). In the last few years it has also been used for ventral herniae. Even large defects can be bridged with the mesh (Figure 7). Here as well, shear forces between the prosthesis and the abdominal wall are of decisive importance for successful hernioplasty (Figure 7). When shear forces exceed the mesh's retention strength, the mesh glides into the opening and the abdominal wall hernia is reexposed. Furthermore, soft materials may cause wide bulging so that the abdominal organs may reenter at the level of the abdominal wall and cause hernia recurrence (Figure 9).

6.638.6. Requirements for Hernia Meshes

The challenge for hernia meshes lies in the various requirements that a foreign body must fulfill in order to reinforce

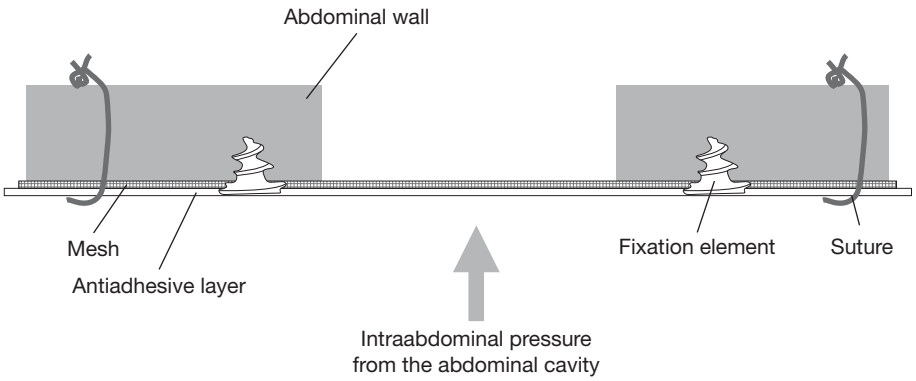

Figure 7 IPOM (Intraperitoneal onlay technique).

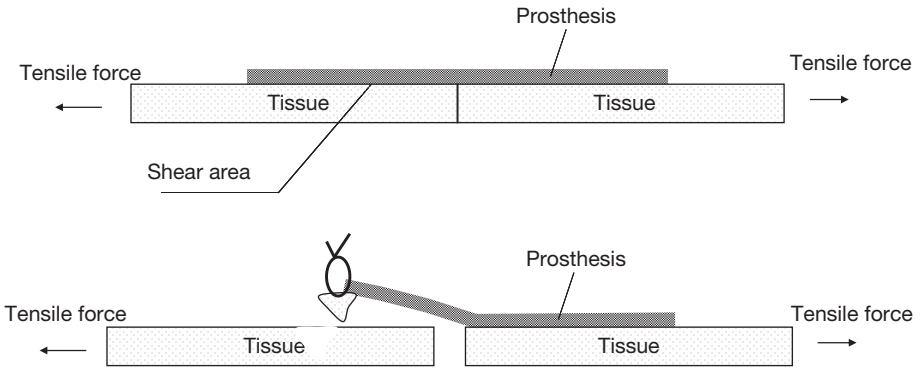

Figure 8 Recurrence after mesh repair always arise due to mesh tear-off rather than mesh rupture.

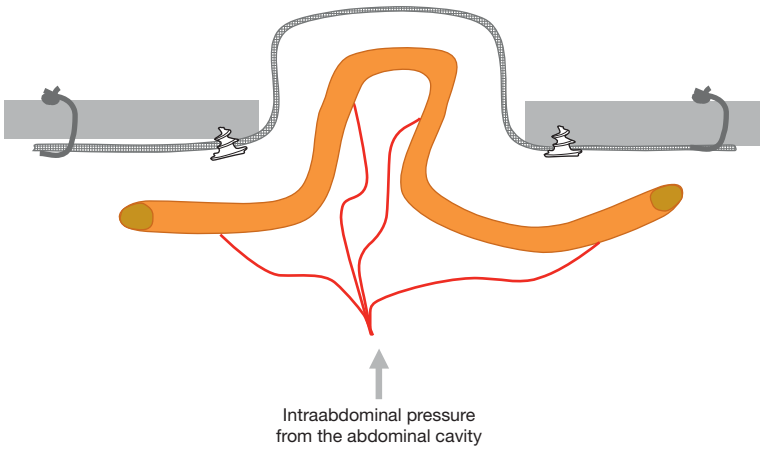

Figure 9 The mesh bulge into the opening and cause hernia recurrence.

the abdominal wall. These demands on the mesh are, in part, contradictory. The surgeon is therefore compelled to make a compromise as regards the properties of the mesh. The required criteria for polymers used in hernia surgery are listed in the following sections.

6.638.6.1. Physical Stability to Tissue Secretions

Hernia meshes should not be absorbable. When meshes started to be widely used some 20 years ago, fully absorbable meshes were used in order to leave no residual foreign substances in the body. After absorption of the meshes, however, the newly formed scar tissue was not sufficiently stable. Nearly all of the herniae reappeared.[59] Only partially absorbable meshes such as those made of polypropylene and polyglactin (e.g., Vicryl and Vicryl II) achieve sufficient stability because of their polypropylene content. Therefore, these meshes expand the spectrum of otherwise nonabsorbable hernia meshes.[60,61]

6.638.6.2. Biocompatibility

Polymers cause an inflammatory reaction in the body directly after implantation.[24] In hernia surgery we try to use meshes that cause minimal and brief inflammatory reactions in the body. Acute as well as chronic pain can be minimized by this approach.

6.638.6.3. No Carcinogenicity

Some of the polymers employed in hernia surgery have been in use for about 50 years (polypropylene and polyester) and have, to date, caused no carcinoma – neither in studies nor in clinical application. Meshes are therefore considered to be noncarcinogenic.[21,22]

6.638.6.4. Tensile Strength

Currently used meshes were shown to possess a tensile strength of 50–200 N when a 1 cm strip of mesh was subjected to tensile loads (DIN 53857) until it ruptured. One of the reasons for this diversity is the fact that the required stability of synthetic meshes has not been clearly established among hernia specialists.[10,58] Furthermore, the mesh stabilities required for various applications are very diverse. In cases of midline herniae one may anticipate horizontal loads of up to 10 N mm^{-2} which are mainly exerted on the oblique muscles of the abdominal wall. Several surgical techniques for midline closure are aided by the use of a synthetic mesh. As it is positioned on fascia or between muscle and fascia, the mesh is primarily subjected to shear forces. Meshes used at the present time are sufficiently resilient to tensile forces. Mesh rupture is practically nonexistent whereas mesh tear-off from tissue is more likely to occur. Therefore, in addition to the tensile strength of meshes, the

problem of fixation should be given greater attention in the field of technical advancement because an enormous improvement potential exists in this area.

In contrast, in the groin the synthetic mesh is fixed nearly exclusively through intraperitoneal pressure in the preperitoneal cavity. Therefore, tensile loads on the mesh in this region are of secondary importance.

6.638.6.5. Elasticity

Due to their large pores (>1.5 mm), modern meshes are very elastic and remain so even after incorporation. This is especially important in cases of ventral herniae because stiffening of the anterior abdominal wall would cause significant limitation of mobility. Likewise, the marked ductility of the mesh reduces the load on fixations. Therefore, mesh tear-off is a rare occurrence.

6.638.6.6. Thickness and Bending Properties

The thickness of the mesh markedly influences its flexion behavior. Especially for those surgical techniques in which the gap remains open and the mesh is only placed on the hernia, its thickness is inversely proportional to its flexion.[62] Very thin meshes of 0.2 or 0.3 mm are therefore unsuitable to cover large defects. In these cases, more stable meshes (in terms of flexion) of 0.4–0.6 mm should be used.[62]

6.638.6.7. Mesh Weight

Depending on their weight, a distinction is made between light (up to 45 g m^{-2}), moderate (45–75 g m^{-2}), and heavy (>75 g m^{-2}) meshes. In some studies, light-weight meshes proved valuable in terms of causing less postoperative pain than heavy meshes.[63] They are preferentially used for small and mid-sized herniae. Owing to their poor stability in terms of flexion, excessively thin meshes are overstrained when used for large herniae. In the latter case, more stable meshes of moderate to heavy weight should be used in order to avoid bulging.[62]

6.638.6.8. Surface Properties

The mesh's surface properties are responsible for the severity and duration of the foreign body reaction, especially in the adjacent tissue. The surface consistency also determines the mesh's friction properties. Especially in the first few postsurgery days, when connective tissue ingrowth of the mesh has not yet started, it is more likely to slip. After this time it is stably fixed in the surrounding connective tissue. Therefore, friction is only significant during the first few postsurgery days.

6.638.6.8.1. Mesh coating

In order to minimize the foreign body reaction, one manufacturer developed a fine titanium coat for the polypropylene mesh (Figure 10). As titanium is an inert substance, the coating was expected to reduce the tissue's reaction to polypropylene. The published literature contains studies that confirm this theory as well as others that provide no indication of the efficacy of this titanium coat in respect of foreign body reaction.[24,41]

6.638.6.8.2. Microhooks

To avoid dislocation, meshes with microhooks made of polylactic acid on their underside were developed (Figure 11). These are stably fixed to the surrounding tissue so that additional fixation elements are not required. In a study on rats it was shown that these microhooks achieve the tensile strength of fixation elements (such as the hernia stapler).[64] The advantage of these polylactin microhooks (Figure 12) is their absorbability – they are degraded within 1 year and cause no chronic nerve irritation, which is occasionally encountered when fixation elements are used.[65]

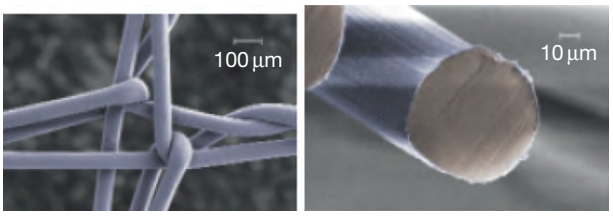

Figure 10 TiMesh: a thin layer of Titan coats the polypropylene.

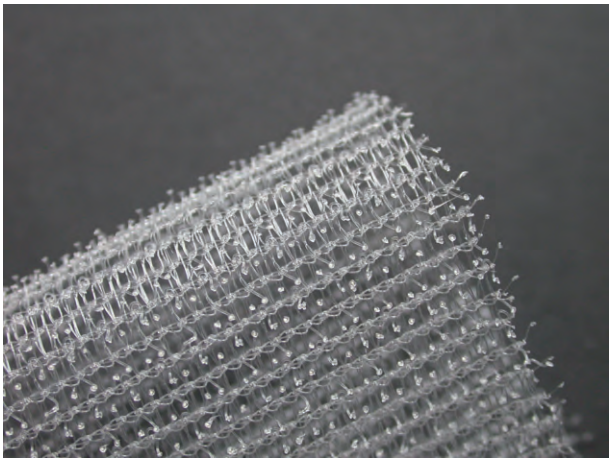

Figure 11 Mesh with microhooks on their underside.

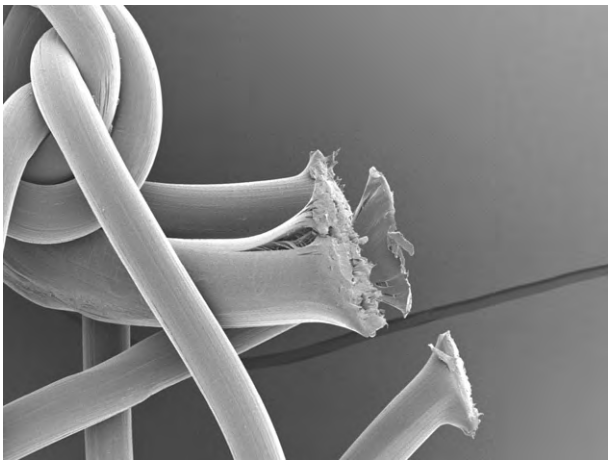

Figure 12 Electron microscopic view of the mesh-microhooks.

6.638.6.8.3. Antiadhesive coat

Meshes for intraperitoneal use are provided with an absorbable coat; one of the materials used to produce the coat is porcine collagen. Adhesion of internal organs such as the bowel, stomach, or liver is largely avoided by this measure (also see Section 6.638.4.2.2).

6.638.6.9. Mesh to Hernia Size Relation

Meshes that overlap the hernia margin should be directly proportional to the size of the hernia. Initially this point was underestimated. Many recurrences occurred because the mesh became detached from the margin and slipped into the hernia. Likewise, recurrences occurred when static friction was inferior to tensile loads because of the small size of the overlapping surface and poor fixation of the mesh.[38,66]

6.638.6.9.1. Surgical techniques with closure of the hernia

For reinforcement of the closed hernia, currently an overlap of at least 4–5 cm on each side is recommended.[38,67] In cases of ventral herniae, the fact that horizontal tensile forces are twofold higher than vertical tensile forces should be taken into account: the defect should be overlapped generously on its sides.[58]

6.638.6.9.2. The mesh overlaps the defect

This type of hernia treatment is given preference, especially when using laparoscopic techniques, and is associated with a low recurrence rate of about 1% in the treatment of groin herniae.[5,6] These favorable results are attributed to the fact that defects in this region are usually <2 cm in diameter and larger herniae are rarely encountered in this location. In the groin, the mesh is inserted in the preperitoneal space and fixed on both sides through the abdominal wall and through the peritoneum. In cases of ventral herniae, even large defects are treated by this approach, although the recurrence rate for these herniae is much higher than 10%.[68] This is due to insufficient lateral mesh overlap which, for anatomical reasons, frequently does not achieve the required dimensions. The mesh is fixed on the peritoneum so that ingrowth of the material is confined to the side facing the abdominal wall. Mesh dislocation and slippage into the hernia are the most common causes of recurrence when this technique is used. Despite stable and widespread fixation, hernia recurrence cannot be avoided. Therefore, in cases of very large defects the indication for laparoscopic IPOM should be established very stringently.

6.638.6.10. Costs of Meshes

Polypropylene and polyester meshes measuring 15 cm × 15 cm cost about 100€ at the present time (this is a rough estimate). Freudenberg *et al.*'s study is noteworthy in respect of mesh costs. In their study in Burkina Faso they showed that sterilized nylon mosquito nets achieve equivalent results as commercially used polypropylene meshes (Ultrapro®).[69] The sole difference was the price – which was 0.0043 US dollars for locally purchased nylon meshes compared to 108 US dollars for the commercial mesh. Therefore, Kingsnorth[70] has emphasized the importance of nylon mosquito meshes in developing countries.

Coated meshes are much more expensive because the protective antiadhesive coat is laborious and costly in terms of production. Meshes measuring 15 cm × 15 cm cost about 300–400€. Biological meshes made of porcine acellular collagen or bovine pericardium are very expensive – a mesh of the above mentioned size costs more than 1000€. This is one of the main reasons why biological hernia meshes are very rarely used at the present time.

6.638.7. Mesh Fixations

As currently used meshes do not tear under physiological loads, hernia recurrence is caused by mesh tear-off or dislocation. Fixation of the mesh in tissue is therefore of decisive importance. Particularly in the early postoperative phase, the prosthesis is stabilized by the fixation elements alone. Additional connective tissue ingrowth of the mesh occurs after about 2 weeks. Once the prosthesis has been well incorporated into the surrounding tissue, recurrences secondary to this structural reinforcement usually do not occur.

6.638.7.1. Nonabsorbable Devices

Early mesh fixations were made of nonabsorbable material in order to ensure sustained fixation.

6.638.7.1.1. Suture

The nonabsorbable suture is still an important tool for fixation of the prosthesis. As it permits fixation through several layers of the abdominal wall, it is the type of fixation that is able to withstand by far the greatest tensile loads.[33] Quite often it is combined with other fixation elements in order to achieve widespread attachment of the prosthesis.[71,72]

6.638.7.1.2. Hernia stapler

These fixation elements are similar to an ordinary desk stapler and function in the same manner. The two metal ends penetrate the tissue by about 4 mm and are then bent by the stapler device when pressed (Figure 13). The prosthesis is thus fixed into the tissue. This fixation technique has been in use for

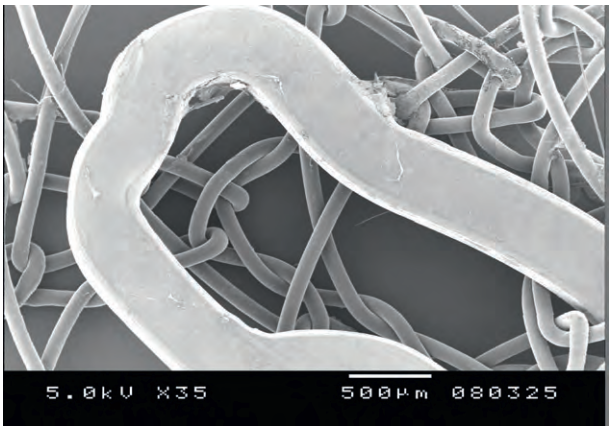

Figure 13 Electron microscopic view of a mesh fixed with a hernia stapler.

about 20 years and is gradually being replaced with more innovative devices. This is because stapler fixation may be associated with a few disadvantages. The nonabsorbable elements may cause chronic pain due to nerve irritation.[73] Likewise, 12 mm trocars are needed to introduce the staples. The high cost of the method has been another reason for developing absorbable and more economical fixation techniques.

6.638.7.1.3. Spiral tacker

These spiral fixation elements have been in use for more than 10 years and achieve stable fixation.[74] They are particularly suitable for fixation of the prosthesis in bone, such as the symphysis or the xiphoid process. Their marked tendency toward adhesion when used in intraperitoneal location is a disadvantage.[33,75]

6.638.7.2. Absorbable Fixation Systems

Absorbable fixation techniques were developed to avoid chronic foreign body reactions and chronic pain.

6.638.7.2.1. Absorba tack

These fixation elements consist of 4-mm-long screws made of polylactic acid and are fully degraded after about 1 year. The formation of adhesions to intraperitoneal organs is thus markedly reduced. Therefore, the elements are given preference when using the IPOM technique for widespread mesh fixation. In respect of retention strength they are as effective as spiral fixation elements.[35]

6.638.7.2.2. Microhooks

These small barbed hooks made of polyactic acid are fixed on the underside of the prosthesis and are equivalent to the hernia stapler in terms of retention strength.[64] The meshes (Progrip®) are used to treat groin herniae.

6.638.7.2.3. Fibrin glue

Fibrin glue is marked by its low rate of complications. Chronic pain due to nerve irritation is avoided by this fixation technique.[73] The prosthesis can be fixed well over a large surface. However, stable fixation of the mesh in tissue immediately after surgery (i.e., in the vulnerable phase) could not be proven in all studies.[64]

6.638.7.2.4. Suture

Nonabsorbable sutures complete the list of fixation techniques. They are preferentially used in those areas in which stable fixation of the prosthesis in tissue is anticipated. Furthermore, to bridge the first few postsurgery months, they provide additional retention and promote integration of tissue into the prosthesis. Nonabsorbable sutures for margins subjected to tensile loads are frequently combined with absorbable sutures for widespread fixation of the prosthesis.[72]

6.638.8. Potential Complications of Hernia Meshes

The advantage of reducing recurrence rates by providing tissue reinforcement must be viewed in the light of a few potential complications.

6.638.8.1. Perioperative Complications

6.638.8.1.1. Rejection

Rejection or intolerance of the prosthesis are extremely rare events and have been reported in isolated cases.[76–78]

6.638.8.1.2. Infection

Infection of the prosthesis is a much more frequent and very unpleasant complication (Lit). Especially when using open techniques,[79] skin pathogens may collect on the prosthesis and necessitate its removal in many cases.[80] To avoid this complication, antibiotics are administered perioperatively to protect the prosthesis when using open techniques.

6.638.8.2. Chronic Complications

6.638.8.2.1. Hernia recurrence

Hernia recurrence rates have been significantly reduced by the use of mesh techniques as opposed to suture techniques. Nevertheless, the treatment of ventral herniae is still reported to be associated with high recurrence rates. Therefore, surgical techniques for this type of hernia need to be optimized.

6.638.8.2.2. Chronic pain

Apart from hernia recurrence, chronic pain after mesh implantation must be avoided. The use of modern meshes and modern fixation techniques has reduced the number of patients who experience chronic pain to about 5%. In cases of proven nerve irritation due to the mesh or mesh fixation, the cause of pain should be eliminated by surgery. Success rates for this type of pain treatment, however, are still unsatisfactory.[81]

6.638.8.2.3. Stiffening of the abdominal wall

Stiffening of the ventral abdominal wall has occurred after implantation of small-pore meshes. This complication can be largely avoided by the use of modern large-pore meshes: the patient is able to move the abdominal wall in all directions despite widespread reinforcement of the abdominal wall with the mesh.

6.638.9. Conclusion and Future Perspectives

6.638.9.1. Further Developments

A wide spectrum of options for improvement exist, especially in the field of prosthesis fixation. Fixation elements or sutures of maximum ductility could markedly reduce mesh tear-off. More exact determination of the forces acting on the prosthesis might enhance our understanding of tensile loads on the foreign body and consequently optimize the characteristics of the prosthesis as well as its dimensions.

6.638.9.2. Conclusion

Hernia meshes have become an integral aspect of surgical techniques for the treatment of abdominal wall herniae and are currently used in two-thirds of all hernia operations. Synthetic meshes represent the artificial fascia and tendons aspired for by Billroth, and have significantly improved the outcome of hernia surgery. Nevertheless, a long pathway of research lies ahead of us if we wish to reduce, or even eliminate, the accompanying negative effects of synthetic meshes.

References

1. Read, R. *Hernia* **2004**, *8*(1), 8–14.
2. Burger, J.; Luijendijk, R.; Hop, W.; Halm, J.; Verdaasdonk, E.; Jeekel, J. *Ann. Surg.* **2004**, *240*(4), 578–583; discussion 583–585.
3. Cassar, K.; Munro, A. *Br. J. Surg.* **2002**, *89*(5), 534–545.
4. Bisgaard, T.; Bay-Nielsen, M.; Christensen, I.; Kehlet, H. *Br. J. Surg.* **2007**, *94*(8), 1038–1040.
5. Amato, B.; Moja, L.; Panico, S.; *et al. Cochrane Database Syst. Rev.* **2009**, *4*, CD001543.
6. Scott, N.; McCormack, K.; Graham, P.; Go, P.; Ross, S.; Grant, A. *Cochrane Database Syst. Rev.* **2002**, *4*, CD002197.
7. Sauerland, S.; Schmedt, C.; Lein, S.; Leibl, B.; Bittner, R. *Langenbecks Arch. Surg.* **2005**, *390*(5), 408–412.
8. Klinge, U.; Conze, J.; Klosterhalfen, B.; *et al. Langenbecks Arch. Chir.* **1996**, *381*(6), 323–332.
9. Klinge, U.; Klosterhalfen, B.; Birkenhauer, V.; Junge, K.; Conze, J.; Schumpelick, V. *J. Surg. Res.* **2002**, *103*(2), 208–214.
10. Klinge, U.; Klosterhalfen, B.; Conze, J.; *et al. Eur. J. Surg.* **1998**, *164*(12), 951–960.
11. Klosterhalfen, B.; Junge, K.; Hermanns, B.; Klinge, U. *Br. J. Surg.* **2002**, *89*(8), 1043–1048.
12. Preston, D.; Richards, C. *Surg. Clin. North Am.* **1973**, *53*(3), 549–554.
13. Witzel, O. *Zentralbl. Chir.* **1900**, *10*, 257–260.
14. Schumpelick, V.; Klinge, U.; Welty, G.; Klosterhalfen, B. *Chirurg* **1999**, *70*(8), 876–887.
15. Usher, F. *Arch. Surg.* **1962**, *84*, 325–328.
16. Usher, F. C.; Fries, J. G.; Ochsner, J. L.; Tuttle, L. L. D. *Arch. Surg.* **1959**, *78*(1), 138–145.
17. Lichtenstein, I.; Shulman, A. *Int. Surg.* **1986**, *71*(1), 1–4.
18. Corbitt, J. J. *Surg. Laparosc. Endosc.* **1991**, *1*(1), 23–25.
19. Schumpelick, V. *Langenbecks Arch. Chir.* **1993**, *378*(6), 321.
20. Schumpelick, V.; Arlt, G.; Schlachetzki, A.; Klosterhalfen, B. *Chirurg* **1997**, *68*(12), 1297–1300.
21. Ghadimi, B.; Langer, C.; Becker, H. *Chirurg* **2002**, *73*(8), 833–837.
22. Witherspoon, P.; Bryson, G.; Wright, D.; Reid, R.; O'Dwyer, P. *Br. J. Surg.* **2004**, *91*(3), 368–372.
23. Aufenacker, T.; Schmits, S.; Gouma, D.; Simons, M. *Hernia* **2009**, *13*(1), 35–39.
24. Weyhe, D.; Belyaev, O.; Müller, C.; *et al. World J. Surg.* **2007**, *31*(1), 234–244.
25. Klinge, U.; Junge, K.; Spellerberg, B.; Piroth, C.; Klosterhalfen, B.; Schumpelick, V. *J. Biomed. Mater. Res.* **2002**, *63*(6), 765–771.
26. Conze, J.; Kingsnorth, A.; Flament, J.; *et al. Br. J. Surg.* **2005**, *92*(12), 1488–1493.
27. Zieren, J.; Proske, J. M.; Neuss, H.; Paul, M.; Muller, J. M. *Ann. Chir.* **2004**, *129*(6–7), 343–346.
28. Beets, G. L.; Go, P.; vanMameren, H. *Eur. J. Surg.* **1996**, *162*(10), 823–825.
29. Bernatchez, S. F.; Parks, P. J.; Gibbons, D. F. *Biomaterials* **1996**, *17*(21), 2077–2086.
30. Bleichrodt, R. P.; Simmermacher, R. K. J.; Vanderlei, B.; Schakenraad, J. M. *Surg. Gynecol. Obstet.* **1993**, *176*(1), 18–24.
31. Matloub, H. S.; Jensen, P.; Grunert, B. K.; Sanger, J. R.; Yousif, N. J. *Ann. Plast. Surg.* **1992**, *29*(6), 508–511.
32. Aguayo-Albasini, J.; Moreno-Egea, A.; Torralba-Martínez, J. *Cir. Esp.* **2009**, *86*(3), 139–146.
33. Hollinsky, C.; Kolbe, T.; Walter, I.; *et al. Surg. Endosc.* **2010**, *24*(6), 1318–1324.
34. Altuntas, I.; Tarhan, O.; Delibas, N.; Cetin, R.; Sutcu, R. *Am. Surg.* **2002**, *68*(9), 759–761.
35. Hollinsky, C.; Kolbe, T.; Walter, I. *Surg. Endosc.* **2009**, *24*, 1318–1324.
36. Judge, T.; Parker, D.; Dinsmore, R. *J. Am. Coll. Surg.* **2007**, *204*(2), 276–281.
37. Leber, G.; Garb, J.; Alexander, A.; Reed, W. *Arch. Surg.* **1998**, *133*(4), 378–382.
38. Schumpelick, V.; Junge, K.; Rosch, R.; Klinge, U.; Stumpf, M. *Chirurg* **2002**, *73*(9), 888–894.
39. Göretzlehner, U.; Müllen, A. *Biomaterialien* **2007**, *8*(S1), 28–29.
40. Junge, K.; Binnebösel, M.; Rosch, R.; *et al. Surg. Endosc.* **2009**, *23*(2), 327–333.
41. Scheidbach, H.; Tamme, C.; Tannapfel, A.; Lippert, H.; Köckerling, F. *Surg. Endosc.* **2004**, *18*(2), 211–220.
42. Oliver, R. F.; Barker, H.; Cooke, A.; Grant, R. A. *Biomaterials* **1982**, *3*(1), 38–40.
43. Oliver, R. F.; Grant, R. A.; Cox, R. W.; Hulme, M. J.; Mudie, A. *Clin. Orthop. Relat. Res.* **1976**, *115*, 291–302.
44. Helton, W. S.; Fisichella, P. M.; Berger, R.; Horgan, S.; Espat, N.; Abcarian, H. *Arch. Surg.* **2005**, *140*, 549–560.
45. Ueno, T.; Pickett, L. C.; de la Fuente, S. G.; Lawson, D. C.; Pappas, T. N. *J. Gastrointest. Surg.* **2004**, *8*(1), 109–112.
46. Rutkow, I.; Robbins, A. *Surgery* **1993**, *114*(1), 3–8.
47. Wauschkuhn, C.; Schwarz, J.; Boekeler, U.; Bittner, R. *Surg. Endosc.* **2010**, *24*, 3026–3030.
48. Hawn, M.; Snyder, C.; Graham, L.; Gray, S.; Finan, K.; Vick, C. *J. Am. Coll. Surg.* **2010**, *210*(5), 648–655 655–657.
49. Kurzer, M.; Kark, A.; Selouk, S.; Belsham, P. *World J. Surg.* **2008**, *32*(1), 31–36; discussion 37.
50. Schumpelick, V.; Klinge, U.; Junge, K.; Stumpf, M. *Langenbecks Arch. Surg.* **2004**, *389*(1), 1–5.
51. Bingener, J.; Buck, L.; Richards, M.; Michalek, J.; Schwesinger, W.; Sirinek, K. *Arch. Surg.* **2007**, *142*(6), 562–567.
52. Goodney, P.; Birkmeyer, C.; Birkmeyer, J. *Arch. Surg.* **2002**, *137*(10), 1161–1165.
53. McGreevy, J.; Goodney, P.; Birkmeyer, C.; Finlayson, S.; Laycock, W.; Birkmeyer, J. *Surg. Endosc.* **2003**, *17*(11), 1778–1780.
54. Dilege, E.; Coskun, H.; Gunduz, B.; Sakiz, D.; Mihmanli, M. *Eur. Surg. Res.* **2006**, *38*(3), 358–364.
55. Gonzalez, R.; Rodeheaver, G.; Moody, D.; Foresman, P.; Ramshaw, B. *Hernia* **2004**, *8*(3), 213–219.
56. Zinther, N.; Wara, P.; Friis-Andersen, H. *Hernia* **2010**, *14*(3), 283–289.
57. Frantzides, C.; Carlson, M.; Loizides, S.; *et al. Surg. Endosc.* **2010**, *24*(5), 1017–1024.
58. Hollinsky, C.; Sandberg, S. *Clin. Biomech. (Bristol, Avon)* **2007**, *22*(1), 88–92.
59. Ramadwar, R.; Carachi, R.; Young, D. *J. Pediatr. Surg.* **1997**, *32*(12), 1708–1710.
60. Bellón, J.; Rodríguez, M.; García-Honduvilla, N.; Pascual, G.; Buján, J. *Am. J. Surg.* **2007**, *194*(1), 68–74.
61. Rosch, R.; Junge, K.; Quester, R.; Klinge, U.; Klosterhalfen, B.; Schumpelick, V. *Eur. Surg. Res.* **2003**, *35*(5), 445–450.
62. Hollinsky, C.; Sandberg, S.; Koch, T.; Seidler, S. *Surg. Endosc.* **2008**, *22*, 2679–2685.
63. Cobb, W.; Kercher, K.; Heniford, B. *Surg. Innov.* **2005**, *12*(1), 63–69.
64. Hollinsky, C.; Kolbe, T.; Walter, I.; *et al. J. Am. Coll. Surg.* **2009**, *208*(6), 1107–1114.
65. Taylor, C.; Layani, L.; Liew, V.; Ghusn, M.; Crampton, N.; White, S. *Surg. Endosc.* **2008**, *22*(3), 757–762.
66. Millikan, K. *Surg. Clin. North Am.* **2003**, *83*(5), 1223–1234.
67. Wheeler, A.; Matz, S.; Bachman, S.; Thaler, K.; Miedema, B. W. *Hernia* **2009**, *13*(6), 597–603.
68. DiCocco, J.; Magnotti, L.; Emmett, K.; *et al. J. Am. Coll. Surg.* **2010**, *210*(5), 686–695; 695–698.
69. Freudenberg, S.; Sano, D.; Ouangré, E.; Weiss, C.; Wilhelm, T. *World J. Surg.* **2006**, *30*(10), 1784–1789 dicussion 1790.
70. Kingsnorth, A. *World J. Surg.* **2007**, *31*(4), 859.
71. Eriksen, J.; Poornoroozy, P.; Jørgensen, L.; Jacobsen, B.; Friis-Andersen, H.; Rosenberg, J. *Hernia* **2009**, *13*(1), 13–21.
72. Wassenaar, E.; Schoenmaeckers, E.; Raymakers, J.; van der Palen, J.; Rakic, S. *Surg. Endosc.* **2010**, *24*(6), 1296–1302.
73. Lovisetto, F.; Zonta, S.; Rota, E.; *et al. Ann. Surg.* **2007**, *245*(2), 222–231.
74. Hollinsky, C.; Göbl, S. *Surg. Laparosc. Endosc. Percutan. Tech.* **1999**, *9*(2), 110–114.
75. Peach, G.; Tan, L. *Hernia* **2008**, *12*(3), 303–305.
76. Foschi, D.; Corsi, F.; Cellerino, P.; Trabucchi, A.; Trabucchi, E. *Surg. Endosc.* **1998**, *12*(5), 455–457.
77. Hofbauer, C.; Andersen, P.; Juul, P.; Qvist, N. *Surg. Endosc.* **1998**, *12*(9), 1164–1165.
78. Jani, K.; Palanivelu, C.; Malladi, V.; *et al. Indian J. Gastroenterol.* **2005**, *24*(5), 219–220.
79. Karthikesalingam, A.; Markar, S.; Holt, P.; Praseedom, R. *Br. J. Surg.* **2010**, *97*(1), 4–11.
80. Stremitzer, S.; Bachleitner-Hofmann, T.; Gradl, B.; *et al. World J. Surg.* **2010**, *34*, 1702–1709.
81. Amid, P. *Hernia* **2004**, *8*(4), 343–349.